Instituto de Fisiología Celular

UNAM La Universidad de la Nación



INFORME DE ACTIVIDADES 2019

Dr. Félix Recillas Targa
Instituto de Fisiología Celular, UNAM



Instituto de Fisiología Celular

UNIVERSIDAD NACIONAL AUTÓNOMA DE MÉXICO

INFORME DE LABORES

2019

DR. FELIX RECILLAS TARGA

UNIVERSIDAD NACIONAL AUTÓNOMA DE MÉXICO

Dr. Enrique Graue Wiechers
Rector

Dr. Leonardo Lomelí Vanegas
Secretario General

Ing. Leopoldo Silva Gutiérrez
Secretario Administrativo

Dr. Alberto Ken Oyama Nakagawa
Secretario de Desarrollo Institucional

Mtro. Javier de la Fuente Hernández
Secretario de Prevención Atención y Seguridad Universitaria

Dr. William Henry Lee Alardín
Coordinador de la Investigación Científica

Dra. Mónica González Contró
Abogada General

INSTITUTO DE FISIOLOGÍA CELULAR

Dr. Félix Recillas Targa
Director

Dra. María de Lourdes Massieu Trigo
Secretaria Académica

L.A.E. María del Pilar Martínez Martínez
Secretaria Administrativa

Dr. Jorge Ramírez Salcedo
Secretario Técnico

Dra. María Soledad Funes Argüello
Coordinadora de Enseñanza

Dr. Luis Vaca Domínguez
Secretario de Vinculación y Gestión

JEFES DE DEPARTAMENTO

- ***División de Investigación Básica***

  Dr. Alfredo Torres Larios
  Bioquímica y Biología Estructural

  Dr. Roberto Coria Ortega
  Genética Molecular

  Dra. Marina Macías Silva
  Biología Celular y Desarrollo

- ***División de Neurociencias***

  Dr. Federico Bermúdez Rattoni
  Neurociencia Cognitiva

  Dra. Diana Escalante Alcalde
  Neurodesarrollo y Fisiología

  Dr. Julio Morán Andrade
  Neuropatología Molecular

CONSEJO INTERNO

Presidente
Dr. Félix Recillas Targa

Secretaria
Dra. María de Lourdes Massieu Trigo

Consejeros
Dr. Alfredo Torres Larios

Dr. Roberto Coria Ortega

Dra. Marina Macías Silva

Dr. Federico Bermúdez Rattoni

Dra. Diana Escalante Alcalde

Dra. Julio Morán Andrade

Dra. María Soledad Funes Argüello

Dra. Rosa Navarro González

Dra. Dr. Raúl Aguilar Roblero

Dra. Bertha González Pedrajo

Biól. Gustavo Sánchez Chávez

- *Representante ante el Consejo Técnico de la Investigación Científica*
  Dra. Bertha González Pedrajo

- *Representantes ante el Consejo Universitario*
  Dra. Ana María López Colomé
  Dr. Diego González Halphen

- *Representantes ante el Consejo Académico del Área de las Ciencias Biológicas Químicas y de la Salud (CAABQyS)*
  Dra. Xóchitl Pérez Martínez
  Dr. Fernando López Casillas

- *Colegio del Personal Académico del Instituto de Fisiología Celular*
  Dra. Susana Castro Obregón
  Presidente

  Dra. Ruth Rincón Heredia
  Secretaria

  Q.F.B. Beatriz Aguirre López
  Vocal

COMISIÓN DICTAMINADORA

Dra. Adela Rodríguez Romero
Instituto de Química, UNAM

Dr. Lorenzo Patrick Segovia Forcella
Instituto de Biotecnología, UNAM

Dr. Enrique Merino Pérez
Instituto de Biotecnología, UNAM

Dra. María Elena Teresa Medina-Mora Icaza
Facultad de Medicina, UNAM

Dr. José Víctor Segovia Vila
CINVESTAV, IPN

Dr. Hugo Merchant Nancy
Instituto de Neurobiología, UNAM

COMISIÓN DEL PRIDE

Dra. María Eugenia Gonsebatt Bonaparte
Instituto de Investigaciones Biomédicas, UNAM

Dr. Salvador Uribe Carvajal
Instituto de Fisiología Celular, UNAM

Dr. David René Romero Camarena
Centro de Ciencias Genómicas, UNAM

Dra. Martha Lilia Escobar Rodríguez
Facultad de Psicología, UNAM

Dr. José Bargas Díaz
Instituto de Fisiología Celular, UNAM

CONSEJO ASESOR

Dr. Carlos Belmonte
Universidad Miguel Hernández-CSIC (Consejo Superior de Investigaciones Científicas), Alicante, España.

Dr. Gabriel Guarneros Peña
Departamento de Genética y Biología Molecular, CINVESTAV, IPN, México.

Dr. Luis Herrera Estrella
Unidad de Biotecnología e Ingeniería Genética, CINVESTAV, IPN Unidad Irapuato,
Irapuato, Guanajuato, México.

Dra. Susana López Charretón
Instituto de Biotecnología, UNAM,
Cuernavaca, Morelos, México.

Dr. Joan Massagué
Cell Biology Program and Howard Hughes Medical Institute, Memorial Sloan-Kettering Cancer Center,
New York, NY, USA.

Dr. Ricardo Miledi
Departamento de Neurobiología Celular y Molecular,
Instituto de Neurobiología, UNAM, Campus Juriquilla
Juriquilla, Querétaro, México.

Dra. Estela Sánchez
División de Estudios de Posgrado, Facultad de Química, UNAM. Ciudad Universitaria, México.

Dr. José Sarukhán
Instituto de Ecología, UNAM,
Ciudad Universitaria, México.

COMISIONES DE LAS UNIDADES DE APOYO

CÓMPUTO:

Dr. Luis Lemus Sandoval
M.I. Manuel T. Figueroa
Dr. Marcelino Arciniega
Dra. Xóchitl Pérez M.
Biól. Gerardo Coello C.
Secretario Ejecutivo:
Dr. Diego González H.

BIBLIOTECA:

Dra. Rosa Navarro
Dr. Julián Valdés
Odont. Javier Gallegos
Mtra. Sandra Moncada
Secretario Ejecutivo:
Dr. Raúl Aguilar

HISTOLOGÍA:

Biól. Teresa Montiel
Dra. Rocío Salceda S.
Dra. Leticia Ramírez L.
Secretario Ejecutivo:
Dr. Julio Morán

IMAGENOLOGÍA:

Dr. Luis Vaca D.
Dra. Yazmín Ramiro C.
Dra. Ruth Rincón H.
Dr. Miguel Tapia (externo, Biomédicas)
Secretaria Ejecutiva:
Dra. Diana Escalante

CICUAL (BIOTERIO):

Dra. Paula Licona
MVZ. Claudia Rivera
Dr. Fatuel Tecuapetla
Dra. Rocio Alcántara
Secretaria Ejecutiva:
Dra. Diana Escalante

TALLER DE MANTENIMIENTO:

M. I. Bruno Méndez
Dr. Jesús Alvarez
Dr. Fernando Suaste
Secretario Ejecutivo:
Dr. Jorge Ramírez

BIOLOGÍA MOLECULAR:

Dra. Mayra Furlan
Biól. Gustavo Sánchez
Dra. Laura Ongay
Dr. Luis Bernardo Tovar
Secretaria Ejecutiva:
Dra. Susana Castro

DIFUSIÓN Y DIVULGACIÓN

Dra. Soledad Funes
M. en C. Blanca Delgado
Dra. Luz Lazos/ Dra. Cecilia Rosen
Dra. Gabriela Loyden
Mtro. Felipe Zenil Ongay
Secretaria Ejecutiva:
Dra. Herminia Pasantes

EDUCACIÓN CONTÍNUA

Dr. Ricardo Tapia
Dr. Luis Vaca
Dra. Laura Ongay
MVZ Claudia Rivera
Dra. Lourdes Massieu
Secretaria Ejecutiva:
Dra. Luz Lazos / Dra. Cecilia Rosen

SUBCOMISIÓN CON PERSPECTIVA DE GÉNERO

Dra. Mayra Furlan Magaril
Biól. Georgina Guerrero Avendaño
Dra. Beatríz Aguilar Maldonado
Odont. Javier Gallegos Infante
Lic. Francisco Pérez Eugenio
Dr. Francisco Sotres Bayón
María Celeste Sánchez Sugía
Brenda Vianey García Hernández
Ameyalli Gómez Illescas

COMISIÓN DE ÉTICA CIENTÍFICA Y BIOÉTICA

Dr. Ricardo Tapia
Dra. Tamara Rosenbaum
Dra. Soledad Funes
MVZ. Claudia Rivera
Dr. Samuel Ponce de León

COMISIÓN DE BIOSEGURIDAD

Dra. Bertha González Pedrajo
Dr. Fatuel Tecuapetla Aguilar
Dra. Diana Escalante Alcalde
Dr. Julio Morán Andrade
Dr. Rolando Hernández
Dr. Jorge Ramírez
MVZ. Claudia Rivera

COMISIÓN LOCAL DE SEGURIDAD:

Coordinador General:	Dr. Félix Recillas Targa
Secretaria:	L.A.E. Pilar Martínez Martínez
Cuerpo Técnico:	Dr. Jorge Ramírez Salcedo
Invitados:	Dra. Diana Escalante Alcalde
	Ing. Armando Canto Canto
	Ing. Aurey Galván Lobato

COMISIÓN DE MICROARREGLOS

Dr. Félix Recillas
Dra. Alicia González
Dr. Luis Tovar y Romo
Dr. Leonardo Peraza
Dr. Gabriel del Río
Responsable:
Dr. Jorge Ramírez

COMISIÓN DE BIOINFORMÁTICA Y MANEJO DE LA INFORMACIÓN

Dr. Félix Recillas
Dra. Mayra Furlan Magaril
Dr. Julián Valdés
Dr. Román Rossi
Dr. Marcelino Arciniega
Dr. Gabriel del Río
Responsable:
Dr. César Poot Hernández

COMISIÓN DE EDICIÓN GENÉTICA Y CRIOPRESERVACIÓN

Dr. Félix Recillas
Dra. Diana Escalante
Dra. Caudia Rivera
Dra. Ariadna Aparicio (Técnica Académica adscrita a la Unidad)
Responsable:
Dra Paula Licona

ÍNDICE

PRESENTACIÓN 9

PERSONAL ACADÉMICO 11

Organización Académica del Instituto 17

Departamento de Biología Celular y del Desarrollo 17

Departamento de Bioquímica y Biología Estructural 19

Departamento de Genética Molecular 20

Departamento de Neurociencia Cognitiva 22

Departamento de Neurodesarrollo y Fisiología 24

Departamento de Neuropatología Molecular 25

LÍNEAS DE INVESTIGACIÓN 26

ACTIVIDADES ACADÉMICO ADMINISTRATIVAS 39

PROGRAMAS DE SUPERACIÓN ACADÉMICA 57

Programas de Superación Académica en la UNAM 57

Programas de Superación Académica Fuera de la UNAM 62

INVESTIGADORES VISITANTES 65

COMISIÓN DICTAMINADORA Y ASUNTOS ACADÉMICO-ADMINISTRATIVOS 67

BECARIOS POSDOCTORALES 70

PERSONAL ADMINISTRATIVO 72

FORMACIÓN DE RECURSOS HUMANOS 77

Estudiantes 77

Graduados 80

DOCENCIA 81

Cursos Impartidos 81

REVISIÓN DE ACTIVIDADES ACADÉMICAS DE DOCTORADO 82

PRODUCCIÓN ACADÉMICA 84

Artículos Publicados en Revistas Internacionales 88
Artículos en Prensa 101
Artículos de Divulgación 102
Capítulos en Libros 103
Capítulos en Prensa 104
Libros Publicados y Reimpresiones 104
Revistas Nacionales 105
Patente Nacional concluída 105
Convenios con otras Instituciones 106
Apoyo a Eventos Académicos Externos 110
PONENCIAS **111**
EVENTOS ACADÉMICOS INSTITUCIONALES **114**
Seminarios Institucionales 114
Seminarios Extraordinarios 119
Feria de Carteles Anual del IFC 121
ACTIVIDADES DE DIFUSIÓN Y DIVULGACIÓN **125**
Participaciones en Programas de Radio o Televisión 125
Participaciones en Medios Impresos 127
Otras actividades de Difusión o Divulgación 129
PREMIOS Y DISTINCIONES **135**
FUENTES DE FINANCIAMIENTO **137**
Proyectos Financiados por DGAPA 137
Proyectos Financiados por CONACyT 142
Proyectos Financiados por Otras Empresas de Gobierno Federal y Local 146
Proyectos Financiados por Organismos y Empresas Nacionales 146
Proyectos Financiados por Organismos y Empresas Internacionales 147

CONVENIOS E INTERCAMBIOS **148**

Convenios Suscritos por Personal del IFC 148

UNIDADES DE SERVICIO **150**

Unidad de Biología Molecular 150

Unidad de Cómputo 152

Unidad de Imagenología 154

Laboratorio Nacional De Canalopatías 155

Coordinación de Difusión Y Divulgación 156

Biblioteca "Armando Gómez Puyou" 157

Bioterio 158

Taller de Mantenimiento 159

Unidad de Histología 160

Unidad de Servicio de Microarreglos de ADN de la UNAM 161

Laboratorio de investigación y desarrollo de Aplicaciones interactivas para la Neuro-Rehabilitación (LANR) 163

Unidad de Bioinformática y Manejo de la Información (UBMI) 165

Unidad de Edición Genética y Criopreservación 167

CONSTRUCCIÓN, REMODELACIÓN, AMPLIACIÓN, ADECUACIÓN DE ESPACIOS Y PROYECTOS ESPECÍFICOS **168**

PRESENTACIÓN

Como lo marca la Legislación Universitaria presento ante las autoridades, a las y los miembros de nuestro Instituto y a la Comunidad Universitaria el Informe de Labores del Instituto de Fisiología Celular correspondiente al año 2019.

En este año el Instituto mantuvo su compromiso con la labor docente de alta calidad impulsando un enfoque moderno de la ciencia y de los temas de investigación que se cultivan en nuestra entidad. Particular atención fue puesta en la transmisión del conocimiento por parte de jóvenes investigadores, apoyándonos en la experiencia de las y los investigadores consagrados, todos ellos líderes en su campo de investigación, en la impartición de cursos de licenciatura y posgrado.

Un total de 508 estudiantes asistieron a nuestras aulas y laboratorios. De los cuales 75 obtuvieron el grado: 14 de Licenciatura, 36 de Maestría y 25 de Doctorado. Afianzamos nuestra relación y participación en los posgrados de Ciencias Bioquímicas, Ciencias Biomédicas y Ciencias Biológicas. Como entidad responsable, junto con la Facultad de Medicina, tuvimos una activa participación en la Licenciatura de Neurociencias organizando e impartiendo un gran número de cursos. Además, renovamos nuestra participación en la Licenciatura en Investigación Biomédica Básica.

En el ámbito de la investigación científica publicamos 117 artículos en revistas indizadas lo que representa 2.05 artículos por grupo de investigación, con un índice de impacto promedio de 5.02. En el 2019 el 71% de nuestras publicaciones se encuentran el Cuartil 1 (Q1), 21% en el Cuartil 2 (Q2) lo cual implica que el 92% de nuestras publicaciones se encuentran en los cuartiles Q1+Q2. Por otra parte, en el mismo periodo se publicaron 6 capítulos (8 en prensa), 9 artículos de divulgación, 2 libros y 6 artículos en revistas nacionales. El análisis de nuestra productividad muestra que en este año publicamos 25 artículos menos en comparación con el 2018, sin embargo, el factor de impacto promedio pasó de 4.263 a 5.02 en el 2019. Considero que la disminución en el número de artículos refleja el momento de cambio generacional que vive nuestro Instituto, sin que esta disminución sea en detrimento de la calidad de nuestras investigaciones al incrementar en casi un punto el factor de impacto promedio de nuestras publicaciones.

Como una consecuencia de nuestro compromiso por realizar investigaciones del más alto nivel, los miembros de nuestra comunidad recibieron diversos premios y reconocimientos. Se destacan la medalla *Sor Juana Inés de la Cruz* otorgada a la Dra. Teresa Montiel Montes, el Dr. Ranulfo Romo fue reconocido con el Premio Crónica de Ciencia y Tecnología, el Dr. Jaime Mas Oliva fue galardonado con el *Premio Universidad Nacional 2019* en el área de Investigación en Ciencias Naturales, el Dr. Fatuel Tecuapetla Aguilar obtuvo la *Cátedra Marcos Moshinsky 2019*, y la Dra. Claudia Álvarez Carreño y el Dr. Luis Vaca Domínguez fueron acreedores a la beca *Fullbright-García Robles* para realizar estancias de Investigación en Estados Unidos.

En este año se mantuvo la distribución por género del personal del Instituto. De este análisis se desprenden datos interesantes que muestran que en la población académica del Instituto 40% de los investigadores son mujeres y 60% hombres. En cuanto a los Técnicos Académicos la relación es de 2 a 1 en favor de las mujeres. Cabe resaltar que la relación en Investigadores Titular A y B entre mujeres y hombres es prácticamente de 1:1, mientras que el 70% de los Investigadores Titulares C son hombres, mostrando una tendencia histórica. Sin embargo, en las nuevas generaciones la equidad de género se va asentando en nuestro Instituto. En cuanto al personal de base y de confianza, el Instituto está compuesto mayoritariamente por mujeres y la relación es 1:1 en cuanto al personal administrativo. A todo lo anterior se suma un esfuerzo por realizar actividades coordinadas a través del trabajo comprometido de la Comisión Interna de Igualdad de Género.

Un hecho que deseo destacar es la creación y puesta en funcionamiento de dos nuevas Unidades de Servicio en nuestro Instituto. Se construyó y equipó la Unidad de Edición Genética (CRISPR-Cas) y Criopreservación. Se equipó el edificio anexo para albergar a la Unidad de Bioinformática y Manejo de la Información. Además, un hecho fundamental para el funcionamiento de nuestro Instituto fue la puesta en marcha de la nueva Red de Cómputo. En el 2019 el edificio anexo entró en funcionamiento albergando al Laboratorio Nacional de Canalopatías, y además se construyeron dos aulas y la Unidad para albergar a los ratopines, un modelo único en México para estudios de envejecimiento. Finalmente, el Instituto y sus investigadores obtuvieron un apoyo para Infraestructura por parte del CONACyT de más de 25 millones de pesos para el Fortalecimiento de las Unidades de Bioterio, y de Edición Genética y Criopreservación, así como equipo para estudios de célula única. Además de una serie de adecuaciones y mantenimiento de la infraestructura del Instituto.

Finalmente, agradezco el apoyo brindado por parte del Sr. Rector, el Dr. Enrique Graue Wiechers, el Coordinador de la Investigación Científica, el Dr. William Lee Alardín y el Secretario Administrativo de la UNAM, el Ing. Leopoldo Silva Gutiérrez.

Solo me queda reiterar mi agradecimiento a las autoridades por su apoyo constante, consejos y atenciones hacia nuestro Instituto, a la comunidad estudiantil y a las y los miembros del Instituto de Fisiología Celular de la UNAM.

Dr. Félix Recillas Targa
Director

PERSONAL ACADÉMICO

En el 2019 la plantilla académica del Instituto de Fisiología Celular cuenta con 160 miembros, 66 son Investigadores, 94 son Técnicos Académicos y uno es Catedrático CONACyT. Del total de Investigadores, 59 son Jefes de Grupo y 10 son Investigadores Asociados. Los Técnicos Académicos adscritos a algún laboratorio son 65 y 29 se encuentran en las Unidades de Servicio del Instituto, cuatro de ellos están contratados por honorarios.

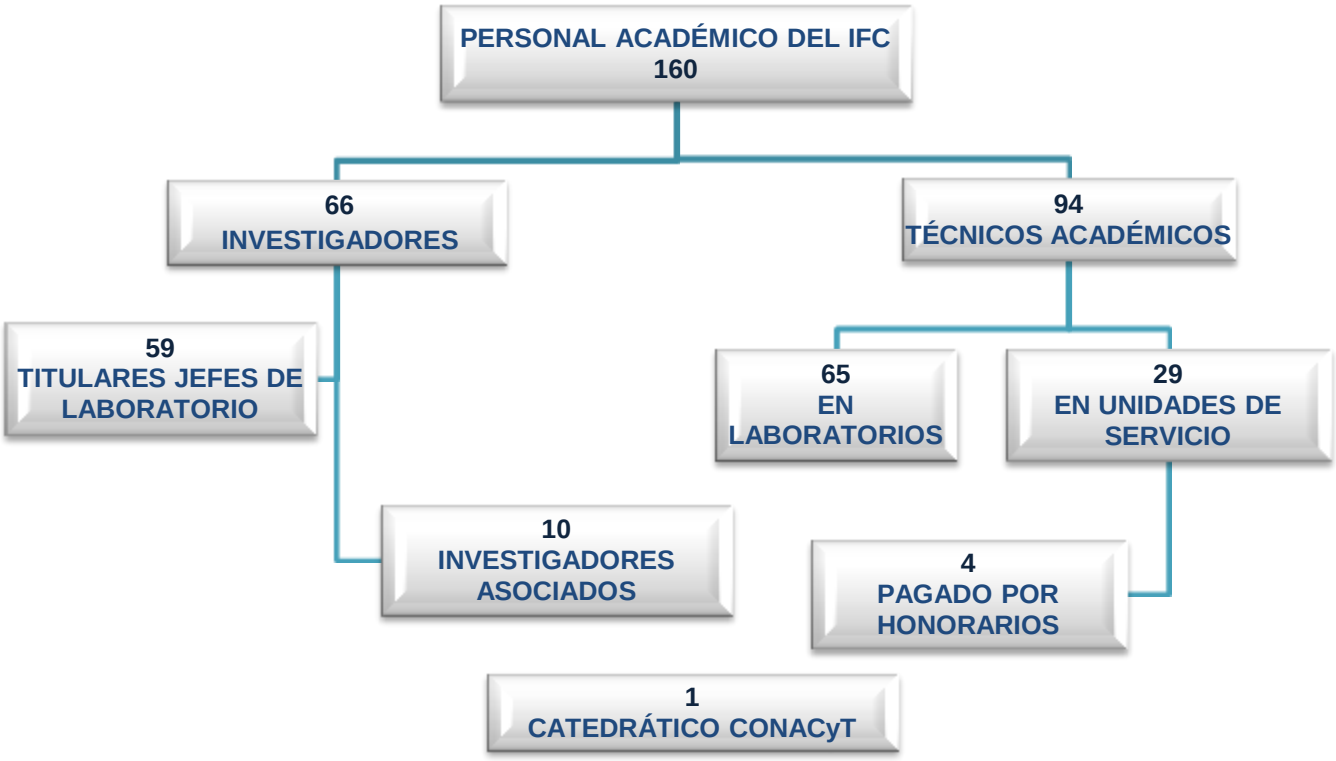

La distribución de equidad de género entre el Personal Académico se muestra en la siguiente gráfica.

Distribución del Personal Académico por Género

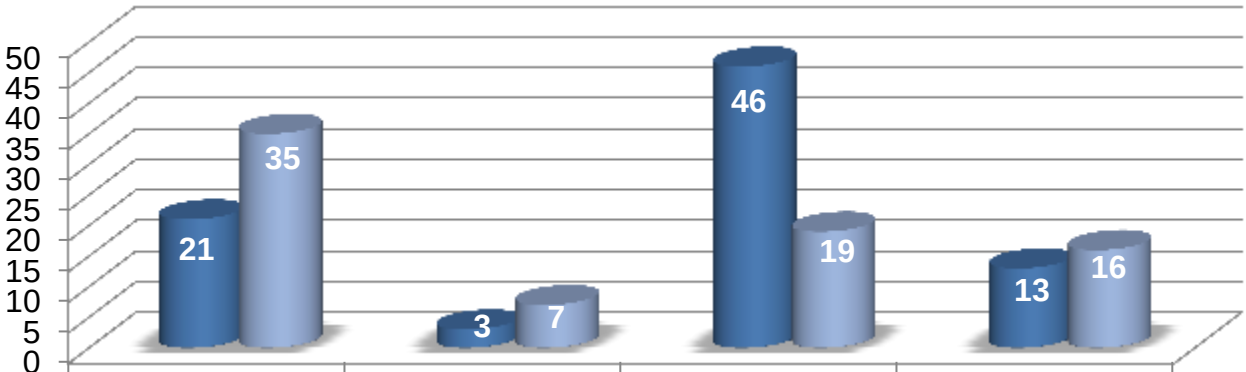

	INV. TITULARES	INV. ASOCIADOS	TEC. EN LABORATORIO	TEC. EN UNIDADES ACADEMICAS
MUJER	21	3	46	13
HOMBRE	35	7	19	16

Distribución de Investigadores por Género

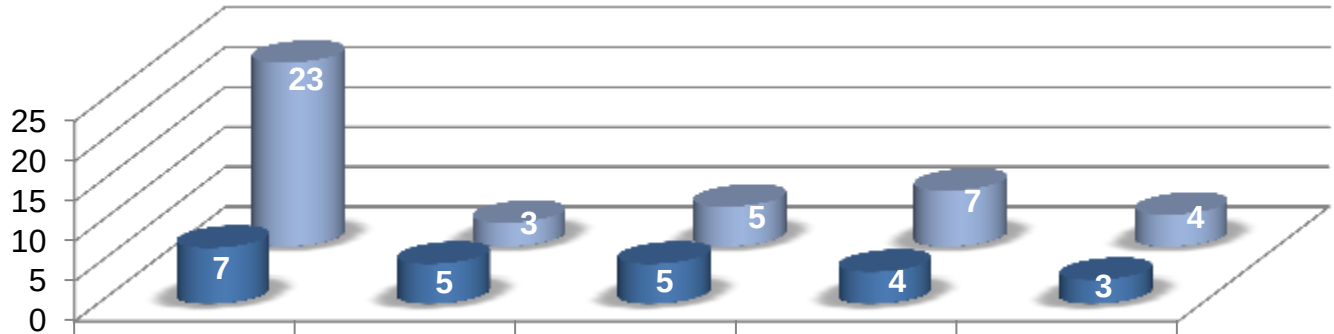

	INV TIT "C"	INV TIT "B"	INV TIT "A"	INV ASO "C"	INV EMÉRITO
Mujeres	7	5	5	4	3
Hombres	23	3	5	7	4

En 2019, el IFC cuenta con 7 Investigadores Eméritos, el nombramiento con mayor número de integrantes fue Titular C con 30 miembros que representan el 46% del total, 8 investigadores son Titular B, 10 tienen el nombramiento Titular A y 10 Asociado C.

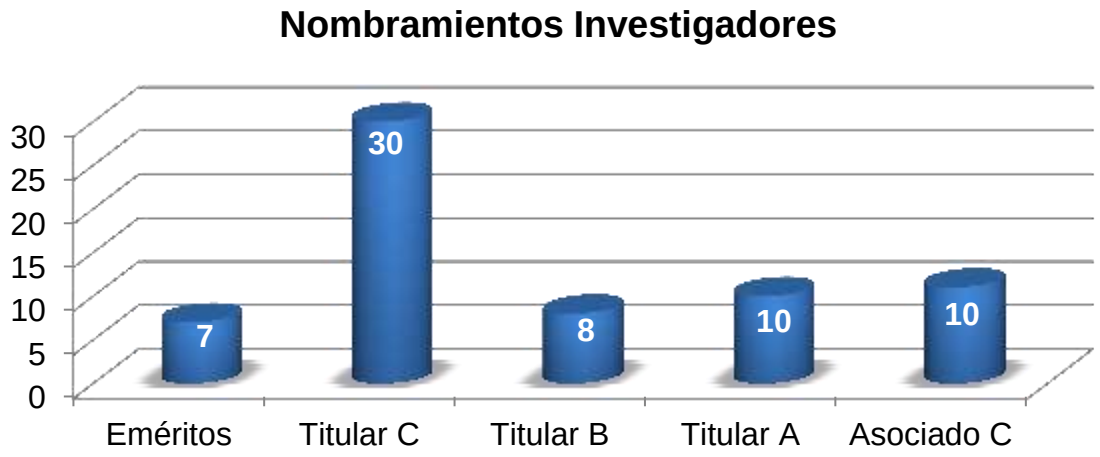

En el mismo periodo, 27 Técnicos Académicos tuvieron nombramiento de Titular C, Titular B y Titular A. 12 son Asociado C, 1 tiene el nombramiento de Asociado A y 4 tienen un contrato por honorarios.

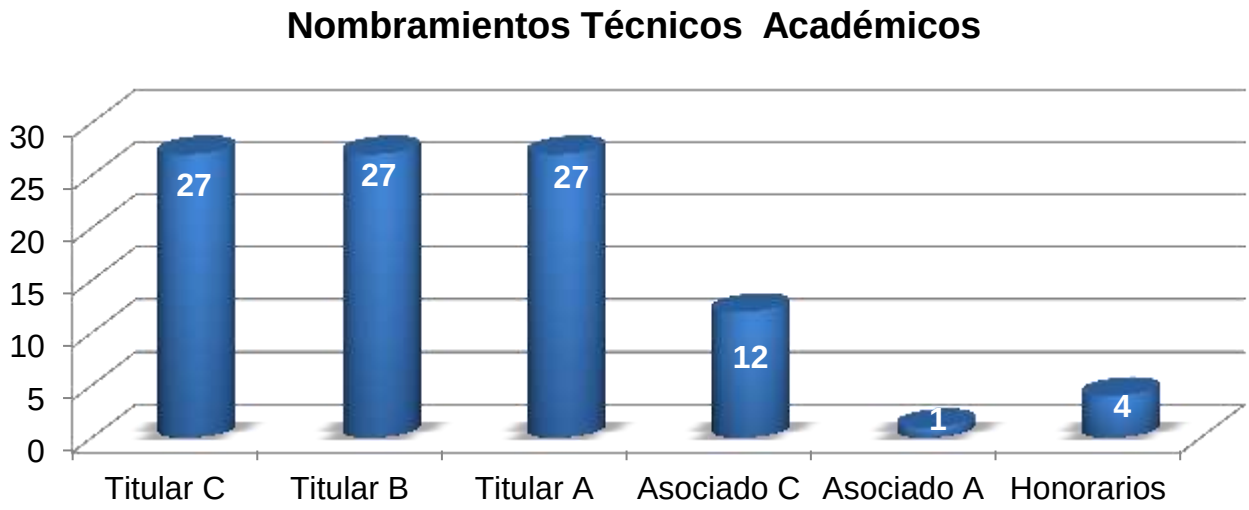

En lo que respecta al programa de Primas al Desempeño del Personal Académico (PRIDE) en el caso de los investigadores predomina el Nivel D, ya que 29 de ellos tienen el nivel, le siguen 24 investigadores en el Nivel C, 12 tienen el nivel B del PRIDE o equivalente y solo un investigador perdió dicho estímulo.

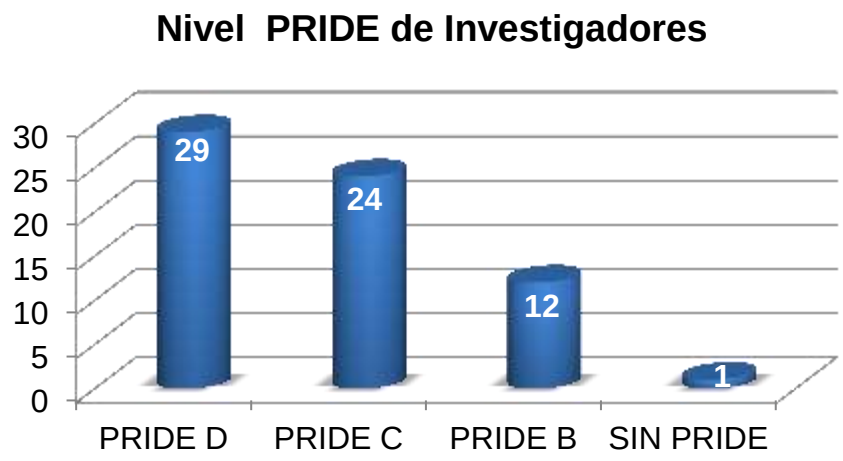

En el caso de los Técnicos Académicos, 41 tiene Nivel C del PRIDE, 30 tiene Nivel B o equivalente, 22 Técnicos Académicos han logrado el Nivel D y 1 no tiene el estimulo.

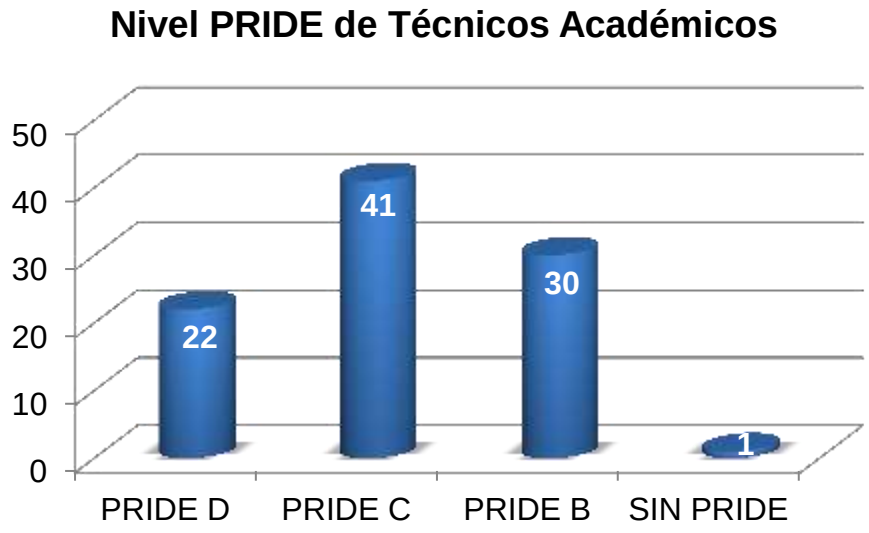

En el Sistema Nacional de Investigadores (SNI), 7 Investigadores han sido reconocidos con el máximo nivel, es decir, como Eméritos, 21 Investigadores poseen el nivel III, 14 tienen el nivel II, el nivel I lo obtuvieron 21 Investigadores y 1 es Candidato.



Son 22 Técnicos Académicos que se encuentran en el nivel I del SNI y 3 son candidatos.

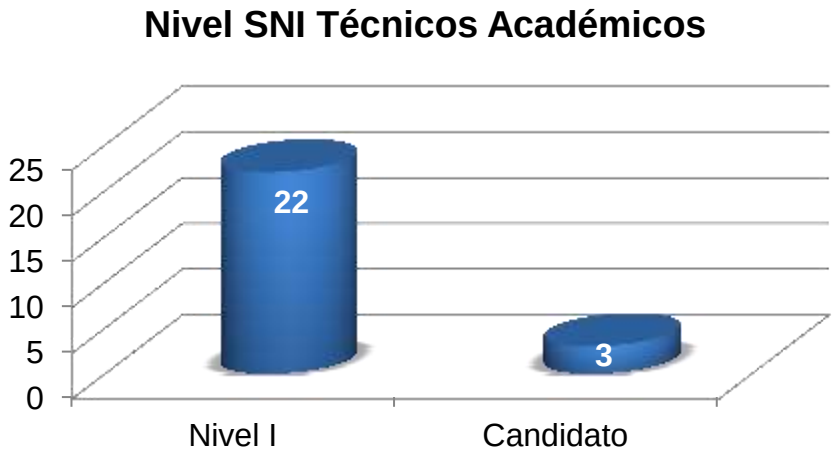

Personal Académico		
	Investigadores	**Técnicos Académicos**
Total	66	94
Jefes de grupo	59	
Asociados a un laboratorio	7	
Nombramiento		
• Eméritos	7	
• Titular C	30	27
• Titular B	8	27
• Titular A	10	27
• Asociado C	11	12
• Asociado A		1
• Contrato por honorarios		4
• Catedrático CONACyT	1	
Nivel de PRIDE		
• Nivel D	29	22
• Nivel C	24	41
• Nivel B	12	30
• Sin PRIDE	1	1
Nivel de SNI		
• Emérito	7	
• Nivel III	21	
• Nivel II	14	
• Nivel I	21	22
• Candidato	1	3
Grado académico		
• Doctorado	66	37
• Maestría		17
• Licenciatura		40

Organización Académica del Instituto

El Instituto de Fisiología Celular esta organizado en dos divisiones: Investigación Básica y Neurociencias, cada una de las divisiones tiene tres departamentos:

DIVISIÓN DE INVESTIGACIÓN BÁSICA	Biología Celular y del Desarrollo Bioquímica y Biología Estructural Genética Molecular
DIVISIÓN DE NEUROCIENCIA	Neurociencia Cognitiva Neurodesarrollo y Fisiología Neuropatología Molecular

Departamento de Biología Celular y del Desarrollo

Aguirre Linares Jesús, Dr.	**Investigador Titular C. PRIDE C. SNI nivel II.**
Sánchez González Alma Olivia, Biól.	Técnico Académico Titular B. PRIDE C.
Chagoya de Sánchez Victoria, Dra.	**Investigador Emérito.PRIDE D. Emérito del SNI.**
Chávez Jiménez Enrique, Dr.	Técnico Académico Titular A. PRIDE B
Velasco Loyden Gabriela, Dra.	Técnico Académico Titular B. PRIDE B.
García Sáinz Jesús Adolfo Dr.	**Investigador Emérito. PRIDE D. Emérito del SNI.**
Alcántara Hernández Rocío, Dra.	Técnico Académico Titular C. PRIDE C. SNI nivel I.
Romero Ávila María Teresa, Dra.	Técnico Académico Titular C. PRIDE D. SNI nivel I.
Hansberg Torres Wilhelm, Dr.	**Investigador Titular C. PRIDE D. SNI nivel II.**
Peña Segura Claudia, Biól.	Técnico Académico Titular A. PRIDE C.

Hernández Muñoz Rolando, Dr.	**Investigador Titular C. PRIDE D. SNI nivel III.**
Contreras Zentella Martha Lucinda, Dra.	Técnico Académico Titular C. PRIDE D. SNI nivel I.
Sánchez Sevilla María de Lourdes, M. en C.	Técnico Académico Titular B. PRIDE C.
Licona Limón Paula, Dra.	**Investigador Titular A. PRIDE B. SNI nivel I.**
Ramos Balderas José Luis, Biól.	Técnico Académico Titular A. PRIDE C.
López Casillas Fernando, Dr.	**Investigador Titular C. PRIDE C. SNI nivel II.**
Mendoza Rodríguez Valentín, Med. Cir.	Técnico Académico Titular A. PRIDE C.
Macías Silva Marina, Dra.	**Investigador Titular C. PRIDE D. SNI nivel III.**
Sosa Garrocho Marcela, Biól.	Técnico Académico Titular C. PRIDE C.
Navarro González Rosa Estela, Dra.	**Investigador Titular B. PRIDE D. SNI nivel I.**
Salinas Velázquez Laura Silvia, M. en C.	Técnico Académico Titular A. PRIDE C.
Vaca Domínguez Luis Alfonso, Dr.	**Investigador Titular C. PRIDE D. SNI nivel III.**
Sampieri García Alicia, Dra.	Técnico Académico Titular C. PRIDE D.
Valdés Rodríguez Víctor Julián, Dr.	**Investigador Titular A. PRIDE B. SNI nivel I.**
Cano Domínguez Nallely, Dra.	Técnico Académico Titular A. PRIDE B.

Departamento de Bioquímica y Biología Estructural

Arciniega Castro Marcelino, Dr.	**Investigador Asociado C. PRIDE B. SNI nivel I.**
Del Río Guerra Gabriel, Dr.	**Investigador Titular B. PRIDE C. SNI nivel II.**
Lara Ortiz María Teresa, Dra.	Técnico Académico Titular A. PRIDE C.
González Manjarrez María Alicia, Dra.	**Investigador Titular C. PRIDE C. SNI nivel III.**
Aguirre López Beatriz, Q.F.B.	Técnico Académico Titular B. PRIDE C.
Mas Oliva Jaime, Dr.	**Investigador Titular C. PRIDE D. SNI nivel III.**
Delgado Coello Blanca Alicia, M. en C.	Técnico Académico Titular C. PRIDE C.
Molinari Soriano José Luis, Dr.	**Investigador Titular C. PRIDE C. SNI nivel II.**
Copitin Niconova Natalia Ivanovna, M. en C.	Técnico Académico Titular B. PRIDE C.
Peraza Reyes Leonardo, Dr.	**Investigador Asociado C. PRIDE B. SNI nivel I.**
Suaste Olmos Fernando, Dr.	Técnico Académico Titular B. PRIDE B.
Pérez Montfort Ruy Enrique, Dr.	**Investigador Titular C. PRIDE D. SNI nivel III.**
Cabrera González E. Nallely, Biól.	Técnico Académico Titular C. PRIDE D.
Torres Larios Alfredo, Dr.	**Investigador Titular B. PRIDE C. SNI nivel II.**
Torres Martínez Marilú, Dra.	Técnico Académico Asociado C. PRIDE B. Candidato SNI.
Torres Quiroz Francisco, Dr.	**Investigador Asociado C. PRIDE C. SNI nivel I.**
Moreno Alvares Paola, Dra.	Técnico Académico Titular A. PRIDE B.
Tuena de Gómez Marietta, Dra.	**Investigador Emérito. PRIDE D. Emérito del SNI.**
José Núñez Concepción, QFB.	Técnico Académico Titular A. PRIDE B.

Departamento de Genética Molecular

Celis Sandoval Heliodoro, Dr.	**Investigador Titular C. SNI nivel I.**
Coria Ortega Roberto, Dr.	**Investigador Titular C. PRIDE C. SNI nivel II.**
Kawasaki Watanabe Laura, Dra.	Técnico Académico Titular C. PRIDE C. SNI nivel I.
Dreyfus Cortés Georges, Dr.	**Investigador Titular C. PRIDE D. SNI nivel III.**
Ballado Nava Socorro Ma. Teresa, QFB.	Técnico Académico Titular C. PRIDE C.
De la Mora Bravo Francisco Javier, Dr.	Técnico Académico Titular B. PRIDE D. SNI nivel I.
Funes Argüello María Soledad, Dra.	**Investigador Titular A. PRIDE C. SNI nivel I.**
Mendoza Martínez Ariann, Dra. .	Técnico Académico Asociado C. PRIDE B.
Furlan Magaril Mayra, Dra.	**Investigador Titular A. PRIDE B. SNI nivel I.**
Pérez Molina Rosario, Lic.	Técnico Académico Titular A. PRIDE B.
Georgellis Dimitrios, Dr.	**Investigador Titular C. PRIDE C. SNI nivel III.**
Álvarez Adrián Fernando, Dr.	**Investigador Asociado C. PRIDE B. SNI nivel I.**
Rodríguez Rangel Claudia, M. en C.	Técnico Académico Titular B. PRIDE B.
González Halphen Diego, Dr.	**Investigador Titular C. PRIDE D. SNI nivel III.**
Vázquez Acevedo Miriam, QBP.	Técnico Académico Titular C. PRIDE D. SNI nivel I.
Santillán Torres José Luís, Dr.	Técnico Académico Titular B. PRIDE C.
González Pedrajo Bertha, Dra.	**Investigador Titular B. PRIDE D. SNI nivel II.**
Espinosa Sánchez Norma, Dra.	Técnico Académico Titular C. PRIDE C.
Peña Díaz Antonio, Dr.	**Investigador Emérito. PRIDE D. Emérito del SNI.**
Calahorra Fuertes Martha, Dra.	Técnico Académico Titular C. PRIDE D. SNI nivel I.
Sánchez Sánchez Norma Silvia, M. en C.	Técnico Académico Titular C. PRIDE D.
Pérez Martínez Xóchitl, Dra.	**Investigador Titular B. PRIDE C. SNI nivel I.**
Camacho Villasana Yolanda, Dra.	Técnico Académico Titular B. PRIDE D. SNI I.

Recillas Targa Félix, Dr.	**Investigador Titular C. PRIDE D. SNI nivel III.**
Guerrero Avendaño Georgina, Biól.	Técnico Académico Titular C. PRIDE D.
Uribe Carvajal Salvador, Dr.	**Investigador Titular C. PRIDE D. SNI nivel III.**
Chiquete Félix Natalia, Dra.	Técnico Académico Titular B. PRIDE C. SNI I.

Departamento de Neurociencia Cognitiva

Aguilar Roblero Raúl Antonio, Dr.	**Investigador Titular C. PRIDE C. SNI nivel III.**
Chávez Juárez José Luis, M. en C.	Técnico Académico Titular A. PRIDE B.
Bargas Díaz José, Dr.	**Investigador Titular C. PRIDE D. SNI nivel III.**
Laville Conde Juan Antonio, Fis.	Técnico Académico Titular A. PRIDE C.
Bermúdez Rattoni Federico, Dr.	**Investigador Emérito. PRIDE D. Emérito del SNI.**
Osorio Gómez Daniel, Dr.	**Investigador Asociado C. PRIDE B. SNI nivel I.**
Rodríguez Durán Luis Francisco, Dr.	Técnico Académico Titular B. PRIDE B.
Fernández De Miguel Francisco, Dr.	**Investigador Titular C. PRIDE C. SNI nivel II.**
Méndez Ambrosio Bruno, M. en I.	Técnico Académico Titular A. PRIDE B.
Galarraga Palacio María Elvira, Dra.	**Investigador Titular C. PRIDE D. SNI nivel III.**
Tapia Ramírez Dagoberto, Biól.	Técnico Académico Titular C. PRIDE D. SNI nivel I.
Hernández Cruz Arturo, Dr.	**Investigador Titular C. PRIDE D. SNI nivel III.**
Luis Baltazar Enoch, Dr.	Catedratico CONACyT. Candidato al SNI.
Millan Aldaco Diana Alicia, Lic.	Técnico Académico Titular C. PRIDE D.
Hiriart Urdanivia Marcia, Dra.	**Investigador Titular C. PRIDE D. SNI nivel III.**
Velasco Torres Myrian, Dra.	**Investigador Asociado C. PRIDE C. SNI nivel I.**
Sánchez Soto Carmen, Biól.	Técnico Académico Titular C. PRIDE C.
Lemus Sandoval Luis Alonso, Dr.	**Investigador Titular A. PRIDE B.**
Figueroa Vanegas Tonatiuh, M. en I.	Técnico Académico Asociado C. PRIDE B.
Pérez de la Mora Miguel, Dr.	**Investigador Titular C. PRIDE C. SNI nivel III.**
Crespo Ramírez Minerva, QFB.	Técnico Académico Titular A. PRIDE C.

Romo Trujillo Ranulfo, Dr.	**Investigador Titular C. PRIDE D. SNI nivel III.**
Rossi Pool Román, Dr.	**Investigador Asociado C. PRIDE B. SNI nivel I.**
Álvarez López Manuel, Dr.	Técnico Académico Titular B. PRIDE C. SNI nivel I.
Díaz Osornio Jaime Héctor, Ing.	Técnico Académico Asociado C. PRIDE B.
Zainos Rosales Antonio, Dr.	Técnico Académico Titular B. PRIDE D. SNI nivel I.
Rosenbaum Emir Tamara, Dra.	**Investigador Titular B. PRIDE D. SNI nivel II.**
Morales Lázaro Sara Luz, Dra.	**Investigador Asociado C. PRIDE C. SNI nivel I.**
Llorente Gil Itzel Alejandra, Biól.	Técnico Académico Titular A. PRIDE C.

Departamento de Neurodesarrollo y Fisiología

Castro Obregón Susana, Dra.	**Investigador Titular A. PRIDE C. SNI nivel II.**
Aguilar Maldonado Beatriz, Dra.	Técnico Académico Titular A. PRIDE B.
Escalante Alcalde Diana, Dra.	**Investigador Titular B. PRIDE C. SNI nivel II.**
Martínez Silva Ana Valeria, Dra.	Técnico Académico Titular A. PRIDE C.
Pasantes Ordóñez Herminia, Dra.	**Investigador Emérito. PRIDE D. Emérito del SNI.**
Salceda Sacanelles Rocío, Dra.	**Investigador Titular C. PRIDE C. SNI nivel II.**
Sánchez Chávez Gustavo, Biól.	Técnico Académico Titular B. PRIDE C.
Velasco Velázquez Iván, Dr.	**Investigador Titular C. PRIDE D. SNI nivel II.**
Escobedo Ávila Itzel, Dra.	Técnico Académico Titular A. PRIDE B. Candidato a SNI
López Huerta Violeta Gisselle, Dra.	**Investigador Asociado C. PRIDE B. SNI nivel I.**
Palomero Rivero Marcela, Biól.	Técnico Académico Titular C. PRIDE D.
Ramiro Cortés Yazmín, Dra.	**Investigador Asociado C. PRIDE B. Candidato al SNI.**

Departamento de Neuropatología Molecular

Gómora Martínez Juan Carlos, Dr.	**Investigador Titular B. PRIDE C. SNI nivel I.**
Ramírez Aragón Miguel, M. en C.	Técnico Asociado C. PRIDE B.
López Colomé Ana María, Dra.	**Investigador Titular C. PRIDE D. SNI nivel III**.
Lee Rivera Irene, Dra.	Técnico Académico Titular B. PRIDE C. SNI nivel I.
López Hernández Edith Catalina, QFB.	Técnico Académico Titular C. PRIDE C. SNI nivel I.
Massieu Trigo Lourdes, Dra.	**Investigador Titular C. PRIDE D. SNI nivel III.**
Montiel Montes Teresa, Biól.	Técnico Académico Titular C. PRIDE D. SNI nivel I.
Morán Andrade Julio, Dr.	**Investigador Titular C. PRIDE D. SNI nivel III.**
Olguín Albuerne Mauricio, Dr.	**Investigador Asociado C. PRIDE B.**
Domínguez Macouzet Guadalupe, M. en C.	Técnico Académico Titular C. PRIDE D.
Sotres Bayón Francisco, Dr.	**Investigador Titular A. PRIDE C. SNI nivel I.**
Ramírez Lugo Leticia, Dra.	Técnico Académico Titular A. PRIDE C. SNI nivel I
Tapia Ibargüengoytia Ricardo, Dr.	**Investigador Emérito. PRIDE D. Emérito del SNI.**
Prior González Mara Guadalupe, M. en C.	Técnico Académico Asociado C. PRIDE B.
Tecuapetla Aguilar Fatuel, Dr.	**Investigador Titular A. PRIDE C. SNI nivel I.**
Ramírez Jarquin Josué O., Dr.	Técnico Académico Titular A. PRIDE B. SNI nivel I
Tovar y Romo Luis Bernardo, Dr.	**Investigador Titular A. PRIDE C. SNI nivel I.**
Aranda Fraustro Cristina, QFB.	Técnico Académico Titular B. PRIDE C.
***Guerra Crespo Magdalena, Dra.**	**Investigador Titular A. PRIDE C. SNI nivel I.**

*Académica que depende del Jefe de Departamento.

LÍNEAS DE INVESTIGACIÓN

BIOLOGÍA CELULAR Y DEL DESARROLLO

Aguirre Linares Jesús

- Diferenciación celular y regulación genética en microorganismos eucariotas: transducción de señales, respuestas al estrés oxidativo y regulación del metabolismo secundario en los hongos.

Chagoya de Sánchez Victoria

- Caracterización y función del ciclo circádico de la adenosina.
- Hepatoxicidad aguda y crónica con etanol, tetracloruro de carbono y dietilnitrosamina, cirrosis, cáncer hepatocelular y síndrome metabólico.
- Cardiotoxicidad durante el infarto de miocardio experimental y la insuficiencia cardiaca.

García Sáinz Jesús Adolfo

- Receptores acoplados a proteínas G.

Hansberg Torres Wilhelm

- Diferenciación celular en microorganismos.
- Especies reactivas del oxígeno.
- Relación estructura función de las catalasas.

Hernández Muñoz Rolando

- Regulación del metabolismo intermedio durante la proliferación celular *in vivo*.
- Identificación de moléculas involucradas en la comunicación inter-órganos y su repercusión en el metabolismo general.
- Mecanismos de producción y potencial reversión de la cirrosis experimental.
- Caracterización del metabolismo nitrogenado en eritrocitos humanos y de las enzimas involucradas en dichas vías.

Licona Limón Paula

- Papel del factor de crecimiento transformante beta (TGF-β) y de la vía de PKA en la diferenciación de subtipos celulares de linfocitos T.
- Caracterización de los mecanismos efectores de defensa y las vías de señalización que controlan la respuesta inmune contra parásitos.
- Estudio de los mecanismos de co-evolución parasito-hospedero.

- Estudio de la respuesta inmune a cepas bacterianas multidrogoresistentes para el diseño de inmunoterapias.
- Estudio del papel de IL-9 en contextos de infección parasitaria, alergias y autoinmunidad.
- Identificación de marcadores moleculares asociados a poblaciones linfoides productoras de IL-9.

López Casillas Fernando

- Mecanismos moleculares de acción y señalamiento de factores autócrinos y parácrinos de crecimiento celular, en particular del TGF-β (*Transforming Growth Factor type beta*).
- Caracterización estructura-función del betaglicano, también llamado el receptor tipo III del TGF-β.
- Participación del betaglicano en el desarrollo embrionario del pez cebra.

Macías Silva Marina

- Vías de transducción de señales de la citocina TGF-β.
- Regulación de la expresión de genes.
- Modificaciones Postraduccionales.
- Plasticidad celular.

Navarro González Rosa

- Regulación de la formación de gránulos de RNA en la gónada del nematodo *Caenorhabditis elegans*.
- Mecanismos de inducción de apoptosis de las células germinales del *Caenorhabditis elegans*.

Vaca Domínguez Luis

- Canales TRP.
- Entrada de calcio capacitiva.
- Desarrollo de sensores nanomoleculares para investigación y diagnostico.

Valdés Víctor Julián

- Neuroepigenética de la conducta en modelos de aprendizaje y memoria.
- Estudio de cambios epigenéticos y transcripcionales inducidos por alta glucosa.

BIOQUÍMICA Y BIOLOGÍA ESTRUCTURAL

Arciniega Castro Marcelino

- Desarrollo de algoritmos bayesianos para búsqueda de inhibidores a gran escala.
- Estimaciones de cambios en energía libre asociados con cambios conformacionales en proteínas.
- Estudios de alostería emplando simulaciones de dinámica molecular y teoría de redes.

Del Río Guerra Gabriel

- Estudio de la relación estructura-función en sistemas biológicos mediante el análisis de redes.
- Diseño asistido por computadora de péptidos capaces de inducir muerte celular selectiva.

González Manjarrez Alicia

- Duplicación génica y evolución en la levadura *Saccharomyces cerevisiae*.
- Diversificación funcional de genes parálogos: Papel de la localización subcelular, regulación transcripcional y propiedades bioquímicas de los productos codificados.
- Caracterización de genes tipo ancestral en *Kluyveromyces lactis* y *Lacchancea kluyveri*.
- Organización de proteínas paralogas hetero-oligomericas: Una instancia de diversificación funcional.
- Papel de Leu3 en la determinación del "lifespan" de la levadura *Saccharomyces cerevisiae*.
- Estudio de la organización y papel regulatorio de los complejos transcripcionales híbridos.

Mas Oliva Jaime

- Membranas biológicas y su función.
- Correlación estructura/función en proteínas.

Molinari Soriano José Luis

- Cisticercosis experimental.

Peraza Reyes Leonardo

- La regulación de la biogénesis peroxisomal durante el desarrollo sexual de *Podospora anserina*.
- La función de los peroxisomas durante el desarrollo meiótico de *Podospora anserina*.

- La dinámica y las interacciones de las mitocondrias, los peroxisomas y el retículo endoplásmico durante el desarrollo de los hongos.
- La dinámica y función del retículo endoplásmico durante el desarrollo sexual de *Podospora anserina*.
- La dinámica y las interacciones de los endosomas y los peroxisomas durante el desarrollo de los hongos.

Pérez Montfort Ruy

- Identificación de amino ácidos importantes para diferentes propiedades bioquímicas en triosafosfato isomerasas de tripanosomas.
- Inactivación selectiva de triosafosfato isomerasas de tripanosomátidos.

Torres Larios Alfredo

- Cristalografía de macromoléculas.
- Interacciones macromolécula-ligando.

Torres Quiroz Francisco

- Producción de ácido sulfhídrico en levadura y la regulación de procesos celulares.
- Regulación del proteosoma por modificaciones postraduccionales.
- Efecto del ácido sulfhídrico en un modelo de isquemia cerebral transitoria.
- Papel de la persulfuración de proteínas en la producción de leche en rumiantes.

Tuena de Gómez Marietta

- Regulación de la actividad de la ATPasa mitocondrial y de su estado oligomérico.
- Estudio sobre Triosafosfato isomerasa, regulación de la síntesis.
- Evolución de triosafosfato isomerasa.
- Estudio de la remodelación cardiaca subsecuente al infarto del miocardio inducido por isoproterenol y el efecto de un derivado de adenosina.

GENÉTICA MOLECULAR

Álvarez Adrián Fernando

- Estudio intergral de microdominios membranales bacterianos.
- Estudio del sistema de dos componentes ArcB/ArcA de *Escherichia coli*.
- Estudio del sistema de dos componentes BarA/UvrY y su relación con el sistema de regulación global Csr.

Celis Sandoval Heliodoro

- Estructura, función y regulación de las pirofosfatasas de bacterias fotosintéticas.
- Caracterización de los centros de reacción de bacterias fotosintéticas.

Coria Ortega Roberto

- Sistemas de transducción en levaduras y *Dictyostelium*. Mecanismos moleculares de la respuesta a estrés de retículo endoplásmico en levaduras y en *Dictyostelium*.

Dreyfus Cortés Georges

- Motilidad en bacterias.

Funes Argüello Soledad

- Respuestas mitocondriales ante condiciones de estrés y durante la regulación de la longevidad celular en *Saccharomyces cerevisiae.*
- Mecanismos de importación co-traduccional de proteínas a la mitocondria.

Furlan Magaril Mayra

- Relación entre la estructura 3D del genoma y la regulación de la actividad transcripcional.
- Topología genómica, accesibilidad cromatínica y modulación transcripcional durante la maduración y diferenciación eritroide.
- Topología genómica y regulación transcripcional de genes circadianos.
- Caracterización molecular y funcional de fronteras entre dominios topológicamente asociados.

Georgellis Dimitris

- Control of microbial gene expression by extra-cellular stimuli.
- Structure and function of proteins involved in bacterial signal transduction.

- Bacterial plasma membrane microdomains: Control of two-component system signaling and beyond.
- Characterization of the BarA/UvrY and ArcB/ArcA two component signal transduction systems of *Escherichia coli*.

González Halphen Diego

- Caracterización bioquímica y de genética molecular de los componentes de la fosforilación oxidativa del alga clorofícea incolora *Polytomella sp*.
- Relaciones estructura-función de los complejos mitocondriales.
- Expresión alotópica de genes mitocondriales.
- Caracterización de la maquinaria importadora de proteínas de los amiloplastos del alga incolora *Polytomella sp*.

González Pedrajo Bertha

- Sistema de secreción tipo III en bacterias Gram negativas.
- Mecanismos moleculares de la secreción de efectores de virulencia en *Escherichia coli* enteropatógena.
- Patogénesis bacteriana.
- Desarrollo de terapias para tratar infecciones bacterianas.

Peña Díaz Antonio

- Transporte y homeostasis de iones en distintas levaduras, así como su relación con el metabolismo energético, en particular ante condiciones extremas de salinidad y pH.
- Efectos de diferentes antimicóticos en levaduras patógenas.
- Mecanismos de adaptación de la levadura *Debaryomyces hansenii* a las condiciones del agua marina o de mayor salinidad y valores elevados del pH; cambios del metabolismo y de la expresión genética.
- Transporte y metabolismo de la xilosa en levaduras no convencionales.
- Mecanismos del transporte de calcio en *Candida albicans*.
- Caracterización estructural, cinética y fisiológica de las NADH deshidrogenasas externas de *Saccharomyces cerevisiae*.

Pérez Martínez Xóchitl

- Mecanismos de biogénesis del citocromo b mitocondrial.
- Mecanismos de control traduccional y de ensamblaje de Cox1 en mitocondrias de *Saccharomyces cerevisiae*.
- Estudio del papel de la compleja regulación de la síntesis de Cox1 en la fisiología de células de *Saccharomyces cerevisiae*.
- Estudio de los mecanismos de acoplamiento entre la traducción citosólica y la mitocondrial.

Recillas Targa Félix

- Estructura de la cromatina y actividad reguladora de la región 3’ no-codificante del dominio α-globina de pollo.
- Caracterización y estudio de los mecanismos de la formación de un dominio transcripcionalmente activo.
- Regulación epigenética de la expresión de genes supresores de tumores y secuencias repetidas.
- Regulación epigenética mediada por RNAs largos no-codificantes.
- Estudio de la organización tri-dimensional del genoma en la regulación de la expresión génica.

Uribe Carvajal Salvador

- Bioenergética de levaduras.
- Coordinación del catabolismo en *Saccharomyces cerevisiae*.
- Bioquímica de *Wolbachia sp*.

NEUROCIENCIA COGNITIVA

Aguilar Roblero Raúl

- Regulación neuroendócrina de los ritmos circadianos en mamíferos.

Bargas Díaz José

- Modulación presináptica de la transmisión entre neuronas.
- Estudio del funcionamiento de los microcircuitos cerebrales.
- Arquitectura funcional de la corteza motora del ratón.

Bermúdez Rattoni Federico

- Mecanismos moleculares y estructurales en la formación y evocación de la memoria de reconocimiento.
- Detección de señales moleculares tempranas que subyacen a los trastornos cognitivos en ratones transgénicos con enfermedad de Alzheimer.

Fernández De Miguel Francisco

- Secreción de serotonina somática y sináptica.
- Enseñanza experimental de las ciencias.
- Arte y cerebro.
- Determinantes moleculares de las sensaciones de tacto y dolor.

Galarraga Palacio Elvira

- Comparación de las oscilaciones en el potencial de membrana en neuronas corticales y en neuronas intralaminares del tálamo.
- Control del mecanismo de disparo neuronal y su neuromodulación: acciones directas e indirectas.
- Integración Sináptica de diferentes tipos neuronales en respuesta a aferentes de distinto origen: talámicas y corticales.

Hernández Cruz Arturo

- Homeostasis del calcio intracelular en neuronas y células endocrinas.
- Participación de las células cromafines de la glándula suprarrenal en la fisiopatología de la hipertensión.
- Estudio de la señalización por calcio intracelular en células foliculares durante el ciclo estral en rebanadas de ovario de ratón.
- Papel de canales iónicos selectivos al potasio implicados en la biología de distintos tipos de cáncer.

- Papel de los transportadores aniónicos en la regulación por GABA de la función de las células cromafines de la médula adrenal.
- El papel del GABA endógeno actuando sobre receptores GABAA en las fluctuaciones espontáneas de [$Ca2^{+}$]i, la transmisión colinérgica y la secreción de catecolaminas de las células cromafines adrenales *in situ*.
- La encefalitis asociada a la presencia de anticuerpos contra el receptor de N-metil-D-aspartato (NMDA-R): Una canalopatía inducida con pérdida de función.
- Estudios de señalización por calcio intracelular en centenares de células únicas empleando agonistas específicos y dispositivos de microfluídica (Colaboración con el grupo del Dr. José Luis García Cordero. CINVESTAV-Monterrey).
- Estudios funcionales de cardiomiocitos humanos diferenciados de células pluripotentes inducidas de sujetos normales y pacientes con síndrome de Andersen-Tawil, una cardio-canalopatía del canal de potasio Kir2.1 que cursa con arritmia y muerte súbita.

Hiriart Urdanivia Marcia

- Modulación del acoplamiento entre el estímulo y la secreción hormonal de células beta pancreáticas sanas y en condiciones diabéticas.
- Regulación del desarrollo, la plasticidad y el funcionamiento de las células beta pancreáticas.
- Mecanismos fisiopatológicos de desarrollo de la resistencia a la insulina, obesidad, síndrome metabólico y diabetes.
- Efecto de tóxicos sobre la secreción de insulina y desarrollo de las células beta.

Lemus Sandoval Luis

- Representación cortical de objetos auditivos.
- Representación de estímulos amodales.

Morales Lázaro Sara Luz

- Regulación de la expresión de canales TRPs asociados a la generación de dolor.
- Regulación del canal TRPV1 por endocanabinoides.
- Regulación del canal TRPV1 por efecto de moléculas esteroideas.

Osorio Gómez Daniel

- Efecto de la obesidad en los mecanismos celulares y moleculares del aprendizaje y la memoria.
- Evaluación por optogenética de la participación de la proyección amígdala-corteza insular en el establecimiento de la valencia de los estímulos.

Pérez de la Mora Miguel

- Interacciones de neurotransmisores dentro de la amígdala de la rata y su relevancia en la modulación de la ansiedad.
- Diabetes y ansiedad.
- Papel de los sistemas oxitocinérgicos y vasopresinérgicos en la modulación amigdalina de la ansiedad.
- Papel de la neurotrasmisión dopaminérgica en la modulación amigdalina de la ansiedad.
- Papel de los sistemas de neurotransmisión catecolaminérgicos en el mecanismo de la acción ansiolítica y prosocial de la 3’4’ Metilen-dioxi-metanfetamina (éxtasis).
- Alteraciones neurocognitivas en la adolescencia temprana por el consumo de inhalantes.
- Sobre-expresión específica del gene de la triptofano 5 hidroxilasa (TPH2) en neuronas serotoninérgicas y evaluación de la producción de serotonina.

Romo Trujillo Ranulfo

- Neurobiología de la percepción.

Rosenbaum Emir Tamara

- Relaciones entre la estructura y la función de los canales de tipo TRPV1.
- Estudios sobre la regulación de la actividad de canales TRP por hormonas y lípidos.

Rossi Pool Román

- Neurociencia computacional.
- Análisis estadístico de mediciones electrofisiológicas.
- Modelado de sistemas dinámicos y redes neuronales.
- Mediciones electrofisiológicas en primates entrenados.
- Decodificación de actividad de neuronas individuales y poblaciones.

Velasco Torres Myrian

- Modulación de la secreción de insulina por canales de potasio.
- Actividad de canales iónicos en el síndrome metabólico.

NEURODESARROLLO Y FISIOLOGÍA

Castro Obregón Susana

- Papel de la autofagia durante el desarrollo y envejecimiento del sistema nervioso, así como en la estabilidad del genoma.

Escalante Alcalde Diana

- Papel de la fosfatasa de fosfolípidos-3 (PLPP3, antes LPP3) en el desarrollo y en enfermedades.

López Huerta Violeta Gisselle

- Patrones de conectividad en circuitos talámicos control y en modelos de autismo.
- Control inhibitorio de circuitos talámicos en el adulto y durante el desarrollo.

Pasantes Ordóñez Herminia

- Mecanismos moleculares del edema cerebral.
- Taurina y células progenitoras neuronales y transdiferenciación neuronal.

Ramiro Cortés Yazmín

- Plasticidad sináptica y sus correlatos estructurales en el autismo en hipocampo y corteza visual.
- Actividad neuronal de corteza visual primaria *in vivo* en ratones despiertos en el autismo.

Salceda Sacanelles Rocío

- Neurotransmisión glicinérgica en la retina de los vertebrados.
- Relación funcional entre el epitelio pigmentario de la retina y la retina neural.
- Retinopatía diabética.
- Neuropatía diabética.

Velasco Velázquez Iván

- Biología de células troncales neurales en el desarrollo del cerebro.
- Uso de las células troncales embrionarias en el tratamiento de enfermedades del sistema nervioso.
- Reprogramación de células somáticas a estado pluripotencial.
- Regeneración del sisema nervioso del ajolote.

NEUROPATOLOGÍA MOLECULAR

Gómora Martínez Juan Carlos

- Relación estructura-función de canales de calcio activados por voltaje.
- Participación de los canales de sodio en las propiedades metastásicas del cáncer cervicouterino.

Guerra Crespo Magdalena

- Estudio de la diferenciación de células pluripotentes inducidas humanas *in vitro* e *in vivo* en patologías cardiacas.
- Estudio del potencial neuronal y dopaminérgico de células troncales embrionarias y células pluripotentes inducidas humanas *in vitro* e *in vivo* en el contexto de la enfermedad de Parkinson

López Colomé Ana María

- Neurotransmisión excitadora en la retina: mecanismos y regulación.
- El glutamato y la trombina como agentes causales de patologías que producen ceguera.

Massieu Trigo Lourdes

- Mecanismos de muerte neuronal asociados a la isquemia/hipoglucemia.
- Respuestas al estrés energético en neuronas. Estrés oxidante, estrés del retículo endoplásmico y autofagia.

Morán Andrade Julio

- Mecanismos moleculares de la muerte neuronal programada.
- Papel de las especies reactivas del oxígeno en la muerte y diferenciación neuronal.
- Papel de la NADPH-oxidasa en la muerte y diferenciación neuronal.

Olguin Albuerne Mauricio

- Crecimiento axonal y dendrítico.
- Migración neuronal.

Sotres Bayón Francisco

- Neurobiología de la supresión activa del miedo en busca de una recompensa.
- Neurobiología de conductas de elección guiadas por motivaciones gustativas.
- Neurobiología de la expresión e inhibición pasiva del miedo condicionado.

Tapia Ibarguengoytia Ricardo

- Modelos experimentales de epilepsia y enfermedades neurodegenerativas.
- Mecanismos de muerte neuronal.
- Bioética y neuroética.

Tecuapetla Aguilar Fatuel

- Subcircuitos de la corteza-ganglios basales-tálamo en condiciones normales y neuropatológicas.

Tovar y Romo Luis Bernardo

- Regulación trófica de la viabilidad neuronal; mecanismos endógenos de recuperación después del infarto cerebral isquémico.
- Estudio de las respuestas moleculares de los astrocitos en la isquemia cerebral.
- Regulación epigenómica y transcriptómica del infarto cerebral isquémico.
- Mecanismos de recuperación neuronal mediados por interacciones con el endotelio vascular.

ACTIVIDADES ACADÉMICO ADMINISTRATIVAS

Aguilar Roblero Raúl

- Revisor Externo del PAPIIT.
- Revisor Externo del CONACyT.
- Revisor externo de Biomedical Physics & Engineering Express.
- Revisor Externo Frontiers in Integrative Neuroscience.

Aguirre Linares Jesús

- Revisor de proyectos para CONACyT, PAPIIT,y de artículos para las revistas PLoS One, Frontiers in Microbiology, Scientific Reports, Fungal Biology and Applied and Environmental Microbiology.
- Miembro de la comisión dictaminadora externa del CICESE desde el 2013 (duración indeterminada).
- Miembro del Comité Evaluador del PAPIIT-UNAM.

Arciniega Castro Marcelino

- Participación en la comisión de cómputo del IFC-UNAM.
- Participación como evaluador en el proceso de selección de candidatos a cursar estudios de posgrado en el extranjero en el marco de la convocatoria CONACyT-Regional Sur-Oriente y Noroeste.
- Participación como evaluador de proyectos PAPIIT.

Bargas Díaz José

- Comisión Evaluadora del PRIDE. Instituto de Fisiología Celular, UNAM.
- Comisión Evaluadora PRIDE Instituto de Ecología, UNAM.
- Revisor de Artículos de Investigación para su publicación en Revistas Internacionales y Nacionales: Brain Research, Trends in Neuroscience, Journal of Neuroscience, Journal of Neurophysiology, Synapse, BMC-Neuroscience, Neuroscience, Journal of Pharmacy and Pharmacology, Proceedings of the Nacional Academy of Sciences, European Journal of Neuroscience, Journal of Neuroscience Research, Revista de Neurología, Neuropsychopharmacology, Experimental Neurology, Frontiers in Cellular Neuroscience, Frontiers in Systems Neuroscience, Journal of Physiology (London), PLoS Computational Biology, Neurocomputing, Biological Psychiatry, Movement Disorders, Neurochemical Research, Learning and Memory, Nature, Scientific Reports, Neurobiology of Disease,

Neuroscience Letters, Revista Biomédica, Frontiers in Neuroanatomy, Revista Mexicana de Ingeniería Biomédica, Basal Ganglia, Journal of Applied Research and Technology, e-Life.

- Revisión de Proyectos de Investigación para dictaminar su apoyo: Proyectos de PAPIIT-UNAM.
- Revisión de Proyectos de Investigación para dictaminar su apoyo: Proyectos de CONACyT.
- Proyectos Internacionales: Netherlands, Colombia, Argentina, New Zealand.
- Miembro y actual presidente de la Internacional Basal Ganglia Society (IBAGS).

Bermúdez Rattoni Federico

- Comisión Evaluadora PRIDE del Instituto de Neurobiología, 2018-2020.
- Comité de Evaluación del PAPIIT.
- Comisión Dictaminadora del Instituto de Neurobiología, 2017-2019.
- Jefe de Departamento de Neurociencia Cognitiva, Instituto de Fisología Celular, 16 de noviembre, 2017-.

Castro Obregón Susana

- Presidenta la Comisión Permanente de Ingreso, Egreso y Permanencia (CPIEP) del Posgrado en Ciencias Bioquímicas.
- Miembro del subcomité Académico de la Licenciatura en Neurociencias.
- Secretaria Ejecutiva de la Comisión de la Unidad de Biología Molecular.
- Miembro de la Comisión de Seminarios del IFC.
- Jurado Evaluador del Concurso de Oposición Abierto para una plaza de Técnico Académico Titular A de tiempo completo.
- Comité Organizador del III Congreso Nacional de Neurobiología de la Sociedad Mexicana de Bioquímica.
- Coordinación de la Red CYTED-NeuroSur.

Chagoya Hazas Victoria Eugenia

- Miembro de la cartera de evaluadores del CONACyT.
- Apoyo a diferentes programas de posgrado como profesor, tutor y asesor: Facultad de Ciencias: Posgrado en Ciencias Biológicas. Facultad de Química: Posgrado en Ciencias Bioquímicas y Químicas. Facultad de Medicina: Posgrado en Ciencias Biomédicas.
- Revisor de Archivos de Cardiología de México.

- Comisión Multidisciplinaria de la Facultad de Química UNAM.
- Revisor de proyectos de la Fundación Glaxo Smith Kline y Fundación Mexicana para la Salud.
- Revisor de la revista Journal of Pharmacy and Pharmacology.

Coria Ortega Roberto

- Árbitro de proyectos PAPIIT.
- Revisor Proyectos de Ciencia Básica de CONACyT.
- Jefe del Departamento de Genética Molecular del IFC.
- Revisor de manuscritos para publicación en revistas internacionales indizadas: Cells, Journal of Microbiology and Biotechnology, Molecular and Cellular Biology, FEBS Letters.

Del Río Guerra Gabriel

- Miembro de la comisión de cómputo del Instituto de Fisiología Celular.
- Revisor para las revistas Bioinformatics, Microbial Cell Factories, ACS Synthetic Biology, Entropy, Molecules, Scientific Reports, Nucleic Acids Research, Polymers, PeerJ.
- Revisor de proyectos CONACyT.
- Revisor de proyectos PAPIIT.
- Revisor de proyectos Facultad de Medicina-UNAM.
- Organizador del simposium internacional realizado en Canadá, titulado "Mathematics and Computer Science in Modeling and Understanding of Structure and Dynamics of Biomolecules".

Dreyfus Cortés Georges

- Miembro del Subcomité Académico de la Licenciatura en Investigación Biomédica Básica 2010- 2019.
- Miembro Titular de la Academia Nacional de Medicina de México, A.C.
- Evaluador del Área de las Ciencias Biológicas, Químicas y de la Salud del Programa de Apoyo a Proyectos de Investigación e Innovación Tecnológica.
- Evaluador de proyectos CONACyT-Ciencia Básica.
- Evaluador de la XXIX edición del Programa "El Verano de la Investigación Científica" 2019.
- Revisor de diversas revistas Internacionales sobre Microbiología.
- Evaluador de proyectos PAPIIT.

- Colaborador Externo de la editorial Fondo de Cultura Económica.

Escalante Alcalde Diana María

- Jefa del departamento de Neurodesarrollo y Fisiología, Enero 2014 a la fecha.
- Miembro del Subcomité Académico de la Licenciatura en Neurociencias.
- Elaboración de una propuesta institucional de infraestrutura del CONACyT para la compra de equipo especializado para el nuevo vivario del IFC. Se otorgaron más de 18 millones de pesos.
- Miembro de Comité de entrevistas para la admisión a la Licenciatura en Neurociencias.
- Miembro del Comité de admisión al Doctorado en Ciencias Biomédicas.
- Miembro del CICUAL.
- Miembro de la Comisión de Bioseguridad.
- Secretaria Ejecutiva de la Unidad de Imagenología del IFC.
- Evaluador de proyectos CONACyT (Ciencia Básica y Fronteras) y PAPIIT.
- Miembro del Comité Editorial del IFC. Creado en Octubre del 2016.
- Miembro de la Comisión Local de Bioseguridad.

Fernández De Miguel Francisco

- Editor Revisor de la revista “Frontiers in Physiology”, sección Membrane Biophysics and Physiology.
- Revisor *ad hoc* de artículos científicos para BMC Neuroscience, Frontiers in Physiology, Frontiers in Cellular Neurosciences, Frontiers in Developmental Neurosciences, Frontiers in Physics, Journal of Neurophysiology, Neuroscience.
- Guest Associate Editor. Frontiers in Physiology. Membrane Physiology and Membrane Biophysics.
- Evaluador de proyectos para el CONACyT.
- Guest Associate Editor. Fundamentals in the 21st Century. Frontiers in Molecular Neuroscience. Suiza.
- Coordinador del Programa de Neurociencias del Centro de Ciencias de la Complejidad.
- Miembro del Comité Académico del Centro de Ciencias de la Complejidad (C3), UNAM.
- Coordinador de la sexta edición del libro de texto "From Neuron to Brain" de Martin, AR., Brown, DA, Diamond, M, Cattaneo, A, y De Miguel FF. Oxford UNiversity Presss. Reino Unido.
- Evaluador de Proyectos de investigación científica y tecnológica presentados al FONCYT, Ministerio de Ciencia, Tecnologia e Innovacion Productiva, Agencia Nacional de

Promoción Científica y Tecnológica, Fondo para la Investigación Científica y Tecnológica, Argentina.

- Evaluador de proyectos PAPIIT.
- Miembro del Consejo Directivo del Consejo Mexicano para la Cultura y las Artes AC (COMCA).

Funes Argüello María Soledad

- Representante del Director del Instituto de Fisiología Celular ante el Comité Académico del Programa de Maestría y Doctorado en Ciencias Bioquímicas (UNAM).
- Coordinadora de enseñanza del Instituto de Fisiología Celular.
- Representante del Director del Instituto de Fisiología Celular ante el Comité Académico del Programa de Maestría y Doctorado en Ciencias Biológicas (UNAM).
- Participación en las entrevistas de admisión del Programa de Doctorado en Ciencias Biológicas. Admisión 2020-1 y 2020-2.
- Tesorera de la Sociedad Mexicana de Bioquímica. Mesa Directiva 2019-2021.
- Responsable de Entidad (Instituto de Fisiología Celular) ante el Programa de Doctorado en Ciencias Biomédicas (UNAM).
- Subsecretaria Tesorera de la Sociedad Mexicana de Bioquímica. Mesa directiva 2017-2019.
- Miembro de la Comisión de Difusión y Divulgación del Instituto de Fisiología Celular.

Furlan Magaril Mayra

- Miembro de la comisión de seminarios. Invitación y coordinación de seminarios institucionales nacionales e internacionales en el Insituto de Fisiología Celular.
- Representate del IFC en la generación de la Orientación Interdisciplinaria de Posgrado en Bioinformática y Biomatemáticas.
- Comisión de la Unidad de Biología Molecular.
- Miembro de la Comisión con perspectiva de Género.
- Evaluación de proyectos PAPIIT y CONACyT.
- Referí de artículos internacionales: Journals: Scientific Reports, Cellular & Molecular Biology Letters y BMC journal.

Galarraga Palacio María Elvira

- Como Miembro y Vicepresidenta de la Sociedad Internacional de Ganglios Basales (IBAGS) apoyar a esta sociedad con el cambio de Presidencia para 2019.

- Revisora de Proyectos de Investigación de PAPIIT-UNAM y CONACyT.
- Revisora de articulos en revistas internacionales para su publicación.

García Sáinz Jesús Adolfo

- Revisor de Proyectos para DGAPA y CONACyT.
- Miembro del Comité Editorial de: European Journal of Pharmacology, Molecular Pharmacology y de Archivos del Instituto Nacional de Cardiología.
- Revisor *Ad Hoc*: Psicopharmacology, Annals of the Brazilian Academy of Sciences, Biochemistry Research International.

Georgellis Dimitris

- Participación en el subcomité de admisión de alumnos del Programa de Maestría y Doctorado en Ciencias bioquímicas, semestre 2019-2.
- Comisión Dictaminadora Instituto de Biotecnología, UNAM. (2018-).
- Representante de Tutores del Instituto de Fisiología Celular ante el Comité Académico del Programa de Maestría y Doctorado en Ciencias Bioquímicas de la UNAM. (2019-) .

Gómora Martínez Juan Carlos

- Miembro de la Comisión de Seminarios institucionales del IFC, desde el 2010.

González Halphen Diego

- Miembro de la Comisión Dictaminadora del Centro de Ciencias Genómicas, Campus Cuernavaca, UNAM, del 27 de junio de 2016 a la fecha.
- Consejero Universitario suplente, representante de los investigadores del Instituto de Fisiología Celular ante el H. Consejo Universitario, UNAM, del 18 de agosto de 2016 a la fecha.
- Miembro de la Comisión de Legislación Universitaria, comisión permanente del H. Consejo Universitario, UNAM; designado por el propio Consejo, del 18 de agosto de 2016 a la fecha.

González Manjarrez Alicia

- Participacion en el programa jovenes hacia la investigacion. alumna: Sheyla Sabel Cruz Cruz y Karen Peralta Estancia del 4 al 29 de Junio de 2019.
- Integrante de la Comisión externa de evaluación del Centro de Investigación Científica de Yucatán (CICY) CONACyT.

- Coordinadora Regional de la Red Latinoamericana de Biología.
- Miembro de la Comisión de Premios de Ciencias Naturales de la Academia Mexicana de Ciencias.
- Miembro de la Comisión Dictaminadora del Instituto de Ecología desde Diciembre de 2015.
- Coordinador del ciclo científico de la Feria Internacional del Libro del Palacio de Minería. Febrero/Marzo 2019.

González Pedrajo Bertha

- Representante del personal académico del Instituto de Fisiología Celular ante el Consejo Técnico de la Investigación Científica.
- Miembro de las comisiones de Reglamentos Internos y de Posgrado del CTIC.
- Miembro del Consejo Interno del IFC.
- Participación del grupo en el seminario departamental de la División de Ciencia Básica del IFC.
- Evaluación de proyectos de investigación para DGAPA, Israel Science Foundation, el Medical Research Council, UK y la Fundación Marcos Moshinsky. Revisora de artículo para las revistas Brazilian Journal of Microbiology y TIP (FES Zaragoza).
- Miembro del Comité Organizador del XLI Congreso Nacional de Microbiología.
- Miembro de la Mesa Directiva de la Sociedad Mexicana de Bioquímica (Subsecretaria Tesorera).
- Miembro de la comisión de bioseguridad del Instituto de Fisiología Celular.

Guerra Crespo Magdalena

- Participación en la inauguración del Laboratorio de Medicina Regenerativa en el Departamento de Cirugía de la Facultad de Medicina de la UNAM, como investigador responsable del laboratorio. marzo de 2019.
- Participación en la reinauguración del Departamento de Cirugía de la Facultad de Medicina de la UNAM.marzo de 2019.
- Evaluador proyectos de investigación de la convocatoria DGAPA-PAPIIT 2019.
- Miembro del comité editorial de la revista Tecnología Digital. Tuxtla Gutiérrez, Chiapas desde su creación (abril del 2011). ISSN: 2007-9400.
- Nombramiento como Representante de los Tutores y Alumnos del IFC en el Comité Académico del Posgrado en Ciencias Biológicas. Periodo 2017-2019.

Hansberg Torres Wilhelm

- Arbitraje de artículos de investigación para revistas Internacionales.
- Arbitraje de proyecto para el PAPIIT.
- Evaluador Fondo SEP-CINVESTAV, Proyecto de Investigación, Área de Ciencias Biológicas y de la Salud.
- Comisión Evaluadora del PRIDE y PAIPA de la Facultad de Química, UNAM.
- Revisión de proyecto de Investigación para la Cátedra Moshinsky.

Hernández Cruz Arturo

- Miembro del Comité Institucional para el Cuidado y Uso de Animales de Laboratorio del IFC 2013-.
- Evaluador de Proyectos de CONACyT y DGAPA 2015-.
- Responsable Técnico del Laboratorio Nacional de Canalopatías del IFC. 2019-.
- Miembro del Subcomité de Admisión al Posgrado en Ciencias Biomédicas 2012-.

Hernández Muñoz Rolando

- Encargado de Seguridad Radiológica del Instituto de Fisiología Celular ante la Comisión Nacional de Seguridad Nuclear y Salvaguardas (CNSNS).

Hiriart Urdanivia Marcia

- Miembro de la Comisión *Ad hoc* para revisar candidatos a plazas en el Centro de Ciencias de la Atmósfera.
- Miembro del Comité Evaluador de la Fundación Miguel Alemán Velasco (2012-2019).
- Miembro del Comité del PECEM, Facultad de Medicina, UNAM.
- Arbitro externo en la evaluación de proyectos PAPIIT, evaluación de proyectos de CONACyT.
- Miembro de la Comisión Dictaminadora del Instituto de Ciencias Físicas, UNAM, Cuernavaca, Mor (2019-2021).
- Miembro del Jurado de las Cátedras Moshinsky.
- Editora Asociada del Frontiers in Pharmacology, revisión de varios artículos al mes y de muchos otros artículos de revistas internacionales como Diabetes Care, Diabetes, J Cell Physiol, J Mol Endocrinology, Am J Physiology, etc.
- Presidente del Jurado del Premio UNAM PUNJA y RNDJA. Docencia 2019.

- Miembro de la Comisión Dictaminadora de Biología, Facultad de Ciencias, UNAM (2019-2021).

Lemus Luis

- Comisión organizadora de seminarios del Instituto de Fisiología Celular. De enero del 2013 a la fecha.
- Miembro de la Comisión de Cómputo del IFC.
- Reviewer editor Frontiers in Psychology. Revisor de cuatro artículos publicados.
- Reviewer editor Frontiers in Integrative Neuroscience (doce artículos revisados).
- Revisor invitado para la revista Neuroscience.
- Revisor invitado para Cerebral Cortex.
- Organizador de la Feria de Carteles del IFC del 2015 a la fecha.

Licona Limon Paula

- Comité Interno para el Cuidado y Uso de Animales de Laboratorio del Instituto de Fisiología Celular.
- Comisión de seminarios institucionales.

López Casillas Fernando

- Integrante del subcomite de admision del Doctorado en Ciencias Biomédicas. Mayo de 2019.
- Miembro de la Comisión Revisora del Área II: Biología y Química (Inconformidades de Dictamines) del Sistema Nacional de Investogadores (Noviembre y Diciembre 2019).
- Representante del Personal Académico del IFC ante el CAABQYS para el periodo agosto 2016 a agosto 2019.
- Miembro de la Comisión Evaluadora del Área de las Ciencias Biológicas, Químicas y de la Salud del Programa de Apoyos para la Superacion del Personal Académico de la UNAM (PASPA) para el periodo mayo 2018 a mayo 2021.

López Colomé Ana María

- Miembro del Patronato de la Fundación "Conde de Valenciana”.
- Jefe de la Unidad de Investigación del Instituto de Oftalmología Conde de Valenciana.
- Miembro de la Comisión Dictaminadora de la Facultad de Medicina, UNAM.
- Editor Regional de la revista "Molecules" (Basilea, Suiza).

- Evaluador de Proyectos PAPIIT/UNAM.
- Consejera Universitaria, Instituto de Fisiología Celular.
- Evaluador de Proyectos CONACyT: Fronteras de la Ciencia.
- Miembro del Comité Directivo de la Maestría México / Francia en "Ciencias de la Visión". Facultad de Medicina, UNAM.
- Jurado del "Premio Estatal de Ciencia y Tecnología 2016, 2017, 2018, 2019: Ciencias de la Salud.
- Miembro de la Comisión Dictaminadora de la Facultad de Veterinaria: Ciencias Aplicadas.
- Revisor de publicaciones para: Cellular Physiology and Biochemistry; Investigative Ophthalmology and Visual Science; Experimental Eye Research; Journal of Cellular Biochemistry.

Macías Silva Marina

- Jefe del Departamento de Biología Celular y Desarrollo del IFC, UNAM.
- Miembro la Comisión Dictaminadora del CAABQYS, de la Facultad de Química, UNAM (a partir de octubre del 2018).
- Miembro del Comité de Seguimiento a Nuevos Investigadores, en particular de la Dra. Daniela Araiza Olivera Toro, del Instituto de Química de la UNAM.
- Evaluador *Ad Hoc* de proyectos de investigación PAPIIT-DGAPA, UNAM.
- Evaluador *Ad Hoc* de proyectos de investigación CONACyT.
- Miembro de la Comisión del Bioterio y del CICUAL del IFC.
- Colaborador del Laboratorio Nacional LaNSBioDyt (Laboratorio Nacional de Soluciones Biomiméticas para Diagnóstico y Terapia) de la Facultad de Ciencias, UNAM.
- Revisor *Ad Hoc* para las revistas internacionales: Neurochemical Research, Cell Biol Int, y Science Signalling.

Mas Oliva Jaime

- Miembro del Comité Editorial de Gaceta Médica de México. Academia Nacional de Medicina.
- Revisor de proyectos presentados al CONACyT dentro de las convocatorias de Problemas Nacionales y Ciencias Básicas.
- Presidente del Jurado Calificador del Premio Dr. Jorge Rosenkranz 2019 (Roche México).
- Miembro del Consejo Consultor de Archives of Medical Research (Elsevier).
- Revisor de proyectos de investigación presentados al programa PAPIIT de la Dirección General de Asuntos del Personal Académico (DGAPA) de la UNAM.

Massieu Trigo María de Lourdes

- Secretaria Académica del Instituto de Fisiología Celular a partir de enero del 2018.
- Miembro de la Comisión del PRIDE de la Facultad de Medicina.
- Arbitro de artículos en revistas internacionales: CNS and Therapeutics, Neurochemistry International (2 revisiones), Journal of Biological Inorganic Chemistry, Frontiers in Cellular Neuroscience, Chemical Research in Toxicology.
- Revisor de proyectos para la Agencia de Promoción Científica y Tecnológica.
- Fondo para la investigación Científica y Tecnológica (FONCyT) Argentina.
- Revisor de proyectos PAPIIT.

Morán Andrade Julio

- Jefe del Departamento de Neuropatología Molecular del Instituto de Fisiología Celular, UNAM. A partir de enero 2018- .
- Miembro del Comité Editorial de la revista Escuela Nacional Preparatoria 2015- .
- Miembro de la Comisión Dictaminadora Facultad de Psicología, UNAM, 2014- .
- Miembro de la Comisión Evaluadora del PRIDE de la Facultad de Ciencias, UNAM, 2016-.
- Miembro de la Comisión Dictaminadora Instituto de Investigaciones Biomédicas, UNAM, 2010- .
- Miembro de la Comisión Evaluadora del PRIDE del Instituto de Química, UNAM, 2015- .
- Miembro de la Comisión de Investigación y Ética de la Facultad de Medicina, UNAM, 2016- .
- Miembro de la Comisión Evaluadora del PRIDE del Instituto de Ecología, UNAM, 2016-.
- Miembro de la Comisión Evaluadora del PRIDE del Centro de Ciencias Genómicas, UNAM, 2016-.
- Miembro de la Comisión Dictaminadora Instituto de Neurobiología, UNAM, 2018-.

Navarro González Rosa Estela

- Miembro del Comité Organizador del Simposio Teórico-Práctico de Edición Genética por CRISPR-Cas9. Realizado en el Instituto de Fisiología Celular de la UNAM. Octubre de 2019.
- Revisora de artículos para la revista Peer J.
- Representante de Tutores ante el Program de Maestría y Doctorado en Ciencias Bioquímicas (2019-).
- Participante de la Red de evaluación del efecto tóxico de nanopartículas Sinanotox.

- Revisora de varios Proyectos de PAPIIT.
- Miembro del Comité Editorial del Instituto de Fisiología Celular, UNAM. Desde 2016.
- Revisora de artículos para la revista PLoS One.
- Participación en la Mesa Redonda: De Estudiante de Doctorado a Investigador. Instituto de Química. Marzo de 2019.
- Miembro de la Comisión de Biblioteca desde 2018.

Pasantes Ordóñez Herminia

- Participación en el subcomité académico de la Licenciatura en Neurociencias.

Peraza Reyes Leonardo

- Miembro de la comisión de seminarios del Instituto de Fisiología Celular, UNAM. 2015-2019.
- Comisión *Ad Hoc* para la elección de representantes de los tutores y alumnos para el Comité Académico del Programa de Maestría y Doctorado en Ciencias Bioquímicas, UNAM. 2019.
- Miembro del Comité central de la Rama de Biología Molecular y Celular de Hongos de la Sociedad Mexicana de Bioquímica, Noviembre 2017 a la fecha.
- Comisión Ad Hoc para la elección para representantes de los tutores y alumnos para el Comité Académico del Programa de Posgrado en Ciencias Biológicas, UNAM. 2019.

Pérez de la Mora Miguel

- Árbitro de la revista Behavioural Brain Research.
- Árbitro externo en la evaluación de proyectos inscritos en el programa de Apoyo a Proyectos de Investigación e Innovación Tecnológica (PAPIIT).
- Árbitro de la revista: Molecular Neurobiology.
- Árbitro de la revista: Neuropharmacoloy.
- Arbitro de la revista: Pharmacological Reports.
- Arbitro de la revista: Neuroscience Letters.
- Evaluador de proyectos de investigación correspondientes a la Convocatoria de Ciencias Básicas del CONACyT.
- Dirección de la Revista Ciencia de la Academía Mexicana de Ciencias A.C. a partir del 2000.

Pérez Martínez Xóchitl

- Miembro de la Comisión de Cómputo del IFC, UNAM.
- Participación en los exámenes de Admisión del Posgrado en Ciencias Biomédicas. Mayo de 2019.
- Representante vocal de investigadores ante el Consejo Académico del Área de las Ciencias Biológicas, Químicas y de la Salud (CAABQYS).

Pérez Montfort Ruy

- Miembro del Comité de Reconsideración Académica del Programa de Apoyo a Proyectos de investigación e Innovación Tecnológica PAPIIT de la Convocatoria 2020.
- Miembro del Editorial Board de la Revista Current Medicinal Chemistry de Bentham Science Publishers, Ltd. (período de nombramiento indefinido).
- Miembro del Editorial Board de la Revista The Open Medicinal Chemistry Journal de Bentham Science Publishers, Ltd. (periodo de nombramiento indefinido).
- Miembro del Editorial Board de la Revista Letters in Drug Design & Discovery (periodo de nombramiento indefinido).
- Miembro del Consejo Editorial de la Revista Investigación en Salud (período de nombramiento indefinido).
- Miembro del Comité Editorial Externo de la Revista Ciencia UANL (período de nombramiento indefinido).
- Evaluador externo de proyectos de investigación del PAPIIT, UNAM, 2019.

Recillas Targa Félix

- Director del Instituto de Fisiología Celular de la UNAM a partir del 17 de Octubre de 2017.
- Miembro del “Editorial Board” de la revista Epigenetics, febrero 2014 a la fecha.
- Miembro del "Editorial Board" de la Revista Epigenetics Insights a partir de 2018.
- Miembro del Comité Editorial de la Revista Ciencia UANL, revista de divulgación científica y tecnológica de la Universidad de Nuevo León, marzo 2014 a la fecha.
- Revisor *Ad Hoc* de las revistas: Epigenetics, Bioinformatics; Epigenetics & Chromatin; BMC Genomics y Frontiers in Genetics (RNA section).
- Miembro de la Comisión Especial del Programa de Primas al Desempeño del Personal Académico de Tiempo Completo nivel D de la UNAM (PRIDE D) del Área de las Ciencias Biológicas, Química y de la Salud (CAABQyS), UNAM. 27 de Junio 2016-.

- Miembro del Consejo Académico del Área de las Ciencias Biológicas, Química y de la Salud (CAABQyS) y formo parte de la Comisión Permanente de Planeación y Evaluación, de la Comisión Permanente de Personal Académico y del Pleno de este Consejo, como Director del Instituto de Fisiología Celular de la UNAM, a partir del 17 de Octubre del 2017.
- Consejero Universitario, Universidad Nacional Autónoma de México, a partir del 17 de Octubre de 2017.
- Consejero Técnico de la Investigación Científica de la UNAM, con participación en las comisiones especiales: Comisión para el Estímulo Especial "Efrén C. Del Pozo" para Técnicos Académicos del Instituto de Investigaciones Biomédicas (Presidente), Comisión para la Evaluación de Técnicos Académicos; Comisión de Evaluación Asuteso UPEID y Cátedra para profesores "Jesús Romo Armería" perteneciente al Instituto de Química, a partir de Octubre de 2017.
- Miembro de la Comisión de Incorporación y Revalidación de Estudios y de Títulos y Grados del Consejo Universitario de la UNAM a partir del 7 de Junio de 2018.
- Miembro de la Comisión de Asuntos Académico Administrativo (CAAA) de la Coordinación de la Investigación Científica, UNAM a partir del 1 de Junio de 2018 al 24 de octubre de 2019.
- Miembro de la Comisión Ampliada de Becas posdoctorales de la CAAA de la Coordinación de la Investigación Científica, UNAM a partir del 11 de Abril de 2018.
- Evaluador de proyectos científicos: CONACyT y DGAPA-PAPIIT.
- Presidente de la Comisión *ad hoc* para Premios y Distinciones del CTIC, relativo a la propuesta del Consejo Interno del Centro de Ciencias Genómicas, para que el Dr. Pedro Julio Collado Vides, adscrito a dicha entidad, sea nombrado Investigador Emérito. Octubre 2019.

Romo Trujillo Ranulfo

- Editor de la sección Beharioral and Cognitive Neuroscicnce de la revista Neuroscience (IBRO).
- Editor asociado: eLife y eNeuro.
- Revisor *ad hoc*: Nature Reviews Neuroscience, Journal of Neuroscience, Current Biology, European Journal of Neuroscience, Journal of Neurophysiology, Journal of Computational Neuroscience, Cerebral Cortex, Experimental Brain Research, Neuroimage, Brain, PLoS Biology, PNAS (editor asociado), Science, Nature, Nature Neuroscience.
- Editor Asociado: Proress in Neurobiology y Neuroscience Research.
- Miembro del comité editorial de la revista Neuron.
- Coordinador del comité de evaluación de Proyectos Milenio del Gobierno de Chile.
- Editor Asociado de la revista Journal of Cognitive Neuroscience, MIT, E.U.A.
- Editor Asociado de la revista Journal de Physiologie, Paris, Francia.

Rosenbaum Emir Tamara

- Miembro de la Comisión de Bioética y Ética Científica del IFC.
- Representante de investigadores electa ante el Consejo Interno del IFC.

Rossi Pool Román

- Revisor *ad hoc*: Neuroscience (IBRO).
- Revisor *ad hoc*: Frontiers in Computational Neuroscience.
- Revisor *ad hoc*: Plos Biology.
- Revisor *ad hoc*: Frontiers in Systems Neuroscience.

Salceda Sacanelles Rocío

- Participación, como representante del Dr. Félix Recillas Targa, en el Seminario Universitario Interdisciplinario sobre Envejecimiento y Vejez (SUIEV).
- Miembro de la Comisión del PASPA, UNAM.
- Miembro de la Comisión Evaluadora del programa de Becas Posdoctorales DGAPA, UNAM.
- Evaluadora en la Convocatoria ConTex CONACYT 2019 para Proyectos de Investigación Conjunta.
- Evaluadora en la Convocatoria para Estancias Posdoctorales en Instituciones Académicas o de investigación con sede en Europa o América, 2019. Secretaría de Educación Ciencia, Tecnología e Innovación.
- Miembro Comisión Dictaminadora para el concurso de oposición abierto para una plaza de Técnico Académico Asociado C (Biología Celular, microscopía electrónica) Facultad de Ciencias, UNAM. 2019.
- Miembro del Comité Editorial de la Revista de Educación Bioquímica.
- Revisor *ad hoc* de distintas revistas, como: IOVS, Cell Physiol Biochem, Peer J, Arch Biochem Biophys, Frontiers Aging Neurosci, Frontiers Cellular Neurosci, Bioscience Report.
- Revisor *ad hoc* del CONACyT y PAPIIT- UNAM.
- Participación en el Subcomité de Admisión del Posgrado en Ciencias Biomédicas, semestre 2019-1.
- Participación en el Subcomité de Admisión Posgrado en Ciencias Biológicas, semestre 2020-2.

Sotres Bayón Francisco

- Revisor de Manuscritos en: Nature Neuroscience, Journal of Neuroscience, eNeuro, Biological Psychiatry, Neuropshychopharmacology, The International Journal of Neuropshychopharmacology, Frontiers in Behavioral Neuroscience, Frontiers in Neural Circuits, Frontiers in Molecular Neuroscience ,Neuroscience, Behavioral Neuroscience, Behavioral Brain Research, Psychopharmacology , Neurobiology of Learning and Memory, Physiology & Behavior, Neuroscience Letters, Progress in Neuro psychopharmacology and Biological Psychiatry, Molecular Psychiatry, Salud Mental.
- Tutor de los siguientes programas: doctorado en Ciencias Biomédicas (UNAM), maestría y doctorado en Ciencias Bioquímicas (UNAM), maestría en Ciencias Biológicas (UNAM), maestría del Instituto de Neurobiología (UNAM), doctorado en Psicología (UNAM) y maestría y doctorado de Farmacologia del CINVESTAV (IPN).
- Subcomisión con perspectiva de género (noviembre 2018 a la fecha).
- Comité Académico del Posgrado de Ciencias Bioquímicas (octubre 2016-2019).
- Comisión Institucional para el Cuidado y Uso de Animales de Laboratorio (agosto 2015 a la fecha).

Tapia Ibargüengoytia Ricardo

- Jurado del Premio Dra. Aurora Arnaiz Amigo a la mejor tesis de doctorado en Bioética, UNAM.

Tecuapetla Aguilar Fatuel

- CONACyT Revisor de proyectos en la convocatoria de Ciencia Básica.
- Revisor de artículo científico para la revista Neuroscience (https://www.journals.elsevier.com/neuroscience/).
- Revisor de artículo científico para la revista Neuron (http://www.cell.com/neuron/home).
- CONACyT Revisor de proyecto de la convocatoria "PDC Problemas Nacionales".
- PAPIIT-DGAPA-UNAM Revisor de proyectos del Área de las Ciencias Biológicas, Químicas y de la Salud del Programa de Apoyo a Proyectos de Investigación e Innovación Tecnológica (PAPIIT - UNAM).
- Revisor de artículo científico para la revista eLife (http://elifesciences.org/).

Torres Larios Alfredo

- Jefe del Departamento de Bioquímica y Biología Estructural del Instituto de Fisiología Celular, UNAM. A partir de Noviembre 2017.
- Revisor de proyectos para el Advanced Photon Source (APS) en Argonne, Illinois, USA.

- Miembro del subcomité de admisión al Doctorado en Ciencias Biomédicas. Semestre, 2020-2.

Torres Quiroz Francisco

- Representante de tutores del IFC ante el Programa de Doctorado en Ciencias Biomédicas. Desde diciembre 2017.
- Participación como evaluador de proyecto del Programa de Apoyo a Proyectos de Investigación e Innovación Tecnológica (PAPIIT) convocatoria 2020.

Tovar y Romo Luis Bernardo

- Miembro de los subcomités de admisión al PDCB en el semestre 2020-2.
- Miembro del subcomité de admisión a la Licenciatura en Neurociencias 2019.
- Revisor de las revistas: Frontiers in Cellular Neuroscience, Neurodegenerative Diseases, Brain Research, Molecular Neurodegeneration, Neuroscience, Stems Cells International, Molecular Neurobiology, Mediators of Inflammation, Journal of Neuroinflammation, Cellular Physiology and Biochemistry, Neurochemical Research, Neurochemistry International, IUBMB Life, Biomedicine & Pharmacotherapy, Frontiers in Cell and Developmental Biology, Neurotoxicity Research.
- Miembro del Subcomité Académico de la Licenciatura en Investigación Biomédica Básica como encargado de la Licenciatura en el Instituto de Fisiología Celular.
- Miembro de la Comisión de la Unidad de Biología Molecular del Instituto de Fisiología Celular.
- Miembro del Editorial Board de Neurochemical Research.
- Editor Asociado Invitado de la sección Molecular Medicine de Frontiers in Cell and Developmental Biology.
- Miembro del Committee for Aid and Education in Neurochemsitry de la International Society for Neurochemistry (2019-2022).
- Editor del Reserach Topic "Mechanisms of neuronal recovery in the central nervous system" en las Revistas Frontiers in Cell and Developmental Biology and Frontiers in Cellular Neuroscience.

Uribe Carvajal Salvador

- Comisión Dictaminadora de la Facultad de Medicina, UNAM. Desde Noviembre de 2019.
- Evaluador de Proyectos de la Fundación Fulbright-García Robles. Noviembre, 2019.
- Comisión del PRIDE en el Instituto de Fisiología Celular. Desde Febrero de 2016.

Vaca Domínguez Luis

- Miembro del Comité de contratación del Instituto de Neurobiología, UNAM.
- Secretario de Vinculación del Instituto de Fisiología Celular.

Velasco Veláquez Iván

- Miembro de subcomité de admisión N° 3 que evaluó a los aspirantes de la Convocatoria 2020-2 al Programa de Doctorado en Ciencias Biomédicas. Octubre 2019.
- Invitaciones aceptadas para arbitrar manuscritos enviados a Bioscience Reports, Cell Biology International y PLoS Neglected Tropical Diseases.
- Representante suplente del personal académico del Instituto de Fisiología Celular ante el Consejo Técnico de la Investigación Científica.
- Designación por parte del Consejo Académico del Área de las Ciencias Biológicas, Químicas y de la Salud para participar en el Comité Evaluador del Área de las Ciencias Biológicas, Químicas y de la Salud del Programa de Apoyo a Proyectos de Investigación e Innovación Tecnológica (PAPIIT) de la Dirección General de Asuntos del Personal Académico, UNAM .
- Co-orgnizador del Simposio Chemical transmission: “The key to understand brain function”, en homenaje al Dr. Ricardo Tapia, Investigador emérito del IFC. Evento organizado por la Facultad de Química y el IFC. UNAM 23 y 24 de abril de 2019.
- Miembro del Comité básico de la XXXIII Reunión Anual de Investigación del Instituto Nacional de Neurología y Neurocirugía "Manuel Velasco Suárez". Abril 2019.
- Miembro de la Comisión Dictaminadora del área Biomédica, Facultad de Medicina, UNAM.

Valdés Rodríguez Julián

- Coordinador de los Seminarios Semanales de la División de Investigación Básica del Instituto de Fisiología Celular.
- Miembro del comité organizador del Simposio Teórico-Práctico de edición genética por CRISPR-Cas9. IFC, UNAM 2019.
- Obtención de Concurso de Oposición Abierto (COA) para la plaza de Investigador Titula A de T.C en el departamento de Biología Celular y del Desarrollo.
- Integrante de la comisión *ad hoc* para el proceso de elección de representantes de tutores y alumnos del comité académico del programa de Doctorado en Ciencias Biomédicas.

PROGRAMAS DE SUPERACIÓN ACADÉMICA

Programas de Superación Académica en la UNAM

1. Alcántara Hernández Rocío. Curso Introducción a la Bioética. Comisión de ética académica y responsabilidad científica (CEARC) a través de Secretaría de Educación Abierta y Continua de la Facultad de Ciencias, UNAM, 19 de noviembre 2019 al 5 de febrero de 2020.

2. Aparicio Juárez Ariadna. Taller de Manejo de roedores de Laboratorio. Instituto de Fisiología Celular, UNAM. Unidad Académica Bioterio, 11 al 13 de febrero, 4 al 6 de marzo, 19 al 21 de agosto, 28 al 30 de octubre, 2 al 4 de diciembre de 2019.

3. Ayala Méndez Xóchitl Gabriela. Taller de Manejo de roedores de Laboratorio. Instituto de Fisiología Celular, UNAM. Unidad Académica Bioterio, 11 al 13 de febrero, 4 al 6 de marzo, 19 al 21 de agosto, 28 al 30 de octubre, 2 al 4 de diciembre de 2019.

4. Códiz Huerta María Guadalupe. Curso-taller de Introducción al Análisis de Fragmentos (Microsatélites). Instituto de Biología, UNAM, 20 y 21 de junio de 2019.

5. Coello Coutiño Gerardo. Curso Diseño y administración de redes segmentadas con VLANs, impartido por el contratista Beamliners, sobre el manejo y administración de la nueva infraestructura de red del IFC, noviembre y diciembre 2019.

6. Delgado Coello Blanca Alicia. Curso Elaboración de material didáctico digital. Facultad de Medicina, UNAM, 14 de mayo al 27 de Junio de 2019.

7. Domínguez Macouzet María Guadalupe. Curso de reentrenamiento de personal ocupacionalmente expuesto a radiación (POE). Auditorio 2 de Neurociencias del Instituto de Fisiología Celular, UNAM, 2019.

8. Escalante Gonzalbo Ana María. Curso Diseño y administración de redes segmentadas con VLANs, impartido por el contratista Beamliners, sobre el manejo y administración de la nueva infraestructura de red del IFC, noviembre y diciembre 2019.

9. Escobedo Avila Itzel. Curso Estrategias didácticas para reforzar conocimientos en el laboratorio de química y biología. DGAPA, UNAM, 22 al 26 julio de 2019.

10. Escobedo Avila Itzel. Curso Introducción a la Bioseguridad. División de Investigación, Facultad de Medicina, UNAM, 19 de febrero de 2019.

11. Guerrero Avendaño Georgina. Curso de reentrenamiento de personal ocupacionalmente expuesto a radiación (POE). Auditorio 2 de Neurociencias del Instituto de Fisiología Celular, UNAM, 2019.

12. Guerrero Avendaño Georgina. Instructor en el Simposio Teórico-Práctico de edición Genética por CRISPR-Cas9. Instituto de Fisiología Celular, UNAM, 28 al 31 de octubre de 2019.

13. Jiménez Pérez Nicolás. Asistencia al curso de capacitación Microscopía electrónica de transmisión y barrido aplicada a las ciencias biológicas. Impartido por la Secretaria de Educación Continua de la Facultad de Medicina Veterinaria y Zootecnia de la UNAM, 21 al 23 de octubre de 2019.

14. Malagón Rivero Héctor Alfonso. Taller de manejo de roedores de laboratorio. Instituto de Fisiología Celular, UNAM. Unidad Académica Bioterio, 11 al 13 de febrero, 4 al 6 de marzo, 19 al 21 de agosto, 28 al 30 de octubre, 2 al 4 de diciembre de 2019.

15. Malagón Rivero Héctor Alfonso. Manejo y Cuidados de animales de Laboratorio. clase impartida en el Taller: Investigación en plantas medicinales de la etnobotánica a los fitomedicamentos, en la Facultad de Ciencias-UNAM, 6 de noviembre de 2019.

16. Malagón Rivero Héctor Alfonso. 3 °Coloquio Estudiantil de Fisiología Animal Comparada, Ponente con el tema “Técnicas en el estudio del corazón en modelos animales”, en la Facultad de Ciencias-UNAM, 4 de diciembre de 2019.

17. Mendoza Martínez Ariann. Obtención de grado de Doctorado mediante defensa de Tesis con el titulo “El papel de los factores transcripcionales NapA y SrrA en la respuesta antioxidante y la diferenciación celular en el hongo Aspergillus nidulans”. Programa de Doctorado en Ciencias Bioquímicas. Tutor: Dr. Jesús Aguirre Linares. Fecha de obtención de grado 13 de junio de 2019.

18. Moncada Hernández Sandra Guillermina. Seminarios mensuales de actualización dirigidos a profesores de la asignatura Informática Biomédica. Facultad de Medicina, Departamento de Informática Biomédica, UNAM, 2019.

19. Moncada Hernández Sandra Guillermina. Asistencia a la XVII Conferencia Internacional sobre Bibliotecas Universitarias. Coordinación de Humanidades, UNAM, 23 al 25 de octubre de 2019.

20. Moncada Hernández Sandra Guillermina. Reuniones convocadas por la D.G.B. para la operación y uso de las adquisiciones de libros a través del Sistema Institucional de Compras. Dirección General de Proveduría, UNAM, febrero 2019.

21. Moncada Hernández Sandra Guillermina. Curso “Capacitación en serio. Haz de tus cursos un aprendizaje inolvidable y entretenido”. Programa de Actualización Profesional 2019, Dirección General de Bibliotecas, UNAM, 12 al 31 de agosto de 2019.

22. Moreno Alvarez Paola. Asistencia al Taller de formación y actualización docente en ciencias de la salud. Modalidad virtual. Facultad de Medicina, UNAM, 25 de abril al 27 de mayo de 2019.

23. Ongay Larios Laura María. Curso taller Introducción al análisis de fragmentos (Microsatélites). Impartido por especialistas de los Institutos de Biología y de Investigaciones Biomédicas, así como de Thermofisher Scientific. Instituto de Biología, UNAM, 21 de junio de 2020.

24. Paredes Díaz Rodolfo. Asistencia al curso de Microscopía electrónica de barrido y microanálisis por dispersión de energía. Impartido por Jeol de México, S.A. de C.V. en el Instituto de Fisiología Celular, UNAM, 29 al 30 de enero de 2019.

25. Peña Segura Claudia. Curso de reentrenamiento de personal ocupacionalmente expuesto a radiación (POE). Auditorio 2 de Neurociencias del Instituto de Fisiología Celular, UNAM, 2019.

26. Pérez Molina Rosario. Simposio Teórico-Práctico de edición Genética por CRISPR-Cas9. Instituto de Fisiología Celular, UNAM, 28 al 31 de octubre de 2019.

27. Prior González Mara Guadalupe. Curso de manejo de Crióstato. Impartido en la Unidad de Histología. Instituto de Fisiología Celular, UNAM, 12 al 14 de Febrero de 2019.

28. Prior González Mara Guadalupe. Curso Teórico de Microscopia óptica y electrónica Curso Práctico de los microscopios Axio Zoom y Confocal LSM 800. Impartido en la Unidad de Imagenología, Instituto de Fisiología Celular, UNAM, 18 al 22 de febrero de 2019.

29. Prior González Mara Guadalupe. Taller de manejo de roedores de laboratorio. Unidad Académica del Bioterio del Instituto de Fisiología Celular, UNAM, 27 al 29 de mayo de 2019.

30. Ramírez Graullera Yoás Saimon. Primer semestre del Programa de Maestría en Ciencia e Ingeniería de la Computación, UNAM, semestre 2020-1.

31. Ramos Balderas José Luis. Curso Dominio del idioma inglés nivel 4. Escuela Nacional de Lenguas, Lingüística y Traducción. UNAM, 15 de enero al 20 de junio de 2019.

32. Rincón Heredia Ruth. Impartición un curso *ad-hoc* “Curso Teórico-Práctico de Inmunohistoquímica”. Unidad de Imagenología, IFC-UNAM, 2019.

33. Rincón Heredia Ruth. Instructor en Latin American Training Program 2019. Enlightening the brain: light as a tool for understanding the function of the nervous system. Instituto de Fisiología Celular, UNAM, 26 de agosto al 13 de septiembre de 2019.

34. Rincón Heredia Ruth. Ponente en el XIII Curso Institucional de Microscopía del Instituto de Investigaciones Biomédicas, Unidad de Microscopía del Instituto de Investigaciones Biomédicas, UNAM, 22 al 26 de abril de 2019.

35. Rincón Heredia Ruth. Organización del Curso teórico práctico de microscopía fotónica y electrónica. Instituto de Fisiología Celular, UNAM, 18 al 22 de febrero de 2019.

36. Rincón Heredia Ruth. Ponente del Curso teórico práctico de microscopía fotónica y electrónica. Instituto de Fisiología Celular, UNAM, 19 de febrero de 2019.

37. Rincón Heredia Ruth. Asistencia al curso de capacitación Microscopía electrónica de transmisión y barrido aplicada a las ciencias biológicas. Impartido por la Secretaria de Educación Continua de la Facultad de Medicina Veterinaria y Zootecnia de la UNAM, 21 al 23 de octubre de 2019.

38. Rincón Heredia Ruth. Asistencia al curso de Microscopía electrónica de barrido y microanálisis por dispersión de energía. Impartido por Jeol de México, S.A. de C.V. en el Instituto de Fisiología Celular, UNAM, 29 al 30 de enero de 2019.

39. Rincón Heredia Ruth. Asistencia al XIII Curso Institucional de Microscopia IIBO-UNAM, Instituto de Investigaciones Biomédicas, UNAM, 22 al 26 de abril de 2019.

40. Rivera Cerecedo Claudia Verónica. Médico Veterinario Certificado por CONCERVET A.C. en la Práctica de la Medicina Veterinaria y Zootecnia en Animales de Laboratorio (2016-2021).

41. Rivera Cerecedo Claudia Verónica. Taller de Manejo de roedores de Laboratorio. Instituto de Fisiología Celular, UNAM. Unidad Académica Bioterio, 11 al 13 de febrero, 4 al 6 de marzo, 19 al 21 de agosto, 28 al 30 de octubre, 2 al 4 de diciembre de 2019.

42. Rivera Cerecedo Claudia Verónica. Curso Prácticas de Higiene y Seguridad, para el Trabajo en Laboratorios de Investigación Científica. Instituto de Fisiología Celular, UNAM, 4 de marzo y 5 de septiembre de 2019.

43. Rivera Cerecedo Claudia Verónica. Curso de Cirugía Básica en Roedores. Instituto de Fisiología Celular, UNAM. Unidad Académica Bioterio, 27 al 29 de mayo, 7 al 9 de octubre de 2019.

44. Rivera Cerecedo Claudia Verónica. Estancia práctica en producción, cuidado y uso de animales de laboratorio. Instituto de Fisiología Celular, UNAM. Unidad Académica Bioterio, 2019.

45. Rodríguez Montaño Sandra Daniela. Asistencia a la transmisión del curso Cerebro, emociones y violencia. impartió la Dra. Feggy Ostrosky, en sede AAPAUNAM, 12 y 14 de noviembre del 2019.

46. Rodríguez Rangel Claudia. Curso de reentrenamiento de personal ocupacionalmente expuesto a radiación (POE). Auditorio 2 de Neurociencias del Instituto de Fisiología Celular, UNAM, 2019.

47. Rosas Arellano Abraham. Latin American training program, Society for Neurosciences. Instituto de Fisiología Celular, UNAM, 2019.

48. Rosas Arellano Abraham. Workshop on muscle ear dissection and electron microscopy. Instituto de Neurobiología, UNAM, noviembre 2019.

49. Rosas Arellano Abraham. Asistencia al curso de capacitación Microscopía electrónica de transmisión y barrido aplicada a las ciencias biológicas. Impartido por la Secretaria de Educación Continua de la Facultad de Medicina Veterinaria y Zootecnia de la UNAM, 21 al 23 de octubre de 2019.

50. Rosas Arellano Abraham. Asistencia al curso de Microscopía electrónica de barrido y microanálisis por dispersión de energía. Impartido por Jeol de México, S.A. de C.V. en el Instituto de Fisiología Celular, UNAM, 29 al 30 de enero de 2019.

51. Salinas Velázquez Laura Silvia. Instructor en el Simposio Teórico-Práctico de edición Genética por CRISPR-Cas9. Instituto de Fisiología Celular, UNAM, 28 al 31 de octubre de 2019.

52. Sánchez Chávez Gustavo. Curso de reentrenamiento de personal ocupacionalmente expuesto a radiación (POE). Auditorio 2 de Neurociencias del Instituto de Fisiología Celular, UNAM, 2019.

53. Sánchez González Olivia. Curso práctico del microscopio confocal LSM800. Instituto de Fisiología Celular, UNAM, 21 y 22 de febrero de 2019.

54. Sánchez Sánchez Norma. Asistencia al Simposio Teórico-Práctico de edición Genética por CRISPR-Cas9. Instituto de Fisiología Celular, UNAM, 28 al 31 de octubre de 2019.

55. Sánchez Soto María del Carmen. Curso de reentrenamiento de personal ocupacionalmente expuesto a radiación (POE). Auditorio 2 de Neurociencias del Instituto de Fisiología Celular, UNAM, 2019.

56. Sosa Garrocho Marcela. Asistencia al Simposio Teórico-Práctico de edición Genética por CRISPR-Cas9. Instituto de Fisiología Celular, UNAM, 28 al 31 de octubre de 2019.

Programas de Superación Académica Fuera de la UNAM

1. Alcántara Hernández Rocío. Curso PreCongreso VII de la Rama de Transducción de Señales de la SMB. CINVESTAV Sur, 29 al 31 de julio de 2019.

2. Aparicio Juárez Ariadna. Curso introductorio de edición genética por CRISPR/Cas 9. Instalaciones de Thermo Fisher Scientific en la Ciudad de México. 24 al 27 de septiembre de 2019.

3. Aparicio Juárez Ariadna. Primer seminario de CRISPR. Instalaciones de Thermo Fisher Scientific en la Ciudad de México. 30 de agosto de 2019.

4. Aparicio Juárez Ariadna. Participación en las jornadas científicas de actualización en Biología Molecular y Biología Celular. Organizado por Uniparts en la Ciudad de México. 26 y 27 de agosto de 2019.

5. Aparicio Juárez Ariadna. Estancia en el laboratorio del Dr. Lluís Montoliu. Investigador Científico del CNB-CSIC de Madrid, España. 18 de mayo al 8 de junio de 2019.

6. Aparicio Juárez Ariadna. Curso de técnicas de Ingeniería Reproductiva en el ratón método CARD. Lluís Montoliu. Universidad de Salamanca, España. 29 al 31 de mayo de 2019.

7. Ayala Méndez Xóchitl Gabriela. Minicourse On Line. Basics of Mouse Genetics. The Jackson Laboratory. 26 de Agosto de 2019.

8. Barbosa Castillo Juan Manuel. Certificación en el programa Microsoft Word 2016. Word 2016 Academic. Folio: CAL4T-VHPGX. Serie: CLSS1801CT. Diplomado registro: STPS CTE-050608QL5-001. 2 de marzo de 2019.

9. Chiquete Félix Natalia. 4° Simposio Científica Senna-ATCC; "Cultivo Celular, Inmunidad y Medicina Traslaciona". INMEGEN. 8 de mayo de 2019.

10. Crespo Ramírez Minerva. Curso de Biología Molecular. Unidad de investigación CMN La Raza. 7 de enero al 4 de marzo de 2019.

11. Crespo Ramírez Minerva. Curso de Inmunilogía. Unidad de investigación CMN La Raza. 25 de marzo al 17 de junio de 2019.

12. Galván Lobato Aurey. Curso de AutoCAD. eduMAC. Digital Arts Center. 2019.

13. Jiménez Pérez Nicolas. Curso de capacitación para el manejo del Microscopio Electrónico de Barrido JSM-5410LV. Impartido por Ingenieros de la compañía JEOL de México. Febrero de 2019.

14. Jiménez Pérez Nicolas. Curso de capacitación para el manejo del Microscopio estereoscópico con fluorescencia Axio ZoomV16 con sistema Apotome. Impartido por Ingenieros de la compañía Carl Zeiss de México. Febrero 2019.

15. Lee Rivera Irene. Curso PreCongreso VII de la Rama de Transducción de Señales de la SMB. CINVESTAV Sur, 29 al 31 de julio de 2019.

16. Llorente Gil Itzel Alejandra. Platica Cell Culture Fundamentals: Your Questions Answered. Impartido por Científica Senna S.A de C.V. y ATCC. 2019.

17. López Hernández Edith. Curso PreCongreso VII de la Rama de Transducción de Señales de la SMB. CINVESTAV Sur, 29 al 31 de julio de 2019.

18. Mendoza Rodríguez Valentin. Curso de Excel. Impartido por eduMac, Digital Arts Center. Ciudad de México, 11 de noviembre de 2019.

19. Moncada Hernández Sandra Guillermina. Certificación de “Google for Education”, a través de una beca otorgada en el Departamento de Informática Biomédica como Educador Google Nivel 1, 29 de noviembre de 2018 a enero de 2019.

20. Moncada Hernández Sandra Guillermina. Gamification. University of Pennsylvania. USA. En línea, 2 de septiembre al 5 de diciembre de 2019.

21. Ortínez Benavides Manuel. Curso de AutoCAD. eduMAC. Digital Arts Center. 2019.

22. Poot Hernández Augusto César. Curso precongreso: 1er Simposio de Mapeo y Navegación Cerebral. XXY Congreso Mexicano e Internacional de Cirugía Neurológica 2019. Sociedad Mexicana de Cirugía Neurológica, A.C. Centro Médico Siglo XXI. Julio 2019.

23. Rodríguez Montaño Sandra Daniela. Asistencia al Curso-Taller Histotecnología, Generalidades y Aplicaciones en Tópicos Selectos de: Dermatopatología, Enfermedades del Hígado, Cáncer de Mama y Cérvico- Uterino, Celaya, Guanajuato, del 1 al 3 de febrero de 2019.

24. Rodríguez Montaño Sandra Daniela. Asistencia al Curso-Taller Tópicos Selectos de Histotecnología, Oaxaca de Juárez, del 20 al 22 de septiembre de 2019.

25. Romero Ávila María Teresa. Curso PreCongreso VII de la Rama de Transducción de Señales de la SMB. CINVESTAV Sur, 29 al 31 de julio de 2019.

26. Rosas Arellano Abraham. Course 219R - ES&H Refresher - Orientation. National Accelerator Laboratory, SLAC - Stanford University, USA. Cyber course. Julio 2019.

27. Rosas Arellano Abraham. Course 115 - GERT. National Accelerator Laboratory, SLAC - Stanford University, USA. Cyber course. Julio 2019.

28. Rosas Arellano Abraham. Course CS100 - Cyber Security for Lab Users. National Accelerator Laboratory, SLAC - Stanford University, USA. Cyber course.

29. Sánchez Sevilla Maria de Luordes. Curso teórico-práctico Cromatografía de líquidos-espectometría de masas y sus aplicaciones en productos naturales. Centro de Investigación Científica de Yucatán, A.C. 4 al 8 de febrero del 2019.

INVESTIGADORES VISITANTES

1) Fernández De Miguel Francisco: Sanz Martín Araceli, Dra. Sanz Martín. Procedencia: Universidad de Guadalajara. Motivo de la visita: Impartió conferencia: La neurobiología de la violencia infant. Fecha inicio: 30-mayo-2019. Fecha término: 30-mayo-2019.

2) Fernández De Miguel Francisco: del Bel Elaine, Dra. Procedencia: Universidad de Sao Paulo. Ribeirao Preto. Brasil. Motivo de la visita: Impartir conferencia: Doxycycline restrains neuroinflammation and confers neuroprotection in Parkinson disease model. Fecha inicio: 27-octubre-2019. Fecha término: 28-octubre-2019.

3) Furlan Magaril Mayra: Martínez Pachec Mónica, Dra. Procedencia: Centro de Ciencias Genómicas. Motivo de la visita: Colaboración. Fecha inicio: 01-marzo-2019.

4) García Sáinz Jesús Adolfo: Medina Bañuelos Luz del Carmen. Procedencia: Universidad Autónoma Metropolitana - Iztapalapa. Motivo de la visita: Estancia-Proyecto en colaboración. Fecha inicio: 01-enero-2019. Fecha término: 31-diciembre-2019.

5) González Halphen Diego: Giraud Marie-France. Procedencia: Institut de Biochimie et Génétique Cellulaires, CN. Motivo de la visita: en el marco de la Cooperación Internacional México-Francia apoyado por el Fondo FONCICYT 2 del CONACyT. Fecha inicio: 21-mayo-2019. Fecha término: 03-junio-2019.

6) Hernández Cruz Arturo: Hernández Guijo Jesús Miguel. Procedencia: Facultad de Medicina, Universidad Autónoma de Madrid. Motivo de la visita: Impartir curso para el posgrado "Modulación de la transmisión sináptica en sistema nervioso central y periférico". Fecha inicio: 06-mayo-2019. Fecha término: 17-mayo-2019.

7) Hernández Cruz Arturo: Montes de Oca Pavel. Procedencia: Unidad de Neurobiología Dinámica, Instituto Nacional de Neurología y Neurocirugía. Motivo de la visita: Estancia de Investigacion. Fecha inicio: 07-enero-2019. Fecha término: 15-diciembre-2020.

8) Peña Díaz Antonio: Calderón Marissa, Dra. Procedencia: FES Iztacala, UNAM. Motivo de la visita: Proyecto en colaboración. Fecha inicio: 01-enero-2019. Fecha término: 31-diciembre-2020.

9) Pérez de la Mora Miguel: Borroto Escuela Dasiel, Dr. Procedencia: Karolinska Institutet. Motivo de la visita: Seminario Extraordinario y taller sobre la técnica del PLA. Fecha inicio: 26-noviembre-2019. Fecha término: 29-noviembre-2019.

10) Tecuapetla Aguilar Fatuel: Rozas Salas Carlos, Dr. Procedencia: Universidad Santiago de Chile. Motivo de la visita: Aprender técnicas de optogenética. Fecha inicio: 01-febrero-2019. Fecha término: 23-febrero-2019.

11) Tecuapetla Aguilar Fatuel: Reyes Mendez Miriam Edith. Procedencia: Universidad de Colima. Motivo de la visita: Aprender técnicas de optogenética. Fecha inicio: 15-agosto-2019. Fecha término: 30-septiembre-2019.

12) Tecuapetla Aguilar Fatuel: Jiménez Mejía Juan Carlos, Dr. Procedencia: FES Iztacala, UNAM. Motivo de la visita: Aprender técnicas de optogenética. Fecha inicio: 01-junio-2019. Fecha término: 30-junio-2019.

13) Velasco Iván: Benvenisty Nissim. Procedencia: Hebrew University, Jerusalem, Israel. Motivo de la visita: Seminario para la Sociedad Mexicana para la Investigación en Células Troncales. Fecha inicio: 30-junio-2019. Fecha término: 03-julio-2019.

14) Velasco Iván: González Pérez Óscar. Procedencia: Universidad de Colima. Motivo de la visita: Impartición del seminario institucional del 31 de mayo de 2019. Fecha inicio: 30-mayo-2019. Fecha término: 31-mayo-2019.

COMISIÓN DICTAMINADORA Y ASUNTOS ACADÉMICO-ADMINISTRATIVOS

La Comisión Dictaminadora del Instituto de Fisiología Celular, está conformada de la siguiente manera:

Por el Rector:

(Consejo Académico del Área de las Ciencias Biológicas y de la Salud).

- Dra. María Elena Teresa Medina-Mora Icaza
- Dr. Enrique Merino Pérez

Por el Consejo Interno:

- Dra. Adela Rodríguez Romero
- Dr. José Víctor Segovia Vila

Por el Colegio del Personal Académico:

- Dr. Lorenzo Patrick Segovia Forcella
- Dr. Hugo Merchant Nancy

Durante el año 2019 la Comisión dictaminó y en su caso opinó sobre los siguientes casos:

PROMOCIONES

Guadalupe Domínguez Macouzet	a Técnico Académico Titular	"C"
Norma Espinosa Sánchez	a Técnico Académico Titular	"C"
José Luis Ramos Balderas	a Técnico Académico Titular	"A"

OBRAS DETERMINADAS

Daniel Osorio Gómez	Investigador Asociado	"C"
C. Leonardo Peraza Reyes	Investigador Asociado	"C"
Román Rossi Pool	Investigador Asociado	"C"
Violeta Gisselle López Huerta	Investigador Asociado	"C"

Jesús Manuel Álvarez López	Técnico Académico Titular	“B”
Luz Lazos Ramírez	Técnico Académico Titular	“B”
Ana Cecilia Rosen Ferlini	Técnico Académico Titular	“B”
Luis Francisco Rodríguez Durán	Técnico Académico Titular	“B”
Beatriz Aguilar Maldonado	Técnico Académico Titular	“A”
Rosario Pérez Molina	Técnico Académico Titular	“A”
Enrique Chávez Jiménez	Técnico Académico Titular	“A”
Arturo Picones Medina	Técnico Académico Titular	“A”
Itzel Escobedo Ávila	Técnico Académico Titular	“A”
Nallely Cano Domínguez	Técnico Académico Titular	“A”
J. Héctor Díaz Osornio	Técnico Académico Asociado	“C”
M. Tonotiuh Figueroa Vanegas	Técnico Académico Asociado	“C”
Augusto César Poot Hernández	Técnico Académico Asociado	“C”
Arriann E. Mendoza Martínez	Técnico Académico Asociado	“C”
Ruth Rincón Heredia	Técnico Académico Asociado	“C”
Mara G. Prior González	Técnico Académico Asociado	“C”
Yoás Saimon Ramírez Graullera	Técnico Académico Asociado	“C”
Ariadna Aparicio Juárez	Técnico Académico Asociado	“C”
Miguel Ramírez Aragón	Técnico Académico Asociado	“C”
Sandra Daniela Rodríguez Montaño	Técnico Académico Asociado	“A”

CONTRATO

Juan Carlos Gómora Martínez	Investigador Titular	“B”
Fatuel Tecuapetla Aguilar	Investigador Titular	“B”
Magdalena Guerra Crespo	Investigador Titular	“A”
Fracisco Sotres Bayón	Investigador Titular	“A”
Luis Bernardo Tovar y Romo	Investigador Titular	“A”
Mayra Furlan Magaril	Investigador Titular	“A”
Paula Licona Limón	Investigador Titular	“A”
Luis Alonso Lemus Sandoval	Investigador Titular	“A”

Adrián Fernando Alvarez	Investigador Asociado	“C”
Sara Luz Morales Lázaro	Investigador Asociado	“C”
Yazmín Ramiro Cortes	Investigador Asociado	“C”
J. Francisco Torres Quiroz	Investigador Asociado	“C”
Myrian Velasco Torres	Investigador Asociado	“C”
Marcelino Arciniega Castro	Investigador Asociado	“C”
Abraham Rosas Arellano	Técnico Académico Titular	“B”
Ana Valeria Martínez Silva	Técnico Académico Titular	“A”
José Luis Ramos Balderas	Técnico Académico Titular	“A”
Josué Orlando Ramírez Jarquín	Técnico Académico Titular	“A”
Ivett Rosas Arciniega	Técnico Académico Asociado	“C”

CONCURSO

Víctor Julián Valdés Rodríguez	Investigador Titular	“A”
Irene Lee Rivera	Técnico Académico Titular	“B”
Beatriz Aguilar Maldonado	Técnico Académico Titular	“A”
Enrique Chávez Jiménez	Técnico Académico Titular	“A”

POSDOCTORALES

Ulises Carrasco Navarro

Mario Alberto Sánchez García

CÁTEDRA CONACyT

Enoch Luis Baltazar

BECARIOS POSDOCTORALES

Tipo de Beca	Número de Becarios Posdoctorales
Beca DGAPA	5
Beca CONACyT	2
Otras Becas	5

1) Aguirre Linares Jesús: Carrasco Navarro Ulises. Procedencia: UAM-Iztapalapa. **Beca DGAPA**. Fecha inicio: 01-septiembre-2019. Fecha término: 31-agosto-2020.

2) Bermúdez Rattoni Federico: Salcedo Tello Ana Pamela. Procedencia: Universidad Nacional Autónoma de México. **Proyecto: OBETEEN.** Fecha inicio: 04-enero-2016. Fecha término: 07-enero-2019.

3) Castro Obregón Susana: Hüttenrauch Melanie. Procedencia: Universidad de Göttingen, Alemania. **Proyecto: Alexander von Humboldt**. Fecha inicio: 01-octubre-2018. Fecha término: 30-septiembre-2020.

4) Del Río Guerra Gabriel: Juárez Arellano Vladimir. Procedencia: Instituto de Fisiología Celular, UNAM. **Proyecto: Alexander von Humboldt**. Fecha inicio: 01-junio-2019. Fecha término: 15-diciembre-2019.

5) Fernández De Miguel Francisco: Moore Corona Sharlen. Procedencia: Universidad Nacional Autónoma de México. **Proyecto: Human Frontiers Science Program**. Fecha inicio: 01-enero-2019. Fecha término: 31-octubre-2019.

6) González Halphen Diego: García Rincón Juan. Procedencia: Instituto de Biotecnología, UNAM. **Beca DGAPA**. Fecha inicio: 01-septimbre-2017. Fecha término: 31-agosto-2019.

7) Hiriart Urdanivia Marcia: Sánchez Zamora Yuriko Itzel. Procedencia: Doctorado Ciencias Biomédicas, Iztacala. **Beca DGAPA**. Fecha inicio: 01-febrero-2018. Fecha término: 31-enero-2020.

8) Licona Limón Paula: Flores Alvarez Luis José. Procedencia: Universidad Michoacana. **Beca CONACyT.** Fecha inicio: 05-agosto-2019. Fecha término: 05-agosto-2021.

9) Macías Silva Marina: Ortega Domínguez Bibiana. Procedencia: Facultad de Quimica, UNAM. **Proyecto: CONACyT-ANR.** Fecha inicio: 01-agosto-2018. Fecha término: 31-enero-2019.

10) Massieu Trigo Lourdes: Rivero Segura Nadia Alejandra. Procedencia: Facultad de Química, UNAM. **Beca DGAPA**. Fecha de inicio: 01-septiembre-2018. Fecha de término: 31-agosto-2019.

11) Tapia Ibarguengoytia Ricardo: Ramirez Jarquin Uri Nimrod. Procedencia: Scripps Institute, Florida. **Proyecto: Posdoctoral asociado al proyecto.** Fecha inicio: 01-enero-2019. Fecha término: 31-diciembre-2019.

12) Tovar y Romo Luis Bernardo: Santana Martínez Ricardo Alberto. Procedencia: Instituto Nacional de Neurología y Neurocirugía “Manuel Velasco Suárez”. **Beca DGAPA**. Fecha inicio: 01-marzo-2019. Fecha término: 28-febrero-2021.

PERSONAL ADMINISTRATIVO

Dirección
Dominga Vera García, Asistente Ejecutivo
Gabriela Valdés Silva, Asistente Ejecutivo
Ubaldo Rodríguez Lagunes, Oficial de Transporte Especializado

Secretaría Académica
Diana Osorio Icaza, Asistente Ejecutivo

Secretaría Administrativa
L.A.E. María del Pilar Martínez Martínez, Secretaria Administrativa
Laura Itzel Méndez Guerrero, Asistente Ejecutivo

Departamento de Personal
L.A.I. María del Carmen Ruiz Valderrábano, Jefe de Departamento
Nancy Lizette Islas Vargas, Asistente Ejecutivo
Lizette Monserrat Saavedra Martínez, Asistente Ejecutivo

Departamentos de Biología Celular y Desarrollo, Genética Molecular y Bioquímica y Biología Estructural
María del Rosario Villaseñor Ávila, Asistente Ejecutivo
Gabriela Valdés Silva, Asistente Ejecutivo
María del Rocío Romualdo Martínez, Asistente Ejecutivo

Departamentos de Neurodesarrollo y Fisiología, Neurociencia Cognitiva y Neuropatología Molecular
Olivia Angélica Farfán Osornio, Secretario Bilingüe
Arleth Gómez Vásquez, Asistente Ejecutivo
Miriam Morales Gómez, Secretario

Coordinación de Enseñanza
Sara Elena Méndez Ibañez, Asistente de Procesos

Departamento de Control Presupuestal
Ángel Cedillo Hernández, Jefe de Departamento
Sabina Rojas Escandón, Secretario
Erika Gisela Vázquez Castro, Auxiliar de Contabilidad

Departamento de Ingresos Extraordinarios
Lic. Claudia Ivette Islas Vargas, Jefe de Departamento
Lina Arreguín Guerrero, Jefe de Sección
Miguel Angel Reyes Montoro, Auxiliar de Contabilidad
Francisco Tomás Márquez Escalona, Secretario

Departamento de Bienes y Suministros
Ing. Mario Arredondo Rivera, Encargado del Despacho del Depto. De Bienes y Suministros
Héctor Antonio Pineda Balcazar, Jefe de Área
Marisela Almanza Villagomez, Secretario Bilingüe
Alfredo Octaviano Martínez, Secretario
María Lidia Sánchez Alpizar, Secretario
Beatriz Fragoso Álvarez, Secretario
Carlos Alberto Hernández Valadez, Oficial de Servicios Administrativo
Virginia Rivera Alvarado, Oficial de Servicios Administrativos

Departamento de Servicios Generales
Ing. Armando Rosalio Canto Canto, Jefe de Departamento
Maria del Carmen Pérez Hernández, Asistente Ejecutivo
Fanny García Guerrero, Secretario
Adriana Camacho Bandera, Secretario
Luis Fernando Molina Martínez, Jefe de Taller
Rocío Arreguín Guerrero, Jefe de Sección
Horacio Cortés Sánchez, Oficial de Servicios Administrativos
José Luis Garduño Garduño, Oficial de Transporte Especializado
Bernardo Castillo López, Oficial de Transporte Especializado
Fabián Domínguez García, Oficial de Transporte

Oficina de DGAPA
Pablo Montiel González, Jefe de Área
Irma Aracelí Santos Cueto, Jefe de Oficina
Jasmín Guerrero Arelio, Oficial de Servicios Administrativos
Domitila Ramírez Rojas, Auxiliar de Contabilidad

Biblioteca
Nadia Brisa Robles Vidal, Bibliotecario
Javier Antonio Robles Durán, Bibliotecario
Marisela Buitrón Cruz, Secretario

Almacén
Irene Rios Castro, Jefe de Oficina
María del Rosario Aguilar Oliver, Secretario
Sergio Méndez Serna, Auxiliar de Intendencia
Abril Jasso Ruiz, Almacenista
Jorge Guerrero Morales, Oficial de Servicios Administrativos

Bioterio
Miriam Pedraza Alanís, Secretario
Alma Rosa Solis Ibarra, Laboratorista
Liliana Bolaños Granda, Laboratorista
Lino Méndez Laso, Laboratorista
Miguel Hernández Cedillo, Laboratorista
Alejandro Monroy Badillo, Laboratorista
Miguel Ángel Monroy Badillo, Auxiliar de Laboratorio
Jesús Moya Jaime, Auxiliar de Laboratorio
José Carlos Lugo Márquez, Auxiliar de Laboratorio
Humberto Quintero Cortés, Laboratorista
Hugo Zenteno Alba, Auxiliar de Laboratorio
José René Flores Rodríguez, Auxiliar de Laboratorio
Erika Cazandra Ávila García, Auxiliar de Intendencia

Laboratoristas
Héctor Zenteno Alba
María Gianelli Cortés González
Marina Cristóbal Ortiz
José Fabián Márquez Escalona
Víctor Manuel Méndez Ramos
Concepción Núñez Vázquez
Patricia Hernández García
Mario Zamora Jiménez
María José Zamora Jiménez
Alejandro Flores Rodríguez
Sergio Méndez Franco
Juan Carlos Molina Martínez
Félix Sierra Ramírez

Auxiliares de Laboratorio
Adrián Alvarado Martínez
Cristina Jardínez Godínez
Rosa María Arelio Nápoles
César Alejandro Bolaños Vidal
Xóchitl Castrejón Galindo
Miguel Angel Enríquez Correa
Fermín Domínguez Díaz
Sara Flores González
José Agustín Flores González
Alicia Cubos Ordaz
Marcelino Hernández González
Alejandra Hernández Trujillo
Esmeralda Isaura Hernández Morales
Verónica Montes Trujillo
Marisela Hernández Aguilar

María Guadalupe Jiménez
Guadalupe Márquez Real
Ramón Méndez Franco
Angélica Montes Trujillo
Alfredo Octaviano García
Rosa Rivera Alvarado
Inés Sánchez Ortega
María Epifanía Martínez Hernández
Laura Vargas Carrillo
Lucía Vázquez Gutiérrez
Salustia Salgado Guzmán
Tonatiuh Mondragón Cerón
María Teresa Constantino Velázquez
Antonio Rivera Alvarado

Vigilantes
María Luisa Constantino Velázquez
Luis Martínez Hernández
Jorge Carmona Aranda
David Carreño Arrazola
Emma Cortés Vargas
María Gladiola Magaña Naranjo
Alfredo Olivar Cecaldi
Daniel Quintero Enríquez
César Rodríguez Miguel
Abdiel Gregorio Sanjuan Raymundo
Concepción Núñez Constantino
Benito Villegas Guemes
Gerardo Montes Trujillo
Verónica López Aguilar
Guillermina Matilde Ruiz Praxediz

Auxiliar de Intendencia
Miguel Ángel Zamora Jiménez, Jefe de Servicio
Jesús Joaquín Salgado Cortés, Jefe de Servicio
Marlen Espitia Salgado
Carlota Guerrero y Fuentes
Iris Adriana Ibarra Sánchez
Andrés Pablo Lugo Hernández
Blanca Leticia Octaviano Martínez
Raúl González López
Araceli Vázquez Gutiérrez
Moni Ybeth Zenteno Alba
Sergio Méndez Serna
Juan Abraham Cruz Hernández
Héctor Uriel Ibarra Sánchez

Abigail Flores González
Julio César Luna Quintero
Pablo César Lugo Márquez
Alicia Aguilar Oliver
Zury Saraí Carmona Camacho
Diego Cedeño Valdez
Saúl González Mendoza
Eduardo Jardinez Godínez
Berenice Olivares Vázquez
Ariadna García Vázquez
Rodrigo Rodriguez Buitrón
Rafael Oliver Romero
Angel Montes Medel

La distribución de equidad de género entre el personal administrativo y de confianza se representa en la siguiente gráfica.

Distribución del Personal Administrativo y de Confianza por Género

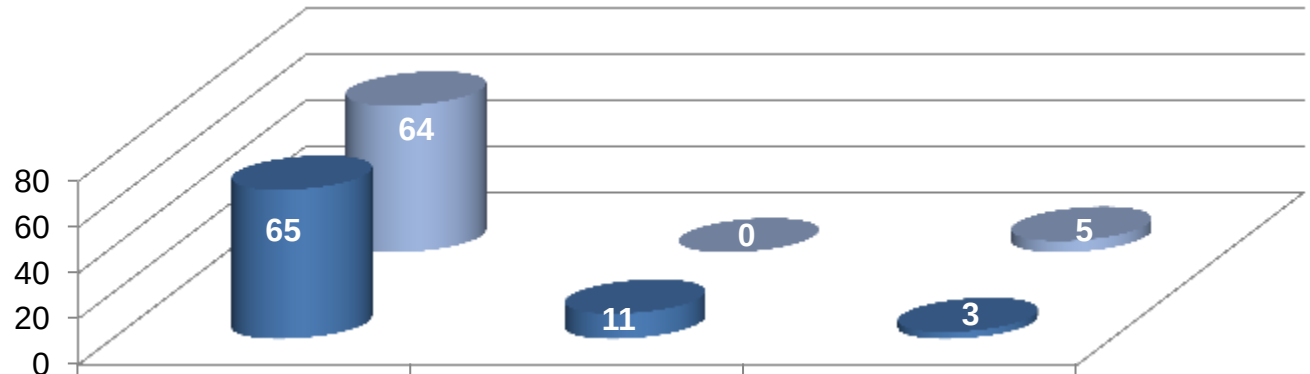

	ADMINISTRATIVO	CONFIANZA	FUNCIONARIO
MUJER	65	11	3
HOMBRE	64	0	5

FORMACIÓN DE RECURSOS HUMANOS

Estudiantes

Los estudiantes son una parte fundamental en las actividades académicas y de investigación en el Instituto. Son colaboradores de los diversos proyectos de investigación que se desarrollan. Durante 2019, el IFC recibió un total de 508 estudiantes de los cuales 15 estudiantes son de Taller, 10 estudiantes de LIBB estuvieron de rotación en laboratorios, 31 alumnos relizaron su estancia de investigación en alguno de nuestros laboratorios, 65 tesistas de Licenciatura, 81 alumnos inscritos a la Licenciatura en Neurociencias, 120 estudiantes de Maestría en Ciencias Bioquímicas, 9 estudiantes de Maestría en Ciencias Biológicas, 86 alumnos son de Doctorado en Ciencias Biomédicas, 76 estudiantes de Doctorado en Ciencias Bioquímicas, 9 estudiantes de Doctorado en Ciencias Biológicas y 3 estudiantes de otro programa de Doctorado y Maestría, respectivamente.

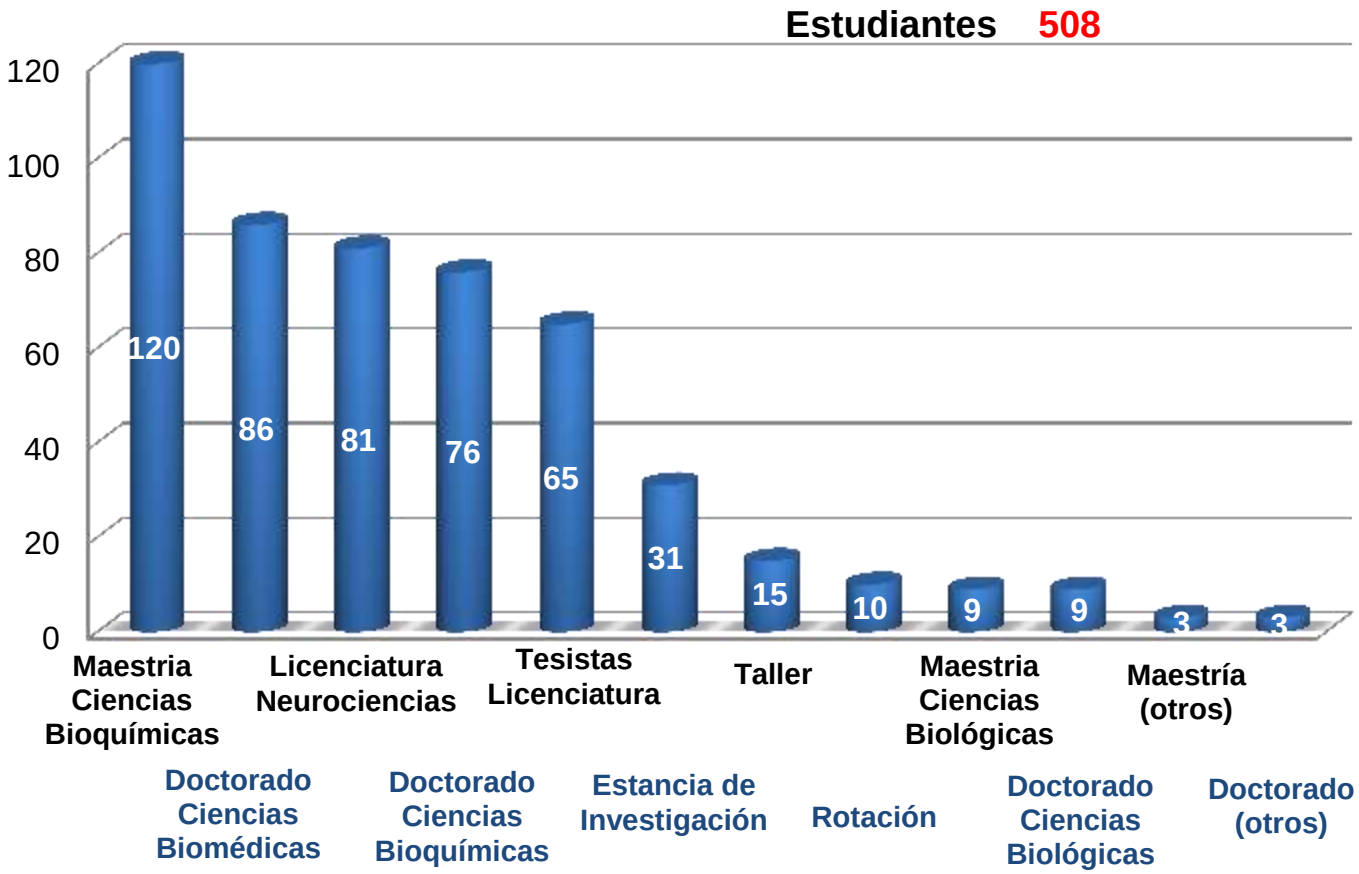

15	• Alumnos de taller
10	• Alumnos de rotación LIBB
31	• Alumnos de estancia de investigación
65	• Alumnos tesistas de Licenciatura
81	• Licenciatura en Neurociencia
120	• Alumnos de Maestría en Ciencias Bioquímicas
9	• Alumnos de Maestría en Ciencias Biológicas
86	• Alumnos de Doctorado en Ciencias Biomédicas
76	• Alumnos de Doctorado en Ciencias Bioquímicas
9	• Alumnos de Doctorado en Ciencias Biológicas
3	• Alumnos de Doctorado (otros)
3	• Alumnos de Maestría (otros)

NEUROCIENCIAS UNAM

Facultad de Psicología | Instituto de Neurobiología | Facultad de Medicina | Instituto de Fisiología Celular UNAM | Ciencias

2018	Seleccionados
Concurso de Selección	15
Pase reglamentado	19
Total	34

2019	Seleccionados
Concurso de Selección	21
Pase reglamentado	12
Cambio de carrera	1
Total	34



Investigación Biomédica Básica

LIBB

LIBB en el IFC	
Alumnos Graduados	3
Alumnos en Rotación	11
Alumnos en Estancia	2

Graduados

Durante 2019 se graduaron en total 75 estudiantes, 14 estudiantes de Licenciatura, 29 estudiantes de Maestría en Ciencias Bioquímicas, 5 de ellos por defensa de proyecto, 7 estudiantes de Maestría en Ciencias Biológicas, 12 estudiantes de Doctorado en Ciencias Biomédicas, 11 estudiantes de Doctorado en Ciencias Bioquímicas y 2 estudiantes de Doctorado en Ciencias Biológicas.

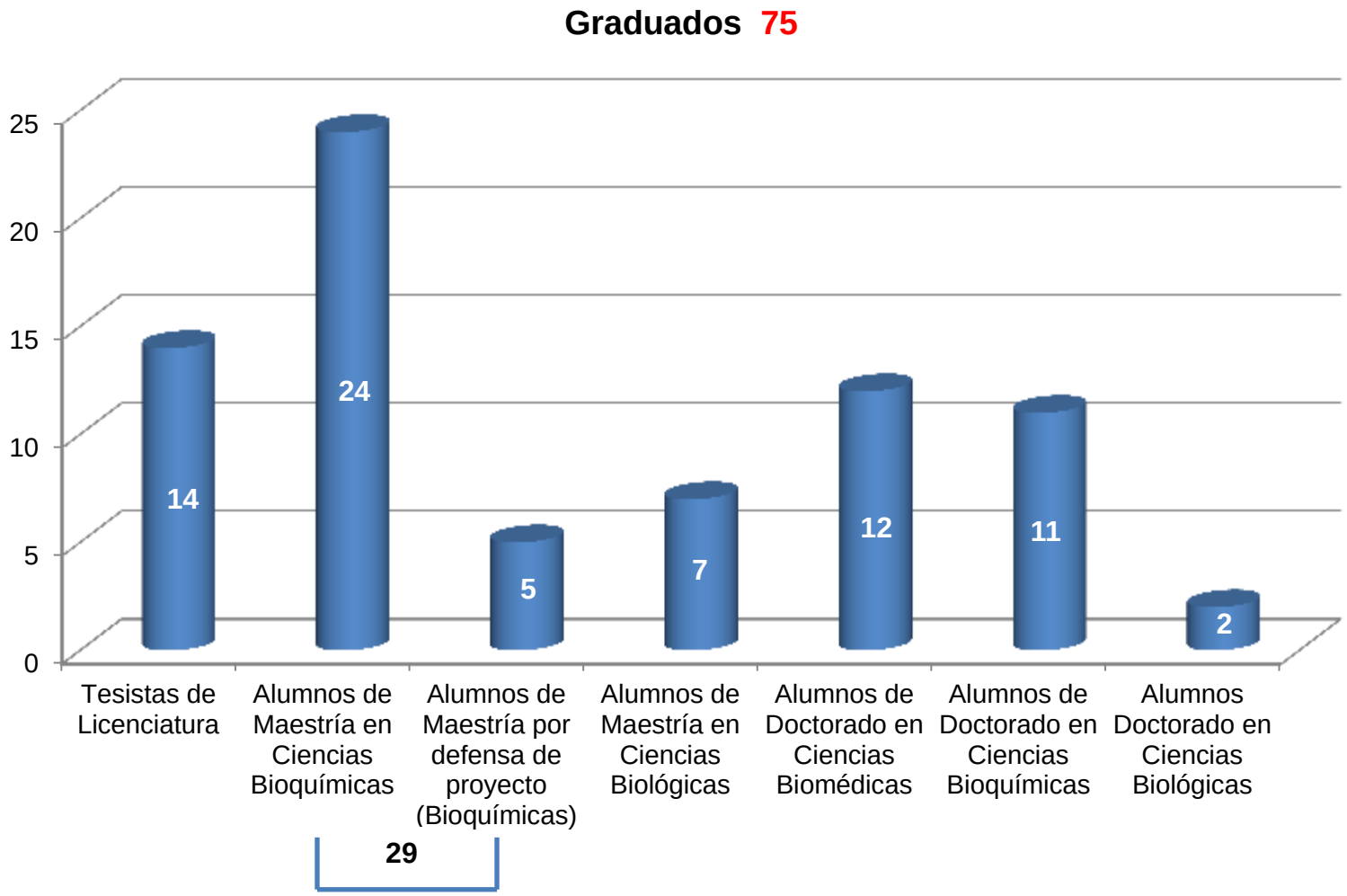

*para la lista de estudiantes y graduados ver el Archivo Anexo-1

DOCENCIA

Cursos Impartidos

La docencia es una de las actividades sustanciales del IFC porque contribuye al desarrollo de recursos humanos. El personal académico del Instituto ha tenido un gran desempeño en la impartición de diversos cursos de Posgrado y Licenciatura, dentro y fuera de la UNAM.

Debido a la participación del IFC en los diversos programas de Maestría y Doctorado y a la colaboración de los académicos con otras dependencias de la UNAM, se impartieron cursos en la Facultad de Ciencias, Facultad de Medicina y la Facultad de Ingeniería principalmente, también se dieron cursos en la Facultad de Psicología, en el Centro de Ciencias Genómicas, en el Instituto de Neurobiología y en el Instituto de Investigaciones Biomédicas.

De igual manera se impartieron cursos fuera de la UNAM, en otras instituciones educativas y universidades como la Universitat Autónoma de Barcelona, el CINVESTAV del IPN, por mencionar algunas.

El total de cursos impartidos durante el 2019 suman 136, 117 fueron impartidos en diversas dependencias de la UNAM, 48 cursos de nivel posgrado y 69 de licenciatura. Dentro del Instituto de Fisiología Celular se impartieron 39 cursos de los 117 dictados dentro de la UNAM. Los que fueron impartidos fuera de la UNAM sumaron un total de 19, de los cuales 15 fueron de posgrado y 4 de licenciatura.

TOTAL DE CURSOS IMPARTIDOS				
CURSOS DICTADOS EN LA UNAM	**Total**	**Académicos del IFC como responsables**	**Participación de algún miembro del IFC**	**Impartidos en el IFC**
Cursos impartidos a nivel posgrado	**48**	26	22	25
Cursos impartidos a nivel licenciatura	**69**	53	16	14
CURSOS DICTADOS FUERA DE LA UNAM				
Cursos impartidos a nivel posgrado	**15**	3	12	*
Cursos impartidos a nivel licenciatura	**4**	*	4	*
Total general	**136**			

*para la lista de Cursos ver el Archivo Anexo-2

REVISIÓN DE ACTIVIDADES ACADÉMICAS DE DOCTORADO

- **Aguilar Roblero Raúl**
  Estudiante: Armida Miranda Riestra.
  Programa: Posgrado en Ciencias Biomédicas.
  Trabajo revisado: Artículo de revisión: La melatonina como factor de diferenciación neuronal.

- **Castro Obregón Susana**
  Estudiante: José Rolando Lara Rodarte.
  Programa: Posgrado en Ciencias Biomédicas.
  Trabajo revisado: Use of inducible expression systems in embryonic stem cells for the expresión of neurorophic factors.

- **Funes Argüello Soledad**
  Estudiante: Carlos Alberto Ayhllon Osorio.
  Programa: Posgrado en Ciencias Biomédicas.
  Trabajo revisado: Artículo de revisión: AZT, a double-edged sword: A summary of its intracellular repercussions.

- **González Pedrajo Bertha**
  Estudiante: Greta Isabel Reynoso Cereceda.
  Programa: Posgrado en Ciencias Biomédicas.
  Trabajo revisado: A look inside the bioreactor: Molecular response of *E. coli* productive cells.

- **González Pedrajo Bertha**
  Estudiante: Nelly Araceli Aburto Rodríguez.
  Programa: Posgrado en Ciencias Biomédicas.
  Trabajo revisado: Quorum sensing and type III secretion system inhibitors as an alternative therapy to treat drug resistant bacterial infections.

- **Massieu Trigo Lourdes**
  Estudiante: Karina Sánchez Alegría.
  Programa: Posgrado en Ciencias Biomédicas.
  Trabajo revisado: Effects of saturated fatty acids on brain function.

- **Peraza Reyes Leonardo**
  Estudiante: Carlos Alberto Ayhllon Osorio.
  Programa: Posgrado en Ciencias Biomédicas.
  Trabajo revisado: AZT, a double-edged sword: A summary of its intracellular repercussions.

- **Ramiro Cortés Yazmín**
  Estudiante: Ana Silvia Báez Cordero.
  Trabajo revisado: Tesis de maestria: Integración de la vía directa e indirecta en la actividad de la sustancia nigra reticulata de los ganglios basales y su modulación por canabinoides.

- **Ramiro Cortés Yazmín**
  Estudiante: Daniel Pérez Torres.
  Trabajo revisado: Tesis de maestria: Evaluación de la actividad intrínseca de las células del núcleo ventro-basal talámico en ratas cegadas al nacimiento.

- **Ramiro Cortés Yazmín**
  Estudiante: Mildred Salgado Ménez.
  Trabajo revisado: Tesis de maestria: Modulación catecolaminérgica en evocación y actualización de la memoria espacial.

- **Ramiro Cortés Yazmín**
  Estudiante: Esteban Urrieta Chávez.
  Trabajo revisado: Tesis de maestria: Regulación metaplástica de la depresión de largo plazo in vivo en la corteza insular debida al condicionamiento.

- **Tovar y Romo Luis Bernardo**
  Estudiante: Jorge Luis Ochoa.
  Programa: Posgrado en Ciencias Biomédicas.
  Trabajo revisado: Receptores de citocinas inflamatorias sobre sinápsis hipocampales.

PRODUCCIÓN ACADÉMICA

El crecimiento de la planta académica y el desempeño del personal académico han tenido como resultado una constante productividad científica, obteniendo en el 2019 un total de 117 artículos indizados con índice de impacto promedio de 5.02, lo que representa 2.05 artículos por grupo de investigación.

Además, 14 artículos se encuentran en prensa, se publicaron 9 artículos de divulgación, 6 capítulos en libros, 8 capítulos en prensa, 1 libro publicado y reimpreso, 6 revistas nacionales y 1 Patente Nacional concluida son parte del resultado de la investigación en el IFC en 2019.

117	•Artículos en Revistas Internacionales
14	•Artículos en Prensa
9	•Artículos de Divulgación
6	•Capítulos de libros
8	•Capítulos en Prensa
1	•Libros publicados y reimpresiones
6	•Revistas Nacionales
1	•Patente Nacional concluida

Producción Académica Histórica

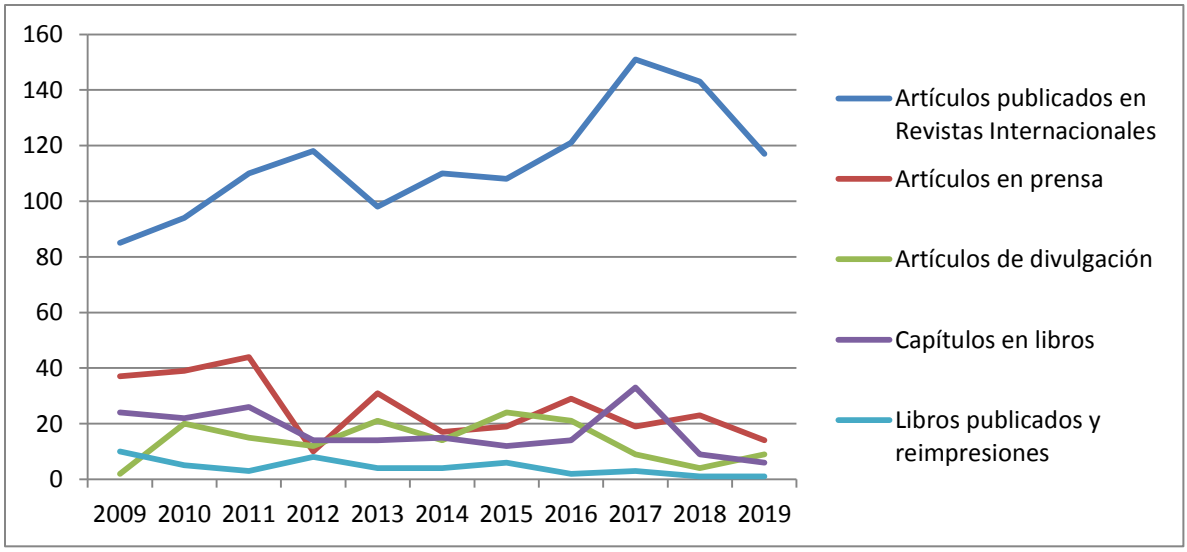

Producción Académica Histórica											
	2019	2018	2017	2016	2015	2014	2013	2012	2011	2010	2009
1. Artículos publicados en Revistas Internacionales	117	142	150	121	108	110	98	118	110	94	85
2. Artículos en prensa	14	23	19	29	19	17	31	10	44	39	37
3. Artículos en memorias	*	2	5	2	7	3	*	*	*	*	*
4. Artículos de divulgación	9	4	9	21	24	14	21	12	15	20	2
5. Capítulos en libros	6	9	32	14	12	15	14	14	26	22	24
6. Capítulos en prensa	8	5	2	9	3	6	*	*	2	5	16
7. Libros publicados y reimpresiones	1	1	3	2	6	4	4	8	3	5	10
8. Patentes nacionales concluidas	1	1	2	2	*	2	2	1	*	*	*
9. Patentes nacionales en trámite	*	*	*	1	3	1	3	4	*	*	*
10. Patentes internacionales concluidas	*	*	1	*	1	1	1	*	*	*	*
11. Patentes Internacionales en Trámite	*	1	*	*	3	4	*	1	*	*	*
12. Revistas Nacionales	6	4	1	4	*	*	*	*	*	2	5

Publicaciones IFC 2017-2019 por cuartiles

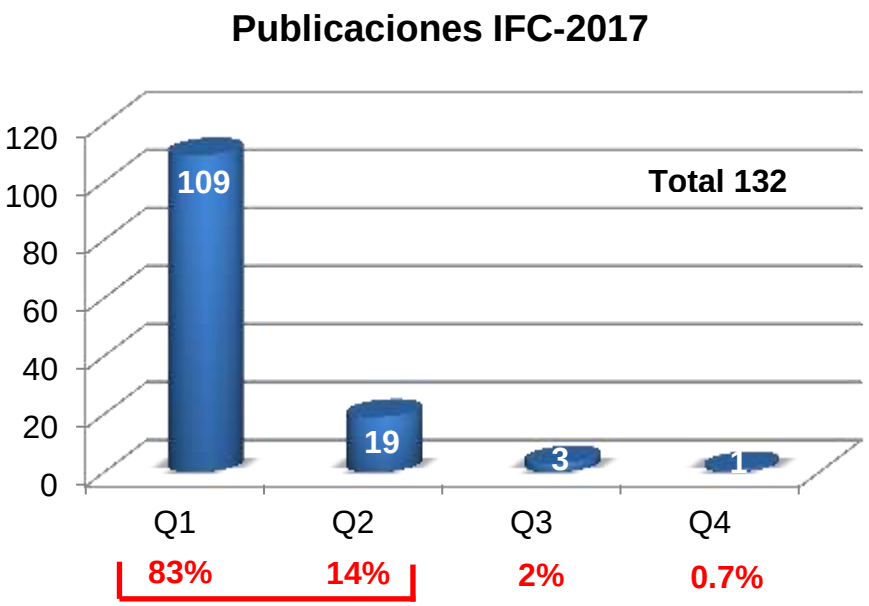

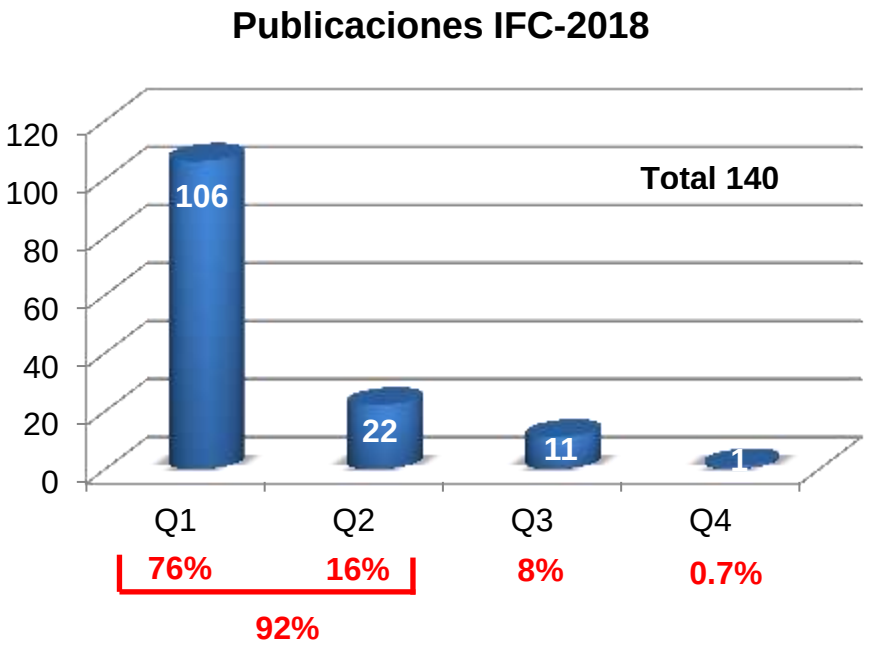

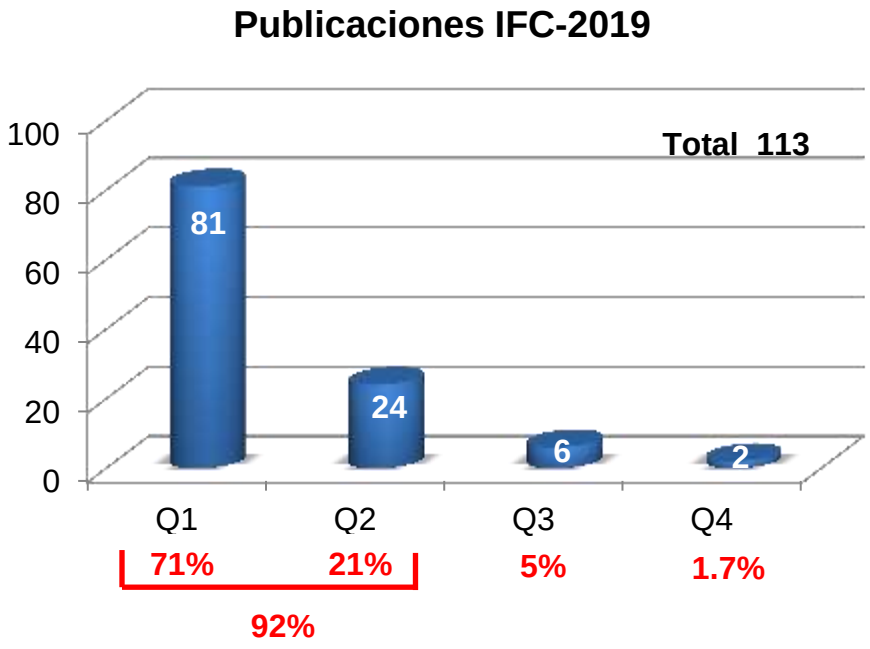

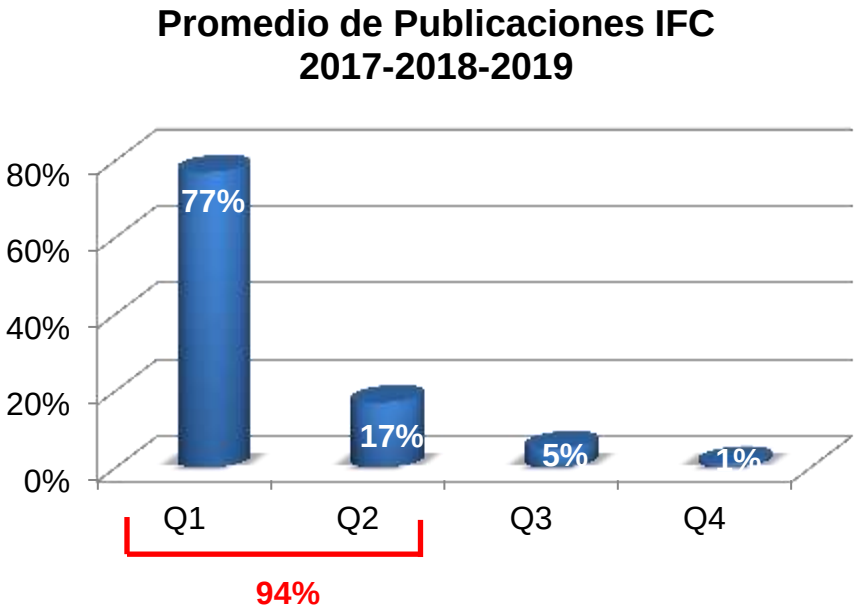

Fuente SJR
https://www.scimagojr.com/journalrank.php

Artículos Publicados en Revistas Internacionales

1) Acosta Montaño, P; Ibarra López, E; Mas Oliva, J; Delgado Coello, B; Rivero, I; Alatorre Meda, M; Aguilera, J; Rodríguez Velázquez, E; Guevara Olaya, E; García González, V. (2019). Fatty acid and lipopolysaccharie effect on beta cells proteostasis and its impacto n insulin secretion. *Cell*. **8**: 884. **FI: 36.216; Q1**.

2) Akinaga, J; García Sáinz, J; Pupo, S. A. (2019). Updates in the function and regulation of α1 –adrenoceptors. *Brit. J. Pharmacol*. **176**: 2343-2357. **FI: 6.583; Q1**.

3) Almanza, A; Segura Chama, P; León Olea, M; Luis, E; Garduño Gutiérrez, R; Mercado Reyes, J; Simón Arceo, K; Coffeen, U; Hernández Cruz, A; Pellicer, F; Mercado, F. (2019). Cellular mechanism for specific mechanical antinociception by D2-like receptor at the spinal cord level. *Neuroscience*. **417**: 81-94. **FI: 3.244; Q2**.

4) Amezcua Vesely, M; Pallis, P; Bielecki, P; Low, J; Zhao, J; Harman, C; Kroehling, L; Jackson, R; Bailis, W; Licona Limón, P; Xu, H; Iijima, N; Pillai, P; Kaplan, D; Weaver, C; Kluger, Y; Kowalczyk, M; Iwasaki, A; Pereira, J; Esplugues, E; Gagliani, N; Flavell, R. (2019). Effector TH17 cells give rise to long-lived TRM cells that are essential for an immediate response against bacterial infection. *Cell*. **178**: 1176-1188.el5. **FI: 36.216; Q1**.

5) Aparicio Juárez, A; Duhne, M; Lara González, E; Ávila Cascajares, F; Calderón, V; Galarraga, E; Bargas, J. (2019). Cortical stimulation relieves parkinsonian pathological activity *in vitro*. *European Journal and Neuroscience*. **49**: 834-848. **FI: 2.832; Q2**.

6) Arroyo Pérez, E. E; González Cerón, G; Soberón Chávez, G; Georgellis, D; Servin Gonzalez, L. (2019). A novel two-component system, encoded by the sco5282/sco5283 genes, affects *streptomyces coelicolor* morphology in liquid culture. *Frontiers in Micobiology*. **10**: 1568. **FI: 4.259; Q1**.

7) Arzate, D; Guerra Crespo, M; Covarrubias, L. (2019). Induction of typical and atypical neurogenesis in the adult substantia nigra after mouse embryonic stem cells transplantation. *Neuroscience*. **408**: 308-326. **FI: 3.244; Q2**.

8) Azuara Medina, P. M; Sandoval Duarte, A. M; Morales Lázaro, S. L; Modragón González, R; Vélez Aguilera, G; Gómez López, J. D; Jiménez Gutiérrez, G. E; Tiburcio Félix, R; Martínez Vieyra, I; Suárez Sánchez, R; Längst, G; Javier Magaña, J; Winder, S. J; Ortega, A; Ramos Perlingeiro, R. C; Jacobs, L. A; Cisneros, B. (2019). The intracellular domain of β-dystroglycan mediates the nucleolar stress response by suppressing UBF transcriptional activity. *Cell Death & Disease.* **10**(196). **FI: 5.959; Q1**.

9) Bahena Alvarez, D; Rincón Heredia, R; Millán Aldaco, D; Fiordelisio, T; Hernández Cruz, A. (2019). Calcium signaling and expression of voltage-gated calcium channels in the mouse ovary throughout the estrous cycle. *Biology of reproduction*. **100**: 1018-1034. **FI: 2.96; Q1**.

10) Barbosa Nascimento Viana, J; Alcántara Hernández, R; Oliveira Barros, E; Castello Branco, L. A; Feijó, P. R; Soares Romeiro, L. A; Nasciutti, L. E; Noël, F; García Sáinz, J. A; Martins Silva, C. L. (2019). The alpha 1-adrenoceptor-mediated human hyperplastic prostate cells proliferation is impaired by EGF receptor inhibition. *Life Sci*. **239**: 117048. **FI: 3.448; Q1**.

11) Barriga Montoya, C; de la O Martínez, A; Picones, A; Hernández Cruz, A; Fuentes Pardo, B; Gómez Lagunas, F. (2019). Desensitization and recovery of crayfish photoreceptors upon delivery of a light stimulus. *J. Vis. Exp*. **153**: e56258. **FI: 1.108; Q2**.

12) Bastián Eugenio, C; Bohórquez Hernández, A; Pacheco, J; Sampieri, A; Asanov, A; Ocelotl Oviedo, J; Guerrero, A; Darszon, A; Vaca, L. (2019). Heterologous calcium-dependent inactivation of orai1 by neighboring TRPV1 channels modulates cell migration and wound healing. *Communications Biology*. **2**: 88. **FI: 2.5; Q1**.

13) Binh Nguyen, M; Valdes, V. J; Cohen, I; Pothula, V; Zhao, D; Zheng, D; Ezhkova, E. (2019). Dissection of Merkel cell formation in hairy and glabrous skin reveals a common requirement for FGFR2-mediated signalling. *Experimetal Dermatology*. **28**: 374-382. **FI: 2.868; Q1**.

14) Borroto Escuela, D; Narvaez, M; Zannoni, M; Contri, C; Crespo Ramírez, M; di Palma, M; Ambrogini, P; Brito, I; Pita Rodríguez, M; Valladolid Acebes, I; de la Mora, M; Fuxe, K. (2019). Isolation and detection of G protein-coupled receptor (GPCR) heteroreceptor complexes in rat brain synaptosomal preparation using a combined brain subcellular fractionation/co-immunoprecipitarion (Co-IP) procedures. Co-Immunoprecipitation Methods for Brain Tissue. *Neuromethods*. **144**: 123-135. **FI: 3.00; Q3**.

15) Cano Domínguez, N; Bowman, B; Peraza Reyes, L; Aguirre, J. (2019). Neurospora crassa NADPH oxidase NOX-1 is localized in the vacuolar system and the plasma membrane. *Frontiers in Microbiology*. **10**: 1825. **FI: 4.259; Q1**.

16) Carbone, E; Borges, R; Eiden, L. E; Garcia, A. G; Hernández Cruz, A. (2019). Chromaffin cells of the adrenal medulla: physiology, pharmacology, and disease*. Comprehensive. Physiol*. **9**: 1443-1502. **FI: 6.246; Q1**.

17) Cárdenas Rivera, A; Campero Romero, A. N; Heras Romero, Y; Penagos Puig, A; Rincón Heredia, R; Tovar y Romo, L. B. (2019). Early post-stroke activation of vascular endothelial growth factor receptor 2 hinders the receptor 1-dependent neuroprotection afforded by the endogenous ligand. *Front. Cell. Neurosci*. **13**: 1-15. **FI: 3.900; Q2**.

18) Carmona Rosas, G; Alcántara Hernández, R; Hernández Espinosa, D. A. (2019). The role of beta-arrestins in G protein-coupled receptor heterologous desensitization: A brief story. *Methods Cell Biol*. **149**: 195-204. **FI: 1.698; Q2**.

19) Carmona Rosas, G; Hernández Espinosa, D. A; Alcántara Hernández, R; Alfonzo Méndez, M. A; García Sainz, J. A. (2019). Distinct phosphorylation sites/clusters in the carboxyl terminus regulate α1D-adrenergic receptor subcellular localization and signaling. *Cellular Signalling*. **53**: 374-389. **FI: 3.388; Q2**.

20) Carranza García, E; Navarro, R. E. (2019). Apoptosis contributes to protect germ cells from the oogenic germline starvation response but is not essential for the gonad shrinking or recovery observed during adult reproductive diapause in *C. elegans*. *PLoS one*. **14**: e0218265. **FI: 2.776; Q1**.

21) Castillo, X; Castro Obregón, S; Gutiérrez Becker, B; Gutiérrez Ospina, G; Karalis, N; Khalil, A. A; López Noguerola, J. S; Lozano Rodríguez, L; Martínez Martínez, E; Pérez Cruz, C; Pérez Velázquez, J; Piña, A. L; Rubio, K; Salazar Garcia, H. P; Syeda, T; Vanoye Carlo, A; Villringer, A; Winek, K; Zille, M. (2019). Re-thinking the etiological framework of neurodegeneration. *Frontiers in Neuroscience*. **13**: 728. **FI: 3.648; Q1**.

22) Castillo Bautista, C. M; Torres Tapia, L. W; Rangel Méndez, J. A; Peraza Sánchez, S. R; Cortes, D; Velasco, I; Moo Puc, R. E. (2019). Neuroprotective effect of Mayan medicinal plant extracts against glutamate-induced toxicity. *J. Natural Medicines*. **73**: 672-678. **FI: 1.966; Q1**.

23) Castro Torres, E; Jiménez Sandoval, P; Romero Romero, S; Fuentes Pascacio, A; López Castillo, L. M; Díaz Quezada, C; Fernández Velasco, A. D; Torres Larios, A; Brieba, L. G. (2019). Structural basis for the modulation of plant cytosolic triosephosphate isomerase activity by mimicry of redox-based modifications. *Plant J*. **99**: 950-964. **FI: 5.726; Q1**.

24) Chiquete Felix, N; Uribe Alvarez, C; Pedroza Davila, U; Cruz Cruz, I; Uribe Carvajal, S. (2019). Wolbachia pipientis colonizes S. cerevisiae with high yields. Effects on the host. *Biophysical Journal*. **116**: 324a. **FI: 3.665; Q1**.

25) Colina Tenorio, L; Miranda Astudillo, H; Dautant, A; Vazquez Acevedo, M; Giraud, M. F; Gonzalez Halphen, D. (2019). Subunit Asa3 ensures the attachment of the peripheral stalk to the membrane sector of the dimeric ATP synthase of *Polytomella* sp. *Biochem. Biophys. Res. Commun*. **509**: 341-347. **FI: 2.705; Q1**.

26) Collazo Navarrete, O; Hernández García, D; Guerrero Flores, G; Drucker Colin, R; Guerra Crespo, M; Covarrubias, L. (2019). The substantia nigra is permissive and gains inductive signals when lesioned for dopaminergic differentiation of embryonic stem cells**.** *Stem. Cells. Dev*. **28**: 1104-1115. **FI: 3.147; Q1**.

27) Contreras Zentella, M. L; Sánchez Sevilla, L; Suárez Cuenca, J. A; Olguín Martínez, M; Alatriste Contreras, M. G; García García, N; Orozco, L; Hernández Muñoz, R. (2019). The role of oxidant stress and gender in the erythrocyte arginine metabolism and ammonia management in patients with type 2 diabetes. *PLoS one*. **14**(7). **FI: 2.776; Q1**.

28) Cortés Fernández de Lara, J; Arzate Mejía, R; Recillas Targa, F. (2019). Enhance RNAs: Insights into their biological role. *Epigenetics Insights*. **12**: 1-7. **FI: 2.91; Q4**.

29) Cortes Medina, L. V; Pasantes Morales, H; Aguilera Castrejón, A; Picones, A; Lara Figueroa, C; Enoch, L; Montesinos, J; Cortés Morales, V. A; de la Rosa Ruiz, M. P; Hernández Estévez, E; Bonifaz, L. C; Álvarez Pérez, M. A; Ramos Mandujano, G. (2019). Neuronal transdifferentiation potential of human mesenchymal stem cells from neonatal and adult sources by a small molecule cocktail. *Stem. Cell. International*. Article ID 7627148. **FI: 3.902; Q2**.

30) Cruz Ramos, E; Macías Silva, M; Sandoval Hernández, A; Tecalco Cruz, A. C. (2019). Non-muscle myosin IIA is post-traslationally modified by interferón-stimulated gene 15 in breast cancer cells. *Int. J. Biochem. Cell. Biol*. **107**: 14-26. **FI: 3.144; Q1**.

31) Domínguez Pérez, M; Simoni Nieves, A; Rosales, P; Nuno Lambarri, N; Rosas Lemus, M; Souza, V; Miranda, R. U; Bucio, L; Uribe Carvajal, S; Marquardt, J. U; Seo, D; Gómez Quiroz, L. E; Gutiérrez Ruiz, M. C. (2019). Cholesterol burden in the liver induces mitochondrial dynamic changes and resistance to apoptosis. *J. Cellular Physiology*. **234**: 7213-7223. **FI: 4.522; Q1**.

32) Escalera Fanjul, X; Quezada, H; Riego Ruiz, L; González, A. (2019). Whole-genome duplication and yeast's fruitful way of life. *Trends in Genetics*. **35**: 42-54. **FI: 10.627; Q1**.

33) Flores Cruz, R; López Arteaga, R; Ramírez Vidal, L; López Casillas, F; Jiménez Sánchez, A. (2019). Unravelling the modus-operandi of chromenylium-cyanine fluorescent probes: a case study. *Phys. Chem. Chem. Phys*. **21**: 15779-15786. **FI: 3.567; Q1**.

34) García Aguirre, I; Alamillo Iniesta, A; Rodríguez Pérez, R; Vélez Aguilera, G; Amaro Encarnación, E; Jiménez Gutiérrez, E; Vásquez Limeta, A; Laredo Cisneros, M. S; Morales Lázaro, S. L; Tiburcio Félix, R; Ortega, A; Magaña, J. J; Winder, S. J; Cisneros, B. (2019). Enhanced nuclear protein export in premature aging and rescue of the progeria phenotype by modulation of CRM1 activity. *Aging Cell*. **18**: e13002. **FI: 7.346; Q1**.

35) García Montes, J. R; Solís, O; Enríquez Traba, J; Ruiz DeDiego, I; Drucker Colín, R; Moratalla, R. (2019). Genetic knockdown of mGluR5 in striatal D1R-containing neurons attenuates L-DOPA-Induced dyskinesia in aphakia mice. *Mol. Neurobiol*. **56**: 4037-4050. **FI: 4.586; Q1**.

36) García Ulloa, M; Ponce Soto, G; González Valdez, A; González Pedrajo, B; Díaz Guerrero, M; Souza, V; Soberón Chávez, G. (2019). Two Pseudomonas aeruginosa clonal groups belonging to the PA14 clade are indigenous to the Churince system in Cuatro Ciénegas Coahuila, México. *Environ. Microbiol*. **21**: 2964-2976. **FI: 5.147; Q1**.

37) Geronimo Olvera, C; Massieu, L. (2019). Autophagy as a homeostatic mechanism in response to stress conditions in the central nervous system. *Mol. Neurobiol*. **56**: 6594-6608. **FI: 4.586; Q1**.

38) Glotfelty, E. J; Delgado, T; Tovar y Romo, L. B; Luo, Y; Hoffer, B; Olson, L; Karlsson, T; Mattson, M. P; Harvey, B; Tweedie, D; Li, Y; Greig, N. H. (2019). Incretin mimetics as rational candidates for the treatment of traumatic brain injury. *ACS* Pharmacol. Transl. Sci. **2**: 66-91.

39) Gómez Verjan, J. C; Rivero Segura, N. A; Estrella Parra, E; Rincón Heredia, R; Madariaga Mazón, A; Flores Soto, E; González Meljem, M; Cerbón, M; Reyes Chilpa, R. (2019). Network pharmacology uncovers anticancer activity of mammea-type coumarins from *Calophyllum brasiliense*. *Planta Médica*. **85**: 14-23. **FI: 2.580; Q1**.

40) González Barbosa, E; García Aguilar, R; Vega, L; Cabañas Cortés, M; González, F; Segovia, J; Morales Lázaro, S; Cisneros, B; Elizondo, G. (2019). Parkin is transcriptionally regulated by the aryl hydrocarbon receptor: Impact on α-synuclein protein levels. *Biochem. Pharmacol*. **168**: 429-437. **FI: 4.825; Q1**.

41) Gutiérrez Vidal, R; Delgado Coello, B; Méndez Acevedo, K; Calixto Tlacomulco, S; Damián Zamacona, S; Mas Oliva, J. (2019). Therapeutic intranasal vaccine HB-ATV-8 prevents atherogenesis and non-alcoholic fatty liver disease in a pig model of atherosclerosis. *Archives of Medical Reserch*. **49**: 456-470. **FI: 1.895; Q2**.

42) Guzmán Flores, J; Steinemann Hernández, L; González de la Vara, L; Gavilanes Ruiz, M; Romeo, T; Alvarez, A; Georgellis, D. (2019). Proteomic analysis of Escherichia coli detergent-resistant membranes (DRM). *PloS one*. **14**: e0223794. **FI: 2.776; Q1**.

43) Hernández Álvarez, D. M; Fernández Cáceres, C; Zapata Téllez, J; Crespo Ramírez, M; González García, N. (2019). Caracterización cognitiva y conductual de una muestra de adolescentes consumidores de inhalables de la ciudad de México. *Health and Addictions* (salud y drogas). **19**: 19-28. **FI: 0.510.**

44) Hernández Elvira, M; Martínez Gómez, R; Domínguez Martin, E; Méndez, A; Kawasaki, L; Ongay Larios, L; Coria, R. (2019). Tunicamycin sensitivity-suppression by high gene dosage reveals new functions of the yeast Hog1 MAP kinase. *Cells*. **8**: 710. **FI: 5.656.**

45) Hernández, G; Osnaya, V. G; Pérez Martínez, X. (2019). Conservation and variability of the AUG initiation codon context in eukaryotes. *Trends Biochem. Sci*. **44**: 1009-1021. **FI: 16.889; Q1**.

46) Hernández Espinosa, D; Carmona Rosas, G; Alfonzo Méndez, M; Alcántara Hernández, R; García Sáinz, J. (2019). Sites phosphorylated in human α1b-adrenoceptors in response to noradrenaline and phorbol myristate acetate. *BBA-Mol. Cell. Res*. **1866**: 1509-1519. **FI: 4.739; Q1**.

47) Hernández Espinosa, D. R**;** Massieu, L; Montiel, T; Moran, J. (2019). Role of NADPH oxidase-2 in the progression of the inflammatory response secondary to striatum excitotoxic damage. *Journal Neuroinflammation*. **16**: 1-19. **FI: 5.700; Q1**.

48) Hernández Muñoz, R; Contreras Zentella, M. L. (2019). Involvement of cell oxidant status and redox state in the increased non-enxymatic etanol oxidation by the regenerating rat liver. *Biochemical Pharmacology*. **161**: 63-72. **FI: 4.825; Q1**.

49) Hernández Plata, E; Velázquez Wong, A. C; Jiménez Ramírez, C; Fernández Ramírez, F; Galicia Sánchez, L. M; Flores García, C. A; Hernández Hernández, J. M; Rosas Vargas, H; Huicochea Montiel, J. C; Espinosa Poblano, E. (2019). Identification of genomic copy number variations in lung benign metastasizing leiomyomatosis. *Clinical Respiratory Jorunal*. **13**: 105-113. **FI: 1.751; Q3**.

50) Herrera Morales, W. V; Ramírez Lugo, L; Santiago Rodríguez, E; Reyes López, J. V; Núñez Jaramillo, L. (2019). Hazardous alcohol consumption and risk of alcohol dependence present different neurophysiological correlates. *Revista de Neurología*. **68**: 137-146. **FI: 0.485; Q3**.

51) Herrera Zamora, J. M; Castro Sánchez, L. A; Reyes Méndez, M; Aguilar Martínez, I; Osuna López, F; Moreno Galindo, E. G; Navarro Polanco, R. A; Aguilar Roblero, R. A; Sánchez Pastor, E; Alamilla, J. (2019). Development-dependent changes in the NR2 subtype of the N-Methyl-D-Aspartate receptor in the suprachiasmatic nucleus of the rat. *J. Biological Rhythms*. **34**: 39-50. **FI: 2.473; Q1**.

52) Izaguirre, G; Arciniega, M; Quezada, A. G. (2019). Specific and selective inhibitors of protein convertases engineered by transferring serpin B8 reactive-site and exosite determinants of reactivity to the serpin slpha 1PDX. *Biochemistry*. **58**: 1679-1688. **FI: 2.952; Q1**.

53) Jáidar, O; Carrillo Reid, L; Nakano, Y; López Huerta, V; Hernández Cruz, A; Bargas, J; García Muñoz, M; Arbuthnott, G. (2019). Synchronized activation of striatal direct and indirect pathways underlies the behavior in unilateral dopamine-depleted mice. *European Journal and Neuroscience*. **49**: 1512-1528. **FI: 2.784; Q2**.

54) Jiménez Jiménez, S; Hashimoto, K; Santana, O; Aguirre, J; Kuchitsu, K; Cárdenas, L. (2019). Emerging roles of tetraspanins in plant inter-cellular and inter-kingdom communication. *Plant Signaling & Behavior*. **14**: e1581559. **FI: 1.644; Q1**.

55) Jiménez Jiménez, S; Santana, O; Lara Rojas, F; Arthikala, M. K; Armada, E; Hashimoto, K; Kuchitsu, K; Salgado, S; Aguirre, J; Quinto, C; Cárdenas, L. (2019). Differential tetraspanin genes expression and subcellular localization during mutualistic interactions in *Phaseolus vulgaris*. *PLoS One*. **14**: e0219765. **FI: 2.776; Q1**.

56) Juárez Hernández, E; Casados Vázquez, L; Brieba, L; Torres Larios, A; Jiménez Sandoval, P; Barboza Corona, J. (2019). The cristal structure of the Chitinase CHIA74 of *Bacillus Thuringiensis* has a multidomain assembly. *Scientific Reports*. **9**:2591. **FI: 4.011; Q1**.

57) Kim, S; Whitley, M; Krzysiak, T; Hinck, C; Taylor, A; Zwieb, C; Byeon, C; Zhou, X; Mendoza, V; López Casillas, F; Furey, W; Hinck, A. (2019). Structural adaptation in its orphan domain engenders betaglycan with an alternate mode of growth factor binding relative to endoglin. *Structure*. **27**: 1427-1442. e4. **FI: 4.576; Q1**.

58) Krol, A; López Huerta, V. G; Corey, T. E. C; Deisseroth, K; Ting, J. T; Feng, G. (2019). Two eARCHT3.0 lines for optogenetic silencing of dopaminergic and serotonergic neurons. *Frontiers in Neural Circuits*. **13**:4. **FI: 3.101; Q1.**

59) Languren, G; Montiel, T; Ramírez Lugo, L; Balderas, I; Sánchez Chávez, G; Sotres Bayón, F; Bermúdez Rattoni, F; Massieu, L. (2019). Recurrent moderate hypoglycemia exacerbates oxidative damage and neuronal death leading to cognitive dysfunction after the hypoglycemic coma. *Journal of Cerebral Blood Flow & Metabolism*. **39**: 808-821. **FI: 6.040; Q1**.

60) Lara González, E; Duhne, M; Ávila Cascajares, F; Cruz, S; Bargas, J. (2019). Comparison of actions between L-DOPA and different dopamine agonists in striatal da-depleted microcircuits in vitro: pre-clinical insights. *Neuroscience***. 410**: 76-96. **FI: 3.244; Q2**.

61) León Aparicio, D; Salvador, C; Aparicio Trejo, O. E; Briones Herrera, A; Pedraza Chaverri, J; Vaca, L; Sampieri, A; Padilla Flores, T; López González, Z; León Contreras, J. C; Hernández Pando, R; Escobar, L. I. (2019). Novel potassium channels in kidney mitochondria: the hyperpolarization-activated and cyclic nucleotide-gated HCN channels. *Int. J. Mol. Sci*. **20**: 4995. **FI: 4.183; Q1**.

62) López, E; Lee Rivera, I; Alvarez Arce, A; López Colomé, A. M. (2019). Thrombin induces ca2+-dependent glutamate release from RPE cells mediated by PLC/PKC and reverse Na+/Ca2+ exchange. *Molecular Vision*. **25**: 546-558. **FI: 2.174; Q2**.

63) López Jácome, E; Franco Cendejas, R; Quezada, H; Morales Espinosa, R; Castillo Juárez, I; González Pedrajo, B; Fernández Presas, A; Tovar García, A; Angarita Zapata, V; Licona Limón, P; Martínez Vázquez, M; García Contreras, R. (2019). The race between drug introduction and appearance of microbial resistance. Current balance and alternative approaches. *Curr. Opin. Pharmacol*. **48**: 48-56. **FI: 5.203; Q1**.

64) López Jácome, L. E; Garza Ramos, G; Hernández Durán, M; Franco Cendejas, R; Loarca, D; Romero Martínez, D; Thi Dong Nguyen, P; Toshinari, M; González Pedrajo, B; Díaz Guerrero, M; Sánchez Reyes, J. L; Díaz Ramírez, D; García Contreras, R. (2019). AiiM lactonase strongly reduces quorum sensing controlled virulence factors in clinical strains of pseudomonas aeruginosa isolated from burned patients. *Front Microbiol*. **10**: 2657. **FI: 4.259; Q1**.

65) López Romero, A. E; Hernández Araiza, I; Torres Quiroz, F; Tovar y Romo, L. B; Islas, L. D; Rosenbaum, T. (2019). TRP ion channels: Proteins with conformational flexibility. *Channels* (Austin) **13**: 207-226. **FI: 2.289; Q1**.

66) Lozano Rosas, M. G; Chávez, E; Velasco Loyden, G; Domínguez López, M; Martínez Pérez, L; Chagoya De Sánchez, V. (2019). Diminished S-adenosylmethionine biosynthesis and its metabolism in a model of hepatocellular carcinoma is recuperated by an adenosine derivative. *Cancer Biol. Ther*. **20**: 81-94. **FI: 2.879; Q1**.

67) Luis, E; Fernández, Y; Alvarado, M; Juárez Santacruz, L; García Nieto, E; Anaya Hernández, A. (2019). Differential expression and immunoreactivity of thyroid hormone transporters MCT8 and OATP1C1 in rat ovary. *Acta Histochemica*. **121**: 151440. **FI: 1.719; Q2**.

68) Madrigal Carrillo, E; Díaz Tufinio, C; Santamaría Suárez, H; Arciniega, M; Torres Larios, A. (2019). A screening platform to monitor RNA processing and protein-RNA interactions in ribonuclease P uncovers a small molecule inhibitor. *Nucleic acids research*. **47**: 6425-6438. **FI: 11.501; Q1**.

69) Martínez Canabal, A; López Oropeza, G; Gaona Gamboa, A; Ballesteros Zebadua, P; Galvan de la Cruz, O; Moreno Jiménez, S; Sotres Bayón, F. (2019). Hippocampal neurogenesis regulates recovery of defensive responses by recruiting threat-and extinction-signalling brain networks. *Scientific Reports*. **9** (2939). **FI: 4.120; Q1**.

70) Martínez Martínez, M. L. A; González Pedrajo, B; Dreyfus, G; Soto Urzúa, L; Martínez Morales, L. J. (2019). Phasin Pha P1 is involved in polyhydroxybutyrate granules morphology and in controlling early biopolymer accumulation in *Azospirillum brasilense* Sp7. *AMB Express*. **9**: 155. **FI: 2.310; Q2**.

71) Jeffri Noelle, M; Camacho Villasana, Y; García Villegas, R; Pérez Martínez, X; Barrientos, A; Fontanesi, F. (2019). The mitoribosome-specific protein mS38 is preferentially required for synthesis of cytochrome c oxidase subunits. *Nucleic Acids Res*. **47**: 5746-5760. **FI: 11.501; Q1**.

72) García Medel, P. L; Baruch Torres, N; Peralta Castro, A; Trasviña Arenas, C. H; Torres Larios, A; Brieba, L. G. (2019). Plant organellar DNA polymerases repair double-stranded breaks by microhomology-mediated end-joining. *Nucleic Acids Research*. **47**: 3028-3044. **FI: 11.501; Q1**.

73) Melo, Z; Castillo, X; Moreno Carranza, B; Ledesma Colunga, M. G; Arnold, E; López Casillas, F; Ruiz Herrera, X; Clapp, C; Martinez de la Escalera, G. (2019). Vasoinhibin suppresses nerve growth factor-induced differentiation and survival of PC12 pheochromocytoma cells. *Neuroendocrinology*. **109**: 152-164. **FI: 5.950; Q1**.

74) Mendez Romero, O; Uribe Carvajal, S; Chiquete Felix, N; Muhlia Almazan, A. (2019). Mitochondrial uncoupling proteins UCP4 and UCP5 from the Pacific white shrimp *Litopenaeus vannamei*. *Journal of Bioenergetics and Biomembranes*. **51**: 103-119. **FI: 2.800; Q2**.

75) Mendoza Martínez, A; Cano Domínguez, N; Aguirre, J. (2019). Yap1 homologs mediate more than the redox regulation of the antioxidant response in filamentous fungi. *Fungal Biology-UK*. **124**: 253-262. **FI: 2.699; Q1**.

76) Morales Calixto, E; Velázquez Flores, M. A; Sánchez Chávez, G; Ruiz Esparza Garrido, R; Salceda, R. (2019). Glycine receptor is differentially expressed in the rat retina at early stages of streptozotocin-induced diabetes. *Neurosci. Lett*. **712**: 134506. **FI: 2.173; Q3**.

77) Morales Lázaro, S; González Ramírez, R; Rosenbaum, T. (2019). Molecular interplay between the sigma-1 receptor, steroids, and ion channels. *Frontiers in Pharmacology*. **10** (419). **FI: 3.860; Q1**.

78) Morales Lázaro, S. L; Rosenbaum, T. (2019). Cholesterol as a key molecule that regulates TRPV1 channel function. *Adv. Exp. Med. Biol*. **1135**: 105-117. **FI: 6.640; Q2**.

79) Moreno Blas, D; Gorostieta Salas, E; Pommer Alba, A; Muciño Hernández, G; Gerónimo Olvera, C; Maciel Barón, L. A; Konigsberg, M; Massieu, L; Castro Obregon, S. (2019). Cortical neurons develop a senescence-like phenotype promoted by dysfunctional autophagy. *Aging* (Albany NY). **11**: 6175-6198. **FI: 5.440; Q1**.

80) Morf, J; Wingett, S. W; Farabella, I; Cairns, J; Furlan Magaril, M; Jiménez García, L. F; Liu, X; Craig, F. F; Walker, S; Segonds Pichon, A; Andrews, S; Marti Renom, M. A; Fraser, P. (2019). RNA proximity sequencing reveals the spatial organization of the transcriptome in the nucleus. *Nat. Biotechnol*. **37**: 793-802. **FI: 16.910; Q1**.

81) Mueller, P. A; Yang, L; Ubele, M; Mao, G; Brandon, J; Vandra, J; Nichols, T. C; Escalante Alcalde, D; Morris, A. J; Smyth, S. S. (2019). Coronary artery disease risk-associated Plpp3 gene and its product lipid phosphate phosphatase 3 regulate experimental atherosclerosis. *Arterioscler. Thromb. Vasc. Biol*. **39**: 2261-2272. **FI: 4.940; Q1**.

82) Nava Lara, R. A; Aguilera Mendoza, L; Brizuela, C. A; Peña, A; Del Rio, G. (2019). Heterologous machine learning for the identification of antimicrobial activity in human-targeted drugs. *Molecules*. **24**: 1258. **FI: 3.010, Q1**.

83) Noguez, P; Miguel Rubi, J; De Miguel, F. F. (2019).Thermodynamic efficiency of somatic exocytosis of serotonin. *Frontiers in Physiology*. **10**: 1-15. **FI: 3.160; Q2**.

84) Olivas Aguirre, M; Torres López, L; Valle Reyes, J. S; Hernández Cruz, A; Pottosin, I; Dobrovinskaya, O. (2019). Cannabidiol directly targets mitochondria and disturbs calcium homeostasis in acute lymphoblastic leukemia. *Cell Death and Disease*. **10**: 779. **FI: 5.910; Q1**.

85) Osorio Gómez, D; Bermúdez Rattoni, F; Guzmán Ramos, K. (2019). Artificial taste avoidance memory induced by coactivation of NMDA and β-adrenergic receptors in the amygdala. *Behav. Brain Res*. **376**: 112193. **FI: 2.77; Q1**.

86) Osorio Gómez, D; Saldivar Mares, K. S; Perera López, A; McGaugh, J. L; Bermúdez Rattoni, F. (2019). Early memory consolidation window enables drugs induced state-dependent memory. *Neuropharmacology*. **146**: 84-94. **FI: 4.367; Q1**.

87) Pérez Estrada, J. R; Hernández García, D; Leyva Castro, F; Ramos León, J; Cuevas Benítez, O; Díaz Muñoz, M; Castro Obregón, S; Ramírez Solís, R; García, C; Covarrubias, L. (2019). Reduced lifespan of mice lacking catalase correlates with altered lipid metabolism without oxidative damage or premature aging. *Free Radical Biology and Medicine*. **135**: 102-115. **FI: 5.657; Q1**.

88) Pérez González, C; Domenzain, C; Poggio, S; González Halphen, D; Dreyfus, G; Camarena, L. (2019). Characterization of FlgP, an essential protein form flagellar assembly in *Rhodobacter sphaeroides. Journal of Bacteriology*. **201**: 1-16. **FI: 3.130; Q1**.

89) Piatkevich, K. D; Bensussen, S; Tseng, H; Shroff, S; Lopez Huerta, V. G; Park, D; Jung, E; Shemesh, O; Straub, C; Gritton, H; Romano, M; Costa, E; Sabatini, B; Fu, Z; Boyden, E; Han, X. (2019). Population imaging of neural activity in awake behaving mice. *Nature*. **574**: 413-417. **FI: 24.360; Q1**.

90) Polo Castillo, L. E; Villavicencio, M; Ramírez Lugo, L; Illescas Huerta, E; Gil Moreno, M; Ruiz Huerta, L; Gutiérrez, R; Sotres Bayón, F; Caballero Ruiz, A. (2019). Reimplantable microdrive for long-term chronic extracellular recordings in freely moving rats. *Frontiers in Neuroscience*. **13**: 128. **FI: 3.810; Q1**.

91) Rivero Segura, N. A; Coronado Mares, Ma. I; Rincón Heredia, R; Pérez Torres, I; Montiel, T; Pavón, N; Cabrera Reyes, E. A; Massieu, L; Cerbón, M. (2019). Prolactin prevents miyochondrial dysfunction induced by glutamate excitotoxicity in hippocampal neurons. *Neurosciences Letters*. **701**: 58-64. **FI: 2.274; Q1**.

92) Rodríguez Bolaños, M; Pérez Montfort, R. (2019). Medical and veterinary importance of the moonlighting functions of triosephosphate isomerase. *Current Protein and Peptide Science*. **20**: 304-315. **FI: 1.470; Q2**.

93) Roig Puiggros, S; Vigouroux, R. J; Beckman, D; Bocai, N. I; Chiou, B; Davimes, J; Gomez, G; Grassi, S; Hoque, A; Karikari, T. K; Kiffer, F; Lopez, M; Lunghi, G; Mazengenya, P; Meier, S; Olguín Albuerne, M; Oliveira, M. M; Paraíso Luna, J; Pradhan, J; Radiske, A; Ramos Hryb, A. B; Ribeiro, M. C; Schellino, R; Selles, M. C; Singh, S; Theotokis, P; Chédotal, A. (2019). Construction and reconstruction of brain circuits: normal and pathological axon guidance. *J. Neurochem*. **153**: 10-32. **FI: 4.830; Q1**.

94) Rossi Pool, R; Romo, R. (2019). Low dimensionality, high robustness in neural population dynamics. *Neuron*. **103**: 177-179. **FI: 14.403; Q1**.

95) Rossi Pool, R; Zizumbo, J; Alvarez, M; Vergara, J; Zainos, A; Romo, R. (2019). Temporal signals underlying a cognitive process in the dorsal premotor cortex. *Proc. Natl. Acad. Sci. USA*. **116**: 7523-7532. **FI: 9.350; Q1**.

96) Rubalcava Gracia, D; García Rincón, J; Pérez Montfort, R; Hamel, P. P; González Halphen, D. (2019). Key within-membrane residues and precursor dosage impact the allotopic expression of yeast subunit II of cytochrome c oxidase. *Mol. Biol Cell*. **30**: 2358-2366. **FI: 3.905; Q1**.

97) Saavedra Montañez, M; Vaca, L; Ramírez Mendoza, H; Gaitán Peredo, C; Bautista Martínez, R; Segura Velázquez, R; Cervantes Torres, J; Sánchez Betancourt, J. I. (2019). Identification and genomic characterization of influenza viruses with different origin in Mexican pigs. *Transboundary and Emerging Diseases*. **66**: 186-194. **FI: 3.554; Q1**.

98) Saldaña Meyer, R; Rodriguez Hernaez, J; Escobar, T; Nishana, M; Jacome López, K; Nora, E. P; Bruneau, B. G; Tsirigos, A; Furlan Magaril, M; Skok, J; Reinberg, D. (2019). RNA interactions are essential for CTCF-mediated genome organization. *Mol. Cell*. **76**: 412-422.e5. **FI: 14.548; Q1**.

99) Sánchez Sandoval, A. L; Gomora, J. C. (2019). Contribution of voltaje-gated sodium cannel beta-subunits to cervical cancer cells metastatic behavior. *Cancer Cell International*. **19**: 1-13. **FI: 3.630; Q2**.

100) Serratos, I. N; López Macay, A; Castellanos, P; Córdoba Herrera, J. G; Pérez Montfort, R; Cabrera, N; Arechavaleta Velasco, F; Domínguez López, P; Santamaría, A. (2019). Co-localization of the receptor for advanced glycation end products (RAGE) with S100 calcium-binding protein B (S100B) in human umbilical vein endothelial. *Journal of the Mexican Chemical Society*. **63**: 25-32. **FI: 0.490; Q3**.

101) Sharma, M; Ramírez Jarquín, U. N; Rivera, O; Kazantzis, M; Eshraghi, M; Shahani, N; Sharma, V; Tapia, R; Subramaniam, S. (2019). Rhes, a striatal-enriched protein, promotes mitophagy via nix. *Proc. Natl. Acad. Sci. USA*. **116**: 23760-23771. **FI: 9.350; Q1**.

102) Soto Aceves, M. P; Cocotl Yañez, M; Merino, E; Castillo Juárez, I; Cortés López, H; González Pedrajo, B; Díaz Guerrero, M; Servín González, L; Soberón Chávez, G. (2019). Inactivation of the quorum-sensing transcriptional regulators LasR OR RhlR does not suppress the expression of virulence factors and the virulence of pseudomonas aeruginosa PAO1. *Microbiology* (Reading, England). **165**: 425-432. **FI: 0.990; Q2**.

103) Tapia Vieyra, J. V; Mas Oliva, J. (2019). Descubrimiento de la proteína reguladora de apoptosis 2 como determinante en la muerte de células tumorales. *Gac. Med. Mex*. **155**: 546-553. **FI: 0.290; Q4**.

104) Tapia, D; Suárez, P; Arias García, M. A; Garcia Vilchis, B; Serrano Reyes, M; Bargas, J; Galarraga, E. (2019). Localization of chloride co-transporters in striatal neurons. *Neuroreport*. **30**: 457-462. **FI: 1.200**.

105) Tauste Campo, A; Vázquez, Y; Alvarez, M; Zainos, A; Rossi Pool, R; Deco, G; Romo, R. (2019). Feed-forward information and zero-lag synchronization in the sensory thalamocortical circuit are modulated during stimulus perception. *Natl. Acad. Sci. USA*. **116**: 7513-7522. **FI: 9.350; Q1**.

106) Tecalco Cruz, A. C; Cortés González, C. C; Cruz Ramos, E; Ramírez Jarquín, J. O; Romero Mandujano, A. K; Sosa Garrocho, M. (2019). Interplay between interferon-stimulated gene 15/ISGYlation and interferon gamma signaling in breast cancer cell. *Cellular Signalling*. **54**: 91-101. **FI: 3.388; Q2**.

107) Tecalco Cruz, A. C; Ramírez Jarquín, J. O; Cruz Ramos, E. (2019). Estrogen receptor alpha and its ubiquitination in breast cancer cells. *Current Drug Targets*. **20**: 690-704. **FI: 2.290; Q2**.

108) Torres López, L; Maycotte, P; Liñán Rico, A; Liñán Rico, L; Donis Maturano, L; Delgado Enciso, I; Meza Robles, C; Vásquez Jiménez, C; Hernández Cruz, A; Dobrovinskaya, O. (2019). Tamoxifen induces toxicity, causes autophagy, and partially reverses dexamethasone resistance in Jurkat T cells. *Journal of Leukocyte Biology*. **105**: 983-998. **FI: 4.012; Q1**.

109) Trastoy Pena, R; Blasco, L; Ambroa, A; González Pedrajo, B; Fernández García, L; López, M; Bleriot, I; Bou, G; García Contreras, R; Wood, T. K; Tomas, M. (2019). Relationship between quorum sensing and secretion systems. *Frontiers in Microbiology*. **10**: 1100. **FI: 4.190; Q1**.

110) Uribe Alvarez, C; Chiquete Félix, N; Morales García, L; Bohórquez Hernández, A; Delgado Buenrostro, N. L; Vaca, L; Peña, A; Uribe Carvajal, S. (2019). *Wolbachia pipientis* grows in *Saccharomyces cerevisiae* evoking early death of the host and deregulation of mitochondrial metabolism. *MicrobiologyOpen*. **8**: e00675. **FI: 2.710; Q2**.

111) Valencia Sánchez, S; Nava Castro, K. E; Palacios Arreola, M. I; Prospéro García, O; Morales Montor, J; Drucker Colín, R. (2019). Chronic exercise modulates the cellular immunity and its cannabinoid receptors expression. *PLoS ONE*. **14**: e0220542. **FI: 2.870; Q1**.

112) Vargas Romero, F; González Barrios, R; Guerra Calderas, L; Escobedo Avila, I; Cortes Pérez, D; López Ornelas, A; Rocha, L; Soto Reyes, E; Velasco, I. (2019). Histamine modulates midbrain dopamine neuron differentiation though the regulation of epigenetic marks. *Frontiers in Cellular Neurociences*. **13**: 215. **FI: 3.910**.

113) Villalobos García, D; Hernández Muñoz, R. (2019). Lactate-stimulated ethanol oxidation: Revisiting an old hypothesis. *Biochemical Pharmacology*. **164**: 283-288. **FI: 4.825; Q1**.

114) Villegas Comonfort, S; Guzmán Silva, A; Romero Ávila, M. T; Takei, Y; Tsujimoto, G; Hirasawa, A; García Sáinz, J. A. (2019). Receptor tyrosyne kinase activation induced free fatty acid 4 receptor phosphorylation, beta-arrestin interaction, and internalization. *European Journal of Pharmacology*. **855**: 267-275. **FI: 3.17; Q1**.

115) Zarate Romero, A; Stojanoff, V; Cohen, A. E; Hansberg, W; Rudiño Piñera, E. (2019). X-ray driven reductionof Cpd I of Catalase-3 from N. *crassa* reveals differential sensitivity of actives sites and formation of ferrous state. *Archives of Biochemistry and Biophysics*. **666**: 107-115. **FI: 3.559; Q1**.

116) Zepeda, N; Copitin, N; Chávez, J. L; García, F; Jaimes Miranda, F; Rincón Heredia, R; Paredes, R; Solano, S; Fernández, A. M; Molinari, J. L. (2019). Hippocampal sclerosis induced in mice by a *Taenia crassiceps* metacestode factor. *J. Helminthol*. **93**: 690-696. **FI: 1.300; Q2**.

117) Zepeda Cervantes, J; Cruz Reséndiz, A; Sampieri, A; Carreón Nápoles, R; Sánchez Betancourt, J. I; Vaca, L. (2019). Incorporation of ORF2 from porcine circovirus type 2 (PCV2) into genetically encoded nanoparticles as a novel vaccine using a self-aggregating peptide. *Vaccine*. **37**: 1928-1937. **FI: 3.269; Q1**.

Factor de Impacto promedio: 5.02[1]
5.06[2]

1- Promedio de las 117 publicaciones totales.
2- Promedio de 116 publicaciones que tienen factor de Impacto.

Artículos en Prensa

1) Alatriste León, H; Verma Rodríguez, A. K; Ramírez Jarquín, J. O; Tecuapetla, F. (2019). Perturbations in the activity of cholinergic interneurons in the dorsomedial striatum impairs the update of actions to an Instrumental contingency change. Neuroscience. doi: 10.1016/j.neuroscience.2019.11.023.

2) Ávila Rodríguez, D; Segura Villalobos, D. L; Ibarra Sánchez, A; González Espinosa, C; Macías Silva, M. (2019). TGF-beta y células cebadas: reguladores del desarrollo del tumor. TIP Revista Especializada en Ciencias Químico-Biológicas. doi.org/10.22201/fesz.23958723e.2020.0.200.

3) Bernal Conde, L. D; Ramos Acevedo, R; Reyes Hernández, M. A; Balbuena Olvera, A; Morales Moreno, I. D; Argüero Sánchez, R; Schüle, B; Guerra Crespo, M. (2019). Alpha-synuclein physiology and pathology: A perspective on cellular structures and organelles. Frontiers in Neurosciences. doi.org/10.3389/fnins.2019.01399.

4) Bielecki, P; Riesenfeld, S. J; Kowalczyk, M. S; Amezcua Vesely, M. C; Kroehling, L; Yaghoubi, P; Dionne, D; Jarret, A; Steach, H. R; McGee, H. M; Porter, C. B. M; Licona Limón, P; Bailis, W; Jackson, R. P; Gagliani, N; Locksley, R. M; Regev, A; Flavell, R. A. (2019). Skin inflammation driven by differentiation of quiescent tissue-resident ILCs into a spectrum of pathogenic effectors. BioRxiv. doi: https://doi.org/10.1101/461228.

5) Hernández Mendoza, G. A; Aguirre Olivas, D; González Gutiérrrez, M; Leal, H. J; Qureshi, N; Treviño Palacios, C. G; Peón, J; De Miguel, F. F. (2019). Fluorescence of serotonin in the visible spectrum upon multiphotonic photoconversion. Biomedical Optics Express. doi.org/10.1364/BOE.380412.

6) Ladrón de Guevara, E; Domínguez, L; Rangel Yescas, G. E; Fernández Velasco, D. A; Torres Larios, A; Rosenbaum, T; Islas, L. D. (2019). The Contribution of the Ankyrin Repeat Domain of TRPV1 as a Thermal Module. Biophysical Journal. doi.org/10.1016/j.bpj.2019.10.041.

7) Melchor, J; Morán, I; Figueroa, T; Lemus, L. (2019). Perceptual invariance of words and other learned sounds in non-human primates. BioRxiv. doi.org/10.1101/805218.

8) Milham, M; Petkov, C; ... Rossi-Pool, R; .... Zhou, Y. (2020). Accelerating the evolution of nonhuman primate neuroimaging. Neuron. doi.org/10.1016/j.neuron.2019.12.023.

9) Pérez de la Mora, M; Hernández Mondragón, C; Crespo Ramírez, M; Rejón Orantes, J; Borroto Escuela, D; Fuxe, K. (2019). Conventional and novel Pharmacological approaches to treat dopamine-related disorders: Focus on Parkinson´s disease and schizophrenia. Neuroscience. doi.org/10.1016/j.neuroscience.2019.07.026

10) Rebolledo Solleiro, D; Solleiro Villavicencio, H; Velasco, M; Roldán Roldán, G. (2019). Obesidad, síndrome metabólico y percepción olfativa. Rev Neurol. doi:10.33588/rn.XXXX.2019204.

11) Ríos López, D. G; Aranda López, Y; Sosa Garrocho, M; Macías Silva, M. (2019). La plasticidad del hepatocito y su relevancia en la fisiología hepática. TIP Revista Especializada en Ciencias Químico-Biológicas. doi.org/10.22201/fesz.23958723e.2020.0.225.

12) Romo, R; Rossi Pool, R. (2020). Toward a conscious model of consciousness. Cognitive Neuropsychology. doi: 10.1080/02643294.2020.1728241.

13) Romo, R; Rossi Pool, R. (2020). Turning Touch into Perception. Neuron. doi.org/10.1016/j.neuron.2019.11.033.

14) Santillán Doherty, P; Grether González, P; Medina Arellano, M. J; Chan, S; Tapia Ibargüengoitia, R; Brena Sesma, I; Fuente, R. C; Linares Salgado, J; Mendoza Cárdenas, H; Muñoz Fernández, L; Schiavon, R. (2020). Reflexiones sobre la ingeniería genética a propósito del nacimiento de gemelas sometidas a edición génica Gac Med Mex. 2020;156(1):53-59. doi: 10.24875/GMM.19005182.

Artículos de Divulgación

1) Lemus, L. (2019). ¡Por las barbas de Platón! Explicando la biología de las emociones.Oikos. http://web.ecologia.unam.mx/oikos3.0/index.php/articulos/biologia-de-las-emociones.

2) Massieu, L. (2019). La glucosa, básica para el funcionamiento neurona. Gaceta UNAM, 6 de junio, 2019.

3) Massieu, L. (2019). Hipoglucemia y muerte neuronal. El Universal, 24 de mayo de 2019.

4) Pérez de la Mora, M. (2019). Desde el Comité Editorial. Revista de la Academia Mexicana de Ciencias**.** enero-marzo 2019, volumen 70, número 1.

5) Pérez de la Mora, M. (2019). Desde el Comité Editorial. Revista de la Academia Mexicana de Ciencias**.** julio-septiembre 2019, volumen 70.

6) Pérez de la Mora, M. (2019). La Ciencia mexicana, ¿requiescat in pace**?** Revista de la Academia Mexicana de Ciencias**.** abril-junio 2019, volumen 70m número 2.

7) Pérez de la Mora, M. (2019). Desde el Comité Editorial. Revista de la Academia Mexicana de Ciencias**.** octubre-diciembre 2019, volumen 69, número 4.

8) Salinas, L. S; Navarro, R. E. (2019). Sydney Brenner: el hombre visionario que nos hizo mirar al Caenorhabditis elegans. Revista de Educación Bioquímica (REB), 38(2):60-61.

9) Tapia, R. (2019). La ciencia no es compatible con la religión. *Nexos*, junio de 2019, p. 26.

Capítulos en Libros

1) Hiriart Urdanivia, M; Díaz García, C. M. (2020). Fisiología Celular. en: Fisiología Humana, 4ª Ed. en Tresguerras J.A.F. Ed., Cap. 2.

2) Hiriart Urdanivia, M; Díaz García, C. M. (2020). Principios generales de fisiología endocrina. en: Fisiología eLibro Editores, David E. García, Sofía Xaviera García González, Daniel Guzmán Toledo, LCC QP34.5 (libro electrónico) DDC 612—dc23, Universidad Nacional Autónoma de México. LIBRUNAM 2009386 (libro electrónico) ISBN 9786073022200.

3) Ortiz Huidobro, R. I; Sabido Barrera, J. I; Sánchez Zamora, Y; Samario Román, J. S; Laqué Velázquez, C. L; Velasco, M; Hiriart Urdanivia, M. (2019). Resistencia a la insulina en el síndrome metabólico. en: Manual práctico para la detección y el tratamiento integral del síndrome metabólico. 2ª Ed. A González Chávez, R. López Espinosa y JA Mesa Pérez, Cap. 6, p.p. 67-81, Editorial Alfil, ISBN 978-607-741-244-1.

4) Rodríguez Aguilera, J. R; Pérez Cabeza de Vaca, R; Guerrero Celis, N; Velasco Loyden, G; Domínguez López, M; Recillas Targa, F; Chagoya de Sánchez, V. (2019). Molecular and cellular aspects of cirrhosis and how an adenosine derivative could reverse fibrosis. In: Liver Cirrhosis - Debates and CurrentChallenges, IntechOpen, 1-22.

5) Rossi Pool, R; Vergara, J; Romo, R. (2020). Constructing Perceptual Decision-Making across Cortex. In: The Cognitive Neuroscience 6ta Edición. (Ed. D. Poeppel, G. Mangun y M. Gazzaniga). The MIT Press. pp. 413-427.

6) Velasco, M; Larqué, C. A; Hiriart Urdanivia, M. (2019). Páncreas. en: Fisiología eLibro (Ed. Dr. David Garcia). Facultad de Medicina UNAM. ISNB: 978-607-30-2220-0.

Capítulos en Prensa

1) Galarraga, E; Bargas, J. (2019). El potencial de membrana y el Potencial de Acción. Ch-6 in: Fisiología Humana 5Th. Tresguerras JAF McGraw Hill Interamericana. México City p. p. 63-73.

2) Martin, A. R; Brown, D. A; Diamond, M; Cattaneo, A; De Miguel, F. F. (2019). Extrasynaptic communication. in: From Neuron to Brain. 6 Ed. Oxford University Press. Oxford, UK. Reino Unido.

3) Martin, A. R; Brown, D. A; Diamond, M; Cattaneo, A; De Miguel, F. F. (2019). Glia. in: From Neuron to Brain. 6 Ed. Oxford University Press. Oxford, UK. Reino Unido.

4) Martin, A. R; Brown, D. A; Diamond, M; Cattaneo, A; De Miguel, F. F. (2019). Walking, Flying and Swimming. Cellular Mechanisms of sensory-motor behavior in invertebrates. in: From Neuron to Brain. 6 Ed. Oxford University Press. Oxford, UK. Reino Unido.

5) Martin, A. R; Brown, D. A; Diamond, M; Cattaneo, A; De Miguel, F. F. (2019). Principles of signalling, in: From Neuron to Brain. 6 Ed. Oxford University Press. Oxford, UK. Reino Unido.

6) Martin, A. R; Brown, D. A; Diamond, M; Cattaneo, A; De Miguel, F. F. (2019). Retina. in: From Neuron to Brain. 6 Ed. Oxford University Press. Oxford, UK. Reino Unido.

7) Martin, A. R; Brown, D. A; Diamond, M; Cattaneo, A; De Miguel, F. F. (2019). Signalling in the visual system. in: From Neuron to Brain. 6 Ed. Oxford University Press. Oxford, UK. Reino Unido.

8) Martin, A. R; Brown, D. A; Diamond, M; Cattaneo, A; De Miguel, F. F. (2019). Synaptic release of transmitters. in: From Neuron to Brain. 6 Ed. Oxford University Press. Oxford, UK. Reino Unido.

Libros Publicados y Reimpresiones

1) Martin, A. R; Brown, D. A; Diamond, M; Cattaneo, A; De Miguel, F. F. (2019). From Neuron to Brain. 6 Ed. Sinauer Associates, Sunderland, MA. Oxford University Press.

Revistas Nacionales

1) Guzmán Flores, J. E; Georgellis, D; Álvarez, A. F. (2019). Microdominios membranales bacterianos semejantes a balsas lipídicas. TIP Revista Especializada en Ciencias Químico-Biológicas. 22: 1-10. doi: 10.22201/fesz. 23958723.2019.0.163.

2) Hiriart Urdanivia, M; Sánchez Soto, C; Velasco, M; Sabido Barrera, J; Ortiz Huidobro, R. (2019). El receptor soluble de insulina y el síndrome metabólico. Gac. Med. Mex. 155(5): 541-545. doi: 10.24875/GMM.19005185.

3) Morán, J; Olguín Albuerne, M. (2019). Role of reactive oxygen species in the development of central nervous system. Mens. Bioquim. 43: 50-60.

4) Rivera, A; Villalva, S; Vázquez, I; Bárcenas, O; Pinzón, C; Moran, J; Arriaga Pizano, L; Guzmán, A; Silva, E; Gutiérrez Pabello, J. (2019). Mycobacterium tuberculosis and mycobacterium bovis derived proteins induce caspase-independent apoptosis in bovine macrophages. Vet México. 6(1): 1-12. doi: 10.22201/fmvz.24486760e.2019.1.560.

5) Tapia Vieyra, J; Mas Oliva, J. (2019). Descubrimiento de la proteína reguladora de apoptosis 2 como determinante en la muerte de células tumorales. Gac. Med. Mex. 155(5): 546-553. doi:10.24875/GMM.19005186.

6) Teran Melo, J. L; Rodríguez, C; Álvarez, A. F; Georgellis, D. (2019). Mecanismos de autofosforilación y transfosforilación en sistemas de dos componentes bacterianos. TIP Revista Especializada en Ciencias Químico-Biológicas. 22: 1-11. doi:10.22201/fesz. 23958723e.2019.0.162.

Patente Nacional concluída

1) Hernández Muñoz, R. Composición farmacéutica de adenosina y antiretrovirales para el tratamiento de daño hepático. 363153. Oxford, UK. Reino Unido.

Convenios con otras Instituciones

Convenios Externos

NO.	FIGURA CONTRACTUAL	AÑO	NO. DE REGISTRO	INVESTIGADORES RESPONSABLES	OBJETO	DEPENDENCIAS INVOLUCRADAS	FECHA DE FIRMA	VIGENCIA	FECHA DE VENCIMIENTO	MONTO
1	Acuerdo.	2015	41145-855-13-IV-15.	Dr. Miguel Angel Pérez de la Mora.	Entender el papel de los complejos de heteroreceptores OXTR-D2R y OXTR-alpha2AR en el miedo y la ansiedad.	Instituto Karolinska.	5 de junio de 2015.	7 Meses.	31 de diciembre de 2017. Prorr. 31 enero 2019.	330,000.00 CORONAS SUECAS
2	Convenio Específico de Colaboración.	2017	48244-1068-24-IV-17.	Dr. Julio Eduardo R. Morán Andrade.	Establecer el marco de colaboración entre la INC-UAB y el IFC-UNAM en los aspectos de investigación académicos. 1) Promover las relaciones de investigación y profesional entre la INC-UAB y el IFC-UNAM, 2) Desarrollar actividades de investigación en materias de interés común para estos centros de investigación, 3) Fomentar el intercambio de profesores y de alumnos en el marco de estas actividades de investigación de interés común, 4) Fomentar el debate e intercambio de experiencias sobre todos aquellos temas que pueda beneficiar a estos centros de investigación.	Universidad Autónoma de Barcelona.	25 de febrero de 2019.	4 años.	25 de febrero de 2023.	N/A.
3	Convenio de Colaboración.	2017	48183-999-18-IV-17.	Dr. Arturo Hernández Cruz.	Establecer la colaboración con la UNAM, con el fin de promover y desarrollar programas de superación académica, formación y capacitación profesional, desarrollo de proyectos de investigación, asesoría técnica y/o divulgación del conocimiento en todas aquellas áreas de coincidencia, acciones de interés y beneficios mutuos que refuercen la vinculación en un espacio común entre estas instituciones de origen que están en la oferta de asignaturas por el estudiante.	Tecnológico de Estudios Superiores de Huixquilucan.	11 de agosto de 2017.	3 años.	11 de agosto de 2020.	N/A.
4	Acuerdo de Confidencialidad.	2017	DGAJ-DPI-220617-330.	Dras. María de Lourdes Massieu.	Establecer los términos y condiciones que regirán el intercambio de información confidencial efectuado por las partes con motivo de la evaluación de una posible colaboración entre ellas para "Sintetizar y purificar péptidos neuroprotectores desarrollados por la Dra. Díaz-Guerra con el fin de realizar estudios conjuntos sobre eficacia neuroprotectora en procesos de hipoglucemia y otras situaciones asociadas con la excitotoxicidad".	Agencia Estatal del Consejo de Investigaciones Científicas y el Centro de Investigaciones de Estudios Avanzados del Instituto Politécnico Nacional.	16 de octubre de 2017.	5 años.	15 de octubre de 2022.	N/A.
5	Convenio de Colaboración.	2017	48955-1771-25-VII-17.	Dr. Ivan Velasco Velázquez.	Estudios de diferenciación neuronal de células troncales humanas y se producirán células troncales pluripotenciales inducidas, con biopsias de pacientes con enfermedad de parkinson, mediante donación por consentimiento informado.	Instituto Nacional de Neurología y Neurocirugía.	30 de noviembre de 2017.	3 años.	29 de noviembre de 2020.	N/A.

NO.	FIGURA CONTRACTUAL	AÑO	NO. DE REGISTRO	INVESTIGADORES RESPONSABLES	OBJETO	DEPENDENCIAS INVOLUCRADAS	FECHA DE FIRMA	VIGENCIA	FECHA DE VENCIMIENTO	MONTO
6	Convenio Específico de Colaboración.	2018	54204-3264-29-X-18	Dr. Carlos Leonardo Peraza Reyes.	Crosstalk between peroxisomes endoplasmic reticulum and endosoes during polar growth and development in fung	Centro de Investigación Científica y Educación Superior de Ensenada	01 de octubre de 2018.	2 años 5 meses .	01 de marzo de 2021.	$820,300.00
7	Acuerdo de Colaboración.	2017	49754-2570-04-X-17.	Dr. Federico Bermúdez Rattoni.	Obeteen-Neurocognitive impact of juvenile obesity: experimental and clinical approaches	UAM-Lerma, CINVESTAV.	24 de julio de 2017.	2 años 6 meses.	02 de enero de 2020.	N/A
8	Convenio de Colaboración	2017	47682-508-24-II-17	Dra. Rosa Navarro González	Sistema Nacional de Evaluación Toxicológica de Nanomateriales "SINANOTOX"	UNAM,CINVESTAV,UASLP,UG,CIATEJ,ITESM	10 de junio de 2017	10 años	10 de junio de 2027	N/A
9	Convenio Modificatorio al Acuerdo de Colaboración.	2018	49754-2570-4-X-17/1	Dr. Federico Bermúdez Rattoni.	Obeteen-Neurocognitive impact of juvenile obesity: experimental and clinical approaches	UAM-Lerma, CINVESTAV.	23 de julio de 2018.	2 años.	14 de julio de 2020.	N/A
10	Formato de carta de aceptación	2019	55142-643-24-IV-19	Dr. Francisco Fernández de Miguel.	Taller internacional de fotonica titulado: Enlightening the brain	The society for neurosciences	30 de abril de 2019	11 meses	31 de marzo de 2020	50,000.00 USD
11	Formato de Agreement for research HFSP Grants	2019	55587-1088-24-VII-19	Dr. Francisco Fernández de Miguel.	Molecular approaches to study individually identified mechanosensory neurons of the leech	Human frontier science program organization	7 de mayo de 2019	3 años.	7 de mayo de 2022	450,00.00 USD
12	Convenio de Desarrollo Tecnológico.	2019	DGAJ-DPI-170119-567	Dr. Luis Alfonso Vaca Domínguez.	Polihedrina modificada, polihedras y productos biotecnológicos obtenidos a partir de la misma.	GRIMANN, S.A. de C.V.	23 de agosto de 2019	11 meses	23 de julio de 2020	$464,000.00
13	colaborative grants program	2019	N/A	Dr. Iván Velasco Velázquez	Liberación de factores quimioatrayentes para axones dopaminergicos humanos por nanoesferas vacias de dioxido de titanio	UC-MEXUS-CONACYT 2019	01 de julio de 2019	17 meses	31 de diciembre de 2020	25,000.00USD
14	Convenio de Colaboración.	2019	56023-1524-2-x-19	Dr. Arturo Hernández Cruz.	Laboratorio Nacional de Canalopatías (LANCA)Consolidación III.	CINVESTAV-Monterrey	09 de septiembre de 2019	2 meses.	30 de noviembre de 2019	$100,000.00

Convenios CONACyT

NO.	FIGURA CONTRACTUAL	NO. DE REGISTRO	INVESTIGADORES RESPONSABLES	OBJETO	NO. DE CONVENIO CONACYT	DEPENDENCIAS INVOLUCRADAS	FECHA DE FIRMA	VIGENCIA	FECHA DE VENCIMIENTO
1	CONVENIO CONACYT	41305-1073-06-V-15	DRA. ROSA ESTELA NAVARRO GONZALEZ	MECANISMOS DE REGULACION DE LA RESPUESTA AL ESTRES DE LAS CELULAS GERMINALES DEL NEMATODO C ELEGANS	220987	CONACYT	24/04/2015	36 MESES	24/04/2018 01/01/2019
2	CONVENIO CONACYT	41581-1291-29-V-15	DR. JESUS AGUIRRE LINARES	LAS ESPECIES DE OXIGENO REACTIVAS, LA RESPUESTA ANTIOXIDANTE Y LA DIFERENCIACION CELULAR EN LOS HONGOS	238492	CONACYT	15/05/2015	36 MESES	15/05/2018 14/05/2019
3	CONVENIO CONACYT	41607-1317-02-VI-15	DR. DIEGO GONZALEZ HALPHEN	ESTUDIOS SOBRE LA ESTRUCTURA Y BIOGENESIS DE LAS SUBUNIDADES DE LA ATP SINTASA MITOCONDRIAL DEL ALGA CLOROFICEA INCOLORIA POLYTOMELLA SP.	239219	CONACYT	15/05/2015	36 MESES	15/05/2018 14/05/2019
4	CONVENIO CONACYT	41855-1585-22-VI-15	DR. RANULFO ROMO TRUJILLO	CORRELATOS NEURONALES ASOCIADOS CON LA INTEGRACION DE ESTIMULOS VIBROTACTILES Y ACUSTICOS EN EL LOBULO FRONTAL DURANTE LA TOMA DE DECISIONES	240892	CONACYT	05/06/2015	36 MESES	05/06/2018 17/07/2019
5	CONVENIO CONACYT	42118-1828-03-VIII-15	DR. GEORGES DREYFUS CORTES	ESTUDIO SOBRE LA REGULACION DE LA EXPRESION DEL SISTEMA FLEGELAR 2 EN RHODOBACTER SPHAEROIDES	235996	CONACYT	13/07/2015	36 MESES	13/07/2018 24/02/2019
6	CONVENIO CONACYT	44109-0379-03-II-16	DR. ANTONIO CALVIN PEÑA DIAZ	EFECTOS DE AGENTES CATIONICOS, SAL Y PH SOBRE SACCHAROMYCES CEREVISIAE Y DEBARYOMYCES HANSENII CULTIVO DE METANOLISMO Y BIOENERGETICA DE WOLBACHIA PIPIENTIS	238497	CONACYT	24/11/2015	36 MESES	24/11/2018 23/09/2019
7	CONVENIO CONACYT	44832-1102-05-V-16	DR. GABRIEL DEL RIO GUERRA	MULTIFUNCIONALIDDAD Y PROPIEDADES EMERGENTES EN PROTEINAS	219	CONACYT	05/04/2016	24 MESES	13/05/2019
8	CONVENIO CONACYT	44833-1103-05-V-16	DR. FELIX RECILLAS TARCA	LA ORGANIZACIÓN TRIDIMENSIONAL DEL GENOMA EN LA REGULACION DE LA EXPRESION GENICA	290	CONACYT	05/04/2016	24 MESES	13/05/2019
9	CONVENIO CONACYT	44834-1104-V-16	DR. JESUS AGUIRRE LINARES	LA DINAMICA Y FUNCION DE LAS MITOCONDRIAS Y EL CITOESQUELETO COMO INTEGRADORES DE LA SEÑALIZACION POR ESPECIES DE OXIGENO REACTIVAS	319	CONACYT	07/04/2016	24 MESES	13/05/2019
10	CONVENIO CONACYT	47469-0305-07-II-17	DR. JESUS ADOLFO GARCIA SAINZ	REGULACION DE LA FUNCION DE RECEPTORES ACOPLADOS A PROTEINAS G	253156	CONACYT	18/07/2016	36 MESES	15/08/2019
11	CONVENIO CONACYT	45776-2046-25-VIII-16	DR. FERNANDO LOPEZ CASILLAS	ANALISIS GENETICO REVERSO (CRISPR/CAS9) DE LA FUNCION DEL INTAGLIO/ANO EN EL DESARROLLO EMBRIONARIO DEL PEZ CEBRA	254046	CONACYT	18/07/2016	36 MESES	15/08/2019 15/07/2020
12	CONVENIO CONACYT	45769-2069-26-VIII-16	DRA. PAULA LUCINA LIMON	MECANISMOS MOLECULARES EN EL CONTROL DE LA DIFERENCIACION DE LOS LINAJES LINFOIDES: REGULACION POR LA CITOCINA TGF-B Y LA CINASA PKA	255267	CONACYT	18/07/2016	36 MESES	15/08/2019
13	CONVENIO CONACYT	45626-1896-15-VIII-16	DR. JAIME MAS OLIVA	ESTUDIO DE LA CORRELACION ESTRUCTURA/FUNCION DE CEPTI COMO UNA NUEVA PROTEINA DE UNION A LIPOPOLISACARIDOS BACTERIANOS	255778	CONACYT	18/07/2016	36 MESES	15/08/2019

NO.	FIGURA CONTRACTUAL	NO. DE REGISTRO	INVESTIGADORES RESPONSABLES	OBJETO	NO. DE CONVENIO CONACYT	DEPENDENCIAS INVOLUCRADAS	FECHA DE FIRMA	VIGENCIA	FECHA DE VENCIMIENTO
14	CONVENIO CONACYT	45766-2036-24-VIII-16	DR. ALFREDO TORRES LARIOS	ESTUDIOS ESTRUCTURALES SOBRE COMPLEJOS RIBONUCLEOPROTEICOS	253323	CONACYT	18/07/2016	36 MESES	15/08/2019
15	CONVENIO CONACYT	46119-2389-23-IX-16	DR. RUY ENRIQUE PEREZ MONFORT	ESTUDIOS EN ENFERMEDADES HUMANAS DE LA TRIOSAFOSFATO ISOMERASA	254994	CONACYT	18/07/2016	36 MESES	15/08/2019 15/02/2020
16	CONVENIO CONACYT	45777-2047-25-VIII-16	DR. ROBERTO CORIA ORTEGA	PAPEL DE LAS PROTEINAS G EN LA RESPUESTA AL ESTRES DE RETICULO ENDOPLASMICO EN LEVADURAS	254078	CONACYT	18/07/2016	36 MESES	15/08/2019 15/12/2019
17	CONVENIO CONACYT	45704-1974-18-VIII-16	DRA. MARCIA HIRIART URDANIVIA	ANALISIS DE LOS CAMBIOS QUE EXPERIMENTAN LAS CELULAS BETA PANCREATICAS EN LA RESISTENCIA A LA INSULINA	253222	CONACYT	18/07/2016	36 MESES	15/08/2019
18	CONVENIO CONACYT	45627-1897-15-VIII-16	DRA. YAZMIN RAMIRO CORTES	PLASTICIDAD SINAPTICA Y ESTRUCTURAL EN UN MODELO DE AUTISMO	254878	CONACYT	18/07/2016	36 MESES	15/08/2019
19	CONVENIO CONACYT	45778-2048-25-VIII-16	DR. JAIME IVAN VELASCO VELAZQUEZ	DIFERENCIACION DOPAMINERGICA DE CELULAS TRONCALES: ESTUDIOS DE CRECIMIENTO AXONAL Y SUPERVIVENCIA EN RATAS QUE MODELAN LA ENFERMEDAD DE PARKINSON	256932	CONACYT	18/07/2016	36 MESES	15/08/2019
20	CONVENIO CONACYT	46441-2701-18-X-16	DR. FEDERICO BERMUDEZ RATTONI	ESTUDIO DE LA CONSOLIDACION, EVOCACION Y ACTUALIZACION DE LA MEMORIA: MECANISMOS NEUROBIOLOGICOS Y SUS IMPLICACIONES EN PROCESOS NEUROPATOLOGICOS	250870	CONACYT	15/09/2016	36 MESES	27/10/2019
21	CONVENIO CONACYT	46461-2731-18-X-16	DR. LUIS ALONSO LEMUS SANDOVAL	CODIFICACION NEURONAL DE OBJETOS AUDITIVOS	256767	CONACYT	14/09/2016	36 MESES	27/10/2019
22	CONVENIO CONACYT	46501-2771-21-X-16	DRA. MARIA ELVIRA GALARRAGA PALACIO	CARACTERIZACION FUNCIONAL DE LA VIA TALAMO ESTRIATAL	251144	CONACYT	14/09/2016	36 MESES	17/10/2019 17/01/2020 17/07/2020
23	CONVENIO CONACYT	46460-2730-18-X-16	DR. GABRIEL DEL RIO GUERRA	ESTUDIO DEL MECANISMO DE ACCION DE PEPTIDOS ANTIMICROBIANOS POR AUTOFAGICOS	252316	CONACYT	14/09/2016	36 MESES	17/10/2019 27/04/2020
24	CONVENIO CONACYT	46442-2712-18-X-16	DRA. DIANA MARIA ESCALANTE ALCALDE	LA LIPPS, UNA ENZIMA REGULADORA DE LA ACTIVIDAD DE LIPIDOS BIOACTIVOS, COMO ENZIMA FUNDAMENTAL PARA EL DESARROLLO TEMPRANO DEL SISTEMA NERVIOSO Y LA NEUROGENESIS ADULTA	250813	CONACYT	14/09/2016	36 MESES	27/10/2019
25	CONVENIO CONACYT	48375-2191-25-VIII-17	DR. JAIME IVAN VELASCO VELAZQUEZ	ESTUDIOS DE SECUENCIACION MASIVA Y PROTEOMICA PARA LA IDENTIFICACION DE REGULADORES MOLECULARES DE LA REGENERACION POSTERIOR AL DAÑO EN LA MEDULA ESPINAL DEL AJOLOTE (NEXT GENERATION SEQUENCING AND PROTEOMICS TO IDENTIFY MOLECULAR REGULATORS OF REGENERAT)	280793	CONACYT	14/09/2016	36 MESES	10/10/2019 10/04/2020

NO.	FIGURA CONTRACTUAL	NO. DE REGISTRO	INVESTIGADORES RESPONSABLES	OBJETO	NO. DE CONVENIO CONACYT	DEPENDENCIAS INVOLUCRADAS	FECHA DE FIRMA	VIGENCIA	FECHA DE VENCIMIENTO
26	CONVENIO CONACYT	47399-0215-25-I-17	DRA. SUSANA CASTRO OBREGON	PROBANDO LA HIPOTESIS DE QUE DURANTE EL ENVEJECIMIENTO FISIOLOGICO EMERGEN NICHOS PARA EL DESARROLLO DE ENFERMEDADES CRONICAS	921	CONACYT	01/11/2016	24 MESES	31/10/2018 31/10/2019
27	CONVENIO CONACYT	47715-0531-27-II-17	DR. JAIME IVAN VELASCO VELAZQUEZ	DIFERENCIACION DE CELULAS TRONCALES PLURIPOTENCIALES HUMANAS A NEURONAS DOPAMINERGICAS PARA GENERAR MODELOS CELULARES DE LA ENFERMEDAD DE PARKINSON Y REALIZAR PRE-CLINICOS DE TRANSPLANTE	272835	CONACYT	09/12/2016	36 MESES	07/02/2020 07/08/2020
28	CONVENIO CONACYT	48167-0983-17-IV-17	DR. DIEGO GONZALEZ HALPHEN	HACIA LA CRISTALIZACION DE UNA ATP SINTASA MITOCONDRIAL DIMERICA, EFECTOS DE UN DETERGENTE DE NUEVA GENERACION DERIVADO DEL LAURIL MALTOSIDO	279125	CONACYT	22/03/2017	48 MESES	15/06/2021
29	CONVENIO CONACYT	49729-2545-02-X-17	DR. FATUEL TEQUIAPETLA AGUILAR	OPTOGENCIA: VISUALIZACION Y EVALUACION DE LOS SUBCIRCUITOS DEL CONTROL MOTOR IN VIVO	239	CONACYT	18/09/2017	24 MESES	19/10/2019
30	CONVENIO CONACYT	52242-1302-19-IV-18	DR. VICTOR JULIAN VALDES RODRIGUEZ	PAPEL DE LA EPIGENETICA EN CIRCUITOS NEURONALES INVOLUCADROS EN CONDUCTA DE C. ELEGANS	284867	CONACYT	21/03/2018	36 MESES	21/03/2021
31	CONVENIO CONACYT	52245-1305-19-IV-18	DRA. BERTHA MARIA JOSEFINA GONZALEZ PEDRAJO	REGULACION DE LA SECRECION DE PROTEINAS A TRAVES DEL INYECTISOMA DE ESCHERICHIA COLI ENTEROPATOGENA ESTUDIO DEL RECONOCIMIENTO Y JERARQUIZACION DE SUSTRATOS	284081	CONACYT	21/03/2018	36 MESES	21/03/2021
32	CONVENIO CONACYT	52244-1304-19-IV-18	DRA. XOCHITL PEREZ MARTINEZ	ESTUDIO DE LOS MECANISMOS DE ACOPLAMIENTO ENTRE LA SINTESIS DE PROTEINAS MITOCONDRIAL Y CITOSOLICA	284514	CONACYT	21/03/2018	36 MESES	21/03/2021
33	CONVENIO CONACYT	52243-1303-19-IV-18	DR. JULIO EDUARDO ROQUE MORAN ANDRADE	SEÑALIZACION REDOX EN EL DESARROLLO NEURONAL: PAPEL EN LA MUERTE NEURONAL Y EL CRECIMIENTO AXONAL	285184	CONACYT	21/03/2018	36 MESES	21/03/2021
34	CONVENIO CONACYT	53930-2990-13-IX-18	DR. CARLOS LEONARDO PERAZA REYES	CROSSTALK BETWEEN PEROXISOMES, ENDOPLASMIC RETICULUM AND ENDOSOMES DURING POLAR GROWTH AND DEVELOPMENT	277869	CONACYT	22/03/2018	24 MESES	22/03/2020
35	CONVENIO CONACYT	52583-1643-25-V-18	DR. FRANCISCO XAVIER SOTRES BAYON	PREVINIENDO EL REGRESO DEL MIEDO: CONTRIBUCION DE LA NEUROGENESIS HIPOCAMPAL	2463	CONACYT	09/05/2018	24 MESES	09/05/2020
36	CONVENIO CONACYT	47404-0220-25-I-17	DRA. ANA MARIA LOPEZ COLOME	LA TROMBINA COMO AGENTE INDUCTOR DE GLIOSIS EN LA RETINA	254333	CONACYT	19/10/2016	36 MESES	13/12/2019
37	CONVENIO CONACYT	56147-1648-14-X-19	DR. RICARDO TAPIA IBARGUENGOITIA	MECANISMOS CELULARES DE LA DEGENERACION Y REGENERACION NEURONAL	A1-S-12135	CONACYT	17/09/2019	36 MESES	17/09/2022

NO.	FIGURA CONTRACTUAL	NO. DE REGISTRO	INVESTIGADORES RESPONSABLES	OBJETO	NO. DE CONVENIO CONACYT	DEPENDENCIAS INVOLUCRADAS	FECHA DE FIRMA	VIGENCIA	FECHA DE VENCIMIENTO
38	CONVENIO CONACYT	56135-1636-10-X-19	DR. LUIS BERNARDO TOVAR Y ROMO	REGULACION TROFICA DE LA VIABILIDAD NEURONAL MECANISMOS ENDOGENOS DE RECUPERACION DESPUES DEL INFARTO CEREBRAL ISQUEMICO	A1-S-13219	CONACYT	13/09/2019	36 MESES	13/09/2022
39	CONVENIO CONACYT	56115-1616-10-X-19	DRA. MARIA DE LOURDES MASSIEU TRIGO	PERDIDA DE LA PROTEOSTASIS POR LA PRIVACION Y REINTRODUCCION DE GLUCOSA EN NEURONAS, SU PAPEL EN LA MUERTE NEURONAL Y SU POSIBLE RESTABLECIMIENTO POR ACCION DEL BETA-HIDROXIBUTIRATO	A1-S-11357	CONACYT	17/09/2019	36 MESES	17/09/2022
40	CONVENIO CONACYT	56143-1644-11-X-19	DRA. MAGDALENA GUERRA CRESPO	DESARROLLO DE UNA NUEVA ESTRATEGIA DE DIFERENCIACION DE CELULAS TRONCALES PLURIPOTENTES HUMANAS TRASPLANTADAS EN UN MODELO DE ENFERMEDAD DE PARKINSON	A1-S-10064	CONACYT	13/09/2019	36 MESES	13/09/2022
41	CONVENIO CONACYT	56125-1621-10-X-19	DRA. TAMARA LUTI ROSENBAUM EMIR	REGULACION DEL CANAL TRPV4 POR FOSFOLIPIDOS	A1-S-08780	CONACYT	13/09/2019	36 MESES	13/09/2022
42	CONVENIO CONACYT	56164-1665-14-X-19	DR. JUAN CARLOS GOMORA MARTINEZ	BASES MOLECULARES Y FUNCIONALES EN LA MODULACION DE CANALES DE CALCIO TIPO T DE HUMANO POR COMPUESTOS ESTRUCTURALMENTE DIVERSOS	A1-S-10171	CONACYT	12/09/2019	36 MESES	12/09/2022
43	CONVENIO CONACYT	56291-1792-24-X-19	DR. FELIX RECILLAS TARGA	FORTALECIMIENTO DE LAS UNIDADES BIOTERIO Y EDICION GENETICA Y CRIOPRESERVACION DEL INSTITUTO DE FISIOLOGIA CELULAR	C-462/2019	CONACYT	08/10/2019	2 MESES	30/11/2019
44	CONVENIO CONACYT	56289-1790-24-X-19	DR. JULIAN VALDES RODRIGUEZ	ADQUISICION DE LA CAPACIDAD PARA AISLAR POBLACIONES CELULARES PARA ENSAYOS DE TRANSCRIPTOMICA EN CELULA UNICA	C-464/2019	CONACYT	08/10/2019	2 MESES	30/11/2019
45	CONVENIO CONACYT	56369-1870-4-XI-19	DR. ENOCH LUIS BALTAZAR	EL CANCER COMO CANALOPATIA: IDENTIFICACION Y CARACTERIZACION DE NUEVOS COMPUESTOS CON EFECTO MODULADOR SOBRE CANALES ONCOGENICOS DE K+	A1-S-13648	CONACYT	02/10/2019	36 MESES	02/10/2022
46	CONVENIO CONACYT	56148-1649-14-X-19	DR. FELIX RECILLAS TARGA	REGULACION EPIGENETICA Y TRANSCRIPCIONAL DE DOS RNAS LARGOS NO-CODIFICANTES DIVERGENTES EN LINEAS CELULARES DE CANCER DE MAMA	A1-S-11844	CONACYT	25/09/2019	36 MESES	25/09/2022
47	CONVENIO CONACYT	55965-1464-25-IX-19	DR. ARTURO HERNANDEZ CRUZ	LABORATORIO NACIONAL DE CANALOPATIAS (LANCA) CONSOLIDACION III	299651	CONACYT	13/08/2019	3 MESES	30/11/2019

Bases de Colaboración

NO.	FIGURA CONTRACTUAL	AÑO	NO. DE REGISTRO	INVESTIGADORES RESPONSABLES	OBJETO	DEPENDENCIAS INVOLUCRADAS	FECHA DE FIRMA	VIGENCIA	FECHA DE VENCIMIENTO
1	Bases de Colaboración.	2017	49588-2404-14-IX-17.	Dra. Marina Macías Silva.	Laboratorio Nacional de soluciones biomiméticas para diagnóstico y terapia LanBioDyT.	Facultad de Ciencias.	25 de julio de 2017.	3 años.	24 de julio de 2020.
2	Bases de Colaboración	2012	N/A	Dra. María de Lourdes Massieu Trigo	Transplantes al cerebro	UNAM	01 de enero de 2012		
3	Bases de Colaboración.	2017	49675-2491-27-IX-17.	Dr. Arturo Hernández Cruz.	Colaboración entre las partes a través de la Unidad de Investigación preclínica y el Laboratorio Nacional de Canalopatías para llevar a cabo de manera conjunta actividades en materia de investigación, desarrollo tecnológico, estancias de investigación, proyectos científicos, formación y capacitación de recursos humanos, intercambio de investigadores y estudiantes, prestación de servicios tecnológicos.	Unidad de Investigación preclínica (UNIPREC) Facultad de Química.	07 de agosto de 2017.	5 años.	06 de agosto de 2022.
4	Bases de Colaboración.	219	56198-1699-16-X-19	Dr. Arturo Hernández Cruz.	Laboratorio Nacional de Canalopatías (LANCA)Consolidación III.	Instituto de Ciencias del Mar y Limnología	13/09/2019	2 meses	30 de noviembre de 2019

Donaciones

NO.	FIGURA CONTRACTUAL	AÑO	NO. DE REGISTRO	INVESTIGADORES RESPONSABLES	OBJETO	EMPRESA	FECHA DE RECEPCION DE RECURSOS
1	Donación	2018	N/A	Dra. Victoria Eugenia Chagoya y Hazas	Donativo para el proyecto de investigación de la cirrosis hepática	Vela Advisor, S.A. de C.V.	12 de octubre de 2018

Apoyo a Eventos Académicos Externos

INSTITUCION	MONTO	ENLACE	CONGRESO/ MOTIVO	FECHA
Sociedad Mexicana de Bioquímica	$35,000.00	Dra. Susana Castro Obregón	Tercer Congreso Nacional de la Rama de Neurobiología	22 al 25 de septiembre
Asociación Mexicana de Microbiología	$20,000.00	Dra. Bertha González Pedrajo	XLI y VI Congresos Nacionales	27 al 31 de octubre de 2019
Sociedad Mexicana de Bioquímica	$30,000.00	Dr. Félix Recillas Targa	Transducción de señales	4 al 7 de noviembre de 2019
Sociedad Mexicana de Bioquímica	$20,000.00	Dr. Félix Recillas Targa	Rama radicales libres y especies reactivas del oxigeno	9 al 11 de septiembre de 2019
Sociedad Mexicana de Bioquímica	$10,000.00	Dra. Soledad Funes Argüello	XVIII Congreso Nacional de la rama de Bioquímica y Biología Molecular de Plantas	28 al 31 de octubre de 2019
Sociedad Mexicana para la Investigación de Células Troncales	$25,000.00	Dr. Iván Velasco Velázquez	5th International meeting on stem cells and regenerative medicine	14 de agosto de 2019 21 al 23 de octubre de 2019
TOTAL	$140,000.00			

PONENCIAS

El personal académico del IFC asistió a 15 Congresos Nacionales con 35 participaciones con ponencias y 78 presentaciones en forma de cartel; en 35 Congresos Internacionales donde se presentaron 39 carteles y 24 ponencias. Además, 20 participaciones con ponencia en 16 simposios internacionales y 7 presentaciones de carteles. 11 Simposios Nacionales donde se tuvieron 15 participaciones en ponencias.

Se impartieron 30 Conferencias Nacionales y 5 Internacionales, 30 seminarios dentro de la UNAM y 22 seminarios fuera de ella.

CONGRESOS NACIONALES	35 Participaciones con ponencia 78 Participaciones con cartel
2nd Epigenomics Meeting, 2019. Epigenetic Regulation in Human Disease.	
CEMUS XIV. Congreso de estudiantes de medicina del noroeste. Neurociencias.	
III Neurobiology Meeting of the Mexican Society for Biochemistry. SMB.	
LXII Congreso Nacional de la Sociedad Mexicana de Ciencias Fisiológicas A.C.	
Taller Multidisciplinario de Redes. Taller de análisis de señales neurofisiológicas.	
XLI Congreso Nacional de Microbiología y VI Congreso de Bioquímica y Biología Molecular de Bacterias.	
VII Congreso de Especies Reactivas del Oxígeno en Biología y Medicina SMB.	
VII Congreso Nacional de la Rama de Transducción de Señales de la Sociedad Mexicana de Bioquímica.	
XIII Congreso de Posgrado en Psicología.	
XIII Congreso Nacional de Biología Molecular y Celular de Hongos.	
XXI Congreso de Bioenergética y Biomembranas de la SMB.	
XXVII Congreso Mexicano de Psicología. Sociedad Mexicana de Psicología y el Instituto de Neurociencias de la Universidad de Guadalajara.	
XVIII Congreso Nacional de Biotecnología y Bioingeniería.	
XXXIV Reunión Anual de Investigación. Instituto Nacional de Neurología y Neurocirugía "Manuel Velasco Suárez" (INNN).	
VI Latin American Protein Society Meeting (LAPSM). VII Congreso de Fisicoquímica, Estructura y Diseño de Proteínas.	

CONGRESOS INTERNACIONALES	24 Participaciones con ponencia 39 Participaciones con cartel
37 SMYTE (Small Meeting on Yeast Transport and Energetics).	
1er Congreso Internacional de Ciencias Químico Biológicas.	
27th Meeting of the International Society for Neurochemistry.	
30th Fungal Genetics Conference.	
63 Annual Meeting of the Biophysical Society.	
7th International Urogenital Science Meeting.	
FASEB-The Lysophospholipid and Related Mediators Conference: from bench to clinic.	
Humboldt Kolleg “Rompiendo Paradigmas: Hacia una Ciencia Multi, Inter y Transdisciplinaria”.	
Humboldt Kolleg: Symposium on Natural Science.	
III International Congress of Psychobiology.	
III International Symposium on Fungal Stress.	
XIII International Basal Ganglia Meeting.	
26th Meeting, Society for Redox Biology and Medicine. (SfRBM 2019).	
II Pan American Congress of Physiological Sciences - PANAM 2019.	
SGP 73 Annual Symposium/Sobla Annual Meeting. Reunión de la Sociedad Biofísica Latinoamericana y la Society for General Physiologists.	
3er Congreso Internacional de la Federación de Sociedades y Asociaciones Hispanas de América del Norte, Centroamérica y el Caribe de la Ciencia de los Animales de Laboratorio, A.C. (FeSAHANCCCAL).	
Federation of European Neuroscience Societies (FENS).	
XXIX International Conference on Yeast Genetics and Molecular Biology.	
20th International Symposium on Cells of the Hepatic Sinusoid (ISCHS).	
21th European Congress of Endocrinology (ECE 2019).	
22nd International *C. elegans* Conference.	
50th Annual meeting Society for Neuroscience.	
eGMD - Epigenetics in Metabolic Diseases // 3rd LIMIOR - Leipzig International Meeting for Interdisciplinary Obesity Research.	

5th International Meeting on Stem Cells and Regenerative Medicine.
EMBO Workshop: Protein Synthesis and Translational Control.
EMBO workshop Bridging cell and tissue mechanics to fate specification and development.
International Stroke Conference 2019.
3rd International Summer Symposium on Systems Biology.
ISSCR 2019 Annual Meeting
Parasitic helminths new perspectives in biology and infection.
VII Meeting of Reactive Oixgen Species in Biology and Medicine.
XIV European Meeting on Glial Cells in health and Disease.
BLAST XV. Bacterial, Locomotion and signal Transduction Meeting.
Association for Research in Vision and Ophthalmology (ARVO) Annual Meeting.
6 to. Congreso Internacional RedBiot.

Numero	Simposios, Conferencias y Seminarios	Participaciones
11	Simposios Nacionales con ponencia	15
	Simposios Nacionales con cartel	0
16	Simposios Internacionales con ponencia	20
	Simposios Internacionales con cartel	7
30	Conferencias Nacionales con ponencia	31
5	Conferencias Internacionales con ponencia	5
30	Seminarios dictados en la UNAM	30
22	Seminarios dictados fuera de la UNAM	22

*para todas las Ponencias ver el Archivo Anexo-3

EVENTOS ACADÉMICOS INSTITUCIONALES

Los principales eventos académicos que se llevan a cabo en el Instituto de Fisiología Celular son fundamentalmente seminarios institucionales, que se realizan semana a semana, seminarios extraordinarios y la Feria Anual de Carteles.

En 2019 se llevaron a cabo 41 seminarios institucionales y 10 seminarios extraordinarios.

Seminarios Institucionales

ENERO

11 Dr. Richard Flavell, Yale University.
"To code or not to code: what is the Linc?".

18 Dr. Darío Lupiañez, Max Planck Institute for Molecular Genetics.
"Structural variation in the 3D genomic era: Implications for disease and evolution".

25 M. en C. Ana María Escalante Gonzalbo, Instituto de Fisiología Celular, UNAM.
"Los olvidados. ¿Puede la tecnología contribuir a la neuro-rehabilitación?".

FEBRERO

1 Dr. Víctor Manuel Valdés López, Facultad de Ciencias, UNAM.
"Teorías Evolutivas del Genoma Humano". Feria de Carteles.

8 Dr. Braulio Gutiérrez Medina, IPICYT (Instituto Potosino de Investigación Científica y Tecnológica A.C.).
"Luz y sombra en la proteína Vivid".

15 Dra. Yazmin Ramiro Cortes, Departamento de Neurodesarrollo y Fisiología, Instituto de Fisiología Celular, UNAM.
"Actividad sináptica y neuronal en ratones SHANK3 como modelo genético de autismo: de las espinas a la conducta".

22 Dra. Karina Acevedo Whitehouse, Facultad de Ciencias Naturales de la Universidad Autónoma de Querétaro.
"La carcinogénesis espontánea en un modelo marino".

MARZO

1 Dr. Stewart Gillmor, Langebio CINVESTAV Irapuato.
"Zygotic genome activation and pattern formation in early *Arabidopsis* embryogenesis".

8 Dra. Claudia Pérez Cruz, CINVESTAV-IPN.
"Modulación del eje intestino-cerebro como estrategia para combatir la enfermedad de Alzheimer".

15 Dr. Luis Téllez, Neurobiología de la Conducta Motivada, Instituto de Neurobiología, UNAM.
"El eje víscero-cerebral como parte del sistema de recompensa".

22 Dr. Luis Vaca, Departamento de Biología Celular y del Desarrollo, Instituto de Fisiología Celular, UNAM.
“Restricciones en el espacio-tiempo a nivel de moléculas individuales”.

29 Dr. Leonardo Peraza, Departamento de Bioquímica y Biología estructural, Instituto de Fisiología Celular, UNAM.
"Orquestando la dinámica intracelular durante el desarrollo sexual del hongo *Podospora*".

ABRIL

5 Dra. Paola Maycotte González, Investigadora Cátedras CONACyT. Centro de Investigación Biomédica de Oriente, IMSS.
"Secreción regulada por autofagia en cáncer de mama: implicaciones terapéuticas".

12 Dra. Daniela Araiza Olivera Toro, Departamento de Química de Biomacromoléculas, Instituto de Química, UNAM.
"Una molécula… un blanco terapéutico en el microambiente tumoral".

26 Dr. Luis Carrillo Reid, Instituto de Neurobiologia, UNAM.
“Cambios en el comportamiento inducidos por la activación selectiva de ensambles corticales.”

MAYO

3 Dra. Rocío Angeles García Becerra, Departamento de Biología Molecular y Biotecnología, Instituto de Investigaciones Biomédicas, UNAM.
“Restablecimiento de la respuesta a la terapia antiestrogénica en células de cáncer de mama receptor de estrógenos negativo.”

9 Dr. Carlos Manlio Díaz García, Department of Neurobiology, Harvard Medical School, Boston, MA.
"La estimulación neuronal promueve la glucólisis y no el consumo de lactato en las neuronas".

24 Dr. Francisco Torres Quiroz, Departamento de Bioquímica y Biología Estructural, Instituto de Fisiología Celular, UNAM.
"Papel del H2S durante la fermentación".

31 Dr. Óscar González-Pérez, Universidad de Colima.
"Consecuencias de la hidrocefalia crónico-obstructiva sobre los progenitores neurales y la citoarquitectura cerebral".

JUNIO

7 Dr. Diego Cortez Quezada, Centro de Ciencias Genómicas CCG, UNAM.
“Genomics of sexuality in vertebrates”.

14 Dr. José Everardo Avelino Cruz, Instituto de Fisiología, BUAP.
“Remodelación cardiaca en el síndrome metabólico y la diabetes”.

21 Dra. Tamara Rosenbaum Emir, Departamento de Neurociencia Cognitiva, Instituto de Fisiología Celular, UNAM.
"Canales TRP: moléculas que exhiben fenómenos biofísicos novedosos".

JULIO

26 Dra. Diana Guallar Artal, Principal Investigator at CiMUS (Center for Research in Molecular Medicine and Chronic Diseases). Santiago De Compostela, Galicia, España.
"Epitranscriptomics: shaping the cell through RNA modifications".

AGOSTO

2 Dr. Abimael Cruz Migoni, Universidad de Oxford.
“Finding small molecules inhibitors against oncogenic proteins”.

9 Dr. James L. McGaugh, Distinguished Professor Emeritus Department of Neurobiology and Behavior. Center for the Neurobiology of Learning and Memory. University of California, Irvine.
"Highly superior autobiographical memory research: A neurobiological puzzle".

16 Dr. Roberto Coria, Departamento de Genética Molecular, Instituto de Fisiología Celular, UNAM.
"Estrés de Retículo Endoplásmico y Autofagia en la Amiba Social *Dictyostelium discoideum".*

23 Dra. Diane Lipscombe, Brown University, USA.
"RNA and DNA binding proteins control the composition of calcium channels in nociceptors in normal and neuropathic pain states".

30 Dra. Maria Angela Franceschini, Associate Professor, Harvard Medical School, Massachusetts General Hospital.
"Imaging brain activity with diffuse optics: opportunities and future directions".

SEPTIEMBRE

6 Dra. Edda Lydia Scuitto Conde, Instituto de Investigaciones Biomédicas, UNAM.
"Hacia el desarrollo de nuevas estrategias para el control de la neuroinflamación: Implicaciones terapéuticas".

13 Dr. Francisco Barrantes, Pontifical Catholic University of Argentina, Buenos Aires, Argentina.
"Exploring the brain at the Nanoscale, in Health and Disease".

20 Dr. Joshua Johansen, RIKEN Center for Brain Science.
"Teaching the brain to fear".

27 Dr. Marcelo Wood, Universidad de California, Irvine, USA.
"Epigenetics: Pushing the boundaries of learning and memory".

OCTUBRE

4 Dr. Fatuel Tecuapetla, Departamento de Neuropatología Molecular, Instituto de Fisiología Celular, UNAM.
"Sub-circuitos neuronales detrás de la generación de movimientos/acciones".

11 Dr. Diego González Halphen, Departamento de Genética Molecular, Instituto de Fisiología Celular, UNAM.
"Cuando la subunidad 2 de la citocromo c oxidasa entra a la membrana interna mitocondrial por la puerta de atrás".

18 Dra. Rosaura Hernández Rivas, Departamento de Biomedicina Molecular CINVESTAV.
"El procesamiento de la histona H3: nuevo mecanismo epigenético que regula la expresión de genes que participan en la replicación del ADN en *Plasmodium falciparum*".

25 Dra. Carmen Sandi, Laboratory of Behavioral Genetics. Brain Mind Institute.
"Papel de la mitocondria en circuitos neurales que codifican conductas de ansiedad y depresión".

NOVIEMBRE

8 Dr. Ben Deverman, Stanley Center for psychiatric research en el Broad Institute of Harvard and MIT.
"Engineering AAV vectors for central nervous system gene therapy".

15 Dr. Félix Recillas Targa, Departamento de Genética Molecular, Instituto de Fisiología Celular, UNAM.
"Participación de la estructura tri-dimensional del genoma en la regulación transcripcional".

22 Dra. Alicia González Manjarrez, Departamento de Bioquímica y Biología Estructural, Instituto de Fisiología Celular, UNAM.
“Reguladores Híbridos: Una alternativa para provocar respuestas transcripcionales innovadoras en *S. cerevisiae*”.

29 Dra. Tatiana Fiordelisio, Laboratorio de Neuroendocrinología Comparada, Facultad de Ciencias, UNAM.
“La Unidad endocrino vascular en la vida real de la hipófisis de un ratón”.

DICIEMBRE

6 Dr. Jesús Chimal Monroy, Departamento de Medicina Genómica y Toxicología ambiental, Instituto de Investigaciones Biomédicas, UNAM.
"Del desarrollo embrionario y regeneración de las extremidades a la formación de organoides".

Seminarios Extraordinarios

ENERO

22 Dr. André S. Pupo, Departamento de Farmacología de la Universidad Estatal Paulista, Brasil.
"Therapeutic potential for biased agonism at alpha-1 adrenoceptors".

ABRIL

9 Dr. Alessandro Sette, Division of Vaccine Discovery, La Jolla Institute for Allergy and Immunology, California, USA.
"The relationship between alfa-synuclein-specific T cell reactivity and Parkinson Disease clinical onset".

25 Dr. Ya-Xiong Tao, Professor, Auburn University College of Veterinary Medicine, Alabama, USA.
"Chaperoning G protein-coupled receptors: From cell biology to therapeutics".

JULIO

31 Dr. Miguel Fidalgo, CIMUS-U de Santiago de Compostela, España.
"Deciphering the crosstalk of cellular metabolism and chromatin dynamics in pluripotency".

SEPTIEMBRE

12 Dra. Saydi Núñez Cetina, UAM-Xochimilco.
"De la violencia conyugal al feminicidio. Reflexiones sobre género y crimen pasional en el siglo XX mexicano".

26 Dr. Víctor G. Corces, Profesor Howard Hughes Medical Institute (HHMI), Investigador en la Universidad de Emory en Atlanta, GA.
"Herencia Transgeneracional de Epi-Fenotipos de Obesidad".

OCTUBRE

24 Dra. Lydiette Carrión Rivera.
"Femicidios y violencia de género: un fenómeno sistémico".

NOVIEMBRE

28 Dr. Dasiel Borroto-Escuela, Department of Neuroscience-Karolinska Institutet, Stockholm, Sweden.
"Molecular integration in the CNS through formation of GPCR heteroreceptor complexes: Relevance for diseases".

DICIEMBRE

4 Dr. Itay Tirosh, Department of Molecular Cell Biology, Weizmann Institute of Science.
"An integrated model of cellular heterogeneity in glioblastoma".

9 Dr. Pedro Bekinschtein, Instituto de Neurociencia Cognitiva y Translacional del CONICET, Argentina.
"Mecanismos biológicos de la memoria de reconocimiento y su olvido".



Feria de Carteles Anual del IFC

En la feria de Carteles 2019 se presentaron 62 trabajos. Se realizarón mini simposios y exposiciones cortas de los carteles, con lo que se promovío la discusión científica y el intercambio académico.

	Nombre	Laboratorio	Título del cartel
1	Roberto Alexander Bahena Cerón	Dr. Alfredo Torres Larios	Estudios estructurales sobre la proteína PyrR
2	Jesús Ruiz Flores	Dr. Francisco Torres Quiroz	Caracterización de los mecanismos post-traduccionales en las regiones de baja complejidad involucradas en la agregación reversible de proteínas en *Saccharomyces cerevisiae*
3	Rodrigo Andrés Nava Lara	Dr. Gabriel Del Río Guerra	Heterologous machine learning for the identification of antimicrobial activity in human-targeted drugs
4	Raful Navarro Espíndola	Dr. Leonardo Peraza Reyes	La dinámica peroxisomal y mitocondrial regulada por DNM1 es necesaria para el desarrollo sexual en el hongo *Podospora anserina*
5	Pamela Amancio Rojas	Dr. Leonardo Peraza Reyes	La dinámica de los endosomas y los peroxisomas regulada por Hok1 es necesaria para el desarrollo sexual del hongo *Podospora anserina*
6	Melisa Selene Álvarez Sánchez	Dr. Leonardo Peraza Reyes	La función del complejo de encuentro entre la mitocondria y el retículo endoplásmico (ERMES) en el hongo *Podospora anserina*
7	Oscar Eduardo Gutiérrez Castañeda	Dr. Marcelino Arciniega Castro	Simulaciones de dinámica molecular en canales iónicos
8	Sergio Campos Ortega Rendón	Dr. Marcelino Arciniega Castro	Detección de similitudes locales entre proteínas con dinámica molecular y teoría de gráficas
9	Francisco Javier Padilla Garfias	Dr. Antonio Peña Díaz	Efectos de la ε-poli-l-lisina sobre la fisiología de *saccharomyces cerevisiae*
10	Mariana Ríos Vázquez	Dra. Bertha González Pedrajo	Molecular characterization of rOrf1 protein of enteropathogenic *Escherichia coli*
11	Ameyalli Gómez Ilescas	Dr. Félix Recillas Targa	The role of CTCF in the nervous system of *Drosophila melanogaster*
12	Carlos Alberto Peralta Alvarez	Dr. Félix Recillas Targa	Regulación epigenética y transcripcional de RNAs no codificantes divergentes involucrados en cáncer
13	Andrés Arenas Navarro	Dr. Heliodoro Celis Sandoval	Caracterización del espectro de los centros de reacción de *Rhodovibrio salinarum*
14	Ayerim Alma Esquivel López	Dra. Mayra Furlán Magaril	Analysis of the chromosomal genomic interactions of homeotic genes in *Drosophila melanogaster* using different cross-linking reagents

	Nombre	Laboratorio	Título del cartel
15	Marintia Mayola Nava García	Dra. Mayra Furlán Magaril	3D organization of the SHH chromatin locus during feather bud formation in *Gallus gallus*
16	José Ernesto Bravo Arévalo	Dra. Soledad Funes	Regulación metabólica de las subunidades β-NAC en *Saccharomyces cerevisiae*
17	Hilario Ruelas Ramírez – Josué Miguel Julián Ramírez Reyes	Dra. Soledad Funes	El enigma de Slm35: de la mitocondria a la autofagia
18	Cristian Alberto Vergara Gerónimo	Dra. Xochitl Pérez Martínez	El factor de inicio de la traducción citoplasmática 4G1 es un regulador de la síntesis mitocondrial de Cox1
19	Diana Grisel Ríos López	Dra. Marina Macías	Regulación de la expresión de TAZ y el fenotipo del hepatocito
20	Karla Ameyali Gómez Ceja	Dra. Marina Macías	Regulación de la estabilidad de la proteína Ski por el antibiótico puromicina
21	Nallely Cano Domínguez	Dr. Jesús Aguirre Linares	Neurospora crassa multifunctional nadph oxidase Nox-1 is localized in the vacuolar system and the plasma membrane
22	Diego Pérez Vázquez	Dra. Paula Licona Limón	Función de TIF1-gamma en poblaciones de linfocitos Th1 y CTL
23	María Fernanda Maldonado	Dra. Paula Licona Limón	Regulación de la expresión de CD25 por TIF1g en linfocitos T reguladores
24	Eugenio Contreras Castillo	Dra. Paula Licona Limón	Regulación de la expresión de Foxp3 por TIF1g en linfocitos Treg
25	Emmanuel Flores Espinoza	Dra. Paula Licona Limón	Expresión del receptor de IL-9 en basófilos
26	Enrique Olguín Martínez	Dra. Paula Licona Limón	Participación de PKIB y la vía de PKA en la diferenciación y función de las células linfoides innatas tipo 2
27	Ofelia Muñoz Paleta	Dra. Paula Licona Limón	PKA y PKIB en la diferenciación y función de los linfocitos Th
28	Jose Luis Ramos Balderas	Dra. Paula Licona Limón	Caracterización de la respuesta inmune contra cepas de *Pseudomonas aeruginosa* resistentes a Galio
29	Alan Anuart González Rangel	Dra. Rosa Navarro González	Searching for regulators of lin-35/Rb expression during starvation in *C. elegans*
30	Laura Silvia Salinas Velázquez	Dra. Rosa Navarro González	PEK-1, ABCF-3 and GCN-1/-2 kinases are required for RNA granules formation during stress in the germline of *C. elegans*
31	Gisselle Angélica Campos Martínez	Dra. Rosa Navarro González	Stress induces mitochondrial aggregation in *Caenorhabditis elegans* adult gonad

	Nombre	Laboratorio	Título del cartel
32	Ángel Armando Dámazo Hernández	Dra. Rosa Navarro González	The RNA binding protein GLA-3/TTP is important for germ cell protection from stress
33	Eduardo Daniel Aguilar Solis	Dr. Víctor Julián Valdés Rodríguez	Caracterización epigenética de un circuito neuronal involucrado en la memoria asociativa de *C. elegans*
34	Marti David Wilson Verdugo	Dr. Víctor Julián Valdés Rodríguez	Characterization of epigenetic changes associated with the metabolic memory *in vitro*
35	Teresa Beatriz Nava Ramírez	Dr. Wilhelm Hasnberg Torres	La función de chaperona de las catalasas de subunidad grande
36	Sammy Israel Gutiérrez Terrazas	Dr. Wilhelm Hasnberg Torres	La actividad de fosfodiesterasa en *Neurospora crassa* está involucrada en formación de la pared celular
37	Oscar Giovanny Urrego Morales	Dr. Federico Bermúdez Rattoni	Effect of the inhibition of palmitoylation on the formation and maintenance of spatial memory
38	Beatríz Sarahí Méndez Rodríguez.	Dra. Elvira Galarraga Palcio	Posible comunicación sináptica entre las neuronas de los núcleos intralaminares del tálamo parafascicular y central lateral (Possible synaptic communication between neurons of Parafascicular and Central lateral intralaminar thalamic nuclei)
39	Rosa María Reyes Chapero	Dra. Elvira Galarraga Palcio	Cortical persistent activity in pyramidal and interneurons of layer 5 motor cortex *in vitro*
40	Yuriko Itzel Sánchez Zamora	Dra. Marcia Hiriart Urdanivia	Dimorfismo sexual en la inflamación presente en un modelo de síndrome metabólico en rata
41	Jazmín Selene Samario Román	Dra. Marcia Hiriart Urdanivia	El papel de NGF en la expresión y actividad de GLUT2 y glucocinasa en células beta pancreáticas
42	Zyanya Sarai Sánchez Salazar	Dra. Marcia Hiriart Urdanivia	Análisis del desarrollo y la distribución de las células α y células PP en el páncreas de rata después del destete
43	Rosa Isela Ortiz Huidobro	Dra. Marcia Hiriart Urdanivia	En la resistencia a la insulina...el sexo si importa.
44	Carla Huezca Carbajal	Dra. Tamara Rosenbaum Emir	Dimorfismo sexual en la respuesta de dolor asociada al canal TRPV1 por efecto del 17B-estradiol
45	Iskra Anai Cruz Cruz	Dra. Myrian Velasco Torres	Efecto del síndrome metabólico sobre el funcionamiento de los canales de potasio sensibles a ATP
46	Germán Alonso Bernate Obando	Dra. Myrian Velasco Torres	Red de co-expresión de los canales de potasio dependientes de voltaje Kv2 en célula beta a diferentes estadios del desarrollo
47	Viridiana Belen Meza González	Dra. Diana Escalante Alcalde	Generación de dos líneas de ratones con mutaciones en la PLPP3
48	Beetsi Eugenia Urrieta Chávez	Dr. Iván Velasco Velázquez	Uso de un hidrogel biocompatible para el direccionamiento de axones de neuronas dopaminérgicas humanas

	Nombre	Laboratorio	Título del cartel
49	Pilar Sarah Acevo Rodríguez	Dra. Susana Castro Obregón	La autofagia podría cooperar con las metaloproteínasas de la matriz en el cierre del tubo neural del ratón
50	Daniel Moreno Blas	Dra. Susana Castro Obregón	Autophagy dysfunction during neuronal senescence
51	Emiliano Jimenez Marquez	Dra. Yazmín Ramiro Cortés	Actividad neuronal en corteza visual de ratones SHANK3+/- en respuesta a una tarea visual de sobre-especificidad
52	Rubén Darío Contreras López	Dr. Fatuel Tecuapetla Aguilar	Ciurcuitos de interacción cerebelo - ganglios basales
53	Luis Antonio Rodríguez Sibrian	Dr. Fatuel Tecuapetla Aguilar	Caracterización de los circuitos paralelos o divergentes de salida del tálamo
54	Anil Kumar Verma Rodríguez	Dr. Fatuel Tecuapetla Aguilar	Disección de circuitos neurales involucrados en la estimulación cerebral profunda con técnicas de optogenética
55	Alejandra Aidaly Hernández Jaramillo	Dr. Francisco Sotres Bayón	Basolateral amygdala and ventral pallidum (but not orbitofrontal cortex) are necessary for motivational conflict responses guided by previous experiences
56	Diana Lizbeth Elías López	Dr. Juan Carlos Gómora Martínez	Efecto de compuestos con propiedades anti metastásicas en el canal Nav1.6 de humano
57	Luis Ángel Montes Ortega	Dra. Lourdes Massieu Trigo	Effect of D-hydroxybutyrate in autophagy induction by exitototxicity
58	Juan Carlos Gómora García	Dra. Lourdes Massieu Trigo	La respuesta a proteínas mal plegadas inducido por la ausencia de glucosa en neuronas corticales ¿Amigo o Enemigo?
59	Aura Nirva Campero Romero	Dr. Luis Tovar y Romo	Proteomic profiling of exosomes derived from brain microvascular endothelial cells under hypoxia
60	Diana Elizabeth Colín Martínez	Dr. Ricardo Tapia	Efectos de la administración aguda y crónica de inhibidores de la glutamato descarboxilasa en la médula espinal de rata
61	Ximena Ameyalli Escutia Macedo, David Andrade Morales, María Fernanda Gutiérrez García y José Jonathan Aguilar Chalé.	M. C. Ana María Escalente Gonzalbo	Hágalo usted mismo: autonomía y motivación con el uso de la tecnología en la neuro-rehabilitación
62	Edgar Gerardo Milo Rocha	Dr. Enoch Luis Baltazar	Estudio electrofisiológico y farmacológico del canal de potasio Kv10.1

ACTIVIDADES DE DIFUSIÓN Y DIVULGACIÓN

Participaciones en radio y televisión	**30**
Participaciones en medios impresos	**24**
Otras actividades de Difusión o divulgación (Conferencias, simposios, ferias)	**72**

Participaciones en Programas de Radio o Televisión

1. Aguilar Roblero Raúl. Entrevista en Mitos y Realidades de Canal Once, para tratar el tema del Cambio de Horario (ventajas y desventajas) tanto en el terreno de impacto en la salud para el ser humano como el impacto económico por el ahorro de energía.

2. Bermúdez Rattoni Federico. Entrevista en 24 horas. “Alzheimer, afecta a 800 mil mexicanos”. https://www.24-horas.mx/2019/09/23/alzheimer-afecta-a-800-mil-mexicanos/

3. Bermúdez Rattoni Federico. Entrevista en Acrópolis. “Se deben prevenir casos de Alzheimer en México: especialistas”. https://acropolismultimedios.mx/se-deben-prevenir-casos-de-alzheimer-en-mexico-especialistas/

4. Bermúdez Rattoni Federico. Entrevista en ADN Sureste. ” ¿Mala memoria o falta de atención?”. https://www.adnsureste.info/mala-memoria-o-falta-de-atencion-1000-h/

5. Bermúdez Rattoni Federico. Entrevista en AFMedios. “En México, padecen Alzheimer 800 mil personas; retos cognitivos una opción para retrasar aparición”. https://www.afmedios.com/2019/09/en-mexico-padecen-alzheimer-800-mil-personas-retos-cognitivos-una-opcion-para-retrasar-aparicion/

6. Bermúdez Rattoni Federico. Entrevista en Bajo Palabra. “Epidemia de Alzheimer amenaza a México”. https://bajopalabra.com.mx/epidemia-de-alzheimer-amenaza-a-mexico

7. Castro Obregón Susana. Entrevista en ADN Sureste. “¿Se pueden crear nuevas neuronas?” http://adnsureste.info/se-pueden-crear-nuevas-neuronas-1600-h/

8. Escalante Alcalde Diana. Entrevista en Diálogos en Confianza, Canal Once. “Avances en el uso y tratamiento con células madre”.

9. Escalante Gonzalbo Ana María. Entrevista en Agencia EFE. “México utiliza videojuegos para sanar a pacientes con daños neuronales”.

10. Escalante Gonzalbo Ana María. Entrevista en CCNews. “UNAM crea videojuegos para rehabilitar a pacientes con daño cerebral”. https://news.culturacolectiva.com/ciencia/unam-crea-videojuego-para-rehabilitar-a-pacientes-con-dano-cerebral/

11. Georgellis Dimitris y Álvarez F. Adrián. Entrevista en RT en español. “Qué “sienten” las bacterias y por qué es importante para acabar con la resistencia a los antibióticos”. https://actualidad.rt.com/actualidad/330445-sienten-bacterias-importante-acabar-resistencia-antibioticos.

12. Hiriart Urdanivia Marcia. Entrevista en ADN 40. “Día Internacional de la Mujer y la Niña en la Ciencia”.

13. Hernández Cruz Arturo. Reportaje en Factor Ciencia, Canal 11. "Células Madre”. https://youtu.be/ns82zY9MT9w.

14. Hernández Muñoz Rolando. Entrevista en 20 minutos. “UNAM obtiene patente para proteger hígado en pacientes con VIH”. 20minutos.com.mx/noticia/

15. Hernández Muñoz Rolando. Entrevista en CND Cadena Digital de Noticias. “UNAM patenta medicamento para proteger hígado de personas con SIDA”. https://www.cdnoticias.com.mx/articulos/unam-patenta-medicamento-proteger-higado-personas-sida/portada

16. López Colomé Ana María. Entrevista en TV UNAM, Espacio académico AAPAUNAM TV. Cápsula de 5 minutos dirigida al público en general.

17. Osorio Gómez Daniel. Entrevista en Radio Educación, programa Paisaje Interno con el tema memoria. Locutora Ana Leticia Vargas.

18. Pasantes Ordóñez Herminia. Entrevista en Canal Once. “El amor es como la materia”. 22 febrero 2019.

19. Pasantes Ordóñez Herminia. Serie Hipócrates 2.0 coproducida por el Programa Universitario de Investigación en Salud y Radio UNAM. “Neurociencias, la licenciatura en la UNAM”.

20. Pérez de la Mora Miguel. Entrevista en ADN 40. “Más de 264 millones de personas en el mundo viven con ansiedad”.

21. Ramirez Graullera Yoas Saimon. Entrevista en ADN 40. “UNAM desarrolla videojuegos para terapia virtual de rehabilitación”. https://www.adn40.mx/noticia/salud/nota/2019-03-31-12-15/unam-desarrolla-videojuegos-para-terapia-virtual-de-rehabilitacion/

22. Recillas Targa Félix. Entrevista en ADN Sureste. “Estudio del genoma del ajolote ayudará en la lucha contra el cáncer”. https://www.adnsureste.info/estudio-del-genoma-del-ajolote-ayudara-en-la-lucha-contra-el-cancer-1100-h/

23. Recillas Targa Félix. Entrevista en Creadores Universitarios, TV UNAM. “Implicaciones de la modificación genética en humanos”.

24. Recillas Targa Félix. Entrevista en Data Noticias. “El estudio del ajolote podría ser clave para ayudar a curar el cáncer”. https://www.datanoticias.com/2019/08/24/el-estudio-del-ajolote-podria-ser-clave-para-ayudar-a-curar-el-cancer/

25. Romo Trujillo Ranulfo. Entrevista en 20 minutos. “Ranulfo Romo: un científico que ha educado sus neuronas”. https://www.20minutos.com.mx/noticia/503376/0/ranulfo-romo-un-cientifico-que-ha-educado-sus-neuronas/

26. Rosenbaum Emir Tamara. Entrevista en ADN Sureste. “Descifrando los mecanismos del dolor y otros transtornos”. https://www.adnsureste.info/basicamente-ciencia-descifrando-los-mecanismos-del-dolor-y-otros-trastornos-0900-h/

27. Tapia Ibargüengoytia Ricardo. Entrevista en el canal 11, con Javier Solórzano.

28. Tapia Ibargüengoytia Ricardo. Participación en la serie de televisión Observatorio Semanal de TV-UNAM, con el tema “Modificación genética”.

29. Tapia Ibargüengoytia Ricardo. Entrevista en ADN 40 en el programa “No hay lugar común”.

30. Velasco Velázquez Iván. Entrevista en América Retail. “Neuromarketing: se pueden crear neuronas *in vitro* similares a las humanas”. https://www.america-retail.com/featured/neuromarketing-se-pueden-crear-neuronas-in-vitro-similares-a-las-humanas/

Participaciones en Medios Impresos

1. Aguilar Roblero Raúl. Entrevista en Periódico Reforma. https://www.playbuzz.com/gruporeforma/cambio-de-hora-un-debate-mexicano-y-mundial.

2. Aguilar Roblero Raúl. Entrevista en El Heraldo de Tabasco. “Horario de Verano, mame de los diputados”. https://www.elheraldodetabasco.com.mx/analisis/horario-de-verano-mame-de-los-diputados-3284149.html.

3. Álvarez Adrián Fernando. Entrevista en Actualidad RT. https://actualidad.rt.com/actualidad/330445-sienten-bacterias-importante-acabar-resistencia-antibioticos.

4. Álvarez Adrián Fernando. Entrevista en Excélsior. “Comprendiendo cómo sienten las bacterias”. https://www.excelsior.com.mx/nacional/comprendiendo-como-sienten-las-bacterias/1327538.

5. Bermúdez Rattoni Federico. Entrevista en DGCS. "Padecen alzhéimer unas 800 mil personas en México”. Día Mundial del Alzheimer.

6. Bermúdez Rattoni Federico. Entrevista en UNAM Global. “¿Mala memoria o falta de atención? “http://www.unamglobal.unam.mx/?p=69829.

7. Bermúdez Rattoni Federico. Entrevista en El Universal. “¿Por qué recuerdas tu primer beso? La ciencia te lo explica”. https://www.tangible-eluniversal.com.mx/por-que-recuerdas-tu-primer-beso-la-ciencia-te-lo-explica.

8. Del Río Guerra Gabriel. Entrevista en la revista Análisis jurídico, en torno al tema de la inteligencia artificial (análisis previo a las implicaciones normativas). https://www.youtube.com/watch?v=TS2P8WSzNw4&t=3s.

9. López Colomé Ana María. Entrevista con Paco Zea. “Cinco mexicanas que destacan en la ciencia”. https://www.pacozea.com/cinco-mexicanas-que-destacan-en-la-ciencia.

10. López Colomé Ana María. “10 mexicanas científicas que con sus conocimientos han puesto al país en alto”. htpps://www.sinembargo.mx/03-01-2019/3517715.

11. López Huerta Violeta. Entrevista en Gaceta UNAM. “Nuevas opciones para tratar males psiquiátricos”. https://www.gaceta.unam.mx/tag/optogenetica/.

12. Massieu Trigo Lourdes. Entrevistas en El Universal. "Hipoglucemia y muerte neuronal".

13. Massieu Trigo Lourdes. Entrevista en Gaceta UNAM. "La glucosa, básica para el funcionamiento neurona".

14. Pasantes Ordóñez Herminia. Entrevista en Colima noticias. “Las mujeres tenemos en mayor porcentaje un cerebro creativo: Herminia Pasantes”. http://www.colimanoticias.com/las-mujeres-tenemos-en-mayor-porcentaje-un-cerebro-creativo-herminia-pasantes/.

15. Peña Díaz Antonio. Entrevista en Una Mirada a la Ciencia, DGDC, UNAM. “Las levaduras: ¿Cómo han servido a la humanidad?”.

16. Peña Díaz Antonio. Entrevista en El Universal. “Cómo las levaduras benefician a la humanidad”. https://www.eluniversal.com.mx/ciencia-y-salud/como-las-levaduras-benefician-la-humanidad.

17. Pérez de la Mora Miguel. Entrevista en Gaceta UNAM. “La ansiedad ¿Amiga o Enemiga?”. No.5036 ISSN 01885138 Pag.10.

18. Pérez de la Mora Miguel. Entrevista en Diario de Morelos. “Trastorno de ansiedad”. https://www.diariodemorelos.com/noticias/trastorno-de-ansiedad.

19. Ramirez Graullera Yoas Saimon. Entrevista en Crónica. “UNAM registra videojuegos para rehabilitar a personas con accidentes cerebrovasculares”. http://www.cronica.com.mx/notas/2019/1113609.html.

20. Recillas Targa Félix. Entrevista en el periódico Milenio. “Avances genéticos que están revolucionando a la ciencia”. https://www.milenio.com/especiales/la-revolucion-genetica.

21. Romo Trujillo Ranulfo. Entrevista en Gaceta UNAM. “El amor y el cerebro”. http://www.gaceta.unam.mx/el-amor-y-el-cerebro/.

22. Rosenbaum Emir Tamara. Entrevista en La Crónica. “Los canales iónicos determinan como las células perciben y reaccionan a su entorno”. https://www.cronica.com.mx/notas-los_canales_ionicos_determinan_como_las__celulas_perciben_y_reaccionan_a_su_entorno_tamara_luti_rosenbaum_emir-1135603-2019.

23. Rosenbaum Emir Tamara. Entrevista en Gaceta UNAM. "La emoción, respuesta fisiológica y aprendida". https://www.gaceta.unam.mx/la-emocion-respuesta-fisiologica-y-aprendida/.

24. Valdés Rodríguez Julián. Entrevista en El Heraldo de México. “El cordón umbilical, ¿es un mito?”. https://heraldodemexico.com.mx/estados/el-cordon-umbilical-es-un-mito/.

Otras actividades de Difusión o Divulgación

1. Aguilar Roblero Raúl. Conferencia. "Llevando el ritmo de vida: Los relojes que gobiernan la vida". Ciclo: Los Domingos en la Ciencia. Academia Mexicana de Ciencias.

2. Aguirre Linares Jesús. Charla. “De toxicidad y regulación: El papel de especies reactivas de oxígeno en la diferenciación celular”. Fiesta de las Ciencias y las Humanidades. Museo de las Ciencias Universum, UNAM.

3. Álvarez Adrián Fernando. Conferencia. "Más de cinco sentidos: cómo sienten las bacterias por medio de su membrana celular." Fiesta de las Ciencias y las Humanidades. Museo de las Ciencias Universum, UNAM.

4. Álvarez Adrián Fernando. Conferencia. “¿Cómo sienten las bacterias?”. Sitio UNAM global. http://www.unamglobal.unam.mx/?p=69576.

5. Arciniega Castro Marcelino. Conferencia. “Opsinas: Proteínas de la visión”. Museo de la Luz.

6. Castro Obregón Susana. Conferencia. “Biología comparada para estudiar el envejecimiento”. Humboldt Kolleg: “El cosmos Mexicano de Humboldt”. El Colegio Nacional.

7. Castro Obregón Susana. Conferencia magistral. “¿Cómo hacer ratones fluorescentes y para qué?” en el 6to curso teórico-práctico de Biología Molecular para profesores de bachillerato: regulación de la expresión génica

8. Crespo Ramírez Minerva. Semana de la Ciencia y Tecnología dando unas platicas en el centro cultural COP,S.C del 11 al 15 de marzo del 2019 con número de adscripción a la SEP 51-3309-561-Px-02 CCT.09PPR1951Y

9. Escalante Alcalde Diana. Semana del Cerebro, IFC-UNAM.

10. Fernández de Miguel Francisco. Conferencia magistral. “¿Qué nos enseñan los murales prehispánicos de nuestra percepción visual?” XXVII Congreso Nacional de la Sociedad Mexicana de Psicología, A.C.Universidad de Guadalajara.

11. Funes Argüello Soledad. Charla. ¡Quiero ser científica! Centro Cultural España.

12. Georgellis Dimitris, Álvarez Adrián Fernando. Conferencia. “Cómo “sienten” las bacterias”. sección Campus–Ciencia, UNAM global. http://www.unamglobal.unam.mx/?p=69576.

13. González Manjarrez Alicia. Seminario. “Cómo influyen nuestros genes en lo que comemos: en la salud y la enfermedad”. 40 edición de la Feria Internacional del Libro del Palacio de Minería.

14. González Manjarrez Alicia. Coordinadora del Programa de Divulgación de la Ciencia. En la 40 edición de la Feria Internacional del Libro del Palacio de Minería.

15. González Pedrajo Bertha. Participación en el video de promoción del IFC. TV UNAM.

16. Hiriart Urdanivia Marcia. Conferencia. "Lo amargo del Azúcar". Centro Regional de Cultura Chimalpahin, Chalco, Edo. de México. Programa de la Academia Mexicana de Ciencias "Domingo en las Ciencias".

17. Lemus Sandoval Luis. Conferencia. “Sensación y percepción: nada es lo que parece”. Curso para profesores de bachillerato.

18. Lemus Sandoval Luis. Conferencia. “Alexa: ¿cómo reconoce el cerebro las palabras?”. Facultad de Medicina, UNAM.

19. López Huerta Violeta Gisselle. Panel. “Mujeres en Ciencia e Investigación”. Talent Woman.

20. López Huerta Violeta Gisselle. Plática de divulgación. “¿Se puede manipular el cerebro vía control remoto?”. Semana del Cerebro, IFC-UNAM.

21. López Huerta Violeta Gisselle. Plática de divulgación. “Cerebros a control remoto” Neurofest. Universum, UNAM.

22. Luis Baltazar Enoch. Visita guiada a alumnos y profesores de la Escuela Nacional Preparatoria, durante la Tercera jornada académica de estudiantes de la ENP y el Instituto de Fisiología Celular de la UNAM. Semana del Cerebro.

23. Mas Oliva Jaime. Participación en Infografía en el sitio Ciencia UNAM de la Dirección General de Divulgación de la Ciencia (DGDC). “¿Cómo funciona el calcio en nuestro cuerpo?”. http://ciencia.unam.mx/contenido/infografia/76/el-calcio-en-nuestro-cuerpo.

24. Navarro González Rosa Estela. Charla. ¡Quiero ser científica! Centro Cultural España.

25. Osorio Gómez Daniel. Charla. “Desvelos Científicos: Inception”. Noches de ciencia para adultos. Centro Cultural España.

26. Pasantes Ordóñez Herminia. Conferencia inaugural. “Las drogas y el cerebro”. Diplomado en Política de Drogas, Salud y Derechos Humanos. Aguascalientes Auditorio CIDE.

27. Pasantes Ordóñez Herminia. Conferencia. “¿Qué pasa en nuestro cerebro cuando nos enamoramos?”. IPN.

28. Pasantes Ordóñez Herminia. Conferencia. “Un viaje a tu cerebro”. Museo de Ciencias Universum, UNAM.

29. Pasantes Ordóñez Herminia. Conferencia. “Cerebro y creatividad”. Archivo Histórico del Municipio de Colima.

30. Pasantes Ordóñez Herminia. Conferencia. “Marihuana, cerebro y sociedad”. Seminario de Cultura Mexicana, Corresponsalía Córdoba, Veracruz.

31. Pasantes Ordóñez Herminia. Conferencia. “El cerebro y los límites de la libertad”. Escuela Nacional de Antropología e Historia.

32. Pasantes Ordóñez Herminia. Conferencia. “Dr. Ricardo Tapia: scientist, university profesor and my friend”. Facultad de Química e Instituto de Fisiología Celular, UNAM.

33. Pasantes Ordóñez Herminia. Conferencia. “El cerebro y los límites de la libertad”. Universidad Autónoma del Estado de México.

34. Pasantes Ordóñez Herminia. Conferencia. “Las funciones cerebrales y las adicciones”. Universidad Pedagógica Nacional.

35. Pasantes Ordóñez Herminia. Conferencia. “El cerebro y los límites de la libertad”. Auditorio del Centro de las Artes de la Universidad de Sonora.

36. Pasantes Ordóñez Herminia. Conferencia. “El funcionamiento del cerebro humano”. Universidad Etac, Aliat Universidades, Campus Coacalco.

37. Pasantes Ordóñez Herminia. Conferencia. “El amor y las neuronas espejo”. Universidad Don Vasco, Uruapan Michoacán.

38. Pasantes Ordóñez Herminia. “Seminario de Política de Drogas”. Universidad Autónoma de San Luis Potosí.

39. Pasantes Ordóñez Herminia. Conferencia. “De neuronas, emociones y motivaciones”. Escuela Nacional Preparatoria, Secretaría de Difusión Cultural, San Ildefonso.

40. Pasantes Ordóñez Herminia. Conferencia. “Retos y perspectivas de las neurociencias”. Auditorio del HGZ no. 7 del IMSS.

41. Pasantes Ordóñez Herminia. Conferencia. “Marihuana, cerebro y sociedad”. Aula Magna Carlos Helguera.

42. Pasantes Ordóñez Herminia. Conferencia. “Retos y perspectivas de las Neurociencias”. Museo del Ferrocarril, Empalme, Sonora.

43. Pasantes Ordóñez Herminia. Conferencia. “Creatividad y cerebro”. Seminario de Cultura Mexicana, Corresponsalía La Paz, Baja California Sur.

44. Pasantes Ordóñez Herminia. Conferencia. “Mariguana, cerebro y sociedad”. Universidad de Colima.

45. Pasantes Ordóñez Herminia. Conferencia. “Cerebro y creatividad”. 4° festival de Neurociencias ¡Prende tu cerebro! (NEUROFEST). Foro de Química en Universum, UNAM.

46. Pasantes Ordóñez Herminia. Conferencia. “El cerebro y los límites de la libertad”. Leamos la Ciencia para todos. Preparatoria 6 UNAM.

47. Pasantes Ordóñez Herminia. Conferencia Magistral. “El cerebro y los límites de la libertad”. Instituto Nacional de Medicina Genómica, 5° encuentro estudiantil.

48. Pasantes Ordóñez Herminia. Conferencia. "Cerebro y creatividad". Sociedad Mexicana de Dermatología.

49. Pérez de la Mora Miguel. Conferencia. “Transtorno de Ansiedad”. Semana del Cerebro, IFC-UNAM.

50. Pérez Martínez Xochitl. Conferencia. "Máquinas moleculares, luces y comunicaciones celulares". Jornada de conferencias y evento de puertas abiertas del IFC.

51. Pérez Martínez Xochitl. Charla. ¡Quiero ser científica! Centro Cultural España.

52. Peña Segura Claudia. Taller. “¡No todo es verde! Fotosíntesis bacteriana!” Desvelos científicos, noches de ciencia para adultos. Centro Cultural España.

53. Ramirez Graullera Yoas Saimon. Conferencia. “Desarrollo de videojuegos para la neurorehabilitación”. Semana del Cerebro, IFC-UNAM.

54. Ramiro Cortés Yazmín. Conferencia. “Las espinas del cerebro de un ratón tipo autista”. Semana del Cerebro, IFC-UNAM.

55. Ramiro Cortés Yazmín. Charla. ¡Quiero ser científica! Centro Cultural España.

56. Recillas Targa Félix. Participación en el Café Científico, Ciencia+Cultura. “Edición genética en humanos: alcances y riesgos”. Centro Cultural UNAM, Morelia.

57. Romo Trujillo Ranulfo. Conferencia. “¿Estás seguro que tu tomas tus decisiones?”. San Luis Potosí.

58. Romo Trujillo Ranulfo. Conferencia. “El cerebro arquitecto de realidades”. Universidad de Sonora.

59. Sotres Francisco. Participación en el video de promoción del IFC. TV UNAM.

60. Tapia Ibargüengoytia Ricardo. Conferencia. “Las Neurociencias y las drogas: ¿por qué no deben estar prohibidas?”. Charlas con premios nacionales en colaboración con consejo consultivo de ciencias.

61. Tapia Ibargüengoytia Ricardo. Taller Somos cerebro. “Neuroética: ¿Qué hacer con el conocimiento de las neurociencias?”. Festival de la salud emocional.

62. Tapia Ibargüengoytia Ricardo. Conferencia. Neuroética: ¿Qué hacer con el conocimiento de las neurociencias? Semana del Cerebro.

63. Tecuapetla Aguilar Fatuel. Conferencia. “Para iniciar acciones se requiere a los circuitos dopaminérgicos y a los del tálamo”. Evento De sinapsis, ensambles y sistemas dinámicos.

64. Tovar y Romo Luis Bernardo. Conferencia. “Participación de las vesículas extracelulares en el proceso de recuperación después del infarto cerebral isquémico”. Evento De sinapsis, ensambles y sistemas dinámicos.

65. Tuena de Gómez Marietta. Presentaciónes del libro del Dr. Gómez Puyou. "Conociendo las Moléculas de la Vida ´un viaje inesperado". IFC- UNAM. Museo Universum-UNAM y XXI Congreso de Bioenergética y Biomembranas, San Luis Potosí.

66. Uribe Carvajal Salvador. Conferencia. “Endosimbiosis y enfermedades por organismos intracelulares”. Fiesta de las Ciencias y las Humanidades. Museo de las Ciencias Universum, UNAM.

67. Vaca Dominguez Luis Alfonso. Conferencia. “Debates en torno al futuro de la educación, la ciencia y la tecnología en México”. 40 Feria Internacional del Libro del Palacio de Minería.

68. Velasco Loyden Nora Gabriela. Charla. ¡Quiero ser científica! Centro Cultural España.

69. Velasco Velazquez Iván. Conferencia. “¿Cómo podemos producir neuronas de nuestro cerebro fuera del cuerpo?” Programa de Divulgación Científica "Domingos en la Ciencia" de la Academia Mexicana de Ciencias. Universidad Autónoma Metropolitana, campus Iztapalapa.

70. Valdés Rodríguez Víctor Julián. Plática de divulgación. "Epigenética y Medio Ambiente". Preparatoria No. 6, UNAM.

71. Valdés Rodríguez Julián. Conferencia. “Epigenética y memoria: en busca de las claves de la interacción entre genes y ambiente”. Fiesta de las ciencias y las humanidades. Museo de las Ciencias Universum, UNAM.

72. Valdés Rodríguez Julián. Mesa Redonda. “Ethics Dumping ¿El fin justifica los medios?”. Jueves de Ciencia. Casa de Francia. IFAL CdMx.

PREMIOS Y DISTINCIONES

1) Ayala Méndez Xóchitl Gabriela. Prórroga del Estímulo Especial “Federico Fernández Cancino”. Universidad Nacional Autónoma de México. Consejo Técnico de la Investigación Científica. 15-Febrero- 2019.

2) Bargas José. Mejor Servicio Social Gustavo Baz Prada. Alumno Yael Chavarría. UNAM. Facultad de Medicina. CdMx. 14-noviembre-2019.

3) Lara González, Esther; Duhne, Mariana; Ávila Cascajares, Fátima; Cruz, Silvia; Bargas, José. Implementación de un nuevo bioensayo farmacologico in vitro utilizando imagenología de calcio. Premio de la cámara nacional de la industria farmacéutica. CdMx. 31-octubre-2019.

4) Mas Oliva Jaime. Premio Universidad Nacional 2019. Área Ciencias Naturales. Universidad Nacional Autónoma de México. CdMx. 31-octubre-2019.

5) Méndez Maldonado, Karla; Vega López, Guillermo; Caballero Chacón, Sara;. Aybar, Manuel J; Velasco, Iván. Tercer lugar de la categoría Investigación Básica por el trabajo: “Células Troncales embrionarias de ratón que expresan MSX1 y HES1 incrementan la diferenciación a derivados de cresta neural” en la XXXIV Reunión anual de Investigación del Instituto. Instituto Nacional de Neurología y Neurocirugía "Manuel Velasco Suárez". CdMx. 17-mayo-2019.

6) Montiel Montes Teresa. Medalla “Sor Juana Inés de la Cruz”. Universidad Nacional Autónoma de México. CdMx. 8-marzo-2019.

7) Pérez Martínez Xochitl. Medalla José Laguna García. Reconocimiento por sus contribuciones a la Bioenergética y a las Biomembranas, otorgado a científicos menores de 50 años de edad. Rama de Bioenergética y Biomembranas de la Sociedad Mexicana de Bioquímica. San Luis Potosí. 10-noviembre-2019.

8) Pérez Martínez Xochitl. Apoyo económico otorgado a un grupo selecto de 15 científicos para asistir al EMBO Workshop on Protein Synthesis and Translational Control. EMBL Corporate Partnership Programme Fellowship. Alemania. 4-septiembre-2019.

9) Romo Trujillo Ranulfo. Cátedra Hugo Aréchiga. El Colegio de Sinaloa. Culiacán, Sinaloa. 11-marzo-2019.

10) Romo Trujillo Ranulfo. Premio Crónica 2019 en Ciencia y Tecnología. Revista Crónica, CdMx.

11) Sosa Garrocho Marcela. Renovación por tercera ocasión del Estímulo especial “Guillermo Massieu”, obtenido por desempeño.

12) Tapia Ricardo. Symposium en honor de Ricardo Tapia “Chemical transmission: the key to understanding brain function”. Facultad de Química, Instituto de Fisiología Celular, UNAM. CdMx. 23-abril-2019.

13) Tecuapetla Aguilar Fatuel. Cátedra de investigación para jóvenes científicos Moshinsky 2019. Fundación Moshinsky. Instituto de Física. UNAM. CdMx. 21-noviembre- 2019.

FUENTES DE FINANCIAMIENTO

Proyectos Financiados por DGAPA

1. Aguilar Roblero Raúl. Proyecto: "Manejo del cloro en neuronas del Núcleo Supraquiasmático y su participación en el reloj circadiano". IN205917. 01/2017-12/2019. Monto: $ 260,000.

2. Aguirre Linares Jesús. Proyecto: "La comunicación intracelular, intercelular e inter-reino en los hongos". IV200519. 01/2019-12/2019. Monto: $ 3, 479,004.

3. Aguirre Linares Jesús. Proyecto: "Las especies de oxígeno reactivas como señales reguladoras del citoesqueleto de actina y la dinámica y comunicación entre organelos celulares en los hongos". IN200719. 01/2019-12/2019. Monto: $ 240,000.

4. Álvarez Adrián Fernando. Proyecto: " Organización y función de microdominios membranales bacterianos". IN208718. 01/2018-12/2020. Monto: $ 240,000.

5. Arciniega Castro Marcelino. Proyecto: "Identificación de rutas alostéricas en la proteína PyrR de *Bacillus Halodurans* emplenado simulaciones de dinámica molecular, teoría de gráficase e información mutua". IN213320. 01/2020-01/2021. Monto: $ 246,280.

6. Bargas Díaz José. Proyecto: "Signos electrofisiológicos de la enfermedad de Parkinson en los Ganglios Basales: su posible uso como bioensayo farmacológico". IN201417. 03/2017- 12/2019. Monto: $ 250,000.

7. Bargas Díaz José. Proyecto: "Estudio de las discinesias inducidas por L-DOPA y de la modulación muscarínica de los canales de Ca2+ en las neuronas estriatales de roedor en un modelo Parkinsoniano". IN222920. 01/2020-12/2022. Monto: $ 260,000.

8. Castro Obregón Susana. Proyecto: "Estudio de la autofagia nuclear como respuesta al daño al DNA y en la senescencia celular". IN206518. 01/2019-12/2019. Monto: $ 240,000.

9. Chagoya de Sánchez Victoria. Proyecto: "Regulación de los genes mitocondriales durante la carcinogénesis en un modelo secuencial de cirrosis - carcinoma hepatocelular y el efecto del hepatoprotector IFC-305". IN214419. 01/2019-31/2019. Monto: $ 260,000.

10. Coria Ortega Roberto. Proyecto: "Mecanismos moleculares de la participación de los reguladores de respuesta Ssk1 y Skn7 en el estrés de retículo endoplásmico en la levadura". IN210519. 01/2019-12/2019. Monto: $ 240,000.

11. Del Río Guerra Gabriel. Proyecto: "Estudio del mecanismo de acción del péptido Iztli 1 en levadura y células de mamifero". IN208817. 01/2017-12/2019. Monto: $ 140,000.

12. Dreyfus Georges. Proyecto: "Caracterización de nuevos componentes involucrados en la formación y funcionamiento de los flagelos 1 y 2 de *Rhodobacter sphaeroides*". IN 204317. 01/2017-12/2019. Monto: $ 260,000.

13. Fernández De Miguel Francisco. Proyecto: “Liberación de serotonina del cuerpo neuronal”. IN210317. 01/2017-12/2019. Monto: $ 238,618.

14. Funes María Soledad. Proyecto: "Estudio de la biogénesis mitocondrial en respuesta a cambios metabólicos y condiciones de estrés en *Saccharomyces cerevisiae*". IN207518. 01/2018-12/2020. Monto: $ 240,000.

15. Furlan Magaril Mayra. Proyecto: "Dinámica de la arquitectura genómica y accesibilidad cromatínica durante la diferenciación y maduración eritroide". IN207319. 01/2019-01/2021. Monto: $ 240,000.

16. Galarraga Palacio Elvira. Proyecto: "Papel de la transmisión GABAérgica en el circuito de los Ganglios Basales y la excitabilidad neuronal”. IN201517. 01/2017-12/2019. Monto: $ 250,000.

17. Galarraga Palacio Elvira. Proyecto: "Comparación de las oscilaciones en el potencial de membrana en neuronas corticales y en neuronas intralaminares del tálamo". IN203020. 02/2020-12/2022. Monto: $ 260,000.

18. García Sáinz Jesús Adolfo. Proyecto: "Receptores acoplados a proteínas G". IN200718. 01/2017-12/2020. Monto: $ 260,000.

19. Georgellis Dimitrios. Proyecto: Control de la expresión génica microbiana por estímulos extracelulares". IN209918. 01/2018- 12/2020 Monto: $ 240,000.

20. Gómora Martínez Juan Carlos. Proyecto: "Contribución diferencial del canal Nav1.6 y las subunidades beta de los canales Nav a las propiedades metastásicas del cáncer cervicouterino". IN206917. 01/2019-12/2019. Monto: $ 250,000.

21. González Halphen Diego. Proyecto: "Estudios topológicos y estructurales de la ATP sintasa mitocondrial de un alga clorofícea". IN208917. 01/2017-12/2019. Monto: $ 250,000.

22. González Manjarrez Alicia. Proyecto: "Diversificación e interrelación funcional de los parálogos leu4-leu9 y bat1-bat2: su influencia sobre la actividad del regulador codificado por leu3 en la levadura *Saccharomyces cerevisiae*". IN204018. 01/2018-12/2020. Monto: $ 240,000.

23. González Pedrajo Bertha. Proyecto: "Estudio del reconocimiento de sustratos de secreción en el inyectisoma de *Escherichia coli* enteropatógena". IN209617. 01/2019-12/2019. Monto: $ 240,000.

24. Guerra Crespo Magdalena. Proyecto: “Estudio del desarrollo temprano de la enfermedad de Parkinson en un modelo *in vitro* de células troncales pluripotentes inducidas provenientes de un paciente con triplicación del gen de alfa-sinucleína". IN211419. 01/2019-12/2021. Monto: $ 189,986.

25. Hansberg Torres Wilhelm. Proyecto: "Diferenciación celular como respuesta a la tensión oxidante en *Neurospora crassa*". IN208717. 01/2017-12/2019. Monto: $ 240,000.

26. Hansberg Torres Wilhelm. Proyecto: “Los mecanismos de la diferenciación celular en la formación de las esporas asexuales de *Neurospora crassa”*. IN216920. 01/2020-12/2022. Monto: $ 240,000.

27. Hernández Cruz Arturo. Proyecto: "Estudios funcionales de cardiomiocitos humanos diferenciados de células pluripotentes inducidas de sujetos normales y pacientes con síndrome de Andersen-Tawil, una cardio-canalopatía del canal de potasio Kir2.1 que cursa con arritmia y muerte súbita". IG200119. 01/2019-12/2021. Monto: $ 200,000.

28. Hernández Muñoz Rolando. Proyecto: "Caracterización de la participación de los eritrocitos en el metabolismo del nitrógeno en humanos y su posible involucramiento en la fisiopatología de enfermedades metabólicas como la diabetes tipo 2 y la cirrosis". IN203217. 02/2018-01/2019. Monto: $ 246,000.

29. Hernández Muñoz Rolando. Proyecto: “Toxicidad por la administración crónica de tres anti-retrovirales sobre el metabolismo hepático de glucosa y lípidos en la generación de esteatosis hepática en ratas”. IT200420. 11/2019-10/2020. Monto: $ 200,000.

30. Hiriart Urdanivia Marcia. Proyecto: "La insulina, el receptor soluble de insulina y el factor de crecimiento neuronal como participantes del síndrome metabólico". IN208720. 01/2020-12/2023. Monto: $ 210,000.

31. Lemus Sandoval Luis. Proyecto: "Circuitos neuronales que representan sonidos complejos en monos *Rhesus*". IN207919. 01/2019-12/2021. Monto: $ 240,000.

32. Licona Limón Paula. Proyecto: "Evaluación del papel de la cinasa PKA y de su inhibidor PKIB en el desarrollo y función de linajes linfoides productores de IL-9". IN209919. 01/2019-12/2021. Monto: $ 260,000.

33. López Colomé Ana María. Proyecto: "Regulación de la actividad de los "Receptores Activados por Proteasa (PARs)" por la calpaína en el epitelio pigmentado de la retina". IN205317. 12/2016-12/2019. Monto: $ 260,000.

34. Macías Silva Marina. Proyecto: "Regulación de los cofactores transcripcionles Ski y SnoN en hepatocitos normales y transformados". IN208118. 01/2018- 12/2020. Monto: $ 240,000.

35. Mas Oliva Jaime. Proyecto: "Proteína CETPI descrita originalmente por nuestro grupo en el IFC, como novedosa molécula marcadora en septicemia y choque séptico". IN206619. 01/2019-12/2020. Monto: $ 240,000.

36. Massieu Trigo Lourdes. Proyecto: "Respuestas al estrés energético inducido por la privación de glucose en neuronas. Dinámica mitocondrial, mitofagia y función lisosomal y su modificación por el beta-hidroxibutirato". IN204919. 01/2019-12/2021. Monto: $ 240,000.

37. Morales Lázaro Sara Luz. Proyecto: "Mecanismos moleculares que participan en la respuesta de dolor mediada por el canal TRPV1 y los receptores de estrógenos". IN206819. 01/2019-12/2019. Monto: $ 200,000.

38. Morán Andrade Julio. Proyecto: "Mecanismos de muerte y diferenciación neuronal: papel de la señalización redox". IN212019. 01/2019-12/2021. Monto: $ 240,000.

39. Navarro González Rosa. Proyecto: "El papel de los gránulos de RNA, las mitocondrias y la apoptosis en la gónada del *C. elegans*.". IN208918. 01/2019-12/2019. Monto: $ 190,000.

40. Osorio Gómez Daniel. Proyecto: “Evaluación por optogenética de la participación de la proyección amígdala-corteza insular en el establecimiento de la valencia de los estímulos”. IA201420. 01/2020-12/2021. Monto: $ 190,000.

41. Pasantes Ordóñez Herminia. Proyecto: Desarrollo de aplicaciones y dispositivos para apoyar las terapias de rehabilitación en pacientes con discapacidad neurológica”. IT200318. 01/2019-12/2019. Monto: $ 211,124.

42. Peraza Reyes Leonardo. Proyecto: "La comunicación intracelular, intercelular e ínter-reinos en los hongos". IV200519. 01/2019-12/2021. Monto: $ 375,000.

43. Pérez de la Mora Miguel. Proyecto: "Papel de la interacción entre los receptores para la oxitocina y los receptores dopaminérgicos D2 y a2 adrenérgicos en la modulación amigdalina de la ansiedad en la rata". IN205217. 01/2017-12/2019. Monto: $ 259,520.

44. Pérez Martínez Xóchitl. Proyecto: "Estudio de los mecanismos de traducción en mitocondrias de *Saccharomyces cerevisiae*". IN209217. 01/2017-12/2019. Monto: $ 250,000.

45. Ramiro Cortés Yazmín. Proyecto: “Dinámica de la actividad neuronal de corteza visual primaria en respuesta a una tarea visual de sobre-especificidad en un modelo genético de autismo (ratones SHANK3)”. IN207420. 01/2020-12/2022. Monto: $ 200,000.

46. Recillas Targa Félix. Proyecto: "Participación de RNAs no-codificantes en la regulación diferencial de los genes α-globina y en la formación de sub-dominios cromatínicos". IN203917. 01/2017-12/2019. Monto: $ 150,000.

47. Recillas Targa Félix. Proyecto: "Organización tridimensional del genoma en la regulación transcripcional del gen *Notch1* humano". IN203620. 10/2019-10/2022. Monto: $ 260,000.

48. Romo Trujillo Ranulfo. Proyecto: “Decodificación de información de más de una modalidad sensorial en las poblaciones neuronales del lóbulo frontal durante la toma de decisiones”. IN210819. 01/2019-12/2021. Monto: $ 260,000.

49. Rosenbaum Emir Tamara. Proyecto: "Caracterización de regiones que sufren cambios conformacionales ante agonistas en el canal TRPV1 por ácido lisofosfatídico". IN200717. 01/2017-12/2019. Monto: $ 250,000.

50. Rosenbaum Emir Tamara. Proyecto: "Inhibición del canal iónico TRPV4 por compuestos broncodilatadores". IN200720. 01/2020-12/2022. Monto: $ 230,000.

51. Sotres Bayón Francisco Xavier. Proyecto: "Mecanismos cerebrales que subyacen la obtención de una recompensa a pesar del peligro". IN214520. 01/2020-12/2022. Monto: $ 189,900.

52. Sotres Bayón Francisco Xavier. Proyecto: "Contribución de la neurogénesis hipocampal al regreso del miedo condicionado después de la extinción". IN205417. 01/2017-12/2019. Monto: $ 270,000.

53. Tapia Ibargüengoytia Ricardo. Proyecto: "Mecanismos de degeneración neuronal y de regeneración axonal". IN206719. 01/2019-12/2019. Monto: $ 260,000.

54. Tecuapetla Aguilar Fatuel. Proyecto: "Monitoreo óptico de la actividad de los ganglios basales durante el inicio/selección de acciones *in vivo* por medio de microendoscopios, sensores de calcio y microscopia de dos fotones". IN226517. 01/2017-12/2019. Monto: $ 240,000.

55. Torres Quiroz Francisco. Proyecto: "Modificaciones post-traduccionales en residuos de cisteína y su dinámica en *Saccharomyces cerevisiae*". IN209219. 01/2019-12/2021. Monto: $ 204,000.

56. Tovar y Romo Luis Bernardo. Proyecto: "Estudio de las respuestas moleculares de los astrocitos en la isquemia cerebral". IN226617. 01/2017-12/2019. Monto: $ 260,000.

57. Uribe Carvajal Salvador. Proyecto: "Metabolismo aerobio de la levadura y de *Wolbachia sp*". IN203018. 01/2018-12/2020. Monto: $ 200,000.

58. Valdés Víctor Julián. Proyecto: "El papel del ciclo celular y el represor epigenético Polycomb en el establecimiento, mantenimiento y perdida de la memoria metabólica inducida por alta glucosa en células troncales embrionarias (mES)". IA202118. 01/2018-12/2019. Monto: $ 200,000.

59. Velasco Velázquez Iván. Proyecto: "La influencia de factores transcripcionales, factores de crecimiento y moléculas que guían el crecimiento axonal sobre neuronas diferenciadas de células troncales embrionarias". IN213719. 01/2019-12/2021. Monto: $ 255,000.

60. Velasco Torres Myrian. Proyecto: "Análisis funcional de los canales de potasio sensibles a ATP en el síndrome metabólico". IN210118. 01/2018-12/2019. Monto: $ 180,000.

Proyectos Financiados por CONACyT

1. Bargas Díaz José. Proyecto: "CONACyT Fronteras". "Estructura funcional de un microcircuito cortical". Fronteras-57. 17/2017-17/2019.

2. Bermúdez Rattoni Federico. Proyecto: "Estudio de la consolidación, evocación y actualización de la memoria. Mecanismos Neurobiológicos y sus implicaciones en procesos neuropatológicos". Ciencia Básica 250870. 2016-2019. Monto: $ 1,500,000.

3. Bermúdez Rattoni Federico. Proyecto: "La corteza insular como nuevo blanco para estudiar los mecanismos celulares de la formación y mantenimiento de las memorias adictivas". Fronteras de la Ciencia 474. 2015-2019. Monto: $ 4,000,000.

4. Bermúdez Rattoni Federico. Proyecto: "Proyecto de Investigación en colaboración Franco-Mexicano". OBETEEN. 2016-2020. Monto: € 500,000.

5. Castro Obregón Susana. Proyecto: "Probando la hipótesis de que en el envejecimiento fisiológico emergen nichos para el desarrollo de enfermedades crónicas". Fronteras 015-2#921. 12/2016-10/2019. Monto: $ 3,000,000.

6. Coria Ortega Roberto. Proyecto: "Papel de las proteínas G en la respuesta al estrés de retículo endoplásmico en levaduras". 254078. 07/2018-07/2019. Monto: $ 315,000.

7. Dreyfus Cortés Georges. Proyecto: "Estudio sobre la regulación de la expresión del sistema flagelar 2 en *Rhodobacter sphaeroides*". 235996. 07/2015-02/2019. Monto: $ 430,000.

8. Escalante Alcalde Diana. Proyecto: "La LPP3, una enzima reguladora de la actividad de lípidos bioactivos, como enzima fundamental para el desarrollo del sistema nervioso y en la neurogénesis adulta". CB-250613. 11/2016-10/2019. Monto: $ 560,000.

9. Galarraga Palacio Elvira. Proyecto: "Caracterización funcional de la vía tálamo estriatal". 251144. 08/2017-07/2020. Monto: $ 450,000.

10. García Sáinz Jesús Adolfo. Proyecto: "Regulación de la función de receptores acoplados a proteínas G". 253156. 07/2017-06/2019. Monto: $ 500,000.

11. Gómora Martínez Juan Carlos. Proyecto: "Bases moleculares y funcionales en la modulación de canales de calcio tipo T de humano por compuestos estructuralmente diversos". A1-S-19171. 09/2019-09/2022. Monto: $ 666,000.

12. González Halphen Diego. Proyecto: "Hacia la cristalización de una atp sintasa mitocondrial dimérica: efectos de un detergente de nueva generación derivado del lauril-maltósido". 279125. 01/2017-12/2020. Monto: $ 20,000.

13. González Pedrajo Bertha. Proyecto: "Regulación de la secreción de proteínas a través del inyectisoma de *Escherichia coli* enteropatógena: estudio del reconocimiento y jerarquización de sustratos". 284081. 06/2018-06/2021. Monto: $ 666,000.

14. Guerra Crespo Magdalena. Proyecto: "Desarrollo de una nueva estrategia de diferenciación de células troncales pluripotentes humanas trasplantadas en un modelo de enfermedad de Parkinson". A1-S-10064. 10/2019-09/2021. Monto: $ 858,387.

15. Hernández Cruz Arturo. Proyecto: "Laboratorio Nacional de Canalopatias consolidacion III". 299051. 05/2019-11/2019. Monto: $ 1,500,000.

16. Lemus Luis. Proyecto: "Procesamiento de información rio-arriba y rio-abajo en el circuito audiomotor durante el seguimiento del ritmo de un metrónomo en primates humanos y no-humanos". Fronteras de la Ciencia 196. 06/2015-06/2019. Monto: $ 800,000.

17. Lemus Luis. Proyecto: "Codificación Neuronal de Objetos Auditivos". 256767. 01/2016-01/2019. Monto: $ 498,700.

18. Licona Limón Paula. Proyecto: "Mecanismos moleculares en el control de la diferenciación de los linajes linfoides: regulación por la citocina TGF-β y la cinasa PKA". 255287. 07/2016-07/2019. Monto: $ 685,000.

19. López Casillas Fernando. Proyecto: "Análisis genético reverso (CRISPR-Cas9) de la función del Betaglicano en el desarrollo embrionario del pez cebra". 254046. 01/2019-02/2020. Monto: $ 500,000.

20. López Colomé Ana María. Proyecto: "La trombina como agente inductor de gliosis en la retina". 254333. 10/2016-10/2019. Monto: $ 1,370,000.

21. Luis Baltazar Enoch. Proyecto: "El cancer como canalopatia: identificación y caracterización de nuevos compuestos con efecto modulador sobre canales oncogénicos de K^+". A1-S-13646. 01/2019-01/2020. Monto: $ 376,308.

22. Mas Oliva Jaime. Proyecto: "Estudio de correlación estructura/función de CETPI como una nueva proteína de unión a lipopolisacáridos bacterianos". 255778. 06/2016-07/2019. Monto: $ 660,000.

23. Massieu Trigo Lourdes. Proyecto: "Pérdida de la proteostasis por la privación y reintroducción de glucosa en neuronas, su papel en la muerte neuronal y su posible restablecimiento por acción del β-hidroxibutirato". CB A-1S-17357. 11/2019-11/2020. Monto: $ 507,333.

24. Morán Andrade Julio. Proyecto: "Señalización redox en el desarrollo neuronal: papel en la muerte neuronal y el crecimiento axonal". 285184. 06/2018-06/2021. Monto: $ 1,800,000.

25. Navarro González Rosa. Proyecto: "Mecanismos de regulación de la respuesta al estrés de las células germinales del nematodo *Caenorhabditis elegans*". 220987. 03/2015-06/2019. Monto: $ 500,000.

26. Peña Díaz Antonio. Proyecto: "Efectos de agentes catiónicos, sal y pH sobre *Saccharomyces cerevisiae* y *Debaryomyces hansenii*. Cultivo de metabolismo y bioenergética de *Wolbachia pipientis*" 238497. 07/2016-09/2019. Monto: $ 600,000.

27. Peraza Reyes Leonardo. Proyecto: "Crosstalk between peroxisomes, endoplasmic reticulum, and endosomes during polar growth and development in fungi". 277869. 03/2018-02/2021. Monto: $ 803,000.

28. Pérez Martínez Xochitl. Proyecto: "Estudio de los mecanismos de acoplamiento entre la síntesis de proteínas mitocondrial y citosólica". 284514. 02/2018-02/2020. Monto: $ 908,000.

29. Pérez Montfort Ruy. Proyecto: "Estudios en enfermedades humanas de la triosafosfato isomerasa". 254694. 10/2016-02/2020. Monto: $ 500,000.

30. Ramiro Cortés Yazmín. Proyecto: "Plasticidad sináptica y estructural en un modelo de autismo". 254878. 09/2016-08/2019. Monto: $ 412,500.

31. Recillas Targa Félix. Proyecto: "La organización tridimensional de genoma en la regulación de la expresión génica". Fronteras de la Ciencia 2015-290. 01/2017-12/2019. Monto: $ 2,000,000.

32. Recillas Targa Félix. Proyecto: "Papel del factor nuclear CTCF y RNAs no-codificantes en la regulación de la expresión génica y la estructura de la cromatina". 220503. 03/2017-02/2018. Monto: $ 500,000.

33. Recillas Targa Félix. Proyecto: "Regulación epigenética y transcripcional de dos RNAs largos no codificantes divergentes en líneas de cáncer de mama". CONACyT Básica A1-S-11844. 09/2018-08/2021. Monto: $ 1,900,000.

34. Rosenbaum Emir Tamara. Proyecto: “Regulación del canal TRPV4 por fosfolípidos ". A1-S-8760. 01/2019-01/2021.

35. Sotres Bayón Francisco. Proyecto: "Previniendo el regreso del miedo: contribución de la neurogénesis hipocampal". 2463. 05/2018-05/2020. Monto: $ 1,500,00.

36. Tapia Ibargüengoytia Ricardo. Proyecto: "Mecanismos celulares de la degeneración y regeneración neuronal". A1-S-12135. 09/2019-08/2020. Monto: $ 560,000.

37. Tecuapetla Aguilar Fatuel. Proyecto: "Optogenética: visualización y evaluación de los subcircuitos del control motor *in vivo*". Fronteras de la Ciencia 2022. 10/2017-10/2019. Monto: $ 200,000.

38. Torres Larios Alfredo. Proyecto: "Estudios estructurales sobre complejos ribonucleoproteicos". CB2015-253323. 06/2016-06/2019. Monto: $ 800,000.

39. Tovar y Romo Luis Bernardo. Proyecto: "Regulación trófica de la viabilidad neuronal; mecanismos endógenos de recuperación después del infarto cerebral isquémico". A1-S-13219. 10/2019-10/2022. Monto: $ 500,000.

40. Valdés Víctor Julián. Proyecto: "Papel de la epigenética en circuitos neuronales involucrados en conducta de *Caenorhabditis elegans*". 284867. 01/2018-12/2020. Monto: $ 500,000.

41. Velasco Velázquez Iván. Proyecto: "Diferenciación de células troncales pluripotenciales humanas a neuronas dopaminérgicas para generar modelos celulares de la enfermedad de parkinson y realizar estudios pre-clínicos de trasplante". 272815. 12/2016-05/2020. Monto: $ 3,000,000.

42. Velasco Velázquez Iván. Proyecto: "Diferenciación dopaminérgica de células troncales: estudios de crecimiento axonal y superviviencia en ratas que modelan la enfermedad de Parkinson". CB15-256092. 07/2016-06/2019. Monto: $ 1,500,000.

43. Velasco Velázquez Iván. Proyecto: "Estudios de secuenciación masiva y proteómica para la identificación de reguladores moleculares de la regeneración posterior al daño en la médula espinal del ajolote. Convocatoria bilateral CONACyT-Tubitak (Turquía) del Fondo CONACyT-Secretaría de Relaciones Exteriores". 265793. 12/2017-04/2020. Monto: $ 1,735,000.

44. Velasco Velázquez Iván. Proyecto: "Liberación de factores quimioatrayentes para axones dopaminérgicos humanos por nanoesferas vacías de dióxido de Titanio". UC-MEXUS CN 19-163. 07/2019-12/2020. Monto: 25,000 USD.

Proyectos Financiados por Otras Empresas de Gobierno Federal y Local

1. Castro Obregón Susana. Proyecto: “Investigación sobre el potencial papel terapéutico de inducir la autofagia con una combinación de ayuno intermitente, dieta cetogénica e ingesta de trehalosa para aminorar síntomas relacionados al envejecimiento". INGER-DI-CRECITES-008-2018. 11/2018-10/2019. Monto: $ 1,292,760.

2. Mas Oliva Jaime. Proyecto: "Secretaría de Desarrollo Institucional (UNAM). Supercómputo (MIZTLI)". LANCAD-UNAM-DGTIC-352. 02/2019-12/2019. Monto: $ 153,000.

3. Massieu Trigo Lourdes. Proyecto: "Potencial papel terapéutico de inducir la autofagia con una combinación de ayuno intermitente, dieta cetogénica e ingesta de trehalosa para aminorar síntomas relacionados al envejecimiento fisiológico y la enfermedad de Alzheimer. Resp. S. Castro". INGER-DI-CRECITES-008-2018. 11/2018-11/2019. Monto: $ 1,292 760.

4. Rosenbaum Emir Tamara. Proyecto: "Potenciales blancos terapéuticos para evitar la progresión de daño renal en la enfermedad poliquística del adulto". 9625c19. 01/2020-12/2020. Monto: $ 1,000,000.

5. Salceda Sacanelles Rocío. Proyecto: "Red Colaborativa de Investigación Traslacional para el Envejecimiento Saludable de la Ciudad de México". INGER-DI-CRECITES-006-2018. 10-2018/10-2019. Monto: $ 375,000.

Proyectos Financiados por Organismos y Empresas Nacionales

1. Chagoya de Sánchez Victoria. Proyecto: "Vela Advisor SA". CIE 1407279. 01/2019-12/2019. Monto: $ 1,500,000.

2. Mas Oliva Jaime. Proyecto: "Estímulo a la Investigación Médica, Miguel Alemán Valdés”. 01/2019-12/2019. Monto: $ 100,000.

3. Recillas Targa Félix. Proyecto: "Estímulo a la Investigación Médica, Miguel Alemán Valdés”. 12/2018-12/2019. Monto: $ 100,000.

4. Valdés Rodriguez Víctor Julián. Proyecto: "Premio Ruben Lisker 2018". 4ta edición. 11/2018-11/2020. Monto: $ 1,000,000.

Proyectos Financiados por Organismos y Empresas Internacionales

1. Bermúdez Rattoni Federico. Proyecto: "Transcriptional signatures of cognitive decline in an Alzheimer´s disease model". The Royal Society. 07/2017-07/2019. Monto: £11,953.

2. Del Río Guerra Gabriel. Proyecto: "Alexander von Humboldt foundation. Study of anastasis in yeast". 06/2019-12/2019. Monto: $ 400,000.

3. Fernández De Miguel Francisco. Proyecto: "Human Frontiers Science Program". RGP0060/2019. 07/2019-06/2021. Monto: 110,000 USD.

4. Fernández De Miguel Francisco. Proyecto: "Society for Neuroscience". 2019-3276. 08/2019. Monto: 70,000 USD.

5. Licona Limón Paula. Proyecto: "Unión Iberoamericana de Universidades. Second Research Collaboration Fund 2019.". USP-05-2019. 09/2019-08/2020. Monto: 2,000 USD.

6. Tovar y Romo Luis Bernardo. Proyecto: "Committee for Aid and Education in Neurochemistry - International Society for Neurochemistry". Cat 1B. 10/2019-09/2020. Monto: 4,500 USD.

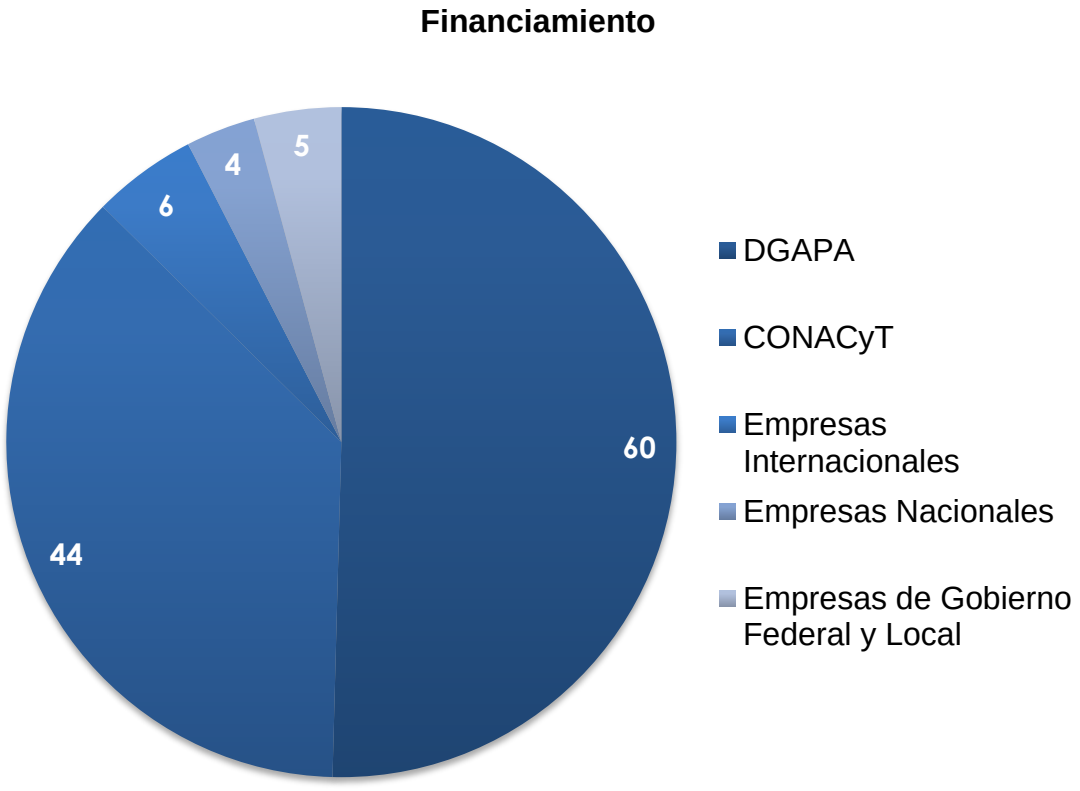

CONVENIOS E INTERCAMBIOS

Convenios Suscritos por Personal del IFC

1. Bermúdez Rattoni Federico. Efectuado con: Francia (ANR)-México (CONACyT). Proyecto: Evaluación de daños cognitivos en animales jóvenes sometidos a dietas hipercalóricas. De investigación. Fecha: 2016-2020. Financiado por: CONACyT. Monto: € 500,000.

2. Gómora Martínez Juan Carlos. Efectuado con: Dr. Sebastien Roger. Proyecto: Pharmacological and nutritional targeting of voltage-gated sodium channels in the treatment of epithelial cancers. Fecha: 09/2017-08/2019. Financiado por: Le Studium Research Consortium.

3. Hernández Cruz Arturo. Efectuado con: Centro Universitario de Investigaciones Biomédicas de la Universidad de Colima. Proyecto: Laboratorio Nacional de Canalopatías (consolidación III), Participación como Unidad Asociada. De investigación. Fecha: 06/2019-12/2019. Financiado por: CONACyT. Monto: $ 1,500,000.

4. Hernández Cruz Arturo. Efectuado con: Instituto de Ciencias del Mar y Limnologia, UNAM. Proyecto: Laboratorio Nacional de Canalopatías (Consolidación III). Participación como Unidad Asociada de Investigación. Fecha: 06/2019-11/2019. Financiado por: CONACyT. Monto: $ 1,500,000.

5. Hernández Cruz Arturo. Efectuado con: CINVESTAV Unidad Monterrey. Proyecto: Laboratorio Nacional de Canalopatías (Consolidación III). Participación como Unidad Asociada. De investigación. 06/2019-11/2019. Financiado por: CONACyT. Monto: $ 1,500,000.

6. Hernández Cruz Arturo. Efectuado con: Facultad de Química/Unidad de Investigación Preclínica. Proyecto: para llevar a cabo de manera conjunta actividades en materia de investigación, desarrollo tecnológico, estancias de investigación, proyectos científicos, formación y capacitación de recursos humanos. De investigación. Fecha: 08/2018-08/2022.

7. López Colomé Ana María. Efectuado con: Dr. Luis Fernando Hernández Zimbrón. Proyecto: Desarrollo y aplicación de materiales avanzados en la producción de Bio-Membranas artificiales funcionales para su uso en medicina traslacional: DMRE (MEMBRANAS V1 090818). Financiado por: Asociación para evitar la ceguera en México, IAP.

8. Rossi Pool Román. Efectuado con: Dr. Nestor Parga Carballeda. Proyecto: Performance, behavioral biases and confidence in the two-interval forced-choice paradigm. De investigación. Fecha: 10/2018-10/2021. Financiado por: ANPCYT - Madrid, España.

9. Tovar y Romo Luis Bernardo. Efectuado con: Dr. Nigel H Greig. Proyecto: Single cell transcriptomics of microglial responses to traumatic brain injury. De investigación. Fecha: 07/2019-09/2019.

10. Velasco Velázquez Iván. Efectuado con: Instituto Nacional de Neurología y Neurocirugía "Manuel Velasco Suárez" (INNN-MVS). Proyecto: Convenio para continuar con el funcionamiento del Laboratorio de Reprogramación Celular del Instituto de Fisiología Celular-UNAM en el INNN-MVS. Convenio con número de registro 48955-1771-25-VII-17. 11/2017-11-2020.

UNIDADES DE SERVICIO

Unidad de Biología Molecular



Responsable:

Laura María Ongay Larios, Dra.	**Técnico Académico Titular C. PRIDE D. SNI I.**
María Guadalupe Códiz Huerta, Biól.	Técnico Académico Titular B. PRIDE C.
Dolores Minerva Mora Cabrera, M. en C.	Técnico Académico Titular B. PRIDE C.

En esta unidad se ofrecieron los siguientes servicios técnicos:

- Síntesis de oligonucleótidos.
- Secuenciación capilar automatizada.
- Tipificación de fragmentos por electroforesis capilar.
- Secuenciación masiva (NGS).
- Purificación de DNA.
- Clonación de DNA.
- Analizadores de muestras marcadas con radioactividad, quimioluminiscencia o quimiofluorescencia.
- PCR en tiempo real.
- Analizador de imágenes.
- Electroforesis en campo ortogonal.
- Termocicladores.
- Citómetro de flujo.
- Espectrofotómetro
- Banco de plásmidos y cepas bacterianas.

Durante 2019 se sintetizaron 897 oligonucleótidos con un total de 24,542 bases (usuarios internos 613 oligonucleótidos (16,089 bases), usuarios externos 244 oligonucleótidos (17,809 bases), usuarios externos 284 oligonucleótidos (6,733 bases). Algunos oligonucleótidos fueron purificados por PAGE. El servicio fue utilizado por 28 grupos de investigación del instituto, 6 dependencias de la UNAM y 11 fuera de la UNAM. También se secuenciaron plásmidos,

cósmidos, productos de PCR, se realizaron 2,101 secuencias (servicio interno 1,307 reacciones, servicio externo 794). Se realizó la electroforesis de 273 reacciones listas para correr (servicio interno 20 reacciones, externo 253). El servicio de secuenciación fue utilizado por 26 grupos de investigación del instituto, 7 por dependencias de la UNAM y 14 de fuera de la UNAM. En este año se corrieron 16 análisis de fragmentos para análisis de Fragile X. Se purificaron 26 productos de PCR, el servicio fue usado por 2 grupos de investigación fuera de la UNAM. En 2019 se realizaron 208 “scans”, este servicio fue utilizado por 5 grupos de investigación de este Instituto. Se llevaron a cabo 338 corridas de PCR en tiempo real. El 92% fueron realizadas por 16 grupos de investigación del IFC, y el 8% por 4 grupos de investigadores de otras dependencias de la UNAM y uno externo. El Analizador de imágenes fue utilizado 530 veces por 25 grupos de investigación de este Instituto. En los Termocicladores el servicio fue utilizado por 18 grupos de investigación del IFC. En el Citómetro de flujo se hicieron un total de 91 corridas de citrometría y el servicio fue utilizado por 10 grupos de investigación del IFC. Los equipos de Espectrofotómetro fueron utilizados 1,054 veces por grupos de investigación del IFC y 1 de una dependencia de la UNAM. Los bancos de plásmidos y cepas bacterianas de uso común en técnicas de Biología Molecular se han mantenido y actualizado.

Asesoría y apoyo técnico. La unidad proporcionó asesoría y entrenamiento a estudiantes, técnicos e investigadores en diferentes técnicas de Biología Molecular como purificación de DNA mitocondrial y nuclear, purificación de plásmidos, productos de PCR, amplificación de secuencias de DNA y RNA mediante las técnicas de PCR y RT-PCR, clonación de DNA en sistemas bacterianos, análisis de DNA recombinante, análisis de patrones de restricción, electroforesis en geles de agarosa y acrilamida, electroforesis en campo ortogonal, hibridaciones tipo Southern, “Dot Blot” y Northern, marcaje de sondas, análisis de oligonucleótidos en geles de acrilamida, purificación de RNA total y mensajero. Así como asesoría y entrenamiento en secuenciación capilar automatizada de DNA y secuenciación de siguiente generación (NGS). En 2019 la Unidad recibió 32 agradecimientos; tanto para la unidad como individuales, 17 agradecimientos en 8 artículos internacionales y 24 en tesis (2 de licenciatura, 8 de maestría y 14 de doctorado). Así como 1 publicación en 1 artículo internacional. Se impartieron 8 cursos en la UNAM y se asistió a diversas reuniones académicas.

Comisión de la Unidad de Biología Molecular:

Dra. Mayra Furlan Magaril
Biól. Gustavo Sánchez Chávez
Dra. Laura Ongay
Dr. Luis Tovar y Romo
Secretaria Ejecutiva: Dra. Susana Castro

Unidad de Cómputo





Responsable:

José Gerardo Coello Coutiño, Biól.	**Técnico Académico Titular C. PRIDE D.**
Ana María Escalante Gonzalbo, M. en C.	**Técnico Académico Titular C. PRIDE D.**
Juan Manuel Barbosa Castillo, Ing.	Técnico Académico Titular A. PRIDE C.
Francisco Pérez Eugenio, Lic.	Técnico Académico Titular A. PRIDE D.
Ivett Rosas Arciniega, Ing.	Técnico Académico, Asociado C. PRIDE B.
Pablo Rangel Silva, Méd. Cir.	Técnico Académico Titular A. PRIDE B.
Yoas Saimon Ramírez Graullera, Lic.	Técnico Académico, Asociado C. PRIDE B.

La unidad de Cómputo es responsable del mantenimiento, implementación y desarrollo de todos los recursos de cómputo generales del IFC. Esto incluye mantenimiento de servidores, comunicaciones, videoconferencia, páginas de internet, herramientas de bioinformática mantenimiento y actualización de equipos, así como el soporte técnico a los miembros de la comunidad. Así mismo da asesoría a los usuarios del instituto y a externos, imparten cursos y preparan personal en el área, quienes realizan su servicio social y sus tesis. También se administra el servicio de videoconferencia.

En 2019 se supervisó y se llevaron a cabo trabajos de canalización, cableado e instalación de equipos de comunicación de la nueva red de datos del Instituto. Se configuraron los equipos de comunicación y se instalaron en cada uno de los 14 closets de datos para la nueva red. Se instaló el nuevo firewall de red, se configuraron las reglas de acceso y migración de las reglas de otros 2 firewall que funcionaban con la antigua red. Se realizó la migración de todas las cuentas de correo electrónico del IFC del servidor Zimbra a una cuenta institucional de Gmail. Se administró, actualizó y monitoreó de los más de 30 servidores de red que hay en el Instituto. También se llevó a cabo el mantenimiento correctivo de varios equipos del IFC. También se apoyó en la transmisión por streaming, grabación y almacenamiento de cursos y seminarios dictados por videoconferencia. Se brindó apoyo de videoconferencia para la impartición de 8 cursos de posgrado con Institutos de la UNAM y para la realización de 142 exámenes tutorales, 24 de grado y 16 candidaturas. Se llevaron a cabo enlaces de videoconferencia para la transmisión de más de 65 seminarios institucionales. Se realizaron 40 enlaces de videoconferencias para reuniones de trabajo, comisiones dictaminadoras y juntas de diversa índole. Se actualizó el programa del Informe de labores del IFC. Se impartieron 3 cursos de Licenciatura en la Facultad de Ingeniería. La Unidad recibió 4

agradecimientos en artículos internacionales, 1 agradecimiento en tesis de licenciatura, 1 de maestría y 5 de doctorado. Se brindó apoyo logístico al Laboratorio de Neuro-Rehabilitación que participó en diversas actividades académicas.

Comisión de la Unidad de Cómputo:
Dr. Luis Lemus Sandoval
M.I. Manuel Tonatiuh Figueroa Vanegas
Dra. Xóchitl Pérez Martínez
Dr. Marcelino Arciniega
Biól. Gerardo Coello
Secretario Ejecutivo: Dr. Diego González Halphen

Imagenes de la Nueva Red de Computo del IFC






Unidad de Imagenología






Responsable:

Ruth Rincón Heredia, Dra.	**Técnico Académico Asociado C. PRIDE B. SNI I**
Rodolfo Paredes Díaz, Méd. Cir.	Técnico Académico Titular A. PRIDE C.
Abraham Rosas Arellano, Dr.	Técnico Académico Titular B. SNI I.
Nicolás Jimenez Pérez, Dr.	Técnico Académico Titular B. PRIDE C.

Página de internet:
https://sites.google.com/email.ifc.unam.mx/imagenologa-ifcunam/p%C3%A1gina-principal

La unidad provee el acceso a tecnología de punta, en el área de microscopia a estudiantes e investigadores del Instituto de Fisiología Celular y otras dependencias de la UNAM, e instituciones externas, así como a la industria. De manera general la Unidad de Imagenología se divide en dos grandes ramas de la microscopia: 1) la microscopía fotónica y 2) la microscopía electrónica. Es también función de la unidad apoyar la divulgación de las investigaciones que se llevan a cabo en el Instituto, por medio de la participación en congresos especializados en el área y en recibir visitas guiadas de estudiantes de nivel superior.

Actividades realizadas en 2019:

- En el área de microscopía electrónica de barrido y transmisión se procesaron un total de 77 muestras epon, 12 muestras para tinción negativa y 3 muestras para inmunogold, para diferentes grupos de investigación del Instituto. Se atendieron un total de 176 horas en el Microscopio Electrónico de Transmisión.
- La microscopía electrónica de barrido se atendieron un total de 20 usuarios, también se procesaron 2 muestras recubiertas de oro. El personal también participó en 3 publicaciones científicas internacionales. El trabajo de la unidad fue reconocido con agradecimientos en 12 publicaciones científicas, en 2 agradecimientos en tesis de licenciatura, 16 de maestría y 6 de doctorado. También se recibieron 2 visitas guiadas.

Comisión de la Unidad de Microscopía (Imagenología):

Dr. Luis Vaca Domínguez
Dra. Yazmín Ramiro Coirtés
Dra. Ruth Rincón Heredia
Dr. Miguel Tapia (externo, Biomédicas)
Secretaria Ejecutiva: Dra. Diana Escalante

Laboratorio Nacional De Canalopatías



Laboratorio Nacional de Canalopatías

Responsable:

Arturo Hernández Cruz, Dr. — **Investigador Titular C. PRIDE D. SNI III.**
Arturo Picones Medina, Dr. — Técnico Académico Titular A. PRIDE B.
Enoch Luis Baltazar, Dr. — Catedrático CONACyT.
Arlet del Carmen Loza Huerta, Dra. — Técnico Especializado por honorarios.Cand. SNI.
César Oliver Lara Figueroa, Fís. — Técnico Especializado por honorarios.

En el Laboratorio Nacional de Canalopatías (LaNCa) se brindan servicios de citometría de flujo, fluorometría, electrofisiología e imagenología automatizada, a grupos de investigación del Instituto, así como de la UNAM y fuera de ella y también a sus instituciones asociadas.

Cuenta con equipamiento automatizado para ensayos electrofisiológicos y fluorométricos y de citometría de flujo rápidos y de alto rendimiento, así como el registro electrofisiológico tradicional (manual), que sigue siendo el “gold estándar” para validar resultados.

Durante el año 2019 el LaNCa participó en 3 actividades de difusión y divulgación, participó en 2 reuniones académicas nacionales y 2 internacionales; así como en congresos nacionales e internacionales. Se publicaron 5 artículos internacionales en revistas indizadas. También recibieron 2 agradecimientos en publicaciones internacionales. Se graduaron 3 estudiantes de licenciatura. Se dictaron 6 cursos de licenciatura y se participó en 6 actividades de apoyo a la docencia.

Coordinación de Difusión Y Divulgación

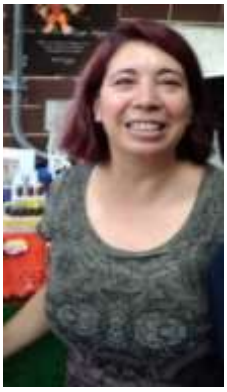



Responsable:

Luz Lazos, Dra. — **Técnico Académico Titular B. PRIDE B.**
Ana Cecilia Rosen Ferlini, Dra. — **Técnico Académico Titular B. PRIDE B. Cad. SNI.**
Felipe Zenil Ongay, M. en C. — Técnico Especializado por honorarios.

En esta Coordinación se diseña, planea y coordinan las actividades para la divulgación de las investigaciones en ciencias biológicas y neurociencias del Instituto. También se incluyen aspectos como el diseño de materiales educativos y de comunicación dirigido a profesores, estudiantes y público en general, en versiones impresas y digitales, la planeación y diseño de cursos presenciales y a distancia para profesores. También la vinculación con diferentes dependencias universitarias para la colaboración en proyectos conjuntos de comunicación, educación, arte y cultura. Durante el año 2019 se participó en diferentes eventos de difusión de la ciencia en la UNAM y fuera de ella, se diseñaron carteles para la difusión de los eventos académicos que se llevaron a cabo en el IFC y su adaptación para los distintos formatos con son: web, pantallas del IFC y redes sociales. Se elaboraron notas informativas diversas. Se apoyó en la coordinación a los investigadores que participaron en diferentes charlas y se coordinaron las visitas guiadas de Jóvenes hacía la Investigación.

Comisión de Difusión y Divulgación:

Dra. Soledad Funes
M. en C. Blanca Delgado
Dra. Gabriela Loyden
Secretaria Ejecutiva: Dra. Herminia Pasantes

https://sites.google.com/ifc.unam.mx/comunicacion



Biblioteca “Armando Gómez Puyou”



Responsable:

Sandra G. Moncada Hernández, Mtra. — **Técnico Académico Titular B. PRIDE C.**
Javier Gallegos Infante, Cir. Dent. — Técnico Académico Titular B. PRIDE C.

Durante el año 2019 la Biblioteca contó con el siguiente acervo bibliográfico y hemerográfico: 58 libros adquiridos para acervo, 199 suscripciones a publicaciones periódicas vigentes, 3 suscripciones de publicaciones periódicas impresas y además 3 libros adquiridos para el personal académico.

Servicios Bibliotecarios:
Consulta Electrónica. Se apoyó a los usuarios tanto internos como externos, en los servicios de información generados por la biblioteca (catálogo electrónico de las colecciones bibliográfica y hemerográfica), de la Dirección General de Bibliotecas y de otras fuentes de información, así como también realizando búsquedas en fuentes especializadas. Tanto el personal académico como los bibliotecarios asisten a los usuarios a través de asesorías u orientación en el uso de estas herramientas de búsqueda.

En 2019 se apoyó en los servicios de información electrónicos, como catálogo electrónico de las colecciones bibliográfica y hemerográfica. También se adquirió bibliografía para la Licenciatura en Neurociencias. Se asesoró a los usuarios internos y externos para el uso eficiente de los recursos de información electrónica. Se recibieron agradecimientos en tesis: 1 de licenciatura, 3 de maestría y 3 de doctorado. Se atendieron 15 solicitudes de búsquedas de citas, en las diferentes bases de datos especializados, 11 para usuarios del IFC y 4 externos.

Comisión de la Biblioteca:

Dra. Rosa Navarro
Dr. Julián Valdés
Odont. Javier Gallegos
Mtra. Sandra Moncada
Secretario Ejecutivo: Dr. Raúl Aguilar

Bioterio



Responsable:

Claudia V. Rivera Cerecedo, MVZ — **Técnico Académico Titular C. PRIDE D.**
Héctor Alfonso Malagón Rivero, MVZ — Técnico Académico Titular A. PRIDE C.
Gabriela X. Ayala Méndez, M. en IBB — Técnico Académico Titular B. PRIDE C.

En el bioterio se llevan a cabo actividades relacionadas con el cuidado de animales para experimento. Durante el 2019 se cumplieron los requerimientos de animales para los protocolos aprobados por el CICUAL. El promedio en producción al año de ratas (*Ratus norvergicus)* fue de 3,682. Una de las actividades más importantes de esta unidad es brindar apoyo a los investigadores y estudiantes de posgrado que utilizan animales en sus protocolos de investigación. Durante este año, 88 protocolos de los 156 que fueron aprobados por el CICUAL permanecieron vigentes. En 2019 se utilizaron 6,933 *Ratus norvergicus,* 8,066 *Mus musculus* y 12 *Oryctolagus cuniculus.* Además de dar mantenimiento a los animales en fase experimental. En el año 2019 los investigadores de otras instituciones de la UNAM y fuera de ella, continuaron adquiriendo roedores producidos en el bioterio de este Instituto. Durante 2019, el personal académico impartió y asistió a diversos cursos. Se impartieron 4 asesorías sobre diferentes temas relacionados con la ciencia de los animales, 5 cursos talleres teórico práctico de manejo de roedores de laboratorio. También se impartió el curso de Cirugía Básica en Roedores. En este año 1 alumno concluyó su servicio social.

Comisión del Bioterio (CICUAL):

Dra. Paula Licona
MVZ. Claudia Rivera
Dr. Fatuel Tecuapetla
Dra. Rocio Alcántara
Secretaria Ejecutiva: Dra. Diana Escalante

Taller de Mantenimiento



Responsable:
Aurey Galván Lobato, Ing. **Técnico Académico Titular C. PRIDE C.**
Manuel Ortínez Benavides, Ing. Técnico Académico Titular B. PRIDE C.

En esta área se realizan labores de mantenimiento correctivo y preventivo al equipo de investigación, así como también apoyar las necesidades de los investigadores que requieren mantenimiento correctivo y preventivo a sus equipos. Se diseñan y construyen equipos totales o partes de los mismos, para su uso en los diferentes laboratorios de investigación.

Durante 2019 se atendieron un total de 300 solicitudes de servicio, incluyendo 218 de pipetas; para el Instituto. También algunas solicitudes de fabricación de piezas de acuerdo a los requerimientos de los usuarios. Se llevó a cabo el mantenimiento a las subestaciones eléctricas y autoclaves. Se tiene un programa preventivo constante y correctivo, para las centrífugas de piso de todas las áreas comunes que se tienen en el Instituto y para las máquinas fabricadoras de hielo, cuartos de temperatura controlada, refrigeradores y agitadores de cultivo. Se dio supervisión en el funcionamiento de los sistemas de agua desionizada. Durante este periodo se obtuvieron agradecimientos en 3 publicaciones internacionales; así como también en 3 tesis de doctorado y 1 de maestría. También se participó en dos cursos.

Además se apoya al Departamento de mantenimiento del IFC, en asesoría técnica, supervisión de trabajos con personal interno y externo, además de la planeación de mejoras en equipo e inmueble, en coordinación con el Departamento de Servicios Generales del Instituto de Fisiología Celular.

Comisión de Taller de Mantenimiento:

M. I. Bruno Méndez Ambrosio
Dr. Jesús Alvarez López
Dr. Fernando Suaste Olmos
Secretario Ejecutivo: Dr. Jorge Ramírez





Unidad de Histología



Responsable:
Ma. Teresa Guadalupe Cortés Flores, Lic. **Honorarios.**
Sandra Daniela Rodríguez Montaño, Lic. Técnico Académico Asociado A. PRIDE B.

Esta unidad apoya las labores de investigación del Instituto de Fisiología Celular. Cuenta con el servicio de procesamiento de muestras histológicas para microscopía de luz, utilizando las técnicas de cortes en parafina y cortes por congelación, se realizan también las diferentes tinciones en cortes hechos en las técnicas de parafina y congelación, preparación de diferentes soluciones, utilizando reactivos y colorantes para las diferentes técnicas histológicas. Durante 2019 se atendieron un total de 152 solicitudes. Se recibió 1 agradecimiento en 1 publicación internacional y se participó en 2 reuniones académicas.

Comisión de la Unidad de Histología:

Biól. Teresa Montiel
Dra. Rocío Salceda
Dra. Leticia Ramírez Lugo
Secretario Ejecutivo: Dr. Julio Morán

Unidad de Servicio de Microarreglos de ADN de la UNAM



Responsable:

Jorge Ramírez Salcedo, Dr.	**Técnico Académico Titular C. PRIDE D. SNI I**
Lorena Chávez González, Lic.	Técnico Académico Titular A. PRIDE C.
Simón Guzmán León, M.en C.	Técnico Académico Titular B. PRIDE C.

Dependiente de la Coordinación de la Investigación Científica, UNAM con sede en el Instituto de Fisiología Celular, UNAM.

Servicios:

- Manejo de bancos y cepas.
- Amplificación de genes y purificación de plásmidos.
- Fabricación de microarreglos de ADN.
- Marcaje de sondas e hibridización de microarreglos de ADN.
- Lectura de microarreglos de ADN.
- Análisis de microarreglos de ADN.

Actividades realizadas durante el año 2019

- Fabricación de microarreglos del genoma completo de levadura.
- Fabricación de microarreglos del genoma completo de *E. coli.*
- Fabricación de microarreglos del genoma completo de H. pylori.
- Fabricación de microarreglos de cáncer humano 2K genes.
- Fabricación de microarreglos de hígado de rata 2K genes.
- Fabricación de microarreglos de ratón 22K genes.
- Fabricación de microarreglos de humano 10K genes.
- Fabricación de microarreglos del genoma humano completo 35K genes.
- Fabricación de microarreglos del genoma completo de *A. thaliana* 30K genes.
- Fabricación de microarreglos del genoma completo de *c. elegans* 20K genes.
- Fabricación de microarreglos de una colección de mini RNAs.
- Diseño y fabricación de un chip para detección de organismos patógenos.

- Diseño y fabricación de un chip para detección de OGMs.
- Diseño y fabricación de un chip para detección de polimorfismos.

En 2019 se recibieron 42 solicitudes de trabajo, de las cuales se entregaron 21 proyectos terminados y pagados. Esto representó más de 180 marcados de sondas, hibridizaciones, lecturas y cuantificaciones de microarreglos para diferentes grupos de investigación de la UNAM y fuera de ella. También se recibieron agradecimientos en 3 trabajos publicados en revistas internacionales y en 1 tesis de doctorado y se dictaron 7 cursos y 4 conferencias.

Comisión de la Unidad de Microarreglos:

Dr. Félix Recillas Targa
Dra. Alicia González
Dr. Luis Tovar y Romo
Dr. Leonardo Peraza
Dr. Gabriel del Río
Secretario Ejecutivo: Dr. Jorge Ramírez

Laboratorio de investigación y desarrollo de Aplicaciones interactivas para la Neuro-Rehabilitación (LANR)



Responsable:

Dra. Herminia Pasantes — **Investigadora Emérita**

M. en C. Ana María Escalante — **Técnico Académico Titular C. PRIDE D**

El Laboratorio de Investigación y Desarrollo de Aplicaciones Interactivas para la Neuro-rehabilitación (LANR) comenzó a funcionar en junio de 2014, en un espacio asignado por la entonces Directora del Instituto de Fisiología Celular (IFC), la Dra. Marcia Hiriart, y con el apoyo decidido de la Dra. Herminia Pasantes, investigadora emérita del IFC, en el edificio de Neurociencias del mismo instituto. La motivación para establecer este laboratorio surge del proyecto de creación de la Licenciatura en Neurociencias en la UNAM, como un espacio para diversificar la preparación de los egresados, en este caso en la línea de la innovación tecnológica para la salud.

El LARN contempla el diseño y el uso de tecnologías en apoyo de las terapias de rehabilitación de pacientes con algún tipo de discapacidad de origen neurológico, congénita o adquirida. En su primera etapa, se ha enfocado a la utilización de sensores de posición y movimiento, conectados a computadoras, tabletas o teléfonos inteligentes, que puedan guiar al paciente en la realización de ejercicios de rehabilitación física, sin requerir el acompañamiento constante de un especialista en rehabilitación. Se trata de desarrollos en lo que se conoce como “juegos serios”, que son interfaces gráficas semejantes a los videojuegos, pero con una finalidad terapéutica y con movimientos y objetivos cuidadosamente trazados.

Hasta el momento se han desarrollado aplicaciones enfocadas a la rehabilitación de pacientes con daño ocasionado por un accidente cerebro vascular (ACV). Se han concluido los prototipos de seis aplicaciones para rehabilitación de extremidad superior y uno para rehabilitación de cabeza y cuello y coordinación ojo-mano. También se han desarrollado prototipos de hardware para un guante de datos, un mouse ergonómico y sensores de posición y movimiento para los pies. Se cuenta ya con el registro de diez de estos programas ante el INDAUTOR y se iniciará el proceso para el registro de al menos otras tres aplicaciones que están en sus etapas finales de elaboración.

Se ha establecido un acuerdo de colaboración entre el IFC con la Unidad de Rehabilitación del Instituto Nacional de Neurología y Neurocirugía Manuel Velasco Suárez de la Ciudad de México, mismo que estamos en el proceso de formalizar mediante un convenio. A través de esta colaboración se llevará a cabo la validación de los beneficios de las aplicaciones desarrolladas en el LANR, así como los ajustes que el personal de salud del INNN considere necesarios, para aplicarlos a los pacientes. Tomando en cuenta la prevalencia del ACV y sus secuelas, y la precariedad de los recursos humanos en salud para atender este problema, creemos que el tipo de aplicaciones elaboradas por el LARN, actualmente y en el futuro, beneficiará a un número grande de pacientes.

Se finalizó el diseño de un guante interactivo y se registraron los diseños de 2 versiones de mouse ergonómico. Se enriqueció la plataforma de juegos a cinco terminados y otros cinco con un avance importante.

Con 4 programas de Servicio Social registrados, contamos con una composición multidisciplinaria: ingenieros en computación, electrónicos, mecatrónicos, diseñadores gráficos, industriales, psicólogos, terapeutas físicos y físicos biomédicos.

Una tesis de licenciatura concluida y 15 estudiantes terminaron el Servicio Social.







Página web del LARN: https://lanr.ifc.unam.mx/colaboradores.html

Unidad de Bioinformática y Manejo de la Información (UBMI)

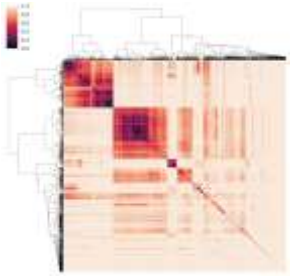



Responsable:

César Augusto Poot Hernández, Dr. **Técnico Académico Asociado C. PRIDE B**

Esta Unidad tiene como objetivo el apoyo a la investigación y a la docencia que se realizan en el Instituto. Se llevan a cabo actividades como la administración continua de los servidores de análisis de la Unidad. También se da asesoría continua y seguimiento a estudiantes en temas de manejo y procesamientos de datos de secuenciación masiva en paralelo, análisis y visualización de datos, estadística y métodos de aprendizaje automático. Se colabora con grupos de investigación recomendando métodos alternativos de visualización y análisis de datos fundamentados en el campo de la ciencia de datos. Se asesora al personal académico del IFC, en el manejo de sistemas operativos GNU/Linux y en la conexión remota con los servidores de análisis.

En 2019 se trabajó en la creación de la Unidad de Bioinformática y Manejo de la Información del IFC (UBMI-IFC). En un principio, la Unidad asumió la responsabilidad de la administración y manejo de los dos servidores de análisis del IFC. Posteriormente, se gestionó la migración e instalación de ambos equipos al Site 2 del Edificio Anexo del Instituto y se gestionó la compra de un tercer servidor de análisis. En conjunto, los 3 equipos suman 192 cores de procesamiento y 576 GB de RAM. Durante este periodo, los servidores fueron usados en aproximadamente entre un 40 a 50% de la capacidad sumada total. Adicionalmente se adquirió un sistema de almacenamiento en red (NAS) con 42 TB de almacenamiento redundante para uso interno de la Unidad.

Concomitantemente, se comenzó el desarrollo de un Sistema Estandarizado de Instalación de Software (SEIS) científico basado en la distribución de *software* Anaconda, el cual está dirigido a sistemas operativos GNU/Linux. El objetivo de este sistema es generar un ambiente de trabajo robusto y de fácil instalación que favorezca la implementación de *pipelines* de análisis y la reproducibilidad de resultados.

En tema de servicios, la Unidad prestó servicios de asesoría y/o colaboración con aproximadamente 15 estudiantes de 8 laboratorios de investigación en temas variados como: análisis de datos de secuenciación masiva en paralelo, programación, visualización de datos, aprendizaje de máquina y estadística.

En tema de la docencia, participé como profesor invitado en 2 cursos de la Licenciatura en Neurociencias, en 1 curso del Posgrado de Ciencias Bioquímicas y cómo titular en 2 cursos del posgrado en Ciencias de la Computación del IIMAS, UNAM. Finalmente, se organizó el 1er Simposio de Bioinformática y Biología Computacional del IFC.





Comisión de la Unidad de Bioinofrmática y Manejo de la Información (UBMI):

Dra. Mayra Furlan Magaril
Dr. Julián Valdés
Dr. Marcelino Arciniega
Dr. Gabriel del Rio
Dr. Román Rossi
Secretario Ejecutivo: Dr. Félix Recillas

Página web de la UBMI: https://sites.google.com/ifc.unam.mx/ubmi-ifc

Unidad de Edición Genética y Criopreservación





Responsable:
Paula Licona Limón, Dra. **Investigador Titular A. PRIDE B. SNI nivel I.**
Ariadna Aparicio Juárez, Dra. **Técnico Académico Asociado "C"**

Las actividades realizadas en la Unidad de Edición Genética y Criopreservación el año 2020 son las siguientes:

Actualmente la Unidad de Edición Genética y Criopreservación brinda **soporte técnico** y **asesorías** en el manejo de diferentes colonias de ratones transgénicos en el Instituto de Fisiología Celular de la Universidad Nacional Autónoma de México.

Se realizaron los primeros ensayos con la técnica de **criopreservación de esperma** en las líneas de ratones CD1, C57/BL6 y 4 Get. Se evaluó la **descongelación de esperma criopreservado** por medio del conteo de viabilidad espermática y los porcentajes de supervivencia. Se realizaron 2 ensayos de **descontaminación de cigotos** murinos en la línea transgénica CHAT-CRE pertenecientes al laboratorio del Dr. Fatuel Tecuapetla. En la **Vasectomización** se utilizaron machos C57/BL6 para la obtención de machos estériles y poder usarlos en la estimulación de las hembras receptoras en la transferencia embrionaria. La **súper ovulación** de hembras murinas C57/BL6 y CD1 para la producción de ovocitos que nos permitieron calibrar el equipo de **microinyección en pronúcleo**. Se hicieron dos ensayos de **rederivación, transferencia embrionaria** e **implantación** de la línea transgénica CHAT-CRE que se mantiene en heterocigosis y se encuentra contaminada por algún agente patógeno. Ensayos de **microinyección** en pronúcleos de cigotos de ratón La Unidad de Edición Genética y Criopreservación junto con le Unidad de Bioterio organizó y participó en 4 ocasiones, con el curso titulado "**Manejo de Animales de Laboratorio en Investigación Biomédica"** para estudiantes, técnicos y académicos del IFC, UNAM con valor curricular de 18 horas.







CONSTRUCCIÓN, REMODELACIÓN, AMPLIACIÓN, ADECUACIÓN DE ESPACIOS Y PROYECTOS ESPECÍFICOS

Programa Institucional de Mantenimiento Verano 2019	**Memoria Fotográfica**
Importe asignado: $149,998.78	 
Trabajos desarrollados: • Sistema de Alarma de Emergencia Edificio Anexo.	

Programa Institucional de Mantenimiento Verano 2019	Memoria Fotográfica
• Pintura vinílica y barniz marino en muros diversas áreas. • Sustitución de lámparas a sistema led de 16 y 36 watts sin balastro en diversos laboratorios	   

Programa Institucional de Mantenimiento Invierno 2019	**Memoria Fotográfica**
Importe asignado: $148,596.05	
Trabajos desarrollados: • Reja metálica de protección en Unidad de Edición Genómica y Criopreservación.	  

Rehabilitación de laboratorios 204 Norte, Dra. Marina Macías y AL-201, Dra. Marcia Hiriart	**Memoria Fotográfica**
Importe aproximado: $400,000.00	
Trabajos desarrollados: • Rehabilitación de mobiliario existente. • Fabricación de mobiliario nuevo. • Trabajos de albañilería, acabados y pintura. • Rehabilitación de Instalaciones • Cambio de lámparas a sistemas led. • Mudanzas. Los trabajos se concluyeron durante el mes de agosto de 2019	**Lab. 224 Norte.- Dra. Marina Macías** 





Lab. AL-201.- Dra. Marcia Hiriart









Cambio de domos en vestíbulo del Edificio Principal y en el sótano Div. Neurociencias	**Memoria Fotográfica**
Importe aproximado: $142,000.00	
Trabajos desarrollados: • Suministro y colocación de domo de policarbonato en vestíbulo del Edificio Principal. • Suministro y colocación de domo de policarbonato en sotáno Div. Neurociencias.	

Cambio de 220 gabinetes de lámparas a sistema led	**Memoria Fotográfica**
Importe aproximado: $80,000.00	
Trabajos desarrollados: • Cambio de 224 gabinetes de lámparas a sistema led de 16 watts sin balastro electrónico en diversos laboratorios y áreas comunes del Instituto	

Resguardo de acervo de la Biblioteca a Almacén de la Administración ubicado en P.B., detrás del Auditorio	**Memoria Fotográfica**
Importe aproximado: $90,000.00	
Trabajos desarrollados: • Adquisición de mas de 300 rejas de plástico para almacenaje del acervo. • Adquisición de tarimas de madera. • Movimiento de libreros metálicos • Tres mudanzas de la Biblioteca al Almacén. • Protección de libreros y rejas con plásticos protectores.	

Impermeabilización de 2,882.00 m2 de azoteas de Edificios Sur, Norte, Biblioteca y Bioterio	**Memoria Fotográfica**
Importe aproximado: $1,123,000.00	
Trabajos desarrollados: • Demolición y retiro de impermeabilizante existente. • Suministro y colocación de Impermeabilizante con sistema prefabricado APP de 4.5 mm. espesor Marca Fester con 15 años de garantía.	

Reacondicionamiento de 2 Aulas y 2 Oficinas en Edificio Anexo	**Memoria Fotográfica**
Importe aproximado: $587,000.00	
Trabajos desarrollados: • Reacondicionamiento de 2 Aulas. • Reacondicionamiento de 2 Oficinas. • 2 Pantallas de 70". • 4 Pizarrones blancos. • 40 butacas y 2 escritorios para profesores.	 

Rejas metálicas de protección junto a artesa y portón de acceso a estacionamiento	**Memoria Fotográfica**
Importe aproximado: $68,000.00	
Trabajos desarrollados: • Reja metálica de protección entre Unidad de Edición Genómica y artesa. • Portón en acceso a estacionamiento	 

ANEXOS

Anexo 1

Alumnos

Alumnos de Doctorado en Ciencias Biomédicas

	Alumno	Tutor
1	Achouna Angele Sorel	Fernández de Miguel Francisco
2	Agoitia Polo Andrés	Bermúdez Rattoni Federico
3	Aguilar Solis Eduardo Daniel	Valdés Rodríguez Víctor Julián
4	Alatriste León Héctor	Tecuapetla Aguilar Fatuel
5	Albert Garay Jesús Silvestre	Salceda Sacanelles Rocío
6	Álvarez Arce Erik Alejandro	López Colomé Ana María
7	Aparicio Juárez Ariadna	Bargas Díaz José
8	Arteaga Tlecuitl Rogelio	Gómora Martínez Juan Carlos
9	Arzate Mejía Rodrigo Gacel	Recillas Targa Félix
10	Avilés Rosas Víctor Hugo	Bargas Díaz José
11	Ayhllon Osorio Carlos Alberto	Hernández Muñoz Rolando Efraín
12	Bahena Alvarez Daniel	Hernández Cruz Arturo
13	Benítez Angeles Miguel	Rosenbaum Emir Tamara Luti
14	Cabrera Ruiz Elizabeth	Lemus Sandoval Luis
15	Cáceres Chávez Verónica Alejandra	Bargas Díaz José
16	Calderon Ortiz Bladimir Melecio	Bargas Díaz José
17	Campero Romero Aura Nirva	Tovar y Romo Luis Bernardo
18	Cárdenas Rivera Alfredo	Tovar y Romo Luis Bernardo
19	Carmona Aldana Francisco Javier	Recillas Targa Félix
20	Carmona Rosas Gabriel	García Sáinz Jesús Adolfo
21	Carranza García Emilio	Navarro González Rosa Estela
22	Cerecedo Castillo Angel Josué	Recillas Targa Félix
23	Chávez Maldonado Juan Pablo	Hiriart Urdanivia Marcia
24	Collazo Navarrete Omar	Drucker Colin René/Guerra Crespo
25	Contreras López Rubén Darío	Tecuapetla Aguilar Fatuel
26	Cortés Fernández de Lara Josué Daniel	Recillas Targa Félix
27	Damián Zamacona Salvador	Mas Oliva Jaime
28	Díaz de León Benbow Gabriel	Romo Trujillo Ranulfo
29	Diaz Hernández Edgar Arturo	Tecuapetla Aguilar Fatuel
30	Díaz Mazariegos Selma	Pérez Montfort Ruy

31	Díaz Osornio Jaime Héctor	Romo Trujillo Ranulfo
32	Duhne Ramírez Mariana	Bargas Díaz José
33	Equihua Benítez Ana Clementina	Drucker Colí René
34	Fuentes Ramírez Emma Oliva	González Halphen Diego
35	García Hernández Brenda Vianey	Morán Andrade Julio
36	García Patiño María Guadalupe	Licona Limón Paula
37	García Vilchis Ana Brisa	Galarraga Palacio Elvira
38	Garza Domínguez Ramiro	Torres Quiroz José Francisco
39	Gil Lievana Elvi	Bermúdez Rattoni Federico
40	Gómez Paz Alejandra Liliana	Drucker Colín René
41	González García Sergio Diego	Pérez de la Mora Miguel
42	Gorostieta Salas Gently Elisa	Castro Obregon Susana
43	Guerrero Celis Nuria	Chagoya Hazas Victoria
44	Gutiérrez Terrazas Sammy Israel	Hansberg y Torres Wilhelm Ludwig
45	Guzmán Vázquez Khalil	Drucker Colin René
46	Heras Romero Yessica Rosalinda	Tovar y Romo Luis Bernardo
47	Hernández Espinosa Diego Rolando	Morán Andrade Julio
48	Hernández Jaramillo Alejandra Aidaly	Sotres Bayón Francisco Xavier
49	Hernández Jiménez Ana María	Chagoya Hazas Victoria
50	Hernández Mondragón Juan Carlos	Pérez de la Mora Miguel
51	Illescas Huerta Elizabeth Sarahi	Sotres Bayón Francisco Xavier
52	Lara González Esther	Bargas Díaz José
53	Lara Rodarte Ernesto José Rolando	Velasco Velázquez Jaime Iván
54	Lazo Gómez Rafael Esaid	Tapia Ibargüengoytia Ricardo
55	Mata Herrera Miguel Ángel	Lemus Sandoval Luis
56	Maya Espinosa María Guadalupe	Drucker Colin René
57	Melchor Hernández Jonathan	Lemus Sandoval Luis
58	Méndez Rodríguez Beatríz Sarahí	Galarraga Palacio Elvira
59	Morales García Norma Lilia	Uribe Carvajal Salvador
60	Morán Martínez Isaac	Lemus Sandoval Luis
61	Noguez Garrido Paula Leticia	Fernández de Miguel Francisco
62	Núñez Martínez Hober Nelson	Recillas Targa Félix
63	Padilla Orozco Montserrat	Bargas Díaz José
64	Palacios Lagunas Daniel Alejandro	Pérez de la Mora Miguel
65	Parada Parra Oscar Javier	Hernández Cruz Arturo
66	Parra Sánchez Sergio	Romo Trujillo Ranulfo
67	Peláez Coyotl Erika Alejandra	Del Río Guerra Gabriel
68	Peña Del Castillo Johanna Guadalupe	Hernández Cruz Arturo
69	Peralta Alvarez Carlos Alberto	Recillas Targa Félix

70	Ramírez López María Fernanda	Drucker Colin René
71	Ramírez Vidal Lizbeth Rocío	López Casillas Fernando
72	Reyes Chapero Rosa María	Galarraga Palacio Elvira
73	Rosendo Pineda Margarita Jacaranda	Vaca Domínguez Luis Alfonso
74	Ruvalcava Gracia Medrano Diana	González Halphen Diego
75	Sánchez Fuentes Asaí	Tecuapetla Aguilar Fatuel
76	Sánchez Sugia María Celeste	Fernández de Miguel Francisco
77	Sánchez Zavaleta Minerva	Salceda Sacanelles Rocío
78	Serrano Reyes Miguel	Bargas Díaz José
79	Solís González Karina Helivier	García Sáinz Jesús Adolfo
80	Torres Esquivel María del Carmen	Massieu Trigo María de Lourdes
81	Valencia Sánchez Salvador	Drucker Colín René
82	Vázquez Vázquez Héctor Aarón	Galarraga Palacio Elvira
83	Velázquez Hernández Leon Gerónimo	Sotres Bayón Francisco Xavier
84	Vergara de la Fuente José	Romo Trujillo Ranulfo
85	Zepeda Cervantes Jesús	Vaca Domínguez Luis Alfonso
86	Zizumbo Colunga Gerónimo	Rossi Pool Román

Alumnos de Doctorado en Ciencias Bioquímicas

	Alumno	Tutor
1	Acevo Rodríguez Pilar Sarah	Castro Obregón Susana
2	Angel Lerma Lidia Esmeralda	Georgellis Dimitris
3	Avendaño Monsalve María Clara	Funes Argüello María Soledad
4	Bastian Eugenio Carlos Ernesto	Vaca Domínguez Luis Alfonso
5	Bernal Vicente Berenice Nohemi	Tovar y Romo Luis Bernardo
6	Campos Martínez Gisselle Angélica	Navarro González Rosa Estela
7	Castillo Casaña Yaisa	Coria Ortega Roberto
8	Cid Castro Carolina	Morán Andrade Julio
9	Contreras Castillo Eugenio	Licona Limón Paula
10	De la Fuente León Rosa Luz	López Casillas Fernando
11	De las Peñas Rincón Ana Paulina	Sotres Bayón Francisco Xavier
12	Díaz Guerrero Miguel Ángel	González Pedrajo Bertha
13	Espinosa Molina Gabriela	Salceda Sacanelles Rocío
14	Espinosa Simon Emilio	Uribe Carvajal Salvador
15	Flores Mireles Daniel	Pérez Martínez Xochitl
16	Flores Ponce Xochitl Natalia	Velasco Velázquez Jaime Iván
17	Franco Juárez Berenice	Castro Obregón Susana
18	Fuentes Jiménez Daniel Alberto	Navarro González Rosa Estela
19	Gálvez Márquez Donovan Kevin	Bermudez Rattoni Federico
20	García Chávez Diana María	Coria Ortega Roberto
21	González Rangel Alan Anuart	Navarro González Rosa Estela
22	Guzmán Flores José Enrique	Georgellis Dimitris
23	Guzmán Silva Alejandro	García Sáinz Jesús Adolfo
24	Hernández Araiza Ileana Raquel	Rosenbaum Emir Tamara Luti
25	Hernández Elvira Mariana	Coria Ortega Roberto
26	Hernández Espinosa David Alejandro	García Sáinz Jesús Adolfo
27	Jiménez Suárez Alejandra	González Halphen Diego
28	López Niño Janintzitzic	Bargas Díaz José
29	Lozano Rosas María Guadalupe	Chagoya Hazas Victoria
30	Luna Reyes Ismael	Mas Oliva Jaime
31	Madrigal Carrillo Ezequiel Alejandro	Torres Larios Alfredo
32	Marcos Vilchis Arely Ivonne	González Pedrajo Bertha
33	Márquez Gutiérrez Dariel	González Manjarrez María Alicia
34	Martínez Morales Juan Carlos	García Sáinz Jesús Adolfo
35	Martínez Pastor David	Macias Silva Marina

36	Mendoza Martínez Ariann Elizabeth	Aguirre Linares Jesús
37	Molina Villa Tonatiuh	López Casillas Fernando
38	Montane Romero Martha Elizabeth	Escalante Alcalde Diana
39	Mora Zenil Janeth	Morán Andrade Julio
40	Morales Tarré Orlando	Torres Quiroz José Francisco
41	Moreno Blas Daniel	Castro Obregón Susana
42	Muciño Hernández Gabriel	Castro Obregón Susana
43	Muñoz Paleta Ofelia	Licona Limón Paula
44	Nava Ramírez Teresa Beatriz	Hansberg y Torres Wilhelm Ludwig
45	Nieto Panqueva Christian Felipe	González Halphen Diego
46	Olguín Martínez Enrique	Licona Limón Paula
47	Ortiz Huidobro Rosa Isela	Hiriart Urdanivia Marcia
48	Penagos Puig Andrés	Furlán Magaril Mayra
49	Pérez Hernández Eréndira Guadalupe	Mas Oliva Jaime
50	Pérez Molina Rosario	Recillas Targa Félix
51	Ramírez Armenta Kathia Itzel	Tecuapetla Aguilar Fatuel
52	Ramírez Mejía Gerardo	Bermudez Rattoni Federico
53	Rendón Ochoa Ernesto Alberto	Bargas Díaz José
54	Reyes Hernández Mario Alberto	Guerra Crespo Magdalena
55	Ríos López Diana Grisel	Macias Silva Marina
56	Rodríguez Aguilera Jesús Rafael	Chagoya Hazas Victoria
57	Rodríguez Bolaños Mónica	Pérez Montfort Ruy
58	Rodríguez Chamorro Daniel Eduardo	Torres Larios Alfredo
59	Rodríguez González Miriam Beatriz	Coria Ortega Roberto
60	Rojo Rodríguez Juliana Berenice	Coria Ortega Roberto
61	Román Figueroa Abraham	Furlán Magaril Mayra
62	Romo Casanueva Hernán	Funes Argüello María Soledad
63	Salas Delgado Griselda Edith	Coria Ortega Roberto
64	Sánchez Sánchez Norma Silvia	Peña Díaz Antonio
65	Sánchez Sandoval Ana Laura	Gómora Martínez Juan Carlos
66	Tapia Urzúa Gustavo	Recillas Targa Félix
68	Terán Melo Juan Luis	Georgellis Dimitris
68	Toledo Ibelles Paola	Mas Oliva Jaime
69	Urias Contreras Silvia Fernanda	Georgellis Dimitris
70	Urrego Morales Oscar Giovanny	Bermúdez Rattoni Federico
71	Vázquez Ciros Oscar Jair	Georgellis Dimitris
72	Vazquez Ibarra Araceli Berenice	Coria Ortega Roberto
73	Vega García Vanessa	Hansberg y Torres Wilhelm Ludwig
74	Villalobos García Daniel	Hernández Muñoz Rolando Efraín

75	Wilson Verdugo Marti David	Valdés Rodríguez Víctor Julián
76	Zaragoza Campillo Marco Antonio	Morán Andrade Julio

Alumnos de Doctorado en Ciencias Biológicas

	Alumno	Tutor
1	Alejandre García Maria Mildred Tzitzitlini	Hernández Cruz Arturo
2	Garrido Bazán Verónica	Aguirre Linares Jesús
3	Jacome López Karina	Furlan Magaril Mayra
4	Medina Ruiz Gabriela Itzel	Morán Andrade Julio
5	Méndez Maldonado Karla M. del Carmen	Velasco Velázquez Jaime Iván
6	Perera Murcia Gerardo	Ramiro Cortés Yazmín
7	Salgado Bernabe Manuel Eduardo	Hiriart Urdanivia Marcia
8	Samario Román Jazmin Selene	Hiriart Urdanivia Marcia
9	Zepeda Córdova Nadia	Molinari Soriano José Luis

Alumnos de otro Doctorado

	Alumno	Tutor
1	Cruz Reséndiz Adolfo	Vaca Domínguez Luis Alfonso
2	Hernández Mendoza Guillermo	Fernández de Miguel Francisco
3	Levario Ramírez Elvia Noemí	Pérez de la Mora Miguel

Alumnos de Maestría en Ciencias Bioquímicas

	Alumno	Tutor
1	Aguilar Lomas Oscar Amaury	Furlán Magaril Mayra
2	Álvarez Esquinca María Fernanda	Arciniega Castro Marcelino
3	Álvarez Sánchez Melisa Selene	Peraza Reyes Carlos Leonardo
4	Amancio Rojas Pamela	Peraza Reyes Carlos Leonardo
5	Amezola Chávez Francisco Manuel	Arciniega Castro Marcelino
6	Anaya Rubio Angélica Isabel	Macías Silva Marina
7	Aparicio Cadena Alejandro Rusbel	Chagoya Hazas Victoria
8	Bahena Cerón Roberto Alexander	Torres Larios Alfredo
9	Balbuena Olvera Andrea Joselin	Guerra Crespo Magdalena
10	Becerra Velez José Fernando	Velasco Velázquez Jaime Iván
11	Bellido Vargas Citlali Belen	Tecuapetla Aguilar Fatuel
12	Bernal Conde Luis Daniel	Guerra Crespo Magdalena
13	Bernate Obando Germán Alonso	Velasco Torres Myrian
14	Busto García Brandon	Valdés Rodríguez Víctor Julián
15	Calixto Tlacomulco Sandra Daniela	Mas Oliva Jaime
16	Campiño Arias Daniela	Aguirre Linares Jesús
17	Campos Martínez Gisselle Angélica	Navarro González Rosa Estela
18	Castillo González David Alejandro	Del Rio Guerra Gabriel
19	Castillo Hernández Kevin Antonio	Coria Ortega Roberto
20	Castillo Huitrón Humberto Rafael	Gómora Martínez Juan Carlos
21	Catalán Bello Ana Isabel	Escalante Alcalde Diana María
22	Ceballos Martínez Laura Georgina	Vaca Domínguez Luis Alfonso
23	Claudio Galeana Giovana Sherlyn	Furlan Magaril Mayra
24	Colín Martínez Diana Elizabeth	Tapia Ibargüengoytia Ricardo
25	Contreras Castillo Eugenio	Licona Limón Paula
26	Cruz Cruz Iskra Anai	Velasco Torres Myrian
27	Cruz Ramos Juan Eduardo	Macías Silva Marina
28	Dámazo Hernández Ángel Armando	Navarro González Rosa Estela
29	Del Ángel Muñoz Carlos Miguel	Castro Obregón Susana
30	Delgado Herrera Deborah de la Caridad	Gómora Martínez Juan Carlos
31	Dimas Torres Jorge Uriel	Torres Larios Alfredo
32	Esquivel López Ayerim Alma	Furlan Magaril Mayra
33	Flores Reyes Josiff Samuel	Del Río Guerra Gabriel
34	Franco Cea Luz Areli	Dreyfus Cortés Georges
35	Gálvez Márquez Donovan Kevin	Bermúdez Rattoni Federico

36	Gomez Ceja Karla Ameyali	Macías Silva Marina
37	Gómez Ilescas Ameyalli	Recillas Targa Félix
38	Gómora García Juan Carlos	Massieu Trigo María de Lourdes
39	González López Minerva Igrein	Aguirre Linares Jesús
40	González Núñez Bruno Axel	Torres Quiroz José Francisco
41	Granados Davalos Estefany	González Manjarrez María Alicia
42	Gutiérrez Alejandre Ana Paulina	Pérez Martínez Xochitl
43	Gutiérrez Chávez Laura Gabriela	Valdés Rodríguez Víctor Julián
44	Hernández Ortíz Jorge Eduardo	Bermúdez Rattoni Federico
45	Hernández Ponce Itzel	Velasco Velázquez Jaime Iván
46	Hernández Rojas Diana Iris	Coria Ortega Roberto
47	Herrera Ruiz Rodolfo Emilio	Álvarez Adrián Fernando
48	Hersch González Jaqueline	González Manjarrez María Alicia
49	Isaias Tizapa Raúl Augusto	García Sáinz Jesús Adolfo
50	Jara Servín Angélica Mariana	González Manjarrez María Alicia
51	Juárez González Emmanuel	Rosenbaum Emir Tamara Luti
52	López del Carpio Juárez Kevin	Coria Ortega Roberto
53	López Durán Brian Saidel	Torres Larios Alfredo
54	López Fuentes Antonio de Jesús	Peraza Reyes Carlos Leonardo
55	López Romero Ana Elena	Rosenbaum Emir Tamara Luti
56	Luna Leal Aldo	Bargas Díaz José
57	Luna Leal Angélica	Escalante Alcalde Diana María
58	Luna Reyes Ismael	Mas Oliva Jaime
59	Maldonado Guerrero María Fernanda	Licona Limón Paula
60	Martínez Becerril Hilda Angélica	Tecuapetla Aguilar Fatuel
61	Martínez Flores Daniel	Vaca Domínguez Luis Alfonso
62	Martínez Sandoval Emilio Alonso	Aguirre Linares Jesús
63	Meléndez Ramírez César Daniel	Velasco Velázquez Jaime Iván
64	Mendoza Cabrera Sofía Natali	Del Río Guerra Gabriel
65	Merino Vázquez Luis Javier	Uribe Carvajal Salvador
66	Minguer Uribe Alan Gerardo	Sotres Bayón Francisco Xavier
67	Montes Ortega Luis Ángel	Massieu Trigo María de Lourdes
68	Morales Castelán Nestor Ricardo	Del Río Guerra Gabriel
69	Morales Oliva Enrique	Navarro González Rosa Estela
70	Morán Torres Rafael Ubaldo	Del Río Guerra Gabriel
71	Muñoz Montero Said Alejandro	Pérez Montfort Ruy
72	Nava Lara Rodrigo Andrés	Del Río Guerra Gabriel
73	Nebreda Corona Adriana	Morán Andrade Julio
74	Ojeda Bello Juan Amado	Tapia Ibargüengoytia Ricardo

75	Olivares Resendis Abiram Eliab	Coria Ortega Roberto
76	Omaña Guzmán Tania Verónica	Recillas Targa Félix
77	Ortega Gurrola Alonso	Velasco Velázquez Jaime Iván
78	Ortiz Renteria Miguel	Morales Lazaro Sara Luz
79	Ostolga Chavarría Marcos	González Halphen Diego
80	Pacheco Martínez María Elena	Hansberg Torres Wilhelm
81	Pedroza Dávial Ulrik Hiram	Uribe Carvajal Salvador
82	Penagos Puig Andrés	Furlán Magaril Mayra
83	Pérez López José Luis	Tecuapetla Aguilar Fatuel
84	Pommer Alba Alexander Michael	Castro Obregón Susana
85	Ponce Arias Alfredo Isacc	Tovar y Romo Luis Bernardo
86	Poot Vélez Albros Hermes	Del Río Guerra Gabriel
87	Ramirez Reyes Josué Miguel Julián	Funes Argüello María Soledad
88	Ramos Acevedo Rodrigo	Guerra Crespo Magdalena
89	Reza Noyola Marlene	Recillas Targa Félix
90	Rodríguez Hernández Adriana	Macías Silva Marina
91	Rodríguez Sibrian Luis Antonio	Tecuapetla Aguilar Fatuel
92	Rojo Rodríguez Juliana Berenice	Coria Ortega Roberto
93	Roldan Blancas Alan Gerardo	Mas Oliva Jaime
94	Romo Casanueva Hernán	Funes Argüello María Soledad
95	Ruelas Ramírez Hilario	Funes Argüello María Soledad
96	Ruiz Flores Jesús	Torres Quiroz José Francisco
97	Sabido Barrera Jean Imanol	Hiriart Urdanivia Marcia
98	Salazar Salgado Alejandro	Valdés Rodríguez Víctor Julián
99	Salgado Menez Mildred	Bermúdez Rattoni Federico
100	Sánchez Contreras Juan Manuel	Uribe Carvajal Salvador
101	Sánchez Durán Alejandro	Hiriart Urdanivia Marcia
102	Sánchez Hernández Raúl	Rosenbaum Emir Tamara Luti
103	Sánchez Salazar Zyanya Saraí	Hiriart Urdanivia Marcia
104	Sandoval Hernández José Antonio	Macías Silva Marina
105	Soltero Echauri Cintia	Macías Silva Marina
106	Soto Beltran Ana María	Coria Ortega Roberto
107	Steinemann Hernández Lidia	Georgellis Dimitris
108	Stephenson Gussinye Aura	Furlan Magaril Mayra
109	Toca de Muga Paulina	Del Río Guerra Gabriel
110	Torres Morales Erika Monserrat	Hernández Cruz Arturo
111	Torres Reyes María del Pilar	González Pedrajo Bertha
112	Trejo Hernández Diana Laura	Recillas Targa Félix
113	Urrieta Chávez Beetsi Eugenia	Velasco Velázquez Jaime Iván

114	Velázquez Delgado Cintia	Bermúdez Rattoni Federico
115	Vergara Gerónimo Cristian Alberto	Pérez Martínez Xochitl
116	Villafuerte Peralta Rafael	Sotres Bayón Francisco Xavier
117	Vivar Cortés Israel César	Bargas Díaz José
118	Wilson Verdugo Marti David	Valdés Rodríguez Víctor Julián
119	Zavala Sánchez José Hugo	Hiriart Urdanivia Marcia
120	Zepeda Gutiérrez Paula	Macías Silva Marina

Alumnos de Maestría en Ciencias Biológicas

	Alumno	Tutor
1	Cortés Escamilla Cicilia Estrella	Gómora Martínez Juan Carlos
2	Garcia Ramos Mariela	Dreyfus Cortés Georges
3	Jiménez Marquez Emiliano	Ramiro Cortés Yazmín
4	Juárez Contreras Rebeca	Morales Lazaro Sara Luz
5	Landa Navarro Lucía	Bermúdez Rattoni Federico
6	Linares Garcia Carlos Iván	Tecuapetla Aguilar Fatuel
7	Ortiz Cruz Carlos Alberto	Ramiro Cortés Yazmín
8	Perera Murcia Gerardo	Ramiro Cortés Yazmín
9	Verma Rodríguez Anil Kumar	Tecuapetla Aguilar Fatuel

Alumnos de otra Maestria

	Alumno	Tutor
1	Albor Ramírez Efraín	Vaca Domínguez Luis Alfonso
2	Mejía López Adriana	Aguilar Roblero Raúl
3	Sánchez Evangelista Grecia	Morán Andrade Julio

Alumnos Tesistas de Licenciatura

	Alumno	Tutor
1	Abarca Magaña Julio Cesar	Massieu Trigo María Lourdes
2	Abelar Cámara Abelardo	Picones Medina Arturo
3	Acevedo Huerta Cecilia Gabriela	Bermúdez Rattoni Federico
4	Acosta Galeana Maria Isabel	Tapia Ibargüengoytia Ricardo Jorge
5	Aguilar Cámara Abelardo	Picones Medina Arturo
6	Aguilar Quiroz Diana Mitzi	Hernández Cruz Arturo
7	Amezola Chávez Francisco Manuel	Torres Quiroz José Francisco
8	Arenas Navarro Andrés	Castro Obregón Susana
9	Beltrán Calderón Yesica	Torres Larios Alfredo
10	Bernal Servín Aida	Hernández Cruz Arturo
11	Bustamante Carrera Manuel Alejandro	Escalante Gonzalbo Ana
12	Bustos Vázquez Cinthya Dafne	Bermúdez Rattoni Federico
13	Caballero Escamilla Brenda Aurora	González Manjarrez Alicia
14	Campos Ortega Rendón Sergio	Arciniega Castro Marcelino
15	Cruz Mendoza Leticia	Dreyfus Cortés Georges
16	Cruz Montesinos Luis Ángel	Pérez de la Mora Miguel
17	De los Santos Cocotle Gustavo	Garcia Sainz Jesús Adolfo
18	Delgado Gómez Giselle Alexa	Guerra Crespo Magdalena
19	Elias López Diana Lizbeth	Gómora Martínez Juan Carlos
20	Enciso Pablo Oscar	Morales Lazaro Sara Luz
21	Escudero Reyes Juan Raúl	González Manjarrez Alicia
22	Estrada Rosales Ana Lilia	Escalante Gonzalbo Ana
23	Felipe González Víctor Martín	Aguilar Roblero Raúl
24	García Cordero Itzel Abil	Pérez Martínez Xochitl
25	García Fidencio Víctor Alejandro	Arciniega Castro Marcelino
26	García Mata Martín	Bargas Díaz José
27	Gasca Aguilera Luis Enrique	Navarro González Rosa Estela
28	Godinez López Victoria	Torres Larios Alfredo
29	Gómez Martínez Cecilia Gabriela	Ramiro Cortés Yazmín
30	González Ríos Axel Rubén	López Huerta Violeta Gissell
31	González Ruiz Karla Daniela	Garcia Sainz Jesús Adolfo
32	Gutierrez Castañeda Oscar Eduardo	Arciniega Castro Marcelino
33	Gutiérrez López Ernesto Saúll	Bermúdez Rattoni Federico
34	Hernández Matias Arturo	Osorio Gómez Daniel
35	Herrera Xithe Gabriela	Bermúdez Rattoni Federico

36	Jaimes Cabrera José	Osorio Gómez Daniel
37	Linares Caballero Brenda	Osorio Gómez Daniel
38	Martínez Cruz Jadir Isaí	Tapia Ibargüengoytia Ricardo Jorge
39	Martínez Velasco Rosario Paulina	Torres Quiroz José Francisco
40	Meza González Viridiana Belén	Escalante Alcalde Diana María
41	Meza Razo Rodrigo	López Casillas Fernando
42	Morales Moreno Ishbelt Denisse	Guerra Crespo Magdalena
43	Moreno de la Rosa Dinorah Ileana	Torres Quiroz José Francisco
44	Navarro Espindola Raful	Peraza Reyes Carlos Leonardo
45	Nieto Zaragoza Elias	Torres Quiroz José Francisco
46	Padilla Garfias Francisco Javier	Peña Díaz Antonio
47	Pérez Rivera Iván Dessaeu	Escalante Gonzalbo Ana
48	Pérez Velázquez Diego	Licona Limón Paula
49	Polanco Maldonado Ángel Lizandro	Velasco Velázquez Jaime Iván
50	Portillo Pérez Luisa María	Gómora Martínez Juan Carlos
51	Pulido Arteaga Rafael	Romo Trujillo Ranulfo
52	Ramirez Rivera Viridiana Guadalupe	Pérez de la Mora Miguel
53	Reyes Becerril Luis Uriel	Hansberg Torres Wilhelm Ludwig
54	Ríos Vázquez Mariana	González Pedrajo Bertha
55	Rodríguez Pié Adrian Antonio	Arciniega Castro Marcelino
56	Romero Enriquez Kébek	Dreyfus Cortés Georges
57	Ruiz Juárez Mariana	Sotres Bayón Francisco Xavier
58	Salazar Ortiz Claudia	Pérez Montfort Ruy
59	Salazar Rios Iván Moisés	Escalante Gonzalbo Ana
60	Salcido Gómez Ashley Michel	Massieu Trigo María Lourdes
61	Sánchez Castillo Gloria Ixchel	Escalante Gonzalbo Ana
62	Sánchez Ramos Arizbeth	Ramiro Cortés Yazmín
63	Soriano Rosales Eric Dilan	Recillas Targa Félix
64	Vázquez Ayala Uriel de Jesus	Gómora Martínez Juan Carlos
65	Zambrano Trejo Daniela	González Manjarrez Alicia

Alumnos de Estancia de Investigación

	Alumno	Tutor
1	Álvarez Carreño Claudia	Arciniega Castro Marcelino
2	Bernal Reza Mauricio	Fernández de Miguel Francisco
3	Campos Oliver Brisa Aranzanzú	González Manjarrez Alicia
4	Cancino Bello Amairani	Chagoya Hazas Victoria Eugenia
5	Cárdenas Rodríguez Mauricio	Funes Argüello María Soledad
6	Chaverri Herrera Miriam	Rivera Cerecedo Claudia
7	Escutia Macedo Ximena Ameyalli	Escalante Gonzalbo Ana
8	Eslava Torres Viridiana Guadalupe	Escalante Gonzalbo Ana
9	Florentino Moreno Alejandra	Fernández de Miguel Francisco
10	Franco Castro Paulina	Escalante Gonzalbo Ana
11	Gutiérrez García María Fernanda	Escalante Gonzalbo Ana
12	Juárez Segura Lizbeth	Rivera Cerecedo Claudia
13	Llanos Mis Jessica Klauzeen	Escalante Gonzalbo Ana
14	Loeza Loeza Jacqueline	Recillas Targa Félix
15	Martínez Cervantes Juan Carlos	López Huerta Violeta Gissell
16	Olmos Ojeda Paola Gabriela	Escalante Gonzalbo Ana
17	Pérez Estrada José Raúl	Castro Obregón Susana
18	Pérez Herrera Carlos Alexis	Escalante Gonzalbo Ana
19	Ramírez Cordero Belén Ernestina	Gómora Martínez Juan Carlos
20	Ramírez Guzmán Sergio Sebastián	Escalante Gonzalbo Ana
21	Robles Hernández Eva María	Escalante Gonzalvo Ana
22	Rodríguez González Mario Raúl	Morán Andrade Julio Eduardo Roque
23	Rodríguez Muñoz Diana Laura	López Huerta Violeta Gissell
24	Rodriguez Plaza Jonathan Gabriel	Del Río Guerra Gabriel
25	Rojas Pacheco Erick Antonio	López Huerta Violeta Gissell
26	Román Carraro Fiordaliso Cardina	Morán Andrade Julio Eduardo Roque
27	Salcedo Tello Pamela	Bermúdez Rattoni Federico
28	Schroder Sara	Peraza Reyes Carlos Leonardo
29	Tapia Vieyra Juana Virginia	Mas Oliva Jaime
30	Torres Zavaleta José Manuel	Hernández Muñoz Rolando Efraín
31	Vazquez Abundes Sandra Elizabeth	Escalante Gonzalbo Ana

Alumnos de Taller

	Alumno	Tutor
1	Avila Tapia Sara Iram	Bermúdez Rattoni Federico
2	Balbuena García Brenda Valeria	Bermúdez Rattoni Federico
3	Canizales Ontiveros Alejandro	Salceda Sacanelles Rocío
4	Carrillo Lorenzo José Alberto	Bermúdez Rattoni Federico
5	González Urzúa Erika Vianey	Bermúdez Rattoni Federico
6	Hernandez Mojica Jorge Efren	Peraza Reyes Carlos Leonardo
7	Jesús Valencia Sanchez Katherine Alide	Georgellis Dimitris
8	Jiménez Negrete Celina	Georgellis Dimitris/Adrian Alvarez Fernando
9	Manzanita Quintero Katya	López Colomé Ana María
10	Mendoza Rodríguez Edgar	López Colomé Ana María
11	Montiel Alcazar Andrea	López Colomé Ana María
12	Rogerio Rios Jaime Emiliano	Tovar y Romo Luis Bernardo
13	Saenz Rodríguez Fernando	Salceda Sacanelles Rocío
14	Tenorio Hernández Luis	Ramiro Cortés Yazmín
15	Torres Torralba Erick Nicolas	Salceda Sacanelles Rocío

Alumnos de Rotación de LIBB

	Alumno	Tutor
1	Blanco Salazar María José	Recillas Targa Félix
2	Bravo Arevalo José Ernesto	Funes Arguello María Soledad
3	Campos Chávez Eduardo	Torres Larios Alfredo
4	Cristino Miranda Arianne Melisa	Castro Obregón Susana
5	Flores Espinosa Emannuel	Garcia Sainz Jesús Adolfo
6	Marroquin Rodríguez Montserrat	Navarro González Rosa Estela
7	Moreno Yllescas Christopher Levitt Alejandro	González Halphen Diego
8	Nava García Marintia Mayola	Furlan Magaril Mayra
9	Peredes Chiquini Yamilé	González Manjarrez Alicia
10	Soriano Rodríguez Carla Itzel	Velasco Velázquez Jaime Iván

Alumnos de Licenciatura en Neurociencias

	Alumno
1	Abrego Islas Iván de Jesús
2	Acevedo Garduño Nuri
3	Albanes Sánchez Cesar Ulises
4	Andrade Ortega Bernardo
5	Avilez Poblador Karla Gabriela
6	Barreras Maldonado José Carlos
7	Batiz Slazak Pola Luz
8	Bautista Galicia Ramssés Jair
9	Becerril Huerta Bibiana Carolina
10	Bravo Lanz Carolina
11	Buendía Sánchez Luis Antonio
12	Cabrera Castro Maricela
13	Campos Pérez Andrea Fernanda
14	Cano Gómez Montserrat
15	Casas Rosas Karla Patricia
16	Castañeda Ferrer Lolbe
17	Castilla Jiménez Jaiver Francisco
18	Chávez Blancas Isaac
19	Cruz Sánchez Oscar Apolinar
20	Cuellar Torres José Manuel
21	De La Cruz Magaña Mauricio
22	Del Río Castro Camila
23	Diaz Zarate Xarenny Yazmin
24	Espinosa Rodríguez Andrea
25	Figueroa Cruz Julio Cesar
26	Franceschi Jiménez Luis Arturo
27	García Kroepfly Aidee Lashmi
28	García López Paulina
29	Garduño Almaraz Angel
30	Gómez García Ozmar Saul
31	Gómez Mendoza Juan Carlos
32	Gómez Villatoro Johana Paulina
33	González Martínez Salvador Eduardo
34	Hernández Real Fernando

35 Herrera Zahar Daniela Michelle
36 Jiménez Gallardo Alejandro
37 Jiménez Pérez Angela Renata
38 Linares García Ana Paola
39 Lombardi Martínez Daniel
40 Lora Marín Obed Ricardo
41 Manriquez Cejudo Alejandra
42 Martínez Guadarrama Andrea
43 Martínez Mata Karina
44 Martínez Pérez Michelle
45 Mejía Ortiz Regina Andrea
46 Mendoza Madrigal Rodrigo
47 Montes Montiel José María
48 Montiel González Valeria
49 Navarrete Hernandez Vania Lizeth
50 Navarro Magallón Javier
51 Novela Maciel Ana Teresa
52 Núñez García Diana
53 Ocampo Romero Ana Gabriela
54 Quintero Hernández Dariana Guadalupe
55 Rico Becerra Allan Irasek
56 Rocha Estrada Karla Patricia
57 Rodríguez López Blanca Estela
58 Rodríguez Vera Andrea
59 Rodríguez Vertiz Fatima Itzel
60 Rubio Galicia Angel
61 Ruiz Alanis Emilio
62 Ruiz Antonio Diana Lizeth
63 Ruiz Ortega Montserrat
64 Salazar Castro Marelly
65 Sánchez Calderon Eder Raziel
66 Sánchez Cortes Flor Erendira
67 Sánchez Velázquez Alan
68 Sandoval González Cesar
69 Santana Roman Estefanía
70 Santiago Bustos Ángel Eduardo
71 Silvas Baltazar Diana Monserrat
72 Torres Leyva Itzel Beatriz
73 Treviño Juárez Denisse Monserrat

74 Tripp Avalos Joseph Marino
75 Trujillo Carreno Santiago
76 Valencia Morales Arisbeth Citlali
77 Vázquez Lechuga Arenski Sugel
78 Vázquez Zuloeta Samantha
79 Velasco Orozco Miguel
80 Vilchis Macias Erik Hazel
81 Zavaleta Zamora Carlos Rafael

Alumnos Graduados

Graduados de Doctorado en Ciencias Biomédicas

	Alumno	Tutor
1	Aparicio Juárez Ariadna	Bargas Díaz José
2	Arteaga Tlecuitl Rogelio	Gómora Martínez Juan Carlos
3	Cáceres Chávez Verónica Alejandra	Bargas Díaz José
4	Cárdenas Rivera Alfredo	Tovar y Romo Luis Bernardo
5	Carmona Aldana Francisco Javier	Recillas Targa Félix
6	Carmona Rosas Gabriel	García Sáinz Jesús Adolfo
7	Carranza García Emilio	Navarro González Rosa Estela
8	Díaz Hernández Edgar Arturo	Tecuapetla Aguilar Fatuel
9	Hernández Espinosa Diego Rolando	Morán Andrade Julio
10	Maya Espinosa María Guadalupe	Drucker Colin René
11	Ruvalcava Gracia Medrano Diana	González Halphen Diego
12	Zepeda Cervantes Jesús	Vaca Domínguez Luis Alfonso

Graduados de Doctorado en Ciencias Bioquímicas

	Alumno	Tutor
1	Guzmán Flores José Enrique	Georgellis Dimitris
2	Hernández Araiza Ileana Raquel	Rosenbaum Emir Tamara Luti
3	Hernández Elvira Mariana	Coria Ortega Roberto
4	Juárez Arellano Vladimir	Del Río Guerra Gabriel
5	Mendoza Martínez Ariann Elizabeth	Aguirre Linares Jesús
6	Rendón Ochoa Ernesto Alberto	Bargas Díaz José
7	Rodríguez Bolaños Mónica	Pérez Montfort Ruy
8	Rodríguez González Miriam Beatriz	Coria Ortega Roberto
9	Terán Melo Juan Luis	Georgellis Dimitris
10	Vazquez Ibarra Araceli Berenice	Coria Ortega Roberto
11	Zaragoza Campillo Marco Antonio	Morán Andrade Julio

Graduados de Doctorado en Ciencias Biológicas

	Alumno	Tutor
1	Alejandre García Maria Mildred Tzitzitlini	Hernández Cruz Arturo
2	Méndez Maldonado Karla M. del Carmen	Velasco Velázquez Jaime Iván

Graduados de Maestría en Ciencias Bioquímicas

	Alumno	Tutor
1	Bahena Cerón Roberto Alexander	Torres Larios Alfredo
2	Campos Martínez Gisselle Angélica	Navarro González Rosa Estela
3	Castañeda Arroyo Aurora Angélica	Hernández Muñoz Rolando
4	Contreras Castillo Eugenio	Licona Limón Paula
5	Cruz Ramos Juan Eduardo	Macías Silva Marina
6	Del Ángel Muñoz Carlos Miguel	Castro Obregón Susana
7	Dimas Torres Jorge Uriel	Torres Larios Alfredo
8	Gálvez Márquez Donovan Kevin *	Bermúdez Rattoni Federico
9	Jara Servín Angélica Mariana	González Manjarrez Alicia
10	López Fuentes Antonio de Jesús	Peraza Reyes Leonardo
11	López Romero Ana Elena	Rosenbaum Emir Tamara Luti
12	Luna Reyes Ismael	Mas Oliva Jaime
13	Montes Ortega Luis Ángel	Massieu Trigo María de Lourdes
14	Morán Torres Rafael Ubaldo	Del Río Guerra Gabriel
15	Nava Lara Rodrigo Andrés	Del Río Guerra Gabriel
16	Olivares Reséndiz Abiram Eliab	Coria Ortega Roberto
17	Ortega Gurrola Alonso	Velasco Velázquez Jaime Iván
18	Ortiz Renteria Miguel	Morales Lazaro Sara Luz
19	Pacheco Martínez María Elena	Hansberg Torres Wilhelm Ludwig
20	Penagos Puig Andrés *	Furlán Magaril Mayra
21	Ramírez Reyes Josué Miguel Julián	Funes Argüello Soledad
22	Rodríguez Sibrian Luis Antonnio	Tecuapetla Aguilar Fatuel
23	Rojo Rodríguez Juliana Berenice	Coria Ortega Roberto
24	Romo Casanueva Hernán *	Funes Argüello Soledad
25	Salgado Ménez Mildred	Bermúdez Rattoni Federico
26	Stephenson Gussinye Aura	Furlán Magaril Mayra
27	Torres Morales Erika Montserrat	Hernández Cruz Arturo
28	Vergara Gerónimo Cristian Alberto *	Pérez Martínez Xochitl
29	Wilson Verdugo Marti David *	Valdés Rodríguez Víctor

***** Alumnos que se graduaron por defensa de proyecto.

Graduados de Maestría en Ciencias Biológicas

	Alumno	Tutor
1	Alejandre García María Mildred Tzitzitlini	Hernández Cruz Arturo
2	García Ramos Mariela	Dreyfus Cortés Georges
3	Juárez Contreras Rebeca	Morales Lazaro Sara Luz
4	Landa Navarro Lucía	Bermúdez Rattoni Federico
5	Linares García Carlos Iván	Tecuapetla Aguilar Fatuel
6	Perera Murcia Gerardo	Ramiro Cortés Yazmín
7	Verma Rodríguez Anil Kumar	Tecuapetla Aguilar Fatuel

Graduados de Licenciatura

	Alumno	Tutor
1	Arenas Navarro Andrés	Celis Sandoval Heliodoro
2	Bravo Arévalo José Ernesto	Funes Argüello María Soledad
3	Calixto Tlacomulco Sandra Daniela	Mas Oliva Jaime
4	Campos-Ortega Rendón Sergio	Arciniega Castro Marcelino
5	Gutiérrez Jaber Inés Fernanda	Bermúdez Rattoni Federico
6	Jiménez Marquez Emiliano	Ramiro Cortés Yazmín
7	Llanos Moreno Argelia Itzel	Tecuapetla Aguilar Fatuel
8	Morales Ramírez Elena	Salceda Sacanelles Rocío
9	Padilla Garfias Francisco Javier	Peña Díaz Antonio
10	Pérez Vázquez Diego	Licona Limón Paula
11	Ricardez García Carolina	Celis Sandoval Heliodoro
12	Ríos Vázquez Mariana	González Pedrajo Bertha
13	Rodríguez Pié Adrian Antonio	Arciniega Castro Marcelino
14	Serrano Solis David Michel	Fernández de Miguel Francisco Rafael

Anexo 2

Docencia

Cursos de Licenciatura

Miembros del IFC como responsables

1. **Bases moleculares del dolor. Taller**
   Responsable: Rosenbaum Emir Tamara.
   Facultad de Ciencias, UNAM.

   Participantes:
   Morales Lázaro Sara Luz
   Llorente Gil Itzel Alejandra

2. **Biofísica**
   Responsable: Hernández Cruz Arturo.
   Lic. Neurociencias.
   Instituto de Fisiología Celular, UNAM.

   Participantes:
   Tecuapetla Aguilar Fatuel
   Picones Medina Arturo

3. **Biología celular**
   Responsable: Castro Obregón Susana.
   Lic. Neurociencias.
   Instituto de Fisiología Celular, UNAM.

   Participantes:
   Gómora Martínez Juan Carlos
   Valdés Rodríguez Víctor Julián
   Peraza Reyes Leonardo

4. **Biología molecular de la célula III**
   Responsable: Salceda Sacanelles Rocío.
   Facultad de Ciencias, UNAM.

5. **Bioquímica**
   Responsable: García Sáinz Jesús Adolfo.
   Lic. IBB.
   Instituto de Fisiología Celular, UNAM.

   Participantes:
   Peña Díaz Antonio
   López Casillas Fernando

6. **Comunicación neuronal**
   Responsable: Tecuapetla Aguilar Fatuel.
   Lic. Neurociencias.
   Instituto de Fisiología Celular, UNAM.

   Participantes:
   Tovar y Romo Luis Bernardo
   Massieu Trigo Lourdes
   Morales Lázaro Sara Luz
   Velasco Torres Myrian
   Ramiro Cortés Yazmín
   Fernández De Miguel Francisco

7. **Curso de Bioquímica y biología molecular**
   Responsable: Pérez de la Mora Miguel.
   Facultad de Medicina, UNAM.

8. **Epigenética**
   Responsable: Recillas Targa Félix.
   Centro de Ciencias Genómicas, UNAM.

9. **Fisiología humana**
   Responsable: Hiriart Urdanivia Marcia.
   Facultad de Medicina, UNAM.

10. **Fisiología**
    Responsable: Aguilar Roblero Raúl.
    Lic. IBB.
    Instituto de Fisiología Celular, UNAM.

11. **Histología y microscopía**
Responsable: Escalante Alcalde Diana.
Lic. Neurociencias.
Instituto de Fisiología Celular, UNAM.

Participantes:
Ramiro Cortés Yazmín
Martínez Silva Ana Valeria
Paredes Díaz Rodolfo
Rincón Heredia Ruth
Rosas Arellano Abraham
Rodríguez Montaño Sandra Daniela
Montiel Montes Teresa

12. **Introducción a las neurociencias**
Responsable: Bargas Díaz José.
Lic. Neurociencias.
Instituto de Fisiología Celular, UNAM.

Participantes:
Sotres Bayón Francisco
Velasco Velázquez Iván
Tecuapetla Aguilar Fatuel
Zainos Rosales Antonio Paulino

13. **Neurobiología**
Responsable: Morán Andrade Julio.
Facultad de Ciencias, UNAM.

Participantes:
Tapia Ibargüengoytia Ricardo
Tecuapetla Aguilar Fatuel
Ramiro Cortés Yazmín
Velasco Velázquez Iván

14. **Bioquímica y biología molecular**
Responsable: Uribe Carvajal Salvador.
Facultad de Medicina, UNAM.

15. **Taller Diferenciación celular en hongos**
Responsable: Aguirre Linares Jesús.
Facultad de Ciencias, UNAM.

Participantes:
Coria Ortega Roberto
Wilhelm Hansberg
Kawasaki Watanabe Laura
Sánchez González Alma Olivia

16. **Taller de Fisiología de canales iónicos**
Responsable: Hernández Cruz Arturo.
Facultad de Ciencias, UNAM.

Participantes:
Picones Medina Arturo

17. **Taller, Transducción de señales y quimiotaxis microbiana**
Responsable: Dreyfus Georges.
Responsable: Georgellis Dimitris.
Facultad de Ciencias, UNAM.

Participantes:
Álvarez Adrián Fernando

18. **Taller: Mecanismos de muerte neuronal**
Responsable: Morán Andrade Julio.
Facultad de Ciencias, UNAM.

19. **Taller: Neurobiología sensorial**
Responsable: Salceda Sacanelles Rocío.
Facultad de Ciencias, UNAM.

20. **Epistemología**
Responsable: Bargas Díaz José.
Lic. Neurociencias.
Instituto de Fisiología Celular, UNAM.

21. **Modelos computacionales**
Responsable: Rossi Pool Román.
Lic. Neurociencias.
Facultad de Medicina, UNAM.

Participantes:
Poot Hernández Augusto César

22. **Neuropatología**
Responsable: Massieu Trigo Lourdes.
Lic. Neurociencias.
Instituto de Fisiología Celular, UNAM.

Participantes:
Velasco Torres Myrian
Velasco Velázquez Iván

23. **Neuroplasticidad**
Responsable: Sotres Bayón Francisco.
Lic. Neurociencias.
Instituto de Fisiología Celular, UNAM.

Participantes:
Ramiro Cortés Yazmín
Ramírez Lugo Leticia
Rodríguez Durán Luis Francisco

24. **Psicofisiología**
Responsable: Osorio Gómez Daniel.
Lic. Neurociencias.
Instituto de Fisiología Celular, UNAM.

Participantes:
Sotres Bayón Francisco

25. **Técnicas y herramientas I**
Responsable: López Huerta Violeta Gisselle.
Lic. Neurociencias.
Instituto de Fisiología Celular, UNAM.

Participantes:
Tovar y Romo Luis Bernardo
Valdés Rodríguez Víctor Julián
Osorio Gómez Daniel
Escalante Alcalde Diana
Jiménez Pérez Nicolás
Palomero Rivero Marcela
Montiel Montes Teresa

26. **Bioética**
Responsable: Tapia Ibargüengoytia Ricardo.
Lic. Neurociencias.
Instituto de Fisiología Celular, UNAM.

27. **Técnicas y herramientas II**
Responsable: Ongay Larios Laura.
Lic. Neurociencias.
Instituto de Fisiología Celular, UNAM.

Participantes:
López Casillas Fernando
Coria Ortega Roberto
Tovar y Romo Luis Bernardo
Códiz Huerta Guadalupe
Velasco Loyden Gabriela
Poot Hernández Augusto César

28. **Introducción a la Biofísica**
Responsable: Álvarez López Jesús Manuel.
Facultad de Ingeniería, UNAM.

29. **Laboratorio de fundamentos de instrumentación Biomédica**
Responsable: Álvarez López Jesús Manuel.
Responsable: Díaz Osornio Jaime Héctor.
Facultad de Ingeniería, UNAM.

30. **Laboratorio de medición e instrumentación**
Responsable: Barbosa Castillo Juan Manuel.
Facultad de Ingeniería, UNAM.

31. **Biología de Hongos**
Responsable: Cano Domínguez Nallely.
Facultad de Ciencias, UNAM.

32. **Algebra lineal**
Responsable: Díaz Osornio Jaime Héctor.
Facultad de Ingeniería, UNAM.

33. **Proyecto de ingeniería**
Responsable: Escalante Gonzalbo Ana María
División de Ingeniería mecánica e industrial, licenciatura en mecatrónica, UNAM.

34. **Biología III**
Responsable: Escobedo Ávila Itzel.
Colegio de Ciencias y Humanidades, Plantel Sur, UNAM.

35. **Biología IV**
Responsable: Escobedo Ávila Itzel.
Colegio de Ciencias y Humanidades, Plantel Sur, UNAM.

36. **Biología molecular de la célula I**
Responsable. Guzmán León Simón.
Facultad de Ciencias, UNAM.

37. **Curso de biotecnología I**
Responsable: Kawasaki Watanabe Laura.
Licenciatura en Biología.
Facultad de Ciencias, UNAM.

38. **Biología molecular de la célula I**
Responsable: Lara María Teresa.
Licenciatura en Biología.
Facultad de Ciencias, UNAM.

39. **Biología y técnicas de animales de laboratorio**
Responsable: Malagón Rivero Héctor Alfonso.
Facultad de Ciencias, UNAM.

40. **Biología celular e histología médica**
Responsable: Millán Aldaco Diana Alicia.
Carrera de Médico Cirujano.
Facultad de Medicina, UNAM.

41. **Práctica de Medicina zootecnia en animales de laboratorio**
Responsable: Rivera Cerecedo Claudia Verónica.
Facultad de Medicina Veterinaria y Zootecnia, UNAM.

42. **Informática biomédica I**
Responsable: Moncada Hernández Sandra
Departamento de Informática Biomédica
Facultad de Medicina, UNAM.

43. **Informática biomédica II**
Responsable: Moncada Hernández Sandra
Departamento de Informática Biomédica
Facultad de Medicina, UNAM.

44. **Biofísica**
Responsable: Picones Medina Arturo.
Licenciatura en Biología.
Facultad de Ciencias, UNAM.

45. **Biología Molecular de la Célula II**
Responsable: Ramírez Jarquín Josué Orlando.
Licenciatura en Biología.
Facultad de Ciencias, UNAM.

46. **Biología de animales II**
Responsable: Ramírez Jarquín Josué Orlando.
Licenciatura en Biología.
Facultad de Ciencias, UNAM.

47. **Fisiología animal**
Responsable: Ramírez Jarquín Josué Orlando.
Licenciatura en Biología.
Facultad de Ciencias, UNAM.

48. **Curso-taller de Neurobiología del aprendizaje y la memoria**
Responsable: Rodríguez Durán Luis Francisco.
Departamento de Biología celular.
Facultad de Ciencias, UNAM.

49. **Prácticas de Psicobiología**
Responsable: Zainos Rosales Antonio Paulino.
Licenciatura en Psicología.
Facultad de Psicología, UNAM.

50. **Neurocognición**
Responsable: Zainos Rosales Antonio Paulino.
Licenciatura en Psicología.
Facultad de Psicología, UNAM.

51. **Neurociencias Cognoscitivas**
Responsable: Zainos Rosales Antonio Paulino.
Licenciatura en Psicología.
Facultad de Psicología, UNAM.

52. **Taller de Psicofisiología**
Responsable: Zainos Rosales Antonio Paulino.
Licenciatura en Psicología.
Facultad de Psicología, UNAM.

53. **Temas selectos en Psicobiolgía III**
Responsable: Zainos Rosales Antonio Paulino.
Licenciatura en Psicología.
Facultad de Psicología, UNAM.

Con participación de miembros del IFC

1. **Fisiología microbiana**
   Participa: González Pedrajo Bertha.
   Facultad de Química, UNAM.

2. **Genómica funcional 2**
   Participa: Furlan Magaril Mayra.
   Centro de Ciencias Genómicas, UNAM.

3. **Taller de Ciencias: Astroglia y el cerebro: funciones y enfermedades**
   Participa: López Huerta Violeta Gisselle.
   Luis Baltazar Enoch.
   Hernández Cruz Arturo.
   Picones Medina Arturo.
   Facultad de Ciencias, UNAM.

4. **Genética**
   Participa: Furlan Magaril Mayra.
   Álvarez Adrián Fernando.
   Facultad de Medicina, UNAM.

5. **Taller de Neurobiología del aprendizaje y la memoria**
   Participa: Osorio Gómez Daniel.
   Facultad de Ciencias, UNAM.

6. **Aplicaciones de bioquímica y biología molecular**
   Participa: Valdés Rodríguez Víctor Julián.
   Torres Quiroz Francisco.
   González Pedrajo Bertha.
   Facultad de Química, UNAM.

7. **Inmunología**
   Participa: Licona Limón Paula.
   Instituto de Investigaciones Biomédicas, UNAM.

8. **Mecanismos que participan en la regulación de la traducción de proteínas**
   Participa: Martínez Silva Ana.
   LBB, UNAM.

9. **Taller de Titulación Biofísica de células excitables**
   Participa: Jiménez Pérez Nicolás.
   Licenciatura en Biología de la Facultad de Ciencias, UNAM.

10. **Métodos computacionales I: Métodos numéricos**
    Participa: Laville Conde Antonio.
    Facultad de Medicina, UNAM.

11. **Taller introductorio al análisis de la actividad eléctrica cerebral**
    Participa: Méndez Ambrosio Bruno.
    Facultad de Psicología, UNAM.

12. **Métodos en Neurociencias**
    Participa: Méndez Ambrosio Bruno.
    Facultad de Psicología, UNAM.

13. **Farmacología**
    Participa: Moncada Hernández Sandra.
    Facultad de Medicina, UNAM.

14. **Curso teórico-práctico: Técnicas en Sistemática Molecular de Plantas**
    Participa: Ongay Larios Laura.
    Instituto de Biología, UNAM.

15. **Taller Nivel III y IV. Caracterización de las Pirofosfatasas de proteobacterias**
    Participa: Peña Segura Claudia.
    Facultad de Ciencias, UNAM.

16. **Taller Neurobiología Sensorial**
    Participa: Sánchez Chávez Gustavo.
    Licenciatura en Biología.
    Facultad de Ciencias, UNAM.

Cursos de Posgrado

Miembros del IFC como responsables

1. **Bases moleculares de la síntesis de proteínas**
   Responsable: Pérez Martínez Xochitl.
   Posgrado en Ciencias Biomédicas.
   Instituto de Fisiología Celular, UNAM.

2. **Biofísica de la actividad eléctrica celular**
   Responsable: Gómora Martínez Juan Carlos.
   Posgrado en Ciencias Biomédicas.
   Instituto de Fisiología Celular, UNAM.

   Participantes:
   Sotres Bayón Francisco
   Velasco Torres Myrian
   Hernández Cruz Arturo
   Galarraga Palacio Elvira
   Fernández de Miguel Francisco
   Méndez Ambrosio Bruno
   Laville Conde Juan Antonio

3. **Biología estructural de las membranas celulares**
   Responsable: González Halphen Diego.
   Posgrado en Ciencias Biomédicas.
   Instituto de Fisiología Celular, UNAM.

   Participantes:
   Funes Soledad

4. **Biología molecular**
   Responsable: Recillas Targa Félix.
   Posgrado en Ciencias Biomédicas.
   Instituto de Fisiología Celular, UNAM.

   Participantes:
   Torres Larios Alfredo
   Álvarez Adrián Fernando
   Furlan Magaril Mayra

5. **Biología molecular**
   Responsable: Funes Soledad.
   Posgrado en Ciencias Bioquímicas.
   Instituto de Fisiología Celular, UNAM.

   Participantes:
   Valdés Rodríguez Víctor Julián

6. **Biología molecular**
   Responsable: González Pedrajo Bertha.
   Posgrado en Ciencias Bioquímicas.
   Instituto de Fisiología Celular, UNAM.

   Participantes:
   Coria Ortega Roberto
   Aguirre Linares Jesús
   Ongay Larios Laura María
   De la Mora Bravo Francisco Javier
   Georgellis Dimitris

7. **Biología molecular de la célula eucarionte**
   Responsable: Castro Obregón Susana.
   Posgrado en Ciencias Biomédicas.
   Instituto de Fisiología Celular, UNAM.

   Participantes:
   Silva Marina Macías
   Funes Soledad
   Torres Quiroz Francisco
   Escalante Alcalde Diana
   Peraza Reyes Leonardo
   Mas Oliva Jaime
   Hansberg Torres Wilhelm

8. **Bioquímica**
   Responsable: Torres Larios Alfredo.
   Posgrado en Ciencias Bioquímicas.
   Instituto de Fisiología Celular, UNAM.

   Participantes:
   Licona Limón Paula

9. **Bioquímica**
Responsable: García Sáinz Jesús Adolfo.
Posgrado en Ciencias Bioquímicas.
Facultad de Química, UNAM.

Participantes:
Macías Silva Marina

10. **Bioquímica**
Responsable: Pérez Martínez Xochitl.
Posgrado en Ciencias Bioquímicas.
Instituto de Fisiología Celular, UNAM.

Participantes:
Torres Quiroz Francisco
Pérez Montfort Ruy

11. **Canales iónicos: Máquinas moleculares**
Responsable: Rosenbaum Emir Tamara.
Posgrado en Ciencias Bioquímicas.
Instituto de Fisiología Celular, UNAM.

Participantes:
Llorente Gil Itzel Alejandra
Morales Lázaro Sara Luz
Arciniega Marcelino

12. **Células troncales: repercusiones en biomedicina**
Responsable: Velasco Velázquez Iván.
Posgrado en Ciencias Biomédicas.
Instituto de Fisiología Celular, UNAM.

Participantes:
Navarro González Rosa
Valdés Rodríguez Víctor Julián
Furlan Magaril Mayra

13. **Tópico Selecto: Bases conceptuales de la epigenómica**
Responsable: Recillas Targa Félix.
Posgrado en Ciencias Biomédicas.
Instituto de Fisiología Celular, UNAM.

Participantes:
Furlan Magaril Mayra
Poot Hernández Augusto César

14. **Optogenética: conceptos y aplicaciones**
Responsable: Tecuapetla Aguilar Fatuel.
Posgrado en Ciencias Bioquímicas.
Instituto de Fisiología Celular, UNAM.

Participantes:
López Huerta Violeta Gisselle
Velasco Torres Myrian
Ramírez Jarquín Josué Orlando

15. **Papel de los rearreglos genómicos como generadores de diversidad genética**
Responsable: González Manjarrez Alicia.
Posgrado en Ciencias Biomédicas.
Instituto de Investigaciones Biomédicas, UNAM.

16. **Fisiopatología del síndrome metabólico y la diabetes**
Responsable: Velasco Torres Myrian.
Posgrado en Ciencias Biomédicas.
Instituto de Fisiología Celular, UNAM.

17. **Neurobiología del aprendizaje y la memoria**
Responsable: Osorio Gómez Daniel.
Posgrado en Ciencias Biológicas.
Instituto de Fisiología Celular, UNAM.

18. **Modulación de la transmisión sináptica en sistema nervioso central y periférico**
Responsable: Hernández Cruz Arturo.
Posgrado en Ciencias Biomédicas.
Instituto de Fisiología Celular, UNAM.

19. **Neuroquímica básica**
Responsable: Massieu Trigo Lourdes.
Morán Andrade Julio.
Posgrado en Ciencias Biomédicas/Bioquímicas.
Instituto de Fisiología Celular, UNAM.

Participantes:
Velasco Velázquez Iván
Tecuapetla Aguilar Fatuel
Sotres Bayón Francisco
Bargas Díaz José
Ramiro Cortés Yazmín

20. **Técnicas selectas de biología molecular**
Responsable: Torres Quiroz Francisco.
Posgrado en Ciencias Bioquímicas.
Instituto de Fisiología Celular, UNAM.

Participantes:
Coria Ortega Roberto
Arciniega Castro Marcelino
Licona Limón Paula
Ongay Larios Laura María
Furlan Magaril Mayra
Moreno Alvarez Paola

21. **Uso e interpretación de la información tridimensional de macromoléculas, modelado y dinámica molecular**
Responsable: Arciniega Castro Marcelino.
Posgrado en Ciencias Bioquímicas.
Instituto de Fisiología Celular, UNAM.

Participantes:
Torres Larios Alfredo

22. **Comunicación nerviosa**
Responsable: Fernández de Miguel Francisco.
Posgrado en Ciencias Biomédicas.
Instituto de Fisiología Celular, UNAM.

23. **Diplomado en Biología molecular.**
Responsable: Contreras Zentella Martha Lucinda.
Posgrado en Ciencias Médicas Odontológicas y de la Salud.
Facultad de Odontología, UNAM.

24. **Biología molecular I**
Responsable: Contreras Zentella Martha Lucinda.
Posgrado en Ciencias Médicas Odontológicas y de la Salud.
Facultad de Odontología, UNAM.

25. **Biología molecular II**
Responsable: Contreras Zentella Martha Lucinda.
Posgrado en Ciencias Médicas Odontológicas y de la Salud.
Facultad de Odontología, UNAM.

26. **Curso Algoritmos Bioinspirados y Bioinformática.**
Responsable: Poot Hernández Augusto César.
Posgrado en Ciencia e Ingeniería de la Computación.
Instituto de Investigaciones en Matemáticas Aplicadas y en Sistemas, UNAM.

Con participación de miembros del IFC

1. **Bioenergética mitocondrial**
   Participa: Uribe Carvajal Salvador.
   Pérez Martínez Xochitl.
   Posgrado en Ciencias Biomédicas.
   Facultad de Medicina, UNAM.

2. **Biología molecular**
   Participa: Peraza Reyes Leonardo.
   Torres Quiroz Francisco.
   Furlan Magaril Mayra.
   Posgrado en Ciencias Bioquímicas.
   Instituto de Investigaciones Biomédicas, UNAM.

3. **Biología molecular aplicada para el estudio de la regulación genética en eucariontes**
   Participa: Morales Lázaro Sara Luz.
   Escalante Alcalde Diana.
   Posgrado en Ciencias Biológicas.
   Instituto de Fisiología Celular, UNAM.

4. **Bioquímica avanzada**
   Participa: Pérez Martínez Xochitl.
   Posgrado en Ciencias Biológicas.
   Facultad de Ciencias, UNAM.

5. **Creadores de la ciencia moderna**
   Participa: González Halphen Diego.
   Posgrado en Ciencias Biomédicas.
   Instituto de Neurobiología, UNAM.

6. **Cristalografía de macromoléculas**
   Participa: Torres Larios Alfredo.
   Posgrado en Ciencias Biomédicas.
   Instituto de Química, UNAM

7. **Fundamentos de células troncales, ingeniería tisular y medicina regenerativa**
   Participa: Velasco Velázquez Iván.
   Maestría y Doctorado en Ciencias de la Producción y de la salud animal.
   Facultad de Medicina Veterinaria y Zootecnia, UNAM.

8. **Inmunología avanzada: Moléculas de la respuesta inmune**
   Participa: Torres Quiroz Francisco.
   Posgrado en Ciencias Biomédicas.
   Facultad de Medicina, UNAM.

9. **Neurobiología celular y neurodesarrollo**
   Participa: Massieu Trigo Lourdes.
   Instituto de Neurobiología, UNAM.

10. **Neurodegeneración y deterioro cognitivo**
    Participa: Osorio Gómez Daniel.
    Posgrado en Ciencias Biológicas.
    Instituto de Fisiología Celular, UNAM.

11. **Proteínas: Estructura, estabilidad y función**
    Participa: Torres Larios Alfredo.
    Posgrado en Ciencias Biomédicas.
    Instituto de Química, UNAM.

12. **Regulación de la expresión génica en bacterias**
    Participa: Georgellis Dimitris.
    Posgrado en Ciencias Biomédicas.
    Centro de Ciencias Genómicas, UNAM.

13. **Relación de estructura-función de proteínas de membrana**
    Participa: González Halphen Diego.
    Posgrado en Ciencias Biomédicas.
    Instituto de Neurobiología, UNAM.

14. **Respuesta a proteínas mal plegadas en cáncer**
    Participa: Massieu Trigo Lourdes.
    Posgrado en Ciencias Biológicas.
    Instituto de Investigaciones Biomédicas, UNAM.

15. **Sistemas globales de regulación génica en bacterias**
    Participa: Georgellis Dimitris.
    Posgrado en Ciencias Bioquímicas.
    Instituto de Fisiología Celular, UNAM

16. **Temas selectos: Biología del envejecimiento**
    Participa: Licona Limón Paula.
    Posgrado en Ciencias Biológicas.
    UNAM

17. **Fundamentos de Biología Molecular**
Participa: Martínez Silva Ana Valeria.
Posgrado en Ciencias Biomédicas.
Instituto de Investigaciones Biomédicas, UNAM.

18. **Bioinformática y Biología Molecular de la Expresión Genética de un Organismo Extremófilo**
Participa: Ongay Larios Laura.
Posgrado en Ciencias Biológicas.
Instituto de Fisiología Celular, UNAM.

19. **Canales Iónicos: Bases y Metodologías para su Estudio**
Participa: Picones Medina Arturo.
Posgrado en Ciencias Bioquímicas.
Instituto de Biotecnología, UNAM.

20. **Biomembranas y Bioenergética, dentro del curso obligatorio de Bioquímica**
Participa: Sánchez Sánchez Norma.
Posgrado en Ciencias Bioquímicas.
Facultad de Medicina, UNAM.

21. **Bioenergética Mitocondrial**
Participa: Sánchez Sánchez Norma.
Posgrado en Ciencias Biomédicas.
Facultad de Medicina, UNAM.

22. **Introducción a las Neurociencias Cognitivas**
Participa: Zainos Rosales Antonio Paulino.
Posgrado en Ciencias Biomédicas.
Instituto de Fisiología Celular, UNAM.

Cursos de Licenciatura impartidos fuera de la UNAM

Con participación de miembros del IFC

1. **Transducción de señales**
   Participa: García Sáinz Jesús Adolfo
   Facultad de Medicina, Universidad Autónoma de San Luis Potosí.

2. **Seminarios para la Licenciatura en Ciencias**
   Participa: Castro Obregón Susana
   Centro de Dinámica Celular, Universidad Autónoma del Estado de Morelos.

3. **Técnicas de Biología Molecular 2**
   Participa: Mendoza Martínez Ariann Elizabeth.
   Universidad Autónoma Metropolitana (UAM)-Cuajimalpa.

4. **Curso- Taller Tópicos Selectos de Histotecnología**
   Participa: Rodríguez Montaño Sandra Daniela.
   Facultad de Ciencias Químicas.
   Universidad Autónoma Benito Juárez de Oaxaca U.A.B.J.O.

Cursos de Posgrado impartidos fuera de la UNAM

Miembros del IFC como responsables

1. **I Curso Internacional NeuroSur-CYTED "Nuevas Rutas de Señalización en Neurodegeneración"**
   Responsable: Castro Obregón Susana.
   Instituto de Investigaciones Científicas y Servicios de Alta Tecnología-AIP, Ciudad del Saber, Panamá.

2. **Taller. Fijación por perfusión para roedores**
   Responsable: Rosas Arellano Abraham.
   CINVESTAV- Instituto Politécnico Nacional.

3. **Curso Computación**
   Responsable: Poot Hernández Augusto César.
   Posgrado en Fisiología y Neurobiología Celular y Molecular.
   Departamento de Fisiología Biofísica y Neurociencias.
   CINVESTAV- Instituto Politécnico Nacional.

Con participación de miembros del IFC

1. **4º Diplomado de Bioética "Humanismo, cimiento de la salud". Interrupción legal del embarazo**
   Participa: Tapia Ibargüengoytia Ricardo.
   Hospital General Xoco, CDMX.

2. **Diplomado Bioética y Bioderecho, Estatus del embrión humano, células troncales y clonación**
   Participa: Tapia Ibargüengoytia Ricardo.
   Poder Judicial del Estado de Chihuahua y Colegio de Bioética. Chihuahua, Chih.

3. **Biología Molecular de Eucariontes**
   Participa: Recillas Targa Félix.
   Centro de Investigaciones de Estudios Avanzados (CINVESTAV) del IPN, Departamento de Biomedicina Molecular.

4. **Bioquímica Avanzada, con el tema cadena respiratoria y fosforilación oxidativa**
   Participa: González Halphen Diego.
   Departamento de Bioquímica, Escuela Nacional de Ciencias Biológicas, IPN.

5. **Cuso pre-congreso de la Rama de Transducción de Señales de la SMB. Clase: La citocina TGF-beta y la plasticidad celular**
   Participa: Macías Silva Marina.
   CINVESTAV-IPN y Sociedad Mexicana de Bioquímica, IPN.

6. **IBRO Course in Neuroscience**
   Participa: Fernández de Miguel Francisco.
   Universidad de Antioquía, Colombia.

7. **Neurociencias**
   Participa: Morán Andrade Julio.
   Universitat Autónoma de Barcelona.

8. **Biología Celular y Molecular**
   Participa: Chiquete Félix Natalia.
   ENCB-Instituto Politécnico Nacional.

9. **Bioinformatica**
   Participa: Guzmán León Simón.
   Programa de Maestría en Biología Molecular del Departamento de Genética y Biología Molecular del Centro de Investigación y de Estudios Avanzados del Instituto Politécnico Nacional.

10. **Regulación de la Expresión Genética**
    Participa: Funes Argüello Soledad.
    Departamento de Biología Celular del CINVESTAV-Zacatenco.

11. **Curso de Microscopia**
    Participa: Rincón Heredia Ruth
    Maestría en Ciencias del Departamento de Fisiología, Biofísica y Neurociencias del CINVESTAV- Instituto Politécnico Nacional.

12. **Microscopia (Teoría y Práctica)**
    Participa: Rosas Arellano Abraham.
    CINVESTAV- Instituto Politécnico Nacional.

Anexo 3

Ponencias

Participación en Congresos Nacionales

1. **2nd Epigenomics Meeting, 2019. Epigenetic Regulation in Human Disease. Instituto de Investigaciones Biomédicas, UNAM. 26-27 de septiembre 2019.**

   Ponencia:

   Valdés, Julián. “Epidermal Stem cell Differentiation”. 27-septiembre-2019.

   Cartel:

   Rodríguez Aguilera, J. R; Ecsedi, S; Goldsmith, C; Cros, M.P; Domínguez López, M; Guerrero Celis, N; Pérez Cabeza de Vaca, R; Chemin, R; Recillas Targa, F; Chagoya de Sánchez, V; Hernández Vargas, H. “Genome-wide 5-hydroxymethylcytosine emerges at early stage of in vitro hepatocyte differentiation”. 26-septiembre-2019.

2. **CEMUS XIV. Congreso de estudiantes de medicina del noroeste. Neurociencias. Universidad de Sonora.**
   30 de septiembre-4 de octubre 2019.

   Ponencia:

   Romo, Ranulfo. “Neurociencia y su impacto en las neuroprótesis”. 3-octubre-2019.

3. **III Neurobiology Meeting of the Mexican Society for Biochemistry. SMB. Guanajuato, México. 22-26 de septiembre 2019.**

   Ponencia:

   Alatriste León, Hector; Verma, Anil K; Ramírez Jarquín, Josué O; Tecuapetla Aguilar, Fatuel. “Perturbations in the Activity of Cholinergic Interneurons in the Dorsomedial Striatum Impairs the Encoding of an Instrumental Contingency Change”. 25-septiembre-2019.

   Escalante Alcalde, D; Cotzomi Ortega, I; Rivera Álvarez, J; Castro Hernández, R; Gómez López, S; Martínez Silva, V; Luna Leal, A. “Phospholipid phosphatase-3, a novel marker of neural stem cells, participates in the ventricular system remodeling and adult neurogenesis in mice”. 23-septiembre-2019.

   Romo, Ranulfo. “The neural code”. 25-septiembre-2019.

Montes Oca Balderas, Pavel; Gómora García, Juan Carlos; Massieu Trigo, Lourdes; Hernández Cruz, Arturo. “Effects of Anti-NMDA receptor antibodies on NMDA-induced intracellular Ca2+ rise: possible implications for anti-NMDAR encephalitis”. 23-septiembre-2019.

Violeta G. Lopez Huerta, Yinqing Li, Xian Adiconis, Kirsten Levandowski, Soonwook Choi, Mario A. Arias Garcia, Annie Y. Yao, Ralf D. Wimmer, Tomomi Aida, Alex Atamian, Tina Naik, Xuyun Sun, Dasheng Bi, Diya Malhotra, Marcos Gomes, Eunjin Hwang. “Integrated single-cell analysis reveals coupled molecular gradient and functional subnetworks in the thalamic reticular nucleus”. 24-septiembre-2019.

Morán, J; Cid Castro, C. “Role of ROS produced by mitochondria and NADPH-oxidase (NOX) in the apoptotic death of cerebellar granule neurons”. 22-septiembre-2019.

Sotrés Bayon, F. “Prefrontal "brake during conflict choice behavior”. 25-septiembre-2019.

Cartel:

Acevo Rodríguez, Pilar Sarah; Cabrera Benítez, Sandra; Escalante Alcalde, Diana; Castro Obregón, Susana. “The role of the autophagy during the early nervous system development”. 22-septiembre-2019.

Gómora García, Juan Carlos; Massieu Trigo, Lourdes. “Friend or Foe? Participation of IRE1 in the unfolded protein response induced by glucose deprivation in cortical neurons”. 23-septiembre-2019.

Gorostieta Salas, Elisa; Moreno Blas, Daniel; Domínguez Bautista, Jorge; Cisneros Vega, Bulmaro; Bermúdez Rattoni, Federico; Castro Obregón, Susana. “Autophagy induction reduces features of cellular senescence in the hippocampus of old rats”. 22-septiembre-2019.

Hüttenrauch, Melanie; Camberos Luna, Lucy Anita; Massieu Trigo, Lourdes; Castro Obregón, Susana. “Investigation of the therapeutic potential of autophagy induction in a mouse model of Alzheimer’s disease”. 23-septiembre-2019.

Jiménez Márquez, E; Ramiro Cortés, Y. “Neuronal activity in the primary visual cortex of SHANK3+/- in response to an over-specificity visual task”. 24-septiembre-2019.

Moreno Blas, Daniel; Gorostieta Salas, Elisa G; Muciño Hernández, Gabriel; Pommer Alba, Alexander M; Castro Obregón, Susana. “Neuronal Senescence is promoted by Dysfunctional Autophagy”. 22-septiembre-2019.

Ortiz Cruz, C.A; Ramiro Cortés, Y. “Behavioral correlates of atypical V1 neurons activity in a genetic mouse model of autism (SHANK3)”. 24-septiembre-2019.

Perera Murcia, G.R; Ramiro Cortés, Y. “Synaptic long-term depression mediated by mGlu and NMDA receptors in individual dendritic spines from SHANK3 mice”. 24-septiembre-2019.

Torres Esquivel, Carmen; Montiel Montes, Teresa; Flores Méndez, Marco; Massieu Trigo, Lourdes. “The Ketone body beta-hydroxybutyrate restores autophagic degradation in the brain of hypoglycemic rats”. 23-septiembre-2019.

Lara González. E; Duhne, M; Laville, A; Bargas, J. “Comparison of actions between L-DOPA and different dopamine agonists in striatal DA-depleted microcircuits in vitro: pre-clinical insights”. 24-septiembre-2019.

Duhne, M; Lara González, E; Laville, A; Padilla Orozco, M; Ávila Cascajares, F; Arias García, M; Galarraga, E; Bargas, J. “Activation of parvalbumin expressing neurons reconfigures neuronal ensembles in murine striatal microcircuits”. 24-septiembre-2019.

Alejandra Liliana Gómez Paz; Marcela Palomero Rivero; Diana Millán Aldaco; René Drucker Colín; Jose Bargas Diaz. “Allosteric modulation of nicotinic receptors reduces L-DOPA induced dyskinesias in parkinsonian mice”. 23-septiembre-2019.

Prior González, Mara; Lazo Gómez, Rafael; Tapia, Ricardo. “Inhibition of HDAC4 with sodium butyrate does not prevent AMPA-induced excitotoxic degeneration of spinal motoneurons *in vivo*”. 24-septiembre-2019.

Acosta Galeana, Isabel; Prior González, Mara; Tapia, Ricardo. “4-Aminopyridine protects against motor alterations in a chronic excitotoxic model of spinal motor neuron degeneration”. 24-septiembre-2019.

Díaz Hernández, Edgar Arturo; Sánchez Fuentes, Asaí; Ramírez Armenta, Kathia; Ramírez Jarquín, Josué Orlando; Tecuapetla Aguilar, Fatuel. “Thalamo-striatal contribution to switch between actions sequences”. 22-septiembre-2019.

Alatriste León, Héctor; Ramírez Jarquín, Josué Orlando; Tecuapetla Aguilar, Fatuel. “Striatal sub-circuits and cholinergic interneurons activity in behavioral flexibility”. 23-septiembre-2019.

Llanos Moreno, Argelia; Cuevas Vicente, Nisa; Alatriste León, Héctor; Valdez Fernández, Yiatzir; Ramírez Jarquín, Josué Orlando; Tecuapetla, Fatuel. “Optogenetic inhibition of the dorsomedial versus dorsolateral striatum”. 24-septiembre-2019.

Sánchez Fuentes, Asai; Ramírez Armenta, Kathia; Díaz Hernández, Edgar; Ramírez Jarquín, Josué Orlando; Tecuapetla, Fatuel. “Cortico–striatal contribution to execution of a chain of sequences”. 25-septiembre-2019.

Contreras López, Rubén Darío; Días Hernández, Edgar Arturo; Ramírez Jarquín, Josué Orlando; Tecuapetla, Fatuel. “Cerebellum–basal ganglia interactions circuits”. 26-septiembre-2019.

Emiliano Tesoro Cruz, Norma Oviedo De Anda, Leticia Manuel Apolinar, Sandra Orozco Suárez, Carolina Bekker Méndez, Gloria Martínez Pérez, Francisco Guerra Castillo, Chamina Aguirre Alvarado, Minerva Crespo Ramírez, Miguel Pérez de la Mora. “Ophthalmic administration of a DNA plasmid harboring the murine Tph2 gene: evidence for exogenous recombinant Tph2.FLAG in brain structures”. 22-septiembre-2019.

Hernández Mondragón Juan Carlos, Crespo Ramírez Minerva, Apolinar Manuel Leticia, Tesoro Cruz Emiliano, Pérez de la Mora Miguel. “Neuro-inmuno-endocrine changes induced by high-fat diet are associated with increased anxiety-like behavior in Wistar rats”. 22-septiembre-2019.

Medina Ruiz Gabriela Itzetl, Morán Julio. “Regulation of actin cytoskeleton by p47 overexpression in cerebellar granule neurons”. 23-septiembre-2019.

Diego Rolando Hernández Espinosa, Lourdes Massieu, Julio Morán. “Role of NADPH oxidase-2 in the progression of the inflammatory response secondary to striatum excitotoxic damage”. 24-septiembre-2019.

E. Colín, R. Tapia. “Chronic administration of glutamate decarboxylase inhibitors in the rat spinal cord induces motor alteration and motor neuron death”. 23-septiembre-2019.

4. **LXII Congreso Nacional de la Sociedad Mexicana de Ciencias Fisiológicas A.C. Universidad Autónoma de Querétaro. 12-15 de agosto 2019.**

Ponencia:

Bermúdez Rattoni, F. “Avances recientes en el estudio del aprendizaje y la memoria”. 14-agosto-2019.

Guzmán Ramos, K; Osorio Gómez, D; Rodríguez, F; Velasco, M; Bermúdez Rattoni, F; Hiriart, M. “Rescate de las alteraciones hipocampales asociadas al síndrome metabólico: participación dopaminérgica”. 13-agosto-2019.

Cartel:

Milo Rocha, Edgar Gerardo; Loza Huerta, Arlet; Lara Figueroa, Cesar Oliver; Picones, Arturo; Hernández Cruz, Arturo; Enoch, Luis. “Nuevos inhibidores del canal oncogénico de potasio Kv10.1”. 14-agosto-2019.

Cruz Cruz, Iskra Anai; Sánchez Zavala, José Hugo; Hiriart, Marcia; Velasco Torres, Myrian. “Efecto del síndrome metabólico en rata sobre el funcionamiento del canal KATP”. 12-agosto-2019.

Bernate Obando, Germán Alonso; Barajas Olmos, Francisco; Hiriart Urdanivia, Marcia; Velasco Torres, Myrian. “Los canales Kv2.1 y Kv2.2 y su regulación transcripcional en célula beta durante el desarrollo”. 12-agosto-2019.

Sánchez Soto, Carmen; Velasco, M; Chávez Maldonado, Juan Pablo; Hiriart Urdanivia, Marcia. “EL NGF plasmático aumenta durante el síndrome metabólico y viaja unido a sus dos receptores”. 12-agosto-2019.

Zavala Sánchez, José Hugo; Hiriart Urdanivia, Marcia; Sánchez Soto, María del Carmen; Velasco Torres, Myrian; Zambrano González, Elena. “El receptor soluble de insulina se encuentra aumentado en enfermedad de hígado graso no alcohólico”. 12-agosto-2019.

Cortes Escamilla, Cecilia Estrella; Sánchez Sandoval, Ana Laura; Gómora Martínez, Juan Carlos. “Participación de la subunidad NaVβ3 en la apoptosis de líneas celulares de cáncer”. 12-agosto-2019.

Elías López, Diana Lizbeth; Hernández Plata, Everardo; Gómora Martínez, Juan Carlos. “Evaluación electrofisiológica de antagonistas del canal NaV1.6 con potencial anti-metastásico en el cáncer cervico-uterino”. 12-agosto-2019.

5. **Taller Multidisciplinario de Redes. Taller de análisis de señales neurofisiológicas. Hotel Hacienda Cocoyoc, Morelos. 6-8 de noviembre 2019.**

Ponencia:

Miguel Serrano, Brisa García, Rosa María Reyes, Alejandra Cáceres, Elvira Galarraga, José Bargas. “Reconfiguración de ensambles neuronales durante eventos epileptiformes en la corteza motora del ratón”. 8-noviembre-2019.

Vladimir Calderón, Aldo Luna, Alejandra Gómez, Fernanda Ramírez, Elvira Galarraga, Jose Bargas. “Acciones de amantadina y clozapina en el microcircuito estriatal del ratón discinético”. 6-noviembre-2019.

Rossi Pool, R; Romo, R. “Código neuronal en la corteza somatosensorial secundaria (S2): dualidad sensorial y categórica” 7-noviembre-2019.

Montes Oca Balderas, Pavel; Gómora García, Juan Carlos; Massieu Trigo, Lourdes; Hernández Cruz, Arturo. “Efectos de anticuerpos anti-NMDA sobre la señal de iCa2+ inducida por NMDA: implicaciones para la encefalitis autoinmune por anticuerpos anti-NMDAR”. 8-noviembre-2019.

6. XLI Congreso Nacional de Microbiología y VI Congreso de Bioquímica y Biología Molecular de Bacterias. Oaxaca, México. 27-31 de octubre 2019.

Ponencia:

Vazquez Ciros, O. J; Rodríguez Rangel, C; Alvarez, A. F; Georgellis, D. "ZMP dependent activation of response regulators in Escherichia coli". 29-octubre-2019.

Hernández Valle, José; Sánchez Flores, Alejandro; Poggio, Sebastian; Dreyfus, Georges; Camarena, Laura. "The CtrA regulon of *Rhodobacter sphaeroides* favors adaptation to particular life styles". 27-octubre-2019.

Cartel:

Urias Contreras, F. A; Pannuri, A; Romeo, T; Alvarez, A. F; Georgellis, D. "Spatiotemporal regulation of the BarA/UvrY two component signaling system". 29-octubre-2019.

Marcos Vilchis, A.I; Espinosa Sánchez, N; González Pedrajo, B. "Substrate recognition by the sorting platform in the injectisome". 29-octubre-2019.

Vega Baray, B; Poggio, S; Dreyfus, G; Camarena, L. "Outer membrane vesicles from *Rhodobacter sphaeroides*". 29-octubre-2019.

Rodríguez Méndez, D; Domenzain, C; Poggio, S; Osorio, A; Dreyfus, G; Camarena, L. "Analysis of the FlgT-MotF interaction in the flagellar system 1 of *Rhodobacter sphaeroides*". 28-octubre-2019.

Vélez González, F; Vega Baray, B; Poggio, S; Dreyfus, G; Camarena, L. "Characterization of the open reading frame rsp_1315 present in the flagellar set 2 of *Rhodobacter sphaerodes*". 29-octubre-2019.

Benítez, J. M; González Vera, M; Poggio, S; Dreyfus, G; Camarena, L. "Expression of the Fla2 flagellin in *R. sphaeroides*: analysis of the control mechanisms". 28-octubre-2019.

Cruz Mendoza, L; de la Mora, F. J; Dreyfus, G. "Study of the motility of bacteria of the genus *Vibrio under* different salinity conditions". 29-octubre-2019.

Domenzain, C; Gómez César, E; Dreyfus, G; Poggio, S; Camarena, L. "CtrA regulation mediated by ClpXP in *Rhodobacter sphaeroides*". 29-octubre-2019.

Reyes Nicolau, J; Osorio, A; Domenzain, C; Poggio, S; Dreyfus, G; Camarena, L. "Evaluation of the open reading frame RSWS8N_09490 in the function of Fla2 of *Rhodobacter sphaeroides*". 29-octubre-2019.

7. **VII Congreso de Especies Reactivas del Oxígeno en Biología y Medicina SMB. Instituto de Investigaciones Biomédicas, UNAM. 9-11 de septiembre 2019.**

   Ponencia:

   Chagoya de Sánchez, Victoria. "Especies reactivas de oxígeno y nitrógeno en hepatotoxicidad: Cirrosis y Carcinoma hepatocelular". 9-septiembre-2019.

   Wilhelm Hansberg, Elisa Domínguez-Hüttinger **. "**Dioxygen Avoidance Theory: An experimentally validated mathematical model for the conidiation process in *Neurospora crassa*". 11-septiembre-2019.

8. **VII Congreso Nacional de la Rama de Transducción de Señales de la Sociedad Mexicana de Bioquímica. Centro Académico Cultural. Campus UNAM Juriquilla, México. 4-7 de noviembre 2019.**

   Ponencia:

   Ríos López, Diana; Ortega Domínguez, Bibiana; Aranda López, Yuli; Martínez Pastor, David; Macías Silva, Marina. "El contexto celular en la regulación transcripcional". 5-noviembre-2019.

   Cartel:

   Martínez Pastor, D; Ríos López, D; Macías Silva, M. "El eje Rho/Rock/F-actina promueve la estabilidad del co-regulador transcripcional SnoN". 5-noviembre-2019.

   Anaya Rubio, I. A; Ávila Rodríguez, D.G; González Espinosa, C; Ibarra Sánchez, A; Sosa Garrocho, M; Vázquez Victorio, G; Macías Silva, M. "La secreción de TGF-beta en células de melanoma y su comunicación con células cebadas". 5-noviembre-2019.

   Gómez Ceja, K. A; Sosa Garrocho, M; Macías Silva, M. "Regulación de la estabilidad de las proteínas Ski y SnoN por el antibiótico puromicina". 5-noviembre-2019.

   Díaz Bello, B; Serna Márquez, N; Macías Silva, M; Vázquez Victorio, G; Hautefeuille, M. "Efecto de la rigidez del sustrato y el factor TGF-beta en la TEM y la senescencia en hepatocitos primarios de rata". 5-noviembre-2019.

   Rodríguez Hernández, A; García Vargas, A.G; Macías Silva, M; Hautefeuille, M; Vázquez Victorio, G. "Respuesta de los hepatocitos primarios de hígado de rata a la rigidez en hidrogeles de poliacrilamida". 5-noviembre-2019.

   Gustavo de los Santos Cocotle, Juan Carlos Martínez Morales, María Teresa Romero Ávila, Jesús Adolfo García Sáinz. "Interacción del receptor α 1A adrenérgico con proteínas Rab durante la desensibilización". 4-noviembre-2019.

Emmanuel Flores Espinoza, Aldo Meizoso Huesca, Sócrates Villegas Comonfort, María Teresa Romero Ávila, Guadalupe Reyes Cruz, Jesús Adolfo García Sainz. “FFA4 receptor association with endocytic Rab proteins by homologous and heterologous receptor desensitization”. 5-noviembre-2019.

Guzmán Silva, Alejandro; Romero Ávila, Tere; Solís, Karina Helivier; Villegas Comonfort, Sócrates; Medina, Luz del Carmen; Martínez Morales, Juan Carlos; García Sainz, J. Adolfo. “Regulación del receptor para ácidos grasos tipo 1, FFA1”. 5-noviembre-2019.

9. **XIII Congreso de Posgrado en Psicologia UNAM 2019. Facultad de Estudios Superiores Iztacala, UNAM. 9-10 de octubre 2019.**

Ponencia:

Hernández Álvarez, Dailett; Pérez de la Mora, Miguel; Prospero García, Oscar; González García, Nadia. “Menor eficiencia en la conectividad cerebral funcional en adolescentes consumidores de inhalables”. 9-octubre-2019.

10. **XIII Congreso Nacional de Biología Molecular y Celular de Hongos. Centro de Investigación Científica y de Educación Superior de Ensenada. CICESE, Baja California, México. 1-5 de octubre 2019.**

Ponencia:

Peraza Reyes, L; López Fuentes, A; Álvarez Sánchez, M; Suaste Olmos, F; Mendieta Romero, A; Meizoso Huesca, A. “Endoplasmic reticulum-mitochondria dynamics and interactions during growth and development in *Podospora anserina*”. 2-octubre-2019.

González Manjarrez, Alicia. “Transcriptional reprogramming: a major mechanism shaping paralogous subfunctionalization”. 3-octubre-2019.

Saldaña de la Cruz, Daisy Ali; Osnaya, Vincent G; Camacho Villasana, Yolanda; Altman, Michael; Pérez Martínez, Xochitl; Hernández Ramírez, Greco. “Med9: A new eIF4E-interacting protein in *Saccharomyces cerevisiae*”. 3-octubre-2019.

Cano Domínguez, Nallely; Bowman, Barry; Peraza Reyes, Leonardo; Aguirre, Jesús. “*Neurospora crassa* NADPH Oxidase NOX-1 is localized in the vacuolar system and the plasma membrane”. 3-octubre-2019.

Aguirre Linares, Jesús; Ramos Balderas, José Luis; Sánchez, Olivia; Martínez Sandoval, Emilio Alonso. “The homologs of Cps1 double adenylation domain protein regulate growth and development in *Aspergillus nidulans* and *Neurospora crassa*”. 3-octubre-2019.

Cartel:

Suaste Olmos, F; Peraza Reyes, L. “Cell dynamics of the peroxisomal protein Pex13 of *Podospora anserine*”. 2-octubre-2019.

Amancio Rojas, P; Peraza Reyes, L. “The role of Hok1 in intracellular dynamics during development of the filamentous fungus *Podospora anserina*”. 3-octubre-2019.

Álvarez Sánchez, M.S; Peraza Reyes, L. “The role of the Endoplasmic Reticulum-Mitochondria Encounter Structure in the sexual development of the fungus *Podospora anserina*”. 2-octubre-2019.

Navarro Espíndola, R; Suaste Olmos, F; Peraza Reyes, L. “Proper development in the fungus *Podospora anserina* depends on organelle dynamics regulated by fission protein DNM1”. 2-octubre-2019.

Moreno Álvarez, P; Cándido López, A. A; Torres Quiroz, F. “Effect of hydrogen sulfide on yeast autophagy”. 2-octubre-2019.

Trejo Zambrano, D. “Subcellular relocalization of proteins as a divergence mechanism of paralogous proteins Bat1 and Bat2 in *Saccharomyces cerevisiae*”. 4-octubre-2019.

Aguirre, B; Márquez, D; Martínez de la Escalera, X; Scazzocchio, C; El-Hafidi, M; Riego, L; González, A. “Analysis of the subfunctionalization pathway followed by *Kluyveromyces lactis* paralogous KlLEU4 and KlLEU4BIS which originated from a Small Scale duplication event”. 4-octubre-2019.

Hersch González, J. “Impact of subcellular localization on LEU4 and Leu9 paralogous proteins subfunctionalization in the yeast *Saccharomyces cerevisiae*”. 4-octubre-2019.

Márquez, D. “GABA shunt: the importance of the ALT1-encoded alanine transaminase in oxidative stress control”. 4-octubre-2019.

Gutiérrez Alejandre, P; Camacho Villasana, Y; García Villegas, R; Flores Herrera, O; De Luna, A; Pérez Martínez, X. “Effect of the regulation of Cox1 biogenesis in yeast phenotype and mitochondrial function”. 4-octubre-2019.

Garrido Bazán, V; Aguirre Linares, J. “DnmA and FisA regulate mitocondrial and peroxisomal dynamics and development in *Aspergillus nidulans*”. 2-octubre-2019.

Sánchez, O; Aguirre, J. “The *Aspergillus nidulans* poly (A) binding protein FabM roles in RNA binding, polar growth and development”. 3-octubre-2019.

Rojo Rodríguez, J; Kawasaki, L; Coria, R. “Effect of endoplasmic reticulum stress induction on the yeast mating pathway”. 1-octubre-2019.

Hernández Rojas, I; Olivarez Resendiz, A; Kawasaki, L; Coria, R. “Transcriptional regulation of FKS2, PMC1 and GDT1 genes by Crz1 and Skn7 transcriptional factors under ER stress conditions”. 1-octubre-2019.

Gutiérrez Terrazas, S. I; Hansberg Torres, W. “cAMP, ergosterol, and deposition of cell wall components”. 3-octubre-2019.

Nava Ramírez, T; Hansberg Torres, W. “Chaperone function of the C-terminal domain of large-subunit catalases”. 3-octubre-2019.

11. XXI Congreso de Bioenergética y Biomembranas de la SMB. San Luis Potosí, SLP, México. 10-14 de noviembre 2019.

Ponencia:

Vázquez Acevedo, M; González Halphen, D. “Structure of the mitochondrial ATP synthase of the colorless alga *Polytomella sp*”. 11-noviembre-2019.

Fuentes Ramírez, E.O; Vázquez Acevedo, M; Guerrero Castillo, S; Cabrera Orefice, A; González Halphen, D. “Characterization of the amyloplasts of the Structure of the colorless alga *Polytomella parva*”. 13-noviembre-2019.

Peña, A; Sánchez, N. S; Calahorra, M. “The use of thioflavin T to estimate and measure the plasma membrane potential in *Saccharomyces cerevisiae*”. 14-noviembre-2019.

Ruelas Ramírez, Hilario; Funes, Soledad. “Mitochondrial network dynamics during Slm35-mediated mitophagy in *Saccharomyces cerevisiae*”. 13-noviembre-2019.

Pedroza Dávila, Ulrik; Uribe Alvarez, Cristina; Morales García, Lilia; Espinosa Simón, Emilio; Muhlia Almazán, Adriana; Chiquete Felix, Natalia; Uribe Carvajal, Salvador. “Staphylococcus epidermidis metabolic adaptation and biofirm formation in respone to varying oxygen”. 12-noviembre-2019.

Morales García, Lilia; Chiquete Felix, Natalia; Uribe Carvajal, Salvador. ”The ScMUC as a cellular protection system but not as an inducer of cell death”. 11-noviembre-2019.

Cartel:

Padilla Garfias, F; Sánchez, N. S; Calahorra, M; Peña, A. “Effects of ε-poly-L-lysine on *Candida albicans* and *Saccharomyces cerevisiae*”. 12-noviembre-2019.

María Concepción José Núñez, Silvia Laura Salinas Velázquez, Rosa Estela Navarro González, Marietta Tuena Sangri. “Validation of a simple method to analyze the content of monomers and dimers of F1F0 -ATP synthase in mitochondria of the complete worm *C.elegans*”. 11-noviembre-2019.

Ostolga Chavarría, M; Vázquez Acevedo, M; González Halphen, D. “Purification and characterization of the F1 sector of the F1Fo-ATP mitochondrial synthase of the colorless alga *Polytomella sp*.” 13-noviembre-2019.

Nieto Panqueva, F; Rubalcava Gracia, D; García Rincón, J; González Halphen, D. “Crucial factors may enhance import of subunit II of cytochrome c oxidase into mitochondria”. 14-noviembre-2019.

Yolanda Camacho Villasana, Rodolfo García Villegas, Xochitl Pérez Martínez. “Has Mss51 a conserved function in mitocondria?”. 12- noviembre-2019.

Natalia Chiquete Felix, Ulrik Pedroza Dávila, Lilia Morales García, Carolina Ricardez García, Salvador Uribe Carvajal. “Meeting the respiratory chain from Rhodotorula mucilaginosa, “gifted yeast””. 11-noviembre-2019.

12. **XXVII Congreso Mexicano de Psicología. Sociedad Mexicana de Psicología y el Instituto de Neurociencias de la Universidad de Guadalajara. Guadalajara, Jalisco, México. 16-18 de octubre 2019.**

Ponencia:

Fernández de Miguel, F. “¿Qué nos enseñan los murales prehispánicos acerca de nuestra percepción visual?”. 17-octubre-2019.

13. **XVIII Congreso Nacional de Biotecnología y Bioingeniería. León, Guanajuato, México. 23-28 de junio 2019.**

Cartel:

Martínez Morales, Luis Javier; Martínez Martínez, María de los Ángeles; Soto Urzúa, Lucía; González Pedrajo, Bertha; Dreyfus, Georges. “El papel de PhaP1 en la síntesis de bioplástico por Azospirillum brasilense Sp7”. 24-junio-2019.

14. **XXXIV Reunión Anual de Investigación. Instituto Nacional de Neurología y Neurocirugía "Manuel Velasco Suárez". Ciudad de México. 16-17 de mayo 2019.**

Cartel:

Karla Méndez Maldonado, Guillermo Vega López, Sara Caballero Chacón, Manuel J. Aybar, Iván Velasco. “Células troncales embrionarias de ratón que expresan MSX1 y HES1 incrementan la diferenciación a derivados de cresta neural”. 17-mayo-2019.

Rosaura Debbie Saldaña Salinas, Karla Cristina Razón Hernández, Alejandro Corzo Cruz, Marina Martínez Vargas, Iván Velasco Velázquez, Karla Berenice Sánchez Huerta, Jesús Enrique Estudillo Hernández. “Efecto del consumo de sacarosa en la neurogénesis del giro dentado ventral en ratas adultas”. 16-mayo-2019.

Beetsi Urrieta Chávez, Oscar Carballo Molina, Verónica Cáceres Chávez, Adolfo López Ornelas, Yazmín Ramiro Cortés, José Bargas Díaz, Iván Velasco Velázquez. “Uso de un hidrogel biocompatible para el direccionamiento de axones de neuronas dopaminérgicas humanas”. 17-mayo-2019.

15. **VI Latin American Protein Society Meeting (LAPSM). VII Congreso de Fisicoquímica, Estructura y Diseño de Proteínas. Ciudad de México. 20-23 de octubre 2019.**

Ponencia:

Rosenbaum, Tamara. “TRPV1: a flexible ion channel”. 21-octubre-2019.

Torres Larios, Alfredo. “Thoughts on the evolution of an ancestral protein”. 20-octubre-2019.

Cartel:

Moreno Álvarez, Paola; Díaz Salazar, Alma Jessica; Garza Ramos, Georgina; Ríos Castro, Emmanuel; Torres Quiroz, Francisco. “Effect of hydrogen sulfide (H_2S) on the activity of glycolytic enzymes from *Saccharomyces cerevisiae*”. 20-octubre-2019.

Adelaida Díaz Vilchis, Vanessa Vega García, Enrique Rudiño Piñera, Wilhelm Hansberg. “Crystal structure of catalase-peroxidase (CAT-2) from *Neurospora crassa*”. 21-octubre-2019.

Teresa Nava Ramirez, Wilhelm Hansberg. “Chaperone function of the large size-subunit catalases”. 21-octubre-2019.

Participación en Congresos Internacionales

1. **37 SMYTE (Small Meeting on Yeast Transport and Energetics). Nove Hrady, Czech Republic. 11-15 de septiembre 2019.**

   Ponencia:

   Peña, A; Sánchez, N. S; Calahorra, M. “The use of thioflavin T to estimate and measure the plasma membrane potential in *Saccharomyces cerevisiae*”. 15-septiembre-2019.

2. **1er Congreso Internacional de Ciencias Químico Biológicas. Cd. Juárez. 4-6 de noviembre 2019.**

   Cartel:

   Arzate Vázquez, Dulce María; Valencia García, Concepción; Guerra Crespo, Magdalena; Covarrubias, Luis. “Inducción de neurogénesis típica y atípica en la sustancia nigra de roedores adultos”. 4-noviembre-2019.

3. **27th Meeting of the International Society for Neurochemistry. Montréal. 4-8 de Agosto 2019.**

   Ponencia:

   Luis B. Tovar y Romo, Isaac Ponce. “DNA methylation and gene expression of astroglia before, during and after oxygen and glucose deprivation”. 4-agosto-2019.

   Lourdes Massieu, Teresa Montiel, Cristian Geronimo, Susana Flores, Berenice Bernal, Yessica Heras, Luis Tovar y Romo. “Beta-hydroxybutyrate attenuates the unfolded protein response and stimulates the autophagic flux after cerebral ischemia” 7-agosto-2019.

   Cartel:

   Campero Romero, A; Ríos Castro, E; Cárdenas Rivera, A; Tovar y Romo, L. B. “Proteomic profiling of exosomes derived from brain microvascular endothelial cells under hypoxia: potential role in remyelination”. 4-agosto-2019.

4. **30th Fungal Genetics Conference. Pacific Grove, CA. 12-17 de marzo 2019.**

   Ponencia:

   Aguirre Jesús. Co-Chair/Organizer of Concurrent Session "Fungal Stress". 14-marzo-2019.

   Peraza Reyes, L; Lopez Fuentes, A; Suaste, Olmos, F; Nachon Garduño, K; Mendieta Romero, A; Meizoso Huesca, A. “Meiotic development in Podospora anserina requires the endoplasmic reticulum shaping protein RTN1”. 15-marzo-2019.

   Cartel:

   V. Garrido, R. Jaimes, O. Sánchez, F. Lara, J. Aguirre. “Stress activated MAP kinases SakA and MpkC interact and show opposite functions on stress responses and development in *Aspergillus nidulans*”. 12-marzo-2019.

5. **63 Annual Meeting of the Biophysical Society. Baltimore, Maryland. 2-6 de marzo 2019.**

   Ponencia:

   Natalia Chiquete Felix, Cristina Uribe Alvarez, Ulrik Pedroza Dávila, Isareli Cruz Cruz, Salvador Uribe Carvajal. “Wolbachia Pipientis colonizes S. Cerevisiae with high yields, Effects on the Host”. 5-marzo-2019.

   Cartel:

   Lilia Morales García, Salvador Uribe Carvajal, Natalia Chiquete Felix, Emilio Espinoza Simon. “The reversible opening $_{SC}$MUC demostrates a high potential as a cellular protection system”. 6-marzo-2019.

6. **7th International Urogenital Science Meeting. Universidad de Tlaxcala, Tlaxcala. 5-7 de noviembre 2019.**

   Ponencia:

   Adolfo López Ornelas, Itzel Escobedo Avila, Gabriel Ramírez García, César Meléndez Ramírez, Tonatiuh Barrios, Beetsi Urrieta, Rolando Lara Rodarte, Verónica A. Cáceres Chávez, Francia Carmona, Leticia Verdugo, Luisa Rocha Arrieta, Víctor Treviño. “Human neuron transplants in an animal model of Parkinson disease”. 7-noviembre-2019.

7. **FASEB-The Lysophospholipid and Related Mediators Conference: from bench to clinic. Lisbon, Portugal. 28 de julio-2 de agosto 2019.**

   Ponencia:

   Escalante Alcalde, D; Cotzomi Ortega, I; Rivera Álvarez, J; Castro Hernández, R; Gómez López, S; Martínez Silva, V; Luna Leal, A. "Of lipids and adult neurogenesis: The role of phospholipid phosphatase-3". 30-julio-2019.

8. **Humboldt Kolleg "Rompiendo Paradigmas: Hacia una Ciencia Multi, Inter y Transdisciplinaria. Ibarra, Ecuador. 22-24 de febrero 2019.**

   Ponencia:

   Castro Obregón, Susana. "Role of autophagy during nervous system develoment and aging". 24-febrero-2019.

   Gabriel del Río. "Designing selective polypharmacological cell-penetrating peptides". 24-febrero-2019.

9. **Humboldt Kolleg: Symposium on Natural Science. Cayo Santa María, Cuba. 30 de junio-2 de julio 2019.**

   Ponencia:

   Castro Obregón, Susana. "Autophagy in the development and aging of the nervous system". 2-julio-2019.

10. **III International Congress of Psychobiology. ETS Arquitectua, Granada, España. 29-31 de mayo 2019.**

    Ponencia:

    Bermúdez Rattoni, Federico. "The Role of Dopaminergic Activity on Recognition Memory: Implications fos Alzheimer´s Disease". 29-mayo-2019.

11. **III International Symposium on Fungal Stress. São José dos Campos, SP, Brazil. 20-23 de mayo 2019.**

    Ponencia:

    Ariann E. Mendoza Martínez, Verónica Garrido Bazán, Rafael Jaimes Arroyo, Fernando Lara Rojas, Olivia Sánchez, Jesús Aguirre. "Ros detoxification and sensing during fungal growth and differentiation". 20-mayo-2019.

12. XIII International Basal Ganglia Meeting. IBAGS. Biarritz. 28 de abril-2 de mayo 2019.

Ponencia:

B. S. Méndez Rodríguez, D. Tapia, M. A. Arias García, J. Bargas, E. Galarraga. "Firing properties of intralaminar thalamic neurons". 28-abril-2019.

V.H. Avilés Rosas, E.A. Rendón Ochoa, T. Hernandez Flores, A. Luna Leal, F. Hernández Vázquez , M. Flores León, E. Galarraga, C. Arias, J. Bargas. "Ca2+ current decrease induced by muscarinic M4 receptors in DA-depleted direct striatal projection neurons is reversed by PP-1 inhibition". 28-abril-2019.

13. 26th Meeting, Society for Redox Biology and Medcine. (SfRBM 2019). Las Vegas, NV, USA. 20-23 de noviembre 2019.

Ponencia:

Mina Königsberg, Stefanie Paola López Cervantes, Norma Silvia Sánchez, Martha Calahorra, Beatriz Mena Montes, Gibrán Pedraza Vázquez, David Hernández Álvarez, Mercedes Esparza Perusquia, Antonio Peña Díaz, Armando Luna López, Óscar Flores Herrera. "Moderate exercise and metformin treatment effect on mitochondrial bioenergetics and dynamics, in quadriceps muscle isolated from old wistar female rats. 21-noviembre-2019.

14. II Pan American Congress of Physiological Sciences - PANAM 2019. La Habana, Cuba. 27-31 de mayo 2019.

Ponencia:

Pérez de la Mora, M; Pérez Carrera, D; Crespo Ramírez, M; Fuxe, K; Borroto Escuela, D. "Signaling at D2R-Oxytocin heterocomplexes and their relevance for the anxiolytic effects of D2R-oxytocinR interactions in the amygdala of the rat". 27-mayo-2019.

15. SGP 73 Annual Symposium/Sobla Annual Meeting. Reunión de la Sociedad Biofísica Latinoamericana y la Society for General Physiologists. Valparaíso, Chile. 4-7 de septiembre 2019.

Ponencia:

Rosenbaum Tamara. "The modes of action of an endogenous TRPV1 activator". 6-septiembre-2019.

16. **3er. Congreso Internacional de la Federación de Sociedades y Asociaciones Hispanas de América del Norte, Centroamérica y el Caribe de la Ciencia de los Animales de Laboratorio, A.C. (FeSAHANCCCAL). Antigua, Guatemala. 4-6 de septiembre 2019.**

Ponencia:

López Casillas, F. “Usos del Pez Cebra (Danio rerio) en investigación”. 6-septiembre-2019.

17. **Federation of European Neuroscience Societies (FENS) 2019. Belgrade, Serbia. 10-13 de julio 2019.**

Cartel:

Pérez de la Mora, M; Pérez Carrera, D; Crespo Ramírez, M; Fuxe, K; Borroto Escuela, D. “Understanding the role of GPCR of heterorerceptor complexes in the neuronal networks of the brain both in health and disease" Signaling at D2R-Oxytocin heterocomplexes and their relevance for the anxiolytic effects of D2R-oxytocinR interactions in the amygdala of the rat”. 10-julio-2019.

18. **XXIX International Conference on Yeast Genetics and Molecular Biology. Göteborg, Sweden. 18-22 de agosto 2019.**

Cartel:

Norma Silvia Sánchez, Martha Calahorra, Laura Kawasaki, Roberto Coria, Papon Nicolas, Defosse Tatiana, Peña Antonio. “The role of MAPK HOG1 in the tolerance to saline stress in *Debaryomyces hansenii*”. 22-agosto-2019.

Alicia González, Beatriz Aguirre, Ximena Escalera, Claudio Scazocchio, Alexander DeLuna, Lina Riego, Dariel Márquez, Mohammed El-Hafidi. “Subcellular localization and leucine feedback control of equivalent paralogous *Saccharomyces cerevisiae* and *Kluyveromyces lactis* proteins play key functional roles in subfunctionalization”. 19-agosto-2019.

19. **20th International Symposium on Cells of the Hepatic Sinusoid (ISCHS). Sydney, Australia. 4-7 de septiembre 2019.**

Cartel:

Guerrero Celis, N; Rodríguez Aguilera, J. R; Pérez Cabeza de Vaca, R; Arzate Mejía, R; Domínguez López, M; Velasco Loyden, G; Recillas Targa, F; Chagoya de Sánchez, V. “Could an Anti-fibrotic Adenosine Derivative Regulate the Wnt/β-catenin Pathway in Liver Cells, in vitro?”. 4-septiembre-2019.

20. 21st European Congress of Endocrinology (ECE 2019). Lyon, France. 18-21 de mayo 2019.

Ponencia:

Ortiz Huidobro, R. I; Velasco, M; Hiriart, M. “Sexual dimorphism in the mechanism for insulin resistance”. 21-mayo-2019.

21. 22nd International *C. elegans* Conference. Los Angeles, CA. 20-24 de junio 2019.

Ponencia:

Campos Martínez, G; Navarro, R. E. “Mitochondria aggregation could affect stress granules formation in the *C. elegans* gonad”. 22-junio-2019.

González Rangel, A; Recillas Targa, F; Navarro, R. E. “Regulation of lin-35/Rb gene expression during fasting in adult animals”. 22-junio-2019.

22. 50th Annual meeting Society for Neuroscience. Chicago, IL. 19-23 de octubre 2019.

Ponencia:

Hernández Matias, A; Jaimes Cabrera, J; Guzmán Ramos, K; Bermúdez Rattoni, F; Osorio Gómez, D. “Optogenetic stimulation of BLA-IC projections induces long-term avoidance memories”. 19-octubre-2019.

Cartel:

Salcedo Tello, P; Hernández Ramírez, S; Hernández Matias, A; Osorio Gómez, D; Perez, C. I; Gutiérrez, R; Bermudez Rattoni, F; Guzman Ramos, K. “The metabolic changes induced by high-fat diet intake during adolescence affect spatial and odor long-term memories”. 23-octubre-2019.

Gutiérrez López, E. S; Rodríguez, L. F; Hernández Ramírez, S; Osorio Gómez, D; Salcedo Tello, P; Velasco, M; Hiriart, M; Bermúdez Rattoni, F; Guzmán Ramos, K. “Increasing dopaminergic activity improves synaptic plasticity and memory performance in cognitively impaired animals due to chronic exposure to a high-sugar diet”. 19-octubre-2019.

Isaac Ponce, Ricardo Santana Martínez, Luis Tovar y Romo. “DNA methylation inhibition promotes axonal growth and neuronal survival in a murine cerebral ischemia model”. 19-octubre-2019.

Aura Campero Romero, Emmanuel Ríos Castro, Luis Tovar y Romo. “Proteomic characterization and protective effect against brain ischemia by adult mouse neural progenitor cells-derived extracellular vesicles”. 19-octubre-2019.

L. Landa Navarro, C. Velázquez Delgado, F. Bermúdez Rattoni. “Intrahippocampal administration of amyloid beta 42 diminishes catecholaminergic axons and disrupts spatial contextual memory”. 19-octubre-2019.

O. Urrego Morales, I. Delint Ramírez, F. Bermúdez-Rattoni. “Inhibition of cellular palmitoylation impairs the formation and maintenance of spatial memory and synaptic plasticity”. 23-octubre-2019.

L. Ayala Guerrero, F. Bermudez RattonI, K. Guzman Ramos. “Impact of high-fat diet and aging on cognitive function: Relation with glial fibrillary acidic protein levels”. 23-octubre-2019.

C. I. Pérez, A. I. Hernández Coss, M. G. Moreno, G. Ferreira, G. Pacheco López, F. Bermúdez Rattoni, R. Gutiérrez. “Electrophysiological recording on basolateral amygdala and ventral hippocampus during memory tasks induced by high fat diet during adolescence”. 23-octubre-2019.

A. Gómez, M. Palomero Rivero, D.A. Millán Aldaco, R. Drucker-Colín, J. Bargas. “Allosteric modulation of nicotinic receptors reduces L-DOPA induced dyskinesias in Parkinsonian mice”. 22-octubre-2019.

23. 5th International Meeting on Stem Cells and Regenerative Medicine. Organizado por la Sociedad Mexicana para la Investigación en Células Troncales y la International Society for Cell and Gene Therapy. Facultad de Medicina, UNAM, Ciudad de México. 21-23 de octubre 2019.

Ponencia:

Adolfo López Ornelas, Itzel Escobedo Ávila, Gabriel Ramírez García, Rolando Lara Rodarte, Tonatiuh Barrios García, César Meléndez Ramírez, Beetsi Urrieta Chávez, Verónica A. Cáceres Chávez, Francia Carmona, Carlos Alberto Reynoso, Carlos Aguilar, Nora E. Kerik, Luisa Rocha, Leticia Verdugo Díaz, Víctor Treviño, José Bargas, Verónica Ramos Mejía, Juan Fernández Ruiz, Aurelio Campos Romo, Iván Velasco. “Human embryonic stem cells-derived dopaminergic neurons transplanted in parkinsonian monkeys recover dopamine levels and motor behavior”. 21-octubre-2019.

Cartel:

Sara Caballero, Daniel Cortés, Baldomero Esquivel, Linaloe Manzano, Israel Pérez, Carlos Ramírez, Iván Velasco. “Antioxidant and neuroprotective effect of an extract rich in antocyanin derived of Hibiscus sabdariffa in a neurotoxicity oxidative stress model in rat (E17) primary neural cultures”. 21-octubre-2019.

Angel Polanco, Iván Velasco, Itzel Escobedo. “Comparison of Two-Dimensional and Three-Dimensional cell cultures for the generation of an in vitro model of ventral midbrain”. 21-octubre-2019.

César Meléndez, Raquel Cuevas, Tonatiuh Barrios, Víctor Treviño, Iván Velasco. “Expression paterns of CTCF and characterization of active enhancers during dopaminergic neuronal differentiation of human embryonic stem cells”. 21-octubre-2019.

Rolando Lara Rodarte, Daniel Cortés, Karla Itzel Soriano, Iván Velasco. “Effects of transgenic gdnf on differentiation and survival of dopaminergic neurons produced from mouse embryonic stem cells”. 22-octubre-2019.

Beetsi Urrieta Chávez, Oscar Carballo Molina, Vladimir Calderón Ortíz, Verónica Cáceres Chávez, Adolfo López Ornelas, Yazmín Ramiro Cortés, José Bargas Díaz, Iván Velasco Velazquez. “Use of a biocompatible hydrogel for directing axonal growth and assessing maturation of human dopaminergic neurons”. 22-octubre-2019.

Montané Romero, Martínez Silva, Escalante Alcalde. “Phospholipid phosphatase 3 enables pluripotency escape during endodermal differentiation”. 22-octubre-2019.

Germán Atzin Mora Roldán, Dalia Ramírez, Diana Millan Aldaco, Rosana Pelayo, Karlen Gazarian, Arturo Hernández-Cruz. “Delivered the talk: From blood to heart: a study of hematopoietic differentiation from human pluripotent stem cells using 2d and 3d cultures”. 22-octubre-2019.

24. eGMD - Epigenetics in Metabolic Diseases // 3rd LIMIOR - Leipzig International Meeting for Interdisciplinary Obesity Research. 11-13 de diciembre 2019.

Cartel:

Rodríguez Aguilera, J. R; Guerrero Hernández, C. A; Pérez Molina, R; Cadena del Castillo, C. E; Pérez Cabeza de Vaca, R; Guerrero Celis, N; Domínguez López, M; Murillo de Ozores, A. R; Arzate Mejía, R; Ecsedi, S; Goldsmith, C; Cros, M. P; Hernández Vargas, H. “Epigenetic alterations in cirrhosis and how an adenosine derivative could revert liver fibrosis”. 11-diciembre-2019.

25. EMBO Workshop: Protein Synthesis and Translational Control. Heidelberg, Alemania. 4-7 de septiembre 2019.

Cartel:

Cristian Vergara, Yolanda Camacho Villasana, Lindsay Burwell, Thomas D. Fox, Xochitl Pérez Martínez. “Defects on translation of the mitochondrial COX1 mRNA are bypassed by a nuclear suppressor”. 6-septiembre-2019.

Greco Hernandez, Vincent G. Osnaya, Xochitl Pérez Martínez. “Diversification of the AUG codon context across eukaryotes”. 6-septiembre-2019.

26. EMBO workshop Bridging cell and tissue mechanics to fate specification and development. Santiago de chile. 2-5 de abril 2019.

Cartel:

Pilar Sarah Acevo Rodríguez, Sandra Cabrera Benitez, Diana Esalante Alcalde, Susana Castro Obregón. “How can autophagy contribute during mouse neural tube closure?” 2-abril-2019.

27. International Stroke Conference 2019. Honolulu, Hawaii. 6-8 de febrero 2019.

Cartel:

Ximena Castillo, Luis Tovar y Romo, Carmen Clapp, Gonzalo Martínez de la Escalera. “Vasoinhibins overexpression in the central nervous system leads to an increased damage after an ischaemic insult, while endogenous prolactin is neuroprotective”. 6-febrero-2019.

28. 3 rd. International Summer Symposium on Systems Biology. INMEGEN, Ciudad de México. 5-6 de Agosto 2019.

Cartel:

Bernate Obando, Germán Alonso; Barajas Olmos, Francisco; Hiriart Urdanivia, Marcia; Velasco Torres, Myrian. “Kv2 Channels and their transcriptional regulation in beta cells throughout development”. 6-agosto-2019.

29. ISSCR 2019 Annual Meeting. Los Angeles, California. 26-29 de junio 2019.

Cartel:

Adolfo López Ornelas, Itzel Escobedo Ávila, Gabriel Ramírez García, César Meléndez Ramírez, Tonatiuh Barrios, Beetsi Urrieta, Rolando Lara Rodarte, Verónica A. Cáceres Chávez, Francia Carmona, Leticia Verdugo, Luisa Rocha Arrieta, Víctor Treviño. “Intracerebral transplantation of dopamine neurons differentiated from human embryonic stem cells to parkinsonian non-human primates promotes functional recovery”. 27-junio-2019.

30. Parasitic helminths new perspectives in biology and infection. Hydra, Greece. 1-6 de septiembre 2019.

Cartel:

Emmanuel Flores Espinoza, José Luis Ramos Balderas, Paula Licona Limón. “Study of the role of IL-9 in basophil differentiation and function”. 1-septiembre-2019.

31. VII Meeting of Reactive Oixgen Species in Biology and Medicine. septiembre 2019.

Cartel:

Cid Castro, C; Morán J. “Role of ROS produced by mitochondria and NOX (N nadph-oxidase) in the apoptotic death of cerebellar granule neurons”. 9-septiembre-2019.

32. XIV European Meeting on Glial Cells in health and Disease. Portugal. 10-13 de julio 2019.

Cartel:

J. Albert Garay, R. Salceda. “High glucose concentrations induce oxidative stress in retinal Müller cells by altering Nrf2”. 11-julio-2019.

M. A. Castro, E. Papic, A. Covarrubias-Pinto, A. Rosas-Arellano, F. Court, A. Rojas-Fernandez. “Huntingtin and Rab27a are involved in the secretion of exosomes from astroglial cells”. 10-julio-2019.

33. BLAST XV. Bacterial, Locomotion and signal Transduction Meeting.New Orleans, USA. 20-25 de enero 2019.

Cartel:

Javier de la Mora, Mariela García Ramos, Teresa Ballado, Laura Camarena, Georges Dreyfus. “Biochemical and phylogenetic study of Sltf, a flagellar lytic transglycosylase from *Rhodobacter sphaeroides*”. 21-enero-2019.

Mariela García Ramos, Javier de la Mora, Laura Camarena, Georges Dreyfus. “The role and regulation of the flagellar lytic transglycosylase (SltF) during rod formation in *Rhodobacter sphaeroides*”. 22-enero-2019.

34. Association for Research in Vision and Ophthalmology (ARVO) Annual Meeting. Vancouver Convention Centre, Canadá. 28 de abril-2 de mayo 2019.

Cartel:

Irene Lee Rivera, Edith López Hernández, Ana María López Colomé. “PAR1 activation induces Glutamate release from RPE cells that is Ca^{+2} and PKC-dependent”. 29-abril-2019.

35. 6to Congreso Internacional RedBiot. Facultad de Ciencias Biológicas, UANL. 16-18 de octubre 2019.

Cartel:

Margarita Linares Zapién, Fernando Suaste Olmos, Patricia González Alva, Vicente Garibay Febles, Diana María Escobar García, Héctor Eduardo Flores Reyes, José Arturo Garrocho Rangel, Marco Antonio Alvarez Pérez, Amaury de Jesús Pozos Guillén. “Respuesta de células inmunes murinas a materiales metálicos de uso biomédico”. 16-octubre-2019.

Participación en simposios Nacionales

1. **1er. Encuentro de Biología Computacional del IFC. Auditorio "Antonio Peña Díaz", Instituto de Fisiología Celular, UNAM. Ciudad de México. 9 de octubre 2019.**

   Ponencia:

   Valdés Rodriguez, J. "Mapeo de cromatina abierta mediante ATAC-seq para identificar dinámicas epigenéticas y scSEQ". 9-octubre-2019.

   Furlan Magaril, M. "Explorando las conexiones genómicas de genes circadianos durante las 24 horas". 9-octubre-2019.

   Del Río Guerra, G. "Diseño bioinspirado de blockchains : De cómo la muerte es necesaria para la sobrevivencia de sistemas complejos". 9-octubre-2019.

2. **Avances Biomédicos en Cáncer y Enfermedades Crónico Degenerativas. Auditorio Unidad de Biomedicina. Facultad de Estudios Superiores Iztcala, UNAM. Ciudad de México. 18- 20 de junio 2019.**

   Ponencia:

   Recillas Targa, F. "De la genética a la epigenética en cáncer". 18-junio-2019.

3. **Ciclo de conferencias de investigación en neurociencias. auditorio "Dra. Silvia Macotela", Licenciatura de Psicología en línea. UNAM. Ciudad de México. 26- 28 de noviembre 2019.**

   Ponencia:

   López Huerta, V. G. "Intervención genética para el estudio del cerebro". 26-noviembre-2019.

4. **De la gran explosión al surgimiento de las civilizaciones. Colegio Nacional. 22-23 de abril 2019.**

   Ponencia:

   Recillas Targa, F. "La aparición de los seres multicelulares". 23-abril-2019.

5. **Docencia, complejidad y prácticas transdisciplinarias. 25 de junio 2019.**

   Ponencia:

   Fernández de Miguel, F. **“**Experimenta: proyecto para vivir la ciencia desde adentro”. 25-junio-2019.

6. **Epigenetic Regulation in Human Disease. Instituto de Investigaciones Biomédicas, UNAM. Ciudad de México. 26- 27 de septiembre 2019.**

   Ponencia:

   Penagos Puig Andres, Claudio Sherlyn, Stephenson Aura, Furlan Magaril Mayra. **“**Genome 3D architecture during erythroid development”. 26-septiembre-2019.

7. **Maquinas Moleculares, Luces y Comunicaciones Celulares. Anfiteatro Alfredo Barrera, Facultad de Ciencias, UNAM. 27-28 de agosto 2019.**

   Ponencia:

   Del Río Guerra, G. “Usos del aprendizaje de máquina en la biomedicina”. 28-agosto-2019.

8. **Sesión General del Instituto Nacional de Cancerología. 5 de marzo 2019.**

   Ponencia:

   López Colomé, Ana María. **“**El camino de la mujer en las Ciencias Médicas”. 5-marzo-2019.

9. **Simposio Teórico-Práctico de Edición Genética por CRISPR-CAs9. Auditorio “Antonio Peña Díaz”, Instituto de Fisiología Celular, UNAM. Ciudad de México. 28 de octubre 2019.**

   Ponencia:

   Rosa Estela Navarro. “Edición Genética por CRISPR-CAs9 para estudiar la función de genes en la gónada del *C. elegans*”. 28-octubre-2019.

   Paula Licona, Ariadna Aparicio Juárez. “Presentación de la Unidad de Edición Genética y Criopreservación del IFC”. 30-octubre-2019.

   Félix Recillas, Rodrigo Arzate. “Estudio de elementos regulatorios mediante el sistema CRISPR-Cas”. 29-octubre-2019.

10. **Taller Multidisciplinario 2019. CINVESTAV, Ciudad de México. 6-8 de noviembre 2019.**

Ponencia:

Sorel Achouna, Dilia Aguirre Olivas, Guillermo Hernández Mendoza y Francisco Fernandez de Miguel. “Transporte y fusión de vesículas electrodensas estudiados con tomografía electrónica y ultramicroscopía”. 6-noviembre-2019.

11. **XIV Congreso de Ciencias Naturales- IBQ. Universidad de Aguascalientes. 11-13 de septiembre 2019.**

Ponencia:

Alfredo Torres Larios.

Participación en simposios Internacionales

1. **20 Aniversario del Instituto de Neurociencias. Alicante, España. 4-5 de julio 2019.**

   Ponencia:

   Ranulfo Romo. "Constructing perceptual decision-making across cortex". 4-julio-2019.

2. **26th American Peptide Symposium. Monterey, California, E.U. A. 22-27 de junio 2019.**

   Ponencia:

   Jaime Mas Oliva. **"**Workshop. A Sustainable Synthetic Methodology for Peptides and Peptidomimetics". 22-junio-2019.

3. **5th International Symposium on Adipobiology and Adipopharmacology. Merida, Yucatán. 1-5 de mayo 2019.**

   Ponencia:

   Myrian Velasco, Rosa Isela Ortiz Huidobro, Larqué Carlos, Marcia Hiriart. "Sexual dimorphism: a factor in the insulin resistance mechanism in metabolic syndrome model". 2-mayo-2019.

   Marcia Hiriart. "Organización del simposio. Academic opening session y Academic Closing Session". 1-mayo-2019.

   Cartel:

   Sánchez Zamora, Y. I; Velasco Torres, M; Hiriart, M. "Sugar, metabolic syndrome and low-grade inflammation: an unsweet combination" 3-mayo-2019.

   Ortiz Huidobro, Rosa Isela; Chávez Maldonado, Juan Pablo; Sabido Barrera, Jean; Larqué, Carlos; Velasco, Myrian; Hiriart, Marcia. "Relevant role of sex in the molecular mechanism of physiological insulin resistance in adipose tissue". 3-mayo-2019.

   Sabido Barrera, Jean Imanol; Ortíz Huidobro, Rosa Isela; Velasco Torres, Myrian; Larqué Velázquez, Carlos; Hiriart Urdanivia, Marcia. "Role of ADAM 10 and 17 in the release of soluble insulin receptor". 3-mayo-2019.

   Samario Roman, J. S; Sánchez Maldonado, J. P; Ortiz Huidobro, R. I; Larque, C; Hiriart, M. "NGF increases glucose uptake in pancreatic beta cells and adipose tissue of 20 day posnatal life". 2-mayo-2019.

4. **Brainhack Non Human Primate Analysis Tools. Londres, UK. 5-6 de septiembre 2019.**

   Ponencia:

   Rossi Pool, R; Romo, R. “Coding and Temporal signals during a cognitive process in the dorsal premotor cortex”. 6-septiembre-2019.

5. **Chemical Transmission: the key to understand brain function. Facultad de Química, Instituto de Fisiología Celular, UNAM. 23-24 de abril 2019.**

   Ponencia:

   Ricardo Tapia. “From GABA to glutamate neurotransmission: excitotoxicity and neurodegeneration”. 23-abril-2019.

   Iván Velasco. “Differentiation of stem cells to dopamine neurons: Relevance for Parkinson disease”. 24-abril-2019.

   Lourdes Massieu. “Unfolded protein response and autophagy during energy stress conditions”. 24-abril-2019.

   Luis Tovar y Romo. “Trophic regulation of neuronal survival”. 24-abril-2019.

   Herminia Pasantes. “Dr. Ricardo Tapia: scientist, university professor and my friend”. 24-abril-2019.

6. **Conferencia Internacional de Educación en Cambio Climático. Santiago de Chile. 6-7 de mayo 2019.**

   Ponencia:

   Alicia González. “Caso práctico: Biorremediacion y cambio climático”. 6-mayo-2019.

7. **IBRO- ICPBR Summer School of Primate Neurobiology. Shanghai, China. 8-14 de julio 2019.**

   Ponencia:

   Ranulfo Romo. “The primate somatosensory system as a model for studying cognitive functions”. 8-julio-2019.

8. **Mathematics and Computer Science in Modeling and Understanding of Structure and Dynamics of Biomolecules. 9-11 de Agosto 2019.**

   Ponencia:

   Marcelino Arciniega, Fernanda Alvarez, Adrian Gutierrez. “Pruning false positives from small molecule docking results using machine learning techniques”. 10-agosto-2019.

   Cartel:

   Fernando Fontove, Gabriel Del Río. “De novo Protein Structure Prediction using Residue Cluster Class”. 10-agosto-2019.

9. **Molecular Biosystems Simposia. Puerto Varas, Chile. 30 de septiembre-4 de octubre 2019.**

   Ponencia:

   Mayra Furlan Magaril. “Gene promoter long-range interaction dynamics during a circadian cycle”. 4-octubre-2019.

10. **Pharmacological and nutritional targeting voltage-gated sodium channels in the treatment of epithelial cancers. Villa Rabelais, Francia. 4-8 de noviembre 2019.**

    Ponencia:

    Juan Carlos Gomora. **“**Nav channels in cervical cancer and effect of potential anti-metastatic compounds on Nav1.6 and Nav1.7 channels”. 5-noviembre-2019.

    Juan Carlos Gomora. “Non-canonical functions of voltage-gated sodium channels in the metastatic behavior of cervical cancer”. 6-noviembre-2019.

11. **Reactive oxygen species and nontransmissible diseases.**

    Ponencia:

    Julio Morán. “Role of reactive oxygen species and their sources in neuronal death”. 11-septiembre-2019.

12. **SciLifeLab Seminar Series. Karolinska Institute. Noviembre 2019.**

    Ponencia:

    Furlan Magaril, Mayra. “Circadian gene promoter chromatin contacts around the clock”. 19-noviembre-2019.

13. **14th Annual Peptide Therapeutics Symposium. The Salk Institute, La Jolla, CA. E.U.A. 24-25 de octubre 2019.**

Ponencia:

Jaime Mas Oliva. **"**Participation in round table". 24-octubre-2019.

14. **The mistery of the mind.**

Ponencia:

Ranulfo Romo. **"**Subjective sensory experience and uncertainty of perceptual decisions: where and how in the brain?". 17-septiembre-2019.

15. **9th Bonn Humboldt Award Winners' Forum. 16-20 de octubre 2019.**

Cartel:

Gabriel Del Río. "Anastasis: exploring the limits of cell death". 17-octubre-2019.

16. **Symposium on Translational Neuroscience. Instituto de Neurobiología, UNAM. 20-21 de junio 2019.**

Cartel:

Ramos Acevedo, R; Morato Torres, C. A; Bernal Conde, L. D; Palomero Rivero, M; Sánchez Argüero, R; Schüle, B; Guerra Crespo, M. "In vivo characterization of dopaminergic potential of human embryonic and induced pluripotent stem cells in a model of Parkinson´s disease". 21-junio-2019.

Conferencias Nacionales

1. **Ciclo de conferencias de divulgación científica, Instituto Nacional de Investigaciones Nucleares, Centro Nuclear Dr. Nabor Carrillo Flores.**

   Ponencia:

   Ricardo Tapia. “El cerebro y la mente”. 5-septiembre-2019.

2. **Fondo de Cultura Económica. En la XX Muestra bibliográfica de la ENP, Plantel 8 “Miguel E. Schultz”, UNAM.**

   Ponencia:

   Ricardo Tapia. Presentación del libro “Las células de la mente”. 7-febrero-2019.

3. **Foro sobre la regulación de la marihuana con fines lúdicos, médicos, ceremoniales y comerciales. Senado de la República.**

   Ponencia:

   Ricardo Tapia. “Marihuana y salud”. 20-marzo-2019.

4. **Charlas con Premios Nacionales. Consejo Consultivo de Ciencias. Librería Octavio Paz, FCE.**

   Ponencia:

   Ricardo Tapia. “Las neurociencias y las drogas: ¿Por qué no deben estar prohibidas?”. 28-agosto-2019.

5. **Homenaje a Ruy Pérez Tamayo. Colegio de Bioética, Instituto de Fisiología Celular, UNAM.**

   Ponencia:

   Ricardo Tapia. “Diez razones para hacer Bioética”. 3-junio-2019.

6. **Coloquio Estudiantil de Bioquímica, Facultad de Ciencias, UNAM.**

   Ponencia:

   Ricardo Tapia. “Mente y cerebro”. 7-noviembre-2019.

7. **VI Foro de la "La ética y la ley en Cirugía". Academia Mexicana de Cirugía.**

   Ponencia:

   Ricardo Tapia. "Pérdida de la vida: una visión desde las neurociencias". 16-marzo-2019.

8. **Encuentro Internacional de Investigación en Ciencias de la Salud. Facultad de Medicina, UNAM.**

   Ponencia:

   Ricardo Tapia. "Neurociencias y drogas". 28-mayo-2019.

9. **1^{era} Conferencia interdisciplinaria de Cátedras CONACYT.**

   Ponencia:

   Enoch Luis. "Canales iónicos: funciones más allá de la generación de potenciales de acción". 13-agosto-2019.

10. **Ciclo de seminarios en el Centro de Investigación Biomédica de Oriente (CIBIOR) del IMSS.**

    Ponencia:

    Enoch Luis. "El cáncer como oncocanalopatía: ¿pueden los canales iónicos ser blancos moleculares contra el cáncer?" 18-octubre-2019.

11. **7° Reunión de Nutrición, UPAEP Puebla.**

    Ponencia:

    Salvador Uribe Carvajal. "La bioenergética en el tratamiento del cáncer". 29-octubre-2019.

12. **Bioenergética, Instituto de Neurociencias, Juriquilla Querétaro.**

    Ponencia:

    Salvador Uribe Carvajal. "Bioenergética mitocondrial". 9-mayo-2019.

13. **Centro de Ciencias Genómicas de la UNAM.**

    Ponencia:

    Félix Recillas Targa. "Organización tri-dimensional del genoma en la expresión diferencial de los genes". 3-octubre-2019.

14. **Instituto de Fisiología Celular, UNAM.**

Ponencia:

Félix Recillas Targa. “Participación de la estructura tri-dimensional del genoma en la regulación transcripcional”. 15-noviembre-2019.

15. **Instituto Nacional de Medicina Genómica**

Ponencia:

Félix Recillas Targa. “Organización tri-dimensional del genoma en la expresión diferencial de los genes”. 31-mayo-2019.

16. **De sinapsis, ensambles y sistemas dinámicos.**

Ponencia:

Luis B. Tovar y Romo. “Participación de las vesículas extracelulares en el proceso de recuperación después del infarto cerebral isquémico”. 22-enero-2019.

17. **Conferencia Magistral del Premio en Investigación y Nutrición 2019, FUNSALUD, Nestlé, INCMNSZ .**

Ponencia:

Marcia Hiriart Urdanivia. “Diferencias en el desarrollo del metabolismo de acuerdo al sexo”. 8-octubre-2019.

18. **Construyendo el Futuro, Encuentro de Ciencia 2019, Academia Mexicana de Ciencias.**

Ponencia:

Marcia Hiriart Urdanivia. “La secreción y acciones de la insulina en la obesidad por exceso de azúcar en la dieta”. 3-diciembre-2019.

19. **Congreso de Transducción de Señales de la SMB.**

Ponencia:

Victoria Chagoya. “Fisiopatología de la señalización celular”. 30-julio-2019.

20. Conversatorios entre Filosofía y Ciencia.

Ponencia:

Violeta Gisselle López Huerta. “Intervención genética para el estudio del cerebro”. 2-mayo-2019.

21. Fiesta de las Ciencias y las Humanidades, Universum, UNAM.

Ponencia:

Adrian F. Alvarez. “Más de cinco sentidos: cómo sienten las bacterias por medio de su membrana celular”. 25-octubre-2019.

Marieta Tuena Sangri. “Conociendo las moléculas de la vida”. 25-octubre-2019.

22. Máquinas Moleculares, Luces y Comunicaciones Celulares, Jornada de Conferencias del Instituto de Fisiología Celular.

Ponencia:

Adrian F. Alvarez. “¿Cómo sienten las bacterias? La membrana bacteriana y sus más de 5 sentidos”. 27-agosto-2019.

23. Métodos ópticos en el estudio de la liberación de transmisores en el cerebro.

Ponencia:

Francisco Fernández de Miguel. “Métodos ópticos en el estudio de la liberación de transmisores en el cerebro”. 10-septiembre-2019.

24. Neurociencias y Arte.

Ponencia:

Francisco Fernández de Miguel. “Neurociencia y Arte”. 15-febrero-2019.

25. Neurofest, UNIVERSUM, UNAM.

Ponencia:

Francisco Fernández de Miguel. “Comunicación Nerviosa”. 23-noviembre-2019.

26. Semana del Cerebro (CCDMX-SfN).

Ponencia:

Francisco Sotrés Bayon. “¿Cómo el cerebro usa memorias emocionales para tomar decisiones?” 1-abril-2019.

27. Seminario Institucional CICY, conmemorativo a 40 años.

Ponencia:

Gabriel del Río. “Anastasis: explorando los límites de la muerte celular”. 23-agosto-2019.

28. Seminario Institucional Hospital General. Dr. M Gea Gonzalez.

Ponencia:

Julián Valdés. “Diferenciación de células troncales epidermales: una aproximación epigenética”. 16-mayo-2019.

29. Seminario Semanal de la Dirección de Investigación. Hospital Juárez de México.

Ponencia:

Julián Valdés. “Control epigenético de la diferenciación de células madre de la piel”. 8-febrero-2019.

30. XXXIV Reunión Annual de Investigación. Instituto Nacional de Neurología y Neurocirugía Manuel Velasco Suárez.

Ponencia:

Lourdes Massieu. “Mecanismos de daño neuronal”. 16-mayo-2019.

Conferencias Internacionales

1. **Biblioteca Nacional, Valparaíso, Chile.**

   Ponencia:

   Ranulfo Romo. “La construcción de la realidad en el cerebro”. 9-abril-2019.

2. **VI Festival de Ciencia, Puerto de Ideas, Antofagasta, Chile.**

   Ponencia:

   Ranulfo Romo. “El cerebro, arquitecto de realidades”. Conferencia de apertura del festival. 12-abril-2019.

3. **III Curso Internacional de Medicina del Sueño, Dr. Mario Skurovich Zaslavsky: “El sueño en la práctica médica”.**

   Ponencia:

   Raúl Aguilar Roblero. “Ciclo circadiano y sueño: Su influencia en la terapia farmacológica”. 8-octubre-2019.

4. **Latin American Training Program 2019 Enlightening the brain: light as a tool for understanding the function of the nervous system.**

   Ponencia:

   Yazmin Ramiro Cortés. “From spines to behavior using two-photon microscopy: an approach to study autism”. 2-septiembre-2019.

5. **Segundo congreso Internacional CILCA, BUAP.**

   Ponencia:

   Fatuel Tecuapetla Aguilar. “Optogenetica: controlando la actividad neuronal con luz para entender las funciones del cerebro”. 16-mayo-2019

Seminarios dictados en la UNAM

1. Aguirre Linares Jesús. “Las especies reactivas del oxígeno, como señales de diferenciación en los hongos”. Facultad de Ciencias, UNAM. 31-octubre-2019. https://www.youtube.com/watch?v=OiUDYrY_IZY.

2. Arciniega Marcelino. “Aproximaciones al acoplamiento molecular desde el aprendizaje de máquina”. Departamento de matemáticas, Facultad de ciencias, UNAM. 31-octubre-2019.

3. Coria Ortega Roberto. “Estrés de retículo endoplásmico y autofagia en la amiba social *Dictyostelium discoideum*”. Instituto de Fisiología Celular, UNAM. 16-agosto-2019.

4. Del Río Guerra Gabriel. “Introducción al robot Evo 150 Tecan”. Instituto de Fisiología Celular, UNAM. 14-marzo-2019.

5. Funes Soledad. “Todos los caminos llevan a la mitocondria: estrés, autofagia y muerte celular”. Facultad de Ciencias, UNAM. 27-agosto-2019.

6. Funes Soledad. “La proteína mitocondrial Slm35: una pieza del rompecabezas entre la autofagia y la longevidad en la levadura *Saccharomyces cerevisiae*”. Facultad de Química, UNAM. 21-juni-2019.

7. Funes Soledad. “Relación entre mitocondrias, autofagia y longevidad”. Facultad de Ciencias, UNAM. 7-noviembre-2019.

8. Funes Soledad. “Ética Científica”. Instituto de Fisiología Celular, UNAM. 22-enero-2019 y 29-julio-2019.

9. Georgellis Dimitris. “Bacterial two-component system signaling; Sensing and responding to the environment”. Departamental de Bioquímica, Facultad de Química, UNAM. 20-septiembre-2019.

10. González Halphen Diego. “Cuando la subunidad II de la citocromo oxidasa entra a la mitocondria por la puerta de atrás”. Departamento de Bioquímica, Facultad de Química, UNAM. 27-septiembre-2019.

11. González Halphen Diego. “Cuando la subunidad II de la citocromo oxidasa entra a la mitocondria por la puerta de atrás”. Instituto de Fisiología Celular, UNAM. 11-octubre-2019.

12. González Manjarrez Alicia. “Reguladores híbridos: Una alternativa para provocar respuestas transcripcionales innovadoras en *S. cerevisiae*. “Instituto de Fisiología Celular, UNAM. 22-noviembre-2019.

13. González Manjarrez Alicia. “Impacto de la retención selectiva de genes paralogos en la adquisición del metabolismo facultativo en la levadura *Saccharomyces cerevisiae*” Whole-Genome Duplication and Yeast´s Fruitful Way of Life. Centro de Ciencias Genómicas. 4-abril-2019.

14. González Pedrajo Bertha. “Regulación de la secreción de proteínas a través del inyectisoma”. Instituto de Investigaciones Biomédicas, UNAM. 14-octubre-2019.

15. López Huerta Violeta Gisselle. “Integrated single-cell analysis reveals coupled molecular gradient and functional subnetworks in the thalamic reticular nucleus”. Instituto de Neurobiología, Quéretaro. 11-junio-2019

16. Navarro González Rosa. “Las aventuras de una célula germinales: cómo se forman los gametos del nematodo *C. elegans*”. Facultad de Ciencias, UNAM. 27-agosto-2019.

17. Peraza Reyes Leonardo. “Orquestando la dinámica intracelular durante el desarrollo sexual del hongo Podospora”. Instituto de Fisiología Celular, UNAM. 29-marzo-2019.

18. Peraza Reyes Leonardo. “La dinámica y las interacciones de los organillos durante el desarrollo celular”. Facultad de Ciencias, UNAM. 28-agosto-2019.

19. Peraza Reyes Leonardo. “El crecimiento de la célula fungía”. Facultad de Ciencias, UNAM. 05-noviembre-2019.

20. Pérez Martínez Xochitl. “Cómo es que la mitocondria acopla la síntesis de proteínas al ensamblaje de complejos respiratorios? El caso del complejo bc1”. Facultad de Química, UNAM. 14-junio-2019.

21. Pérez Martínez Xochitl. “Efecto de la desregulación de la biogénesis de Cox1 en la función mitocondrial de la levadura *Saccharomyces cerevisiae*”. Instituto de Fisiología Celular. 17-junio-2019.

22. Ramiro Cortés Yazmín. “Actividad sináptica y neuronal en ratones SHANK3 como modelo genético de autismo: de las espinas a la conducta”. Instituto de Fisiología Celular, UNAM. 15-febrero-2019.

23. Rosenbaum Emir Tamara. “Canales TRP: moléculas que exhiben fenómenos biofísicos novedosos”. Instituto de Fisiología Celular, UNAM. 21-junio-2019.

24. Rossi Pool Román. “1er. Encuentro de Biología Computacional del IFC”. Instituto de Fisiología Celular, UNAM. 9-octubre-2019.

25. Tecuapetla Aguilar Fatuel. “To initiate actions, the dopaminergic and thalamus circuits are required”. Center for complex sciences C3, UNAM. 22-enero-2019.

26. Tecuapetla Aguilar Fatuel. “How do we test the functions of the brain using light?”. Latin American Training Program 2019. 10-septiembre-2019.

27. Torres Quiroz Francisco. “Papel del H2S durante la fermentación”. Instituto de Fisiología Celular, UNAM. 24-mayo-2019.

28. Tovar y Romo Luis Bernardo. “Trophic regulation of neuronal survival”. Auditorio Alfonso Caso. 24-abril-2019.

29. Tovar y Romo Luis Bernardo. “Participación de las vesículas extracelulares en el proceso de recuperación después del infarto cerebral isquémico”. Centro de Ciencias de la Complejidad C3, UNAM. 22-enero-2019.

30. Velasco Iván. “El nacimiento, la degeneración y el reemplazo de las neuronas dopaminérgicas”. Departamento de Bioquímica, Facultad de Química, UNAM. 18-septiembre-2019.

Seminarios dictados fuera de la UNAM

1. Aguilar Roblero Raúl. “Cronostasia: Regulación Fisiológica en el Tiempo”. Instituto Nacional de Ciencias Médicas y Nutrición "Salvador Zubiran". 26-septiembre-2019.

2. Aguirre Linares Jesús. “Reactive oxygen species signaling and fungal cell differentiation, distinguished lectures in microbiology”. Madison, Wisconsin, USA. 11-abril-2019.

3. Arciniega Marcelino. “Identificación de falsos positivos en resultados de acoplamiento molecular”. Instituto de Física de la Universidad Autónoma de San Luis Potosí. 10-octubre-2019.

4. Castro Obregón Susana. “El papel de la Autofagia en el desarrollo y envejecimiento del sistema nervioso de mamíferos”. Seminario Interdisciplinario en Biomedicina en el Instituto Nacional de Ciencias Médicas y Nutrición “Salvador Zubirán”. 10-octubre-2019.

5. Furlan Magaril Mayra. “Chromatin state and 3D conformation during erythroid differentiation”. Instituto de Medicina Genómica. 14-junio-2019.

6. Furlan Magaril Mayra. “La dinámica circadiana de la organización 3D del genoma”. UAEM, Cuernavaca Morelos. 29-marzo-2019.

7. Gómora Martínez Juan Carlos. “Funciones no canonicas de canales de sodio activados por voltaje en la metastasis del cáncer”. Departamento de Bioquímica, Instituto Nacional de Cardiología. 13-junio-2019.

8. Gómora Martínez Juan Carlos. “Funciones no canonicas de canales de sodio activados por voltaje en la metastasis del cáncer”. Facultad de Medicina, Universidad Autónoma de San Luis Potosí. 6-diciembre-2019.

9. González Halphen Diego. “Cuando la subunidad 2 de la citocromo c oxidasa entra a la membrana interna mitocondrial por la puerta de atrás”. Departamento de Biomedicina Cardiovascular, Instituto Nacional de Cardiología. 29-marzo-2019.

10. López Huerta Violeta Gisselle. “De los genes a la función: Disección de circuitos implicados en enfermedades psiquiátricas”. Universidad Autónoma de San Luis Potosí. 25-octubre-2019.

11. Macías Silva Marina. “Ski y SnoN: Cofactores Transcripcionales Negativos de la Señales de la Citocina TGF-beta”. Departamento de Bioquímica del Instituto Nacional de Cardiología. 10-octubre-2019.

12. Navarro González Rosa. “La gónada del C. elegans como modelo para estudiar la formación de gránulos de RNA por estrés”. Instituto Nacional de Medicina Genómica.

13. Ramiro Cortés Yazmín. “Actividad sináptica y neuronal en ratones SHANK3 como modelo genético de autismo: de las espinas a la conducta”. Clínica de Trastornos del Sueño de la Universidad Autónoma Metropolitana, Unidad Iztapalapa. 25-junio-2019.

14. Romo Trujillo Ranulfo. “¿Estás seguro que tú tomas tus decisiones?”. Centro de las Artes de San Luis Potosí, SLP, México. 21-febrero-2019.

15. Romo Trujillo Ranulfo. “El cerebro, arquitecto de realidades”. Universidad de Sonora, Hermosillo, Sonora. 2-mayo-2019.

16. Romo Trujillo Ranulfo. “Constructing perceptual decision-making across cortex”. Boston, MA, E.U.A. 22-mayo-2019.

17. Rossi Pool Román. “De las neuronas individuales a la dinámica poblacional: baja dimensionalidad en alta heterogeneidad de respuestas”. Instituto Balseiro - San Carlos de Bariloche - Argentina. 17-diciembre-2019.

18. Velasco Iván. “¿Cómo podemos producir neuronas de nuestro cerebro fuera del cuerpo?”. Universidad Autónoma Metropolitana Iztapalapa, como parte del Programa de Divulgación Científica "Domingos en la Ciencia" de la Academia Mexicana de Ciencias. 3-junio-2019.

19. Velasco Iván. “Neuronas dopaminérgicas humanas diferenciadas de células troncales: Relevancia para la enfermedad de Parkinson”. Facultad de Medicina de la Universidad Autónoma de Yucatán. Mérida, Yucatán. 22-mayo-2019.

20. Velasco Iván. Conferencia Magistral: “Neuronas dopaminérgicas humanas diferenciadas de células troncales: Relevancia para la enfermedad de Parkinson”. Universidad Marista. Mérida, Yucatán. 22-mayo-2019.

21. Velasco Iván. “La expresión transgénica en células troncales embrionarias de ratón dirige su diferenciación”. Facultad de Química de la Universidad Autónoma de Yucatán. Mérida, Yucatán. 23-mayo-2019.

22. Velasco Iván. “Neuronas dopaminérgicas humanas diferenciadas de células troncales: Relevancia para la enfermedad de Parkinson”. Hospital de Especialidades CMN “Ignacio García Téllez”, Mérida, Yucatán. 23-mayo-2019.

cells

MDPI

Article

Fatty Acid and Lipopolysaccharide Effect on Beta Cells Proteostasis and its Impact on Insulin Secretion

Paloma Acosta-Montaño [1], Eustolia Rodríguez-Velázquez [2,3], Esmeralda Ibarra-López [1], Héctor Frayde-Gómez [1,4], Jaime Mas-Oliva [5], Blanca Delgado-Coello [5], Ignacio A. Rivero [6], Manuel Alatorre-Meda [7], Jorge Aguilera [6], Lizbeth Guevara-Olaya [1] and Victor García-González [1,*]

1 Departamento de Bioquímica, Facultad de Medicina Mexicali, Universidad Autónoma de Baja California, 21000 Mexicali, Mexico
2 Facultad de Odontología, Universidad Autónoma de Baja California, 22390 Tijuana, Mexico
3 Tecnológico Nacional de México/I.T. Tijuana, Centro de Graduados e Investigación en Química-Grupo de Biomateriales y Nanomedicina, 22510 Tijuana, Mexico
4 Hospital General de Zona No. 30, Instituto Mexicano del Seguro Social, 21100 Mexicali, Mexico
5 Instituto de Fisiología Celular, Universidad Nacional Autónoma de México, 04510 Ciudad de México, Mexico
6 Tecnológico Nacional de México/I.T. Tijuana, Centro de Graduados e Investigación en Química, 22000 Tijuana, Mexico
7 Cátedras CONACyT- Tecnológico Nacional de México/I.T. Tijuana. Centro de Graduados e Investigación en Química-Grupo de Biomateriales y Nanomedicina, 22000 Tijuana, Mexico
* Correspondence: vgarcia62@uabc.edu.mx; Tel.: +52-1-686-557-1622 (ext. 121); Fax: +52-1-686-557-1622 (ext. 109)

Received: 15 July 2019; Accepted: 6 August 2019; Published: 13 August 2019



Abstract: Metabolic overload by saturated fatty acids (SFA), which comprises β-cell function, and impaired glucose-stimulated insulin secretion are frequently observed in patients suffering from obesity and type 2 diabetes mellitus. The increase of intracellular Ca^{2+} triggers insulin granule release, therefore several mechanisms regulate Ca^{2+} efflux within the β-cells, among others, the plasma membrane Ca^{2+}-ATPase (PMCA). In this work, we describe that lipotoxicity mediated mainly by the saturated palmitic acid (PA) (16C) is associated with loss of protein homeostasis (proteostasis) and potentially cell viability, a phenomenon that was induced to a lesser extent by stearic (18C), myristic (14C) and lauric (12C) acids. PA was localized on endoplasmic reticulum, activating arms of the unfolded protein response (UPR), as also promoted by lipopolysaccharides (LPS)-endotoxins. In particular, our findings demonstrate an alteration in PMCA1/4 expression caused by PA and LPS which trigger the UPR, affecting not only insulin release and contributing to β-cell mass reduction, but also increasing reactive nitrogen species. Nonetheless, stearic acid (SA) did not show these effects. Remarkably, the proteolytic degradation of PMCA1/4 prompted by PA and LPS was avoided by the action of monounsaturated fatty acids such as oleic and palmitoleic acid. Oleic acid recovered cell viability after treatment with PA/LPS and, more interestingly, relieved endoplasmic reticulum (ER) stress. While palmitoleic acid improved the insulin release, this fatty acid seems to have more relevant effects upon the expression of regulatory pumps of intracellular Ca^{2+}. Therefore, chain length and unsaturation of fatty acids are determinant cues in proteostasis of β-cells and, consequently, on the regulation of calcium and insulin secretion.

Keywords: fatty acids; lipopolysaccharides; β-cells; proteostasis; insulin secretion

INFORME DE LABORES 2019

1. Introduction

Type 2 diabetes mellitus (T2DM) is a metabolic disorder characterized by dysfunction and progressive loss of pancreatic β-cells, which are responsible for insulin synthesis, originating tissue damage and several long-term complications [1]. This pathology could occur in conditions of obesity accompanied with a decrease in cellular response of insulin-dependent tissues. Phenomena such as β-cells proliferation and hyperinsulinemia seem to have a compensatory effect. However, these conditions possibly lead to β-cell dysfunction [2]. Indeed, in obesity and insulin resistance, β-cells are able to modulate the energetic metabolism in order to increase insulin synthesis and release [3].

Packaged in small granules, each β-cell has approximately 10,000 granules of insulin, of which only a fraction is released in response to an increase in glycemia [4–6]. After translation, pre-proinsulin polypeptides are translocated to the endoplasmic reticulum (ER) to acquire the native folding [7]. However, under conditions of high protein demand, ER stress is triggered. Therefore, the transducers of the unfolded protein response (UPR), IRE1, ATF6α, and PERK, promote the transcription and translation of target chaperones through XBPIs, ATF6α and CHOP transcription factors, respectively, when unfolded proteins accumulate in the lumen [8,9]. The three branches of UPR are essential in β-cells homeostasis to reduce ER stress and to ensure adequate synthesis of peptides such as insulin [6].

The key triggering factor for release of insulin granules is the increase of intracellular Ca^{2+}, associated with increased extracellular glucose [10]. Several mechanisms regulate the flux of Ca^{2+} in cells, such as the plasma membrane Ca^{2+}-ATPase (PMCA) and the Na^{+}/Ca^{2+} exchanger (NCX) [11]. PMCA belongs to the P-type ATPases whose function is critical to maintain the concentration of cytosolic calcium below 300 nM [12]; it is encoded by four different genes (*ATP2B1-ATP2B4*) and the isoforms expressed differentially in excitable and non-excitable cells [13,14]. On the other hand, the NCX uses the electrochemical Na^{+} gradient to export Ca^{2+} against gradient concentration [15]. Four isoforms have been identified for NCX (NCX1-4) and NCX1 is the most expressed in rat β-cells. The role of PMCA and NCX1 in β-cells is critical; both contribute to the extrusion of Ca^{2+}, therefore to the regulation of insulin release.

Lipotoxicity is associated with deleterious effects due to an increase of circulating fatty acids when the storage capacity of triglycerides in adipose tissue is overloaded. Indeed, lipotoxicity is related to β-cell dysfunction, wherein the capacity of protein folding may be compromised [16]. Lipotoxicity represses the protein trafficking from ER to the Golgi apparatus [17,18]. The palmitic (PA) and oleic (OA) fatty acids have been reported to induce apoptosis of β-cells, but only palmitic acid activates the PERK and IRE1 pathways [19]. Although the mechanism responsible for lipoapoptosis induced by ER stress is complex, it could involve alterations in Ca^{2+} [20]. Dysfunction of pancreatic β-cells has been associated with a low-grade inflammatory condition (meta-inflammation) associated with the excess of white adipose tissue in obesity [21]. It has been proposed that lipopolysaccharides (LPS) activate a signaling pathway mediated by TLR-4 [22], and this has been identified as a factor in obesity-associated metabolic disorders [23]. Additional evidence suggests that patients with T2DM show an altered intestinal microbiota in which Gram-negative bacteria predominate, then LPS, a critical component of its outer membrane, might promote inflammation [24]. Accordingly, the gut microbiota may play a role as a risk factor in the development of T2DM [25].

In this work, the effect of LPS on the UPR pathway in addition to free fatty acids was characterized, which modifies several key processes related to insulin secretion. Specifically, the properties that provide to fatty acids with their ER stress-inducing or protective role with a concomitant effect of LPS were described, through modulation of specific targets that regulate homeostasis of proteins (proteostasis), and then insulin secretion.

INFORME DE LABORES 2019

2. Materials and Methods

2.1. Reagents

RPMI-1640 medium (Gibco, Waltham, MA, USA), fetal bovine serum (FBS), penicillin, streptomycin, amphotericin B, palmitic acid (PA), oleic acid (OA), palmitoleic acid (PAO), stearic acid (SA), myristic acid (MA), lauric acid (LA), fatty acid-free bovine serum albumin (BSA) (Fraction V), lipopolysaccharides (from *Escherichia coli* O111:B4), trypsin, phosphate buffer saline (PBS), (3-(4,5-Dimethylthiazol-2-yl)-2,5-Diphenyltetrazolium Bromide (MTT) and tunicamycin (Tum) were obtained from Sigma-Aldrich.

2.2. Cell Culture

The established rat β-cell line RIN-m5F (American Type Culture Collection, ATCC, Manassas, VA, USA) was grown in RPMI-1640 medium supplemented with 10% FBS, 10 U/mL penicillin, 10 µg/mL streptomycin and 25 µg/mL amphotericin B. Cultures were maintained at 37 °C in a humidified atmosphere of 95% air and 5% CO_2. The culture medium was changed every 3 to 4 days and also passaged once per week, according to ATCC recommendations.

2.3. Fatty Acid and LPS Preparation

Stock solutions were prepared as follows: fatty acids were dissolved in ethanol:H_2O (1:1, vol:vol) at 60 °C at a final concentration of 75 mM. Stock solutions were complexed with fatty-acid-free BSA (3 mM in H_2O) by stirring for 1.5 h at 37 °C, then diluted in culture media and filtered by a 0.22-µm pore membrane. The final molar ratio of fatty acid:BSA was 4:1 with a final concentration of 300 µM BSA. LPS O111:B4 were dissolved in ultrapure water (1 mg/mL), and then diluted to a final concentration of 100 ng/mL, as previously reported [26].

2.4. Cell Viability Assays

Cell viability was evaluated using the MTT assay according to previous protocols [27]. Formazan crystals were dissolved in a lysis buffer containing 20% SDS and 50% N,N-dimethylformamide (pH 3.7) for 12 h at 37 °C, and absorbance readings were acquired at 560/530 nm.

2.5. Western Blotting Analysis

Proteins were extracted from cell cultures under different conditions, using ice-cold protein lysis buffer (150 mM NaCl, 10 mM Tris, pH 7.4, 1% Triton X-100, 0.5% NP40, 1 mM EDTA, 1 mM EGTA, 0.2 mM sodium orthovanadate, 10 mM benzamidine, 10 µg/mL leupeptin, 10 µg/mL aprotinin, and 250 µM PMSF). An average of 25 µg of protein samples from RIN-m5F cells were separated on 10% SDS-PAGE electrophoresis and transferred to polyvinylidene difluoride (PVDF) membranes. The membranes were blocked with 5% non-fat milk in Tris-buffered saline 0.1% Tween-20 (TBS-T) for 1 h at 37 °C, and incubated at 4 °C overnight with primary antibody (anti-XBP1s, anti-c-Jun, anti-ATF6α, anti-CHOP, anti-PMCA1/4, anti-Lamin-B, anti-β-adaptin, anti-BiP, anti-SPT, anti-SERCA2, anti-PMCA3, anti-NCX1, and anti-β-actin). Following washing with TBS-T, the membranes were further incubated for 1 h at 37 °C with the corresponding horseradish peroxidase-conjugated secondary antibodies. Proteins were detected with the enhanced chemiluminescence reagent (Immobilon Western from Millipore, Burlington, MA, USA).

2.6. Immunoprecipitations on Nucleus Extracts

Nuclei separation was carried out using a buffer containing sucrose (250 mM) and imidazole (3 mM) pH 7.4, supplemented with protease and phosphatase inhibitors. Cells were scraped from culture dishes and 21 passages were performed through a 22-G syringe. For the recovery of nuclei, lysates were centrifuged at 3400 rpm for 15 min. Then, nucleus fractions (200 µg) were incubated with

an anti-c-Jun antibody (1:400) for 2 h at 4 °C. Immune complexes were precipitated with protein G agarose Fast Flow (Millipore) 12 h at 4 °C. Immuno-precipitated proteins were washed 3 times and suspended in Laemmli buffer, separated by SDS-PAGE gels and transferred to PVDF membranes for Western-blot analysis. Protein detection was performed based on a previous protocol [26].

2.7. Insulin ELISA Assays

Cells were proliferated in 20 mm cell culture plates at a density of 2.3×10^5 cells/mL (2 mL). Cells were maintained in proliferation for 72 h, and later different treatments were performed on a volume of 1 mL. Cell culture medium was recovered, and centrifuged for 5 min at 5000 rpm. Supernatant medium was recovered and diluted (1/3) in PBS. Insulin concentrations were quantified with the Rat Ultrasensitive Insulin ELISA kit (80-INSRTU-E01, E10; ALPCO Diagnostics, Salem, NH, USA) through several adaptations according to manufacturer recommendations. Absorbance readings were performed at 450 nm, and results were reported as ng/mL.

2.8. Immunocytochemistry Assays

Treated cells were fixed in ethanol:acetone (1:1) at −20 °C and permeabilized with 0.01% Triton X-100. Slides were processed for immunocytochemical detection of transcription factors XBP1s and CHOP using the mouse/rabbit Polydetector HRP/DAB (BioSB, Santa Barbara, CA, USA). Slides were blocked with a horseradish peroxidase-conjugated antibody for 5 min and 1% bovine serum for 20 min, then incubated at 4 °C with the primary antibody. Following washing with PBS, the slides were further incubated for 40 min at room temperature with the secondary antibody. Immunostaining was performed with free-floating diaminobenzidine (DAB) for 2 min. After stopping the reaction, sections were embedded in Entellan and analyzed with the Axiovert.A1 FL-LED Microscope (Carl Zeiss, Oberkochen, Germany) and AxioCam ERc 5s (Carl Zeiss, Oberkochen, Germany). Image acquisition software ZEN-Blue edition was employed for image processing (Carl Zeiss, Oberkochen, Germany).

2.9. Fractionation of Cultured Cells and Determination of Triglycerides

Cells were processed as elsewhere reported [28]. Briefly, cells were washed with PBS 1×, scraped from the plate and transferred into a 2-mL tube, then centrifuged at 2000× *g* for 2 min. The pellet was resuspended in 200 µL of 60% sucrose dissolved in lysis buffer (10 mM HEPES and 1 mM EDTA, pH 7.4). After mixing, samples were incubated on ice for 10 min. Next, 800 µL of ice-cold lysis buffer was added, and incubated on ice for another 10 min. Cells were lysed by 5 passes through a 27-G needle and centrifuged at 100× *g* for 2 min. A mixture consisting of 2 µL of methylene blue mix per mL of lysis buffer was prepared. Then, 600 µL of this mixture were carefully layered on top of the cell homogenate and centrifuged at 20,000× *g* at 4 °C for 2 h. Tubes were frozen at −70 °C, the dye layer containing lipids (floating layer) was recovered by cutting the tube and transferred to a new tube where 100 µL of lysis buffer was added. Triglyceride content of fractions was measured using the Triglyceride-LQ kit (Giorna, Spain).

2.10. Calcium Quantification

Cells were processed according to a previous protocol [29] and intracellular calcium levels were calculated according to Patel et al. [30]. After treatments, cells were washed with PBS 1× and incubated at 37 °C with Opti-MEM/1.5 µM Fura-2/AM (fluorescent Ca^{2+} indicator) for 75 min. Subsequently, cells were washed with PBS 1× and incubated for 20 min at room temperature. Cells were washed with PBS 1×, and fluorescence measurements were carried out at 340 and 380 nm excitation wavelengths, and a 510 nm emission wavelength, employing a Cary Eclipse Fluorescence Spectrophotometer (Santa Clara, CA, USA).

2.11. Nitrite Assay

Nitrites were measured in the extracellular culture medium from treated cells as an index of reactive nitrogen species (RNS) formation, using the Griess reaction (40 mg/mL). Absorbance readings were performed at 450 nm in an ELISA plate.

2.12. Fluorescence-Probe Synthesis

Based in a methodology developed by our group, BODIPY (BDP) coupled to palmitic acid (BDP-PA), BODIPY coupled to stearic acid (BDP-SA), and BODIPY coupled to myristic acid (BDP-MA) were synthesized. Briefly, BODIPY-8-Ethylendiamine (0.436 mM) [31] in dichloromethane anhydrous (8 mL) was added to *N*′-ethylcarbodiimide hydrochloride (0.524 mM), hydroxybenzotriazole (0.524 mm), *N*-methylmorpholine (1.308 mM) and the corresponding fatty acid (0.48 mM). The mixture reaction was stirred for 5 h under argon atmosphere at 25 °C. Solvent was eliminated under reduced pressure, and the product was dissolved in water (20 mL) and extracted with dichloromethane. The combined organic extracts were washed with brine and dried over anhydrous Na_2SO_4, and later the product was concentrated. The crude product was purified by flash chromatography. All structures were confirmed by mass spectroscopy and nuclear magnetic resonance (NMR).

2.13. Confocal Microscopy

A LEICA TCS-SP8 confocal scanning biological microscope (LEICA Microsystems Heidelberg GmbH, Nussloch, Germany) was employed in order to characterize the BDP-MA, BDP-PA and BDP-SA sub-cellular localization. After different experiments with BDP-fatty acids (10–100 μM), cells were washed with PBS 1× 3 times, and then incubated with Aza-2-DBP for 30 min (0.8 μM). Later, cells were washed extensively and fixed with cold paraformaldehyde, and mounted for observation. Macroscopically different zones were recorded, preferentially at the center of the specimens, in order to depict representative images. Images were recorded at excitation/emission wavelengths of 488/495-545 and 638/650–750 nm for detection of BDP-fatty acids (green) and AZA-2-BDP (red), respectively.

2.14. Colocalization of ER-Tracker Probe and BDP-SFA

RIN-m5F cells were proliferated to 90% of confluence, and treated with BDP-PA (5–25 μM) for 12 h. Later, culture cells were washed with HBSS buffer and then ER-tracker (1 μM) was added and incubated for 25 min at 37 °C. Cells were washed once with HBSS buffer and fixed with 4% formaldehyde, for 2 min at 37 °C. Finally, cells were washed twice with PBS 1×. Images were recorded at excitation/emission wavelengths of 488/495-545 and 587/615 nm for detection of BDP-PA (green) and ER-tracker (red), respectively.

2.15. Quantitative PCR Methods

Total RNA from RIN-5mF cells was obtained with Trizol following the supplier's instructions. cDNA was synthesized using 1 μg of RNA and the iScript RT Supermix from Bio-Rad (Hercules, CA, USA). cDNA concentration was standardized to be used for qPCR with the PowerUp Sybr Green Master Mix 2X (Applied Biosystems) according to manufacturer's instructions. Primer sequences were: *RPL13*fwd 5′-AAAGCCTGCCAGAATTTCTCT-3′, *RPL13*rev 5′-GGGCTCCAAGGACTCTCTG-3′, *ATP2B1*fwd: 5′-GCAATTGAAAATCGCAACAA-3′; *ATP2B1*rev: 5′-TTCAGAGGCTGCATCTCCAT-3′; *ATP2B2*fwd: 5′-CGGAGTGTGGACTAAC AGCA-3′, *ATP2B2*rev: 5′-CTAGGGACTGCGTGACCAAG-3′; *ATP2B3*fwd: 5′-CAATCTTTCTA CCCCTACTCACATC; *ATP2B3*rev: 5′-GATGCAACTCTTGGATTCTGG; *ATP2B4*fwd: 5′-CTCTG AAAATCGCAACAAAGC-3′, *ATP2B4*rev: 5′-AGTGGCTGGATTTCCAAGG-3′. qPCR reactions were performed in triplicate using an ABI PRISM 7000. qPCR data were analyzed with the $2^{-\Delta\Delta Ct}$ method with *RPL13* (ribosomal protein L13) as reference calibrator, and reported as fold change.

INFORME DE LABORES 2019

2.16. Statistical Analysis

Data are expressed as mean ± SD. The statistical analyses were conducted with one-way ANOVA, and differences among means were compared with the Bonferroni test using a level of significance of $p < 0.001$ unless otherwise specified. The software used was GraphPad Prism version 6 (San Diego, CA, USA). For the analysis of the expression of proteins by Western blot, a semiquantitative analysis was performed using β-actin as loading control with the software ImageJ (Bethesda, MD, USA). Likewise, ImageJ was employed in the processing of immunocytochemistry results.

3. Results

First, we examined the effects of LPS upon the UPR pathway in β-cells. Although increasing concentrations of LPS did not modify cell viability (Figure 1A), LPS promoted an increase in the expression levels of transcription factors associated with diminishing ER stress, such as XBP1s and c-Jun. However, the ATF6α branch that showed a basal expression in the control condition showed a diminished expression by effect of LPS treatment (Figure 1B). Upon proving that LPS cause ER stress through the modification of the UPR pathway without affecting cell viability, we decided to evaluate the effect of the most representative saturated fatty acids (SFA). The four main saturated fatty acids (SFA) found in the phospholipid membranes and neutral lipids—lauric acid, myristic acid, palmitic acid, and stearic acid—were studied in order to characterize the role of the fatty acid acyl-chain length on β-cell physiology. In a first approach, we evaluated the effect of increasing concentrations of SFA (0–600 μM) on cell viability, considering a ratio of albumin/SFA of 1/4, which is in the range of reported plasmatic concentrations of fatty acids (350–500 μM) [32]. Results suggest PA as the most lipotoxic fatty acid, followed by SA, as demonstrated by the cellular viability measured by the MTT assay (Figure 1C), which is associated with mitochondrial activity. Although the UPR pathway was activated by the three SFA tested (Figure 1D), palmitic acid showed the major effect on CHOP expression. In this case, tunicamycin (Tun) was used as a positive control inducing ER stress, by inhibition of N-glycosylation protein process [33].

In order to evaluate the intracellular distribution of SFA, our working group carried out the chemical synthesis of three fluorescent probes to be tracked by confocal microscopy: BODIPY-PA (referred to as BDP-PA), BODIPY-SA (referred to as BDP-SA) and BODIPY-MA (referred to as BDP-MA). After the treatments, the internalization of BDP-PA (Figure 1F) was higher compared to detection with BDP-MA or BDP-SA (Figure 1E,G). This phenomenon supports the results obtained for cell viability, wherein PA was the most lipotoxic fatty acid.

PA is the most abundant SFA in the human body distributed in neutral lipids, the phospholipids of plasma membrane, organelles such as ER, and as a free fatty acid bound to albumin in plasma. Although the UPR activation by the three fatty acids was observed, PA treatment was more evident in the activation of UPR. In the endoplasmic reticulum, one-third of cellular proteins are synthesized, membrane and extracellular proteins are also folded, and, importantly, the ER is the main site of calcium storage [34,35]. In order to characterize the cellular distribution of PA, we employed the specific probe ER-tracker, performing the co-localization of ER-tracker (red channel) and BDP-PA (green channel) (Figure 2A–E). Results show that BDP-PA is located in the endoplasmic reticulum. In a complementary way, under a PA dose-dependent stimulus (0–600 μM), we corroborated the activation of IRE1 branch of the UPR through XBP1s expression (Figure 2G), and concomitantly the effect on insulin secretion function (Figure 2H). At 150 and 300 μM PA, the UPR activation was more evident, which agrees with the drop of cell viability observed previously.

INFORME DE LABORES 2019

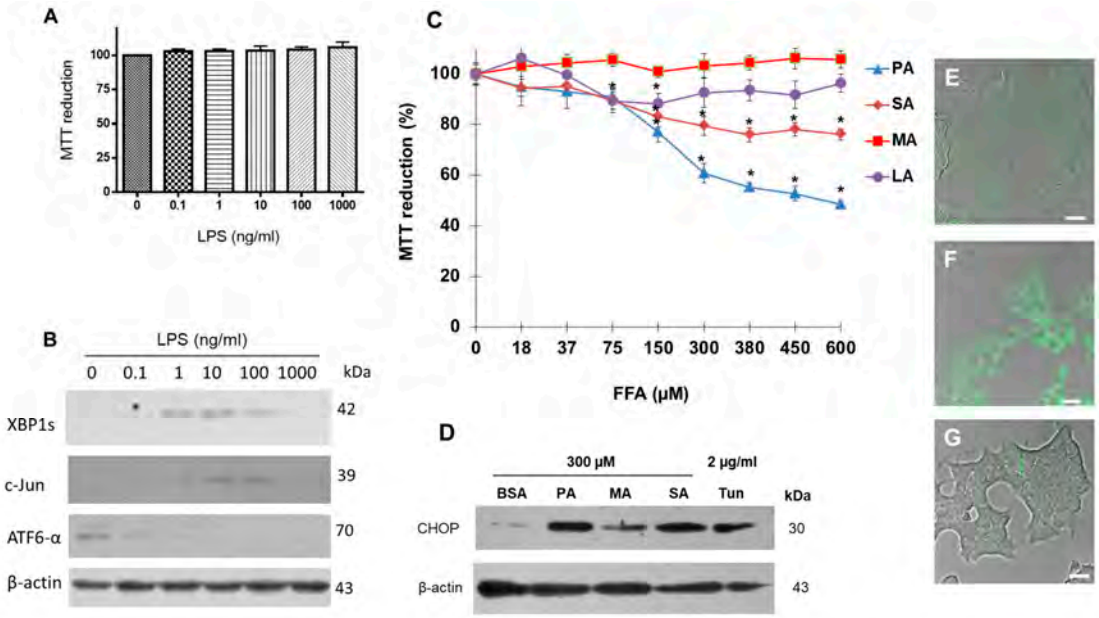

Figure 1. Lipopolysaccharides (LPS) and saturated fatty acids (SFA) trigger the unfolded protein response (UPR) pathway in β-cells, with 16C-pamitic acid (PA) the most lipotoxic. (**A**) Effect of increasing concentrations of LPS (0.1–1000 ng/mL) on cell viability. (**B**) Under the same conditions, expression of proteins XBP1s, c-Jun, and ATF6α analyzed by Western blot. (**C**) Effect of the treatment of saturated PA, stearic acid (SA), myristic acid (MA) and lauric acid (LA) (0–600 μM) on cell viability. (**D**) Effect of SFA treatment on CHOP expression. Tunicamycin (Tum) was used as a control. (**E**) Cellular distribution of BODIPY (BDP)-MA probe (green channel) (**E**), BDP-PA (**F**) and BDP-SA (**G**) in β-cells. Bars correspond to 20 μm. In panel B and D, β-actin was used as a loading control. In panel A and C, mean values are presented (n = 6, mean ± SD), * $p < 0.0005$ with respect to control.

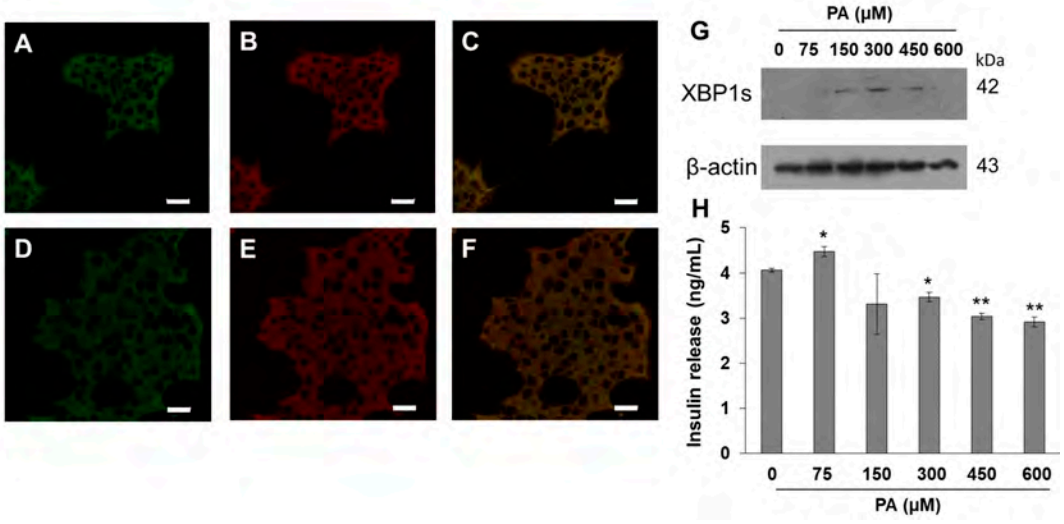

Figure 2. BDP-PA probe colocalizes with endoplasmic reticulum (ER)-tracker, and UPR is activated. (**A**,**D**) Confocal images of β-cells treated with BDP-PA (green channel). (**B**,**E**) Localization of ER-tracker probe (1 μM) (red channel). (**C**,**F**) Images corresponding to the merge. Bars correspond to 20 μm. (**G**) Under increasing concentrations of PA, UPR activation was evaluated through XBP1s activation, as well as the insulin release (**H**). Mean ± SD are presented (n = 3), * $p < 0.05$, **** $p < 0.005$.

Aiming to elucidate the combined effect of saturated fatty acids and LPS on cell viability as well as their intracellular location, which has not been described in the literature so far, β-cells were treated with PA and LPS. Cell viability was evaluated after a 24-h incubation with 300 μM palmitic

acid and 100 ng/mL LPS, and results show a significant decrease in cell viability, as compared to controls (Figure 3A). In addition, we characterized the intracellular distribution of BDP-PA probe and Aza-2-BODIPY (used as a counterstain; both were synthesized by our group). Interestingly, the counterstain probe Aza-2-BODIPY showed a cytoplasmic localization within the β-cells. By contrast, the BDP-PA signal was rather concentrated around the perinuclear area, wherein ER is localized, a phenomenon that was slightly increased under the treatment with LPS (Figure 3B–G). These results were corroborated, now employing the ER-tracker probe (Supplementary Figure S1).

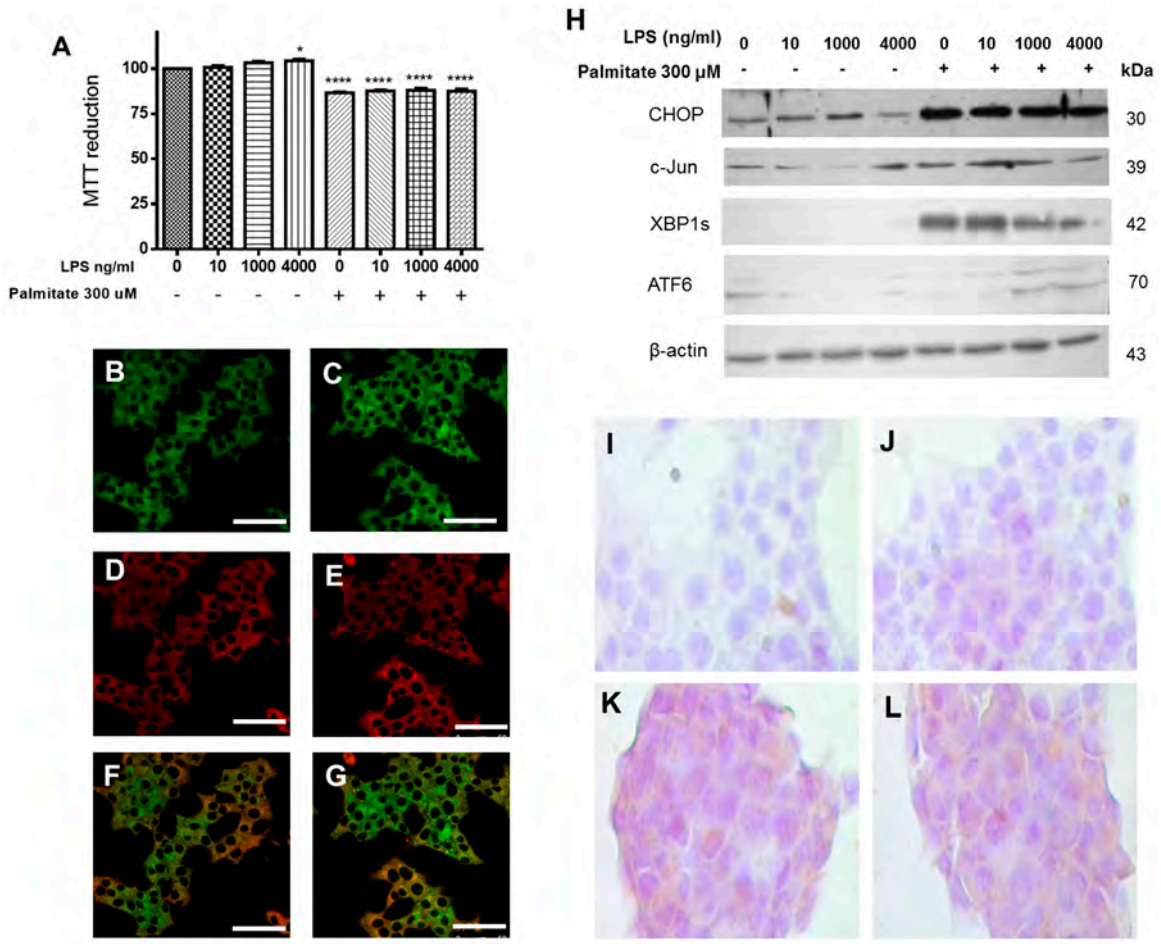

Figure 3. The combined treatment of LPS and PA potentiate the UPR activation in β-cells. (**A**) Effect of treatments with LPS and PA on cell viability ($n = 6$, mean ± SD), * $p < 0.05$, **** $p < 0.001$. Confocal images of β-cells treated with BDP-PA (**B**), Aza-2-BDP (**D**) and the merge (**F**). Under the same conditions, β-cells treated with BDP-PA plus LPS (**C**), Aza-2-BDP plus LPS (**E**), and the merge (**G**). Bars correspond to 50 µm. (**H**) Expression of CHOP, c-Jun, XBP1s, and ATF6α under increasing concentrations of LPS and PA (300 µM). β-actin was used as a loading control. (**I**,**J**) Detection of XBP1s by immunocytochemistry in control cells (negative signal). (**K**,**L**) Detection of XBP1s on PA-treated cells, positive signal (++) is determined by brown areas.

Although the LPS stimulus did not cause a decrease in cell viability, it slightly activated the UPR pathway through CHOP. However, when LPS and PA treatments were evaluated together, the UPR pathway was significantly activated by this transcription factor (CHOP). In parallel, it also increases the expression of XBP1s and ATF6a, as well as c-Jun (Figure 3H), which might be a possible response associated with the decrease in cell viability. Changes observed in cellular viability and the increase in XBP1s expression induced by PA agree with the analysis by immunocytochemistry of XBP1s (Figure 3I–L), where positive signals are observed as brown areas. Together, these data show

INFORME DE LABORES 2019

the activation of the UPR branches induced by LPS and the SFA most abundant in neutral lipids, as well as the ER localization of PA.

To assess if lipotoxicity could be extended to unsaturated fatty acids, the effect of oleic acid was evaluated. Unlike palmitic acid treatment, the exposure to OA neither modified the cell viability nor caused ER stress by activation of CHOP or XBP1s (Figure 4A,B). In this case, immunocytochemistry for CHOP in the presence of LPS and PA evidenced an increase in their expression (Figure 4C–F). Considering the stressor effect of palmitic acid and that OA did not produce ER stress, the possible protective or restorative role of OA was assessed under cytotoxicity induced by palmitic acid. With both fatty acids' stimuli, the effect of palmitic acid is reversed and cell viability is maintained (Figure 4G,H). Additionally, 12-h treatment with palmitic acid and followed by 12 h with OA alone, CHOP is not activated, but cell viability decreases (Figure 4H). However, treatment with OA prior to palmitic acid does not affect viability, but it activates CHOP, which may be a consequence of treatment with palmitic acid. These data suggest that OA could play a partial protective role.

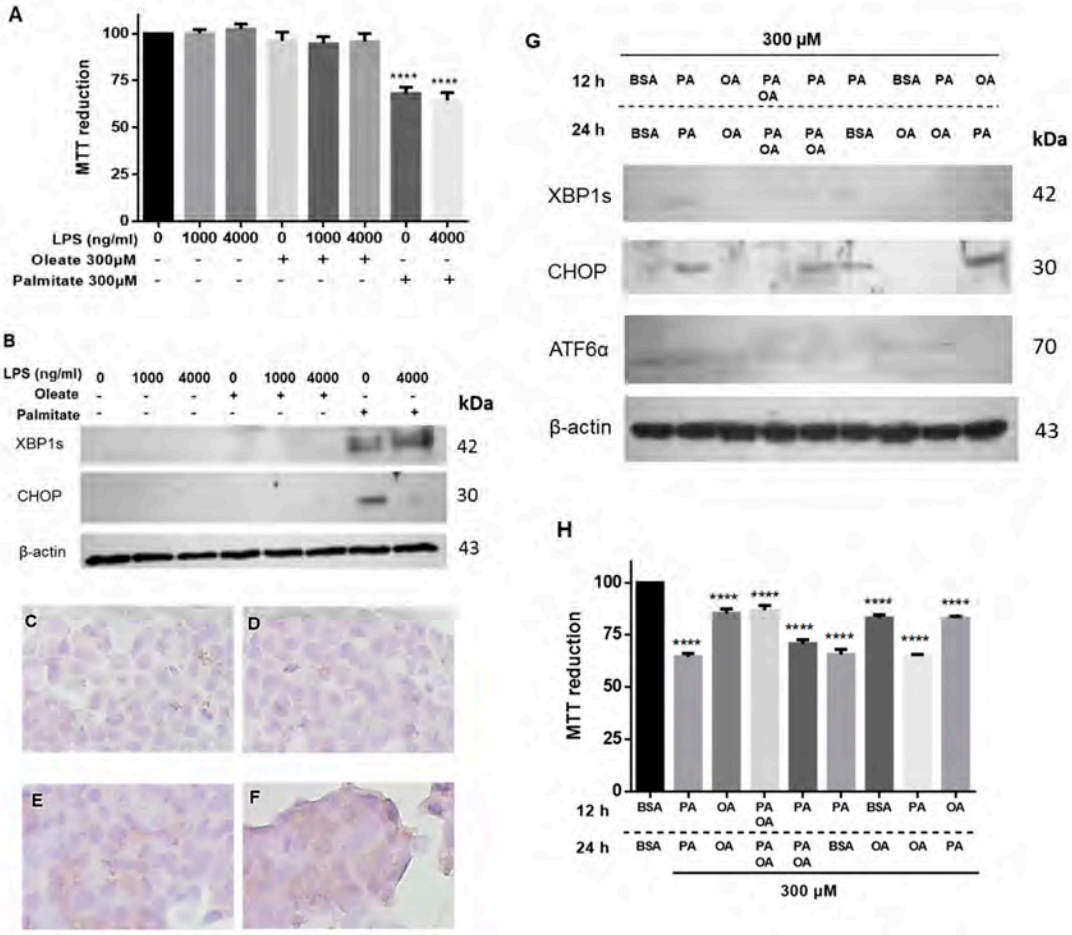

Figure 4. Oleic acid (OA) treatment does not trigger UPR and shows a partial protective role on lipotoxicity induced by PA. (**A**) MTT assay performed in β-cells exposed to different concentrations of LPS in the presence of 300 μM of PA or OA. (**B**) Under the same conditions, expression of XBP1s and CHOP. (**C**,**D**) Detection of CHOP by immunocytochemistry in control cells (negative signal). (**E**,**F**) Immunocytochemistry for CHOP under LPS and PA stimuli, positive signal (+) corresponds to brown areas. (**G**) Characterization of XBP1s, CHOP and ATF6α under a pre-treatment with fatty acids for 12 h, followed by the next treatment. (**H**) Under the same conditions, cell viability was characterized. β-actin was used as a loading control. In panel (**A**) and (**H**), (n = 6, mean ± SD), **** $p < 0.001$ with respect to control.

Aiming to evaluate one of the most relevant functions of β-cells, the insulin release, as we reported previously, we found a decrease in β-cell function with PA treatment, now using tunicamycin (Tum) as a control (Figure 5A). This characterization was complemented with the evaluation of CHOP, ATF6α and c-Jun in a time range (0–36 h), upon which a gradual activation was evidenced (Supplementary Figure S2). Considering that an increase of cytoplasmic [Ca^{2+}] in β-cells is the triggering factor for insulin release, a slight modification in PMCA expression isoforms 1 and 4 (PMCA 1/4) was observed (Figure 5B). Contrary to what was expected, the decrease in PMCA expression may favor an increase in insulin release due to a rise in intracellular [Ca^{2+}], however, other regulatory systems may be involved. The decrease in insulin secretion induced by PA matches with the cell viability decrease (Figure 5C). In order to broaden the effect of main saturated fatty acids, under a dose-dependent administration of PA, the decrease of PMCA1/4 expression was confirmed (Figure 5D), however, this change was not found in SA stimulus (Figure 5E). This phenomenon was supported through the UPR activation mediated by IRE1 only with PA treatment as previously described (Figure 2G), and not with SA treatment (Figure 5E).

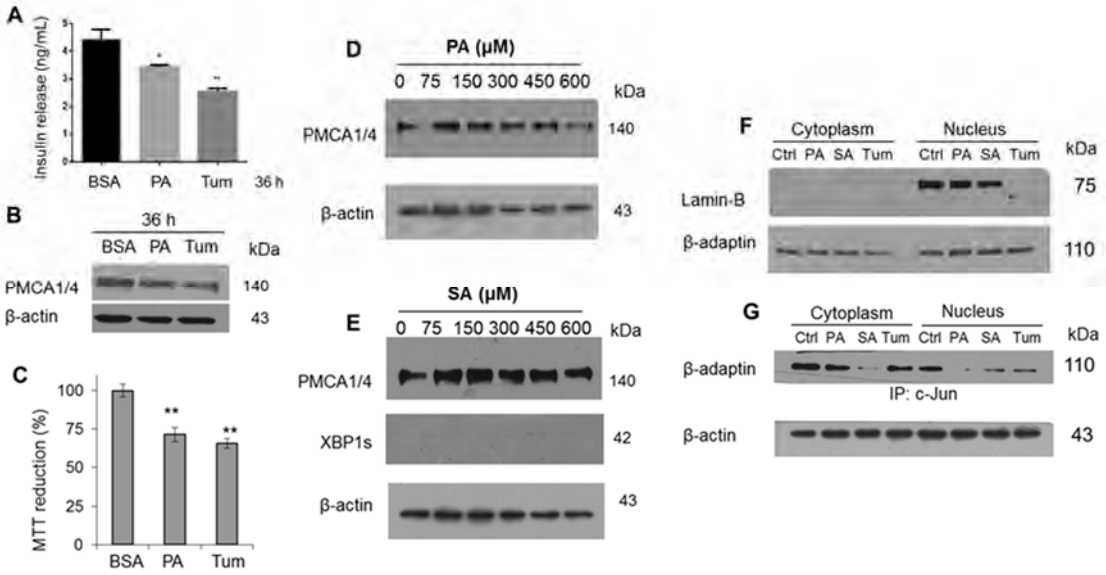

Figure 5. Endoplasmic reticulum stress reduces insulin secretion modifying the expression of PMCA1/4 and nuclear complexes. (**A**) Effect of treatment with PA and Tum on insulin secretion (n = 3, mean ± SD) * $p < 0.05$, ** $p < 0.01$. (**B**) Western blot characterization of PMCA1/4 isoforms. (**C**) Cellular viability assay, ** $p < 0.001$ with respect to control (n = 6, mean ± SD). Expression of PMCA1/4 and XBP1s in the presence of (**D**) PA or (**E**) SA. (**F**) Expression of Lamin-B and β-adaptin in nucleus extracts. (**G**) Evaluation of the complex formed by c-Jun and β-adaptin. β-actin was used as a loading control.

The specific case of the cytotoxicity exerted by Tum may be associated with an alteration in the nuclear structure (Figure 5F), considering the involvement of Lamin-B, a similar phenomenon that we have described in macrophages treated with LPS [36]. It should be noted that our group has described the function of new protein complexes formed by the adapter protein β-adaptin and transcriptional activators such as c-Myc and c-Jun that regulate the cell cycle and mechanisms such as endocytosis [36]. This condition was found to be affected in the nucleus under the stimuli with PA and Tum (Figure 5G), which we have correlated with the presence of an oxidative imbalance [37] implicating critical functions in the cells.

Expanding the characterization of this phenomenon, we found that stimulation with PA and LPS promotes the formation of RNS in the extracellular medium (Figure 6A). In a previous publication, we correlated the formation of RNS with the oxidative damage phenomenon and UPR activation in macrophages treated with LPS [36]. In our conditions, a drastic drop in insulin release was observed upon the treatment with palmitic acid and LPS (Figure 6B), associated with an increase in RNS

formation in the culture medium. In this case, the activation of BiP and XBP1s matches with an increase of nitrites (Figure 6C). Taking into account a partial protective function of OA under lipotoxicity conditions, the role of other unsaturated fatty acids such as PAO was evaluated. In both cases, the data suggest that treatment with unsaturated fatty acids prevents the drop of insulin release that is generated under the conditions of lipotoxicity by PA and LPS (Figure 6B). Interestingly, there is a mild increase of insulin release with PAO treatment with respect to controls. Data suggest that there is no metabolic effect that could modulate the treatment with unsaturated fatty acids, considering the quantification of triglycerides wherein only a slight increase in treatment of PA and LPS was registered, as well as the evaluation of targets such as serine palmitoyl-transferase (SPT), a key enzyme that uses palmitoyl-CoA and serine during ceramide synthesis (Figure 6D), which has been involved in several pathological diseases [38]. Then, our results suggest that under the cellular conditions evaluated, there was no significant metabolic alteration in β-cells.

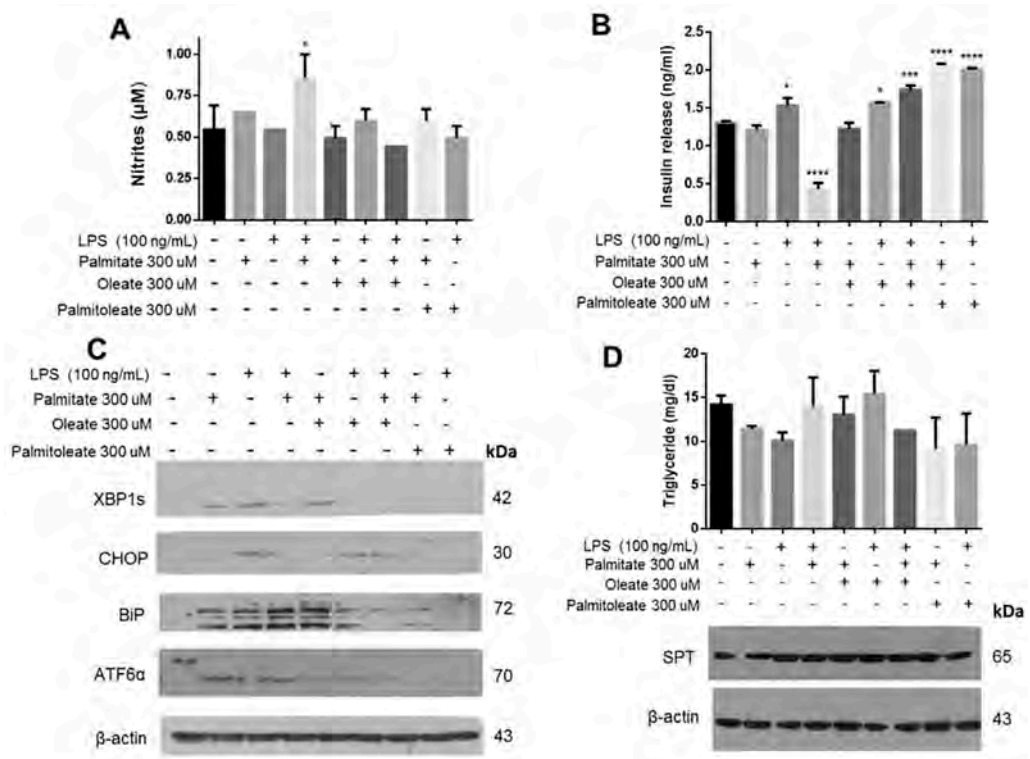

Figure 6. Unsaturated fatty acids could regulate the insulin secretion. (**A**) Quantification of nitrites in the extracellular medium under the incubation with several fatty acids and LPS. (**B**) Insulin secretion in cells exposed to the same treatments. (**C**) Western blot of UPR targets, XBP1s, CHOP, BiP and ATF6α. (**D**) Effect of treatments on metabolic regulation through intracellular quantification of triglycerides and evaluation of SPT. β-actin was used as a loading control. In panels (**A**) and (**B**), (n = 3, mean ± SD), * $p < 0.05$, *** $p < 0.01$, **** $p < 0.001$ compared to control.

To elucidate the correlation of the lipotoxicity phenomenon directly with the main β-cell function, the intracellular [Ca^{2+}] was evaluated under the same treatments (Figure 7A). We found that palmitic acid and LPS induced a decrease in [Ca^{2+}], which was demonstrated to be stabilized under incubation with oleic acid. Importantly, treatment with palmitoleic acid avoids the alteration in [Ca^{2+}] levels that induced the lipotoxicity. The most important proteins regulating intracellular [Ca^{2+}] were assessed, which in turn could explain this phenomenon. Importantly, a decrease in the expression of isoforms 1 and 4 of PMCA was induced by the presence of palmitic acid and LPS (Figure 7B). Although these isoforms maintain a ubiquitous expression, they show a low Ca^{2+} affinity in comparison to PMCA2 and PMCA3 isoforms [39]. Specifically, a second band of lower molecular weight was detected in the Western blot of PMCA1/4 (Figure 7B). This could suggest a proteolytic cleavage mediated by calpain,

which has been described to induce its degradation [40], as analyzed by our group in a previous work [41], therefore altering Ca^{2+} homeostasis, which affects key functions such as insulin secretion. Under our experimental conditions, the expression of PMCA3 in β-cells was undetectable (Figure 7B), although the expression of this isoform has been reported elsewhere [42]. The efficacy of the antibody was evaluated using brain tissue as a positive control where it is abundantly expressed, and in the liver tissue considering that the presence of transcripts has been reported before [43] (Figure 7D).

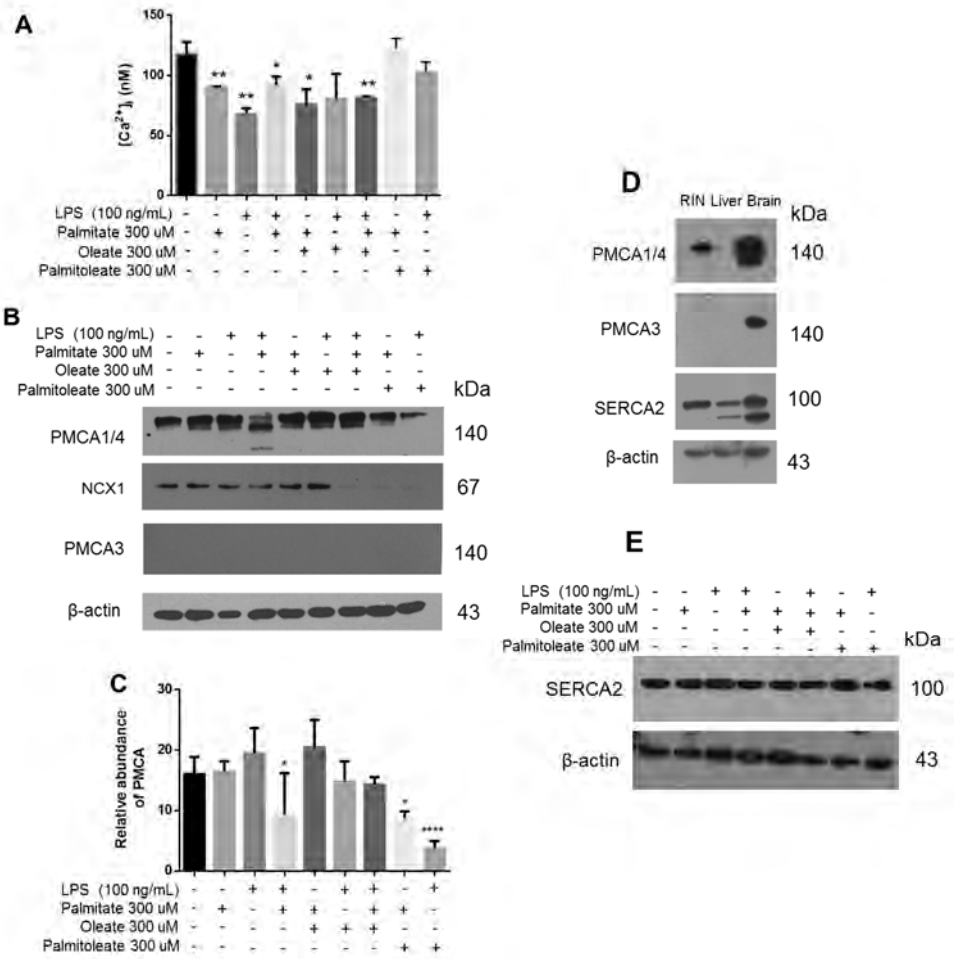

Figure 7. The treatment with unsaturated fatty acids regulates the expression of calcium transporting proteins. (**A**) Quantification of intracellular [Ca^{2+}] under lipotoxicity conditions. * $p < 0.05$, ** $p < 0.01$ compared to control ($n = 3$, mean ± SD). (**B**) Expression of targets PMCA1/4, NCX1 and PMCA3, which are regulated by oleic and palmitoleic acid. (**C**) Quantitative characterization of the expression of PMCA1/4, the analysis was based on three different experiments. * $p < 0.05$, **** $p < 0.001$ compared to control ($n = 3$, mean ± SD). (**D**) Validation of antibodies anti-PMCA1/4, anti-PMCA3 and anti-SERCA2 in RIN-m5F cells, liver and brain tissues. (**E**) Western blot of SERCA2. β-actin was used as a loading control.

Extending our characterization associated with PMCA1/4, the treatment with OA prevented the alteration of PMCA1/4 expression, which was evidenced through the statistical analysis (Figure 7C). However, a decrease in the expression of PMCA1/4 was found under PAO treatment, without evidence of degradation (Figure 7B). Furthermore, cytoplasmic Ca^{2+} levels were maintained at the same levels with respect to controls (Figure 7A). Notwithstanding this, under these conditions an increase in insulin release was recorded (Figure 6B). In order to expand the characterization of this phenomenon, other relevant proteins regulating intracellular [Ca^{2+}] were evaluated. A decrease in NCX1 expression was found under treatment with unsaturated fatty acids, which is responsible for Ca^{2+} output against the

gradient (Figure 7B). This phenomenon could represent a key condition in the regulation of insulin release. With respect to the evaluation of other targets, which could contribute to the explanation of the effect with unsaturated fatty acids, importantly, significant changes were not registered in the expression of SERCA2 (Figure 7E).

Taking into account these results, the role of SA, the second most abundant SFA in biological membranes, was evaluated. In particular, the stimulation with SA did not significantly decrease cell viability, contrary to what was observed with LPS, which caused a slight decrease in the viability (Figure 8A). In fact, insulin release is only modified under SA treatment (Figure 8B), and the incubation with PAO prevents this decrease and maintains insulin levels similar to controls. Under these same experimental conditions, PMCA1/4 expression remained constant (Figure 8C) and in none of the conditions, even upon treatment with SA and LPS, was a second band associated with the degradation of PMCA1/4 present; moreover, the PMCA3 isoform was not identified. An increase in insulin release was observed with the combination of PAO and SA, when compared with PAO. In order to extend this phenomenon associated with the maintenance of $[Ca^{2+}]$, no modifications were found in the SERCA2 expression. Remarkably, the cellular internalization of SA was diminished compared to PA (Figure 8D–I).

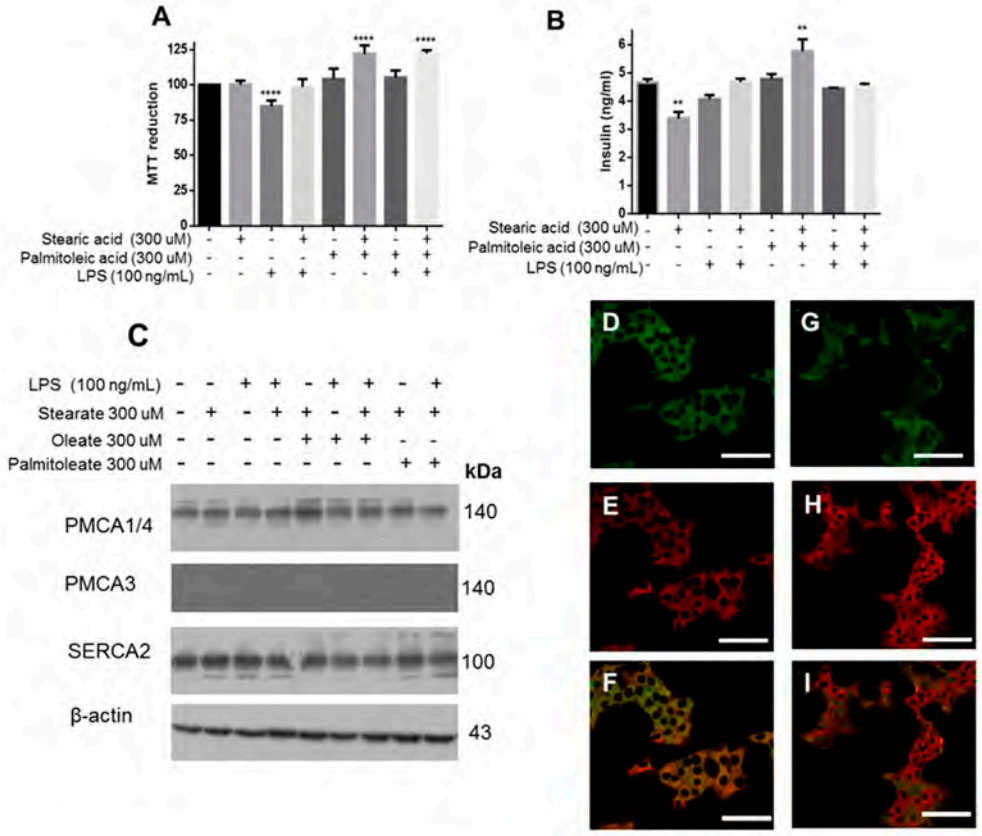

Figure 8. Stearic acid does not modify the homeostasis of calcium in β-cells. (**A**) Viability assay experimentation under treatment with different fatty acids. **** $p < 0.01$ with respect to control ($n = 6$, mean ± SD). (**B**) Determination of insulin concentrations in supernatant medium. ** $p < 0.05$ with respect to control ($n = 3$, mean ± SD). (**C**) Expression of targets that regulate the intracellular calcium concentration. β-actin was used as a loading control. Confocal images of β-cells treated with BDP-PA (**D**), Aza-2-BDP (**E**) and the merge (**F**). Under the same conditions, β-cells treated with BDP-SA (**G**), Aza-2-BDP (**H**), and the merge (**I**). Bars correspond to 50 µm.

4. Discussion

Considering that the ER lumen is the main site where protein folding and post-translational modifications take place, a decrease of insulin secretion attributed to fatty acid and LPS lipotoxicity could be identified by ER stress through UPR activation. Particularly, XBP1s is associated with the regulation of chaperones and protein degradation [44], relevant to mediate the ER stress that may be related to insulin processing. A similar pattern was observed in the activation of c-Jun, CHOP, and ATF6α transcription factors, which allow reduction of ER stress. Although in our conditions cell viability remains basal even in high concentrations of LPS, this could be associated with the fact that cells are trying to recover homeostasis by activating the UPR.

In an important manner, when main SFAs were evaluated, the most lipotoxic was PA (16C) which, according to our results, is mainly located in the endoplasmic reticulum. Although SA (18C), MA (14C) and LA (12C) were evaluated under the same conditions, possibly the length of PA is the optimal for recognition, and then for cellular internalization. In an attempt to extend the characterization of SFAs on key processes of β-cell physiology, our group has designed new materials based on surfaces functionalized with a layer of a fatty acid covalently bound. Results suggest that mainly PA affects the cell adhesion on surfaces compared to other saturated fatty acids (personal communication).

An association between ER stress and the development of DM2 has been previously described [45]. Nevertheless, no influence of SFAs and LPS on β-cell physiology has been reported hitherto. Our data suggest that LPS activated the UPR pathway, but did not reduce cell viability. However, cell viability was reduced significantly with PA and LPS stimuli, associated with cell internalization of the BDP-PA probe, activating the UPR pathway through CHOP, c-Jun, ATF6α and XBP1s. Considering that unsaturated fatty acids could prevent or even restore cell damage caused by lipotoxicity [46,47], our data suggest that oleic acid could have a partial protective role against lipotoxicity caused by PA/LPS. It is likely that a competition between oleic and palmitic acid for receptors such as FFAR1 or CD36 might occur; in fact, CD36 facilitates fatty acid transport and overexpression affects insulin secretion [48]. In an important way, we previously reported that small molecules with terpene structure could regulate ER stress induced by PA, through inhibition of the eukaryotic initiation factor-4A, with an effect in CHOP and XBP1s expression [49]. Therefore, protein translation is a target that could modulate ER stress induced by lipotoxicity.

Our results showed the activation of the UPR pathway by PA and its accumulation in organelle membranes, mainly in the ER area (Figures 2 and 3), generating stress conditions. Also, we observed a decrease in the PMCA1/4 expression, in correlation with an alteration of insulin secretion. It should be noted that the monoclonal antibody employed here recognizes isoforms 1 and 4, which show a ubiquitous expression. Although PMCA3 isoform has been detected specifically in β-cells by other authors [42], this is a controversial issue since we and others have not detected this isoform. In this work, PMCA3 was not detected at the protein level and, importantly, its absence was confirmed also when transcripts were measured by qPCR in all experimental conditions (data not shown). Regarding other PMCA transcripts expression, the observed pattern corresponds to the maximal expression of *ATP2B1* which is the most abundant in all tissues, but also when high intracellular [Ca^{2+}] levels are present. By itself, this finding can be related to the specific PMCA1 affinity for Ca^{2+} that is lower with respect to isoforms PMCA2 and PMCA3; when [Ca^{2+}] is elevated in the cytoplasm, cells do not require the function of the sensitive isoforms to extrude calcium, as we have observed before [14]. Since PMCA is responsible for intracellular Ca^{2+} removal and Ca^{2+} entry is a trigger factor for insulin release, a decrease in PMCA expression would be expected to generate the opposite effect. This may be due to other mechanisms responsible for [Ca^{2+}] regulation in the β-cells, such as the NCX1 exchanger and SERCA. The possibility of studying the expression of transcripts and activity of these proteins in the near future is open.

In our conditions, SERCA2 shows a basal expression, suggesting the importance of maintaining [Ca^{2+}] in the ER. Results suggest that there is not severe alteration in the ER. Importantly, the decrease in insulin release upon treatment with the PA/LPS was accompanied by the decrease in PMCA1/4

expression, wherein the detection of a lower molecular weight band of PMCA was a major finding. This effect could be correlated with the degradation of PMCA due to a proteolytic cleavage, a condition mediated by calpains and caspases under oxidative conditions [40], as corroborated by the formation of RNS. In this sense, a phenomenon related to oxidative phenomenon in β-cells is the lipid peroxidation by the generation of α, β-unsaturated 4-hydroxyalkenals (4-HNE, 4-HHE and 4-DDE) [50]. However, oleic and palmitoleic acid avoided this phenomenon, which could improve under the co-treatment with chalcone and flavone analogs recently synthetized by our group [51]. Interestingly, when the combination of palmitic acid plus LPS and the treatment with palmitoleic acid were tested, the UPR activation was minimal. Specifically, palmitoleic acid promoted an increase in insulin secretion without inducing CHOP over-activation, indicating a possible restorative role.

On the other hand, unlike palmitic acid, stearic acid alone did not cause severe ER stress and cell viability remained in basal conditions. In fact, treatment with SA and PAO increases cell viability; this was corroborated by the null modification in PMCA1/4 expression and insulin release. Therefore, we demonstrated that fatty acids exert a differential effect on the physiology of β-cells, with the length of the hydrocarbon chain a contributing factor. Palmitic acid caused the most harmful condition, affecting cell viability and activating the UPR pathway, wherein the saturation and, specifically, the 16C length chain are critical properties. Also, in combination with LPS, it generated a greater deleterious effect in all evaluated parameters: it decreased insulin release, promoted the proteolytic degradation of PMCA, and increased RNS. By contrast, SA did not cause any significant damage, but it decreased insulin secretion.

However, the effect of oleic acid and palmitoleic acid was different in insulin release, PMCA expression, and Ca^{2+} storage. Oleic acid had the ability to restore insulin release, but the expression of PMCA and NCX1 increased. Nevertheless, PMCA and NCX1 expression decreased with PAO/PA and PAO/LPS treatments, and insulin secretion increased maintaining the basal levels of Ca^{2+}. Therefore, oleic acid seemed to play a restorative role for the damage induced by SFAs, mainly ER stress, while palmitoleic acid improves insulin release and has more relevant effects upon intracellular calcium regulatory pumps.

Although free fatty acid proportions in the diet are a condition associated with the development of several diseases associated with alterations in metabolism [16,38,49], it is important to consider the adipose tissue as a buffering of lipid fluxes, which could be impaired in obesity by defects in response to the dynamic metabolism that occurs after meals [52], then modifying the relationship in concentrations of saturated/unsaturated plasmatic fatty acids. Therefore, the characterization of the main effects fatty acids have upon pancreatic β-cell physiology and the UPR pathway, and the repercussion on calcium homeostasis and insulin release, allow us to broaden our understanding of the different roles of fatty acids inside β-cells, which are important metabolites to take into account in explaining the damage and treatment of novel therapeutic targets in T2DM.

Supplementary Materials: The following are available online at http://www.mdpi.com/2073-4409/8/8/884/s1, Figure S1: LPS treatment increases the signal of DBP-PA on endoplasmic reticulum; Figure S2: Activation of UPR arms induced by PA treatment (300 μM); Figure S3: Full Western-blot of XBP1s, c-Jun, and ATF6α under LPS increasing concentrations (0.1-1000 ng/mL); Figure S4: Full Western blot of PMCA1/4 under different conditions of treatment with stearic acid, oleic acid and LPS.

Author Contributions: Conceived and designed the experiments: P.A.-M., and V.G.-G. Performed experiments: P.A.-M., E.R.-V., E.I.-L., H.F.-G., B.D.-C., M.A.-M., J.A., L.G.-O. and V.G.-G. Analyzed data: P.A.-M., J.M.-O., B.D.-C., I.A.-R. and V.G.-G. Contributed reagents/materials/analysis tools: M.A.-M. and V.G.-G. Wrote the paper: P.A.-M. and V.G.-G.

Funding: This research was funded by Coordinación de Posgrado e Investigación-UABC (grant no. 106/2/N/57/1; 1983).

Acknowledgments: The authors recognize the administrative support of Josue Villegas Sandoval. M.A.-M. thanks funding from CONACYT (Mexico) through Research Projects INFR-2015-251863 and PDCPN-2015-89.

Conflicts of Interest: The authors declare no conflict of interest.

References

1. Remedi, M.S.; Emfinger, C. Pancreatic beta-cell identity in diabetes. *Diabetes Obes. Metab.* **2016**, *18*, 110–116. [CrossRef]
2. Ashcroft, F.M.; Rorsman, P. Diabetes mellitus and the beta cell: The last ten years. *Cell* **2012**, *148*, 1160–1171. [CrossRef]
3. Seino, S.; Shibasaki, T.; Minami, K. Dynamics of insulin secretion and the clinical implications for obesity and diabetes. *J. Clin. Investig.* **2011**, *121*, 2118–2125. [CrossRef]
4. Scheuner, D.; Kaufman, R.J. The unfolded protein response: A pathway that links insulin demand with beta-cell failure and diabetes. *Endocr. Rev.* **2008**, *29*, 317–333. [CrossRef]
5. Rorsman, P. Insulin granule dynamics in pancreatic beta cells. *Diabetologia* **2003**, *46*, 1029–1045. [CrossRef]
6. Schuit, F.C.; Veld, P.A.I.; Pipeleers, D.G. Glucose stimulates proinsulin biosynthesis by a dose-dependent recruitment of pancreatic beta cells. *Proc. Natl. Acad. Sci. USA* **1988**, *85*, 3865–3869. [CrossRef]
7. Hasnain, S.Z.; Prins, J.B.; McGuckin, M.A. Oxidative and endoplasmic reticulum stress in beta-cell dysfunction in diabetes. *J. Mol. Endocrinol.* **2016**, *56*, R33–R54. [CrossRef]
8. Schuck, S.; Prinz, W.A.; Thorn, K.S.; Voss, C.; Walter, P. Membrane expansion alleviates endoplasmic reticulum stress independently of the unfolded protein response. *J. Cell Boil.* **2009**, *187*, 525–536. [CrossRef]
9. Díaz-Villanueva, J.F.; Díaz-Molina, R.; García-González, V. Protein Folding and Mechanisms of Proteostasis. *Int. J. Mol. Sci.* **2015**, *16*, 17193–17230. [CrossRef]
10. Bratanova-Tochkova, T.K.; Cheng, H.; Daniel, S.; Gunawardana, S.; Liu, Y.J.; Mulvaney-Musa, J.; Schermerhorn, T.; Straub, S.G.; Yajima, H.; Sharp, G.W. Triggering and Augmentation Mechanisms, Granule Pools, and Biphasic Insulin Secretion. *Diabetes* **2002**, *51*, S83–S90. [CrossRef]
11. Herchuelz, A.; Kamagate, A.; Ximenes, H.; Eylen, F.V. Role of Na/Ca exchange and the plasma membrane Ca^{2+}-ATPase in beta cell function and death. *Ann. N. Y. Acad. Sci.* **2007**, *1099*, 456–467. [CrossRef]
12. Carafoli, E. Calcium pump of the plasma membrane. *Physiol. Rev.* **1991**, *71*, 129–153. [CrossRef]
13. Bruce, J.I. Metabolic regulation of the PMCA: Role in cell death and survival. *Cell Calcium* **2018**, *69*, 28–36. [CrossRef]
14. Bravo-Martínez, J.; Delgado-Coello, B.; García, D.E.; Mas-Oliva, J. Analysis of plasma membrane Ca2+-ATPase gene expression during epileptogenesis employing single hippocampal CA1 neurons. *Exp. Biol. Med.* **2011**, *236*, 409–417. [CrossRef]
15. Brini, M.; Carafoli, E. The plasma membrane Ca^{2+} ATPase and the plasma membrane sodium calcium exchanger cooperate in the regulation of cell calcium. *Cold Spring Harb. Perspect. Biol.* **2011**, *3*, a004168. [CrossRef]
16. Acosta-Montaño, P.; García-González, V. Effects of Dietary Fatty Acids in Pancreatic Beta Cell Metabolism, Implications in Homeostasis. *Nutrients* **2018**, *10*, 393. [CrossRef]
17. Boslem, E.; MacIntosh, G.; Preston, A.M.; Bartley, C.; Busch, A.K.; Fuller, M.; Laybutt, D.R.; Meikle, P.J.; Biden, T.J. A lipidomic screen of palmitate-treated MIN6 beta-cells links sphingolipid metabolites with endoplasmic reticulum (ER) stress and impaired protein trafficking. *Biochem. J.* **2011**, *435*, 267–276. [CrossRef]
18. Preston, A.M.; Gurisik, E.; Bartley, C.; Laybutt, D.R.; Biden, T.J.; Biden, T. Reduced endoplasmic reticulum (ER)-to-Golgi protein trafficking contributes to ER stress in lipotoxic mouse beta cells by promoting protein overload. *Diabetologia* **2009**, *52*, 2369–2373. [CrossRef]
19. Karaskov, E.; Scott, C.; Zhang, L.L.; Teodoro, T.; Ravazzola, M.; Volchuk, A. Chronic palmitate but not oleate exposure induces endoplasmic reticulum stress, which may contribute to INS-1 pancreatic beta-cell apoptosis. *Endocrinology* **2006**, *147*, 3398–33407. [CrossRef]
20. Gwiazda, K.S.; Yang, T.L.B.; Lin, Y.; Johnson, J.D. Effects of palmitate on ER and cytosolic Ca^{2+} homeostasis in beta-cells. *Am. J. Physiol. Endocrinol. Metab.* **2009**, *296*, E690–E701. [CrossRef]
21. Fortis, Á.; García-Macedo, R.; Maldonado-Bernal, C.; Alarcón-Aguilar, F.; Cruz, M. El papel de la inmunidad innata en la obesidad. *Salud Pública México* **2012**, *54*, 171–177. [CrossRef]
22. Amyot, J.; Semache, M.; Ferdaoussi, M.; Fontés, G.; Poitout, V. Lipopolysaccharides impair insulin gene expression in isolated islets of Langerhans via Toll-Like Receptor-4 and NF-kappaB signalling. *PLoS ONE* **2012**, *7*, e36200. [CrossRef]
23. Guerville, M.; Boudry, G. Gastrointestinal and hepatic mechanisms limiting entry and dissemination of lipopolysaccharide into the systemic circulation. *Am. J. Physiol. Gastrointest. Liver Physiol.* **2016**, *311*, G1–G15. [CrossRef]

24. Larsen, N.; Vogensen, F.K.; Berg, F.W.J.V.D.; Nielsen, D.S.; Andreasen, A.S.; Pedersen, B.K.; Abu Al-Soud, W.; Sørensen, S.J.; Hansen, L.H.; Jakobsen, M. Gut Microbiota in Human Adults with Type 2 Diabetes Differs from Non-Diabetic Adults. *PLoS ONE* **2010**, *5*, e9085. [CrossRef]
25. Cani, P.D.; Delzenne, N.M. Gut microflora as a target for energy and metabolic homeostasis. *Curr. Opin. Clin. Nutr. Metab. Care* **2007**, *10*, 729–734. [CrossRef]
26. García-González, V.; Gutiérrez-Quintanar, N.; Mas-Oliva, J. The C-terminal Domain Supports a Novel Function for CETPI as a New Plasma Lipopolysaccharide-Binding Protein. *Sci. Rep.* **2015**, *5*, 16091. [CrossRef]
27. García-González, V.; Mas-Oliva, J. Amyloidogenic Properties of a D/N Mutated 12 Amino Acid Fragment of the C-Terminal Domain of the Cholesteryl-Ester Transfer Protein (CETP). *Int. J. Mol. Sci.* **2011**, *12*, 2019–2035. [CrossRef]
28. Harris, L.A.L.S.; Shew, T.M.; Skinner, J.R.; Wolins, N.E. A single centrifugation method for isolating fat droplets from cells and tissues. *J. Lipid Res.* **2012**, *53*, 1021–1025. [CrossRef]
29. Alfonzo-Mendez, M.A.; Hernández-Espinosa, D.A.; Carmona-Rosas, G.; Romero-Ávila, M.T.; Reyes-Cruz, G.; García-Sáinz, J.A. Protein kinase c activation promotes alpha1b-adrenoceptor internalization and late endosome trafficking through rab9 interaction. Role in heterologous desensitization. *Mol. Pharmacol.* **2017**, *91*, 296–306. [CrossRef]
30. Patel, A.; Hirst, R.A.; Harrison, C.; Hirota, K.; Lambert, D.G. Measurement of [Ca^{2+}] i in whole cell suspensions using Fura-2. *Methods Mol. Biol.* **2013**, *937*, 37–47.
31. Ma, D.H.; Kim, D.; Akisawa, T.; Lee, K.H.; Kim, K.T.; Ahn, K.H. An FITC-BODIPY FRET Couple: Application to Selective, Ratiometric Detection and Bioimaging of Cysteine. *Chem. Asian J.* **2014**, *10*, 894–902. [CrossRef]
32. Engin, A.B. What is lipotoxicity? *Adv. Exp. Med. Biol.* **2017**, *960*, 197–220.
33. Savage, K.E.; Baur, P.S. Effect of tunicamycin, an inhibitor of protein glycosylation, on division of tumour cells in vitro. *J. Cell Sci.* **1983**, *64*, 295–306.
34. Melloul, D.; Marshak, S.; Cerasi, E. Regulation of insulin gene transcription. *Diabetologia* **2002**, *45*, 309–326. [CrossRef]
35. Poitout, V.; Robertson, R.P.; Harmon, J.S.; Hagman, D.; Stein, R.; Artner, I. Regulation of the Insulin Gene by Glucose and Fatty Acids. *J. Nutr.* **2006**, *136*, 873–876. [CrossRef]
36. García-González, V.; Mas-Oliva, J. A Novel β-adaptin/c-Myc Complex Formation Modulated by Oxidative Stress in the Control of the Cell Cycle in Macrophages and its Implication in Atherogenesis. *Sci. Rep.* **2017**, *7*, 13442. [CrossRef]
37. Damián-Zamacona, S.; García-González, V.; Avila-Barrientos, L.P.; Delgado-Coello, B.; Reyes-Grajeda, J.P.; Mas-Oliva, J. Cell survival regulation during receptor-mediated endocytosis of chemically-modified lipoproteins associated to the formation of an Amphiphysin 2 (Bin1)/c-Myc complex. *Biochem. Biophys. Res. Commun.* **2018**, *505*, 365–371. [CrossRef]
38. García-González, V.; Díaz-Villanueva, J.F.; Galindo-Hernández, O.; Martínez-Navarro, I.; Hurtado-Ureta, G.; Pérez-Arias, A.A. Ceramide Metabolism Balance, a Multifaceted Factor in Critical Steps of Breast Cancer Development. *Int. J. Mol. Sci.* **2018**, *19*, 2527. [CrossRef]
39. Delgado-Coello, B.; Trejo, R.; Mas-Oliva, J. Is there a specific role for the plasma membrane Ca^{2+}-ATPase in the hepatocyte? *Mol. Cell. Biochem.* **2006**, *285*, 1–15. [CrossRef]
40. Zaidi, A. Plasma membrane Ca^{2+}-ATPases: Targets of oxidative stress in brain aging and neurodegeneration. *World J. Boil. Chem.* **2010**, *1*, 271–280. [CrossRef]
41. Pulido-Capiz, A.; Díaz-Molina, R.; Martínez-Navarro, I.; Guevara-Olaya, L.A.; Casanueva-Pérez, E.; Mas-Oliva, J.; Rivero, I.A.; García-González, V. Modulation of Amyloidogenesis Controlled by the C-Terminal Domain of Islet Amyloid Polypeptide Shows New Functions on Hepatocyte Cholesterol Metabolism. *Front. Endocrinol.* **2018**, *9*, 331. [CrossRef]
42. García, M.E.; del Zotto, H.; Caride, A.J.; Filoteo, A.G.; Penniston, J.T.; Rossi, J.P.F.C.; Gagliardino, J.J. Expression and Cellular Distribution Pattern of Plasma Membrane Calcium Pump Isoforms in Rat Pancreatic Islets. *J. Membr. Boil.* **2002**, *185*, 17–23. [CrossRef]
43. Delgado-Coello, B.; Bravo-Martinez, J.; Sosa-Garrocho, M.; Briones-Orta, M.A.; Macías-Silva, M.; Mas-Oliva, J. Plasma membrane calcium ATPase isoform 3 expression in single cells isolated from rat liver. *Mol. Cell. Biochem.* **2010**, *344*, 117–124. [CrossRef]

44. Bertolotti, A.; Zhang, Y.; Hendershot, L.M.; Harding, H.P.; Ron, D. Dynamic interaction of BiP and ER stress transducers in the unfolded-protein response. *Nat. Cell Biol.* **2000**, *2*, 326–332. [CrossRef]
45. Ron, D.; Walter, P. Signal integration in the endoplasmic reticulum unfolded protein response. *Nat. Rev. Mol. Cell Boil.* **2007**, *8*, 519–529. [CrossRef]
46. Parillo, M.; Rivellese, A.; Ciardullo, A.; Capaldo, B.; Giacco, A.; Genovese, S.; Riccardi, G. A high-monounsaturated -fat/low-carbohydrate diet improves peripheral insulin sensitivity in non-insulin-dependent diabetic patients. *Metabolism* **1992**, *41*, 1373–1378. [CrossRef]
47. Ryan, M.; McInerney, D.; Owens, D.; Collins, P.; Johnson, A.; Tomkin, G. Diabetes and the Mediterranean diet: A beneficial effect of oleic acid on insulin sensitivity, adipocyte glucose transport and endothelium-dependent vasoreactivity. *QJM Int. J. Med.* **2000**, *93*, 85–91. [CrossRef]
48. Wallin, T.; Ma, Z.; Ogata, H.; Jørgensen, I.H.; Iezzi, M.; Wang, H.; Wollheim, C.B.; Björklund, A. Facilitation of fatty acid uptake by CD36 in insulin-producing cells reduces fatty-acid-induced insulin secretion and glucose regulation of fatty acid oxidation. *Biochim. Biophys. Acta BBA Mol. Cell Biol. Lipids* **2010**, *1801*, 191–197. [CrossRef]
49. Galindo-Hernández, O.; Córdova-Guerrero, I.; Díaz-Rubio, L.J.; Pulido-Capiz, Á.; Díaz-Villanueva, J.F.; Castañeda-Sánchez, C.Y.; Serafín-Higuera, N.; García-González, V. Protein translation associated to PERK arm is a new target for regulation of metainflammation: A connection with hepatocyte cholesterol. *J. Cell. Biochem.* **2019**, *120*, 4158–4171.
50. Maulucci, G.; Daniel, B.; Cohen, O.; Avrahami, Y.; Sasson, S. Hormetic and regulatory effects of lipid peroxidation mediators in pancreatic beta cells. *Mol. Asp. Med.* **2016**, *49*, 49–77. [CrossRef]
51. Díaz-Rubio, L.; Hernández-Martínez, R.; Estolano-Cobián, A.; Chávez-Velasco, D.; Salazar-Aranda, R.; De Torres, N.W.; Rivero, I.A.; García-González, V.; Ramos, M.A.; Córdova-Guerrero, I. Synthesis, Biological Evaluation and Docking Studies of Chalcone and Flavone Analogs as Antioxidants and Acetylcholinesterase Inhibitors. *Appl. Sci.* **2019**, *9*, 410. [CrossRef]
52. Frayn, K. Adipose tissue as a buffer for daily lipid flux. *Diabetologia* **2002**, *45*, 1201–1210. [CrossRef]



© 2019 by the authors. Licensee MDPI, Basel, Switzerland. This article is an open access article distributed under the terms and conditions of the Creative Commons Attribution (CC BY) license (http://creativecommons.org/licenses/by/4.0/).

Received: 17 September 2018 | Revised: 19 December 2018 | Accepted: 21 January 2019

DOI: 10.1111/bph.14617

Themed Section: Adrenoceptors—New Roles for Old Players

REVIEW ARTICLE

Updates in the function and regulation of α_1-adrenoceptors

Juliana Akinaga[1] | J. Adolfo García-Sáinz[2] | André S. Pupo[1]

[1] Department of Pharmacology, Instituto de Biociências, UNESP, Botucatu, Brazil

[2] Instituto de Fisiología Celular, Universidad Nacional Autónoma de México, Ciudad de México, Mexico

Correspondence
André S. Pupo, Department of Pharmacology, Instituto de Biociências, UNESP, Rua Prof. Dr. Antônio Celso Wagner Zanin, 250, Botucatu, 18618-689 SP, Brazil.
Email: andre.pupo@unesp.br; andrepupo94@gmail.com

Funding information
Fundação de Amparo à Pesquisa do Estado de São Paulo - FAPESP, Grant/Award Numbers: 2008/50423-7 and 2017/15175-1; Coordenação de Aperfeiçoamento de Pessoal de Nível Superior – Brasil (CAPES), Grant/Award Number: 23038.007773/2014-07; Dirección General de Personal Académico-UNAM, Grant/Award Number: IN200915; Consejo Nacional de Ciencia y Tecnología (CONACYT), Grant/Award Numbers: 253156 and FDC-882

α_1-Adrenoceptors are seven transmembrane domain GPCRs involved in numerous physiological functions controlled by the endogenous catecholamines, noradrenaline and adrenaline, and targeted by drugs useful in therapeutics. Three separate genes, whose products are named α_{1A}-, α_{1B}-, and α_{1D}- adrenoceptors, encode these receptors. Although the existence of multiple α_1-adrenoceptors has been acknowledged for almost 25 years, the specific functions regulated by each subtype are still largely unknown. Despite the limited comprehension, the identification of a single class of subtype-selective ligands for the α_{1A}- adrenoceptors, the so-called α-blockers for prostate dysfunction, has led to major improvement in therapeutics, demonstrating the need for continued efforts in the field. This review article surveys the tissue distribution of the three α_1-adrenoceptor subtypes in the cardiovascular system, genitourinary system, and CNS, highlighting the functions already identified as mediated by the predominant activation of specific subtypes. In addition, this review covers the recent advances in the understanding of the molecular mechanisms involved in the regulation of each of the α_1-adrenoceptor subtypes by phosphorylation and interaction with proteins involved in their desensitization and internalization.

LINKED ARTICLES: This article is part of a themed section on Adrenoceptors—New Roles for Old Players. To view the other articles in this section visit http://onlinelibrary.wiley.com/doi/10.1111/bph.v176.14/issuetoc

1 | INTRODUCTION

The actions of **adrenaline** and **noradrenaline** result from the activation of nine different **adrenoceptors**. All nine adrenoceptors belong to the superfamily of **GPCRs**, the most numerous family of membrane proteins (Fredriksson, Lagerstrom, Lundin, & Schioth, 2003; Fredriksson & Schioth, 2005). Adrenoceptors are classified into three subfamilies, α_1-, α_2-, and β- adrenoceptors, based on their pharmacological profiles, major coupling to signalling pathways (Hieble et al., 1995) and phylogeny. Using the latter criteria, adrenoceptors belong to the amine receptor cluster of the rhodopsin family (Fredriksson & Schioth, 2005) or to subfamily A, group 17 (Joost & Methner, 2002). For the accepted nomenclature, classification, databases, and other tools, see the following: IUPHAR/BPS guide for pharmacology (Harding et al., 2018; Sharman et al., 2018; and http://www.guidetopharmacology.org).

This review deals with advances in the function and regulation of each of the α_1-adrenoceptor subtypes; for additional aspects, readers are directed mainly to the reviews mentioned in this text, the references therein, and to Alexander et al. (2017).

Abbreviations: BPH, benign prostatic hyperplasia; GRK, GPCR kinase

 © 2019 The British Pharmacological Society

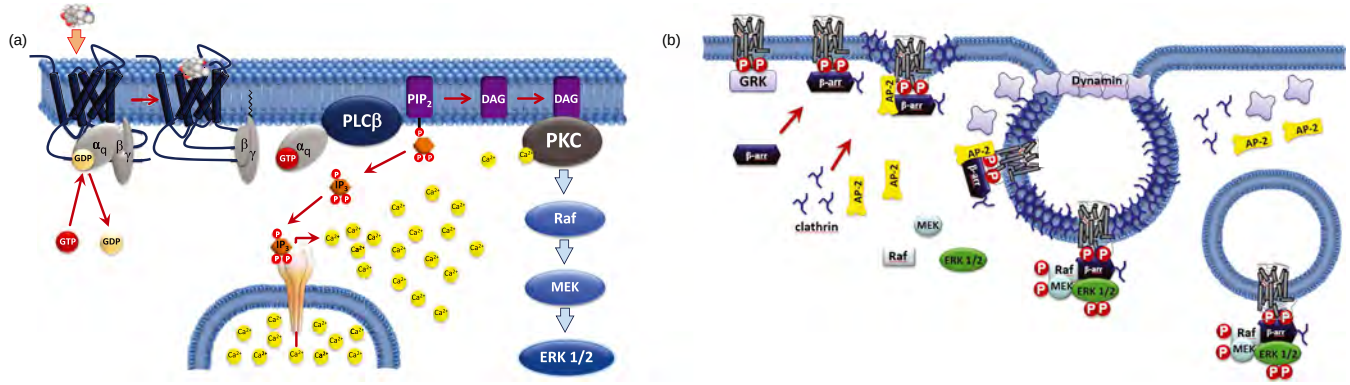

FIGURE 1 (a) Schematic representation of the classical Gq protein dependent signalling triggered by α_1-adrenoceptor subtypes and (b) of the signalling triggered by receptor phosphorylation and interaction with β-arrestin, which is also involved in receptor internalization. IP_3: inositol trisphosphate; PIP_2: phosphatidylinositol 4,5-bisphosphate; PLC: phospholipase Cβ

2 | INTRACELLULAR SIGNALLING BY α_1-ADRENOCEPTOR SUBTYPES

The classical intracellular signalling pathway triggered by all three α_1-adrenoceptor subtypes results from coupling to $G_{q/11}$ proteins, leading to the activation of **phospholipase Cβ**, hydrolysis of phosphatidylinositol 4,5-bisphosphate into DAG/**inositol trisphosphate**, intracellular calcium mobilization, and **PKC** activation (Figure 1a; Hieble et al., 1995). Upon receptor activation, GPCR kinases (GRKs) and/or PKC phosphorylate α_1-adrenoceptors, leading to the recruitment of β-arrestins. Moreover, β-arrestins act as a scaffolding for other proteins triggering a distinct array of G-protein independent signalling through the activation of **ERK1/2** (Figure 1b; Perez-Aso et al., 2013; Segura et al., 2013).

It is worth mentioning that constitutive activity has been observed for native **α_{1D}- adrenoceptors** in rat arteries (Gisbert et al., 2002; Gisbert, Noguera, Ivorra, & D'Ocon, 2000; Noguera, Ivorra, & D'Ocon, 1996; Ziani, Gisbert, Noguera, Ivorra, & D'Ocon, 2002) and in cells overexpressing recombinant α_{1D}- adrenoceptors (García-Sáinz & Torres-Padilla, 1999; Rodríguez-Pérez, Romero-Ávila, Reyes-Cruz, & García-Sáinz, 2009); meanwhile, weak inverse agonism has been observed in some cells expressing native **α_{1A}-** or **α_{1B}- adrenoceptors** (Cotecchia, 2007). However, using site-directed mutagenesis, constitutively active mutants have been generated and inverse agonism has been detected (Cotecchia, 2007). Many of the currently used α_1-adrenoceptor antagonists are, in fact, inverse agonists (Cotecchia, 2007; García-Sáinz & Torres-Padilla, 1999; Rodríguez-Pérez et al., 2009).

3 | α_1-ADRENOCEPTORS IN PHYSIOLOGY AND PHYSIOPATHOLOGY

The α_1-adrenoceptor subfamily is composed of three members, that is, α_{1A}-, α_{1B}-, and α_{1D}- adrenoceptors (Hieble et al., 1995). These receptors participate in a large number of physiological processes and in the pathogenesis of diseases (for reviews, see García-Sáinz, Vázquez-Prado, & Medina, 2000; Garcia-Sainz, Vazquez-Prado, & Villalobos-Molina, 1999; Michelotti, Price, & Schwinn, 2000; Tanoue et al., 2003; Toews, Prinster, & Schulte, 2003). The latter has been regarded as the "dark side" of these transducers' actions, but, in our opinion, a better understanding of the molecular pharmacology of these receptors might lead to a path of light and hope, offering opportunities for novel therapeutic interventions. The sections below survey the roles of α_1-adrenoceptor subtypes in the cardiovascular system, genitourinary system, and CNS with regard to health and disease. Figure 2 summarizes some of the important functions controlled by α_1-adrenoceptor subtypes in these systems.

3.1 | α_1-Adrenoceptors in arteries

Among the best characterized α_1-adrenoceptor-mediated actions are those in the vascular system, where they are distributed across adventitial, medial smooth muscle, and endothelial cells (see McGrath, 2015). However, information on the role of each of the individual α_1-adrenoceptor subtype is limited to receptors expressed in vascular smooth muscle. Exceptions are the clear identification of **NO** production in endothelial cells from the rat aorta by α_{1A}- adrenoceptors (Arce et al., 2017), by α_{1B}-adrenoceptors in cultured endothelial cells from coronary arteries (Jensen, Swigart, Montgomery, & Simpson, 2010), and by α1D- adrenoceptors in endothelial cells from the rat mesenteric vascular bed and carotid artery (de Andrade et al., 2006; Filippi et al., 2001). With the increasing recognition of the importance of the perivascular adipose tissue for normal vascular function (Bulloch & Daly, 2014), it is expected that the roles of individual α_1-adrenoceptor subtypes in the tunica adventitia will be soon elucidated.

Although the vascular system expresses all three α_1-adrenoceptors, there is a predominance of specific subtypes in different arteries. An interesting view emerged in which the prevalence of an α_1-adrenoceptor subtype in a vessel depends on the density of sympathetic innervation and on the vessel calibre (Stassen, Maas, Schiffers, Janssen, & De Mey, 1998). The α_{1A}- adrenoceptors predominate in resistance arteries such as the small mesenteric artery (Marti et al., 2005; Methven, McBride, Wallace, & McGrath, 2009; Nourian et al., 2008; Philipp & Hein, 2004) and distributing arteries such as the renal (Hrometz et al., 1999) and tail (Kamikihara et al., 2005; Lachnit, Tran,

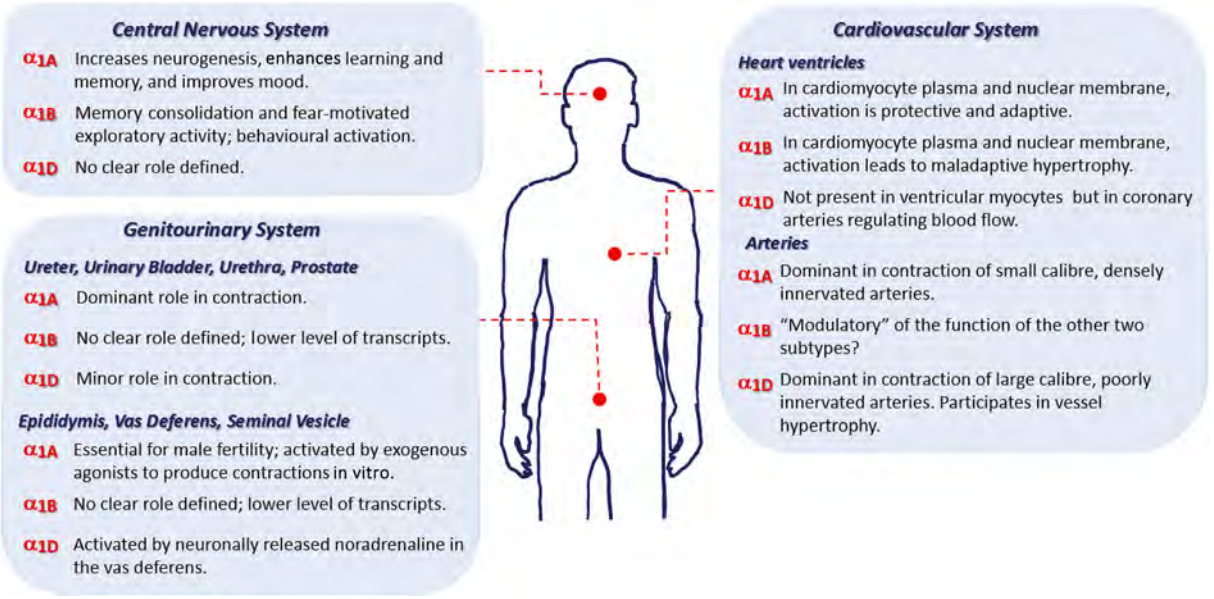

FIGURE 2 Summary of the main functions identified for each of the α_1-adrenoceptors subtypes in the cardiovascular system, genitourinary system, and CNS. Readers are referred to the text for the bibliography

Clarke, & Ford, 1997; Taki et al., 2004) arteries. Conversely, α_{1D}-adrenoceptors are more prevalent on less innervated conductance arteries including the aorta, femoral, iliac, carotid, pulmonary, and superior mesenteric arteries (Arevalo-Leon, Gallardo-Ortiz, Urquiza-Marin, & Villalobos-Molina, 2003; Gisbert et al., 2000; Hussain & Marshall, 1997; Marti et al., 2005; Methven, Simpson, & McGrath, 2009; Nourian et al., 2008; Piascik et al., 1995; Rudner et al., 1999). This differential distribution of α_{1A}-adrenoceptors indicates physiological relevance; the dominant α_{1D}- adrenoceptors in conductance arteries result in high sensitivity to catecholamines, and the activation of this subtype leads to persistent vasoconstriction that tends to continue even after agonist removal, preventing sudden changes in the vessel calibre during variations in the circulating levels of catecholamines (Flacco et al., 2013; Gisbert et al., 2000; Noguera et al., 1996; Ziani et al., 2002). On the other hand, in the more densely innervated smaller resistance arteries, noradrenaline released from sympathetic terminals activates α_{1A}- adrenoceptors and causes less sustained vasoconstriction allowing rapid vascular tonus adjustment in response to autonomic activation. The positive relationship between the density of adrenergic fibres and dominance of α_{1A}- adrenoceptors is reversible, as sympathetic denervation increases the expression and participation of the other two subtypes in vasoconstriction (Kamikihara et al., 2005; Kamikihara et al., 2007; Stassen et al., 1998; Taki et al., 2004). In addition, the potencies of antipsychotics in producing orthostatic hypotension correlated with their affinities for α_{1A}- adrenoceptors but not for α_{1D}- adrenoceptors (Nourian et al., 2008), as most of the antipsychotics behave as competitive antagonists of α_1-adrenoceptors, and this positive correlation further indicates that noradrenaline released from sympathetic terminals targets the α_{1A}- adrenoceptors to increase peripheral vascular resistance.

Whereas the roles of the α_{1A}- and α_{1D}- adrenoceptors in vasoconstriction were promptly recognized, evidence for the participation of α_{1B}-adrenoceptors is scarce. The lack of subtype-selective α_{1B}-adrenoceptor ligands limits the understanding of the role of this subtype in the vascular system. Nevertheless, studies in α_{1B}-adrenoceptor knockout mice indicate that this subtype plays a minor role in vascular homeostasis, acting mainly as a modulator of the other two receptors' activities (Cavalli et al., 1997; Cotecchia, 2010; Daly et al., 2002; Docherty, 2010; Tanoue et al., 2003).

In several animal models, hypertension has been associated with increased α_{1D}- adrenoceptor signalling (Gisbert et al., 2002; Ibarra, Terrón, López-Guerrero, & Villalobos-Molina, 1997; Villalobos-Molina et al., 2008; Villalobos-Molina & Ibarra, 1999; Villalobos-Molina & Ibarra, 2005; Villalobos-Molina, López-Guerrero, & Ibarra, 1999). Activation of α_{1D}-adrenoceptors increases protein synthesis and vascular wall growth (Erami, Zhang, Ho, French, & Faber, 2002; Xin, Yang, Eckhart, & Faber, 1997). In an **angiotensin II**-induced hypertension and aortic hypertrophy model, α_{1D}- adrenoceptor antagonists do not prevent hypertension, but do inhibit vascular hypertrophy, dissociating both events and suggesting a role for α_{1D}- adrenoceptors in the long-term vascular hypertrophic process (Gallardo-Ortiz et al., 2015).

The roles of catecholamines and α_1-adrenoceptors in pulmonary hypertension induced by chronic exposure to reduced oxygen was examined in wild-type (WT) and knockout mice. The decreased luminal area and increased wall thickness of the arteries induced by hypoxic conditions in WT mice were markedly reduced in **dopamine β-hydroxylase** knockouts as well as in α_{1A}- or α_{1B}-adrenoceptor-deficient mice, strongly suggesting that the activation of these receptors by noradrenaline/adrenaline contributes to the vascular remodelling in hypoxic pulmonary hypertension (Faber et al., 2007).

Although α_1-adrenoceptor antagonists are antihypertensive, orthostatic hypotension and the worsening of heart failure, along with the availability of better alternatives, have considerably decreased their prescription. Currently, the α_1-adrenoceptors in the vascular system

are targets for agonists to promote vasoconstriction. Thus, α_1-adrenoceptor agonists such as **phenylephrine**, are components of oral over-the-counter medications to alleviate the congestive symptoms of the common cold and influenza. In addition, the imidazolines, **oxymetazoline** and **naphazoline,** are common components of topical nasal decongestants, mydriatic eye drops, and more recently dermatological formulations for the treatment of facial erythema in rosacea (Kircik et al., 2018; Mota & Norris, 2016; Vaidyanathan, Williamson, Clearie, Khan, & Lipworth, 2010). Interestingly, oxymetazoline and naphazoline are low efficacy agonists with reasonable selectivity for α_{1A}- adrenoceptors (10- to 30-fold; Akinaga et al., 2013; Minneman, Theroux, Hollinger, Han, & Esbenshade, 1994), further supporting the relevance of this subtype in vasoconstriction. However, the prolonged use of these topical agonists is limited by tachyphylaxis leading to rebound congestion and hyperaemia, opening the possibility for the development of better agonists that are less tachyphylactic than those currently available.

Intravenous α_1-adrenoceptor agonists are indispensable medications in emergency and intensive care units to raise BP in shock (Colling, Banton, & Beilman, 2018; Jentzer et al., 2018). The most used α_1-adrenoceptor agonists to revert hypotension are noradrenaline, adrenaline, **dopamine,** and phenylephrine. Recently, a shortage in the noradrenaline supply to US hospitals was associated with increased mortality among patients with septic shock (Vail et al., 2017). In septic shock, reversal of hypotension with the currently available vasoconstrictors is limited by tachyphylaxis because vasoconstriction diminishes as treatment continues, resulting in inadequate blood perfusion and vital organ failure. It has been proposed that the loss of vasoconstriction due to α_1-adrenoceptor agonists in septic patients might result from receptor desensitization (Geloen et al., 2015; Hwang, Lau, Huang, Chen, & Liu, 1994), and again, the development of ligands that are less tachyphylactic than the natural catecholamines and phenylephrine would be a significant improvement in the emergency treatment of hypotension by providing more sustained elevation of BP.

3.2 | α_1- Adrenoceptors in the heart

α_1- Adrenoceptors participate in the development, growth, and function of the heart. Current evidence indicates that the α_{1A}- and α1B-adrenoceptors are present in the myocardium, modulating contractility, whereas the α_{1D} subtype is found in coronary arteries, regulating heart perfusion (O'Connell, Jensen, Baker, & Simpson, 2014). It has been recently proposed that all ventricular myocytes in the mouse heart express the α_{1B}-adrenoceptors (and β_1-adrenoceptors), whereas the α_{1A}- adrenoceptors are present in half of these cells and co-expressed with α_{1B}-adrenoceptors (Myagmar et al., 2017). These receptors also play an important role in cardiac hypertrophy (reviewed in Cotecchia, Del Vescovo, Colella, Caso, & Diviani, 2015; O'Connell et al., 2014; Woodcock, Du, Reichelt, & Graham, 2008). Cardiac hypertrophy is characterized by an abnormally large myocardial mass that reflects, among other changes, an increased cardiomyocyte size and is often accompanied by heart failure. The development of α_1-adrenoceptor-mediated cardiomyocyte hypertrophy depends on classical signalling through Gq proteins and, probably, through β-arrestins, leading to the activation of **MAPKs**, modulation of transcription factors, and ultimately to hypertrophy (Cotecchia et al., 2015; O'Connell et al., 2014; Woodcock et al., 2008). Interestingly, in addition to this canonical signalling pathway, there is evidence indicating that α_1-adrenoceptors are also present in cardiomyocyte nuclei, from where they signal likely through Gq, phospholipase Cβ, inositol trisphosphate, and calcium to induce hypertrophy (Dahl et al., 2018; O'Connell et al., 2014; Wu & O'Connell, 2015). This is an interesting new paradigm that might have important physiological and pharmacological implications, including ligand transport into the cells, ligand lipophilicity, and the possible roles of transporters (O'Connell et al., 2014).

Surprisingly, the activation of α_1-adrenoceptors appears to be beneficial for some cardiac conditions. This sounds counterintuitive and, in fact, runs contrary to some relatively recent medical ideas. Agonists of α_1-adrenoceptors ameliorate ischaemia reperfusion injury, chemotherapy-induced cardiotoxicity, and calcium overload, among other noxious events or drugs (reviewed in Jensen, O'Connell, & Simpson, 2011; Perez & Doze, 2011). Similarly, experimental and clinical trial data have suggested that α_1-adrenoceptor antagonists might worsen some cases of heart failure (Jensen et al., 2011). It has been suggested that α_1-adrenoceptor agonists could provide cardioprotection (Jensen et al., 2011; Perez & Doze, 2011), particularly those selective for the α_{1A} subtype (Cowley et al., 2017). Consistent with this, in transgenic mice adrenergic-induced ischaemic-preconditioning is mediated by α1A- adrenoceptors (Perez & Doze, 2011).

3.3 | α_1-Adrenoceptors in the genitourinary system: Ureter, urinary bladder, urethra, and prostate

Benign prostatic hyperplasia (BPH), an enlarged prostate frequently accompanied by lower urinary tract symptoms, such as acute urine retention, is very common in men 40 years old and older. The prostate expresses α_1-adrenoceptors, predominantly the α_{1A} subtype (Price et al., 1993; Faure, Pimoule, Vallancien, Langer, & Graham, 1994) and this subtype mediates prostate contraction (Forray et al., 1994), and the enlarged prostate compresses the urethra leading to difficulties in micturition. **Tamsulosin**, the first α_{1A}- adrenoceptor selective drug used to alleviate the symptoms of BPH, was a major step in improving the pharmacological treatment of patients. This and related drugs are recommended as first-line treatments for patients with BPH by medical associations (McVary et al., 2011; Oelke et al., 2013). Although most of the patients have a good clinical response, others require additional treatments. Among those are the use of **5-α-reductase** inhibitors and antagonists of other receptors, which could be involved in the pathogenesis of the disease and its symptoms, such as α_{1D}- adrenoceptors and **5-HT receptors** (McVary et al., 2011; Oelke et al., 2013). The development of drugs with selectivity for several of these receptors is in progress (see Chagas-Silva et al., 2014; Nascimento-Viana et al., 2016).

All three α_1-adrenoceptors are present in the human ureter, albeit the α_{1A}- and α_{1D}- adrenoceptors seem to be more abundant than the α_{1B}-subtype (Sigala et al., 2005). This forms the basis for one of the

several off-label uses of **prazosin** and other α_1-adrenoceptor antagonists in facilitating stone expulsion in urolithiasis through the relaxation of the ureter smooth muscle.

α_1- Adrenoceptors are expressed in both the bladder and urethra from different species and are described to be involved in dysfunctions of these organs (Alexandre et al., 2017; Michel & Vrydag, 2006). Phenylephrine contracts the bladder neck, indicating that the control of the tonus of this region involves activation of α_1-adrenoceptors (Michel & Vrydag, 2006). A recent study showed that male and female proximal urethra from mice and marmoset present striking differences in the presence of α_1-adrenoceptor subtypes, indicating that urinary retention might involve different mechanisms depending on gender (Alexandre et al., 2017). Although α_{1A}-adrenoceptors seem to be the main functional subtype in both genders, the contractions in response to phenylephrine are more vigorous in male, compared with those in female, urethra.

3.4 | α_1-Adrenoceptors in the genitourinary system: Epididymis, vas deferens, and seminal vesicle

From a biological and evolutionary perspective, α_1-adrenoceptors in the reproductive system are essential for male fertility and therefore for the existence of a species. Knocking out both α_{1A}- adrenoceptors and **P2X1** purinoceptors in male mice leads to complete infertility (White et al., 2013). During the emission phase of ejaculation, sympathetically released noradrenaline and **ATP** produce forceful contractions of the epididymis, vas deferens, seminal vesicles, urethra, and prostate, propelling the semen towards the urethral meatus. The complete infertility of the α_{1A}- P2X1 knockout mice results from the lack of contractility of these organs, as sperm collected from the epididymis still fertilizes ova in vitro. The key role for α_{1A}- adrenoceptors in reproduction is also demonstrated by the fact that the knockout of either α_{1B}- or α_{1D}-adrenoceptors has no effect on male fertility (Cavalli et al., 1997; Sanbe et al., 2007; Tanoue, Koshimizu, & Tsujimoto, 2002). On the other hand, knocking out only the α_{1A}-adrenoceptors reduces the fertility rate by 50%, whereas the triple α_1-adrenoceptor knockout male mice are infertile (Sanbe et al., 2007).

Transcripts encoding all three α_1-adrenoceptors have been found in organs of the male reproductive tract from rodents and humans, albeit in different proportions with relatively similar levels for α_{1A}- and α_{1D}- but lower levels for α_{1B}-adrenoceptors (Avellar, Lazari, & Porto, 2009; Burt, Chapple, & Marshall, 1995; Mendes, Hamamura, Queiroz, Porto, & Avellar, 2004; Pacini, Castilho, Hebeler-Barbosa, Pupo, & Kiguti, 2018; Pupo, 1998; Queiroz, Mendes, Porto, & Avellar, 2002; Silva, Megale, Avellar, & Porto, 1999; Yono et al., 2012). However, in isolated tissue preparations, the contractions of these organs in response to α_1-adrenoceptor agonists are often described as mediated by the α_{1A}-subtype (Avellar et al., 2009; Burt et al., 1995; Mendes et al., 2004; Pacini et al., 2018; Pupo, 1998; Silva et al., 1999; Yono et al., 2012). Importantly, the contractions of the mouse and rat vas deferens in response to electrical field stimulation have been described to involve α_{1D}- adrenoceptors, and at least in the mouse vas deferens, these receptors seem to play a role in contractions to exogenous noradrenaline (Bexis et al., 2008; Cleary, Slattery, Bexis, & Docherty, 2004; Mallard, Marshall, Sithers, & Spriggs, 1992). Therefore, it has been proposed that the α_{1A}- and α_{1D}- adrenoceptors are differentially located in relation to the sympathetic neuro-effector junction in the vas deferens, where the latter is more readily accessed by noradrenaline released from sympathetic nerve terminals than the former (Docherty, 2010).

3.5 | α_1- Adrenoceptors in the CNS

α_1- Adrenoceptors are the most abundant adrenoceptors in the CNS. However, knowledge on their localization and function has been hampered by the lack of subtype-selective antibodies, selective ligands with good brain barrier permeability, and the intrinsic complexity of brain functions. Despite these difficulties, significant knowledge has been gained with the use of genetically engineered mice (Koshimizu, Tanoue, & Tsujimoto, 2007; Perez & Doze, 2011; Tanoue et al., 2002, 2003; Zuscik et al., 2000). Studies with α_{1B}-adrenoceptor knockout mice showed the involvement of this subtype in memory consolidation and fear-motivated exploratory activity (Tanoue et al., 2002, 2003), whereas the overexpression of these receptors results in marked apoptotic neurodegeneration accompanied by locomotor impairment and seizures (Zuscik et al., 2000). Interestingly, the behavioural activation produced by **modafinil**, one of the most prescribed drugs for attention-deficit disorder and hyperactivity syndrome, is markedly attenuated in α_{1B}-adrenoceptor knockout mice, whereas in WT mice, this effect is blocked by **terazosin** (a non-selective α1-adrenoceptor antagonist) but not by **WB-4101** (selective α_{1A}-/α_{1D}-adrenoceptor antagonist) or **BMY-7378** (selective α_{1D}- adrenoceptor antagonist; Stone, Cotecchia, Lin, & Quartermain, 2002). These findings implicate the α_{1B}-adrenoceptors in the mechanism of action of modafinil. Changes in the seizure thresholds to chemoconvulsants have also been observed in mice expressing constitutively active α_{1A}- or α_{1B}-adrenoceptors (Perez & Doze, 2011). Alterations in cognitive functions have also been detected in α_{1A}- adrenoceptor knockout mice, whereas chronic stimulation of α_{1A}- adrenoceptors increases neurogenesis, enhances learning and memory, and improves the mood (reviewed in Perez & Doze, 2011). It has been suggested that the brain α_1-adrenergic system could be altered in depression (Stone, Lin, Rosengarten, Kramer, & Quartermain, 2003) and post-traumatic stress disorder (Roepke et al., 2017).

4 | REGULATION OF α_1-ADRENOCEPTORS BY PHOSPHORYLATION

Protein phosphorylation is among the major regulators of cell function. Initially discovered as a process that modulates glycogen metabolism, it later became clear that protein phosphorylation/dephosphorylation cycles regulate essentially all major life processes in cells, including overall metabolism, cell cycle, secretion and motility (see historical perspective in Cohen, 2002).

The α_1-adrenoceptors are phosphorylated, and this is a key regulatory process for these receptors (Cotecchia et al., 2004; Cotecchia, Scheer, Diviani, Fanelli, & De Benedetti, 1998; García-Sáinz et al., 2000; Vázquez-Prado, Casas-González, & García-Sáinz, 2003). The activation of PKC in rat hepatocytes blocked or desensitized α_1-adrenoceptor activity, suggesting that the receptor activity could be regulated by phosphorylation (Corvera & García-Sáinz, 1984). Receptor phosphorylation was later experimentally shown using DDT1-MF-2 cells, a hamster smooth muscle cell line (Leeb-Lundberg et al., 1985) that, like the rat hepatocytes, expresses the α_{1B} subtype. It is now known that α_{1B}-adrenoceptors are phosphorylated in response to α_1-adrenoceptor agonists and to a large variety of other agonists that act through different receptors, including GPCRs, **receptor tyrosine kinases**, **receptors with serine/threonine kinase activity** (**TGF-β**), and **intracellular receptors** (see Cotecchia et al., 1998; Cotecchia et al., 2004; García-Sáinz et al., 2000; García-Sáinz, Romero-Ávila, & Alcántara-Hernández, 2011; Vázquez-Prado et al., 2003). Evidence that the other α_1-adrenoceptors are also phosphorylated was subsequently reported (García-Sáinz, Rodríguez-Pérez, & Romero-Ávila, 2004; García-Sáinz, Vázquez-Cuevas, & Romero-Ávila, 2001; Vazquez-Prado, Medina, Romero-Avila, Gonzalez-Espinosa, & Garcia-Sainz, 2000).

Figure 3 illustrates the substrates for phosphorylation (serine/threonine residues; large red, yellow, and blue circles) in the intracellular domains of the three human α_1-adrenoceptor subtypes identified by mutagenesis and functional analysis (Diviani et al., 1996; Lattion, Diviani, & Cotecchia, 1994) or through MS and functional work (Alcantara-Hernandez et al., 2017; Alfonzo-Méndez, Carmona-Rosas, Hernández-Espinosa, Romero-Ávila, & García-Sáinz, 2018; Carmona-Rosas, Hernández-Espinosa, Alcántara-Hernández, Alfonzo-Méndez, & García-Sáinz, 2018).

The pioneer work of Diviani, Lattion, and Cotecchia (1997) and Lattion et al. (1994) showed that the key phosphorylation sites of the α_{1B}-adrenoceptor activated by adrenaline were located in the intracellular C-tail and correspond to five serines: three of them are substrates for GRKs and the remaining two for PKC (Figure 3).

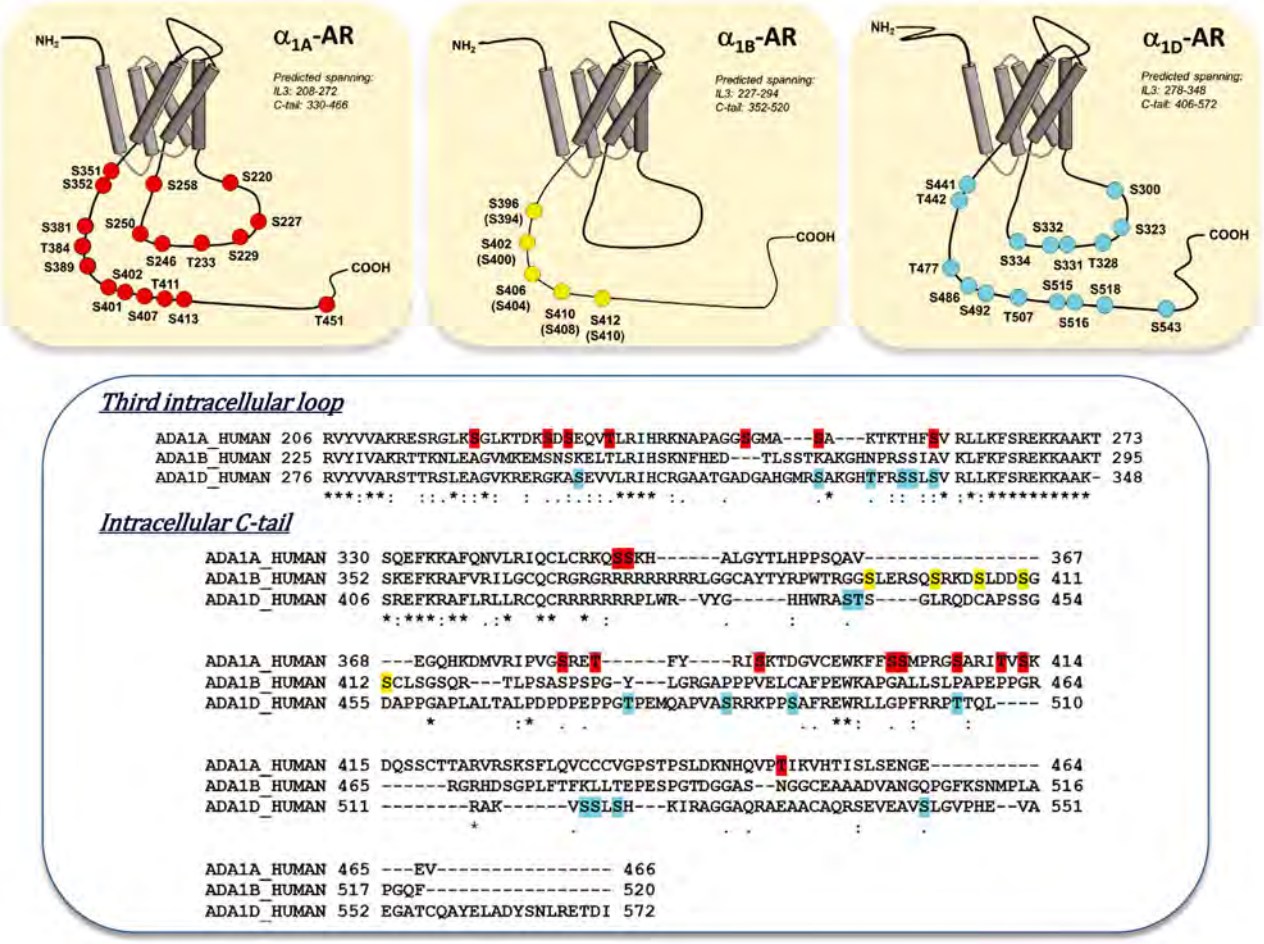

FIGURE 3 Schematic representation of the substrates for phosphorylation currently identified in the three human α_1-adrenoceptors (AR) subtypes (large red, yellow, and blue circles). Phosphorylated residues in the α_{1A}- and α_{1D}- adrenoceptors were identified by MS (Alcantara-Hernandez et al., 2017; Alfonzo-Méndez et al., 2018), whereas for the α_{1B}-adrenoceptor, the residues were identified by site-directed mutagenesis and functional analysis of the hamster orthologue (Diviani et al., 1997; in parenthesis are the sites defined for the hamster receptor). Below the diagram are the sequence alignments of the third intracellular loop and the carboxyl terminus (C-tail) of the three human α_1-adrenoceptor subtypes. Phosphorylated amino acids are marked in colour. Symbols: (a) "*" indicates single fully conserved residue; (b) ":" indicates conservative among subtypes; and (c) "." non-conservative among subtypes

However, truncation of the C-tail of the α_{1A}- (Price, Morris, Biswas, Smith, & Schwinn, 2002) and α_{1D}- adrenoceptor (Rodríguez-Pérez et al., 2009) rendered receptors that could be phosphorylated in response to agonists and PKC activation by phorbol esters, indicating the existence of phosphorylation sites in addition to those in the C-tail of these subtypes.

Considerable evidence indicates that the bulk and charge changes induced by receptor phosphorylation are not enough to explain the outcomes in signalling and cellular location. Therefore, it was hypothesized that the phosphorylation of specific residues results in a "barcode" pattern that in turn determines a receptor's fate (reviewed in Tobin, 2008; Tobin, Butcher, & Kong, 2008; see also Butcher et al., 2011). It has been proposed that the residues that are phosphorylated in a given receptor may change according to the cell type in which it is expressed, the type of stimulus to which such cells are subjected, and most importantly, the long-term response observed (Tobin, 2008; Tobin et al., 2008). This has markedly increased the interest in defining the phosphorylated sites and their functional importance. Considerable effort has been made during recent years to define this for a variety of receptors, mainly using partial affinity purification and MS (see some recent examples: Alfonzo-Méndez, Alcántara-Hernández, & García-Sáinz, 2017; Alvarez-Curto et al., 2016; Bouzo-Lorenzo et al., 2016; Bradley et al., 2016; Butcher et al., 2011; Butcher et al., 2014; Prihandoko et al., 2016; Zindel et al., 2016).

The phosphorylation sites of α_{1A}- and α_{1D}-adrenoceptors were only recently identifed (Alcantara-Hernandez et al., 2017;Alfonzo-Méndez et al., 2018;Carmona-Rosas et al., 2018). These adrenoceptors are phosphorylated in both the third intracellular loop and C-tail. Figure 3 illustrates the residues phosphorylated under baseline conditions and after stimulation by agonists or phorbol ester. The large number of phosphorylated residues (18 in α_{1A}- and 16 in α_{1D}-subtypes) and their distribution impose a considerable challenge to define their biological significance. For α_{1A}- adrenoceptors, there were differences in the phosphorylation patterns induced by noradrenaline and oxymetazoline (Alcantara-Hernandez et al., 2017). Not surprisingly, in silico analysis indicated the possible roles for GRK and PKC isoforms, but other kinases may also be involved (Alcantara-Hernandez et al., 2017; Alfonzo-Méndez et al., 2018). It is interesting that the phosphorylation sites detected for the α_1-adrenoceptor subtypes are not conserved among them and in only a few cases are the sites are conserved between two subtypes (α_{1A} S250/α_{1D} S323; α_{1A} S258/α_{1D} S334; α_{1A} S407/α_{1D} T507; see Figure 3).

In recombinant systems, α_{1D}- adrenoceptors are mainly misfolded or unable to undergo proper ligand binding and intracellularly located due to a motif present within the first N-terminal 79 amino acids of the receptor (Hague, Chen, et al., 2004; Hague, Uberti, et al., 2004; Pupo, Uberti, & Minneman, 2003). Recent evidence has indicated that N-terminal proteolysis of the α_{1D}- adrenoceptors could be an endogenous mechanism for proper plasma membrane expression (Kountz et al., 2016). To increase membrane expression of this receptor, we used N-terminally truncated receptors with additional mutations in the third intracellular loop and C-tail to gain insights on the phosphorylated residues. Among the major findings are the following: noradrenaline increased the intracellular calcium in cells expressing C-tail truncated α_{1D}- adrenoceptors to a similar extent as that seen in cells expressing these receptors with an intact C-tail (Alfonzo-Méndez et al., 2016; Alfonzo-Méndez et al., 2018). In contrast, α_{1D}- adrenoceptors in which the phosphorylated residues in the third intracellular loop were replaced by non-phosphorylatable amino acids presented a markedly decreased calcium response to noradrenaline (Alfonzo-Méndez et al., 2018). The data indicated that the third loop is important for signalling through G-protein coupling, as proposed for many GPCRs, and raises the possibility that phosphorylation of these residues might be important for receptor G-protein activation. The possibility that the C-tail could also participate in calcium signalling was not discarded, because in cells expressing C-tail-truncated α_{1D}- adrenoceptors with the third intracellular loop mutated, the calcium response to noradrenaline was decreased even further (Alfonzo-Méndez et al., 2018; Carmona-Rosas et al., 2018). ERK 1/2 phosphorylation in cells expressing these mutants was also studied. In cells expressing the control receptor, noradrenaline induced a rapid ERK 1/2 phosphorylation that decreased at 30 and 60 min, whereas in cells with the different mutants, the response was also rapid but either decreased much more slowly or remained elevated during the entire 60 min (Alfonzo-Méndez et al., 2018; Carmona-Rosas et al., 2018). This indicates that some of the phosphorylated residues, in both the third intracellular loop and C-tail, might participate in turning off the signal in the MAPK pathway (Alfonzo-Méndez et al., 2018; Carmona-Rosas et al., 2018).

An important additional finding was that although C-tail-truncated α_{1D}- adrenoceptors were able to mobilize calcium in response to noradrenaline, they were mainly detected in intracellular vesicles, and only a minor fraction was detected at the plasma membrane (Alfonzo-Méndez et al., 2016; Alfonzo-Méndez et al., 2018; Carmona-Rosas et al., 2018). The mutation of a motif in the C-tail of the α_{1D}- adrenoceptors which interacts with the post synaptic density protein (PSD95)/drosophila disc large tumour suppressor/zonula occludens-1 protein domain of syntrophins markedly decreased these receptorsat the plasma membrane (Chen, Hague, Hall, & Minneman, 2006). Furthermore, it has been observed that the knockout of syntrophins results in the loss of α_{1D}-adrenoceptor function in mouse aortic smooth muscle cells and the block of α_{1D}- adrenoceptor-mediated increases in BP in mice (Lyssand et al., 2008). These data support a role for the C-tail of the α_{1D}- adrenoceptors, not only in post-transcriptional regulation by phosphorylation but also in proper receptor insertion in the membrane.

5 | ASSOCIATION OF α_1-ADRENOCEPTORS WITH RAB PROTEINS

GPCRs are synthesized and properly folded in the rough endoplasmic reticulum, from where they reach the plasma membrane via intracellular traffic (anterograde transport). GPCRs are transported to the intracellular compartment (retrograde transport) and recycled back to the plasma membrane through constitutive and signal-triggered internalization and externalization processes. These latter events can take

place several times until the GPCRs are degraded in the lysosome or proteasome. Therefore, interaction with proteins that govern traffic is critical, and the signatures that define receptors' destinations are far from completely known. **Rab proteins** are among the master modulators of vesicular traffic. These comprise a large family of more than 60 monomeric GTPases that favour docking, fusion, cargo exchange, and vesicle transport along the cytoskeleton through interactions with the cytoplasmic face of vesicles with the aid of molecular motors (Hutagalung & Novick, 2011; Schwartz, Cao, Pylypenko, Rak, & Wandinger-Ness, 2007; Stenmark, 2009; Zerial & McBride, 2001).

Anterograde GPCR traffic has been studied by several groups, particularly that of Wang, Wei, and Wu (2018) and Wang and Wu (2012). Rab1, 2, and 6 modulate GPCR transit from the endoplasmic reticulum to the Golgi, whereas Rab8 and some ARF GTPases regulate the transfer to the plasma membrane (Wang et al., 2018; Wang & Wu, 2012). The anterograde traffic of α_1-adrenoceptors has also been studied, and it has been observed that the attenuation of Rab1 function inhibits the transit of α_{1A}- and α_{1B}-adrenoceptors to the plasma membrane, whereas augmented Raf1 function increases transit (Filipeanu, Zhou, Fugetta, & Wu, 2006; Wang & Wu, 2012). In addition, the overexpression of Rab1 selectively enhances ERK 1/2 activation and leads to cardiomyocyte hypertrophy in response to phenylephrine (Filipeanu et al., 2006).

To the best of our knowledge, the role of Rab proteins in the retrograde transport of α_{1B}-adrenoceptors was only recently reported. Agonist-activated α_{1B}-adrenoceptors (associated with homologous desensitization) mainly interacted with proteins present in early endosomes, such as early endosome antigen 1, Rab5, Rab4, and Rab11, but not with the late endosome markers Rab9 and Rab7 (Alfonzo-Méndez et al., 2017; Castillo-Badillo et al., 2015). In contrast, the activation of other receptors (such as sphingosine 1-phosphate receptors) or direct activation of PKC by phorbol esters (heterologous desensitization) induced a brief α_{1B}-adrenoceptor–Rab5 interaction, a more pronounced and sustained one with Rab9, and some interaction with Rab7 (Alfonzo-Méndez, Hernández-Espinosa, et al., 2017; Castillo-Badillo et al., 2015). It is worth mentioning that the action of **sphingosine-1-phosphate** on the phosphorylation/desensitization/internalization of α_{1B}-adrenoceptors mainly depended on the activation of PKC (Alfonzo-Méndez, Hernández-Espinosa, et al., 2017). These data suggested that agonist-activated α_{1B}-adrenoceptors undergo rapid internalization and recycling back to the plasma membrane, whereas heterologous desensitization was associated with a slower recycling pathway. However, preliminary work with non-adrenergic receptors indicates that although some similarities might exist with internalization and Rab protein association to other GPCRs, the findings with the α_{1B}-adrenoceptors cannot be generalized; in fact, different Rab protein association was observed using different agonists for the same receptor (García-Sáinz et al., 2016 unpublished observations). A major question arises from these observations regarding the nature of the "signal" or "tag" that defines the immediate destiny of a given receptor, that is, is the receptor interaction with a given Rab protein defined by conformational changes induced by the distinct ligands, by covalent (receptor phosphorylation, palmitoylation, or other) or non-covalent modifications, or by all of these? Our current hypothesis is that the so-called phosphorylation "barcode" (Tobin, 2008; Tobin et al., 2008) could be a major participant.

6 | DESENSITIZATION AND INTERNALIZATION OF α_1-ADRENOCEPTORS

Receptor desensitization, a decreased cell responsiveness to agonists, has been operationally divided into homologous and heterologous types. In homologous desensitization, the decreased responsiveness results from the previous activation of the same receptor affected, whereas in heterologous desensitization, the decreased responsiveness is not limited to the previously activated receptor type and may result from the activation of protein kinases and other molecular entities. The present review emphasizes the mechanisms involved in the homologous desensitization of α_1-adrenoceptors.

The interaction of α_1-adrenoceptors with proteins such as β-arrrestins and other molecular entities during these processes has been reported, and readers are directed to those publications (Cotecchia, Stanasila, & Diviani, 2012; Perez-Aso et al., 2013; Segura et al., 2013; Stanasila, Abuin, Dey, & Cotecchia, 2008).

There are significant differences in the degrees of desensitization and in the kinetics of internalization among the α_1-adrenoceptors. Studies comparing the internalization of these receptors in the same cellular background have shown that α_{1B}- and α_{1D}- adrenoceptors activated by noradrenaline, adrenaline, or phenylephrine internalize at a much faster rate than the α_{1A}- adrenoceptors (Cabrera-Wrooman, Romero-Avila, & Garcia-Sainz, 2010; Chalothorn et al., 2002; Stanasila et al., 2008; Wang et al., 2007). Conversely, the α_{1A}- adrenoceptors were much more resistant to desensitization induced by noradrenaline or phorbol ester than were the α_{1B}- and α_{1D}- adrenoceptors (Cabrera-Wrooman et al., 2010; Vazquez-Prado et al., 2000; Vazquez-Prado & Garcia-Sainz, 1996). Therefore, the general view is that the α_{1A}- adrenoceptors are less tightly regulated than the other two subtypes (Cotecchia, 2010).

More recent studies have shown that the α_{1A}- adrenoceptors can indeed undergo fast desensitization and internalization, but this depends on the agonist activating the receptor. In HEK293 cells, α_{1A}-adrenoceptors activated by oxymetazoline internalized at a much faster rate (~5 min) than when activated by noradrenaline (>45 min; Akinaga et al., 2013). Moreover, there was significant tachyphylaxis in the contractions of smooth muscles in response to oxymetazoline, whereas no tachyphylaxis was observed for noradrenaline. In addition, short exposures of cells or tissues to oxymetazoline (5 min) reduced the potency of noradrenaline in a subsequent exposure (Akinaga et al., 2013; Alcantara-Hernandez et al., 2017). The phosphorylation and faster desensitization/internalization of the α_{1A}- adrenoceptors activated by oxymetazoline largely depended on GRK2, whereas the phosphorylation and slower desensitization/internalization produced by noradrenaline depended on PKCα. In LNCap cells, the co-localization and co-immunoprecipitation of α_{1A}- adrenoceptors and β-arrestin produced by oxymetazoline was as strong as those produced by noradrenaline, despite the weak partial agonism of oxymetazoline for Ca^{2+} mobilization (Alcantara-Hernandez et al., 2017). Strikingly, oxymetazoline was more efficacious and potent than noradrenaline

for the phosphorylation of ERK 1/2 in LNCap cells but differed from what was observed in HEK293 cells (da Silva Junior et al., 2017). The superagonism of oxymetazoline for the ERK pathway in LNCap cells was unrelated to 5-HT receptor activation and was antagonized by prazosin (Alcantara-Hernandez et al., 2017). One of the most accentuated manifestations of biased agonism is the reversal in the order of potencies and/or efficacies for agonists in the production of different effects mediated by a receptor (Kenakin & Christopoulos, 2013; Pupo et al., 2016). This is a clear example of efficacy reversal and therefore of the biased agonism for oxymetazoline towards the ERK pathway versus Ca^{2+} mobilization at the α_{1A}- adrenoceptors.

Analysis of the phosphorylated α_{1A}- adrenoceptors activated by oxymetazoline and noradrenaline in LNCap cells revealed that two residues located in the C-tail (S381 and T384; see Figure 3) were exclusively phosphorylated when the receptor was activated by oxymetazoline, implicating this region in the differential effects of these two agonists (Alcantara-Hernandez et al., 2017). On the other hand, there were residues that were exclusively phosphorylated when the α_{1A}- adrenoceptors were activated by noradrenaline (S220 and S229), and these are in the beginning of the third intracellular loop. Therefore, depending on the agonist, clearly distinct phosphorylation barcodes are formed in these adrenoceptors.

The understanding of the phosphorylation barcoding produced by different ligands and their functional repercussions may provide the rationale for the development of α_1-adrenoceptor ligands more suited to some needed therapeutic purposes, such as less tachyphylactic ligands for more sustained rises in BP for the treatment of shock or vasoconstrictors without rebound effects.

7 | CONCLUDING REMARKS

In these nearly 45 years since the pharmacological separation of α_1-adrenoceptors from the α_2-adrenoceptors (Dubocovich & Langer, 1974; Langer, 1974; Starke, Montel, Gayk, & Merker, 1974) and 30 years after the cloning of the first α_1-adrenoceptor (the hamster α_{1B}-adrenoceptor; Cotecchia et al., 1988; for a historical perspective, see Langer, 1999), considerable progress has been made towards the understanding of the physiological roles of the α_1-adrenoceptor subtypes and their recognition as well as regulation by drugs. This knowledge translated into a few drugs that are safe and efficacious; the most relevant of them in our opinion being the so-called α-blockers for BPH and other micturition dysfunctions, which benefit a large proportion of the human population at some point in their lives.

The array of functions controlled by α_1-adrenoceptors has not been completely covered in this review, but enough has been presented to demonstrate the immense potential of these subtypes for innovative pharmacological interventions. The discoveries during the past two decades showing that drugs do not fit into simple agonist or antagonist categories and that receptors can regulate multiple signalling pathways further encourage the search for new drugs that target the α_1-adrenoceptor subtypes for new therapeutic purposes. For the success of this endeavour, continuous effort and sharp pharmacological reasoning are essential.

7.1 | Nomenclature of targets and ligands

Key protein targets and ligands in this article are hyperlinked to corresponding entries in http://www.guidetopharmacology.org, the common portal for data from the IUPHAR/BPS Guide to PHARMACOLOGY (Harding et al., 2018), and are permanently archived in the Concise Guide to PHARMACOLOGY 2017/18 (Alexander, S. P. H., Christopoulos et al., 2017; Alexander, Cidlowski et al., 2017; Alexander, Fabbro et al., 2017; Alexander, Peters et al., 2017).

ACKNOWLEDGEMENTS

Research in JAG's laboratory is supported by Grants from Consejo Nacional de Ciencia y Tecnología (CONACYT) [Grant 253156 and FDC-882] and Dirección General de Personal Académico-UNAM [PAPIIT, Grant IN200915]. This study was financed in part by the Coordenação de Aperfeiçoamento de Pessoal de Nível Superior – Brasil (CAPES) – 23038.007773/2014-07, as J.A. received a CAPES Drug Discovery fellowship and during the preparation of this review was at the University of Nottingham, UK. Research in ASP's laboratory is supported by Grants from Fundação de Amparo à Pesquisa do Estado de São Paulo – FAPESP [2008/50423-7 and 2017/15175-1]. The authors are thankful to Dr. Vanessa Lima for kindly providing Figure 1.

CONFLICT OF INTEREST

The authors declare no conflicts of interest

ORCID

Juliana Akinaga https://orcid.org/0000-0002-5235-0657
J. Adolfo García-Sáinz http://orcid.org/0000-0002-5235-0657
André S. Pupo https://orcid.org/0000-0001-6627-3448

REFERENCES

Akinaga, J., Lima, V., Kiguti, L. R., Hebeler-Barbosa, F., Alcantara-Hernandez, R., Garcia-Sainz, J. A., & Pupo, A. S. (2013). Differential phosphorylation, desensitization, and internalization of α1A-adrenoceptors activated by norepinephrine and oxymetazoline. *Molecular Pharmacology*, *83*(4), 870–881. https://doi.org/10.1124/mol.112.082313

Alcantara-Hernandez, R., Hernandez-Mendez, A., Romero-Avila, M. T., Alfonzo-Mendez, M. A., Pupo, A. S., & Garcia-Sainz, J. A. (2017). Noradrenaline, oxymetazoline and phorbol myristate acetate induce distinct functional actions and phosphorylation patterns of α_{1A}-adrenergic receptors. *Biochimica et Biophysica Acta*, *1864*(12), 2378–2388. https://doi.org/10.1016/j.bbamcr.2017.09.002

Alexander, S. P. H., Christopoulos, A., Davenport, A. P., Kelly, E., Marrion, N. V., Peters, J. A., … CGTP Collaborators (2017). The Concise Guide to PHARMACOLOGY 2017/18: G protein-coupled receptors. *British Journal of Pharmacology*, *174*, S17–S129. https://doi.org/10.1111/bph.13878

Alexander, S. P. H., Cidlowski, J. A., Kelly, E., Marrion, N. V., Peters, J. A., Faccenda, E., … CGTP Collaborators (2017). The Concise Guide to PHARMACOLOGY 2017/18: Nuclear hormone receptors. *British Journal of Pharmacology*, *174*, S208–S224. https://doi.org/10.1111/bph.13880

Alexander, S. P. H., Fabbro, D., Kelly, E., Marrion, N. V., Peters, J. A., Faccenda, E., … CGTP Collaborators (2017). The Concise Guide to PHARMACOLOGY 2017/18: Enzymes. *British Journal of Pharmacology*, *174*, S272–S359. https://doi.org/10.1111/bph.13877

Alexander, S. P. H., Peters, J. A., Kelly, E., Marrion, N. V., Faccenda, E., Harding, S. D., … CGTP Collaborators (2017). The Concise Guide to PHARMACOLOGY 2017/18: Ligand-gated ion channels. *British Journal of Pharmacology*, *174*, S130–S159.

Alexandre, E. C., de Oliveira, M. G., Campos, R., Kiguti, L. R., Calmasini, F. B., Silva, F. H., … Antunes, E. (2017). How important is the α_1-adrenoceptor in primate and rodent proximal urethra? Sex differences in the contribution of α_1-adrenoceptor to urethral contractility. *American Journal of Physiology. Renal Physiology*, *312*(6), F1026–F1034. https://doi.org/10.1152/ajprenal.00013.2017

Alfonzo-Méndez, M. A., Alcántara-Hernández, R., & García-Sáinz, J. A. (2017). Novel structural approaches to study GPCR regulation. *International Journal of Molecular Sciences*, *18*, 27.

Alfonzo-Méndez, M. A., Carmona-Rosas, G., Hernández-Espinosa, D. A., Romero-Ávila, M. T., & García-Sáinz, J. A. (2018). Different phosphorylation patterns regulate α_{1D}-adrenoceptor signaling and desensitization. *Biochimica et Biophysica Acta*, *1865*(6), 842–854.

Alfonzo-Méndez, M. A., Castillo-Badillo, J. A., Romero-Ávila, M. T., Rivera, R., Chun, J., & García-Sáinz, J. A. (2016). Carboxyl terminus-truncated α_{1D}-adrenoceptors inhibit the ERK pathway. *Naunyn-Schmiedeberg's Archives of Pharmacology*, *389*(8), 911–920.

Alfonzo-Méndez, M. A., Hernández-Espinosa, D. A., Carmona-Rosas, G., Romero-Ávila, M. T., Reyes-Cruz, G., & García-Sáinz, J. A. (2017). Protein kinase C activation promotes α_{1B}-adrenoceptor internalization and late endosome trafficking through Rab9 interaction. Role in heterologous desensitization. *Molecular Pharmacology*, *91*(4), 296–306.

Alvarez-Curto, E., Inoue, A., Jenkins, L., Raihan, S. Z., Prihandoko, R., Tobin, A. B., & Milligan, G. (2016). Targeted elimination of G proteins and arrestins defines their specific contributions to both intensity and duration of G protein-coupled receptor signaling. *The Journal of Biological Chemistry*, *291*(53), 27147–27159. https://doi.org/10.1074/jbc.M116.754887

Arce, C., Vicente, D., Segura, V., Flacco, N., Monto, F., Almenar, L., … Ivorra, M. D. (2017). Activation of alpha1A-adrenoceptors desensitizes the rat aorta response to phenylephrine through a neuronal NOS pathway, a mechanism lost with ageing. *British Journal of Pharmacology*, *174*(13), 2015–2030. https://doi.org/10.1111/bph.13800

Arevalo-Leon, L. E., Gallardo-Ortiz, I. A., Urquiza-Marin, H., & Villalobos-Molina, R. (2003). Evidence for the role of alpha1D- and alpha1A-adrenoceptors in contraction of the rat mesenteric artery. *Vascular Pharmacology*, *40*(2), 91–96. https://doi.org/10.1016/S1537-1891(02)00336-1

Avellar, M. C., Lazari, M. F., & Porto, C. S. (2009). Expression and function of G-protein-coupled receptors in the male reproductive tract. *Anais da Academia Brasileira de Ciências*, *81*(3), 321–344. https://doi.org/10.1590/S0001-37652009000300002

Bexis, S., Cleary, L., McGrath, J. C., Tanoue, A., Tsujimoto, G., & Docherty, J. R. (2008). Alpha(1D)-adrenoceptors mediate nerve and agonist-evoked contractions in mouse vas deferens: Evidence obtained from knockout technology. *Autonomic & Autacoid Pharmacology*, *28*(2–3), 81–85. https://doi.org/10.1111/j.1474-8673.2008.00420.x

Bouzo-Lorenzo, M., Santo-Zas, I., Lodeiro, M., Nogueiras, R., Casanueva, F. F., Castro, M., … Camiña, J. P. (2016). Distinct phosphorylation sites on the ghrelin receptor, GHSR1a, establish a code that determines the functions of ss-arrestins. *Scientific Reports*, *6*, 22495.

Bradley, S. J., Wiegman, C. H., Iglesias, M. M., Kong, K. C., Butcher, A. J., Plouffe, B., … Tobin, A. B. (2016). Mapping physiological G protein-coupled receptor signaling pathways reveals a role for receptor phosphorylation in airway contraction. *Proceedings of the National Academy of Sciences of the United States of America*, *113*(16), 4524–4529. https://doi.org/10.1073/pnas.1521706113

Bulloch, J. M., & Daly, C. J. (2014). Autonomic nerves and perivascular fat: Interactive mechanisms. *Pharmacology & Therapeutics*, *143*(1), 61–73.

Burt, R. P., Chapple, C. R., & Marshall, I. (1995). Evidence for a functional alpha 1A-(alpha 1C-) adrenoceptor mediating contraction of the rat epididymal vas deferens and an alpha 1B-adrenoceptor mediating contraction of the rat spleen. *British Journal of Pharmacology*, *115*(3), 467–475.

Butcher, A. J., Hudson, B. D., Shimpukade, B., Alvarez-Curto, E., Prihandoko, R., Ulven, T., … Tobin, A. B. (2014). Concomitant action of structural elements and receptor phosphorylation determine arrestin-3 interaction with the free fatty acid receptor FFA4. *The Journal of Biological Chemistry*, *289*(26), 18451–18465. https://doi.org/10.1074/jbc.M114.568816

Butcher, A. J., Prihandoko, R., Kong, K. C., McWilliams, P., Edwards, J. M., Bottrill, A., … Tobin, A. B. (2011). Differential G-protein-coupled receptor phosphorylation provides evidence for a signaling bar code. *The Journal of Biological Chemistry*, *286*(13), 11506–11518. https://doi.org/10.1074/jbc.M110.154526

Cabrera-Wrooman, A., Romero-Avila, M. T., & Garcia-Sainz, J. A. (2010). Roles of the alpha1A-adrenergic receptor carboxyl tail in protein kinase C-induced phosphorylation and desensitization. *Naunyn-Schmiedeberg's Archives of Pharmacology*, *382*(5–6), 499–510. https://doi.org/10.1007/s00210-010-0569-7

Carmona-Rosas, G., Hernández-Espinosa, D. A., Alcántara-Hernández, R., Alfonzo-Méndez, M. A., & García-Sáinz, J. A. (2018). Distinct phosphorylation sites/clusters in the carboxyl terminus regulate α_{1D}-adrenergic receptor subcellular localization and signaling. *Cellular Signalling*, *53*, 374–389.

Castillo-Badillo, J. A., Sánchez-Reyes, O. B., Alfonzo-Méndez, M. A., Romero-Ávila, M. T., Reyes-Cruz, G., & García-Sáinz, J. A. (2015). α1B-Adrenergic receptors differentially associate with Rab proteins during homologous and heterologous desensitization. *PLoS ONE*, *10*(3), e0121165. https://doi.org/10.1371/journal.pone.0121165

Cavalli, A., Lattion, A. L., Hummler, E., Nenniger, M., Pedrazzini, T., Aubert, J. F., … Cotecchia, S. (1997). Decreased blood pressure response in mice deficient of the alpha1b-adrenergic receptor. *Proceedings of the National Academy of Sciences of the United States of America*, *94*(21), 11589–11594. https://doi.org/10.1073/pnas.94.21.11589

Chagas-Silva, F., Nascimento-Viana, J. B., Romeiro, L. A., Barberato, L. C., Noel, F., & Silva, C. L. (2014). Pharmacological characterization of N1-(2-methoxyphenyl)-N4-hexylpiperazine as a multi-target antagonist of α1A/α1D-adrenoceptors and 5-HT1A receptors that blocks prostate contraction and cell growth. *Naunyn-Schmiedeberg's Archives of Pharmacology*, *387*(3), 225–234. https://doi.org/10.1007/s00210-013-0935-3

Chalothorn, D., McCune, D. F., Edelmann, S. E., Garcia-Cazarin, M. L., Tsujimoto, G., & Piascik, M. T. (2002). Differences in the cellular localization and agonist-mediated internalization properties of the alpha(1)-adrenoceptor subtypes. *Molecular Pharmacology*, *61*(5), 1008–1016.

Chen, Z., Hague, C., Hall, R. A., & Minneman, K. P. (2006). Syntrophins regulate alpha1D-adrenergic receptors through a PDZ domain-mediated interaction. *The Journal of Biological Chemistry*, *281*(18), 12414–12420.

Cleary, L., Slattery, J., Bexis, S., & Docherty, J. R. (2004). Sympathectomy reveals alpha 1A- and alpha 1D-adrenoceptor components to contractions to noradrenaline in rat vas deferens. *British Journal of Pharmacology*, *143*(6), 745–752.

Cohen, P. (2002). The origins of protein phosphorylation. *Nature Cell Biology*, *4*(5), E127–E130.

Colling, K. P., Banton, K. L., & Beilman, G. J. (2018). Vasopressors in sepsis. *Surgical Infections*, *19*(2), 202–207. https://doi.org/10.1089/sur.2017.255

Corvera, S., & García-Sáinz, J. A. (1984). Phorbol esters inhibit alpha1 adrenergic stimulation of glycogenolysis in isolated rat hepatocytes. *Biochemical and Biophysical Research Communications*, *119*(3), 1128–1133. https://doi.org/10.1016/0006-291X(84)90892-1

Cotecchia, S. (2007). Constitutive activity and inverse agonism at the alpha1adrenoceptors. *Biochemical Pharmacology*, *73*(8), 1076–1083. https://doi.org/10.1016/j.bcp.2006.10.024

Cotecchia, S. (2010). The α1-adrenergic receptors: Diversity of signaling networks and regulation. *Journal of Receptor and Signal Transduction Research*, *30*(6), 410–419. https://doi.org/10.3109/10799893.2010.518152

Cotecchia, S., Del Vescovo, C. D., Colella, M., Caso, S., & Diviani, D. (2015). The alpha1-adrenergic receptors in cardiac hypertrophy: Signaling mechanisms and functional implications. *Cellular Signalling*, *27*(10), 1984–1993. https://doi.org/10.1016/j.cellsig.2015.06.009

Cotecchia, S., Scheer, A., Diviani, D., Fanelli, F., & De Benedetti, P. G. (1998). Molecular mechanisms involved in the activation and regulation of the alpha 1-adrenergic receptor subtypes. *Farmaco*, *53*(4), 273–277. https://doi.org/10.1016/S0014-827X(98)00021-4

Cotecchia, S., Schwinn, D. A., Randall, R. R., Lefkowitz, R. J., Caron, M. G., & Kobilka, B. K. (1988). Molecular cloning and expression of the cDNA for the hamster alpha 1-adrenergic receptor. *Proceedings of the National Academy of Sciences of the United States of America*, *85*(19), 7159–7163.

Cotecchia, S., Stanasila, L., & Diviani, D. (2012). Protein–protein interactions at the adrenergic receptors. *Current Drug Targets*, *13*(1), 15–27. https://doi.org/10.2174/138945012798868489

Cotecchia, S., Stanasila, L., Diviani, D., Bjorklof, K., Rossier, O., & Fanelli, F. (2004). Structural determinants involved in the activation and regulation of G protein-coupled receptors: Lessons from the alpha1-adrenegic receptor subtypes. *Biology of the Cell*, *96*(5), 327–333. https://doi.org/10.1111/j.1768-322X.2004.tb01422.x

Cowley, P. M., Wang, G., Joshi, S., Swigart, P. M., Lovett, D. H., Simpson, P. C., & Baker, A. J. (2017). α1A-Subtype adrenergic agonist therapy for the failing right ventricle. *American Journal of Physiology. Heart and Circulatory Physiology*, *313*(6), H1109–H1118. https://doi.org/10.1152/ajpheart.00153.2017

Dahl, E. F., Wu, S. C., Healy, C. L., Harsch, B. A., Shearer, G. C., & O'Connell, T. D. (2018). Subcellular compartmentalization of proximal Galphaq-receptor signaling produces unique hypertrophic phenotypes in adult cardiac myocytes. *The Journal of Biological Chemistry*, *293*(23), 8734–8749. https://doi.org/10.1074/jbc.RA118.002283

Daly, C. J., Deighan, C., McGee, A., Mennie, D., Ali, Z., McBride, M., & McGrath, J. C. (2002). A knockout approach indicates a minor vasoconstrictor role for vascular alpha1B-adrenoceptors in mouse. *Physiological Genomics*, *9*(2), 85–91. https://doi.org/10.1152/physiolgenomics.00065.2001

de Andrade, C. R., Fukada, S. Y., Olivon, V. C., de Godoy, M. A., Haddad, R., Eberlin, M. N., … de Oliveira, A. M. (2006). Alpha1D-adrenoceptor-induced relaxation on rat carotid artery is impaired during the endothelial dysfunction evoked in the early stages of hyperhomocysteinemia. *European Journal of Pharmacology*, *543*(1–3), 83–91.

Diviani, D., Lattion, A. L., & Cotecchia, S. (1997). Characterization of the phosphorylation sites involved in G protein-coupled receptor kinase- and protein kinase C-mediated desensitization of the alpha1B-adrenergic receptor. *The Journal of Biological Chemistry*, *272*(45), 28712–28719.

Diviani, D., Lattion, A. L., Larbi, N., Kunapuli, P., Pronin, A., Benovic, J. L., & Cotecchia, S. (1996). Effect of different G protein-coupled receptor kinases on phosphorylation and desensitization of the alpha1B-adrenergic receptor. *The Journal of Biological Chemistry*, *271*(9), 5049–5058.

Docherty, J. R. (2010). Subtypes of functional alpha1-adrenoceptor. *Cellular and Molecular Life Sciences: CMLS*, *67*(3), 405–417. https://doi.org/10.1007/s00018-009-0174-4

Dubocovich, M. L., & Langer, S. Z. (1974). Negative feed-back regulation of noradrenaline release by nerve stimulation in the perfused cat's spleen: Differences in potency of phenoxybenzamine in blocking the pre- and post-synaptic adrenergic receptors. *The Journal of Physiology*, *237*(3), 505–519.

Erami, C., Zhang, H., Ho, J. G., French, D. M., & Faber, J. E. (2002). Alpha(1)-adrenoceptor stimulation directly induces growth of vascular wall in vivo. *American Journal of Physiology. Heart and Circulatory Physiology*, *283*(4), H1577–H1587. https://doi.org/10.1152/ajpheart.00218.2002

Faber, J. E., Szymeczek, C. L., Cotecchia, S., Thomas, S. A., Tanoue, A., Tsujimoto, G., & Zhang, H. (2007). Alpha1-adrenoceptor-dependent vascular hypertrophy and remodeling in murine hypoxic pulmonary hypertension. *American Journal of Physiology. Heart and Circulatory Physiology*, *292*(5), H2316–H2323. https://doi.org/10.1152/ajpheart.00792.2006

Faure, C., Pimoule, C., Vallancien, G., Langer, S. Z., & Graham, D. (1994). Identification of alpha 1-adrenoceptor subtypes present in the human prostate. *Life Sciences*, *54*(21), 1595–1605. https://doi.org/10.1016/0024-3205(94)90031-0

Filipeanu, C. M., Zhou, F., Fugetta, E. K., & Wu, G. (2006). Differential regulation of the cell-surface targeting and function of beta- and alpha1-adrenergic receptors by Rab1 GTPase in cardiac myocytes. *Molecular Pharmacology*, *69*(5), 1571–1578. https://doi.org/10.1124/mol.105.019984

Filippi, S., Parenti, A., Donnini, S., Granger, H. J., Fazzini, A., & Ledda, F. (2001). Alpha(1D)-adrenoceptors cause endothelium-dependent vasodilatation in the rat mesenteric vascular bed. *The Journal of Pharmacology and Experimental Therapeutics*, *296*(3), 869–875.

Flacco, N., Pares, J., Serna, E., Segura, V., Vicente, D., Perez-Aso, M., … D'Ocon, P. (2013). Alpha1D-adrenoceptors are responsible for the high sensitivity and the slow time-course of noradrenaline-mediated contraction in conductance arteries. *Pharmacology Research & Perspectives*, *1*(1), e00001. https://doi.org/10.1002/prp2.1

Forray, C., Bard, J. A., Wetzel, J. M., Chiu, G., Shapiro, E., Tang, R., et al. (1994). The alpha 1-adrenergic receptor that mediates smooth muscle contraction in human prostate has the pharmacological properties of the cloned human alpha 1c subtype. *Molecular Pharmacology*, *45*(4), 703–708.

Fredriksson, R., Lagerstrom, M. C., Lundin, L. G., & Schioth, H. B. (2003). The G-protein-coupled receptors in the human genome form five main families. Phylogenetic analysis, paralogon groups, and fingerprints. *Molecular Pharmacology*, *63*(6), 1256–1272.

Fredriksson, R., & Schioth, H. B. (2005). The repertoire of G-protein-coupled receptors in fully sequenced genomes. *Molecular Pharmacology*, *67*(5), 1414–1425. https://doi.org/10.1124/mol.104.009001

Gallardo-Ortiz, I. A., Rodriguez-Hernandez, S. N., Lopez-Guerrero, J. J., Del Valle-Mondragon, L., Lopez-Sanchez, P., Touyz, R. M., & Villalobos-Molina, R. (2015). Role of alpha1D-adrenoceptors in vascular wall hypertrophy during angiotensin II-induced hypertension. *Autonomic & Autacoid Pharmacology*, *35*(3), 17–31. https://doi.org/10.1111/aap.12035

García-Sáinz, J. A., Rodríguez-Pérez, C. E., & Romero-Ávila, M. T. (2004). Human alpha-1D adrenoceptor phosphorylation and desensitization. *Biochemical Pharmacology*, *67*, 1853–1858.

García-Sáinz, J. A., Romero-Ávila, M. T., & Alcántara-Hernández, R. (2011). Mechanisms involved in alpha(1B)-adrenoceptor desensitization. *IUBMB Life*, *63*, 811–815. https://doi.org/10.1002/iub.519

García-Sáinz, J. A., & Torres-Padilla, M. E. (1999). Modulation of basal intracellular calcium by inverse agonists and phorbol myristate acetate in rat-1 fibroblasts stably expressing alpha1d-adrenoceptors. *FEBS Letters*, *443*(3), 277–281. https://doi.org/10.1016/S0014-5793(98)01738-4

García-Sáinz, J. A., Vázquez-Cuevas, F. G., & Romero-Ávila, M. T. (2001). Phosphorylation and desensitization of alpha1d-adrenergic receptors. *The Biochemical Journal*, *353*(Pt 3), 603–610.

García-Sáinz, J. A., Vázquez-Prado, J., & Medina, L. C. (2000). Alpha 1-adrenoceptors: Function and phosphorylation. *European Journal of Pharmacology*, *389*(1), 1–12.

Garcia-Sainz, J. A., Vazquez-Prado, J., & Villalobos-Molina, R. (1999). Alpha 1-adrenoceptors: Subtypes, signaling, and roles in health and disease. *Archives of Medical Research*, *30*(6), 449–458.

Geloen, A., Pichot, C., Leroy, S., Julien, C., Ghignone, M., May, C. N., & Quintin, L. (2015). Pressor response to noradrenaline in the setting of septic shock: Anything new under the sun-dexmedetomidine, clonidine? A minireview. *BioMed Research International*, *2015*, 863715. https://doi.org/10.1155/2015/863715

Gisbert, R., Noguera, M. A., Ivorra, M. D., & D'Ocon, P. (2000). Functional evidence of a constitutively active population of alpha(1D)-adrenoceptors in rat aorta. *The Journal of Pharmacology and Experimental Therapeutics*, *295*(2), 810–817.

Gisbert, R., Ziani, K., Miquel, R., Noguera, M. A., Ivorra, M. D., Anselmi, E., & D'Ocon, P. (2002). Pathological role of a constitutively active population of alpha(1D)-adrenoceptors in arteries of spontaneously hypertensive rats. *British Journal of Pharmacology*, *135*(1), 206–216.

Hague, C., Chen, Z., Pupo, A. S., Schulte, N. A., Toews, M. L., & Minneman, K. P. (2004). The N terminus of the human {alpha}1D-adrenergic receptor prevents cell surface expression. *The Journal of Pharmacology and Experimental Therapeutics*, *309*(1), 388–397.

Hague, C., Uberti, M. A., Chen, Z., Hall, R. A., & Minneman, K. P. (2004). Cell surface expression of {alpha}1D-adrenergic receptors is controlled by heterodimerization with {alpha}1B-adrenergic receptors. *The Journal of Biological Chemistry*, *279*(15), 15541–15549. https://doi.org/10.1074/jbc.M314014200

Harding, S. D., Sharman, J. L., Faccenda, E., Southan, C., Pawson, A. J., Ireland, S., … NC-IUPHAR. (2018). The IUPHAR/BPS guide to PHARMACOLOGY in 2018: Updates and expansion to encompass the new guide to IMMUNOPHARMACOLOGY. *Nucleic Acids Research*, *46*(D1), D1091–D1106. https://doi.org/10.1093/nar/gkx1121

Hieble, J. P., Bylund, D. B., Clarke, D. E., Eikenburg, D. C., Langer, S. Z., Lefkowitz, R. J., … Ruffolo, R. R. Jr. (1995). International Union of Pharmacology. X. Recommendation for nomenclature of alpha 1-adrenoceptors: Consensus update. *Pharmacological Reviews*, *47*(2), 267–270.

Hrometz, S. L., Edelmann, S. E., McCune, D. F., Olges, J. R., Hadley, R. W., Perez, D. M., & Piascik, M. T. (1999). Expression of multiple alpha1-adrenoceptors on vascular smooth muscle: Correlation with the regulation of contraction. *The Journal of Pharmacology and Experimental Therapeutics*, *290*(1), 452–463.

Hussain, M. B., & Marshall, I. (1997). Characterization of alpha1-adrenoceptor subtypes mediating contractions to phenylephrine in rat thoracic aorta, mesenteric artery and pulmonary artery. *British Journal of Pharmacology*, *122*(5), 849–858. https://doi.org/10.1038/sj.bjp.0701461

Hutagalung, A. H., & Novick, P. J. (2011). Role of Rab GTPases in membrane traffic and cell physiology. *Physiological Reviews*, *91*(1), 119–149.

Hwang, T. L., Lau, Y. T., Huang, S. F., Chen, M. F., & Liu, M. S. (1994). Changes of alpha 1-adrenergic receptors in human liver during intraabdominal sepsis. *Hepatology*, *20*(3), 638–642. https://doi.org/10.1002/hep.1840200314

Ibarra, M., Terrón, J. A., López-Guerrero, J. J., & Villalobos-Molina, R. (1997). Evidence for an age-dependent functional expression of alpha 1D-adrenoceptors in the rat vasculature. *European Journal of Pharmacology*, *322*(2–3), 221–224.

Jensen, B. C., O'Connell, T. D., & Simpson, P. C. (2011). Alpha-1-adrenergic receptors: Targets for agonist drugs to treat heart failure. *Journal of Molecular and Cellular Cardiology*, *51*(4), 518–528.

Jensen, B. C., Swigart, P. M., Montgomery, M. D., & Simpson, P. C. (2010). Functional alpha-1B adrenergic receptors on human epicardial coronary artery endothelial cells. *Naunyn-Schmiedeberg's Archives of Pharmacology*, *382*(5–6), 475–482. https://doi.org/10.1007/s00210-010-0558-x

Jentzer, J. C., Vallabhajosyula, S., Khanna, A. K., Chawla, L. S., Busse, L. W., & Kashani, K. B. (2018). Management of refractory vasodilatory shock. *Chest*, *154*(2), 416–426.

Joost, P., & Methner, A. (2002). Phylogenetic analysis of 277 human G-protein-coupled receptors as a tool for the prediction of orphan receptor ligands. *Genome Biology*, *3*(11), research0063.1–0063.16.

Kamikihara, S. Y., Mueller, A., Lima, V., Akinaga, J., Nojimoto, F. D., Castilho, A., … Pupo, A. S. (2007). Alpha1-adrenoceptors in proximal segments of tail arteries from control and reserpinised rats. *Naunyn-Schmiedeberg's Archives of Pharmacology*, *376*(1–2), 117–126.

Kamikihara, S. Y., Mueller, A., Lima, V., Silva, A. R., da Costa, I. B., Buratini, J. Jr., … Pupo, A. S. (2005). Differential distribution of functional alph}1-adrenergic receptor subtypes along the rat tail artery. *The Journal of Pharmacology and Experimental Therapeutics*, *314*(2), 753–761. https://doi.org/10.1124/jpet.105.087502

Kenakin, T., & Christopoulos, A. (2013). Signalling bias in new drug discovery: Detection, quantification and therapeutic impact. *Nature reviews. Drug Discovery*, *12*(3), 205–216. https://doi.org/10.1038/nrd3954.

Kircik, L. H., DuBois, J., Draelos, Z. D., Werschler, P., Grande, K., Cook-Bolden, F. E., … Ahluwalia, G. (2018). pivotal trial of the efficacy and safety of oxymetazoline cream 1.0% for the treatment of persistent facial erythema associated with rosacea: Findings from the first REVEAL trial. *Journal of Drugs in Dermatology: JDD*, *17*(1), 97–105.

Koshimizu, T. A., Tanoue, A., & Tsujimoto, G. (2007). Clinical implications from studies of alpha1 adrenergic receptor knockout mice. *Biochemical Pharmacology*, *73*(8), 1107–1112. https://doi.org/10.1016/j.bcp.2006.11.002

Kountz, T. S., Lee, K. S., Aggarwal-Howarth, S., Curran, E., Park, J. M., Harris, D. A., … Hague, C. (2016). Endogenous N-terminal domain cleavage modulates α1D-adrenergic receptor pharmacodynamics. *The Journal of Biological Chemistry*, *291*(35), 18210–18221. https://doi.org/10.1074/jbc.M116.729517

Lachnit, W. G., Tran, A. M., Clarke, D. E., & Ford, A. P. (1997). Pharmacological characterization of an alpha 1A-adrenoceptor mediating contractile responses to noradrenaline in isolated caudal artery of rat. *British Journal of Pharmacology*, *120*(5), 819–826. https://doi.org/10.1038/sj.bjp.0700983

Langer, S. Z. (1974). Presynaptic regulation of catecholamine release. *Biochemical Pharmacology*, *23*(13), 1793–1800.

Langer, S. Z. (1999). History and nomenclature of alpha1-adrenoceptors. *European Urology*, *36*(Suppl 1), 2–6.

Lattion, A. L., Diviani, D., & Cotecchia, S. (1994). Truncation of the receptor carboxyl terminus impairs agonist-dependent phosphorylation and desensitization of the alpha 1B-adrenergic receptor. *The Journal of Biological Chemistry*, *269*(36), 22887–22893.

Leeb-Lundberg, L. M., Cotecchia, S., Lomasney, J. W., DeBernardis, J. F., Lefkowitz, R. J., & Caron, M. G. (1985). Phorbol esters promote alpha 1-adrenergic receptor phosphorylation and receptor uncoupling from inositol phospholipid metabolism. *Proceedings of the National Academy of Sciences of the United States of America*, *82*(17), 5651–5655.

Lyssand, J. S., Defino, M. C., Tang, X. B., Hertz, A. L., Feller, D. B., Wacker, J. L., … Hague, C. (2008). Blood pressure is regulated by an {alpha}1D-adrenergic receptor/dystrophin signalosome. *The Journal of Biological Chemistry*, *283*(27), 18792–18800. https://doi.org/10.1074/jbc.M801860200

Mallard, N. J., Marshall, R. W., Sithers, A. J., & Spriggs, T. L. (1992). Separation of putative alpha 1A- and alpha 1B-adrenoceptor mediated components in the tension response of the rat vas deferens to electrical field stimulation. *British Journal of Pharmacology*, *105*(3), 727–731. https://doi.org/10.1111/j.1476-5381.1992.tb09046.x

Marti, D., Miquel, R., Ziani, K., Gisbert, R., Ivorra, M. D., Anselmi, E., … D'Ocon, P. (2005). Correlation between mRNA levels and functional role of alpha1-adrenoceptor subtypes in arteries: Evidence of alpha1L as a functional isoform of the alpha1A-adrenoceptor. *American journal of physiology. Heart and Circulatory Physiology*, *289*(5), H1923–H1932. https://doi.org/10.1152/ajpheart.00288.2005

McGrath, J. C. (2015). Localization of α-adrenoceptors: JR Vane Medal Lecture. *British Journal of Pharmacology*, *172*(5), 1179–1194.

McVary, K. T., Roehrborn, C. G., Avins, A. L., Barry, M. J., Bruskewitz, R. C., Donnell, R. F., … Wei, J. T. (2011). Update on AUA guideline on the management of benign prostatic hyperplasia. *The Journal of Urology*, *185*(5), 1793–1803. https://doi.org/10.1016/j.juro.2011.01.074

Mendes, F. R., Hamamura, M., Queiroz, D. B., Porto, C. S., & Avellar, M. C. (2004). Effects of androgen manipulation on alpha1-adrenoceptor subtypes in the rat seminal vesicle. *Life Sciences*, *75*(12), 1449–1463. https://doi.org/10.1016/j.lfs.2004.03.011

Methven, L., McBride, M., Wallace, G. A., & McGrath, J. C. (2009). The alpha 1B/D-adrenoceptor knockout mouse permits isolation of the vascular alpha 1A-adrenoceptor and elucidates its relationship to the other subtypes. *British Journal of Pharmacology*, *158*(1), 209–224. https://doi.org/10.1111/j.1476-5381.2009.00269.x

Methven, L., Simpson, P. C., & McGrath, J. C. (2009). Alpha1A/B-knockout mice explain the native alpha1D-adrenoceptor's role in vasoconstriction and show that its location is independent of the other alpha1-subtypes. *British Journal of Pharmacology*, *158*(7), 1663–1675.

Michel, M. C., & Vrydag, W. (2006). Alpha1-, alpha2- and beta-adrenoceptors in the urinary bladder, urethra and prostate. *British Journal of Pharmacology*, *147*(Suppl 2), S88–S119. https://doi.org/10.1038/sj.bjp.0706619

Michelotti, G. A., Price, D. T., & Schwinn, D. A. (2000). Alpha 1-adrenergic receptor regulation: Basic science and clinical implications. *Pharmacology & Therapeutics*, *88*(3), 281–309. https://doi.org/10.1016/S0163-7258(00)00092-9

Minneman, K. P., Theroux, T. L., Hollinger, S., Han, C., & Esbenshade, T. A. (1994). Selectivity of agonists for cloned alpha 1-adrenergic receptor subtypes. *Molecular Pharmacology*, *46*(5), 929–936.

Mota, P. M., & Norris, J. H. (2016). Review on surgical management of ptosis and the use of phenylephrine: A national survey of British Oculoplastic Surgery Society (BOPSS) UK Consultants. *Orbit*, *35*(6), 339–342. https://doi.org/10.1080/01676830.2016.1193547

Myagmar, B. E., Flynn, J. M., Cowley, P. M., Swigart, P. M., Montgomery, M. D., Thai, K., … Simpson, P. C. (2017). Adrenergic receptors in individual ventricular myocytes: The beta-1 and alpha-1B are in all cells, the alpha-1A is in a subpopulation, and the beta-2 and beta-3 are mostly absent. *Circulation Research*, *120*(7), 1103–1115. https://doi.org/10.1161/CIRCRESAHA.117.310520

Nascimento-Viana, J. B., Carvalho, A. R., Nasciutti, L. E., Alcántara-Hernández, R., Chagas-Silva, F., Souza, P. A., … Silva, C. L. (2016). New multi-target antagonists of α1A-, α1D-adrenoceptors and 5-HT1A receptors reduce human hyperplastic prostate cell growth and the increase of intraurethral pressure. *The Journal of Pharmacology and Experimental Therapeutics*, *356*(1), 212–222. https://doi.org/10.1124/jpet.115.227066

Noguera, M. A., Ivorra, M. D., & D'Ocon, P. (1996). Functional evidence of inverse agonism in vascular smooth muscle. *British Journal of Pharmacology*, *119*(1), 158–164. https://doi.org/10.1111/j.1476-5381.1996.tb15689.x

Nourian, Z., Mow, T., Muftic, D., Burek, S., Pedersen, M. L., Matz, J., … Mulvany, M. J. (2008). Orthostatic hypotensive effect of antipsychotic drugs in Wistar rats by in vivo and in vitro studies of alpha1-adrenoceptor function. *Psychopharmacology*, *199*(1), 15–27. https://doi.org/10.1007/s00213-007-1064-9

O'Connell, T. D., Jensen, B. C., Baker, A. J., & Simpson, P. C. (2014). Cardiac alpha1-adrenergic receptors: Novel aspects of expression, signaling mechanisms, physiologic function, and clinical importance. *Pharmacological Reviews*, *66*(1), 308–333. https://doi.org/10.1124/pr.112.007203

Oelke, M., Bachmann, A., Descazeaud, A., Emberton, M., Gravas, S., Michel, M. C., … European Association of Urology (2013). EAU guidelines on the treatment and follow-up of non-neurogenic male lower urinary tract symptoms including benign prostatic obstruction. *European Urology*, *64*(1), 118–140. https://doi.org/10.1016/j.eururo.2013.03.004

Pacini, E. S. A., Castilho, A. C. S., Hebeler-Barbosa, F., Pupo, A. S., & Kiguti, L. R. A. (2018). Contraction of rat cauda epididymis smooth muscle to α1-adrenoceptor activation is mediated by α1A-adrenoceptors. *The Journal of Pharmacology and Experimental Therapeutics*, *366*(1), 21–28.

Perez, D. M., & Doze, V. A. (2011). Cardiac and neuroprotection regulated by α(1)-adrenergic receptor subtypes. *Journal of Receptor and Signal Transduction Research*, *31*(2), 98–110. https://doi.org/10.3109/10799893.2010.550008

Perez-Aso, M., Segura, V., Monto, F., Barettino, D., Noguera, M. A., Milligan, G., & D'Ocon, P. (2013). The three α1-adrenoceptor subtypes show different spatio-temporal mechanisms of internalization and ERK1/2 phosphorylation. *Biochimica et Biophysica Acta*, *1833*(10), 2322–2333. https://doi.org/10.1016/j.bbamcr.2013.06.013

Philipp, M., & Hein, L. (2004). Adrenergic receptor knockout mice: Distinct functions of 9 receptor subtypes. *Pharmacology & Therapeutics*, *101*(1), 65–74. https://doi.org/10.1016/j.pharmthera.2003.10.004

Piascik, M. T., Guarino, R. D., Smith, M. S., Soltis, E. E., Saussy, D. L. Jr., & Perez, D. M. (1995). The specific contribution of the novel alpha-1D adrenoceptor to the contraction of vascular smooth muscle. *The Journal of Pharmacology and Experimental Therapeutics*, *275*(3), 1583–1589.

Price, D. T., Schwinn, D. A., Lomasney, J. W., Allen, L. F., Caron, M. G., & Lefkowitz, R. J. (1993). Identification, quantification, and localization of mRNA for three distinct alpha 1 adrenergic receptor subtypes in human prostate. *The Journal of Urology*, *150*(2 Pt 1), 546–551. https://doi.org/10.1016/S0022-5347(17)35544-1

Price, R. R., Morris, D. P., Biswas, G., Smith, M. P., & Schwinn, D. A. (2002). Acute agonist-mediated desensitization of the human alpha 1a-adrenergic receptor is primarily independent of carboxyl terminus regulation: implications for regulation of alpha 1aAR splice variants. *The Journal of Biological Chemistry*, *277*(11), 9570–9579.

Prihandoko, R., Alvarez-Curto, E., Hudson, B. D., Butcher, A. J., Ulven, T., Miller, A. M., … Milligan, G. (2016). Distinct phosphorylation clusters determine the signaling outcome of free fatty acid receptor 4/G protein-coupled receptor 120. *Molecular Pharmacology*, *89*(5), 505–520. https://doi.org/10.1124/mol.115.101949

Pupo, A. S. (1998). Functional effects of castration on alpha1-adrenoceptors in rat vas deferens. *European Journal of Pharmacology*, *351*(2), 217–223. https://doi.org/10.1016/S0014-2999(98)00315-X

Pupo, A. S., Duarte, D. A., Lima, V., Teixeira, L. B., Parreiras, E. S. L. T., & Costa-Neto, C. M. (2016). Recent updates on GPCR biased agonism. *Pharmacological Research*, *112*, 49–57.

Pupo, A. S., Uberti, M. A., & Minneman, K. P. (2003). N-terminal truncation of human alpha1D-adrenoceptors increases expression of binding sites but not protein. *European Journal of Pharmacology*, *462*(1–3), 1–8.

Queiroz, D. B., Mendes, F. R., Porto, C. S., & Avellar, M. C. (2002). Alpha1-adrenoceptor subtypes in rat epididymis and the effects of sexual maturation. *Biology of Reproduction*, *66*(2), 508–515. https://doi.org/10.1095/biolreprod66.2.508

Rodríguez-Pérez, C. E., Romero-Ávila, M. T., Reyes-Cruz, G., & García-Sáinz, J. A. (2009). Signaling properties of human alpha(1D)-adrenoceptors lacking the carboxyl terminus: Intrinsic activity, agonist-mediated activation, and desensitization. *Naunyn-Schmiedeberg's Archives of Pharmacology*, *380*(2), 99–107.

Roepke, S., Danker-Hopfe, H., Repantis, D., Behnia, B., Bernard, F., Hansen, M. L., & Otte, C. (2017). Doxazosin, an α-1-adrenergic-receptor antagonist, for nightmares in patients with posttraumatic stress disorder and/or borderline personality disorder: A chart review. *Pharmacopsychiatry*, *50*(1), 26–31. https://doi.org/10.1055/s-0042-107794

Rudner, X. L., Berkowitz, D. E., Booth, J. V., Funk, B. L., Cozart, K. L., D'Amico, E. B., … Schwinn, D. A. (1999). Subtype specific regulation of human vascular alpha(1)-adrenergic receptors by vessel bed and age. *Circulation*, *100*(23), 2336–2343.

Sanbe, A., Tanaka, Y., Fujiwara, Y., Tsumura, H., Yamauchi, J., Cotecchia, S., … Tanoue, A. (2007). Alpha1-adrenoceptors are required for normal male sexual function. *British Journal of Pharmacology*, *152*(3), 332–340. https://doi.org/10.1038/sj.bjp.0707366

Schwartz, S. L., Cao, C., Pylypenko, O., Rak, A., & Wandinger-Ness, A. (2007). Rab GTPases at a glance. *Journal of Cell Science*, *120*(Pt 22), 3905–3910. https://doi.org/10.1242/jcs.015909

Segura, V., Perez-Aso, M., Monto, F., Carceller, E., Noguera, M. A., Pediani, J., … D'Ocon, P. (2013). Differences in the signaling pathways of alpha(1A)- and alpha(1B)-adrenoceptors are related to different endosomal targeting. *PLoS ONE*, *8*(5), e64996. https://doi.org/10.1371/journal.pone.0064996

Sharman, J. L., Harding, S. D., Southan, C., Faccenda, E., Pawson, A. J., Davies, J. A., & NC-IUPHAR. (2018). Accessing expert-curated pharmacological data in the IUPHAR/BPS guide to PHARMACOLOGY. *Current Protocols in Bioinformatics*, *61*(1), 1.34.1–1.34.46. https://doi.org/10.1002/cpbi.46

Sigala, S., Dellabella, M., Milanese, G., Fornari, S., Faccoli, S., Palazzolo, F., … Muzzonigro, G. (2005). Evidence for the presence of alpha1 adrenoceptor subtypes in the human ureter. *Neurourology and Urodynamics*, *24*(2), 142–148.

da Silva Junior, E. D., Sato, M., Merlin, J., Broxton, N., Hutchinson, D. S., Ventura, S., … Summers, R. J. (2017). Factors influencing biased agonism in recombinant cells expressing the human alpha1A-adrenoceptor. *British Journal of Pharmacology*, *174*(14), 2318–2333. https://doi.org/10.1111/bph.13837

Silva, M. A., Megale, A., Avellar, M. C., & Porto, C. S. (1999). Expression and pharmacological characterization of alpha1-adrenoceptors in rat seminal vesicle. *European Journal of Pharmacology*, *381*(2–3), 141–149.

Stanasila, L., Abuin, L., Dey, J., & Cotecchia, S. (2008). Different internalization properties of the alpha1a- and alpha1b-adrenergic receptor subtypes: The potential role of receptor interaction with beta-arrestins and AP50. *Molecular Pharmacology*, *74*(3), 562–573. https://doi.org/10.1124/mol.107.043422

Starke, K., Montel, H., Gayk, W., & Merker, R. (1974). Comparison of the effects of clonidine on pre- and postsynaptic adrenoceptors in the rabbit pulmonary artery. Alpha-sympathomimetic inhibition of Neurogenic vasoconstriction. *Naunyn-Schmiedeberg's Archives of Pharmacology*, *285*(2), 133–150. https://doi.org/10.1007/BF00501149

Stassen, F. R., Maas, R. G., Schiffers, P. M., Janssen, G. M., & De Mey, J. G. (1998). A positive and reversible relationship between adrenergic nerves and alpha-1A adrenoceptors in rat arteries. *The Journal of Pharmacology and Experimental Therapeutics*, *284*(1), 399–405.

Stenmark, H. (2009). Rab GTPases as coordinators of vesicle traffic. *Nature Reviews. Molecular Cell Biology*, *10*(8), 513–525. https://doi.org/10.1038/nrm2728

Stone, E. A., Cotecchia, S., Lin, Y., & Quartermain, D. (2002). Role of brain alpha 1B-adrenoceptors in modafinil-induced behavioral activity. *Synapse*, *46*(4), 269–270.

Stone, E. A., Lin, Y., Rosengarten, H., Kramer, H. K., & Quartermain, D. (2003). Emerging evidence for a central epinephrine-innervated alpha 1-adrenergic system that regulates behavioral activation and is impaired in depression. *Neuropsychopharmacology*, *28*(8), 1387–1399. https://doi.org/10.1038/sj.npp.1300222

Taki, N., Tanaka, T., Zhang, L., Suzuki, F., Israilova, M., Taniguchi, T., … Muramatsu, I. (2004). Alpha-1D adrenoceptors are involved in reserpine-induced supersensitivity of rat tail artery. *British Journal of Pharmacology*, *142*(4), 647–656.

Tanoue, A., Koshimizu, T. A., Shibata, K., Nasa, Y., Takeo, S., & Tsujimoto, G. (2003). Insights into alpha1 adrenoceptor function in health and disease from transgenic animal studies. *Trends in Endocrinology and Metabolism: TEM*, *14*(3), 107–113. https://doi.org/10.1016/S1043-2760(03)00026-2

Tanoue, A., Koshimizu, T. A., & Tsujimoto, G. (2002). Transgenic studies of alpha(1)-adrenergic receptor subtype function. *Life Sciences*, *71*(19), 2207–2215.

Tobin, A. B. (2008). G-protein-coupled receptor phosphorylation: Where, when and by whom. *British Journal of Pharmacology*, *153*(Suppl 1), S167–S176.

Tobin, A. B., Butcher, A. J., & Kong, K. C. (2008). Location, location, location…site-specific GPCR phosphorylation offers a mechanism for cell-type-specific signalling. *Trends in Pharmacological Sciences*, *29*(8), 413–420.

Toews, M. L., Prinster, S. C., & Schulte, N. A. (2003). Regulation of alpha-1B adrenergic receptor localization, trafficking, function, and stability. *Life Sciences*, *74*(2–3), 379–389.

Vaidyanathan, S., Williamson, P., Clearie, K., Khan, F., & Lipworth, B. (2010). Fluticasone reverses oxymetazoline-induced tachyphylaxis of response and rebound congestion. *American Journal of Respiratory and Critical Care Medicine*, *182*(1), 19–24.

Vail, E., Gershengorn, H. B., Hua, M., Walkey, A. J., Rubenfeld, G., & Wunsch, H. (2017). Association between US norepinephrine shortage and mortality among patients with septic shock. *JAMA: The Journal of the American Medical Association*, *317*(14), 1433–1442. https://doi.org/10.1001/jama.2017.2841

Vázquez-Prado, J., Casas-González, P., & García-Sáinz, J. A. (2003). G protein-coupled receptor cross-talk: Pivotal roles of protein phosphorylation and protein–protein interactions. *Cellular Signalling*, *15*(6), 549–557.

Vazquez-Prado, J., & Garcia-Sainz, J. A. (1996). Effect of phorbol myristate acetate on alpha 1-adrenergic action in cells expressing recombinant alpha 1-adrenoceptor subtypes. *Molecular Pharmacology*, *50*(1), 17–22.

Vazquez-Prado, J., Medina, L. C., Romero-Avila, M. T., Gonzalez-Espinosa, C., & Garcia-Sainz, J. A. (2000). Norepinephrine- and phorbol ester-

induced phosphorylation of alpha(1a)-adrenergic receptors. Functional aspects. *The Journal of Biological Chemistry*, *275*(9), 6553–6559.

Villalobos-Molina, R., & Ibarra, M. (1999). Vascular alpha 1D-adrenoceptors: Are they related to hypertension? *Archives of Medical Research*, *30*(5), 347–352. https://doi.org/10.1016/S0188-0128(99)00047-0

Villalobos-Molina, R., & Ibarra, M. (2005). Increased expression and function of vascular alpha1D-adrenoceptors may mediate the prohypertensive effects of angiotensin II. *Molecular Interventions*, *5*(6), 340–342.

Villalobos-Molina, R., López-Guerrero, J. J., & Ibarra, M. (1999). Functional evidence of alpha1D-adrenoceptors in the vasculature of young and adult spontaneously hypertensive rats. *British Journal of Pharmacology*, *126*(7), 1534–1536. https://doi.org/10.1038/sj.bjp.0702468

Villalobos-Molina, R., Vazquez-Cuevas, F. G., Lopez-Guerrero, J. J., Figueroa-Garcia, M. C., Gallardo-Ortiz, I. A., Ibarra, M., … Elizondo, G. (2008). Vascular alpha-1D-adrenoceptors are overexpressed in aorta of the aryl hydrocarbon receptor null mouse: Role of increased angiotensin II. *Autonomic & Autacoid Pharmacology*, *28*(2–3), 61–67.

Wang, G., Wei, Z., & Wu, G. (2018). Role of Rab GTPases in the export trafficking of G protein-coupled receptors. *Small GTPases*, *9*(1–2), 130–135. https://doi.org/10.1080/21541248.2016.1277000

Wang, G., & Wu, G. (2012). Small GTPase regulation of GPCR anterograde trafficking. *Trends in Pharmacological Sciences*, *33*(1), 28–34.

Wang, S. Y., Song, Y., Xu, M., He, Q. H., Han, Q. D., & Zhang, Y. Y. (2007). Internalization and distribution of three alpha1-adrenoceptor subtypes in HEK293A cells before and after agonist stimulation. *Acta Pharmacologica Sinica*, *28*(3), 359–366.

White, C. W., Choong, Y. T., Short, J. L., Exintaris, B., Malone, D. T., Allen, A. M., … Ventura, S. (2013). Male contraception via simultaneous knockout of alpha1A-adrenoceptors and P2X1-purinoceptors in mice. *Proceedings of the National Academy of Sciences of the United States of America*, *110*(51), 20825–20830. https://doi.org/10.1073/pnas.1318624110

Woodcock, E. A., Du, X. J., Reichelt, M. E., & Graham, R. M. (2008). Cardiac alpha 1-adrenergic drive in pathological remodelling. *Cardiovascular Research*, *77*(3), 452–462.

Wu, S. C., & O'Connell, T. D. (2015). Nuclear compartmentalization of alpha1-adrenergic receptor signaling in adult cardiac myocytes. *Journal of Cardiovascular Pharmacology*, *65*(2), 91–100.

Xin, X., Yang, N., Eckhart, A. D., & Faber, J. E. (1997). Alpha1D-adrenergic receptors and mitogen-activated protein kinase mediate increased protein synthesis by arterial smooth muscle. *Molecular Pharmacology*, *51*(5), 764–775. https://doi.org/10.1124/mol.51.5.764

Yono, M., Tanaka, T., Tsuji, S., Hori, M., Irie, S., Sakata, Y., … Latifpour, J. (2012). A comparison of the expression and contractile function of alpha1-adrenoceptors in seminal vesicle and vas deferens from normotensive and hypertensive rats. *European Journal of Pharmacology*, *694*(1–3), 104–110. https://doi.org/10.1016/j.ejphar.2012.08.005

Zerial, M., & McBride, H. (2001). Rab proteins as membrane organizers. *Nature Reviews. Molecular Cell Biology*, *2*(2), 107–117.

Ziani, K., Gisbert, R., Noguera, M. A., Ivorra, M. D., & D'Ocon, P. (2002). Modulatory role of a constitutively active population of alpha(1D)-adrenoceptors in conductance arteries. *American Journal of Physiology. Heart and Circulatory Physiology*, *282*(2), H475–H481.

Zindel, D., Engel, S., Bottrill, A. R., Pin, J. P., Prezeau, L., Tobin, A. B., … Butcher, A. J. (2016). Identification of key phosphorylation sites in PTH1R that determine arrestin3 binding and fine-tune receptor signaling. *The Biochemical Journal*, *473*(22), 4173–4192. https://doi.org/10.1042/BCJ20160740

Zuscik, M. J., Sands, S., Ross, S. A., Waugh, D. J., Gaivin, R. J., Morilak, D., & Perez, D. M. (2000). Overexpression of the alpha1B-adrenergic receptor causes apoptotic neurodegeneration: Multiple system atrophy. *Nature Medicine*, *6*(12), 1388–1394.

How to cite this article: Akinaga J, García-Sáinz JA, S. Pupo A. Updates in the function and regulation of α_1-adrenoceptors. *Br J Pharmacol*. 2019;176:2343–2357. https://doi.org/10.1111/bph.14617

NEUROSCIENCE
RESEARCH ARTICLE
A. Almanza et al. / Neuroscience 417 (2019) 81–94

Cellular Mechanism for Specific Mechanical Antinociception by D2-like Receptor at the Spinal Cord Level

Angélica Almanza,[a1] Pedro Segura-Chama,[a,b1] Leon-Olea Martha León-Olea,[c] Enoch Luis,[d,e] Garduno-Gutierrez René Garduño-Gutiérrez,[c] Jonathan Mercado-Reyes,[a] Simon-Arceo Karina Simón-Arceo,[f] Ulises Coffeen,[f] Hernandez-Cruz Arturo Hernández-Cruz,[d,g] Francisco Pellicer[f] and Francisco Mercado[a,*]

[a] *Laboratorio de Fisiología Celular, Dirección de Investigaciones en Neurociencias, Instituto Nacional de Psiquiatría Ramón de la Fuente Muñiz, Ciudad de México, Mexico*

[b] *Cátedras CONACyT – Instituto Nacional de Psiquiatría Ramón de la Fuente Muñiz, Ciudad de México, Mexico*

[c] *Departamento de Neuromorfología Funcional, Dirección de Investigaciones en Neurociencias, Instituto Nacional de Psiquiatría Ramón de la Fuente Muñiz, Ciudad de México, Mexico*

[d] *Laboratorio Nacional de Canalopatías, Instituto de Fisiología Celular, Universidad Nacional Autónoma de México, Ciudad de México, Mexico*

[e] *Cátedras CONACyT – Instituto de Fisiología Celular, Universidad Nacional Autónoma de México, Ciudad de México, Mexico*

[f] *Laboratorio de Neurofisiología Integrativa, Dirección de Investigaciones en Neurociencias, Instituto Nacional de Psiquiatría Ramón de la Fuente Muñiz, Ciudad de México, Mexico.*

[g] *Departamento de Neurociencia Cognitiva, División de Neurociencias, Instituto de Fisiología Celular, Universidad Nacional Autónoma de México, Ciudad de México, Mexico*

Abstract—Intrathecal (i.t.) administration of quinpirole, a dopamine (DA) D2-like receptor agonist, produces antinociception to mechanonociceptive stimuli but not to thermonociceptive stimuli. To determine a cellular mechanism for the specific antinociceptive effect of D2-like receptor activation on mechanonociception, we evaluated the effect of quinpirole on voltage-gated Ca^{2+} influx in cultured dorsal root ganglion (DRG) neurons and the D2 DA receptor distribution in subpopulations of rat nociceptive DRG neurons. Small-diameter DRG neurons were classified into IB_4+ (nonpeptidergic) and IB_4- (peptidergic). Intracellular [Ca^{2+}] microfluorometry and voltage-clamp experiments showed that quinpirole reduced Ca^{2+} influx and inhibited the high voltage-activated Ca^{2+} current (HVA-I_{Ca}) in half of IB_4+ neurons, leaving Ca^{2+} entry and HVA-I_{Ca} in IB_4- neurons nearly unaffected. Pretreatment with ω-conotoxin MVIIA prevented the effect of quinpirole on HVA-I_{Ca} from IB_4+ neurons, indicating that quinpirole mainly inhibits $Ca_V2.2$ channels. Immunofluorescence experiments showed that D2 DA receptor was present mainly in IB_4+ small DRG neurons. Finally, in behavioral experiments in rats, the clinically approved D2-like receptor agonist pramipexole produced spinal antinociception in a similar fashion to quinpirole, with a significant effect only in the mechanonociceptive test. Our results explain, at least in part, why D2-like receptor agonists produce antinociception on mechanonociceptors. **© 2019 IBRO. Published by Elsevier Ltd. All rights reserved.**

Key words: dopamine, D2-like receptors, mechanonociception, $Ca_V2.2$ channels, neurotransmitter release, antinociception.

INTRODUCTION

The use of dopamine (DA) receptor agonists has been a useful treatment for a diversity of experimental and clinical pain conditions (Dickey and Minton, 1972; Kernbaum and Hauchecorne, 1981; Coffeen et al., 2008; Pellicer et al., 2010; Cobacho et al., 2014; Almanza et al., 2015). Some efforts have been made to determine the cellular and molecular mechanisms by which DA agonists produce their antinociceptive effect (Fleetwood-Walker et al., 1988; Tamae et al., 2005; Charbit et al., 2009; Taniguchi et al., 2011; Galbavy et al., 2013; Lu et al., 2018), but it is still incompletely understood. At the dorsal horn spinal cord level (lamina I and lamina II), it has been suggested that presynaptic and postsynaptic effects are responsible for the antinociceptive effect of DA and are mediated mainly by D2-like receptors (Tamae et al., 2005; Taniguchi et al., 2011; Lu et al., 2018).

In rodents, increasing evidence has demonstrated that *in vivo* DRG neurons respond specifically to one type of nociceptive stimulus (heat, cold, mechanical, *etc.*) (Cavanaugh et al., 2009; Le Pichon and Chesler,

*Corresponding author at: Francisco Mercado, Calzada México-Xochimilco 101, Col. San Lorenzo Huipulco, Tlalpan, Ciudad de México, CP 14360, Mexico Tel.: + 52 554 160 5106.
E-mail address: fmercado@imp.edu.mx (F. Mercado).
[1] These authors contribute equally to this work.

https://doi.org/10.1016/j.neuroscience.2019.08.019
0306-4522/© 2019 IBRO. Published by Elsevier Ltd. All rights reserved.

2014; Emery et al., 2016). This specific response also occurs with different modulatory neurotransmitters. For example, intrathecal (i.t.) administration of a specific delta-opioid receptor (DOR) agonist produces antinociception only against mechanical nociceptive stimuli (Scherrer et al., 2009). DOR is expressed only in mechanonociceptive DRG neurons, which explains the modality-specific antinociception induced by DOR activation.

A similar effect is observed with the administration of quinpirole, a D2-like DA receptor agonist. Quinpirole i.t. administration at low doses (1.8 nmol) produces mechanical antinociception, leaving unaffected the peripheral processing of thermonociceptive stimuli (Almanza et al., 2015). The mechanical antinociceptive effect is completely abolished by i.t administration of D2-like receptor antagonists, suggesting that the antinociceptive effect is due to the activation of D2, D3 and D4 DA receptors, which are expressed in primary sensory neurons and the spinal cord (Xie et al., 1998; Zhu et al., 2007; Kawamoto et al., 2012).

To extend our understanding of the cellular and molecular mechanisms by which D2-like receptor agonists exert their effect only on mechanonociceptive pathways, we evaluated 1) the effect of quinpirole on voltage-gated Ca^{2+} channels (VGCC) and on the electrical properties of small IB_4+ and IB_4- DRG neurons, 2) determined the D2 receptor expression by Western blot and their expression pattern by immunohistochemistry in lumbar DRG, and 3) assessed the behavioral response to the clinically relevant D2-like receptor agonist pramipexole in nociceptive tests in rats.

EXPERIMENTAL PROCEDURES

The present work was conducted following the recommendations of the *Guide for the Care and Use of Laboratory Animals* of the National Academy of Sciences (USA), the International Association for the Study of Pain (IASP) (Zimmermann, 1983), and the local regulations for the use and care of laboratory animals (NOM-062-ZOO-1999). All the protocols in this work were approved by the *Comité de Ética en Investigación* from *Instituto Nacional de Psiquiatría Ramón de la Fuente Muñiz*. The work adhered to the ARRIVE guidelines for studies reporting the results from *in vivo* animal experiments (Kilkenny et al., 2010).

Animals

Wistar rats used for this work were produced and maintained in our institutional animal care facilities. The animals were kept in acrylic cages (sawdust bedding) with *ad libitum* access to food (rat chow) and water. Room temperature was set to 22 °C, with dark/light cycles of 12 h. For neuronal cell-culture and Western blot experiments, animals from P21 to P25 were used (either sex), and for immunohistochemistry and behavioral tests, male rats weighing 250–350 g were used.

DRG neuron isolation and culture

For cell culture, the rats were anesthetized with isoflurane (Sofloran Vet, PISA, México) and then decapitated. Under a stereomicroscope, DRGs were isolated from the L4 to the L6 level and immersed in ice-chilled Dulbecco's Modified Eagle Medium (DMEM; Gibco, Life Technologies, Rockville MD, USA). Isolated ganglia were incubated for 30 min in DMEM containing trypsin (1 mg/mL; Affimetrix-ThermoFisher, Waltham, MA, USA), and collagenase type IA (1 mg/mL; Sigma-Aldrich, St Louis MO, USA) at 37 °C. Then, ganglia were washed and triturated with a fire-polished Pasteur pipette. The cell suspension was centrifuged (5 min, 5000 rpm), and the medium was replaced with fresh, sterile DMEM. After three washouts, isolated DRG neurons were plated on glass coverslips (Corning, New York, NY, USA) pretreated with poly-L-lysine (0.01%; Sigma Aldrich), which were placed onto 35-mm culture dishes (Trueline, USA) containing DMEM supplemented with N2 (Gibco, Life Technologies) and penicillin–streptomycin-amphotericin B (100 U/mL, 0.1 mg/mL, 0.25 μg/mL; respectively; Sigma-Aldrich). The neurons were maintained at 37 °C (NuAire Inc., Plymouth, MN, USA) in a 10% CO_2 atmosphere until the recording (18–24 h).

Calcium imaging recordings

For these experiments, five rats were used. The DRG neurons were incubated with Fluo-4 AM (1 μM; Molecular Probes, Life Technologies; 50 min at 37 °C), and placed in a recording chamber attached to the stage of a microscope (Nikon Eclipse 80i, Japan); the DRG neurons were perfused with extracellular solution (Table 1; 2 mL/min). Fluo-4 AM was excited at 488 nm and the emitted fluorescence was bandpassed at 510 nm. The images were acquired at 1 Hz frequency (20 ms exposure) with a CCD camera (Andor Technology iXon 897, Oxford Instruments, High Wycombe, UK) controlled by the software Andor iQ version 1.10.2, at room temperature (22–25 °C).

The increase of $[Ca^{2+}]_i$ was induced by local depolarization (3 s; 10 min between stimuli) with a high K^+ solution (60 mM; Table 1). As methodological control, a Ca^{2+}-free extracellular solution was used, and the increment in $[Ca^{2+}]_i$ elicited by high K^+ was prevented (data not shown). The fluorescence amplitude (ΔF) produced in control was compared with ΔF produced in the presence of an agonist or antagonist of the D2-like DA receptors or DAMGO, as well as after the washout of the drug. In both, calcium imaging and patch-clamp experiments, when the recording finished, the neurons were incubated for 10 min with the IB_4 Alexa-fluor 488 conjugate (10 μg/mL; Life Technologies-ThermoFisher, Waltham, MA, USA), rinsed for 5 min and observed to determine their binding to IB_4.

Images files were converted to TIFF and imported into FIJI for *post hoc* analysis (Schindelin et al., 2012). Basal fluorescence was obtained from areas of the cell displaying the most uniform and least intense fluorescence (F_0). The amplitude of the rise of $[Ca^{2+}]_i$ was expressed as ΔF arbitrary units (a.u.), where ΔF represents the difference

Table 1. Solutions used for patch-clamp and microfluorometry experiments. Concentrations are expressed in mM.

Microfluorometry	NaCl	KCl	$CaCl_2$	$MgCl_2$	HEPES	Glucose	EGTA	$ATPMg^{2+}$	$GTPNa^{+}$
Extracellular	140	5	1.8	1.2	10	10	-	-	-
High K^{+}	85	60	1.8	1.2	10	10	-	-	-
AP									
Extracellular	140	5	1.8	1.2	10	10	-	-	-
Intracellular	10	125	0.134	-	5	-	10	2	1
I_{Ca}	$CaCl_2$	CsCl	$MgCl_2$	TEACl	HEPES	Glucose	EGTA	$ATPMg^{2+}$	$GTPNa^{+}$
Extracellular	5	95	1	30	10	10	-	-	-
Intracellular	0.1	120	-	5	5	-	10	2	1

between instantaneous Ca^{2+} fluorescence less the basal Ca^{2+} fluorescence (F_0). Analysis of the area under the curve (AUC) of the ΔF transient was performed with Origin 2016 software (OriginLab Corp., Northampton, MA, USA). We assessed the first 25 s of the trace, which represents the Ca^{2+} influx from bath solution during high K^{+}-induced depolarization. Although mechanonociceptive neurons belong to both A-delta (medium-size neurons) and C-fibers (small-size neurons), we choose to only record small-size neurons to be sure that we were recording nociceptors, for this reason neurons with diameter $\leq$ 26 μm were considered for the analysis (Taddese et al., 1995; Stucky and Lewin, 1999; Blair and Bean, 2002).

Whole-cell patch-clamp recording

A total of 47 animals were used in these experiments. The coverslips containing DRG neurons were placed inside a recording chamber adapted to the mechanical stage of an inverted microscope (TS100) equipped with a mercury lamp and filters for fluorescence observation (Nikon Corporation, Tokyo, Japan). The recording chamber was bathed with external solution at a constant flow (0.5 mL/min) maintained with a peristaltic pump (Cole-Parmer, Vernon Hills IL, USA). The solutions used for the recordings are listed in Table 1.

Patch pipettes were pulled from Clark custom patch borosilicate glass (Harvard Apparatus, MA, USA) with a P-97 puller (Sutter Instruments, Palo Alto, CA, USA). Pipette resistances were 2–3 MΩ when filled with the internal solution (Table 1). To drug delivery, a perfusion system VC-6 couplet to a fast-step solution changer was used (SF-77B; Warner Instruments, Hamden, CT, USA).

Voltage-clamp and current-clamp recordings were obtained in whole-cell configuration at room temperature (21–22 °C). Acquisition and stimulation were performed using a PC-505B patch-clamp amplifier (Warner Instruments, Hamden, CT, USA), Digidata 1440 (Molecular Devices, Sunny Valley, CA, USA) and the software WinWCP (v. 4.7; John Dempster; University of Strathclyde, Glasgow, Scotland). Data were acquired at 20 kHz, and the low-pass filter was set at 5 kHz. Since C_m is an indirect measure of the cell size, neurons were classified as small when their C_m was 45 pF or less (Stucky and Lewin, 1999; Baccei and Kocsis, 2000).

In all cases, a control trace (average of 3 traces recorded) of action potential (AP) or voltage-clamp recording was compared with the trace after perfusion of the drug (average of 3 traces recorded). Then, the neuron was left to recovery from the drug effect, and the washout response was recorded.

The HVA-I_{Ca} was isolated and recorded in small-diameter DRG neurons with a CsCl-based intra and extracellular solutions (Table 1). HVA-I_{Ca} was elicited with a depolarizing pulse to −10 mV for 30 ms, from a holding potential (V_H) of −60 mV (25 s between voltage steps). Data are shown as an inhibition percentage with respect to the control condition.

For current-clamp experiments, internal and extracellular solutions were used (AP solutions, Table 1). APs were elicited with a square pulse of 164 ± 23 pA in IB_4+ and 106 ± 16 pA in IB_4- small DRG neurons (500 ms of duration) and a current ramp from 0 to 558 ± 37 pA in IB_4+ and from 0 to 446 ± 55 pA in IB_4- small DRG neurons (750 ms of duration). Current was injected to set the V_H close to −60 mV in every cell. The duration of the AP was measured at 50% of the peak amplitude from resting potential.

Immunofluorescence

Under anesthesia with sodium pentobarbital (63 mg/kg), rats were transcardially perfused with a clearing solution (0.9% NaCl + 5 IU/mL of heparin; 50–200 mL) followed by 350–400 mL of 4% paraformaldehyde in PBS 1x (Sigma Chemical Co., St. Louis, MO). Lumbar DRGs from 4 rats were removed and postfixed in the same fixative for 2 h at 4 °C. Then, they were cryoprotected in 30% sucrose and stored at 4 °C until their use. Ganglia were immersed in Tissue Freezing Medium (Leica Instruments, Nussloch, Germany). Subsequently, 14-μm-thick serial sections were cut in a cryostat

INFORME DE LABORES 2019

microtome (Microm HM 525, Microm International GmbH, Germany) and mounted on gelatin-coated slides. Double immunofluorescence protocol was done as previously reported (León-Olea et al., 2013). Briefly, after blocking to minimize nonspecific staining, random sections were incubated with rabbit D2 receptor antibody (Chemicon, cat. AB5084P, 1:300) and mouse Calcitonin-Gene Related Peptide (CGRP) antibody (Pierce, cat. MA1–20209, 1:300) in the same blocking solution for 48 h at 4 °C. After washing, tissue was incubated with Alexa Fluor 647 donkey anti-rabbit and Alexa Fluor 555 donkey anti-mouse secondary antibodies (Invitrogen Corp., Carlsbad, CA, USA) at 1:300 dilution in blocking solution, in a humidified chamber at 37 °C for 1.5 h. Afterward, the sections were incubated with IB_4 at 10 μg/mL for 10 min, washed (3 × 10 min) with PBS, and finally mounted onto glass slides with ProLong Diamond Antifade mounting medium with 4′,6-diamidino-2-phenylindole (DAPI; ProLong Antifade Kit, Molecular Probes; Eugene, ON, USA). In several random sections, the primary antibody was replaced by blocking solution, representing methodological control sections.

Sections were analyzed with a Plan-Apochromat 63x/1.40 oil DIC M27 objective (Carl Zeiss) in a Zeiss LSM 800 Airyscan laser scanning confocal microscope attached to an Axio Observer.Z1/7 microscope. All the pinholes were calibrated at 1 airy unit. Confocal images were converted to 8-bit TIFF format with a ZEN (blue edition, v2.3 Carl Zeiss microscopy GmbH, 2011).

Western blot

Lumbar DRGs (L3-L6) from 4 rats were collected for each experiment, and 3 experiments were carried out (n = 3), for a total of 12 rats used in these experiments. For striatum control blots (positive expression control), left or right striatum from three rat brains were used (n = 3). The protocol was the same as previously reported (Ortega-Legaspi et al., 2011), with mouse anti D1 receptor (Santa Cruz, Cat sc-33,660, 1:1000), rabbit anti D2 receptor (Chemicon, cat. AB5084P, 1:1200) and goat anti-actin (Santa Cruz, cat. sc-1616, 1:8000) in the blocking solution. After three washes, the membrane was incubated with secondary antibodies: HRP donkey anti-mouse (Santa. Cruz, cat. sc-2314, 1:2500), HRP donkey anti-rabbit (Jackson Immunoresearch, cat. 711–035-152, 1:5000) and HRP donkey anti-goat (Santa Cruz, cat. sc-2020, 1:10,000) in blocking solution for 2 h at room temperature. Bound antibody was visualized on films (Kodak, cat 604–0331) using an enhanced chemiluminescence kit (Perkin Elmer, Waltham, MA USA).

Nociceptive behavioral test

All experiments were carried out between 9 AM and 3 PM. A total of 35 animals were used in these experiments. All animals were caged individually in acrylic boxes and were habituated 2 days 30 min each, previous to behavioral tests. The animals were randomly assigned to one of the five experimental groups: control group (VH 50 μL), pramipexole at doses of 3, 10 or 30 nmol (D2-like agonist) and SKF-38393 30 nmol (D1-like agonist). Paw withdrawal latencies (PWL) were tested prior to the i.t. administration to determine the nociceptive threshold. Mechanical and thermonociceptive responses were measured 15, 30, 60 and 120 min after drug administration. Drug administration was done as previously described (Almanza et al., 2015). The method for the acute i.t. administration was chosen because it is of our interest to compare the effect of pramipexole with the effect of the quinpirole used in our previous works (Almanza et al., 2015; Mercado-Reyes et al., 2019). In brief, rats were anesthetized (isoflurane 2% + medical oxygen 98%; Pisa Vet., México) and a small incision (~3 mm) was made at L4-L6 level, a 25 G needle connected to a 50 μL Hamilton syringe was used to i.t. drug delivery, the deposit of the drug was made in ~3 s; after the injection, one shot of Xylocaine 10% was sprayed on the wound. The effect of the anesthetic disappeared within 5 min after the animal was left for recovery, then behavioral testing started 15 min after the drug administration. The experimenter was blinded for the formulation of the administered solution.

For mechanonociception, animals were tested in the dynamic plantar aesthesiometer (Ugo Basile, Varese, Italy). Briefly, a metallic filament pressed the mid-plantar surface of a hind limb with a ramp stimulus (from 0 to 50 g in a lapse of 10 s). The latency and the force used to produce the flexor reflex were recorded automatically. Four consecutive trials were averaged to determine the PWL. Cut-off time was 25 s to avoid tissue damage. For thermonociception, animals were tested in the Hargreaves apparatus (Plantar test; Ugo Basile, Varese, Italy). Animals were exposed to a heat source to hind paws, and the latency of the flexor reflex was automatically recorded. Cut-off time was 25 s to avoid tissue damage. Measurements from three consecutive trials were averaged to determine the hind PWL. All the animals were euthanized immediately after the experiments within a CO_2 chamber.

Drugs

± Quinpirole (D2-like receptor agonist), sulpiride (D2-like receptor antagonist), DAMGO ([D-Ala2, N-Me-Phe4, Gly5-ol]-enkephalin; mu-opioid receptor selective agonist), pramipexole (clinically approved D2-like receptor agonist), SKF-38393 (D1-like receptor agonist) and ω-conotoxin MVIIA (ω-CMVIIA; specific and irreversible $Ca_V2.2$ blocker (Feng et al., 2003)) were obtained from Sigma Aldrich (St. Louis, MO, USA). Stock solution of sulpiride was prepared in absolute ethanol, while the other drugs were dissolved in distilled water. The final concentration of ethanol administered i.t. was always $\leq$0.2%. For i.t. administration, the drugs at the desired concentrations were dissolved in sterile saline solution (NaCl 0.9%) and filtered through a 0.22 μm pore membrane. The vehicle (VH), consisting of sterile saline solution containing 0.1% absolute ethanol was used as a control. Drugs were dissolved in normal extracellular solution for current-clamp experiments and I_{Ca} extracellular solution for voltage-clamp experiments (Table 1).

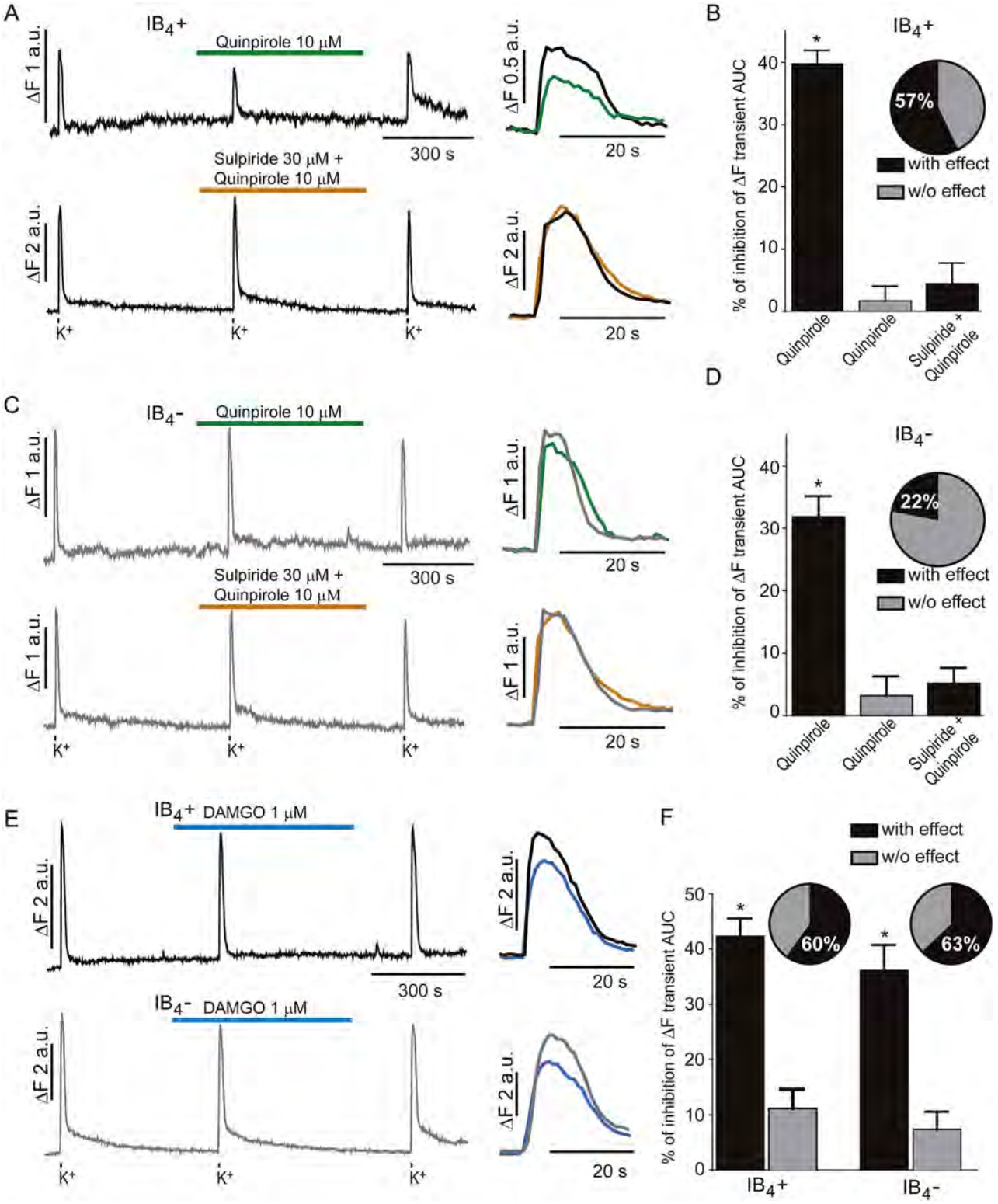

Fig. 1. *Quinpirole's effect on the intracellular Ca^{2+} transient in IB_4+ and IB_4- DRG neurons*. In A and C, representative traces of ΔF transient induced by high K^+ in control, in the presence of 10 μM quinpirole (top) with or without sulpiride 30 μM (bottom), in IB_4+ (A) and IB_4- (C) neurons; right panels show a magnification of superposed ΔF transient in control (black traces), during 10 μM quinpirole application (green traces) or with sulpiride (orange traces). In B and D, the percentage of inhibition of ΔF transient AUC induced by quinpirole in IB_4+ and IB_4- DRG neurons, respectively. In E, representative traces of ΔF transient induced by high K^+ in control, in the presence of 1 μM DAMGO in IB_4+ (top) or in IB_4- (bottom) neurons, right panels show a magnification of superposed ΔF transient in control (black traces) and during DAMGO perfusion (blue traces). In F, the percentage of inhibition of ΔF transient AUC induced by DAMGO in IB_4+ and IB_4- DRG neurons. The pie charts inserts show the percentage of affected (black) or unaffected (gray) neurons by quinpirole or DAMGO. Statistical differences were determined using one-way-ANOVA (denoted by *). (For interpretation of the references to color in this figure legend, the reader is referred to the web version of this article.)

INFORME DE LABORES 2019

Data analysis

All the data are presented as the mean ± standard error of the mean (S.E.M.). In patch-clamp and Ca^{2+} microfluorometry experiments, the *n* of each group represents the number of DRG neurons recorded. In immunofluorescence and behavioral experiments, the *n* of each group represents the number of animals studied. In Western blot, the *n* represents the number of

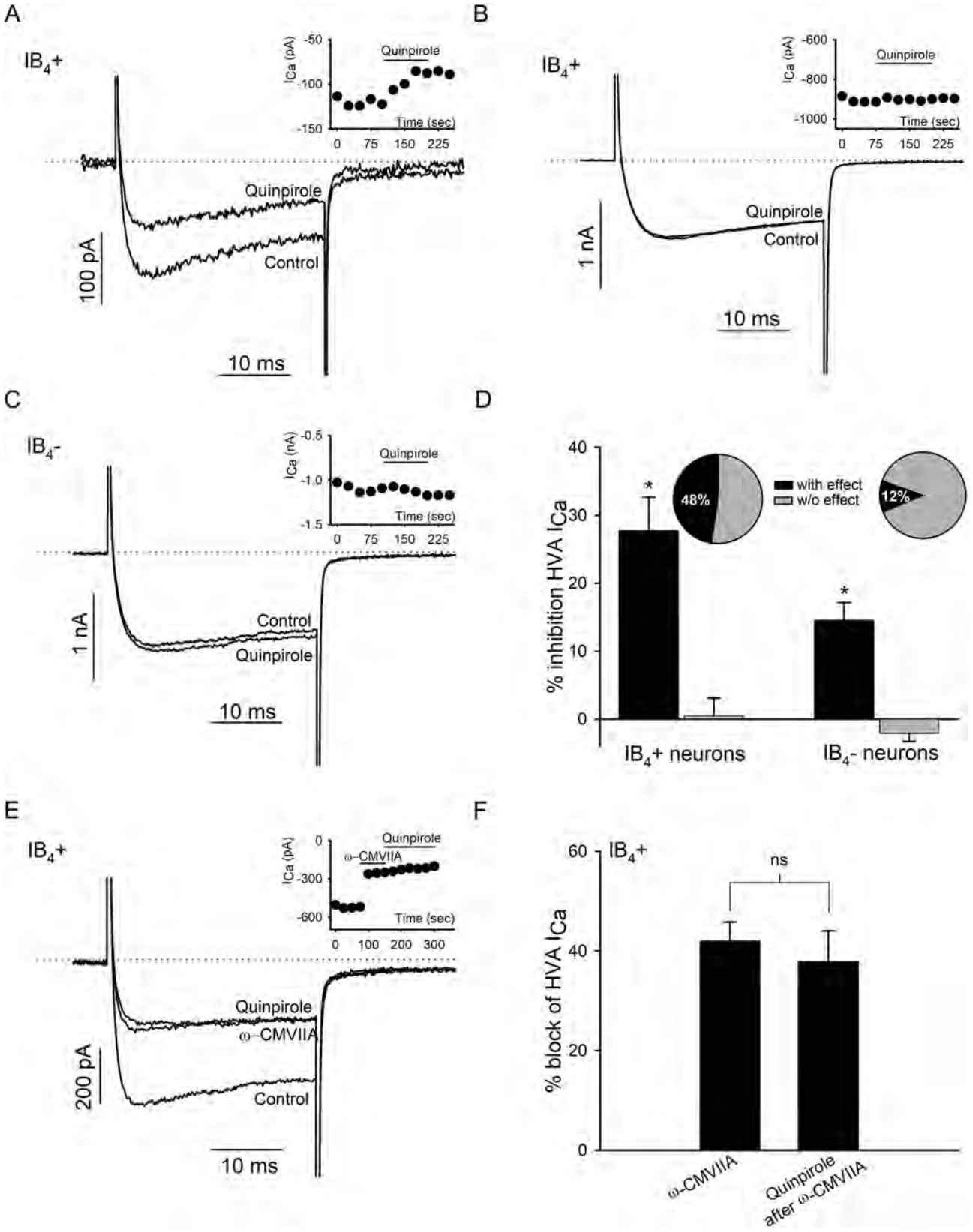

INFORME DE LABORES 2019

experiments. In each experiment, tissue was collected from various animals.

More than two standard deviations of the mean (more than 20%) obtained in control experiments (data not shown) was taken as significant effect induced by test solutions in Ca^{2+} microfluorometry.

In Western blot, the optical densities of the bands were quantified with ImageJ (NIH, USA). In behavioral tests, data were normalized to obtain the maximum drug effect and the AUC. When comparing proportions, statistical significance was assessed by the χ^2 test. Normal distribution and equal variance of data were verified before statistical tests. Comparisons between groups were done with ANOVA and Student's *t*-tests (when two groups were compared). Differences were considered significant when $P < .05$.

RESULTS

D2-like receptor activation effect on $[Ca^{2+}]_i$ in small DRG neurons

In 57% of small IB_4+ neurons (38 of 67), 10 μM quinpirole reduced the ΔF transient AUC induced by high K^+ depolarization by 40 ± 2% (n = 67; $P < .0001$, one-way ANOVA, $F_{10,148} = 38.1$) (Fig. 1A, B top, C). Meanwhile, quinpirole reduced the ΔF transient AUC by 32 ± 3% only in 22% of IB_4- small DRG neurons (5 of 22), a lower percentage of quinpirole sensitive neurons compared with IB_4+ neurons (χ^2 test, $P = .007$). The inhibitory effect of quinpirole was analogous in both IB_4+ and IB_4- small DRG neurons ($P = .92$, one-way ANOVA) (Fig. 1B, D). Sulpiride 30 μM prevented the effect of quinpirole in both IB_4+ and IB_4- nociceptive sensory neurons (Fig. 1A bottom, B; C bottom, D).

As positive control, we used DAMGO (1 μM), which produced a significant decrement in the ΔF transient AUC after high K^+ depolarization in both, IB_4+ (42 ± 3%; n = 12; $P < .0001$, one-way ANOVA, $F_{10,148} = 38.1$) and IB_4- neurons (36 ± 5; n = 10; $P < .0001$, one-way ANOVA; $F_{10,148} = 38.1$) (Fig. 1 E, F); in both populations, the effect of DAMGO on ΔF transient AUC was not different ($P = .97$, one-way ANOVA) (Fig. 1F), and the percentage of IB_4+ and IB_4- neurons that responded to DAMGO was similar (χ^2 test, $P = .9$) (Fig. 1F).

D2-like agonist effect on HVA I_{Ca} from small-diameter DRG neurons

HVA-I_{Ca} in small DRG neurons displayed little inactivation during 30 ms of the voltage pulse to −10 mV, with similar temporal courses in IB_4- and IB_4+ neurons (Fig. 2). In IB_4+ neurons, 10 μM quinpirole reduced the HVA-I_{Ca} amplitude by 27 ± 5% in 10 of 21 neurons (t(9) = −4.741, $P = .000529$, Student's *t* test; $C_m = 30$ ± 3 pF) (Fig. 2A, D), while in the remaining neurons, quinpirole produced no changes in the HVA-I_{Ca} amplitude (change percent 1 ± 3%; t(10) = −1.160, $P = .136$, paired Student's *t* test; $C_m = 31$ ± 7 pF) (Fig. 2B, D). In IB_4- neurons, quinpirole did not affect the HVA-I_{Ca} amplitude in 30 of 34 neurons, with a nonsignificant current amplitude increment of 2 ± 1% (t(29) = 0.0703, $P = .472$, paired Student's *t* test; $C_m = 37$ ± 4 pF) (Fig. 2C, D). In only 4 out of 34 neurons did quinpirole produce a significant inhibition of the HVA-I_{Ca}, whose reduction was 14 ± 3% (t(3) = −2.489, $P = .0443$, paired Student's *t* test; $C_m = 35$ ± 8 pF) (Fig. 2D). The percentage of HVA-I_{Ca} inhibition by quinpirole in IB_4+ neurons was not different respect to the observed in the four IB_4- neurons (t(12) = 1.585, $P = .139$, paired Student's *t* test), but, the proportion of neurons in which quinpirole inhibited the HVA-I_{Ca} was higher in IB_4+ compared to IB_4- neurons (χ^2 test, $P = .008$).

To evaluate if the quinpirole effect was on the N-type VGCC ($Ca_V2.2$), we tested in IB_4+ neurons the effect of the quinpirole after pretreating the neurons with a blocker of the N-type Ca^{2+} channel. Perfusion of 1 μM ω-CMVIIA by itself reduced the HVA-I_{Ca} in 42 ± 4% (n = 11; $C_m = 34$ ± 3 pF; $P < .001$, one-way ANOVA, $F_{2,\ 30} = 67.250$) (Fig. 2E, F). Following ω-CMVIIA pretreatment, 10 μM quinpirole was unable to induce its inhibitory effect: the percentage of blocked HVA-I_{Ca} remained similar to the ω-CMVIIA effect (38 ± 6%; n = 11; $P = .501$, one-way ANOVA $F_{2,\ 30} = 67.250$) (Fig. 2E, F), suggesting that quinpirole's main effect was on ω-CMVIIA-sensitive Ca^{2+} channels (Fig. 2F).

D2-like agonist effect on action potential firing of small-diameter DRG neurons

In the presence of 10 μM quinpirole, there was no significant change in the number of APs produced by a depolarizing square pulse (500 ms) in IB_4+ neurons (6 ± 0.7 APs in control, 5.9 ± 0.8 APs after quinpirole treatment; n = 16; $C_m = 26$ ± 2 pF; t(21) = 0.05, $P = .95$) (Fig. 3A, C). Similar results were obtained in IB_4- neurons (6.2 ± 0.5 APs in control, 6.2 ± 0.6 APs after quinpirole treatment; n = 22; $C_m = 20$ ± 2 pF; t(15) = 0.85, $P = .41$) (Fig. 3B, C). To unmask a possible quinpirole's effect, a ramp current pulse was used for stimulation. Quinpirole did not affect the AP discharge in IB_4+ neurons (9 ± 2 APs in control, 9 ± 2 APs after quinpirole; n = 6; $C_m = 26$ ± 2 pF; t(5) = 0.55, $P = .61$) (Fig. 3D, F), nor in IB_4- neurons (10

Fig. 2. *Quinpirole's effect on HVA-I_{Ca} in IB_4+ and IB_4- DRG neurons.* In A and B, traces of HVA-I_{Ca} ($V_H = -60$ mV, voltage step to −10 mV) recorded in IB_4+ DRG neurons before (control trace) and after 10 μM quinpirole perfusion. In C, traces of HVA-I_{Ca} recorded in IB_4- neurons before (control trace) and after 10 μM quinpirole perfusion. Inserts in A, B and C show the time course of quinpirole's effect on HVA-I_{Ca} amplitude. In D, the percentage of HVA-I_{Ca} inhibition by quinpirole in IB_4+ and IB_4- DRG neurons is showed, in which there was an effect (black bars) and those where did not (gray bars). The pie graph shows the percentage of DRG neurons where quinpirole inhibited (black) or not (gray) the HVA-I_{Ca} for each population. Statistically significant changes are denoted with * ($P < .05$, paired Student's t test). In E, representative traces of HVA-I_{Ca} recorded in IB_4+ DRG neurons in control conditions, after 1 μM ω-conotoxin MVIIA and posterior perfusion of 10 μM quinpirole. Time course of drug's effect on HVA-I_{Ca} amplitude is shown in the insert. In F, bar graphs show the percent of blockade of HVA-I_{Ca} by ω-conotoxin MVIIA and quinpirole in presence of N-type Ca^{2+} channel blocker. Differences were not significant ($P > .05$, paired Student's t test).

INFORME DE LABORES 2019

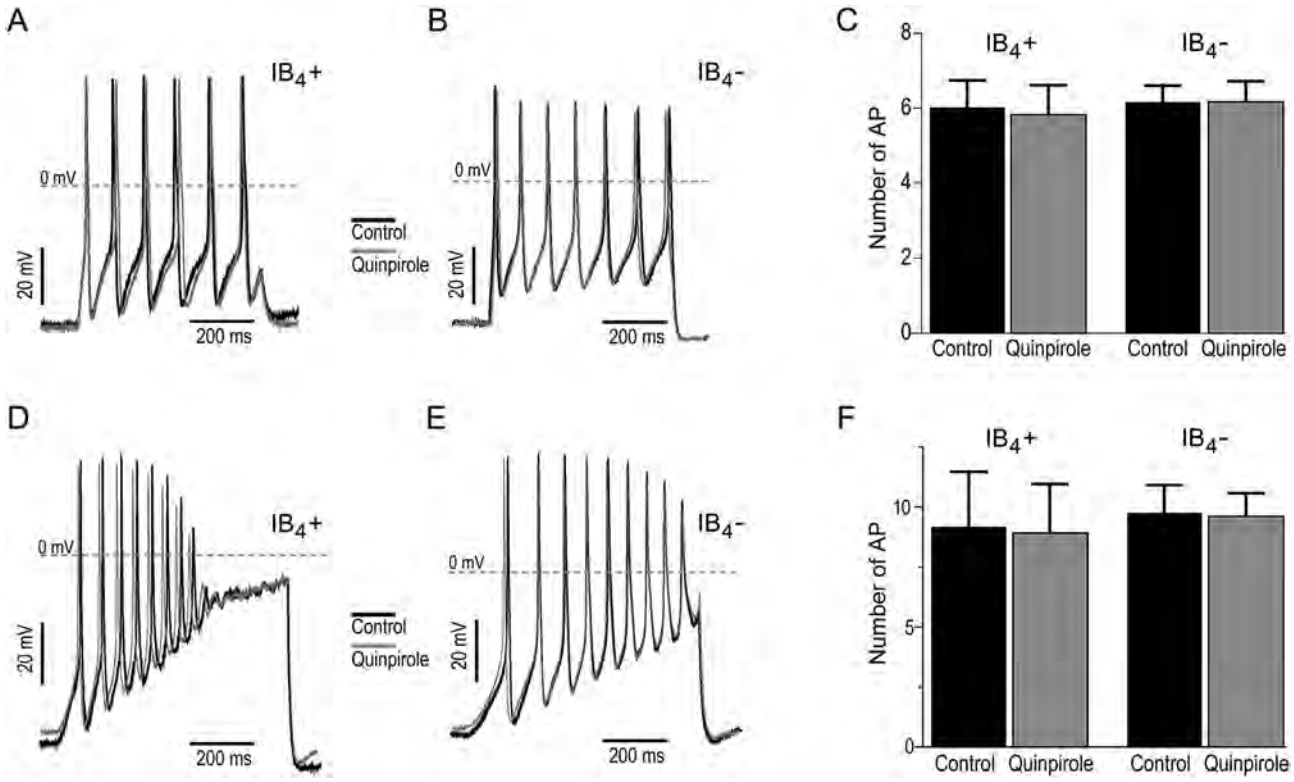

Fig. 3. *Effect of quinpirole on AP firing in small-diameter DRG neurons.* In A and B, representative AP firing obtained with a square pulse stimulation, recorded before (black traces) and after quinpirole perfusion (10 μM; gray traces), in IB_4+ (A) and IB_4- (B) neurons. In C, summary of the effect of quinpirole on the number of APs in IB_4+ and IB_4- small DRG neurons during square pulse stimulation. In D and E, representative AP firing obtained with a ramp current stimulation, recorded before (black traces) and after quinpirole perfusion (10 μM; gray traces), in IB_4+ (D) and IB_4- (E) neurons. In F summary of the effect of quinpirole on the number of APs in IB_4+ and IB_4- small DRG neurons during ramp stimulation.

± 1 APs in control, 9.6 ± 1 APs after quinpirole; n = 12; C_m = 25 ± 3 pF; t(11) = 0.53, P = .61) (Fig. 3E, F).

As positive control DAMGO (1 μM), produced no significant change in the discharge of AP during a depolarizing square pulse (500 ms) in IB_4+ (4.7 ± 1 APs in control, 4.2 ± 1 APs after DAMGO; n = 10; t(9) = 1.37, P = .21) or IB_4- neurons (6.6 ± 1 APs in control, 6 ± 1 APs after DAMGO; n = 8; t(7) = 2.1, P = .07), similar to quinpirole (not shown).

Immunolocalization of D2 DA receptor in the DRG population

To determine the distribution of D2 DA receptor between peptidergic and nonpeptidergic subpopulations of nociceptive DRG neurons, D2 DA receptor was immunolocalized in thin DRG sections (14 μm) of adult rats, and we observed its colocalization with CGRP (peptidergic neuron marker) and IB_4 (nonpeptidergic neurons marker). The antibody raised against D2 DA receptor produced a staining pattern of tiny dots preferentially on or near the membranes of neuron soma (Fig. 4, arrows), but the staining was not homogeneous among all the DRG neurons, since it was absent in many of them. CGRP antibody stained the cytoplasm of small-diameter neurons (< 26 μm) (Fig. 4, arrowhead), and those CGRP-positive neurons were not stained by the marker IB_4 (Fig. 4, arrows), as has been extensively reported (Scherrer et al., 2009). D2 DA receptor staining correlated with IB_4 staining, however some CGRP neurons have scarse D2 DA receptor staining (Fig. 4), suggesting that D2 DA receptor is expressed preferentially in nonpeptidergic DRG neurons. Control sections where 1st antibody was omitted are showed in Fig. 4F-H.

Western blot

To determine the expression of D2 DA receptor in the lumbar DRG, Western blot experiments were done. As reported in earlier reports and above, we found significant expression of D2 DA receptor in the lumbar DRGs (n = 3) (Fig. 5). Rat striatum was used as the positive control of D2 DA receptor expression (n = 3), and the negative control (secondary antibody omission) produced no band staining. The band pattern for D2 DA receptor it was consistent with the MW in previous reports (Galbavy et al., 2013; Stojanovic et al., 2017).

Because D1-like DA receptors have been identified in DRGs (Galbavy et al., 2013), we used an antibody against D1 DA receptor as a positive control and performed Western blot experiments. We found a significant expression of D1 DA receptor in both lumbar DRGs and the rat striatum; the negative control produced no band staining (n = 3) (omission of the secondary antibody).

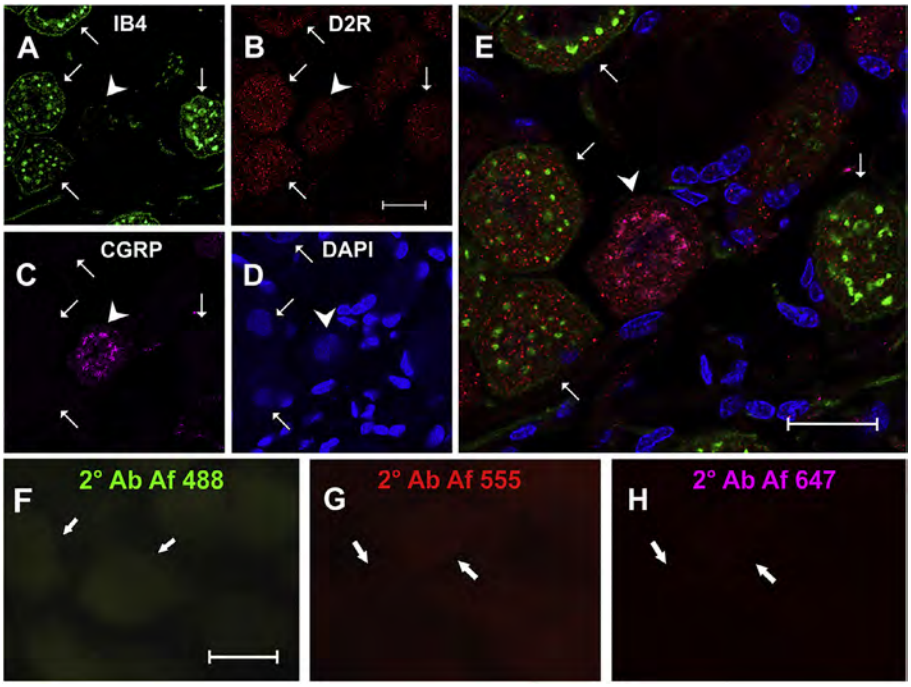

Fig. 4. *Immunostaining of D2 DA receptor in DRG neurons*. Photomicrographs of rat DRG showing in A, IB_4 fluorescence (IB_4; green), B, D2 DA receptor immunoreactivity (D2R; red), C, CGRP immunoreactivity (magenta), D, DAPI fluorescence (blue), E, merge of the images from the same optical fields. Thin arrows indicate IB_4+ small neurons. The arrowhead points to a CGRP-immunoreactive neuron, which is IB_4-. Notice that IB_4+ neurons contain a higher D2 DA receptor immunoreactivity density compared to CGRP-positive neuron. At the bottom (F-H), methodological control of immunostaining omitting primary antibodies, showing the absence of specific immunoreactivity and the background of the second antibodies used, slices were observed with their specific filters (Af, Alexa fluor). Scale bar: 20 μm. (For interpretation of the references to color in this figure legend, the reader is referred to the web version of this article.)

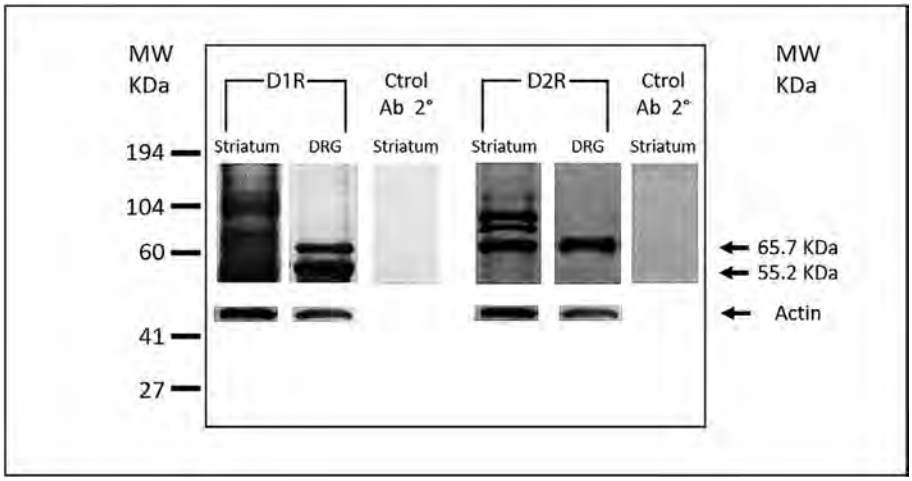

Fig. 5. *D1 and D2 DA receptor protein expression in lumbar DRG neurons*. Western immunoblot analysis with antibodies against D1 and D2 DA receptors of membrane protein extracts from lumbar DRG neurons. Striatum membranes were used as a positive control. As loading control actin was used. For the negative control, the secondary antibody was omitted.

Behavioral tests

Finally, we tested the D2/D3 agonist drug pramipexole (doses tested: 1, 10, and 30 nmol). The use of pramipexole only in the behavioral tests was aimed at evaluating whether a clinically approved D2-like agonist produced antinociceptive effect similar to those of the gold standard D2-like agonist quinpirole, tested in our previous behavioral studies (Almanza et al., 2015; Mercado-Reyes et al., 2019). This experiment is of clinical relevance, as positive results could encourage the potential usage of D2-like agonists as analgesic adjuvants at the spinal cord level.

Pramipexole i.t. administration reached its maximum antinociceptive effect after 15 min and disappeared during the experiment (within 2 h). Pramipexole 30 nmol i.t. administration produced a significant increment of 43 ± 14% in the PWL in mechanonociceptive tests (n = 8; two-way ANOVA, $F_{4, 35} = 4.125$; $P = .002$) (Fig. 6A), while 1 and 10 nmol i.t. produced nonsignificant changes in the PWL. In the thermonociceptive test, pramipexole produced no effect in the PWL at the same doses tested in mechanonociception (Fig. 6B), consistent with the findings previously reported for quinpirole (Almanza et al., 2015). AUC analysis yielded the same conclusions (One-way ANOVA, $F_{4, 30} = 2.75$; $P = .04$; Fig. 6C-F).

Because there was a significant expression of D1-like receptors in DRGs, we tested whether i.t. administration of SKF-38393 (highly selective D1-like agonist) at a high dose (30 nmol) would modify both mechano- and thermonociceptive responses. After SKF-38393 i.t. administration, there were no changes in the PWL from either nociceptive test at any evaluated time (Fig. 6A, B). This finding was best represented in the maximum effect and AUC analysis (Fig. 6C-F).

DISCUSSION

We found that the D2-like DA receptor agonist, quinpirole, inhibits the Ca^{2+} influx in a set of small IB_4+ DRG neurons, mainly through Ca_V 2.2 channels, those neurons are predominantly associated with

INFORME DE LABORES 2019

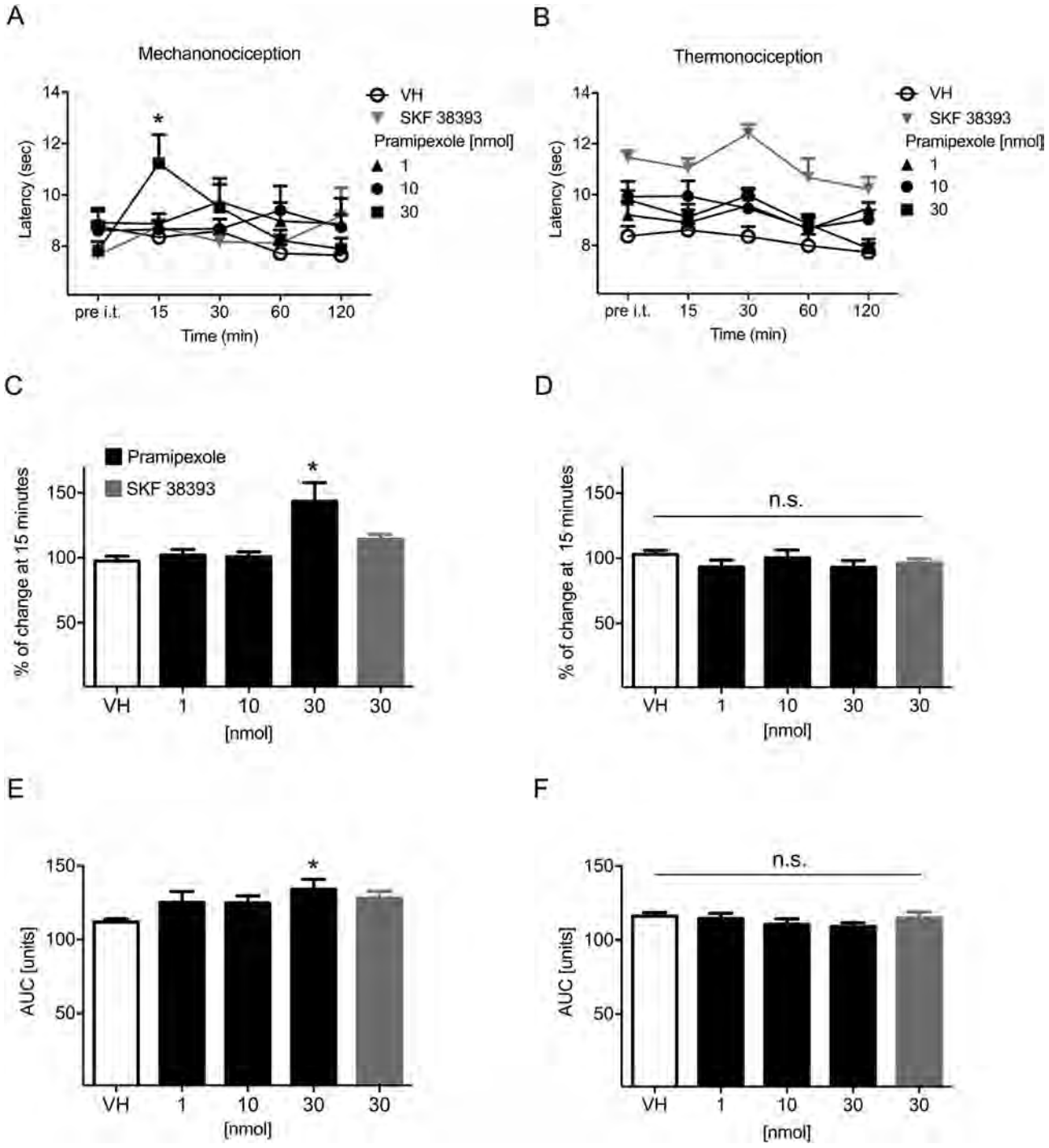

Fig. 6. *The effects of pramipexole and SKF 38393 on the mechanonociceptive and thermonociceptive test*. In A and B, time courses of the effect of i.t. application of vehicle (VH), pramipexole (1, 10 and 30 nmol) and the D1-like DA receptor agonist (SKF 38393, 30 nmol) on PWL in mechano- and thermonociceptive tests, respectively. In C and D, latencies percentage of change (normalized to the basal latency) of VH, pramipexole and SKF 38393 obtained 15 min after i.t. administration in mechano- and thermonociceptive tests. In E and F, area under the curve (AUC) from A and B graphs for each drug and VH in mechano- and thermonociceptive tests, respectively. * denotes significant differences *versus* VH ($P < .05$, one-way ANOVA).

mechanonociception. Western blot revealed a significant expression of D2 DA receptors in the lumbar DRG and immunofluorescence experiments showed that D2 DA receptors were expressed mainly in IB_4+ small DRG neurons. Interestingly, pramipexole produced spinal antinociception in a similar fashion to quinpirole. Our results explain, at least in part, why D2-like receptor agonists produce antinociception specific on mechanonociceptive stimuli.

D2-like DA receptor agonists produce antinociception in different pain models (Tamae et al., 2005; Cobacho et al., 2010, 2014; Rodgers et al., 2019) and clinical con-

ditions that involve intense pain (Dickey and Minton, 1972; Nixon, 1975; Kernbaum and Hauchecorne, 1981; Ertas et al., 1998). Some studies have been done to determine the mechanism by which DA receptor agonists produce antinociception (Fleetwood-Walker et al., 1988; Tamae et al., 2005; Charbit et al., 2009; Taniguchi et al., 2011; Lu et al., 2018), but, at least at the spinal cord level, it is not completely understood.

Neurons from the dorsal horn and DRG express DA receptors; there are evidences that supports the presence of D2-like and D1-like DA receptors in both structures (Xie et al., 1998; Zhu et al., 2007; Barraud et al., 2010; Kawamoto et al., 2012; Galbavy et al., 2013). Our previous work suggests that the distribution of DA receptors in DRG neurons is not homogeneous, and DA receptors must be expressed predominantly in mechanonociceptive neurons (Almanza et al., 2015; Mercado-Reyes et al., 2019).

Results in this work provide evidence that D2-like DA receptor agonist inhibits both, the rise of transient $[Ca^{2+}]_i$ induced by high-K^+ depolarization, and the HVA-I_{Ca} in a significantly higher proportion of IB_4+ neurons than IB_4- neurons. IB_4 stains nonpeptidergic DRG neurons population denominate as IB_4+, its activation mediate mechanonociception (Price and Flores, 2007; Cavanaugh et al., 2009 ; Havelin et al., 2017). While peptidergic that are not stained by IB_4 (IB_4-), mostly express the heat-sensing receptor TRPV1 (Cavanaugh et al., 2009; Havelin et al., 2017) and mediate the thermonociception. Although, grouping neurons by their binding to IB_4 is not perfect to classify neurons by their physiological role (thermonociceptive, mechanonociceptive, *etc.*), and it is less exact in rats than in mouse (Price and Flores, 2007), there is a clear trend of the quinpirole effect to inhibit Ca^{2+} current in those neurons that bind IB_4, which has been related to transduced mechanical nociception (Cavanaugh et al., 2009; Le Pichon and Chesler, 2014). The Ca^{2+} microfluorometry and the electrophysiological data agree with the behavioral effect of the i.t. delivery of D2-like DA receptor agonists (quinpirole in previous work and pramipexole in this report) in nociceptive tests (Cobacho et al., 2014; Almanza et al., 2015).

The immunofluorescence data further support our idea of D2-like DA receptor expression in a population of neurons that are associated with mechanonociception; our results show higher expression of D2 DA receptor mostly in IB_4+ neurons, which could explain the specific antinociception seen in the previous behavioral data and agrees with our findings in Ca^{2+} imaging and patch-clamp experiments.

VGCCs are expressed in the soma and in nerve terminals of DRG neurons, where they regulate neurotransmitter release in the presynaptic terminals of the dorsal horn in the spinal cord through $Ca_V2.2$ channels. In this work, our results show that the major effect of quinpirole on the electrophysiological properties of DRG neurons was the inhibition of HVA-I_{Ca}. Thus, our results support the idea that Ca^{2+} entry through $Ca_V2.2$ channels is reduced due to the activation of D2-like DA receptors, and this can be the presynaptic mechanism by which quinpirole produces –at least in part- its antinociceptive effect when delivered i.t.

VGCC modulation or blocking in nociceptive DRG neurons is one of the most sought-after targets for analgesic drug development. The U.S. Food & Drug Administration (FDA) has approved drugs such as opioids, gabapentinoids and ziconotide that produce analgesia by reducing the HVA-I_{Ca} in DRG neurons (Sluka, 1998; Hendrich et al., 2008; Scherrer et al., 2009). In agreement with the inhibition of HVA-I_{Ca} in DRG by quinpirole shown here, similar results in other neuronal types have been reported (Ramanathan et al., 2008; Kline et al., 2009).

In DRG nociceptors, $Ca_V2.2$ channels are associated with the neurotransmitter release to the spinal dorsal horn and not directly with the neuronal excitability modulation (Bao et al., 1998; Altier and Zamponi, 2004; Takasu et al., 2016); probably explaining why the N-type Ca^{2+} channels inhibition by quinpirole did not modify the neuronal discharge pattern.

T-type Ca^{2+} channels have been described in both, small and medium size DRG neurons and are associated with cellular excitability regulation, its activation determines the after-depolarizing potential which could lead to a burst firing of action potentials. Modulation of these channels would affect the neuronal discharge pattern (Todorovic and Jevtovic-Todorovic, 2007; François et al., 2015). Our results show that quinpirole has no apparent effect on DRG nociceptor excitability, nevertheless, it is important to consider that in our current-clamp conditions, at the membrane potential of about −60 mV, most of T-type channels are in inactivated-state, so, from the current clamp results we can not to determinate if quinpirole had or not effect on them, ultimately changing the neuronal discharge pattern. However, quinpirole exhibits two traits of the mu-opioid agonists: it produces significant inhibition of $Ca_V2.2$ channels (Taddese et al., 1995; Baillie et al., 2015), and it produces modest changes in the electrophysiological firing properties of small DRG neurons (IB_4+ and IB_4- populations, as shown in this work), suggesting an analogous mechanism of antinociception.

Previous studies using DA at 10–100 μM showed a significant inhibition of HVA-I_{Ca} in almost all small-diameter DRG neurons of rat and chicken (Marchetti et al., 1986; Formenti et al., 1998), but DA at those concentrations is an agonist of other amine receptors, particularly α-adrenergic receptor (Cornil and Ball, 2008; Cilz et al., 2014), which are abundant in small-diameter DRG neurons (peptidergic and nonpeptidergic nociceptors). It is worth noting that α-adrenergic agonists (for example, clonidine) produce I_{Ca} inhibition and antinociception when they are administered i.t. (Eisenach et al., 2005; Nguyen et al., 2017). In our work, quinpirole only produced I_{Ca} inhibition in ~50–60% of small-diameter neurons within the IB_4+ population, and it only produced mechanical antinociception. One reasonable conclusion is that D2-like DA receptor expression is confined to the subpopulation of mechanonociceptors (Le Pichon and Chesler, 2014).

INFORME DE LABORES 2019

Our results reveal the cellular mechanism by which mechanonociceptive DRG neurons are inhibited by D2-like DA receptor agonists. They are in agreement with studies reporting the effect of DA or quinpirole on the dorsal horn neurons from superficial layers (Tamae et al., 2005; Taniguchi et al., 2011). Patch-clamp recordings of *substantia gelatinosa* neurons have shown that D2-like DA receptor activation produced the opening of an outward K^+ current, which in turn hyperpolarized the resting membrane potential of dorsal horn neurons, reducing their excitability (Tamae et al., 2005). The frequency of postsynaptic excitatory currents can be reduced by DA application when C-fibers are stimulated, which suggests that D2-like DA receptor activation produces inhibition of the neurotransmitter release (presynaptic inhibition), in lamina I (Lu et al., 2018), and lamina II dorsal horn neurons (Taniguchi et al., 2011), which can be explained with our finding that D2-like DA receptor agonist decreased the HVA-I_{Ca} (most probably $Ca_V2.2$) in IB_4+ small-diameter DRG neurons.

D1 DA receptor activation was linked to reduction of the excitability of small-diameter DRG neurons (Galbavy et al., 2013), but i.t. administration of a high dose of the selective D1/D5 DA receptor agonist SKF-38393 produced no effect on the latency of flexor reflex in nociceptive tests, which is in agreement with a previous report (Tamae et al., 2005). In contrast, D1/D5 DA receptor activation has been linked to the genesis and maintenance of chronic pain conditions, leaving its role in the spinal cord most likely pronociceptive under pathological conditions (Kim et al., 2015; Megat et al., 2018) with little or uncertain participation in the modulation of nociceptive entry in healthy animals.

Thus, differential expression of dopaminergic receptors in primary nociceptive neurons could have physiological and clinical relevance. Our findings are in accordance with the hypothesis of labeled lines for the nociceptive stimulus codification and modulation at the peripheral level (Cavanaugh et al., 2009; Emery et al., 2016). They also provide a better description of the antinociceptive effect of DA at the spinal cord level by suggesting that the mechanism that underlies the mechanical antinociception is elicited by the activation of D2-like DA receptors in primary nociceptive neurons. Together with previous data that demonstrate that D2-like DA receptor agonists produce antinociception in other pain-related CNS structures (López-Avila et al., 2004; Coffeen et al., 2008; Wood, 2008; Pellicer et al., 2010), our work reinforces the hypothesis that dopaminergic agonists could be useful as adjuvants in the treatment of painful conditions resistant to conventional treatments.

ACKNOWLEDGMENTS

The authors thank Dr. José Nicolás Jiménez Pérez and Diana Millán Aldaco for their valuable technical assistance and Claudia V. Rivera-Cerecedo, Francisco Ruiz and Mario A. Aguilar for expert animal husbandry and Francisco Perez Eugenio for expert computing advice.

RESEARCH FUNDING

This work was supported by INPRFM [grant number NC12165994.0], la Fundación Ramón de la Fuente A.C. and CONACyT [grant numbers 165994 and 266249] to FM. CONACyT grant CB-240305 and Laboratorio Nacional de Canalopatías grant 299051 to AH-C and grant PAPIIT AG200119 from Dirección General de Asuntos del Personal Académico of Universidad Nacional Autónoma de México (DGAPA-UNAM).

CONFLICT OF INTEREST

The authors have no conflicts of interest to declare.

REFERENCES

Almanza A, Simón-Arceo K, Coffeen U, Fuentes-García R, Contreras B, Pellicer F, Mercado F (2015) A D2-like receptor family agonist produces analgesia in mechanonociception but not in thermonociception at the spinal cord level in rats. Pharmacol Biochem Behav 137:119–125. available at:Available from: http://www.ncbi.nlm.nih.gov/pubmed/26303304.

Altier C, Zamponi GW (2004) Targeting Ca2 + channels to treat pain: T-type versus N-type. Trends Pharmacol Sci 25:465–470. available at:Available from: http://www.ncbi.nlm.nih.gov/pubmed/15559248.

Baccei ML, Kocsis JD (2000) Voltage-gated calcium currents in axotomized adult rat cutaneous afferent neurons. J Neurophysiol 83:2227–2238. available at:Available from: http://www.ncbi.nlm.nih.gov/pubmed/10758131.

Baillie LD, Schmidhammer H, Mulligan SJ (2015) Peripheral μ-opioid receptor mediated inhibition of calcium signaling and action potential-evoked calcium fluorescent transients in primary afferent CGRP nociceptive terminals. Neuropharmacology 93:267–273. available at:Available from: http://www.ncbi.nlm.nih.gov/pubmed/25721395.

Bao J, Li JJ, Perl ER (1998) Differences in ca 2 + channels governing generation of miniature and evoked excitatory synaptic currents in spinal laminae I and II. J Neurosci 18:8740–8750. Available at: Available from: https://doi.org/10.1523/JNEUROSCI.18-21-08740.1998.

Barraud Q, Obeid I, Aubert I, Barrière G, Contamin H, McGuire S, Ravenscroft P, Porras G, Tison F, Bezard E, Ghorayeb I (2010) Neuroanatomical study of the A11 diencephalospinal pathway in the non-human primate. PLoS One 5 e13306.

Blair NT, Bean BP (2002) Roles of tetrodotoxin (TTX)-sensitive Na + current, TTX-resistant Na + current, and Ca2 + current in the action potentials of nociceptive sensory neurons. J Neurosci 22:10277–10290. available at:Available from: http://www.ncbi.nlm.nih.gov/pubmed/12451128.

Cavanaugh DJ, Lee H, Lo L, Shields SD, Zylka MJ, Basbaum AI, Anderson DJ (2009) Distinct subsets of unmyelinated primary sensory fibers mediate behavioral responses to noxious thermal and mechanical stimuli. Proc Natl Acad Sci U S A 106:9075–9080. available at:Available from: http://www.ncbi.nlm.nih.gov/pubmed/19451647.

Charbit AR, Akerman S, Holland PR, Goadsby PJ (2009) Neurons of the dopaminergic/calcitonin gene-related peptide A11 cell group modulate neuronal firing in the trigeminocervical complex: an electrophysiological and immunohistochemical study. J Neurosci 29:12532–12541.

Cilz NI, Kurada L, Hu B, Lei S (2014) Dopaminergic modulation of GABAergic transmission in the entorhinal cortex: concerted roles of 1 Adrenoreceptors, inward rectifier K +, and T-type Ca2 + channels. Cereb Cortex 24:3195–3208. Available at:Available from: https://doi.org/10.1093/cercor/bht177.

Cobacho N, De la Calle JL, González-Escalada JR, Paíno CL (2010) Levodopa analgesia in experimental neuropathic pain. Brain Res Bull 83:304–309.

Cobacho N, de la Calle JL, Paíno CL (2014) Dopaminergic modulation of neuropathic pain: analgesia in rats by a D2-type receptor agonist. Brain Res Bull 106:62–71.

Coffeen U, López-Avila A, Ortega-Legaspi JM, del Angel R, López-Muñoz FJ, Pellicer F (2008) Dopamine receptors in the anterior insular cortex modulate long-term nociception in the rat. Eur J Pain 12:535–543.

Cornil CA, Ball GF (2008) Interplay among catecholamine systems: dopamine binds to α 2 -adrenergic receptors in birds and mammals. J Comp Neurol 511:610–627. Available at:Available from: https://doi.org/10.1002/cne.21861.

Dickey RP, Minton JP (1972) Levodopa relief of bone pain from breast cancer. N Engl J Med 286:843.

Eisenach JC, Zhang Y, Duflo F (2005) alpha2-adrenoceptors inhibit the intracellular Ca2 + response to electrical stimulation in normal and injured sensory neurons, with increased inhibition of calcitonin gene-related peptide expressing neurons after injury. Neuroscience 131:189–197. available at:Available from: http://www.ncbi.nlm.nih.gov/pubmed/15680702.

Emery EC, Luiz AP, Sikandar S, Magnúsdóttir R, Dong X, Wood JN (2016) In vivo characterization of distinct modality-specific subsets of somatosensory neurons using GCaMP. Sci Adv 2: e1600990 available at: http://www.ncbi.nlm.nih.gov/pubmed/27847865.

Ertas M, Sagduyu A, Arac N, Uludag B, Ertekin C (1998) Use of levodopa to relieve pain from painful symmetrical diabetic polyneuropathy. Pain 75:257–259.

Feng Z-P, Doering CJ, Winkfein RJ, Beedle AM, Spafford JD, Zamponi GW (2003) Determinants of inhibition of transiently expressed voltage-gated calcium channels by omega-conotoxins GVIA and MVIIA. J Biol Chem 278:20171–20178. available at: Available from: http://www.ncbi.nlm.nih.gov/pubmed/12654924.

Fleetwood-Walker SM, Hope PJ, Mitchell R (1988) Antinociceptive actions of descending dopaminergic tracts on cat and rat dorsal horn somatosensory neurones. J Physiol 399:335–348.

Formenti A, Martina M, Plebani A, Mancia M (1998) Multiple modulatory effects of dopamine on calcium channel kinetics in adult rat sensory neurons. J Physiol 509 (Pt 2:395–409.

François A, Schüetter N, Laffray S, Sanguesa J, Pizzoccaro A, Dubel S, Mantilleri A, Nargeot J, Noël J, Wood JN, Moqrich A, Pongs O, Bourinet E (2015) The low-threshold Calcium Channel Cav3.2 determines low-threshold mechanoreceptor function. Cell Rep 10:370–382. Available at:Available from: https://linkinghub.elsevier.com/retrieve/pii/S221112471401095X.

Galbavy W, Safaie E, Rebecchi MJ, Puopolo M (2013) Inhibition of tetrodotoxin-resistant sodium current in dorsal root ganglia neurons mediated by D1/D5 dopamine receptors. Mol Pain 9:60.

Havelin J, Imbert I, Sukhtankar D, Remeniuk B, Pelletier I, Gentry J, Okun A, Tiutan T, Porreca F, King TE (2017) Mediation of movement-induced breakthrough Cancer pain by IB4-binding nociceptors in rats. J Neurosci 37:5111–5122. available at: Available from: http://www.ncbi.nlm.nih.gov/pubmed/28438966.

Hendrich J, Van Minh AT, Heblich F, Nieto-Rostro M, Watschinger K, Striessnig J, Wratten J, Davies A, Dolphin AC (2008) Pharmacological disruption of calcium channel trafficking by the alpha2delta ligand gabapentin. Proc Natl Acad Sci U S A 105:3628–3633.

Kawamoto K, Otsuguro K, Ishizuka M, Ito S (2012) Inhibitory effects of dopamine on spinal synaptic transmission via dopamine D1-like receptors in neonatal rats. Br J Pharmacol 166:788–800.

Kernbaum S, Hauchecorne J (1981) Administration of levodopa for relief of herpes zoster pain. JAMA 246:132–134. available at: Available from: http://www.ncbi.nlm.nih.gov/pubmed/7017177.

Kilkenny C, Browne WJ, Cuthill IC, Emerson M, Altman DG (2010) Improving bioscience Research reporting: the ARRIVE guidelines for reporting animal Research. PLoS Biol 8. Available at:Available from: https://doi.org/10.1371/journal.pbio.1000412 e1000412.

Kim J-YV, Tillu DV, Quinn TL, Mejia GL, Shy A, Asiedu MNK, Murad E, Schumann AP, Totsch SK, Sorge RE, Mantyh PW, Dussor G, Price TJ (2015) Spinal dopaminergic projections control the transition to pathological pain plasticity via a D1/D5-mediated mechanism. J Neurosci 35:6307–6317.

Kline DD, Hendricks G, Hermann G, Rogers RC, Kunze DL (2009) Dopamine inhibits N-type channels in visceral afferents to reduce synaptic transmitter release under normoxic and chronic intermittent hypoxic conditions. J Neurophysiol 101:2270–2278. available at:Available from: http://www.ncbi.nlm.nih.gov/pubmed/19244351.

Le Pichon CE, Chesler AT (2014) The functional and anatomical dissection of somatosensory subpopulations using mouse genetics. Front Neuroanat 8. https://doi.org/10.3389/fnana.2014.00021/abstract. Available at:.

León-Olea M, Miller-Pérez C, Sánchez-Islas E, Mendoza-Sotelo J, Garduño-Gutiérrez R, de Gortari P, Amaya MI (2013) The nociceptin/orphanin FQ-like opioid peptide in nervous periesophageal ganglia of land snail *Helix aspersa*. Brain res 1505:22–46. available at:Available from: http://www.ncbi.nlm.nih.gov/pubmed/23419890.

López-Avila A, Coffeen U, Ortega-Legaspi JM, del Angel R, Pellicer F (2004) Dopamine and NMDA systems modulate long-term nociception in the rat anterior cingulate cortex. Pain 111:136–143.

Lu Y, Doroshenko M, Lauzadis J, Kanjiya MP, Rebecchi MJ, Kaczocha M, Puopolo M (2018) Presynaptic inhibition of primary nociceptive signals to dorsal horn Lamina I neurons by dopamine. J Neurosci 38:8809–8821. Available at:Available from: https://doi.org/10.1523/JNEUROSCI.0323-18.2018.

Marchetti C, Carbone E, Lux HD (1986) Effects of dopamine and noradrenaline on ca channels of cultured sensory and sympathetic neurons of chick. Pflugers Arch 406:104–111.

Megat S, Shiers S, Moy JK, Barragan-Iglesias P, Pradhan G, Seal RP, Dussor G, Price TJ (2018) A critical role for dopamine D5 receptors in pain chronicity in male mice. J Neurosci 38:379–397.

Mercado-Reyes J, Almanza A, Segura-Chama P, Pellicer F, Mercado F (2019) D2-like receptor agonist synergizes the μ-opioid agonist spinal antinociception in nociceptive, inflammatory and neuropathic models of pain in the rat. Eur J Pharmacol 853:56–64. Available at:Available from: https://linkinghub.elsevier.com/retrieve/pii/S001429991930175X.

Nguyen V, Tiemann D, Park E, Salehi A (2017) Alpha-2 Agonists. Anesthesiol Clin 35:233–245. Available at:Available from: http://linkinghub.elsevier.com/retrieve/pii/S1932227517300149.

Nixon DW (1975) Letter: use of L-dopa to relieve pain from bone metastases. N Engl J Med 292:647.

Ortega-Legaspi JM, de Gortari P, Garduño-Gutiérrez R, Amaya MI, León-Olea M, Coffeen U, Pellicer F (2011) Expression of the dopaminergic D1 and D2 receptors in the anterior cingulate cortex in a model of neuropathic pain. Mol pain 7(97). available at: Available from: http://www.ncbi.nlm.nih.gov/pubmed/22171983.

Pellicer F, Ortega-Legaspi JM, López-Avila A, Coffeen U, Jaimes O (2010) Dopamine pathways and receptors in nociception and pain. In: Beaulieu J-M, Lussier D, Porreca F, Dickenson A, editors. Pharmacology of pain. Washington, D.C.: IASP. p. 241–252.

Price TJ, Flores CM (2007) Critical evaluation of the colocalization between calcitonin gene-related peptide, substance P, transient receptor potential vanilloid subfamily type 1 immunoreactivities, and isolectin B4 binding in primary afferent neurons of the rat and mouse. J pain 8:263–272. available at:Available from: http://www.ncbi.nlm.nih.gov/pubmed/17113352.

Ramanathan S, Tkatch T, Atherton JF, Wilson CJ, Bevan MD (2008) D2-like dopamine receptors modulate SKCa channel function in subthalamic nucleus neurons through inhibition of Cav2.2 channels. J Neurophysiol 99:442–459. available at:Available from: http://www.ncbi.nlm.nih.gov/pubmed/18094105.

Rodgers HM, Yow J, Evans E, Clemens S, Brewer KL (2019) Dopamine D1 and D3 receptor modulators restore morphine analgesia and prevent opioid preference in a model of neuropathic pain. Neuroscience 406:376–388. Available at:

INFORME DE LABORES 2019

Available from: https://linkinghub.elsevier.com/retrieve/pii/S0306452219301927.

Scherrer G, Imamachi N, Cao Y-Q, Contet C, Mennicken F, O'Donnell D, Kieffer BL, Basbaum AI (2009) Dissociation of the opioid receptor mechanisms that control mechanical and heat pain. Cell 137:1148–1159.

Schindelin J, Arganda-Carreras I, Frise E, Kaynig V, Longair M, Pietzsch T, Preibisch S, Rueden C, Saalfeld S, Schmid B, Tinevez J-Y, White DJ, Hartenstein V, Eliceiri K, Tomancak P, Cardona A (2012) Fiji: an open-source platform for biological-image analysis. Nat Methods 9:676–682. Available at:Available from: http://www.nature.com/articles/nmeth.2019.

Sluka KA (1998) Blockade of N- and P/Q-type calcium channels reduces the secondary heat hyperalgesia induced by acute inflammation. J Pharmacol Exp Ther 287:232–237.

Stojanovic T, Orlova M, Sialana FJ, Höger H, Stuchlik S, Milenkovic I, Aradska J, Lubec G (2017) Validation of dopamine receptor DRD1 and DRD2 antibodies using receptor deficient mice. Amino acids 49:1101–1109. available at:Available from: http://www.ncbi.nlm.nih.gov/pubmed/28316027.

Stucky CL, Lewin GR (1999) Isolectin B(4)-positive and -negative nociceptors are functionally distinct. J Neurosci 19:6497–6505. available at:Available from: http://www.ncbi.nlm.nih.gov/pubmed/10414978.

Taddese A, Nah SY, McCleskey EW (1995) Selective opioid inhibition of small nociceptive neurons. Science 270:1366–1369.

Takasu K, Ogawa K, Minami K, Shinohara S, Kato A (2016) Injury-specific functional alteration of N-type voltage-gated calcium channels in synaptic transmission of primary afferent C-fibers in the rat spinal superficial dorsal horn. Eur J Pharmacol 772:11–21. available at:Available from: http://www.ncbi.nlm.nih.gov/pubmed/26708163.

Tamae A, Nakatsuka T, Koga K, Kato G, Furue H, Katafuchi T, Yoshimura M (2005) Direct inhibition of substantia gelatinosa neurones in the rat spinal cord by activation of dopamine D2-like receptors. J Physiol 568:243–253.

Taniguchi W, Nakatsuka T, Miyazaki N, Yamada H, Takeda D, Fujita T, Kumamoto E, Yoshida M (2011) In vivo patch-clamp analysis of dopaminergic antinociceptive actions on substantia gelatinosa neurons in the spinal cord. Pain 152:95–105.

Todorovic SM, Jevtovic-Todorovic V (2007) Regulation of T-type calcium channels in the peripheral pain pathway. Channels 1:238–245. Available at:Available from: https://doi.org/10.4161/chan.4953.

Wood PB (2008) Role of central dopamine in pain and analgesia. Expert Rev Neurother 8:781–797.

Xie GX, Jones K, Peroutka SJ, Palmer PP (1998) Detection of mRNAs and alternatively spliced transcripts of dopamine receptors in rat peripheral sensory and sympathetic ganglia. Brain Res 785:129–135.

Zhu H, Clemens S, Sawchuk M, Hochman S (2007) Expression and distribution of all dopamine receptor subtypes (D(1)-D(5)) in the mouse lumbar spinal cord: a real-time polymerase chain reaction and non-autoradiographic in situ hybridization study. Neuroscience 149:885–897.

Zimmermann M (1983) Ethical guidelines for investigations of experimental pain in conscious animals. Pain 16:109–110.

(Received 26 March 2019, Accepted 8 August 2019)
(Available online 17 August 2019)

Article

Cell

Effector T_H17 Cells Give Rise to Long-Lived T_{RM} Cells that Are Essential for an Immediate Response against Bacterial Infection

Graphical Abstract

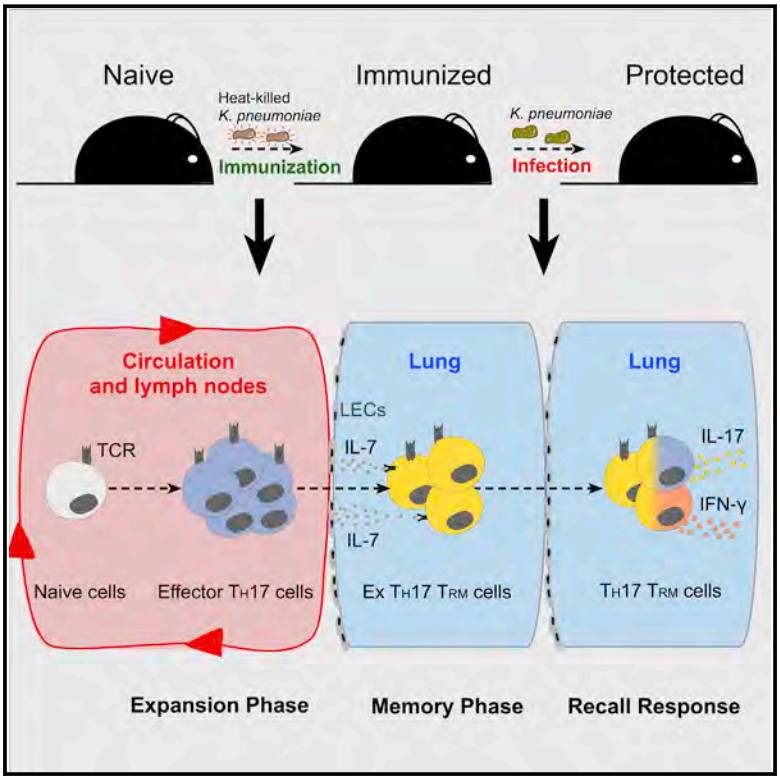

Highlights

- A significant fraction of CD4 T_{RM} cells derive from effector T_H17 cells
- Maintenance of resting ex T_H17 T_{RM} cells is mediated by IL-7
- Ex T_H17 T_{RM} cells play an important role in bacterial clearance

Authors

Maria Carolina Amezcua Vesely, Paris Pallis, Piotr Bielecki, ..., Enric Esplugues, Nicola Gagliani, Richard A. Flavell

Correspondence

n.gagliani@uke.de (N.G.), richard.flavell@yale.edu (R.A.F.)

In Brief

Fate-mapping studies reveal that $CD4^+$ tissue resident-memory cells are derived from effector T_H17 cells and play essential roles in response to bacterial infections.

Amezcua Vesely et al., 2019, Cell *178*, 1176–1188
August 22, 2019 © 2019 Elsevier Inc.
https://doi.org/10.1016/j.cell.2019.07.032

CellPress

Effector T_H17 Cells Give Rise to Long-Lived T_{RM} Cells that Are Essential for an Immediate Response against Bacterial Infection

Maria Carolina Amezcua Vesely,[1,2] Paris Pallis,[1] Piotr Bielecki,[1] Jun Siong Low,[1] Jun Zhao,[1,3,4] Christian C.D. Harman,[1,2] Lina Kroehling,[1] Ruaidhrí Jackson,[1] Will Bailis,[1] Paula Licona-Limón,[5] Hao Xu,[1] Norifumi Iijima,[1] Padmini S. Pillai,[1,12] Daniel H. Kaplan,[6] Casey T. Weaver,[7] Yuval Kluger,[3,4,8] Monika S. Kowalczyk,[9] Akiko Iwasaki,[1,2] Joao P. Pereira,[1] Enric Esplugues,[1,13] Nicola Gagliani,[1,10,11,14,*] and Richard A. Flavell[1,2,14,15,*]

[1]Department of Immunobiology, School of Medicine, Yale University, New Haven, CT, USA
[2]Howard Hughes Medical Institute, Yale University School of Medicine, New Haven, CT, USA
[3]Department of Pathology, Yale School of Medicine, New Haven, CT 06510, USA
[4]Program of Computational Biology and Bioinformatics, Yale University, New Haven, CT 06520, USA
[5]Departamento de Biología Celular y del Desarrollo, Instituto de Fisiología Celular, Universidad Nacional Autónoma de México, Ciudad de México, México
[6]Department of Dermatology and Immunology, University of Pittsburgh, Pittsburgh, PA 15261, USA
[7]Departments of Pathology, University of Alabama at Birmingham, Birmingham, AL 35294, USA
[8]Applied Mathematics Program, Yale University, New Haven, CT 06511, USA
[9]Broad Institute of MIT and Harvard, Cambridge, MA, USA
[10]I. Medical Department and Department of General, Visceral and Thoracic Surgery, University Medical Center Hamburg-Eppendorf 20246 Hamburg, Germany
[11]Immunology and Allergy Unit, Department of Medicine Solna, Karolinska Institute, 17176 Stockholm, Sweden
[12]Koch Institute for Integrative Cancer Research and Department of Chemical Engineering, Massachusetts Institute of Technology, Cambridge, MA 02142, USA
[13]Laboratory of Molecular and Cellular Immunology, Principe Felipe Research Center (CIPF), 46012 Valencia, Spain
[14]These authors contributed equally
[15]Lead Contact
*Correspondence: n.gagliani@uke.de (N.G.), richard.flavell@yale.edu (R.A.F.)
https://doi.org/10.1016/j.cell.2019.07.032

SUMMARY

Adaptive immunity provides life-long protection by generating central and effector memory T cells and the most recently described tissue resident memory T (T_{RM}) cells. However, the cellular origin of CD4 T_{RM} cells and their contribution to host defense remain elusive. Using IL-17A tracking-fate mouse models, we found that a significant fraction of lung CD4 T_{RM} cells derive from IL-17A-producing effector (T_H17) cells following immunization with heat-killed *Klebsiella pneumonia (Kp)*. These exT_H17 T_{RM} cells are maintained in the lung by IL-7, produced by lymphatic endothelial cells. During a memory response, neither antibodies, γδ T cells, nor circulatory T cells are sufficient for the rapid host defense required to eliminate Kp. Conversely, using parabiosis and depletion studies, we demonstrated that exT_H17 T_{RM} cells play an important role in bacterial clearance. Thus, we delineate the origin and function of airway CD4 T_{RM} cells during bacterial infection, offering novel strategies for targeted vaccine design.

INTRODUCTION

Adaptive immunity provides life-long protection from infection by establishing an enduring reservoir of memory cells. Upon infection, CD4 and CD8 T cells undergo clonal expansion followed by a subsequent contraction and ultimately, memory formation (Kaech et al., 2002; Mueller et al., 2013). While central memory T (T_{CM}) cells have long since been known to mainly reside and circulate through secondary lymphoid tissues and effector memory T (T_{EM}) cells to circulate through non-lymphoid tissues, the identification of T_{RM} cells within peripheral organs has opened new concepts about tissue-specific protective immunity (Schenkel and Masopust, 2014).

CD4 T_{RM} cells serve at the frontline at different barrier sites such as vagina (Iijima and Iwasaki, 2014; Stary et al., 2015), lung (Teijaro et al., 2011; Turner et al., 2014; Hondowicz et al., 2016), and skin (Glennie et al., 2017), and their main host-protective mechanism is mediated by the production of effector cytokines such as interferon-γ (IFN-γ) and interleukin-4 (IL-4).

While most of the studies have focused on the biology of virus-specific CD8 T_{RM} cells, basic questions regarding CD4 T_{RM} still remain unanswered. For example: Where do these cells come from; What is the cellular origin of CD4 T_{RM} cells; Which environmental signals maintain them into the tissue; and finally, Are CD4 T_{RM} cells able to rapidly respond to a second challenge?

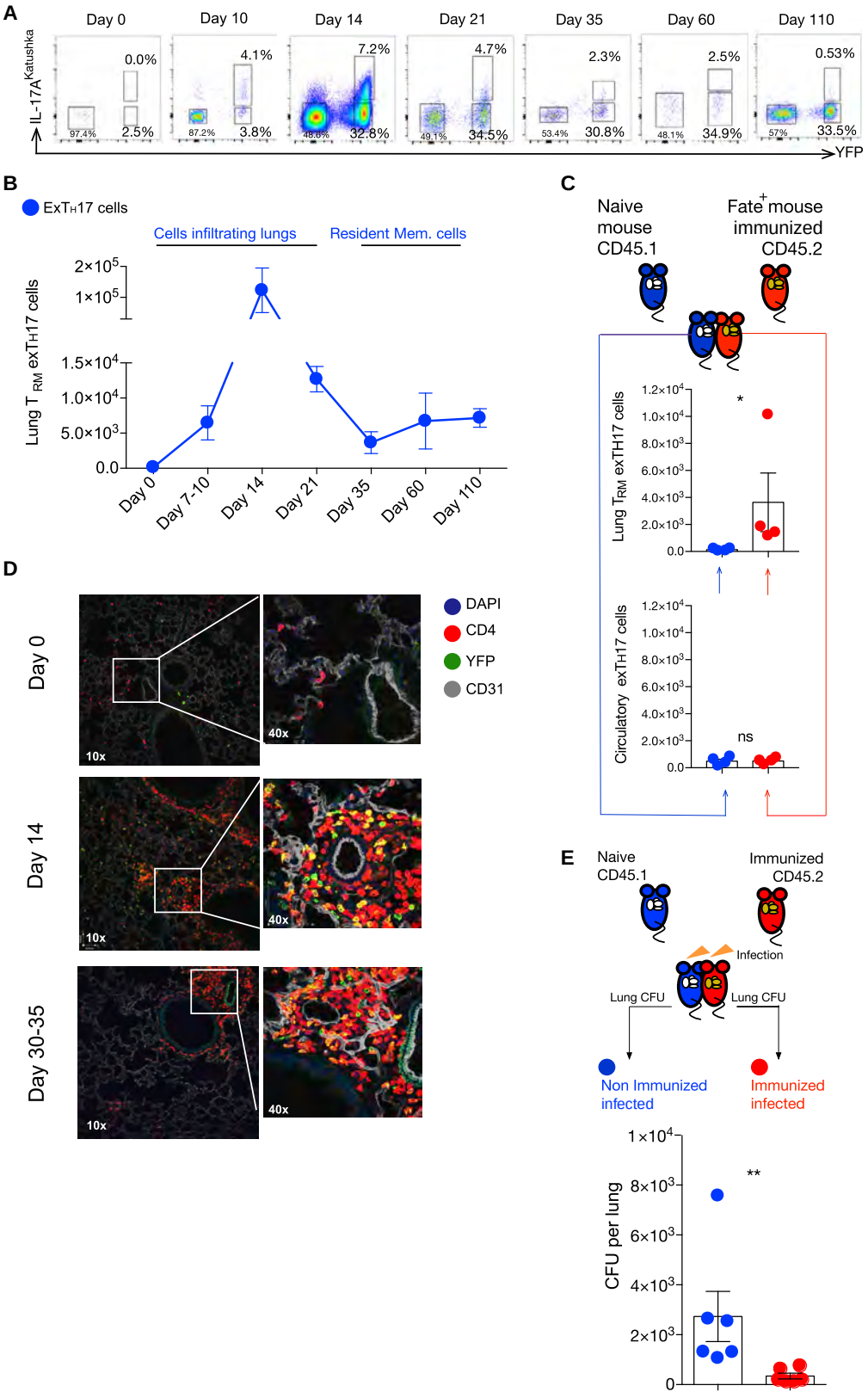

(legend on next page)

To address these questions, we devised an experimental plan combining the use of two complementary fate reporter mouse models, next-generation T cell receptor (TCR) and single-cell sequencing approaches.

We consider that understanding CD4 T_{RM} cell development and function is imperative, particularly as they may represent the key target cells to design specific and efficacious vaccination against the growing number of antibiotic-resistant bacterial strains emerging in the clinic. This might also help to reduce antibiotic use, avoiding the evolution of antibiotic-resistant bacteria. For instance, there is currently no targeted treatment strategy for carbapenem-resistant *Enterobacteriaceae*-like *Klebsiella pneumoniae* (Kp). This is a leading cause of nosocomial and community-acquired gram-negative bacterial pneumonia, which results in a severe pyrogenic infection with high mortality rates (Falagas et al., 2014). Despite the fact that IL-17A cytokine is critical to deal with Kp infection (Moore et al., 2000; Happel et al., 2005; Chen et al., 2011), the function of T_H17 memory cells have been underestimated because of their short-term survival (Pepper et al., 2010).

Considering all this, we hypothesized that CD4 T_{RM} cells derive from the first wave of effector cells generated during the first encounter with a pathogen. Furthermore, since CD4 T_{RM} cells localize at the site of immunization, we also hypothesized that some of them acquire a poised while others a more plastic status (Lee et al., 2009; Wei et al., 2009; Harrison et al., 2019), which allows them to mount a fast and essential immune response against bacterial infection.

Here, by using an immunization-infection model with different serotypes of *Kp*, we show that a significant fraction of the lung long-lived CD4 T_{RM} cells (ex$T_H17$cells) derive from specific effector T_H17 cells. We observed that exT_H17 T_{RM} cells are maintained by IL-7, which is mainly produced by lymphatic endothelial cells (LECs) in the lung. Finally, we reveal that exT_H17 T_{RM} cells are important players that can resist an antibiotic-resistant strain of Kp.

RESULTS

T_{RM} Cells Can Derive from Effector Cells and Protect against Carbapenem-Resistant Klebsiella Pneumoniae Infection

We started by characterizing the kinetics of the development of lung T_{RM} cells. To this end, wild-type (WT) mice were immunized twice with heat-killed serotype 2 *Klebsiella pneumoniae* (Figure S1A), and the presence of CD4 T_{RM} cells was evaluated at multiple time points. An *in vivo* antibody (Ab)-labeling technique was used to differentiate between circulatory and lung-infiltrating CD4 T cells (Anderson et al., 2014). Lung-infiltrating CD4 T cells began accumulating as early as day 5 post-immunization and persisted through day 110 (Figure S1B). CD69 and CD103 have been used as markers for T_{RM} cells. We found that CD4 T_{RM} cells were $CD103^-$ but characterized by high levels of CD69 expression compared with circulatory CD4 T cells (Figures S1C and S1D). Similar to classic CD8 and CD4 memory formation, lung-infiltrating CD4 cells underwent robust expansion upon immunization, followed by an acute contraction phase. Then, a stable lung T_{RM} CD4 population was observed during the memory phase (Figure S1E).

We next aimed to further characterize the origin of T_{RM} CD4 cells, a point that still remained elusive. T_H17 cells have previously been shown to provide protection against Kp infection (Ye et al., 2001; Chen et al., 2011); however, it is unclear whether these cells are short lived and whether they contribute to the memory pool (Pepper et al., 2010; Chen et al., 2011; Muranski et al., 2011). Considering the plasticity of T_H17 cells and instability of IL-17A production, their main marker, one possible explanation for the unknown origin of CD4 T_{RM} cells could be that T_H17 cells lose the expression of their signature cytokine, becoming "exT_H17" cells, when they mature into long-lived memory cells. We therefore used the *Il17a* $Fate^+$-mapping mouse model (Gagliani et al., 2015), which allowed us to track the fate of T_H17 cells independently from the actual expression of IL-17A and from the need of *in vitro* re-stimulation. To generate these mice, $Il17a^{CRE}$ crossed with a $R26STOP^{flox/flox}$ YFP ($R26^{YFP}$) (Hirota et al., 2011) were further crossed with a triple-reporter mouse strain, consisting of $Il17a^{Katushka}$ $Il10^{eGFP}$ $Foxp3^{RFP}$ alleles (Gagliani et al., 2015). In addition, the $Fate^+$ mice allowed us to exclude Foxp3 and IL-10-producing cells from our analysis. By using these mice, we observed that Kp immunization resulted in the generation of T_H17 and exT_H17 cell populations, with the latter persisting in the lung as a population of T_{RM} cells for at least 110 days (Figures 1A and 1B).

To specifically track T_H17 cells generated in response to Kp immunization, rather than all cells with a history of IL-17A expression, we took advantage of an inducible *Il17a* fate model (Gagliani et al., 2015). $R26^{YFP}$ mice were crossed with $Il17a^{eGFP\text{-}Cre\text{-}ERT2}$ mice, such that cells expressing *Il17a* are labeled GFP^+YFP^+ upon tamoxifen administration and persist as a $GFP^{neg}YFP^+$ population after the expression of *Il17a* is

Figure 1. Origin and Function of T_{RM} exT_H17 Cells

(A and B) Dot plots show (A) percentage of T_H17, exT_H17, and YFP^{neg} $IL\text{-}17^{neg}$ cells and (B) absolute number of T_{RM} exT_H17 cells in lungs at different time points after immunization in $Fate^+$ mice (gated on CD4 *in vitro*$^+$ CD4 *in vivo* ^{neg} TCR-β^+ $Foxp3^{neg}$) (n = 4 per time point). One out of two independent experiments is shown.

(C) Naive $CD45.1^+$ and day 35 immunized $Fate^+$ $CD45.2^+$ mice were surgically joined for 3 weeks. Before sacrifice, the anti-CD4 antibody was injected to distinguish T_{RM} and circulating cells. The graph shows the absolute number of lung T_{RM} $CD45.2^+$ and circulatory exT_H17 cells in naive CD45.1 mice (blue) and in $Fate^+$ immunized mice (red).

(D) Representative immunofluorescent sections of lungs from naive (day 0) and immunized mice (day 14 and day 30) showing the presence of CD4 T cells (red) and exTh17/Th17 cells (yellow) surrounding the airways only in the lungs of immunized mice. AW, airway; BV, blood vessel; blue: DAPI, gray: CD31 (n = 3 per time point)

(E) Parabiotic pairs were infected with live carbapenem-resistant *Kp* 3 weeks after surgery. The graph shows the CFU count in total lung 24 h after infection of naive-infected (blue) or immunized-infected (red). Each dot represents one mouse. Data are cumulative of 2 experiments.

Data are represented as mean ± SEM. Mann-Whitney U test; ns (non-significant); *p = 0.0286; **p = 0.0022.

See also Figures S1, S2, and S3.

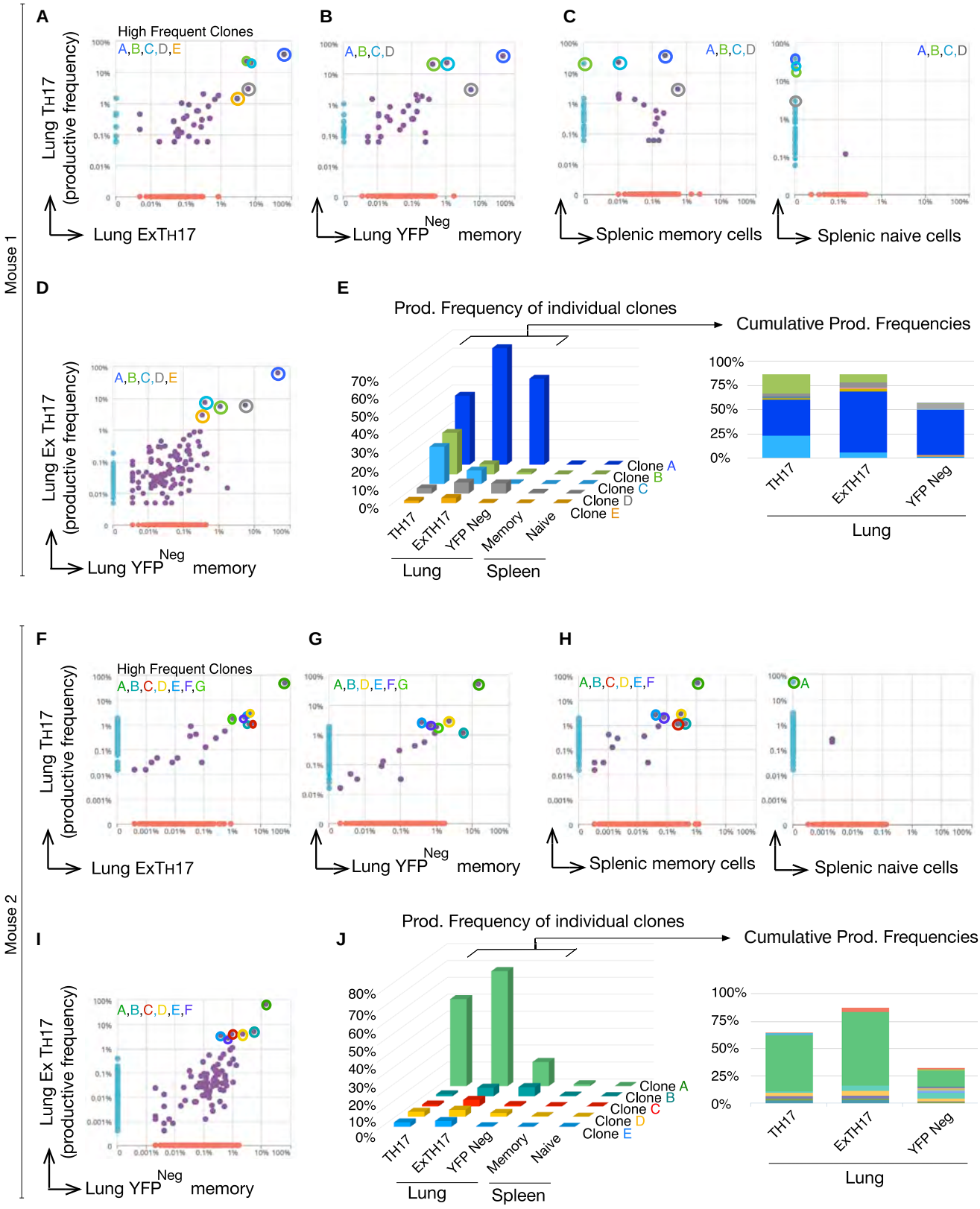

(legend on next page)

terminated. As expected, Kp immunization resulted in the induction of a newly generated T_H17 cell population (Figure S1F). Notably, 60 days after immunization most of these cells lost *Il17a*^{eGFP} expression and persisted as YFP$^+$ exT_H17 cells in the lung of immunized mice (Figure S1G).

To test whether the accumulation of T_{RM} was associated with long-term protection, the immunized mice were infected with a second serotype of live *K. pneumoniae*, characterized as being resistant to carbapenems (Figure S2A). Immunized mice showed protection against carbapenem-resistant Kp compared with non-immunized mice (Figure S2B).

CD4 T cells, antibodies, and γδ T cells are all important components of the immune response against Kp. However, whether memory T cells alone are sufficient to orchestrate a proper immune response, especially at the early phase of memory activation, remains unknown. Here, we found that despite the absence of B cell and γδ T cells—using genetically deficient mice—immunized animals were still more efficiently protected from acute live carbapenem-resistant Kp infection than non-immunized controls (Figures S2C and S2D).

Next, to further test whether exT_H17 cells were residing in the lung as bona fide T_{RM} cells, we performed parabiosis experiments with naive WT CD45.1$^+$ and immunized Fate$^+$ CD45.2$^+$ mice in combination with an *in vivo* Ab-labeling technique. Naive CD45.1$^+$ and immunized CD45.2$^+$ mice were surgically paired, and 3–4 weeks later we observed shared specific Kp antibodies and CD4 T cells in the circulation (Figures S2E–S2G). We observed that, although the two mice shared memory exT_H17 T cells in circulation, the large majority of exT_H17 cells were present in the lungs of the immunized Fate$^+$ mice and not in the lungs of the naive WT mice (Figure 1C). In addition, immunofluorescent imaging of lungs from immunized mice showed that exT_H17 cells (depicted by yellow) resided in close proximity to the airways and blood vessels at 14 and 30–35 days after immunization forming a potential network of tissue resident cells (Figure 1D).

Finally, to test the hypothesis that the observed resident cells act as the crucial mediators of tissue-specific adaptive immunity, we conducted parabiosis studies infecting both naive and immunized mice with antibiotic-resistant Kp. Despite displaying Kp-specific antibodies and circulatory memory cells, the respective naive mice of the joined pairs failed to efficiently clear live carbapenem-resistant Kp infection. In contrast, we found a very low bacterial burden in the immunized partners (Figure 1E). Moreover, we observed that when the recruitment of memory cells from lymphoid organs is impaired, using FTY720 (S1PR1 antagonist that blocks lymphocyte egress from lymph nodes), the immunized mice still appeared to be more protected compared with naive mice (Figure S2H).

We extended our findings to different pathogens and found long-lived exT_H17 cells after *Candida albicans* and Bacillus Calmette-Guérin (BCG) infections (Figure S3), supporting the hypothesis that the longevity and presence of T_H17 effector-derived T_{RM} cells not only occur in the Kp setting but they are also generated in other infections where IL-17A plays an important role (Khader et al., 2007; Igyártó et al., 2011).

Taken together, these data show that effector T_H17 can give rise to T_{RM} cells and tissue resident cells play a key protective role in the early phase of *Klebsiella pneumoniae* infection.

TCR Specificity and Transcriptome Analysis of Lung T_{RM} Cells

The expansion of certain clones in response to a bacterial infection is a prototypical feature of a memory response. To test whether the development of these T_{RM} cells follows this classic path, we sequenced the CDR3 region of the TCR-β genes of T_H17 and exT_H17 cells present in the lung 35 days after immunization. Thus, this CDR3 sequencing also allowed us to elucidate the clonal origin of exT_H17 T_{RM} cells.

We found that the small population of T_H17 cells present at day 35 post-immunization was represented by highly restricted oligo-clonal expanded TCR clones, and these clones were shared with exT_H17 cells (Figures 2A and 2F), further indicating a common origin between these two populations. Then, we selected the most expanded clones among lung T_H17 cells and tracked them in all the other populations of T_{RM} cells in the lung and also in naive and memory cells in the spleen (Figures 2B, 2C, 2E, 2G, 2H, and 2J). When we evaluated the clonality of those lung T_{RM} cells that never expressed IL-17A (YFP^{neg}), we found that they share some degree of clonality with both T_H17 and exT_H17 T_{RM} cells, but to a lower degree compared with what T_H17 and exT_H17 T_{RM} cells share between one another (Figure 2B, 2D, 2G, and 2I). This suggests that both type of cells were generated during the effector immune response, but unknown differences led them to become YFP^{pos} or YFP^{neg} cells. Finally, some of the expanded clones represented in the T_H17 cells were also present, albeit at a very low frequency in splenic CD4 memory cells, but they were not detectable in naive CD4 T cells, denoting the generation of a specific and systemic immune response after immunization (Figures 2C and 2H).

Tissue and cell-type-specific expression of genes, including T_{RM} "core" genes, can be commonly suggestive of corresponding specific functions and cell origin. To evaluate the presence of a tissue-related specific gene profile in memory cells residing at the lung or lymph nodes, we performed RNA sequencing. We hypothesized that, based on their location, different transcriptomes will be expressed by these memory CD4 T cell populations. We

Figure 2. TCR-β Sequencing of Lung T_{RM} Cells

(A–C and F–H) TCR-β sequencing of (A and F) lung T_H17 T_{RM} versus lung exT_H17 T_{RM} cells, (B and G) lung T_H17 T_{RM} versus lung YFP^{neg} T_{RM}, and (C and H) lung T_H17 T_{RM} versus splenic CD4 memory cells and versus splenic CD4 naive cells at day 35 after immunization in 2 different mice.

(D and I) TCR-β sequencing of lung exT_H17 versus lung YFP^{neg} cells at day 35 after immunization in 2 different mice. The dots plots graphs show the common shared CDR3 amino acid sequences of TCR-β chains between all the populations. The most expanded clones among T_H17 cells were colored and followed across all the comparisons between different populations.

(E and J) The bar graphs on the left show percentage of the most expanded clones in each population. The bar graphs on the right show the cumulative productive frequency of the most expanded clones in lung T_{RM} cells. The colors of the clones followed the same colors used for the dot plots graphs.

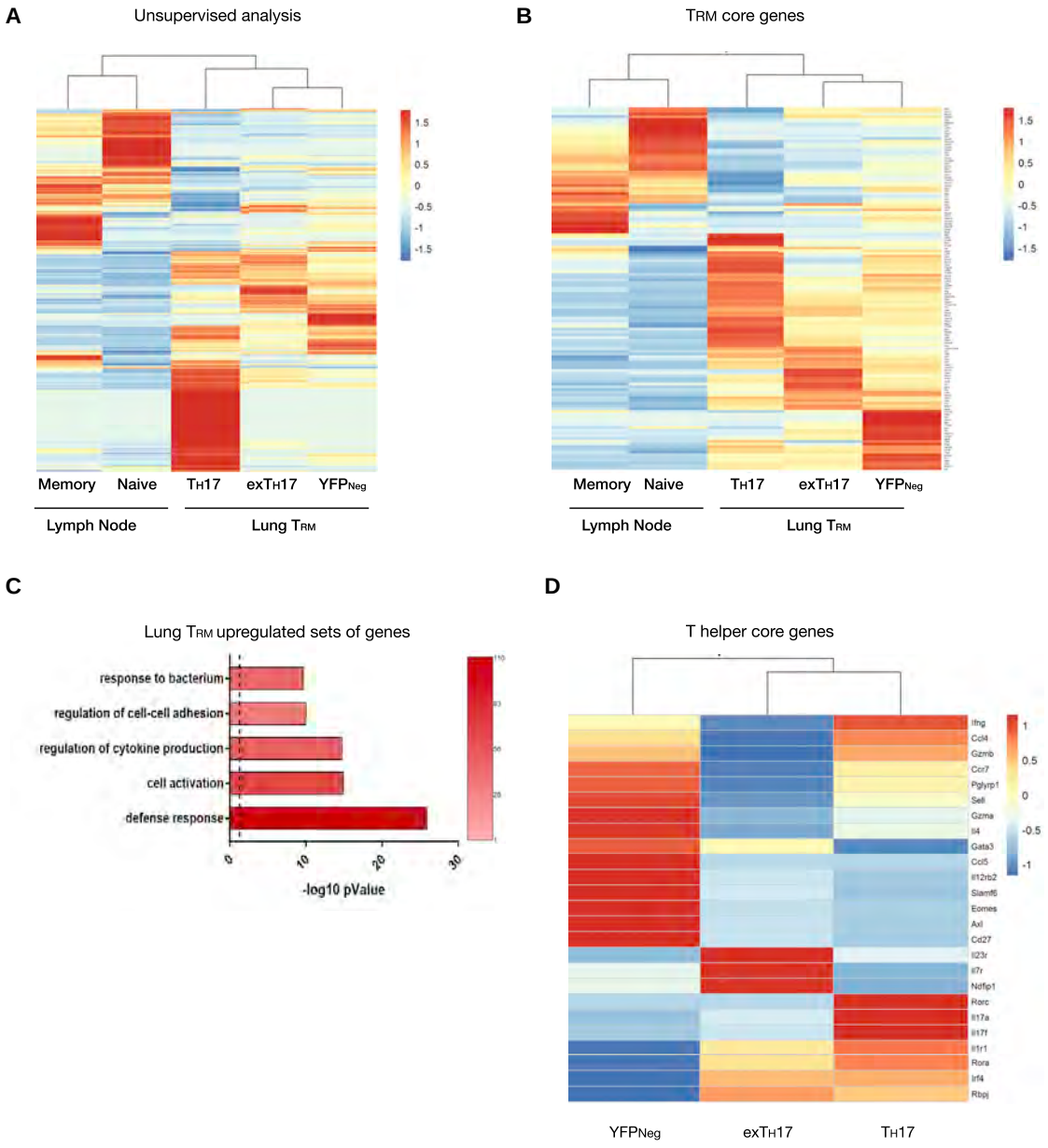

Figure 3. RNA Sequencing of Lung T_{RM} and Lymph Node Memory and Naive CD4 Populations Illustrates Key Features of Lung T_{RM} Populations

(A) Heatmap of genes significantly differentially expressed (>4-fold cutoff) between the lymph node and lung populations.

(B) Heatmap of a selected subset of genes known to be involved in tissue resident memory cell-biology.

(C) Bar graph of gene ontology assignments of genes overexpressed 4-fold in lung T_{RM} cells relative to lymph node memory cells. The dashed line represents p = 0.05, Fisher's exact test. The intensity of the color bar on the right indicates the amount of genes in each pathway.

(D) Heatmap of a selected subset of genes known to be involved in T helper subset and memory biology.

profiled the transcriptome of draining lymph node (LN)-naive CD4 T cells, memory CD4 T cells, and the 3 populations of T_{RM} cells present in the lung 35 days after immunization (T_H17, exT_H17, and YFP^{neg} cells).

We used either an unsupervised list of genes that were significantly differentially expressed (>4-fold) (Figure 3A; GEO: GSE130446) or a core of T_{RM} signature genes (Table S1; Figure 3B; Wakim et al., 2012; Mackay et al., 2013; Pan et al., 2017) to test similarities and differences among the transcriptomes of these cell populations. We found that lung T_{RM} cells (T_H17 cells, ex-T_H17 and YFP^{neg} cells) share a similar pattern of gene expression, which, in contrast, differs from the expression pattern of the peripheral memory LN cells, independently of the approach used to analyze them (Figures 3A and 3B).

To search for different functional features among all lung T_{RM} cells and peripheral LN memory cells, we performed gene

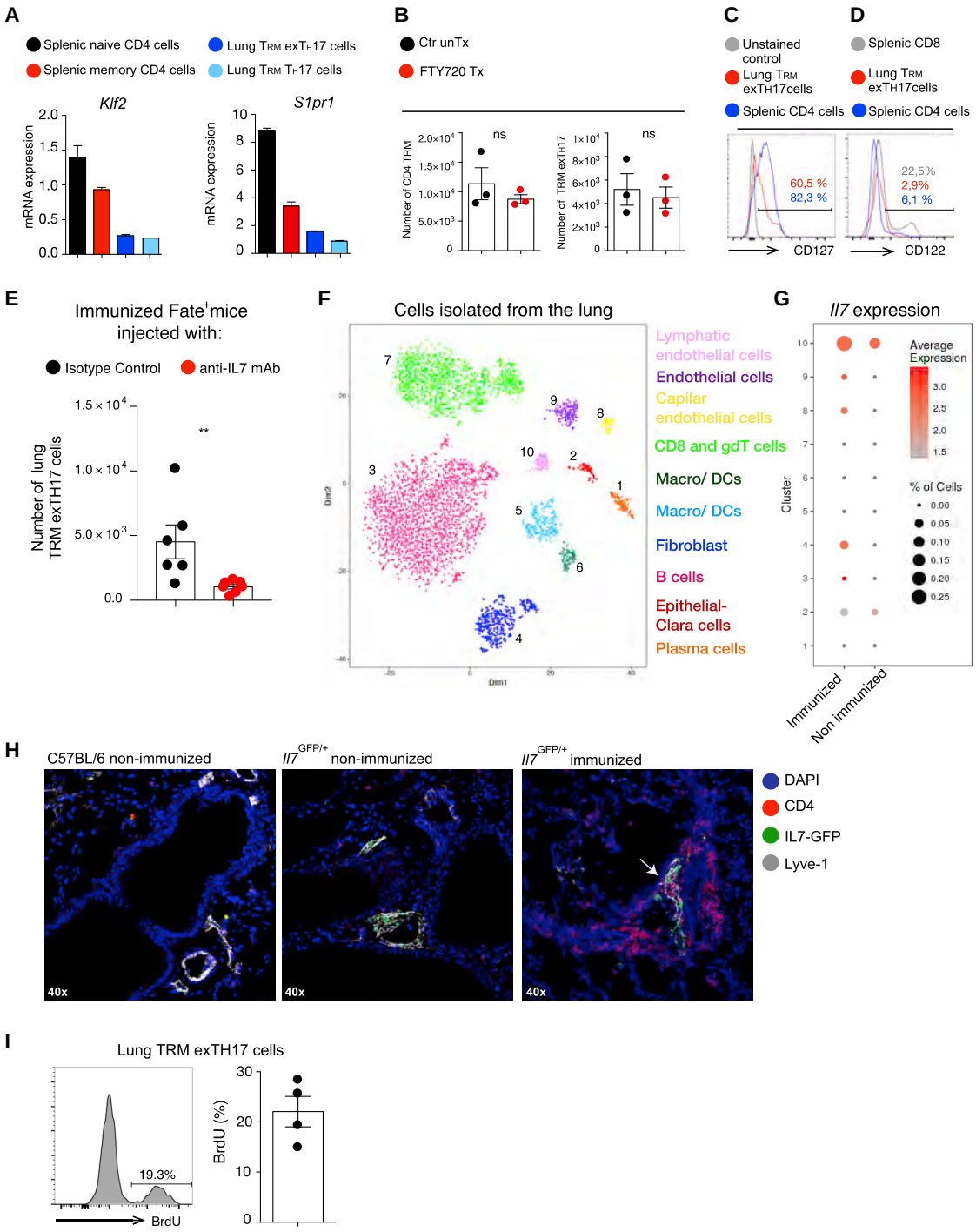

Figure 4. LECs Maintain Effector-Derived Lung T_{RM} Cells

(A) Relative RNA expression of KLF2 and S1PR1 on day 30 in immunized mice is shown. Splenic naive CD4 cells (black bars), splenic memory CD4 cells (red bars), lung exT_H17 cells (dark blue bars), and lung T_H17 cells (light blue bars). Technical replicates of one representative experiment out of two are shown, and data are represented as mean ± SD.

(B) The graphs show the absolute number of total CD4 T_{RM} (left) and exT_H17 T_{RM} cells (right) in lungs (gated on CD4 *in vitro*$^+$ CD4 *in vivo*^{Neg} TCR-β$^+$ Foxp3$^-$) after FTY720 treatment (red circles). Ctr unTx mice = normal drinking water (black circles). Each dot represents one mouse. One out of two independent experiments is shown.

(legend continued on next page)

ontology (GO) analysis of genes upregulated in lung T_{RM} cells using DAVID (Huang et al., 2009). Interestingly, GO terms showing statistically significant enrichment were mainly related with immune process such as defense response, cell-to-cell adhesion, cell activation, regulation of cytokine production, and response to bacteria (Figure 3C). All this suggests that lung T_{RM} cells present a profile more focused toward a rapid immune response compared with peripheral memory cells.

We then focused on the different populations of lung T_{RM} cells and evaluated the expression of a selected list of genes involved in specific T-helper cell subset and memory T cell-biology. Interestingly, based on the expression of the genes from this list, we found that T_H17 and exT_H17 cells cluster more closely together than to the YFP^{neg} cells (Figure 3D; Table S2). In particular, the expression patterns of *Il1r*, *Rora*, *Irf4*, and *Rbpj* suggested that some of the exT_H17 T_{RM} cells have acquired a prime signature state that could allow them to rapidly respond by producing IL-17.

Interestingly, we also found that Ndfip1, which was recently shown to be essential to balance the potential tissue related pathogenicity of T_H17 cells (Layman et al., 2017), was highly expressed in exT_H17 cells. We also observed that the expression of *Il7r* was higher in exT_H17 cells than in YFP^{neg} cells. Finally, regarding the population that never activates the production of *Il17a* (YFP^{neg} cells), the expression of a $T_H1/2$-memory signature transcriptome (e.g., *Eomes*, *Ifng*, *Ccr7*, *Sell*, *Il4*, *Gata3*, *Ccr3*, *Ccr5*) suggests that these cells might be a heterogeneous population composed of T_H1 and T_H2 effector-derived memory cells (Figure 3D; Chang et al., 2007; Bannard et al., 2009).

Effector-Derived T_{RM} Cells Depend on IL-7, which Is Produced by Lung LECs

We next interrogated the possible mechanisms that might be involved in the maintenance of exT_H17 T_{RM} cells in the lung. The residency and establishment of T_{RM} cells at peripheral tissues correlates with downregulation of KLF2 and S1PR1 and the concomitant inability to follow a gradient of S1P and leave the tissue (Carlson et al., 2006; Skon et al., 2013). Consistently, lower levels of KLF2 and S1PR1 expression were found in lung T_{RM} exT_H17 cells and in the small population of T_H17 cells compared to CD4 splenic memory or naive CD4 T cells from $Fate^+$ immunized mice (Figure 4A).

Then, to evaluate whether a continuous supply of circulating lymphocytes is required for the maintenance of the pool of CD4 T_{RM}, we treated day 35 immunized mice with FTY720. Decreased numbers of circulating total white blood cells were found after 2 weeks of FTY720 treatment, while, by contrast, the total number of CD4 T_{RM} and exT_H17 T_{RM} cells in the lung remained unchanged (Figure 4B). All these data pointed toward *in situ* mechanisms that might sustain the survival of CD4 T_{RM} cells. Therefore, we investigated the possible role of the cytokine milieu. Both IL-7 and IL-15 signaling are understood to be key mediators of CD4 T cell homeostatic proliferation, a mechanism that could explain the long-term and circulatory independent maintenance of T_{RM} (Mackay et al., 2013; Iijima and Iwasaki, 2014; Adachi et al., 2015; Hondowicz et al., 2016). In line with the data obtained from the RNA sequencing experiment, we found that a fraction of T_{RM} exT_H17 cells expressed IL-7Rα, but they lacked IL-15Rβ expression (Figures 4C and 4D). To test the role of IL-7 in the maintenance of T_{RM} exT_H17 cells, we intranasally administered anti-IL-7 antibodies (Abs) or isotype control antibodies into immunized mice. The local treatment with anti-IL-7 Abs did not diminish CD4 T cell numbers systemically (Figure S4A). However, the number of lung T_{RM} exT_H17 cells was reduced after IL-7 blockade (Figure 4E).

Then, considering the key role of IL-7, we also investigated the cellular source of IL-7 in the lungs of immunized mice. By performing single-cell RNA sequencing of total lung cells and unsupervised clustering (Figure S4B; GEO: GSE131450), we observed first that *Il7* was preferentially expressed by lymphatic endothelial cells (LECs, Figure 4F) and second that the percentage of $Il7^+$ LECs increased in immunized mice (Figure 4G). By using $IL\text{-}7^{GFP/+}$ reporter mice, we found that lung CD4 T_{RM} cells are located in close proximity to $IL\text{-}7^+$ LECs in the lung of *Klebsiella* immunized mice (Figure 4H). Finally, as IL-7 is known to promote the homeostatic proliferation of T cells, $Fate^+$ mice were immunized and 60 days later given bromo-2-deoxyuridine (BrdU) in the drinking water for 2 weeks. Approximately 20% of exT_H17 T_{RM} cells were labeled with BrdU, suggesting that homeostatic proliferation plays a role in maintaining CD4 T_{RM} cells (Figure 4I).

Function of Effector-Derived T_{RM} Cells

T_H17 cells are a distinct subset of effector CD4 T cells with a degree of plasticity (O'Shea and Paul, 2010; Schlapbach et al.,

(C and D) Histograms show the expression of CD127 and CD122 in lung exT_H17 T_{RM} cells (red line) 60 days after immunization and in total spleen CD4 cells (blue line). For CD127 unstained control (grey line) is shown. CD122 expression in total CD8 spleen cells is shown as a positive control (grey line) (n = 4 mice). One out of 2 independent experiments is shown.

(E) $Fate^+$ immunized mice were intra-nasally treated with anti-IL-7 Ab or with an isotope control on days 35, 37, and 39 after immunization, and the mice were sacrificed on day 40. The graph shows the absolute number of lung exT_H17 T_{RM} cells in the isotype ctrl-treated group (black circles) and in the anti-IL-7-treated group (red circles). Each dot represents one mouse. Three combined experiments are shown.

(F) Single-cell RNA sequencing of total lung tissue cells from immunized mice with total $CD4^+$ cells and circulatory $CD45^+$ removed by fluorescence-activated cell sorting (FACS). Lung cells were profiled by droplet-based scRNA-seq (Drop-Seq). t-distributed stochastic neighbor embedding (t-SNE) plots show 1,500 cells (dots) in a nonlinear representation of the top 50 PCs. Cells are colored by cluster. The clusters were identified by specific genes (Figure S7).

(G) Representation of differentially expressed *Il7* gene by cluster (y axis) in immunized and naive conditions (x axis). The dot size represents the fraction of cells in the cluster that express *Il7*; the dot color represents the intensity of *Il7* expression.

(H) Representative immunofluorescent sections of lungs from B6-non-immunized (left), $IL\text{-}7^{GFP/+}$ non- immunized (middle) or day 35-immunized mice (right). Colocalization of CD4 T cells (red) and $IL\text{-}7^+$ LECs (gray + green) in the lungs of immunized mice. Blue: DAPI, gray: Lyve-1, green: IL-7, red: CD4.

(I) The histogram shows the percentage of lung exT_H17 T_{RM} $BrdU^+$ cells. Each dot represents one mouse. One out of 2 independent experiments is shown.

Data are represented as mean ± SEM. Mann-Whitney U test; ns (non-significant) (B); **p = 0.0082 (E).

See also Figure S4.

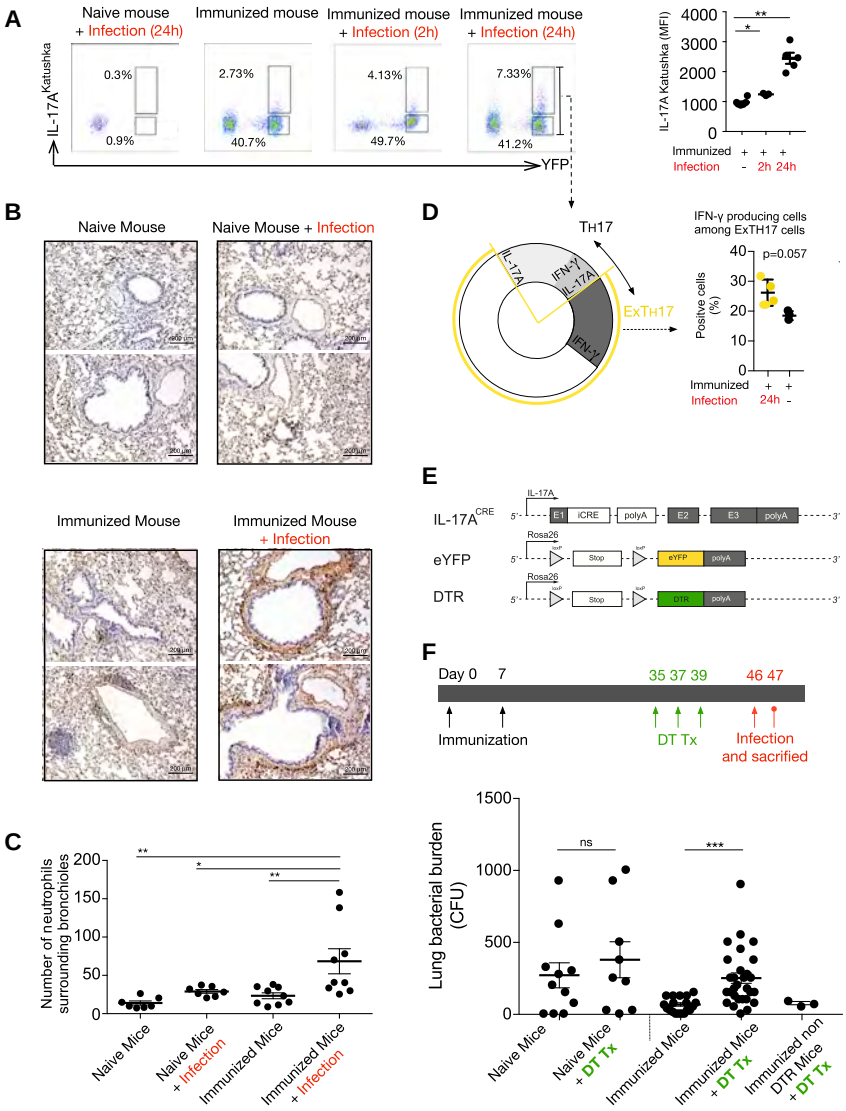

Figure 5. Function of T_{RM} exTh17 Cells

(A) Dot plots show the frequencies of T_H17 T_{RM} and of exT_H17 T_{RM} cells (CD4 *in vitro*$^+$, CD4 *in vivo*^{neg}, TCR-β^+ Foxp3^{neg}, YFP$^+$) in naive + infection mouse, immunized mouse (day 35), immunized mouse + infection (2 h), and immunized mouse + infection (24 h) (n = 3 mice per group). The right graph shows the MFI of IL-17^{kata} in T_H17 T_{RM} cells.

(B) Peroxidase immune staining of mouse Ly6B in naive, naive + infected, immunized (day 35), and immunized (day 35) + infection lungs, 2 h after Kp infection. Representative slides are shown for each group.

(C) Quantification of neutrophils surrounding bronchioles from (B).

(D) Cake graph shows the percentage of INF-γ^+ (dark gray) among the population of YFP$^+$ cells 24 h after infection with live Kp (after PMA-ionomycin stimulation). Double-positive cells (IL-17A$^+$, INF-γ^+ middle gray) and IL-17A$^+$ cells (light gray) are shown separately. The graph on the right shows the percentage of INF-γ^+ single positive cells in immunized + infection (yellow circles) and in immunized mice not infected (day 35 after immunization).

(E) Constructs of Fate-DTR mice.

(F) Scheme depicting the time plan of immunization, DT treatment (DT Tx), and infection of Fate-DTR mice (Top). The graph shows the CFU counts in the indicated groups. For the first 4 groups (from left to right) Fate-DTR mice were used, while for the last group Fate$^+$ immunized mice were used. Each symbol represents one mouse.

Data are represented as mean ± SEM. Kruskal-Wallis ($p < 0.0001$) and post hoc Mann-Whitney U test with Bonferroni correction *p = 0.0238 **p = 0.0043 (A); one-way ANOVA, and post hoc Dunnett *$p < 0.05$; **$p < 0.005$ (C); Mann-Whitney U test (D) and Kruskal-Wallis (p = 0.0009) and post hoc Mann-Whitney U test with Bonferroni correction, ns (non-significant), ***$p < 0.0001$ (F).

See also Figure S5.

2014; DuPage and Bluestone, 2016). However, whether exT_H17 T_{RM} cells can maintain their ability to express their original cytokine profile when re-challenged with antigen remained to be addressed. If so, this could be interpreted as an evolutionary advantage to be able to maintain a population of memory cells at the previously infected barrier to provide a quick response to eventual subsequent infections. We therefore determined the expression of IL-17A and observed that only previously immunized mice show a rapid (i.e., 2 and 24 h) increase in IL-17A^{Kata} expression following infection with carbapenem-resistant Kp (Figure 5A). One feature of T_H17 cells is their ability to recruit neutrophils (Fossiez et al., 1996; Schwarzenberger et al., 1998). In line with this, immunized mice showed a significantly increased number of neutrophils surrounding the bronchial lung barrier, within 2 h after infection (Figures 5B and 5C).

Although IL-17A activity is sufficient to control spread of the bacteria, IFN-γ seems to be necessary to fully promote efficient control of Kp (Happel et al., 2005). In parallel, it has also been shown that T_H17 cells have the ability to acquire a T_H1-like phenotype (Wei et al., 2009; Hirota et al., 2011; Zielinski et al., 2012). We therefore wondered whether some exT_H17 cells were capable of expressing IFN-γ rather than IL-17A upon reencountering bacterial-derived antigens. Our data show that a fraction of exT_H17 cells do not re-express the original cytokine IL-17A but instead IFN-γ within 24 h after infection (Figure 5D). These data reveal that T_{RM} cells also have the ability to maintain a degree of flexibility as other CD4 T cells.

Finally, we wanted to test whether exT_H17 T_{RM} cells and their several functions are necessary to orchestrate the tissue resident memory immune response. We therefore developed a mouse model to delete cells with a history of IL-17A production such as exT_H17 and their inherent ability to rapidly produce IL-17A at a desired time point. We crossed *Il17a*^{CRE} R26^{YFP} *Foxp3*^{RFP} with conditional diphtheria toxin receptor (DTR) mice

(R26STOP$^{flox/flox}$ DTR; referred to here as Fate-DTR) (Figure 5E). In this mouse model, only the YFP^{+} cells express DTR and can therefore be selectively deleted at the time of diphtheria toxin (DT) treatment. We first tested the efficacy of the DT mediated depletion and observed that exT_H17 cells were depleted in the lung after three injections with the toxin (Figure S5A). As expected, $\gamma\delta$ exIL-17 T cells were also deleted. However, they did not appear to play an obvious role during memory response against Kp (Figure S2D).

We then took advantage of this model to test whether other tissue resident cells in the lung (i.e., CD4^{+} YFP^{neg}) are sufficient to provide a reservoir for the generation and in turn the maintenance of exT_H17 T_{RM} cells. Therefore, day 35 immunized mice were treated or not treated with DT and rested for 21 days (Figure S5B). Then, the absolute number of exT_H17 cells and total CD4 T_{RM} cells were evaluated. No new generation or differentiation of exT_H17 cells was observed 21 days after DT treatment suggesting that a new wave of effector CD4 T cells is required to re-establish long-lived exT_H17 T_{RM} cells following depletion (Figures S5C–S5).

Finally, immunized Fate-DTR mice were infected with live carbapenem-resistant Kp and the bacteria burden was tested 24 h later. Mice depleted of exT_H17 cells before infection were impaired in their ability to control bacterial load. As expected, the non-depleted mice, whose lungs still contained exT_H17 T_{RM} cells, were able to effectively control the bacterial infection (Figure 5F). These data suggest that effector-derived T_H17 cells are indeed required to rapidly control this bacterial infection. Naive depleted and naive non-depleted mice were used as controls, and both groups behaved as the immunized exT_H17 cell depleted group. Moreover, immunized Fate^{+} (non DTR) mice were used as additional controls for non-specific DT effects, showing protection after infection.

DISCUSSION

Several studies have focused on the molecules and or transcription factors needed for the arrival and or retention of T_{RM} cells (Mackay et al., 2013; Skon et al., 2013; Mackay et al., 2016). However, whether T_{RM} cells derive from effector T cells remained unclear. Here, we showed that lung-infiltrating CD4 T cells became T_{RM} cells at later time points after *Klebsiella pneumoniae* immunization and protected immunized mice from carbapenem-resistant *Klebsiella pneumoniae* infection. By using two state-of-the-art IL-17A fate mouse models, we demonstrated that effector T_H17 cells were capable of persisting as a long-lived exT_H17 population, creating a resident cellular network in the lung airways. We observed a similar phenomenon, although at a lower magnitude, using other T_H17-induced pathogens such us *Candida albicans* and BCG. Using parabiosis experiments, we showed that T_H17 effector-derived T_{RM} cells persisted in the lung of immunized mice, despite reaching an equilibrium in the circulation of both paired parabionts. Infecting both parabionts or blocking the recruitment of circulatory cells from the periphery, we proved the fundamental advantage to an organism of having a local memory immune response over a systemic memory response.

We sought to compare and contrast the clonality and the whole transcriptome of lung T_{RM} cells versus periphery memory and naive cells. Here, we found that lung T_{RM} cells comprise 3 distinct populations: (1) exT_H17 cells, derived from effector T_H17 cells generated during effector immune response, (2) a low percentage of T_H17 cells, and (3) YFP^{neg} cells or cells that despite their never having been IL-17A producers also became T_{RM} cells. Moreover, the TCR sequencing (TCR-seq) analysis revealed a common clonal origin of T_H17 and exT_H17 T_{RM} cells with highly frequent clones that first expanded then contracted and finally generated a bona fide T_H17 T_{RM} response. The frequency of YFP^{neg} T_{RM} clones is in line with some previous studies where a T_H1 population was also generated during the first immune response against *Klebsiella pneumoniae* (Happel et al., 2005). Additionally, our whole-transcriptomic analysis revealed similarities among all lung T_{RM} cells, distinguishing them from peripheral memory cells. Nevertheless, some effector-derived exT_H17 cells still maintained a "T_H17-prone memory status" (Muranski et al., 2011; Youngblood et al., 2017), which may explain their fast response.

A more detailed analysis of YFP^{neg} T_{RM} cells unveiled possible distinct origins for this population. Based on their T_H1/ T_H2 and T_{CM}-related transcriptome and in line with previous human studies (Sathaliyawala et al., 2013; Becattini et al., 2015), we speculate that some YFP^{neg} T_{RM} cells may have derived from effector/effector memory T_H1 and T_H2 cells and some from central memory cells. However, more studies using polyclonal and combined cytokine fate-mapping systems are needed to clarify the origin of this heterogeneous population of cells. Previous studies, using TCR-seq or skin injections of TCR transgenic T cells have suggested that central memory CD8 T cells are the the origin of skin CD8 T_{RM} cells (Gaide et al., 2015; Kirsch et al., 2015). Our results show that CD4 T_{RM} cells were also able to derive from the first wave of effector cells generated at the beginning of the immune response.

The mechanisms elucidated for CD8 T_{RM} cell maintenance indicate that cytokines, transcription factors, and even some free fatty acid binding proteins could be involved in these processes (Adachi et al., 2015; Mackay et al., 2015; Schenkel et al., 2016; Pan et al., 2017). Nevertheless, little is known about CD4 T_{RM} cell maintenance. We hypothesized that, based on the tissue and the environment where T_{RM} cells are located, different mechanisms will operate to maintain their survival. In our models, we observed that there was no contribution from peripheral memory cells when it comes to maintenance of exT_H17 cells in the lung. By antibody-blocking and by performing single-cell RNA-seq experiments, we demonstrated that IL-7 derived from LECs was needed to maintain the survival and location of lung exT_H17 T_{RM} cells. Our results highlight the importance of stromal cells in the maintenance of exT_H17 T_{RM} cells, resembling similar mechanism by which IL-7 support other cells in the bone marrow (Cordeiro Gomes et al., 2016).

Another key aspect is the mechanisms whereby T_{RM} cells induce protection during infection. Our *in vivo* results are in line with the "primed status" of T_{RM} cells, usually viewed as a front-line branch of the adaptive immune system that "seeds" mucosal tissues. The kinetic experiments suggested that some of the lung exT_H17 T_{RM} cells transcribe high levels of *Il17a* as rapidly as 2 h after challenge with carbapenem-resistant *Klebsiella pneumoniae* infection. Our data are in line with previous

studies where CD4 T_{RM} cells express IFN-γ or IL-4 in their membrane or quickly release these cytokines after viral, parasite, or house dust mite re-challenge to better control infections or contribute to the pathology associated with asthma (Teijaro et al., 2011; Iijima and Iwasaki, 2014; Hondowicz, et al., 2016). In addition some of the lung exT_H17 T_{RM} cells also maintain the flexibility to produce only IFN-γ, the other key cytokine for an efficient response to *Klebsiella pneumoniae*. The plasticity of T_H17 cells is well characterized (Wei et al., 2009; Hirota et al., 2011; Zielinski et al., 2012), but for the first time our data show that the capacity to adapt to the environment is maintained also in exT_H17 T_{RM} cells.

We also hypothesized that the tissue environment created by the reactivation of T_{RM} exT_H17 cells commits neutrophils to extravasate and rapidly clear the bacteria.

One caveat of the functional experiments in which we used DT to delete both exT_H17 and T_H17 T_{RM} cells is that the IL-17A-producing γδ T cells were also deleted. However, using knockout mice for γδ T cells, we showed that γδ T cells do not appear to play a key role during the memory response, therefore supporting a major role for exT_H17 and T_H17 T_{RM} cells during this memory phase. In contrast, our data suggest that γδ T cells play a key role during the first response to the infection in a naive mouse (Figure S2D). Our data therefore support the hypothesis that T_H17 T_{RM} cells and IL-17A γδ T respond to this pathogen at different times of exposure; however, further studies are required to fully dissect the "division of labor" between these two types of IL-17A producer cells during *Klebsiella pneumoniae* infection. All this is also the case for circulatory IL-17A producer memory cells.

Taken together, our results indicate for the first time that a long-lived exT_H17 T_{RM} population originates from polarized T_H17 effector cells. This population is maintained by non-stromal LECs that produce IL-7. Furthermore, we underline the importance of having an effector-derived T_{RM} cell population as frontline cells that together with other T_{RM} cells, mediate the rapid clearance of threatening strains of antibiotic-resistant bacterial infections. We suggest that this cell population plays a central role in the cellular basis of immunological memory.

Finally, our study may hopefully pave the way for future studies in human tissues to design better strategies aimed to deliver more effective vaccines. Hospitalized patients infected with carbapenem-resistant *Klebsiella pneumoniae* do not respond to carbapenem antibiotic treatment and thus represent a serious clinical problem. Our data provide basic knowledge that may provide a possible solution to such a problem: vaccination for prophylaxis of carbapenem-resistant Kp especially in patients at risk.

STAR★METHODS

Detailed methods are provided in the online version of this paper and include the following:

- KEY RESOURCES TABLE
- LEAD CONTACT AND MATERIALS AVAILABILITY
- EXPERIMENTAL MODEL AND SUBJECT DETAILS
  - Mice
  - Heat killed *Klebsiella pneumoniae*
- METHOD DETAILS
  - Immunization and infection with *Klebsiella pneumoniae*
  - *In vivo* labeling of circulating CD4 T cells
  - Lymphocyte Preparation and Flow Cytometry
  - BrdU labeling
  - Tamoxifen, FTY720 and Diphtheria toxin treatments
  - Antibodies and chemicals administered to the mice
  - Immunofluorescence staining
  - Real time PCR
  - K.pneumoniae antibody titers
  - Cutaneous Candida albicans infection
  - Bacillus Calmette-Guérin (BCG) infection
  - Parabiosis
  - RNA sequencing
  - Single cell RNA sequencing
  - CDR3 TCRβ sequencing
- QUANTIFICATION AND STATISTICAL ANALYSIS
  - Statistical Analysis
- DATA AND CODE AVAILABILITY

SUPPLEMENTAL INFORMATION

Supplemental Information can be found online at https://doi.org/10.1016/j.cell.2019.07.032.

ACKNOWLEDGMENTS

We thank Jason Weinstein, Lidia Bosurgi, Jacek Puchałka, Liang Shan, Angel Solis, Nancy Ruddle, and Aviv Regev for helpful discussion, and Roni Nowarski for disucssion and microscopy assistance. We thank Katie Bolland for assistance during TCR-seq analysis, Brigitta Stockinger for providing the Fate mice and Ewa Menet and Geoffrey Lyon for sorting assistance. We would also like to thank Judy Stein for the design of iFate plasmids, and Jon Alderman, Caroline Lieber, and the Amezcua Vesely family for general assistance. We acknowledge support from HHMI for M.C.A.V. and R.A.F.; Karolinska Institute Professor fellowship for N.G., NIH RO1AI113040 for J.P.P., NIH R01AR060744 for D.H.K.; NIH R01HG008383 and R01GM131642 for Y.K.; and NIH R01DK103744 for C.T.W.

AUTHOR CONTRIBUTIONS

M.C.A.V. designed and performed the experiments, analyzed the data, and wrote the manuscript. R.A.F. designed experiments, wrote the manuscript, and supervised the project. N.G. designed experiments, discussed and interpreted the results, and wrote the paper. P.S.P. performed the immunofluorescence. P.B. and J.S.L. performed microscopy experiments. N.G., E.E., and H.X. generated Fate$^+$ mice. C.T.W. provided the Thy1.1 IL-10 reporter model. P.L.-L., R.J., W.B., P.S.P., P.B., C.C.D.H., and J.P.P. made key suggestions for experiments and edited the manuscript. P.B. performed single-cell experiment, and M.S.K. provided key suggestion for the single-cell experiment. C.C.D.H., J.Z., Y.K., and L.K. performed RNA-seq and single-cell analysis. A.I. and N.I. helped with parabiosis experiments. D.H.K. provided *Candida albicans*. M.C.A.V. did parabiosis and performed all the other experiments.

DECLARATION OF INTERESTS

R.A.F. is a recipient of a grant from Abbvie Inc., and is a consultant of GSK Vaccines and Hatteras Venture Partners. No other authors have a competing interest.

Received: March 8, 2018
Revised: March 19, 2019
Accepted: July 17, 2019
Published: August 22, 2019

REFERENCES

Adachi, T., Kobayashi, T., Sugihara, E., Yamada, T., Ikuta, K., Pittaluga, S., Saya, H., Amagai, M., and Nagao, K. (2015). Hair follicle-derived IL-7 and IL-15 mediate skin-resident memory T cell homeostasis and lymphoma. Nat. Med. *21*, 1272–1279.

Anderson, K.G., Mayer-Barber, K., Sung, H., Beura, L., James, B.R., Taylor, J.J., Qunaj, L., Griffith, T.S., Vezys, V., Barber, D.L., and Masopust, D. (2014). Intravascular staining for discrimination of vascular and tissue leukocytes. Nat. Protoc. *9*, 209–222.

Bannard, O., Kraman, M., and Fearon, D.T. (2009). Secondary replicative function of CD8+ T cells that had developed an effector phenotype. Science *323*, 505–509.

Becattini, S., Latorre, D., Mele, F., Foglierini, M., De Gregorio, C., Cassotta, A., Fernandez, B., Kelderman, S., Schumacher, T.N., Corti, D., et al. (2015). T cell immunity. Functional heterogeneity of human memory CD4+ T cell clones primed by pathogens or vaccines. Science *347*, 400–406.

Carlson, C.M., Endrizzi, B.T., Wu, J., Ding, X., Weinreich, M.A., Walsh, E.R., Wani, M.A., Lingrel, J.B., Hogquist, K.A., and Jameson, S.C. (2006). Kruppel-like factor 2 regulates thymocyte and T-cell migration. Nature *442*, 299–302.

Carlson, C.S., Emerson, R.O., Sherwood, A.M., Desmarais, C., Chung, M.W., Parsons, J.M., Steen, M.S., LaMadrid-Herrmannsfeldt, M.A., Williamson, D.W., Livingston, R.J., et al. (2013). Using synthetic templates to design an unbiased multiplex PCR assay. Nat. Commun. *4*, 2680.

Chang, J.T., Palanivel, V.R., Kinjyo, I., Schambach, F., Intlekofer, A.M., Banerjee, A., Longworth, S.A., Vinup, K.E., Mrass, P., Oliaro, J., et al. (2007). Asymmetric T lymphocyte division in the initiation of adaptive immune responses. Science *315*, 1687–1691.

Chen, K., McAleer, J.P., Lin, Y., Paterson, D.L., Zheng, M., Alcorn, J.F., Weaver, C.T., and Kolls, J.K. (2011). Th17 cells mediate clade-specific, serotype-independent mucosal immunity. Immunity *35*, 997–1009.

Cordeiro Gomes, A., Hara, T., Lim, V.Y., Herndler-Brandstetter, D., Nevius, E., Sugiyama, T., Tani-Ichi, S., Schlenner, S., Richie, E., Rodewald, H.R., et al. (2016). Hematopoietic Stem Cell Niches Produce Lineage-Instructive Signals to Control Multipotent Progenitor Differentiation. Immunity *45*, 1219–1231.

DuPage, M., and Bluestone, J.A. (2016). Harnessing the plasticity of CD4(+) T cells to treat immune-mediated disease. Nat. Rev. Immunol. *16*, 149–163.

Falagas, M.E., Tansarli, G.S., Karageorgopoulos, D.E., and Vardakas, K.Z. (2014). Deaths attributable to carbapenem-resistant Enterobacteriaceae infections. Emerg. Infect. Dis. *20*, 1170–1175.

Fossiez, F., Djossou, O., Chomarat, P., Flores-Romo, L., Ait-Yahia, S., Maat, C., Pin, J.J., Garrone, P., Garcia, E., Saeland, S., et al. (1996). T cell interleukin-17 induces stromal cells to produce proinflammatory and hematopoietic cytokines. J. Exp. Med. *183*, 2593–2603.

Gagliani, N., Amezcua Vesely, M.C., Iseppon, A., Brockmann, L., Xu, H., Palm, N.W., de Zoete, M.R., Licona-Limón, P., Paiva, R.S., Ching, T., et al. (2015). Th17 cells transdifferentiate into regulatory T cells during resolution of inflammation. Nature *523*, 221–225.

Gaide, O., Emerson, R.O., Jiang, X., Gulati, N., Nizza, S., Desmarais, C., Robins, H., Krueger, J.G., Clark, R.A., and Kupper, T.S. (2015). Common clonal origin of central and resident memory T cells following skin immunization. Nat. Med. *21*, 647–653.

Glennie, N.D., Volk, S.W., and Scott, P. (2017). Skin-resident CD4+ T cells protect against Leishmania major by recruiting and activating inflammatory monocytes. PLoS Pathog. *13*, e1006349.

Happel, K.I., Dubin, P.J., Zheng, M., Ghilardi, N., Lockhart, C., Quinton, L.J., Odden, A.R., Shellito, J.E., Bagby, G.J., Nelson, S., and Kolls, J.K. (2005). Divergent roles of IL-23 and IL-12 in host defense against Klebsiella pneumoniae. J. Exp. Med. *202*, 761–769.

Harrison, O.J., Linehan, J.L., Shih, H.Y., Bouladoux, N., Han, S.J., Smelkinson, M., Sen, S.K., Byrd, A.L., Enamorado, M., Yao, C., et al. (2019). Commensal-specific T cell plasticity promotes rapid tissue adaptation to injury. Science *363*, eaat6280.

Hirota, K., Duarte, J.H., Veldhoen, M., Hornsby, E., Li, Y., Cua, D.J., Ahlfors, H., Wilhelm, C., Tolaini, M., Menzel, U., et al. (2011). Fate mapping of IL-17-producing T cells in inflammatory responses. Nat. Immunol. *12*, 255–263.

Hondowicz, B.D., An, D., Schenkel, J.M., Kim, K.S., Steach, H.R., Krishnamurty, A.T., Keitany, G.J., Garza, E.N., Fraser, K.A., Moon, J.J., et al. (2016). Interleukin-2-Dependent Allergen-Specific Tissue-Resident Memory Cells Drive Asthma. Immunity *44*, 155–166.

Huang, W., Sherman, B.T., and Lempicki, R.A. (2009). Systematic and integrative analysis of large gene lists using DAVID bioinformatics resources. Nat. Protoc. *4*, 44–57.

Igyártó, B.Z., Haley, K., Ortner, D., Bobr, A., Gerami-Nejad, M., Edelson, B.T., Zurawski, S.M., Malissen, B., Zurawski, G., Berman, J., and Kaplan, D.H. (2011). Skin-resident murine dendritic cell subsets promote distinct and opposing antigen-specific T helper cell responses. Immunity *35*, 260–272.

Iijima, N., and Iwasaki, A. (2014). T cell memory. A local macrophage chemokine network sustains protective tissue-resident memory CD4 T cells. Science *346*, 93–98.

Kaech, S.M., Wherry, E.J., and Ahmed, R. (2002). Effector and memory T-cell differentiation: implications for vaccine development. Nat. Rev. Immunol. *2*, 251–262.

Khader, S.A., Bell, G.K., Pearl, J.E., Fountain, J.J., Rangel-Moreno, J., Cilley, G.E., Shen, F., Eaton, S.M., Gaffen, S.L., Swain, S.L., et al. (2007). IL-23 and IL-17 in the establishment of protective pulmonary CD4+ T cell responses after vaccination and during Mycobacterium tuberculosis challenge. Nat. Immunol. *8*, 369–377.

Kirsch, I.R., Watanabe, R., O'Malley, J.T., Williamson, D.W., Scott, L.L., Elco, C.P., Teague, J.E., Gehad, A., Lowry, E.L., LeBoeuf, N.R., et al. (2015). TCR sequencing facilitates diagnosis and identifies mature T cells as the cell of origin in CTCL. Sci. Transl. Med. *7*, 308ra158.

Layman, A.A.K., Sprout, S.L., Phillips, D., and Oliver, P.M. (2017). Ndfip1 restricts Th17 cell potency by limiting lineage stability and proinflammatory cytokine production. Sci. Rep. *7*, 39649.

Lee, Y.K., Turner, H., Maynard, C.L., Oliver, J.R., Chen, D., Elson, C.O., and Weaver, C.T. (2009). Late developmental plasticity in the T helper 17 lineage. Immunity *30*, 92–107.

Mackay, L.K., Rahimpour, A., Ma, J.Z., Collins, N., Stock, A.T., Hafon, M.L., Vega-Ramos, J., Lauzurica, P., Mueller, S.N., Stefanovic, T., et al. (2013). The developmental pathway for CD103(+)CD8+ tissue-resident memory T cells of skin. Nat. Immunol. *14*, 1294–1301.

Mackay, L.K., Wynne-Jones, E., Freestone, D., Pellicci, D.G., Mielke, L.A., Newman, D.M., Braun, A., Masson, F., Kallies, A., Belz, G.T., and Carbone, F.R. (2015). T-box Transcription Factors Combine with the Cytokines TGF-β and IL-15 to Control Tissue-Resident Memory T Cell Fate. Immunity *43*, 1101–1111.

Mackay, L.K., Minnich, M., Kragten, N.A., Liao, Y., Nota, B., Seillet, C., Zaid, A., Man, K., Preston, S., Freestone, D., et al. (2016). Hobit and Blimp1 instruct a universal transcriptional program of tissue residency in lymphocytes. Science *352*, 459–463.

Macosko, E.Z., Basu, A., Satija, R., Nemesh, J., Shekhar, K., Goldman, M., Tirosh, I., Bialas, A.R., Kamitaki, N., Martersteck, E.M., et al. (2015). Highly Parallel Genome-wide Expression Profiling of Individual Cells Using Nanoliter Droplets. Cell *161*, 1202–1214.

Miller, C.N., Hartigan-O'Connor, D.J., Lee, M.S., Laidlaw, G., Cornelissen, I.P., Matloubian, M., Coughlin, S.R., McDonald, D.M., and McCune, J.M. (2013). IL-7 production in murine lymphatic endothelial cells and induction in the setting of peripheral lymphopenia. Int. Immunol. *25*, 471–483.

Moore, T.A., Moore, B.B., Newstead, M.W., and Standiford, T.J. (2000). Gamma delta-T cells are critical for survival and early proinflammatory cytokine gene expression during murine Klebsiella pneumonia. J. Immunol. *165*, 2643–2650.

Mueller, S.N., Gebhardt, T., Carbone, F.R., and Heath, W.R. (2013). Memory T cell subsets, migration patterns, and tissue residence. Annu. Rev. Immunol. *31*, 137–161.

Muranski, P., Borman, Z.A., Kerkar, S.P., Klebanoff, C.A., Ji, Y., Sanchez-Perez, L., Sukumar, M., Reger, R.N., Yu, Z., Kern, S.J., et al. (2011). Th17 cells are long lived and retain a stem cell-like molecular signature. Immunity *35*, 972–985.

O'Shea, J.J., and Paul, W.E. (2010). Mechanisms underlying lineage commitment and plasticity of helper CD4+ T cells. Science *327*, 1098–1102.

Pan, Y., Tian, T., Park, C.O., Lofftus, S.Y., Mei, S., Liu, X., Luo, C., O'Malley, J.T., Gehad, A., Teague, J.E., et al. (2017). Survival of tissue-resident memory T cells requires exogenous lipid uptake and metabolism. Nature *543*, 252–256.

Pepper, M., Linehan, J.L., Pagán, A.J., Zell, T., Dileepan, T., Cleary, P.P., and Jenkins, M.K. (2010). Different routes of bacterial infection induce long-lived TH1 memory cells and short-lived TH17 cells. Nat. Immunol. *11*, 83–89.

Sathaliyawala, T., Kubota, M., Yudanin, N., Turner, D., Camp, P., Thome, J.J., Bickham, K.L., Lerner, H., Goldstein, M., Sykes, M., et al. (2013). Distribution and compartmentalization of human circulating and tissue-resident memory T cell subsets. Immunity *38*, 187–197.

Schenkel, J.M., and Masopust, D. (2014). Tissue-resident memory T cells. Immunity *41*, 886–897.

Schenkel, J.M., Fraser, K.A., Casey, K.A., Beura, L.K., Pauken, K.E., Vezys, V., and Masopust, D. (2016). IL-15-Independent Maintenance of Tissue-Resident and Boosted Effector Memory CD8 T Cells. J. Immunol. *196*, 3920–3926.

Schlapbach, C., Gehad, A., Yang, C., Watanabe, R., Guenova, E., Teague, J.E., Campbell, L., Yawalkar, N., Kupper, T.S., and Clark, R.A. (2014). Human TH9 cells are skin-tropic and have autocrine and paracrine proinflammatory capacity. Sci. Transl. Med. *6*, 219ra8.

Schwarzenberger, P., La Russa, V., Miller, A., Ye, P., Huang, W., Zieske, A., Nelson, S., Bagby, G.J., Stoltz, D., Mynatt, R.L., et al. (1998). IL-17 stimulates granulopoiesis in mice: use of an alternate, novel gene therapy-derived method for in vivo evaluation of cytokines. J. Immunol. *161*, 6383–6389.

Shekhar, K., Lapan, S.W., Whitney, I.E., Tran, N.M., Macosko, E.Z., Kowalczyk, M., Adiconis, X., Levin, J.Z., Nemesh, J., Goldman, M., et al. (2016). Comprehensive Classification of Retinal Bipolar Neurons by Single-Cell Transcriptomics. Cell *166*, 1308–1323.

Skon, C.N., Lee, J.Y., Anderson, K.G., Masopust, D., Hogquist, K.A., and Jameson, S.C. (2013). Transcriptional downregulation of S1pr1 is required for the establishment of resident memory CD8+ T cells. Nat. Immunol. *14*, 1285–1293.

Stary, G., Olive, A., Radovic-Moreno, A.F., Gondek, D., Alvarez, D., Basto, P.A., Perro, M., Vrbanac, V.D., Tager, A.M., Shi, J., et al. (2015). VACCINES. A mucosal vaccine against Chlamydia trachomatis generates two waves of protective memory T cells. Science *348*, aaa8205.

Teijaro, J.R., Turner, D., Pham, Q., Wherry, E.J., Lefrançois, L., and Farber, D.L. (2011). Cutting edge: Tissue-retentive lung memory CD4 T cells mediate optimal protection to respiratory virus infection. J. Immunol. *187*, 5510–5514.

Trapnell, C., Roberts, A., Goff, L., Pertea, G., Kim, D., Kelley, D.R., Pimentel, H., Salzberg, S.L., Rinn, J.L., and Pachter, L. (2012). Differential gene and transcript expression analysis of RNA-seq experiments with TopHat and Cufflinks. Nat. Protoc. *7*, 562–578.

Turner, D.L., Bickham, K.L., Thome, J.J., Kim, C.Y., D'Ovidio, F., Wherry, E.J., and Farber, D.L. (2014). Lung niches for the generation and maintenance of tissue-resident memory T cells. Mucosal Immunol. *7*, 501–510.

Wakim, L.M., Woodward-Davis, A., Liu, R., Hu, Y., Villadangos, J., Smyth, G., and Bevan, M.J. (2012). The molecular signature of tissue resident memory CD8 T cells isolated from the brain. J. Immunol. *189*, 3462–3471.

Wei, G., Wei, L., Zhu, J., Zang, C., Hu-Li, J., Yao, Z., Cui, K., Kanno, Y., Roh, T.Y., Watford, W.T., et al. (2009). Global mapping of H3K4me3 and H3K27me3 reveals specificity and plasticity in lineage fate determination of differentiating CD4+ T cells. Immunity *30*, 155–167.

Ye, P., Rodriguez, F.H., Kanaly, S., Stocking, K.L., Schurr, J., Schwarzenberger, P., Oliver, P., Huang, W., Zhang, P., Zhang, J., et al. (2001). Requirement of interleukin 17 receptor signaling for lung CXC chemokine and granulocyte colony-stimulating factor expression, neutrophil recruitment, and host defense. J. Exp. Med. *194*, 519–527.

Youngblood, B., Hale, J.S., Kissick, H.T., Ahn, E., Xu, X., Wieland, A., Araki, K., West, E.E., Ghoneim, H.E., Fan, Y., et al. (2017). Effector CD8 T cells dedifferentiate into long-lived memory cells. Nature *552*, 404–409.

Zielinski, C.E., Mele, F., Aschenbrenner, D., Jarrossay, D., Ronchi, F., Gattorno, M., Monticelli, S., Lanzavecchia, A., and Sallusto, F. (2012). Pathogen-induced human TH17 cells produce IFN-γ or IL-10 and are regulated by IL-1β. Nature *484*, 514–518.

STAR★METHODS

KEY RESOURCES TABLE

REAGENT or RESOURCE	SOURCE	IDENTIFIER
Antibodies		
Mouse IgG2a anti-mouse CD45.1 PECy7 clone A20	Biolegend	Cat# 110730; RRID: AB_1134168
Rat IgG2a anti- mouse CD19 APC clone 6D5	Biolegend	Cat# 115512; RRID: AB_313647
Armenian Hamster IgG anti-mouse TCR gd APC, clone GL3	Biolegend	Cat# 118116; RRID: AB_1731813
Armenian Hamster IgG anti-CD69 PE/Cy7 clone H1.2F3	Biolegend	Cat# 104511; RRID: AB_493564
Armenian Hamster IgG anti-CD69 APC clone H1.2F3	Biolegend	Cat# 104513; RRID: AB_492843
Armenian Hamster IgG anti-mouse CD69 APCCy7 clone H1.2F3	Biolegend	Cat# 104525; RRID: AB_10679041
Armenian Hamster IgG anti-mouse TCRb PECy7 clone H57-597	Biolegend	Cat# 109222; RRID: AB_893625
Armenian Hamster IgG anti-mouse TCRb APC clone H57-597	Biolegend	Cat# 109212; RRID: AB_313435
Rat IgG2b anti-mouse CD4 Pacific Blue clone RM4/4	Biolegend	Cat# 116008; RRID: AB_11149680
Rat IgG2a anti-mouse CD4 Alexa 700 clone RM4/5	Biolegend	Cat# 100536; RRID: AB_493701
Rat IgG2a anti-mouse CD127PeCy7 clone A7R34	Biolegend	Cat# 135014; RRID: AB_1937265
Armenian Hamster IgG anti-mouse CD103 APC clone 2E7	Biolegend	Cat# 121414; RRID: AB_1227502
Mouse IgG2a anti-mouse CD45.2 Alexa 700 clone 104	Biolegend	Cat# 109822; RRID: AB_493730
Rat IgG1 anti-mouse IL17a Pacific blue TC11-18H10.1	Biolegend	Cat# 506917; RRID: AB_893545
Rat IgG1 anti mouse IFNg APC clone XMG1.2	BD PHARMIGEN	Cat# 554413 ; RRID: AB_398551
Rat IgG2a anti-mouse CD122 PE clone 5H4	Biolegend	Cat# 105905; RRID: AB_2125737
Purified anti-mouse CD16/CD32 clone 93	Thermo Fisher	Cat# 14-0161-85; RRID: AB_467134
Rat IgG1 anti-mouse Lyve-1 eFlour 660 clone ALY7	Invitrogen, Thermo Fisher	Cat# 50-0443-82; RRID: AB_10597449
Rat IgG2a anti-mouse CD31 Alexa 488 clone 390	Biolegend	Cat# 102413; RRID: AB_493409
Rat IgG2a anti-mouse CD31 Alexa 488 clone MEC13.3	Biolegend	Cat# 102514; RRID: AB_2161031
Anti GFP (polyclonal antibody)	invitrogen	Cat# A11122; RRID: AB_221569
Donkey anti Rabbit IgG Alexa 488	Invitrogen, Thermo Fisher	Cat# A21206; RRID: AB_2535792
Mouse IgG2b Anti mouse/human IL7 clone M25	Bio X cell	Cat# BE0048; RRID: AB_1107711
Mouse IgG2b isotype control, unknown specificity clone MCP-11	Bio X cell	Cat# BE0086; RRID: AB_1107791
Rat IgG2b anti-mouse/human CD44 PeCy7 clone IM7	Biolegend	Cat# 103030; RRID: AB_830787
Rat IgG2a anti-mouse CD62L APC clone MEL-14	Biolegend	Cat# 104412; RRID: AB_313099
Bacterial and Virus Strains		
Klebsiella pneumoniae 43816	ATCC	ATCC 43816
Klebsiella pneumoniae BAA-2146 (NDM1+)	ATCC	ATCC BAA-2146
Candida albicans SC5314 strain	Daniel Kaplan	Igyártó et al., 2011 #39
BCG	Lauren Cohn	Yale PCCSM
Chemicals, Peptides, and Recombinant Proteins		
Tamoxifen	Sigma-Aldrich	Cat#T5648
FTY720	Cayman Chemichal Company	162359-56-0
Diphtheria toxin	Sigma-Aldrich	D0564
BrdU	Sigma-Aldrich	B5002
Collagenase D	Roche/ Sigma-Aldrich	11088882001
DNase I	Sigma	9003989
Percoll	GE Healthcare	17089101

(*Continued on next page*)

Continued

REAGENT or RESOURCE	SOURCE	IDENTIFIER
UltraPure BSA (50 mg/mL)	ThermoFisher	AM2616
Ficol 20%	Sigma-Aldrich	F5415-50ML
Sarkosyl	Sigma-Aldrich	L7414-10ML
UltraPure 0.5M EDTA	Life Tech	15575-020
Trizma® hydrochloride solution, 2M Tris ph 7,5	Sigma-Aldrich	T2944-100ML
RNase Inhibitor NxGwn	Lucigen	Lucigen
Maxima H Minus Reverse Transcriptase	ThermoFisher	EP0753
1M DTT (Dithiothreitol)	Teknova	D0060
1H,1H,2H,2H-Perfluorooctan-1-ol	Synquest	Synquest
Critical Commercial Assays		
BrdU flow kit	BD PharMingen	552598
ELISA plates for KP titers	Corning	3590
Nextera XT 96	Illumina	FC-131-1002
NextSeq® 500 High Output v2 Kit (75 cycles)	Illumina	FC 404 2005
HotStart ReadyMix, 500 × 25 μL reactions	KAPA	KM2602
RNeasy Plus Micro Kit	QIAGEN	74034
Deposited Data		
RNA Sequencing	This paper	GEO: GSE130446
Single cell RNA Sequencing	This Paper	GEO: GSE131450
TCR Sequencing	This Paper	https://clients.adaptivebiotech.com
Experimental Models: Organisms/Strains		
Mouse: C57BL/6	Yale University	N/A
Mouse: Fate^{+}	Gagliani et al., 2015	N/A
Mouse: iFate	Gagliani et al., 2015	N/A
Mouse: ROSA26iDTR	The Jackson Laboratories	007900
Mouse: IL7$^{GFP/+}$	Yale University	N/A
Oligonucleotides		
Primer for quantitative RT-PCR: Hprt	Sigma–Aldrich	NM 013556
Primer for quantitative RT-PCR: Klf2) (F, cattgcaactggg aaggatg; R, aaagggtctgtgacctgtgtg)	Sigma–Aldrich	
Primer for quantitative RT-PCR: S1pr1 (F, accttccgcaa gaacatctc; R, ttgcagcccacatctaacag)	Sigma–Aldrich	
DropSeq Barcoded Bead SeqB 5′ –Bead–Linker-TTTTT TTAAGCAGTGGTATCAAC GCAGAGTACJJJJJJJJJJJJ NNNNNNNN TTTTTTTTTTTTTTTTTTTTTTTTTTTTTT-3′	ChemeGenes, Macosko et al., 2015	Cat# *Macosko-2011-10*
Template_Switch_Oligo AAGCAGTGGTATCAACGCAG AGTGAATrGrGrG	Macosko et al., 2015	IDT
SMART PCR primer AAGCAGTGGTATCAACGCAGAGT	Macosko et al., 2015	Sigma
New-P5-SMART PCR hybrid oligo AATGATACGGCG ACCACCGAGATCTACACGCCT GTCCGCGGAAGCAGT GGTATCAACGCAGAGT* A*C	Macosko et al., 2015	IDT
Custom Read 1 primer GCCTGTCCGCGGAAGCAGTGG TATCAACGCAG AGTAC	Macosko et al., 2015	Sigma
Software and Algorithms		
Prism 6.0	GraphPad	https://www.graphpad.com
FlowJo	Tree Star	https://www.flowjo.com/solutions/flowjo/downloads
Leica LAS X software	to be completed this	
Ask Jun or who did the analysis to complete this		

(*Continued on next page*)

Continued

REAGENT or RESOURCE	SOURCE	IDENTIFIER
FastQC	Babraham Institute	https://www.bioinformatics.babraham.ac.uk/projects/fastqc/
Tophat2	Johns Hopkins/University of Washington	Trapnell et al., 2012
Cufflinks	Trapnell Lab	Trapnell et al., 2012
Drop-seq tools	Macosko et al., 2015	http://mccarrolllab.org/dropseq/
R	R foundation for statistical computing	https://www.R-project.org
CummeRbund R Package	MIT/Harvard University	http://compbio.mit.edu/cummeRbund/
Pheatmap R package	Raivo Kolde (CRAN)	https://cran.r-project.org/web/packages/pheatmap/pheatmap.pdf
Rtsne R package	Jesse H. Krijthe	https://github.com/jkrijthe/Rtsne
DBSCAN R package	Michael Hahsler	https://github.com/mhahsler/dbscan
Excel	Microsoft	www.microsoft.com/Microsoft/Excel
Other		
PDMS co-flow microfluidic droplet generation device	Nanoshift	Cat# Drop-Seq
100-micron cell strainer	VWR	Cat# 21008-950
40-micron cell strainer	VWR	Cat#21008-949
Fuchs-Rosenthal hemocytometer	Incyto	#DHC-F01
Droplet generation oil	Bio-Rad	Cat# 186-4006

LEAD CONTACT AND MATERIALS AVAILABILITY

Further information and requests for resources and reagents should be directed to Richard Flavell (richard.flavell@yale.edu).

EXPERIMENTAL MODEL AND SUBJECT DETAILS

Mice

C57BL/6 mice 8–12 weeks of age were obtained from Charles River (USA).

As previously described (*1*) the Fate^{+} model was obtained by crossing the original Foxp3^{RFP} IL-10^{eGFP} IL-17A^{Kata} mice with IL-17a$^{CRE+/+}$ R26YFP$^{+/+}$ mice (kindly provided by Prof B. Stockinger). The iFate mice were generated in our Lab (Gagliani et al., 2015). The iFate mice were used in heterozygosis for the IL-17a$^{IRES\text{-}eGFP\text{-}CRE\text{-}ERT2}$ allele (Gagliani et al., 2015).

ROSA26iDTR were acquired from the Jackson laboratories (007900) and crossed with IL17$^{CRE\ +/+}$ FoxP3 RFP$^{+/+}$ R26STOP$^{flox/flox}$ YFP$^{+/+}$ to obtain the Fate-DTR mice. Heterozygous IL7GFP/+ mice (Miller et al., 2013) were provided by Joao Pereira. We always used females in our studies because it is not allowed to do parabiosis experiments with males.

Animal procedures were approved by the Institutional Animal Care and Use Committee of Yale University

Heat killed *Klebsiella pneumoniae*

K. pneumoniae (Kp) ATCC strain 43816, serotype 2 was expanded over night at 37 C in nutrient broth. 200 ul of the bacterial suspension were added to 50 mL of nutrient broth and grown for 3.5/4 hr at 37 C, allowing the culture to reach log phase. The concentration of Kp was determined by measuring the absorbance at 600 nm. Bacteria were pelleted by centrifugation at 4,500 rpm for 8 min, washed twice in sterile PBS, and re-suspended in 5 mL of sterile PBS. To heat kill the bacteria we incubated the suspension for 2 hr at 70 C. Then we calculate the amount of protein by Biorad kit (DC protein assay) and keep our stock of 1mg/ml of heat killed Kp at −20 C. Cultures in solid nutrient broth confirm that the bacteria were death.

METHOD DETAILS

Immunization and infection with *Klebsiella pneumoniae*

For immunizations, 40 ug of heat killed Kp (43816) were intranasally administered into anesthetized mice (Ketamine/Xylazine (100 mg/kg and 10 mg/kg respectively)) on day 0 and 7 (Figure S1A).

For infections *Klebsiella pneumoniae* BAA-2146 (NDM1+) (ATCC) was expanded over night at 37 C in nutrient broth. 200 ul of the bacterial suspension were added to 50 mL of nutrient broth and grown for 3.5/4 hr at 37 C, allowing the culture to reach log phase. The

concentration of Kp was determined by measuring the absorbance at 600 nm (OD_{600} = 2 resemble $2x10^9$ bacteria/ml). Bacteria were pelleted by centrifugation at 4,500 rpm for 8 min, washed twice in sterile PBS, and re-suspended at the desired concentration with sterile PBS. $5x10^5$ bacteria (40 ul) were intranasally administered on anesthetized mice. 24 hours after infection mice were sacrificed (Figure S2A). The lungs were re-suspended in 500 ul of sterile PBS and homogenized using gentleMACS dissociator. Different dilutions of lungs were plated in agar nutrient broth. CFU numbers were counted 24 hours later (Figure S2B).

In vivo labeling of circulating CD4 T cells

To distinguish between circulating $CD4^+$ T cells and $CD4^+$ T cells infiltrating into the lung parenchyma, we injected fluorochrome labeled antibody specific for CD4 (CD4-A700) into the bloodstream of mice. Briefly, naive or immunized mice were injected intravenously with 5 μg Alexa 700 conjugated anti-CD4 Ab (clone RM4-5) in PBS, and after 7 min, mice were euthanized. For *in vitro* CD4 staining, Pacific Blue conjugated anti-CD4 Ab (clone RM4-4) was used. In all the experiments blood staining controls were used and around 96%–99% of $CD4^+$ T cells were labeled.

Lymphocyte Preparation and Flow Cytometry

Spleen, mediastinal lymph nodes (medLNs), and bone marrow (BM) were removed from immunized (day 35) or naive euthanized mice, placed into RPMI media supplemented with 5% fetal calf serum (FCS), and passed through a cell strainer (70mm).

For isolation of lung infiltrates, cells were collected after 1 hr digestion in RPMI media supplemented with 5% FCS, 1 mg/ml Collagenase D (Roche), and 10 mg/ml DNase I (Sigma) at 37 C. Homogenates were passed through a cell strainer, and ammonium- chloride-potassium lysing buffer was used. Immune cells were separated with a Percoll gradient by centrifugation at 450 g for 20 min. Cells were removed from the interface, washed and stained with the indicated FACS antibodies. Cells were acquired on an LRS II Flow Cytometer (BD Biosciences), and data were analyzed with FlowJo software (Tree Star).

For intracellular IL-17A and IFN-γ staining in Figure 4C, cells were re-stimulated for 3 hr with phorbol 12-myristate 13-acetate (20 ng/ml) and ionomycin (1 mg/ml) in the presence of monensin (1 mg/ml). Then cells were fixed with BD fixation protocol and perm for 4 min with NP-40. Cells were washed and stained with intracellular antibodies described above.

The gating strategy shown in Figure S1 was preceded by gating on the typical physical parameters of the lymphocyte (FSC, SSC), exclusion of the doublets and by gating on CD4 in-vitro$^+$ and TCRβ$^+$ cells.

The gating strategy shown in Figures 1, 4, 5,8, S2, and S5 was preceded by gating on the typical physical parameters of the lymphocyte, exclusion of the doublets and by gating on CD4 in-vitro$^+$, TCRβ$^+$, $Foxp3^{RFP\ neg}$.

In all the experiments the gating strategy of every time point was based on negative and single positive controls.

BrdU labeling

For analysis of homeostatic proliferation, Fate$^+$ mice were given BrdU (0.8 mg/ml; Sigma-Aldrich)/1% sucrose in the drinking water *ad libitum*. The water was carefully protected from light and change every other day. After 15 days, organs were collected, processed and cells were stained with surface Abs and incorporated BrdU was detected with a BrdU flow kit (BD PharMingen) according to the manufacturer's specifications.

Tamoxifen, FTY720 and Diphtheria toxin treatments

Tamoxifen (Sigma) was dissolved in corn or sesame oil (Fluka, Sigma). Naive or immunized Inducible IL17A Fate mice were i.p. injected with 2 mg of tamoxifen on day 3, 7 and 10 after immunization.

Fate$^+$ mice were immunized with heat killed Kp. 35 days later mice were given 4 μg/ml of FTY720 (Cayman Chemical Company) in the drinking water for two weeks.

For the FTY720 and infections studies, the mice were given FTY720 in the drinking water for 14 days before infection. After the infection the mice kept under FTY720 treatment for 1 more day and then sacrificed (Figure S2H)

Diphtheria toxin was administered i.p. at 50 μg/kg body weight on day 35, 37 and 39 after immunization. On day 45, mice were infected i.n. with Kp BAA-2146 and sacrificed 24 hr after infection.

Antibodies and chemicals administered to the mice

All antibodies for flow cytometry analysis were from Biolegend.

Diphteria toxin, BrdU and Tamoxifen were from Sigma.

See Key Resources Table for the details.

Immunofluorescence staining

Lungs were inflated with a perfusion buffer (1% PFA; 50% OCT; 1x PBS). Incubations at 4°C with sucrose gradients were done sequentially (10% sucrose 1 hour, 20% sucrose 1 hour, 30% sucrose 1 hour) and then the lungs were flash frozen in Tissue Freezing Medium (Jung). Cryosections (8 μm) were mounted on glass slides, fixed with 4% PFA and blocked with αCD32/CD16 (BioLegend) at a dilution of 1/200. Staining was performed for 2h at room temperature for primary antibodies and 1h at room temperature for

secondary antibodies. The following antibodies were used: rabbit anti-GFP (Life technologies) was used at 1/100, followed by polyclonal goat anti-rabbit-Alexa Fluor 488 (Life Technologies) at 1/2000 for detecting YFP. Anti-CD4-Pe (BioLegend) and anti-CD31-APC (BioLegend) were used at 1/70.

The images were captured by a confocal microscope at room temperature, using 40x and 10x lenses and were processed using Volocity 6.3 software (Perkin Elmer).

For IL7 detection in $IL7^{GFP/+}$ mice cryosections (40 μm) were mounted on glass slides, fixed with 4% PFA and blocked with αCD32/CD16 (BioLegend) at a dilution of 1/200. Staining was performed for 2h at room temperature for primary anti-GFP antibody and 1h at room temperature for secondary antibodies. The following antibodies have been used rabbit anti-GFP (Thermo/A11122), and donkey anti rabbit IgG-A488 (Thermo/A21206). The images were captured by a confocal microscope (Leica TCS SP5), using 40x and were processed using Leica LAS X software.

Real time PCR

RNA from cells was isolated using TRIzol LS reagent (Life Technology) according to the manual. RNA was subjected to reverse transcription with SuperScript II (Invitrogen) with oligo(dT) primer. cDNA was semi quantified using commercially available primer/probe sets from Applied Biosystems. Samples were analyzed with the change in cycle threshold method. Results were normalized to hypoxanthine phosphoribosyltransferase (*Hprt*).

K.pneumoniae antibody titers

Flat bottom high binding 96-well plates (Costar) were coated with 10 ug/ml of heat killed Kp in PBS at 4°C overnight, and then washed with PBS-Tween 20 0.05%. Each plate was blocked with PBS plus 1% BSA (blocking buffer) overnight at 4°C. Serum samples were diluted in blocking buffer and incubated for 2 h at room temperature. Detection of IgM or IgG was done using goat anti-mouse IgM-Biotin or anti-mouse IgG-Biotin (Southern Biotech) for 1 h at room temperature followed by incubation with streptavidin coupled to Horseradish peroxidase (Vector laboratories) for 30 minutes at room temperature. The reaction was developed with 3, 3′, 5, 5′-tetramethylbenzidine substrate-chromogen (BD Bioscience) and stopped with 1N H2SO4. Anti-Kp titers were determined by serial dilutions of plasma and the titer was defined as the highest dilution that yielded an OD at 450 nm that was 2-fold greater than the background level.

Cutaneous Candida albicans infection

C. albicans (kindly provided by J. Craft and D. Kaplan, (Yale University and University of Pittsburg respectively) was grown in YPAD medium at 30°C until the OD_{600} reached 1.5–1.8. After washing with sterile PBS, *C. albicans* were counted using a hemocytometer.

Mice were anesthetized with ketamine and xylazine (100/10 mg/kg body weight), shaved on the back with electric clipper, then chemically depilated with Nair hair remover lotion (Church & Dwight) for 3 minutes and cleaned. The stratum corneum was removed with 20 strokes with 220 grit sandpaper (3M). $2x10^8$ *C. albicans* in 50 ul of sterile PBS was applied to the skin. 30 days after infection mice were sacrificed and 1 cm^2 of infected skin was excised, minced and then digested for 1 h at 37°C in RPMI medium containing liberase (400 μg/ml; Roche) collagenase D (1 mg/ml; Roche) and DNase I (10 mg/ml Sigma) with continuous stirring. Cells were separated via a Percoll gradient by centrifugation at 450 g for 20 min. Cells were then removed from the interface, washed, stained with specifics abs and analyzed by FACS.

Bacillus Calmette-Guérin (BCG) infection

Mycobacterium bovis BCG (kindly provided by Dr Lauren Cohn, Yale School of Medicine, Pulmonary, Critical Care and Sleep Medicine) was grown in Middlebrook 7H9 broth base (Difco) supplemented with 10% Bacto Middlebrook OADC enrichment (Remel) for 2 weeks at 37°C. Mice were infected intranasaly with $1x10^6$ viable bacteria in 20ul of PBS or with PBS alone as a control. The final concentration of viable bacteria was enumerated by plate counts of CFU with Middlebrook 7H10 agar (Difco) supplemented with 0.5% glycerol (Difco) and 10% Bacto Middlebrook OADC enrichment.

After 30 days of infection mice were sacrificed, the lungs were harvested and processed as described above for the experiments with *K. pneumoniae.*

Parabiosis

In short, females were anesthetized with a mixture of Ketamine/Xylazine (100 mg/kg and 10 mg/kg respectively). After shaving the corresponding lateral aspects of each mouse, matching skin incisions were made from behind the ear to the hip and sutured together with nylon and collagen (5-0,ETHICON, VICRYL*) absorbable suture. Then these areas were clipped with 7-mm stainless-steel wound clips (Reflex7).

RNA sequencing

All cells used for bulk RNA-sequencing were obtained from mice immunized with heat-killed Kp (described above) 35 days post-immunization. Purified lymphocyte populations were obtained from lymph nodes as described above, lymphocytes populations

from lung tissue were obtained via collagenase digestion and percoll separation as described above. Purified RNA was obtained using QIAGEN Kits.

Libraries for RNA sequencing were generated using Illumina TruSeq mRNA-Seq Sample Prep Kits. Library concentration and quality was assessed using a Bioanalyzer, and sequencing performed on an Illumina HiSeq 2500 at the Yale Center for Genome Analysis.

Analysis performed using the Tuxedo suite, with splice junction mapping performed using TopHat and transcript quantification using Cufflinks (Trapnell et al., 2012). Downstream analysis was performed in R using CummeRbund (http://compbio.mit.edu/cummeRbund/) analysis software, heatmaps were produced using the package (https://cran.r-project.org/web/packages/pheatmap/pheatmap.pdf) "pheatmap" in R. Gene ontology analysis was performed using DAVID (Huang et al., 2009).

Single cell RNA sequencing

Naive or immunized (day 35) C57BL/6 mice were injected intravenously with 2.5 ug Alexa 700 conjugated anti-CD45.2 Ab in PBS, and after 7 min, mice were euthanized. For *in vitro* CD45.2 staining, PECy7 conjugated anti-CD45.2 Ab was used. For isolation of total lung cells, cells were collected after 1 hr digestion in RPMI media supplemented with 5% FCS, 1 mg/ml Collagenase D (Roche), 10 mg/ml DNase I (Sigma) and 0.1 mg/ml Dispase II (Sigma) at 37 C 250 rpm. Homogenates were passed through a cell strainer, and ammonium- chloride-potassium lysing buffer was used. After *in vitro* staining with PECy7 anti-CD45.2 and Pacific blue anti-CD4 Abs, CD45.2 *in vivo* ^{neg}, CD4 ^{neg} cells were sorted into PBS plus 0.01% BSA. The cells were diluted to concentration of 100 cells/μl and 1 mL aliquots were used as input to the Drop-seq protocol. Cells were processed for Drop-seq within ~30 min of collection.

Drop-seq was performed as described previously (Macosko et al. 2015; Shekhar et al., 2016) with minor modifications. The beads were purchased from ChemGenes Corporation, Wilmington MA (catalog number Macosko201110) and the PDMS co-flow microfluidic droplet generation device was generated by Nanoshift, Emeryville CA. The cDNA was generated using Template Switch Oligo and the populations of 5,000 beads (~150 cells) were separately amplified for 16 cycles of PCR (conditions identical to those previously described) with SMART PCR primer and PCR products were purified by the addition of 0.6x AMPure XP beads (Beckman Coulter). For each condition the cells from multiple mice were pooled together. The immunized group consisted of cells from 3 mice and naive condition consisted of 5 mice. Each sample was collected by Drop-seq. For immunized conditions two 1 mL collections were performed and for naive mouse one collection was performed. For immunized group the cDNA from an estimated 4000 cells was prepared and tagmented by Nextera XT using 1000 pg of cDNA input, and the custom primers New-P5-SMART-hybrid [3] and Nextera XT primers - N701 and N702 (Illumina). For naive group, cDNA from an estimated 2000 cells was used as input into the Nextera XT tagmentation with New-P5-SMART-hybrid oligoand N704. The concentration and the quality of libraries was measured with Qubit HS DNA assay and Agilent TapeStation Three libraries were sequenced on the Illumina NextSeq 500 using 2.0 pM in a volume of 1.3 mL HT1, and 2 mL of 0.3 μM Custom Read 1 primer (*3*) for priming of read 1. Read 1 was 20 bp; read 2 (paired end) was 60 bp.

Single cell RNA-seq data was processed as described previously (Macosko et al., 2015) with Drop-seq tools. After the generation of the digital expression matrix, data was normalized in terms of log (*CPM* / 10 + 1), where *CPM* stands for counts per million (meaning that the sum of all gene-levels is equal 1,000,000). Subsequently, to visualize the cell subpopulations in two dimensions, PCA (principal component analysis) followed by t-SNE (t-Distributed Stochastic Neighbor Embedding), a non-linear dimension reduction method, were applied on the normalized data. DBSCAN (Density-based spatial clustering of applications with noise) was then used on the t-SNE coordinates to investigate cell subpopulations. Marker genes for each cluster of cells were identified based on binary classifiers trained with Logistic Regression with the R package "*glm*" (https://www.R-project.org/). In order to analyze behaviors of specific genes in different clusters and conditions (Figure 4F), fraction of cells expressing the gene of interest and average expression values among expressing cells were calculated.

CDR3 TCRβ sequencing

Spleen and lung were removed from immunized mouse. Tissue resident cells from the lung were isolated by cell sorting CD4 $^{in\ vitro+\ in\ vivo\ neg}$ (YFP^{neg}, exTh17 and Th17). Memory and naive CD4 T cells were isolated from spleen of the same mouse by cell sorting.

DNA extraction, amplification and TCRβ-chain sequencing was conducted by Adaptive Biotechnologies based on the ImmunoSEQ platform (Carlson et al., 2013)

QUANTIFICATION AND STATISTICAL ANALYSIS

Statistical Analysis

Statistical analyses were calculated in Prism 6.0 (Graphpad Software). According to the experimental set-up and the distribution of the means (normal versus non parametric) we used ANOVA or Kruskal-Wallis followed by Dunnett and Mann - Whitney U test, respectively, for the multiple comparisons; $p < 0.05$ was considered significant. Bonferroni correction was used to counteract the problem in case of multiple comparisons. The specific statistical analyses used in each figure are further described in the figure legends.

DATA AND CODE AVAILABILITY

The datasets of the RNA-Seq, single cell RNA-Seq and CDR3 TCRβ-Seq generated during this study are available at GEO: GSE130446; GEO: GSE131450 and http://clients.adaptivebiotech.com/login respectively. The accession number for RNA-seq in Fig.3 reported in this paper is GEO: GSE130446. The accession number for Single cell RNA-seq in Fig.4 reported in this paper is GEO: GSE131450. The DOI for Immuno-seq in Fig.2 reported in this paper is https://doi.org/10.21417/MCAV2019CELL. For further details see the Key Resources Table.

Supplemental Figures

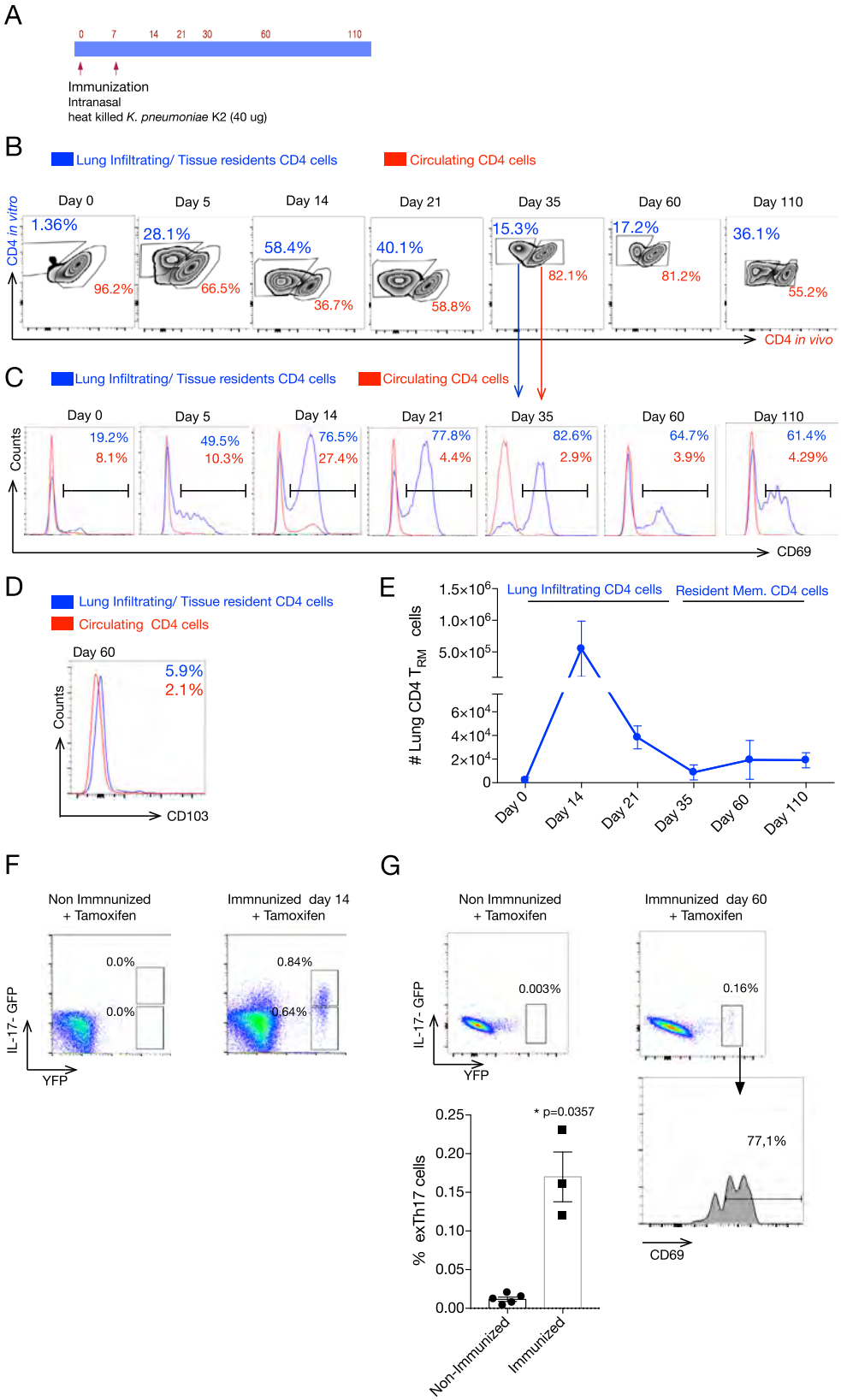

(legend on next page)

Figure S1. Related to Figure 1

(**A**) Scheme of immunization with heat killed *Klebsiella pneumoniae* (serotype K2) on day 0 and 7. At different time points C57BL/6 mice were sacrificed and the presence of CD4 T_{RM} was evaluated using an *in vivo* antibody labeling technique. (**B**) Zebra plots show accumulation of infiltrating/tissue resident CD4 *in vitro*$^{+}$ TCR-β^{+}, CD4 *in vivo*^{neg}, Foxp3 ^{neg} T cells in lung after immunization with heat killed *K. pneumoniae* in C57BL/6 mice at different time points. *In vivo* labeling delineates infiltrating/resident (CD4 *in vivo*^{neg}, CD4 *in vitro*$^{+}$) and circulating (CD4 *in vivo*$^{+}$, CD4 *in vitro*$^{+}$) polyclonal lung CD4 T cell subsets. (**C**) CD69 and (**D**) CD103 expression in infiltrating/ T_{RM} (blue line) and circulatory (red line) CD4^{+} TCR β^{+} T cells. (**E**) Absolute number of lung CD4 infiltrating/resident (CD4 *in vitro*$^{+}$, CD4 *in vivo*^{neg}, TCRb^{+}) T cells at different time points after immunization (n = 3 per time point). One out of 2 independent experiments is shown. (**F**) The dot plots show the frequency of lung exT_H17 cells in non-immunized (left) and day 14 immunized inducible IL17A Fate mice (right). Both groups of mice were treated with tamoxifen. (**G**) The dot plots show the frequency of lung exT_H17 cells in non-immunized (left) and day 60 immunized inducible IL17A Fate^{+} mice (right). Both groups of mice were treated with tamoxifen. The bottom histogram shows the expression of CD69 in exT_H17 cells of immunized + tamoxifen mouse. The bar graphs on the right show the frequency of exT_H17 cells in the lung of non-immunized and immunized mice (Day 60). Each dot represents one mouse. Representative dot plots are shown (n: 3 mice per group). One out of 3 experiments is shown. Data are represented as mean ± SEM. Mann-Whitney U test, *p = 0.0357

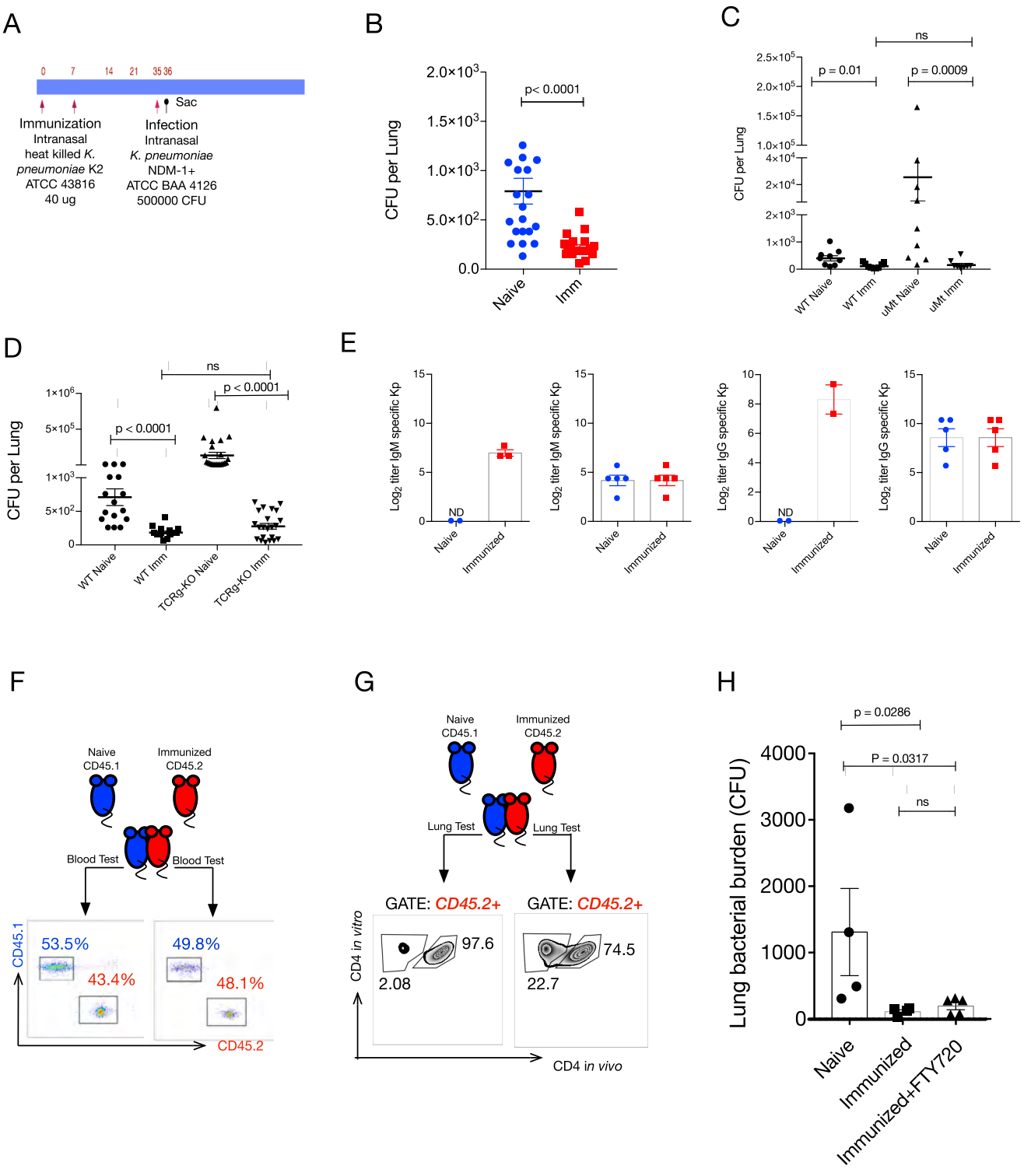

Figure S2. Related to Figure 1

A) Scheme of immunization with heat killed *Klebsiella pneumoniae* (K2 serotype) on day 0 and 7 and infection with Cre (carbapenem-resistant enterobacteriaceae) Kp (NDMI$^+$) on day 35. 24 hours later the mice where sacrificed. (**B**) The graphs show the amount of Cre Kp (NDMI$^+$) CFU after 24 hs of infection of C57BL/6 WT naive mice (blue circles) or immunized mice (red squares). **C and D)** The graphs show the amount of Cre Kp (NDMI$^+$) CFU after 24 hs of infection. WT, uMT and TCR$\gamma\delta$ KO mice were immunized at day 0 and 7 with heat killed Kp serotype 2 (ATCC 43816) and on day 35 infected with live 5x10^5 CFU of Cre Kp (NDMI$^+$ ATCC BAA 2146). Each dot represents one mouse. Data is cumulative of 4 experiments for C, and 2 experiments in D. (**E**) The graphs show the titer of specific antibodies

(legend continued on next page)

against Kp, IgM and IgG before parabiosis in naive and day 30 immunized mice. 30 days after parabiosis the titer of specific antibodies against Kp, IgM and IgG were measure in naive and immunized mice. (**F**) Naive CD45.1^{+} and day 35 immunized CD45.2^{+} mice were surgically joined for 3 weeks. Before sacrifice anti CD4 antibody was injected to distinguish tissue infiltrating/resident and circulating cells. Dot plots showing blood full chimerism 3 weeks after surgery. (**G**) Dot plots showing the percentage of CD4^{+} CD45.2^{+} cells in the lung of naive CD45.1 mouse (left) and in the lung of immunized CD45.2 mouse (right). (**H**) The graphs show the amount of Cre Kp (NDMI^{+}) CFU after 24 hs of infection. Immunized mice were given FTY720 in the drinking water from day 35 until the day of sacrificed (14 days) (Immunized + FTY720). Naive and Immunized mice drinking normal water were also infected and used as controls.

Data are represented as mean ± SEM and ± SD.

Mann-Whitney U test (B), Kruskal-Wallis ($p = 0.0004$) and post hoc Mann-Whitney U test with Bonferroni correction (C), Kruskal-Wallis ($p < 0.0001$) and post hoc Mann- Whitney U test with Bonferroni correction (D). Kruskal-Wallis ($p = 0.0134$) and post hoc Mann Whitney U test with Bonferroni correction (H).

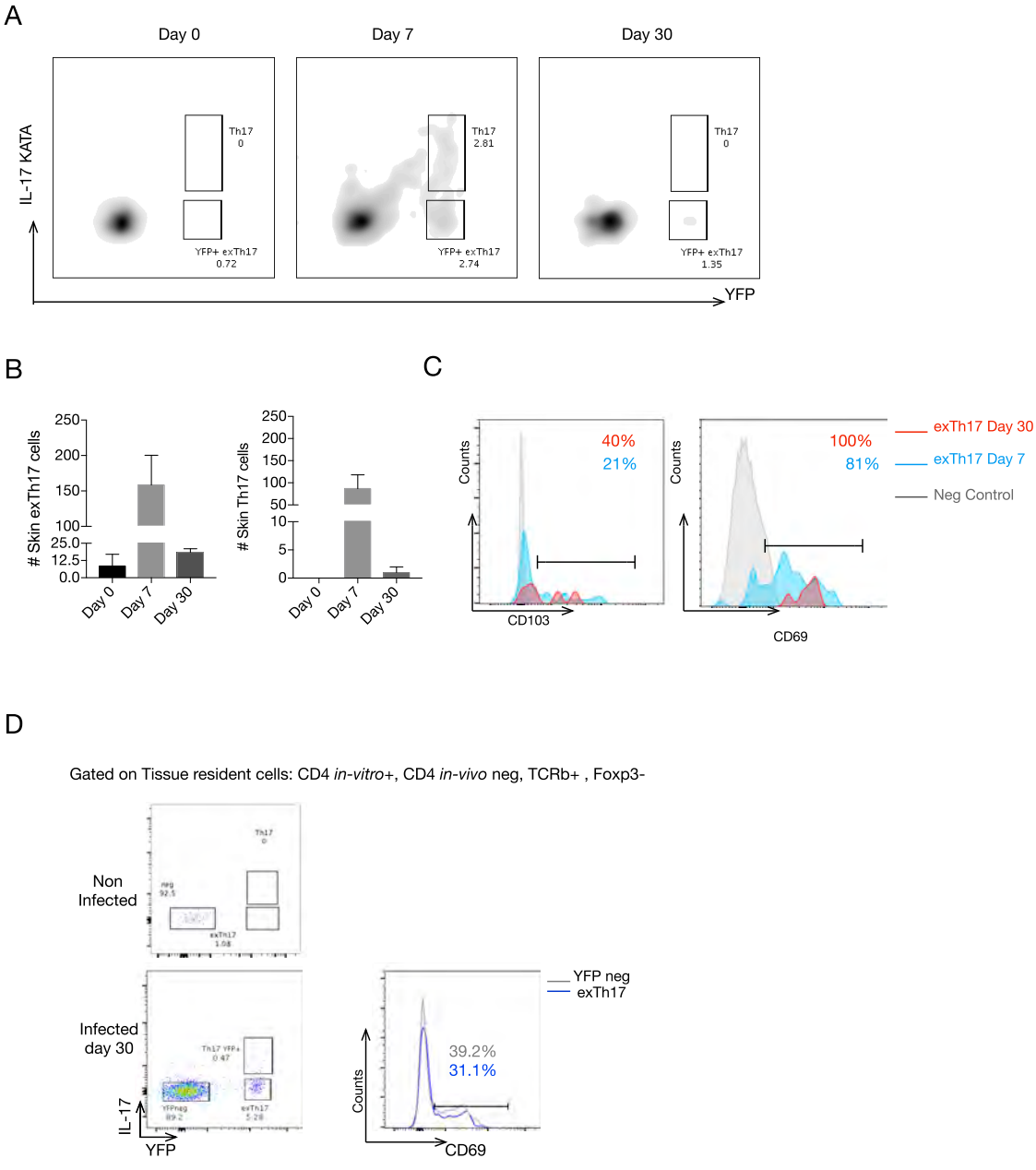

Figure S3. Related to Figure 1

Fate^{+} mice where infected in the skin with *C. albicans*. **A, B)** Dot plots show the percentage and (**B**) absolute numbers of Th17 and exTh17 after infection at day 7 and day 30. Non infected Fate^{+} mice where used as controls (day 0). (**C**) Histograms show the percentage of skin exTh17 cells that express CD103 (left graph) and CD69 (right graph) at day 7 (blue histogram) and day 30 (red histogram) after infection. Grey histograms represent negative control. (**D**) Dot plots show the frequency of T_{RM} exT_H17 cells in the lung of naive (top) or BCG infected Fate^{+} mice after 30 days of infection (bottom). The histogram shows the expression of CD69 in lung exT_H17 cells (blue line) and YFP negative cells (gray line). Representative dot plots are shown (n:3 mice per group).

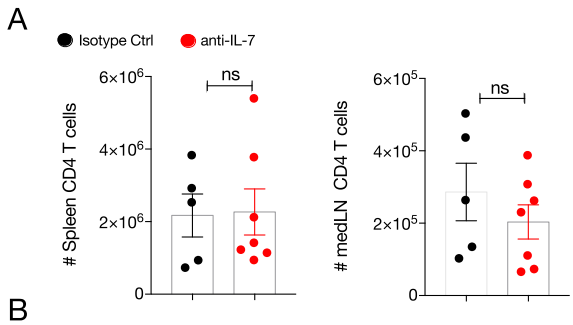

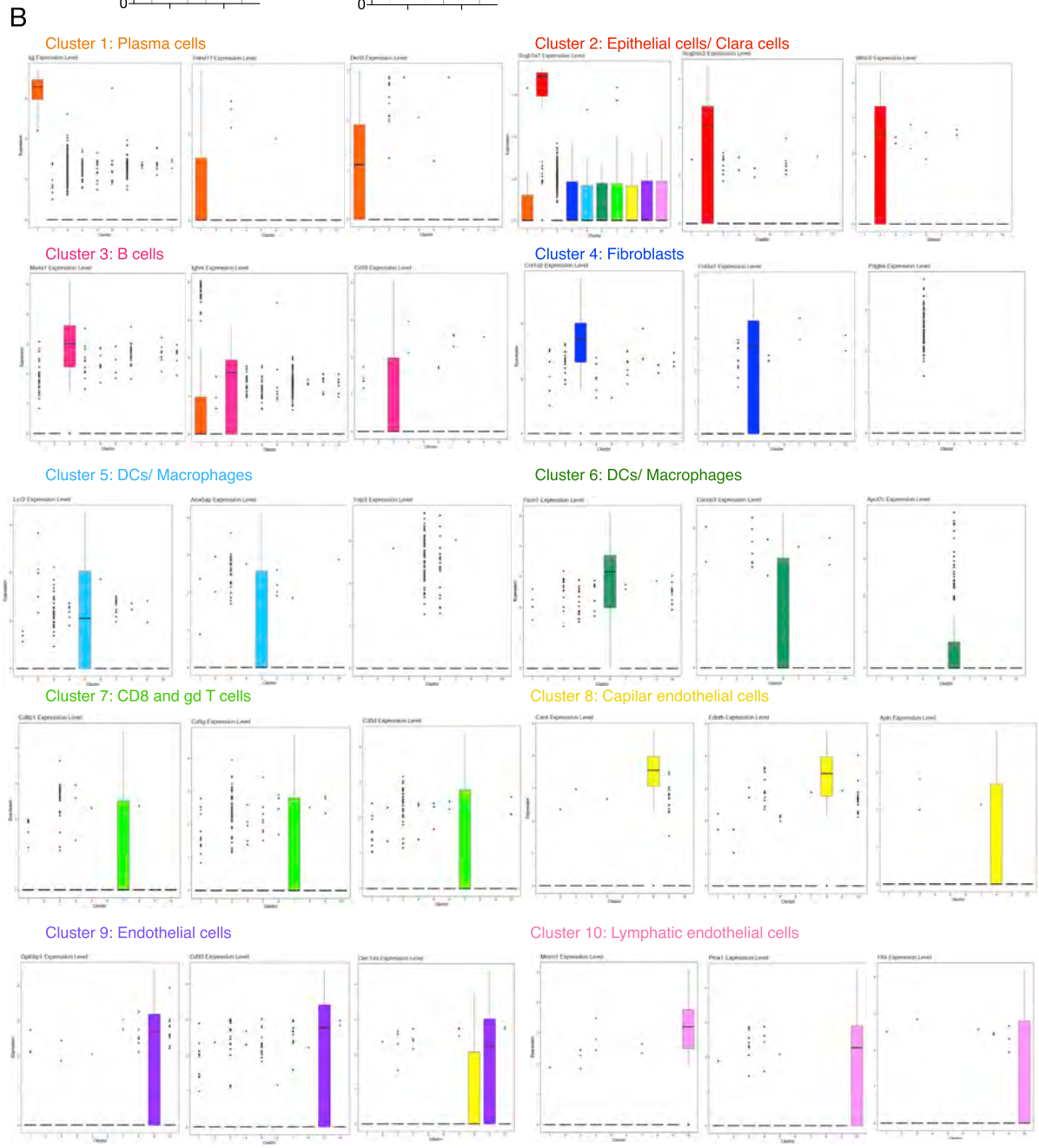

(legend on next page)

Figure S4. Related to Figure 4

(**A**) Fate+ immunized mice were intra-nasally treated with anti-IL-7 Ab, or with an isotope control on day 35, 37 and 39 after immunization and the mice were sacrificed on day 40. The graph shows the absolute number of spleen (left) and dLN (right) exT_H17 cells in the isotype ctrl treated group (black circles) and in the anti-IL-7 treated group (red circles). Each dot represents one mouse. Two combined experiments are shown. Data are represented as mean ± SEM. Mann-Whitney U Test ns (non-significant). (**B**) The Boxplots show the specific genes for each cluster, with cluster labels on the x axis; normalized expression values on the y axis. The same color codes as in Figure 4F were used. Three markers are shown for each cluster.

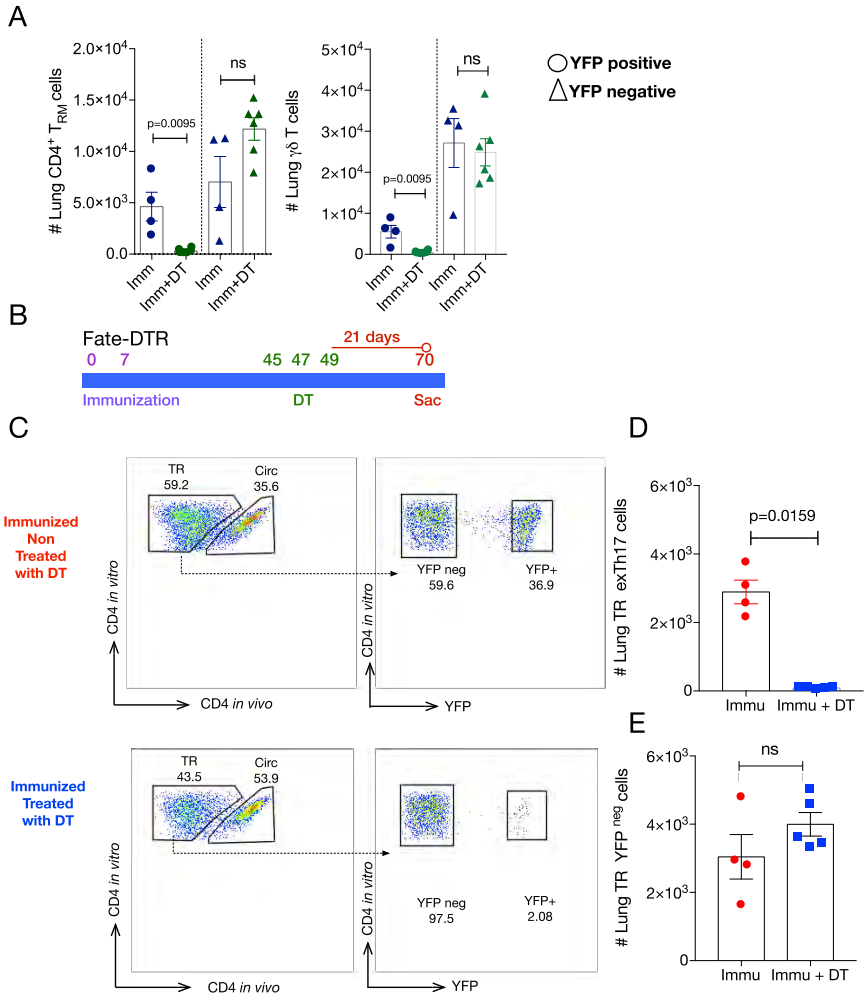

Figure S5. Related to Figure 5

Immunized Fate-DTR mice were either treated (Tx) with diphtheria toxin (DT) (Figure 5E) or with PBS and were sacrificed 7 days after the last DT treatment. (**A**) Absolute number of Lung T_{RM} cells (CD4 *in vitro*$^{+}$, CD4 *in vivo*^{neg} TCRβ^{+}, FoxP3^{neg}) and $\gamma\delta$T cells. The circles and triangles represent YFP positive (exT_H17, ex$\gamma\delta$IL17) and YFP negative cells respectively. Blue symbols and green symbols represent immunized PBS Tx or immunized DT Tx mice respectively. Each symbol represents one mouse (Immu n = 4; Imm+DT n = 6). Showing one out of 2 representative experiments. Data are represented as mean ± SEM. Mann-Whitney U test, ns (non-significant). (**B**) Immunized Fate-DTR mice were either treated (Tx) with diphtheria toxin (DT) on Day 45, 47 and 49 or with PBS and were sacrificed 21 days after the last DT treatment. (**C**) Representative dot plots showing the percentage of YFP negative and YFP positive cells (Gate CD4 *in vitro*$^{+}$, CD4 *in vivo*^{neg} TCRβ^{+}, FoxP3^{neg}) (Imm = 4; Imm+DT n = 5). Each dot plot represents one mouse. (**D**) Absolute number of YFP^{+} (exT_H17) Lung T_{RM} cells. Data are represented as mean ± SEM. Mann- Whitney U test. (**E**) Absolute number of YFP^{neg} Lung T_{RM} cells. Data are represented as mean ± SEM. Mann- Whitney U test, ns (non-significant).

European Journal of Neuroscience, Vol. 49, pp. 834–848, 2019

Cortical stimulation relieves parkinsonian pathological activity *in vitro*

Ariadna Aparicio-Juárez,* Mariana Duhne,* Esther Lara-González, Fátima Ávila-Cascajares, Vladimir Calderón, Elvira Galarraga and José Bargas
División Neurociencias, Instituto de Fisiología Celular, Universidad Nacional Autónoma de México, P.O. Box 70-253, CDMX, Mexico City 04510, México

Keywords: 6-OHDA, L-DOPA, microcircuit analysis, *Mus Musculus*, Parkinson's disease, striatum

Abstract

Previously, we have shown that chemical excitatory drives such as *N*-methyl-D-aspartate (NMDA) are capable of activating the striatal microcircuit exhibiting neuronal ensembles that alternate their activity producing temporal sequences. One aim of this work was to demonstrate whether similar activity could be evoked by delivering cortical stimulation. Dynamic calcium imaging allowed us to follow the activity of dozens of neurons with single-cell resolution in *mus musculus* brain slices. A train of electrical stimuli in the cortex evoked network activity similar to the one induced by bath application of NMDA. Previously, we have also shown that the dopamine-depleted striatal microcircuit increases its spontaneous activity generating dominant recurrent ensembles that interrupt the temporal sequences found in control microcircuits. This activity correlates with parkinsonian pathological activity. Several cortical stimulation protocols such as transcranial magnetic stimulation reduce motor signs of Parkinsonism. Here, we show that cortical stimulation *in vitro* temporarily eliminates the pathological activity from the dopamine-depleted striatal microcircuit by turning off some neurons that sustain this activity and recruiting new ones that allow transitions between network states, similar to the control circuit. When cortical stimulation is given in the presence of L-DOPA, parkinsonian activity is eliminated during the whole recording period. The present experimental evidence suggests that cortical stimulation such as that generated by transcranial magnetic stimulation, or otherwise, may allow reduce L-DOPA dosage.

Introduction

Parkinson's disease (PD) is a movement disorder characterized by bradykinesia, rigidity, resting tremor and postural, locomotor and cognitive deficits (Dauer & Przedborski, 2003; Thomas & Beal, 2010; Kalia & Lang, 2015). These signs and symptoms appear as a result of dopamine depletion in the basal ganglia following dopaminergic cell loss in the substantia nigra pars compacta (SNc; Ehringer & Hornykiewicz, 1960; Andén *et al.*, 1964; Bernheimer *et al.*, 1973). Striatal neurons receive monosynaptic glutamatergic connections from the cortex and thalamus (Kemp & Powell, 1971; Bernard *et al.*, 1997; Bernard & Bolam, 1998; Bolam *et al.*, 2000; Gerfen & Surmeier, 2011; Arias-García *et al.*, 2017). These connections have proven to be important in action selection, habits and goal-directed behavior (Znamenskiy & Zador, 2013). Deficiencies in *N*-methyl-D-aspartate (NMDA) receptors affect action selection, learning, procedural memory, habits, coordination and storage of motor commands (Beutler *et al.*, 2011; Lambot *et al.*, 2016).

In dopamine-depleted animal models, alterations in the synaptic integration of corticostriatal commands have been reported, such as differences in neuronal excitability (Fieblinger *et al.*, 2014), distinct corticostriatal synaptic integration (Flores-Barrera *et al.*, 2011), changes in NMDA receptor subunits (Feng *et al.*, 2014), altered responses to somatosensory inputs (Ketzef *et al.*, 2017) and changes in long-term plasticity (Picconi *et al.*, 2012). Cortical stimulation by several means temporarily improves the parkinsonian state (e.g., Dileone *et al.*, 2017), leading some researchers think that the cortex is a main player in the disease (Arbuthnott & Garcia-Munoz, 2016; Pérez-Ortega *et al.*, 2016).

Previous reports have described microcircuit behavior of the striatal network in control (using NMDA as excitatory drive) and parkinsonian conditions (Carrillo-Reid *et al.*, 2008; Jáidar *et al.*, 2010; Pérez-Ortega *et al.*, 2016). Microcircuit alterations are reversed by L-DOPA administration (Plata *et al.*, 2013a) as *in vivo* conditions (Ketzef *et al.*, 2017). However, there is no experimental work in animal models that observes whether cortical stimuli may change the striatal microcircuit activity during the parkinsonian

Correspondence: J. Bargas, as above.
E-mail: jbargas@ifc.unam.mx

*These authors contributed equally to the work.

Received 14 September 2017, revised 21 November 2017, accepted 11 December 2017

Edited by Yoland Smith

Reviewed by Jérôme Baufreton, University of Bordeaux, France; and Charles Wilson, Texas University at San Antonio, USA

The associated peer review process communications can be found in the online version of this article.

© 2017 Federation of European Neuroscience Societies and John Wiley & Sons Ltd

state. Therefore, the aims of this work were, first, to evoke prolonged microcircuit activity without using chemical stimulation such as bath application of NMDA and second, to characterize the alteration of microcircuit activity due to cortical stimulation in dopamine-depleted (DA-depleted) striatal circuitry after unilateral 6-OHDA lesions, a commonly used hemiparkinsonian model in rodents. Finally, we report the mechanisms by which cortical stimulation alone, or together with L-DOPA administration, acts to improve parkinsonian pathological activity at the microcircuit level.

Materials and methods

Animal use and care

All experiments were carried out in accordance with the international guidelines for the ethical use of experimental animals established in the NIH guidelines, and detailed protocols were submitted and approved by the Institutional Committee for Laboratory Animals Care and Use of the Instituto de Fisiología Celular (IFC), UNAM (NOM-062-Z00-1999; project protocol JBD-59-15). Experiments were performed in male C57BL/6 mice breaded in the animal facilities of the IFC. Mice were housed in a temperature-controlled, pathogen-free room, on a 12 : 12 light: dark cycle and allowed food and water *ad libitum*. P21-P23 mice were used for stereotaxic surgery. P29-P40 brain slices were prepared for calcium imaging experiments. Slices from at least four to seven different animals were used in each experimental sample (control $n = 5$ slices, hemiparkinsonian $n = 7$ slices and hemiparkinsonian + L-DOPA *in vitro*, $n = 4$ slices). In both surgical and perfusion protocols, animals were anesthetized with ketamine (85 mg/kg)–xylazine (15 mg/kg) and all measures were taken to minimize pain and discomfort trough every protocol. Body temperature was modulated peri- and post-operatively until full recovery. Mice were killed by decapitation, and the brains were rapidly dissected and processed. To prevent bias, mice from each litter were randomly chosen for surgery. DA-depleted animals were randomly used for either DA-depleted or DA-depleted + L-DOPA experiments. A total of six animals were used to complete the control group experiments, four intact and two sham. To perform the DA-depleted experimental groups, 22 mice were used to perform the surgical procedure described below. Nineteen mice met the DA-depleted selection criteria, and these were used for slice preparation.

6-OHDA model

Mice P21-P23 were administered intra-peritoneal ketamine (85 mg/kg)–xylazine (15 mg/kg) and placed under a stereotaxic instrument. Once the skull was cleared and the coordinates located, 0.6 μL of 6-OHDA (0.1 mg/mL) was injected at a 0.2 μL/min rate in −2.6 mm AP, −1.5 mm LM and −4.7 mm DV from bregma. Coordinates were previously optimized in the laboratory for better accuracy. The whole procedure was also performed in *sham* mice, except that saline solution (NaCl 0.9%) without 6-OHDA was used. Body temperature was modulated peri- and post-operatively until full recovery. Caution was taken to minimize animal pain and discomfort through all the procedures.

Post-operatively mice were allowed to recover for 7 days in the vivarium in a temperature-controlled, pathogen-free room, on a 12 : 12 light: dark cycle and allowed food and water *ad libitum*.

After full recovery, lesion was confirmed by the apomorphine-induced turning behavior test (Ungerstedt & Arbuthnott, 1970). Mice were placed in rotameter bowls and were allowed to acclimatize for 5 min. Spontaneous rotations were measured for at least 30 min by the program RotaCount 2.0. After that time, mice received a subcutaneous injection of apomorphine hydrochloride (0.05 mg/kg) in vehicle (normal saline with 0.02% ascorbate). Rotations were measured for 60 min. Clockwise (CW) and counterclockwise (CCW) rotations were contrasted between and within spontaneous/ apomorphine conditions. Mice CW/CCW ratio was inverted between spontaneous and apomorphine conditions. Monitored for 60 min, mice showing > 80% of contralateral turning unbalance (contralateral/total rotations) were considered for further experiments. To minimize the effects of dopamine receptor priming, experiments were performed at least 10 days after the evaluation (Morelli *et al.*, 1989).

Slice preparation

Mice P29-P40 were anesthetized intra-peritoneally with ketamine (85 mg/kg)–xylazine (15 mg/kg) and perfused intracardially with chilled sucrose solution (sucrose 234 mM, $NaHCO_3$ 28 mM, dextrose 7 mM, pyruvate 4.54 mM, ascorbic acid 0.28 mM, KCl 2.5 mM, $MgCl_2$ 7 mM, NaH_2PO_4 1.44 mM, $CaCl_2$ 0.4 mM, 4 °C). Mice were rapidly decapitated and brains extracted. A total of 250-μm-thick horizontal slices with a 30° angle were taken in a vibratome (PELCO easiSlicer Ted Pella, Redding, CA, USA). For the rest of the procedures, the slices were maintained in artificial cerebrospinal fluid (NaCl 126 mM, dextrose 15 mM, $NaHCO_3$ 26 mM, thiourea 0.2 mM, ascorbic acid 0.2 mM, KCl 2.5 mM, $MgCl_2$ 1.3 mM, NaH_2PO_4 1.2 mM and $CaCl_2$ 2 mM; pH = 7.4; 300 ± 5 mOsm/L) and continually perfused with 95% O_2 and 5% CO_2. The procedure was identically performed for both control and DA-depleted animals, except that only the right hemisphere was taken in DA-depleted animals, while both hemispheres from control animals were used.

Data acquisition

Slices were incubated for a 40-min period at 37 °C in a Calcium Orange solution (Calcium Orange 8.2 μM, 0.1% DMSO, 0.67% Pluronic Acid in ACSF). Calcium Orange was chosen for this set of experiments because long-term data acquisition is required and Calcium Orange has very low photobleaching (Thomas *et al.*, 2000). Later, slices were placed in a perfusion chamber with constant ACSF flow under a 20× immersion objective (N20X-PFH—20× Olympus XLUMPLFLN Objective, 1.00 NA, 2.0 mm WD, Center Valley, PA, USA). Observation field was 750 × 750 μm. A Lambda LS Illuminator (Sutter Instruments, Petaluma, CA, USA) and a 570/30-nm light filter were used for fluorophore stimulation and signal acquisition. Fluorescence videos were recorded using a CoolSnap K4 camera (Photometrics, Tucson, AZ, USA) controlled trough Im-Patch ©, an open-access software designed in the LabView environment (http://www.im-patch.com), taking 4–6 frames/s and 720–2160 frames per video. Each experiment consisted of 7–10 videos accounting for up to 60 min per experiment. Three slice conditions were used: control (Ctrl), dopamine-depleted (DA-depleted) and DA-depleted +L-DOPA. In all of them, spontaneous activity was recorded before and after the administration of a single stimulation train (CtxS = 10 pulses, 40 Hz, 1.1–1.3 mA) using a bipolar concentric electrode (FHC, #CBCFE75, Bowdoin, ME, USA) inserted in cortex layer V. When required, 10 μM L-DOPA was added to superfusion bath prior to stimulation and maintained until the end of the experiment. A 0.5 mM KCl solution was administered at the end of each experiment to count all viable cells during the experiment. Only slices in which 85% of the cells participating in the experiment were still viable were taken into account.

© 2017 Federation of European Neuroscience Societies and John Wiley & Sons Ltd

INFORME DE LABORES 2019

Data analyses

Videos were processed with Im-Patch ©. Using this software, single cells were identified. Calcium entry into the cell (Ca^{2+} signals or transients) and its time derivative were calculated for each cell along time and during the whole experiment. Using time derivatives of Ca^{2+} transients, moments of neuronal electrical activity were inferred as previously reported (Carrillo-Reid *et al.*, 2008, 2009, 2011, 2015; Jáidar *et al.*, 2010; López-Huerta *et al.*, 2013; Plata *et al.*, 2013a,b; Hernandez-Flores *et al.*, 2015; Pérez-Ramírez *et al.*, 2015; Pérez-Ortega *et al.*, 2016). Frames whose time derivative exceeded two standard deviations from the noise or basal activity were considered as active frames due to neuronal ensembles. Frame activity was transferred into an activity matrix where 1 denotes an active and 0 a not active frame for each cell. Whole experiments are contained in these matrices and expressed as raster plots, where each row shows the activity of a single cell and each dot a frame in which that cell was active. Matrices together with their coordinates were processed to determine statistically significant coactivity peaks. The activity of all the cells in every frame was added to build a coactivity histogram. To determine significant coactivity peaks, Monte Carlo simulations were used (see Pérez-Ortega *et al.*, 2016). Briefly, the activity of every cell was shuffled over time and new randomized coactivity histograms were obtained (1000 iterations); the randomized histograms were compared to the original one, by counting the frames with a given number of coactive cells (from 0 to the number of cells). The threshold to consider significant activity peaks is established at the minimal value in which the experimental data showed greater occurrence of coactive cell events than 95% of the randomized data. The significant activity peaks were built from the frames in which the threshold was overcome and a 12- to 18-frame time bin was used. Coactivity peaks were compared based on a similarity index calculated as the cosine of the angle between vectors obtained with the dot product of each pair of vectors with significant activity normalized by their magnitude (Carrillo-Reid *et al.*, 2008) retrieving a similarity matrix. Peaks were grouped using hierarchical clustering analysis to determine neuronal ensembles or network states shown with different colors or tones in raster plots as previously reported (Pérez-Ortega *et al.*, 2016). To compare individual cell activity through different sections of the experiment, activity of each cell was determined simply as the total number of active frames/total number of frames.

To quantify the amount of activity per experiment, a cumulative activity plot was built; the value of the coactivity histogram per frame was added over time during the experiment. To compare the activity of multiple experiments, a linear fit was approximated to cumulative activity plots. Slopes of fitted lines represent the cumulative activity/time over the course of the experiment. This value was used to compare different experiments and experimental conditions. To quantify the significant activity peaks/min, the number of frames in which the coactivity histogram value was greater than the threshold determined by the Monte Carlo method was divided by the total length of the experiment in minutes. To compare the cellular activity among different experimental conditions, a cumulative distribution function was made with the cellular activity of all the active cells in all of the experiments per section, namely control (Ctrl), control plus cortical stimulation (Ctrl + CtxS), DA-depleted, DA-depleted + CtxS, DA-depleted + L-DOPA and DA-depleted + L-DOPA + CtxS.

For neurons that belong to different groups, their cellular activity on each fragment of the experiment was determined as described above. To consider an activity increase or decrease, a 20% activity change was necessary, otherwise the neuron was considered with constant activity. The parkinsonian state is characterized by a dominant more recurrent state interrupting ensembles sequences (Jáidar *et al.*, 2010; Pérez-Ortega *et al.*, 2016). To detect the appearance of these pathological network states across a sample of experiments, we calculated a recurrence index for every state with respect to the other states in each condition. The recurrence index is the relative proportion of recurrence of any state:

$$R_{\text{Index}} = \frac{R_i}{\sum \mathrm{R}_{n \neq i}}$$

where R_i is the recurrence of a given state; the appearance of the state has values 1 (one appearance) to p, where p is the number of times in which the state appeared repeatedly without alternation. This number was divided by the sum of recurrences of the other states in the experiment. In the case some network states have an excess of recurrence (dominant pathological states) circuits will be divided into two populations of network states those with high and those with low recurrence and the variance of that sample will reflect this sampling separation. In the cases where there is no predominance of any network state, all of them would have a similar recurrence index and sample variance would be smaller. In this way, we could compare all different states through sampling different experiments using neuronal ensembles no matter the duration of the particular conditions. In this case, recurrence of network states of compared samples used the O'Brien Homogeneity of Variance test.

Statistical analysis

To determine the significance threshold for coactivity peaks, Monte Carlo simulations were used; this test was programmed into a MATLAB script (MATLAB R2015a; The MathWorks, Inc. Natick, MA, USA). GraphPad Prism (GraphPad Software, Inc. La Jolla, CA, USA) was used to compare the different activity metrics among the four groups: Ctrl, DA-depleted, Ctrl + CtxS and DA-Depleted + CtxS. Tests used and their purposes are indicated as follows: multiple comparison Kruskal–Wallis ANOVA test with the *post hoc* Dunn test for pairwise comparisons, paired Wilcoxon *t*-test with a one-tail Spearman approximation to compare the activity of the same sample from one condition to another, the contingency pie chart test to compare the proportion of activity from each cellular population, the Friedman ANOVA test with *post hoc* Dunn test to compare the activity of individual cells in experiments with three different treatments, Kolmogorov–Smirnov tests to compare distributions of data sets (MATLAB) and O'Brien Homogeneity of Variance test to compare the recurrence index in the different conditions (MATLAB). Note that samples with dominant states have their variance increased.

Suppliers & reagents

The reagents used were as follows: Calcium Orange (Molecular Probes®, Life technologies, Mexico City, Mexico); pluronic acid (pluronic TM F-127, P3000MP; Life Technologies Corporation, OR, USA); 6-OHDA (6-hydroxydopamine hydrochloride; Sigma-Aldrich H4381-100MG); L-DOPA (3,4-dihydroxy-L-phenylalanine, Sigma-Aldrich D9628); and apomorphine (R-(-)-apomorphine hydrochloride hemihydrate Sigma-Aldrich A4393-250MG).

Results

Cortical stimulation in brain slices

The spontaneous cellular activity in the dorsal striatum was recorded for several minutes (Ctrl; Fig. 1A). A single train of 10 pulses at

© 2017 Federation of European Neuroscience Societies and John Wiley & Sons Ltd

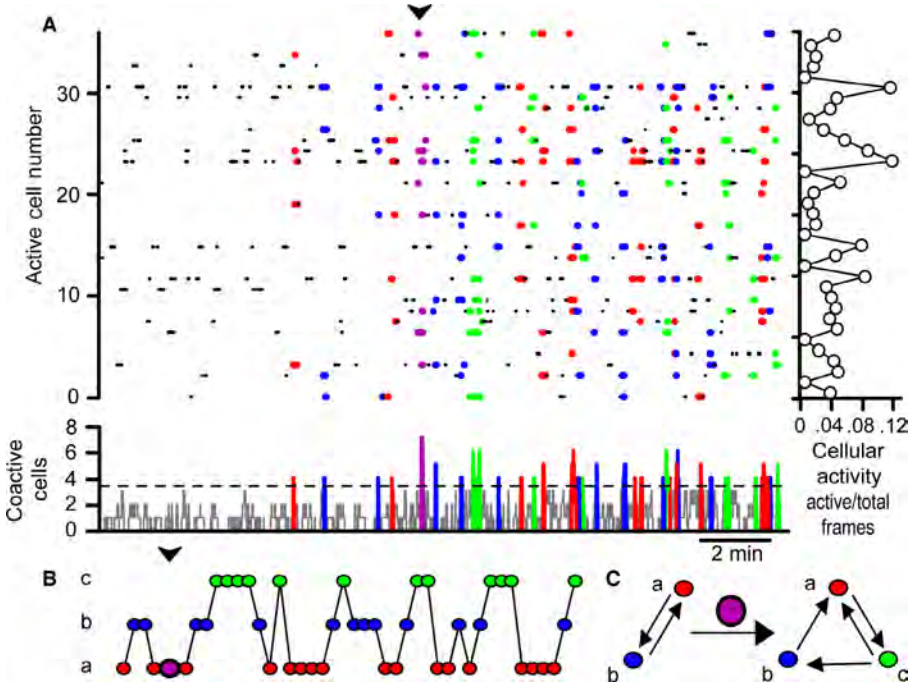

FIG. 1. Cortical stimulation activates the striatal microcircuit. (A) Raster plot of a cortical stimulation (CtxS) protocol. The moment of stimulation is shown with an arrowhead on top. Each row represents the activity of a single cell over time. Colored dots represent cells that activate together significantly. At the bottom, a coactivity histogram with the sum of active neurons per frame is shown. The dotted line shows the threshold for significant coactivity peaks ($P < 0.05$, after Monte Carlo simulations). Significant activity peaks were classified as neuronal ensembles using hierarchical cluster analyses. Different ensembles are shown in the histogram and raster plot with different tones and thicker lines. The right histogram represents individual cellular activity: the sum of the active frames divided by the total number of frames. (B) Once ensembles were identified, each dot in the sequence graph represents its activation: ensembles time sequence. Note network states that alternate their activity (a–c: bottom, middle and top). The stimulus is represented by the larger (purple) dot with an arrowhead at the top. (C) Transitions summary: before the stimulus, only two ensembles were significant and rarely active. After the stimulus, there were three ensembles that activate more frequently showing transitions between them.

40 Hz in motor cortex layer V or in cortical afferents (CtxS; Fig. 1A arrowhead) could activate the striatal microcircuit revealing continuous sequences of significant peaks of neuronal coactivity for at least 30 min. In this way the evoked activity of dozens of neurons was observed simultaneously, using calcium imaging with single-cell resolution in horizontal mouse brain slices without adding any drugs to the preparation (cf. Carrillo-Reid *et al.*, 2008). A raster plot of this activity is shown in Fig. 1A following such stimulus; each row represents the activity of a single neuron. At the bottom, a histogram of the summed activity along time shows significant peaks of coactivity where the dashed line represents the significance threshold determined with Monte Carlo simulations ($P < 0.05$). Significant coactivity peaks are marked in the raster plot and bottom histogram with thicker (or colored) dots or lines. In the plot to the right, individual cellular activity over the course of the experiment measured as the sum of activity per cell divided by the number of frames is illustrated. The moment of CtxS evokes a significant activity peak which is composed by stimulated neurons and is different to the spontaneous peaks of coactivity that follow. The significant coactivity peaks were grouped according to their similarity (see Methods) and classified, using hierarchical cluster analysis, as neuronal ensembles (raster plot) or network states (temporal sequences). The temporal sequence of ensembles activation is shown in Fig. 1B. Clearly, CtxS activates the microcircuit increasing the number of spontaneously active ensembles ($n = 5$ slices from different animals). The time sequence is summarized into network states transition cycles before and after CtxS (Fig. 1C). Note a change in the number of active ensembles after CtxS, thus generating reverberating microcircuit dynamics (Carrillo-Reid *et al.*, 2008).

In the DA-depleted striatum, there is an excess of neuronal activity as compared to the non-stimulated control striatum (Jáidar *et al.*, 2010; Plata *et al.*, 2013a,b; Pérez-Ortega *et al.*, 2016).This can be observed in the raster plot and coactivity histogram in Fig. 2 before CtxS is given. This hyperactivity is characterized by the excessive recurrence of one of the network states (Jáidar *et al.*, 2010; Pérez-Ortega *et al.*, 2016). After CtxS, alternations between network states become more balanced and transitions are recovered; this new dynamics is maintained for several minutes after stimulation (Fig. 2A; CtxS is marked with an arrowhead). Time sequence of ensembles activation (Fig. 2B) shows that before CtxS, there are several coactivity peaks with one of them exhibiting high recurrence (state 'c' at top), as though the microcircuit is trapped in state 'c'. As a consequence, transitions cycles per 3 min are commonly open (Fig. 2C left). After CtxS transitions, cycles became closed (Fig. 2C right; Pérez-Ortega *et al.*, 2016).

To compare global activity in the striatal microcircuit under different treatments, we analyzed cumulative activity (summed activity of coactive cells over time; from histograms at the bottom in Figs 1A and 2A) taking all the cells from each experiment. Solid lines in Fig. 3A illustrate cumulative activity in a representative experiment. Straight lines were fitted to experimental data (dashed). The non-stimulated striatal microcircuit (Ctrl) shows the lowest spontaneous activity along time. Significant higher activity appears after cortical stimulation (CtxS) in control conditions ($n = 5$; Wilcoxon *t*-test; $P < 0.01$), and the DA-depleted striatal microcircuit was confirmed to have higher spontaneous activity than the non-stimulated control (Fig. 3B; slopes of fitted straight lines were used to show box plots of samples distributions; $P < 0.05$; $n = 7$; Kruskal–

© 2017 Federation of European Neuroscience Societies and John Wiley & Sons Ltd

INFORME DE LABORES 2019

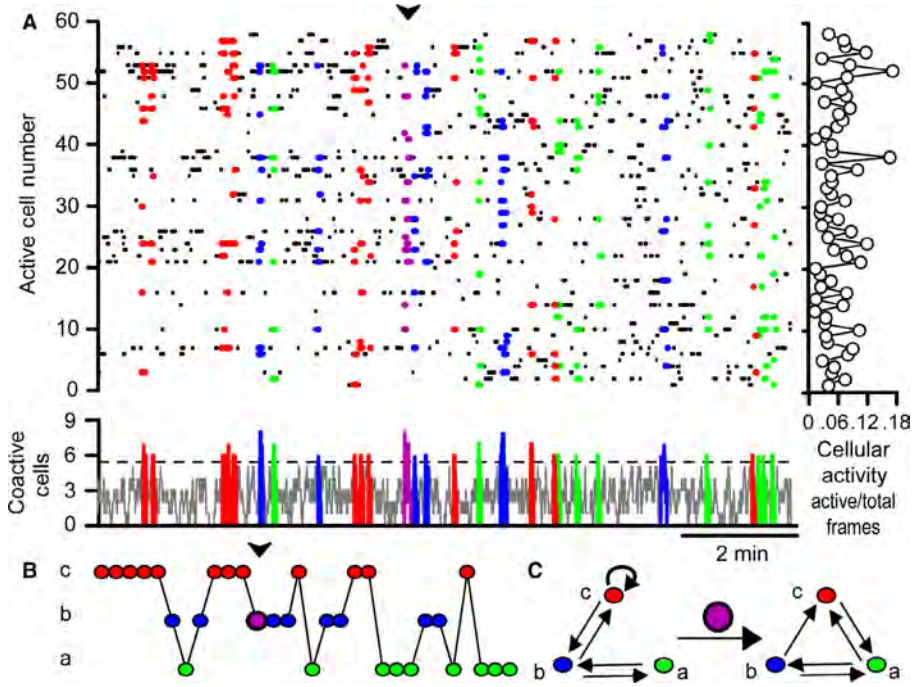

FIG. 2. Cortical stimulation modifies network state transitions in the DA-depleted striatal microcircuit. (A) Raster plot of a DA-depleted slice microcircuit before and after CtxS. Stimulation is signaled with an arrowhead on top. Each row represents the activity of a single neuron over time. Coactivity histogram is at the bottom with the sum of active neurons per frame. The dotted line shows the threshold for significant activity peaks. The significant activity peaks were classified into neuronal ensembles after hierarchical clustering. Different ensembles are shown in the histogram and raster plot with different tones (or colors) and thicker dots and lines. Individual cellular activity, the sum of all the active frames divided by the total number of frames, is at right. (B) Time sequence of ensembles activation showing significant peaks of coactivity represented by circles. The position and letters represent the ensembles to which they belong, a–c (bottom, middle and top). The stimulation is signaled by a larger circle with an arrowhead on top. Note that in the DA-depleted microcircuit, a dominant ensemble activates more recurrently than the others (c). However, after CtxS, activity of ensembles alternates more between different ensembles. (C) Network states transition cycles. Before the CtxS, a network state activates recurrently (pseudo-loop) with little participation of other states. After the stimulus, transitions between states become more frequent showing closed cycles and reverberating dynamics.

Wallis ANOVA with *post hoc* Dunn tests). After cortical stimulation, the DA-depleted microcircuit did not significantly increase its cumulative activity in spite of the changes induced in circuit behavior (Fig. 2). Similar results were found when we measured significant peaks of coactivity (Fig. 3C). Only the analysis of cumulative distributions of individual cellular activity showed that, first, non-stimulated control circuit activity distribution is different from all other distributions ($P \leq 0.0000124$), and second, that cellular activity distribution of the DA-depleted microcircuit was different to the one found after CtxS, both in control ($P = 0.000205$) and in DA-depleted stimulated circuits ($P = 0.000043$; Fig. 3D; Ctrl $n = 116$ cells, Ctrl + CtxS $n = 161$ cells, DA-depleted $n = 440$ cells, DA-depleted + CtxS $n = 180$ cells; Kolmogorov–Smirnov tests). We conclude that the differences between control and pathological microcircuits do not mainly consist of differences in global neuronal activity but more subtle differences in network behavior and composition.

Cellular activity in the DA-depleted striatum before and after cortical stimulation

Because changes in global neuronal activity cannot explain changes in circuit behavior in the DA-depleted microcircuit after CtxS, we asked whether CtxS induces change in the neuronal subpopulations making up circuit activity by comparing neuronal activity present in the circuit before and after CtxS. Simply, cells were classified into three classes (i, ii, iii) according to their activity before and after CtxS (Fig. 4A): cells that decreased or stopped their activity after CtxS (i), cells with constant activity before and after CtxS (ii) and cells whose activity increased or that became recruited into the circuit after CtxS (iii). A decrease or increase in 20% of cellular activity was used as threshold to classify neurons into the different groups. If the activity changed in a smaller proportion, cells were considered as constant activity cells (ii). Cells that changed their activity (i, iii) are illustrated in Fig. 4B. This analysis showed that while some cells stopped or decreased their activity, others began or increased their activity after CtxS. Finally, we quantified the contribution of each population before and after CtxS, for all the experiments. Before CtxS, most of the activity was generated by group 'i' (62%). After CtxS, most of activity (64%) came from group 'iii'. This change in active neuronal subpopulations might explain the changes in microcircuit dynamics observed in Fig. 2. Therefore, besides changing the microcircuit's activity, CtxS recruits a new neuronal subpopulation while stopping the firing of another subpopulation; this effect of CtxS lasted for at least 30 min. Over longer periods of time (> 30 min), the effects of the stimulus were lost.

Figure 5 shows an experiment in which neuronal activity was followed over a longer period of time. Figure 5A is the raster plot of neuronal activity. Each row represents the activity of a single cell over the course of the experiment, and three temporal segments or epochs of activity are shown divided by vertical dotted lines (1–3). Epoch 1 is a sample of the activity before stimulation, Epoch 2 is the period right after the stimulus, and Epoch 3 is at least 30 min after the stimulation. According to the activity in each epoch, cells were divided into five groups (i-v, right part of the raster), according to their decrease, increase or no change in their activity in any of

© 2017 Federation of European Neuroscience Societies and John Wiley & Sons Ltd

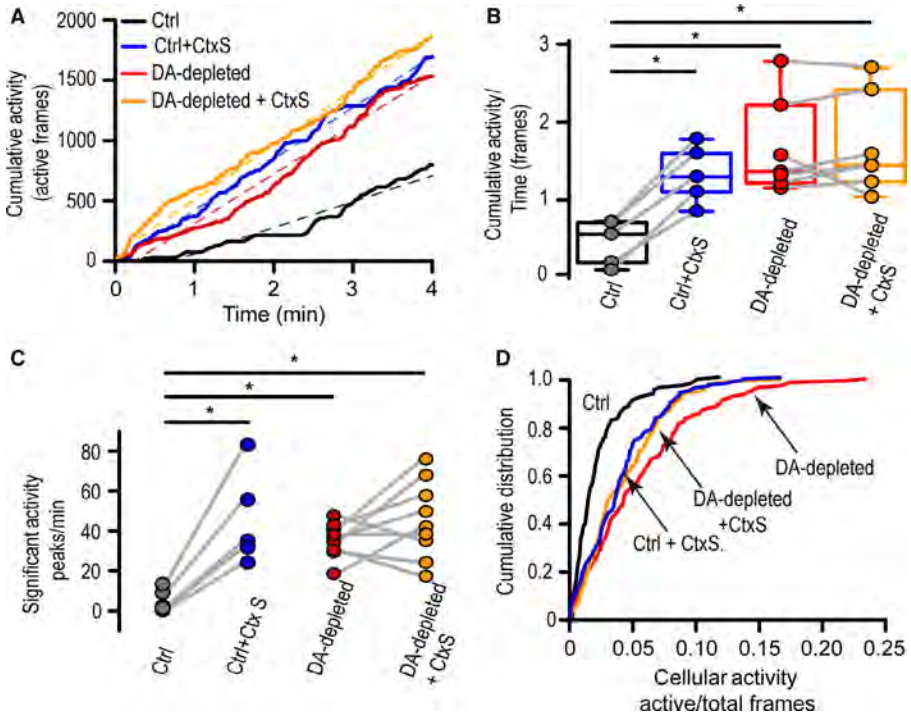

FIG. 3. Neuronal cumulative activity in the striatal microcircuit under different conditions. (A) Continuous lines: cumulative activity (sum of coactive cells per frame along time) of single representative experiments under different conditions: control without stimulus (Ctrl), cortical stimulation in control conditions (Ctrl + CtxS), DA-depleted striatal microcircuit without stimulus (DA-depleted) and DA-depleted striatal microcircuit after a cortical stimulus (DA-depleted + CtxS). Straight lines (dashed) are fitted to the data. (B) Cumulative activity over time for all the experiments. Box plots show the distribution of slopes from the lines fitted to cumulative activity (shown in A) for all of the experiments and conditions. There is a significant increase in neuronal activity after CtxS in control conditions ($P < 0.05$). DA depletion also shows increased activity compared to the controls without stimulation ($P < 0.05$). There is no significant increase in activity between the stimulated control and DA-depleted microcircuits. CtxS does not significantly increase the total activity of the DA-depleted microcircuit; it only changes the behavior of the circuit (Fig. 2). (C) Number of significant coactivity peaks before and after CtxS in Ctrl and DA-depleted microcircuits ($P < 0.05$). (D) Average cumulative distribution functions of cellular activity over time for all experiments and conditions. The cumulative distribution of cellular activity in non-stimulated controls is different to all other conditions ($P \leq 0.0000124$). The activity distribution of the stimulated control circuit is similar to that from the stimulated DA-depleted microcircuits ($P \leq 0.000205$; Ctrl $n = 116$ cells, Ctrl+CtxS $n = 161$ cells, DA-depleted $n = 440$ cells, DA-depleted + CtxS $n = 180$ cells; Kolmogorov–Smirnov tests) (Global Kruskal–Wallis ANOVA for (B) and (C): $P < 0.05$). '*' indicates statistical significance.

the three epochs, using a 20% change as threshold. As shown in Fig. 5C, group i reduced its activity after CtxS but has high activity before and 30 min after CtxS (epochs 1 and 3). Cells in group ii have high activity before CtxS, but their activity goes down after CtxS, and it does not return at a later time (epochs 2 and 3). Group iii becomes more active right after CtxS and even more active 30 min after CtxS (epochs 2 and 3). Group iv cells show the highest activity right after CtxS. Group v has nearly constant activity at all times. We made coactivity histograms for each population and compared them with the whole coactivity histogram (Fig. 5B; gray histogram in the background) to better illustrate the contribution of each neuron group to the whole circuit activity. For example, the greater contribution right after the CtxS was from group iv. To conclude, individual neuronal activity changes after CtxS and this change is reverted 30 min after the stimulus. We next investigated how these changes in neuronal activity rearrange microcircuit dynamics after CtxS.

Changes in architecture and dynamics of the DA-depleted microcircuit after cortical stimulation

Functional neuronal network connectomics was used to follow the changes that CtxS induces in the DA-depleted striatum (Fig. 6). In each graph, the nodes are active neurons during an epoch represented by circles in the periphery of a circular visualization, and functional connections were chosen as the moments of neuronal coactivity in an activity peak. One type of graph used the groups of cells as defined in Fig. 5; neurons were grouped according to the changes in activity they undergo after CtxS (Fig. 6A2 and 30 min after CtxS; Fig. 6A3). It can be seen that some neuron groups get most connections before CtxS (i and ii), while after CtxS, other groups come into action and become highly connected (iii and iv) although groups i and ii remain active. However, 30 min after CtxS, most connected groups change again: Group i recovers its connections, and surprisingly, group iii remains strongly connected while group iv is severely reduced in the number of neurons and connections (Fig. 6A3). Taken together, these data indicate that the microcircuit is temporarily remodeled by CtxS.

We also used a more traditional way to group the same neurons: those neurons making up the significant activity peaks in the coactivity histograms built from raster plots of neuronal activity in Figs 1 and 2 defined as neuronal ensembles (Carrillo-Reid *et al.*, 2008, 2011; Pérez-Ortega *et al.*, 2016). This neuronal ensemble definition is based on the proved Hebbian assumption that neurons that fire together have preferential connections with each other (Carrillo-Reid *et al.*, 2016), nodes again are seen as circles in the perimeter. These different ways of analyzing neuron groups do not coincide because in this case, neurons may belong to more than one

© 2017 Federation of European Neuroscience Societies and John Wiley & Sons Ltd

INFORME DE LABORES 2019

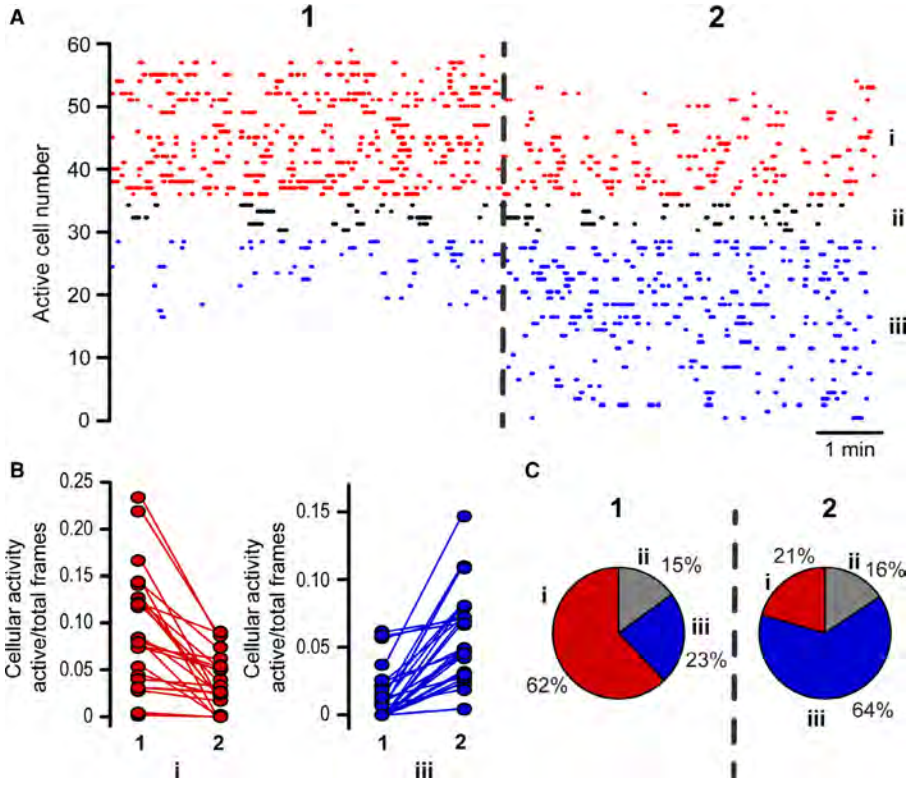

FIG. 4. Changes in neuronal subpopulations before and after cortical stimulation in the DA-depleted striatal microcircuit. (A). Raster plot of a representative experiment of CtxS in a DA-depleted slice. Each row represents the activity of a single neuron over time. Neurons were sorted and grouped according to the activity before (1) and after CtxS (2, dashed line). The neurons at the top: had greater activity before the stimulus and reduced or stopped their activity after the stimulus (i). Neurons at the bottom enhanced their activity after the stimulus or were even recruited by the stimulus; hence, they were not active before (iii). Middle neurons had similar activity in both conditions (ii). The threshold to consider a change in activity as significant was a decrease or increase in 20% from one epoch to the other. (B) Activity of the neurons classified into each group before and after the stimulation. Cells in group "i" decreased their activity after CtxS. Some of these cells stopped their activity. Activity of cells in group iii increased after CtxS, while many other cells in this group began their activity after CtxS. C. Pie plots illustrating percentages of activity generated by neurons classified into groups i–iii, in each epoch, for all the experiments. There was significant change in neuronal subpopulations active (n = 10 microcircuits, 451 cells, contingency of pie charts $P < 0.0001$) after CtxS.

ensemble or significant peak of coactivity (neurons that participated in more than one ensemble are indicated by labels). Functional connections are still defined as moments of coactivity. In spite of the different grouping methods, both networks show similar phenomena after CtxS, suggesting intrinsic robustness. Before CtxS (Fig. 6B1), most connections were monopolized by ensemble 'b'; this state of affairs changed after CtxS (Fig. 6B2) when several ensembles connect with each other and a group of neurons participate in all ensembles. Finally, 30 min after the stimulus (Fig. 6B3), ensemble 'b' becomes again the one with more neurons and gets most of the connections. To summarize, both methods of graphing show that CtxS changes both the neurons participating in the circuit as neuronal ensembles and their connectivity. Moreover, if each main group from the ensembles coactivity networks is taken as a network state, we can see that transitions between network states show a different evolution after CtxS.

Thus, time sequences of transitions between network states show that before CtxS (Fig. 6C1), state 'b' is dominant as it is the most recurrent and attracts more transitions. Right after the stimulus (Fig. 6C2), transitions between all three main ensembles are more balanced; 30 min after the stimulus (Fig. 6C3), the pathological dynamics returns: Network state 'b' becomes the most recurrent and transitions decrease as though the circuit gets trapped in one state. To conclude, a cortical stimulus changes the architecture and dynamics of the DA-depleted microcircuit even if neuronal activity remains high as compared to the control non-stimulated microcircuit (Fig. 3B). Previous work has shown that application of L-DOPA turns the DA-depleted microcircuit less active, similar to the control non-stimulated microcircuit (Plata *et al.*, 2013a). However, it has not been shown whether this less active microcircuit would resemble the control-stimulated microcircuit upon CtxS (Fig. 3B).

Effects of cortical stimulation in the presence of L-DOPA actions in a DA-depleted microcircuit

Figure 7 is similar to Fig. 5; it shows changes in neuronal activity in the DA-depleted microcircuit under two different treatments, first, the administration of 10 μM L-DOPA, and second, a cortical stimulation (CtxS) during L-DOPA actions. The aim was to see whether the evoked circuit activity during L-DOPA corresponds more to a control-stimulated circuit or, else, better resembles the pathological network. Experiments were followed more than 30 min. Neurons were divided into five groups (i–v), according to their change in activity during the different epochs of the experiment. The raster plot (Fig. 7A1) and the histogram of coactivity (Fig. 7B1) show what neuronal subpopulations were preferentially activated in the DA-depleted microcircuit before the stimuli i and ii. After adding L-DOPA to the superfusion, activity of all neurons decreased (Figs 7A,B2; Plata *et al.*, 2013a); thus, Epoch 2 when L-DOPA was administered was not considered for measuring activity changes as

© 2017 Federation of European Neuroscience Societies and John Wiley & Sons Ltd

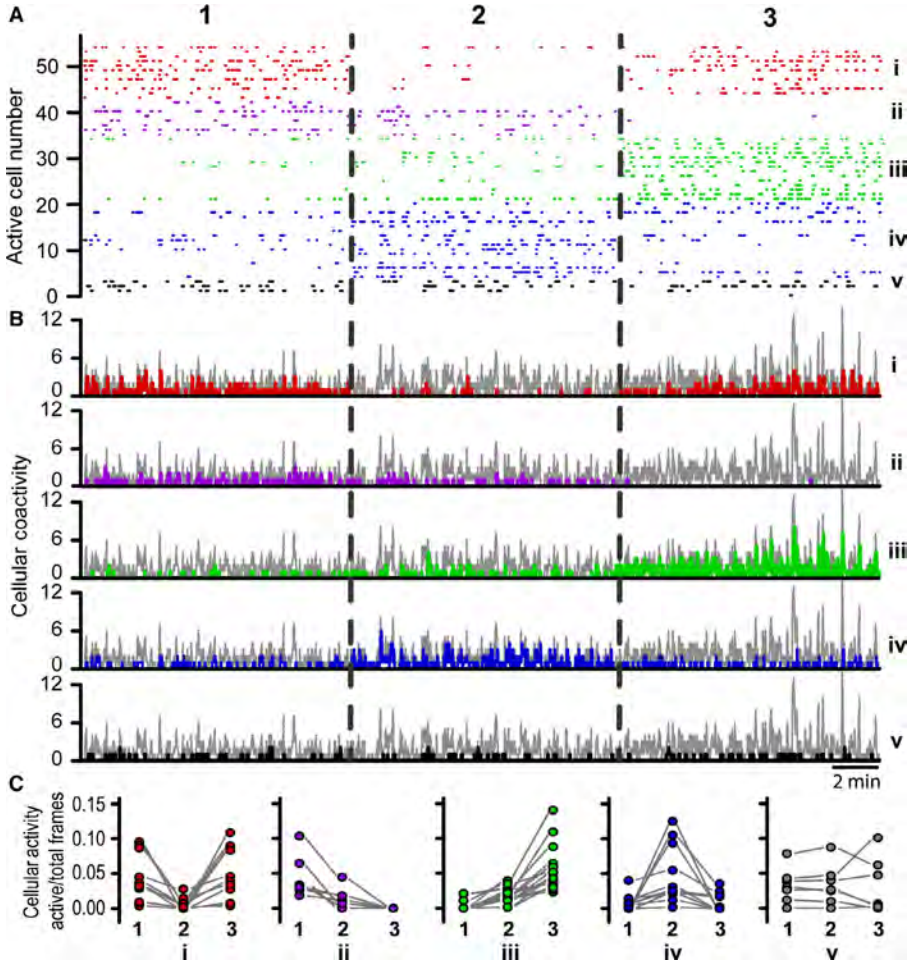

FIG. 5. The effects of cortical stimulation on the DA-depleted microcircuit are temporary. Thirty minutes after CtxS, the active neuronal subpopulations change again. The present representative experiment was divided into three epochs (1–3). (1) Before stimulation, (2) right after CtxS and (3) > 30 min after CtxS. (A) The raster plot of neuronal activity shows three fragments of each epoch divided by vertical dashed lines, the moment of CtxS was removed. Each row represents the activity of a neuron during the three epochs. Neurons were divided into five subpopulations according to their activity in each epoch: (i) Neurons that had high activity before CtxS, low activity right after CtxS, and recovered or had larger activity 30 min after CtxS. (ii) Neurons that had high activity before CtxS, less activity right after CtxS and that did not recover their activity 30 min after CtxS. (iii) Neurons with low or no activity before CtxS, which increase their activity right after CtxS and even more activity 30 min after CtxS. (iv) Neurons with the greatest activity right after CtxS but less activity before and 30 min after CtxS. (v) Neurons that kept constant activity before and after CtxS. The threshold to consider a significant change in activity was 20%. (B) Contribution of each neuronal subpopulation to the whole coactivity histogram. The histogram of each neuronal subpopulation (i–v) is shown over the total histogram (light gray) to demonstrate the contribution of each subpopulation per epoch. (C) Activity of each cell group per epoch (1–3) divided into the different subpopulations (i–v).

no significant peaks of coactivity were present. After CtxS (Figs 7A,B3) activity clearly increased, however, a recruitment of different neuronal subpopulations which now contribute to the circuit activity resembling a control-stimulated circuit is observed (e.g., iii and iv), these subpopulations do not participate in the initial pathological dynamics. Thirty minutes after CtxS in the presence of L-DOPA (Figs 7A,B4), a set of neurons that were active before the administration of the drug and CtxS reactivate. A subpopulation of neurons (v) did not change its activity along the experiment. The contribution of each subpopulation to the total histogram of activity is shown in Fig. 7B. Figure 7C shows the activity of each neuron set during epochs 1, 3 and 4. We conclude that the DA-depleted microcircuit reconfigures itself after L-DOPA plus CtxS differentially changing the activity of diverse neuronal subpopulations.

Next, we asked how the architecture and dynamics of the remodeled microcircuit change under these conditions. To appreciate the remodeling in microcircuit architecture and dynamics, we built two types of networks (Fig. 8; cf. Fig. 6). One points out the subpopulations of neurons that change their activity after L-DOPA and CtxS (Fig. 8A epochs 1, 3, 4), and the other one shows the neurons that form part of the neuronal ensembles during the significant peaks of coactivity (Fig. 8B epochs 1, 3, 4). In the first case, the number of elements making the groups as well as their connections changed after L-DOPA and CtxS and tended to return to the original circuit after 30 min. In the second case, there is a dominant ensemble 'b' in the original DA-depleted microcircuit (Jáidar *et al.*, 2010; Pérez-Ortega *et al.*, 2016) that clearly stays after L-DOPA plus CtxS. However, it allows more transitions between ensembles after CtxS in the presence of L-DOPA, and its preponderance does not return after 30 min. When we make the time sequence of transitions between main ensembles or network states (Fig. 8C epochs 1, 3, 4), clearly the number of transitions between the three states increases. In contrast to the experiment without L-DOPA, they remain alternating their activity after 30 min. We conclude, first, that L-DOPA decreases the activity of the DA-depleted microcircuit in a way that significant peaks of coactivity become hard to observe,

© 2017 Federation of European Neuroscience Societies and John Wiley & Sons Ltd

INFORME DE LABORES 2019

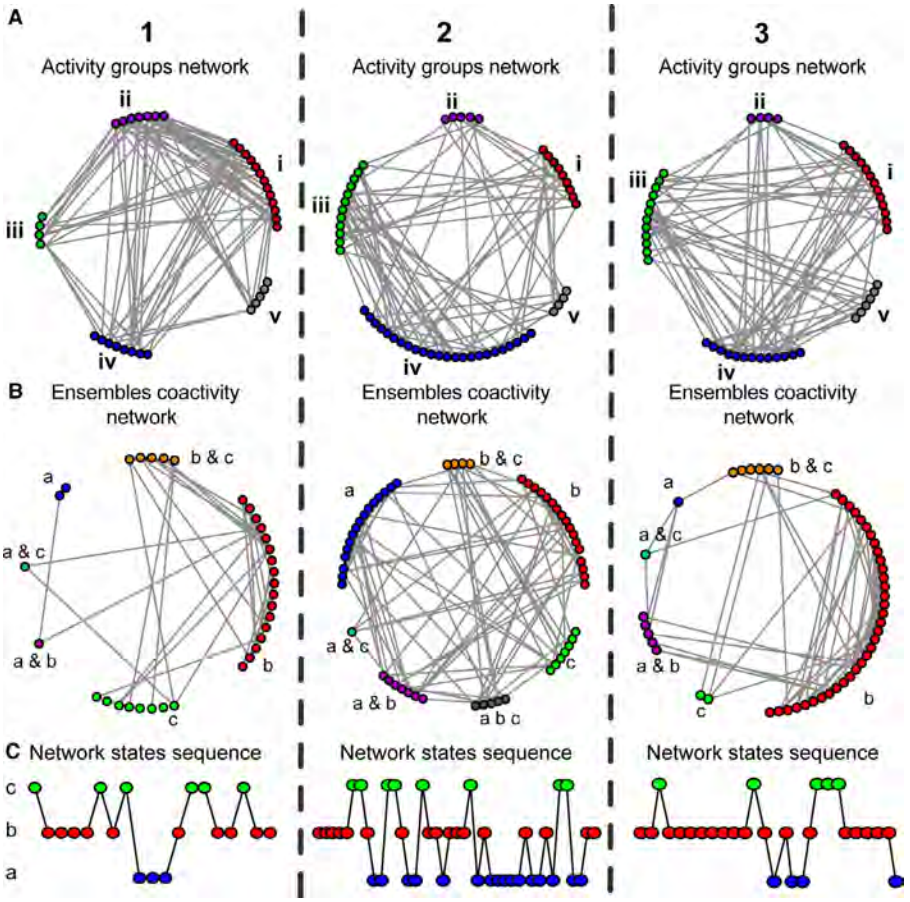

FIG. 6. The effect of corticostriatal stimulation on microcircuit architecture and dynamics. We illustrate microcircuit architecture with two types of graphs: activity group networks and ensembles coactivity networks. (A) Activity group networks separate groups of neurons (nodes represented by circles in the perimeter) according to their activity before (1), right after (2) and 30 min after (3) the cortical stimulus (Fig. 5). The functional connections between them (gray lines, see Methods) indicate moments of coactivation in significant activity peaks. Only active neurons during a given epoch are represented. Before CtxS groups i and ii get most connections, after CtxS group iii and iv have most connections but members of groups i and ii remain connected. Thirty minutes after CtxS, group i recovers many connections and surprisingly group iii remains strongly connected while group iv is severely decreased. (B) Ensemble coactivity networks are sets of neurons (nodes seen as circles in the periphery) that form significant peaks of coactivity in the coactivity histograms obtained from the raster plots (Figs 1 and 2). There can be neurons belonging to more than one ensemble. Functional connections are also defined as moments of coactivity. Groups of neurons in (A) and (B) do not coincide since they illustrate divergent ways to define neuronal groups; however, they show similar phenomena. Neurons that participated in more than one ensemble are indicated by labels. Still, note that before CtxS (1), most connections are monopolized by ensemble b, right after the stimulus (2) several ensembles share connections and one of them has neurons that belong to all ensembles, and finally, 30 min after the stimulus (3) the b ensemble has recruited more members and gets most connections again. C. Time sequences of network states illustrate the dynamics of such architectures: before CtxS most transitions occupy state b (1), right after CtxS (2) the number of transitions increases between the three major ensembles and 30 min after CtxS (3) the dominant ensemble returns, transitions decrease and the network gets trapped most time in network state b.

thus dissolving the most recurrent activity of the dominant ensemble (Plata *et al.*, 2013a). In addition, when the circuit was turned on by a CtxS in the presence of L-DOPA actions, it did not behave as the pathological DA-depleted circuit but showed alternating behavior between ensembles. In contrast to CtxS without L-DOPA, it remains behaving this way after 30 min. Thus, the striatal microcircuit became functional for a longer period of time.

Because cumulative distributions of cellular activity showed statistical differences between different treatments (Fig. 3D), we compared these distribution with those obtained with both cortical stimulus and L-DOPA (Fig. 9) taking into account all cells from all samples. In the case of CtxS only, cumulative distributions for DA-depleted microcircuits have a significant difference with the initial distribution right after CtxS ($P \leq 0.0135$; Figs 3D and 9A). However, this difference is lost 30 min after the stimulus (Fig. 9A).

In the case of CtxS plus L-DOPA, Fig. 9B shows, first, that L-DOPA reduced cellular activity in the DA-depleted microcircuit ($n = 7$, Wilcoxon t-test $P = 0.015$, data not shown). Second, after CtxS during L-DOPA actions, cumulative distribution of cellular activity increased as the circuit was turned on (Figs 2, 7, 8); however, it remained significantly different to the original cellular activity distribution of the DA-depleted microcircuit ($P = 0.00000003$). Third, in contrast with the case without L-DOPA, the circuit remained with this level of activity after 30 min. This means that in the presence of L-DOPA, the evoked activity by CtxS resembles that of a control-stimulated circuit and remains for longer periods of time. That is, L-DOPA reduces the activity to that of a control not activated circuit, and upon stimulation, it behaves as a control-stimulated circuit. Pie charts of Fig. 9C and D show the contribution of neuron groups as defined by their cellular activity (Figs 5, 7: i–v) under each condition and for all of experiments. Pie chart contingency chart tests show that there is no significant difference between equivalent experimental conditions in both sets of experiments: DA-depleted + CtxS (Fig. 9C) vs. DA-depleted + L-DOPA + CtxS (Fig. 9D). For DA-depleted neurons, most activity comes from subpopulations i and ii across all experiments ($P = 0.6227$ comparing

© 2017 Federation of European Neuroscience Societies and John Wiley & Sons Ltd

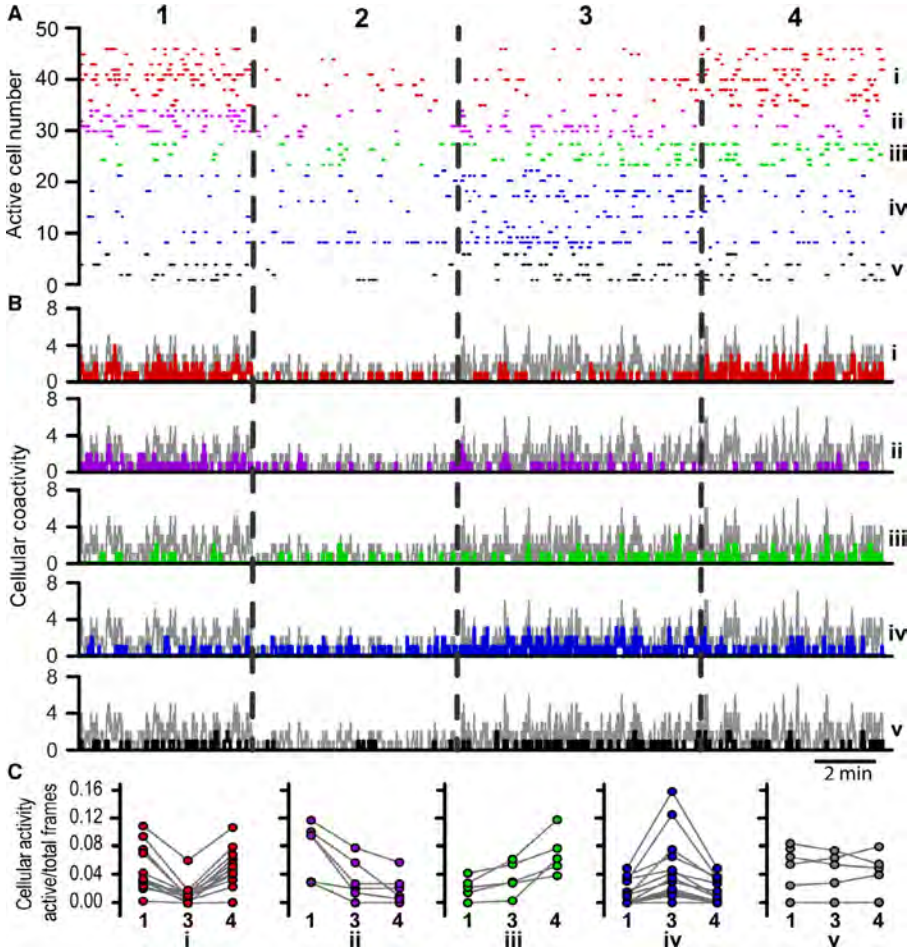

FIG. 7. Corticostriatal stimulation of the DA-depleted microcircuit during L-DOPA action. During the increased spontaneous neuronal activity of a DA-depleted microcircuit (1), 10 μM L-DOPA was administered in the bath saline (2); then, cortical stimulation was delivered (3), and activity was followed after 30 min (4). As in Fig. 5, neurons were sorted in the raster plot (A) and in the histograms of coactivity (B) according to their decrease or increase in activity and their participation in the whole activity is illustrated (pale histogram in the background). The threshold to consider a significant change in activity is 20%. During L-DOPA administration, all neuronal activity decreased to levels found in non-stimulated control microcircuits (2) and no significant peaks of coactivity were found in this experiment. Therefore, activity changes were compared only for epochs 1, 3 and 4 and neurons were divided into five subpopulations. (A) Sorted raster plot where each row is the activity of a single cell along time. (B) Coactivity histograms. Before stimulation (1), activity was high in neuron groups i and ii (C), after L-DOPA (2), activity decreased in all groups, and after CtxS in the presence of L-DOPA (3), activity returned; however, other neuron groups, iii and iv, contribute to the activity together with some neurons from groups i and ii. After 30 min of CtxS (3), activity in groups i and iii returned while that in groups ii and iv decreased. Neurons in group v did not change their activity except during L-DOPA. C. Activity of neuronal subpopulations during epochs 1, 3 and 4.

DA-depleted circuits from both sets of experiments). After CtxS without (Fig. 9C2) or with L-DOPA (Fig. 9D3), a significant renovation ($P = 0.0001$) of the neuronal subpopulations contributing to the circuit occurred: now group iv and part of group iii contribute with most neurons in the microcircuit, and there were no significant differences with or without L-DOPA ($P = 0.16$). Thirty minutes after CtxS, group i returns and group iv activity decreases in both samples while many neurons from group iii remain showing no significant differences with or without L-DOPA (Figs 9C3, D4; $P = 0.2078$). We conclude that CtxS reconfigures the active neuronal populations in the presence or absence of L-DOPA, but that 30 min after the stimulus, neuronal groups that sustained the DA-depleted microcircuit return. However, it is shown below that dynamics of these circuits differ depending on L-DOPA actions.

Figure 10A and B illustrates patterns of network states recurrence under different conditions in two samples of experiments (see recurrence index in Methods): DA-depleted + CtxS (Fig. 10A) and DA-depleted + L-DOPA + CtxS Fig. 10B). When a network state has a high pathological recurrence (Jáidar *et al.*, 2010; Pérez-Ortega *et al.*, 2016) with respect to the other states, the sample exhibits two different clusters and augmented variance as that seen in the left box of Fig. 10A, B (DA-depleted microcircuit). When no network states has a significant higher recurrence than the other states, sample distribution appears homogenous as a single cluster with no dominant network state, as seen in the middle box plots of Fig. 10A,B (DA-depleted circuits + CtxS and DA-depleted circuits + L-DOPA + CtxS). That is, CtxS eliminates the pathological ensemble in both cases: without ($P = 0.007586$; O'Brien test for Homogeneity of Variance in this and other P values of this section) and with L-DOPA ($P = 0.03712$), restoring ensembles alternation ($n = 12$ network states from four experiments in each condition obtained from eight different slices and animals). However, a difference between the two conditions was evident 30 min after CtxS: without L-DOPA highly recurrent pathological ensembles returned (Fig. 10A right box; $P = 0.01532$ compared with CtxS). In addition, highly recurrent ensembles appeared to be more recurrent than in the initial DA-

© 2017 Federation of European Neuroscience Societies and John Wiley & Sons Ltd

INFORME DE LABORES 2019

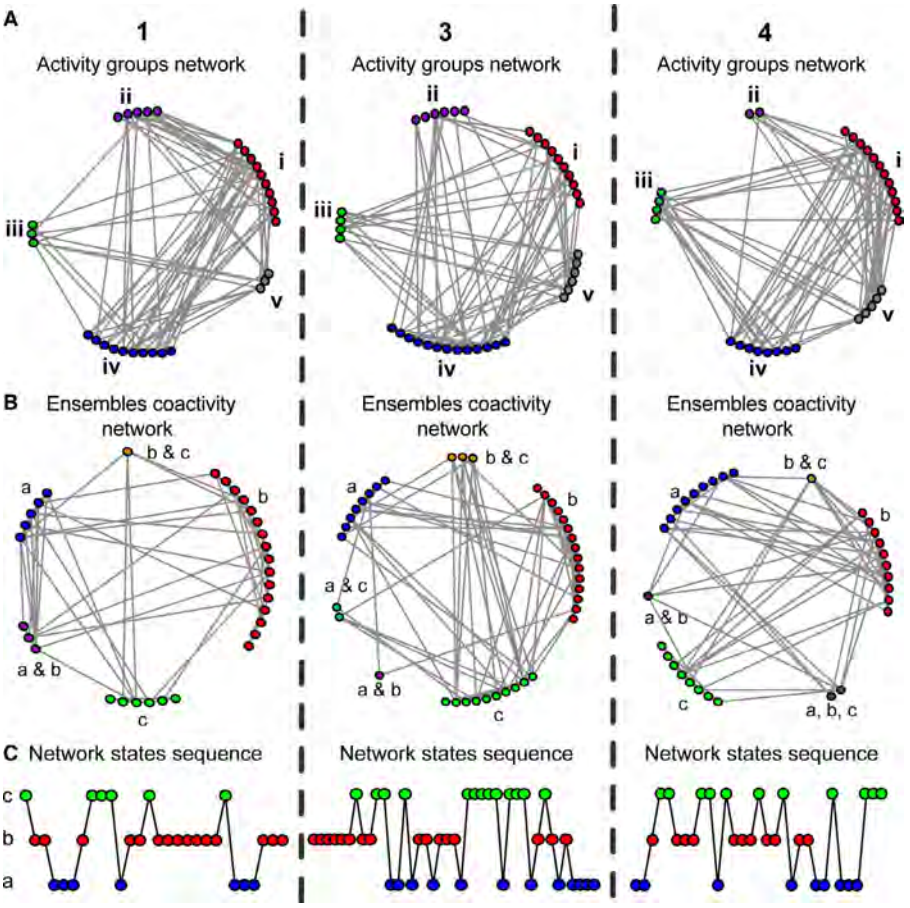

FIG. 8. The effects of L-DOPA and corticostriatal stimulation on the DA-depleted microcircuit architecture and dynamics. (A) Microcircuit built with neuronal subpopulations that changed their activity after the treatments: neuronal networks per epoch: (1) DA-depleted microcircuit before CtxS, circuit while L-DOPA is administered is omitted (2), (3) In the presence of L-DOPA, microcircuit right after CtxS and (4) 30 min after stimulation. Each neuron is a node (circles in the perimeter), each link is a moment of coactivity. Only active neurons in a given epoch are represented, and they are classified into groups according to Fig. 7 (i–v). See the changes in the number of elements and connections of each group after CtxS. (B) Ensembles coactivity networks composed by neurons that make significant peaks of coactivity: main ensembles a–c, neurons that participated in more than one ensemble are grouped separately as indicated by labels. Changes in ensembles and connectivity are obvious after CtxS in the presence of L-DOPA. (C) Network states time sequences per epoch. A more recurrent state (b) is not lost but allows more transitions to other states after L-DOPA and CtxS (3). In contrast to CtxS alone (cf. Fig. 6), transitions persist after 30 min.

depleted condition ($P = 0.01869$) as though the parkinsonian state returned worse than before. In contrast, in the presence of L-DOPA, the microcircuit remained without highly recurrent ensembles 30 min after CtxS (Fig. 10B right box; $P = 0.03582$ as compared to the original DA-depleted circuits). Taken together, these results demonstrate that even when neuronal subpopulation activity or neuronal ensembles tend to return after being temporarily reconfigured by CtxS (Figs 6, 8, 9), L-DOPA prevents the circuit to regain its pathological activity.

Discussion

Cortical stimulation in control and DA-depleted microcircuits

It is being discussed whether the signs and symptoms of parkinsonism have a cortical origin (Arbuthnott & Garcia-Munoz, 2016) as abnormal neuronal correlations are recorded in the motor cortex before motor signs of the disease are apparent (Li *et al.*, 2012). Some cortical influences over striatal circuitry and its changes during parkinsonism have been described (Calabresi *et al.*, 1996, 2015; Hammond *et al.*, 2007; Pérez-Ortega *et al.*, 2016). Accordingly, extradural cortical stimulation in patients (Cilia *et al.*, 2007; Bentivoglio *et al.*, 2012), transcranial magnetic stimulation of the cortex in patients and rodents (Kanno *et al.*, 2004; González-García *et al.*, 2011; Dileone *et al.*, 2017), direct motor cortex stimulation in primates and patients (Drouot *et al.*, 2004; Benninger *et al.*, 2010), optogenetic cortical stimulation in rodents (Gradinaru *et al.*, 2008; Sanders & Jaeger, 2016) and antidromic stimulation of corticofugal axons in rodents (Li *et al.*, 2007, 2012) all relieve parkinsonian signs. In the present work, we asked what the mechanisms are. Therefore, our aim was to observe the changes produced in the striatal microcircuit by cortical stimulation in *in vitro* brain slices of DA-depleted striata.

The control striatal microcircuit is characterized by having low spontaneous activity which increases during action initiation (e.g., Cui *et al.*, 2013). *In vitro*, we have shown that activity increases with network-related behavior after adding an excitatory drive to the superfusion saline such as NMDA at low concentrations (Grillner, 2006). Once turned on, microcircuit activity is characterized by exhibiting significant spontaneous peaks of neuronal coactivity that resemble neuronal ensembles, whose neurons work in concert. This allowed us to use neuronal coactivity in a given time frame to build functional connections and microcircuit representations (Carrillo-Reid *et al.*, 2008; Pérez-Ortega *et al.*, 2016). Network activity

© 2017 Federation of European Neuroscience Societies and John Wiley & Sons Ltd

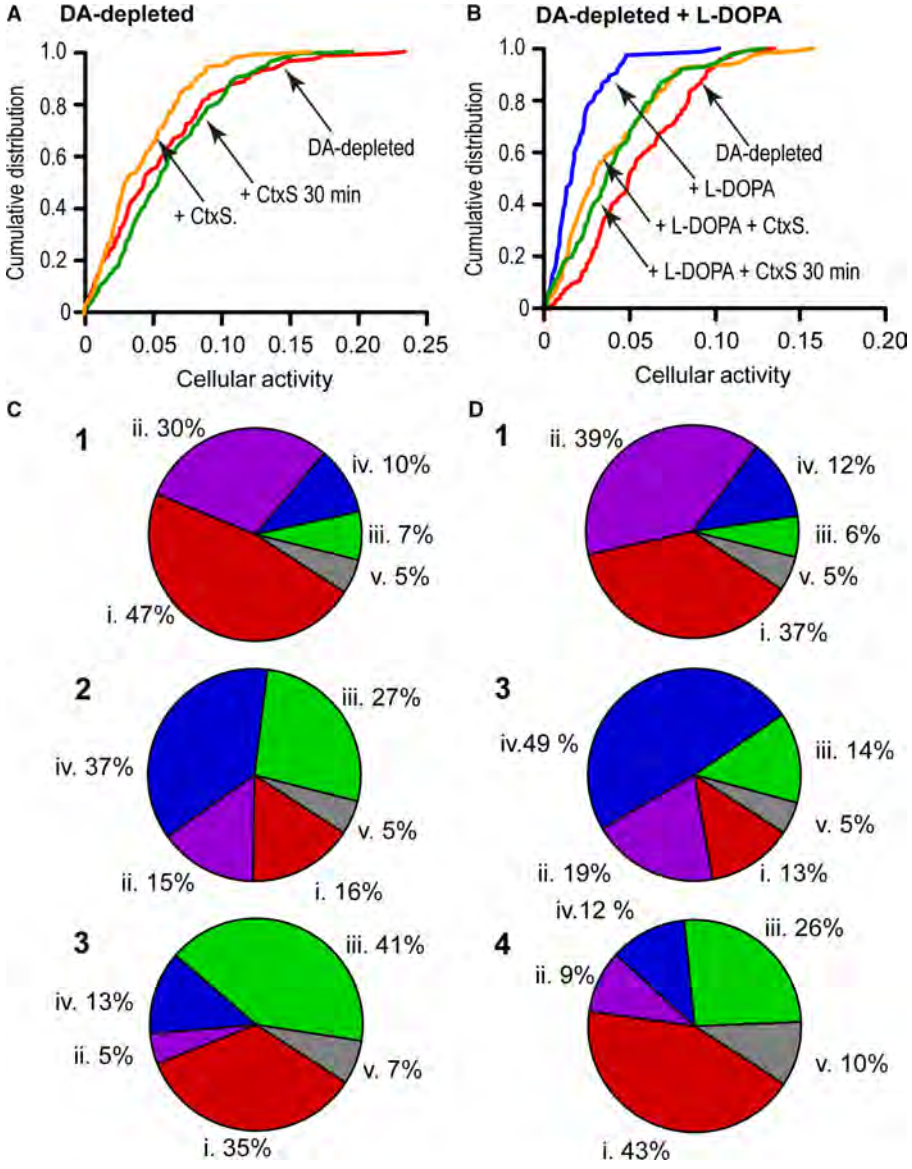

FIG. 9. Cellular activity groups under different conditions for all experiments. (A) Cumulative activity distribution of the cellular activity for the DA-depleted microcircuit treated with CtxS only: there is a significant difference between DA-depleted activity and DA-depleted plus CtxS distributions ($P \leq 0.0135$), this difference disappears after 30 min of the stimulus. (B) Cumulative activity distribution of the cellular activity for the cases of L-DOPA plus CtxS; there is a significant difference in activity after L-DOPA administration ($P = 9.4 \times 10^{-15}$). Activity is recovered after CtxS in the presence of L-DOPA and remains significantly different than that of the DA-depleted microcircuit ($P = 0.00025$). In contrast to CtxS alone, activity distribution remains significantly different after 30 min when L-DOPA was present ($P = 0.0253$; Kolmogorov–Smirnov tests). (C, D) Pie charts illustrating the contribution of different neuronal subpopulations as classified by their activity before and after CtxS (see Figs 5 and 7) for all experiments pooled together. (1) Groups i and ii were predominant in DA-depleted circuits in both cases ($P = 0.6227$). After CtxS, a significant renovation in the neuron subpopulations making up the circuits was observed without (C2) and with L-DOPA (D3). A rise in the neurons of group iv was evident in both cases ($P < 0.0001$), but there was no significant difference in this neuronal redistribution without or with L-DOPA ($P = 0.16$). Thirty minutes after CtxS, group i returns and group iv decreases in both cases ($P = 0.2078$ comparing C3 and D4). Contingency pie chart tests.

revealed high-order processing as ensembles show recurrence and alternating activity with reverberating closed cycles during various minutes, and are modulated in different ways by cholinergic or dopaminergic agonists (Carrillo-Reid *et al.*, 2009, 2011). *In vivo* research has shown that, indeed, this activity encodes motor actions in space (Klaus *et al.*, 2017). Here, we show that it is possible to evoke this network behavior without adding chemical excitatory drives such as NMDA, and instead, using an adequate cortical electrical stimulus (see Methods and Fig. 1). Once it is evoked, microcircuit activity can be followed for more than 30 min in brain slices *in vitro*. Activity recorded in the striatal microcircuit arises from several neuronal subpopulations. Some cholinergic and GABAergic interneurons have spontaneous activity (Goldberg & Wilson, 2010; Tepper *et al.*, 2010), which suggests that they are participating in the microcircuit. Additionally, both low threshold spiking interneurons and cholinergic interneurons communicate with each other through ionotropic and metabotropic receptors (Elghaba *et al.*, 2016).

The DA-depleted parkinsonian microcircuit has dynamics that radically differ from that of the control microcircuit (Jáidar *et al.*, 2010; López-Huerta *et al.*, 2013; Plata *et al.*, 2013a; Pérez-Ortega *et al.*, 2016). A dominant neuronal ensemble with a high level of

© 2017 Federation of European Neuroscience Societies and John Wiley & Sons Ltd

INFORME DE LABORES 2019

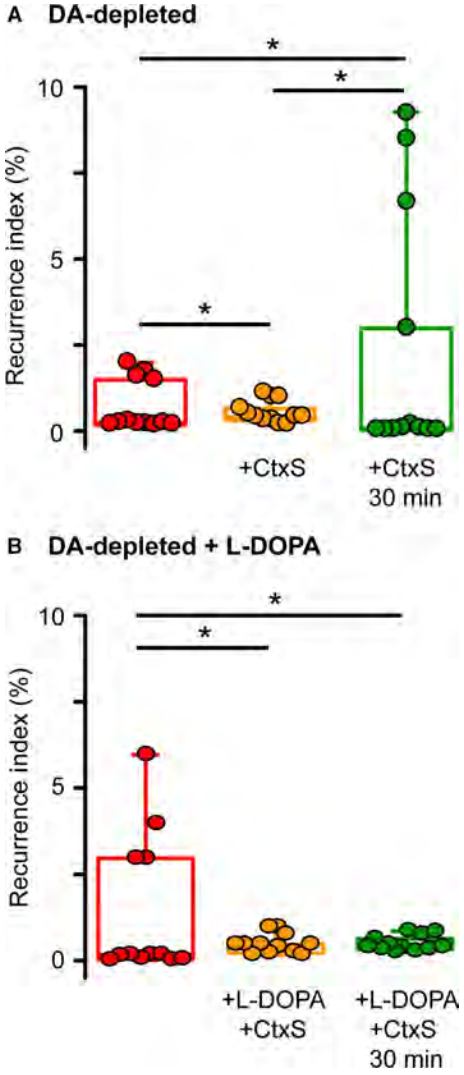

FIG. 10. Recurrence of network states. To test whether the recurrence is predominant in certain network states, we calculated the recurrence of each network state with respect to the others across all experiments (see Materials and methods). In the case some network states have an excess of recurrence (dominant pathological states), the circuit will be divided into two populations of network states those with high and those with low recurrence and the variance of that sample will reflect this separation. In the cases where there is no predominance of any network state, all of them would have similar recurrence and sample variance would be smaller. (A) Box plots comparing recurrence of network states in DA-depleted circuits before and after CtxS: before CtxS, there clearly are two subpopulations of network states one of them with higher recurrence than the others (left). After CtxS, all networks states tended to group together (middle; $P = 0.007586$ with respect to DA-depleted circuits). However, 30 min after CtxS, network states separated again and dominant networks states became even more recurrent (right; $P = 0.01532$ with respect to CtxS and $P = 0.01869$ with respect to DA-depleted circuits before CtxS), suggesting that the parkinsonian state returned worse than before. (B) Comparison of network states recurrence before and after CtxS plus L-DOPA. DA-depleted circuits showed network states with high and low recurrence (left). After CtxS during L-DOPA actions, all network states tended to have the same recurrence (middle; $P = 0.03712$ with respect to DA-depleted circuits). In contrast to the case without L-DOPA, 30 min after CtxS in the presence of L-DOPA, the circuits remained with network states with the same incidence of recurrence (right; $P = 0.03582$ with respect to the DA-depleted circuits). $N = 12$ network states taken from four different circuits and slices from different animals. (O'Brien Homogeneity of Variance test). '*' indicates statistical significance.

recurrence absorbs most neurons and connections in the observed circuits, thus trapping them in a single network state during most of the time (Figs 2, 9, 10). Transitions between network states become scarce, which is very metaphorically, as it corresponds to the motor impairment shown by parkinsonian subjects. By obtaining a recurrence index (see Materials and methods and Fig. 10), we found that DA-depleted microcircuits divide their ensembles into those with high and those with low recurrence, thus increasing the variance. Because previous reports show that cortical stimulation ameliorates Parkinsonism, we wanted to confirm this *in vitro*. Observing whether ensembles with high recurrence are decreased. Thus, another finding of this work is that cortical stimulation releases the microcircuit activity from the parkinsonian state, allowing the circuit to return to ensembles alternation and transitions. By observing graphed microcircuits built with single neurons as nodes and coactivity time frames as the functional connections, it is seen that highly recurrent ensembles that monopolize most activity and connections decrease, leaving way to more balanced connections among different ensembles. In patients, this phenomenon can be related to events of *Kinesia Paradoxa*, in which a strong sensory input may temporarily alleviate the signs of PD (Banou, 2015). In addition, new neuronal subpopulations are recruited into the active circuit and other neuronal subpopulations, that sustain the pathological state, stop firing. Some neurons lower their activity while others increase it. A working hypothesis to explain how some neurons are either silenced or recruited probably would involve the action of striatal inhibitory interneurons known to receive special large numbers of cortical synapses (Bennett & Bolam, 1994; Gittis *et al.*, 2010; Planert *et al.*, 2010). These interneurons have also been reported to connect densely with striatal projection neurons (Straub *et al.*, 2016). Apparently, these interneurons are necessary to observe control network activity such as neuronal ensembles alternation and reverberatory behavior (Pérez-Ortega *et al.*, 2016). To conclude, a cellular substrate that may explain how cortical stimulation may be acting to alleviate parkinsonism was encountered. This finding correlates with changes in long-term synaptic plasticity found in DA-depleted striatal synapses (Calabresi *et al.*, 1996; Ghiglieri *et al.*, 2012). Nonetheless, the effects of CtxS on the DA-depleted microcircuit only last for a few minutes. After 30 min, most tested microcircuits had returned to the parkinsonian state.

The most used treatment for PD is L-DOPA which greatly ameliorates motor signs (Mercuri & Bernardi, 2005) and improves somatosensorial responses (Ketzef *et al.*, 2017). *In vitro*, L-DOPA has been shown to help in the recovery of control long-term synaptic plasticity (Ghiglieri *et al.*, 2012). In agreement with previous data, the present results demonstrate that L-DOPA returns the DA-depleted striatal microcircuit into a low-activity circuit, similar to the one found in control conditions (Plata *et al.*, 2013a). Therefore, a main question to ask was whether in the presence of L-DOPA, activity evoked in the striatal DA-depleted microcircuit corresponds to the alternating activity between neuronal ensembles similar to the one found in control conditions or else the pathological circuit comes into action. We found that cortical stimulation during L-DOPA actions induces new subpopulations of neurons to activate while many neurons that were active during pathological activity become silent.

In the presence of L-DOPA, CtxS produced network activity similar to control-stimulated circuits and similar to CtxS of DA-depleted circuits. However, in contrast to CtxS without L-DOPA, L-DOPA allowed circuits to remain as in control conditions for longer periods of time. Cumulative distribution of cellular activity did not return to

© 2017 Federation of European Neuroscience Societies and John Wiley & Sons Ltd

resemble the DA-depleted microcircuit during the rest of the recording period even though cells that participated in the pathological state reactivated. Therefore, not all phenomena can be explained with changes in neuronal participation. In the presence of L-DOPA, changes in network dynamics evoked by cortical stimulation such as alternation between neuronal ensembles and closed cycles of reverberatory activity lasted for the rest of the recording period (more than 30 min), even when much activity of original subpopulations of neurons returned. Neuronal ensembles that monopolized most activity in the pathological microcircuit were dissolved, and more balanced connections and alternations with other ensembles remain.

If we think of the cortical stimulation as the command that initiates action, the action initiated in the presence of L-DOPA was more similar to the control-stimulated microcircuit, than to the pathological one.

In conclusion, L-DOPA and cortical stimulation work synergically. Therefore, the question becomes whether the two treatments may be balanced somehow as to reduce L-DOPA dosage if continuous cortical stimulation devices are developed.

Supporting Information

Additional supporting information can be found in the online version of this article:
Video S1. Unstimulated striatal control activity.
Video S2. Stimulated striatal control activity.
Video S3. Parkinsonian striatal activity.
Data S1. Supplementary material.

Acknowledgements

This work was supported by public grants: CONACyT Frontera 57 and DGAPA-UNAM IN201417. Ariadna Aparicio -Juárez and Mariana Duhne both are students from the Programa de Doctorado en Ciencias Biomedicas, Universidad Nacional Autónoma de México (UNAM), and received doctoral fellowships 210319 and 270245 from CONACyT. Data in this work are part of their doctoral dissertation. We thank Juan Antonio Laville Conde, Garbriela Xochitl Ayala and Yazmín Ramiro Cortés for their technical support and Claudia Rivera for her help at the animal facility.

Conflict of interest

The authors declare they have no conflict of interest.

Author contributions

Ariadna Aparicio -Juárez and Mariana Duhne worked equally in the study conception, experiments, design, data analysis and manuscript drafting. Esther Lara-González worked in the study conception, design, data acquisition, data analysis and provided critical review. Fátima Ávila-Cascajares contributed in data acquisition, analysis and manuscript drafting. Vladimir Calderón, contributed in data acquisition. Elvira Galarraga and Jose Bargas contributed to study conception and design providing critical revision.

Data accessibility

All of the raw data and videos cannot be uploaded into a server due to the high storage requirements for videos, but will be made available upon request.

Abbreviations

6-OHDA, 6-hydroxydopamine; AP, anterior–posterior; CCW, counterclockwise; Ctrl, control; CtxS, cortical stimulation; CW, clockwise; DA, dopamine; DV, dorsal–ventral; IFC, Instituto de Fisiología Celular; L-DOPA, L-3,4-dihydroxyphenylalanine or levodopa; LM, lateral–medial; NMDA, *N*-methyl-D-aspartate; PD, Parkinson's disease; SNc, substantia nigra pars compacta.

References

Andén, N.E., Carlsson, A., Dahlström, A., Fuxe, K., Hillarp, N.-Å. & Larsson, K. (1964) Demonstration and mapping out of nigro-neostriatal dopamine neurons. *Life Sci.*, **3**, 523–530.

Arbuthnott, G.W. & Garcia-Munoz, M. (2016) Are the symptoms of parkinsonism cortical in origin? *Comput. Struct. Biotechnol. J.*, **15**, 21–25.

Arias-García, M.A., Tapia, D., Laville, J.A., Calderón, V.M., Ramiro-Cortés, Y., Bargas, J. & Galarraga, E. (2017) Functional comparison of corticostriatal and thalamostriatal postsynaptic responses in striatal neurons of the mouse. *Brain Struct. Funct.*, **223**, 1229–1253.

Banou, E. (2015) Kinesia paradoxa: a challenging Parkinson's phenomenon for simulation. *Adv. Exp. Med. Biol.*, **822**, 165–177.

Bennett, B.D. & Bolam, J.P. (1994) Synaptic input and output of parvalbumin-immunoreactive neurons in the neostriatum of the rat. *Neuroscience*, **62**, 707–719.

Benninger, D.H., Lomarev, M., Lopez, G., Wassermann, E.M., Li, X., Considine, E. & Hallett, M. (2010) Transcranial direct current stimulation for the treatment of Parkinson's disease. *J. Neurol. Neurosurg. Psychiatry*, **81**, 1105–1111.

Bentivoglio, A.R., Fasano, A., Piano, C., Soleti, F., Daniele, A., Zinno, M., Piccininni, C., De Simone, C. *et al.* (2012) Unilateral extradural motor cortex stimulation is safe and improves Parkinson disease at 1 year. *Neurosurgery*, **71**, 815–825.

Bernard, V. & Bolam, J.P. (1998) Subcellular and subsynaptic distribution of the NR1 subunit of the NMDA receptor in the neostriatum and globus pallidus of the rat: co-localization at synapses with the GluR2/3 subunit of the AMPA receptor. *Eur. J. Neurosci.*, **10**, 3721–3736.

Bernard, V., Somogyi, P. & Bolam, J.P. (1997) Cellular, subcellular, and subsynaptic distribution of AMPA-type glutamate receptor subunits in the neostriatum of the rat. *J. Neurosci.*, **17**, 819–833.

Bernheimer, H., Birkmayer, W., Hornykiewicz, O., Jellinger, K. & Seitelberger, F. (1973) Brain dopamine and the syndromes of Parkinson and Huntington. Clinical, morphological and neurochemical correlations. *J. Neurol. Sci.*, **20**, 415–455.

Beutler, L.R., Eldred, K.C., Quintana, A., Keene, C.D., Rose, S.E., Postupna, N., Montine, T.J. & Palmiter, R.D. (2011) Severely impaired learning and altered neuronal morphology in mice lacking NMDA receptors in medium spiny neurons. *PLoS One*, **6**, e28168.

Bolam, J.P., Hanley, J.J., Booth, P.A. & Bevan, M.D. (2000) Synaptic organisation of the basal ganglia. *J. Anat.*, **196**, 527–542.

Calabresi, P., Pisani, A., Mercuri, N.B. & Bernardi, G. (1996) The corticostriatal projection: from synaptic plasticity to dysfunctions of the basal ganglia. *Trends Neurosci.*, **19**, 19–24.

Calabresi, P., Ghiglieri, V., Mazzocchetti, P., Corbelli, I. & Picconi, B. (2015) Levodopa-induced plasticity: a double-edged sword in Parkinson's disease? *Philos. T. Roy. Soc. B*, **370**, 20140184.

Carrillo-Reid, L., Tecuapetla, F., Tapia, D., Hernández-Cruz, A., Galarraga, E., Drucker-Colín, R. & Bargas, J. (2008) Encoding network states by striatal cell assemblies. *J. Neurophysiol.*, **99**, 1435–1450.

Carrillo-Reid, L., Tecuapetla, F., Ibáñez-Sandoval, O., Hernández-Cruz, A., Galarraga, E. & Bargas, J. (2009) Activation of the cholinergic system endows compositional properties to striatal cell assemblies. *J. Neurophysiol.*, **101**, 737–749.

Carrillo-Reid, L., Hernández-López, S., Tapia, D., Galarraga, E. & Bargas, J. (2011) Dopaminergic modulation of the striatal microcircuit: receptor-specific configuration of cell assemblies. *J. Neurosci.*, **31**, 14972–14983.

Carrillo-Reid, L., Lopez-Huerta, V.G., Garcia-Munoz, M., Theiss, S. & Arbuthnott, G.W. (2015) Cell assembly signatures defined by short-term synaptic plasticity in cortical networks. *Int. J. Neural Syst.*, **25**, 1550026.

Carrillo-Reid, L., Yang, W., Bando, Y., Peterka, D.S. & Yuste, R. (2016) Imprinting and recalling cortical ensembles. *Science*, **353**, 691–694.

Cilia, R., Landi, A., Vergani, F., Sganzerla, E., Pezzoli, G. & Antonini, A. (2007) Extradural motor cortex stimulation in Parkinson's disease. *Mov. Disord.*, **22**, 111–114.

Cui, G., Jun, S.B., Jin, X., Pham, M.D., Vogel, S.S., Lovinger, D.M. & Costa, R.M. (2013) Concurrent activation of striatal direct and indirect pathways during action initiation. *Nature*, **494**, 238–242.

© 2017 Federation of European Neuroscience Societies and John Wiley & Sons Ltd

INFORME DE LABORES 2019

Dauer, W. & Przedborski, S. (2003) Parkinson's disease: mechanisms and models. *Neuron*, **11**, 889–909.

Dileone, M., Carrasco-López, M.C., Segundo-Rodriguez, J.C., Mordillo-Mateos, L., López-Ariztegui, N., Alonso-Frech, F., Catalan-Alonso, M.J., Obeso, J.A. *et al.* (2017) Dopamine-dependent changes of cortical excitability induced by transcranial static magnetic field stimulation in Parkinson's disease. *Sci. Rep.*, **7**, 4329.

Drouot, X., Oshino, S., Jarraya, B., Besret, L., Kishima, H., Remy, P., Dauguet, J., Lefaucheur, J.P. *et al.* (2004) Functional recovery in a primate model of Parkinson's disease following motor cortex stimulation. *Neuron*, **44**, 769–778.

Ehringer, H. & Hornykiewicz, O. (1960) Distribution of noradrenaline and dopamine (3-hydroxytyramine) in the human brain and their behavior in diseases of the extrapyramidal system. *Klin. Wochenschr.*, **15**, 1236–1239.

Elghaba, R., Vautrelle, N. & Bracci, E. (2016) Mutual control of cholinergic and low-threshold spike interneurons in the striatum. *Front. Cell Neurosci.*, **10**, 111.

Feng, Z.J., Zhang, X. & Chergui, K. (2014) Allosteric modulation of NMDA receptors alters neurotransmission in the striatum of a mouse model of Parkinson's disease. *Exp. Neurol.*, **255**, 154–160.

Fieblinger, T., Graves, S.M., Sebel, L.E., Alcacer, C., Plotkin, J.L., Gertler, T.S., Chan, C.S., Heiman, M. *et al.* (2014) Cell type-specific plasticity of striatal projection neurons in parkinsonism and L-DOPA-induced dyskinesia. *Nat. Commun.*, **31**, 5316.

Flores-Barrera, E., Vizcarra-Chacón, B.J., Bargas, J., Tapia, D. & Galarraga, E. (2011) Dopaminergic modulation of corticostriatal responses in medium spiny projection neurons from direct and indirect pathways. *Front. Syst. Neurosci.*, **5**, 15.

Gerfen, C.R. & Surmeier, D.J. (2011) Modulation of striatal projection systems by dopamine. *Annu. Rev. Neurosci.*, **34**, 441–466.

Ghiglieri, V., Bagetta, V., Pendolino, V., Picconi, B. & Calabresi, P. (2012) Corticostriatal plastic changes in experimental L-DOPA-induced dyskinesia. *Parkinsons Dis.*, **2012**, 1–10.

Gittis, A.H., Nelson, A.B., Thwin, M.T., Palop, J.J. & Kreitzer, A.C. (2010) Distinct roles of GABAergic interneurons in the regulation of striatal output pathways. *J. Neurosci.*, **30**, 2223–2234.

Goldberg, J.A. & Wilson, C.J. (2010) The cholinergic interneurons of the striatum: intrinsic properties underlie multiple discharge patterns. In Steiner, H. & Tseng, K.Y. (Eds), *Handbook of Basal Ganglia Structure and Function*. Elsevier, San Diego, CA, pp. 137–157.

González-García, N., Armony, J.L., Soto, J., Trejo, D., Alegría, M.A. & Drucker-Colín, R. (2011) Effects of rTMS on Parkinson's disease: a longitudinal fMRI study. *J. Neurol.*, **258**, 1268–1280.

Gradinaru, V., Mogri, M., Thompson, K.R., Henderson, J.M. & Deisseroth, K. (2008) Optical deconstruction of parkinsonian neural circuitry. *Science*, **324**, 354–359.

Grillner, S. (2006) Biological pattern generation: the cellular and computational logic of networks in motion. *Neuron*, **52**, 751–766.

Hammond, C., Bergman, H. & Brown, P. (2007) Pathological synchronization in Parkinson's disease: networks, models and treatments. *Trends Neurosci.*, **30**, 357–364.

Hernandez-Flores, T., Hernandez-Gonzalez, O., Perez-Ramirez, M.B., Lara-Gonzalez, E., Arias-Garcia, M.A., Duhne, M., Perez-Burgos, A., Prieto, G.A. *et al.* (2015) Modulation of direct pathway striatal projection neurons by muscarinic M4-type receptors. *Neuropharmacology*, **89**, 232–244.

Jáidar, O., Carrillo-Reid, L., Hernández, A., Drucker-Colín, R., Bargas, J. & Hernández-Cruz, A. (2010) Dynamics of the Parkinsonian striatal microcircuit: entrainment into a dominant network state. *J. Neurosci.*, **30**, 11326–11336.

Kalia, L.V. & Lang, A.E. (2015) Parkinson's disease. *Lancet*, **386**, 896–912.

Kanno, M., Matsumoto, M., Togashi, H., Yoshioka, M. & Mano, Y. (2004) Effects of acute repetitive transcranial magnetic stimulation on dopamine release in the rat dorsolateral striatum. *J. Neurol. Sci.*, **217**, 73–81.

Kemp, J.M. & Powell, T.P.S. (1971) The termination of fibres from the cerebral cortex and thalamus upon dendritic spines in the caudate nucleus: a study with the Golgi method. *Phillos. T. Roy. Soc. B.*, **262**, 429–439.

Ketzef, M., Spigolon, G., Johansson, Y., Bonito-Oliva, A., Fisone, G. & Silberberg, G. (2017) Dopamine depletion impairs bilateral sensory processing in the striatum in a pathway-dependent manner. *Neuron*, **94**, 855–865.

Klaus, A., Martins, G.J., Paixao, V.B., Zhou, P., Paninski, L. & Costa, R.M. (2017) The spatiotemporal organization of the striatum encodes action space. *Neuron*, **95**, 1171–1180.

Lambot, L., Chaves Rodriguez, E., Houtteman, D., Li, Y., Schiffmann, S.N., Gall, D. & de Kerchove d'Exaerde, A. (2016) Striatopallidal neuron NMDA receptors control synaptic connectivity, locomotor and goal-director behaviors. *J. Neurosci.*, **36**, 4976–4992.

Li, S., Arbuthnott, G.W., Jutras, M.J., Goldberg, J.A. & Jaeger, D. (2007) Resonant antidromic cortical circuit activation as a consequence of high-frequency subthalamic deep-brain stimulation. *J. Neurophysiol.*, **98**, 3525–3537.

Li, Q., Ke, Y., Chan, D.C., Qian, Z.M., Yung, K.K., Ko, H., Arbuthnott, G.W. & Yung, W.H. (2012) Therapeutic deep brain stimulation in Parkinsonian rats directly influences motor cortex. *Neuron*, **76**, 1030–1041.

López-Huerta, V.G., Carrillo-Reid, L., Galarraga, E., Tapia, D., Fiordelisio, T., Drucker-Colin, R. & Bargas, J. (2013) The balance of striatal feedback transmission is disrupted in a model of parkinsonism. *J. Neurosci.*, **33**, 4964–4975.

Mercuri, N.G. & Bernardi, G. (2005) The 'magic' of L-dopa: why is it the gold standard Parkinson's disease therapy?. *Trends Pharm. Sci.*, **26**, 341–344.

Morelli, M., Fenu, S., Garau, L. & Di Chiara, G. (1989) Time and dose dependence of the "priming" of the expression of dopamine receptor supersensitivity. *Eur. J. Pharmacol.*, **162**(2), 329–335.

Pérez-Ortega, J., Duhne, M., Lara-González, E., Plata, V., Gasca, D., Galarraga, E., Hernández-Cruz, A. & Bargas, J. (2016) Pathophysiological signatures of functional connectomics in parkinsonian and dyskinetic striatal microcircuits. *Neurobiol. Dis.*, **91**, 347–361.

Pérez-Ramírez, M.B., Laville, A., Tapia, D., Duhne, M., Lara-González, E., Bargas, J. & Galarraga, E. (2015) KV7 channels regulate firing during synaptic integration in GABAergic striatal neurons. *Neural. Plast.*, **2015**, 1–18.

Picconi, B., Piccoli, G. & Calabresi, P. (2012) Synaptic dysfunction in Parkinson's disease. *Adv. Exp. Med. Biol.*, **970**, 553–572.

Planert, H., Szydlowski, S.N., Hjorth, J.J., Grillner, S. & Silberberg, G. (2010) Dynamics of synaptic transmission between fast-spiking interneurons and striatal projection neurons of the direct and indirect pathways. *J. Neurosci.*, **30**, 3499–3507.

Plata, V., Duhne, M., Pérez-Ortega, J.E., Barroso-Flores, J., Galarraga, E. & Bargas, J. (2013a) Direct evaluation of L-DOPA actions on neuronal activity of Parkinsonian tissue in vitro. *Biomed. Res. Int.*, **2013**, 1–7.

Plata, V., Duhne, M., Pérez-Ortega, J., Hernández-Martinez, R., Rueda-Orozco, P., Galarraga, E., Drucker-Colín, R. & Bargas, J. (2013b) Global actions of nicotine on the striatal microcircuit. *Front. Syst. Neurosci.*, **7**, 78.

Sanders, T.H. & Jaeger, D. (2016) Optogenetic stimulation of cortico-subthalamic projections is sufficient to ameliorate bradykinesia in 6-OHDA lesioned mice. *Neurobiol. Dis.*, **95**, 225–237.

Straub, C., Saulnier, J.L., Bègue, A., Feng, D.D., Huang, K.W. & Sabatini, B.L. (2016) Principles of synaptic organization of GABAergic interneurons in the striatum. *Neuron*, **92**, 84–92.

Tepper, J.M., Tecuapetla, F., Koós, T. & Ibáñez-Sandoval, O. (2010) Heterogeneity and diversity of striatal GABAergic interneurons. *Front. Neuroanat.*, **4**, 150.

Thomas, B. & Beal, M.F. (2010) Mitochondrial therapies for Parkinson's disease. *Mov. Disord.*, **25**, S155–S160.

Thomas, D., Tovey, S.C., Collins, T.J., Bootman, M.D., Berridge, M.J. & Lipp, P. (2000) A comparison of fluorescent Ca^{2+} indicator properties and their use in measuring elementary and global Ca^{2+} signals. *Cell Calcium*, **28**, 213–223.

Ungerstedt, U. & Arbuthnott, G.W. (1970) Quantitative recording of rotational behavior in rats after 6-hydroxy-dopamine lesions of the nigrostriatal dopamine system. *Brain Res.*, **24**, 485–493.

Znamenskiy, P. & Zador, A.M. (2013) Corticostriatal neurons in auditory cortex drive decisions during auditory discrimination. *Nature*, **497**, 482–485.

© 2017 Federation of European Neuroscience Societies and John Wiley & Sons Ltd

frontiers in Microbiology

INFORME DE LABORES 2019

published: 09 July 2019
doi: 10.3389/fmicb.2019.01568

A Novel Two-Component System, Encoded by the *sco5282/sco5283* Genes, Affects *Streptomyces coelicolor* Morphology in Liquid Culture

*Erick Eligio Arroyo-Pérez[1], Gabriela González-Cerón[1], Gloria Soberón-Chávez[1], Dimitris Georgellis[2] and Luis Servín-González[1]**

[1] *Instituto de Investigaciones Biomédicas, Departamento de Biología Molecular y Biotecnología, Universidad Nacional Autónoma de México, Mexico City, Mexico,* [2] *Instituto de Fisiología Celular, Departamento de Genética Molecular, Universidad Nacional Autónoma de México, Mexico City, Mexico*

Streptomyces are mycelial bacteria adapted to grow in soil. They have become important producers of biomolecules with medical applications, but their growth in industrial fermenters is challenged by their peculiar morphology in liquid culture: the hyphae tend to clump and grow as large pellets, which are oxygen- and nutrient-limited, grow slowly and present diminished protein production. Here, by implementing an experimental evolution strategy, a *S. coelicolor* strain, 2L12, with dispersed morphology and reduced pellet size in liquid culture and no defects in either differentiation or secondary metabolism was selected. Genome sequencing revealed a single amino acid substitution in a sensor kinase, Sco5282, of unknown function to be responsible for the morphological changes. Moreover, genetic and biochemical scrutiny identified Sco5283 as the cognate response regulator and demonstrated that the acquired mutation activates this two-component system. Finally, transcriptomic analysis of the mutant strain revealed changes in expression of genes involved in central processes such as glycolysis, gluconeogenesis, stress-signaling pathways, proteins secretion and cell envelope metabolism. Thus a novel two-component system is proposed to play a key role in the control of *Streptomyces* extracellular metabolism.

Keywords: *Streptomyces*, morphology, two-component systems, HAMP domain, aggregation, biofilm

OPEN ACCESS

Edited by:
Marie-Joelle Virolle, Centre National de la Recherche Scientifique (CNRS), France

Reviewed by:
Angel Manteca, Universidad de Oviedo, Spain
Dennis Claessen, Leiden University, Netherlands
Giselda Bucca, University of Brighton, United Kingdom
Andrew Hesketh, University of Brighton, United Kingdom

****Correspondence:***
Luis Servín-González
servin@biomedicas.unam.mx

Specialty section:
This article was submitted to Microbial Physiology and Metabolism, a section of the journal Frontiers in Microbiology

Received: *16 May 2019*
Accepted: *24 June 2019*
Published: *09 July 2019*

Citation:
Arroyo-Pérez EE, González-Cerón G, Soberón-Chávez G, Georgellis D and Servín-González L (2019) A Novel Two-Component System, Encoded by the sco5282/sco5283 Genes, Affects Streptomyces coelicolor Morphology in Liquid Culture. Front. Microbiol. 10:1568. doi: 10.3389/fmicb.2019.01568

INTRODUCTION

Streptomyces is a genus of soil-dwelling mycelial actinobacteria (Hopwood, 2007). In the presence of nutritious substrates in the soil, their spores are able to germinate, leading to growth of hyphae that adhere to the soil particles and to each other, and grow as a packed vegetative mycelium (Bobek et al., 2017). When conditions become suboptimal, they go through a developmental program, growing out of the soil and forming the reproductive aerial mycelium (Flärdh and Buttner, 2009). There is a concerted lysis of the vegetative hyphae, which releases nutrients for the growing aerial mycelium (Manteca et al., 2005). During this stage antibiotics are also produced preventing

competitors from feeding on the lysed mycelium. Subsequently aerial hyphae septate by undergoing synchronous cell divisions, which later become chains of spores. This is the only stage of the *Streptomyces* life cycle in which unigenomic cells exist (Bush et al., 2015; Zhang et al., 2016).

This genus has been widely studied because of the vast array of antibiotics they produce. In recent years many species have also been exploited for the production of heterologous proteins. Because of their mycelial morphology, *Streptomyces* growth in liquid media is unlike that of unicellular bacteria. For example, germinating spores of the model organism *S. coelicolor* tend to clump together, and the hyphae stick to each other, leading to growth as tight mycelial pellets (Zacchetti et al., 2016). As a consequence, the inner hyphae have limited access to nutrients and oxygen (Walisko et al., 2015), leading to slower growth rates. This morphology in liquid cultures has also a clear impact on production of different molecules: while pelleted forms present increased antibiotic synthesis (Martin and Bushell, 1996; Manteca et al., 2008) they are disadvantageous for protein production, because of the reduced contact with inducer molecules (van Wezel et al., 2006).

For this reason, strategies have been developed to control the morphology of mycelia in liquid culture. Increasing agitation or viscosity of the medium (by addition of sucrose, for example) are simple methods that intensify shear forces, reducing aggregation but also increasing energy input and mechanical stress on the cells (van Dissel et al., 2014). A different approach has been to engineer strains where hyphae do not aggregate. For example, deletion of *cslA*, which encodes a cellulose synthase-like enzyme, leads to pellet dispersion. However, this mutant also exhibits pleiotropic effects on growth and differentiation (Xu et al., 2008). A different set of genes, *matAB*, were identified among the mutations in a dispersed-growing strain of *S. lividans*, a close relative of *S. coelicolor*, isolated from a chemostat after 100 generations (van Dissel et al., 2015). These genes were initially identified for their similarity to a biofilm operon of *Staphylococcus* spp., and their deletion was sufficient to induce dispersed growth in both *S. lividans* and *S. coelicolor* (van Dissel et al., 2015). More recently the *mat* genes have been shown to be responsible for synthesis of extracellular poly-β-1,6-*N*-acetylglucosamine, which provides hyphal adhesion to hydrophylic surfaces (van Dissel et al., 2018).

We sought to isolate new strains of *S. coelicolor* with a dispersed-growth phenotype through directed evolution. A study about the origin of multicellularity in the unicellular yeast *Saccharomyces cerevisiae* described an experimental evolution method to isolate aggregating mutants, based on the selection of fast-sedimenting cell clumps, eventually obtaining "multicellular" strains (Ratcliff et al., 2012). We adapted this method to obtain slower sedimenting *S. coelicolor* strains by applying the opposite selection: subculturing the slower sedimenting pellets. One of the obtained strains, 2L12, showed significantly reduced pellet size and dispersed growth even in medium without sucrose, although its secondary metabolism and differentiation in solid medium was not affected. We show that this phenotype is caused by an activating mutation in a histidine kinase of a novel two-component system. Finally, transcriptomic analysis of the 2L12 mutant strain revealed molecular targets able to explain the dispersed growth phenotype of the selected mutant strain.

MATERIALS AND METHODS

Streptomyces Cultures

Streptomyces spores were obtained from MS agar plates and preserved in 20% glycerol at −20°C (Kieser et al., 2000). Liquid cultures were grown in LB + 25% sucrose or 2xYT (Kieser et al., 2000), without sucrose. Growth curves were performed in 2xYT or YEME media (Kieser et al., 2000), using freshly harvested spores to give an initial OD_{450} = 0.01. Samples (10 mL) were taken at the indicated times and filtered through 0.45 μm cellulose acetate filters (Millipore, HAWP02500); the mycelium was then dried at 100°C for dry weight determination. Total actinorhodin was determined by lysing 1 mL aliquots of the culture with 1 M KOH, which were then centrifuged to remove debris and measuring OD_{640} (Kieser et al., 2000).

Experimental Evolution

Spores of *S. coelicolor* M145 were used to inoculate test tubes (16x150 mm) containing 2.5 mL of LB + 25% sucrose, which were incubated with orbital shaking at 30° C. After 48 h of growth, the tubes were left standing without shaking for 10 min to allow most of the mycelial pellets to sediment. Then, the upper 0.2 mL of each culture was transferred to a new tube with fresh medium and incubated as before. The process was repeated every 48 h until the culture consisted of slow sedimenting mycelium which appeared visibly dispersed. When this stage was reached, the mycelium was transferred to MS agar plates and allowed to sporulate. Spores were then streaked onto fresh plates for single colony strain purification. Spores from individual colonies were tested in LB + 25% sucrose, and spore preparations were made of those strains maintaining dispersed morphology after single colony purification.

Microscopy and Pellet Size Determination

Six independent cultures of M145 and 2L12 were grown in non-viscous medium (2xYT), and the morphology of mycelial pellets was analyzed using a Nikon Eclipse 6000 microscope. In order to measure the complete pellets of strain M145, consecutive bright-field images under 10× amplification were taken and stitched together using the ImageJ plugin Stitching (Preibisch et al., 2009) as pellets of the wild type were often too large to fit in a single field. The area of the cross-section of the pellet was measured using ImageJ tools.

DNA Extraction, Genome Sequencing and Mutation Analysis

For total DNA isolation, a modification of procedure 4 of Hopwood et al. (1985) was used. Briefly, 25 mL cultures of strains M145 and 2L12 were grown in LB+25% sucrose medium for 48 h, the mycelium was then harvested by centrifugation, washed with 25 mL of a 10% sucrose solution, and resuspended in 5 mL of lysis

buffer (25 mM Tris–Hcl, 25 mM EDTA, pH = 8.0) containing 5 mg of freshly dissolved lysozyme and 250 μg of RNase A, and incubated at 37 C for 1 h. After lysis, 2.5 mL of a 2% SDS solution was added followed by vortexing for 30 s. The resulting lysed mycelium was extracted several times with an equal volume of saturated phenol:chloroform until a clear interphase was observed after centrifugation. Total DNA was then precipitated with ethanol, dried and resuspended in 0.5 mL of distilled water. The libraries were constructed with a TrueSeq DNA PCR-Free Library Prep kit (Illumina, 215962), and sequenced in an Illumina MiSeq equipment at a 2 × 150 cycles configuration at the Unidad Universitaria de Secuenciación Masiva y Bioinformática of the Universidad Nacional Autónoma de México[1].

For variant calling, pair-end reads were aligned to the reference *S. coelicolor* A3(2) genome (NC_003888.3) using Bowtie 2 software (Langmead and Salzberg, 2012). Variant calling was performed using Samtools (Li, 2011) and VCFtools (Danecek et al., 2011). Only variants with a quality score above 100 were considered, and analyzed individually against the reference genome using Artemis (Carver et al., 2012). Variants present in both M145 and 2L12 were filtered out, as were variants with a lower quality score not present in at least 95% of all individual reads. The bam files used for variant calling, which contain all the sorted and aligned reads, are available from the NCBI with accession no. PRJNA499125.

Sedimentation Time Determination

Spores of the strains to be tested were used to inoculate liquid LB + 25% sucrose medium to obtain dispersed mycelium, which was then used to inoculate 2xYT medium at a 1:20 ratio. Mycelial pellets were cultured for 48 h at 30°C. To measure the sedimentation time of the pellets, cultures were diluted with one volume of water and left to settle at the bottom of the tube before taking 0.5 mL to overlay on top of a 2 cm column of a 10% sucrose solution in a 13 × 100 mm test tube. The time reported in this work is the time it took for the first pellet in each tube to reach the bottom of the solution.

Genetic Manipulation

PCR targeting (Datsenko and Wanner, 2000) was performed as described by Gust et al. (2004). The *aac3(IV)-oriT* (apra) cassette described by Gust et al. (2004), which confers resistance to apramycin, was amplified with oligonucleotides SCO5282For and SCO5282Rev (**Table 1**) and used to replace the *sco5282* gene in cosmid StCB12 (Redenbach et al., 1996). This cosmid (StCB12Δ*sco5282*::apra) was introduced by conjugation from the non-methylating *Escherichia coli* strain ET12567/pUZ8002 (Gust et al., 2004) into the wild type strain M145 to obtain apramycin-resistant exconjugants, which were then tested for kanamycin resistance. A kanamycin sensitive exconjugant was purified and confirmed by PCR as a Δ*sco5282*::apra null mutant (strain IB94). The StCB12Δ*sco5282*::apra cosmid was also used to clone the *sco5282-D125G* allele by introducing it into strain 2L12, and selecting exconjugants resistant to both apramycin and kanamycin, in order to obtain strains with the cosmid inserted into the chromosome. These strains were grown non-selectively in liquid culture, and covalently closed circular DNA was purified, which was then introduced into *E. coli* strain DH5α by transformation, with selection for kanamycin and ampicillin resistance. About half of the colonies were resistant to apramycin and carried the StCB12D*sco5282*::apra cosmid, whereas the other half were apramycin-sensitive and therefore carried the StCB12*sco5282-D125G* allele, which was confirmed by DNA sequencing. The StCB12*sco5282-D125G* cosmid was introduced into strain IB94 to replace the apramycin resistance cassette with the cloned *sco5282-D125G* allele, yielding strain M145*sco5282-D125G*. Allele replacement was confirmed by sequencing the PCR product obtained from chromosomal DNA of the resulting

TABLE 1 | Oligonucleotides used in this work.

Name	Sequence 5′ →3′
SCO5282For	GCACGGCGTGGGCTACGCCTTGGAGACGCCGACGCC ATGATTCCGGGGATCCGTCGACC
SCO5282Rev	CGCAGTGGATCTTGACGCTCCGCTTCGAACCCTACG TCATGTAGGCTGGAGCTGCTTC
SCO5282Up	GTGGACAGCCACATCAAGG
SCO5282Down	GTTCATCGTCGCGTAAGTCA
SCO5283For	CCACGGATTCCGGAAAGCACACCTCAGGGGCGGGCG ATGATTCCGGGGATCCGTCGACC
SCO5283Up	GGATCATTCAAGCGTCAAGC
cl5282For	CATATGAGCAGCAGAGGACGGGA
cl5282Rev	GAATTCAACCGGACGTCGACGGCA
cl5282Sol	CATATGTCGCTGACCGCCCCGCTG
cl5283For	CATATGGAGCAGACACAGACCTCC
cl5283Rev	GAATTCATGGCGTCGGCGTCTCC
ATTB_FOR	CCATGCATGCACAGCTCAGGCAGACGTTA
ATTB_REV	GTGTGCATGCGACCGGTACTTGTCATGG
For RT-qPCRs	
0753for	GAAATGGCTATACGAAGGGAAG
0753rev	GACGGCGTTCACGTTCAG
0754for	ACCTCGAAGTCCACGAAGAG
0754rev	AGGGTCATGGAGGTCAGTTC
mbl2for	GGCATGATCCTCGACGTG
mbl2rev	TGGGTGTCGACGATGGAG
gap3for	CGATCGTCGAGCTGAACAC
gap3rev	GTGATGTCGGAGGAGACCAG
gap2for	GACGACTCGTTCACCAACTG
gap2rev	CTGACCACCGACTTGTTCAC
pckGfor	GAGGGCTTCTTCGTCAAGG
pckGrev	GCGAGATGTACTTGGTGCTG
whiDfor	AAGGAGGTCTGCATGAGGTG
whiDrev	CCCGTCCCATGAGTTCTTC
matBfor	ACGCCATGGACAACAAGTC
matBrev	TGTTGACGACGACGAGGTAG
sigBfor	GGGAGTTGTCGAAGCTGTTC
sigBrev	ATCTCGATCAGCGTGTTGC
hrdBfor	GGTCGAGGTCATCAACAAGC
hrdBrev	TGGACCTCGATGACCTTCTC
secDF-for	TCATTCTGGTCGGTGTGTTC
secDF-rev	GAGTCGTTCACCGAGTAGCC

[1]www.uusmd.unam.mx

strain with primers SCO5282Up and SCO5282Down, which flank the kinase gene.

The apramycin resistance gene of strain IB94 was removed by recombination between the FLP sites of the cassette, resulting in a 81 bp non-polar scar sequence (Gust et al., 2004). This apramycin-sensitive Δ*sco5282*::*scar* strain (IB95) was used in subsequent studies. The same procedure was followed to obtain strains lacking both genes for the two-component system, resulting in strains IB96 (Δ*sco5282-sco5283*::apra) and IB97 (Δ*sco5282-sco5283*::*scar*), using primers SCO5283For and SCO5282Rev.

Genetic Complementation

Wild-type and mutant *sco5282* kinase genes were amplified by PCR with *Pfu* Ultra DNA polymerase (Agilent Technologies) from chromosomal DNA of M145 and 2L12, respectively, using primers clSCO5282For and clSCO5282Rev, which add an in-frame NdeI site at the start codon, and an EcoRI site at the 3′ end after the stop codon. The blunt-end PCR products were cloned in plasmid pBlueScript II SK (Alting-Mees and Short, 1989) digested with EcoRV, and their DNA sequence was confirmed using universal M13 primers. The wild type and mutant genes were then subcloned in vector pIJ6902 (Huang et al., 2005) using NdeI and EcoRI, thereby placing them under control of the inducible promoter P_{tipA}. The resulting plasmids were transferred to *S. coelicolor* via conjugation with *E. coli* ET12567/pUZ8002. Sedimentation times of the mycelial pellets of the complemented strains were measured in the absence of thiostrepton.

Merodiploid Strains

The ampicillin-resistance gene of cosmids StCB12 and StCB12*sco5282-D125G* were replaced by PCR targeting with the apramycin-resistance cassette from pIJ784 bearing the origin of transfer *oriT* (Gust et al., 2004), so that they could be introduced to *Streptomyces* by conjugation. Exconjugants for each cosmid were selected and maintained in the presence of both kanamycin and apramycin, to select for the presence of the integrated cosmids. Sedimentation times of the mycelial pellets grown in the presence of 25 μg/mL kanamycin were determined as described above.

Phosphorylation Assays

The *sco5283* gene coding for the response regulator was amplified by PCR with primers clSCO5283for and clSCO5283rev (**Table 1**) and cloned in pET28a using the NdeI and EcoRI sites. The region encoding the cytosolic domain of the wild type and mutant sensor kinases (amino acids 80-375), were amplified by PCR from the wild type *sco5282* and mutant *sco5282-D125G* genes, respectively, with primers clSCO5282sol and clSCO5282rev (**Table 1**) and also cloned in pET28a with NdeI and EcoRI. The plasmids were then introduced into *E. coli* Rosetta 2 (Novagen) for protein expression. Protein purification was carried out using a Ni-NTA Superflow Cartridge (QIAGEN, 30721) in an FPLC system (ÄKTAprime plus; GE Healthcare) according to the manufacturer instructions.

Autophosphorylation and transphosphorylation assays were performed as described by Álvarez and Georgellis (2012).

RNA Extraction, Sequencing and Analysis

For RNA extraction, three independent cultures of strains IB97 and M145-D125G were grown in 2xYT medium until mid-log phase (24 h), in shaking flasks without coils to allow pellet formation. Mycelium was harvested by filtration as described in Hopwood et al. (1985) and RNA isolation was carried out as described in Kieser et al. (2000), but using a modified Kirby mixture (1% SDS, 6% EDTA, 6% saturated phenol solution, 150 mM β-mercaptoethanol, 50 mM Tris–Hcl, pH = 8.3) as follows: pellets were filtered through ice-cold Whatman paper after pouring the cultures over a funnel containing ice, placed above the filter; the filter was washed with ice-cold water and the mycelium was then scraped into ice-cold modified Kirby solution and vortexed with an equal volume of 4 mm glass beads for 2 min, then five pulses of 30 s. The suspension was extracted with equal volumes of phenol:chloroform until the interphase was clear, then precipitated with sodium acetate and isopropanol. Total nucleic acids were treated with RNAse-free DNAse I (Ambion, AM2222; Thermo Fisher Scientific) until no PCR product was detected after 30 cycles using primers ATTB_FOR and ATTB_REV (**Table 1**). rRNA was depleted by subtractive hybridization with the Ribo-Zero Gram-positive kit (Illumina, MRZGP126); mRNA libraries for each of the three independent cultures of each strain were constructed using the TrueSeq stranded mRNA Library Prep kit (Illumina 20020594) and sequenced in an Illumina NextSeq 500 equipment, with up to 10^7 paired reads/sample. Raw RNA sequencing reads are available through the NCBI Sequence Read Archive (BioProject Accession No. PRJNA499125).

Sequences were mapped to the reference genome of *S. coelicolor* A3(2) (NC_003888.3) and differential expression evaluated with packages DESeq2 1.18.1 (Love et al., 2014), edgeR 3.20.9 (Robinson et al., 2010) and NOISeq 2.22.1 (Tarazona et al., 2011). Genes were considered differentially expressed if they showed a $\log_2$ fold-change above 1 and an FDR-controlled *p*-value below 0.05. Genes that resulted positive with at least two tests were annotated with eggNOG-mapper (Huerta-Cepas et al., 2017).

RT-qPCRs to Validate Differential Gene Expression

RNA obtained as described before was used in RT-qPCR using the Luna Universal One-Step RT-qPCR kit (NEB, E3005S), following the manufacturer's instructions with 100 ng total RNA/reaction plus 5% DMSO (NEB, B0515). Differential expression was calculated according to the ΔΔCt method (Livak and Schmittgen, 2001), using the *hrdB* gene as calibrator. Primers used are listed in **Table 1**.

Statistical Analysis

Pellet size and differential gene expression were compared by Student's *t*-test. Due to the asymmetrical distribution of the sedimentation time, the corresponding assays were analyzed by the non-parametric Kruskal-Wallis test for multiple comparisons, with *post hoc* Dunn test with Benjamini-Hochberg

correction of experiment-wise error rate. Statistical significance was determined at p-value < 0.05. All statistical procedures were performed using R version 3.4.4 (R Core Team, 2018).

RESULTS

Experimental Evolution for Selection of Slow-Sedimenting Strains

Since wild type *S. coelicolor* grows in liquid medium as tight, dense mycelial pellets that settle quickly when the culture is left without shaking, we sought to isolate mutants showing dispersed growth by adapting a gravity-based sedimentation strategy used previously by Ratcliff et al. (2012). Our strategy consisted of sequentially transferring the uppermost part of settled cultures for reinoculation, as opposed to the strategy used to isolate multicellular derivatives of *S. cerevisiae*, which consisted of sequentially transferring the lower part of the settled cultures. Thus, any mutation which allowed for more dispersed mycelium and less dense mycelial pellets would be positively selected. By applying this selection to independent cultures of the wild type M145 strain, we observed more dispersed morphologies appearing after 12–56 transfers. The different isolates were transferred to solid medium and purified from single colonies after one sporulation round. Most of the purified strains no longer showed dispersed growth in liquid medium, or showed increased antibiotic production and reduced spore viability and were no longer considered. Only one strain, which was named 2L12, was phenotypically indistinguishable from M145 on solid MS medium and retained the slower sedimenting, dispersed growth phenotype when reinoculated in liquid medium.

Microscopically, the main difference between strain 2L12 and the parental strain M145 was the pellet size when both were grown in liquid media without sucrose (**Figure 1**). The pellets of 2L12 were smaller, like the one shown in **Figure 1** (with an area of 0.242 mm^2), and frequently appeared breaking apart, suggesting increased fragility. Pellets of the wild type M145 frequently reached at least the size of the pellet shown in **Figure 1** (with an area of 0.621 mm^2). It is worth noting that, under these conditions, we never found in the 2L12 strain a pellet of the size depicted for M145, whereas on almost every experiment the wild type pellets reached at least this size (**Supplementary Table S1**) The growth rate of 2L12 was indistinguishable from that of M145, either in liquid YEME medium with 34% sucrose or in 2xYT medium (**Figures 2A,B**), indicating that the reduced pellet size was not due to a major growth defect.

In order to have an objective way to compare the phenotypes of the M145 and 2L12 strains, we measured the time it took for the pellets of either strain to settle through a 2 cm high column of a 10% sucrose solution in a 1 cm wide test tube, since loose and smaller pellets would take longer to settle to the bottom of the tube because of their lower density. As expected, the selected

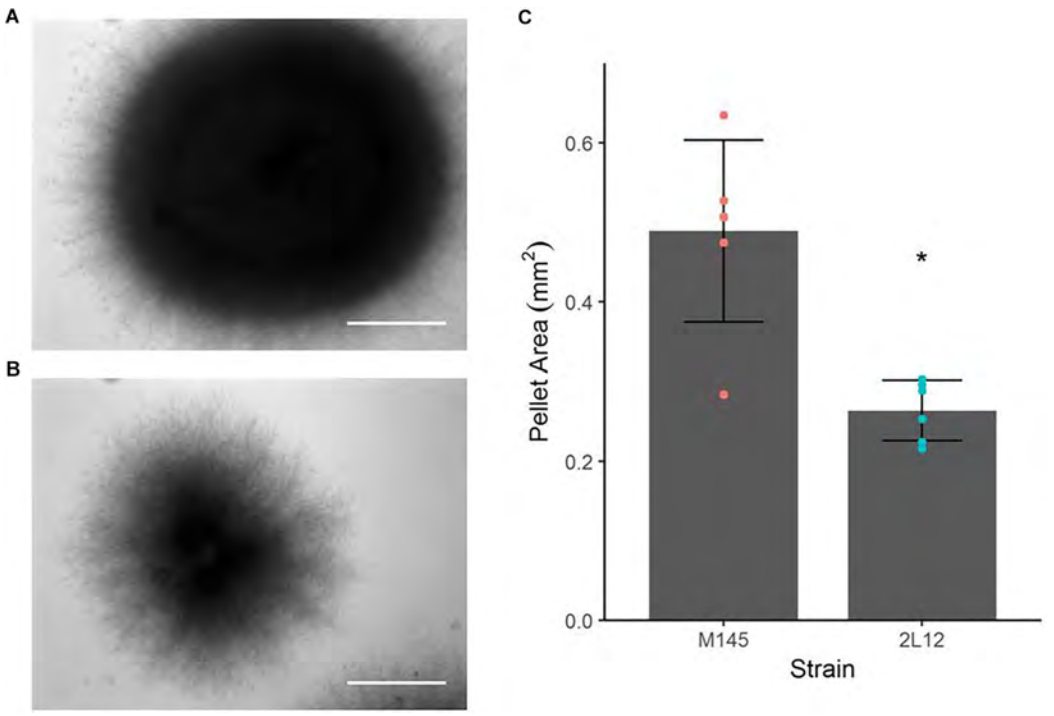

FIGURE 1 | Pellet morphology of strains M145 and 2L12. Bright field microscopy of representative pellets, grown in 2xYT medium. **(A)** M145 pellet with an area of 0.621 mm^2 and **(B)** 2L12 pellet with an area of 0.242 mm^2. These areas are around the average of the distribution for each strain. It is worth noting that under these conditions, no pellets were found in the 2L12 strain of the size shown for M145, whereas in almost every experiment the M145 pellets reached at least this size. The scale bar corresponds to 0.2 mm. **(C)** Pellet area quantification. Each dot represents the average area of pellets from an independent culture; the raw data for each independent culture are shown in **Supplementary Table S1**. Bars represent mean ± standard deviation. An asterisk indicates significant difference at $p < 0.01$.

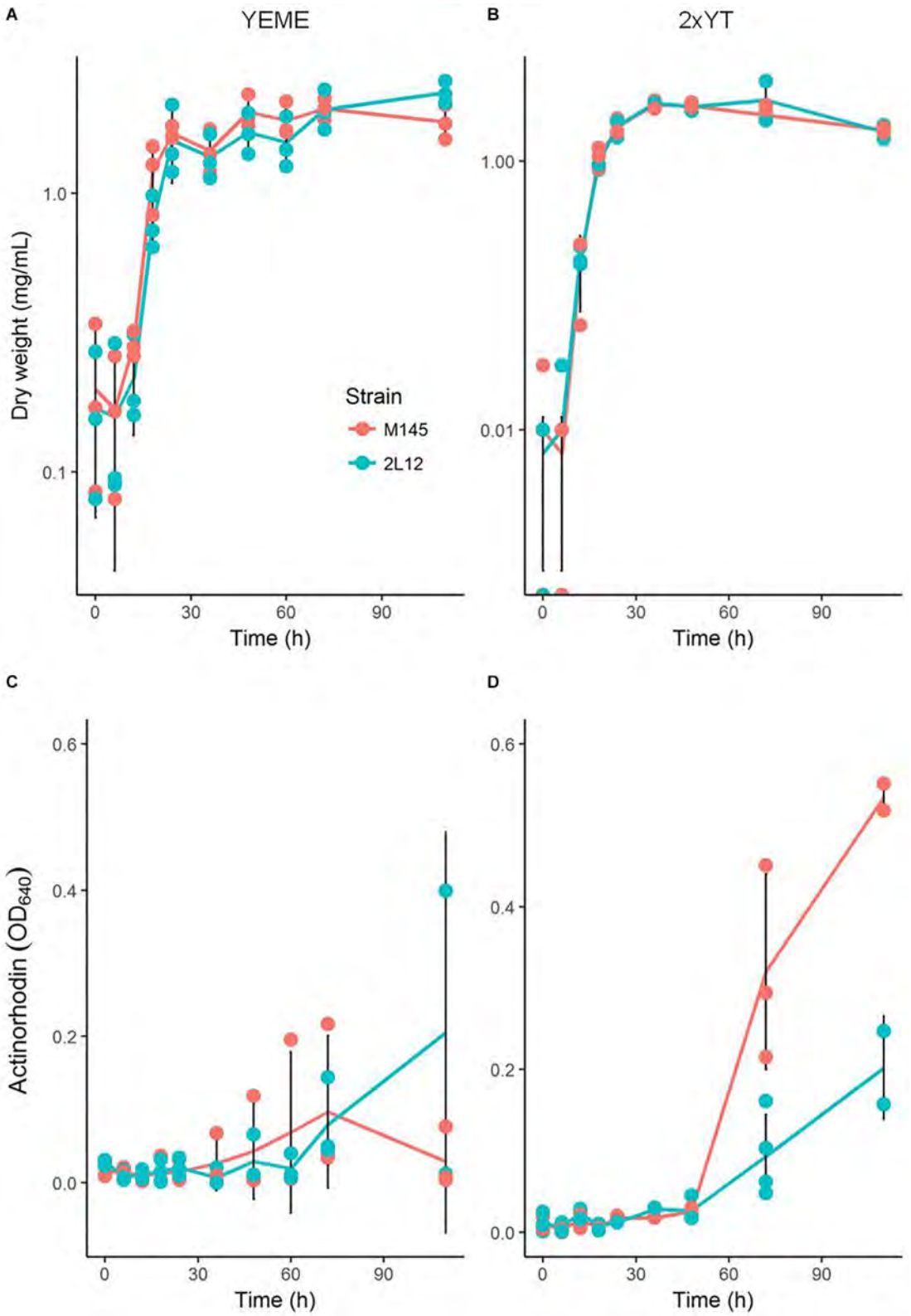

FIGURE 2 | Growth and actinorhodin production by M145 and 2L12 strains. **(A,B)** show the growth curves in YEME and 2xYT media, respectively; **(C,D)** show actinorhodin production in YEME and 2xYT media. Each dot represents a measurement from each of three independent cultures; black vertical lines represent the means ± standard deviation.

2L12 strain settled significantly slower to the bottom of the tube than the M145 wild type strain (**Figure 3**), confirming the validity of our experimental evolution strategy (i.e., slower sedimentation due to increased mycelial dispersion).

We also measured total actinorhodin production of both strains grown in liquid media. In YEME, where neither strain forms large pellets due to the increased viscosity caused by the 34% sucrose present in the medium, there was no significant difference in actinorhodin production (**Figure 2C**). On the other hand, in 2xYT, where the wild type strain forms large, dense, pellets, only M145 produced actinorhodin (**Figure 2D**). This is consistent with previous studies which showed that most antibiotic production takes place inside pellets (Manteca et al., 2008). Together, these results demonstrate that, although strain 2L12 produces less actinorhodin under this condition, this difference is due to its morphology and is not caused by a mutation specifically affecting synthesis of this antibiotic.

A Single Amino Acid Substitution Is Responsible for the Dispersed Growth Phenotype of Strain 2L12

In order to determine the genetic change responsible for the phenotype of 2L12, we sequenced the genome of this strain and also the genome of the isogenic M145 wild-type strain, grown from the same spore vial used for the evolution experiment that led to isolation of 2L12. After variant calling and filtering, a single nucleotide change, a T to C transition in nucleotide 5,754,703 of the *S. coelicolor* genome sequence (GenBank accession NC_003888) appeared as the likely mutation responsible for the differences observed between both strains (**Supplementary Table S2**). This mutation lies in the *sco5282* gene, which encodes a histidine kinase of a two-component system of unknown function. This kinase gene is translationally coupled to an upstream gene, *sco5283*, which encodes an OmpR-type response regulator. The Sco5282 kinase is predicted to be membrane-anchored by two transmembrane domains, followed by a cytosol located HAMP domain, which functions as a signal transmitter domain in many two-component sensor kinases (Parkinson, 2010). The HAMP domain is followed by the histidine kinase (HisKA) domain and a C-terminal HATPase domain (**Figure 3A**). The mutation found in 2L12 causes a substitution of an aspartate to a glycine (D125G) in the second helix of the HAMP domain of the kinase (herein referred to as *sco5282-D125G*). Analysis of the variants between genome sequences revealed two other possible mutations: one inside the *sco4820* gene and the other one in the intergenic region between *sco6571* and *sco6572*. However, these variants had much lower quality scores (179 and 160, vs. 222 of *sco5282-D125G*) and, in the case of the variant in the *sco4820* gene, not all the

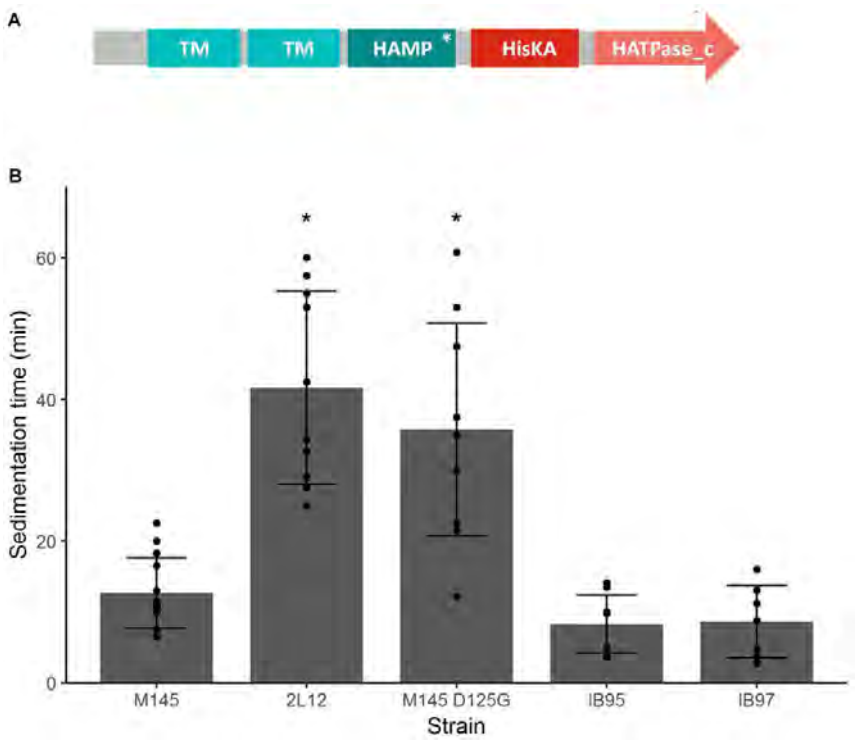

FIGURE 3 | (A) Domain structure of the Sco5282 histidine kinase. TM, transmembrane domain; HAMP, HAMP domain; HisKA, histidine kinase domain, HATPase_c; ATPase domain. An asterisk shows the position of the D125G mutation. **(B)** Sedimentation time of *sco5282* mutants. Spores were germinated in viscous medium, then grown in thin medium. Pellets were deposited on top of a 2 cm tall 10% sucrose solution, and the time it took for the first pellet to reach the bottom of the tube was measured. Each dot represents the measurement from an independent culture; bars show the mean ± standard deviation; asterisks indicate statistical significance ($p < 0.01$).

aligned reads showed the presence of this putative mutation, as opposed to *sco5282-D125G* where the mutation was present in all the aligned reads (**Supplementary Table S2**). For this reason, we focused on the mutation in the *sco5282* gene. Interestingly, when the presence of Sco5282/Sco5283 orthologs was analyzed by reciprocal BLASTP searches using the Actinoblast database (Chandra and Chater, 2014[2]) this two-component system was found to be prevalent in the *Streptomycineae*, but not in other actinomycetes suborders (**Supplementary Figure S1**).

To demonstrate that the *sco5282-D125G* allele was responsible for the phenotype of strain 2L12, we transferred it to the wild type M145 background by recombining this mutation *in vivo*, using the StCB12 cosmid (which carries the *sco5282* and *sco5283* genes) as described in Materials and Methods. This resulting strain, M145*sco5282-D125G*, was grown in liquid culture and its sedimentation time was measured. It was found that this strain had the same slow-sedimentation phenotype as the 2L12 strain, demonstrating that the mutation in the histidine kinase gene *sco5282* is sufficient to cause a dispersed, slow-sedimenting morphology (**Figure 3B**). We also constructed a mutant carrying an in-frame deletion of the *sco5282* gene, IB95, and a mutant lacking both the kinase and response regulator genes (Δ*sco5282-5283*), IB97, and tested their sedimentation time. Interestingly, a wild-type phenotype, with fast sedimentation times was obtained for both the IB95 and IB97 mutant strains (**Figure 3B**). This result suggested that the *sco5282-D125G* allele is a gain-of-function mutation. It also implies that, during normal growth this two-component system is most likely inactive, since the absence of the Sco5282 kinase resulted in wild-type growth. To confirm that the *sco5282-D125G* allele is responsible for the dispersed morphology phenotype, we cloned the mutant allele under the control of the P_{tipA} promoter in the integrative expression vector pIJ6902, and introduced it into strain IB95, to complement the Δ*sco5282* null mutation. As can be seen in **Figure 4**, expression *in trans* of the mutant allele restored the dispersed growth phenotype, even without adding thiostrepton as inducer. This indicates that the mutant *sco5282-D125G* allele is able to produce a dispersed morphology even when it is expressed at the low constitutive level observed for the P_{tipA} promoter in the absence of thiostrepton (Ali et al., 2002). When the same plasmid was introduced into strain IB97, the mutant kinase alone did not cause the slow-sedimenting phenotype (**Figure 4**), indicating that the Sco5282-D125G mutant kinase exerts its effect through the Sco5283 cognate response regulator.

The D125G Mutation Is Recessive

Since the *sco5282-D125G* allele appeared to be a gain of function mutation, we decided to determine whether it was dominant over the wild type gene. To this end, we introduced the pIJ6902 plasmid derivative carrying the mutant *sco5282-D125G* allele into the wild type M145 strain. Surprisingly, the mutant allele did not promote dispersed growth in the presence of the wild type gene (**Figure 4**) and therefore appeared to be recessive. To confirm this, we constructed merodiploid strains by inserting either the wild type StCB12 or the mutant StCB12*sco5282-D125G* cosmids into both the M145 and 2L12 strains, through homologous recombination. In this way, two copies of the two-component system, each one expressed from its own promoter, could be

[2]http://streptomyces.org.uk/actinoblast

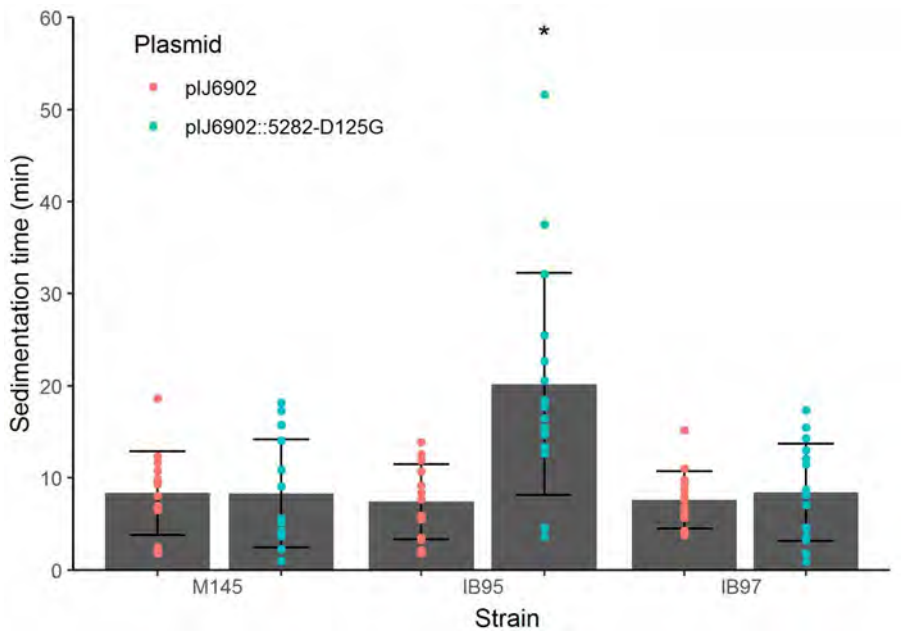

FIGURE 4 | Sedimentation times of complemented strains. Vector pIJ6902 was introduced either empty or with the cloned *sco5282-D125G* gene into the indicated strains. Each dot represents the measurement from an independent culture; bars show the mean ± standard deviation; an asterisk indicates statistical significance ($p < 0.01$).

tested in the proper homozygous or heterozygous combinations. Measuring the sedimentation time of these strains revealed that insertion of a wild-type cosmid in strain 2L12 resulted in a wild-type phenotype, whereas insertion of the D125G cosmid did not result in a dispersed-growth phenotype in M145 (**Figure 5**). Both wild-type and mutant cosmids were also introduced into strain IB97, resulting in wild-type and mutant phenotypes, respectively (**Figure 5**). Taken together these results confirm that the *sco5282-D125G* mutation is recessive and also rule out the possibility that doubling the gene dose of the neighbor genes which are present in the cosmid might affect the growth phenotype.

The D125G Substitution in the HAMP Domain Results in Activation of the Sco5282 Kinase

As mentioned above, the D^{125} to G mutation in Sco5282 appears to result in enhanced phosphorylation of the Sco5282/Sco5283 two-component system. To test this, His_6-tagged versions of the Sco5283 protein and also of the cytosolic portions of the wild-type and mutant Sco5282 proteins were overexpressed in *E. coli*, purified by Ni-NTA-agarose affinity chromatography and used in *in vitro* autophosphorylation and transphosphorylation assays with [γ-^{32}P]ATP (**Figure 6**). Although both the wild type and the mutant kinase proteins had similar kinetics regarding their autophosphorylation, the mutant Sco5282-D125G kinase exhibited a significantly higher transphosphorylation rate of the Sco5283 response regulator as compared to the wild type Sco5282 kinase protein. Net phosphorylation of Sco5282-D125G was also higher in the presence of Sco5283 as compared to Sco5282. Thus the D125G substitution in the Sco5282 kinase appears to be an activating mutation.

Transcriptomic Differences Between Dispersed and Pelleting Strains

Since strain 2L12 is carrying an activating mutation in the Sco5282/Sco5283 two-component system, it is reasonable to argue that its dispersed growth is caused by the activation of genes that are normally not expressed or that have a low expression level. To investigate which genes were affected, we decided to analyze the transcriptomes of a strain with wild-type morphology and one with dispersed morphology. In order to maximize the differences in expression of target genes of the two-component system, we chose the strain M145*sco5282-D125G* as the strain exhibiting dispersed slow-sedimenting growth, and IB97 (i.e., the null Δ*sco5282-5283* mutant) as the tightly pelleting fast-sedimenting strain. Total RNA was extracted from three independent cultures of each strain at mid-log phase grown in 2xYT, the medium where morphological differences are maximal. After rRNA subtraction the samples were sequenced and gene abundances were compared using three statistical packages: DESeq2 (Love et al., 2014), edgeR (Robinson et al., 2010) and NOISeq (Tarazona et al., 2011). Comparisons were made between M145*sco5282-D125G* and IB97, so that positive $\log_2$ Fold Change represents genes that were either highly overexpressed in the dispersed strain, or repressed in the pelleting strain. 437 genes were found to be differentially expressed, and 354 of them were identified by all three statistical tests. Genes

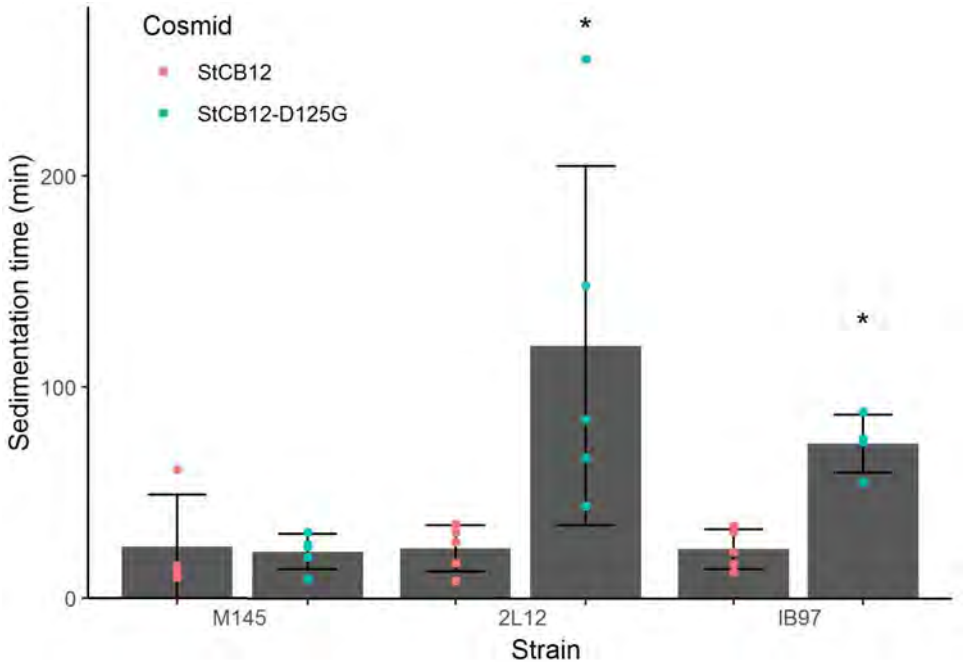

FIGURE 5 | Sedimentation times of merodiploid strains. Merodiploid strains were constructed by insertion of the StCB12 cosmid harboring either a wild-type or mutant version of *sco5282-sco5283* as indicated. Each dot represents the measurement from an independent culture; bars show the mean ± standard deviation; asterisks indicate statistical significance ($p < 0.05$).

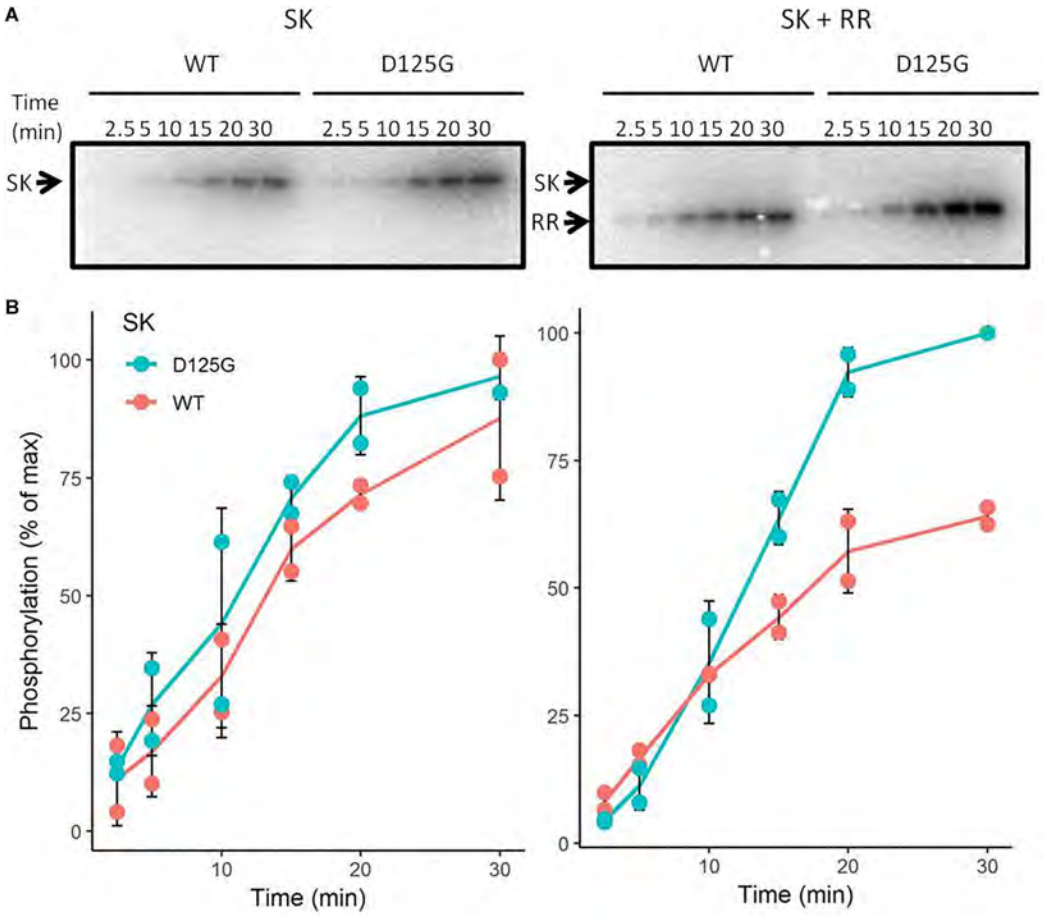

FIGURE 6 | *In vitro* phosphorylation assays. Wild-type and mutant Sco5282 kinases were overexpressed in *E. coli*, purified and incubated with [γ-32P]ATP. **(A)** shows a time course of autophosphorylation in the absence of the Sco5283 response regulator and **(B)** shows a time course of transphosphorylation in its presence. Each dot represents an individual phosphorylation assay. The positions of the cytosolic portion of the Sco5282 histidine kinase and Sco5283 response regulator are indicated by SK and RR, respectively.

identified by at least two tests were annotated with the program eggNOG-mapper (Huerta-Cepas et al., 2017) to assign functional categories (**Figure 7**). Differential expression of relevant genes mentioned in the sections below and shown in **Tables 2–4**, was validated by qPCR as described in "Materials and Methods," and shown in **Table 5**. A table showing the differentially expressed genes identified by all three statistical packages is provided as **Supplementary Table S4**.

Genes Involved in Envelope Maintenance

Among the most overexpressed genes in the dispersed M145*sco5282-D125G* strain were many involved in protein secretion and envelope maintenance (**Table 2**). The single most overexpressed gene was *sco0753* which encodes a 77 amino acid peptide of unknown function. This gene is located upstream of an operon for a secretion system (*sco0754-sco0756*), homologous to a type I secretion system and similar to bacteriocin secretion systems (Håvarstein et al., 1995). The Sco0753 peptide has been predicted as a probable bacteriocin-like ribosomal lanthipeptide (van Keulen and Dyson, 2014). It is predicted to be very hydrophobic (57% of hydrophobic amino acids) reminiscent of the hydrophobic proteins that coat the hyphae during differentiation helping them to break free from the aqueous medium (Flärdh and Buttner, 2009). The fact that these four genes are conserved in many *Streptomyces* species, with the same genomic organization, suggests that this hydrophobic peptide is exported by the above mentioned secretion system.

Another gene with upregulated expression in the dispersed strain was *mbl2* (*sco6166*), which encodes one of the three MreB homologs present in *S. coelicolor*. Previous studies have shown that *mbl2* was expressed only in vegetative mycelium and repressed during differentiation (Heichlinger et al., 2011), in contrast to the other two paralogs, MreB and Mbl1, which were found to regulate cell wall deposition during sporogenic cell division, with a similar role to the one played by homologous proteins in unicellular bacteria.

The Sec system component SecDF (*sco6160*) was also greatly overexpressed in the dispersed strain. This protein consists of domains paralogous to SecD and SecF, but fused into a single

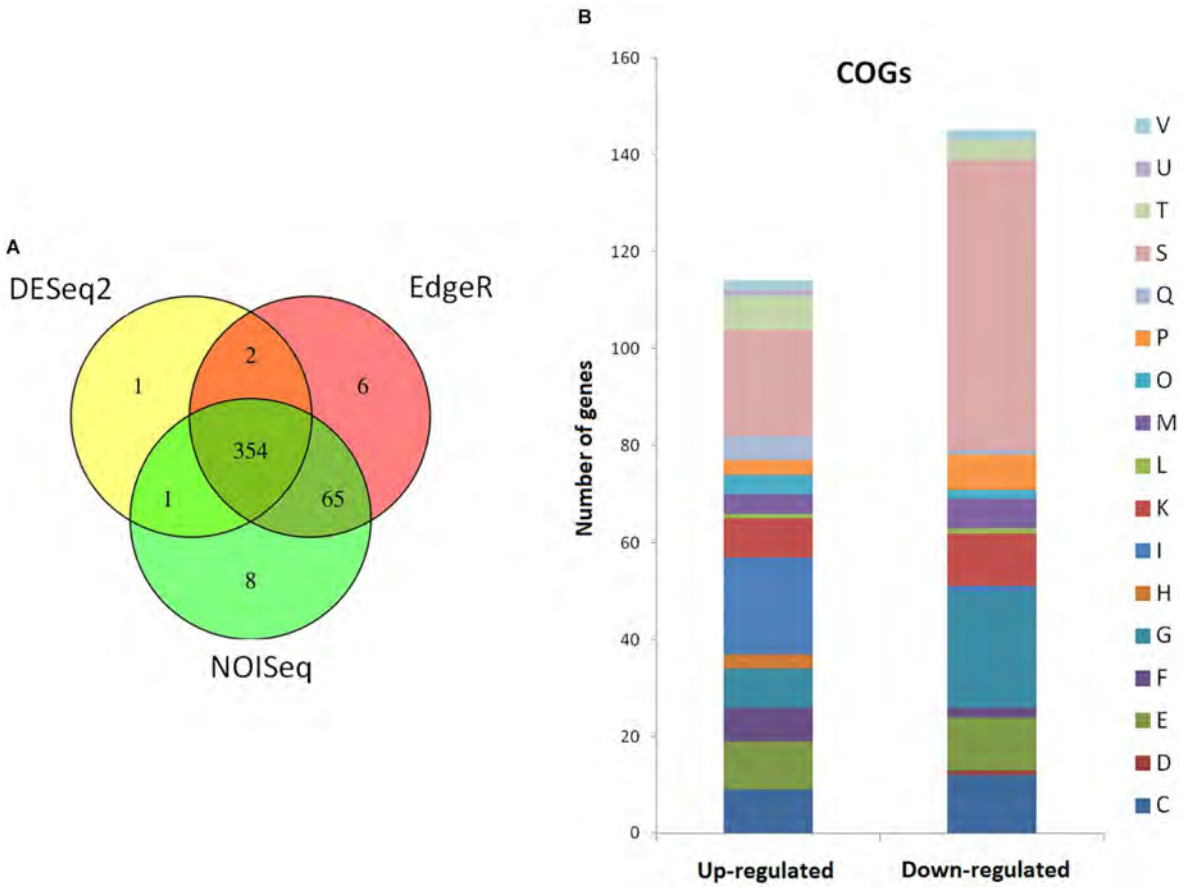

FIGURE 7 | Summary of the differentially expressed genes. **(A)** Venn diagram showing the number of differentially expressed genes as analyzed by the statistical analysis packages DESeq2, EdgeR, and NOISeq. **(B)** Cluster of orthologous groups (COG) annotation of RNAseq-identified differentially expressed genes. C, energy production and conversion; D, cell cycle control and mitosis; E, amino acid metabolism and transport; F, nucleotide metabolism and transport; G, carbohydrate metabolism and transport; H, coenzyme metabolism; I, lipid metabolism; K, transcription; L, replication and repair; M, cell wall/membrane/envelop biogenesis; O, post-translational modification, protein turnover, chaperone functions; P, inorganic ion transport and metabolism; Q, secondary structure; T, signal transduction; U, intracellular trafficking and secretion; V, defense mechanisms; S, function unknown.

polypeptide, which is normally expressed at very low levels (Zhou et al., 2014). It appears to be part of an operon which includes a two-component system, since all these genes had similar expression levels. SecDF promotes the release of secreting polypeptides, providing the proton motive force and enhancing protein secretion (Tsukazaki et al., 2011). This suggests that the dispersed strain is dealing with protein secretion stress, although it is not yet possible to tell whether this is a cause or a consequence of the mutant morphology.

On the other hand, exopolysaccharide synthesis proteins were repressed in the dispersed-growing strain. Of special interest is the gene encoding the MatB protein (*sco2962*), whose absence is known to lead to mycelial dispersion (van Dissel et al., 2015). However, the upstream gene, *matA*, was not differentially expressed. Further analysis is required to determine whether these genes are transcribed as a single unit, and in that case, the mechanism by which the system Sco5282-Sco5283 could be affecting such differential regulation. Even though *cslA* and *glxA* were not part of the set of genes identified by all three statistical analysis packages as differently expressed, their expression levels were lower in the dispersed mutant, and in the case of *cslA* this reduced expression was found to be statistically significant by two of the packages (see **Supplementary Table S3**).

Primary Metabolism Genes

A majority of the genes identified as differentially expressed were annotated in the primary metabolism category. This was not surprising, since pellet formation is known to exert stress on the cells and limit the amount of oxygen and nutrients available to hyphae. Therefore, cell metabolism must adapt to the different conditions imposed by the morphology.

The main metabolic routes affected were those for branched-chain amino acids and purine degradation, which were stimulated in the dispersed strain, along with the regulatory enzymes of gluconeogenesis (**Table 3**). Glycolysis, on the contrary, was repressed in this strain. Together, these findings suggest that strain M145 *sco5282-D125G* is taking up carbon from amino acids and purines, the main components of 2xYT

TABLE 2 | Differentially expressed genes involved in cell envelope maintenance.

Gene	Function	Log_2 fold change	COG[1]	FDR-controlled *p*-value		
				EdgeR	DESeq2	NOISeq
SCO0753	Natural ribosomal product; predicted secretion signal peptide	6.3		1.5E-91	4.1E-15	1.0E-13
SCO0754	Secreted protein; homolog of type I secretion system protein HlyD	4.4	M	7.6E-51	1.5E-47	2.1E-14
SCO0755	ABC transporter component	4.25	V	2.6E-49	3.6E-60	2.9E-15
SCO0756	ABC transporter component	4.25	V	1.8E-50	1.1E-58	5.6E-16
SCO0757	Exopolyphosphatase; involved in phosphate metabolism	1.58	F, P	2.7E-08	7.8E-09	6.2E-06
SCO6160	*secDF*; alternative secretion system protein	2.89	U	1.4E-26	3.8E-02	0.0E+00
SCO6161	Secreted protein	1.51	–	1.4E-07	4.0E-06	2.8E-03
SCO6162	Response regulator	2.21	T	1.8E-16	5.3E-02	0.0E+00
SCO6163	Histidine kinase	2.13	T	1.7E-15	1.2E-01	0.0E+00
SCO1741	Secreted serine protease	4.10	O	5.3E-41	1.3E-36	1.1E-16
SCO0381	Polyprenyl glycosyl transferase; involved in exopolysaccharide syntesis	−1.86	M	3.3E-10	2.8E-01	1.5E-02
SCO0382	UDP-glucose/GDP-mannose dehydrogenase (*algD*); catalyzes the reaction GDP-mannose + NAD+ → GDP-mannuronate + NADH	−1.37	M	7.1E-06	3.7E-01	2.0E-02
SCO0836	Mechanosensitive ion channel	−1.31	M	1.2E-05	5.0E-09	1.6E-03
SCO2589	CDP-glycerol poly(glycerophosphate) glycerophosphotransferase; involved in teichoic acid biosynthesis	2.24	M	5.1E-17	7.6E-39	0.0E+00
SCO2590	CDP-glycerol poly(glycerophosphate) glycerophosphotransferase; involved in teichoic acid synthesis	2.37	M	7.6E-19	5.5E-41	3.3E-15
SCO2591	N-acetylmuramoyl-L-alanine amidase	−3.77	M	2.3E-41	3.0E-125	5.3E-14
SCO2962	Transferase (*matB*); involved in exopolysaccharide synthesis	−1.73	M	3.0E-10	2.0E-23	1.1E-16
SCO6131	*D-alanyl-D-alanine carboxypeptidase*; penicillin-binding protein family 4	2.93	M	2.9E-27	5.9E-47	0.0E+00
SCO6164	*dksA*-like zinc-finger protein	2.53	K	5.7E-21	3.0E-01	0.0E+00
SCO6165	*dksA*-like protein	2.71	K	1.5E-23	1.7E-01	0.0E+00
SCO6166	*mreB/mbl2*; cell wall synthesis regulator	2.77	S	1.3E-24	9.1E-02	5.8E-04
SCO6167	Proline rich protein	1.48	S	5.6E-08	8.8E-05	5.6E-16

[1] *The cluster of orhologous groups (COG) categories in this table are: F, nucleotide metabolism and transport; K, transcription; M, cell wall/membrane/envelope biogenesis; O, post-translational modification, protein turnover, chaperone functions; P, inorganic ion transport and metabolism; T, signal transduction; U, intracellular trafficking and secretion; V, defense mechanisms; S, function unknown.*

medium, while the pelleting IB97 strain is using carbohydrates. Most likely this is a consequence of the lysis occurring inside the pellets, which releases murein for the growing hyphae to feed on.

It is noteworthy that the genes for glyceraldehyde-3-phosphate dehydrogenase, for which *S. coelicolor* has three copies, were all differentially expressed. Two of them, including the most important *gap* gene during vegetative growth (*sco1947*, Li and Townsend, 2006) were repressed in the dispersed strain, while *sco7040* was overexpressed. This suggests specialized functions for the enzyme encoded by each gene, that may be related to their role in glycolysis and gluconeogenesis.

Other genes, strongly repressed in the dispersed strain, are those of the pentose-phosphate pathway.

Regulatory Genes

The genes for 24 transcriptional regulators were found to be differentially expressed. Of those with known function, regulators of stress responses that indirectly promote differentiation and sporulation stand out. For example, SigB (*sco0600*) is an osmotic stress response sigma factor (Cho et al., 2001), which promotes differentiation by activating SigM (*sco7314*, Lee et al., 2005) and its own anti-anti-sigma factor RsbV (*sco4005*, Lee et al., 2004). Although SigK is a negative regulator of sporulation, its transcript is accumulated at the onset of the differentiation process (Mao et al., 2009). RamR is an orphan response regulator which also promotes sporulation indirectly (Keijser et al., 2002). All of these stress-response sporulation-promoting genes are overexpressed in the pelleting IB97 strain (**Table 4**), in agreement with previous knowledge that tight clumping induces stress in the mycelium.

No direct regulators of sporulation were identified, with the exception of WhiD, a regulator required for sporulation that normally is not expressed in liquid media, where no sporulation takes place (Molle et al., 2000). Nevertheless, this regulator was overexpressed in the dispersed mutant (**Table 4**), opposite to the trend of the indirect sporulation regulators. It has to be mentioned that little is known about

TABLE 3 | Differentially expressed genes for primary metabolism.

Gen	Function	Log_2 fold change	Metabolic pathway	COG[1]	FDR-controlled *p*-value		
					EdgeR	DESeq2	NOISeq
SCO4979	Phosphoenolpyruvate carboxykinase	2.37	Gluconeogenesis	C	7.45E-19	3.81E-03	0.00E+00
SCO7040	Glyceraldehyde-3-phosphate dehydrogenase	1.48	Glycolysis/Gluconeogenesis	G	5.98E-08	1.18E-01	3.03E-05
SCO5047	Fructose-1,6-bisphosphatase	1.45	Gluconeogenesis	G	1.11E-07	3.97E-04	1.67E-15
SCO7638	Enolase	−1.22	Glycolysis/Gluconeogenesis	G	5.90E-05	2.76E-03	5.66E-03
SCO5423	Pyruvate kinase	−1.38	Glycolysis	G	7.14E-07	1.21E-04	2.89E-15
SCO1947	Glyceraldehyde-3-phosphate dehydrogenase	−1.67	Glycolysis/Gluconeogenesis	G	9.66E-10	8.63E-07	1.44E-15
SCO7511	Glyceraldehyde-3-phosphate dehydrogenase	−5.22	Glycolysis/Gluconeogenesis	G	2.49E-69	1.56E-09	1.01E-14
SCO6659	Phosphohexose isomerase	−4.00	Glycolysis/Gluconeogenesis	G	1.45E-45	1.41E-03	1.44E-15
SCO2774	Acyl-CoA dehydrogenase	1.56	Amino acid degradation	I	8.90E-09	1.41E-04	4.44E-16
SCO2776	Carboxylase	2.11	Amino acid degradation	I	3.14E-15	1.33E-01	3.77E-15
SCO2777	Carboxylase	2.12	Amino acid degradation	I	1.85E-15	1.16E-01	0.00E+00
SCO2778	Hydroxymethylglutaryl-CoA lyase	1.96	Amino acid degradation	I	2.54E-13	2.75E-01	1.06E-03
SCO2779	Acyl-CoA dehydrogenase	2.08	Amino acid degradation	I	6.17E-15	1.50E-01	0.00E+00
SCO4800	Isobutiryl-CoA mutase	1.16	Amino acid degradation	I	4.36E-05	2.09E-04	2.03E-03
SCO5398	Methylmalonyl-CoA epimerase	1.38	Amino acid degradation	I	5.03E-07	1.03E-05	0.00E+00
SCO5399	Acetyl-CoA acetyltransferase	1.63	Amino acid degradation	I	1.63E-09	1.41E-09	0.00E+00
SCO5415	Methylmalonyl-CoA mutasa	1.47	Amino acid degradation	I	7.03E-08	2.39E-01	0.00E+00
SCO6701	Acetyl-CoA acetyltransferase	1.44	Amino acid degradation	I	7.60E-07	4.84E-04	4.18E-03
SCO6702	Acetyl-CoA acetyltransferase subunit B	1.81	Amino acid degradation	I	3.26E-10	4.79E-02	8.24E-03
SCO4972	Xanthine dehydrogenase	2.65	Purine degradation	F	7.57E-23	1.38E-02	2.22E-15
SCO6209	OHCU decarboxylase	3.11	Purine degradation	F	8.62E-27	9.16E-19	5.50E-09
SCO6247	Dihydroorotase	2.92	Purine degradation	F	2.17E-26	7.02E-20	0.00E+00
SCO6248	Allantoate amidinohydrolase	2.43	Purine degradation	F	4.30E-19	2.53E-13	1.51E-11
SCO1679	Gluconokinase	−2.54	Pentose phosphate	G	5.38E-20	4.82E-02	6.66E-16
SCO6497	Transketolase	−1.99	Pentose phosphate	G	1.32E-12	3.37E-16	0.00E+00
SCO6658	6-phosphogluconate dehydrogenase	−3.92	Pentose phosphate	G	2.50E-44	1.07E-03	3.33E-16
SCO6661	glucose-6-phosphate 1-dehydrogenase	−4.84	Pentose phosphate	G	9.78E-62	1.86E-04	0.00E+00
SCO6662	Transaldolase	−5.33	Pentose phosphate	G	2.54E-71	1.10E-04	0.00E+00
SCO6663	Transketolase	−6.12	Pentose phosphate	G	1.51E-87	3.66E-05	4.33E-15
SCO1224	Ribose-5-phosphate isomerase	1.55	Pentose phosphate	G	1.33E-08	1.09E-06	0.00E+00

[1] *The cluster of orhologous groups (COG) categories in this table are: C, energy production and conversion; G, carbohydrate transport and metabolism; I, lipid transport and metabolism; F, nucleotide metabolism and transport.*

the role of WhiD, other than the fact that it possesses a [4Fe-4S] nucleus capable of binding oxygen and nitric oxide (Jakimowicz et al., 2005; Crack et al., 2009).

Recently, it has been revealed that cytosolic copper is a major modulator of germination and development in *S. coelicolor*, and that its levels depend on the copper export system, encoded by the *sco2730* and *sco2731* genes. As is shown in **Supplementary Table S3**, no significant differences in the expression of these genes was observed in the dispersed mutant.

No regulators of antibiotic biosynthesis were differentially expressed, which is probably due to the fact that the RNA samples were taken at mid-log phase, when there is no antibiotic biosynthesis.

Gas Vesicles

Among the most differentially expressed genes was one of the two clusters of gas vesicle genes in the *S. coelicolor* genome (genes *sco6499-sco6508*). Despite being widespread among actinobacteria, there are no reports of functional gas vesicles in these organisms (van Keulen et al., 2005). Transcriptional activation of this cluster has been seen in mutants of the arginine-synthesis regulator gene *argR* (Botas et al., 2018), of the nitrogen sensor *glnK* (Waldvogel et al., 2011), in response to saline stress, in a SigB dependent manner (Lee et al., 2005) and in the presence of antibiotics that target cell wall biosynthesis (Hesketh et al., 2011). These genes were greatly overexpressed in strain IB97, suggesting that their expression might be related to the general stress response shown by this strain.

DISCUSSION

In this study, we set up an experimental approach to focus on the factors governing mycelial aggregation in liquid culture. By working with liquid *S. coelicolor* cultures, it is possible to restrict the phenomenon to the non-sporulating vegetative mycelium. By applying a very general selective pressure, as is sedimentation speed, it was possible to isolate many

TABLE 4 | Differentially expressed genes for transcriptional regulators.

Gene	Function	Log_2 fold change	COG[1]	FDR-controlled *p*-value		
				EdgeR	DESeq2	NOISeq
SCO6164	*dksA*-like zinc-finger protein	2.53	K	5.72E-21	3.03E-01	0.00E+00
SCO6165	*dksA*-like protein	2.71	K	1.50E-23	1.67E-01	0.00E+00
SCO6166	*mreB/mbl2*; cell wall synthesis regulator	2.77	S	1.34E-24	9.08E-02	5.81E-04
SCO6167	Proline-rich protein	1.48	S	5.63E-08	8.79E-05	5.55E-16
SCO1897	DeoR-type regulator	2.15	K	3.20E-15	1.14E-06	2.21E-05
SCO0864	ECF sigma factor	1.69	K	1.27E-08	5.50E-05	7.98E-03
SCO4767	WhiD; sporulation regulator	1.45	K	7.60E-07	1.45E-04	7.85E-03
SCO6685	RamR; sporulation regulator	−1.48	T	7.25E-05	2.15E-02	1.33E-02
SCO3198	DeoR-type regulator	−1.59	K	1.13E-08	2.03E-01	9.10E-03
SCO6520	SigK; differentiation sigma factor	−1.65	K	4.32E-09	8.41E-07	4.09E-03
SCO0600	SigB; stress sigma factor	−1.70	K	4.36E-10	3.06E-23	3.22E-15
SCO7325	RsbV; SigB anti-anti-sigma factor	−1.28	T	7.68E-06	2.38E-03	4.55E-03
SCO4005	ECF sigma factor	−1.81	K	3.10E-11	4.31E-17	0.00E+00
SCO1658	GylR; glycerol responsive regulator	−2.05	K	2.88E-14	1.36E-07	1.78E-15
SCO2845	GntR-type regulator	−2.62	K	1.17E-16	2.93E-02	5.13E-03
SCO7314	SigM; differentiation sigma factor	−2.75	K	2.56E-22	7.35E-18	0.00E+00
SCO2846	ROK-type regulator	−3.49	K	3.83E-36	1.03E-02	4.44E-16

[1] *The cluster of orhologous groups (COG) categories in this table are: K, transcription; T, signal transduction; S, function unknown.*

different slow-sedimenting strains with dispersed morphology. Even though none of them reached a level of dispersion or fragmentation like the one seen in *S. venezuelae*, the fact that several different mutational events could be found, even in such a relatively short time (12 transfers), indicates that submerged culture morphology is a multifactorial trait that can be affected through many different ways. Initial concerns that too many mutations could arise in such experiments, complicating further analysis, were dissipated upon discovery that few generations were needed to obtain a visibly distinct phenotype, given that many different independent cultures were set up since the beginning. Strain 2L12 appeared on the 12th transfer, the fastest of all cultures used in this study, and it is most likely because of this that it differed from the wild type strain by a single point mutation.

It was important to identify mutations that did not have pleiotropic effects that could be causing fragmentation as a secondary effect to other major metabolic changes or that showed altered viability or differentiation. In this regard, we chose to work with strain 2L12 because it did not have any differentiation or sporulation problems. Even more so, growth kinetics showed that it was indistinguishable from wild-type M145, proving that it had no major defects in primary metabolism. It was surprising to find that in medium without sucrose, where morphological differences are the most pronounced between the two strains, growth proceeded at exactly the same rate, since pelleted forms are known to show reduced growth (Walisko et al., 2015). Nevertheless, it has been reported previously that those differences are especially seen in bioreactors, and not in cultures grown in shake flasks (van Dissel et al., 2015).

Metabolic adaptations were expected to take place in order to compensate for the different morphologies. Indeed, a third of the functional categories assigned to the differentially expressed genes belong to primary metabolism (**Figure 7**). Thus, the two different strains were on two different metabolic states despite growing at the same rate: the slow-sedimenting dispersed strain was using the carbon source in the medium through gluconeogenesis, whereas the fast-sedimenting tight-pelleting strain was using carbohydrates. This difference is probably due to the increased lysis that the pelleting strain is going through, since it has a larger proportion of hyphae inside the pellets, which is where lysis takes place (Manteca et al., 2008). Nonetheless, the pellets continue to grow (Manteca et al., 2008), which is the reason that they reach the same final biomass (**Figure 2A**).

TABLE 5 | qRT-PCR validation of selected differentially expressed genes.

Gene name	log_2 fold change (M145-D125G vs. IB97)[1]
SCO0753	8.10 ± 2.62*
SCO0754	5.79 ± 1.60*
SCO6166 (mbl)	5.27 ± 3.14*
SCO7511 (gap3)	−2.89 ± 1.81*
SCO7040 (gap2)	3.59 ± 2.58*
SCO4979 (pckA)	4.35 ± 2.99*
SCO4767 (whiD)	0.65 ± 2.73
SCO2962 (matB)	−0.86 ± 1.40
SCO0600 (sigB)	1.97 ± 3.76
SCO6160 (secDF)	3.68 ± 2.17*

[1] *Values represent the average of four biological replicates ± 95% confidence interval. An asterisk indicates statistical significance. Correlation between RNAseq and qRT-PCR resulted in* $R^2 = 0.9129$.

An Activating Mutation in the HAMP Domain

Genome sequencing revealed that strain 2L12 had a single point mutation that caused a substitution of an aspartate residue for a glycine in the HAMP domain of a histidine kinase of a two-component system of unknown function. Transferring the mutant allele to a wild-type background demonstrated that this mutation was sufficient to confer the dispersed slow-sedimenting phenotype. Further genetic analysis showed that this is not a loss-of-function mutation, that it does not change the specificity of the kinase for its cognate response regulator, and that it is a recessive allele. These are interesting findings for a HAMP domain mutation. The HAMP domain is composed of two helices, AS1 and AS2 that form a 4 helix-bundle when the kinase dimerizes. A phase-stutter at the contact of the helices allows them to rotate upon detection of the signal (Parkinson, 2010). Aspartate 125 is located in the membrane-distal part of the AS2 helix, opposite to the contact side of the helices, suggesting that it is probably not directly involved in the conformational changes of signal transmission.

Nevertheless, a substitution for a glycine is likely to interrupt the helical structure. Previously, destabilizing mutations in the membrane-distal half of the AS1 helix were identified as activating mutations of the PhoQ kinase (Matamouros et al., 2015). A model was proposed in which interactions between the HAMP and catalytic domains repress kinase activity. Extracellular signaling would disrupt these interactions, leading to kinase activation (Matamouros et al., 2015). Therefore, destabilizing mutations in the HAMP domain could lead to increased kinase activity. In this work, a similar mutation was found in the AS2 helix, with the same activating effect. Even though *in vitro* autophosphorylation was almost identical between the wild-type Sco5282 and Sco5282-D125G kinases, transphosphorylation of the response regulator by Sco5282-D125G was greatly increased, with a maximal phosphorylation level of the target almost twice that of the wild type. A possibility could be that the equilibrium between phosphorylation and dephosphorylation in the mutant kinase is displaced toward phosphorylation, resulting in increased activation *in vivo*.

This model could also explain why the activating D125G mutation is recessive. The HAMP domain is where the kinase dimerizes. In a heterozygous cell, both wild-type and mutant monomers are produced, which entails formation of heterodimers. These molecules would have one destabilized HAMP domain and one functional, which may still interact with the catalytic domain and repress it. Thus, heterodimers would display wild-type transphosphorylation activity, and consequently a wild-type phenotype.

Transcriptional Changes Related to the Dispersed Morphology

Streptomyces morphology is a complex trait. Even though all species have a common life cycle in the soil, growing as a multicellular vegetative mycelium, their growth in the laboratory reveals widely different morphologies. *S. venezuelae* and *S. coelicolor* can form similar vegetative mycelia on solid medium, and yet they represent opposite sides of the morphology spectrum in liquid media: the first grows as fragmented, separate hyphae, while mycelium of the latter becomes inextricably matted in giant nets (van Dissel et al., 2014), which results in formation of large, dense pellets. Many parallels have been drawn between pelleted growth and biofilm formation: like a biofilm, a pellet's matrix is composed of different polymers, at least extracellular DNA and polysaccharides (Xu et al., 2008). Polysaccharides are produced in germinating hyphal tips, to allow adhesion to the substrate and to each other (Zacchetti et al., 2016). Most surprisingly, when faced with nutrient scarcity, pellets disassemble, like a starving biofilm (Zacchetti et al., 2018).

Perhaps because most morphological studies of this genus have focused on sporulation, the part of the life cycle that occurs outside of the substrate, little is known about the importance of hyphal aggregation and biofilm-like mycelial growth. Some components of this extracellular matrix, however, are already known to be important in the *Streptomyces* life cycle: the polysaccharide synthesized by CslA is necessary to guide the hydrophobic chaplin layer that allows aerial hyphae to erect out of the water (de Jong et al., 2009). The other polysaccharide known to be a part of the *Streptomyces* extracellular matrix, synthesized by MatAB, seems to be non-essential for surface growth (van Dissel et al., 2015). Of course, nothing is known about the timing and regulation of these events.

The phenotype of strain 2L12 could be explained by the reduced expression observed in the *matB* gene, whose deletion is known to be sufficient to obtain dispersed growth. This is an important finding, since the Sco5282/Sco5283 two-component system would be the first identified regulator which affects expression of these exopolysaccharide synthases. Since *clsA* and *glxA* expression is also reduced, it is likely that reduced aggregation caused by lower expression of these genes also contributes to the phenotype. Even, though there is reduced expression of *matB,* the expression of the upstream *matA* gene is not altered, suggesting that changes in *matB* expression are most likely not caused by direct regulation by Sco5283. Therefore it appears it is more probable that reduced expression of *matB* is an indirect effect, probably exerted by one of the 24 transcriptional regulators identified as differentially expressed (**Figure 7**), 16 of which have no known targets. Further indication that *matAB* is not part of the direct regulon of Sco5282/Sco5283 is its narrow distribution among *Streptomyces* species: whereas *matAB* is lacking in some species like *S. venezuelae*, *sco5282-sco5283* has orthologs in all *Streptomyces* genomes present in StrepDB (Chandra and Chater, 2014).

Other genes identified as differentially expressed are more likely to be direct targets of the Sco5282-Sc05283 system. The lantibiotic-like peptide Sco0753 was the single most overexpressed gene in the strain carrying the activating Sco5282-D125G allele, with over 60-fold overexpression. Together with its putative secretion system encoded downstream, these genes were almost completely silent in the null mutant. *S. coelicolor* is known to produce another lantibiotic-like peptide

with morphogenic properties, SapB, which is a surfactant peptide required for aerial mycelium erection in some conditions (Willey et al., 2006). It is possible that the Sco0753 peptide could induce changes in the surface of hyphae, although it is unlikely to function exactly as SapB, since it has no cysteins, which lantibiotics require to be processed (Sahl and Bierbaum, 1998).

Another morphogenic protein identified as differentially expressed was the MreB paralog Mbl2. Of the three paralogs encoded in the *S. coelicolor* genome, Mbl2 seems to be expressed exclusively in the vegetative mycelium and its deletion does not affect sporulation in solid medium (Heichlinger et al., 2011). Given the role of MreB coordinating synthesis of the cell wall, it is an obvious candidate to contribute to the alterations observed in strain 2L12.

Other genes differentially expressed suggest an activated protein secretion stress response. SecDF, which is normally not expressed, was activated in the presence of the constitutive kinase. It is interesting that a previous study considered the two-component system Sco5282-Sco5283 as a candidate homolog of *Bacillus subtilis* CssRS, which responds to the Sec secretion pathway stress. It was dismissed because its transcript levels remained unchanged after induction of protein secretion stress (Gullón et al., 2012), although that does not disprove the possibility that it may act as a sensor in this route. Sco5282 has only four amino acids in its extracellular loop, leaving the transmembrane helices as the only regions that could act as a sensor domain, for example to detect stalled Sec complexes. Curiously, among the overexpressed genes in our RNA-seq experiment, there was a serine protease, Sco1741, like the HtrA-like proteases of the CssRS response (Gullón et al., 2012). Protein secretion rate is bound to affect cell envelope structure, since it controls the rate at which remodeling enzymes can be translocated. Thus, strain 2L12 could have a weaker extracellular matrix due to improved secretion of polysaccharide-degrading enzymes.

Further research will be needed to discern the role of these proteins in vegetative mycelium morphology.

In general, our study provides insight into the molecular adaptations to morphological constraints. Most transcriptomic studies are performed in viscous media, where *Streptomyces* forms few or small pellets. In our experiment, RNA samples were specifically taken from 2xYT, a medium that promotes pellet formation, so that the main difference between strains was the pellet size. It is interesting that our results provide further confirmation that pelleted growth induces stress in the cells, as seen by the activation of many stress sigma factors in the null mutant. Surprisingly, gas vesicle genes were also activated in this condition. This cluster had been seen to be activated upon saline stress, in a SigB-dependent manner. SigB is also activated during pelleted growth, suggesting that it may also be regulating gas vesicle genes in this condition, which is unrelated to saline stress. A simple explanation could be that inner hyphae are lacking oxygen, and gas vesicles are formed in an attempt to find shallow waters with greater oxygen pressure. Another explanation is that gas vesicle proteins have a different role in a more generalized stress response, as has been previously suggested (Lee et al., 2005; Hesketh et al., 2011; Botas et al., 2018), in a process thus far unknown.

Even though this study has been carried out only with *S. coelicolor*, the prevalence of orthologs of the Sco5282/Sco5283 two-component system among different members of the *Streptomycineae* raises the possibility that genetic manipulation to activate this system could be used to modify morphology of *Streptomyces* species that grow in a pelleted form. It will also be interesting to explore whether the altered morphology can be used as a tool to increase extracellular enzyme production.

DATA AVAILABILITY

The datasets generated for this study are available in the NCBI Sequence Read Archive accession number PRJNA499125.

AUTHOR CONTRIBUTIONS

EA-P, DG, GS-C, and LS-G designed the experiments. EA-P, GG-C, DG, and LS-G performed the experiments. EA-P carried out the statistical analysis. EA-P and LS-G wrote the first draft of the manuscript. All authors contributed to the manuscript revision, and read and approved the submitted version.

FUNDING

This work was supported in part by the grant 220020 from the CB2013 fund of the Consejo Nacional de Ciencia y Tecnología (México), and received additional funding from the Programa Institucional La Producción de Biomoléculas de Interés Biomédico en Bacterias y Hongos, of the Instituto de Investigaciones Biomédicas.

ACKNOWLEDGMENTS

We are grateful to the Consejo Nacional de Ciencia y Tecnología (Mexico) for the funding provided. EA-P received a scholarship from the Consejo Nacional de Ciencia y Tecnología as a postgraduate student in the Programa de Maestría y Doctorado en Ciencias Bioquímicas of the Universidad Nacional Autónoma de México.

SUPPLEMENTARY MATERIAL

The Supplementary Material for this article can be found online at: https://www.frontiersin.org/articles/10.3389/fmicb.2019.01568/full#supplementary-material

REFERENCES

Ali, N., Herron, P. R., Evans, M. C., and Dyson, P. J. (2002). Osmotic regulation of the *Streptomyces lividans* thiostrepton-inducible promoter, *ptipA*. *Microbiology* 148, 381–390.

Alting-Mees, M. A., and Short, J. M. (1989). pBluescript II: gene mapping vectors. *Nucleic Acids Res.* 17:9494.

Álvarez, A. F., and Georgellis, D. (2012). *In vitro* and *in vivo* analysis of the ArcB/A redox signaling pathway. *Methods Enzymol.* 471, 205–228. doi: 10.1016/S0076-6879(10)71012-0

Bobek, J., Šmídová, K., and Čihák, M. (2017). A waking review: old and novel insights into the spore germination in *Streptomyces*. *Front. Microbiol.* 8:2205. doi: 10.3389/fmicb.2017.02205

Botas, A., Pérez-Redondo, R., Rodríguez-García, A., Álvarez-Álvarez, R., Yagüe, P., Manteca, A., et al. (2018). ArgR of *Streptomyces coelicolor* is a pleiotropic transcriptional regulator: effect on the transcriptome, antibiotic production, and differentiation in liquid cultures. *Front. Microbiol.* 9:361. doi: 10.3389/fmicb.2018.00361

Bush, M. J., Tschowri, N., Schlimpert, S., Flärdh, K., and Buttner, M. J. (2015). c-di-GMP signaling and the regulation of developmental transitions in streptomycetes. *Nat. Rev. Microbiol.* 13, 749–760. doi: 10.1038/nrmicro3546

Carver, T., Harris, S. R., Berriman, M., Parkhill, J., and McQuillan, J. A. (2012). Artemis: an integrated platform for visualization and analysis of high-throughput sequence-based experimental data. *Bioinformatics* 28, 464–469. doi: 10.1093/bioinformatics/btr703

Chandra, G., and Chater, K. F. (2014). Developmental biology of *Streptomyces* from the perspective of 100 actinobacterial genome sequences. *FEMS Microbiol. Rev.* 38, 345–379. doi: 10.1111/1574-6976.12047

Cho, Y. H., Lee, E. J., Ahn, B. E., and Roe, J. H. (2001). SigB, an RNA polymerase sigma factor required for osmoprotection and proper differentiation of *Streptomyces coelicolor*. *Mol. Microbiol.* 42, 205–214.

Crack, J. C., den Hengst, C. D., Jakimowicz, P., Subramanian, S., Johnson, M. K., Buttner, M. J., et al. (2009). Characterization of [4Fe-4S]-containing and cluster-free forms of *Streptomyces* WhiD. *Biochemistry* 48, 12252–12264. doi: 10.1021/bi901498v

Danecek, P., Auton, A., Abecasis, G., Albers, C. A., Banks, E., DePristo, M. A., et al. (2011). The variant call format and VCFtools. *Bioinformatics* 27, 2156–2158. doi: 10.1093/bioinformatics/btr330

Datsenko, K. A., and Wanner, B. L. (2000). One-step inactivation of chromosomal genes in *Escherichia coli* K-12 using PCR products. *Proc. Natl. Acad. Sci. U.S.A.* 97, 6640–6645.

de Jong, W., Wösten, H. A., Dijkhuizen, L., and Claessen, D. (2009). Attachment of *Streptomyces coelicolor* is mediated by amyloidal fimbriae that are anchored to the cell surface via cellulose. *Mol. Microbiol.* 73, 1128–1140. doi: 10.1111/j.1365-2958.2009.06838.x

Flärdh, K., and Buttner, M. J. (2009). *Streptomyces* morphogenetics: dissecting differentiation in a filamentous bacterium. *Nature Rev. Microbiol.* 7, 36–49. doi: 10.1038/nrmicro1968

Gullón, S., Vicente, R. L., and Mellado, R. P. (2012). A novel two-component system involved in secretion stress response in *Streptomyces lividans*. *PLoS One* 7:e48987. doi: 10.1371/journal.pone.0048987

Gust, B., Chandra, G., Jakimowicz, D., Yuqing, T., Bruton, C. J., and Chater, K. F. (2004). λ Red-mediated genetic manipulation of antibiotic-producing *Streptomyces*. *Adv. Appl. Microbiol.* 54, 107–128.

Håvarstein, L. S., Diep, D. B., and Nes, I. F. (1995). A family of bacteriocin ABC transporters carry out proteolytic processing of their substrates concomitant with export. *Mol. Microbiol.* 16, 229–240.

Heichlinger, A., Ammelburg, M., Kleinschnitz, E. M., Latus, A., Maldener, I., Flärdh, K., et al. (2011). The MreB-Like protein Mbl of *Streptomyces coelicolor* A3(2) depends on MreB for proper localization and contributes to spore wall synthesis. *J. Bacteriol.* 193, 1533–1542. doi: 10.1128/JB.01100-10

Hesketh, A., Hill, C., Mokhtar, J., Novotna, G., Tran, N., Bibb, M., et al. (2011). Genome-wide dynamics of a bacterial response to antibiotics that target the cell envelope. *BMC Genomics* 12:226. doi: 10.1186/1471-2164-12-226

Hopwood, D. A. (2007). *Streptomyces in Nature and Medicine*. New York, NY: Oxford University Press.

Hopwood, D. A., Bibb, M. J., Chater, K. F., Kieser, T., Bruton, C. J., Kieser, H. M., et al. (1985). *Genetic Manipulation of Streptomyces. A Laboratory Manual*. Norwich: The John Innes Foundation.

Huang, J., Shi, J., Molle, V., Sohlberg, B., Weaver, D., and Bibb, M. J. (2005). Cross-regulation among disparate antibiotic biosynthetic pathways of *Streptomyces coelicolor*. *Mol. Microbiol.* 58, 1276–1287.

Huerta-Cepas, J., Forslund, K., Coelho, L. P., Szklarczyk, D., Jensen, L. J., von Mering, C., et al. (2017). Fast genome-wide functional annotation through orthology assignment by eggNOG-mapper. *Mol. Biol. Evol.* 34, 2115–2122. doi: 10.1093/molbev/msx148

Jakimowicz, P., Cheesman, M. R., Bishai, W. R., Chater, K. F., Thomson, A. J., and Buttner, M. J. (2005). Evidence that the *Streptomyces* developmental protein WhiD, a member of the WhiB family, binds a [4Fe-4S] cluster. *J. Biol. Chem.* 280, 8309–8315.

Keijser, B. J., van Wezel, G. P., Canters, Q. W., and Vijgenboom, E. (2002). Developmental regulation of the *Streptomyces lividans ram* genes: involvement of RamR in regulation of the *ramCSAB* operon. *J. Bacteriol.* 184, 4420–4429.

Kieser, T., Bibb, M. J., Buttner, M. J., Chater, K., and Hopwood, D. A. (2000). *Practical Streptomyces Genetics*. Norwich: John Innes Foundation.

Langmead, B., and Salzberg, S. (2012). Fast gapped-read alignment with Bowtie 2. *Nat. Methods* 9, 357–359. doi: 10.1038/nmeth.1923

Lee, E. J., Cho, Y. H., Kim, H. S., Ahn, B. E., and Roe, J. H. (2004). Regulation of sigmaB by an anti- and an anti-anti-sigma factor in *Streptomyces coelicolor* in response to osmotic stress. *J. Bacteriol.* 86, 8490–8498.

Lee, E. J., Karoonuthaisiri, N., Kim, H. S., Park, J. H., Cha, C. J., Kao, C. M., et al. (2005). A master regulator sigmaB governs osmotic and oxidative response as well as differentiation via a network of sigma factors in *Streptomyces coelicolor*. *Mol. Microbiol.* 57, 1252–1264.

Li, H. (2011). A statistical framework for SNP calling, mutation discovery, association mapping and population genetical parameter estimation from sequencing data. *Bioinformatics* 27, 2987–2993. doi: 10.1093/bioinformatics/btr509

Li, R., and Townsend, C. A. (2006). Rational strain improvement for enhanced clavulanic acid production by genetic engineering of the glycolytic pathway in *Streptomyces clavuligerus*. *Metab. Eng.* 8, 240–252.

Livak, K. J., and Schmittgen, T. D. (2001). Analysis of relative gene expression data using real-time quantitative PCR and the 2(-Delta Delta C(T)) Method. *Methods* 25, 402–408.

Love, M. I., Huber, W., and Anders, S. (2014). Moderated estimation of fold change and dispersion for RNA-seq data with DESeq2. *Genome Biol.* 15:550.

Manteca, A., Alvarez, R., Salazar, N., Yagüe, P., and Sanchez, J. (2008). Mycelium differentiation and antibiotic production in submerged cultures of *Streptomyces coelicolor*. *Appl. Environ. Microbiol.* 72, 3877–3886.

Manteca, A., Fernandez, M., and Sanchez, J. (2005). A death round affecting a young compartmentalized mycelium precedes aerial mycelium dismantling in confluent surface cultures of *Streptomyces antibioticus*. *Microbiology* 151, 3689–3697.

Mao, X. M., Zhou, Z., Hou, X. P., Guan, W. J., and Li, Y. Q. (2009). The reciprocal regulation between SigK and differentiation programs in *Streptomyces coelicolor*. *J. Bacteriol.* 191, 6473–6481. doi: 10.1128/JB.00875-09

Martin, S. M., and Bushell, M. E. (1996). Effect of hyphal micromorphology on bioreactor performance of antibiotic-producing *Saccharopolyspora erythraea* cultures. *Microbiology* 142, 1783–1788.

Matamouros, S., Hager, K. R., and Miller, S. (2015). HAMP domain rotation and tilting movements associated with signal transduction in the PhoQ sensor kinase. *MBio* 6:e00616-15. doi: 10.1128/mBio.00616-15

Molle, V., Palframan, W. J., Findlay, K. C., and Buttner, M. J. (2000). WhiD and WhiB, homologous proteins required for different stages of sporulation in *Streptomyces coelicolor* A3(2). *J. Bacteriol.* 182, 1286–1295.

Parkinson, J. S. (2010). Signaling mechanisms of HAMP domains in chemoreceptors and sensor kinases. *Annu. Rev. Microbiol.* 64, 101–122. doi: 10.1146/annurev.micro.112408.134215

Preibisch, S., Saalfeld, S., and Tomancak, P. (2009). Globally optimal stitching of tiled 3D microscopic image acquisitions. *Bioinformatics* 25, 1463–1465. doi: 10.1093/bioinformatics/btp184

R Core Team (2018). *R: A Language and Environment for Statistical Computing*. Vienna: R Foundation for Statistical Computing. Available at: https://www.R-project.org

Ratcliff, W. C., Denison, R. F., Borrello, M., and Travisano, M. (2012). Experimental evolution of multicellularity. *Proc. Natl. Acad. Sci. U.S.A.* 109, 1595–1600. doi: 10.1073/pnas.1115323109

Redenbach, M., Kieser, H. M., Denapaite, D., Eichner, A., Cullum, J., Kinashi, H., et al. (1996). A set of ordered cosmids and a detailed genetic and physical map for the 8 Mb *Streptomyces coelicolor* A3(2) chromosome. *Mol. Microbiol.* 21, 77–96.

Robinson, M. D., McCarthy, D. J., and Gordon, K. (2010). edgeR: a bioconductor package for differential expression analysis of digital gene expression data. *Bioinformatics* 26, 139–140. doi: 10.1093/bioinformatics/btp616

Sahl, H. G., and Bierbaum, G. (1998). Lantibiotics: biosynthesis and biological activities of uniquely modified peptides from gram-positive bacteria. *Annu. Rev. Microbiol.* 52, 41–79.

Tarazona, S., García-Alcalde, F., Dopazo, J., Ferrer, A., and Conesa, A. (2011). Differential expression in RNA-seq: a matter of depth. *Genome Res.* 21, 2213–2223. doi: 10.1101/gr.124321.111

Tsukazaki, T., Mori, H., Echizen, Y., Ishitani, R., Fukai, S., Tanaka, T., et al. (2011). Structure and function of a membrane component SecDF that enhances protein export. *Nature* 474, 235–238. doi: 10.1038/nature09980

van Dissel, D., Claessen, D., Roth, M., and van Wezel, G. P. (2015). A novel locus for mycelial aggregation forms a gateway to improved *Streptomyces* cell factories. *Microb. Cell Fact.* 14:44. doi: 10.1186/s12934-015-0224-6

van Dissel, D., Claessen, D., and van Wezel, G. P. (2014). Morphogenesis of *Streptomyces* in submerged cultures. *Adv. Appl. Microbiol.* 89, 1–45. doi: 10.1016/B978-0-12-800259-9.00001-9

van Dissel, D., Willemse, J., Zacchetti, B., Claessen, D., Pier, G. B., and van Wezel, G. P. (2018). Production of poly-β-1,6-N-acetylglucosamine by MatAB is required for hyphal aggregation and hydrophilic surface adhesion by *Streptomyces*. *Microb. Cell* 5, 269–279. doi: 10.15698/mic2018.06.635

van Keulen, G., and Dyson, P. J. (2014). Production of specialized metabolites by *Streptomyces coelicolor* A3(2). *Adv. Appl. Microbiol.* 89, 217–266. doi: 10.1016/B978-0-12-800259-9.00006-8

van Keulen, G., Hopwood, D. A., Dijkhuizen, L., and Sawers, R. G. (2005). Gas vesicles in actinomycetes: old buoys in novel habitats? *Trends Microbiol.* 13, 350–354.

van Wezel, G., Krabben, P., Traag, B., Keijser, B., Kerste, B., Vijgenboom, E., et al. (2006). Unlocking *Streptomyces* spp. for use as sustainable industrial production platforms by morphological engineering. *Appl. Environ. Microbiol.* 72, 5283–5288.

Waldvogel, E., Herbig, A., Battke, F., Amin, R., Nentwich, M., Nieselt, K., et al. (2011). The PII protein GlnK is a pleiotropic regulator for morphological differentiation and secondary metabolism in *Streptomyces coelicolor*. *Appl. Microbiol. Biotechnol.* 92, 1219–1236. doi: 10.1007/s00253-011-3644-1

Walisko, R., Moench-Tegeder, J., Blotenberg, J., Wucherpfennig, T., and Krull, R. (2015). The taming of the shrew–controlling the morphology of filamentous eukaryotic and prokaryotic microorganisms. *Adv. Biochem. Eng. Biotechnol.* 149, 1–27.

Willey, J. M., Willems, A., Kodani, S., and Nodwell, J. R. (2006). Morphogenetic surfactants and their role in the formation of aerial hyphae in Streptomyces coelicolor. *Mol. Microbiol.* 59, 731–742.

Xu, H., Chater, K. F., Deng, Z., and Tao, M. (2008). A cellulose synthase-like protein involved in hyphal tip growth and morphological differentiation in *Streptomyces*. *J. Bacteriol.* 190, 4971–4978. doi: 10.1128/JB.01849-07

Zacchetti, B., Smits, P., and Claessen, D. (2018). Dynamics of pellet fragmentation and aggregation in liquid-grown cultures of *Streptomyces lividans*. *Front. Microbiol.* 9:943. doi: 10.3389/fmicb.2018.00943

Zacchetti, B., Willemse, J., Recter, B., van Dissel, D., van Wezel, G. P., Wösten, H. A., et al. (2016). Aggregation of germlings is a major contributing factor towards mycelial heterogeneity of *Streptomyces*. *Sci. Rep.* 6:27045. doi: 10.1038/srep27045

Zhang, L., Willemse, J., Claessen, D., and van Wezel, G. P. (2016). SepG coordinates sporulation-specific cell division and nucleoid organization in *Streptomyces coelicolor*. *Open Biol.* 6:150164. doi: 10.1098/rsob.150164

Zhou, Z., Li, Y., Sun, N., Sun, Z., Lv, L., Wang, Y., et al. (2014). Function and evolution of two forms of SecDF homologs in *Streptomyces coelicolor*. *PLoS One* 9:e105237. doi: 10.1371/journal.pone.0105237

Conflict of Interest Statement: The authors declare that the research was conducted in the absence of any commercial or financial relationships that could be construed as a potential conflict of interest.

Copyright © 2019 Arroyo-Pérez, González-Cerón, Soberón-Chávez, Georgellis and Servín-González. This is an open-access article distributed under the terms of the Creative Commons Attribution License (CC BY). The use, distribution or reproduction in other forums is permitted, provided the original author(s) and the copyright owner(s) are credited and that the original publication in this journal is cited, in accordance with accepted academic practice. No use, distribution or reproduction is permitted which does not comply with these terms.

NEUROSCIENCE
RESEARCH ARTICLE

Dulce María Arzate et al. / Neuroscience 408 (2019) 308–326

Induction of typical and atypical neurogenesis in the adult substantia nigra after mouse embryonic stem cells transplantation

Dulce María Arzate,[a] Magdalena Guerra-Crespo[b1] and Luis Covarrubias[a]*

[a]*Instituto de Biotecnología, UNAM. Av. Universidad 2001, Col. Chamilpa, 62210, Cuernavaca, Morelos, Mexico*

[b]*Instituto de Fisiología Celular, UNAM. Circuito Exterior s/n Ciudad Universitaria, Coyoacán, 04510. Ciudad de México, Mexico*

Abstract—Neurogenesis in the substantia nigra (SN) has been a controversial issue. Here we report that neurogenesis can be induced in the adult rodent SN by transplantation of embryoid body cells (EBCs) derived from mouse embryonic stem cells. The detection of Sox2$^+$ dividing (BrdU$^+$) putative host neural precursor cells (NPCs) between 1 and 6 days post-transplantation (dpt) supported the neurogenic capacity of the adult SN. In agreement with the awakening of NPCs by EBCs, only host cells from implant-bearing SN were able to generate neurosphere-like aggregates in the presence of Egf and Fgf2. Later, at 15 dpt, a significant number of SN Dcx$^+$ neuroblasts were detected. However, a continuous BrdU administration after transplantation showed that only a fraction (about 20–30%) of those host Dcx$^+$ progeny derived from dividing cells and few BrdU$^+$ cells, some of them NeuN$^+$, survived up to 30 dpt. Unexpectedly, 25–30% of Dcx$^+$ or Psa-Ncam$^+$ cells at 15 dpt displayed astrocytic markers such as Gfap and S100b. Using a genetic lineage tracing strategy, we demonstrated that a large proportion of host Dcx$^+$ and/or Tubb3$^+$ neuroblasts originated from Gfap$^+$ cells. Remarkably, new blood vessels formed in association with the neurogenic process that, when precluded, caused a reduction in neuroblast production. Accordingly, two proteins secreted by EBCs, Fgf2 and Vegf, were able to promote the emergence of Dcx$^+$/Psa-Ncam$^+$, Tubb3$^+$ and NeuN$^+$/BrdU$^+$ cells *in vivo* in the absence of EBCs. We propose that the adult SN is a mostly silent neurogenic niche with the ability to generate new neurons by typical and atypical mechanisms. **© 2019 IBRO. Published by Elsevier Ltd. All rights reserved.**

Key words: neurogenesis, astrocytes, substantia nigra, transdifferentiation, transplantation.

INTRODUCTION

In the mammalian adult brain only two neurogenic regions show abundant production of new neurons (Alvarez-Buylla and Lois, 1995;Alvarez-Buylla and Garcia-Verdugo, 2002). The neurogenic niches that harbor dividing neural stem cells (NSC) are the subventricular zone (SVZ) lining the lateral ventricles (Lois and Alvarez-Buylla, 1993) and the subgranular zone (SGZ) in the hippocampus (Cameron et al., 1993). Adult neurogenesis in other brain areas, especially in those affected by neurodegenerative diseases, has been the focus of recent studies (Gould, 2007). In particular, evidence that supports neurogenesis in the substantia nigra (SN) remains controversial. While there is evidence that the SN contains proliferating precursor cells with a demonstrated plasticity to generate new neurons when transplanted to a neurogenic niche (Lie DC et al., 2002), others postulate that dopaminergic neurogenesis continue throughout life, though at a low rate (Albright et al., 2016;Morrison, 2016) and could be increased by a lesion (Zhao et al., 2003;Shan et al., 2006). Conversely, Frielingsdorf et al. (2004) reported the absence of dopaminergic neurogenesis. Alternatively, evidence has been provided to support that new neurons in the SN upon damage may originate from NPCs (neural precursor cells) residing in the aqueduct periventricular region (Hermann et al., 2006;L'Episcopo et al., 2014).

Commonly, neurogenesis in the adult brain is estimated by detecting dividing cells and the presence of neural markers. The caveat of approaches based in these determinations is the assumption that neuronal differentiation in all regions and conditions occurs by a similar mechanism. It is worth considering that the inability to detect neurogenesis in certain

*Corresponding author.
E-mail address: covs@ibt.unam.mx (Luis Covarrubias).
[1] Present address: Facultad de Medicina, UNAM. Circuito Interior Ciudad Universitaria, Av. Universidad 3000. Coyoacán, 04510. Ciudad de México, México.

Abbreviations: SN, substantia nigra; EBs, embryoid bodies; EBCs, embryoid body cells; ESCs, embryonic stem cells; MEFs, mouse embryonic fibroblasts; NPCs, neural precursor cells; NSCs, neural stem cells; dpt, days post-transplantation; dpi, days post-injection; SGZ, subgranular zone; SVZ, subventricular zone; Lif, leukemia inhibitory factor; Fgf2, fibroblast growth factor; Vegf, vascular endothelial growth factor; Egf, epidermal growth factor; Egfp, enhanced green fluorescent protein; CypA, cyclosporine A.

https://doi.org/10.1016/j.neuroscience.2019.03.042
0306-4522/© 2019 IBRO. Published by Elsevier Ltd. All rights reserved.

regions may be related to the poor environment for NPC differentiation or for survival of mature neurons under regular physiological conditions. A pro-neurogenic environment may be constantly present or emerge upon particular physiological conditions or damage. We recently showed that the capacity of the adult brain to support neurogenesis could be determined by transplanting cells with neurogenic potential. Embryoid body cells (EBCs) derived from mouse embryonic stem cells (ESCs), which possess a high neurogenic potential (Baizabal and Covarrubias, 2009), efficiently differentiate into neurons in distinct adult brain host regions and conditions. The striatum shows poor capacity to support neurogenesis, but this capacity improves after an experimental damage. Interestingly, the intact SN promotes neurogenesis of transplanted cells with high efficiency, similar to that determined within a classical neurogenic area. Therefore, new neurons in the SN could originate from either migrating NPCs or latent NSCs awaiting for activation signals.

In the present study, we tested the hypothesis that cells with neurogenic potential exist in the adult SN. This consideration arose from the observation of putative Dcx^+/$Psa\text{-}Ncam^+$ neuroblasts surrounding implanted EBCs, particularly abundant in the SN. We provide evidence of the emergence of cells with NPC characteristics in the SN few days after transplantation. Interestingly, many of those Dcx^+/$Psa\text{-}Ncam^+$ neuroblasts appeared to derive from non-dividing glial cells, which are coincident with recent reports supporting that astrocytes are the source of new neurons (Magnusson et al., 2014;Nato et al., 2015). We conclude that new neurons in the SN could originate from residing cells through typical and atypical mechanisms in the presence of proper inducing signals, some of which could be angiogenic factors.

EXPERIMENTAL PROCEDURES

Embryoid body formation

Two mouse ESC lines were used to generate embryoid body aggregates (EBs): the R1 and its derivative R1B5 that constitutively expresses the enhanced green fluorescent protein (Egfp). To generate EBs, we followed the protocol described by Maya-Espinosa et al. (2015). Briefly, ESCs were seeded on gelatin-coated culture plates covered with mitomycin-treated mouse embryonic fibroblasts (MEFs) as feeder cells and grown in M15 medium (DMEM medium supplemented with 15% FBS, 1 mM sodium pyruvate 1X glutamax, 0.1 mM non-essential amino acids, 0.1 mM 2-mercaptoethanol from Gibco). After two days *in vitro*, ESCs were seeded on plates without feeder cells but supplemented with 1000 U of leukemia inhibitory factor (Lif; Chemicon) for 3 days. To form EBs, 5×10^5 ESCs were transferred to non-adherent 10 cm bacterial culture dishes and cultivated during 4 days without Lif; during this time evident aggregates were formed most of them surrounded by endodermal-like cells (Maya-Espinosa et al., 2015). For transplantation, 4-day EBs (Fig. 1A) were disaggregated with 0.25% trypsin, centrifuged and resuspended in Optimem medium (Gibco).

Animals

We used 2–3 months old Wistar male rats (300 g) or 2–3 months old wild-type mice (28–30 g). Depending on the transplantation protocol, in some cases host mice were those of the 129/Sv strain carrying the *Egfp*, the *tdTomato/Egfp* [B6.129(Cg)-*Gt(ROSA)26Sor* $^{tm4(ACTB\text{-}tdTomato\text{-}EGFP)Luo}$/J, https://www.jax.org/strain/007676; referred ahead as tdTomato mice], or two transgenes *Gfap-cre/ERT2* [B6.Cg-Tg (*GFAP-cre/ERT2*)505Fmv/J, https://www.jax.org/strain/012849] and *–tdTomato/Egfp*. In tdTomato mice, all cells constitutively express *tdTomato*, whereas in *Gfap-cre/ERT2*;*Gt(ROSA)26Sor* $^{tm4(ACTB\text{-}tdTomato,\text{-}EGFP)}$ double transgenic mice, after CreERT2-induced recombination in the presence of tamoxifen, only *Gfap* expressing cells turn off *tdTomato* and turn on *Egfp* expression. One week before surgery, double transgenic mice were administered with i.p. tamoxifen (200 mg/kg), five doses in total, one every other day. All animals were maintained under standard colony conditions (12-h light/12-h dark cycle) with food and water *ad libitum*. Animals were sacrificed by a pentobarbital overdose and underwent transcardiac perfusion with a 0.1 M PBS solution followed by a 4% PFA solution. The experiments were carried out in accordance with the local bioethical committee (project number 293) of the Instituto de Biotecnología (Universidad Nacional Autónoma de México).

Transplantation of EBCs and infusion of Fgf2 and Vegf

Stereotaxic coordinates for SN were obtained from Paxinos and Watson (2005) for adult rats (AP −5.0, L −2, DV −8.0) and from Franklin and Paxinos (2013) for adult mice (AP −3.0, L −1.2, DV −4.2). Animals were transplanted under ketamine (10 mg/kg)–xylazine (1 mg/kg) anesthesia by injection of 1 µl of the cell suspension (approximately 1.5×10^5 cells in rats and 5×10^4 cells in mice) using a 5-µl Hamilton syringe. As controls, we considered the intact contralateral SN and animals injected with the delivery medium Optimem. For cell proliferation analysis, rats were injected with one 50 mg/kg i.p. dose of BrdU per day during the first 6 days post-trasplantation (dpt), whereas mice were injected with one 50 mg/kg i.p. dose of BrdU every day from day 3 to day 15. For Fgf2 (fibroblast growth factor) and Vegf (vascular endothelial growth factor) infusions in the SN, 10 ng of recombinant human Fgf2 (Peprotech) and 10 ng of recombinant human Vegf (Peprotech) were embedded in Puramatrix hydrogel (BD) (1:1) and injected in the same coordinates used for EBCs under ketamine–xylazine anesthesia. Angiogenesis inhibition was attained by administering 20 mg/kg i.p. of cyclosporine A (CypA; Sandimmune, Novartis) diluted in saline solution (0.9% *w/v* NaCl), one every other day during 15 days, to tdTomato mice previously transplanted with R1B5 EBCs, as described above.

Neurosphere culture

Neurosphere formation assays were performed on 6-day transplanted and intact contralateral SN in the presence of Egf (epidermal growth factor) and Fgf2 (20 ng/ml each;

INFORME DE LABORES 2019

Peprotech). We followed a protocol similar to the one described by Baizabal et al. (2012). Briefly, we dissected the SN, and the SVZ as a positive control, under a stereoscopic microscope. The dissected tissue was placed in a 6-cm culture dish containing DMEM/F12 and cut into ≈1-mm pieces. Then, the tissue was transferred to a dissociation solution [124 mM NaCl, 5 mM KCl, 3.2 mM $MgCl_2$, 0.1 mM $CaCl_2$, 26 mM $NaHCO_3$, 10 mM D-glucose, 0.2 mg/ml kynurenic acid, 0.67 mg/ml type IV hyaluronidase (SIGMA) and 1.33 mg/ml trypsin (ThermoFisher Scientific)] and incubated for 1 h at 37 °C. This step was followed by the addition of a trypsin inhibitor solution (1 mg/ml; SIGMA) and mechanical dissociation. The cell suspension derived from each tissue fragments was centrifuged at 1500 rpm for 7 min and the pellet was resuspended in 1 ml neurosphere culture media [DMEM/F12 supplemented with 25 μg/ml insulin (Gibco), glutamax 1× (ThermoFisher Scientific), 100 μg/ml transferrin, 20 nM progesterone, 60 μM putrescine, 30 nM selenium, and 2 μg/ml heparin (SIGMA)] containing Fgf2 and Egf (20 ng/ml each). To remove undissociated tissue fragments and debris, the suspension obtained was filtered through a 70-μm nylon membrane (BD Falcon). 1.8×10^5 cells were seeded in 35-mm culture dishes. Cultures were maintained at 37 °C in humidified 5% CO_2–95% atmospheric air incubators for 18 days.

A similar procedure was followed to evaluate the generation of neurospheres from SN cells that were exposed *in vitro* to Vegf and Fgf2 delivered from a Puramatrix hydrogel (BD). Briefly, 20 ng of Vegf and Fgf2 were embedded in a proportion 1:1 with hydrogel. Then, the mixture was left to settle down for 30 min and hydrogel polymerization was induced by adding 50 μl of neurosphere culture media. Finally, 5×10^4 cells were seeded per well (24-well microplate) and cultured for 12 days at 37 °C in a humidified 5% CO_2–95% atmospheric air incubator to allow the formation of neurospheres. At the end of the culture, the number of neurospheres was determined.

Tissue preparation and immunolabeling

All brains were removed and cryopreserved in a 30% sucrose solution. Brain 30-μm coronal sections were obtained using a cryostat and stored as free-floating in an antifreeze solution (25% ethylene glycol, 25% glycerol and 50% 0.1 M PBS) until immunolabeling. We followed a standard technique for immunochemistry, except for BrdU detection in which we added a 1-N HCl incubation step at 37 °C for 30 min after permeabilization. Three slices per brain were selected for analysis of each immunophenotypical marker. Brain slices were rinsed three times with 0.1 M TBS, followed by a 0.1% Triton X-100 incubation and treated with 1× immune DNA-retriever citrate buffer (Bio SB) at 65 °C for 30 min, and washed three times with TBS. After blocking in a 10% donkey serum/0.1% TX-100 solution, the slices were incubated in the corresponding primary antibody (Table 1) solution (containing 1% donkey serum/ 0.1% TX-100) overnight at 4 °C. After three times rinsing in TBS, slices were incubated for 2 h at room temperature with the appropriate secondary antibody (Table 1) 1:1500 in a solution containing 2% donkey serum/ 2% TX-100. Finally, the brain slices were counterstained with a 1:10,000 DAPI solution, rinsed with TBS and mounted in glass slides with Prolong Gold (ThermoFisher Scientific) mounting medium. We used typical neurogenic zones and regions (SVZ-OB and SGZ-dentate gyrus) as internal controls for the proliferation marker BrdU, and NSC and neuroblast markers.

Imaging and cell counting

Since no difference in response to EBC transplantation was evident for cells in the SN pars compacta or the SN pars reticulata portions, the whole SN was considered for the analysis. Endogenous reporter gene expression such as *Egfp* from the R1B5 cell line or the *tdTomato/Egfp* from the transgenic mice allowed us to discriminate between the host and the transplanted cells. We use an Olympus FV1000 confocal microscope for image acquisition. Cell and blood vessel counting was carried out in coronal sections considering the area comprised within the adjacent 600 μm to the transplanted cells or the hydrogel and covering their rostrocaudal distribution. We obtained three brain slices from at least three independent subjects, and two photomicrographs were taken from each slice with a 20× objective; Z stack images were taken with a 60× objective to analyze co-expression when required. All results are expressed as the mean ± SEM (cells/mm^2, blood vessels/mm^2 or transplant diameter) or as the percentage (mean ± SEM) of double positive cells from the total Gfap or Egfp positive cells when applicable.

Statistical analysis

Cell count data were analyzed with the Shapiro–Wilk normality test and Levene equal variance test to confirm their normal distribution. To compare two groups the t-student test was done and to compare three or more groups we performed a one way-ANOVA test. SIGMAPLOT V12.0 software (Systat Software, Inc.) was used for all statistical analysis of data. For comparisons between the number of $BrdU^+$ cells at two subsequent time points (i.e. 2 hpt vs 24 hpt; 24 hpt vs 48 hpt), the multiple comparison procedure (Fisher LSD Method) was applied. P values of statistically significant differences are indicated as: *$p < 0.05$ or **$p < 0.01$.

RESULTS

Transplantation of EBCs stimulates neurogenesis in the adult rat and mouse SN

Proliferation of putative NPCs has been associated with active neurogenesis. Accordingly, BrdU incorporation occurred above basal levels immediately (2 h) after transplantation of EBCs to the adult rat SN increasing, with an apparent synchrony (considering a 20-h cell cycle), up to 48 h post-transplantation (hpt; Fig. 1B, C and Table 2). After this period, incorporation rate diminished by 72 hpt, but a significant number of $BrdU^+$ cells continued to be detected the following days and few remained at 30 dpt (Fig. 1C and Table 2). Very few cells incorporated BrdU in the contralateral

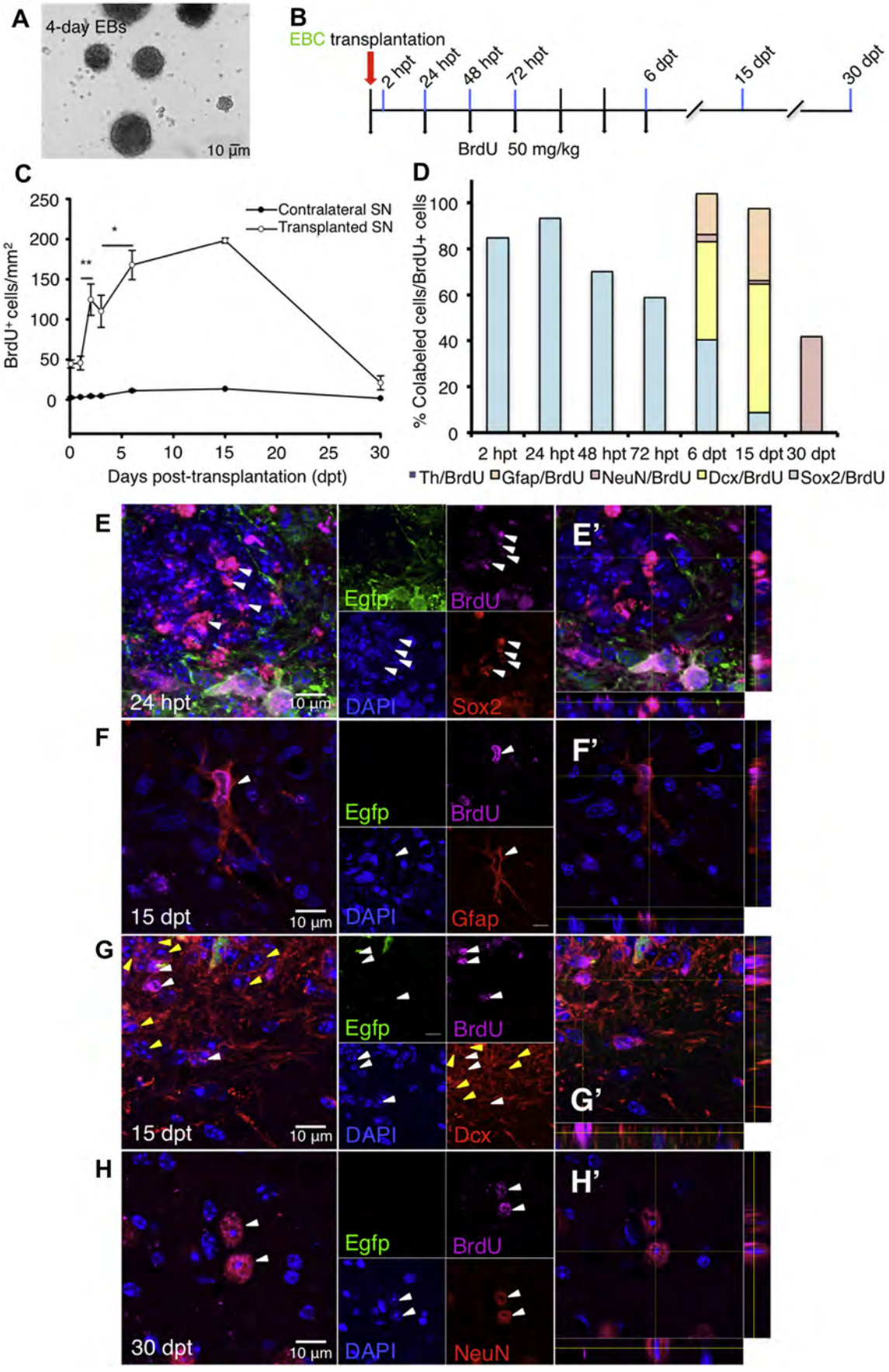
A
4-day EBs
10 µm
B
EBC transplantation
2 hpt
24 hpt
48 hpt
72 hpt
6 dpt
15 dpt
30 dpt
BrdU 50 mg/kg
C
Contralateral SN
Transplanted SN
BrdU+ cells/mm2
Days post-transplantation (dpt)
D
% Colabeled cells/BrdU+ cells
2 hpt 24 hpt 48 hpt 72 hpt 6 dpt 15 dpt 30 dpt
Th/BrdU Gfap/BrdU NeuN/BrdU Dcx/BrdU Sox2/BrdU
E
E'
24 hpt
Egfp
BrdU
DAPI
Sox2
F
F'
15 dpt
Gfap
G
G'
Dcx
H
H'
30 dpt
NeuN

INFORME DE LABORES 2019

Table 1. Antibodies employed for immunohistochemistry procedures.

Antibody Name	Dilution	Vendor and Catalog Number	Research Resource Identifier (RRID)
Rabbit anti-Gfp polyclonal	1:1000	Santa Cruz Biotechnology Cat# sc-8334	AB_641123
Mouse anti-BrdU monoclonal	1:100	BD Biosciences Cat# 347580	AB_400326
Goat anti-Sox2 polyclonal	1:200	Santa Cruz Biotechnology Cat# sc-17,320	AB_2286684
Goat anti-Sox1 polyclonal	1:200	Santa Cruz Biotechnology Cat# sc-17,318	AB_2195365
Mouse anti-Nestin monoclonal	1:500	Millipore Cat# MAB353	AB_94911
Goat anti-Dcx polyclonal	1:200	Santa Cruz Biotechnology Cat# sc-8067	AB_2088491
Mouse anti-Psa-Ncam monoclonal	1:200	Millipore Cat# MAB5324	AB_95211
Rabbit anti-Gfap polyclonal	1:5000	Dako Cat# Z0334	AB_10013382
Rabbit anti-S100b polyclonal	1:5000	Abcam Cat# ab41548	AB_956280
Rabbit anti-Tubb3 polyclonal	1:500	Covance Research Products Inc. Cat# PRB-435P-100	AB_291637
Mouse anti-NeuN monoclonal	1:200	Millipore Cat# MAB377	AB_2298772
Rabbit anti-NeuN polyclonal	1:500	Novus Cat# NBP1–92716	AB_11033614
Rabbit anti-Th polyclonal	1:1000	Millipore Cat# AB152	AB_390204
Rat anti-CD31 monoclonal	1:100	BD Biosciences Cat# 550274	AB_393571
Mouse anti-O4 monoclonal	1:100	R&D Systems Cat# MAB1326	AB_357617
Rabbit anti-NG2 monoclonal	1:100	Millipore Cat# AB5320	AB_11213678
Rabbit anti-Lmx1a polyclonal	1:1000	Millipore Cat# AB10533	AB_10805970
Goat anti-Neurog2 polyclonal	1:100	Santa Cruz Biotechnology Cat# sc-19,233	AB_2149513
Anti-rat Cy3 polyclonal antibody	1:1000	Rockland Cat# 612–104-120	AB_218631
Goat anti-mouse IgG Alexa Fluor 488	1:3000	Thermo Fisher Scientific Cat# A11001	AB_2534069
Goat anti-mouse IgG Alexa Fluor 594	1:3000	Thermo Fisher Scientific Cat# A11005	AB_2534073
Goat anti-mouse IgG Alexa Fluor 647	1:3000	Thermo Fisher Scientific Cat# A21235	AB_2535804
Goat anti-rabbit IgG Alexa Fluor 488	1:1250	Thermo Fisher Scientific Cat# A11008	AB_143165
Goat anti-rabbit IgG Alexa Fluor 594	1:1250	Thermo Fisher Scientific Cat# A11012	AB_2534079
Goat anti-rabbit IgG Alexa Fluor 647	1:1250	Thermo Fisher Scientific Cat# A21244	AB_2535812
Donkey anti-goat IgG Alexa Fluor 488	1:1250	Thermo Fisher Scientific Cat# A11055	AB_2534102
Donkey anti-goat IgG Alexa Fluor 594	1:1250	Thermo Fisher Scientific Cat# A11058	AB_2534105
Donkey anti-goat IgG Alexa Fluor 647	1:1250	Thermo Fisher Scientific Cat# A21447	AB_2535864

SN (Fig. 1C and Table 2). The NPC identity of most $BrdU^+$ cells detected shortly after transplantation (i.e., up to 72 hpt) is supported by the detection of Sox2 in the majority of them (Fig. 1D, E, E' and Table 3).

Sox2 expression, as well as other similar markers, is not exclusive of NPCs. In particular, reactive astrocytes proliferate upon brain damage and express several NPC markers (Gotz et al., 2015). Actually, many glial cells with reactive astrocyte characteristics (i.e., high levels of Gfap, hypertrophy and proliferation) were found after EBCs transplantation (Fig. 1D, F, F' and Table 3). However, since reactive astrocytes have no neurogenic potential *in vivo*, the NPC identity of the proliferating $Sox2^+$ cells emerging in response to EBCs transplantation can be determined by tracing the neuronal progeny from them (i.e., those retaining the incorporated BrdU). In agreement with this possibility, as incorporation of BrdU diminished, an increasing number of $BrdU^+$ cells were also positive for the immature neuronal marker Dcx (white arrowheads in Fig. 1G; see also Fig. 1D and Table 3) but, in addition, many endogenous Dcx^+ cells detected were not positive for BrdU (yellow arrowheads in Fig. 1G; see also Table 3). In coincidence with the disappearance of transplanted cells, very few cells derived from the proliferating NPCs remained in the long term (30 dpt; Fig. 1C). Occasionally, $BrdU^+$ cells containing the mature neuronal marker NeuN were found at this time (Fig. 1D, H, H' and Table 3). Similar to the fate of NPCs derived from the transplanted cells (Maya-Espinosa et al., 2015), no cell positive for Th, an early marker of dopaminergic neurons, derived from dividing NPCs.

Similar results were obtained when transplantations were performed in the mouse (Fig. 2A). Several $BrdU^+$ cells were detected at 6 dpt, their number increased by 15 dpt, but very few were found at 30 dpt (Fig. 2B and Table 4). NPCs were detected by the presence of Sox1 and Nes (also named Nestin), markers more restricted to activated NPCs than Sox2 (Venere et al., 2012;Codega et al., 2014). At 6 dpt, a significant proportion of $BrdU^+$ cells expressed *Nes* and *Sox1* (Fig. 2C–E and Table 5). Supporting the NPC identity of these proliferating cells, nearly half of the $BrdU^+$ cells detected at 15 dpt expressed *Dcx* (Fig. 2C, F, F' and Table 5) but, in addition, many endogenous Dcx^+ cells detected were not positive for BrdU (yellow arrowheads in Fig. 2F). Since administration of BrdU was maintained from

Fig. 1. Transplantation of EBCs induces neurogenesis in the adult rat SN. (A) ESCs form spherical aggregates (EBs) under non-adherent conditions. For transplantation, 4-day EBs were disaggregated. (B) Schematic representation of the experimental strategy in the rat; EBCs from R1B5 cells ($Egfp^+$) were used for these experiments. (C) BrdU-labeled cells in the adult rat transplanted SN (white circles) and contralateral SN (dark circles). Error bars indicate SEM; P values are indicated as $*p < 0.05$ and $**p < 0.01$. (D) Percentage of $BrdU^+$ cells colabeled with: Sox2, Gfap, Dcx, NeuN and Th in the rat SN at different time points after transplantation. (E–H) Confocal Z-projections showing $BrdU^+$ cells colabeled with the neural markers Sox2 (at 24 hpt), Gfap (at 15 dpt), Dcx (at 15 dpt) and NeuN (at 30 dpt) in the rat SN. White arrowheads indicate cells colabeling with BrdU and yellow arrowheads in (G) indicate those only labeled with Dcx. (E'–H') Orthogonal views. Scale bar 10 μm. (For interpretation of the references to color in this figure legend, the reader is referred to the web version of this article.)

INFORME DE LABORES 2019

Table 2. BrdU-labeled cells per mm^2 (mean ± SEM) in the transplanted adult rat SN.

Post-transplantation period	Rat	
	Contralateral SN	Transplanted SN
2 hpt (n = 2)	1.23, 3.70	39.56, 49.45
24 hpt (n = 3)	3.29 ± 0.41	45.74 ± 8.56
48 hpt (n = 4)	4.32 ± 1.28	124.56 ± 19.58
72 hpt (n = 4)	4.63 ± 1.05	110.04 ± 20.05
6 dpt (n = 5)	11.20 ± 1.21	167.68 ± 18.12
15 dpt (n = 3)	13.51 ± 2.55	198.20 ± 3.17
30 dpt (n = 2)	1.63, 1.63	12.36, 29.67

BrdU-labeled cells were counted (see Material and Methods) at different times post-transplantation. The corresponding contralateral SN was used as control for each time. The number of subjects (n) per group is specified between parentheses.

the 3 to 15 dpt, and up to just 2 h before sacrifice, neuroblasts without detectable BrdU unlikely emerged due to incorporated BrdU dilution after extensive proliferation. At 30 dpt, some $BrdU^+$ expressed *NeuN* (Fig. 2C, G ,G' and Table 5) but, again no $BrdU^+$ cell was found positive for Th (Fig. 2C). Furthermore, no cell positive for Lmx1a or Neurog2, two early markers of mesencephalic dopaminergic progenitors detected in embryos before *Th* expression (Guerrero-Flores et al., 2017), was found. It is relevant to mention that in mice, in contrast with observations in rats [present report and in Maya-Espinosa et al., 2015], transplanted EBCs continued proliferating and a large mass of transplanted cells was commonly observed at 30 dpt, a condition that might affect the final outcome.

Transplanted EBCs efficiently differentiate into Dcx^+ neuroblasts in the SN (Maya-Espinosa et al., 2015). To discard the possibility that the Dcx^+ cells detected in previous experiments were not the result of EBCs progeny that downregulated *Egfp* expression, we transplanted wild-type EBCs to an $Egfp^+$ host brain (Fig. 3A, A') or the $Egfp^+$ R1B5 EBCs to the brain of tdTomato mice (Fig. 3B, B'). As expected for the host origin of Dcx^+ cells surrounding the implant, a high proportion of them were $Egfp^+$ cells (315.6 ± 26.7 cells/mm^2) or $tdTomato^+$ (358.24 ± 42.18 cells/mm^2), respectively. Nonetheless, EBCs carried the inducing neurogenic factor, since very few cells incorporated BrdU and no Dcx^+ cell was found in the contralateral intact SN or after injecting the basal culture medium (Optimem) without EBCs (Figs. 1C, 2B and Tables 2 and 4). In agreement with this conclusion, mouse embryonic fibroblasts (MEFs) transplantation to the SN of $Egfp^+$ mice produced a moderate glial reaction but no Dcx^+ cell was found at 15 dpt (Fig. 3C).

Table 3. BrdU-labeled cells per mm^2 (mean ± SEM) colabeling with neural, neuronal and glial cell markers in the transplanted adult rat SN.

Post-transplantation period	Cell markers	Number of cells (% $BrdU^+$ cells)
2 hpt	$Sox2^+/BrdU^+$	35.85 (84.72%)
(n = 2)	$Sox2^+/BrdU^-$	80.98
24 hpt	$Sox2^+/BrdU^+$	41.62 ± 6.3 (93.15 ± 3.43%)
(n = 3)	$Sox2^+/BrdU^-$	91.08 ± 20.81
48 hpt	$Sox2^+/BrdU^+$	89.09 ± 13.66 (70.12 ± 7.17%)
(n = 4)	$Sox2^+/BrdU^-$	146.24 ± 11.45
72 hpt	$Sox2^+/BrdU^+$	61.2 ± 6.26 (58.87 ± 4.75%)
(n = 4)	$Sox2^+/BrdU^-$	130.44 ± 24.79
6 dpt	$Sox2^+/BrdU^+$	68.85 ± 14.18 (46.08 ± 5.99%)
(n = 5)	$Sox2^+/BrdU^-$	233.2 ± 46.27
15 dpt	$Sox2^+/BrdU^+$	12.71 ± 4.75 (8.87 ± 4.87%)
(n = 3)	$Sox2^+/BrdU^-$	7.24 ± 4.64
6 dpt	$Nes^+/BrdU^+$	30.91 ± 6.18 (28.84 ± 9.61%)
(n = 3)	$Nes^+/BrdU^-$	90.25 ± 8.65
6 dpt	$Dcx^+/BrdU^+$	68.92 ± 6.02 (48.73 ± 6.65%)
(n = 4)	$Dcx^+/BrdU^-$	106.33 ± 11.95
15 dpt	$Dcx^+/BrdU^+$	91.84 ± 23.95 (55.83 ± 4.64%)
(n = 3)	$Dcx^+/BrdU^-$	175.21 ± 44.06
6 dpt	$Gfap^+/BrdU^+$	39.56 ± 2.47 (17.46 ± 0.60%)
(n = 3)	$Gfap^+/BrdU^-$	77.48 ± 23.56
15 dpt	$Gfap^+/BrdU^+$	51.1 ± 4.36 (30.11 ± 3.66%)
(n = 3)	$Gfap^+/BrdU^-$	97.26 ± 27.98
6 dpt (n = 4)		4.94 ± 0.8 (3.05 ± 1.27%)
15 dpt (n = 3)	$NeuN^+/BrdU^+$	2.47 ± 0 (1.42 ± 0.85%)
30 dpt (n = 2)		8.65 (41.87%)
30 dpt (n = 2)	$Th^+/BrdU^+$	0%

BrdU-labeled cells that also showed the markers indicated were counted (see Material and Methods) at different times post-transplantation; cells positive for the marker but negative for BrdU were also counted. The number of subjects (n) per group and the percentage (mean ± SEM) of total $BrdU^+$ cells are specified between parentheses.

INFORME DE LABORES 2019

Cells of the transplanted adult mouse SN generate neurospheres

To confirm the emergence of cells with NPC characteristics after transplantation of EBCs, we performed a neurosphere formation assay for cells derived from the intact and transplanted SN at 6 dpt (Fig. 4A). In agreement with the abundant number of cells expressing NPC markers found at this stage in the transplanted SN, neurospheres-like aggregates were formed with cells from the host tissue (51.0 ± 10.8 neurospheres from 1.8 × 10^5 total cells; Fig. 4B, C) but none from cells of the intact SN. The time to form these neurospheres was longer than that required to form neurospheres from SVZ cells (15 vs. 7 days, respectively; Fig. 4B, C). In addition, they were generally smaller in size in comparison with those derived from the SVZ (around 80 vs. 250 μm diameter) and evidently different from those flat colonies formed by the EB-derived cells (Egfp$^+$; Fig. 4B, bottom panel). Nonetheless, to confirm their NPC properties and similarity to SVZ cells they were able to produce secondary neurospheres (Fig. 4D) and expressed typical neurosphere markers such as *Nes* and *Gfap* (Fig. 4E; right panel).

Non-dividing resident Gfap$^+$/S100b$^+$ cells acquire neuroblast markers after EBCs transplantation

The number of total Dcx$^+$ cells detected in the rat SN after EBCs transplantation moderately increased (1.5-fold) from 6 dpt to 15 dpt (Table 3). However, although BrdU was applied during the first 6 days after transplantation, only a fraction of those Dcx$^+$ cells colabeled with BrdU (approximately 30% at 15 dpt). Thus, activation of NPCs and generation of Dcx$^+$ cells might occur after 6 dpt. However, for transplantation to mouse SN, BrdU was applied daily from 3 to 15 dpt and, yet, the proportion of Dcx$^+$/BrdU$^+$ was not larger than 20% of total Dcx$^+$ cells (Table 5). This would mean that the remaining 80% Dcx$^+$ cells originated from non-dividing progenitor cells. Accordingly, many Sox2$^+$ cells emerging at 6 dpt did not show BrdU incorporation (Tables 3 and 5). These observations opened the possibility to the participation of a differentiated cell type (e.g., astrocytes) as a precursor of neuroblasts by a mechanism that does not involve cell divisions. In the adult brain, Gfap$^+$ cells represent either parenchymal astrocytes or NSCs in the neurogenic areas. In the intact SN, Gfap$^+$ cells are scattered mainly within the SNpr and the glia limitans layer (Fig. 3D, left panel). Interestingly, we found many Gfap$^+$ cells around the implanted cells (Fig. 3D, right panel), with a corresponding reduction in the glia limitans layer, some of which were also labeled for Dcx at 6 dpt (4.15 ± 0.97% of total Gfap$^+$ cells within 600 μm from the transplant border, n = 3; Fig. 5H), which number markedly increased by 15 dpt (25.46 ± 2.37%, n = 7; Fig. 5B, B', F, F′, I). Similar results were obtained in Dcx colabeling determinations with S100b at 15 dpt (29.42 ± 4.4% S100b$^+$/Dcx$^+$, n = 7, Fig. 5G, G', I; see also S100b/Psa-Ncam colabeling, n = 3, in Fig. 5E, I), a marker that characterizes a terminal maturation stage of astrocytes (Raponi et al., 2007) and is not expressed by SVZ NSC (Codega et al., 2014).

The fact that the number of Dcx$^+$ cells increased while the proportion of Dcx$^+$ cells also positive for Gfap remained constant (17.51 ± 3.38% at 6 dpt and 18.15 ± 2.29% at 15 dpt) suggests that the co-expression of astrocytic and neuroblast markers is a transient event. As expected, Psa-Ncam$^+$/Sox2$^+$ cells were rarely detected (0.75 ± 0.29% of total Psa-Ncam$^+$ cells, n = 4; Fig. 5A, I), but a significant proportion of cells Sox2$^+$/Gfap$^+$, (39.85 ± 4.02% at 6 dpt, and 32.16 ± 1.09% at 15 dpt, n = 3; Fig. 5C, C', H, I) or Nes$^+$/Gfap$^+$ (38.83 ± 4.36% at 6 dpt and 57.02 ± 3.05% at 15 dpt, n = 3; Fig. 5D, D', H, I) were found. Many of those cells might be reactive astrocytes, but the possibility that some of them represent a transient event to become a neuroblast should be considered. In concordance with data of a recent report by Magnusson et al. (2014), these observations suggest that fully differentiated parenchymal astrocytes can give rise to new neurons, in our case, possibly through a direct transdifferentiation process that does not require cell divisions. It is important to mention that at 15 dpt Dcx$^+$/Tubb3$^+$ cells or Dcx$^+$/Th$^+$ positive cells were not detected discarding a neuronal dedifferentiation process. Tubb3 is a neuronal marker present in young and mature neurons that emerges as Dcx disappears.

Resident Gfap$^+$ cells give rise to new neurons in the transplanted SN

To confirm our previous findings, EBCs from wild-type ESC (R1 line) were transplanted to the SN of double transgenic mice Gfap-Cre/ERT2;*Gt(ROSA)26Sor$^{tm4(ACTB-tdTomato,-EGFP)}$*. Before transplantation, these mice were treated with tamoxifen such that the tdTomato sequence was floxed by the Cre/ERT2 and *Egfp* expression occurred in Gfap$^+$ cells (Fig. 6A). Using this protocol, the recombination efficiency obtained was around 30% of all Gfap$^+$ cells detected in the SN; full recombination might not be achieved likely due to a variable *Gfap* expression among astrocytes (Ganat et al., 2006), but it is relevant to mention that >85% of Egfp$^+$ expressed *Gfap* in the contralateral SN. We were not able to detect any Egfp$^+$/NG2$^+$ (oligodendrocyte precursor cell) or Egfp$^+$/O4$^+$ (oligodendrocyte), while some Egfp$^+$/Nes$^+$ and many Egfp$^+$/Dcx$^+$ cells (Fig. 6C, C', E) were detected after transplantation. At 15 dpt, 70.48 ± 2.79% (519.78 ± 89.65 cells/mm^2; n = 3) of the Egfp$^+$ cells were also positive for Gfap (Fig. 6B, E) and 29.35 ± 3.29% (196.32 ± 25.10 cells/mm^2; n = 3) at 30 dpt (Fig. 6E). Interestingly, among the Egfp$^+$ cells, 53.49 ± 8.07% (484.49 ± 76.13 cells/mm^2) and 24.46 ± 4.82% (152.69 ± 33.5 cells/mm^2) at 15 dpt (n = 4), and 23.98 ± 1.90% (132.68 ± 33.03 cells/mm^2) and 27.27 ± 2.97% (189.38 ± 56.18 cells/mm^2) at 30 dpt (n = 4) cells were Dcx$^+$ or Tubb3$^+$, respectively (Fig. 6C–E). Consistent with the above determinations showing that some Gfap$^+$ cells were also expressing neuroblast markers (Fig. 5), the percentage of cells with neuroblast/neuronal markers among the Egfp$^+$ cells was larger than the percentage of cells that were Egfp$^+$/Gfap$^-$. These results confirm that a high percentage of putative neuroblasts emerging around the implanted EBCs in the SN derived from Gfap$^+$ cells and could generate new neurons. In fact, in addition to the detection of Egfp$^+$ cells colabeling with neuronal markers, a neuronal morphology could be revealed in some of them (Fig. 6F).

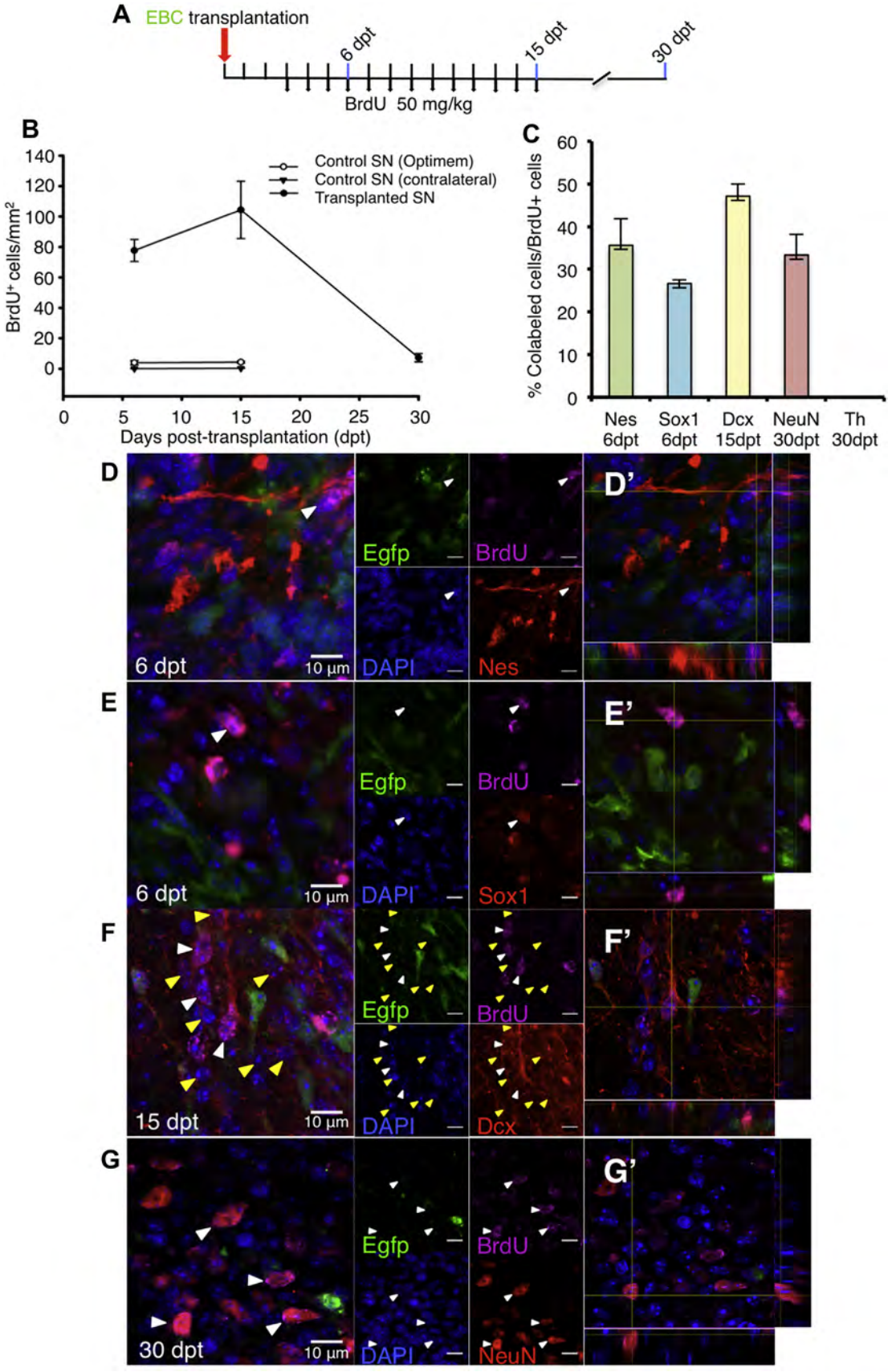
A
EBC transplantation
6 dpt
15 dpt
30 dpt
BrdU 50 mg/kg
B
Control SN (Optimem)
Control SN (contralateral)
Transplanted SN
BrdU+ cells/mm2
Days post-transplantation (dpt)
C
% Colabeled cells/BrdU+ cells
Nes 6dpt
Sox1 6dpt
Dcx 15dpt
NeuN 30dpt
Th 30dpt
D
D'
Egfp
BrdU
6 dpt
10 µm
DAPI
Nes
E
E'
Sox1
F
F'
15 dpt
Dcx
G
G'
30 dpt
NeuN

INFORME DE LABORES 2019

Angiogenic EBC-secreted factors induce neurogenesis in the SN in the absence of EBC transplantation

In comparison with the intact SN (Fig. 7A), an increased immunoreactivity to CD31, a blood vessel marker, was associated with the emerging Dcx$^+$ cells in the EBCs transplanted SN (Fig. 7B). Furthermore, some of these Dcx$^+$ cells showed a tight association with blood vessels (Fig. 7C; white arrowheads in inset Fig. 7C'), suggesting an interaction similar to the one observed in migrating neuroblasts from the SVZ to the olfactory bulb (Bovetti et al., 2007;Whitman et al., 2009). It is relevant to note that blood vessels are evident in the tdTomato mouse without any specific labeling (see Figs. 7 and 8). To determine the role of blood vessels in the EBC-induced neurogenic process, tdTomato mice were treated with CypA, a calcineurin inhibitor that reduces Vegf-mediated angiogenesis (Hernandez et al., 2001;Rafiee et al., 2004), after transplanting R1B5 EBCs to the SN. In comparison to controls (Fig. 7D, D'), mice treated with CypA (Fig. 7E, E') showed a marked reduction in transplant growth (Fig. 7F; 252.48 ± 15.14 μm vs. 432.26 ± 89.0 μm, n = 3) in association with a decreased number of CD31$^+$ blood vessels around it (Fig. 7G; 256.23 ± 11.11 blood vessels/mm^2 vs. 212.51 ± 0.786 blood vessels/mm^2, n = 3). Interestingly, these effects were accompanied by a significant reduction in the number of Dcx$^+$ putative neuroblasts (Fig. 7D, E, H; 101.05 ± 8.59 cells/mm^2 vs. 358.24 ± 42.18 cells/mm^2, n = 3). In agreement with these observations, a reduction in blood vessels (control group, 366.15 ± 18.31 blood vessels/mm^2 vs. CypA group, 323.24 ± 7.72 blood vessels/mm^2; n = 3) and in the number of Dcx$^+$ cells (control group, 43.39 ± 2.06 cells per field vs CypA group, 36.46 ± 6.58 cells per field; n = 3) was also observed in the neurogenic dentate gyrus of CypA-treated mice.

Considering these latter observations and the soluble factors secreted by EBCs in culture (Fathi et al., 2009;Ngangan et al., 2014), we tested Vegf and Fgf2 as molecules contributing to the activation of neurogenesis in the SN, both with angiogenic (Cuevas et al., 1993;Seo et al., 2013) and neurogenic (Kim et al., 2006;Luo et al., 2015;Shen et al., 2016) properties. Interestingly, we observed that Vegf alone or in combination with Fgf2 (embedded in Puramatrix hydrogel) promoted the generation of neurospheres from SN cells, whereas no neurosphere was formed in presence of the hydrogel vehicle alone (data not shown). Therefore, Vegf and Fgf2 were embedded in hydrogel and implanted in the SN of tdTomato mice for their *in vivo* delivery and testing of their neurogenic inducing activity. Fifteen days postinjection (dpi), in contrast with the SN injected with the vehicle (Fig. 8A), though in a smaller quantity than that generated by transplanted EBCs (185.15 ± 5.39 cells/mm2, n = 4 vs. 358.24 ± 42.18 cells/mm^2, n = 4), many Dcx$^+$ cells were detected (Fig. 8B). Furthermore, and similar to the SN with transplanted EBCs, we detected an association between Dcx$^+$ cells and blood vessels (Fig. 8C, C'). At 30 dpi the number of Dcx$^+$ cells decreased (92.17 ± 3.77 cells/mm^2, n = 3; Fig. 8D, D', I) while NeuN$^+$ (82.52 ± 20.29 cells per mm^2, n = 5; Fig. 8E, E', G–I) and Tubb3$^+$ cells (146.51 ± 6.8 cells/mm^2, n = 3; Fig. 8F, I) appeared around the implanted hydrogel (those within a 600-μm distance from the implanted hydrogel) suggesting a progressive neurogenic process, going from Dcx neuroblast, transiting through Tubb3 immature neurons, up to becoming Tubb3/NeuN mature neurons (Zhang and Jiao, 2015).

Table 4. BrdU-labeled cells per mm^2 (mean ± SEM) in the transplanted and control adult mouse SN.

Post-transplantation period	Mouse		
	Vehicle	Contralateral SN	Transplanted SN
6 dpt	3.98 ± 1.43 (n = 3)	0.09 ± 0.03 (n = 5)	77.67 ± 7.2 (n = 10)
15 dpt	4.32 ± 0.61 (n = 3)	0.29 ± 0.02 (n = 4)	104.4 ± 18.85 (n = 4)
30 dpt	ND	ND	7.21 ± 2.71 (n = 7)

BrdU-labeled cells were counted (see Material and Methods) at different times post-transplantation. The corresponding contralateral SN and the SN injected with the vehicle (Optimem medium) were used as controls for 6 and 15 dpt (ND, not determined). The number of subjects (n) per group is specified between parentheses.

However, in mice that were continuously administered with BrdU after injection of factors, only 16% of all NeuN$^+$ cells around the hydrogel colabeled with BrdU (13.18 ± 2.62 NeuN$^+$/BrdU$^+$ cells/mm^2, n = 3; Fig. 8E, E', I), possibly meaning poor survival of new neurons. We traced the possible astrocytic origin of new neurons induced by Vegf and Fgf2 by searching for Egfp$^+$ neurons/neuroblasts around the growth factors-embedded hydrogel in the SN of mice Gfap-Cre/ERT2;*Gt(ROSA)26Sor* $^{tm4(ACTB-tdTomato,-EGFP)}$ previously treated with tamoxifen. Interestingly, some Dcx$^+$/Egfp$^+$ at 15 dpi (Fig. 9A, A') and Tubb3$^+$/Egfp$^+$ cells at 30 dpi (Fig. 9B, B') were detected, as well as some Egfp$^+$ cells with neuronal morphology (Fig. 9C), though the proportion was apparently low. Therefore, the combination of Vegf and Fgf2 is capable of inducing a conversion from poorly dividing Gfap$^+$ cells to new neurons in the SN, as observed after EBCs transplantation, although with much lower efficiency. Accordingly, very few cells co-localizing Gfap and Psa-Ncam (4.56 ± 1.94%, n = 3; Fig. 9D) were found, in comparison with the high frequency of co-localization between the neuroblast markers Psa-Ncam and Dcx (97.59 ± 2.58%, n = 3; Fig. 9E). These latter data suggest that, unlike the effect of EBCs transplantation, Vegf and Fgf2 promoted mostly a neurogenic process through the activation of NSCs.

Fig. 2. Transplantation of EBCs induces neurogenesis in the adult wild-type mouse SN. (A) Schematic representation of the experimental strategy in the mouse; EBCs from R1B5 cells (Egfp$^+$) were used for these experiments. (B) BrdU-labeled cells in the transplanted adult mouse SN (dark circles), contralateral SN (dark triangles) and Optimem-injected SN (white circles). Error bars indicate the SEM. (C) Percentage of BrdU$^+$ cells colabeled with: Nes and Sox1 at 6 dpt, Dcx at 15 dpt, NeuN and Th at 30 dpt; ND, not detected. (D–G) Confocal Z-projections showing BrdU$^+$ cells colabeled with Sox1, Nes, Dcx and NeuN markers in the mouse SN. White arrowheads indicate cells colabeling with BrdU and yellow arrowheads in (F) indicate those only labeled with Dcx. (D'–G') Orthogonal views. Scale bar 10 μm.

INFORME DE LABORES 2019

Table 5. Number of BrdU-labeled cells per mm^2 (mean ± SEM) colabeling with neural and neuronal markers in the transplanted adult mouse SN.

Post-transplantation period	Cell markers	Number of cells (percentage of $BrdU^+$ cells)
6 dpt	$Sox1^+/BrdU^+$	20.71 ± 5.18 (35.61 ± 0.89%)
(n = 3)	$Sox1^+/BrdU^-$	36.47 ± 11.17
6 dpt	$Nes^+/BrdU^+$	21.26 ± 4.39 (26.66 ± 6.31%)
(n = 4)	$Nes^+/BrdU^-$	37.09 ± 6.72
15 dpt	$Dcx^+/BrdU^+$	58.11 ± 8.47 (47.13 ± 2.87%)
(n = 4)	$Dcx^+/BrdU^-$	274.48 ± 25.77
30 dpt	$NeuN^+/BrdU^+$	2.47 ± 0.9 (33.33 ± 4.81%)
(n = 3)	$Th^+/BrdU^+$	0%

BrdU-labeled cells that also showed the markers indicated were counted (see Material and Methods) at different times post-transplantation; cells positive for the marker but negative for BrdU were also counted. The number of subjects (n) per group and the percentage (mean ± SEM) of total $BrdU^+$ cells are specified between parentheses.

DISCUSSION

Adult neurogenesis in the mammalian brain seems to be a restricted process to specific regions. However, based on experimental evidence it has been proposed that, albeit at a low rate, several brain areas possess a neurogenic capacity or nest an NSC population that is prompted to initiate a neurogenic process upon the emergence of activating signals (Lie et al., 2002;Zhao et al., 2003;Gould, 2007;Albright et al., 2016;Morrison, 2016). The present work was focused on evaluating the neurogenic capacity of the adult SN taking advantage of factors produced by EBCs which, in the context of embryonic (Baizabal and Covarrubias, 2009) and adult brain (Maya-Espinosa et al., 2015) environments, carry out a neurogenic process. Our results reveal the presence of quiescent NSCs and the induction of what appears to be an astrocyte to neuron transdifferentiation phenomenon in the adult SN.

Activation of quiescent NSCs

Activation of quiescent NSCs (Codega et al., 2014) in neurogenic niches is a constant process that can be modulated by specific signals (Alvarez-Buylla and Lim, 2004;Conover and Notti, 2008). In particular, injury activates NSCs in both hippocampus and SVZ. Interestingly, blood vessels are commonly associated with neurogenic niches and angiogenesis increases upon NSC activation (Palmer et al., 2000;Licht and Keshet, 2015). These relationships could also be present in other regions in which neurogenesis is not a constant

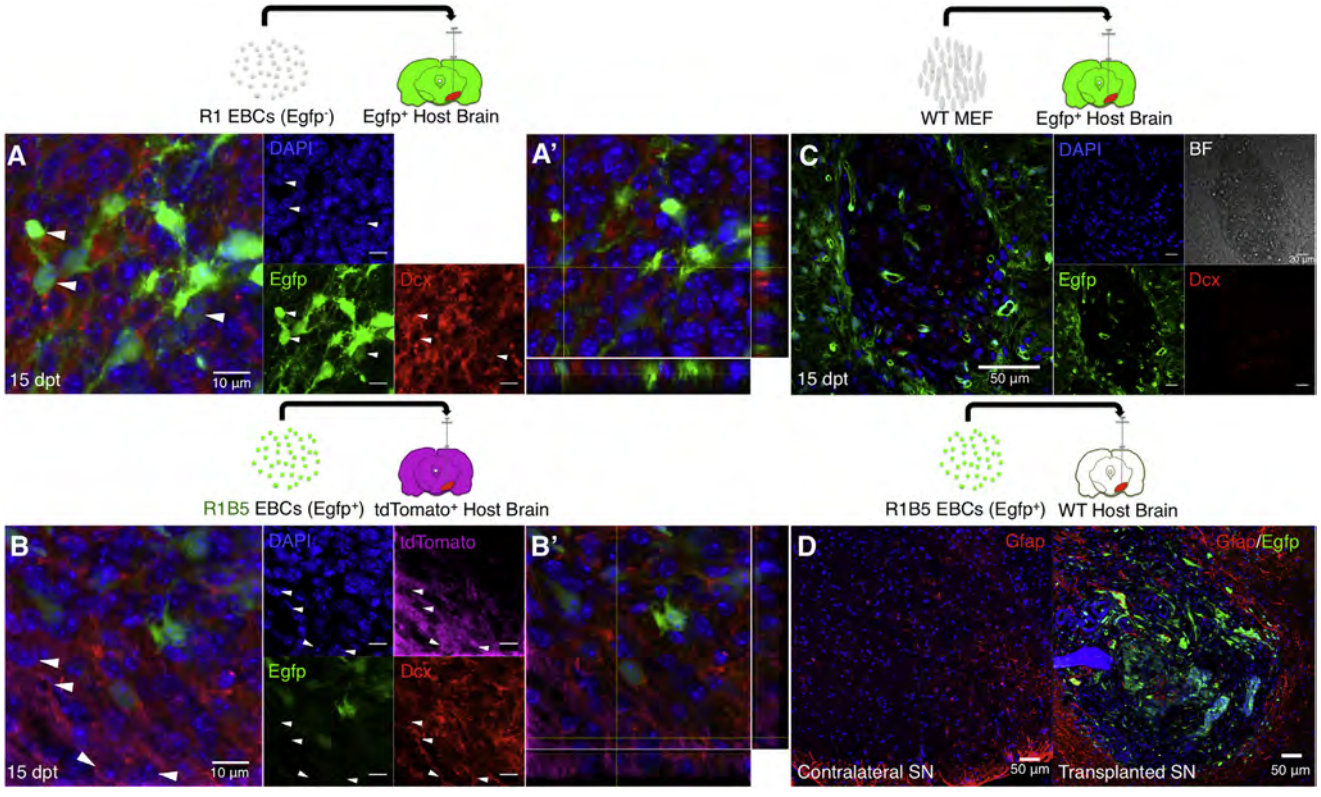

Fig. 3. Putative neuroblasts (Dcx^+ cells) and astrocytes ($Gfap^+$ cells) around the transplanted EBCs in the SN are of host origin. Confocal Z-projections of: (A) Endogenous $Egfp^+/Dcx^+$ cells (white arrowheads) detected 15 days after transplantation of R1 EBCs (no fluorescent marker present) to an $Egfp^+$ host brain (A', orthogonal view); (B) Endogenous $tdTomato^+/Dcx^+$ cells (white arrowheads) detected 15 days after transplantation of R1B5 EBCs ($Egfp^+$) to a $tdTomato^+$ host brain (B′, orthogonal view). (C) No Dcx^+ cell was detected 15 days after transplantation of wild-type MEFs to an $Egfp^+$ host brain. (D) In contrast with the contralateral intact SN, many $Gfap^+$ cells were detected in the transplanted SN parenchyma of wild-type mice 15 days after transplantation of R1B5 EBCs.

INFORME DE LABORES 2019

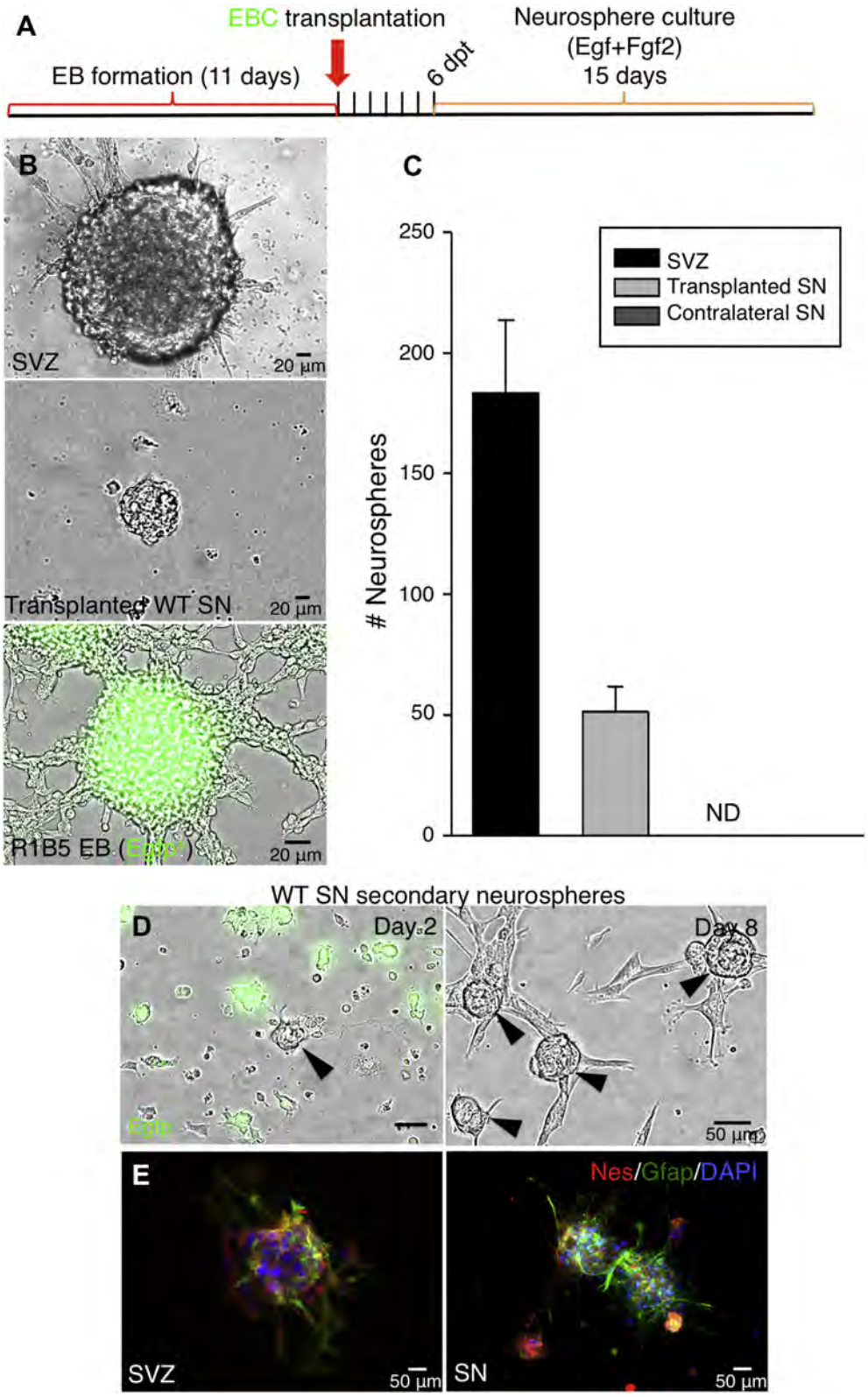

Fig. 4. Cells of the transplanted adult mouse SN generate neurospheres. (A) Schematic representation of the experimental strategy; transplanted EBCs were from R1B5 cells ($Egfp^+$). (B) Representative neurospheres from different cell sources: the SVZ (top) and the transplanted SN (middle). Note the formation of flat colonies derived from $Egfp^+$ EBCs (bottom). Scale bar 20 µm. (C) Number of neurospheres after 7 days *in vitro* for cells from the SVZ (positive control) and after 15 days *in vitro* for cells from the transplanted SN and contralateral SN (ND, not detected). Error bars indicate the SEM. (D) Secondary neurospheres (black arrowheads) formed from cells of the transplanted SN cultured for 2 or 8 days. (E) The SN neurospheres expressed *Gfap* and *Nes,* as typical neurospheres from the SVZ. Scale bar 50 µm.

INFORME DE LABORES 2019

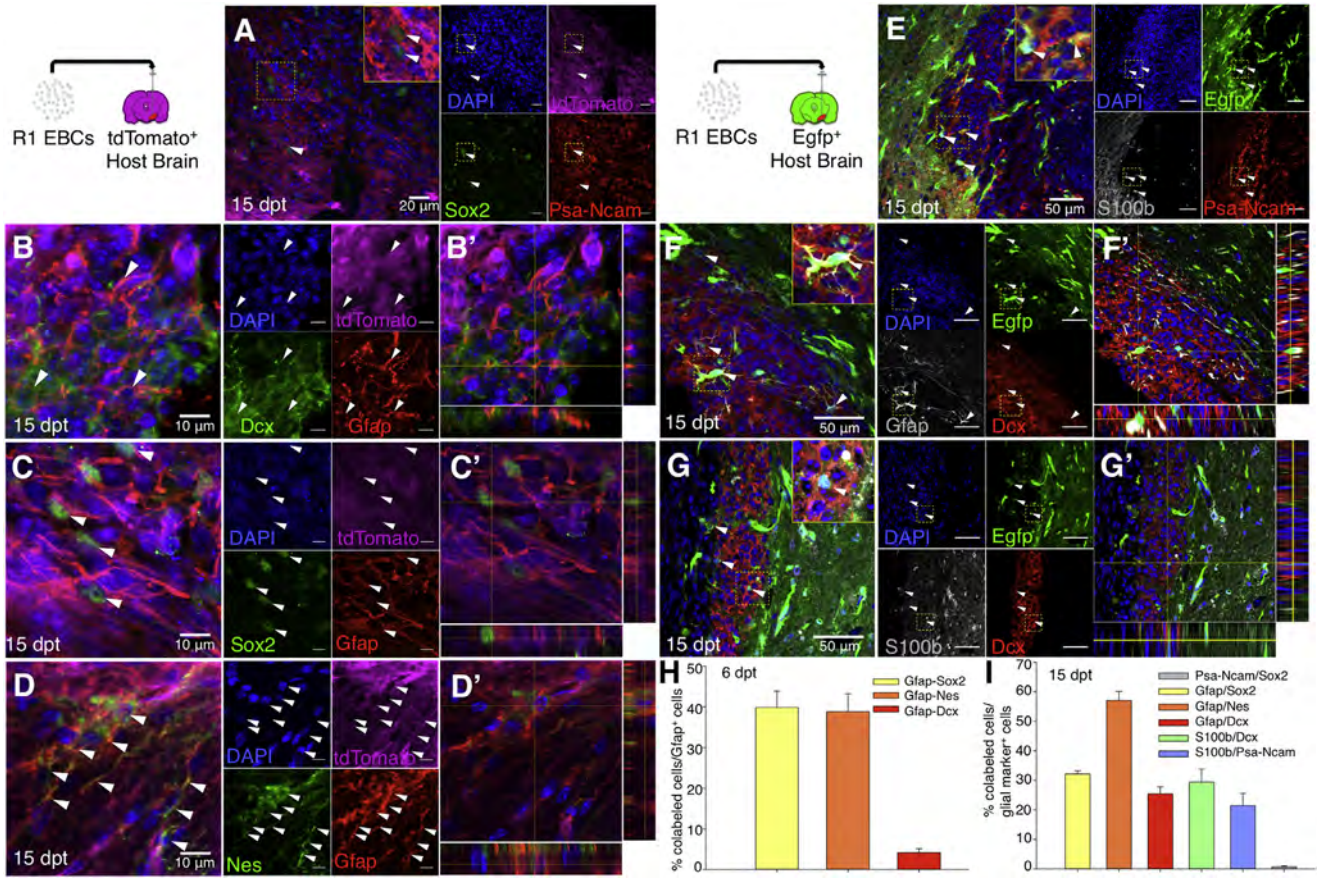

Fig. 5. Resident putative astrocytes express neuroblast and NPC markers after EBC transplantation. EBCs from R1 cells (no fluorescent marker present) were transplanted to the SN of tdTomato (A–D) mice or Egfp mice (E–G) and neural markers determined after 6 and 15 dpt. (A) Confocal Z-projection of Psa-Ncam$^+$/Sox2$^+$/tdTomato$^+$ cells at 15 dpt. (B–D) Confocal Z-projections showing host Gfap$^+$ cells (tdTomato$^+$) in the SN that colabeled with Dcx (B; B′, orthogonal view), Sox2 (C; C′, orthogonal view) and Nes (D; D', orthogonal view). Scale bar 10 µm. (E) Confocal Z-projection of S100b$^+$/Psa-Ncam$^+$/Egfp$^+$ cells at 15 dpt. (F, G) Confocal Z-projections showing host Gfap$^+$ (F) or S100b$^+$ (G) cells (Egfp$^+$) that colabeled with Dcx (F′ and G', orthogonal views). White arrowheads indicate colabeled cells. Scale bar 50 µm. (H) Percentage of colabeled Gfap$^+$/Sox2$^+$(n = 3), Gfap$^+$/Nes$^+$ (n = 3) and Gfap$^+$/Dcx$^+$ (n = 3) cells with respect to total host Gfap$^+$ cells at 6 dpt. (I) Percentage of colabeled Gfap$^+$/Sox2$^+$(n = 3), Gfap$^+$/Nes$^+$ (n = 3) and Gfap$^+$/Dcx$^+$ (n = 7) cells with respect to total Gfap$^+$ cells at 15 dpt. Additionally, the percentage of S100b$^+$/Dcx$^+$ (n = 7) and S100b$^+$/Psa-Ncam$^+$ (n = 3) is shown with respect to total S100b$^+$ cells and Psa-Ncam$^+$/Sox2$^+$ (n = 4) cells with respect to total Psa-Ncam$^+$ cells at 15 dpt.

process but only occurs under specific physiological conditions or damage.

Finding NSCs in regions with low neurogenic activity may not be an easy task, since they are expected to be scarce. Interestingly we found that, upon EBCs transplantation, dividing Sox2$^+$ and Nes$^+$ cells emerged in the SN. Migration of these cells from a putative neurogenic niche such as the aqueduct periventricular region seems unlikely since Sox2$^+$ cells were distributed evenly around the transplant and emerged only few days after transplantation. This kinetics is not in agreement with NPC migration from the aqueduct, a putative neurogenic niche that shows apparent capacity to populate the SN with new dopaminergic neurons 45–65 days after MPTP-induced injury (L'Episcopo et al. (2014). The identity of the dormant NSC found is uncertain since *Sox1*/*Sox2*/*Nes* expression was very infrequent in the intact SN; thus, common NSC markers may not be present or be expressed at low levels in these putative NSCs. In addition, although NSC markers appeared to emerge before cell division (detected as Sox1$^+$/Sox2$^+$/BrdU$^-$ NSCs), at least some of these 'activated' NSCs (Sox1$^+$/Sox2$^+$/BrdU$^+$) divide before differentiation into Dcx$^+$ neuroblasts (Dcx$^+$/BrdU$^+$) and neurons (NeuN$^+$/BrdU$^+$). Supporting the activation of quiescent NSCs, neurospheres could be generated from cells of the transplanted SN; interestingly, these neurospheres resemble those that can be generated from the SGZ (Guo et al., 2012). As in typical neurogenic regions, survival of terminally differentiated neurons was low and only few mature neurons were found. However, this outcome was also determined by the continuous growth of the transplant that made it difficult to track new neurons and determine the capacity for integration into established neuronal circuits.

EBC-induced neurogenesis involved the participation of blood vessels since the number of Dcx$^+$ neuroblast was reduced by an angiogenesis inhibitor and neurogenesis in the SN could also be induced by the infusion of angiogenic factors (i.e., Vegf and Fgf2). Interestingly, a strong association between NSCs and blood vessels has been observed in the SGZ (Palmer et al., 2000) and the SVZ (Shen et al., 2008). In agreement with a relevant role of this association,

INFORME DE LABORES 2019

the intracerebroventricular infusion of Vegf stimulates neurogenesis in these regions (Jin et al., 2002) and the ectopic expression of Vegf increases neurogenesis and blood vessels in the SGZ (Licht et al., 2016). Furthermore, as it appeared to occur in the SN, the simultaneous administration of Vegf and Fgf2 in the fourth ventricle activates a dormant NSCs population (Luo et al., 2015). In our experiments, the capacity of Fgf2 and Vegf for stimulating the generation of new neurons was lower than that of EBCs and, in addition, transdifferentiation from astrocytes to neurons appeared to occur at lower levels (see below); therefore, other factors secreted by EBCs contribute to promote the full neurogenic capacity of the SN.

Glial cells as a source of new neurons

NPC proliferation is a characteristic of activated neurogenesis such that new neuroblasts and neurons are typically identified by tracing the incorporation of nucleotide analogs. Therefore, it was unexpected to find that only around 20–30% of Dcx cells colabeled with BrdU, even when this latter nucleotide analog was constantly applied during most of the neurogenic process. This result suggests that these neuroblasts/young neurons do not emerge from highly dividing NPCs. In addition, many of those Dcx$^+$ and Psa-Ncam$^+$ neuroblasts colabeled with astrocytic markers such as Gfap and S100b. The presence of S100b was particularly relevant

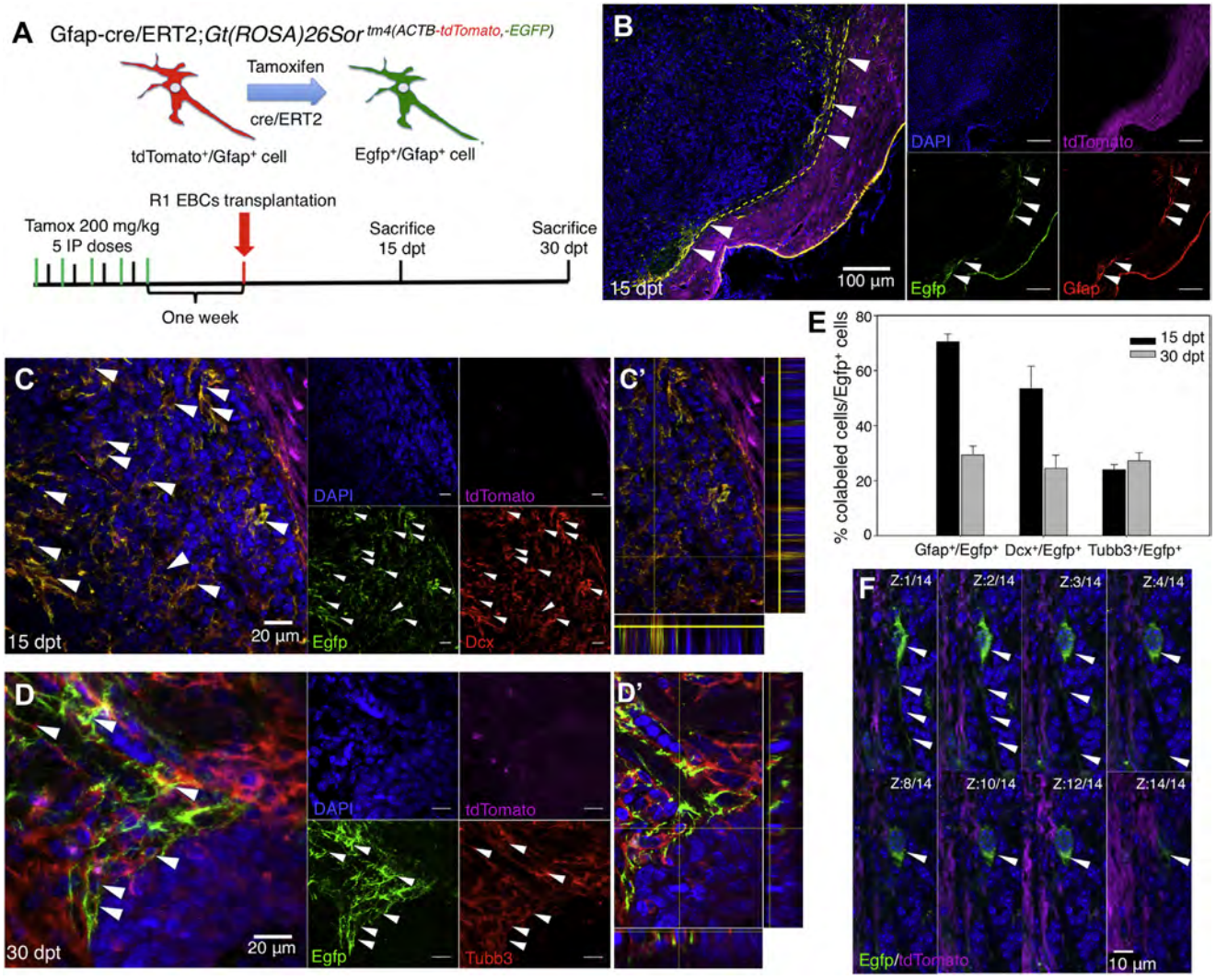

Fig. 6. Resident Gfap$^+$ cells acquire a neuronal fate after EBC transplantation to the SN. (A) Schematic representation of the experimental strategy. R1 EBCs (no fluorescent marker present) were transplanted to the SN of Gfap-cre/ERT2;*Gt(ROSA)26Sor* $^{tm4(ACTB\text{-}tdTomato,\text{-}EGFP)}$ double transgenic mice 1 week after tamoxifen treatment and neuronal markers determined at 15 and 30 dpt. (B) Confocal Z-projection showing the recombined cells Egfp$^+$/Gfap$^+$ (white arrowheads) around the transplantation site (dashed yellow line) at 15 dpt. (C) Dcx-labeled cells derived from Gfap$^+$ cells (Egfp$^+$; white arrowheads) at 15 dpt (C', orthogonal view). (D) Tubb3-labeled cells derived from Gfap$^+$ cells (Egfp$^+$; white arrowheads) at 30 dpt (D', orthogonal view). (E) Percentage of colabeled Gfap$^+$/Egfp$^+$, Dcx$^+$/Egfp$^+$, and Tubb3$^+$/Egfp$^+$ cells with respect to the total Egfp$^+$ cells at 15 and 30 dpt (n = 3–4). Error bars indicate SEM. (F) Z-plane trajectory of a representative Egfp$^+$ cell found around the transplantation site (30 dpt); note the projection that emerges from the cell body (white arrowheads).

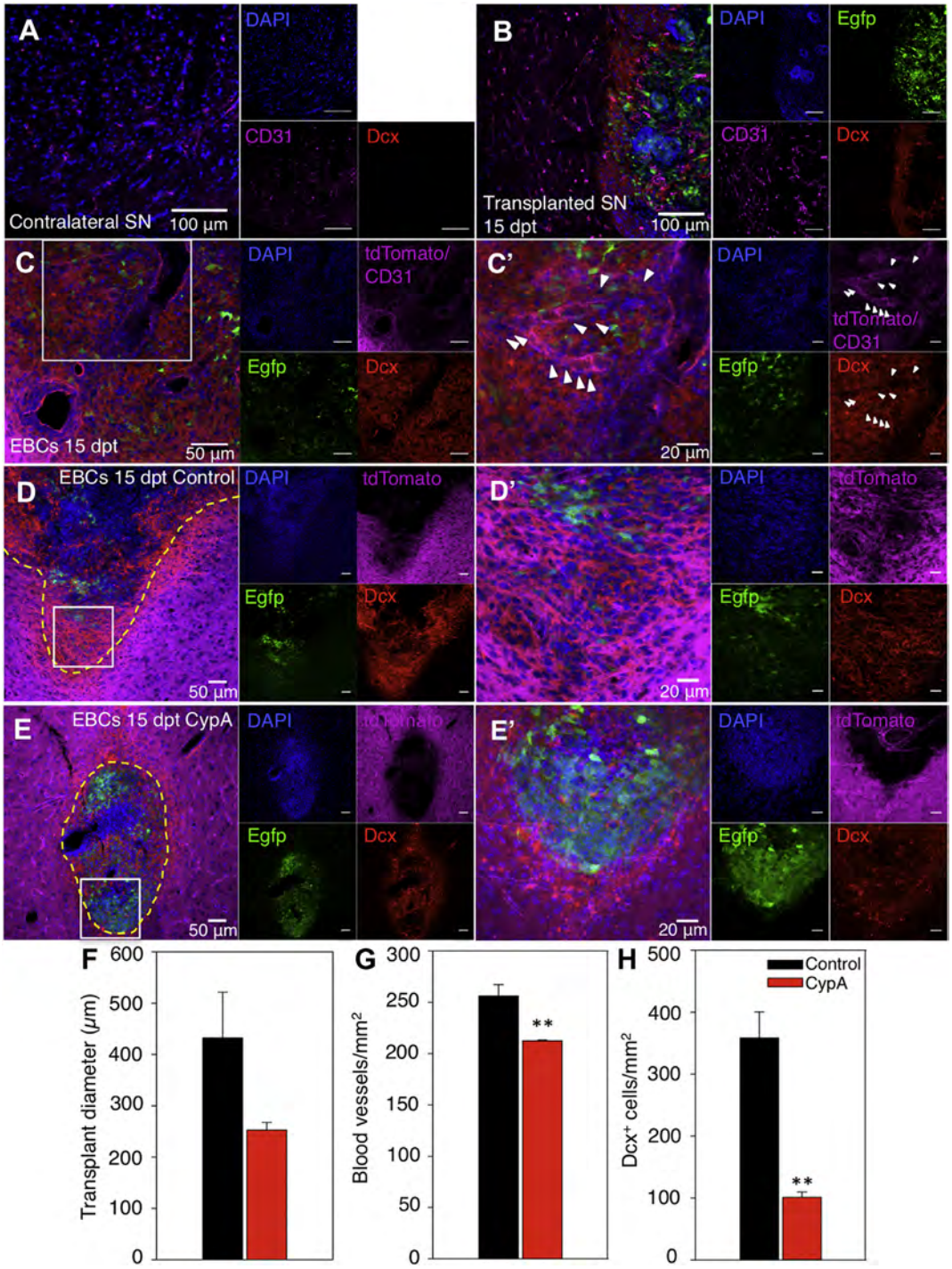

Fig. 7. Angiogenesis inhibition reduces transplant growth and induced neurogenesis in the SN. (A–B) R1B5 EBCs were transplanted to the SN of wild type mice. Dcx^+ cells were not found in the contralateral SN and CD31 immunoreactivity (magenta) appeared less evident (A), in comparison with the significant number of Dcx^+ cells (red) and blood vessels (magenta) in the SN with implanted EBCs (B). (C) Dcx^+ cells (red) were found tightly associated with $CD31^+$ blood vessels (magenta; white arrowheads in C'). (D–H) tdTomato mice previously transplanted with R1B5 EBCs ($Egfp^+$) were treated with CypA or injected with the vehicle solution (Control) and, after 15 dpt, the number of Dcx^+ cells generated was determined. (D) Confocal images showing neuroblasts (Dcx^+/$tdTomato^+$) surrounding the R1B5 EBC transplant ($Egfp^+$) in the tdTomato SN (magenta) at 15 dpt (Control). (E) Equivalent images from mice treated with CypA. Dcx^+ cells are shown in red and the transplant limited in picture by a yellow dashed line. Inset in (D) and (E) is shown in (D') and (E'), respectively. Determinations in the Control and CypA-treated mice of: (F) transplant diameter, (G) the number of blood vessels per mm^2, and (H) Dcx^+ cells per mm^2 are shown. Error bars indicate SEM; **$p < 0.01$.

INFORME DE LABORES 2019

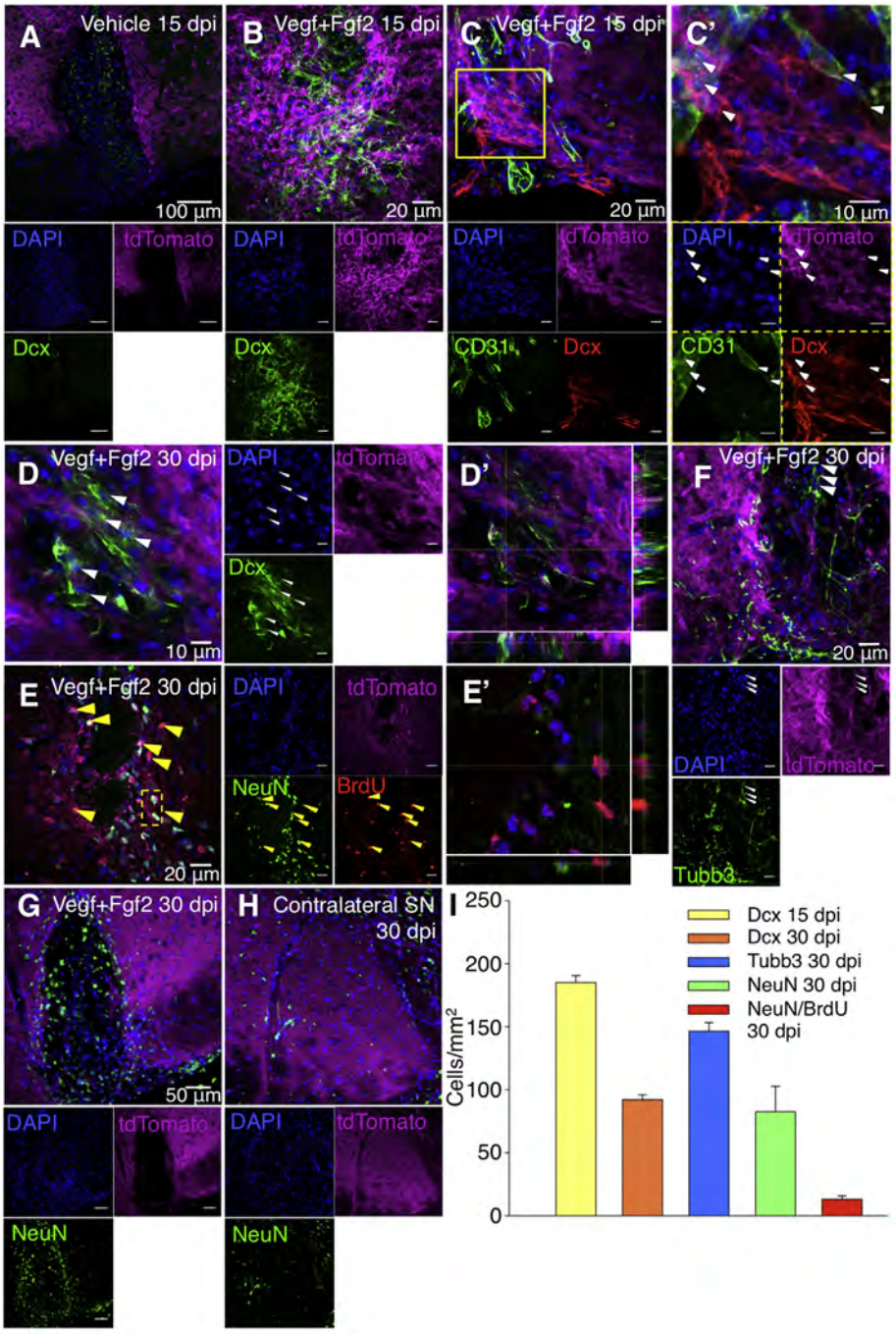

Fig. 8. Angiogenic factors promote neurogenesis in the SN. Vegf and Fgf2 were embedded in a Puramatrix hydrogel and then implanted in the SN of tdTomato mice; neuronal markers were determined at 15 and 30 dpi. (A, B) Confocal Z-projections showing the absence of Dcx^+ cells in the SN injected with a hydrogel without growth factors (Vehicle; A), and the presence of Dcx^+ cells emerging around the Fgf2 + Vegf-embedded hydrogel at 15 dpi (B). (C) Dcx^+ cells (red) are associated with thick blood vessels ($CD31^+$; green) in the Vegf+Fgf2 injected SN at 15 dpi (white arrowheads in C′ inset). (D, E) Confocal Z-projections showing Dcx^+ neuroblasts (D, white arrowheads; D', orthogonal view) and $NeuN^+$ cells (E; E', orthogonal view of inset in E) around the Vegf+Fgf2-embedded hydrogel in the SN of tdTomato mice at 30 dpi (n = 3–5); in E, yellow arrowheads indicate $NeuN^+$ cells that were also positive for BrdU. (F) Confocal Z-projection showing $Tubb3^+$ cells (white arrowheads) at 30 dpi. (G, H) $NeuN^+$ cells around the Vegf+Fgf2 injection site in the SN of tdTomato mice at 30 dpi (G) and in the contralateral non-injected SN (H); note that, although only 16% of the $NeuN^+$ cells were colabeled with BrdU, the density of NeuN labeled cells increased around the Vegf+Fgf2 containing hydrogel in comparison with the contralateral SN. (I) Quantification of labeled cells for the markers indicated (n = 3) near the injection site at 15 and 30 dpi is shown. Error bars indicate SEM.

since its gene is repressed in adult SVZ NSCs and is a chracteristic of 'mature' $Gfap^+$ astrocytes with reduced NSC properties (Raponi et al., 2007). It is relevant to mention that the level of Dcx detection in the SN was similar to the one obtained in the rostral migratory stream and the dentate gyrus (data not shown); thus these cells hardly correspond

INFORME DE LABORES 2019

to the ones previously reported in the SN (Worlitzer et al., 2013). Therefore, these results open the possibility that parenchymal Gfap$^+$ cells are transdifferentiating into neurons. Supporting this conclusion, lineage tracing in Gfap-cre/ERT2; *Gt(ROSA)26Sor* $^{tm4(ACTB-tdTomato,-EGFP)}$ double transgenic mice showed that Dcx$^+$ and Tubb3$^+$ cells can derive from Gfap$^+$ cells.

The conversion of astrocytes into neurons has been achieved by the forced expression of pro-neural factors such as neurogenin-2 and Ascl1 (Mash1) *in vitro* (Berninger et al., 2007) and *in vivo* (Torper et al., 2013;Rivetti di Val Cervo et al., 2017). However, the actual intrinsic potential of astrocytes for converting into neurons has been demonstrated mainly in the striatum after injury (Magnusson et al., 2014;Nato et al., 2015). In particular, Magnusson et al. (2014) showed that the conversion observed initiates by the downregulation of Notch1 signaling and the upregulation of *Ascl1*, and transits through cells that retain astrocytic markers (Gfap, S100b) at the time gain neuroblast markers (Dcx). This is similar to what we found in our study, though in this case, it is apparent that cell division is required before neuronal conversion (Fig. 10).

It is worth mentioning that early in the EBCs-induced neurogenesis, Gfap$^+$/Sox2$^+$ cells were abundant (6 dpt), but later (15 dpt) this population decreased while Gfap$^+$/Dcx$^+$ cells emerged. This contrasts with the increasing number of Gfap$^+$/Nes$^+$ cells which likely represent reactive astrocytes. Therefore, it is possible that non-dividing cells with NPC markers (Sox2$^+$/BrdU$^-$) emerge before becoming Dcx$^+$/Psa-Ncam$^+$ neuroblasts, and also that astrocytes are a candidate source of the dividing NPCs detected upon EBCs transplantation. Due to the sharing of phenotypic markers, complete discrimination of fully differentiated astrocytes from resident quiescent NSCs still requires further investigation. On the other hand, the infusion of Vegf and Fgf2 apparently was not as efficient as EBCs transplantation to induce the direct conversion of Gfap$^+$ cells into neuroblasts since few cells colabeled with markers of neuroblasts and astrocytes. However, not all neuroblasts/neurons appeared to originate from dividing NPCs, since few of these cells around the injected hydrogel incorporated BrdU along the neurogenic process. The astrocytic origin was supported by tracing Dcx$^+$ and Tubb3$^+$ cells from Egfp$^+$-labeled Gfap$^+$ cells. Therefore, a

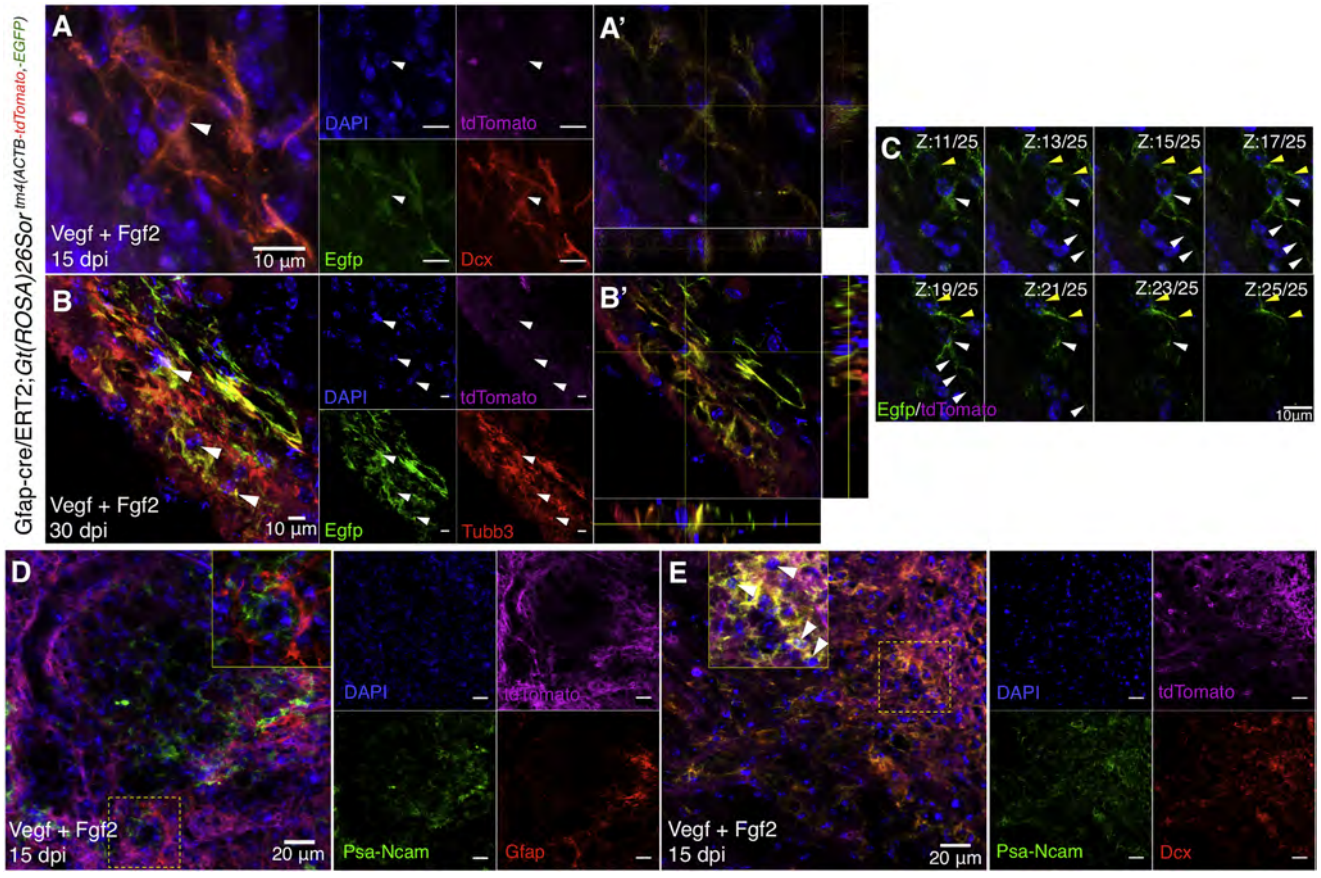

Fig. 9. Some SN putative astrocytes (Gfap$^+$ cells) derive into neurons in response to soluble angiogenic factors. The SN of Gfap-cre/ERT2;*Gt(ROSA)26Sor* $^{tm4(ACTB-tdTomato,-EGFP)}$ double transgenic mice, 1 week after tamoxifen treatment, was injected with a Fgf2 + Vegf-embedded hydrogel and neuronal markers determined at 15 and 30 dpi. (A) Some Dcx$^+$/Egfp$^+$ cells (white arrowheads; A', orthogonal view) were identified at 15 dpi. (B) Tubb3$^+$/Egfp$^+$ cells (white arrowheads; B′, orthogonal view) were identified at 30 dpi. (C) Z-plane trajectories of two representative Egfp$^+$ cells (white and yellow arrowheads) found around the implanted hydrogel (15 dpi); note the projections that emerge from the two cell bodies indicated. (D) Evaluation of the colabeling between Psa-Ncam and Gfap markers in neuroblasts detected around the injection site; only 4.56 ± 1.94% Psa-Ncam$^+$/Gfap$^+$ cells of total Psa-Ncam$^+$ cells were identified (n = 3). (E) Evaluation of the colabeling between Psa-Ncam and Dcx markers in neuroblasts detected around the injection site; colabeling (white arrowheads) was observed in most neuroblast identified (97.59 ± 2.58%; n = 3).

INFORME DE LABORES 2019

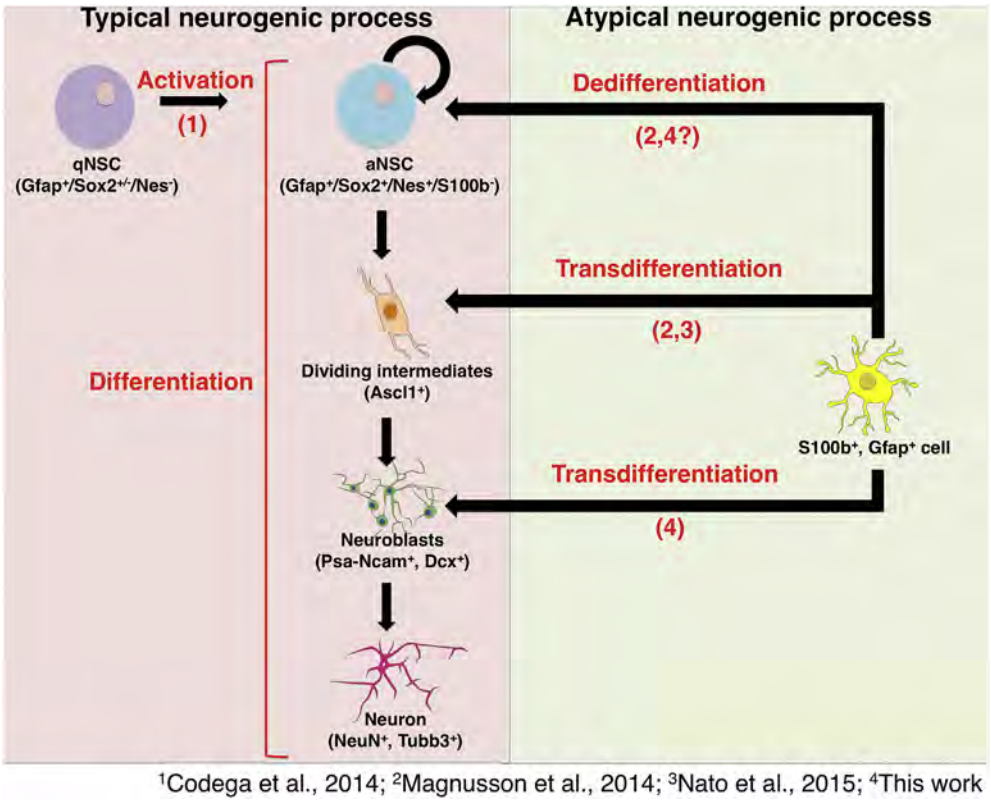

Fig. 10. Typical and atypical neurogenesis in the adult brain. A typical neurogenic process involves the participation of NSCs (aNSC) with self-renewal capacity, which give rise to highly dividing intermediates (Ascl1$^+$), which in turn originate new neuroblasts (Psa-Ncam$^+$/Dcx$^+$) that mature into fully differentiated neurons (Tubb3$^+$/NeuN$^+$). Regions with high neuronal renewal rate appear to have quiescent NSC-like cells (qNSC) that become active upon specific stimuli. In contrast with this typical neurogenic process, in the SN as well as in the striatum and medial cortex, cells with mature post-mitotic astrocytic markers (S100b$^+$/Gfap$^+$) can transdifferentiate or dedifferentiate into cells with neurogenic capacity upon certain inputs. These atypical neurogenic processes involve the acquisition by parenchymal astrocytes of NPC properties with or without the requirement of cell division. Whether these latter cells represent a specific class of quiescent NSCs remains to be determined (see text for details).

significant number of Tubb3$^+$ and NeuN$^+$ cells can emerge upon induction by either EBCs or Vegf+Fgf2 administration from non-dividing cells. Although we cannot discard that these are parenchymal astrocytes, an interesting possibility is that they are equivalent to the Gfap$^+$/S100b$^+$/Nes$^+$/Sox2$^+$ adult NSCs found in the intact zebrafish telencephalon, which are mostly quiescent and convert directly into neurons without a cell division phase (Barbosa et al., 2015).

Neurogenesis in the adult SN

Dopaminergic neurons might renew throughout life at a low rate and the process could be accelerated by induced neurodegeneration (e.g., disease-associated or provoked by a toxic compound). This perception derives from experimental observations whose interpretation is yet inconclusive. One issue that remains to be determined is the origin of these new neurons. BrdU incorporation has been detected during the generation of new dopaminergic neurons in the adult SN (Zhao et al., 2003). Without considering the possibility of BrdU incorporation due to a DNA repair process, this has been interpreted as an indicative of the presence of NPCs in the SN though, strictly, this only indicates that, during the process of renewal or repair, cell divisions occur. In another study, based on the tracing of dopaminergic neurons with deleted floxed *Th* alleles due to the activation in the adult of CreER, whose expression was driven by either the Nes or Sox2 promoter, it was proposed that the source of new dopaminergic neurons are cells Nes$^+$/Sox2$^-$ (Albright et al., 2016). We have not been able to detect Nes$^+$ cells within the intact SN, thus leaving the possibility that these precursors are recruited from "nearby" neurogenic sites [e.g., periaqueduct; L'Episcopo et al., 2014]. Alternatively, transient *Nes* expression could have occurred in putative active precursors in the SN during tamoxifen treatment as it occurs in some striatal astrocytes (Nato et al., 2015).

Here we show that scarce dividing cells or cells with NPC markers were present in the intact SN, but cells with NPC or neuroblast markers rapidly emerge upon EBCs transplantation or Vegf+Fgf2 infusion. However, although these cells showed neurogenic capacity, expression of the essential *Th* dopaminergic gene and of genes required for mesencephalic dopaminergic differentiation (i.e., *Lmx1a*, *Neurog2*; Guerrero-Flores et al., 2017) was not found in neuronal derivatives at any time. The inability of the precursors identified here for deriving new dopaminergic neurons might be due to an inhibitory effect of EBCs-secreted factors or missing factors required for correct specification not activated under the conditions tested. In this regard, it will be interesting to determine whether the missing factors activate upon induced

dopaminergic neurodegeneration though, at the moment, it cannot be discarded that the neuronal fate of activated NPCs is restricted to non-dopaminergic phenotypes.

Homeostatic renewal of neurons has been proposed for many brain regions, including the striatum and the SN. However, an evident neurogenic niche has not been found in these regions. On the other hand, it has been proposed that a neurogenic process activates upon injury. Our data support that new neurons can originate in the SN from either dormant NSCs or parenchymal astrocytes that upon a transdifferentiation phenomenon are converted into NPCs or directly into neuroblasts (Fig. 10). However, our data do not provide evidence on the adult SN capacity to generate new dopaminergic neurons. Due to the biological and medical interest, ongoing work is focused to determine whether SN glial cells could be the source of new dopaminergic neurons.

ACKNOWLEDGMENTS

DMA is a doctoral student of the Programa de Doctorado en Ciencias Biomédicas, Universidad Nacional Autónoma de México (UNAM) and received the fellowship 366700 from CONACyT. We appreciate the technical support of Concepción Valencia and Rubén Blancas at the Instituto de Biotecnología and of Marcela Palomero Rivero at the Instituto de Fisiología Celular. We also acknowledge the assistance of the LNMA facility core members, especially that of Xóchitl Alvarado-Affantranger, and of the Animal Care Facility members, particularly Graciela Cabeza Pérez, Sergio González Trujillo and Elizabeth Mata Moreno, of the Instituto de Biotecnología, UNAM. We are grateful to José Segovia for his comments and the careful reading of the manuscript.

AUTHOR'S CONTRIBUTION

D.M.A., acquisition of data, analysis and interpretation of data, drafting of manuscript; M.G.C., study conception and design, critical revision; L.C., study conception and design, analysis and interpretation of data, drafting of manuscript, critical revision.

FUNDING

This work was supported by CONACyT grants CB131031 and FOINS1723.

REFERENCES

Albright JE, Stojkovska I, Rahman AA, Brown CJ, Morrison BE. (2016) Nestin-positive/SOX2-negative cells mediate adult neurogenesis of nigral dopaminergic neurons in mice. Neurosci Lett 615:50-54.

Alvarez-Buylla A, Garcia-Verdugo JM. (2002) Neurogenesis in adult subventricular zone. J Neurosci 22:629-634.

Alvarez-Buylla A, Lim DA. (2004) For the long run: maintaining germinal niches in the adult brain. Neuron 41:683-686.

Alvarez-Buylla A, Lois C. (1995) Neuronal stem cells in the brain of adult vertebrates. Stem Cells 13:263-272.

Baizabal JM, Covarrubias L. (2009) The embryonic midbrain directs neuronal specification of embryonic stem cells at early stages of differentiation. Dev Biol 325:49-59.

Baizabal JM, Cano-Martinez A, Valencia C, Santa-Olalla J, Young KM, Rietze RL, Bartlett PF, Covarrubias L. (2012) Glial commitment of mesencephalic neural precursor cells expanded as neurospheres precludes their engagement in niche-dependent dopaminergic neurogenesis. Stem Cells Dev 21:1047-1058.

Barbosa JS, Sanchez-Gonzalez R, Di Giaimo R, Baumgart EV, Theis FJ, Gotz M, Ninkovic J. (2015) Neurodevelopment. Live imaging of adult neural stem cell behavior in the intact and injured zebrafish brain. Science 348:789-793.

Berninger B, Costa MR, Koch U, Schroeder T, Sutor B, Grothe B, Gotz M. (2007) Functional properties of neurons derived from in vitro reprogrammed postnatal astroglia. J Neurosci 27:8654-8664.

Bovetti S, Hsieh YC, Bovolin P, Perroteau I, Kazunori T, Puche AC. (2007) Blood vessels form a scaffold for neuroblast migration in the adult olfactory bulb. J Neurosci 27:5976-5980.

Cameron HA, Woolley CS, McEwen BS, Gould E. (1993) Differentiation of newly born neurons and glia in the dentate gyrus of the adult rat. Neuroscience 56:337-344.

Codega P, Silva-Vargas V, Paul A, Maldonado-Soto AR, Deleo AM, Pastrana E, Doetsch F. (2014) Prospective identification and purification of quiescent adult neural stem cells from their in vivo niche. Neuron 82:545-559.

Conover JC, Notti RQ. (2008) The neural stem cell niche. Cell Tissue Res 331:211-224.

Cuevas P, Gimenez-Gallego G, Carceller F, Cuevas B, Crespo A. (1993) Single topical application of human recombinant basic fibroblast growth factor (rbFGF) promotes neovascularization in rat cerebral cortex. Surg Neurol 39:380-384.

Fathi A, Pakzad M, Taei A, Brink TC, Pirhaji L, Ruiz G, Sharif Tabe Bordbar M, Gourabi H, et al. (2009) Comparative proteome and transcriptome analyses of embryonic stem cells during embryoid body-based differentiation. Proteomics 9:4859-4870.

Franklin KBJ, Paxinos G. (2013) Paxinos and Franklin's the mouse brain in stereotaxic coordinates. Amsterdam: Academic Press, an imprint of Elsevier, 2013.

Frielingsdorf H, Schwarz K, Brundin P, Mohapel P. (2004) No evidence for new dopaminergic neurons in the adult mammalian substantia nigra. Proc Natl Acad Sci U S A 101:10177-10182.

Ganat YM, Silbereis J, Cave C, Ngu H, Anderson GM, Ohkubo Y, Ment LR, Vaccarino FM. (2006) Early postnatal astroglial cells produce multilineage precursors and neural stelm cells in vivo. J Neurosci 26:8609-8621.

Gotz M, Sirko S, Beckers J, Irmler M. (2015) Reactive astrocytes as neural stem or progenitor cells: in vivo lineage, in vitro potential, and genome-wide expression analysis. Glia 63:1452-1468.

Gould E. (2007) How widespread is adult neurogenesis in mammals? Nat Rev Neurosci 8:481-488.

Guerrero-Flores G, Bastidas-Ponce A, Collazo-Navarrete O, Guerra-Crespo M, Covarrubias L. (2017) Functional determination of the differentiation potential of ventral mesencephalic neural precursor cells during dopaminergic neurogenesis. Dev Biol 429:56-70.

Guo W, Patzlaff NE, Jobe EM, Zhao X. (2012) Isolation of multipotent neural stem or progenitor cells from both the dentate gyrus and subventricular zone of a single adult mouse. Nat Protoc 7:2005-2012.

Hermann A, Maisel M, Wegner F, Liebau S, Kim DW, Gerlach M, Schwarz J, Kim KS, et al. (2006) Multipotent neural stem cells from the adult tegmentum with dopaminergic potential develop essential properties of functional neurons. Stem Cells 24:949-964.

Hernandez GL, Volpert OV, Iniguez MA, Lorenzo E, Martinez-Martinez S, Grau R, Fresno M, Redondo JM. (2001) Selective inhibition of vascular endothelial growth factor-mediated angiogenesis by cyclosporin a: roles of the nuclear factor of activated T cells and cyclooxygenase 2. J Exp Med 193:607-620.

Jin K, Zhu Y, Sun Y, Mao XO, Xie L, Greenberg DA. (2002) Vascular endothelial growth factor (VEGF) stimulates neurogenesis in vitro and in vivo. Proc Natl Acad Sci U S A 99:11946-11950.

Kim BK, Kim SE, Shim JH, Woo DH, Gil JE, Kim SK, Kim JH. (2006) Neurogenic effect of vascular endothelial growth factor during germ layer formation of human embryonic stem cells. FEBS Lett 580:5869-5874.

L'Episcopo F, Tirolo C, Testa N, Caniglia S, Morale MC, Serapide MF, Pluchino S, Marchetti B. (2014) Wnt/beta-catenin signaling is required to rescue midbrain dopaminergic progenitors and promote

neurorepair in ageing mouse model of Parkinson's disease. Stem Cells 32:2147-2163.
Licht T, Keshet E. (2015) The vascular niche in adult neurogenesis. Mech Dev 138(Pt 1):56-62.
Licht T, Rothe G, Kreisel T, Wolf B, Benny O, Rooney AG, Ffrench-Constant C, Enikolopov G, et al. (2016) VEGF preconditioning leads to stem cell remodeling and attenuates age-related decay of adult hippocampal neurogenesis. Proc Natl Acad Sci U S A 113:E7828-E7836.
Lie DC, Dziewczapolski G, Willhoite AR, Kaspar BK, Shults CW, Gage FH. (2002) The adult substantia nigra contains progenitor cells with neurogenic potential. J Neurosci 22:6639-6649.
Lois C, Alvarez-Buylla A. (1993) Proliferating subventricular zone cells in the adult mammalian forebrain can differentiate into neurons and glia. Proc Natl Acad Sci U S A 90:2074-2077.
Luo Y, Coskun V, Liang A, Yu J, Cheng L, Ge W, Shi Z, Zhang K, et al. (2015) Single-cell transcriptome analyses reveal signals to activate dormant neural stem cells. Cell 161:1175-1186.
Magnusson JP, Goritz C, Tatarishvili J, Dias DO, Smith EM, Lindvall O, Kokaia Z, Frisen J. (2014) A latent neurogenic program in astrocytes regulated by notch signaling in the mouse. Science 346:237-241.
Maya-Espinosa G, Collazo-Navarrete O, Millan-Aldaco D, Palomero-Rivero M, Guerrero-Flores G, Drucker-Colin R, Covarrubias L, Guerra-Crespo M. (2015) Mouse embryonic stem cell-derived cells reveal niches that support neuronal differentiation in the adult rat brain. Stem Cells 33:491-502.
Morrison BE. (2016) Discovery of nigral dopaminergic neurogenesis in adult mice. Neural Regen Res 11:878-881.
Nato G, Caramello A, Trova S, Avataneo V, Rolando C, Taylor V, Buffo A, Peretto P, et al. (2015) Striatal astrocytes produce neuroblasts in an excitotoxic model of Huntington's disease. Development 142:840-845.
Ngangan AV, Waring JC, Cooke MT, Mandrycky CJ, McDevitt TC. (2014) Soluble factors secreted by differentiating embryonic stem cells stimulate exogenous cell proliferation and migration. Stem Cell Res Ther 5:26.
Palmer TD, Willhoite AR, Gage FH. (2000) Vascular niche for adult hippocampal neurogenesis. J Comp Neurol 425:479-494.
Paxinos G, Watson C. (2005) The rat brain in stereotaxic coordinates. Amsterdam: Elsevier Academic Press, 2005.
Rafiee P, Heidemann J, Ogawa H, Johnson NA, Fisher PJ, Li MS, Otterson MF, Johnson CP, et al. (2004) Cyclosporin A differentially inhibits multiple steps in VEGF induced angiogenesis in human microvascular endothelial cells through altered intracellular signaling. Cell Commun Signal 2:3.
Raponi E, Agenes F, Delphin C, Assard N, Baudier J, Legraverend C, Deloulme JC. (2007) S100B expression defines a state in which GFAP-expressing cells lose their neural stem cell potential and acquire a more mature developmental stage. Glia 55:165-177.
Rivetti di Val Cervo P, Romanov RA, Spigolon G, Masini D, Martin-Montanez E, Toledo EM, La Manno G, Feyder M, et al. (2017) Induction of functional dopamine neurons from human astrocytes in vitro and mouse astrocytes in a Parkinson's disease model. Nat Biotechnol 35:444-452.
Seo JH, Yu JH, Suh H, Kim MS, Cho SR. (2013) Fibroblast growth factor-2 induced by enriched environment enhances angiogenesis and motor function in chronic hypoxic-ischemic brain injury. PLoS One 8e74405.
Shan X, Chi L, Bishop M, Luo C, Lien L, Zhang Z, Liu R. (2006) Enhanced de novo neurogenesis and dopaminergic neurogenesis in the substantia nigra of 1-methyl-4-phenyl-1,2,3,6-tetrahydropyridine-induced Parkinson's disease-like mice. Stem Cells 24:1280-1287.
Shen Q, Wang Y, Kokovay E, Lin G, Chuang SM, Goderie SK, Roysam B, Temple S. (2008) Adult SVZ stem cells lie in a vascular niche: a quantitative analysis of niche cell-cell interactions. Cell Stem Cell 3:289-300.
Shen SW, Duan CL, Chen XH, Wang YQ, Sun X, Zhang QW, Cui HR, Sun FY. (2016) Neurogenic effect of VEGF is related to increase of astrocytes transdifferentiation into new mature neurons in rat brains after stroke. Neuropharmacology 108:451-461.
Torper O, Pfisterer U, Wolf DA, Pereira M, Lau S, Jakobsson J, Bjorklund A, Grealish S, et al. (2013) Generation of induced neurons via direct conversion in vivo. Proc Natl Acad Sci U S A 110:7038-7043.
Venere M, Han YG, Bell R, Song JS, Alvarez-Buylla A, Blelloch R. (2012) Sox1 marks an activated neural stem/progenitor cell in the hippocampus. Development 139:3938-3949.
Whitman MC, Fan W, Rela L, Rodriguez-Gil DJ, Greer CA. (2009) Blood vessels form a migratory scaffold in the rostral migratory stream. J Comp Neurol 516:94-104.
Worlitzer MM, Viel T, Jacobs AH, Schwamborn JC. (2013) The majority of newly generated cells in the adult mouse substantia nigra express low levels of doublecortin, but their proliferation is unaffected by 6-OHDA-induced nigral lesion or minocycline-mediated inhibition of neuroinflammation. Eur J Neurosci 38:2684-2692.
Zhang J, Jiao J. (2015) Molecular biomarkers for embryonic and adult neural stem cell and neurogenesis. Biomed Res Int 2015727542.
Zhao M, Momma S, Delfani K, Carlen M, Cassidy RM, Johansson CB, Brismar H, Shupliakov O, et al. (2003) Evidence for neurogenesis in the adult mammalian substantia nigra. Proc Natl Acad Sci U S A 100:7925-7930.

Glossary

Adult Neurogenesis*:* Process by which new mature and functional neurons are generated in the brain of adult animals.

Dedifferentiation*:* Process by which a differentiated and specialized cell regresses to an undifferentiated state, as a progenitor or stem cell.

Embryoid bodies*:* ESC aggregations formed *in vitro* that emulate the early developmental stage of embryo gastrulation. It is used to promote ESC differentiation into ectodermal, mesodermal and endodermal cells.

Transdifferentiation*:* Conversion of one fully differentiated cell into another cell type without undergoing a proliferation step.

(Received 10 December 2018, Accepted 19 March 2019)
(Available online 26 April 2019)

Azuara-Medina et al. *Cell Death and Disease* (2019)10:196
https://doi.org/10.1038/s41419-019-1454-z

Cell Death & Disease

ARTICLE Open Access

The intracellular domain of β-dystroglycan mediates the nucleolar stress response by suppressing UBF transcriptional activity

Paulina Margarita Azuara-Medina[1], Ariana María Sandoval-Duarte[1], Sara L. Morales-Lázaro[2], Ricardo Modragón-González[1], Griselda Vélez-Aguilera[1], Juan de Dios Gómez-López[1], Guadalupe Elizabeth Jiménez-Gutiérrez[1], Reynaldo Tiburcio-Félix[1], Ivette Martínez-Vieyra[3], Rocío Suárez-Sánchez[4], Gernot Längst[5], Jonathan Javier Magaña[4], Steve J. Winder[6], Arturo Ortega[7], Rita de Cassia Ramos Perlingeiro[8], Laura A. Jacobs[6] and Bulmaro Cisneros[1]

Abstract

β-dystroglycan (β-DG) is a key component of multiprotein complexes in the plasma membrane and nuclear envelope. In addition, β-DG undergoes two successive proteolytic cleavages that result in the liberation of its intracellular domain (ICD) into the cytosol and nucleus. However, stimuli-inducing ICD cleavage and the physiological relevance of this proteolytic fragment are largely unknown. In this study we show for the first time that β-DG ICD is targeted to the nucleolus where it interacts with the nuclear proteins B23 and UBF (central factor of Pol I-mediated rRNA gene transcription) and binds to rDNA promoter regions. Interestingly DG silencing results in reduced B23 and UBF levels and aberrant nucleolar morphology. Furthermore, β-DG ICD cleavage is induced by different nucleolar stressors, including oxidative stress, acidosis, and UV irradiation, which implies its participation in the response to nucleolar stress. Consistent with this idea, overexpression of β-DG elicited mislocalization and decreased levels of UBF and suppression of rRNA expression, which in turn provoked altered ribosome profiling and decreased cell growth. Collectively our data reveal that β-DG ICD acts as negative regulator of rDNA transcription by impeding the transcriptional activity of UBF, as a part of the protective mechanism activated in response to nucleolar stress.

Introduction

Regulated proteolysis of cell surface receptors that liberates biologically active proteins/peptides from the plasma membrane (PM) to the cytosol is a critical step in a variety of different signaling pathways that respond to external stimuli. γ-Secretase is an intramembranous cleaving protease complex consisting of at least four proteins: presenilin-1, nicastrin, anterior pharynx-defective phenotype 1, and presenilin enhancer 2[1]. γ-Secretase is known to be required for the activation of many transmembrane proteins, including the amyloid precursor protein, cadherins, Notch1[2], and recently, dystroglycan[3,4]. Dystroglycan, a key component of the dystrophin-associated protein complex (DAPC), is transcribed from the *DAG1* gene and translated as a single propeptide, which is proteolytically processed to generate the extracellular subunit α-dystroglycan (α-DG) and the transmembrane subunit β-dystroglycan (β-DG)[5]. α-DG binds to different extracellular matrix proteins

Correspondence: Bulmaro Cisneros (bcisnero@cinvestav.mx)
[1]Departamento de Genética y Biología Molecular, Centro de Investigación y de Estudios Avanzados Del Instituto Politécnico Nacional, 07360 Ciudad de México, Mexico
[2]Departamento de Neurociencia Cognitiva, Instituto de Fisiología Celular, Universidad Nacional Autónoma de México, 04510 Ciudad de México, Mexico
Full list of author information is available at the end of the article.
Edited by S. Lavandero

© The Author(s) 2019
Open Access This article is licensed under a Creative Commons Attribution 4.0 International License, which permits use, sharing, adaptation, distribution and reproduction in any medium or format, as long as you give appropriate credit to the original author(s) and the source, provide a link to the Creative Commons license, and indicate if changes were made. The images or other third party material in this article are included in the article's Creative Commons license, unless indicated otherwise in a credit line to the material. If material is not included in the article's Creative Commons license and your intended use is not permitted by statutory regulation or exceeds the permitted use, you will need to obtain permission directly from the copyright holder. To view a copy of this license, visit http://creativecommons.org/licenses/by/4.0/.

INFORME DE LABORES 2019

including laminin, agrin, or perlecan[6], while β-DG connects actin through various cytolinker proteins including dystrophin or utrophin. Thereby, dystroglycan serves as a link between the extracellular matrix and the actin-based cytoskeleton, acting also as an adhesion and signaling receptor[5,7].

Besides its structural role in the maintenance of membrane integrity, dystroglycan localization is not static but dynamic. Phosphorylation of β-DG at Y^{890} triggers its retrograde trafficking from PM to the nucleus, via the membranous endosome-endoplasmic reticulum (ER) network, with ezrin activation enhancing the intracellular trafficking and translocon Sec61 facilitating the exit of β-DG from the ER membrane to be accessible for importin-dependent nuclear import through the nuclear pore[8–10]. In the nucleus, β-DG is assembled with nuclear envelope (NE) components, including emerin, and lamins A/C and B1, to preserve the nuclear structure/function[11,12] and where it can also indirectly regulate gene expression[13]. This functional diversity of β-DG, acting as a platform for both PM- and NE-associated processes, is further expanded by proteolytic cleavage of the protein. β-DG is subjected to proteolytic cleavage by MMP-2 and MMP-9 to liberate its extracellular domain[14,15], while the remaining fragment, containing the transmembrane stub and the cytoplasmic portion is thought to be subsequently processed by γ-secretase to deliver an intracellular domain (ICD; 12 kDa in mass but runs aberrantly on SDS-PAGE at ~26 kDa) into the cytosol[3,4]. Recent evidence showed that β-DG ICD is targeted to the nucleus in prostate cancer cells[3,13,16] nonetheless the biological significance of such localization is largely unknown. The nucleus is organized into distinct functional compartments containing specific macromolecules that govern nuclear processes;[16] for instance, the nucleolus is a prominent non-membranous nuclear organelle primarily involved in ribosome biogenesis and cellular homeostasis[17]. Thus, identification of the destination of β-DG ICD within the nucleus could facilitate further elucidation of its function.

In this study we demonstrate for the first time that β-DG ICD is target to the nucleolus where it plays a negative role in the regulation of ribosomal RNA (rRNA) transcription. We provide evidence that full-length β-DG is proteolytically processed into β-DG ICD in response to nucleolar stress, via the Notch signaling pathway. Remarkably, β-DG ICD binds to the rDNA promoter to suppress rRNA synthesis by impairing the expression, localization, and ultimately activity of the RNA polymerase I (Pol I) transcription factor UBF (upstream binding factor), which further results in the down-regulation of rRNA expression and cell proliferation. Thus, β-DG ICD appears to be a key contributor to the nucleolar stress response.

Results

The γ-secretase-generated intracellular domain of β-DG is targeted to the nucleolus

We previously observed localization of β-DG to the nucleoli in C2C12 myoblasts[11]; but no role for β-DG has been described in this nuclear organelle. As a first step, we analyzed whether β-DG colocalizes with proteins that define functionally distinct compartments of the nucleolus. Cells were double-stained for β-DG (C20 antibody) along with UBF, fibrillarin (markers of the fibrillar center, FC), or B23 (marker of the granular component, GC) and further analyzed by confocal microscopy. The nucleolar immunostaining of β-DG colocalized at certain extent with all three nucleolar proteins analyzed, as confirmed by the line intensity scan analysis and Manders' overlapping coefficients (Fig. 1a). The specificity of C20 antibody was demonstrated using both DG knockout C2C12 cells and primary fibroblasts from a subject with Walker–Warburg syndrome that do not express *DAG1* gene all[18]. Nucleoli were strongly staining by C20 in C2C12 wild-type cells, while a faint nuclear staining that was excluded from nucleoli was observed in DG knockout C2C12 cells (Supplementary Figure 1A, left panel). Furthermore, the immunoreactive band corresponding to β-DG (~43 kDa), which was observed in primary fibroblast lysates from a healthy subject, was absent in Walker–Warburg syndrome primary fibroblast lysates (Supplementary Figure 1A, right panel). Finally, pre-incubation with a blocking peptide virtually eliminated C20 immunostaining in wild-type cells (Supplementary Figure 1B). In addition, nucleolar localization of β-DG was confirmed using another anti-β-DG antibody (G5; Supplementary Figure 1C). The nucleolus is a highly dynamic organelle that responds to a variety of cellular stresses with morphological changes[19] and redistribution of proteins implicated in ribosome biogenesis form perinuclear caps upon inhibition of rDNA transcription[20]. C2C12 cells were therefore treated with actinomycin D (0.08 μg/ml) or DRB (0.3 μM) to cause nucleolar stress, and the effect of treatments on β-DG distribution was evaluated by confocal microscopy. The formation of nucleolar caps and nucleolar segregation/nucleolar necklaces was found after treatment with Act D and DRB, respectively, as shown by immunostaining for UBF and B23 (Fig. 1b). Treatment with the vehicle alone dimethyl sulfoxide (DMSO) produced no change in the immunostaining pattern of nucleolar proteins. Interestingly, nucleolar labeling of β-DG also underwent redistribution in response to Act D and DRB but remained in colocalization partially with UBF and barely with B23, as shown by Manders' overlapping coefficient analysis (Fig. 1b), suggesting that β-DG might be involved in nucleolar organization/plasticity. Next, we investigated whether the nucleolar localization of β-DG is dependent on nucleic acid integrity. C2C12

INFORME DE LABORES 2019

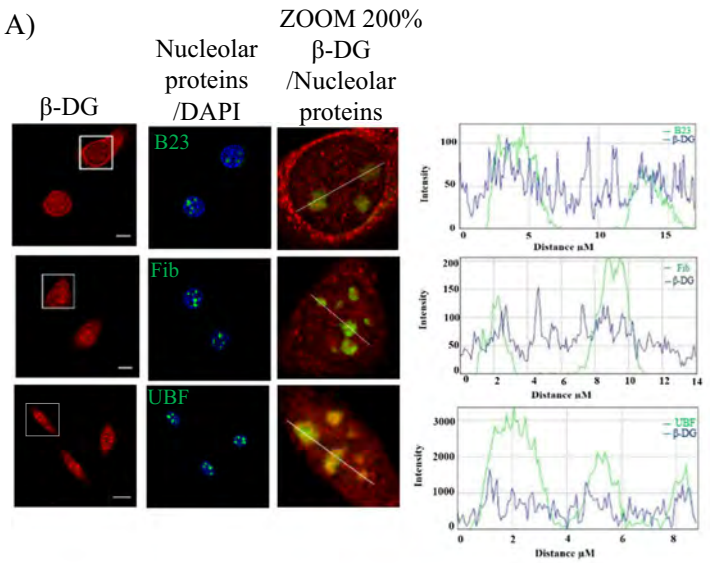

Manders' Coefficient	M1	M2
β-DG - B23	0.092	0.89
β-DG - Fib	0.390	0.279
β-DG - UBF	0.787	0.564

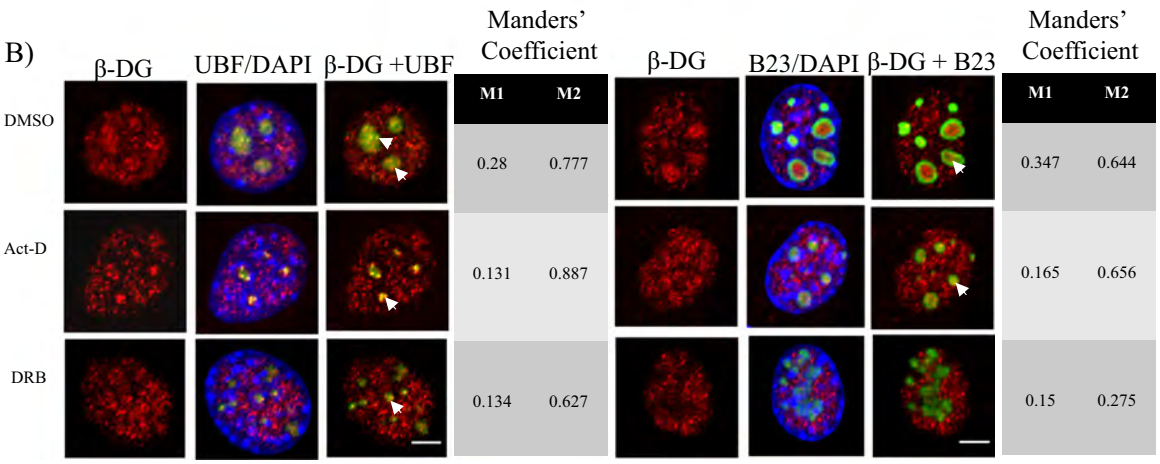

	Manders' Coefficient M1	Manders' Coefficient M2	Manders' Coefficient M1	Manders' Coefficient M2
DMSO	0.28	0.777	0.347	0.644
Act-D	0.131	0.887	0.165	0.656
DRB	0.134	0.627	0.15	0.275

Fig. 1 β-DG colocalizes with nucleolar proteins before and after induced nucleoli disorganization. a C2C12 cells were double immunostained for β-DG (C20 antibodies) and B23, fibrillarin (Fib), or UBF. Cells were stained with DAPI for nuclei visualization prior to being subjected to confocal laser scanning microscopy (CLSM; scale bar = 5 μm). Colocalization of β-DG with nucleolar proteins is denoted by arrowheads in the magnified images. A line intensity scan along the white line in the merge images was carried using ROI manager Multiplot (middle graphs). *Right*: The Manders overlap coefficient was calculated on double labeling inmunofluorescences: M1 denotes the fraction of the β-DG signal coincident with the nucleolar proteins signal over its total intensity, and M2 denotes the fraction of the nucleolar proteins signal coincident with the β-DG signal over its total intensity. **b** Cells were treated with actinomycin D (Act D) or DRB for 3 h, fixed and then double immunostained for β-DG and either UBF or B23. Nuclei were stained with DAPI before CLSM analysis (scale bar = 1 μm). Typical single Z-sections are shown and colocalization of β-DG with nucleolar proteins after drug-induced nucleoli disruption is indicated by arrowheads in the merge images. The Manders overlap coefficient was calculated for each experimental condition as peer **a**

myoblasts were immunolabeled for β-DG before and after nuclease treatment, and stained with DAPI to monitor DNA degradation, or immunolabeled for hnRNP C1/C2 antibody (RNA-binding protein) to monitor RNA removal. DNase digestion completely removed DAPI-labeled DNA, while treatment with RNase caused hnRNP C1/C2 redistribution from the nucleoplasm to the nuclear periphery and cytoplasm, thus confirming the effectiveness of nucleases treatment. DNase treatment completely abrogated the nucleolar distribution of β-DG, while treatment with RNase apparently increased the intensity of β-DG nucleolar immunostaining, compared with untreated cells (Supplementary Figure 2A and B). These results suggest that the nucleolar localization of β-DG is dependent on DNA.

To demonstrate conclusively that β-DG resides in the nucleolus, C2C12 were fractionated into total, cytoplasmic, nuclear, and nucleolar fractions to be further analyzed by SDS-PAGE/WB. A prominent ~30 kDa β-DG band was found enriched, together with fibrillarin, in the

INFORME DE LABORES 2019

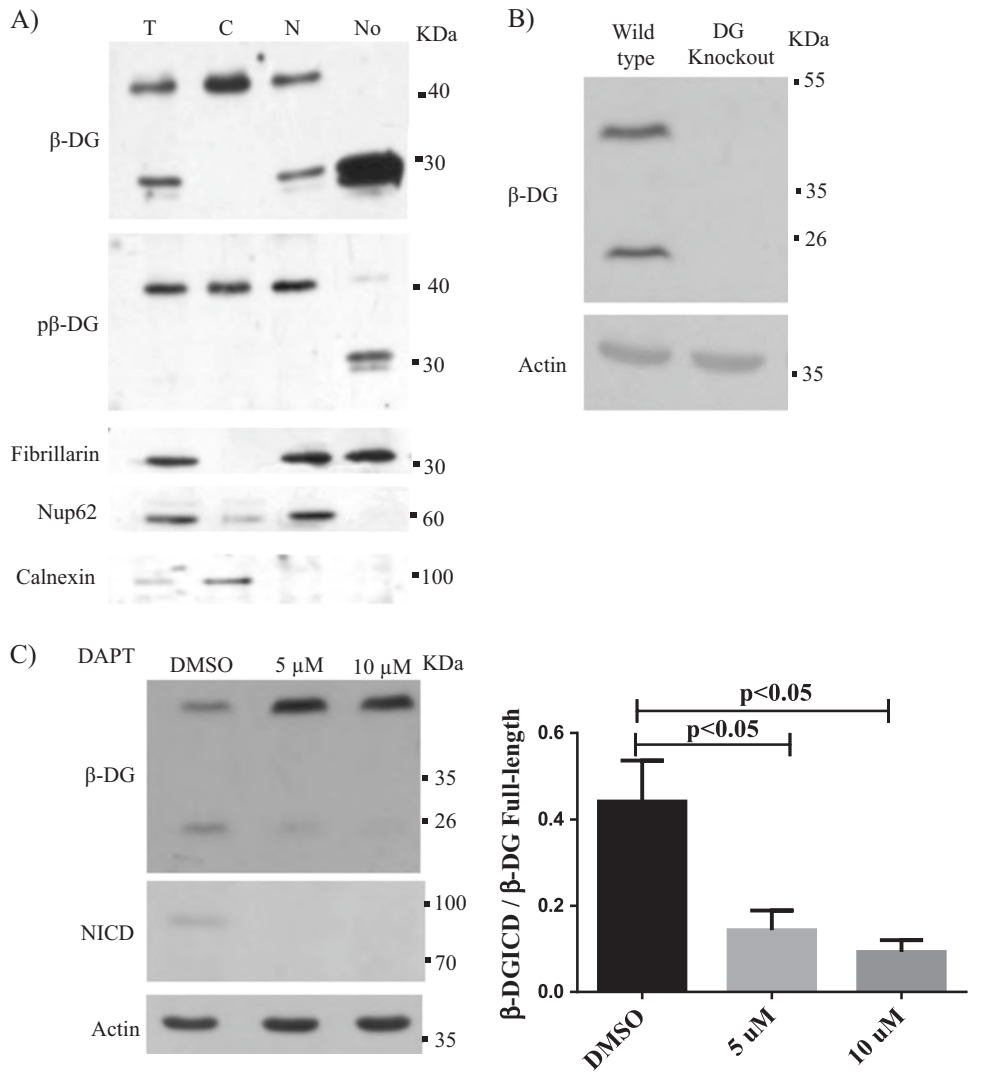

Fig. 2 β-DG ICD resides in the nucleolus. a Cells were partitioned to obtain total (T), cytoplasmic (C), nuclear (N), and nucleolar (No) fractions, prior to SDS-PAGE/WB analysis, using specific antibodies for β-DG (Mandag) or its phosphorylated counterpart (pβ-DG). Fibrillarin (nucleolar protein), Nup62 (nuclear membrane protein), and calnexin (reticulum endoplasmic protein) were used as cellular fraction markers. **b** Lysates from wild-type and DG knockout C2C12 cells were analyzed by SDS-PAGE/WB using antibodies for β-DG (Mandag) and actin (loading control), to demonstrate β-DG antibody specificity. **c** Lysates from C2C12 cells treated for 24 h with the indicated concentrations DAPT (γ-secretase inhibitor) or the vehicle alone (DMSO) were analyzed by SDS-PAGE/WB, using antibodies for β-DG, Notch intracellular domain (NICD; positive control for DAPT action), and actin (loading control). Representative gel from three independent experiments is shown. *Right*. Data correspond to the mean ± SEM from three independent experiment, with *p* values indicating significant differences (unpaired *t*-test)

nucleolar fraction, as revealed using three different anti-β-DG antibodies: MANDAG (mouse mab that recognizes total β-DG levels), pTyr890 (rabbit pAb that specifically recognizes β-DG phosphorylated at Tyr^{890}) (Fig. 2a), and C20 (rabbit antibody that recognizes the total β-DG pool Supplementary Figure 1D). Nup62 (nuclear pore protein) and calnexin (endoplasmic reticulum protein) were recovered in the nuclear and cytoplasmic fractions, respectively, and the two proteins were absent from the nucleolar fraction demonstrating that no cross-contamination occurred during cellular fractionation. Control experiments using both DG knockout C2C12 cells and Walker–Warburg syndrome primary fibroblasts yield no immunoreactive bands after incubation with MANDAG antibody (Fig. 2b and Supplementary Figure 1A, right panel), which demonstrated the specificity of this antibody for β-DG detection. We hypothesized that the ~30 kDa band correspond to the ICD of β-DG generated by γ-secretase cleavage as has been described previously[3,13,16]. Compatible with this assumption, lysates from cells treated with DAPT (γ-secretase inhibitor) resulted in a dose-dependent decrease in β-DG ICD levels that paralleled with

INFORME DE LABORES 2019

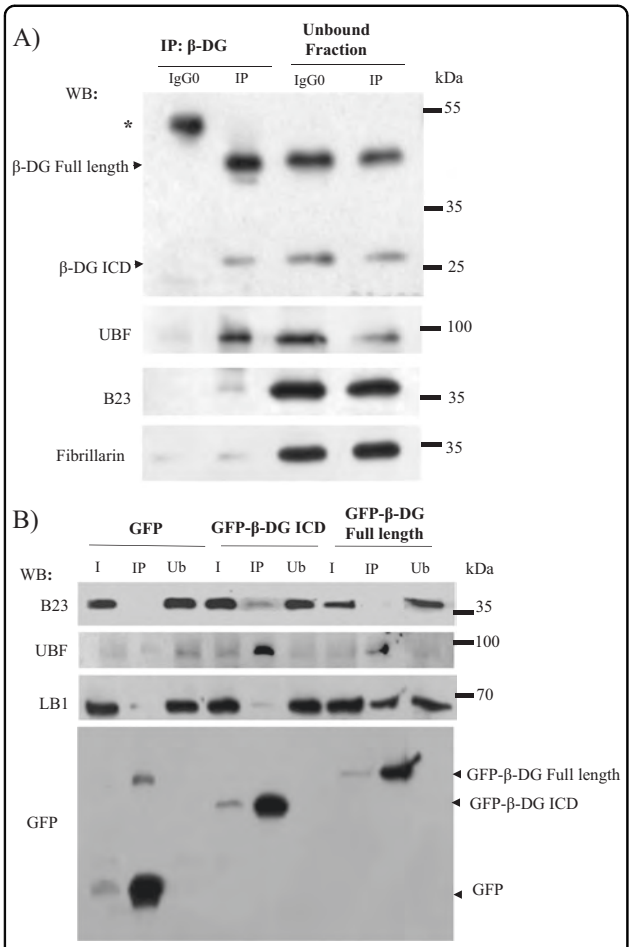

Fig. 3 β-DG ICD interacts with the nucleolar proteins UBF and B23. a C2C12 cell lysates were subjected to immunoprecipitation (IP) using anti-β-DG antibody (Mandag) and the precipitated proteins were subsequently analyzed by western blotting using primary antibodies against β-DG, UBF, B23, or fibrillarin. **b** Lysates from cells transiently expressing GFP-β-DG full-length, β-DG ICD, or GFP alone were subjected to immunoprecipitation using the GFP-Trap system, and the captured proteins were analyzed by western blotting using antibodies against B23, UBF, lamin B1 (LB1), and GFP. **a**, **b** Ub, unbound proteins, IP immunoprecipitated fraction, IgG0, nonspecific antibody. Input corresponds to 10% of protein lysates prior to immunoprecipitation

dose-dependent reduction of the intracellular domain of Notch (NICD), a well-characterized γ-secretase substrate (Fig. 2c). Collectively these data support the idea that the γ-secretase-derived cleavage fragment of β-DG (~30 kDa), named hereafter as β-DG ICD, is targeted to the nucleolus where it possibly has a role in regulating nucleoli structure/function.

β-DG ICD interacts with UBF and B23

Colocalization of β-DG with nucleolar proteins even after induced nucleolar disruption (Fig. 1b), suggests their physical interaction. Consistent with this notion, UBF and traces of B23 but not fibrillarin were recovered in complex with β-DG after immunoprecipitation (IP) of C2C12 lysates with anti-β-DG antibody (Fig. 3a). None of the nucleolar proteins were immunoprecipitated using non-specific IgG antibodies. Because anti-β-DG antibody immunoprecipitated both β-DG full-length and β-DG ICD, we wondered what form is bound to nucleolar proteins. To approach this, C2C12 cells were transiently transfected to express GFP-β-DG full-length or GFP-β-DG ICD and subjected to GFP-based IP assays. Both UBF and B23 were found preferentially bound to GFP-β-DG ICD, with UBF interaction predominant over that with B23 (Fig. 3b). GFP alone interacted with neither B23 nor UBF, while lamin B1 (β-DG nuclear partner) was bound to GFP-β-DG full-length but not GFP-β-DG ICD, demonstrating the specificity of GFP-Trap assays.

Silencing of DG disrupts nucleolar morphology and decreases B23 and UBF levels

To elucidate whether nucleolar localization of β-DG is physiologically relevant, the impact of knocking down of β-DG expression on nucleolar structure and expression of nucleolar proteins was examined. Significant reduction of dystroglycan mRNA levels and the consequent decrease in β-DG full-length and β-DG ICD levels were observed upon stably transfection of C2C12 cells with a vector expressing a short hairpin RNA against *DAG1* gene (DG shRNA), compared to cells expressing an unspecific shRNA (control shRNA) (Fig. 4a, b). Remarkably, the depletion of β-DG resulted in decreased proteins levels of B23 (80%), fibrillarin (30%), and UBF (60%) (Fig. 4b). Such effects were accompanied by a clear alteration in nucleolar morphology; while control shRNA cells contain numerous relatively small nucleoli, β-DG-depleted cells exhibited fewer larger and more amorphous nucleoli, as shown by immunostaining for UBF and B23 (Fig. 4c, d) and quantification of nucleolar area (right panels).

β-DG binds to the rDNA promoter to possibly regulate rRNA expression

Because knockdown of β-DG resulted in decreased levels of UBF, a key component of the RNA polymerase I preinitiation complex in rRNA transcription, we sought to determine the expression of 28 S and 18 S pre-rRNAs in β-DG knockdown cells by quantitative RT-PCR (Figure 4a). β-DG knockdown cells exhibited an ~40% decrease in 18 S levels, while 28 S expression showed a slight but significant increase, compared with control shRNA (Fig. 5a). To provide insight into the mechanism by which β-DG depletion influences rDNA gene expression, we analyzed whether β-DG is physically associated with the rDNA promoter. Chromatin was immunoprecipitated from wild-type and DG knockout (negative control) C2C12 cells, using β-DG or nonspecific IgG

INFORME DE LABORES 2019

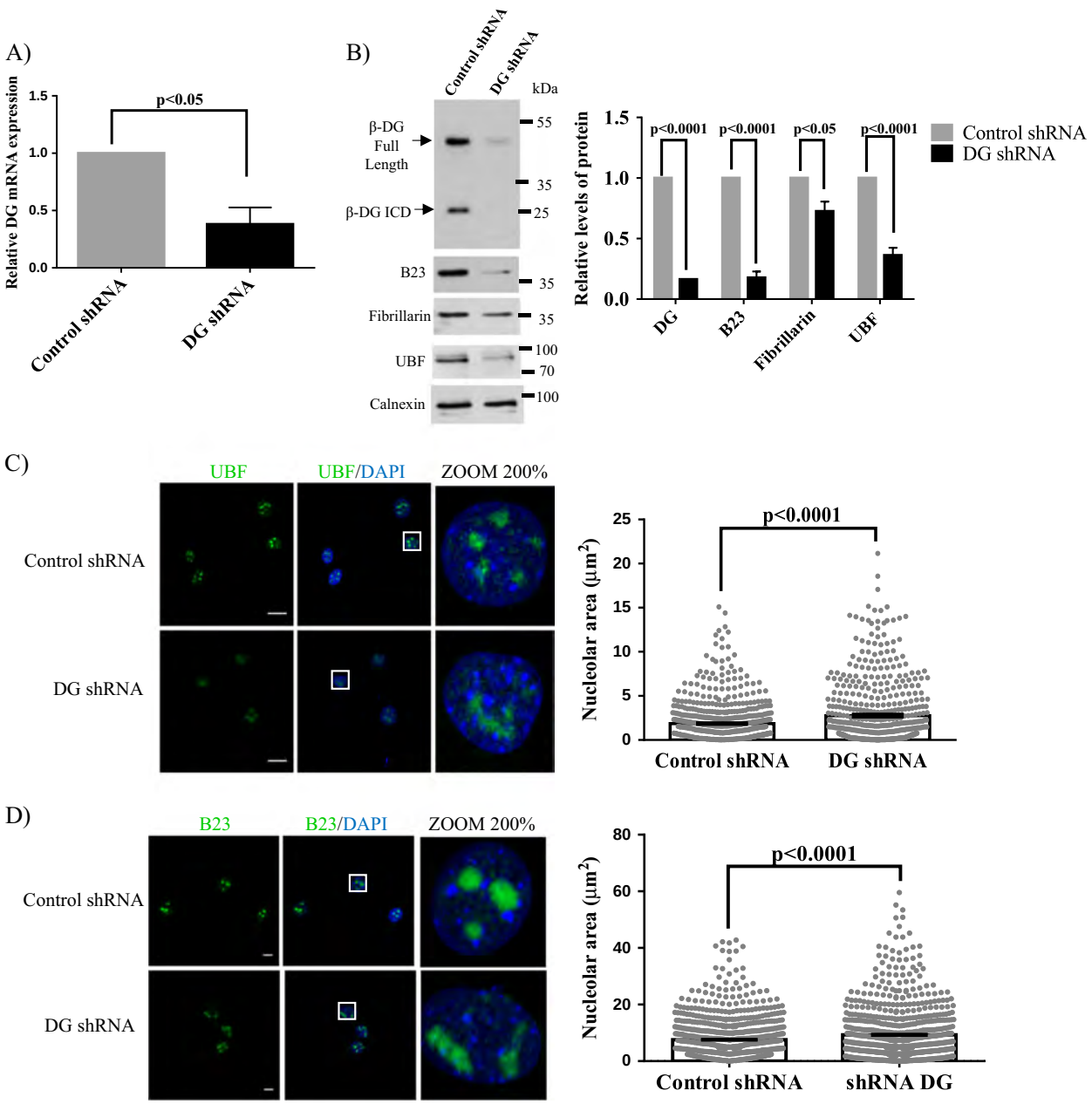

Fig. 4 Silencing of dystroglycan results in altered nucleoli structure and reduced levels of B23 and UBF. a Messenger RNA expression of dystroglycan and GAPDH (endogenous control) was assessed by qRT-PCR in C2C12 cells stably expressing DG shRNA or control shRNA, as described in Methods. Relative mRNA levels obtained in control cells were set at 1. Results are the mean ± standard deviation of three independent experiments, with *P* value indicating significance difference (unpaired *t*-test). **b** Lysates from C2C12 cells stably transfected with DG shRNA or control shRNA were analyzed by western blotting using primary antibodies against DG, B23, fibrillarin, UBF, and calnexin (loading control). Blots were stripped and reprobed successively with each protein antibody. Relative protein levels from control shRNA cells were set at 1 for comparison. Results are the mean ± SEM of three independent experiments (right panel), with *p* value denoting significance differences (unpaired *t*-test). **c**, **d** Nucleolar morphology was analyzed in cells stably expressing DG shRNA or control shRNA, using specific antibodies against UBF and B23 respectively. Cells were counterstained with DAPI to visualize nuclei prior to CLSM analysis. The nucleolar area (μm^2) was determined in each cell condition as described in Methods (graphs at right). Data are the mean ± SEM from three independent experiments ($n = 600$ nucleoli), with *p* values indicating significant differences (unpaired *t*-test)

antibodies; moreover, ChIP assays using RNA polymerase I (Pol I) antibodies were performed in parallel (positive control). Then, rDNA was amplified using primers specific for the rDNA promoter, 5.8 S or intergenic spacer (IGS) regions. ChIP assays revealed the presence of β-DG in the 5.8 S and IGS regions, while Pol I was found to

INFORME DE LABORES 2019

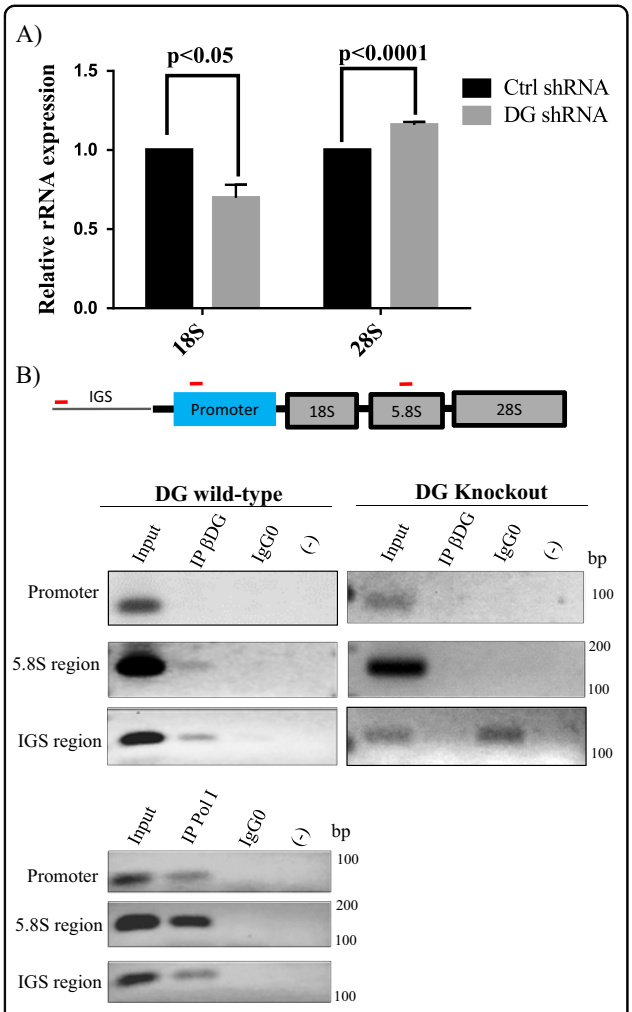

Fig. 5 β-DG binds to the rDNA gene regulatory region and knockdown of DG expression alters rRNA expression. a Total RNA was isolated from control shRNA and DG shRNA stably transfected cells and the expression of 18 S and 28 S pre-rRNAs was assessed by qRT-PCR using GAPDH as endogenous control. The expression levels obtained in control shRNA cells were set at 1 for comparison. Data correspond to the mean ± SEM from three independent experiments with duplicates; *p* values denoted significant differences (unpaired *t*-test). **b** Wild-type and DG knockout C2C12 cells were subjected to chromatin immunoprecipitation (ChIP) with antibody anti-β-DG (MANDAG), followed by PCR assays for the promoter, 5.8 S and IGS (intergenic sequence) regions of rDNA gene. ChIP assays using anti-PolI antibody were carried out in wildtype C2C12 cells as positive control. The drawing at the top shows the organization of the rDNA gene (bottom panel). IgG0 nonspecific antibodies, (-) mock reaction without antibodies

occupy all three regions of the rDNA (Fig. 5b). As expected, no PCR amplification was detected upon ChIP assays on DG knockout cells (right panel), which demonstrated the specificity of Mandag antibody for immunoprecipitating β-DG from chromatin. Overall these data suggest that β-DG may modulate rRNA transcript expression through its binding to the rDNA regulatory region.

Nucleolar stress-induced β-DG ICD cleavage correlates with impaired ribosome biogenesis

In an effort to understand the potential role of β-DG ICD in the nucleolus, we investigated whether β-DG ICD cleavage is induced by nucleolar stress. C2C12 cells were subjected to different kind of stresses, namely oxidative stress, acidosis, and UV irradiation, and effectiveness of treatments was monitored by p53 activation. Interestingly, the ratio of β-DG ICD/full-length β-DG was augmented in response to all treatments with concomitant decrease in UBF content, with H_2O_2 and UV being the most efficient inductors (Fig. 6a, b). As expected, H_2O_2-induced nucleolar stress resulted in nucleolar segregations, with a formation of UBF-stained nucleolar caps at the periphery of B23-stained nucleoli (Supplementary Figure 3), which elicited ultimately downregulation of 45 S rRNA expression (Fig. 6c) and abnormal ribosomal profiling characterized by decreased monosomes and polysome absorbance peaks (Fig. 6d). We hypothesized that augmented β-DG ICD levels could be reflected in a higher binding activity to the rDNA promoter; consistent with this idea, occupancy of the three rDNA regulatory regions by β-DG markedly increased after H_2O_2 treatment, as revealed by ChIP-qPCR assays (Fig. 6e).

Overexpression of β-DG ICD impairs ribosomal biogenesis by suppressing UBF function

To analyze directly the implication of β-DG ICD in ribosome biogenesis, we stably transfected C2C12 cells with a GFP-β-DG ICD vector, to mimic high levels of the cleavage fragment. GFP-β-DG ICD localization was restricted to the nucleus showing homogenous distribution throughout the nucleoplasm, with less intense staining in nucleoli (Fig. 7a). Remarkably, the significant number of GFP-β-DG ICD-transfected cells exhibited mislocalization of UBF foci to the cytoplasm, compared to GFP alone (50% and 20%, respectively), while the nucleolar distribution of B23 remained unaltered (Fig. 7a, bottom panel and right panel). Impaired nucleolar localization of UBF due to exogenous β-DG ICD expression was confirmed by transfecting FLAG-tagged β-DG ICD (Supplementary Figure 4, top rows). Furthermore, overexpression of GFP-β-DG ICD resulted in decreased levels of UBF with no effect on B23, compared to GFP alone (Fig. 7b and right panel). We have demonstrated previously that the phosphorylation of β-DG at Tyr890 is not only a signal for the proteolysis and internalization of dystroglycan[3,16,22] but also acts to target dystroglycan to the nucleus[10]. We considered therefore whether phosphorylation of β-DG ICD at the PPxY motif (Tyr^{890}) plays a role in UBF mislocalization. Thus, FLAG-β-DG ICD

INFORME DE LABORES 2019

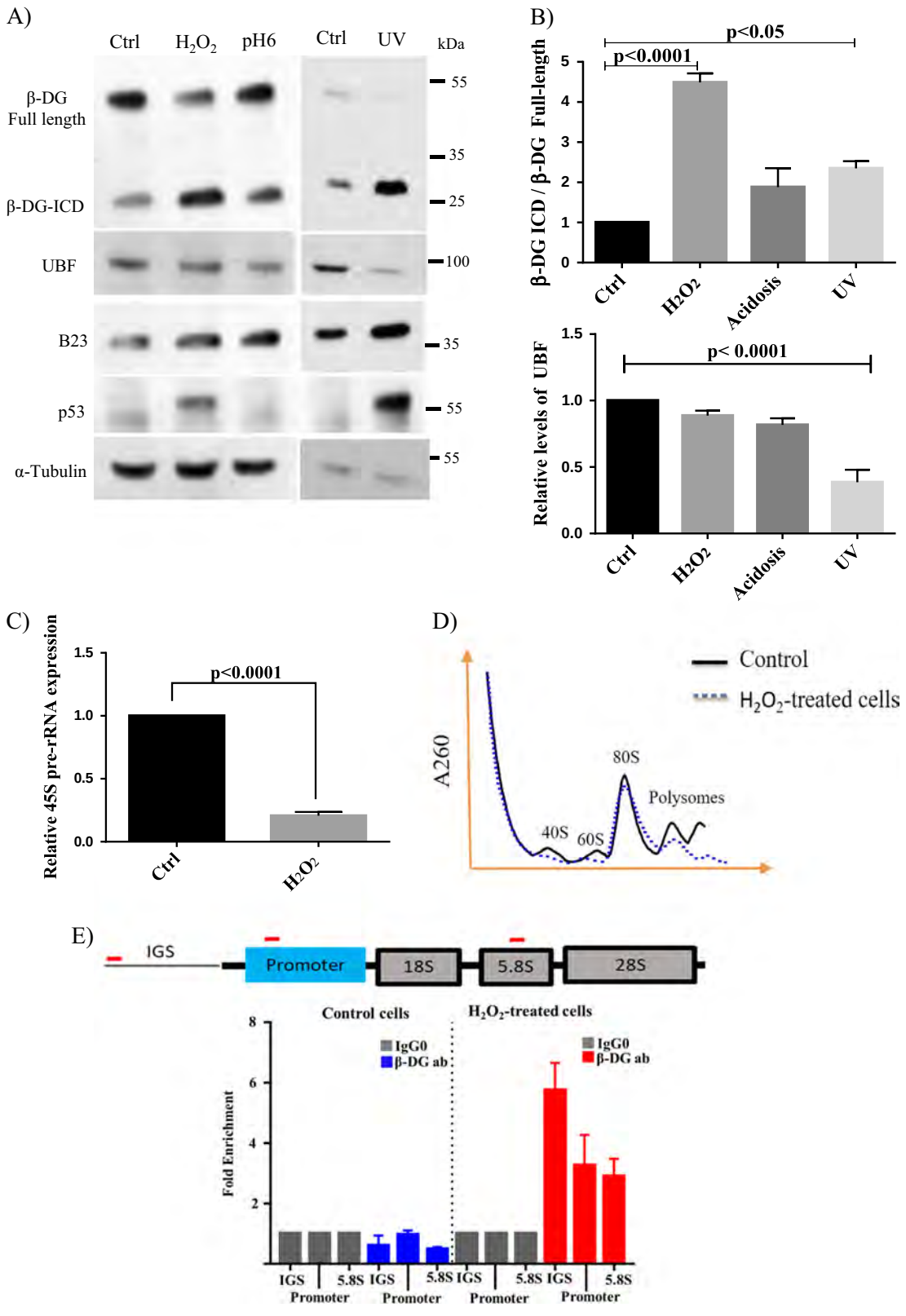

Fig. 6 (See legend on next page.)

INFORME DE LABORES 2019

(see figure on previous page)

Fig. 6 Nucleolar stress triggers β-DG ICD and disturbs rRNA expression and ribosome profile. a Lysates from control (ctrl, untreated) cells or cells induced to nucleolar stress response by H_2O_2 treatment, UV irradiation or acidosis (pH 6) (see Methods for details) were analyzed by western blotting using specific antibodies against β-DG, UBF, B23, p53, and α-tubulin. **b** Quantification of β-DG ICD/β-DG full-length ratio and UBF levels was carried out using α-tubulin as loading control. Results correspond to the mean ± SEM of three independent experiments with *p* values denoting significant differences (ordinary one-way ANOVA). **c** The 45 S rRNA precursor expression was assessed by qRT-PCR using GAPDH as endogenous control. The expression levels obtained in control cells were set at 1 for comparison. Data correspond to the mean ± SEM from three independent experiments with duplicates; *p* values denoted significant differences (unpaired *t*-test). **d** Ribosome profiling from control and H_2O_2-treated cells are shown. **e** Chromatin immunoprecipitation assays on control and H_2O_2-treated C2C12 cells were performed, with specific antibody against β-DG (Mandag), followed by SYBR green-based qPCR assays for the promoter, 5.8 S and IGS (intergenic sequence) regions of rDNA gene. Scheme of rDNA gene regulatory regions is shown at the top

variants that either mimic (Y890E) or block (Y890A) the Tyr^{890} phosphorylation were analyzed for UBF localization. Similar percentage of transfected cells showing UBF outside of the nucleus were observed between β-DG ICD FLAGY890A and β-DG ICD-FLAGY890E; thus, overexpression of β -DG ICD resulted in UBF mislocalization irrespective of a charged residue at residue 890 that mimics phosphorylation (Supplementary Figure 4). We hypothesized that decreased expression/mislocalization of UBF through β-DG ICD overexpression would ultimately impact rRNA expression. Consistent with this idea, an ~50% decrease in 45 S rRNA and 28 S but not 18 S was found in cells stably overexpressing β-DG ICD, compared with those expressing GFP alone (Fig. 8a). To ascertain whether β-DG ICD overexpression influences Pol I transcription, functional rRNA promoter reporter assays were carried out in β-DG ICD stably transfected cells, using a vector that expresses Firefly luciferase under the control of the mouse rRNA promoter and a vector that expresses Renilla luciferase to normalize transfection efficiency. Pol I promoter activity was found to decrease by 40% in GFP-β-DG ICD-transfected, compared with those with GFP alone (Fig. 8b). Because the rRNA content is a crucial point of regulation for ribosome biogenesis, we hypothesized that decreased 40 S and 60 S levels would impact the ribosome profile. Consistent with this notion, altered ribosome profiles devoid of the peaks corresponding to free 40 S and 60 S ribosomal subunits were observed in cells expressing β-DG ICD (Fig. 8c). Such impairment in rRNA expression and polysome profiling ultimately leads to defective proliferative capacity of β-DG ICD overexpressing cells, as shown by MTT-based proliferation assays (Fig. 8d). Collectively these data indicate that β-DG ICD acts as negative regulator of rRNA expression by affecting both the levels and transcriptional activity of UBF.

Discussion

β-DG is a key component of both PM and NE, acting as a platform for the proper anchorage of organelle-specific protein assemblies. At the PM β-DG modulates adhesion/signaling by connecting extracellular matrix proteins with the actin-based cytoskeleton[5,7], while in the nucleus β-DG interacts with the NE proteins emerin and lamins A/C and B1 to regulate nuclear structure and function[11,12]. This functional diversity could be wider than originally thought, due to the potential function of β-DG proteolytic fragments. Recent in vitro and in vivo evidence showed that β-DG undergoes two successive and possibly coordinate proteolytic cleavages that result in the liberation of the intracellular domain (ICD) into the cytosol; first matrix metalloproteinases, MMP-2 and MMP-9 cleave the extracellular domain of β-DG[23] and create a membrane-tethered intermediate that is subsequently processed by γ-secretase, a PM-embedded protease complex, to render a final cleavage product that approximates the entire ICD[21]. Except for cell density[21], other cellular stimuli inducing β-DG ICD release as well as the physiological consequences of such processing event are largely unknown. In this study we showed that β-DG ICD associates to nucleoli and its cleavage is promoted by the induction of a different kind of nucleolar stresses. We also ascribed for the first time a role for β-DG ICD in regulating rRNA transcription through negative regulation of the expression and transcriptional activity of UBF, in the context of the response to nucleolar stress.

We show herein that β-DG colocalizes and interacts with the key nucleolar proteins B23 and UBF, and, based on the converging redistribution of β-DG with B23, fibrillarin, or UBF in response to both actinomycin- and DRB-induced nucleoli disorganization, we hypothesized that β-DG participates in the functional plasticity of nucleoli. Interestingly, cell fractionation experiments revealed the presence of β-DG ICD but not β-DG full-length in the nucleolar fraction of C2C12 cells; however, GFP-based IP experiments revealed that both β-DG ICD and β-DG full-length are able to bind UBF. Because full-length β-DG is an NE protein associated with nuclear lamin and because the interaction of intranuclear filaments of lamins with nuclear compartments (including nucleoli) has been well established[24–26] it is possibly that IP of β-DG full-length pulled down a nuclear

INFORME DE LABORES 2019

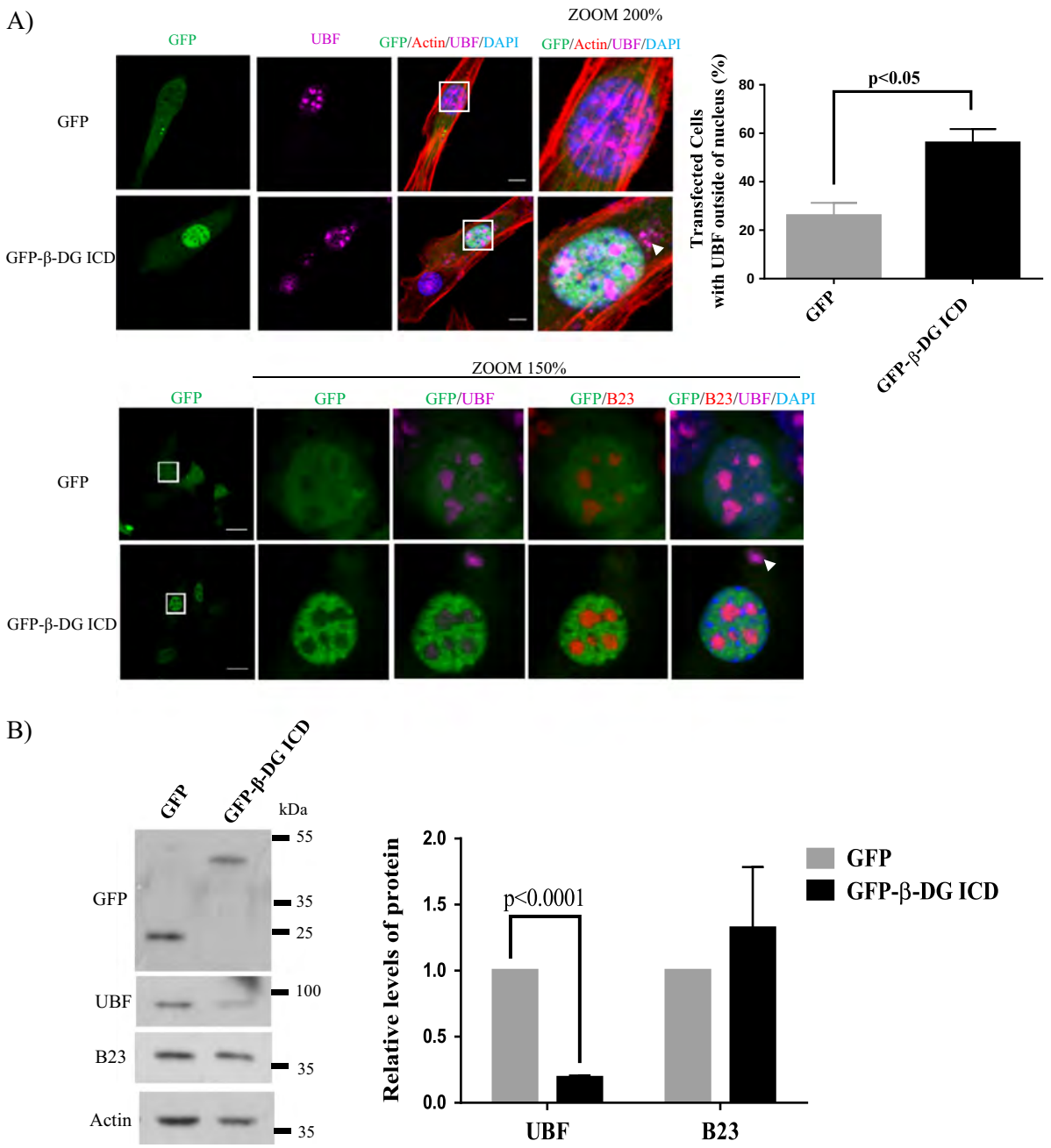

Fig. 7 Overexpression of β-DG ICD induces mislocalization and reduces UBF levels. a C2C12 cells transiently expressing GFP or GFG-β-DG ICD were immunolabeling for UBF at 24 h post-transfection. Cells were then fixed, stained with phalloidin and DAPI to visualize actin and nuclei, respectively, and subjected to CLSM analysis. In parallel experiments transfected cells were double immunostained for UBF and B23 and counterstained with DAPI to visualize nuclei prior to CLSM analysis (bottom panels). Scale bar = 10 µm. Mislocalized UBF is denoted by arrowheads. Quantification of cells transfected with GFP and GFP-β-DG ICD that showed UBF outside of the nucleus (right panel). Results correspond to the mean ± SEM of three independent experiments with *p* values denoting significant differences (unpaired *t*-test), *n* = 50 per experiment. **b** Lysates from GFP- or GFG-β-DG-ICD-transfected cells were analyzed by western blotting using specific antibodies against GFP, UBF, B23, and actin (loading control). *Right*: Data correspond to the mean ± SEM from three independent experiments, with *p* values indicating significant differences (unpaired *t*-test)

macromolecular complex containing NE (lamin B1) and nucleolar (UBF) proteins. The trafficking pathway underlying nucleolar targeting of β-DG ICD remains to be deciphered. Full-length β-DG is translocated to the nucleus through recognition of its NLS by importins α2/β1[9], therefore it is likely that β-DG ICD enters the nucleus by virtue of the NLS that is still present in the cleaved fragment, or alternatively by passive diffusion

INFORME DE LABORES 2019

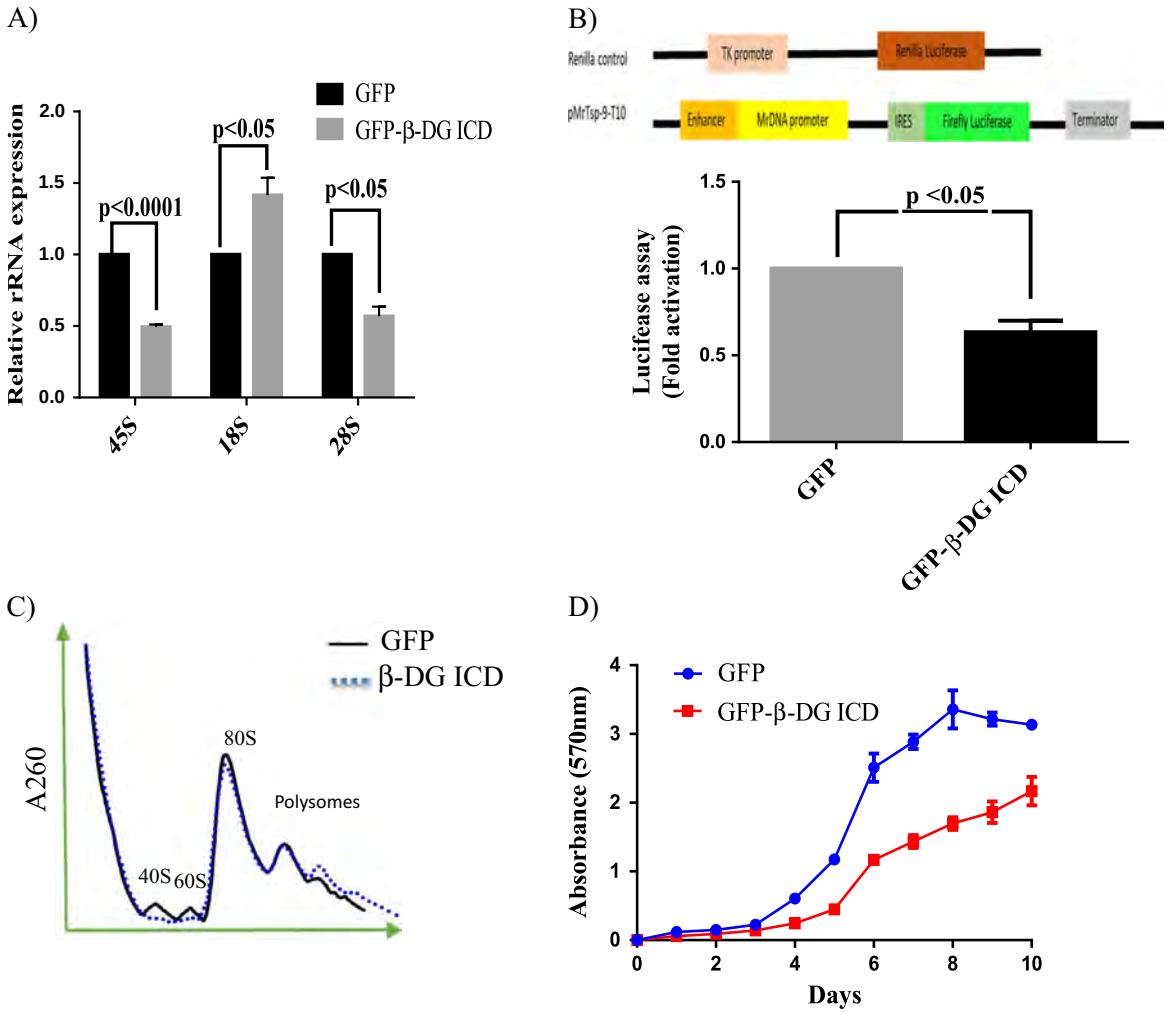

Fig. 8 Exogenous expression of β-DG ICD impairs ribosome biogenesis by affecting transcriptional activity of UBF. C2C12 cells were transfected to stably express GFP-β-DG ICD or GFP alone (empty vector). **a** The expression of 45 S, 18 S, and 28 S rRNAs was analyzed in the transfected cell cultures, using GAPDH as endogenous control. **b** Schematic representation of the mouse rDNA promoter construct (pMrTsp-9-T10) and *Renilla* luciferase control vector is shown at the top. Cell cultures stably expressing GFP-β-DG ICD or GFP alone were co-transfected with both luciferase reporter constructs and transcriptional activities were estimated after incubation for 48 h, as described in Methods. Control condition obtained in cells transfected with GFP alone was set at 1 for comparison. Data represent mean ± SEM of three independent experiments; *p* values denote a significant difference (unpaired *t*-test). **c** The ribosomal gradient profiles obtained from transfected cell cultures are shown. **d** Cell proliferation of the stably transfected cell cultures was monitored over a 10-day period using the MTT assay. Data represent mean ± SEM of three independent experiments

through the nuclear pore complex (NPC), because its molecular mass (<30 kDa) is clearly below the NPC permissive size[27]. No obvious nucleolar localization signal is found in β-DG ICD, thus, its nucleolar accumulation might be mediated by a retention mechanism via interaction with nucleolar components. Supporting this idea, β-DG ICD was found to interact with B23, a shuttle protein that transports cargos between the cytoplasm and the nucleolus and mediates nucleolar retention of other proteins[28]. Furthermore, binding of β-DG to the rDNA gene regulatory region (see below) could serve to anchor β-DG ICD to nucleoli too. Owing to the main contribution of nucleoli in ribosome biogenesis[16], we wondered whether β-DG is involved in this process. We provide here solid evidence supporting this hypothesis: first, β-DG interacts with UBF, an HMG box-containing protein that binds directly with rDNA and plays an important role in the recruitment of SL1 (selectivity factor 1) and Pol I to the rRNA promoter to constitute the Pol I preinitiation machinery complex[29]; second, ChIP assays with anti-β-DG antibody demonstrated β-DG recruitment to the rDNA 5.8 S and IGS regulatory regions; and third, DG silencing resulted in reduced UBF levels, decreased 18 S pre-rRNA expression but not 28 S pre-rRNA

INFORME DE LABORES 2019

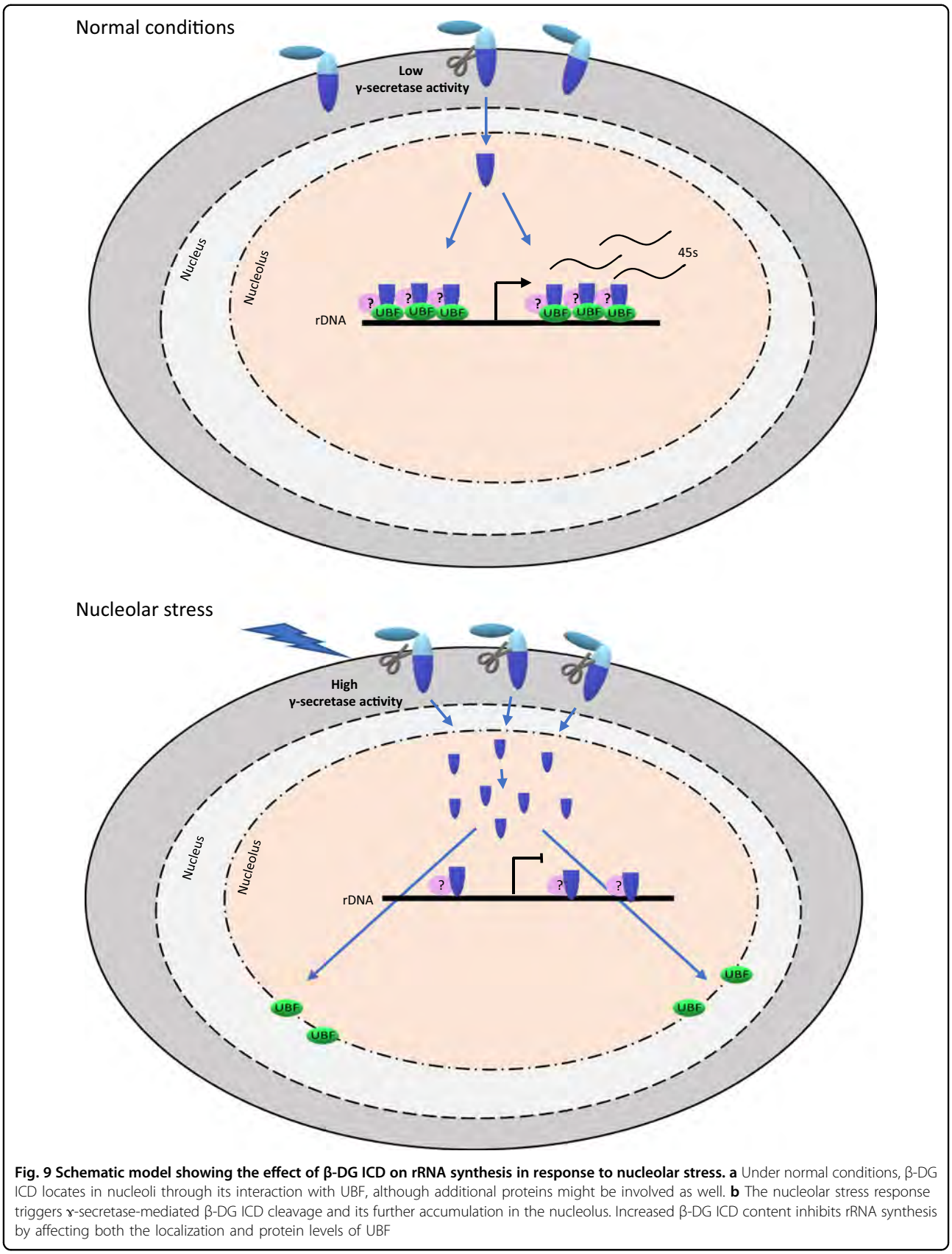

Fig. 9 Schematic model showing the effect of β-DG ICD on rRNA synthesis in response to nucleolar stress. a Under normal conditions, β-DG ICD locates in nucleoli through its interaction with UBF, although additional proteins might be involved as well. **b** The nucleolar stress response triggers ɤ-secretase-mediated β-DG ICD cleavage and its further accumulation in the nucleolus. Increased β-DG ICD content inhibits rRNA synthesis by affecting both the localization and protein levels of UBF

INFORME DE LABORES 2019

expression, and aberrant nucleolar morphology. Discordant expression between 28 S and 18 S rRNAs is intriguingly. Even though both 28 S rRNA and 18 S rRNA are originated from 45 S rRNA precursor, their processing/maturation pathways differ from each other, and each one is assisted by specific exo and endoribonucleasas[30]. Therefore, we argue that aside from its effect on rDNA basal transcription machinery (as shown here), β-DG ICD might modulate processing pathways of 18 S rRNA and 28 S rRNA differentially by indirect mechanisms. Additional experiments are needed to clear this issue.

The nucleolus is a central hub for orchestrating stress response, with downregulation of rRNA synthesis taking place as a part of ribosome biogenesis surveillance[31], furthermore, numerous proteins that functions are not generally ascribed to ribosome biogenesis are recruited to the nucleolus in response to environmental stimuli[32]. Therefore, we ascertained whether β-DG ICD cleavage is coupled to the response to nucleolar stress. Remarkably, triggers of β-DG ICD cleavage by Notch signaling activation occurred in response to different nucleolar stressor treatments, including oxidative stress, acidosis, and UV irradiation. Supporting a role for β-DG ICD in the response to nucleolar stress, β-DG ICD overexpression was sufficient to elicit several features of nucleolar stress, including mislocalization and decreased levels of UBF, repression of rRNA transcription, altered ribosome profile, and decreased cell proliferation.

The results raise the question of how β-DG ICD exerts a negative regulation on rDNA expression. β-DG lacks DNA-binding motifs or enzymatic activity and is considered as a scaffold protein, due to the presence of protein modules supporting interactions with diverse proteins (e.g. SH3, SH2, and WW domains)[5]. Therefore, we postulate that binding of β-DG ICD to UBF may lead to mislocalization and decreased levels of the latter protein, possibly by altering its stability, thereby interfering with the assembly of the Pol I initiation complex and the subsequent UBF-dependent activation of rDNA transcription (Fig. 9). Because the occupancy of rDNA regulatory regions by β-DG increased in response to nucleolar stress, it is also possible that β-DG ICD exerts its suppressive effect by displacing UBF from the Pol I transcription complex, which is consistent with mislocalization of UBF to the nucleolar periphery and cytoplasm that was observed in H_20_2-treated cells. Further ChIP assays to ascertain whether β-DG and UBF coexist or not in the rDNA promoter region under nucleolar stress conditions are needed to solve this question. Furthermore, since β-DG has multiple partners in the nucleus, the existence of an indirect mechanism by which β-DG ICD represses UBF activity cannot be ruled out. The implication of β-DG ICD in rDNA expression could be envisioned as an extension of the homeostatic role of β-DG, where induction of ICD cleavage and its further targeting to the nucleolus in response to environmental stress, like oxidative stress, acts as a protective response to inhibit rDNA transcription and further proliferation of damaged cells.

In summary, our data are compatible with the paradigm that β-DG ICD functions as a negative regulator of rRNA transcription by impeding the transcriptional activity of UBF, as a part of the nucleolar stress response mechanisms that are activated under physiologically relevant stress conditions. Thus, in addition to its roles as PM and NE signaling scaffold, β-DG should be regarded as a regulator of Pol I transcription in the nucleolus.

Materials and methods

Cell culturing and treatments

Mouse C2C12 myoblasts (ATCC® CRL-1772™) were grown as previously (Vásquez-Limeta, et al 2014). Generation of C2C12-derivative DG knockout cell lines with the CRISP/Cas9 system will be published elsewhere. For nucleoli disorganization treatments, cells were treated for 3 h with 0.01 μg/ml Act D (Sigma-Aldrich, St Louis, Missouri) or 25 μg/ml DRB (5,6 dichloro-1–d-ribofuranosylbenzimidazole; Sigma-Aldrich, St Louis, Missouri) or vehicle alone (DMSO), prior to confocal laser scanning microscopy (CLSM) analysis. The ɤ-secretase inhibitor N-(N-(3,5-difluorophenacetyl)-L-alanyl). S-phenylglycine t-butyl ester (DAPT; Sigma-Aldrich, St Louis, Missouri) was used at 10 μM for 24 h. For induction of the nucleolar stresses response, cells were cultured in DMEM supplemented with serum adjusted to pH 6, treated with 1.4 mM H_2O_2 (7722-84-1,Sigma-Aldrich) for 4 h or subjected to UV radiation using a pulse of 20 J/cm^2 each 24 h for 2 days. For nuclease digestion assays, cells grown on coverslips were treated with either 100 μg/ml protease-free RNase A in CSK buffer (10 mM Pipes pH 6.8, 100 mM NaCl, 30 mM sucrose, 3 mM $MgCl_2$, 1 mM EGTA, 0.5% (v/v) Triton X-100) for 40 min at 37 °C or with 200 μg/ml protease-free DNase I in PBS with 5 mM $MgCl_2$ for 1 h at 37 °C, then the cells were fixed with PFA 4% and immunolabeled using primary antibodies and the corresponding fluorochrome-conjugated secondary antibodies. Negative control experiments were carried out by incubating cells only with CSK buffer (RNase) or PBS with 5 mM $MgCl_2$ (DNase) prior to fixation.

Plasmids and transfection

The expression vectors Flag-β-DG ICD WT, Flag-β-DG ICDY890E, and Flag-β-DG ICDY890A were generated by PCR amplification using DGWT-DG, DGY890E-GFP, and DGY890A-GFP plasmids as template, respectively[10]. The cDNA sequence encoding the intracellular domain of β-DG (ICD, amino acids 774–895) was amplified using an

INFORME DE LABORES 2019

M-MLV reverse transcriptase coupled to a high-fidelity polymerase (*Pfu* turbo; Strategene) and primers containing Hind III and EcoRI restriction sites. Forward primer was 5′-CCTAAGCTTTATCGCAAGAAGAGGAAGGGC-3′ and the respective reverse primers were 5′-CTGAATTCTTAAGGGGGAACATACGGAGGG-3′ (ICD WT), 5′-CTGGAATCCTTAAGGGGGAAC**CTC**CGGAGGG-3′ (ICD Y890E mutation), and 5′-CTGAATTCTTAAGGGGGAAC**TGC**CGGAGGG-3′ (ICD Y890A mutation). PCR products were double digested with Hind III and EcoRI and cloned into the Hind III-EcoRI digested pFlag-CMV-10 vector. The integrity of the constructs was confirmed by DNA sequencing. Transfection was performed following supplier's recommendations. Briefly, cells seeded onto glass coverslips were incubated overnight and then transfected with 3 µg of the corresponding vector premixed with 3 µl of Lipofectamine 2000 (Invitrogen, Carlsbad, CA, USA). Transiently transfected cells were analyzed at 24 h post-transfection. When indicated, cells were stably transfected by culturing them for 12 days in the presence of 2 µg/ml puromycin (Invitrogen) or for 5 days in the presence of 800 µg/ml gentamicin (G418), prior to being used for further experiments. For knockdown experiments, cells were stably transfected with psiMH1 vector expressing a small interfering RNA (RNAi) specific for mouse DAG1 gene or a scrambled RNAi, as negative control (GeneCopoeia, Inc., Rockville, MD). For overexpression analysis, cells were stably transfected with GFP constructions as previously reported[9].

Antibodies

The following anti-β-DG primary antibodies were used: rabbit polyclonal antibodies G5 (Royuela et al, 2001) and Dystroglycan pTyr892 (Ilsley et al, 2002); goat polyclonal antibody C20 (Santa Cruz Biotechnology, CA), and mouse monoclonal antibodies MANDAG2[33] and 7D11 (Santa Cruz). Rabbit polyclonal antibodies anti-B23 (C19-R), anti-Nup62 (H-122), anti-calnexin (H70), anti-fibrillarin (Ab5821), anti-GFP (sc8334) and mouse monoclonal antibodies anti-UBF (F9), anti-B23 (NPM1-FC-61991) (anti-RNA polymerase I (sc-46699), anti-lamin B1 (Ab16048), anti-and anti-RPA(sc-46699), and α-Tubulin (sc-32293) were purchased from Santa Cruz Biotechnology, CA, USA. Rabbit polyclonal anti-Flag (2368) and rabbit monoclonal anti-Notch1 (4147) antibodies were acquired from cell signaling, while mouse monoclonal anti-actin antibody was a gift from Dr. Manuel Hernández (CINVESTAV, Mexico City).

Immunofluorescence and confocal microscopy analysis

Cells grown on coverslips were fixed with 4% paraformaldehyde for 10 min in PBS, permeabilized with 0.2% Triton X-100-PBS, blocked with 0.5% fetal bovine serum and 3% bovine serum albumin (BSA) in PBS and incubated overnight at 4 °C with the appropriate primary antibodies. The following day, cells were washed with 0.2% Triton X-100-PBS for 5 min and then with PBS alone three times, prior to be incubated for 1 h at room temperature with the appropriate fluorochrome-conjugated secondary antibody. For double immunolabeled samples, this was followed by overnight incubation at 4 °C with corresponding primary antibodies and the next day, cells were incubated with secondary fluorochrome-conjugated antibodies. Where indicated F-actin was labeled using TRITC-conjugated Phalloidin (Sigma-Aldrich St. Louis, Mo. USA) diluted 1:500 in PBS for 10 min at room temperature. For nuclease digestion assays, cells grown on coverslips were treated with either 100 µg/ml protease-free RNase A in CSK buffer (10 mM Pipes pH 6.8, 100 mM NaCl, 30 mM sucrose, 3 mM $MgCl_2$, 1 mM EGTA, 0.5% (v/v) Triton X-100) for 40 min at 37 °C or with 200 µg/ml protease-free DNase I in PBS with 5 mM MgCl2 for 1 h at 37 °C. Cells were then immunolabeled using primary antibodies and the corresponding fluorochrome-conjugated secondary antibodies. Finally, coverslip preparations were incubated for 20 min at room temperature with 0.2 µg/ml diamidino-2-phenylindole (DAPI; Sigma-Aldrich) for nuclei visualization, mounted on microscope slides with VectaShield (Vector Laboratories Inc. Burlingame, CA, USA) and further analyzed by CLSM (TCP-SP5, Leica Microsystems, Heidelberg, Germany) using a Plan Neo Fluor 63 × (NA = 1.4) oil-immersion objective. Analyses of digitized images were carried out using ImageJ 1.62 software. The nucleolar area (μm^2) of 600 nucleoli was analyzed in maxima projection using 3D objects counter and the data were analyzed using Prism6 software. Manders overlap coefficients were calculated for double labeling inmunofluorescences, using red (Alexa 594 nm) and green (FITC 488 nm) channels and the ImageJ plugin JACoB. A line intensity scan analysis was performed by ROI manager Multiplot.

Western blotting

Cell lysates were electrophoresed on 10% SDS-polyacrylamide gels and transferred onto nitrocellulose membranes (Hybond-Nb, Amersham Pharmacia, GE Healthcare, Bukinghamshire, UK). Membranes were blocked in TBST (100 mM Tris-HCl pH 8.0, 150 mM NaCl, 0.5 % (v/v) Tween-20) with low fat-dried milk and then incubated overnight at 4 °C with the appropriate primary antibodies. The specific protein signal was developed using the corresponding secondary antibodies and enhanced chemiluminescence western blotting detection system (ECL™; Amersham Pharmacia, GE Healthcare), according to the manufacturer's instructions.

Cell fractionation

Total cell extracts were obtained with lysis Buffer (10 mM Tris-HCl pH 8, 30 mM NaCl, 0.2% Triton X-100, 4

INFORME DE LABORES 2019

mM Na_3O_4V, 50 mM NaF, 20 mM Na_2MoO_4, 1 mM PMSF, 1X complete protease inhibitor) sonicated three times at 3.5 µm with 15 s bursts and analyzed by western blotting. Purification of the cytosolic, nuclear, and nucleolar fractions was performed as previously reported[34]. A total amount of fifteen 100 mm dishes grown to 90% confluence were used; cells were washed twice with 1 ml of ice-cold PBS and collected by centrifugation at 15,000 rpm for 15 min at 4 °C. The pellet was resuspended in 1 ml of buffer TM (10 mM Tris-HCl pH 8, 2 mM $MgCl_2$, 25 mM NaF, 10 mM Na_2MoO_4, 2 mM Na_3VO_4, 1 mM PMSF), supplemented with 1× complete protease inhibitor mixture (Roche Applied Science, Indianapolis, USA), and incubated on ice for 10 min. Then, 2% Triton X-100-PBS was added, and the homogenate incubated for 10 min on ice, transferred to a glass Dounce homogenizer, stroked 30 times with B pestle, and centrifuged at 5,000 rpm for 15 min at 4 °C. The supernatant was recovered as the cytosolic fraction and the nuclear pellet was resuspended in 1 ml of buffer I (0.32 M Sucrose, 3 mM $CaCl_2$, 2 mM $Mg(CH_3COO)_2$, 0.1 mM EDTA, 10 mM Tris-HCl pH 8, 1 mM DTT, 0.5 mM PMSF, 0.5% (v/v) NP40) and 1 ml of Sucrose buffer II (2 M Sucrose, 5 mM $Mg(CH_3COO)_2$, 0.1 mM EDTA, 10 mM Tris-HCl pH 8.0, 1 mM DTT, 0.5 mM PMSF), and further purified by sucrose gradient centrifugation at 16,000 rpm for 1 h at 4 °C. The pellet was resuspended in 600 µl of buffer III (0.34 M Sucrose, 1 mM $MgCl_2$, 0.1 mM EDTA, 10 mM Tris-HCl pH 8.0, 1 mM DTT, 0.5 mM PMSF) and aliquots collected for extraction of nuclear and nucleolar proteins. For nuclear proteins, the aliquot was centrifuged at 1,000 rpm for 5 min at 4 °C and the pellet resuspended in 200 µl of lysis buffer (50 mM Tris-HCl pH 8.0, 150 mM NaCl, 1 mM PMSF, 1% (v/v) Triton X-100), supplemented with protease inhibitor cocktail and phosphatase inhibitors, sonicated 3 times at 4µm with 15 s bursts and 4 min on ice between intervals, and then pre-cleared at 13,000 rpm for 2 min at 4 °C. For purification of nucleoli, the remaining 350 µl aliquot was sonicated 5 times at 5 µm with 30 s bursts and analyzed under a light microscope to ensure nucleoli integrity, prior to purification by centrifugation at 3,000 g for 20 min at 4 °C through a sucrose gradient, using buffer III and four volumes of Sucrose buffer IV (0.88 M Sucrose, 0.1 mM EDTA, 10 mM Tris-HCl pH 8.0, 1 mM DTT, 0.5 mM PMSF). Finally, the pellet was washed in 500 µl of buffer III and centrifuged at 2,000 g for 2 min at 4 °C, to save the supernatant as the nucleolar fraction[34].

Immunoprecipitation

Recombinant protein G-agarose beads (10 µl per sample; Invitrogen, Carlsbab, CA, USA) were equilibrated by gently agitation in lysis buffer (50 mM Tris-HCl pH 8, 150 mM NaCl, 1% Triton X-100, 2 mM Na_3VO_4, 25 mM NaF, 10 mM Na_2MoO_4, 1 mM PMSF, and 1× complete protease inhibitor mixture). We quantified 500 ug of protein and the lysates were pre-cleared with equilibrated beads for 2 h at 4 °C, the beads were removed by centrifugation at 3,500 rpm for 5 min and the pre-cleared extracts incubated overnight at 4 °C with the appropriate antibody. Incubations with an irrelevant IgG antibody were carried out in parallel. Thereafter, equilibrated protein G-agarose beads blocked previously with 4% BSA were added to the lysates and incubated overnight at 4 °C. Immune complexes were collected by centrifugation at 3,500 rpm for 5 min, washed twice for 10 min with 500 µl of washing buffer (50 mM Tris-HCl, 150 mM NaCl, 5 mM EDTA, 1% Tritón X-100, 1X complete protease inhibitor, 1 mM PMSF). Bound proteins were eluted from beads by boiling in sample buffer (50 mM Tris-HCl pH 6.8, 2% (w/v) SDS, 10% (v/v) glycerol, 0.1% (v/v) 2-mercaptoethanol, 0.001% bromophenol blue), prior to being subjected to western blot analysis. C2C12 cell lysates expressing GFP-tagged proteins were subjected to IP using the GFP-Trap® system (Chromotek, Germany), according to the manufacturer's instructions.

Quantitative reverse PCR (RT-qPCR)

For analysis of rRNA transcripts, total RNA was extracted using Direct-zol ™ RNA Miniprep Kit (Zymo Research, Irvine, CA, USA), according to the manufacturer's instructions. And further analyzed by qRT-PCR with specific primers amplifying 45 S pre-rRNA (forward, 5′-GTGTCCAAGTGTTCATGCCA; reverse, 5′-CGATCTAAGAGTGAGCAACGAC), 18 S rRNA (forward, 5′-TTCCGACCATAAACGATGCC; reverse, 5′-GCTCCACCAACTAAGAACGG), 28 S rRNA (forward, 5′-GATGGTGAACTATGCTTGGG; reverse, 5′-GAATAGGTTGAGATCGTTTCGG), and GAPDH mRNA (forward, 5′-CTTGGGCTACACTGAGGACC; reverse, 5′-CTGTTGCTGTAGCCGTATTC). For analysis of *DAG1* mRNA expression, the following primers were used: forward, 5′-GAGATCATCAAGGTGTCTGCA and reverse, 5′-GTGGCTCATTGTGGTCTTCAG. RT-qPCR reactions were carried out in the StepOneplus System (Life technologies), using KAPA SYBR® FAST One-Step qRT-PCR Master Mix (2 ×) Kit, and further analyzed with the StepOne Software v2.3. The data were analyzed by comparative method $2^{-\Delta\Delta CT}$.

RNA pol I reporter assays

C2C12 cells stably expressing GFP-ICD-βDG or GFP alone were co-transfected with both the Renilla Luciferase vector (transcribed by RNA polymerase II) as a control to normalize for differences in transfection efficiency and with the firefly luciferase RNA polymerase I reporter vector (pMrTsp-9-T10). The two vectors were kindly donated by Gernot Längst Lab., Regensburg University,

INFORME DE LABORES 2019

Germany. After 48 h, the luciferase activity was measured using Dual Luciferase Assay kit (Promega). The firefly luciferase counts of the RNA polymerase I reporter were divided by the Renilla luciferase counts and compared to GFP control transfections.

Cell proliferation assays

C2C12 cells stably expressing GFP-ICD-βDG or GFP alone were harvested and plated in triplicate onto 12 wells microplates at 1×10^3 cells/mL confluence. Proliferation was measured for 13 days using the MTT (3-(4,5-dimethylthiazole)− 2–5-diphenyl tetrazolium bromide) commercial kit (Sigma-Aldrich), following the manufacturer's instructions.

Chromatin immunoprecipitation assays

C2C12 cells were incubated with 1% formaldehyde in PBS for 10 min at room temperature. Cross-link reaction was stopped by adding glycine to a final concentration of 125 mM. Cells were washed and harvested with cold PBS. After centrifugation at 1500 g, the pellet was resuspended in sonication buffer (50 mM Hepes pH 7.9, 140 mM NaCl, 1 mM EDTA, 1% Triton X-100, 0.1% sodium deoxycholate, 0.1% SDS and protease inhibitors). Soluble and sheared chromatin were obtained by applying five cycles of sonication on ice at 10% of amplitude for 20 s (Q55 sonicator, Qsonica) and recovered by centrifugation. Soluble chromatin was pre-clarified by mixing with 50 µl of recombinant protein G-agarose beads (rPGA Invitrogen) and incubated with shaking for 1 h at 4 °C. The mix was centrifuged at 3,000 × g for 1 min to remove rPGA. Twenty five micrograms of pre-clarified chromatin diluted 1:10 in sonication buffer were mixed with 7.8 µg of mouse purified serum anti-β-dystroglycan or 7.8 µg of mouse IgG (irrelevant control). Finally 25 µl of rPGA were added to each sample and incubate with shaking overnight at 4 °C. Immunoprecipitated DNA-protein complexes were extensively and sequentially washed with sonication buffer, wash buffer A (50 mM Hepes pH 7.9, 500 mM NaCl, 1 mM EDTA, 1% Triton X-100, 0.1% sodium deoxycholate, 0.1% SDS), wash buffer B (20 mM Tris-Cl pH 8, 1 mM EDTA, 250 mM LiCl, 0.5% NP40, 0.5% deoxycholate), and TE buffer. Finally, the pellet was incubated with shaking for 10 min at 65 °C in elution buffer (50 mM Tris-Cl pH 8, 1 mM EDTA, 1% SDS, 50 mM $NaHCO_3$). Supernatant was recovered by centrifugation and the cross-link reversion was carried out by adding RNAase A and Proteinase K to each sample and incubating with shaking for 4 h at 65 °C. DNA was recovered by phenol–chloroform extraction and ethanol precipitation. Twenty nanograms of DNA was used to perform quantitative PCR (qPCR), using SYBR green and rDNA-specific primers as previously reported[35,36].

Ribosomal profile analysis

Cells grown at 80–90% confluency were harvested, washed with PBS with 100 µg/mL cycloheximide and centrifuged at 5,000 rpm for 5 min at 4 °C, prior to suspension in 200 µl of lysis buffer containing 100 µg/mL cycloheximide and 1× complete protease inhibitor mixture. Thereafter cells were centrifuged for 10 min at 10,000 rpm and the supernatant was layered on top of a 15–50% sucrose gradient to be centrifuged at 25,000 rpm for 5:30 h at 4 °C in a Beckman SW28Ti rotor. All gradients were scanned at 260 nm from the top with an ISCO gradient collector. Collected fractions were precipitated with ethanol and centrifuged at 15,000 rpm for 30 min to obtain ribosomal particles.

Acknowledgments

This work was funded by CONACYT Mexico, a grant to BC (237123) and MRC PhD studentship to LAJ (G1000405-1/1 MR//J500513/1.

Author details

[1]Departamento de Genética y Biología Molecular, Centro de Investigación y de Estudios Avanzados Del Instituto Politécnico Nacional, 07360 Ciudad de México, Mexico. [2]Departamento de Neurociencia Cognitiva, Instituto de Fisiología Celular, Universidad Nacional Autónoma de México, 04510 Ciudad de México, Mexico. [3]Laboratorio de Hematobiología, Escuela Nacional de Medicina y Homeopatía, Instituto Politécnico Nacional, 07320 Ciudad de México, Mexico. [4]Laboratorio de Medicina Genómica, Instituto Nacional de Rehabilitación, 14389 Ciudad de México, Mexico. [5]Biochemistry Centre Regensburg (BCR), Universität Regensburg, 93053 Regensburg, Germany. [6]Department of Biomedical Science, University of Sheffield, Sheffield S10 2TN, UK. [7]Departamento de Toxicología, Centro de Investigación y de Estudios Avanzados Del Instituto Politécnico Nacional, 07000 Ciudad de México, Mexico. [8]Department of Medicine, Lillehei Heart Institute, University of Minnesota, Minneapolis, MN, USA

Conflict of interest

The authors declare that they have no conflict of interest.

Publisher's note

Springer Nature remains neutral with regard to jurisdictional claims in published maps and institutional affiliations.

Supplementary Information accompanies this paper at (https://doi.org/10.1038/s41419-019-1454-z).

Received: 26 September 2018 Revised: 21 January 2019 Accepted: 11 February 2019
Published online: 27 February 2019

References

1. Vieceli Dalla Sega, F. et al. Context-dependent function of ROS in the vascular endothelium: The role of the Notch pathway and shear stress. *Biofactors* **43**, 475–485 (2017).
2. Walter, J., Kemmerling, N., Wunderlich, P. & Glebov, K. γ-Secretase in microglia - implications for neurodegeneration and neuroinflammation. *J. Neurochem.* **143**, 445–454 (2017).
3. Leocadio, D., Mitchell, A. & Winder, S. J. γ-Secretase dependent nuclear targeting of dystroglycan. *J. Cell. Biochem.* **117**, 2436 (2016).
4. Leiton, C. V. et al. Laminin promotes metalloproteinase-mediated dystroglycan processing to regulate oligodendrocyte progenitor cell proliferation. *J. Neurochem.* **135**, 522–538 (2015).
5. Moore, C. J. & Winder, S. J. Dystroglycan versatility in cell adhesion: a tale of multiple motifs. *Cell. Commun. Signal.* **8**, 3 (2010).

INFORME DE LABORES 2019

6. Moore, C. J. & Winder, S. J. The inside and out of dystroglycan post-translational modification. *Neuromuscul. Disord.* **22**, 959–965 (2012).
7. Bozzi, M., Morlacchi, S., Bigotti, M. G., Sciandra, F. & Brancaccio, A. Functional diversity of dystroglycan. *Matrix Biol.* **28**, 179–187 (2009).
8. Vásquez-Limeta, A. et al. Nuclear import of β-dystroglycan is facilitated by ezrin-mediated cytoskeleton reorganization. *PLoS ONE* **9**, e90629 (2014).
9. Lara-Chacón, B. et al. Characterization of an importin alpha/beta-recognized nuclear localization signal in beta-dystroglycan. *J. Cell. Biochem.* **110**, 706–717 (2010).
10. Gracida-Jiménez, V. et al. Retrograde trafficking of β-dystroglycan from the plasma membrane to the nucleus. *Sci. Rep.* **7**, 9906 (2017).
11. Martínez-Vieyra, I. A. et al. A role for β-dystroglycan in the organization and structure of the nucleus in myoblasts. *Biochim. Biophys. Acta* **1833**, 698–711 (2013).
12. Vélez-Aguilera, G. et al. Control of nuclear β-dystroglycan content is crucial for the maintenance of nuclear envelope integrity and function. *Biochim. Biophys. Acta* **1865**, 406–420 (2018).
13. Mathew, G. et al. Nuclear targeting of dystroglycan promotes the expression of androgen regulated transcription factors in prostate cancer. *Sci. Rep.* **3**, 2792 (2013).
14. Sbardella, D. et al. Enzymatic processing by MMP-2 and MMP-9 of wild-type and mutated mouse β-dystroglycan. *IUBMB Life* **64**, 988–994 (2012).
15. Sbardella, D. et al. α-dystroglycan is a potential target of matrix metalloproteinase MMP-2. *Matrix Biol.* **41**, 2–7 (2015).
16. Mitchell, A. et al. Dystroglycan function is a novel determinant of tumor growth and behavior in prostate cancer. *Prostate* **73**, 398–408 (2013).
17. Sleeman, J. E. & Trinkle-Mulcahy, L. Nuclear bodies: new insights into assembly/dynamics and disease relevance. *Curr. Opin. Cell Biol.* **28**, 76–83 (2014).
18. Sharifi, S. & Bierhoff, H. Regulation of RNA polymerase I transcription in development, disease, and aging. *Annu. Rev. Biochem.* https://doi.org/10.1146/annurev-biochem-062917-012612 (2018).
19. Riemersma, M. et al. Absence of α- and β-dystroglycan is associated with Walker-Warburg syndrome. *Neurology* **84**, 2177–2182 (2015).
20. Tsekrekou, M., Stratigi, K. & Chatzinikolaou, G. The Nucleolus: In Genome Maintenance and Repair. *Int. J. Mol. Sci.* **18**, https://doi.org/10.3390/ijms18071411 (2017).
21. Shav-Tal, Y. et al. Dynamic sorting of nuclear components into distinct nucleolar caps during transcriptional inhibition. *Mol. Biol. Cell.* **16**, 2395–2413 (2005).
22. Lipscomb, L., Piggott, R. W., Emmerson, T. & Winder, S. J. Dasatinib as a treatment for Duchenne muscular dystrophy. *Hum. Mol. Genet.* **25**, 266–274 (2016).
23. Bozzi, M. et al. Enzymatic processing of beta-dystroglycan recombinant ectodomain by MMP-9: identification of the main cleavage site. *IUBMB Life* **61**, 1143–1152 (2009).
24. Martin, C. et al. Lamin B1 maintains the functional plasticity of nucleoli. *J. Cell. Sci.* **122**, 1551–1562 (2009).
25. Legartová, S. et al. Nuclear structures surrounding internal lamin invaginations. *J. Cell. Biochem.* **115**, 476–487 (2014).
26. Sen Gupta, A. & Sengupta, K. Lamin B2 modulates nucleolar morphology, dynamics, and function. *Mol. Cell. Biol.* **37**, https://doi.org/10.1128/MCB.00274-17 (2017).
27. Christie, M. et al. Structural biology and regulation of protein import into the nucleus. *J. Mol. Biol.* **428**, 2060–2090 (2016).
28. Lindström, M. S. NPM1/B23: a multifunctional chaperone in ribosome biogenesis and chromatin remodeling. *Biochem. Res. Int.* **2011**, 195209 (2011).
29. Panov, K. I., Friedrich, J. K., Russell, J. & Zomerdijk, J. C. UBF activates RNA polymerase I transcription by stimulating promoter escape. *EMBO J.* **25**, 3310–3322 (2006).
30. Aubert, M., O'Donohue, M. F., Lebaron, S. & Gleizes, P. E. Pre-ribosomal RNA processing in human cells: from mechanisms to congenital diseases. *Biomolecules* **8**, https://doi.org/10.3390/biom8040123 (2018).
31. Yang Kai, Y. J. & Jing, Ji Nucleolar Stress: hallmarks, sensing mechanism and diseases. *Cell Stress* **2**, 125–140 (2018).
32. Németh, A. & Grummt, I. Dynamic regulation of nucleolar architecture. *Curr. Opin. Cell Biol.* **52**, 105–111 (2018).
33. Pereboev, A. V., Ahmed, N., thi Man, N. & Morris, G. E. Epitopes in the interacting regions of beta-dystroglycan (PPxY motif) and dystrophin (WW domain). *Biochim. Biophys. Acta* **1527**, 54–60 (2001).
34. Hernández-Ibarra, J. A., Laredo-Cisneros, M. S., Mondragón-González, R., Santamaría-Guayasamín, N. & Cisneros, B. Localization of α-dystrobrevin in cajal bodies and nucleoli: a new role for α-dystrobrevin in the structure/stability of the nucleolus. *J. Cell. Biochem.* **116**, 2755–2765 (2015).
35. Todd, M. A., Huh, M. S. & Picketts, D. J. The sub-nucleolar localization of PHF6 defines its role in rDNA transcription and early processing events. *Eur. J. Hum. Genet.* **24**, 1453–1459 (2016).
36. Hisaoka, M., Ueshima, S., Murano, K., Nagata, K. & Okuwaki, M. Regulation of nucleolar chromatin by B23/nucleophosmin jointly depends upon its RNA binding activity and transcription factor UBF. *Mol. Cell. Biol.* **30**, 4952–4964 (2010).

Biology of Reproduction, 2019, 100(4), 1018–1034
doi:10.1093/biolre/ioy250
Research Article
Advance Access Publication Date: 28 November 2018

OXFORD

Research Article

Calcium signaling and expression of voltage-gated calcium channels in the mouse ovary throughout the estrous cycle†

Daniel Bahena-Alvarez [1], Ruth Rincón-Heredia [2], Diana Millán-Aldaco [1], Tatiana Fiordelisio [3] and Arturo Hernández-Cruz [1,4,*]

[1]Departamento Neurociencia Cognitiva, Instituto de Fisiología Celular, UNAM, Circuito de la Investigación Científica s/n, Ciudad Universitaria, Ciudad de México, D.F., México; [2]Unidad de Imagenología, Instituto de Fisiología Celular, UNAM, Circuito de la Investigación Científica s/n, Ciudad Universitaria, Ciudad de México, D.F. México; [3]Laboratorio de Neuroendocrinología Comparada, Departamento de Ecología y Recursos Naturales, Biología, Facultad de Ciencias, UNAM, Ciudad Universitaria, Ciudad de México, D.F., México and [4]Laboratorio Nacional de Canalopatías, Instituto de Fisiología Celular, UNAM, Circuito de la Investigación Científica s/n, Ciudad Universitaria, Ciudad de México, D.F., México

*__Correspondence:__ Departamento de Neurociencia Cognitiva, Instituto de Fisiología Celular, Universidad Nacional Autónoma de México, Circuito de la Investigación Científica, Col. UNAM, Ciudad Universitaria, CP 04510 CDMX, México. Tel: 52–556225623; E-mail: ahernan@ifc.unam.mx

†__Grant support:__ This work was funded by Mexico's Consejo Nacional de Ciencia y Tecnología grants CB-240305, Fronteras 71 39908-Q and Laboratorio Nacional de Canalopatías 279820. We also thank support from Dirección General de Asuntos del Personal Académico of Universidad Nacional Autónoma de México (DGAPA-UNAM) Programa de Apoyo a Proyectos de Investigación e Innovación Tecnológica-IN211616, IG200119 and Coordinación de la Investigación Científica /Dr W. Lee. Edited by Dr. Jodi Flaws

Received 14 June 2018; Revised 31 October 2018; Accepted 27 November 2018

Abstract

The estrous cycle is an iterative change in the anatomy, endocrinology, physiology, and behavior to provide maximum fecundity. Ovarian steroid production involves gonadotropin-induced $[Ca^{2+}]_i$ raises due in part to voltage-gated Ca^{2+} channels (VGCCs) whose identity and tissue distribution *in situ* is largely unknown. Using fluorescence Ca^{2+} imaging and confocal microscopy, we recorded both spontaneous and depolarization-induced Ca^{2+} signals in living mouse ovarian slices. They were most prominent in theca cells (TCs) and oocytes. The presence of Ca^{2+} channel subunits Ca_V 1.2, Ca_V 1.3, Ca_V 2.1, Ca_V 2.2, and Ca_V 3 was examined with immunofluorescence of ovarian sections. Ca_V 1.2 and Ca_V 1.3 (L-type Ca^{2+} channels) are present in the stroma, granulosa cells (GCs), and corpora lutea (CL). Intriguingly subunits that are characteristic of nerve cells are also expressed: P/Q-type (Ca_V 2.1; α1A) in the stroma and CL cells and N-type (Ca_V 2.2; α1B) in perifollicular smooth muscle cells. The expression of α1 subunits fluctuates along the estrous cycle: in metestrus-diestrus (the quiescent stage of the cycle), CL and GCs are similarly stained, while in proestrus (stage of maximal ovarian stimulation) CL staining increases relatively to GCs. Also in proestrus, Ca_V 3 Ca^{2+} channel subunits are expressed more in CL compared to GC suggesting a more significant role of Ca^{2+} channels. In estrus, Ca_V 3 subunits from mesenchymal and interfollicular stromal cells

© The Author(s) 2018. Published by Oxford University Press on behalf of Society for the Study of Reproduction. All rights reserved.
For permissions, please e-mail: journals.permissions@oup.com

Downloaded from https://academic.oup.com/biolreprod/article/100/4/1018/5212287 by Universidad Nacional Autonoma de Mexico user on 14 October 2020

become intensely stained. Our study represents an important step in understanding the role of VGCCs in ovarian physiology and possibly in ovarian cancer and other reproductive pathologies.

Summary Sentence

Calcium signaling and the expression of voltage-gated Ca^{2+} channels in the ovary is heterogeneous and varies considerably along the estrous cycle.

Key words: estrous cycle, follicle, granulosa cells, ion channels, calcium signaling, ovary, ovulatory cycle, follicular development, immunofluorescence.

Introduction

Ion channels perform a diversity of important functions in mammalian cells. The ovary is not an exception. However, a detailed understanding of the molecular identity, cellular distribution, and functional role of the majority of ovarian ion channels is still absent. Such understanding would greatly improve our comprehension of the role of ion channels in ovarian physiology and physiopathology. Moreover, ion channels are emerging as important and specific targets of novel therapeutic approaches. A better knowledge of their role in ovarian function could allow the development of new treatments for fertility control and ovarian diseases. Ovarian theca and granulosa cells (GCs) are the main steroid-producing cells in the ovary. Along with the oocyte, they coordinate folliculogenesis, steroidogenesis, and ovulation [1]. TCs form a sheet of elongated endocrine cells approximately 3–5 cell layers thick immediately adjacent to the basal lamina known as the theca interna. The role of ion channels subtypes in ovarian function is incomplete and fragmentary. To this date GCs are the only ovarian cell type (besides the oocyte itself) studied in some detail with electrophysiological and molecular biology techniques [2, 3]. This is probably due to the fact that GCs escort the oocytes after ovulation and are easily obtained as a pure, uniform cell population for in vitro experiments. Nonetheless, these GCs originate from mature follicles and are at the final stage of their development, and they lack responsiveness to follicle-stimulating hormone (FSH) and no longer produce estrogen, but progesterone in response to stimulation with luteinizing hormone (LH) and human Chorionic Gonadotropin (hCG). Therefore, information on ion channels expression and function collected from mature GCs cells is likely to be incomplete.

Ion channels expressed in ovarian cells

Voltage-dependent and independent K^+ channels have been characterized molecularly, electrophysiologically, and pharmacologically in porcine GCs [4]. There is no doubt that ovarian K^+ channels are functionally relevant, since their antagonists disrupt several GCs functions, including steroid production [5, 6]. Several types of K^+ channels have also been identified in human GCs from in vitro fertilization patients, including the three types of Ca^{2+}-activated K^+ channels; IK, SK, and BK(Ca) [7, 8], and the ATP-sensitive potassium channel, K(ATP), which couples metabolic state and membrane potential. Glibenclamide, a K(ATP) channel blocker, depolarizes GCs and inhibits hCG-induced progesterone production [9].

The presence of voltage-gated tetrodotoxin (TTX)-sensitive Na^+ channels (Nav 1.7) has also been demonstrated in human GCs, where its functional role is subject of some debate [10]: it has been reported that veratridine (an Na^+ channel opener) reduces progesterone production and triggers the presence of secondary lysosomes, an autophagocytic process involved in the regression of the corpus luteum [2]. Conversely, TTX (a specific Na^+ channel blocker) does not seem to affect the GCs phenotype. Several Cl^- currents, both voltage-dependent and voltage-independent, have been recorded in chicken GCs, where they contribute to the negative resting membrane potential essential for action potential generation [11]. Expression of Cl^- currents has not been reported yet in mammalian GCs. Finally, two types of voltage-gated Ca^{2+} channels (VGCCs; T-type: low voltage activated [LVA] and L-type: high voltage activated [HVA]) have been described in porcine, chicken, and human GCs (see below) [11–17].

Data collected from over 30 years of research support the notion that $[Ca^{2+}]_i$ elevations, either from intracellular or extracellular sources, participate in the stimulation by gonadotropins of ovarian follicle steroid production, and several of these reports suggest a role of VGCCs in these phenomena [18]. Nonetheless, a comprehensive assessment about the identity and tissue distribution of VGCCs the ovary *in situ* is still lacking. Also, it is not known if Ca^{2+} channel expression and/or $[Ca^{2+}]_i$ signaling undergoes variations along the estrous cycle.

Ca^{2+} imaging experiments reported here for the first time revealed patterns of spontaneous and depolarization-induced Ca^{2+} signals in living ovarian slices in vitro. The information obtained with the Ca^{2+} indicator fluo-4 and confocal fluorescence microscopy suggests the participation of VGCCs in TCs. Spontaneous oocyte Ca^{2+} signals were also recorded. The results from these physiological experiments underscore the importance of understanding the expression of VGCCs in ovarian tissue. Immunofluorescence from ovarian frozen sections unveiled the diverse expression patterns of specific HVA and LVA Ca^{2+} channel subtypes at different stages of the estrous cycle. The information reported here is relevant to the understanding of Ca^{2+} signaling in ovary cells *in situ* and its regulation by gonadotropins. Also, it is of great interest in physiopathology, since increasing evidence demonstrates that the disruption of Ca^{2+} homeostasis underlies certain ovarian malignant phenotypes and ovarian reproductive pathologies.

Materials and methods

Animals

Female CD1 mice, 8 weeks of age, were used. They were maintained under controlled conditions of light and temperature (12 h light, 12 h dark), with free access to food and water. All animal studies were performed in accordance with the SSR's specific guidelines and standards and under the supervision of an Institutional Committee for the Use of and Care of Laboratory Animals (CICUAL Protocol # AHC115 (46)-17) and the Official Mexican Guide from the Secretary of Agriculture (SAGARPA NOM-062-Z00–1999). Mice were maintained in the animal facility and fed ad libitum. The stage of the estrous cycle was determined at the same time of day (10:00) for 8 to 10 consecutive days through vaginal smears [19]. Only mice that showed two consecutive estrous cycles of the same duration were selected. Animals were sacrificed at 12 o'clock on the expected day of metestrus-diestrus, proestrus, or estrus.

Downloaded from https://academic.oup.com/biolreprod/article/100/4/1018/5212287 by Universidad Nacional Autonoma de Mexico user on 14 October 2020

INFORME DE LABORES 2019

Preparation of acute ovarian slices

After decapitation under CO_2 anesthesia, the ovaries were rapidly removed and then carefully dissected, cleaned, and embedded in 3.0% low-melting point agarose (Invitrogen Catlab, CA) dissolved in Krebs–Ringer Bicarbonate buffer (KRB) at 37°C containing (125 mM NaCl, 2.5 mM KCl, 2 mM $CaCl_2$, 1 mM $MgCl_2$, 1.25 mM NaH_2PO_4, 26 mM $NaHCO_3$, and 12 mM glucose, gassed with 5% CO_2 and 95% O_2 to pH ~7.4). The agarose with embedded ovaries was hardened by immersion in ice-cold physiological solution, and the agar block was glued with cyanoacrylate onto the plate of a microtome. The slicing chamber was filled with physiological solution at 3°C, and transverse slices 150 μm in thickness were prepared using a vibrating blade microtome (Leica Microsystems VT 1000S GmbH). Freshly cut slices were transferred to an incubation beaker containing physiological solution at room temperature and continuously gassed (5% CO_2 and 95% O_2). Slices remained viable for up to 6 h after preparation.

Intracellular Ca^{2+} imaging of living ovarian slices

$[Ca^{2+}]$i changes were determined as previously described [31]. Briefly, mouse ovarian sections were incubated with 10 μM of the cell-permeable fluorescent Ca^{2+} indicator fluo-4 AM (Molecular Probes, Eugene, OR) for 35 min at room temperature in KRB. Slices were washed twice and placed in the bottom of a plexiglass recording chamber attached to the stage of an upright microscope (Nikon Eclipse 80i; Nikon Corp., Tokyo, Japan) and continuously superfused (2 ml/min) with KRB by gravity-fed perfusion. Fluo-4 was excited at 488 nm with monochromatic light from an argon laser (Laser Physics, Reliant 100 s488, West Jordan, UT), coupled to a Yokogawa spin-disk confocal scan head (CSU10B, Yokogawa Electronic Co., Tokyo, Japan and Solamere Technology Group, Salt Lake City). Excitation light was band passed to 488 nm with a filter cube placed in the light path, and emitted fluorescence was band passed (510 nm) before its reflection into the camera port. Fluorescence images were acquired with a water-immersion, Nikon objective (20x, 0.5 NA), and a cooled digital CCD camera (Andor Technology iXon 897, Oxford Instruments, High Wycombe, UK) controlled by the iQ software (Andor iQ version 1.10.2). Fluorescence images were acquired at 10 ms exposure and 500 ms intervals. All Ca^{2+} imaging experiments were performed at room temperature (22–24°C). Fluorescence image sequences 300 s in duration (movies) were acquired from imaging field during perfusion with normal KRB solution. Movies were acquired and saved in multi-tiff format and processed and analyzed with Fiji (Image J version 1.52 g; National Institutes of Health). Fluo-4 is a single wavelength dye and its fluorescence is a function of dye concentration, illumination pathway, and $[Ca^{2+}]$i. Nonetheless, our experiments are designed to maximize fluorescence changes associated to fluctuations of $[Ca^{2+}]$i. Raw movies were converted to ΔF movies: $\Delta F = F(i) - F_0$, where F_0 is the result of averaging the first five frames of the sequence, and F(i) represents each (i) fluorescence image of the set. No attempts were made to calculate absolute $[Ca^{2+}]$i from these data. The values obtained are expressed as arbitrary fluorescence units. Regions of interest (ROIs) were drawn around selected cells that showed spontaneous or induced fluorescence increases (SD > 5 ± 0.5). These ROIs were used for single-cell quantification of ΔF over time.

Solution exchange

KRB solution was continuously applied to the recording chamber (2 ml/min) by a gravity-fed perfusion. To assess the presence of functional VGCCs, a high $[K^+]$ solution (KCl 120 mM, NaCl 20 mM, $CaCl_2$ 2 mM, and HEPES 10 mM, pH = 7.4) was pressure applied (10 psi; 0.5 s) via a glass puffer pipette (tip diameter ~ 7 μm) connected to a Picospritzer II device (General Valve, Fairfield, NJ) and placed within 100 μm from the surface of the slice with a micromanipulator. Control experiments showed that with this procedure, the external medium surrounding the slice surface is replaced within 100 ms.

Immunofluorescence of ovarian frozen sections

Three mice from each stage of the estrous cycle were injected with a terminal dose of pentobarbital (60 mg/kg, I.P.) and perfused transcardially with 50 ml of phosphate-buffered saline (PBS, 0.1 M), and then with 50 ml of ice-cold 4% paraformaldehyde in PBS. Ovaries were then removed, cleaned, and post-fixed in 4% paraformaldehyde in PBS for 5 h at 4°C. Thereafter, they were placed overnight in 10%, 20%, and 30% sucrose solution in PBS. Finally, they were included in Tissue-Tek (Sakura Finetek) for sectioning in a cryostat (Leica Microsystems CM1900, Wetzlar, Germany). Frozen sections (10 μm in thickness) were then mounted on superfrost glass slides (Fisher Scientific). Frozen sections were washed with PBS and incubated with a blocking solution (2% BSA (weight/volume)) and permeabilized with 0.1% triton 100 in PBS for 30 min at room temperature. After washing with PBS, sections were incubated in a humid chamber for 24 h in the dark at 4°C with one of the following primary rabbit antibodies from Alomone Labs (Jerusalem, Israel): anti Ca_V 2.1 (α1A; validation number 2039764, lot # AN-09), anti Ca_V 2.2 (α1B; validation number 2039766, lot # AN-015), anti Ca_V 1.2 (α1C; validation number 2039771, lot # AN-19) or anti Ca_V 1.3 (α1D; validation number 2039775, lot # AN-09), together with goat anti-SMAα (vascular smooth muscle cell marker α actin) at a 1:250 dilution (validation number 10980764, lot # PA5–18292; Thermo Scientific, Rockford, IL). In separate experiments, sections were incubated with primary goat antibodies against Ca_V 3.1, Ca_V 3.2, and Ca_V 3.3 (validation numbers: 660887, 2259540, and 660891: lot # Sc-16259, Sc-16264, and Sc-16261, respectively; Santa Cruz Biotechnology, Inc. Dallas, TX) at a dilution of 1:250 in PBS. Each of the anti Ca_V 3 subunits gave specific, but weak staining, with patterns indistinguishable from one another. To increase the sensitivity of detection, the immunostaining was carried out with antibodies raised against the three subunits α1G, α1H, and α1I combined.

Sections were washed and incubated for 2 h at room temperature with a $F(ab')_2$ Alexa 488 fraction of donkey anti-rabbit IgG (1:150 dilution, validation number 2340586 cat # 705–006-147; Jackson ImmunoResearch Lab, West Grove, PA) and $F(ab')_2$ Alexa 647 fraction of donkey anti-goat IgG (H + L) (1:150 dilution; validation number 2340386 cat # 705–006-152; Jackson ImmunoResearch Lab) in PBS. Finally, stained sections were washed with PBS and mounted with Dako Glycergel (Dako North American, Inc., CA) for microscopic observation. Several negative controls were required to achieve a reliable double-immunolabeling. Negative control of Ca_V primary antibodies was accomplished by pre-adsorbing each of them with the corresponding synthetic antigenic peptides (2 μg peptide per 1 μg antibody). This procedure completely blocked specific immunofluorescence. In addition, incubation with either secondary antibody alone produced weak, nonspecific fluorescence. Possible interactions between unmatched secondary antibodies were ruled out by incubating samples: first with the rabbit primary anti-CaV antibody, or the goat anti-SMAα, and then with the Alexa 488 F(ab')2 fraction of donkey anti-rabbit IgG and Alexa 647 F(ab')2 fraction

Downloaded from https://academic.oup.com/biolreprod/article/100/4/1018/5212287 by Universidad Nacional Autonoma de Mexico user on 14 October 2020

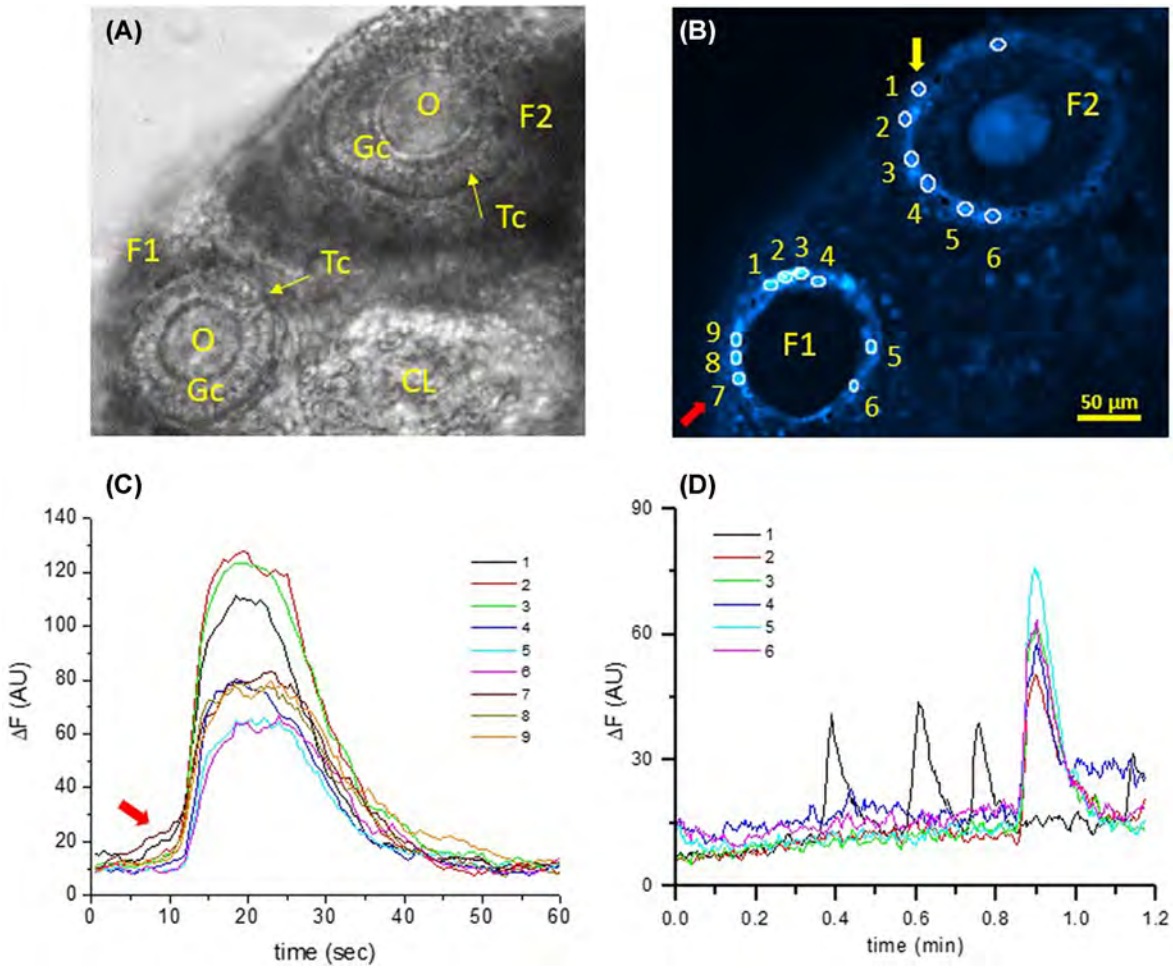

Figure 1. Spontaneous $Ca^{2\pm}$ fluctuations in intact ovarian follicles. (A) Bright-field image of a living mouse ovarian slice. Two intact primary follicles (F1 and F2) are shown. GC: granulosa cells. TC: theca cells. O: oocyte; CL corpus luteum. A 500-frame-long ΔF movie was obtained (see Methods section). (B) Standard deviation image (SD) where regions of interest (ROIs) were drawn on individual cells. (C) ΔF recordings corresponding to follicle # 1 that involves the whole external theca (ROIs 1 to 9). Cell # 7 (red arrow) shows an early response that propagates clockwise, reaching cell # 6 after a delay of ~ 1.2 s. (D) ΔF recordings in follicle #2 also show a spontaneous synchronous Ca^{2+} fluctuation in five out of six TCs. Cell #1 that shows random, unrelated Ca^{2+} spikes.

of donkey anti-goat IgG. As expected, reaction with rabbit primary anti-CaV antibody gave fluorescence at 488 nm excitation, but not at 647 nm excitation and with the presence of goat anti-SMAα antibody gave fluorescence at 647 nm excitation, but not at 488 nm excitation (data not shown).

Mounted sections from three mice were viewed by epifluorescence microscopy, and a representative section from each condition was chosen for analysis and display. Images were acquired with an LSM700 Zeiss confocal laser scanning microscope (Gottingen, Germany), equipped with a 20x/1.0 NA Plan Apochromat water-immersion objective, Samples were excited for Alexa 488 with an Argon-488 nm laser, 490–600 emission range and MBS 488/543 and for Alexa 647 an He/Ne-633 nm laser, 650–750 emission range and MBS 543/633. Exposures were adjusted according to range of fluorescence intensities of each primary antibody, and then imaging parameters (laser power, gain, and pinhole size) remained fixed throughout the session of observation of each set of ovarian section. Images were acquired with Leica ZEN blue software and stored in CVS or TIFF image format (8 bits, 1024 × 1024 pixels). For reconstruction of a complete ovarian section, 1024 × 1024 pixels images were acquired using the "tile scan mode" and a motorized stage. Each tile corresponds to the image summarizing 15 z-stack images spaced by 1 micron. In our case, a tile of 6 × 6 frames was required to completely map an ovarian section. Raw images were normalized so that no more than 0.1% of pixels were saturated. Some of the figures were digitally processed (i.e. multiplied by a factor of 1.25 or 1.5) to emphasize certain aspects or weakly stained structures that are difficult to appreciate. As a result, some areas may appear saturated. However, for the digital quantification performed with some images (see below) we took care that the pixel intensities of the areas involved were far for saturation. Fluorescence quantification was carried out with Fiji ImageJ v.1.52 [20]. The mean fluorescence intensity (arbitrary units) was determined in six different areas of interest on every structure present (either ovarian follicles or corpora lutea [CL]) in each ovarian section. The mean fluorescence measured on CL or GC was used to calculate the fluorescence ratio CL/GC.

Results

Spontaneous follicle Ca^{2+} fluctuations in living ovarian slices

The bright-field image of a living ovarian slice obtained from a mouse in metestrus shows two intact primary follicles (Figure 1A, F1 and

Downloaded from https://academic.oup.com/biolreprod/article/100/4/1018/5212287 by Universidad Nacional Autonoma de Mexico user on 14 October 2020

INFORME DE LABORES 2019

Table 1. Incidence of voltage-gated Ca^{2+} signals in ovarian slices at different stages of the estrous cycle

	Proestrus	Estrus	Metestrus	Diestrus	**Total**
Number of follicles recorded	66	72	157	164	459
Number of follicles with spontaneous Ca^{2+} signals	7	4	12	19	42
% of follicles with Ca^{2+} signals	**1.53**	**0.87**	**2.61**	**4.14**	**9.18**
Number of follicles recorded	31	25	31	60	147
Number of follicles with induced* Ca^{2+} signals	4	2	4	8	18
% of follicles with induced* Ca^{2+} signals	**2.72**	**1.36**	**2.72**	**5.44**	**12.24**

* High K^+ depolarization-induced Ca^{2+} signals

F2). Ca^{2+} signals, in the form of ΔF movies, were obtained with confocal microscopy and in fluo-4 loaded ovarian slices (see the Methods section). Supplementary Movie 1 (SM1) displays spontaneous Ca^{2+} fluctuations observed in both follicles. The oocyte from follicle # 2 showed a spontaneous Ca^{2+} oscillation. Regions of interest were drawn in the standard deviation (SD) image, which summarizes the events of the entire movie (Figure 1B). These ROIs correspond to individual cells that showed large ΔF fluctuations. ΔF recordings from ROIs drawn on follicle #1 are shown in Figure 1C. This spontaneous Ca^{2+} fluctuation involves the whole external theca, as nine cells at different locations activate at once. A closer examination reveals that cell #7 had an early small response (red arrow) followed by a large ΔF signal that propagated clockwise, and until after a delay of about 1.2 s, cell #6 is reached and the wave stops. Follicle #2 also showed a spontaneous Ca^{2+} fluctuation. The ΔF recordings in Figure 1D show that five out of six TCs are recruited. Cell #1 shows random, unrelated Ca^{2+} spikes. Ca^{2+} fluctuations of the external theca layer in ovarian follicles is a relatively infrequent phenomenon. Its incidence in ovarian slices from mice at different stages of the estrous cycle is summarized in Table 1. The percentage of follicles with theca Ca^{2+} oscillations ranged from 0.87 to 4.14%, with the highest frequency observed in diestrus. From 459 follicles examined, 42 showed theca Ca^{2+} oscillations.

Spontaneous oocyte Ca^{2+} signals in intact follicles from living ovarian slices

Bright-field and fluorescence images (Figure 2A and B, respectively) were obtained from a slice containing two intact secondary follicles. The oocyte from the larger follicle displayed the spontaneous Ca^{2+} oscillations shown in Figure 2C. Similar "spike-like" fluctuations resulting from Ca^{2+} influx and release from intracellular stores have been reported in isolated oocytes, where they trigger spontaneous exit from diplotene and M-II arrest (reviewed in [21]). Nonetheless, this is the first report where such oscillations have been observed in *intact* secondary follicles from acutely isolated mammalian ovarian slices. In a different slice, the oocyte of another follicle displayed four Ca^{2+} oscillations over the course of several minutes, as depicted in the inset of Figure 2D. The first two of such oscillations can be observed in Supplementary Movie 2 (SM2). Interestingly, these oscillations begin in the edge of the oocyte, spreading inwards as a wave. Figure 2E shows the traces of ΔF over time of the first oscillation, obtained from the ROIs drawn in the inset. ROI # 1 is the initiation site, and the Ca^{2+} wave reaches ROIs 4–5 with a delay of ~2.5 s. The image sequence in Figure 2F illustrates the initiation and spreading of the Ca^{2+} wave during the first Ca^{2+} oscillation. Strictly speaking, oocyte Ca^{2+} signals cannot be explained by the expression of specific Ca^{2+} channel subunits.

Depolarization-induced Ca^{2+} signals

Spontaneous Ca^{2+} oscillations of the TCs layer are fast, appear abruptly, and spread rapidly, properties that are reminiscent of excitable tissues. We conjectured that the opening of VGCCs could be involved in these phenomena. Figure 3A illustrates the result of applying with a puffer pipette a depolarizing solution to an ovarian slice (see the Methods section). In the SD image in Figure 3B, 12 cells were chosen to examine Ca^{2+} signals triggered by the stimulus. Cells 9 and 10, located directly in front of the pipette tip respond first, with a large Ca^{2+} signal. Then, with a 5 s delay, TCs 1 to 8 respond with a rapid, synchronous Ca^{2+} rise. Notice that cells 11 and 12, located away from the pipette tip, also respond to the depolarizing stimulus. The incidence of voltage-gated Ca^{2+} signals in ovarian slices at different stages of the estrous cycle is summarized in Table 1. They were observed more frequently in diestrus (5.4%). Out of 147 follicles examined, 18 responded with Ca^{2+} signals. These experiments suggest the presence of functional VGCCs in specific populations of the ovarian cells *in situ*. Further studies should focus on the physiological and pharmacological characterization of these Ca^{2+} signals.

It is remarkable that GCs do not exhibit spontaneous Ca^{2+} fluctuations nor responses to the depolarizing stimulus, even though the expression of VGCCs has been reported in porcine, chicken, and human GCs [11–14, 16, 17], and both LH/FSH and hCG trigger elevations of $[Ca^{2+}]i$ in GCs that stimulate steroid production [28–30]. Conversely, porcine TCs in vitro display diverse forms of $[Ca^{2+}]_I$ signaling in response to increasing doses of LH, from single spikes to spike-plateau and oscillations.

Immunofluorescence of ovarian frozen sections

Metestrus-diestrus

Ca_V 1.2 (α1C). The presence of L-type, sustained dihidropyridine-sensitive Ca^{2+} currents has been amply documented in GCs from mammalian ovary by both electrophysiology and molecular biology. The tissue distribution of Ca_V 1.2 in metestrus-diestrus (the catabolic or quiescent phases of the cycle, see below) was examined first. Figure 4A illustrates the specific immunolabeling for Ca_V 1.2 and smooth muscle actin (SMAα) in the same ovarian section (A_1 and A_2, respectively). As expected, SMAα immunostaining labels a layer of smooth muscle cells in the theca externa surrounding ovarian follicles (Figure 4A_2) and CL, forming a network of interconnected smooth muscle cells (Figure 4A_2). Ca_V 1.2 immunostaining is widely distributed throughout the ovary, with some regions showing stronger labeling than others, like unidentified stromal cells in the ovarian medulla (Figure 4A_1, yellow arrows; see Figure 5A). Also, the GCs adjacent to the basal lamina of ovarian follicles appear more intensely labeled (Figure 4A_1, red arrows). Higher magnifica-

Downloaded from https://academic.oup.com/biolreprod/article/100/4/1018/5212287 by Universidad Nacional Autonoma de Mexico user on 14 October 2020

INFORME DE LABORES 2019

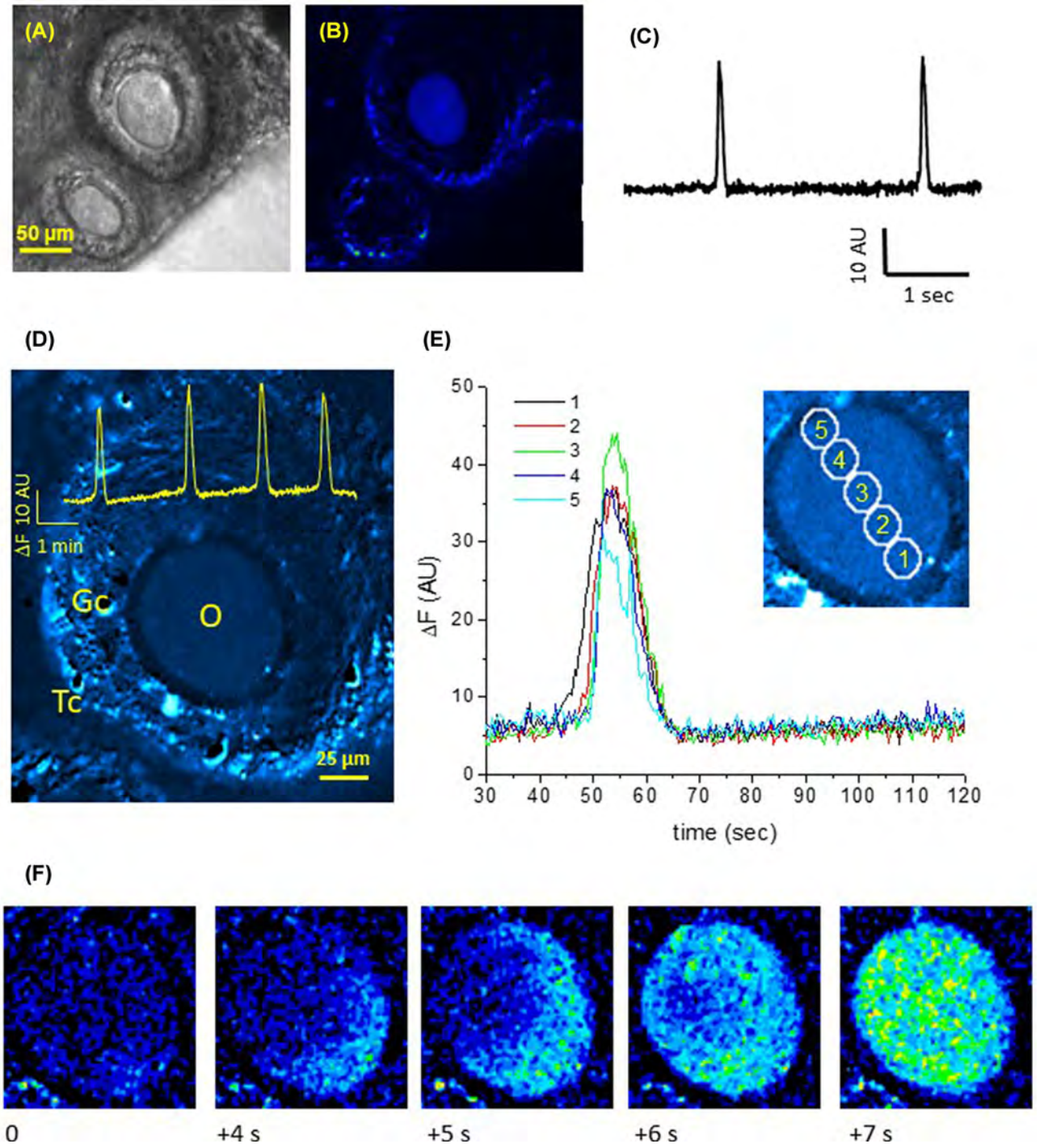

Figure 2. Spontaneous $Ca^{2\pm}$ fluctuations in intact oocytes. (A and B) Bright-field and fluorescence images were obtained from a slice containing two intact secondary follicles. (C) Spontaneous Ca^{2+} oscillations recorded from the oocyte in the larger follicle. (D) Another follicle where the oocyte displayed four Ca^{2+} oscillations (inset). (E) ΔF recordings over time of the first of such oscillations, obtained from the ROIs on the inset. Clearly the oscillation begins in the perimeter of the oocyte (ROI #1), spreading inwards as a wave. (F) Image sequence showing the initiation and spreading of the Ca^{2+} wave during the first Ca^{2+} oscillation. The labels indicate the corresponding delay in seconds.

tion shows that GCs labeling is confined to the plasma membrane (Figure 5B and D; GC), and that the stronger peripheral staining of ovarian follicles (Figure 4A_1, red arrows) is a palisade of elongated GCs perpendicular to the basal lamina (Figure 5B, red stars). In some cases, this pattern is somewhat confusing: they appear as slender processes, running perpendicular to the basal lamina and extending several microns inward, forming ramifications (Figure 5B and D, yellow stars). The fluorescence intensity of several ROIs comprising these peripheral GCs was measured and compared with ROIs of the same size from the central GCs. A ratio of peripheral versus

Downloaded from https://academic.oup.com/biolreprod/article/100/4/1018/5212287 by Universidad Nacional Autonoma de Mexico user on 14 October 2020

INFORME DE LABORES 2019

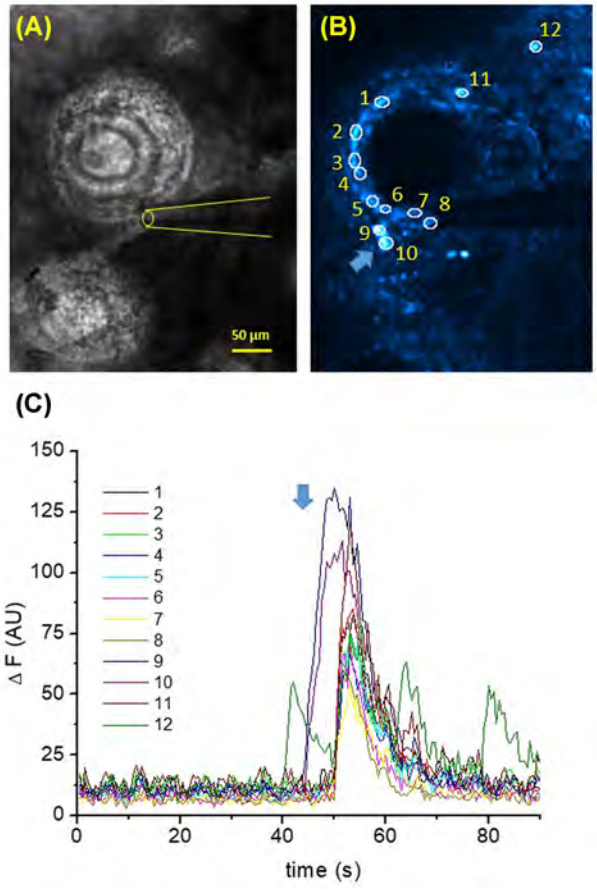

Figure 3. Ca^{2+} signals triggered by a depolarizing stimulus in an ovarian slice. (A) Bright-field image of an ovarian slice with two intact follicles. The diagram indicates the position of the puffer pipette (B) SD image showing the 12 ROIs that were chosen to record Ca^{2+} signals triggered by the depolarizing stimulus (see Methods section). (C) ΔF recordings over time from cells 1 to 12. Cells 9 and 10, located directly in front of the pipette tip, respond promptly to the application of the high K^+ solution (10 psi; 0.5 s; time indicated with a blue arrow) with large Ca^{2+} signals Then, after a ~5 s delay, TCs 1 to 8 also respond with a rapid, synchronous Ca^{2+} rise. Even cells 11 and 12, located away from the pipette tip, respond to the depolarizing stimulus with about same delay.

central GCs staining of 1.77 is obtained (i.e. peripheral GCs were 77% brighter than central GCs). In contrast, CL cells are stained more uniformly (Figure 5C and D, CL). Excluding the periphery of ovarian follicles, central GCs and CL cells are stained similarly (Figure 5C and D). Accordingly, when the mean fluorescence was measured in GCs and CL cells, a ratio CL/GC of 1.06 was obtained (see Table 2). Slender processes resembling unmyelinated nerve fibers can be seen both inside (Figure 5C, red arrows) and around CL and ovarian follicles (Figure 5D, red arrows). As shown in Figure $4A_3$, Ca_V 1.2 and SMAα do not co-localize, implying that this subunit is absent in perifollicular smooth muscle cells (see below).

Ca_V 1.3 (α1D). The expression pattern of Ca_V 1.3 (α1D) subunits, also capable of generating L-type, dihidropyridine-sensitive Ca^{2+} currents in model systems, was examined next (Figure $4B_1$). Similar to Ca_V 1.2, unidentified medulla stromal cells show cytoplasmic Ca_V 1.3 staining (Figure $4B_1$, yellow arrows; see also Figure 6A). Both CL cells and GCs are weakly labeled (Figure $4B_1$: see Figure 6B, GC and CL). Hence, a fluorescence ratio CL/Gc of 1.12 close to unity is obtained (see Table 2). Ca_V 1.3 and SMAα do not co-localize either (see Figure $4B_3$). The anti-Ca_V 1.3 antibody labels GCs in the plasma membrane and CL cells in the cytoplasm (Figure 6B). Thin filaments reminiscent of unmyelinated nerve fibers are not stained with the Ca_V 1.3 antibody (Figure 6B).

Ca_V 2.1 (α1A). Ca_V 2.1, α1A pore-forming subunits expressed in model systems lead to the generation of HVA sustained Ca^{2+} currents also known as P/Q-type Ca^{2+} channels blocked by ω-Agatoxin IVA and abundantly expressed in CNS neurons. The presence of this Ca^{2+} channel subunit had not been previously reported in ovarian tissue. Ca_V 2.1 and SMAα immunolabeling are illustrated in Figure $4C_1$ and C_2, respectively. Ca_V 2.1 staining is markedly nonuniform (Figure $4C_1$): similarly to Ca_V 1.2 and Ca_V 1.3, Ca_V 2.1-positive cells are present in the stroma of ovarian medulla (Figure $4C_1$, yellow arrows). Ca_V 2.1 does not co-localize with SMAα either (see Figure $4C_1$–C_3). However, Ca_V 2.1 immunostaining differs from Ca_V1.2 and Ca_V1.3 in that CL cells are more intensely stained than GCs (see Figure $4C_1$). Accordingly, a fluorescence ratio CL/GC of 1.4 is obtained (CL cells are 40% brighter than GCs; see Table 2). Nerve fiber-like structures inside and around CL and ovarian follicles are not stained with Ca_V 2.1 (data not shown).

Ca_V 2.2 (α1B). Ca_V 2.2 (α1B) subunits expressed in heterologous cell models generate an HVA sustained Ca^{2+} current, also known as N-type, typically expressed in central and peripheral neurons and blocked by ω-Conotoxin GVIA. The presence of this Ca^{2+} channel subtype had not been previously reported in ovarian tissue. Ca_V 2.2 and SMAα immunolabeling are shown in Figure $4D_1$ and D_2, respectively. The expression pattern of Ca_V 2.2 is weak throughout the entire ovary, but unequivocally strong in smooth muscle cells, as revealed by their characteristic anatomical disposition, and evident co-expression with the anti SMAα antibody (see Figure $4D_1$–D_3). This is the only Ca^{2+} channel subunit detected in the ovarian perifollicular smooth muscle. The distribution of Ca_V 2.2 and SMAα immunolabeling are shown enlarged in Figure 6C and D. Co-localization is obvious for the most part, but few cells are only positive to Ca_V 2.2 and other cells are only SMAα positive. The presence of this α1 Ca^{2+} channel subunit had not been reported in ovarian tissue nor in any other smooth muscle cells elsewhere [22]. Although in Ca_V 2.2 labeling is weak in most ovarian structures, CL cells are more intensely stained than GCs from ovarian follicles (Figure $4D_1$; see Figure 6C and D, GCs and CL); accordingly, a mean fluorescence ratio CL/GC of 1.24 (a 24% difference) is obtained (see Table 2). The apparent staining of some oocytes (i.e. Figure 6C and D) probably results from nonspecific antibody binding or autofluorescence of either cytoplasmic lipid droplets or reduced nicotinamide adenine dinucleotide (phosphate) (NAD(P)H) [31].

Proestrus. The anabolic phase of the estrous cycle begins with proestrus, which is characterized by maximal concentrations of plasma of 17β-estradiol, which triggers the surge of pituitary LH and FSH that initiates ovulation and the recruitment of the next cohort of ovarian follicles, respectively. Since proestrus is the stage of maximal stimulation of the ovary, we examined the expression pattern of Ca_Vs subunits in comparison with the more quiescent stage of metestrous-diestrus.

Ca_V 1.2 (α1C). The ovarian distribution of Ca_V 1.2 and SMAα immunostaining in proestrus are shown in Figure $7A_1$ and A_2, respec-

Downloaded from https://academic.oup.com/biolreprod/article/100/4/1018/5212287 by Universidad Nacional Autonoma de Mexico user on 14 October 2020

INFORME DE LABORES 2019

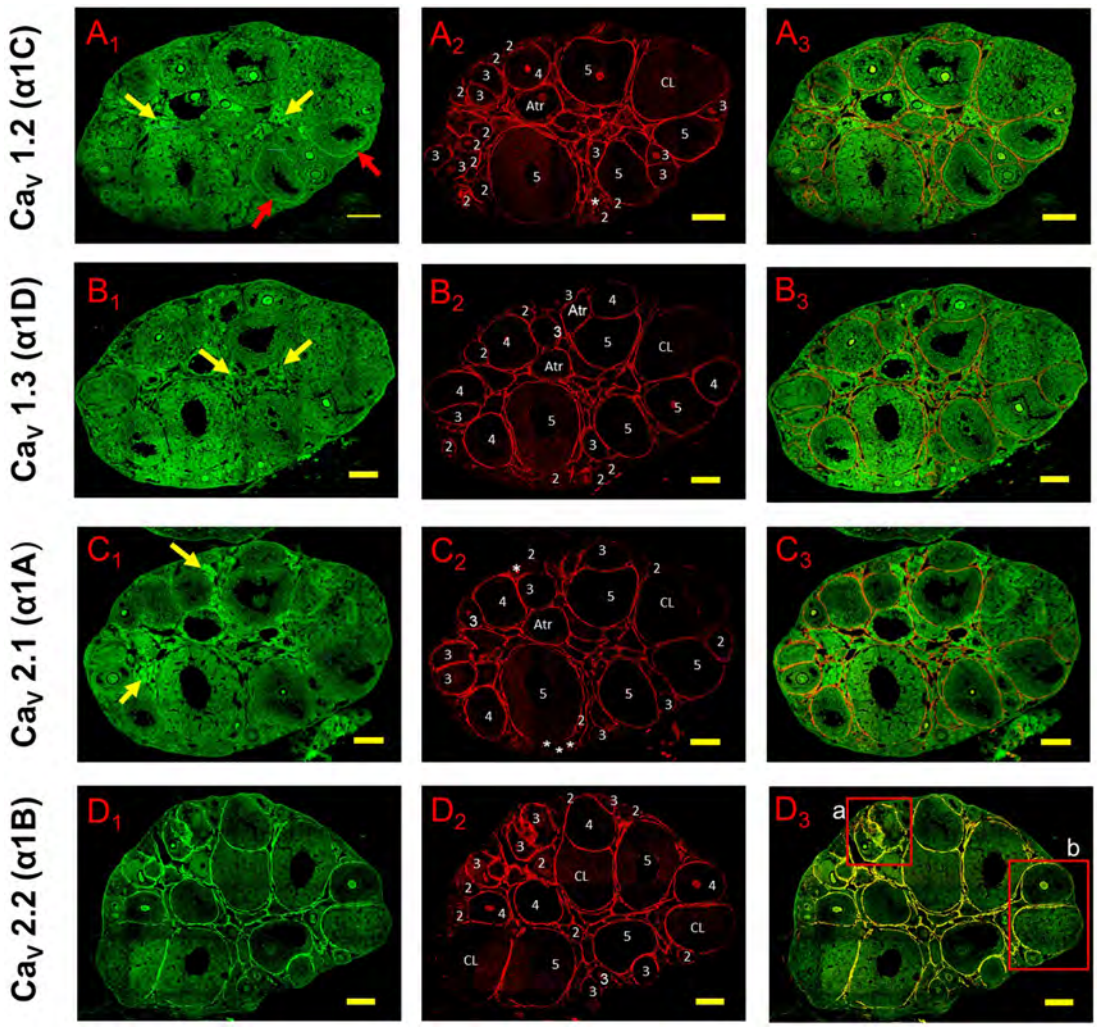

Figure 4. Specific immunolabeling of mouse ovarian sections in metestrus-diestrus. A_1: Ca_V 1.2 staining; yellow arrows, unidentified stromal cells in the ovarian medulla; red arrows, intensely labeled GCs adjacent to the basal lamina of ovarian follicles. A_2: smooth muscle actin (SMAα) staining: A_3: images A_1 and A_2 superimposed. B_1: Ca_V 1.3 staining; yellow arrows, unidentified stromal cells in the ovarian medulla. B_2: SMAα staining: B_3: images B_1 and B_2 superimposed. C_1: Ca_V 2.1 staining; yellow arrows, unidentified stromal cells. C_2: SMAα staining. C_3: images C_1 and C_2 superimposed. D_1: Ca_V 2.2 staining. D_2: SMAα staining. D_3: images C_1 and C_2 superimposed. (a, b) Regions of interest shown enlarged in Figure 6C and D. Denotation of labels in A_2, B_2, C_2, and D_2: asterisk: primary follicle, 2: secondary follicle, 3: secondary preantral follicle, 4: antral follicle 5: preovulatory follicle. CL: corpora lutea. Atr: atresic follicle. Calibration bar: 200 μm.

tively. Ca_V 1.2 does not co-express with SMAα (compare Figure 7A_1 and A_2 and Figure 7A_3). The stronger staining of GCs observed in the periphery of ovarian follicles is present (red arrows in Figure 7A_1) although less conspicuously than in metestrous-diestrus (compare Figure 7A_1 and 4A_1). An obvious difference between metestrous-diestrus and proestrus is that in the latter, CL cells are considerably more intensely stained than GCs (Figure 7A_1). The mean fluorescence ratio CL/GC of 1.49 is obtained(a 49% difference; see Table 2). Thin nerve fiber-like structures positive to Ca_V 1.2 can be seen inside and around CLs and ovarian follicles, but they are less distinctly labeled than in metestrous-diestrus (data not shown).

Ca_V 1.3 (α1D). The staining patterns of Ca_V 1.3 and SMAα in proestrus are illustrated in Figure 7B_1 and B_2, respectively. Ca_V 1.3 does not co-localize with SMAα (see Figure 7B_1–B_3). This is confirmed by comparing the SMAα-positivity of smooth muscle fibers of the hilum (Figure 7B, yellow asterisk) and the lack of Ca_V 1.3 staining of the same structure (Figure 7B_1, yellow asterisk). In metestrus-diestrus, Ca_V 1.3 staining is weak and uniform throughout the ovary (see Figure 4B_1), while in proestrus the expression pattern of Ca_V 1.3 is rather inhomogeneous. As seen in Figure 7B_1, CL cells display the strongest immunostaining, while GCs from ovarian follicles show the weakest. In general, the staining pattern of Ca_V 1.3 and Ca_V 1.2 in proestrus is similar (compare Figure 7A_1 and B_1), but the staining ratio CL/GC for Ca_V 1.3 is higher than for Ca_V 1.2 (fluorescence ratio CL/GC of Ca_V 1.3 in proestrus gave 2.04 (a 104% difference: see Table 2)).

Ca_V 2.1 (α1A). The staining patterns of Ca_V 2.1 and SMAα in proestrus are shown in Figure 7C_1 and C_2, respectively. As seen in the composite image in Figure 7C_3, SMAα-positive cells apparently do not co-express Ca_V 2.1, although smooth muscle fibers in the hilum appear weakly Ca_V 2.1 positive (blue asterisk in Figure 7C_1 and C_2). Ca_V 2.1 immunofluorescence pattern in proestrus is similar to that of metestrous, except for the absence of stained cells in the stroma and the even greater differential expression of CL cells versus

Downloaded from https://academic.oup.com/biolreprod/article/100/4/1018/5212287 by Universidad Nacional Autonoma de Mexico user on 14 October 2020

INFORME DE LABORES 2019

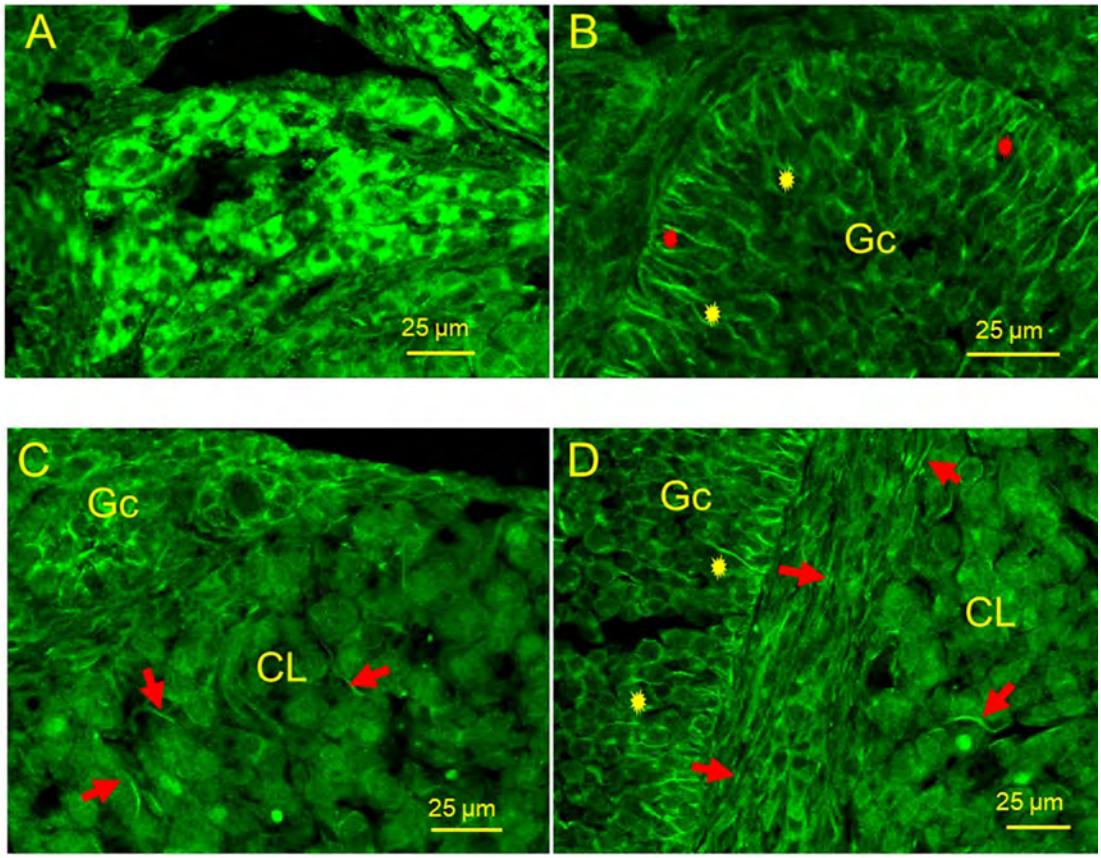

Figure 5. High magnification images of Ca_V 1.2-specific immunolabeling. (A) Unidentified Ca_V 1.2 positive stromal cells in the ovarian medulla (Figure 1A_1; red arrows). (B, C) Ca_V 1.2 labeling of GCs from ovarian follicles is confined to the plasma membrane (Gc). (B) Peripheral staining from ovarian follicles results from the presence of elongated GCs arranged perpendicularly to the basal lamina (red stars), or processes extending into the follicle, forming ramifications (yellow stars). (C, D) Red arrows: thin processes, resembling unmyelinated nerve fibers seen both inside and around CL and ovarian follicles. (D) Corpora lutea (CL) cells express Ca_V 1.2 uniformly in the cytoplasm while GCs express Ca_V 1.2 in the plasma membrane.

GCs. The expression pattern of Ca_V 2.1 in proestrus appears to be an *intensification* of that observed in metestrus-diestrus (compare Figures 4C_1 and 7C_1). Accordingly, the Ca_V 2.1 ratio CL/GC rises from 1.39 in metestrus-diestrus to 2.08 in proestrus (see Table 2).

Ca_V 2.2 (α1B). Ca_V 2.2 and SMA*α* immunostaining patterns in proestrus are illustrated in Figure 7D_1 and D_2, respectively. It is obvious that Ca_V 2.2 immunostaining in proestrus co-localizes with SMA*α*, as judged by the network-like perifollicular disposition around ovarian follicles and CL, and the unequivocal superposition of red and green signals in Figure 7D_3. Nonetheless, in proestrus, not only the smooth muscle cells express Ca_V 2.2 but also the CL. In fact, the differential Ca_V 2.2 staining of CL versus GC in proestrus is stronger than in metestrus-diestrus (compare Figures 4D_1 and 7D_1). Hence, the mean Ca_V 2.2 fluorescence ratio CL/GC obtained in proestrus is 1.94 (see Table 2).

Estrus

Estrus begins shortly after the pre-ovulatory LH/FSH surge and ends the anabolic phase of the cycle. It has been reported that these gonadotropins, as well as hCG, increase intracellular Ca^{2+} concentration in GCs and stimulate steroid production. Thus, we wondered if the expression pattern of VGCCs in the ovary changes as a result of gonadotropin stimulation. As shown in Figure 8, the overall staining pattern for Ca_V 1.2, Ca_V 1.3, and Ca_V 2.1 in the ovary at estrus suggests a *decline* from the peak expression reached in proestrus, and a progressive return to the baseline condition of metestrus-diestrus. The staining intensity of Ca_V 1.2 and Ca_V 1.3 in estrus is still higher in CL cells compared to GCs. The mean fluorescence CL/GC ratio obtained is 1.34 for Ca_V 1.2 and 1.91 for Ca_V 1.3 (see Table 2). The stronger Ca_V 1.2 labeling of GCs in the edge of ovarian follicles described in Figure 1A_1 is also noticeable in Figure 8A_1. In estrus, Ca_V 2.2 antibody strongly labels smooth muscle cells just as in metestrus-diestrus, but labeling now appears more dispersed throughout the ovary (see Figure 8D_1), with a fluorescence ratio CL/GC still relatively high: 1.31 (see Table 2; compare Figures 7D_1 and 8D_1). Bundles of Ca_V 2.2-positive and SMA*α*-positive smooth muscle cells are clearly visible in a bundle of smooth muscle cells from the hilum (Figure 8D1 and D2, blue asterisks).

Regardless of the stage of estrus cycle, Ca_V 1.2 and SMA*α* do not co-localize, implying that this subunit is absent from perifollicular smooth muscle cells. This result is contrary to reports that Ca_V 1.2 subunits are expressed in smooth muscle. To address this issue, an ovarian section containing a large longitudinal section of the oviduct was immunostained both with Ca_V 1.2 and SMA*α*. The doubly stained section is shown in Supplementary Figure S1. In the smooth muscle fibers of the oviduct Cav1.2 and SMA*α* clearly co-localize (see orange and yellow hues in Supplementary Figures S1A_1 and

Downloaded from https://academic.oup.com/biolreprod/article/100/4/1018/5212287 by Universidad Nacional Autonoma de Mexico user on 14 October 2020

Table 2. Level of expression of voltage-gated Ca^{2+} channel subunits in corpora lutea cells and granule cells in mouse ovary at different stages of the estrus cycle.

	Cav 1.2 $\alpha 1C$			Cav 1.3 $\alpha 1D$			Cav 2.1 $\alpha 1A$			Cav 2.2 $\alpha 1B$			Cav 3.1, 2,3 $\alpha 1G$, I, H			
	Mean ± s.e.	N	CL/CG	Mean ± s.e.	N	CL/CG	Mean ± s.e.	N	CL/CG	Mean ± s.e.	N	CL/CG	Mean ± s.e.	N	CL/CG	
CL	54.67 ± 4.1	12	1.06	28.27 ± 2.42	12	1.12	105.23 ± 10.92	12	1.39	14.54 ± 1.19	18	1.24	44.78 ± 1.32	30	1.84	Metestrus
GC	51.7 ± 1.95	54		25.22 ± 0.87	48		75.85 ± 2.74	54		11.74 ± 0.65	54		24.29 ± 0.79	60		diestrus
CL	141.5 ± 8.97	66	1.49	159.41 ± 8.63	18	2.04	52.66 ± 1.12	36	2.08	48.79 ± 2.37	12	1.94	42.32 ± 2.13	24	4.24	Proestrus
GC	94.6 ± 3.56	18		78.071 ± 2.79	66		25.28 ± 0.66	42		25.2 ± 0.97	42		9.97 ± 0.6	66		
CL	58.08 ± 2.01	12	1.34	141.53 ± 8.54	12	1.91	31.3 ± 0.93	6	1.15	114.59 ± 4.8	6	1.31	54.45 ± 2.73	18	0.77	Estrus
GC	43.39 ± 1.04	48		74.01 ± 1.9	42		27.18 ± 0.95	42		87.37 ± 3.39	36		70.27 ± 7.2	60		

Arbitrary fluorescence units. N is the number of areas of interest measured (6 areas per structure, either ovarian follicle or corpora lutea). CL/GC: fluorescence ratio of corpora lutea *versus* granular cells.

A_3). In contrast, SMAα-positive interfollicular smooth muscle fibers in the same section do not co-localize with Cav1.2, displaying a red color only (Supplementary Figure S1A_2, yellow arrow).

Presence of LVA α1 subunits (Ca_V 3.1; α1G, 3.2; α1H and 3.3; α1I)

Metestrus-diestrus

The predominant Ca^{2+} current component recorded with patch-clamp electrophysiology from porcine, chicken, and human GCs is an LVA T-type Ca^{2+} current. Pore-forming α1 subunits Ca_V 3.1, Ca_V 3.2, and Ca_V 3.3, when expressed in heterologous systems, generate LVA T-type Ca^{2+} currents with slightly different biophysical properties. Accordingly, mRNAs encoding for Cav 3.2 subunits have been isolated from human luteinized GCs [16, 17]. Experiments conducted with antibodies raised against each of the three Ca_V 3 α1 subunits (Ca_V3.1, Ca_V3.2, and Ca_V3.3) separately gave weak, but specific staining patterns indistinguishable from one another. To increase the sensitivity of detection, the immunostaining was carried out with antibodies raised against the three subunits combined. Figure 9A illustrates the Ca_V 3 staining pattern in mouse ovarian sections in metestrus-diestrus. This pattern resembles that of Ca_V 2.1 (compare Figures 9A and 4C_1): the strongest Ca_V 3 immunostaining is visible in medulla stroma cells (red arrows in Figure 9A and A_1) and perifollicular stroma cells forming an incomplete multilayer envelope around secondary and antral follicles (see blue arrows in Figure 9A and A_3). It would be interesting to perform double immunolabeling (Ca_V 3 and Ca_V 2.1) to find out if these subunits are co-expressed in the same cells.

Some of the cells associated with ovarian follicles probably correspond to TCs, which produce the androgen substrate required for ovarian estrogen biosynthesis [23]. Substantial Ca_V 3 staining is present in CL (Figure 9A and A_2: CL), in agreement with electrophysiological and molecular biology studies in human luteinized GCs [16, 17]. In contrast, the staining is weak or absent in GCs from ovarian follicles (yellow asterisks in Figure 9A and A_3). Accordingly, the fluorescence ratio CL/GC obtained is 1.84 (84% difference; see Table 2). Ca_V 3-positive cells do not display the characteristic anatomical arrangement of smooth muscle cells (compare Figures 9A and 4D_2, which are contiguous sections from the same ovary); nonetheless, we cannot rule out that some perifollicular Ca_V 3-positive cells are smooth muscle cells, since RNAs encoding for Ca_V 3 α1 subunits have been reported in smooth muscle cells [24]. Substantial differences in the distribution pattern or Ca_V 3 expression were observed along the estrous cycle (see below).

Proestrus

Ca_V 3 immunostaining in proestrus is shown in Figure 9B. At this stage of the estrus cycle, CL staining is stronger than in any other ovarian structure, while ovarian follicles (yellow asterisks) display the weakest. Accordingly the fluorescence ratio CL/GC obtained is 4.2 (324% difference). Staining of CL cells is not uniform, with patches of stronger immunofluorescence (Figure 9B and B_1). Another peculiarity of proestrus is that medullar and interfollicular stroma cells are weakly stained. Ca_V 3-positive flat cells around CL and ovarian follicles are probably theca and/or smooth muscle cells. In Figure 9B, a cross section of the hilum is weakly Ca_V 3-positive (red asterisk). This structure is clearly SMAα-positive as seen in the adjacent section from the same ovary (Figure 5B_2 and C_2). Bundles of smooth muscle-like fibers in a longitudinal section (red arrow in Figure 9B and B_2) are also Ca_V 3-positive.

Downloaded from https://academic.oup.com/biolreprod/article/100/4/1018/5212287 by Universidad Nacional Autonoma de Mexico user on 14 October 2020

INFORME DE LABORES 2019

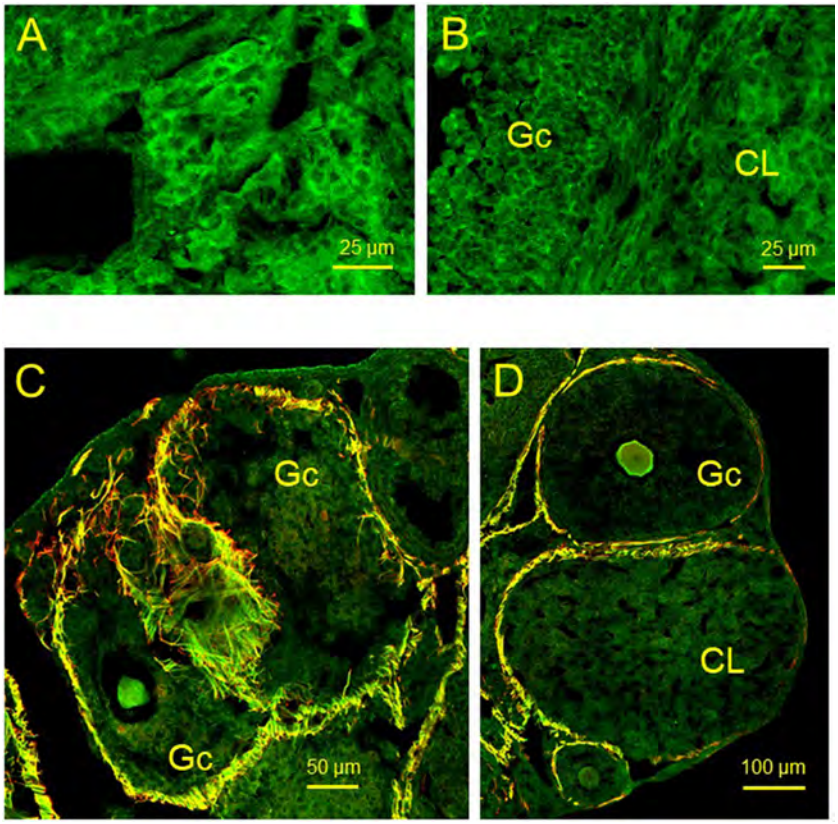

Figure 6. High magnification images of Ca_V 1.3- and Ca_V 2.2-specific immunolabeling. (A) Ca_V 1.3-positive unidentified medulla stromal cells (Figure 1B_1, yellow arrows). (B) Both corpora lutea (CL) and granule cells (Gc) are weakly labeled with anti-Ca_V 1.3. Thin filaments resembling unmyelinated nerve fibers are not stained with anti-Ca_V 1.3. (C, D) High magnification views of regions *a* and *b* from Figure 1D_3. (C) Superimposed images of Ca_V 2.2 and SMAα staining reveal that both labels co-localize, but some cells are either positive to Ca_V 2.2 only and other cells are SMAα positive only. (D) Ca_V 2.2 labeling is weak in most ovarian structures, but CL cells are more intensely stained than GCs from ovarian follicles.

Estrus

The distribution pattern of Ca_V 3 immunostaining in estrus is shown in Figure 10. Here, the most remarkable feature is the intense cytoplasmic staining of mesenchymal and interfollicular cells in the ovarian stroma, stronger than CL and ovarian follicles (asterisks: see Figure 10A). At this stage both CL and GCs from ovarian follicles are stained weakly. This is the only example where GCs are slightly more intensely stained than CL cells (fluorescence ratio CL/GC = 0.77). The majority of the strongly stained Ca_V 3-positive cells in the stroma are round and arranged in clusters (see Figure 10A_1). Perifollicular cells of the internal theca are also stained, but their anatomical distribution is not compatible with that of smooth muscle cells (Figure 10A_2). In fact, smooth muscle cells of the hilum (red asterisk in Figure 10A) are negative for Ca_V 3 at this stage of the estrous cycle.

Discussion

The estrous cycle in mice comprises a series of physiological and behavioral events that repeats every 4–6 days throughout the reproductive life span unless interrupted by pregnancy or anestrus. The cycle length is variable and affected by a number of factors, including stress, diet, and social cues. The estrous cycle affects the entire reproductive tract, and can be regarded as comprised of three phases: *anabolic, catabolic, and quiescent phase*. In the ovary, the anabolic phase concludes with the release of oocytes, while the catabolic phase is characterized by degenerative changes. The quiescent phase is regarded as a resting state of the reproductive tract. The estrous cycle is also classically divided, based on the vaginal smears, into four stages: metestrus, diestrus, proestrus, and estrus [19, 25].

At metestrus, CL formation and atresia are widespread among the remaining follicles. Metestrus-diestrus can be regarded as the quiescent phase of the cycle: estradiol concentrations remain low, and in the absence of mating, CL does not activate completely, producing little progesterone. Metestrus-diestrus represents the catabolic phase of the cycle and coincides with declining concentrations of estradiol following ovulation. Near the end of diestrus, ovarian follicles begin to grow [25]. Proestrus signals the increase in functional activity of both GCs and TCs: the peak concentration of estrogen (typically late in the afternoon) triggers the pre-ovulatory surge of pituitary LH and FSH. LH stimulates in TCs a cAMP signaling pathway that increases the synthesis of key steroidogenic enzymes that synthesize androstenedione, which diffuses across the basal lamina and into the ovarian follicle. FSH by a cAMP-mediated mechanism then stimulates the synthesis of aromatase cytochrome P450 and 17 β-hydroxysteroid dehydrogenase in GCs. With these enzymes, GCs metabolize androstenedione to estradiol. Estrus ends the anabolic phase of the cycle. During estrus the female is receptive to the male because of the elevated concentration of estrogen. Estrus typically occurs during the night, and mating occurs near the mid-point of the dark phase. Ovulation also occurs during estrus, about 12 h after the LH surge.

Downloaded from https://academic.oup.com/biolreprod/article/100/4/1018/5212287 by Universidad Nacional Autonoma de Mexico user on 14 October 2020

INFORME DE LABORES 2019

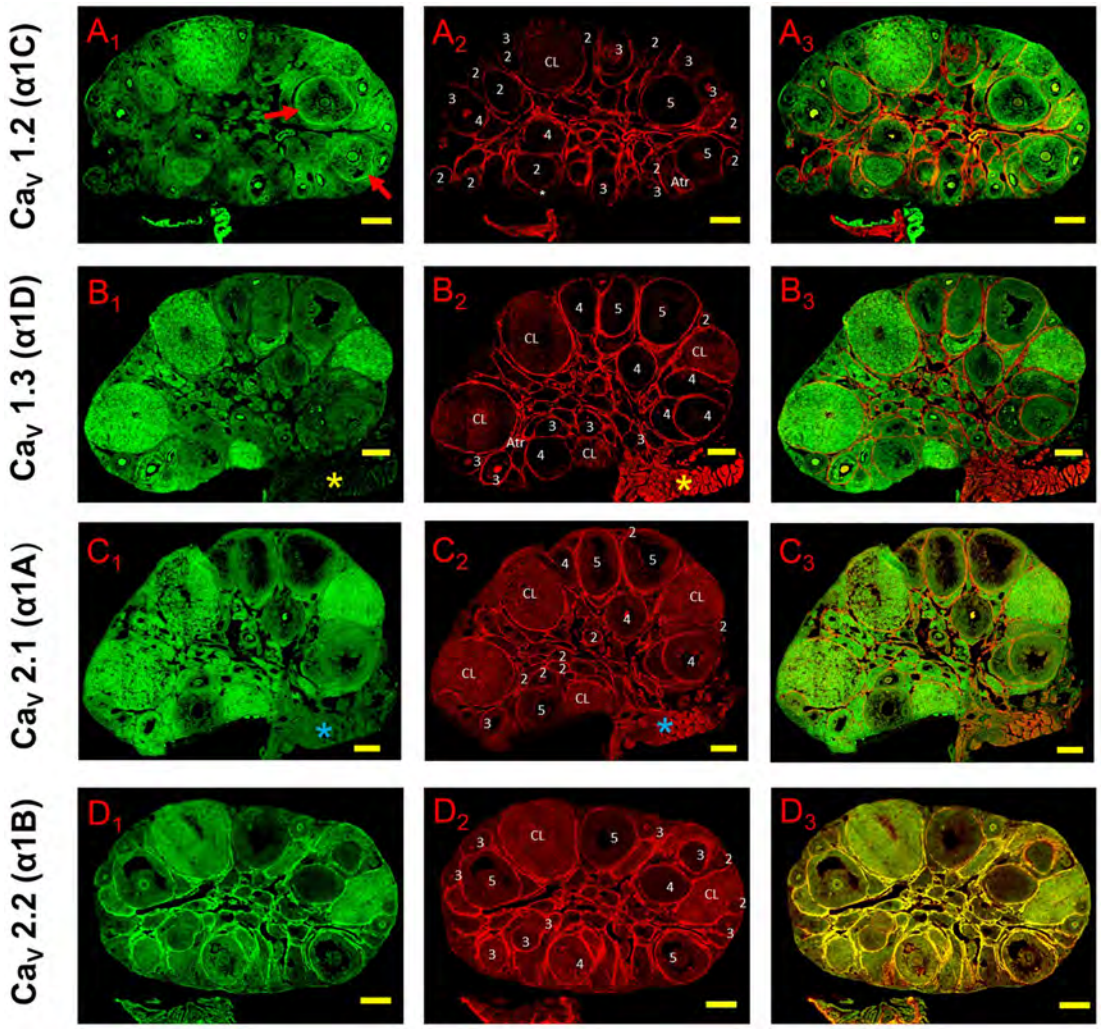

Figure 7. Specific immunolabeling of mouse ovarian sections in proestrus. A_1: Ca_V 1.2 staining; red arrows, intensely labeled GCs adjacent to the basal lamina of ovarian follicles. A_2: smooth muscle actin (SMAα) staining: A_3: images A_1 and A_2 superimposed. B_1: Ca_V 1.3 staining; yellow asterisk, lack of Ca_V 1.3 immunostaining in smooth muscle fibers of the hilum. B_2: SMAα staining; yellow asterisk, SMAα-positivity of smooth muscle fibers of the hilum. B_3: images B_1 and B_2 superimposed. C_1: Ca_V 2.1 immunostaining; blue asterisk, weak Ca_V 2.1 staining of smooth muscle fibers of the hilum. C_2: SMAα immunostaining; blue asterisk, SMAα-positive smooth muscle fibers of the hilum. C_3: images C_1 and C_2 superimposed. D_1: Ca_V 2.2 immunostaining. D_2: SMAα immunostaining. D_3: images D_1 and D_2 superimposed. Denotation of labels in A_2, B_2, C_2, and D_2: asterisk: primary follicle, 2: secondary follicle, 3: secondary preantral follicle, 4: antral follicle, 5: preovulatory follicle. CL: corpora lutea. Atr: atresic follicle. Calibration bar: 200 μm.

Role of Ca^{2+} in ovarian endocrine cell function

A role for extracellular Ca^{2+} in hCG-induced ovulation was discovered more than 30 years ago in the perfused rabbit ovary: the infusion the Ca^{2+} channel blocker verapamil did not suppress hCG-induced ovulation; however, the infusion of hCG together with EGTA (an extracellular Ca^{2+} chelator) greatly reduces the ovulatory efficiency (17%) in comparison to hCG alone (80%) [26]. Reducing the extracellular Ca^{2+} concentration disrupts LH-stimulated steroidogenesis [27] in isolated ovarian cells, possibly by preventing transmembrane Ca^{2+} influx. Also, hCG-induced, but not basal testosterone production was impaired in goldfish follicles after incubation with Ca^{2+}-deficient media, or a variety of Ca^{2+} channel blockers (verapamil, nifedipine, nicardipine, and $CoCl_2$) [18].

More recent reports showed that inhibitors of VGCCs attenuate hCG-induced steroid production in co-cultures of TCs and GCs from carp [28]. These findings are consistent with earlier reports showing that application of FSH elevates intracellular Ca^{2+} concentration ($[Ca^{2+}]_i$) in swine GCs [29–31], and that both diacylglycerol and inositol trisphosphate trigger $[Ca^{2+}]_i$ mobilization in pig GCs [32]. Strong $[Ca^{2+}]_i$ elevations, like those induced by exposure to the Ca^{2+} ionophore A23187, increase by fivefold the release of progesterone in rat GCs in culture [33] and by twofold basal testosterone and estradiol (E_2) production in co-cultured TCs/GCs from carp. A23187 also significantly potentiates hCG-stimulated production of testosterone and E_2 [32].

It has been reported that both LH/FSH and hCG trigger elevations of $[Ca^{2+}]$i in GCs that stimulate steroid production [28–30]. Porcine TCs in vitro display diverse forms of $[Ca^{2+}]_I$ signaling in response to increasing doses of LH, from single spikes to spike-plateau and oscillations. Removal of extracellular Ca^{2+} or treatment with 100 μM $CoCl_2$ inhibits the maintenance, but not the initiation of these responses, suggesting the participation of VGCCs [35]. The

Downloaded from https://academic.oup.com/biolreprod/article/100/4/1018/5212287 by Universidad Nacional Autonoma de Mexico user on 14 October 2020

INFORME DE LABORES 2019

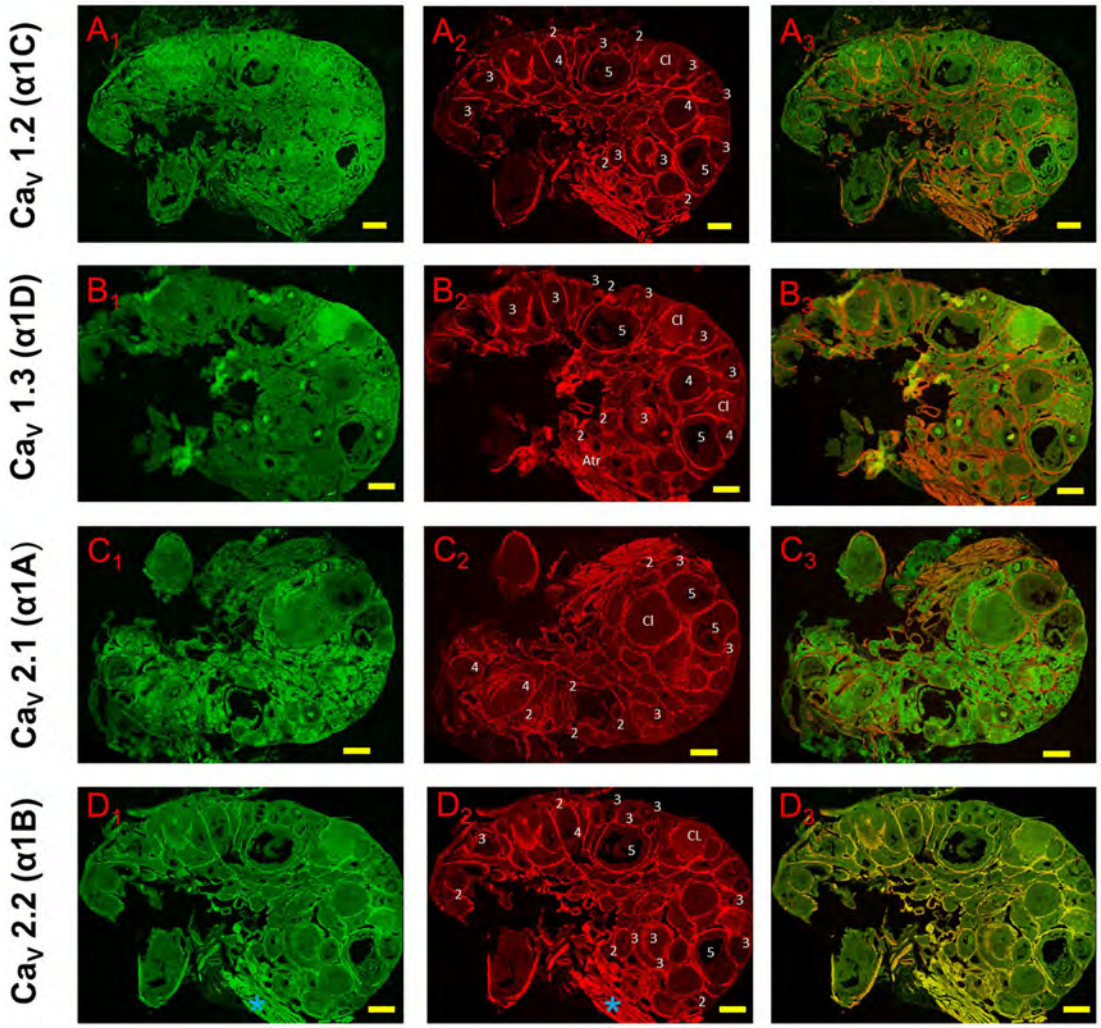

Figure 8. Specific immunolabeling of mouse ovarian sections in estrus. A_1: Ca_V 1.2 staining. A_2: smooth muscle actin (SMAα) staining. A_3: images A_1 and A_2 superimposed. B_1: Ca_V 1.3 immunostaining. B_2: SMAα immunostaining: B_3: images B_1 and B_2 superimposed. C_1: Ca_V 2.1 immunostaining. C_2: SMAα immunostaining. C_3: images C_1 and C_2 superimposed. D_1: Ca_V 2.2 immunostaining. D_2: SMAα immunostaining. D_3: images C_1 and C_2 superimposed. Denotation of labels in A_2, B_2, C_2, and D_2: asterisk, primary follicle, 2: secondary follicle, 3: secondary preantral follicle, 4: antral follicle 5: preovulatory follicle. CL: corpora lutea. Atr: atresic follicle. Calibration bar: 200 μm.

diversity of the $[Ca^{2+}]$i signals elicited by LH in porcine TCs is in contrast to the stereotyped responses to LH in GCs where $[Ca^{2+}]_i$ oscillations have not been reported nor observed here [34]. The increased expression of Ca_V3 $\alpha1$ subunits in TCs and its relative scarcity in GCs and CL cells (see figure 4A_3) could explain in part these functional differences. In the neuronal cell line NG108–15, overexpression of $Ca_V3.1$ and $Ca_V3.3$ channels produces repetitive action potentials and spontaneous $[Ca^{2+}]$i oscillations [36]. It remain to be seen if the presence of Ca_V3 Ca^{2+} channels underlies the spontaneous and depolarization-induced Ca^{2+} signals recorded in the TCs layer (Figures 1 and 2).

Types of VGCC identified electrophysiologically in ovarian endocrine cells

Using patch-clamp electrophysiology in isolated cultured GCs, a LVA T type Ca^{2+} current has been recorded in porcine and chicken GCs [12, 13]. A smaller HVA L-type Ca^{2+} current component has also been identified in chicken GCs [14, 15]. More recently, Ca^{2+} channels expressed in human GCs (cultured human luteinized GCs obtained from patients undergoing in vitro fertilization) were characterized electrophysiologically, and their regulation by hormones [16] and muscarinic receptors [17] was examined. The most predominant Ca^{2+} current, identified by their biophysical and pharmacological properties, is a LVA T-type Ca^{2+} current [16,17]. In some GCs a high-voltage-activated Ca^{2+} current sensitive to dihydropyridine (L-type Ca^{2+} current) was also recorded. These results are similar to those obtained in GCs from other species [12–14]. These electrophysiological findings are supported by the isolation of mRNAs encoding pore-forming $\alpha1$ subunits Cav 3.2 and Cav 1.2 (T- and L-type Ca^{2+} channels, respectively). Further progress in this area requires (1) identification of the different subtypes of VGCCs present in the ovary *in situ*, (2) evaluation of the expression levels of Ca^{2+} channels subunits in the different types of ovarian cells and their variations along the estrous cycle, and (3) characterization of $[Ca^{2+}]_i$ signals

Downloaded from https://academic.oup.com/biolreprod/article/100/4/1018/5212287 by Universidad Nacional Autonoma de Mexico user on 14 October 2020

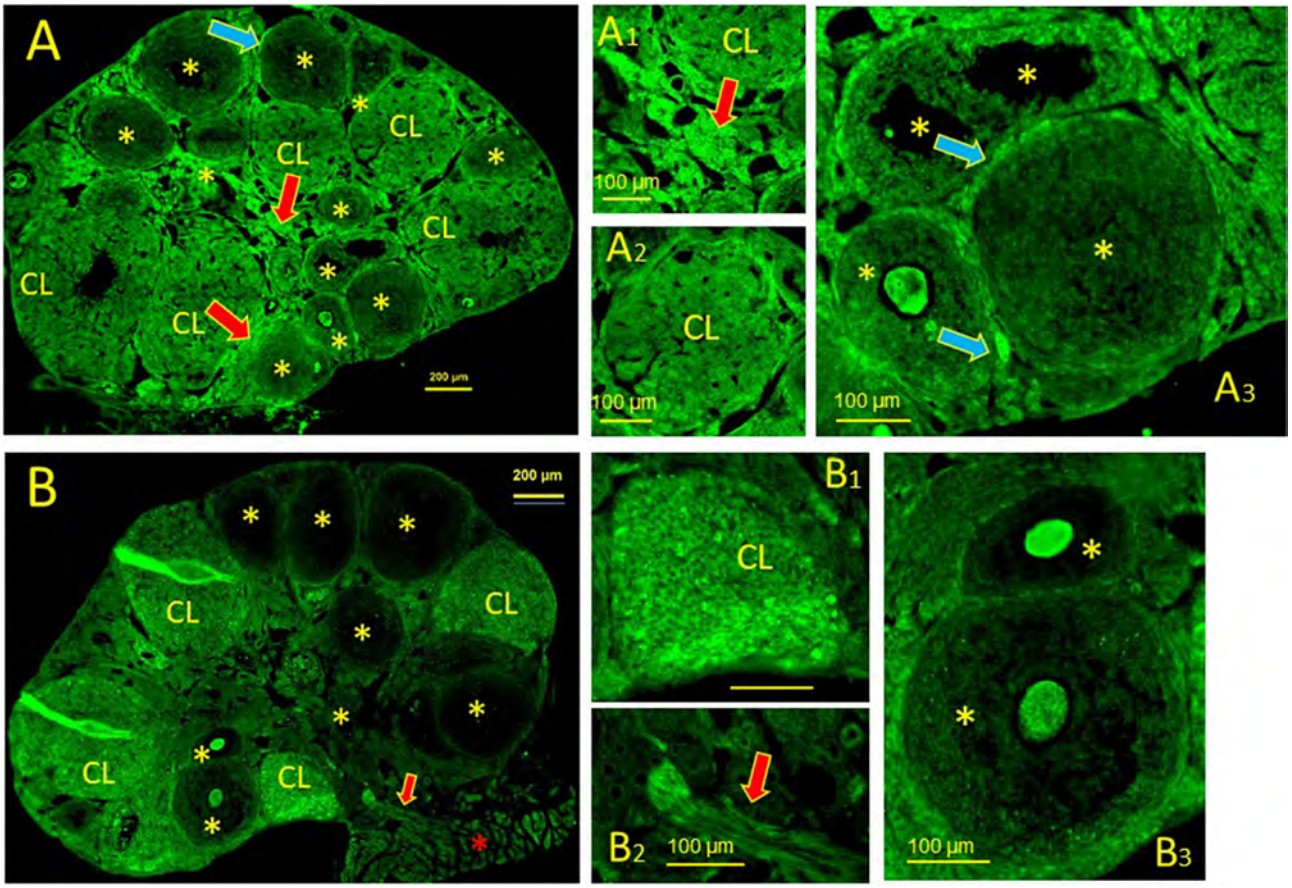

Figure 9. (A) Ca_V 3 immunostaining of mouse ovarian sections in metestrus-diestrus and proestrus. (A) Metestrus-diestrus. Staining of medullar stroma cells (red arrows) and interfollicular stroma cells forming an incomplete multilayer envelope around secondary and antral follicles (blue arrow). Corpora lutea (CL) are more intensely labeled than ovarian follicles (asterisks). A_1: enlarged view of medullar stroma cells (red arrow). A_2: enlarged view of a corpus luteum (CL). A_3: enlarged view showing Ca_V 3-positive interfollicular stroma cells (blue arrows) forming an incomplete multilayer envelope around secondary and antral ovarian follicles. (B) Proestrus. At this stage, corpora lutea (CL) staining is the strongest and ovarian follicles (yellow asterisk) is the weakest (>300% difference). Smooth muscle cells of the hilum (red asterisk) and bundles of smooth muscle-like fibers (red arrow) are weakly Ca_V 3-positive. B_1: enlargement of corpus luteum showing patchy staining (CL). B_2: enlargement of Ca_V 3-positive bundles of smooth muscle-like fibers (red arrow). B_3: enlargement of ovarian follicles (yellow asterisks) to show lack of Ca_V 3 staining in GCs.

displayed by ovarian cells in situ at different stages of the estrous cycle, including responses to LH and FSH. Our study represents a crucial step forward in addressing these important questions.

In the "quiescent" stage of the estrous cycle (metestrous-diestrus), L-type Ca^{2+} channel subunits Ca_V 1.2 (α1C) and Ca_V 1.3 (α1D) are widely distributed throughout the ovary, particularly in stromal medulla cells, GCs, and CL cells. At the follicle's edge GCs are more strongly labeled with Ca_V 1.2. Ca^{2+} channel subunits abundant in nerve cells (P/Q-type and N-type Ca^{2+} channel subunits Ca_V 2.1 and Ca_V 2.2) are reported for the first time in ovarian tissue. The former are abundant in stroma and CL cells, while the latter are unequivocally expressed in perifollicular smooth muscle cells. Subunits encoding LVA T-type Ca^{2+} channels (Ca_V 3.1, 3.2, and 3.3) are expressed in CL cells and medullar and interfollicular stroma cells, with GCs displaying the weakest staining. Remarkably, the expression level of HVA and LVA Ca^{2+} channel subunits fluctuates significantly along the estrus cycle. The ratio CL/GC is used here for comparison (see Table 1), but other ovarian structures like mesenchymal and interfollicular stroma cells also display marked variations. The description of the Ca^{2+} signals and the expression of VGCCs in the ovary and their variations throughout the estrous cycle opens a new chapter in ovarian physiology.

A relevant question is how VGCCs participate in ovarian endocrine cells. For instance, GCs have a resting membrane potential of around –42 mV [3, 4]. At this potential more than 75% of LVA T-type Ca^{2+} channels should be inactivated [16]. Nonetheless, voltage clamp experiments indicate that a small fraction (about 4%) of these channels could be available for activation, because of the "window current" formed at the crossing between activation and inactivation curves [16]. Thus, a small, continuous Ca^{2+} influx across the plasma membrane is likely to occur at the GC resting potential [37]. Interestingly, chicken GCs, which possess a more negative resting potential than mammalian GCs, are excitable, i.e. capable of generating Ca^{2+}-dependent action potentials [11]. It is conceivable that luteinized mammalian GCs could become excitable as the expression level of VGCCs increases, in some cases up to 240% in proestrus (see Table 1). The large spontaneous Ca^{2+} fluctuations reported here strongly suggest that the resting membrane potential of perifollicular TCs is probably more negative than –55 mV, so that a significant number of Ca^{2+} channels are available for activation. A similar

Downloaded from https://academic.oup.com/biolreprod/article/100/4/1018/5212287 by Universidad Nacional Autonoma de Mexico user on 14 October 2020

INFORME DE LABORES 2019

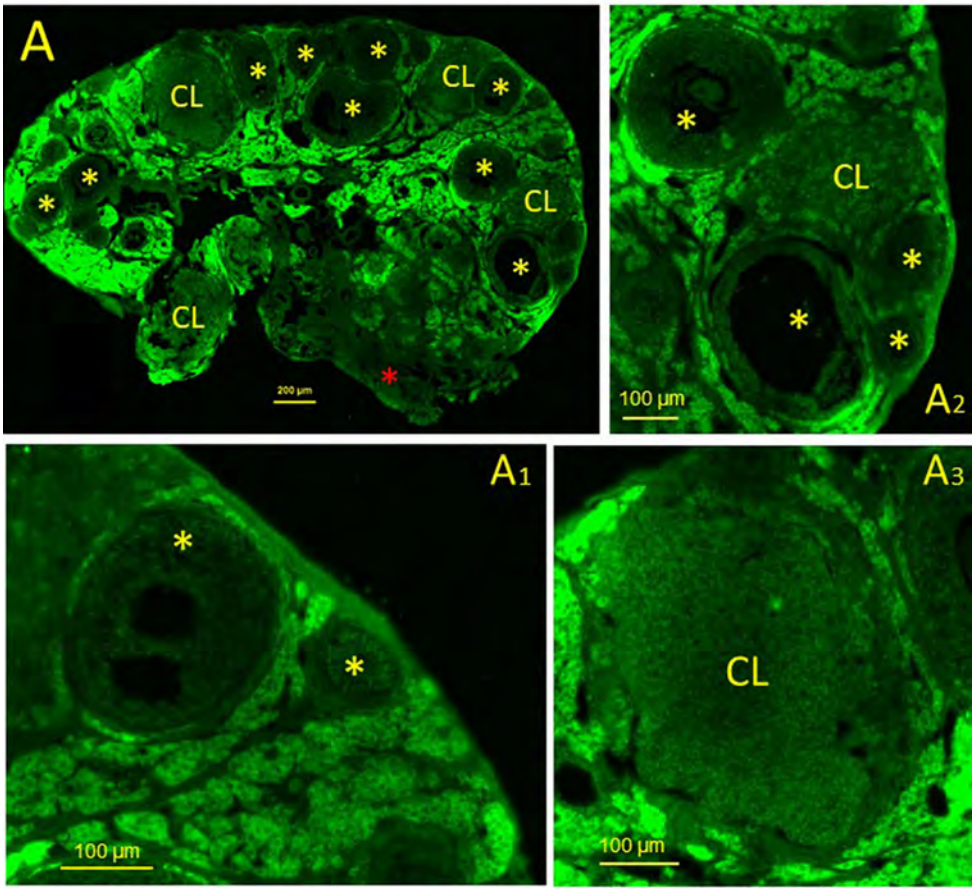

Figure 10. (A) Ca_V 3 immunostaining of mouse ovarian sections in estrus. At this stage, the most notable feature is the cytoplasmic staining of mesenchymal and interfollicular cells in the ovarian stroma, much stronger than corpora lutea (CL) and ovarian follicles (yellow asterisks). Smooth muscle cells of the hilum (red asterisk) are Ca_V 3-negative. A_1: detail of Ca_V 3-positive cells in the stroma. A_2: Ca_V 3-positive perifollicular cells of the internal theca do not resemble perifollicular smooth muscle cells. Corpus luteum (CL) is slightly more stained than ovarian follicles (yellow asterisks). A_2: enlargement of corpus luteum and surrounding Ca_V 3-positive stromal cells.

study focused on the ovarian expression of intracellular Ca^{2+} release channels—inositol 1, 4, 5-trisphosphate receptors and ryanodine receptors [38] together with plasma membrane Ca^{2+} ATPases (PMCA) and sarco-endoplasmic reticulum Ca^{2+} ATPases (SERCA)—is needed to achieve a comprehensive view of the Ca^{2+} handling proteins responsible for Ca^{2+} homeostasis and dynamics [39].

The functional role of the numerous transporting molecules responsible for Ca^{2+} mobilization and signaling in the different ovarian cell types is only begging to unfold. Moreover, in spite of convincing evidence that the disruption of Ca^{2+} homeostasis underlies certain ovarian malignant phenotypes [40–42] and the identification of Ca^{2+} transporters whose altered function underlies different pathologies, a rational therapeutic application of these findings is still at its infancy. However, the rapid development of the field warrants the development of improved molecular Ca^{2+} transport-targeting tools for diagnosis and treatment of ovarian cancer and other reproductive pathologies. This study represents an important step in the definition of the specific physiological questions that need to be addressed.

Supplemental data

Supplementary data are available at *BIOLRE* online.

Supplementary Figure S1. A_1: An ovarian section containing a large longitudinal section of the oviduct (white star) was immunostained both with Ca_V 1.2 and SMAα. **A2** and **A3**: Higher magnification images of the areas marked in yellow in **A_1**. SMAα-positive interfollicular smooth muscle fibers are not stained with the Cav1.2 antibody (A_2, yellow arrow). In contrast, Cav1.2 and SMAα clearly co-localize in the smooth muscle fibers of the oviduct (see orange and yellow hues in A_3).

Supplementary Movie 1 (SM1). This file shows the spontaneous Ca^{2+} fluctuations recorded in two follicles. A series of confocal microscopy images (ΔF movie) was obtained from an ovarian slice containing two intact follicles (F1 and F2 in Figure 1). This movie represents 1.2 min of recording. Scale 100 μm.

Supplementary Movie 2 (SM2). This file shows two spontaneous Ca^{2+} fluctuations in the oocyte from an intact follicle. These oscillations begin in the edge of the oocyte, spreading inwards as a wave. See additional information in Figure 2D–F. Scale 20 μm.

Acknowledgment

We would like to thank Claudia V. Rivera-Cerecedo for expert animal husbandry, Nicolas Jimenez-Perez for technical support, and Francisco Perez Eugenio and Ana María Escalante for advice and support in computing and videoconferencing. We also thank Drs Alberto Darszon and Marcia Hiriart

Downloaded from https://academic.oup.com/biolreprod/article/100/4/1018/5212287 by Universidad Nacional Autonoma de Mexico user on 14 October 2020

for advice and encouragement. Daniel Bahena Alvarez is a Ph.D. student from the Programa de Doctorado en Ciencias Biomédicas, Universidad Nacional Autónoma de México (UNAM) and was supported by Ph. D. fellowship 389732 from CONACyT (México). This study was conducted as part of the requirements to obtain his Ph.D.

References

1. Gougeon A. Dynamics of human follicular growth: morphologic, dynamic, and functional aspects. In: Adashi EY, Leung PCK (eds.). *The Ovary*, 2nd ed. San Diego: Elsevier Academic Press; 2004:25–38.
2. Bulling A, Berg FD, Berg U, Duffy DM, Stouffer RL, Ojeda SR, Gratzl M, Mayerhofer A. Identification of an ovarian voltage-activated Na+ channel type: hints to involvement in luteolysis. *Mol Endocrinol* 2000; **14**(7):1064–1074.
3. Mattioli M, Barboni B, Bacci ML, Seren E. Maturation of pig oocytes: observations on membrane potential. *Biol Reprod* 1990; **43**(2):318–322.
4. Mason DE, Mitchell KE, Li Y, Finley MR, Freeman LC. Molecular basis of voltage-dependent potassium currents in porcine granulosa cells. *Mol Pharmacol* 2002; **61**(1):201–213.
5. Manikkam M, Li Y, Mitchell BM, Mason DE, Freeman LC. Potassium channel antagonists influence porcine granulosa cell proliferation, differentiation, and apoptosis. *Biol Reprod* 2002; **67**(1):88–98.
6. Li Y, Ganta S, von Stein FB, Mason DE, Mitchell BM, Freeman LC. 4-aminopyridine decreases progesterone production by porcine granulosa cells. *Reprod Biol Endocrinol* 2003; **1**(1):31.
7. Kunz L, Thalhammer A, Berg FD, Berg U, Duffy DM, Stouffer RL, Dissen GA, Ojeda SR, Mayerhofer A. Ca^{2+}-activated, large conductance K^+ channel in the ovary: identification, characterization, and functional involvement in steroidogenesis. *J Clin Endocrinol Metab* 2002; **87**(12):566–5574.
8. Traut MH, Berg D, Berg U, Mayerhofer A, Kunz L. Identification and characterization of Ca^{2+}-activated K^+ channels in granulosa cells of the human ovary. *Reprod Biol Endocrinol* 2009; **7**(1):8.
9. Kunz L, Richter JS, Mayerhofer A. The adenosine 5′-triphosphate-sensitive potassium channel in endocrine cells of the human ovary: role in membrane potential generation and steroidogenesis. *J Clin Endocrinol Metab* 2006; **91**(5):1950–1955.
10. Brackenbury WJ. Voltage-gated sodium channels and metastatic disease. *Channels* 2012; **6**(5):352–361.
11. Mealing G, Morley P, Whitfield JF, Tsang BK, Schwartz JL. Granulosa cells have calcium-dependent action potentials and a calcium-dependent chloride conductance. *Pflugers Arch* 1994; **428**(3-4):307–314
12. Mattioli M, Barboni B, DeFelice LJ. Calcium and potassium currents in porcine granulosa cells maintained in follicular or monolayer tissue culture. *J Membr Biol* 1993; **134**(1):75–83.
13. Kusaka M, Tohse N, Nakaya H, Tanaka T, Kanno M, Fujimoto S. Membrane currents of porcine granulosa cells in primary culture: characterization and effects of luteinizing hormone. *Biol Reprod* 1993; **49**(1):95–103.
14. Schwartz JL, Asem EK, Mealing GA, Tsang BK, Rousseau EC, Whitfield JF, Payet MD. T- and L- calcium channels in steroid-producing chicken granulosa cells in primary culture. *Endocrinology* **125**(4):1973–1982.
15. Asem EK, Qin W, Rane SG. Effect of basal lamina of ovarian follicle on T- and L- type Ca^{2+} currents in differentiated granulosa cells. *Am J Physiol Endocrinol Metab* 2002; **282**(1):E184–E196.
16. Agoston A, Kunz L, Krieger A, Mayerhofer A. Two types of calcium channels in human ovarian endocrine cells: involvement in steroidogenesis. *J Clin Endocrinol Metab* 2004; **89**(9):4503–4512.
17. Platano D, Magli MC, Pia Ferraretti A, Gianaroli L, Aicardi G. L-and T-type voltage- gated Ca^{2+} channels in human granulosa cells: functional characterization and cholinergic regulation. *J Clin Endocrinol Metab* 2005; **90**(4):2192–2197.
18. Van der Kraak G. Role of calcium in the control of steroidogenesis in preovulatory ovarian follicles of the goldfish. *Gen Comp Endocrinol* 1991; **81**(2):268–275.
19. Byers SL, Wiles MV, Dunn SL, Taft RA. Mouse estrous cycle identification tool and images. *PLoS One* 2012; **7**(4):e35538.
20. Schindelin J, Arganda-Carreras I, Frise E, Kaynig V, Longair M, Pietzsch T, Preibisch S, Rueden C, Saalfeld S, Schmid B, Tienevez JY, White DJ et al. Fiji: an open-source platform for biological-image analysis, *Nat Methods*. 2012; **9**(7):676–682.
21. Tiwari M, Prasad S, Shrivastav TG, Chaube SK. Calcium signaling during meiotic cell cycle regulation and apoptosis in mammalian oocytes. *J Cell Physiol* 2017; **232**(5):76–981.
22. Hill-Eubanks DC, Werner ME, Heppner TJ, Nelson MT. Calcium signaling in smooth muscle. *Cold Spring Harb Perspect Biol* 2011; **3**(9):a004549.
23. Magoffin DA. Ovarian theca cell. *Int J Biochem Cell Biol* 2005; **37**(7):1344–1349.
24. Perez-Reyes E. Molecular physiology of low-voltage-activated T-type calcium channels. *Physiol Rev* 2003; **83**(1):117–161.
25. Pritchett KR, Taft RA. Reproductive biology of the laboratory mouse In: Fox JG, Davisson MT, Quimby FW, Barthold SW, Newcomer CE, Smith AL (eds.), *The Mouse in Biomedical Research*, Vol III, 2nd ed. Academic Press. Cambridge Massachusetts USA; 2007:91–121.
26. Kitai H, Santulli R, Wright KH, Wallach EE. Examination of the role of calcium in ovulation in the in vitro perfused rabbit ovary with use of ethyleneglycol-bis(beta-aminoethyl ether)-n,n′-tetraacetic acid and verapamil. *Am J Obstet Gynecol* 1985; **152**(6):705–708.
27. Veldhuis JD, Klase PA. Mechanisms by which calcium ions regulate the steroidogenic actions of luteinizing hormone in isolated ovarian cells *in vitro*. *Endocrinology* 1982; **111**(1):1–6.
28. Paul S, Kundu S, Pramanick K, Bandyopadhyay A, Mukherjee D. Regulation of ovarian steroidogenesis in vitro by gonadotropin in common carp *Cyprinus carpio*: interaction between calcium- and adenylate cyclase-dependent pathways and involvement of ERK signaling cascade. *J Mol Endocrinol* 2010; **45**(4):207–218.
29. Flores JA, Veldhuis JD, Leong DA. Follicle-stimulating hormone evokes an increase in intracellular free calcium ion concentrations in single ovarian (granulosa) cells. *Endocrinology* 1990; **127**(6):3172–3179.
30. Flores JA, Leong DA, Veldhuis JD. Is the calcium signal induced by follicle-stimulating hormone in swine granulosa cells mediated by adenosine cyclic 3′,5′-monophosphate-dependent protein kinase?. *Endocrinology* 1992; **130**:1862–1866.
31. Sutton-McDowall ML, Mottershead DG, Gardner DK, Gilchrist RB, Thompson JG. Metabolic differences in bovine cumulus-oocyte complexes matured in vitro in the presence or absence of follicle-stimulating hormone and bone morphogenetic protein 151. *Biol Reprod* 2012 **87**(4):1–8.
32. Sadighian JJ, Kearns WG, Waddell BJ, Dimino MJ. Effects of diacyiglycerol and inositol trisphosphate on steroidogenesis by ovarian granulosa from pigs. *Biol Reprod* 1989; **40**(2):294–299.
33. Chen JJ, Wang SW, Chien EJ, Wang PS. Direct effect of propylthiouracil on progesterone release in rat granulosa cells. *Br J Pharmacol* 2003; **139**(8):1564–1570.
34. Aguirre C, Jayes FC, Veldhuis JD. Luteinizing hormone (LH) drives diverse intracellular calcium second messenger signals in isolated porcine ovarian thecal cells: preferential recruitment of intracellular Ca^{2+} oscillatory cells by higher concentrations of LH. *Endocrinology* 2000; **141**(6):2220–2228.
35. Flores JA, Aguirre C, Sharma OP, Veldhuis JD. Luteinizing hormone (LH) stimulates both intracellular calcium ion ($[Ca^{2+}]i$) mobilization and transmembrane cation influx in single ovarian (granulosa) cells: recruitment as a cellular mechanism of LH-$[Ca^{2+}]i$ dose response. *Endocrinology* 1998; **139**(8):3606–3612.
36. Chevalier M, Lory P, Mironneau C, Macrez N, Quignard JF. T-type $Ca_V3.3$ calcium channels produce spontaneous low-threshold action potentials and intracellular calcium oscillations. *Eur J Neurosci* 2006; **23**(9):2321–2329.
37. Schwartz JL, Asem EK, Mealing GA Tsang BK, Rousseau EC, Whitfield JF, Payet MD. T- and L- calcium channels in steroid-producing chicken granulosa cells in primary culture. *Endocrinology* 1989; **125**(4):1973–1982.
38. Díaz-Muñoz M, de la Rosa Santander P, Juárez-Espinosa AB, Arellano RO, Morales-Tlalpan V. Granulosa cells express three inositol 1,4,5-

Downloaded from https://academic.oup.com/biolreprod/article/100/4/1018/5212287 by Universidad Nacional Autonoma de Mexico user on 14 October 2020

INFORME DE LABORES 2019

trisphosphate receptor isoforms: cytoplasmic and nuclear Ca^{2+} mobilization. *Reprod Biol Endocrinol* 2008; **6**(1):60.
39. Carafoli E. Intracellular calcium homeostasis. *Annu Rev Biochem* 1987; **56**(1):395–433.
40. Monteith GR, Davis FM, Roberts-Thomson SJ. Calcium channels and pumps in cancer: changes and consequences. *J Biol Chem* 2012; **14**(38):31666–31673.
41. Jang SJ, Choi HW, Choi DL, Cho S, Rim HK, Choi HE, Kim KS, Huang M, Rhim H, Lee KT, Lee JY. In vitro cytotoxicity on human ovarian cancer cells by T-type calcium channel blockers. *Bioorg Med Chem Lett* 2013; **15**(24):6656–6662.
42. Bose T, Cieślar-Pobuda A, Wiechec E. Role of ion channels in regulating Ca^{2+} homeostasis during the interplay between immune and cancer cells. *Cell Death Dis* 2015;**19** (2):e1648.

Downloaded from https://academic.oup.com/biolreprod/article/100/4/1018/5212287 by Universidad Nacional Autonoma de Mexico user on 14 October 2020

INFORME DE LABORES 2019

Life Sciences 239 (2019) 117048

Contents lists available at ScienceDirect

Life Sciences

journal homepage: www.elsevier.com/locate/lifescie

The α1-adrenoceptor-mediated human hyperplastic prostate cells proliferation is impaired by EGF receptor inhibition

Jessica Barbosa Nascimento-Viana[a], Rocío Alcántara-Hernández[b], Eliane Oliveira-Barros[c], Luiza A. Castello Branco[c], Priscilla R. Feijó[a], Luiz Antonio Soares Romeiro[d], Luiz Eurico Nasciutti[c], François Noël[a], J. Adolfo García-Sáinz[b], Claudia Lucia Martins Silva[a,*]

[a] Laboratory of Biochemical and Molecular Pharmacology, Universidade Federal do Rio de Janeiro, Brazil
[b] Instituto de Fisiología Celular, Universidad Nacional Autónoma de México, Mexico
[c] Cell Biology and Development Research Program, Universidade Federal do Rio de Janeiro, Brazil
[d] Pharmaceutical Sciences, Universidade de Brasília, Brazil

ARTICLE INFO

Keywords:
Adrenoceptor
Benign prostatic hyperplasia
EGF
N-phenylpiperazine

ABSTRACT

Benign prostatic hyperplasia (BPH) is an aging-related and progressive disease linked to an up-regulation of α_1-adrenoceptors. The participation of EGF receptors (EGFR) in the GPCRs' signalosome has been described but so far data about the contribution of these receptors to prostatic stromal hyperplasia are scanty. We isolated and cultured vimentin-positive prostate stromal cells obtained from BPH patients. According to intracellular Ca^{2+} measurements, cell proliferation and Western blotting assays, these cultured hyperplastic stromal cells express functional α_1-adrenoceptors and EGFR, and proliferate in response to the α_1-adrenoceptor agonist phenylephrine. Interestingly, in these cells the inhibition of EGFR signaling with GM6001, CRM197, AG1478 or PD98059 was associated with full blockage of α_1-adrenoceptor-mediated cell proliferation, while cell treatment with each inhibitor alone did not alter basal cell growth. Moreover, the co-incubation of AG1478 (EGFR inhibitor) with α_{1A}/α_{1D}-adrenoceptor antagonists showed no additive inhibitory effect. These findings highlight a putative role of EGFR signaling to α_1-adrenoceptor-mediated human prostate hyperplasia, suggesting that the inhibition of this transactivation cascade could be useful to reduce BPH progression.

1. Introduction

Benign prostatic hyperplasia (BPH) is a progressive condition that affects aging men. The epithelial and stromal hyperplasia occurs in the periurethral prostatic transition zone favoring the occurrence of the lower urinary tract symptoms suggestive of BPH (LUTS/BPH). Prostate enlargement and the enhanced prostatic smooth muscle contraction are responsible for the static and dynamic components of BPH, respectively, and both components reduce bladder outflow favoring urinary retention [1–3].

The α_1-adrenoceptor belongs to the G protein-coupled receptors (GPCRs) family being composed by three receptor subtypes known as α_{1A}-, α_{1B}- and α_{1D}-adrenoceptors [4]. The adult human prostate expresses mainly α_{1A}-adrenoceptors particularly in the stroma, and its expression is increased during BPH [5–9]. Therefore, it is well accepted that the mechanism underlying the BPH-related raise of smooth muscle contraction involves mainly the increased prostate expression of α_{1A}-adrenoceptors [5,6]. On the other hand, α_{1D}-adrenoceptors have been implicated in prostatic cell proliferation [6,10,11] and their mRNA expression is also up regulated in BPH patients [5,6]. α_{1A}-adrenoceptor blockers such as tamsulosin and silodosin are the first line drugs to treat low to moderate LUTS/BPH favoring bladder emptying, but they do not modify prostatic enlargement progression or the risk of BPH complications [12].

The etiology of prostate enlargement is complex with some evidence pointing to the involvement of metabolic and endocrine disorders, including roles of peptide growth factors, such as the epidermal growth factor (EGF) [2,13,14].

Two large families of membrane receptors, namely GPCRs and receptor tyrosine kinases, regulate cell proliferation among other cell functions. G protein-coupled receptors' signaling involves canonical and non-canonical pathways. In the case of α_1-adrenoceptor, the canonical pathway mediated by G protein involves the activation of phospholipase Cβ and the increase of intracellular Ca^{2+} [4]. On the other hand, the non-canonical receptor signaling activates other intracellular pathways including growth factor receptors signaling in a

* Corresponding author. Av. Carlos Chagas Filho, 373, CCS, room J-17, Cidade Universitária, Zip code 21941-902, Rio de Janeiro, Brazil.
E-mail addresses: silva.claudiamartins.ufrj@gmail.com, cmartins@icb.ufrj.br (C.L.M. Silva).

https://doi.org/10.1016/j.lfs.2019.117048
Received 17 June 2019; Received in revised form 24 October 2019; Accepted 5 November 2019
Available online 12 November 2019
0024-3205/ © 2019 Elsevier Inc. All rights reserved.

Abbreviations

AG	AG1478
BPH	benign prostatic hyperplasia
CK	cytokeratin
EGF	epidermal growth factor
EGFR	epidermal growth factor receptor
GM	GM6001
GPCR	G protein-coupled receptor
HB-EGF	pro-ligand heparin-binding epidermal growth factor
LUTS	lower urinary tract symptoms
NA	noradrenaline
Phe	phenylephrine
Vim	vimentin
5-HT	serotonin

process known as transactivation [15–17].

The participation of EGF receptors in the GPCRs' signalosome is essential for physiological and disease-related conditions such as mitogenesis, inflammation, and muscle contraction [17–23]. Moreover, the pioneer work of Oganesian and colleagues [23] showed that the constitutive activity of naturally occurring variant of α_{1A}-adrenoceptor transfected to Rat-1 fibroblasts lead to cell proliferation. EGF receptors belong to the ErbB/HER protein family and are expressed in normal human prostate mainly in the epithelial cells [24,25]. However, the expression of these receptors in prostate from BPH patients expands to stromal cells [25], where α_1-adrenoceptors are mainly expressed, with EGF inducing stromal cell proliferation [26,27]. Besides, the availability of EGF receptor ligand depends on matrix metalloproteinases activity, which in turn may be activated by GPCR [15,24].

Previously we characterized two *N*-phenylpiperazine derivatives named LDT3 and LDT5 as new α_{1A}/α_{1D}-adrenoceptor antagonists, and we showed that the α_{1D}-adrenoceptor antagonist BMY7378 as well as LDT3 and LDT5 inhibit human prostatic cell proliferation *in vitro* [28,29], while another α_{1D}-adrenoceptor antagonist, naftopidil, inhibits cell proliferation *in vivo* [30]. Therefore, we explored the possible role of α_1-adrenoceptor-mediated transactivation of EGF receptor leading to mitogenesis of stromal cells from BPH patients. Our results indicate that EGF receptor transactivation is involved in the α_1-adrenoceptor-mediated proliferation of human hyperplastic prostatic cells providing insight into the understanding of BPH physiopathology, and suggesting that this transactivation cascade could be a target to reduce BPH progression.

2. Material and methods

2.1. Cell culture maintenance

Prostate tissue samples were collected from three patients with LUTS/BPH during transurethral resection and immediately placed in ice-cold Dulbecco's modified Eagle's medium (DMEM) and transported to the Laboratory. The inclusion criteria of the patients were IPSS greater than 8 points, 50–70 years of age and PSA less than 2.5 ng/mL. Exclusion criteria were: previous prostatic surgery, prostate cancer, use of drugs that interfere with the function of adrenoceptors such as antagonists, anti-androgens and antidepressants, herbal extract, bladder catheter or neurogenic bladder. This study was approved by the ethics committee of the Federal University of Rio de Janeiro (UFRJ; CAAE-0029.0.197.000–05; 2009) and all experiments were performed in accordance with relevant guidelines and regulations. Informed written consent was signed by all donors. Briefly, prostate tissue was washed in phosphate buffer solution (PBS) before minced. The prostate fragments (1 mm^3) were added to DMEM supplemented with 10% heat-inactivated fetal bovine serum containing 1 mg/mL type I collagenase. Tissue specimens were dissociated by magnetic bar constant stirring for 2–4 h at 37 °C. The recovered cells were seeded in 25 mm^3 flasks cultured in DMEM supplemented with 10% heat-inactivated fetal bovine serum, 1% sodium pyruvate and 1% penicillin/streptomycin (100 IU/mL and 0.1 mg/mL, respectively), and fungizone (25 µg/mL) at 37 °C and 5% CO_2. Cells were observed at phase contrast microscopy (x250) to analyze morphology and confluence. At sub-confluence (approximately 90% confluence), cells were harvested using 0.05% trypsin/EDTA, and plated. A homogeneous stromal cell culture was obtained after six passages. The subsequent steps were the sub-culture of the cells and storage at −70 °C until use. Cells were used at 9th - 11th passage since the initial cell harvesting [31].

Rat-1 fibroblasts stably expressing human α_{1A}- or α_{1D}-adrenoceptors were cultured in DMEM supplemented with 10% fetal bovine serum, 300 µg/mL neomycin analogue G418 sulfate, 1% penicillin/streptomycin (100 IU/mL and 0.1 mg/mL, respectively; 37 °C, 5% CO_2) until confluence. The receptor density of α_1-adrenoceptors estimated with [^{3}H]-prazosin is in the range of 1.0–1.5 pmol/mg of protein [28].

2.2. Immunofluorescence assay

To analyze BPH cell morphology we used an anti-human cytokeratin (CK) monoclonal antibody (Dako) and anti-vimentin (Vim) monoclonal antibody (Sigma) as primary antibodies. For this procedure, 2×10^4 cells (11th passage) were plated and incubated for four days. Following, the culture medium was removed and cells were fixed with absolute cold ethanol for 20 min at room temperature, and then washed three times with PBS. The nonspecific binding was blocked with PBS/BSA 5% and then primary antibodies were added to the cultures and incubated for 2 h at room temperature. After that, cells were washed with PBS and incubated for an additional 2 h with goat anti-mouse Alexa 546 secondary antibody (Invitrogen). Cell nuclei were counterstained with DAPI (Santa Cruz Biotechnology). Finally, cells were washed in distilled water and mounted on histological slides with *N*-propylgallate (Sigma). Negative control conditions were performed by omitting the primary antibodies. No reactivity was observed when the primary antibody was absent. Images were captured using an inverted microscopy (Olympus IX81) and a Hamamatsu ORCA-R2 digital CCD camera using a 40× objective.

2.3. Intracellular [Ca^{2+}] measurement

In order to verify if primary stromal cell cultures from BPH patients express functional α_1-adrenoceptors we used a fluorimetric assay to measure the intracellular Ca^{2+} concentration ($[Ca^{2+}]_i$), a robust marker of the canonical Gq signaling. Cells were serum-starved overnight. In the next day, cells were washed with PBS and loaded with 2.5 µM fura-2/AM in the dark for 60 min at 37 °C in Krebs-Ringer-HEPES solution containing (mM) NaCl 120, KH_2PO_4 1.2, $MgSO_4$ 1.2, KCl 4.75, glucose 10, $CaCl_2$ 1.2, HEPES 20, and 0.05% bovine serum albumin (pH 7.4). Thereafter, the cells were washed to remove the unincorporated dye, detached by gentle trypsinization, centrifuged (200 × *g*, 7 min, 4 °C), and incubated (10^6 cells/condition) for 100 s (baseline) and then stimulated with 10 µM noradrenaline (NA) or 100 µM phenylephrine (Phe). The antagonists (BMY7378, 50 nM; WB4101, 50 nM or tamsulosin, 5 nM) were pre-incubated for 100 s before addition of the agonists, and their concentrations were previously defined based on their affinities [28]. Fluorescence measurements were performed at 340 and 380 nm excitation wavelengths and 510 nm emission wavelength, with a chopper interval set at 0.5 s, using an Aminco-Bowman Series 2 luminescence spectrometer (Rochester, NY). Peak fluorescence values were used for data analysis, and the

intracellular Ca^{2+} concentration ($[Ca^{2+}]_i$) was calculated, as described by Grynkiewicz et al. [32].

2.4. Cell growth assays

Briefly, cells (3×10^3 cells/well) were plated in 96-well plates in serum-free DMEM for 24 h. Sub-confluent cells were kept in DMEM (basal) or stimulated with 3 μM phenylephrine (Phe) for 48 h in the absence or presence of GM6001 (10 μM; metalloproteinase inhibitor), CRM197 (200 ng/mL; HB-EGF inhibitor), AG1478 (5 μM; selective EGFR tyrosine kinase inhibitor) or the MEK inhibitor PD98059 (1 μM) added 30 min before addition of the agonist. EGF 100 ng/mL (48 h) was used as positive control. All concentrations were chosen based on their affinities for the targets and previously reported in the literature [19,22]. Alternatively, cells were also treated with 3 μM phenylephrine for 48 h in the absence or presence of LDT3 or LDT5 (50 nM) alone, or in combination with AG1478 (5 μM), added 30 min before. The medium was changed every 24 h with fresh dilutions of drugs. Cell growth was evaluated by counting of viable cells using Trypan blue as an exclusion dye or by the 3-(4,5-dimethythiazol-2-yl)-2,5-diphenyl tetrazolium bromide (MTT) assay [28]. Otherwise indicated, each assay was performed in quadruplicate to calculate the mean value of one experiment. Data were expressed as the percentage of the basal condition which was considered as 100%.

2.5. Western blot assays

BPH cells (1×10^6) seeded on 6-well plate were incubated with 100 μM phenylephrine (Phe) or 10 μM noradrenaline (NA; in the presence of 1 μM propranolol added 2 min before) for 2, 5, 15, and 30 min in serum free medium. After treatment, cells were lysed with 200 μL of RIPA buffer (150 mM NaCl, 1 mM EGTA, 10% glycerol, 1% Triton X-100, 0.1% SDS, 1.5 mM $MgCl_2$, 10 mM sodium pyrophosphate, 1 mM sodium orthovanadate, 100 mM NaF, 10 mg/mL aprotinin, 10 mg/mL leupeptin, and 50 mM Tris-HCl, pH 7.4) under agitation, centrifuged at 13,000 × *g* for 5 min (4 °C) and the supernatants were used for evaluation of activation (phosphorylation) of extracellular signal-regulated kinases 1 and 2 (ERK 1/2). Protein content was determined according to the method of Lowry et al. Twenty μg of proteins were boiled for 5 min and resolved using 10% SDS/PAGE. After electrophoresis, proteins were transferred to nitrocellulose membranes and incubated for 1 h with Tris buffered saline (TBS) containing 0.1% Tween-20 (TBS-T) and 5% non-fat milk. Then, membranes were washed 3 times in TBS-T and incubated overnight with the primary monoclonal antibodies phospho-p44/p42 MAPK (p-ERK 1/2 Thr202/Tyr204, #9101; 1:1000), or p44/p42 MAPK Total (ERK 1/2, #4695; 1:1000) diluted in TBS-T with 5% non-fat milk at 4 °C with gentle shaking. The peroxidase-conjugated anti-rabbit IgG secondary antibody (#7074; 1:10000) was diluted in cold TBS-T and incubated for 1 h. Membranes were washed in TBS-T and detection of immunoreactivity was performed by enhanced chemiluminescence (ECL, Westar Cyanagen). Protein blot images were scanned and the optical density was obtained using ImageJ software (NIH, USA). The relative expression of p-ERK was normalized in relation to total ERK (also used as loading control).

2.6. Human androgen receptor binding assay

Filtration based radioligand binding assays for human prostate androgen receptors (LNCap cells; catalogue number 0933) using 1 nM [^{3}H]-methyltrienolone (4 °C, 24 h) were performed by Eurofins Cerep SA, France (Study 100018032). Mibolerone (1 μM) was used as positive control and showed an IC_{50} value of 1.9 nM. LDT3 and LDT5 were tested at the final concentration of 1 μM and the results were expressed as the percentage of the specific binding of [^{3}H]-methyltrienolone (considered as 100%).

2.7. Reagents and antibodies

LDT3 and LDT5 were synthesized as previously described [28]. The following reagents were acquired from the sources indicated between parenthesis: (R)-(−)-phenylephrine hydrochloride, (±)-propranolol hydrochloride, (−)-noradrenaline, fungizone, EGF, CRM197 and reagents for RIPA buffer (Sigma Aldrich, USA). Fura 2/AM (Molecular Probes, USA). Dulbecco's modified Eagle's medium (DMEM), fetal

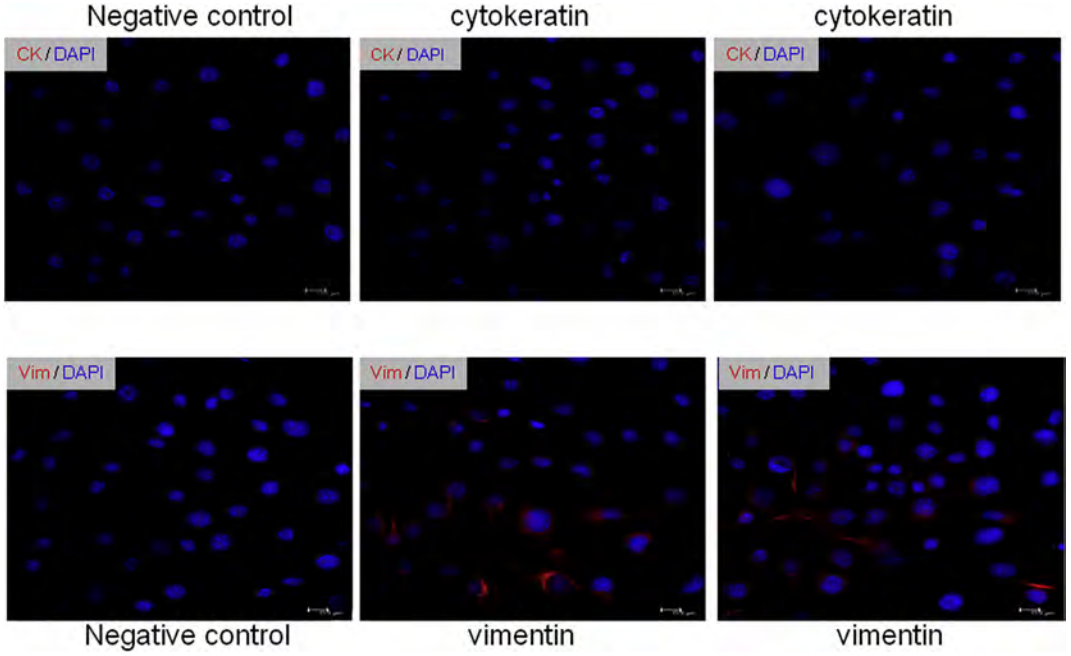

Fig. 1. BPH cells are positive for vimentin and negative for cytokeratin staining. Cells were incubated with anti-human primary monoclonal antibodies against cytokeratin (upper panels, CK) or vimentin (lower panels, Vim, red). In all immunostaining-negative controls, reactions were performed by omitting the primary antibody. No reactivity was observed when the primary antibody was absent. Blue staining = DAPI. Bars = 150 μm, objective 40×. (For interpretation of the references to colour in this figure legend, the reader is referred to the Web version of this article.)

bovine serum (South America), trypsin, penicillin (10000 IU/mL)/ streptomycin (10 mg/mL), PD98059 and other reagents for cell culture (Life Technologies, USA). AG1478 (Calbiochem, USA). GM6001 (Merck Millipore, USA). Rabbit monoclonal primary antibodies against extracellular signal-regulated kinases (ERK) 1/2 (#4695), and phospho-ERK 1/2 (#9101) (Cell Signaling, USA). Monoclonal anti-human cytokeratin antibody (#0821, Dako, USA). Monoclonal anti-human vimentin antibody (#V2258, Sigma Aldrich, USA). Anti-rabbit IgG secondary antibody (#7074, Cell Signaling, USA) and anti-mouse Alexa 546 secondary antibody (#A11003, Invitrogen, USA).

2.8. Statistical analysis

Otherwise indicated, data are expressed as mean and S.E.M. of 3–5 independent experiments. Independent experiments were performed using different primary cell cultures. The significance of the differences among two or more conditions was determined by two-tailed Student's *t*-test or one-way analysis of variance (one way ANOVA), respectively. ANOVA was followed by Dunnett's multiple comparisons test using the software GraphPad Prism 6.0 (Graphpad, La Jolla, CA, USA). Differences were considered statistically significant if $P < 0.05$.

3. Results

3.1. BPH stromal cells express functional α_1-adrenoceptors

The cultured hyperplastic cells are positive for vimentin and negative for cytokeratin staining which is a signature of stromal cells (Fig. 1). The canonical α_1-adrenoceptor signaling is linked to the increase of intracellular Ca^{2+} concentration $[Ca^{2+}]_i$. As shown in Fig. 2, the stimulation of BPH cells expressing native α_1-adrenoceptors with either 100 μM phenylephrine or 10 μM noradrenaline induced similar increments of $[Ca^{2+}]_i$ in relation to basal, which indicates that the receptors are functional. We chose the selective agonist of α_1-adrenoceptor phenylephrine to perform the subsequent experiments.

The agonist specificity for α_1-adrenoceptor was confirmed by measuring the intracellular Ca^{2+} concentration in Rat-1 fibroblasts stably expressing α_{1A}- or α_{1D}-adrenoceptors subtypes, the two adrenoceptor subtypes relevant for BPH. Cell pre-incubation with the antagonists WB 4101 (50 nM; α_{1A}-adrenoceptor antagonist) and tamsulosin (5 nM, $\alpha_{1A/1D}$-adrenoceptor antagonist), but not with BMY7378 (50 nM, α_{1D}-adrenoceptor antagonist), blocked the effect of 100 μM phenylephrine in cells expressing α_{1A}-adrenoceptors, while BMY7378 (50 nM) blocked the agonist effect only in cells expressing α_{1D}-adrenoceptors (Fig. 3A and B).

3.2. The EGF receptor modulates the α_1-adrenoceptor-mediated BPH cell growth

The presence of EGF receptors in the stromal cells was evaluated by cell proliferation. Cells were stimulated with EGF (100 ng/mL) in the absence and presence of an antagonist. As shown in Fig. 4A, the EGF-induced BPH cell proliferation was blocked by the EGF receptor tyrosine kinase inhibitor (AG1478, 5 μM). AG1478 *per se* did not alter basal cell growth discarding a putative cytotoxicity. Interestingly, phenylephrine (3 μM) increased BPH cell proliferation similarly to EGF. Then, in order to evaluate a possible dependence on the EGF receptor for the α_1-adrenoceptor-mediated BPH cell proliferation, we investigated if the blockage of downstream EGF receptor signaling could alter phenylephrine-mediated cell growth.

GM6001 (10 μM) is a pan inhibitor of the matrix metalloproteinases involved in pro-ligand heparin-binding epidermal growth factor (HB-EGF) cleavage, and consequently EGF receptor signaling [23]. GM6001 treatment did not alter the basal cell proliferation but prevented cell proliferation induced by phenylephrine (Fig. 4B), and the specific inhibitor of human HB-EGF, CRM197 (200 ng/mL) [18], had the same effect. The selective EGF receptor tyrosine kinase inhibitor AG1478 (5 μM) also prevented completely the effect of phenylephrine, without altering the basal cell proliferation. Cells were treated with the MEK inhibitor PD98059 (1 μM) which also inhibited cell proliferation in response to phenylephrine (Fig. 4B). Similar qualitative results were obtained using the MTT assay (Fig. 4C). Moreover AG1478, GM6001 and PD98059 blunted the EGF-mediated cell growth (Fig. 4D). None of the inhibitors *per se* inhibited cell growth. Altogether, the inhibition of sequential steps of EGF receptor signaling impaired the proliferative effect of the α_1-adrenoceptor agonist phenylephrine.

3.3. α_1-adrenoceptor agonists induce ERK phosphorylation in BPH cells

Since BPH cell proliferation induced by activation of α_1-adrenoceptor was prevented by the inhibition of EGF receptor signaling, which usually involves activation of the mitogen-activated protein kinase pathway, we then evaluated the impact of phenylephrine on ERK 1/2 activation by quantifying the ratio of phospho-ERK (p-ERK) to total ERK protein. Due to BPH cell limitation, we used only one concentration of phenylephrine (100 μM) which has been used elsewhere to activate ERK 1/2 pathway [33,34]. Moreover, previous data obtained from different cell systems showed that this concentration usually induces the maximal effect of the agonist [33,34].

Phenylephrine stimulated ERK 1/2 activity in stromal BPH cells in a time-dependent manner, and its effect peaked after 15 min. A similar stimulatory effect was also observed with the α_1-adrenoceptor agonist noradrenaline (10 μM, in the presence of propranolol 1 μM). In these experiments, EGF (100 ng/mL, 5 min stimulation) was used as a positive control and it stimulated ERK 1/2 activation (Fig. 5A–C). In isometric contraction assays, 100 μM phenylephrine added in the plateau of the contraction induced by 1 μM 5-HT, and in the presence of 1 μM prazosin, failed to relax rat aorta therefore discarding a putative β-adrenergic effect (*data not shown*). Previously we showed that the selective α_{1D}-adrenoceptor antagonist BMY7378, as well as the α_{1A}-/α_{1D}-adrenoceptor antagonists LDT3 and LDT5, inhibited human hyperplastic prostate stromal cell growth mediated by phenylephrine [28]. Current data showed that AG1478 (5 μM) inhibited the proliferative effect of phenylephrine, and the association with the α_{1A}/α_{1D}-adrenoceptor antagonists LDT3 or LDT5 (50 nM) resulted in similar inhibition suggesting that in this model the EGF receptor pathway is necessary for α_1-adrenoceptor-mediated BPH cell proliferation (Fig. 6). Of note, this inhibitory effect of LDT3 or LDT5 (50 nM) did not involve the inhibition of prostate androgen receptors (AR) since even at a much higher

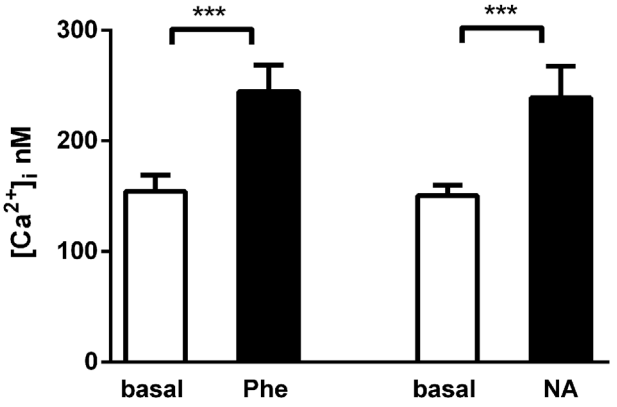

Fig. 2. Phenylephrine and noradrenaline increase intracellular Ca^{2+} concentration ($[Ca^{2+}]_i$) in hyperplastic prostatic stromal cells obtained from BPH patients. Cells were loaded with 2.5 μM fura-2 AM for 60 min before stimulation with the agonists (10 μM NA, 100 μM Phe). Data were expressed as mean and S.E.M. (n = 7–10 replicates from 3 individual experiments). ***P = 0.007 vs. basal (two-tailed Student's *t*-test). Phe = phenylephrine; NA = noradrenaline.

INFORME DE LABORES 2019

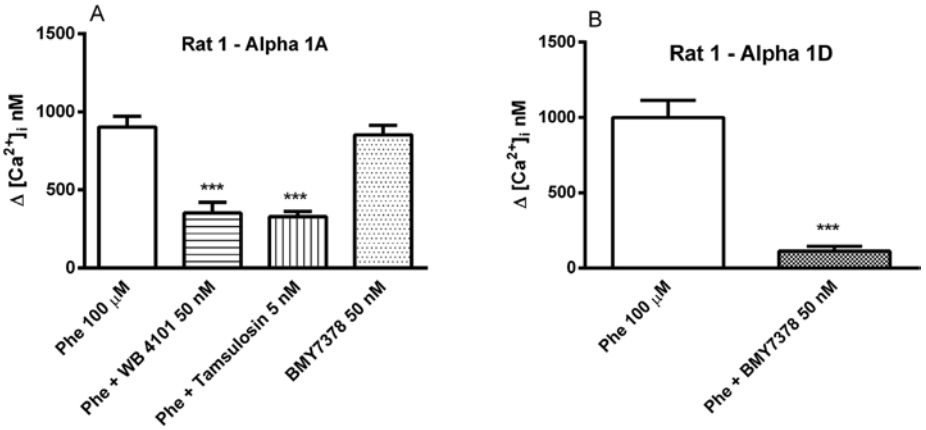

Fig. 3. The increase of intracellular Ca^{2+} concentration ($[Ca^{2+}]_i$) in Rat-1 cells transfected with human α_{1A}- or α_{1D}-adrenoceptors induced by phenylephrine is inhibited by selective antagonists added 100 s before. Cells were loaded with 2.5 μM fura-2 AM for 60 min before stimulation with phenylephrine (100 μM Phe). WB 4101 (50 nM): α_{1A}-adrenoceptor antagonist; tamsulosin (5 nM): $\alpha_{1A/D}$-adrenoceptor antagonist; BMY7378 (50 nM): α_{1D}-adrenoceptor antagonist. Data represent the difference (Δ) between the basal and agonist-induced increase of fluorescence, and were expressed as mean and S.E.M. (n = 6–8 replicates from 3 individual experiments). ***P < 0.001 vs. Phe (A, one way ANOVA followed by Dunnett's multiple comparisons test; B, two-tailed Student's *t*-test).

concentration (1 μM) they did not inhibit the specific binding of the AR agonist (LDT3: 6.9 ± 4.9%, n = 2; LDT5: 17.7 ± 8.1%, n = 2).

4. Discussion

BPH is an aging-related disease linked to an imbalance between prostate cell proliferation and apoptosis, favoring hyperplastic stromal cell growth [35]. Mounting evidence points to the importance of GPCRs for cell proliferation in pathological conditions [17,22,23]. Here we showed that the α_1-adrenoceptor-mediated proliferation of human hyperplastic prostatic stromal cells is fully inhibited by EGF receptor and MEK inhibitors suggesting the transactivation of the EGF receptors by α_1-adrenoceptors as an important event for BPH cell proliferation. To the best of our knowledge this is the first report about the stromal α_1-adrenoceptor-EGF receptor signaling in BPH.

The prostatic stroma makes up a large percentage of prostate volume during BPH, and the use of human stromal cells is considered valuable for BPH studies [35,36]. However, the isolation of stromal

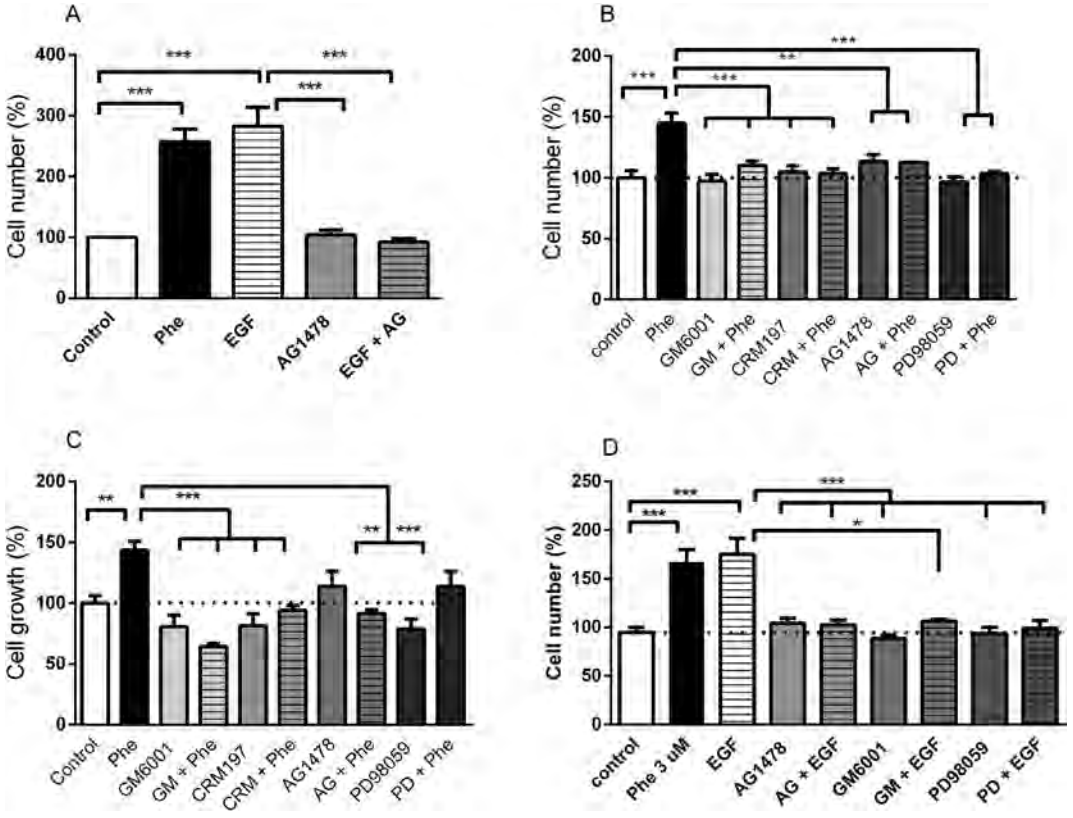

Fig. 4. The BPH cell proliferative effect of phenylephrine depends on the activation of EGF receptors. A) Hyperplastic stromal cells in culture were treated with 3 μM phenylephrine (Phe) or 100 ng/mL EGF for 48 h in the absence (control, white bar) or presence of the EGF receptor tyrosine kinase inhibitor AG1478 5 μM ***P < 0.001 Phe and EGF vs. control; AG1478 and EGF + AG vs. EGF (one way ANOVA followed by Dunnett's multiple comparisons test).
B and C) Hyperplastic stromal cells were treated with 3 μM phenylephrine (black bar) for 48 h in the absence (control, white bar) or presence of the following inhibitors of EGF receptor signaling: GM = GM6001 10 μM; CRM = CRM197 200 ng/mL; AG = AG1478 5 μM; PD = PD98059 1 μM. Cell proliferation was accessed by cell counting using Trypan Blue exclusion dye (B) and MTT assays (C). D. The EGF-mediated cell growth (100 ng/mL) is fully inhibited by AG1478, GM6001 and PD98059. The inhibitors alone did not alter basal cell proliferation (P > 0.05). Data were expressed as mean and S.E.M. of 3 experiments (performed in duplicate (A) or quadruplicate (B)), or 4 experiments performed in quadruplicate (C, D). B and C: **P < 0.01 and ***P < 0.001 vs. Phe; D: *P < 0.05 and ***P < 0.001 vs. control or EGF (one way ANOVA followed by Dunnett's multiple comparisons test).

INFORME DE LABORES 2019

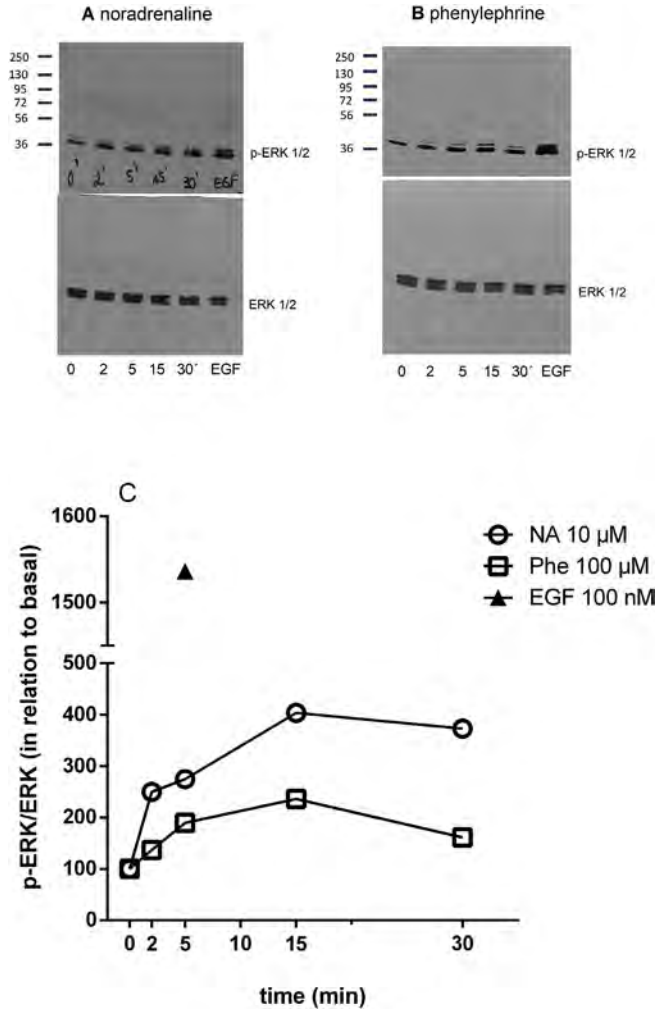

Fig. 5. Time-dependent activation of ERK 1/2 by phenylephrine and noradrenaline in hyperplastic stromal cells obtained from BPH patients (full-length representative blots). Cells were treated with 100 µM phenylephrine (Phe; A), 10 µM noradrenaline (NA) in the presence of 1 µM propranolol (B), for the indicated times or 100 ng/mL EGF (5 min, A-C). C. Densitometric analysis. Data were expressed as mean of 2 individual experiments.

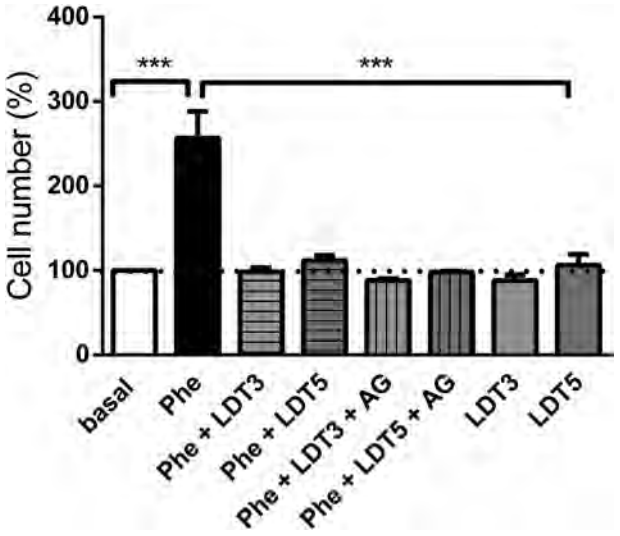

Fig. 6. The BPH cell proliferative effect of phenylephrine is completely inhibited by α_1-adrenoceptor antagonists (LDT3 and LDT5) or AG1478, an EGF receptor tyrosine kinase inhibitor, alone or in association. The co-incubation of AG1478 (5 µM) with the α_1-adrenoceptor antagonists did not potentiate the inhibitory effect of LDT3 and LDT5. Phe = phenylephrine. Data were expressed as mean and S.E.M. of 2 individual experiments performed in triplicate. ***P < 0.001 all conditions vs. Phe (one way ANOVA followed by Dunnett's multiple comparisons test).

cells from human prostate yields a small quantity of material. The cell immortalization frequently causes the loss of cell characteristics, making the screening of immortalized cell clones for lines that keep the phenotypic characteristics needed. For instance, immortalized human prostate stromal cells show an increased expression of α_{1B}-adrenoceptors which is not observed in human prostate or primary cultured cells [37]. Therefore we used primary cell culture obtained from BPH patients (*i.e.*, non-transformed cells). In our model, cultured cells stained positively for vimentin, and negatively for the epithelial cell marker cytokeratin, indicating the predominance of stromal cells.

The proposed ratio of α_{1A}:α_{1B}:α_{1D}-adrenoceptors mRNA in normal human prostate is approximately 63:6:31%, respectively [6]. In support to these data real time RT-PCR assays corroborate the predominance of α_{1A}- and α_{1D}-adrenoceptors mRNA [5]. Moreover, an increased expression of α_{1A}- and α_{1D}-adrenoceptors mRNA has been reported in BPH, and the α_{1D}-adrenoceptor mRNA has a more pronounced increased expression (as high as three times) [5,6]. Therefore these upregulated receptors are supposed to participate in the pathophysiology of BPH. However, most, if not all, commercially available antibodies against each subtype of α_1-adrenoceptor lacks selectivity, which limits the quantification of the protein at cellular level [38], and the identification of functional α_1-adrenoceptor subtypes relies on the use of selective drugs.

Our data showed that BPH stromal cells express functional α_1-adrenoceptors since phenylephrine, a selective α_1-adrenoceptor agonist, activated the canonical signaling pathway involving the increase of $[Ca^{2+}]_I$. Similar data were obtained using the endogenous non-selective adrenoceptor agonist noradrenaline, when tested in the presence of propranolol for blocking its β–adrenoceptor effects. Moreover, functional data suggest that α_{1D}-adrenoceptor is involved in the BPH cell proliferative effect of phenylephrine since BMY7378, a selective α_{1D}-adrenoceptor antagonist, blocked the agonist effect [28].

EGF receptor is a membrane-bound glycoprotein expressed in normal and hyperplastic human prostate [39,40] including stromal cells [27,35, and present data]. One of the proposed mechanisms leading to EGF receptor transactivation by GPCR includes the action of metalloproteinases promoting the shedding of members of EGF family such as HB-EGF, and consequently the binding to its cognate receptor [15,18,20]. As a consequence, metalloproteinase inhibition is reported as a strategy to interrupt EGF receptor transactivation. Here we showed that inhibition of metalloproteinase prevented BPH cell growth mediated by phenylephrine, which could suggest that the activation of α_1-adrenoceptor induces EGF receptor transactivation. In support of these data it was previously shown in rat lacrimal gland epithelial cells that α_{1D}-adrenoceptor mediates the shedding of EGF and EGF receptor activation [41].

In our model EGF induced stromal cell proliferation. As shown by Duque and colleagues [27], both HB-EGF and EGF (100 ng/mL) induce a similar mitogenic effect upon human prostate stromal cell suggesting a role of these agonists in BPH. Moreover, stromal cells express HB-EGF mRNA and the HB-EGF inhibitor CRM197 inhibits in a concentration-dependent manner the stromal cell growth [27].

There is evidence that a naturally occurring human α_{1A}-adrenoceptor genetic variant is constitutively coupled to EGFR transactivation [23]. In support of our hypothesis that α_1-adrenoceptors might induce transactivation of EGF receptor in BPH cells, the HB-EGF inhibitor CRM197, as well as the EGF tyrosine kinase receptor inhibitor AG1478, prevented hyperplastic cell growth induced by phenylephrine. Of note, the concentration of AG1478 used (5 µM) fully inhibited the

phenylephrine- and the EGF-induced cell proliferation. As ERK 1/2 activation is important for cell proliferation, and it may be activated by EGF receptor signaling, we investigated the effect of the MEK inhibitor PD98059, which also inhibited the proliferative effect of phenylephrine. Accordingly, in Western blotting assays, besides EGF (positive control), phenylephrine (and noradrenaline) also stimulated ERK 1/2 phosphorylation corroborating functional data. Therefore, our results suggest that α_1-adrenoceptors (most probably α_{1D}-subtype) transactivate EGF receptors in stromal cells from BPH patients leading to cell proliferation. However, present data do not rule out that the canonical signaling of α_1-adrenoceptor (*i.e.*, Gq canonical signaling) could also activate ERK pathway. On the other hand, as the inhibition of EGF receptor signaling did not reduce cell proliferation in the absence of phenylephrine, we could suggest that α_1-adrenoceptor-mediated EGF receptor transactivation is mainly agonist-dependent, rather than constitutively active as previously shown in cardiomyoblasts [42].

Different sets of evidence obtained by others indicate that transactivation of EGF receptors is involved in α_1-adrenoceptor signaling. For instance, it has been shown that α_{1D}-adrenoceptor activation induces the shedding of biologically active EGF and subsequent EGF receptor transactivation, and an EGF neutralizing antibody reduces phenylephrine-induced ERK activation in rat lacrimal gland [41]. Moreover, α_1-adrenoceptor activation induces ERK 1/2 activity in rat aorta myocytes (mainly α_{1D}-adrenoceptor type) [19], and in human epithelial prostatic cells where ERK 1/2 activity was related to cell volume regulation [43]. In good accordance with our data, the metalloproteinase inhibitor GM6001 [41] and the EGF receptor inhibitor AG1478 [19] blocked ERK 1/2 activation in response to phenylephrine linking α_1-adrenoceptor to EGF receptor transactivation. On the other hand, the β-adrenoceptor-mediated EGF receptor transactivation may involve (COS-7) or not (brown adipocytes) ERK 1/2 pathway [44,45]. Therefore ERK 1/2 activation during EGF receptor transactivation depends both on GPCR and cell type.

It is noteworthy that the co-incubation of EGF receptor inhibitor AG1478 with the α_{1A}-/α_{1D}-adrenoceptor antagonists LDT3 or LDT5 resulted in full inhibition of cell proliferation, which was similar to the inhibition promoted by each drug alone. A putative nonspecific inhibition of androgen receptors by these α_1 adrenoceptor antagonists was ruled out by binding assays. Moreover, as previously shown by our group or by others, the α_{1D}-adrenoceptor selective antagonists BMY7378 and naftopidil also fully inhibited the proliferative effect of phenylephrine in BPH cells [28,30]. However, in these models tamsulosin, a benzenesulfonamide derivative, showed no effect [28,30]. Furthermore, tamsulosin alone did not inhibit the increase of volume of the cell line BPH-1 in response to phenylephrine [43]. In common, BMY7378, naftopidil, LDT3 and LDT5 are α_{1D}-adrenoceptors antagonists that share the *N*-phenylpiperazine moiety which could shape some inhibitory functional selectivity upon BPH cell proliferation, and therefore other experiments would be welcome. Patients' adherence to current pharmacotherapy is low, a fact that favors BPH progression [46] and stimulates the search for new drugs. Understanding the mechanisms involved in prostate cell proliferation may help the development of new drugs.

In conclusion, our findings demonstrate that α_1-adrenoceptor activation in human hyperplastic prostate cells induces canonical and non-canonical signaling. The α_1-adrenoceptor non-canonical signaling involved in mitogenesis of BPH cells depends on EGF receptor transactivation. This mechanism could contribute to prostate enlargement and to the development of LUTS/BPH, and therefore our data give new insight into the physiopathology of BPH. We therefore propose that blockage of this transactivation cascade could be a putative non-hormonal pharmacological strategy to reduce concomitantly LUTS and BPH progression.

Author contributions

Conducted experiments: JBNV, RAH, LACB.

Contributed with reagents or cell culture: LASR, LEN, EOB, JAGS.

Participated in research design and coordinated experiments: CLMS, JAGS.

Performed data analysis, discussion, revised the manuscript: JBNV, RAH, PRF, FN, JAGS, CLMS.

Wrote the manuscript with important contributions by all authors: CLMS. All authors read and approved the final version of the manuscript.

Declaration of competing interest

None.

Acknowledgements

Supported by The Brazilian National Council for Scientific and Technological Development (CNPq, Brazil; Grants #306431/2015-7, #455436/2014-2, #312709/2017-0). JBNV was a PDJ fellow of CNPq (#166215/2015-5). CLMS, FN, LEN, and LASR are senior fellows of CNPq (Brazil). The Study 100018032 was sponsored by Biozeus Desenvolvimento de Produtos Biofarmacêuticos S.A. (Brazil). The funding source had no role in the study design, collection, analysis or interpretation of data, writing or submission of the manuscript. Orlando R. Moreira (UFRJ) for technical assistance.

References

[1] M. Speakman, R. Kirby, S. Doyle, C. Ioannou, Burden of male lower urinary tract symptoms (LUTS) suggestive of benign prostatic hyperplasia (BPH) - focus on the UK, BJU Int. 115 (4) (2015) 508–519.

[2] C.G. Roehrborn, Pathology of benign prostatic hyperplasia, Int. J. Impot. Res. 20 (Suppl 3) (2008) S11–S18.

[3] M. Marberger, The MTOPS study: new findings, new insights, and clinical implications for the management of BPH, Eur. Urol. 5 (9) (2006) 628–633.

[4] S. Cotecchia, The α1-adrenergic receptors: diversity of signaling networks and regulation, J. Recept. Signal Transduct. Res. 30 (6) (2010) 410-409.

[5] Y. Kojima, S. Sasaki, H. Shinoura, Y. Hayashi, G. Tsujimoto, K. Kohri, Quantification of alpha1-adrenoceptor subtypes by real-time RT-PCR and correlation with age and prostate volume in benign prostatic hyperplasia patients, The Prostate 66 (7) (2006) 761–767.

[6] K. Nasu, N. Moriyama, K. Kawabe, G. Tsujimoto, M. Murai, T. Tanaka, J. Yano, Quantification and distribution of alpha 1-adrenoceptor subtype mRNAs in human prostate: comparison of benign hypertrophied tissue and non-hypertrophied tissue, Br. J. Pharmacol. 119 (5) (1996) 797–803.

[7] J. Tseng-Crank, T. Kost, A. Goetz, S. Hazum, K.M. Roberson, J. Haizlip, N. Godinot, C.N. Robertson, D. Saussy, The alpha 1C-adrenoceptor in human prostate: cloning, functional expression, and localization to specific prostatic cell types, Br. J. Pharmacol. 115 (8) (1995) 1475–1485.

[8] C. Forray, J.A. Bard, J.M. Wetzel, G. Chiu, E. Shapiro, R. Tang, H. Lepor, P.R. Hartig, R.L. Weinshank, et al., The alpha 1-adrenergic receptor that mediates smooth muscle contraction in human prostate has the pharmacological properties of the cloned human alpha 1c subtype, Mol. Pharmacol. 45 (4) (1994) 703–708.

[9] D.T. Price, D.A. Schwinn, J.W. Lomasney, L.F. Allen, M.G. Caron, R.J. Lefkowitz, Identification, quantification, and localization of mRNA for three distinct alpha 1 adrenergic receptor subtypes in human prostate, J. Urol. 150 (2 Pt 1) (1993) 546–551.

[10] H. Kanda, K. Ishii, Y. Ogura, T. Imamura, M. Kanai, K. Arima, Y. Sugimura, Naftopidil, a selective alpha-1 adrenoceptor antagonist, inhibits growth of human prostate cancer cells by G1 cell cycle arrest, Int. J. Cancer 122 (2) (2008) 444–451.

[11] J. Kim, Y. Yanagihara, T. Kikugawa, M. Ji, N. Tanji, Y. Masayoshi, M.R. Freeman, A signaling network in phenylephrine-induced benign prostatic hyperplasia, Endocrinology 150 (8) (2009) 3576–3583.

[12] K.T. McVary, C.G. Roehrborn, A.L. Avins, M.J. Barry, R.C. Bruskewitz, R.F. Donnell, H.E. Foster Jr., C.M. Gonzalez, S.A. Kaplan, et al., Update on AUA guideline on the management of benign prostatic hyperplasia, J. Urol. 185 (5) (2011) 1793–1803.

[13] C. Füllhase, O. Hakenberg, New concepts for the treatment of male lower urinary tract symptoms, Curr. Opin. Urol. 25 (1) (2015) 19–26.

[14] A. Sciarra, G. Mariotti, S. Salciccia, A. Autran Gomez, S. Monti, V. Toscano, F. Di Silverio, Prostate growth and inflammation, J. Steroid Biochem. Mol. Biol. 108 (3–5) (2008) 254–260.

[15] A.C. Overland, P.A. Insel, Heterotrimeric G proteins directly regulate MMP14/membrane type-1 matrix metalloprotease: a novel mechanism for GPCR-EGFR transactivation, J. Biol. Chem. 290 (16) (2015) 9941–9947.

[16] C. Marty, R.D. Ye, Heterotrimeric G protein signaling outside the realm of seven transmembrane domain receptors, Mol. Pharmacol. 78 (1) (2010) 12–18.
[17] H. Daub, F.U. Weiss, C. Wallasch, A. Ullrich, Role of transactivation of the EGF receptor in signalling by G-protein-coupled receptors, Nature 379 (6565) (1996) 557–560.
[18] N. Prenzel, E. Zwick, H. Daub, M. Leserer, R. Abraham, C. Wallasch, A. Ullrich, EGF receptor transactivation by G-protein-coupled receptors requires metalloproteinase cleavage of proHB-EGF, Nature 402 (6764) (1999) 884–888.
[19] N. Ulu, H. Gurdal, S.W. Landheer, M. Duin, M.O. Guc, H. Buikema, R.H. Henning, α1-Adrenoceptor-mediated contraction of rat aorta is partly mediated via transactivation of the epidermal growth factor receptor, Br. J. Pharmacol. 161 (6) (2010) 1301–1310.
[20] C. Liebmann, EGF receptor activation by GPCRs: a universal pathway reveals different versions, Mol. Cell. Endocrinol. 331 (2) (2011) 222–231.
[21] L. Hao, M. Du, A. Lopez-Campistrous, C. Fernandez-Patron, Agonist-induced activation of matrix metalloproteinase-7 promotes vasoconstriction through the epidermal growth factor-receptor pathway, Circ. Res. 94 (1) (2004) 68–76.
[22] H. Zhang, D. Chalothorn, L.F. Jackson, D.C. Lee, J.E. Faber, Transactivation of epidermal growth factor receptor mediates catecholamine-induced growth of vascular smooth muscle, Circ. Res. 95 (10) (2004) 989–997.
[23] A. Oganesian, V. Yarov-Yarovoy, W.C. Parks, D.A. Schwinn, Constitutive coupling of a naturally occurring human alpha1a-adrenergic receptor genetic variant to EGFR transactivation pathway, Proc. Natl. Acad. Sci. U.S.A. 108 (49) (2011) 19796–19801.
[24] M.J. Wieduwilt, M.M. Moasser, The epidermal growth factor receptor family: biology driving targeted therapeutics, Cell. Mol. Life Sci. 65 (10) (2008) 1566–1584.
[25] M.P. De Miguel, Royuela, R. Bethencourt, A. Ruiz, B. Fraile, R. Paniagua, Immunohistochemical comparative analysis of transforming growth factor α, and epidermal growth factor receptor in normal, hyperplastic and neoplastic human prostates, Cytokine 11 (9) (1998) 722–727.
[26] R.M. Adam, J.G. Borer, J. Williams, J.A. Eastham, K.R. Loughlin, M.R. Freeman, Amphiregulin is coordinately expressed with heparin-binding epidermal growth factor-like growth factor in the interstitial smooth muscle of the human prostate, Endocrinology 140 (12) (1999) 5866–5871.
[27] J.L. Duque, R.M. Adam, J.S. Mullen, J. Lin, J.P. Richie, M.R. Freeman, Heparin-binding epidermal growth factor-like growth factor is an autocrine mediator of human prostate stromal cell growth in vitro, J. Urol. 165 (1) (2001) 284–288.
[28] J.B. Nascimento-Viana, A.R. Carvalho, L.E. Nasciutti, R. Alcántara-Hernández, F. Chagas-Silva, P.A. Souza, L.A. Romeiro, J.A. García-Sáinz, F. Noël, C.L. Silva, New Multi-target antagonists of α1A-, α1D-adrenoceptors and 5-HT1A receptors reduce human hyperplastic prostate cell growth and the increase of intraurethral pressure, J. Pharmacol. Exp. Ther. 356 (1) (2016) 212–222.
[29] F. Chagas-Silva, J.B. Nascimento-Viana, L.A. Romeiro, L.C. Barberato, F. Noël, C.L. Silva, Pharmacological characterization of N1-(2-methoxyphenyl)-N4-hexylpiperazine as a multi-target antagonist of α1A/α1D-adrenoceptors and 5-HT1A receptors that blocks prostate contraction and cell growth, Naunyn Schmiedebergs Arch. Pharmacol. 387 (3) (2014) 225–234.
[30] Y. Kojima, S. Sasaki, N. Oda, T.A. Koshimizu, Y. Hayashi, M. Kiniwa, G. Tsujimoto, K. Kohri, Prostate growth inhibition by subtype-selective alpha(1)-adrenoceptor antagonist naftopidil in benign prostatic hyperplasia, The Prostate 69 (14) (2009) 1521–1528.
[31] P.A. De Souza, A. Palumbo Jr., L.M. Alves, V.P. de Souza, L.M. Cabral, P.D. Fernandes, C.M. Takiya, F.S. Menezes, L.E. Nasciutti, Effects of a nano-composite containing Orbignya speciosa lipophilic extract on Benign Prostatic Hyperplasia, J. Ethnopharmacol. 135 (1) (2011) 135–146.
[32] G. Grynkiewicz, M. Poenie, R.Y. Tsien, A new generation of Ca2+ indicators with greatly improved fluorescence properties, J. Biol. Chem. 260 (6) (1985) 3440–3450.
[33] M. Perez-Aso, V. Segura, F. Montó, D. Barettino, M.A. Noguera, G. Milligan, P. D'Ocon, The three α1-adrenoceptor subtypes show different spatio-temporal mechanisms of internalization and ERK1/2 phosphorylation, Biochim. Biophys. Acta 1833 (2013) 2322–2333.
[34] D.F. McCune, S.E. Edelmann, J.R. Olges, G.R. Post, B.A. Waldrop, D.J. Waugh, D.M. Perez, M.T. Piascik, Regulation of the cellular localization and signaling properties of the alpha(1B)- and alpha(1D)-adrenoceptors by agonists and inverse agonists, Mol. Pharmacol. 57 (4) (2000) 659–666.
[35] T.M. Nicholson, W.A. Ricke, Androgens and estrogens in benign prostatic hyperplasia: past, present and future, Differentiation 82 (2011) 184–199.
[36] J.P. Hieble, Animal models for benign prostatic hyperplasia, Handb. Exp. Pharmacol. 202 (2011) 69–79.
[37] Price, D.T., Rudner, X., Michelotti, G.A. & Schwinn, D.A. Immortalization of a human prostate stromal cell line using a recombinant retroviral approach. J. Urol. 164: 2145-2150.
[38] B.C. Jensen, P.M. Swigart, P.C. Simpson, Ten commercial antibodies for alpha-1-adrenergic receptor subtypes are nonspecific, Naunyn Schmiedebergs Arch. Pharmacol. 379 (4) (2009) 409–412.
[39] P. Davies, C.L. Eaton, Binding of epidermal growth factor by human normal, hypertrophic, and carcinomatous prostate, The Prostate 14 (2) (1989) 123–132.
[40] G.L. Morris, J.G. Dodd, Epidermal growth factor receptor mRNA levels in human prostatic tumors and cell lines, J. Urol. 143 (6) (1990) 1272–1274.
[41] L. Chen, R.R. Hodges, C. Funaki, D. Zoukhri, R.J. Gaivin, D.M. Perez, D.A. Dartt, Effects of alpha1D-adrenergic receptors on shedding of biologically active EGF in freshly isolated lacrimal gland epithelial cells, Am. J. Physiol. Cell Physiol. 291 (5) (2006) C946–C956.
[42] M. Kleine-Brueggeney, I. Gradinaru, E. Babaeva, D.A. Schwinn, A. Oganesian, Alpha1a-adrenoceptor genetic variant induces cardiomyoblast-to-fibroblast-like cell transition via distinct signaling pathways, Cell. Signal. 26 (2014) 1985–1997.
[43] M. Wang, Y. Daaka, A. Dey, Biased α-adrenergic receptor and βarrestin signaling in a cell culture model of benign prostatic hyperplasia, Biochem. Biophys. Res. Commun. 471 (1) (2016) 41–46.
[44] S. Maudsley, K.L. Pierce, A.M. Zamah, W.E. Miller, S. Ahn, Y. Daaka, R.J. Lefkowitz, L.M. Luttrell, The beta(2)-adrenergic receptor mediates extracellular signal-regulated kinase activation via assembly of a multi-receptor complex with the epidermal growth factor receptor, J. Biol. Chem. 275 (13) (2000) 9572–9580.
[45] Y. Wang, J.M. Fälting, C.L. Mattson, T.E. Holmström, J. Nedergarrd, In brown adipocytes, adrenergically induced β_1-/β_3-(G_s)-, α_2-(G_i)- and α_1-(G_q)-signalling to Erk1/2 activation is not mediated via EGF receptor transactivation, Exp. Cell Res. 319 (2013) 2718–2767.
[46] T. Zabkowski, M. Saracyn, Drug adherence and drug-related problems in pharmacotherapy for lower urinary tract symptoms related to benign prostatic hyperplasia, J. Physiol. Pharmacol. 69 (2018) 639–645.

INFORME DE LABORES 2019

Video Article

Desensitization and Recovery of Crayfish Photoreceptors Upon Delivery of a Light Stimulus

Carolina Barriga-Montoya[1], Araceli de la O-Martínez[1], Arturo Picones[2], Arturo Hernández-Cruz[2], Beatriz Fuentes-Pardo[1], Froylán Gómez-Lagunas[1]

[1]Departamento de Fisiología, Facultad de Medicina, Universidad Nacional Autónoma de México

[2]Laboratorio Nacional de Canalopatías, Instituto de Fisiología Celular, Universidad Nacional Autónoma de México

Correspondence to: Froylán Gómez-Lagunas at froylangl@yahoo.com

URL: https://www.jove.com/video/56258
DOI: doi:10.3791/56258

Keywords: Neuroscience, Issue 153, Light-elicited current, desensitization, recovery from desensitization, intracellular recording, voltage-clamp, two-pulse protocol, crayfish, circadian rhythms.

Date Published: 11/9/2019

Citation: Barriga-Montoya, C., de la O-Martínez, A., Picones, A., Hernández-Cruz, A., Fuentes-Pardo, B., Gómez-Lagunas, F. Desensitization and Recovery of Crayfish Photoreceptors Upon Delivery of a Light Stimulus. *J. Vis. Exp.* (153), e56258, doi:10.3791/56258 (2019).

Abstract

A method to study desensitization and recovery of crayfish photoreceptors is presented. We performed intracellular electrical recordings of photoreceptor cells in isolated eyestalks using the discontinuous single electrode-switched voltage-clamp configuration. First, with a razor blade we made an opening in the dorsal cornea to get access to the retina. Thereafter, we inserted a glass electrode through the opening, and penetrated a cell as reported by the recording of a negative potential. Membrane potential was clamped at the photoreceptor's resting potential and a light-pulse was applied to activate currents. Finally, the two light-flash protocol was employed to measure current desensitization and recovery. The first light-flash triggers, after a lag period, the transduction ionic current, which after reaching a peak amplitude decays towards a desensitized state; the second flash, applied at varying time intervals, assesses the state of the light-activated conductance. To characterize the light-elicited current, three parameters were measured: 1) latency (the time elapsed between light flash delivery and the moment in which current achieves 10% of its maximum value); 2) peak current; and 3) desensitization time constant (exponential time constant of the current decay phase). All parameters are affected by the first pulse.

To quantify recovery from desensitization, the ratio p2/p1 was employed versus time between pulses. p1 is the peak current evoked by the first light-pulse, and p2 is the peak current evoked by the second pulse. These data were fitted to a sum of exponential functions. Finally, these measurements were carried out as function of circadian time.

Video Link

The video component of this article can be found at https://www.jove.com/video/56258/

Introduction

In order to be perceived as a visual stimulus, light reaching the eyes must be transduced into an electrical signal. Hence, in all visual organisms, light triggers a transduction ion-current, which in turn produces a change in the membrane potential of photoreceptor cells, the so-called receptor potential. Due to this, the light sensitivity of the eye primarily depends on the state of the light activated conductance, which can be either available to be activated or desensitized.

In crayfish photoreceptors, light triggers a slow, transient, ionic current[1]. Upon illumination, the transduction current arises after a lag or latency before reaching its maximum; thereafter it decays, as the transduction channels fall into a desensitized state in which they are unresponsive to further light stimulus[2]. That is, light, in addition to activating the transduction current responsible of vision, also induces a transient decrement of the sensitivity of photoreceptor cells. Desensitization may represent a general protective mechanism against overexposure to an adequate stimulus. The eye's sensitivity to light is recovered as the transduction conductance recovers from desensitization.

Intracellular recording is a useful technique for measuring electrical activity of excitable cells[3,4,5,6,7,8]. Although intracellular recording has become less frequent with the advent of the patch-clamp technique[9], it is still a convenient approach when cells are either difficult to isolate, or present a geometry that makes the formation of the patch-clamping giga-seals difficult (*i.e.*, seals or tight-contacts between the patch electrode and membranes with electrical resistance of the order of 10^9ohms). Examples of the latter are sperm cells[10] and the photoreceptor cells herein studied. In our experience, *Procambarus clarkii* photoreceptors are difficult to isolate and keep in primary culture; additionally, they are thin rods that make giga-seal formation difficult to achieve. In intracellular recordings, a sharp electrode is advanced into a cell that is kept in place by the surrounding tissue. The electrode is chopped by the high-speed switching circuitry of the amplifier, so current is sampled between voltage pulses. This mode is known as discontinuous single-electrode voltage clamp (dSEVC mode)[11]. The high resistance (small opening) of the electrode hinders the diffusional exchange between the cell and the pipette solutions, yielding a minimal disturbance of the intracellular milieu[3]. A potential drawback of this technique is that electrode insertion may produce a non-selective leak current; therefore, care must be taken to avoid recording from cells where the size of the leak current may interfere with the intended measurements[4,12].

Copyright © 2019 Journal of Visualized Experiments

Herein, we use isolated crayfish eyestalks to assess desensitization and recovery of the light-activated ion conductance by performing intracellular electrical recordings of photoreceptor cells under voltage clamp conditions.

Protocol

NOTE: The experiments comply with the Laws of Animal Protection of Mexico.

1. Experimental Setup

1. General connections
    1. Connect the amplifier to a suitable computer through an analog-to-digital converter and use an oscilloscope to monitor the experiment (**Figure 1**).
    2. Connect the photostimulator to the A/D converted.

2. Recording chamber
    1. Place the recording chamber on top of an anti-vibration table and locate it inside a Faraday cage.
    NOTE: This prevents mechanical vibration and electrical noise that may affect the recording. Our Faraday cage was made of darkened wire mesh. A homemade, 2 mL, acrylic recording chamber is used (**Figure 2**).
    2. Prepare the bath solution to keep the preparation alive[13]: 205 mM NaCl; 5 mM KCl; 2 mM $MgSO_4$; 13 mM $CaCl_2$; 5 mM Hepes-NaOH, pH 7.3.
    NOTE: Solution does not include dextrose or any bubbling by 95% O_2, 5% CO_2 mixture because the experimental procedure is short enough to detect damage by the electrical recording (see step 4.2.3 for completeness).

3. Electrodes
    1. Use a chloride-coated silver-wire electrode as the reference electrode
    NOTE: Silver chloride coating is necessary to allow the electrode reaction: $AgCl(s) + e^- \leftrightarrow Ag(s) + Cl^-$.
    2. Sand a silver wire (thickness ~ 1 mm, length ~ 10 cm) with a fine grade emery paper in order to clean its surface.
    3. Rinse the silver wire with distilled water.
    4. Immerse the clean silver-wire in a 4-6% sodium hypochlorite solution (NaClO) until it appears dark (approximately 20 min).
    5. Use thin glass pipettes filled with an electrolyte solution (2.7 M KCl) as the intracellular electrode.
    6. Pull a glass capillary tube (internal diameter ≈ 1 mm) with a micro-pipette puller to obtain a thin tip with a small opening (0.01-0.1 µm)[14].
    7. Fill the pulled capillary glass with a 2.7 M KCl solution. First fill it by capillarity (immerse the pipette tip into the 2.7 M KCl solution) and then fill the half of the pipette with a fine injection needle. If necessary, tap the electrode pipette to eliminate air bubbles.
    8. Connect the electrode to its holder. Connect the holder to the amplifier headstage with the amplifier. Position the electrode-holder-headstage with a stable 3-D micromanipulator. Lower the electrode until bath solution covers its tip.
    NOTE: The electrode must have a vertical orientation

4. Select the Bridge Mode of the amplifier (in the Mode section of the amplifier, press the Bridge button) and measure the electrode resistance. Make sure that the resistance is about 50 MΩ[11].
NOTE: This electrode size allows a good-quality electrical recording with limited damage to the cell.
5. Null the offset current and compensate capacitive transients using the Holding Position button in the section Voltage Clamp of the amplifier, and the Capacitance Neutralization button in Microelectrode 1 section of the amplifier.
6. Superfusion system
    1. Pour the bath solution (step 1.2.2) into a suitable receptacle (a 250 mL serum bottle) and connect it to an irrigation tubing set (3.2 mm of internal diameter), thus connecting the recording chamber. Use a gravity driven superfusion system. Regulate the flow rate to ~ 0.5 mL/s.
    2. Connect the chamber to a suction device. Regulate the solution suction system in such a way that the total volume of the recording chamber does not vary. Use a vacuum pump for suction.
    NOTE: A constant volume in the recording chamber is important to keep stray capacitances constant throughout the experiment.

2. Biological Material

Note: Use adult crayfishes *P. clarkii* (7-10 cm long) in the intermolt stage of indistinct sex.

1. Circadian time
    1. One month prior to the experiments, maintain 100 crayfishes under a 12-h light/12-h dark cycle[15] (white light, 2.4 kW/m^2).
    NOTE: One month is sufficient time to synchronize the crayfish population.
    2. Determine the circadian time of the crayfish population by assessing the amplitude of electroretinograms of five randomly chosen animals[15].
    NOTE: 0 h circadian time (CT 0) indicates the beginning of a subjective day, *i.e.*, time during which an organism is normally active[16,17,18,19] (**Figure 3**). The crayfish is a nocturnal animal, so under a 12-h light/12-h dark cycle, it is active during the dark phase.

2. Eyestalk isolation procedure
    1. At the desired circadian time, anesthetize a selected crayfish by immersion in tap water at 0-4 °C, for 15 min.
    2. By means of a fine scissor, detach the eyestalk from the base.
    3. Access the retina using a razor blade to make an opening (~ 1-mm^2) in the dorsal cornea.

4. Place the eyestalk in the center of the recording chamber (the hole covered with silicone) with the access opening to the retina on the top of the chamber.

3. Keep the eyestalk under constant darkness for 20 min.
NOTE: 20 min is sufficient time for the photoreceptor cell to be fully dark adapted.

3. Photoreceptor Impaling

1. Put the microelectrode and the eyestalk's longitudinal axis parallel in such a way that the microelectrode is centered for access to the retina. Use a stereoscopic microscope (10X) to place the devices in the correct configuration.
2. Monitor the voltage difference between the reference and recording electrodes by selecting the Bridge Mode[11] of the amplifier.
3. Lower the electrode into the bath and thereafter place it right over the retina.
4. Move away the microscope and position the photostimulator lamp parallel to the eyestalk's longitudinal axis.
NOTE: Distance between lamp and superfusion chamber is approximately 15 cm.
5. Slowly lower the microelectrode until a sudden voltage drop is detected.
NOTE: A voltage drop of around −50 mV indicates the impalement of a healthy photoreceptor cell.
6. Deliver a test light-flash (white light, 7.2 kW/m^2, 10 µs duration) to record the photoreceptor's receptor potential.
NOTE: The photoreceptor's receptor potential is a depolarizing potential of 10-15 mV amplitude and 300 ms duration (**Figure 4**).

4. Electrical Recording

1. Ensure that the photoreceptor cells are totally adapted to dark conditions (see step 2.3).
    1. Deliver a test-light flash every 2 min. Automate the time between flashes by choosing an adequate value (120 s) of "time between episodes" in the data acquisition software.
    NOTE: 2 min is the necessary time to allow the total recovery of the currents underlying the photoreceptor's electrical response.
    2. Monitor the resting membrane potential, as well as the amplitude and duration of the receptor potential. Assume that the photoreceptor is completely adapted once the membrane potential, amplitude, and duration of the receptor potential remain unchanged. Eyestalks previously kept under constant darkness for 20 min (step 2.3) complete their adaptation in approximately 5 min.
    3. Stop stimulating the cell 2 min before recording the light-elicited current.

2. Current recording
    1. Clamp the voltage at the measured resting membrane potential value of the cell by selecting "Holding amplitude" in the data acquisition software (in Waveform on the Analog Output Channel section).
    2. Select the dSEVC mode of the amplifier. In the Mode section of the amplifier, select the SEVC button and switch the lever to the Discont SEVC position.
    3. Set the switching rate to 500-1,000 Hz (by using the Rate Adjust button of the amplifier), as determined by the speed of the electrode[11].
    4. Deliver a light-flash, and observe the evoked ion influx.
    NOTE: This is the light-elicited or transduction current (**Figure 5**).
    5. Return to the Bridge mode on the amplifier and record a receptor potential by sending a light flash (see section 3). Make sure that the photoreceptor cell is totally adapted to dark conditions. Measure the receptor potential characteristics (amplitude and duration) and compare with the first measurements. Assume that the impaled photoreceptor cell is a healthy cell if they have the same characteristics.
    NOTE: After eyestalk ablation, biological preparation is viable during the following 2 h.

3. Two pulse protocol: Measure the recovery from desensitization with a two light-flash protocol.
NOTE: The two light-flash protocol is similar to the standard two-pulse voltage protocol used to measure recovery from inactivation of voltage-gated channels[20]. The first light-flash causes a temporary change in the sensitivity of the photoreceptor cell and the second flash evaluates the state of the light-activated conductance.
    1. Deliver a pair of light pulses. Apply the second flash after a desired time interval (from 300 ms to 2 min).
    2. Digitize the currents at 10 KHz sampling with the data acquisition software and save the data for off-line analysis[11].
    NOTE: A table with the configuration values of the software is included as supplementary material.

5. Data Analysis

1. Kinetics of the light-elicited current
    1. Measure three current parameters: activation latency L, the time elapsed from the light-flash delivery until the current attains 10% of its maximal amplitude (**Figure 5**); peak or maximal current amplitude I_p; and desensitization time constant T. Measure the desensitization time constant (T) by fitting the current decay phase to:
    $$i(t) = -Ae^{\frac{-t}{T}}$$
    where, A = -I(t=0) is a positive constant (**Figure 5**).

2. Desensitization and recovery
Note: Recovery from desensitization was assessed as the ratio p_2/p_1, where p_1 is the relevant parameter (either L, I_p, or T) of the control current, and p_2 is the corresponding parameter of the second test-current.
    1. Plot p_2/p_1 (either L, I_p, or T) as a function of time between pulses.
    2. Depending on the parameter, fit the points of each plot to:

$$\frac{p_2}{p_1} = \sum_{1}^{n} 1 - e^{\frac{-t}{\tau_n}}$$

or to:

$$\frac{p_2}{p_1} = \sum_{1}^{n} 1 + A_n e^{\frac{-t}{\tau_n}}$$

3. Use an appropriate statistical test to determine the number of exponential terms required to fit the experimental data.

Representative Results

First, a representative receptor potential of crayfish photoreceptor cells is obtained (**Figure 4**). Afterwards, a test light-flash was applied to trigger the light transduction current (**Figure 5**). The cationic transduction current[1] activates after a lag, reaching a maximal and thereafter slowly drops into an absorbing desensitized state from which it slowly recovers.

It is reasonable to suppose that the long latency L (tens of milliseconds) of the light-elicited current depends on the biochemical events triggered by light, which involve G-protein pathways. The amplitude of the peak current I_p depends on the fraction of channels available to be opened, and the relative rates of current activation and inactivation. The latter is assessed by the decay time constant T.

On the other hand, the L recovery should be related to the rate of recovery of the biochemical phototransduction cascade; I_p recovery depends both, on the intrinsic conformational changes of the proteins responsible for the ion conductance, and on the rate of recovery of the biochemical phototransduction cascade. The latter could also be related to the recovery of T. Furthermore, the parallel variation of L and T suggest that a common biochemical factor (or factors; *e.g.*, the phosphorylation state of the channel) can affect both parameters[1].

A two-flash protocol (**Figure 6**) was applied subsequently to determine the kinetics of recovery from desensitization (**Figure 7**) at different moments in the circadian cycle (**Figure 8**).

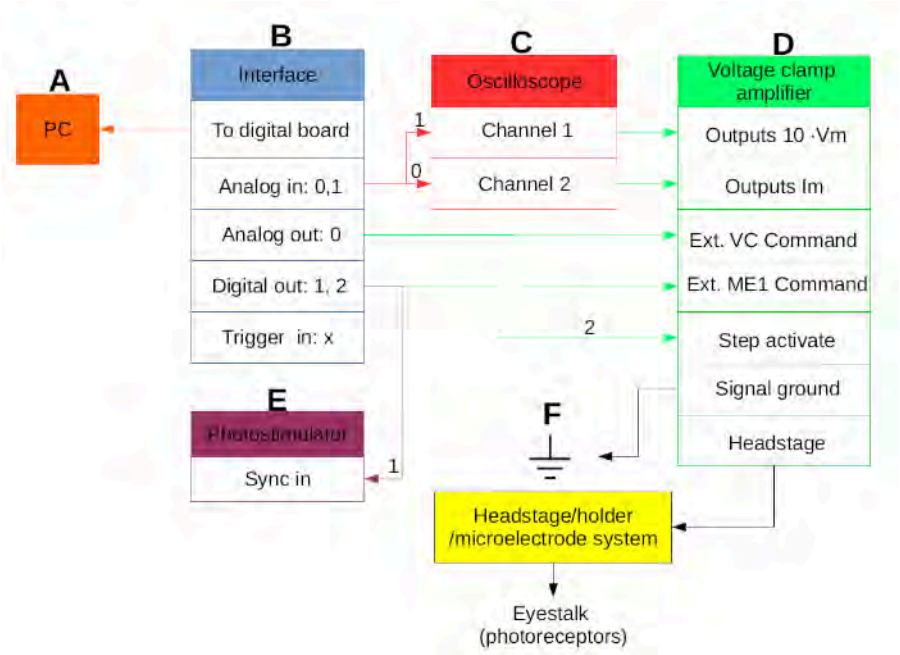

Figure 1. **Line diagram of the equipment setup**. Connections among personal computer (PC) (**A**), interface (**B**), oscilloscope (**C**), voltage-clamp amplifier (**D**), photostimulator (**E**), and the headstage/holder/microelectrode system of the equipment setup (**F**). Please click here to view a larger version of this figure.

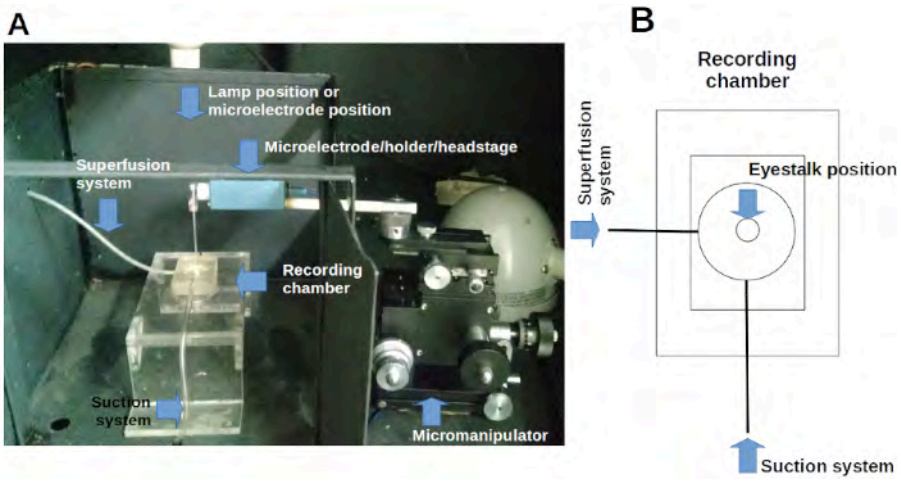

Figure 2. **Recording chamber.** (**A**) The recording chamber inside a Faraday cage with its superfusion-suction system. It is also shown the position of photostimulator, microscope, and micromanipulator-headstage-microelectrode system. (**B**) Diagram of the recording chamber. Please click here to view a larger version of this figure.

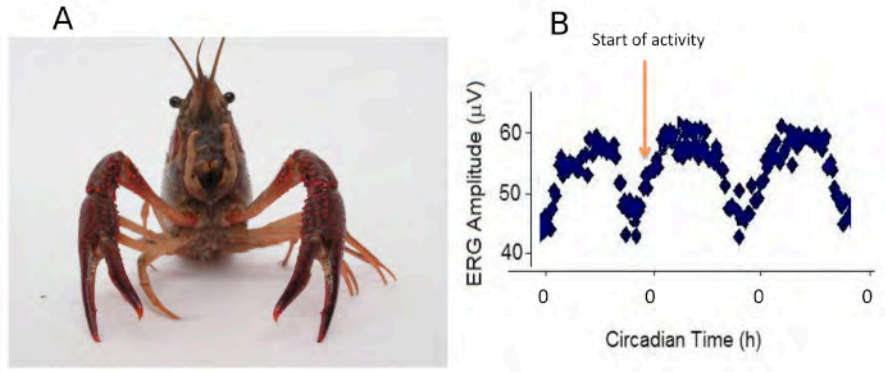

Figure 3. **Electroretinogram (ERG) amplitude.** (**A**) Crayfish. (**B**) Representative plot of the ERG amplitude of crayfish photoreceptors (data were taken every 20 min) as a function of circadian time. The existence of a circadian rhythm can be clearly appreciated. Note that for each cycle, the beginning of activity coincides with circadian time 0. Please click here to view a larger version of this figure.

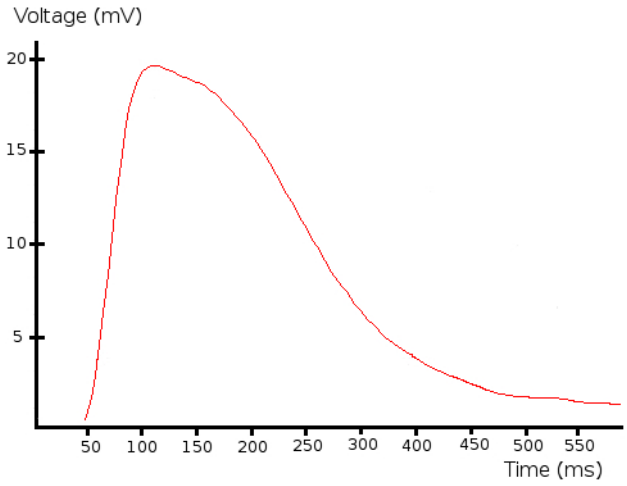

Figure 4. Receptor potential. Representative receptor potential evoked by a light flash (white light, 7.2 kW/m^2, 10 µs duration). This figure has been modified from Barriga-Montoya, C, *et al.*[2]. Please click here to view a larger version of this figure.

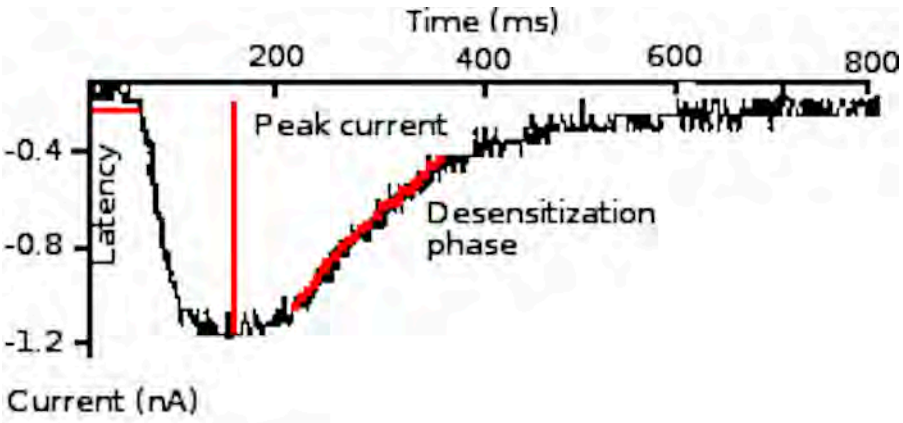

Figure 5. Transduction current. Representative transduction current triggered by a light flash (white light, 7.2 kW/m^2, 10 µs duration) applied with the voltage kept constant at the photoreceptor resting potential. Current latency, peak amplitude, and desensitization phase are indicated. This figure has been modified from Barriga-Montoya, C, *et al.*[2]. Please click here to view a larger version of this figure.

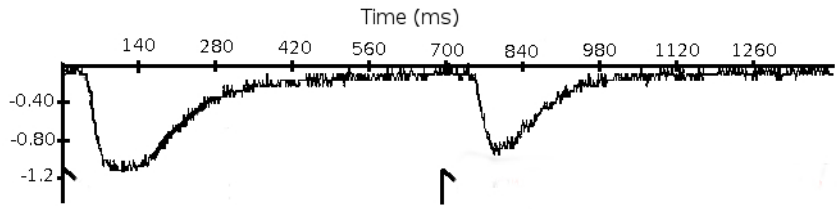

Figure 6. Two-pulse protocol. Currents elicited by a pair of light flashes. Light stimuli were applied at 0 ms and 700 ms (indicated by arrows). This figure has been modified from [2]. Please click here to view a larger version of this figure.

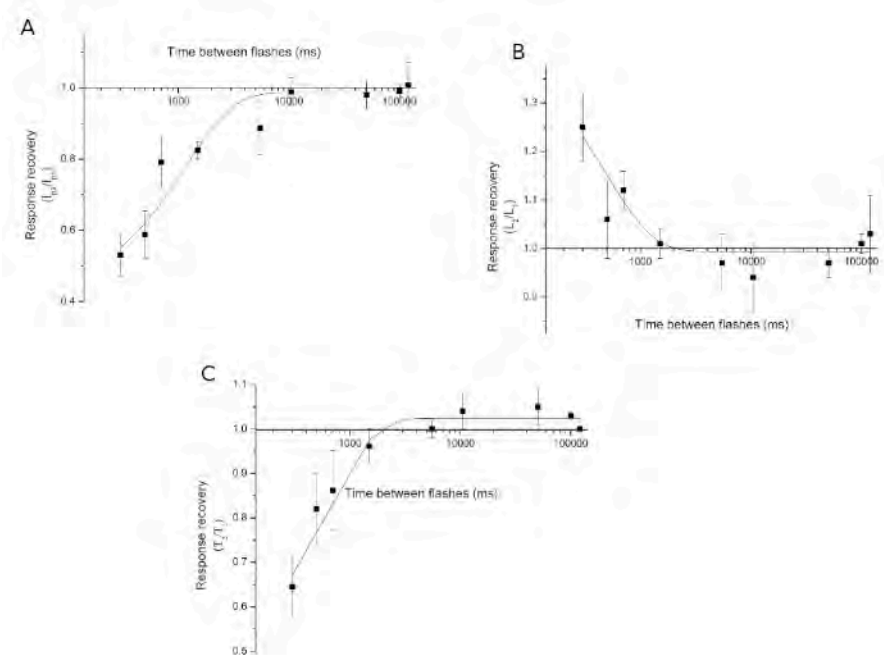

Figure 7. Recovery from desensitization. (**A**) I_p: peak current recovery, (**B**) L: latency recovery, (**C**) T: Desensitization time constant T recovery. Experiments were performed at 0 h CT. This figure has been modified from Barriga-Montoya, C, *et al.*[2]. Results are expressed as the mean ± standard deviation of the number of experiments (n = 11). Please click here to view a larger version of this figure.

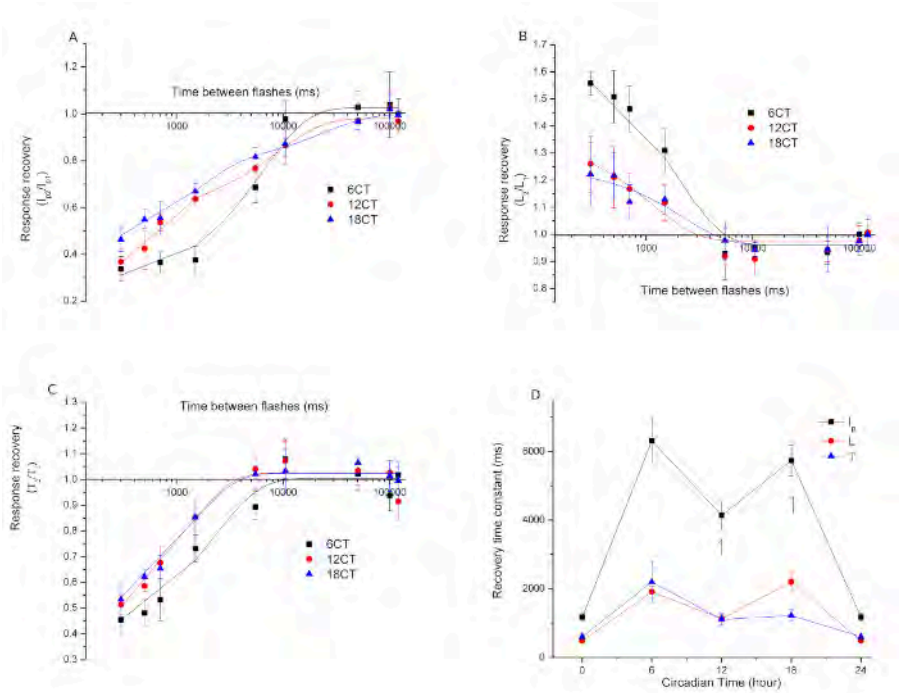

Figure 8. **Recovery from desensitization as a function of CT.** (**A**) I_p recovery, (**B**) L recovery, (**C**) T recovery. (**D**) Weighted time constants. Biphasic processes are marked with an arrow. This figure has been modified from Barriga-Montoya, C, *et al.*[2]. Results are expressed as the mean ± standard deviation of the number of experiments (n = 11). Please click here to view a larger version of this figure.

Discussion

The crayfish has proven to be an excellent model due to its ability to survive under non-natural conditions. There is easy access to *in vivo* and *in vitro* electrophysiological analyses. In addition, crustaceans are a favorable group for neurobiological research in the field of comparative chronobiology[21].

In this paper, the study of desensitization and recovery of the light-activated transduction-current of crayfish photoreceptor cells is shown using the intracellular recording technique. However, we believe that the same technique could be adapted to other invertebrate visual systems as long as it is possible to access photoreceptor cells.

To obtain acceptable experimental results, it is important to consider some critical steps in the protocol, including eliminating electrical noise by grounding all equipment, building an electrode with a sufficiently fine tip, and ensuring that the photoreceptor cell is completely dark-adapted before the two-pulse protocol begins.

Despite the limitations of intracellular recording such as the damage of membrane, it is possible to go further and obtain detailed information about the biophysical mechanism underlying crayfish (or another animal) photoreceptor electrical signal. As in other invertebrate photoreceptors, in crayfish photoreceptors, light triggers a graded depolarization, or receptor potential, produced by the activation of a cationic conductance. The light-activated conductance begins after a lag or latency, and after reaching its maximal amplitude, it slowly drops following an exponential time course, as the channels enter an absorbing desensitized state.

The kinetics of recovery from desensitization of the light-elicited ion conductance of crayfish were obtained using a two-light flash protocol (similar to the standard two-voltage pulse protocol used to study recovery from inactivation of voltage-gated channels)[20]. Interestingly, and in contrast to the well-known case of voltage-gated channels, not only the peak amplitude, but also all the current parameters (I_p, L, T) change after the first light stimulus, recovering with characteristic exponential time courses to the original, first flash values, as reported elsewhere[20]. This variation of all the parameters that characterize the current indicates the participation of second messengers in the visual transduction system of crayfish[1,2,22,23,24].

Additionally, and interestingly, as **Figure 8** shows, recovery of L, I_p, and T depends on the circadian time at which experiments are realized. Further studies are needed to determine the molecular basis of this phenomenon. Of course, it is possible to obtain similar information using another technique, such as patch clamp. However, the intracellular milieu can be greatly disturbed in other techniques, and this could be critical, if, for example, internal elements like proteins, amino acids, nucleotides, among many others, play a relevant role in the electrical signal generation or in the interaction with hormones or neuromodulators.

Disclosures

We have nothing to disclose.

Acknowledgments

This work was supported by DGAPA-UNAM IN224616-RN224616 grant. The authors want to thank Mrs. Josefina Bolado, Head of the Scientific Paper Translation Department, from División de Investigación at Facultad de Medicina, UNAM, for editing the English-language version of this manuscript.

References

1. Barriga-Montoya, C., Gómez-Lagunas, F., Fuentes-Pardo, B. Effect of pigment dispersing hormone on the electrical activity of crayfish visual photoreceptors during the 24-h cycle. *Comp. Biochem. Physiol. A Comp. Physiol*. **157** (4), 338-345, (2010).
2. Barriga-Montoya, C., de la O-Martínez, A., Fuentes-Pardo, B., Gómez-Lagunas, F. (2017). Desensitization and recovery of crayfish photoreceptors. Dependency on circadian time, and pigment-dispersing hormone. *Comp. Biochem. Physiol. A Comp. Physiol.* **203**, 297-303, (2017).
3. Wickenden, A. D. Overview of electrophysiological techniques. *Curr. protoc. pharmacol.* **11:11.1**, **11.1.1**-11.1.17, (2014).
4. Brette, R., Destexhe, A. Intracellular recording. *Handbook of Neural Activity Measurement.* 44-91, (2012).
5. Cummins, D., Goldsmith, T.H. Cellular identification of the violet receptor in the crayfish eye. *J. Comp. Physiol.* **142**(2), 199-202, (1981).
6. Eguchi, E. Rhabdom structure and receptor potentials in single crayfish retinular cells. *J. Cell and Comp. Physiol.* **66**, 411-430, (1965).
7. Nosaki, H. Electrophysiological study of color encoding in the compound eye of crayfish, Procambarus clarkii. *Z. vergl. Physiologie*. **64**(3), 318-323 (1969).
8. Miller, C. S., Glantz, R.M. Visual adaptation modulates a potassium conductance in retinular cells of the crayfish. *Vis Neurosci.* **17**(3), 353-368 (2000).
9. Hamill, O. P., Marty, A., Neher, E., Sakmann, B., Sigworth, F. J. Improved patch-clamp techniques for high-resolution current recording from cells and cell-free membrane patches. *Pflugers Arch.* **391**(2), 85-100, (1981).
10. Lishko, P., Clapham, D. E., Navarro, B., Kirichok, Y. Sperm patch-clamp. *Methods Enzymol.* **525**, 59-79, (2013).
11. Finkel, A. Axoclamp-2A microelectrode clamp theory and operation. *Axon Instruments, Inc.* (1990).
12. Sakmann, B. (Ed.). Single-channel recording. *Springer Science & Business Media.* (2013).
13. Van Harreveld, A. A physiological solution for freshwater crustacea. *Proc. Soc. Exp. Biol. Med*. **34** (4), 428-432, (1936).
14. Oesterle, A. P-97 pipette cookbook. *Sutter Instruments, Novato, CA*. (2008).
15. Fuentes-Pardo, B., Ramos-Carvajal, J. The phase response curve of electroretinographic circadian rhythm of crayfish. *Comp. Biochem. Physiol. A Comp. Physiol*. **74**(3), 711-714, (1983).
16. Pace-Schott, E.F., Hobson, J.A. The neurobiology of sleep: genetics, cellular physiology and subcortical networks. *Nat. Rev. Neurosci.* **3**(8), 591-605, (2002).
17. Pittendrigh, C.S., On the mechanism of the entrainment of a circadian rhythm by light cycles. In: Aschoff, J. (Ed.), *Circadian Clocks.* North Holland, Amsterdam, pp. 277-297 (1965).
18. Pittendrigh, C.S.,. Circadian systems: entrainment. In: Aschoff, J. (Ed.), *Handbook Behavioral Neurobiology Biological Rhythms.* **4**. Plenum, New York, pp. 94-124, (1981).
19. Vitaterna, M.H., Takahashi, J.S., Turek, F.W. Overview of circadian rhythms. *Alcohol Res. Health*. **25**(2), 85-93, (2001).
20. Hille, B. *Ion channels of excitable membranes.* (Vol. 507). Sunderland, MA: Sinauer, (2001).
21. Dircksen, H., Strauss, J. Circadian clocks in crustaceans: identified neuronal and cellular systems. *Front Biosci.* **15**, 1040-1074, (2010).
22. Terakita, A., Hariyama, T., Tsukahara, Y., Katsukura, Y., Tashiro, H. Interaction of GTP-binding protein G_q with photoactivated rhodopsin in the photoreceptor membranes of crayfish. *FEBS Lett.* **330**, 197-200, (1993).
23. Terakita, A., Takahama, H., Hariyama, T., Suzuki, T., Tsukahara, Y. Light regulated localization of the beta-subunit of G_q-type G-protein in the crayfish photoreceptors. *J Comp Physiol A*. **183**(4), 411-417, (1998).
24. Terakita, A., Takahama, H., Tamotsu, S., Suzuki, T., Hariyama, T., Tsukahara, Y. Light-modulated subcellular localization of the alpha-subunit of GTP-binding protein G_q in crayfish photoreceptors. *Vis Neurosci.* **13**(3), 539-547, (1996).

INFORME DE LABORES 2019

COMMUNICATIONS BIOLOGY

ARTICLE

https://doi.org/10.1038/s42003-019-0338-1 OPEN

Heterologous calcium-dependent inactivation of Orai1 by neighboring TRPV1 channels modulates cell migration and wound healing

Carlos Ernesto Bastián-Eugenio[1], Arlette Bohórquez-Hernández[1], Jonathan Pacheco[1], Alicia Sampieri[1], Alexander Asanov[2], Jose Pablo Ocelotl-Oviedo[3], Adán Guerrero[4], Alberto Darszon[3] & Luis Vaca[1]

Store-operated calcium entry (SOCE) is an essential calcium influx mechanism in animal cells. One of the most important auto regulatory control systems involves calcium-dependent inactivation (CDI) of the Orai channel, which prevents excessive calcium influx. In the present study we analyze the role of two channels in the induction of CDI on Orai1. Here we show that calcium entering through freely diffusing TRPV1 channels induce strong CDI on Orai1 while calcium entering through $P2X_4$ channel does not. TRPV1 can induce CDI on Orai1 because both channels were found in close proximity in the cell membrane. This was not observed with $P2X_4$ channels. To our knowledge, this is the first study demonstrating that calcium arising from different channels may contribute to the modulation of Orai1 through CDI in freely diffusing single channels of living cells. Our results highlight the role of TRPV1-mediated CDI on Orai1 in cell migration and wound healing.

[1] Departamento de Biología Celular y del Desarrollo, Instituto de Fisiología Celular, Universidad Nacional Autónoma de México, Mexico City 04510, Mexico. [2] TIRF Labs Inc., 106 Grendon Place, Cary 27519 NC, USA. [3] Departamento Genética del Desarrollo y Fisiología Molecular, Instituto de Biotecnología, Universidad Nacional Autónoma de México, Mexico City 62250, Mexico. [4] Laboratorio Nacional de Microscopía Avanzada, Universidad Nacional Autónoma de México, Mexico City 62250, Mexico. Correspondence and requests for materials should be addressed to L.V. (email: lvaca@ifc.unam.mx)

The calcium ion (Ca^{2+}) is a second messenger with a key role in numerous cellular processes[1]. Cells have developed many mechanisms to regulate this ion[2]. Store-operated calcium entry (SOCE) is the principal mechanism for calcium mobilization in non-excitable cells[3,4]. The prototypical store-operated calcium channel is the Ca^{2+} release-activated Ca^{2+} (CRAC) channel[5,6]. The essential components of CRAC are the endoplasmic reticulum (ER) Ca^{2+} sensor STIM1[7,8] and the plasma membrane (PM) channel Orai[9]. In general, activation of inositol 1,4,5-triphosphate (IP_3) receptors on the ER produces a rapid and transient release of Ca^{2+} from ER store. The resulting decrease of the Ca^{2+} concentration inside the ER is sensed by the EF-hand motif of STIM1, which then translocates to the PM, associating to Orai and inducing channel activation.

Orai activity is regulated through a negative feedback mechanism that maintains intracellular Ca^{2+} homeostasis and prevents excessive Ca^{2+} influx. Such a mechanism is known as Ca^{2+}-dependent inactivation (CDI).

CDI consists of slow CDI (SCDI) and fast CDI (FCDI), which have different kinetics and sites of action. SCDI occurs gradually in tens of seconds after channel activation and has been reported to occur by global increases in cytosolic calcium concentrations[10]. The most important regulator of SCDI is the SOCE-associated regulatory factor (SARAF)[11]. Moreover, SCDI can be regulated by other factor such as caveolin, E-syt1, septin4, and $PI(4,5)P_2$[12,13].

FCDI take place within ~10–100 ms after channel activation and is controlled by Ca^{2+} binding to a site located ~8 nm from the channel pore[14,15]. FCDI is modulated by various factors, including the STIM1-Orai1 expression ratio[16], an amino acid region negatively charged in STIM1 (residues 475–483)[17–19], the intracellular loop II–III of Orai1[20], the N-terminus of Orai1 (residues 68–91)[17,21], and also probably the first 63 amino acids from Orai1[22]. Most interestingly, a single amino acid mutation alters FCDI in Orai1 channels rendering the channel CDI insensitive[21].

To our knowledge, all the studies carried out to this date to understand and explore CDI have been conducted by artificially increasing intracellular Ca^{2+} via the patch clamp pipette or by measuring CDI with normal and reduced extracellular calcium concentrations, which reflects CDI induced by Ca^{2+} entering through the Orai channel pore (homologous CDI). Less studied are physiological sources of Ca^{2+}, such as the contribution of other channels to CDI in Orai.

In the present study, we have explored other sources of Ca^{2+} arising from different channels that may play a role in Orai's CDI. We have found that Ca^{2+} entering the cell through TRPV1 channels induce strong CDI in Orai1, while Ca^{2+} entering through $P2X_4$ purinergic channels does not. Super resolution studies indicate that Orai1 and TRPV1 are associated and move in close proximity to each other at the PM, while $P2X_4$ and Orai1 do not. These results were confirmed by co-immunoprecipitation (CoIP) and Förster resonance energy transfer (FRET) studies between Orai1-TRPV1 and Orai1-$P2X_4$.

All the results presented here strongly suggest that a close association between TRPV1 and Orai1 results in an elevated Ca^{2+} microenvironment near the Orai1 pore when TRPV1 channels are activated, which enhances CDI in Orai1. Because $P2X_4$ and Orai1 are not found in close proximity at the PM, Ca^{2+} entering $P2X_4$ channels do not induce CDI in Orai1, in spite the fact that Ca^{2+} entering through $P2X_4$ channels contribute to increments in cytosolic Ca^{2+} concentrations.

These results have important physiological implications in the modulation of calcium influx in cells where TRPV1 and Orai1 channels coexist, such as astrocytes. We show that TRPV1 is an important modulator of Orai1 channel activity in cortical astrocytes by controlling CDI in this channel and thus reducing the amount of Ca^{2+} entering to the cell when TRPV1 and Orai1 are simultaneously or sequentially activated. This heterologous modulation of CDI plays a role in controlling cell migration and wound healing mediated by astrocytes.

Results

Engineering of Orai1-GCaMP3 to characterize CDI. In an attempt to identify how Orai1 may sense changes of Ca^{2+} in its vicinity, we engineered a fusion protein consisting of the green genetically encoded calcium indicator (GCaMP3) fused to the amino terminus of Orai1 channel (Orai1-GCaMP3). We use the red calcium indicator (R-GECO) to simultaneously measure changes in global calcium in the cytosol and compare it to local calcium changes reported by the fusion protein Orai1-GCaMP3, which would presumably report only calcium changes near the channel pore from Orai1.

Firstly, we characterize Orai1-GCaMP3 to determine if the fusion protein behaves like a wild type Orai1 channel. Orai1-GCaMP3 is found primarily at the PM, similarly to Orai1 alone or Orai1-GFP used as controls (Fig. 1a). The expression of the fusion protein was identified also by western blot (Fig. 1b, for full-length blot see Supplementary Fig. 1). As expected, cells overexpressing Orai1-GCaMP3 or Orai1-GFP showed enhanced SOCE (Fig. 1c, d), indicating that the functionality of Orai1-GCaMP3 is indistinguishable from that of Orai1-GFP. This was clear when measuring the area under the curve (AUC) for calcium entry (Fig. 1d), but also with the peak increments in Fura-2 fluorescence from the same data (endogenous 0.43 ± 0.15, Orai1-GCaMP3 0.92 ± 0.18, and Orai1-GFP 0.99 ± 0.16, Fig. 1c).

Furthermore, Orai1-GCaMP3 forms regular puncta with STIM1 when internal calcium stores are depleted with thapsigargin (TG) (Fig. 1e–g). These results indicate that the function of Orai1 is unaltered by fusing the GCaMP3 calcium indicator.

We characterize further the calcium changes sensed by Orai1-GCaMP3 or by R-GECO present in the cytosol as a soluble protein. We proceeded to explore the ability of Orai1-GCaMP3 to sense calcium increments when other channels that permeate calcium are activated. We explored several channels and found that Orai1-GCaMP3 senses calcium arising from the activation of TRPV1 channel (Fig. 2a, b) but not from the $P2X_4$ purinergic receptor (Fig. 2c, d). Most interestingly, a PM targeted calcium sensor (Lck-GCaMP5)[23] detects calcium increments derived from the activation of both, TRPV1 and $P2X_4$ channels (Supplementary Fig. 2). These results suggest that, even though both fusion proteins (Orai1-GCaMP3 and Lck-GCaMP5) are located at the PM, they may be contained within different microdomains conferring them differential sensitivity to calcium increments arising from different sources.

We decided to characterize in greater detail the interactions between Orai1-TRPV1 and Orai1-$P2X_4$ in an attempt to identify the molecular mechanism responsible for the differential sensing of calcium by Orai1-GCaMP3 when TRPV1 or $P2X_4$ are activated.

If Orai1-GCaMP3 is sensing increments in calcium upon activation of TRPV1 but not $P2X_4$, then the calcium accumulating in the proximity from Orai1 should have an effect on Orai1 CDI. To explore this hypothesis, we developed a sequential activation patch clamp protocol to induce channel activity first on TRPV1 or $P2X_4$ followed by the activation of Orai1 with TG and measure whole-cell currents in the perforated patch clamp mode. Control experiments consisting of perfusion with extracellular solution (Methods) provided a basal Orai1 activity and a control for CDI (Fig. 3a, b).

Activation of TRPV1 with capsaicin (Cap) followed by the activation of Orai1 with TG resulted in strong CDI (Fig. 3b, c).

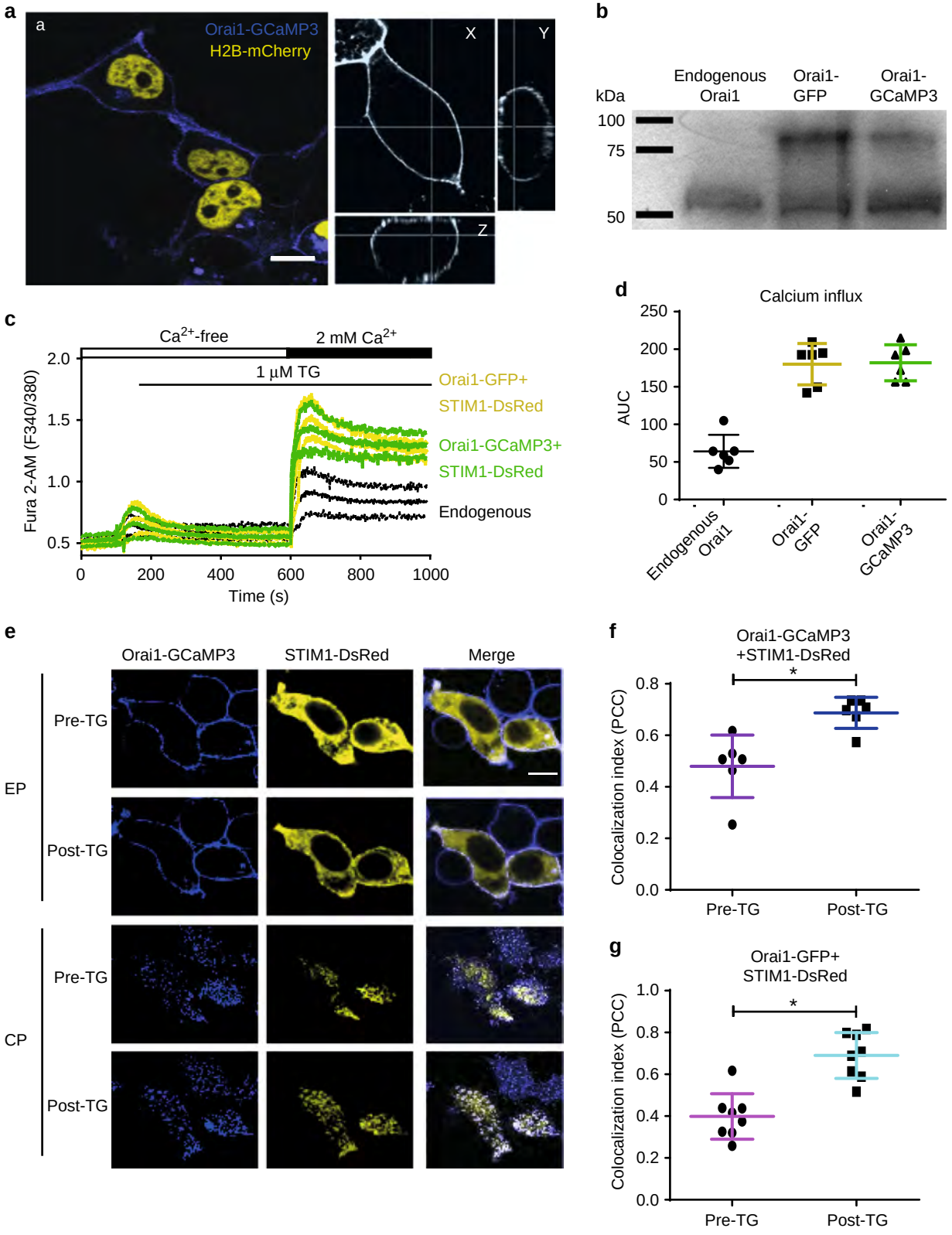

This phenomenon was not observed when we activated $P2X_4$ with cytidine triphosphate (CTP) followed by the activation of Orai1 with TG (Fig. 3d, e). To further demonstrate that the rapid decay in Orai1 current was the result of CDI, we conducted experiments with the Orai1 mutant insensitive to CDI (Orai1-Y80W)[21]. Activation of TRPV1 followed by activation of Orai1-Y80W with TG did not induce significant CDI (Fig. 3f, g). Furthermore, using strong calcium buffering with BAPTA inside the cell (BAPTA-AM) further confirmed that the rapid reduction in Orai1 current was the result of CDI (Fig. 3b, d). The CDI observed in Orai1 after TRPV1 activation was evident at all voltages explored (Fig. 3h).

Fig. 1 Developing and testing the Orai1-GCaMP3 sensor. **a** Representative confocal images of the fluorescence obtained with Orai1-GCaMP3 (blue) and histone 2B fused to mCherry as nuclear marker (yellow) expressed in HEK293 cells obtained from at least 3 independent transfections. Left panels show the 3D (*x*, *y*, and *z* axes) confocal projections from Orai1-GCaMP3 to illustrate its plasma membrane localization. Scale bar 5 μM. **b** Western blot analysis from HEK293 cells expressing the Orai1-GCaMP3 sensor and Orai1-GFP (representative blot from 3 independent blots). Notice the 55 kDa band corresponding to endogenous Orai1 and the 79 kDa band from Orai1-GFP and the Orai1-GCaMP3 sensor. **c** Cell population calcium measurements using a spectrofluorometer with HEK293 cells expressing Orai1-GFP + STIM1-DsRed (yellow) or Orai1-GCaMP3 + STIM1-DsRed (green) or measuring the endogenous SOCE (black). Measurements obtained from at least 5 independent transfections. Calcium increments induced by the application of thapsigargin (TG) in free extracellular calcium and SOCE measured after re-addition of 2 mM calcium to the extracellular solution. **d** Area under the curve (AUC) for fluorescence obtained after re-addition of 2 mM calcium (calcium influx) with endogenous Orai1 (gray), Orai1-GFP (yellow), and Orai1-GCaMP3 (green). **e** Representative confocal images of the puncta formation after TG application in cells expressing Orai1-GCaMP3 (blue) and STIM1-DsRed (yellow). Images shown before the application of thapsigargin (pre-TG) and after (post-TG) for the equatorial plane (middle) of the cell (EP) and the cortical plane (CP, the plane closest to the Petri dish bottom). Scale bar 5 μM. **f** Co-localization index (PC, Pearson's correlation coefficient) for Orai1-GCaMP3 + STIM1-DsRed before and after TG. **g** Co-localization index (PCC) for Orai1-GFP + STIM1-DsRed before and after TG. In all cases, data shows the mean ± standard deviation from at least 6 independent transfections. Asterisks show *p* values of < 0.01. The statistical significance was $p < 0.05$. Statistics was performed by Student's *t*-test

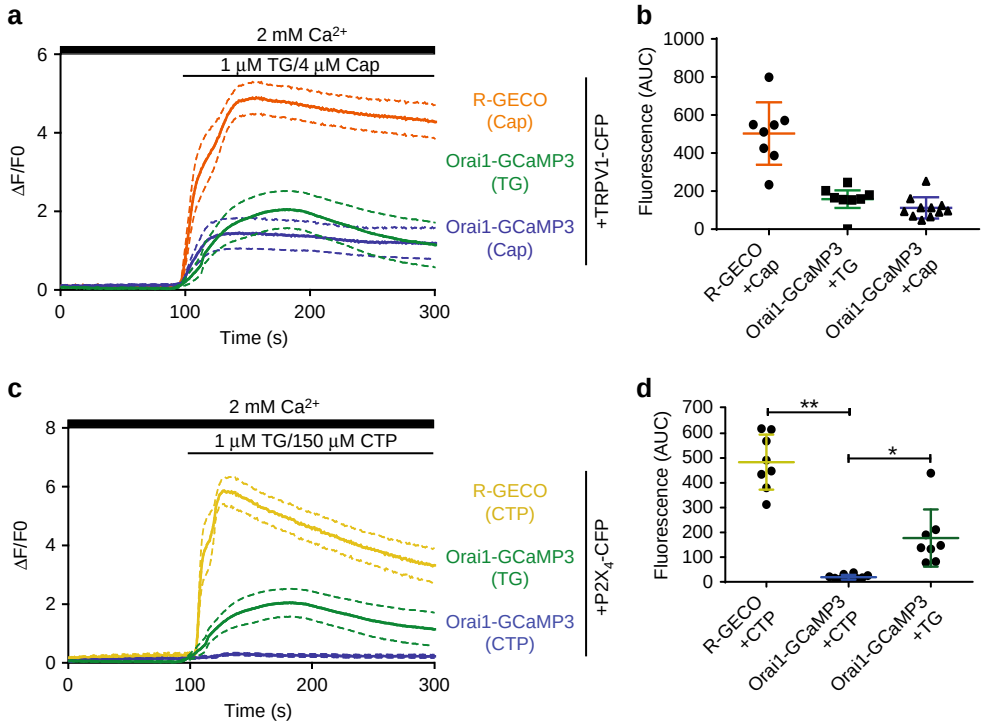

Fig. 2 Orai1-GCaMP3 senses local calcium increments through TRPV1 but not through $P2X_4$. **a** Calcium increments reported by R-GECO when the cells were exposed to capsaicin, Orai1-GCaMP3 with capsaicin and Orai1-GCaMP3 with thapsigargin (TG) from at least 12 independent transfections. **b** Area under the curve (AUC) for fluorescence of R-GECO with capsaicin (orange), Orai1-GCaMP3 with capsaicin (blue), and Orai1-GCaMP3 with TG (green). **c** Calcium increments reported by R-GECO when the cells were exposed to CTP, Orai1-GCaMP3 with CTP, and Orai1-GCaMP3 with thapsigargin (TG). **d** Area under the curve (AUC) for fluorescence of R-GECO with CTP (yellow, $n = 8$), Orai1-GCaMP3 with CTP (blue, $n = 10$), and Orai1-GCaMP3 with TG (green, $n = 8$). Notice that Orai1-GCaMP3 does not sense calcium increments with CTP while the R-GECO reports large calcium increments. In all cases, data shows the mean ± s.e.m. $^{**}p < 0.01$, $^{*}p < 0.05$. The statistical significance was $p < 0.05$. Statistics was performed by one-way ANOVA with Tukey's post hoc test

Orai1 is in close proximity to TRPV1 but not to $P2X_4$. If calcium entering TRPV1 is inducing strong CDI in Orai1 but not calcium entering through $P2X_4$, this result strongly suggests that TRPV1 and Orai1 must be in close proximity from each other. Indeed FRET analysis indicates that Orai1-YFP and TRPV1-CFP are within less than 10 nm from each other (Fig. 4a, c). FRET was not observed between Orai1-YFP and CFP-$P2X_4$ (Fig. 4b, c). These results were confirmed by CoIP studies with Orai1-TRPV1 and Orai1-$P2X_4$ (Fig. 4d, for full-length blots see Supplementary Fig. 3).

To explore at the single channel level how calcium entering TRPV1 is sensed by our Orai1-GCaMP3 fusion protein, we conducted super resolution studies. Super resolution imaging showed individual Orai1, TRPV1, and $P2X_4$ channels freely diffusing at the PM of living cells (Fig. 5a and Supplementary Movies 1 and 2). Measuring the distance between Orai1-TRPV1 and Orai1-$P2X_4$ confirmed the results obtained by FRET and CoIP. The distance between individual Orai1 and TRPV1 channels was significantly smaller than that between Orai1-$P2X_4$ (Fig. 5b). Average distances over time obtained from hundreds of single channels showed at least a 4-fold greater distance between Orai1 and $P2X_4$ compared to Orai1 and TRPV1 (Fig. 5c). Furthermore, super resolution imaging of fluorescence increments using Orai1-GCaMP3 single channels showed that

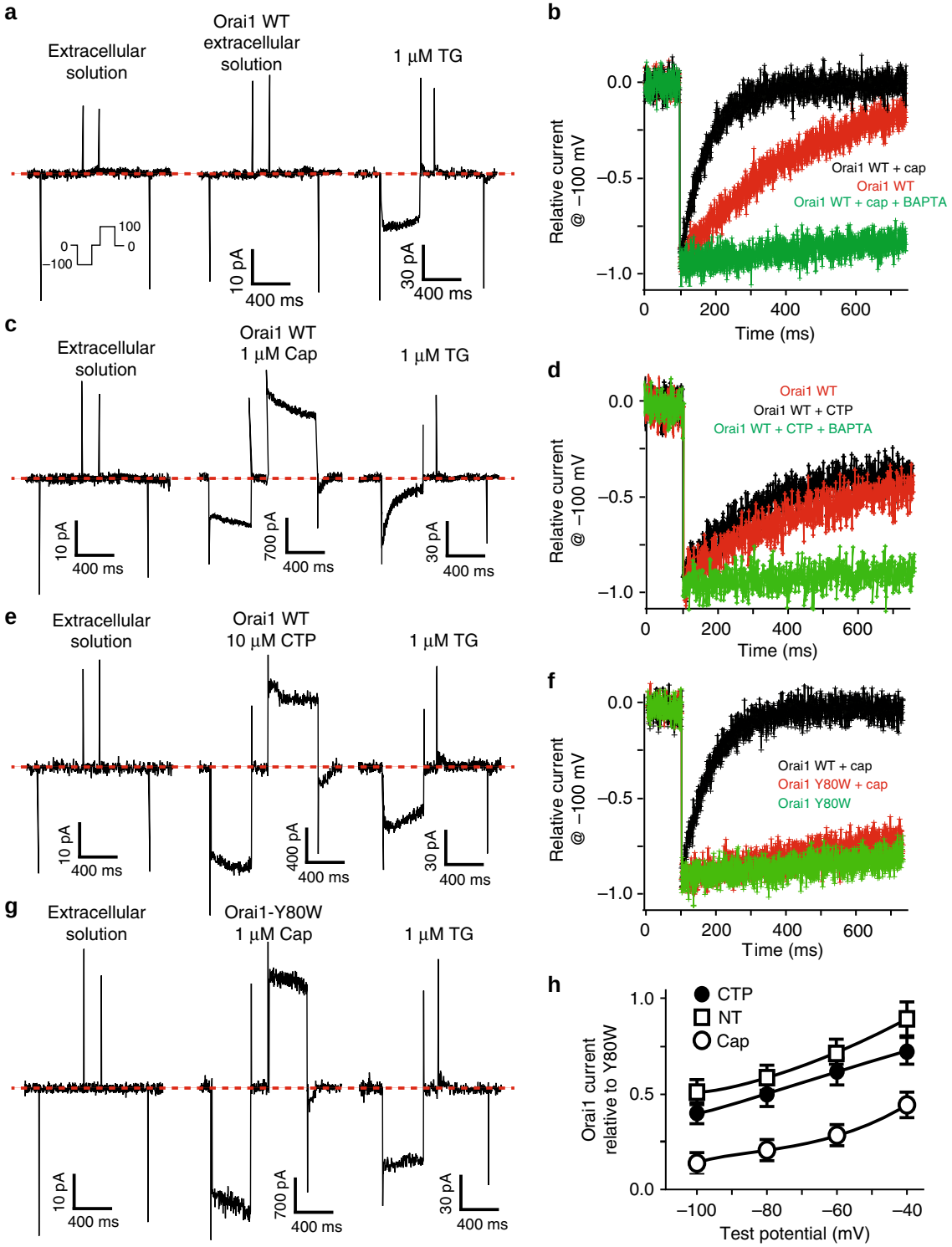

this fusion protein could sense calcium increments arising from TRPV1 but not $P2X_4$ channels (Fig. 5d, e and Supplementary Movies 1 and 2). These differences in sensing calcium from TRPV1 or $P2X_4$ were evident also when measuring the average change in fluorescence from hundreds of single Orai1-GCaMP3 channels (Fig. 5f, g).

ANK1 of TRPV1 is essential for the association to Orai1 C terminus. To identify the molecular structures responsible for the association between Orai1 and TRPV1 channels, we conducted a wide screening using peptide microarrays with a platform we have previously developed and tested[24] (data available here[25]). Previous studies have highlighted the role of the ankyrin domains from TRPV1 in the association to regulatory proteins and scaffolds[26]. To evaluate the role of each of the 6 ankyrin domains from TRPV1 we produced fusion proteins of each domain to the green fluorescent protein (GFP) and conducted CoIP studies using Orai1 as bait. CoIP analysis indicated that the first 3 ankyrin domains associate to Orai1, although the first ankyrin domain (ANK1) showed to strongest interaction (Fig. 6a, for full-length blots see Supplementary Fig. 4). To explore further to what sequence from Orai1 was the ANK1 associating, we produced

Fig. 3 Activation of TRPV1 induces strong CDI in Orai1. **a** Perforated patch measurements in HEK293 cells expressing Orai1-GFP and STIM-DsRed. The sequential protocol consisted in the application of extracellular solution followed by a second control application of extracellular solution (ES) and finally thapsigargin. The second ES application will be replaced by either capsaicin or cytidine triphosphate (CTP) in the following experiments. In all cases, capsaicin or CTP were incubated for 3 min and then the cells were washed with fresh ES for 1–2 min prior to TG stimulation (TG was present for the remaining duration of the experiment). **b** Relative current illustrating the activation by applying a voltage step from 0 to −100 mV for cells expressing Orai1 and TRPV1 pre-stimulated with capsaicin (cap, black), Orai1 only with thapsigargin (red), and Orai1 and TRPV1 pre-stimulated with capsaicin in cells incubated with BAPTA-AM (green). **c** Perforated patch measurements using the sequential protocol pre-simulating with capsaicin in cells expressing Orai1-GFP and TRPV1-CFP. The middle panel shows the currents elicited by capsaicin stimulation (TRPV1). Panel to the right shows the subsequent activation of Orai1 with TG. **d** Relative current illustrating the activation of current by applying a voltage step from 0 to −100 mV for cells expressing Orai1 and activated by TG (red), cells expressing Orai1 and $P2X_4$ and pre-stimulated with CTP (black) and cells expressing Orai1 and $P2X_4$ and pre-stimulated with CTP and previously incubated with BAPTA-AM (green). Lines show mean ± standard deviation from at least 31 cells. **e** Perforated patch measurements using the sequential protocol in a cell expressing Orai1 and $P2X_4$. **f** Relative current illustrating the activation for cells expressing Orai1 wild type (WT) with pre-stimulation with capsaicin (black) and cells expressing the CDI-resistant mutant Orai1 Y80W with (red) or without pre-stimulation (green). **g** Perforated patch measurements using the sequential protocol in cells expressing Orai1 Y80W and TRPV1. **h** Orai1 currents relative to mutant Orai1 Y80W at different voltages. Cells pre-stimulated with CTP (black circle), with capsaicin (open circle) or cells not exposed to capsaicin, only TG (NT). All experiments show the mean ± standard deviation from at least 20 cells

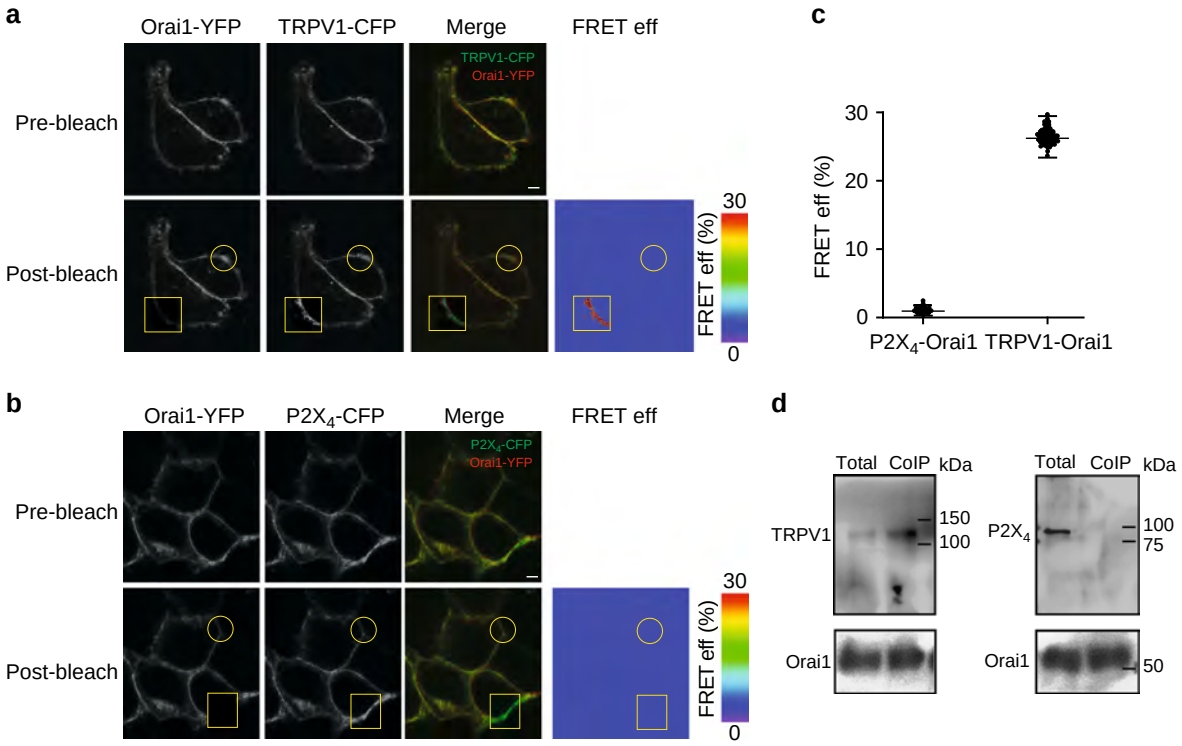

Fig. 4 TRPV1 is in close proximity to Orai1. **a** Representative confocal images illustrating the expression of Orai1-YFP and TRPV1-CFP before (pre-bleach) or after (post-bleach) photobleaching of the acceptor (YFP). The square shows the area photobleached and the circle a control area not exposed to the photobleach procedure. We used both areas to calculate the FRET efficiency as indicated in Methods. Right panel shows the FRET efficiency (FRET eff) in pseudo color calculated from the acceptor photobleaching protocol (Methods). Scale bar 1 μM. **b** Representative confocal images illustrating the expression of Orai1-YFP and $P2X_4$-CFP before (pre-bleach) or after (post-bleach) photobleaching of YFP. The square shows the area photobleached and the circle a control area not exposed to the photobleach procedure. FRET efficiency (FRET eff) in pseudo color calculated from the acceptor photobleaching protocol (Methods). Scale bar 1 μM. **c** FRET eff (%) obtained from at least 45 cells for $P2X_4$-Orai1 and TRPV1-Orai1. Data show the mean ± standard deviation. **d** Co-immunoprecipitation analysis of cells expressing c-Myc-Orai1 and TRPV1-YFP or $P2X_4$-CFP (for the entire blots check Supplementary Figures). Total indicates the protein that was not retained in the affinity column, thus reflects the protein that did not co-immunoprecipitate (Methods). Blots are representative examples from at least 3 independent blots

fusion proteins between the amino terminus from Orai1 and GFP (Orai1-NH2-GFP) and the carboxyl terminus from Orai1 (Orai1-COOH-GFP). Peptide microarray studies showed that the strongest interaction was between ANK1 and COOH-GFP (Fig. 6b). COOH-GFP interacts with the first 3 ankyrin domains from TRPV1, but the strongest interaction is with ANK1 (Fig. 6c). To ensure that the amount of Orai1-COOH deposited on each microarray spot was not affecting the binding of the different ankyrin domains, we produced a fusion protein of the carboxyl terminus from Orai1 fused to the red fluorescent protein (Orai1-COOH-DsRed). In this way, we can determine how much of the Orai1-COOH-DsRed was deposited on each microarray spot (using the red fluorescence channel) and the binding from the 6-ankyrin domains fused to GFP (using the green fluorescence channel), simultaneously (Methods). Below the strips of the microarray from the 6 ankyrin domains are illustrated examples

INFORME DE LABORES 2019

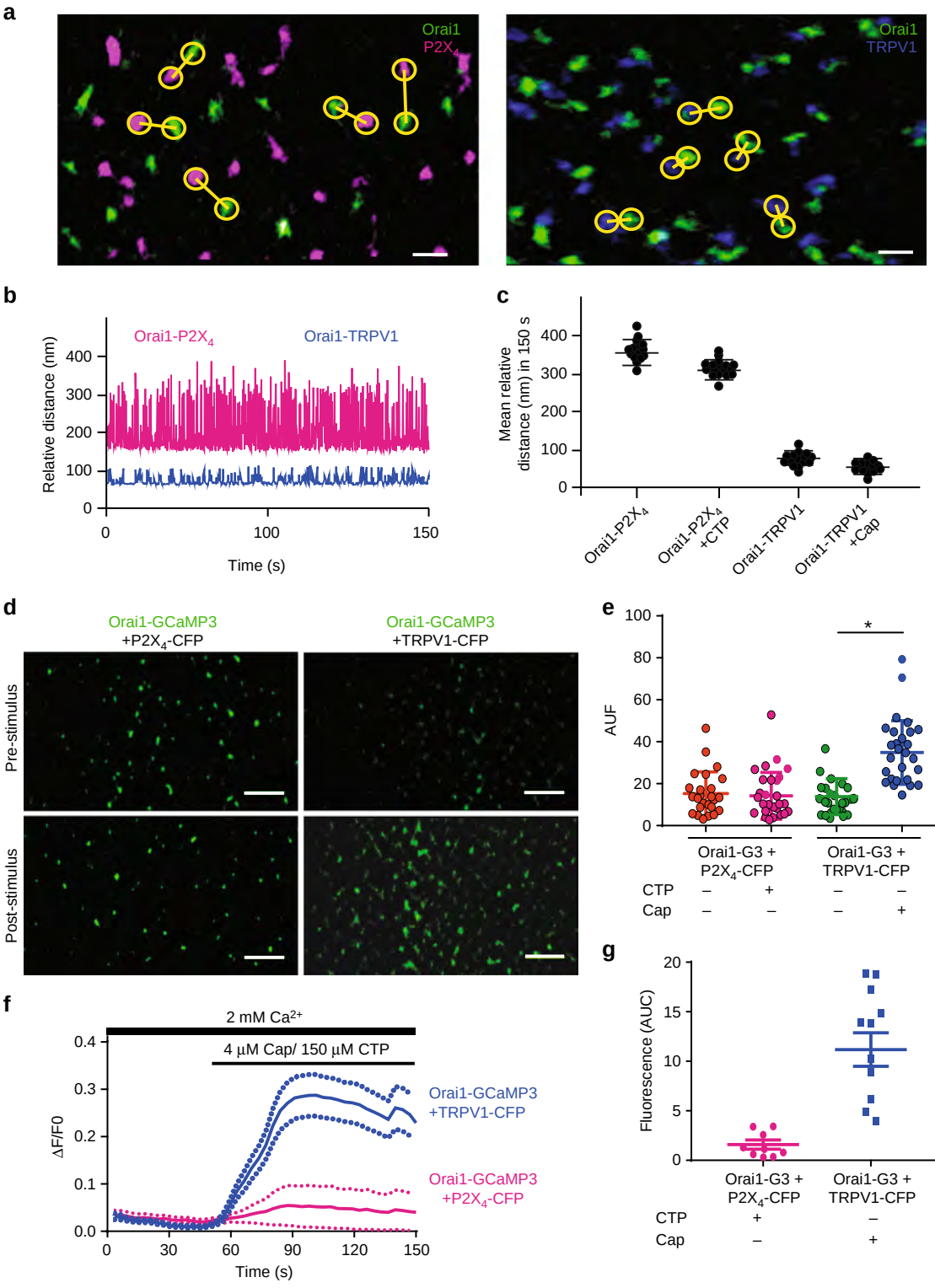

of the Orai1-COOH-DsRed deposited on the microarray coverslip for each condition (Fig. 6c, lower panels labeled Orai1-COOH-DsRed)[25].

To explore the role of the first 3 ankyrin domains in the entire TRPV1 protein, we produced individual deletions of these 3 ankyrin domains. Unfortunately, only the deletion of the first ankyrin domain produced channels that reached the PM, deleting beyond this first ankyrin domain resulted in channels that were retained in intracellular compartments. This finding was previously reported, showing that only the first amino acids from the amino terminus of TRPV1 can be deleted without affecting channel localization and function[26]. In particular, the ankyrin domain 3 plays a key role in channel tetramerization[27]. Nevertheless, we could explore the role of the first ankyrin domain on CDI using the deletion mutant TRPV1-ΔANK1, which is lacking the first ankyrin domain (Methods).

Fig. 5 Super resolution studies reveal that TRPV1 and Orai1 move in close proximity in the plasma membrane. **a** Super resolution single channel TIRFM images from cells expressing Orai1 (green) and $P2X_4$ (magenta) in the left panel or Orai1 (green) and TRPV1 (blue, right panel). Yellow circles show measurements between the nearest two channels for Orai1-$P2X_4$ (left panel) or Orai1-TRPV1 (right panel). Scale bar 60 nm. **b** Relative distance over time for a single pair of channels measured in cells expressing Orai1-$P2X_4$ (magenta) and Orai1-TRPV1 (blue). **c** Mean relative distance obtained from several hundred channels in cells expressing Orai1-$P2X_4$ (magenta) with or without CTP and Orai1-TRPV1 (blue) with or without capsaicin. Notice that agonist stimulation (CTP or capsaicin) did not alter mean distances. **d** Super resolution single channel TIRFM images from cells expressing Orai1-GCaMP3 (green) + $P2X_4$-CFP (left panels) or TRPV1-CFP (right panels) before and after stimulation with CTP or capsaicin. Notice the increment in the fluorescence of single Orai1-GCaMP3 channels after capsaicin stimulation but not with CTP. Scale bar 200 nm. **e** Fluorescence intensity in arbitrary units (AUF) reported by the Orai1-GCaMP3 sensor under the different stimulations. Notice that only cells expressing TRPV1 (T1-CFP) exposed to capsaicin produced an increment in fluorescence (blue bar). Capsaicin stimulation in cells without TRPV1 (orange and magenta bar) or cells expressing TRPV1-CFP but not exposed to capsaicin (green bar) did not result in changes in the fluorescence of Orai1-GCaMP3. **f** Fluorescence measurements of the entire field of view (containing dozens of individual channels) over time with cells expressing the Orai1-GCaMP3 sensor and TRPV1 with capsaicin (blue line) or cells expressing $P2X_4$ and stimulated with CTP (magenta line). Lines show the mean ± standard deviations (dotted lines). Fluorescence from Orai1-GCaMP3 sensor increases only after capsaicin stimulation in cells expressing TRPV1. **g** Area under the curve (AUC) for the different conditions shown in panel **f**. Notice that only the fluorescence is observed in cells expressing the Orai1-GCaMP3 sensor + the TRPV1 channel and stimulated with capsaicin (green bar). $^*p < 0.01$. The statistical significance was $p < 0.05$. Statistics was performed by Student's *t*-test

Super resolution imaging analysis showed that the relative distance between TRPV1-ΔANK1 and Orai1 was greater than that between TRPV1 wild type (TRPV1-WT) and Orai1 (Fig. 6d–f). Most interestingly, Orai1-GCaMP3 partially sense changes in calcium when TRPV1-ΔANK1 was activated with capsaicin compared to TRPV1-WT (Fig. 6g). Activation of TRPV1-WT and TRPV1-ΔANK1 with capsaicin results in robust increments in intracellular calcium reported by R-GECO produced as a soluble protein in the cytosol (Supplementary Fig. 5), discarding the possibility that the reduced sensing of calcium entering via TRPV1-ΔANK1 by Orai1-GCaMP3 may be the result of reduced calcium influx by the TRPV1-ΔANK1 deletion mutant. Furthermore, TRPV1-ΔANK1 does not co-immunoprecipitate with Orai1 (Supplementary Fig. 5).

Activation of TRPV1-ΔANK1 using our sequential activation patch clamp protocol showed only reduced CDI in Orai1 while TRPV1-WT produced strong CDI as previously shown (Fig. 3 and Supplementary Fig. 6). To discard any nonspecific effects of capsaicin on ionic currents, we conducted additional controls using the synthetic antagonist of capsaicin, capsazepine (Supplementary Fig. 5). Capsazepine stimulation had no effect on Orai1 CDI. Furthermore, the activation of TRPV1 with capsaicin in cells incubated with BAPTA-AM showed no effect on Orai1 CDI, strongly supporting the hypothesis that the CDI observed on Orai1 is the result of increments in intracellular calcium mediated by TRPV1 (Supplementary Fig. 5).

These results highlight the role of the first ankyrin domain in the association of TRPV1 to the carboxyl terminus from Orai1. This molecular interaction supports the formation of a complex between Orai1 and TRPV1, bringing the two channels in close proximity. This association between both channels favors the generation of a calcium microenvironment near the Orai1 channel pore when TRPV1 is activated, which modulates CDI on Orai1. The strong CDI observed in Orai1 channels induced by the activation of TRPV1 remains even after TRPV1 is not active anymore (Fig. 3c). These results suggest that calcium entering TRPV1 triggers the initial steps of CDI on Orai1 channels, but a sustained mechanism maintains CDI even when the influx of calcium through TRPV1 has been stopped (by washing out capsaicin). The sustain CDI can be explained by the fact that FCDI is modulated by Orai1-STIM1 interactions and not only high calcium near the Orai1 pore. Such Orai1-STIM1 interactions are mediated by the STIM1-Orai1 expression ratio[16] an amino acid region negatively charged in STIM1 (residues 475–483)[17–21] from Orai1[22].

CDI may prevent excessive calcium entry into the cell when both channels (TRPV1 and Orai1) are activated simultaneously or sequentially.

To facilitate the study of the interactions between TRPV1 and Orai1 and the identification of the amino acid domains involved in this association, we conducted all the experiments described to this point in HEK293 cells. However, in order to assess the effect of TRPV1-induced CDI on Orai1 channels in a physiological model, we implemented a scratch-wound assay (SWA) using primary cultures of cortical astrocytes. We have previously shown that the majority of thrombin-activated calcium influx in cortical astrocytes is carried by Orai1 channels[28]. Cortical astrocytes express TRPV1 channels[29]. Furthermore, thrombin plays a key role in astrocyte migration and wound healing[30–32].

First, we validated that our Orai1-GCaMP3 sensor behaved in astrocytes similarly to what we have observed in HEK293 cells. Indeed, primary cultures of cortical astrocytes expressing our Orai1-GCaMP3 calcium sensor responded to capsaicin stimulation but not to the activation of $P2X_4$ purinergic receptors with CTP (Fig. 7a). Nevertheless, astrocytes respond normally to CTP with a robust increment in intracellular calcium measured with the soluble calcium sensor R-GECO (Fig. 7a). Orai1-GCaMP3 senses also calcium increments induced with TG (Fig. 7a). All these results recapitulate what we observed with HEK293 cells expressing our Orai1-GCaMP3 construct (Fig. 2).

Capsaicin induces CDI on endogenous Orai1 currents from cortical astrocytes but not CTP stimulation (Fig. 7b). Furthermore, expression of the first ankyrin domain in astrocytes (ANK1-GFP) reduces the amount of CDI obtained with capsaicin pre-stimulation in our sequential perforated patch clamp protocol (Fig. 7c, d). Endogenous TRPV1 immunoprecipitate with endogenous Orai1 in cortical astrocytes (Supplementary Fig. 7), similarly to what we observed with the overexpression of these channels in HEK293 cells (Fig. 4d).

Using the SWA model, we have found that endogenous Orai1 participates in thrombin-induced cell migration and wound healing with cortical astrocytes, since transfection with a selective siRNA for Orai1[28] prevents the effects of thrombin on wound healing (Supplementary Fig. 7).

Capsaicin stimulation previous to activation of Orai1 with thrombin significantly reduces wound healing (Fig. 7e, f), this effect is not observed with the synthetic antagonist of capsaicin, capsazepine (Supplementary Fig. 7). Expressing the ANK1-GFP domain in cortical astrocytes prevents the effect of capsaicin on thrombin-induced wound healing (Fig. 7e, f).

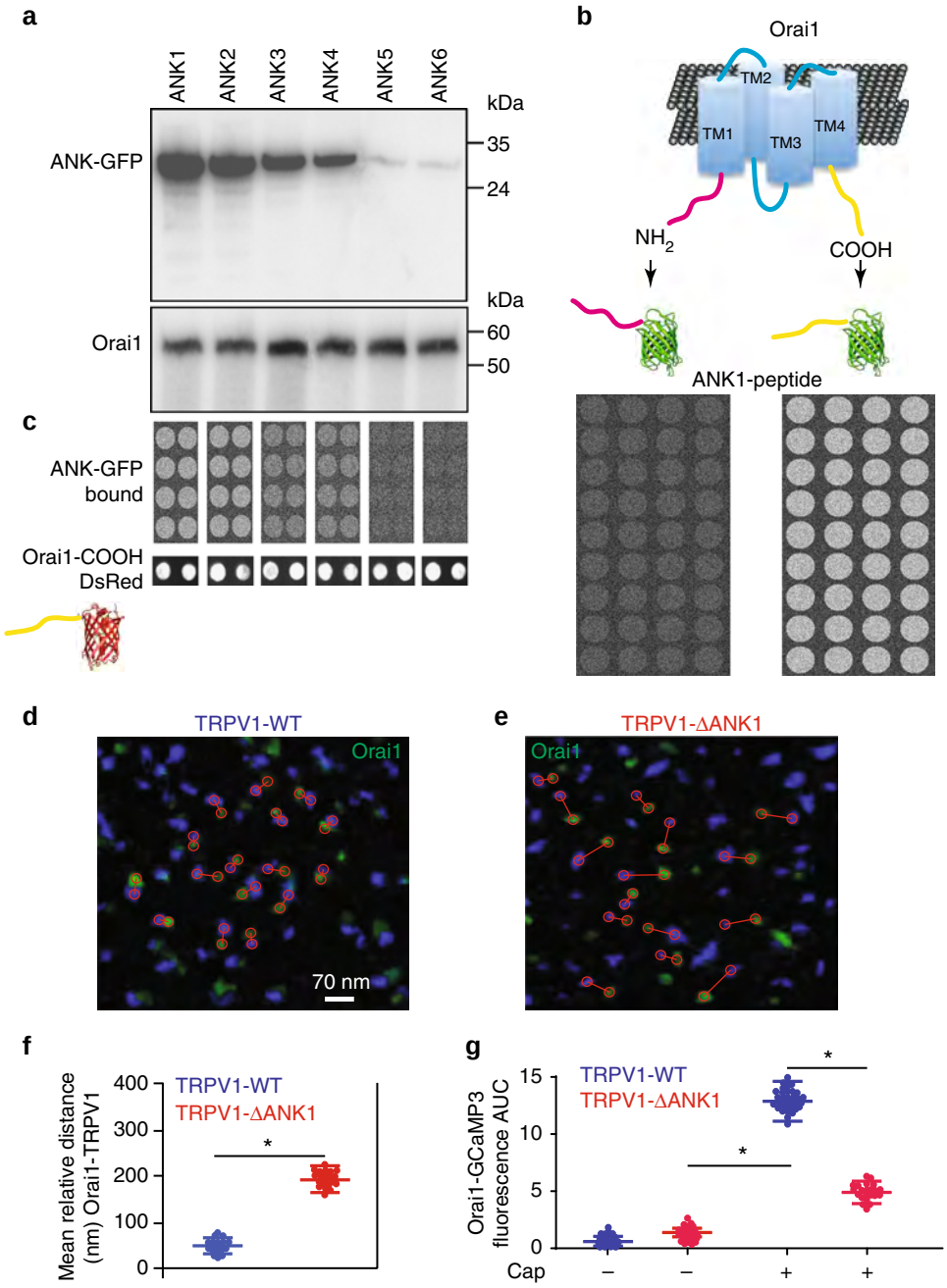

Fig. 6 The first ankyrin domain from TRPV1 associates to the carboxyl domain from Orai1 to favor TRPV1-Orai1 association. **a** Co-immunoprecipitation analysis of cells expressing c-Myc-Orai1 and the 6 ankyrin domains fused to GFP (ANK1-ANK6). **b** Cartoon showing the fusion of the amino or the carboxyl terminus from Orai1 to GFP. Lower panels show the results of the peptide microarrays using ANK1 as bait. Notice that only COOH-GFP is captured by ANK1 but not NH2-GFP. **c** Peptide microarrays using the 6 ankyrin domains individually fused to GFP. In this case Orai1-COOH is used as bait (printed on the glass coverslip). Notice that Orai1-COOH retained ANK1-GFP, ANK2-GFP and less efficiently ANK3 and ANK4 but not ANK5 and ANK6. **d** Super resolution TIRFM images of cells expressing TRPV1 wild type (TRPV1-WT, blue) and Orai1 (green) or cells expressing TRPV1-ΔANK1 (right panel, **e**). Red circles show the distance between the closest pair of channels and the lines connect the pair. **f** Mean relative distance obtained from hundreds of individual channels for Orai1 with TRPV1-WT (blue) or TRPV1-ΔANK1 (red). Data shows the mean ± standard deviation. **g** Fluorescence increments reported by the Orai1-GCaMP3 sensor with and without capsaicin stimulation. Notice that the Orai1-GCaMP3 increases about half the fluorescence after capsaicin in cells expressing TRPV1-ΔANK1 (red bar) compared to the cells stimulated with capsaicin and expressing TRPV1-WT (green). This indicates that deletion of the first ANK domain results in Orai1 moving apart from TRPV1 and the Orai1-GCaMP3 sensor reporting less of the calcium that enters through the TRPV1 channel. $^{*}p < 0.01$. The statistical significance was $p < 0.05$. Statistics was performed by one-way ANOVA with Tukey's post hoc test

All these results strongly suggest that the activation of endogenous TRPV1 channels in cortical astrocytes modulate the activity of endogenous Orai1 channels by inducing CDI and reducing calcium entry through Orai1 channels. Enhanced CDI reduces thrombin-induced cell migration and wound healing. The results presented here provide the first evidence, to our knowledge, of the role of Orai1 in thrombin-activated cell migration and wound healing, while highlighting the role of CDI on Orai1 activity during this physiological process.

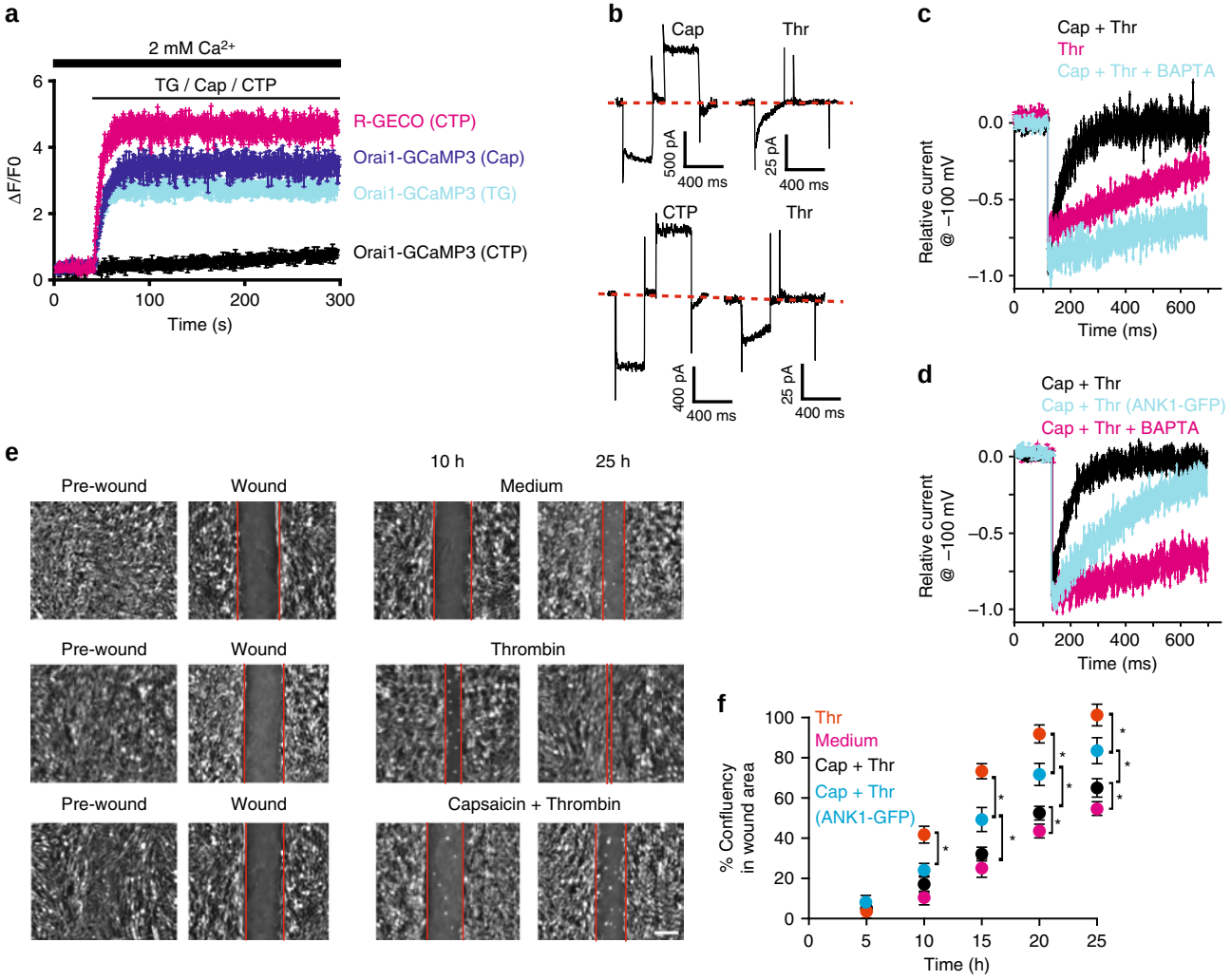

Fig. 7 TRPV1 induced CDI on Orai1 modulates wound healing. **a** Cell population calcium measurements obtained with cortical astrocytes primary cultures transfected with Orai1-GCaMP3. Endogenous TRPV1 and $P2X_4$ were used. Orai1-GCaMP3 senses calcium increments evoked with capsaicin (500 nM, blue) and TG (1 μM, cyan) but not with CTP (black). CTP induces robust calcium increments as reported by R-GECO (magenta). Data shows the mean ± standard deviation from at least 10 independent measurements obtained from 5 different cultures. **b** Stimulation with capsaicin (500 nM) prior to activation of Orai1 with thrombin induces strong CDI. CTP stimulation induces large $P2X_4$ currents, however not CDI in Orai1 (activated by thrombin). **c** Perforated patch measurements of currents evoked by a voltage step from 0 to −100 mV in response to capsaicin followed by thrombin (black lines), thrombin alone (magenta) and capsaicin + thrombin in cells incubated with BAPTA-AM (cyan). BAPTA incubation strongly reduces CDI in cells stimulated with capsaicin and thrombin. Capsaicin incubated for 3 min and then the cells were washed with fresh PBS for 3 min prior to thrombin stimulation. **d** Perforated patch measurements of currents evoked by a voltage step from 0 to −100 mV in response to capsaicin + thrombin in cells expressing TRPV1 (black) and cells expressing also the ANK1-GFP domain (cyan) and cells incubated with BAPTA-AM (magenta). **e** Scratch-wound assay in cortical astrocytes. Representative photographs of the cell culture around the wound area are shown for 10 and 25 h after wound. Medium shows the cells that were maintained in DMEM. Thrombin indicates cells treated with thrombin (5 U mL^{-1} thrombin) for 3 min[42]. Cell cultures were exposed to capsaicin (500 nM) for 3 min and then incubated with thrombin (5 U mL^{-1} thrombin) for 3 min. **f** Percentage of confluency in wound area under the different treatments shown in **e**. Cells were also transfected with a construct carrying ANK1-GFP (blue). Data points show the mean ± standard deviation from at least 5 cell culture dishes for each condition. *$p < 0.01$. The statistical significance was $p < 0.05$ according to ANOVA

Discussion

The present study identifies the molecular determinants of the association between TRPV1 and Orai1 channels, which favor heterologous CDI of Orai1 by calcium entering through single TRPV1 channels. Using super resolution studies on living cells, we observed that both channels move associated at the PM. This physical interaction results in relevant physiological modulation of channel activity (TRPV1 contributes to CDI on Orai1). This was not observed for another channel that does not associate to Orai1, the purinergic $P2X_4$ receptor, even though activation of this receptor/channel results in robust increments in cytosolic calcium as reported by our cytosolic soluble sensor, R-GECO.

CDI is a regulatory process that prevents excessive calcium influx via Orai channels, which may have deleterious or toxic effects in the cell. Up until now, this phenomenon has been studied using electrophysiological whole-cell current measurements evoked by Orai channels. To induce CDI under these conditions, the extracellular and/or intracellular calcium concentrations have been artificially controlled. To our knowledge, this is the first report showing that a physiological source of calcium (e.g., activation of TRPV1) can induce CDI on Orai1 both in an heterologous expression system (HEK293 cells) and in cell that naturally express both channels (cortical astrocytes). We have shown that the induction of CDI is the result of the close

proximity between Orai1 and TRPV1 at the PM, since the activation of a different channel ($P2X_4$) did not induce CDI on Orai1. Furthermore, super resolution studies show that both channels (TRPV1 and Orai1) move in close proximity to each other. This was not observed for $P2X_4$ and Orai1. The use of our local calcium reporter Orai1-GCaMP3 in super resolution studies shows that Orai1 single channels detect increments in calcium mediated by the activation of TRPV1 while freely diffusing at the PM. However, our Orai1-GCaMP3 sensor does not detect increments in calcium mediated after the activation of $P2X_4$. These results obtained with super resolution studies indicate that Orai1 and TRPV1 are moving in close proximity to each other, maintaining a microenvironment where calcium entering via TRPV1 accumulates and induces CDI in Orai1.

Super resolution analysis showed at least a 4-fold greater distance between $P2X_4$ and Orai1, when compared to the distance between TRPV1 and Orai1 (Fig. 5). The average distance between individual TRPV1 and Orai1 channels obtained from super resolution studies was around 50 nm. This distance contrasts to that observed with our FRET studies (less than 10 nm). The discrepancy can be explained by the resolution limits attained by both methods. While FRET detects distances between two proteins smaller than 10 nm (100 Å), the super resolution method (even though has gone beyond the light diffraction limit) it is still far away from the resolution of FRET. For example, STED (stimulated emission depletion) imaging has achieved a resolution of 20 nm when using organic dyes and 50–70 nm resolution when using fluorescent proteins[33]. The association of Orai1 and TRPV1 channels was evaluated also with CoIP studies. Even though all CoIP studies presented here are in agreement with the FRET and super resolution results, we would like to highlight the fact that the molecular weight obtained from Orai1 (≈55 kDa) differs from the predicted molecular weight for this protein (≈33 kDa). Thus, we would like to take the CoIP studies with caution, even though other reports have found similar discrepancies in the molecular weight for Orai1[34,35]. Feasible explanations for the higher molecular weight observed may involve glycosylation, phosphorylation, and other post-translational modifications of Orai1[36–38].

We have identified the first ankyrin domain (ANK1) as a structure responsible for the association of TRPV1 to the carboxyl terminus from Orai1. Deletion of this ANK1 domain (TRPV1-ΔANK1) prevents TRPV1-mediated CDI on Orai1. Single Orai1-GCaMP3 channels do not longer sense calcium entering through TRPV1-ΔANK1.

A previous study shows that capsaicin inhibits Jurkat T-cell activation by blocking I_{CRAC}[39]. Other studies have also shown that capsaicin or TRPV1 activation inhibits SOCE[40–43]. However, the molecular mechanism for these observations remained unknown until now.

CDI is a complex process, which involves the participation of several proteins such as SARAF[11], caveolin, E-syt1, septin4, and $PI(4,5)P_2$[13]. Furthermore, several amino acid regions have been identified in Orai1 and STIM1 to play a role in CDI[17–21]. This may be one of the reasons why CDI remained for several minutes after TRPV1 was not active anymore. Calcium entering through TRPV1 channel was the triggering event that initiated CDI in neighboring Orai1 channels, but other factors were involved in the sustained CDI even after the calcium source (TRPV1) was not active anymore (after washing out capsaicin).

In the present study, we focused our attention on the role of a different channel (TRPV1) in the induction of CDI on Orai1, to induced what we have named here heterologous CDI (as opposed to homologous CDI, which is induced by calcium entering via the Orai1 channel pore). We identified the ankyrin 1 domain from TRPV1 and the carboxyl terminus from Orai1 as sequences required for the association of these two channels. We cannot discard the participation of other proteins (as those mentioned above) or other amino acid regions in CDI. Further studies are required to evaluate the participation of other proteins and/or amino acid regions in Orai1 and TRPV1 in CDI.

Many cells and tissues express both TRPV1 and Orai1 channels, in particular cortical astrocytes. In these cells, activation of TRPV1 may modulate the subsequent (or concomitant) activation of Orai1 channels[44]. The role of astrocytes in chronic pain is well established[44]. We have previously shown that Orai1 mediates the thrombin response in cortical astrocytes[28]. Furthermore, thrombin induces cell migration and proliferation in astrocytes[30–32].

In the present study, we have shown that the activation of endogenous TRPV1 channels with capsaicin induces CDI on endogenous Orai1 channels from cortical astrocytes. In this study, we showed that the heterologous modulation of Orai1 by TRPV1 via CDI plays a role in controlling injury-promoted astrocyte migration (Fig. 7). All these results provide the first evidence highlighting the role of heterologous CDI in controlling calcium entry via Orai1 and how this modulates migration in astrocytes primary cultures.

Methods

Plasmids and reagents. Capsaicin and the synthetic antagonist of capsaicin, capsazepine and cytidine triphosphate (CTP) were purchased from Sigma (St. Louis, MO). TG was purchased from Calbiochem (La Jolla, CA).

Plasmids Orai1-GFP, GCaMP3, STIM1-DsRed, H2B-mCherry, and Lck-GCaMP5 were purchased from Addgene (Cambridge, MA), R-GECO was a generous gift from Dr. Takeharu Nagai (Osaka University, Japan), TRPV1-CFP and TRPV1-YFP were kindly donated by Dr. Leon Islas-Suárez (Facultad de Medicina, UNAM), CFP-$P2X_4$ was a generous gift of Dr. Jorge Arreola (Instituto de Fisica, UASLP). Full length complementary DNA of human-Orai1 was inserted into GCaMP3 between BamHI and EcoRI to generate Orai1-GCaMP3. All constructs were fully sequenced before using them.

Ankyrin domains fused to GFP. Oligonucleotides were synthesized (Integrated DNA Technologies, Skokie, IL) to generate peptides corresponding to the amino acid sequences for the 6 ankyrin (ANK) domains from rat TRPV1 (Genbank NM_031982). Ankyrin domains were obtained from ref. [45].

Oligonucleotides were cloned in the pDrive plasmid after PCR amplification and cloned in frame at the 5′ of GFP. The resulting peptides were:

ANK1 110.152 (42 aa) RLYDRRSIFDAVAQSNCQELESLLPFLQRSKKRLTDSEFKDPE

ANK2 153.199 (46 aa) TGKTCLLKAMLNLHNGQNDTIALLLDVARKTDSLKQFVNASYTDSYY

ANK3 200.246 (46 aa) KGQTALHIAIERRNMTLVTLLVENGADVQAAANGDFFKKTKGRPGFY

ANK4 247.282 (35 aa) FGELPLSLAACTNQLAIVKFLLQNSWQPADISARDS

ANK5 283.331 (48 aa) VGNTVLHALVEVADNTVDNTKFVTSMYNEILILGAKLHPTLKLEEITNR

ANK6 332.358 (26 aa) KGLTPLALAASSGKIGVLAYILQREIH

Followed by the enhanced GFP sequence. All fusion genes were fully sequenced prior to use. For CoIP studies, the pcDNA 3.1 plasmid containing the nucleotide sequences for the 6 ankyrin domains individually fused to the GFP sequence (above) were transfected in HEK293 cells combined with the plasmid containing Orai1. For peptide microarray studies, the plasmids mentioned above were transfected in HEK293 cells maintained in suspension in 500 mL flasks to produce fusion proteins. Cells were harvested and sonicated to disrupt the cell membrane. Supernatants were immunoprecipitated using the commercial anti-GFP antibody (632376, Clontech, Mountain View, CA). Aliquots of the 6 ankyrin domains fused to GFP were utilized for TIRFM peptide microarray studies as previously described[46]. Briefly, silica glass was coated with a 0.01 mg mL^{-1} poly-D-lysine (Sigma, St. Louis, MO). Orai1-dsRED-COOH peptide was spotted on the microarray slide using a peptide solution of 500 ng in 50 µL. Approximately 2 µL were manually deposited on each spot using a pipette. Spots were allowed to dry for 20 min at room temperature prior to starting the TIRFM microarray experiment. Microarray slides were mounted on the lg-TIRFM closed chamber (TIRF Labs, Cary, NC).

A similar PCR strategy was conducted to produce the fusion proteins between the amino terminus from Orai1 and GFP (NH_2-GFP), the carboxyl terminus from Orai1 (COOH-GFP), and the carboxyl terminus from Orai1 fused to the red fluorescent protein (DsRed, Takara Bio, USA). Production and purification of recombinant fused proteins followed the procedure described above. The Orai1-COOH domain contained the last 38 amino acids (amino acid 200–238) with the sequence: HKTDRQFQELNELAEFARLQDQLDHRGDHPLTPGSHYA (Genbank:

AAH13386.1). Followed by the GFP or dsRED protein (Takara Bio, USA). The amino terminus of Orai1 contained the first 54 amino acids (1–54, Genbank: AAH13386.1): MSLNEHSMQALSWRKLYLSRAKLKASSRTSALLSGFAMVAMV EVQLDADHDYPP. Followed by the GFP protein. The deletion mutant TRPV1-RPV1-was produced by PCR amplification of TRPV1 cDNA using a forward oligonucleotide that started after nucleotide 536 (amino acid 153).

Cell culture and transfection. Human embryonic kidney 293 cells (HEK293; ATCC) were cultured using Dulbecco's modified Eagle's medium (DMEM) (GIBCO) supplemented with 10% (V/V) fetal bovine serum, 50 μg mL^{-1} penicillin–streptomycin and maintained at 37 °C in a humidified atmosphere with 5% CO_2.

Transient transfection was performed using Lipofectamine 2000 (Invitrogen) according to manufacturer instruction using cells seeded to 80% confluence in Optimem medium (GIBCO). Before imaging, culture medium was changed in Krebs solution (119 mM NaCl, 2.5 mM KCl, 1 mM NaH_2PO_4, 1.3 mM $MgCl_2$, 20 mM HEPES, 11 mM glucose, 1.8 mM $CaCl_2$, 500 μM EGTA and adjusted to 7.4 pH).

Western blot. Proteins of cells transfected with Orai1-GCaMP3 or Orai1-GFP were separated using SDS-Page with 10% acrylamide and transferred to the membrane using 110 V for 60 min in a wet chamber. A specific antibody was used to identify Orai1 (ab59330, Abcam) and for TRPV1 the antibody used was VR1 (sc-398417) from Santa Cruz Biotechnology. Primary antibody was incubated with agitation at 4 C° for 1 h. The secondary antibody was incubated for 2 h with agitation at room temperature. Signal was acquired using X-ray films and then the image was digitalized and analyzed using ImageJ software. Full-length blots are included in Supplementary Figures.

Confocal microscopy. HEK293 cells transfected with the different constructs and channels were plated on 25 mm coverslips. Cells were imaged in Krebs–Ringer's solution. TG (1 μM; Calbiochem) was used for store depletion. Image acquisition for co-localization experiments was conducted 12 min after store depletion. Enhanced GFP (EGFP), GCaMP3, DsRed, and R-GECO were excited at 488, 488, 494, and 594 nm, respectively. Fluorescence emission was collected at 500–540 nm for EGFP and GCaMP3 and 605–650 nm for DsRed and R-GECO. All images were captured at room temperature with a ×60, 1.40 numerical aperture oil-immersion objective lens controlled by Fluoview Olympus software on a FV10i confocal microscope (Olympus imaging). Pearson's correlation coefficient was calculated with Fluoview Olympus software.

Ca^{2+} measurements. Calcium imaging was performed in 25 mm coverslip with cells transfected with the plasmid of choice indicated in the figures. Cells expressing Orai1-GCaMP3 in Krebs–Ringer solution with Ca^{2+} were exposed to TG (1 μM) to induce store depletion. Capsaicin (4 μM) was utilized to activate TRPV1 channels and 150 μM cytidine triphosphate (CTP) to open $P2X_4$ channels. Calcium dynamics were measured in individual cells (at least 20 per coverslip per condition) using a wide-field inverted IX81 Olympus® microscope with a ×60 1.42 NA oil immersion objective, MT-20 illumination system, 420/10, 484/25 excitation filter, and 450, 550/25, 520 nm/40 bandpass and 605/40 bandpass emission filter with an EMCCD camera iXon-897 (Andor Technology, South Windsor, CT, USA). Sampling was acquired each second during 300 s. The acquired images were analyzed using Olympus Cell-R software. To measure calcium increments in cell populations, we loaded HEK293 cells with FURA-2 AM (Molecular Probes) at 2 μM final concentration. FURA-2 AM was incubated for 30 min at 25 °C. Calcium-free Krebs solution contained (119 mM NaCl, 2.5 mM KCl, 1 mM NaH_2PO_4, 1.3 mM $MgCl_2$, 20 mM HEPES, 11 mM glucose, 1 mM EGTA and adjusted to 7.4 pH). Then cells were rinsed with the same solution and were exposed to 1 μM TG to induce store depletion and Orai1 activation. Ca^{2+} entry was measured through an Aminco-Bowman luminescence spectrometer (Thermo Electron, Madison, WI). Dual excitation wavelength was selected at 340 and 380 nm and emission was collected at 510 nm. Fluorescence sampling was acquired each 10 s during 1000 s.

FRET measurements. The cells were seeded on 25 mm coverslips and co-transfected with TRPV1-CFP and Orai1-YFP. We performed FRET measurements using the acceptor photobleaching protocol with TRPV1-CFP as donor and Orai1-YFP as acceptor, as previously described[4].

For acceptor photobleaching, the images were acquired with an inverted Olympus FV1000 confocal microscope. The photobleaching of the acceptor was performed exposing the selected ROI to the laser at 50% of its maximum intensity (ROI indicated by a yellow square in Fig. 4), at a wavelength of 492 nm. This wavelength does not affect the donor as the excitation of GFP beyond 480 nm is negligible. The photobleaching protocol consisted of continuous excitation at 492 nm for 4 min, during this time, the fluorescence emission of CFP and YFP were monitored using the confocal microscope. Photobleaching excitation was alternated with image acquisition of CFP (460 nm) and YFP (520 nm). We used a 1.45 NA ×100 objective (Olympus, Japan) for image acquisition.

FRET efficiency, which indicates the percentage of excitation photons that contribute to FRET, was calculated measuring the fluorescence intensity in a ROI, before and after photobleaching the acceptor (Orai1-YFP), we also measured the fluorescence of acceptor and donor in a different ROI (without the photobleaching protocol applied, indicated by a yellow circle in Fig. 4) to correct for photobleaching that might occur during acquisition unrelated to the photobleaching protocol. FRET efficiency was calculated with the formula $E_{FRET} = (D_{post} - D_{pre})/D_{post}$, where D_{pre} and D_{post} are YFP fluorescence before and after the photobleaching protocol, respectively. The E_{FRET} calculated from the area not subjected to photobleaching (indicated by a yellow circle in Fig. 4) was considered the baseline. This baseline value was indistinguishable from the E_{FRET} obtained between Orai1-YFP and CFP-$P2X_4$ (Fig. 4). For a detailed description of the protocol, please refer to ref. [47].

Electrophysiology. HEK293 cells expressing the different constructs described in Fig. 3 were placed on coverslips coated with poly-lysine (Sigma). Cells were studied between 24 and 48 h post-transfection. Coverslips were mounted on an open perfusion chamber (TIRF Labs, Cary, NC). The patch clamp amplifier used for whole-cell recordings was the EPC-10 (Heka Electroniks, Germany). The patch clamp pipettes were prepared from Corning 7052 glass and had a resistance of 1–5 MΩ when filled with the pipette solution (see below). An Ag/AgCl electrode was utilized to attain electrical continuity and was connected to the bath solution via a KCl-agar bridge. TG was applied using a multibarrel perfusion system driven by gravity (TIRF Labs, Cary, NC).

Whole-cell currents were studied in the perforated patch mode. Amphotericin B was dissolved in 50 μL DMSO to give a 60 mg mL^{-1} stock solution and stored at −20 °C until use. The amphotericin B stock solution was dissolved to a final concentration of 0.24 mg mL^{-1} in a syringe containing the pipette solution: cesium aspartate 120 mM, EGTA 5 mM, HEPES 10 mM, $MgCl_2$ 2 mM, and NaCl 8 mM; pH to 7.2 adjusted with CsOH. The bath solution contained NaCl 120 mM, tetraethylammonium chloride (TEA-Cl) 10 mM, $CaCl_2$ 10 mM, $MgCl_2$ 2 mM, glucose 30 mM, and HEPES 10 mM; pH to 7.2 adjusted with NaOH. Osmolarity of both solutions was adjusted to 310 mOsm with mannitol (Sigma).

To determine Orai1 current inactivation, the cell was first stimulated with either 1 μM capsaicin (Cap) or 10 μM cytidine triphosphate (CTP) for approximately 1 min. The solution was removed and washout for 1–2 min with bathing solution before stimulation with 1 μM TG. Relative inactivation was obtained after obtaining the current density relative to the non-inactivating Orai1 Y80W mutant.

Current density was obtained after dividing the current from each cell by the cell capacitance (measured directly from the amplifier readout). The amplifier provided current density in real time calculated via the Patchmaster software and EPC10 electronics (Heka Electroniks, Germany). For time courses studying Orai1 whole-cell current activation, TG was applied while the cell membrane potential was held at −100 mV. All whole-cell current illustrated in Fig. 3 represents the mean ± standard deviation (SD) from at least 30 independent cells obtained from 4 different days and transfections.

Orai1 whole-cell currents were imported into Igor pro v. 7 (Wavemetrics, Oregon) for further analysis and plotting. Final figures were created with Adobe Illustrator (Adobe Systems).

Super-resolution microscopy. The total internal reflection fluorescence (TIRF) excitation (cellTIRF Illuminator; Olympus) system was mounted on an Olympus IX81 inverted microscope for all super resolution experiments reported here. The excitation angle was set up to attain the critical angle for total internal reflection, which provided a penetration of less than 100 nm. Cells were continuously illuminated using excitation sources depending on the fluorophore studied. Blue (CFP-$P2X_4$) and green (Orai1-YFP) were excited with either a 405 and 491-nm diode-pumped solid-state laser, respectively. Cells were continuously illuminated using the following excitation sources: blue (CFP-$P2X_4$) and green (Orai1-YFP) were excited with either a 405 and 491-nm diode-pumped solid-state laser, respectively. The maximum laser power, measured at the back of the focal plane of the objective lens, ranged between 20 and 25 mW, depending on the laser line used. Excitation wavelength and intensity were modulated using the Xcellence software v.1.2. A multiband laser cube set was used to discriminate the selected light sources (LF 405/488/561/635 A-OMF, Bright Line; Semrock). The microscope was equipped with an Olympus UApo N ×100/1.49-numerical-aperture oil-immersion objective lens with an extra ×1.6 intermediate magnification lens. All movies were recorded on a crop chip mode (512 × 32 pixels) of an EMCCD camera (Andox, Ixon 888) at 100 nm per pixel.

For each independent experiment, sub-diffraction images were derived from the Super Resolution Radial Fluctuation (SRRF) analysis[48]. Reconstructions contained thousands of TIRF images acquired within the evanescent field. All images were collected using stroboscopic illumination, alternating between laser lines in a per-frame basis, each with an exposure time of 1–5 ms.

Each serial stack (300 images block) was analyzed using the NanoJ-core and NanoJ-SRRF plugins of Image J[48,49]. For the analysis the following parameters were utilized: ring radius 0.5, radiality magnification 5, axes in ring 10; all other parameters were set up as the default options in NanoJ-core and NanoJ-SRRF plugins. The radiality maps were drift corrected using pre-calculated drift tables obtained with the Estimate Drift tool of NanoJ-SRRF, considering an average of 300 images. These drift-corrected radiality maps were then finally integrated on a super-resolution image by calculating the Temporal Radiality Pairwise Product Mean.

To obtain distances between Orai1 and TRPV1 or Orai1 and $P2X_4$ overtime, we used the tracking image correlation method[50]. For this purpose, HEK293 cells were transfected with a combination of Orai1-YFP and TRPV1-CFP or Orai1-YFP and CFP-$P2X_4$, respectively. The signal of individual fluorophores was tracked overtime by alternating the excitation wavelengths, as described above. Temporal blocks of 300 images were analyzed. Tracking image correlation (TrIC) computes a colocalization analysis on single particles along their trajectory based on local image cross-correlation. The accuracy of the correlation is limited to the SRRF, which in our case is between 40 and 60 nm. All of the analysis was programmed with MATLAB (The MathWorks, Natick, MA) using the original algorithms described by Dupont and collaborators[50]. Unlike the original study, which tracked particles in the 3D space, we conducted only 2D tracking within the depth of the evanescent wave (less than 100 nm). The depth resolution of TIRFM (less than 100 nm) provided high accuracy when determining the 2D spatial localization of the particles when compared to confocal microscopy, which in the best case scenario has a depth resolution of around 600 nm[51].

TIRFM microarrays. For peptide microarrays studies using ankyrin domains fused to GFP, we utilized a novel system specifically developed for this purpose based on total internal reflection microscopy (TIRFM)[46]. We have documented extensively this method elsewhere[46]. Briefly, purified peptides (either the ANK1 domain (see above) or the Orai1-COOH-DsRed terminal domain) were printed using a micropipette on conventional glass microarray slides previously coated with a film of 0.01 mg mL^{-1} poly-D-lysine (Sigma, St. Louis, MO). The microarray-closed chamber was bathed with a solution containing the ANK domains fused to GFP (see above) at a final concentration of 1 µM. After 3 min incubation, the chamber was bathed with saline solution and fluorescence signal was collected for 1 min. Excitation was in TIRFM mode using the LG-TIRFM system (TIRF Labs, Cary, NC). Excitation was alternated between 405 nm (GFP excitation) and 594 nm (DsRed excitation). DsRed emission was used to evaluate the amount of Orai1-COOH-dsRED deposited on each microarray spot. Microarray spots containing less than 80% of the average DsRed fluorescence were discarded because insufficient Orai1-COOH-dsRED was deposited in those spots. Emission of GFP (D505/40 m) and DsRed (ET620/60 m) were collected using high-quality single band emission filter from Chroma (Chroma Technology Corporation, Bellows Falls, VT, USA). For details on our TIRFM microarray system and protocols for microperfusion and fluorescence detection, please refer to ref. [24].

Co-immunoprecipitation. Plasmids c-Myc-Orai1 and TRPV1-YFP or CFP-$P2X_4$ were overexpressed in HEK293 cells. Cells were washed twice with PBS, then the cells were lysed with TNI lysis buffer[52] (0.5% Igepal CA-630, 50 mM Tris pH 7.5, 250 mM NaCl, 1 mM EDTA, 1× Complete ULTRA-EDTA-free protease Inhibitor cocktail) during 30 min at 4 °C with agitation and sonicated using a bath sonicator (55 kHz, 5 min). The samples were centrifuged 40 min (4 °C, 18,000×*g*) and the supernatant was incubated overnight with sepharose resin beads coupled to anti-c-myc antibody. Proteins were recovered by centrifuging the beads (4 °C, 500×*g*). Bound proteins were eluted with elution buffer[52] (0.2 M glycine pH 2.3 and 0.5% Igepal CA-630) during 30 min at 37 °C. The proteins were analyzed by western blot using specific antibodies c-myc (Invitrogen, MA1-21316) for c-Myc-Orai1 (50 kDa), VR1 (Santa Cruz, 398417) for TRPV1-YFP (125 kDa) and $P2X_4$ (Abcam, 134559) for CFP-$P2X_4$ (71 kDa), all the antibodies were used according to the manufacturer's recommendations. For endogenous Orai1 and TRPV1 from astrocytes we use the following protocol. Cells from 5 to 7 100 mm Petri dishes with confluent monolayers of primary culture astrocytes were rinsed and cells were detached mechanically. All cells from the Petri dishes were concentrated and lysed using TNI lysis buffer during 30 min with agitation at 4 °C and sonicated using a bath sonicator (55 kHz, 5 min). The samples were centrifuged 40 min (4 °C, 18,000×*g*) and the supernatant was incubated overnight with sepharose resin beads coupled to anti-Orai1 antibody. Proteins were recovered by centrifuging the beads (4 °C, 500×*g*). Bound proteins were eluted with elution buffer during 30 min at 37 °C. The proteins were analyzed by western blot using the specific antibodies described above.

Scratch-wound assay. Primary cortical astrocytes were isolated from rat brains[28]. All procedures for maintaining the rats and for isolation of astrocytes were approved by the Animal Care Committee of the Instituto de Fisiología Celular, Universidad Nacional Autónoma de México. Animal care was performed according to the International Guiding Principles for Biomedical Research Involving Animals (Council for International Organizations of Medical Sciences, 2010). Cortical astrocytes cultures were obtained from 1-day-old Wistar rat pups provided by our animal facility center. The astrocytes were isolated from the brain cortex of 6–8 pups. Brains were placed in Krebs solution and cut in small slices. The tissue was dissociated with a solution containing trypsin (4800 U mL^{-1}, Sigma, St. Louis, MO) for 10 min. Cells were mechanically dispersed by passage through 80 µm nylon mesh and resuspended in Eagle's medium (Gibco, Grand Island, NY) supplemented with 10% heat-inactivated fetal bovine serum (Gibco), 2 mM glutamine (Sigma), 50 U mL^{-1} penicillin (Gibco), and 50 µg mL^{-1} streptomycin (Gibco). The dissociated astrocytes were plated on 35 mm plastic Petri dishes and incubated at 37 °C in humidified 5% CO_2, 95% air atmosphere for 2 weeks.

When indicated astrocytes were transfected with the constructs described in the figure legends[28]. For RNA interference experiments, astrocytes cultures of 80% confluence in 35 mm plates were transfected with a set of three oligonucleotides of Stealth siRNAs for Orai1 (RSS357633, RSS357634, RSS357635) purchased from Invitrogen. A Stealth RNAi scramble negative control (Invitrogen) was used in parallel experiments. siRNAs transfection was carried out on primary astrocytes using Lipofectamine 2000 and Opti-MEM reduced serum medium according to the manufacturer's instructions (Invitrogen).

For the SWA, we followed the next protocol. Cover glass chambers (ThermoScientific, Rochester, NY) were coated with 0.01 mg mL^{-1} poly-D-lysine (Sigma, St. Louis, MO). Confluent primary cortical astrocytes were seeded onto chambers[28]. Once confluent, astrocytes were serum-deprived overnight. A single scratch with a 1 mL pipet tip was made through the astrocyte monolayer, cells were rinsed three times with serum-free media. The scratch area was marked with a sharpie for later identification and positioning in the microscope. Images of cells were obtained with a low magnification ×10 objective attached to an inverted IX81 microscope (Olympus). A low-resolution 5 MP USB c-mount microscope camera (Zowaysoon) attached to the microscope c-port was used to acquire individual images of the scratch wound area at 0 time (pre-wound), immediately after the scratch wound, 5, 10, 15, 20, and 25 h after scratch wound. After every image acquisition cells were placed in the CO_2 incubator.

Reporting summary. Further information on experimental design is available in the Nature Research Reporting Summary linked to this article.

Data availability

All constructs used in the present study are available upon request. Super resolution image files are too big (each file is over 1 terabyte in size) to be included in any archiving system but are available upon request. Microarray data is publicly available (https://doi.org/10.6084/m9.figshare.7621955.v1). Other data that support the findings of this study are available from the corresponding author upon reasonable request.

Received: 10 August 2018 Accepted: 5 February 2019
Published online: 04 March 2019

References

1. Berridge, M. J., Lipp, P. & Bootman, M. D. The versatility and universality of calcium signalling. *Nat. Rev. Mol. Cell Biol.* **1**, 11–21 (2000).
2. Bagur, R. & Hajnóczky, G. Intracellular Ca^{2+} sensing: its role in calcium homeostasis and signaling. *Mol. Cell* **66**, 780–788 (2017).
3. Redondo, P. C. & Rosado, J. A. Store-operated calcium entry: unveiling the calcium handling signalplex. *Int. Rev. Cell Mol. Biol.* **316**, 183–226 (2015).
4. Bohórquez-Hernández, A., Gratton, E., Pacheco, J., Asanov, A. & Vaca, L. Cholesterol modulates the cellular localization of Orai1 channels and its disposition among membrane domains. *Biochim. Biophys. Acta Mol. Cell Biol. Lipids* **1862**, 1481–1490 (2017).
5. Muik, M., Schindl, R., Fahrner, M. & Romanin, C. Ca^{2+} release-activated Ca^{2+} (CRAC) current, structure, and function. *Cell. Mol. Life Sci.* **69**, 4163–4176 (2012).
6. Mullins, F. M. & Lewis, R. S. The inactivation domain of STIM1 is functionally coupled with the Orai1 pore to enable Ca^{2+}-dependent inactivation. *J. Gen. Physiol.* **147**, 153–164 (2016).
7. Roos, J. et al. STIM1, an essential and conserved component of store-operated Ca^{2+} channel function. *J. Cell Biol.* **169**, 435–445 (2005).
8. Liou, J. et al. STIM is a Ca^{2+} sensor essential for Ca^{2+}-store-depletion-triggered Ca^{2+} influx. *Curr. Biol.* **15**, 1235–1241 (2005).
9. Feske, S. et al. A mutation in Orai1 causes immune deficiency by abrogating CRAC channel function. *Nature* **441**, 179–185 (2006).
10. Zweifach, A. & Lewis, R. S. Slow calcium-dependent inactivation of depletion-activated calcium current. Store-dependent and -independent mechanisms. *J. Biol. Chem.* **270**, 14445–14451 (1995).
11. Palty, R., Raveh, A., Kaminsky, I., Meller, R. & Reuveny, E. SARAF inactivates the store operated calcium entry machinery to prevent excess calcium refilling. *Cell* **149**, 425–438 (2012).
12. Li, X. et al. Calmodulin dissociates the STIM1-Orai1 complex and STIM1 oligomers. *Nat. Commun.* **8**, 1042 (2017).
13. Maléth, J., Choi, S., Muallem, S. & Ahuja, M. Translocation between PI(4,5) P2-poor and PI(4,5)P2-rich microdomains during store depletion determines STIM1 conformation and Orai1 gating. *Nat. Commun.* **5**, 1–10 (2014).
14. Zweifach, A. & Lewis, R. S. Rapid inactivation of depletion-activated calcium current (ICRAC) due to local calcium feedback. *J. Gen. Physiol.* **105**, 209–226 (1995).

15. Fierro, L. & Parekh, A. B. Membrane biology fast calcium-dependent inactivation of calcium release-activated calcium current. *J. Membr. Biol.* **168**, 9–17 (1999).
16. Scrimgeour, N., Litjens, T., Ma, L., Barritt, G. J. & Rychkov, G. Y. Properties of Orai1 mediated store-operated current depend on the expression levels of STIM1 and Orai1 proteins. *J. Physiol.* **587**, 2903–2918 (2009).
17. Mullins, F. M., Park, C. Y., Dolmetsch, R. E. & Lewis, R. S. STIM1 and calmodulin interact with Orai1 to induce Ca^{2+}-dependent inactivation of CRAC channels. *Proc. Natl. Acad. Sci. U.S.A.* **106**, 15495–15500 (2009).
18. Lee, K. P. et al. Molecular determinants of fast Ca^{2+}-dependent inactivation and gating of the Orai channels. *Proc. Natl. Acad. Sci. U.S.A.* **106**, 14687–14692 (2009).
19. Derler, I. et al. A Ca^{2+} release-activated Ca^{2+} (CRAC) modulatory domain (CMD) within STIM1 mediates fast Ca^{2+}-dependent inactivation of ORAI1 channels. *J. Biol. Chem.* **284**, 24933–24938 (2009).
20. Srikanth, S., Jung, H. J., Ribalet, B. & Gwack, Y. The intracellular loop of Orai1 plays a central role in fast inactivation of Ca^{2+} release-activated Ca^{2+} channels. *J. Biol. Chem.* **285**, 5066–5075 (2010).
21. Mullins, F. M., Yen, M. & Lewis, R. S. Orai1 pore residues control CRAC channel inactivation independently of calmodulin. *J. Gen. Physiol.* **147**, 137–152 (2016).
22. Desai, P. N. et al. Multiple types of calcium channels arising from alternative translation initiation of the Orai1 message. *Sci. Signal.* **8**, ra74 (2015).
23. Shigetomi, E., Kracun, S. & Khakh, B. S. Monitoring astrocyte calcium microdomains with improved membrane targeted GCaMP reporters. *Neuron Glia Biol.* **6**, 183–191 (2010).
24. Asanov, A., Zepeda, A. & Vaca, L. A platform for combined DNA and protein microarrays based on total internal reflection fluorescence. *Sensors* **12**, 1800–1815 (2012).
25. Vaca, L. Microarrays showing binding of the six ankyrin domains from TRPV1 to Orai1 carboxyl terminus. Figshare. Fileset. https://doi.org/10.6084/m9.figshare.7621955.v1 (2019).
26. Lishko, P. V., Procko, E., Jin, X., Phelps, C. B. & Gaudet, R. The ankyrin repeats of TRPV1 bind multiple ligands and modulate channel sensitivity. *Neuron* **54**, 905–918 (2007).
27. Erler, I., Hirnet, D., Wissenbach, U., Flockerzi, V. & Niemeyer, B. A. Ca^{2+}-selective transient receptor potential V channel architecture and function require a specific ankyrin repeat. *J. Biol. Chem.* **279**, 34456–34463 (2004).
28. Moreno, C., Sampieri, A., Vivas, O., Pena-Segura, C. & Vaca, L. STIM1 and Orai1 mediate thrombin-induced Ca(2+) influx in rat cortical astrocytes. *Cell Calcium* **52**, 457–467 (2012).
29. Huang, C. et al. Existence and distinction of acid-evoked currents in rat astrocytes. *Glia* **58**, 1415–1424 (2010).
30. Wang, H., Ubl, J. J., Stricker, R. & Reiser, G. Thrombin (PAR-1)-induced proliferation in astrocytes via MAPK involves multiple signaling pathways. *Am. J. Physiol. Cell Physiol.* **283**, C1351–C1364 (2002).
31. Ebrahimi, S. et al. Role of thrombin in the pathogenesis of central nervous system inflammatory diseases. *J. Cell. Physiol.* **232**, 482–485 (2017).
32. Lin, C.-C. et al. Thrombin mediates migration of rat brain astrocytes via PLC, Ca^{2+}, CaMKII, PKCα, and AP-1-dependent matrix metalloproteinase-9 expression. *Mol. Neurobiol.* **48**, 616–630 (2013).
33. Hell, S. W. Far-field optical nanoscopy. *Science* **316**, 1153–1158 (2007).
34. Sahu, I. et al. NFAT5-sensitive Orai1 expression and store-operated Ca^{2+} entry in megakaryocytes. *FASEB J.* **31**, 3439–3448 (2017).
35. Michiels, C. F., Fransen, P., De Munck, D. G., De Meyer, G. R. Y. & Martinet, W. Defective autophagy in vascular smooth muscle cells alters contractility and Ca^{2+} homeostasis in mice. *Am. J. Physiol. Heart Circ. Physiol.* **308**, H557–H567 (2015).
36. Henke, N. et al. The plasma membrane channel ORAI1 mediates detrimental calcium influx caused by endogenous oxidative stress. *Cell Death Dis.* **4**, e470 (2013).
37. Fukushima, M., Tomita, T., Janoshazi, A. & Putney, J. W. Alternative translation initiation gives rise to two isoforms of Orai1 with distinct plasma membrane mobilities. *J. Cell Sci.* **125**, 4354–4361 (2012).
38. Penna, A. et al. The CRAC channel consists of a tetramer formed by Stim-induced dimerization of Orai dimers. *Nature* **456**, 116–120 (2008).
39. Fischer, B. S., Qin, D., Kim, K. & McDonald, T. V. Capsaicin inhibits Jurkat T-cell activation by blocking calcium entry current I(CRAC). *J. Pharmacol. Exp. Ther.* **299**, 238–246 (2001).
40. Choi, S. Y. & Kim, K. T. Capsaicin inhibits phospholipase C-mediated Ca(2+) increase by blocking thapsigargin-sensitive store-operated Ca(2+) entry in PC12 cells. *J. Pharmacol. Exp. Ther.* **291**, 107–114 (1999).
41. Wang, J. P. et al. Capsaicin stimulates the non-store-operated Ca^{2+} entry but inhibits the store-operated Ca^{2+} entry in neutrophils. *Toxicol. Appl. Pharmacol.* **209**, 134–144 (2005).
42. Fischer, B. S. et al. Capsaicin inhibits Jurkat T-cell activation by blocking calcium entry current I CRAC. *J. Pharmacol. Exp. Ther.* **299**, 238–246 (2001).
43. Gouin, O. et al. Major role for TRPV1 and InsP3R in PAR2-elicited inflammatory mediator production in differentiated human keratinocytes. *J. Invest. Dermatol.* **138**, 1564–1572 (2018).
44. Zhang, E. & Liao, P. Brain transient receptor potential channels and stroke. *J. Neurosci. Res.* **93**, 1165–1183 (2015).
45. Cao, E., Liao, M., Cheng, Y. & Julius, D. TRPV1 structures in distinct conformations reveal activation mechanisms. *Nature* **504**, 113–118 (2013).
46. Asanov, A., Zepeda, A. & Vaca, L. A novel form of Total Internal Reflection Fluorescence Microscopy (LG-TIRFM) reveals different and independent lipid raft domains in living cells. *Biochim. Biophys. Acta Mol. Cell Biol. Lipids* **1801**, 147–155 (2010).
47. Van Munster, E. B., Kremers, G. J., Adjobo-Hermans, M. J. W. & Gadella, T. W. J. Fluorescence resonance energy transfer (FRET) measurement by gradual acceptor photobleaching. *J. Microsc.* **218**, 253–262 (2005).
48. Gustafsson, N. et al. Fast live-cell conventional fluorophore nanoscopy with ImageJ through super-resolution radial fluctuations. *Nat. Commun.* **7**, 12471 (2016).
49. Schindelin, J. et al. Fiji: an open-source platform for biological-image analysis. *Nat. Methods* **9**, 676–682 (2012).
50. Dupont, A., Stirnnagel, K., Lindemann, D. & Lamb, D. C. Tracking image correlation: combining single-particle tracking and image correlation. *Biophys. J.* **104**, 2373–2382 (2013).
51. Cox, G. & Sheppard, C. J. R. Practical limits of resolution in confocal and non-linear microscopy. *Microsc. Res. Tech.* **63**, 18–22 (2004).
52. Pankow, S., Bamberger, C., Calzolari, D., Bamberger, A. & Yates, J. R. Deep interactome profiling of membrane proteins by co-interacting protein identification technology. *Nat. Protoc.* **11**, 2515–2528 (2016).

Acknowledgements

L.V. and A.D. were supported by grants from Direccion General de Asuntos del Personal Academico (DGAPA) UNAM and the Consejo Nacional de Ciencia y Tecnologia (Conacyt). C.E.B.-E. (CVU 486558) performed this study in partial fulfillment of the requirements for the PhD in Programa de Maestría y Doctorado en Ciencias Bioquímicas at the Universidad Nacional Autónoma de México and he is recipient of PhD fellowship (277682) from CONACYT. The authors would like to thank the imaging, the molecular biology, computing center and animal facility center from the Instituto de Fisiologia Celular, UNAM for their support on image acquisition and analysis and for sequencing and primer synthesis for molecular biology and providing animals for this study. The authors thank the Laboratorio Nacional de Microscopía Avanzada, UNAM for their assistance on image acquisition and analysis for the super resolution studies.

Author contributions

C.E.B.-E., A.B.-H., J.P., A.S., A.A., J.P.O.-O., A.G., and A.D. performed experiments. C.E.B.-E., A.G., J.P., and L.V. analyzed data. C.E.B.-E., J.P., A.B.-H., and L.V. produced figures. C.E.B.-E. and L.V. wrote the manuscript. All authors revised and approved the final version.

Additional information

Supplementary information accompanies this paper at https://doi.org/10.1038/s42003-019-0338-1.

Competing interests: Dr. Alexander Asanov is the CEO of TIRF Labs. The lg-TIRFM system is the property of TIRF Labs. TIRF Labs did not provide any financial support for this study, only equipment. The remaining authors declare no competing interests.

Reprints and permission information is available online at http://npg.nature.com/reprintsandpermissions/

Publisher's note: Springer Nature remains neutral with regard to jurisdictional claims in published maps and institutional affiliations.

Open Access This article is licensed under a Creative Commons Attribution 4.0 International License, which permits use, sharing, adaptation, distribution and reproduction in any medium or format, as long as you give appropriate credit to the original author(s) and the source, provide a link to the Creative Commons license, and indicate if changes were made. The images or other third party material in this article are included in the article's Creative Commons license, unless indicated otherwise in a credit line to the material. If material is not included in the article's Creative Commons license and your intended use is not permitted by statutory regulation or exceeds the permitted use, you will need to obtain permission directly from the copyright holder. To view a copy of this license, visit http://creativecommons.org/licenses/by/4.0/.

© The Author(s) 2019

Received: 17 September 2018 | Revised: 4 February 2019 | Accepted: 5 February 2019

DOI: 10.1111/exd.13901

ORIGINAL ARTICLE

WILEY Experimental Dermatology

Dissection of Merkel cell formation in hairy and glabrous skin reveals a common requirement for FGFR2-mediated signalling

Minh Binh Nguyen[1,2] | Victor Julian Valdes[1,2] | Idan Cohen[1,2] | Venu Pothula[1,2] | Dejian Zhao[3] | Deyou Zheng[4] | Elena Ezhkova[1,2]

[1]Department of Cell, Developmental, and Regenerative Biology, Black Family Stem Cell Institute, The Tisch Cancer Institute, New York City, New York

[2]Icahn School of Medicine at Mount Sinai, New York City, New York

[3]Department of Genetics, Albert Einstein College of Medicine, Bronx, New York

[4]Departments of Genetics, Neurology, and Neuroscience, Albert Einstein College of Medicine, Bronx, New York

Correspondence
Elena Ezhkova, Icahn School of Medicine at Mount Sinai, New York, NY.
Email: elena.ezhkova@mssm.edu

Present addresses
Victor Julian Valdes, Department of Cell Biology and Development, Instituto de Fisiologia Celular, UNAM, Mexico City, Mexico

Dejian Zhao, Department of Genetics, Yale University School of Medicine, New Haven, Connecticut

and

Yale Center for Genome Analysis, Yale University, New Haven, Connecticut

Funding information
Cancer Center Support; NIH/NHBLI, Grant/Award Number: R01HL133120

Abstract

Merkel cells are mechanosensory cells involved in tactile discrimination. Merkel cells have been primarily studied in the murine back skin, where they are found in specialized structures called touch domes located around primary hair follicles. Yet, little is known about the morphogenesis of Merkel cells in areas of the skin devoid of hair, such as the glabrous paw skin. Here, we describe Merkel cell formation in the glabrous paw skin during embryogenesis. We first found in the glabrous paw skin that Merkel cells were specified at E15.5, 24 hours later, compared to in the back skin. Additionally, by performing lineage-tracing experiments, we found that unlike in the back skin, SOX9(+) cells do not give rise to Merkel cells in the glabrous paw skin. Finally, we compared the transcriptomes of Merkel cells in the back and the glabrous paw skin and showed that they are similar. Genetic and transcriptome studies showed that the formation of Merkel cells in both regions was controlled by similar regulators. Among them was FGFR2, an upstream factor of MAPK signalling that was reported to have a critical function in Merkel cell formation in the back skin. Here, we showed that FGFR2 is also required for Merkel cell development in the glabrous paw skin. Taken together, our results demonstrate that Merkel cells in the murine back skin and glabrous paw skin are similar, and even though their formation is controlled by a common genetic programme, their precursor cells might differ.

KEYWORDS
FGFR2, glabrous skin, hair follicle, Merkel cells

1 | INTRODUCTION

Merkel cells were first described by Friedrich Merkel in 1875 as cells that may serve as "touch cells."[1] It took over 100 years to prove that Merkel cells have a function in skin sensation.[2] Merkel cells are mechanosensory cells, which are innervated by afferent neurons and play a key role in the tactile discrimination of the shape and texture of objects.[2,3] Functional studies in mutant mice, in which Merkel cells were not formed, have demonstrated that the animals were unable to discriminate between different textures when performing behavioural tasks.[4] In humans, Merkel cells are most abundant on the fingertips, lips and face.[5–7] In mice, they are found mainly in the back skin, paws and whiskers.[8]

Most of our knowledge about Merkel cells comes from studies focused on the murine back skin, where these cells are found in specialized structures called touch domes which are located exclusively around primary hair follicles.[9] Recently, we discovered that a subset of SOX9-expressing cells located inside of developing hair follicles are Merkel cell progenitors that give rise to Merkel cells at embryonic day (E) 14.5.[10] We also found that fibroblast growth

 © 2019 John Wiley & Sons A/S. Published by John Wiley & Sons Ltd

factor receptor 2 (FGFR2) plays an essential function in Merkel cell specification in the back skin, as loss of *Fgfr2* leads to drastic decreases in the number of Merkel cells but does not affect the formation of SOX9-positive (+) cells.[10] To further our investigations, we sought to determine whether our recent findings in the murine back skin apply to other types of skin in the mouse such as the glabrous skin. When do Merkel cells first appear in glabrous skin? Do they share common progenitors with Merkel cells in the hairy skin? How similar are the Merkel cells among these different anatomical regions? These are some of the unanswered questions we wanted to take on.

In this study, we characterized Merkel cell formation in the glabrous paw skin during embryogenesis and determined how known Merkel cell regulators in the back skin affect Merkel cell formation in the glabrous paw skin to uncover common regulators of Merkel cells.

2 | METHODS

2.1 | Mice

All mice were housed in the Center for Comparative Medicine and Surgery (CCMS) at Icahn School of Medicine at Mount Sinai (ISMMS) in accordance with the Institutional Animal Care and Use Committee (IACUC) approved protocol LA11-0020. At least three animals from independent litters were used for each analysis. $Fgfr2^{flox}$ mice were generously provided by Dr. Philippe Soriano.[11] Sox9-CreER mice were described in Ref. [12] R26-mT/mG (stock number: 007676), Atoh1-GFP (stock number: 013593), Gli1-CreER (stock number: 007913) and Krt14-Cre (stock number: 004782) mice were obtained from Jackson Laboratories. For tamoxifen treatment, pregnant females carrying Sox9-CreER; R26-mT/mG or Gli1-CreER; R26-mT/mG embryos were injected with tamoxifen (Sigma-Aldrich; St. Louis, MO) doses totalling 40 μg/g body weight at E13.5 and E14.5. Pups were collected at E17 and P0 for further analysis. Mice were genotyped mice by PCR using DNA extracted from tail skin.

2.2 | Immunofluorescence staining and microscopy

For immunofluorescence staining, tissues were collected and embedded into OCT (Tissue-Tek; Torrance, CA) and subsequently cut into 10-μm sections using a Leica Cryostat. Slides were fixed for 10 minutes in 4% paraformaldehyde (PFA; Electron Microscopy Sciences) in PBS and blocked for 1 hour at room temperature or overnight at 4°C in PBS with 1% Triton X-100, 1% BSA and 0.25% normal donkey serum (NDS). Primary antibodies were diluted in blocking solution, and incubations were carried out for one hour at room temperature or overnight at 4°C, followed by incubation in secondary antibodies for one hour at room temperature. Slides were counterstained with DAPI, mounted using antifade mounting media and then imaged using a Leica DM5500 upright slide microscope using 10x, 20x or 40x objectives.

2.3 | Antibodies

The following antibodies were used: KRT14 (generously gifted by Dr. Julie Segre of the National Human Genome Research Institute, USA, 1/20,000), KRT8 (Developmental Studies Hybridoma Bank, TROMA-1, 1/500), KRT20 (Dako, M7019, 1/70), SOX2 (Stemgent, 09–0024, 1/150), GFP (Abcam, ab13970, 1/1000), SOX9 (Abcam, ab185966, 1/500) and FGFR2 (Cell Signaling, 23328, 1/150). For immunofluorescence staining, secondary antibodies were coupled with Alexa 488, 549 or 649 from Jackson Laboratories (1/1000).

2.4 | Quantifications

Merkel cells were quantified by counting the number of KRT8(+) cells per millimetre (mm) of skin. Briefly, the length of each section was measured, and the number of positively stained cells was counted. Typical section lengths were between 7 and 14 mm, and at least 100 mm of skin was counted for each condition. A large number of Merkel cells were counted in control conditions (> 200 KRT8(+) cells), and subsequently, the number of Merkel cells in a similar length of back and paw skin was counted for the knockout condition. Comparisons and statistics were performed between matching knockout and control littermates.

2.5 | Statistics

In column bar graphs in Figure 4D and E, mean value ± one standard deviation was presented. Box-and-whisker plots show first to third quartiles around the median, with whiskers showing a 5%-95% range and outliers presented as individual data points. To determine the significance between two groups, a Mann-Whitney test was performed. For all statistical tests, $P < 0.05$ was considered for statistical significance, and furthermore, the actual *P*-values (to four decimal places) are provided in the figure legends. Significance levels were defined as $^{*}P < 0.05$, $^{**}P < 0.01$, $^{***}P < 0.001$. n.s., not significant. For statistical analyses, GraphPad Prism 5 was used.

2.6 | Fluorescence-activated cell sorting (FACS)

Interfollicular epidermis (IFE) and Merkel cells were isolated and pooled from multiple *Atoh1-GFP* newborn mice from more than 3 litters (about 50-100 newborn mice) using FACS. Briefly, P0 *Atoh1-GFP* back skins were collected and incubated for 4-6 hours in 1.26U/mL dispase (Invitrogen) at 4°C. The epidermis was then gently peeled from the underlying dermis, dissociated by 0.25% Trypsin with 1 mmol/L EDTA (Corning Cellgro; Manassas, Virginia, USA) and washed with 1x PBS. To collect glabrous skin, P0 *Atoh1-GFP* paws were collected and incubated in 1.26U/mL dispase (Invitrogen) and 0.3% type 1 collagenase (Worthington) overnight at 4°C. The paw epidermis was then separated from the dermis, dissociated in 0.25% Trypsin with 1 mmol/L EDTA (Corning Cellgro; Manassas, Virginia, USA) for 15 minutes at 37°C and washed with 1x PBS.

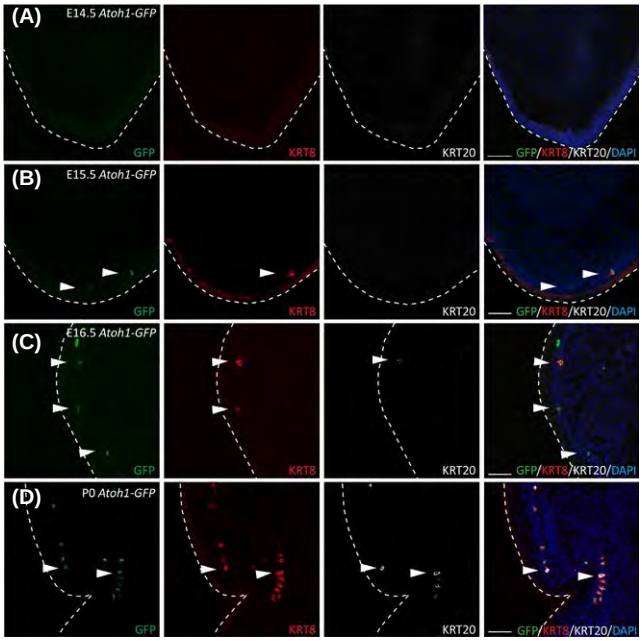

FIGURE 1 Merkel cells are formed at embryonic day 15.5 in the glabrous paw skin. (A–D) Immunofluorescence analysis of early, intermediate and late Merkel cell differentiation markers ATOH1-GFP (green), KRT8 (red) and KRT20 (white), respectively, in the glabrous paw skin of *Atoh1-GFP* mice 14.5 (A), E15.5 (B), E16.5 (C) and P0 (D). White arrows indicate Merkel cells. White dotted lines indicate the edges of the tissue. Note that ATOH1-GFP(+) and KRT8(+) Merkel cells were first observed at E15.5, and KRT20(+) Merkel cells were first observed at E16.5. Scale = 50 μm in all panels

The cell suspension was stained in HBSS + 2%FBS with 1:100 SCA1-PerCP-Cy5.5 (Biolegend) and 1:500 EPCAM-APC (Biolegend) for 20 minutes at room temperature and washed with 1x HBSS prior to cell sorting in HBSS with DAPI. IFE was sorted as ATOH1-GFP(−), EPCAM(+) and SCA1(+). Merkel cells were sorted as ATOH1-GFP(+), EPCAM(+) and SCA1(−). Note that alpha6 integrin was not used in the flow sorting scheme to isolate Merkel cells, but alpha6-integrin(+) cells were included in FACS purification of hair follicle cells.[13] All cell isolations were performed on a BD FACSAria II instrument (BD, Franklin Lakes, New Jersey, USA) in the Flow Cytometry Core Facility at ISMMS.

2.7 | RNA purification, RT-qPCR and library preparation

FACS-purified cells were collected directly into RLT Plus buffer (QIAGEN), and RNA was purified from these sorted cells with the RNeasy Plus Micro Kit (QIAGEN) according to manufacturer's instructions. To perform RT-qPCR, complimentary DNA was reverse-transcribed from total RNA using qScript cDNA SuperMix (Quanta Biosciences, Gaithersburg, Maryland, USA). Prior to library construction, sample quality was measured using an Agilent Bioanalyzer. Only samples with RNA integrity numbers > 8 were used for library preparation. Briefly, 10 ng of RNA was first reverse-transcribed and amplified using the Ovation RNA-seq System V2 (Nugen). Libraries from 100 ng of sonicated cDNA (Covaris) were then constructed using the Ovation Ultra-Low DR Multiplex system (Nugen). All RNA libraries were sequenced on an Illumina HiSeq platform at GENEWIZ.

2.8 | RNA-Seq analysis and data visualization

RNA-seq reads were aligned to the mouse reference genome (mm10) using Tophat (v2.0.13).[14] The mouse gene models of Refgene were downloaded from the UCSC genome browser (genome.uscs.edu) on 13 March 2017. FPKM (fragments per kilobase of transcript per million mapped reads) values were generated using Cufflinks (v2.2.1).[15] Lowly expressed genes (mean FPKM values < 2) were excluded from differential expression analysis. For each gene, read counts were obtained using the counts feature in the subread package (v1.4.6).[16] Differentially expressed genes were identified with absolute fold change > 5 and adjusted *P*-value < 0.01 by DESeq2.[17] The sample PCA plot was generated using the plotPCA function in DESeq2 package after a variance stabilizing transformation of the count data by the variance Stabilizing Transformation function in DESeq2 package. The heatmap was generated using the heatmap.2 function in gplots package with normalized counts from the DESeq2 package scaled by row.

2.9 | Gene ontology enrichment analysis

Significantly over-represented functional categories were identified using DAVID Bioinformatics Resources 6.8.[18] Selected gene ontology (GO) terms and KEGG pathways were considered significant with *P* values < 0.05 and are showed in Figure 4 and Table S1-S5.

2.10 | Data availability

RNA-seq data of back skin/paw glabrous skin Merkel cells and IFE at P0 were uploaded to the GEO database (GSE122598; this study). RNA-seq data of hair follicle cells at P0 were obtained from the previous publication[13] and in the GEO database (GSM3069360, GSM3069361 and GSM3069362). Additional data that support the findings of this study are available from the corresponding author upon request.

3 | RESULTS

3.1 | Merkel cells are formed at embryonic day 15.5 in the glabrous paw skin

While Merkel cells in the back skin, which contains hair follicles, have been extensively studied, little is known about the development of Merkel cells in glabrous skin, which is devoid of hair follicles. To characterize Merkel cell formation in glabrous skin, we used *Atoh1-GFP* mice, in which an enhanced green fluorescent protein (GFP) is fused to the 3′-end of the atonal homolog 1 gene (*Atoh1*).[19] We collected paws from *Atoh1-GFP* pups at embryonic day (E) 14.5, E15.5, E16.5

and postnatal day (P) 0 and performed immunofluorescence analyses of ATOH1-GFP and the keratin intermediate filaments 8 and 20 (KRT8 and KRT20, respectively) that are expressed in more mature Merkel cells.[20,21] At E14.5, when Merkel cells were already formed inside of the hair placode of the back skin,[10,21] we could not detect any ATOH1-GFP(+), KRT8(+) or KRT20(+) Merkel cells in the mouse paw (Figure 1A). At E15.5, a few ATOH1-GFP(+) and KRT8(+) Merkel cells were observed in the mouse paw (Figure 1B). At E16.5, we detected more cells positive for ATOH1-GFP and KRT8, as well as a few cells that were also positive for KRT20 (Figure 1C). At P0, the number of Merkel cells positive for ATOH1-GFP, KRT8 and KRT20 drastically increased (Figure 1D). Similar to in the back skin,[21] induction of expression of ATOH1, KRT8 and KRT20 markers was temporally regulated in the glabrous paw skin as out of more than 200 Merkel cells analysed, no KRT20(+)/KRT8(−) cells were observed and only a small number of KRT8(+)/ATOH1-GFP(−) cells were detected (Figure S1A, B). Thus, similar to in the back skin, the formation of Merkel cells in the glabrous paw skin is a temporally regulated process, although the timing of the induction of Merkel cell formation in the glabrous paw skin occurs 1 day later compared to in the back skin.

3.2 | SOX9(+) cells do not give rise to Merkel cells in the glabrous paw skin at E14.5

In the back skin, we previously found that Merkel cells formed from SOX9(+) cells present in primary hair placodes.[10] Therefore, we sought to determine whether Merkel cells in glabrous skin are also formed from SOX9(+) cells. By performing immunofluorescence studies at previously examined time points E14.5-E16.5 and P0, we observed in the glabrous paw skin that Merkel cells were not near SOX9(+) cells (Figure 2A-D), suggesting that SOX9(+) cells may not be a common precursor cell population for Merkel cells in all of the different regions of the body.

To test this hypothesis, we used *Sox9-CreER; R26-mT/mG* mice to fate map cells originating from SOX9(+) cells. We treated embryos with tamoxifen at E13.5-E14.5, when Merkel cells had not yet been specified, and collected paws and back skins at E17.5 (Figure 2E). Immunofluorescence analysis showed that GFP staining was found in approximately 85% of KRT8(+) Merkel cells in the back skin (Figure 2F, G), which is consistent with our previous report that showed that Merkel cells originate from SOX9(+) precursor cells in the back skin.[10] In contrast, KRT8(+) Merkel cells were not GFP(+) in the glabrous paw skin (Figure 2H, I; Figure S1C). In fact, GFP(+) cells were negative for E-Cadherin, a marker of epithelial cells (Figure S1D). These fate-mapping studies show that at E14.5, when SOX9(+) cells give rise to Merkel cells in the back skin, SOX9(+) cells do not give rise to Merkel cells in the glabrous paw skin.

3.3 | Differential requirement of SHH for Merkel cell formation in the back and glabrous paw skin

In the back skin, Merkel cells are located around primary hair follicles and during development originate from SOX9(+) cells located

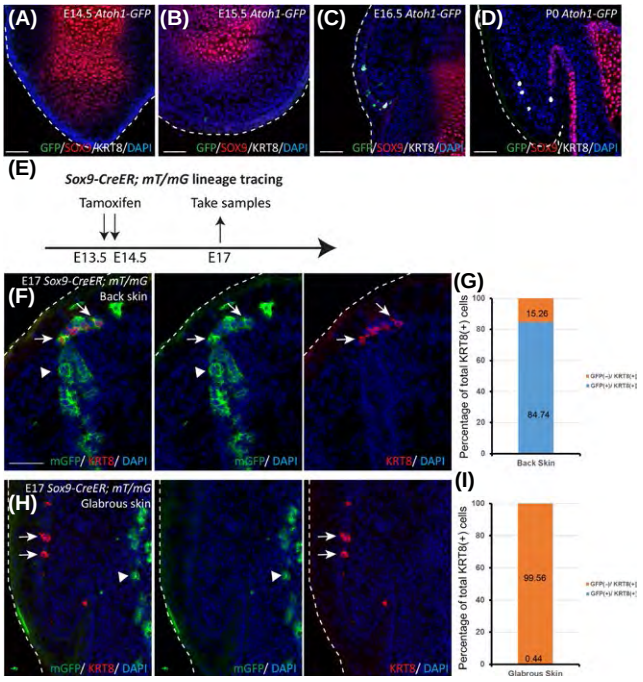

FIGURE 2 During embryogenesis, SOX9(+) cells do not give rise to Merkel cells in the glabrous paw skin at E14.5. (A–D) Immunofluorescence analysis of SOX9 (red), Merkel cell markers ATOH1-GFP (green) and KRT8 (white) at E14.5 (A), E15.5 (B), E16.5 (C) and at P0 (D) in the glabrous paw skin of *Atoh1-GFP* mice. White dotted lines indicate the edges of the tissue. Note that ATOH1-GFP(+) and KRT8(+) Merkel cells do not overlap with SOX9(+) cells. (E) Experimental design for *Sox9-CreER; mT/mG* lineage-tracing experiment. (F) *Sox9-CreER; mT/mG* lineage tracing in the back skin. White arrows point to Merkel cells; arrow heads point to SOX9-traced cells. SOX9-traced cells are GFP(+) (green). KRT8(+) Merkel cells are stained in red. Note the overlap between SOX9 progenies and KRT8 staining. (G) Quantification of Merkel cells positive for KRT8 and GFP in *Sox9-CreER; mT/mG* back skin sections at E17. n = 6. Data are presented as a percentage of the total 401 cells quantified. The bar graph shows the percentage of KRT8(+) cells, which are co-labelled with GFP (blue) or not co-labelled with GFP (orange). (H) *Sox9-CreER; mT/mG* lineage tracing in the glabrous paw skin. White arrows point to Merkel cells; white arrow heads point to SOX9-traced cells. SOX9-traced cells are GFP(+) (green). KRT8(+) Merkel cells are stained in red. Right side panels show separated colour channels. (I). Quantification of Merkel cells positive for KRT8 and GFP in *Sox9-CreER; mT/mG* glabrous paw skin sections at E17. n = 6. Data are presented as percentages of the total 325 cells quantified. The bar graph shows the percentage of KRT8(+) cells that are co-labelled with GFP (blue) or not co-labelled with GFP (orange). White dotted lines indicate the edges of the tissue. Scale bar is 50 μm in (A-D), (F) and (H)

in developing hair follicles.[9,10] In contrast, our data showed that Merkel cells in the glabrous paw skin do not originate from SOX9(+) cells. We therefore tested whether the formation of Merkel cells in the back and glabrous skin is similarly affected in mouse mutants with impaired hair follicle formation and loss of SOX9(+) cells. SHH and Smoothened (SMO), two critical factors of the SHH signalling pathway, are essential for hair follicle formation and specification of

TABLE 1 Table of genes encoding for the critical regulator of Merkel cell formation in the back skin but not in the glabrous paw skin

Gene symbol(s)	Mouse models used to study the gene loss of function effects	Merkel cell phenotype in the back skin	Merkel cell phenotype in the glabrous skin
Shh	*Shh*$^{EGFPcre/EGFPcre}$ *Krt14-Cre; Shh*$^{flox/flox}$	Merkel cells are not formed (Perdigoto et al., 2016; Xiao et al., 2016)	Reduced number of Merkel cells (Perdigoto et al., 2016)
Smo	*Krt14-Cre; Smo*$^{flox/flox}$ *Krt5-tTA; TRE-Cre; Smo*$^{flox/flox}$	Merkel cells are not formed (Perdigoto et al., 2016; Xiao et al., 2016)	Reduced number of Merkel cells (Perdigoto et al., 2016)
Eed, Smo	*Krt14-Cre; Eed*$^{flox/flox}$; *Smo*$^{flox/flox}$	Reduced number of Merkel cells (Perdigoto et al., 2016)	Increased number of Merkel cells (Perdigoto et al., 2016)

SOX9(+) cells.[22,23] In mouse mutants that lack *Shh* or *Smo* genes in the skin epithelium, Merkel cells are not formed in the back skin.[22,23] However, in the glabrous paw skin, loss of *Shh* or *Smo* had much less of an effect on Merkel cell formation as these cells were still formed, and their total count was only slightly reduced, compared to control[23] (Table 1). This lesser effect on Merkel cell formation was also found in the glabrous paw skin when coupling the loss of *Smo* with the loss of *EED*, a component of the Polycomb repressive complex (PRC) 2 that temporally restricts Merkel cell formation.[23,24] Loss of *EED* leads to an ectopic expansion of Merkel cells in both the back and glabrous paw skin.[23,24] Concurrent loss of *EED* and *Smo* in the skin epithelium depleted Merkel cells in the back skin; however, it leads to a slight increase in the number of Merkel cells in the glabrous paw skin[23] (Table 1).

These observations encouraged us to test whether SHH-responding cells, known to serve as Merkel cell precursors in the back skin,[22] are also the precursors of Merkel cells in glabrous skin. By performing lineage-tracing experiments using *Gli1-CreER*, *mT/mG* reporter mice, we demonstrated that at E14.5, GLI1(+) cells do not give rise to Merkel cells in the glabrous paw skin (Figure S2A-C). In fact, GFP(+) cells were negative for E-cadherin, suggesting that they are not of epithelial origin (Figure S2D). Thus, during development, SHH signalling is important for Merkel cell formation in the back skin but to a lesser extent in the glabrous paw skin. Together, these results show that in the back skin, SHH signalling is required for hair follicle formation, SOX9(+) cell specification and Merkel cell development; however, in the glabrous paw skin, SHH signalling makes minor contributions to Merkel cell development.

3.4 | Transcriptome profiles of Merkel cells isolated from the back and glabrous paw skin are similar

To look further into the mechanisms of Merkel cell formation, we performed transcriptional profiling of Merkel cells isolated from the back and glabrous skin regions. By performing FACS, we purified Merkel cells from the back and glabrous paw skins of P0 *Atoh1-GFP* mice and collected IFE cells from corresponding regions. We next isolated total RNAs from these FACS-purified cells and subjected them to high-throughput RNA sequencing (RNA-seq). We also included in the analysis hair follicle cells from the back skin for comparative reference purposes.[13] Principal component analysis (PCA) of the top 5000 most variable genes (across all samples) showed that Merkel cell populations from back and glabrous paw skins clustered near each other but away from the epidermal and hair follicle populations (Figure 3A). Hierarchical clustering of the significantly differentially expressed genes between Merkel cells and IFE cells also showed that Merkel cell populations from the back skin and glabrous skin clustered together and that they are distinct from the epidermis and hair follicle cells (Figure 3B). It should be noted that since the

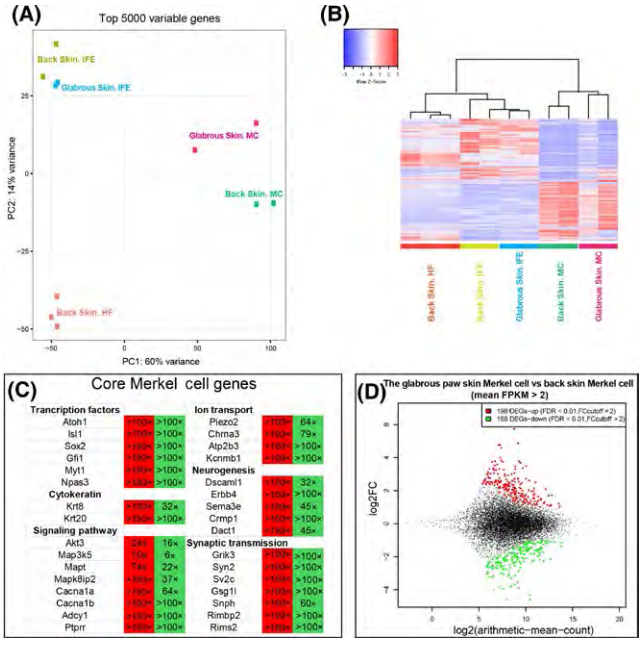

FIGURE 3 RNA-seq transcriptional profiling of Merkel cells isolated from back and glabrous paw skins revealed common core Merkel cell genes. (A) Principal component analysis based on the top 5000 most variable genes in the back skin and the glabrous paw skin. (B) Hierarchical clustering of the significantly differentially expressed genes between Merkel cells and IFE in either the back skin or glabrous paw skin (Figure S3), indicating distinct clusters of genes with either shared or unique gene expression in all isolated skin cell types. (C) List of core Merkel cell genes. Selected signature genes from the 514 genes that were commonly upregulated in Merkel cells of back and the glabrous paw skin regions, compared to IFE of the corresponding skin region and selected by these criteria, FPKM > 2, fold change > 5 and adjusted *P*-value < 0.01, are organized according to functional categories. (D) Differential expression analysis of genes expressed in Merkel cells in the glabrous paw skin vs. the back skin. Genes with mean FPKM > 2, absolute fold change > 2 and adjust *P*-value < 0.01 were considered as differentially expressed genes

TABLE 2 Table of genes encoding critical regulators of Merkel cell formation in both the back skin and the glabrous paw skin

Gene symbol(s)	Mouse models used to study the gene loss of function effects	Merkel cell phenotype in the back skin	Merkel cell phenotype in the glabrous skin
Atoh1	*Hoxb1^{Cre}; Atoh1$^{flox/flox}$Krt14-Cre; Atoh1$^{flox/flox}$*	Merkel cells are not formed (Maricich et al., 2009; Perdigoto et al., 2014; Van Keymeulen et al., 2009)	Merkel cells are not formed (Maricich et al., 2009; Van Keymeulen et al., 2009)
Sox2	*Krt14-Cre; Sox2$^{flox/flox}$*	Reduced number of Merkel cells (Lesko et al., 2013; Bardot et al., 2013)	Reduced number of Merkel cells (Bardot et al., 2013)
Ezh1/2	*Krt14-Cre; Ezh1/2$^{flox/flox}$*	Increased number of Merkel cells (Bardot et al., 2013)	Increased number of Merkel cells (Bardot et al., 2013)
Eed	*Krt14-Cre; Eed$^{flox/flox}$*	Increased number of Merkel cells (Dauber et al., 2016; Perdigoto et al., 2016)	Increased number of Merkel cells (Dauber et al., 2016; Perdigoto et al., 2016)
Suz12	*Krt14-Cre; Suz12$^{flox/flox}$*	Increased number of Merkel cells (Dauber et al., 2016)	Increased number of Merkel cells (Dauber et al., 2016)

RNA-seq data of purified hair follicle cell populations are obtained from a previous study,[13] there could be a batch effect in the PCA and hierarchical clustering analysis.

Seeking to determine which genes are specifically expressed in the back skin and glabrous skin, we first identified 1151 genes that were significantly upregulated in Merkel cells in the back skin compared to adjacent IFE cells and 753 genes that were significantly upregulated in Merkel cells in the glabrous paw skin compared to adjacent IFE cells, by fold change > 5 and adjusted *P*-value < 0.01 (Figure S3, Table S1 and Table S2). By performing KEGG pathway analysis of genes enriched in Merkel cells of the back skin and the glabrous paw skin, we observed common enrichment for genes of the cholinergic synapse, synaptic vesicle cycle and MAPK signalling pathways (Table S1 and Table S2). Gene ontology (GO) term analysis also showed similar enrichment for genes of ion transport, nervous system development and synaptic transmission in both back skin and glabrous paw skin Merkel cell populations (Table S1 and Table S2).

In line with our PCA and hierarchical clustering analyses which showed similarity in the Merkel cell populations of the back skin and glabrous paw skin, we observed a large overlap between upregulated genes in Merkel cells in the back and glabrous paw skins, in comparison to their corresponding IFE. We identified 514 upregulated genes in common and classified them as core Merkel cell genes (Figure 3C and Table S3). Among them were *Atoh1*, *Isl1*, *Sox2*, *Krt20* and *Piezo2*, genes with known roles in Merkel cells of the back and glabrous skin[19,21,25–27] (Figure 3C and Table 2).

We next performed differential expression analysis between Merkel cells in the glabrous paw skin and those in the back skin using FDR < 0.01 and fold change cut-off > 2. The analysis showed 198 genes that were more highly expressed in glabrous paw skin Merkel cells and 168 genes that were more highly expressed in back skin Merkel cells, out of more than 11 000 genes expressed in these cells (Figure 3D; Table S4 and S5). We also observed expression of *Hox* family genes, exclusive to the back skin or glabrous paw skin. Among these were *Hoxb3*, *Hoxb7* and *Hoxb5* in back skin Merkel cells and *Hoxc9* and *Hoxc10* in glabrous paw skin Merkel cells. Additionally, KEGG pathway and GO term analyses of genes expressed higher in glabrous paw skin Merkel cells showed enrichment of genes pertaining to focal adhesion, cell division and cell cycle pathways (Table S5), while genes expressed higher in back skin Merkel cells showed enrichment of genes pertaining to focal adhesion and cell adhesion pathways (Table S4). We did not observe any enrichment for the SHH signalling pathway or its components, which could explain the differing requirement of SHH signalling of Merkel cell formation in the glabrous paw skin and the back skin. Together, this result suggests that Merkel cells in the glabrous paw skin and back skin are very similar, and differences in gene expression between these two populations are likely due to their distinct localizations within the body such as *Hox* genes.

3.5 | FGFR2 is critical for Merkel cell formation in both back and glabrous paw skin

As described above, KEGG pathway analysis of Merkel cell core genes revealed enrichment for genes of MAPK signalling pathways (Figure 4A and Table S3). Interestingly, we recently reported that FGFR2-mediated signalling is required for Merkel cell specification in the back skin,[10] and it is known that the MAPK signalling pathway is a downstream effector of FGFR2-mediated signalling.[28] To test whether FGFR2 signalling also controls Merkel cell formation in the glabrous paw skin, we analysed *Fgfr2* cKO mice in which *Fgfr2* is conditionally ablated in the skin epithelium.[10] Immunofluorescence analysis of mouse glabrous paw skin confirmed the loss of FGFR2 in P0 *Fgfr2 cKO* mice compared to control (Figure 4B) and revealed significant reductions in the numbers of KRT8(+) and KRT20(+) Merkel cells (Figure 4C-E). Thus, FGFR2-mediated signalling is required for Merkel cell formation in both back and glabrous paw skin.

4 | DISCUSSION

Merkel cells are important epidermal mechanoreceptors involved in tactile recognition of shapes and textures of objects.[4,29] In the

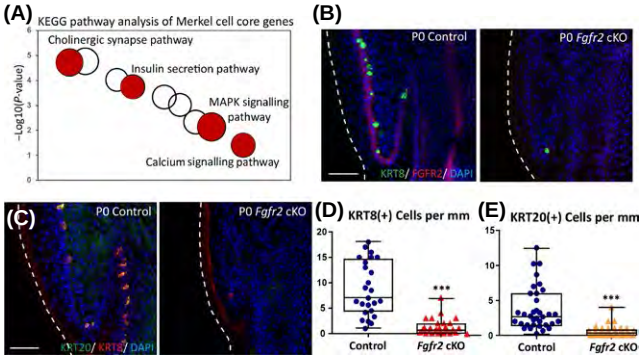

FIGURE 4 FGFR2 is critical for Merkel cell formation in the glabrous paw skin. (A) KEGG pathway analysis of Merkel cell core genes from the back skin and glabrous paw skin. Selected KEGG terms are in red. The size of a circle indicates the number of genes in a KEGG term. (B) Immunofluorescence analysis of a Merkel cell marker KRT8 (green) and FGFR2 (red) in P0 control and *Fgfr2* cKO glabrous paw skin. Note that FGFR2 (red) is completely gone in P0 *Fgfr2* cKO. (C) Immunofluorescence analysis of Merkel cell markers KRT20 (green) and KRT8 (red) in P0 control and P0 *Fgfr2* cKO glabrous paw skin. (D). Quantification of KRT8 (+) Merkel cells in P0 control and P0 *Fgfr2* cKO, $P < 0.0001$, n = 4. (E). Quantification of KRT20(+) Merkel cells in P0 control and P0 *Fgfr2* cKO, $P < 0.0001$, n = 4. White dotted lines indicate the edges of the tissue. Scale = 50 μm in (B) and (C). The data presented in box plots (D, E) show the median with 25th and 75th percentile borders. Whiskers extend from minimum to maximum. ***$P < 0.001$ (per Mann-Whitney test)

body, Merkel cells are innervated by afferent neurons and located in touch-sensitive areas, which in mice are located on their back skin, whisker pads and footpads. Merkel cells in the back skin are located in touch domes around primary hair follicles and are innervated by two types of neurofilament fibres, NFH+/TrkC+ and Ret+/TrkA+ fibres.[30] In contrast to in the back skin, Merkel cells in the glabrous paw skin are mainly innervated by NFH+/TrkC+ fibres.[30]

The majority of studies on Merkel cells have been done on the murine back skin. Our recent study revealed that Merkel cells within the back skin arise from SOX9(+) precursors located in hair placodes.[10] In contrast, there is little understanding of the mechanisms that control Merkel cell formation in areas of the skin devoid of hair, such as the glabrous paw skin.

In this paper, we performed a comparative analysis of Merkel cells located in the back skin and the glabrous paw skin. Our study shows that in the glabrous paw skin, the formation of Merkel cells occurs one day later than it does in the back skin, but it follows the same maturation process characterized by progressive expression of early (*Atoh1*), mid (*Krt8*) and late (*Krt20*) differentiation markers.[21]

We performed transcriptional profiling of Merkel cells isolated from back and glabrous paw skins of newborn mice and identified that these cells share similar transcriptomes. Consistent with previous studies, among commonly expressed genes were transcription factors *Atoh1* and *Sox2*,[31,32] which have been shown to be essential for Merkel cell formation in glabrous and back skin.[19,21,26,27] In epidermal progenitors, *Atoh1* and *Sox2* are regulated by the epigenetic repressor PRC2. The loss of PRC2 by knocking out their critical components *Ezh1/2*, *Eed* or *Suz12* in the skin epithelium leads to activation of Atoh1 and Sox2 expression, which results in the formation of ectopic Merkel cells.[23,26] As in the back skin, we observed a similar phenotype in the glabrous paw PRC2-null skin epithelium.[23,24,26] To gain further insight into the general regulators of Merkel cell control, we performed KEGG pathway analysis of commonly upregulated genes and identified enrichment for genes in the MAPK signalling pathway. One of the pathways that activates the MAPK kinase cascade is the FGF signalling pathway.[28] As our recent study shows that FGFR2 is critical for Merkel cell formation in the back skin,[10] we thus examined FGFR2's role in the glabrous paw skin and demonstrated that the loss of *Fgfr2* leads to a drastic decrease in the number of Merkel cells, highlighting a general requirement for the FGFR2 signalling pathway in Merkel cell formation. Thus, Merkel cells in newborn back skin and glabrous paw skin are similar and share some common regulators that control Merkel cell formation.

Our studies also uncover the differences between Merkel cell development in both back and glabrous skin. Although SOX9(+) cells were recently shown to give rise to Merkel cells in the back skin at E14.5,[10] our fate-mapping experiments showed that SOX9(+) cells do not give rise to Merkel cell in the glabrous paw skin at a similar time point. Furthermore, we found that SHH signalling, which is essential for Merkel cell formation in the back skin,[22,23] is important but has minor roles in Merkel cell development in the glabrous skin.

How can we reconcile between these differences? In the back skin, SHH signalling is essential for proper hair follicle development, including SOX9(+) cell specification.[22,23] Because glabrous skin lacks hair follicles, the mechanisms regulating Merkel cell formation through control of hair follicle development should have no effect on Merkel cell formation in this region. Because SOX9(+) cells do not give rise to Merkel cells in the glabrous paw skin, there could be a different precursor population in this region. Alternatively, the back and glabrous paw skins might share a common Merkel cell progenitor population, with SOX9 expression within this progenitor population occurring only in the back skin. In support of the latter hypothesis, previous studies have shown that the loss of *Sox9* in the skin epithelium does not affect Merkel cell formation in the back skin, suggesting that even in this region, SOX9 is not required for Merkel cell development and serves simply as a marker.[10] Future work on uncovering a population of Merkel cell precursors in glabrous skin will reconcile these possibilities.

Future studies on the morphogenesis of Merkel cells are important not only for our understanding of the biology of the skin as a sensory organ but also for uncovering processes that lead to human pathologies. Hyper- or hypo-sensitivity to touch have long been reported in patients with diabetes, inflammation or autism.[33–36] Recent studies have shown that Merkel cells can inhibit alloknesis, a disease state where mechanical light touch stimuli provoke itching.[37] Finally, these discoveries might help us uncover which

mechanisms control Merkel cell carcinoma, a deadly skin disease with no effective treatment.[38–41]

ACKNOWLEDGEMENTS

For help, critical suggestions, reagents and experimental input, we are grateful to Dr. Ya-Chieh Hsu, Dr. Julie Segre and Sergei Ezhkov. We would like to thank Dr. Philippe Soriano for the *Fgfr2* floxed mice. We also thank the personnel of the Microscope Facility at ISMMS. Research reported in this publication was supported by the National Institute of Arthritis and Musculoskeletal and Skin Diseases of the National Institutes of Health under award number R01 AR063724 (to E.E.). We also thank the NCI P30 Cancer Center Support Grant (to E.E.) for their support, as well as the NIH/NHBLI grant, the R01HL133120 (to D.Zheng.). This content is solely the responsibility of the authors and does not necessarily represent the official views of the National Institute of Health.

CONFLICT OF INTERESTS

The authors have declared no conflicting interests.

AUTHOR CONTRIBUTIONS

MBN, VJV, IC and EE conceived the experimental plan. MBN, VJV and IC carried out the experiments. DZ and DZ analysed RNA-seq data. MBN, IC, VP and EE wrote the manuscript with input from all authors.

ORCID

Elena Ezhkova https://orcid.org/0000-0003-4154-1615

REFERENCES

[1] R. K. Winkelmann, A. S. Breathnach, *J Invest Dermatol.* **1973**, *60*(1), 2.
[2] H. Haeberle, E. A. Lumpkin, *Chemosens. Percept.* **2008**, *1*, 110.
[3] E. A. Lumpkin, K. L. Marshall, A. M. Nelson, *J. Cell Biol.* **2010**, *191*, 237.
[4] S. M. Maricich, K. M. Morrison, E. L. Mathes, B. M. Brewer, *J. Neurosci.* **2012**, *32*, 3296.
[5] A. Iggo, A. R. Muir, *J. Physiol.* **1969**, *200*, 763.
[6] P. M. Boot, G. Rowden, N. Walsh, *Am. J. Dermatopathol.* **1992**, *14*, 391.
[7] J. P. Lacour, D. Dubois, A. Pisani, J. P. Ortonne, *Br. J. Dermatol.* **1991**, *125*, 535.
[8] I. Moll, R. Paus, R. Moll, *J Invest Dermatol.* **1996**, *106*, 281.
[9] Z. Halata, M. Grim, K. I. Bauman, *Anat Rec Part A.* **2003**, *271a*(1), 225.
[10] M. B. Nguyen, I. Cohen, V. Kumar, Z. Xu, C. Bar, K. L. Dauber-Decker, P. C. Tsai, P. Marangoni, O. D. Klein, Y. C. Hsu, T. Chen, M. L. Mikkola, E. Ezhkova, *Nat. Commun.* **2018**, *9*(1), 2333.
[11] A. Molotkov, P. Mazot, J. R. Brewer, R. M. Cinalli, P. Soriano, *Dev. Cell* **2017**, *41*, 511.
[12] Z. Xu, W. Wang, K. Jiang, Z. Yu, H. Huang, F. Wang, B. Zhou, T. Chen, *eLife*. **2015**, *4*, e10567.
[13] I. Cohen, D. Zhao, C. Bar, V. J. Valdes, K. L. Dauber-Decker, M. B. Nguyen, M. Nakayama, M. Rendl, W. A. Bickmore, H. Koseki, D. Zheng, E. Ezhkova, *Cell Stem Cell* **2018**, *22*, 726.
[14] D. Kim, G. Pertea, C. Trapnell, H. Pimentel, R. Kelley, S. Salzberg, *Genome Biol.* **2013**, *14*, R36.
[15] C. Trapnell, A. Roberts, L. Goff, G. Pertea, D. Kim, D. R. Kelley, H. Pimentel, S. L. Salzberg, J. L. Rinn, L. Pachter, *Nat Protocols*. **2012**, *7*, 562.
[16] Y. Liao, G. K. Smyth, W. Shi, *Bioinformatics* **2014**, *30*(7), 923-930.
[17] M. I. Love, W. Huber, S. Anders, *Genome Biol.* **2014**, *15*, 550.
[18] W. da Huang, B. T. Sherman, R. A. Lempicki, *Nat. Protoc.* **2009**, *4*(1), 44.
[19] S. M. Maricich, S. A. Wellnitz, A. M. Nelson, D. R. Lesniak, G. J. Gerling, E. A. Lumpkin, H. Y. Zoghbi, *Science* **2009**, *324*, 1580.
[20] I. Moll, C. Kuhn, R. Moll, *J Invest Dermatol.* **1995**, *104*, 910.
[21] C. N. Perdigoto, E. S. Bardot, V. J. Valdes, F. J. Santoriello, E. Ezhkova, *Development* **2014**, *141*, 4690.
[22] Y. Xiao, D. T. Thoresen, L. L. Miao, J. S. Williams, C. C. Wang, R. P. Atit, S. Y. Wong, I. Brownell, *PLoS Genet*. **2016**, *12*(7), e1006150.
[23] C. N. Perdigoto, K. L. Dauber, C. Bar, P. C. Tsai, V. J. Valdes, I. Cohen, F. J. Santoriello, D. Zhao, D. Zheng, Y. C. Hsu, E. Ezhkova, *PLoS Genet*. **2016**, *12*, e1006151.
[24] K. L. Dauber, C. N. Perdigoto, V. J. Valdes, F. J. Santoriello, I. Cohen, E. Ezhkova, *J Invest Dermatol.* **2016**, *136*, 1647.
[25] A. Van Keymeulen, G. Mascre, K. K. Youseff, I. Harel, C. Michaux, N. De Geest, C. Szpalski, Y. Achouri, W. Bloch, B. A. Hassan, C. Blanpain, *J. Cell Biol.* **2009**, *187*(1), 91.
[26] E. S. Bardot, V. J. Valdes, J. S. Zhang, C. N. Perdigoto, S. Nicolis, S. A. Hearn, J. M. Silva, E. Ezhkova, *EMBO J.* **2013**, *32*, 1990.
[27] M. H. Lesko, R. R. Driskell, K. Kretzschmar, S. J. Goldie, F. M. Watt, *Dev. Biol.* **2013**, *382*(1), 15.
[28] D. M. Ornitz, N. Itoh, *Wires Dev Biol.* **2015**, *4*, 215.
[29] D. M. Owens, E. A. Lumpkin, *Cold Spring Harb. Perspect Med.* **2014**, *4*(6), a013656.
[30] J. Niu, A. Vysochan, W. Luo, *PLoS ONE* **2014**, *9*, e92027.
[31] H. Haeberle, M. Fujiwara, J. Chuang, M. M. Medina, M. V. Panditrao, S. Bechstedt, J. Howard, E. A. Lumpkin, *Proc Natl Acad Sci U S A.* **2004**, *101*, 14503.
[32] B. U. Hoffman, Y. Baba, T. N. Griffith, E. V. Mosharov, S. H. Woo, D. D. Roybal, G. Karsenty, A. Patapoutian, D. Sulzer, E. A. Lumpkin, *Neuron* **2018**, *100*, 1401.
[33] S. J. Blakemore, T. Tavassoli, S. Calo, R. M. Thomas, C. Catmur, U. Frith, P. Haggard, *Brain Cogn.* **2006**, *61*(1), 5.
[34] S. D. Tomchek, W. Dunn, *Am. J. Occup. Ther.* **2007**, *61*, 190.
[35] K. F. Richards, A. Guastafierro, M. Shuda, T. Toptan, P. S. Moore, Y. Chang, *J. Gen. Virol.* **2015**, *96*, 3532.
[36] W. Chang, H. Kanda, R. Ikeda, J. Ling, J. J. DeBerry, J. G. Gu, *Proc Natl Acad Sci U S A.* **2016**, *113*, E5491.
[37] J. Feng, J. Luo, P. Yang, J. Du, B. S. Kim, H. Hu, *Science* **2018**, *360*, 530.
[38] M. Samimi, A. Touze, *Presse Med.* **2014**, *43*(12 Pt 2), e405.
[39] M. Thakuria, N. R. LeBoeuf, G. Rabinowits, *Am Soc Clin Oncol Educ Book*. **2014**, e405-e410.
[40] K. Boyse, E. H. Foley, V. Bradley, D. Scarborough, *Cutis* **2004**, *74*, 350.
[41] S. V. Porceddu, M. J. Veness, A. Guminski, *J. Clin. Oncol.* **2015**, *33*, 3338.

SUPPORTING INFORMATION

Additional supporting information may be found online in the Supporting Information section at the end of the article.

Figure S1. *Sox9-CreER; mT/mG* lineage tracing in the glabrous paw skin.
Figure S2. *Gli1-CreER; mT/mG* lineage tracing in the glabrous paw skin.
Figure S3. Volcano plots of differentially expressed genes between Merkel cells and IFE in the back skin and glabrous paw skin.

Table S1. Differentially expressed genes in MC compared with IFE in the glabrous paw skin

Table S2. Differentially expressed genes in MC compared with IFE in the back skin

Table S3. Common upregulated genes in Merkel cells compared with IFE in the glabrous paw skin and back skin

Table S4. Differentially expressed genes at the back skin Merkel cell compared with the glabrous paw skin Merkel cell

Table S5. GO Biological Process analysis of differentially expressed genes at the glabrous paw skin MC compared with back skin MC

How to cite this article: Nguyen MB, Valdes VJ, Cohen I, et al. Dissection of Merkel cell formation in hairy and glabrous skin reveals a common requirement for FGFR2-mediated signalling. *Exp Dermatol*. 2019;28:374–382. https://doi.org/10.1111/exd.13901



Chapter 10

Isolation and Detection of G Protein-Coupled Receptor (GPCR) Heteroreceptor Complexes in Rat Brain Synaptosomal Preparation Using a Combined Brain Subcellular Fractionation/Co-immunoprecipitation (Co-IP) Procedures

Dasiel O. Borroto-Escuela, Manuel Narvaez, Martina Zannoni, Chiara Contri, Minerva Crespo-Ramírez, Michael di Palma, Patrizia Ambrogini, Daily Y. Borroto-Escuela, Ismel Brito, Mariana Pita-Rodríguez, Ismael Valladolid-Acebes, Miguel Pérez de la Mora, and Kjell Fuxe

Abstract

The isolation and characterization of GPCR heteroreceptor complexes, specially those present at the central nervous system, are of crucial relevance for the understanding of the molecular mechanisms behind several mental and neurodegenerative disorders. The existence of homo- and heteroreceptor complexes with allosteric receptor-receptor interactions increases the diversity of receptor function including recognition, trafficking, and signaling. This phenomenon increases our understanding of how brain function is altered through molecular integration of receptor signals. An alteration in specific heteroreceptor complexes or their neuronal localization is considered to have a role in the pathogenic mechanisms that lead to mental and neurological diseases, including drug addiction, depression, Parkinson's disease, and schizophrenia. Therefore, it is fundamental to understand the appropriate localization and synaptic clustering of these GPCR heteroreceptor complexes. This chapter represents a workflow for the analysis of GPCR heteroreceptor complexes by means of combined use of differential centrifugation/co-immunoprecipitation in rat brain tissue. The combination of differential centrifugation/co-immunoprecipitation allows the separation and detection of GPCR heteroreceptor complexes present at synaptic sites from those found in intracellular compartments and vesicular pools. It is a reproducible protocol and produces reliable quantitative data.

Key words G protein-coupled receptors (GPCRs), GPCR heteroreceptor complexes, Receptor-receptor interactions, Heterodimerization, Co-immunoprecipitation, Subcellular, Synaptic membrane protein, Ultracentrifugation

Yuji Odagaki and Dasiel O. Borroto-Escuela (eds.), *Co-Immunoprecipitation Methods for Brain Tissue*, Neuromethods, vol. 144, https://doi.org/10.1007/978-1-4939-8985-0_10, © Springer Science+Business Media, LLC, part of Springer Nature 2019

INFORME DE LABORES 2019

1 Introduction

Mental and neurological diseases, including drug addiction, depression, Parkinson's disease, and schizophrenia, are highly complex in their etiology. It is not surprising that the underlying pathological processes are poorly understood, and treatment possibilities are inadequate. One emerging concept is that direct physical interactions of different receptors named homo−/heteroreceptor complexes may be involved with disease onset and progression [1–3]. Among all membrane receptor complexes, the G protein-coupled receptors (GPCR) heteroreceptor complexes are of special relevance [4–8].

In the last decades, GPCR heteroreceptor complexes were demonstrated through diverse biophysical, biochemical, or microscopy-based procedures (e.g., co-immunolocalization, co-immunoprecipitation, radioligand binding, co-internalization analysis, fluorescence resonance energy transfer (FRET) or bioluminescence resonance energy transfer (BRET) methods) [9–11]. Each methodology used has provided precise and valuable information which was considered with caution in view of the limitations of the techniques. Some controversy regarding some approaches also emerged [12, 13].

In this chapter, we will describe how the combined use of brain tissue subcellular fractionation procedure and co-immunoprecipitation method may make it possible in a highly selective and sensitive assay to study and characterize also the GPCR homo- and heteroreceptor complexes, specially their existence and distribution within a subcellular compartment. Although the combined procedures of brain tissue subcellular fractionation by differential centrifugation and co-immunoprecipitation require a great deal of optimization and troubleshooting, in most cases the method allows the study of the synaptic clustering of GPCR heteroreceptor complexes in a fine-tuning manner.

2 Materials

2.1 Animals

3- to 4-week-old male Sprague Dawley rats (Scanbur, Sweden). All studies involving animals are performed in accordance with the Stockholm North Committee on Ethics of Animal Experimentation, the Swedish National Board for Laboratory Animal, and the European Communities Council Directive (Cons 123/2006/3) guidelines for accommodation and care of laboratory animals. Thus, animals are housed in standard cages with ad libitum access to food and water and maintained under controlled standard conditions (12 h dark/light cycle, 22 °C temperature, and 66% humidity).

2.2 Reagents

Protein A-immobilized agarose fast flow, 50% (v/v) (Sigma-Aldrich); TrueBlot™ anti-mouse IgG IP resin (eBioscience); Protease Inhibitor Cocktail Set III (Millipore), phosphatase inhibitors (aprotinin, β-glycerophosphate, pefabloc, leupeptin); acrylamide/bis-acrylamide (30%/0.8% w/v) (Bio-Rad); ammonium persulfate (APS) (Sigma-Aldrich); tetramethylethylenediamine (TEMED) (Sigma-Aldrich), sodium dodecyl sulfate (SDS) (Sigma-Aldrich); methanol 99.8% (Pancreac Química SL, Barcelona, Spain); Precision Plus Protein Standards (Bio-Rad); Tween 20 (Sigma-Aldrich); nonfat dry milk or bovine serum albumin (BSA) or commercial blocking buffer (e.g., Odyssey blocking buffer from LI-COR Biosciences, cat. nr. 927–40,000); SuperSignal West Pico Chemiluminescent Substrate (Thermo Fisher Scientific Inc.); BCA Protein Assay Kit (Pierce Biotechnology). *Antibodies specific for subcellular fractions*: e.g., anti-synaptophysin (Chemicon) or anti-VAMP (Stressgen) for synaptic vesicles, anti-Na^+/K^+-ATPase (Transduction Laboratories) for plasma membranes, and anti-Lactate Dehydrogenase (anti-LDH, Abcam) for cytosol. *Primary antibodies*: rabbit monoclonal anti-5HT1A (vtg544, 1 μg/mL, VTG Biosciences), goat monoclonal anti-5HT1A (ab101914, 1:500, Abcam, Sweden), rabbit monoclonal anti-5HT2A (HPA014011, 1 μg/mL; Human Atlas Project, Stockholm, Sweden), and goat monoclonal anti-5HT2A (ab140824, 1:500, Abcam, Sweden). *Secondary antibodies*: horseradish peroxidase (HRP)-conjugated goat anti-rabbit IgG (Thermo Fisher Scientific) and HRP-conjugated anti-mouse IgG TrueBlot™ (eBioscience).

2.3 Buffers

1. *Phosphate-buffered saline (PBS)*: 137 mM NaCl, 2.7 mM KCl, 1.4 mM KH_2PO_4, 17 mM Na_2HPO_4, pH 7.2.
2. *Percoll gradients*: To create a discontinuous gradient, carefully layer 2 mL of each Percoll solution in an 11 mL (16 × 100 mm) polycarbonate high-speed centrifuge tube, starting with 23% at the bottom. Prepare gradients on the day of or the day before the experiment, and keep at 4 °C until use. *23% Percoll*: 12 mL 100% Percoll and 14 mL H_2O in 26 mL 2× sucrose buffer. Adjust solutions to pH 7.4 and store up to 5 days at 4 °C. *15% Percoll*. 30 mL 23% Percoll in 16 mL 1× sucrose buffer. Adjust solutions to pH 7.4 and store up to 5 days at 4 °C. *10% Percoll*: 20 mL 15% Percoll in 10 mL 1× sucrose buffer. Adjust solutions to pH 7.4 and store up to 5 days at 4 °C. *3% Percoll*: 6 mL 10% Percoll in 14 mL 1× sucrose buffer. Adjust solutions to pH 7.4 and store up to 5 days at 4 °C.
3. *Sucrose gradients* in thin-walled ultracentrifuge tubes (ultra-clear tubes, 38.5 mL capacity, 25 × 89 mm). 7 mL 1.2 M sucrose. 6 mL 1.0 M sucrose. 6 mL 0.8 M sucrose. 6 mL 0.6 M sucrose. 6 mL 0.4 M sucrose. Prepare sucrose solutions

INFORME DE LABORES 2019

individually in Medium L, and store up to 5 days at 4 °C. On the day of experiment, layer solutions on top of each other in a thin-walled 38.5 mL, 25 × 89 mm ultracentrifuge tube, starting with 1.2 M at the bottom. Keep at 4 °C until use.

4. *Wash buffer*: 6.142 mL 2 M NaCl (122 mM final). 500 µL 1 M KCl (5 mM final). 460 µL 0.25 M NaH_2PO_4 (1.15 mM final). 4 mL 0.5 M PIPES (20 mM final). 0.1 g D-(+)-glucose (1 mg/mL final). 100 mL H_2O. Adjust to pH 6.8. Prepare fresh on the day of use and keep at 4 °C.
5. *Hypoosmotic Medium L*. 0.174 g K_2HPO_4 (1 mM final). 2 mL 0.5 M EDTA (0.1 mM final). 1 L H_2O. Adjust to pH 8.0. Store up to several months at 4 °C.
6. *Radioimmunoprecipitation assay (RIPA) lysis buffer*: 50 mM Tris–HCl, pH 7.4, 100 mM NaCl, 1% Triton X-100, 0.5% sodium deoxycholate, 0.2% SDS, and 1 mM EDTA.
7. *Sodium dodecyl sulfate polyacrylamide gel electrophoresis (SDS-PAGE) sample buffer*: 125 mM Tris–HCl, pH 6.8, 4% SDS, 20% glycerol, 0.004% bromophenol blue, and freshly prepared 50 mM dithiothreitol (DTT).
8. *Urea sample buffer*: 375 mM Tris–HCl, pH 6.8, 8 M Urea, 50 mM DTT, 2% SDS, 0.004% bromophenol blue.
9. *Glycine buffer*: 0.1–0.2 M glycine, pH 2.0–3.0.
10. *Electrophoresis buffer*: 25 mM Tris base, pH 8.0, 380 mM Glycine, 0.1% SDS.
11. *Anode buffer*: 300 mM Tris base, 20% methanol.
12. *Cathode buffer*: 40 mM 6-Aminocaproic acid, 20% methanol.
13. *IB blocking solution*: PBS containing 0.05% Tween 20 and 5% (w/v). You can also use the commercial blocking buffer (e.g., Odyssey blocking buffer from LI-COR Biosciences, cat. nr. 927-40000).
14. *Immunoblot (IB) washing solution*: PBS containing 0.05% Tween 20.

2.3.1 Instrumentation, Equipment, and Software

1. Rat guillotine.
2. Surgical tools for isolation of the cortex.
3. 25 and 55 mL Potter-Elvehjem homogenizers (Teflon glass).
4. High-speed centrifuge (e.g., Sorvall RC-5C with SS-34 rotor and adaptors for eight 16 × 100 mm tubes).
5. 50 mL (29 × 102 mm) polycarbonate high-speed centrifuge tubes.
6. Ultracentrifuge capable of 100,000 × *g* with swinging-bucket rotor (e.g., Beckman SW 28) and 31 mL, 25 × 89 mm, thick-walled polycarbonate ultracentrifuge tubes.

INFORME DE LABORES 2019

7. Fixed angle rotor (e.g., Beckman 70.1 Ti or 50 Ti) with 10 mL, 16 × 76 mm thick-walled polycarbonate ultracentrifuge tubes.
8. 10,000 MWCO dialysis membranes.
9. Centriprep 10 centrifugal concentrations (Millipore).
10. Mini-PROTEAN casting frame (Bio-Rad).
11. Immobilon-P transfer membrane (pore 0.45 μm, Millipore).
12. Extra thick blot paper, filter paper (Bio-Rad).
13. Western blot equipment (Bio-Rad).
14. Proper detection equipment, for instance, for Kodak Image Station 440 CF from Kodak for HRP-coupled antibodies and Odyssey from LI-COR Biosciences for infrared dye-coupled antibodies.

3 Methods

3.1 Synaptosomes Preparation (Fig. 1)

1. Sacrifice 4–8 rats weighting 200–250 g under ether anesthesia by decapitation with a guillotine. Remove carefully the brains and place in ice-cold 1× sucrose buffer.
2. Dissect quickly the brain area of interest (e.g., hippocampus, raphe nucleus, striatum (dorsal and ventral components)). Pools 4–8 are of interest together, and place in 9 mL ice-cold 1× sucrose buffer containing the Protease Inhibitor Cocktail.
3. Homogenize with the polytron for four periods of 20 s each.
4. Centrifuge the homogenate for 10 min at 1000 × *g* (3000 rpm in an SS-34 rotor) at 4 °C to remove the nucleus and tissue debris.
5. Recover the supernatant containing the membrane extracts, and carefully load 2 mL supernatant onto each of four Percoll gradients. Centrifuge gradients for exactly 5 min at 32,500 × *g* (17,250 rpm in an SS-34 rotor), 4 °C. Alternatively, the supernatant may be loaded onto a discontinuous sucrose gradient consisting of 1.2/1.0/0.8 M sucrose layers and centrifuged for 20 min at 48,200 × *g*.
6. Collect synaptosomes from the interface at 15%/23% using a Pasteur pipet. In this case, the synaptosome fraction will be collected from a discontinuous sucrose gradient consisting of 1.2/1.0/0.8 M sucrose; the synaptosomes will be collected from the interface between the 1.2 and 1.0 M sucrose layers. Synaptosomes are visible as a cloud of material concentrated at the bottom interface (15%/23% for Percoll or 1.2/1.0 M for sucrose). Use a separate Pasteur pipet to remove upper layers before collecting the synaptosome layer.

INFORME DE LABORES 2019

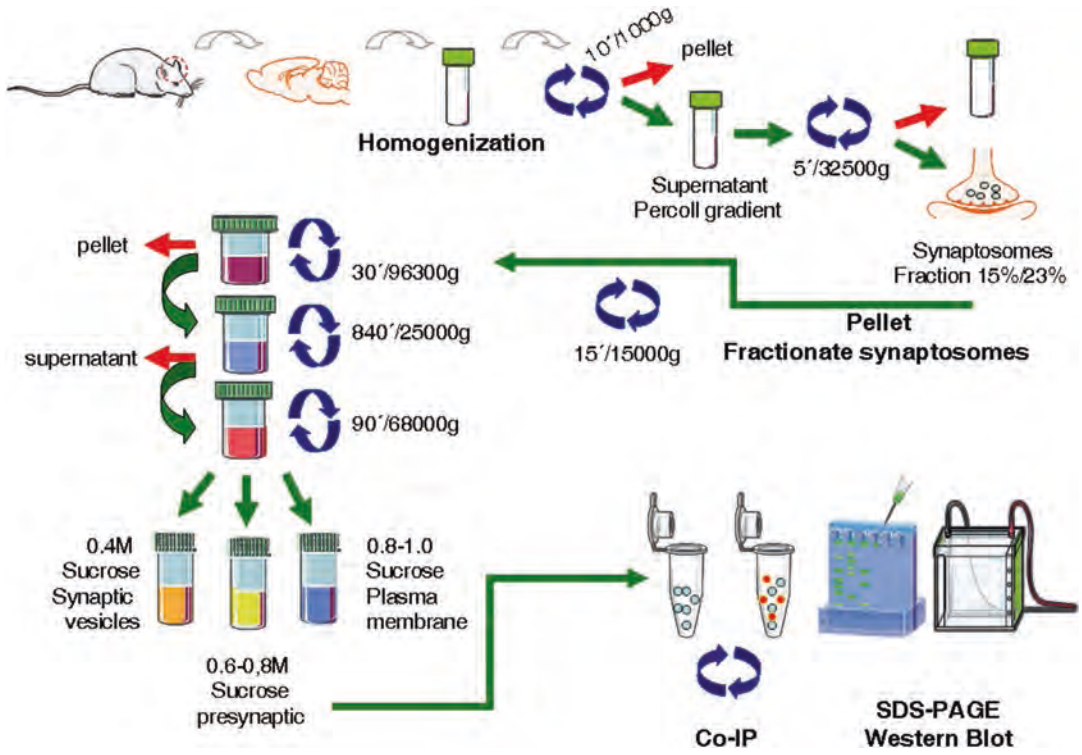

Fig. 1 Illustration of the flow chart for synaptosomes preparation and co-immunoprecipiation (Co-IP) experiment which is done using these fractions. The method is represented step by step. It includes the brain region dissection, the synaptosomes isolation, and the subcellular fraction of the synaptosomes samples by differential centrifugation and the co-immunoprecipitation, electrophoresis, and Western blot. Each of these steps is described in more details in the corresponding method section

7. Transfer the synaptosomes to a 50 mL polycarbonate centrifuge tube, and add 30 mL chilled wash buffer. Centrifuge 15 min at 15,000 × *g* (11,000 rpm in an SS-34 rotor), 4 °C.
8. Carefully discard the supernatant, and use immediately the synaptosomes pellet for fractionation (see below) or alternatively frozen down in liquid nitrogen and stored at −80 °C until use.
9. Determine the total protein content of each pellet (synaptosomes) by means of the BCA Protein Assay Kit (Pierce, USA). Adjust all membrane extracts to the same final concentration, normally between 1 and 2 mg/mL in wash buffer containing the Protease Inhibitor Cocktail.

3.2 Fractionate Synaptosomes (Fig. 1)

1. Resuspend the synaptosomes pellet (Step 8) in 12–15 mL ice-cold hypoosmotic Medium L. Save a 0.5 mL aliquot of this synaptosomal suspension for validation of the fractionation procedure.

INFORME DE LABORES 2019

2. Homogenize with the polytron for three periods of 10 s each, and then incubate suspension on ice for 15 min.
3. Repeat homogenization once more, then adjust pH to 8.0 with 1 M KOH, and incubate homogenized synaptosomal suspension on ice for another 45 min.
4. Layer, as much as you need, 5 mL synaptosomal suspension onto 5 mL of 1.0 M sucrose in Medium L in a 31 mL thick-walled polycarbonate ultracentrifuge tube.
5. Centrifuge 30 min at 96,300 × *g* (27,000 rpm in an SW 28 rotor), 0° to 4 °C. Collect the supernatant in fresh 31 mL ultracentrifuge tubes. Discard the pellet, which contain the crude synaptosomal mitochondrial fraction.
6. Cover the supernatant tubes with Parafilm and gently mix by inverting. Centrifuge 14 h at 25,000 × *g* (14,000 rpm in an SW 28 rotor), 4 °C. Collect the pellet on ice and discard the supernatant (cytosolic fraction).
7. Resuspend the pellet from Step 6 in Medium L (1.0–4.0 mL). Layer 5 mL of suspension onto separate sucrose gradients prepared in 38.5 mL thin-walled ultracentrifuge tubes. Mark phase interfaces on the tubes to facilitate recognition of the desired fractions after centrifugation.
8. Centrifuge sucrose gradients 90 min at 68,000 × *g* (23,000 rpm in an SW 28 rotor), 0° to 4 °C. Collect each fraction carefully with a Pasteur pipet. The synaptic vesicle fraction is located above the 0.4 M sucrose layer. The fraction enriched with the presynaptic plasma membrane proteins is located at the phase interfaces between 0.6/0.8, 0.8/1.0, and 1.0/1.2 M sucrose. The 0.8/1.0 M interface usually contains the purest plasma membrane fraction.
9. Transfer each fraction to a thick-walled 10 mL ultracentrifuge tube. Add Medium L to fill 3/4 of each tube. Centrifuge 45 min at 106,500 × *g* (40,000 rpm in 50 Ti rotor), 0° to 4 °C.
10. Collect each pellet, and resuspend in 0.5–1 mL of 20 mM Tris·Cl, pH 7.4, containing protease inhibitors. Store in 50–100 µL aliquots for up to several years at −20 °C.
11. Determine the total protein content of each synaptosomes fraction by means of the BCA Protein Assay Kit (Pierce, USA). Analyze aliquots containing equal amounts of protein from each fraction by SDS-PAGE. Aliquots containing 10 µg total protein should be sufficient to detect most synaptic vesicle proteins. Detect proteins of interest by immunoblotting with the appropriate specific antibodies.

3.3 Detection and Visualization of Synaptic Vesicle GPCR Heteroreceptor Complexes by Co-immuno-precipitation (A General Scheme for the Co-immuno-precipitation Procedure Is Provided in Fig. 1 (Note 1))

1. Take 0.5–1 mL membrane fraction (e.g., synaptosomes or the fraction enriched with the presynaptic plasma membrane proteins) for each antibody to be tested in the experiment.
2. Centrifuge during 30 min at 12,000 × *g* at 4 °C.
3. Resuspend pellet in 1 mL of RIPA buffer containing the Protease Inhibitor Cocktail, and homogenize using the polytron (**Note 2**).
4. Incubate during 60–120 min in constant rotation at 4 °C.
5. Centrifuge for 15 min at 10,000 × *g* at 4 °C. The membrane receptors will mainly be in the supernatant fraction.
6. Collect each supernatant in a new microcentrifuge tubes, and add 1–4 μg of the indicated primary antibody (**Note 3**).
7. Incubate the sample with the antibody overnight at 4 °C, upon constant rotation. The length of the incubation period depends on the amount of protein and affinity properties of the antibody.
8. Meanwhile prepare the Sepharose beads (**Note 4**) or use ready-to-use protein A beads (delivered as a 50% slurry). These beads are first washed three times (centrifugation after each washing step: 110 × *g*, 4 °C, 1 min) with RIPA buffer supplemented with protease and phosphatase inhibitors.
9. The washed beads are added to the incubate samples (Step 7) and incubated 2 h with rotation at 4 °C.
10. The beads are again washed. Wash the resin three times in 1 mL of ice-cold RIPA buffer (supplemented with protease and phosphatase inhibitors) by centrifuging at 10,000 × *g* for 1 min at 4 °C. In the last wash, aspirate the supernatant to dryness with a 28-gauge needle. The protein of interest should now be specifically bound to the antibody coating the beads.
11. Resuspend the resin and elute the beads. There are several possibilities: *glycine buffer elution (go to Step 5), SDS buffer elution (go to Step 6), or urea buffer elution (go to Step 7)*. In the glycine buffer, the complex is eluted from the beads by acidification using a buffer containing 0.1–0.2 M glycine, pH 2.0–3.0. The low pH of glycine weakens the interaction between the antibody and the beads. This method is advantageous as beads can be reused after removal of the glycine buffer. However, the eluted sample should be immediately neutralized with Tris, pH 8.0–8.5. On the other hand, the SDS buffer is the harshest, which will also elute non-covalently bound antibodies and antibody fragments along with the protein of interest. The Ag-Ab complex is eluted from the beads by heating or boiling samples in loading buffer with denaturant SDS. This method is advantageous because the extraction method is highly efficient and the resulting sample is more concentrated. The urea elu-

tion is advantageous for mass spectrometry because the sample can be digested by proteolytic enzymes.

12. Elute the beads (50 µL) with 3 × 50 µL 0.2 M glycine pH 2.6 (1:1) by incubating the sample for 10 min with frequent agitation before gentle centrifugation. Pool the eluate and neutralize by adding equal volume of Tris pH 8.0. Neutralize the beads by washing 2× with 150 µL lysis buffer (without detergent), and pool with eluate. Run the samples on SDS-PAGE (see below Step 8).
13. Elute 50 µL of beads by heating in 50 µL of 2× SDS loading buffer without DTT for 10 min at 50 °C. Pellet beads, transfer supernatant to a new tube, and add DTT at 100 mM (elution 1). Add 50 µL 2× SDS buffer with DTT to pelleted beads (elution 2). Boil the eluted samples for 5 min, and analyze content of the sample by SDS-PAGE and Western blot (see below Step 8).
14. Wash beads with pre-urea wash buffer (50 mM Tris pH 8.5, 1 mM EGTA, 75 mM KCl). Remove all residual supernatant. Add 2–5 volumes urea elution buffer (6–8 M Urea, 20 mM Tris pH 7.5, and 100 mM NaCl), and rotate for 30 min at room temperature with frequent agitation before gentle centrifugation. Repeat this process at least twice more to ensure that the entire captured complex has been released from the beads. Pellet beads and remove urea to a new tube. Run the samples on SDS-PAGE (see below Step 8).
15. Finally, when the receptors are eluted from the beads, standard SDS-PAGE can be performed to separate the receptors according to their molecular weight. Prepare samples for SDS-PAGE. Load the mini-PROTEAN tetra cell with electrophoresis buffer. Load protein marker and samples into the gel wells.
16. Run the gels at 75 V until samples reach the separating gel, and then increase voltage until 150 V. Stop SDS-PAGE running when the downmost band of the protein marker reaches the foot line of the glass plate.
17. Following electrophoresis, separate glass plates, recover the gel, and equilibrate it in anode buffer for 5 min.
18. Cut two immunoblot thick filter papers in 6.25 × 9.25 cm sheet. Soak one of them in anode buffer and the other in cathode buffer.
19. Cut Immobilon-P transfer membranes in 9 cm × 6 cm sheets. Completely soak membranes in methanol for 3 s to activate them and finally equilibrate in anode buffer.
20. Prepare the Western blot sandwich by placing (a) the anode buffer pre-soaked sheet of filter paper onto the anode cassette; (b) the anode buffer pre-wetted transfer membrane on top of

the filter paper; (c) the anode buffer equilibrated gel on top of the transfer membrane, aligning the gel on the center of the membrane; and finally (d) the other cathode buffer pre-soaked extra thick filter paper on top of the gel.

21. Roll a plastic pipet over the surface of the filter paper in both directions to eliminate air bubbles and to ensure complete contact between polyacrylamide gel and the transfer membrane.
22. Carefully place the cathode top onto the cassette.
23. Turn on the power and transfer mini gels for 30 min at 25 V.
24. Following transfer, discard filter papers and polyacrylamide gel.
25. Block transfer membrane in IB blocking solution for 30 min at room temperature with continuous shacking.
26. Incubate the membrane overnight at 4 °C with the indicated primary antibody diluted in IB blocking solution with continuous shaking. You can also use the commercial blocking buffer (e.g., Odyssey blocking buffer from LI-COR Biosciences, cat. nr. 927–40,000).
27. Make three washes of 10 min with IB washing solution to eliminate unbound primary antibody.
28. Incubate with the indicated secondary antibody for 90 min at room temperature in continuous shaking. For instance, the horseradish peroxidase (HRP)-conjugated goat anti-rabbit IgG (Thermo Fisher Scientific), HRP-conjugated anti-mouse IgG TrueBlot™ (eBioscience), or Odyssey for infrared dye-coupled antibodies from LI-COR.
29. Make three washes of 10 min with IB washing solution to eliminate unbound secondary antibody.
30. If using the horseradish peroxidase (HRP)-conjugated antibodies, incubate membrane with SuperSignal West Pico Chemiluminescent Substrate (prepare the mix following the proportion 1:1 of solution A and B provided by the manufacturer in dark conditions).
31. Develop membrane in, for instance, Kodak Image Station 440 CF from Kodak for HRP-coupled antibodies and Odyssey from LI-COR Biosciences for infrared dye-coupled antibodies.

4 Notes

1. There are a few different methods to co-immunoprecipitate GPCRs. One approach consists in the pre-mixture of the pri-

mary antibody with your membrane fraction sample, followed by addition of protein A/G support. This method yields high purity of receptor; however, the antibodies are also co-eluted with receptor of interest which sometimes creates difficulties in Western blot detection. The other approach is to bind the primary antibody that recognizes one of the protomers of interest to the protein A/G beads and then mix with the antigen. This method gives lesser yield than the first one but avoids the problem of co-elution of antibodies. Herein we will describe the first approach.

2. There are a lot of possibilities concerning detergent choice for the solubilization of membrane receptors. For instance, CHAPS buffer (30 mM Tris–HCl pH 7.5; 150 mM NaCl; 1% CHAPS), TNT buffer (20 mM Tris/HCl pH 7.5; 200 mM NaCl; 0.1% Tween 20), NP-40 buffer (0.5% NP-40; 140 mM NaCl; 1.5 mM $MgCl_2$; 10 mM Tris HCl pH 7.5), and Triton X-100 buffer (10% glycerol; 1% Triton X-100; 160 mM NaCl; 50 mM Tris HCl pH 7.5; 1 mM EDTA; 1 mM EGTA). So far, for GPCR the RIPA buffer (150 mM NaCl; 50 mM Tris HCl pH 7.5; 1% NP-40; 0.1% SDS; 0.5% deoxycholic acid) seemed to be the optimal choice, because it gave the best signal. The RIPA lyses buffer is based on moderate concentrations of the nonionic detergent NP-40 that will disrupt the integrity of the cell membrane, causing the extraction of membrane proteins in their native form. The buffer also contains a low concentration of the harsh denaturing anionic detergent SDS and ionic detergent sodium deoxycholate. SDS and sodium deoxycholate will help to disrupt the membrane, resulting in a higher yield of extracted membrane proteins. The concentration of these two is however quite low and will not be able to disrupt the protein–protein interactions. In addition, the detergent digitonin (0.1%) can also be added to optimize the solubilization of the membrane receptors.
3. Typically in a pilot experiment, a fixed amount of protein is precipitated by increasing amounts of antibody. Check the antibody datasheet for recommended antibody concentration. As a guideline use 1–5 μL polyclonal antiserum, 1 μg affinity purified polyclonal antibody, 0.2–1 μL ascites fluid (monoclonal antibody), or 20–100 μL culture supernatant (monoclonal antibody).
4. If using a monoclonal antibody choose protein G-coupled Sepharose beads. If using a polyclonal antibody, protein A-coupled Sepharose beads are usually a better option. If the beads come as a powder, incubate 100 mg of beads in 1 mL 0.1 M PBS, wash for 1 h so they swell up, and then centrifuge, remove the supernatant, and discard. Add 1 mL PBS 0.1% BSA, mix for 1 h using an Eppendorf rotator and rinse twice in

PBS. Remove the supernatant and add 400 μL of buffer made with protease inhibitors. The slurry is now ready for use. It can be stored at 4 °C for a few days. You can also buy pre-swollen beads as slurry ready for use. If use IgM antibodies, do not use protein A- or protein G-conjugated beads. Use, instead, anti-IgM coupled protein A or protein G beads. The IgM will bind to the beads by binding to the anti-IgM antibody.

Acknowledgments

This work has been supported by the Karolinska Institutets Forskningsstiftelser 2014/2015 to DOBE, by the Swedish Medical Research Council (62X-00715-50-3) and AFA Försäkring (130328) to KF and DOBE. DOBE belongs to Academia de Biólogos Cubanos.

References

1. Borroto-Escuela DO, Narvaez M, Perez-Alea M, Tarakanov AO, Jimenez-Beristain A, Mudo G, Agnati LF, Ciruela F, Belluardo N, Fuxe K (2014) Evidence for the existence of FGFR1-5-HT1A heteroreceptor complexes in the midbrain raphe 5-HT system. Biochem Biophys Res Commun 456(1):489–493. https://doi.org/10.1016/j.bbrc.2014.11.112
2. Fuxe K, Guidolin D, Agnati LF, Borroto-Escuela DO (2015) Dopamine heteroreceptor complexes as therapeutic targets in Parkinson's disease. Expert Opin Ther Targets 19(3):377–398. https://doi.org/10.1517/14728222.2014.981529
3. Fuxe K, Borroto-Escuela D, Fisone G, Agnati LF, Tanganelli S (2014) Understanding the role of heteroreceptor complexes in the central nervous system. Curr Protein Pept Sci 15(7):647
4. Borroto-Escuela DO, Tarakanov AO, Brito I, Fuxe K (2018) Glutamate heteroreceptor complexes in the brain. Pharmacol Rep 70(5):936–950. https://doi.org/10.1016/j.pharep.2018.04.002
5. Borroto-Escuela DO, DuPont CM, Li X, Savelli D, Lattanzi D, Srivastava I, Narvaez M, Di Palma M, Barbieri E, Andrade-Talavera Y, Cuppini R, Odagaki Y, Palkovits M, Ambrogini P, Lindskog M, Fuxe K (2017) Disturbances in the FGFR1-5-HT1A heteroreceptor complexes in the Raphe-Hippocampal 5-HT system develop in a genetic rat model of depression. Front Cell Neurosci 11:309. https://doi.org/10.3389/fncel.2017.00309
6. Borroto-Escuela DO, Li X, Tarakanov AO, Savelli D, Narvaez M, Shumilov K, Andrade-Talavera Y, Jimenez-Beristain A, Pomierny B, Diaz-Cabiale Z, Cuppini R, Ambrogini P, Lindskog M, Fuxe K (2017) Existence of brain 5-HT1A-5-HT2A isoreceptor complexes with antagonistic allosteric receptor-receptor interactions regulating 5-HT1A receptor recognition. ACS Omega 2(8):4779–4789. https://doi.org/10.1021/acsomega.7b00629
7. Borroto-Escuela DO, Narváez M, Jiménez-Beristain A, Fuxe K (2016) FGFR1–5-HT1A heteroreceptor complexes in the hippocampus and midbrain raphe as a novel targets for antidepressant drugs. Paper presented at the 30th CINP World Congress of Neuropsychopharmacology, Seoul, Republic of Korea, July 5, 2016
8. Fuxe K, Borroto-Escuela DO (2016) Heteroreceptor complexes and their allosteric receptor-receptor interactions as a novel biological principle for integration of communication in the CNS: targets for drug development. Neuropsychopharmacology 41(1):380–382. https://doi.org/10.1038/npp.2015.244
9. Borroto-Escuela DO, Flajolet M, Agnati LF, Greengard P, Fuxe K (2013) Bioluminescence resonance energy transfer methods to study G protein-coupled receptor-receptor tyrosine kinase heteroreceptor complexes. Methods Cell Biol 117:141–164. https://doi.org/10.1016/B978-0-12-408143-7.00008-6

10. Fernandez-Duenas V, Llorente J, Gandia J, Borroto-Escuela DO, Agnati LF, Tasca CI, Fuxe K, Ciruela F (2012) Fluorescence resonance energy transfer-based technologies in the study of protein-protein interactions at the cell surface. Methods 57(4):467–472. https://doi.org/10.1016/j.ymeth.2012.05.007
11. Skieterska K, Duchou J, Lintermans B, Van Craenenbroeck K (2013) Detection of G protein-coupled receptor (GPCR) dimerization by coimmunoprecipitation. Methods Cell Biol 117:323–340. https://doi.org/10.1016/B978-0-12-408143-7.00017-7
12. James JR, Oliveira MI, Carmo AM, Iaboni A, Davis SJ (2006) A rigorous experimental framework for detecting protein oligomerization using bioluminescence resonance energy transfer. Nat Methods 3(12):1001–1006. https://doi.org/10.1038/nmeth978
13. Bouvier M, Heveker N, Jockers R, Marullo S, Milligan G (2007) BRET analysis of GPCR oligomerization: newer does not mean better. Nat Methods 4(1):3–4. https://doi.org/10.1038/nmeth0107-3; author reply 4

frontiers in Microbiology

INFORME DE LABORES 2019

published: 14 August 2019
doi: 10.3389/fmicb.2019.01825

Neurospora crassa NADPH Oxidase NOX-1 Is Localized in the Vacuolar System and the Plasma Membrane

*Nallely Cano-Domínguez[1], Barry Bowman[2], Leonardo Peraza-Reyes[3] and Jesús Aguirre[1]**

[1] Departamento de Biología Celular y del Desarrollo, Instituto de Fisiología Celular, Universidad Nacional Autónoma de México, Mexico City, Mexico, [2] Department of Molecular, Cell and Developmental Biology, University of California, Santa Cruz, Santa Cruz, CA, United States, [3] Departamento de Bioquímica y Biología Estructural, Instituto de Fisiología Celular, Universidad Nacional Autónoma de México, Mexico City, Mexico

The NADPH oxidases (NOX) catalyze the production of superoxide by transferring electrons from NADPH to O_2, in a regulated manner. In *Neurospora crassa* NOX-1 is required for normal growth of hyphae, development of aerial mycelium and asexual spores, and it is essential for sexual differentiation and cell-cell fusion. Determining the subcellular localization of NOX-1 is a critical step in understanding the mechanisms by which this enzyme can regulate all these different processes. Using fully functional versions of NOX-1 tagged with mCherry, we show that in growing hyphae NOX-1 shows only a minor association with the endoplasmic reticulum (ER) markers Ca^{2+}-ATPase NCA-1 and an ER lumen-targeted GFP. Likewise, NOX-1 shows minor co-localization with early endosomes labeled with YPT-52, a GTPase of the Rab5 family. In contrast, NOX-1 shows extensive co-localization with two independent markers of the entire vacuolar system; the vacuolar ATPase subunit VMA-1 and the fluorescent molecule carboxy-DFFDA. In addition, part of NOX-1 was detected at the plasma membrane. The NOX-1 regulatory subunit NOR-1 displays a very different pattern of localization, showing a fine granular distribution along the entire hypha and some accumulation at the hyphal tip. In older hyphal regions, germinating conidia, and conidiophores it forms larger and discrete puncta some of which appear localized at the plasma membrane and septa. Notably, co-localization of NOX-1 and NOR-1 was mainly observed under conidial cell-cell fusion conditions in discrete vesicular structures. NOX functions in fungi have been evaluated mainly in mutants that completely lacked this protein, also eliminating interactions between hyphal growth regulatory proteins NOR-1, the GTPase RAC-1 and the scaffold protein BEM-1. To dissect NOX-1 roles as scaffold and as ROS-producing enzyme, we analyzed the function of NOX-1::mCherry proteins carrying proline 382 by histidine (P382H) or cysteine 524 by arginine (C524R) substitutions, predicted to only affect NADPH-binding. Without notably affecting NOX-1 localization or protein levels, each of these substitutions resulted in lack of function phenotypes, indicating that NOX-1 multiple functions are all dependent on its oxidase activity. Our results open new interpretations to possible NOX functions, as components of the fungal vacuolar system and the plasma membrane, as well as to new vacuolar functions.

Keywords: NOR-1, ROS, fungal development, cell fusion, fungal growth, CAT fusion

OPEN ACCESS

Edited by:
Luis F. Larrondo, Pontifical Catholic University of Chile, Chile

Reviewed by:
Stephen J. Free, University at Buffalo, United States
Irina Druzhinina, Vienna University of Technology, Austria

****Correspondence:***
Jesús Aguirre
jaguirre@ifc.unam.mx

Specialty section:
This article was submitted to Fungi and Their Interactions, a section of the journal Frontiers in Microbiology

Received: *15 May 2019*
Accepted: *24 July 2019*
Published: *14 August 2019*

Citation:
Cano-Domínguez N, Bowman B, Peraza-Reyes L and Aguirre J (2019) Neurospora crassa NADPH Oxidase NOX-1 Is Localized in the Vacuolar System and the Plasma Membrane. Front. Microbiol. 10:1825. doi: 10.3389/fmicb.2019.01825

INTRODUCTION

Many years ago we proposed reactive oxygen species (ROS) as signaling molecules and regulators of cell differentiation (Hansberg and Aguirre, 1990; Aguirre et al., 2005). The existence of NADPH oxidase (NOX) enzymes, capable of producing ROS in a highly regulated fashion, became particularly interesting to us in this context. NOX2 (gp91*phox*), the catalytic component of the first and most studied NOX was reported as a novel cytochrome *b*558 in phagocytic vacuoles of human granulocytes (Segal and Jones, 1978), where phagocytosis is associated with the production of superoxide and other derived ROS, necessary for the efficient killing of invading pathogens. Defects in NOX components cause the immunodeficiency syndrome called granulomatous disease or CGD (Babior, 1995). Later, it was found that NOX2 was part of a larger family of enzymes that were ubiquitous in eukaryotic cells, where they were related not only to innate immunity but also to other processes such as modifications of the extracellular matrix, cell-cell signaling, development, and morphogenesis (Lambeth et al., 2000; Lara-Ortiz, 2004; Aguirre and Lambeth, 2010).

We reported the presence of three different NOX subfamilies in fungi and the Amoebozoa, and demonstrated that NOX enzymes were essential for ROS production and sexual development in the Ascomycetes *Aspergillus nidulans* (Lara-Ortiz et al., 2003; Aguirre et al., 2005), *Neurospora crassa* (Cano-Dominguez et al., 2008), and *Sordaria macrospora* (Dirschnabel et al., 2014). Independently, Malagnac et al. (2004) found that in *Podospora anserina* PaNox1 and PaNox2 were needed for sexual development and ascospore germination, respectively (Malagnac et al., 2004). Since then, fungal NOX enzymes have been linked to other critical functions such as growth, asexual development, cell-cell fusion (Cano-Dominguez et al., 2008; Fu et al., 2011; Read et al., 2012; Roca et al., 2012; Dirschnabel et al., 2014), pathogenicity (Egan et al., 2007; Segmuller et al., 2008; Kim et al., 2011; Schurmann et al., 2013; Yang and Chung, 2013; Zhang et al., 2016; Rossi et al., 2017; Zhou et al., 2017), endosymbiosis (Tanaka et al., 2006), and the asexual reproduction induced by injury in *Trichoderma atroviride* (Hernandez-Onate et al., 2012). More recently the functions of other NOX enzymes, originally considered as ferric reductases, have been reported in *Saccharomyces cerevisiae* (Rinnerthaler et al., 2012) and *Candida albicans* (Rossi et al., 2017), while bioinformatic analysis and *in vitro* experiments suggest the presence of NOX enzymes in prokaryotes (Hajjar et al., 2017). Such ubiquity of NOX enzymes supports the idea that the controlled production of ROS as signaling molecules appeared early in life evolution as an important mechanism to regulate cell physiology and differentiation.

In mammalian phagocytic cells part of NOX2 is localized in the plasma membrane, where it interacts with subunits p22*phox*, p40*phox*, p47*phox*, p67*phox*, and the GTPase Rac1 for its activation [reviewed in Aguirre and Lambeth (2010)]. Fungal A and B NOX subfamilies belong to the NOX2 family (Lara-Ortiz et al., 2003; Aguirre et al., 2005), and interact with equivalent subunits. Indeed, p67*phox* homolog NoxR interacts with RacA (Takemoto et al., 2006), and together with p22*phox* homolog NoxD (Lacaze et al., 2015; Siegmund et al., 2015) are required for NOX functions (Takemoto et al., 2006; Cano-Dominguez et al., 2008). Membrane proteins of the tetraspanin family have also been linked to NOX function (Lambou et al., 2008; Schurmann et al., 2013; Siegmund et al., 2013; Lacaze et al., 2015; Zhao et al., 2016) and suggested to play roles analogous to p22*phox* for NoxB family members. Finally, it has been proposed that fungal Bem1 proteins play roles analogous to animal p40*phox* and p47*phox* (Takemoto et al., 2011).

Although little is known about how NOX and ROS can regulate so many seemingly different functions in fungi, some NOX functions have been related to actin organization and calcium signaling. In yeast, mutants lacking the NOX Yno1p are hypersensitive to drugs that inhibit F-actin nucleation and elongation, and this phenotype is rescued by non-toxic concentrations of H_2O_2, suggesting that Yno1p is necessary for proper F-actin function (Rinnerthaler et al., 2012). In the phytopathogen *Magnaporthe grisea Δnox1* and *Δnox2* mutants are able to differentiate the leaf penetration structure called appressorium, but fail to penetrate the plant cuticle (Egan et al., 2007). Nox2 and NoxR are required to organize a septin ring at the base of the appressorium pore, which in turn is necessary for the assembly of a toroidal F-actin network at the point of penetration peg emergence, while Nox1 is needed to maintain the cortical F-actin network (Ryder et al., 2013). A similar situation occurs in the fungus *Verticillium dahlia*, which only infects plant roots using a structure called hyphopodium, from which a penetration peg develops. Mutants lacking NOX VdNoxB are impaired in the formation of a septin ring that partitions the hyphopodium and the invasive hyphae, which is critical for the secretion of effector proteins (Zhou et al., 2017). Moreover, tetraspanin VdPls1 and NOX VdNoxB are specifically expressed in hyphopodia, where they colocalize and are necessary for ROS production and the development of the penetration peg. The nuclear targeting of the calcium-regulated transcription factor VdCrz1, which normally occurs in hyphopodia, was prevented in mutants lacking VdPls1 or VdNoxB, linking NOX function and calcium signaling in this process (Zhao et al., 2016).

Neurospora crassa is a particularly interesting model to study NOX function, as it contains two NOX enzymes (NOX-1 and NOX-2), both requiring the regulatory subunit encoded by *nor-1* (NCU07850). While *nox-2* (NCU10775) elimination only affects ascospore germination, *nox-1* (NCU02110) deletion has more pleitropic effects in this fungus than in any other fungus studied. Indeed, NOX-1 is required for normal growth of vegetative hyphae, growth of the aerial mycelium and conidia production, and it is essential for sexual differentiation and hyphal fusion (Cano-Dominguez et al., 2008; Read et al., 2012). To understand how NOX-1 might regulate so many different cellular processes, it is critical to know the subcellular localization of this enzyme. Here we compare the subcellular localization of NOX-1 and its regulatory subunit NOR-1 during different conditions of growth and development and provide genetic evidence supporting that all critical NOX-1 functions require its oxidase activity.

MATERIALS AND METHODS

Strains, Media, Growth Conditions, and Phenotypic Characterization

Neurospora crassa strains used in this work are listed in **Table S1**. All strains were grown on Vogel's minimal medium (VMM) solidified with 1.8% agar at 30°C (Davies and deSerres, 1970). For histidine auxotrophic strains, VMM was supplemented with 0.002% of L-histidine. To determine the production of conidia, 1×10^4 conidia were inoculated on borosilicate tubes containing 3 mL of solid VMM and incubated at 30°C during 3 days in the dark plus 2 days at 25°C in the light. Conidia from these tube cultures were collected with 1 mL of sterile water, diluted and counted using a Neubauer chamber. For radial growth analysis, 1×10^3 conidia were inoculated on the center of a Petri dish containing Vogel's solid minimal medium. Radial growth was measure after 24 h at 30°C and plates were photographed. For observation of conidial anastomosis tube (CAT) formation and fusion, 8×10^6 conidia were inoculated on solid MMV medium using a glass handle, and incubated at 37°C for 4–5 h. An agar block sectioned from these cultures was directly observed under the microscope. To induce sexual crosses, conidia were inoculated on synthetic crossing medium and incubated for 6 days at 25°C in the light (Westergaard and Mitchell, 1974). After that time, a conidial suspension from the opposite mating type was laid over this culture. To follow fruiting body primordia (protoperithecia) development, 1×10^3 conidia were used to initiate cultures according to the method of Bistis (Bistis, 1983; Cano-Dominguez et al., 2008).

Plasmids Construction

The list of plasmids obtained in this work is given in **Table S2**. To construct plasmid pNCNOX-1::mCherry4, *nox-1* (NCU02110) ORF (1659 pb) was amplified using *N. crassa* genomic DNA as template and primers NOX-1 XbaIF2 and NOX-1 PacIR2 (**Table S3**). The generated PCR product fragment was cloned as a *Xba*I/*Pac*I fragment into plasmid pJV15-2 (Verdin et al., 2009). Plasmids pNCNOX-1P382H and pNCNOX-1C524R were generated using In-Fusion® HD Cloning Kit-Clonetech and primers Nox-1 P382HF and Nox-1 P382HR for pNCNOX-1P382H, and Nox-1 C524RF and Nox-1 C524RR for pNCNOX-1C524R. These primers contain point mutations and 15 pb overlap with adjoining fragments. Plasmid pNCNOX-1::mCherry4 was used as template for the In-Fusion® reaction. To replace *ccg-1* promoter by *nox-1* native promoter in pNCNOX-1::mCherry4, we used genomic DNA to amplify a 1226 pb upstream of *nox-1* ORF with primes NOX-1PROM NATF and PromNatR. Then, we amplified the host plasmid pNCNOX-1::mCherry4 using primers PNC-NOX-1mCherry PromNatF and PNC-NOX-1mCherry PromNatR. The amplified host plasmid lacks the *ccg-1* promoter and contains 15 pb overlap with the 1226 pb *nox-1* promoter region. In the last step, we used In-Fusion® HD Cloning Kit-Clonetech to perform the ligation. To fuse NOR-1 to GFP, we amplified *nor-1* (NCU07850) ORF as a 1893 pb fragment, using primers NOR-1BAMHIUP and NOR-1PacILOW and genomic DNA as template. This PCR product was purified and cloned into pGEM®-T Easy Vector (Promega, Madison, WI) to yield plasmid pGemNOR-1-2. A *nor-1 PacI-BamHI* fragment obtained from pGemNOR-1-2 was cloned into plasmid pMF272 (Freitag et al., 2004), digested with *XbaI*/*PacI*, to generate pNCNOR-1::GFP18.

Neurospora crassa Transformation

Conidia were collected from VMM slant cultures using cold sterile water. After determining their concentration, 1.25×10^8 conidia were collected by centrifugation and washed two times with 500 μL of 1 M cold sorbitol and finally resuspended in 40 μL of the same solution. This spore suspension was incubated with DNA (plasmids or PCR products, during 30 min at 4°C) and electroporated using the Gene Pulser II and Pulser Controller II (Bio-Rad, Hercules, CA) set to 1.5 kV, 600 Ω, and 2.5 μF, as reported (Colot et al., 2006). After electroporation, 960 μL of 1 M cold sorbitol were added, mixed with 25 mL of recovery solution (liquid Vogel's medium) and incubated at 30°C and 100 RPM, for 2 h. This solution was mixed with 25 mL of regeneration agar (Vogel's medium with 1 M sorbitol, 2% L-sorbose, 0.05% glucose, 0.05% fructose, and 1% agar) and plated immediately on solid CA medium (2% L-sorbose, 0.05% glucose, 0.05% fructose in Vogel media, and 1% agar) containing hygromycin (200 μg/mL) or phleomycin (80 μg/mL) (Colot et al., 2006). Transformants were purified to obtain homokaryotic strains through three monosporic passes on CA medium plus hygromycin (200 μg/mL) or phleomycin (80 μg/mL).

Heterokaryon Formation

To observe hypha with two proteins labeled with different fluorophores, we constructed heterokaryons using strains with the same mating types. We inoculated 4×10^6 conidia of each strain on a solid VMM. Cultures were incubated at 37°C for 4–5 h to induce CAT fusion. Cell fusion was verified under epifluorescence microscopy and then agar blocks were transferred to solid VMM and incubated for 12 h at 30°C. The margins of the colony were used to detect hyphae expressing both markers and observed under confocal microscopy.

Microscopy

Primordia (protoperithecia) and mature sexual fruiting bodies (perithecia) were photographed using a Nikon stereoscopic microscope. Live-cell imaging was carried out using the "inverted agar block" method (Hickey et al., 2002) and a Zeiss LSM-800-Inverted Laser Scanning Confocal Microscope with a Plan-Apochromatic 63x/1.4 oil immersion objective and 488 and 561 nm laser lines, or a Zeiss LSM-800-Inverted Laser Scanning Confocal Microscope with a 30°C temperature chamber and the same parameters. Time-lapse images were recorded simultaneously by bright field microscopy and fluorescence confocal microscopy. The images were processed using ZEN 2012 (Carl Zeiss, Jena, Germany) software. Latrunculin A (Lat A) (Tocris Bioscience, Bristol, UK: 100 μg) was use to inhibit actin polymerization and endocytosis. A 2 μg/μL stock solution in DMSO was diluted with VMM to a final 20 μg/mL working concentration. Fifty microliter of this solution were placed onto a coverslip and mycelium on an agar block was placed in contact

with the latrunculin. After 10 min, the sample was observed using confocal microscopy. Oregon Green 488 carboxylic acid diacetate (carboxy-DFFDA; Molecular Probes) was used to visualize the vacuolar system. A 1 mM stock solution in DMSO was diluted with VMM to a final 10 μM concentration. Fifty microliter of this solution were placed onto a coverslip and conidia or mycelium on agar blocks were placed in contact with the dye. The sample was observed immediately in the Zeiss LSM-800 Confocal Microscope equipped with a 30°C temperature chamber.

RESULTS

NOX-1::mCherry Expressed From *ccg*-1 Promoter Fully Complements *Δnox-1* Mutant Multiple Defects

To determine NOX-1 subcellular localization we decided to use fluorescent protein mCherry, an improved version of mRFP1, showing higher photostability and pH resistance (Shaner et al., 2004). First, we generated plasmid pNCNOX-1::mCherry4, which contains a *nox-1::mCherry* gene fusion under the control the *ccg-1* constitutive promoter and allows integration at the *his-3* locus. We used this plasmid to transform strain *Δnox-1 his-3*, and four His-3$^+$ transformants were analyzed by PCR to confirm the presence of this plasmid at the *his-3* locus. Strains *Δnox-1 nox-1::mCherry d* and *e* were selected for further experiments (**Figure S1**). As reported before (Cano-Dominguez et al., 2008), *Δnox-1* mutants showed a severe decrease in aerial mycelium growth and conidiation, reduced radial growth and were unable to develop perithecia, with these phenotypes being somewhat enhanced by the presence of *his-3* mutation (**Figures S2A–E**). The *nox-1::mCherry* allele was able to fully complement the defects in aerial mycelium growth and conidiation (**Figures S2A,B)** and restored radial growth (**Figures S2C,D**, **S7D**). Moreover, *Δnox-1* complemented strains were able to produce protoperithecia (not shown) that were competent for fertilization and able to develop mature perithecia (**Figure S2E**), containing viable ascospores (not shown).

When inoculated at high density, conidia from *N. crassa* and other fungi develop specialized structures, called conidial anastomosis tubes or CATs, for cell-cell fusion (Fischer and Glass, 2019). Although *Δnox-1* mutants differentiate CAT structures, these cannot undergo cell-cell fusion (Cano-Dominguez et al., 2008; Read et al., 2012). We used confocal microscopy to determine NOX-1::mCherry localization during germination, and to assess if this allele complemented *Δnox-1* cell fusion defects. Results in **Figure 1A** show that in germinating conidia the NOX-1::mCherry signal, largely absent from the hyphal tip, was localized in discrete round and tubular structures behind the hyphal tip, which moved very fast and showed very dynamic shape changes. CATs from strain *Δnox-1 nox-1::mCherry* were competent for cell-cell fusion (**Figure 1B)** and NOX-1::mCherry labeled structures were exchanged freely between the fusion partners (**Video S1**). This shows that NOX-1::mCherry expressed from *ccg*-1 promoter complements all *Δnox-1* mutant phenotypes, and its localization in mobile globular and filamentous structures during conidial germination.

In Growing Hyphae NOX-1 Is Localized in Pleomorphic Structures Consistent With the Morphology of the Entire Vacuolar System

Having shown NOX-1::mCherry fusion functionality, we next determined NOX-1 localization during hyphal growth using *in vivo* confocal microscopy. **Figure 2** shows the reconstruction of a single hyphae in which three major characteristic regions can be distinguished; the actively growing tip, a central region and an older region that contains large spherical vacuoles. In contrast to the simpler pattern observed in germinated conidia (**Figures 1A,B**), NOX-1::mCherry signal displayed a highly differentiated pattern within these three regions. First, mCherry signal was very low closer to the hyphal tip and then gradually increased behind the tip, defining small round structures, some presenting u- or o-ring shapes (white arrow in **Figure 2B**). Second, the intensity and density of fluorescent signal increased toward the second hyphal segment up to the first septum, displaying a well-defined tubular network. Third, a more discrete pattern, including large round structures, was observed in the older region of the hyphae, where proteins that belong to the vacuolar system such as CAX, NCA-2, and some times VMA-1 have been localized (Bowman et al., 2009). Considering that the pattern of these three regions is notably similar to the one recently reported for the entire vacuolar system in *N. crassa* (Bowman et al., 2015), we also delimited them as the prevacuolar compartment, tubular vacuolar network and large spherical vacuolar regions, respectively (**Figure 2A**). In turn, the prevacuolar region was divided in regions I, II, III, and IV (**Figure 2B**), according to the population of vacuoles, distance from the hyphal tip and Bowman's nomenclature (Bowman et al., 2015). **Figure 2B** shows an enlarged image of the prevacuolar region shown in **Figure 2A**. As indicated before, NOX-1::mCherry signal was low in regions I and II. In zone III it became more visible, being located in small structures and some rings or u-shaped structures (**Figure 2B** and **Video S2**). Zone IV shows a transition between the morphology of zone III and the beginning of the dense network of interconnected filaments that extends backwards until the position of the first septum. These results are consistent with NOX-1 being localized in the entire vacuolar system.

NOX-1 Shows Minor Co-localization With Endoplasmic Reticulum and Endosome Markers

In filamentous fungi *P. anserina* (Lacaze et al., 2015) and *Botrytis cinerea* (Siegmund et al., 2013, 2015), NOX-1 has been detected mainly in the ER and in vesicles proposed to derive from the ER (Schurmann et al., 2013; Siegmund et al., 2013, 2015; Lacaze et al., 2015). To explore this in *N. crassa*, we performed co-localization experiments following NOX-1::mCherry and NCA-1, a homolog of the SERCA-type Ca^{2+}-ATPase, as an ER marker (Bowman et al., 2009), tagged with GFP. Heterokaryotic mycelia from NCA-1::GFP and NOX-1::mCherry strains were analyzed by confocal microscopy. Results in **Figure 3A** show that, as reported before, NCA-1 is

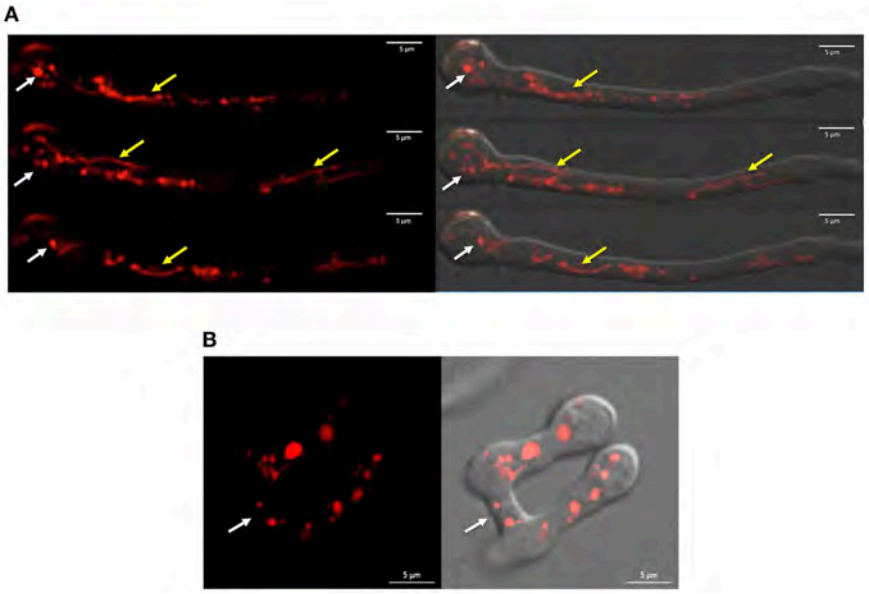

FIGURE 1 | NOX-1::mCherry expressed from *ccg*-1 promoter is localized in discrete compartments and complements *Δnox-1* cell fusion defects. **(A)** Conidia from strain *Δnox-1 nox-1-mCherry e* were induced to germinate and observed using confocal microscopy. NOX-1::mCherry is localized in round (white arrows) and tubular (yellow arrows) organelles. Images belong to a series of frames from a movie (not shown). **(B)** Conidia from strain *Δnox-1 nox-1-mCherry e* were induced to develop CATs and observed using confocal microscopy. Figures represent still images from **Video S1**. Left panel shows NOX-1-mCherry fluorescence signal of two conidia with CATs fused at the indicated point (white arrow). The right panel shows the same image merged to the corresponding bright field image.

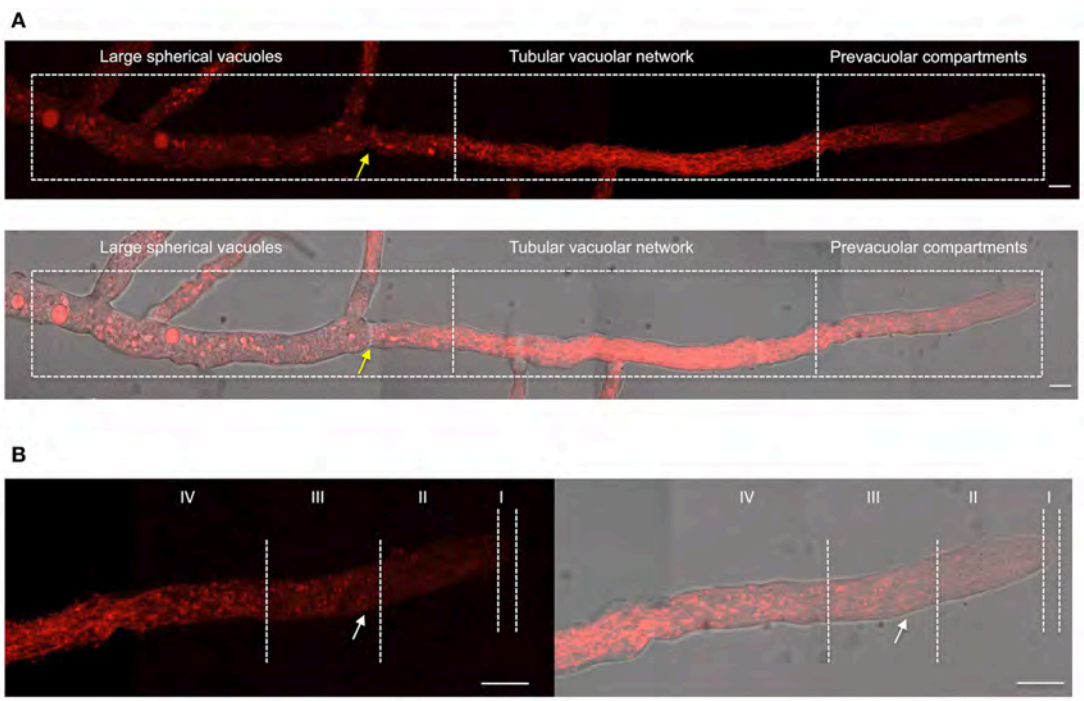

FIGURE 2 | NOX-1 localization during hyphal growth. **(A)** A single hyphae from strain *Δnox-1 nox-1-mCherry e* composed using nine overlapping pictures obtained with fluorescent microscopy (upper panel) and the overlap with the bright field image (lower panel). **(B)** Enlargement of the prevacuolar compartment shown in **(A)** divided in subcompartments I to IV, using the hyphal tip as reference, according to Bowman et al. (2015). Yellow arrows indicate the position of the septum and the white arrow points to one of several u-shaped structures observed. White bars represent 10 μm.

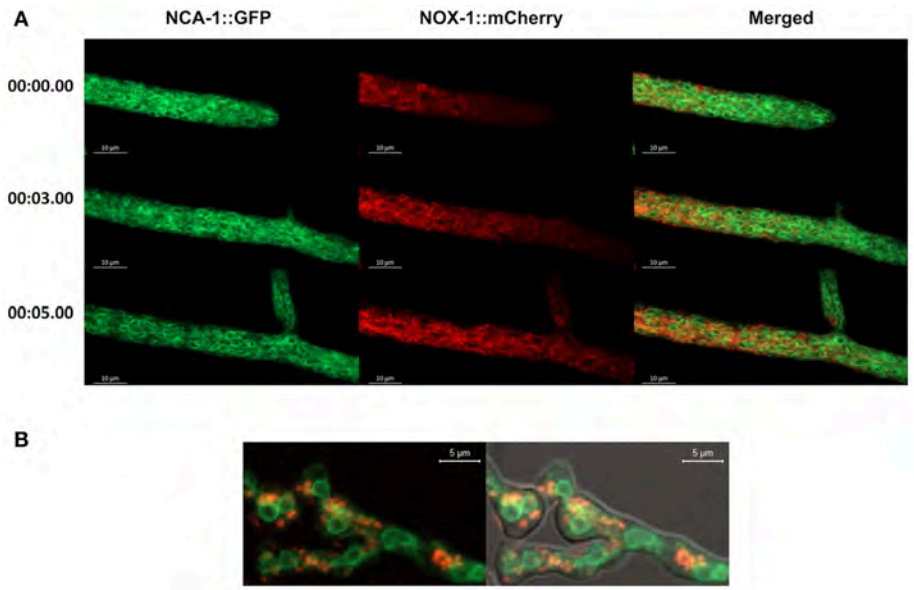

FIGURE 3 | ER-marker NCA-1-GFP shows limited co-localization with NOX-1::mCherry. **(A)** Heterokaryotic hyphae from strains expressing NCA-1::GFP and NOX-1::mCherry were observed by confocal microscopy. Images correspond to time frames from a movie (not shown), as indicated in the left. **(B)** Conidia from NCA-1::GFP and NOX-1::mCherry strains were inoculated under CAT inducing conditions and heterokaryotic germlings observed by confocal microscopy.

observed as ring structures, previously shown to represent the nuclear envelope, distributed along the entire hyphae, including the growing tip. Although NOX-1 is also seen in some ring structures, these are fewer and smaller than NCA-1-labeled nuclear envelopes. Furthermore, double label experiments showed virtually no co-occurrence between NCA-1-GFP and NOX-1-mCherry labeled structures. If any, co-localization was limited to areas with high GFP and mCherry labeling density, while NOX-1 was mostly localized in filamentous structures and largely excluded from the hyphal tip. Likewise, NCA-1 and NOX-1::mCherry showed limited co-localization during CAT induction, where NCA-1 can be observed around putative nuclei and NOX-1 in round structures (**Figure 3B**). This suggested that *N. crassa* NOX-1 is not largely associated to the ER. To confirm this result, we generated strains in which the ER was labeled using a different marker. For this, we transformed wild-type strain 4200 with plasmid pAM01, encoding an ER-lumen targeted GFP (ER-GFP), containing ER-signal and ER-retention sequences from *P. anserina* BiP chaperone protein, a classical ER-marker (Pidoux and Armstrong, 1992; Plemper et al., 1997), fused to *gfp* and expressed from *A. nidulans gpdA* promotor (Meizoso-Huesca A. and Peraza-Reyes L., unpublished). Results in **Figure S3**, show that this protein labeled a reticular network along the entire hyphae, as well as putative nuclear envelope structures, consistent with ER labeling. The difference with NCA-1 ER signal, mostly enriched in putative nuclear envelope structures suggest that NCA-1 and ER-GFP might be enriched in different ER domains. As in the case of NCA-1 (**Figure 3**), NOX-1 presented very limited co-localization with ER-GFP labeled structures in both growing hyphae (**Figure S3A**) and under CAT inducing conditions (**Figure S3B**).

To explore NOX-1 localization in early endosomes, defined as Rab5-labeled organelles, we produced heterokaryons between the NOX-1::mCherry strain and a strain containing the Rab5 GTPase early endosome protein YPT-52 labeled with GFP (Seidel et al., 2013). **Figure 4A** shows that as reported before, in growing hyphae YPT-52 shows a punctate pattern distributed along the entire hyphae, including the tip. Again, it was difficult to appreciate a co-localization of NOX-1 and YPT-52. Furthermore, YPT-52-stained puncta tended to accumulate toward hyphal apical segments in inverse correlation to NOX-1-labeled structures. However, some limited but clear co-localization was observed under CAT inducing conditions. **Figure 4B** and **Video S3** show heterokaryotic conidia formed by cell-cell fusion, one of which shows three initial points of contact between endosomes and NOX-1-labeled organelles (blue arrows). Two of these contact points quickly disappear, while the upper one is maintained for a longer time and finally released. Notably, under these conditions NOX-1 labeled structures were highly pleomorphic, shifting between long filaments (yellow arrows) and dotted structures that were isolated or arranged in circles that assembled and disassembled (white arrows). Moreover, NOX-1 labeled structures seen first as a continuous circular filament a few seconds later become individual round structures, maintaining the circular arrangement (**Video S3**). In summary, these results show that NOX-1 is localized in structures that are consistent with the vacuolar system, and these are very dynamic and pleomorphic, changing their shape during hyphal aging, development, and cell fusion. Moreover, results indicate

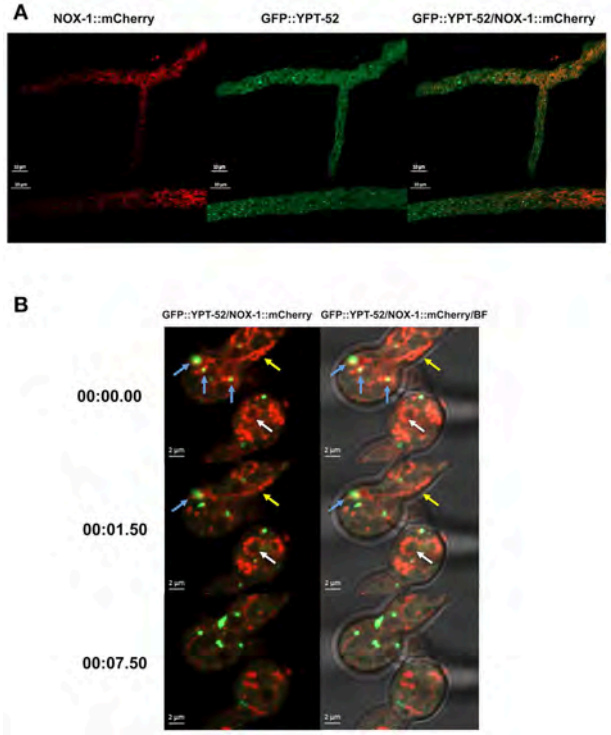

FIGURE 4 | Early endosome marker GFP-YPT-52 shows minor co-localization with NOX-1::mCherry. **(A)** Heterokaryotic hyphae from strains expressing GFP-YPT-52 and NOX-1::mCherry were observed by confocal microscopy. **(B)** Conidia from strains expressing NOX-1::mCherry and GFP-YPT-52 were inoculated under CAT inducing conditions and heterokaryotic germlings were observed by confocal microscopy. Blue arrows indicate co-localization points between GFP-YPT-52 and NOX-1::mCherry, yellow arrows point to NOX-1::mCherry filamentous structures and white arrows point to NOX-1::mCherry structures arranged in a circular shape that change between continuous and dotted patterns (see corresponding **Video S3**).

that NOX-1 shows limited co-localization with early endosomes and the ER.

NOX-1 Co-localizes With Vacuolar ATPase VMA-1

VMA-1 corresponds to subunit "A" of the vacuolar ATPase (V-ATPase). V-ATPases are membrane proteins that hydrolyze ATP to pump protons across the membrane and acidify the lumen of vacuoles and other cell compartments. In *N. crassa*, VMA-1 has been localized in the entire vacuolar system (Bowman et al., 2015), displaying a pattern very similar to the one we report here for NOX-1. To determine if these two proteins co-localize, a *Δ*nox-1 NOX-1-mCherry/VMA-1-GFP heterokaryon was analyzed by confocal microscopy. As reported, we detected VMA-1 in ring and tubular structures that correspond to the vacuolar system. Notably, VMA-1 and NOX-1 co-localized in the same structures **(Figure 5)**, except in the region of large spherical vacuoles in which NOX-1 was localized in the luminal part of the vacuoles and VMA-1 in the periphery.

To further confirm NOX-1 localization in the vacuolar system, we stained the *Δnox-1 NOX-1::mCherry* strain with carboxy-DFFDA, a molecule that accumulates in fungal acidic vacuolar compartments, producing a fluorescencent signal (Richards et al., 2012; Bowman et al., 2015; Rico-Ramirez et al., 2018). As shown in **Figure 6A**, NOX-1::mCherry localized in the same compartments stained by carboxy-DFFDA, including the luminal region of the large spherical vacuoles. The same co-localization was observed during conidia germination and CAT fusion, and as before, the shape of the vacuolar system was composed of larger and less filamentous structures (**Figure 6B**).

NOX-1 Is Also Partially Localized at the Plasma Membrane

In plants, NOX AtrbohC has been detected at the plasma membrane of root hair cells, where it plays a critical role in polar growth (Takeda et al., 2008). We addressed the possibility that in our experiments NOX-1 membrane localization was being overshadowed by the strong NOX-1::mCherry organellar signal, derived from its constitutive expression. First, we used latrunculin A to inhibit the endocytic process, as a strategy to increase possible NOX-1 plasma membrane signal. As expected, latrunculin A delayed hyphal tip growth and under these conditions some NOX-1::mCherry signal was detected at the plasma membrane (not shown).

To further confirm our NOX-1 localization results, we generated strains in which *nox-1::mCherry* was expressed from its native promoter. As shown in **Figures S4A–E**, expression of NOX-1::mCherry from *nox-1* promoter also resulted in full complementation of all *Δnox-1* defects. When strain *Pnox-1-nox-1::mCherry* was analyzed by confocal microscopy, it was evident that the fluorescence signal produced from the *nox-1* promoter was lower than the one produced from *ccg-1* promoter. Nevertheless, it could be appreciated that NOX-1::mCherry was largely absent from hyphal tips and formed a tubular network behind the tip, showing a vacuolar system pattern very similar to the one observed before (not shown). After increasing laser intensity, it was possible to confirm that NOX-1::mCherry signal also localized to the entire vacuolar system (**Figure 7A**), showing a pattern virtually identical to the one observed using the *ccg-1* promoter (**Figure 2**). Notably, under these conditions NOX-1 also was detected at the cell surface, consistent with plasma membrane localization. This was reproducibly observed in hyphal regions corresponding to the tubular vacuolar network and large spherical vacuole regions (**Figures 7A,B**). However, NOX-1 plasma membrane localization at the prevacuolar compartment region and hyphal tip was not as consistent, and only in some cases NOX-1 localized to the cell surface at the hyphal tip (**Figure S3A**, white arrows). After confirming that NOX-1::mCherry localization is alike whether expressed from *ccg-1* or *nox-1* promoters, we continued our NOX-1 localization studies using strains that expressed NOX-1::mCherry from *ccg-1* promoter, as their stronger signal allowed longer imaging acquisition and lower photo-bleaching.

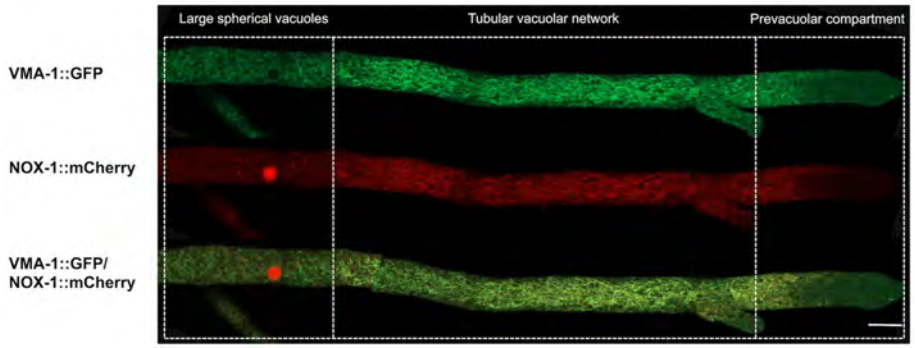

FIGURE 5 | NOX-1::mCherry co-localizes with the vacuolar system marker VMA-1 ATPase. **(A)** Heterokaryotic hyphae from strains expressing NOX-1::mCherry and VMA-1::GFP were observed by confocal microscopy. Bar corresponds to 20 μm.

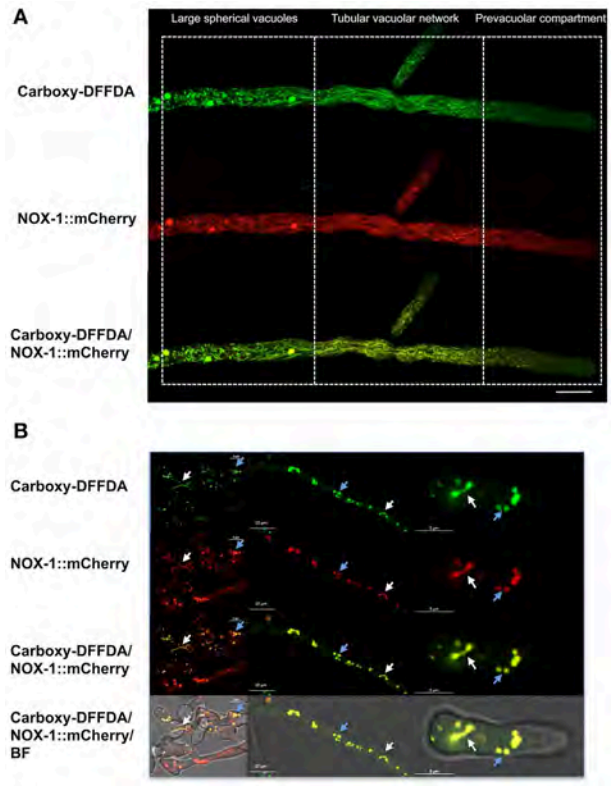

FIGURE 6 | NOX-1::mCherry co-localizes with the vacuolar system marker carboxy-DFFDA. **(A)** Hyphae from strains expressing NOX-1::mCherry were stained with carboxy-DFFDA and observed by confocal microscopy. **(B)** Conidia from strain NOX-1::mCherry were induced to form CATs (left panels) or to germinate (middle and right panels), stained with carboxy-DFFDA, and observed by confocal microscopy.

NOX-1 and Regulatory Subunit NOR-1 Co-localize Only at Very Discrete Compartments

While NOX-1 contains 6 putative transmembrane domains, its regulatory subunit NOR-1 lacks any clear signal peptide or transmembrane domain. However, since NOR-1 is required for NOX-1 function, we decide to compare the localization of both proteins. For this purpose, we generated a PCR construct coding for NOR-1 fused to GFP at the C-terminus and used it to transform strain FGSC-9718. Three homokaryotic strains were obtained in which the *nor-1::GFP* construct replaced the *nor-1* gene, as confirmed by Southern blot analysis (not shown). These strains showed a wild type phenotype, indicating that GFP tagging of NOR-1 did not affect its activity. However, when these strains were observed by confocal microscopy GFP signal was very low and difficult to detect (not shown). Therefore, we expressed *nor-1::GFP* from the *ccg-1* promoter as we did for NOX-1::mCherry. For this, we generated plasmid pNCNOR-1::GFP18 and used it to transform *Δnor-1* mutant strain Nc28nor-1. Ten transformants were obtained, from which GFP fluorescence positive strains were screened using epifluorescence microscopy. Two of these were confirmed by PCR (**Figure S5**) and used for NOR-1 localization experiments. This *nor-1::gfp* allele was able to restore all asexual, sexual and growth defects of *Δnor-1* mutants, indicating its full functionality (**Figure S6**).

NOR-1::GFP fluorescence pattern was very different form the one observed for NOX-1. In growing hyphae, it was detected as a fine granular pattern along the entire hyphae and also in a few larger puncta. NOR-1 was clearly present in the hyphal tip, very likely at the plasma membrane and mainly confined to the apical dome (**Figure 8A** and **Figure S7A**). Notably, NOR-1 did not show any clear co-localization with NOX-1 in growing hyphae **(Figure 8A)** or germinating conidia (**Figure S8B**), where NOR-1::GFP was observed in punctate structures close to the plasma membrane (**Figure S7C**). In older hyphal regions (**Figure S7B**) and in intact conidia (**Figure S8A**), NOR-1::GFP displayed a punctuate pattern. In conidiophores (**Figure S8A**) both NOR-1 and NOX-1 showed the circular dotted structures described before for NOX-1 under CAT inducing conditions (**Figure 4B**). In some cases, NOR-1 and NOX-1 dotted structures seemed to be intercalated and in few cases the two signals co-localized, suggesting that NOR-1 and NOX-1 localize to specific domains of these structures, where they can eventually converge. Because both NOX-1 and NOR-1 are essential for CAT fusion, we incubated conidia from NOX-1::mCherry and NOR-1::GFP

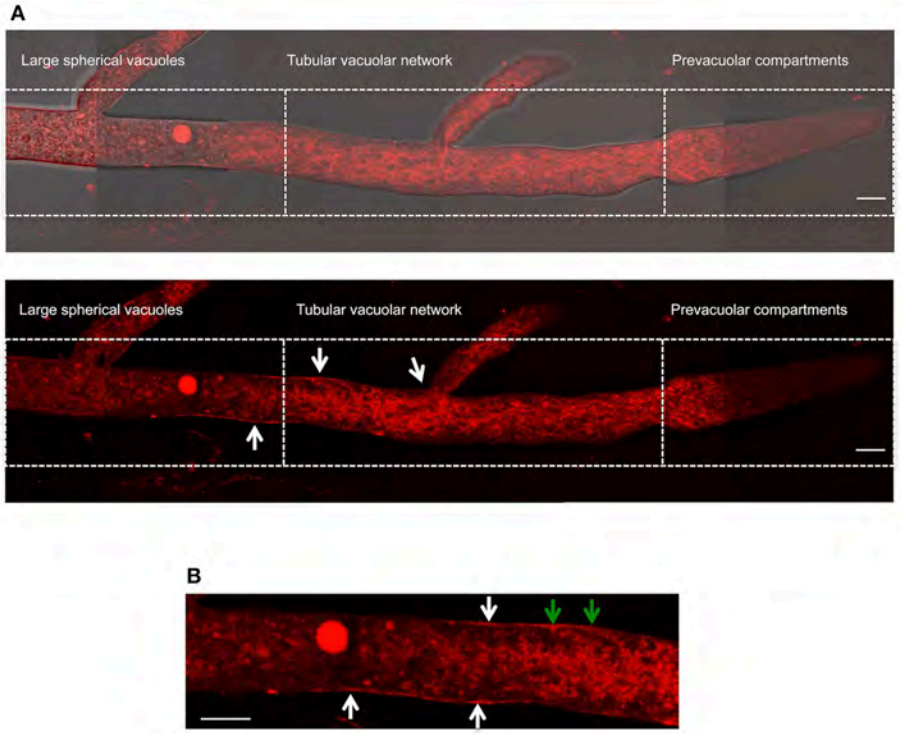

FIGURE 7 | Localization of NOX-1::mCherry expressed from native *nox-1* promoter during hyphal growth. **(A)** Composition of a hypha using overlapping pictures obtained with fluorescent microscopy (lower panel) merged with the corresponding bright field image (upper panel), and divided in compartments as in **Figure 2**. The bars indicate 10 μm. **(B)** Enlargement of a region around the intersection between large spherical vacuoles and tubular vacuolar network compartments shown in **(A)** (lower panel). White arrows point to NOX-1::mCherry plasma membrane localization. Green arrows point to places that suggest endocytic activity. The bar indicates 10 μm.

strains at high density and made observations after 4 h, where profuse CAT fusions take place. Under these conditions, we observed both clear segregation and co-localization of NOR-1 and NOX-1 signals. **Figure 8B** shows three heterokaryotic conidia (i.e., after cell fusion) at different germination stages. The two top conidia show a NOX-1 pattern, consisting of strands and puncta located within cells and at the cell surface. In addition, NOX-1 also decorated the periphery of what appears to be large vacuolar structures. In these conidia NOR-1::GFP displays a different pattern, with isolated puncta located at the cell surface and a septum. In the conidium at the bottom of the figure, which is in a more advanced stage of germination and has fused with a contiguous conidium, NOX-1 localization pattern is similar to the one described above. However, NOR1-GFP more conspicuously stained the hyphal tip at this stage (white arrow), and clear co-localization of NOR-1 and NOX-1 was observed in puncta located at the cell surface, the cytoplasm and the cell-cell fusion interface, as well as some associated with putative large vacuoles (yellow arrows). Together, these results suggest a dynamic localization of NOR-1 and NOX-1 at specific domains of the plasma membrane and the cytoplasm–notably including the vacuolar system–, where they interact at specific compartments, which are enriched during the cell-fusion interactions that occur under CAT inducing conditions.

NOX-1 Single Amino Acid Substitutions in NADPH-Binding Sites Result in a Complete Lack of Function

We took advantage of the functionality of NOX::mCherry to evaluate the effects of specific amino acid substitutions in NOX-1 function. The analysis of mutations in human CYBB gene, encoding gp91phox catalytic subunit, or NOX2, showed that the substitution of proline 415 by histidine resulted in a lack of oxidase enzyme activity but preservation of the inactive protein. The same was observed with mutations replacing arginine 537 by cysteine (Rae et al., 1998). These amino acids, which are part of the NADPH-binding sites, are highly conserved in the NOX from filamentous fungi (**Figure S9**), and correspond to NOX-1 proline 382 and cysteine 524. We used plasmid pNCNOX-1::mCherry4 to introduce point mutations by PCR in the corresponding codons, to generate NOX-1-mCherry proteins with P382H and C524R substitutions. The resulting plasmids were confirmed by DNA sequencing and used to transform *Δnox-1 his-3* strain. Two transformants confirmed by PCR were named *NOX-1P382H-mCherry Δnox-1* and *NOX-1C524R-mCherry Δnox-1* and used for further experiments. The analysis of the corresponding strains by confocal microscopy showed that the signal intensity and localization of the mutant proteins was very similar to wild type NOX-1 (**Figure S10**). Nevertheless, *nox-1*^{P382H}*-mCherry*

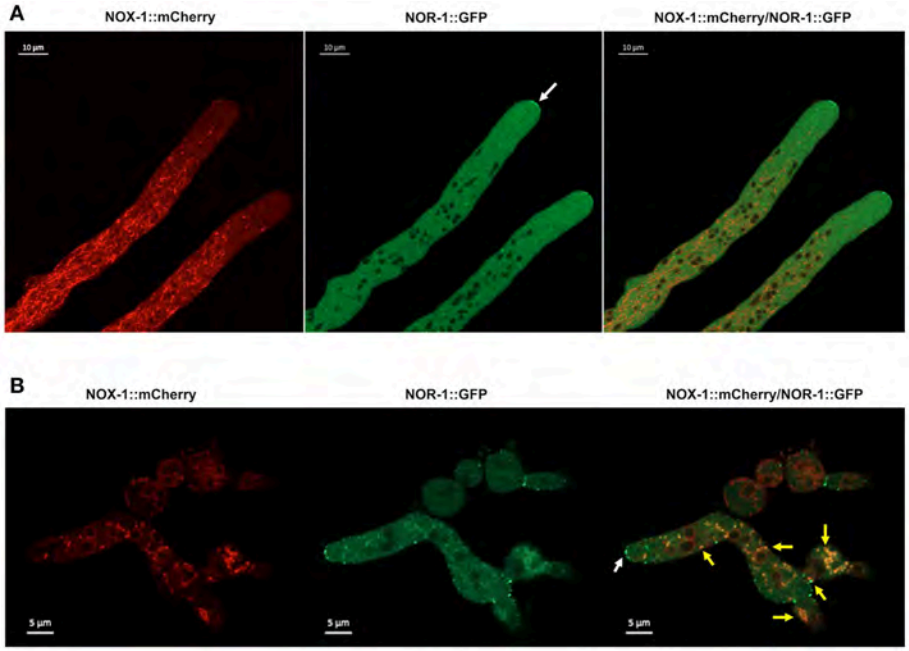

FIGURE 8 | NOX-1::mCherry co-localizes with NOR-1::GFP during CAT inducing conditions. **(A)** Heterokaryotic hyphae from strains expressing NOX-1::mCherry and NOR-1::GFP were observed by confocal microscopy. A white arrow points to NOR-1::GFP enrichment at the hyphal tip. **(B)** Conidia from NOX-1::mCherry and NOR-1::GFP strains were incubated under CAT inducing conditions and observed by confocal microscopy. The white arrow indicates NOR-1::GFP localized at the hyphal tip in a dotted pattern and yellow arrows indicate single dot or dotted regions where NOX-1 and NOR-1 co-localize.

and *nox-1*^{C524R}*-mCherry* alleles were unable to complement any of the defects observed in *Δnox-1* mutants (**Figures S11A–F**). These results indicate that all NOX functions depend on its oxidase activity.

DISCUSSION

NOX-1 Is Localized in the Vacuolar System

The localization of a protein is a determinant of its functions. Previous reports on NOX subcellular localization in different filamentous fungi concluded that these enzymes are mainly associated to the ER. In *P. anserina*, PaNox1-GFP tagging resulted in a reticulate pattern, in some cases perinuclear, showing high co-localization with an ER marker in young hyphae, while in older hyphae a cortical punctuated pattern was more frequent. The authors concluded that PaNox1 is mainly localized in the ER, as well as in cortical vesicles originated from the ER and presumably involved in the vacuolar network (Lacaze et al., 2015). However, the ER marker consisted of mCherry tagged with the predicted secretion signal from NOX subunit PaNoxD and the KDEL ER-retention signal, and no other independent ER marker was used.

In *B. cinerea*, BcNoxA and BcNoxB GFP fusions expressed constitutively were localized in similar structures in germinated conidia. Both GFP-NoxA and NoxB-GFP showed partial co-localization with an ER-tracker signal, in some cases in structures surrounding nuclei (Siegmund et al., 2013). In *Claviceps purpurea*, mCherry fusions of CpNox1 and CpNox2, not tested for functionality, were expressed constitutively and localized using epifluorescence microscopy. Using ER-Tracker Blue-White DPX, these authors concluded that CpNox1 and CpNox2 appeared to be located mainly in the ER while CpNox2 also showed a tendency to accumulate in unspecified vacuoles (Schurmann et al., 2013). In support of ER localization, Siegmund et al. (2015) showed that a *B. cinerea* GFP::BcNoxA fusion designed to be artificially retained in the ER, by addition of the HDEL motif, restored the pathogenicity defects of a *ΔbcnoxA* mutant. However, the fact that this fusion failed to complement *ΔbcnoxA* CAT fusion and sclerotia formation defects, led the authors to propose that BcNoxA has functions both inside and outside the ER (Siegmund et al., 2015). However, the possibility that GFP::BcNoxA::HDEL could leak from the ER cannot be excluded, as it is known that some KDEL bearing proteins are localized outside the ER (Soares Moretti and Martins Laurindo, 2017). In search of possible NOX functions at the ER, Marschall and Tudzynski (2017) detected physical interaction between BcNoxA and putative ER disulfide isomerase protein BcPdi1, and showed that *ΔbcnoxA* and *Δbcpdi1* mutants display similar phenotypes (Marschall and Tudzynski, 2017). However, there is increasing evidence indicating that disulfide isomerases can be located and have functions outside the ER (Soares Moretti and Martins Laurindo, 2017).

Our results using confocal microscopy show that functional versions of *N. crassa* NOX-1, expressed either from a constitutive promoter or from its own promoter, display limited co-localization with the ER and early endosomes and

are mainly associated to the entire vacuolar system, as defined by the organellar system labeled by the vacuolar ATPase VMA-1 and the fluorescent molecule carboxy-DFFDA. The fact that in older hyphal regions the NOX-1::mCherry signal is located in the lumen of large vesicles suggests that NOX-1 degradation might occur in these cell compartments, as it has been observed for other vacuolar membrane proteins such as NCA-2, NCA-3, and CAX but not for VMA-1, which does not contain transmembrane domains (Bowman et al., 2009). In addition, NOX-1 proteolysis could result in cleavage of the mCherry tag. Although the reasons for these differences in fungal NOX localization (mainly ER *vs.* mainly vacuolar) are not known, they might be related to (i) the biological dissimilarity between *N. crassa* and the other fungi studied; (ii) the fact that different cell types or regions were studied in different fungi or (iii) technical and methodological reasons.

As shown before (Bowman et al., 2015; Rico-Ramirez et al., 2018) and in this work, *N. crassa* vacuolar system is a highly dynamic and pleomorphic structure, showing dramatic changes in shape during growth, aging, and development. In growing hyphae, the tubular vacuolar region has also been named as network of elongated cisternae or NEC. Studying the co-expression of CSE-7, a chaperone required for ER exit of some proteins, and different ER markers, Rico-Ramirez et al. (2018) concluded that what has been defined as ER and NEC show some overlap. How extensive this overlap is, structurally as well as functionally, is yet to be defined. However, it should be noted that while the subcellular localization of proteins depends mainly on their targeting signals, the accumulation of DFFDA and its fluorescence depends on specific transporters and an acidic pH, both associated with vacuolar compartments and not with the ER. Indeed, DFFDA never stains the nuclear envelope or the hyphal tip regions, while ER markers are readily detected in these regions. As NOX-1, VMA-1, and DFFDA largely stain the same compartments, we conclude that such compartments correspond to the vacuolar network. Interestingly, NOX2 and V-ATPase not only are both located in mammalian phagosomes, but V-ATPase activity is required for NOX2 oxidase activity (Rybicka et al., 2012).

Fungal vacuoles have functions similar to animal lysosomes and plant vacuoles (Richards et al., 2012). They play essential roles in protein and organelle degradation, xenobiotic detoxification, cellular pH, and osmotic homeostasis, and the storage of metabolites and critical ions like iron and calcium. We propose that some of these processes are ROS-regulated by NOX enzymes capable to produce low levels of ROS in the vacuolar lumen (see below), as exemplified by the redox regulation of cysteine cathepsin proteases in phagosomes (Rybicka et al., 2012).

NOX-1 Is Also Localized at the Plasma Membrane

Although in growing hyphae most of the NOX-1-mCherry fluorescence signal was associated to the vacuolar system, we also detected part of NOX-1 at the plasma membrane, particularly in areas that correspond to the tubular vacuolar network and large spherical vacuoles regions. Polarized growth in plants has been associated with plasma membrane enrichment of specific NOX enzymes at the tip of root hair cells (Takeda et al., 2008). As *Δnox-1* mutants are affected in radial growth and growth of aerial mycelium, this suggests that NOX-1 plasma membrane localization might be linked to polar growth in this fungus. However, NOX-1 localization at the plasma membrane of the hyphal tip was observed only in some instances, including when latrunculin was used to partially inhibit endocytosis, and even in these cases the enzyme was not particularly enriched at the tip. This might be related to the fact that this region moves out of focus during growth, or it could indicate that NOX-1 membrane localization at the hyphal tip is transient and highly dynamic. In contrast, the NOX-1 regulatory subunit NOR-1 was indeed enriched at the hyphal tip (see below). In *M. oryzae*, using a NOX1-GFP fusion expressed from its own promoter and epifluorescence microscopy, Egan et al. (2007) detected faint GFP fluorescence at the periphery of appressoria, suggesting that NOX1 was localized at the plasma membrane. Notably, this fusion was also partially localized in the appressorium central vacuole, but its localization was not studied in other conditions. Although in *B. cinerea*, NoxA and NoxB were associated to the ER, faint fluorescence was also detected at the plasma membrane (Siegmund et al., 2013). It is not uncommon that only a portion of the total amount of cellular NOX is localized at the plasma membrane. In resting dendritic cells, only about 10% of total NOX2 is present on the plasma membrane and this increases to about 22% after zymosan stimulation, while a significant amount of this enzyme is detected in late endosomes and lysosomes (Dingjan et al., 2017).

NOX-1 and NOR-1 Co-localize Only in Some Specific Compartments

As *Δnor-1* mutant phenotypes recapitulate the phenotypes of both *Δnox-1* and *Δnox-2* mutants, it has been considered that NOR-1 is necessary for the activity of both enzymes. Therefore, it was unexpected to find that NOX-1 and NOR-1 co-localize in only some cell compartments. Our NOR-1 localization results are largely consistent with the localization of NOR-1 orthologs in other fungi. In the plant symbiont *Epichloë festucae* grown in axenic culture, a NoxR-GFP fusion, not tested for functionality and expressed from a constitutive promoter, was detected in septa and hyphal tips showing both punctuated and more homogeneous patterns behind the tip. The hyphal tip localization depended on the presence of NoxR PB1 domain (Takemoto et al., 2011). In *B. cinerea*, a constitutively expressed functional GFP-BcNoxR fusion was detected in granules irregularly distributed throughout the vegetative hyphae. In some cases these granules were moving toward the hyphal tip, and no co-localization with BcNoxA or BcNoxB was observed (Siegmund et al., 2013). In *C. purpurea* a CpNoxR::mCherry fusion, not tested for functionality and expressed constitutively was detected equally distributed in the cytoplasm as well as within mobile particles (Schurmann et al., 2013). In *P. anserina*, PaNoxR was detected in a diffuse cytoplasmic pattern in young hyphal regions and in a punctuated pattern in older regions. In some cases PaNoxR was detected at

the tip of growing hyphae, as well as the tip of hyphae undergoing anastomosis, and PaNox1 and PaNoxR co-localization was only observed in vesicles and never at ER-type structures or the hyphal tip (Lacaze et al., 2015).

We found that NOX-1 and NOR-1 co-localization is mainly observed in vesicular structures formed during CAT formation and cell-cell fusion conditions. It is possible that all the defects observed in *Δnor-1* and *Δnox-1* mutants could be explained by their inability to undergo cell fusion, both during hyphal growth and CAT fusion. Indeed, many mutants screened as defective for cell fusion were also affected in radial growth, aerial mycelium growth and were female sterile during sexual differentiation (Fu et al., 2011). CAT development is a complex process and more than 70 genes involved in cell recognition, chemotropic interactions and cell fusion have been identified in filamentous fungi. Among these NOX-1 and NOR-1 are essential for cell fusion in different fungi [see (Fischer and Glass, 2019) for a comprehensive review]. Interestingly, we have found that *Δnox-1* conidia cannot fuse with wild type conidia, indicating that a functional NOX-1 is needed in the fusing cells and highlighting the importance of NOX-1 during this process.

NOX-1 Oxidase Activity Is Essential to Regulate Growth and Development in *N. crassa*

We have demonstrated that the substitution of a single amino acid in two different NADPH-binding sites is enough to render NOX-1 inactive. This indicates that the oxidase activity of NOX-1 is essential for its functions, as opposed to NOX-1 possible roles as a scaffolding protein, capable to interact with several proteins. NOX transport of the electrons taken form NADPH across a membrane not only produces superoxide and derived ROS, but can also affect the pH on either side of the membrane. This, in turn, affects electrochemical-driven ion fluxes and cell turgor (Segal, 2016). Because these two functions cannot be separated, the critical question on which NOX functions are attributed to the production of ROS and which to the associated changes in pH remains unanswered and therefore, it cannot be ignored that NOX enzyme function has these two effects.

The fact that electron transport activity can be induced *in vitro* by adding NADPH to purified and relipidated NOX2 (Koshkin and Pick, 1993) indicates that there is a low basal activity that seems independent of its regulatory subunits. Therefore, it is possible that the NOX-1 we observe in the vacuolar network could have some NOR-1 independent activity in this cell compartment, which might be important to regulate the acidic pH and contents of the vacuolar system, as well as cell turgor.

In addition, some NOX-1 targeted to the plasma membrane might be endocyted and fused with NOR-1 containing vesicles to generate a fully active enzyme and produce high ROS levels inside these vesicles. Some of these vesicles could travel back to the plasma membrane and release ROS to the extracellular space, where they could participate in cell-wall remodeling, defense and cell-cell communication (Aguirre and Lambeth, 2010). Some of these vesicles containing fully active NOX-1 could also be directed to specific cell compartments, where they could fuse and release ROS, as a way of generating different oxidation conditions in time and space.

In dendritic cells, where a sustained production of ROS is needed in the phagosome, it has been recently shown that lysosomes contain a large portion of inactive NOX2, which is recruited to the phagosome to replenish inactive oxidized NOX2 (Dingjan et al., 2017). Therefore, it is possible that part of the NOX-1 present in the fungal vacuolar system could also be a NOX-1 reservoir to be directed to NOR-1-containing or other cell compartments.

DATA AVAILABILITY

The raw data supporting the conclusions of this manuscript will be made available by the authors, without undue reservation, to any qualified researcher.

AUTHOR CONTRIBUTIONS

JA designed experiments, wrote the manuscript, and obtained funding. NC-D performed and designed experiments, and contributed to manuscript writing. BB and LP-R contributed materials, and to discussion and manuscript writing.

FUNDING

This work was supported by CONACYT grants Investigación en Fronteras de la Ciencia 2015-I-319, CONACYT-DFG 277869 and PAPIIT-UNAM IN200719 and IV200519.

ACKNOWLEDGMENTS

We are deeply grateful to Meritxell Riquelme (CICESE), for providing the endosome labeled strain, Oregon Green, and helpful discussions and Olivia Sánchez and Mariana Angélica Robledo (supported by a postdoctoral fellowship form DGAPA-UNAM) for technical assistance. We also thank Dr. Fernando García and Dr. Abraham Rosas-Arellano from IFC Imagenology unit for help with confocal microscopy, as well as to IFC-UNAM Molecular Biology and Computer Units.

SUPPLEMENTARY MATERIAL

The Supplementary Material for this article can be found online at: https://www.frontiersin.org/articles/10.3389/fmicb.2019.01825/full#supplementary-material

Video S1 | Conidia expressing NOX-1::mCherry undergoing cell-cell fusion.

Video S2 | Growing hyphae expressing NOX-1::mCherry.

Video S3 | Heterokaryotic conidia expressing endosome marker GFP-YPT-52 and NOX-1::mCherry under CAT inducing conditions.

REFERENCES

Aguirre, J., and Lambeth, J. D. (2010). Nox enzymes from fungus to fly to fish and what they tell us about Nox function in mammals. *Free Radic. Biol. Med.* 49, 1342–1353. doi: 10.1016/j.freeradbiomed.2010.07.027

Aguirre, J., Rios-Momberg, M., Hewitt, D., and Hansberg, W. (2005). Reactive oxygen species and development in microbial eukaryotes. *Trends Microbiol.* 13, 111–118. doi: 10.1016/j.tim.2005.01.007

Babior, B. M. (1995). The respiratory burst oxidase. *Curr. Opin. Hematol.* 2, 55–60. doi: 10.1097/00062752-199502010-00008

Bistis, G. N. (1983). Synchronous induction and development of ascogonia. *Neurospora Newslett.* 30:14. doi: 10.4148/1941-4765.1624

Bowman, B. J., Draskovic, M., Freitag, M., and Bowman, E. J. (2009). Structure and distribution of organelles and cellular location of calcium transporters in *Neurospora crassa*. *Eukaryot. Cell* 8, 1845–1855. doi: 10.1128/EC.00174-09

Bowman, B. J., Draskovic, M., Schnittker, R. R., El-Mellouki, T., Plamann, M. D., Sanchez-Leon, E., et al. (2015). Characterization of a novel prevacuolar compartment in *Neurospora crassa*. *Eukaryot. Cell* 14, 1253–1263. doi: 10.1128/EC.00128-15

Cano-Dominguez, N., Alvarez-Delfin, K., Hansberg, W., and Aguirre, J. (2008). NADPH oxidases NOX-1 and NOX-2 require the regulatory subunit NOR-1 to control cell differentiation and growth in *Neurospora crassa*. *Eukaryot. Cell* 7, 1352–1361. doi: 10.1128/EC.00137-08

Colot, H. V., Park, G., Turner, G. E., Ringelberg, C., Crew, C. M., Litvinkova, L., et al. (2006). A high-throughput gene knockout procedure for Neurospora reveals functions for multiple transcription factors. *Proc. Natl. Acad. Sci. U.S.A.* 103, 10352–10357. doi: 10.1073/pnas.0601456103

Davies, R. H., and deSerres, D. (1970). Genetic and microbial research techniques for *Neurospora crassa*. *Methods Enzymol.* 27A, 79–143. doi: 10.1016/0076-6879(71)17168-6

Dingjan, I., Linders, P. T. A., van den Bekerom, L., Baranov, M. V., Halder, P., ter Beest, M., et al. (2017). Oxidized phagosomal NOX2 complex is replenished from lysosomes. *J. Cell Sci.* 130, 1285–1298. doi: 10.1242/jcs.196931

Dirschnabel, D. E., Nowrousian, M., Cano-Dominguez, N., Aguirre, J., Teichert, I., and Kuck, U. (2014). New insights into the roles of NADPH oxidases in sexual development and ascospore germination in *Sordaria macrospora*. *Genetics* 196, 729–744. doi: 10.1534/genetics.113.159368

Egan, M. J., Wang, Z. Y., Jones, M. A., Smirnoff, N., and Talbot, N. J. (2007). Generation of reactive oxygen species by fungal NADPH oxidases is required for rice blast disease. *Proc. Natl. Acad. Sci. U.S.A.* 104, 11772–11777. doi: 10.1073/pnas.0700574104

Fischer, M. S., and Glass, N. L. (2019). Communicate and fuse: how filamentous fungi establish and maintain an interconnected mycelial network. *Front. Microbiol.* 10:619. doi: 10.3389/fmicb.2019.00619

Freitag, M., Hickey, P. C., Raju, N. B., Selker, E. U., and Read, N. D. (2004). GFP as a tool to analyze the organization, dynamics and function of nuclei and microtubules in *Neurospora crassa*. *Fungal Genet Biol.* 41, 897–910. doi: 10.1016/j.fgb.2004.06.008

Fu, C., Iyer, P., Herkal, A., Abdullah, J., Stout, A., and Free, S. J. (2011). Identification and characterization of genes required for cell-to-cell fusion in *Neurospora crassa*. *Eukaryot. Cell* 10, 1100–1109. doi: 10.1128/EC.05003-11

Hajjar, C., Cherrier, M. V., Dias Mirandela, G., Petit-Hartlein, I., Stasia, M. J., Fontecilla-Camps, J. C., et al. (2017). The NOX family of proteins is also present in bacteria. *MBio* 8:e01487–17. doi: 10.1128/mBio.01487-17

Hansberg, W., and Aguirre, J. (1990). Hyperoxidant states cause microbial cell differentiation by cell isolation from dioxygen. *J. Theor. Biol.* 142, 201–221. doi: 10.1016/S0022-5193(05)80222-X

Hernandez-Onate, M. A., Esquivel-Naranjo, E. U., Mendoza-Mendoza, A., Stewart, A., and Herrera-Estrella, A. H. (2012). An injury-response mechanism conserved across kingdoms determines entry of the fungus *Trichoderma atroviride* into development. *Proc. Natl. Acad. Sci. U.S.A.* 109, 14918–14923. doi: 10.1073/pnas.1209396109

Hickey, P. C., Jacobson, D., Read, N. D., and Glass, N. L. (2002). Live-cell imaging of vegetative hyphal fusion in *Neurospora crassa*. *Fungal Genet Biol.* 37, 109–119. doi: 10.1016/S1087-1845(02)00035-X

Kim, H. J., Chen, C., Kabbage, M., and Dickman, M. B. (2011). Identification and characterization of Sclerotinia sclerotiorum NADPH oxidases. *Appl. Environ. Microbiol.* 77, 7721–7729. doi: 10.1128/AEM.05472-11

Koshkin, V., and Pick, E. (1993). Generation of superoxide by purified and relipidated cytochrome b559 in the absence of cytosolic activators. *FEBS Lett.* 327, 57–62. doi: 10.1016/0014-5793(93)81039-3

Lacaze, I., Lalucque, H., Siegmund, U., Silar, P., and Brun, S. (2015). Identification of NoxD/Pro41 as the homologue of the p22phox NADPH oxidase subunit in fungi. *Mol. Microbiol.* 95, 1006–1024. doi: 10.1111/mmi.12876

Lambeth, J. D., Cheng, G., Arnold, R. S., and Edens, W. A. (2000). Novel homologs of gp91phox. *Trends Biochem. Sci.* 25, 459–461. doi: 10.1016/S0968-0004(00)01658-3

Lambou, K., Malagnac, F., Barbisan, C., Tharreau, D., Lebrun, M. H., and Silar, P. (2008). The crucial role of the Pls1 tetraspanin during ascospore germination in *Podospora anserina* provides an example of the convergent evolution of morphogenetic processes in fungal plant pathogens and saprobes. *Eukaryot. Cell* 7, 1809–1818. doi: 10.1128/EC.00149-08

Lara-Ortiz, T. (2004). *NoxA, una NADPH Oxidasa Homóloga a Gp91phox, Regula El Desarrollo Sexual En El Hongo Aspergillus Nidulans*. Ph.D., Universidad Nacional Autónoma de México.

Lara-Ortiz, T., Riveros-Rosas, H., and Aguirre, J. (2003). Reactive oxygen species generated by microbial NADPH oxidase NoxA regulate sexual development in *Aspergillus nidulans*. *Mol. Microbiol.* 50, 1241–1255. doi: 10.1046/j.1365-2958.2003.03800.x

Malagnac, F., Lalucque, H., Lepere, G., and Silar, P. (2004). Two NADPH oxidase isoforms are required for sexual reproduction and ascospore germination in the filamentous fungus *Podospora anserina*. *Fung. Genet. Biol.* 41, 982–997. doi: 10.1016/j.fgb.2004.07.008

Marschall, R., and Tudzynski, P. (2017). The protein disulfide isomerase of *Botrytis cinerea*: an ER protein involved in protein folding and redox homeostasis influences NADPH oxidase signaling processes. *Front. Microbiol.* 8:960. doi: 10.3389/fmicb.2017.00960

Pidoux, A. L., and Armstrong, J. (1992). Analysis of the BiP gene and identification of an ER retention signal in *Schizosaccharomyces pombe*. *EMBO J.* 11, 1583–1591. doi: 10.1002/j.1460-2075.1992.tb05203.x

Plemper, R. K., Bohmler, S., Bordallo, J., Sommer, T., and Wolf, D. H. (1997). Mutant analysis links the translocon and BiP to retrograde protein transport for ER degradation. *Nature* 388, 891–895. doi: 10.1038/42276

Rae, J., Newburger, P. E., Dinauer, M. C., Noack, D., Hopkins, P. J., Kuruto, R., et al. (1998). X-Linked chronic granulomatous disease: mutations in the CYBB gene encoding the gp91-phox component of respiratory-burst oxidase. *Am. J. Hum. Genet.* 62, 1320–1331. doi: 10.1086/301874

Read, N. D., Goryachev, A. B., and Lichius, A. (2012). The mechanistic basis of self-fusion between conidial anastomosis tubes during fungal colony initiation. *Fung. Biol. Rev.* 26, 1–11. doi: 10.1016/j.fbr.2012.02.003

Richards, A., Gow, N. A., and Veses, V. (2012). Identification of vacuole defects in fungi. *J. Microbiol. Methods* 91, 155–163. doi: 10.1016/j.mimet.2012.08.002

Rico-Ramirez, A. M., Roberson, R. W., and Riquelme, M. (2018). Imaging the secretory compartments involved in the intracellular traffic of CHS-4, a class IV chitin synthase, in *Neurospora crassa*. *Fungal Genet Biol.* 117, 30–42. doi: 10.1016/j.fgb.2018.03.006

Rinnerthaler, M., Buttner, S., Laun, P., Heeren, G., Felder, T. K., Klinger, H., et al. (2012). Yno1p/Aim14p, a NADPH-oxidase ortholog, controls extramitochondrial reactive oxygen species generation, apoptosis, and actin cable formation in yeast. *Proc. Natl. Acad. Sci. U.S.A.* 109, 8658–8663. doi: 10.1073/pnas.1201629109

Roca, M. G., Weichert, M., Siegmund, U., Tudzynski, P., and Fleissner, A. (2012). Germling fusion via conidial anastomosis tubes in the grey mould *Botrytis cinerea* requires NADPH oxidase activity. *Fungal Biol.* 116, 379–387. doi: 10.1016/j.funbio.2011.12.007

Rossi, D. C. P., Gleason, J. E., Sanchez, H., Schatzman, S. S., Culbertson, E. M., Johnson, C. J., et al. (2017). *Candida albicans* FRE8 encodes a member of the NADPH oxidase family that produces a burst of ROS during fungal morphogenesis. *PLoS Pathog.* 13:e1006763. doi: 10.1371/journal.ppat.1006763

Rybicka, J. M., Balce, D. R., Chaudhuri, S., Allan, E. R. O., and Yates, R. M. (2012). Phagosomal proteolysis in dendritic cells is modulated by NADPH oxidase in a pH-independent manner. *Embo J.* 31, 932–944. doi: 10.1038/emboj.2011.440

Ryder, L. S., Dagdas, Y. F., Mentlak, T. A., Kershaw, M. J., Thornton, C. R., Schuster, M., et al. (2013). NADPH oxidases regulate septin-mediated cytoskeletal remodeling during plant infection by the rice blast fungus. *Proc. Natl. Acad. Sci. U.S.A.* 110, 3179–3184. doi: 10.1073/pnas.1217470110

Schurmann, J., Buttermann, D., Herrmann, A., Giesbert, S., and Tudzynski, P. (2013). Molecular characterization of the NADPH oxidase complex in the ergot fungus *Claviceps purpurea*: CpNox2 and CpPls1 are important for a balanced host-pathogen interaction. *Mol. Plant Microbe Interact.* 26, 1151–1164. doi: 10.1094/MPMI-03-13-0064-R

Segal, A. W. (2016). NADPH oxidases as electrochemical generators to produce ion fluxes and turgor in fungi, plants and humans. *Open Biol.* 6:160028. doi: 10.1098/rsob.160028

Segal, A. W., and Jones, O. T. (1978). Novel cytochrome b system in phagocytic vacuoles of human granulocytes. *Nature* 276, 515–517. doi: 10.1038/276515a0

Segmuller, N., Kokkelink, L., Giesbert, S., Odinius, D., van Kan, J., and Tudzynski, P. (2008). NADPH oxidases are involved in differentiation and pathogenicity in *Botrytis cinerea*. *Mol Plant Microbe Interact.* 21, 808–819. doi: 10.1094/MPMI-21-6-0808

Seidel, C., Moreno-Velasquez, S. D., Riquelme, M., and Fischer, R. (2013). *Neurospora crassa* NKIN2, a kinesin-3 motor, transports early endosomes and is required for polarized growth. *Eukaryot Cell* 12, 1020–1032. doi: 10.1128/EC.00081-13

Shaner, N. C., Campbell, R. E., Steinbach, P. A., Giepmans, B. N., Palmer, A. E., and Tsien, R. Y. (2004). Improved monomeric red, orange and yellow fluorescent proteins derived from Discosoma sp. red fluorescent protein. *Nat. Biotechnol.* 22, 1567–1572. doi: 10.1038/nbt1037

Siegmund, U., Heller, J., van Kan, J. A., and Tudzynski, P. (2013). The NADPH oxidase complexes in *Botrytis cinerea*: evidence for a close association with the ER and the tetraspanin Pls1. *PLoS ONE* 8:e55879. doi: 10.1371/annotation/84c258cf-4f98-43d8-a4f0-7032cba36f22

Siegmund, U., Marschall, R., and Tudzynski, P. (2015). BcNoxD, a putative ER protein, is a new component of the NADPH oxidase complex in *Botrytis cinerea*. *Mol. Microbiol.* 95, 988–1005. doi: 10.1111/mmi.12869

Soares Moretti, A. I., and Martins Laurindo, F. R. (2017). Protein disulfide isomerases: redox connections in and out of the endoplasmic reticulum. *Arch. Biochem. Biophys.* 617, 106–119. doi: 10.1016/j.abb.2016.11.007

Takeda, S., Gapper, C., Kaya, H., Bell, E., Kuchitsu, K., and Dolan, L. (2008). Local positive feedback regulation determines cell shape in root hair cells. *Science* 319, 1241–1244. doi: 10.1126/science.1152505

Takemoto, D., Kamakura, S., Saikia, S., Becker, Y., Wrenn, R., Tanaka, A., et al. (2011). Polarity proteins Bem1 and Cdc24 are components of the filamentous fungal NADPH oxidase complex. *Proc. Natl. Acad. Sci. U.S.A.* 108, 2861–2866. doi: 10.1073/pnas.1017309108

Takemoto, D., Tanaka, A., and Scott, B. (2006). A p67Phox-like regulator is recruited to control hyphal branching in a fungal-grass mutualistic symbiosis. *Plant Cell* 18, 2807–2821. doi: 10.1105/tpc.106.046169

Tanaka, A., Christensen, M. J., Takemoto, D., Park, P., and Scott, B. (2006). Reactive oxygen species play a role in regulating a fungus-perennial ryegrass mutualistic interaction. *Plant Cell* 18, 1052–1066. doi: 10.1105/tpc.105.039263

Verdin, J., Bartnicki-Garcia, S., and Riquelme, M. (2009). Functional stratification of the Spitzenkorper of *Neurospora crassa*. *Mol. Microbiol.* 74, 1044–1053. doi: 10.1111/j.1365-2958.2009.06917.x

Westergaard, M., and Mitchell, H. K. (1974). A synthetic medium favoring sexual reproduction. *Amer. J. Bot.* 34, 573–577. doi: 10.1002/j.1537-2197.1947.tb13032.x

Yang, S. L., and Chung, K. R. (2013). Similar and distinct roles of NADPH oxidase components in the tangerine pathotype of *Alternaria alternata*. *Mol. Plant Pathol.* 14, 543–556. doi: 10.1111/mpp.12026

Zhang, C., Lin, Y., Wang, J., Wang, Y., Chen, M., Norvienyeku, J., et al. (2016). FgNoxR, a regulatory subunit of NADPH oxidases, is required for female fertility and pathogenicity in *Fusarium graminearum*. *FEMS Microbiol. Lett.* 363:fnv223. doi: 10.1093/femsle/fnv223

Zhao, Y. L., Zhou, T. T., and Guo, H. S. (2016). Hyphopodium-specific VdNoxB/VdPls1-dependent ROS-Ca2+ signaling is required for plant infection by *Verticillium dahliae*. *PLoS Pathog* 12:e1005793. doi: 10.1371/journal.ppat.1005793

Zhou, T. T., Zhao, Y. L., and Guo, H. S. (2017). Secretory proteins are delivered to the septin-organized penetration interface during root infection by *Verticillium dahliae*. *PLoS Pathog.* 13:e1006275. doi: 10.1371/journal.ppat.1006275

Conflict of Interest Statement: The authors declare that the research was conducted in the absence of any commercial or financial relationships that could be construed as a potential conflict of interest.

Copyright © 2019 Cano-Domínguez, Bowman, Peraza-Reyes and Aguirre. This is an open-access article distributed under the terms of the Creative Commons Attribution License (CC BY). The use, distribution or reproduction in other forums is permitted, provided the original author(s) and the copyright owner(s) are credited and that the original publication in this journal is cited, in accordance with accepted academic practice. No use, distribution or reproduction is permitted which does not comply with these terms.

Chromaffin Cells of the Adrenal Medulla: Physiology, Pharmacology, and Disease

Emilio Carbone,[1] *Ricardo Borges,*[2] *Lee E. Eiden,*[3] *Antonio G. García,*[4] *and Arturo Hernández-Cruz*[*5]

ABSTRACT

Chromaffin cells (CCs) of the adrenal gland and the sympathetic nervous system produce the catecholamines (epinephrine and norepinephrine; EPI and NE) needed to coordinate the bodily "fight-or-flight" response to fear, stress, exercise, or conflict. EPI and NE release from CCs is regulated both neurogenically by splanchnic nerve fibers and nonneurogenically by hormones (histamine, corticosteroids, angiotensin, and others) and paracrine messengers [EPI, NE, adenosine triphosphate, opioids, γ-aminobutyric acid (GABA), etc.]. The "stimulus-secretion" coupling of CCs is a Ca^{2+}-dependent process regulated by Ca^{2+} entry through voltage-gated Ca^{2+} channels, Ca^{2+} pumps, and exchangers and intracellular organelles (RE and mitochondria) and diffusible buffers that provide both Ca^{2+}-homeostasis and Ca^{2+}-signaling that ultimately trigger exocytosis. CCs also express Na^+ and K^+ channels and ionotropic (nAChR and $GABA_A$) and metabotropic receptors (mACh, PACAP, β-AR, 5-HT, histamine, angiotensin, and others) that make CCs excitable and responsive to autocrine and paracrine stimuli. To maintain high rates of E/NE secretion during stressful conditions, CCs possess a large number of secretory chromaffin granules (CGs) and members of the soluble NSF-attachment receptor complex protein family that allow docking, fusion, and exocytosis of CGs at the cell membrane, and their recycling. This article attempts to provide an updated account of well-established features of the molecular processes regulating CC function, and a survey of the as-yet-unsolved but important questions relating to CC function and dysfunction that have been the subject of intense research over the past 15 years. Examples of CCs as a model system to understand the molecular mechanisms associated with neurodegenerative diseases are also provided. Published 2019. *Compr Physiol* 9:1443-1502, 2019.

Didactic Synopsis

Major teaching points

1. During stress, chromaffin cells (CCs) from the adrenal medulla release a surge of catecholamines (CAs) [epinephrine (EPI) and norepinephrine (NE)] into the bloodstream, which serves to prepare the different organs of the body for the fight-or-flight response, to escape from danger and survive.

2. Classically, the secretory response of CCs is triggered by a rapid elevation of the Ca^{2+} concentration in the cytosol, mainly contributed by Ca^{2+} entry via voltage-activated Ca^{2+} channels that open upon membrane depolarization as a consequence of the activation of postsynaptic cholinergic receptors by the neurotransmitter acetylcholine (ACh) that is released from splanchnic nerve terminals. Pituitary adenylate cyclase-activating polypeptide (PACAP) co-released with ACh at the adrenomedullary synapse contributes to CA secretion from the adrenal medulla during stress.

3. CCs express many types of Na^+, Ca^{2+}, and K^+ channels that are also able to generate spontaneous "neuronal-like" tonic and burst-firing patterns that can drive a sustained "nonneurogenic" release of CAs upon stimulation by various secretagogues.

4. The Ca^{2+} signal due to Ca^{2+} entry is subsequently modulated by Ca^{2+} uptake and release in mitochondria and endoplasmic reticulum (ER). Intracellular Ca^{2+} controls

*Correspondence to ahernan@ifc.unam.mx

[1]Laboratory of Cellular and Molecular Neuroscience, Department of Drug Science, N.I.S. Centre, University of Torino, Torino, Italy

[2]Unidad de Farmacología, Facultad de Medicina, Universidad de La Laguna, Tenerife, Spain

[3]Section on Molecular Neuroscience, National Institute of Mental Health, Bethesda, Maryland, USA

[4]Departamento de Farmacología y Terapéutica, Facultad de Medicina, Instituto Teófilo Hernando, Universidad Autónoma de Madrid, Madrid, Spain

[5]Departamento de Neurociencia Cognitiva and Laboratorio Nacional de Canalopatías, Instituto de Fisiología Celular, Universidad Nacional Autonoma de México, Ciudad Universitaria, CDMX, México

Published online, October 2019 (*comprehensivephysiology.com*)

DOI:10.1002/cphy.c190003

This article is a U.S. Government work and is in the public domain in the U.S.A.

granule movement to the plasma membrane, exocytosis and endocytosis, and couples cell activity to adenosine triphosphate (ATP) generation.

5. CAs, chromogranins, ATP, GABA, opioids, and other peptides are tightly packaged in secretory granules (SGs) that release their contents by fusion with the plasmalemma. In this process (exocytosis) several soluble NSF-attachment receptor complex (SNARE) proteins participate in regulating the formation of a membrane fusion pore and its subsequent expansion to release the granule content.

6. CAs are preferentially released from newly synthetized granules. Older granules may act as CA donors for newly formed granule reloading.

7. Secretagogues of the adrenal medulla stimulate both CA/peptide synthesis and release via "stimulus-secretion-synthesis coupling." CC excitability, Ca^{2+} channel currents and the ensuing secretory responses are regulated further by several receptors for opioids, PACAP, ATP, GABA, and various other neurotransmitters.

8. Altered cell excitability, Ca^{2+}-handling, and exocytosis defects have been reported in CCs from rodent models of diseases such as hypertension, Alzheimer's disease, Huntington's disease (HD), autism, and amyotrophic lateral sclerosis, suggesting that the defective proteins of the disease also have an impact on CC function.

Introduction

The adrenal glands are endocrine organs that reside above the kidneys in mammals and, as such, have also been called "suprarenal" glands. The inner part of the adrenal is the medulla, a tissue originating from the neural crest, and surrounded by the cortex. Both cortex and medulla contribute critically to the body's responses to stress. At the beginning of the 19th century, Alfred Kohn coined the term "chromaffin" for adrenal medulla catecholamine-containing cells, which can be stained by a chemical reaction to chromium (113). Since then, CCs have provided one of the most successful models for the study of nerve cells, especially for the stimulus-secretion coupling process and its regulation (394).

During intense fear, metabolic stress, exercise, or struggle, adrenal CCs release into the blood stream EPI and NE necessary for regulating the "fight-or-flight" response (96). These potent chemical messengers bind to their molecular targets, the adrenergic receptors, distributed throughout the entire organism, and prepare it for maximal muscle performance and motor responsiveness by increasing heart pumping strength and blood pressure, producing vasodilation in the blood supply of skeletal muscles and heart, and vasoconstriction in the skin and gastrointestinal vasculature. At the same time, mobilization of glucose from the liver is enhanced, while bronchioles dilate to optimize blood oxygenation and pupils dilate to improve visual acuity. Released CAs also promote relaxation of smooth muscle in tissues not required for a stress response such as the intestinal tract or the uterus (570).

The adrenal medulla performs these tasks, by virtue of its unique functional organization: Preganglionic sympathetic nerve fibers originating from cell bodies in the thoracolumbar segments of the spinal cord bypass the celiac ganglion without making synapses and form the splanchnic nerve, which innervates CCs directly. These synaptic terminals release ACh, that upon binding to postsynaptic nicotinic receptors in CCs, induces a rapid membrane depolarization. This triggers action potentials (APs) that allow Ca^{2+} influx, followed by rapid elevation of the intracellular Ca^{2+} concentration ($[Ca^{2+}]_i$). Ca^{2+} elevation then triggers the fusion of SGs with the plasma membrane and the exocytotic release of CAs. The neurogenic control of CCs permits a continuum of CA output, from a firing rate of splanchnic nerve impulses of about 1 Hz, sufficient to maintain resting cardiovascular, respiratory, and metabolic functions (247, 249, 506), to nerve fiber discharges at maximum rates equal or higher than 10 Hz producing a massive release of CAs during stress (569).

The first synapse described electron microscopically was the splanchnicoadrenomedullary synapse (139). Earlier, the storage of CAs within SGs of adrenal medulla was characterized (299). The concept of exocytosis was developed from the observation of the secretion of a highly charged, >70 kDa protein, chromogranin A (CgA), unlikely to be released by diffusion across cell membranes, from the adrenal medulla following splanchnic nerve stimulation (280, 673). Ca^{2+}-dependence of exocytosis was also demonstrated in the adrenal medulla (176), culminating in Douglas's concept of stimulus-secretion coupling (172), analogous to the muscle stimulus-contraction coupling.

CCs resemble neurons in many ways. Besides their synaptic input, they receive chemical signals both from their neighbors (paracrine signal) and from themselves (autocrine signal). Some of them are electrically coupled (261). Their excitable properties originate from a surprisingly wide variety of ion channels, comparable to those of many central neurons (389, 394). Thus, far from being passive followers of their neurogenic input, these cells can decode and integrate different types of extra- and intracellular signals to generate complex patterns of electrical and cytoplasmic second messenger signaling that culminate in the regulated release by exocytosis of potent chemical messengers, which include CAs, opioids and other peptides, ATP, and GABA.

The unique properties of CCs derive from their embryological origin: they belong to both the nervous and the endocrine systems (16, 628). Their neuron-like phenotype has been particularly valuable over more than 30 years of research to understand excitability, nerve impulse generation, synaptic transmission, regulated neurotransmitter secretion, and the actions of drugs that regulate central nervous system (CNS)

function (70). CCs have also been crucial for understanding the basic mechanisms of intracellular Ca^{2+} dynamics and neurochemical transmission through secretory vesicles or CGs. The CGs were first isolated from the bovine adrenal medulla and their releasable cargo analyzed (215). Most of the vesicular proteins involved in the secretory machinery were first definitively characterized in CCs (86, 163, 301, 583, 601). CCs, together with the pheochromocytoma cell line (PC12) isolated from a rat tumor of adrenomedullary origin in 1976 (257), have been the major cell types employed in the development and refinement of patch-clamp and amperometric recording techniques. These two independent but complementary electrophysiological approaches have been indispensable in clarifying most of the now-known molecular mechanisms that regulate cell excitability, Ca^{2+}-dependent secretion, and the molecular apparatus that regulates vesicle fusion (394, 667).

Starting with the seminal work of Levi-Montalcini and Unsicker (16, 628), showing that CCs can transdifferentiate into sympathetic neurons when exposed to nerve growth factor (320, 325), adrenal CCs have extended our understanding of neural development. Much of our present knowledge of the physiology and pathophysiology of neuropeptide and monoamine neurotransmitters stems from studies in CCs. More recently, CCs have been valuable in studies of neurodegenerative processes, tumorigenesis, and drug development (157, 435). This article aims at providing the reader with a broad view of both classical and recent advances concerning the molecular mechanisms regulating the secretory function of these remarkable cells, as well as their concerted role within the adrenal medulla as an endocrine organ responsible for integrating physiological responses to a range of homeostatic challenges.

The sympathoadrenal medulla connection

It is recognized that in higher organisms the brain regulates the "milieu interieur" (60) and body homeostasis (95). This regulation ensures that under normal conditions, blood glucose, oxygen, electrolyte concentrations, body temperature, blood pressure, heart rate, respiration, and blood flow to vital organs do not vary much or for very long. To maintain the integrity of the organism, the brain controls the inner world via feedback-regulated systems. Cannon introduced three concepts focused on the adrenal medulla that are well known and widely accepted: homeostasis, the "fight-or-flight" response, and the functionally unitary nature of the sympathoadrenal system. The autonomic nervous system has two divisions, parasympathetic and sympathetic. The sympathetic nervous system (SNS) comprises a large variety of cells. Thus, sympathetic neurons form the pre- and paravertebral ganglia and their axonal noradrenergic nerve terminals innervate and regulate most organs and blood vessels through the release of NE. A second SNS component is the collection of CCs within the adrenal medulla that, upon ACh and PACAP release from the splanchnic nerve, trigger the secretion of NE and EPI. CCs are also located in paraganglia close to large blood vessels and along sympathetic nerves that innervate pelvic organs (296, 366, 437). Finally, paraganglionic cells also include chemoreceptive type I cells of the carotid body, which are peripheral oxygen sensors.

Unique to the SNS is that a quite low firing frequency (less than 1 AP per second), is sufficient to maintain constant cardiovascular, respiratory, and metabolic functions of the body. Full activation during stress occurs when nerve fibers discharge at maximum rates equal or higher than 10 Hz (2, 50, 155, 515). The splanchnic nerve innervates the adrenal medullary CCs and is cholinergic. Through the release of ACh at the cholinergic-CC synapse, the human adrenal medulla secretes about 0.05 $\mu g\,kg^{-1}\,min^{-1}$ NE and 0.2 $\mu g\,kg^{-1}\,min^{-1}$ EPI (i.e. about 75% EPI and 25% NE), similar to the ratios reported in adrenal glands of cats, dogs, and calves (576). Thus, NE release from sympathetic nerve terminals throughout the body, and NE plus EPI release from the adrenal medulla maintains the basal circulating CA levels at about 250 and 100 $pg\,mL^{-1}$, (1.25 and 0.55 nM), respectively, for NE and EPI. This dual mechanism of stimulation represents a safety mechanism to maintain body homeostasis. The sympathetic neurons releasing NE locally at tissues they innervate and the adrenal medulla CCs releasing NE and EPI into the circulation augment the metabolic rate of practically every cell in the organism (250, 268).

Classical and modern histochemical, morphological, and functional studies have shown the existence of separate populations of NE- and EPI-secreting CCs in the adrenal medulla of mammals (140, 300, 456). The activity of these two cell subtypes seems to be regulated by separate neuronal pathways to the adrenal medulla. Nerve terminals on NE CC cells are morphologically distinct from terminals on EPI cells (259). Double-virus transneuronal labeling shows that the secretory activity of CCs is regulated by a set of neurons at the brainstem and the hypothalamus (323). Cumulative evidence supports the view that NE and EPI release from their respective adrenal medullary CCs is tightly regulated at three different levels, namely the brain, the spinal cord, and the CCs themselves. Thus, burst-pattern stimulation of the trigeminal nucleus caudalis in the cat brain stem preferentially releases EPI (59). The selective release of EPI is also regulated by autonomic areas in the cerebral cortex (648), hypothalamus (228, 540), and medulla oblongata (388, 438). Furthermore, the stimulation of other regions of the hypothalamus (228, 540) and medulla oblongata (438) selectively regulates the release of NE. This occurs probably because distinct preganglionic neurons innervate NE and EPI CCs (457). In addition, separate populations of preganglionic neurons, originating in different segments of the intermediolateral column of the spinal cord, differentially innervate CC subtypes, with the more cephalic preganglionic outputs innervating EPI cells and the more caudal ones innervating NE cells (187).

Thus, the different secretion of NE and EPI seems to be regulated by the distinct innervation of NE and EPI cells and

by the different input patterns that each cell type receives from the brain during stress. This may lead to selective recruitment of different subtypes of voltage-gated Ca^{2+} channels (Ca_V) expressed by CCs (240, 417). Thus, in two studies, different stimulation patterns caused differential secretion of EPI or NE; in bovine CCs stimulated with KCl, $Ca_V2.1$ (P/Q-type) channels were associated more tightly with EPI release, while Ca_V1 (L-type) channels were linked to selective NE release (400). The type of cholinergic receptor targeted by ACh may also condition the selective amine release; while nAChRs mediate the release of both CAs, muscarinic receptors preferentially mediate the release of EPI (173).

The differential secretion of NE and EPI may find a physiological and pathophysiological explanation in the different stressors or pathological situations that disrupt the organism's homeostasis. During the "flight-or-fight" response described by Cannon, an alarming acute stressful conflict causes a massive discharge of the sympathoadrenal axis, with the ensuing a large surge of NE and EPI release. Pupils and bronchioles dilate; heart rate, myocardial contraction, and blood pressure increase to switch blood to skeletal muscles that must increase the vigor of their activity; glucose is mobilized from muscle and liver to increase glycemia and metabolic activity is augmented in practically all cells of the organism. In this way, the organism is prepared as a whole to fight or run away from danger, two highly coordinated physiological responses.

From a pathophysiological perspective, the differential secretion of NE and EPI may also occur as a response to specific stressors (252). For instance, hemorrhage in cat causes a preferential release of NE, a situation in which vasoconstriction is required; however, insulin-induced hypoglycemia causes a selective EPI release because of its stronger capability to mobilize glucose from the liver (225). Other studies in the rat also demonstrate a preferential EPI release during hypoglycemia (597, 645). This contrasts with the preferential release of NE observed in rats exposed to cold stress (646). Histamine releases preferentially EPI through the activation of H1 receptors (68). Muscarinic stimulation also preferentially releases EPI (164).

Synthesis, Storage, and Metabolism of CAs

Synthesis and storage of CAs

Winkler and colleagues first introduced the concept of the "secretory cocktail" of CCs: the complement of proteins, peptides, cations, ATP, and CAs that are released from the CG as the major effector function of the CC of the adrenal medulla. Here, we describe briefly CA and protein/peptide biosynthesis and granule storage, as a necessary prelude to the more elaborate description of how this secretory cargo is released from the CC of the adrenal medulla to exert the unique physiological function of this essential endocrine organ.

The CA content of the CG depends on two processes: CA biosynthesis and CA vesicular transport and storage. The story of the discovery of the biosynthetic pathways of CAs is one of the most fascinating in neuroscience that, in spite of the enormous technical limitations was started in the latest 1930s of the past century. The detailed description of all the steps involved in the transformation of the amino acid tyrosine in the three natural CAs, DA, NE, and EPI, is beyond the aim of this article. A comprehensive description of the enzymes, cofactors, and kinetics associated with CA biosynthesis can be found elsewhere (647).

The adrenal medulla is the paradigm for the full CA synthetic pathway from the amino acid tyrosine to the final major CA product of the adrenal medulla, EPI. The conversion of tyrosine to DA occurs via the sequential actions of tyrosine hydroxylase (importantly, the rate-limiting enzyme in CA biosynthesis) to produce L-dopa and aromatic amino acid decarboxylase (AADC, a.k.a. dopa decarboxylase) to produce DA. DA is transported into the storage vesicle by vesicular monoamine transporters (VMATs) (see below) and converted to NE by DBH within the SG. Sequestration of DA into the SG accomplishes two important cellular goals: presenting DA to dopamine-β-hydroxylase (DBH) for its conversion to NE and removal of DA from the cytoplasm, where its metabolism by monoamine oxidase (MAO) creates potentially toxic oxidation products which, in the brain, have been implicated in the neurodegeneration of Parkinson's disease (293). The only synthetic step that must occur inside the CG is the conversion of DA into NE as DBH is an intragranular protein, in fact, one of the intragranular proteins that, along with CgA, helped to first establish the concept of exocytosis itself (62, 283). Once DA is converted to NE, NE diffuses from the SG and is converted in the cytoplasm to EPI [in cells that express the cytoplasmic enzyme phenylethanolamine-*N*-methyltransferase (PNMT)], which is then transported back into the CG and stored mainly in an osmotically inert compartment prior to exocytotic release. The proportion of NE/EPI varies depending on the species where it is measured; for instance, the proportion of EPI found in rats is around 90%, whereas this ratio drops to ≈73% in dogs, mice, and cows and 60% in cats and goats. The CA content of the human adrenal medulla is about 80% EPI. As described earlier in this article, EPI and NE are found mainly in separate CCs, that is most NE in PNMT-containing CCs is converted to EPI.

Almost all CAs are stored in CGs. This process occurs via transport by the VMAT. VMAT is at the heart of CC function because it is responsible for accumulation of EPI and NE into CGs at the concentrations required for hormonal action at distant targets, following exocytotic secretion into the general circulation. The free catechol concentration in the cytosol is 50 to 500 μM, comprising 10% CAs (458), while the measured concentration of catechols in CGs is 0.8 to 1.0 M, depending on the mammalian species (9, 454, 455). Thus, the CG concentrates CAs more than 10,000-fold against their concentration gradient, a thermodynamic feat whose accomplishment defines the function of the CC.

Understanding how VMAT transports CAs began with the work of Scarpa, Johnson, and colleagues (329, 330).

CA uptake and storage in CGs is a two-step process in which CA transport into the CG is followed by its osmotic inactivation via complexation with other granule components including ATP, chromogranins, and Ca^{2+} (282, 517, 629). To study the first process in isolation, workers employed CG ghost granules lysed to release their contents, and then resealed as empty vesicles (330). Accumulation of CAs into these "ghosts" was the model system in which Scarpa and Johnson worked out the now-famous formula for CA transport via proton exchange, where the proton-motive force $\Delta p = \Delta\Psi - [2.30\ RT/F \times \Delta p\mathrm{H}]$, with proton-motive force generated by the vacuolar ATPase of the CG membrane (331). The laboratories of Schuldiner and Henry made seminal contributions to the pharmacological characterization of amine uptake in the granule "ghost" system, identifying the approximate molecular weight of the transporter via reconstitution and explaining the amine-depleting effects of reserpine and tetrabenazine based on their inhibition of CA transport. It was deduced that there were two forms of VMAT—now known as VMAT1 and VMAT2—based on the universal uptake-inhibition properties of reserpine, but the species and tissue-specific inhibition by tetrabenazine (for reviews, see Refs. 286 and 559). The uptake of quaternary amines such as the Parkinsonogenic MPP+ confirmed the likelihood of amine transport through the carrier as a positively charged species (559). All of these pharmacological properties were used to allow the eventual cloning of VMAT1 and VMAT2 cDNAs in *in cellula* expression systems (208, 393). VMAT1 and VMAT2 are expressed in all mammalian species, while *Caenorhabditis elegans* contains only one VMAT, with the properties of VMAT2 (uptake of histamine and inhibition by tetrabenazine). This suggests that the evolutionary selection of the properties of VMAT1 allows it to function as a selective transporter for serotonin, to the exclusion of histamine, in the enterochromaffin cells of the gut that supply serotonin for utilization as a neurotransmitter in the enteric nervous system (179). Although VMAT1 was originally characterized as the "endocrine" VMAT and VMAT2 as the "neuronal" VMAT (664), the CG contains VMAT1, VMAT2, or both VMATs, depending on species and (in the rat), on the state of stress of the organism. Immobilization stress causes an upregulation of VMAT2 expression in the rat adrenal medulla, mainly within EPI cells (616). VMAT2, however, is the exclusive transporter for CAs in the CNS (209, 210). VMAT is a structurally highly conserved protein across species—both isoforms possess twelve vesicular membrane-spanning domains, with the residues contributing to specificity for histamine located to several discrete regions within the transporter that contributes to an amine-binding domain (226). The essential proton-exchange function of the VMATs is found even in bacterial proton antiporters, leading to the inclusion of the VMATs in an evolutionarily distinguishable superfamily called the toxin-extruding antiporters (TEXANS). This suggests that amine uptake into vesicles is a coopted function of toxin extrusion from single-celled organisms (560), and presaging the function of VMAT2 as a "vesicle-sequestering" protein protecting CA-containing CCs, as well as dopaminergic neurons, from oxidative damage caused by CA metabolites resulting from CA degradation by MAO and other oxidative enzymes (253).

The parallel process of biosynthesis and storage in SGs for the protein and peptide exportable products of the CC is discussed later. Synthesized as the so-called preprohormones in the rough ER, proteins of the SG are imported into the granule through the trans-Golgi network (TGN) and condensed into nascent CGs at that location through a process that is still ill-defined (312). The CC has been a model system for understanding the role(s) of proteolytic converting enzymes (PCs) as well as "trimming" and amidating enzymes in the production of bioactive peptides in neuroendocrine cells. For an overall historical perspective, see Ref. 672; for prohormone convertases, see Ref. 459; for carboxypeptidase processing enzyme (CPE), see Refs. 307 and 231; and for peptidylglycine α-amidating monooxygenase (PAM), see Ref. 192.

An important factor that largely contributes to the accumulation of amines is the vesicular ATP. ATP is present, and highly concentrated, in almost all secretory vesicles from all animal species (67). Although its physiological role in the concentration of CA was suggested since the 1960s and demonstrated *in vitro* (361, 603), it was not easy to test its role *in vivo*, as the removal of cellular ATP would mean the death of the cell. However, the cloning of the vesicular nucleotide transporter (VNUT, Figure 9) by the group of Moriyama (554) allowed the study of the contribution of vesicular ATP in the accumulation of CA. Thus, using siRNA against VNUT, Estevez-Herrera and collaborators demonstrated that the reduction of vesicular ATP largely reduced the accumulation of CA (214).

The result of amine uptake and storage, protein processing, and the collaboration of granins, ATP and Ca^{2+} in the production of the SG core is the "secretory cocktail" of the adrenal medulla: proteins, bioactive peptides, and small molecules, including CAs, GABA, and ATP that are released upon depolarization of the CC. The remainder of this article describes the molecular, cellular, and system biology of how the release of this secretory cocktail, via hormonal, neuronal, and inflammatory first messengers, affects mammalian organisms in both normal and pathophysiological states.

Metabolism of CAs

Two different mechanisms terminate CA activity: active cell membrane transporters and metabolizing enzymes. The final disposal of CAs and their metabolites is achieved by renal excretion. In neurons, 90% of released NE is taken back up into the cell by the NE transporter at the presynaptic membrane (193), while EPI released from the adrenal medulla is removed from the circulation by nonneuronal monoamine transporters (198). CAs taken up into neurons or CCs can either be metabolized by intracellular enzymes or sequestered into storage vesicles (194). Sympathetic neurons and CCs, contain monoamine oxidase (MAO), whose

principal substrates are, as the name implies, the CAs DA, NE, and EPI. The major deaminated metabolite of NE is 3,4-dihydroxyphenylglycol (DHPG) (194). The adrenal medulla contains catechol-*O*-methyltransferase (COMT). This enzyme is responsible for the intramedullary conversion of EPI into metanephrine and NE into normetanephrine (198). Over 90% of metanephrine and about 23% of normetanephrine in circulation are formed within the adrenal medulla from CA leaking from granules into the cytosol (198). The remainder of the circulating metanephrine derives from extra-adrenal metabolism by COMT after adrenal release of EPI.

Chromaffin Cell Excitability

What makes CCs excitable? The ion channels controlling the resting potential and action potential generation in CCs

As explained above, adrenal CCs release CA into blood circulation in response to sympathetic stressful stimuli. Typically, CA secretion is regulated neurogenically by the activity of the splanchnic nerve whose nerve terminals in the adrenal medulla release ACh sufficiently close to CCs to induce postsynaptic responses well above the threshold to activate *all-or-none* APs (303). This excitatory response is associated with the activation of nicotinic excitatory postsynaptic currents (48, 304, 334) that cause cell depolarization and AP trains of the same frequency as splanchnic nerve stimulation, with no evidence of fatigue or desensitization when stimulated at low rates (0.3–3 Hz) (303). In this way, CCs act as "relay elements." They couple splanchnic nerve activity to CA secretion by generating AP trains that trigger Ca^{2+} entry through voltage-gated Ca^{2+} channels and regulate the Ca^{2+}-dependent cascade of events leading to neurotransmitter release.

To accomplish this task, CCs contain a "palette" of ion channels that is as rich as that found in neurons (389), appearing even excessive for a "relay element" that should passively follow the neural input. Despite the central importance of neurogenically evoked release of CAs (155), it is possible that the ion channel "palette" can also sustain an *intrinsic electrical activity* of CCs that, under humoral conditions, may contribute to characteristic forms of CA secretion. Consistent with this, recent work on mouse models reveals that mouse CCs exhibit several voltage patterns of intrinsic excitability, including a slow-wave burst activity that may be significant for CA secretion (12, 260, 263, 426, 434, 633).

In this section, we will describe all the ion channels expressed by CCs that contribute to the resting membrane potential and generate the patterns of APs and slow-wave burst activity under physiological and pathological conditions. Table 1 summarizes all the ion channels that will be described and that are proposed to play specific roles in the function of CCs.

Na^+ channels (Nav1.3 and Nav1.7)

CCs of most mammalian species exhibit robust voltage-dependent Na^+ (Nav) currents (222, 407, 633) that are entirely tetrodotoxin (TTX)-sensitive. Na^+ currents in CCs start activating at around −35 mV and reaches maximal amplitude at −10 mV in 2 mM extracellular Ca^{2+}. They activate in less than 1 ms and inactivate quickly within 5 ms at 0 mV. At this potential, the AP reaches its maximal rate of rise (dV/dt_{max}) and decay ($-dV/dt_{max}$) before and after reaching its peak amplitude between +20 and +40 mV in mouse CCs (51, 633). Recovery from full inactivation of Nav channels is relatively fast and complete at −90 mV (90% in 100 ms) and at resting potentials of −50 mV (70% in 100 ms) (633). In this way, the Nav channels of CCs are designed to sustain the fast response to sympathetic nerve stimulation repeated at its maximal rate of 20 Hz with no decay of AP amplitude (303).

Na^+ currents in CCs have been reported to be carried by Nav1.7 channels (358, 654, 655), but evidence on this point is incomplete. Recent work, using quantitative PCR and western blots, suggests a contribution of both Nav1.3 and Nav1.7 in MCCs, with a preponderance of the Nav1.3 isoform (633). However, the voltage dependence of both activation and steady-state inactivation of mouse Nav currents is consistent with one type of sodium channel (633). Based on the studies of heterologously expressed Nav1.3 and Nav1.7, both channels share similar functional properties, but the voltage at which Nav1.3 is half inactivated is shifted to the right compared to that for Nav1.7 (146, 297, 638). Thus, if both isoforms are expressed in mouse CCs in similar proportions, the Nav currents should exhibit double rather than single Boltzmann inactivation functions. However, this is not the case in either rat or mouse CCs (633). Thus, Nav currents seem most consistent with a dominant Nav1.3 channel in MCCs. Indeed, preliminary results using Nav1.3 KO mice confirm that Nav current is completely lost in MCCs (Chris Lingle, personal communication) (389). Interestingly, Nav1.3 channels have strong structural homologies to Nav1.1 and Nav1.2, which are the Nav channels of brain neurons implicated in AP initiation, AP conduction, and repetitive firing (117).

Ca^{2+} channels (Cav1, Cav2, and Cav3)

Following the early patch-clamp recordings of voltage-dependent Ca^{2+} currents (32, 222, 309), the gating properties, pharmacological diversity, and modulation of these currents in CCs have been the subjects of extensive investigation using different CC species (7, 30, 31, 35, 36, 74, 98, 103, 121, 136, 236, 404, 406, 411, 417, 419, 427, 484, 495, 509, 510, 542, 575, 634). Nearly all known subtypes of high-voltage-activated Ca^{2+} current, including Cav1 (L-type) and Cav2 (P/Q-, N-, and R-type) channels have been described in rat (523), mouse (11, 417), cat (7), cow (30, 411) and human (510) CCs. Cav3.2 T-type Ca^{2+} channels are also expressed, particularly during immature stages and stressful conditions preserving their particular low-voltage range of activation

and fast-inactivating kinetics in rat and mouse CCs (74, 103, 107, 108, 298, 379, 479).

The expression density of Cav channels varies remarkably among animal species studied (human, bovine, pig, cat, mouse, and rat; 224), cell conditions, and development. In adult animals, L-, N-, P/Q-, and R-type channels are the dominant species (240, 262, 426, 427). They shape AP waveforms and regulate CA secretion and vesicle retrieval. Despite the many reports, there is still no convincing proof of a specific colocalization of any of the expressed Cav channel subtypes with the secretory apparatus. Each channel type controls CA release with the same linear Ca^{2+}-dependence (30, 100, 103, 206, 248, 352, 417, 543, 609, 627). Why do simple relay elements like CCs need so many different Ca^{2+} channel types for their task? A possibility is that depending on their different sensitivity to voltage, external signaling, and intracellular second messengers, the many expressed Cav channel types (see Table 1) permit compensatory paracrine and autocrine responses to regulate the proper CA release during different CC functioning conditions. The large number of Cav channels also derives from the dual role (chemical and electrical) that Ca^{2+} channels exert in the control of both CA release and AP firing (426, 631, 632).

Cav channel contributions to AP firing are conditioned by the voltage dependence of activation of the different Cav channel isoforms. Cav2.1 (P/Q-), Cav2.2 (N-), and Cav2.3 (R-type) channels activate at significantly more positive voltages than Cav1.2 and Cav1.3 (L-type) channels and therefore contribute mostly to the fast AP upstroke. Cav1.2 and Cav1.3 channels activate at more negative potentials and thus contribute to the slow phase of depolarization between consecutive APs (interspike potential). It is also important to notice that L-type channels are expressed at high densities in CCs. They inactivate slowly and carry about half of the total current in mouse, rat, and cat CCs (46, 121, 240, 428) and, most likely, also in human CCs (see Ref. 631). For this reason, they pass sufficient currents at very negative potentials and are thus favored to set the "pacemaking" current regulating the repetitive AP firing of CCs near resting potential. Looking more closely at the biophysical properties of these two L-type

Table 1 Na^+, Ca^{2+}, and K^+ Channel Types Expressed in CCs

Current	Channel type	Function	Animal	References
INa	Nav1.3	AP upstroke	Mouse	(389, 633)
	Nav1.7		Rat	(358, 654, 655, 681)
ICa	Cav1.2 (L)	AP upstroke, pacemaking, neurosecretion	Mouse, rat, bovine, human	(46, 429)
	Cav1.3 (L)			(429, 632, 635)
	Cav2.1 (P/Q)	AP upstroke, neurosecretion	Mouse, rat, bovine, human	(12, 30, 35, 240, 418)
	Cav2.2 (N)			(12, 30, 35, 240, 418)
	Cav2.3 (R)			(11, 121, 418)
	Cav3.2 (T)	AP threshold, neurosecretion	Mouse, rat	(104, 107, 427)
IKCa	BK (Slo1)	V_{rest}, burst generation, AP repolarization	Mouse, rat	(429, 434, 436, 468, 632)
	SK1-3	V_{rest}, burst duration, burst repolarization	Mouse, rat	(436, 468, 504, 635)
IKv	Kv1-3	V_{rest}, AP repolarization	Bovine, rat, mouse	(564)
	Kv4 (IA)	V_{rest}, AP repolarization, AP trains	Bovine, rat, mouse	(564)
	Kv7 (KCNQ)	V_{rest}, AP repolarization, burst generation	Bovine, mouse, rat	(660)
	Kv11 (ERG)	V_{rest}, AP repolarization	Mouse, rat	(263)
IK_{ATP}	Kir6.1 Kir6.2	V_{rest} repolarization during hypoxia	Rat	(73, 550)
IK	K2P (TASK)	V_{rest}, pH sensitive	Mouse, rat	(260, 316)

channels, it appears evident that Cav1.3 possesses the proper parameters to act as a pacemaker channel. Data derived from heterologously expressed channels indicate that (i) Cav1.3 activates with steeper voltage dependence and at more negative voltages than Cav1.2 (362, 679) and (ii) Cav1.3 has slower and less-complete voltage-dependent inactivation as compared to Cav1.2 (362).

Given the lack of specific blockers for either Cav1.2 or Cav1.3 (both are nifedipine-sensitive) in CCs, the dominant role of Cav1.3 as a pacemaker channel could only be revealed using the Cav1.3 KO mouse ($Cav1.3^{-/-}$) (516). Previous studies on the role of L-type channels in CC pacemaking showed that these channels could pass 10 to 20 pA of current in WT MCCs at rest, and nifedipine could either decrease the firing frequency or block the spontaneous firing (426, 428). A subthreshold inward Ca^{2+} current of this size passing through the high input resistance of CCs (3–5 GΩ) (222, 428, 429) is sufficient to generate pacemaker potentials of 10 to 20 mV in amplitude to drive the cell from resting (−50 mV) to the threshold of the AP upstroke (~−30 mV). Deletion of Cav1.3 drastically reduces the amplitude of this pacemaker current and the fraction of MCCs firing spontaneously (429). Loss of Cav1.3 (i) decreases markedly the level of the nifedipine-sensitive currents driving spike generation, (ii) raises the rheobase (the minimal amount of current required to elicit a train of APs) from 4 to 6.6 pA, and (iii) decreases the extent of spike frequency adaptation during sustained current injections (635). In conclusion, Cav1.3 in CCs plays a key role in the control of AP firing either spontaneous or evoked during step depolarization. Compared with other neuronal pacemaker channels that carry mostly Na^+ currents, like the hyperpolarization-activated cation channels (HCN) (502), the persistent (143) and resurgent (527) Na^+ channels, and background channels (409), Cav1.3 appears unique and worthy of being further studied in cardiac cells and brain neurons.

Ca^{2+}-dependent SK and BK potassium channels

CCs were among the first cells from both rat and cow in which Ca^{2+}-dependent small- and big-conductance (SK and BK) potassium currents were recorded (29, 408, 434, 436, 467, 468). SK currents are voltage independent and blocked by the bee-venom toxin apamin (319). They activate robust outward currents following the release of cytosolic Ca^{2+} stores (467). Single SK channels have small K^+ conductance and are half activated at ~0.7 μM cytosolic Ca^{2+} (503). Mouse CCs express all the identified SK channel subtypes: SK1, SK2, and SK3 (635). SK are open at any potential if sufficient cytosolic Ca^{2+} is available, and therefore they contribute to setting the CC resting potential. Their current builds up between successive APs and sets the basal frequency of spontaneous repetitive firing. In fact, block of SK channels by apamin usually increases the spontaneous firing rate of CCs, suggesting that there is sufficient SK activation between spontaneous APs to prolong the interspike interval (ISI) (635). SK channels respond to small and persistent increases in cytosolic Ca^{2+} (218). In this way, they play a negative feedback role in response to Ca^{2+} influx and set the firing frequency in resting CCs. SK currents build up markedly during high-frequency firing or prolonged bursts and help terminate the firing or the burst (635). More specifically, SK channels are the main K^+ channel types that activate near rest, which is with mild depolarization, or during the ISI, with a degree of activation proportional to the amount of Ca^{2+} entering the cell during the repeated APs or a burst. In this way, SK channels act as an effective "brake" on firing cells, to promote more regular firing and adapting the AP for constant maximal amplitude during sustained cell activity.

BK channels are voltage dependent. They activate following cytosolic Ca^{2+} elevation, but their probability of opening depends on the degree of cell depolarization. BK channels are also less sensitive to Ca^{2+} with respect to SK, requiring ≥10 μM cytosolic Ca^{2+} to be activated (218). Given the diversity and multiplicity of intracellular Ca^{2+} buffering systems, and their tight regulation, such high concentrations occur only within Ca^{2+} "nanodomains" near Ca^{2+} sources, that is in the vicinity of Cav channels (218). This implies that BK channels are localized near a Cav channel, and usually they are colocalized with more than one Cav channel (522, 632). In CCs, upon sufficient Ca^{2+} elevation and depolarization, the BK current is typically the most prominent outward current in CCs of all mammalian species (408, 429, 434, 468). This greatly conditions the shape of single APs that exhibit a marked afterhyperpolarization (AHP) during the falling phase of the action potential, depending on the number of BK channels open upon cell repolarization. In CCs, BK currents can be either inactivating (BK_i) or noninactivating (BK_s) (429, 434, 468, 522) in varying degrees, from completely inactivating to completely noninactivating.

BK channel inactivation rate in CCs depends on the presence of a regulatory β2 subunit (661, 676) whose cytosolic N-terminus mediates a pore occlusion type of inactivation (677). Genetic ablation of β2 subunit expression results in complete loss of inactivation of BK current in mouse CCs (434). The functional role of BK channel inactivation *per se* remains unclear (598). BK channel inactivation is very slow (>35 ms, when 2 β2 subunits are bound to the channel); thus, during trains of APs at 10 Hz, there is little cumulative BK channel inactivation (167, 434). However, besides producing inactivation, the regulatory β2 subunit also shifts the range of channel activation to more negative voltages (676). With a full set of four β2 subunits bound, the activation of BK channels shifts by about 60 mV to more negative voltages with 10 μM cytosolic Ca^{2+}. This shift is critical for the effective range of channel gating and results in different AP firing patterns between CCs with BK_i or BK_s currents (434, 581, 598). In the absence of any β2 subunit bound, BK channels will activate less at a given Ca^{2+} (434), causing an increased AP amplitude, slowed AP repolarization, and reduced AHP. This, in turn, slows the rate of recovery of Nav channels from inactivation and reduces the contribution of Nav channels to the next AP. This, eventually, results in AP

block after sufficient cumulative Nav inactivation (390). How these properties of BK channels affect burst firing will be considered in the following sections.

Voltage-dependent Kv (Kv1–3, Kv4, Kv7, and Kv11), K_{2P} TASK, and K_{ATP} potassium channels

CCs express a variety of voltage-gated Kv channels that mainly control the resting potential, the AP repolarization phase, and the mode of AP firing (tonic vs. burst) of the cells. Bovine rat, and mouse CCs express Kv currents that are either slowly (Kv1–3) or rapidly inactivating (Kv4; I_A current) (429, 436, 468, 564). Kv4 currents are prominent in bovine CCs and possess activation/inactivation characteristics that suggest that they may play a key role in the regulation of repetitive AP firing frequency during sustained stimulation (564).

CCs also express Kv7 (KCNQ; M-currents) and the Kv11 (ERG) channels. Kv7 is highly expressed in cardiac cells, postganglionic sympathetic neurons, and brain and blocked by mAChR activation through a membrane-delimited PIP_2 depletion mechanism mediated by Gq/PLC-β [for review, see (161)]. Kv7 are "low-threshold" K^+ channels that are already open at rest, activate very slowly with membrane depolarization, and do not inactivate during prolonged depolarization. In bovine CCs, there is evidence of an M-current inhibited by histamine (660). The existence of Kv7 in CCs, along with mAChRs, suggests a role for Kv7 channels in cell depolarizations induced by mAChR activation. However, data on this issue do not lead to a firm conclusion on this point (489). This derives most likely from the existence of different isoforms of mAChRs and different coupling to Kv7. In MCCs, muscarine causes either hyperpolarization plus a depolarization (31%), a depolarization alone (30%), hyperpolarization alone (21%), or no effects (18%). In contrast, blockade of Kv7 channels by XE991 causes a sizeable depolarization in 100% of the cells, followed by an increased firing frequency or a switch of spontaneous firing from tonic to bursts (402) (I. Méndez-López, A.G. García, and E. Carbone, unpublished observations). ERG or Kv11 channels have been identified in rat CCs (263). Block of Kv11 by the selective blocker WAY-123,398 causes marked cell depolarization, increased spontaneous firing frequency, and even burst firing in some cases, indicating that Kv11 channels may have an important role in regulating CC excitability (263).

Rat and mouse CCs also express the pH-sensitive K^+ channels TASK-1 and TASK-3 that are two-pore "leak" channels (K_{2P}) contributing to the membrane potential and firing activity of cells at rest (260, 316). In rat CCs, TASK-1 channels are blocked by the activation of mAChRs, and thus are postulated to be targets of the mAChR stimulatory action that leads to increased CA secretion (316). In mouse CCs, blockade of TASK-1 channels by the selective blocker A1899 and BK channels by paxilline mimics the effect of lowering the extracellular pHo causing cell depolarization, burst firing, and increased CA release (260). Given the expression of TASK channels, MCCs act as "pH sensors" which trigger an effective physiological response that compensates for the acute acidosis and hyperkalemia generated after vigorous exercise and muscle fatigue (441).

CCs also express K_{ATP} (Kir6.1 and Kir6.2) channels (73, 375, 550, 615). As in other cells, these channels are expressed to protect the cell during low O_2 pressure (PO_2) conditions that lower cytoplasmic ATP. In rat CCs, K_{ATP} channels are effectively activated during acute hypoxia, most likely due to the transient reduction of ATP at low PO_2. The involvement and upregulation of these channels is evident in rat CCs when acute hypoxia is tested in the presence of the K_{ATP} channel blocker glibenclamide. The addition of glibenclamide has no direct effect on K^+ current but enhances the inhibitory action of acute hypoxia on K^+ currents (550), suggesting that K_{ATP} channels are recruited only in response to low O_2.

The neuron-like spontaneous action potentials: tonic versus burst firing

In CCs, like in neurons, spontaneous firing takes place when sufficient inward current is driven by small voltage perturbations near resting potential. Critical for triggering spontaneous AP oscillations is the net balance between inward (leak, Na^+, and Ca^{2+}) and outward K^+ currents near resting potential. When the inward depolarizing current exceeds the outward current, a more positive unstable potential is reached at the start of the "negative conductance" region of the IV characteristics (680). At this unstable potential, any small depolarization causes a small inward current that depolarizes the cell further and triggers a train of APs. Subthreshold spontaneous membrane potential oscillations occur easily if the cell possesses high input resistance (3–5 GΩ) and is equipped with sufficiently large densities of Nav and Cav channels that activate readily at low voltages as in CCs (222, 418, 428). An additional critical requirement for driving spontaneous APs in slowly firing cells (~1 Hz) is the presence of a weakly inactivating inward current that sustains the slow pacemaker potential. Spontaneous firing is rather variable in CCs regardless of whether the cells are isolated and plated in culture or in adrenal gland slices (for a review, see Refs. 389 and 631). In many CCs, the repetitive firing is "irregular," that is spikes occur at a variable frequency (Figure 1A). In mouse CCs, the degree of regularity is somehow correlated with spike frequencies. Fast spiking cells are typically more tonic and display "regular" repetitive firings (Figure 1B).

As in neurons, a small fraction of CCs can also undergo spontaneous bursts at normal physiological conditions (434, 633). Burst firing occurs as trains of APs on top of a sustained plateau potential of variable duration (Figure 1C). The burst terminates with a robust AHP whose amplitude sets the duration of the ISI. Deeper AHPs generate longer ISI. The origin of this "neuron-like" bursting mode in CCs is largely unknown, but one can speculate that it derives from a combination of accumulated BK- and Kv-channel inactivation and sizeable slowly inactivating Na^+ and Ca^{2+} currents that sustain the plateau potential and part of the spike amplitude.

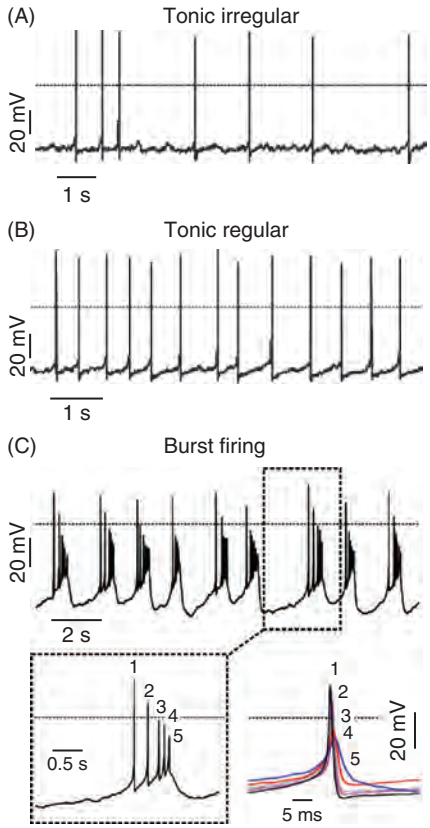

Figure 1 Different firing modes of spontaneously active chromaffin cells. (A, B) Spontaneous AP trains recorded from two different rat CCs displaying "irregular" and "regular" tonic firings, respectively. (C) Spontaneous AP trains exhibiting slow-wave bursting recorded from a mouse CC. Below is shown a single burst at an expanded time scale (dashed rectangle) and the overlap of consecutive APs within a burst. Numbers indicate the sequential position in the burst. Adapted, with permission, from Vandael DH, et al., 2015 (633).

Any reduction of the K^+ currents activated during the first AP attenuates the AHP to less negative values (plateau potential) where Cav and Nav channels can sustain the series of AP during bursts. Several ion channels contribute to set the plateau potentials and spike amplitudes. The key issue is to uncover how the degree of expression, gating properties, and sensitivity to endogenous and exogenous modulators of these channels may alter the equilibrium between repetitive and burst-firing modes in CCs.

Tonic firing in CCs

The first intracellular and extracellular recordings of spontaneous firing activity in rat CCs were reported almost 50 years ago (61, 76). In these studies, the emphasis was on the identification of the current components that participate in nerve-evoked depolarization and could influence the Ca^{2+} influx required for CA secretion. Subsequent reports confirmed that CCs can generate APs when stimulated and that they fire spontaneously both *in situ* or when isolated from the glands (47, 263, 467). In some cases, they exhibited considerable rhythmic complexity suggestive of bursting (263). The existence of a spontaneous (nonneurogenic) firing activity was compelling and received strong experimental attention. The leading idea was to identify the resting currents that control the timing of repetitive AP firing, after having observed that the block of L-type channels by 3 µM nifedipine reduced or fully blocked the spontaneous activity of mouse CCs (426, 428). Given this, the primary issue was to determine whether the slowly inactivating Cav1.3 channel was the main L-type channel responsible for the spontaneous firing activity. This could be done using the Cav1.3 KO mouse generated by the Striessnig laboratory (516). By comparing the ionic conductances and firing properties of WT and Cav1.3 KO mice, it was possible to show that both a Cav1.3-mediated inward current and a BK-mediated outward current are active during the interspike interval and the initial rising phase of an individual AP (429). The two currents balance each other with a slight predominance of Cav1.3 that drives the spontaneous firing. The time course of the subthreshold inward Cav1.3 current became evident in WT cells after blocking BK channels with 1 µM paxilline or 5 mM TEA, while this current was clearly absent in Cav1.3 KO cells.

A dominance of subthreshold Cav1.3 currents in regulating AP firing is also evident when studying their functional coupling with SK currents and how the coupling effectively adapts sustained AP trains during prolonged cell depolarizations. The Cav1.3-dependent SK currents that build up during the interspike intervals in WT cells lead to spike frequency adaptation that is strongly attenuated in Cav1.3 KO cells (635). Low adaptation ratios due to reduced SK channels activation associated with Cav1.3 channel deficiency prevent the effective recovery of Nav1.3 channels from inactivation. This promotes a rapid decline in AP amplitudes and facilitates early onset of depolarization block following prolonged stimulation. Thus, in Cav1.3 KO mice, both the spontaneous and evoked AP firing are significantly altered.

The involvement of Cav1.3 in regulating AP firing in mouse CCs is also supported by the altered firing properties observed in mutated CCs in which the C-terminal automodulatory (CTM) domain is interrupted with a hemagglutinin tag (556). The CTM domain regulates the Ca^{2+}-dependent inactivation (CDI) of the channel and the replacement of the "distal C-terminal regulatory domain" (DCRD) with an HA-epitope generates a mouse ($Cav1.3DCRD^{HA/HA}$) that displays faster CDI. Indeed, the mutated CCs exhibited L-type currents with faster inactivation and reduced CDI. Spontaneous cell firing was significantly altered. An increased percentage of cells lost their spontaneous activity due to their more negative resting potential (silent cells), and evoked AP bursts had increased firing frequency due most likely to the reduced number of SK channels activated by the accelerated CDI of $Cav1.3DCRD^{HA/HA}$ channels (556). In conclusion, łoss or mutations of Cav1.3 channel gating induce significant changes in the spontaneous and evoked CC activity, suggesting a key role of these L-type channels in the generation and maintenance of AP firing.

Slow-wave bursting in CCs

Slow-wave bursting activity is an intrinsic firing pattern that can be recorded in 15% of WT MCCs either grown in culture (633) or in adrenal medulla slices (434). Burst firing may become dominant when CCs need to release CAs to sustain several physiological responses such as acute acidosis and hyperkalemia during heavy exercise and muscle fatigue (441) (see below).

AP bursts have variable shapes. In general, an initial AP of usual amplitude exhibits a slow and reduced repolarization. The slow repolarization leads to a depolarized plateau potential upon which a series of truncated, presumably Ca^{2+}-dependent secondary, APs develops before terminating with a strong repolarization. The number of secondary APs varies from burst to burst, but it is likely the amplitude and duration of the plateau potential that determines the amount of Ca^{2+} entry during the burst. Given that a slow-wave bursting lasts more than 300 ms and the plateau potential varies between −30 and −20 mV, the quantity of Ca^{2+} entering a cell is likely to be more than an order of magnitude larger than the Ca^{2+} entering during a single AP. This is far more than the Ca^{2+} entering by simply increasing the frequency of firing from 1 Hz to its maximal value (20–30 Hz). This implies that any cell manipulation, ion channel blocker, or channel agonist able to switch the spontaneous firing of a CC from tonic to bursting can induce a significant Ca^{2+} overload that boosts massive CA release during stress or perhaps some ongoing pathological condition (i.e. hypertension). In this view, an increased percentage of burst-firing CCs could be a marker of an increased functionality or a pathological state for the adrenal CCs.

It is of key importance to understand how Na^+, K^+, and Ca^{2+} channels contribute to the generation of slow-wave bursting. Figure 2 shows the time course of Nav, Cav, Kv, BK, and SK currents during burst firing using as voltage-clamp commands three different AP bursts previously recorded in current clamp (see Ref. 633). It is evident that Nav, BK, and Kv currents are maximal during the first and second AP, while they decrease rapidly during the remaining APs (Figures 2A, 2B, and 2D). At the end of the burst, their contribution falls drastically. Quite different is the time course of inward Cav currents that decreases slowly during the burst but keep contributing significantly to Ca^{2+} entry almost up to the end of the burst (Figures 2C and 2D). Conversely, the SK currents build up progressively during the burst to reach a critical size that terminates it (Figures 2C and 2D).

Recent studies have highlighted cell manipulations that enhance or unmask this slow-wave burst (260, 434, 633). In one case, reducing Nav1.3 channel availability by either slow depolarizations that induce partial Nav channel inactivation or application of low concentrations of TTX to reduce the number of active Nav1.3 channels unmasked bursting activity (633). In the second case, when the β2 auxiliary subunit of BK channels is genetically deleted, almost all CCs exhibit repetitive slow-wave bursting which occurs at a frequency (~1 Hz) similar to the spontaneous AP frequency of WT cells (434). In the third case, lowering of extracellular pH (pHo) from 7.4 to 6.6 causes a marked cell depolarization that induces sustained slow-wave bursts (Figure 3) and a nearly sevenfold increase in CA secretion. Cell depolarization is attributed to the blockade of pH-sensitive TASK and BK channels (260). As summarized in Table 2, burst firing is also induced when Kv7 channels are blocked by histamine (660), Kv11 channels are blocked by their specific blocker WAY-123,398 (263), and Kv, SK, and BK channels are blocked by acute hypoxia (550). Burst firing is also induced in mouse CCs when Kv and BK channels are blocked by TEA (464) and when Cav1 channels are potentiated with the selective agonist Bay K 8644 (260). There is also evidence that the pronounced depolarization

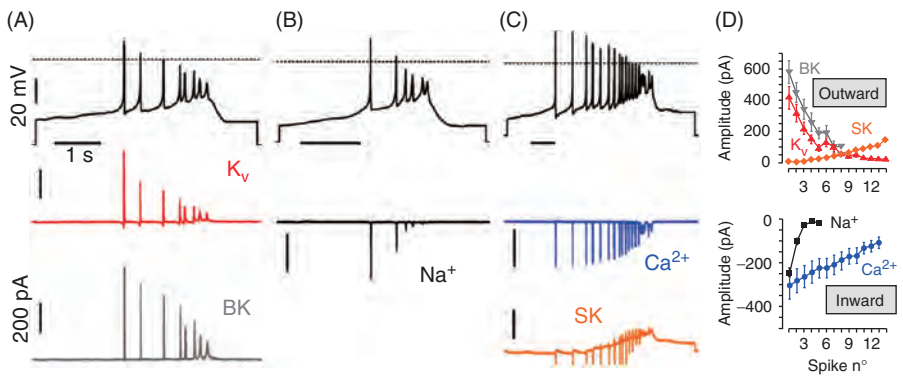

Figure 2 Time course of Na^+, Ca^{2+}, and K^+ currents during slow-wave bursts in mouse CCs. (A) AP-clamp experiment measuring Kv and BK currents. Top: AP bursts elicited by current steps were recorded at current-clamp mode and used as voltage command (black trace) in voltage-clamp experiments. Bottom: Kv currents are shown in red and BK currents in gray. (B, C) As in (A), but the currents isolated were Ca^{2+} currents (blue), SK (orange), and Na^+ (black). (D) Top: BK, SK, and Kv outward current amplitudes versus the spike number of the burst. Bottom: Same, but for the Na^+ and Ca^{2+} inward currents. Adapted, with permission, from Vandael DH, et al., 2015 (633).

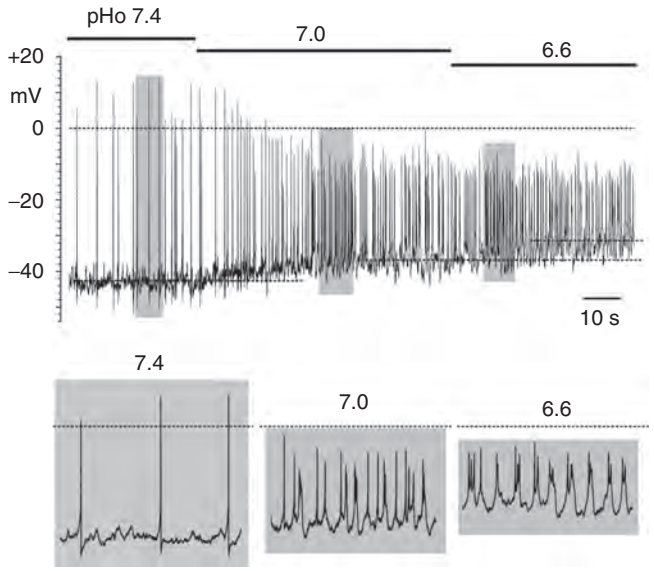

Figure 3 Low pHo induces burst firing in mouse CCs. Spontaneous firing (no current injection) recorded in mouse CCs at pHo 7.4, 7.0, and 6.6. Bottom: AP recordings on an expanded time scale corresponding to the gray window above. A decrease in pHo results in resting membrane depolarization and the switch of firing modes from tonic (pHo 7.4) to mildly bursting (pHo 7.0), to sustained bursting (pHo 6.6). Intermittent and sustained burst firing are accompanied by a net decrease of AP peak amplitude associated with the slow inactivation of Nav1.3 channels at depolarized potentials. The dotted line indicates the 0-mV level. Adapted, with permission, from Guarina L, et al., 2017 (260).

induced by 10 µM muscarine drives the spontaneous firing of a large percentage of mouse CCs into a slow-wave bursting mode (I. Méndez-López, A.G. García, and E. Carbone, unpublished results).

Burst firing occurs typically when CCs are either depolarized by blockade of Kv, SK, TASK, or BK channels or when Cav1 channels are potentiated. In the first case, Nav1.3 channels are steadily inactivated by the sustained cell depolarization and are thus unable to activate a sufficient number of BK and Kv channels to produce marked AHP that warrants the fast recovery of Nav1.3 and Cav channels from their inactivation and the generation of the next AP. In the second case, the increase of slowly inactivating Cav1 currents is sufficient to produce enough inward current to sustain the plateau potential of the burst. It seems likely that other cases of channel modulation or cell manipulation that induce bursting will be discovered, to join those listed in Table 2.

Action potentials elicited by current injection

The ability of CCs to generate different patterns of spontaneous firing is helpful in understanding the causes of altered CC excitability and identifying the molecular targets that are altered. In some cases, CCs do not fire spontaneously (for a review, see Ref. 155), and when it does occur, spontaneous firing never reaches the high-frequency levels obtained during intense sympathetic stimulation (20–30 Hz). In addition, detailed analysis of CC firing during sustained high-frequency sympathetic stimulation is often required to obtain a more physiological view of stimulation-secretion coupling (153). In these cases, an alternative to recording spontaneous firing is to elicit trains of APs by applying step depolarizations of increasing current amplitude (2–20 pA) and variable length (0.1–10 s) to induce AP firing of increasing frequencies. Using current steps above 2 to 4 pA, CCs from all animal species examined undergo AP firing and CA secretion, confirming

Table 2 Cell Conditions, Hormones, Neurotransmitters, Blockers, and Agonists That Induce Slow-Wave Bursting in CCs

Stimuli, compound	Action on channels	Intensity of depolarization	Animal	References
Cell depolarization	Slowly inactivated Nav1.3	+++	Mouse	(633)
TTX	Block of Na1.3	+	Mouse	(633)
Bay K 8644	Potentiation of Cav1.2 & Cav1.3	++	Mouse	(260)
Low pHo	Block of TASK and BK	+++	Mouse	(260)
Paxilline	Block of BK	+	Mouse	(260)
A1899	Block of TASK-1	+	Mouse	(260)
Deletion of BK-β2	Removal of fast inactivation; leftward shift of BK activation	+	Mouse (slices)	(434)
TEA	Block of Kv and BK	++	Mouse (slices)	(464)
Acute hypoxia	Block of Kv, SK and BK	+++	Rat	(550)
Histamine	Block of Kv7 (IM)	+++	Bovine	(660)
Muscarine	Block of Kv7 (IM)	+++	Mouse	I. Méndez-López, A.G. García, and E. Carbone (unpublished results)
WAY-123,398	Block of Kv11 (ERG)	++	Rat	(263)

that CCs, like neurons, are highly excitable cells whose firing frequency controls Ca^{2+}-dependent CA secretion (303).

Evoked AP firing with step depolarization was first recorded 40 years ago (61, 76) using sharp glass microelectrodes. With the advent of the patch-clamp technique, evoked AP firing was detected in CCs of many animal species with variable results (153). AP recordings were used to identify the ion channel types involved in CC excitability (389). As in neurons, the analysis of AP trains with increasing step depolarizations furnishes a detailed view of the ion channels involved and their role in sustaining the firing. Well-resolved recordings of current-evoked AP firing have been reported in cow (153), rat (178, 581, 689), and mouse CCs (244, 434, 556, 635).

Figure 4 shows an example of AP recordings evoked with increasing current steps (from 5 to 15 pA) illustrating how CCs respond to constant depolarizations. Current injections induce trains of APs that gradually decrease in frequency (Figure 4A). The instantaneous firing frequency toward the end of the pulse (f_{ss}) is always smaller than one measured at the onset (f_o), giving rise to an adaptation ratio f_o/f_{ss} always >1 (Figure 4B). Increasing the injected current (from 5 to 15 pA), the CC responds with a marked increase of f_o (from 8 to 16 Hz) and f_{ss} that rises with the same proportion (from 2 to 4 Hz), indicative of the adapting behavior of these cells. The maximal f_o at very large depolarizations (15–20 pA) reaches values (16–18 Hz) that are comparable with those recorded in adrenal medulla slices (434) and with those induced by maximal sympathetic stimulation. The frequency of the adapted APs is significantly lower in mouse CCs (4–6 Hz) than in rat CCs (10–12 Hz) (178, 303, 689), most likely due to the different expression of BK channels in the two cell preparations (434). In all cases, the AP peak adapts steadily to a lower value, due to the incomplete recovery of Nav channels and BK channel activation induced by the constant (20 mV) cell depolarization.

AP firing adaptation is the result of an ionic equilibrium between ion channels carrying inward and outward currents. Figure 4C shows clearly that when SK channels are blocked with 100 nM apamin, the AP firing increases remarkably. The cell adapts more slowly to higher f_{ss}, and the AP amplitude falls even below overshoot (Figure 4B). Thus, the current-evoked AP firing is a potent tool to identify the key molecular components of CC excitability. Current-evoked AP firing has been successfully used to highlight the key roles of some ion channel and modulatory pathways in regulating CC excitability. Specifically, they have revealed: (i) the role of SK channels in setting firing frequency of mouse CCs (635), (ii) the dual action of leptin-mediated upregulation of BK channels through the activation of an IP3K pathway regulating spontaneous and evoked AP firing in mouse CCs (244), (iii) the BK channel inactivation regulating AP firing in rat CCs (581), (iv) the Cav1.3 channel regulation of AP firing in KO (635) and KI Cav1.3 in mouse CCs (556) and, (v) the existence of burst firing during sustained cell depolarization (434) and its block by nifedipine in mouse CCs (260).

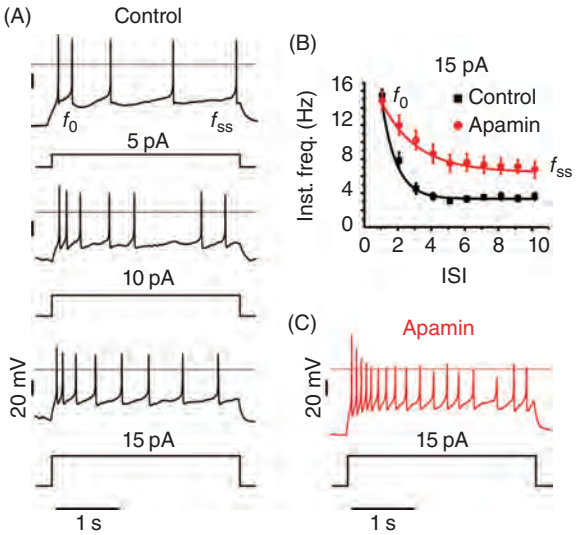

Figure 4 Spike frequency adaptation during current injections in mouse CCs. (A) Representative current-clamp recordings from WT mouse CCs in response to 5, 10, or 15 pA current injection from Vh = –70 mV (from top to bottom). (B) Evolution of the instantaneous firing frequency in WT mouse CCs at 15 pA in control (black squares) and in the presence of the SK channel blocker apamin (200 nM; red circles). (C) AP recordings in the presence of 200 nM apamin during 15 pA current injection, to be compared with the control trace to the left. Adapted, with permission, from Vandael DHF, et al., 2012 (635).

Action potentials elicited by splanchnic nerve stimulation and pulses of ACh

APs in CCs are generated by sympathetic splanchnic nerve stimulation that releases ACh and activates the nAChRs of the cells. Opening of nAChRs triggers excitatory postsynaptic potentials that initiate synchronous APs following splanchnic nerve stimulation. Alternatively, APs can be activated directly by brief pulses of ACh on cultured cells or adrenal gland slices (240). These two forms of stimulation are used sometimes for studying the modulatory effects of hormones, neurotransmitters, and drugs, which affect the stimulus-secretion coupling machinery in a cell system near physiological conditions (for a review, see Ref. 153). In the first case, recordings of APs are performed on the CCs of isolated bisected adrenal glands, which preserve their splanchnic innervation intact. CCs respond to low-frequency sympathetic stimulation (0.3, 1, and 3 Hz) with single APs that follow each stimulus synchronously, with no evidence of fatigue or desensitization (303). At higher frequencies (10 Hz), some stimuli fail to evoke a response. Failures of synaptic transmission are also observed in the superior cervical ganglion neurons during continuous stimulation at 10 and 20 Hz (58), suggesting strong similarities between the responses to splanchnic nerve stimulation of CCs *in situ* and sympathetic ganglion cells, and a weak linear correspondence between splanchnic stimulation and CC responses at a higher frequency. This approach has been used in the past to establish a correlation between the frequency of neuronal stimulation and the amount of released CA, with contrasting results on whether the two parameters

are linearly related or not in the range of physiological frequencies (0.3–30 Hz) (303, 658). Presently, this approach is not often used due to the complexity of the preparation and the technical difficulties to record stable APs, but it remains nevertheless a valuable tool to study stimulus-secretion coupling in intact innervated glands. A recent work, using a modified version of this technique, has shown remarkable spatial and activity-dependent differences in stimulus-secretion coupling between CCs releasing EPI and cells releasing NE (674).

APs induced by short puffs of ACh have been used recently for the purpose of mimicking the quantal release of ACh during single splanchnic nerve stimulation. de Diego et al. were first to design a protocol made of a train of brief pulses of 30 μM ACh lasting 25 ms of variable frequency (154) that mimicked the CC responses to trains of splanchnic nerve stimulations (153). In bovine CCs, the protocol could elicit trains of APs with similar waveforms to those recorded using either brief step depolarizations or single splanchnic nerve stimulations. All-or-none APs had a proper amplitude (65 mV from V_{rest}), half-width (2.7 ms), and well-resolved AHP (−17 mV from V_{rest}) indicative of the excellent state of excitability of the cells. Tonic firings with no sign of adaptation and failures could be achieved with frequencies ≤1 Hz. At higher frequencies (≥3 Hz), APs occurred irregularly and resting potential became unstable, most likely due to the incomplete fast washout of ACh after each brief application (153). Accumulation of ACh during repeated stimulation could induce nAChRs desensitization, activation of mAChRs, cell depolarization, and Nav channel inactivation. Thus, ACh-evoked APs appear to be a physiologically interesting way to induce cell firing in CCs, although the method requires technical improvements to study stimulus-secretion coupling mechanisms using AP frequencies above 3 Hz.

Nicotinic acetylcholine receptors of chromaffin cells

Stimulation of the sympathetic splanchnic nerve elicits the release of ACh from their nerve endings. ACh binds to nAChRs and mAChRs present in the CCs membrane. Membrane depolarization and AP firing were initially recorded in rat CCs upon activation of nAChRs (349). nAChRs play a central role in triggering fast CA secretion from adrenal CCs in response to ACh (175, 220). Pharmacological and immunological studies support the view that nAChRs expressed by CCs are of the neuronal type (142). nAChRs are formed by five subunits that span the membrane four times with the agonist-binding site located at the extracellular region, which is also structurally and functionally linked to the ion channel (152). Crystal structures of complete receptors reveal a cylinder-like structure made of five subunits symmetrically located around the ion channel. Single-channel nAChR conductance is ∼44 pS (221). The channel is permeable to Na^+, K^+, and Ca^{2+}, the latter contributing only 2% to 4% of the current (691).

The most conspicuous nAChR subtype involved in CA secretion is the heteromeric receptor formed by α3 and β4 subunits. In bovine CCs, two nAChR subtypes have been described. The main subtype is a heteromeric assembly of α3, β4, and possibly α5 subunits insensitive to α-bungarotoxin. The other subtype is α-bungarotoxin-sensitive homomeric α7 nAChRs (142). The transcription factor Sp1 (specificity protein 1) coordinates the synthesis of α3, β4, and α5 subunits that form the α-bungarotoxin-resistant nAChRs (57), while the transcription factor Egr-1 (early growth response protein 1) controls the differential expression of both α7 nAChR (114) and PNMT (185) in adrenergic CCs.

In addition to the typical nicotinic ligands, several unrelated substances of clinical relevance bound to nAChRs in CCs act as agonists, antagonists, or allosteric modulators. *Agonists* include ACh, carbachol, dimethylphenylpiperazinium, cytosine, and (+)-anatoxin-a that act on α3β4 receptors (142). Choline elicits $[Ca^{2+}]_c$ signals and secretion by acting on α7 receptors in bovine CCs (159, 232). A study on human CCs showed that the α7 nAChR-selective agonist PNU-282987 elicited whole-cell inward currents that were potentiated by allosteric α7 modulators 5-hydroxyindole and PNU-120596. Since α7 nAChR agonists choline and ONU-282987 augment secretion, it was concluded that human CCs express functional α7 nAChRs (508). In a similar study in bovine CCs, the authors conclude that CA release might be regulated by α7 and α3β47 nAChRs, depending on agonist concentrations and the presence of allosteric modulators of α7 nAChRs (159). The *antagonist* pharmacology of CCs nAChRs shows a classical "ganglionic" profile, with some additional blockers, like the spasmolytic otilonium (237), nanomolar concentrations of atropine (256), or the diuretic cyclothiazide (478). The involvement of α7 nAChRs in human CCs is supported by its partial blockade of CA secretion with α-bungarotoxin (405, 508). Some neuropeptides, that is catestatin, a fragment of CgA (294), substance P (132), and calcitonin gene-related peptide (CGRP) (164) also modulate the nAChRs of CCs.

In conclusion, although various subunits of nAChRs have been cloned and are expressed by CCs, the α3β4 is the predominant nAChR subtype in mediating the whole-cell nicotinic currents, $[Ca^{2+}]_c$ signaling, and the release of CA triggered by ACh in CCs. The α7 nAChR is also expressed by CCs, although its function is not yet fully characterized. A rich pharmacology is at hand either for activation or blockade of CC nAChRs, or to modulate them allosterically.

Ca^{2+} and Stimulus-Secretion Coupling

Ca^{2+} channel-secretion coupling

Ca^{2+} channel regulation by neurotransmitters: a historical background

Douglas and Rubin (172, 176) working in CCs and Katz and Miledi (337, 338) in presynaptic nerve terminals were the first to identify the role of Ca^{2+} influx as the key regulator of hormone and neurotransmitter release. Later studies uncovered the steep dependence of neurotransmitter release on Ca^{2+}

influx (169) and demonstrated the link between presynaptic Ca^{2+} currents and postsynaptic responses using the squid giant synapse (398). These results focused interest on Cav channels and their physiological role, with special emphasis on neurotransmitter and hormone release. It soon became evident that Cav channels are plastic and can be modulated by neurotransmitters, hormones, second messengers, and other intracellular chemicals, as well as by pharmacological agents. The first hormone-mediated pathway was described in cardiac cells where EPI or elevation of intracellular cyclic adenosine monophosphate (cAMP) facilitated Ca^{2+} channel activity (531, 621). The second neurotransmitter-mediated pathway was reported in chick sensory neurons where the addition of NE inhibited Ca^{2+} channel activity, the amplitude of Ca^{2+} currents, and the duration of APs (182, 183). In this section, we will describe a variety of mechanisms for the regulation of Cav channels of CCs by autocrine/paracrine neurotransmitters, hormones, and other modulators.

The role of Cav2.1 and Cav2.2 on excitation-secretion coupling in CCs

Cav2 channels (N, P/Q, and R) are highly expressed in the nervous system, where they carry the presynaptic Ca^{2+} currents that trigger neurotransmitter release and synaptic transmission (216, 530). Neurotransmitter release controlled by these voltage-gated channels is steeply Ca^{2+} dependent (third to fourth power) (169), making them an important locus of synaptic regulation. Among Cav2 channels, Cav2.1 and Cav2.2 are the main sources of the Ca^{2+} that initiates the rapid release of glutamate, ACh, and GABA from neurons. In addition, Cav2.1 and Cav2.2 contain a synprint region that binds to syntaxin 1A and SNAP-25 (115), suggesting that they colocalize to regions of the membrane where the SNARE complex is formed and synaptic vesicle fusion occurs to initiate neurotransmitter release. Cav2 channel activation is also critically regulated by several G-protein subunits (686), which form the basis of Ca^{2+}- and voltage-dependent signal transduction at the synaptic terminal (116).

In CCs, Cav2.1 and Cav2.2 are highly expressed, but at different densities, in all animal species (240). The two channels are effectively coupled to secretion, with Ca^{2+} dependence of secretion not as steep as in presynaptic terminals. The dependence on Ca^{2+} is nearly linear and comparable to that seen with the other Ca^{2+} channels expressed in CCs (L, R, and T types) (100, 103, 248, 308, 352, 543, 609). This means that Cav2 channel opening is loosely coupled to readily releasable secretory vesicles, which is consistent with the idea that Ca^{2+} channels and release sites in CCs are not closely colocalized as in presynaptic neuronal terminals (130). Ca^{2+} channels and release sites are distributed within nanometric distances (200–300 nm) to form specialized membrane regions with dimensions of several micrometers (357, 469). In this way, the dominant Ca^{2+} signal regulating vesicle fusion and neurotransmitter release derives from the activation of several Cav channel subtypes distributed over areas covering tens of square micrometers, rather than from dense Ca^{2+} channel clusters localized near some readily releasable vesicles at the presynaptic secretion sites similar to the active zones (469, 470).

Regarding the regulatory role of Cav2.1 and Cav2.2 channels in secretion, most electrophysiological studies support the idea that both channels are equally accessible to the secretory apparatus, without any preferential coupling (30, 100, 206, 230, 352). Nonetheless, using Cav2.1 KO mice, a predominant role of P/Q-type channels in regulating the fast release of vesicles from the immediately releasable pool (IRP; see below for an accurate definition) has been proposed (20). Using short square pulses (10 ms) to 0 mV from −80 mV to specifically recruit vesicles from the IRP, it was shown that Cav2.1 channels control most of the IRP. Finally, it is worth noticing that depending on the activation gating of Cav2 channels, it is likely than Cav2.1 channels exert a key role in secretion when using trains of triangular APs rather than square pulses (122). This is likely associated with the fast activation of Cav2.1 with respect to the other Cav channels, which is more evident with short stimuli since less affected by the fast Ca^{2+}-dependent inactivation (CDI) of the channel. This suggests that channel activation and the type of stimuli applied, rather than the specific colocalization of the secretory apparatus with Ca^{2+} channels, critically regulate exocytosis in CCs.

The voltage-dependent modulation of Cav2.1 and Cav2.2 by neurotransmitters: physiological significance

As shown in the previous section, due to their higher threshold of activation, Cav2 channels contribute mainly to the upstroke and falling phase of APs, while Cav1 channels (Cav1.2 and Cav1.3) control the subthreshold current regulating AP firing in rat and mouse CCs (426, 429). Cav2 channels are also uniquely modulated in a voltage-dependent manner by G-protein-coupled receptor (GPCR) pathways (314). In CCs, Cav2.1 and Cav2.2 are autocrinally inhibited by ATP and opioids that are released together with CAs during cell activity (8, 10, 149, 235). The inhibition occurs in membrane microdomains, without the involvement of diffusible second messengers, and is manifested by a delay of channel openings (slow activation) at low potentials (Figures 5A and 5B) (98, 102). This effect, however, can be reversed by depolarizing voltage steps. The normal fast activation is recovered during strong depolarizations to +100 mV (52, 430) or when a strong depolarizing prepulse anticipates a test depolarization to 0 mV (Figures 5A-5C) (201). This phenomenon is called "voltage-dependent facilitation" and is attributed to a protein-protein interaction between the activated GPCR βγ subunit and several sites on both the Cav2 α1 subunits: the N-terminus, the I–II linker domain, and probably the C-terminus (see Ref. 686 for a recent review). Remarkably, this inhibition of Cav2.1 and Cav2.2 can be partially recovered during brief depolarizations repeated at high frequency (150) as it occurs during high-frequency AP

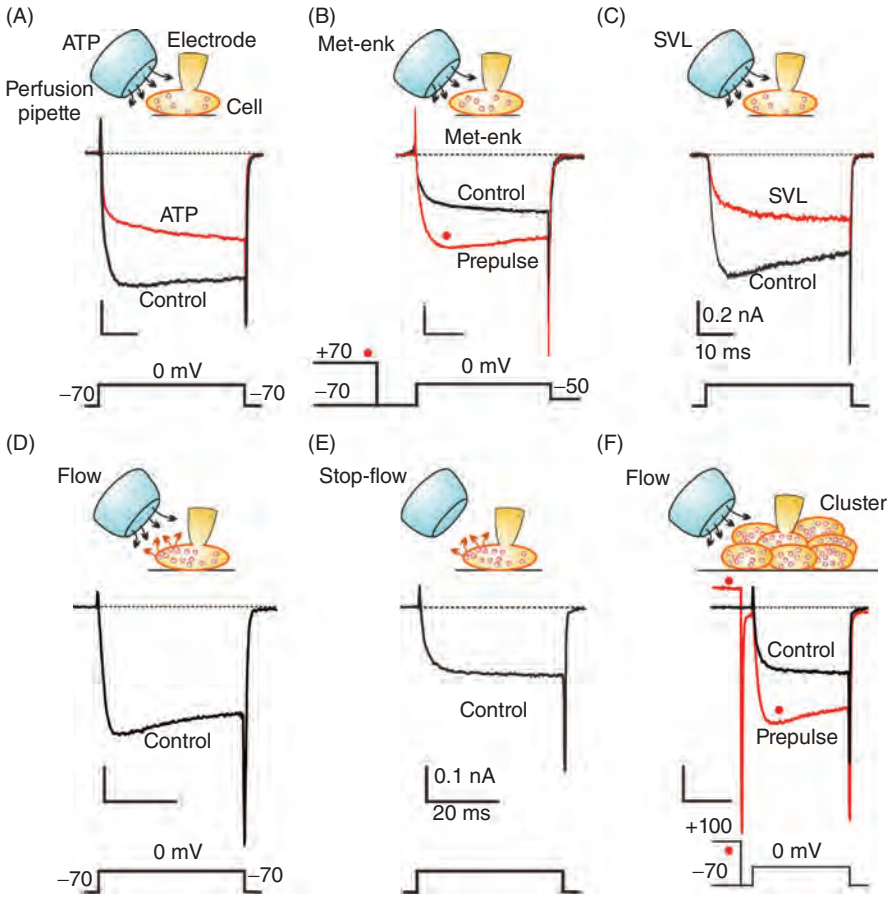

Figure 5 Voltage-dependent modulation of $Ca_V2.1$ and $Ca_V2.2$ in CCs. (A) Acute application of ATP (50 μM) slows down the activation of N- and P/Q-type Ba^{2+} currents recorded at 0 mV in a bovine CC (for details, see Ref. 98). (B) The delayed activation of N- and P/Q-type Ba^{2+} currents induced by the acute application of met-enkephalin (10 μM; black trace; control) is recovered by a 50-ms prepulse step depolarization to +70 mV (red dot; red trace) (for details, see Ref. 573). (C) Acute application of the soluble vesicle lysate (SVL) containing (EPI, NE, opioids, and ATP) causes N- and P/Q-type current delayed activation in bovine CCs (for details, see Ref. 10). (D, E) Autocrine inhibition of N- and P/Q-type channels revealed by changing cell superfusion from "stop-flow" to "flow" condition, in bovine CCs. In the "flow" condition, there is no autocrine inhibition. Ba^{2+} currents at 0 mV are fast activating. In the "stop-flow" condition, the autocrine-released material inhibits through GPCRs the opening of Ca_V2 (N- and P/Q-type) channels, inducing marked activation delay. Adapted, with permission, from Carabelli V, et al., 1998 (98). (F) Ba^{2+} currents recorded from a cell that is part of a cluster undergo robust autocrine modulation (black trace, control). A prepulse to +100 mV is able to rescue the fast channel activation by removing the autocrine inhibition induced by the neurotransmitters released by the surrounding cells (for details, see Ref. 290).

trains occurring during stress-mimicking conditions. The result is that the reduced Ca^{2+} entry through $Ca_V2.1$ and $Ca_V2.2$ at rest, due to the downregulation induced by the released opioids and ATP, can be partially recovered during sustained cell activity. This "autocrine inhibition" of Ca_V2 channels was first discovered by applying the purified low molecular weight components of secretory vesicles (soluble vesicle lysate, SVL), containing EPI, NE, opioids, and ATP, directly onto bovine CCs (Figure 5C) (10). Application of SVL caused the typical slowdown of Ca_V currents induced by applied neurotransmitters that could be removed by strong pre-step depolarizations. This report also showed that the same autocrine inhibition occurs by stopping the flow of external solution perfusing the cell (*stop-flow*), allowing the unwashed released neurotransmitters (ATP and opioids) to activate the inhibitory GPCR pathway that slows down Ca_V2 currents (Figure 5E). This resting autocrine inhibition of Ca_V2 channels is particularly evident in clusters of bovine CCs (290) (Figure 5F) and in mouse adrenal gland slices (292). In these tissue preparations, the packed organization of the cells is well preserved and the released neurotransmitters can accumulate in the extracellular space to exert a basal tonic inhibition on cell firing and CA secretion that is facilitated by prepulse depolarizations. The application of opioids or ATP

directly on bovine CCs mimics the effects of SLV application (Figures 5C and 5F).

The effective action of this autocrine modulation derives from the high concentration of neurotransmitters stored in the CC granules (0.8–1 M CA, ~200 mM ATP, and 1–2 mM met-enk; see below) and the high density of adrenergic (α_2-AR, β_1-AR, and β_2-AR) (78, 121, 355), opioidergic (μ and δ) (8, 355, 624), and purinergic (P_{2y}) receptors (98, 149, 519, 627) expressed in bovine, rat, and mouse CCs. It is noteworthy that rat CCs also possess ligand-gated purinergic receptors (P_{2X3} and P_{2X7}), which are upregulated during pain-induced stress in chronic pain rat models (28). This suggests a key role of P_{2Y} and P_{2X} receptors in regulating cell depolarization, AP firing, and CA release. The role of secreted ATP modulating the quantum characteristics of CA exocytosis through purinergic receptor activation has also been recently demonstrated (421).

In conclusion, it seems that the autocrine inhibition of the Ca_V2 channel acts primarily as negative feedback to regulate the amount of secretion. With increased firing rates, the autocrine inhibition may still act to prevent excessive CA release, but when under intense APs stimulation, a large surge of CAs is required. CCs are able to overcome the inhibition by facilitating Ca_V2 currents in an activity-dependent manner.

The voltage-independent modulation of $Ca_V2.1$ and $Ca_V2.2$ by neurotransmitters

Voltage-independent inhibition of Ca_V2 channels also exists and likely includes several distinct modulatory mechanisms. In CCs, the neuronal Ca^{2+} sensor-1 (NCS-1) exerts a tonic voltage-independent inhibition of $Ca_V2.1$ channels (665). NCS-1 acts through an autocrine, purinergic, and opioidergic receptor-mediated pathway and the activation of PTX-insensitive G-proteins. To complete the $Ca_V2.1$ channel inhibition in CCs, it is also necessary that the $Ca_V2.1$ α1-subunit be phosphorylated at the tyrosine residues by a Src-like kinase, strictly controlling Ca^{2+}-dependent exocytosis through a series of biochemical steps (665). Specifically, NCS-1 is shown to regulate CC secretion by favoring PIP_2 production, leading to $InsP_3$ increases and Ca^{2+} release from intracellular stores (500). A similar voltage-independent inhibition of $Ca_V2.1$ and $Ca_V2.2$ channels mediated by PIP_2 and PKC has been reported in the sympathetic superior cervical ganglion and transfected TsA201 cells (596). Voltage-independent inhibition of Ca_V2 channels is also produced by Gq-coupled H1-histamine receptors in bovine CCs (151).

Modulation of $Ca_V2.1$ and $Ca_V1.3$ channels in CCs: a role in stimulus-secretion coupling

The important participation of L-type channels in the Ca^{2+}-dependent release of CAs from the adrenal medulla was first reported in a pioneering set of experiments (243). Subsequent reports confirmed this observation and showed that due to their slow inactivation, Ca_V1 are the Ca^{2+} channels mostly contributing to CA secretion when long-lasting stimuli are applied. Sustained depolarization with high KCl solutions (404), prolonged applications of ACh (325, 461), or repeated splanchnic nerve stimulation (6) in isolated cells or intact adrenal glands of various animal species revealed a predominant L-type channel regulation of CA release (see Refs. 70, 240, 417, 463, 634 for recent reviews). This slow action occurs independently of the expression densities of Ca_V1 channels and it is associated with the unique gating properties of these channels. Two features, in particular, are the slow Ca^{2+}-dependent inactivation that allows sustained Ca^{2+} fluxes during prolonged (or repeated) depolarizations and the weak steady-state inactivation of both channels at −50 and −60 mV, the latter favoring channel availability near the resting membrane potentials. When exocytosis is evaluated using capacitance changes on single isolated cells, the L-type Ca^{2+} current possesses the same Ca^{2+} sensitivity of Ca_V2 and Ca_V3 channels and contributes proportionally to their density of expression (100, 103, 206).

The voltage-independent direct and remote autocrine modulation of L-type channels

The Ca_V1 (L-type) channels, like the Ca_V2 type, experience basal and stimulus-induced autocrine modulation, which affects the amount of Ca^{2+} entry that regulates CA secretion. This autocrine effect is mediated by a variety of GPCRs, including adrenergic, opioidergic, and purinergic, expressed in CCs. It occurs in isolated CCs (Figures 5A-5C) (10, 121, 288, 419) but is more prominent in cell clusters (236) and in adrenal gland slices (292), in which, as *in vivo*, released neurotransmitters accumulate between closely packed CCs (Figure 5F).

The autocrine modulation of L-type channels in CCs is mainly voltage independent and occurs through two opposing distinct pathways (see Refs. 109 and 417 for a review): (i) rapid inhibition of Ca_V1 channel gating via PTX-sensitive G-proteins (*direct inhibition*) or (ii) slow upregulation of Ca_V1 channel activity through a cAMP/PKA-mediated phosphorylation (*remote upregulation*), similar to the upregulation of cardiac $Ca_V1.2$ channels under β1-AR-mediated sympathetic stimulation. The *direct inhibition* is fully apparent in membrane microdomains where Ca_V1 channels and GPCRs interact to reduce the open channel probability and Ca^{2+} entry (98, 101, 288, 292). The *remote upregulation* requires the presence of β-adrenoceptors (β-ARs), functional adenylate cyclases, PKA, and Ca_V1 channels and occurs in nearly all the CCs of all animal species including humans (101, 121, 138, 229, 428); for a review, see Refs. 46, 109, 417, 426, 427, and 634.

L-type channels are also regulated by a remote mechanism, in addition to neurotransmitter-mediated modulation, involving the NO/cGMP/PKG pathway which tonically inhibits Ca_V1 channels and CA release in bovine (99, 561) and mouse CCs (419). The NO/cGMP/PKG-mediated downregulation of L-type channels and cAMP/PKA-mediated upregulation act oppositely, just as they act on cardiac $Ca_V1.2$ channels. An interesting question is whether $Ca_V1.2$ and $Ca_V1.3$,

which are equally expressed in both mouse and rat CCs, are both modulated by NO/cGMP/PKG- and cAMP/PKA-driven mechanisms. Using $Ca_V1.3^{-/-}$ KO mice, it was demonstrated that both channels are equally up- or downregulated by the two opposing pathways (419). The two pathways act independently on the two channels and may induce almost an order of magnitude variation of L-type current amplitudes when concomitantly regulated. Figure 6 illustrates the cascade of events of the two opposing modulatory pathways. The upper part shows cAMP/PKA-mediated upregulation driven by the autocrine activation of β-ARs. The lower part shows the NO/cGMP/PKG-mediated downregulation driven by different stimuli. Figure 7 summarizes the two main experiments that showed how Ca_V1 currents in WT mouse CCs can be upregulated by inhibiting the NO/cGMP/PKG cascade and activating the cAMP/PKA pathway (bottom part) or drastically downmodulated by inhibiting cAMP/PKA pathway and stimulating the NO/cGMP/PKG cascade (top part) (see Figure 7 legend for further details).

Concerning the functional relevance of this dual modulation of $Ca_V1.2$ and $Ca_V1.3$ L-type channels, we point out that cAMP/PKA and cGMP/PKC are likely active even at rest due to the basal activity of the two kinases. PKA can be stimulated by PACAP (526), Ca^{2+} entry, and G-protein subunits that are activated by the basal activity of first messengers released from sympathetic neurons (24), surrounding capillaries (431, 670), and by the autocrine activity of CCs (10, 121). The soluble GC is activated by the resting NO levels generated by the Ca^{2+}-calmodulin-mediated activation of NO synthase (NOS) expressed in most CCs (494, 561). Under these conditions, cGMP/PKG appears to work as a "brake" to limit the potentiating effects of cAMP/PKA and helps set the resting levels of $Ca_V1.2$ and $Ca_V1.3$ currents, which regulate the resting potential and basal repetitive firing.

A *synergistic potentiation* of Ca_V1 channels could occur during sustained splanchnic nerve stimulation that releases PACAP (*vide infra*) and induces a massive release of EPI from CCs, which would further elevate the levels of cAMP/PKA

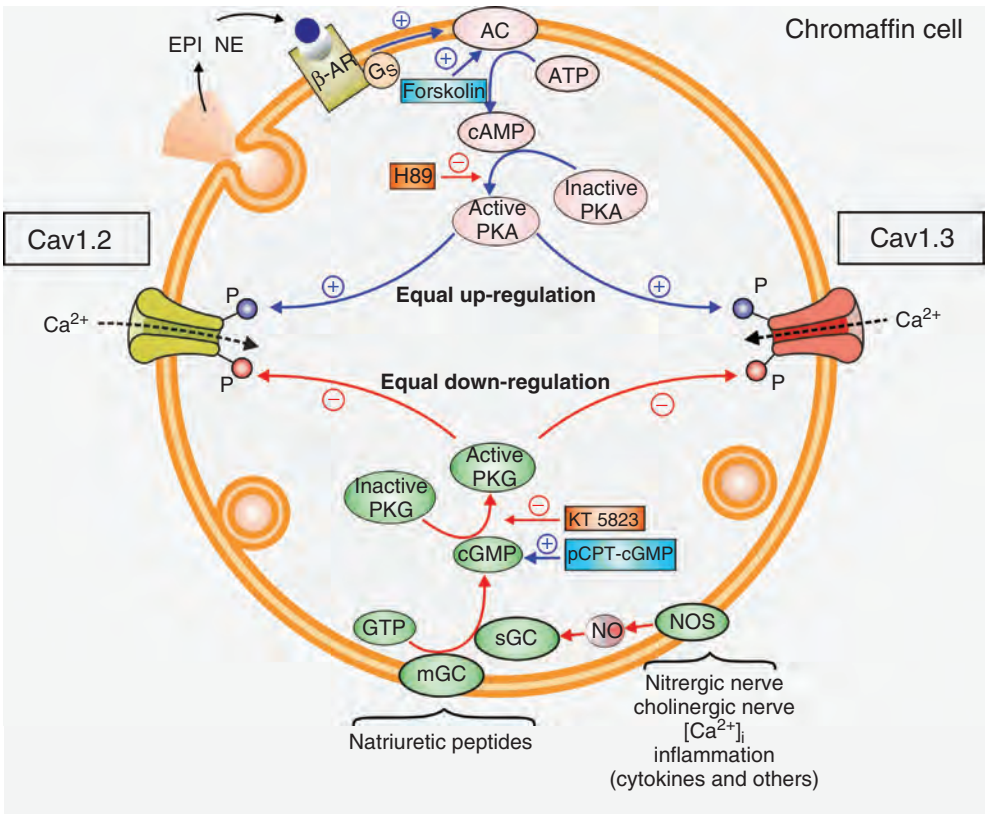

Figure 6 Up- and downmodulation of $Ca_V1.2$ and $Ca_V1.3$ channels by the cAMP/PKA and NO/cGMP/PKG pathways in mouse CCs. The top half illustrates the molecular components and the sequential steps of the β-AR-mediated upregulation of $Ca_V1.2$ and $Ca_V1.3$ L-type channels through the activation of adenylate cyclase (AC), leading to cAMP production, activation of PKA, and Ca_V1 channel phosphorylation, causing an increase in open channel probability. The bottom part shows the molecular components and the sequential steps of the NO-mediated downregulation of $Ca_V1.2$ and $Ca_V1.3$ L-type channels through the activation of a soluble guanylate cyclase (sGC), leading to cGMP production, activation of PKG, and Ca_V1 channels phosphorylation, causing a decrease in open channel probability. NO is produced by membrane NO-synthases. cGMP is also produced by a membrane guanylate cyclase (mGC). Adapted, with permission, from Mahapatra S, et al., 2012 (417).

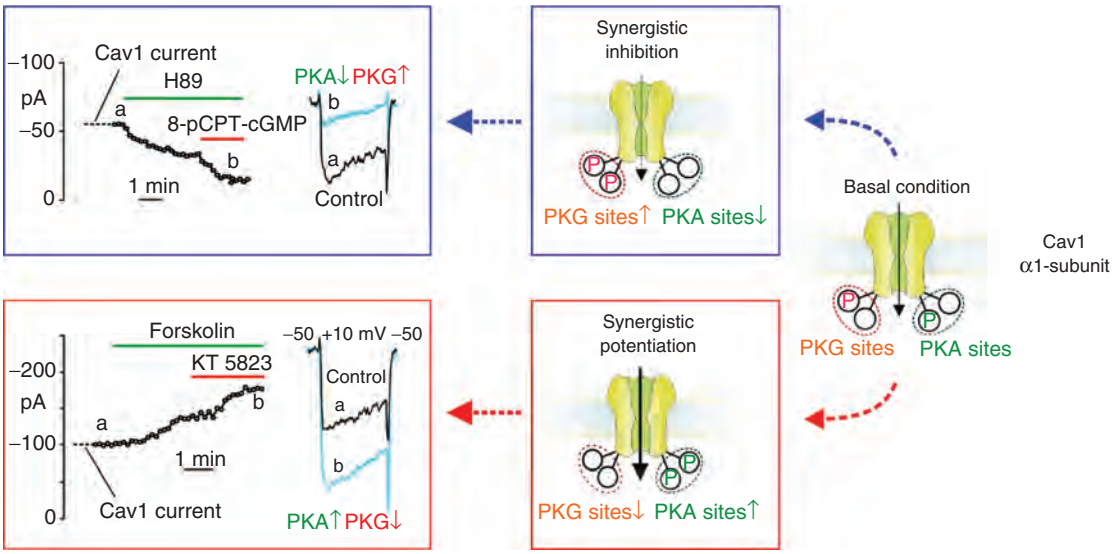

Figure 7 Synergistic effects of cAMP/PKA and cGMP/PKG pathways on Cav1 currents of WT mouse CCs. The right side is a schematic representation of Ca_V1 channel α1 subunit with two hypothetical PKA and PKG phosphorylation sites (P). The schemes represent the situation under basal conditions (middle), a synergistic potentiation (top), and a synergistic inhibition (bottom) of Ca_V1 channel. PKA and PKG P-sites are partially phosphorylated (P) or unphosphorylated under resting conditions. Phosphorylation and dephosphorylation drove by up- and downregulation of PKA and PKG proceed independently of each other and can reach two extreme conditions. In one case, the two PKA P-sites are dephosphorylated and the two PKG P-sites are phosphorylated (minimal Ca_V1 current; cyan trace, on the top left panel). Alternatively, the PKA sites are phosphorylated and PKG P-sites are dephosphorylated (maximal Ca_V1 current; cyan trace, on the bottom left panel). The two panels to the left show the time course of synergistic downregulation of Ca_V1 channels induced by the sequential application of the PKA inhibitor H-89 and the PKG activator 8-pCPT-cGMP (top) and the synergistic upregulation of Ca_V1 channels by sequential application of the PKA activator forskolin and PKG inhibitor KT 5823 (bottom). Adapted, with permission, from Mahapatra S, et al., 2012 (417); Adapted, with permission, from Vandael DHF, et al., 2013 (634) (drawing and experimental data).

through the autocrine activation of the β_1-ARs (121, 428). The increased Ca^{2+} entry could, in turn, upregulate PDE1, the cGMP-hydrolyzing and Ca^{2+}-calmodulin-activated PDE that controls the resting levels of cGMP (561, 637). Activation of a cGMP-specific PDE that lowers cGMP, inhibiting PKG, and the parallel activation of PKA during PACAP release and β_1-AR stimulation could markedly boost the L-type Ca_V1 currents. This regulation would overall serve to sustain the rapid increase of cell firing activity and CA release during the "fight-or-flight" response to stressors in CCs. On the other hand, a *synergistic inhibition* could occur if, as in mammalian ventricular myocytes, CCs possess cGMP-activated PDE2 isoforms that hydrolyze cAMP (410). Any robust upregulation of the NO/cGMP/PKG pathway under these conditions would enhance cGMP and downregulate cAMP, rapidly depressing $Ca_V1.2$ and $Ca_V1.3$ channel gating. The existence of various PDEs acting on cAMP in CCs is supported by the observation, in mouse CCs, that the nonspecific PDE blocker IBMX increases basal cAMP levels more potently than the PDE-4-specific blocker rolipram (428).

Regulation of endocytosis by L-type Ca^{2+} channels

To ensure that the size of nerve terminals and neuroendocrine cells is preserved during cell activity, excess vesicle membrane incorporation into the cytosolic membrane during exocytosis must be compensated by an equivalent membrane retrieval during subsequent endocytosis (see the following section). This mechanism ensures that a given number of vesicles are available to replenish the secretory vesicle pool and participate in subsequent rounds of exocytosis during repetitive cell activation (33, 118, 284). Like exocytosis, endocytosis is a Ca^{2+}-dependent process in CCs (33, 481). The question is whether some Ca_V channels (Ca_V1 and Ca_V2) are preferentially coupled to endocytosis or not.

In bovine CCs stimulated with long depolarizing pulses, there is a preferential coupling of L-type Ca_V1 channels to endocytosis (541). In spite of the small contribution of Ca_V1 channels to the whole-cell Ca^{2+} current, this shows that nifedipine abolishes the endocytotic response, without significantly affecting exocytosis that is also sustained by $Ca_V2.1$ and $Ca_V2.2$ channels. In the presence of FPLA64176 (an L-type Ca_V channel agonist), the increased Ca^{2+} entry doubles the endo/exocytosis ratio, indicating a selective augmentation of endocytosis associated with the selective Ca^{2+} entry increase through Ca_V1 channels (543). In mouse CCs, the membrane excess retrieval following strong Ca^{2+} entry is suppressed by nitrendipine, suggesting the direct involvement of Ca_V1 channels (511).

Immunofluorescence experiments on bovine CCs have shown negligible colocalization of clathrin and dynamin to

L-type Ca^{2+}-channels (543). This, and the additional studies in CCs (136), support the idea that a low-rate, non-inactivating Ca^{2+}-entry through Ca_V1 channels ($Ca_V1.3$) might be more critical to trigger compensatory as well as excess exocytosis. These data also support the idea that not all Ca^{2+} that enters CCs during depolarization through slow-inactivating Ca_V1 channels or through fast-inactivating $Ca_V2.1$ and $Ca_V2.2$ channels has the same physiological function (463).

Ca^{2+} handling by CCs: impact on exocytosis

That Ca^{2+} is the coupling agent in the stimulation-secretion process was established in pioneering experiments in perfused cat adrenal glands: ACh stimulation triggered a Ca^{2+}-dependent CA release (176) that was associated with enhanced Ca^{2+} entry via Ca_V channels (174). Since then, we have learned much more about the complexities of enhanced Ca^{2+} entry and secretion. The details of the stimulus-secretion coupling process (172) have been amply clarified using Ca^{2+}-sensitive probes, particularly aequorins targeted to different organelles (537) as well as patch-clamp (271) and amperometric techniques (668) to measure the exocytotic release of CAs with high temporal resolution.

Several ion channels and transporters tightly regulate Ca^{2+} handling in excitable cells. This exquisite control of the cycling of Ca^{2+} is vital to cell function and survival. Concerning CCs, we will review the cycle of Ca^{2+} that comprises four processes: Ca^{2+} entry, Ca^{2+} efflux, Ca^{2+} redistribution into organelles, and Ca^{2+} release from those organelles.

Ca^{2+} entry

Ca^{2+} entry through the various Ca_V channels is the primary determinant in shaping the $[Ca^{2+}]_c$ elevations occurring during CC activation. Although Ca^{2+} entry through the plasmalemma is mainly associated with Ca_V channels, Ca^{2+} can reach the cytosol through the nAChRs as well as the store-operated Ca^{2+} channels (SOCCs). The characteristics and functions of Ca_V channel subtypes and their role in the regulation of CA release have been described earlier (*Ca^{2+} channel-secretion coupling*). Those of nAChR and SOCC channels in Ca^{2+}-handling and transport have been discussed in detail elsewhere (242).

Ca^{2+} efflux

There are two plasmalemma transporters for pumping Ca^{2+} out of the CCs. These are the plasma membrane Ca^{2+}-ATPase or Ca^{2+} pump (PMCA) and the Na^+/Ca^{2+} exchanger (NCX). The Ca^{2+} pump, inhibited by vanadate and lanthanum, has a high affinity for Ca^{2+} (submicromolar K_D) and transports one Ca^{2+} ion for each ATP hydrolyzed (79). The H^+/Ca^{2+} transport ratio for PMCA in reconstituted *in vitro* systems has been estimated at 1:1 (165), and therefore PMCA pumping would be electrogenic (551) and sensitive to membrane potential. Nevertheless, in neurons, PMCA exchanges two H^+ for each Ca^{2+} ion extruded, that is it is electroneutral (612). PMCA is modulated by numerous factors, but mainly calmodulin. When intracellular Ca^{2+} increases, calmodulin binds to PMCAs, increasing their Ca^{2+} affinity. The PMCAs are encoded by four different genes: PMCA1 and PMCA4, which are ubiquitously expressed, and PMCA2 and PMCA3, expressed predominantly in the CNS (106). The Na^+/Ca^{2+} exchanger uses the energy of the Na^+ gradient, to exchange three external Na^+ ions for one internal Ca^{2+} ion (42); its function is, therefore, electrogenic. The exchanger can also work in the "reverse mode," moving Na^+ out of the cell and Ca^{2+} into the cell; this occurs during membrane depolarization and/or when intracellular Na^+ concentration increases, for instance after intense AP firing (63).

Using plasma membrane purified from bovine adrenal medullae, a first functional characterization of the two transporters was achieved (335). Later, it was found that bovine CCs express NCX1, the major isoform of the exchanger (497). NCX1 can adopt two functional modes: the forward mode that favors Ca^{2+} efflux (520) and the reverse mode that favors Na^+-dependent Ca^{2+} influx (391). Changes in the Na^+ gradient, either directly through manipulation of ion concentrations (499, 501, 536) or indirectly through inhibition of the Na^+ pump with ouabain (213, 241), augment Ca^{2+} entry and the release of CAs. This has suggested a role of the NCX in the regulation of Ca^{2+} signaling and exocytosis in CCs. However, an alternative explanation in the case of experiments with ouabain involves its ability to release Ca^{2+} from the ER (443).

Ca^{2+} sequestration

The membrane of the ER and sarcoplasmic reticulum (SR) contains a Ca^{2+} pump, the sarcoendoplasmic reticulum Ca^{2+}-dependent ATPase (SERCA), of which there are three major isoforms (SERCA1–3). SERCA1a-b and SERCA2a are present in skeletal and cardiac muscles, while SERCA2b is expressed in all nonmuscle tissues including nerve cells. SERCA keeps intracellular Ca^{2+} concentration low and Ca^{2+} concentration high inside the ER/SR, creating the conditions for cytosolic Ca^{2+} transients and oscillations in response to a variety of external stimuli that allow ER Ca^{2+} release. Phospholamban (PLB), a small protein expressed in muscle and integral to the ER/SR membrane, when nonphosphorylated, binds to SERCA and decreases its affinity for Ca^{2+}, and when phosphorylated, it detaches from the pump, relieving the inhibition. The activity of all SERCA isoforms is specifically inhibited by thapsigargin with half-maximal inhibitory potency of 10 to 20 nM (106).

Redistribution of Ca^{2+} into, and release of Ca^{2+} from, the endoplasmic reticulum

Several laboratories have approached the study of Ca^{2+} circulation in and out of the cytoplasm and ER Ca^{2+} store of CCs. Upon cell activation, increased cytoplasmic Ca^{2+} concentration ($[Ca^{2+}]_c$) activates Ca^{2+} uptake into the ER lumen

through the SERCA. For instance, upon stimulation of bovine CCs (17, 640, 678) or rat CCs (295), Ca^{2+} is effectively taken up by the ER, to reach concentrations as high as half millimolar within the ER lumen (17).

Various stimuli are known to release Ca^{2+} from the ER through two channels, namely, the inositol tris-phosphate receptor ($InsP_3R$) and the ryanodine receptor (RyR). Carbachol, histamine, bradykinin, and angiotensin II augment the synthesis of $InsP_3$ in bovine CCs (477, 518, 553) in parallel with $[Ca^{2+}]_c$ increase (589). These ER Ca^{2+}-mobilizing actions are mimicked by direct stimulation with $InsP_3$, suggesting that they are mediated by the plasmalemmal receptors for these first messengers to generate $InsP_3$ that will finally elicit Ca^{2+} release via $InsP_3Rs$ (589, 590).

The functional correlation of the $InsP_3$ ER Ca^{2+} release pathway has been studied in more detail with agonists for metabotropic receptors. Thus, stimulation of bovine CCs with histamine (29) or guinea-pig CCs with muscarine (487) augments $[Ca^{2+}]_c$ to elicit the activation of Ca^{2+}-dependent SK and BK channels that gives rise to cell hyperpolarization. In line with this is the observation that SK and BK channels regulate the nicotinic and muscarinic secretory responses of cat and bovine CCs (371, 625, 626). A short application of histamine causes a transient mild secretory response (83), while a longer application causes a greater effect (83, 397, 476). Most likely, the histamine-elicited $[Ca^{2+}]_c$ elevation has two components: an initial transient phase linked to ER Ca^{2+} release and a late, sustained phase due to Ca^{2+} entry (485, 589, 590, 687); but see (64). The second component has been linked to the inhibition of a K_V7 (M-current) potassium channel with an associated depolarization and augmented Ca^{2+} entry through open Ca_V channels (660). Angiotensin II also increases cytosolic Ca^{2+} and stimulates exocytosis in bovine CCs, but to a lesser extent than histamine (126, 590).

The second pathway for Ca^{2+} release from the ER is the RyR Ca^{2+}-release channel. An activator of this channel, caffeine, causes rapid Ca^{2+} release in bovine CCs (126). Caffeine effects displayed a "quantal" pattern as if Ca^{2+} release from the ER occurred in steps; thus, it was concluded that the caffeine-sensitive Ca^{2+} pool is composed of different functionally discrete stores (124, 126, 127). The presence of separate or overlapping Ca^{2+} stores sensitive to histamine or caffeine and their functional significance have been under debate since the 1990s (123, 392, 538, 589).

How the $InsP_3$-sensitive and the caffeine-sensitive Ca^{2+} stores interact was partly clarified in bovine CCs transfected with ER-targeted aequorin (17, 640). These experiments suggest that in CCs, the ER behaves as a single thapsigargin-sensitive Ca^{2+} pool that releases Ca^{2+} through a Ca^{2+}-induced Ca^{2+} release (CICR) mechanism mediated by RyR or $InsP_3Rs$. Later reports suggested that in mouse CCs in the intact adrenal gland, CICR is either small or nonexistent (535), but in another study in cultured mouse CCs, a functional CICR mechanism was found (675). The contribution of the ER Ca^{2+} store to the regulation of exocytosis has been studied by several laboratories. In voltage-clamped bovine CCs, depletion of the ER Ca^{2+} store with a SERCA blocker either did not affect exocytosis (451) or depressed it (498). In a third study also in bovine CCs, ER Ca^{2+} depletion depressed the ACh secretory responses but not that triggered by depolarizing high-K^+ solution. This difference was explained assuming that ACh produces discrete and more localized $[Ca^{2+}]_c$ transients at sub-plasmalemmal regions, while high K^+ elicits greater $[Ca^{2+}]_c$ transients that spread quickly throughout the cytosol (145). Nevertheless, sustained stimulation of bovine CCs with caffeine caused ER Ca^{2+} depletion and a decrease of the K^+-elicited secretory responses. It seems, therefore, that depending on its grade of filling, the ER may behave as a Ca^{2+} sink when empty, or to augment $[Ca^{2+}]_c$ signals and exocytosis by a CICR mechanism when full (370).

The ER Ca^{2+} store could also have a regulatory function on Ca^{2+}-dependent pre-exocytotic steps, that is promoting the flow of secretory vesicles from a reserve pool (RP) toward the sub-plasmalemmal readily release vesicle pool. This is supported by experiments in voltage-clamped bovine CCs that use histamine to elicit mild $[Ca^{2+}]_c$ elevations elicited by ER Ca^{2+} release; although these $[Ca^{2+}]_c$ elevations were subthreshold for exocytosis, they caused a clear augmentation of the exocytotic response elicited by depolarizing pulses (652).

Redistribution of Ca^{2+} into, and release of Ca^{2+} from, mitochondria

Mitochondria use the driving force of the large electrical potential across their membrane (nearly −180 mV) to import vast amounts of Ca^{2+} through their Ca^{2+} uniporter (532). Mitochondria behave as a temporary Ca^{2+} store and export Ca^{2+} back into the cytosol by exchanging one Ca^{2+} for 2 Na^+ ions via the mitochondrial electroneutral Na^+/Ca^{2+} exchanger (mNCX). A less-active H^+/Ca^{2+} exchanger has also been described (105, 264). As the uniporter has a low affinity for Ca^{2+}, mitochondria take up large quantities of this cation efficiently only when overall intracellular Ca^{2+} concentrations are high, or if mitochondria are close to cytosolic high Ca^{2+} microdomains (HCMDs) that build-up upon Ca^{2+} entry through Ca_V channels at sub-plasmalemmal sites (640). This also occurs with HCMDs close to $InsP_3$ receptors that are sensed by neighboring mitochondria (537).

During stimulation, mitochondria of rat CCs behave as rapid and reversible Ca^{2+} buffers (40, 504). However, the use of Ca^{2+} probes in these experiments to monitor Ca^{2+} concentrations in the mitochondrial matrix ($[Ca^{2+}]_m$) revealed increases only in the low micromolar range (40). This is likely due to an underestimation due to the saturation of the Ca^{2+} probe. In bovine CCs, mitochondria also contribute to the clearance of large cytosolic Ca^{2+} loads (640, 678). Mitochondria-targeted aequorins with different Ca^{2+} affinities in bovine CCs revealed surprisingly rapid $[Ca^{2+}]_m$ transients, nearly in the millimolar range upon stimulation with ACh, caffeine, or high K^+ (453).

The impact on exocytosis of such avid mitochondrial Ca^{2+} uptake has been explored in several laboratories. For instance, dissipation of the proton gradient by protonophores, which drastically decreases the Ca^{2+} buffering capacity of mitochondria (453, 682), results in a pronounced augmentation of the exocytotic responses (452, 453). Such potentiated secretion has also been observed in fast-perifused bovine CCs stimulated with ACh, caffeine, or K^+ (112, 144, 145, 453), as well as in embryonic and adult rat CCs (636) and in mouse CCs after pharmacological interfering with the mitochondrial Ca^{2+} uniporter (MICU) and the mNCX (402). The inhibition of the Ca^{2+} uniporter also augments the secretory response of bovine CCs (682). However, in mouse CCs, the protonophores depressed the K^+-evoked $[Ca^{2+}]_c$ signals and the secretory responses (112). This could be due to a different expression of Ca_V channel subtypes and different inactivation rates during the blockade of mitochondrial Ca^{2+} sequestration by the protonophores (291).

An integrative view of Ca^{2+} handling by CCs

The rates of Ca^{2+} entry, its redistribution into CC organelles, its release back to the cytosol, and its extrusion to the extracellular space have been calculated with both direct and indirect approaches (640). Ca^{2+} entry into CCs through the various Ca_V channel subtypes is the primary determinant of the initial $[Ca^{2+}]_c$ transient. Thus, for a 15-µm diameter bovine CC, the rate of Ca^{2+} entry can be calculated from the measured Ca^{2+} inward current (692) or from the rate of $^{45}Ca^{2+}$ uptake into K^+ depolarized cells (32). The mean rate of Ca^{2+} entry from the two sets of experiments is around 500 µmol L cell^{-1} s^{-1}. After generating the sub-plasmalemmal HCMDs, which can reach concentrations as high as 10 to 100 µM (38, 471), Ca^{2+} redistributes into various intracellular compartments, particularly at the ER and mitochondria. This $[Ca^{2+}]_c$ elevation activates the SERCA and the ER avidly takes up Ca^{2+}; thus, during stimulation of bovine CCs (17, 640, 678) and rat CCs (295), the rate of uptake by the ER is about 60 µmol L cell^{-1} s^{-1}.

Mitochondria are highly effective in clearing $[Ca^{2+}]_c$ transients. Using mitochondria-targeted aequorin in bovine CCs maximally stimulated with K^+, it was found that mitochondria took up Ca^{2+} through their uniporter at about a rate of 1100 µmol L cells^{-1} s^{-1} (452, 453, 640). This value is close to that found for Ca^{2+} entry through Ca_V channels, meaning that most Ca^{2+} entering the bovine CC during stimulation is initially taken up by mitochondria and then released back into the cytosol through the mNCX. The rate of Ca^{2+} efflux through this transporter at 37 °C in bovine CCs is about 800 µmol L cells^{-1} s^{-1}; its kinetics are exponential and K_{50} approaches 20 µM Ca^{2+} (640). Finally, Ca^{2+} extrusion from the cytosol to the extracellular space depends on the activity of both SERCA and NCX. The joint action of both transporters decreases $[Ca^{2+}]_c$ at a maximal rate of 20 µmol L cells^{-1} s^{-1} in rat CCs at 27 °C (295, 504). In bovine CCs at 37 °C, this rate is close to 100 µmol L cells^{-1} s^{-1}.

After a brief opening of Ca_V channels in bovine CCs, an HCMD is formed near sub-plasmalemmal exocytotic sites (Figure 8). This HCMD has been estimated to have about 0.3-µM diameter and reach 10 µM or higher $[Ca^{2+}]_c$ (38, 129, 357, 442, 471–473). The formation of HCMDs is favored by colocalization of Ca_V channel clusters and secretory vesicles (490, 539, 690) to trigger fast exocytosis (54).

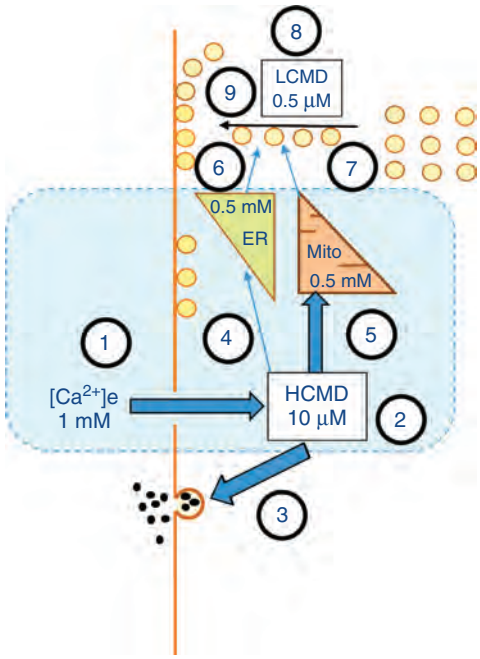

Figure 8 The concept of functional triads that regulate the generation of local $[Ca^{2+}]c$ transients and exocytosis responses upon stimulation of CCs. (1) After cell depolarization with the physiological neurotransmitter ACh, the voltage-dependent Ca^{2+} channels open. (2) Ca^{2+} enters the cell through a huge electrochemical gradient, giving rise to the formation of a high-Ca^{2+} microdomain (HCMD) of about 10 µM or higher near the sub-plasmalemmal exocytotic sites. (3) High Ca^{2+} is required to trigger the fast exocytotic release of CAs. (4) The HCMD quickly dissipates initially by mobile Ca^{2+} buffers (not drawn) and more slowly by Ca^{2+} uptake by the ER Ca^{2+}-ATPase (SERCA). (5) The second more relevant pathway for the clearance of the $[Ca^{2+}]c$ transient is the mitochondrial Ca^{2+} uniporter, which has a low-affinity high-capacity for Ca^{2+} sequestration into the mitochondrial matrix. (6, 7) In both ER and mitochondria (Mito), the matrix $[Ca^{2+}]c$ can reach near half a millimolar. ER Ca^{2+} can be released back into the cytosol through a CICR mechanism via ryanodine receptors, $InsP_3$ receptors (6), or through the mitochondrial Na^+/Ca^{2+} exchanger (7). (8) Ca^{2+} diffusion serves to redistribute Ca^{2+} at inner areas of the cell core to generate low-Ca^{2+} microdomains (LCMD) of around half micromolar that are required for the cytoskeleton-mediated Ca^{2+}-dependent vesicle traffic. (9) The Ca^{2+} levels of the LCMD refills with new vesicles the RRP at sub-plasmalemmal exocytotic sites, securing that new rounds of exocytosis take place, thus completing the exocytotic process.

The dissipation of HCMDs has two components. The fast one occurs in the time range of milliseconds and is associated to nearby cytosolic mobile Ca^{2+} buffers that accelerate Ca^{2+} diffusion and oppose the development of HCMDs (287, 480, 692). Consistent with this is the observation that added external Ca^{2+} buffers such as fura-2 increase the apparent rate of Ca^{2+} diffusion about fourfold (692).

The slower component of the $[Ca^{2+}]_c$ transient clearance is linked to the redistribution of Ca^{2+} into the ER and

mitochondria. This occurs particularly under conditions of intense stimulation of CCs. Using mitochondria-targeted aequorins with different Ca^{2+} affinities, two pools of mitochondria, M1 and M2, were characterized in bovine CCs (453). Mitochondrial pool M1, located near sub-plasmalemmal sites can sense the HCMDs occurring during physiological stimulation (295, 453, 504, 639, 640) (a local $[Ca^{2+}]_c$ rise of about 20 μM) and tune the mitochondrial generation of ATP to match the local energy needed for ATP-dependent vesicle docking at the plasmalemma and later exocytosis. Pool M2 exhibits a much lower rate of Ca^{2+} redistribution, which moves to inner regions to serve other functions, for instance, the intracellular transport of secretory vesicles from a RP to the readily releasable pool of vesicles (RRP) at sub-plasmalemmal sites (453, 640).

Concerning the functional role of ER Ca^{2+}, it is noteworthy that using ER-targeted aequorins, a reduction of 60 to 100 μM ER Ca^{2+} was observed in bovine CCs stimulated with high K^+, suggesting that CICR takes place during cell depolarization (17). RyR channels mediating CICR seem to colocalize with Ca_V channels and the mitochondrial uniporter of the M1 pool. Finally, after stimulation of CCs, the residual $[Ca^{2+}]_c$ released from the M1 pool of mitochondria and through the CICR mechanism from the ER is extruded out of the cytosol through the SERCA and the NCX.

We summarize our simplified view of the global Ca^{2+} handling by CCs in terms of what we refer to as a "functional triad" to shape the $[Ca^{2+}]_c$ transients. It has been proposed that functional triads formed by clusters of Ca_V channels, the ER RyR, and the mitochondrial Ca^{2+} uniporter are responsible for the generation and shaping of local sub-plasmalemmal $[Ca^{2+}]_c$ transients at the HCMDs that control the rate of exocytosis (17, 453, 640). Ca_V channels will act as the initiating signal, the RyR as the signal amplifier through CICR, and mitochondria as a barrier to limit diffusion further into the cell's core, where such HCMDs are not required. Ca^{2+} uptake into mitochondria has at least three functions, namely, to serve as a Ca^{2+} buffer, thus dissipating the large local Ca^{2+} transient; to redistribute the matrix Ca^{2+} into other mitochondria and the ER compartment into the cytosol; and to stimulate mitochondrial respiration and couple increased energy production to finely regulate the exocytotic machinery of the CC. As mitochondria release their matrix Ca^{2+} into the cytosol slowly, respiratory stimulation lags behind the cessation of cell stimulation, until the mitochondria Ca^{2+} load is completely cleared. Most Ca^{2+} taken up by mitochondria at sub-plasmalemmal sites may diffuse to other cell locations through the mitochondrial network, and eventually will be released near the cell core. Thus, mitochondrial Ca^{2+} release likely contributes, in a spatially specific way, to maintaining elevation of $[Ca^{2+}]_c$ after cell stimulation ends, to facilitate vesicle transport from a RP to a RRP (652). Ca^{2+} diffusion from sub-plasmalemmal sites to inner cytosolic sites is achieved by the propagation of a Ca^{2+} wave assisted by diffusible Ca^{2+} buffers and maintained by the CICR mechanism of the ER (17) (Figure 8).

From a physiological point of view, the concept of a functional triad suggests that plasma membrane Ca_V channels, together with the uptake and release of Ca^{2+} by ER and mitochondria, regulate Ca^{2+} handling in CCs. Ca^{2+} fluxes through these channels, and reservoirs are strongly activated during cell depolarization, but they also operate during inter-stimulation periods contributing to the Ca^{2+} homeostasis. Dysregulation of Ca^{2+} fluxes under pathological conditions at, for instance, the mitochondria will alter energy production and the exocytotic release of CAs. Recent experiments have demonstrated that Ca^{2+} handling and exocytosis of the sympathoadrenal axis and adrenal medullary CCs are altered in hypertension and various transgenic mouse models of neurodegenerative diseases (see below).

Exocytosis and endocytosis in CCs

Chromaffin granules

CCs are secretory cells and their most characteristic organelles are the CGs, which are very similar to the large dense-core vesicles (LDCVs) found in most neuroendocrine cells and neurons. In contrast to the synaptic vesicles found in neurons, CGs contain an intravesicular matrix that is visualized by electron microscopy as a dark structure within the CG. Granules are also of a larger size (≈200 nm) than synaptic vesicles (≈50 nm). Not only the size and matrix define CG, also the nature of their releasable cargo as they, beside amines and ATP, also release GABA, peptides, and granins. CGs contain astonishing concentrations of solutes whose resulted osmolarity would be expected to cause the swelling of CGs and their lysis. The ways used by nature to overcome the theoretical osmotic gradient from granule toward the cytosol have fascinated scientists for over five decades. A typical CG contains 0.8 to 1 M CAs, an estimated concentration of ATP of ≈200 mM, 40 mM Ca^{2+}, and significant amounts of peptides, nucleotides, and chromogranins. This inner cocktail, whose interaction enables the accumulation of neurotransmitters, is crucial for neurotransmission and for the successful secretion of hormones; processes that require the packaging of highly concentrated releasable cargo. Two components, chromogranins (166) and ATP (214), are essential for the accumulation of solutes. A concise description of the role of ATP and chromogranins contributing to the accumulation of adrenal CAs has been recently published (215).

The general view is that proteins that will form the granule matrix are synthesized in the ER, and protein assembly continues through the Golgi. CGs are produced in the trans-Golgi network by a budding process encapsulating the organized proteins that will form the matrix. The trans-Golgi network is also the sorting place for newly formed organelles. CGs are differentially sorted toward the regulated exocytosis pathway. A detailed description of the biogenesis and sorting processes occurring in neurosecretory cells is out of the scope of this article. However, excellent reviews have been published elsewhere (37, 604).

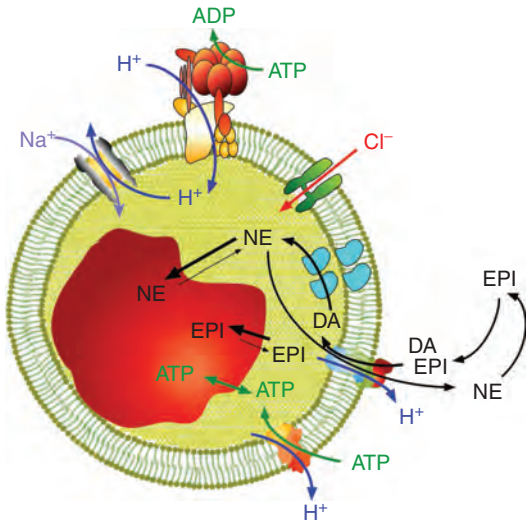

Figure 9 Main mechanisms involved in the accumulation of amines and ATP into the CG. A specific vesicular carrier (V-ATPase) pumps H^+ against a concentration and voltage gradient. To reduce the Ψ gradient, Cl^- channels open, allowing the pH to drop. The pH gradient is also regulated by Na^+ (and probably K^+) channels. Protons are used for exchange with CAs (dopamine, DA, or NE) or ATP. The synthesis of NE must occur inside the CG by the enzyme dopamine-β-hydroxylase (DBH, light blue) using DA as a substrate. In adrenergic cells, NE must leave the granule to be transformed into EPI in the cytosol (by an enzyme called phenylethanolamine-*N*-methyltransferase, PNMT, not shown) Most solutes bind the granule matrix, thus permitting their accumulation by maintaining the isotonicity of CG versus cytosol. Ca^{2+} is accumulated and released by a combination of H^+/Ca^{2+} exchange, Ca^{2+} pump, $InsP_3$-receptors (683), and ryanodine receptors (552). For clarity, Ca^{2+} turnover is not shown.

The inner milieu of CG is then further acidified from the Golgi value (pH ≈ 6.5) (555), and the matrix condenses to allow the uptake of amines, ATP, and Ca^{2+}. It is generally accepted that acidification will occur rapidly and that the uptake of cargo species starts immediately. This process is driven by an ATP-dependent specific H^+ pump, the vesicular proton pump (V-ATPase), which accumulates H^+ until the Ψ gradient reaches around +80 mV. To obtain the requisite lowering of pH, Cl^- enters CG acting as a counterion, and finally, the interior milieu reaches pH ≈ 5.5. Protons are then used as a counter-carrier to concentrate CAs, ATP, and Ca^{2+}. Thus, any alteration in the pH gradient will result in a loss of accumulation of these three species (94, 552). Most solutes will bind chromogranins, thus forming the granule matrix (Figure 9). It has been estimated that more than 90% of amines (669) and Ca^{2+} (552) are tightly bound to the matrix, thus forming a bicompartmental store, which will become important to determine the kinetics of exocytosis (558) and the participation of CGs in cellular Ca^{2+} dynamics (93). It should be noted that although CGs constitute approximately 20% of CC volume and contain Ca^{2+} at 40 mM, they do not appear to be a functionally important part of Ca^{2+}dynamics/regulation as are the ER, mitochondria, and plasma membrane (683) (Figure 9).

The complex process of secretion

As CCs are cellular machines evolutionarily optimized for secretion, they contain all the elements necessary to readily release solutes to the bloodstream. Each CC possesses around 12,000 CGs (671). The total amount of CAs present in both adrenal glands, if released instantly, would be a lethal dose for the organism. To prevent CA poisoning, CCs have multiple mechanisms to regulate secretion. An important initial limiting factor is that only a small fraction of CGs are available (the "readily releasable pool") for immediate release, with 70% to 80% of granules requiring further priming before they are available for secretion.

CG release occurs by regulated exocytosis, a Ca^{2+}-dependent process that entails the fusion of a CG with the plasma membrane. Roughly, exocytosis starts with the approach of a CG to the membrane, docking it and the formation of a fusion pore, and the expansion of the fusion pore allowing the release of CG products (cargo), followed by CG membrane recapture from the plasma membrane by a process called endocytosis. Exocytosis is common to most secretory cells, including neurons, and most of the molecular steps leading to vesicle exocytosis are shared by neurons and CCs. This has been one of the historical reasons for the use of CCs to unveil the mechanisms underlying secretion (470). Probably, the first evidence indicating that the secretion of neurotransmitters occurs by exocytosis was the finding of intravesicular proteins in the extracellular media after the stimulation of adrenal medulla. No other mechanism could easily explain how CgA (a soluble protein of ~70 kDa discovered in CGs) could cross the plasma membrane together with CAs (62). Once the mandatory role of Ca^{2+} for secretion was established (176, 360), the main question was to determine how Ca^{2+} entry could trigger a very energy-unfavorable reaction like the fusion of two membranes. The elucidation, mainly in CCs, of the main steps of protein-protein, lipid, and lipid-protein interactions involved in triggering and regulating exocytosis has taken more than 40 years of extensive research.

The sites of exocytosis, either in CCs and in synapses, are not widely distributed along the plasmalemma but restricted to specialized areas, active zone-like release sites. These regions, characterized by cytoskeletal elements arranged to direct SGs toward docking and fusion sites, are specifically enriched in lipids like cholesterol and PIP_2 (306, 363, 662), contain the acceptor proteins for fusion, and are relatively close to Ca_V channels, hence the fusion machinery is in close proximity to the Ca^{2+} source. Contrary to active zones in neurons, where the probability of exocytosis is high, the role or even the presence of the piccolo/bassoon anchoring proteins has not been described in CCs so far. Consequently, the transport of CGs to active zone-like release sites likely performed sequentially by tubulin and actin. F-actin was initially considered to fulfill a role as a cortical barrier that prevents the access of granules to the plasmalemma (39, 125, 642). This concept has evolved, and the cytoskeleton is currently considered a dynamic element, where a close interaction of actin filaments

with granules occurs (326, 369, 486, 592). Myosins II, V, and VI also seem essential for the delivery of granules from the Golgi to the periphery of the cell (545, 618, 641). Figure 10A illustrates our current view of the SG cycle in CCs. The F-actin cytoskeleton and myosin II could also be important for providing the "extrusion, squeezing" force needed for the fast release of neurotransmitters through the open fusion pore (466, 666).

The secretory machinery

The discovery that exocytosis can be selectively blocked by proteolytic neurotoxins like tetanus and botulinum toxins (359) indicated the existence of specific exocytotic proteins, as these toxins do not affect endocytosis (465). In addition, the discovery of the *N*-ethylmaleimide-sensitive factor (NSF) and the protein complexes involved in its action (the soluble NSF-attachment receptor complex or SNARE) (594, 595) started a stimulating scientific race to elucidate the molecular steps of regulated exocytosis. Although not all of the exocytotic steps have been defined, there is a general consensus about the main actors and steps involved in the process, which are summarized in Figure 10B (685). The so-called SNARE complex is formed by the interaction of one specific protein in the membrane of the granule (synaptobrevin or VAMP)

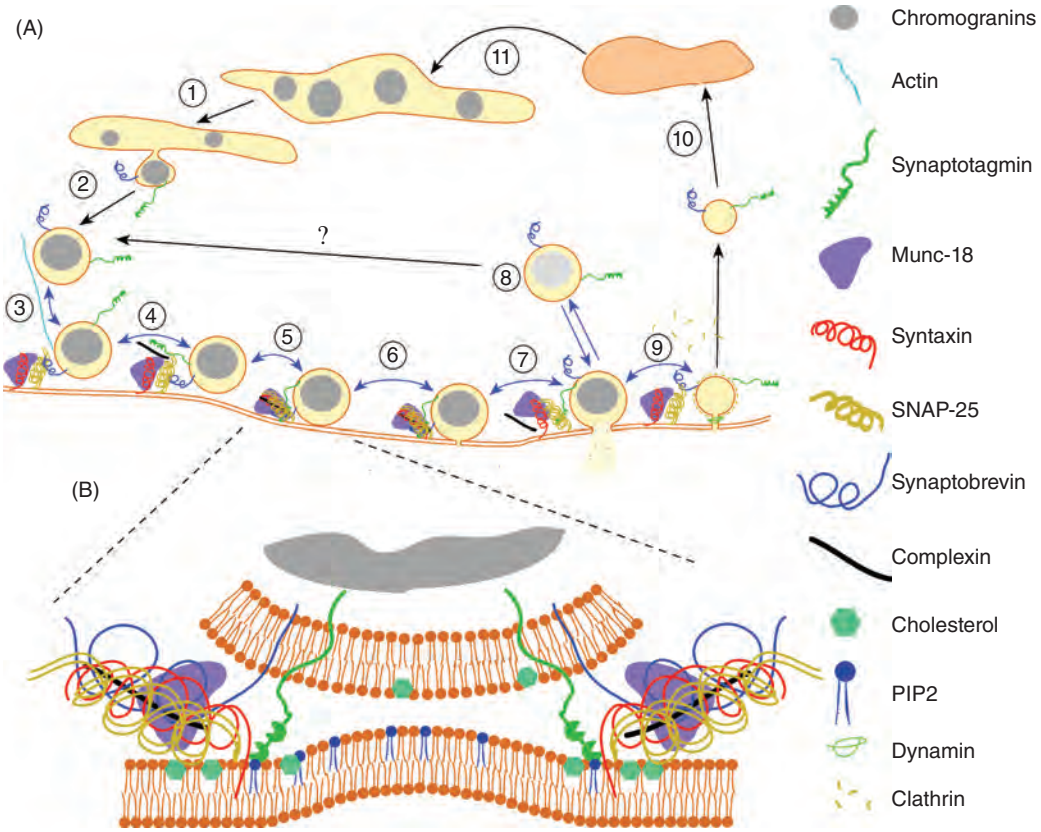

Figure 10 Exocytosis and endocytosis of CGs. (A) For clarity, only one SNARE complex is shown, while some of the accessory proteins are omitted: (1) granule proteins are sorted and packaged into the Golgi apparatus; (2) granules are transported to the release sites by tubulin (not shown); (3) actin filaments drive granules to specific tethering points; (4) "granule docking," the SNARE complex starts to organize and the granule docks to the plasmalemma; (5) priming, mediated by Munc-18 and complexin, thus allowing a tighter interaction of SNARE complexes. Munc13 acts on syntaxin changing its conformation, thereby leading to SNARE proteins zippering and the formation of fusion pore; (6) the initial fusion pore allows a limited exchange of water and solutes; (7) fusion pore dilatation allowing the partial or complete release of the granule content; depending on the extent of dilatation and duration of the Ω state, more or fewer solutes will be released. The SNARE complex is disassembled; (8) cavicapture. This partial exocytosis occurs when a dilated, but reversible, fusion pore allows the partial release of small molecules like peptides. Whether these granules can go to the SRP or get exocytosed again is unknown; (9) membrane recovery by endocytosis. Two major mechanisms might be involved: depending on clathrin and dynamin 2 or clathrin-independent that uses dynamin 1 to promote granule fission. The inner content of the granule rapidly acidifies; (10) clathrin is disassembled and the granule can travel deeper inside the cell toward either endosomes or lysosomes from where they can reenter in the secretory cycle after sorting in the Golgi (11). Note that sizes of the resulted endocytotic granules are now smaller, and granule matrices are clearer as a result of protein loss during exocytosis. Note also that some of the steps are reversible (blue double head arrows). (B) Organization of the SNARE complex in the priming state. The presence of cholesterol and lysophospholipids allows the curvature of the cell membrane. Note the lateral disposition of coiled-coil of proteins and the proposed situation of Munc-18 and complexin.

and two proteins at the plasma membrane (syntaxin and SNAP-25) (see Ref. 163 for a recent review). The exocytosis of CGs is much slower than that of synaptic vesicles, probably because despite using similar Ca^{2+}-triggering mechanisms and exocytosis machinery, they differ in the degree of preparation (docking) for fusion and in the composition of their vesicular matrix. Only six proteins, syntaxin, synaptobrevin, SNAP-25, Munc18-1, synaptotagmin, and complexin, form the core of the exocytosis machinery. Once the energetic barrier opposing membrane fusion is overcome, the interior of the granule is connected to the external media, thus starting the release of its contents.

The following are the currently most accepted steps involved in exocytosis (Figure 10B). The remodeling of the actin cytoskeleton allows SGs to get in contact with the plasma membrane (docking). At this stage, SNARE proteins are not yet fully associated. Ca^{2+} and the interaction of Munc13 and CAPS are crucial mechanisms involved in the priming process (423). Then, complexin binds to the SNARE complex, hence leaving it ready for Ca^{2+} action (super priming). Ca^{2+} will subsequently bring synaptotagmin to bind syntaxin, thereby promoting fusion pore opening (partial fusion). If Ca^{2+} concentration is sufficiently large or maintained long enough, the process evolves to "full fusion." Probably, there are intermediate steps between partial and full fusion. CCs possess two types of synaptotagmin (1 and 7), which have been implicated in the fast and slow components of the secretory response, respectively (528, 557). Ca^{2+} binds synaptotagmin at two binding sites (C1 and C2) to trigger granule fusion.

Pools of secretory granules

Since the first rudimentary recording of the time course of CA release (Figure 11A), it became clear that adrenal response decreased progressively regardless of stimulus persistence. This signaling "fatigue" is probably a physiological mechanism of defense to avoid the deleterious effect of oversecretion of CAs into the bloodstream, as occurs in some forms of adrenal pheochromocytoma (see below). This phenomenon is partially dependent on desensitization of nAChRs as well as Na_V and Ca_V channels (45). However, the "fatigue of secretory response" was also observed in the so-called leaky cell using either electroporation (43) or detergents like digitonin (184), indicating that the secretory machinery cannot maintain secretion for long periods of time, especially during strong stimuli (Figure 11B).

With the arrival of electrophysiological techniques, especially whole-cell capacitance, the phenomenon of "fatigue" was localized to the existence of distinct pools of granules (Figure 11C) with different probabilities of fusion (277, 387, 472). The nomenclature used to classify the differences in the release rate of CG populations varies from one research group to another, with sometimes confusing results. Hence, the granules that were ready to enter exocytosis in the first seconds after depolarization, as they are close to the "open mouths of Ca^{2+} channels" were considered to be in the immediately releasable pool (IRP). This pool would comprise only about 17 granules per cell in mouse CCs (582), although its exact size is difficult to determine as most studies were carried out in cultured cells whose channel distribution is significantly affected by denervation and adhesion to the cell culture surface.

Large Ca^{2+} entry, or sudden elevation of Ca^{2+} experimentally caused by uncaging of trapped Ca^{2+} using light pulses, will promote the release of about 200 granules from a CC within 20 to 40 ms when intracellular Ca^{2+} levels are around 20 μM (644). This is the rapidly releasable pool (RRP), which is observed by whole-cell capacitance as a rapid increase in cell surface resulting from the addition of granular membranes to the plasmalemma (Figure 11C). The analysis of the kinetics of release observed either by whole-cell capacitance or by integrating amperometric recordings shows that the rapid secretion from the RRP is followed by a slow phase of release from an RP or slowly releasable pool (SRP) with a time constant of ≈200 ms (644).

Finally, it should be noted that most CGs are either nonreleasable or are exocytosed only very slowly. The physiological role of this unreleasable pool has received little attention from scientists. Historically, it was considered as formed by immature granules that progressively move toward the releasable pools. However, novel experimental approaches have concluded that young granules will "jump the queue" and be the first released. This was shown using either total internal reflection fluorescent microscopy (TIRFM) with fluorescent dyes that changed color with age (180) or by analyzing the secretion of EGFP from CCs expressing EGFP-tagged neuropeptide Y (214) (Figure 11D). The classical theory uses a geographical distribution of granules to explain the kinetics of release, assigning to the RRP those granules situated near the membrane and to the RP those that are behind the actin barrier. TIRFM analysis suggests that only a small fraction of the granules that are already within the evanescent plane (<200 nm from membrane) do not get exocytosed and remain immobile for minutes regardless of the presence of stimuli. The unreleasable pool in CCs is about 70% to 80% of the whole population (≈10,000 granules per cell), and its physiological role is still unknown. Furthermore, it is the RRP that requires repletion, after its reduction by stimulation. Theoretically, refilling the RRP could be accomplished by (i) refilling of granules only partially exocytosed (kiss-and-run or cavicapture), (ii) formation of new granules after a short travel through endosomes, or (iii) the arrival of new granules to the cortical domain of the CCs. The precise contribution of each alternative is still under debate.

The exact contribution of the different pools to secretion is difficult to establish because of the Ca^{2+} dependence of both exocytosis and granule motion processes. However, the latter requires lower intracellular Ca^{2+} levels (≈1 μM) compared with the higher concentration required for exocytosis (>2 μM). These features have been used to determine the

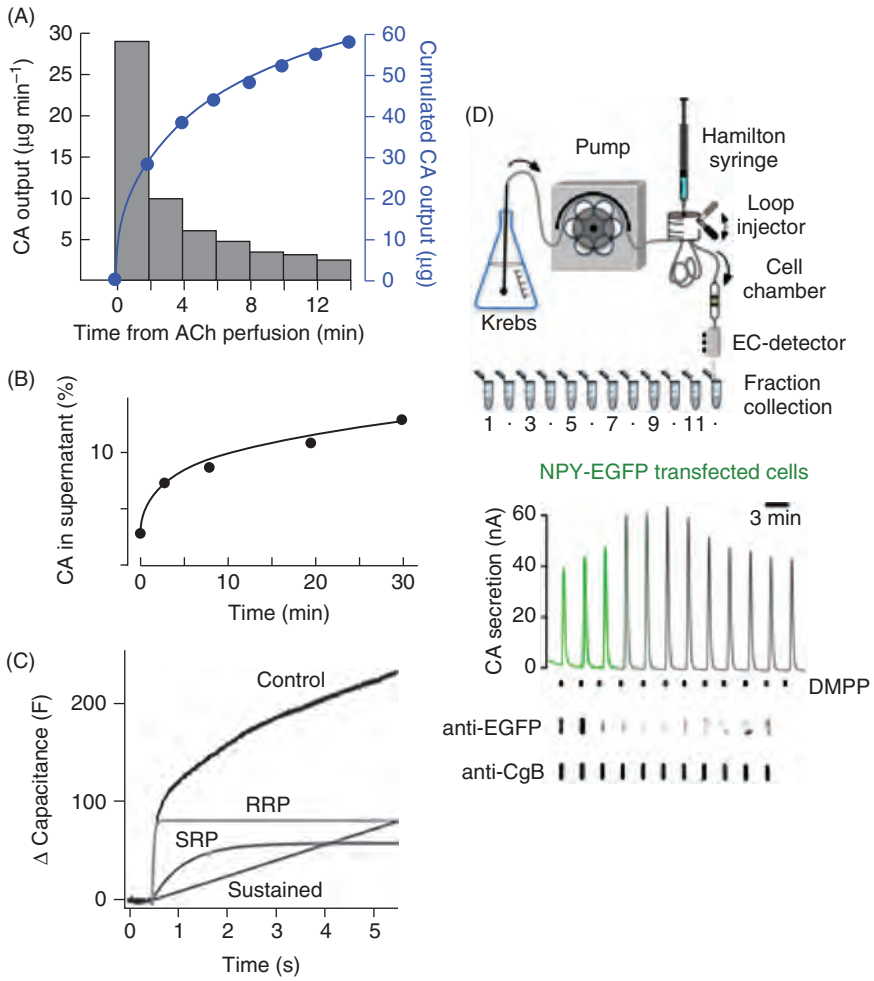

Figure 11 Different pools of granules are involved in the secretory responses. (A) Even in the continuous presence of Ach, the secretion of CA from perfused cat adrenals progressively decays (gray bars). Cumulative CA secretion is superimposed (blue trace). Modified, with permission, from Douglas WW, and Rubin RP, 1961 (176). (B) Although the time courses are different, a similar situation occurs when secretion is elicited by rising intracellular Ca^{2+} in permeabilized CCs (leaky cell). Modified, with permission, from Baker PF, and Knight DE, 1981 (44). (C) Recordings of whole-cell capacitance from mouse CCs evidence the presence of at least two exocytotic kinetics: rapid (RRP) and slow (SRP). Authors tested the effect of rising intracellular Ca^{2+} by flash photolysis of NP-EGTA (taken from Figure 2A in Ref. 591). Notice the different time course compared with panels A and B. (D) Newly produced granules are the first to be released. Perfused CCs are stimulated with a nicotinic agonist and CA secretion continuously recording by an electrochemical detector. The analysis of the perfusate shows that EGFP (labeling neuropeptide Y) is released only during the first pulses. Modified, with permission, from Estevez-Herrera J, et al., 2016 (214).

size and contribution to the secretion of RRP and SRP, that is by low versus high levels of intracellular Ca^{2+} released dose-dependently by controlled flash photolysis of Ca^{2+}-caged compounds (168, 643). An important limitation of the capacitance measurements to indicate the extent of CG release is the difficulty in determining, and subtracting, the contribution of endocytosis to the recordings. Capacitance change recordings might overestimate secretion as it also detects the fusion of granules that are devoid of CAs, a phenomenon observed when capacitance and amperometry measurements of exocytosis are compared (599).

Measuring exocytosis

Exocytosis from CCs has been measured by several methods including the chemical analysis of secreted products. However, the latter occurs too slowly for assessing a phenomenon that occurs in tens of milliseconds. For this reason, only modern live imaging, electrophysiological or electrochemical techniques, and the combination of them get a reliable time resolution. TIRFM uses the evanescent wave principle, by which excitation is restricted to ~150 nm beneath the cell surface situated in direct contact with the bottom coverslip. This noninvasive technique also allows examining the movement

of a granule prior to exocytosis and also membrane recapture. However, it requires the use of fluorescent dyes (170).

Cell capacitance change (ΔC) measurements with the patch-clamp are based on the notion that the cell membrane is a capacitor and its capacitance increases when the granule membrane fuses with the plasmalemma (or decreases when a portion of the membrane is retrieved during endocytosis). Modern equipment incorporates lock-in amplifiers to resolve exocytosis occurring at the whole-cell level. This is an invasive technique that permits control of the intracellular media but in general, is unable to resolve single-granule fusion events and is also blind to all phenomena occurring prior to fusion. The advantage of ΔC measurements is the monitoring of the whole-cell secretion and not just that restricted to the area covered by an amperometric electrode or the attached surface of a glass cover slide as in TIRFM measurements. The capacitance changes observed from a whole cell are the sum of two phenomena (exocytosis and endocytosis) that usually overlap. The RRP can be measured by applying strong stimuli to promote the fusion of the entire pool, whereas the refilling of this pool could be measured by the slower kinetics that follows the initial rise in capacitance (Figure 11C). One variation of the technique uses the cell-attached patch-clamp configuration to resolve single exocytotic events, allowing the study of the initial stages of fusion pore formation. These observations, however, are restricted to the patched area (386).

Electrochemical methods comprise amperometry and cyclic voltammetry. They detect the CAs released with a precise time resolution but do not detect other secreted species like ATP or peptides. This technique is noninvasive (the cell integrity is preserved), but it does not provide information about what happens to granules prior to exocytosis nor after their recapture (endocytosis). Voltammetry has less time resolution but allows the quantification of the released CAs. Single-cell electrochemistry also allows the analyses of the kinetics of exocytosis, including the pre-spike phenomenon—the so-called foot—that is associated with the escape of CAs through the fusion pore. However, some of the published data should be taken with caution unless proper calibration and correction for artifacts (e.g. use of the same calibrated electrode throughout the experiment, reduction of bias caused by changes in electrode responsiveness, and appropriate statistical analyses) are employed (69, 412). The kinetics of the exocytotic fusion pore can be resolved with high-resolution amperometric techniques (668). Thus, with a carbon-fiber microelectrode placed on the surface of a CC, several modes of exocytosis can be distinguished: (i) CA release occurs through a transient fusion pore that opens and closes without giving rise to full fusion and pore expansion, the so-called kiss-and-run; (ii) formation of a more stable fusion pore that, however, does not give rise to full fusion, the so-called kiss-and-stay exocytosis; (iii) formation of a fusion pore with subsequent expansion to release all vesicle content, followed by the collapse of the vesicle membrane and its integration in the plasmalemma, referred to as "full fusion" (630). Another interesting feature of the individual amperometric spikes is that many of them are preceded by a small "foot" (fusion pore formation) before the abrupt upstroke occurs (pore expansion and full fusion, see below) (130).

Finally, amperometry and cell-attached capacitance measurements have been successfully combined for simultaneous measurements (9). This technique, called patch amperometry, allows the direct characterization of fusion pore and the direct measurement of granule content of CAs (254, 454). The main disadvantage of this procedure is its technical difficulty.

Partial versus full exocytosis

Classically, exocytosis has been considered as an all-or-none process. The concept of partial exocytosis, that is when only one part of the granule content is released upon fusion, was first suggested by Bruno Ceccarelli in frog neuromuscular junction (119). This phenomenon, however, received real attention only after it was observed in mast cells and CCs (9, 18) and has finally gained acceptance as a technology for measuring secretion evolved. The stable and reversible formation of a fusion pore allows the release of cargo species through its limited diameter and lasting duration (170). There is not a general consensus about the definition of the fusion pore: the concept ranges from a channel-like structure (with a diameter of 1–2 nm), measurable by capacitance, to a wider Ω-shaped vesicle as observed by electron microscopy (of about 20–30 nm in size). The former probably is governed by a mixture of lipids and proteins, whereas the expanded pore seems to be composed only of lipids (574). Nevertheless, it is now accepted that most of the exocytotic events are partial, and the granule usually retains a significant fraction of its content after fusion. This comprises both low molecular weight species such as CAs and high molecular weight proteins such as chromogranins and their fragments.

The comparison of the quantum size measured in the same cell cultures by amperometry and patch amperometry (455) or by "electrochemical cytometry" (181) indicates that only about 30% of CAs are released in most of the exocytotic events. In addition, the monitoring of fluorescent-labeled CgA (chromogranin coupled with EGFP) by TIRFM shows that most granules retain some fluorescence after fusion (170). An emerging novel concept about the regulation of secretion of CAs comes from the amount released during partial exocytosis (491). It seems that strong stimuli tend to favor full release, whereas mild stimulation triggers partial release. The main regulators of this process seem to be the intracellular Ca^{2+} concentration (199) and cAMP (413). The nature and physiology of the fusion pore have been recently reviewed (19).

Endocytosis

The increase of membrane resulting from secretion or constitutive exocytosis has to be compensated by membrane retrieval. This fission process is called endocytosis, and it is necessary not only to maintain constant the membrane surface

but also for renewal of proteins and lipids from the membrane. This latter type of endocytosis, named "constitutive," is common to all cells and it is not dependent on Ca^{2+}. Constitutive endocytosis is used to retrieve receptors, carriers, and channels, and it is essential for downregulation processes common to transporter activity, receptor desensitization, and, more generally, cellular responsivity (285, 649). This is a slow process, and does not necessarily occur at the site of exocytosis even for proteins involved in the exocytotic process itself.

Triggered endocytosis occurs in CCs rapidly after exocytosis (Figure 10). Plasma membrane internalization does not occur randomly to maintain the total surface stable. Rather, despite full fusion, exocytosed granules and plasmalemma maintain their specific protein and lipid composition. This exo-endocytosis coupling was first observed by morphological studies showing that granule membrane-bound components are retrieved after exocytosis (507). Also, a large increase of *coated pit* structures containing granule components immediately after stimulation of CCs was observed by electron microscopy (245). The endocytosis process seems to occur at the same lipid-raft structures where exocytosis took place. These areas are enriched in both cholesterol and phospholipids like PIP_2 (322). Taken together, these data indicate that exocytosis and endocytosis are tightly coupled phenomena intended not only to maintain the cell surface constant but also to recapture most of the granule membrane components and part of the granule matrix.

In CCs, two endocytic pathways exist: a rapid endocytosis, which takes place in tens of milliseconds to a few seconds, and it is probably associated with cavicapture and kiss-and-run secretory modes (605), and a slow clathrin-mediated exocytosis (200). Rapid endocytosis does not require clathrin and seems to involve GTP, Ca^{2+} (85, 541), and dynamin-1 (34). The clathrin-mediated endocytosis is the best-studied and involves clathrin and dynamin-2, but not Ca^{2+}; this slow endocytosis occurs in tenths of seconds and can last for minutes (200). Dynamins are envisaged to function in constricting the fusion pore and promoting the formation of an endocytic vesicle capable of traveling toward the cell interior. It is, therefore, possible that these proteins can also regulate the amount of cargo released during each exocytotic event. Data derived from dynamin manipulation in CCs are still contradictory (128, 233). Even the expression of dynamin-1 in CCs has been questioned (255). Likewise, the functional role of amphiphysin, another protein involved in fusion pore constriction in other tissues, has not been conclusively established in CCs.

Endocytosis often results in retrieving more membrane than that previously incorporated during exocytosis. This excess retrieval is faster than rapid endocytosis and seems to be triggered by different mechanisms (207, 579) unlinked to exocytosis and at a rate that could internalize approximately 10% of the total cell surface within a few seconds (49). Excess retrieval is frequently accompanied by the formation of large nonreleasable endosomes (611). This formation of large endosomes during excess retrieval is called "bulk" endocytosis (111, 533) (for clarity, this is not shown in Figure 10).

Clathrin-dependent membrane retrieval produces vesicles of 50 to 100 nm, notably smaller than CGs (180–250 nm). The discrepancy in size suggests that the membrane from CGs can be recaptured as small pieces rather than as a whole (311). Both recycling from partial exocytosis and a degradation pathway from full granule collapse coexist, and their fraction may depend on secretory activity, as mentioned above. Vesicles resulting from the endocytotic clathrin-mediated pathway might go to early endosomes to produce new granules or fuse with lysosomes for degradation. The degree of contribution of both pathways and their regulation is not known. Since retrieved vesicles are composed of pieces from CGs and not as a whole, the early endosomes could be a transient organelle where endocytic vesicles are repackaged to reconstitute functional granules before going to the retrograde transport pathway to the trans-Golgi network (311). Using specific antibodies against membrane-bound granule proteins, it was shown that they were taken up through clathrin-mediated vesicles and internalized toward lysosomes (56). These proteins were then found in the trans-Golgi, and a few hours later were localized in newly formed granules (507, 649) (Figure 10A).

From *kiss-and-run* to full granule collapse, there are different degrees of exocytotic modes. The same can be said for endocytosis where several mechanisms for membrane retrieval coexist. Capacitance changes and patch-amperometry studies conclude that the fusion pore can open and close (or "flicker"); this suggests that this transient structure can be reversible at least up to certain pore size. Therefore, kiss-and-run retains membrane and most of the matrix proteins of CGs. The limit for reversibility for CGs is around 3.4 nm, as larger sizes convert fusion to an irreversible process (9, 15). However, observations using TIRFM (512) and fluid-phase capture (650) suggest that even larger pores are reversible. Many CGs reseal in a few seconds after exocytosis. These granules are rapidly acidified (606) and might be partially or completely empty of CAs and other soluble components (599). The physiological contribution and importance of the cell mechanisms operating, for the various modes of exocytosis/endocytosis, opens exciting research prospects for the coming years.

The Sympathoadrenal Medulla Axis in Stress Responding: Roles of PACAP, Other Transmitters and Peptides, and Organ Remodeling

PACAP as a stress transmitter at the splanchnicoadrenomedullary synapse

The ability to generate an AP via nAChR-dependent Na^+ channel activation on CCs explains how ACh acts as a secretagogue for EPI release from the adrenal medulla (see the

preceding sections). In the late 1970s, however, the possibility of adrenomedullary CA secretion by first messengers other than ACh began to emerge. The Wakade laboratory in particular, explored the long-term changes in CC content driven by high stimulation rates thought to be typical of the frequency of firing of the splanchnic nerve during stress. It was discovered that the adrenal medulla releases an amount of CAs equivalent to its entire initial content during a bout of secretion lasting several hours. Yet even after such prolonged secretion, CCs remain able to continue CA secretion, due to constant CA repletion via biosynthesis during the secretory episode (see (576, 659) for similar observations in the calf adrenal gland). How the adrenal gland resynthesizes its entire store of accumulated EPI, as well as its complement of releasable proteins and peptides, following prolonged and even acute but intense secretion, has been a subject of considerable investigation, subsumed under the rubric of "stimulus-secretion-synthesis coupling" (3, 190). One mechanism for enhanced repletion of CAs linked to increased depletion by secretion was discovered in the 1970s by Costa and Chuang. They learned that exposure to cold, which is associated with massive sympathoadrenal activation, causes an increase in the total capacity to convert tyrosine to L-Dopa within the adrenal medulla (126), due to induction of tyrosine hydroxylase (TH), the rate-limiting step in CA biosynthesis (131). Since nicotinic cholinergic stimulation has a limited ability to induce TH as well as peptide synthesis in the gland, it was concluded that this "stimulus-secretion-synthesis coupling" might be afforded by activation of mAChRs on CCs following enhanced splanchnic nerve stimulation during episodes of stress (217). It was noted subsequently, however, that reflex stimulation of the splanchnic nerve *in vivo*, by pharmacological treatment with reserpine, caused an induction of TH that could not be reversed by blockade of either nicotinic or muscarinic receptors, and these authors concluded that either a novel type of cholinergic receptor was expressed on CCs, or that a noncholinergic substance might be released along with ACh from the splanchnic nerve, to allow TH induction under conditions of stress (610). Similarly, stimulation of the sympathetic trunk at high frequency also causes TH induction in the postganglionic sympathetic neurons of the superior cervical ganglion, and this also occurs by a mechanism only partially accounted for by action of ACh released from preganglionic terminals (318).

The discovery of the neuropeptide PACAP (447) by Miyata, Arimuraa, and colleagues in 1989 finally offered a clue to the identity of this additional sympathetic neurotransmitter. PACAP, as its name implies, was initially discovered as a hypothalamic peptide able to stimulate cAMP production in cells of the anterior pituitary. However, it was subsequently learned that the physiological role of PACAP extends far beyond its role as a hypothalamic releasing factor, to that of neurotransmitter in both brain and autonomic nervous system (26). In particular, and consistent with a potential role as a splanchnicoadrenomedullary transmitter along with ACh, PACAP potently stimulates EPI secretion from the adrenal gland *in vivo*, from the perfused adrenal gland, and from CCs in primary culture (155, 265, 270, 302, 600, 663; and references therein).

The localization of PACAP to the splanchnic nerve innervating the adrenal medulla required the creation of mice genetically deficient in PACAP expression. This in turn allowed the certification of antibodies to PACAP that could be shown clearly to detect PACAP specifically, especially compared to the very closely related neuropeptide VIP, in the cholinergic nerve terminals of the splanchnic nerve (269). The role of PACAP in stress-induced CA release and biosynthesis in the adrenal medulla was further examined with the aid of PACAP-deficient mice. Injection of insulin lowers blood glucose levels and stimulates maximal reflex firing of the splanchnic nerve, causing greatly elevated blood EPI levels and enhanced TH activity in the adrenal gland: these effects were blunted or abolished in PACAP-deficient mice. PACAP-deficient mice could be rescued from death after prolonged hypoglycemia by treatment with either PACAP or glucose (269). In adrenal slices taken from the mouse, EPI secretion upon splanchnic nerve stimulation at high frequency (2 Hz), but not at low stimulation rates (0.2 Hz), is blocked by the PACAP antagonist $PACAP_{(6\text{-}38)}$ and is abrogated by PACAP deficiency (i.e. is absent in slices from PACAP-deficient mice) (368, 593).

In summary, PACAP is colocalized with ACh (i.e. the cholinergic vesicular marker VAChT) at nerve terminals of the splanchnic nerve that innervate CCs in the mouse. Stress-induced CA secretion and TH regulation require the expression of PACAP. Experiments with adrenal slices *ex vivo* show that this PACAP dependence occurs at the level of the splanchnic nerve itself, and is probably due directly to the release of PACAP there, since the morphology and chemical neuroanatomy of the splanchnicoadrenomedullary synapse in PACAP-deficient mice are otherwise normal. These experiments suggest that PACAP released at the adrenomedullary synapse mediates CA secretion from the adrenal medulla during stress (see Figure 12) (189, 580). Residual CA release provoked by prolonged hypoglycemia even in the PACAP-deficient mouse suggests that ACh also contributes to stress-induced CC CA secretion *in vivo* (269), consistent with the many previous reports of high-frequency CA secretion from the adrenal glands of various mammalian blocked by nicotinic and muscarinic antagonists (342, 356, 364, 374, 623, 658, 684). Of relevance to this issue are the observations of Arun Wakade's lab on isolated perfused adrenal glands from rats (657). The group reports that prolonged high-frequency splanchnic nerve stimulations (10 Hz for >3 h) produce the massive release of CA that is almost completely abolished (>80%) by cholinergic receptor antagonists, while sustained low-frequency stimulations (1 Hz for >6 h) are effectively controlled (>60%) by noncholinergic receptors activation (PACAP and VIP) (422, 656).

It is evident from the above arguments that the relative contributions of ACh and PACAP at the splanchnicoadrenomedullary synapse during high levels of splanchnic

INFORME DE LABORES 2019

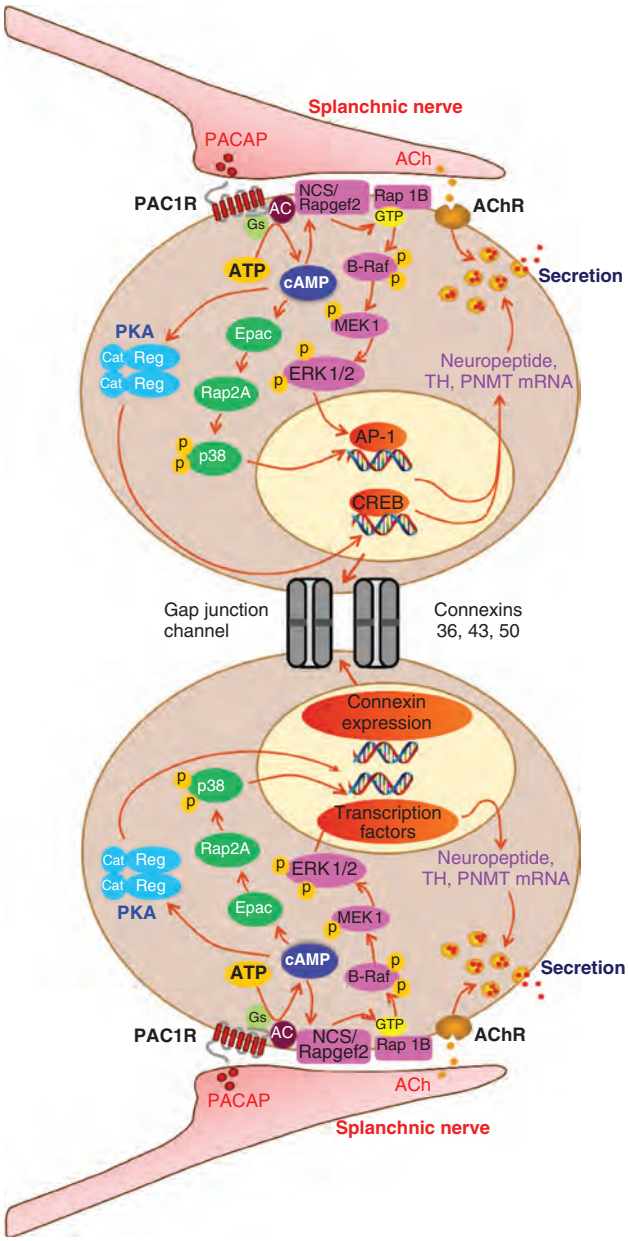

Figure 12 Intracellular signaling pathways and physiology of the chromaffin cell. Acetylcholine and PACAP (sympathetic preganglionic) release from splanchnic nerve activates the nicotinic (AChR) and PACAPergic (PAC1R) receptors, triggering catecholamine and neuropeptide secretion from CG, and increased transcription of genes encoding biosynthetic enzymes for catecholamines (TH, PNMA), and prohormones from which processing to mature neuropeptides occurs, and stimulus-secretion-synthesis coupling in the chromaffin cell. PAC1R activation promotes Gs coupling to adenylate cyclase (AC), the elevation of cyclic AMP (cAMP), and the activation of three separate cAMP effectors. Protein kinase A (PKA) mediates CREB-dependent gene transcription; Epac mediates Rap-dependent activation of the MAP kinase p38, leading to activation of transcription factors including AP1; NCS-Rapgef2 mediates Rap-dependent activation of the mixed-function kinase B-Raf, allowing MEK upregulation of the MAP kinase ERK (extracellularly regulated kinase) and gene activation through a combination of transcription factors. Stimulus-secretion-synthesis coupling also involves on the intercellular level increased expression of connexins that form gap junctions, which help to amplify chromaffin cell secretion from the adrenal gland as a whole. There is as yet no direct proof for PACAP or acetylcholine as the principal mediator of what might be termed the "gap-junction response." IFN, TNF, IL-1, and IL-6 effects on cognate receptors on chromaffin cells and cellular sequelae in the chromaffin cell are not shown, but synergize with PACAP stimulation to modulate both catecholamine and peptide secretion and chromaffin cell gene transcription. Splanchnic nerve input affords synergistic as well as antagonistic interactions between cytokines and PACAP under physiological conditions in which both stress and inflammation may play a role. Finally, secretory products of the chromaffin cell itself, including substance P, other neuropeptides, and chromogranin-derived peptides such as catestatin, modulate chromaffin cell secretion via paracrine actions, in part through modulation of AChR function. See text, and references in text, for further details.

nerve stimulation that occurs during stress may vary significantly across mammalian species. Like ACh, PACAP stimulates secretion of CAs from the adrenal *in vivo* or from CCs in primary culture, in mice, rats, cows, dogs, humans, and other mammals (reviewed in Ref. 270). In terms of PACAP action at other sympathetic ganglia/synapses, there are well-documented PACAP actions at sympathetic postganglionic neurons, at least in culture, that include secretion and changes in gene expression, suggestive of a role for PACAP in stimulus-secretion-synthesis coupling at sympathetic as well as sympathoadrenal synapses (53, 440). Postganglionic parasympathetic neurons of intrinsic ganglia of the heart are also PACAP-responsive (620). These findings support the concept that PACAP acts as an effective neurotransmitter, along with ACh and NE, in the autonomic nervous system. It is also evident that understanding the details of the specific roles of this stress-inducing neurotransmitter in supporting ACh-driven secretion and gene expression in the adrenal medulla deserves further investigation.

Implications of PACAP transmission for GPCR-mediated stimulus-secretion-synthesis coupling in the CC during stress

Endocrine cells, in general, the must maintain their stores of secretable material, even during intense episodes of stimulation and secretion, to preserve their efficacy for future homeostatic responding. Secretion and synthesis need not be coupled processes if they occur at about the same rate constitutively. This is rarely the case, however, as hormone secretion is commonly episodic, occurring in response to varying homeostatic demands. Repletion of hormone content lost by secretion from endocrine cells could occur by several mechanisms, but two mechanisms seem to dominate for the CCs of the adrenal medulla. The first is a chronic overproduction of prohormone protein relative to the storage capacity. In this case, the excess hormone is degraded at times of low secretory activity, and diverted to the secretory pathway at times of high secretory activity and demand. CgA, the major protein constituent of the CG, appears to be regulated in this way. Since CgA is a component in the process of SG biogenesis itself, the CC can package no more CgA than there are available vesicular membranes to contain it. At rest, and when the CG complement is maximal, excess chromogranin is apparently degraded in the trans-Golgi network, and when the CG complement is depleted by an episode of secretion, this excess is redirected toward granule production. This mechanism allows CgA levels (and CGs) to be maintained at a sufficient level across even prolonged episodes of secretion without the need for compensatory increases in chromogranin mRNA abundance and protein synthesis (191, 227). For (pro)hormones that represent a smaller fraction of total SG protein content, and are therefore not "rate-limiting" for CG biosynthesis, and also for CAs, however, a regulatory mechanism must exist to compensate hormone lost from the cell by secretion, via enhanced hormone biosynthesis.

The hypothesis of stimulus-secretion-synthesis coupling arose during the search for this second mechanism of the hormone loss and repletion cycle, which centered on whether or not secretagogues, while stimulating the release of stored hormones, signal at the same time to the nucleus to activate transcription of the specific genes responsible for hormone biosynthesis (190). For bioactive peptides produced by prohormone processing within the CG, this is accomplished by an increased rate of transcription of the prohormone gene and subsequent increase in translation of its mRNA into the prohormone, which is then processed into mature peptide(s). In the adrenal medulla, the "secretory cocktail" is a mixture of protein (chromogranins and processed neuropeptides) and small molecules (CAs, ATP, and GABA), and stimulus-secretion synthesis coupling must occur for both categories of secreted material. Thus, binding of secretagogues to their receptors stimulates Ca^{2+} influx, activation of CG exocytosis, and release of CG contents. Simultaneously, secretagogue signaling stimulates transcription of prohormone protein-encoding genes as well as biosynthetic enzymes responsible for CA and another small-molecule biosynthesis. In the case of CA production, this means activation of TH through phosphorylation at key serine/threonine residues, and increased production of the TH protein itself, through enhanced transcription of the TH gene (276).

The cellular mechanisms for stimulus-secretion-synthesis coupling in the adrenal medulla have been well investigated throughout the 20th century and have functioned as a model for understanding this process in other types of endocrine cells (Figure 12). The second messenger most prominent in regulation of stimulus-synthesis coupling is Ca^{2+}, consistent with its role in stimulating secretion in most endocrine cells. In the adrenal medulla, cAMP was implicated early in both the transcriptional and posttranslational phases of TH activation. Study of stimulus-secretion-synthesis coupling related to co-stored peptides such as substance P, NPY, enkephalin, and galanin revealed that while cAMP appears to be the main second messenger for activation of gene transcription of the genes associated with these peptides, cAMP-dependent gene activation by the classical third messenger protein kinase A (PKA) was not always clearly identified as a regulated step in the process.

Kuo and Greengard (367) initially proposed that PKA was the sole effector for cAMP in mammalian cells. It was later discovered that cAMP gates Ca^{2+} channels on some mammalian cells (81), and that in addition, many non-PKA and non-Ca^{2+}-dependent cAMP-initiated signaling events exist in mammalian cells, especially neuroendocrine cells. In the 1990s, two proteins within the family of Rapgefs (rap-activating guanine-nucleotide-exchange factors) were identified as cAMP-regulated enzymes. These two proteins are most commonly called EPAC1 and EPAC2 (other names include Rapgef 3 and 4, or cAMP—GEF1 and 2 (72, 158, 341). The EPACs extended the range of cAMP effectors—from protein kinases to guanine-nucleotide-exchange factors—and also brought into the

stimulus-secretion-synthesis coupling pathway downstream signaling molecules activated preferentially by Rapgefs, such as the MAP kinase ERK (Figure 12) (202, 204, 205).

For example, galanin biosynthesis in the CC was found to be regulated by PACAP via a non-PKA-dependent cAMP signaling pathway acting through ERK (203). Experiments in cellula allowed the identification of a Rapgef cAMP effector molecule, Rapgef2, in this pathway, by both loss-of-function after gene ablation and gain-of-function after expression in nonendocrine cells (202). The Rapgef2 gene emits two classes of transcripts by alternative splicing, now called NN (for nonneuronal)- and NCS (for neuritogenic cAMP sensor)-Rapgef2. NCS-Rapgef2 is expressed mainly in neuronal and endocrine cell types/tissues in adult rodents and other mammals, and links cAMP elevation to ERK activation in CCs, in neurons, and in pancreatic beta cells (324). The initial discovery of NCS-Rapgef2 in the CC has led to the understanding that cAMP signaling in these and other endocrine cells and neurons is parcellated among at least three effectors, NCS-Rapgef2, EPAC, and PKA, that independently signal through distinct Rap isoforms (NCS-Rapgef2 and EPAC), and through CREB and other threonine/serine kinase acceptor proteins, to mediate distinct and separate cellular functions (204, 305, 324, 347, 403, 544).

A relevant emerging question is how PACAP receptor activation, since it does not involve the opening of sodium channels, engages the machinery for Ca^{2+} influx in the CC. A plethora of reports on this subject convey the general impression that Ca^{2+} channel opening via activation of the PAC1 receptor (PAC1R) is likely to involve initial cAMP-dependent phosphorylation of Ca^{2+} channels themselves, albeit the mechanisms ultimately responsible for secretion and regulation of gene expression for CA and secretory protein biosynthesis by PACAP in CCs will require additional investigation (*vide supra*).

The role of peptides secreted from the adrenal medulla

The discovery that bioactive neuropeptides, in particular opioid peptides are released along with CAs from the CCs of the adrenal medulla provided a source tissue for the isolation of the prohormones for the enkephalins, and later the mRNAs encoding them (135, 380, 381, 395). These developments were in turn made possible by the earlier identification of chromogranins as secreted proteins of the adrenal medulla (*vide infra*) and the discovery that enkephalin peptides are a major constituent of CGs (380, 395). Progress in understanding the generation of small opioid peptides from larger precursors led in turn to the realization that CgA is itself a prohormone, generating the bioactive peptides pancreastatin, vasostatin, catestatin, and others (188, 281, 313, 608). One of the proenkephalin-derived peptides found to exist in CGs BAM-22P was structurally identified through a systematic peptidomics analysis of the CG (448). Likewise, the novel bioactive peptide adrenomedullin was identified, in extracts of CC-derived human pheochromocytoma tissue, similar to PACAP extracted from the hypothalamus, via a proteomics-based search for novel cAMP-elevating neuropeptides (354). The finding of a highly variegated secretory cocktail, including CgA and enkephalin-derived peptides, as well as substance P, galanin, and NPY, also later shown to be prohormone derived, increased appreciation that the CC might participate in organismic endocrine regulation through these peptides as well as via the release of CAs. The ability to determine where, and how, these peptides exerted their physiological roles was initially made difficult by ignorance of the location of their receptors, which might suggest their autocrine, paracrine, or hormonal actions *in vivo* (281). Indeed, the molecular nature of the receptor for catestatin, one of the CgA-derived peptides of the adrenal medulla, is still uncertain. Catestatin, for example, inhibits ACh-induced CA secretion from CCs, but not that caused by potassium depolarization, by the Ca^{2+} "agonist" barium, or by ionophores that mobilize Ca^{2+}, suggesting that catestatin acts through a receptor that either is or acts immediately downstream of the nAChR of CCs (420). In PC12 cells, catestatin affects not only ACh-induced but also PACAP-induced CA secretion, suggesting that it may act to modulate both resting and stress-induced adrenomedullary secretion (549). Thus, catestatin may function as an autocrine regulator of CA secretion and biosynthesis, based on its negative modulation of nAChR activation in CCs, as has been suggested for substance P produced in CCs (84, 310, 396).

Catestatin has multiple effects on distant organs, suggesting a hormonal role, in addition to its autocrine functions within the adrenal medulla itself. It is noteworthy that, given the presence of several other bioactive peptides within the CgA primary sequence, administration of catestatin alone rescues the major aspects of the CgA-deficiency phenotype in CgA-knockout mice (416). Catestatin and other chromogranin-derived peptides affect virtually all stages of the secretory function of the CC (416), including CG biogenesis (353), and this function appears to be shared with other granin proteins in CCs (455). Modulation of CA release is a major function of catestatin that is increasingly well defined pharmacologically (622). Physiologically, catestatin not only modulates CA release, but, as a hormone in its own right, acts in synergy with CAs on cardiovascular function and metabolism, and regulation of other endocrine cells and immunocytes, and their metabolism and secretory morphology (348, 588). Other CgA-derived peptides with potent effects on heart and vasculature are reported, including vasostatin, and these potential hormones create multiple regulatory linkages among adrenomedullary secretion, metabolic function, and muscle performance, and therefore between stress transduction and cardiovascular and metabolic physiology (279).

Another adrenal medulla-derived neuropeptide worthy of consideration is adrenomedullin, which was discovered as a constituent of human pheochromocytoma (354). Adrenomedullin activates a GPCR linked to Gs, and its receptors are found throughout the cardiovascular system.

It has profound hypotensive properties and thus could be envisaged as a counter-regulator or modulator of CA actions. Unlike peptides present at only low levels in CCs, for which autocrine and paracrine are more likely than hormonal ones (*vide supra*), adrenomedullin, like catestatin, may function as a bona fide hormone, like the CAs, in mammalian physiology, as well as a paracrine/autocrine factor in the adrenal medulla itself (25) in addition to actions at sites of local synthesis outside of the adrenal medulla. The possible functional role of adrenomedullin in the regulation of the heart, vasculature, and kidney has been studied, and this peptide shows some promise for clinical utility (186).

The role of peptide hormones of the adrenal medulla, including CgA, CgA-derived peptides, opioid peptides, NPY, substance P, adrenomedullin, and others, has opened a new and important avenue of adrenal medulla physiology. These peptides and their receptors represent adaptive components of the endocrine network and their fine-tuning of homeostasis, throughout mammalian evolution, including the tissue-specific production of specific hormones and the tissue-specific expression of their receptors. BAM22P, for example is a 22-amino acid peptide that is proteolytically processed from proenkephalin almost exclusively in the adrenal medulla, perhaps because the uniquely slow or incomplete processing of this opioid prohormone in the adrenal CC, unlike in neurons, generates a multitude of peptide "processing intermediates," which are characteristic of the adrenal medulla. BAM22P appears to be one of these which is uniquely bioactive upon release, because its receptor is expressed mainly within sensory neurons. This receptor prefers BAM22P to met-enkephalin with a potency ratio of greater than 50-fold. Consistent with this preference, the BAM22 receptor is only distantly related to the μ-opioid receptor, for which enkephalin pentapeptides are thought to be the main endogenous ligands (377). The expression of the BAM22P receptor in sensory neurons, together with high concentrations of BAM22P contained in and therefore secreted from the adrenal medulla, invites the speculation that BAM22P may act as a transmitter or paracrine factor for cross-communication between CCs and the sensory nerves that innervate the adrenal gland (505) (see Figures 12 and 13).

The concept of organ plasticity in stress responding of the adrenal medulla

During development, endocrine organs arise as cell colonies with a very specific secretory mission. Some are spatially quite compact, as the adrenal medulla, and others dispersed throughout other organs, such as the cells of the endocrine pancreas and the entero CCs of the gut. Regardless of their physical coherence, it is generally considered that each cell within an endocrine organ acts in parallel with, but independently of, its neighbors in hormone secretion in response to the presence of secretagogues. The detailed study of vasopressin secretion from the posterior lobe of the pituitary, however, caused a reappraisal of this point of view. Several investigators began to advance the idea of a concerted function of the secretory cells as a cohort, through cell-cell communication about the secretory status of individual cells, with integration to the function of the entire gland (80). This perspective allows endocrine organs to be viewed not only as a "massively parallel" system, but takes into account plasticity in the secretory status and responsivity of individual cells in response to secretory demand and even organismic

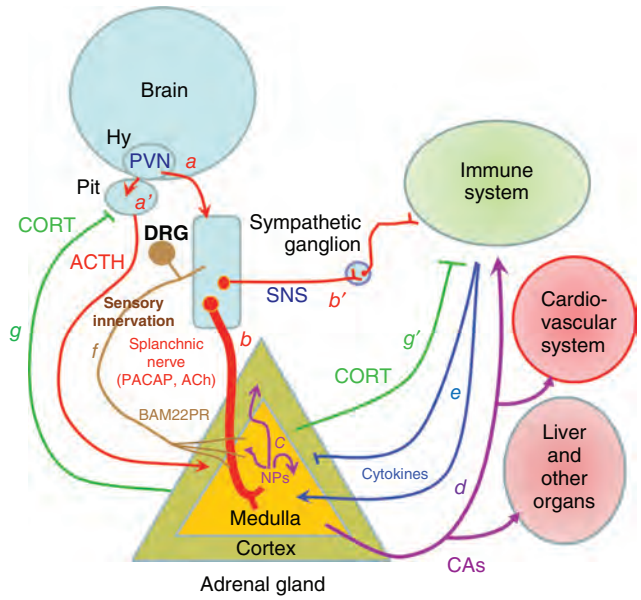

Figure 13 The adrenal medulla as a stress transducer and neuroimmunoinflammatory and cardiovascular regulator. Lower figure. a. The "final common pathway" for stress responding in the CNS is the activation of neurons in the paraventricular nucleus (PVN) of the hypothalamus (Hy), which projects both to the cell bodies of sympathetic preganglionic neurons in the intermediolateral column of the spinal cord and to the median eminence: a′. for ACTH release from the pituitary (Pit) to stimulate corticosterone/cortisol (CORT) release from adrenal cortex; b′. cell bodies in the intermediolateral column of the spinal cord innervate the CCs of the adrenal medulla via the splanchnic nerve, and sympathetic postganglionic nerve targets via para- and prevertebral postganglionic sympathetic neurons b. via the splanchnic nerve, releasing ACh basally, and ACh and PACAP during stress, with activation of both secretion by ACh and PACAP, and of CC signaling pathways by PACAP increasing expression of genes encoding neuropeptides (NPs), additional mediators, catecholamine biosynthetic enzymes, and adhesion factors and connexins that increase cell-cell communication among CCs and amplify CA, neuropeptide, and chromogranin output in response to stress; c. NP (neuropeptide) release from CCs has autocrine effects on CA secretion from CCs themselves (e.g. catestatin, substance P, and others), activation of sensory neurons (e.g. BAM22P, acting on specific receptors expressed in sensory nerves), and modulation of CORT secretion from the adrenal cortex (galanin, VIP, and other peptides), as well as hormonal effects on distant organs; d. CA release from CCs into the general circulation, and affecting metabolism, heart rate, blood pressure, and immune cell mobilization; e. *Cytokines* released as blood-borne molecules or locally from circulating monocyte macrophages act as inhibitors of CORT secretion in the adrenal cortex, and as modulators of peptide secretion in adrenal cortex via receptors on CCs themselves; f. Sensory inputs to adrenal medulla sense CC secretory activity via release of BAM-22P, for which sensory neurons express specific receptors. Also depicted are the targets of glucocorticoid (CORT) release from the adrenal cortex at the pituitary g and immune system g′, the latter decreasing in turn cytokine secretion, which affects adrenomedullary function during stress. For a further explication of the figure, see the text.

conditions. Paracrine/autocrine regulation, discussed above, is one way in which the activity of individual cells can be aggregated and modulated. This autocrine/paracrine regulatory concept may explain the roles of several of the peptide hormones produced by and released from the adrenal medulla (see previous section), in particular, those that are released at concentrations too low, relative to their potencies, to be active at distant receptors.

A second mode of regulating the collective secretory response of cells within an endocrine organ involves altered cellular adhesion, through the formation of gap junctions among secretory cells themselves (Figure 12). Gap junctions lower the resistance between adjacent cells through physical connections between them. This occurs, at the molecular level, through the dynamic expression of connexins, proteins that form hexameric hemichannels to promote the spread of electrical excitability. Connexins are expressed by rat adrenal CCs (433) and are regulated *in vivo* by changes in splanchnic nerve activity in response to stress (see Ref. 133 for a comprehensive review). It was initially observed that cellular resistances of isolated CCs in primary culture are greater than those of CCs in intact adrenal glands, and this difference inferred to exist due to loss of gap junctions in dissociated cells (120, 433). A series of *in vivo* experiments assessed changes in gap-junction formation in the adrenal medulla *in vivo* as a function of cold stress (summarized in Ref. 261). Rat adrenomedullary slices examined before and after five days of cold stress (134) showed morphological remodeling of both synapses onto CCs and CC cell-cell borders; increased dye permeation between CCs; and increased electrical coupling between CCs after depolarization of single cells. Finally, application of a several-day stress paradigm *in vivo* caused a noticeable increase in CA secretion after an applied electrical stimulation that was attenuated by pharmacological inhibition of gap-junction formation. Further investigation of the detailed biochemical constitution of gap junctions in the adrenal medulla, and the modulation of gap-junction formation in concert with altered secretory function after stress, has been reported (133, 162). Thus, in addition to shifts between the balance of cholinergic and PACAPergic neurotransmission from rest to stress, physical reorganization of the gland itself anticipates further episodes of stress. The actual first messengers mediating this adaptive response, whether the neurotransmitters ACh and/or PACAP, or autocrine factors released from the CCs in response to stress transduction, are as yet unidentified.

The role of gap junctions in adrenomedullary function may well apply to other endocrine organs (219). It is worth noting that the stress stimuli so far selected for the study of gap-junction-driven plasticity of the adrenal medulla are not among the most "selective" for that organ (252). Cold stress, for example, activates NE secretion rather more than EP secretion, suggesting that its major effect is on postganglionic sympathetic neuronal activity rather than CC activation. It remains to be seen if principal ganglion cells of the SNS respond to stress as the adrenal medulla does. An additional unresolved issue is whether PACAP, or ACh, or both are the principal regulator(s) of either type of adrenomedullary stress-induced plasticity. Stress also regulates CC responsiveness through alteration of other components of the CC. Two important examples are the recruitment of T-type ($Ca_V3.2$) Ca^{2+} channels during chronic hypoxia and β-AR stimulation of cultured rat CCs that cause a pronounced reduction of the threshold of CA release associated with the low threshold of activation of newly recruited Ca^{2+} channels (104, 479) (see below). It is also noteworthy that CCs from mice previously stressed by exposure to rats express a high density of T-type channels as determined by Ca^{2+} current patch-clamp studies (Emilio Carbone, Chiara Calorio, and Daniela Gavello, unpublished observation).

Adrenomedullary function during inflammatory responses

Inflammatory responses involve multiple organs and are mediated largely by cytokines that act hormonally on virtually all tissues via the circulation, as well as locally through the mobile and ubiquitous cytokine-secreting cells of the immune system, which can migrate to various locations during and after infection. Lipopolysaccharide and cytokine receptors have been identified functionally and biochemically on CCs, suggesting a role for the adrenal medulla in responding to inflammation, and potentially coordinating various phases of the immune response (Figures 12 and 13). In fact, this signaling system may hold the key to explaining how stress and immune function mutually modify one another, although definitive experiments in this direction remain to be reported (82, 171).

Two inflammatory cytokines, interleukin type 1 (IL-1) and tumor necrosis factor-alpha (TNF-α), have been shown to regulate CC neuropeptide expression, increasing expression of VIP and decreasing that of met-enkephalin in bovine CCs in primary culture. These cytokines also amplify the effects of cAMP on VIP and substance P biosynthesis (211). The TNF-α receptor is expressed in the bovine adrenal medulla *in vivo* (4, 5), and TNF-α regulates gene transcription and elevates production, of both galanin and secretogranin II (SgII) (5). Bunn and colleagues have postulated a role for TNF-α in VIP biosynthesis and TH induction, based on inflammation-induced elevation in mRNA encoding the neuropeptide prohormone and the TH protein, in the rodent adrenal medulla *in vivo* (82, 171). Additional studies support a physiological role for cytokine regulation of adrenomedullary peptide production, in particular in counter-regulation of inflammation. Thus, cytokine-induced production of galanin (4) may counter-regulate cytokine actions elsewhere in the body via enhancement of glucocorticoid production in the adrenal cortex (483) (see Figure 13). IL-1 and TNF (82), themselves inflammatory cytokines, increase the production of IL-6 mRNA in CCs. As IL-6 has anti-inflammatory properties, its production by the adrenal medulla may also function as a counter-regulator of excess cytokine action associated with the pathogenesis of sepsis.

Interactions between cytokines and CC neuropeptides may also be more or less pronounced in the presence of PACAP and CC autocoids (Figure 13), thus linking anti-inflammatory mechanisms to stress and potentially allowing a better understanding of multiorgan involvement in pathophysiological states including inflammation and hypertension (88).

GABAergic regulation of CA release

Excessive response to stress can be harmful. Therefore, adequate control of CA secretion by CCs is essential for normal physiological function and appropriate stress response. Substances secreted by CCs can either augment or decrease CA exocytosis. Receptors for ATP (P2Y receptors), CA (α-adrenergic receptors), and enkephalin (μ-opioid receptors) coupled to Gi-type G-proteins inhibit Ca_V channels and CA release (148) (see also *Ca^{2+} channel-secretion coupling* above). Conversely, D1 dopamine and β-adrenergic receptors augment CA release by increasing Ca^{2+} influx through L-type Ca^{2+} channels or by phosphorylating components of the exocytosis apparatus (30, 100). A regulatory mechanism mediated by gamma-aminobutyric acid (GABA, the main inhibitory neurotransmitter of the CNS) was also described in the adrenal gland (493).

GABA inhibition in the CNS is mediated by ionotropic $GABA_A$ receptors ($GABA_A$-Rs), permeable to Cl^- ions and metabotropic G-protein-coupled $GABA_B$ receptors, which control cellular excitability by regulating Ca^{2+} and K^+ ion channels (22, 71, 75). When GABA (or the $GABA_A$-R agonist muscimol) is injected intravenously, heart rate and blood pressure increase (75). These cardiovascular actions are prevented by adrenalectomy or a $GABA_A$-Rs antagonist, suggesting stimulation of CA secretion by $GABA_A$-Rs. In the isolated adrenal gland, muscimol increases baseline CA release but reduces synaptically evoked CA secretion (317). This paradoxical effect reflects the "dual action" of $GABA_A$-R activation (273, 439). GABA is stored in dense core granules (274) and it is likely released together with CA, ATP, and opioids in response to physiological stimuli (493). Functional tests with $GABA_A$-R antagonists indicate that GABA is present in the milieu of adrenal medulla slices (14, 273).

Acute application of GABA or muscimol to CCs in culture causes membrane potential depolarization, AP firing, opening of Cav channels, and a transient $[Ca^{2+}]_i$ rise that initiates CA exocytosis (87, 240, 317, 493, 513). GABA-induced adrenal CA secretion is likely due to this excitatory mechanism. Conversely, $GABA_A$-Rs tonically inhibits spontaneous cholinergic transmission (14) and shunts CC membrane electrical resistance, weakening synaptic excitation and impairing AP firing (13, 14, 87, 350). These effects explain the GABA inhibition of synaptically evoked CA release (317).

In neurons, intracellular chloride concentration ($[Cl^-]_i$) results from the interplay between Cl^- accumulation by the $Na^+/K^+/2Cl^-$ cotransporter NKCC1 and Cl^- extrusion by the cation-chloride cotransporter KCC2. Immature neurons display excitatory responses to GABA (55) because of Cl^- efflux due to a high $[Cl^-]_i$, resulting from a greater functionality of NKCC1 (Figure 14). Conversely, in mature neurons, the GABA response is inhibitory because $[Cl^-]_i$ is low due to a dominant activity of KCC2, and Cl^- enters the cell ((336); Figure 14B). In rat adrenal CCs ~44% of $GABA_A$-Rs-mediated response comprises depolarization and $[Ca^{2+}]_i$ elevation (Figure 14C), while in ~26% it includes hyperpolarization and $[Ca^{2+}]_i$ drop (Figure 14D) (13, 14); the remaining CCs are unresponsive. Since muscimol-induced $[Ca^{2+}]_i$ rises are not inhibited by bumetanide (13), NKCC1 is probably not responsible for Cl^- accumulation in rat CCs. This role could be played by the anion-exchanger AE3 or by Pendrin, a member of the SLC26A family of Cl^-/HCO_3^- exchangers that is expressed in adrenal CCs and can modulate CA release (373). Pendrin would be most active in CCs that respond to GABA with membrane depolarization and $[Ca^{2+}]_i$ rise (Figure 14C). The dynamic reciprocal regulation of AE3/Pendrin and KCC2 underlies the variance in $[Cl^-]_i$. It is plausible that the proportion of CCs responding to GABA with excitation or inhibition varies depending on how $[Cl^-]_i$ is controlled (333).

Experiments in isolated rat adrenal gland suggest that GABA regulates CA secretion differently depending on the functional state: Under nonstressful conditions, the activation of $GABA_A$-Rs by endogenous GABA inhibits cholinergic transmission and reduces CC excitability (14), thus preventing excessive CA release. During intense stress, strong synaptic stimulation initially causes a vigorous CA release, which then declines (240). Activation of postsynaptic $GABA_A$-R by released GABA can then depolarize CCs and maintain CA exocytosis even under acute stress. These findings emphasize the importance of GABAergic regulation as another CA secretion controlling agent.

The Stimulus-Secretion Coupling of the Adrenal Medulla and CCs in Disease

A role of adrenal CCs in essential hypertension?

Essential hypertension, the most common manifestation of high blood pressure, is also the most insidious since it leads to cardiac hypertrophy, congestive heart failure, stroke, and retina and kidney damage. It has several possible causes, but an augmented sympathetic tone has been implied in many studies (23, 212). Higher levels of plasma CAs resulting from increased release from sympathetic synaptic terminals and adrenal CCs is a common finding in essential hypertension (147, 251). In the spontaneously hypertensive rat (SHR), an animal model (488) widely used to investigate hypertension, blood pressure rises above 150 mm Hg at 6 to 9 weeks of age, reaching ~200 mm Hg by 15 weeks (376). At 45 weeks of age, SHRs develop cardiac hypertrophy and heart failure (137). Chemical sympathectomy of newborn SHRs delays the onset of hypertension, and when this procedure is combined with demedullation (bilateral removal of the adrenal medulla), adult SHRs become normotensive

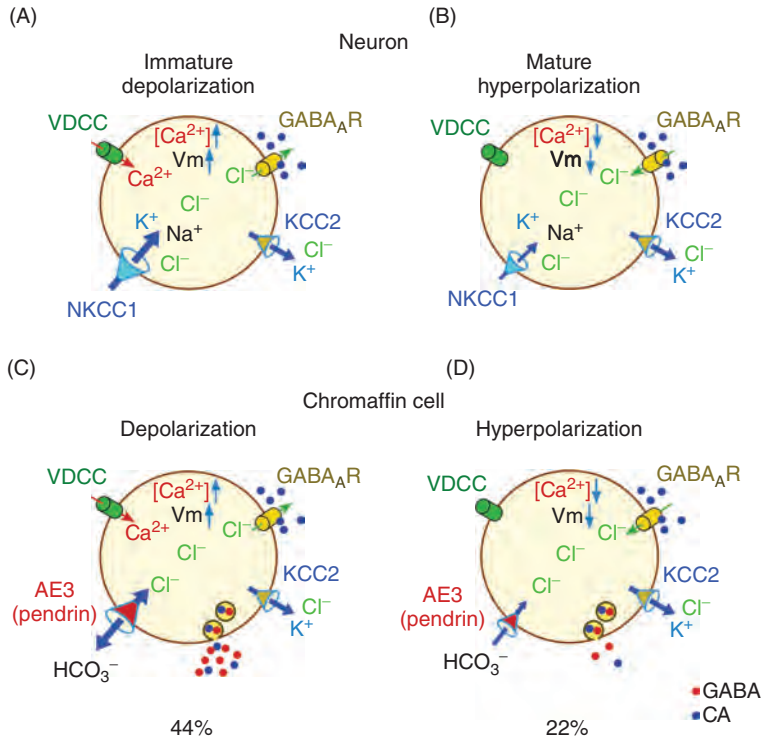

Figure 14 Divergent responses of rat CCs to $GABA_A$ receptor activation. (A) GABA response is excitatory in immature neurons because of a greater functionality of NKCC1. (B) In mature neurons, GABA response is inhibitory because of the dominant activity of the KCC2. (C) $GABA_A$-Rs-mediated response is depolarizing with $[Ca^{2+}]_i$ elevation in ~44% of rat adrenal CCs. (D) in ~26% of CCs, GABA response is hyperpolarizing and causes $[Ca^{2+}]_i$ drop. The scheme also represents the anion-exchanger AE3 (pendrin), which accumulates Cl^- in exchange for intracellular $HCO3^-$ and participates in Cl^- transport into CCs as a replacement for NKCC1. VDDC: voltage-dependent Ca^{2+} channel.

(376). In fact, in young SHR, both EPI and NE plasma levels are elevated compared to age-matched normotensive Wistar-Kyoto rats (WKY) (496), and isolated adrenal glands from SHR secrete more CA than those from normotensive rats in response to depolarizing agents (ACh or high K^+) (385). In cultured CCs, the CA secretion (cumulative charge) measured with single-cell amperometry (see the section titled "Measuring exocytosis") is 2.3-fold higher and the number of spikes 2.4-fold larger in SHR versus WKY CCs (65, 445). Likewise, massive intracellular Ca^{2+} release from the ER or mitochondria triggers long-lasting bursts of spikes, threefold larger in SHR CCs compared to WKY CCs (444). Among the mechanisms suggested to explain the enhanced CA secretion in adult hypertensive SHRs (16-weeks old) are the augmented capacity of the ER Ca^{2+} store due to impaired mitochondrial Ca^{2+} uptake; greater cytosolic and mitochondrial Ca^{2+} transients; larger microdomains of high-$[Ca^{2+}]_i$ at sub-plasmalemmal sites; augmented vesicle pool; and greater quantal size of amperometric events (65, 444–446, 460).

In early hypertensive SHRs (9–12 weeks of age), spontaneous amperometric events are more numerous and of larger mean amplitude in SHR CCs than in WKY. A brief stimulation with high K^+ or caffeine (which causes voltage-gated Ca^{2+} influx or intracellular Ca^{2+} release, respectively) triggers a burst of spikes with greater mean amplitude in SHR CCs. Therefore, CA secretion for both stimuli was approximately twofold higher in SHR CCs (566). Treatment with ryanodine, a specific blocker of RyRs, reduced depolarization-induced CA secretion by 77% in SHR CCs and 10% in WKY, suggesting a greater contribution of Ca^{2+}-induced Ca^{2+} release to CA exocytosis in SHR CCs (Figure 15). Also, $[Ca^{2+}]_i$ signals elicited by a brief stimulation with high K^+ or caffeine were 3.2- and 2.5-fold larger, respectively (566). Together, these findings implicate an enhancement of CA release in the origin of hypertension in this model in SHR and support the notion that a key mechanism involved in the enhanced secretion of CA at early stage of hypertension is a "gain-of-function" of the RyR, an intracellular Ca^{2+} release channel from the ER.

The hypothesis that SHR CCs could have Ca_V currents of greater magnitude was discarded. Electrophysiological recordings showed that this current is either indistinguishable in both strains (565) or reduced by ~39% in SHR CCs

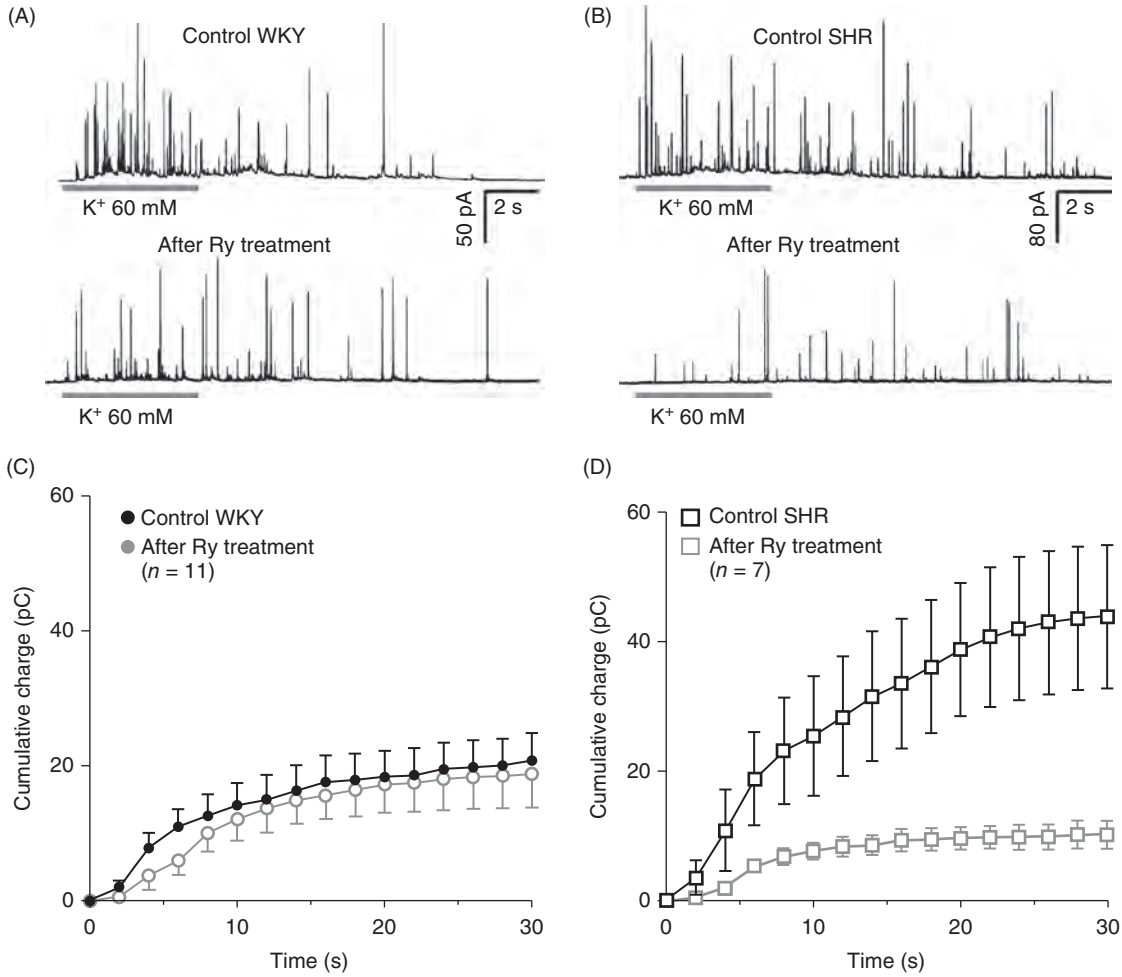

Figure 15 Ryanodine effects on depolarization-induced CA secretion. (A, B) Burst of amperometric spikes elicited by a 5-s-long depolarizing pulse in a WKY (A) and an SHR CCs (B) before (top) and after (bottom) incubation with 10 μM ryanodine. (C, D) Mean cumulative charge in WKY and SHR CCs, respectively, before and after ryanodine treatment. The cumulative charge after RyR blockade was not significantly affected in WKY CCs (20.8 vs. 18.8 pC; $p = 0.274$), but it was drastically reduced in SHR CCs (from 43.9 to 10.1 pC; $p = 0.0001$). The number of cells examined is shown in parentheses. Reused, with permission, from Segura-Chama P, et al., 2015 (566).

compared to WKY (460). A comprehensive analysis revealed that CA hypersecretion in SHR CCs results from the combination of larger depolarization-induced Ca^{2+} transients, more exocytosis events per time unit, and a greater proportion of medium and large amperometric spikes due to a higher CA content per granule (566). A study in prehypertensive SHRs and WKY CCs at 4 weeks of age revealed that all changes found in early hypertensive rats (566) are already present, but to a lesser degree (Peña-del Castillo, JG, in preparation). The cumulative secretion elicited by high K^+ and caffeine is 2- and 1.6-fold larger, respectively, in SHR, compared to WKY CCs. Ryanodine treatment reduces CA secretion by 48% in SHR and by 10% in WKY, and $[Ca^{2+}]_i$ signals elicited by stimulation with either high K^+ or caffeine were 1.4-fold larger in SHC CCs. These data suggest that the "gain-of-function" of the Ca^{2+}-induced Ca^{2+} release mechanism is already present in prehypertensive stages in SHR CCs and that it intensifies with age. It remains to be established to what extent the dysfunctional CA secretion by the adrenal medulla and possibly the SNS are involved in the origin of essential hypertension. Identifying the most likely molecular targets of adrenal and sympathetic hyperfunction in SHR rats leading to hypertension, and their potential dysfunction in human hypertension, is an area in which further advances will have major clinical implications.

Pheochromocytoma

Pheochromocytoma is a tumor arising from CCs in the adrenal medulla and sympathetic paraganglia, which can synthesize and secrete NE, EPI, and, to a lesser extent, DA (21, 617). By acting on their target receptors, these CAs cause significant physiological changes in the body, most often severe hypertension, which can cause devastating cardiovascular and cerebrovascular effects, if untreated (77). Pheochromocytomas are more prevalent than paragangliomas. Yet, the combined

prevalence of these tumors is less than 0.05% in the general population (27, 492). Most pheochromocytomas are benign tumors: the prevalence of malignancy varies between 10% and 15%. In contrast to the normal adrenal medulla, negative feedback of TH on CA synthesis is absent in pheochromocytoma, thus contributing to the uncontrolled and autonomous synthesis of CAs (462). The surgical treatment represents the only modality of ultimate cure, but timely diagnosis and pharmacological treatment is the basis of a successful outcome. Several laboratories have devoted considerable effort to validating markers for pheochromocytoma and especially in distinguishing its benign and malignant forms (378).

While the most common sign of pheochromocytoma is hypertension (90), additional symptoms include episodes of headache, palpitation, anxiety, and sweating related to excess CA secretion (21). The duration of paroxysms varies from a few minutes to 30 min, separated by asymptomatic intervals, from many times per day to a few times per month. Other less well-known symptoms are nausea, vomiting, weight loss, and diabetes mellitus. The secretory profile of pheochromocytoma can be useful in its diagnosis. Extra-adrenal tumors secrete NE and rarely DA (525), while adrenal pheochromocytomas primarily secrete EPI, with or without NE. DA-secreting tumors are rare and occur only in extra-adrenal tumors. Patients with tumors that produce high concentrations of NE are likely to incur sustained hypertension, while patients with elevated levels of EPI often experience paroxysmal and orthostatic hypertension (321). DA-secreting tumors are often asymptomatic (525). Pheochromocytomas can also produce adrenomedullin, vasoactive intestinal polypeptide (VIP), ACTH, NPY, endothelin-1, somatostatin, atrial natriuretic factor, and parathyroid hormone-related peptide. The resulting clinical picture will depend on the combination of increased CA and the amount released of these vasoactive substances (424).

CA metabolism is crucial to protect the organism against excessive CAs. In pheochromocytoma, more than 94% of the metanephrines derive from CA metabolism within tumor cells (195). Production and secretion of metanephrines is continuous and independent from CA secretion. Dopamine is also O-methylated by COMT to 3-methoxytyramine (3-MT), which is also continuously released from the tumor (195, 197). While free metanephrines are excreted in urine, the sulfate-conjugated metanephrines (194) represent 30-fold higher levels than free metanephrines, and are the principal form in which they are finally eliminated in the urine. Some of these metanephrines are oxidized to 3-methoxy-4-hydroxyphenylglycol (MHPG) (194). Both DHPG and MHPG are oxidized in the liver to vanillylmandelic acid (VMA), the major end product of CA metabolism (196). This unconjugated metabolite, excreted in the urine, has been used for many decades as a marker of the presence of CC tumors. However, VMA has insufficient diagnostic accuracy and has been removed from the diagnostic checklist of CC tumors (378).

It is impossible to predict when and how much CA a particular tumor will release during a secretory episode, but it is known that hypertensive paroxysms can be precipitated by physical activity (exercise and postural change) or tumor manipulation (77, 289). One of the few physiological studies conducted on cultured human pheocromocytoma cells (289) revealed that they express densities and proportions of L, N, and P/Q types of voltage-gated Ca^{2+} channels similar to those of normal human CCs. Nonetheless, the extent of downmodulation of Ca^{2+} currents by ATP and opioids is quite heterogeneous in these cells. The pattern of exocytotic events is also heterogeneous; some cells secrete spontaneously and continuously, while others evoke a normal secretory pattern after a brief pulse of high K^+. Cell heterogeneity suggests that normal CCs coexist with pathological CCs that escape the autocrine/paracrine downmodulation of Ca^{2+} channels and hence, may produce abnormal Ca^{2+} signals and CA hypersecretion. Hyperexcitability of CCs is also likely, given the reported peak of CA secretion often observed during tumor manipulation (288). These alterations could underlie the uncontrolled CA peaks suffered by patients with pheochromocytoma, which are responsible for the typical symptoms produced by this tumor. There is much to be learned about the physiopathology of tumoral CCs. This knowledge will certainly provide a basis for better understanding of the pathogenesis and treatment of this disease.

The molecular mechanism regulating CA release during acute, chronic, and intermittent hypoxia

In mammals, low oxygen pressure (hypoxia) is an environmental stressor that triggers CA release from adrenal CCs, depending on the extent and duration of the hypoxic exposure (97, 332). The acute response is initiated by the O_2-sensitive glomus cells of the carotid body that through the activation of SNS triggers the release of CAs from CCs. Acute hypoxia causes sustained cell depolarization, repetitive firing, Ca^{2+} entry, and CA release (73, 239, 449, 482, 550, 602, 615).

In most animal species, adrenal CCs play a critical role during fetal and perinatal life when sympathetic innervation is absent or immature. CCs possess inborn chemosensitivity to O_2 that allows them to control directly the release of CAs from the adrenal gland under nonneurogenic conditions (567, 578). In CCs of fetal and neonatal rodents, the hypoxia-induced release of CAs plays a key role in setting heart rates and oxygen delivery to the growing tissues (529). This is particularly evident during the transition from intra- to extrauterine life when the fetus experiences episodic asphyxia, and the hypoxia-induced release of CAs helps to regulate the cardiac function through the activation of β-ARs and prepare the lungs for air-breathing (567, 578). As the adrenal gland acquires cholinergic innervation, typically during the seventh to tenth postnatal days in rodents (619), the acute hypoxia-sensing mechanism of CCs is gradually suppressed with the same time course (567, 578). Remarkably, direct O_2-sensitivity is reestablished after adrenal gland denervation (567). How this occurs is not yet fully understood. There is likely a developmental loss of hypoxia chemosensitivity in CCs (343, 450, 534, 613, 614) that can

reemerge after prolonged deprivation of neural input in adult rat adrenal glands. However, there is also evidence that a fraction of CCs intrinsically possess an O_2-sensing mechanism regardless of cholinergic innervation, which is also effective in adult rat CCs (239, 315, 375, 449, 602). This issue, and the remodeling of cell function that occurs in response to chronic and intermittent hypoxia, will be explored and clarified in the following sections.

The role of K^+ channel in O_2-sensing in perinatal and mature CCs

The first cellular studies addressing the K^+ channel types involved in the nonneurogenic mechanisms of the hypoxia-induced secretory response in cultured rat CCs date to the late 1990s (449, 450, 614). It appeared evident that the Ca^{2+}-dependent release of CA was triggered by a hypoxia-induced block of K^+ channels that generated membrane depolarization, cell firing, and Ca^{2+} entry through voltage-gated Ca_V channels (449, 613). Early findings suggested the involvement of BK and K_V channels. In voltage-clamp experiments, acute hypoxia reversibly inhibited both Ca^{2+}-dependent BK currents and voltage-gated K_V currents (449, 602, 615). Later findings also implicated SK (346, 375) and K_{ATP} (Kir6.1, Kir6.2) ATP-sensitive K channels (73, 375, 550, 615). Acute hypoxia clearly inhibited SK channels, while activating K_{ATP} channels, most likely due to the transient reduction of ATP during low O_2. In the case of SK channels, voltage-clamp recordings showed that hypoxia reduced the outward K^+ currents of neonatal rat CCs and apamin largely prevented these effects (375). In the case of K_{ATP} channels, their involvement and upregulation were evident in rat CCs when acute hypoxia was tested in the presence of the K_{ATP} channel blocker glibenclamide. The addition of glibenclamide did not affect K^+ current, but the inhibitory action of acute hypoxia was enhanced (Figure 2a in Ref. 550), suggesting that K_{ATP} channels are upregulated only in response to low O_2. Current-clamp recordings confirmed this view. The hypoxia-induced cell depolarization caused burst firing in the control condition that was further enhanced in the presence of glibenclamide (Table 2) (see Figure 2b in Ref. 550). Apparently, K_{ATP} channels play a protective role in the hypoxia-induced response of CCs. These channels hyperpolarize the cell during hypoxia and have a maximal expression at mid-gestation decreasing toward late gestation, while BK channels show an opposite trend. Thus, the hypoxia-evoked CA release is attenuated at mid-gestation due to high K_{ATP} expression and more hyperpolarized membrane potential, but is facilitated at birth as K_{ATP} expression decreases and BK expression increases (73).

Likely, heteromeric TASK-1/3 channels are also involved in hypoxia-induced CA secretion in CCs. TASK-1/3 channels are highly expressed in rat and mouse CCs (316, 389) and their activity is moderately reduced (30%–40% inhibition) by acute hypoxia (351). Given the key role that these channels play in setting the resting potential of rat and mouse CCs, it is likely that the hypoxia-evoked reduction of their resting current is sufficient to induce cell depolarization, burst firing, Ca^{2+} entry, and CA release during acute hypoxia. In conclusion, it seems that, although to different extents, nearly all K^+ channels expressed in mammalian CCs are involved in O_2-sensing, suggesting a common mechanism acting on a protein domain shared by all of the K^+ channels of CCs.

Concerning the O_2-sensing mechanism, significant progress has been made in the past decade to understand the downstream events in the signal transduction cascade regulating the hypoxia-evoked response in CCs, nicely described in recent reviews (401, 482). Briefly, there is strong support for the involvement of complexes I and IV of the mitochondrial electron transport chain (ETC) coupled to the alteration of reactive oxygen species (ROS) (344, 450). Recently, it has been proposed that loss of the mitochondrial subunit *Ndufs2* of complex I, which encodes a protein that participates in ubiquinone binding, is critical for the O_2-sensing mechanism in glomus cells and adrenal CCs (223). An important role is also played by the cytochrome c oxidase subunit IV isoform 2 (*Cox4i2*) and the NADH dehydrogenase (ubiquinone)1 alpha subcomplex, 4-like2 (*Ndufa4l2*) (238). Unresolved and controversial issues still exist concerning the role of ROS generated by complex I in the O_2 signaling pathway. It is not clear, for instance, whether acute hypoxia induces an *increase* (223) or a *decrease* in ROS (238) and how ROS interact with K^+ channels. Further studies will clarify this issue.

Ca_V channel types responsible for hypoxia-induced release of CAs at embryo and perinatal life CCs and their roles

Ca_V channels have a key role in the hypoxia-evoked response of neonatal CCs (see Refs. 482 and 495 for recent reviews). They convert the hypoxia-induced mild depolarization (73, 550) and associated repetitive firing into Ca^{2+} influx that drives vesicle fusion and release of CAs (224, 550, 602). Thus, the question is: which Ca^{2+} channel types are expressed in neonatal CCs and how they contribute to the release of CAs. As nifedipine strongly attenuates the response of neonatal CCs to acute hypoxia, L-type channels would appear to be critical for the regulation of the hypoxia-induced release of CAs (1, 602, 614). Neonatal CCs of rats, mice, and sheep express different percentages of the same Cav channels expressed in adult CCs (L, N, and P/Q) (20, 73, 224, 379, 495) with relative percentages similar to those found in adult CCs (240, 417), except for a net increase in expression of Cav3.2 (T-type) channels in adults (73, 345, 379). T-type channels are typically upregulated in adult CCs under stressful conditions (107, 298, 368, 479), including chronic (103) and intermittent hypoxia (584) (see below and Table 1 in Ref. 417).

Concerning the specific role of Ca_V channel subtypes on the quantal release of CAs measured with carbon-fiber microelectrodes on embryonic and neonatal CCs, two reports indicate the involvement of L-, N-, P/Q-, and T-type channels that contribute differently to the acute hypoxia-evoked response (417). In one case (224), exposure of cultured rat embryo

CCs to 1 min hypoxia elicits transient bursts of amperometric secretory spikes followed by dispersed spikes during the period of O_2 deprivation. This bulk response is blocked 85% by nimodipine and 35% by combined ω-conotoxin GVIA and ω-agatoxin IVA, suggesting that the acute hypoxic response in early life is initially controlled by both Cav1 (L) and Ca_V2 (N- and P/Q-type) channels. However, due to the fast inactivation of $Ca_V2.1$ (P/Q-type) and Ca_V 2.2 (N-type) channels, their contribution is blunted after a few seconds so that the slowly inactivating $Ca_V1.3$ L-type channels remain the main ones responsible for the hypoxia response. In the second case (379), recording of secretory events with amperometry performed in neonate rat adrenal slices reveals a pronounced spontaneous generation of spike events. Acute hypoxia increases the frequency of spikes, and the hypoxia-induced response is triggered by Ca^{2+}-influx through T-type ($Ca_V3.2$) channels, giving rise to what is commonly indicated as the "low-threshold exocytosis" that also occurs in adult rat CCs exposed to chronic cAMP (110, 479) or chronic hypoxia (104, 107). Interestingly, T-type channel expression, as well as CC responsiveness to hypoxia decreases with postnatal maturation, and adrenal medulla denervation restores the sensitivity to hypoxia in parallel with the recruitment of T-type channels.

Ion channel remodeling in CCs following chronic and intermittent hypoxia

Exposure to chronic hypoxia, as it occurs in patients with chronic pulmonary obstructive disease causes elevated sympathetic activity, increased circulating CAs, and hypertension (432). Recent studies have shown that exposure to sustained or chronic hypoxia *in vivo* and in cultured cells leads to a functional remodeling of CCs excitability and CA secretion (89), and this may occur regardless of the increased sympathetic activity (104, 160). In this regard, exposure of cultured adult rat CCs to chronic hypoxia (3% O_2 for 12–18 h) causes a hypoxia-inducible factor (HIF)-dependent upregulation of $Ca_V3.2$ T-type Ca^{2+} channels that results in enhanced CA secretion during prolonged mild depolarizations (2–10 mM KCl) (104). T-type channels are absent in control normoxic conditions (20% O_2), and high-threshold Ca^{2+} currents (L, N, P/Q, and R) are insensitive to low O_2, suggesting that the hypoxia-induced recruitment of T-type channels is the only Ca^{2+} source that during chronic hypoxia sustains vesicle secretion at "low-threshold" voltages. This unique channel remodeling is similar to that occurring with another stressor stimuli (417). Interestingly, an HIF-2α-dependent increased expression of $Ca_V3.2$ T-type channel activity is also reported in PC12 cells following exposure to chronic hypoxia (160).

Chronic hypoxia also causes an upregulation of the brain-derived neurotrophic factor (BDNF)-TrkBs signaling pathway in CCs that leads to an increased voltage-gated Ca^{2+} entry and CA secretion (562). TrkBs are usually expressed in CCs and are upregulated during chronic hypoxia. Addition of BDNF causes increased burst firing, elevation of intracellular Ca^{2+}, and enhancement of CA release. Addition of the selective blocker of T-type Ca^{2+} channels TTA-P2 attenuates the BDNF-induced response, suggesting a key role of T-type channels in the upregulation of the Ca^{2+}-dependent CC response during chronic hypoxia. Since chronic hypoxia and stressors in general cause increased levels of circulating plasma BDNF (278), the facilitation of the BDNF-TrkB signaling pathway provides an alternative non-neurogenic mechanism that may contribute to the enhanced CA release during chronic hypoxia.

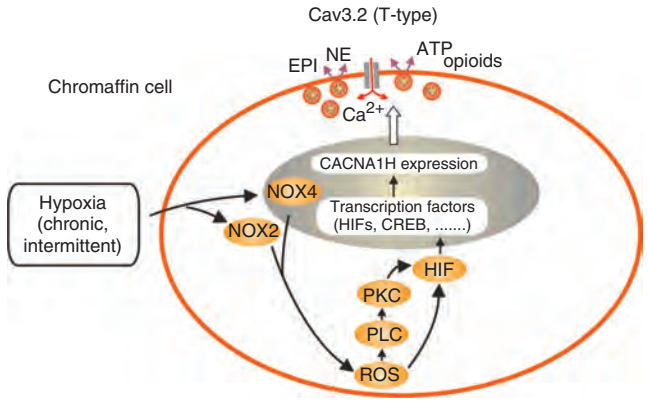

Figure 16 Cell signaling pathways leading to CACNA1H gene expression and Cav3.2 channels recruitment during chronic or intermittent hypoxia. Schematic pathway of the activation of transcription factors (HIF, CREB, etc.) and CACNA1H gene expression through a NOX, ROS, PLC, and PKC cascade leading to Cav3.2 channels recruitment during chronic/intermittent hypoxia. Adapted, with permission, from Mahapatra S, et al., 2012 (417).

Recurrent apnea with chronic intermittent hypoxia occurs in patients with sleep-disordered breathing and is associated with an increased sympathetic activity, enhanced levels of circulating CAs, and increased risk to develop hypertension and stroke (572). In adult rats, exposure to intermittent hypoxia leads to the potentiation of CA secretion from CCs during acute hypoxia. The mechanism involves a PKC-dependent increase of the RRP of SGs and an HIF-2α-dependent cell function remodeling (521). A similar potentiation of CA secretion in response to acute hypoxia is evident in neonatal CCs after exposure to intermittent hypoxia. The effect is associated with an increase of voltage-gated Ca^{2+} entry and intracellular Ca^{2+} stores (585) driven by a NOX-ROS-PLC-PKC signaling pathway, culminating in HIF-dependent upregulation of NADPH oxidase. The result is an increased expression of both $Ca_V3.1$ and $Ca_V3.2$ T-type channels and RyR_2 and RyR_3 (Figure 16).

Altered CC exocytosis by mutated proteins linked to human neurodegenerative diseases

A limited but increasing number of studies support the hypothesis that altered synaptic neurotransmitter release in various brain nuclei during the progression of neurodegenerative diseases is paralleled by changes in secretion in the sympathoadrenal axis (157). Below, we address how

proteins associated with neurodegeneration in various neurological diseases, including Parkinson's, Huntington's, and Alzheimer's diseases, autism, and amyolateral sclerosis, may function, or contribute to dysfunction, including the stages of exocytotic CA release from CCs (for complete details, see the section titled "Measuring exocytosis").

Altered CA exocytosis by the expression of proteins associated with neurodegenerative diseases

α-*Synuclein* The protein α-synuclein is located at presynaptic nerve terminals under physiological conditions. However, duplication and triplications of the WT human α-synuclein gene are present in familial forms of Parkinson's disease (PD) and dementia with Lewy bodies (577). Diminution of spontaneous synaptic responses (563), and of neurotransmitter release due to a reduction in size of the vesicle recycling pool (475), occurs in neurons overexpressing human α-synuclein. Also, this overexpression leads to synaptic dysfunction and diminished exocytosis in the striatum (258, 571). Pathology associated with α-synuclein has also been found in the adrenal medulla of PD patients and mouse CCs endogenously expressing the protein (234). Furthermore, the overexpression of α-synuclein in mouse CCs decreases CA release by acting at a late exocytotic step (372) that is associated with an acceleration of exocytosis by promoting fusion pore dilation (399). Thus, it seems that striatal synaptic pathology linked to α-synuclein also exists in adrenal medullary CCs, causing altered fusion pore kinetics and decreased exocytosis.

Huntingtin Expansion of CAG trinucleotide repeats (CAG repeats) in the N-terminal part of the huntingtin gene is the main pathological feature of HD. Huntingtin-associated protein 1 (HAP1) is the first interacting partner of huntingtin, and the degree of binding correlates with the length of the polyglutamine (CAG) repeats and primarily localizes to synaptic vesicles (382). Peripherally, HAP1 also localizes in secretory vesicles of endocrine cells, including adrenal medullary CCs (177, 384). This generated the hypothesis that HAP1 could contribute to the regulation of exocytosis. Adrenal CCs from mice with the HAP1 gene deleted discharged fewer amperometric secretory spikes and total secretion was decreased, upon stimulation with high K^+; this correlated well with a smaller RRP and a smaller fraction of docked vesicles, indicating that HAP1 reduces full fusion exocytosis by affecting vesicle docking and control of fusion pore stabilization (414). HAP1 also decreases endocytosis by interacting with some proteins of the exocytotic machine and binding to clathrin (415).

Altered excitability and exocytosis in mouse models of neurodegenerative diseases

The APP/PS1 mouse model of Alzheimer's disease

Senile plaques of amyloid-beta (Aβ) and neurofibrillary tangles due to tau hyperphosphorylation are the pathogenic hallmarks of Alzheimer's disease (AD) (275). Synaptic deficits correlate with this disease (568). Presenilin 1 (PS1) is the catalytic subunit of the multimolecular complex ϒ-secretase; PS1 contributes to the regulation of Ca^{2+} movements from the ER (474) and of neurotransmitter release (688). Mutations in the amyloid precursor protein (APP) and PS1 have been linked to early onset AD and to alterations of Ca^{2+} signaling and synaptic transmission. *APP/PS1* mice carry the Swedish mutation and the human PS1 mutation A246E (66). These mice develop an AD-like disease consisting of early Aβ plaques (66), diminished long-term potentiation (266), impairment of hippocampal synaptic transmission (524), and decreased synaptic plasticity (246). About 60% of amperometric secretory spikes generated with K^+ depolarizing pulses in CCs are preceded by an observable "foot." In aged mice, four of the characteristics of single exocytotic events were substantially smaller in *APP/PS1* mice with respect to wild-type mice, namely, peak current (Imax; −30%), decay time (−40%), $t_{1/2}$ (−45%), and quantal size (−50%). Thus, the fusion pore stabilization, expansion, and closure are faster in *APP/PS1* mice, but CA secretion is less. Although these mice exhibited brain Aβ deposition, Aβ pathology was not observed in their adrenal medullary tissue (156).

The SOD1^{G93A} mouse model of amyotrophic lateral sclerosis

Selective loss of motor neurons in amyotrophic lateral sclerosis (ALS) patients leads to paralysis, respiratory insufficiency, and death 3 to 5 years after diagnosis (546). Around 10% of patients have a mutation of glycine to alanine at codon 93 at Cu^{2+}/Zn^{2+}-dependent superoxide dismutase 1 (SOD1^{G93A}). In model mice, this mutation produces ALS paralytic symptoms at postnatal day 90, mimicking the human disease onset (267). Pathogenic features of ALS include augmented glutamate release (141, 339, 607), disturbed Ca^{2+} handling, overproduction of free radicals, and motor neuron death by apoptosis (651).

In adrenal CCs from SOD1^{G93A} mice at ages P90-P120, ACh elicited a 47% higher exocytosis burst secretion compared to WT mice. The kinetic analysis of single-vesicle amperometric events revealed notable differences in SOD1^{G93A} CCs. There was a 36% lower rise rate and 61% slower decay with 55% wider half-width and 52% higher quantal size, giving rise to single-vesicle exocytotic spikes with a slower release rate but greater CA release (92).

The R6/2 and R6/1 mouse models of Huntington's disease

HD is an autosomal dominant neurodegenerative disease with clinical symptoms of hyperkinetic involuntary movements, progressive dementia, aggressiveness, and paranoid psychosis. The disease is associated with mutated huntingtin, consisting of an anomalous expansion of CAG repeats giving rise to extended polyglutamine stretch and resulting in the formation of misfolded huntingtin aggregates that accumulate in the nucleus and the cytoplasm. These pathological features

are associated with neuronal loss in the caudate nucleus and putamen, in cortical layers III, IV, and VI and the lateral tuberal nucleus of the hypothalamus (365, 653). Mutated huntingtin aggregates and neuronal death are the two relevant markers of human HD that have been modeled in mice. For instance, transgenic mice R6/1 and R6/2 express the human huntingtin gene with, respectively, around 115 and 150 CAG repeats (425). In comparison with other HD mouse models, the R6/2 is the one that develops widespread huntingtin inclusions in the brain and early phenotypic symptoms (383). The R6/1 model reproduces several features of HD in older animals (272, 547, 548). Synaptic dysfunction and altered neurotransmitter release have been found in these HD mice models. For instance, electrically evoked dopamine release is attenuated in brain slices of 6-week-old R6/2 mice (327). The same group found that K^+ stimulation triggered a secretory response with similar spike number but lower vesicle quantal size (328) in CCs of R6/2 mice 3-months old. In a recent study performed in R6/1 mice, several alterations in CCs were reported; some of them were already present in 2-month-old mice at a phenotypic pre-disease stage, but they were more pronounced in 7-month-old mice when motor deficits were already established. CCs from R6/1 mice exhibited the following features: (i) mutated huntingtin overexpression as nuclear aggregates; (ii) smaller CC size with decreased dopamine-β-hydroxylase, indicating a decreased number of chromaffin SG; (iii) reduced adrenal medulla CA content; (iv) reduced peak Na_V currents; (v) membrane hyperpolarization and decreased ACh-evoked APs; (vi) diminished $[Ca^{2+}]_c$ transients with faster Ca^{2+} clearance; (vii) decreased quantal secretion with smaller single-vesicle quantal size; and (viiii) faster kinetics of the exocytotic fusion pore, pore expansion, and closure. These data suggest that the primary event in these alterations is the deposition of mutated huntingtin in the nucleus of adrenal CCs of R6/1 mice that could be responsible for less Na_V channel expression and function, giving rise to decreased cell excitability, altered Ca^{2+} handling and exocytosis, and eventually, cell damage and loss of CCs. These data suggest that in HD, the sympathoadrenal axis, which is tightly controlled by cortical neurons via hypothalamus, brain stem, and spinal cord is also significantly affected, predicting dysfunctional stress responses in HD patients (435).

The autistic TS2-neo mouse model carrying the G406R missense mutation on Cav1.2 channel

Timothy syndrome (TS) is a rare multiorgan channelopathy characterized by cardiac arrhythmias, long QTs, immune deficiencies, and autism spectrum disorder (ASD) (586, 587). TS is associated with a *de novo* single point mutation in the pore-forming subunit of $Ca_V1.2$ L-type Ca^{2+} channels (*CACNA1C*) and exists in two major forms (TS1 and TS2), depending on whether the point mutation appears on exon 8a (587) or exon 8 (586). The two exons code for the IS6 helix of $Ca_V1.2$ channel controlling the voltage-dependence of activation and inactivation. In the TS2, one mutation occurs at gly406 (G406R) within exon 8 that is highly expressed in the brain and the heart (80%) and to a lesser degree in the adrenal glands (586). The mutation causes reduced channel inactivation and shifts the voltage dependence of activation toward more negative potentials, thus causing increased Ca^{2+} influx during rest and cell activity. TS2 patients with the G406R mutation exhibit ASD-type behaviors (586).

The recent availability of the autistic TS2-neo mouse (41) made it possible to study the origins of neuronal firing and Ca^{2+} signaling mistuning that might generate autism. CCs possess high densities of L-type Cav1.2 channels (46, 426, 429) and are thus an excellent cell model to study the role of Cav1.2 channels on AP firing and CA secretion (100, 389). Interest in the effects of the TS2 mutation on CC function is intensified by a recent case report of a 2-month-old TS patient, whose post-mortem autopsy revealed remarkable bilateral adrenal glands dystrophy, possibly caused by the increased intracellular Ca^{2+} associated with the $Ca_V1.2$ channel mutation that occurred mainly in the adrenal medulla (340).

Recently, it has been reported that L-type currents in TS2-neo mouse CCs exhibit slower inactivation, voltage-dependent activation and inactivation shifted toward negative potentials, and large "window" current at rest (91). The increased "window" current is a likely cause of the increased resting Ca^{2+} that lowers the density of functioning Na_V channels, promotes AP switching from tonic to bursting firing mode alters cell morphology and reduces both mitochondrial metabolism and CA secretion. Extended cytoplasmic vacuolization and cell swelling is also observed by high-resolution electron microscopy in intact adrenal glands of TS2-neo mice. The findings of Calorio et al. (91), provide evidence that CCs are an excellent cell model for studying the effects of the Cav1.2 G406R mutation on AP firing and on Ca^{2+} signaling associated with autism.

A hypothesis concerning the alterations undergone by the sympathoadrenal axis in neurodegenerative diseases

Evidence is accumulating to support the hypothesis that some of the pathogenic features occurring in the CNS of patients suffering from certain neurodegenerative disease are also expressed in the sympathoadrenal axis. Those alterations may occur for the following reasons: (i) the sympathoadrenal axis may undergo impaired stress responses imposed by the limitations of body functions associated with neurodegeneration, (ii) "propagation" via cortico-hypothalamic-sympatho-adrenal axis of pathogenic synaptic dysfunctions occurring in the brain, (iii) mutant proteins linked to neurodegenerative diseases are expressed in CCs themselves, altering cell excitability, ion currents, Ca^{2+} signaling, and exocytosis, and (iv) leading to chronic alterations of blood pH, hormones, and their metabolites or hypoxic conditions that may further change CC function (see above). These four pathogenic pathways may ultimately give rise to altered exocytotic release at sympathetic neurons, and of NE and EPI at adrenal CCs, thus leading to poor adaptation to stressful conflicts in patients with neurodegenerative diseases.

Conclusion

Being the amplifying arm of the cortico-hypothalamic-sympatho-adrenal axis during the fight-or-flight response, the study of the physiological aspects of adrenal CCs has fundamental and intrinsic interest. Additionally, due to their accessibility and easy preparation of primary cultures from embryos, neonates, or adult mammals, CCs have been used widely as biological models to study exocytosis in fine detail, both ultrastructurally and molecularly. Ever since 1961 when Douglas and Rubin pioneered the discovery that Ca^{2+} entry was the trigger for ACh-mediated explosive release of CAs from perfused cat adrenal glands, we have learned much about cellular excitability, ion channels, Ca^{2+} signaling, SG pools, exocytosis, and endocytosis, both in normal and in animal models of disease, from the CC.

By now, a quite complete list of ion channels has been identified and characterized in CCs from various mammalian species, including humans. However, although the role of most channels has been defined in physiological processes (i.e. cell excitability, exocytosis, and endocytosis), only a few studies have approached how certain pathological states (i.e. hypoxia, hypertension, neurodegenerative diseases, and diabetes) affect these physiological parameters. It is not surprising that, as part of the sympathoadrenal axis that regulates body homeostasis, the adrenal medullary CCs are affected in various disorders, particularly brain disease. There is, therefore, ample scientific motivation to investigate the alterations undergone by CCs in animal models of disease as well as in humans. Recently, ion currents from CCs have been successfully recorded with automated patch-clamp technology and instrumentation (514). Given their relevance as proven models of CNS neurons, CCs could be a suitable preparation for high-throughput screening for the discovery and development of new drug candidates targeting therapeutically relevant ion channels.

The regulation of the rapid exocytotic release of CAs into the circulation during stress is particularly critical for two reasons: first, EPI is the most powerful secreted molecule of the organism and its release must be adapted to the degree of stress; and second, if extensively released, EPI may give rise to hypertensive crises and cardiac arrhythmias. Regulation of exocytosis has various control steps both centrally through afferent sympathetic output to CCs and at the level of the splanchnic-nerve-CC synapse, and in regulating the firing rate of the CC itself. There are also local regulatory loci, for example the activity of Ca_V channels by neurotransmitters acting on surface receptors on CCs. A second important type of regulation, particularly relevant under conditions of chronic stress occurs intracellularly and rests on the rate of secretory vesicle transport and the refilling of the exocytotic machinery with new vesicles. Future experiments should focus this problem in models closer to physiology, namely, in adrenal slices and *in vivo*. As proteins and ion channels are remodeled in cultures of CCs, efforts should be made to clarify this issue using the more complex preparation of adrenal slices.

The simple and classical view that the adrenal medulla releases CAs under acute and chronic stress in response to ACh release from the splanchnic nerve supported the investigation of the detailed cellular physiology underlying the function of this endocrine tissue for many years, and continues to do so. This view has been vastly expanded over the past 20 years, the adrenal medulla is now viewed as a more complex, and more integrative, stress transducer. Basal secretion, under the influence of ACh, is seen as important to cardiovascular function as well. Additional first messengers besides ACh, including GABA, PACAP, bradykinin, angiotensin, histamine, cytokines, and others, provide regulation of the CC and integration of inputs from the immune as well as the nervous system during stress to produce a complex output, including proteins, peptides, and CAs, that likely affects sensory neurons, and perhaps even the brain, as well as liver, heart, vasculature, and other CA target organs. The secretory products of CCs also have important, yet-to-be-discovered paracrine, autocrine, and hormonal roles, and this is especially true for CgA and its processed peptides including catestatin. The roles of ACh at the splanchnicoadrenomedullary synapse may require reassessment, especially regarding a potential role in modulation of gap junctions, nAChR- and mAChR-mediated gene regulation, and subtle but important regulation of the tempo of PACAP-induced CA release during both acute and chronic stress.

For over half a century, the CC has been a unique model to study basic mechanisms of cell excitability, ion channels, Ca^{2+} signaling, exocytosis, and endocytosis, all linked to basic principles of neuronal communication. We predict that CCs, particularly those of transgenic murine models of disease, and after genetic manipulation of SNARE and other proteins of the secretory machinery will continue to be an invaluable tool to explore those mechanisms with complementary genetic and molecular biology techniques, and with electrophysiological and neuropharmacological approaches. The future of CCs as a neuronal model is assured.

The abbreviations used throughout this review are listed in Table 3.

Acknowledgements

We are very grateful to all members of the CC club (*International Symposium of Chromaffin Cell Biology*) who have devoted so much of their research effort to the chromaffin cell. This group meets every 2 years at different locations worldwide in an outstanding scientific and friendly atmosphere. This work has been partially funded by grants from i) CONACyT Laboratorio Nacional de Canalopatías 299051 and PAPIIT AG200119 (DGAPA-UNAM) to A.H-C. ii) MH002386 to L.E.E., iii) SAF 2016-78892R from MINECO, Spain, European Union Horizon2020 Research and Innovation Programme under the Marie Skoldowska-Curie Grant Agreement No. 766124, and Fundación Teófilo Hernando, Spain to A.G.G., iv) Ministerio de Ciencia, Innovación y Universidades BFU2017-82618-P to R.B. and v) Telethon Foundation, Italy (GGP 15110) and local grants from the University of Torino to E.C.

Table 3 List of Abbreviations

Abbreviation	Definition	Abbreviation	Definition
AADC	Aromatic amino acid decarboxylase	DCRD	Distal C-terminal regulatory domain
AE3	Anion exchanger	EGFP	Enhanced green fluorescent protein
Aβ	Amyloid beta-protein	Egr-1	Early growth response protein 1
AC	Adenylate cyclase	EPI	Epinephrine
ACh	Acetylcholine	EPAC	Exchange protein activated by cAMP
ACTH	*Adrenocorticotropic hormone*	ER	Endoplasmic reticulum
AD	Alzheimer's disease	ERG	Ether-à-go-go-related gene
AHP	Afterhyperpolarization	ERK	Extracellularly regulated kinase
AP	Action potential	GABA	γ-Aminobutyric acid
ALS	Amyotrophic lateral sclerosis	$GABA_A$-R	$GABA_A$ receptor
APP	Amyloid precursor protein	GPCR	G-protein-coupled receptor
AR	Adrenergic receptor	HAP1	Huntingtin-associated protein 1
ASD	Autism spectrum disorder	HCMDs	High calcium microdomains
ATP	Adenosine triphosphate	HD	Huntington's disease
BK	Big-conductance potassium channels	HIF	Hypoxia-inducible factor
BAM22P	Peptide (aa210-231) of proenkephalin-A	Kv	Voltage-gated potassium channels
BDNF	Brain-derived neurotrophic factor	IBMX	3-Isobutyl-1-methylxanthine
β-AR	Beta-adrenergic receptor	IL-1	Interleukin type 1
CAs	Catecholamines	$InsP_3$	Inositol tris-phosphate
Cav	Voltage-gated calcium channels	$InsP_3R$	Inositol tris-phosphate receptor
$[Ca^{2+}]_i$	Intracellular calcium concentration	IRP	Immediately releasable pool
$[Cl^-]_i$	Intracellular chloride concentration	ISI	Interspike interval
CC	Chromaffin cell	K_{ATP}	ATP-sensitive K channel
CDI	Calcium-dependent inactivation	KCC2	Cation-chloride cotransporter
CGRP	Calcitonin gene-related peptide	LDCV	Large dense core vesicles
CGs	Chromaffin granules	L-Dopa	Levorotatory form of dopa, L-3,4-dihydroxyphenylalanine
CgA	Chromogranin A	mAChR	Muscarinic cholinergic receptor
cGMP	Cyclic guanosine monophosphate	MAO	Mono amine oxidase
cAMP	Cyclic adenosine monophosphate	MHPG	3-Methoxy-4-hydroxyphenylglycol
CICR	Calcium-induced calcium release	MAPK	Mitogen-activated protein kinase, also called ERK,
CNS	Central nervous system		extracellular signal-regulated kinase
CPE	Carboxypeptidase processing enzyme	mNCX	Mitochondrial electroneutral Na^+/Ca^{2+} exchanger
COMT	Catechol-*O*-methyltransferase	MICU	Mitochondrial Ca^{2+} uniporter
CREB	cAMP response element-binding protein	MCCs	Mouse chromaffin cells
DA	Dopamine	nAChR	Nicotinic cholinergic receptor
DR1	Dopamine receptor type 1	Nav	Voltage-gated sodium channels
DBH	Dopamine-beta-hydroxylase	NE	Norepinephrine

(*continued*)

Table 3 (*Continued*)

Abbreviation	Definition	Abbreviation	Definition
NCS-1	Neuronal calcium sensor-1	SG	Secretory granule
NCX	Na^+/Ca^{2+} exchanger	SHR	Spontaneously hypertensive rat
NCS	Neuritogenic cAMP sensor	SNARE	Soluble NSF-attachment receptor complex
NKCC	$Na^+/K^+/2Cl^-$ cotransporter	SNS	Sympathetic nervous system
NO	Nitric oxide	Sp1	Specificity protein 1
NOS	NO synthase	SK	Small-conductance potassium channels
NPY	Neuropeptide Y	SOCCs	Store-operated calcium channels
NSF	*N*-Ethylmaleimide-sensitive factor	SOD	Superoxide dismutase
PACAP	Pituitary adenylate cyclase-activating polypeptide	SR	Sarcoplasmic reticulum
PAC1R	PACAP type 1 receptor	SRP	Slow releasable pool of vesicles
PAM	Peptidylglycine alpha-amidating monooxygenase	TEA	Tetraethylammonium
PD	Parkinson's disease	TH	Tyrosine hydroxylase
PDE	Phosphodiesterase	TS	Timothy syndrome
PIP_2	Phosphatidylinositol (4,5)-bisphosphate	TIRFM	Total internal reflection fluorescence microscopy
PKA	Protein kinase A	TNF-α	Tumor necrosis factor-alpha
PKC	Protein kinase C	TrkB	Tyrosine receptor kinase B
PKG	cGMP-dependent protein kinase	TTX	Tetrodotoxin
PLB	Phospholamban	VAMP	Vesicular monoamine transporter
PMCA	Plasma membrane Ca^{2+}-ATPase or Ca^{2+} pump	VAChT	Vesicular acetylcholine transporter
PNMT	Phenylethanolamine-*N*-methyltransferase	VNUT	Vesicular nucleotide transporter
PS1	presenilin 1	VIP	Vasoactive intestinal polypeptide
Rapgef	Rap-activating guanine-nucleotide-exchange factor	V-ATPase	Vesicular proton pump
ROS	Reactive oxygen species	VMA	Vanillylmandelic acid
RP	Reserve pool of vesicles	VMAT	Vesicular monoamine transporter
RRP	Readily releasable pool of vesicles	WT	Wild type
RyR	Ryanodine receptor	WKY	Wistar-Kyoto rats
SERCA	Sarco-endoplasmic reticulum Ca^{2+}-dependent ATPase		

References

1. Adams MB, Simonetta G, McMillen IC. The non-neurogenic catecholamine response of the fetal adrenal to hypoxia is dependent on activation of voltage sensitive Ca^{2+} channels. *Brain Res Dev Brain Res* 94: 182-189, 1996.
2. Adrian ED, Bronk DW, Phillips G. Discharges in mammalian sympathetic nerves. *J Physiol* 74: 115-133, 1932.
3. Affolter H-U, Giraud P, Hotchkiss AJ, Eiden LE. Stimulus-secretion-synthesis coupling: A model for cholinergic regulation of enkephalin secretion and gene transcription in adrenomedullary chromaffin cells. In: Fraioli F, editor. *Opiate Peptides in the Periphery*. Amsterdam: Elsevier, 1984, p. 23-30.
4. Ait-Ali D, Turquier V, Grumolato L, Yon L, Jourdain M, Alexandre D, Eiden LE, Vaudry H, Anouar Y. The proinflammatory cytokines tumor necrosis factor-alpha and interleukin-1 stimulate neuropeptide gene transcription and secretion in adrenochromaffin cells via activation of extracellularly regulated kinase 1/2 and p38 protein kinases, and activator protein-1 transcription factors. *Mol Endocrinol* 18: 1721-1739, 2004.
5. Ait-Ali D, Turquier V, Tanguy Y, Thouennon E, Ghzili H, Mounien L, Derambure C, Jegou S, Salier JP, Vaudry H, Eiden LE, Anouar Y. Tumor necrosis factor (TNF)-alpha persistently activates nuclear factor-kappaB signaling through the type 2 TNF receptor in chromaffin cells: Implications for long-term regulation of neuropeptide gene expression in inflammation. *Endocrinology* 149: 2840-2852, 2008.
6. Akiyama T, Yamazaki T, Mori H, Sunagawa K. Effects of Ca^{2+} channel antagonists on acetylcholine and catecholamine releases in the in vivo rat adrenal medulla. *Am J Physiol Regul Integr Comp Physiol* 287: R161-R166, 2004.
7. Albillos A, Artalejo AR, Lopez MG, Gandia L, Garcia AG, Carbone E. Calcium channel subtypes in cat chromaffin cells. *J Physiol* 477 (Pt 2): 197-213, 1994.
8. Albillos A, Carbone E, Gandia L, Garcia AG, Pollo A. Opioid inhibition of Ca^{2+} channel subtypes in bovine chromaffin cells: Selectivity of action and voltage dependence. *Eur J Neurosci* 8: 1561-1570, 1996.
9. Albillos A, Dernick G, Horstmann H, Almers W, Alvarez de Toledo G, Lindau M. The exocytotic event in chromaffin cells revealed by patch amperometry. *Nature* 389: 509-512, 1997.
10. Albillos A, Gandia L, Michelena P, Gilabert JA, delValle M, Carbone E, Garcia AG. The mechanism of calcium channel facilitation in bovine chromaffin cells. *J Physiol* 494: 687-695, 1996.
11. Albillos A, Neher E, Moser T. R-Type Ca^{2+} channels are coupled to the rapid component of secretion in mouse adrenal slice chromaffin cells. *J Neurosci* 20: 8323-8330, 2000.

12. Albinana E, Segura-Chama P, Baraibar AM, Hernandez-Cruz A, Hernandez-Guijo JM. Different contributions of calcium channel subtypes to electrical excitability of chromaffin cells in rat adrenal slices. *J Neurochem* 133: 511-521, 2015.
13. Alejandre-Garcia T, Pena-Del Castillo JG, Hernandez-Cruz A. GABAA receptor: A unique modulator of excitability, Ca(2+) signaling, and catecholamine release of rat chromaffin cells. *Pflug Archiv: Eur J Physiol* 470: 67-77, 2018.
14. Alejandre-Garcia T, Segura-Chama P, Perez-Armendariz EM, Delgado-Lezama R, Hernandez-Cruz A. Erratum to: Modulation of spontaneous intracellular Ca(2+) fluctuations and spontaneous cholinergic transmission in rat chromaffin cells in situ by endogenous GABA acting on GABAA receptors. *Pflug Archiv: Eur J Physiol* 469: 1413, 2017.
15. Ales E, Tabares L, Poyato JM, Valero V, Lindau M, Alvarez de Toledo G. High calcium concentrations shift the mode of exocytosis to the kiss-and-run mechanism. *Nat Cell Biol* 1: 40-44, 1999.
16. Aloe L, Levi-Montalcini R. Nerve growth factor-induced transformation of immature chromaffin cells in vivo into sympathetic neurons: Effect of antiserum to nerve growth factor. *Proc Natl Acad Sci USA* 76: 1246-1250, 1979.
17. Alonso MT, Barrero MJ, Michelena P, Carnicero E, Cuchillo I, Garcia AG, Garcia-Sancho J, Montero M, Alvarez J. Ca^{2+}-induced Ca^{2+} release in chromaffin cells seen from inside the ER with targeted aequorin. *J Cell Biol* 144: 241-254, 1999.
18. Alvarez de Toledo G, Fernandez-Chacon R, Fernandez JM. Release of secretory products during transient vesicle fusion. *Nature* 363: 554-558, 1993.
19. Alvarez de Toledo G, Montes MA, Montenegro P, Borges R. Phases of the exocytotic fusion pore. *FEBS Lett* 592: 3532-3541, 2018.
20. Alvarez YD, Ibanez LI, Uchitel OD, Marengo FD. P/Q Ca^{2+} channels are functionally coupled to exocytosis of the immediately releasable pool in mouse chromaffin cells. *Cell Calcium* 43: 155-164, 2008.
21. Amar L, Servais A, Gimenez-Roqueplo AP, Zinzindohoue F, Chatellier G, Plouin PF. Year of diagnosis, features at presentation, and risk of recurrence in patients with pheochromocytoma or secreting paraganglioma. *J Clin Endocrinol Metab* 90: 2110-2116, 2005.
22. Amenta F, Collier WL, Erdo SL, Giuliani S, Maggi CA, Meli A. GABAA receptor sites modulating catecholamine secretion in the rat adrenal gland: Evidence from 3H-muscimol autoradiography and in vivo functional studies. *Pharmacology* 37: 394-402, 1988.
23. Anderson EA, Sinkey CA, Lawton WJ, Mark AL. Elevated sympathetic nerve activity in borderline hypertensive humans. Evidence from direct intraneural recordings. *Hypertension* 14: 177-183, 1989.
24. Anderson K, Robinson PJ, Marley PD. Cholinoceptor regulation of cyclic AMP levels in bovine adrenal medullary cells. *Br J Pharmacol* 106: 360-366, 1992.
25. Andreis PG, Neri G, Prayer-Galetti T, Rossi GP, Gottardo G, Malendowicz LK, Nussdorfer GG. Effects of adrenomedullin on the human adrenal glands: An in vitro study. *J Clin Endocrinol Metab* 82: 1167-1170, 1997.
26. Arimura A. Pituitary adenylate cyclase-activating polypeptide (PACAP): Discovery and current status of research. *Regul Pept* 37: 287-303, 1992.
27. Ariton M, Juan CS, AvRuskin TW. Pheochromocytoma: Clinical observations from a Brooklyn tertiary hospital. *Endocr Prac: Off J Am Coll Endocrinol Am Assoc Clin Endocrinol* 6: 249-252, 2000.
28. Arribas-Blazquez M, Olivos-Ore LA, Barahona MV, Sanchez de la Muela M, Solar V, Jimenez E, Gualix J, McIntosh JM, Ferrer-Montiel A, Miras-Portugal MT, Artalejo AR. Overexpression of P2X3 and P2X7 receptors and TRPV1 channels in adrenomedullary chromaffin cells in a rat model of neuropathic pain. *Int J Mol Sci* 20 (1): 155, 2019.
29. Artalejo AR, Garcia AG, Neher E. Small-conductance Ca(2+)-activated K+ channels in bovine chromaffin cells. *Pflug Archiv: Eur J Physiol* 423: 97-103, 1993.
30. Artalejo CR, Adams ME, Fox AP. Three types of Ca^{2+} channel trigger secretion with different efficacies in chromaffin cells. *Nature* 367: 72-76, 1994.
31. Artalejo CR, Dahmer MK, Perlman RL, Fox AP. Two types of Ca^{2+} currents are found in bovine chromaffin cells: Facilitation is due to the recruitment of one type. *J Physiol* 432: 681-707, 1991.
32. Artalejo CR, Garcia AG, Aunis D. Chromaffin cell calcium channel kinetics measured isotopically through fast calcium, strontium, and barium fluxes. *J Biol Chem* 262: 915-926, 1987.
33. Artalejo CR, Henley JR, McNiven MA, Palfrey HC. Rapid endocytosis coupled to exocytosis in adrenal chromaffin cells involves Ca2+, GTP, and dynamin but not clathrin. *Proc Natl Acad Sci USA* 92: 8328-8332, 1995.
34. Artalejo CR, Lemmon MA, Schlessinger J, Palfrey HC. Specific role for the PH domain of dynamin-1 in the regulation of rapid endocytosis in adrenal chromaffin cells. *EMBO J* 16: 1565-1574, 1997.
35. Artalejo CR, Mogul DJ, Perlman RL, Fox AP. Three types of bovine chromaffin cell Ca^{2+} channels: Facilitation increases the opening probability of a 27 pS channel. *J Physiol* 444: 213-240, 1991.
36. Artalejo CR, Perlman RL, Fox AP. Omega-conotoxin GVIA blocks a Ca^{2+} current in bovine chromaffin cells that is not of the "classic" N type. *Neuron* 8: 85-95, 1992.
37. Arvan P, Castle D. Sorting and storage during secretory granule biogenesis: Looking backward and looking forward. *Biochem J* 332 (Pt 3): 593-610, 1998.
38. Augustine GJ, Neher E. Calcium requirements for secretion in bovine chromaffin cells. *J Physiol* 450: 247-271, 1992.
39. Aunis D, Bader MF. The cytoskeleton as a barrier to exocytosis in secretory cells. *J Exp Biol* 139: 253-266, 1988.
40. Babcock DF, Herrington J, Goodwin PC, Park YB, Hille B. Mitochondrial participation in the intracellular Ca^{2+} network. *J Cell Biol* 136: 833-844, 1997.
41. Bader PL, Faizi M, Kim LH, Owen SF, Tadross MR, Alfa RW, Bett GC, Tsien RW, Rasmusson RL, Shamloo M. Mouse model of Timothy syndrome recapitulates triad of autistic traits. *Proc Natl Acad Sci USA* 108: 15432-15437, 2011.
42. Baker PF, Blaustein MP, Hodgkin AL, Steinhardt RA. The influence of calcium on sodium efflux in squid axons. *J Physiol* 200: 431-458, 1969.
43. Baker PF, Knight DE. Calcium-dependent exocytosis in bovine adrenal medullary cells with leaky plasma membranes. *Nature* 276: 620-622, 1978.
44. Baker PF, Knight DE. Calcium control of exocytosis and endocytosis in bovine adrenal medullary cells. *Philos Trans R Soc Lond B Biol Sci* 296: 83-103, 1981.
45. Baker PF, Rink TJ. Catecholamine release from bovine adrenal medulla in response to maintained depolarization. *J Physiol* 253: 593-620, 1975.
46. Baldelli P, Hernandez-Guijo JM, Carabelli V, Novara M, Cesetti T, Andres-Mateos E, Montiel C, Carbone E. Direct and remote modulation of L-channels in chromaffin cells – Distinct actions on alpha(1C) and alpha(1D) subunits? *Mol Neurobiol* 29: 73-96, 2004.
47. Barbara JG, Poncer JC, McKinney RA, Takeda K. An adrenal slice preparation for the study of chromaffin cells and their cholinergic innervation. *J Neurosci Methods* 80: 181-189, 1998.
48. Barbara JG, Takeda K. Quantal release at a neuronal nicotinic synapse from rat adrenal gland. *Proc Natl Acad Sci USA* 93: 9905-9909, 1996.
49. Barg S, Machado JD. Compensatory endocytosis in chromaffin cells. *Acta Physiol (Oxf)* 192: 195-201, 2008.
50. Barman SM, Gebber GL. Sympathetic nerve rhythm of brain stem origin. *Am J Physiol* 239: R42-R47, 1980.
51. Bean BP. The action potential in mammalian central neurons. *Nat Rev Neurosci* 8: 451-465, 2007.
52. Bean BP. Neurotransmitter inhibition of neuronal calcium currents by changes in channel voltage dependence. *Nature* 340: 153-156, 1989.
53. Beaudet MM, Parsons RL, Braas KM, May V. Mechanisms mediating pituitary adenylate cyclase-activating polypeptide depolarization of rat sympathetic neurons. *J Neurosci* 20: 7353-7361, 2000.
54. Becherer U, Moser T, Stuhmer W, Oheim M. Calcium regulates exocytosis at the level of single vesicles. *Nat Neurosci* 6: 846-853, 2003.
55. Ben-Ari Y, Gaiarsa JL, Tyzio R, Khazipov R. GABA: A pioneer transmitter that excites immature neurons and generates primitive oscillations. *Physiol Rev* 87: 1215-1284, 2007.
56. Benedeczky I, Somogyi P. Cytochemical localization of exogenous peroxidase in adrenal medullary cells of hamster. *Acta Biol Acad Sci Hung* 29: 155-163, 1978.
57. Benfante R, Flora A, Di Lascio S, Cargnin F, Longhi R, Colombo S, Clementi F, Fornasari D. Transcription factor PHOX2A regulates the human alpha3 nicotinic receptor subunit gene promoter. *J Biol Chem* 282: 13290-13302, 2007.
58. Bennett MR, McLachlan EM. An electrophysiological analysis of the synthesis of acetylcholine in preganglionic nerve terminals. *J Physiol* 221: 669-682, 1972.
59. Bereiter DA, Engeland WC, Gann DS. Adrenal secretion of epinephrine after stimulation of trigeminal nucleus caudalis depends on stimulus pattern. *Neuroendocrinology* 45: 54-61, 1987.
60. Bernard C. *Decons sur les phénomenes de la vie communs aux animaux et auc végétaux*. Paris: Bailliere, 1878.
61. Biales B, Dichter M, Tischler A. Electrical excitability of cultured adrenal chromaffin cells. *J Physiol* 262: 743-753, 1976.
62. Blaschko H, Comline RS, Schneider FH, Silver M, Smith AD. Secretion of a chromaffin granule protein, chromogranin, from the adrenal gland after splanchnic stimulation. *Nature* 215: 58-59, 1967.
63. Blaustein MP, Lederer WJ. Sodium/calcium exchange: Its physiological implications. *Physiol Rev* 79: 763-854, 1999.
64. Bödding M. Histamine evoked sustained elevations of cytosolic Ca^{2+} in bovine adrenal chromaffin cells independently of Ca^{2+} entry. *Cell Calcium* 27: 139-151, 2000.
65. Bomfim GHS, Mendez-Lopez I, Fernandez-Morales JC, Padin JF, Jurkiewicz A, Jurkiewicz NH, Garcia AG. Electrophysiological

properties and augmented catecholamine release from chromaffin cells of WKY and SHR rats contributing to the hypertension development elicited by chronic EtOH consumption. *Eur J Pharmacol* 803: 65-77, 2017.
66. Borchelt DR, Ratovitski T, van Lare J, Lee MK, Gonzales V, Jenkins NA, Copeland NG, Price DL, Sisodia SS. Accelerated amyloid deposition in the brains of transgenic mice coexpressing mutant presenilin 1 and amyloid precursor proteins. *Neuron* 19: 939-945, 1997.
67. Borges R. The ATP or the natural history of neurotransmission. *Purinergic Signal* 9: 5-6, 2013.
68. Borges R. Histamine H1 receptor activation mediates the preferential release of adrenaline in the rat adrenal gland. *Life Sci* 54: 631-640, 1994.
69. Borges R, Camacho M, Gillis KD. Measuring secretion in chromaffin cells using electrophysiological and electrochemical methods. *Acta Physiol (Oxf)* 192: 173-184, 2008.
70. Borges R, Gandia L, Carbone E. Old and emerging concepts on adrenal chromaffin cell stimulus-secretion coupling. *Pflug Archiv: Eur J Physiol* 470: 1-6, 2018.
71. Bormann J. Electrophysiology of GABAA and GABAB receptor subtypes. *Trends Neurosci* 11: 112-116, 1988.
72. Bos JL. Epac: A new cAMP target and new avenues in cAMP research. *Nat Rev Mol Cell Biol* 4: 733-738, 2003.
73. Bournaud R, Hidalgo J, Yu H, Girard E, Shimahara T. Catecholamine secretion from rat foetal adrenal chromaffin cells and hypoxia sensitivity. *Pflug Archiv: Eur J Physiol* 454: 83-92, 2007.
74. Bournaud R, Hidalgo J, Yu H, Jaimovich E, Shimahara T. Low threshold T-type calcium current in rat embryonic chromaffin cells. *J Physiol* 537: 35-44, 2001.
75. Bowery N. GABAB receptors and their significance in mammalian pharmacology. *Trends Pharmacol Sci* 10: 401-407, 1989.
76. Brandt BL, Hagiwara S, Kidokoro Y, Miyazaki S. Action potentials in the rat chromaffin cell and effects of acetylcholine. *J Physiol* 263: 417-439, 1976.
77. Bravo EL, Tagle R. Pheochromocytoma: State-of-the-art and future prospects. *Endocr Rev* 24: 539-553, 2003.
78. Brede M, Nagy G, Philipp M, Sorensen JB, Lohse MJ, Hein L. Differential control of adrenal and sympathetic catecholamine release by alpha 2-adrenoceptor subtypes. *Mol Endocrinol (Baltimore, Md)* 17: 1640-1646, 2003.
79. Brini M, Carafoli E. The plasma membrane Ca(2)+ ATPase and the plasma membrane sodium calcium exchanger cooperate in the regulation of cell calcium. *Cold Spring Harb Perspect Biol* 3, 2011. DOI: 10.1101/cshperspect.a004168.
80. Brown CH, Scott V, Ludwig M, Leng G, Bourque CW. Somatodendritic dynorphin release: Orchestrating activity patterns of vasopressin neurons. *Biochem Soc Trans* 35: 1236-1242, 2007.
81. Brown RL, Strassmaier T, Brady JD, Karpen JW. The pharmacology of cyclic nucleotide-gated channels: Emerging from the darkness. *Curr Pharm Des* 12: 3597-3613, 2006.
82. Bunn SJ, Ait-Ali D, Eiden LE. Immune-neuroendocrine integration at the adrenal gland: Cytokine control of the adrenomedullary transcriptome. *J Mol Neurosci* 48: 413-419, 2012.
83. Bunn SJ, Boyd TL. Characterization of histamine-induced catecholamine secretion from bovine adrenal medullary chromaffin cells. *J Neurochem* 58: 1602-1610, 1992.
84. Bunn SJ, Marley PD, Livett BG. Receptor stimulated formation of inositol phosphates in cultures of bovine adrenal medullary cells: The effects of bradykinin, bombesin and neurotensin. *Neuropeptides* 15: 187-194, 1990.
85. Burgoyne RD. Fast exocytosis and endocytosis triggered by depolarisation in single adrenal chromaffin cells before rapid Ca^{2+} current run-down. *Pflug Archiv: Eur J Physiol* 430: 213-219, 1995.
86. Burgoyne RD. Mechanisms of catecholamine secretion from adrenal chromaffin cells. *J Physiol Pharmacol* 46: 273-283, 1995.
87. Busik J, Nakamura M, Abe Y, Shibuya I, Kanno T. Effects of GABA on spontaneous $[Ca^{2+}]$c dynamics and electrical properties of rat adrenal chromaffin cells. *Brain Res* 739: 97-103, 1996.
88. Byrne CJ, Khurana S, Kumar A, Tai TC. Inflammatory signaling in hypertension: Regulation of adrenal catecholamine biosynthesis. *Front Endocrinol* 9: 343, 2018.
89. Calbet JA. Chronic hypoxia increases blood pressure and noradrenaline spillover in healthy humans. *J Physiol* 551: 379-386, 2003.
90. Calhoun DA, Jones D, Textor S, Goff DC, Murphy TP, Toto RD, White A, Cushman WC, White W, Sica D, Ferdinand K, Giles TD, Falkner B, Carey RM. Resistant hypertension: Diagnosis, evaluation, and treatment. A scientific statement from the American Heart Association Professional Education Committee of the Council for High Blood Pressure Research. *Hypertension* 51: 1403-1419, 2008.
91. Calorio C, Gavello D, Guarina L, Salio C, Sassoe-Pognetto M, Riganti C, Bianchi FT, Hofer NT, Tuluc P, Obermair GJ, Defilippi P, Balzac F, Turco E, Bett GC, Rasmusson RL, Carbone E. Impaired chromaffin cell excitability and exocytosis in autistic Timothy syndrome TS2-neo mouse rescued by L-type calcium channel blockers. *J Physiol* 597: 1705-1733, 2019.
92. Calvo-Gallardo E, de Pascual R, Fernandez-Morales JC, Arranz-Tagarro JA, Maroto M, Nanclares C, Gandia L, de Diego AM, Padin JF, Garcia AG. Depressed excitability and ion currents linked to slow exocytotic fusion pore in chromaffin cells of the SOD1(G93A) mouse model of amyotrophic lateral sclerosis. *Am J Physiol Cell Physiol* 308: C1-C19, 2015.
93. Camacho M, Machado JD, Alvarez J, Borges R. Intravesicular calcium release mediates the motion and exocytosis of secretory organelles: A study with adrenal chromaffin cells. *J Biol Chem* 283: 22383-22389, 2008.
94. Camacho M, Machado JD, Montesinos MS, Criado M, Borges R. Intragranular pH rapidly modulates exocytosis in adrenal chromaffin cells. *J Neurochem* 96: 324-334, 2006.
95. Cannon WB. Organization for physiological homeostasis. *Physiol Rev* 9: 399-431, 1929.
96. Cannon WB. *Wisdom of the Body*. New York: W. W. Norton & Company, 1932.
97. Cannon WB, Hoskins RG. The effects of sphyxia, hyperpnea, and sensory stimulation on adrenal secretion. *Am J Physiol* 29: 274-279, 1911.
98. Carabelli V, Carra I, Carbone E. Localized secretion of ATP and opioids revealed through single Ca2+ channel modulation in bovine chromaffin cells. *Neuron* 20: 1255-1268, 1998.
99. Carabelli V, D'Ascenzo M, Carbone E, Grassi C. Nitric oxide inhibits neuroendocrine Ca(v)1 L-channel gating via cGMP-dependent protein kinase in cell-attached patches of bovine chromaffin cells. *J Physiol-Lond* 541: 351-366, 2002.
100. Carabelli V, Giancippoli A, Baldelli P, Carbone E, Artalejo AR. Distinct potentiation of L-type currents and secretion by cAMP in rat chromaffin cells. *Biophys J* 85: 1326-1337, 2003.
101. Carabelli V, Hernandez-Guijo JM, Baldelli P, Carbone E. Direct autocrine inhibition and cAMP-dependent potentiation of single L-type Ca2+ channels in bovine chromaffin cells. *J Physiol-Lond* 532: 73-90, 2001.
102. Carabelli V, Lovallo M, Magnelli V, Zucker H, Carbone E. Voltage-dependent modulation of single N-type Ca^{2+} channel kinetics by receptor agonists in IMR32 cells. *Biophys J* 70: 2144-2154, 1996.
103. Carabelli V, Marcantoni A, Comunanza V, Carbone E. Fast exocytosis mediated by T- and L-type channels in chromaffin cells: Distinct voltage-dependence but similar Ca^{2+}-dependence. *Eur Biophys J Biophys Lett* 36: 753-762, 2007.
104. Carabelli V, Marcantoni A, Comunanza V, De Luca A, Diaz J, Borges R, Carbone E. Chronic hypoxia up-regulates alpha(1H) T-type channels and low-threshold catecholamine secretion in rat chromaffin cells. *J Physiol* 584: 149-165, 2007.
105. Carafoli E. The calcium cycle of mitochondria. *FEBS Lett* 104: 1-5, 1979.
106. Carafoli E, Fedrizzi L, Domi T, Di Leva F, Brini M. Caclium pumps part II. Transmission: Effectors and cytosolic events. In: *Handbook of Cell Signaling* (2nd ed). New York: Academic Press, 2010, p. 943-947.
107. Carbone E, Calorio C, Vandael DH. T-type channel-mediated neurotransmitter release. *Pflug Archiv: Eur J Physiol* 466: 677-687, 2014.
108. Carbone E, Carabelli V. O_2 sensing in chromaffin cells: New duties for T-type channels. *J Physiol* 587: 1859-1860, 2009.
109. Carbone E, Carabelli V, Cesetti T, Baldelli P, Hernandez-Guijo JM, Giusta L. G-protein- and cAMP-dependent L-channel gating modulation: A manyfold system to control calcium entry in neurosecretory cells. *Pflug Archiv: Eur J Physiol* 442: 801-813, 2001.
110. Carbone E, Giancippoli A, Marcantoni A, Guido D, Carabelli V. A new role for T-type channels in fast "low-threshold" exocytosis. *Cell Calcium* 40: 147-154, 2006.
111. Cardenas AM, Marengo FD. Rapid endocytosis and vesicle recycling in neuroendocrine cells. *Cell Mol Neurobiol* 30: 1365-1370, 2010.
112. Caricati-Neto A, Padin JF, Silva-Junior ED, Fernandez-Morales JC, de Diego AM, Jurkiewicz A, Garcia AG. Novel features on the regulation by mitochondria of calcium and secretion transients in chromaffin cells challenged with acetylcholine at 37 °C. *Physiol Rep* 1: e00182, 2013.
113. Carmichael SW, Winkler H. The adrenal chromaffin cell. *Sci Am* 253: 39-49, 1985.
114. Carrasco-Serrano C, Campos-Caro A, Viniegra S, Ballesta JJ, Criado M. GC- and E-box motifs as regulatory elements in the proximal promoter region of the neuronal nicotinic receptor alpha7 subunit gene. *J Biol Chem* 273: 20021-20028, 1998.
115. Catterall WA. Interactions of presynaptic Ca^{2+} channels and snare proteins in neurotransmitter release. *Ann NY Acad Sci* 868: 144-159, 1999.
116. Catterall WA. Voltage-gated calcium channels. *Cold Spring Harbor Perspect Biol* 3: 23, 2011.
117. Catterall WA, Goldin AL, Waxman SG. International Union of Pharmacology. XLVII. Nomenclature and structure-function relationships of voltage-gated sodium channels. *Pharmacol Rev* 57: 397-409, 2005.
118. Ceccarelli B, Hurlbut WP. Ca^{2+}-dependent recycling of synaptic vesicles at the frog neuromuscular junction. *J Cell Biol* 87: 297-303, 1980.

119. Ceccarelli B, Hurlbut WP, Mauro A. Turnover of transmitter and synaptic vesicles at the frog neuromuscular junction. *J Cell Biol* 57: 499-524, 1973.
120. Cena V, Nicolas GP, Sanchez-Garcia P, Kirpekar SM, Garcia AG. Pharmacological dissection of receptor-associated and voltage-sensitive ionic channels involved in catecholamine release. *Neuroscience* 10: 1455-1462, 1983.
121. Cesetti T, Hernandez-Guijo JM, Baldelli P, Carabelli V, Carbone E. Opposite action of beta 1- and beta 2-adrenergic receptors on Ca(V)1 L-channel current in rat adrenal chromaffin cells. *J Neurosci* 23: 73-83, 2003.
122. Chan SA, Polo-Parada L, Smith C. Action potential stimulation reveals an increased role for P/Q-calcium channel-dependent exocytosis in mouse adrenal tissue slices. *Arch Biochem Biophys* 435: 65-73, 2005.
123. Cheek TR, Barry VA, Berridge MJ, Missiaen L. Bovine adrenal chromaffin cells contain an inositol 1,4,5-trisphosphate-insensitive but caffeine-sensitive Ca^{2+} store that can be regulated by intraluminal free Ca^{2+}. *Biochem J* 275 (Pt 3): 697-701, 1991.
124. Cheek TR, Berridge MJ, Moreton RB, Stauderman KA, Murawsky MM, Bootman MD. Quantal Ca^{2+} mobilization by ryanodine receptors is due to all-or-none release from functionally discrete intracellular stores. *Biochem J* 301 (Pt 3): 879-883, 1994.
125. Cheek TR, Burgoyne RD. Nicotine-evoked disassembly of cortical actin filaments in adrenal chromaffin cells. *FEBS Lett* 207: 110-114, 1986.
126. Cheek TR, Moreton RB, Berridge MJ, Stauderman KA, Murawsky MM, Bootman MD. Quantal Ca^{2+} release from caffeine-sensitive stores in adrenal chromaffin cells. *J Biol Chem* 268: 27076-27083, 1993.
127. Cheek TR, Murawsky MM, Stauderman KA. Histamine-induced Ca^{2+} entry precedes Ca^{2+} mobilization in bovine adrenal chromaffin cells. *Biochem J* 304 (Pt 2): 469-476, 1994.
128. Chen TT, Li L, Chung DH, Allen CD, Torti SV, Torti FM, Cyster JG, Chen CY, Brodsky FM, Niemi EC, Nakamura MC, Seaman WE, Daws MR. TIM-2 is expressed on B cells and in liver and kidney and is a receptor for H-ferritin endocytosis. *J Exp Med* 202: 955-965, 2005.
129. Chow RH, Klingauf J, Neher E. Time course of Ca^{2+} concentration triggering exocytosis in neuroendocrine cells. *Proc Natl Acad Sci USA* 91: 12765-12769, 1994.
130. Chow RH, von Ruden L, Neher E. Delay in vesicle fusion revealed by electrochemical monitoring of single secretory events in adrenal chromaffin cells. *Nature* 356: 60-63, 1992.
131. Chuang D-M, Costa E. Biosynthesis of tyrosine hydroxylase in rat adrenal medulla after exposure to cold. *Proc Natl Acad Sci USA* 71: 4570-4574, 1974.
132. Clapham DE, Neher E. Substance P reduces acetylcholine-induced currents in isolated bovine chromaffin cells. *J Physiol* 347: 255-277, 1984.
133. Colomer C, Martin AO, Desarmenien MG, Guerineau NC. Gap junction-mediated intercellular communication in the adrenal medulla: An additional ingredient of stimulus-secretion coupling regulation. *Biochim Biophys Acta* 1818: 1937-1951, 2011.
134. Colomer C, Olivos Ore LA, Coutry N, Mathieu MN, Arthaud S, Fontanaud P, Iankova I, Macari F, Thouennon E, Yon L, Anouar Y, Guerineau NC. Functional remodeling of gap junction-mediated electrical communication between adrenal chromaffin cells in stressed rats. *J Neurosci* 28: 6616-6626, 2008.
135. Comb M, Seeburg PH, Adelman J, Eiden L, Herbert E. Primary structure of the human Met- and Leu-enkephalin precursor and its mRNA. *Nature* 295: 663-666, 1982.
136. Comunanza V, Marcantoni A, Vandael DHF, Mahapatra S, Gavello D, Navarro-Tableros V, Carabelli V, Carbone E. Ca(V)1.3 as pacemaker channels in adrenal chromaffin cells. *Channels* 4: 440-446, 2010.
137. Conrad CH, Brooks WW, Hayes JA, Sen S, Robinson KG, Bing OH. Myocardial fibrosis and stiffness with hypertrophy and heart failure in the spontaneously hypertensive rat. *Circulation* 91: 161-170, 1995.
138. Cortez V, Santana M, Marques AP, Mota A, Rosmaninho-Salgado J, Cavadas C. Regulation of catecholamine release in human adrenal chromaffin cells by beta-adrenoceptors. *Neurochem Int* 60: 387-393, 2012.
139. Coupland RE. Electron microscopic observations on the structure of the rat adrenal medulla. I. The ultrastructure and organization of chromaffin cells in the normal adrenal medulla. *J Anat* 99: 231-254, 1965.
140. Coupland RE, Pyper AS, Hopwood D. A method for differentiating between noradrenaline- and adrenaline-storing cells in the light and electron microscope. *Nature* 201: 1240-1242, 1964.
141. Couratier P, Hugon J, Sindou P, Vallat JM, Dumas M. Cell culture evidence for neuronal degeneration in amyotrophic lateral sclerosis being linked to glutamate AMPA/kainate receptors. *Lancet* 341: 265-268, 1993.
142. Criado M. Acetylcholine nicotinic receptor subtypes in chromaffin cells. *Pflug Archiv: Eur J Physiol* 470: 13-20, 2018.
143. Crill WE. Persistent sodium current in mammalian central neurons. *Annu Rev Physiol* 58: 349-362, 1996.
144. Cuchillo-Ibanez I, Lejen T, Albillos A, Rose SD, Olivares R, Villarroya M, Garcia AG, Trifaro JM. Mitochondrial calcium sequestration and protein kinase C cooperate in the regulation of cortical F-actin disassembly and secretion in bovine chromaffin cells. *J Physiol* 560: 63-76, 2004.
145. Cuchillo-Ibanez I, Olivares R, Aldea M, Villarroya M, Arroyo G, Fuentealba J, Garcia AG, Albillos A. Acetylcholine and potassium elicit different patterns of exocytosis in chromaffin cells when the intracellular calcium handling is disturbed. *Pflug Archiv: Eur J Physiol* 444: 133-142, 2002.
146. Cummins TR, Aglieco F, Renganathan M, Herzog RI, Dib-Hajj SD, Waxman SG. Nav1.3 sodium channels: Rapid repriming and slow closed-state inactivation display quantitative differences after expression in a mammalian cell line and in spinal sensory neurons. *J Neurosci* 21: 5952-5961, 2001.
147. Currie G, Freel EM, Perry CG, Dominiczak AF. Disorders of blood pressure regulation-role of catecholamine biosynthesis, release, and metabolism. *Curr Hypertens Rep* 14: 38-45, 2012.
148. Currie KP. Inhibition of Ca^{2+} channels and adrenal catecholamine release by G protein coupled receptors. *Cell Mol Neurobiol* 30: 1201-1208, 2010.
149. Currie KP, Fox AP. ATP serves as a negative feedback inhibitor of voltage-gated Ca2+ channel currents in cultured bovine adrenal chromaffin cells. *Neuron* 16: 1027-1036, 1996.
150. Currie KP, Fox AP. Differential facilitation of N- and P/Q-type calcium channels during trains of action potential-like waveforms. *J Physiol* 539: 419-431, 2002.
151. Currie KP, Fox AP. Voltage-dependent, pertussis toxin insensitive inhibition of calcium currents by histamine in bovine adrenal chromaffin cells. *J Neurophysiol* 83: 1435-1442, 2000.
152. Dani JA. Neuronal nicotinic acetylcholine receptor structure and function and response to nicotine. *Int Rev Neurobiol* 124: 3-19, 2015.
153. de Diego AM. Electrophysiological and morphological features underlying neurotransmission efficacy at the splanchnic nerve-chromaffin cell synapse of bovine adrenal medulla. *Am J Physiol Cell Physiol* 298: C397-C405, 2010.
154. de Diego AM, Arnaiz-Cot JJ, Hernandez-Guijo JM, Gandia L, Garcia AG. Differential variations in Ca^{2+} entry, cytosolic Ca^{2+} and membrane capacitance upon steady or action potential depolarizing stimulation of bovine chromaffin cells. *Acta Physiol (Oxford)* 194: 97-109, 2008.
155. de Diego AM, Gandia L, Garcia AG. A physiological view of the central and peripheral mechanisms that regulate the release of catecholamines at the adrenal medulla. *Acta Physiol (Oxford, England)* 192: 287-301, 2007.
156. de Diego AM, Lorrio S, Calvo-Gallardo E, Garcia AG. Smaller quantal size and faster kinetics of single exocytotic events in chromaffin cells from the APP/PS1 mouse model of Alzheimer's disease. *Biochem Biophys Res Commun* 428: 482-486, 2012.
157. de Diego AMG, Garcia AG. Altered exocytosis in chromaffin cells from mouse models of neurodegenerative diseases. *Acta Physiol (Oxford, England)* 224: e13090, 2018.
158. de Rooij J, Zwartkruis FJT, Verheijen MHG, Cool RH, Jijman SMB, Witinghofer A, Bos JL. Epac is a Rap1 guanine-nucleotide-exchange factor directly activated by cyclic AMP. *Nature* 396: 474-477, 1998.
159. del Barrio L, Egea J, Leon R, Romero A, Ruiz A, Montero M, Alvarez J, Lopez MG. Calcium signalling mediated through alpha7 and non-alpha7 nAChR stimulation is differentially regulated in bovine chromaffin cells to induce catecholamine release. *Br J Pharmacol* 162: 94-110, 2011.
160. Del Toro R, Levitsky KL, Lopez-Barneo J, Chiara MD. Induction of T-type calcium channel gene expression by chronic hypoxia. *J Biol Chem* 278: 22316-22324, 2003.
161. Delmas P, Brown DA. Pathways modulating neural KCNQ/M (Kv7) potassium channels. *Nat Rev Neurosci* 6: 850-862, 2005.
162. Desarmenien MG, Jourdan C, Toutain B, Vessieres E, Hormuzdi SG, Guerineau NC. Gap junction signalling is a stress-regulated component of adrenal neuroendocrine stimulus-secretion coupling in vivo. *Nat Commun* 4: 2938, 2013.
163. Dhara M, Mohrmann R, Bruns D. v-SNARE function in chromaffin cells. *Pflug Archiv: Eur J Physiol* 470: 169-180, 2018.
164. Di Angelantonio S, Giniatullin R, Costa V, Sokolova E, Nistri A. Modulation of neuronal nicotinic receptor function by the neuropeptides CGRP and substance P on autonomic nerve cells. *Br J Pharmacol* 139: 1061-1073, 2003.
165. Di Leva F, Domi T, Fedrizzi L, Lim D, Carafoli E. The plasma membrane Ca^{2+} ATPase of animal cells: Structure, function and regulation. *Arch Biochem Biophys* 476: 65-74, 2008.
166. Diaz-Vera J, Camacho M, Machado JD, Dominguez N, Montesinos MS, Hernandez-Fernaud JR, Lujan R, Borges R. Chromogranins A and B are key proteins in amine accumulation, but the catecholamine secretory pathway is conserved without them. *FASEB J* 26: 430-438, 2012.
167. Ding JP, Li ZW, Lingle CJ. Inactivating BK channels in rat chromaffin cells may arise from heteromultimeric assembly of distinct inactivation-competent and noninactivating subunits. *Biophys J* 74: 268-289, 1998.

168. Dinkelacker V, Voets T, Neher E, Moser T. The readily releasable pool of vesicles in chromaffin cells is replenished in a temperature-dependent manner and transiently overfills at 37 °C. *J Neurosci* 20: 8377-8383, 2000.
169. Dodge FA Jr., Rahamimoff R. Co-operative action a calcium ions in transmitter release at the neuromuscular junction. *J Physiol* 193: 419-432, 1967.
170. Dominguez N, Estevez-Herrera J, Borges R, Machado JD. The interaction between chromogranin A and catecholamines governs exocytosis. *FASEB J* 28: 4657-4667, 2014.
171. Douglas SA, Sreenivasan D, Carman FH, Bunn SJ. Cytokine interactions with adrenal medullary chromaffin cells. *Cell Mol Neurobiol* 30: 1467-1475, 2010.
172. Douglas WW. Stimulus-secretion coupling: The concept and clues from chromaffin and other cells. *Br J Pharmacol* 34: 451-474, 1968.
173. Douglas WW, Poisner AM. Preferential release of adrenaline from the adrenal medulla by muscarine and pilocarpine. *Nature* 208: 1102-1103, 1965.
174. Douglas WW, Poisner AM. Stimulation of uptake of calcium-45 in the adrenal gland by acetylcholine. *Nature* 192: 1299, 1961.
175. Douglas WW, Rubin RP. Mechanism of nicotinic action at the adrenal medulla: Calcium as a link in stimulus-secretion coupling. *Nature* 192: 1087-1089, 1961.
176. Douglas WW, Rubin RP. The role of calcium in the secretory response of the adrenal medulla to acetylcholine. *J Physiol* 159: 40-57, 1961.
177. Dragatsis I, Dietrich P, Zeitlin S. Expression of the Huntingtin-associated protein 1 gene in the developing and adult mouse. *Neurosci Lett* 282: 37-40, 2000.
178. Duan K, Yu X, Zhang C, Zhou Z. Control of secretion by temporal patterns of action potentials in adrenal chromaffin cells. *J Neurosci: Off J Soc Neurosci* 23: 11235-11243, 2003.
179. Duerr JS, Frisby DL, Gaskin J, Duke A, Asermely K, Huddleston D, Eiden LE, Rand JB. The cat-1 gene of *Caenorhabditis elegans* encodes a vesicular monoamine transporter required for specific monoamine-dependent behaviors. *J Neurosci* 19: 72-84, 1999.
180. Duncan RR, Greaves J, Wiegand UK, Matskevich I, Bodammer G, Apps DK, Shipston MJ, Chow RH. Functional and spatial segregation of secretory vesicle pools according to vesicle age. *Nature* 422: 176-180, 2003.
181. Dunevall J, Fathali H, Najafinobar N, Lovric J, Wigstrom J, Cans AS, Ewing AG. Characterizing the catecholamine content of single mammalian vesicles by collision-adsorption events at an electrode. *J Am Chem Soc* 137: 4344-4346, 2015.
182. Dunlap K, Fischbach GD. Neurotransmitters decrease the calcium conductance activated by depolarization of embryonic chick sensory neurones. *J Physiol* 317: 519-535, 1981.
183. Dunlap K, Fischbach GD. Neurotransmitters decrease the calcium component of sensory neurone action potentials. *Nature* 276: 837-839, 1978.
184. Dunn LA, Holz RW. Catecholamine secretion from digitonin-treated adrenal medullary chromaffin cells. *J Biol Chem* 258: 4989-4993, 1983.
185. Ebert SN, Balt SL, Hunter JP, Gashler A, Sukhatme V, Wong DL. Egr-1 activation of rat adrenal phenylethanolamine N-methyltransferase gene. *J Biol Chem* 269: 20885-20898, 1994.
186. Edwards RM, Trizna W, Aiyar N. Adrenomedullin: A new peptide involved in cardiorenal homeostasis? *Exp Nephrol* 5: 18-22, 1997.
187. Edwards SL, Anderson CR, Southwell BR, McAllen RM. Distinct preganglionic neurons innervate noradrenaline and adrenaline cells in the cat adrenal medulla. *Neuroscience* 70: 825-832, 1996.
188. Eiden LE. Is chromogranin a prohormone? *Nature* 325: 301, 1987.
189. Eiden LE, Emery AC, Zhang L, Smith CB. PACAP signaling in stress: Insights from the chromaffin cell. *Pflug Archiv: Eur J Physiol* 470: 79-88, 2018.
190. Eiden LE, Giraud P, Dave J, Hotchkiss JA, Affolter H-U. Nicotinic receptor stimulation activates both enkephalin release and biosynthesis in adrenal chromaffin cells. *Nature* 312: 661-663, 1984.
191. Eiden LE, Iacangelo A, Hsu C-M, Hotchkiss AJ, Bader M-F, Aunis D. Chromogranin A synthesis and secretion in chromaffin cells. *J Neurochem* 49: 65-74, 1987.
192. Eipper BA, Milgram SL, Husten EJ, Yun HY, Mains RE. Peptidylglycine alpha-amidating monooxygenase: A multifunctional protein with catalytic, processing, and routing domains. *Protein Sci: Publ Protein Soc* 2: 489-497, 1993.
193. Eisenhofer G. The role of neuronal and extraneuronal plasma membrane transporters in the inactivation of peripheral catecholamines. *Pharmacol Ther* 91: 35-62, 2001.
194. Eisenhofer G, Huynh TT, Hiroi M, Pacak K. Understanding catecholamine metabolism as a guide to the biochemical diagnosis of pheochromocytoma. *Rev Endocr Metab Disord* 2: 297-311, 2001.
195. Eisenhofer G, Keiser H, Friberg P, Mezey E, Huynh TT, Hiremagalur B, Ellingson T, Duddempudi S, Eijsbouts A, Lenders JW. Plasma metanephrines are markers of pheochromocytoma produced by catechol-O-methyltransferase within tumors. *J Clin Endocrinol Metab* 83: 2175-2185, 1998.
196. Eisenhofer G, Kopin IJ, Goldstein DS. Catecholamine metabolism: A contemporary view with implications for physiology and medicine. *Pharmacol Rev* 56: 331-349, 2004.
197. Eisenhofer G, Lenders JW, Siegert G, Bornstein SR, Friberg P, Milosevic D, Mannelli M, Linehan WM, Adams K, Timmers HJ, Pacak K. Plasma methoxytyramine: A novel biomarker of metastatic pheochromocytoma and paraganglioma in relation to established risk factors of tumour size, location and SDHB mutation status. *Eur J Cancer (Oxford, England: 1990)* 48: 1739-1749, 2012.
198. Eisenhofer G, Rundquist B, Aneman A, Friberg P, Dakak N, Kopin IJ, Jacobs MC, Lenders JW. Regional release and removal of catecholamines and extraneuronal metabolism to metanephrines. *J Clin Endocrinol Metab* 80: 3009-3017, 1995.
199. Elhamdani A, Azizi F, Artalejo CR. Double patch clamp reveals that transient fusion (kiss-and-run) is a major mechanism of secretion in calf adrenal chromaffin cells: High calcium shifts the mechanism from kiss-and-run to complete fusion. *J Neurosci: Off J Soc Neurosci* 26: 3030-3036, 2006.
200. Elhamdani A, Azizi F, Solomaha E, Palfrey HC, Artalejo CR. Two mechanistically distinct forms of endocytosis in adrenal chromaffin cells: Differential effects of SH3 domains and amphiphysin antagonism. *FEBS Lett* 580: 3263-3269, 2006.
201. Elmslie KS, Zhou W, Jones SW. LHRH and GTP-gamma-S modify calcium current activation in bullfrog sympathetic neurons. *Neuron* 5: 75-80, 1990.
202. Emery A, Eiden MV, Mustafa T, Eiden LE. GPCR-Gs signaling to ERK is controlled by the cAMP-sensing guanine nucleotide exchange factor NCS/Rapgef2 in neuronal and endocrine cells. *Sci Signal* 6: ra51, 2013.
203. Emery AC, Eiden LE. Signaling through the neuropeptide GPCR PAC1 induces neuritogenesis via a single linear cAMP- and ERK-dependent pathway using a novel cAMP sensor. *FASEB J* 26: 3199-3211, 2012.
204. Emery AC, Liu XH, Xu W, Eiden MV, Eiden LE. Cyclic adenosine 3′,5′-monophosphate elevation and biological signaling through a secretin family Gs-coupled G protein-coupled receptor are restricted to a single adenylate cyclase isoform. *Mol Pharmacol* 87: 928-935, 2015.
205. Emery AC, Xu W, Eiden MV, Eiden LE. Guanine nucleotide exchange factor Epac2-dependent activation of the GTP-binding protein Rap2A mediates cAMP-dependent growth arrest in neuroendocrine cells. *J Biol Chem* 292: 12220-12231, 2017.
206. Engisch KL, Nowycky MC. Calcium dependence of large dense-cored vesicle exocytosis evoked by calcium influx in bovine adrenal chromaffin cells. *J Neurosci: Off J Soc Neurosci* 16: 1359-1369, 1996.
207. Engisch KL, Nowycky MC. Compensatory and excess retrieval: Two types of endocytosis following single step depolarizations in bovine adrenal chromaffin cells. *J Physiol* 506 (Pt 3): 591-608, 1998.
208. Erickson JD, Eiden LE, Hoffman B. Expression cloning of a reserpine-sensitive vesicular monoamine transporter. *Proc Natl Acad Sci USA* 89: 10993-10997, 1992.
209. Erickson JD, Eiden LE, Schäfer MK-H, Weihe E. Reserpine- and tetrabenazine-sensitive transport of 3H-histamine by the neuronal isoform of the vesicular monoamine transporter. *J Mol Neurosci* 6: 277-287, 1995.
210. Erickson JD, Schäfer MK-H, Bonner TI, Eiden LE, Weihe E. Distinct pharmacological properties and distribution in neurons and endocrine cells of two isoforms of the human vesicular monoamine transporter. *Proc Natl Acad Sci USA* 93: 5166-5171, 1996.
211. Eskay RL, Eiden LE. Interleukin-1 alpha and tumor necrosis factor alpha differentially regulate enkephalin, vasoactive intestinal polypeptide, neurotensin, and substance P biosynthesis in chromaffin cells. *Endocrinology* 130: 2252-2258, 1992.
212. Esler M, Rumantir M, Kaye D, Jennings G, Hastings J, Socratous F, Lambert G. Sympathetic nerve biology in essential hypertension. *Clin Exp Pharmacol Physiol* 28: 986-989, 2001.
213. Esquerro E, Garcia AG, Herandez M, Kirpekar SM, Prat JC. Catecholamine secretory response to calcium reintroduction in the perfused cat adrenal gland treated with ouabain. *Biochem Pharmacol* 29: 2669-2673, 1980.
214. Estevez-Herrera J, Dominguez N, Pardo MR, Gonzalez-Santana A, Westhead EW, Borges R, Machado JD. ATP: The crucial component of secretory vesicles. *Proc Natl Acad Sci USA* 113: E4098-E4106, 2016.
215. Estevez-Herrera J, Gonzalez-Santana A, Baz-Davila R, Machado JD, Borges R. The intravesicular cocktail and its role in the regulation of exocytosis. *J Neurochem* 137: 897-903, 2016.
216. Evans RM, Zamponi GW. Presynaptic Ca^{2+} channels – integration centers for neuronal signaling pathways. *Trends Neurosci* 29: 617-624, 2006.
217. Evinger MJ, Ernsberger P, Regunathan S, Joh TH, Reis DJ. A single transmitter regulates gene expression through two separate mechanisms: Cholinergic regulation of phenylethanolamine N-methyltransferase mRNA via nicotinic and muscarinic pathways. *J Neurosci* 14: 2106-2116, 1994.

218. Fakler B, Adelman JP. Control of K-Ca channels by calcium nano/microdomains. *Neuron* 59: 873-881, 2008.
219. Farnsworth NL, Benninger RK. New insights into the role of connexins in pancreatic islet function and diabetes. *FEBS Lett* 588: 1278-1287, 2014.
220. Feldberg W, Gaddum JH. The chemical transmitter at synapses in a sympathetic ganglion. *J Physiol* 81: 305-319, 1934.
221. Fenwick EM, Marty A, Neher E. A patch-clamp study of bovine chromaffin cells and of their sensitivity to acetylcholine. *J Physiol* 331: 577-597, 1982.
222. Fenwick EM, Marty A, Neher E. Sodium and calcium channels in bovine chromaffin cells. *J Physiol* 331: 599-635, 1982.
223. Fernandez-Aguera MC, Gao L, Gonzalez-Rodriguez P, Pintado CO, Arias-Mayenco I, Garcia-Flores P, Garcia-Perganeda A, Pascual A, Ortega-Saenz P, Lopez-Barneo J. Oxygen sensing by arterial chemoreceptors depends on mitochondrial complex I signaling. *Cell Metab* 22: 825-837, 2015.
224. Fernandez-Morales JC, Padin JF, Arranz-Tagarro JA, Vestring S, Garcia AG, de Diego AM. Hypoxia-elicited catecholamine release is controlled by L-type as well as N/PQ types of calcium channels in rat embryo chromaffin cells. *Am J Physiol Cell Physiol* 307: C455-C465, 2014.
225. Feuerstein G, Gutman Y. Preferential secretion of adrenaline or noradrenaline by the cat adrenal in vivo in response to different stimuli. *Br J Pharmacol* 43: 764-775, 1971.
226. Finn JP, 3rd, Edwards RH. Individual residues contribute to multiple differences in ligand recognition between vesicular monoamine transporters 1 and 2. *J Biol Chem* 272: 16301-16307, 1997.
227. Fischer-Colbrie R, Iacangelo A, Eiden LE. Neural and humoral factors separately regulate neuropeptide Y, enkephalin, and chromogranin A and B mRNA levels in rat adrenal medulla. *Proc Natl Acad Sci USA* 85: 3240-3244, 1988.
228. Folkow B, Von Euler US. Selective activation of noradrenaline and adrenaline producing cells in the cat's adrenal gland by hypothalamic stimulation. *Circ Res* 2: 191-195, 1954.
229. Foucart S, Nadeau R, Dechamplain J. Local modulation of adrenal catecholamines release by beta-2 adrenoceptors in the anesthetized dog. *Naunyn-Schmiedeberg's Arch Pharmacol* 337: 29-34, 1988.
230. Fox AP, Cahill AL, Currie KP, Grabner C, Harkins AB, Herring B, Hurley JH, Xie Z. N- and P/Q-type Ca^{2+} channels in adrenal chromaffin cells. *Acta Physiol (Oxf)* 192: 247-261, 2008.
231. Fricker LD, Snyder SH. Enkephalin convertase: Purification and characterization of a specific enkephalin-synthesizing carboxypeptidase localized to adrenal chromaffin granules. *Proc Natl Acad Sci USA* 79: 3886-3890, 1982.
232. Fuentealba J, Olivares R, Ales E, Tapia L, Rojo J, Arroyo G, Aldea M, Criado M, Gandia L, Garcia AG. A choline-evoked $[Ca^{2+}]c$ signal causes catecholamine release and hyperpolarization of chromaffin cells. *FASEB J* 18: 1468-1470, 2004.
233. Fulop T, Doreian B, Smith C. Dynamin I plays dual roles in the activity-dependent shift in exocytic mode in mouse adrenal chromaffin cells. *Arch Biochem Biophys* 477: 146-154, 2008.
234. Fumimura Y, Ikemura M, Saito Y, Sengoku R, Kanemaru K, Sawabe M, Arai T, Ito G, Iwatsubo T, Fukayama M, Mizusawa H, Murayama S. Analysis of the adrenal gland is useful for evaluating pathology of the peripheral autonomic nervous system in lewy body disease. *J Neuropathol Exp Neurol* 66: 354-362, 2007.
235. Gandia L, Garcia AG, Morad M. ATP modulation of calcium channels in chromaffin cells. *J Physiol* 470: 55-72, 1993.
236. Gandia L, Mayorgas I, Michelena P, Cuchillo I, de Pascual R, Abad F, Novalbos JM, Larranaga E, Garcia AG. Human adrenal chromaffin cell calcium channels: Drastic current facilitation in cell clusters, but not in isolated cells. *Pflug Archiv: Eur J Physiol* 436: 696-704, 1998.
237. Gandia L, Villarroya M, Lara B, Olmos V, Gilabert JA, Lopez MG, Martinez-Sierra R, Borges R, Garcia AG. Otilonium: A potent blocker of neuronal nicotinic ACh receptors in bovine chromaffin cells. *Br J Pharmacol* 117: 463-470, 1996.
238. Gao L, Bonilla-Henao V, Garcia-Flores P, Arias-Mayenco I, Ortega-Saenz P, Lopez-Barneo J. Gene expression analyses reveal metabolic specifications in acute O_2-sensing chemoreceptor cells. *J Physiol* 595: 6091-6120, 2017.
239. Garcia-Fernandez M, Mejias R, Lopez-Barneo J. Developmental changes of chromaffin cell secretory response to hypoxia studied in thin adrenal slices. *Pflug Archiv: Eur J Physiol* 454: 93-100, 2007.
240. Garcia AG, Garcia-De-Diego AM, Gandia L, Borges R, Garcia-Sancho J. Calcium signaling and exocytosis in adrenal chromaffin cells. *Physiol Rev* 86: 1093-1131, 2006.
241. Garcia AG, Garcia-Lopez E, Horga JF, Kirpekar SM, Montiel C, Sanchez-Garcia P. Potentiation of K+-evoked catecholamine release in the cat adrenal gland treated with ouabain. *Br J Pharmacol* 74: 673-680, 1981.
242. Garcia AG, Padin F, Fernandez-Morales JC, Maroto M, Garcia-Sancho J. Cytosolic organelles shape calcium signals and exo-endocytotic responses of chromaffin cells. *Cell Calcium* 51: 309-320, 2012.
243. Garcia AG, Sala F, Reig JA, Viniegra S, Frias J, Fonteriz R, Gandia L. Dihydropyridine BAY-K-8644 activates chromaffin cell calcium channels. *Nature* 309: 69-71, 1984.
244. Gavello D, Vandael D, Gosso S, Carbone E, Carabelli V. Dual action of leptin on rest-firing and stimulated catecholamine release via phosphoinositide 3-kinase-driven BK channel up-regulation in mouse chromaffin cells. *J Physiol* 593: 4835-4853, 2015.
245. Geisow MJ, Childs J, Burgoyne RD. Cholinergic stimulation of chromaffin cells induces rapid coating of the plasma membrane. *Eur J Cell Biol* 38: 51-56, 1985.
246. Gengler S, Hamilton A, Holscher C. Synaptic plasticity in the hippocampus of a APP/PS1 mouse model of Alzheimer's disease is impaired in old but not young mice. *PLoS One* 5: e9764, 2010.
247. Gerra G, Zaimovic A, Mascetti GG, Gardini S, Zambelli U, Timpano M, Raggi MA, Brambilla F. Neuroendocrine responses to experimentally-induced psychological stress in healthy humans. *Psychoneuroendocrinology* 26: 91-107, 2001.
248. Giancippoli A, Novara M, de Luca A, Baldelli P, Marcantoni A, Carbone E, Carabelli V. Low-threshold exocytosis induced by cAMP-recruited Ca(V)3.2 (alpha(1H)) channels in rat chromaffin cells. *Biophys J* 90: 1830-1841, 2006.
249. Goldstein DS. Catecholamines and stress. *Endocr Regul* 37: 69-80, 2003.
250. Goldstein DS. Concepts of scientific integrative medicine applied to the physiology and pathophysiology of catecholamine systems. *Compr Physiol* 3: 1569-1610, 2013.
251. Goldstein DS. Plasma catecholamines and essential hypertension. An analytical review. *Hypertension* 5: 86-99, 1983.
252. Goldstein DS, Kopin IJ. Adrenomedullary, adrenocortical, and sympathoneural responses to stressors: A meta-analysis. *Endocr Regul* 42: 111-119, 2008.
253. Goldstein DS, Sullivan P, Holmes C, Miller GW, Alter S, Strong R, Mash DC, Kopin IJ, Sharabi Y. Determinants of buildup of the toxic dopamine metabolite DOPAL in Parkinson's disease. *J Neurochem* 126: 591-603, 2013.
254. Gong LW, Hafez I, Alvarez de Toledo G, Lindau M. Secretory vesicles membrane area is regulated in tandem with quantal size in chromaffin cells. *J Neurosci* 23: 7917-7921, 2003.
255. Gonzalez-Jamett AM, Momboisse F, Guerra MJ, Ory S, Baez-Matus X, Barraza N, Calco V, Houy S, Couve E, Neely A, Martinez AD, Gasman S, Cardenas AM. Dynamin-2 regulates fusion pore expansion and quantal release through a mechanism that involves actin dynamics in neuroendocrine chromaffin cells. *PLoS One* 8: e70638, 2013.
256. Gonzalez-Rubio JM, Garcia de Diego AM, Egea J, Olivares R, Rojo J, Gandia L, Garcia AG, Hernandez-Guijo JM. Blockade of nicotinic receptors of bovine adrenal chromaffin cells by nanomolar concentrations of atropine. *Eur J Pharmacol* 535: 13-24, 2006.
257. Greene LA, Tischler AS. Establishment of a noradrenergic clonal line of rat adrenal pheochromocytoma cells which respond to nerve growth factor. *Proc Natl Acad Sci USA* 73: 2424-2428, 1976.
258. Greten-Harrison B, Polydoro M, Morimoto-Tomita M, Diao L, Williams AM, Nie EH, Makani S, Tian N, Castillo PE, Buchman VL, Chandra SS. αβγ-Synuclein triple knockout mice reveal age-dependent neuronal dysfunction. *Proc Natl Acad Sci USA* 107: 19573-19578, 2010.
259. Grynszpan-Winograd O. Adrenaline and noradrenaline cells in the adrenal medulla of the hamster: A morphological study of their innervation. *J Neurocytol* 3: 341-361, 1974.
260. Guarina L, Vandael DH, Carabelli V, Carbone E. Low pHo boosts burst firing and catecholamine release by blocking TASK-1 and BK channels while preserving Cav1 channels in mouse chromaffin cells. *J Physiol* 595: 2587-2609, 2017.
261. Guerineau NC. Gap junction communication between chromaffin cells: The hidden face of adrenal stimulus-secretion coupling. *Pflug Archiv: Eur J Physiol* 470: 89-96, 2018.
262. Guerineau NC, Desarmenien MG, Carabelli V, Carbone E. Functional chromaffin cell plasticity in response to stress: Focus on nicotinic, gap junction, and voltage-gated Ca^{2+} channels. *J Mol Neurosci* 48: 368-386, 2012.
263. Gullo F, Ales E, Rosati B, Lecchi M, Masi A, Guasti L, Cano-Abad MF, Arcangeli A, Lopez MG, Wanke E. ERG K+ channel blockade enhances firing and epinephrine secretion in rat chromaffin cells: The missing link to LQT2-related sudden death? *FASEB J* 17: 330-332, 2003.
264. Gunter TE, Pfeiffer DR. Mechanisms by which mitochondria transport calcium. *Am J Physiol* 258: C755-C786, 1990.
265. Guo X, Wakade AR. Differential secretion of catecholamines in response to peptidergic and cholinergic transmitters in rat adrenals. *J Physiol* 475: 539-545, 1994.
266. Gureviciene I, Ikonen S, Gurevicius K, Sarkaki A, van Groen T, Pussinen R, Ylinen A, Tanila H. Normal induction but accelerated decay of LTP in APP + PS1 transgenic mice. *Neurobiol Dis* 15: 188-195, 2004.
267. Gurney ME, Pu H, Chiu AY, Dal Canto MC, Polchow CY, Alexander DD, Caliendo J, Hentati A, Kwon YW, Deng HX, et al. Motor neuron

degeneration in mice that express a human Cu. Zn superoxide dismutase mutation. *Science* 264: 1772-1775, 1994.
268. Guyton AC, Hall JE. The autonomic nervous system and the adrenal medulla. In: *Textbook of Medical Physiology*, 13th ed. New York: Saunders, 2016.
269. Hamelink C, Tjurmina O, Damadzic R, Young WS, Weihe E, Lee H-W, Eiden LE. Pituitary adenylate cyclase activating polypeptide is a sympathoadrenal neurotransmitter involved in catecholamine regulation and glucohomeostasis. *Proc Natl Acad Sci USA* 99: 461-466, 2002.
270. Hamelink C, Weihe E, Eiden LE. PACAP: an 'emergency response' co-transmitter in the adrenal medulla. In: Vaudry H, Arimura A, editors. *Pituitary Adenylate Cyclase-Activating Polypeptide*. Norwell, MA: Kluwer-Academic Press, 2003, p. 227-250.
271. Hamill OP, Marty A, Neher E, Sakmann B, Sigworth FJ. Improved patch-clamp techhniques for high-resolution current recording from cells and cell-free membrane patches. *Pflug Arch* 391: 85-100, 1981.
272. Hansson O, Guatteo E, Mercuri NB, Bernardi G, Li XJ, Castilho RF, Brundin P. Resistance to NMDA toxicity correlates with appearance of nuclear inclusions, behavioural deficits and changes in calcium homeostasis in mice transgenic for exon 1 of the huntington gene. *Eur J Neurosci* 14: 1492-1504, 2001.
273. Harada K, Matsuoka H, Fujihara H, Ueta Y, Yanagawa Y, Inoue M. GABA signaling and neuroactive steroids in adrenal medullary chromaffin cells. *Front Cell Neurosci* 10: 100, 2016.
274. Harada K, Matsuoka H, Nakamura J, Fukuda M, Inoue M. Storage of GABA in chromaffin granules and not in synaptic-like microvesicles in rat adrenal medullary cells. *J Neurochem* 114: 617-626, 2010.
275. Hardy J, Selkoe DJ. The amyloid hypothesis of Alzheimer's disease: Progress and problems on the road to therapeutics. *Science* 297: 353-356, 2002.
276. Haycock JW, Wakade AR. Activation and multiple-site phosphorylation of tyrosine hydroxylase in perfused rat adrenal glands. *J Neurochem* 58: 57-64, 1992.
277. Heinemann C, von Ruden L, Chow RH, Neher E. A two-step model of secretion control in neuroendocrine cells. *Pflug Archiv: Eur J Physiol* 424: 105-112, 1993.
278. Helan M, Aravamudan B, Hartman WR, Thompson MA, Johnson BD, Pabelick CM, Prakash YS. BDNF secretion by human pulmonary artery endothelial cells in response to hypoxia. *J Mol Cell Cardiol* 68: 89-97, 2014.
279. Helle KB. The chromogranin A-derived peptides vasostatin-I and catestatin as regulatory peptides for cardiovascular functions. *Cardiovasc Res*, 2009.
280. Helle KB. The granin family of uniquely acidic proteins of the diffuse neuroendocrine system: Comparative and functional aspects. *Biol Rev Camb Philos Soc* 79: 769-794, 2004.
281. Helle KB, Angeletti RH. Chromogranin A: A multipurpose prohormone? *Acta Physiol Scand* 152: 1-10, 1994.
282. Helle KB, Reed RK, Pihl KE, Serck-Hanssen G. Osmotic properties of the chromogranins and relation to osmotic pressure in catecholamine storage granules. *Acta Physiol Scand* 123: 21-33, 1985.
283. Helle KB, Serck-Hanssen G. The adrenal medulla: A model for studies of hormonal and neuronal storage and release mechanisms. *Mol Cell Biochem* 6: 127-146, 1975.
284. Henkel AW, Almers W. Fast steps in exocytosis and endocytosis studied by capacitance measurements in endocrine cells. *Curr Opin Neurobiol* 6: 350-357, 1996.
285. Henkel AW, Meiri H, Horstmann H, Lindau M, Almers W. Rhythmic opening and closing of vesicles during constitutive exo- and endocytosis in chromaffin cells. *Embo J* 19: 84-93, 2000.
286. Henry JP, Botton D, Sagne C, Isambert MF, Desnos C, Blanchard V, Raisman-Vozari R, Krejci E, Massoulie J, Gasnier B. Biochemistry and molecular biology of the vesicular monoamine transporter from chromaffin granules. *J Exp Biol* 196: 251-262, 1994.
287. Hernandez-Cruz A, Sala F, Adams PR. Subcellular calcium transients visualized by confocal microscopy in a voltage-clamped vertebrate neuron. *Science* 247: 858-862, 1990.
288. Hernandez-Guijo JM, Carabelli V, Gandia L, Garcia AG, Carbone E. Voltage-independent autocrine modulation of L-type channels mediated by ATP, opioids and catecholamines in rat chromaffin cells. *Eur J Neurosci* 11: 3574-3584, 1999.
289. Hernandez-Guijo JM, Gandia L, Cuchillo-Ibanez I, Albillos A, Novalbos J, Gilsanz F, Larranaga E, de Pascual R, Abad F, Garcia AG. Altered regulation of calcium channels and exocytosis in single human pheochromocytoma cells. *Pflug Archiv: Eur J Physiol* 440: 253-263, 2000.
290. Hernandez-Guijo JM, Gandia L, Lara B, Garcia AG. Autocrine/paracrine modulation of calcium channels in bovine chromaffin cells. *Pflug Archiv: Eur J Physiol* 437: 104-113, 1998.
291. Hernandez-Guijo JM, Maneu-Flores VE, Ruiz-Nuno A, Villarroya M, Garcia AG, Gandia L. Calcium-dependent inhibition of L, N, and P/Q Ca^{2+} channels in chromaffin cells: Role of mitochondria. *J Neurosci* 21: 2553-2560, 2001.
292. Hernandez A, Segura-Chama P, Jimenez N, Garcia AG, Hernandez-Guijo JM, Hernandez-Cruz A. Modulation by endogenously released ATP and opioids of chromaffin cell calcium channels in mouse adrenal slices. *Am J Physiol Cell Physiol* 300: C610-C623, 2011.
293. Herrera A, Munoz P, Steinbusch HWM, Segura-Aguilar J. Are dopamine oxidation metabolites involved in the loss of dopaminergic neurons in the nigrostriatal system in Parkinson's disease? *ACS Chem Neurosci* 8: 702-711, 2017.
294. Herrero CJ, Ales E, Pintado AJ, Lopez MG, Garcia-Palomero E, Mahata SK, O'Connor DT, Garcia AG, Montiel C. Modulatory mechanism of the endogenous peptide catestatin on neuronal nicotinic acetylcholine receptors and exocytosis. *J Neurosci: Off J Soc Neurosci* 22: 377-388, 2002.
295. Herrington J, Park YB, Babcock DF, Hille B. Dominant role of mitochondria in clearance of large Ca^{2+} loads from rat adrenal chromaffin cells. *Neuron* 16: 219-228, 1996.
296. Hervonen A, Partanen S, Vaalasti A, Partanen M, Kanerva L, Alho H. The distribution and endocrine nature of the abdominal paraganglia of adult man. *Am J Anat* 153: 563-572, 1978.
297. Herzog RI, Cummins TR, Ghassemi F, Dib-Hajj SD, Waxman SG. Distinct repriming and closed-state inactivation kinetics of Nav1.6 and Nav1.7 sodium channels in mouse spinal sensory neurons. *J Physiol* 551: 741-750, 2003.
298. Hill J, Chan SA, Kuri B, Smith C. Pituitary adenylate cyclase-activating peptide (PACAP) recruits low voltage-activated T-type calcium influx under acute sympathetic stimulation in mouse adrenal chromaffin cells. *J Biol Chem* 286: 42459-42469, 2011.
299. Hillarp NA. Isolation and some biochemical properties of the catechol amine granules in the cow adrenal medulla. *Acta Physiol Scand* 43: 82-96, 1958.
300. Hillarp NA, Hokfelt B. Evidence of adrenaline and noradrenaline in separate adrenal medullary cells. *Acta Physiol Scand* 30: 55-68, 1953.
301. Hohne-Zell B, Gratzl M. Adrenal chromaffin cells contain functionally different SNAP-25 monomers and SNAP-25/syntaxin heterodimers. *FEBS Lett* 394: 109-116, 1996.
302. Holgert H, Holmberg K, Hannibal J, Fahrenkrug J, Brimijoin S, Hartman BK, Hökfelt T. PACAP in the adrenal gland – relationship with choline acetyltransferase, enkephalin and chromaffin cells and effects of immunological sympathectomy. *NeuroReport* 20: 297-301, 1996.
303. Holman ME, Coleman HA, Tonta MA, Parkington HC. Synaptic transmission from splanchnic nerves to the adrenal medulla of guinea-pigs. *J Physiol* 478 (Pt 1): 115-124, 1994.
304. Holman ME, Tonta MA, Coleman HA, Parkington HC. Currents caused by the spontaneous release of quanta of acetylcholine onto chromaffin cells in guinea-pig adrenal medulla. *Neurosci Lett* 184: 75-78, 1995.
305. Holz GG, Kang G, Harbeck M, Roe MW, Chepurny OG. Cell physiology of cAMP sensor Epac. *J Physiol* 577: 5-15, 2006.
306. Honigmann A, van den Bogaart G, Iraheta E, Risselada HJ, Milovanovic D, Mueller V, Mullar S, Diederichsen U, Fasshauer D, Grubmuller H, Hell SW, Eggeling C, Kuhnel K, Jahn R. Phosphatidylinositol 4,5-bisphosphate clusters act as molecular beacons for vesicle recruitment. *Nat Struct Mol Biol* 20: 679-686, 2013.
307. Hook VY, Eiden LE, Brownstein MJ. A carboxypeptidase processing enzyme for enkephalin precursors. *Nature* 295: 341-342, 1982.
308. Horrigan FT, Bookman RJ. Releasable pools and the kinetics of exocytosis in adrenal chromaffin cells. *Neuron* 13: 1119-1129, 1994.
309. Hoshi T, Rothlein J, Smith SJ. Facilitation of Ca^{2+}-channel currents in bovine adrenal chromaffin cells. *Proc Natl Acad Sci USA* 81: 5871-5875, 1984.
310. Houchi H, Teraoka K, Oka M, Murakumo Y, Morita K. Substance P inhibits catecholamine biosynthesis stimulated by carbamylcholine in cultured adrenal chromaffin cells. *Biochem Pharmacol* 45: 1165-1167, 1993.
311. Houy S, Croise P, Gubar O, Chasserot-Golaz S, Tryoen-Toth P, Bailly Y, Ory S, Bader MF, Gasman S. Exocytosis and endocytosis in neuroendocrine cells: Inseparable membranes! *Front Endocrinol* 4: 135, 2013.
312. Huttner WB, Gerdes HH, Rosa P. The granin (chromogranin/secretogranin) family. *Trends Biochem Sci* 16: 27-30, 1991.
313. Iacangelo AL, Eiden LE. Chromogranin A: Current status as a precursor for bioactive peptides and a granulogenic/sorting factor in the regulated secretory pathway. *Regul Pept* 58: 65-88, 1995.
314. Ikeda SR, Dunlap K. Voltage-dependent modulation of N-type calcium channels: Role of G protein subunits. *Adv Second Messenger Phosphoprotein Res* 33: 131-151, 1999.
315. Inoue M, Fujishiro N, Imanaga I. Hypoxia and cyanide induce depolarization and catecholamine release in dispersed guinea-pig chromaffin cells. *J Physiol* 507 (Pt 3): 807-818, 1998.
316. Inoue M, Harada K, Matsuoka H, Sata T, Warashina A. Inhibition of TASK1-like channels by muscarinic receptor stimulation in rat adrenal medullary cells. *J Neurochem* 106: 1804-1814, 2008.
317. Inoue M, Harada K, Matsuoka H, Warashina A. Paracrine role of GABA in adrenal chromaffin cells. *Cell Mol Neurobiol* 30: 1217-1224, 2010.

318. Ip NY, Perlman RL, Zigmond RE. Acute transsynaptic regulation of tyrosine 3-monooxygenase activity in the rat superior cervical ganglion: Evidence for both cholinergic and noncholinergic mechanisms. *Proc Natl Acad Sci USA* 80: 2081-2085, 1983.
319. Ishii TM, Maylie J, Adelman JP. Determinants of apamin and d-tubocurarine block in SK potassium channels. *J Biol Chem* 272: 23195-23200, 1997.
320. Islas-Suarez L, Gomez-Chavarin M, Drucker-Colin R, Hernandez-Cruz A. Properties of the sodium current in rat chromaffin cells exposed to nerve growth factor in vitro. *J Neurophysiol* 72: 1938-1948, 1994.
321. Ito Y, Fujimoto Y, Obara T. The role of epinephrine, norepinephrine, and dopamine in blood pressure disturbances in patients with pheochromocytoma. *World J Surg* 16: 759-763; discussion 763-754, 1992.
322. Jackson LP, Kelly BT, McCoy AJ, Gaffry T, James LC, Collins BM, Honing S, Evans PR, Owen DJ. A large-scale conformational change couples membrane recruitment to cargo binding in the AP2 clathrin adaptor complex. *Cell* 141: 1220-1229, 2010.
323. Jansen AS, Nguyen XV, Karpitskiy V, Mettenleiter TC, Loewy AD. Central command neurons of the sympathetic nervous system: Basis of the fight-or-flight response. *Science* 270: 644-646, 1995.
324. Jiang SZ, Xu W, Emery AC, Gerfen CR, Eiden MV, Eiden LE. NCS-Rapgef2, the protein product of the neuronal Rapgef2 gene, is a specific activator of D1 dopamine receptor-dependent ERK phosphorylation in mouse brain. *eNeuro* 4, 2017. DOI: 10.1523/ENEURO.0248-17.2017.
325. Jimenez RR, Lopez MG, Sancho C, Maroto R, Garcia AG. A component of the catecholamine secretory response in the bovine adrenal gland is resistant to dihydropyridines and omega-conotoxin. *Biochem Biophys Res Commun* 191: 1278-1283, 1993.
326. Johns LM, Levitan ES, Shelden EA, Holz RW, Axelrod D. Restriction of secretory granule motion near the plasma membrane of chromaffin cells. *J Cell Biol* 153: 177-190, 2001.
327. Johnson MA, Rajan V, Miller CE, Wightman RM. Dopamine release is severely compromised in the R6/2 mouse model of Huntington's disease. *J Neurochem* 97: 737-746, 2006.
328. Johnson MA, Villanueva M, Haynes CL, Seipel AT, Buhler LA, Wightman RM. Catecholamine exocytosis is diminished in R6/2 Huntington's disease model mice. *J Neurochem* 103: 2102-2110, 2007.
329. Johnson RG, Carty SE, Scarpa A. Proton: Substrate stoichiometries during active transport of biogenic amines in chromaffin ghosts. *J Biol Chem* 256: 5773-5780, 1981.
330. Johnson RG, Pfister D, Carty SE, Scarpa A. Biological amine transport in chromaffin ghosts. Coupling to the transmembrane proton and potential gradients. *J Biol Chem* 254: 10963-10972, 1979.
331. Johnson RG, Scarpa A. Protonmotive force and catecholamine transport in isolated chromaffin granules. *J Biol Chem* 254: 3750-3760, 1979.
332. Johnson TS, Young JB, Landsberg L. Sympathoadrenal responses to acute and chronic hypoxia in the rat. *J Clin Invest* 71: 1263-1272, 1983.
333. Kahle KT, Rinehart J, Lifton RP. Phosphoregulation of the Na-K-2Cl and K-Cl cotransporters by the WNK kinases. *Biochim Biophys Acta* 1802: 1150-1158, 2010.
334. Kajiwara R, Sand O, Kidokoro Y, Barish ME, Iijima T. Functional organization of chromaffin cells and cholinergic synaptic transmission in rat adrenal medulla. *Jpn J Physiol* 47: 449-464, 1997.
335. Kao LS, Cheung NS. Mechanism of calcium transport across the plasma membrane of bovine chromaffin cells. *J Neurochem* 54: 1972-1979, 1990.
336. Kataoka Y, Fujimoto M, Alho H, Guidotti A, Geffard M, Kelly GD, Hanbauer I. Intrinsic gamma aminobutyric acid receptors modulate the release of catecholamine from canine adrenal gland in situ. *J Pharmacol Exp Ther* 239: 584-590, 1986.
337. Katz B, Miledi R. Ionic requirements of synaptic transmitter release. *Nature* 215: 651, 1967.
338. Katz B, Miledi R. A study of synaptic transmission in the absence of nerve impulses. *J Physiol* 192: 407-436, 1967.
339. Kawahara Y, Ito K, Sun H, Aizawa H, Kanazawa I, Kwak S. Glutamate receptors: RNA editing and death of motor neurons. *Nature* 427: 801, 2004.
340. Kawaida M, Abe T, Nakanishi T, Miyahara Y, Yamagishi H, Sakamoto M, Yamada T. A case of Timothy syndrome with adrenal medullary dystrophy. *Pathol Int* 66: 587-592, 2016.
341. Kawasaki H, Springett GM, Mochizuki N, Toki S, Nakaya M, Matsuda M, Housman DE, Graybiel AM. A family of cAMP-binding proteins that directly activate Rap1. *Science* 282: 2275-2279, 1998.
342. Kayaalp SO, McIsaac RJ. Muscarinic component of splanchnic-adrenal transmission in the dog. *Br J Pharmacol* 36: 286-293, 1969.
343. Keating DJ, Rychkov GY, Adams MB, Holgert H, McMillen IC, Roberts ML. Opioid receptor stimulation suppresses the adrenal medulla hypoxic response in sheep by actions on Ca(2+) and K(+) channels. *J Physiol* 555: 489-502, 2004.
344. Keating DJ, Rychkov GY, Giacomin P, Roberts ML. Oxygen-sensing pathway for SK channels in the ovine adrenal medulla. *Clin Exp Pharmacol Physiol* 32: 882-887, 2005.
345. Keating DJ, Rychkov GY, Roberts ML. The contribution of voltage-gated Ca^{2+} currents to K+ channel activation during ovine adrenal chromaffin cell development. *Int J Dev Neurosci* 27: 357-363, 2009.
346. Keating DJ, Rychkov GY, Roberts ML. Oxygen sensitivity in the sheep adrenal medulla: Role of SK channels. *Am J Physiol Cell Physiol* 281: C1434-C1441, 2001.
347. Keiper M, Stope MB, Szatkowski D, Bohm A, Tysack K, Vom Dorp F, Saur O, Oude Weernink PA, Evellin S, Jakobs KH, Schmidt M. Epac- and Ca^{2+}-controlled activation of Ras and extracellular signal-regulated kinases by Gs-coupled receptors. *J Biol Chem* 279: 46497-46508, 2004.
348. Kennedy BP, Mahata SK, O'Connor DT, Ziegler MG. Mechanism of cardiovascular actions of the chromogranin A fragment catestatin in vivo. *Peptides* 19: 1241-1248, 1998.
349. Kidokoro Y, Miyazaki S, Ozawa S. Acetylcholine-induced membrane depolarization and potential fluctuations in the rat adrenal chromaffin cell. *J Physiol* 324: 203-220, 1982.
350. Kidokoro Y, Ritchie AK. Chromaffin cell action potentials and their possible role in adrenaline secretion from rat adrenal medulla. *J Physiol* 307: 199-216, 1980.
351. Kim D, Kang D. Role of K(2)p channels in stimulus-secretion coupling. *Pflug Archiv: Eur J Physiol* 467: 1001-1011, 2015.
352. Kim SJ, Lim W, Kim J. Contribution of L- and N-type calcium currents to exocytosis in rat adrenal medullary chromaffin cells. *Brain Res* 675: 289-296, 1995.
353. Kim T, Tao-Cheng J-H, Eiden LE, Loh YP. Chromogranin A, an "on/off" switch controlling dense-core secretory granule biogenesis. *Cell* 106: 499-509, 2001.
354. Kitamura K, Kangawa K, Kawamoto M, Ichiki Y, Nakamura S, Matsuo H, Eto T. Adrenomedullin: A novel hypotensive peptide isolated from human pheochromocytoma. *Biochem Biophys Res Commun* 192: 553-560, 1993.
355. Kleppisch T, Ahnert-Hilger G, Gollasch M, Spicher K, Hescheler J, Schultz G, Rosenthal W. Inhibition of voltage-dependent Ca^{2+} channels via alpha 2-adrenergic and opioid receptors in cultured bovine adrenal chromaffin cells. *Pflug Archiv: Eur J Physiol* 421: 131-137, 1992.
356. Klevans LR, Gebber GL. Comparison of differential secretion of adrenal catecholamines by splanchnic nerve stimulation and cholinergic agents. *J Pharmacol Exp Therap* 172: 69-76, 1970.
357. Klingauf J, Neher E. Modeling buffered Ca^{2+} diffusion near the membrane: Implications for secretion in neuroendocrine cells. *Biophys J* 72: 674-690, 1997.
358. Klugbauer N, Lacinova L, Flockerzi V, Hofmann F. Structure and functional expression of a new member of the tetrodotoxin-sensitive voltage-activated sodium channel family from human neuroendocrine cells. *EMBO J* 14: 1084-1090, 1995.
359. Knight DE. Botulinum toxin types A, B and D inhibit catecholamine secretion from bovine adrenal medullary cells. *FEBS Lett* 207: 222-226, 1986.
360. Knight DE, Baker PF. Calcium-dependence of catecholamine release from bovine adrenal medullary cells after exposure to intense electric fields. *J Membr Biol* 68: 107-140, 1982.
361. Kopell WN, Westhead EW. Osmotic pressures of solutions of ATP and catecholamines relating to storage in chromaffin granules. *J Biol Chem* 257: 5707-5710, 1982.
362. Koschak A, Reimer D, Huber I, Grabner M, Glossmann H, Engel J, Striessnig J. alpha 1D (Cav1.3) subunits can form L-type Ca^{2+} channels activating at negative voltages. *J Biol Chem* 276: 22100-22106, 2001.
363. Koseoglu S, Love SA, Haynes CL. Cholesterol effects on vesicle pools in chromaffin cells revealed by carbon-fiber microelectrode amperometry. *Anal Bioanal Chem* 400: 2963-2971, 2011.
364. Kovacic B, Robinson RL. Drug-induced secretion of catecholamines by the perfused adrenal gland of the dog during nicotine blockade. *J Pharmacol Exp Therap* 175: 178-182, 1970.
365. Kremer HP, Roos RA, Dingjan G, Marani E, Bots GT. Atrophy of the hypothalamic lateral tuberal nucleus in Huntington's disease. *J Neuropathol Exp Neurol* 49: 371-382, 1990.
366. Kummer W, Neuhuber WL. Vagal paraganglia of the rat. *J Electr Microsc Techn* 12: 343-355, 1989.
367. Kuo JF, Greengard P. Cyclic nucleotide-dependent protein kinases. IV. Widespread occurrence of adenosine 3′,5′-monophosphate-dependent protein kinase in various tissues and phyla of the animal kingdom. *Proc Natl Acad Sci USA* 64: 1349-1355, 1969.
368. Kuri BA, Chan SA, Smith CB. PACAP regulates immediate catecholamine release from adrenal chromaffin cells in an activity-dependent manner through a protein kinase C-dependent pathway. *J Neurochem* 110: 1214-1225, 2009.
369. Lang T, Wacker I, Wunderlich I, Rohrbach A, Giese G, Soldati T, Almers W. Role of actin cortex in the subplasmalemmal transport of secretory granules in PC-12 cells. *Biophys J* 78: 2863-2877, 2000.
370. Lara B, Lopez MG, Villarroya M, Gandia L, Cleeman L, Morad M, Garcia AG. A caffeine-sensitive Ca^{2+} store modulates K+-evoked secretion in chromaffin cells. *Am J Physiol* 272: C1211-C1221, 1997.

371. Lara B, Zapater P, Montiel C, de la Fuente MT, Martinez-Sierra R, Ballesta JJ, Gandia L, Garcia AG. Density of apamin-sensitive Ca(2+)-dependent K+ channels in bovine chromaffin cells: Relevance to secretion. *Biochem Pharmacol* 49: 1459-1468, 1995.
372. Larsen KE, Schmitz Y, Troyer MD, Mosharov E, Dietrich P, Quazi AZ, Savalle M, Nemani V, Chaudhry FA, Edwards RH, Stefanis L, Sulzer D. Alpha-synuclein overexpression in PC12 and chromaffin cells impairs catecholamine release by interfering with a late step in exocytosis. *J Neurosci* 26: 11915-11922, 2006.
373. Lazo-Fernandez Y, Aguilera G, Pham TD, Park AY, Beierwaltes WH, Sutliff RL, Verlander JW, Pacak K, Osunkoya AO, Ellis CL, Kim YH, Shipley GL, Wynne BM, Hoover RS, Sen SK, Plotsky PM, Wall SM. Pendrin localizes to the adrenal medulla and modulates catecholamine release. *Am J Physiol Endocrinol Metab* 309: E534-E545, 2015.
374. Lee FL, Trendelenburg U. Muscarinic transmission of preganglionic impulses to the adrenal medulla of the cat. *J Pharmacol Exp Therap* 158: 73-79, 1967.
375. Lee J, Lim W, Eun SY, Kim SJ, Kim J. Inhibition of apamin-sensitive K+ current by hypoxia in adult rat adrenal chromaffin cells. *Pflug Archiv: Eur J Physiol* 439: 700-704, 2000.
376. Lee RM, Borkowski KR, Leenen FH, Tsoporis J, Coughlin M. Combined effect of neonatal sympathectomy and adrenal demedullation on blood pressure and vascular changes in spontaneously hypertensive rats. *Circulat Res* 69: 714-721, 1991.
377. Lembo PM, Grazzini E, Groblewski T, O'Donnell D, Roy MO, Zhang J, Hoffert C, Cao J, Schmidt R, Pelletier M, Labarre M, Gosselin M, Fortin Y, Banville D, Shen SH, Strom P, Payza K, Dray A, Walker P, Ahmad S. Proenkephalin A gene products activate a new family of sensory neuron – specific GPCRs. *Nat Neurosci* 5: 201-209, 2002.
378. Lenders JW, Eisenhofer G. Pathophysiology and diagnosis of disorders of the adrenal medulla: Focus on pheochromocytoma. *Compr Physiol* 4: 691-713, 2014.
379. Levitsky KL, Lopez-Barneo J. Developmental change of T-type Ca^{2+} channel expression and its role in rat chromaffin cell responsiveness to acute hypoxia. *J Physiol* 587: 1917-1929, 2009.
380. Lewis RV, Stern AS, Kilpatrick DL, Gerber LD, Rossier J, Stern S, Udenfriend S. Marked increases in large enkephalin-containing polypeptides in the rat adrenal gland following denervation. *J Neurosci* 1: 80-82, 1981.
381. Lewis RV, Stern AS, Kimura S, Rossier J, Stein S, Udenfriend S. An about 50,000-dalton protein in adrenal medulla: A common precursor of [Met]- and [Leu]enkephalin. *Science* 208: 1459-1461, 1980.
382. Li H, Li SH, Cheng AL, Mangiarini L, Bates GP, Li XJ. Ultrastructural localization and progressive formation of neuropil aggregates in Huntington's disease transgenic mice. *Hum Mol Genet* 8: 1227-1236, 1999.
383. Li H, Wyman T, Yu ZX, Li SH, Li XJ. Abnormal association of mutant huntingtin with synaptic vesicles inhibits glutamate release. *Hum Mol Genet* 12: 2021-2030, 2003.
384. Liao M, Shen J, Zhang Y, Li SH, Li XJ, Li H. Immunohistochemical localization of huntingtin-associated protein 1 in endocrine system of the rat. *J Histochem Cytochem* 53: 1517-1524, 2005.
385. Lim DY, Jang SJ, Park DG. Comparison of catecholamine release in the isolated adrenal glands of SHR and WKY rats. *Auton Autacoid Pharmacol* 22: 225-232, 2002.
386. Lindau M. Time-resolved capacitance measurements: Monitoring exocytosis in single cells. *Q Rev Biophys* 24: 75-101, 1991.
387. Lindau M, Neher E. Patch-clamp techniques for time-resolved capacitance measurements in single cells. *Pflug Arch* 411: 137-146, 1988.
388. Lindgren P, Rosen A, Uvnas B. The release of catechols from the adrenal medulla on activation of the bulbar part of the sympathetic vasodilator outflow in cats. *Acta Physiol Scand* 47: 233-242, 1959.
389. Lingle CJ, Martinez-Espinosa PL, Guarina L, Carbone E. Roles of Na(+), Ca(2+), and K(+) channels in the generation of repetitive firing and rhythmic bursting in adrenal chromaffin cells. *Pflug Archiv: Eur J Physiol* 470: 39-52, 2018.
390. Lingle CJ, Solaro CR, Prakriya M, Ding JP. Calcium-activated potassium channels in adrenal chromaffin cells. *Ion Channels* 4: 261-301, 1996.
391. Liu PS, Kao LS. Na(+)-dependent Ca^{2+} influx in bovine adrenal chromaffin cells. *Cell Calcium* 11: 573-579, 1990.
392. Liu PS, Lin YJ, Kao LS. Caffeine-sensitive calcium stores in bovine adrenal chromaffin cells. *J Neurochem* 56: 172-177, 1991.
393. Liu Y, Peter D, Roghani A, Schuldiner S, Prive GG, Eisenberg D, Brecha N, Edwards RH. A cDNA that suppresses MPP+ toxicity encodes a vesicular amine transporter. *Cell* 70: 539-551, 1992.
394. Livett BG. Chromaffin cells: Model cells for neuronal cell biology. In: Squire LR, editor. *Encyclopedia of Neuroscience*. Burlington, MA: Elsevier, vol. 2, 2009.
395. Livett BG, Dean DM, Whelan LG, Udenfriend S, Rossier J. Co-release of enkephalin and catecholamines from cultured chromaffin cells. *Nature* 289: 317-319, 1981.
396. Livett BG, Kozousek V, Mizobe F, Dean DM. Substance P inhibits nicotinic activation of chromaffin cells. *Nature* 278: 256-257, 1979.
397. Livett BG, Marley PD. Effects of opioid peptides and morphine on histamine-induced catecholamine secretion from cultured, bovine adrenal chromaffin cells. *Br J Pharmacol* 89: 327-334, 1986.
398. Llinas R, Steinberg IZ, Walton K. Relationship between presynaptic calcium current and postsynaptic potential in squid giant synapse. *Biophys J* 33: 323-351, 1981.
399. Logan T, Bendor J, Toupin C, Thorn K, Edwards RH. alpha-Synuclein promotes dilation of the exocytotic fusion pore. *Nat Neurosci* 20: 681-689, 2017.
400. Lomax RB, Michelena P, Nunez L, Garcia-Sancho J, Garcia AG, Montiel C. Different contributions of L- and Q-type Ca^{2+} channels to Ca^{2+} signals and secretion in chromaffin cell subtypes. *Am J Physiol* 272: C476-C484, 1997.
401. Lopez-Barneo J, Gonzalez-Rodriguez P, Gao L, Fernandez-Aguera MC, Pardal R, Ortega-Saenz P. Oxygen sensing by the carotid body: Mechanisms and role in adaptation to hypoxia. *Am J Physiol Cell Physiol* 310: C629-C642, 2016.
402. Lopez-Gil A, Nanclares C, Mendez-Lopez I, Martinez-Ramirez C, de Los RC, Padin-Nogueira JF, Montero M, Gandia L, Garcia AG. The quantal catecholamine release from mouse chromaffin cells challenged with repeated ACh pulses is regulated by the mitochondrial Na(+)/Ca(2+) exchanger. *J Physiol* 595: 2129-2146, 2017.
403. Lopez De Jesus M, Stope MB, Oude Weernink PA, Mahlke Y, Borgermann C, Ananaba VN, Rimmbach C, Rosskopf D, Michel MC, Jakobs KH, Schmidt M. Cyclic AMP-dependent and Epac-mediated activation of R-Ras by G protein-coupled receptors leads to phospholipase D stimulation. *J Biol Chem* 281: 21837-21847, 2006.
404. Lopez MG, Albillos A, de la Fuente MT, Borges R, Gandia L, Carbone E, Garcia AG, Artalejo AR. Localized L-type calcium channels control exocytosis in cat chromaffin cells. *Pflug Archiv: Eur J Physiol* 427: 348-354, 1994.
405. Lopez MG, Montiel C, Herrero CJ, Garcia-Palomero E, Mayorgas I, Hernandez-Guijo JM, Villarroya M, Olivares R, Gandia L, McIntosh JM, Olivera BM, Garcia AG. Unmasking the functions of the chromaffin cell alpha7 nicotinic receptor by using short pulses of acetylcholine and selective blockers. *Proc Natl Acad Sci USA* 95: 14184-14189, 1998.
406. Lopez MG, Villarroya M, Lara B, Martinez Sierra R, Albillos A, Garcia AG, Gandia L. Q- and L-type Ca2+ channels dominate the control of secretion in bovine chromaffin cells. *FEBS Lett* 349: 331-337, 1994.
407. Lou XL, Yu X, Chen XK, Duan KL, He LM, Qu AL, Xu T, Zhou Z. Na+ channel inactivation: A comparative study between pancreatic islet beta-cells and adrenal chromaffin cells in rat. *J Physiol* 548: 191-202, 2003.
408. Lovell PV, James DG, McCobb DP. Bovine versus rat adrenal chromaffin cells: Big differences in BK potassium channel properties. *J Neurophysiol* 83: 3277-3286, 2000.
409. Lu BX, Su YH, Das S, Liu J, Xia JS, Ren DJ. The neuronal channel NALCN contributes resting sodium permeability and is required for normal respiratory rhythm. *Cell* 129: 371-383, 2007.
410. Lugnier C. Cyclic nucleotide phosphodiesterase (PDE) superfamily: A new target for the development of specific therapeutic agents. *Pharmacol Ther* 109: 366-398, 2006.
411. Lukyanetz EA, Neher E. Different types of calcium channels and secretion from bovine chromaffin cells. *Eur J Neurosci* 11: 2865-2873, 1999.
412. Machado JD, Montesinos MS, Borges R. Good practices in single cell amperometry. *Methods Mol Biol* 440: 297-313, 2008.
413. Machado JD, Morales A, Gomez JF, Borges R. cAMP modulates exocytotic kinetics and increases quantal size in chromaffin cells. *Mol Pharmacol* 60: 514-520, 2001.
414. Mackenzie KD, Duffield MD, Peiris H, Phillips L, Zanin MP, Teo EH, Zhou XF, Keating DJ. Huntingtin-associated protein 1 regulates exocytosis, vesicle docking, readily releasable pool size and fusion pore stability in mouse chromaffin cells. *J Physiol* 592: 1505-1518, 2014.
415. Mackenzie KD, Lim Y, Duffield MD, Chataway T, Zhou XF, Keating DJ. Huntingtin-associated protein-1 (HAP1) regulates endocytosis and interacts with multiple trafficking-related proteins. *Cell Signal* 35: 176-187, 2017.
416. Mahapatra NR, O'Connor DT, Vaingankar SM, Hikim AP, Mahata M, Ray S, Staite E, Wu H, Gu Y, Dalton N, Kennedy BP, Ziegler MG, Ross J, Mahata SK. Hypertension from targeted ablation of chromogranin A can be rescued by the human ortholog. *J Clin Invest* 115: 1942-1952, 2005.
417. Mahapatra S, Calorio C, Vandael DHF, Marcantoni A, Carabelli V, Carbone E. Calcium channel types contributing to chromaffin cell excitability, exocytosis and endocytosis. *Cell Calcium* 51: 321-330, 2012.
418. Mahapatra S, Marcantoni A, Vandael DHF, Striessnig J, Carbone E. Are Ca(v)1.3 pacemaker channels in chromaffin cells? Possible bias from resting cell conditions and DHP blockers usage. *Channels* 5: 219-224, 2011.
419. Mahapatra S, Marcantoni A, Zuccotti A, Carabelli V, Carbone E. Equal sensitivity of Cav1.2 and Cav1.3 channels to the opposing modulations of PKA and PKG in mouse chromaffin cells. *J Physiol-Lond* 590: 5053-5073, 2012.

420. Mahata SK, Mahata M, Parmer RJ, O'Connor DT. Desensitizaton of catecholamine release. The novel catecholammine release-inhibitory peptide catestatin (chromogranin A344-364) acts at the receptor to prevent nicotinic cholinergic tolerance. *J Biol Chem* 274: 2920-2928, 1999.
421. Majdi S, Larsson A, Najafinobar N, Borges R, Ewing AG. Extracellular ATP regulates the vesicular pore opening in chromaffin cells and increases the fraction released during individual exocytosis events. *ACS Chem Neurosci* 10 (5): 2459-2466, 2019.
422. Malhotra RK, Wakade AR. Non-cholinergic component of rat splanchnic nerves predominates at low neuronal activity and is eliminated by naloxone. *J Physiol* 383: 639-652, 1987.
423. Man KN, Imig C, Walter AM, Pinheiro PS, Stevens DR, Rettig J, Sorensen JB, Cooper BH, Brose N, Wojcik SM. Identification of a Munc13-sensitive step in chromaffin cell large dense-core vesicle exocytosis. *eLife* 4, 2015. DOI: 10.7554/eLife.10635.
424. Manger WM, Eisenhofer G. Pheochromocytoma: Diagnosis and management update. *Curr Hypertension Rep* 6: 477-484, 2004.
425. Mangiarini L, Sathasivam K, Seller M, Cozens B, Harper A, Hetherington C, Lawton M, Trottier Y, Lehrach H, Davies SW, Bates GP. Exon 1 of the HD gene with an expanded CAG repeat is sufficient to cause a progressive neurological phenotype in transgenic mice. *Cell* 87: 493-506, 1996.
426. Marcantoni A, Baldelli P, Hernandez-Guijo JM, Comunanza V, Carabelli V, Carbone E. L-type calcium channels in adrenal chromaffin cells: Role in pace-making and secretion. *Cell Calcium* 42: 397-408, 2007.
427. Marcantoni A, Carabelli V, Comunanza V, Hoddah H, Carbone E. Calcium channels in chromaffin cells: Focus on L and T types. *Acta Physiol* 192: 233-246, 2008.
428. Marcantoni A, Carabelli V, Vandael DH, Comunanza V, Carbone E. PDE type-4 inhibition increases L-type Ca2+ currents, action potential firing, and quantal size of exocytosis in mouse chromaffin cells. *Pflug Archiv: Eur J Physiol* 457: 1093-1110, 2009.
429. Marcantoni A, Vandael DHF, Mahapatra S, Carabelli V, Sinnegger-Brauns MJ, Striessnig J, Carbone E. Loss of Cav1.3 channels reveals the critical role of L-type and BK channel coupling in pacemaking mouse adrenal chromaffin cells. *J Neurosci* 30: 491-504, 2010.
430. Marchetti C, Carbone E, Lux HD. Effects of dopamine and noradrenaline on Ca channels of cultured sensory and sympathetic neurons of chick. *Pflug Archiv: Eur J Physiol* 406: 104-111, 1986.
431. Marley PD. Mechanisms in histamine-mediated secretion from adrenal chromaffin cells. *Pharmacol Ther* 98: 1-34, 2003.
432. Marshall JM. Peripheral chemoreceptors and cardiovascular regulation. *Physiol Rev* 74: 543-594, 1994.
433. Martin AO, Mathieu MN, Chevillard C, Guerineau NC. Gap junctions mediate electrical signaling and ensuing cytosolic Ca^{2+} increases between chromaffin cells in adrenal slices: A role in catecholamine release. *J Neurosci* 21: 5397-5405, 2001.
434. Martinez-Espinosa PL, Yang C, Gonzalez-Perez V, Xia XM, Lingle CJ. Knockout of the BK beta2 subunit abolishes inactivation of BK currents in mouse adrenal chromaffin cells and results in slow-wave burst activity. *J Gen Physiol* 144: 275-295, 2014.
435. Martinez-Ramirez C, Baraibar AM, Nanclares C, Mendez-Lopez I, Gomez A, Munoz MP, de Diego AMG, Gandia L, Casarejos MJ, Garcia AG. Altered excitability and exocytosis in chromaffin cells from the R6/1 mouse model of Huntington's disease is linked to over-expression of mutated huntingtin. *J Neurochem*, 2018.
436. Marty A, Neher E. Potassium channels in cultured bovine adrenal chromaffin cells. *J Physiol* 367: 117-141, 1985.
437. Mascorro JA, Yates RD, Chen IL. A glutaraldehyde/potassium dichromate tracing method for the localization and preservation of abdominal extra-adrenal chromaffin tissues. *Stain Technol* 50: 391-396, 1975.
438. Matsui H. Effect of myelencephalic stimulation on the secretion of noradrenaline and adrenaline of the adrenal gland in the cat. *Tohoku J Exp Med* 87: 332-337, 1965.
439. Matsuoka H, Harada K, Endo Y, Warashina A, Doi Y, Nakamura J, Inoue M. Molecular mechanisms supporting a paracrine role of GABA in rat adrenal medullary cells. *J Physiol* 586: 4825-4842, 2008.
440. May V, Beaudet MM, Parsons RL, Hardwick JC, Gauthier EA, Durda JP, Braas KM. Mechanisms of pituitary adenylate cyclase activating polypeptide (PACAP)-induced depolarization of sympathetic superior cervical ganglion (SCG) neurons. *Ann N Y Acad Sci* 865: 164-175, 1998.
441. Medbo JI, Sejersted OM. Plasma potassium changes with high-intensity exercise. *J Physiol-Lond* 421: 105-122, 1990.
442. Michelena P, Vega T, Montiel C, Lopez MG, Garcia-Perez LE, Gandia L, Garcia AG. Effects of tyramine and calcium on the kinetics of secretion in intact and electroporated chromaffin cells superfused at high speed. *Pflug Archiv: EurJ Physiol* 431: 283-296, 1995.
443. Milla J, Montesinos MS, Machado JD, Borges R, Alonso E, Moreno-Ortega AJ, Cano-Abad MF, Garcia AG, Ruiz-Nuno A. Ouabain enhances exocytosis through the regulation of calcium handling by the endoplasmic reticulum of chromaffin cells. *Cell Calcium* 50: 332-342, 2011.
444. Miranda-Ferreira R, de Pascual R, Caricati-Neto A, Gandia L, Jurkiewicz A, Garcia AG. Role of the endoplasmic reticulum and mitochondria on quantal catecholamine release from chromaffin cells of control and hypertensive rats. *J Pharmacol Exp Therap* 329: 231-240, 2009.
445. Miranda-Ferreira R, de Pascual R, de Diego AM, Caricati-Neto A, Gandia L, Jurkiewicz A, Garcia AG. Single-vesicle catecholamine release has greater quantal content and faster kinetics in chromaffin cells from hypertensive, as compared with normotensive, rats. *J Pharmacol Exp Therap* 324: 685-693, 2008.
446. Miranda-Ferreira R, de Pascual R, Smaili SS, Caricati-Neto A, Gandia L, Garcia AG, Jurkiewicz A. Greater cytosolic and mitochondrial calcium transients in adrenal medullary slices of hypertensive, compared with normotensive rats. *Eur J Pharmacol* 636: 126-136, 2010.
447. Miyata A, Arimura A, Dahl RR, Minamino N, Uehara A, Jiang L, Culler MD, Coy DH. Isolation of a novel 38 residue-hypothalamic polypeptide which stimulates adenylate cyclase in pituitary cells. *Biochem Biophys Res Commun* 164: 567-574, 1989.
448. Mizuno K, Minamino N, Kangawa K, Matsuo H. A new family of endogenous "big" Met-enkephalins from bovine adrenal medulla: Purification and structure of docosa- (BAM-22P) and eicosapeptide (BAM-20P) with very potent opiate activity. *Biochem Biophys Res Commun* 97: 1283-1290, 1980.
449. Mochizuki-Oda N, Takeuchi Y, Matsumura K, Oosawa Y, Watanabe Y. Hypoxia-induced catecholamine release and intracellular Ca^{2+} increase via suppression of K+ channels in cultured rat adrenal chromaffin cells. *J Neurochem* 69: 377-387, 1997.
450. Mojet MH, Mills E, Duchen MR. Hypoxia-induced catecholamine secretion in isolated newborn rat adrenal chromaffin cells is mimicked by inhibition of mitochondrial respiration. *J Physiol* 504 (Pt 1): 175-189, 1997.
451. Mollard P, Seward EP, Nowycky MC. Activation of nicotinic receptors triggers exocytosis from bovine chromaffin cells in the absence of membrane depolarization. *Proc Natl Acad Sci USA* 92: 3065-3069, 1995.
452. Montero M, Alonso MT, Albillos A, Cuchillo-Ibanez I, Olivares R, Garcia AG, Garcia-Sancho J, Alvarez J. Control of secretion by mitochondria depends on the size of the local $[Ca^{2+}]$ after chromaffin cell stimulation. *Eur J Neurosci* 13: 2247-2254, 2001.
453. Montero M, Alonso MT, Carnicero E, Cuchillo-Ibanez I, Albillos A, Garcia AG, Garcia-Sancho J, Alvarez J. Chromaffin-cell stimulation triggers fast millimolar mitochondrial Ca2+ transients that modulate secretion. *Nat Cell Biol* 2: 57-61, 2000.
454. Montesinos MS, Camacho M, Machado JD, Viveros OH, Beltran B, Borges R. The quantal secretion of catecholamines is impaired by the accumulation of beta-adrenoceptor antagonists into chromaffin cell vesicles. *Br J Pharmacol* 159: 1548-1556, 2010.
455. Montesinos MS, Machado JD, Camacho M, Diaz J, Morales YG, Alvarez de la Rosa D, Carmona E, Castaneyra A, Viveros OH, O'Connor DT, Mahata SK, Borges R. The crucial role of chromogranins in storage and exocytosis revealed using chromaffin cells from chromogranin A null mouse. *J Neurosci:Off J Soc Neurosci* 28: 3350-3358, 2008.
456. Moro MA, Garcia AG, Langley OK. Characterization of two chromaffin cell populations isolated from bovine adrenal medulla. *J Neurochem* 57: 363-369, 1991.
457. Morrison SF, Cao WH. Different adrenal sympathetic preganglionic neurons regulate epinephrine and norepinephrine secretion. *Am J Physiol Regul, Integr Comp Physiol* 279: R1763-R1775, 2000.
458. Mosharov EV, Gong LW, Khanna B, Sulzer D, Lindau M. Intracellular patch electrochemistry: Regulation of cytosolic catecholamines in chromaffin cells. *J Neurosci: Off J Soc Neurosci* 23: 5835-5845, 2003.
459. Muller L, Lindberg I. The cell biology of the prohormone convertases PC1 and PC2. *Progr Nucl Acid Res Mol Biol* 63: 69-108, 1999.
460. Musial DC, Bomfim GH, Arranz-Tagarro JA, Mendez-Lopez I, Miranda-Ferreira R, Jurkiewicz A, Jurkiewicz NH, Garcia AG, Padin JF. Altered mitochondrial function, calcium signaling, and catecholamine release in chromaffin cells of diabetic and SHR rats. *Eur J Pharmacol* 815: 416-426, 2017.
461. Nagayama T, Matsumoto T, Kuwakubo F, Fukushima Y, Yoshida M, Suzuki-Kusaba M, Hisa H, Kimura T, Satoh S. Role of calcium channels in catecholamine secretion in the rat adrenal gland. *J Physiol* 520 (Pt 2): 503-512, 1999.
462. Nakada T, Furuta H, Katayama T. Catecholamine metabolism in pheochromocytoma and normal adrenal medullae. *J Urol* 140: 1348-1351, 1988.
463. Nanclares C, Baraibar AM, Gandia L. L-type calcium channels in exocytosis and endocytosis of chromaffin cells. *Pflug Archiv: Eur J Physiol* 470: 53-60, 2018.
464. Nassar-Gentina V, Pollard HB, Rojas E. Electrical activity in chromaffin cells of intact mouse adrenal gland. *Am J Physiol* 254: C675-C683, 1988.

465. Neale EA, Bowers LM, Jia M, Bateman KE, Williamson LC. Botulinum neurotoxin A blocks synaptic vesicle exocytosis but not endocytosis at the nerve terminal. *J Cell Biol* 147: 1249-1260, 1999.
466. Neco P, Giner D, Viniegra S, Borges R, Villarroel A, Gutierrez LM. New roles of myosin II during the vesicle transport and fusion in chromaffin cells. *J Biol Chem*, 2004.
467. Neely A, Lingle CJ. Effects of muscarine on single-rat adrenal chromaffin cells. *J Physiol-Lond* 453: 133-166, 1992.
468. Neely A, Lingle CJ. Two components of calcium-activated potassium current in rat adrenal chromaffin cells. *J Physiol* 453: 97-131, 1992.
469. Neher E. A comparison between exocytic control mechanisms in adrenal chromaffin cells and a glutamatergic synapse. *Pflug Archiv: Eur J Physiol* 453: 261-268, 2006.
470. Neher E. Neurosecretion: What can we learn from chromaffin cells. *Pflug Archiv: Eur J Physiol* 470: 7-11, 2018.
471. Neher E. Usefulness and limitations of linear approximations to the understanding of Ca++ signals. *Cell Calcium* 24: 345-357, 1998.
472. Neher E. Vesicle pools and Ca2+ microdomains: New tools for understanding their roles in neurotransmitter release. *Neuron* 20: 389-399, 1998.
473. Neher E, Augustine GJ. Calcium gradients and buffers in bovine chromaffin cells. *J Physiol* 450: 273-301, 1992.
474. Nelson O, Tu H, Lei T, Bentahir M, de Strooper B, Bezprozvanny I. Familial Alzheimer disease-linked mutations specifically disrupt Ca^{2+} leak function of presenilin 1. *J Clin Invest* 117: 1230-1239, 2007.
475. Nemani VM, Lu W, Berge V, Nakamura K, Onoa B, Lee MK, Chaudhry FA, Nicoll RA, Edwards RH. Increased expression of alpha-synuclein reduces neurotransmitter release by inhibiting synaptic vesicle reclustering after endocytosis. *Neuron* 65: 66-79, 2010.
476. Noble EP, Bommer M, Liebisch D, Herz A. H1-histaminergic activation of catecholamine release by chromaffin cells. *Biochem Pharmacol* 37: 221-228, 1988.
477. Noble EP, Bommer M, Sincini E, Costa T, Herz A. H1-histaminergic activation stimulates inositol-1-phosphate accumulation in chromaffin cells. *Biochem Biophys Res Commun* 135: 566-573, 1986.
478. Nooney JM, Feltz A. Inhibition by cyclothiazide of neuronal nicotinic responses in bovine chromaffin cells. *Br J Pharmacol* 114: 648-655, 1995.
479. Novara M, Baldelli P, Cavallari D, Carabelli V, Giancippoli A, Carbone E. Exposure to cAMP and beta-adrenergic stimulation recruits Ca(V)3 T-type channels in rat chromaffin cells through Epac cAMP-receptor proteins. *J Physiol* 558: 433-449, 2004.
480. Nowycky MC, Pinter MJ. Time courses of calcium and calcium-bound buffers following calcium influx in a model cell. *Biophys J* 64: 77-91, 1993.
481. Nucifora PG, Fox AP. Tyrosine phosphorylation regulates rapid endocytosis in adrenal chromaffin cells. *J Neurosci: Off J Soc Neurosci* 19: 9739-9746, 1999.
482. Nurse CA, Salman S, Scott AL. Hypoxia-regulated catecholamine secretion in chromaffin cells. *Cell Tissue Res* 372: 433-441, 2018.
483. Nussdorfer GG. Paracrine control of adrenal cortical function by medullary chromaffin cells. *Pharmacol Rev* 48: 495-530, 1996.
484. O'Farrell M, Marley PD. Different contributions of voltage-sensitive Ca^{2+} channels to histamine-induced catecholamine release and tyrosine hydroxylase activation in bovine adrenal chromaffin cells. *Cell Calcium* 25: 209-217, 1999.
485. O'Sullivan AJ, Burgoyne RD. A comparison of bradykinin, angiotensin II and muscarinic stimulation of cultured bovine adrenal chromaffin cells. *Biosci Rep* 9: 243-252, 1989.
486. Oheim M, Stuhmer W. Tracking chromaffin granules on their way through the actin cortex. *Eur Biophys J* 29: 67-89, 2000.
487. Ohta T, Ito S, Nakazato Y. Ca^{2+}-dependent K+ currents induced by muscarinic receptor activation in guinea pig adrenal chromaffin cells. *J Neurochem* 70: 1280-1288, 1998.
488. Okamoto K, Aoki K. Development of a strain of spontaneously hypertensive rats. *Jpn Circul J* 27: 282-293, 1963.
489. Olivos L, Artalejo AR. Muscarinic excitation-secretion coupling in chromaffin cells. *Acta Physiol (Oxford, England)* 192: 213-220, 2007.
490. Olivos Ore L, Artalejo AR. Intracellular Ca^{2+} microdomain-triggered exocytosis in neuroendocrine cells. *Trends Neurosci* 27: 113-115, 2004.
491. Omiatek DM, Dong Y, Heien ML, Ewing AG. Only a fraction of quantal content is released during exocytosis as revealed by electrochemical cytometry of secretory vesicles. *ACS Chem Neurosci* 1: 234-245, 2010.
492. Omura M, Saito J, Yamaguchi K, Kakuta Y, Nishikawa T. Prospective study on the prevalence of secondary hypertension among hypertensive patients visiting a general outpatient clinic in Japan. *Hypertens Res: Off J Jpn Soc Hypertens* 27: 193-202, 2004.
493. Oset-Gasque MJ, Castro E, Gonzalez MP. Mechanisms of [3H] gamma-aminobutyric acid release by chromaffin cells in primary culture. *J Neurosci Res* 26: 181-187, 1990.
494. Oset-Gasque MJ, Parramon M, Hortelano S, Bosca L, Gonzalez MP. Nitric oxide implication in the control of neurosecretion by chromaffin cells. *J Neurochem* 63: 1693-1700, 1994.
495. Padin JF, Fernandez-Morales JC, de Diego AM, Garcia AG. Calcium channel subtypes and exocytosis in chromaffin cells at early life. *Curr Mol Pharmacol* 8: 81-86, 2015.
496. Pak CH. Plasma adrenaline and noradrenaline concentrations of the spontaneously hypertensive rat. *Jpn Heart J* 22: 987-995, 1981.
497. Pan CY, Chu YS, Kao LS. Molecular study of the Na^+/Ca^{2+} exchanger in bovine adrenal chromaffin cells. *Biochem J* 336 (Pt 2): 305-310, 1998.
498. Pan CY, Fox AP. Rundown of secretion after depletion of intracellular calcium stores in bovine adrenal chromaffin cells. *J Neurochem* 75: 1132-1139, 2000.
499. Pan CY, Huang CH, Lee CH. Calcium elevation elicited by reverse mode Na^+/Ca^{2+} exchange activity is facilitated by intracellular calcium stores in bovine chromaffin cells. *Biochem Biophys Res Commun* 342: 589-595, 2006.
500. Pan CY, Jeromin A, Lundstrom K, Yoo SH, Roder J, Fox AP. Alterations in exocytosis induced by neuronal Ca^{2+} sensor-1 in bovine chromaffin cells. *J Neurosci* 22: 2427-2433, 2002.
501. Pan CY, Kao LS. Catecholamine secretion from bovine adrenal chromaffin cells: The role of the Na^+/Ca^{2+} exchanger and the intracellular Ca^{2+} pool. *J Neurochem* 69: 1085-1092, 1997.
502. Pape HC. Queer current and pacemaker: The hyperpolarization-activated cation current in neurons. *Annu Rev Physiol* 58: 299-327, 1996.
503. Park YB. Ion selectivity and gating of small conductance Ca(2+)-activated K+ channels in cultured rat adrenal chromaffin cells. *J Physiol* 481 (Pt 3). 555-570, 1994.
504. Park YB, Herrington J, Babcock DF, Hille B. Ca^{2+} clearance mechanisms in isolated rat adrenal chromaffin cells. *J Physiol* 492 (Pt 2): 329-346, 1996.
505. Parker TL, Kesse WK, Mohamed AA, Afework M. The innervation of the mammalian adrenal gland. *J Anat* 183 (Pt 2): 265-276, 1993.
506. Patel JN, Coppack SW, Goldstein DS, Miles JM, Eisenhofer G. Norepinephrine spillover from human adipose tissue before and after a 72-hour fast. *J Clin Endocrinol Metab* 87: 3373-3377, 2002.
507. Patzak A, Winkler H. Exocytotic exposure and recycling of membrane antigens of chromaffin granules: Ultrastructural evaluation after immunolabeling. *J Cell Biol* 102: 510-515, 1986.
508. Perez-Alvarez A, Hernandez-Vivanco A, Alonso YGS, Tabernero A, McIntosh JM, Albillos A. Pharmacological characterization of native alpha7 nicotinic ACh receptors and their contribution to depolarization-elicited exocytosis in human chromaffin cells. *Br J Pharmacol* 165: 908-921, 2012.
509. Perez-Alvarez A, Hernandez-Vivanco A, Caba-Gonzalez JC, Albillos A. Different roles attributed to Cav1 channel subtypes in spontaneous action potential firing and fine tuning of exocytosis in mouse chromaffin cells. *J Neurochem* 116: 105-121, 2011.
510. Perez-Alvarez A, Hernandez-Vivanco A, Cano-Abad M, Albillos A. Pharmacological and biophysical properties of Ca^{2+} channels and subtype distributions in human adrenal chromaffin cells. *Pflug Archiv: Eur J Physiol* 456: 1149-1162, 2008.
511. Perez Bay AE, Belingheri AV, Alvarez YD, Marengo FD. Membrane cycling after the excess retrieval mode of rapid endocytosis in mouse chromaffin cells. *Acta Physiol (Oxford, England)* 204: 403-418, 2012.
512. Perrais D, Kleppe IC, Taraska JW, Almers W. Recapture after exocytosis causes differential retention of protein in granules of bovine chromaffin cells. *J Physiol* 560: 413-428, 2004.
513. Peters JA, Lambert JJ, Cottrell GA. An electrophysiological investigation of the characteristics and function of GABAA receptors on bovine adrenomedullary chromaffin cells. *Pflug Archiv: Eur J Physiol* 415: 95-103, 1989.
514. Picones A, Loza-Huerta A, Segura-Chama P, Lara-Figueroa CO. Contribution of automated technologies to ion channel drug discovery. *Adv Protein Chem Struct Biol* 104: 357-378, 2016.
515. Pitts RF, Bronk DW. Excitability cycle of the hypothalamus-sympathetic neurone system. *Am J Physiol* 135 (2): 504-522, 1941.
516. Platzer J, Engel J, Schrott-Fischer A, Stephan K, Bova S, Chen H, Zheng H, Striessnig J. Congenital deafness and sinoatrial node dysfunction in mice lacking class D L-type Ca^{2+} channels. *Cell* 102: 89-97, 2000.
517. Pletscher A, Da Prada M, Berneis KH, Steffen H, Lütold B, Weder HG. Molecular organization of amine storage organelles of blood platelets and adrenal medulla. In: Ceccarelli B, Clementi F, Meldolesi J, editors. *Advances in Cytopharmacology*. New York: Raven Press, 1974, p. 257-264.
518. Plevin R, Boarder MR. Stimulation of formation of inositol phosphates in primary cultures of bovine adrenal chromaffin cells by angiotensin II, histamine, bradykinin, and carbachol. *J Neurochem* 51: 634-641, 1988.
519. Powell AD, Teschemacher AG, Seward EP. P2Y purinoceptors inhibit exocytosis in adrenal chromaffin cells via modulation of voltage-operated calcium channels. *J Neurosci: Off J Soc Neurosci* 20: 606-616, 2000.

520. Powis DA, O'Brien KJ, Von Grafenstein HR. Calcium export by sodium-calcium exchange in bovine chromaffin cells. *Cell Calcium* 12: 493-504, 1991.
521. Prabhakar NR, Kumar GK, Peng YJ. Sympatho-adrenal activation by chronic intermittent hypoxia. *J Appl Physiol* 113: 1304-1310, 2012, 1985.
522. Prakriya M, Lingle CJ. Activation of BK channels in rat chromaffin cells requires summation of Ca(2+) influx from multiple Ca(2+) channels. *J Neurophysiol* 84: 1123-1135, 2000.
523. Prakriya M, Lingle CJ. BK channel activation by brief depolarizations requires Ca^{2+} influx through L- and Q-type Ca^{2+} channels in rat chromaffin cells. *J Neurophysiol* 81: 2267-2278, 1999.
524. Priller C, Mitteregger G, Paluch S, Vassallo N, Staufenbiel M, Kretzschmar HA, Jucker M, Herms J. Excitatory synaptic transmission is depressed in cultured hippocampal neurons of APP/PS1 mice. *Neurobiol Aging* 30: 1227-1237, 2009.
525. Proye C, Fossati P, Fontaine P, Lefebvre J, Decoulx M, Wemeau JL, Dewailly D, Rwamasirabo E, Cecat P. Dopamine-secreting pheochromocytoma: An unrecognized entity? Classification of pheochromocytomas according to their type of secretion. *Surgery* 100: 1154-1162, 1986.
526. Przywara DA, Guo X, Angelilli ML, Wakade TD, Wakade AR. A noncholinergic transmitter, pituitary adenylate cyclase-activating polypeptide, utilizes a novel mechanism to evoke catecholamine secretion in rat adrenal chromaffin cells. *J Biol Chem* 271: 10545-10550, 1996.
527. Raman IM, Bean BP. Resurgent sodium current and action potential formation in dissociated cerebellar Purkinje neurons. *J Neurosci: Off J Soc Neurosci* 17: 4517-4526, 1997.
528. Rao TC, Santana Rodriguez Z, Bradberry MM, Ranski AH, Dahl PJ, Schmidtke MW, Jenkins PM, Axelrod D, Chapman ER, Giovannucci DR, Anantharam A. Synaptotagmin isoforms confer distinct activation kinetics and dynamics to chromaffin cell granules. *J Gen Physiol* 149: 763-780, 2017.
529. Ream MA, Chandra R, Peavey M, Ray AM, Roffler-Tarlov S, Kim HG, Wetsel WC, Rockman HA, Chikaraishi DM. High oxygen prevents fetal lethality due to lack of catecholamines. *Am J Physiol Regul Integr Comp Physiol* 295: R942-R953, 2008.
530. Reid CA, Bekkers JM, Clements JD. Presynaptic Ca^{2+} channels: A functional patchwork. *Trends Neurosci* 26: 683-687, 2003.
531. Reuter H. The dependence of slow inward current in Purkinje fibres on the extracellular calcium-concentration. *J Physiol* 192: 479-492, 1967.
532. Reynafarje B, Lehninger AL. Electric charge stoichiometry of calcium translocation in mitochondria. *Biochem Biophys Res Commun* 77: 1273-1279, 1977.
533. Richards DA, Guatimosim C, Betz WJ. Two endocytic recycling routes selectively fill two vesicle pools in frog motor nerve terminals. *Neuron* 27: 551-559, 2000.
534. Rico AJ, Prieto-Lloret J, Gonzalez C, Rigual R. Hypoxia and acidosis increase the secretion of catecholamines in the neonatal rat adrenal medulla: An in vitro study. *Am J Physiol Cell Physiol* 289: C1417-C1425, 2005.
535. Rigual R, Montero M, Rico AJ, Prieto-Lloret J, Alonso MT, Alvarez J. Modulation of secretion by the endoplasmic reticulum in mouse chromaffin cells. *Eur J Neurosci* 16: 1690-1696, 2002.
536. Rink TJ. The influence of sodium on calcium movements and catecholamine release in thin slices of bovine adrenal medulla. *J Physiol* 266: 297-325, 1977.
537. Rizzuto R, Brini M, Murgia M, Pozzan T. Microdomains with high Ca^{2+} close to IP3-sensitive channels that are sensed by neighboring mitochondria. *Science* 262: 744-747, 1993.
538. Robinson IM, Burgoyne RD. Characterisation of distinct inositol 1,4,5-trisphosphate-sensitive and caffeine-sensitive calcium stores in digitonin-permeabilised adrenal chromaffin cells. *J Neurochem* 56: 1587-1593, 1991.
539. Robinson IM, Yamada M, Carrion-Vazquez M, Lennon VA, Fernandez JM. Specialized release zones in chromaffin cells examined with pulsed-laser imaging. *Cell Calcium* 20: 181-201, 1996.
540. Robinson RL, Culberson JL, Carmichael SW. Influence of hypothalamic stimulation on the secretion of adrenal medullary catecholamines. *J Auton Nerv Syst* 8: 89-96, 1983.
541. Rosa JM, de Diego AM, Gandia L, Garcia AG. L-type calcium channels are preferentially coupled to endocytosis in bovine chromaffin cells. *Biochem Biophys Res Commun* 357: 834-839, 2007.
542. Rosa JM, Gandia L, Garcia AG. Inhibition of N and PQ calcium channels by calcium entry through L channels in chromaffin cells. *Pflug Archiv: Eur J Physiol* 458: 795-807, 2009.
543. Rosa JM, Torregrosa-Hetland CJ, Colmena I, Gutierrez LM, Garcia AG, Gandia L. Calcium entry through slow-inactivating L-type calcium channels preferentially triggers endocytosis rather than exocytosis in bovine chromaffin cells. *Am J Physiol Cell Physiol* 301: C86-C98, 2011.
544. Roscioni SS, Elzinga CR, Schmidt M. Epac: Effectors and biological functions. *Naunyn Schmiedeberg's Arch Pharmacol* 377: 345-357, 2008.
545. Rose SD, Lejen T, Casaletti L, Larson RE, Pene TD, Trifaro JM. Molecular motors involved in chromaffin cell secretion. *Ann N Y Acad Sci* 971: 222-231, 2002.
546. Rowland LP, Shneider NA. Amyotrophic lateral sclerosis. *N Engl J Med* 344: 1688-1700, 2001.
547. Rozas JL, Gomez-Sanchez L, Tomas-Zapico C, Lucas JJ, Fernandez-Chacon R. Increased neurotransmitter release at the neuromuscular junction in a mouse model of polyglutamine disease. *J Neurosci* 31: 1106-1113, 2011.
548. Rubio I, Rodriguez-Navarro JA, Tomas-Zapico C, Ruiz C, Casarejos MJ, Perucho J, Gomez A, Rodal I, Lucas JJ, Mena MA, de Yebenes JG. Effects of partial suppression of parkin on huntingtin mutant R6/1 mice. *Brain Res* 1281: 91-100, 2009.
549. Sahu BS, Mahata S, Bandyopadhyay K, Mahata M, Avolio E, Pasqua T, Sahu C, Bandyopadhyay GK, Bartolomucci A, Webster NJG, Van Den Bogaart G, Fischer-Colbrie R, Corti A, Eiden LE, Mahata SK. Catestatin regulates vesicular quanta through modulation of cholinergic and peptidergic (PACAPergic) stimulation in PC12 cells. *Cell Tissue Res*, 2018.
550. Salman S, Buttigieg J, Zhang M, Nurse CA. Chronic exposure of neonatal rat adrenomedullary chromaffin cells to opioids in vitro blunts both hypoxia and hypercapnia chemosensitivity. *J Physiol* 591: 515-529, 2013.
551. Salvador JM, Inesi G, Rigaud JL, Mata AM. Ca^{2+} transport by reconstituted synaptosomal ATPase is associated with H+ countertransport and net charge displacement. *J Biol Chem* 273: 18230-18234, 1998.
552. Santodomingo J, Vay L, Camacho M, Hernandez-Sanmiguel E, Fonteriz RI, Lobaton CD, Montero M, Moreno A, Alvarez J. Calcium dynamics in bovine adrenal medulla chromaffin cell secretory granules. *Eur J Neurosci* 28: 1265-1274, 2008.
553. Sasakawa N, Nakaki T, Kato R. Formation of inositol polyphosphates in cultured adrenal chromaffin cells. *Adv Exp Med Biol* 287: 111-123, 1991.
554. Sawada K, Echigo N, Juge N, Miyaji T, Otsuka M, Omote H, Yamamoto A, Moriyama Y. Identification of a vesicular nucleotide transporter. *Proc Natl Acad Sci USA* 105: 5683-5686, 2008.
555. Schapiro FB, Grinstein S. Determinants of the pH of the Golgi complex. *J Biol Chem* 275: 21025-21032, 2000.
556. Scharinger A, Eckrich S, Vandael DH, Schonig K, Koschak A, Hecker D, Kaur G, Lee A, Sah A, Bartsch D, Benedetti B, Lieb A, Schick B, Singewald N, Sinnegger-Brauns MJ, Carbone E, Engel J, Steiessnig J. Cell-type-specific tuning of Cav1.3 Ca2+-channels by a C-terminal automodulatory domain. *Front Cellular Neurosci* 9: 18, 2015.
557. Schonn JS, Maximov A, Lao Y, Sudhof TC, Sorensen JB. Synaptotagmin-1 and -7 are functionally overlapping Ca^{2+} sensors for exocytosis in adrenal chromaffin cells. *Proc Natl Acad Sci USA* 105: 3998-4003, 2008.
558. Schroeder TJ, Borges R, Finnegan JM, Pihel K, Amatore C, Wightman RM. Temporally resolved, independent stages of individual exocytotic secretion events. *Biophys J* 70: 1061-1068, 1996.
559. Schuldiner S. A molecular glimpse of vesicular transporters. *J Neurochem* 62: 2067-2078, 1994.
560. Schuldiner S, Shirvan A, Stern-Bach Y, Steiner-Mordoch S, Yelin R, Laskar O. From bacterial antibiotic resistance to neurotransmitter uptake. A common theme of cell survival. *Ann N Y Acad Sci* 733: 174-184, 1994.
561. Schwarz PM, Rodriguez-Pascual F, Koesling D, Torres M, Forstermann U. Functional coupling of nitric oxide synthase and soluble guanylyl cyclase in controlling catecholamine secretion from bovine chromaffin cells. *Neuroscience* 82: 255-265, 1998.
562. Scott AL, Zhang M, Nurse CA. Enhanced BDNF signalling following chronic hypoxia potentiates catecholamine release from cultured rat adrenal chromaffin cells. *J Physiol* 593: 3281-3299, 2015.
563. Scott DA, Tabarean I, Tang Y, Cartier A, Masliah E, Roy S. A pathologic cascade leading to synaptic dysfunction in alpha-synuclein-induced neurodegeneration. *J Neurosci* 30: 8083-8095, 2010.
564. Scott RS, Bustillo D, Olivos-Oré LA, Cuchillo-Ibanez I, Barahona MV, Carbone E, Artalejo AR. Contribution of BK channels to action potential repolarisation at minimal cytosolic Ca2+ concentration in chromaffin cells. *Pflug Archiv: Eur J Physiol* 462: 545-557, 2011.
565. Segura-Chama P, Hernandez A, Jimenez-Perez N, Alejandre-Garcia T, Rivera-Cerecedo CV, Hernandez-Guijo J, Hernandez-Cruz A. Comparison of Ca^{2+} currents of chromaffin cells from normotensive Wistar Kyoto and spontaneously hypertensive rats. *Cell Mol Neurobiol* 30: 1243-1250, 2010.
566. Segura-Chama P, Lopez-Bistrain P, Perez-Armendariz EM, Jimenez-Perez N, Millan-Aldaco D, Hernandez-Cruz A. Enhanced Ca-induced Ca release from intracellular stores contributes to catecholamine hypersecretion in adrenal chromaffin cells from spontaneously hypertensive rats. *Pflug Archiv: Eur J Physiol*, 2015.
567. Seidler FJ, Slotkin TA. Adrenomedullary function in the neonatal rat: Responses to acute hypoxia. *J Physiol* 358: 1-16, 1985.

568. Selkoe DJ. Alzheimer's disease is a synaptic failure. *Science* 298: 789-791, 2002.
569. Selye H. The evolution of the stress concept. *Am Scientist* 61: 692-699, 1973.
570. Selye H. *Stress In Health and Disease*. Butterworths, 1976.
571. Senior SL, Ninkina N, Deacon R, Bannerman D, Buchman VL, Cragg SJ, Wade-Martins R. Increased striatal dopamine release and hyperdopaminergic-like behaviour in mice lacking both alpha-synuclein and gamma-synuclein. *Eur J Neurosci* 27: 947-957, 2008.
572. Shahar E, Whitney CW, Redline S, Lee ET, Newman AB, Nieto FJ, O'Connor GT, Boland LL, Schwartz JE, Samet JM. Sleep-disordered breathing and cardiovascular disease: Cross-sectional results of the Sleep Heart Health Study. *Am J Respir Crit Care Med* 163: 19-25, 2001.
573. Sher E, Cesare P, Codignola A, Clementi F, Tarroni P, Pollo A, Magnelli V, Carbone E. Activation of delta-opioid receptors inhibits neuronal-like calcium channels and distal steps of Ca2+-dependent secretion in human small-cell lung carcinoma cells. *J Neurosci* 16: 3672-3684, 1996.
574. Shin W, Ge L, Arpino G, Villarreal SA, Hamid E, Liu H, Zhao WD, Wen PJ, Chiang HC, Wu LG. Visualization of membrane pore in live cells reveals a dynamic-pore theory governing fusion and endocytosis. *Cell* 173: 934-945, e912, 2018.
575. Shukla R, Wakade AR. Functional aspects of calcium channels of splanchnic neurons and chromaffin cells of the rat adrenal medulla. *J Neurochem* 56: 753-758, 1991.
576. Silver M. The output of adrenaline and noradrenaline from the adrenal medulla of the calf. *J Physiol* 152: 14-29, 1960.
577. Singleton AB, Farrer M, Johnson J, Singleton A, Hague S, Kachergus J, Hulihan M, Peuralinna T, Dutra A, Nussbaum R, Lincoln S, Crawley A, Hanson M, Maraganore D, Adler C, Cookson MR, Muenter M, Baptista M, Miller D, Blancato J, Hardy J, Gwinn-Hardy K. alpha-Synuclein locus triplication causes Parkinson's disease. *Science* 302: 841, 2003.
578. Slotkin TA, Seidler FJ. Adrenomedullary catecholamine release in the fetus and newborn: Secretory mechanisms and their role in stress and survival. *J Dev Physiol* 10: 1-16, 1988.
579. Smith C, Neher E. Multiple forms of endocytosis in bovine adrenal chromaffin cells. *J Cell Biol* 139: 885-894, 1997.
580. Smith CB, Eiden LE. Is PACAP the major neurotransmitter for stress transduction at the adrenomedullary synapse? *J Mol Neurosci* 48: 403-412, 2012.
581. Solaro CR, Prakriya M, Ding JP, Lingle CJ. Inactivating and noninactivating Ca^{2+}- and voltage-dependent K^+ current in rat adrenal chromaffin cells. *J Neurosci* 15: 6110-6123, 1995.
582. Sorensen JB. Formation, stabilisation and fusion of the readily releasable pool of secretory vesicles. *Pflug Archiv: Eur J Physiol* 448: 347-362, 2004.
583. Sorensen JB, Matti U, Wei SH, Nehring RB, Voets T, Ashery U, Binz T, Neher E, Rettig J. The SNARE protein SNAP-25 is linked to fast calcium triggering of exocytosis. *Proc Natl Acad Sci USA* 99: 1627-1632, 2002.
584. Souvannakitti D, Kumar GK, Fox A, Prabhakar NR. Neonatal intermittent hypoxia leads to long-lasting facilitation of acute hypoxia-evoked catecholamine secretion from rat chromaffin cells. *J Neurophysiol* 101: 2837-2846, 2009.
585. Souvannakitti D, Nanduri J, Yuan G, Kumar GK, Fox AP, Prabhakar NR. NADPH oxidase-dependent regulation of T-type Ca^{2+} channels and ryanodine receptors mediate the augmented exocytosis of catecholamines from intermittent hypoxia-treated neonatal rat chromaffin cells. *J Neurosci* 30: 10763-10772, 2010.
586. Splawski I, Timothy KW, Decher N, Kumar P, Sachse FB, Beggs AH, Sanguinetti MC, Keating MT. Severe arrhythmia disorder caused by cardiac L-type calcium channel mutations. *Proc Natl Acad Sci USA* 102: 8089-8096, 2005.
587. Splawski I, Timothy KW, Sharpe LM, Decher N, Kumar P, Bloise R, Napolitano C, Schwartz PJ, Joseph RM, Condouris K, Tager-Flusberg H, Priori SG, Sanguinetti MC, Keating MT. Ca(v)1.2 calcium channel dysfunction causes a multisystem disorder including arrhythmia and autism. *Cell* 119: 19-31, 2004.
588. Stadinski BD, Delong T, Reisdorph N, Reisdorph R, Powell RL, Armstrong M, Piganelli JD, Barbour G, Bradley B, Crawford F, Marrack P, Mahata SK, Kappler JW, Haskins K. Chromogranin A is an autoantigen in type 1 diabetes. *Nat Immunol* 11: 225-231.
589. Stauderman KA, Murawsky MM, Pruss RM. Agonist-dependent patterns of cytosolic Ca^{2+} changes in single bovine adrenal chromaffin cells: Relationship to catecholamine release. *Cell Regul* 1: 683-691, 1990.
590. Stauderman KA, Pruss RM. Different patterns of agonist-stimulated increases of 3H-inositol phosphate isomers and cytosolic Ca^{2+} in bovine chromaffin cells: Comparison of the effects of histamine and angiotensin II. *J Neurochem* 54: 946-953, 1990.
591. Stevens DR, Schirra C, Becherer U, Rettig J. Vesicle pools: Lessons from adrenal chromaffin cells. *Front Synap Neurosci* 3: 2, 2011.
592. Steyer JA, Almers W. Tracking single secretory granules in live chromaffin cells by evanescent-field fluorescence microscopy. *Biophys J* 76: 2262-2271, 1999.
593. Stroth N, Kuri BA, Mustafa T, Chan SA, Smith CB, Eiden LE. PACAP controls adrenomedullary catecholamine secretion and expression of catecholamine biosynthetic enzymes at high splanchnic nerve firing rates characteristic of stress transduction in male mice. *Endocrinology* 154: 330-339, 2013.
594. Sudhof TC, Rizo J. Synaptic vesicle exocytosis. *Cold Spring Harb Perspect Biol* 3, 2011.
595. Sudhof TC, Rothman JE. Membrane fusion: Grappling with SNARE and SM proteins. *Science* 323: 474-477, 2009.
596. Suh BC, Leal K, Hille B. Modulation of high-voltage activated Ca(2+) channels by membrane phosphatidylinositol 4,5-bisphosphate. *Neuron* 67: 224-238, 2010.
597. Sun CL, Thoa NB, Kopin IJ. Comparison of the effects of 2-deoxyglucose and immobilization on plasma levels of catecholamines and corticosterone in awake rats. *Endocrinology* 105: 306-311, 1979.
598. Sun L, Xiong Y, Zeng X, Wu Y, Pan N, Lingle CJ, Qu A, Ding J. Differential regulation of action potentials by inactivating and noninactivating BK channels in rat adrenal chromaffin cells. *Biophys J* 97: 1832-1842, 2009.
599. Tabares L, Ales E, Lindau M, Alvarez de Toledo G. Exocytosis of catecholamine (CA)-containing and CA-free granules in chromaffin cells. *J Biol Chem* 276: 39974-39979, 2001.
600. Tabarin A, Chen D, Hakanson R, Sundler F. Pituitary adenylate cyclase-activating peptide in the adrenal gland of mammals: Distribution, characterization and responses to drugs. *Neuroendocrinology* 59: 113-119, 1994.
601. Tagaya M, Toyonaga S, Takahashi M, Yamamoto A, Fujiwara T, Akagawa K, Moriyama Y, Mizushima S. Syntaxin 1 (HPC-1) is associated with chromaffin granules. *J Biol Chem* 270: 15930-15933, 1995.
602. Takeuchi Y, Mochizuki-Oda N, Yamada H, Kurokawa K, Watanabe Y. Nonneurogenic hypoxia sensitivity in rat adrenal slices. *Biochem Biophys Res Commun* 289: 51-56, 2001.
603. Taleat Z, Estevez-Herrera J, Machado JD, Dunevall J, Ewing AG, Borges R. Electrochemical investigation of the interaction between catecholamines and ATP. *Anal Chem* 90: 1601-1607, 2018.
604. Tanguy E, Carmon O, Wang Q, Jeandel L, Chasserot-Golaz S, Montero-Hadjadje M, Vitale N. Lipids implicated in the journey of a secretory granule: From biogenesis to fusion. *J Neurochem* 137: 904-912, 2016.
605. Taraska JW, Almers W. Bilayers merge even when exocytosis is transient. *Proc Natl Acad Sci USA* 101: 8780-8785, 2004.
606. Taraska JW, Perrais D, Ohara-Imaizumi M, Nagamatsu S, Almers W. Secretory granules are recaptured largely intact after stimulated exocytosis in cultured endocrine cells. *Proc Natl Acad Sci USA* 100: 2070-2075, 2003.
607. Tateno M, Sadakata H, Tanaka M, Itohara S, Shin RM, Miura M, Masuda M, Aosaki T, Urushitani M, Misawa H, Takahashi R. Calcium-permeable AMPA receptors promote misfolding of mutant SOD1 protein and development of amyotrophic lateral sclerosis in a transgenic mouse model. *Hum Mol Genet* 13: 2183-2196, 2004.
608. Taylor CV, Taupenot L, Mahata SK, Mahata M, Wu H, Yasothornsrikul S, Toneff T, Caporale C, Jiang Q, Parmer RJ, Hook VY, O'Connor DT. Formation of the catecholamine release-inhibitory peptide catestatin from chromogranin A. Determination of proteolytic cleavage sites in hormone storage granules. *J Biol Chem* 275: 22905-22915, 2000.
609. Thiagarajan R, Tewolde T, Li Y, Becker PL, Rich MM, Engisch KL. Rab3A negatively regulates activity-dependent modulation of exocytosis in bovine adrenal chromaffin cells. *J Physiol* 555: 439-457, 2003.
610. Thoenen H, Mueller RA, Axelrod J. Trans-synaptic induction of adrenal tyrosine hydroxylase. *J Pharm Exp Ther* 169: 249-254, 1969.
611. Thomas P, Lee AK, Wong JG, Almers W. A triggered mechanism retrieves membrane in seconds after Ca(2+)-stimulated exocytosis in single pituitary cells. *J Cell Biol* 124: 667-675, 1994.
612. Thomas RC. The plasma membrane calcium ATPase (PMCA) of neurones is electroneutral and exchanges 2 H+ for each Ca2+ or Ba2+ ion extruded. *J Physiol* 587: 315-327, 2009.
613. Thompson RJ, Farragher SM, Cutz E, Nurse CA. Developmental regulation of O(2) sensing in neonatal adrenal chromaffin cells from wild-type and NADPH-oxidase-deficient mice. *Pflug Archiv: Eur J Physiol* 444: 539-548, 2002.
614. Thompson RJ, Jackson A, Nurse CA. Developmental loss of hypoxic chemosensitivity in rat adrenomedullary chromaffin cells. *J Physiol* 498 (Pt 2): 503-510, 1997.
615. Thompson RJ, Nurse CA. Anoxia differentially modulates multiple K+ currents and depolarizes neonatal rat adrenal chromaffin cells. *J Physiol* 512 (Pt 2): 421-434, 1998.
616. Tillinger A, Sollas A, Serova LI, Kvetnansky R, Sabban EL. Vesicular monoamine transporters (VMATs) in adrenal chromaffin cells: Stress-triggered induction of VMAT2 and expression in epinephrine synthesizing cells. *Cell Mol Neurobiol* 30: 1459-1465, 2010.
617. Tischler AS. Pheochromocytoma and extra-adrenal paraganglioma: Updates. *Arch Pathol Lab Med* 132: 1272-1284, 2008.

618. Tomatis VM, Papadopulos A, Malintan NT, Martin S, Wallis T, Gormal RS, Kendrick-Jones J, Buss F, Meunier FA. Myosin VI small insert isoform maintains exocytosis by tethering secretory granules to the cortical actin. *J Cell Biol* 200: 301-320, 2013.
619. Tomlinson A, Coupland RE. The innervation of the adrenal gland. IV. Innervation of the rat adrenal medulla from birth to old age. A descriptive and quantitative morphometric and biochemical study of the innervation of chromaffin cells and adrenomedullary neurons in Wistar rats. *J Anat* 169: 209-236, 1990.
620. Tompkins JD, Ardell JL, Hoover DB, Parsons RL. Neurally released pituitary adenylate cyclase-activating polypeptide enhances guinea pig intrinsic cardiac neurone excitability. *J Physiol* 582: 87-93, 2007.
621. Tsien RW, Giles W, Greengard P. Cyclic AMP mediates the effects of adrenaline on cardiac purkinje fibres. *Nat: New Biol* 240: 181-183, 1972.
622. Tsigelny IF, Kouznetsova VL, Biswas N, Mahata SK, O'Connor DT. Development of a pharmacophore model for the catecholamine release-inhibitory peptide catestatin: Virtual screening and functional testing identify novel small molecule therapeutics of hypertension. *Bioorg Med Chem* 21: 5855-5869, 2013.
623. Tsujimoto A, Nishikawa T. Further evidence for nicotinic and muscarinic receptors and their interaction in dog adrenal medulla. *Eur J Pharmacol* 34: 337-344, 1975.
624. Twitchell WA, Rane SG. Opioid peptide modulation of Ca(2+)-dependent K+ and voltage-activated Ca^{2+} currents in bovine adrenal chromaffin cells. *Neuron* 10: 701-709, 1993.
625. Uceda G, Artalejo AR, de la Fuente MT, Lopez MG, Albillos A, Michelena P, Garcia AG, Montiel C. Modulation by L-type Ca2+ channels and apamin-sensitive K^+ channels of muscarinic responses in cat chromaffin cells. *Am J Physiol* 266: C1432-C1439, 1994.
626. Uceda G, Artalejo AR, Lopez MG, Abad F, Neher E, Garcia AG. Ca(2+)-activated K+ channels modulate muscarinic secretion in cat chromaffin cells. *J Physiol* 454: 213-230, 1992.
627. Ulate G, Scott SR, Gonzalez J, Gilabert JA, Artalejo AR. Extracellular ATP regulates exocytosis in inhibiting multiple Ca(2+) channel types in bovine chromaffin cells. *Pflug Archiv: Eur J Physiol* 439: 304-314, 2000.
628. Unsicker K, Habura-Fluh O, Zwarg U. Different types of small granule-containing cells and neurons in the guinea-pig adrenal medulla. *Cell Tissue Res* 189: 109-130, 1978.
629. Uvnäs B, Aborg C-H. The ability of ATP-free granule material from bovine adrenal medulla to bind inorganic cations and biogenic amines. *Acta Physiol Scand* 99: 476-483, 1977.
630. van Kempen GT, vanderLeest HT, van den Berg RJ, Eilers P, Westerink RH. Three distinct modes of exocytosis revealed by amperometry in neuroendocrine cells. *Biophys J* 100: 968-977, 2011.
631. Vandael DH, Marcantoni A, Cav1 CE. 3 Channels as key regulators of neuron-like firings and catecholamine release in chromaffin cells. *Curr Mol Pharmacol* 8: 149-161, 2015.
632. Vandael DH, Marcantoni A, Mahapatra S, Caro A, Ruth P, Zuccotti A, Knipper M, Carbone E. Ca(v)1.3 and BK channels for timing and regulating cell firing. *Mol Neurobiol* 42: 185-198, 2010.
633. Vandael DH, Ottaviani MM, Legros C, Lefort C, Guerineau NC, Allio A, Carabelli V, Carbone E. Reduced availability of voltage-gated sodium channels by depolarization or blockade by tetrodotoxin boosts burst firing and catecholamine release in mouse chromaffin cellslabilit. *J Physiol* 593: 905-927, 2015.
634. Vandael DHF, Mahapatra S, Calorio C, Marcantoni A, Carbone E. Cav1.3 and Cav1.2 channels of adrenal chromaffin cells: Emerging views on cAMP/cGMP-mediated phosphorylation and role in pacemaking. *Biochim Biophys Acta-Biomembr* 1828: 1608-1618, 2013.
635. Vandael DHF, Zuccotti A, Striessnig J, Carbone E. Ca(V)1.3-driven SK channel activation regulates pacemaking and spike frequency adaptation in mouse chromaffin cells. *J Neurosci* 32: 16345-16359, 2012.
636. Vestring S, Fernandez-Morales JC, Mendez-Lopez I, CM D, AM GD, Padin JF, GG A. Tight mitochondrial control of calcium and exocytotic signals in chromaffin cells at embryonic life. *Pflug Archiv: Eur J Physiol* 467: 2589-2601, 2015.
637. Vicente S, Gonzalez MP, Oset-Gasque MJ. Neuronal nitric oxide synthase modulates basal catecholamine secretion in bovine chromaffin cells. *J Neurosci Res* 69: 327-340, 2002.
638. Vijayaragavan K, O'Leary ME, Chahine M. Gating properties of Na(v)1.7 and Na(v)1.8 peripheral nerve sodium channels. *J Neurosci* 21: 7909-7918, 2001.
639. Villalobos C, Nunez L, Chamero P, Alonso MT, Garcia-Sancho J. Mitochondrial [Ca(2+)] oscillations driven by local high [Ca(2+)] domains generated by spontaneous electric activity. *J Biol Chem* 276: 40293-40297, 2001.
640. Villalobos C, Nunez L, Montero M, Garcia AG, Alonso MT, Chamero P, Alvarez J, Garcia-Sancho J. Redistribution of Ca^{2+} among cytosol and organella during stimulation of bovine chromaffin cells. *FASEB J* 16: 343-353, 2002.
641. Villanueva J, Torres V, Torregrosa-Hetland CJ, Garcia-Martinez V, Lopez-Font I, Viniegra S, Gutierrez LM. F-actin-myosin II inhibitors affect chromaffin granule plasma membrane distance and fusion kinetics by retraction of the cytoskeletal cortex. *J Mol Neurosci* 48: 328-338, 2012.
642. Vitale ML, Rodriguez Del Castillo A, Tchakarov L, Trifaro JM. Cortical filamentous actin disassembly and scinderin redistribution during chromaffin cell stimulation precede exocytosis, a phenomenon not exhibited by gelsolin. *J Cell Biol* 113: 1057-1067, 1991.
643. Voets T. Dissection of three Ca^{2+}-dependent steps leading to secretion in chromaffin cells from mouse adrenal slices. *Neuron* 28: 537-545, 2000.
644. Voets T, Neher E, Moser T. Mechanisms underlying phasic and sustained secretion in chromaffin cells from mouse adrenal slices. *Neuron* 23: 607-615, 1999.
645. Vollmer RR, Balcita JJ, Sved AF, Edwards DJ. Adrenal epinephrine and norepinephrine release to hypoglycemia measured by microdialysis in conscious rats. *Am J Physiol* 273: R1758-R1763, 1997.
646. Vollmer RR, Baruchin A, Kolibal-Pegher SS, Corey SP, Stricker EM, Kaplan BB. Selective activation of norepinephrine- and epinephrine-secreting chromaffin cells in rat adrenal medulla. *Am J Physiol* 263: R716-R721, 1992.
647. Von Euler US. Pathophysiological aspects of catecholamine production. *Clin Chem* 18: 1445-1448, 1972.
648. Von Euler US, Folkow B. The effect of stimulation of autonomic areas in the cerebral cortex upon the adrenaline and noradrenaline secretion from the adrenal gland in the cat. *Acta Physiol Scand* 42: 313-320, 1958.
649. von Grafenstein H, Borges R, Knight DE. The effect of botulinum toxin type D on the triggered and constitutive exocytosis/endocytosis cycles in cultures of bovine adrenal medullary cells. *FEBS Lett* 298: 118-122, 1992.
650. von Grafenstein H, Knight DE. Membrane recapture and early triggered secretion from the newly formed endocytotic compartment in bovine chromaffin cells. *J Physiol* 453: 15-31, 1992.
651. von Lewinski F, Keller BU. Ca^{2+}, mitochondria and selective motoneuron vulnerability: Implications for ALS. *Trends Neurosci* 28: 494-500, 2005.
652. von Ruden L, Neher E. A Ca-dependent early step in the release of catecholamines from adrenal chromaffin cells. *Science* 262: 1061-1065, 1993.
653. Vonsattel JP, DiFiglia M. Huntington disease. *J Neuropathol Exp Neurol* 57: 369-384, 1998.
654. Wada A, Wanke E, Gullo F, Schiavon E. Voltage-dependent Na(v)1.7 sodium channels: Multiple roles in adrenal chromaffin cells and peripheral nervous system. *Acta Physiol (Oxford, England)* 192: 221-231, 2008.
655. Wada A, Yanagita T, Yokoo H, Kobayashi H. Regulation of cell surface expression of voltage-dependent Nav1.7 sodium channels: mRNA stability and posttranscriptional control in adrenal chromaffin cells. *Front Biosci* 9: 1954-1966, 2004.
656. Wakade AR. Multiple transmitter control of catecholamine secretion in rat adrenal medulla. *Adv Pharmacol (San Diego, CA)* 42: 595-598, 1998.
657. Wakade AR. Noncholinergic transmitter(s) maintains secretion of catecholamines from rat adrenal medulla for several hours of continuous stimulation of splanchnic neurons. *J Neurochem* 50: 1302-1308, 1988.
658. Wakade AR. Studies on secretion of catecholamines evoked by acetylcholine or transmural stimulation of the rat adrenal gland. *J Physiol* 313: 463-480, 1981.
659. Wakade AR, Wakade TD, Malhotra RK. Restoration of catecholamine content of previously depleted adrenal medulla in vitro: Importance of synthesis in maintaining the catecholamine stores. *J Neurochem* 51: 820-829, 1988.
660. Wallace DJ, Chen C, Marley PD. Histamine promotes excitability in bovine adrenal chromaffin cells by inhibiting an M-current. *J Physiol* 540: 921-939, 2002.
661. Wallner M, Meera P, Toro L. Molecular basis of fast inactivation in voltage and Ca^{2+}-activated K^+ channels: A transmembrane beta-subunit homolog. *Proc Natl Acad Sci USA* 96: 4137-4142, 1999.
662. Wang N, Kwan C, Gong X, de Chaves EP, Tse A, Tse FW. Influence of cholesterol on catecholamine release from the fusion pore of large dense core chromaffin granules. *J Neurosci* 30: 3904-3911, 2010.
663. Watanabe T, Masuo Y, Matsumoto H, Suzuki N, Ohtaki T, Masuda Y, Kitada C, Tsuda M, Fujino M. Pituitary adenylate cyclase activating polypeptide provokes cultured rat chromaffin cells to secrete adrenaline. *Biochem Biophys Res Commun* 182: 403-411, 1992.
664. Weihe E, Schafer MK, Erickson JD, Eiden LE. Localization of vesicular monoamine transporter isoforms (VMAT1 and VMAT2) to endocrine cells and neurons in rat. *J Mol Neurosci* 5: 149-164, 1994.
665. Weiss JL, Burgoyne RD. Voltage-independent inhibition of P/Q-type Ca^{2+} channels in adrenal chromaffin cells via a neuronal Ca^{2+} sensor-1-dependent pathway involves Src family tyrosine kinase. *J Biol Chem* 276: 44804-44811, 2001.

666. Wen PJ, Grenklo S, Arpino G, Tan X, Liao HS, Heureaux J, Peng SY, Chiang HC, Hamid E, Zhao WD, Shin W, Nareoja T, Evergren E, Jin Y, Karlsson R, Ebert SN, Jin A, Liu AP, Shupliakov O, Wu LG. Actin dynamics provides membrane tension to merge fusing vesicles into the plasma membrane. *Nat Commun* 7: 12604, 2016.
667. Westerink RH, Ewing AG. The PC12 cell as model for neurosecretion. *Acta Physiol (Oxford)* 192: 273-285, 2008.
668. Wightman RM, Jankowski JA, Kennedy RT, Kawagoe KT, Schroeder TJ, Leszczyszyn DJ, Near JA, Diliberto EJ Jr., Viveros OH. Temporally resolved catecholamine spikes correspond to single vesicle release from individual chromaffin cells. *Proc Natl Acad Sci USA* 88: 10754-10758, 1991.
669. Wightman RM, Schroeder TJ, Finnegan JM, Ciolkowski EL, Pihel K. Time-course of release of catecholamines from individual vesicles during exocytosis at adrenal-medullary cells. *Biophys J* 68: 383-390, 1995.
670. Wilson SP. Vasoactive intestinal peptide elevates cyclic AMP levels and potentiates secretion in bovine adrenal chromaffin cells. *Neuropeptides* 11: 17-21, 1988.
671. Winkler H. The adrenal chromaffin granule: A model for large dense core vesicles of endocrine and nervous tissue. *J Anat* 183 (Pt 2): 237-252, 1993.
672. Winkler H, Apps DK, Fischer-Colbrie R. The molecular function of adrenal chromaffin granules: Established facts and unresolved topics. *Neuroscience* 18: 261-290, 1986.
673. Winkler H, Fischer-Colbrie R. The chromogranins A and B: The first 25 years and future perspectives. *Neuroscience* 49: 497-528, 1992.
674. Wolf K, Zarkua G, Chan SA, Sridhar A, Smith C. Spatial and activity-dependent catecholamine release in rat adrenal medulla under native neuronal stimulation. *Physiol Rep* 4, 2016.
675. Wu PC, Fann MJ, Kao LS. Characterization of Ca^{2+} signaling pathways in mouse adrenal medullary chromaffin cells. *J Neurochem* 112: 1210-1222, 2010.
676. Xia X-M, Ding JP, Lingle CJ. Molecular basis for the inactivation of Ca^{2+}- and voltage-dependent BK channels in adrenal chromaffin cells and rat insulinoma tumor cells. *J Neurosci* 19: 5255-5264, 1999.
677. Xia XM, Ding JP, Lingle CJ. Inactivation of BK channels by the NH2 terminus of the beta2 auxiliary subunit: An essential role of a terminal peptide segment of three hydrophobic residues. *J Gen Physiol* 121: 125-148, 2003.
678. Xu T, Naraghi M, Kang H, Neher E. Kinetic studies of Ca^{2+} binding and Ca^{2+} clearance in the cytosol of adrenal chromaffin cells. *Biophys J* 73: 532-545, 1997.
679. Xu WF, Lipscombe D. Neuronal Ca(v)1.3 alpha(1) L-type channels activate at relatively hyperpolarized membrane potentials and are incompletely inhibited by dihydropyridines. *J Neurosci* 21: 5944-5951, 2001.
680. Yamada-Hanff J, Bean BP. Persistent sodium current drives conditional pacemaking in CA1 pyramidal neurons under muscarinic stimulation. *J Neurosci: Off J Soc Neurosci* 33: 15011-15021, 2013.
681. Yanagita T, Kobayashi H, Uezono Y, Yokoo H, Sugano T, Saitoh T, Minami S, Shiraishi S, Wada A. Destabilization of Na(v)1.7 sodium channel alpha-subunit mRNA by constitutive phosphorylation of extracellular signal-regulated kinase: Negative regulation of steady-state level of cell surface functional sodium channels in adrenal chromaffin cells. *Mol Pharmacol* 63: 1125-1136, 2003.
682. Yang DM, Kao LS. Relative contribution of the Na(+)/Ca(2+) exchanger, mitochondria and endoplasmic reticulum in the regulation of cytosolic Ca(2+) and catecholamine secretion of bovine adrenal chromaffin cells. *J Neurochem* 76: 210-216, 2001.
683. Yoo SH. Secretory granules in inositol 1,4,5-trisphosphate-dependent Ca^{2+} signaling in the cytoplasm of neuroendocrine cells. *FASEB J* 24: 653-664, 2010.
684. Yoshizaki T. Participation of muscarinic receptors on splanchnic-adrenal transmission in the rat. *Jpn J Pharmacol* 23: 813-816, 1973.
685. Zachowski A, Henry JP, Devaux PF. Control of transmembrane lipid asymmetry in chromaffin granules by an ATP-dependent protein. *Nature* 340: 75-76, 1989.
686. Zamponi GW, Currie KP. Regulation of Ca(V)2 calcium channels by G protein coupled receptors. *Biochim Biophys Acta* 1828: 1629-1643, 2013.
687. Zerbes M, Bunn SJ, Powis DA. Histamine causes Ca^{2+} entry via both a store-operated and a store-independent pathway in bovine adrenal chromaffin cells. *Cell Calcium* 23: 379-386, 1998.
688. Zhang C, Wu B, Beglopoulos V, Wines-Samuelson M, Zhang D, Dragatsis I, Sudhof TC, Shen J. Presenilins are essential for regulating neurotransmitter release. *Nature* 460: 632-636, 2009.
689. Zhou Z, Misler S. Action potential-induced quantal secretion of catecholamines from rat adrenal chromaffin cells. *J Biol Chem* 270: 3498-3505, 1995.
690. Zhou Z, Misler S. Amperometric detection of stimulus-induced quantal release of catecholamines from cultured superior cervical ganglion neurons. *Proc Natl Acad Sci USA* 92: 6938-6942, 1995.
691. Zhou Z, Neher E. Calcium permeability of nicotinic acetylcholine receptor channels in bovine adrenal chromaffin cells. *Pflug Archiv: Eur J Physiol* 425: 511-517, 1993.
692. Zhou Z, Neher E. Mobile and immobile calcium buffers in bovine adrenal chromaffin cells. *J Physiol* 469: 245-273, 1993.

frontiers in Cellular Neuroscience

INFORME DE LABORES 2019

published: 02 July 2019
doi: 10.3389/fncel.2019.00270

Early Post-stroke Activation of Vascular Endothelial Growth Factor Receptor 2 Hinders the Receptor 1-Dependent Neuroprotection Afforded by the Endogenous Ligand

*Alfredo Cárdenas-Rivera[1], Aura N. Campero-Romero[1], Yessica Heras-Romero[1], Andrés Penagos-Puig[1], Ruth Rincón-Heredia[2] and Luis B. Tovar-y-Romo[1]**

[1] *Division of Neuroscience, Instituto de Fisiología Celular, Universidad Nacional Autónoma de México, Mexico City, Mexico,*
[2] *Microscopy Core Unit, Instituto de Fisiología Celular, Universidad Nacional Autónoma de México, Mexico City, Mexico*

OPEN ACCESS

Edited by:
Victoria Campos-Peña, National Institute of Neurology and Neurosurgery (INNN), Mexico

Reviewed by:
Sharon DeMorrow, The University of Texas at Austin, United States
Ertugrul Kilic, Istanbul Medipol University, Turkey

***Correspondence:**
Luis B. Tovar-y-Romo
ltovar@ifc.unam.mx

Specialty section:
This article was submitted to Cellular Neuropathology, a section of the journal Frontiers in Cellular Neuroscience

Received: *21 March 2019*
Accepted: *03 June 2019*
Published: *02 July 2019*

Citation:
Cárdenas-Rivera A, Campero-Romero AN, Heras-Romero Y, Penagos-Puig A, Rincón-Heredia R and Tovar-y-Romo LB (2019) Early Post-stroke Activation of Vascular Endothelial Growth Factor Receptor 2 Hinders the Receptor 1-Dependent Neuroprotection Afforded by the Endogenous Ligand. Front. Cell. Neurosci. 13:270. doi: 10.3389/fncel.2019.00270

Vascular endothelial growth factor (VEGF) has long been connected to the development of tissue lesion following ischemic stroke. Contradictory findings either situate VEGF as a promoter of large infarct volumes or as a potential attenuator of damage due to its well documented neuroprotective capability. The core of this discrepancy mostly lies on the substantial number of pleiotropic functions driven by VEGF. Mechanistically, these effects are activated through several VEGF receptors for which various closely related ligands exist. Here, we tested in an experimental model of stroke how the differential activation of VEGF receptors 1 and 2 would modify functional and histological outcomes in the acute phase post-ischemia. We also assessed whether VEGF-mediated responses would involve the modulation of inflammatory mechanisms and how this trophic factor acted specifically on neuronal receptors. We produced ischemic infarcts in adult rats by transiently occluding the middle cerebral artery and induced the pharmacological inhibition of VEGF receptors by i.c.v. administration of the specific VEGFR2 inhibitor SU1498 and the pan-VEGFR blocker Axitinib. We evaluated the neurological performance of animals at 24 h following stroke and the occurrence of brain infarctions analyzed at the gross metabolic and neuronal viability levels. We also assessed the induction of peripheral pro- and anti-inflammatory cytokines in the cerebrospinal fluid and blood and assessed the polarization of activated microglia. Finally, we studied the direct involvement of cortical neuronal receptors for VEGF with *in vitro* assays of excitotoxic damage. Preferential VEGFR1 activation by the endogenous ligand promotes neuronal protection and prevents the presentation of large volume infarcts that highly correlate with neurological performance, while the concomitant activation of VEGFR2 reduces this effect, even in the presence of exogenous ligand. This process partially involves the polarization of microglia to the state M2. At the cellular level, neurons also responded better to the preferential activation of VEGFR1 when challenged to *N*-methyl-D-aspartate-induced excitotoxicity.

Endogenous activation of VEGFR2 hinders the neuroprotective mechanisms mediated by the activation of VEGFR1. The selective modulation of these concurrent processes might enable the development of therapeutic approaches that target specific VEGFR1-mediated signaling during the acute phase post-stroke.

Keywords: Axitinib, ischemia, MCAO, stroke, SU1498, VEGF, VEGFR1, VEGFR2

INTRODUCTION

The neuroprotective molecular mechanisms that drive endogenous adaptive responses to injury in the central nervous system (CNS) are mostly unknown, and their elucidation would ideally open new avenues for rehabilitation. A very promising process to target therapeutically is driven by vascular endothelial growth factor A (VEGF), which has long been implicated in the regulation of several events that take place following ischemic stroke, the leading cause of acquired disability in the developed world.

VEGF regulates a series of molecular processes that allow tissue to adapt to the conditions that prevail after stroke, such as neurovascular remodeling and repair, neuroprotection, brain plasticity and the recruitment and proliferation of neuronal precursors (Zhang et al., 2000; Ma et al., 2012; Dzietko et al., 2013; Greenberg and Jin, 2013). However, VEGF is also responsible for some damaging processes, such as cerebral edema and exacerbated blood-brain barrier leakage (Eliceiri et al., 1999; van Bruggen et al., 1999; Paul et al., 2001; Weis and Cheresh, 2005; Kim et al., 2018; Wu et al., 2018). Such opposing findings have, thus far, impeded the utilization of VEGF in a clinical setting aimed at alleviating the sequels of ischemic stroke.

VEGF acts by activating tyrosine kinase receptors 1 (VEGFR1, also known as FMS-like tyrosine kinase; Flt1) and 2 (VEGFR2, also known as kinase domain receptor; KRD, and fetal liver kinase 1; Flk-1). Both receptors are structurally closely related, each composed with seven immunoglobulin-like domains on the extracellular portion, a transmembrane motif, and an intracellular tyrosine kinase domain with conserved tyrosine phosphorylation sites (Grassot et al., 2006; Rahimi, 2006; Simons et al., 2016), although the ultimate biological actions driven by these receptors individually are somewhat different. Traditionally, VEGFR2 has been considered the canonical receptor for VEGF (Geiseler and Morland, 2018), and for a very long time, VEGFR1 has been thought to function as a decoy signal that counter-regulates VEGFR2 actions by sequestering the ligand, thus reducing its availability to binding VEGFR2 (Park et al., 1994; Meyer et al., 2006). Also, VEGFR1 is preferably activated by other members of the VEGF family, such as VEGF-B (Olsson et al., 2006).

An open question in all these molecular events is whether VEGF can also modulate the neuroinflammation elicited by ischemia (Geiseler and Morland, 2018). Neuroinflammation is an important component of the pathophysiology of stroke and other neurodegenerative processes where microglia, the resident macrophages of the CNS, play a central role.

Here we studied the mechanisms of VEGF-mediated neuroprotection in the acute phase of stroke using an *in vivo* model produced by the transitory occlusion of the middle cerebral artery in the rat (MCAO). The i.c.v. administration of VEGF in the early phase after stroke results in a significant reduction of infarct volume and increased neuronal survival. We found that if VEGFR1 gets preferably activated when VEGFR2 is inhibited, there is a reduction of infarct volume and edema, and an increase of neuronal survival and neurological outcome. Given the role of VEGFR1 on microglial responses to altered brain homeostasis, the underlying mechanisms of the VEGFR1-mediated protection partially involve also the modulation of the inflammatory response and microglial polarization to a neuroprotector phenotype. These results point toward VEGFR1 as an attractive therapeutic target for stroke.

MATERIALS AND METHODS

Animals

In this study, we used young (1.5 months old; 270–290 g) Wistar rats that were subjected to MCAO as described below. Animals were housed in individual cages in a 12 h light/dark cycle with food and water *ad libitum*. All rats were killed at 24 h during the acute phase post-stroke. All experimental procedures were conducted under the current Mexican law for the use and care of laboratory animals (NOM-062-ZOO-1999) with the approval of the Institutional Animal Care and Use Committee (CICUAL-IFC-LTR93-16).

Study Design

Animals were randomly divided into seven groups with an $n = 10–13$ for MCAO groups and 7 shams. The sample size was calculated *a priori* to detect a medium Cohen's d effect size > 0.3, β power of 0.8 and significance of 0.05. Mortality rate was assumed to be 0.4 based on pilot experiments. These parameters were chosen to reduce the number of animals used. Inclusion criteria in analyzes considered the reduction of blood perfusion below 50% of basal values, which roughly corresponds to the effect of occluding the common carotid artery, no immediate recovery of reperfusion (above 50% baseline values within 3 min), total occlusion time between 90–95 min, absence of subarachnoid or intraparenchymal hemorrhages and survival at 24 h after stroke. This study is limited to assess effects on males.

MCAO

Rats were put under isoflurane anesthesia (5% for induction followed by $\leq$1.5% during surgery) with oxygen as the carrier. Normal ventilation was autonomously maintained. Focal cerebral ischemia was induced with the Longa method (Longa et al., 1989) using a nylon monofilament with a silicone-dipped tip

(403734, Doccol, Sharon, MA, United States) that was inserted in a stump created by cutting the ligated left external carotid artery and intraluminally advanced through the internal carotid artery until it reached and occluded the MCA at its inception in the Circle of Willis. MCA occlusion was kept for 90 min after which the monofilament was removed. Body temperature was maintained at 37°C with a heating pad for the duration of surgery. At the end of the procedure, the skin of the neck was sutured, and rats were returned to their cages. During the entire experimental procedure, the cerebral blood flow (CBF) was monitored in the territory irrigated by MCA with laser-Doppler flowmetry. For this, the parietal skull bone was thinned using a small mototool drill bit (Dremel, Racine, WI, United States) and a probe holder was glued onto it at stereotaxic coordinates (AP −1.5 L +3.5 from Bregma). A laser-Doppler probe (model 407, Perimed, Järfälla, Sweden) was inserted into the holder and connected to a Periflux System 5010 (Perimed). CBF was continuously monitored with an acquisition interval of 0.3 s using the Perisoft software (Perimed).

Administration of VEGF and Pharmacological Inhibitors

VEGF and the VEGFRs inhibitors were administered by intracerebroventricular (i.c.v.) injections in the corresponding animal groups 30 min after intraluminal filament removal, which marked the beginning of reperfusion, with the following stereotaxic coordinates: AP −0.8 and L −1.5 from Bregma and V -4 from dura matter. Injections were performed with graduated glass microcapillary pipettes that were pulled to produce a tip < 50 μm in diameter (McCluskey et al., 2008) at a flux rate of 0.8 μL/min. Because of the non-polar nature of the inhibitors used in this study, we injected a corresponding volume of DMSO in all experimental groups to control for DMSO possible effects. Control sham- and MCAO-operated animals were injected with vehicle solutions consisting of 2 μL DMSO followed by 2 μL 0.1% BSA (4 μL final volume). Recombinant rat VEGF-A_{164} (Sigma) was prepared in a 0.1% BSA at a final concentration of 25 ng/μL, 2 μL VEGF were injected followed by 2 μL DMSO. SU1498 and Axitinib (both from Sigma) were prepared in DMSO at a concentration of 6.4 mM. Two μL of each inhibitor were administered in the corresponding groups followed by 2 μL 0.1% BSA or 25 ng/μL VEGF depending on the experimental condition.

Infarct Volume Calculation

Animals were sedated with sodium pentobarbital and transcardially perfused with 200 mL 0.9% NaCl at 4°C, after which brains were collected and immediately sectioned into seven coronal slices (2 mm thick) that were incubated in 2% 2,3,5-triphenyltetrazolium chloride (TTC) at 37°C for 10 min. Images of sections were digitally acquired with a Lexmark scanner (Lexmark X2650, Lexmark, Canada) using Imaging Studio software (Lexmark, Canada). The infarcted and individual hemisphere areas of each section were measured with a semi-automatized macro routine executed in Fiji (Fiji-ImageJ, version 1.52i, NIH, United States) (Schindelin et al., 2012). Infarct volume was then calculated and corrected for edema with the following formula:

$$IV = \sum_{i=1}^{n} \left[\left(\frac{clHA_i \times IA_i}{ilHA_i} \right) t \right]$$

Where IV is the volume of infarct in mm^3, n is the number of sections, $clHA$ is the area of the contralateral hemisphere in mm^2, IA is the area of the damaged tissue in mm^2, $ilHA$ is the area of ipsilateral hemisphere in mm^2, and t is the thickness of each section in mm.

Post-stroke Neuronal Viability Evaluation

For histological analyses, three rats per group were transcardially perfused with 200 mL ice-cold 0.9% NaCl followed by 250 mL ice-cold 4% paraformaldehyde (PFA). Brains were collected and post-fixed in 4% PFA for 24 h and then cryoprotected in 30% sucrose. Whole PFA-fixed brains were cut into 40 μm thick sections in a cryostat to produce 10 series of consecutive sections that were 400 μm apart. An entire series was mounted on gelatin-coated slides and stained with 1% cresyl violet. Digital images of a section series were acquired in an Olympus IX71 microscope with a 20X magnification using a 12 Megapixel Evolution UVF camera (Media Cybernetics, Buckinghamshire, United Kingdom). Images were processed in Image-Pro Plus 6.0 (Media Cybernetics). Soma diameters and shapes of pyramidal neurons within an area of 250 × 350 μm in layers IV and V of the somatosensory cortex in 3 consecutive sections were analyzed with an automatized macro routine executed in Fiji. Healthy cells were defined by circularity values of 0.47 – 0.88 and area of 30 – 250 μm^2. Neuronal viability is reported as a survival index, which was calculated from each count of ipsilateral live neurons expressed as a proportion of the count in the respective contralateral area. The resulting values were normalized to the pooled indexes of the sham group. This algorithm is calculated with the following formula:

$$SI = p\left(\sum_{1}^{t} \left(\frac{\sum_{i=1}^{n} \left(C_i^{il} / C_i^{cl} \right)}{n} \right)_t \right) \Big/ t\left(\sum_{1}^{p} \left(\frac{\sum_{0=1}^{m} \left(S_o^{il} / S_o^{cl} \right)}{m} \right)_p \right)$$

Where SI is the survival index, C^{il} is the number of live neurons in the ipsilateral side, C^{cl} is the number of live neurons in the respective confraternal side, n is the number of coronal sections analyzed for each brain, t is the number of animals analyzed per experimental group, S^{il} is the number of neurons in the left side of the sham group, S^{cl} is the number of neurons in the right side of the sham group and, m is the number of sections analyzed for each sham brain and p is the number of sham rats. No statistical differences were detected in absolute numbers of live neurons among contralateral sides across experimental groups.

Behavioral Testing

Animals were evaluated with a battery of neurological tests to assess sensorimotor deficits 24 h after stroke. The severity of functional deficits was scored by assessing eight items described in **Table 1** with slight modifications from previous reports (Mattsson et al., 1997; Schallert et al., 2000; Burguete et al., 2006; Zhang et al., 2015). Maximum score (32 total) was assigned to animals without neurological deficits. All evaluations were cross-validated by a trained observer blinded to the experimental treatment that analyzed recorded videos of the tests.

Peripheral Cytokines Determination

Blood samples were obtained by cardiac puncture right before transcardial perfusion to determine circulating cytokine levels 24 h after stroke. Plasma was prepared from blood by adding 50 μL/mL 0.5 M EDTA and samples were stored at −80°C until used. Cytokine detection was carried out with a custom-made rat cytokine/chemokine magnetic bead Milliplex MAP panel (Millipore, Temecula, CA, United States) following the manufacturer instructions. A 96-well plate was used to simultaneously determine the concentrations of IL-1β, IL-4, IL-6, IL-10, IL-12p70, IL-17, TNF-α, CCL11, INFγ, CX3CL1, MIP-1α, and VEGF. The plate was read on a MAGPIX system (EMD Millipore, Darmstadt, Germany). Results were analyzed using the xPONENT software (Luminex, Madison, WI, United States). Standards of 200–16,000 pg/mL were used for generating the corresponding concentration curve of each analyte. Determinations were done in duplicates per biological replicate ($n = 3$).

Cytokine mRNA Expression

Cytokine mRNA levels were determined 24 h after stroke by real-time quantitative PCR (RT-qPCR). For this, 1 mL of blood was combined with 50 μL 0.5 M EDTA and 10 mL of red blood cells lysis buffer (155 mM NH_4Cl, 12 mM $NaCO_3$, 0.1M EDTA, pH 7). Samples were centrifuged at 1,900 × *g* for 8 min at RT in a Sorvall ST8 centrifuge (Thermo Fisher Scientific. Karlsruhe, Germany) to obtain white blood cells pellet. Total RNA was isolated with 5:1 TRIzol (Ambion Life Technologies. Austin, TX, United States)-chloroform by phase separation centrifugation at 12,000 × *g* for 15 min at 4°C. RNA was precipitated in 500 μL isopropanol and washed in 75% ethanol. After air-drying, the pellet was reconstituted in RNAse and DNAse free ultra-pure water (Thermo Scientific). RNA concentration and purity were assessed using OD 260/280 ratios and gel electrophoresis. RT-qPCR was performed with One-step NZYSpeed RT-qPCR Green kit, ROX (nzyTECH, Lisbon, Portugal) according to the manufacturer directions. RT-qPCRs were run in 96-well plates in an Applied Biosystems StepOne RT-qPCR System (Thermo Fisher) with the following parameters: 20 min reverse transcription at 50°C, 2 min cDNA denaturing at 95°C, 40 cycles of 5 s denaturation at 95°C, 30 s annealing/amplification at 61°C. Relative quantification of gene expression was performed using the $2^{-\Delta\Delta C_T}$ method, with glyceraldehyde 3-phosphate dehydrogenase as a reference gene. Melting curve analyzes and gel electrophoresis evaluation of the RT-qPCR products were routinely performed to determine the specificity of the RT-qPCR reaction. Primer information for each gene is contained in **Table 2**.

Immunohistochemistry and Confocal Microscopy

PFA-fixed brain sections containing infarct core and penumbra were blocked with 5% bovine serum albumin in Tris-buffered saline with 0.5% v/v Triton X-100 (TBS-T) and incubated with anti-Iba-1 (1:200; Wako, Richmond, VA, United States) and anti-arginase-1 antibodies (1:200; Invitrogen) for 48 h. Sections were washed three times with TBS followed by 2 h incubation at RT with Alexa Fluor 488-conjugated anti-mouse and Alexa 546-conjugated anti-rabbit antibodies (1:2000 each; Invitrogen, Carlsbad, CA, United States) in TBS. Images were obtained in a Zeiss LSM 800 confocal microscope using a 63X objective. An average of 45 optical slices was obtained every 0.5 μm for each Z-stack.

Cortical Neuronal Cultures

Cortical neuronal cultures were prepared from embryonic day 17 Wistar rats as previously described (Tovar-y-Romo et al., 2012). Briefly, cortices were isolated and trypsinized, and cells were dissociated by trituration in a Ca^{2+} and Mg^{2+} free Hanks' balanced salt solution (Gibco, Carlsbad, CA, United States). Neurons were plated at a density of 1.3×10^5 cells/cm^2 in polyethyleneimine-coated 24-well plates in Neurobasal medium supplemented with B-27 (Gibco) and 1% antibiotic/antimycotic solution (104 U of penicillin G/ml, 10 mg of streptomycin/ml, and 25 μg of amphotericin B/ml) (Sigma). Ten μM cytosine β–D-arabinofuranoside (Sigma) was added on DIV 3 to prevent the proliferation of astrocytes.

Immunofluorescent staining was performed in cells plated on glass coverslips and fixed with 100% methanol for 10 min at −20°C on DIV 7. Neurons were incubated with anti-VEGFR1 or anti-VEGFR2 (1:100 each, LifeSpan Biosciences, Seattle, WA, United States) and anti-microtubule-associated protein 2 (MAP2; 1:100, Sigma) overnight at 4°C. Labeled cells were incubated with Alexa Fluor 546- and Alexa Fluor 488-conjugated antibodies (1:200 each, Life Technologies), for 1 h at RT, after three washes, neurons were incubated with DAPI for 5 min and mounted on glass slides. Cells were imaged with confocal microscopy as described above with a 40X objective. An average of 30 optical slices was obtained every 0.5 μm for each Z-stack.

Cortical Neurons Excitotoxicity Assays

Neuronal cultures were challenged on DIV 11 with 1, 10, or 100 μM NMDA + 1 μM glycine for 24 h to induce excitotoxic damage or neuronal death. Rat recombinant VEGF-A_{164} was added to some experimental wells at a concentration of 10 ng/mL for 24 h. In some experiments, we added, 2 μM SU1498 or 2 μM Axitinib for the same time. Neuronal viability was inferred from metabolic activity determined by standard 3-(4,5-dimethylthiazol-2-yl)-2,5-diphenyltetrazolium bromide (MTT) reduction. For this, neurons were incubated with 0.1 mg/mL

TABLE 1 | Items evaluated in neurofunctional assessments.

Neurological assessment	Reflex	Score	Previously reported
Spontaneous activity	Exploring an open arena more than 20 s	3	Burguete et al., 2006
	Exploring between 10 and 20 s	2	
	Exploring less than 10 s	1	
	Not exploring or moving only when stimulated	0	
Contralesioned- wise circling	None	3	Burguete et al., 2006
	Spontaneous circling	2	
	Stimulus-induced circling	1	
	Not moving	0	
Prehensile grip of forepaws to a wire	Symetrical grip	4	Mattsson et al., 1997
	Asymetrical, preferably use of non-lesioned forelimb	3	
	Asymetrical, unable to hold body weight	2	
	Unable to hold grip with lesioned forelimb	1	
	Fall from wire	0	
Ability to rise while suspended from the tail	Unskewed side to rise	4	Zhang et al., 2015
	Rise preferably to the non-lesioned side	3	
	Able to rise only until reached the horizontal plane	2	
	Unable to rise	1	
	Unresponsive while suspended	0	
Cylinder test	Steading with both forelimbs at even height	4	Schallert et al., 2000
	Unable to bring lesioned forelimb to equal height of contralesioned forelimb	3	
	Does not support body weight on lesioned forelimb	2	
	Unable to rear	1	
	Unresponsive	0	
Protective retraction of forelimbs after poking	Symmetrical flex and move from the site	4	NA
	Asymmetrical flex of the ipsilateral forelimb and move from the site	3	
	Asymmetrical flex of the ipsilateral forelimb but stays on site	2	
	Slight movement of ipsilateral forelimb and stays on site	1	
	Does not flex forelimb and stays on site	0	
Body posture	Balanced	5	NA
	Head tilted to the right (lesioned flank)	4	
	Head tilted to the right and forearm extended	3	
	Body tilted to the right	2	
	Unable to keep posture with lesioned hindlimb	1	
	Unable to stand from lay down position	0	
March coordination	Symetrical movement	5	NA
	Forepaws extended during march	4	
	Support on ulnar side of lesioned forelimb	3	
	Dragging fingers during march	2	
	Dragging lesioned forelimb on dorsal side	1	
	Does not stand on lesioned forelimb	0	

The neurological performance of every individual was assessed 24 h after stroke in eight items, and for each one, a corresponding value was assigned. Behavioral evaluations were cross-validated by a trained analyst blind to the experimental conditions.

TABLE 2 | Primer sequences for RT-PCR analyses of cytokine transcripts.

Gene	Primer sequence	Amplicon length (bp)	Accession number
IL-1b	F: 5′-CCCTGCAGCTGGAGAGTGTGG-3′	153	NM_031512.2
	R: 5′-TGTGCTCTGCTTGAGAGGTGCT-3′		
IL-6	F: 5′-CGAGCCCACCAGGAACGAAAGTC-3′	84	M26744.1
	R: 5′-CTGGCTGGAAGTCTCTTGCGGAG-3′		
TGFb	F: 5′-ACCTGCAAGACCATCGACAT-3′	154	NM_021578.2
	R: 5′-TGTTGTACAAAGCGAGCACC-3′		
GAPDH	F: 5′-GCATCTTCTTGTGCAGTGCC-3′	278	NM_017008.4
	R: 5′-GATCTCGCTCCTGGAAGATGG-3′		

MTT for 2 h at 37°C at the end of the analyzed period. Media was removed, and formazan precipitations were dissolved in a 4 mM HCl isopropanol solution. The absorbance of cell debris-free supernatants was read in a spectrophotometer (Beckman Coulter) with a 570 nm wavelength. Data are presented as percentage relative to the absorbance of control conditions. In some experimental conditions we corroborated neuronal viability with the life/dead fluorescence assay (Thermo Fisher Scientific) that stain live cells with calcein AM (green) and dead cells with ethidium homodimer-1 (red), following manufacturers directions.

In an independent series of experiments, neurons were subjected to the same conditions and dendritic spines were stained with the Neurite Outgrowth Staining kit (Life Technologies, Carlsbad, CA, United States) following the manufacturer directions. Briefly, neurons plated on glass coverslips were fixed with 3.7% PFA for 30 min at RT, and 1X bright orange-fluorescent dye was added to stain the outer cell membrane surfaces. After incubation with a background suppression solution, coverslips were mounted on glass slides with a permanent mounting medium with antifading agents (DAKO, Santa Clara, CA, United States). Dendritic branches were visualized using a Leica DM1000 microscope under epifluorescence illumination (568-nm excitation and 580-nm emission) with a 40X objective. A minimum of 10 neurons from 3 independent experiments was analyzed for each condition. The number of dendritic spines, defined as thin protrusions emerging from dendritic processes, extending from two to five primary dendrites/neuron was quantified for a distance of approximately 20 μm from the cell soma. Neurite lengths and spine numbers were quantified with ImageJ (NIH, United States). Spine density across all measured dendritic segments was normalized to the length of the primary dendrite.

Statistics

R- Feather Spray version 3.5.1, (R Foundation for Statistical Computing, Vienna, Austria) was used to analyze all data from *in vivo* experiments. Normal distribution in each data set was corroborated using the Shapiro–Wilk normality test. Data were tested by one-way analysis of variance (ANOVA) followed by Tukey *post hoc* test. Data were considered significant at $\alpha \leq 0.05$ level. All data are shown as mean ± 2SD. For *in vitro* experiments without normal distribution we did a Kruskal–Wallis, followed by Dunn *post hoc* test. Results are expressed as mean ± SEM.

RESULTS

VEGF Mediates Neuroprotection in the Acute Phase of Stroke

There are contradictory findings on the neuroprotective effects of VEGF in stroke. Most of the reported discrepancies can be grounded on time, dose and route of administration of exogenous VEGF in several models of stroke (Ma et al., 2012; Tovar-y-Romo et al., 2016). Because of this, we first tested the effect of administering a single bolus of 50 ng rat recombinant VEGF-A_{164} by i.c.v. injection 30 min after the beginning of reperfusion (**Figure 1**), the dose was chosen based on pilot experiments, and also on a previous study showing that this dose and method of administration is protective in other models of neurodegeneration (Tovar-y-Romo and Tapia, 2012). This protocol was carried out using a pulled glass microcapillary pipette to minimize mechanical damage in order to prevent the activation of inflammatory processes merely associated with the injection procedure. Twenty four hours after stroke, animals were evaluated in a series of neurobehavioral and motor tasks to determine the level of neurological alterations produced by the stroke (**Figure 1A**). Animals that were injected with vehicle only (DMSO + 0.1% BSA; 4 μl) showed a noticeable weakness and impaired movement of the lesioned side forelimb. These animals were unable to climb a grid and support their body weight and had a noticeable difficulty rising when placed on their sides, plus ∼60% of animals had epileptiform seizures, mostly represented by tonic-clonic convulsions, barrel rolls and running fits. Stroked rats also displayed signs of neuropathic pain when stimulated by slightly poking the affected flank. Administration of 50 ng recombinant VEGF at the beginning of reperfusion did not improve significantly the neurological deficits presented after stroke and also failed to prevent seizures.

Nonetheless, VEGF did reduce infarct volumes by about 20% in comparison to the group that received vehicle only (**Figures 1B,C**). Moreover, neuronal viability was also preserved as revealed by analyzing the somatosensory region of the parietal cortex, in which ∼50% neurons remain alive at 24 h post-stroke (**Figures 1D,E**). Therefore, with this experimental settings, we found a condition in which exogenous VEGF did produce a protective impact on brain tissue without translating into a better neurobehavioral outcome at this short time point after stroke.

VEGFR2 Activation Hinders VEGFR1-Driven Neuroprotection Elicited by Endogenous Ligand in the Acute Phase Post-stroke

It has been known for a long time that VEGF synthesis is upregulated by ischemia immediately after an experimental stroke (Hayashi et al., 1997; Plate et al., 1999; Hai et al., 2003), and this phenomenon has also been reported to occur in human patients (Issa et al., 1999). It is suspected that such VEGF increase is mechanistically involved in neuroprotection. Considering the large body of evidence that involves VEGFR2 participation in neuroprotection (Olsson et al., 2006; Tovar-y-Romo et al., 2016; Geiseler and Morland, 2018), we set out to determine whether VEGFR2 would be primordially responsible for the protection seen here. For this, we administered i.c.v. 13 nmoles of SU1498, a selective VEGFR2 inhibitor (Strawn et al., 1996), 30 min after the beginning of reperfusion and analyzed the overall effects of this procedure 24 h after stroke. Animals in this group displayed signs of neurological deficits mainly characterized by paresis of the lesioned forelimb. However, all animals in this group performed better in the neurological tests and showed significantly fewer alterations than rats that were

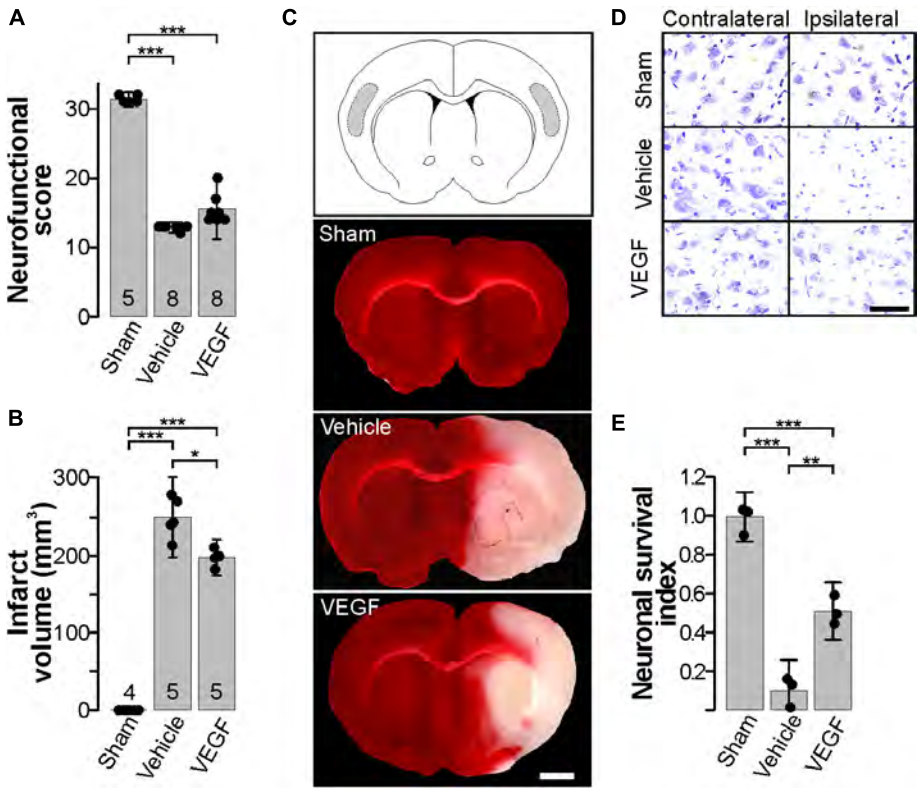

FIGURE 1 | Exogenous VEGF administration in the acute phase post-stroke is neuroprotective. **(A)** Behavioral performance of sham-operated animals and stroked rats treated with vehicle or VEGF 24 h post-stroke. Animals were assessed individually in 8 items with scoring values that added up to 32 points that corresponded to neurologically unaffected performance, see **Table 1**. **(B)** Mean infarct volume ± 2 SD of the indicated experimental groups. In **(A,B)**, the number of experiments analyzed in each group is indicated at the bottom of each column; individual data points are plotted for each group. **(C)** Representative images of thick coronal sections of brains stained with TTC from a sham-operated animal and stroked rats treated with vehicle or VEGF. The unstained (pinkish) portion of the tissue depicts the infarct. Images show brain structures at around Bregma level in the anteroposterior axis. Bar equals 2 mm. **(D)** Representative photomicrographs of Nissl-stained thin sections of the cortical areas shaded in the diagram in (top **C**). Alive neurons have a pyramidal morphology and cytosolic light violet stain, while damaged neurons appear as condensed pycnotic nuclei with enhanced concentration of the dye. Bar equals 50 μm. **(E)** Survival index represents the portion of alive neurons present at 24 h post-stroke relative to the same region in the corresponding contralateral side normalized to the number of alive neurons in sham-operated animals. $^{*}p < 0.05$, $^{**}p < 0.01$, and $^{***}p < 0.001$ in one-way ANOVA followed by Tukey *post hoc* test.

administered with vehicle alone (**Figures 2A**, **3**). Furthermore, co-administration of VEGFR2 antagonist together with a bolus of 50 ng exogenous agonist also resulted in a noticeable improvement in neurological function as compared to animals that received vehicle alone but also to the group that was administered with VEGF, which displayed better recoveries (**Figures 2A**, **3**) – thus pointing to a VEGFR2-independent effect driven by the endogenous ligand.

Given the lack of a specific pharmacological inhibitor of VEGFR1, we employed the general VEGFR inhibitor Axitinib that blocks all VEGF receptors (Inai et al., 2004). The MCAO group that received 13 nmoles of Axitinib at 30 min of the beginning of reperfusion presented exacerbated neurological symptoms described above that were followed by a lethargic state in which animals laid on their right side. As expected, infarct volumes in this group were large and comparable to the vehicle group (**Figures 1B,C**, **2B,C**). Finally, blocking all VEGFRs prevented any protection mediated by the i.c.v. administration of exogenous VEGF and animals displayed neurological impairments characteristic of large infarctions (**Figures 2A–C**). Brain damage seen in TTC stainings in this group was of proportions similar to the ones seen in the control untreated group (**Figures 2B,C**). Accordingly, neuronal death was reduced in the animals that received SU1498 alone or in combination with VEGF and was increased in animals treated with Axitinib (**Figures 2D,E**).

Correlating the neurological performance of animals 24 h after stroke to the extent of brain tissue damage allowed us to clearly segregate groups by experimental treatment and show that blocking VEGFR2 and potentiating the activation of VEGFR1 by the administration of exogenous ligand, afforded the best level of neuroprotection, closely followed by only blocking VEGFR2 (**Figure 3**). This analysis shows a strong correlation of $R^2 = 0.8747$ with a $p = 3.33 \times 10^{-16}$. The sole administration of the exogenous ligand, while still protective, does not result in a very different outcome as compared to all the non-protected experimental conditions, in which we either not treated animals or inhibited all VEGFRs (**Figure 3**).

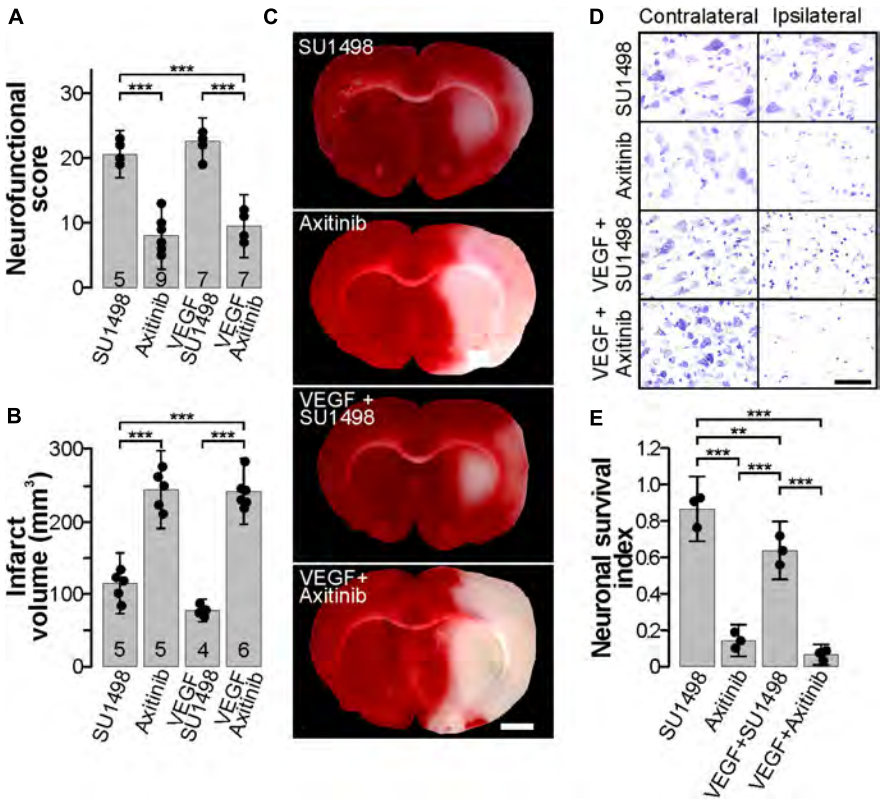

FIGURE 2 | Blocking the VEGFR2 in the acute phase post-stroke is neuroprotective. **(A)** Behavioral performance of stroked rats treated with the VEGFR2 specific inhibitor SU1498 and the pan-VEGFR inhibitor Axitinib with and without exogenous VEGF, 24 h post-stroke. **(B)** Mean infarct volume ± 2 SD of the indicated experimental groups treated with SU1498 or Axitinib alone or in combination with exogenous VEGF. In **(A,B)**, the number of experiments analyzed in each group is indicated at the bottom of each column; individual data points are plotted for each group. **(C)** Representative images of thick coronal sections of brains stained with TTC from stroked animals treated with SU1498 and Axitinib with or without exogenous VEGF. The unstained (pinkish) portion of the tissue depicts the infarct. Images show brain structures at around Bregma level in the anteroposterior axis. Bar equals 2 mm. **(D)** Representative photomicrographs of Nissl-stained thin sections of cortical areas in the somatosensory region. Alive neurons have a pyramidal morphology and cytosolic light violet stain, while damaged neurons appear as condensed pycnotic nuclei with enhanced concentration of the dye. Bar equals 50 μm. **(E)** Survival index represents the portion of live neurons present at 24 h post-stroke relative to the same region in the corresponding contralateral side normalized to the number of live neurons in sham-operated animals. $^{**}p < 0.01$ and $^{***}p < 0.001$ in one-way ANOVA followed by Tukey *post hoc* test.

VEGFR1-Mediated Neuroprotection Partially Involves M2 Polarization of Microglia With a Minimal Discernible Impact on Systemic Markers of Inflammation

VEGF drives the migration of macrophages and microglia to the damaged CNS through VEGFR1-mediated signaling (Forstreuter et al., 2002; Huang et al., 2013; Lelli et al., 2013). Therefore, we decided to study whether the neuroprotection exerted by the preferential activation of VEGFR1 would also involve the modulation of neuroinflammatory processes. We first assessed changes in inflammatory markers, both in CSF and in plasma, at 24 h post-stroke. We analyzed the content of IL-1β, IL-4, IL-6, IL-10, IL-12p70, IL-17, TNF-α, CCL11, INFγ, CX3CL1, and MIP-1α with a multiplex array for these cytokines in samples collected prior transcardial perfusion. None of the detected cytokines in CSF (IL-1β, INFγ, CXCL-3) showed a significant change compared to the values seen in the vehicle-treated group (**Figure 4A**). Likewise, for most of the peripheral markers of inflammation that produced a readable measurement in plasma, we did not find differences among experimental groups. However, we detected with this array that the inhibition of all VEGFRs with Axitinib blunted the release of peripheral markers of inflammation IL-12, TNFα, and CCL11. This blockade did not happen to the same degree when we selectively inhibited VEGFR2 (**Figure 4B**). Since under our experimental conditions we were not able to have reliable measurements of peripheral IL-1β, IL-6, and TGFβ, which have been previously identified as central players of the neuroinflammatory processes that happen after stroke, we decided to evaluate the levels of transcriptional expression of these cytokines in white blood cells collected 24 h after stroke. With RT-qPCR analyses, we determined that there are no significant changes in the level of transcription for neither of these molecules at the time point of our investigations and that VEGF or its receptors are not modifiers of these molecular responses (**Figures 4C–E**).

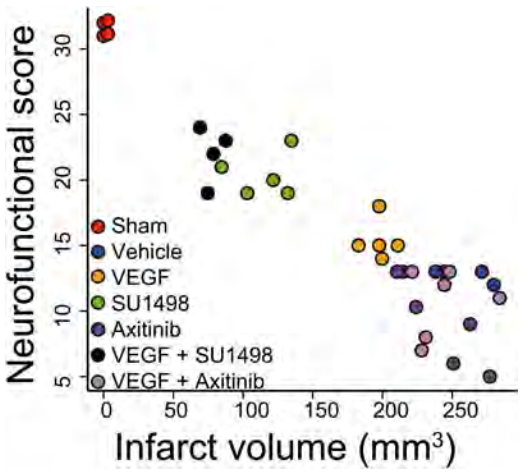

FIGURE 3 | Activation of VEGFR2 hinders VEGFR1-dependent neuroprotection afforded by the endogenous ligand. The plot shows the correlation of neurofunctional score to the infarct volume produced by MCAO in animals injected i.c.v. 30 min after the beginning of reperfusion with vehicle, or exogenous VEGF alone or in combination with VEGFR2 specific inhibitor SU1498 or VEGFR general inhibitor Axitinib. Two groups of animals that received the inhibitors individually are also presented. Each data point represents the values obtained in a single animal. Groups segregate by experimental condition and produce a strong correlation with an adjusted R^2 = 0.8747. Animals in which VEGFR2 early activation was prevented show the best levels of protection, both neurofunctional and histological, inhibiting VEGFR1 in addition to VEGFR2 blocked this effect.

Next, we looked into the polarization of microglial cells to the anti-inflammatory phenotype M2, which is known to occur in the first 24 h after stroke (Hu et al., 2012). For this, we co-stained brain sections for the microglial marker Iba-1 and the M2 marker arginase-1. Strikingly, resting state morphologically looking microglia were found to express arginase-1 in sham animals at 24 h of transiently occluding the common carotid artery (**Figure 5**). In the control MCAO group, microglia in the lesioned cortical region looked morphologically activated, mainly with shortened cellular processes and rounded somas but cells in these regions lacked the expression of arginase-1. VEGF-treated animals, however, showed activated microglia expressing the M2 polarization marker and this was also the scenario in the groups treated with the VEGFR2 inhibitor SU1498 with and without VEGF. In the case of animals injected with Axitinib, we found fewer activated microglia expressing arginase-1, suggesting that VEGFR1 blockade also reduced the polarization of microglia to the anti-inflammatory phenotype.

VEGF Acts Directly on Neurons Through the Activation of VEGFR1

In the last part of our study, we analyzed whether the effects of preferentially activating VEGFR1 and the neuroprotection seen in the *in vivo* model of ischemic stroke were derived from the direct stimulation of neuronal receptors. Using an *in vitro* model of cultured cortical neurons we first determined the expression of both, VEGFR1 and VEGFR2 in these cells. **Figure 6A** shows the expression of both TRKs at 7 DIV, specifically in neurons. Expression of both receptors is clear in neuronal somas as well as in neurites. Then, we tested whether the addition of VEGF to neuronal cultures could rescue neurons from excitotoxicity, one of the primary mechanisms underlying neuronal death after ischemia. For this, we incubated the neurons with different concentrations of the glutamatergic agonist NMDA for 24 h in the same culture media in which cells were grown for 11 days. At the lowest concentration assayed (1 μM), neuronal death is not apparent and increasing the concentration of NMDA to 10, and 100 μM gradually increased the level of neuronal death (**Figures 6B,C**). Addition of 10 ng/mL recombinant VEGF reduced in about 20% the loss of metabolic activity in the neuronal cultures, which relates to the overall health of the cells and their survivability.

Even though the lower concentrations of NMDA tested here did not produce a substantial decrease of neuronal viability, neurons exposed to these conditions developed morphological signs of structural damage, mainly characterized by dendritic spine loss. Addition of VEGF to the culture media also prevented this morphological change and preserved spine structures although it did not modify the length of primary neurites (**Figures 6D–F**). With these experiments, we showed that VEGF executes trophic effects on cortical neurons to allow them to grow healthy in culture and make them less susceptible to excitotoxic death.

Finally, in an independent set of experiments, we tested the role of VEGFR1 and VEGFR2 in driving the pro-survival effects. Strikingly, blocking VEGFR2 activation by addition of SU1498 also resulted in a significant increase in neuronal protection, which was further potentiated by the co-administration of VEGF (**Figure 6G**). By contrast, inhibiting the activation of both receptors with Axitinib prevented entirely the neuroprotection exerted by VEGF (**Figure 6G**). These results replicated well the effects that we described first with the *in vivo* model, therefore, proving that the mechanisms of protection seen partially encompassed a direct involvement of neuronal receptors.

DISCUSSION

Since VEGF is a molecule with pleiotropic actions that can execute its functions by binding a number of different receptors, the exact role of VEGF increased expression after stroke in neuroprotective mechanisms has been the core of a controversy. The prevailing idea on the dual effects exerted by VEGF states that the dominant actions of this trophic factor, whether neuroprotective or detrimental, are chiefly dictated by the timing, dosage, and route of administration in experimental models of stroke (Wittko-Schneider et al., 2013; Geiseler and Morland, 2018). Moreover, it has been amply described that excessive levels of VEGF in the early phase following stroke promote BBB alterations and a general state that favors neurodegeneration. Interestingly, delayed administration of VEGF is more likely to result in neuroprotection (Sun et al., 2003; Dzietko et al., 2013), even though, others have also reported the protective effect of an early VEGF i.c.v. administration (Kaya et al., 2005).

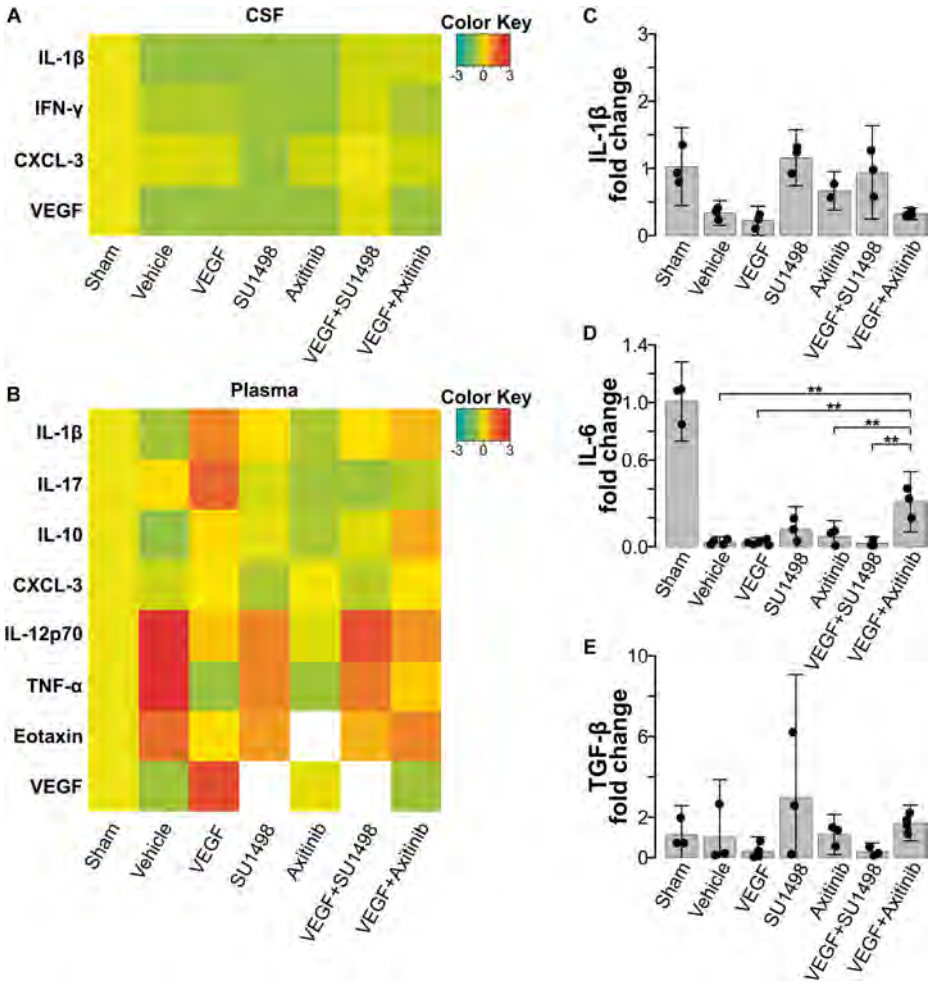

FIGURE 4 | VEGFR1-dependent neuroprotection does not reflect on changes in peripheral inflammatory markers. **(A)** Heatmap of cytokines and VEGF detected in CSF 24 h after stroke. **(B)** Heatmap of peripheral cytokines and VEGF detected in plasma 24 h after stroke. No significant differences were detected in these markers in the acute phase following stroke. White colored areas are from groups with undetectable readings. Changes in transcriptional expression of **(C)** IL-1β, **(D)** IL-6, and **(E)** TGF-β, determined by RT-qPCR relative to GAPDH in blood 24 h following stroke. No differences were found among experimental groups.

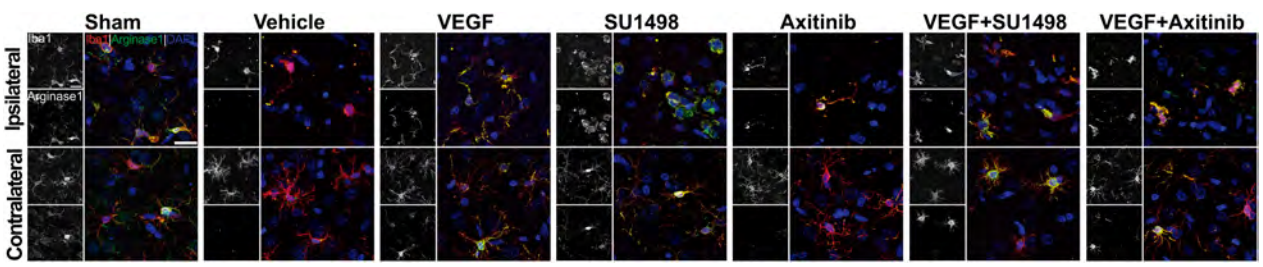

FIGURE 5 | Blockade of VEGFR1 impedes the polarization of microglia to the M2 phenotype. Representative images of brain sections co-labeled with the microglia marker Iba-1 (red) and the M2 phenotype indicator arginase-1 (green). Images were taken from the somatosensory cortex adjacent to infarct core. Ameboid-like activated morphology is present under all MCAO conditions in the ipsilateral side. M2 polarizations are evident in most of the Iba-1 positive cells in the MCAO groups treated with vehicle, VEGF, SU1498 and the combination of VEGF and SU1498. Animals injected with the pan-VEGFR blocker Axitinib do not show labeling of M2 polarization in the activated microglia on the ipsilateral side. Bar equals 20 μm.

In the brain, VEGFR1 and VEGFR2 are the most expressed receptors, with VEGFR1 showing a higher density in neurons (Yang et al., 2003; Du et al., 2010). Several reports have been published over the years indicating that VEGFR2 is the receptor predominantly responsible for neuroprotective actions, mainly by driving pro-survival signaling mediated by

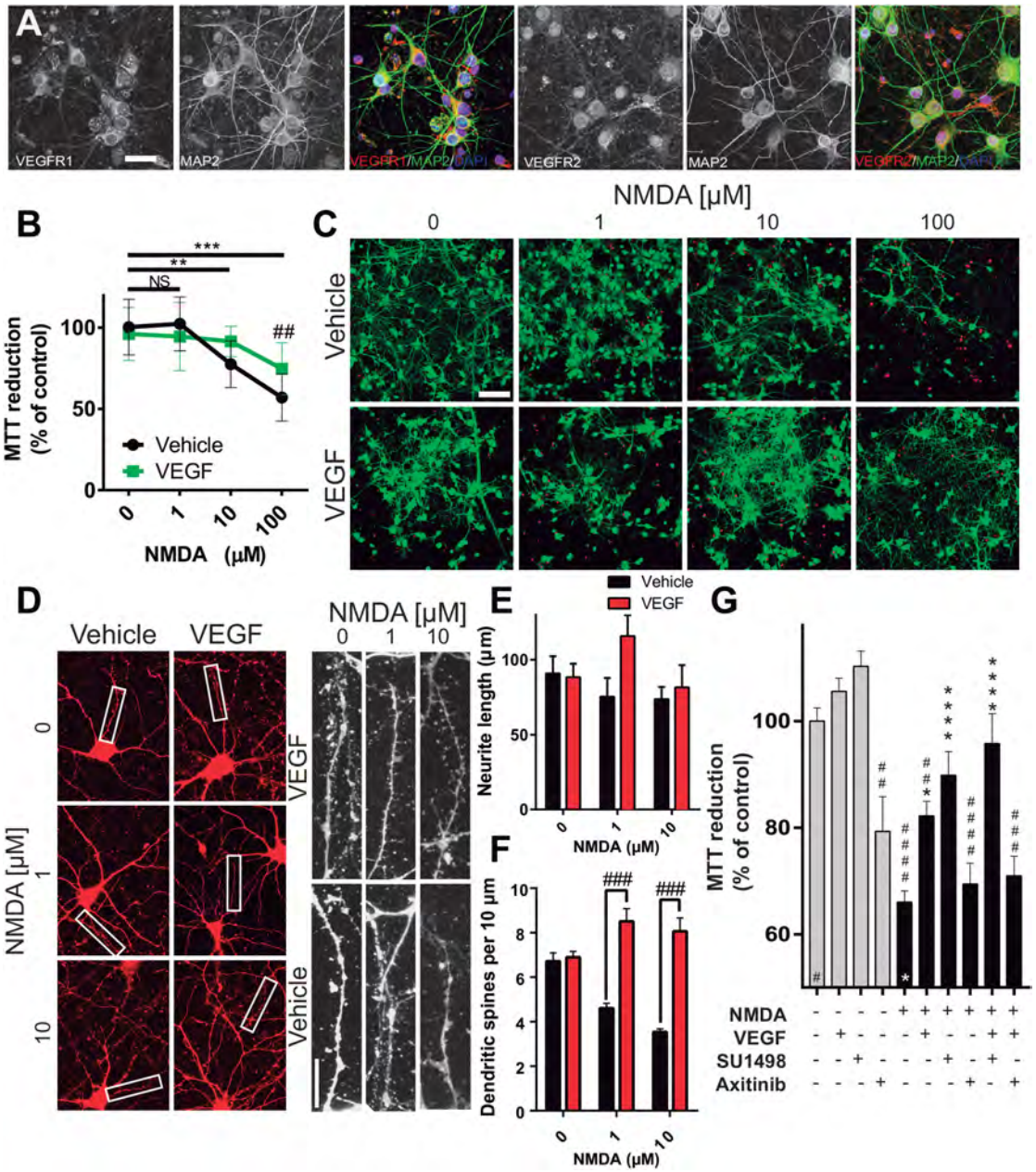

FIGURE 6 | Neuronal VEGFR1 drives neuroprotection under excitotoxic stress. **(A)** Representative photomicrographs of cultured cortical neurons labeled with the neuronal marker MAP2 (green), and VEGFR1 and VEGFR2 (red). Bar equals 25 μm. **(B)** Neuronal survival assessed by MTT reduction of cultures exposed to increasing concentrations of NMDA for 24 h and 10 ng/mL VEGF. The graph shows the mean ± SEM of three independent experiments. **(C)** Representative images of cortical neurons exposed to increasing concentrations of NMDA for 24 h with or without 10 ng/mL VEGF, calcein stain labels alive neurons green, while dead cells are marked by the nuclear staining of bromide homodimer in red. Bar equals 200 μm. **(D)** Representative micrographs of neurons exposed to sublethal concentrations of NMDA for 24 h and stained with a membrane dye. VEGF preserved the structural integrity of neurites and dendritic spines. Images on the right are magnifications of the indicated areas on the left. Scale bar equals 10 μm. Quantifications of neurite length **(E)** and dendritic spines **(F)** of the experiments described in **(D)**. Each column represents the mean ± SEM of the neurites of 5 neurons analyzed in three independent experiments. **(G)** Neuronal survival assessed by MTT reduction of cultures exposed to 100 μM NMDA for 24 h and 10 ng/mL VEGF alone or in combination with 2 μM SU1498 and 0.2 μM Axitinib. The graph shows the mean ± SEM of three independent experiments. $^{*}p < 0.05$, $^{**}p < 0.01$, $^{***}p < 0.001$, and $^{****}p < 0.0001$ compared to NMDA alone, and $^{\#\#}p < 0.01$, $^{\#\#\#}p < 0.001$, and $^{\#\#\#\#}p < 0.0001$ compared to untreated neurons in Kruskal–Wallis followed by Dunn *post hoc* test.

PI-3K/PKB and MEK/Erk pathways (Greenberg and Jin, 2013). Here, we found that the preferential activation of VEGFR1 by the endogenous ligand promotes neuronal protection and prevents the presentation of large volume infarcts; this is highly correlated with neurological performance. Of note, the concurrent activation of VEGFR2 prevents this effect, even in the

presence of excess ligand. Strikingly, such protection still happens at the cellular level, where neurons are better protected when challenged to NMDA-induced excitotoxicity by the activation of VEGFR1 if VEGFR2 is blocked.

VEGF along with its receptors 1 and 2 are transcriptionally upregulated following stroke (Hayashi et al., 1997; Issa et al., 1999; Plate et al., 1999; Marti et al., 2000; Hai et al., 2003; Stowe et al., 2007, 2008) in a long-lasting fashion (Zhang et al., 2002), through the stabilization and subsequent binding of hypoxia-inducible factor 1 (HIF-1) to the hypoxia response element sequence in their promoters (Forsythe et al., 1996). Also, it has been shown that exogenous administration of VEGF causes the upregulation of VEGFR1 and VEGFR2 (Krum et al., 2008). Cellular distribution of VEGFRs might be key in understanding the temporal regulation of vasculature adaptations in the acute phase post-stroke. In this regard, the apicobasal localization of VEGFR1 and VEGFR2 is different, where VEGFR2 is predominantly expressed in the basal side and VEGFR1 in the apical pole that produces a differential response when the ligand acts at the circulation or the parenchymal sides of endothelial cells (Hudson et al., 2014). It has also been reported that the expression of VEGFR1 is upregulated while VEGFR2 is downregulated in endothelial cells following hypoxia, which changes the VEGFR1:VEGFR2 ratio altering the ultimate responses on cell viability and recovery (Ulyatt et al., 2011). It is also important to point out that the affinity of VEGFR1 for VEGF is about 1 order of magnitude higher than the one for VEGFR2 (K_d 2–10 pM for VEGFR1 and 75–250 pM for VGFR2) (de Vries et al., 1992; Ferrara, 2004; Shibuya, 2006). Although VEGFR3 is expressed in the adult rat brain (Hou et al., 2011), we ruled out the participation of this receptor in the neuroprotection seen here, even when it can also be inhibited by Axitinib, because it does not get activated by VEGF-A (Olsson et al., 2006; Leppänen et al., 2013) and its expression is primarily restricted to lymphatic endothelial cells (Iljin et al., 2001), which have a very low relative abundance in the brain (Louveau et al., 2015).

Our observations lead to reaffirm the critical role of VEGFR1 in the endogenous neuroprotective mechanisms elicited after ischemic insults to the brain. In this regard, it is known that the deletion of VEGF-B, a specific ligand for VEGFR1, produces 50% larger infarcts in mice when subjected to the permanent occlusion of the MCA in comparison to WT animals, by inhibition of apoptotic executioner molecules (Li et al., 2008). Protein analysis identified a significant increase of VEGF-B in CSF and the ischemic hemispheres, with increased VEGFR1 activation that also correlated with an increase in Akt phosphorylation, whereas an increase in VEGF in the contralateral hemisphere correlates with a significant increase in vascular density 7 days post-stroke (Guan et al., 2011). VEGFR1 activation in pericytes promotes the formation of stable new vessels in a mechanistic way independent of endothelial cells, and also slightly attenuated inflammation when administered in the sub-acute phase post-stroke (Jean LeBlanc et al., 2018). In this sense, it has also been shown that PlGF, a specific ligand for VEGFR1, is the most efficient promoter of angiogenesis, which produces mature non-leaky new vessels (Luttun et al., 2002; Gaál et al., 2013).

The direct VEGFR1 activation in neurons might be a mechanism more relevant than promoting healthy angiogenesis (Poesen et al., 2008; Dhondt et al., 2011; Ishrat et al., 2018). In this regard, it is noteworthy that VEGF associates to neurons in infarct and peri-infarct brain regions in a non-human primate model of stroke (Stowe et al., 2007), and interestingly, such association can even be more relevant than the interaction of this growth factor with astrocytes (Shen et al., 2018). Our results, however, indicate that all these neuroprotective mechanisms driven by VEGFR1 are suppressed in the first hours following stroke by the activation of VEGFR2. The exact mechanisms underlying this phenomenon are not fully elucidated, but they might involve the suppression of endoplasmic reticulum stress and apoptosis (Feng et al., 2019).

VEGF has some interesting roles in regulating neuroinflammation. It has been shown that macrophages express more VEGF in response to disturbances in brain metabolic homeostasis, especially responding to decreased glucose incorporation (Jais et al., 2016), and microglia in chronically affected regions of CNS upregulate their expression of VEGF (Nikodemova et al., 2014). However, not much is known about the involvement of VEGF, or its receptors, in the polarization of macrophages/microglia under inflammation. Interestingly, very recent evidence indicates that the antiangiogenic VEGF isoform $VEGF_{164}b$ is capable of blocking VEGFR1 prompting the M1 polarization of peripheral macrophages (Ganta et al., 2019), although it is known that this form of VEGF has neuroprotective effects in the CNS (Beazley-Long et al., 2013). Also, M2-polarized peripheral macrophages in culture are known to upregulate their VEGFR1 mRNA expression (Melton et al., 2015), which in microglial cells could lead to the inhibition of the expression of the scavenger receptor A following stroke (Xu et al., 2017). With the determinations carried out in the present study, we were unable to obtain reliable readings of the levels of soluble mediators of inflammation poured on CSF and plasma, however, many of these markers, like IL-6, have been disregarded as important predictors of the outcome (Clark Wayne et al., 2000; Worthmann et al., 2010). Nonetheless, we could characterize the overall response of microglia polarizing to the anti-inflammatory phenotype under the experimental conditions that allow the activation of VEGFR1. More detailed analyses are required to characterize these responses at the molecular and cellular levels.

CONCLUSION

We found that the activation of VEGFR2 in the first hours post-stroke obstructs endogenously-coded mechanisms of adaptation to injury in the brain. We propose here the existence of a VEGFR2-mediated antagonism of VEGFR1, which has not been reported previously. This process would constitute a fundamental mechanism of endogenous operations that drive adaptive responses in the brain after stroke that is worthy of further exploration. Our results also strengthen the notion that VEGFR1 has a critical role in neuroprotection, and that targeting this receptor would be useful at developing restorative therapies for stroke.

DATA AVAILABILITY

The datasets used and/or analyzed during the current study are available from the corresponding author on reasonable request.

ETHICS STATEMENT

This study was carried out in accordance with the Mexican law for the use and care of laboratory animals (NOM-062-ZOO-1999) with the approval of the Institutional Animal Care and Use Committee (CICUAL-IFC-LTR93-16).

AUTHOR CONTRIBUTIONS

AC-R and LT-y-R conceived the project and designed the experiments. AC-R conducted the *in vivo* experiments, wrote the R-based scripts to process data, and carried out statistical analyses. YH-R cross-validated the neurological assessments. ANC-R and AP-P conducted the *in vitro* experiments. RR-H was responsible for confocal microscopy acquisition and analyses. AC-R, ANC-R, YH-R, and LT-y-R analyzed the data. LT-y-R wrote the manuscript. All authors read and approved the final version of the manuscript.

FUNDING

This work was supported by the Programa de Apoyo a Proyectos de Investigación e Innovación Tecnológica, Dirección General de Asuntos del Personal Académico (IN226617), Consejo Nacional de Ciencia y Tecnología (CONACYT; CB219542/13219), and the Committee for Aid and Education in Neurochemistry of the International Society for Neurochemistry and the International Brain Research Organization Return Home Program (2014) grants to LT-y-R. AC-R, ANC-R, and YH-R are recipients of doctoral scholarships from the CONACYT (280986/277660/428473).

ACKNOWLEDGMENTS

We thank Jaime Rogerio Ríos for his contribution with microglia immunofluorescence stainings, Cristina Aranda Fraustro for administrative assistance, Dr. Laura Ongay-Larios for her expert aid with RT-qPCR, and Gabriela Meneses and Dr. Edda Sciutto for their helpful assistance with the MAGPIX system. AC-R conducted this study in partial fulfillment of the requirements of the Programa de Doctorado en Ciencias Biomédicas of Universidad Nacional Autónoma de México.

REFERENCES

Beazley-Long, N., Hua, J., Jehle, T., Hulse, R. P., Dersch, R., Lehrling, C., et al. (2013). VEGF-A165b is an endogenous neuroprotective splice isoform of vascular endothelial growth factor A in vivo and in vitro. *Am. J. Pathol.* 183, 918–929. doi: 10.1016/j.ajpath.2013.05.031

Burguete, M. C., Torregrosa, G., Pérez-Asensio, F. J., Castelló-Ruiz, M., Salom, J. B., Gil, J. V., et al. (2006). Dietary phytoestrogens improve stroke outcome after transient focal cerebral ischemia in rats. *Eur. J. Neurosci.* 23, 703–710. doi: 10.1111/j.1460-9568.2006.04599.x

Clark Wayne, M., Rinker Lisa, G., Lessov Nikola, S., Hazel, K., Hill, J. K., Stenzel-Poore, M., et al. (2000). Lack of interleukin-6 expression is not protective against focal central nervous system ischemia. *Stroke* 31, 1715–1720. doi: 10.1161/01.STR.31.7.1715

de Vries, C., Escobedo, J. A., Ueno, H., Houck, K., Ferrara, N., and Williams, L. T. (1992). The fms-like tyrosine kinase, a receptor for vascular endothelial growth factor. *Science* 255, 989–991. doi: 10.1126/science.1312256

Dhondt, J., Peeraer, E., Verheyen, A., Nuydens, R., Buysschaert, I., Poesen, K., et al. (2011). Neuronal FLT1 receptor and its selective ligand VEGF-B protect against retrograde degeneration of sensory neurons. *FASEB J.* 25, 1461–1473. doi: 10.1096/fj.10-170944

Du, H., Li, P., Pan, Y., Li, W., Hou, J., Chen, H., et al. (2010). Vascular endothelial growth factor signaling implicated in neuroprotective effects of placental growth factor in an in vitro ischemic model. *Brain Res.* 1357, 1–8. doi: 10.1016/j.brainres.2010.07.015

Dzietko, M., Derugin, N., Wendland, M. F., Vexler, Z. S., and Ferriero, D. M. (2013). Delayed VEGF treatment enhances angiogenesis and recovery after neonatal focal rodent stroke. *Transl. Stroke Res.* 4, 189–200. doi: 10.1007/s12975-012-0221-6

Eliceiri, B. P., Paul, R., Schwartzberg, P. L., Hood, J. D., Leng, J., and Cheresh, D. A. (1999). Selective requirement for Src kinases during VEGF-induced angiogenesis and vascular permeability. *Mol. Cell* 4, 915–924. doi: 10.1016/S1097-2765(00)80221-X

Feng, S.-Q., Zong, S.-Y., Liu, J.-X., Chen, Y., Xu, R., Yin, X., et al. (2019). VEGF antagonism attenuates cerebral ischemia/reperfusion-induced injury via inhibiting endoplasmic reticulum stress-mediated apoptosis. *Biol. Pharm. Bull.* 42, 692–702. doi: 10.1248/bpb.b18-00628

Ferrara, N. (2004). Vascular endothelial growth factor: basic science and clinical progress. *Endocr. Rev.* 25, 581–611. doi: 10.1210/er.2003-0027

Forstreuter, F., Lucius, R., and Mentlein, R. (2002). Vascular endothelial growth factor induces chemotaxis and proliferation of microglial cells. *J. Neuroimmunol.* 132, 93–98. doi: 10.1016/s0165-5728(02)00315-6

Forsythe, J. A., Jiang, B. H., Iyer, N. V., Agani, F., Leung, S. W., Koos, R. D., et al. (1996). Activation of vascular endothelial growth factor gene transcription by hypoxia-inducible factor 1. *Mol. Cell. Biol.* 16, 4604–4613. doi: 10.1128/mcb.16.9.4604

Gaál, E. I., Tammela, T., Anisimov, A., Marbacher, S., Honkanen, P., Zarkada, G., et al. (2013). Comparison of vascular growth factors in the murine brain reveals placenta growth factor as prime candidate for CNS revascularization. *Blood* 122, 658–665. doi: 10.1182/blood-2012-07-441527

Ganta, V. C., Choi, M., Farber, C. R., and Annex, B. H. (2019). Antiangiogenic VEGF165b regulates macrophage polarization via S100A8/S100A9 in peripheral artery disease. *Circulation* 139, 226–242. doi: 10.1161/CIRCULATIONAHA.118.034165

Geiseler, S. J., and Morland, C. (2018). The janus face of VEGF in stroke. *Int. J. Mol. Sci.* 19:1362. doi: 10.3390/ijms19051362

Grassot, J., Gouy, M., Perrière, G., and Mouchiroud, G. (2006). Origin and molecular evolution of receptor tyrosine kinases with immunoglobulin-like domains. *Mol. Biol. Evol.* 23, 1232–1241. doi: 10.1093/molbev/msk007

Greenberg, D. A., and Jin, K. (2013). Vascular endothelial growth factors (VEGFs) and stroke. *Cell. Mol. Life Sci.* 70, 1753–1761. doi: 10.1007/s00018-013-1282-8

Guan, W., Somanath, P. R., Kozak, A., Goc, A., El-Remessy, A. B., Ergul, A., et al. (2011). Vascular protection by angiotensin receptor antagonism involves differential VEGF expression in both hemispheres after experimental stroke. *PLoS One* 6:e24551. doi: 10.1371/journal.pone.0024551

Hai, J., Li, S.-T., Lin, Q., Pan, Q.-G., Gao, F., and Ding, M.-X. (2003). Vascular endothelial growth factor expression and angiogenesis induced by chronic cerebral hypoperfusion in rat brain. *Neurosurgery* 53, 963–970; discussion 970–972.

Hayashi, T., Abe, K., Suzuki, H., and Itoyama, Y. (1997). Rapid induction of vascular endothelial growth factor gene expression after transient middle cerebral artery occlusion in rats. *Stroke* 28, 2039–2044. doi: 10.1161/01.str.28.10.2039

Hou, Y., Shin, Y.-J., Han, E. J., Choi, J.-S., Park, J.-M., Cha, J.-H., et al. (2011). Distribution of vascular endothelial growth factor receptor-3/Flt4 mRNA in adult rat central nervous system. *J. Chem. Neuroanat.* 42, 56–64. doi: 10.1016/j.jchemneu.2011.06.001

Hu, X., Li, P., Guo, Y., Wang, H., Leak, R. K., Chen, S., et al. (2012). Microglia/macrophage polarization dynamics reveal novel mechanism of injury expansion after focal cerebral ischemia. *Stroke* 43, 3063–3070. doi: 10.1161/STROKEAHA.112.659656

Huang, H., Parlier, R., Shen, J.-K., Lutty, G. A., and Vinores, S. A. (2013). VEGF receptor blockade markedly reduces retinal microglia/macrophage infiltration into laser-induced CNV. *PLoS One* 8:e71808. doi: 10.1371/journal.pone.0071808

Hudson, N., Powner, M. B., Sarker, M. H., Burgoyne, T., Campbell, M., Ockrim, Z. K., et al. (2014). Differential apicobasal VEGF signaling at vascular blood-neural barriers. *Dev. Cell* 30, 541–552. doi: 10.1016/j.devcel.2014.06.027

Iljin, K., Karkkainen, M. J., Lawrence, E. C., Kimak, M. A., Uutela, M., Taipale, J., et al. (2001). VEGFR3 gene structure, regulatory region, and sequence polymorphisms. *FASEB J.* 15, 1028–1036. doi: 10.1096/fj.00-0383com

Inai, T., Mancuso, M., Hashizume, H., Baffert, F., Haskell, A., Baluk, P., et al. (2004). Inhibition of vascular endothelial growth factor (VEGF) signaling in cancer causes loss of endothelial fenestrations, regression of tumor vessels, and appearance of basement membrane ghosts. *Am. J. Pathol.* 165, 35–52. doi: 10.1016/s0002-9440(10)63273-7

Ishrat, T., Soliman, S., Eldahshan, W., Pillai, B., Ergul, A., and Fagan, S. C. (2018). Silencing VEGF-B diminishes the neuroprotective effect of candesartan treatment after experimental focal cerebral ischemia. *Neurochem. Res.* 43, 1869–1878. doi: 10.1007/s11064-018-2604-x

Issa, R., Krupinski, J., Bujny, T., Kumar, S., Kaluza, J., and Kumar, P. (1999). Vascular endothelial growth factor and its receptor, KDR, in human brain tissue after ischemic stroke. *Lab. Invest.* 79, 417–425.

Jais, A., Solas, M., Backes, H., Chaurasia, B., Kleinridders, A., Theurich, S., et al. (2016). Myeloid-cell-derived VEGF maintains brain glucose uptake and limits cognitive impairment in obesity. *Cell* 165, 882–895. doi: 10.1016/j.cell.2016.03.033

Jean LeBlanc, N., Guruswamy, R., and ElAli, A. (2018). Vascular endothelial growth factor isoform-B stimulates neurovascular repair after ischemic stroke by promoting the function of pericytes via vascular endothelial growth factor receptor-1. *Mol. Neurobiol.* 55, 3611–3626. doi: 10.1007/s12035-017-0478-6

Kaya, D., Gürsoy-Ozdemir, Y., Yemisci, M., Tuncer, N., Aktan, S., and Dalkara, T. (2005). VEGF protects brain against focal ischemia without increasing blood–brain permeability when administered intracerebroventricularly. *J. Cereb. Blood Flow Metab.* 25, 1111–1118. doi: 10.1038/sj.jcbfm.9600109

Kim, E., Yang, J., Park, K. W., and Cho, S. (2018). Inhibition of VEGF signaling reduces diabetes-exacerbated brain swelling, but not infarct size, in large cerebral infarction in mice. *Transl. Stroke Res.* 9, 540–548. doi: 10.1007/s12975-017-0601-z

Krum, J. M., Mani, N., and Rosenstein, J. M. (2008). Roles of the endogenous VEGF receptors flt-1 and flk-1 in astroglial and vascular remodeling after brain injury. *Exp. Neurol.* 212, 108–117. doi: 10.1016/j.expneurol.2008.03.019

Lelli, A., Gervais, A., Colin, C., Chéret, C., Ruiz de Almodovar, C., Carmeliet, P., et al. (2013). The NADPH oxidase Nox2 regulates VEGFR1/CSF-1R-mediated microglial chemotaxis and promotes early postnatal infiltration of phagocytes in the subventricular zone of the mouse cerebral cortex. *Glia* 61, 1542–1555. doi: 10.1002/glia.22540

Leppänen, V.-M., Tvorogov, D., Kisko, K., Prota, A. E., Jeltsch, M., Anisimov, A., et al. (2013). Structural and mechanistic insights into VEGF receptor 3 ligand binding and activation. *Proc. Natl. Acad. Sci. U.S.A.* 110, 12960–12965. doi: 10.1073/pnas.1301415110

Li, Y., Zhang, F., Nagai, N., Tang, Z., Zhang, S., Scotney, P., et al. (2008). VEGF-B inhibits apoptosis via VEGFR-1-mediated suppression of the expression of BH3-only protein genes in mice and rats. *J. Clin. Invest.* 118, 913–923. doi: 10.1172/JCI33673

Longa, E. Z., Weinstein, P. R., Carlson, S., and Cummins, R. (1989). Reversible middle cerebral artery occlusion without craniectomy in rats. *Stroke* 20, 84–91. doi: 10.1161/01.str.20.1.84

Louveau, A., Smirnov, I., Keyes, T. J., Eccles, J. D., Rouhani, S. J., Peske, J. D., et al. (2015). Structural and functional features of central nervous system lymphatic vessels. *Nature* 523, 337–341. doi: 10.1038/nature14432

Luttun, A., Tjwa, M., and Carmeliet, P. (2002). Placental growth factor (PlGF) and its receptor Flt-1 (VEGFR-1): novel therapeutic targets for angiogenic disorders. *Ann. N. Y. Acad. Sci.* 979, 80–93. doi: 10.1111/j.1749-6632.2002.tb04870.x

Ma, Y., Zechariah, A., Qu, Y., and Hermann, D. M. (2012). Effects of vascular endothelial growth factor in ischemic stroke. *J. Neurosci. Res.* 90, 1873–1882. doi: 10.1002/jnr.23088

Marti, H. J. H., Bernaudin, M., Bellail, A., Schoch, H., Euler, M., Petit, E., et al. (2000). Hypoxia-induced vascular endothelial growth factor expression precedes neovascularization after cerebral ischemia. *Am. J. Pathol.* 156, 965–976. doi: 10.1016/s0002-9440(10)64964-4

Mattsson, B., Sørensen, J. C., Zimmer, J., and Johansson, B. B. (1997). Neural grafting to experimental neocortical infarcts improves behavioral outcome and reduces thalamic atrophy in rats housed in enriched but not in standard environments. *Stroke* 28, 1225–1231; discussion 1231–1232.

McCluskey, L., Campbell, S., Anthony, D., and Allan, S. M. (2008). Inflammatory responses in the rat brain in response to different methods of intra-cerebral administration. *J. Neuroimmunol.* 194, 27–33. doi: 10.1016/j.jneuroim.2007.11.009

Melton, D. W., McManus, L. M., Gelfond, J. A. L., and Shireman, P. K. (2015). Temporal phenotypic features distinguish polarized macrophages in vitro. *Autoimmunity* 48, 161–176. doi: 10.3109/08916934.2015.1027816

Meyer, R. D., Mohammadi, M., and Rahimi, N. (2006). A single amino acid substitution in the activation loop defines the decoy characteristic of VEGFR-1/FLT-1. *J. Biol. Chem.* 281, 867–875. doi: 10.1074/jbc.M506454200

Nikodemova, M., Small, A. L., Smith, S. M. C., Mitchell, G. S., and Watters, J. J. (2014). Spinal but not cortical microglia acquire an atypical phenotype with high VEGF, galectin-3 and osteopontin, and blunted inflammatory responses in ALS rats. *Neurobiol. Dis.* 69, 43–53. doi: 10.1016/j.nbd.2013.11.009

Olsson, A.-K., Dimberg, A., Kreuger, J., and Claesson-Welsh, L. (2006). VEGF receptor signalling? in control of vascular function. *Nat. Rev. Mol. Cell Biol.* 7, 359–371. doi: 10.1038/nrm1911

Park, J. E., Chen, H. H., Winer, J., Houck, K. A., and Ferrara, N. (1994). Placenta growth factor. Potentiation of vascular endothelial growth factor bioactivity, in vitro and in vivo, and high affinity binding to Flt-1 but not to Flk-1/KDR. *J. Biol. Chem.* 269, 25646–25654.

Paul, R., Zhang, Z. G., Eliceiri, B. P., Jiang, Q., Boccia, A. D., Zhang, R. L., et al. (2001). Src deficiency or blockade of Src activity in mice provides cerebral protection following stroke. *Nat. Med.* 7, 222–227. doi: 10.1038/84675

Plate, K. H., Beck, H., Danner, S., Allegrini, P. R., and Wiessner, C. (1999). Cell type specific upregulation of vascular endothelial growth factor in an MCA-occlusion model of cerebral infarct. *J. Neuropathol. Exp. Neurol.* 58, 654–666. doi: 10.1097/00005072-199906000-00010

Poesen, K., Lambrechts, D., Van Damme, P., Dhondt, J., Bender, F., Frank, N., et al. (2008). Novel role for vascular endothelial growth factor (VEGF) receptor-1 and its ligand VEGF-B in motor neuron degeneration. *J. Neurosci.* 28, 10451–10459. doi: 10.1523/JNEUROSCI.1092-08.2008

Rahimi, N. (2006). VEGFR-1 and VEGFR-2: two non-identical twins with a unique physiognomy. *Front. Biosci.* 11, 818–829.

Schallert, T., Fleming, S. M., Leasure, J. L., Tillerson, J. L., and Bland, S. T. (2000). CNS plasticity and assessment of forelimb sensorimotor outcome in unilateral rat models of stroke, cortical ablation, parkinsonism and spinal cord injury. *Neuropharmacology* 39, 777–787. doi: 10.1016/s0028-3908(00)00005-8

Schindelin, J., Arganda-Carreras, I., Frise, E., Kaynig, V., Longair, M., Pietzsch, T., et al. (2012). Fiji: an open-source platform for biological-image analysis. *Nat. Methods* 9, 676–682. doi: 10.1038/nmeth.2019

Shen, Y., Gu, J., Liu, Z., Xu, C., Qian, S., Zhang, X., et al. (2018). Inhibition of HIF-1α reduced blood brain barrier damage by regulating MMP-2 and VEGF during acute cerebral ischemia. *Front. Cell. Neurosci.* 12:288. doi: 10.3389/fncel.2018.00288

Shibuya, M. (2006). Vascular endothelial growth factor receptor-1 (VEGFR-1/Flt-1): a dual regulator for angiogenesis. *Angiogenesis* 9, 225–230; discussion 231.

Simons, M., Gordon, E., and Claesson-Welsh, L. (2016). Mechanisms and regulation of endothelial VEGF receptor signalling. *Nat. Rev. Mol. Cell Biol.* 17, 611–625. doi: 10.1038/nrm.2016.87

Stowe, A. M., Plautz, E. J., Eisner-Janowicz, I., Frost, S. B., Barbay, S., Zoubina, E. V., et al. (2007). VEGF protein associates to neurons in remote regions following cortical infarct. *J. Cereb. Blood Flow Metab.* 27, 76–85. doi: 10.1038/sj.jcbfm.9600320

Stowe, A. M., Plautz, E. J., Nguyen, P., Frost, S. B., Eisner-Janowicz, I., Barbay, S., et al. (2008). Neuronal HIF-1 alpha protein and VEGFR-2 immunoreactivity in functionally related motor areas following a focal M1 infarct. *J. Cereb. Blood Flow Metab.* 28, 612–620. doi: 10.1038/sj.jcbfm.9600560

Strawn, L. M., McMahon, G., App, H., Schreck, R., Kuchler, W. R., Longhi, M. P., et al. (1996). Flk-1 as a target for tumor growth inhibition. *Cancer Res.* 56, 3540–3545.

Sun, Y., Jin, K., Xie, L., Childs, J., Mao, X. O., Logvinova, A., et al. (2003). VEGF-induced neuroprotection, neurogenesis, and angiogenesis after focal cerebral ischemia. *J. Clin. Invest.* 111, 1843–1851. doi: 10.1172/JCI17977

Tovar-y-Romo, L. B., Bumpus, N. N., Pomerantz, D., Avery, L. B., Sacktor, N., McArthur, J. C., et al. (2012). Dendritic spine injury induced by the 8-hydroxy metabolite of efavirenz. *J. Pharmacol. Exp. Ther.* 343, 696–703. doi: 10.1124/jpet.112.195701

Tovar-y-Romo, L. B., Penagos-Puig, A., and Ramírez-Jarquín, J. O. (2016). Endogenous recovery after brain damage: molecular mechanisms that balance neuronal life/death fate. *J. Neurochem.* 136, 13–27. doi: 10.1111/jnc.13362

Tovar-y-Romo, L. B., and Tapia, R. (2012). Delayed administration of VEGF rescues spinal motor neurons from death with a short effective time frame in excitotoxic experimental models in vivo. *ASN Neuro* 4:e00081. doi: 10.1042/AN20110057

Ulyatt, C., Walker, J., and Ponnambalam, S. (2011). Hypoxia differentially regulates VEGFR1 and VEGFR2 levels and alters intracellular signaling and cell migration in endothelial cells. *Biochem. Biophys. Res. Commun.* 404, 774–779. doi: 10.1016/j.bbrc.2010.12.057

van Bruggen, N., Thibodeaux, H., Palmer, J. T., Lee, W. P., Fu, L., Cairns, B., et al. (1999). VEGF antagonism reduces edema formation and tissue damage after ischemia/reperfusion injury in the mouse brain. *J. Clin. Invest.* 104, 1613–1620. doi: 10.1172/JCI8218

Weis, S. M., and Cheresh, D. A. (2005). Pathophysiological consequences of VEGF-induced vascular permeability. *Nature* 437, 497–504. doi: 10.1038/nature03987

Wittko-Schneider, I. M., Schneider, F. T., and Plate, K. H. (2013). Brain homeostasis: VEGF receptor 1 and 2-two unequal brothers in mind. *Cell. Mol. Life Sci.* 70, 1705–1725. doi: 10.1007/s00018-013-1279-3

Worthmann, H., Tryc, A. B., Goldbecker, A., Ma, Y. T., Tountopoulou, A., Hahn, A., et al. (2010). The temporal profile of inflammatory markers and mediators in blood after acute ischemic stroke differs depending on stroke outcome. *Cerebrovasc. Dis.* 30, 85–92. doi: 10.1159/000314624

Wu, L., Ye, Z., Pan, Y., Li, X., Fu, X., Zhang, B., et al. (2018). Vascular endothelial growth factor aggravates cerebral ischemia and reperfusion-induced blood-brain-barrier disruption through regulating LOC102640519/HOXC13/ZO-1 signaling. *Exp. Cell Res.* 369, 275–283. doi: 10.1016/j.yexcr.2018.05.029

Xu, Z., Han, K., Chen, J., Wang, C., Dong, Y., Yu, M., et al. (2017). Vascular endothelial growth factor is neuroprotective against ischemic brain injury by inhibiting scavenger receptor A expression on microglia. *J. Neurochem.* 142, 700–709. doi: 10.1111/jnc.14108

Yang, S.-Z., Zhang, L.-M., Huang, Y.-L., and Sun, F.-Y. (2003). Distribution of Flk-1 and Flt-1 receptors in neonatal and adult rat brains. *Anat. Rec. A Discov. Mol. Cell. Evol. Biol.* 274, 851–856. doi: 10.1002/ar.a.10103

Zhang, H., Shen, Y., Wang, W., and Gao, H. (2015). Rat model of focal cerebral ischemia in the dominant hemisphere. *Int. J. Clin. Exp. Med.* 8, 504–511.

Zhang, Z. G., Zhang, L., Jiang, Q., Zhang, R., Davies, K., Powers, C., et al. (2000). VEGF enhances angiogenesis and promotes blood-brain barrier leakage in the ischemic brain. *J. Clin. Invest.* 106, 829–838. doi: 10.1172/JCI9369

Zhang, Z. G., Zhang, L., Tsang, W., Soltanian-Zadeh, H., Morris, D., Zhang, R., et al. (2002). Correlation of VEGF and angiopoietin expression with disruption of blood-brain barrier and angiogenesis after focal cerebral ischemia. *J. Cereb. Blood Flow Metab.* 22, 379–392. doi: 10.1097/00004647-200204000-00002

Conflict of Interest Statement: The authors declare that the research was conducted in the absence of any commercial or financial relationships that could be construed as a potential conflict of interest.

Copyright © 2019 Cárdenas-Rivera, Campero-Romero, Heras-Romero, Penagos-Puig, Rincón-Heredia and Tovar-y-Romo. This is an open-access article distributed under the terms of the Creative Commons Attribution License (CC BY). The use, distribution or reproduction in other forums is permitted, provided the original author(s) and the copyright owner(s) are credited and that the original publication in this journal is cited, in accordance with accepted academic practice. No use, distribution or reproduction is permitted which does not comply with these terms.

CHAPTER

12 The role of β-arrestins in G protein-coupled receptor heterologous desensitization: A brief story

Gabriel Carmona-Rosas[1], **Rocío Alcántara-Hernández, David Alejandro Hernández-Espinosa**

Instituto de Fisiologia Celular (UNAM), Mexico City, Mexico

[1]*Corresponding author: e-mail address: gcarmona@email.ifc.unam.mx*

CHAPTER OUTLINE

1 Introduction....196

2 The Formation of GPCR/β-Arrestin Complexes During the Homologous and Heterologous Desensitization Processes....196

2.1 The Role of β-Arrestins in GPCR Regulation....197

3 The Role of β-Arrestins in Heterologous Desensitization: Describing a Few Number of Studies....199

4 Coda/Future Directions....200

Acknowledgments....201

Author Contributions....201

Conflicts of Interest....201

References....201

Further Reading....204

Abstract

G protein-coupled receptors (GPCRs) are transmembrane proteins that have an important impact in a myriad of cellular functions. Posttranslational modifications on GPCRs are a key processes that allow these proteins to recruit other intracellular molecules. Among these modifications, phosphorylation is the most important way of desensitization of these receptors. Several research groups have described two different desensitization mechanisms: heterologous and homologous desensitization. The first one involves the phosphorylation of the receptors by protein kinases, such as PKC, following the desensitization and internalization of the receptor, while the second one involves the phosphorylation of the receptors by GRKs, allowing for the receptor to recruit β-arrestins to be desensitized and internalized.

Methods in Cell Biology, Volume 149, ISSN 0091-679X, https://doi.org/10.1016/bs.mcb.2018.08.004

© 2019 Elsevier Inc. All rights reserved.

Interestingly, a few number of studies have described the participation of β-arrestins during the heterologous desensitization process. Hence, the aim of this review is to briefly explore the role that β-arrestins play during the heterologous desensitization of several GPCRs.

1 INTRODUCTION

G protein-coupled receptors (GPCRs) have an important impact in a great variety of cellular processes (Bockaert & Pin, 1999; Kumari, Gosh, & Shukla, 2015; Miao & McCammon, 2016). The superfamily of GPCRs involves almost 1000 members that are encoded by the genome (Ikeda, Sugihara, & Suwa, 2018; Santos et al., 2017), and they are well known to be the target of almost 20–40% of the current therapeutic drugs in the market (Celebiro & Godbole, 2018; Insel et al., 2018; Smith, Lefkowitz, & Rajagopal, 2018). Currently, almost 30 GPCRs have been crystalized, allowing not only for a high resolution view of the receptor in order to design more specific drugs with less side effects (Grisshammer, 2017; Kruse, Manglik, Kobilka, & Weis, 2013; Stauch & Cherezov, 2018) but also to elucidate the residues and the intracellular domains that are responsible for the binding to other intracellular proteins (Deupi, 2014; Kang et al., 2015; Lu & Wu, 2016). One of the molecules that are known to bind GPCRs after being phosphorylated, is β-arrestins. These proteins were originally discovered due to their ability to desensitize and internalize several activated GPCRs during homologous desensitization (Carmona-Rosas, Alcantara-Hernandez, & Hernandez-Espinoza, 2018), however, recent studies have demonstrated that β-arrestins are also able to desensitize and internalize receptors during heterologous desensitization (Shi et al., 2017; Zhang & Kim, 2017). This means that the recruitment of β-arrestins to a GPCR may occur when the receptor is phosphorylated both in ligand-dependent and -independent fashions (Bohn, Lefkowitz, & Caron, 2002; Chaturvedi et al., 2018; Ranjan, Dwivedi, Baidya, Kumar, & Shukla, 2017). In addition to this, we recently described that β-arrestins are important scaffold proteins that need to be recruited to a receptor in order to form the multi-protein complex GPCR/β-arrestin/ERK1/2, which is able to activate different downstream signaling pathways (Carmona-Rosas et al., 2018). We do not pretend to present a vast analysis of the few studies that reported the recruitment of β-arrestins to the receptor during the heterologous desensitization process, but rather, describing the key elements of such interaction and the subsequent signaling pathways that are activated.

2 THE FORMATION OF GPCR/β-ARRESTIN COMPLEXES DURING THE HOMOLOGOUS AND HETEROLOGOUS DESENSITIZATION PROCESSES

GPCR desensitization is understood as a decrease in the coupling between the phosphorylated receptor and the G proteins. This process allows for the receptor to be internalized through the endocytic machinery, resulting in an important decline of

the receptor response (Magalhaes, Dunn, & Ferguson, 2012). Currently, there are two main types of desensitization: (1) homologous desensitization, which is the result of the activation of the receptor by a ligand and the phosphorylation of the receptor intracellular domains, by G protein-coupled receptor kinases (GRKs), hence, resulting in the internalization of the receptor by their coupling to β-arrestin proteins (Shenoy & Lefkowitz, 2011). The latter proteins were described as scaffold elements that the GPCRs employ to amplify their signaling pathways and to be internalized into clathrin-coated pits (Delom & Fessart, 2011; Irannejad et al., 2013; Puthenveddu & Von Zastrow, 2006) and (2) heterologous desensitization, which is a ligand-independent process where the receptor is phosphorylated in its intracellular domains by second messenger-dependent protein kinases, such as protein kinase A (PKA) or protein kinase C (PKC) (Benovic et al., 1985).

Understanding the interaction between the homologous and heterologous desensitization of GPCRs is currently an important field of study. Several reports have related GRK2 and β-arrestins with the PKA/PKC-mediated regulatory pathway. For example, the activated GRK2 is able to bind PKCβ through its pleckstrin homology domain, resulting in the inhibition of PKC. In addition, β-arrestins are able to inhibit the PKC-mediated regulatory pathways through the recruitment and activation of the diacylglycerol (DAG) kinase, which subsequently regulates the conversion of DAG into phosphatidic acid (PA). Besides, it has been reported that β-arrestins can recruit cAMP phosphodiesterases to ligand-activated receptors, promoting the degradation of cAMP, and inhibiting the activation of PKC (Fig. 1A) (Zhang & Kim, 2017).

2.1 THE ROLE OF β-ARRESTINS IN GPCR REGULATION

Even though β-arrestins are known to hinder the binding of the receptor with the G protein, different studies have reported that the conformation of the supercomplex GPCR-β-arrestin–G protein exists, which allows the receptor to keep signaling in a β-arrestin- and G protein-dependent fashion while internalized. It is important to mention that the formation of this multi-protein complex is particular of class B receptors, which have a great number of serine and threonine residues in the C-terminal tail, enabling the recruitment of β-arrestins (Thomsen et al., 2016). On the other hand, class A receptors are known to have less phosphorylated residues in the C-terminal tail, which impairs the binding of β-arrestins to the receptors. In addition, class B receptors may undergo homologous and heterologous desensitization, being the phosphorylation of the receptor the main signal that allows the binding of β-arrestins and the subsequent internalization and trafficking of the receptors (Oakley, Laporte, Holt, Caron, & Barak, 2000). This process has been demonstrated with several GPCRs, in particular with the β2-adrenergic receptor, (β2-AR), a class A receptor, where the addition of phosphoacceptor residues in the C-terminal tail, improves the binding of β-arrestin 2 to the receptor (Zindel et al., 2015). The participation of β-arrestins in the regulation of GPCRs is a key process that allows for the regulation of these receptors and the activation of different signaling

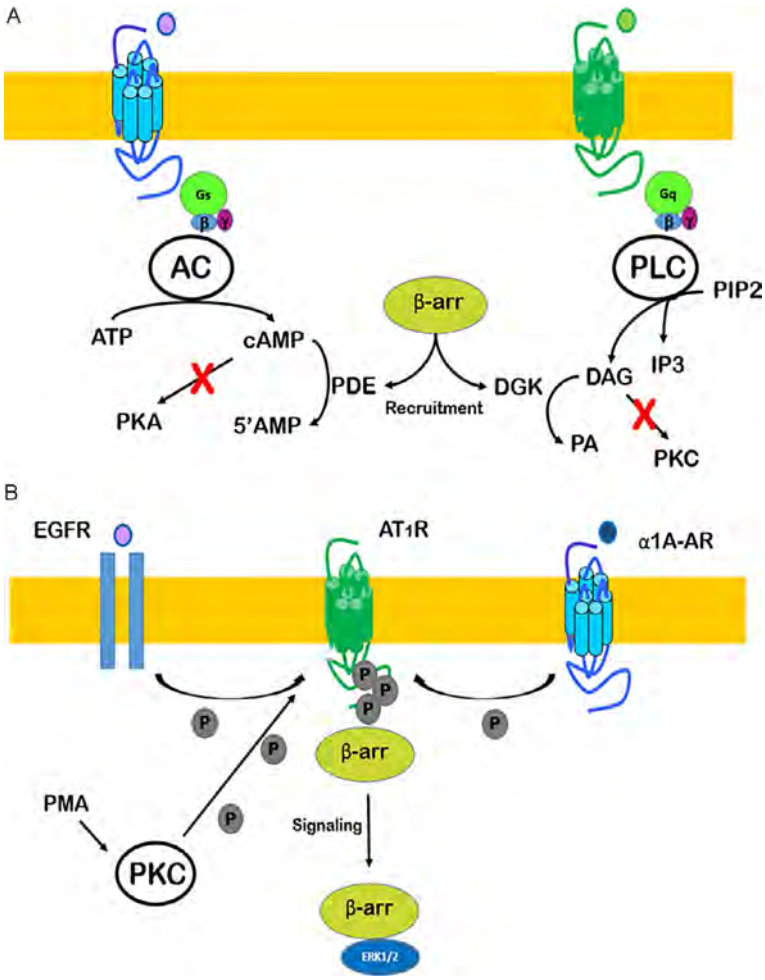

FIG. 1

Schematic representations of the putative roles of β-arrestins during GPCR heterologous desensitization. (A) β-Arrestins are able to inhibit the PKC-mediated signaling pathways through the activation of the diacylglycerol (DAG) kinase, which is responsible for the conversion of DAG into phosphatidic acid (PA), hence, decreasing the activity of PKC. In addition, β-arrestins are able to activate and recruit cAMP phosphodiesterases to ligand-activated receptors, fostering the degradation of cAMP, and inhibiting the activity of PKC. (B) The recruitment of β-arrestin 2 to the unstimulated angiotensin 1 receptor (AT1) is regulated by the activation of PKC, the α1A-adrenergic receptor (α1A-AR), and the epidermal growth factor receptor (EGFR), which in turn, promotes the phosphorylation of the AT1 receptor and the recruitment of β-arrestin 2.

pathways, such as the MAPK cascade (Carmona-Rosas et al., 2018). Interestingly, a few number of studies have reported the participation of these scaffold proteins during the heterologous desensitization of several GPCRs, opening a new way of studying the regulation of these transmembrane proteins.

3 THE ROLE OF β-ARRESTINS IN HETEROLOGOUS DESENSITIZATION: DESCRIBING A FEW NUMBER OF STUDIES

During the last years, several studies have reported the participation of β-arrestins during the homologous desensitization. However, little is known about the role that these proteins play during the heterologous desensitization process. Our research group recently reported that the activation of the sphingosine-1-phosphate receptor (S1P) allows for the binding of β-arrestin 2 to the α1B-adrenergic receptor (α1B-AR) (Castillo-Badillo et al., 2015). In addition, we also reported that the phosphorylation of the α1A-adrenergic receptor (α1A-AR) by PKC induces the binding of endogenous β-arrestin 1/2 to the receptor. These results were further confirmed by coimmunoprecipitation assays of the α1A-AR and the endogenous β-arrestins 1/2 (Alcántara-Hernández et al., 2017). Along the same lines, it has been reported that the activation of some GPCRs coupled to the G_s and G_q proteins promotes the phosphorylation of cardiac β2-AR by PKA and PKC. This process allows for the binding of the phosphodiesterase 4D (PDE4D) to the phosphorylated receptor in a β-arrestin-dependent manner. Subsequently, the PDE4D will have the role of hydrolyzing the cAMP generated by the activation of the β2-AR.

Another study reported that in neurons from the locus curelous, the brief stimulation of the μ-opioid receptor with Met^5-enkephalin, causes its homologous desensitization, however, longer times of stimulation produces the heterologous desensitization of the α2-adrenergic receptors (α2-ARs). Such heterologous process is regulated by β-arrestin 2 and the activation of ERK1/2. Interestingly, the inhibition in the expression of β-arrestin 2 does not have an effect in the internalization of the μ-opioid receptor, but does have an impact in the heterologous desensitization of the α2-ARs (Dang, Chieng, & Christie, 2012). This interesting study suggests that the recruitment of β-arrestin to the α2-ARs by heterologous desensitization, enables the formation of a multi-protein complex that involves the α2-ARs, β-arrestin 2, and ERK1/2. Disruption at any protein level inhibits the assemble of such complex. In addition, the activation of the neuropeptide FF2 receptor was sufficient to recruit β-arrestin 2 to the μ-opioid receptor, but not to induce its internalization. Besides, this recruitment of β-arrestin is the result of the phosphorylation of the receptor at serine 377 by GRK2, but not by PKA or PKC as would be expected in a heterologous desensitization model (Mouledous et al., 2012). Along the same lines, the phosphorylation of the δ-opioid receptor at serine 344 by PKC leads to the heterologous desensitization of this receptor, which is also regulated by the recruitment of β-arrestins and the internalization of the receptor into clathrin-coated vesicles (Xiang et al., 2001).

Interestingly, another study reported the participation of PKC in the phosphorylation and internalization of the dopamine 2 receptor (D2). In such study, it was described that the pharmacological activation of PKC induces the phosphorylation of multiple sites within two main domains in the C-terminal tail of the D2 receptor, resulting in the recruitment of β-arrestins and the desensitization and internalization of the receptor (Namkung & Sibley, 2004). Similarly, this was not the only study that related the activation of PKC with the phosphorylation and subsequent internalization of the D2 receptor. The activation of the neurotensin receptor 1 (NT1R) leads to the PKC-mediated phosphorylation of the D2 receptor, triggering the recruitment of β-arrestin 1, and the uncoupling of the receptor with the G protein (Thibault, Albert, Pineyro, & Trudeau, 2011).

Recently, it was also described that the activation of PKC, $G_{q/11}$ GPCRs, and epidermal growth factor receptor (EGFR), promotes the recruitment of β-arrestin 2 to the unstimulated angiotensin 1 receptor AT1 (Fig. 1B). This process enables for the formation of a stability lock, which depends on the phosphorylated residues located in the C-terminal tail of the receptor and two conserved phospho-binding lysines in the β-arrestin 2 N-terminal domain. This process also promotes the activation of the MAPK pathway, which depends on the internalization of the receptor by β-arrestin 2. This study suggests that the solely phosphorylation of the receptor is sufficient to recruit and activate β-arrestins, which may serve as a novel mechanism of β-arrestin activation (Toth et al., 2018).

Finally, it has been described that chronic insulin treatment of Rat1 fibroblast leads to the downregulation of β-arrestin 1 through ubiquitination and proteosomal degradation, which is associated with a decrease in insulin growth factor receptor I (IGF-I), lysophosphatidic acid (LPA), and β2-AR stimulation of the MAP kinase pathway. This deficit in the activation of such kinases was restored by the expression of exogenous wild-type β-arrestin 1 in insulin-treated cells. This suggests that the insulin-induced decrease in β-arrestin 1 plays a role in the activation of the MAP kinase signaling pathway triggered by some GPCRs (Dalle et al., 2002).

4 CODA/FUTURE DIRECTIONS

The regulation of GPCRs by β-arrestins is a process that has been extensively described for many research groups. It has been proposed that several receptors have a particular phosphorylation bar code, which allows the receptors to bind β-arrestins and use this interaction to activate other signaling pathways (Zhou et al., 2017). Even though this interaction has been characterized in homologous desensitization models, little is known about such interaction during the heterologous desensitization process. Efforts have to be done in order to further understand this cellular process. Additionally, it would be of great interest to explore the heterologous desensitization of other RTKs and their binding to β-arrestin 1/2, which could open the possibility to design new drugs with less side effects.

ACKNOWLEDGMENTS

The authors thank Dr. J. Adolfo García-Sáinz (Instituto de Fisiologia Celular) for suggestions and comments in the manuscript.

AUTHOR CONTRIBUTIONS

The draft of this review was initially conceived by G.C.-R. and was jointly written by G.C.-R., R.A.-H., and D.A.H.E.. G.C.-R. is a student of the Programa de Doctorado en Ciencias Biomédicas-UNAM and a recipient of a fellowship from Consejo Nacional de Ciencia y Tecnología (CONACyT).

CONFLICTS OF INTEREST

The authors declare no conflict of interest.

REFERENCES

Alcántara-Hernández, R., Hernández-Méndez, A., Romero-Avila, M. T., Alfonzo-Méndez, M. A., Pupo, A. S., & García-Sainz, J. A. (2017). Noradrenaline, oxymetazoline and phorbol myristate acetate induce distinct functional actions and phosphorylation patterns of α_{1A}-adrenergic receptors. *Biochimica et Biophysica Acta (BBA)—Molecular Cell Research*, *1864*(12), 2378–2388. https://doi.org/10.1016/j.bbamcr.2017.09.002.

Benovic, J. L., Pike, L. J., Cerione, R. A., Staniszewski, C., Yoshimasa, T., Codina, J., et al. (1985). Phosphorylation of the mammalian beta-adrenergic receptor by cyclic AMP-dependent protein kinase. Regulation of the rate of receptor phosphorylation and dephosphorylation by agonist occupancy and effects on coupling of the receptor to the stimulatory guanine nucleotide regulatory protein. *The Journal of Biological Chemistry*, *260*(11), 7094–7101.

Bockaert, J., & Pin, J. P. (1999). Molecular tinkering of G protein coupled receptors: An evolutionary success. *The EMBO Journal*, *18*(7), 1723–1729. https://doi.org/10.1093/emboj/18.7.1723.

Bohn, L. M., Lefkowitz, R. J., & Caron, M. G. (2002). Differential mechanisms of morphine antinociceptive tolerance revealed in (beta)-arrestin-2 knock-out mice. *Journal of Neuroscience*, *22*(23), 10494–10500. https://doi.org/10.1523/JNEUROSCI.22-23-10494.2002.

Carmona-Rosas, G., Alcantara-Hernandez, R., & Hernandez-Espinoza, D. A. (2018). Dissecting the signaling features of the multi-protein complex GPCR/β-arrestin/ERK1/2. *European Journal of Cell Biology*. https://doi.org/10.1016/j.ejcb.2018.04.001. Epub ahead of print.

Castillo-Badillo, J. A., Sánchez-Reyes, O. B., Alfonzo-Méndez, M. A., Romero-Ávila, M. T., Reyes-Cruz, G., & García-Sainz, J. A. (2015). α1B-adrenergic receptors differentially associate with Rab proteins during homologous and heterologous desensitization. *PLoS One*, *10*(3), 1–27. https://doi.org/10.1371/journal.pone.0121165.

Celebiro, D., & Godbole, A. (2018). Internalization of G-protein-coupled receptors: Implication in receptor function, physiology and diseases. *Best Practice & Research Clinical Endocrinology & Metabolism*, *32*(2), 83–91. https://doi.org/10.1016/j.beem.2018.01.004.

Chaturvedi, M., Schilling, J., Beautrait, A., Bouvier, M., Benovic, J. L., & Shukla, A. K. (2018). Emerging paradigm of intracellular targeting of G protein-coupled receptors. *Trends in Biochemical Sciences*, *43*(7), 533–546. https://doi.org/10.1016/j.tibs.2018.04.003.

Dalle, S., Imamura, T., Rose, D. W., Worrall, D. S., Ugi, S., Hupfeld, C. J., et al. (2002). Insulin induces heterologous desensitization of G-protein-coupled receptor and insulin-like growth factor I signaling by downregulating beta-arrestin-1. *Molecular and Cell Biology*, *22*(17), 6272–6285. https://doi.org/10.1128/MCB.22.17.6272-6285.2002.

Dang, V. C., Chieng, B. C., & Christie, M. J. (2012). Prolonged stimulation of μ-opioid receptors produces β-arrestin-2-mediated heterologous desensitization of α2-adrenoceptor function in locus ceruleus neurons. *Molecular Pharmacology*, *82*(3), 473–480. https://doi.org/10.1124/mol.112.079350.

Delom, F., & Fessart, D. (2011). Role of phosphorylation in the control of clathrin-mediated internalization of GPCR. *International Journal of Cell Biology, 2011*, 246954. https://doi.org/10.1155/2011/246954.

Deupi, X. (2014). Relevance of rhodopsin studies for GPCR activation. *Biochimica et Biophysica Acta (BBA)—Bioenergetics*, *1837*(5), 674–682. https://doi.org/10.1016/j.bbabio.2013.09.002.

Grisshammer, R. (2017). New approaches towards the understanding of integral membrane proteins: A structural perspective on G protein-coupled receptors. *Protein Science*, *26*(8), 1493–1504. https://doi.org/10.1002/pro.3200.

Ikeda, M., Sugihara, M., & Suwa, M. (2018). SEVENS: A datebase for comprenhesive GPCR genes obtained from genomes: Update to 68 eukaryotes. *Byophysics and Physicobiology*, *15*, 104–110. https://doi.org/10.2142/biophysico.15.0_104.

Insel, P. A., Sriam, K., Wiley, S. Z., Wilderman, A., Katakia, T., McCann, T., et al. (2018). GPCRomics: GPCR expression in cancer cells and tumors identifies new, potential biomarkers and therapeutic targets. *Frontiers in Pharmacology*, *9*, 431–475. https://doi.org/10.3389/fphar.2018.00431.

Irannejad, R., Tomshine, J. C., Tomshine, J. R., Chevalier, M., Mahoney, J. P., Steyaert, J., et al. (2013). Conformational biosensors reveal GPCR signaling from endosomes. *Nature*, *495*(7442), 534–538. https://doi.org/10.1038/nature12000.

Kang, Y., Zhou, X. E., Gao, X., He, Y., Liu, W., Ishchenko, A., et al. (2015). Crystal structure of rhodopsin bound to arrestin by femtosecond X-ray laser. *Nature*, *523*(7562), 561–567. https://doi.org/10.1038/nature14656.

Kruse, A. C., Manglik, A., Kobilka, B. K., & Weis, W. I. (2013). Applications of molecular replacement to G protein-coupled receptors. *Acta Crystals*, *69*(Pt 11), 2287–2292. https://doi.org/10.1107/S090744491301322X.

Kumari, P., Gosh, E., & Shukla, A. K. (2015). Emerging approaches to GPCR ligand screening for drug discovery. *Trends Molecular Medicine*, *21*(11), 687–701. https://doi.org/10.1016/j.molmed.2015.09.002.

Lu, M., & Wu, B. (2016). Structural studies of G protein-coupled receptors. *IUBMB Lifestyles*, *68*(11), 894–903. https://doi.org/10.1002/iub.1578.

Magalhaes, A. C., Dunn, H., & Ferguson, S. S. (2012). Regulation of GPCR activity, trafficking and localization by GPCR-interacting proteins. *British Journal de Pharmacologie*, *165*(6), 1717–1736. https://doi.org/10.1111/j.1476-5381.2011.01552.x.

Miao, Y., & McCammon, J. A. (2016). G-protein coupled receptors: advances in simulation and drug discovery. *Current Opinion in Structural Biology*, *41*, 83–89. https://doi.org/10.1016/j.sbi.2016.06.008.

Mouledous, L., Froment, C., Dauvillier, S., Burlet-Schitlz, O., Zajac, J. M., & Mollereau, C. (2012). GRK2 protein-mediated transphosphorylation contributes to loss of function of μ-opioid receptors induced by neuropeptide FF (NPFF2) receptors. *Journal of Biological Chemistry*, *287*(16), 12736–12749. https://doi.org/10.1074/jbc.M111.314617.

Namkung, Y., & Sibley, D. R. (2004). Protein kinase C mediates phosphorylation, desensitization, and trafficking of the D2 dopamine receptor. *Journal of Biological Chemistry*, *279*(47), 49533–49541. https://doi.org/10.1074/jbc.M408319200.

Oakley, R. H., Laporte, S. A., Holt, J. A., Caron, M. G., & Barak, L. S. (2000). Differential affinities of visual arrestin, beta arrestin1, and beta arrestin2 for G protein-coupled receptors delineate two major classes of receptors. *Journal of Biological Chemistry*, *275*(22), 17201–17210. https://doi.org/10.1074/jbc.M910348199.

Puthenveddu, M. A., & Von Zastrow, M. (2006). Cargo regulates clethrin-coated pit dynamics. *Cell*, *127*(1), 113124. https://doi.org/10.1016/j.cell.2006.08.035.

Ranjan, R., Dwivedi, H., Baidya, M., Kumar, M., & Shukla, A. K. (2017). Novel structural insights into GPCR–β-arrestin interaction and signaling. *Trends in Cell Biology*, *27*(11), 851–862. https://doi.org/10.1016/j.tcb.2017.05.008.

Santos, R., Ursu, O., Gaulton, A., Bento, A. P., Donadi, R. S., Bologa, C. G., et al. (2017). A comprehensive map of molecular drug targets. *Nature Reviews Drug Discovery*, *16*(1), 19–34. https://doi.org/10.1038/nrd.2016.230.

Shenoy, S. K., & Lefkowitz, R. J. (2011). β-arrestin-mediated receptor trafficking and signal transduction. *Trends in Pharmacological Science*, *32*(9), 5214–5233. https://doi.org/10.1016/j.tips.2011.05.002.

Shi, Q., Li, M., Mika, D., Fu, Q., Kim, S., Phan, J., et al. (2017). Heterologous desensitization of cardiac β-adrenergic signal via hormone-induced βAR/arrestin/PDE4 complexes. *113*(6), 656–670. https://doi.org/10.1093/cvr/cvx036.

Smith, J. S., Lefkowitz, R. J., & Rajagopal, S. (2018). Biased signaling: from simple switches to allosteric microprocessors. *Nature Reviews Drug Discovery*, *17*, 243–260. https://doi.org/10.1038/nrd.2017.229.

Stauch, B., & Cherezov, V. (2018). Serial femtosecond crystallography of G protein-coupled receptors. *Annual Review of Biophysics*, *47*, 377–397. https://doi.org/10.1146/annurev-biophys-070317-033239.

Thibault, D., Albert, P. R., Pineyro, G., & Trudeau, L. E. (2011). Neurotensin triggers dopamine D2 receptor desensitization through a protein kinase C and beta-arrestin1-dependent mechanism. *Annual Review of Biophysics*, *286*(1), 9174–9187. https://doi.org/10.1074/jbc.M110.166454.

Thomsen, A. R. B., Plouffe, B., Cahill, T. J., 3rd., Shukla, A. K., Tarrasch, J. T., Dosey, A. M., et al. (2016). GPCR-G protein-β-arrestin super-complex mediates sustained G protein signaling. *Cell*, *166*(4), 907–919. https://doi.org/10.1016/j.cell.2016.07.004.

Toth, A. D., Prokop, S., Gyombolai, P., Varnai, P., Balla, A., Gurevich, V. V., et al. (2018). Heterologous phosphorylation-induced formation of a stability lock permits regulation of inactive receptors by β-arrestins. *The Journal of Biological Chemistry*, *293*(3), 876–892. https://doi.org/10.1074/jbc.M117.813139.

Xiang, B., Yu, G. H., Guo, L., Chen, L., Hu, W., Pei, G., et al. (2001). Heterologous activation of protein kinase C stimulates phosphorylation of delta-opioid receptor at serine 344, resulting in beta-arrestin- and clathrin-mediated receptor internalization. *The Journal of Biological Chemistry*, *247*(7), 4709–4716. https://doi.org/10.1074/jbc.M006187200.

Zhang, Z., & Kim, K.-M. (2017). Multifactorial regulation of G protein-coupled receptor endocytosis. *Biomolecules Therapeutics*, *25*(1), 26–43. https://doi.org/10.4062/biomolther.2016.186.

Zhou, X. E., He, Y., de Waal, P. W., Gao, X., Kang, Y., Van Eps, N., et al. (2017). Identification of phosphorylation codes for arrestin recruitment by G protein-coupled receptors. *Cell*, *170*(3), 457–469. https://doi.org/10.1016/j.cell.2017.07.002.

Zindel, D., Butcher, A. J., Al-Sabah, S., Lanzerstorfer, P., Weghuber, J., Tobin, A. B., et al. (2015). Engineered hyperphosphorylation of the β2-adrenoceptor prolongs arrestin-3 binding and induces arrestin internalization. *Molecular Pharmacology*, *87*(2), 349–362. https://doi.org/10.1124/mol.114.095422.

FURTHER READING

Bjarnadottir, T. K., Gloriam, D. E., Hellstrand, S. H., Kristiansson, H., Fredriksson, R., & Schioth, H. B. (2006). Comprehensive repertoire and phylogenetic analysis of the G protein-coupled receptors in human and mouse. *Genomics*, *88*(3), 263–273. https://doi.org/10.1016/j.ygeno.2006.04.001.

Gurevich, E. V., Uversky, E. V., & V. N. (2018). Arrestins: Structural disorder creates rich functionality. *Protein Cell*. https://doi.org/10.1007/s13238-017-0501-8. Epub ahead of print.

Yu, J., Arttamangkul, S., Evans, C. J., Williams, J., & von Zastrow, M. (2009). Neurokinin1 receptors regulate morphine-induced endocytosis and desensitization of mu opioid receptors in CNS neurons. *Journal of Neuroscience*, *29*(1), 222–233. https://doi.org/10.1523/JNEUROSCI.4315-08.2009.

INFORME DE LABORES 2019

Cellular Signalling 53 (2019) 374–389

Contents lists available at ScienceDirect

Cellular Signalling

journal homepage: www.elsevier.com/locate/cellsig

Distinct phosphorylation sites/clusters in the carboxyl terminus regulate α_{1D}-adrenergic receptor subcellular localization and signaling

Gabriel Carmona-Rosas, David A. Hernández-Espinosa, Rocío Alcántara-Hernández, Marco A. Alfonzo-Méndez[1], J. Adolfo García-Sainz*

Departamento de Biología Celular y Desarrollo, Instituto de Fisiología Celular, Universidad Nacional Autónoma de México, Ap. Postal 70-248, Ciudad de México 04510, Mexico

ARTICLE INFO

Keywords:
α_{1D}-adrenergic receptor phosphorylation
α_{1D}-adrenergic receptor
Receptor phosphorylation
Membrane localization
Phosphorylation clusters

ABSTRACT

The human α_{1D}-adrenergic receptor is a seven transmembrane-domain protein that mediates many of the physiological actions of adrenaline and noradrenaline and participates in the development of hypertension and benign prostatic hyperplasia. We recently reported that different phosphorylation patterns control α_{1D}-adrenergic receptor desensitization. However, to our knowledge, there is no data regarding the role(s) of this receptor's specific phosphorylation residues in its subcellular localization and signaling. In order to address this issue, we mutated the identified phosphorylated residues located on the third intracellular loop and carboxyl tail. In this way, we experimentally confirmed α_{1D}-AR phosphorylation sites and identified, in the carboxyl tail, two groups of residues in close proximity to each other, as well as two individual residues in the proximal (T442) and distal (S543) regions. Our results indicate that phosphorylation of the distal cluster (T507, S515, S516 and S518) favors α_{1D}-AR localization at the plasma membrane, i. e., substitution of these residues for non-phosphorylatable amino acids results in the intracellular localization of the receptors, whereas phospho-mimetic substitution allows plasma membrane localization. Moreover, we found that T442 phosphorylation is necessary for agonist- and phorbol ester-induced receptor colocalization with β-arrestins. Additionally, we observed that substitution of intracellular loop 3 phosphorylation sites for non-phosphorylatable amino acids resulted in sustained ERK1/2 activation; additional mutations in the phosphorylated residues in the carboxyl tail did not alter this pattern. In contrast, mobilization of intracellular calcium and receptor internalization appear to be controlled by the phosphorylation of both third-intracellular-loop and carboxyl terminus-domain residues. In summary, our data indicate that a) both the phosphorylation sites present in the third intracellular loop and in the carboxyl terminus participate in triggering calcium signaling and in turning-off α_{1D}-AR-induced ERK activation; b) phosphorylation of the distal cluster appears to play a role in receptor's plasma membrane localization; and c) T442 appears to play a critical role in receptor phosphorylation and receptor-β-arrestin colocalization.

1. Introduction

G protein-coupled receptors (GPCRs) are the most abundant class of sensors of the external (light, odors, tastants) and the internal (hormone, neurotransmitters, autacoids) mileaux [1]. These receptors participate in essentially all key physiological processes and are involved in the development of many diseases, making them the target of 20–40% of current therapeutic drugs on the market [2,3]. Among the GPCR family are the adrenergic receptors. These receptors have been classified into α_1-, α_2-, and β-adrenergic subfamilies on the basis of their structure and signaling; each subfamily is formed by three members [4]. In turn, the α_1-adrenergic receptors (α_1-ARs) are composed of the α_{1A}-, α_{1B}- and α_{1D}- subtypes; the latter receptor was the subject of the present work.

As are all the members of the GPCR family, α_{1D}-ARs are constituted of seven membrane-spanning domains connected by three extracellular and three intracellular loops, an extracellular amino terminus, and an intracellular carboxyl tail (CTail) [4]. α_{1D}-ARs have some unique features that have made their study very challenging. For example, α_{1D}-ARs have been difficult to detect in many tissues [5] and, when overexpressed, they have a low level of expression at the plasma membrane, being mainly localized in intracellular vesicles [6–9]. Additionally, α_{1D}-

* Corresponding author at: Inst. Fisiología Celular, UNAM, Ap. Postal 70-248, Ciudad de México 04510, Mexico.
E-mail address: agarcia@ifc.unam.mx (J.A. García-Sainz).
[1] Present Address: Laboratory of Molecular Biophysics, National Heart, Lung, and Blood Institute, NIH, Bethesda, MD 20892, USA.

https://doi.org/10.1016/j.cellsig.2018.11.003
Received 20 September 2018; Received in revised form 8 November 2018; Accepted 8 November 2018
Available online 09 November 2018
0898-6568/ © 2018 Elsevier Inc. All rights reserved.

INFORME DE LABORES 2019

ARs have constitutive activity with physiological and pathophysiological relevance; in particular this receptor subtype appears to be involved in the regulation of tissue perfusion and the control of blood pressure, and in the pathogenesis of hypertension [10–20]. Deletion of the first α_{1D}-AR 79 amino acids increases its localization at the plasma membrane [7,8,21–24]. Interestingly, cleavage in the amino terminus occurs endogenously in human cell lines, which suggests that this could be a physiological mechanism employed by cells to generate functional α_{1D}-ARs localized at the plasma membrane [25]. Once at the plasma membrane, α_{1D}-ARs appear to have a conserved mechanism of action: agonist binding to the receptor's extracellular region induces transmembrane conformational changes, which trigger intracellular $G_{q/11}$ -receptor interactions. This activates phosphatidylinositol 4, 5 bisphosphate hydrolysis by PLC-β, generating inositol 1, 4, 5-trisphosphate and diacylglycerol. Inositol trisphosphate causes the release of calcium from intracellular stores, while diacylglycerol is able to activate protein kinase C (PKC) and together these mediators intracellularly propagate the signal. Sustained α_{1D}-AR stimulation triggers the binding of G protein-coupled receptor kinases (GRKs) and the phosphorylation of α_{1D}-ARs third intracellular loops and carboxyl tails, which reduces responsiveness through a mechanism known as homologous desensitization [22–24,26,27]. Additionally, PKC activation induces α_{1D}-AR phosphorylation and reduces responsiveness, a process known as heterologous desensitization [22–24,26,27]. During the former processes, the scaffold protein, β-arrestin, seems to associate with the receptor-signaling complex, favoring the action of the endocytic machinery, receptor internalization, and putatively switching from G protein-mediated to β-arrestin-mediated signaling [28–33].

As compared to other members of the α_1- subfamily, α_{1D}-AR regulatory mechanisms remain poorly characterized. It is known that agonists, such as noradrenaline (NA), and pharmacological activation of PKC by phorbol 12-myristate 13-acetate (PMA) induce phosphorylation and desensitization of α_{1D}-ARs [10,22,26,27]. Using mass spectrometry analysis, our group recently reported distinct α_{1D}-AR phosphorylation patterns in response to NA or PMA [22]; the data suggested possible roles of GRK2 and conventional PKC isoforms α and β in phosphorylations associated with α_{1D}-AR homologous and heterologous desensitization. Six phosphorylated residues in the α_{1D}-AR third intracellular loop (IL3) and nine in the CTail were detected consistently and with high probability [22]. This large number of phosphorylation sites and their location in different receptor domains complicate the experimental analysis of their functional relevance. Hence, the aim of the present work was to further explore the role of some of these residues in α_{1D}-AR function. In order to tackle this issue, we generated several receptor mutants and assessed their phosphorylation state, internalization, and β-arrestin binding, as well as activation of ERK 1/2 and calcium signaling. Here we show that residues located in the carboxyl tail play roles in the signaling and subcellular location of this adrenergic receptor. Our data indicate that there are different points of regulation controlled by phosphorylated residues in close proximity in the α_{1D}-AR CTail.

2. Materials and methods

2.1. Reagents

(−)-Noradrenaline (NA), propranolol, BMY 7378, phorbol myristate acetate (PMA), and lysophosphatidic acid (LPA) were obtained from Sigma-Aldrich Chemical. AG1478 was obtained from Calbiochem and EGF was obtained from Preprotech. [^{32}P]Pi (8500–9120 Ci/mmol) was obtained from Perkin-Elmer Life Sciences. Dulbecco's modified Eagle's medium, fetal bovine serum, trypsin, Lipofectamine 2000, amphotericin B, streptomycin, penicillin, doxycycline hyclate, hygromycin B, blasticidin, and Fura-2 AM were purchased from Invitrogen-Life Technologies. Wheat germ agglutinin Alexa Fluor-350 conjugate (catalog number W11263), Super Signal West Pico chemiluminescence kits, small interfering RNA (siRNA) for β-arrestin 1 (catalog number AM16708, lot AS027ZUU), β-arrestin 2 (catalog number AM16708, lot AS027ZUT), and scrambled siRNA (catalog number AM4611, lot AS026WKE) were obtained from Thermo Fisher. Polyvinylidene difluoride and nitrocellulose membranes were obtained from BioRad. Polyethyleneimine was obtained from Polyscience. Agarose-coupled protein A was obtained from Merck-Millipore. Monoclonal anti-GFP was from Clontech (catalog number 632381, lot A5033481) and polyclonal anti-GFP was generated in our laboratory [22,23,34]. Anti-phospho-ERK 1/2 (Thre202/Tyr204) (catalog number 9101S, lot: 30) and anti-total ERK (p42/44) (catalog number 4695S, lot: 21) antibodies were obtained from Cell Signaling Technology; β-Arrestin-1/2 (catalog number sc-7491, lot D1615) monoclonal antibody was obtained from Santa Cruz Biotechnology (Sc-74,591). Tetramethyl-rhodamine-conjugated AffiniPure anti-donkey mouse IgG (code 715-025-150) was from Jackson Immunology. were purchased from Thermo Fisher Scientific. Secondary antibodies were obtained from Jackson ImmunoResearch and Zymed (Thermo Fisher Scientific). Antibody dilutions were 1:1000 for primary antibodies and 1:10,000 for secondary antibodies.

2.2. Plasmids

cDNA coding for either amino terminus-truncated or amino- and carboxyl termini-truncated-α_{1D}-AR-EGFP (Enhanced Green Fluorescent Protein) constructs (Δ1–79 and Δ1–79 and Δ440–572, respectively [24]) were subcloned into pEGFP-N1 (Clontech). These constructs were further subcloned into pCDNA5/FRT/TO to generate pΔN-α_{1D}-AR-EGFP and pΔNΔC-α_{1D}-AR-EGFP (Flp-ln T-Rex expression system, Invitrogen), as previously described [22]. The latter constructs were mutagenized to change the detected phosphorylated serines and threonine 328 in IL3 [22] into alanines or valine, respectively (S300/323/331/332/334A,T328 V) i. e., plasmids: pΔN-α_{1D}-AR-MutIL3-EGFP and pΔNΔC-α_{1D}-AR-MutIL3-α_{1D}-AR-EGFP. The pΔN-MutIL3-α_{1D}-AR-EGFP construct was then used as a template to mutagenize and generate the following mutants: 1) T442V, 2) S543A, 3) T477V,S486/492A, 4) T507V,S515/516/518A, 5) T477V, S486/492A,T507V,S515/516/518A, 6) T442/477V,S486/492A,T507V, S515/516/518/543A, 7) T477D,S486/492D, 8) T507D,S515/516/518D and 9) T442/477D,S486/492D,T507D,S515/516/518/543D. All these constructs were performed by Mutagenex, Inc. and proper modification was confirmed through sequencing by the same company.

2.3. Cells and transfection

HEK293 cells do not seem to express α_1-ARs as evidenced by the absence of calcium response to NA (in the presence of propranolol) [35] and specific radioligand binding (unpublished). Parental Flp-In T-Rex HEK293 cells (Invitrogen) were grown in Dulbecco's modified Eagle's medium supplemented with 10% fetal bovine serum, 100 μg/ml streptomycin, 100 U/ml penicillin, and 0.25 μg/ml amphotericin B. To generate inducible receptor-expressing cells, parental Flp-In T-Rex HEK293 cells were transfected with pCDNA5/FRT/TO, containing the cDNA coding for the previously described α_{1D}-AR mutants, and pOG44 using Lipofectamine 2000 following the manufacturer's instructions. Transfected cells were selected with 100 μg/ml hygromycin B and 5 μg/ml blasticidin, as previously described [22,36]. Receptor expression was induced with 1 μg/ml doxycycline hyclate 14–24 h before performing experiments. In all experiments using NA, 1 μM propranolol was also present, to avoid any β-adrenergic action; the addition of propranolol by itself had no impact on any of the parameters studied. In experiments in which the expression of β-arrestin 1/2 was knocked down, both the β-arrestin 1 and 2 siRNA (50 nmol final of each plasmid for each 3 cm-diameter dishes) were combined and transfected using Lipofectamine 2000, following the manufacturer's instructions, and cells were cultured for 48 h prior to being used.

INFORME DE LABORES 2019

2.4. Receptor phosphorylation

Receptor phosphorylation was performed as previously described [22,24]. In brief, cells, cultured in six well plates, were incubated for 3 h in phosphate-free Dulbecco's Modified Eagle's media supplemented with 50 μCi/ml [^{32}P]Pi. Labeled cells were stimulated with the indicated compounds, washed with ice-cold phosphate-buffered saline (PBS) solution and solubilized for 1 h in the lysis buffer [22,24]. The extracts were centrifuged and supernatants were incubated overnight with protein A-agarose and anti-EGFP antiserum. Samples were subjected to SDS-PAGE, transferred onto nitrocellulose membranes and exposed for 24 h. The amount of phosphorylated receptor was assessed by PhosphorImager analysis. Western blotting for loading controls was performed using monoclonal anti-EGFP antibodies.

2.5. Intracellular calcium determinations

Intracellular calcium concentrations were determined as previously described [22,24]. In brief, cells were serum-starved for 2 h, then loaded with 2.5 μM Fura-2/AM for 1 h at 37 °C. Labeled cells were washed three times to eliminate unincorporated dye. Fluorescence measurements were assessed at 340- and 380-nm excitation wavelengths and at a 510-nm emission wavelength, with a chopper interval set at 0.5 s, using an Aminco-Bowman Series 2 Luminescence Spectrometer. Intracellular calcium levels were calculated as described by Grynkiewicz et al. [37].

2.6. ERK 1/2 phosphorylation

Cells were serum-starved for 2 h before experiments. After stimulation with the indicated compounds, cells were washed with ice-cold PBS and lysed with Laemmli sample buffer [38]. Lysates were centrifuged at 12,000 × *g* for 5 min, and proteins in supernatants were separated by SDS-PAGE. Proteins were electrotransferred onto polyvinylidene difluoride membranes and immunoblotting was performed. Duplicate samples were run in parallel to determine total-ERK and phospho-ERK 1/2. For data normalization, the maximal response was considered as 100%.

2.7. Intracellular fluorescence, receptor internalization and colocalization with endogenous β-arrestin 1/2

Receptor internalization and colocalization assays with endogenous β-arrestin 1/2 were performed as described [22,39]. In brief, cells were seeded to reach 50% confluence into glass-bottomed Petri dishes and were cultured for 24 h at 37 °C in media containing 1% serum and stimulated with NA or PMA. After stimulation, the cells were washed with PBS, fixed with 4% paraformaldehyde in 0.1 M phosphate buffer for 30 min at room temperature, and then washed three times with PBS. To determine intracellular fluorescence and receptor internalization, the plasma membrane was delineated using the differential interference contrast image, and fluorescence in such an area was excluded; intracellular fluorescence was quantified employing ImageJ software [40–42]. To determine membrane-receptor colocalization additional experiments were performed using Alexa Fluor-350-conjugated wheat germ agglutinin (20 μg/ml) for membrane labeling. To determine the colocalization of the α_{1D}-AR with β-arrestin 1/2, the cells were fixed, as indicated previously, and samples were permeabilized with 0.3% Triton X-100 for 15 min at 4 °C. The samples were then incubated with 3% BSA for 1.5 h at room temperature, in the absence or presence of the anti-β-arrestin 1/2 antibody (1:200) with 3% BSA in 50 mM Tris base-buffered saline (pH 7.4) containing 0.1% Tween 20. After this process, the samples were washed twice, were incubated for 2 h in the same buffer containing a tetramethyl-rhodamine-conjugated secondary antibody (1500) and then washed with PBS with soft agitation. Confocal microscopy images were acquired with an Olympus Fluoview FV10 with an oil-immersion objective (60× at 5.0 zoom), 2.0 confocal aperture X16 quality high, and 512 × 512 size. To determine α_{1D}-AR/β-arrestin 1/2 colocalization, the overlap of the two fluorophores (EGFP/rhodamine) was estimated employing ImageJ software [40–42]. Representative images showing green channel fluorescence, red channel

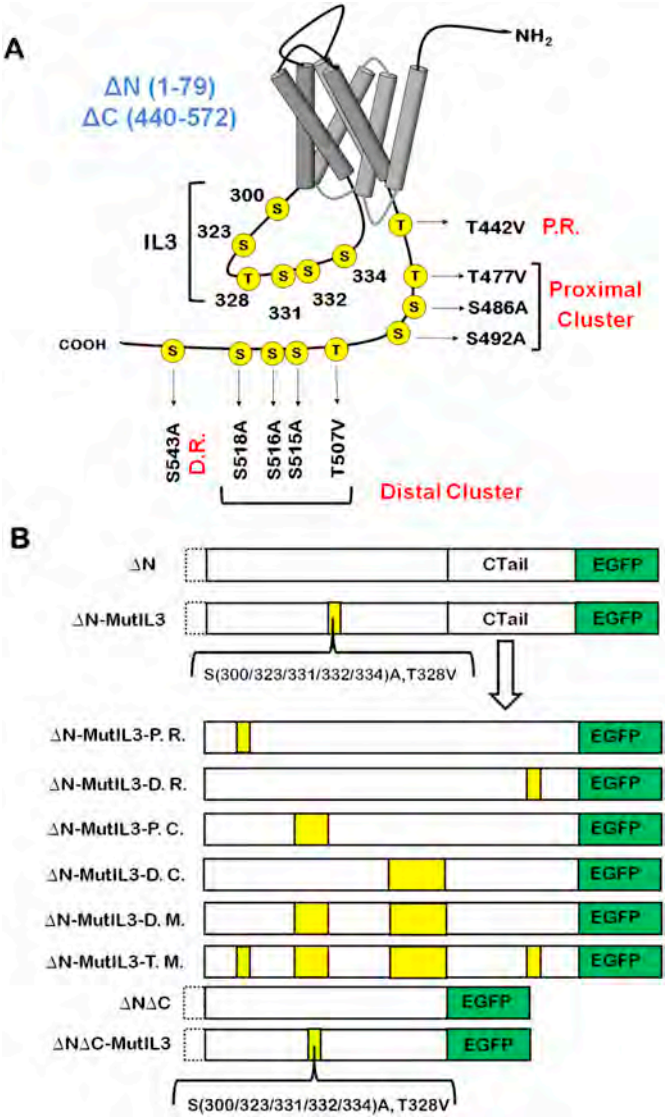

Fig. 1. Schematic representation of the α_{1D}-AR mutants. Panel A: The phosphorylation residues of the α_{1D}-AR detected by MS analysis are located in the IL3 and in the C-terminal tail. Such residues were mutagenized to non-phosphorylatable amino acids: serine residues changed into alanine and threonine residues changed into valine. Panel B: Schematic representation of the α_{1D}-AR mutants. Dotted lines in the constructs represent the deletion of the first 79 amino acids of the N-terminal region (ΔN, 1–79). The mutant ΔN-MutIL3 was generated taking the ΔN receptor as a template. Yellow section in this mutant indicates that the residues S300, S323, S331, S332, S334 and T328 located in the IL3, were mutagenized by non-phosphorylatable residues, as previously described. Subsequently, the ΔN-MutIL3 mutant was mutagenized in T442 (ΔN-MutIL3-P.R.), S543 (ΔN-MutIL3-D.R.), T477, S486, S492 (ΔN-MutIL3-P.C., proximal cluster), T507, S515, S516, and S518 (ΔN-MutIL3-D.C., distal cluster), T477, S486, S492, T507, S515, S516, and S518 (ΔN-MutIL3-D.M.) and T442, T477, S486, S492, T507, S515, S516, S518, and S543 (ΔN-MutIL3-T.M.). Deletion of the last amino acids (440–572) in the CTail (ΔN).

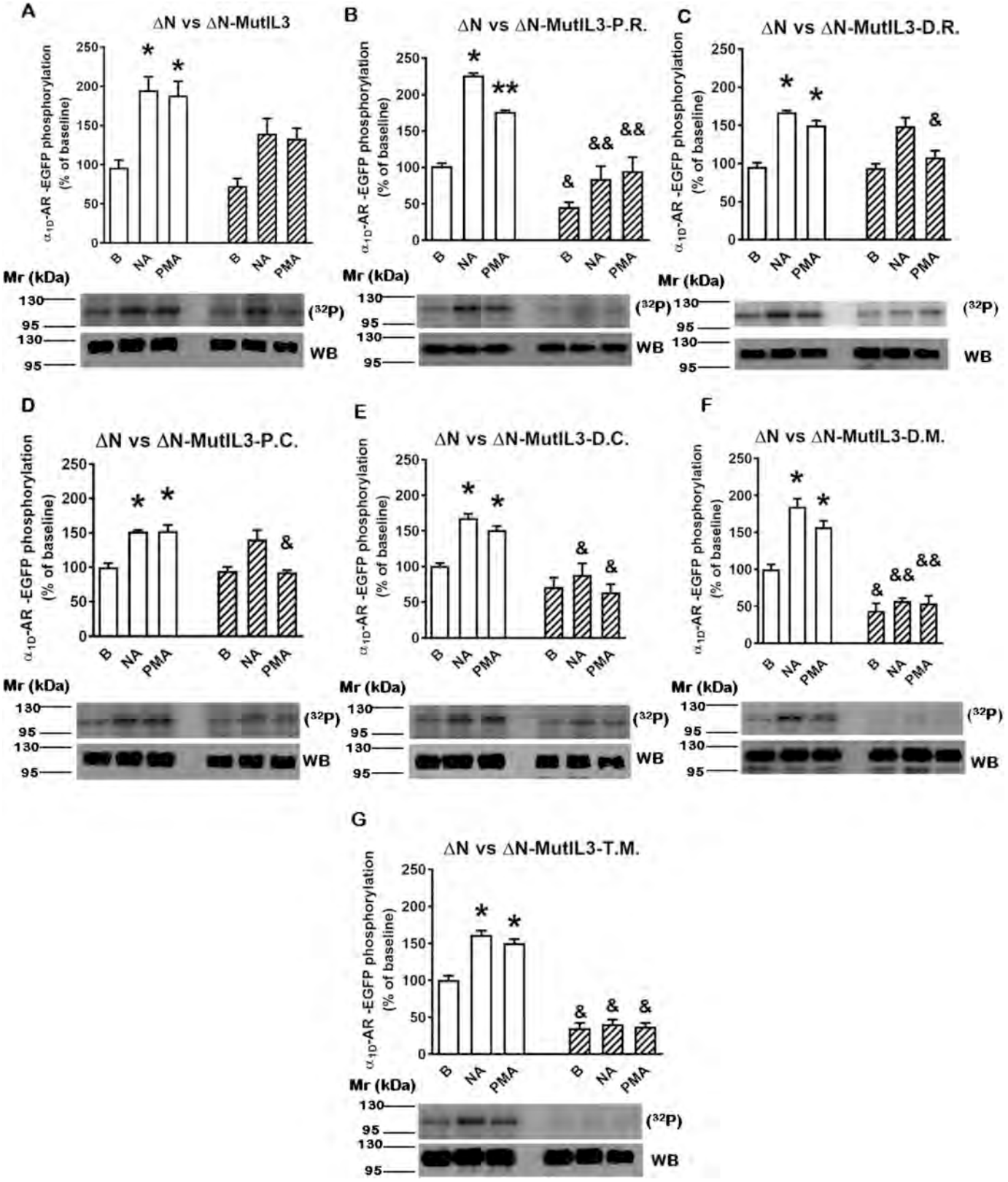

Fig. 2. NA-and PMA-induced phosphorylation of the different α_{1D}-AR mutants. Cells expressing the different constructs were stimulated with NA 10 μM and PMA 1 μM for 15 min and compared to the ΔN receptor. In all cases, cultures were processed in parallel and data were normalized to the percentage of the ΔN receptor's baseline (B) phosphorylation. Plotted lines are the means and vertical lines representing S.E.M. of 3–5 independent experiments. Representative autoradiographs and Western-blots are presented below each graph. Panel 2A, * $P < 0.005$ vs. ΔN receptor's baseline; Panel 2B, *$P < 0.001$ vs, ΔN receptor's baseline, ** $P < 0.005$ vs. ΔN receptor's baseline, & $P < 0.05$ vs. ΔN receptor's baseline, && $P < 0.001$ vs. ΔN receptor's corresponding stimulus; Panel 2C, * $P < 0.001$ vs. ΔN receptor's baseline, & $P < 0.01$ vs. ΔN receptor's PMA; Panel 2D, * $P < 0.005$ vs. ΔN receptor's baseline, & $P < 0.005$ vs. ΔN receptor's PMA; Panel 2E, * $P < 0.005$ vs. ΔN receptor's baseline, & $P < 0.001$ vs. ΔN receptor's corresponding stimulus; Panel 2F, * $P < .005$ vs. ΔN receptor's baseline, & $P < 0.005$ vs. ΔN receptor's baseline, && $P < 0.001$ vs. ΔN receptor's corresponding stimulus; Panel 2G, * $P < 0.001$ vs. ΔN receptor's baseline, & $P < 0.001$ vs. ΔN receptor's corresponding condition.

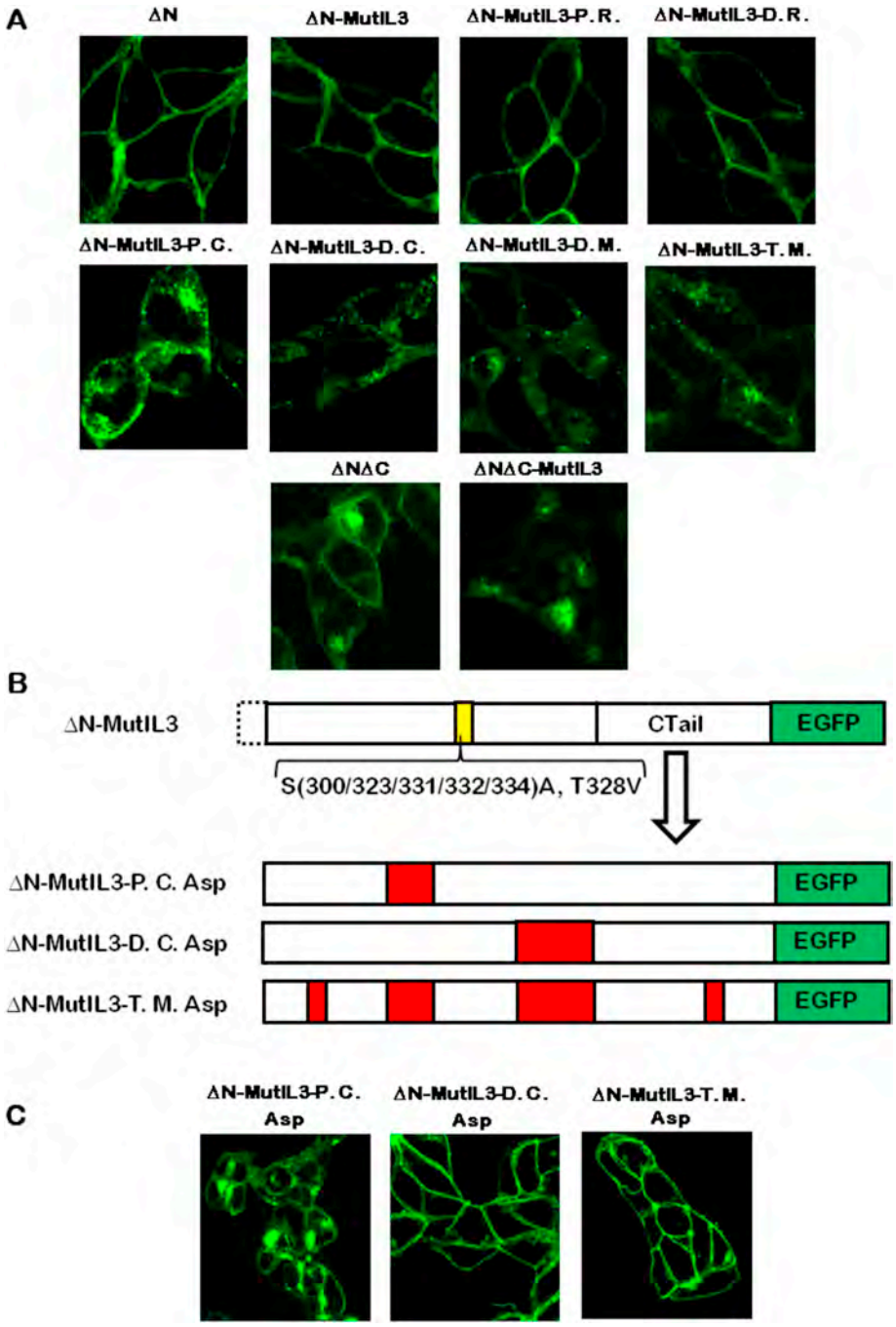

Fig. 3. Subcellular localization of α_{1D}-AR mutants under baseline conditions and schematic representation of the mutants with aspartic acid. Panel A: Cells expressing the different constructs of α_{1D}-AR were analyzed under baseline conditions by confocal microscopy. Images are representative of data of 5–7 experiments using different cell preparations. Panel B: ΔN-MutIL3 was used as a template to change the residues located in the proximal (ΔN-MutIL3-P.C. Asp), and distal cluster (ΔN-MutIL3-D.C. Asp) as well as in both clusters and both proximal and distal residues (ΔN-MutIL3-T.M. Asp), by aspartic acid (phospho-mimetic). Red sections in the constructs represent these mutations. Panel C: ΔN-MutIL3-P.C. Asp, ΔN-MutIL3-D.C. Asp, and ΔN-MutIL3-T.M. Asp mutants were analyzed under baseline conditions by confocal microscopy. Images are representative of data of 5–7 experiments using different cell preparations.

fluorescence, merged images, and pixel-by-pixel colocalization are presented. At least 10 different images per condition were obtained for each experiment.

2.8. Statistical analyses

Statistical comparisons between two conditions was performed employing the Student's *t*-test (Figures 7 and 20; indicated in the text). All other statistical analysis (comparisons between groups with three or more variables) were evaluated using a parametric analysis of variance (ANOVA) with Bonferroni's post-test, assuming Gaussian data distribution (http://www.graphpad.com/guides/prism/7/statistics/index.htm). We utilized the software included in GraphPad Prism 6 software to perform these analyses. A P value < 0.05 was considered statistically significant.

3. Results

3.1. α_{1D}-AR phosphorylation sites and site-directed mutagenesis

Using mass spectrometry, we previously reported that α_{1D}-AR harbors six phosphorylated residues (S300, S323, T328, S331, S332, and S334) in IL3 and nine more on the CTail (see below) [22]. One of the main goals of the present work was to experimentally define the role(s) of the CTail phosphorylation residues. To accomplish this, first we identified that phosphorylation sites in the CTail have a particular arrangement, i.e., two isolated residues (T442 and S543) and two groups of residues with close proximity; we named these groups as proximal cluster (T477, S486, S492) and distal cluster (T507, S515, S516, S518) (Fig. 1A).Taking this arrangement into account, we generated a combination of point mutations and deletions on the α_{1D}-AR (Fig. 1B). As

INFORME DE LABORES 2019

already mentioned, the α_{1D}-AR amino terminus negatively controls its membrane-targeting [7,8,21–24]. Therefore, all of the mutants were designed using the amino-truncated receptor (ΔN; abbreviated names will be used for clarity). Non-phosphorylatable substitutions in the six residues in IL3 (ΔN-MutIL3) were obtained. These two modifications represent a compromise necessary to obtain: a) membrane expression and b) to eliminate the contribution of phosphorylation at the IL3 in our studies. Then, we used this latter mutant as a template to further individually mutagenize the proximal residue T442 V (ΔN-MutIL3-P.R.) and the distal residue S543A (ΔN-MutIL3-D.R.), as well as the proximal and distal clusters (ΔN-MutIL3-P.C. and ΔN-MutIL3-D.C., respectively). We also included a double mutant where both clusters were changed (ΔN-MutIL3-D.M.) and a total mutant (ΔN-MutIL3-T.M.), including all of these substitutions in the CTail. Finally, we employed the previously reported carboxyl tail-truncated receptor (ΔNΔC) [22] and a further mutated form in which IL3 phosphorylated residues were changed into non-phosphorylatable amino acids (ΔNΔC-MutIL3) [22]. All of these mutants were tagged with EGFP for confocal microscopy imaging and biochemical studies.

Next we utilized Flp-In T-Rex HEK293 cells expressing the former mutants to asses receptor phosphorylation during homologous and heterologous desensitization, i.e., in the presence of 10 μM NA or 1 μM PMA for 15 min. Agents, concentrations, and incubation times were selected based on previously reported data [22]. In independent parallel experiments, the phosphorylation of the ΔN receptor was compared with each of the other mutants and all data were normalized to the phosphorylation of the ΔN receptor detected under baseline conditions. ΔN receptor baseline phosphorylation increased approximately 2-fold after stimulation with NA and PMA, as illustrated in Fig. 2A. In cells expressing the ΔN-MutIL3 receptor, baseline phosphorylation and the actions of NA and PMA were marginally decreased when compared to those of the ΔN receptor (not statistically significant). The CTail mutation on the proximal residue (ΔN-MutIL3-P.R.), resulted in a receptor with decreased baseline labeling and phosphorylation in response to NA and PMA (Fig. 2B). On the other hand, the mutant receptor with the non-phosphorylatable distal residue (ΔN-MutIL3-D.R.) did not exhibit any clear difference in baseline or NA-induced phosphorylation when compared with the ΔN mutant, but the effect of PMA was reduced (Fig. 2C). Similarly, the proximal cluster mutant (ΔN-MutIL3-P.C.) increased its phosphorylation in response to NA, but not after PMA stimulation (Fig. 2D). Interestingly, the receptor with the mutated distal cluster, ΔN-MutIL3-D.C., showed a slight decrease in basal phosphorylation but marked attenuation of phosphorylation observed in response to NA or PMA (Fig. 2E). Baseline phosphorylation of the receptor containing the double-cluster mutations (ΔN-MutIL3-D.M.) diminished below ΔN baseline levels and nearly no effect of NA or PMA was detected (Fig. 2F). Very similar results were obtained with the total mutant (ΔN-MutIL3-T.M.) (Fig. 2G). Overall, these data experimentally confirmed that α_{1D}-AR phosphorylation specifically occurs at the residues depicted in Fig. 1A. It appears that phosphorylatable residues in proximal and distal clusters and distal residue, S543, might be phosphorylated during PMA-induced desensitization and that mutations in the distal cluster also disturb NA-induced phosphorylation. Phosphorylation of ΔNΔC and ΔN-MutIL3-ΔC mutants was reported previously [22].

3.2. α_{1D}-AR plasma membrane localization is regulated by CTail distal cluster phosphorylation

Cells expressing the α_{1D}-AR mutants described previously were studied using confocal microscopy. Under baseline conditions, we observed that the control receptor (ΔN) and the mutant containing substitutions in the IL3 (ΔN-MutIL3), as well as receptors additionally containing single mutations in the proximal and distal residues (ΔN-MutIL3-P.R. and ΔN-MutIL3-D.R., respectively) were mainly located at the plasma membrane. In contrast, receptors including non-phosphorylatable substitutions in the CTail proximal or distal clusters were found mainly in vesicles (Fig. 3A). Prompted by this observation, we measured intracellular fluorescence to qualitatively determine the main subcellular location of each mutant. As depicted in Fig. 4, we normalized all data to the signal detected in the control receptor (ΔN), i. e., it was considered as 100%. As Fig. 4 illustrates, we detected some intracellular fluorescence in ΔN, ΔN-MutIL3, ΔN-MutIL3-P.R. and in ΔN-MutIL3-D.R., whereas the following mutants showed approximately a 4-fold increment of fluorescence located intracellularly: ΔN-MutIL3-P.C., ΔN-MutIL3-D.C., ΔN-MutIL3-D.M. and ΔN-MutIL3-T.M. Moreover, the carboxyl truncated mutants (ΔNΔC and ΔNΔC-MutIL3) revealed a 6-fold increase of intracellular fluorescence. In other words, truncation of the entire CTail or substitutions in the phosphorylation clusters contained in this domain blocked the receptor's ability to reach or remain at the plasma membrane.

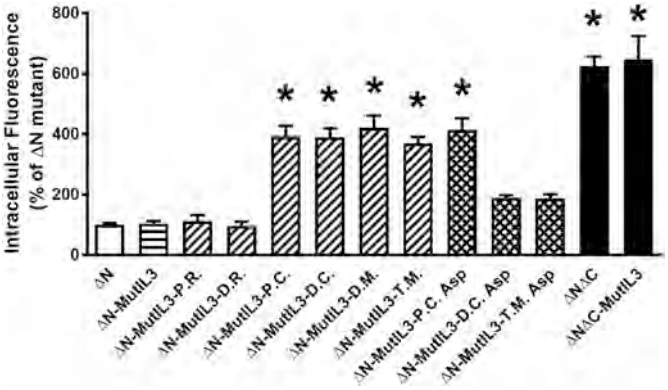

Fig. 4. Intracellular fluorescence quantification (α_{1D}-AR mutants) under baseline conditions. Accumulation of intracellular fluorescence under baseline conditions was quantified for α_{1D}-AR mutants. Data were normalized to that observed in cells expressing the ΔN mutant (100%). Plotted lines are the means and vertical lines representing S.E.M. of 7 independent experiments in each of which 3–5 cells were analyzed (n = 20–35). * $P < 0.001$ vs ΔN.

Under the latter premise, we hypothesized that phosphorylation of such residues in close proximity might regulate receptor subcellular localization. In order to test this, we generated phospho-mimetic mutants containing aspartic acid substitutions. As presented in Fig. 3B, the phosphorylatable residues were changed to aspartic acid in the proximal (ΔN-MutIL3-P.C. Asp) and distal clusters (ΔN-MutIL3-D.C. Asp), as well as in both clusters plus the isolated residues, to generate a total phospho-mimetic mutant (ΔN-MutIL3-T.M. Asp). We observed abundant vesicles in cells expressing ΔN-MutIL3-P.C. Asp (Fig. 3C). This mutant also showed a 4-fold increment of intracellular fluorescence, similar to the mutants lacking phosphorylation clusters (Fig. 4). Surprisingly, ΔN-MutIL3-D.C. Asp and ΔN-MutIL3-T.M. Asp mutants were fully expressed at the plasma membrane (Fig. 3C) and they both showed intracellular fluorescence levels equivalent to the control (intracellular fluorescence quantifications are presented in Fig. 4). In order to confirm these results, colocalization experiments employing Alexa Fluor-350-conjugated wheat germ agglutinin were performed with six of the mutants employed (ΔN, ΔN-MutIL3, ΔN-MutIL3-D.C., ΔN-MutIL3-T.M., ΔN-MutIL3-D.C. Asp and ΔN-MutIL3-T.M. Asp). Wheat germ agglutinin is generally considered as a membrane marker but also binds to glycoproteins present in other organelles [43]. Observations were normalized to the colocalization observed with cells expressing the ΔN mutant. As shown in Fig. 5, in non-permeabilized cells, the lectin labeled the plasma membrane but also some structures present inside the cells; this was much more clearly observed in cells containing large amounts of vesicles. Despite this, the colocalization data (Fig. 5) confirmed the previous findings (Fig. 4). Altogether, these results suggest that, specifically, distal-cluster phosphorylation could be necessary and sufficient to allow α_{1D}-AR plasma membrane localization.

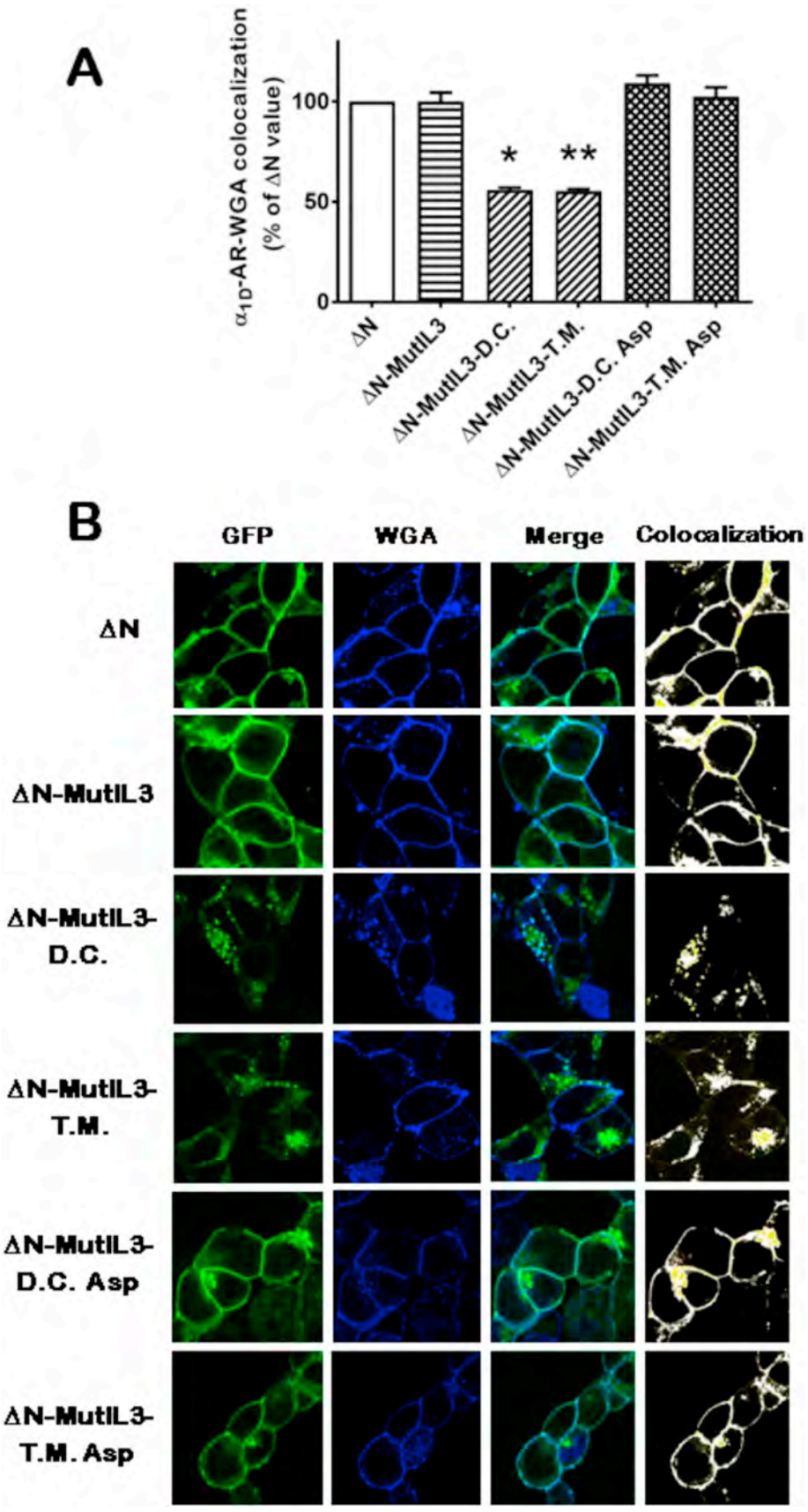

Fig. 5. Colocalization of α_{1D}-AR mutants with Alexa Fluor-350-conjugated wheat germ agglutinin (plasma membrane marker) under baseline conditions. Cells expressing the different constructs of α_{1D}-AR were fixed and stained with Alexa Fluor-350-conjugated wheat germ agglutinin (WGA), as indicated under Material and Methods. Fluorescence was analyzed under baseline conditions by confocal microscopy and ImageJ analysis. Panel A, Receptor-membrane marker colocalization, normalized to ΔN mutant baseline value (100%), is presented. Plotted are the means and vertical lines representing S.E.M. of 4 independent experiments in each of which 10 cells were analyzed ($n = 40$). * $P < 0.001$ vs. ΔN mutant and $P < 0.001$ vs. ΔN-MutIL3-D.C. Asp; ** $P < 0.001$ vs. ΔN mutant and $P < 0.001$ vs. ΔN-MutIL3-T.M. Asp. Panel B, representative images showing: receptor fluorescence (GFP), WGA fluorescence, Merge images and colocalization (white).

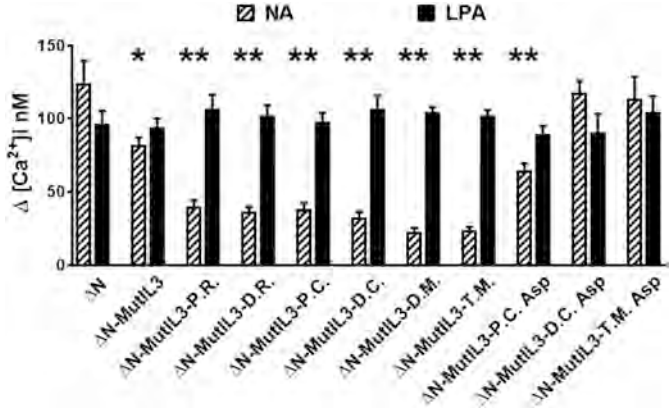

Fig. 6. NA- and LPA-induced mobilization of intracellular calcium in cells expressing the different α_{1D}-AR mutants. Cells expressing the different constructs were stimulated with NA 10 μM (dashed bars) or LPA 1 μM (solid bars) and increases (Δ $[Ca^{2+}]$ i nM; baseline subtracted) in intracellular calcium concentration were determined. Plotted are the means and vertical lines representing S.E.M. of 5–7 independent experiments. * $P < 0.005$ vs. ΔN, NA-stimulation; * $P < 0.001$ vs. ΔN, NA-stimulation. No significant difference was observed when the response to LPA stimulation in the different cell lines was compared.

3.3. Phosphorylation on α_{1D}-AR CTail specific residues regulates the mobilization of intracellular Ca^{2++}

Next, we evaluated agonist-induced mobilization of intracellular calcium to determine the functionality of the receptors previously described. As depicted in Figs. 6, 10 μM NA elicited an increase of over 100 nM intracellular calcium in cells expressing the ΔN receptor, whereas it scarcely reached 100 nM in cells expressing the ΔN-MutIL3 mutant. Remarkably, in CTail mutants lacking phosphorylatable single residues or clusters (ΔN-MutIL3-P.R., ΔN-MutIL3-D.R., ΔN-MutIL3-P.C., and ΔN-MutIL3-D.C.), calcium release was markedly reduced as compared with those expressing the ΔN receptor. Calcium increments were even smaller in double and total mutants (ΔN-MutIL3-D.M. and ΔN-MutIL3-T.M.). As a positive control, we measured the response of endogenously expressed lysophosphatidic acid receptors, using 1 μM LPA, and a consistent increase in calcium concentration (≈ 100 nM) was observed in cells expressing the different mutants. When we examined receptors containing the phospho-mimetic mutations, we observed that the proximal cluster mutant (ΔN-MutIL3-P.C. Asp) partially recovered its ability to mobilize intracellular calcium. Interestingly, distal cluster and total mutants containing the phospho-mimetic mutations (ΔN-MutIL3-D.C. Asp and ΔN-MutIL3-T.M. Asp) were able to increase calcium to concentrations similar to those of the control (ΔN receptor-expressing cells). These data suggest that phosphorylation of the CTail region, mainly at the distal cluster, controls the ability of α_{1D}-AR to trigger the calcium signaling pathway. NA-induced increases in intracellular calcium in cells expressing the ΔNΔC and ΔN-MutIL3-ΔC mutants were reported previously [22]. The effect of NA on intracellular calcium concentration as affected by NA, PMA and BMY 7378 (inverse agonist) [10,11,24] is presented in Supplementary Fig. S1. In agreement with the previous data, NA action was robust in cells expressing the ΔN mutant; this was of smaller magnitude in cells expressing the ΔN-MutIL3 mutant and even smaller in cells expressing the ΔN-MutIL3-T.M. receptors. Similarly, the ability of PMA and BMY 7378 was very clear in cells expressing the ΔN mutant and marginal (but statistically significant) in cells expressing the total mutant (Supplementary Fig. S1).

3.4. α_{1D}-AR mutants' ERK activation kinetics

A different pathway initiated by α_{1D}-AR was investigated. ERK 1/2 phosphorylation was determined under baseline conditions and after 2, 5, 15, 30, and 60 min of incubation with 10 μM noradrenaline. As it is shown in Fig. 7A, the ΔN mutant showed a rapid increase in ERK phosphorylation after 5 and 15 min, and subsequently, this signal decreased at 30 and 60 min. In the same way, the rest of the mutants also presented a quick increase in ERK 1/2 phosphorylation. However, the signal remained elevated in all of these even after 60 min of observation (this trend was statistically significant (Student's *t*-test $P < 0.05$; 60 min vs. ΔN mutant) except for the ΔN-MutIL3-D.R. and ΔN-MutIL3-D.M. mutants). Representative Western blots of the p-ERK 1/2 and total-ERK 1/2 of each mutant are presented (Fig. 7B).

3.5. α_{1D}-AR activation of ERK is regulated by the transactivation of the EGF receptor and β-arrestins

It has been observed that α_{1D}-AR activation induces the shedding of active epidermal growth factor (EGF) that stimulates the EGF receptor and contributes to the activation of ERK 1/2 [44]. Fig. 8A shows that when cells expressing the ΔN receptor are treated with EGF, a robust increase in ERK 1/2 phosphorylation can be detected. AG1478, a specific inhibitor of EGF receptor endogenous tyrosine kinase activity [45] totally abolished the EGF effect. Cells stimulated with NA for 5 min, also showed an important increase in ERK 1/2 phosphorylation; interestingly, this activation was markedly diminished when the cells were pre-incubated with AG1478 and then challenged with NA (Fig. 8A). It has been shown that activation of ERK depends in some cells on the binding of β-arrestins to GPCRs, forming a multi-protein complex: GPCR/β-arrestin/ERK1/2 [32]. In order to explore the possible participation of β-arrestins, we knocked down the expression of β-arrestin 1/2 by using small interfering RNA. Fig. 8B illustrates the increase in ERK 1/2 phosphorylation when cells expressing the ΔN mutant were stimulated with NA for 5 and 60 min. Scrambled small interfering RNA induced a very small decrease (not statistically significant) of NA-induced ERK phosphorylation, as presented in the same figure. In contrast, when β-arrestin1/2 was knocked down, a clear decrease of NA-induced ERK phosphorylation was detected, at 5 and 60 min. β-arrestin 1/2 knock down was confirmed by Western blot analysis (Fig. 8B). The roles of EGF receptor transactivation and of β-arrestin 1/2 knock down were also tested in cells expressing the ΔN-MutIL3-T. M. mutant and the results were very similar, i. e., data confirmed the role of these processes in α_{1D}-AR ERK 1/2 activation (Supplementary Fig. S2). Overall, these experiments suggest that transactivation of EGF receptors and β-arrestins participate in NA-induced ERK 1/2 activation, in cells expressing the receptor mutants employed.

3.6. The α_{1D}-AR mutants have a different kinetic of internalization triggered by NA and PMA

α_{1D}-AR internalization using confocal microscopy was studied next. In order to achieve this, we exclusively studied the mutants that were mainly expressed at the plasma membrane under baseline conditions. Attempts to study this with mutants that were mainly internalized proved to be impossible with this approach. To evaluate the kinetic profiles of internalization, cells were stimulated with NA or PMA. The intracellular fluoresce of cells expressing each mutant, under baseline conditions, was considered as 100% (Figs. 9 and 10); these baseline values were very similar as shown in Fig. 4. As depicted in Fig. 9A, we stimulated the cells with NA 10 μM and detected an increase in the intracellular florescence at 5 and 15 min in the ΔN mutant. Subsequently, the intracellular signal vanished and was barely detected at 30

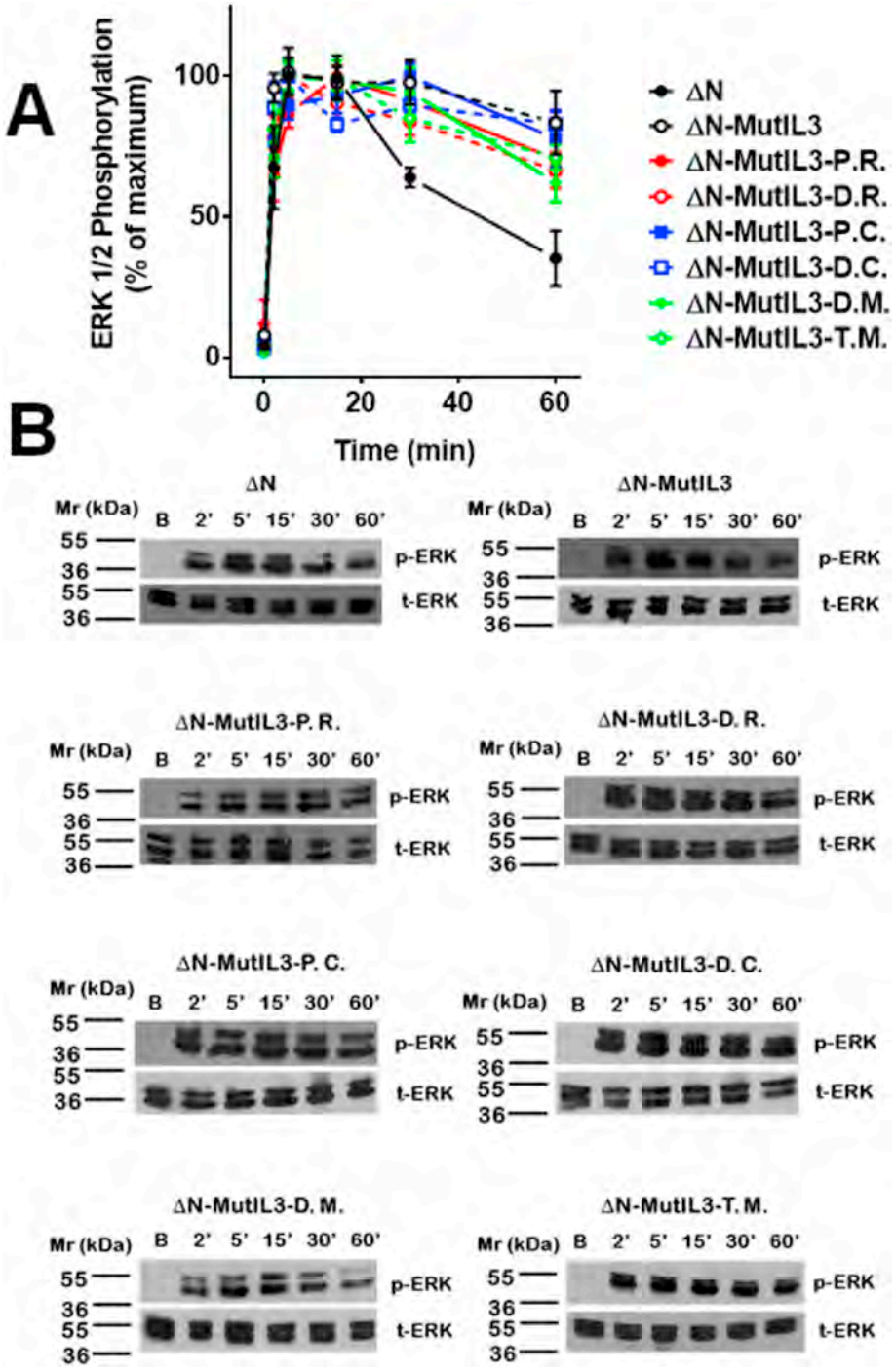

Fig. 7. Time-course of NA-induced activation of ERK1/2 in the different α_{1D}-AR mutants. Cells expressing the different constructs were stimulated for the times indicated with NA 10 μM, and ERK1/2 phosphorylation was determined. Plotted lines are the means and vertical lines representing S.E.M. of at least 4 independent experiments. Representative Western-blots for total-ERK1/2 and phospho-ERK1/2 are presented below the graph.

and 60 min. The ΔN-MutIL3 mutant was also internalized in response to NA, but remained so, along the 60 min of stimulation (Student's *t*-test vs. the ΔN mutant, $P < 0.001$at 60 min). Interestingly, the ΔN-MutIL3-P.R. and ΔN-MutIL3-D.R. mutants behaved in a similar manner to those of the ΔN mutant, i.e., there was an increase in intracellular fluorescence at 5 and 15 min and a partial decrease of such a signal at 30 and 60 min (Student's t-test: $P < 0.001$ vs. the ΔN mutant and $P < 0.001$ vs. the ΔN-MutIL3 mutant at 60 min). Fig. 9B presents the images of the kinetic profiles of internalization of each α_{1D}-AR mutant.

Next, we decided to evaluate the kinetic profile of internalization of the same mutants by stimulating the cells with 1 μM PMA. As shown in Fig. 10A, we detected that the ΔN mutant progressively internalized during the 60 min of incubation. In contrast, the ΔN-MutIL3 reached the maximal internalization at 15 min and then intracellular fluorescence

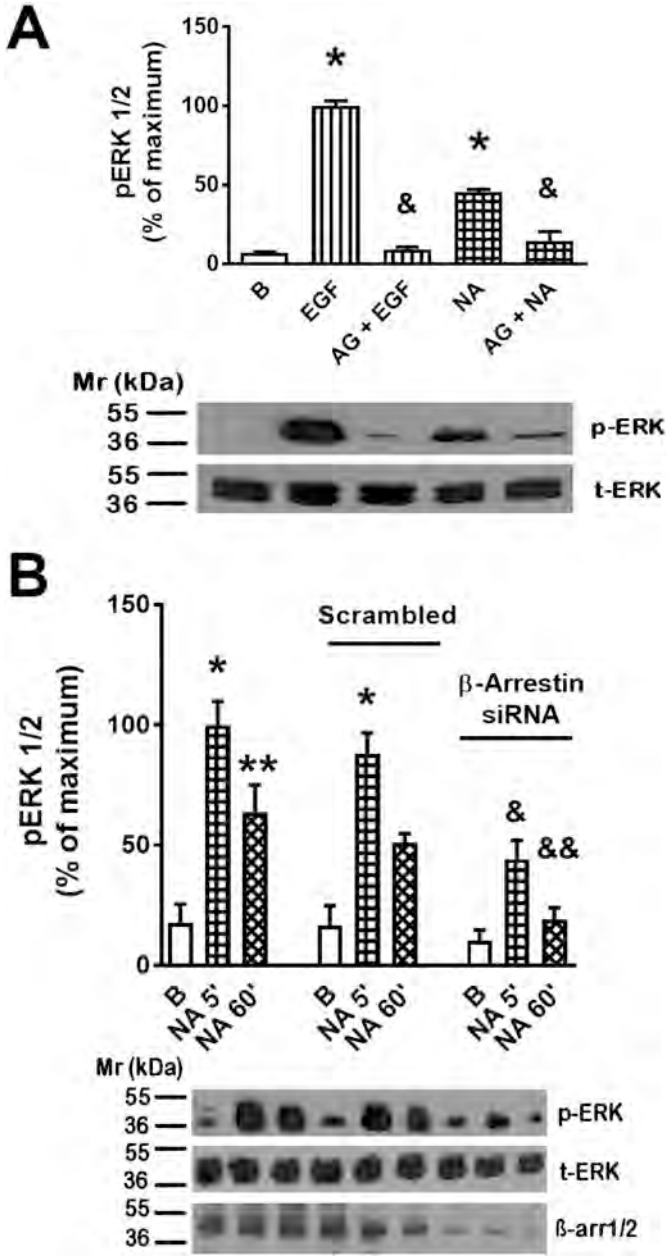

Fig. 8. Regulation of ERK 1/2 phosphorylation by EGF receptor transactivation and β-arrestins in cells expressing the ΔN receptor. Panel A: Cells were pre-incubated in the absence or presence of AG1478 10 μM (AG) and then challenged with EGF 100 ng/ml or NA 10 μM for 5 min. Plotted are the means and vertical lines representing the S.E.M. of 3 independent experiments. * $P < 0.001$ vs. baseline (B); & $P < 0.001$ vs. absence of AG1478. Representative Western-blots for total-ERK 1/2 and phospho-ERK 1/2 are presented below the histogram. Panel B: Cells were nor transfected (first group or bars), or they were transfected with either a scrambled siRNA (second group of bars) or with a specific siRNAs to block the expression of β-arrestin 1/2 (third group of bars) Cells were stimulated with NA 10 μM for 5 (5′) or 60 min (60′). Plotted are the means and vertical lines representing S.E.M. of 3 independent experiments. * $P < 0.001$ vs. respective baseline (B); ** $P < 0.05$ vs. respective baseline (B); & $P < 0.005$ vs NA 5′ non-transfected cells and $P < 0.05$ vs. NA 5′ scrambled siRNA; && $P < 0.05$ vs. NA 60′ non-transfected cells. Representative Western-blots for total-ERK 1/2, phospho-ERK 1/2, and β-arrestins (β-arr1/2) are presented below the histogram.

gradually decreased toward baseline values (Fig. 10A, Student's *t*-test vs. the ΔN mutant, $P < 0.001$ at 60 min). The ΔN-MutIL3-P.R. similarly reached its maximal internalization at 15 min,but intracellular fluorescence remained at that level during the remaining of the incubation (Student's t-test vs. the ΔN mutant and ΔN-MutIL3 mutant, $P < 0.001$ in both comparison, at 60 min). The ΔN-MutIL3-D.R. mutant behaved like the ΔN-MutIL3 mutant (Fig. 10A, Student's t-test vs. the ΔN mutant, $P < 0.001$ at 60 min). Fig. 10B presents representative images of the kinetic profile of internalization of each α_{1D}-AR mutant under the action of PMA.

3.7. The α_{1D}-AR mutants colocalize with endogenous β-arrestin1/2

β-arrestins are scaffold proteins known to bind and participate in the internalization of ligand-activated receptors. This process allows for a GPCR to maintain signaling while internalized in endosomes in a β-arrestin-dependent fashion [29,46,47]. Hence, we examined the colocalization of endogenous β-arrestins with the α_{1D}-AR mutants that are expressed at the plasma membrane, taking into consideration the time at which each mutant was maximally internalized in response to NA or PMA. Data were normalized to the colocalization observed, under baseline conditions, in cells expressing each mutant. As it is shown in Fig. 11A, colocalization was observed under baseline conditions with all of the cells studied and mainly at the plasma membrane (Fig. 11B); this could be due to the α_{1D}-AR intrinsic activity. However, this was less clear with the ΔN-MutIL3-P.R mutant (Fig. 11B). When cells were treated with NA or PMA, the ΔN, ΔN-MutIL3 and ΔN-MutIL3-Δ-D.R. mutants increased their colocalization with endogenous β-arrestin1/2, and colocalization was also clearly observed intracellularly (Fig. 11, panels A and B). Interestingly, the ΔN-MutIL3-ΔP.R. mutant did not increase its colocalization with β-arrestins in response to NA or PMA. Representative images of the colocalization of each mutant with endogenous β-arrestin1/2, under the conditions described, are illustrated in Fig. 11B. When the primary anti-β-arrestin antibody was omitted during the immunostaining procedure, essentially no fluorescence was observed in the red channel and consequently no colocalization was detected; these data indicate that the observed fluorescence was due to detection of the anti-β-arrestin antibody and not to unspecific immunostaining by the secondary antibody (Supplementary Fig. S3). Colocalization of α_{1D}-AR and β-arrestin was absent in cells expressing receptors located in intracellular vesicles (data not shown). It must be stated that colocalization does not necessarily imply physical interaction of these proteins.

4. Discussion

α_{1D}-AR is known for being an elusive GPCR, whose expression, cellular localization, and function, as well as its roles in the development of cardiovascular diseases and other maladies, remain only partially known to date [48–51]. The ability of agonists and phorbol esters to induce α_{1D}-AR phosphorylation and the association of this process with receptor desensitization has been known for some time [22–24,26,27]. A series of α_{1D}-AR phosphorylation sites were recently defined by employing mass spectrometry [22]. This latter work revealed that there are six phosphorylated residues located in the IL3 and nine in the CTail, and that several protein kinases could putatively target such residues, including PKC α/β and GRK2. In our present experiments, we observed that as the phosphorylation sites were substituted by non-phosphorylatable amino acids, baseline phosphorylation, as well as those observed in response to receptor activation (NA) or PKC stimulation (PMA), decreased. Therefore, the identified 15 amino acids seem to be the major targets of the protein kinases involved

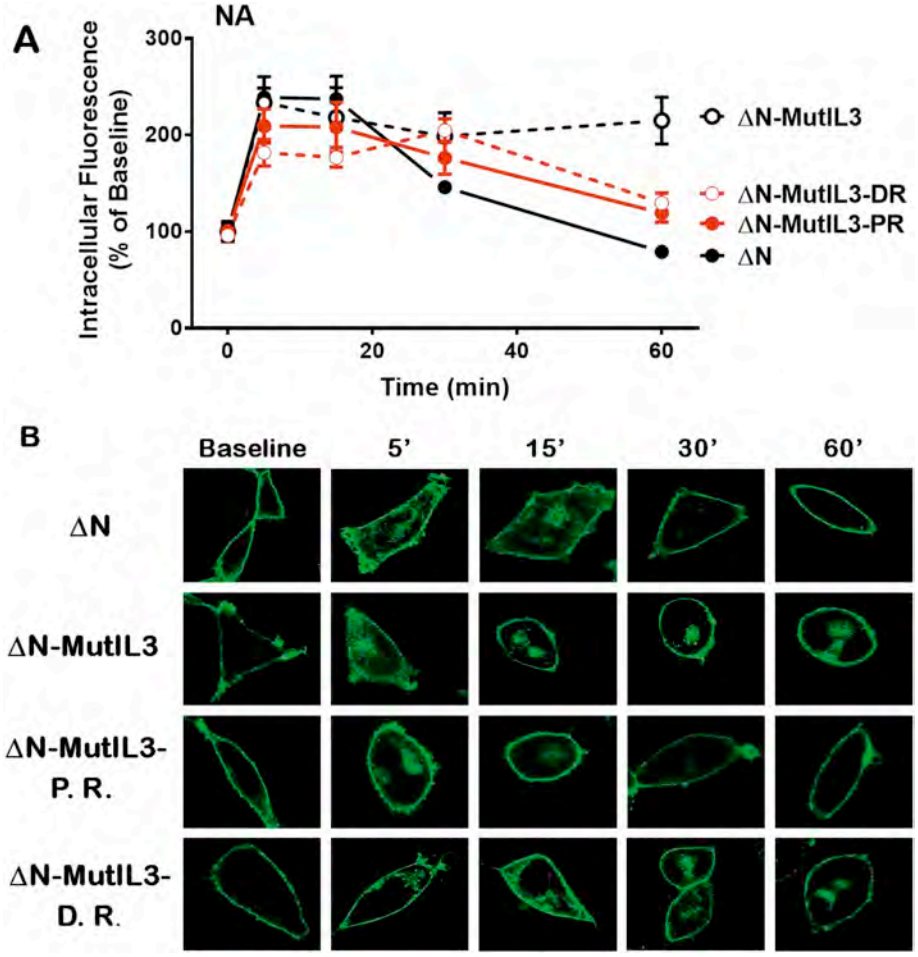

Fig. 9. Time-course of NA-induced internalization of the different α_{1D}-AR mutants. Panel A: Accumulation of intracellular fluorescence in response to NA 10 μM in cells expressing the ΔN, ΔN-MutIL3, ΔN-MutIL3-P.R. and ΔN-MutIL3-D.R. mutants. The intracellular fluorescence observed, under baseline conditions, in cells expressing each of the mutants was considered as 100%. Plotted are the means and vertical lines representing S.E.M. of 7 independent experiments in each of which 3–5 cells were analyzed (n = 20–35). Panel B: Representative images.

in α_{1D}-AR phosphorylation. However, in the total mutant, i. e. in the receptor in which all the 15 detected residues were substituted by non-phosphorylatable amino acids, a very weak but consistent receptor phosphorylation was detected, including some marginal actions of NA and PMA. It is important to consider that the reported phosphorylated residues were those that were consistently detected in the different mass spectrometry analysis performed and with high probability (i. e., high Ascore value [52]) [22]. However, during the course of that study, other phosphorylation sites were detected, although not in all the analysis or with low probability value. Therefore, it is possible that the remaining phosphorylation detected could be due to such sites. It should be mentioned that in our previous experiments using the mutant, ΔNΔC-MutIL3 (in which the amino and carboxyl termini were deleted and the identified phosphorylated sites at the IL3 were substituted by non-phosphorylatable residues), we were unable to detect receptor phosphorylation and no evidence for stimulation by NA or PMA were observed [22]. These data suggest the possibility that the unidentified phosphorylation site(s) could be present at the CTail.

Interestingly, the ΔN-MutIL3-P.R. mutant in which the proximal residue, T442, was modified to valine showed a decrease in baseline as well as in stimulated (NA and PMA) receptor phosphorylation. Such decrease was much larger than could have been anticipated, because only one of the phosphorylation targets was modified. This might suggest that such a residue could be an important regulator of total receptor phosphorylation. In addition, this mutant, although mainly localized at the plasma membrane, appears to colocalize poorly with β-arrestins in response to NA or PMA. This could be related with its decreased phosphorylation, since it has been shown structurally that phosphorylation of CTail peptides is critical for β-arrestin binding [53]. However, we cannot discard the possibility that the amino acid substitution could alter the structure in such a way that both receptor phosphorylation and colocalization with β-arrestins could be perturbed. GPCR association with β-arrestins has been mainly observed during homologous desensitization and the information of such possible interaction during heterologous desensitization is scarce; our present data suggest that this takes place in the course of both processes.

We previously observed that an amino- and carboxyl-termini-truncated receptor (i. e., the ΔNΔC α_{1D}-AR mutant) was able to increase intracellular calcium (G protein signaling) and could be desensitized by PKC activation [18]. The lack of the CTail altered the mitogen activated kinase pathways in some cells (Rat-1 fibroblasts or neuroblastoma B103), but not in the HEK cell line [17]. We also observed that mutants lacking the CTail (i. e., the ΔNΔC and ΔNΔC-MutIL3 receptors) were mainly localized in intracellular vesicles [16], which was confirmed in the present work. It has been reported that the α_{1D}-AR CTail is of importance for this receptor's proper plasma membrane targeting/insertion, because interaction with proteins such as syntrophins seems to be involved and this takes place through the receptor's CTail-located PDZ domain [44,45].

One of the major findings of the present work is the relationship between phosphorylatable residues and α_{1D}-AR cellular localization. As already mentioned, current ideas indicate that GPCR phosphorylation

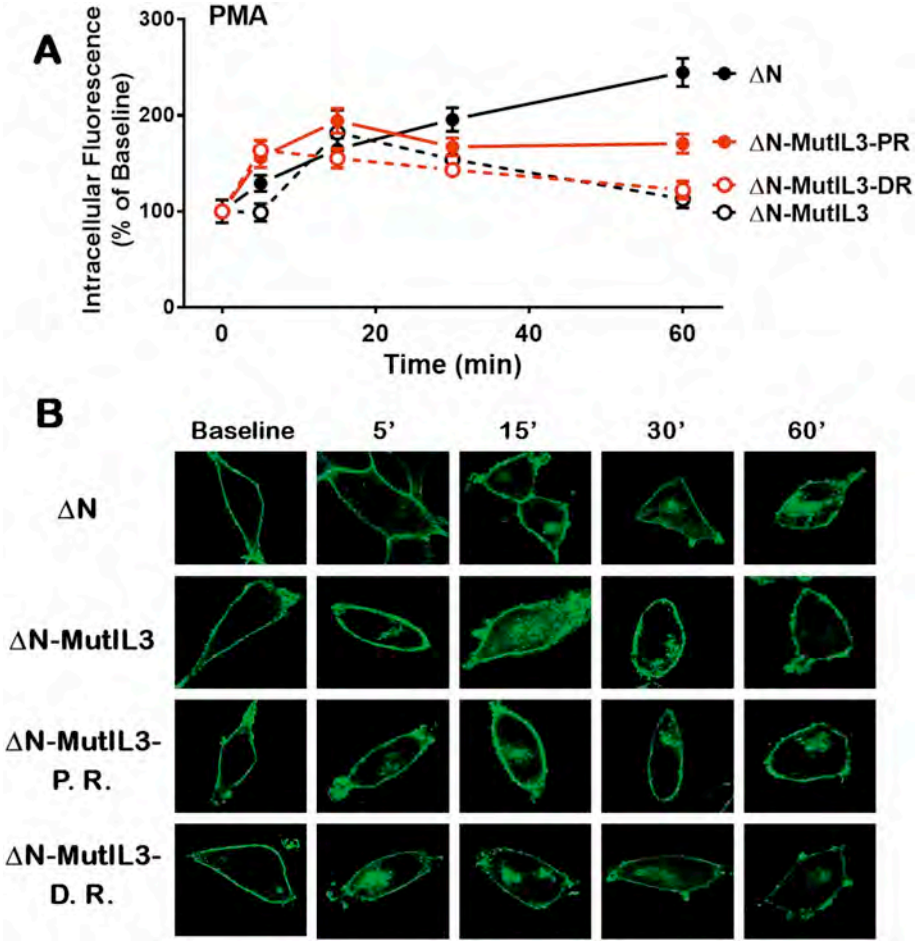

Fig. 10. Time-course of PMA-induced internalization of the different α_{1D}-AR mutants. Panel A: Accumulation of intracellular fluorescence in response to PMA1 μM in cells expressing the ΔN, ΔN-MutIL3, ΔN-MutIL3-P.R. and ΔN-MutIL3-D.R. mutants. The intracellular fluorescence observed, under baseline conditions, in cells expressing each of the mutants was considered as 100%. Plotted are the means and vertical lines representing S.E.M. of 7 independent experiments in each of which 3–5 cells were analyzed (n = 20–35). Panel B: Representative images.

triggers an association with the scaffold protein, β-arrestin, favoring the action of the endocytic machinery, receptor internalization and putatively switching from G protein-mediated signaling to β-arrestin-mediated action [28–33]. Some of the present results indicate that not all GPCR phosphorylations trigger receptor internalization, but rather the opposite: these results were totally unexpected and extremely puzzling, but at the same time, are provocative and their interpretation is challenging.

Our data indicate that the phosphorylation state of residues T507, S515, S516, and S518, which are located in the distal cluster of the C-terminal tail, regulate the subcellular localization of α_{1D}-ARs. When these residues were exchanged for non-phosphorylatable amino acids, the α_{1D}-ARs were localized mainly in intracellular vesicles. This was contrary to our expectations; i. e., we anticipated that the absence of phosphorylation sites would favor receptor retention at the plasma membrane. The possibility that the amino acid substitutions could alter the receptor's conformation was considered, but substitution of these same residues for the phospho-mimetic amino acid, aspartic acid, restored the receptor's plasma membrane localization. This is completely counter to the general idea that all GPCR phosphorylations could be functionally translated into desensitization, internalization, and possible degradation, and that a general action of protein phosphatases might trigger receptor recycling. The present findings suggest that these processes are more complex than anticipated and that it is likely that phosphorylation at some specific sites could lead to internalization, whereas at others this might favor membrane localization. To the best of our knowledge, this is the first study indicating that the phosphorylation of certain residues in a GPCR CTail could favor receptor localization at the plasma membrane. However, it must be mentioned that it has been reported that prolonged inhibition of PKC induces down-regulation of sphingosine 1-phosphate $S1P_1$ receptor surface expression, associated to decreased receptor phosphorylation, but the mechanisms or residues involved were not explored [54]. Similarly, there is evidence that phosphorylation of channel receptor (also called "ionotropic receptors") subunits, such as those of AMPA/Glutamate receptors or $GABA_A$ receptors increase their membrane localization (see, for example [55–58]).

The steady state density of plasma membrane receptors results from a balance between several complex processes, i. e., anterograde transport and insertion into the plasma membrane, internalization and recycling. Intracellular accumulation of receptors might result from decreased plasma membrane insertion, by a reduced time of residence in this organelle due to increased internalization or improper recycling; these events are not mutually exclusive and combinations might exit in response to key structural modification. The absence of α_{1D}-AR phosphorylation sites, in the distal CTail cluster, could render membrane targeting/insertion more difficult or could impede it. Similarly, it is possible that even if membrane insertion takes place, the absence of this phosphorylated sites could reduce the time of residence of these receptors at the plasma membrane by increasing its internalization and/or reducing its recycling back to this organelle. All these possibilities, together with the intrinsic activity of α_{1D}-ARs, might explain why with

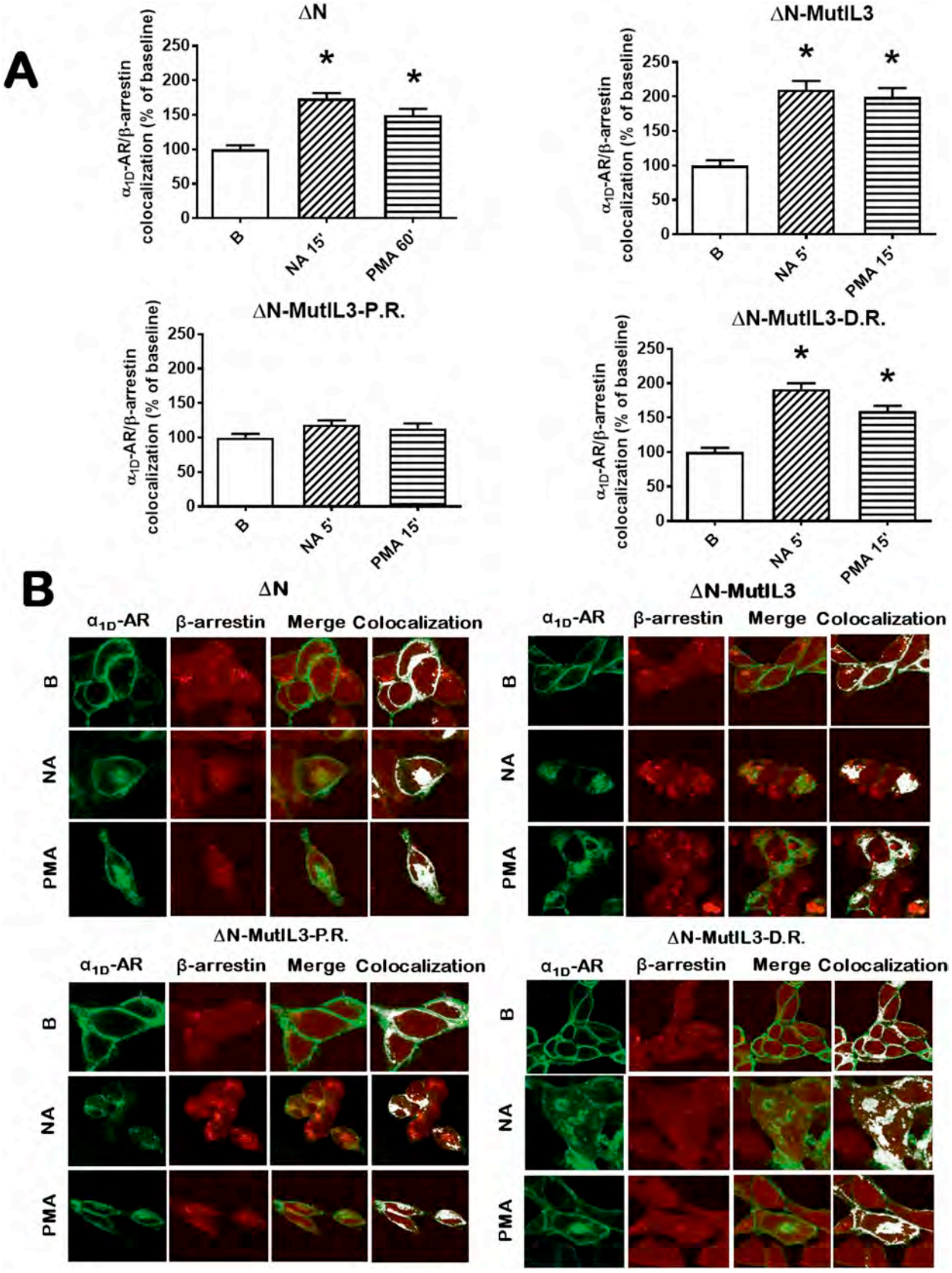

Fig. 11. Colocalization of the α_{1D}-AR mutants with endogenous β-arrestin 1/2. Panel A. Cells expressing the ΔN, ΔN-MutIL3, ΔN-MutIL3-P.R., and ΔN-MutIL3-D.R. mutants were treated without any agent (B, baseline) or stimulated with NA 10 μM or PMA 1 μM for the times at which each mutant showed a higher level of internalization (i. e., 5,. 15 or 30 min, as indicated in each histogram). Data were normalized considering the baseline colocalization observed, under baseline conditions, as 100%. Plotted are the means and vertical lines representing S.E.M. of 7 independent experiments in each of which 3–5 cells were analyzed (n = 20–35). * $P < 0.05$ vs. baseline (B). Panel B. Representative images are presented showing the α_{1D}-AR mutants (α_{1D}-AR, green channel), β-arrestins 1/2 (β-arrestins, red channel), merge images (merge) and colocalization (colocalization, white); treated as indicated; B, baseline, NA 10 μM or PMA 1 μM.

this receptor subtype, a relatively high degree of baseline phosphorylation was consistently observed [22–24,26,27]. In fact, S516 and S518 were detected as phosphorylated under baseline conditions in our work using mass spectrometry [22]. It is possible, therefore, to suggest that during receptor internalization and recycling processes, a series of different protein kinases and phosphatases could participate, forming functional elements of the signaling complexes, in a dynamic fashion.

Modification of the proximal cluster (T477, S486, and S492) with non-phosphorylatable amino acids also induces an important intracellular localization of these receptors, but substitution with aspartate did not favor their presence at the plasma membrane. This suggests that the proximal cluster might also play a role in receptor subcellular distribution but one of minor importance.

Interestingly, the ΔN-ΔC and ΔN-MutIL3-ΔC mutants exhibited a very high degree of internal localization as compared with the remainder of the mutants. This suggests the possibility that the CTail might exert a pivotal influence on the subcellular localization of this receptor. It is possible that, in addition to the detected phosphorylation sites, other undetected phosphorylation sites and/or structural elements in the CTail could have an impact on the expression of this GPCR at the plasma membrane.

The functional data obtained in this work are also worth considering. Previous information had shown that CTail truncation (i.e., the ΔNΔC mutants) did not decrease the ability of NA to increase intracellular calcium concentration [22,24], the latter being a G protein-triggered action. However, substitution of the phosphorylation sites with non-phosphorylatable amino acids leads the ΔN-MutIL3 receptor mutant to exhibit a partially decreased ability to increase intracellular calcium in response to NA; similar data were obtained for the ΔNΔC-MutIL3, as previously reported [22]. In addition, it was observed in this work that all of the different mutants of the CTail containing non-phosphorylatable amino acid substitutions exhibited a decreased calcium response to NA. In contrast, mutants with aspartate substitution in the clusters maintain the ability to increase intracellular calcium in response to the adrenergic agonist, either partially (ΔN-MutIL3-P. C. Asp mutant) or completely (ΔN-MutIL3-D. C. Asp and ΔN-MutIL3-T. M. Asp mutants). With these mutants there seems to exist a correlation between their ability to increase intracellular calcium in response to NA and their localization at the plasma membrane. In the case for the ΔNΔC mutant, there was a large accumulation of receptors in intracellular vesicles but nonetheless, a full calcium response was observed [22,24]; with the ΔNΔC-MutIL3 mutant NA-induced calcium response was smaller (confirmed in the present work, data not shown). It is likely, therefore, that membrane localization and an unmodified IL3 are critical for proper α_{1D}-AR-Gq interaction and consequent calcium signaling; however, we cannot discard the possibility that phosphorylatable residues or structural elements in the α_{1D}-AR CTail might participate in the interaction with Gq.

The ability of the different α_{1D}-AR receptor mutants to increase ERK 1/2 phosphorylation was studied. This is a signaling process that governs cell proliferation, differentiation and survival and it is modulated through many cellular pathways [32,59]. Not surprisingly, it was observed that both the expression of β-arrestin 1/2, and EGF receptor transactivation play roles in this action. We evaluated NA-activated ERK 1/2 phosphorylation in cells expressing the different receptors, and our results indicated that the kinetic profile of activation was very similar for all receptors containing the MutIL3 non-phosphorylatable mutation (i. e., a rapid and essentially sustained activation for up to 60 min) but different from what was observed with the ΔN receptor (i. e., a rapid activation that progressively decreased after 30 min); this is consistent with previous observations [22] and suggests the possibility that phosphorylation of IL3 plays a major role in turning off ERK 1/2 activation. Receptors containing the ΔN-MutIL3 mutation and non-phosphorylatable substitutions in the CTail markedly activated the ERK 1/2 pathway, but were defective in increasing intracellular calcium in response to NA, i.e., they behaved as biased receptors.

It has been observed that phosphorylation of a given GPCR can take place at different sites, depending on cell type and other conditions, and that this is associated with different functional outcomes. The possibility that such an association could be causally related has been suggested and has been denominated the bar-code hypothesis [60–62]. Efforts to characterize phosphorylation sites of different GPCRs and their functional significance have been reported (see, for example, [22,39,63–69]). The data presented here, supports the phosphorylation bar-code concept and indicates a new role for GPCR phosphorylation (i. e., one favoring membrane localization). If this is unique feature of α_{1D}-ARs or can be generalized for other GPCRs remains to be determined.

5. Conclusions

Our present results suggests that phosphorylation of a CTail distal cluster (T507, S515, S516 and S518) favors α_{1D}-AR localization at the plasma membrane, i. e., substitution of these residues for non-phosphorylatable amino acids results in the intracellular accumulation of the receptors, whereas phospho-mimetic substitution allows plasma membrane localization. Substitution of IL3 phosphorylation sites for non-phosphorylatable amino acids resulted in agonist-induced sustained ERK1/2 activation, which was not altered by additional mutations in the phosphorylated residues in the CTail. In contrast, mobilization of intracellular calcium appears to be controlled by IL3 and CTail phosphorylation states. IL3 mutation affects, differentially, NA- and PMA-induced receptor internalization and substitution of the CTail phosphorylation sites seems also to participate in this process.

Funding

This research was supported by Grants from Consejo Nacional de Ciencia y Tecnología(CONACYT) [Grant numbers 253156 and Fronteras 882] https://www.conacyt.gob.mx/ and Dirección General de Personal Académico-UNAM [PAPIIT, Grant number IN200915] http://dgapa.unam.mx/.

Declarations of interest

None.

Acknowledgments

The authors express their gratitude for advice and technical support to Dr. Maria Teresa Romero-Ávila from our laboratory and the following members of the indicated service units of our Institute: Dr. Héctor Malagón and Dr. Claudia Rivera (Bioterio); Dr. Fernando García, Dr. Ruth Rincón-Heredia, and Abrahan Rosas-Arellano (Microscopía); Juan Barbosa and Gerardo Coello (Cómputo); Dr. María Luisa Durán-Pastén (Canalopatías); and Aurey Hernández and Manuel Ortín (Taller) for their advice and technical support. Gabriel Carmona-Rosas is a doctoral student from Programa de Doctorado en Ciencias Biomédicas, Universidad Nacional Autónoma de México, and received a doctoral fellowship (CVU: 695329) from Consejo Nacional de Ciencia y Tecnología (CONACyT).

Appendix A. Supplementary data

Supplementary data to this article can be found online at https://doi.org/10.1016/j.cellsig.2018.11.003.

References

[1] R. Fredriksson, H.B. Schioth, The repertoire of G-protein-coupled receptors in fully sequenced genomes, Mol. Pharmacol. 67 (5) (2005) 1414–1425.
[2] J.P. Overington, B. Al-Lazikani, A.L. Hopkins, How many drug targets are there? Nat. Rev. Drug Discov. 5 (12) (2006) 993–996.
[3] K. Sriram, P.A. Insel, G Protein-coupled Receptors as Targets for Approved drugs:

how many Targets and how many drugs? Mol. Pharmacol. 93 (4) (2018) 251–258.
[4] J.P, D.B. Bylund Hieble, D.E. Clarke, D.C. Eikenburg, S.Z. Langer, R.J. Lefkowitz, K.P. Minneman, R.R. Ruffolo, International Union of Pharmacology. X. Recommendation for nomenclature of alpha 1-adrenoceptors: consensus update, Pharmacol. Rev. 47 (2) (1995) 267–270.
[5] M. Yang, F. Verfurth, R. Buscher, M.C. Michel, Is alpha1D-adrenoceptor protein detectable in rat tissues? Naunyn Schmiedeberg's Arch. Pharmacol. 355 (4) (1997) 438–446.
[6] D.F. McCune, S.E. Edelmann, J.R. Olges, G.R. Post, B.A. Waldrop, D.J. Waugh, D.M. Perez, M.T. Piascik, Regulation of the cellular localization and signaling properties of the alpha(1B)- and alpha(1D)-adrenoceptors by agonists and inverse agonists, Mol. Pharmacol. 57 (4) (2000) 659–666.
[7] C. Hague, Z. Chen, A.S. Pupo, N.A. Schulte, M.L. Toews, K.P. Minneman, The N terminus of the human {alpha}1D-adrenergic receptor prevents cell surface expression, J. Pharmacol. Exp. Ther. 309 (1) (2004) 388–397.
[8] A.S. Pupo, M.A. Uberti, K.P. Minneman, N-terminal truncation of human alpha1D-adrenoceptors increases expression of binding sites but not protein, Eur. J. Pharmacol. 462 (1–3) (2003) 1–8.
[9] D. Chalothorn, D.F. McCune, S.E. Edelmann, M.L. García-Cazarin, G. Tsujimoto, M.T. Piascik, Differences in the cellular localization and agonist-mediated internalization properties of the alpha(1)-adrenoceptor subtypes, Mol. Pharmacol. 61 (5) (2002) 1008–1016.
[10] J.A. García-Sáinz, M.E. Torres-Padilla, Modulation of basal intracellular calcium by inverse agonists and phorbol myristate acetate in rat-1 fibroblasts stably expressing alpha1d-adrenoceptors, FEBS Lett. 443 (3) (1999) 277–281.
[11] J.A. García-Sáinz, M.T. Romero-Ávila, L.C. Medina, Alpha(1D)-Adrenergic receptors constitutive activity and reduced expression at the plasma membrane, Methods Enzymol. 484 (2010) 109–125.
[12] R. Gisbert, M.A. Noguera, M.D. Ivorra, P. D'Ocon, Functional evidence of a constitutively active population of alpha(1D)-adrenoceptors in rat aorta, J. Pharmacol. Exp. Ther. 295 (2) (2000) 810–817.
[13] R. Gisbert, K. Ziani, R. Miquel, M.A. Noguera, M.D. Ivorra, E. Anselmi, P. D'Ocon, Pathological role of a constitutively active population of alpha(1D)-adrenoceptors in arteries of spontaneously hypertensive rats, Br. J. Pharmacol. 135 (1) (2002) 206–216.
[14] M.A. Noguera, M.D. Ivorra, P. D'Ocon, Functional evidence of inverse agonism in vascular smooth muscle, Br. J. Pharmacol. 119 (1) (1996) 158–164.
[15] Z. Chen, C. Hague, R.A. Hall, K.P. Minneman, Syntrophins regulate alpha1D-adrenergic receptors through a PDZ domain-mediated interaction, J. Biol. Chem. 281 (18) (2006) 12414–12420.
[16] I.A. Gallardo-Ortiz, S.N. Rodriguez-Hernandez, J.J. Lopez-Guerrero, L. Del Valle-Mondragon, P. Lopez-Sanchez, R.M. Touyz, R. Villalobos-Molina, Role of alpha1D -adrenoceptors in vascular wall hypertrophy during angiotensin II-induced hypertension, Auton. Autacoid Pharmacol. 35 (3) (2015) 17–31.
[17] J.S. Lyssand, M.C. Defino, X.B. Tang, A.L. Hertz, D.B. Feller, J.L. Wacker, M.E. Adams, C. Hague, Blood pressure is regulated by an {alpha}1D-adrenergic receptor/dystrophin signalosome, J. Biol. Chem. 283 (27) (2008) 18792–18800.
[18] A. Tanoue, Y. Nasa, T. Koshimizu, H. Shinoura, S. Oshikawa, T. Kawai, S. Sunada, S. Takeo, G. Tsujimoto, The alpha(1D)-adrenergic receptor directly regulates arterial blood pressure via vasoconstriction, J. Clin. Invest. 109 (6) (2002) 765–775.
[19] R. Villalobos-Molina, M. Ibarra, Alpha 1-adrenoceptors mediating contraction in arteries of normotensive and spontaneously hypertensive rats are of the alpha 1D or alpha 1A subtypes, Eur. Aust. J. Pharm. 298 (3) (1996) 257–263.
[20] R. Villalobos-Molina, M. Ibarra, Increased expression and function of vascular alpha1D-adrenoceptors may mediate the prohypertensive effects of angiotensin II, Mol. Interv. 5 (6) (2005) 340–342.
[21] C. Hague, M.A. Uberti, Z. Chen, R.A. Hall, K.P. Minneman, Cell surface expression of {alpha}1D-adrenergic receptors is controlled by heterodimerization with {alpha} 1B-adrenergic receptors, J. Biol. Chem. 279 (15) (2004) 15541–15549.
[22] M.A. Alfonzo-Méndez, G. Carmona-Rosas, D.A. Hernández-Espinosa, M.T. Romero-Ávila, J.A. García-Sáinz, Different phosphorylation patterns regulate alpha1D-adrenoceptor signaling and desensitization, Biochim. Biophys. Acta 1865 (6) (2018) 842–854.
[23] M.A. Alfonzo-Méndez, J.A. Castillo-Badillo, M.T. Romero-Ávila, R. Rivera, J. Chun, J.A. García-Sáinz, Carboxyl terminus-truncated alpha1D-adrenoceptors inhibit the ERK pathway, Naunyn Schmiedeberg's Arch. Pharmacol. 389 (8) (2016) 911–920.
[24] C.E. Rodríguez-Pérez, M.T. Romero-Ávila, G. Reyes-Cruz, J.A. García-Sáinz, Signaling properties of human alpha(1D)-adrenoceptors lacking the carboxyl terminus: intrinsic activity, agonist-mediated activation, and desensitization, Naunyn Schmiedeberg's Arch. Pharmacol. 380 (2) (2009) 99–107.
[25] T.S. Kountz, K.S. Lee, S. Aggarwal-Howarth, E. Curran, J.M. Park, D.A. Harris, A. Stewart, J. Hendrickson, N.D. Camp, A. Wolf-Yadlin, E.H. Wang, J.D. Scott, C. Hague, Endogenous N-terminal domain cleavage modulates alpha1D-adrenergic receptor pharmacodynamics, J. Biol. Chem. 291 (35) (2016) 18210–18221.
[26] J.A. García-Sáinz, C.E. Rodríguez-Pérez, M.T. Romero-Ávila, Human alpha-1D adrenoceptor phosphorylation and desensitization, Biochem. Pharmacol. 67 (2004) 1853–1858.
[27] J.A. García-Sáinz, F.G. Vázquez-Cuevas, M.T. Romero-Ávila, Phosphorylation and desensitization of alpha1d-adrenergic receptors, Biochem. J. 353 (2001) 603–610 Pt 3.
[28] K. Eichel, M. von Zastrow, Subcellular organization of GPCR signaling, Trends Pharmacol. Sci. 39 (2) (2018) 200–208.
[29] S.K. Shenoy, R.J. Lefkowitz, Beta-Arrestin-mediated receptor trafficking and signal transduction, Trends Pharmacol. Sci. 32 (9) (2011) 521–533.
[30] R.J. Lefkowitz, A brief history of G-protein coupled receptors (Nobel Lecture), Angew Chem. Int. Ed. Engl. 52 (25) (2013) 6366–6378.
[31] A.R. Thomsen, B. Plouffe, T.J. Cahill 3rd, A.K. Shukla, J.T. Tarrasch, A.M. Dosey, A.W. Kahsai, R.T. Strachan, B. Pani, J.P. Mahoney, L. Huang, B. Breton, F.M. Heydenreich, R.K. Sunahara, G. Skiniotis, M. Bouvier, R.J. Lefkowitz, GPCR-G protein-beta-arrestin super-complex mediates sustained G protein signaling, Cell 166 (4) (2016) 907–919.
[32] G. Carmona-Rosas, R. Alcantara-Hernandez, D.A. Hernandez-Espinosa, Dissecting the signaling features of the multi-protein complex GPCR/beta-arrestin/ERK1/2, Eur. J. Cell Biol. 97 (5) (2018) 349–358.
[33] C.A. Moore, S.K. Milano, J.L. Benovic, Regulation of receptor trafficking by GRKs and arrestins, Annu. Rev. Physiol. 69 (2007) 451–482.
[34] S.E. Avendaño-Vázquez, A. García-Caballero, J.A. García-Sáinz, Phosphorylation and desensitization of the lysophosphatidic acid receptor LPA1, Biochem. J. 385 (2005) 677–684 Pt 3.
[35] J.A. Castillo-Badillo, O.B. Sánchez-Reyes, M.A. Alfonzo-Méndez, M.T. Romero-Ávila, G. Reyes-Cruz, J.A. García-Sáinz, alpha1B-adrenergic receptors differentially associate with rab proteins during homologous and heterologous desensitization, PLoS One 10 (3) (2015) e0121165.
[36] R.J. Ward, E. Alvarez-Curto, G. Milligan, Using the Flp-in T-Rex system to regulate GPCR expression, Methods Mol. Biol. 746 (2011) 21–37.
[37] G. Grynkiewicz, M. Poenie, R.Y. Tsien, A new generation of Ca2+ indicators with greatly improved fluorescence properties, J. Biol. Chem. 260 (6) (1985) 3440–3450.
[38] U.K. Laemmli, Cleavage of structural proteins during the assembly of the head of bacteriophage T4, Nature 227 (5259) (1970) 680–685.
[39] R. Alcántara-Hernández, A. Hernández-Méndez, M.T. Romero-Ávila, M.A. Alfonzo-Méndez, A.S. Pupo, J.A. García-Sáinz, Noradrenaline, oxymetazoline and phorbol myristate acetate induce distinct functional actions and phosphorylation patterns of alpha1A-adrenergic receptors, Biochim. Biophys. Acta 1864 (12) (2017) 2378–2388.
[40] T.J. Collins, ImageJ for microscopy, BioTechniques 43 (1 Suppl) (2007) 25–30.
[41] M. Hachet-Haas, N. Converset, O. Marchal, H. Matthes, S. Gioria, J.L. Galzi, S. Lecat, FRET and colocalization analyzer–a method to validate measurements of sensitized emission FRET acquired by confocal microscopy and available as an ImageJ Plug-in, Microsc. Res. Tech. 69 (12) (2006) 941–956.
[42] S.M. Hartig, Basic image analysis and manipulation in ImageJ, Curr. Protoc. Mol. Biol 14 (2013) 15.1–15.12.
[43] B. Chazotte, Labeling membrane glycoproteins or glycolipids with fluorescent wheat germ agglutinin, Cold Spring Harb. Protoc. (5) (2011).
[44] L. Chen, R.R. Hodges, C. Funaki, D. Zoukhri, R.J. Gaivin, D.M. Perez, D.A. Dartt, Effects of alpha1D-adrenergic receptors on shedding of biologically active EGF in freshly isolated lacrimal gland epithelial cells, Am. J. Physiol. Cell Physiol. 291 (5) (2006) C946–C956.
[45] A. Levitzki, E. Mishani, Tyrphostins and other tyrosine kinase inhibitors, Annu. Rev. Biochem. 75 (2006) 93–109.
[46] D.S. Kang, X. Tian, J.L. Benovic, Role of beta-arrestins and arrestin domain-containing proteins in G protein-coupled receptor trafficking, Curr. Opin. Cell Biol. 27 (2014) 63–71.
[47] S.K. Shenoy, R.J. Lefkowitz, Seven-transmembrane receptor signaling through beta-arrestin, Science (308) (2005) cm10.
[48] J.A. García-Sáinz, J. Vázquez-Prado, L.C. Medina, Alpha 1-adrenoceptors: function and phosphorylation, Eur. J. Pharmacol. 389 (1) (2000) 1–12.
[49] J.A. García-Sáinz, R. Villalobos-Molina, The elusive alpha(1D)-adrenoceptor: molecular and cellular characteristics and integrative roles, Eur. J. Pharmacol. 500 (1–3) (2004) 113–120.
[50] R. Villalobos-Molina, M. Ibarra, Vascular alpha 1D-adrenoceptors: are they related to hypertension? Arch. Med. Res. 30 (5) (1999) 347–352.
[51] R. Villalobos-Molina, J.J. López-Guerrero, M. Ibarra, Functional evidence of alpha1D-adrenoceptors in the vasculature of young and adult spontaneously hypertensive rats, Br. J. Pharmacol. 126 (7) (1999) 1534–1536.
[52] S.A. Beausoleil, J. Villen, S.A. Gerber, J. Rush, S.P. Gygi, A probability-based approach for high-throughput protein phosphorylation analysis and site localization, Nat. Biotechnol. 24 (10) (2006) 1285–1292.
[53] A.K. Shukla, A. Manglik, A.C. Kruse, K. Xiao, R.I. Reis, W.C. Tseng, D.P. Staus, D. Hilger, S. Uysal, L.Y. Huang, M. Paduch, P. Tripathi-Shukla, A. Koide, S. Koide, W.I. Weis, A.A. Kossiakoff, B.K. Kobilka, R.J. Lefkowitz, Structure of active beta-arrestin-1 bound to a G-protein-coupled receptor phosphopeptide, Nature 497 (7447) (2013) 137–141.
[54] S.C. Sensken, M.H. Graler, Down-regulation of S1P1 receptor surface expression by protein kinase C inhibition, J. Biol. Chem. 285 (9) (2010) 6298–6307.
[55] A.M. Abramian, E. Comenencia-Ortiz, A. Modgil, T.N. Vien, Y. Nakamura, Y.E. Moore, J.L. Maguire, M. Terunuma, P.A. Davies, S.J. Moss, Neurosteroids promote phosphorylation and membrane insertion of extrasynaptic GABAA receptors, Proc. Natl. Acad. Sci. U. S. A. 111 (19) (2014) 7132–7137.
[56] E. Comenencia-Ortiz, S.J. Moss, P.A. Davies, Phosphorylation of GABAA receptors influences receptor trafficking and neurosteroid actions, Psychopharmacology 231 (17) (2014) 3453–3465.
[57] C. Kibaly, A.Y. Kam, H.H. Loh, P.Y. Law, Naltrexone facilitates learning and delays extinction by increasing AMPA receptor phosphorylation and membrane insertion, Biol. Psychiatry 79 (11) (2016) 906–916.
[58] D.T. Lin, Y. Makino, K. Sharma, T. Hayashi, R. Neve, K. Takamiya, R.L. Huganir, Regulation of AMPA receptor extrasynaptic insertion by 4.1N, phosphorylation and palmitoylation, Nat. Neurosci. 12 (7) (2009) 879–887.
[59] W. Kolch, Meaningful relationships: the regulation of the Ras/Raf/MEK/ERK pathway by protein interactions, Biochem. J. 351 (Pt 2) (2000) 289–305.
[60] A.B. Tobin, G-protein-coupled receptor phosphorylation: where, when and by whom, Br. J. Pharmacol. 153 (Suppl. 1) (2008) S167–S176.
[61] A.B. Tobin, A.J. Butcher, K.C. Kong, Location, location, location...Site-specific GPCR phosphorylation offers a mechanism for cell-type-specific signalling, Trends Pharmacol. Sci. 29 (8) (2008) 413–420.
[62] I. Torrecilla, E.J. Spragg, B. Poulin, P.J. McWilliams, S.C. Mistry, A. Blaukat, A.B. Tobin, Phosphorylation and regulation of a G protein-coupled receptor by protein kinase CK2, J. Cell Biol. 177 (1) (2007) 127–137.
[63] M. Bouzo-Lorenzo, I. Santo-Zas, M. Lodeiro, R. Nogueiras, F.F. Casanueva, M. Castro, Y. Pazos, A.B. Tobin, A.J. Butcher, J.P. Camina, Distinct phosphorylation

sites on the ghrelin receptor, GHSR1a, establish a code that determines the functions of ss-arrestins, Sci. Rep. 6 (2016) 22495.

[64] A.J. Butcher, B.D. Hudson, B. Shimpukade, E. Alvarez-Curto, R. Prihandoko, T. Ulven, G. Milligan, A.B. Tobin, Concomitant action of structural elements and receptor phosphorylation determine arrestin-3 interaction with the free fatty acid receptor FFA4, J. Biol. Chem. 289 (26) (2014) 18451–18465.

[65] A.J. Butcher, R. Prihandoko, K.C. Kong, P. McWilliams, J.M. Edwards, A. Bottrill, S. Mistry, A.B. Tobin, Differential G-protein-coupled receptor phosphorylation provides evidence for a signaling bar code, J. Biol. Chem. 286 (13) (2011) 11506–11518.

[66] R. Prihandoko, E. Alvarez-Curto, B.D. Hudson, A.J. Butcher, T. Ulven, A.M. Miller, A.B. Tobin, G. Milligan, Distinct phosphorylation clusters determine the signaling outcome of free fatty acid receptor 4/G protein-coupled receptor 120, Mol. Pharmacol. 89 (5) (2016) 505–520.

[67] D. Zindel, S. Engel, A.R. Bottrill, J.P. Pin, L. Prezeau, A.B. Tobin, M. Bunemann, C. Krasel, A.J. Butcher, Identification of key phosphorylation sites in PTH1R that determine arrestin3 binding and fine-tune receptor signaling, Biochem. J. 473 (22) (2016) 4173–4192.

[68] X. Chen, B. Bai, Y. Tian, H. Du, J. Chen, Identification of serine 348 on the apelin receptor as a novel regulatory phosphorylation site in apelin-13-induced G protein-independent biased signaling, J. Biol. Chem. 289 (45) (2014) 31173–31187.

[69] L. Bray, C. Froment, P. Pardo, C. Candotto, O. Burlet-Schiltz, J.M. Zajac, C. Mollereau, L. Mouledous, Identification and functional characterization of the phosphorylation sites of the neuropeptide FF2 receptor, J. Biol. Chem. 289 (49) (2014) 33754–33766.

PLOS ONE

RESEARCH ARTICLE

Apoptosis contributes to protect germ cells from the oogenic germline starvation response but is not essential for the gonad shrinking or recovery observed during adult reproductive diapause in *C. elegans*

E. Carranza-García, R. E. Navarro*

Departamento de Biología Celular y Desarrollo, Instituto de Fisiología Celular, Universidad Nacional Autónoma de México, Ciudad de México, México

* rnavarro@ifc.unam.mx

Check for updates

OPEN ACCESS

Citation: Carranza-García E, Navarro RE (2019) Apoptosis contributes to protect germ cells from the oogenic germline starvation response but is not essential for the gonad shrinking or recovery observed during adult reproductive diapause in *C. elegans*. PLoS ONE 14(6): e0218265. https://doi.org/10.1371/journal.pone.0218265

Editor: Myon-Hee Lee, East Carolina University, UNITED STATES

Received: December 17, 2018

Accepted: May 29, 2019

Published: June 13, 2019

Copyright: © 2019 Carranza-García, Navarro. This is an open access article distributed under the terms of the Creative Commons Attribution License, which permits unrestricted use, distribution, and reproduction in any medium, provided the original author and source are credited.

Data Availability Statement: All relevant data are within the manuscript.

Funding: This work was supported by grants from Dirección General de Asuntos del Personal Académico PAPIIT-UNAM (IN207415 and IN208918) and Consejo Nacional de Ciencia y Tecnología-MEXICO (220987) to REN. ECG is a Doctoral Student from Programa de Doctorado en Ciencias Biomédicas, Universidad Nacional

Abstract

When *C. elegans* hermaphrodites are deprived of food during the mid-L4 larval stage and throughout adulthood, they enter an alternative stage termed "adult reproductive diapause (ARD)" in which they halt reproduction and extend their lifespan. During ARD, germ cell proliferation stops; oogenesis is slowed; and the gonad shrinks progressively, which has been described as the "oogenic germline starvation response". Upon refeeding, the shrunken gonad is regenerated, and animals recover fertility and live out their remaining lifespan. Little is known about the effects of ARD on oocyte quality after ARD. Thus, the aim of this study was to determine how oocyte quality is affected after ARD by measuring brood size and embryonic lethality as a reflection of defective oocyte production. We found that ARD affects reproductive capacity. The oogenic germline starvation response protects oogenic germ cells by slowing oogenesis to prevent prolonged arrest in diakinesis. In contrast to a previous report, we found that germ cell apoptosis is not the cause of gonad shrinkage; instead, we propose that ovulation contributes to gonad shrinkage during the oogenic germline starvation response. We show that germ cell apoptosis increases and continues during ARD via *lin-35/Rb* and an unknown mechanism. Although apoptosis contributes to maintain germ cell quality during ARD, we demonstrated that apoptosis is not essential to preserve animal fertility. Finally, we show that IIS signaling inactivation partially participates in the oogenic germline starvation response.

Introduction

To ensure species continuity, animals have developed mechanisms for protecting germ cells during stressful conditions. The *C. elegans* hermaphrodite germline serves as an excellent model for studying cell biology. In *C. elegans* hermaphrodites, 2 identical U-shaped gonad arms contain germ cells (Fig 1A). Under control conditions, L4 hermaphrodites (Fig 1C and

Autónoma de México (UNAM) and received a fellowship from CONACyT (361899). The funders had no role in study design, data collection and analysis, decision to publish, or preparation of the manuscript.

Competing interests: The authors have declared that no competing interests exist.

1E) produce approximately 40 germ cells that give rise 160 spermatids per gonad arm, which are stored within each spermatheca. Thereafter, during the adult stage, the remaining germ cells either differentiate into oocytes or are eliminated by physiological germline apoptosis [1, 2]. Physiological apoptosis is an essential mechanism for maintaining oocyte quality during oogenesis, as it promotes the allocation of nutrients to growing oocytes [3]. The most proximal oocytes arrest in diakinesis until they are fertilized, then complete meiosis and begin embryogenesis [3, 4] (Fig 1A and 1D). During its fertile period, a hermaphrodite produces approximately 300 new organisms in 3 days by self-fertilization with very low embryonic lethality (approx. 1–2 dead embryos/animal). Then, they cease laying eggs and live for 15 more days [4].

The short, highly stereotyped reproductive cycle of *Caenorhabditis elegans* can be altered when animals are deprived of food and enter into reversible states of growth arrest or diapause, depending on the stage in which they are deprived of food [5]. Animals subjected to high temperatures, crowding or fasting during the L1-L2 stage transition develop into a well-studied alternative larval stage known as the "dauer" stage. During dauer diapause, animals seal their orifices and form a thick impermeable cuticle, allowing them to endure stress for months [6].

When mid-L4 larvae or adult hermaphrodites face starvation conditions, they enter into adult reproductive diapause (ARD), characterized by delayed reproduction and an extended lifespan [7, 8]. ARD is a not yet fully elucidated form of diapause and differs from dauer diapause since animals starved at a low population density can enter and maintain this alternate developmental stage [8]. It has been observed that when starvation begins during the late-L4 or adult stage, embryos are retained *in utero*, hatch and cause the hermaphrodite's death [7]; however, this fate can be avoided if embryo viability is inhibited [8]. During ARD, the hermaphrodites' gonad shows a remarkable change; it shrinks in size progressively and the number of germ cells decreases to a small pool of ~35 cells [7] (Fig 1B and 1F). Starvation causes subsequent halting of the cell cycle in mitotically proliferating germ cells, which remain quiescent until conditions are restored [9]. The starved hermaphrodites form a single oocyte per gonad arm and usually carry 1–2 developing embryos within the uterus. These embryos are the result of delayed ovulation and fertilization, which occur approximately every 8 h ([8] and Fig 1B and 1F).

Remarkably, gonad shrinking and delayed reproduction are reversible [7, 8]. Following refeeding, germ cells resume their cell-cycle progression and start dividing, causing gonad regeneration, which, at least morphologically under the microscope, resembles a young adult gonad that never has been starved [7–9]. Hermaphrodites recover fertility and produce progeny by self-fertilization or mating [7]. Angelo and van Gilst (2009) proposed that apoptosis plays a crucial role during ARD, since apoptosis-defective mutants subjected to starvation from the mid-L4 stage do not reduce their gonad size and are unable to recover fertility after ARD [7].

ARD extends not only the total lifespan but also the reproductive period of animals [7]. In *C. elegans*, as in many other organisms, fertility declines with age [10], and oocyte quality is greatly affected during aging [3]. Adult reproductive diapause has been proposed as an anti-aging mechanism for protecting the germline [7]. Despite the numerous unexplained aspects of this phenomenon, whether ARD protects oocyte quality and the mechanisms that control this phenomenon have not yet been determined.

In this report, we use brood size and embryonic lethality to reflect defective oocyte production to investigate the effects of ARD on oocyte quality. We found that ARD affects gametes' reproductive capacity and prevents oogenic germ cells from undergoing prolonged arrest in diakinesis. During ARD, germ cell apoptosis is very active; however, in contrast to a previous report, we found that it is not important for gonad shrinking. We observed that increased

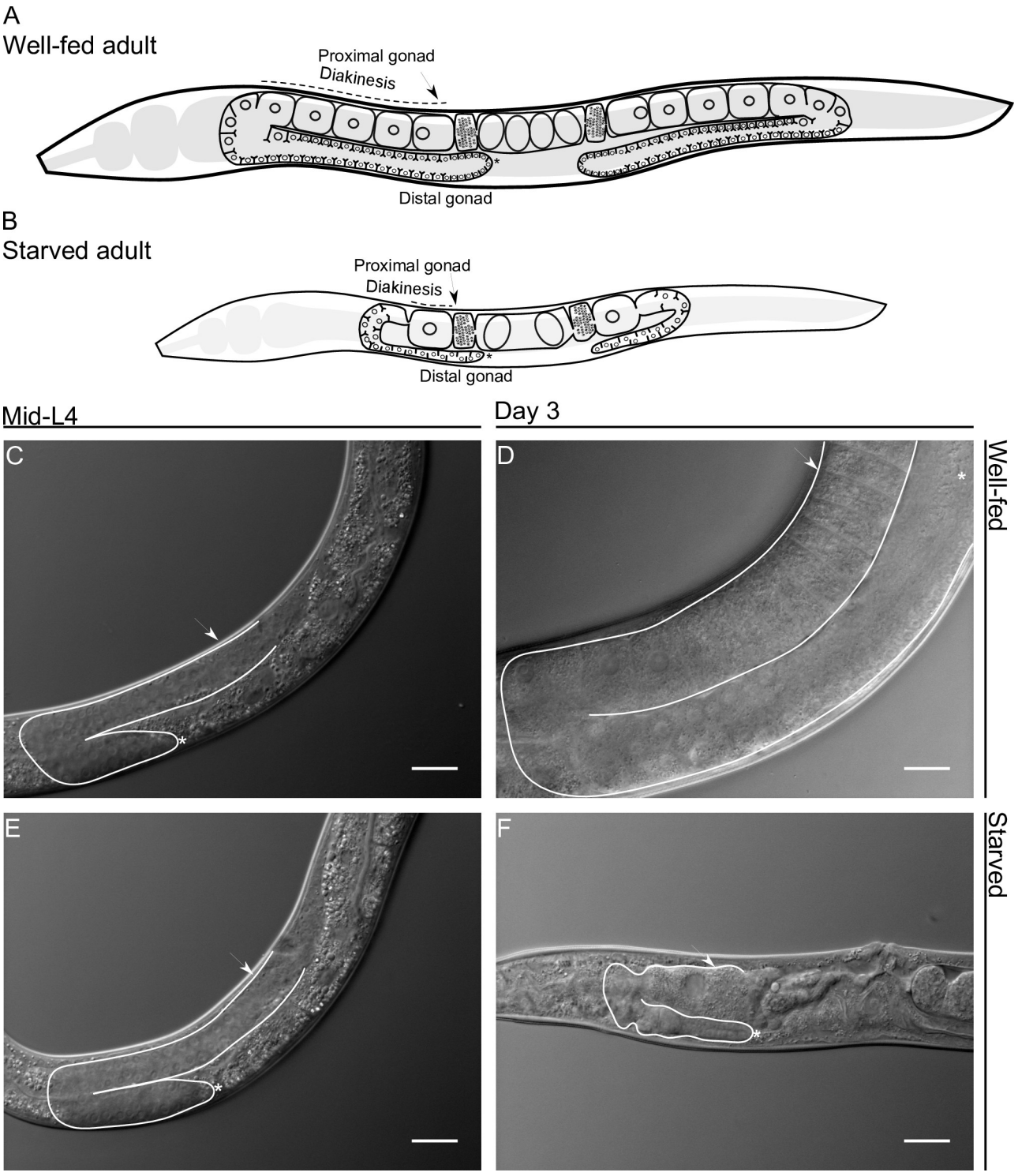

Fig 1. Comparison between well-fed and starved adult hermaphrodite gonad arms in *Caenorhabditis elegans*. Schematic representation of well-fed (A) and starved (B) adult hermaphrodites. (C, E) Nomarski image of mid-L4 gonad arms. (D) Nomarski image of a hermaphrodite that was well-fed for 3 days. (F) Nomarski image of a hermaphrodite that was starved for 3 days from mid-L4. In all images one gonad arm is outlined in white; the distal gonad is marked with an asterisk (*); and the arrow points to the proximal gonad. Scale bar = 20 μm.

https://doi.org/10.1371/journal.pone.0218265.g001

germ cell apoptosis during ARD depends partially on *lin-35*/Rb and an unknown mechanism. We propose that ovulation causes gonad shrinking by exhausting gonad contents when a few oocytes are produced. Finally, DAF-2 inactivation causes gonad shrinking in the presence of food suggesting that it may partially participate in this pathway. Here, we describe the effects of ARD on fertility and the regulation of germ cell apoptosis under starvation conditions.

Materials and methods

Strains

C. elegans strains were maintained as described previously [11]. All strains were grown at 20˚C or the permissive temperature using *Escherichia coli* OP50 as food. The wild-type strain was N2 Bristol. For the *daf-2* experiments, 15˚C and 25˚C were used as the permissive and restrictive temperatures, respectively. For the *pha-4(zu225)* experiments, 24˚C and 15˚C were used as the permissive and restrictive temperatures, respectively. Heterozygous EU31 *skn-1(zu135)* animals segregate as Unc and WT: Unc individuals were picked for maintenance, and WT individuals laid eggs that did not hatch. For the *fog-1(q253)* experiments, 15˚C and 25˚C were used as the permissive and restrictive temperatures, respectively. *fog-1(q253)* worms were maintained at 15˚C and upshifted to 25˚C to feminize their germline. The alleles used were as follows: JK560 *fog-1(q253)*, CB4108 *fog-2(q71)*, MD701 *ced-1*::*gfp(bcIs39)*, *cep-1(gk138);ced-1*::*gfp(bcIs39)*, MT3002 *ced-3(n1286)*, RB2071 *ced-3(ok2734)*, MT1522 *ced-3(n717)*, CB1370 *daf-2(e1370)*, DR1309 *daf-16(m26);daf-2(e1370)*, MT10430 *lin-35(n745)*, GR1307 *daf-16(mgDf50)*, EU31 *skn-1(zu135)*, SM190 *pha-4(zu225)*, VC446 *alg-1(gk214)*, RB1206 *rsks-1(ok1255)*, SS712 *ife-1(bn127)*, WS2973 *gla-3(op212)*, RN083 *daf-2(e1370);ced-1*::*gfp*, and RN084 *lin-35(n745); ced-1*::*gfp*. All the strains were obtained from the *Caenorhabditis* Genetics Center (CGC).

Image acquisition

Animals were mounted with 10 μl of 0.01% tetramisole in M9 on 2% agarose pads and observed using a Nikon Eclipse E600 microscope equipped with an AxioCam MRc camera (Zeiss). Images were obtained using Axio Vision software (Zeiss) and processed with ImageJ software.

Starvation protocol

We performed the starvation protocol described by Seidel and Kimble (2011) [8]. Synchronous L1 populations were obtained by bleaching gravid hermaphrodites. The resulting embryos were washed in M9, transferred to conical tubes and incubated for 18 h at 20˚C in a gyratory rocker. Hatched L1s were collected and placed in 10 cm plates seeded with OP50 at a density of ~1,200 L1s per plate until they reached the mid-L4 stage. To initiate starvation, the animals were collected with M9 medium and washed up to 6 times until no turbidity was observed; they were then placed in 10 cm plates with or without food at a density of ~10,000 animals per plate.

Apoptosis assay

Cell corpses were counted using the MD701 *bcIs39* [*Plim-7*::*ced-1*::*gfp;lin-15(+)*] transgenic strain. After the starvation protocol, animals were placed in seeded plates as the control condition or in unseeded plates as the starvation condition. Animals were transferred daily until they ceased laying eggs and were then picked, anesthetized, mounted and visualized under an epifluorescence microscope.

Germ cell quantification

We used DAPI staining to quantify the germ cells in each gonad arm as described by Silva-García and Navarro (2013) with some modifications [12]. Animals were dissected on glass coverslips, which were then inverted and placed on a polylysine-treated slide. The samples were freeze-cracked, fixed, stained with DAPI, mounted using 10 μl of Vectashield (Vector Lab) and visualized through fluorescence microscopy.

Fertility assay

We determined the brood size and embryonic lethality, resulting from self-fertilization and mating as described by Bukhari *et al*., 2012 [13]. Single mid-L4 hermaphrodites were transferred to seeded NGM plates and maintained at 20˚C. Animals were transferred to fresh plates each day until they ceased laying eggs. For the recovery of self-fertilizing animals following starvation, single hermaphrodites that had spent 5 days under starvation were transferred to seeded NGM plates and then to fresh plates each day until they ceased laying eggs. For mating animals, either mid-L4, well-fed 6-day-old or recovered *fog-(q253)* or *fog-2(q71)* animals were individually transferred to seeded NGM plates and crossed with 4 well-fed 1-day-old wild-type males. Twenty-four hours after the transfer of hermaphrodites, the embryos that did not hatch were scored as dead embryos. Forty-eight hours after the transfer of hermaphrodites, the number of larvae was scored.

Long-term immobilization

We determined the temporal progression of germ cell corpse clearance using a method described by Kim *et al*., 2013 [14]. Briefly, animals were immobilized using 0.5 μl of a suspension of polystyrene beads (Polysciences, 2.5% by volume, 0.1 μm diameter) on 10% agarose pads. Germ cell corpses were visualized and imaged at 60X magnification until they were completely cleared.

Ovulation rate

We followed the methodology described by Huang *et al*., 2012 [15]. Animals were individually scored for the number of embryos within the uterus using Nomarski microscopy, then transferred to fresh plates with food for 4 h and finally scored for the number of embryos within the uterus and those laid on the plate. More than 30 animals were observed for each genotype. The ovulation rate per gonad arm per hour = (embryos at the end of a time interval—embryos at the beginning) / (2 x number of animals x time interval).

Statistical comparisons

The t-test or Mann-Whitney U test was used for comparisons with controls in fertility assays. For multiple comparisons in apoptosis, fertility assays and germ cell corpse clearance assays, the data were analyzed using one way ANOVA and Dunn's test for multiple comparisons.

Results

Animals that undergo ARD do not recover their full fertility because this condition affects germ cell quality

We wanted to study how fertility and germ cell quality are affected after exposing animals to ARD. Although it has been reported that wild-type animals survive up to 30 days in ARD, their self-fertility is severely impaired after 15 days of starvation [7]. Therefore, we decided to

study the effect of ARD when animals are exposed to 5 days of starvation because this period is sufficient to reduce hermaphrodite self-fertility by up to 50% [7]. To conduct our experiments, we used synchronized populations of mid-L4 larvae that were fed (control) or starved (no bacteria) for 5 days and then refed. For simplicity we will refer to starved/refed nematodes as recovered animals. We quantified the brood size of self-fertilizing recovered wild-type hermaphrodites and compared it to that of well-fed nematodes. We found that the recovered wild-type hermaphrodites produced smaller broods than those that grew under control conditions (29% of the wild-type brood size; Table 1, Fig 2A).

When we analyzed the progeny produced by the control and recovered animals by day, we observed that recovered animals produced fewer offspring during the first two days after refeeding, after which progeny production peaked at the third day and ceased at the fifth day (Fig 2B). It is likely that the delay in offspring production in recovered animals was due to the gonad regeneration process, which usually takes two days.

One explanation for the low fertility after ARD is that because the starvation experiments started at the mid-L4 larval stage (approx. 4 h after L4 molting), when spermatogenesis has not yet been completed, insufficient sperm production could occur. To discard this possibility, we quantified sperm production in starved animals once they were close to completing the L4 larval stage (approx. 8 h after L4 molting) by DAPI staining. Control wild-type animals produced an average of 105.11± 1.1 sperm (N = 36, Fig 2C) and starved wild-type animals produced a similar number of 101.89 ± 2.5 (N = 37). After 5 days of L4 larval molting, the control wild-type animals did not have any more sperm in their spermatheca, while 5-day-starved wild-type animals still harbored an average of 102.5 ± 0.68 sperm (N = 28, Fig 2C). We conclude that even during prolonged starvation sufficient sperm are produced, therefore this is not a factor that explains low progeny numbers after ARD.

We also quantified the embryonic lethality of self-fertilizing recovered hermaphrodites after ARD and found that recovered animals exhibited significantly higher embryonic lethality than control animals (3.8 ± 0.3 dead embryos/worm in recovered animals vs. 2.1 ± 0.1 dead embryos/worm in control animals, i.e., 1.8-fold; Table 1, Fig 2D).

To counteract the effect of ARD on sperm, we quantified the brood size and embryonic lethality of wild-type hermaphrodites that were exposed to ARD and later crossed with well-fed wild-type males. Under control conditions, mid-L4 wild-type hermaphrodites were crossed with 4 wild-type males overnight and then transferred daily to new Petri dishes until they ceased laying embryos. For ARD, mid-L4 wild-type animals were deprived of bacteria for 5 days, then transferred to plates with food and immediately crossed with 4 well-fed wild-type males. We observed that the fertility of recovered wild-type animals crossed with well-fed males improved considerably (81% of that in control wild-type animals) even though their brood size never reached that of the control (Fig 2E). Additionally, we did not observe significant differences in embryonic lethality between these two groups of animals (2.6 ± 0.3 dead embryos in control mated animals vs. 2.8 ± 0.6 dead embryos in recovered mated animals; Table 1, Fig 2F). Our results suggest that ARD affects fertility and embryonic survival due to defects in oogenic germ cells; however, we were not able to rule out the possibility that sperm quality is impaired under starvation conditions.

Feminized germlines are more sensitive to ARD than those of wild-type animals

To test the effect of ARD exclusively on oogenic germ cells, we used *fog-1(q253)* and *fog-2(q71)* mutant animals, which have feminized germlines. Female *fog-2(q71)* animals are unable to produce sperm and only reproduce when they are crossed with males [16]. *fog-1(q253)*

Table 1. Fertility assays in diverse genetic backgrounds used in this study.

Genotype	Brood Size				Dead Embryos				N	
WT	231.8	±	2.3		2.1	±	0.1		144	
Recovered WT	67.0	±	2.9	***	3.8	±	0.3	***	69	
Control WT	424.9	±	8.3		2.6	±	0.3		22	
x WT males										
Recovered WT	344.8	±	26.3	n.s	2.8	±	0.6	n.s.	17	
x WT males										
Control *fog-2(q71)*	324.5	±	6.5		2.4	±	0.3		46	
x WT males										
Recovered *fog-2(q71)*	183.2	±	5.6	*	4.0	±	0.3	*	42	
x WT males										
Prolonged diakinesis *fog-2(q71)*	55.8	±	2.3	*	4.8	±	0.2	*	51	
x WT males										
Control *fog-1(q253)*	302.3	±	7.0		2.5	±	0.1		31	
x WT males										
Recovered *fog-1(q253)*	177.1	±	3.3	*	4.4	±	0.2	*	35	
x WT males										
Prolonged diakinesis *fog-1(q253)*	65.0	±	1.6	*	5.6	±	0.1	*	39	
x WT males										
Control *ced-3(n717)*	141.0	±	2.6		8.1	±	0.7		43	
Recovered *ced-3(n717)*	53.1	±	1.8	*	7.3	±	0.5	*	41	
Control *ced-3(n1286)*	143.8	±	3.2		7.5	±	0.4		88	
Recovered *ced-3(n1286)*	52.0	±	2.3	*	12.3	±	0.8	*	58	
Control *ced-3(n717)*	315.6	±	8.6		19.8	±	3.0		11	
x WT males										
Recovered *ced-3(n717)*	248.9	±	12.3	**	19.3	±	1.9	n.s.	20	
x WT males										

Hermaphrodites with the different genetic backgrounds were individually selected at the mid-L4 stage and transferred to new plates every 24 h until they ceased laying embryos. Recovered wild-type hermaphrodites were selected at the mid-L4 stage, starved for 5 days and transferred to new plates every 24 h until they ceased laying embryos. t-test (control vs. recovered). Control *fog-1(q253)* and *fog-2(q71)* animals were individually selected in the mid-L4 stage, mated with well-fed males and transferred to fresh plates daily until they ceased laying embryos. Recovered virgin *fog-1(q253)* and *fog-2(q71)* animals were selected in the mid-L4 stage and starved for 5 days, then individually refed for 1 day, mated with well-fed males and transferred to fresh plates daily until they ceased laying embryos. Virgin *fog-1(q253)* and *fog-2 (q71)* animals were selected in the mid-L4 stage and placed on food for 6 days, then mated with well-fed males and transferred to fresh plates daily until they ceased laying embryos. Plates were scored for dead embryos and total progeny. Embryos that did not hatch within 24 h after being laid were scored as dead. Dunn's test (wild-type values as control). n.s. non significant.

* $P \leq 0.05$

** $P \leq 0.01$

*** $P \leq 0.001$

https://doi.org/10.1371/journal.pone.0218265.t001

hermaphrodites are temperature sensitive and at the restrictive temperature (25˚C) they exhibit feminized gonads [17]. Under control conditions, single mid-L4 virgin *fog-2(q71)* females were crossed with 4 wild-type males overnight and then transferred daily to new Petri dishes until they ceased laying embryos. For ARD, virgin mid-L4 *fog-2(q71)* females were deprived of bacteria for 5 days, then recovered on food for 24 h and crossed with 4 wild-type males overnight. We compared the brood size and embryonic lethality of control and recovered *fog-2* mutant animals. We observed that recovered *fog-2(q71)* animals produced smaller broods than control *fog-2(q71)* animals (56.5% of the brood size of control animals, Table 1,

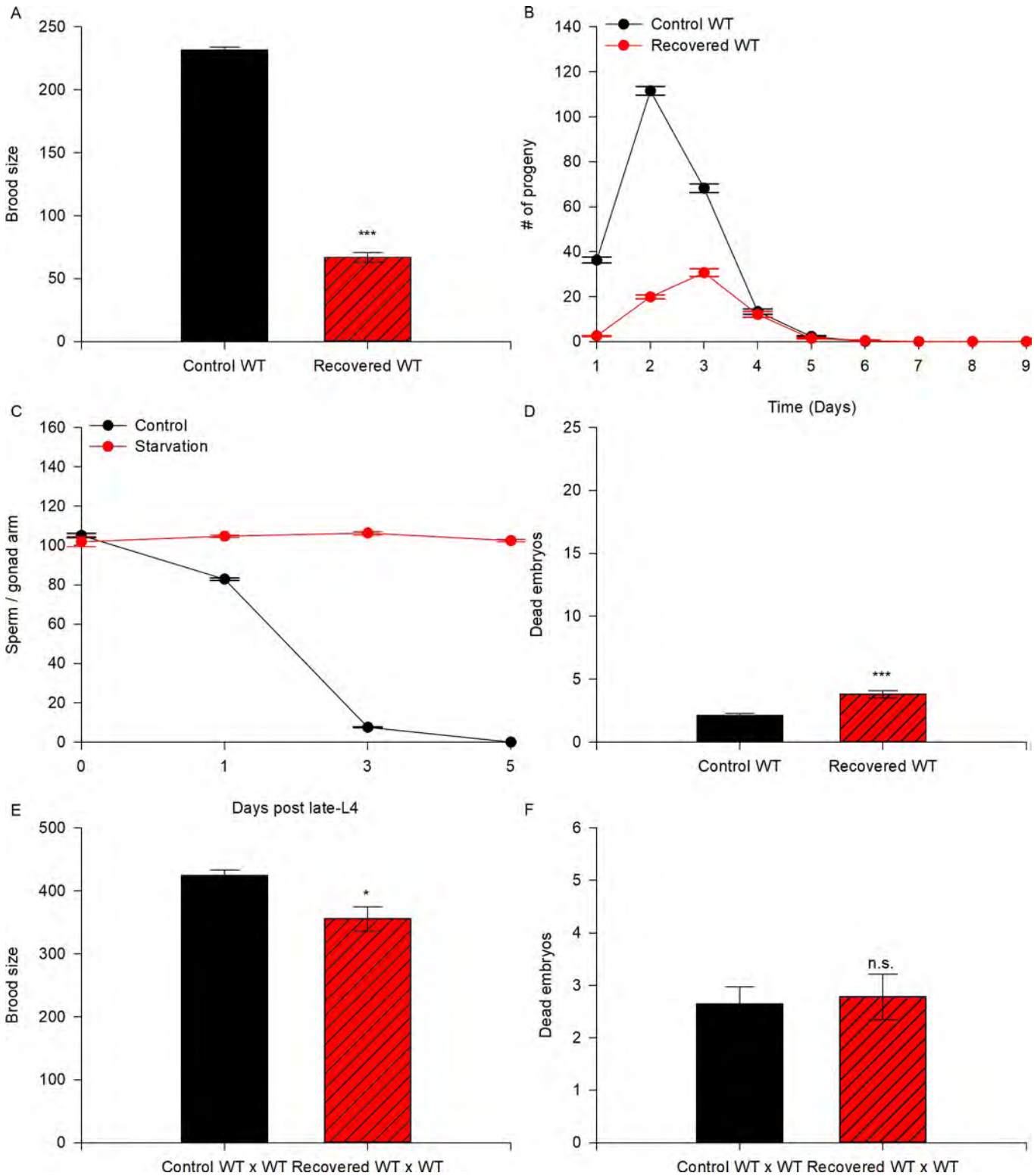

Fig 2. Animals subjected to ARD do not recover their fertility due to defects in germ cells. (A) The graph represents the brood size produced by self-fertilizing control (black) and recovered (red) wild-type animals. Mid-L4 hermaphrodites were allowed to self-fertilize (black) or were starved for 5 days and then refed (red). The data represent the mean brood size (±SEM) per animal. Statistical significance was determined by the Student's t-test ($P \leq 0.001$). (B) Quantification of the progeny produced on each day by self-fertilizing control (black line) and recovered (red line) wild-type animals. Time-course data are displayed as the mean (±SEM) number of progeny per time point. (C) Quantification of sperm produced by wild-type animals under control conditions (black

INFORME DE LABORES 2019

line) or subjected to ARD (red line) at several time points: the late-L4 larval stage and 1, 3 and 5 days after the mid-L4 larval stage. The data are displayed as the mean (±SEM) number of sperm per time point. (D) The number of dead embryos within the progeny of self-fertilizing wild-type animals under control (black) and recovered conditions (red) was calculated. Data represent the mean number of dead embryos (±SEM) per animal. Statistical significance was determined by the Mann-Whitney rank sum test ($P \leq 0.001$). (E) The graph represents the brood size produced by mating control (black) and recovered (red) wild-type animals. Well-fed mid-L4 hermaphrodites were individually mated to 4 well-fed wild-type males overnight and were then transferred individually to fresh plates until they ceased laying eggs (black). For the recovered animals, mid-L4 hermaphrodites were starved for 5 days, then recovered on food and mated to 4 well-fed 1-day-old wild-type males overnight, then transferred individually to fresh plates until they ceased laying eggs (red). The data represent the mean brood size (±SEM) per animal. Statistical significance was determined by the Mann-Whitney rank sum test ($P \leq 0.024$). (F) The number of dead embryos within the progeny produced by mating wild-type animals under control (black) and recovered conditions (red) to well-fed wild-type males was calculated. Data represent the mean number of dead embryos (±SEM) per animal. Statistical significance was determined by the Mann-Whitney rank sum test, and the difference was not significant (n.s.).

https://doi.org/10.1371/journal.pone.0218265.g002

Fig 3A) and showed higher embryonic lethality (1.7-fold; 2.4 ± 0.3 dead embryos/worm in *fog-2* control animals vs. 4 ± 0.3 dead embryos/worm in *fog-2* recovered animals; Table 1, Fig 3B).

To confirm our findings we compared the brood size and embryonic lethality of control and recovered *fog-1(q253)* mutant animals. To do so, a group of synchronized hermaphrodite *fog-1(q253)* animals were grown from L1-mid-L4 at 25˚C and then individually transferred to a plate with bacteria and 4 wild-type males overnight as a control. Another group of *fog-1 (q253)* animals was transferred to plates without bacteria and incubated for 5 days at 25˚C. On the fifth day, the animals were recovered for 24 h in a plate with bacteria and then individually transferred to plates with bacteria and crossed with 4 wild-type males overnight. Recovered *fog-1(q253)* mutant animals showed significantly fewer progeny than control animals (Fig 3A and Table 1). Additionally, recovered *fog-1(q253)* mutant animals showed higher embryonic lethality (1.7-fold; 2.5 ± 0.1 dead embryos/worm in *fog-1* control animals vs. 4.4 ± 0.2 dead embryos/worm in *fog-1* recovered animals; Table 1, Fig 3B). Our results demonstrate that ARD affects oogenic germ cells to an extent that could interfere with embryo survival long after starvation has been ended. Since we observed that the effect of ARD was stronger in feminized mutants, we conclude that some genetic backgrounds could be more sensitive than others.

Oogenic germline starvation response prevents germ cells from entering oogenesis arrest

Well-fed virgin *fog-2* mutant animals' do not produce sperm; instead, all of their germ cells develop as oocytes, and the most proximal remain arrested in diakinesis within the gonad [16]. When *fog-2* mutant animals are mated after prolonged diakinesis arrest, their fertility and embryonic viability are severely affected [3]. By the fifth day after L4 molting, well-fed wild-type hermaphrodites have exhausted their sperm supply and arrested oocytes in diakinesis can be observed in the gonad (approx. 9) (Fig 4A). During the oogenic germline starvation response in wild-type animals, oogenesis is delayed but does not seem to be arrested (at least for the first 3 days after fasting); no stacking oocytes are observed and it is possible to distinguish only one developing oocyte per gonad arm ([8] and Fig 4B). In contrast, we observed stacked oocytes in 5-day-old ARD virgin *fog-2* mutant animals (approx. 7, Fig 4D) although they exhibited fewer stacked oocytes than well-fed 5-day-old virgin *fog-2* animals (approx. 11, Fig 4C). We also observed that *fog-1(q253)* mutant animals that were starved for 5 days at the restrictive temperature showed stacked oocytes within their gonads (approx. 4, Fig 4F) although they presented fewer stacked oocytes than well-fed 5-day-old virgin *fog-1* animals (approx. 8, Fig 4E).

To continue testing whether the oogenic germline starvation response during ARD exerts a protective effect on germ cells, we compared the quality of germ cells when they were exposed to prolonged arrest in meiosis under well-fed conditions vs. ARD. We crossed well-fed 6-day-

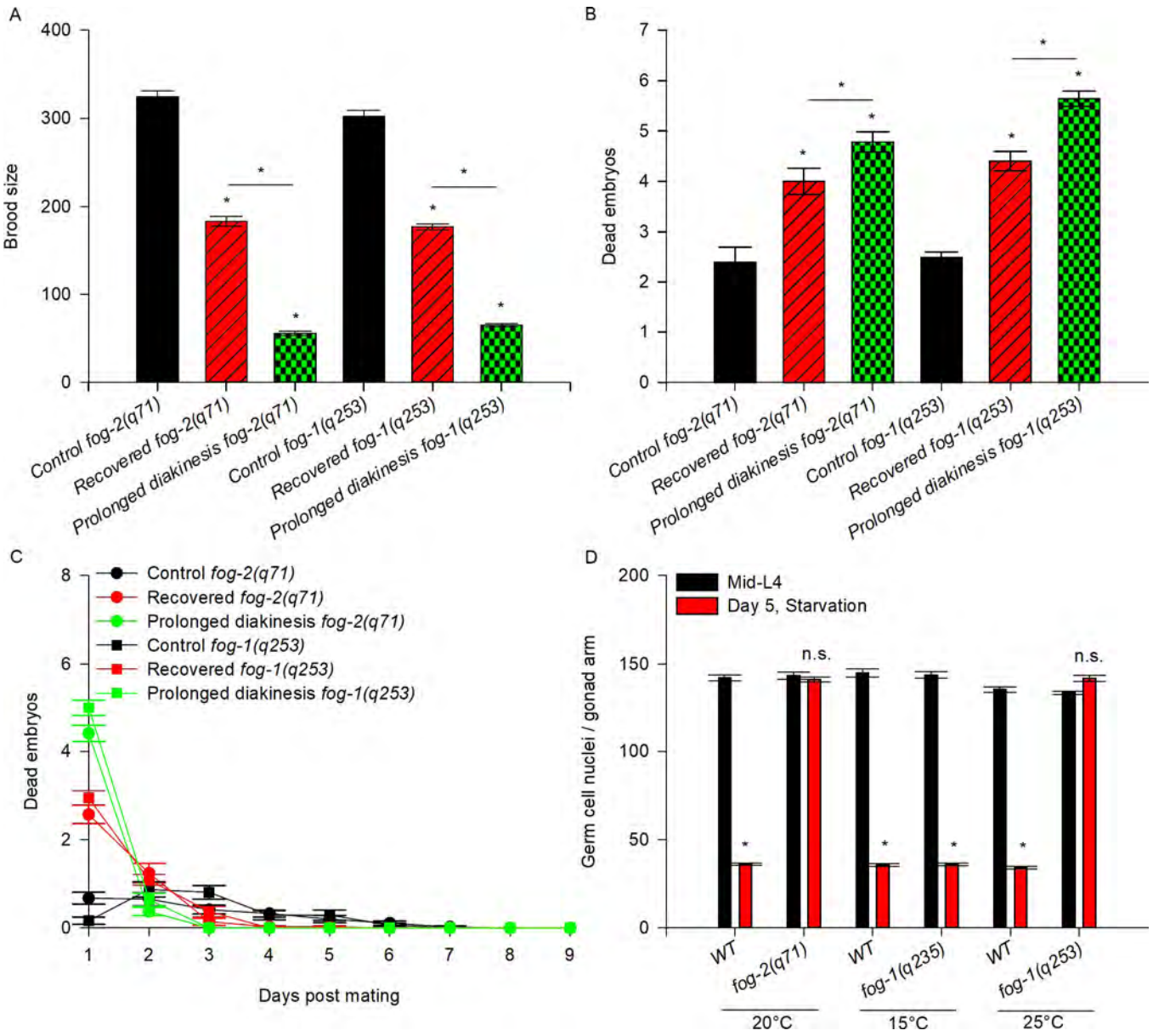

Fig 3. Germlines from feminized mutant backgrounds are more sensitive to ARD that those of wild-type animals. (A) The graph represents the brood size produced by mating virgin *fog-2(q71)* and *fog-1(q253)* mutant animals to well-fed wild-type males. Mid-L4 virgin animals from different genetic backgrounds were mated to 4 well-fed wild-type males overnight, then transferred individually to fresh plates until they ceased laying eggs (black). Mid-L4 virgin mutant animals were starved for 5 days, recovered on food for 24 h and then mated with 4 well-fed 1-day-old wild-type males overnight, after which they were transferred individually to fresh plates until they ceased laying eggs (red). Well-fed 6-day-old virgin mutant animals, which exhibited stacked oocytes arrested in prolonged diakinesis within the gonad, were mated with 4 well-fed 1-day-old wild-type males overnight and then transferred individually to fresh plates until they ceased laying eggs (green). The data represent the mean brood size (±SEM) per animal. Statistical significance was determined by one-way ANOVA on ranks, followed by Dunn's test ($P<0.05$). (B) The graph shows the number of dead embryos within the progeny produced by mating with well-fed wild-type males under control conditions (black), recovered conditions (red) and prolonged arrest in diakinesis (green). The data represent the mean number of dead embryos (±SEM) per animal. Statistical significance was determined by one-way ANOVA on ranks, followed by Dunn's test ($P<0.05$). (C) Quantification of dead embryos within the progeny produced each day by mating with wild-type males under control (black line) and recovered (red line) conditions and prolonged arrest in diakinesis (green line). Time course data are displayed as the mean (±SEM) number of dead embryos per time point. (D) Number of germ cells per gonad arm in wild-type and *fog-2 (q71)* and *fog-1(q253)* mutant animals. The graph represents the average number of germ cells scored using DAPI staining in dissected gonads during the mid-L4 stage (0) and 5 days after the mid-L4 stage under starvation conditions.

https://doi.org/10.1371/journal.pone.0218265.g003

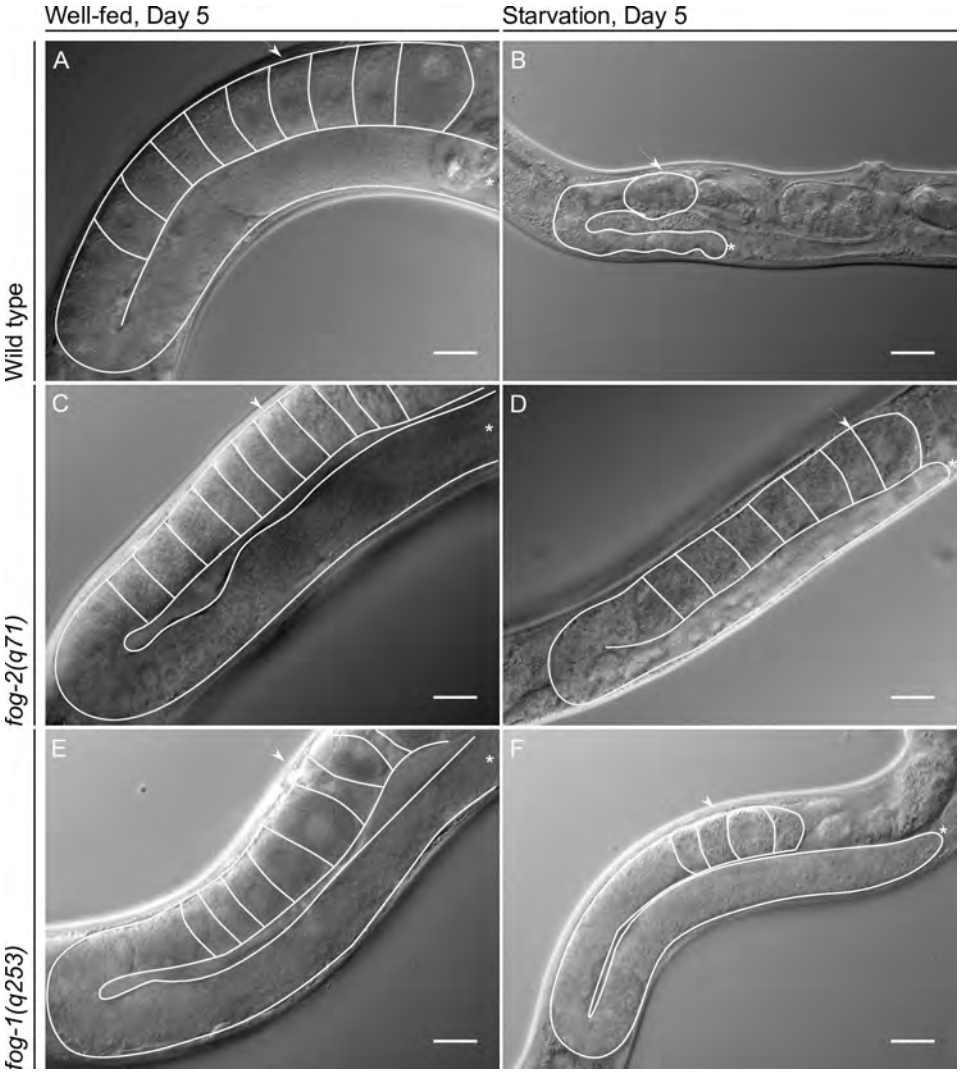

Fig 4. The gonads of feminized germline mutant animals do not shrink during ARD. Nomarski gonad images of the indicated genetic backgrounds and conditions. (A) Representative Nomarski image of a well-fed 5-day-old wild-type hermaphrodite. (B) Nomarski image of a wild-type hermaphrodite that had spent 5 days in ARD. (C) A well-fed 5-day-old virgin *fog-2(q71)* mutant animal. (D) A virgin *fog-2(q71)* animal that had been starved for 5 days. (E) A well-fed 5-day-old virgin *fog-1(q253)* mutant animal. (F) A virgin *fog-1(q253)* animal that had been starved for 5 days. In all images one gonad arm and the oocytes within it are outlined in white; the distal gonad is marked with an asterisk (*); the arrow points to the proximal gonad. Scale bar = 20 μm.

https://doi.org/10.1371/journal.pone.0218265.g004

old virgin *fog-2* and *fog-1* mutant animals with well-fed wild-type males and determined their brood size and embryonic lethality, which were compared to those of *fog-2(q71)* and *fog-1 (q253)* mutant animals crossed under control and recovered conditions. We found that well-fed 6-day-old *fog-2* and *fog-1* mutant animals produced smaller broods (by 17% and 22%, respectively) than the controls and even smaller broods (by 30.5% and 36.7%, respectively) than animals recovered after 5 days of ARD (Fig 3A, Table 1).

Additionally, well-fed 6-day-old *fog-2* and *fog-1* mutant animals exhibited higher embryonic lethality than control (by 2- and 2.2-fold, respectively) and recovered animals (1.2- and 1.3-fold, respectively) (Fig 3B and Table 1). We observed that dead embryos were present mainly during the first day in well-fed 6-day-old *fog-2* and *fog-1* mutant animals (Fig 3C). Similarly, in *fog-2* and *fog-1* mutant recovered animals, the main peak of dead embryos was

Table 2. Germ cell quantification per gonad arm in different genetic backgrounds under control and starvation conditions.

										5 Days post mid-L4							
		mid-L4			N		Control			N		Starvation			N		
	WT	141.9	±	1.8	49		468.2	±	2.0	38	**	36.0	±	0.5	54	**	
20˚C																	
	fog-2(q71)	143.1	±	2.0	42		315.9	±	2.6	47	**	141.0	±	1.5	48	**	
	WT	144.7	±	2.2	30		386.9	±	1.6	20	**	35.5	±	0.8	24	**	
15˚C																	
	fog-1(q253)	143.5	±	1.8	30		386.2	±	1.6	30	**	36.0	±	0.6	25	**	
	WT	135.3	±	1.5	20		388.5	±	1.8	25	**	34.2	±	0.7	25	**	
25˚C																	
	fog-1(q253)	133.5	±	0.8	30		338.5	±	1.8	30	**	141.8	±	1.6	25	n.s.	

The gonads of animals under control conditions or starvation were dissected, stained and scored for the number of germ cells using epifluorescence microscopy. Control animals remained on NGM plates seeded with OP50. For starvation conditions, animals were grown on food from L1 to the mid-L4 larval stage and then starved for 5 days. Animals were subsequently picked and dissected. The dissected gonads were stained with DAPI and the number of germ cells per gonad arm was scored under fluorescence microscopy.

https://doi.org/10.1371/journal.pone.0218265.t002

observed on the first day after the cross (Fig 3C). Apparently, the dead embryos were produced from the oocytes that were arrested in diakinesis for the longest period during ARD. We observed that embryonic lethality in *fog-2(q71)* and *fog-1(q253)* mutant animals was mainly caused by embryos that resulted from the fertilization of the oocytes that were already present or produced during ARD and presumably were arrested for a long period of time. We conclude that because the oogenic germline starvation response during ARD slows oocyte production, oogenic germ cells are prevented from undergoing diakinesis arrest, which preserves oocyte quality. We suggest that this could explain why feminized germline mutant animals are more sensitive to ARD than wild-type animals.

During the course of these experiments, we observed that the gonads of *fog-2* and *fog-1* animals did not shrink during ARD (Fig 4D and 4F). Our results, as well as those of other similar approaches reported previously [18], show that feminized mutant animals' gonads do not decrease in size, suggesting that ovulation is one of the causes of gonad shrinking during ARD. To verify that feminized gonads do not shrink during ARD, we quantified the germ cell number per gonad arm using DAPI staining in control animals and in animals that spent 5 days in ARD. In well-fed conditions, wild-type animals showed an increase in the number of germ cells per gonad arm from 141.9 ± 1.8 (at mid-L4) to 468.23 ± 2.0 (at the fifth day post mid-L4) (Table 2). Additionally, the number of germ cells per gonad arm decreased progressively during starvation from 141.9 ± 1.8 (at the mid-L4) to 36.0 ± 0.5 (at the fifth day post mid-L4) (Fig 3D and Table 2). We found that the number of germ cells in *fog-2* mutant animals that were starved for 5 days remained unchanged compared to the number of germ cells per gonad arm at the mid-L4 stage (143.1 ± 2.0 vs. 141.0 ± 1.5; Fig 3D and Table 2). We confirmed this result using *fog-1(q253)* mutant animals (Fig 3D and Table 2). Moreover, when *fog-1(q253)* animals were maintained at the permissive temperature (15˚C) from L1 to adulthood and subjected to ARD, their gonads were able to shrink similarly to those of the wild-type (Fig 3D and Table 2). Our results suggested that gonad shrinking during ARD is partially due to ovulation.

Germ cell apoptosis is not required to reduce gonad size during prolonged starvation

Caspase CED-3 is required for germ cell apoptosis under control and starvation conditions [19, 20]. Angelo and van Gilst, (2009) previously showed that during ARD, the gonads of *ced-3*

(n1286) mutant animals are not able to shrink and they suggested that apoptosis is required for this process [7]. However, we obtained different results. We exposed mid-L4 *ced-3* mutant animals (alleles *n1286*, *n717* or *ok2734)* to prolonged-starvation and we observed that the gonads of animals harboring all of these alleles were able to shrink during fasting (Fig 5D, 5E, 5G, 5H, 5J and 5K) similarly to those of the wild-type (Fig 5A and 5B).

To verify that the gonads of *ced-3* mutant animals shrink similarly to those of wild-type animals, we quantified the number of germ cells per gonad arm by DAPI staining from the mid-L4 stage over the next 5 days under control and starvation conditions in animals with the wild-type and *ced-3(n717)* and *(1286)* mutant alleles. We found that *ced-3* mutant animals indeed showed a progressive reduction of the germ cell number per gonad arm during starvation similar to that in wild-type animals (Fig 5M and Table 3). Moreover, the gonad size of *ced-3* mutant animals recovered when they were refed as efficiently as that of wild-type animals, as judged by Nomarski microscopy (Fig 5C, 5F, 5I and 5L) and DAPI staining (Table 3). Our data demonstrate that germ cell apoptosis is not required for gonad shrinking during prolonged starvation or gonad regeneration after fasting.

Angelo and van Gilst (2009) also reported that *ced-3(n1286)* caspase mutant animals were unable to produce progeny after 15 days of prolonged starvation and suggested that apoptosis was essential to maintain fertility after fasting [7]. We observed that neither wild-type nor *ced-3(n717 and n1286)* mutant animals produced any progeny after spending 15 days in ARD (N = 37, 39 and 42, respectively), even after they were crossed with wild-type males (N = 27, 29 and 30, respectively).

We quantified the progeny produced by well-fed and recovered *ced-3* animals (alleles *n717* and *n1286*) and compared the number to that in wild-type animals after spending 5 days in ARD. Andux and Ellis (2008) previously reported that *ced-3* mutant animals (with the *n718*, *n2439*, *n2921* alleles) produce fewer progeny and exhibit higher embryonic lethality than wild-type animals in control conditions [3]. Accordingly, we observed that the animals harboring the *ced-3* mutant alleles *n717* and *n1286* exhibited 40% fewer offspring on average than wild-type animals under control conditions (Fig 6A and Table 1). When we compared the number of progeny produced by recovered wild-type animals to that produced by recovered *ced-3* mutant animals, we observed that *ced-3* mutant animals produced 20–24% fewer progeny on average than recovered wild-type animals (Fig 6A and Table 1).

As reported by Andux and Ellis (2008), the embryonic lethality of *ced-3* mutant animals under normal conditions was higher than that of the wild-type (3.9-fold higher than the wild-type for the *ced-3(n717)* allele and 3.6-fold higher for *ced-3(n1286)*) ([3]; Fig 6B and Table 1). After ARD, *ced-3(n717)* mutant animals exhibited 1.9-fold higher embryonic lethality than recovered wild-type animals while *ced-3(n1286)* mutant animals presented 3.2-fold higher embryonic lethality than recovered wild-type animals (Fig 6B and Table 1).

To counteract the effect of ARD on sperm, we quantified the brood size and embryonic lethality of *ced-3(n717)* mutant animals exposed to ARD and subsequently crossed with well-fed wild-type males. We found that the fertility of recovered *ced-3(n717)* mutant animals crossed with well-fed males improved considerably (79% of that in the corresponding control) even though they did not reach the control brood size (Fig 6C). In control conditions, mated *ced-3(n717)* mutant animals exhibited higher embryonic lethality than mated wild-type animals (7-fold) but their embryonic lethality did not increase further after ARD (8-fold) (Fig 6D and Table 1). Our results confirmed that apoptosis is important to maintain oocyte quality under control conditions ([3] and this work). We also observed that apoptosis is important for fertility and to preserve oocyte quality during ARD; however, it is not essential, as previously claimed by Angelo and van Gilst (2009) [7].

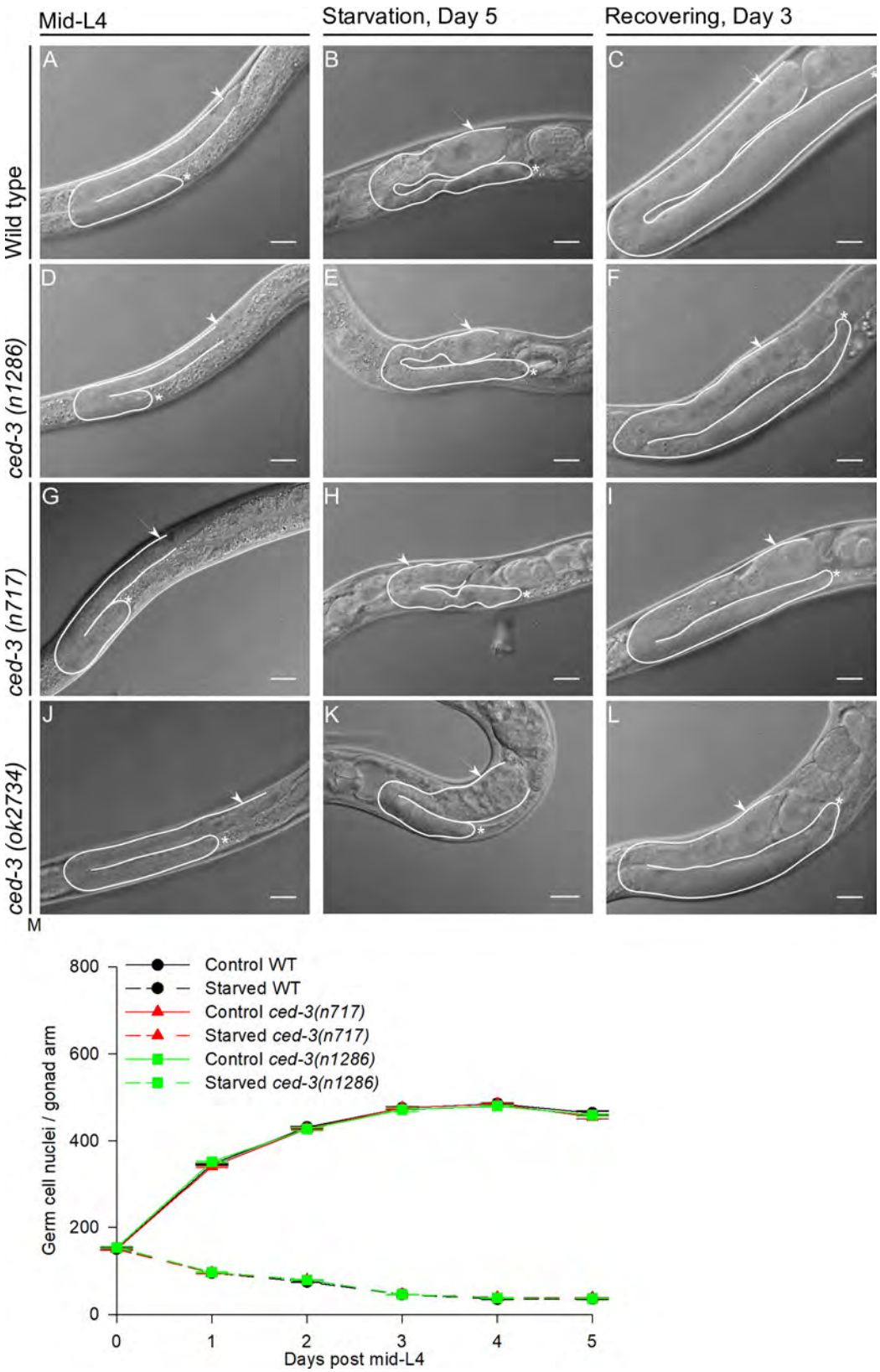

Fig 5. Apoptosis is not required to reduce gonad size during the oogenic germline starvation response. Nomarski images of gonads of mid-L4 wild-type animal and animals with the three different alleles of *ced-3* (A, D, G and J).

Nomarski images of gonads of wild-type and *ced-3* mutant animals starved for 5 days (B, E, H and K). Nomarski images of gonads of wild-type and *ced-3* animals that spent 5 days under starvation and were recovered on food for 3 days (C, F, I and L). In all images one gonad arm is outlined in white; the distal gonad is marked with an asterisk (*); the arrow points to the proximal gonad. Scale bar = 20 μm. (M) Germ cell nuclei per gonad arm scored in wild-type animals and two *ced-3* defective mutants by DAPI staining. The graph shows the average number of germ cell nuclei per gonad arm in control conditions (solid lines) and during starvation (dotted lines) ±SEM at each point.

https://doi.org/10.1371/journal.pone.0218265.g005

High germ cell apoptosis continues during ARD

We investigated germ cell apoptosis dynamics during ARD. To quantify apoptosis, we used a germ cell apoptosis reporter $P_{lim\text{-}7}$*ced-1*::*gfp*, which is expressed in the sheath cells and surrounding germ cell corpses [21]. In well-fed *ced-1*::*gfp* animals, the number of corpses per gonad arm increased with age and peaked at day 4 post-mid-L4 (16.3 ± 0.55 germ cell corpses per gonad arm), with an average of 9.65 ± 0.98 germ cell corpses per gonad over the following

Table 3. Germ cells per gonad arm under control, starvation and recovered conditions.

		WT											
Days post mid-L4		Control			N	Starvation			N	Recovering			N
0		150.4	±	2.5	36	150.4	±	2.5	36	339.2	±	3.5	25
1		346.1	±	2.0	35	95.1	±	1.0	36				
2		431.3	±	1.9	35	74.5	±	0.9	36				
3		475.6	±	2.7	25	45.6	±	0.7	35				
4		485.3	±	1.4	30	35.0	±	0.6	36				
5		463.7	±	4.7	24	35.5	±	0.9	35				
		ced-3(n717)											
Days post mid-L4		Control			N	Starvation			N	Recovering			N
0		145.5	±	4.6	35	145.5	±	4.6	35	342.9	±	2.8	30
1		340.9	±	1.9	36	93.7	±	1.9	35				
2		427.8	±	1.7	36	78.9	±	1.2	35				
3		475.8	±	2.7	24	46.1	±	0.8	35				
4		484.6	±	2.4	25	38.6	±	0.8	36				
5		454.7	±	3.7	25	38.1	±	0.8	35				
		ced-3(n1286)											
Days post mid-L4		Control			N	Starvation			N	Recovering			N
0		153.7	±	2.1	36	153.7	±	2.1	36	342.6	±	2.7	30
1		351.8	±	1.8	25	96.8	±	1.3	35				
2		427.1	±	3.3	26	78.8	±	0.9	36				
3		471.2	±	3.9	25	46.1	±	0.6	35				
4		479.7	±	2.2	25	37.7	±	1.0	36				
5		459.2	±	2.9	25	36.7	±	0.8	35				

The gonads of animals under control conditions, starvation and recovery were dissected, stained and scored for the number of germ cells using epifluorescence microscopy. Control animals were placed in NGM plates seeded with OP50 and transferred to fresh plates daily until they ceased laying eggs. For starvation conditions, animals were placed in NGM plates unseeded and transferred to fresh plates daily, similar to the control animals. Animals were picked and dissected. The dissected gonads were stained with DAPI, and the number of germ cells per gonad arm was scored under fluorescence microscopy. For recovery, animals that had spent 5 days in ARD were transferred to plates seeded with OP50 for 3 days. Animals were then picked and dissected.

https://doi.org/10.1371/journal.pone.0218265.t003

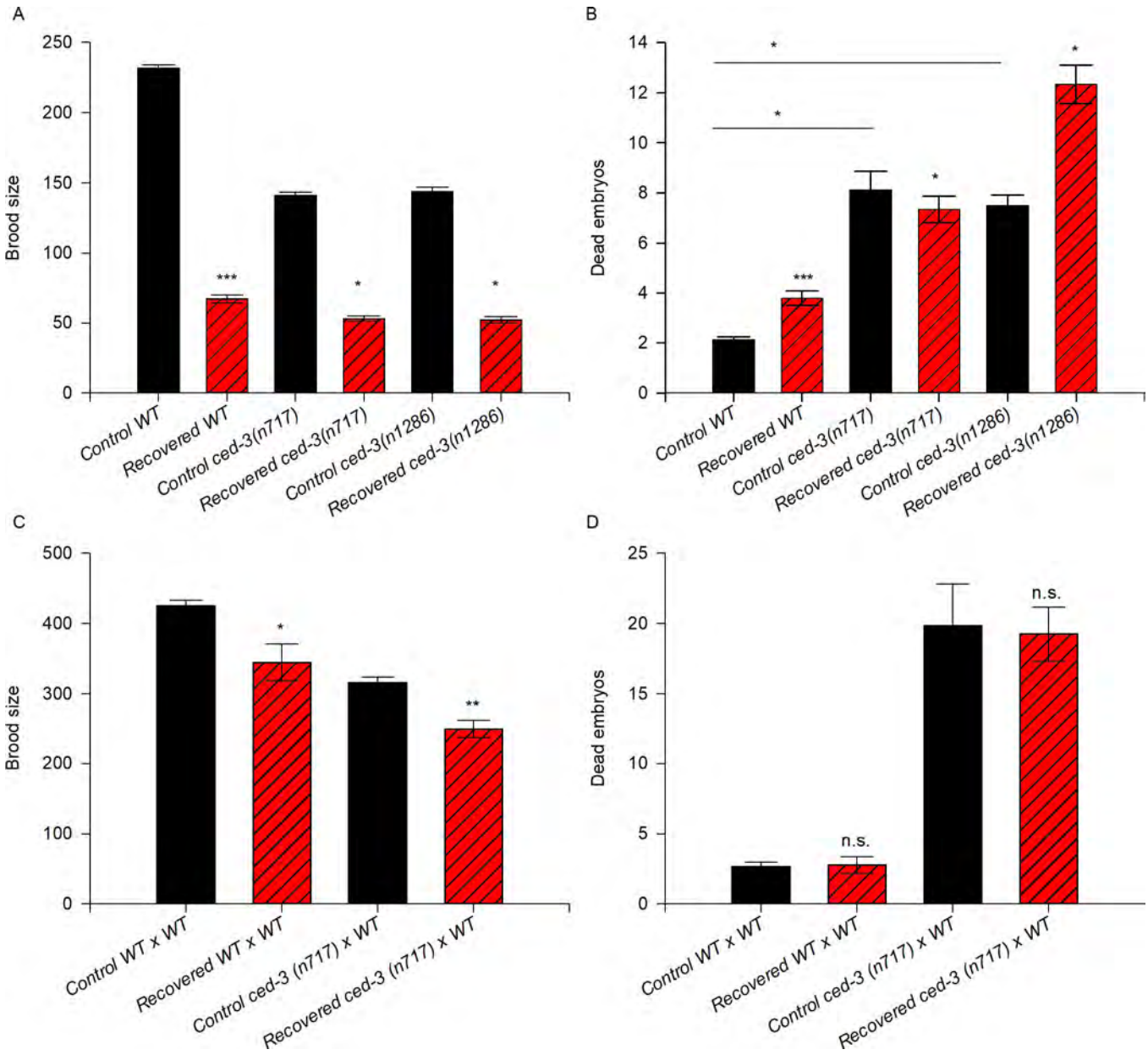

Fig 6. Apoptosis is as important to preserve oocyte quality after ARD as in control conditions but it is not essential for recovering fertility after ARD. (A) The graph represents the brood size produced by control (black) and recovered (red) wild-type and *ced-3* mutant animals. Mid-L4 hermaphrodites of the different genetic backgrounds were allowed to self-fertilize (black) or were starved for 5 days and then refed (red). The data represent the mean brood size (±SEM) per animal. Statistical significance was determined by the t-test (WT control vs. recovered) or by ANOVA on ranks and Dunn's test for multiple comparisons. (B) The number of dead embryos within the progeny of self-fertilizing wild-type and *ced-3* mutant animals under control (black) and recovered conditions (red) was calculated. The data represent the mean number of dead embryos (±SEM) per animal. Statistical significance was determined by the Mann-Whitney rank sum test ($P \leq 0.001$) (WT control vs. recovered) or by ANOVA on ranks and Dunn's test for multiple comparisons. (C) The graph represents the brood size produced by mating control (black) and recovered (red) animals of the different genetic backgrounds. Well-fed mid-L4 hermaphrodites were individually mated with 4 well-fed wild-type males overnight, then transferred individually to fresh plates until they ceased laying eggs (black). For the recovered animals, mid-L4 hermaphrodites were starved for 5 days, then recovered on food and immediately mated with 4 well-fed 1-day-old wild-type males overnight and transferred individually to fresh plates until they ceased laying eggs (red). The data represent the mean brood size (±SEM) per animal. Statistical significance was determined by the Mann-Whitney rank sum test ($P \leq 0.024$) in wild-type populations and by the Student's t-test ($P \leq 0.001$) in *ced-3(n717)* populations. (D) The number of dead embryos within the progeny produced by mating animals of the different genetic backgrounds under control (black) and recovered conditions (red) to well-fed wild-type males was calculated. Data represent the mean number of dead embryos (±SEM) per animal. Statistical significance was determined by the Mann-Whitney rank sum test.

https://doi.org/10.1371/journal.pone.0218265.g006

days (Table 4). After one day of starvation, we observed an increase of 1.6-fold in apoptosis compared to control conditions, with an average of 4.9 germ cell corpses per gonad arm over the following days (Fig 7A and Table 4).

It is remarkable that germ cell apoptosis continues and is very active during prolonged starvation particularly because germ cell proliferation stops after 30 minutes of fasting [9] and the gonad is completely shrunken after the fifth day. To quantify the proportion of germ cells that were being eliminated by apoptosis during starvation versus those that remained in the starved gonad, we determined the number of germ cells per gonad arm in dissected gonads under control and fasting conditions, using DAPI (4',6'-diamino-2-phenylindole) staining. We found that under control conditions the number of germ cells per gonad arm increased gradually with age until day 4 post-mid-L4, after which the numbers of germ cells per gonad arm were similar (approx. 534.2 germ cells/gonad arm) (Fig 7B and Table 5). During prolonged-starvation, the germ cell number decreased gradually until reaching the minimal number at day 6 post-mid-L4, then remained almost unchanged over the course of the experiments (38.1 germ cells/gonad arm on average) (Fig 7B and Table 5).

We quantified the percentage of germ cells eliminated by apoptosis (Table 4) and compared it to the number of germ cells present in the gonad (Table 5) under control conditions and during starvation. We found that under control conditions, approximately 1.91% of the total number of germ cells appeared as germ cell corpses at each time point. However, during starvation the percentage of germ cell corpses was considerably higher at each point compared to the control conditions (average of 9.27% of the total number of germ cells) (Fig 7C). Our data show that germ cell apoptosis increases up to 4.8-fold during the oogenic germline starvation response and continues under these conditions.

To test whether germ cell corpse clearance is affected during starvation, we quantified germ cell corpse engulfment in animals exposed to 1–5 days of starvation by time-lapse microscopy (see methods). We found that the timing of germ cell corpse clearance was not extended during the first 5 days of prolonged starvation compared to the control (approx. 55 minutes (prolonged starvation), similar to the control time of 58 minutes) (Fig 7D, Table 6). Our results demonstrate that the process of germ cell corpse engulfment remains active during prolonged starvation.

Germ cell apoptosis can be triggered by DNA damage or meiosis defects via CEP-1, the *C. elegans* p53 homologue [21–24]. *cep-1* mutant animals do not show increased germ cell apoptosis after DNA damage or meiosis defects. To test whether the germ cell apoptosis during prolonged starvation is regulated by DNA damage or meiosis defects, we quantified germ cell apoptosis in a *cep-1* mutant background [25]. We starved mid-L4 *ced-1*:*gfp* and *cep-1(gk138); ced-1*:*gfp* animals for 5 days and scored the number of germ cell corpses and the number of germ cell nuclei per gonad arm daily (see Methods). *ced-1*:*gfp* and *cep-1(gk138);ced-1*:*gfp* animals showed similar germ cell apoptosis levels in control and starvation conditions (Fig 8A), and the number of germ cell nuclei was progressively reduced during starvation (Fig 8C). Our results indicate that the proportion of germ cells eliminated by cell death was similar in the two genetic backgrounds (Fig 8E) suggesting that the increased germ cell apoptosis observed during ARD is not a consequence of DNA damage or defects during meiosis.

In our previous work, we found that *lin-35*/Rb is essential for inducing germ cell apoptosis during starvation [26]. Hence, we asked whether the high germ cell death triggered during ARD depended on *lin-35* and we found that it partially did. To demonstrate this, we subjected *ced-1*::*gfp* (control) and *lin-35(n745);ced-1*::*gfp* animals to 5 days of starvation beginning in the mid-L4 stage and determined germ cell apoptosis dynamics during ARD (Fig 8B). As previously reported [27], we found that *lin-35(n745);ced-1*::*gfp* mutant animals showed lower germ cell apoptosis compared to *ced-1*:*gfp* animals in well-fed conditions (Fig 8B). As previously

Table 4. Germ cell apoptosis dynamics under control and starvation conditions.

	ced-1::*gfp*								
Days post mid-L4	**Control**			**N**	**Starvation**				**N**
0	0.0	±	0.00	141	0.0	±	0.01	n.s.	140
1	5.4	±	0.21	139	8.8	±	0.20	**	140
2	11.4	±	0.26	129	6.5	±	0.15	**	141
3	13.6	±	0.34	111	6.3	±	0.24	**	129
4	16.3	±	0.55	103	5.6	±	0.18	**	123
5	13.7	±	0.40	111	5.2	±	0.16	**	143
6	11.6	±	0.26	121	4.5	±	0.10	**	135
7	8.5	±	0.22	110	4.2	±	0.11	**	129
8	8.2	±	0.25	119	4.1	±	0.10	**	144
9	7.9	±	0.30	76	3.9	±	0.11	**	124
10	8.0	±	0.21	72	3.6	±	0.08	**	105

The number of germ cell corpses was scored using *ced-1*::*gfp* animals under epifluorescence microscopy. Control mid-L4 hermaphrodites were placed in NGM plates seeded with OP50 and transferred to fresh plates daily until they ceased laying eggs; the animals were picked daily for up to 10 days and mounted with 20 μl of 0.01% tetramisole in M9 on 2% agarose pads. For starvation conditions, mid-L4 animals were placed in unseeded NGM plates and transferred to fresh plates daily similar to the control animals; the animals were picked daily for up to 10 days and mounted with 20 μl of 0.01% tetramisole in M9 on 2% agarose pads. n.s. non significant

* $P \leq 0.05$

** $P \leq 0.01$,.

https://doi.org/10.1371/journal.pone.0218265.t004

reported [26], we also observed that after 24h of starvation, *lin-35(n745);ced-1*::*gfp* animals do not increase their number of germ cell corpses (Fig 8B). However, it is important to remember that during prolonged starvation the number of germ cells progressively decreased (Fig 8D), which could explain why we observed lower apoptosis levels in the *lin-35* mutant background on subsequent days (Fig 8B). We calculated the proportion of germ cells eliminated by apoptosis versus the germ cell number as we did previously (Fig 7C) and observed that germ cell apoptosis increased in the *lin-35* mutant background although it never reach control levels (Fig 8F). We concluded that *lin-35* is partially responsible for germ cell apoptosis induction during ARD, but there is an unknown mechanism that also triggers germ cell apoptosis under these conditions.

The gonads of *daf-2* deficient animals shrink in the presence of food similar to the oogenic germline starvation response

In an attempt to reveal the molecular mechanisms that govern the oogenic germline starvation response, we subjected mid-L4 hermaphrodites of different genetic backgrounds to starvation for 5 days, followed by refeeding for 3 days, to test the capacity of their gonad to shrink and regenerate. We chose the gene candidates based on their known roles in the stress response or in germ cell proliferation. We tested the *C. elegans* retinoblastoma ortholog *lin-35*/Rb because it is essential for inducing apoptosis in short-term starvation [26] and partially required for inducing germ cell apoptosis in ARD (this work). We tested the *daf-16*/FoxO transcription factor due to its implication in the regulation of dauer diapause [28, 29]; the *skn-1*/NrF and *pha-4*/FoxA transcription factors due to their roles in dietary restriction and other types of stress responses [30]; the *alg-1* Argonaut ortholog due to its role in microRNAs pathway regulation and germ cell proliferation [13]; the *rsks-1* putative ribosomal protein S6 kinase, which has been implicated in resistance to starvation and, together with the eIF4E/*ife-1*, which regulates the germline cell cycle progression during development [31, 32]; the gene encoding the

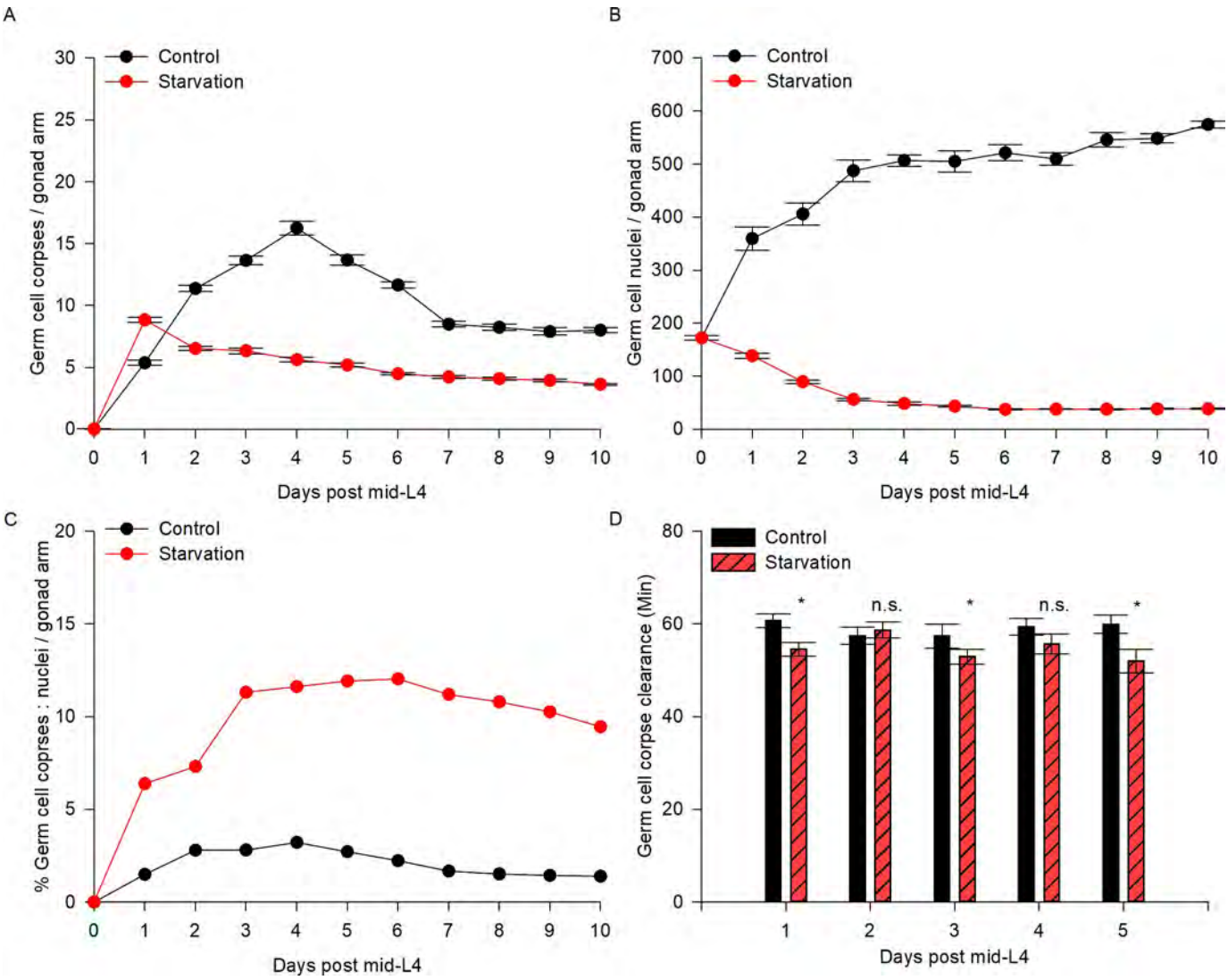

Fig 7. Germ cell apoptosis is increased and continues during ARD. (A) The *ced-1*::*gfp* transgene was used to visualize the number of germ cell corpses per gonad arm (see Materials and methods) for 10 days in control (black line) and starvation conditions (red line). The average number of germ cell corpses per gonad arm is shown with SEM. (B) DAPI staining was used to quantify the number of germ cells per gonad arm (see Materials and methods) for 10 days in control (black line) and starvation (red line) conditions. The average number of germ cells per gonad arm is shown with SEM. (C) The percentage of germ cell corpses among the total germ cells per gonad arm in fed animals (black line) and during starvation (red line) was calculated. (D) The time of germ cell corpse clearance was recorded every day after 1–5 days post-mid-L4 (see Materials and methods) in control (black bars) and starvation (red bars) conditions.

https://doi.org/10.1371/journal.pone.0218265.g007

TIS11-like zinc-finger-containing protein *gla-3* mutant, which exhibits increased germline apoptosis [33]; and the p53 *C. elegans* ortholog *cep-1*, which is required for the DNA damage response [34]. None of the tested genes were required to shrink the gonad during the oogenic germline starvation response or to regenerate upon refeeding (Table 7).

The insulin/insulin receptor signaling (IIS) pathway has been established as a link between nutrient availability and homeostasis in species ranging from worms to humans. This pathway is maintained through the activity of insulin-like molecules that bind to the insulin receptor. In *C. elegans*, more than 40 peptides related to insulin bind to the insulin receptor/DAF-2 to negatively regulate the DAF-16/FoxO transcription factor. Thus, mutations in the insulin receptor/DAF-2 promote the transcription of target genes through the activity of DAF-16/

INFORME DE LABORES 2019

Table 5. The number of germ cells per gonad arm under control and starvation conditions.

	ced-1::gfp							
Days post mid-L4	**Control**			**N**	**Starvation**			**N**
0	172.2	±	4.57	45	172.2	±	4.57	45
1	359.6	±	21.88	15	138.4	±	4.72	42
2	406.1	±	21.23	15	89.4	±	3.04	30
3	487.3	±	20.82	17	56.0	±	1.83	31
4	506.8	±	10.94	15	48.4	±	3.02	27
5	505.1	±	19.53	18	43.6	±	1.37	35
6	521.3	±	14.82	18	37.2	±	1.18	30
7	509.6	±	11.76	16	37.8	±	0.75	24
8	545.9	±	13.44	17	37.8	±	1.04	38
9	548.6	±	8.19	17	38.4	±	1.19	34
10	574.7	±	6.56	15	38.4	±	1.19	38

The gonads of animals under control conditions and starvation were dissected, stained and scored for the number of germ cells using epifluorescence microscopy. Control animals were placed in NGM plates seeded with OP50 and transferred to fresh plates daily until they ceased laying eggs. For starvation conditions, animals were placed in unseeded NGM plates and transferred to fresh plates daily, similar to the control animals. Animals were picked and dissected. The dissected gonads were stained with DAPI and the number of germ cells per gonad arm was scored under fluorescence microscopy.

https://doi.org/10.1371/journal.pone.0218265.t005

FoxO to cope with nutrient scarcity and other types of stress [35]. This pathway regulates entry to dauer diapause, a well-studied diapause stage in *C. elegans* that occurs between larval stages L1-L2 in response to different cues, including a lack of food [36].

To test the role of *daf-2* in the oogenic germline starvation response, we used the temperature-sensitive mutant *daf-2(e1370)* [37]. Synchronous populations of wild-type or *daf-2(e1370)* animals were grown from hatching to mid-L4 at the permissive temperature (15˚C) (Fig 9A and 9D, respectively) and then transferred to the restrictive temperature (25˚C) for 5 days in the absence of food. We found that the gonads of *daf-2(e1370)* mutant animals grown at the restrictive temperature (25˚C) and starved for 5 days were able to shrink similarly to those of the wild-type animals (Fig 9E and 9B; Table 7) suggesting that *daf-2* is not required for the oogenic germline starvation response.

Table 6. Germ cell corpse clearance under control and starvation conditions.

		WT								
Days post mid-L4		**Control**			**N**	**Starvation**				**N**
0		No corpses detected			25	No corpses detected				25
1		60.7	±	1.51	9	54.6	±	1.47	*	9
2		57.4	±	1.89	9	58.7	±	1.74	n.s.	9
3		57.3	±	2.63	9	52.9	±	1.61	*	9
4		59.4	±	1.74	8	55.6	±	2.15	n.s.	8
5		59.9	±	1.97	8	52.0	±	2.50	*	8

The timing of germ cell corpse clearance under control and starvation conditions was scored using a long-term immobilization technique and Nomarski microscopy at 60x magnification. Control mid-L4 hermaphrodites were placed in NGM plates seeded with OP50, picked daily for up to 5 days and immobilized with 0.5 μl of a polystyrene bead suspension on 10% agarose pads to observe an individual germ cell corpse and determine its clearance time in minutes. For starvation conditions, mid-L4 hermaphrodites were placed in unseeded NGM plates, picked daily for up to 5 days and then immobilized with 0.5 μl of a polystyrene bead suspension on 10% agarose pads to observe an individual germ cell corpse and determine its clearance time in minutes. The Holm-Sidak test for comparisons within groups was used. n.s. = non significant

* $P < 0.05$.

https://doi.org/10.1371/journal.pone.0218265.t006

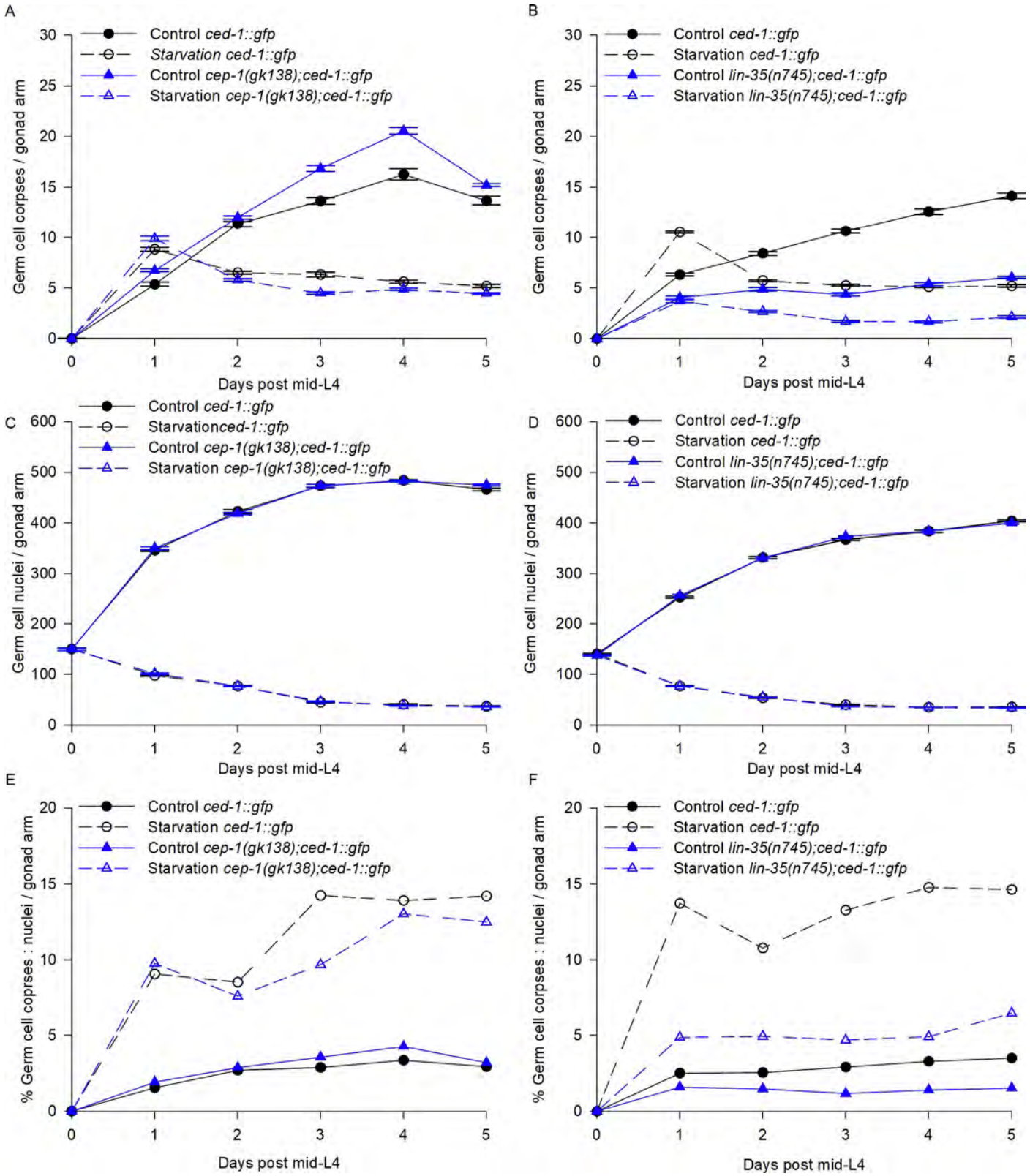

Fig 8. Germ cell apoptosis is p53 independent and partially regulated by *lin-35/Rb* during ARD. (A-B) *cep-1(gk38);ced-1::gfp*, *lin-35(n745);ced-1::gfp* and *ced-1::gfp* animals were used to visualize the number of germ cell corpses per gonad arm (see Materials and methods) for 5 days in control (solid lines) and starvation conditions (dotted lines). The average number of germ cell corpses per gonad arm is shown with the SEM. (C-D) DAPI staining was used to quantify the number of

INFORME DE LABORES 2019

germ cells per gonad arm (see Materials and methods) for 5 days in control (solid lines) and starvation conditions (dotted lines). The average number of germ cells per gonad arm is shown with the SEM. (E-F) The percentage of germ cell corpses among the total germ cells per gonad arm in fed animals (solid lines) and during starvation (red lines) conditions was calculated.

https://doi.org/10.1371/journal.pone.0218265.g008

Unexpectedly, we observed that the well-fed control mid-L4 *daf-2* mutant animals grown at the restrictive temperature for 5 days exhibited shrunken gonads in the presence of food (Fig 9F) when their gonads were compared to those of the wild-type animals (Fig 9C). We decided to quantify the germ cell number per gonad arm at the mid-L4 stage and 5 days after IIS pathway inactivation in the presence of food using *daf-2(e1370)* mutant animals and the wild-type as a control. We found that in wild-type animals, the germ cell number increased from 140.6 ± 1.2 at mid-L4 to 380.8 ± 3.4 5 days post-mid-L4. However, *daf-2(e1370)* mutant animals did not show the same increase; instead, the number of germ cell nuclei per gonad arm was reduced from 137.6 ± 1.0 at mid-L4 to 77.2 ± 1.5 5 days post-mid-L4 (Fig 9I and Table 8).

The transcription factor *daf-16/FoxO* is activated when the *daf-2* signal is absent [38]. As we previously showed, *daf-16* is not required to shrink the gonad during ARD, but we tested whether gonad shrinking induced in the absence of *daf-2* in the presence of food requires *daf-16*. To test this, *daf-16(m26);daf-2(e1370)* double mutant animals were grown from hatching to mid-L4 on food at the permissive temperature and then shifted to 25˚C for 5 days (Fig 9G and 9H). We observed that the gonads of animals lacking *daf-2* did not shrink in the presence of food when *daf-16* was not present. We quantified the germ cell number in this double mutant genetic background and found that the number of germ cells increased from 136.4 ± 0.7 at mid-L4 to 382.2 ± 2.5 5 days after IIS pathway inactivation in the presence of food (Fig 9I and Table 8). These results suggest that inactivation of *daf-2* in well-fed animals might trigger a mechanism similar to ARD that requires *daf-16*/FoxO.

Table 7. The oogenic germline starvation response in different genetic backgrounds.

Genotype	Relevant function for this study	References	Human ortholog	Starvation response	Re-feeding
WT	Control	[7, 8]	-	Shrunken gonad	Completely recovered
ced-3(n1286)	The only effector caspase	[7, 20]	Isoform 1 Caspase-2	Shrunken gonad	Completely recovered
				Not required	Not required
ced-3(n717)	The only effector caspase	[7, 20]	Isoform 1 Caspase-2	Not required	Not required
ced-3(ok2734)	The only effector caspase		Isoform 1 Caspase-2	Not required	Not required
lin-35(n745)	Causes starvation-induced germline apoptosis	[26]	Rb	Not required	Not required
daf-16(mgDf50)	Regulates dauer diapause	[28]	FoxO	Not required	Not required
skn-1(zu135)	Dietary restriction and other stresses response	[30]	Nrf	Not required	Not required
pha-4(zu225)	Dietary restriction and other stresses response	[30]	FoxA	Not required	Not required
alg-1(gk214)	miRNA pathway and proliferation	[13]	Argonaut	Not required	Not required
rsks-1(ok1255)	Increases resistance to starvation	[31]	Putative ribosomal protein S6K	Not required	Not required
ife-1(bn127)	Regulates germline progenitor number	[32]	eIF4e	Not required	Not required
gla-3(op212)	Increased germline apoptosis	[33]	-	Not required	Not required
cep-1(gk138);ced-1::gfp	Regulates DNA-damage-induced germline apoptosis	[34]	p53 transcription factor	Not required	Not required

Hermaphrodites from the different backgrounds were selected at the mid L4, starved for 5 days and observed daily under Nomarski microscopy to compare their gonad size to that under the oogenic germline starvation response using WT hermaphrodites as a control. At day 5, the hermaphrodites were refed for 3 days and observed daily under Nomarski microscopy to determine their gonad recovery, using WT hermaphrodites as a control.

https://doi.org/10.1371/journal.pone.0218265.t007

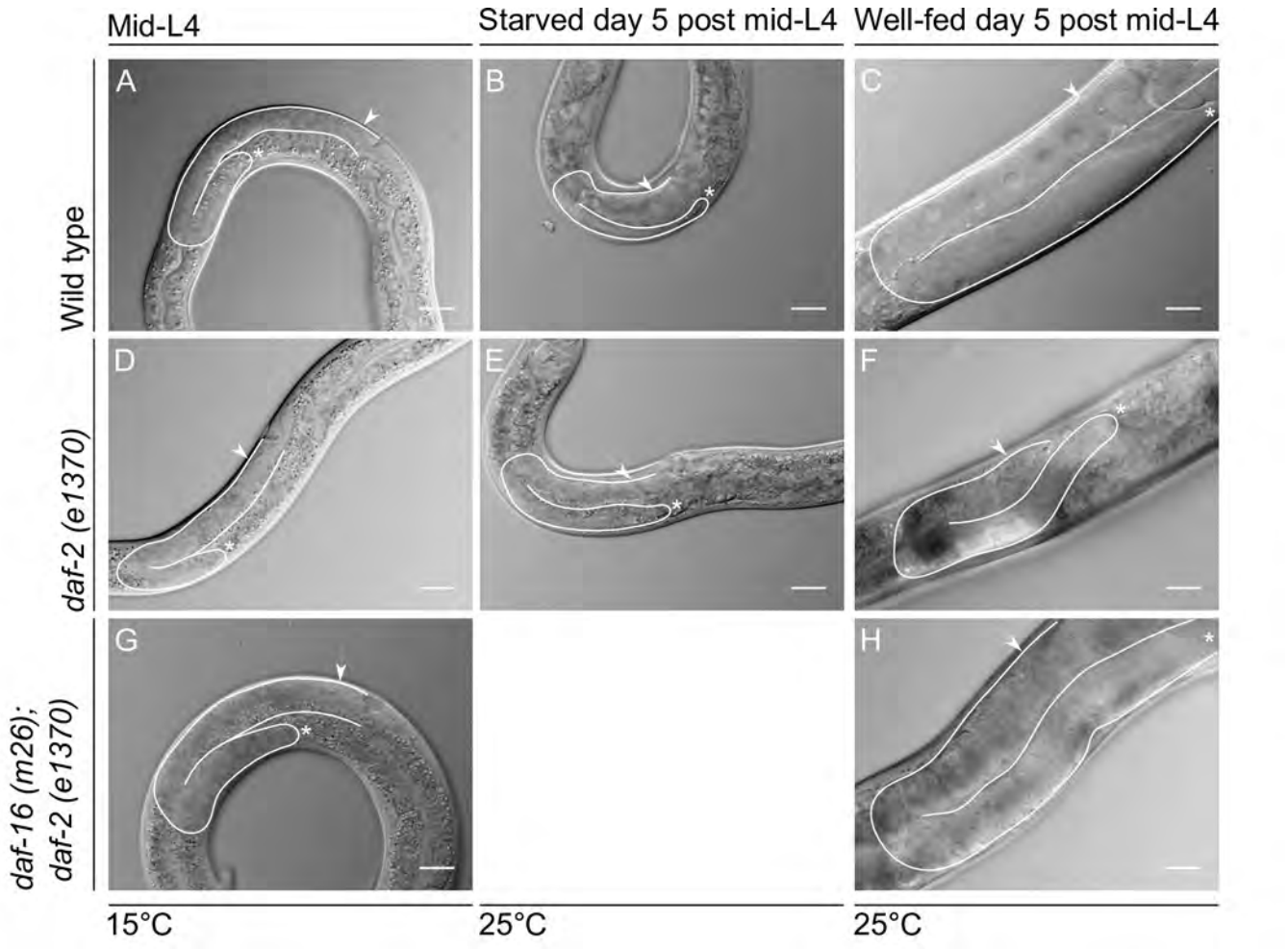
Mid-L4
Starved day 5 post mid-L4
Well-fed day 5 post mid-L4
Wild type
daf-2 (e1370)
daf-16 (m26); daf-2 (e1370)
A
B
C
D
E
F
G
H
15°C
25°C
25°C

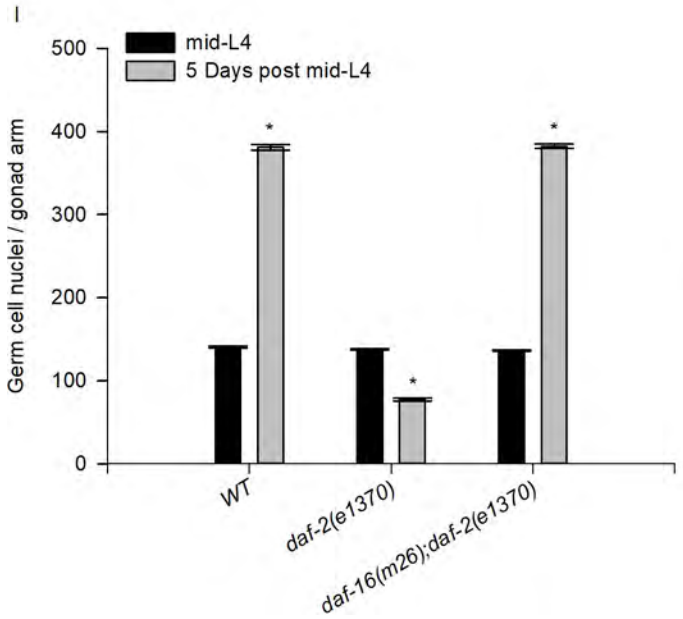
I
mid-L4
5 Days post mid-L4
Germ cell nuclei / gonad arm
500
400
300
200
100
0
WT
daf-2(e1370)
daf-16(m26);daf-2(e1370)

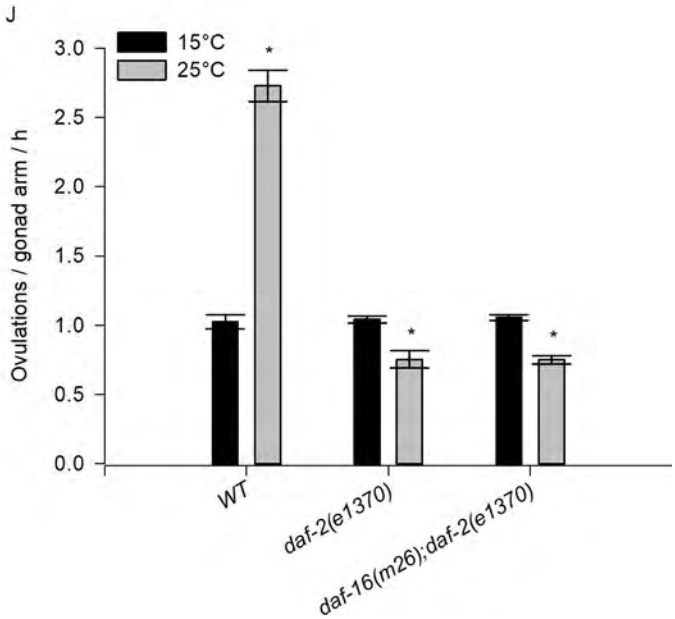
J
15°C
25°C
Ovulations / gonad arm / h
3.0
2.5
2.0
1.5
1.0
0.5
0.0
WT
daf-2(e1370)
daf-16(m26);daf-2(e1370)

Fig 9. Long-term IIS pathway inactivation mimics the entry to ARD in the presence of food. Mid-L4 wild-type, *daf-2(e1370)* and *daf-16(m26); daf-2(e1370)* larvae were fed until mid-L4 at 15˚C (A, D and G, respectively). Wild-type and *daf-2(e1370)* mid-L4 larvae starved for 5 days at 25˚C (B, E). Nomarski images of well-fed wild-type, *daf-2(e1370)* and *daf-16(m26); daf-2(e1370)* animals grown until mid-L4 at 15˚C, then upshifted to 25˚C for 5 days (C, F and H). In all images one gonad arm is outlined in white; the distal gonad is marked with an asterisk (*); and the arrow points to the proximal gonad. Scale bar = 20 μm. (I) Quantification of the number of germ cell nuclei per gonad arm during prolonged IIS pathway inactivation. Animals were grown from L1 to the mid-L4 stage at the permissive temperature and then upshifted to the restrictive temperature for 5 days. Dissected gonads were stained using DAPI in each condition. The graph shows the average number of germ cell nuclei per gonad arm (±SEM). (J) Ovulation rate determination during IIS pathway inactivation. Animals were grown from L1 to the mid-L4 stage at the permissive temperature and then either upshifted to the restrictive temperature or maintained in the permissive temperature for 1 day. Animals were individually picked and scored for the number of embryos *in utero*, then placed in plates for 4 h and finally scored for the number of embryos *in utero*. The ovulation rate was calculated as follows: (final number of embryos—initial number) / (2 * 4 h). The graph shows the average number of ovulations per gonad arm per hour (±SEM).

https://doi.org/10.1371/journal.pone.0218265.g009

To test whether IIS pathway inactivation could mimic entry to ARD even in the presence of food, we determined the ovulation rate in 1-day-old wild-type and *daf-2(e1370)* and *daf-16 (m26);daf-2(e1370)* mutant animals grown from L1 to mid-L4 at 15˚C that were late upshifted to 25˚C in the presence of food. It has been reported that ARD causes a delay in the ovulation rate [8]. Wild-type animals ovulate more frequently when upshifted to 25˚C (N = 30) (Fig 9J). In contrast, *daf-2(e1370)* animals showed no increase in the ovulation rate when upshifted to 25˚C (N = 33). However, *daf-16(m26);daf-2(e1370)* mutant animals continued to exhibit a slowed ovulation rate (N = 33) (Fig 9J).

Another feature of the oogenic germline starvation response is that the ovulation rate is limited by the rate of oocyte growth [8]. Starved animals almost always form only a single oocyte at a time in each gonad arm ([8], Figs 1F and 9B). However, gonads from *daf-2(e1370)* animals grown at 25˚C in the presence of food did not exhibit this phenotype (Fig 9E). We concluded that DAF-2 might participate in the oogenic germline response but that it is not the only signal that participates in this phenomenon. It is also possible that because the *daf-2* mutation results in pleiotropic phenotypes, it is not easy to study its role in the oogenic germline response.

Discussion

Angelo and van Gilst (2009) reported a novel type of adult reproductive diapause for the first time while studying reproduction when nutrients are limited. They showed that crowded populations of mid-L4 larval stage animals subjected to starvation delay their reproductive cycle and are able to live for up to 30 days without food. Furthermore, when conditions are restored, these animals resume their reproductive cycle and live out a normal lifespan. During ARD, the gonad experiences reversible germ cell loss and size reduction; when animals are returned to food, the gonad regenerates in terms of both germ cell number and size [7].

Later, Seidel and Kimble (2011) studied ARD in depth. They showed that germline shrinkage occurs in all oogenic germlines, from the mid-L4 to adult stages, and practically all shrunken gonads regenerate upon refeeding if bagging is prevented. Seidel and Kimble (2011)

Table 8. Quantification of germ cell number per gonad arm in different genetic backgrounds on food.

								5 Days post mid-L4				
	mid-L4			N	15˚C			N	25˚C			N
WT	140.6	±	1.2	37	339.0	±	2.0	35	380.8	±	3.4	20
daf-2(e1370)	137.6	±	1.0	42	337.0	±	1.4	44	77.2	±	1.5	41
daf-16(m26);daf-2(e1370)	136.4	±	0.7	43	342.3	±	1.7	43	382.2	±	2.5	22

The gonads of animals were dissected, stained and scored for the number of germ cells using epifluorescence microscopy. Animals were grown in NGM plates seeded with OP50 from hatching to mid-L4 at 15˚C and then incubated on food at 15˚C or 25˚C for 5 days. Animals were picked and dissected. The dissected gonads were stained with DAPI and the number of germ cells per gonad arm was scored under fluorescence microscopy.

https://doi.org/10.1371/journal.pone.0218265.t008

showed that embryo production continues during prolonged starvation, and it is possible to distinguish one or two viable-looking embryos within the uterus, which are a product of recent fertilizations, indicating that oocyte production and fertilization are active but considerably delayed in starved animals; however, embryo viability is severely impaired during starvation. They also showed that population density is not a prerequisite for inducing or maintaining the starvation response in starved animals and suggested that this phenomenon is not a form of diapause [8].

Despite not supporting the existence of the ARD proposed by Angelo and van Gilst (2009), Seidel and Kimble (2011) coined the term "oogenic germline starvation response" referring to the germline plasticity controlled by nutritional cues [8]. They also reported that starvation causes reversible cell-cycle quiescence in adult germline stem cells, reducing the number of M-phase cells under 30 minutes of starvation and rapidly re-establishing their number upon refeeding [9].

Our results support the following conclusions: Long-term exposure to fasting compromises the animals' reproductive capacity, and the oogenic germline starvation response prevents oogenic germ cells from undergoing prolonged arrest in diakinesis by slowing oocyte production. In contrast to Angelo and van Gilst (2009), we demonstrated that apoptosis is not the cause of gonad shrinkage during ARD and that it is not essential for fertility recovery after ARD. Instead, we propose that once germ cell proliferation stops, ovulation contributes to gonad shrinking during the oogenic germline starvation response. Germ cell apoptosis is increased during ARD and continues during prolonged starvation. Germ cell apoptosis during ARD is not induced by DNA damage or chromosome segregation errors during meiosis but is partially regulated by *lin-35*/Rb. We also found that during ARD an unknown mechanism triggers germ cell apoptosis. Finally, we suggest that inactivation of the IIS signaling pathway triggers gonad shrinking in the presence of food that might resemble the oogenic germline response.

ARD compromises fertility by affecting oogenic germ cells

In the present work, we showed that fertility is affected after ARD (Figs 2, 3 and 6). Although recovered animals exhibit restoration of fertility upon refeeding, none of the genetic backgrounds tested (N2, *fog-1*, *fog-2* and *ced-3*) produced broods that were as large as those of the controls by self-fertilization or mating. Angelo and van Gilst (2009) proposed that the fecundity of self-fertilizing animals depended on the survival of functional sperm during starvation [7]. However, we observed that, at least during the first 5 days of starvation, the sperm number remained unchanged.

Several authors have used embryonic lethality to reflect oocyte quality [3, 39]. Our results showed that animals produce more dead embryos when they use their self-sperm to fertilize oocytes after recovery from 5 days of starvation than their respective controls (Figs 2 and 6). We showed that recovered self-fertilizing hermaphrodites produce dead embryos during the entire reproductive period (Fig 2). However, recovered *fog-1(q253)* and *fog-2(q71)* females produced the majority of dead embryos during the first two days after mating (Fig 3), which suggests that the self-sperm exposed to starvation and used to fertilize oocytes in wild-type animals had been compromised. Moreover, when well-fed male sperm were provided, the oogenic germ cells produced during starvation were prone to produce dead embryos after fertilization. Our results suggest that the self-fertilizing capacity of hermaphrodites is not only compromised by the sperm number, but also by oogenic germ cell exhaustion after ARD. It is worth noting that the effects of ARD on sperm capacity remain unclear. Further studies are needed to determine the effect of ARD on sperm quality.

Oogenesis arrest is prevented by the oogenic germline starvation response

In the *C. elegans* germline, the presence of food and sperm promotes meiotic progression and oogenesis. Sperm depletion causes prolonged diakinesis arrest in the proximal gonad due to oocyte stacking, and starvation halts meiotic progression in the pachytene region [40]. In replete conditions and the presence of sperm, hermaphrodites ovulate every ~20 minutes per gonad arm, while during ARD, hermaphrodites exhibit slowed oogenesis and produce one oocyte at a time, and the next oocyte production starts once the fully grown oocyte is ovulated, which occurs approx. every ~8 h per gonad arm, regardless of the presence of sperm [8]. The oocytes that experience longer arrest in diakinesis are more likely to produce dead embryos [3]. We demonstrated that at day 5 post-mid-L4, in the presence of food, *fog-1* and *fog-2* animals actively produced and stacked as many oocytes as possible, while under starvation conditions *fog-1* and *fog-2* animals produced and stacked fewer oocytes within their gonads (Fig 4). When mated, well-fed 6-day-old *fog-1* and *fog-2* animals produced smaller broods and more dead embryos than *fog-1* and *fog-2* animals recovered from starvation, suggesting that slowing oogenesis during starvation is a beneficial mechanism for preserving the reproductive capacity and oocyte quality.

Apoptosis is important to preserve oocyte quality during ARD; however, it is not essential for fertility and gonad shrinking

In this study, we demonstrated that *ced-3* mutant animals respond to starvation by shrinking their gonads during ARD and partially recover their fertility upon refeeding (Figs 5 and 6). In contrast to Angelo and van Gilst (2009), who reported that apoptosis-deficient *ced-3(n1286)* animals subjected to 15 days of starvation did not show loss of germ cell nuclei or gonad shrinkage, and did not produce progeny after ARD [7]. In fact, we observed that wild-type animals and *ced-3* deficient mutants are unable to produce progeny after spending 15 days under starvation, either by self-fertilization or mating with well-fed wild-type males.

As previously reported [3], we observed that apoptosis-deficient mutants produced fewer offspring and exhibited higher embryonic lethality under control conditions compared to the wild-type animals. In this paper, we show that the apoptosis-deficient animals that were recovered from 5 days of starvation produced even fewer offspring and exhibited higher embryonic lethality than the wild-type animals. Our results suggest that apoptosis is important to preserve oocyte quality in control or prolonged starvation conditions.

Germ cell apoptosis continues during ARD

Our work shows that apoptosis is increased during prolonged starvation and continues to be high during ARD. Germ cell apoptosis is required during oogenesis for properly allocating resources within the gonad and ensuring oocyte quality [3, 41]. Apoptosis increases with age under control conditions and continues in later life contributing to gonad degeneration [41, 42]. We found that increased germ cell apoptosis during ARD is not triggered by *cep-1*/p53, suggesting that it is not caused by DNA damage or meiotic defects.

Furthermore, germ cell apoptosis can be triggered when animals face different types of stress [19]. Previously, we reported that one-day-old animals exposed to 6 h of starvation presented a 2-fold increase in the number of germ cell corpses, for which *lin-35*/Rb is responsible [19, 26]. Unexpectedly, we found that apoptosis seems to be induced during ARD by *lin-35*/Rb and an unknown mechanism.

Why is germ cell apoptosis elevated during ARD? Our results support the notion proposed by Andux and Ellis (2008) that germ cell death serves as a mechanism to redistribute resources

in the gonad [3]. The biological significance of this mechanism might be that it ensures oocyte production only under suitable conditions. At the mid-L4 stage when ARD entry is promoted, some germ cells have already committed to the meiotic oogenic cell fate, which is irreversible; however, completion of meiosis and development into a mature oocyte takes several hours. Thus, we think that the germ cell apoptosis observed during ARD might arise from the germ cells that escape the mitotic cell fate but, due to lack of resources, are eliminated by apoptosis.

DAF-2 inactivation causes gonad size reduction in the presence of food

We sought to investigate the molecular mechanism that governs the oogenic germline starvation response during ARD. We tested some genes involved in the regulation of dauer diapause, L1 arrest and other genes implicated in germ cell apoptosis and proliferation and demonstrated that only IIS in the mid-L4 larval stage caused a reduction in gonad size even in the presence of food (Table 8 and Fig 9). We propose that IIS pathway inactivation might trigger a response that mimics the entry into ARD in well-fed conditions, since animals show a reduced gonad size (Fig 9). Similarly, *daf-2* animals slow ovulation when they reduced their gonad size suggesting that *daf-2* might participate in ARD signaling; however, the shrunken gonads of *daf-2* animals do not form one single oocyte at a time as that of the ARD gonads, and *daf-2* is not essential for the gonad shrinking during ARD. Although our results provide some evidence of the pathway that governs the oogenic germline starvation response, further information is still needed for a better understanding of the precise molecular mechanism that controls reproduction under starvation conditions.

Acknowledgments

We thank the *Caenorhabditis* Genetics Center (CGC), which is funded by NIH Office of Research Infrastructure Programs (P40 OD010440) for kindly providing the strains used in this work. We thank WormBase release WS224 for gathering information and making it available. We also thank Laura Silvia Salinas for technical assistance, members of the Navarro Lab and Dr. Jesús Chimal from the Instituto de Investigaciones Biomédicas-UNAM and Dr. Wilhem Hansberg and Dr. Félix Recillas from the Instituto de Fisiología Celular-UNAM for helpful discussion and comments on this project. Emilio Carranza-García received a CONACyT doctoral fellowship (361899) and data in this work are part of his doctoral dissertation in the Programa de Doctorado en Ciencias Biomédicas, Universidad Nacional Autónoma de México.

Author Contributions

Conceptualization: E. Carranza-García, R. E. Navarro.

Formal analysis: E. Carranza-García, R. E. Navarro.

Funding acquisition: R. E. Navarro.

Investigation: E. Carranza-García, R. E. Navarro.

Methodology: E. Carranza-García.

Project administration: R. E. Navarro.

Supervision: R. E. Navarro.

Validation: E. Carranza-García, R. E. Navarro.

Visualization: E. Carranza-García, R. E. Navarro.

Writing – review & editing: E. Carranza-García, R. E. Navarro.

References

1. Kim S, Spike C, Greenstein D. Control of oocyte growth and meiotic maturation in Caenorhabditis elegans. Advances in experimental medicine and biology. 2013; 757:277–320. https://doi.org/10.1007/978-1-4614-4015-4_10 PMID: 22872481; PubMed Central PMCID: PMC3819423.
2. Pazdernik N, Schedl T. Introduction to germ cell development in Caenorhabditis elegans. Advances in experimental medicine and biology. 2013; 757:1–16. https://doi.org/10.1007/978-1-4614-4015-4_1 PMID: 22872472; PubMed Central PMCID: PMC3781019.
3. Andux S, Ellis RE. Apoptosis maintains oocyte quality in aging Caenorhabditis elegans females. PLoS genetics. 2008; 4(12):e1000295. https://doi.org/10.1371/journal.pgen.1000295 PMID: 19057674; PubMed Central PMCID: PMC2585808.
4. Miller MA, Nguyen VQ, Lee MH, Kosinski M, Schedl T, Caprioli RM, et al. A sperm cytoskeletal protein that signals oocyte meiotic maturation and ovulation. Science. 2001; 291(5511):2144–7. https://doi.org/10.1126/science.1057586 PMID: 11251118.
5. Schindler AJ, Baugh LR, Sherwood DR. Identification of late larval stage developmental checkpoints in Caenorhabditis elegans regulated by insulin/IGF and steroid hormone signaling pathways. PLoS genetics. 2014; 10(6):e1004426. https://doi.org/10.1371/journal.pgen.1004426 PMID: 24945623; PubMed Central PMCID: PMC4063711.
6. Corsi AK, Wightman B, Chalfie M. A Transparent window into biology: A primer on Caenorhabditis elegans. WormBook : the online review of C elegans biology. 2015:1–31. https://doi.org/10.1895/wormbook.1.177.1 PMID: 26087236; PubMed Central PMCID: PMC4781331.
7. Angelo G, Van Gilst MR. Starvation protects germline stem cells and extends reproductive longevity in C. elegans. Science. 2009; 326(5955):954–8. https://doi.org/10.1126/science.1178343 PMID: 19713489.
8. Seidel HS, Kimble J. The oogenic germline starvation response in C. elegans. PloS one. 2011; 6(12): e28074. https://doi.org/10.1371/journal.pone.0028074 PMID: 22164230; PubMed Central PMCID: PMC3229504.
9. Seidel HS, Kimble J. Cell-cycle quiescence maintains Caenorhabditis elegans germline stem cells independent of GLP-1/Notch. eLife. 2015; 4. https://doi.org/10.7554/eLife.10832 PMID: 26551561; PubMed Central PMCID: PMC4718729.
10. Hughes SE, Evason K, Xiong C, Kornfeld K. Genetic and pharmacological factors that influence reproductive aging in nematodes. PLoS genetics. 2007; 3(2):e25. https://doi.org/10.1371/journal.pgen.0030025 PMID: 17305431; PubMed Central PMCID: PMC1797816.
11. Stiernagle T. Maintenance of C. elegans. WormBook : the online review of C elegans biology. 2006:1–11. Epub 2007/12/01. https://doi.org/10.1895/wormbook.1.101.1 PMID: 18050451; PubMed Central PMCID: PMCPMC4781397.
12. Silva-Garcia CG, Estela Navarro R. The C. elegans TIA-1/TIAR homolog TIAR-1 is required to induce germ cell apoptosis. Genesis. 2013; 51(10):690–707. https://doi.org/10.1002/dvg.22418 PMID: 23913578.
13. Bukhari SI, Vasquez-Rifo A, Gagne D, Paquet ER, Zetka M, Robert C, et al. The microRNA pathway controls germ cell proliferation and differentiation in C. elegans. Cell research. 2012; 22(6):1034–45. https://doi.org/10.1038/cr.2012.31 PMID: 22370633; PubMed Central PMCID: PMC3367518.
14. Kim E, Sun L, Gabel CV, Fang-Yen C. Long-term imaging of Caenorhabditis elegans using nanoparticle-mediated immobilization. PloS one. 2013; 8(1):e53419. https://doi.org/10.1371/journal.pone.0053419 PMID: 23301069; PubMed Central PMCID: PMC3536676.
15. Huang J, Wang H, Chen Y, Wang X, Zhang H. Residual body removal during spermatogenesis in C. elegans requires genes that mediate cell corpse clearance. Development. 2012; 139(24):4613–22. https://doi.org/10.1242/dev.086769 PMID: 23172915; PubMed Central PMCID: PMC3509724.
16. Schedl T, Kimble J. fog-2, a germ-line-specific sex determination gene required for hermaphrodite spermatogenesis in Caenorhabditis elegans. Genetics. 1988; 119(1):43–61. PMID: 3396865; PubMed Central PMCID: PMC1203344.
17. Barton MK, Kimble J. fog-1, a regulatory gene required for specification of spermatogenesis in the germ line of Caenorhabditis elegans. Genetics. 1990; 125(1):29–39. PMID: 2341035; PubMed Central PMCID: PMC1204007.
18. Cinquin A, Chiang M, Paz A, Hallman S, Yuan O, Vysniauskaite I, et al. Intermittent Stem Cell Cycling Balances Self-Renewal and Senescence of the C. elegans Germ Line. PLoS genetics. 2016; 12(4): e1005985. https://doi.org/10.1371/journal.pgen.1005985 PMID: 27077385; PubMed Central PMCID: PMCPMC4831802.

19. Salinas LS, Maldonado E, Navarro RE. Stress-induced germ cell apoptosis by a p53 independent pathway in Caenorhabditis elegans. Cell death and differentiation. 2006; 13(12):2129–39. https://doi.org/10.1038/sj.cdd.4401976 PMID: 16729024.

20. Ellis HM, Horvitz HR. Genetic control of programmed cell death in the nematode C. elegans. Cell. 1986; 44(6):817–29. PMID: 3955651.

21. Schumacher B, Schertel C, Wittenburg N, Tuck S, Mitani S, Gartner A, et al. C. elegans ced-13 can promote apoptosis and is induced in response to DNA damage. Cell death and differentiation. 2005; 12 (2):153–61. https://doi.org/10.1038/sj.cdd.4401539 PMID: 15605074.

22. Derry WB, Putzke AP, Rothman JH. Caenorhabditis elegans p53: role in apoptosis, meiosis, and stress resistance. Science. 2001; 294(5542):591–5. https://doi.org/10.1126/science.1065486 PMID: 11557844.

23. Bailly AP, Freeman A, Hall J, Declais AC, Alpi A, Lilley DM, et al. The Caenorhabditis elegans homolog of Gen1/Yen1 resolvases links DNA damage signaling to DNA double-strand break repair. PLoS genetics. 2010; 6(7):e1001025. https://doi.org/10.1371/journal.pgen.1001025 PMID: 20661466; PubMed Central PMCID: PMC2908289.

24. Mateo AR, Kessler Z, Jolliffe AK, McGovern O, Yu B, Nicolucci A, et al. The p53-like Protein CEP-1 Is Required for Meiotic Fidelity in C. elegans. Current biology : CB. 2016; 26(9):1148–58. https://doi.org/10.1016/j.cub.2016.03.036 PMID: 27151662; PubMed Central PMCID: PMC5215890.

25. Lettre G, Kritikou EA, Jaeggi M, Calixto A, Fraser AG, Kamath RS, et al. Genome-wide RNAi identifies p53-dependent and -independent regulators of germ cell apoptosis in C. elegans. Cell death and differentiation. 2004; 11(11):1198–203. https://doi.org/10.1038/sj.cdd.4401488 PMID: 15272318.

26. Lascarez-Lagunas LI, Silva-Garcia CG, Dinkova TD, Navarro RE. LIN-35/Rb causes starvation-induced germ cell apoptosis via CED-9/Bcl2 downregulation in Caenorhabditis elegans. Mol Cell Biol. 2014; 34 (13):2499–516. https://doi.org/10.1128/MCB.01532-13 PMID: 24752899; PubMed Central PMCID: PMCPMC4054308.

27. Schertel C, Conradt B. C. elegans orthologs of components of the RB tumor suppressor complex have distinct pro-apoptotic functions. Development. 2007; 134(20):3691–701. https://doi.org/10.1242/dev.004606 PMID: 17881492.

28. Gottlieb S, Ruvkun G. daf-2, daf-16 and daf-23: genetically interacting genes controlling Dauer formation in Caenorhabditis elegans. Genetics. 1994; 137(1):107–20. PMID: 8056303; PubMed Central PMCID: PMCPMC1205929.

29. Murphy CT. The search for DAF-16/FOXO transcriptional targets: approaches and discoveries. Exp Gerontol. 2006; 41(10):910–21. https://doi.org/10.1016/j.exger.2006.06.040 PMID: 16934425.

30. Smith-Vikos T, de Lencastre A, Inukai S, Shlomchik M, Holtrup B, Slack FJ. MicroRNAs mediate dietary-restriction-induced longevity through PHA-4/FOXA and SKN-1/Nrf transcription factors. Current biology : CB. 2014; 24(19):2238–46. https://doi.org/10.1016/j.cub.2014.08.013 PMID: 25242029; PubMed Central PMCID: PMCPMC4208828.

31. Pan KZ, Palter JE, Rogers AN, Olsen A, Chen D, Lithgow GJ, et al. Inhibition of mRNA translation extends lifespan in Caenorhabditis elegans. Aging Cell. 2007; 6(1):111–9. https://doi.org/10.1111/j.1474-9726.2006.00266.x PMID: 17266680; PubMed Central PMCID: PMCPMC2745345.

32. Korta DZ, Tuck S, Hubbard EJ. S6K links cell fate, cell cycle and nutrient response in C. elegans germline stem/progenitor cells. Development. 2012; 139(5):859–70. https://doi.org/10.1242/dev.074047 PMID: 22278922; PubMed Central PMCID: PMCPMC3274352.

33. Kritikou EA, Milstein S, Vidalain PO, Lettre G, Bogan E, Doukoumetzidis K, et al. C. elegans GLA-3 is a novel component of the MAP kinase MPK-1 signaling pathway required for germ cell survival. Genes Dev. 2006; 20(16):2279–92. https://doi.org/10.1101/gad.384506 PMID: 16912277; PubMed Central PMCID: PMCPMC1553210.

34. Schumacher B, Hofmann K, Boulton S, Gartner A. The C. elegans homolog of the p53 tumor suppressor is required for DNA damage-induced apoptosis. Current biology : CB. 2001; 11(21):1722–7. PMID: 11696333.

35. Templeman NM, Murphy CT. Regulation of reproduction and longevity by nutrient-sensing pathways. J Cell Biol. 2018; 217(1):93–106. https://doi.org/10.1083/jcb.201707168 PMID: 29074705; PubMed Central PMCID: PMCPMC5748989.

36. Riddle DL, Swanson MM, Albert PS. Interacting genes in nematode dauer larva formation. Nature. 1981; 290(5808):668–71. PMID: 7219552.

37. Kenyon C, Chang J, Gensch E, Rudner A, Tabtiang R. A C. elegans mutant that lives twice as long as wild type. Nature. 1993; 366(6454):461–4. https://doi.org/10.1038/366461a0 PMID: 8247153.

38. Henderson ST, Johnson TE. daf-16 integrates developmental and environmental inputs to mediate aging in the nematode Caenorhabditis elegans. Current biology : CB. 2001; 11(24):1975–80. PMID: 11747825.

39. Spike CA, Coetzee D, Eichten C, Wang X, Hansen D, Greenstein D. The TRIM-NHL protein LIN-41 and the OMA RNA-binding proteins antagonistically control the prophase-to-metaphase transition and growth of Caenorhabditis elegans oocytes. Genetics. 2014; 198(4):1535–58. https://doi.org/10.1534/genetics.114.168831 PMID: 25261698; PubMed Central PMCID: PMCPMC4256770.

40. Lopez AL 3rd, Chen J, Joo HJ, Drake M, Shidate M, Kseib C, et al. DAF-2 and ERK couple nutrient availability to meiotic progression during Caenorhabditis elegans oogenesis. Dev Cell. 2013; 27 (2):227–40. https://doi.org/10.1016/j.devcel.2013.09.008 PMID: 24120884; PubMed Central PMCID: PMCPMC3829605.

41. Gumienny TL, Lambie E, Hartwieg E, Horvitz HR, Hengartner MO. Genetic control of programmed cell death in the Caenorhabditis elegans hermaphrodite germline. Development. 1999; 126(5):1011–22. PMID: 9927601.

42. de la Guardia Y, Gilliat AF, Hellberg J, Rennert P, Cabreiro F, Gems D. Run-on of germline apoptosis promotes gonad senescence in C. elegans. Oncotarget. 2016; 7(26):39082–96. https://doi.org/10.18632/oncotarget.9681 PMID: 27256978; PubMed Central PMCID: PMCPMC5129915.

frontiers in Neuroscience

REVIEW
published: 24 July 2019
doi: 10.3389/fnins.2019.00728

Re-thinking the Etiological Framework of Neurodegeneration

*Ximena Castillo[1,2], Susana Castro-Obregón[3], Benjamin Gutiérrez-Becker[4], Gabriel Gutiérrez-Ospina[5], Nikolaos Karalis[6], Ahmed A. Khalil[7,8,9], José Sócrates Lopez-Noguerola[10], Liliana Lozano Rodríguez[11], Eduardo Martínez-Martínez[12], Claudia Perez-Cruz[13], Judith Pérez-Velázquez[14,15], Ana Luisa Piña[16], Karla Rubio[17], Héctor Pedro Salazar García[18], Tauqeerunnisa Syeda[13], America Vanoye-Carlo[19], Arno Villringer[7,8,9], Katarzyna Winek[20,21] and Marietta Zille[22,23,24]**

[1] Instituto de Neurobiología, Universidad Nacional Autónoma de México, Mexico City, Mexico, [2] Institute of Neurobiology, University of Puerto Rico, San Juan, PR, United States, [3] Instituto de Fisiología Celular, Universidad Nacional Autónoma de México, Mexico City, Mexico, [4] Artificial Intelligence in Medical Imaging KJP, Ludwig Maximilian University of Munich, Munich, Germany, [5] Laboratorio de Biología de Sistemas, Departamento de Biología Celular y Fisiología, Instituto de Investigaciones Biomédicas y Coordinación de Psicobiología y Neurociencias, Facultad de Psicología, Universidad Nacional Autónoma de México, Mexico City, Mexico, [6] Friedrich Miescher Institute for Biomedical Research, Basel, Switzerland, [7] Center for Stroke Research Berlin, Charité-Universitätsmedizin Berlin, Berlin, Germany, [8] Berlin School of Mind and Brain, Humboldt-Universität zu Berlin, Berlin, Germany, [9] Department of Neurology, Max Planck Institute for Human Cognitive and Brain Sciences, Leipzig, Germany, [10] School of Health Sciences, Department of Gerontology, Autonomous University of Hidalgo State, Pachuca, Mexico, [11] Departamento de Bioquímica, Facultad de Medicina, Universidad Nacional Autónoma de México, Mexico City, Mexico, [12] Cell Communication & Extracellular Vesicles Laboratory, Instituto Nacional de Medicina Genómica, Mexico City, Mexico, [13] National Polytechnic Institute, Center of Research in Advanced Studies, Mexico City, Mexico, [14] Departamento de Matemáticas y Mecánica, Instituto de Investigaciones en Matemáticas Aplicadas y Sistemas, Universidad Nacional Autónoma de México, Mexico City, Mexico, [15] Mathematische Modellierung Biologischer Systeme, Fakultät für Mathematik, Technische Universität München, Munich, Germany, [16] Department of Neurosurgery, Charité-Universitätsmedizin Berlin, Berlin, Germany, [17] Lung Cancer Epigenetics, Max Planck Institute for Heart and Lung Research, Bad Nauheim, Germany, [18] Leibniz-Forschungsinstitut für Molekulare Pharmakologie, Berlin, Germany, [19] Laboratorio de Neurociencias, Instituto Nacional de Pediatría, Secretaría de Salud, Mexico City, Mexico, [20] The Shimon Peres Postdoctoral Fellow at the Edmond and Lily Safra Center for Brain Sciences, The Hebrew University of Jerusalem, Jerusalem, Israel, [21] Department of Experimental Neurology, Charité-Universitätsmedizin Berlin, Berlin, Germany, [22] Institute for Experimental and Clinical Pharmacology and Toxicology, University of Lübeck, Lübeck, Germany, [23] Institute for Medical and Marine Biotechnology, University of Lübeck, Lübeck, Germany, [24] Fraunhofer Research Institution for Marine Biotechnology and Cell Technology, Lübeck, Germany*

OPEN ACCESS

Edited by:
Aurel Popa-Wagner, University Hospital Essen, Germany

Reviewed by:
Daniela Galimberti, University of Milan, Italy
Jukka Jolkkonen, University of Eastern Finland, Finland

***Correspondence:**
Marietta Zille
marietta.zille@pharma.uni-luebeck.de

Specialty section:
This article was submitted to Neurodegeneration, a section of the journal Frontiers in Neuroscience

Received: *31 March 2019*
Accepted: *28 June 2019*
Published: *24 July 2019*

Citation:
Castillo X, Castro-Obregón S, Gutiérrez-Becker B, Gutiérrez-Ospina G, Karalis N, Khalil AA, Lopez-Noguerola JS, Rodríguez LL, Martínez-Martínez E, Perez-Cruz C, Pérez-Velázquez J, Piña AL, Rubio K, García HPS, Syeda T, Vanoye-Carlo A, Villringer A, Winek K and Zille M (2019) Re-thinking the Etiological Framework of Neurodegeneration. Front. Neurosci. 13:728. doi: 10.3389/fnins.2019.00728

Neurodegenerative diseases are among the leading causes of disability and death worldwide. The disease-related socioeconomic burden is expected to increase with the steadily increasing life expectancy. In spite of decades of clinical and basic research, most strategies designed to manage degenerative brain diseases are palliative. This is not surprising as neurodegeneration progresses "silently" for decades before symptoms are noticed. Importantly, conceptual models with heuristic value used to study neurodegeneration have been constructed retrospectively, based on signs and symptoms already present in affected patients; a circumstance that may confound causes and consequences. Hence, innovative, paradigm-shifting views of the etiology of these diseases are necessary to enable their timely prevention and treatment. Here, we outline four alternative views, not mutually exclusive, on different etiological paths toward neurodegeneration. First, we propose neurodegeneration as being a secondary outcome of a primary cardiovascular cause with vascular pathology disrupting the vital homeostatic interactions between the vasculature and the brain, resulting in

cognitive impairment, dementia, and cerebrovascular events such as stroke. Second, we suggest that the persistence of senescent cells in neuronal circuits may favor, together with systemic metabolic diseases, neurodegeneration to occur. Third, we argue that neurodegeneration may start in response to altered body and brain trophic interactions established via the hardwire that connects peripheral targets with central neuronal structures or by means of extracellular vesicle (EV)-mediated communication. Lastly, we elaborate on how lifespan body dysbiosis may be linked to the origin of neurodegeneration. We highlight the existence of bacterial products that modulate the gut-brain axis causing neuroinflammation and neuronal dysfunction. As a concluding section, we end by recommending research avenues to investigate these etiological paths in the future. We think that this requires an integrated, interdisciplinary conceptual research approach based on the investigation of the multimodal aspects of physiology and pathophysiology. It involves utilizing proper conceptual models, experimental animal units, and identifying currently unused opportunities derived from human data. Overall, the proposed etiological paths and experimental recommendations will be important guidelines for future cross-discipline research to overcome the translational roadblock and to develop causative treatments for neurodegenerative diseases.

Keywords: lifespan, vascular pathology, senescence, body–brain trophism, dysbiosis

INTRODUCTION

Neurological disorders are the leading cause of disability-adjusted life-years and the second-leading cause of deaths worldwide. This burden has increased substantially over the past 25 years because of expanding population numbers and aging (GBD 2015 Neurological Disorders Collaborator Group, 2017) and will continue to grow in the coming decades due to the further increase in life expectancy.

At intermediate and advanced stages, frequently by the time a diagnosis is made, neurodegeneration has affected higher brain areas that control cognitive, sensory, and motor functions. Because the majority of cases are seen by the age of 50 or older in both men and women, many scientists think of neurodegenerative diseases as processes that reflect abnormal aging. Likewise, since neurodegeneration involves the loss of neuronal populations brain-wide, many researchers believe that neuronal death results from altered processes intrinsic to the nervous system, such as neuroinflammation, abnormal accumulation or deteriorated clearance of toxic proteins, and reduced anti-oxidative defenses.

Hence, current explicative models of neurodegenerative diseases account for signs and symptoms already seen in affected patients. In fact, the majority of these causative models have been formulated in retrospect, based on what is already present in the patient's brain. Given the nature of these models, it is difficult to identify real causes from mere consequences and epiphenomena. This is even more puzzling given that neurodegenerative diseases are life-spanning processes that start silently at least 20 to 30 years before the pathological signs and symptoms are recognized by patients and diagnosed by physicians. In addition, accumulating information suggests an extraneural origin of neurodegeneration.

Clearly, the essential premises guiding research on neurodegenerative diseases seem at least partly incorrect and somewhat misleading. This may explain why, despite researchers' best efforts, neurodegeneration is still a growing health concern and the reason why therapeutic measures are currently palliative, while preventive approaches are often ineffective (Crous-Bou et al., 2017; Hsu and Marshall, 2017; Klein and Tyrlikova, 2017).

Here, we outline four different paths as the basis for a paradigm shift toward an etiologic view on neurodegeneration: (1) the vascular origin of neurodegeneration, (2) cellular senescence as the origin of neurodegeneration, (3) body–brain trophic interactions as the origin of neurodegeneration, and (4) lifespan gut dysbiosis as the origin of neurodegeneration. We did not cover here genetic components as risk factors for neurodegeneration, a comprehensive analysis of which can be found elsewhere (Brainstorm et al., 2018). We provide concrete recommendations on how to investigate the discussed etiological paths experimentally in future studies. This work is the result of the discussions that took place during the German-Mexican Roundtable Exploring New Etiological Paths Towards Neurodegeneration in October 2018.

THE VASCULAR ORIGIN OF NEURODEGENERATION

Neurons depend on blood vessels to deliver oxygen and nutrients, for the removal of carbon dioxide and other by-products of metabolism from the brain's interstitial space, which helps to maintain the homeostasis of the cerebral microenvironment. Therefore, to function properly, it is thought that the cerebral circulation has developed adaptive mechanisms to provide the

trophic molecules and energy substrates needed for neuronal cells at different times and regions, depending on neural activity (Girouard and Iadecola, 2006).

The recognition of these mechanisms led to the concept of neurovascular coupling (Roy and Sherrington, 1890), which refers to the dynamic functional change in cerebral blood flow that occurs in response to local neuronal activity (Dirnagl, 1997; Kisler et al., 2017; Villringer, 1997). This response increases cerebral blood flow within the activated brain regions to fulfill energy demands in a process known as functional hyperemia.

The main players of these dynamic adjustments in the cerebral blood flow are neurons, glia, and vascular cells. All of them come together in a functional morphological entity termed the "neurovascular unit". This view explains why cerebrovascular diseases linked to neurodegeneration are considered as stand-alone etiopathological states (Przedborski et al., 2003; Brown et al., 2005). Vascular diseases, however, may be the forerunners of neurodegeneration. In support of this, it has been shown that shifts in blood pressure lead neurons to adjust the excitability thresholds according to brain perfusion levels, safeguarding their homeostasis. Hence, vascular diseases may occur first and then later neurodegeneration may follow, if the process of neurovascular coupling proceeds ineffectively (Moore and Cao, 2008; Kim et al., 2016).

Cerebral blood vessels originate from large cerebral arteries arising from the circle of Willis. As they find the way through the brain, large cerebral arteries divide into pial arteries and arterioles, which grow gradually deeper and form the penetrating arteries and arterioles that become progressively smaller until they turn into cerebral capillaries (Wittko-Schneider et al., 2014). The development of nerves and astrocytes originating from central and peripheral sources is closely associated with cerebral arteries, arterioles, and capillaries as demonstrated by the observation that the inhibition of angiogenesis during development is accompanied by severe developmental defects in specific regions of the central nervous system (CNS) (Hallene et al., 2006). This highlights the importance of blood vessels during brain formation.

There are different steps and mediators underlying neurovascular coupling. Briefly, neurons and interneurons are responsible for the initiation and modulation of the vascular response by the activation of NMDA and AMPA receptors, which leads to an increase of intracellular Ca^{2+} and calcium-dependent enzymes that exert effects on the endothelium, astrocytes, and pericytes. Because of their close association with synapses and microvessels, astrocytes are in charge of the neurovascular transmission of signals to the capillaries and arterioles while endothelial cells exert a retrograde propagation of vasomotor responses to regulate cerebral blood flow (Iadecola, 2017). The endothelium also regulates the vascular tone by releasing potent relaxing and contracting factors that readjust the vascular musculature and maintain a healthy homeostasis of the vascular wall.

Nitric oxide (NO), prostacyclins, endothelial-derived hyperpolarizing factor (EDHF), and endothelin have been proposed as the main vasoactive factors related to the endothelial response to neural activity. NO promotes the vasodilation of cerebral blood vessels by stimulating soluble guanylate cyclase in the vascular muscle, leading to an intracellular increase of cGMP and relaxation (Schmidt and Walter, 1994). NO is generated by three different isoforms of the enzyme NO synthase (NOS): neuronal (nNOS), inducible (iNOS), and endothelial NOS (eNOS).

In the CNS, nNOS is mainly located in neurons, astrocytes, and neuronal stem cells and has been implicated in synaptic plasticity and in the central control of blood pressure. Abnormal NO signaling is likely to contribute to a variety of neurodegenerative pathologies such as excitotoxicity following stroke, multiple sclerosis (MS), Alzheimer's disease (AD), and Parkinson's disease (PD) (Calabrese et al., 2007).

iNOS expression had initially been shown for macrophages, but it is now clear that it can be induced by cytokines in a variety of cell types in the context of inflammation (Li et al., 1991). During episodes of acute inflammation, the role of NO appears to be protective, while chronic iNOS expression is detrimental. The high levels of NO produced by activated macrophages and other cells may not only be toxic to microbes, parasites, or tumor cells, but may also harm healthy cells (Wong and Billiar, 1995).

Endothelial NOS is mostly expressed in endothelial cells, although the isozyme has been detected in certain neurons of the brain (Caviedes et al., 2017). eNOS-derived NO is a well-known physiological vasodilator and an inhibitor of platelet aggregation and adhesion, but it also inhibits leukocyte adhesion and vascular inflammation, controls vascular smooth muscle proliferation, stimulates angiogenesis, and activates endothelial progenitor cells (Forstermann and Sessa, 2012).

In addition to the production and release of NO, cyclooxygenase produces prostacyclin, which induces the relaxation of cerebral vessels by the activation of adenylate cyclase with the accumulation of cAMP and the activation of potassium channels. Similarly, in large cerebral arteries, the production of EDHF by the cytochrome P-450 monooxygenase metabolism of arachidonic acid causes relaxation by hyperpolarizing the underlying vascular muscle through the activation of potassium channels. The contribution of EDHF increases as the vessel size decreases, with a predominance of EDHF activity in resistance vessels and a compensatory upregulation of hyperpolarization in states characterized by reduced NO availability (Ozkor and Quyyumi, 2011).

Besides vasodilatory factors, under certain conditions, the cerebral endothelium produces vasoconstrictive substances such as endothelins leading to a potent and long-lasting contraction of cerebral vessels dependent on extracellular calcium and the activation of protein kinase C (Faraci and Heistad, 1998).

The alterations of any of the cellular players involved in the neurovascular unit may impair its coupling and functional hyperemia, resulting in an alteration of homeostasis leading to brain dysfunction (Iadecola, 2004).

Heart and Vascular Diseases and the Origin of Neurodegeneration

According to the World Health Organization, cardiovascular diseases (CVDs) lead to one-third of all annual deaths globally,

which is about 17.9 million total deaths (Lim et al., 2012). CVDs are disorders of the heart and blood vessels and include among others coronary heart disease, cerebrovascular disease, and rheumatic heart disease. A large number of studies have reported a strong relationship between indices of vascular pathology (such as carotid intima-media thickness, arterial stiffness, and small-artery remodeling) and cognitive impairment and neurodegeneration (Gorelick et al., 2011).

Because the factors contributing to vascular pathology are often preventable or treatable, targeting them may prove useful for preventing or delaying the onset of neurodegenerative diseases. Epidemiological studies show that treating hypertension and hyperlipidemia reduces the incidence of neurodegenerative diseases (Larsson and Markus, 2018) and slows down the rate of cognitive impairment (Deschaintre et al., 2009). Here, we will focus on the main CVDs known to promote changes in the cerebral microvasculature that lead to neurodegeneration in the long run.

Hypertension

Hypertension – or blood pressure at or beyond 130 mmHg/80 mmHg (systolic/diastolic blood pressure) according to the 2017 American College of Cardiology/American Heart Association guidelines (Whelton et al., 2018) – affects one billion people worldwide and leads to nine million deaths every year (Lim et al., 2012). In normotensive individuals, cerebrovascular autoregulation counteracts the cerebrovascular effects of the fluctuations in arterial pressure that occur during normal activities. Cerebral arteries relax when arterial pressure decreases and constrict when arterial pressure rises. The role of this vascular adjustment is the maintenance of a stable cerebral perfusion despite changes in systemic arterial pressure.

Hypertension alters cerebrovascular autoregulation (Sadoshima et al., 1983) by impairing endothelium-dependent relaxation (Faraci and Heistad, 1998). Hypertension promotes vascular hypertrophy, remodeling, and atherosclerosis in large cerebral arteries and lipohyalinosis in penetrating arterioles. These changes are damaging because they reduce the lumen of the vessel and increase vascular resistance (Dickinson, 2001). In humans, longstanding hypertension induces the deposition of collagen and fibronectin as well as elastin fragmentation, leading to an increased stiffness of the wall of large arteries (Henskens et al., 2008). Hypertension also affects neurovascular coupling as shown by a reduction in the normal increase in cerebral blood flow elicited in the posterior parietal and thalamic areas during cognitive tasks in patients with chronic untreated hypertension relative to normotensive individuals (Jennings et al., 2005).

The disruption of the adjustment mechanisms by a sustained increase in the blood pressure has been linked to different neurodegenerative diseases such as stroke (MacMahon et al., 1990). Hypertension is also considered an important modifiable risk factor for late-life cognitive decline and non-amnestic mild cognitive impairment in the mid-aged population (Knopman et al., 2001; Reitz et al., 2007). The Honolulu Asia aging study demonstrated an association between elevated levels of blood pressure in middle age and vascular dementia (Launer et al., 2000).

Atherosclerosis

Atherosclerosis, a progressive disease, characterized by the accumulation of lipids and fibrous elements in the large arteries, is a major cause of heart disease and stroke (Banerjee and Chimowitz, 2017).

The damage leading to atherosclerosis is elicited over years and is highly influenced by lifestyle. The pathogenic sequence starts with the recruitment of circulating monocytes into the intima, where they differentiate into macrophages and internalize modified lipoproteins to become foam cells (fat-laden M2 macrophages). Then, chemokines and growth factors induce the proliferation of neighboring smooth muscle cells and the synthesis of extracellular matrix components within the intimal compartment, generating a fibromuscular plaque that undergoes progressive structural remodeling resulting in the formation of a fibrous cap, overlying a lipid-rich, necrotic core accompanied by varying degrees of matrix remodeling and calcification (Lusis, 2000). If a rupture of the plaque occurs, the highly thrombogenic contents of the necrotic core are released to the lumen of the vessel, promoting atherothrombotic occlusion.

Epidemiological and post-mortem studies have shown that the atherosclerosis of the arteries that supply the brain is associated with a two- to threefold increased odds of dementia (Hofman et al., 1997; van Oijen et al., 2007; Wendell et al., 2012; Dearborn et al., 2017). Interestingly, this association is independent of the effects of cerebral infarction (Dolan et al., 2010), which can result from the atherosclerosis-induced occlusion of vessels.

Cerebral Small-Vessel Disease

Cerebral small-vessel disease comprises white matter lesions (WMLs), lacunar infarcts, and cerebral microbleeds and is a frequent neuroimaging finding (best seen on magnetic resonance images) in elderly people (de Leeuw et al., 2001).

Factors such as arterial stiffness, also related to aging and hypertension, are considered to expose the small vessels in the brain to highly pulsatile pressure and flow (Poels et al., 2012). This causes thickening of the arterial media of these vessels, which gradually narrows the lumen. In addition, atherosclerotic plaques in large arteries can encroach on the origins of smaller arteries, blocking the blood flow to areas supplied by these arteries. Subcortical white matter is particularly susceptible to such changes, as its blood supply depends on small arteries that get progressively smaller as they descend from the cortex to the deeper parts of the brain. Hypoxia ensues, causing edema, demyelination, and infarction of the white matter.

Cerebral small-vessel disease is associated with an increased risk of cognitive decline, dementia, stroke, balance disturbances, and parkinsonism (Bohnen and Albin, 2011). Individuals with an identical WML pattern present clinically heterogeneous complaints in cognitive and motor performance, ranging from no complaints to dementia and parkinsonism, which means other factors determine the cognitive or motor outcome (de Leeuw et al., 2001). Possible explanations for this heterogeneity are the lack of sensitivity of conventional magnetic resonance imaging to the early loss of microstructural integrity in the normal-appearing white matter (Scheltens et al., 1995), the disagreement on how lesions underlying small-vessel disease

are classified (Wardlaw et al., 2013), and the efficiency of compensation mechanisms that prevent further cognitive and motor deterioration (Mondadori et al., 2006).

Atrial Fibrillation

Atrial fibrillation (AF) is the most common arrhythmia affecting 1 to 2% of the general population (Andrade et al., 2014). AF is characterized by disturbances that promote ectopic firing and reentrant mechanisms that lead to impaired atrial function [for a review on the pathophysiology of AF, refer to (Andrade et al., 2014)].

AF can lead to reduced cardiac output, intermittent cerebral hypoperfusion, and transient hypertension in the cerebral capillaries (Anselmino et al., 2016). Such changes have been suggested as possible mediators of AF-related brain damage. On the other hand, AF may be a manifestation of a broader systemic illness that involves widespread inflammation and platelet activation, which can also lead to impaired cerebrovascular function (Dietzel et al., 2018).

AF is associated with increased morbidity and mortality and has long been known as one of the main risk factors for embolic stroke (Kamel et al., 2016). It is now also considered a risk factor for dementia. de Bruijn et al. (2015) analyzed the association of prevalent and incident AF with incident dementia in 6514 dementia-free patients, revealing not only a positive association between AF and the development of dementia but also that the association was strongest for younger participants with the longest duration of AF. These findings have been replicated by several studies (Nishtala et al., 2018), some of which have shown that the association between AF and dementia is independent of the occurrence of embolic stroke (Ryden et al., 2019) and the use of anticoagulants (Graves et al., 2017). Future investigation will determine if optimal treatment of AF can prevent or postpone cognitive decline and dementia.

Vascular Pathology in Neurodegenerative Diseases

The link between vascular risk factors and neurodegenerative disease is strengthened by the evidence showing that vascular and neurodegenerative pathophysiological changes often co-exist in patients with a diverse spectrum of neurodegenerative diseases. Several lines of evidence even suggest that vascular mechanisms are *directly* involved in the pathophysiology of neurodegenerative diseases.

The event that triggers the onset of a stroke, such as the rupture of an atherosclerotic plaque, the embolization of a blood clot, or the damage to a vessel and subsequent bleeding, is often preceded by vascular pathophysiological changes that accumulate over time. One of the earliest changes is endothelial dysfunction induced by oxidative stress (Roquer et al., 2009), which occurs as a result of the aforementioned cerebrovascular risk factors. Immediately after the onset of stroke, a series of overlapping pathophysiological changes occur leading to neuronal death within and beyond the initial area of damage. These include critically low blood flow, the accumulation of free oxygen radicals, the sustained or spreading depolarization of neurons, acidosis, tissue inflammation, damage to the blood–brain barrier (BBB), and regulated cell death (Mergenthaler et al., 2004).

The same vascular mechanisms that lead to acute stroke can also lead to cognitive impairment (Popa-Wagner et al., 2010). In the condition known as vascular dementia (or vascular cognitive impairment), the consequences of these pathophysiological changes are the primary cause of neurodegeneration. They include the development of multiple or strategically located infarcts, damage to the myelin sheath and axons, small cerebral hemorrhages, chronic cerebral hypoperfusion, and brain atrophy (Iadecola, 2013). Each of these represents damaged tissue, and the accumulation of damage eventually manifests as cognitive impairment (Gorelick et al., 2011).

Vascular pathology leading to white matter damage, manifesting as WML, seems to play a particularly important role in the pathogenesis of vascular dementia (Iadecola, 2013). Very often, however, both vascular and neurodegenerative changes contribute to the development of dementia, resulting in a condition known as "mixed" dementia.

The link between vascular pathology and neurodegeneration has also been thoroughly studied in AD. Vascular damage, initiated by vascular and genetic predisposing factors, precedes the accumulation of beta-amyloid (Aβ), which eventually leads to neurodegeneration in AD (Nelson et al., 2016). Neuroimaging studies support this theory, showing that reduced CBF and abnormal neurovascular coupling occurs in elderly people at the risk of AD before they show the hallmarks of the disease such as brain atrophy, cognitive impairment, or accumulation of Aβ (Smith et al., 1999; Bookheimer et al., 2000; Ruitenberg et al., 2005).

Vascular damage may facilitate neurodegeneration by altering a major route through which substances are cleared from the interstitial space of the brain parenchyma. This route is known as the glymphatic system, which facilitates the movement of fluid from perivascular (Virchow-Robin) spaces surrounding pial arterioles to the interstitium into spaces surrounding the brain's deep veins and then to the cervical lymph nodes (Jessen et al., 2015).

Vascular risk factors cause blockages in and around small arteries, which can manifest as an enlargement of the perivascular spaces (Gouw et al., 2011) that are visible on structural magnetic resonance images (Wardlaw et al., 2013). These enlarged spaces are a sign of impeded interstitial fluid flow and hence impaired clearance of substances from the brain parenchyma, and have been linked to an increased risk of dementia (Buerge et al., 2011; Ramirez et al., 2015) and stroke (Mills et al., 2007; Selvarajah et al., 2009).

Interestingly, the spatial distribution of these enlarged perivascular spaces has been linked to different underlying pathologies. A predominant distribution in the basal ganglia indicates vascular disease caused by hypertension (Selvarajah et al., 2009; Charidimou et al., 2013), while a white matter distribution is related to cerebral amyloid angiopathy (Martinez-Ramirez et al., 2013; Charidimou et al., 2014), caused by the accumulation of Aβ protein in the walls of the cerebral and meningeal vessels.

Cerebral amyloid angiopathy, which leads to intracerebral hemorrhage that aggravates the cognitive impairment (Cordonnier, 2011), is found in more than 80% of AD patients (Jellinger, 2010). Aβ itself is a potent vasoconstrictor (Thomas et al., 1996), worsening the hypoperfusion, which, if severe enough, directly injures neurons. However, even milder hypoperfusion alters protein synthesis and plays a role in neurodegeneration (Iadecola, 2004). The critical role of hypoperfusion is supported by the evidence that the induction of chronic global hypoperfusion in animal models causes memory impairment, the accumulation of Aβ, and synaptic dysfunction (Walsh et al., 2002; Koike et al., 2010; Wang et al., 2010).

Blood–brain barrier dysfunction, which involves damage to pericytes and endothelial tight junction molecules, has been observed in several neurodegenerative diseases, including AD, PD, amyotrophic lateral sclerosis (ALS), and Huntington's disease (Zlokovic, 2008; Chao et al., 2009; Duran-Vilaregut et al., 2009; Henkel et al., 2009; Kalaria, 2010; Alvarez et al., 2011). Vascular damage worsens the situation, both by leading to further BBB dysfunction and because low blood flow traps potentially neurotoxic proteins such as Aβ that pass through the leaky barrier. These proteins, which include immunoglobulins, plasmin, thrombin, and albumin, further reduce blood flow and cause vasogenic brain edema, oxidative stress, and axonal demyelination (Chen and Strickland, 1997; Mhatre et al., 2004; Farrall and Wardlaw, 2009; Chen et al., 2010). In patients, this BBB dysfunction is detectable using neuroimaging and the analysis of the biomarkers of neurodegenerative diseases in the cerebrospinal fluid (Olsson et al., 2016; Sweeney et al., 2018).

The presence and severity of vascular damage occurring at the cellular and molecular level, affect the clinical course of neurodegenerative diseases. Large neuropathological studies show the post-mortem presence of infarcts, lacunes, leukoencephalopathy, atherosclerosis, or hemorrhages in 80% of AD patients compared to 67% of similarly aged people without cognitive impairment (Toledo et al., 2013).

Interestingly, the effects of vascular pathology and neurodegeneration on cognitive decline seem to be synergistic, particularly in patients with moderate AD pathology (Zekry et al., 2002; Choi et al., 2011; Lee et al., 2014). Studies show that the worse the vascular pathology in patients with AD, the worse the cognitive impairment (Snowdon et al., 1997; Song et al., 2007; White, 2009). AD patients with infarcts or microangiopathic white matter disease also experience faster cognitive decline (Silvestrini et al., 2006; Helzner et al., 2009).

CELLULAR SENESCENCE AS THE ORIGIN OF NEURODEGENERATION

Since a main feature of aging is the accumulation of senescent cells in various tissues (van Deursen, 2014; Calcinotto et al., 2019), cellular senescence has emerged as a key potential contributor to neurodegenerative and cerebrovascular diseases (Baker and Petersen, 2018; Kritsilis et al., 2018).

Cellular senescence is a phenotype characterized by a durable cell cycle withdrawal (i.e., cells do not respond to mitogens), associated with the expression of tumor suppressors $p21^{CIP1/WAF1}$ (encoded by *Cdkn1a*) and/or $p16^{INK4A}$ (encoded by *Cdkn2a*), as well as by apoptosis resistance (**Figure 1**). Senescent cells display a flattened and vacuolated morphology with abundant stress granules and accumulate lipofuscin. There is a persistent DNA damage response commonly detected by the presence of γH2AX foci, while the most common feature is an increase in the lysosomal activity of the enzyme senescence-associated beta galactosidase isoform (SA-B-Gal), which has been widely used for their detection. Some senescent cells exhibit a formation of senescence-associated heterochromatin

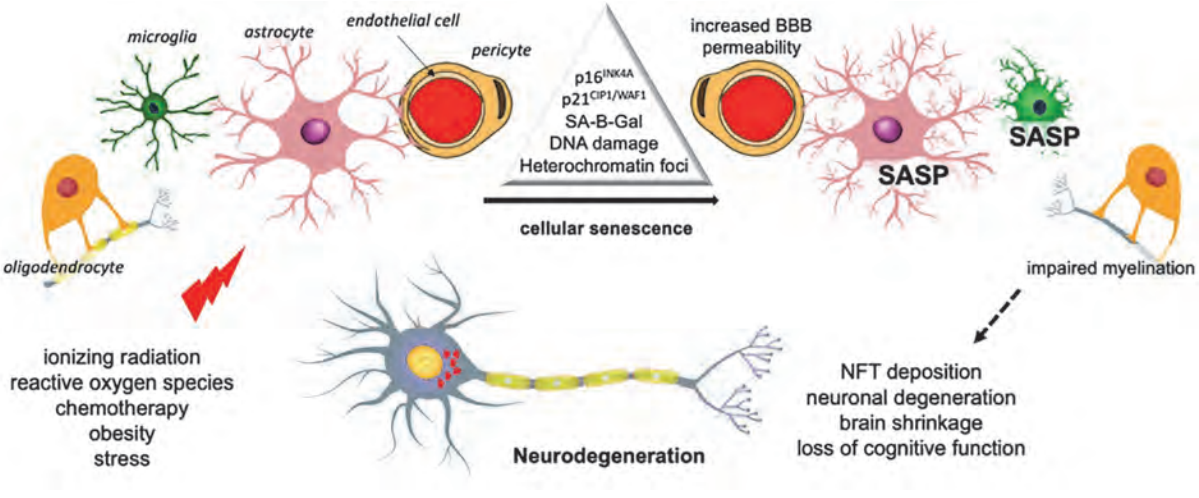

FIGURE 1 | Senescence-mediated neurodegeneration. Cellular senescence can be induced by several stimuli in the different brain cells. Senescence of microglia and astrocytes results in inflammation and the loss of trophic support. Oligodendrocyte senescence reduces myelin, which affects transmission and the BBB may be compromised by endothelial cells senescence. These changes have an impact on the integrity and viability of neurons and ultimately brain function [based on Chinta et al. (2015)]. SASP, senescence-associated secretory phenotype.

foci (SAHF), which are domains enriched in the transcription-silencing histone H2A variant, macroH2A.

However, the most important feature of senescent cells is the secretion of pro-inflammatory cytokines, growth factors, extracellular enzymes, and metalloproteases, collectively known as senescence-associated secretory phenotype (SASP) (Chow and Herrup, 2015; Ask et al., 2018). In early stages, the secretion of cytokines by senescent cells promotes the migration and infiltration of effector immune cells and the secretion of growth factors and proteases, which facilitate tissue repair and remodeling (Munoz-Espin and Serrano, 2014; Davaapil et al., 2017).

Yet, persisting cytokine signaling, as occurs in aging, contributes among other processes to chronic inflammation (*inflammaging*), a major contributor to age-related dysfunctions. SASP molecules also have an autocrine role, fostering the senescent phenotype, and a paracrine role inducing senescence in surrounding cells (Coppe et al., 2010). Notably, during aging, senescent cells accumulate and persist in different organs, including the brain, and are associated with the onset of several diseases (Munoz-Espin and Serrano, 2014).

To avoid confusion, it is however important to differentiate between aging, often termed "senescence" and cellular senescence. Aging is featured by an accumulation of senescent cells, but not all aged cells have the unique cellular senescence phenotype. Further investigations are needed to understand why senescent cells accumulate with aging, perhaps involving a combination of immune system malfunction failing to eliminate them, with changes in senescent cells themselves so that they become less efficiently recognized.

Senescence in Neurodegenerative Diseases

More recent *in vitro* and *in vivo* evidence strengthens the hypothesis of cellular senescence as causative of neurodegeneration. Dysfunctional astrocytes with senescent hallmarks have been detected in post-mortem human brain tissue from patients with ALS, PD, and AD (Bhat et al., 2012; Chinta et al., 2015, 2018; Turnquist et al., 2016). Mouse models and *in vitro* studies provide further evidence of senescence in microglia (Bussian et al., 2018), endothelial cells (Broadwell, 1989), neural stem cells and possibly oligodendrocytes (Kritsilis et al., 2018), which may contribute to neurodegenerative disorders.

Moreover, several senescent features have recently been described in studies of both physiological aging and neurodegenerative diseases using different models, including AD, PD, MS, and stroke (Kritsilis et al., 2018; Walton and Andersen, 2019), supporting the idea that cellular senescence may contribute to neurodegeneration and cerebrovascular disease in a far-reaching way (reviewed by Baker and Petersen, 2018; Walton and Andersen, 2019).

In a recent publication, using weighted gene co-expression analysis, Mukherjee et al. (2019) found a microglial signature of 17 genes that are strongly related with both aging and neurodegenerative diseases, not only in human brains but also in neurodegenerative murine models. An early study from Bhat et al. (2012) suggested that $p16^{INK4A}$-positive astrocytes may increase the risk for sporadic AD, since the prefrontal cortex of AD patients harbors a significant increase of senescent astrocytes expressing $p16^{INK4a}$ and matrix metalloproteinase-1 (MMP-1).

Also, the *in vitro* exposure of astrocytes to $A\beta_{1-42}$ triggers senescence, leading to the secretion of pro-inflammatory cytokines, including interleukin 6 (Bhat et al., 2012). Chinta and colleagues also demonstrated an increase of senescent astrocytes in brain tissue from PD patients, and found that cultured murine and human astrocytes exposed to paraquat (an herbicide associated with sporadic PD) become senescent. Interestingly, the depletion of senescent cells diminished neurodegeneration (Chinta et al., 2018), suggesting that senescence may be the cause, not the consequence of neurodegeneration.

Cellular senescence has also been considered as a therapeutic target in MS (Oost et al., 2018). Although MS is regarded as a classical autoimmune disease, it has been hypothesized that the driver of the autoreactive immune response in MS is actually a primary neurodegenerative process (Trapp and Nave, 2008). The senescence of microglia, T-cells, astrocytes, endothelial cells, and oligodendrocytes, among other cell types, is implicated in MS pathophysiology (Oost et al., 2018). Even though no study has been conducted for senescent cell detection on post-mortem tissue of MS patients, there is initial evidence in animal models about the role of cellular senescence on MS progression (Oost et al., 2018).

Senescence and Synaptic Plasticity

Another common hallmark of neurodegenerative pathologies is the alteration in synaptic structure and function during the early stages of the disease, which is related to subcellular reorganization preceding cell loss. The mechanisms underlying these pathologies are not fully understood. In fact, a decline in synaptic plasticity may be linked to the phenomenon of senescence. Unfortunately, there are only a few studies that have investigated the effect of senescence on the synaptic machinery. However, there is growing evidence of the changes in neuroplasticity caused by inflammation, oxidative stress, and protein misfolding, that may be linked to SASP action as well as the influence of senescence in glial cells, which are associated with an impairment in the neuroplasticity machinery (Gan et al., 2018).

The hippocampus has been pointed out as a brain structure with high plasticity and prone to neurodegeneration with age (Kreutzmann et al., 2015). The neurogenic capacity of the hippocampal dentate gyrus is reduced during aging. This reduction correlates with an impairment in memory formation and is accompanied by other changes, such as an increase of pro-inflammatory cytokines as well as a reduction of neurotrophic and vascular factors (Seib and Martin-Villalba, 2015; Fan et al., 2017).

Aging is also associated with changes in the hippocampal perforant pathway and its synapses, with the dentate gyrus being particularly affected (Wenk and Barnes, 2000). A decrease of synapses and changes in the morphology of dendrites and their spines have been linked to atrophy and a dysfunction of the aged hippocampus (Rogers et al., 1984). A synapto-proteome

study in old animals revealed a general decrease in the expression of neurotransmission regulation proteins, such as post-synaptic density 95, synaptosomal nerve-associated protein 25, shiga toxin 1, synapsin 1 and 2, synaptophysin, and vesicle-associated membrane protein (Wang et al., 2007; VanGuilder et al., 2010; Orock et al., 2019).

Moreover, a recent breakthrough paper, using a classical model of neurodegeneration, shows the accumulation of senescent astrocytes and microglia, but not neurons, in the brains of mice overexpressing human TauP301S. The genetic clearance of senescent glial cells prevented neurofibrillary tangle (NFT) deposition, the degeneration of hippocampal neurons, brain shrinkage, and the thinning of the dentate gyrus, thus preserving cognitive function. The transgenic mice that did not undergo a senescent transformation of microglia cells maintained their cognitive functions (Bussian et al., 2018).

Interestingly, neurogenesis and learning and memory can be impaired when blood and plasma from aged animals are transfused to young animals, showing that systemic factors can affect brain integrity. This phenomenon may be related to chemokine levels, especially the C–C Motif Chemokine Ligand 2 (CCL2), an important SASP component (Villeda et al., 2011). It is possible that when senescent astrocytes accumulate, they release SASP factors that lead to NFT deposition and other neurodegenerative hallmarks in surrounding neurons, oligodendrocytes, microglia, and endothelial cells (**Figure 1**). Investigating senescent cell accumulation in the periphery and in the nervous system should help to understand the process of aging of the brain and, more importantly, neurodegeneration in an integrative way.

Cellular Senescence in Stroke

Cellular senescence accompanying neurological conditions involves many cell types of the CNS (Walton and Andersen, 2019), which may also be of great importance in the case of brain injury following stroke (Buga et al., 2013). Most studies in this field, however, focused on the effects of aging rather than on cellular senescence. The timing of the cellular and genetic response to brain tissue injury is dysregulated in aged animal models due to a premature accumulation of BrdU-positive microglia and astrocytes, activated oligodendrocytes, and degenerated neurons (Popa-Wagner et al., 2007).

There is no consensus whether and to what extent age influences infarct size: several studies reported larger (Popa-Wagner et al., 2011) or smaller ischemic lesions in aged animals when compared to young rodents (Manwani et al., 2013; Ritzel et al., 2018). However, irrespective of the infarct size, aged animals have worse functional when compared to young ones (Popa-Wagner et al., 2011; Ritzel et al., 2018). The slow tissue recovery and rapid development of damage after injuries like stroke in aged animals may be linked to several factors such as a reduced expression of genes linked to neuroprotective pathways, high and accelerated cell death, high oxidative stress by mitochondrial dysfunction, increased permeability of the BBB, high phagocytic activity of brain macrophages, autophagic dysfunction, as well as an imbalanced inflammatory state (Popa-Wagner et al., 2007, 2011; Petcu et al., 2008).

Furthermore, the immune response to ischemic brain injury differs between aged and young mice. In a recent report, older mice displayed an increased number of brain-infiltrating and peripheral neutrophils with decreased phagocytic potential, increased levels of reactive oxygen species and extracellular matrix-degrading enzymes (Ritzel et al., 2018). Rawji and colleagues reported that aging also affects brain-resident immune cells. Aged microglia express excessive amounts of pro-inflammatory cytokines and proliferate at increased rates, but simultaneously display defective phagocytosis and decreased motility. Interestingly, aged peripheral monocytes seem to share the features of impaired phagocytosis and reduced motility, but are less prone to activation and proliferation (Rawji et al., 2016).

Since aging has been linked to the accumulation of senescent cells (van Deursen, 2014; Calcinotto et al., 2019), we speculate that cellular senescence may contribute to the outcome after stroke. However, there is a need for more studies, exploring specifically the impact of cellular senescence rather than the global effects of aging. *In vitro* and *in vivo* experiments show that aging influences the state of endothelial cells, pericytes, and tight junctions, in turn resulting in a compromised function of the BBB (Yamazaki et al., 2016). Acute stroke leads to increased permeability and BBB breakdown, associated with worse outcome in stroke patients (Brouns et al., 2011).

Astrocytes in aged brains display the features of cellular senescence and SASP (Salminen et al., 2011), possibly impacting surrounding cells also in the case of acute brain damage. In the context of senescence hallmarks, human astrocytes are highly sensitive to oxidative stress and trigger a senescence program when faced with multiple types of stressors (Crowe et al., 2016; Liddell, 2017).

Chronic low-grade inflammation contributes to the increased risk of cerebrovascular disease (Lucas et al., 2006) and was shown to be a feature of the aging (Buga et al., 2013). The SASP in many cell types, including peripheral immune cells, astrocytes and microglia may influence a chronic inflammatory state observed in aging (Buga et al., 2013).

Taking into consideration the pathogenesis of cerebrovascular diseases, it is important to mention that cellular senescence may play a role in comorbidities and conditions known as risk factors for stroke (Buga et al., 2013). Cellular senescence impacts the formation and state of atherosclerotic plaques (Ritzel et al., 2018) and endothelial cells showing the hallmarks of senescence triggered by stressors like changes in glucose levels, homocysteine or elevated blood pressure (Tian and Li, 2014) may play a role in age-related vascular diseases. Since cellular stress induces senescence, it remains to be experimentally tested whether stroke itself triggers senescence in brain cells, which may influence the CNS microenvironment, have long-term consequences and an impact on the outcome after cerebral insults.

Systemic Metabolic Disease, Cellular Senescence, and Neurodegeneration

Risk factors in many neurodegenerative disorders include systemic metabolic diseases (see section "Impact of Peripheral Metabolic Disorders on Neurodegeneration"), which, in fact, favor the accumulation of senescent cells by facilitating the

functional changes of cellular distribution and regulation of adipose tissue. As mentioned before, cellular senescence in aging may contribute to a chronic inflammatory state in the brain and peripheral tissues (Buga et al., 2013).

Interestingly, obesity generates an accelerated state of aging, pro-oxidant factors as well as glucotoxicity (Hardie et al., 2006; Eberle and Ament, 2012). It is also associated with an increased senescent cell burden and a wide range of neurodegenerative and neuropsychiatric diseases (Gariepy et al., 2011; Hryhorczuk et al., 2013; Morsi et al., 2018). Ogrodnik and colleagues demonstrated that, in obese mice, glial cells show increased markers of cellular senescence in the periventricular region of the lateral ventricle, a region in close proximity to the neurogenic niche (Ogrodnik et al., 2019).

Furthermore, the affected glial cells in obese mice display excessive fat accumulation, which is in agreement with the role of glial cells on the senescence-mediated induction of neurodegeneration. Since SASP contributes to inflammation, metabolic dysregulation, progeria, pulmonary fibrosis, geriatric syndromes, and the loss of resilience, the clearance of senescent cells may delay or even alleviate multiple age-related diseases (Kirkland and Tchkonia, 2017).

Taking into consideration the increasing body of evidence on the role of cellular senescence in neurodegenerative, cerebrovascular, and metabolic disorders, we propose to investigate senescent cell accumulation in the periphery and in the nervous system as well as the influence of SASP on processes in the CNS, such as neuroplasticity, specific cellular populations, and on the brain–body signaling. This will help to understand the normal process of aging and senescence in an integrative way.

BODY–BRAIN TROPHIC INTERACTIONS AS THE ORIGIN OF NEURODEGENERATION

The disruption of the bidirectional interaction between neurons and the cells they innervate has not been considered as a putative etiologic mechanism of neurodegeneration. According to the trophic theory of neural connections, the body is represented several times within the nervous system along the sensory and motor pathways (Purves, 1988). Thus, changes in size and function of the body must be accompanied by changes in their neural representation at a central level, which may include neurite remodeling and functional adaptations.

Furthermore, novel requirements of the body affect the peripheral and central connections of peripheral neurons. In early phases of metabolic disorders, adipocytes and immune cells are related to peripheral nerve remodeling of both sympathetic and sensory fibers (Pellegrinelli et al., 2018; Yamazaki et al., 2018). In addition, the alteration of the enteric nervous system (ENS) may be a conduit to induce changes in the CNS. Future studies oriented to understand the interactions between neurons and the cells they innervate would help to discover biomarkers for early diagnosis and to monitor disease progression. Here, we present a brief summary of the experimental evidence related to the early events of neurodegeneration in the body and discuss possible mechanisms of intercellular communication that may be operating (**Figure 2**).

Pathological Events in the Peripheral Nervous System

Various neurodegenerative diseases share common molecular and cellular mechanisms including the misfolding of proteins that undergo conformational changes leading to tissue deposition and the formation of inclusion bodies. Increasing evidence suggests that these neurodegenerative proteinopathies may originate in the peripheral nervous system (Wakabayashi et al., 2010) or even across the body.

In PD and dementia with Lewy bodies (DLBs), the histopathological hallmark is the occurrence of neuronal α-synuclein aggregates, also known as Lewy bodies. Lewy bodies are typically found in the substantia nigra in PD. However, LBs can also be present in peripheral organs, neural or not, including the sympathetic ganglia, ENS, cardiac and pelvic plexuses, submandibular gland, adrenal medulla, and the skin (Beach et al., 2010; Wakabayashi et al., 2010). Moreover, in the early pathological stages of PD, α-synuclein pathology is present first in the dorsal motor nucleus of the glossopharyngeal and vagal nerves as well as the anterior olfactory nucleus (Braak et al., 2003a).

In AD, NFTs are observed in the spinal and sympathetic ganglia. However, it seems that they develop independently of the cerebral AD pathology (Shankle et al., 1993). In ALS, TDP-43 is a major component of the ubiquitinated inclusions and also occurs in the neurons of the spinal ganglia (Nishihira et al., 2008).

Sensory abnormalities have been described in neurodegenerative diseases including PD and AD. In this regard, the loss of olfaction represents an important early clinical symptom frequently preceding motor and cognitive impairments typically observed in these neurodegenerative diseases (Driver-Dunckley et al., 2014; Doty, 2017; Marin et al., 2018; Rey et al., 2018). The olfactory system may be particularly affected in neurodegenerative diseases as seen by the accumulation of pathological protein aggregates in olfactory structures including the anterior olfactory nucleus, the olfactory bulb, and the olfactory epithelium (OE) (Doty, 2017; Marin et al., 2018; Rey et al., 2018).

Given that the OE is directly accessible to external factors, it is vulnerable to environmental insults. Thus, external agents (toxins, bacteria, viruses, air pollutants) may trigger neurodegeneration through the OE (Rey et al., 2018). Once these agents enter the brain via the OE, they may cause protein misfolding and the spreading of protein aggregates in a prion-like manner throughout the olfactory pathway to other anatomically connected brain regions (Doty, 2017).

Moreover, xenobiotics and particles in contact with the OE can also induce the production of reactive oxygen species triggering a local inflammatory reaction in a similar way to that induced by misfolded proteins (Lema Tome et al., 2013). Alternatively, the enhanced expression of misfolding-prone proteins in olfactory structures may make those regions prone to develop certain diseases (Duda et al., 1999; Taguchi et al., 2016; Kim et al., 2018).

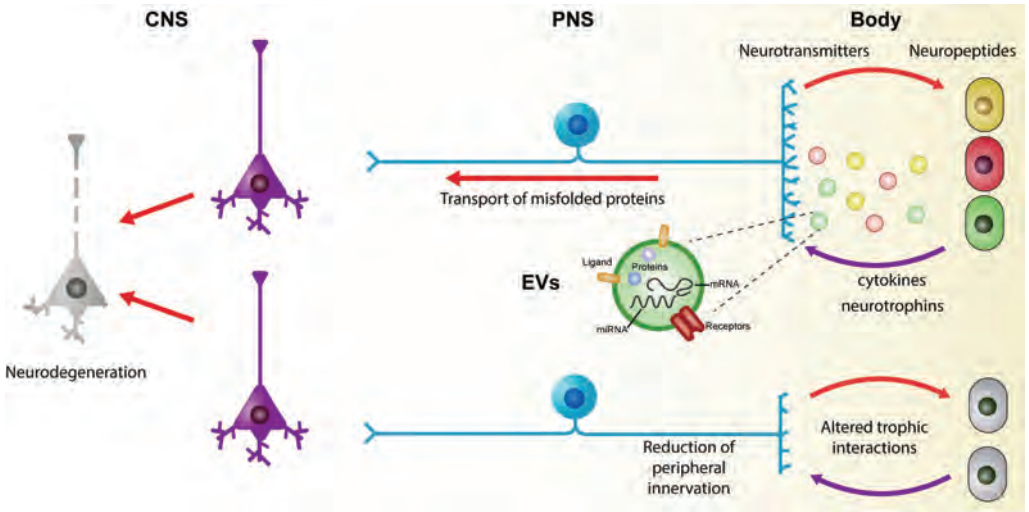

FIGURE 2 | The role of trophic interactions between the brain and the body in the development of neurodegenerative diseases. Under physiologic conditions, there is a continuous exchange of information between neurons and their targets. Neurons control several aspects of the cells they innervate by the release of neuropeptides and neurotransmitters. Reciprocally, peripheral cells modulate neuronal physiology by the release of several molecules including neurotrophins and cytokines. Recently, extracellular vesicles (EVs) have been considered as key players in the development and progression of chronic and degenerative diseases. An alteration of the homeostatic state of peripheral cells is reflected on the molecular cargo of EVs which, in turn, can affect the functioning of the neurons. Common to several chronic and neurodegenerative diseases, there is a reduction of peripheral innervation which leads to a disturbance of the trophic relation between the body and the central nervous system. A continuous alteration of these interactions during maturity of individuals may underlie some of the early events that reflect on neuronal death during aging. CNS, central nervous system; EVs, extracellular vesicles; PNS, peripheral nervous system.

Pain abnormalities are part of the clinical features in patients with PD and the impaired nociceptive processing depends on nociceptor degeneration (Nolano et al., 2008; Reichling and Levine, 2011; Conte et al., 2013). Skin biopsies of PD patients reveal a decrease in cutaneous autonomic innervation, free epidermal nerve endings, and encapsulated sensory endings (Dabby et al., 2006; Nolano et al., 2008). The severity of PD correlates with the loss of Meissner corpuscles and epidermal nerve fibers, accompanied by a reduction in cold and pain perception (Nolano et al., 2008).

The accumulation of misfolded proteins such as α-synuclein and parkin due to a dysfunction of the ubiquitin-proteasome system may partially explain the painful nociceptor dysfunction (Saha et al., 2000). In AD, pain perception seems not to be reduced. However, more studies are necessary to document whether sensory innervation is modified in AD and other neurodegenerative diseases (Cole et al., 2006). Of note, it is important to mention that different mechanisms involving both peripheral and central pain pathways may play a role in sensory dysfunction.

Autonomic dysfunction is present in several neurodegenerative diseases including PD, multiple system atrophy, AD, and other types of dementia such as DLB, PD with dementia, and frontotemporal lobar degeneration (Idiaquez and Roman, 2011; Coon et al., 2018). Orthostatic hypotension has been widely reported in patients with PD and DLBs as seen by the decreased cardiac uptake of the noradrenaline analog meta-iodobenzylguanidine (Orimo et al., 2005).

The presence of orthostatic hypertension may be due to the depletion of cardiac vagal sympathetic nerves as well as the α-synuclein pathology in sympathetic ganglia and adrenal gland that have been reported in Lewy body diseases, which includes PD, PD with dementia, and DLB (Wakabayashi et al., 2010). Interestingly, sympathetic denervation precedes neuronal loss in the sympathetic ganglia (Orimo et al., 2005). Autonomic dysfunction in AD may also be affected by neuropathological changes in central autonomic networks (Collins et al., 2012). Future studies should focus on the temporality of autonomic alterations in neurodegenerative diseases.

Gastrointestinal dysfunction is closely linked to the dysfunction of the ENS. Enteric dysfunction has been reported in PD, AD, ALS, and frontotemporal dementia (Rao and Gershon, 2016). Biopsies of PD patients have demonstrated the presence of Lewy-type pathology in enteric neurons suggesting a role of the ENS in the onset of the disease (Kupsky et al., 1987; Wakabayashi et al., 1988, 1990). The unmyelinated axons of enteric neurons may increase their susceptibility to PD and due to their multiple synaptic terminals may promote the propagation of α-synuclein aggregates via connected ganglia (Chalazonitis and Rao, 2018).

Likewise, in AD patients, Aβ immunoreactivity is found in the submucosa of the intestine (Joachim et al., 1989). In addition, amyloid precursor protein expression is present in the enteric neurons of AD patients (Arai et al., 1991). However, in contrast to PD, data from human samples in AD are still sparse. Other autonomic dysfunctions reported include urinary symptoms, sexual and thermoregulatory, dysfunction, and sleep disturbances (Postuma et al., 2015; Racosta et al., 2015; Pfeiffer, 2016). A better characterization of peripheral damage is required

in those cases where there is evidence of alteration in the peripheral innervation.

Impact of Peripheral Metabolic Disorders on Neurodegeneration

An increasing body of evidence suggests that metabolic disturbances may contribute to neurodegenerative processes in the CNS. We discuss here briefly the impact of diabetes mellitus (DM) and obesity on neurodegeneration.

Diabetes mellitus is one of the most common metabolic diseases and a major disorder of insulin regulation with increasing incidence (Duarte et al., 2012). Especially type 2 diabetes (T2D) is a highly complex, multifactorial metabolic disease, characterized by a progressive pancreatic β-cell failure (relative insulin deficiency), decreased insulin action and peripheral insulin resistance (Campbell, 2011; Carvalho et al., 2012).

T2D develops under a cluster of risk factors that includes high blood glucose, obesity, increased blood triacylglycerols and insulin resistance, which individually or collectively, also increase the risk for neurodegeneration/neuronal death, functional and structural brain changes, culminating in cognitive dysfunction that underlies dementia-type disorders (e.g., AD), which may arise from a complex interplay between T2D and brain aging. Additionally, decreased brain insulin levels/signaling and glucose metabolism in both pathologies further suggests that an effective treatment strategy for one disorder maybe also beneficial in the other (Duarte et al., 2013).

Obesity is clinically identified based on measurements of body mass index, but can be generally defined as the condition in which excess body fat has accumulated to an extent that can negatively affect health. This definition is based on the dramatically enhanced risk for a myriad of disorders, including T2D, CVD, gastrointestinal and respiratory disorders, and several types of cancer (for review, see Haslam and James, 2005). Furthermore, abdominal obesity is a component of the metabolic syndrome, which additionally combines insulin resistance or glucose intolerance, atherogenic dyslipidemia, elevated blood pressure, and increased expression of prothrombotic and proinflammatory markers (for review, see Olufadi and Byrne, 2008) and is an important risk factor for T2D, CVD, and stroke.

While the consequences of obesity on metabolic and cardiovascular pathophysiology are well-studied, epidemiological and experimental data are beginning to reveal that the CNS may also be detrimentally affected by obesity and obesity-induced metabolic dysfunction. In particular, data show that obesity is associated with cognitive decline and enhanced vulnerability to brain injury, while experimental studies in animal models confirm a profile of increased susceptibility to brain damage and decreased cognitive function (Bruce-Keller et al., 2009).

Recent data suggest that both AD and PD can manifest systemic alterations in energy metabolism (e.g., increased insulin resistance and dysregulation of glucose metabolism). Moreover emerging evidence that dietary restriction can forestall the development of AD and PD is consistent with a major "metabolic" component to these diseases, and provides optimism that these devastating brain disorders of aging may be largely preventable (Blum-Degen et al., 1995; Mattson et al., 1999).

Advanced glycation end products generated by chronic hyperglycemia and their receptor RAGE provide critical links between diabetes and AD (Vicente Miranda et al., 2016; Fleitas et al., 2018). Obesity, diabetes, and metabolic syndrome increase the risk of cognitive decline and dementia, including not only vascular dementia, but also AD and PD (Roriz-Filho et al., 2009).

However, due to increased incidence, especially in the aging population, the impact of metabolic disease on neurodegenerative processes will increase tremendously in the upcoming decades. We believe therefore that potential therapeutic approaches aiming at preventing/treating neurodegenerative diseases should include metabolic disorders.

Altered Body–Brain Trophic Communication

Accumulating evidence suggests that patients with neurodegenerative diseases commonly develop sensory and autonomic dysfunctions during maturity. This raises the possibility that the peripheral nervous system may be the gateway to alter brain physiology. The trophic theory of neural connections states that there is a mutual dependence between neurons and their targets (Purves, 1988; Qureshi and Mehler, 2013; Holm et al., 2018). Olfactory or gastrointestinal alterations may reflect a distortion of the communication between a variety of cell types and peripheral neurons. The repercussion of these altered interactions on the development of neurodegenerative diseases are still underexplored. Moreover, the mechanisms of cellular communication between peripheral cells and the nervous system are not fully characterized.

Recently, a novel system of intercellular communication has been proposed to modulate changes in neuronal physiology and to participate in the propagation of misfolded proteins (Fevrier et al., 2004; Asai et al., 2015; Grey et al., 2015; Polanco et al., 2016). This system is mediated by membranous organelles denominated as EVs, which can travel from the periphery to the brain and vice versa (Li et al., 2018).

Apparently, all the cell types of the body can release EVs to transmit information in the form of proteins, RNAs, and lipids. EVs are classified according to their subcellular origin in exosomes when originating from multivesicular bodies and in ectosomes (or microvesicles) when formed from the plasma membrane (Thery et al., 2018). Despite the technical challenges to study the functional role of different EVs subpopulations, their participation in both the maintenance of tissue homeostasis and the progression of chronic degenerative diseases is becoming clearer.

Extracellular vesicles are involved in several processes of brain development and normal functioning, including synapse formation, synaptic plasticity, and communication between glia and neurons. The signaling proteins of hydrophobic nature, such as the Wnt family members and other regulatory proteins, are loaded into EVs (Korkut et al., 2009; Coulter et al., 2018; Lee et al., 2018). During mammalian brain development, the vesicular secretion of the

growth factor sonic hedgehog promotes the proliferation of neural progenitors.

Interestingly, the loss of function of the complex charged multivesicular body proteins 1A reduces the number of intraluminal vesicles and the secretion of a specific subtype of EVs whose functions can be directly related to sonic hedgehog signaling (Coulter et al., 2018). At the *Drosophila* neuromuscular junction, EVs containing the Wnt-binding protein Evennes Interrupt and the Wnt 1 homolog Wingless promote synaptic growth when released from the presynaptic terminal (Korkut et al., 2009; Koles et al., 2012).

There is a constant reciprocal exchange of information through EVs between the pre- and post-synapse to modulate fine aspects of synaptic maturation and remodeling. In rat hippocampal neurons, excitatory synapses can be eliminated by a mechanism dependent on the delivery of Proline-Rich 7 by exosomes to induce the degradation of the post-synaptic density protein-95 (Lee et al., 2018).

Extracellular vesicles contents also influence long-term memory and synaptic plasticity. In neuronal cultures from mouse hippocampus and in neuromuscular junction preparations from *Drosophila*, oligomers of the activity-regulated cytoskeleton-associated protein and its own mRNA are transported through exosomes to the post-synapse (Ashley et al., 2018; Pastuzyn et al., 2018). The translation of the exosomal activity-regulated cytoskeleton-associated protein mRNA increases by the activation of the group 1 metabotropic glutamate receptors (Pastuzyn et al., 2018). The notion that neurons constantly use EV-mediated communication is reinforced by the fact that the release of EVs is activity-dependent and that the delivery of the cargo from presynaptic cells enables retrograde signaling from the post-synaptic cells (Lachenal et al., 2011; Korkut et al., 2013; Lee et al., 2018).

The general hypothesis on the role of EVs related to the development of neurodegenerative diseases relies on their potential to transport protein aggregates, which has been reviewed elsewhere (Howitt and Hill, 2016). Here, we would like to center the discussion on the possibility that a bidirectional exchange of information through EVs between peripheral cells and neurons may have a long-term impact on the brain physiology.

Emerging evidence suggests that both central and peripheral neurons can uptake EVs from a variety of cell types. Thus, under certain circumstances, EVs derived from peripheral cells contain proteins or RNAs that can be deleterious for neuronal functioning. In agreement with this notion, exosomes derived from hyperglycemic Schwann cells contain microRNAs that suppress axonal growth *in vitro* (Jia et al., 2018). Moreover, hyperglycemic Schwann cell-derived exosomes contribute to the development of diabetic peripheral neuropathy when injected into a diabetic mouse (Jia et al., 2018).

Similarly, the CNS can also be affected by the information transported by systemic exosomes. An increase of inflammatory cytokines in the brain and microglial and astrocytic activation is observed after the intravenous injection of serum-derived exosomes from lipopolysaccharide (LPS)-challenged mice (Balusu et al., 2016; Li et al., 2018). Dorsal root ganglion neurons modulate immune cells in the periphery by the release of neuropeptides.

Recent findings also indicate that EV-mediated communication can be an additional mechanism operating during trauma. After nerve injury, dorsal root ganglia neuron-derived exosomes loaded with microRNA-21 increase the infiltration of inflammatory macrophages, which contributes to neuronal sensitization (Simeoli et al., 2017). Further work is required to obtain insights whether EVs from peripheral cells modulate cellular processes in the brain under physiological conditions and which factors can alter the messages coming from the periphery (Ridder et al., 2014).

Despite the few studies focusing on the influence of peripherally derived EVs on peripheral neurons, it is likely that peripheral terminals establish a bidirectional interaction with the cellular elements surrounding them. Both sensory and autonomic axon terminals usually end as free nerve endings in the extracellular matrix intercalated between different cell types. Peripheral neurons are responsive to EVs derived from mesenchymal stem cells and Schwann cells (Lopez-Verrilli et al., 2013, 2016; Ching et al., 2018; Sun et al., 2018; Shiue et al., 2019). The general observation of these studies, performed in conditions of neuronal damage, is that EVs reduce the inflammatory state and have a beneficial role in axonal growth both *in vivo* and *in vitro*.

Taken together, these findings indicate that neurons are susceptible to modify their functioning or gene expression profile as a result of incorporating EVs from neighboring cells. A challenge for future studies is to determine if EVs from any cell source can modify neuronal functioning and how these events are associated with physiological alterations that precede neurodegeneration in the brain.

GUT DYSBIOSIS AS THE ORIGIN OF NEURODEGENERATION

Microbiota is defined as a community of all microorganisms living in our body. Microbiota therefore includes all taxonomic domains such as fungi, protozoa, viruses, and bacteria. Bacterial microbiota living in the gut (further referred as GM) represent about 90% of all microbiota in the body (Thursby and Juge, 2017), with an estimated ratio of human:bacterial cells close to 1:1 (Sender et al., 2016). This large number of bacteria offers different benefits to the host, confers protection against pathogens (Baumler and Sperandio, 2016), regulates host immunity (Gensollen et al., 2016), and products originating from bacterial fermentation can be used as a source of energy for colonocytes (den Besten et al., 2013).

A delicate balance exists between the GM composition and its interaction with the host, while an imbalance in this composition is commonly known as dysbiosis. Gut dysbiosis has been implicated in the development of chronic diseases, such as irritable bowel syndrome (Raskov et al., 2016), coeliac disease (Verdu et al., 2015) as well as metabolic disorders, including obesity, metabolic syndrome, and T2D (Holmes et al., 2011;

TABLE 1 | Alterations in gut microbiota at PHYLUM level in AD patients and AD transgenic mice.

Model	Bacterial phylum INCREASED	Bacterial phylum DECREASED	References
AD patients	Actinobacteria	Bacteroidetes	Zhuang et al., 2018
AD patients	Bacteroidetes	Firmicutes	Vogt et al., 2017
3×TG-AD mice 8 months old	Firmicutes	–	Sanguinetti et al., 2018
3×Tg-AD mice 24 months old	–	Tenericutes Cyanobacteria	Bonfili et al., 2017
APP/PS1 mice 8 months old	Firmicutes	Bacteroidetes Proteobacteria	Park et al., 2017
APP/PS1 mice 1 month old	Firmicutes	Bacteroidetes	Harach et al., 2017
APP/PS1 mice 8 months old	Bacteroidetes Tenericutes	Firmicutes Verrucomicrobia Proteobacteria Actinobacteria	Harach et al., 2017
5×FAD mice 9 weeks old	Firmicutes	Bacteroidetes	Brandscheid et al., 2017

Carding et al., 2015; Zhang et al., 2015; Baothman et al., 2016; Org et al., 2017).

Notably, those metabolic diseases, when developed during adulthood, are considered important risk factors for AD (Alzheimer's Association, 2016; Livingston et al., 2017). Furthermore, metabolic alterations are known to induce peripheral low-grade chronic inflammation, associated with higher incidence of neurodegenerative diseases. In AD, systemic inflammation during prodromal stages shortens disease onset (Tao et al., 2018), whereas dysregulation of the gastrointestinal function and colonic inflammation diminished immune competence and preceded motor symptoms in PD patients (Dobbs et al., 1999; Braak et al., 2003b; Lebouvier et al., 2009; Villaran et al., 2010; Forsyth et al., 2011).

During aging, there is an increased permeability of the gut epithelium (Tran and Greenwood-Van Meerveld, 2013). This condition allows bacteria and bacterial products to translocate through the disrupted gut barrier reaching peripheral organs (Zevin et al., 2016). Newest reports suggest that translocated bacteria may even reach the brain (Roberts et al., 2018), where an exacerbated immune reaction can lead to neurodegeneration. These observations remain however to be investigated in detail.

Gut Microbiota Alterations in Neurodegenerative Diseases

Recent reports concomitantly demonstrate a gut dysbiosis in PD (Minato et al., 2017; Wu et al., 2017), ALS, and AD patients (Cattaneo et al., 2017; Vogt et al., 2017).

Understanding how GM may be implicated in brain pathologies requires a clear comparison among the data reported from different research groups. The GM is mainly dominated by four phyla: Firmicutes, Bacteroidetes, Actinobacteria, and Proteobacteria (Szablewski, 2018). The first studies described GM alterations only at the phylum level. However, recent advances in sequencing techniques allow distinction at the species level, which is advantageous since the different species of bacteria belonging to the same genus affect host physiology in a different manner. We compared previously published GM data obtained from AD patients and AD mice models. We noted a strong variation between studies: at phylum level, most transgenic models coincide with an increased abundance of Firmicutes but a decreased abundance of Bacteriodetes (**Table 1**). Whereas at the family and upper taxonomical levels (i.e., genus/species), there is no more consistency (**Table 2**).

Importantly, variations in the experimental design or the type of samples can be observed. Moreover, differences in the animal model, chronological stage of the pathology (age), handling and diet significantly impact GM (Mueller et al., 2006; Hufeldt et al., 2010; Sanchez-Tapia et al., 2017). Thus, experimental variations among published studies may explain discrepancies in the GM composition in AD.

Despite this strong variation, we can observe a general increased abundance of pro-inflammatory bacteria in AD mice and AD patients (Kountouras et al., 2009; Zhan et al., 2016; Cattaneo et al., 2017; Shen et al., 2017; Vogt et al., 2017; Zhang et al., 2017; Syeda et al., 2018) compared to controls. Furthermore, in AD transgenic mice, longitudinal studies clearly indicate an age-associated gut dysbiosis, culminating in a strong pro-inflammatory environment along the development of brain pathological hallmarks (Shen et al., 2017; Zhang et al., 2017; Syeda et al., 2018).

How Can the GM Affect Brain Function or Even Cause Neurodegeneration?

A bidirectional communication between the gastrointestinal system and the brain has been described and has led to the concept of gut-brain axis (Collins and Bercik, 2013). Recent studies illustrated the role of GM in brain Aβ aggregation, as GM absence in germ-free condition (Harach et al., 2017) or GM partial depletion by antibiotic treatment (Minter et al., 2016) reduced the amyloid burden and microglia activation in AD transgenic mice. However, it is still unclear which factors may be associated with the above described gut-brain axis in brain pathologies.

Several groups have implicated the neurotoxin LPS present in the outer membrane of gram-negative bacteria. LPS plays key roles in the host-pathogen interactions of the innate immune system (Hill and Lukiw, 2015; Maldonado et al., 2016). Alterations in the GM composition/abundance are associated with enhanced plasma levels of LPS (Avila-Nava et al., 2017;

TABLE 2 | Alterations in gut microbiota in AD patients and AD mice at FAMILY, GENUS, and SPECIES levels.

Model	Bacterial family (f.)/genus (g.)/ species (g. s.) INCREASED	Bacterial family (f.)/genus (g.)/ species (g. s.) DECREASED	References
AD patients	*g. Escherichia/Shigella*	*g.s. Eubacterium rectale*	Cattaneo et al., 2017
AD patients	*f. Bacteroidaceae* *f. Rikenellaceae* *f. Gemellaceae* *g. Bilophila* *g. Phascolarctobacterium* *g. Gemella* *g. Bacteroides* *g. Alistipes*	*f. Ruminococcaceae* *f. Turicibacteraceae* *f. Peptostreptococcaceae* *f. Clostridiaceae* *f. Mogibacteriaceae* *f. Bifidobacteriaceae* *g. SMB53* *g. Dialister* *g. Clostridium* *g. Turicibacter* *g. cc115*	Vogt et al., 2017
AD patients	*f. Ruminococcaceae* *f. Enterococcaceae* *f. Lactobacillaceae*	*f. Lanchnospiraceae* *f. Bacteroidaceae* *f. Veillonellaceae*	Zhuang et al., 2018
3XTG-AD mice 24 months old	*g. Prevotellaceae* *g. Enterococcus* *g. Streptococcus* *g. Turicibacter* *g. Ruminococcus* *g. Desulfovibrionaceae* *g. Flexispira*	*g. Turicibacter* *g. Prevotella* *g. Ruminococcus* *g. Flexispira*	Bonfili et al., 2017
APP/PS1 mice 8 months old	*f. Rikenellaceae* *f. S24-7*	*g. Allobaculum* *g. Akkermansia*	Harach et al., 2017
APP/PS1 mice 8 months old	*f. Aerococcaceae* *f. Leuconostocaceae* *f. Lactobacillaceae* *f. Pseudomonadaceae* *f. Caulobacteraceae* *f. Cytophagaceae* *f. Sphingobacteriaceae* *f. Corynebacteriaceae*	*f. Sphingomonadaceae* *f. Comamonadaceae* *f. Rhodocyclaceae* *f. Flavobacteriaceae*	Park et al., 2017
3XTG-AD mice 8 months old	*f. Enterococcaceae* *f. Turicibacteraceae*	*f. S24-7* *f. Bifidobacteriaceae*	Sanguinetti et al., 2018
3XTG-AD mice 9 months old	*g.s. Prevotella copri* *g.s. Lactobacillus ruminis* *g.s. Streptococcus anginosus* *g.s. Actinobacillus parahaemolyticus* *g.s. Haemophilus parainfluenzae*	*g.s. Bacteroides fragilis* *g.s. Faecalibacterium prausnitzii* *g.s. Akkermansia muciniphila*	Syeda et al., 2018

Sanchez-Tapia et al., 2017), which may result in an exacerbated metabolic endotoxemia (Cani et al., 2012), a condition characterized by inflammation and the increased release of pro-inflammatory cytokines.

Systemic infections have been related to a higher possibility to develop AD (Holmes et al., 2009) as well as early motor dysfunction in PD patients (Dobbs et al., 1999). Therefore, long-term gut microbiota alterations and gut dysbiosis resulting in a pro-inflammatory environment and inflammation may be linked to brain dysfunction in aging.

As a proof of concept, LPS is detected in the parenchyma and blood vessels of both, non-demented aged and AD brain samples, but at a higher level in diseased tissues (Zhao et al., 2015, 2017; Zhan et al., 2016). LPS also increases in the plasma of AD transgenic mice compared to wild type controls (Syeda et al., 2018). In PD patients, higher plasma LPS correlates with α-synuclein aggregation (Forsyth et al., 2011). Furthermore, LPS is a well-known neuroinflammatory agent driving the generation of $A\beta_{1-42}$ (Lee et al., 2008; Asti and Gioglio, 2014; Hill and Lukiw, 2015; Zhao et al., 2015). LPS administration to mice results in memory impairment, Aβ aggregation, and astrocyte activation (Lee et al., 2008). Therefore, gut dysbiosis may enhance LPS to the blood circulation and even to the brain, producing glia activation and protein aggregation, both important features of neurodegenerative diseases.

Another bacterial product related to the development of neurodegenerative diseases are short-chain fatty acids (SCFAs). SCFAs are produced by the GM after the degradation of non-digestible polysaccharides, with butyrate, acetate, and propionate being the more abundant fermentation products (Wong et al., 2006). About 95% of the SCFAs produced in the gut are absorbed within the colon (Hoyles et al., 2018), while butyrate is used by the colonocytes as an energy source. In order to maintain an optimal equilibrium between intestinal SCFAs and the concentration in the body, the gut intestinal barrier increases its mucus production

(Rios-Covian et al., 2016), while the liver clears the majority of propionate and butyrate from the portal circulation (Bloemen et al., 2010). However, SCFAs can be transported through the bloodstream to reach the brain.

Some alterations in fecal SCFAs concentration have been described in AD transgenic mice compared to controls (Bonfili et al., 2017; Zhang et al., 2017). Butyrate, a well-known neuroprotective agent (Minamiyama et al., 2004; Govindarajan et al., 2011; Liu et al., 2015), is reduced in the fecal samples of AD mice (Zhang et al., 2017). Other reports show increased propionate levels in brain tissue of AD transgenic mice compared to wild type controls, an event associated with GM dysbiosis (Syeda et al., 2018). Although, propionate has some beneficial effects [e.g., on the BBB (Hoyles et al., 2018)], excessive propionate alters dopamine, serotonin, and glutamate systems in a manner similar to that observed in autism spectrum disorders (El-Ansary et al., 2012; Li et al., 2017).

Fecal samples of children with autism spectrum disorder present an increased level of propionate (Wang et al., 2012). In addition, genetic diseases that affect the function of the enzyme propionyl-CoA carboxylase (such as propionic acidemia) are characterized by high levels of propionate and high incidence of dementia (Grunert et al., 2013), while in AD patients, increased levels of acetate and propionate have been found in saliva samples compared to healthy controls (Figueira et al., 2016; Yilmaz et al., 2017). Although, the effects of butyrate and propionate are still controversially discussed, several data support a role of the imbalance between butyrate and propionate in the pathogenesis of AD (Syeda et al., 2018).

Another important pathway connecting the brain and the GM is the involvement of the immune system (Fung et al., 2017) studied, e.g., in stroke. According to recent reports, in the experimental rodent models, stroke leads to dysbiosis (Benakis et al., 2016; Houlden et al., 2016; Singh et al., 2016; Stanley et al., 2018) and dysbiosis may have an effect on the course of the disease (Benakis et al., 2016; Singh et al., 2016; Stanley et al., 2016). This may be linked to GM-related fine-tuning of the balance between pro-inflammatory/anti-inflammatory immune responses primarily in the gut, followed by an infiltration of immune cells to the CNS after injury. Interestingly, pro-inflammatory T-helper cell 17 and γδ T cells found in the ischemic CNS originate from the intestine and the infiltration of these subpopulations has been linked with unfavorable outcome (Benakis et al., 2016; Singh et al., 2016).

However, the optimal (in terms of prognosis after stroke) composition of the GM has not been identified yet and is possibly difficult to pinpoint. Some findings indicate that the complete absence (in germ-free mice) or deep antibiotic depletion of GM can be detrimental, leading to increased infarct volumes (Singh et al., 2018) or increased mortality not related to lesion size (Winek et al., 2016). Alterations in GM have also been identified in stroke patients (Yin et al., 2015; Stanley et al., 2016). Due to its metabolic capacities, GM can also contribute to the pathogenesis of the diseases considered as the risk factors of stroke, like obesity (for review Torres-Fuentes et al., 2017) and atherosclerosis (Karlsson et al., 2012; Tang et al., 2013) (for review, see Li and Tang, 2017).

We can conclude that a predominantly pro-inflammatory GM and the release of neurotoxic substances may negatively affect brain functions, causing systemic and central inflammation over decades. This is in support of the recent hypothesis of an infectious etiology for neurodegenerative diseases, such as AD (Bhattacharjee and Lukiw, 2013; Little et al., 2014; Maheshwari and Eslick, 2015; Itzhaki et al., 2016). The substances released from the GM (i.e., LPS and SCFAs) may be implicated in the pathogenesis of several neurodegenerative diseases; however, more data are still needed to clearly understand this gut-brain-immune interaction.

FROM CONSEQUENCES TO CAUSES: ACADEMIC AND PRECLINICAL CONSIDERATIONS

As we have described above, the neurocentric view entertained as the predominant focus of our effort in treating neurodegeneration is likely insufficient to ensure successful therapeutic intervention.

The Lack of Adequate Experimental Models to Study the Etiology

Investigating the pathophysiological processes behind neurodegeneration in detail requires the use of animal models. A plethora of animal models of neurodegeneration exists, and the nuances of these models are beyond the scope of this manuscript (for recent reviews, see Gitler et al., 2017; Dawson et al., 2018; Ransohoff, 2018).

However, two general problems with current models seem to be particularly widespread and contribute to our limited success in extrapolating findings from preclinical research to patients. Firstly, they often fail to fully integrate our understanding of the etiology of the diseases they are meant to represent, often being restricted to inducing the disease in a single way, despite multiple inducing factors being responsible for the human disease. Secondly, animals used as the model organism of specific diseases often do not exhibit similar comorbidities and demographic characteristics (such as age or gender) seen in human patients. Examples of such problems are the rodent models of stroke, particularly ones that involve surgical ligation or occlusion of blood vessels in otherwise healthy, young animals (van der Worp et al., 2010; Mergenthaler and Meisel, 2012).

Another important issue is the way these models are characterized. For animal models to be used to study neurodegeneration, two essential steps must be taken. First, the validity of the model for the question at hand should be thoroughly and systematically investigated. This is preferably done in a multi-centric and multi-disciplinary way to ensure the generalizability and robustness of the results. Second, the external (face, construct, and predictive) validity of the model (Willner, 1984) should be empirically and thoroughly tested, as well as the inter-rater agreement on, and replicability of, the model's characteristics (McKinney and Bunney, 1969). Such studies aimed at characterizing the model should be very clearly

and unequivocally separated from experiments using the model to test hypotheses, such as the effect of an intervention on the course of the model's progression.

For these strategies to be successful, research into and using these models must be conducted in the setting of appropriate, rigorous, and transparent experimental design and reporting (Kilkenny et al., 2010; Holman et al., 2016; Percie du Sert et al., 2017). Beyond that, we should make an active effort to think of the drawbacks of the models and methods we have used and how this may restrict or bias the knowledge we gain from such studies (Garner et al., 2017). Finally, we need a framework for integrating the knowledge gained from individual studies using different models and methods to address similar research questions. Systematic reviews and quantitative meta-analyses, widely used for knowledge synthesis in clinical research, may be helpful tools to help us achieve this.

Studying Human Disease in Human Systems

Although animal models are a powerful tool toward understanding the etiology of neurodegenerative diseases, they still present considerable limitations (Jucker, 2010). As a consequence, there has been little success translating the knowledge obtained from model organisms to therapeutically valuable outcomes. This constraint can only be addressed by studying neurodegenerative diseases directly on humans.

The recent increase in the generation of digital data including imaging, genotypic, and phenotypic information coupled with a fast development of computational methods allows us to obtain new insights from this massive amount of data. Major efforts from consortiums such as the Alzheimer's Disease Initiative (ADNI), the Australian Imaging, Biomarkers & Lifestyle Study of Ageing (AIBL), the Parkinson's Progression Markers Initiative (PPMI) or more recently the United Kingdom Biobank have made available an unprecedented amount of data, which can be exploited through the use of big data algorithms.

Having large amounts of information coming from heterogeneous populations and acquisition systems increases the power of statistic approaches and reduces the risk of bias. Big data approaches are inherently limited since in general they cannot be used to perform causal inference, but rather to find correlations or associations between variables. However, these correlations have proven to be an invaluable tool for hypothesis generation, drug and safety surveillance, disease and treatment heterogeneity among many other applications (Lee and Yoon, 2017).

Such computational models have been used for example to build a model of senescence signaling via DNA damage, insulin-TOR, FoxO3a transcription factors, oxidative stress response, mitochondrial regulation, and mitophagy using a systems biology approach (Dalle Pezze et al., 2014). A recent review of mathematical models in neurodegenerative diseases reports several mathematical models involving some of the processes we addressed above, such as energy metabolism and synaptic plasticity (Lloret-Villas et al., 2017). A multivariate Bayesian model of biomarker measurements was used to estimate AD dementia onset age (Bilgel and Jedynak, 2019). Similarly, multivariate models have been used to relate image based morphological features to the risk of dementia (Gutierrez Becker et al., 2018; Cole et al., 2019).

Recent trends in stem cell methods have also opened new possibilities for human brain cell cultures, which can in turn be used to model neurodegeneration. Induced pluripotent stem cells and neural stem cell cultures can now be used to generate human neurons from human and sometimes patient cells (Abud et al., 2017; Korhonen et al., 2018). This has been reviewed extensively elsewhere (Xie and Tang, 2016; Robbins and Price, 2017).

CONCLUSION

Disease is typically defined in juxtaposition to the state of health, which has been even more generally defined as "a state of complete physical, mental, and social well-being" (International Health Conference, 2002). However, in order to characterize a bodily or mental state as diseased, we need a more practical, operational definition of the healthy state, characterized in terms of physiological parameters and defined by the description of the steady state functioning of the body and its subsystems.

Typically, pathophysiological events of neurodegeneration are detected through behavioral observations and self-reporting and subsequently confirmed and classified using neurological examination and diagnostic imaging. The result of this diagnostic approach usually reveals typical defining features for each neurological disease (such as hemorrhage, tumor, or deformations), that allows the classification of the disorder. However, these defining characteristics are not necessarily the root causes of the disease but rather elements of the disease manifestation or even merely epiphenomena. In addition to the complex and usually obscure causal relationships giving rise to brain disorders, a parameter that further complicates the identification of causation is the widespread and intricate comorbidities between presumably distinct and unrelated disorders.

Together, these facts limit the therapeutic potential to treat the symptoms rather than the causes. The complex causality chain hinders the early detection and treatment of the root causes of brain disorders overall and neurodegeneration more specifically. These limitations highlight the critical need for a drastic shift of perspective and the improvement of the models used to investigate and understand neurodegenerative diseases.

Given the complexity of the brain and its disorders, researchers and clinicians have retreated to a highly segregated approach, focusing on describing subsets of the symptoms of each disease and trying to identify mechanistic explanations and treatments for those symptoms. However, the lack of a holistic perspective, taking into account the deviations from the default homeostatic state at an organismal level, renders this endeavor nearly impossible and doomed to fail.

Importantly, characterizing the expected, default healthy brain, is a necessary precondition to being able to identify and meaningfully interpret the deviations from it. Thus, characterizing and understanding the brain function in health is of paramount importance in the attempt to understand and treat the diseased brain.

In summary, there is an identifiable need for an interdisciplinary approach to explore the brain function at multiple levels, from molecular to systems, while maintaining a holistic perspective that treats the brain as an element of a complex system, rather than a separate entity. Using this approach, fundamental research can proceed hand-in-hand and maintain a constant dialogue with clinical research, to propose, improve, and revise current models of health and disease.

We hope that our work inspires the opening of new research avenues among those interested in understanding and pursuing the complexities of the "neuro-degenerating" brain focusing on lifespan processes. Therefore, the proposed etiological paths and suggestions will be important guidelines for future cross-discipline research to overcome the translational roadblock and to develop causative treatments for neurological disorders.

AUTHOR CONTRIBUTIONS

AP, GG-O, and MZ applied for funding and organized the workshop. AK, AP, AV, BG-B, MZ, NK, and XC were participants of the subgroup "The Vascular Origin of Neurodegeneration." AV-C, JP-V, KR, KW, LR, and SC-O of the subgroup "Cellular Senescence as the Origin of Neurodegeneration." CP-C, EM-M, GG-O, HG, and JL-N of the subgroup "Body–Brain Trophic Interactions as the Origin of Neurodegeneration." Accordingly, the authors wrote the respective sections of this manuscript, except CP-C who together with TS wrote the section "Gut Dysbiosis as the Origin of Neurodegeneration" with contributions from KW. AP contributed to the section "Body–Brain Trophic Interactions as the Origin of Neurodegeneration." BG-B wrote the section on "Studying Human Disease in Human Systems." AK on "The Lack of Adequate Experimental Models to Study the Etiology." NK wrote the conclusion. MZ wrote the remaining sections of the manuscript. AV commented on the manuscript. All authors discussed and commented on the final version of the manuscript.

FUNDING

This work was supported by a grant from the German Federal Ministry of Education and Research (BMBF grant number 01DN18054) to MZ, AP, and GG-O.

ACKNOWLEDGMENTS

This is a spin-off article from the workshop "German-Mexican Roundtable Exploring New Etiological Paths Towards Neurodegeneration," which took place at the Instituto de Investigaciones Biomédicas at the National Autonomous University of México, Mexico City, on October 15–17th, 2018. Miguel Morales Pacheco helped in the design of **Figure 1**.

REFERENCES

Abud, E. M., Ramirez, R. N., Martinez, E. S., Healy, L. M., Nguyen, C. H. H., Newman, S. A., et al. (2017). iPSC-derived human microglia-like cells to study neurological diseases. *Neuron* 94, 278–293.e9.

Alvarez, J. I., Cayrol, R., and Prat, A. (2011). Disruption of central nervous system barriers in multiple sclerosis. *Biochim. Biophys. Acta* 1812, 252–264. doi: 10.1016/j.bbadis.2010.06.017

Alzheimer's Association (2016). 2016 Alzheimer's disease facts and figures. *Alzheimers Dement* 12, 459–509. doi: 10.1016/j.jalz.2016.03.001

Andrade, J., Khairy, P., Dobrev, D., and Nattel, S. (2014). The clinical profile and pathophysiology of atrial fibrillation: relationships among clinical features, epidemiology, and mechanisms. *Circ. Res.* 114, 1453–1468. doi: 10.1161/circresaha.114.303211

Anselmino, M., Scarsoglio, S., Saglietto, A., Gaita, F., and Ridolfi, L. (2016). Transient cerebral hypoperfusion and hypertensive events during atrial fibrillation: a plausible mechanism for cognitive impairment. *Sci. Rep.* 6: 28635.

Arai, H., Lee, V. M., Messinger, M. L., Greenberg, B. D., Lowery, D. E., and Trojanowski, J. Q. (1991). Expression patterns of beta-amyloid precursor protein (beta-APP) in neural and nonneural human tissues from Alzheimer's disease and control subjects. *Ann. Neurol.* 30, 686–693. doi: 10.1002/ana.410300509

Asai, H., Ikezu, S., Tsunoda, S., Medalla, M., Luebke, J., Haydar, T., et al. (2015). Depletion of microglia and inhibition of exosome synthesis halt tau propagation. *Nat. Neurosci.* 18, 1584–1593. doi: 10.1038/nn.4132

Ashley, J., Cordy, B., Lucia, D., Fradkin, L. G., Budnik, V., and Thomson, T. (2018). Retrovirus-like gag protein arc1 binds RNA and traffics across synaptic boutons. *Cell* 172, 262–274.e11. doi: 10.1016/j.cell.2017.12.022

Ask, T. F., Lugo, R. G., and Sutterlin, S. (2018). The neuro-immuno-senescence integrative model (NISIM) on the negative association between parasympathetic activity and cellular senescence. *Front. Neurosci.* 12:726. doi: 10.3389/fnins.2018.00726

Asti, A., and Gioglio, L. (2014). Can a bacterial endotoxin be a key factor in the kinetics of amyloid fibril formation? *J. Alzheimers Dis.* 39, 169–179. doi: 10.3233/jad-131394

Avila-Nava, A., Noriega, L. G., Tovar, A. R., Granados, O., Perez-Cruz, C., Pedraza-Chaverri, J., et al. (2017). Food combination based on a pre-hispanic Mexican diet decreases metabolic and cognitive abnormalities and gut microbiota dysbiosis caused by a sucrose-enriched high-fat diet in rats. *Mol. Nutr. Food Res.* 61:1501023. doi: 10.1002/mntr.201501023

Baker, D. J., and Petersen, R. C. (2018). Cellular senescence in brain aging and neurodegenerative diseases: evidence and perspectives. *J. Clin. Invest.* 128, 1208–1216. doi: 10.1172/jci95145

Balusu, S., Van Wonterghem, E., De Rycke, R., Raemdonck, K., Stremersch, S., Gevaert, K., et al. (2016). Identification of a novel mechanism of blood-brain communication during peripheral inflammation via choroid plexus-derived extracellular vesicles. *EMBO Mol. Med.* 8, 1162–1183. doi: 10.15252/emmm.201606271

Banerjee, C., and Chimowitz, M. I. (2017). Stroke caused by atherosclerosis of the major intracranial arteries. *Circ. Res.* 120, 502–513. doi: 10.1161/circresaha.116.308441

Baothman, O. A., Zamzami, M. A., Taher, I., Abubaker, J., and Abu-Farha, M. (2016). The role of gut microbiota in the development of obesity and diabetes. *Lipids Health Dis.* 15, 108.

Baumler, A. J., and Sperandio, V. (2016). Interactions between the microbiota and pathogenic bacteria in the gut. *Nature* 535, 85–93. doi: 10.1038/nature18849

Beach, T. G., Adler, C. H., Sue, L. I., Vedders, L., Lue, L., White Iii, C. L., et al. (2010). Multi-organ distribution of phosphorylated alpha-synuclein histopathology in subjects with Lewy body disorders. *Acta Neuropathol.* 119, 689–702. doi: 10.1007/s00401-010-0664-3

Benakis, C., Brea, D., Caballero, S., Faraco, G., Moore, J., Murphy, M., et al. (2016). Commensal microbiota affects ischemic stroke outcome by regulating intestinal gammadelta T cells. *Nat. Med.* 22, 516–523. doi: 10.1038/nm.4068

Bhat, R., Crowe, E. P., Bitto, A., Moh, M., Katsetos, C. D., Garcia, F. U., et al. (2012). Astrocyte senescence as a component of Alzheimer's disease. *PLoS One* 7:e45069. doi: 10.1371/journal.pone.0045069

Bhattacharjee, S., and Lukiw, W. J. (2013). Alzheimer's disease and the microbiome. *Front. Cell Neurosci.* 7:153. doi: 10.3389/fncel.2013.00153

Bilgel, M., and Jedynak, B. M. (2019). Predicting time to dementia using a quantitative template of disease progression. *Alzheimers Dement* 11, 205–215. doi: 10.1016/j.dadm.2019.01.005

Bloemen, J. G., Olde Damink, S. W., Venema, K., Buurman, W. A., Jalan, R., and Dejong, C. H. (2010). Short chain fatty acids exchange: is the cirrhotic, dysfunctional liver still able to clear them? *Clin. Nutr.* 29, 365–369. doi: 10.1016/j.clnu.2009.10.002

Blum-Degen, D., Frolich, L., Hoyer, S., and Riederer, P. (1995). Altered regulation of brain glucose metabolism as a cause of neurodegenerative disorders? *J. Neural Transm. Suppl.* 46, 139–147.

Bohnen, N. I., and Albin, R. L. (2011). White matter lesions in Parkinson disease. *Nat Rev Neurol* 7, 229–236. doi: 10.1038/nrneurol.2011.21

Bonfili, L., Cecarini, V., Berardi, S., Scarpona, S., Suchodolski, J. S., Nasuti, C., et al. (2017). Microbiota modulation counteracts Alzheimer's disease progression influencing neuronal proteolysis and gut hormones plasma levels. *Sci. Rep.* 7:2426.

Bookheimer, S. Y., Strojwas, M. H., Cohen, M. S., Saunders, A. M., Pericak-Vance, M. A., Mazziotta, J. C., et al. (2000). Patterns of brain activation in people at risk for Alzheimer's disease. *N. Engl. J. Med.* 343, 450–456.

Braak, H., Del Tredici, K., Rub, U., De Vos, R. A., Jansen Steur, E. N., and Braak, E. (2003a). Staging of brain pathology related to sporadic Parkinson's disease. *Neurobiol. Aging* 24, 197–211. doi: 10.1016/s0197-4580(02)00065-9

Braak, H., Rub, U., Gai, W. P., and Del Tredici, K. (2003b). Idiopathic Parkinson's disease: possible routes by which vulnerable neuronal types may be subject to neuroinvasion by an unknown pathogen. *J. Neural Transm.* 110, 517–536. doi: 10.1007/s00702-002-0808-2

Brainstorm, C., Anttila, V., Bulik-Sullivan, B., Finucane, H. K., Walters, R. K., Bras, J., et al. (2018). Analysis of shared heritability in common disorders of the brain. *Science* 360:eaap8757.

Brandscheid, C., Schuck, F., Reinhardt, S., Schafer, K. H., Pietrzik, C. U., Grimm, M., et al. (2017). Altered gut microbiome composition and tryptic activity of the 5xFAD Alzheimer's mouse model. *J. Alzheimers Dis.* 56, 775–788. doi: 10.3233/jad-160926

Broadwell, R. D. (1989). Transcytosis of macromolecules through the blood-brain barrier: a cell biological perspective and critical appraisal. *Acta Neuropathol.* 79, 117–128. doi: 10.1007/bf00294368

Brouns, R., Wauters, A., De Surgeloose, D., Marien, P., and De Deyn, P. P. (2011). Biochemical markers for blood-brain barrier dysfunction in acute ischemic stroke correlate with evolution and outcome. *Eur. Neurol.* 65, 23–31. doi: 10.1159/000321965

Brown, R. C., Lockwood, A. H., and Sonawane, B. R. (2005). Neurodegenerative diseases: an overview of environmental risk factors. *Environ. Health Perspect.* 113, 1250–1256. doi: 10.1289/ehp.7567

Bruce-Keller, A. J., Keller, J. N., and Morrison, C. D. (2009). Obesity and vulnerability of the CNS. *Biochim. Biophys. Acta* 1792, 395–400.

Buerge, C., Steiger, G., Kneifel, S., Wetzel, S., Wollmer, M. A., Probst, A., et al. (2011). Lobar dementia due to extreme widening of virchow-robin spaces in one hemisphere. *Case Rep. Neurol.* 3, 136–140. doi: 10.1159/000329267

Buga, A. M., Di Napoli, M., and Popa-Wagner, A. (2013). Preclinical models of stroke in aged animals with or without comorbidities: role of neuroinflammation. *Biogerontology* 14, 651–662. doi: 10.1007/s10522-013-9465-0

Bussian, T. J., Aziz, A., Meyer, C. F., Swenson, B. L., Van Deursen, J. M., and Baker, D. J. (2018). Clearance of senescent glial cells prevents tau-dependent pathology and cognitive decline. *Nature* 562, 578–582. doi: 10.1038/s41586-018-0543-y

Calabrese, V., Mancuso, C., Calvani, M., Rizzarelli, E., Butterfield, D. A., and Stella, A. M. (2007). Nitric oxide in the central nervous system: neuroprotection versus neurotoxicity. *Nat. Rev. Neurosci.* 8, 766–775. doi: 10.1038/nrn2214

Calcinotto, A., Kohli, J., Zagato, E., Pellegrini, L., Demaria, M., and Alimonti, A. (2019). Cellular senescence: aging, cancer, and injury. *Physiol. Rev.* 99, 1047–1078. doi: 10.1152/physrev.00020.2018

Campbell, R. K. (2011). Clarifying the role of incretin-based therapies in the treatment of type 2 diabetes mellitus. *Clin. Ther.* 33, 511–527. doi: 10.1016/j.clinthera.2011.04.015

Cani, P. D., Osto, M., Geurts, L., and Everard, A. (2012). Involvement of gut microbiota in the development of low-grade inflammation and type 2 diabetes associated with obesity. *Gut Microbes* 3, 279–288. doi: 10.4161/gmic.19625

Carding, S., Verbeke, K., Vipond, D. T., Corfe, B. M., and Owen, L. J. (2015). Dysbiosis of the gut microbiota in disease. *Microb Ecol. Health Dis.* 26:26191.

Carvalho, C., Cardoso, S., Correia, S. C., Santos, R. X., Santos, M. S., Baldeiras, I., et al. (2012). Metabolic alterations induced by sucrose intake and Alzheimer's disease promote similar brain mitochondrial abnormalities. *Diabetes Metab. Res. Rev.* 61, 1234–1242. doi: 10.2337/db11-1186

Cattaneo, A., Cattane, N., Galluzzi, S., Provasi, S., Lopizzo, N., Festari, C., et al. (2017). Association of brain amyloidosis with pro-inflammatory gut bacterial taxa and peripheral inflammation markers in cognitively impaired elderly. *Neurobiol. Aging* 49, 60–68. doi: 10.1016/j.neurobiolaging.2016.08.019

Caviedes, A., Varas-Godoy, M., Lafourcade, C., Sandoval, S., Bravo-Alegria, J., Kaehne, T., et al. (2017). Endothelial nitric oxide synthase is present in dendritic spines of neurons in primary cultures. *Front. Cell Neurosci.* 11:180. doi: 10.3389/fncel.2017.00180

Chalazonitis, A., and Rao, M. (2018). Enteric nervous system manifestations of neurodegenerative disease. *Brain Res.* 1693, 207–213. doi: 10.1016/j.brainres.2018.01.011

Chao, Y. X., He, B. P., and Tay, S. S. (2009). Mesenchymal stem cell transplantation attenuates blood brain barrier damage and neuroinflammation and protects dopaminergic neurons against MPTP toxicity in the substantia nigra in a model of Parkinson's disease. *J. Neuroimmunol.* 216, 39–50. doi: 10.1016/j.jneuroim.2009.09.003

Charidimou, A., Jaunmuktane, Z., Baron, J. C., Burnell, M., Varlet, P., Peeters, A., et al. (2014). White matter perivascular spaces: an MRI marker in pathology-proven cerebral amyloid angiopathy? *Neurology* 82, 57–62. doi: 10.1212/01.wnl.0000438225.02729.04

Charidimou, A., Meegahage, R., Fox, Z., Peeters, A., Vandermeeren, Y., Laloux, P., et al. (2013). Enlarged perivascular spaces as a marker of underlying arteriopathy in intracerebral haemorrhage: a multicentre MRI cohort study. *J. Neurol. Neurosurg. Psychiatry* 84, 624–629. doi: 10.1136/jnnp-2012-304434

Chen, B., Cheng, Q., Yang, K., and Lyden, P. D. (2010). Thrombin mediates severe neurovascular injury during ischemia. *Stroke* 41, 2348–2352. doi: 10.1161/strokeaha.110.584920

Chen, Z. L., and Strickland, S. (1997). Neuronal death in the hippocampus is promoted by plasmin-catalyzed degradation of laminin. *Cell* 91, 917–925. doi: 10.1016/s0092-8674(00)80483-3

Ching, R. C., Wiberg, M., and Kingham, P. J. (2018). Schwann cell-like differentiated adipose stem cells promote neurite outgrowth via secreted exosomes and RNA transfer. *Stem Cell Res. Ther.* 9:266.

Chinta, S. J., Woods, G., Demaria, M., Rane, A., Zou, Y., Mcquade, A., et al. (2018). Cellular senescence is induced by the environmental neurotoxin paraquat and contributes to neuropathology linked to Parkinson's Disease. *Cell Rep.* 22, 930–940. doi: 10.1016/j.celrep.2017.12.092

Chinta, S. J., Woods, G., Rane, A., Demaria, M., Campisi, J., and Andersen, J. K. (2015). Cellular senescence and the aging brain. *Exp. Gerontol.* 68, 3–7.

Choi, B. R., Lee, S. R., Han, J. S., Woo, S. K., Kim, K. M., Choi, D. H., et al. (2011). Synergistic memory impairment through the interaction of chronic cerebral hypoperfusion and amlyloid toxicity in a rat model. *Stroke* 42, 2595–2604. doi: 10.1161/strokeaha.111.620179

Chow, H. M., and Herrup, K. (2015). Genomic integrity and the ageing brain. *Nat. Rev. Neurosci.* 16, 672–684. doi: 10.1038/nrn4020

Cole, J. H., Marioni, R. E., Harris, S. E., and Deary, I. J. (2019). Brain age and other bodily 'ages': implications for neuropsychiatry. *Mol. Psychiatry* 24, 266–281. doi: 10.1038/s41380-018-0098-1

Cole, L. J., Farrell, M. J., Duff, E. P., Barber, J. B., Egan, G. F., and Gibson, S. J. (2006). Pain sensitivity and fMRI pain-related brain activity in Alzheimer's disease. *Brain* 129, 2957–2965. doi: 10.1093/brain/awl228

Collins, O., Dillon, S., Finucane, C., Lawlor, B., and Kenny, R. A. (2012). Parasympathetic autonomic dysfunction is common in mild cognitive impairment. *Neurobiol. Aging* 33, 2324–2333. doi: 10.1016/j.neurobiolaging.2011.11.017

Collins, S. M., and Bercik, P. (2013). Gut microbiota: intestinal bacteria influence brain activity in healthy humans. *Nat. Rev. Gastroenterol. Hepatol.* 10, 326–327. doi: 10.1038/nrgastro.2013.76

Conte, A., Khan, N., Defazio, G., Rothwell, J. C., and Berardelli, A. (2013). Pathophysiology of somatosensory abnormalities in Parkinson disease. *Nat. Rev. Neurol.* 9, 687–697. doi: 10.1038/nrneurol.2013.224

Coon, E. A., Cutsforth-Gregory, J. K., and Benarroch, E. E. (2018). Neuropathology of autonomic dysfunction in synucleinopathies. *Mov. Disord.* 33, 349–358. doi: 10.1002/mds.27186

Coppe, J. P., Desprez, P. Y., Krtolica, A., and Campisi, J. (2010). The senescence-associated secretory phenotype: the dark side of tumor suppression. *Annu. Rev. Pathol.* 5, 99–118. doi: 10.1146/annurev-pathol-121808-102144

Cordonnier, C. (2011). Brain microbleeds: more evidence, but still a clinical dilemma. *Curr. Opin. Neurol.* 24, 69–74. doi: 10.1097/wco.0b013e328341f8c0

Coulter, M. E., Dorobantu, C. M., Lodewijk, G. A., Delalande, F., Cianferani, S., Ganesh, V. S., et al. (2018). The ESCRT-III protein CHMP1A mediates secretion of sonic hedgehog on a distinctive subtype of extracellular vesicles. *Cell Rep.* 24, 973–986.e8. doi: 10.1016/j.celrep.2018.06.100

Crous-Bou, M., Minguillon, C., Gramunt, N., and Molinuevo, J. L. (2017). Alzheimer's disease prevention: from risk factors to early intervention. *Alzheimers Res. Ther.* 9:71.

Crowe, E. P., Tuzer, F., Gregory, B. D., Donahue, G., Gosai, S. J., Cohen, J., et al. (2016). Changes in the transcriptome of human astrocytes accompanying oxidative stress-induced senescence. *Front. Aging Neurosci.* 8:208. doi: 10.3389/fnagi.2016.00208

Dabby, R., Djaldetti, R., Shahmurov, M., Treves, T. A., Gabai, B., Melamed, E., et al. (2006). Skin biopsy for assessment of autonomic denervation in Parkinson's disease. *J. Neural Transm.* 113, 1169–1176. doi: 10.1007/s00702-005-0431-0

Dalle Pezze, P., Nelson, G., Otten, E. G., Korolchuk, V. I., Kirkwood, T. B., Von Zglinicki, T., et al. (2014). Dynamic modelling of pathways to cellular senescence reveals strategies for targeted interventions. *PLoS Comput. Biol.* 10:e1003728. doi: 10.1371/journal.pcbi.1003728

Davaapil, H., Brockes, J. P., and Yun, M. H. (2017). Conserved and novel functions of programmed cellular senescence during vertebrate development. *Development* 144, 106–114. doi: 10.1242/dev.138222

Dawson, T. M., Golde, T. E., and Lagier-Tourenne, C. (2018). Animal models of neurodegenerative diseases. *Nat. Neurosci.* 21, 1370–1379.

de Bruijn, R. F., Heeringa, J., Wolters, F. J., Franco, O. H., Stricker, B. H., Hofman, A., et al. (2015). Association between atrial fibrillation and dementia in the general population. *JAMA Neurol.* 72, 1288–1294.

de Leeuw, F. E., De Groot, J. C., Achten, E., Oudkerk, M., Ramos, L. M., Heijboer, R., et al. (2001). Prevalence of cerebral white matter lesions in elderly people: a population based magnetic resonance imaging study. The rotterdam scan study. *J. Neurol. Neurosurg. Psychiatry* 70, 9–14. doi: 10.1136/jnnp.70.1.9

Dearborn, J. L., Zhang, Y., Qiao, Y., Suri, M. F. K., Liu, L., Gottesman, R. F., et al. (2017). Intracranial atherosclerosis and dementia: the atherosclerosis risk in communities (ARIC) study. *Neurology* 88, 1556–1563. doi: 10.1212/wnl.0000000000003837

den Besten, G., Van Eunen, K., Groen, A. K., Venema, K., Reijngoud, D. J., and Bakker, B. M. (2013). The role of short-chain fatty acids in the interplay between diet, gut microbiota, and host energy metabolism. *J. Lipid Res.* 54, 2325–2340. doi: 10.1194/jlr.r036012

Deschaintre, Y., Richard, F., Leys, D., and Pasquier, F. (2009). Treatment of vascular risk factors is associated with slower decline in Alzheimer disease. *Neurology* 73, 674–680. doi: 10.1212/wnl.0b013e3181b59bf3

Dickinson, C. J. (2001). Why are strokes related to hypertension? Classic studies and hypotheses revisited. *J. Hypertens.* 19, 1515–1521. doi: 10.1097/00004872-200109000-00001

Dietzel, J., Haeusler, K. G., and Endres, M. (2018). Does atrial fibrillation cause cognitive decline and dementia? *Europace* 20, 408–419. doi: 10.1093/europace/eux031

Dirnagl, U. (1997). Metabolic aspects of neurovascular coupling. *Adv. Exp. Med. Biol.* 413, 155–159. doi: 10.1007/978-1-4899-0056-2_17

Dobbs, R. J., Charlett, A., Purkiss, A. G., Dobbs, S. M., Weller, C., and Peterson, D. W. (1999). Association of circulating TNF-alpha and IL-6 with ageing and parkinsonism. *Acta Neurol. Scand.* 100, 34–41. doi: 10.1111/j.1600-0404.1999.tb00721.x

Dolan, H., Crain, B., Troncoso, J., Resnick, S. M., Zonderman, A. B., and Obrien, R. J. (2010). Atherosclerosis, dementia, and Alzheimer disease in the baltimore longitudinal study of aging cohort. *Ann. Neurol.* 68, 231–240.

Doty, R. L. (2017). Olfactory dysfunction in neurodegenerative diseases: is there a common pathological substrate? *Lancet Neurol.* 16, 478–488. doi: 10.1016/s1474-4422(17)30123-0

Driver-Dunckley, E., Adler, C. H., Hentz, J. G., Dugger, B. N., Shill, H. A., Caviness, J. N., et al. (2014). Olfactory dysfunction in incidental Lewy body disease and Parkinson's disease. *Parkinsonism Relat. Disord.* 20, 1260–1262. doi: 10.1016/j.parkreldis.2014.08.006

Duarte, A. I., Candeias, E., Correia, S. C., Santos, R. X., Carvalho, C., Cardoso, S., et al. (2013). Crosstalk between diabetes and brain: glucagon-like peptide-1 mimetics as a promising therapy against neurodegeneration. *Biochim. Biophys. Acta* 1832, 527–541. doi: 10.1016/j.bbadis.2013.01.008

Duarte, A. I., Moreira, P. I., and Oliveira, C. R. (2012). Insulin in central nervous system: more than just a peripheral hormone. *J. Aging Res.* 2012:384017.

Duda, J. E., Shah, U., Arnold, S. E., Lee, V. M., and Trojanowski, J. Q. (1999). The expression of alpha-, beta-, and gamma-synucleins in olfactory mucosa from patients with and without neurodegenerative diseases. *Exp. Neurol.* 160, 515–522. doi: 10.1006/exnr.1999.7228

Duran-Vilaregut, J., Del Valle, J., Camins, A., Pallas, M., Pelegri, C., and Vilaplana, J. (2009). Blood-brain barrier disruption in the striatum of rats treated with 3-nitropropionic acid. *Neurotoxicology* 30, 136–143. doi: 10.1016/j.neuro.2008.10.007

Eberle, C., and Ament, C. (2012). Diabetic and metabolic programming: mechanisms altering the intrauterine milieu. *ISRN Pediatr.* 2012:975685.

El-Ansary, A. K., Ben Bacha, A., and Kotb, M. (2012). Etiology of autistic features: the persisting neurotoxic effects of propionic acid. *J. Neuroinflammation* 9:74.

Fan, X., Wheatley, E. G., and Villeda, S. A. (2017). Mechanisms of hippocampal aging and the potential for rejuvenation. *Annu. Rev. Neurosci.* 40, 251–272. doi: 10.1146/annurev-neuro-072116-031357

Faraci, F. M., and Heistad, D. D. (1998). Regulation of the cerebral circulation: role of endothelium and potassium channels. *Physiol. Rev.* 78, 53–97. doi: 10.1152/physrev.1998.78.1.53

Farrall, A. J., and Wardlaw, J. M. (2009). Blood-brain barrier: ageing and microvascular disease–systematic review and meta-analysis. *Neurobiol. Aging* 30, 337–352. doi: 10.1016/j.neurobiolaging.2007.07.015

Fevrier, B., Vilette, D., Archer, F., Loew, D., Faigle, W., Vidal, M., et al. (2004). Cells release prions in association with exosomes. *Proc. Natl. Acad. Sci. U.S.A.* 101, 9683–9688. doi: 10.1073/pnas.0308413101

Figueira, J., Jonsson, P., Nordin Adolfsson, A., Adolfsson, R., Nyberg, L., and Ohman, A. (2016). NMR analysis of the human saliva metabolome distinguishes dementia patients from matched controls. *Mol. Biosyst.* 12, 2562–2571. doi: 10.1039/c6mb00233a

Fleitas, C., Pinol-Ripoll, G., Marfull, P., Rocandio, D., Ferrer, I., Rampon, C., et al. (2018). proBDNF is modified by advanced glycation end products in Alzheimer's disease and causes neuronal apoptosis by inducing p75 neurotrophin receptor processing. *Mol. Brain* 11:68.

Forstermann, U., and Sessa, W. C. (2012). Nitric oxide synthases: regulation and function. *Eur. Heart J.* 33, 829–837 doi: 10.1093/eurheartj/ehr304

Forsyth, C. B., Shannon, K. M., Kordower, J. H., Voigt, R. M., Shaikh, M., Jaglin, J. A., et al. (2011). Increased intestinal permeability correlates with sigmoid mucosa alpha-synuclein staining and endotoxin exposure markers in early Parkinson's disease. *PLoS One* 6:e28032. doi: 10.1371/journal.pone.0028032

Fung, T. C., Olson, C. A., and Hsiao, E. Y. (2017). Interactions between the microbiota, immune and nervous systems in health and disease. *Nat. Neurosci.* 20, 145–155. doi: 10.1038/nn.4476

Gan, L., Cookson, M. R., Petrucelli, L., and La Spada, A. R. (2018). Converging pathways in neurodegeneration, from genetics to mechanisms. *Nat. Neurosci.* 21, 1300–1309. doi: 10.1038/s41593-018-0237-7

Gariepy, G., Wang, J., Lesage, A., and Schmitz, N. (2011). Obesity and the risk of disability in a 12-year cohort study: the role of psychological distress. *Soc. Psychiatry Psychiatr. Epidemiol.* 46, 1173–1179. doi: 10.1007/s00127-010-0284-1

Garner, J. P., Gaskill, B. N., Weber, E. M., Ahloy-Dallaire, J., and Pritchett-Corning, K. R. (2017). Introducing therioepistemology: the study of how knowledge is gained from animal research. *Lab Anim.* 46, 103–113. doi: 10.1038/laban.1224

GBD 2015 Neurological Disorders Collaborator Group (2017). Global, regional, and national burden of neurological disorders during 1990-2015: a systematic analysis for the global burden of disease study 2015. *Lancet Neurol.* 16, 877–897.

Gensollen, T., Iyer, S. S., Kasper, D. L., and Blumberg, R. S. (2016). How colonization by microbiota in early life shapes the immune system. *Science* 352, 539–544. doi: 10.1126/science.aad9378

Girouard, H., and Iadecola, C. (2006). Neurovascular coupling in the normal brain and in hypertension, stroke, and Alzheimer disease. *J. Appl. Physiol.* 100, 328–335. doi: 10.1152/japplphysiol.00966.2005

Gitler, A. D., Dhillon, P., and Shorter, J. (2017). Neurodegenerative disease: models, mechanisms, and a new hope. *Dis. Model Mech.* 10, 499–502. doi: 10.1242/dmm.030205

Gorelick, P. B., Scuteri, A., Black, S. E., Decarli, C., Greenberg, S. M., Iadecola, C., et al. (2011). Vascular contributions to cognitive impairment and dementia: a statement for healthcare professionals from the american heart association/american stroke association. *Stroke* 42, 2672–2713. doi: 10.1161/str.0b013e3182299496

Gouw, A. A., Seewann, A., Van Der Flier, W. M., Barkhof, F., Rozemuller, A. M., Scheltens, P., et al. (2011). Heterogeneity of small vessel disease: a systematic review of MRI and histopathology correlations. *J. Neurol. Neurosurg. Psychiatry* 82, 126–135. doi: 10.1136/jnnp.2009.204685

Govindarajan, N., Agis-Balboa, R. C., Walter, J., Sananbenesi, F., and Fischer, A. (2011). Sodium butyrate improves memory function in an Alzheimer's disease mouse model when administered at an advanced stage of disease progression. *J. Alzheimers Dis.* 26, 187–197. doi: 10.3233/jad-2011-110080

Graves, K. G., May, H. T., Jacobs, V., Bair, T. L., Stevens, S. M., Woller, S. C., et al. (2017). Atrial fibrillation incrementally increases dementia risk across all CHADS2 and CHA2DS2VASc strata in patients receiving long-term warfarin. *Am. Heart J.* 188, 93–98. doi: 10.1016/j.ahj.2017.02.026

Grey, M., Dunning, C. J., Gaspar, R., Grey, C., Brundin, P., Sparr, E., et al. (2015). Acceleration of alpha-synuclein aggregation by exosomes. *J. Biol. Chem.* 290, 2969–2982. doi: 10.1074/jbc.m114.585703

Grunert, S. C., Mullerleile, S., De Silva, L., Barth, M., Walter, M., Walter, K., et al. (2013). Propionic acidemia: clinical course and outcome in 55 pediatric and adolescent patients. *Orphanet J. Rare Dis.* 8:6. doi: 10.1186/1750-1172-8-6

Gutierrez Becker, B., Klein, T., Wachinger, C., Alzheimer's Disease Neuroimaging Initiative., The Australian Imaging Biomarkers, and Lifestyle flagship study of ageing (2018). Gaussian process uncertainty in age estimation as a measure of brain abnormality. *Neuroimage* 175, 246–258. doi: 10.1016/j.neuroimage.2018.03.075

Hallene, K. L., Oby, E., Lee, B. J., Santaguida, S., Bassanini, S., Cipolla, M., et al. (2006). Prenatal exposure to thalidomide, altered vasculogenesis, and CNS malformations. *Neuroscience* 142, 267–283. doi: 10.1016/j.neuroscience.2006.06.017

Harach, T., Marungruang, N., Duthilleul, N., Cheatham, V., Mc Coy, K. D., Frisoni, G., et al. (2017). Reduction of abeta amyloid pathology in appps1 transgenic mice in the absence of gut microbiota. *Sci. Rep.* 7:41802.

Hardie, D. G., Hawley, S. A., and Scott, J. W. (2006). AMP-activated protein kinase–development of the energy sensor concept. *J. Physiol.* 574, 7–15. doi: 10.1113/jphysiol.2006.108944

Haslam, D. W., and James, W. P. (2005). Obesity. *Lancet* 366, 1197–1209.

Helzner, E. P., Luchsinger, J. A., Scarmeas, N., Cosentino, S., Brickman, A. M., Glymour, M. M., et al. (2009). Contribution of vascular risk factors to the progression in Alzheimer disease. *Arch. Neurol.* 66, 343–348.

Henkel, J. S., Beers, D. R., Wen, S., Bowser, R., and Appel, S. H. (2009). Decreased mRNA expression of tight junction proteins in lumbar spinal cords of patients with ALS. *Neurology* 72, 1614–1616. doi: 10.1212/wnl.0b013e3181a41228

Henskens, L. H., Kroon, A. A., Van Oostenbrugge, R. J., Gronenschild, E. H., Fuss-Lejeune, M. M., Hofman, P. A., et al. (2008). Increased aortic pulse wave velocity is associated with silent cerebral small-vessel disease in hypertensive patients. *Hypertension* 52, 1120–1126. doi: 10.1161/hypertensionaha.108.119024

Hill, J. M., and Lukiw, W. J. (2015). Microbial-generated amyloids and Alzheimer's disease (AD). *Front. Aging Neurosci.* 7:9. doi: 10.3389/fnagi.2015.00009

Hofman, A., Ott, A., Breteler, M. M., Bots, M. L., Slooter, A. J., Van Harskamp, F., et al. (1997). Atherosclerosis, apolipoprotein E, and prevalence of dementia and Alzheimer's disease in the rotterdam Study. *Lancet* 349, 151–154. doi: 10.1016/s0140-6736(96)09328-2

Holm, M. M., Kaiser, J., and Schwab, M. E. (2018). Extracellular vesicles: multimodal envoys in neural maintenance and repair. *Trends Neurosci.* 41, 360–372. doi: 10.1016/j.tins.2018.03.006

Holman, C., Piper, S. K., Grittner, U., Diamantaras, A. A., Kimmelman, J., Siegerink, B., et al. (2016). Where have all the rodents gone? the effects of attrition in experimental research on cancer and stroke. *PLoS Biol.* 14:e1002331. doi: 10.1371/journal.pbio.1002331

Holmes, C., Cunningham, C., Zotova, E., Woolford, J., Dean, C., Kerr, S., et al. (2009). Systemic inflammation and disease progression in Alzheimer disease. *Neurology* 73, 768–774. doi: 10.1212/wnl.0b013e3181b6bb95

Holmes, E., Li, J. V., Athanasiou, T., Ashrafian, H., and Nicholson, J. K. (2011). Understanding the role of gut microbiome-host metabolic signal disruption in health and disease. *Trends Microbiol.* 19, 349–359. doi: 10.1016/j.tim.2011.05.006

Houlden, A., Goldrick, M., Brough, D., Vizi, E. S., Lenart, N., Martinecz, B., et al. (2016). Brain injury induces specific changes in the caecal microbiota of mice via altered autonomic activity and mucoprotein production. *Brain Behav. Immun.* 57, 10–20. doi: 10.1016/j.bbi.2016.04.003

Howitt, J., and Hill, A. F. (2016). Exosomes in the pathology of neurodegenerative diseases. *J. Biol. Chem.* 291, 26589–26597. doi: 10.1074/jbc.r116.757955

Hoyles, L., Snelling, T., Umlai, U. K., Nicholson, J. K., Carding, S. R., Glen, R. C., et al. (2018). Microbiome-host systems interactions: protective effects of propionate upon the blood-brain barrier. *Microbiome* 6:55.

Hryhorczuk, C., Sharma, S., and Fulton, S. E. (2013). Metabolic disturbances connecting obesity and depression. *Front. Neurosci.* 7:177. doi: 10.3389/fnins.2013.00177

Hsu, D., and Marshall, G. A. (2017). Primary and secondary prevention trials in Alzheimer disease: looking back, Moving Forward. *Curr. Alzheimer Res.* 14, 426–440.

Hufeldt, M. R., Nielsen, D. S., Vogensen, F. K., Midtvedt, T., and Hansen, A. K. (2010). Variation in the gut microbiota of laboratory mice is related to both genetic and environmental factors. *Comp. Med.* 60, 336–347.

Iadecola, C. (2004). Neurovascular regulation in the normal brain and in Alzheimer's disease. *Nat. Rev. Neurosci.* 5, 347–360. doi: 10.1038/nrn1387

Iadecola, C. (2013). The pathobiology of vascular dementia. *Neuron* 80, 844–866. doi: 10.1016/j.neuron.2013.10.008

Iadecola, C. (2017). The neurovascular unit coming of age: a journey through neurovascular coupling in health and disease. *Neuron* 96, 17–42. doi: 10.1016/j.neuron.2017.07.030

Idiaquez, J., and Roman, G. C. (2011). Autonomic dysfunction in neurodegenerative dementias. *J. Neurol. Sci.* 305, 22–27. doi: 10.1016/j.jns.2011.02.033

International Health Conference (2002). Constitution of the World Health Organization. 1946. *Bull. World Health Organ.* 80, 983–984.

Itzhaki, R. F., Lathe, R., Balin, B. J., Ball, M. J., Bearer, E. L., Braak, H., et al. (2016). Microbes and Alzheimer's disease. *J. Alzheimers Dis.* 51, 979–984.

Jellinger, K. A. (2010). Prevalence and impact of cerebrovascular lesions in Alzheimer and lewy body diseases. *Neurodegener. Dis.* 7, 112–115. doi: 10.1159/000285518

Jennings, J. R., Muldoon, M. F., Ryan, C., Price, J. C., Greer, P., Sutton-Tyrrell, K., et al. (2005). Reduced cerebral blood flow response and compensation among patients with untreated hypertension. *Neurology* 64, 1358–1365. doi: 10.1212/01.wnl.0000158283.28251.3c

Jessen, N. A., Munk, A. S., Lundgaard, I., and Nedergaard, M. (2015). The glymphatic system: a beginner's guide. *Neurochem. Res.* 40, 2583–2599.

Jia, L., Chopp, M., Wang, L., Lu, X., Szalad, A., and Zhang, Z. G. (2018). Exosomes derived from high-glucose-stimulated schwann cells promote development of diabetic peripheral neuropathy. *FASEB J.* doi: 10.1096/fj.201800597R. [Epub ahead of print].

Joachim, C. L., Mori, H., and Selkoe, D. J. (1989). Amyloid beta-protein deposition in tissues other than brain in Alzheimer's disease. *Nature* 341, 226–230. doi: 10.1038/341226a0

Jucker, M. (2010). The benefits and limitations of animal models for translational research in neurodegenerative diseases. *Nat. Med.* 16, 1210–1214. doi: 10.1038/nm.2224

Kalaria, R. N. (2010). Vascular basis for brain degeneration: faltering controls and risk factors for dementia. *Nutr. Rev.* 68(Suppl 2), S74–87.

Kamel, H., Okin, P. M., Elkind, M. S., and Iadecola, C. (2016). Atrial fibrillation and mechanisms of stroke: time for a new model. *Stroke* 47, 895–900. doi: 10.1161/strokeaha.115.012004

Karlsson, F. H., Fak, F., Nookaew, I., Tremaroli, V., Fagerberg, B., Petranovic, D., et al. (2012). Symptomatic atherosclerosis is associated with an altered gut metagenome. *Nat. Commun.* 3:1245.

Kilkenny, C., Browne, W. J., Cuthill, I. C., Emerson, M., and Altman, D. G. (2010). Improving bioscience research reporting: the arrive guidelines for reporting animal research. *PLoS Biol.* 8:e1000412. doi: 10.1371/journal.pbio.1000412

Kim, J. Y., Rasheed, A., Yoo, S. J., Kim, S. Y., Cho, B., Son, G., et al. (2018). Distinct amyloid precursor protein processing machineries of the olfactory system. *Biochem. Biophys. Res. Commun.* 495, 533–538. doi: 10.1016/j.bbrc.2017.10.153

Kim, K. J., Ramiro Diaz, J., Iddings, J. A., and Filosa, J. A. (2016). Vasculo-neuronal coupling: retrograde vascular communication to brain neurons. *J. Neurosci.* 36, 12624–12639. doi: 10.1523/jneurosci.1300-16.2016

Kirkland, J. L., and Tchkonia, T. (2017). Cellular senescence: a translational perspective. *EBioMedicine* 21, 21–28. doi: 10.1016/j.ebiom.2017.04.013

Kisler, K., Nelson, A. R., Montagne, A., and Zlokovic, B. V. (2017). Cerebral blood flow regulation and neurovascular dysfunction in Alzheimer disease. *Nat. Rev. Neurosci.* 18, 419–434. doi: 10.1038/nrn.2017.48

Klein, P., and Tyrlikova, I. (2017). Prevention of epilepsy: should we be avoiding clinical trials? *Epilepsy Behav.* 72, 188–194. doi: 10.1016/j.yebeh.2017.05.024

Knopman, D., Boland, L. L., Mosley, T., Howard, G., Liao, D., Szklo, M., et al. (2001). Cardiovascular risk factors and cognitive decline in middle-aged adults. *Neurology* 56, 42–48. doi: 10.1212/wnl.56.1.42

Koike, M. A., Green, K. N., Blurton-Jones, M., and Laferla, F. M. (2010). Oligemic hypoperfusion differentially affects tau and amyloid-{beta}. *Am. J. Pathol.* 177, 300–310. doi: 10.2353/ajpath.2010.090750

Koles, K., Nunnari, J., Korkut, C., Barria, R., Brewer, C., Li, Y., et al. (2012). Mechanism of evenness interrupted (Evi)-exosome release at synaptic boutons. *J. Biol. Chem.* 287, 16820–16834. doi: 10.1074/jbc.m112.342667

Korhonen, P., Malm, T., and White, A. R. (2018). 3D human brain cell models: new frontiers in disease understanding and drug discovery for neurodegenerative diseases. *Neurochem. Int.* 120, 191–199. doi: 10.1016/j.neuint.2018.08.012

Korkut, C., Ataman, B., Ramachandran, P., Ashley, J., Barria, R., Gherbesi, N., et al. (2009). Trans-synaptic transmission of vesicular Wnt signals through Evi/Wntless. *Cell* 139, 393–404. doi: 10.1016/j.cell.2009.07.051

Korkut, C., Li, Y., Koles, K., Brewer, C., Ashley, J., Yoshihara, M., et al. (2013). Regulation of postsynaptic retrograde signaling by presynaptic exosome release. *Neuron* 77, 1039–1046. doi: 10.1016/j.neuron.2013.01.013

Kountouras, J., Boziki, M., Gavalas, E., Zavos, C., Grigoriadis, N., Deretzi, G., et al. (2009). Eradication of *helicobacter* pylori may be beneficial in the management of Alzheimer's disease. *J. Neurol.* 256, 758–767.

Kreutzmann, J. C., Havekes, R., Abel, T., and Meerlo, P. (2015). Sleep deprivation and hippocampal vulnerability: changes in neuronal plasticity, neurogenesis and cognitive function. *Neuroscience* 309, 173–190. doi: 10.1016/j.neuroscience.2015.04.053

Kritsilis, M., Sophia, V. R., Koutsoudaki, P. N., Evangelou, K., Gorgoulis, V. G., and Papadopoulos, D. (2018). Ageing, cellular senescence and neurodegenerative disease. *Int. J. Mol. Sci.* 19:E2937.

Kupsky, W. J., Grimes, M. M., Sweeting, J., Bertsch, R., and Cote, L. J. (1987). Parkinson's disease and megacolon: concentric hyaline inclusions (Lewy bodies) in enteric ganglion cells. *Neurology* 37, 1253–1255.

Lachenal, G., Pernet-Gallay, K., Chivet, M., Hemming, F. J., Belly, A., Bodon, G., et al. (2011). Release of exosomes from differentiated neurons and its regulation by synaptic glutamatergic activity. *Mol. Cell. Neurosci.* 46, 409–418. doi: 10.1016/j.mcn.2010.11.004

Larsson, S. C., and Markus, H. S. (2018). Does treating vascular risk factors prevent dementia and Alzheimer's disease? a systematic review and meta-analysis. *J. Alzheimers Dis.* 64, 657–668. doi: 10.3233/jad-180288

Launer, L. J., Ross, G. W., Petrovitch, H., Masaki, K., Foley, D., White, L. R., et al. (2000). Midlife blood pressure and dementia: the honolulu-asia aging study. *Neurobiol. Aging* 21, 49–55. doi: 10.1016/s0197-4580(00)00096-8

Lebouvier, T., Chaumette, T., Paillusson, S., Duyckaerts, C., Bruley Des Varannes, S., Neunlist, M., et al. (2009). The second brain and Parkinson's disease. *Eur. J. Neurosci.* 30, 735–741.

Lee, C. H., and Yoon, H. J. (2017). Medical big data: promise and challenges. *Kidney Res. Clin. Pract.* 36, 3–11. doi: 10.23876/j.krcp.2017.36.1.3

Lee, J. W., Lee, Y. K., Yuk, D. Y., Choi, D. Y., Ban, S. B., Oh, K. W., et al. (2008). Neuro-inflammation induced by lipopolysaccharide causes cognitive impairment through enhancement of beta-amyloid generation. *J. Neuroinflammation* 5:37. doi: 10.1186/1742-2094-5-37

Lee, M. J., Seo, S. W., Na, D. L., Kim, C., Park, J. H., Kim, G. H., et al. (2014). Synergistic effects of ischemia and beta-amyloid burden on cognitive decline in patients with subcortical vascular mild cognitive impairment. *JAMA Psychiatry* 71, 412–422.

Lee, S. H., Shin, S. M., Zhong, P., Kim, H. T., Kim, D. I., Kim, J. M., et al. (2018). Reciprocal control of excitatory synapse numbers by Wnt and Wnt inhibitor PRR7 secreted on exosomes. *Nat. Commun.* 9:3434.

Lema Tome, C. M., Tyson, T., Rey, N. L., Grathwohl, S., Britschgi, M., and Brundin, P. (2013). Inflammation and alpha-synuclein's prion-like behavior in Parkinson's disease–is there a link? *Mol. Neurobiol.* 47, 561–574.

Li, D. Y., and Tang, W. H. W. (2017). Gut microbiota and atherosclerosis. *Curr. Atheroscler. Rep.* 19:39.

Li, J. J., Wang, B., Kodali, M. C., Chen, C., Kim, E., Patters, B. J., et al. (2018). In vivo evidence for the contribution of peripheral circulating inflammatory exosomes to neuroinflammation. *J. Neuroinflammation* 15:8.

Li, L. M., Kilbourn, R. G., Adams, J., and Fidler, I. J. (1991). Role of nitric oxide in lysis of tumor cells by cytokine-activated endothelial cells. *Cancer Res.* 51, 2531–2535.

Li, Q., Han, Y., Dy, A. B. C., and Hagerman, R. J. (2017). The gut microbiota and autism spectrum disorders. *Front. Cell. Neurosci.* 11:120. doi: 10.3389/fncel.2017.00120

Liddell, J. R. (2017). Are astrocytes the predominant cell type for activation of nrf2 in aging and neurodegeneration? *Antioxidants* 6:E65

Lim, S. S., Vos, T., Flaxman, A. D., Danaei, G., Shibuya, K., Adair-Rohani, H., et al. (2012). A comparative risk assessment of burden of disease and injury attributable to 67 risk factors and risk factor clusters in 21 regions, 1990-2010: a systematic analysis for the global burden of disease study 2010. *Lancet* 380, 2224–2260.

Little, C. S., Joyce, T. A., Hammond, C. J., Matta, H., Cahn, D., Appelt, D. M., et al. (2014). Detection of bacterial antigens and Alzheimer's disease-like pathology in the central nervous system of BALB/c mice following intranasal infection with a laboratory isolate of *Chlamydia pneumoniae*. *Front. Aging Neurosci.* 6:304. doi: 10.3389/fnagi.2014.00304

Liu, J., Sun, J., Wang, F., Yu, X., Ling, Z., Li, H., et al. (2015). Neuroprotective effects of clostridium butyricum against vascular dementia in mice via metabolic butyrate. *Biomed Res. Int.* 2015:412946.

Livingston, G., Sommerlad, A., Orgeta, V., Costafreda, S. G., Huntley, J., Ames, D., et al. (2017). Dementia prevention, intervention, and care. *Lancet* 390, 2673–2734.

Lloret-Villas, A., Varusai, T. M., Juty, N., Laibe, C., Le Novere, N., Hermjakob, H., et al. (2017). The impact of mathematical modeling in understanding the mechanisms underlying neurodegeneration: evolving dimensions and future directions. *CPT Pharmacometrics Syst. Pharmacol.* 6, 73–86. doi: 10.1002/psp4.12155

Lopez-Verrilli, M. A., Caviedes, A., Cabrera, A., Sandoval, S., Wyneken, U., and Khoury, M. (2016). Mesenchymal stem cell-derived exosomes from different sources selectively promote neuritic outgrowth. *Neuroscience* 320, 129–139. doi: 10.1016/j.neuroscience.2016.01.061

Lopez-Verrilli, M. A., Picou, F., and Court, F. A. (2013). Schwann cell-derived exosomes enhance axonal regeneration in the peripheral nervous system. *Glia* 61, 1795–1806. doi: 10.1002/glia.22558

Lucas, S. M., Rothwell, N. J., and Gibson, R. M. (2006). The role of inflammation in CNS injury and disease. *Br. J. Pharmacol.* 147 Suppl 1, S232-S240.

Lusis, A. J. (2000). Atherosclerosis. *Nature* 407, 233–241.

MacMahon, S., Peto, R., Cutler, J., Collins, R., Sorlie, P., Neaton, J., et al. (1990). Blood pressure, stroke, and coronary heart disease. Part 1, prolonged differences in blood pressure: prospective observational studies corrected for the regression dilution bias. Lancet 335, 765–774. doi: 10.1016/0140-6736(90)90878-9

Maheshwari, P., and Eslick, G. D. (2015). Bacterial infection and Alzheimer's disease: a meta-analysis. *J. Alzheimers. Dis.* 43, 957–966. doi: 10.3233/jad-140621

Maldonado, R. F., Sa-Correia, I., and Valvano, M. A. (2016). Lipopolysaccharide modification in Gram-negative bacteria during chronic infection. *FEMS Microbiol. Rev.* 40, 480–493. doi: 10.1093/femsre/fuw007

Manwani, B., Liu, F., Scranton, V., Hammond, M. D., Sansing, L. H., and Mccullough, L. D. (2013). Differential effects of aging and sex on stroke induced

inflammation across the lifespan. *Exp. Neurol.* 249, 120–131. doi: 10.1016/j.expneurol.2013.08.011

Marin, C., Vilas, D., Langdon, C., Alobid, I., Lopez-Chacon, M., Haehner, A., et al. (2018). Olfactory dysfunction in neurodegenerative diseases. *Curr. Allergy Asthma Rep.* 18:42.

Martinez-Ramirez, S., Pontes-Neto, O. M., Dumas, A. P., Auriel, E., Halpin, A., Quimby, M., et al. (2013). Topography of dilated perivascular spaces in subjects from a memory clinic cohort. *Neurology* 80, 1551–1556. doi: 10.1212/wnl.0b013e31828f1876

Mattson, M. P., Pedersen, W. A., Duan, W., Culmsee, C., and Camandola, S. (1999). Cellular and molecular mechanisms underlying perturbed energy metabolism and neuronal degeneration in Alzheimer's and Parkinson's diseases. *Ann. N. Y. Acad. Sci.* 893, 154–175. doi: 10.1111/j.1749-6632.1999.tb07824.x

McKinney, W. T. Jr., and Bunney, W. E. Jr. (1969). Animal model of depression. I. Review of evidence: implications for research. *Arch. Gen. Psychiatry* 21, 240–248.

Mergenthaler, P., Dirnagl, U., and Meisel, A. (2004). Pathophysiology of stroke: lessons from animal models. *Metab. Brain Dis.* 19, 151–167. doi: 10.1023/b:mebr.0000043966.46964.e6

Mergenthaler, P., and Meisel, A. (2012). Do stroke models model stroke? Dis Model Mech 5, 718–725. doi: 10.1242/dmm.010033

Mhatre, M., Nguyen, A., Kashani, S., Pham, T., Adesina, A., and Grammas, P. (2004). Thrombin, a mediator of neurotoxicity and memory impairment. *Neurobiol. Aging* 25, 783–793. doi: 10.1016/s0197-4580(03)00192-1

Mills, S., Cain, J., Purandare, N., and Jackson, A. (2007). Biomarkers of cerebrovascular disease in dementia. *Br. J. Radiol.* 80 Spec No 2, S128-S145.

Minamiyama, M., Katsuno, M., Adachi, H., Waza, M., Sang, C., Kobayashi, Y., et al. (2004). Sodium butyrate ameliorates phenotypic expression in a transgenic mouse model of spinal and bulbar muscular atrophy. *Hum. Mol. Genet.* 13, 1183–1192. doi: 10.1093/hmg/ddh131

Minato, T., Maeda, T., Fujisawa, Y., Tsuji, H., Nomoto, K., Ohno, K., et al. (2017). Progression of Parkinson's disease is associated with gut dysbiosis: two-year follow-up study. *PLoS One* 12:e0187307. doi: 10.1371/journal.pone.0187307

Minter, M. R., Zhang, C., Leone, V., Ringus, D. L., Zhang, X., Oyler-Castrillo, P., et al. (2016). Antibiotic-induced perturbations in gut microbial diversity influences neuro-inflammation and amyloidosis in a murine model of Alzheimer's disease. *Sci. Rep.* 6:30028.

Mondadori, C. R., Buchmann, A., Mustovic, H., Schmidt, C. F., Boesiger, P., Nitsch, R. M., et al. (2006). Enhanced brain activity may precede the diagnosis of Alzheimer's disease by 30 years. *Brain* 129, 2908–2922. doi: 10.1093/brain/awl266

Moore, C. I., and Cao, R. (2008). The hemo-neural hypothesis: on the role of blood flow in information processing. *J. Neurophysiol.* 99, 2035–2047. doi: 10.1152/jn.01366.2006

Morsi, M., Maher, A., Aboelmagd, O., Johar, D., and Bernstein, L. (2018). A shared comparison of diabetes mellitus and neurodegenerative disorders. *J. Cell Biochem.* 119, 1249–1256. doi: 10.1002/jcb.26261

Mueller, S., Saunier, K., Hanisch, C., Norin, E., Alm, L., Midtvedt, T., et al. (2006). Differences in fecal microbiota in different European study populations in relation to age, gender, and country: a cross-sectional study. *Appl. Environ. Microbiol.* 72, 1027–1033. doi: 10.1128/aem.72.2.1027-1033.2006

Mukherjee, S., Klaus, C., Pricop-Jeckstadt, M., Miller, J. A., and Struebing, F. L. (2019). A microglial signature directing human aging and neurodegeneration-related gene networks. *Front. Neurosci.* 13:2. doi: 10.3389/fnins.2019.00002

Munoz-Espin, D., and Serrano, M. (2014). Cellular senescence: from physiology to pathology. *Nat. Rev. Mol. Cell Biol.* 15, 482–496. doi: 10.1038/nrm3823

Nelson, A. R., Sweeney, M. D., Sagare, A. P., and Zlokovic, B. V. (2016). Neurovascular dysfunction and neurodegeneration in dementia and Alzheimer's disease. *Biochim. Biophys. Acta* 1862, 887–900. doi: 10.1016/j.bbadis.2015.12.016

Nishihira, Y., Tan, C. F., Onodera, O., Toyoshima, Y., Yamada, M., Morita, T., et al. (2008). Sporadic amyotrophic lateral sclerosis: two pathological patterns shown by analysis of distribution of TDP-43-immunoreactive neuronal and glial cytoplasmic inclusions. *Acta Neuropathol.* 116, 169–182. doi: 10.1007/s00401-008-0385-z

Nishtala, A., Piers, R. J., Himali, J. J., Beiser, A. S., Davis-Plourde, K. L., Saczynski, J. S., et al. (2018). Atrial fibrillation and cognitive decline in the framingham heart study. *Heart Rhythm* 15, 166–172. doi: 10.1016/j.hrthm.2017.09.036

Nolano, M., Provitera, V., Estraneo, A., Selim, M. M., Caporaso, G., Stancanelli, A., et al. (2008). Sensory deficit in Parkinson's disease: evidence of a cutaneous denervation. *Brain* 131, 1903–1911. doi: 10.1093/brain/awn102

Ogrodnik, M., Zhu, Y., Langhi, L. G. P., Tchkonia, T., Kruger, P., Fielder, E., et al. (2019). Obesity-induced cellular senescence drives anxiety and impairs neurogenesis. Cell Metab. 29(5), 1061-1077.e8

Olsson, B., Lautner, R., Andreasson, U., Ohrfelt, A., Portelius, E., Bjerke, M., et al. (2016). CSF and blood biomarkers for the diagnosis of Alzheimer's disease: a systematic review and meta-analysis. *Lancet Neurol.* 15, 673–684. doi: 10.1016/s1474-4422(16)00070-3

Olufadi, R., and Byrne, C. D. (2008). Clinical and laboratory diagnosis of the metabolic syndrome. *J. Clin. Pathol.* 61, 697–706. doi: 10.1136/jcp.2007.048363

Oost, W., Talma, N., Meilof, J. F., and Laman, J. D. (2018). Targeting senescence to delay progression of multiple sclerosis. *J. Mol. Med.* 96, 1153–1166. doi: 10.1007/s00109-018-1686-x

Org, E., Blum, Y., Kasela, S., Mehrabian, M., Kuusisto, J., Kangas, A. J., et al. (2017). Relationships between gut microbiota, plasma metabolites, and metabolic syndrome traits in the METSIM cohort. *Genome Biol.* 18:70.

Orimo, S., Amino, T., Yokochi, M., Kojo, T., Uchihara, T., Takahashi, A., et al. (2005). Preserved cardiac sympathetic nerve accounts for normal cardiac uptake of MIBG in PARK2. *Mov. Disord.* 20, 1350–1353. doi: 10.1002/mds.20594

Orock, A., Logan, S., and Deak, F. (2019). Age-related cognitive impairment: role of reduced synaptobrevin-2 levels in memory and synaptic plasticity deficits. *J. Gerontol. A Biol. Sci. Med. Sci.* doi: 10.1093/gerona/glz013 [Epub ahead of print].

Ozkor, M. A., and Quyyumi, A. A. (2011). Endothelium-derived hyperpolarizing factor and vascular function. *Cardiol. Res. Pract.* 2011:156146.

Park, J. Y., Choi, J., Lee, Y., Lee, J. E., Lee, E. H., Kwon, H. J., et al. (2017). Metagenome analysis of bodily microbiota in a mouse model of Alzheimer disease using bacteria-derived membrane vesicles in blood. *Exp. Neurobiol.* 26, 369–379.

Pastuzyn, E. D., Day, C. E., Kearns, R. B., Kyrke-Smith, M., Taibi, A. V., Mccormick, J., et al. (2018). The neuronal gene arc encodes a repurposed retrotransposon gag protein that mediates intercellular RNA transfer. *Cell* 172, 275-288.e18.

Pellegrinelli, V., Peirce, V. J., Howard, L., Virtue, S., Turei, D., Senzacqua, M., et al. (2018). Adipocyte-secreted BMP8b mediates adrenergic-induced remodeling of the neuro-vascular network in adipose tissue. *Nat. Commun.* 9:4974.

Percie du Sert, N., Alfieri, A., Allan, S. M., Carswell, H. V., Deuchar, G. A., Farr, T. D., et al. (2017). The improve guidelines (Ischaemia models: procedural refinements of in vivo experiments). *J. Cereb. Blood Flow Metab.* 37, 3488–3517. doi: 10.1177/0271678x17709185

Petcu, E. B., Sfredel, V., Platt, D., Herndon, J. G., Kessler, C., and Popa-Wagner, A. (2008). Cellular and molecular events underlying the dysregulated response of the aged brain to stroke: a mini-review. *Gerontology* 54, 6–17. doi: 10.1159/000112845

Pfeiffer, R. F. (2016). Non-motor symptoms in Parkinson's disease. *Parkinsonism Relat. Disord.* 22(Suppl 1), S119-S122.

Poels, M. M. F., Zaccai, K., Verwoert, G. C., Vernooij, M. W., Hofman, A., van der Lugt, A., et al. (2012). Arterial stiffness and cerebral small vessel disease: the rotterdam scan study. *Stroke* 43, 2637–2642. doi: 10.1161/strokeaha.111.642264

Polanco, J. C., Scicluna, B. J., Hill, A. F., and Gotz, J. (2016). Extracellular vesicles isolated from the brains of rTg4510 mice seed tau protein aggregation in a threshold-dependent manner. *J. Biol. Chem.* 291, 12445–12466. doi: 10.1074/jbc.m115.709485

Popa-Wagner, A., Buga, A. M., and Kokaia, Z. (2011). Perturbed cellular response to brain injury during aging. *Ageing Res. Rev.* 10, 71–79. doi: 10.1016/j.arr.2009.10.008

Popa-Wagner, A., Carmichael, S. T., Kokaia, Z., Kessler, C., and Walker, L. C. (2007). The response of the aged brain to stroke: too much, too soon? *Curr. Neurovasc. Res.* 4, 216–227. doi: 10.2174/156720207781387213

Popa-Wagner, A., Pirici, D., Petcu, E. B., Mogoanta, L., Buga, A. M., Rosen, C. L., et al. (2010). Pathophysiology of the vascular wall and its relevance for cerebrovascular disorders in aged rodents. *Curr. Neurovasc. Res.* 7, 251–267. doi: 10.2174/156720210792231813

Postuma, R. B., Adler, C. H., Dugger, B. N., Hentz, J. G., Shill, H. A., Driver-Dunckley, E., et al. (2015). REM sleep behavior disorder and neuropathology in Parkinson's disease. *Mov. Disord.* 30, 1413–1417.

Przedborski, S., Vila, M., and Jackson-Lewis, V. (2003). Neurodegeneration: what is it and where are we? *J. Clin. Invest.* 111, 3–10.

Purves, D. (1988). *Body and Brain: A Trophic Theory of Neural Connections*. Cambridge, MA: Harvard University Press.

Qureshi, I. A., and Mehler, M. F. (2013). Towards a 'systems'-level understanding of the nervous system and its disorders. *Trends Neurosci.* 36, 674–684. doi: 10.1016/j.tins.2013.07.003

Racosta, J. M., Kimpinski, K., Morrow, S. A., and Kremenchutzky, M. (2015). Autonomic dysfunction in multiple sclerosis. *Auton. Neurosci.* 193, 1–6. doi: 10.1016/j.autneu.2015.06.001

Ramirez, J., Berezuk, C., Mcneely, A. A., Scott, C. J., Gao, F., and Black, S. E. (2015). Visible virchow-robin spaces on magnetic resonance imaging of Alzheimer's disease patients and normal elderly from the sunnybrook dementia study. *J. Alzheimers. Dis.* 43, 415–424. doi: 10.3233/jad-132528

Ransohoff, R. M. (2018). All (animal) models (of neurodegeneration) are wrong. Are they also useful? *J. Exp. Med.* 215, 2955–2958. doi: 10.1084/jem.20182042

Rao, M., and Gershon, M. D. (2016). The bowel and beyond: the enteric nervous system in neurological disorders. *Nat. Rev. Gastroenterol. Hepatol.* 13, 517–528. doi: 10.1038/nrgastro.2016.107

Raskov, H., Burcharth, J., Pommergaard, H. C., and Rosenberg, J. (2016). Irritable bowel syndrome, the microbiota and the gut-brain axis. *Gut Microbes* 7, 365–383. doi: 10.1080/19490976.2016.1218585

Rawji, K. S., Mishra, M. K., Michaels, N. J., Rivest, S., Stys, P. K., and Yong, V. W. (2016). Immunosenescence of microglia and macrophages: impact on the ageing central nervous system. *Brain* 139, 653–661. doi: 10.1093/brain/awv395

Reichling, D. B., and Levine, J. D. (2011). Pain and death: neurodegenerative disease mechanisms in the nociceptor. *Ann. Neurol.* 69, 13–21. doi: 10.1002/ana.22351

Reitz, C., Tang, M. X., Manly, J., Mayeux, R., and Luchsinger, J. A. (2007). Hypertension and the risk of mild cognitive impairment. *Arch. Neurol.* 64, 1734–1740.

Rey, N. L., Wesson, D. W., and Brundin, P. (2018). The olfactory bulb as the entry site for prion-like propagation in neurodegenerative diseases. *Neurobiol. Dis.* 109, 226–248. doi: 10.1016/j.nbd.2016.12.013

Ridder, K., Keller, S., Dams, M., Rupp, A. K., Schlaudraff, J., Del Turco, D., et al. (2014). Extracellular vesicle-mediated transfer of genetic information between the hematopoietic system and the brain in response to inflammation. *PLoS Biol.* 12:e1001874. doi: 10.1371/journal.pbio.1001874

Rios-Covian, D., Ruas-Madiedo, P., Margolles, A., Gueimonde, M., De Los Reyes-Gavilan, C. G., and Salazar, N. (2016). Intestinal short chain fatty acids and their link with diet and human health. *Front. Microbiol.* 7:185. doi: 10.3389/fmicb.2016.00185

Ritzel, R. M., Lai, Y. J., Crapser, J. D., Patel, A. R., Schrecengost, A., Grenier, J. M., et al. (2018). Aging alters the immunological response to ischemic stroke. *Acta Neuropathol.* 136, 89–110. doi: 10.1007/s00401-018-1859-2

Robbins, J. P., and Price, J. (2017). Human induced pluripotent stem cells as a research tool in Alzheimer's disease. *Psychol. Med.* 47, 2587–2592. doi: 10.1017/s0033291717002124

Roberts, R. C., Farmer, C. B., and Walker, C. K. (2018). "The human brain microbiome; there are bacteria in our brains!," *Conference Report at the Society for Neuroscience Meeting*, San Diego, CA.

Rogers, J., Zornetzer, S. F., Bloom, F. E., and Mervis, R. E. (1984). Senescent microstructural changes in rat cerebellum. *Brain Res.* 292, 23–32. doi: 10.1016/0006-8993(84)90886-2

Roquer, J., Segura, T., Serena, J., and Castillo, J. (2009). Endothelial dysfunction, vascular disease and stroke: the ARTICO study. *Cerebrovasc. Dis.* 27 (Suppl 1), 25–37. doi: 10.1159/000200439

Roriz-Filho, J. S., Sa-Roriz, T. M., Rosset, I., Camozzato, A. L., Santos, A. C., Chaves, M. L., et al. (2009). (Pre)diabetes, brain aging, and cognition. *Biochim. Biophys. Acta* 1792, 432–443.

Roy, C. S., and Sherrington, C. S. (1890). On the regulation of the blood-supply of the brain. *J. Physiol.* 11, 85-158.17.

Ruitenberg, A., Den Heijer, T., Bakker, S. L., Van Swieten, J. C., Koudstaal, P. J., Hofman, A., et al. (2005). Cerebral hypoperfusion and clinical onset of dementia: the rotterdam study. *Ann. Neurol.* 57, 789–794. doi: 10.1002/ana.20493

Ryden, L., Zettergren, A., Seidu, N. M., Guo, X., Kern, S., Blennow, K., et al. (2019). Atrial fibrillation increases the risk of dementia amongst older adults even in the absence of stroke. *J. Intern. Med.* 286, 101–110

Sadoshima, S., Busija, D. W., and Heistad, D. D. (1983). Mechanisms of protection against stroke in stroke-prone spontaneously hypertensive rats. *Am. J. Physiol.* 244, H406–412.

Saha, A. R., Ninkina, N. N., Hanger, D. P., Anderton, B. H., Davies, A. M., and Buchman, V. L. (2000). Induction of neuronal death by alpha-synuclein. *Eur. J. Neurosci.* 12, 3073–3077. doi: 10.1046/j.1460-9568.2000.00210.x

Salminen, A., Ojala, J., Kaarniranta, K., Haapasalo, A., Hiltunen, M., and Soininen, H. (2011). Astrocytes in the aging brain express characteristics of senescence-associated secretory phenotype. *Eur. J. Neurosci.* 34, 3–11. doi: 10.1111/j.1460-9568.2011.07738.x

Sanchez-Tapia, M., Aguilar-Lopez, M., Perez-Cruz, C., Pichardo-Ontiveros, E., Wang, M., Donovan, S. M., et al. (2017). Nopal (*Opuntia ficus indica*) protects from metabolic endotoxemia by modifying gut microbiota in obese rats fed high fat/sucrose diet. *Sci. Rep.* 7:4716.

Sanguinetti, E., Collado, M. C., Marrachelli, V. G., Monleon, D., Selma-Royo, M., Pardo-Tendero, M. M., et al. (2018). Microbiome-metabolome signatures in mice genetically prone to develop dementia, fed a normal or fatty diet. *Sci. Rep.* 8:4907.

Scheltens, P., Barkhof, F., Leys, D., Wolters, E. C., Ravid, R., and Kamphorst, W. (1995). Histopathologic correlates of white matter changes on MRI in alzheimer's disease and normal aging. *Neurology* 45, 883–888. doi: 10.1212/wnl.45.5.883

Schmidt, H. H., and Walter, U. (1994). NO at work. *Cell* 78, 919–925.

Seib, D. R., and Martin-Villalba, A. (2015). Neurogenesis in the normal ageing hippocampus: a mini-review. *Gerontology* 61, 327–335. doi: 10.1159/000368575

Selvarajah, J., Scott, M., Stivaros, S., Hulme, S., Georgiou, R., Rothwell, N., et al. (2009). Potential surrogate markers of cerebral microvascular angiopathy in asymptomatic subjects at risk of stroke. *Eur. Radiol.* 19, 1011–1018. doi: 10.1007/s00330-008-1202-8

Sender, R., Fuchs, S., and Milo, R. (2016). Revised estimates for the number of human and bacteria cells in the body. *PLoS Biol.* 14:e1002533. doi: 10.1371/journal.pbio.1002533

Shankle, W. R., Landing, B. H., Ang, S. M., Chui, H., Villarreal-Engelhardt, G., and Zarow, C. (1993). Studies of the enteric nervous system in Alzheimer disease and other dementias of the elderly: enteric neurons in Alzheimer disease. *Mod. Pathol.* 6, 10–14.

Shen, L., Liu, L., and Ji, H. F. (2017). Alzheimer's disease histological and behavioral manifestations in transgenic mice correlate with specific gut microbiome state. *J. Alzheimers. Dis.* 56, 385–390. doi: 10.3233/jad-160884

Shiue, S. J., Rau, R. H., Shiue, H. S., Hung, Y. W., Li, Z. X., Yang, K. D., et al. (2019). Mesenchymal stem cell exosomes as a cell-free therapy for nerve injury-induced pain in rats. *Pain* 160, 210–223. doi: 10.1097/j.pain.0000000000001395

Silvestrini, M., Pasqualetti, P., Baruffaldi, R., Bartolini, M., Handouk, Y., Matteis, M., et al. (2006). Cerebrovascular reactivity and cognitive decline in patients with Alzheimer disease. *Stroke* 37, 1010–1015. doi: 10.1161/01.str.0000206439.62025.97

Simeoli, R., Montague, K., Jones, H. R., Castaldi, L., Chambers, D., Kelleher, J. H., et al. (2017). Exosomal cargo including microRNA regulates sensory neuron to macrophage communication after nerve trauma. *Nat. Commun.* 8:1778.

Singh, V., Roth, S., Llovera, G., Sadler, R., Garzetti, D., Stecher, B., et al. (2016). Microbiota dysbiosis controls the neuroinflammatory response after stroke. *J. Neurosci.* 36, 7428–7440. doi: 10.1523/jneurosci.1114-16.2016

Singh, V., Sadler, R., Heindl, S., Llovera, G., Roth, S., Benakis, C., et al. (2018). The gut microbiome primes a cerebroprotective immune response after stroke. *J. Cereb. Blood Flow Metab.* 38, 1293–1298. doi: 10.1177/0271678x18780130

Smith, C. D., Andersen, A. H., Kryscio, R. J., Schmitt, F. A., Kindy, M. S., Blonder, L. X., et al. (1999). Altered brain activation in cognitively intact individuals at high risk for Alzheimer's disease. *Neurology* 53, 1391–1396.

Snowdon, D. A., Greiner, L. H., Mortimer, J. A., Riley, K. P., Greiner, P. A., and Markesbery, W. R. (1997). Brain infarction and the clinical expression of Alzheimer disease. The nun study. *JAMA* 277, 813–817. doi: 10.1001/jama.277.10.813

Song, I. U., Kim, J. S., Kim, Y. I., Eah, K. Y., and Lee, K. S. (2007). Clinical significance of silent cerebral infarctions in patients with Alzheimer disease. *Cogn. Behav. Neurol.* 20, 93–98. doi: 10.1097/wnn.0b013e31805d859e

Stanley, D., Mason, L. J., Mackin, K. E., Srikhanta, Y. N., Lyras, D., Prakash, M. D., et al. (2016). Translocation and dissemination of commensal bacteria in post-stroke infection. *Nat. Med.* 22, 1277–1284. doi: 10.1038/nm.4194

Stanley, D., Moore, R. J., and Wong, C. H. Y. (2018). An insight into intestinal mucosal microbiota disruption after stroke. *Sci. Rep.* 8:568.

Sun, G., Li, G., Li, D., Huang, W., Zhang, R., Zhang, H., et al. (2018). HucMSC derived exosomes promote functional recovery in spinal cord injury mice via attenuating inflammation. *Mater. Sci. Eng. C Mater. Biol. Appl.* 89, 194–204. doi: 10.1016/j.msec.2018.04.006

Sweeney, M. D., Sagare, A. P., and Zlokovic, B. V. (2018). Blood-brain barrier breakdown in Alzheimer disease and other neurodegenerative disorders. *Nat. Rev. Neurol.* 14, 133–150. doi: 10.1038/nrneurol.2017.188

Syeda, T., Sanchez-Tapia, M., Pinedo-Vargas, L., Granados, O., Cuervo-Zanatta, D., Rojas-Santiago, E., et al. (2018). Bioactive food abates metabolic and synaptic alterations by modulation of gut microbiota in a mouse model of Alzheimer's disease. *J. Alzheimers. Dis.* 66, 1657–1682. doi: 10.3233/jad-180556

Szablewski, L. (2018). Human gut microbiota in health and Alzheimer's disease. *J. Alzheimers. Dis.* 62, 549–560. doi: 10.3233/jad-170908

Taguchi, K., Watanabe, Y., Tsujimura, A., and Tanaka, M. (2016). Brain region-dependent differential expression of alpha-synuclein. *J. Comp. Neurol.* 524, 1236–1258. doi: 10.1002/cne.23901

Tang, W. H., Wang, Z., Levison, B. S., Koeth, R. A., Britt, E. B., Fu, X., et al. (2013). Intestinal microbial metabolism of phosphatidylcholine and cardiovascular risk. *N. Engl. J. Med.* 368, 1575–1584. doi: 10.1056/nejmoa1109400

Tao, Q., Ang, T. F. A., Decarli, C., Auerbach, S. H., Devine, S., Stein, T. D., et al. (2018). Association of chronic low-grade inflammation with risk of Alzheimer disease in ApoE4 carriers. *JAMA Netw. Open* 1, e183597. doi: 10.1001/jamanetworkopen.2018.3597

Thery, C., Witwer, K. W., Aikawa, E., Alcaraz, M. J., Anderson, J. D., Andriantsitohaina, R., et al. (2018). Minimal information for studies of extracellular vesicles 2018 (MISEV2018): a position statement of the international society for extracellular vesicles and update of the MISEV2014 guidelines. *J. Extracell. Vesicles* 7:1535750.

Thomas, T., Thomas, G., Mclendon, C., Sutton, T., and Mullan, M. (1996). beta-Amyloid-mediated vasoactivity and vascular endothelial damage. *Nature* 380, 168–171. doi: 10.1038/380168a0

Thursby, E., and Juge, N. (2017). Introduction to the human gut microbiota. *Biochem. J.* 474, 1823–1836. doi: 10.1042/bcj20160510

Tian, X. L., and Li, Y. (2014). Endothelial cell senescence and age-related vascular diseases. *J. Genet. Genom.* 41, 485–495. doi: 10.1016/j.jgg.2014.08.001

Toledo, J. B., Arnold, S. E., Raible, K., Brettschneider, J., Xie, S. X., Grossman, M., et al. (2013). Contribution of cerebrovascular disease in autopsy confirmed neurodegenerative disease cases in the national Alzheimer's coordinating centre. *Brain* 136, 2697–2706. doi: 10.1093/brain/awt188

Torres-Fuentes, C., Schellekens, H., Dinan, T. G., and Cryan, J. F. (2017). The microbiota-gut-brain axis in obesity. *Lancet Gastroenterol. Hepatol.* 2, 747–756.

Tran, L., and Greenwood-Van Meerveld, B. (2013). Age-associated remodeling of the intestinal epithelial barrier. *J. Gerontol. A Biol. Sci. Med. Sci.* 68, 1045–1056. doi: 10.1093/gerona/glt106

Trapp, B. D., and Nave, K. A. (2008). Multiple sclerosis: an immune or neurodegenerative disorder? *Annu. Rev. Neurosci.* 31, 247–269. doi: 10.1146/annurev.neuro.30.051606.094313

Turnquist, C., Horikawa, I., Foran, E., Major, E. O., Vojtesek, B., Lane, D. P., et al. (2016). p53 isoforms regulate astrocyte-mediated neuroprotection and neurodegeneration. *Cell Death. Differ.* 23, 1515–1528. doi: 10.1038/cdd.2016.37

van der Worp, H. B., Howells, D. W., Sena, E. S., Porritt, M. J., Rewell, S., O'collins, V., et al. (2010). Can animal models of disease reliably inform human studies? *PLoS Med.* 7:e1000245. doi: 10.1371/journal.pmed.1000245

van Deursen, J. M. (2014). The role of senescent cells in ageing. *Nature* 509, 439–446. doi: 10.1038/nature13193

van Oijen, M., De Jong, F. J., Witteman, J. C., Hofman, A., Koudstaal, P. J., and Breteler, M. M. (2007). Atherosclerosis and risk for dementia. *Ann. Neurol.* 61, 403–410.

VanGuilder, H. D., Yan, H., Farley, J. A., Sonntag, W. E., and Freeman, W. M. (2010). Aging alters the expression of neurotransmission-regulating proteins in the hippocampal synaptoproteome. *J. Neurochem.* 113, 1577–1588.

Verdu, E. F., Galipeau, H. J., and Jabri, B. (2015). Novel players in coeliac disease pathogenesis: role of the gut microbiota. *Nat. Rev. Gastroenterol. Hepatol.* 12, 497–506. doi: 10.1038/nrgastro.2015.90

Vicente Miranda, H., El-Agnaf, O. M., and Outeiro, T. F. (2016). Glycation in Parkinson's disease and Alzheimer's disease. *Mov. Disord.* 31, 782–790.

Villaran, R. F., Espinosa-Oliva, A. M., Sarmiento, M., De Pablos, R. M., Arguelles, S., Delgado-Cortes, M. J., et al. (2010). Ulcerative colitis exacerbates lipopolysaccharide-induced damage to the nigral dopaminergic system: potential risk factor in Parkinson's disease. *J. Neurochem.* 114, 1687–1700. doi: 10.1111/j.1471-4159.2010.06879.x

Villeda, S. A., Luo, J., Mosher, K. I., Zou, B., Britschgi, M., Bieri, G., et al. (2011). The ageing systemic milieu negatively regulates neurogenesis and cognitive function. *Nature* 477, 90–94. doi: 10.1038/nature10357

Villringer, A. (1997). Understanding functional neuroimaging methods based on neurovascular coupling. *Adv. Exp. Med. Biol.* 413, 177–193. doi: 10.1007/978-1-4899-0056-2_20

Vogt, N. M., Kerby, R. L., Dill-Mcfarland, K. A., Harding, S. J., Merluzzi, A. P., Johnson, S. C., et al. (2017). Gut microbiome alterations in Alzheimer's disease. *Sci. Rep.* 7:13537.

Wakabayashi, K., Mori, F., Tanji, K., Orimo, S., and Takahashi, H. (2010). Involvement of the peripheral nervous system in synucleinopathies, tauopathies and other neurodegenerative proteinopathies of the brain. *Acta Neuropathol.* 120, 1–12. doi: 10.1007/s00401-010-0706-x

Wakabayashi, K., Takahashi, H., Ohama, E., and Ikuta, F. (1990). Parkinson's disease: an immunohistochemical study of Lewy body-containing neurons in the enteric nervous system. *Acta Neuropathol.* 79, 581–583. doi: 10.1007/bf00294234

Wakabayashi, K., Takahashi, H., Takeda, S., Ohama, E., and Ikuta, F. (1988). Parkinson's disease: the presence of Lewy bodies in Auerbach's and *Meissner's plexuses*. *Acta Neuropathol.* 76, 217–221. doi: 10.1007/bf00687767

Walsh, D. M., Klyubin, I., Fadeeva, J. V., Cullen, W. K., Anwyl, R., Wolfe, M. S., et al. (2002). Naturally secreted oligomers of amyloid beta protein potently inhibit hippocampal long-term potentiation in vivo. *Nature* 416, 535–539. doi: 10.1038/416535a

Walton, C. C., and Andersen, J. K. (2019). Unknown fates of (brain) oxidation or UFO: close encounters with neuronal senescence. *Free Radic Biol. Med.* 134, 695–701 doi: 10.1016/j.freeradbiomed.2019.01.012

Wang, L., Christophersen, C. T., Sorich, M. J., Gerber, J. P., Angley, M. T., and Conlon, M. A. (2012). Elevated fecal short chain fatty acid and ammonia concentrations in children with autism spectrum disorder. *Dig. Dis. Sci.* 57, 2096–2102. doi: 10.1007/s10620-012-2167-7

Wang, R., Tang, Y., Feng, B., Ye, C., Fang, L., Zhang, L., et al. (2007). Changes in hippocampal synapses and learning-memory abilities in age-increasing rats and effects of tetrahydroxystilbene glucoside in aged rats. *Neuroscience* 149, 739–746. doi: 10.1016/j.neuroscience.2007.07.065

Wang, X., Xing, A., Xu, C., Cai, Q., Liu, H., and Li, L. (2010). Cerebrovascular hypoperfusion induces spatial memory impairment, synaptic changes, and amyloid-beta oligomerization in rats. *J. Alzheimers Dis.* 21, 813–822. doi: 10.3233/jad-2010-100216

Wardlaw, J. M., Smith, E. E., Biessels, G. J., Cordonnier, C., Fazekas, F., Frayne, R., et al. (2013). Neuroimaging standards for research into small vessel disease and its contribution to ageing and neurodegeneration. *Lancet Neurol.* 12, 822–838.

Wendell, C. R., Waldstein, S. R., Ferrucci, L., O'brien, R. J., Strait, J. B., and Zonderman, A. B. (2012). Carotid atherosclerosis and prospective risk of dementia. *Stroke* 43, 3319–3324. doi: 10.1161/strokeaha.112.672527

Wenk, G. L., and Barnes, C. A. (2000). Regional changes in the hippocampal density of AMPA and NMDA receptors across the lifespan of the rat. *Brain Res.* 885, 1–5. doi: 10.1016/s0006-8993(00)02792-x

Whelton, P. K., Carey, R. M., Aronow, W. S., Casey, D. E. Jr., Collins, K. J., Dennison Himmelfarb, C., et al. (2018). 2017 ACC/AHA/AAPA/ABC/ACPM/AGS/APhA/ASH/ASPC/NMA/PCNA guideline for the prevention, detection, evaluation, and management of high blood pressure in adults: a report of the american college of cardiology/american heart association task force on clinical practice guidelines. *Hypertension* 71, e13-e115.

White, L. (2009). Brain lesions at autopsy in older Japanese-American men as related to cognitive impairment and dementia in the final years of life: a summary report from the Honolulu-Asia aging study. *J. Alzheimers. Dis.* 18, 713–725. doi: 10.3233/jad-2009-1178

Willner, P. (1984). The validity of animal models of depression. *Psychopharmacology* 83, 1–16. doi: 10.1007/bf00427414

Winek, K., Engel, O., Koduah, P., Heimesaat, M. M., Fischer, A., Bereswill, S., et al. (2016). Depletion of cultivatable gut microbiota by broad-spectrum antibiotic pretreatment worsens outcome after murine stroke. *Stroke* 47, 1354–1363. doi: 10.1161/strokeaha.115.011800

Wittko-Schneider, I. M., Schneider, F. T., and Plate, K. H. (2014). Cerebral angiogenesis during development: who is conducting the orchestra? *Methods Mol. Biol.* 1135, 3–20. doi: 10.1007/978-1-4939-0320-7_1

Wong, J. M., and Billiar, T. R. (1995). Regulation and function of inducible nitric oxide synthase during sepsis and acute inflammation. *Adv. Pharmacol.* 34, 155–170. doi: 10.1016/s1054-3589(08)61084-4

Wong, J. M., De Souza, R., Kendall, C. W., Emam, A., and Jenkins, D. J. (2006). Colonic health: fermentation and short chain fatty acids. *J. Clin. Gastroenterol.* 40, 235–243.

Wu, S. C., Cao, Z. S., Chang, K. M., and Juang, J. L. (2017). Intestinal microbial dysbiosis aggravates the progression of Alzheimer's disease in drosophila. *Nat. Commun.* 8:24.

Xie, N., and Tang, B. (2016). The application of human iPSCs in neurological diseases: from bench to bedside. *Stem Cells Int.* 2016:6484713.

Yamazaki, T., Li, W., Yang, L., Li, P., Cao, H., Motegi, S. I., et al. (2018). Whole mount adult ear skin imaging reveals defective neuro-vascular branching morphogenesis in obese and type 2 diabetic mouse models. *Sci. Rep.* 8:430.

Yamazaki, Y., Baker, D. J., Tachibana, M., Liu, C. C., Van Deursen, J. M., Brott, T. G., et al. (2016). Vascular cell senescence contributes to blood-brain barrier breakdown. *Stroke* 47, 1068–1077. doi: 10.1161/strokeaha.115.010835

Yilmaz, A., Geddes, T., Han, B., Bahado-Singh, R. O., Wilson, G. D., Imam, K., et al. (2017). Diagnostic biomarkers of Alzheimer's disease as identified in Saliva using 1H NMR-based metabolomics. *J. Alzheimers. Dis.* 58, 355–359. doi: 10.3233/jad-161226

Yin, J., Liao, S. X., He, Y., Wang, S., Xia, G. H., Liu, F. T., et al. (2015). Dysbiosis of gut microbiota with reduced trimethylamine-N-Oxide level in patients with large-artery atherosclerotic stroke or transient ischemic attack. *J. Am. Heart Assoc.* 4:e002699.

Zekry, D., Duyckaerts, C., Moulias, R., Belmin, J., Geoffre, C., Herrmann, F., et al. (2002). Degenerative and vascular lesions of the brain have synergistic effects in dementia of the elderly. *Acta Neuropathol.* 103, 481–487. doi: 10.1007/s00401-001-0493-5

Zevin, A. S., Mckinnon, L., Burgener, A., and Klatt, N. R. (2016). Microbial translocation and microbiome dysbiosis in HIV-associated immune activation. *Curr. Opin. HIV AIDS* 11, 182–190. doi: 10.1097/coh.0000000000000234

Zhan, X., Stamova, B., Jin, L. W., Decarli, C., Phinney, B., and Sharp, F. R. (2016). Gram-negative bacterial molecules associate with Alzheimer disease pathology. *Neurology* 87, 2324–2332. doi: 10.1212/wnl.0000000000003391

Zhang, C., Yin, A., Li, H., Wang, R., Wu, G., Shen, J., et al. (2015). Dietary modulation of gut microbiota contributes to alleviation of both genetic and simple obesity in children. *EBioMed.* 2, 968–984. doi: 10.1016/j.ebiom.2015.07.007

Zhang, L., Wang, Y., Xiayu, X., Shi, C., Chen, W., Song, N., et al. (2017). Altered gut microbiota in a mouse model of Alzheimer's disease. *J. Alzheimers Dis.* 60, 1241–1257. doi: 10.3233/jad-170020

Zhao, Y., Cong, L., and Lukiw, W. J. (2017). Lipopolysaccharide (LPS) accumulates in neocortical neurons of Alzheimer's disease (AD) brain and impairs transcription in human neuronal-glial primary co-cultures. *Front. Aging. Neurosci.* 9:407. doi: 10.3389/fnagi.2017.00407

Zhao, Y., Dua, P., and Lukiw, W. J. (2015). Microbial sources of amyloid and relevance to amyloidogenesis and alzheimer's disease (AD). *J. Alzheimers. Dis. Parkinsonism* 5:177.

Zhuang, Z. Q., Shen, L. L., Li, W. W., Fu, X., Zeng, F., Gui, L., et al. (2018). Gut microbiota is altered in patients with Alzheimer's disease. *J. Alzheimers. Dis.* 63, 1337–1346.

Zlokovic, B. V. (2008). The blood-brain barrier in health and chronic neurodegenerative disorders. *Neuron* 57, 178–201. doi: 10.1016/j.neuron.2008.01.003

Conflict of Interest Statement: The authors declare that the research was conducted in the absence of any commercial or financial relationships that could be construed as a potential conflict of interest.

Copyright © 2019 Castillo, Castro-Obregón, Gutiérrez-Becker, Gutiérrez-Ospina, Karalis, Khalil, Lopez-Noguerola, Rodríguez, Martínez-Martínez, Perez-Cruz, Pérez-Velázquez, Piña, Rubio, García, Syeda, Vanoye-Carlo, Villringer, Winek and Zille. This is an open-access article distributed under the terms of the Creative Commons Attribution License (CC BY). The use, distribution or reproduction in other forums is permitted, provided the original author(s) and the copyright owner(s) are credited and that the original publication in this journal is cited, in accordance with accepted academic practice. No use, distribution or reproduction is permitted which does not comply with these terms.

Journal of Natural Medicines (2019) 73:672–678
https://doi.org/10.1007/s11418-019-01284-w

NATURAL RESOURCE LETTER

Neuroprotective effect of Mayan medicinal plant extracts against glutamate-induced toxicity

Cristina M. Castillo-Bautista[1] · Luis W. Torres-Tapia[1] · Jorge A. Rangel-Méndez[2] · Sergio R. Peraza-Sánchez[1] · Daniel Cortés[3,4] · Iván Velasco[3,4] · Rosa E. Moo-Puc[2,5]

Received: 11 December 2018 / Accepted: 26 January 2019 / Published online: 16 February 2019
© The Japanese Society of Pharmacognosy 2019

Abstract

Neurological disorders are a public health problem worldwide for which there is currently no direct treatment of the cause of the disorder. The goal of this study was to investigate the potential in vitro neuroprotective property of plants used in Mayan traditional medicine. Plant ethanolic extracts were prepared and tested on models in which neuronal damage was induced by glutamate, i.e., a human neuroblastoma cell line (SH-SY5Y) and rat cortical neurons. HPLC profiles from active extracts were also obtained. A total of 51 plant species were identified in the literature as plant species used in Mayan traditional medicine for the treatment of symptoms suggestive of neurological disorders, and we studied 34 of these in our analysis. Six extracts had a neuroprotective effect on SH-SY5Y cells, with the most active extract being that from *Schwenckia americana* roots (half maximal effective concentration [EC_{50}] 11.3 ± 2.9 µg/mL), and three extracts exhibited a neuroprotective effect in the rat neuron cortical model, with the most active extract being that from *Elytraria imbricata* aerial parts (EC_{50} 6.8 ± 3.1 µg/mL). These results suggest that the active extracts from such plants have the potential to be a great resource. Future studies should be performed that are more extensive and which isolate the active constituents.

Keywords Mayan traditional medicine · Neuroprotective effect · Glutamate · Rat cortical neuron · SH-SY5Y cell line

Introduction

Neurological disorders, such as cerebrovascular and neurodegenerative diseases, are a public health problem worldwide [1]. Damage to and loss of neurons are the main characteristics of these disorders, and the mechanisms involved comprise oxidative stress, inflammation, excitotoxicity, misfolded protein accumulation, and others [2].

Current treatments are palliative, only relieving the symptoms without dealing with the cause of the condition. Thus, neuronal damage remains even during and after treatment, and the disease progresses [3].

There is a vast amount of information available on traditional medicines, including those used in Mayan traditional medicine, and the application of these plants to treat different disorders. Much research has focused on identifying the bioactive extracts/compounds of such plants [4, 5]. However, to date no studies on native plants from the Yucatan Peninsula with neuroprotective effects have been reported.

The goal of this study was to test plants reported to be used in Mayan traditional medicine to treat symptoms related to a neurological disorder in two in vitro models of neuronal

Electronic supplementary material The online version of this article (https://doi.org/10.1007/s11418-019-01284-w) contains supplementary material, which is available to authorized users.

✉ Rosa E. Moo-Puc
moopuc@gmail.com

1 Unidad de Biotecnología, Centro de Investigación Científica de Yucatán (CICY), Calle 43 No. 130 × 32 y 34, Col. Chuburná de Hidalgo, 97205 Mérida, Yucatán, Mexico

2 Unidad de Investigación Médica Yucatán, Unidad Médica de Alta Especialidad, Centro Médico Ignacio García Téllez, Instituto Mexicano del Seguro Social (IMSS), Calle 41 No. 439, Col. Industrial, 97150 Mérida, Yucatán, Mexico

3 Instituto de Fisiología Celular-Neurociencias, Universidad Nacional Autónoma de México, 04510 Mexico City, Mexico

4 Laboratorio de Reprogramación Celular, Instituto Nacional de Neurología y Neurocirugía "Manuel Velazco Suárez", 14269 Mexico City, Mexico

5 Applied Science Research Foundation, A.C. Km 5.5 carretera Sierra Papacal-Chuburna Puerto, 97302 Mérida, Yucatán, Mexico

damage induced by glutamate, namely, in a human neuroblastoma cell line (SH-SY5Y) and in rat cortical neurons.

Materials and methods

Literature search

The selection of the plant species included in this study was based on information derived from Mayan traditional medicine records [4, 5]. Criteria for the selection of the species were as follows: (1) plant species used against symptomatology suggestive of neurological conditions (such as headache, convulsions, depression, dementia, loss of speech, loss of orientation, and neuralgia); (2) plant species mentioned in the ethnobotanical literature with full scientific name; (3) endemic or native plant species of the Yucatan Peninsula; (4) plant species for which no more than ten neuroprotective and/or chemical studies reported.

Plant material and preparation of ethanolic extract

Plant species were collected from different locations around the Yucatan Peninsula in Mexico (see Electronic Supplementary Material [ESM]). The plant material was identified and authenticated by a taxonomist from the Department of Natural Resources of the Centro de Investigación Científica de Yucatán (CICY). Voucher specimens were deposited at CICY's U Najil Tikin Xiw herbarium.

Plant material was dried first at room temperature for 48 h and then at 40 °C in a herbarium drying box for 48 h before being ground into powder. Dried plant material (20 g) was macerated with ethanol (100%) for 72 h at room temperature. The supernatants were filtered and evaporated under vacuum using a rotary evaporator.

Cell culture

Cercopithecus aethiops kidney (Vero cells; ATCC® CCL-81™) and human neuroblastoma SH-SY5Y (ATCC® CRL-2266™) cell lines from the American Type Culture Collection (ATCC; Manassas, VA, USA) were used for the in vitro assays. Vero cells were cultured with Dulbecco's Modified Eagle medium (DMEM) supplemented with fetal bovine serum (FBS) (10%, v/v), 100 U/mL of penicillin G and 100 µg/mL of streptomycin. SH-SY5Y cells were cultured in DMEM/F12 (1:1) medium supplemented with FBS (15%, v/v), 100 U/mL of penicillin G, and 100 µg/mL of streptomycin. Both cell lines were maintained at 37 °C in an atmosphere of 5% CO_2.

Cell viability assay in the Vero and SH-SY5Y cell lines

Cell viability in Vero cells was determined using sulphorhodamine B (SRB; Sigma–Aldrich, St. Louis, MO, USA) and in SH-SY5Y cells using calcein-AM (Sigma–Aldrich). For each assay, 1×10^5 cells per well were seeded in 96-well plates, and the assays were performed 24 h later. Cells were exposed to the plant extracts at concentrations of 500, 250, 125, and 62.5 µg/mL for 48 h. Vero cells were then fixed with 10% trichloroacetic acid at 4 °C for 20 min, following which SRB (0.1%, p/v) was added for 20 min at room temperature; the cells were later washed with acetic acid (1%, v/v). A solution of 10 mM TRIS-base was used to solubilize SRB, and optic density was read in a microplate reader. For the SH-SY5Y cells, calcein-AM (4 µM) was added to the cells and the wells incubated for 30 min at 37 °C. The plates were then washed twice with phosphate buffered saline (PBS) 1×(pH 7.4), and fluorescence was read in the same microplate reader as that used for the assay of Vero cells.

Neuroprotection assay in SH-SY5Y cells

For the assays 1×10^6 cells per well were seeded in 96-well plates, and the assays were performed 24 h later. Cells were pretreated with the extracts at concentrations of 25, 12.5, 6.25, and 3.125 µg/mL for 24 h. Ascorbic acid (Sigma–Aldrich) was employed as positive control due to its antioxidant activity. The cells were then exposed to glutamic acid (Sigma–Aldrich) at 25 mM for 30 min, following which the medium was removed and replaced with fresh medium, and incubated continued for 24 h. Calcein-AM (4 µM) was added and the cells incubated for 30 min at 37 °C before being washed twice with PBS 1×(pH 7.4); fluorescence was read in a microplate reader.

Experimental animals and rat cortical neurons isolation

All procedures were approved by the Institutional Animal Care and Use Committee and complied with Mexican regulations (NOM-062-ZOO-1999). The animals were housed in animal units under a photoperiod of 12 h light/12 h dark and at a temperature of 22 °C; food and water were provided ad libitum. Pregnant Wistar rats (E17–E18 days gestation) were anesthetized with sevoflurane and sacrificed by decapitation. Primary cultures of mixed cortical cells containing both neuronal and glial cells were prepared from the fetal Wistar rats aged E17 to E18 days of gestation. The cortex was dissociated mechanically and with 0.25% trypsin (1 µL/mL), and dissociated cells were cultured in 96-well culture plates coated with poly-L-ornithine at a density of 1×10^5

INFORME DE LABORES 2019

Table 1 Plant species included in this study

Plant species[a] (voucher specimen)	Family	Mayan and common name[a]	Status[b]	Ailments treated[a]
Acalypha unibracteata Muell. Arg. (P. Simá 3165)	Euphorbiaceae	*Ch'ilibtux*	Native	Headache
Adiantum tenerum Sw. (P. Simá 3203)	Pteridaceae	*Ix tel dziu, tel dziu, cilantrillo de pozo*	Native	Headache
Caesalpinia gaumeri Greenm. (P. Simá 3166)	Fabaceae	*Kitam che'*	Native	Epilepsy
Canna indica L. (P. Simá 3200)	Cannaceae	*Chan kaia*	Native	Neuralgia
Clusia flava Jacq. (P. Simá 3175)	Clusiaceae	*K'anchunuup*	Native	Headache
Crateva tapia L. (P. Simá 3176)	Capparaceae	*Kolok max*	Native	Alteration of nerves
Croton schiedeanus Schltdl. (P. Simá 3196)	Euphorbiaceae	*Chul, chulche', ch' ujuche', palo santo*	Native	Convulsions
Dalea carthagenensis (Jacq.) J. F. Macbr. (P. Sima 3178)	Fabaceae	Ch'o'	Native	Depression
Dalechampia scandens L. (P. Simá 3174)	Euphorbiaceae	*Molkoh*	Native	Headache and epilepsy
Diphysa carthagenensis Jacq. (P. Simá 3167)	Fabaceae	*Xts'uts'uk*	Native	Epilepsy
Ehretia tinifolia L. (P. Simá 3180)	Boraginaceae	*Bec o beek, roble*	Native	Headache
Elytraria imbricata (Vahl) Pers. (P. Simá 3187)	Acanthaceae	*Cabal che*	Native	Headache
Harpalyce rupicola Donn. Sm. (P. Simá 3198)	Fabaceae	*K'an chan te'*	Native	Convulsions
Helicteres baruensis Jacq. (P. Simá 3168)	Sterculiaceae	*Tsutsup*	Native	Epilepsy
Isotoma longiflora (L.) Presl. (P. Simá 3201)	Campanulaceae	*Luk'sahtan o sahtahan*	Native	Epilepsy
Justicia spicigera Schltdl. (P. Simá 3183)	Acanthaceae	*Chaklool, ts'I'its, sacatinta o yich can*	Native	Headache and epilepsy
Lasiacis divaricata (L.) Hitchc. (P. Simá 3184)	Poaceae	*Siit*	Native	Dementia, headache, and loss of orientation
Leucaena leucocephala (Lam.) de Wit (P. Simá 3164)	Fabaceae	*Waxim*	Native	Headache
Lisianthus axillaris (Hemsl) Kuntze (P. Simá 3199)	Gentianaceae	*Xputsche*	Endemic	Alteration of nerves
Malvaviscus arboreus Cav. (P. Simá 3172)	Malvaceae	*Bisilk'aax o bisikax*	Native	Epilepsy
Manfreda brachystachya (Cav.) Rose (P. Simá 3188)	Agavaceae	*Pets' kinil*	Endemic	Headache
Metopium brownei (Jacq.) Urb. (P. Simá 3173)	Anacardiaceae	*Kabab, kabalchechem,*	Native	Headache
Mimosa bahamensis Benth. (P. Simá 3169)	Fabaceae	*Katzim*	Native	Headache, epilepsy, stimulant, and fatigue
Pilocarpus racemosus Vahl. (P. Simá 3189)	Rutaceae	*Tankasche'*	Native	Headache and alteration of nerves,
Piper gaumeri Trel. (P. Simá 3197)	Piperaceae	*K'uk'sub, xpeheche*	Native	Headache
Pluchea odorata (L.) Cass. (P. Simá 3171)	Asteraceae	*Chalche', hierba de Santa María*	Native	Convulsions, headache, loss of speech, and neuralgia

INFORME DE LABORES 2019

Table 1 (continued)

Plant species[a] (voucher specimen)	Family	Mayan and common name[a]	Status[b]	Ailments treated[a]
Schwenckia americana (L.) D. Royen (P. Simá 3185)	Solanaceae	*Xayúu lool xiiw*	Native	Depression
Tetramerium nervosum Nees. (P. Simá 3186)	Acanthaceae	*Baak soots', sak ch'ikib, xk'uch'eel,*	Native	Headache
Thouinia paucidentata Radlk. (P. Simá 3170)	Sapindaceae	*K'anchunup*	Endemic	Headache
Tillandsia streptophylla Scheidw. ex C. Morren (P. Simá 3202)	Bromeliaceae	*Hk'olomxal*	Native	Headache
Tradescantia spathacea Sw. (P. Simá 3191)	Commelinaceae	*Chaktsam, maguey morado*	Native	Headache
Urera baccifera (L.) Gaudich. ex Wedd. (P. Simá 3195)	Urticaceae	*Laal, ortiga*	Native	Headache
Vitex gaumeri Greenm. (P. Simá 3182)	Lamiaceae	*Ya'axnik*	Native	Headache
Zanthoxylum caribaeum Lam. (P. Simá 3190)	Rutaceae	*Si na'an ché ik, sinanché*	Native	Epilepsy and anesthesic

[a]Osadao [4]; Arellano-Rodriguez et al. [5]

[b]Fernandez et al. [6]

Table 2 Plant species excluded from analysis in this study

Plant species[a]	Family	Mayan and common name[a]	Status[b]	Ailments treated[a]	CR[c]	BA[c]
Acacia farnesiana (L.) Willd.	Fabaceae	*Kan ix che*	Native	Alterations of nerves	28	14
Ageratum gaumeri B.L. Rob.[d]	Asteraceae	*Ak'umbil, ta'uluum, flor de San Juan, mota morada*	Endemic	Headache	0	0
Asclepias curassavica L.	Apocynaceae	*Sac cancel xiu, anal xiu, cancerillo*	Native	Headache	21	28
Bursera simaruba (L.) Sarg.	Burseraceae	*Chakah, palo chino*	Native	Headache	6	22
Cestrum nocturnum L.	Solanaceae	*Aak'a xiiw*	Native	Epilepsy	5	15
Chenopodium ambrosioides L.	Amaranthaceae	*Lukum, epazote*	Native	Mal de San Vito	47	4
Gliricidia sepium (Jacq.) Kunth ex Walp.	Fabaceae	*Sak ya'ab, cocolito*	Endemic	Headache	17	1
Indigofera suffruticosa Mill.	Fabaceae	*Ch'oj xiiw*	Native	Epilepsy	10	7
Plumeria rubra L.	Apocynaceae	Flor de mayo	Native	Stimulant		
Rauwolfia tetraphylla L.	Apocynaceae	*Chacmukak, cabal muc*	Native	Headache	12	7
Stachytarpheta jamaicensis (L.) Vahl	Verbenaceae	*Ibin xiu, verbena*	Native	Analgesic and calmative	12	9
Tabebuia pentaphylla L.	Bignoniaceae	*Hokab*	Native	Headache	22	8
Turnera diffusa Willd.	Turneraceae	*Misib coc*	Native	Brain weakness	13	12

CR number of compound(s) reported, *BA* number of biological activity reports related to neuroprotection

[a]Osadao [4]; Arellano-Rodríguez et al. [5]

[b]Fernandez et al. [6]

[c]Databases: Napralert™, Pubmed™, and ScienceDirect™

[d]Studied by another research group

cells per well. Cortical cells were grown in N2B25 medium. Cultures were allowed to mature for 10–14 days before being used for the experiments.

Neuroprotection assay in rat cortical neurons

Rat cortical neurons were pretreated with the plant extracts at concentrations of 25, 12.5, 6.25, and 3.125 µg/mL for 24 h. Dizocilpine (MK-801; Sigma–Aldrich) at 10 µM was used

INFORME DE LABORES 2019

Table 3 Neuroprotective effect of the most active plant extracts

Plant species	Plant part[a]	Extraction yield (%)	Neuroprotective effect EC_{50} (µg/mL)	
			SH-SY5Y	Rat cortical neurons
Elytraria imbricata	AP	6.63	18.4 ± 2.3	6.8 ± 3.1
Isotoma longiflora	R	28.55	13.1 ± 1.6	12.4 ± 1.8
Mimosa bahamensis	S	2.75	15.4 ± 3.0	> 25
Schwenckia americana	AP	7.61	16.7 ± 2.2	> 25
	R	2.38	11.3 ± 2.9	> 25
Zanthoxylum caribaeum	S	2.17	23.9 ± 2.1	8.6 ± 2.4
Ascorbic acid (µM)[b]			20 ± 1.53	
MK-801 (µM)[c]				10 ± 2.41

EC_{50} Half maximal effective concentration

[a]*AP* Aerial parts, *R* roots, *S* stem, *B* bark,

[b]Positive control in SH-SY5Y cell assays

[c]Dizocilpine; positive control in rat cortical neuron assays

as the positive control. The neurons were then exposed to glutamic acid (12.5 mM) for 30 min, following which the medium was removed and replaced with fresh medium; the neurons were then incubated for a further 24 h. Calcein-AM (4 µM) was added to the cells and the cells incubated for 30 min at 37 °C. The cells were washed twice with PBS 1×(pH 7.4), and fluorescence was read in a microplate reader.

HPLC profiles

Ethanolic extracts were diluted 1:100, and 10- to 20-µL aliquots were injected into an Agilent Infinity 1260 HPLC system (Agilent Technologies, Santa Clara, CA, USA) equipped with a C-18 pre-column (Zorbax Extend, 12.5 mm × 4.6 mm × 4.5 µm) and a reverse column (Persil Gold C-18, 150 mm × 4.6 mm × 5.0 µm).).

The ultraviolet detector was set at 254–274 nm and the flow rate at 1 mL/min. Samples were eluted with a linear gradient of 1–100% acetonitrile and water with 3% acetic acid.

Statistical analysis

The experiments were performed in duplicate and repeated at least three times. The half maximal effective concentration (EC_{50}) was determined from sigmoidal dose–response variable-slope curves using employing GraphPad Prism ver. 6 statistical software (GraphPad Software Inc., San Diego, CA, USA).

Results and discussion

In this study, we identified 51 plant species from the literature search, of which 38 met the criteria and 34 were collected (Table 1); four species were not collected because the specimens were difficult to find (see ESM), and 13 plant species were excluded (Table 2). Sixty-five ethanolic extracts were prepared using different parts of the plant or whole plant (see ESM). Cytotoxic activity of the ethanolic extracts was tested against the Vero cell line to show that the extracts were innocuous to a normal cell line. Extracts with an CC_{50} of < 125 µg/mL were excluded from the neuroprotective assays. Four extracts were found to be cytotoxic to the Vero cells, 12 extracts were cytotoxic to SH-SY5Y cells, and five extracts were cytotoxic to rat cortical neurons (Table 3).

The viability percentage of SH-SY5Y cells exposed to glutamic acid (25 µM) to induce neuronal damage was 47.29 ± 5.61%, and based on this value we calculated the EC_{50} of the extracts. Ascorbic acid (positive control) had an EC_{50} of 20 µM. Six extracts exerted a neuroprotective effect against glutamate-induced toxicity in this model (Table 3), of which the extract of *Schwenckia americana* roots was the most active (EC_{50} 11.3 µg/mL).

The viability percentage of rat cortical neurons exposed to glutamic acid (12.5 mM) to induce neuronal damage was 47.00 ± 1.82%, and based on this value we calculated the EC_{50} of the extracts. MK-801 (positive control) had an EC_{50} of 10 µM. Three extracts were found to have a neuroprotective effect against glutamate-induced toxicity in this model (Table 3), of which the most active extract was that of *Elytraria imbricata* aerial parts (EC_{50} 6.8 µg/mL).

The chromatographic profile can be used in future studies to isolate the metabolites responsible for the effect of the standardized herbal extract. Therefore, we determined the chromatographic profiles of the six most active extracts (Fig. 1).

To date there are no reports of a phytochemical study of *E. imbricata* nor on the neuroprotective effect of its extracts.

Journal of Natural Medicines (2019) 73:672–678

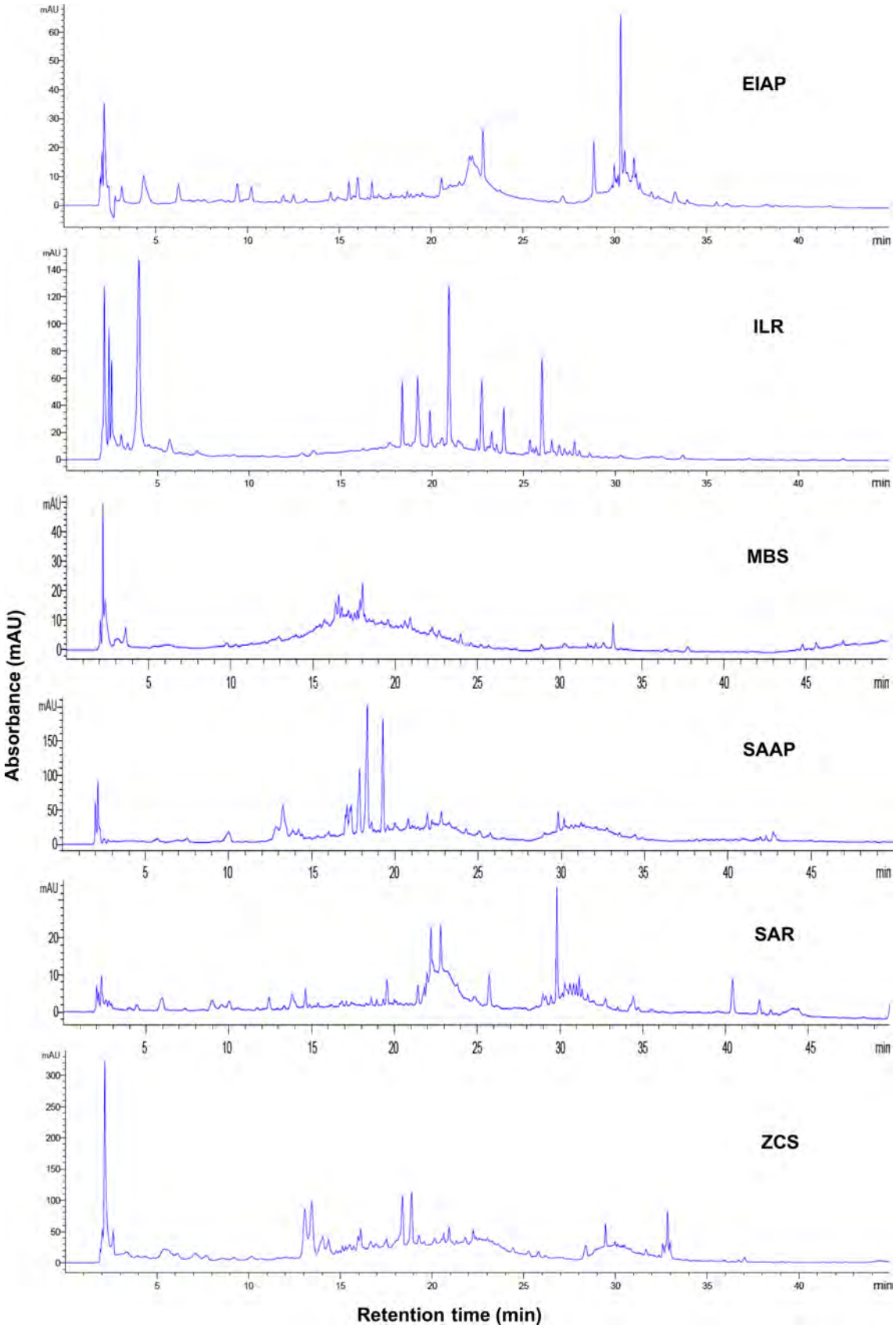

INFORME DE LABORES 2019

◂**Fig. 1** HPLC profiles of active extracts. *EIAP Elytraria imbricata* aerial parts (254 nm), *ILR Isotoma longiflora* roots (254 nm), *MBS Mimosa bahamensis* stems (274 nm), *SAAP Schwenkia americana* aerial parts (254 nm), *SAR Schwenkia americana* roots (254 nm), *ZCS Zanthoxylum caribaeum* stems (254 nm)

Isotoma longiflora is reported to be a Mayan traditional medicine used to treat depression, a disorder which presents high levels of glutamate [7]. Thus, the neuroprotective effect shown by *I. longiflora* in both assays provides support for its use in Mayan traditional medicine. Piperidine and tetrahydropyiridine alkaloids have been isolated from *E. imbricata* plants, and the methanolic extract from whole plant contains saponins and glycosides [8, 9].

There is no report to date on the neuroprotective effect of *M. bahamensis*; however, *M. pudica* has been widely studied in neuroprotective assays [10, 11].

A phytochemical profile of the ethanolic extract from *Schwenckia americana* has been reported in which the presence of alkaloids, tannins, phenols, flavonoids, saponins, terpenoids, steroids, and phytosteroids was shown [12]. Both parts of the plants (aerial parts and roots) were shown to have a neuroprotective effect, suggesting that the active metabolites are distributed throughout the whole plant.

Zanthoxylum caribaeum is reported to be a Mayan traditional medicine used to treat epilepsy and to possess anesthetic properties. There are no reports of a neuroprotective effect but a species of the same genus, *Z. capense*, has been reported to have neuroprotective properties [13].

Conclusion

Traditional medicine is a source of plant species that can be potential novel drugs, including those which could be used to treat neurological disorders. In this study, we analyzed 34 plant species utilized in Mayan traditional medicine to treat symptoms suggestive of neurological disorders and tested these in two models of neuronal damage induced by glutamate, namely, in SH-SY5Y cells and rat cortical neurons. According to our results, five of the plant species tested, i.e., *E. imbricata*, *I. longiflora*, *M. bahamensis*, *S. americana*, and *Z. caribaeum*, have distinct in vitro neuroprotective effect.

Because there is no drug that is currently commercially available to treat directly the causes of neuronal damage observed in neurological diseases, we suggest that it is worthwhile to conduct more in vitro studies on these extracts and to purify the active compounds.

Acknowledgements The research reported herein was partially supported by Red Temática de Células Troncales y Medicina Regenerativa, project number 271609. We are grateful to Paulino Simá-Polanco from the Department of Natural Resources of the Centro de Investigación Científica de Yucatán (CICY) for identifying the specimens and to the Departamento de Nutrición e Inmunología Acuícola of CINVESTAV-Mérida for the facilities provided. We thank the Foundation of Instituto Mexicano del Seguro Social for the grant to Rosa E. Moo-Puc. The authors are grateful to Dr. Margaret Reynolds for an English review of the manuscript.

Compliance with ethical standards

Conflict of interest The authors declare that they have no conflict of interest.

References

1. Chin JH, Vora N (2014) The global burden of neurologic diseases. Neurology 83:349–351
2. Tovar-y-Romo LB, Santa-Cruz LD, Tapia R (2009) Experimental models for the study of neurodegeneration in amyotrophic lateral sclerosis. Mol Neurodegener 4:31
3. Hung AY, Schwarzschild MA (2007) Clinical trials for neuroprotection in Parkinson's disease: overcoming angst and futility? Curr Opin Neurol 20:477–483
4. Osadao R (1834) El Libro del Judío o Medicina Doméstica, Descripción de las Virtudes de las Yerbas Medicinales de Yucatán. Yucatán, Mexico City
5. Arellano-Rodriguez J, Flores-Guido J, Tun-Garrido J, Cruz-Bojorquez M (2003) Leguminosae. Nomenclatura, Forma de Vida, Uso, Manejo y Distribución de las Especies Vegetales de la Península de Yucatán. Universidad Autónoma de Yucatán Press, Mexico City, pp 312–380
6. Fernandez-Concha GC, Tapia Muñoz JL, Duno de Setfano R, Ramírez Morillo IM (2010) Flora ilustrada de la península de Yucatán: listado florístico. CICY, Yucatan, Mexico City
7. Mitani H, Shirayama Y, Yamada T, Maeda K, Ashby CR Jr, Kawahara R (2006) Correlation between plasma levels of glutamate, alanine and serine with severity of depression. Prog Neuro Psychopharmacol Biol Psychiatry 30:1155–1158
8. Kesting JR, Tolderlund IL, Pedersen AF, Witt M, Jaroszewski JW, Staerk D (2009) Piperidine and tetrahydropirydine alkaloids from *Lobelia siphilitica* and *Hippobroma longiflora*. J Nat Prod 72:312–315
9. Chichioco-Hernandez CL, Paguigan ND (2010) Phytochemical profile of selected Philippine plants used to treat asthma. Pharmacogn J 2:198–202
10. Ittiyavirah SP, Pullachol I (2014) Neuroprotective effect of ethanolic extract of *Mimosa pudica* in D-galactose induced Alzheimer's model. World J Pharm Pharm Sci 3:462–470
11. Ngo Bum E, Dawack DL, Schmutz M, Rakotonirina A, Rakotonirina SV, Portet C, Jeker A, Olpe H-R, Herrling P (2004) Anticonvulsant activity of *Mimosa pudica* decoction. Fitoterapia 75:309–314
12. Eriyamremu G, Iorliam BE (2014) Biochemical evaluation of ulcer curative effect of ethanolic and aqueous extracts of *Schwenkia americana* Linn on experimental rats. J. Pharmacogn Phytochem 3:125–130
13. Seoposengwe K, van Tonder JJ, Steenkamp V (2013) In vitro neuroprotective potential of four medicinal plants against rotenone-induced toxicity in SH-SY5Y neuroblastoma cells. BMC Complement Altern Med 13:353

Publisher's Note Springer Nature remains neutral with regard to jurisdictional claims in published maps and institutional affiliations.

the plant journal

INFORME DE LABORES 2019

Society for Experimental Biology

The Plant Journal (2019) **99,** 950–964 doi: 10.1111/tpj.14375

Structural basis for the modulation of plant cytosolic triosephosphate isomerase activity by mimicry of redox-based modifications

Eduardo Castro-Torres[1], Pedro Jiménez-Sandoval[1,†], Sergio Romero-Romero[2,‡], Alma Fuentes-Pascacio[1], Laura M. López-Castillo[1], Corina Díaz-Quezada[1], D. Alejandro Fernández-Velasco[2], Alfredo Torres-Larios[3] and Luis G. Brieba[1,*]

[1]*Laboratorio Nacional de Genómica para la Biodiversidad, Centro de Investigación y de Estudios Avanzados del IPN, Apartado Postal 629, Irapuato, Guanajuato, México CP 36821, México,*

[2]*Departamento de Bioquímica, Facultad de Medicina, Universidad Nacional Autónoma de México, Circuito Exterior s/n, Ciudad Universitaria, Apartado Postal 70-243, Mexico City 04510 México,*

[3]*Departamento de Bioquímica y Biología Estructural, Instituto de Fisiología Celular, Universidad Nacional Autónoma de México, Circuito Exterior s/n, Ciudad Universitaria, Apartado Postal 70-243, México City 04510 México,*

[†]Present address: The Plant Signalling Mechanisms Laboratory, Department of Plant Molecular Biology, University of Lausanne, 1015, Lausanne, Switzerland

[‡]Present address: Department of Biochemistry, University of Bayreuth, 95447, Bayreuth, Germany

Received 3 March 2019; revised 12 April 2019; accepted 23 April 2019; published online 29 April 2019.
*For correspondence (e-mail lgbrieba@langebio.cinvestav.mx).

SUMMARY

Reactive oxidative species (ROS) and *S*-glutathionylation modulate the activity of plant cytosolic triosephosphate isomerases (cTPI). *Arabidopsis thaliana* cTPI (AtcTPI) is subject of redox regulation at two reactive cysteines that function as thiol switches. Here we investigate the role of these residues, AtcTPI-Cys13 and At-Cys218, by substituting them with aspartic acid that mimics the irreversible oxidation of cysteine to sulfinic acid and with amino acids that mimic thiol conjugation. Crystallographic studies show that mimicking AtcTPI-Cys13 oxidation promotes the formation of inactive monomers by reposition residue Phe75 of the neighboring subunit, into a conformation that destabilizes the dimer interface. Mutations in residue AtcTPI-Cys218 to Asp, Lys, or Tyr generate TPI variants with a decreased enzymatic activity by creating structural modifications in two loops (loop 7 and loop 6) whose integrity is necessary to assemble the active site. In contrast with mutations in residue AtcTPI-Cys13, mutations in AtcTPI-Cys218 do not alter the dimeric nature of AtcTPI. Therefore, modifications of residues AtcTPI-Cys13 and AtcTPI-Cys218 modulate AtcTPI activity by inducing the formation of inactive monomers and by altering the active site of the dimeric enzyme, respectively. The identity of residue AtcTPI-Cys218 is conserved in the majority of plant cytosolic TPIs, this conservation and its solvent-exposed localization make it the most probable target for TPI regulation upon oxidative damage by reactive oxygen species. Our data reveal the structural mechanisms by which *S*-glutathionylation protects AtcTPI from irreversible chemical modifications and re-routes carbon metabolism to the pentose phosphate pathway to decrease oxidative stress.

Keywords: *Arabidopsis thaliana*, glutathionylation, thiol-based redox modulation, triosephosphate isomerase, X-ray structure.

INTRODUCTION

Triosephosphate isomerase (TPI) interconverts glyceraldehyde 3-phosphate to dihydroxyacetone near the rate diffusion limit during glycolysis, gluconeogenesis, and the Calvin–Benson cycle (Blacklow *et al.*, 1988; Wierenga *et al.*, 2010; Michelet *et al.*, 2013). TPI folds as a $(\beta-\alpha)_8$ barrel and its dimerization is necessary to assemble a functional active site (Banner *et al.*, 1975; Alber *et al.*, 1987; Wierenga, 2001; Lara-Gonzalez *et al.*, 2015; Jiménez-Sandoval *et al.*, 2017). Dimerization is achieved by an extensive set of protein–protein interactions, and among these, an interaction between loop1 of one subunit with loop 3 from the neighboring subunit is the main contributor to the dimer interface area (Wierenga *et al.*, 2010; Lara-Gonzalez *et al.*, 2015). The role of TPIs in central metabolic

© 2019 The Authors
The Plant Journal © 2019 John Wiley & Sons Ltd

pathways drives the conservation of this enzyme from bacteria to animal and plants. The nuclear genome of flowering plants encodes two fully functional TPIs, one cytosolic and one targeted into the chloroplast (Chen and Thelen, 2010; Dumont *et al.*, 2016; López-Castillo *et al.*, 2016). Chloroplast TPI (pdTPI) arose by a gene duplication event from cytosolic TPI (cTPI) that replaced the cyanobacterial-derived TPI (Reyes-Prieto and Bhattacharya, 2007).

The activity of cytosolic and plastidic TPIs in land plants is subject to diverse regulatory mechanisms. For example, the activity of cTPI increases during growth to provide acetyl-CoA for the citric acid cycle and this enzyme is inhibited by glutathionylation, whereas 2-phosphoglycolate decreases pdTPI activity (Ito *et al.*, 2003; Dorion *et al.*, 2005; Flugel *et al.*, 2017). Yeast and potato (*Solanum tuberosum*) harboring cTPI variants with decreased catalytic activities re-route their carbon flux toward the pentose phosphate pathway (PPP) (Ralser *et al.*, 2007; Dorion *et al.*, 2012; Valancin *et al.*, 2013). In plants, reactive oxidative species (ROS) are produced as metabolic byproducts and by abiotic stress (Kim *et al.*, 2011), targeting a diverse set of enzymes for redox modifications (Dixon *et al.*, 2005; Zaffagnini *et al.*, 2012b, 2013). Specific cysteines from those enzymes play a predominant role as direct redox modifications targets. The thiolate group is reactive to hydrogen peroxide (H_2O_2), hydroxyl radical (OH•), and the superoxide anion (O_2-•). Therefore, oxidative stress can induce progressive post-translational modifications (PTM) of the thiol group to sulfenic (−SOH), sulfinic ($-SO_2H$), and sulfonic acids ($-SO_3H$) (Ito *et al.*, 2003). Oxidation to sulfinic and sulfonic acids is an irreversible, reaction unless is mediated by an enzymatic process involving sulfiredoxins (Jacob *et al.*, 2004; Murray *et al.*, 2012). Also, cysteines can be reversibly modified by glutathionylation, nitrosylation, and disulfide bond formation (Zaffagnini *et al.*, 2012a, 2012b). Different studies have shown that TPIs from photosynthetic organisms are targets for *S*-glutathionylation and nitrosylation (Ito *et al.*, 2003; Dixon *et al.*, 2005; Zaffagnini *et al.*, 2014; Dumont *et al.*, 2016; López-Castillo *et al.*, 2016). However, the effect of glutathionylation differs among these TPIs. For example, *S*-glutationylation in cTPI from *A. thaliana* produces a concomitant loss of enzymatic activity, and this reaction is reverted by the addition of reduced glutathione (GSH) or dithiothreitol (DTT) (Ito *et al.*, 2003), whereas *S*-glutationylation only induces a slight reduction in the activity of chloroplastic from Arabidopsis and *Chlamydomonas* (CrTPI) (Zaffagnini *et al.*, 2014; López-Castillo *et al.*, 2016) and has a negligible effect on the enzymatic activity of the TPI from the photosynthetic bacteria *Synechocystis* (SyTPI) (Zaffagnini *et al.*, 2014; López-Castillo *et al.*, 2016).

With basis on the crystal structure of cTPI from *A. thaliana* (AtcTPI) it was hypothesized that *S*-glutationylation and chemical modifications of residues AtcTPI-Cys13 and AtcTPI-Cys218 would result in enzyme inactivation by promoting the formation an inactive monomeric species or by modifying the enzyme active site (López-Castillo *et al.*, 2016). To understand how *S*-glutathionylation and ROS-mediated modifications at residues AtcTPI-Cys13 and AtcTPI-Cys218 decrease AtcTPI enzymatic activity, we mutated those residues to amino acids that mimic the oxidation of cysteine (Asp) (Miyata *et al.*, 2012), conjugation with thiol-conjugating adducts (Tyr or Lys) and to conserved amino acids. We found that the mutation of AtcTPI-Cys13 to aspartic acid promotes monomer formation. Conversely, mutations to AtcTPI-Cys218 to Tyr, Asp, and Lys result in enzymes with decrease catalytic activities by virtue of conformational changes near the enzyme active site. In summary, our data show that chemical modifications at residues AtcTPI-Cys218 and AtcTPI-Cys13 renders inactive enzymes by two different mechanisms. We propose that cAtTPI glutathionylation may protect the enzyme from irreversible cysteine oxidation and decrease AtcTPI activity to re-route carbon metabolism into the PPP and decrease oxidative stress by modifications of the oligomeric state and the active site of the enzyme (Dumont *et al.*, 2016; López-Castillo *et al.*, 2016).

RESULTS AND DISCUSSION

Residues Cys13 and Cys218 react with thiol-conjugating agents

AtcTPI harbors four cysteines at positions Cys13, Cys67, Cys127, and Cys218. From those residues, Cys13, Cys127, and Cys218 are found to be glutathionylated *in vitro* (Dumont *et al.*, 2016; López-Castillo *et al.*, 2016). The crystal structure of AtcTPI shows that the thiol groups of residues Cys13 and Cys218 are solvent exposed, whereas the thiol groups of residues Cys67 and Cys127 are completely buried (Figure 1a) (López-Castillo *et al.*, 2016). The identity of residue 127 corresponds to a cysteine in all TPIs known to date (Olivares-Illana *et al.*, 2017) and its glutathionylation is unforeseen, as the thiol group of this residue is always buried. Mutations of cysteine 127 decrease thermal stability and dimer association, revealing that this residue is critical to stabilize the dimer interface by interacting with amino acids that assemble this interface (Gonzalez-Mondragon *et al.*, 2004; Samanta *et al.*, 2011). However, proteomic analysis has shown that cysteines analogous to AtcTPI-Cys127 are glutathionylated in TPIs from human, yeast, and *Synechocystis* sp. (SyTPI) (McDonagh *et al.*, 2009; Chardonnet *et al.*, 2015; Dumont *et al.*, 2016). The inaccessibility of the thiol group of residue Cys127 and its tendency to be a target of glutathione are paradoxical. Most TPIs including, *Zea mays* TPI (ZmTPI), dissociate into unfolded monomers, suggesting the possibility that glutathionylation at residue Cys127 may occur at the unfolded state (Tellez *et al.*, 2008; Romero-Romero *et al.*, 2018) or it

© 2019 The Authors
The Plant Journal © 2019 John Wiley & Sons Ltd,

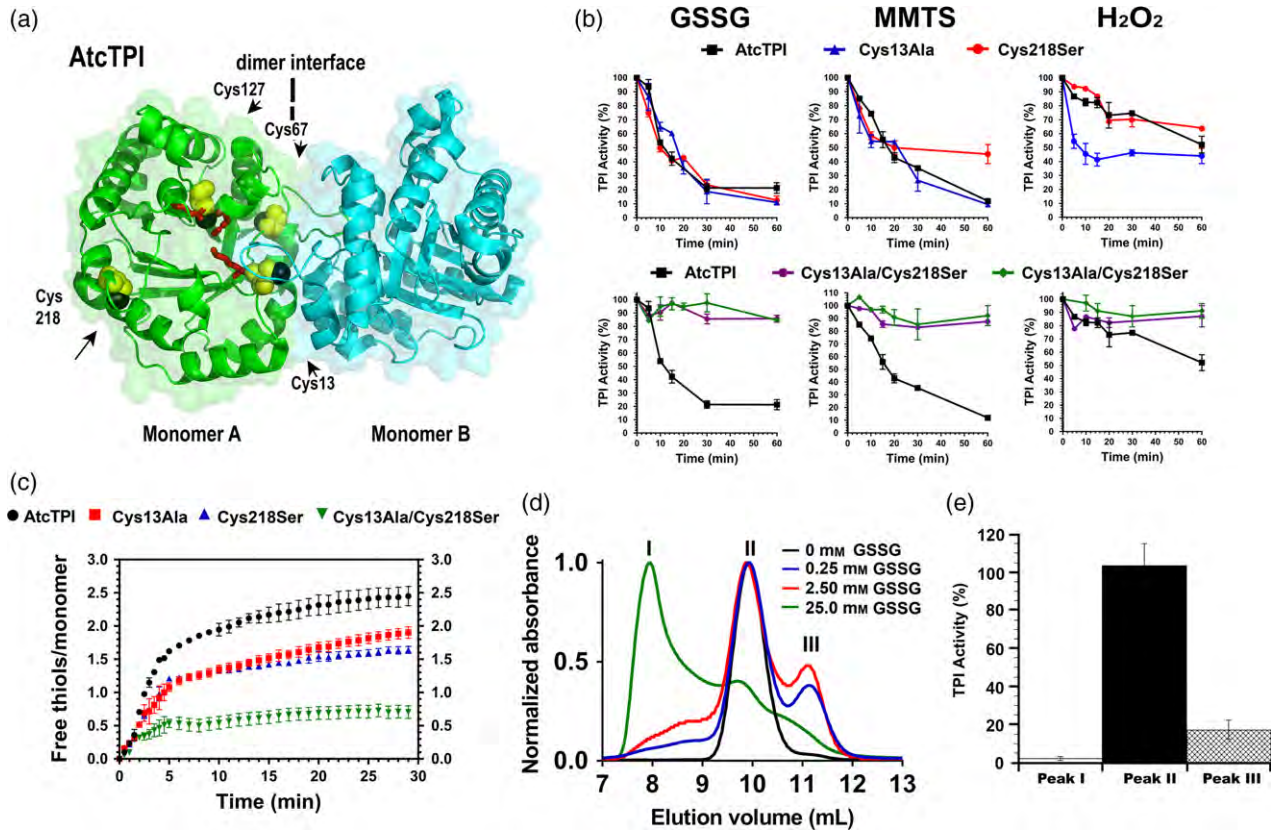

Figure 1. Structural analysis of AtcTPI and its inactivation by thiol-conjugating agents. (a) Ribbon representation of the crystal structure of AtcTPI showing the localization of its four cysteines in monomer A and its dimer interface. The conserved catalytic amino acids are in ball-stick representation and red colored. (b) Time-course experiment showing the inactivation of AtcTPI by thiol-derivatizing agents. AtcTPI present at 0.184 nM was incubated with a 200-fold excess of either MMTS, GSSG or H_2O_2 (36.8 nM). The graphs represent the percentage of AtcTPI activity with respect to an untreated sample during the time course. (c) Thiol content determination of wild-type and AtcTPI mutants by DTNB analysis. The graph shown the total number of reactive thiols per TPI monomer during a 30 min incubation with DTNB. The experiment was performed by triplicate and shows the average data and the corresponding standard deviation. (d) Effect of glutathione incubation on the oligomeric state of AtcTPI. AtcTPI was incubated with three different GSSG concentrations from 0.25 to 25 mM. The AtcTPI oligomeric state was assessed by running the samples on a gel filtration column. Untreated AtcTPI eluted as a dimer with as estimated molecular mass of *c.* 50 kDa (peak II). Incubation with 0.25 and 2.5 mM of GSSG resulted in the appearance of a protein peak with a molecular mass that corresponded to a monomer of 25 kDa (peak III), whereas incubation with 25 mM GSSG resulted migrate in a way that corresponded to protein aggregates (peak I). (e) Enzymatic activity of TPIs recovered from peaks I and II. AtcTPI recovered from peaks I and II exhibited less than 20% and 4% of enzymatic activity untreated samples, respectively. Samples recovered from peak II present similar enzymatic activity as untreated samples. All experiments were conducted in triplicate.

may reflect a transient exposure of its thiol group to the surface, as suggested to occur for SyTPI (Castro-Torres *et al.*, 2018). Residue AtcTPI-Cys13 is located in the middle of loop 1 and forms part of the dimer interface by interacting with residues from loop 3 of the neighboring subunit (Figure 1a). Residue AtcTPI-Cys13 has an accessible surface area (ASA) of *c.* 2.7 $Å^2$ in a dimeric AtcTPI structure, whereas its ASA as a monomer corresponds to 129.3 $Å^2$ (López-Castillo *et al.*, 2016). Residue AtcTPI-Cys218 is located at the N-terminus of α-helix 7, near the phosphate binding loop, and in one monomer exhibits an ASA of 6.7 $Å^2$ (López-Castillo *et al.*, 2016) (Figure 1a). The solvent accessibility of residues AtcTPI-Cys13 and AtcTPI-Cys218 makes them a more plausible target for plant oxidoreductases of the thioredoxins and glutaredoxins families and the subject of study in this work.

To understand if residues AtcTPI-Cys13 and AtcTPI-Cys218 are the main targets for glutathionylation and oxidation we constructed mutants aimed to eliminate their thiol groups and have minimal structural consequences. We designed a recombinant version of wild-type AtcTPI that only contains three extra amino acids before its initial methionine, the latter in contrast with previous recombinant protein versions that harbor a poly-histidine tail or a long non-related sequence (Dumont *et al.*, 2016; López-Castillo *et al.*, 2016). Using this recombinant AtcTPI, that closely resembles the native enzyme, we chose to mutate residue AtcTPI-Cys13 to both serine and alanine. A mutation to serine is expected to have minimal effect on the van der Waals interactions and is predicted to create minimal structural perturbations. The rationale to mutate AtcTPI-Cys13 to alanine is because of the hydrophobic

© 2019 The Authors

INFORME DE LABORES 2019

characteristics of residues surrounding AtcTPI-Cys13 that correlate with the hydrophobic nature of cysteine (Nagano *et al.*, 1999). We initially mutated AtcTPI-Cys218 to serine because of the structural similarities between both amino acids. Steady-state kinetic analysis indicated that AtcTPI-Cys13Ala and AtcTPI-Cys218Ser mutants decreased their catalytic efficiency by 4.3-fold and 2.5-fold, respectively. In contrast, an AtcTPI-Cys13Ser mutant exhibited a 30-fold decrease in catalytic efficiency (Table 1). These data suggest that the introduction of an alanine at position 13 and a serine at position 218 are tolerated in AtcTPI. The observed 2.5-fold reduction in the catalytic activity of the AtcTPI-Cys218Ser mutant contrasts with the 142-fold reduction previously reported using an AtcTPI with a large non-related amino acid sequence in its N-terminal (López-Castillo *et al.*, 2016). This differential in activity correlates with the presence a long sequence tag in the previous constructs that may hamper their activity (Panek *et al.*, 2013; Sabaty *et al.*, 2013; Booth *et al.*, 2018).

To determine if modification in residues AtcTPI-Cys13 and Cys218 affect TPI enzymatic activity, we measured the susceptibly of mutants AtcTPI-Cys13Ala and AtcTPI-Cys218Ser to oxidized glutathione (GSSG), methyl methanethiosulfonate (MMTS), and H_2O_2 in a 1-h time-course experiment instead of the dose-dependent experiment previously conducted (López-Castillo *et al.*, 2016). AtcTPIs carrying individual mutations at residues Cys13 and Cys218 exhibit similar susceptibility with respect to wild-type AtcTPI to thiol-conjugating agents, whereas the AtcTPI-Cys13Ala mutant is more susceptible to H_2O_2 (Figure 1a,b). These data suggest that both AtcTPI-Cys13 and AtcTPI-Cys218 residues react with similar efficiency to thiol derivatizing and oxidative agents, and suggest that both residues are targets for ROS-mediated modifications.

Table 1 Catalytic parameters

Enzyme	K_m (mM)	K_{cat} (sec^{-1})	K_{cat}/K_m (M^{-1} sec^{-1})	Fold decrease
AtcTPI wt	0.47 ± 0.08	1140 ± 46.7	2.40×10^6	–
Cys13Met	0.52 ± 0.03	353 ± 16.7	6.87×10^5	3.49
Cys13Ala	0.37 ± 0.04	209 ± 8.1	5.54×10^5	4.32
Cys13Ser	0.51 ± 0.07	41.6 ± 3.1	8.00×10^4	30.0
Cys13Asp	0.63 ± 0.09	32.1 ± 2.4	5.09×10^4	47.1
Cys218Met	0.82 ± 0.09	468 ± 19.2	5.68×10^5	4.22
Cys218Val	1.03 ± 0.18	642 ± 42.2	6.25×10^5	3.84
Cys218Ser	0.49 ± 0.09	465 ± 26.9	9.44×10^5	2.54
Cys218Lys	0.53 ± 0.02	165 ± 14.2	3.11×10^5	7.71
Cys218Tyr	0.88 ± 0.07	455 ± 37.1	5.11×10^5	4.69
Cys218Asp	0.50 ± 0.12	115 ± 6.67	2.27×10^5	10.5
Cys13Ala/ Cys218Ser	1.75 ± 0.21	789 ± 138	4.51×10^5	5.37
Cys13Ser/ Cys218Ser	3.76 ± 0.45	209 ± 35.9	5.57×10^4	43.5

To further test if those residues are the sole responsible for ROS-mediated inhibition by conjugation or oxidation, we measured the enzymatic activity of the double AtcTPI-Cys13Ala/Cys218Ser and AtcTPI-Cys13Ser/Cys218Ser mutants upon the exposure of thiol-conjugating agents and H_2O_2 using a time-course experiment (Figure 1b).

The observed differential in enzymatic activity with the previously reported AtcTPI mutants is intensified in the double mutants (López-Castillo *et al.*, 2016), further suggesting that non-related sequences in the N-terminal of AtcTPI affect catalysis. The current protein constructs harboring the double mutant AtcTPI-Cys13Ser/AtcTPI-Cys218Ser decreases its catalytic efficiency by 43.5-fold, whereas the double mutant AtcTPI-Cys13Ala/AtcTPI-Cys218Ser only decreases its catalytic efficiency by 5.3-fold (Table 1). As previously reported for the AtcTPI-Cys13Ser/AtcTPI-Cys218Ser mutant, both double mutants are not susceptible to thiol derivatizing agents and H_2O_2, supporting the role of both residues AtcTPI-Cys13 and AtcTPI-Cys218 as the only ROS targets in AtcTPI (López-Castillo *et al.*, 2016) (Figure 1b). To further verify this analysis, we measured the accessibility of cysteine thiols in wild-type and mutant AtcTPIs by 5,5′-dithiobis-(2-nitrobenzoic acid) (DTNB) conjugation. In concordance to a previously report, wild-type AtcTPI contains approximately two accessible thiols per monomer, whereas AtcTPI-Cys13Ala and AtcTPI-Cys218Ser mutants harbors near to one thiol per monomer (Figure 1c). A double mutant AtcTPI-Cys13Ala/Cys218Ser presents limited reactivity to DTNB conjugation indicating that the only exposed thiol groups in AtcTPI is from residues Cys13 and Cys218. Overall the data agree with western blot analysis that identified residues Cys13 and Cys218 as the main targets of glutathione and suggest that the observed glutathionalytion of residue AtcTPI-Cys127 may occur at the unfolded state or as a consequence of a transient solvent exposure of its thiol group (Dumont *et al.*, 2016; López-Castillo *et al.*, 2016).

GSSG incubation promotes the formation of inactive AtcTPI monomers

We have hypothesized that the decrease in activity by AtcTPI upon its incubation with oxidative and thiol-conjugating agents is due to the formation of inactive monomers (López-Castillo *et al.*, 2016).

The reversible characteristics of glutathionylation make this post-translational modification a common modulator of enzymatic activity by conjugation of the glutathione moiety to the thiol groups of a cysteine. We have shown that incubation of AtcTPI with GSSG resulted in conjugated proteins with an apparent molecular mass that is lower than the molecular mass of a monomer (López-Castillo *et al.*, 2016). The aberrant migration of a conjugated AtcTPI on a gel filtration column upon glutathionylation is counterintuitive. Because of this atypical result, we decided to

© 2019 The Authors
The Plant Journal © 2019 John Wiley & Sons Ltd,

test the effect of *S*-glutathionylation using a shorted incubation period and three different GSSG concentrations (Figure 1d). As expected, non-derivatized AtcTPI eluted in a single peak at an elution volume that corresponds to a AtcTPI dimer of ~50 kDa (Figure 1d, peak II). Incubation of AtcTPI with 25 mM of GSSG induced the formation of inactive protein aggregates of high molecular weight (Figure 1d, peak I). These aggregates may be a consequence of dimer dissociation and monomer unfolding, as previously reported for other TPIs (Chanez-Cardenas *et al.*, 2002; Maithal *et al.*, 2002). AtcTPIs incubated with 2.5 or 0.25 mM GSSG resulted in the appearance of a protein peak that corresponds to an AtcTPI monomer of ~25 kDa (Figure 1e, peak III). Proteins from these monomeric fractions displayed less than 20% of enzymatic activity in comparison with the activity of the dimeric fractions that displayed the same activity than untreated AtcTPI samples (Figure 1e). These data further suggest that glutathionylation alters the oligomeric state of cTPI resulting in enzymes with reduced activity because of monomerization or total loss of activity because of aggregation.

Redox modification can be mimicked by site-directed mutagenesis

To understand the fate of AtcTPI upon oxidation and conjugation at residues Cys13 and Cys218, we use site-directed mutagenesis to mimic redox modifications of those cysteines (Figure 2a). We further mutated AtcTPI-Cys13 to aspartic acid that resembles the irreversible chemical modification of cysteine to sulfinic acid and to methionine because human and yeast TPIs harbor this amino acid in an analogous position to AtcTPI-Cys13 (Lolis *et al.*, 1990; Mande *et al.*, 1994; Permyakov *et al.*, 2012). We mutated AtcTPI-Cys218 to Met, Val, and Lys that resemble the

(a)

Chemical specie/amino acid	Structure
Cysteine	-R-CH_2-SH
Methionine	-R-CH_2-CH_2-S-CH_3
Alanine	-R-CH_3
Valine	-R-CH(CH_3)(CH_3)
Serine	-R-CH_2-OH
Lysine	-R-CH_2-CH_2-CH_2-CH_2-NH_3
Tyrosine	-R-CH_2-C$_6$H$_4$-OH
Aspartic acid	-R-CH_2-C(=O)-O^-
Cysteine-GSH	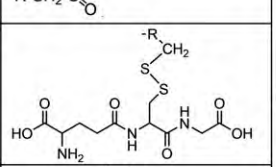
Cysteine-DTNB	-R-CH_2-S-S-C$_6$H$_4$-NO_2-COO^-
Cysteine-MMTS	-R-CH_2-S-S-CH_3
Sulfenic acid	-R-CH_2-S-O^-
Sulfinic acid	-R-CH_2-S(=O)-O^-
Sulfonic acid	-R-CH_2-S(=O)(=O)-O^-

(b)

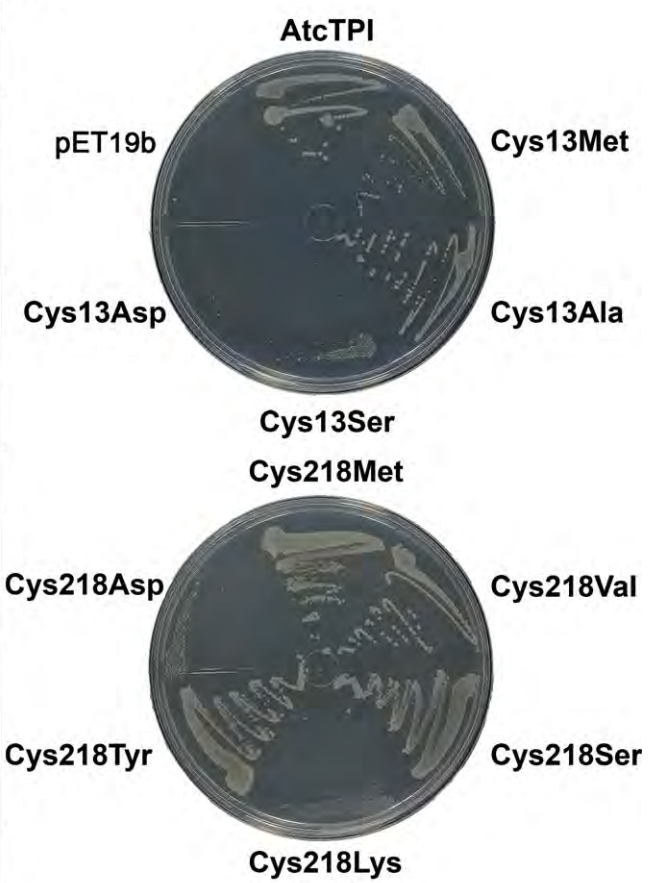

Figure 2. Amino acid mimicry of ROS-mediated oxidation and thiol-conjugated agents. (a) Chemical structure of amino acids used for site-directed mutagenesis and their ROS-mediated modification counterpart that mimic the derivatization or oxidation of the thiol group. As observed, aspartic acid mimics cysteine oxidation to sulfinic acid, lysine MMTS conjugation and tyrosine DTNB conjugation. (b) Bacterial complementation by wild-type and AtcTPI mutants in a Δtpi BL21-DE3 *E. coli* strain. Bacteria transformed with plasmids harboring the indicated constructs were grown on minimal medium and incubated for 48 h at 30°C.

© 2019 The Authors

conjugation to linear adducts like MMTS or *S*-glutathionylation and to Tyr because this modification would resemble the chemical conjugation to a bulky aromatic adduct line DTNB, and finally to aspartic acid that mimics its oxidation to sulfinic acid. We did not mutate residue AtcTPI-Cys13 to bulky amino acids like Tyr or Lys, because amino acids with larger side chains are not present at this position in any TPI reported to date and because the large van der Waals radius of these residues would hamper dimer formation (Lara-Gonzalez *et al.*, 2015; Olivares-Illana *et al.*, 2017) (Figure 2a).

As a first step to assess the effect of modifications in residues Cys13 and Cys218, we measured the complementation of a bacterial strain deficient of endogenous triosephosphate isomerase activity by plasmids harboring AtcTPI mutants (Lara-Gonzalez *et al.*, 2015) (Figure 2b). Wild-type AtcTPI, AtcTPI-Cys13Ala, and AtcTPI-Cys13Met mutants efficiently complemented the transformed bacterial strain. In contrast, construct AtcTPI-Cys13Asp failed to complement the *E. coli* Δ*tpi* strain and construct AtcTPI-Cys13Ser exhibited a decrease in the observed number of colonies (Figure 2b). Bacterial cells harboring AtcTPI-Cys218Asp and AtcTPI-Cys218Lys mutants exhibited a defect in complementation, whereas bacteria harboring AtcTPI-Cys218Val, AtcTPI-Cys218Tyr, AtcTPI-Cys218Ser and AtcTPI-Cys218Met constructs present similar complementation compared with the wild-type AtcTPI (Figure 2b). Steady-state kinetic analysis indicated that AtcTPI-Cys13Asp and AtcTPI-Cys13Ser mutants showed a 47-fold and 30-fold reduction in their catalytic efficiency, whereas mutations to alanine and methionine exhibit less than a five-fold reduction in catalytic efficiency (Table 1). Therefore, the lack of complementation for AtcTPI-Cys13Asp and AtcTPI-Cys13Ser mutants correlated with their decrease in catalytic efficiency (Figure 2b). AtcTPI-Cys218Asp and AtcTPI-Cys218Lys mutants showed a 10.5-fold and 7.7-fold reduction in their catalytic activity, in contrast AtcTPI-Cys218Met, AtcTPI-Cys218Val, and AtcTPI-Cys218Tyr mutants presented enzymatic activities near wild-type AtcTPI levels (Table 1). Therefore, the observed difficulty of Asp and Lys mutants in residue AtcTPI-Cys218 to complement a Δ*tpi* bacterial strain, also correlated with a decrease in catalytic efficiency (Figure 2b). To assess if mutations in residues Cys13 and Cys218 affect the stability of AtcTPI, we measured their thermal stability in comparison with the wild-type enzyme (Table 2). Point mutants in residue Cys13 decreased their melting temperature (T_m) between 4.5–3°C with respect to the T_m exhibited by wild-type AtcTPI. In contrast, mutants in residue Cys218 decrease their T_m between 2–10°C (Table 2). The mutants that decrease the most the catalytic activity of AtcTPI, AtcTPI-Cys13Ser and AtcTPI-Cys13Asp, only present a small decrease in their T_m. In contrast, mutants in residue Cys218 have a large decrease in T_m and only a moderate, 7.7-fold to 10.6-fold, decrease in catalytic activity. These data suggest that modification in residue Cys13 does not present large structural changes, and mutations in residue Cys218 induce structural modification that alters the protein structure, but with only a moderate effect on catalysis.

Table 2 Thermal stability and apparent dissociation constant

Enzyme	T_m, °C	$^{app}Kd_{diss}$ (M)
AtcTPI	52.0 ± 0.0	1.45E-07 ± 2.10E-08
Cys13Met	49.0 ± 0.0	2.40E-07 ± 2.83E-07
Cys13Aal	48.0 ± 0.0	3.22E-07 ± 3.57E-08
Cys13Ser	48.0 ± 0.0	3.12E-06 ± 3.57E-07
Cys13Asp	47.5 ± 0.5	1.40E-05 ± 1.77E-07
Cys218Met	48.0 ± 0.0	3.20E-07 ± 4.09E-08
Cys218Val	50.0 ± 0.0	2.39E-07 ± 3.02E-08
Cys218Ser	50.0 ± 0.0	0.96E-07 ± 3.53E-08
Cys218Lys	42.0 ± 1.0	1.03E-07 ± 2.83E-08
Cys218Tyr	47.0 ± 0.0	1.06E-07 ± 1.71E-08
Cys218Asp	42.5 ± 0.5	1.03E-07 ± 4.97E-08
C13Ala/C218Ser	45.8 ± 0.3	1.15E-07 ± 2.52E-08
C13Ser/C218Ser	46.3 ± 0.1	0.81E-06 ± 1.01E-07

Site-directed mutagenesis of AtcTPI-Cys13 promotes the formation of non-catalytic monomers

To investigate if the loss of enzymatic activity by mutations at residues AtcTPI-Cys13 is due to alterations in the dimeric nature of AtcTPI, we assessed the oligomeric state of purified AtcTPI on a size-exclusion chromatography column at two protein concentrations: 1 mg mL^{-1} and 0.1 mg mL^{-1} (Figure 3a). At a concentration of 1 mg mL^{-1}, wild-type AtcTPI and all AtcTPI-Cys13 and AtcTPI-Cys218 point mutants eluted in a single peak at an elution volume that corresponds to the retention volume of a dimer of ~50 kDa. In contrast, at a concentration of 0.1 mg mL^{-1}, AtcTPI-Cys13Asp, AtcTPI-Cys13Ser, and AtcTPI-Cys13Met mutants exhibited a displacement in their migration profile to an elution volume that corresponds to a monomeric species of 25 kDa. The only AtcTPI-Cys13 mutant that migrates as a dimer is the one corresponding to AtcTPI-Cys13Ala (Figure 3a). In contrast, all mutations in residue AtcTPI-Cys218 eluted in a volume that corresponded to dimers at both protein concentrations (Figure 3a).

In all TPIs studied to date, this enzyme is an obligatory dimer, meaning that TPI monomers are catalytically incompetent (Zarate-Perez *et al.*, 2009; Jiménez-Sandoval *et al.*, 2017). To assess the role of monomerization in catalysis, we measured the specific activities of wild-type and point mutant AtcTPIs incubating the enzymes for 24 h at 25°C at protein concentrations that rank from 50 ng mL^{-1} to 1000 μg mL^{-1} (Table 2). Dilution promotes the concentration-dependent dissociation of active dimeric AtcTPI into inactive monomers, with a concomitant loss in specific activity (Figure 3b) (Mainfroid *et al.*, 1996; Reyes-Vivas

© 2019 The Authors
The Plant Journal © 2019 John Wiley & Sons Ltd,

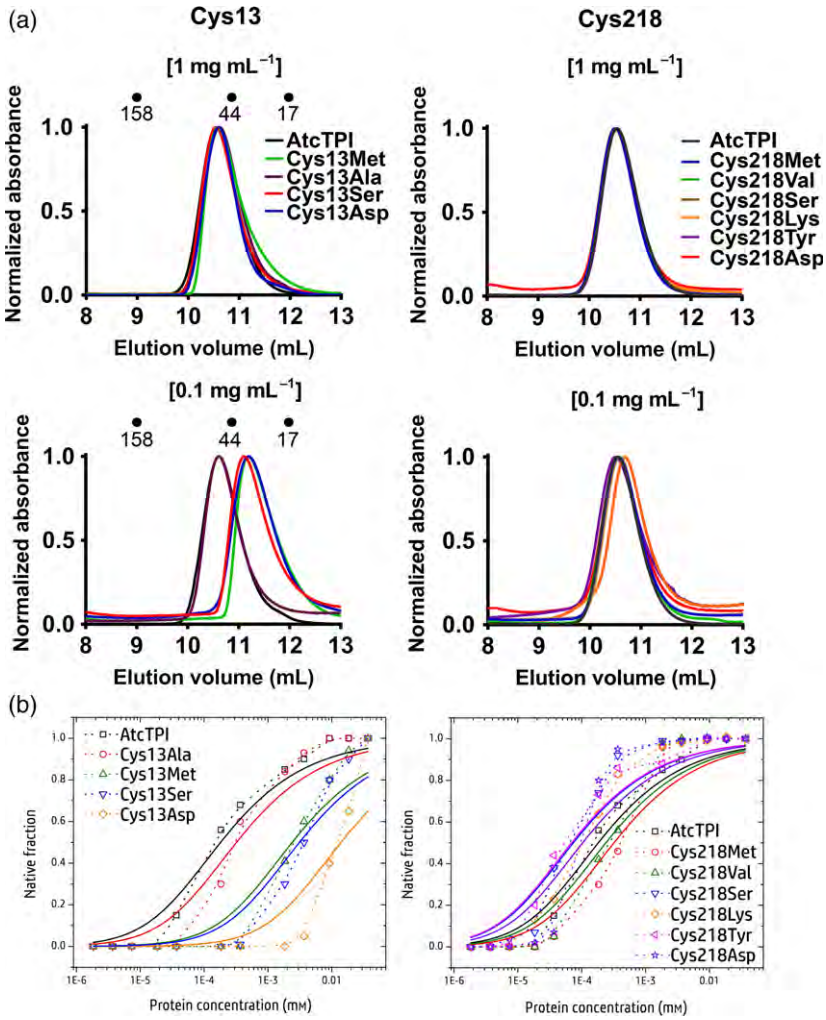

Figure 3. Elution profiles of AtcTPIs upon oxidation mimicry by site-directed mutagenesis. (a) Gel filtration elution profiles of wild-type and point mutants of residues Cys13 and Cys218 at protein concentrations of 1 and 0.1 mg mL^{-1}. The elution profile of Cys13 mutants at 0.1 mg mL^{-1} shows the displacement of the elution profile to one that corresponds to an elution profile of a monomeric species of *c.* 25 kDa. (b) Determination of the apparent K_{diss} of wild-type and point mutants of AtcTPI. The graph represents the relative enzymatic activity after serial dilutions of three independent experiments.

et al., 2002; Romero-Romero *et al.*, 2018). The fraction of native molecules shows a more pronounced transition than the one expected for a reversible two-state equilibrium nevertheless, the midpoint of the transitions (K_{diss}) are well described by this model.

In TPIs as well as in other obligated oligomers, this behavior has been related to reversible and/or irreversible conformational changes in the dissociated monomers such that processes shift the equilibrium towards inactive states (Mainfroid *et al.*, 1996; Reyes-Vivas *et al.*, 2002; Romero-Romero *et al.*, 2018). From these data we calculated an apparent dissociation constant ($^{app}K_{diss}$). Wild-type AtcTPI exhibited an $^{app}K_{diss}$ of 1.5^{-7} M, that is similar to the one observed for other TPIs (Reyes-Vivas *et al.*, 2002). Point mutants AtcTPI-Cys13Ala, AtcTPI-Cys13Met, and AtcTPI-Cys13Ser decrease the binding affinity of the dimer by 2-fold, 16-fold, and 21-fold, respectively. In sharp contrast the AtcTPI-Cys13Asp mutant decreases the dimer stability by more than 100-fold, indicating that a mutation that resembles the oxidation of Cys13 results in stable monomeric enzymes (Figure 3b). In comparison to the influence of residue AtcTPI-Cys13 in promoting the appearance of monomeric species, mutations in residue AtcTPI-Cys218 do not alter their specific activity upon dilution, supporting the finding that mutations in this residue do not alter the dimeric nature of AtcTPI (Figure 3a,b and Table 2). The shift in the dimer–monomer equilibrium of AtcTPI-Cys13Ser and AtcTPI-Cys13Asp mutants correlates with a 30-fold and 47-fold reduction in their catalytic efficiency. Interestingly, a mutant AtcTPI-Cys13Met is only 3.5-fold less active than wild-type AtcTPI (Table 1). The difference in enzymatic activity observed between monomeric AtcTPI-Cys13Ser, AtcTPI-Cys13Asp, and AtcTPI-Cys13Met may be related to the formation of AtcTPI dimers assisted by substrate binding as occurs in TPI from *Trichomonas vaginalis* (Lara-Gonzalez *et al.*, 2015) and meaning that dimer assembly from dissociated monomers is favorable in the AtcTPI-Cys13Met mutant, but not in the AtcTPI-Cys13Ser and AtcTPI-Cys13Asp mutants.

© 2019 The Authors

Structural basis for the formation of non-catalytic monomers by modifications at residue AtcTPI-Cys13

To test how the mimicry of the thiol oxidation of residue AtcTPI-Cys13 induces the formation of non-catalytic monomeric species, we solved the crystal structures of AtcTPI-Cys13Asp and AtcTPI-Cys13Ala mutants (Figure 4a). In comparison with the presence of cysteine at position 13, a mutation to alanine decreases the van der Waals volume by 19 Å^3 and a mutation to aspartic acid increases its volume by 10 Å^3. The crystal structures of AtcTPI-Cys13Ala and AtcTPI-Cys13Asp revealed that these mutations do not significantly alter the AtcTPI structure, as these structures present a root-mean-square deviation (RMSD) of 0.1350 and 0.1750 Å, respectively, with respect to wild-type AtcTPI. The crystal structure of AtcTPI-Cys13Ala only presented a small variation in the amino acids corresponding to loop 3, that is displaced *c.* 0.6 Å, presumably to compensate the smaller alanine side chain (Figure S1). The minimal changes in the crystal structure of AtcTPI-Cys13Ala with respect to wild-type AtcTPI are in agreement with the unaltered catalytic efficiencies and dimeric nature of this mutant, which is resistant to dilution. The crystal structure further showed that the aromatic amino acids from the neighboring subunit that surround residue at position 13 were organized in a similar fashion when an alanine replaces a cysteine (Figure S1). Both AtcTPI-Cys13Ala and AtcTPI-Cys13Asp mutants do not create severe changes in the overall structural of the enzyme or alter its dynamics (Figure S2). The crystal structure of AtcTPI-Cys13Asp shows that a substitution to aspartic acid, that mimics cysteine oxidation by virtue of its negative charge, places the carboxyl side chain in a similar position to the thiol group of the cysteine residue. However, the placement of the carboxylate produced subtle conformational changes in loop 1 and loop 3 of the neighboring subunit

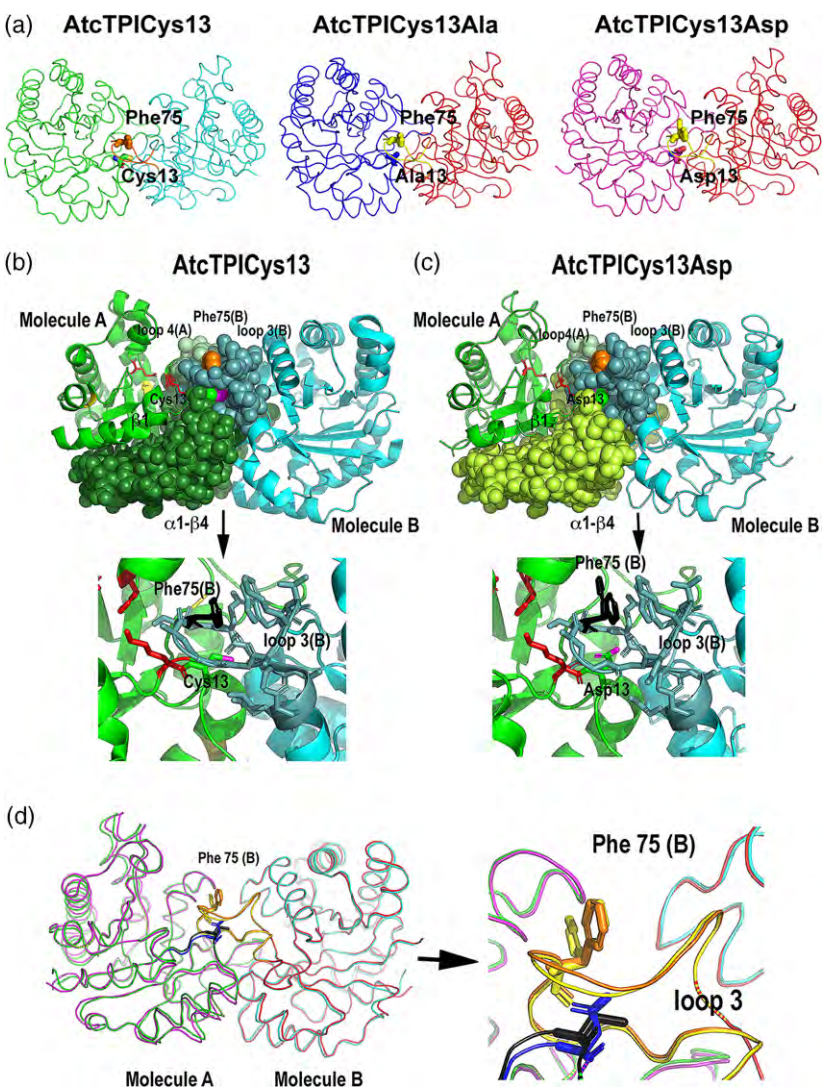

Figure 4. Structural consequences of oxidation mimicry at residue AtcTPICys13. (a) Structural comparison of AtcTPI crystal structures harboring alanine and aspartic acid substitutions at position 13 in a ribbon representation. (b, c) Dimer interface representation. The thiol group and carboxyl groups of residue 13 in wild-type or mutant AtcTPIs are colored in magenta and residues from the loop 3 of the neighboring subunit are colored in cyan in a ball-stick representation. Residue Phe75 is colored in magenta. Residues corresponding to the first-half of the TIM barrel (α1 to β4) present a subtle displacement (colored green and lime in wild-type and AtcTPICys13Asp mutant, respectively). A close-up view (bottom part) of wild-type and AtcTPICys13Asp mutants. Illustrates the dual conformation of residue Phe75 (black) due to presence of the carboxyl group instead of the thiol group at residue 13. (d) Ribbon representation of the superposition between the crystal structures of wild-type and AtcTPICys13Asp and close-up view at loop 3 of their dimer interface. The AtcTPICys13Asp structure illustrates that the oxidative mimicry of residue Cys13 induces a re-orientation of residue Phe75 from the neighboring subunit.

© 2019 The Authors
The Plant Journal © 2019 John Wiley & Sons Ltd,

(Figure 4a). Being the most dramatic consequences of the AtcTPI-Cys13Asp mutation the appearance of residue AtcTPI-Phe75 of the neighbor subunit in two alternate conformations (Figure S2).

Residue AtcTPI-Cys13 exerts inter-subunit interactions with residues from the loop 3 of the neighboring subunit. Residue AtcTPI-Cys13 interacts with the following residues from the neighboring subunit: Gly72, Gly73, Ala74, Phe75, Thr76, Glu78, Ser80, and Met83. These residues form part of conserved GGAFTG motif located in loop 3 (Figure 4b). The interaction between loop 1 from one subunit and loop 3 from the neighbor subunit is critical for dimer formation. For instance, engineered monomeric versions of several TPIs were designed by the decreasing in the length of loop 3 (Borchert *et al.*, 1994; Saab-Rincon *et al.*, 2001; Jiménez-Sandoval *et al.*, 2017). Derivatization of the residue to corresponding AtcTPI-Cys13 with alkylating agents generate TPIs monomers in TPIs from *P. falciparum* and *E. histolytica*, and also protein aggregation in TPIs from *T. cruzi* and *T. brucei* (Garza-Ramos *et al.*, 1998; Maithal *et al.*, 2002; Rodríguez-Romero *et al.*, 2002). The presence of the carboxyl group in the AtcTPI-Cys13Asp mutants displaced the phenyl side chain of residue AtcTPI-Phe75 of the neighboring subunit, so this residue adopts a double conformation. As a consequence of this alternate conformation, half of the α/β triosephosphate isomerase (TIM) barrel ($\alpha1$ to $\beta4$) shifted its orientation relative to AtcTPI (Figure 4b,c). This conformational change is reminiscent of the small changes in subunit orientation observed in pathogenic mutants of superoxide dismutase (Hough *et al.*, 2004). The double conformations of residue AtcTPI-Phe75 of the neighboring subunit displaced loop 3 residues by 1 Å, to accommodate the carboxylate side chain (Figure 4d).

A diagram of the B-factors for the interface residues shows that their overall mobility is conserved (Figure S3). The structural changes observed in the AtcTPI-Cys13Asp mutant correlated with the fact that point mutants Ser, Met, and Asp are monomeric at a concentration of *c.* 1.8 μM (of 0.1 mg mL^{-1}). As the AtcTPI-Cys13Asp mutant resembles the oxidation of Cys13, our data suggest that AtcTPI monomerization is a mechanism to rapidly decrease the enzymatic activity of TPI upon oxidative stress. TPI activity modulation is observed in yeast expressing human TPI variants deficient in dimer assembly that are more resistant to oxidative stress, presumably by re-routing the carbohydrate flux (Ralser *et al.*, 2006). Another example of TPI modulation activity is the stimulation of rice TPI activity by interaction with a transmembrane receptor-like kinase. In this putative allosteric TPI modulation mechanism, a plant resistant to bacterial infection presents a strengthened interaction between the transmembrane receptor-like kinase and TPI, this high interaction stimulates TPI activity with a concomitant increase in ROS production that leads to bacterial infection resistance (Liu *et al.*, 2018).

Modifications at residue AtcTPI-Cys218 decrease enzymatic activity

Two independent studies have shown that residue AtcTPI-Cys218 is a glutathionylation target (Dumont *et al.*, 2016; López-Castillo *et al.*, 2016). Steady-state kinetic analysis indicated that a mutant protein harboring an aspartic acid substitution decreased its catalytic efficiency by 10-fold, whereas replacements with bulky or linear branched amino acids decreases their catalytic efficiency between 5-fold to 8-fold (Table 1). These mutants present similar dimer stability compared with wild-type AtcTPI, ruling out the possibility that an alteration in the dimer–monomer equilibrium is responsible for the observed decrease in catalytic efficiency. Therefore, it is unknown how modifications in residue AtcTPI-Cys218 affect catalysis.

Modifications at residue AtcTPI-Cys218 drive structural rearrangements in loops 6 and 7

To understand the mechanisms by which modifications in residue AtcTPI-Cys218 affect the catalytic activity of AtcTPI, we solved the structures of AtcTPI-Cys218 with residues that mimic cysteine conjugation with bulky or aromatic groups or its oxidation (Table S1). A structural comparison between these crystal structures shows that the point mutations do not induce gross structural changes with respect to wild-type AtcTPI (Figure 5a). However, a close inspection shows that all mutants present alternate conformations in loops 6 (residues 166–176) and 7 (residues 210–218) (Figure 5b,c). These structural changes are localized only in this region and are not observed in other regions, like the active site or the dimer interface (Figure S4). Loop 6 or the phosphate binding loop suffers open to closed transitions upon substrate binding (Wierenga *et al.*, 1991, 1992; Wierenga, 2001) and it is highly flexible structural element. Loop 6 in the AtcTPI-Cys218Ser mutant is partially disordered, whereas this loop moves near 2.5 Å in AtcTPI-Lys and Tyr mutants (Figure 5b). Point mutations of residue AtcTPI-Cys218 also increase the thermal mobility of loop 6, suggesting that point mutants alter the dynamics of the phosphate binding loop (Figure 5c,d). In contrast with the flexibility of loop 6, loop 7 is located in the same position in all TPIs studied to date. Loop 7 harbors the YGGS (residues 209–212) motif whose integrity is indispensable for enzymatic activity, as modifications of this motif reduce TPI catalytic activity more than 1000-fold (Sampson and Knowles, 1992a,1992b). Point mutations, especially substitutions to Asp, Lys and Tyr, also alter the orientation of loop 7 (Figure 5b,c). Residue AtcTPI-Cys218 interacts with residue AtcTPI-Gly211 of the YGGS motif, therefore structural variations in AtcTPI-Cys218 are expected to affect this interaction. A mutation of residue AtcTPI-Cys218 to Ser does not alter the orientation of loop 7 (Figure 5b), in contrast mutations to Asp, Lys, and Tyr

© 2019 The Authors

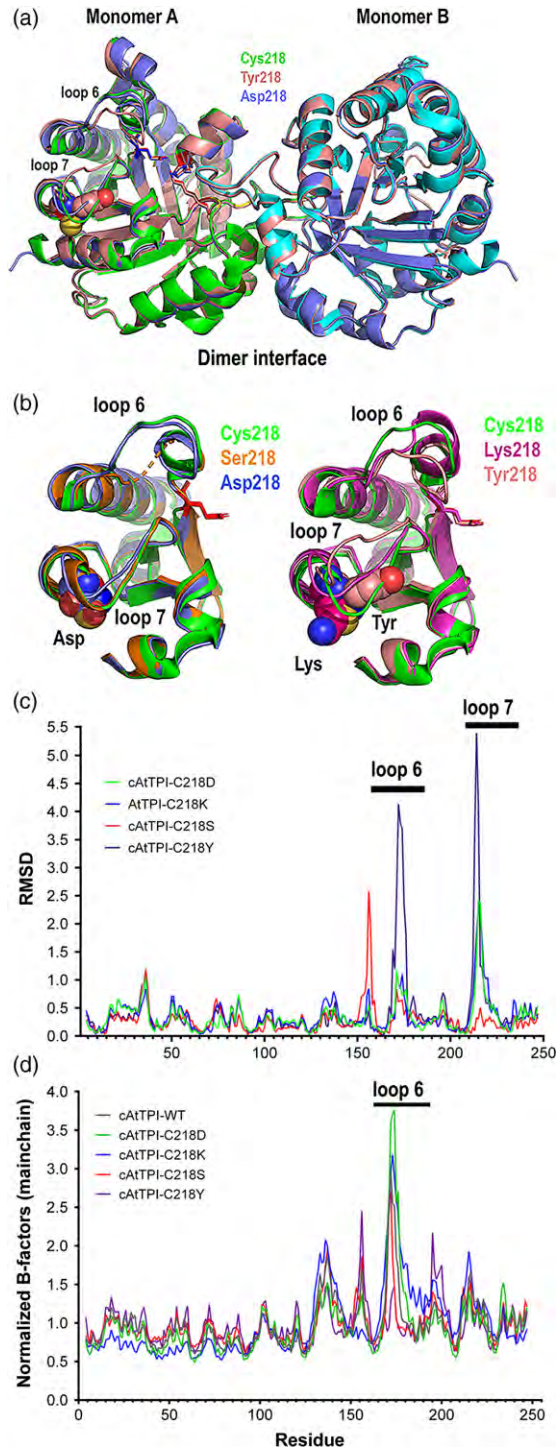

Figure 5. Structural consequences of oxidation and thiol-conjugation mimicry at residue AtcTPICys218. (a) Structural alignment of wild-type AtcTPIs carrying Cys, Asp or Tyr at position 218. (b, c) Close-up of the region corresponding to loops 6 and 7 for cysteine mutants to Ser and Asp (b) and Lys and Try (c). The corresponding point mutant is represented in a ball–stick representation. (c) Structural comparison between wild-type AtcTPI and point mutants. Plot of the RMSD analysis per residue (Roberts *et al.*, 2006) shows the structural differences among the AtcTPI-Cys218 mutants. (d) Structural comparison between wild-type cAtcTPI and the point mutants showing the normalized B-factors for the wild-type and AtcTPI mutants.

that induce conformation changes in the Cα of residues Val213 to Asn217 that are located immediately after the YGGS motif (Figure 5b,c). These conformational changes are subtle in the case of Asp and Lys mutants. In these structures, a segment of loop 7 from residues Val213 to Asn217 moves between 2 to 2.3 Å. In contrast, the AtcTPI-Cys218Tyr mutation results in abrupt re-orientation of 6.3 Å in loop 7 (Figure 5b). The side chains of residue 218 harboring mutations to Asp, Lys, and Ser are in an equivalent position to the side chain of residue Cys218. Distinctly, the side chain of AtcTPI-Cys218Tyr mutant occupies the space that corresponds to residue Val213 located immediately after the YGGS motif (Figure 5b). Mutations in a residue analogous to AtcTPI-Cys218 in *G. lambia* TPI (GlTPI) also exhibit a decrease in their catalytic activity (Hernandez-Alcantara *et al.*, 2013) and crystallographic studies of the GlTPI-Cys222Asp mutant also present structural variation on loops 6 and 7 that correlate with the loss of enzymatic activity (Hernandez-Alcantara *et al.*, 2013). The AtcTPI-Cys218Asp mutant decreases its catalytic efficiency by approximately 11-fold, in contrast the AtcTPI-Cys218Tyr and Lys mutants decrease the catalytic efficiency by 4.7-fold and 7.7-fold, respectively. In contrast with the severe loss in catalytic activity observed by an aspartic acid mutation in residue AtcTPI-Cys13, an aspartate mutation in residue AtcTPI-Cys218 resulted in an 11-fold decrease. Although this loss in activity seems modest, the 4-fold decrease caused by the Ile170Val mutation in human TPI induces hyper-resistance against oxidative stress in yeast (Ralser *et al.*, 2006). This suggests that small changes in enzymatic activity of this key glycolytic enzyme are sufficient to alter and re-route central metabolic pathways (Ralser *et al.*, 2006, 2007).

A dual mechanism for redox-based modulation in plant cytosolic TPIs

The identity of residues Cys 13 and Cys218 is conserved in TPIs from green algae and in the majority of plant cytosolic TPIs, being one exception *Medicago truncatula* (Zaffagnini *et al.*, 2014; López-Castillo *et al.*, 2016) (Figure 6a). However, the identity of the residue corresponding to Cys218 in all plastidic TPIs and TPIs from photosynthetic bacteria is a serine or a hydrophobic amino acid, suggesting that cysteine-based modulation at this position is only conserved in green algae and land plants (López-Castillo *et al.*, 2016). Seminal work by Zaffagnini and coworkers show that TPI from *Chlamydomonas reinhardtii* (CrTPI) harbors a cysteine residue (CrTPI-Cys219) that is structurally analogous to AtcTPI-Cys218 (Zaffagnini *et al.*, 2014). A structural comparison between the crystal structures of CrTPI and AtcTPIs shows that in both TPIs crystal structures, the exposed thiol groups of residues CrTPI-Cys219 and AtcTPI-Cys218 are located at the N-terminal cap of an α-helix and, in both cases, two lysines are in close proximity to the thiol groups

© 2019 The Authors

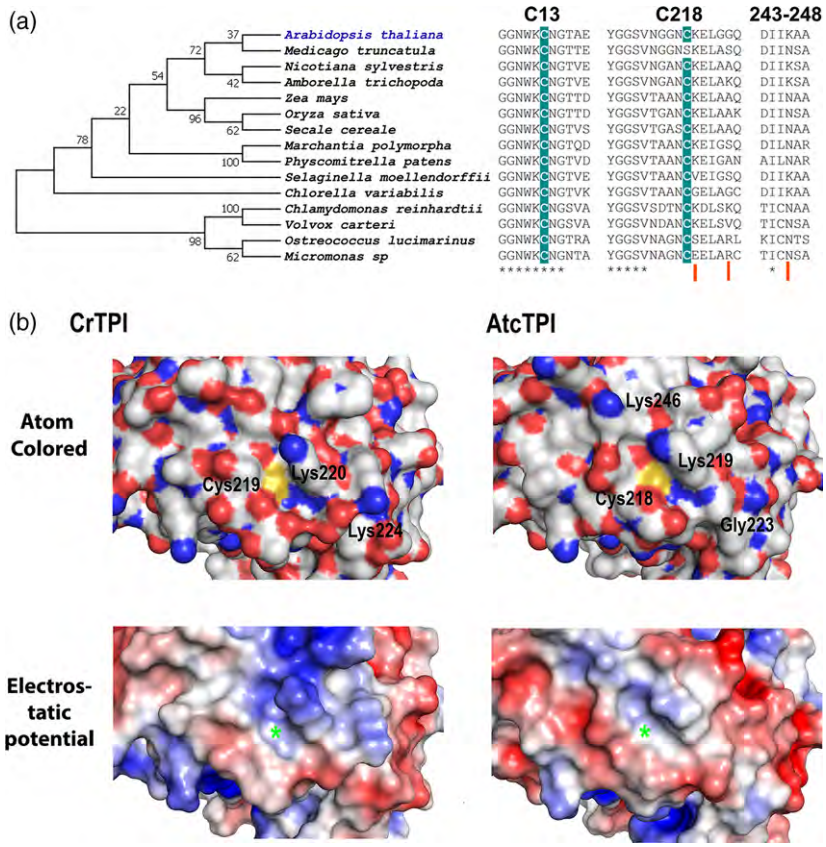

Figure 6. Residue AtcTPI-Cys218 is a conserved *S*-glutathionylation target to modulate glycolysis in land plants and green algae. (a) Multiple sequence alignment of amino acids near AtcTPI in selected green algae and land plants. The identity of residues analogous to AtcTPI-Cys218 and lysines that contribute to create a positively charged region near CrTPI-Cys219 and AtcTPI-Cys218 are indicated. (b) Surface and electrostatic potential representations near residues CrTPI-Cys219 and AtcTPI-Cys218. The thiol group is colored in yellow, nitrogens in blue, oxygen in red and carbons in white. The bottom figure shows the chemical environment near residues CrTPI-Cys219 and AtcTPI-Cys218. Positively charged regions are colored in blue and negatively charged regions in red. The thiol groups are indicated with a green asterisk.

(Figure 6b) (Zaffagnini *et al.*, 2014). These chemical characteristics produce a positively charged environment that may exhibit, as a consequence, a decrease in the pK_a of both cysteines that stabilizes the formation of a deprotonated cysteine form (thiolate) that is prone to react with GSSG. Although the amino acids surrounding CrTPI-Cys219 and AtcTPI-Cys218 are not conserved, the chemical environment of these residues surrounded by positively and negatively charged amino acids is conserved (Figure 6b). Therefore, the three-dimensional structures show that the chemical propensity of the residue corresponding to AtcTPI-Cys218 to be a target of glutathione is conserved from green algae to land plants. The absence of a thiol group in the residue corresponding to AtcTPI-Cys218 in plastidic TPI from land plants may be explained by the need of plastidic TPIs to cope with higher concentrations of oxidative agents (López-Castillo *et al.*, 2016).

In sum, here we elucidated the mechanisms by which cTPI from land plants modulate their activity by modifying two cysteine residues: AtcTPI-Cys13 and AtcTPI-Cys218. Redox-based modifications of those residues result in a decrease in TPI catalytic efficiency. This reduction in enzymatic activity is associated with a reduction in ROS production by re-routing the central metabolism (Ralser *et al.*, 2006, 2007). A crystal structure that mimics cysteine oxidation in residue cATP-Cys13 induces enzymatic inactivation due to monomerization and mimicry of residue AtcATP-Cys218 to sulfinic acid or *S*-thiolation induces a conformation change in the enzyme that is concomitant with a decrease in enzymatic activity. Here, we propose a model in which the solvent-exposed residue AtcTPI-Cys218 is the primary target for ROS and *S*-glutathionylation (Figure 7). The solvent-exposed localization of residue AtcTPI-Cys218 make it a plausible target for plant oxido-reductases of the thioredoxins and glutaredoxins families that could modulate TPI enzymatic activity. Furthermore, this chemical environment is conserved in TPIs from green algae and cytosolic TPIs, suggesting the possibility of a conserved evolutionary mechanism to control glycolysis in plants. *S*-glutathionylation of residue AtcTPI-Cys218 both protect the redox sensitive thiol to non-reversible oxidation products and decreases TPI activity. The localization of residue cATP-Cys13 at the dimer interface makes it a difficult target for enzymatic *S*-glutathionalytion, however conditions of elevated ROS could trigger its oxidation. Oxidation of this amino acid, and the induced loss of dimeric assembly may generate a severe drop in catalysis as a rapid response to oxidative stress, shifting the sugar metabolism into the PPP (Ralser *et al.*, 2006, 2007) (Figure 7). In summary, our study describes how *S*-glutathionylation and thiol oxidation in AtcTPI are part of the tuning mechanism of plant glycolysis based on redox status (Scheibe *et al.*, 2005; Holtgrefe *et al.*, 2008).

© 2019 The Authors

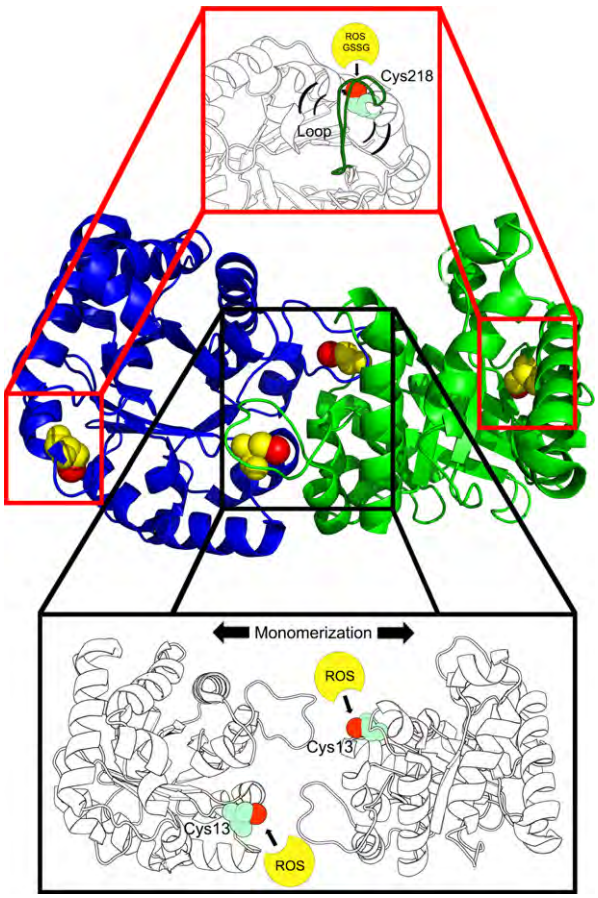

Figure 7. Model for the role of residues AtcTPI-Cys13 and AtcTPI-Cys218 in modulating TPI enzymatic activity by oxidation or glutathionylation. (a) Irreversible oxidation of residue Cys13 at the AtcTPI dimer interface induces subtle conformation changes in loop 3 of the neighboring subunit that lead to dimer dissociation with a concomitant loss in enzymatic activity. Oxidation or glutathionylation at residue Cys218 alters the structure of loops 6 and 7. These structural changes decrease the enzymatic activity of AtcTPI. The reversibility of the *S*-glutathionylation reaction at residue AtcTPI is a potential redox switch to cope with ROS in plants.

EXPERIMENTAL PROCEDURES

Synthetic gene design for AtcTPI expression and site-directed mutagenesis

The open reading frame of AtcTPI was codon optimized for its recombinant expression in *E. coli* and subcloned into *Nde*I and *Bam*HI restriction sites of a modified pET19 vector. Site-directed mutagenesis for residue AtcTPI-Cys13 was performed using the polymerase chain reaction (PCR) and AtcTPI-Cys218 mutants were constructed using the quick-change site-directed mutagenesis protocol (New England Biolabs, Beverly, MA, USA). Oligonucleotides used for site-directed mutagenesis are shown in Table S1.

Protein expression and purification

Bacterial codon optimized AtcTPIs were expressed in BL21 (DE3) *Δtpi E. coli* cells for both crystallographic and biochemical studies (Sullivan *et al.*, 2011). Bacterial pellets were resuspended in lysis buffer (25 mM Tris–acetate–EDTA (TAE) pH 7.4, 150 mM NaCl). Recombinant AtcTPI was purified by metal chelate affinity chromatography (IMAC). Protein eluate was dialyzed in lysis buffer with the addition of 2 mM ethylene diamine tetraacetic acid (EDTA) and 1 mM dithiothreitol (DTT). PreScission protease was added during dialysis at a final concentration of 0.1 mg mL^{-1} to cleavage the histidine tag. After affinity tag removal, AtcTPI and mutant variants were concentrated using centrifugal ultrafiltration units of 10 kDa MWCO (Millipore, Burlington, MA, USA), and further purified by size-exclusion chromatography on a Superdex 75 Column (GE Healthcare, Waukesha, WI, USA). Once the histidine tag is removed recombinantly purified proteins contain only three amino acids (Gly, Pro, His) before the initial methionine.

Protein crystallization

AtcTPI mutants were concentrated to 14 mg mL^{-1} in 20 mM Tris pH 8, 50 mM NaCl and 2 mM DTT. Four sparse matrix crystallization screens of 96 conditions each were used mixing 1 μL of reservoir solution and protein using the sitting drop method. Crystals for each mutant were obtained in specific conditions (Table S2). Datasets for each mutant were collected at the Advanced Photon Source using a single protein crystal. Datasets were processed with MOSFLM (Battye *et al.*, 2011) and scaled with AIMLESS, using the CCP4 Software Suite (McNicholas *et al.*, 2011). The X-ray structures for mutants AtcTPIs were solved by molecular replacement. PDB accession numbers, data collection and refinement statistics are presented in Table S3.

In vivo functional assays and determination of catalytic parameters

In vivo complementation assays, and catalytic activities were measured as previously reported (Sullivan *et al.*, 2011; Figueroa-Angulo *et al.*, 2012). Briefly, catalytic activity of AtTPIs was measured spectrophotometrically by a coupled enzyme assay with α-GDH in the direction G3P to DHAP. Assays were performed according to Benítez-Cardoza *et al.* in 100 μL of 0.1 TAE pH 7.4, containing 10 mM EDTA, 0.01% BSA, 0.2 mM NADH (Sigma, St. Louis, MO, USA), 1 μg α-GDH (Roche, Basel, Switzerland) and 1 mM of D-L glyceraldehyde 3-phosphate (Sigma) (Benítez-Cardoza *et al.*, 2001). The reaction was started by addition of AtTPIs and activity was calculated by the decrease in absorbance at 340 nm, monitored each 30-sec using an Infinite M1000 reader (TECAN, Männedorf, Switzerland). For the determination of the apparent kinetic constants (K_M and K_{cat}), assays were carried out by increasing G3P concentrations, from 0 to 4.0 mM.

© 2019 The Authors
The Plant Journal © 2019 John Wiley & Sons Ltd,

INFORME DE LABORES 2019

Dilution experiments for apparent dissociation constants

The apparent dissociation constants ($^{app}K_{diss}$) of the AtcTPI dimer and those of the Cys-13 and Cys-218 mutants were estimated from dilution experiments followed by catalytic activity. Proteins were incubated for 24 h at 25°C and different protein concentrations (1000 μg mL^{-1} to 50 ng mL^{-1}) in buffer 100 mM TAE, 10 mM EDTA and 1 mM DTT, pH 8.0. Subsequently, activity was determined as indicated previously at 25°C with 5 ng mL^{-1} of TIM and 2 mM G3P. Data were normalized (f_N) to the highest activity value obtained. As TPI is a homodimer, a decrease in total protein concentration favors dimer dissociation. $^{app}K_{diss}$ was calculated from the following equation, derived from the simplest equilibrium two-state model that describes the change in the fraction of active dimers f_N as a function of TPI concentration (P_C expressed on a monomer basis) (Neet and Timm, 1994; Romero-Romero *et al.*, 2015)

$$f_N = \frac{^{app}K_{diss} + 4P_C - \sqrt{^{app}K_{diss}{}^2 + 8K_{diss}P_C}}{4P_C}$$

ACKNOWLEDGEMENTS

This project was supported by CONACYT-Fronteras de la ciencia grant # 11 (LGB). Data were collected at the Life Sciences Collaborative Access Team beam lines 21-ID-G and F at the Advanced Photon Source, Argonne National Laboratory by the Michigan Economic Development Corporation and the Michigan Technology Tri-Corridor (Grant 085P1000817). This research used resources of the Department of Energy (DOE) under Contract No. DE-AC02-06CH11357.

AUTHOR CONTRIBUTIONS

LGB, ECT, and PJS conceived the project. ECT, PJS, SRR, AFP, LMLC, CDQ, DAFV, and ATL performed experiments and data analysis. LGB wrote the manuscript. ECT, PJS, SRR, DAFV, and ATL edited the manuscript.

CONFLICT OF INTEREST

The authors have no conflict of interest to declare.

SUPPORTING INFORMATION

Additional Supporting Information may be found in the online version of this article.

Figure S1. Mutation AtcTPICys13Ala does not create structural changes. Ribbon representation of the superposition between the crystal structures of wild-type and AtcTPICys13Ala mutant and close-up view at loop 3 of the dimer interface.

Figure S2. Structural changes mediated by AtcTPI mutations. (a) Structural comparison between wild-type AtcTPI and point mutants. The RMSD analysis (Roberts *et al.*, 2006) shows the structural differences among the cAtTPI-Cys13 mutants. (b) Structural comparison between cAtTPI-WT and the point mutants showing the normalized B-factors for the wild-type and cAtTPI mutants.

Figure S3. Simulated annealing omit maps at residue Phe75. Difference density contoured at 3σ (mFo-DFc map, green mesh). Residue Phe75 has an alternative conformation and is close to the interface with the other subunit. The 2mFo-DFc map is colored blue and contoured at 1.5σ. TPI subunits A and B are colored in red and gray, respectively.

Figure S4. Modifications in residue Cys 218 do not alter the dimer interface. (a, b) Close-up to the region corresponding to the dimer interface of cysteine mutants to Ser and Asp and Lys.

Table S1. Oligonucleotides for site-directed mutagenesis.

Table S2. Crystal grow conditions.

Table S3. Data collection and refinement statistics.

REFERENCES

Alber, T.C., Davenport, R.C. Jr, Giammona, D.A., Lolis, E., Petsko, G.A. and Ringe, D. (1987) Crystallography and site-directed mutagenesis of yeast triosephosphate isomerase: what can we learn about catalysis from a "simple" enzyme? *Cold Spring Harb. Symp. Quant. Biol.* **52**, 603–613.

Banner, D.W., Bloomer, A.C., Petsko, G.A. *et al.* (1975) Structure of chicken muscle triose phosphate isomerase determined crystallographically at 2.5 angstrom resolution using amino acid sequence data. *Nature*, **255**, 609–614.

Battye, T.G., Kontogiannis, L., Johnson, O., Powell, H.R. and Leslie, A.G. (2011) iMOSFLM: a new graphical interface for diffraction-image processing with MOSFLM. *Acta Crystallogr. D Biol. Crystallogr.* **67**, 271–281.

Benítez-Cardoza, C.G., Rojo-Dominguez, A. and Hernandez-Arana, A. (2001) Temperature-induced denaturation and renaturation of triosephosphate isomerase from Saccharomyces cerevisiae: evidence of dimerization coupled to refolding of the thermally unfolded protein. *Biochemistry*, **40**, 9049–9058.

Blacklow, S.C., Raines, R.T., Lim, W.A., Zamore, P.D. and Knowles, J.R. (1988) Triosephosphate isomerase catalysis is diffusion controlled. Appendix: analysis of triose phosphate equilibria in aqueous solution by 31P NMR. *Biochemistry*, **27**, 1158–1167.

Booth, W.T., Schlachter, C.R., Pote, S., Ussin, N., Mank, N.J., Klapper, V., Offermann, L.R., Tang, C., Hurlburt, B.K. and Chruszcz, M. (2018) Impact of an N-terminal polyhistidine tag on protein thermal stability. *ACS Omega*, **3**, 760–768.

Borchert, T.V., Abagyan, R., Jaenicke, R. and Wierenga, R.K. (1994) Design, creation, and characterization of a stable, monomeric triosephosphate isomerase. *Proc. Natl Acad. Sci. USA*, **91**, 1515–1518.

Castro-Torres, E., Jiménez-Sandoval, P., Fernández-de Gortari, E. *et al.* (2018) Structural basis for the limited response to oxidative and thiol-conjugating agents by triosephosphate isomerase from the photosynthetic bacteria *Synechocystis*. *Front. Mol. Biosci.* **5**, 103.

Chanez-Cardenas, M.E., Fernández-Velasco, D.A., Vazquez-Contreras, E., Coria, R., Saab-Rincon, G. and Perez-Montfort, R. (2002) Unfolding of triosephosphate isomerase from Trypanosoma brucei: identification of intermediates and insight into the denaturation pathway using tryptophan mutants. *Arch. Biochem. Biophys.* **399**, 117–129.

Chardonnet, S., Sakr, S., Cassier-Chauvat, C., Le Marechal, P., Chauvat, F., Lemaire, S.D. and Decottignies, P. (2015) First proteomic study of S-glutathionylation in cyanobacteria. *J. Proteome Res.* **14**, 59–71.

Chen, M. and Thelen, J.J. (2010) The plastid isoform of triose phosphate isomerase is required for the postgerminative transition from heterotrophic to autotrophic growth in Arabidopsis. *Plant Cell*, **22**, 77–90.

Dixon, D.P., Skipsey, M., Grundy, N.M. and Edwards, R. (2005) Stress-induced protein S-glutathionylation in Arabidopsis. *Plant Physiol.* **138**, 2233–2244.

Dorion, S., Jeukens, P.J., Matton, D.P. and Rivoal, J. (2005) Cloning and characterization of a cytosolic isoform of triosephosphate isomerase developmentally regulated in potato leaves. *Plant Sci.* **168**, 183–194.

Dorion, S., Clendenning, A., Jeukens, J., Salas, J.J., Parveen, N., Haner, A.A., Law, R.D., Force, E.M. and Rivoal, J. (2012) A large decrease of cytosolic triosephosphate isomerase in transgenic potato roots affects the distribution of carbon in primary metabolism. *Planta*, **236**, 1177–1190.

Dumont, S., Bykova, N.V., Pelletier, G., Dorion, S. and Rivoal, J. (2016) Cytosolic triosephosphate isomerase from *Arabidopsis thaliana* is

© 2019 The Authors

INFORME DE LABORES 2019

reversibly modified by glutathione on cysteines 127 and 218. *Front. Plant Sci.* **7**, 1942.

Figueroa-Angulo, E.E., Estrella-Hernandez, P., Salgado-Lugo, H. *et al.* (2012) Cellular and biochemical characterization of two closely related triosephosphate isomerases from Trichomonas vaginalis. *Parasitology*, **139**, 1729–1738.

Flugel, F., Timm, S., Arrivault, S., Florian, A., Stitt, M., Fernie, A.R. and Bauwe, H. (2017) The photorespiratory metabolite 2-phosphoglycolate regulates photosynthesis and starch accumulation in Arabidopsis. *Plant Cell*, **29**, 2537–2551.

Garza-Ramos, G., Cabrera, N., Saavedra-Lira, E., Tuena de Gomez-Puyou, M., Ostoa-Saloma, P., Perez-Montfort, R. and Gomez-Puyou, A. (1998) Sulfhydryl reagent susceptibility in proteins with high sequence similarity–triosephosphate isomerase from Trypanosoma brucei, Trypanosoma cruzi and Leishmania mexicana. *Eur. J. Biochem.* **253**, 684–691.

Gonzalez-Mondragon, E., Zubillaga, R.A., Saavedra, E., Chanez-Cardenas, M.E., Perez-Montfort, R. and Hernandez-Arana, A. (2004) Conserved cysteine 126 in triosephosphate isomerase is required not for enzymatic activity but for proper folding and stability. *Biochemistry*, **43**, 3255–3263.

Hernandez-Alcantara, G., Torres-Larios, A., Enriquez-Flores, S. *et al.* (2013) Structural and functional perturbation of Giardia lamblia triosephosphate isomerase by modification of a non-catalytic, non-conserved region. *PLoS One*, **8**, e69031.

Holtgrefe, S., Gohlke, J., Starmann, J., Druce, S., Klocke, S., Altmann, B., Wojtera, J., Lindermayr, C. and Scheibe, R. (2008) Regulation of plant cytosolic glyceraldehyde 3-phosphate dehydrogenase isoforms by thiol modifications. *Physiol. Plant.* **133**, 211–228.

Hough, M.A., Grossmann, J.G., Antonyuk, S.V. *et al.* (2004) Dimer destabilization in superoxide dismutase may result in disease-causing properties: structures of motor neuron disease mutants. *Proc. Natl Acad. Sci. USA*, **101**, 5976–5981.

Ito, H., Iwabuchi, M. and Ogawa, K. (2003) The sugar-metabolic enzymes aldolase and triose-phosphate isomerase are targets of glutathionylation in Arabidopsis thaliana: detection using biotinylated glutathione. *Plant Cell Physiol.* **44**, 655–660.

Jacob, C., Holme, A.L. and Fry, F.H. (2004) The sulfinic acid switch in proteins. *Org. Biomol. Chem.* **2**, 1953–1956.

Jiménez-Sandoval, P., Vique-Sanchez, J.L., Hidalgo, M.L. *et al.* (2017) A competent catalytic active site is necessary for substrate induced dimer assembly in triosephosphate isomerase. *Biochim. Biophys. Acta*, **1865**, 1423–1432.

Kim, Y.J., Kim, D., Illuzzi, J.L., Delaplane, S., Su, D., Bernier, M., Gross, M.L., Georgiadis, M.M. and Wilson, D.M. 3rd (2011) S-glutathionylation of cysteine 99 in the APE1 protein impairs abasic endonuclease activity. *J. Mol. Biol.* **414**, 313–326.

Lara-Gonzalez, S., Estrella, P., Portillo, C. *et al.* (2015) Substrate-induced dimerization of engineered monomeric variants of Triosephosphate Isomerase from Trichomonas vaginalis. *PLoS One*, **10**, e0141747.

Liu, Y., Cao, Y., Zhang, Q., Li, X. and Wang, S. (2018) A cytosolic triosephosphate isomerase is a key component in XA3/XA26-mediated resistance. *Plant Physiol.* **178**, 923–935.

Lolis, E., Alber, T., Davenport, R.C., Rose, D., Hartman, F.C. and Petsko, G.A. (1990) Structure of yeast triosephosphate isomerase at 1.9-A resolution. *Biochemistry*, **29**, 6609–6618.

López-Castillo, L.M., Jiménez-Sandoval, P., Baruch-Torres, N., Trasvina-Arenas, C.H., Díaz-Quezada, C., Lara-Gonzalez, S., Winkler, R. and Brieba, L.G. (2016) Structural basis for redox regulation of cytoplasmic and chloroplastic triosephosphate isomerases from Arabidopsis thaliana. *Front. Plant Sci.* **7**, 1817.

Mainfroid, V., Terpstra, P., Beauregard, M., Frere, J.M., Mande, S.C., Hol, W.G., Martial, J.A. and Goraj, K. (1996) Three hTIM mutants that provide new insights on why TIM is a dimer. *J. Mol. Biol.* **257**, 441–456.

Maithal, K., Ravindra, G., Balaram, H. and Balaram, P. (2002) Inhibition of plasmodium falciparum triose-phosphate isomerase by chemical modification of an interface cysteine. Electrospray ionization mass spectrometric analysis of differential cysteine reactivities. *J. Biol. Chem.* **277**, 25106–25114.

Mande, S.C., Mainfroid, V., Kalk, K.H., Goraj, K., Martial, J.A. and Hol, W.G. (1994) Crystal structure of recombinant human triosephosphate isomerase at 2.8 A resolution. Triosephosphate isomerase-related human genetic disorders and comparison with the trypanosomal enzyme. *Protein Sci.* **3**, 810–821.

McDonagh, B., Ogueta, S., Lasarte, G., Padilla, C.A. and Barcena, J.A. (2009) Shotgun redox proteomics identifies specifically modified cysteines in key metabolic enzymes under oxidative stress in Saccharomyces cerevisiae. *J. Proteomics.* **72**, 677–689.

McNicholas, S., Potterton, E., Wilson, K.S. and Noble, M.E. (2011) Presenting your structures: the CCP4 mg molecular-graphics software. *Acta Crystallogr. D Biol. Crystallogr.* **67**, 386–394.

Michelet, L., Zaffagnini, M., Morisse, S. *et al.* (2013) Redox regulation of the Calvin-Benson cycle: something old, something new. *Front. Plant Sci.* **4**, 470.

Miyata, Y., Rauch, J.N., Jinwal, U.K., Thompson, A.D., Srinivasan, S., Dickey, C.A. and Gestwicki, J.E. (2012) Cysteine reactivity distinguishes redox sensing by the heat-inducible and constitutive forms of heat shock protein 70. *Chem. Biol.* **19**, 1391–1399.

Murray, C.I., Uhrigshardt, H., O'Meally, R.N., Cole, R.N. and Van Eyk, J.E. (2012) Identification and quantification of S-nitrosylation by cysteine reactive tandem mass tag switch assay. *Mol. Cell Proteomics*, **11**, M1110.13441.

Nagano, N., Ota, M. and Nishikawa, K. (1999) Strong hydrophobic nature of cysteine residues in proteins. *FEBS Lett.* **458**, 69–71.

Neet, K.E. and Timm, D.E. (1994) Conformational stability of dimeric proteins: quantitative studies by equilibrium denaturation. *Protein Sci.* **3**, 2167–2174.

Olivares-Illana, V., Riveros-Rosas, H., Cabrera, N., Tuena de Gomez-Puyou, M., Perez-Montfort, R., Costas, M. and Gomez-Puyou, A. (2017) A guide to the effects of a large portion of the residues of triosephosphate isomerase on catalysis, stability, druggability, and human disease. *Proteins*, **85**, 1190–1211.

Panek, A., Pietrow, O., Filipkowski, P. and Synowiecki, J. (2013) Effects of the polyhistidine tag on kinetics and other properties of trehalose synthase from *Deinococcus geothermalis*. *Acta Biochim. Pol.* **60**, 163–166.

Permyakov, S.E., Zernii, E.Y., Knyazeva, E.L., Denesyuk, A.I., Nazipova, A.A., Kolpakova, T.V., Zinchenko, D.V., Philippov, P.P., Permyakov, E.A. and Senin, I.I. (2012) Oxidation mimicking substitution of conservative cysteine in recoverin suppresses its membrane association. *Amino Acids*, **42**, 1435–1442.

Ralser, M., Heeren, G., Breitenbach, M., Lehrach, H. and Krobitsch, S. (2006) Triose phosphate isomerase deficiency is caused by altered dimerization–not catalytic inactivity–of the mutant enzymes. *PLoS One*, **1**, e30.

Ralser, M., Wamelink, M.M., Kowald, A. *et al.* (2007) Dynamic rerouting of the carbohydrate flux is key to counteracting oxidative stress. *J. Biol.* **6**, 10.

Reyes-Prieto, A. and Bhattacharya, D. (2007) Phylogeny of Calvin cycle enzymes supports Plantae monophyly. *Mol. Phylogenet. Evol.* **45**, 384–391.

Reyes-Vivas, H., Martinez-Martinez, E., Mendoza-Hernandez, G., López-Velazquez, G., Perez-Montfort, R., Tuena de Gomez-Puyou, M. and Gomez-Puyou, A. (2002) Susceptibility to proteolysis of triosephosphate isomerase from two pathogenic parasites: characterization of an enzyme with an intact and a nicked monomer. *Proteins*, **48**, 580–590.

Roberts, E., Eargle, J., Wright, D. and Luthey-Schulten, Z. (2006) MultiSeq: unifying sequence and structure data for evolutionary analysis. *BMC Bioinformatics*, **7**, 382.

Rodríguez-Romero, A., Hernández-Santoyo, A., del Pozo Yauner, L., Kornhauser, A. and Fernández-Velasco, D.A. (2002) Structure and Inactivation of Triosephosphate Isomerase from Entamoeba histolytica. *J. Mol. Biol.* **322**, 669–675.

Romero-Romero, S., Costas, M., Rodriguez-Romero, A. and Alejandro Fernández-Velasco, D. (2015) Reversibility and two state behaviour in the thermal unfolding of oligomeric TIM barrel proteins. *Phys. Chem. Chem. Phys.* **17**, 20699–20714.

Romero-Romero, S., Becerril-Sesin, L.A., Costas, M., Rodriguez-Romero, A. and Fernández-Velasco, D.A. (2018) Structure and conformational stability of the triosephosphate isomerase from Zea mays. Comparison with the chemical unfolding pathways of other eukaryotic TIMs. *Arch. Biochem. Biophys.* **658**, 66–76.

Saab-Rincon, G., Juarez, V.R., Osuna, J., Sanchez, F. and Soberon, X. (2001) Different strategies to recover the activity of monomeric triosephosphate isomerase by directed evolution. *Protein Eng.* **14**, 149–155.

© 2019 The Authors
The Plant Journal © 2019 John Wiley & Sons Ltd,

Sabaty, M., Grosse, S., Adryanczyk, G., Boiry, S., Biaso, F., Arnoux, P. and Pignol, D. (2013) Detrimental effect of the 6 His C-terminal tag on YedY enzymatic activity and influence of the TAT signal sequence on YedY synthesis. *BMC Biochem.* **14**, 28.

Samanta, M., Banerjee, M., Murthy, M.R., Balaram, H. and Balaram, P. (2011) Probing the role of the fully conserved Cys126 in triosephosphate isomerase by site-specific mutagenesis–distal effects on dimer stability. *FEBS J.* **278**, 1932–1943.

Sampson, N.S. and Knowles, J.R. (1992a) Segmental motion in catalysis: investigation of a hydrogen bond critical for loop closure in the reaction of triosephosphate isomerase. *Biochemistry*, **31**, 8488–8494.

Sampson, N.S. and Knowles, J.R. (1992b) Segmental movement: definition of the structural requirements for loop closure in catalysis by triosephosphate isomerase. *Biochemistry*, **31**, 8482–8487.

Scheibe, R., Backhausen, J.E., Emmerlich, V. and Holtgrefe, S. (2005) Strategies to maintain redox homeostasis during photosynthesis under changing conditions. *J. Exp. Bot.* **56**, 1481–1489.

Sullivan, B.J., Durani, V. and Magliery, T.J. (2011) Triosephosphate isomerase by consensus design: dramatic differences in physical properties and activity of related variants. *J. Mol. Biol.* **413**, 195–208.

Tellez, L.A., Blancas-Mejia, L.M., Carrillo-Nava, E., Mendoza-Hernandez, G., Cisneros, D.A. and Fernández-Velasco, D.A. (2008) Thermal unfolding of triosephosphate isomerase from Entamoeba histolytica: dimer dissociation leads to extensive unfolding. *Biochemistry*, **47**, 11665–11673.

Valancin, A., Srinivasan, B., Rivoal, J. and Jolicoeur, M. (2013) Analyzing the effect of decreasing cytosolic triosephosphate isomerase on Solanum tuberosum hairy root cells using a kinetic-metabolic model. *Biotechnol. Bioeng.* **110**, 924–935.

Wierenga, R.K. (2001) The TIM-barrel fold: a versatile framework for efficient enzymes. *FEBS Lett.* **492**, 193–198.

Wierenga, R.K., Noble, M.E., Vriend, G., Nauche, S. and Hol, W.G. (1991) Refined 1.83 A structure of trypanosomal triosephosphate isomerase crystallized in the presence of 2.4 M-ammonium sulphate. A comparison with the structure of the trypanosomal triosephosphate isomerase-glycerol-3-phosphate complex. *J. Mol. Biol.* **220**, 995–1015.

Wierenga, R.K., Noble, M.E. and Davenport, R.C. (1992) Comparison of the refined crystal structures of liganded and unliganded chicken, yeast and trypanosomal triosephosphate isomerase. *J. Mol. Biol.* **224**, 1115–1126.

Wierenga, R.K., Kapetaniou, E.G. and Venkatesan, R. (2010) Triosephosphate isomerase: a highly evolved biocatalyst. *Cell. Mol. Life Sci.* **67**, 3961–3982.

Zaffagnini, M., Bedhomme, M., Lemaire, S.D. and Trost, P. (2012a) The emerging roles of protein glutathionylation in chloroplasts. *Plant Sci.* **185–186**, 86–96.

Zaffagnini, M., Bedhomme, M., Marchand, C.H., Morisse, S., Trost, P. and Lemaire, S.D. (2012b) Redox regulation in photosynthetic organisms: focus on glutathionylation. *Antioxid. Redox Signal.* **16**, 567–586.

Zaffagnini, M., Fermani, S., Costa, A., Lemaire, S.D. and Trost, P. (2013) Plant cytoplasmic GAPDH: redox post-translational modifications and moonlighting properties. *Front. Plant Sci.* **4**, 450.

Zaffagnini, M., Michelet, L., Sciabolini, C., Di Giacinto, N., Morisse, S., Marchand, C.H., Trost, P., Fermani, S. and Lemaire, S.D. (2014) High-resolution crystal structure and redox properties of chloroplastic triosephosphate isomerase from Chlamydomonas reinhardtii. *Mol. Plant*, **7**, 101–120.

Zarate-Perez, F., Chanez-Cardenas, M.E., Arreola, R., Torres-Larios, A. and Vazquez-Contreras, E. (2009) Different catalytic properties of two highly homologous triosephosphate isomerase monomers. *Biochem. Biophys. Res. Commun.* **382**, 626–630.

© 2019 The Authors

INFORME DE LABORES 2019

characterize the interplay between tumor cells and angiogenesis, as well as their proliferation, phenotypic transitions, and death. We use this model to predict–early in course of neoadjuvant therapy–the eventual response of the individual patient. Success in this endeavor would enable replacing an ineffective treatment with an alternative regimen, thereby potentially improving outcomes and curtailing unnecessary toxicities. Furthermore, our approach can be applied to any disease site for which neoadjuvant therapy is indicated and the requisite data is accessible.

Platform: Bacterial Mechanics, Cytoskeleton, and Motility

1596-Plat

***Wolbachia pipientis* Colonizes *S cerevisiae* with High Yields. Effects on the Host**

Natalia Chiquete Felix[1], Cristina Uribe-Alvarez[2], Ulrik Pedroza-Dávila[3], Isareli Cruz-Cruz[3], Salvador Uribe-Carvajal[3].
[1]Dept Molec Gene, Inst Cell Physiol, Mexico, Mexico, [2]Molecular, Inst Fisiología Celular UNAM, Mexico, Mexico, [3]Inst Fisiol Celular, Univ Natl Autonoma Mexico, Mexico, Mexico.

Wolbachia pipientis is an obligate-endosymbiotic gram-negative bacterium, that naturally colonizes 40-60% of all insect species. It may be transmitted vertically transmitted via germinal cells or horizontally. Each Wolbachia strain is quite different to the rest, as *Wolbachia* coevolves with the host, where it manipulates protein expression, fertility and metabolism. *Wolbachia* may protect its host against infection by other organisms such as pathogenic viruses or bacteria. A major problem to study *Wolbachia* has been its inability to grow *ex-vivo* and the low yields obtained from insect cell cultures. The unicellular yeast *Saccharomyces cerevisiae* was infected with *Wolbachia pipientis*, obtaining large biomass yields. *Wolbachia* did not contribute to oxidative phosphorylation, but instead it seemed to rely on external supply of ATP, possibly precipitating premature death of the host. In contrast, Wolbachia does seem to contribute some coenzymes to the host. It also modifies the actin cytoskeleton. Premature death has been reported also in the artificially infected mosquito *A. aegypti* probably accounting for the decrease in vector disease activity of this host.

1597-Plat

Time-Lapse Atomic Force Microscopy Reveals New End Take Off (Neto) Dynamics in Mycobacteria

Melanie T.M. Hannebelle[1,2], Joelle X.Y. Ven[1,2], Haig A. Eskandarian[1,2], Chiara Toniolo[2], Adrian P.D. Nievergelt[1], John D. McKinney[2], Georg E. Fantner[1].
[1]Laboratory for Bio- and Nano- Instrumentation, Ecole Polytechnique Federale de Lausanne (EPFL), Lausanne, Switzerland, [2]Laboratory of Microbiology and Microtechnology, Ecole Polytechnique Federale de Lausanne (EPFL), Lausanne, Switzerland.

Tuberculosis is a lung infection caused by *Mycobacterium tuberculosis*. One third of the world population is thought to be infected. Antibiotic treatment with antibiotics lasts 6 month, which is difficult to achieve in low-income countries. The uncommon ability of tuberculosis bacteria to persist during long periods is linked to various factors, one of which potentially being cell growth asymmetry. However, growth symmetry or asymmetry of mycobacteria remains a controversial topic as opposing descriptions have been reported in the literature.

Observing bacterial growth at the single cell level is inherently challenging due to the diffraction limit of optical microscopes and the small size of the cells. We built a new dedicated platform for long-term, correlated Atomic Force Microscopy (AFM) and fluorescence microscopy and obtained time-lapses of bacterial growth at an unprecedented resolution.

Surprisingly, the AFM high-resolution time-lapses did not match any of the two previously reported models of pure symmetry and pure asymmetry. Mycobacterial pole growth dynamics was rather an intermediate between the two, reminiscent of the well-known ''new end take off'' mechanism for fission yeast. Using AFM nanomanipulation we show that growth asymmetry is not a physical occlusion phenomenon, but is inherent to mycobacterial growth. Finally, using fluorescent photoconversion microscopy we identify biomolecular mechanisms linked to growth asymmetry, which in the future could be used to develop novel treatments for tuberculosis infection.

1598-Plat

Molecular Motors Govern Liquid-Like Ordering and Fusion Dynamics of Bacterial Colonies

Tom Cronenberg, Anton Welker, Robert Zöllner, Claudia Meel, Katja Siewering, Niklas Bender, Marc Hennes, Enno R. Oldewurtel, Berenike Maier.
Institute for Biological Physics, University of Cologne, Cologne, Germany.

Many bacteria are able to form communities called biofilms. Within these structured communities, they benefit from various advantages including facilitated gene transfer and increased antibiotic resistance. Bacteria can adjust the structure of colonies and biofilms to enhance their survival rate under external stress. The human pathogen *Neisseria gonorrhoeae* is able to aggregate into spherical colonies due to active retraction of its type 4 pili.Here, we explore the link between bacterial interaction forces and colony structure and dynamics. First, we show that the simultaneous expression of a functional and a nonfunctional variant of the motor protein PilT affects motor activity, namely the retraction velocity and the probability to be in the retracting, elongating or pausing state, respectively. Second, we demonstrate that motor activity enhances local ordering and accelerates fusion dynamics of bacterial colonies. Motor activity strongly affects the probability of two cells to be bound to each other. The radial distribution function of mature colonies shows local fluid-like order. The degree and dynamics of ordering are dependent on motor activity. At a larger scale, the fusion dynamics of two colonies shows liquid-like behavior whereby motor activity strongly affects the ratio between surface tension and viscosity. An estimate of colony surface tension using molecular interaction characteristics shows that surface tension is hardly affected by motor activity, indicating a strong effect on colony viscosity.

1599-Plat

DNA Origami as a Tool in the Targeted Destruction of Bacteria

Ioanna Mela[1], Masayuki Endo[2], Hiroshi Sugiyama[2], Robert M. Henderson[3], Clemens F. Kaminski[1].
[1]Chemical Engineering and Biotechnology, University of Cambridge, Cambridge, United Kingdom, [2]Kyoto University, Kyoto, Japan, [3]Dept Pharmacology, Univ Cambridge, Cambridge, United Kingdom.

Antibiotic resistance is a growing worldwide human health issue. It is now threatening to render us vulnerable once again to infections that have been treatable for decades. Various approaches have been proposed in the effort to overcome this threat and effectively treat bacterial infections. We explore the possibility of creating and using DNA origami nanostructures as a vehicle for delivering functional molecules in a specific and efficient manner, in order to destroy bacterial targets. In the past few years, DNA origami has been used to successfully target eukaryotic cancer cells, with impressive results. However, there are no reports of the use of DNA origami to specifically target bacterial cells. We have created a DNA origami tile with five ''wells'' that can carry up to 10 molecules of antibacterial lysozyme. The origami tile has been modified to carry four aptamers that are specific to *Escherichia coli* bacteria and enable anchoring of tiles onto a bacterium. Each origami tile measures approximately 100 x 100 nm, allowing for multiple tiles to attach to any bacterium. We use direct stochastic optical reconstruction microscopy (dSTORM) to assess the efficiency of targeting the tile to the bacteria and we show that treatment with lysozyme-functionalised tiles slows bacterial growth more effectively than treatment with free lysozyme. We also assess the mechanical properties of the origami-treated bacteria with atomic force microscopy. Our study introduces DNA origami as a tool in the fight against antibiotic resistance, and our results demonstrate the specificity and efficiency of the nanostructure as a drug delivery vehicle.

1600-Plat

3D Fluorescence Microscopy Reveals Geometric Localization of Bacterial Cell Shape Proteins in Straight, Curved and Helical Rods

Benjamin P. Bratton[1,2], Zemer Gitai[1], Joshua W. Shaevitz[2].
[1]Department of Molecular Biology, Princeton University, Princeton, NJ, USA, [2]Lewis-Sigler Institute for Integrative Genomics, Princeton University, Princeton, NJ, USA.

The bacterial kingdom is full of complex cell shapes including straight, curved and helical rods. Using a computational fluorescent imaging approach to reconstruct experimentally obtained 3D shapes of individual cells with 50 nm precision, we have been exploring the geometric localization of the proteins associated with cell shape homeostasis in various species. In straight-rod shaped *E. coli,* for example, the actin-like protein

INFORME DE LABORES 2019

Biochemical and Biophysical Research Communications 509 (2019) 341–347

Contents lists available at ScienceDirect

Biochemical and Biophysical Research Communications

journal homepage: www.elsevier.com/locate/ybbrc

Subunit Asa3 ensures the attachment of the peripheral stalk to the membrane sector of the dimeric ATP synthase of *Polytomella* sp.

Lilia Colina-Tenorio [a], Héctor Miranda-Astudillo [b], Alain Dautant [c, d], Miriam Vázquez-Acevedo [a], Marie-France Giraud [c, d], Diego González-Halphen [a, *]

[a] Departamento de Genética Molecular, Instituto de Fisiología Celular, Universidad Nacional Autónoma de México, Ciudad de México, Mexico
[b] Genetics and Physiology of Microalgae, InBios/PhytoSYSTEMS, Université de Liège, Liège, Belgium
[c] CNRS, UMR5095, IBGC, Bordeaux, France
[d] Energy Transducing Systems and Mitochondrial Morphology, Université de Bordeaux, Bordeaux, France

ARTICLE INFO

Article history:
Received 5 December 2018
Accepted 19 December 2018
Available online 22 December 2018

Keywords:
ATP synthase
Asa subunit
HEAT repeats
Peripheral stalk
Polytomella

ABSTRACT

The mitochondrial ATP synthase of *Polytomella* exhibits a peripheral stalk and a dimerization domain built by the Asa subunits, unique to chlorophycean algae. The topology of these subunits has been extensively studied. Here we explored the interactions of subunit Asa3 using Far Western blotting and subcomplex reconstitution, and found it associates with Asa1 and Asa8. We also identified the novel interactions Asa1-Asa2 and Asa1-Asa7. *In silico* analyses of Asa3 revealed that it adopts a HEAT repeat-like structure that points to its location within the enzyme based on the available 3D-map of the algal ATP synthase. We suggest that subunit Asa3 is instrumental in securing the attachment of the peripheral stalk to the membrane sector, thus stabilizing the dimeric mitochondrial ATP synthase.

© 2018 Elsevier Inc. All rights reserved.

1. Introduction

The F_1F_O-ATP synthase, an electrochemical gradient-driven nanomotor, is crucial for oxidative phosphorylation and its dimerization/oligomerization determines the morphology of mitochondrial cristae [1–3]. In the yeast and mammalian enzymes the rotor is formed by a membrane-embedded *c*-ring and subunits γ/δ/ε; the stator includes subunit *a*, subunits α_3/β_3 of the catalytic core, OSCP/*b*/*d*/F6 of the peripheral stalk (PS), and A6L/*e*/*f*/*g* of the dimerization module. Subunit *a* and the *c*-ring create an interface that defines the proton translocation pathway [4–6]. The divergence and structural heterogeneity of PSs and of the dimer interfaces has prompted the reclassification of mitochondrial F-ATPases into metazoan-type (*i.e.* those of yeast and mammals) and protozoan-type (*i.e.* those of *Trypanosoma brucei*, *Tetrahymena thermophila*, *Paramecium tetraurelia*, *Euglena gracilis*, chlorophycean algae, etc.) [7]. In the ATP synthase of the colorless chlorophycean alga *Polytomella* sp. the PS and the dimer interface are built by subunits Asa1 to 9 [8]. Asa1 to 5 and Asa7 are the PS main building blocks, Asa6, Asa8 and Asa9 have predicted transmembrane segments, and Asa6 and Asa9 participate in the dimerization module [9–11]. Despite the lack of similarity of Asa subunits with orthodox PS components, they share some structural features: *i)* Asa1 spans the whole length of the PS like subunit *b* [12]; *ii)* Asa1, Asa2, Asa4 and Asa7 adopt coiled-coil structures as all PS subunits [13]; and *iii)* Asa6 has a V-shape similar to the membrane-embedded region of subunit *b* [14]. The arrangement of the Asa subunits in the *Polytomella* ATP synthase has been addressed [8,9,11–13] but little is known of Asa3; here we explore its structure, its location, and its association with other PS components.

2. Materials and methods

2.1. Algal strains and growth conditions

Polytomella sp. cells (198.80 Culture Collection of Algae, University of Göttingen, Germany, identical to *Polytomella parva*) were grown as reported [15] and collected in the middle of the logarithmic phase by centrifugation 7000×*g* for 20 min. Cells were stored at −70 °C until use.

2.2. Mitochondria isolation and ATP synthase purification

Algal cells were broken mechanically and mitochondria

* Corresponding author. Departamento de Genética Molecular, Instituto de Fisiología Celular, Universidad Nacional Autónoma de México, Mexico.
E-mail address: dhalphen@ifc.unam.mx (D. González-Halphen).

https://doi.org/10.1016/j.bbrc.2018.12.142
0006-291X/© 2018 Elsevier Inc. All rights reserved.

INFORME DE LABORES 2019

obtained by differential centrifugation [8]. The dimeric ATP synthase was purified as in Ref. [15].

2.3. Cloning of cDNAs encoding ATP synthase subunits in expression vectors

The constructs expressing Asa1 [12], Asa2, Asa4, Asa7 [13], Asa8 [12], OSCP [12,16] and OSCPΔC [9,12,13] were used here to overexpress the proteins with a hexa-histidine tag in the N-terminus (using vector pET28a) or without this tag (using vector pET3a). The cDNAs of Asa1ΔC (Asa1$^{1-367}$ lacking 205 residues from its C-terminus) and Asa3ΔN$_{term}$ (Asa3$^{74-325}$) were amplified by PCR from a *Polytomella* sp. cDNA library cloned in λ-ZapII phages using specific oligonucleotide primers. For Asa1ΔC: forward 5′-GCGGCATGCGCTAGCTACCTTGCCCCCCTCCGCTCTGAT-3′ and reverse 5′-GCGGCCGCTTAAGTGTACCTGTGCTCGGTAAT-3′ and for Asa3ΔN$_{term}$: forward 5′-CGCCATATGTCCTCTGGTCCTTCCCAGAACCTT-3′ and reverse 5′-CGCGGATCCTTAATGACCATGGGCACCTTC-3′. The amplification products were cloned into the pET28a vector with the restriction sites *Nhe*I/*Not*I for Asa1ΔC and *Nde*I/*Bam*HI for Asa3ΔN$_{term}$.

2.4. Overexpression of recombinant subunits

Competent *Escherichia coli* BL21 Codon Plus (DE3) RIL cells (Agilent Technologies) were transformed with the plasmid of interest by heat shock. Transformed cells were grown in LB medium containing 64 μg/mL chloramphenicol and 50 μg/mL kanamycin. Overexpression of proteins was induced with 0.1 mM IPTG (Isopropyl β-D-1-thiogalactopyranoside) for 8 h.

2.5. Purification of recombinant subunits

Asa1, Asa2, Asa4, Asa7, Asa8, OSCP and OSCPΔC were purified as in Refs. [12,13]. The overexpressed proteins ^{6H}Asa1ΔC and ^{6H}Asa3ΔN$_{term}$ were obtained in bacterial inclusion bodies (ICBs), which were isolated, washed and stored as previously described [13]. ICBs were solubilized in PBS buffer (500 mM NaCl50 mM NaH_2PO_4, pH 7.8) with 8.0 M urea under mild agitation for 8 h at 4 °C. The insoluble material was removed by centrifugation at 17,500 g for 10 min. Both proteins were purified under denaturing conditions using affinity chromatography. Samples were diluted to a final concentration of 4.0 M urea with PBS buffer containing 15 mM imidazole and loaded into an equilibrated 5 mL HisTrap FF crude column (GE Healthcare Life Sciences). The column was washed with 30 mM imidazole and proteins were eluted with a 30–500 mM imidazole linear gradient in the same buffer. Resulting fractions were analyzed by Tricine–SDS–PAGE, those enriched with the protein of interest were pooled, concentrated, and stored at −70 °C until used.

2.6. Protein interactions assayed by Far Western Blots

Far Western Blot (FWB) analysis was performed as previously described [13]. The purified algal ATP synthase or the purified recombinant subunits were resolved in Tricine-SDS gels, transferred to nitrocellulose membranes and visualized by Ponceau S red staining (0.1% in 5.0% acetic acid). Membranes were blocked overnight, washed, and incubated for 4 h with the externally added recombinant protein at increasing concentrations in subunit-specific buffers [Asa1/^{6H}Asa1ΔC: 150 mM NaCl, 2% glycerol, 0.05% DDM, 0.5 M urea, 50 mM NaH_2PO_4, pH 7.8; Asa2: 0.5 mM EDTA, 1 mM DTT, 2% glycerol, 0.05% Tween-20, 50 mM CAPS, pH 10; ^{6H}Asa3ΔN$_{term}$: 150 mM NaCl, 5 mM DTT, 2% glycerol, 0.05% DDM, 0.5 M urea, 50 mM Tris, pH 8.4 and Asa4, Asa7 and Asa8 in TBST buffer (500 mM NaCl, 0.05% Tween-20, 20 mM Tris, pH 7.5)] supplemented with 1.0% powdered milk. The protein of interest was recognized using primary and secondary antibodies, both incubated with TBST buffer containing 1.0% powdered milk. Finally, the membranes were immunochemically stained as described in Ref. [13].

2.7. Subcomplex reconstitution from recombinant subunits

All steps were performed at 4 °C. Solubilized ICBs containing the same molar ratio of each protein were mixed (Asa1+^{6H}Asa3ΔN$_{term}$ + OSCP or Asa1+Asa2+^{6H}Asa3ΔN$_{term}$ + Asa4+Asa7+OSCP) and diluted 1:1 with dialysis buffer (150 mM NaCl, 10% glycerol, 0.01% DDM, 50 mM Tris, pH 8.4). Samples were supplemented with a mini protease inhibitor tablet (cOmplete EDTA-free, Roche) and with 10% glycerol, 0.01% DDM and 1.0 mM DTT (final concentrations). Protein refolding was carried out by slow dilution (from 8.0 to 4.0 M urea) followed by sequential dialysis steps yielding final concentrations of 0.5 M urea and 150 mM NaCl. After each dialysis step samples were centrifuged at 20,000 rpm in a Type 70Ti rotor for 20 min. The final supernatant was concentrated to 500 μL with an Amicon Ultra 30,000 MWCO and injected into a Superose 6 10/300 GL column connected to an ÄKTA FPLC (GE Healthcare). After elution at 0.5 mL/min, the resulting fractions were analyzed by Tricine-SDS-PAGE, pooled and incubated with a nickel resin (Ni-NTA Agarose, Qiagen) in the presence of 20 mM imidazole for 7 h. For batch purification the resin was centrifuged at 2000 rpm for 5 min (Centrifuge 5424 R, Eppendorf) and washed ten times. Proteins were eluted with increasing concentrations of imidazole (100–300 mM in steps of 50 mM) and analyzed in Tricine-SDS-PAGE.

2.8. Structural modeling of subunit Asa3

F_1-OSCP-ac_{10}-Asa6 subcomplex was modeled using PDB files 2JDI, 2WSS and 6F36 as templates [14,17,18] and fitted in the cryo-EM map (EMD 2852 [4]) using UCSF Chimera [19]. Approximately sixty helical segments were automatically built into the map with the Phenix suite [20]. Secondary structure (2D) and membrane helix (TM) predictions were carried out on the Asa subunits (Asa1, $\alpha_5\beta_1\alpha_{16}$; Asa2, $\alpha_{18}\beta_2\alpha_1$; Asa3, $\alpha_{13}\beta_1$; Asa4, $\alpha_7\beta_1\alpha_5$; Asa5, $\alpha_3\beta_1$/1TM; Asa6, $\alpha_3\beta_1\alpha_3$/2TM; Asa7, $\beta_3\alpha_4\beta_1\alpha_4$/1TM; Asa8, $\alpha_3\beta_2\alpha_2$/1TM; Asa9, $\alpha_2\beta_2\alpha_1$/1TM) using PsiPred [21] and MEMSAT-SVM [22], respectively. The segments were linked and assigned on the basis of predictions and biochemical data using COOT [23]. The model was finely refined against densities in real space in Phenix.

3. Results and discussion

3.1. On the association of subunit Asa3 with other ATP synthase subunits

The interactions of Asa3 were evaluated with FWB experiments performed on the isolated algal enzyme and on the purified recombinant proteins Asa1, Asa2, Asa4, Asa7, Asa8 and OSCP. Membrane strips with the same protein concentration were incubated with increasing concentrations of purified ^{6H}Asa3ΔN$_{term}$ and decorated with anti-Asa3 antibodies. Besides Asa3, the antibody recognized a degraded form of Asa3 (Asa3$_{deg}$), Asa1, and an oligomeric form of subunit *c* (c_x) [12] (Fig. 1A). The last signal did not increase at higher concentrations of Asa3 and was considered non-specific. Thus, Asa3 seems to bind only to Asa1 in this assay. To confirm the observed Asa1-Asa3 interaction, higher quantities of the purified recombinant subunits Asa1, Asa2, Asa4, Asa7 and OSCP were blotted on a membrane and incubated with the highest amount of ^{6H}Asa3ΔN$_{term}$ used in the previous experiment. After decorating the membrane with anti-Asa3 antibodies only the Asa1

INFORME DE LABORES 2019

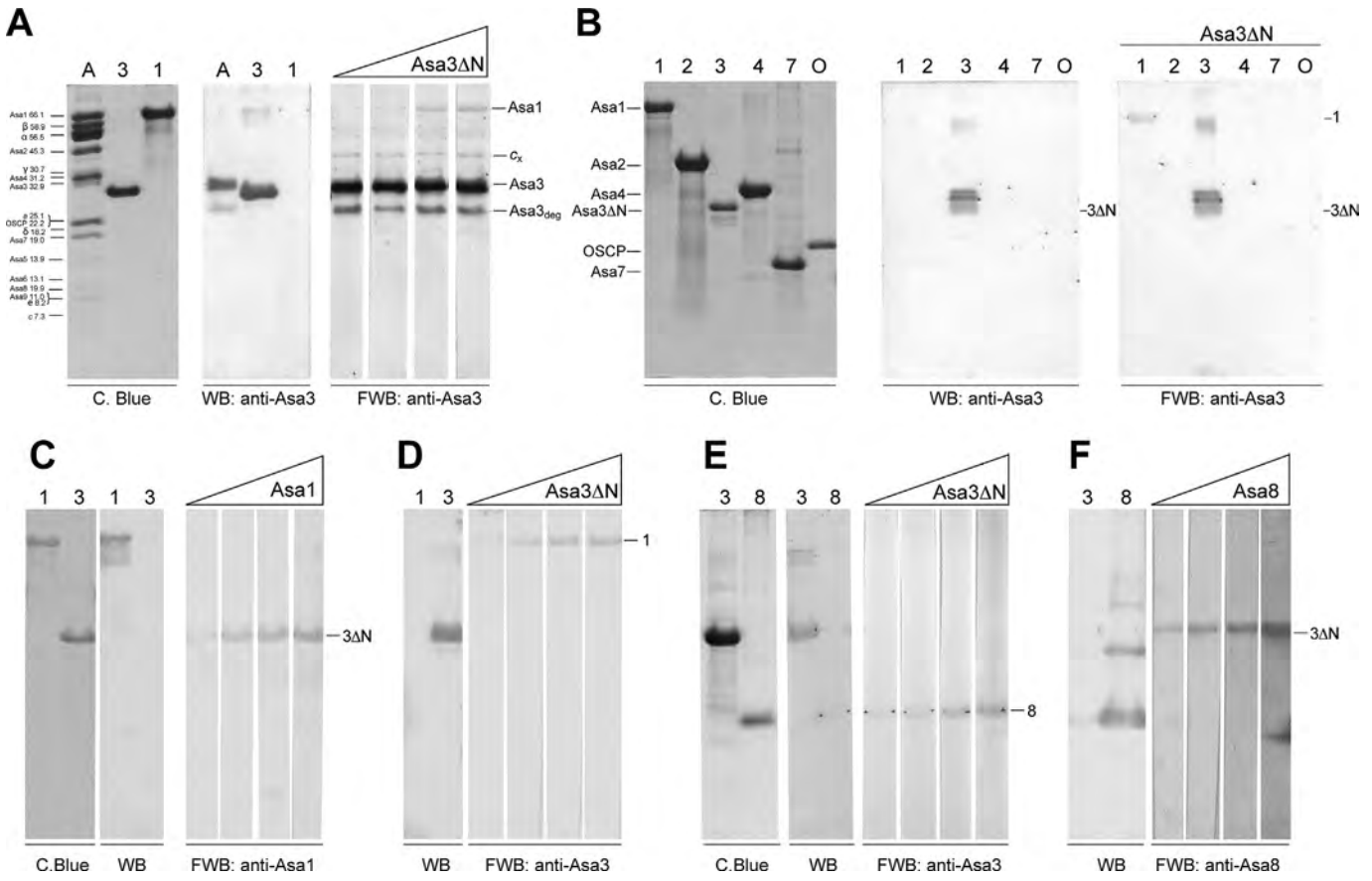

Fig. 1. Associations of subunit Asa3 in the algal ATP synthase. Interactions were assayed by FWB. Lanes labeled as: purified ATP synthase (A), recombinant Asa1 (1), ^{6H}Asa3ΔN$_{term}$ (3), Asa4 (4), Asa7 (7), Asa8 (8) and OSCP (O). **A.** Asa1-Asa3 interaction. Right panel: Coomassie Blue-stained gel with purified ATP synthase and recombinant ^{6H}Asa3ΔN$_{term}$ and Asa1 proteins. Central panel: WB of a parallel gel decorated with anti-Asa3 antibodies. Left panel: FWB of SDS-denatured ATP synthase incubated with increasing concentrations of ^{6H}Asa3ΔN$_{term}$ and decorated with anti-Asa3 antibodies. **B.** Asa1-Asa3 interaction. Right panel: Coomassie Blue-stained gel with the indicated purified recombinant subunits. Central panel: WB of a parallel gel decorated with anti-Asa3 antibodies. Left panel: FWB of a parallel gel incubated with purified recombinant ^{6H}Asa3ΔN$_{term}$ and decorated with anti-Asa3 antibodies. **C.** Asa1-Asa3 interaction. Right panel: Coomassie Blue-stained gel with Asa1 and ^{6H}Asa3ΔN$_{term}$. Central panel: WB of the same gel using anti-Asa1 antibodies. Left panel: FWB of membrane strips containing ^{6H}Asa3ΔN$_{term}$ incubated with increasing concentrations of Asa1 and decorated with anti-Asa1 antibodies. **D.** Asa1-Asa3 interaction. Left panel: WB of a gel parallel to the one shown in C decorated with anti-Asa3 antibodies. Right panel: Membrane strips with Asa1 incubated with increasing concentrations of ^{6H}Asa3ΔN$_{term}$ and decorated with anti-Asa3 antibodies. **E.** Right panel: Coomassie Blue-stained gel with ^{6H}Asa3ΔN$_{term}$ and Asa8. Left panel: WB of the same gel using anti-Asa3 antibodies. Right panel: FWB of membrane strips containing Asa8 incubated with increasing concentrations of ^{6H}Asa3ΔN$_{term}$ and decorated with anti-Asa3 antibodies **F.** Asa3-Asa8 interaction. Left panel: WB of a gel parallel to the one shown in E decorated with anti-Asa8 antibodies, dimeric and tetrameric forms of SDS-resistant Asa8 were observed. Right panel: Membrane strips containing ^{6H}Asa3ΔN$_{term}$ incubated with increasing concentrations of Asa8 and decorated with anti-Asa8 antibodies.

signal was detected (Fig. 1B), confirming the previous result and suggesting ^{6H}Asa3ΔN$_{term}$ does not associate with the other assayed proteins. FWB experiments performed with both recombinant subunits, incubating membrane strips with increasing concentrations of each protein, confirmed the Asa1-Asa3 interaction (Fig. 1C and 1D).

Previous cross-linking experiments revealed an Asa3-Asa8 interaction [11,16]. Asa8 has a predicted transmembrane segment and therefore is likely located in the membrane domain of the PS. We confirmed this Asa3-Asa8 interaction using purified recombinant subunits (Fig. 1E and IF). When testing the binding of ^{6H}Asa3ΔN$_{term}$ on the isolated ATP synthase (see Fig. 1A) we could not detect an Asa8 signal, which may be due to: *i)* the high hydrophobicity of Asa8 that is not ideal when assessing interactions by FWB experiments or *ii)* only faint quantities of Asa8 are being transferred to the membrane.

3.2. On the structure and location of subunit Asa3 in the algal ATP synthase

A 3D model of the dimeric *Polytomella* ATP synthase was built [24] in the available 3D cryo-EM map (EMD 2852 [4]) using map2model, real_space_refine and refine of the Phenix suite [20].

The *Asa3* gene encodes a preprotein of 325 residues. Initially, it was established by Edman degradation that Asa3 from the purified complex starts at residue 74 [8], hence the Asa3ΔN$_{term}^{74-325}$ construct. A MTS of 30 residues predicted for *Polytomella* sp. Asa3 using MitoFates [25] agrees with the MTS of *C. reinhardtii* Asa3 determined experimentally [8].

2D structure predictions of Asa3$^{31-325}$ revealed thirteen consecutive helices made of 12–18 residues (H1-13) linked by short loops (Fig. S1) and threading methods predict an α-solenoid fold [26]. Multiple sequence alignment of Asa3 from different sources revealed a conserved region of 16 aa (196–211) belonging to H8 and the longest loop (208–215), which connects H8 and H9 (see Fig. S1). Only one chain of our 3D model unequivocally matches such a fold and thus was assigned to Asa3 (Fig. 2A). Therefore, Asa3 must be located at the base of the peripheral stalk, lying on top of the matrix side of the mitochondrial inner membrane. Despite the lack of any sequence homology with proteins of known structure, DALI [27] suggests that it is related to HEAT repeat-containing proteins. Six HEAT repeats (helix-loop-helix motif) pack together

INFORME DE LABORES 2019

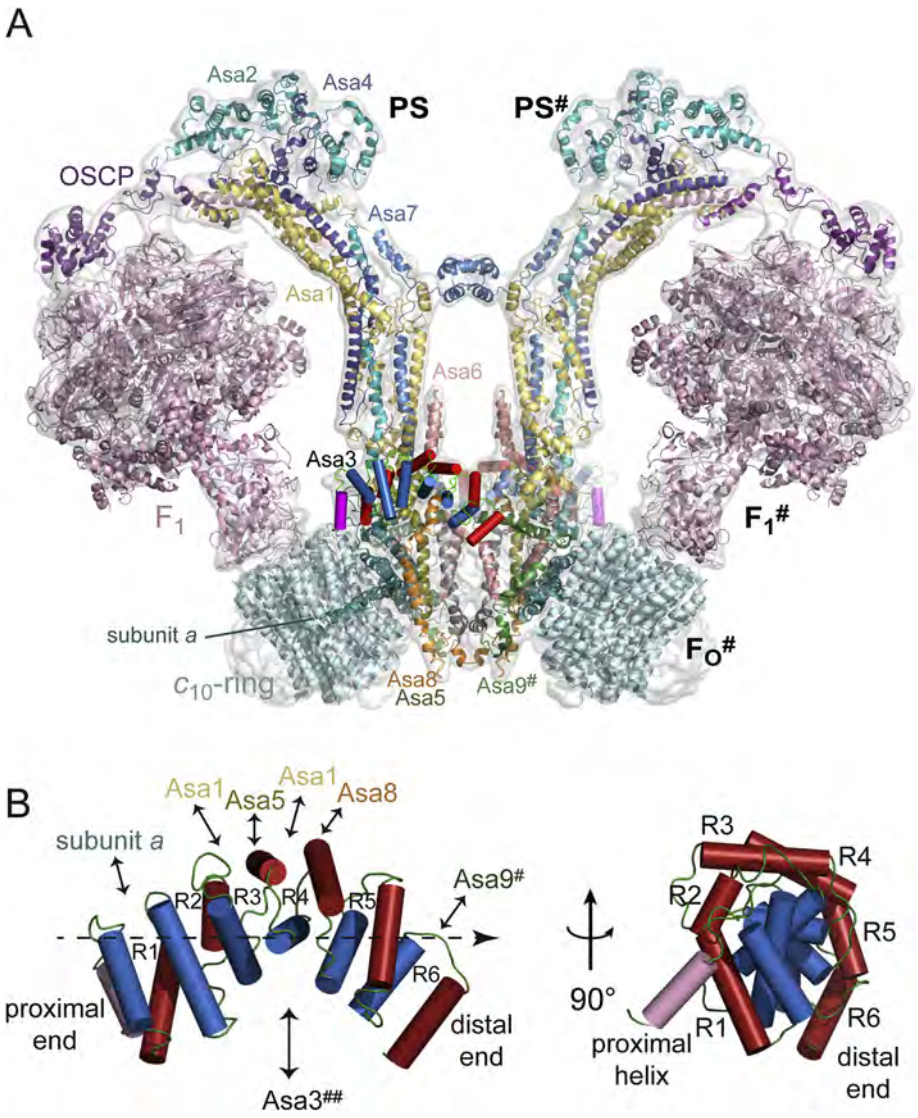

Fig. 2. Molecular model and location of subunit Asa3 in the *Polytomella* ATP synthase. A. Side view of the dimeric ATP synthase model built in the cryo-EM map [4,24]. **B.** Longitudinal (left) and axial (right) schematic views of Asa3. R1-6 HEAT repeats are labeled from the proximal end. Interactions with neighbor subunits are indicated with arrows. # and ## refer to dimeric and oligomeric species, respectively.

forming half a turn of a right-handed super helix of 55 Å length and 20 Å diameter, capped by one helix at the distal extremity (Fig. 2B). Attempts to detect any apparent repetition within successive repeats failed. The low resolution and the regular tandem repeat structure prevent to unambiguously determine the chain orientation. The repeats were labeled R1 to R6 starting at the proximal extremity. The concave face of the super helix groove is shaped by a ladder of 32°–52° tilted helices (Fig. 2B, right panel) turned towards the oligomeric interface, which is likely nested in the neighboring Asa3$^{\#\#}$ (Asa3 of the adjacent dimer). On its convex face, the proximal helix and R1-2 strongly interact with subunit *a* (*a*H2 and *a*C$_{term}$), R3-4 with Asa1, Asa5 and Asa8, whereas R6 interacts with Asa9$^{\#}$ belonging to the neighbor monomer at the dimer interface (Fig. 2B, left panel).

Interestingly, the extended C-terminal domain of the bovine mitochondrial factor B of F-type ATPase is composed of four leucine-rich repeats (LRR, β-strand-loop-helix motif) [28] and cross-linking studies reveal its proximity with subunits *e* and *g* [29] that are involved in dimer stabilization [30]. The N-terminal domain of the H subunit of the *S. cerevisiae* V-type ATPase displays an armadillo fold (three α-helices motif) [31] and links the foot of one of the three peripheral stalks to the soluble domain of the *a* subunit [32]. Thus, it can be argued that three different repeat protein classes, LRR and closely related HEAT and armadillo, were independently selected during the evolution of F- and V-type ATPases to serve as a scaffold for protein-protein interactions.

3.3. Reconstitution of subcomplexes corresponding to the peripheral stalk

Given the Asa1-Asa3 interaction, the previously identified Asa1-OSCP interaction [12], and to further explore these interactions with another approach, a reconstitution protocol was designed to obtain an ^{6H}Asa3ΔN$_{term}$-Asa1-OSCP subcomplex (see Materials and Methods). Starting from solubilized ICBs, proteins were refolded and recovered in a soluble fraction (Fig. 3A). The concentrated sample was subjected to size exclusion cromatography and the elution profile was analyzed by Tricine-SDS-PAGE (Fig. S2). The fractions that corresponded to an ^{6H}Asa3ΔN$_{term}$-Asa1-OSCP subcomplex, identified by SDS-PAGE, were pooled and purified by

INFORME DE LABORES 2019

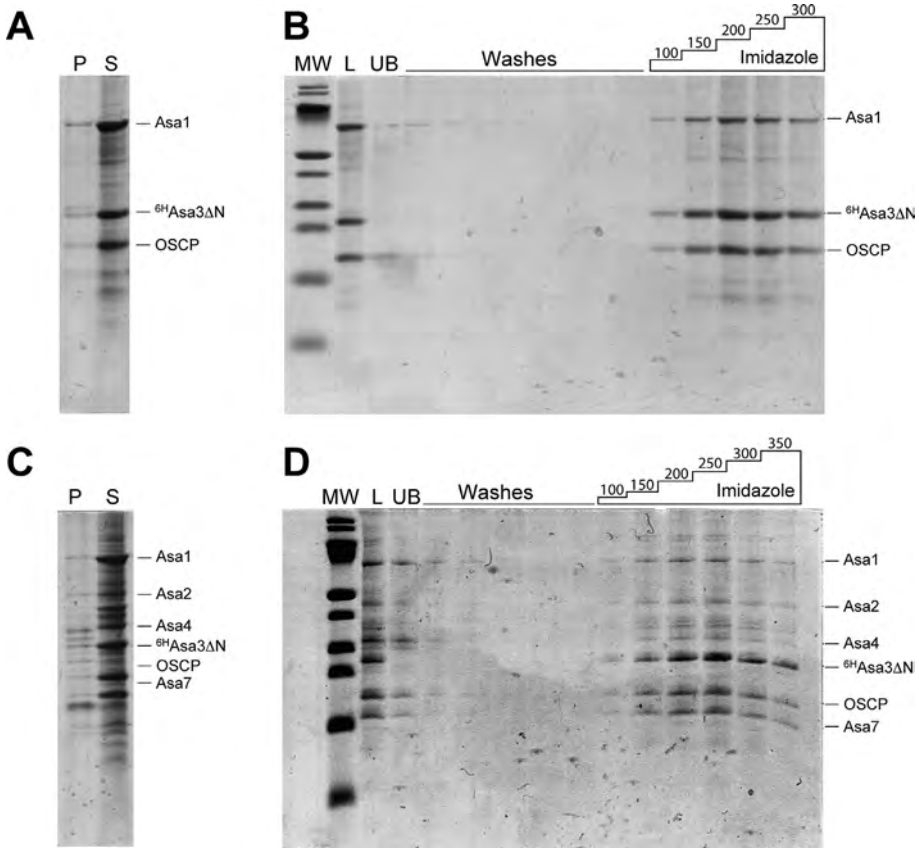

Fig. 3. Reconstitution of subcomplexes from the extrinsic region of the PS of the algal ATP synthase. A. Proteins recovered in the soluble fraction after step-dialysis. P: pellet, S: supernatant. **B.** Co-elution of a reconstituted ^{6H}Asa3ΔN$_{term}$-Asa1-OSCP subcomplex after size exclusion and batch purification. M: molecular weight markers, L: loaded sample mixed with resin, UB: unbound material, the staircase indicates elution with increasing imidazole concentrations (mM). **C.** Proteins recovered in the soluble fraction after step-dialysis. P: pellet, S: supernatant. **D.** Co-elution of a reconstituted ^{6H}Asa3ΔN$_{term}$-Asa1-Asa2-Asa4-Asa7-OSCP subcomplex after size exclusion and batch purification. Abbreviations as in B.

affinity chromatography. After extensively washing the resin to ensure all unbound material was removed, fractions were recovered following a batch procedure eluting at increasing imidazole concentrations, after which the three subunits were recovered together (Fig. 3B). This result supports the idea that Asa1 spans the entire peripheral stalk [12] bridging Asa3 with OSCP.

Asa1, Asa3 and Asa8 seem to connect tightly, since they are consistently found in subcomplexes generated after treating the algal ATP synthase with heat, detergent or amphipol [8,10,12]. The Asa1-Asa3 and Asa3-Asa8 interactions, as well as the previously reported Asa1-Asa8 interaction [11,12], may explain why these proteins remain associated in subcomplexes after dissociating the enzyme. In the 3D map of the dimer Asa3 bridges both PSs [4]; our results suggest that this subunit may act as a clamp that joins the extrinsic part of the PS with its membrane-bound sector, a connection instrumental for enzyme function. Thus, we thought it was feasible to reconstitute the membrane-extrinsic section of the PS, and hypothesized that the ^{6H}Asa3ΔN$_{term}$-Asa1-OSCP subcomplex should interact with the previously identified Asa2-Asa4-Asa7 subcomplex [13]. Following the same reconstitution protocol, now including the recombinant proteins Asa2, Asa4 and Asa7, most of the proteins were recovered in the soluble fraction after refolding (Fig. 3C). The concentrated sample was subjected to size exclusion chromatography and the elution profile was analyzed in Tricine-SDS-PAGE (Fig. S3). The fractions that were consistent with a large subcomplex were pooled and incubated with a nickel resin for a batch purification. At the end of the two-step purification process an ^{6H}Asa3ΔN$_{term}$-Asa1-Asa2-Asa4-Asa7-OSCP subcomplex that represents a large fraction of the PS was recovered (Fig. 3D).

3.4. Other associations of subunit Asa1 in the peripheral stalk

The fact that a six-component subcomplex could be reconstituted suggested Asa1 must associate with other proteins besides Asa3 and OSCP, given the location and interactions of the latter two subunits. We thus explored the interactions of Asa1 with Asa2, Asa4 and Asa7 with FWB analyses. Asa1 and Asa2 were tested having one protein on the membrane and incubating with increasing concentrations of the other protein and vice versa. When the membranes containing Asa1 were incubated with increasing concentrations of Asa2 and decorated with anti-Asa2 antibodies, a signal corresponding to Asa1 was obtained (Fig. 4A); the same happened in the complementary experiment (Fig. 4B). An Asa1-Asa7 interaction was detected using the same approach (Fig. 4C and D). In contrast, an Asa1-Asa4 interaction was not detected (data not shown).

Having previously identified an Asa1-OSCP interaction [12], reminiscent of the *b*-OSCP interaction in orthodox F-ATPases, we explored which part of Asa1 contacts OSCP. Accordingly, a truncated version of Asa1 (Asa1ΔC) was generated to evaluate its binding to OSCP. Membranes containing OSCP or OSCPΔC were incubated with Asa1 or with Asa1ΔC and decorated with anti-Asa1 antibodies. The membranes containing OSCP that were incubated with Asa1 exhibited the expected Asa1-OSCP interaction (Fig. 4E), whereas the ones incubated with Asa1ΔC showed a strongly diminished signal (Fig. 4F); finally, when the membranes containing the truncated OSCPΔC were incubated with Asa1ΔC, no signal

INFORME DE LABORES 2019

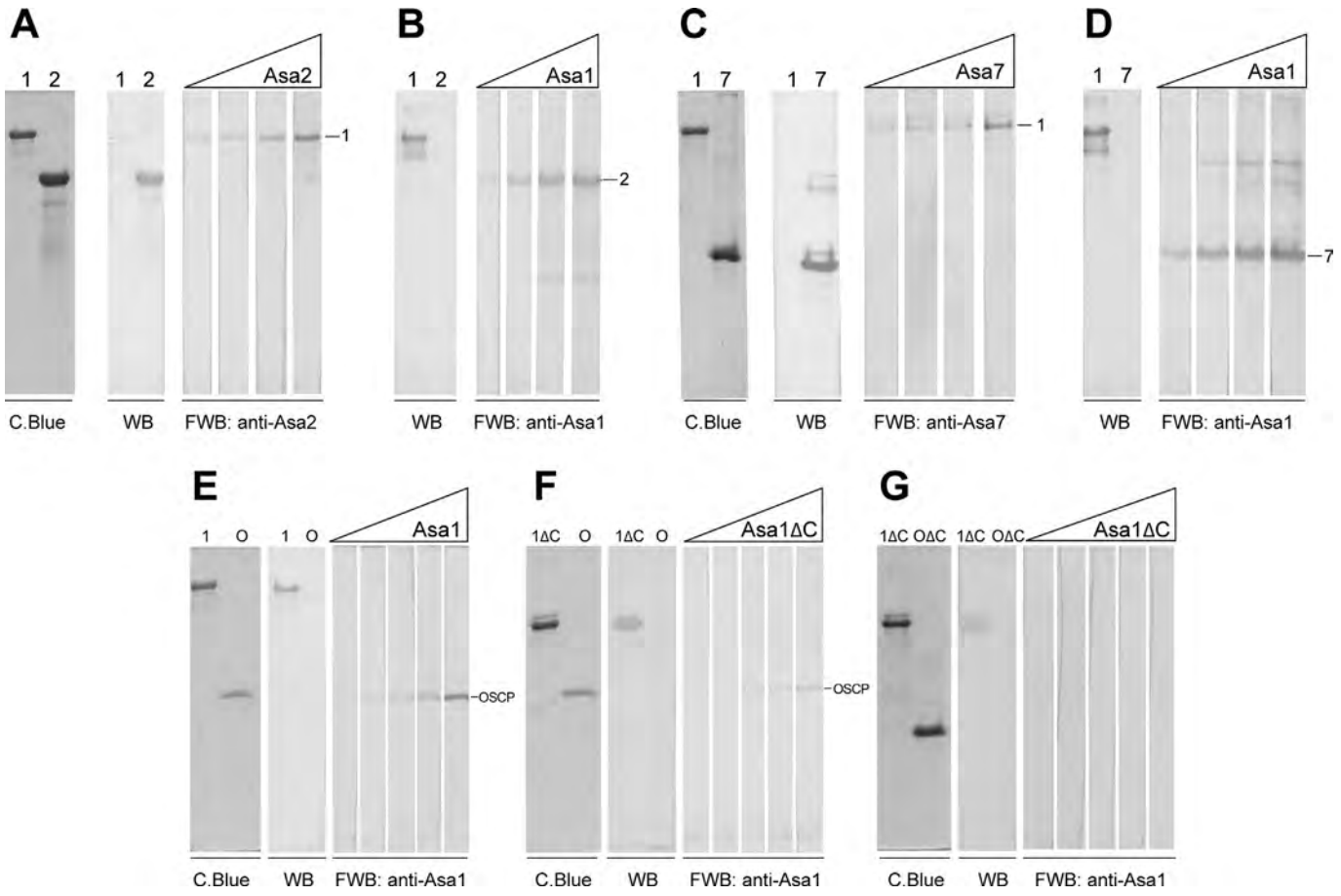

Fig. 4. Associations established by subunit Asa1 assayed by FWB. A-B. Asa1-Asa2 interaction. Asa1 (A) and Asa2 (B) in the membranes incubated with increasing concentrations of Asa2 (A) and Asa1 (B) and decorated with anti-Asa2 (A) and anti-Asa1 (B) antibodies. **C-D.** Asa1-Asa7 interaction. Experiment with Asa1 (C) and Asa7 (D) in the membranes incubated with increasing concentrations of Asa7 (C) and Asa1 (D) and decorated with anti-Asa7 (C) and anti-Asa1 (D) antibodies. **E-F-G.** Asa1-OSCP interaction assayed with complete and truncated subunits. Experiments with OSCP (E and F) and OSCPΔC (G) in the membranes incubated with increasing concentrations of Asa1 (E), Asa1ΔC (F) and Asa1ΔC (G). The membranes were decorated with anti-Asa1 antibodies (E–G).

was obtained (Fig. 4G). This suggests that some of the residues of the C-terminus region of Asa1 must be involved in binding OSCP. Altogether, these results show that Asa1 binds to Asa2 and Asa7, hence their presence in the ^{6H}Asa3ΔN$_{term}$-Asa1-Asa2-Asa4-Asa7-OSCP subcomplex. The fact that we did not detect an Asa1-Asa4 interaction suggests that the presence of Asa4 in the subcomplex occurs through its contact with either Asa2 or Asa7, as previously observed [13]. We also conclude the Asa1-OSCP interaction must occur through the C-terminal regions of both proteins, similar to what happens in the *b*-OSCP interaction in orthodox ATP synthases.

Acknowledgements

We received financial support from grant ECOS Nord-ANUIES-CONACyT 279125, and grants 239219 (Fondo SEP-CONACYT) CONACyT and IN208917 (PAPIIT-DGAPA-UNAM).

Appendix A. Supplementary data

Supplementary data to this article can be found online at https://doi.org/10.1016/j.bbrc.2018.12.142.

References

[1] K.M. Davies, M. Strauss, B. Daum, J.H. Kief, H.D. Osiewacz, A. Rycovska, V. Zickermann, W. Kuhlbrandt, Macromolecular organization of ATP synthase and complex I in whole mitochondria, Proc. Natl. Acad. Sci. 108 (2011) 14121–14126, https://doi.org/10.1073/pnas.1103621108.

[2] P. Paumard, The ATP synthase is involved in generating mitochondrial cristae morphology, EMBO J. 21 (2002) 221–230, https://doi.org/10.1093/emboj/21.3.221.

[3] N.V. Dudkina, J. Heinemeyer, W. Keegstra, E.J. Boekema, H.P. Braun, Structure of dimeric ATP synthase from mitochondria: an angular association of monomers induces the strong curvature of the inner membrane, FEBS Lett. 579 (2005) 5769–5772, https://doi.org/10.1016/j.febslet.2005.09.065.

[4] M. Allegretti, N. Klusch, D.J. Mills, J. Vonck, W. Kühlbrandt, K.M. Davies, Horizontal membrane-intrinsic α-helices in the stator a-subunit of an F-type ATP synthase, Nature 521 (2015) 237–240, https://doi.org/10.1038/nature14185.

[5] H. Guo, S.A. Bueler, J.L. Rubinstein, Atomic model for the dimeric FO region of mitochondrial ATP synthase, Science (80-.) 358 (2017) 936–940, https://doi.org/10.1126/science.aao4815.

[6] W. Kühlbrandt, K.M. Davies, Rotary ATPases: a new twist to an ancient machine, Trends Biochem. Sci. 41 (2016) 106–116, https://doi.org/10.1016/j.tibs.2015.10.006.

[7] A.W. Mühleip, C.E. Dewar, A. Schnaufer, W. Kühlbrandt, K.M. Davies, In situ structure of trypanosomal ATP synthase dimer reveals a unique arrangement of catalytic subunits, Proc. Natl. Acad. Sci. 114 (2017) 992–997, https://doi.org/10.1073/pnas.1612386114.

[8] M. Vázquez-Acevedo, P. Cardol, A. Cano-Estrada, M. Lapaille, C. Remacle, D. González-Halphen, The mitochondrial ATP synthase of chlorophycean algae contains eight subunits of unknown origin involved in the formation of an atypical stator-stalk and in the dimerization of the complex, J. Bioenerg. Biomembr. 38 (2006) 271–282, https://doi.org/10.1007/s10863-006-9046-x.

[9] A. Cano-Estrada, M. Vázquez-Acevedo, A. Villavicencio-Queijeiro, F. Figueroa-Martínez, H. Miranda-Astudillo, Y. Cordeiro, J.A. Mignaco, D. Foguel, P. Cardol, M. Lapaille, C. Remacle, S. Wilkens, D. González-Halphen, Subunit-subunit interactions and overall topology of the dimeric mitochondrial ATP synthase

of Polytomella sp, Biochim. Biophys. Acta Bioenerg. 1797 (2010) 1439–1448, https://doi.org/10.1016/j.bbabio.2010.02.024.
[10] M. Vázquez-Acevedo, F. Vega-deLuna, L. Sánchez-Vásquez, L. Colina-Tenorio, C. Remacle, P. Cardol, H. Miranda-Astudillo, D. González-Halphen, Dissecting the peripheral stalk of the mitochondrial ATP synthase of chlorophycean algae, Biochim. Biophys. Acta Bioenerg. 1857 (2016) 1183–1190, https://doi.org/10.1016/j.bbabio.2016.02.003.
[11] L. Sánchez-Vásquez, M. Vázquez-Acevedo, J. de la Mora, F. Vega-deLuna, P. Cardol, C. Remacle, G. Dreyfus, D. González-Halphen, Near-neighbor interactions of the membrane-embedded subunits of the mitochondrial ATP synthase of a chlorophycean alga, Biochim. Biophys. Acta Bioenerg. 1858 (2017) 497–509, https://doi.org/10.1016/j.bbabio.2017.04.004.
[12] L. Colina-Tenorio, H. Miranda-Astudillo, A. Cano-Estrada, M. Vázquez-Acevedo, P. Cardol, C. Remacle, D. González-Halphen, Subunit Asa1 spans all the peripheral stalk of the mitochondrial ATP synthase of the chlorophycean alga Polytomella sp, Biochim. Biophys. Acta Bioenerg. 1857 (2016) 359–369, https://doi.org/10.1016/j.bbabio.2015.11.012.
[13] H. Miranda-Astudillo, A. Cano-Estrada, M. Vázquez-Acevedo, L. Colina-Tenorio, A. Downie-Velasco, P. Cardol, C. Remacle, L. Domínguez-Ramírez, D. González-Halphen, Interactions of subunits Asa2, Asa4 and Asa7 in the peripheral stalk of the mitochondrial ATP synthase of the chlorophycean alga Polytomella sp, Biochim. Biophys. Acta Bioenerg. 1837 (2014) 1–13, https://doi.org/10.1016/j.bbabio.2013.08.001.
[14] N. Klusch, B.J. Murphy, D.J. Mills, Ö. Yildiz, W. Kühlbrandt, Structural basis of proton translocation and force generation in mitochondrial ATP synthase, Elife 6 (2017) 1–16, https://doi.org/10.7554/eLife.33274.
[15] H. Miranda-Astudillo, L. Colina-Tenorio, A. Jiménez-Suárez, M. Vázquez-Acevedo, B. Salin, M.-F. Giraud, C. Remacle, P. Cardol, D. González-Halphen, Oxidative phosphorylation supercomplexes and respirasome reconstitution of the colorless alga Polytomella sp, Biochim. Biophys. Acta Bioenerg. 1859 (2018) 434–444, https://doi.org/10.1016/j.bbabio.2018.03.004.
[16] A. Cano-Estrada, M. Vázquez-Acevedo, A. Villavicencio-Queijeiro, F. Figueroa-Martínez, H. Miranda-Astudillo, Y. Cordeiro, J.A. Mignaco, D. Foguel, P. Cardol, M. Lapaille, C. Remacle, S. Wilkens, D. González-Halphen, Subunit-subunit interactions and overall topology of the dimeric mitochondrial ATP synthase of Polytomella sp, Biochim. Biophys. Acta Bioenerg. 1797 (2010) 1439–1448, https://doi.org/10.1016/j.bbabio.2010.02.024.
[17] M.W. Bowler, M.G. Montgomery, A.G.W. Leslie, J.E. Walker, Ground state structure of F1-ATPase from bovine heart mitochondria at 1.9 Å resolution, J. Biol. Chem. 282 (2007) 14238–14242, https://doi.org/10.1074/jbc.M700203200.
[18] D.M. Rees, A.G.W. Leslie, J.E. Walker, The structure of the membrane extrinsic region of bovine ATP synthase, Proc. Natl. Acad. Sci. U. S. A 106 (2009) 21597–21601, https://doi.org/10.1073/pnas.0910365106.
[19] E.F. Pettersen, T.D. Goddard, C.C. Huang, G.S. Couch, D.M. Greenblatt, E.C. Meng, T.E. Ferrin, UCSF Chimera - a visualization system for exploratory research and analysis, J. Comput. Chem. 25 (2004) 1605–1612, https://doi.org/10.1002/jcc.20084.
[20] P.D. Adams, R.W. Grosse-Kunstleve, L.W. Hung, T.R. Ioerger, A.J. McCoy, N.W. Moriarty, R.J. Read, J.C. Sacchettini, N.K. Sauter, T.C. Terwilliger, PHENIX: building new software for automated crystallographic structure determination, Acta Crystallogr. Sect. D Biol. Crystallogr. 58 (2002) 1948–1954, https://doi.org/10.1107/S0907444902016657.
[21] D.W.A. Buchan, F. Minneci, T.C.O. Nugent, K. Bryson, D.T. Jones, Scalable web services for the PSIPRED protein analysis workbench, Nucleic Acids Res. 41 (2013) 349–357, https://doi.org/10.1093/nar/gkt381.
[22] T. Nugent, D.T. Jones, Transmembrane protein topology prediction using support vector machines, BMC Bioinf. 10 (2009) 1–11, https://doi.org/10.1186/1471-2105-10-159.
[23] P. Emsley, K. Cowtan, Coot: model-building tools for molecular graphics, Acta Crystallogr. Sect. D Biol. Crystallogr. 60 (2004) 2126–2132, https://doi.org/10.1107/S0907444904019158.
[24] L. Colina-Tenorio, A. Dautant, H. Miranda-Astudillo, M.F. Giraud, D. González-Halphen, The peripheral stalk of rotary ATPases, Front. Physiol. 9 (2018) 1–19, https://doi.org/10.3389/fphys.2018.01243.
[25] Y. Fukasawa, J. Tsuji, S.-C. Fu, K. Tomii, P. Horton, K. Imai, MitoFates: improved prediction of mitochondrial targeting sequences and their cleavage sites, Mol. Cell. Proteomics 14 (2015) 1113–1126, https://doi.org/10.1074/mcp.M114.043083.
[26] J. Yang, R. Yan, A. Roy, D. Xu, J. Poisson, Y. Zhang, The I-TASSER Suite: protein structure and function prediction, Nat. Methods 12 (2014) 7–8, https://doi.org/10.1038/nmeth.3213.
[27] L. Holm, P. Rosenström, Dali server: conservation mapping in 3D, Nucleic Acids Res. 38 (2010) 545–549, https://doi.org/10.1093/nar/gkq366.
[28] J.K. Lee, G.I. Belogrudov, R.M. Stroud, Crystal structure of bovine mitochondrial factor B at 0.96-A resolution, Proc. Natl. Acad. Sci. 105 (2008) 13379–13384, https://doi.org/10.1073/pnas.0805689105.
[29] G.I. Belogrudov, The proximal N-terminal amino acid residues are required for the coupling activity of the bovine heart mitochondrial factor B, Arch. Biochem. Biophys. 473 (2008) 76–87, https://doi.org/10.1016/j.abb.2008.02.022.
[30] J. Habersetzer, W. Ziani, I. Larrieu, C. Stines-Chaumeil, M.F. Giraud, D. Brèthes, A. Dautant, P. Paumard, ATP synthase oligomerization: from the enzyme models to the mitochondrial morphology, Int. J. Biochem. Cell Biol. 45 (2013) 99–105, https://doi.org/10.1016/j.biocel.2012.05.017.
[31] M. Sagermann, T.H. Stevens, B.W. Matthews, B.W. Matthew, Crystal structure of the regulatory subunit H of the V-type ATPase of Saccharomyces V-type ATPase of saccharom', Proc. Natl. Acad. Sci. U. S. A 98 (2001) 7134–7139, https://doi.org/10.1073/pnas.131192798.
[32] J. Zhao, S. Benlekbir, J.L. Rubinstein, Electron cryomicroscopy observation of rotational states in a eukaryotic V-ATPase, Nature 521 (2015) 241–245, https://doi.org/10.1038/nature14365.

STEM CELLS AND DEVELOPMENT
Volume 28, Number 16, 2019
© Mary Ann Liebert, Inc.
DOI: 10.1089/scd.2018.0226

The Substantia Nigra Is Permissive and Gains Inductive Signals When Lesioned for Dopaminergic Differentiation of Embryonic Stem Cells

Omar Collazo-Navarrete,[1,2,*] David Hernández-García,[2] Gilda Guerrero-Flores,[2,*] René Drucker-Colín,[1,†] Magdalena Guerra-Crespo,[1,§] and Luis Covarrubias[2]

Downloaded by Sistemas Biblioinforma S.a De C.v. from www.liebertpub.com at 10/15/20. For personal use only.

Transplantation of dopaminergic (DA) cells into the striatum can rescue from dopamine deficiency in a Parkinson's disease condition, but this is not a suitable procedure for regaining the full control of motor activity. The minimal condition toward recovering the nigrostriatal pathway is the proper innervation of transplanted DA neurons or their precursors from the substancia nigra pars compacta (SNpc) to their target areas. However, functional integration of transplanted cells would require first that the host SNpc is suitable for their survival and/or differentiation. We recently reported that the intact adult SNpc holds a strong neurogenic environment, but primed embryonic stem cells (ie, embryoid body cells, EBCs) could not derive into DA neurons. In this study, we transplanted into the intact or lesioned SNpc, EBCs derived from embryonic stem cells that were prompt to differentiate into DA neurons by the forced expression of *Lmx1a* in neural precursor cells (R1B5/NesE-Lmx1a). We observed that, 6 days post-transplantation (dpt), R1B5 or R1B5/NesE-Lmx1a EBCs gave rise to Nes^+ and Dcx^+ cells within the host SNpc, but a large number of Th^+ cells derived only from EBCs exogenously expressing *Lmx1a*. In contrast, when transplantation was carried out into the 6-hydroxidopamine-lesioned SNpc, the emergence of Th^+ cells from EBCs was independent of exogenous *Lmx1a* expression, although these cells were not found by 15 dpt. These results suggest that the adult SNpc is not only a permissive niche for initiation of DA differentiation of non-neuralized cells but also releases factors upon damage that promote the acquisition of DA characteristics by transplanted EBCs.

Keywords: transplantation, substantia nigra, dopaminergic differentiation, adult neurogenesis

Introduction

Parkinson's disease (PD), the second most common neurodegenerative disease, is characterized by the selective loss of A9-subtype ventral midbrain neurons that project to the striatum [1]. The current therapy for PD is the administration of dopamine analogs that, although effective for reducing some motor symptoms, their effects are lost after long-term administration and, in addition, can generate severe side effects [2]. Hence, there is a pressing demand for more effective therapies.

Among the promising alternative therapies is the replacement of damaged neurons by cell transplantation. Studies in PD patients or animal models have indicated that these therapies can result in significant symptomatic improvements [3–5]. To date, cell transplantation into the striatum is the most common strategy to rescue from dopamine deficiency; however, cell transplantation into the substancia nigra pars compacta (SNpc) followed by a proper rewiring should provide a better condition for the re-establishment of motor functions. In contrast with transplantations to the striatum, the latter strategy requires cells with the potential of getting the full characteristics of mesencephalic dopaminergic (DA) neurons and a host environment for efficient survival and differentiation, the minimal conditions for functional integration.

Pluripotent stem cells (PSCs), self-renewable cells with high differentiation potential, are a promising cell source for the treatment of degenerative disorders, including PD [6]. Although significant improvements in protocols for specific PSC differentiation have been accomplished [7,8], undesirable

[1]Department of Molecular Neuropathology, Instituto de Fisiología Celular, Universidad Nacional Autónoma de México, Mexico City, Mexico.
[2]Department of Developmental Genetics and Molecular Physiology, Instituto de Biotecnología, Universidad Nacional Autónoma de México, Cuernavaca, Mexico.
*Current affiliation: Laboratorio Nacional de Recursos Genómicos, Instituto de Investigaciones Biomédicas, Universidad Nacional Autónoma de México, Mexico City, Mexico.
[§]Current affiliation: Facultad de Medicina, Universidad Nacional Autónoma de México, Mexico City, Mexico.
[†]Deceased.

INFORME DE LABORES 2019

Downloaded by Sistemas Biblioinforma S.a De C.v. from www.liebertpub.com at 10/15/20. For personal use only.

fates or incomplete differentiation could influence functional integration, resulting in poor recovery and/or unwanted side effects after grafting. The in vitro DA differentiation of PSCs goes through several stages including ectodermal specification, neuralization, and neuronal differentiation [7,9,10]. Cells at each stage bear distinct characteristics some of which could fit those required, not only for efficient DA differentiation, but also for their integration after being transplanted.

Of interest, embryoid body cells (EBCs), embryonic stem cell (ESC) derivatives representing the cell population at the epiblast stage of embryonic development, differentiate efficiently into DA neurons when transplanted to the DA niche of the developing mesencephalon. However, the efficiency of this specific differentiation was markedly reduced when cells are differentiated in vitro [11]. These observations indicate that a large proportion of EBCs hold the full potential to acquire the DA neuronal phenotype when they are in a DA differentiation context, but this is lost or affected when in vitro neuronal differentiation is allowed.

The SNpc, site where mesencephalic DA neurons reside in the adult brain, has shown the ability to support DA neuronal survival when mesencephalic fetal cells are implanted after a pharmacological DA neuron depletion. Remarkably, differentiated neurons are able to project axons to the striatum [12–14]. Similarly, DA neurons derived from human ESCs also could survive in the rodent-lesioned adult SNpc [14].

We recently reported that EBCs directly transplanted to the intact adult SNpc, although do not give rise to DA neurons, differentiate into neurons with a similar efficiency to that of EBCs implanted in a well-known neurogenic area, the subventricular zone of lateral ventricles or the rostral migratory tract [15]. In contrast, EBCs cannot differentiate into neurons in the intact striatum, but when they are transplanted after an ischemic lesion, they can derive into neurons, suggesting that a lesion creates a condition that favors neurogenesis [15]. Therefore, the intact SNpc allows EBCs neuronal differentiation, possibly triggered by inductive signals present in this region, but an open question is whether the factors required for directing specific differentiation or survival can emerge upon damage.

In this study, we tested the possibility of in vivo DA neuronal differentiation in the intact and lesioned SNpc of ESCs at their earliest stage of differentiation (ie, after forming EBC) using wild-type ESCs and ESCs prompted to differentiate into DA neurons by the Nestin-enhancer-controlled expression of a *Lmx1a* transgene (R1B5/NesE-Lmx1a cell line). R1B5/NesE-Lmx1a EBCs acquired neuronal and DA markers at 6 days post-transplantation (dpt) in the adult SNpc, whereas wild-type EBCs derived into neural precursors cells (NPCs) and neuroblasts but did not acquire DA markers. Of interest, either R1B5/NesE-Lmx1a or wild-type EBCs efficiently differentiate into Th^+ cells within the 6-hydroxidopamine (6-OHDA)-lesioned SNpc. Therefore, brain damage not only generates conditions that allow neurogenesis of transplanted EBCs but also favor those that promote acquisition of DA characteristics.

Materials and Methods

Generation of the R1B5/NesE-Lmx1a cell line

R1B5 cells (a gift from Andras Nagy) were propagated on mitomycin c-treated mouse embryonic fibroblast cells (feeder cells) in ESC media (also called M15) composed of Dulbecco's modified Eagle's medium (DMEM; Gibco, Grand Island, NY) supplemented with 15% heat-inactivated fetal bovine serum, GPS (1×Glutamax; Gibco; 0.3 mg/mL of penicillin and 0.5 mg/mL of streptomycin; Sigma, St. Louis, MO), 1×MEM nonessential amino acids (from a 100×stock; Gibco), 1 mM sodium pyruvate (Gibco), 0.55 mM 2-mercaptoethanol (Sigma), and 1,000 U/mL of leukemia inhibitor factor (LIF; Chemicon, Temecula, CA). Before differentiation, cells were cultured in the 2i media containing the selective Gsk3β and Mek1/2 inhibitors, CHIR99021 (3 μM) and PDO325901 (1 μM), respectively (Stemgent, Beltsville, MD). To generate R1B5/NesE-Lmx1a ESC line, R1B5 cells were electroporated with the pNesE-Lmx1a vector (gift from Elisabet Andersson), and 24 h after reseeding them, cultured in the presence of 400 μg/mL G418 (Sigma) for clone selection. Individual clones were picked and expanded for 14 days, as described for R1B5 cells.

In vitro differentiation of ESCs

Unbiased neural differentiation was carried out using the one-step short-term protocol based on cells grown as a monolayer [9]. Cells were plated on gelatin-coated dishes and incubated in M15 medium for 12–15 h. Thereafter, cells were washed once with phosphate-buffered saline (PBS) and grown in N2B27 medium, composed of 50% DMEM/nutrient mixture F12 (F12), 50% neurobasal medium, and supplemented with 1×N2 and 1×B27 (from a 100×and 50×stocks, respectively; Gibco). RNA from putative NPCs derived from each clone was extracted to determine the *Lmx1a* transgene expression levels. For specific DA differentiation, we used the progressive 5-stage protocol [7]. In brief, ESCs were expanded on a feeder cell monolayer in M15 medium for 3 days. Then, trypsin-dissociated cells were seeded on gelatinized dishes in feeder-free conditions and cultured in M15 medium supplemented with LIF for 3 days (Stage 1: feeder-free ESC growth). After clearing ESCs from feeder cells, the cells were seeded on non-adherent bacterial culture dishes and cultured for 4 days in M15 media, without LIF or 2i, to form embryoid bodies (EBs; Stage 2). For the selection of NPCs (Stage 3), EBs were seeded on adherent conditions using gelatin-coated culture dishes in M15 medium for 24 h, then, 7 days in the selection medium composed of DMEM/F12 without HEPES (Gibco) plus 1×insulin/transferrin/selenium/sodium pyruvate supplement (100×ITS-A stock; Gibco), 1 mg/mL fibronectin (Gibco) and GPS. For expansion of NPCs (Stage 4), trypsin-dissociated NPCs were seeded on 24-well culture dishes, previously treated with poly-D-lysine (10 μg/mL; Sigma) and fibronectin (1 μg/mL; Gibco), in the expansion medium composed of DMEM/F12 without HEPES supplemented with 10 ng/mL Fgf2, 100 ng/mL Fgf8; and 500 ng/mL Sonic Hedgehog (all growth factors from Peprotech, Rocky Hill, NJ) for 7 days. To promote terminal differentiation (Stage 5), cells were cultured in differentiation medium composed of the expansion medium without growth factors for 6 days. Immunolabeling and real time polymerase chain reaction (PCR) were performed at fourth and fifth stage to detect expression of specific genes of neural or neuronal cells and the transgene expression.

INFORME DE LABORES 2019

Downloaded by Sistemas Biblioinforma S.a De C.v. from www.liebertpub.com at 10/15/20. For personal use only.

Animal and cell transplantation procedures

Animals were housed under a 12-h light/dark cycle with ad libitum access to food and water. All procedures were approved by the bioethical committees of the Instituto de Biotecnología and of the Instituto de Fisiología Celular (MGC08). Embryos used were from CD1 mice at 10.5 days postcoitum (E10.5; 0.5 was the day of mating plug detection); pregnant mice were killed by cervical dislocation. E10.5 midbrain explant cultures and the transplant-into-explant procedure were performed as previously described [11]. The brains of adult male Wistar rats (250 g) were used as the host for EBCs. For transplantation, animals were anesthetized with a mix of xylazine (8 mg/kg; PiSA, Guadalajara, México) and ketamine (10 mg/kg; PiSA) and those with transplanted cells were killed by an overdose of pentobarbital (PiSA) at 6 or 15 dpt. Cell transplantations to adult rat brains were performed by stereotaxic surgery; coordinates for SNpc were obtained from Paxinos and Watson (−4.7, −1.6, and −8.1 mm; posterior, lateral, and ventral to bregma, respectively) [16]. One to two microliters of EB-derived cell suspension (~150,000 cells) was injected using a 5 µL Hamilton syringe. Animals were lesioned with 6-OHDA as previously described [17]. In brief, animals were anesthetized under ketamine–xylazine (as described previously) and 40 µg 6-OHDA (Sigma) in 0.5 µL of saline solution were injected at a rate of 0.1 µL per minute into the left SNpc (coordinates were the same as for cell transplantations). Cell suspensions were obtained from three independent cultures and each transplanted to brains of groups of three rats.

Tissue processing and immunolabeling

Midbrain explants, after 4 or 7 days in culture, were fixed with 4% paraformaldehyde (PFA; Sigma) for 2 h at 4°C. After dehydration with 30% sucrose (J.T.Baker/Avantor Performance Materials S.A. de C.V., Xalostoc, México) for 24 h at 4°C, 10 µm coronal sections were obtained from tissues using a cryostat (Microm HM550; Thermo Scientific, Waltham, MA). For cultured cells, they were fixed with cooled 4% PFA for 20 min and then stored in antifreeze solution. To analyze cells implanted in the adult rat brain, an intracardiac perfusion was performed on the killed animals, first with saline solution (PBS), followed by 4% cooled PFA. Before slicing in frozen conditions, tissues were sequentially dehydrated in 10%, 20%, and 30% sucrose (24 h each). Forty-micrometer slices were obtained from brains and collected in antifreeze solution. After fixation, tissue or cells were subjected to immunolabeling using the protocols described in Maya-Espinosa et al. [15] and Baizabal and Covarrubias [11]. The antibodies used are given in Supplementary Table S1. Processed tissues were analyzed with an epifluorescence or confocal microscope as detailed hereunder.

RNA extraction and quantitative PCR

Total RNA extraction with TRIzol (Invitrogen, Waltham, MA) and complementary DNA (cDNA) synthesis with AMV Reverse Transcriptase (RT; Invitrogen) were carried out following the manufacturer's instructions. Messenger RNA (mRNA) levels were determined by real-time quantitative PCR (qPCR) performed on cDNA produced from total RNA of each sample. The qPCR was carried out using standard protocols with KAPA SYBR® FAST kit (KAPA Biosystems, Wilmington, MA) and Rotor Gene Q thermocycler (Qiagen, Hilden, Germany). To determine relative gene expression levels, a comparative Ct (ΔCt) method was used and the amount of a specific mRNA was normalized based on the estimated amount of Rplp0 or Cyclophilin (Cyc) mRNAs. Primer sequences (forward and reverse) are given in Supplementary Table S2.

Image acquisition and cell counting

For cell quantification in culture, images were captured in a Zeiss AxioVision microscope using AxioVison LE software or direct counting from the microscope eyepieces. We counted at 40× or 60× magnifications in two different fields for each culture. For transplanted cells, images were captured in an Olympus FV1000 multiphoton laser scanning microscope. At least two fields of two slices were analyzed for each transplanted brain (three for each of the three EBC suspensions prepared). Quantifications of double-stained cells were carried out on continuous Z-optical slices. When required, data were statistically analyzed by the Student's *t*-test.

Results

Generation of traceable neural derivatives from ESCs with increased DA differentiation potential

EBCs derived from the R1B5 ESC line, constitutively expressing an *EGFP* transgene, show neural differentiation capacity when transplanted to an adult neurogenic niche, a lesioned striatum or the SNpc; however, in contrast with the specific differentiation observed within the embryonic DA niche [11], their fate was rarely Th^+ neurons [15]. On the contrary, it has been shown that the forced *Lmx1a* expression driven by the chimeric Nestin-enhancer TK-basal promoter (NesE) increases the midbrain DA differentiation capacity of ESCs, as revealed when they are subjected to different DA differentiation protocols [18–20].

To test the capacity of ESCs to carry out DA differentiation in an in vivo context, the *NesE-Lmx1a* transgene was introduced to R1B5 ESCs. Transfected clones were initially selected by the ability to activate the *NesE-Lmx1a* transgene in NPCs (ie, expressing *Nestin*) derived from an unbiased short-term monolayer neural differentiation protocol [9] (Supplementary Fig. S1). From the three ESC clones showing a relatively high *NesE-Lmx1a* transgene expression after 4 days in the neural differentiation medium, two were selected for further analysis (R1B5/NesE-Lmx1a/C3 and R1B5/NesE-Lmx1a/C5) (Supplementary Fig. S1C). Between these two clones, R1B5/NesE-Lmx1a/C3 (referred herein as the R1B5/NesE-Lmx1a) not only had higher *Lmx1a* expression levels but also showed more consistent DA differentiation in culture (see hereunder) and was used for all transplantation experiments.

Overexpression of Lmx1a *leads to DA differentiation in a non-DA embryonic domain*

The capacity of Lmx1a to increase DA differentiation in vitro was previously determined and found that Shh and

INFORME DE LABORES 2019

Downloaded by Sistemas Biblioinforma S.a De C.v. from www.liebertpub.com at 10/15/20. For personal use only.

Fgf8 are still required to lead specific differentiation. To corroborate the increased DA differentiation potential of the selected clones, the five-stage protocol was performed with the R1B5/NesE-Lmx1a line and the DA neuronal differentiation efficiency compared with that obtained with the parental R1B5 line (Fig. 1A). For this, we took advantage of the constitutive presence of GFP to make more evident the changes in cell distribution during the differentiation of live cultures. We did not observe any difference between the two lines in the progress of culture across the differentiation process (Fig. 1B), suggesting that the exogenous Lmx1a or any event during clone selection did not generally affected neural differentiation.

In contrast, a specific effect of exogenous *NesE-Lmx1a* transgene was expected because NPCs derived and expanded from R1B5/NesE-Lmx1a cells showed not only more clusters with Lmx1a but also a greater percentage of $Lmx1a^+/Nes^+$ cells in comparison with that determined for NPCs from R1B5 cells (94.5% vs. 7.8%, $n=3$) (Fig. 1C, D). Accordingly, higher levels of total *Lmx1a* mRNA were detected in samples from R1B5/NesE-Lmx1a cells in comparison with samples at the same stage from R1B5 cells (Fig. 1D).

The DA promoting effect of the exogenous Lmx1a on NPCs was evaluated at the differentiation stage by estimating the number of clusters with Th^+ cells and the proportion of Th^+ cells within each cluster. We found a markedly higher number of cell clusters with Th^+ cells in cultures derived from R1B5/NesE-Lmx1a cells compared with cultures derived from R1B5 cells (94.4%, $n=3$ vs. 38%, $n=2$) (Fig. 1E, F), which correlated very well with the increased number of clusters with Lmx1a at the fourth stage. In addition, the proportion of Th^+ cells in each cluster was also greater for cultures derived from R1B5/NesE-Lmx1a cells than those derived from R1B5 cells (61%, $n=3$ vs. 4%, $n=2$) (Fig. 1F). In agreement with these determinations, differentiated R1B5/NesE-Lmx1a cells showed higher levels of *Th* expression than differentiated R1B5 cells (Fig. 1F). Therefore, Lmx1a in R1B5/NesE-Lmx1a cells can promote DA differentiation at early (estimated by the number of developed Th^+ clusters) and late (estimated by the number of Th^+ neurons within each cluster) stages of differentiation.

The DA promoting function of the *NesE-Lmx1a* transgene was also tested in an in vivo embryonic context. DA neurogenesis in the midbrain occurs from the gestational stage E9.0 to the stage E14.0 [21]. We previously determined that EBCs could be specifically instructed to differentiate into mesencephalic DA neurons by the milieu of the ventral midbrain of E10.5 embryos, passing through a gradual differentiation from NPCs Nes^+ and $Lmx1a^+$ up to becoming neuronal postmitotic Th^+ cells [11]. When donor cells implanted into sites far from the ventral midline, they differentiated in accordance with the implantation site.

EBCs derived from the R1B5 or R1B5/NesE-Lmx1a lines were transplanted to the ventricular surface of E10.5 midbrains and cells analyzed at 4 and 7 days postimplantation (dpi) (Fig. 2). At 4 dpi, as with R1B5 EBCs, implanted cells within the ventral region (the DA domain) acquired Nes and Lmx1a markers in most implantation cases (five of six cases) but no Th^+ cells were detected (zero of six cases) (Fig. 2B, C). In contrast, at this same stage of explant culture, implanted R1B5 EBCs within the dorsal region (non-DA domain) did not develop into $Lmx1a^+$ cells, whereas implanted R1B5/NesE-Lmx1a EBCs within this same region derive into $Lmx1a^+$ cells in some implantation cases (two of four cases) (Fig. 2B, C).

At day 7, R1B5/Nes-Lmx1a EBCs implanted in either the ventral or dorsal region gave rise to cells coexpressing *Lmx1a* and *Th* (6 of 11 cases in the ventral region and 3 of 8 cases in the dorsal region) (Fig. 2B, C), whereas coexpression of these markers was only detected for cells derived from R1B5 EBCs when implanted in the DA domain (3 of 4 cases) (Fig. 2B, C), as previously reported. Because the endogenous *Lmx1a* was only activated when EBCs implanted around the midline, these observations agree with the promotion of DA differentiation by the activation of the *NesE-Lmx1a* transgene upon reaching the NPC differentiation stage. The fact that many NPCs ectopically expressing *Lmx1a* in dorsal regions did not become Th^+ neurons, indicates that additional factors present in the ventral region are required to complete DA differentiation (Fig. 2), as recently reported [22].

Lmx1a overexpression is required for EBCs DA differentiation in the intact SNpc

Although it remains controversial whether the SNpc carries out active neurogenesis for a continuous turnover of DA neurons, we recently propose that, at least, the SNpc holds a silent neurogenic niche that can be detected by EBCs such that they derive into a large number of neurons in this region [15]. Accordingly, R1B5/NesE-Lmx1a EBCs survived in the SNpc and differentiated into a similar proportion of neural cells as transplanted R1B5 EBCs (no significant difference determined). Specifically, transplanted R1B5/NesE-Lmx1a EBCs derived into Nes^+ or Dcx^+ (markers for neural stem cells or neuroblasts, respectively) cells at 6 dpt (Fig. 3). Therefore, exogenous *Lmx1a* does not alter the neurogenic capacity of EBCs in the adult brain.

Strikingly, at 6 dpt many cells expressing *Th* were derived from transplanted R1B5/NesE-Lmx1a EBCs (GFP^+), whereas none was found when R1B5 EBCs were transplanted (Fig. 3) as previously reported [15]. In agreement with the expected effect of Lmx1a in promoting mesencephalic DA neuronal differentiation, several nuclei (at least 16% of total GFP^+ cells) were detected with Pitx3, a transcription factor emerging specifically in the midbrain at an early stage of DA differentiation (Fig. 3E). However, at 15 dpt, the number of GFP^+/Th^+ detected was markedly reduced although the number of Dcx^+ cells was as for R1B5 EBCs ($n=2$) (Fig. 3D) [15]. These observations suggest that Lmx1a can lead EBCs to gain higher DA potential in vivo without the need of exogenous Shh and/or Fgf8, but additional factors seem to be required to complete differentiation and/or increase long-term survival of these putative DA neurons (see Discussion section).

The lesioned SNpc favors DA differentiation of EBCs

In the past, it has been demonstrated that the damaged brain can support neurogenic processes of both endogenous and/or exogenous NPCs or from undifferentiated PSCs [23–25]. To evaluate whether the SNpc can turn into a

Downloaded by Sistemas Biblioinforma S.a De C.v. from www.liebertpub.com at 10/15/20. For personal use only.

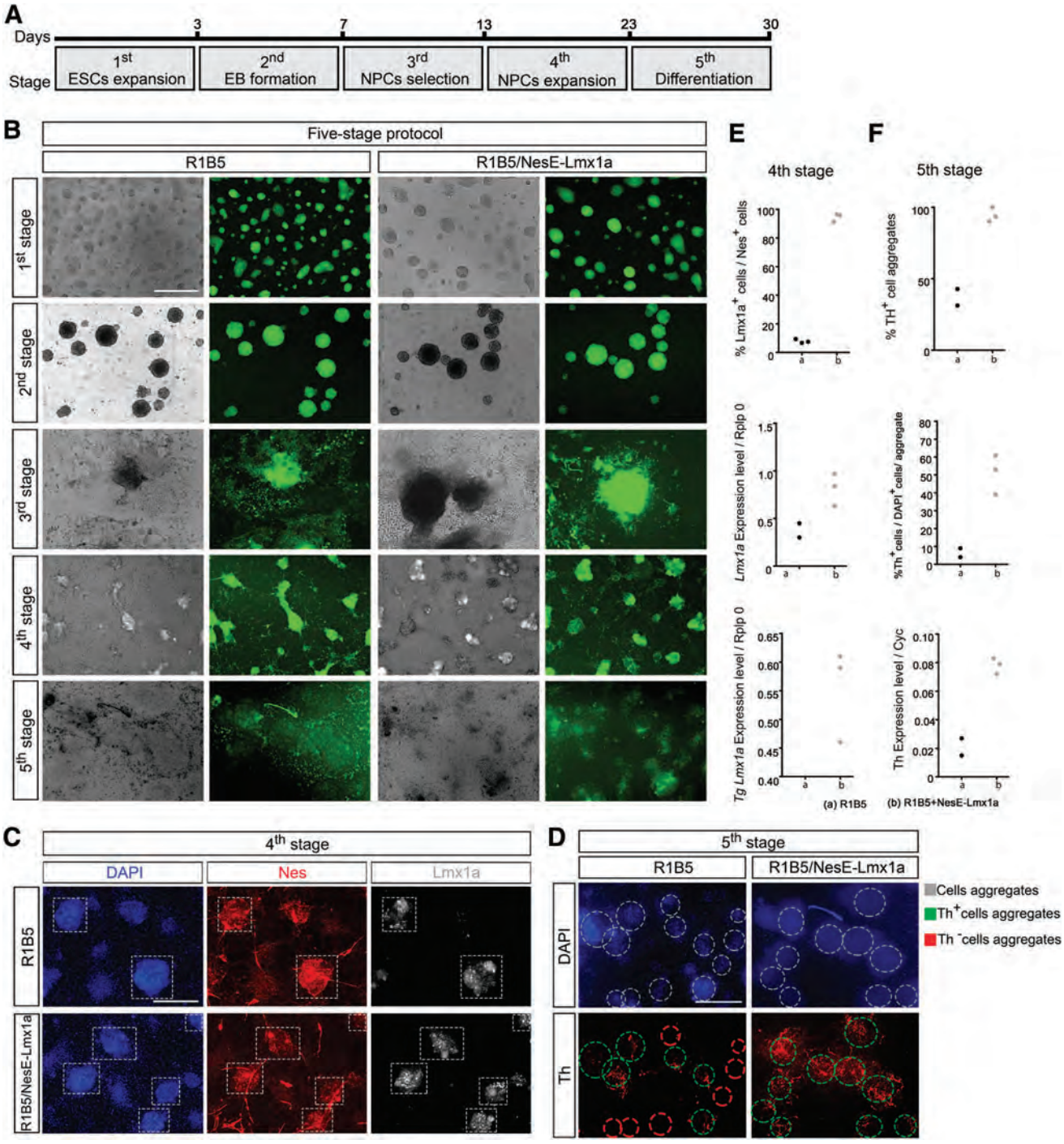

FIG. 1. In vitro DA differentiation of ESCs containing the *NesE-Lmx1a* transgene. **(A)** Scheme of DA neuronal differentiation through the five-stage protocol. R1B5 and R1B5/NesE-Lmx1a ESC were differentiated under the same conditions. **(B)** Bright field and fluorescence (GFP) imaging across each differentiation stage. Low magnification images did not reveal major differences in culture development at any differentiation stage when both cell lines were compared. **(C)** Detection of putative DA NPCs ($Nes^+/Lmx1a^+$). Lmx1a and Nes were detected by specific immunolabeling at the fourth differentiation stage; *dashed squares* indicate $Nes^+/Lmx1a^+$ cell clusters. **(D)** Detection of putative DA neurons (Th^+). Cells immunopositive for Th were found within clusters at the fifth differentiation stage; *dashed circles* delimit distinct cell clusters containing (*green*) or not containing (*red*) Th^+ cells. **(E)** Quantification of the number of putative DA NPCs. Because of the presence of the *Lmx1a* transgene, abundant $Nes^+/Lmx1a^+$ cells were detected at the fourth differentiation stage of R1B5/NesE-Lmx1a differentiation (b, *gray dots*), in contrast with the few found in differentiated R1B5 cells at this same stage (a, *black dots*); determination of *Lmx1a* expression levels by RT-qPCR confirmed this observation. **(F)** Quantification of the number of putative DA neurons. At the fifth differentiation stage, more clusters containing Th^+ cells and more Th^+ cells in each cluster derived from cells of the R1B5/NesE-Lmx1a cell line (b, *gray dots*) than from those of the R1B5 cell line (a, *black dots*); higher *Th* expression levels determined by RT-qPCR confirmed the increased DA differentiation efficiency of R1B5/NesE-Lmx1a cells. Scale bars: 500 µm. DA, dopaminergic; ESCs, embryonic stem cells; NPCs, neural precursors cells; RT-qPCR, reverse transcriptase quantitative PCR. Color images are available online.

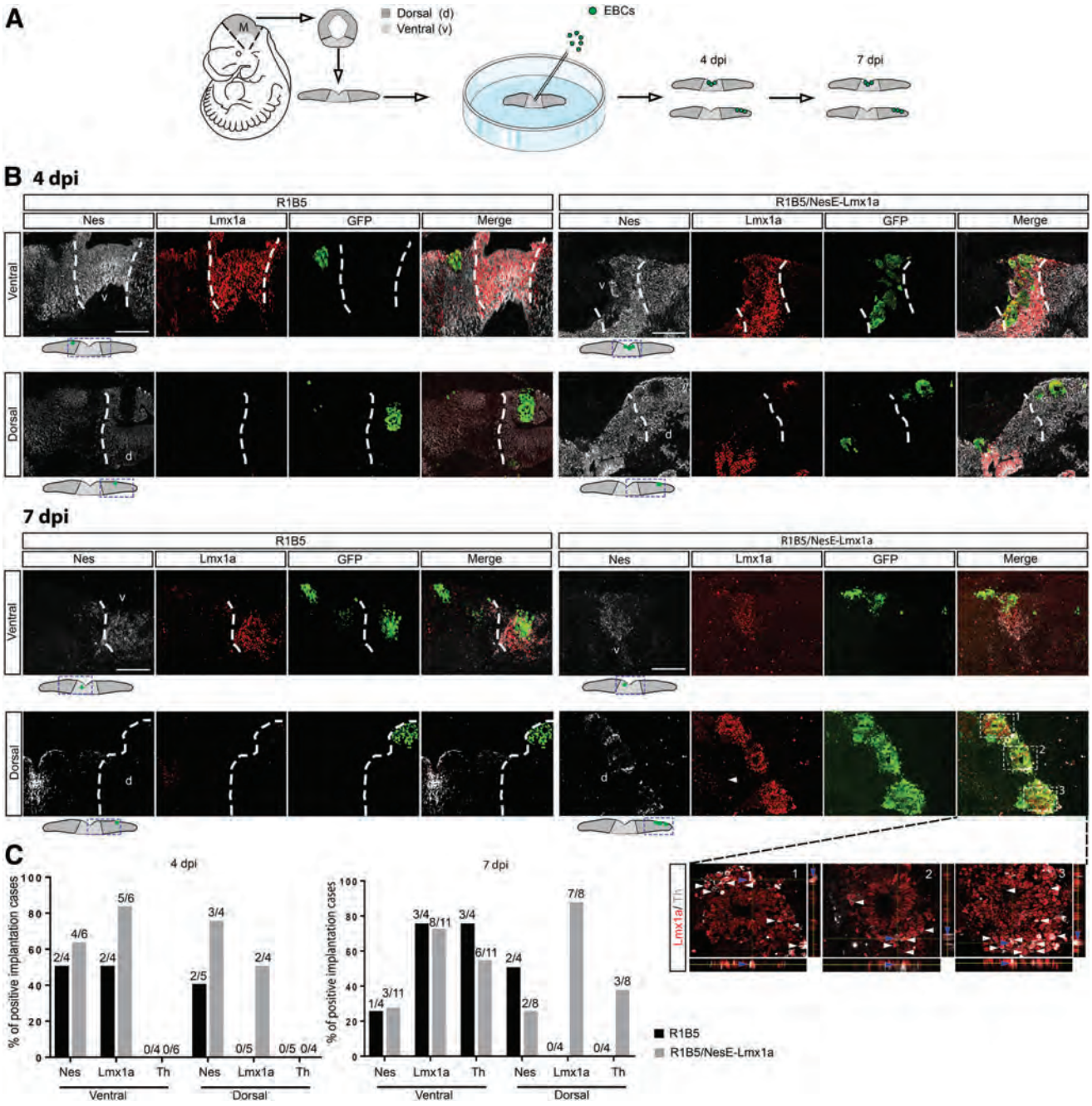

FIG. 2. Evaluation of *Lmx1a* transgene function in the developing midbrain context. **(A)** Schematic representation of the midbrain explant culture and implantation of EBCs into the ventral or dorsal area (DA or non-DA niche, respectively). **(B)** Detection of EBC-derived DA NPCs or neurons in midbrain explants. Nes, Lmx1a and Th were detected by immunolabeling at 4 or 7 days after implanting (dpi) R1B5 or R1B5/NesE-Lmx1a EBCs (GFP^+) into the ventral (4 and 7 dpi, *upper panels*) or dorsal (4 and 7 dpi, *lower panels*) midbrain regions. Magnification of zones are delimited by *dashed squares*; *white arrowheads* indicate implanted cells (GFP^+) coexpressing *Lmx1a* and *Th*, whereas some of these selected for orthogonal analysis are indicated with *blue arrowheads*. **(C)** DA differentiation efficiency of EBCs in the ventral or dorsal midbrain. Number of implantation cases in which implanted cells were positive for Nes, Lmx1a or Th markers at 4 or 7 dpi in ventral or dorsal areas were determined. Note that, whereas EBCs derived from both cell lines behaved similarly once integrated into the ventral region or near to it, only those derived from the R1B5/NesE-Lmx1a cell line gave rise to Nes^+ and/or $Lmx1a^+$ (at 4 dpi) and $Lmx1a^+$ and/or Th^+ (at 7 dpi) cells when implanted in the dorsal region. Scale bars: 200 µm. dpi, days postimplantation; EBC, embryoid body cell. Color images are available online.

stronger neurogenic niche after lesioned with 6-OHDA, the fate of EBCs from R1B5 and R1B5/NesE-Lmx1a lines was determined when transplanted to the lesioned SNpc (Fig. 4). At 6 dpt, a proportion of EBCs implanted at the lesioned area had a neuronal morphology and, unexpectedly, many of those cells were Th^+ (>20%) (Fig. 4 and Supplementary Fig. S2) disregarding whether they derived or not from cells containing the *NesE-Lmx1a* transgene (Fig. 4B–D). A significant proportion of these Th^+ cells coexpressed *Dcx* (>90%) (Fig. 5).

Downloaded by Sistemas Bibliotecarios S.a De C.v. from www.liebertpub.com at 10/15/20. For personal use only.

Downloaded by Sistemas Biblioinforma S.a De C.v. from www.liebertpub.com at 10/15/20. For personal use only.

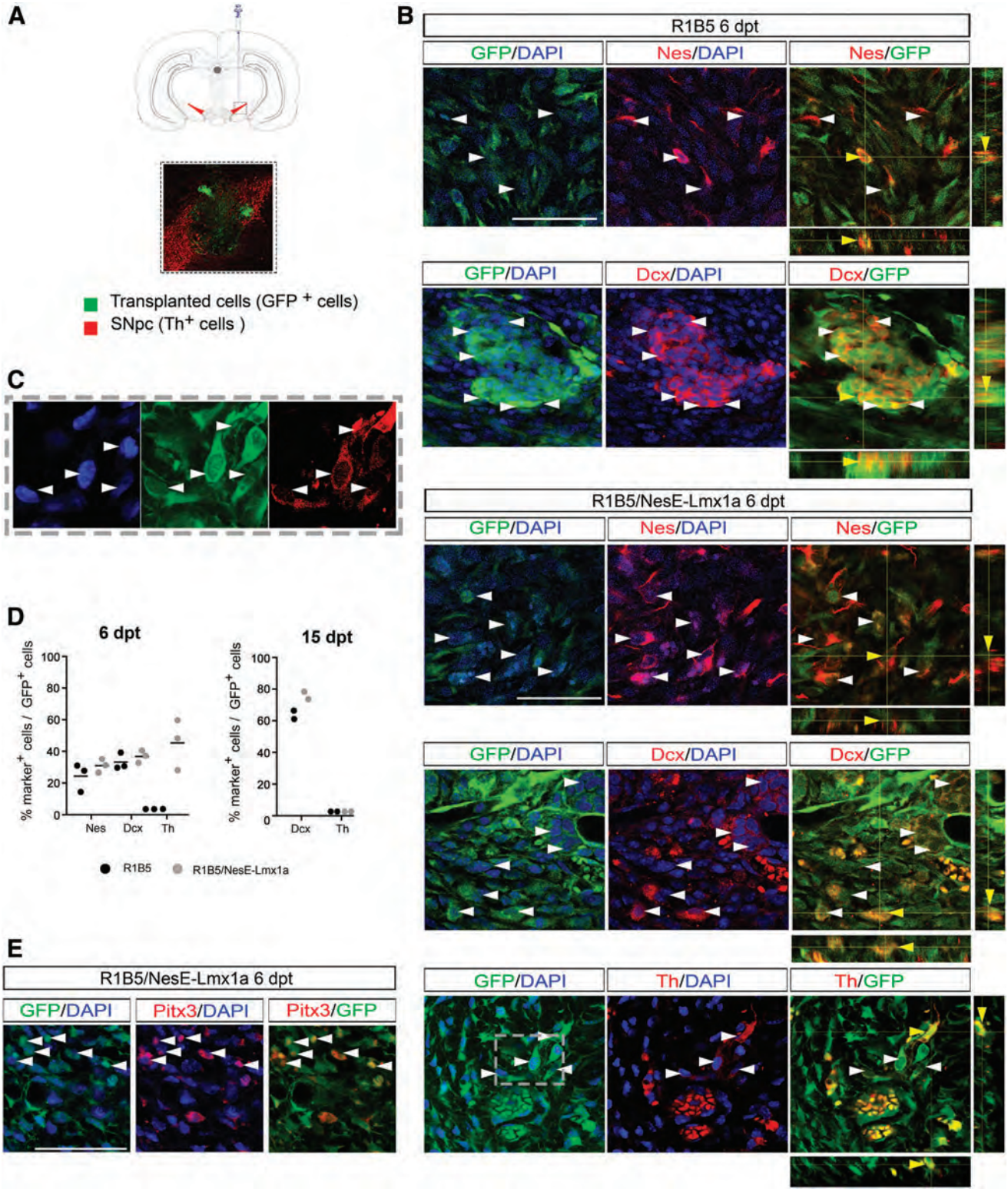

FIG. 3. Effect of *Lmx1a* overexpression on DA differentiation of EBCs in the intact rat SNpc. **(A)** Schematic representation of EBC transplantation to the adult SNpc. A representative image revealing the typical implantation site of EBCs (GFP^+) within the SNpc (Th^+, *red*) is shown. **(B)** DA fate of EBCs in the SNpc at 6 dpt. NPCs (Nes), neuroblast (Dcx), and DA (Th) markers were determined by immunostaining at 6 dpt in cells derived from transplanted R1B5 and R1B5/NesE-Lmx1a EBCs; *white arrowheads* indicate transplanted cells (GFP^+) expressing *Nes*, *Dcx* or *Th*, whereas *yellow arrowheads* indicate those cells selected for orthogonal views. **(C)** A higher magnification of the *dashed square* in *lower panels* of **(B)**. **(D)** Quantification of EBC neural and DA differentiation in the SNpc at 6 and 15 dpt. GFP^+ cells presenting the given marker were manually counted; each point in graph represents the average differentiation efficiency of EBCs derived from an independent culture and transplanted to the brain of three rats. Note that, whereas transplanted EBCs from both lines differentiated into similar number of NPCs and neuroblasts at 6 dpt, only R1B5/pNes-Lmx1a EBCs differentiated into Th^+ cells. **(E)** Detection of the midbrain-specific DA differentiation marker Pitx3. Pitx3 was immunodetected in transplanted cells at 6 dpt; *arrowheads* indicate positive nuclei for this marker. Scale bars: 50 μm. dpt, Days posttransplantation; SNpc, substancia nigra pars compacta. Color images are available online.

INFORME DE LABORES 2019

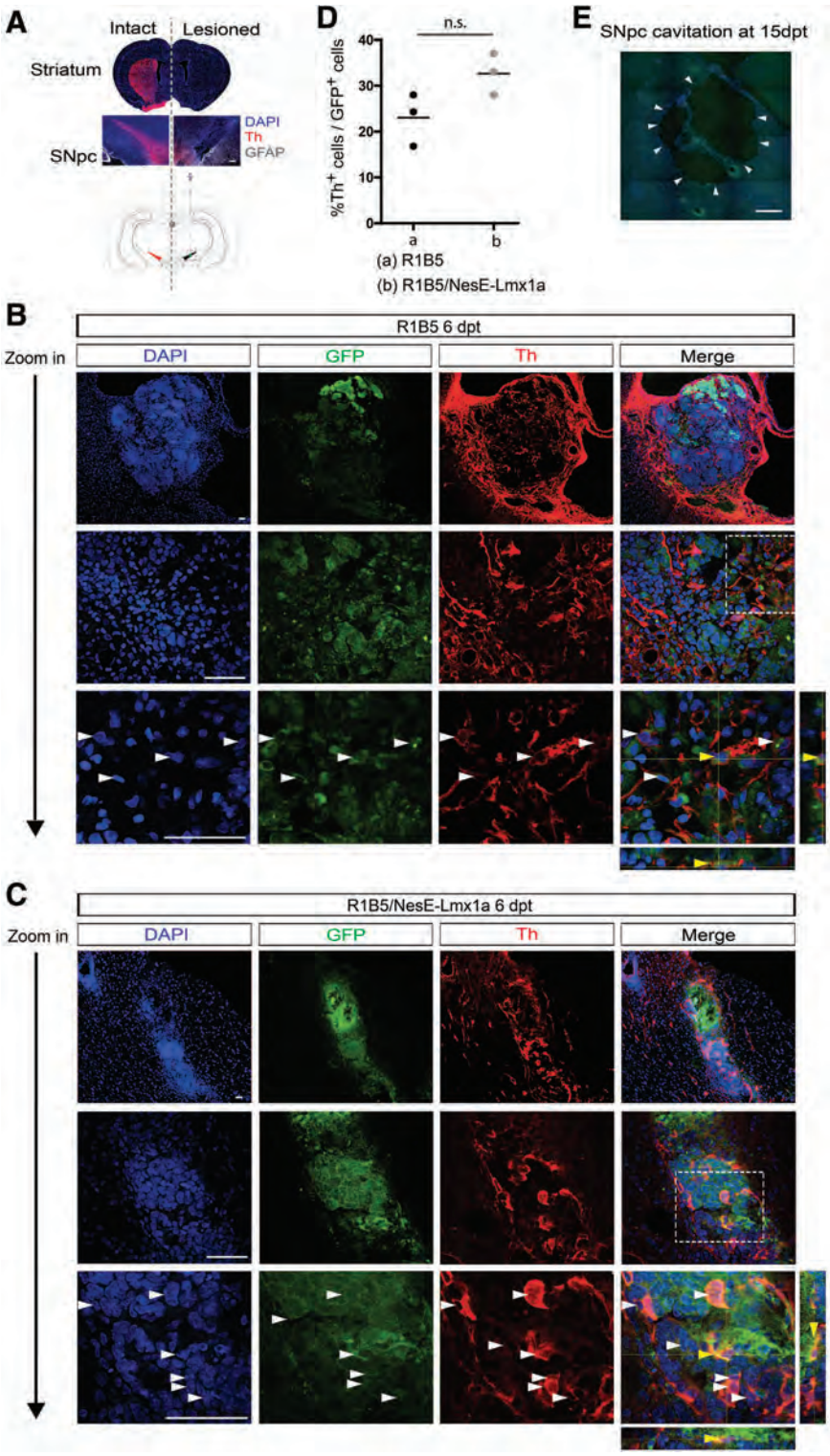

FIG. 4. Effect of lesioned SNpc on EBC DA differentiation. **(A)** Schematic representation of EBC transplantation to the lesioned adult SNpc. Representative images revealing the lack of Th (*red*) in coronal sections containing the SNpc-innervating striatum (*upper image*) or the SNpc (*lower image*) 2 weeks after unilaterally inducing DA neuron depletion are shown; EBCs were transplanted at this stage. Scale bar: 200 μm. **(B, C)** Detection of putative DA EBC-derived cells in the lesioned SNpc. Th was immunodetected at 6 dpt in cells from R1B5 **(B)** and from R1B5/NesE-Lmx1a **(C)** after EBCs were transplanted to lesioned animals. *Dashed squares* delimit the magnified area shown in the *lower panels*; *white arrowheads* indicate Th^+ cells derived from transplanted EBCs, whereas *yellow arrowheads* indicate those cells analyzed in orthogonal views. Scale bars: 50 μm. **(D)** Quantification of EBC DA differentiation in the lesioned SNpc. GFP^+ cells presenting Th were manually counted; each *point* in graph represents the average differentiation efficiency of EBCs derived from an independent culture and transplanted to the brain of three rats; n.s., no significant difference found. Note that, in contrast with the results in the intact SNpc, R1B5 and R1B5/NesE-Lmx1a EBCs differentiated into Th^+ cells in the lesioned region. **(E)** X-Y reconstruction of the lesioned SNpc at 15 dpt. Image is composed of 3 (*x* axis) × 4 (*y* axis) images. *Arrowheads* indicate the cavitated zone. Scale bar: 200 μm. It was apparent that cavitation continued growing after transplantation and no EBCs was found at 15 dpt. Color images are available online.

In contrast with the outcome of transplanted EBCs in the intact SNpc (at least 30 days survival) [15], the lesioned condition did not allow long-term survival of the in vivo-derived EBCs progeny, possibly because of the cavitation of the host tissue resulting from the 6-OHDA-induced neurodegeneration (Fig. 4E). These results suggest that the lesioned SNpc retains a neurogenic environment but, in addition, gains inductive properties that direct differentiation toward a DA phenotype.

Discussion

The common cell transplantation approach to test the dopamine releasing capacity of grafted cells in a PD animal model is to place them within the target striatal region [26]. For successful therapeutic effectiveness, this strategy does not need cells for transplantation with the capacity for nigrostriatal circuit integration; in this case, rather, grafted cells stimulate the host striatum and rescue from dopamine deficiency by

Downloaded by Sistemas Biblioinforma S.a De C.v. from www.liebertpub.com at 10/15/20. For personal use only.

INFORME DE LABORES 2019

Downloaded by Sistemas Biblioinforma S.a De C.v. from www.liebertpub.com at 10/15/20. For personal use only.

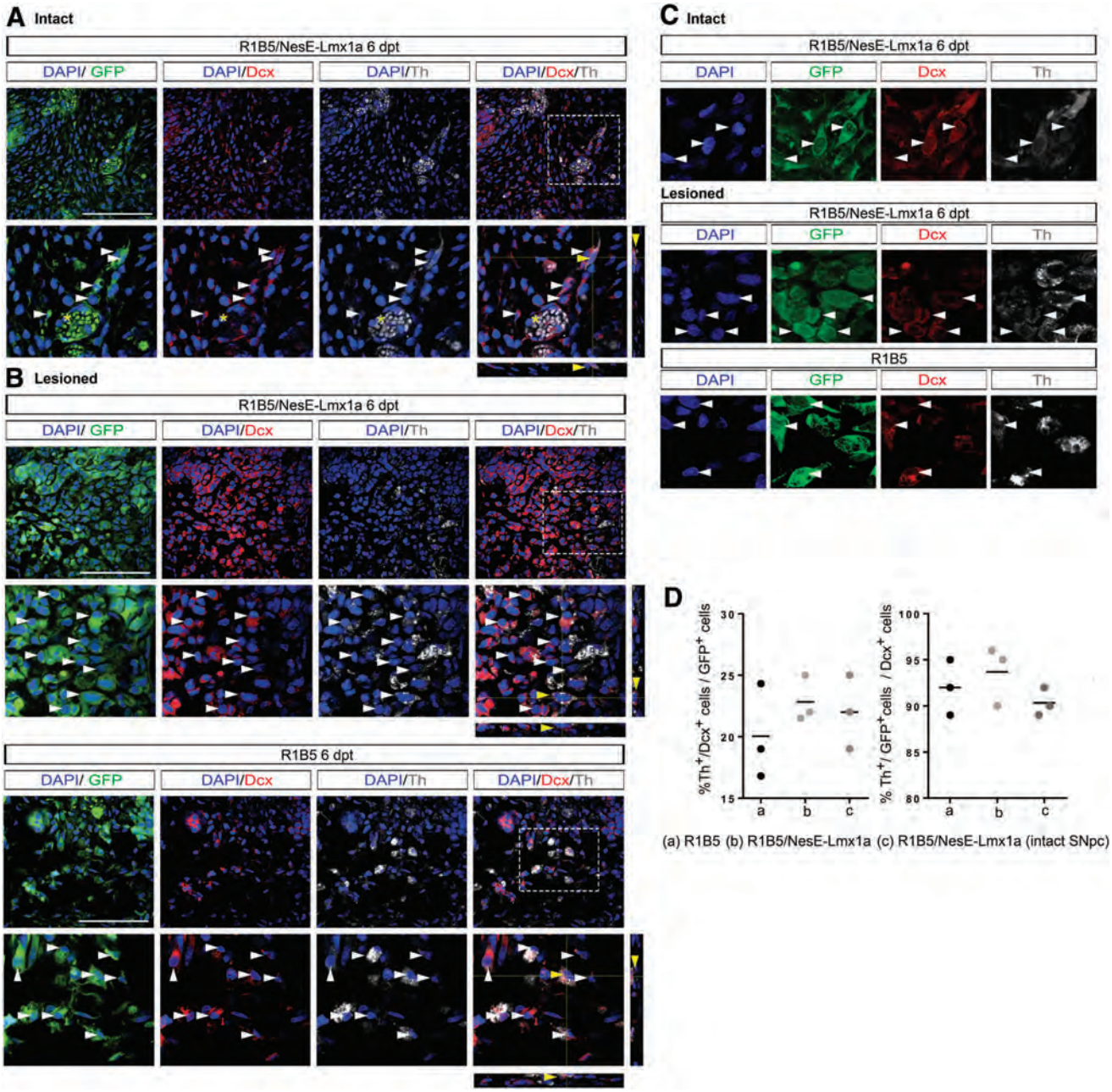

FIG. 5. Differentiation of transplanted EBCs into DA neuroblasts. The Dcx neuroblast marker was immunodetected in Th^+ cells derived from transplanted R1B5 or R1B5/NesE-Lmx1a EBCs in the intact **(A)** or lesioned **(B)** SNpc. *Dashed squares* in *upper panels* delimit the magnified area shown in *lower panels*. *White arrowheads* indicate transplanted cells coexpressing *Th* and *Dcx,* whereas *yellow arrowheads* indicate those cells analyzed in orthogonal views. The *asterisk* indicates a group of Th^+/Dcx^- cells that might represent chromafin-like cells. Scale bars: 100 μm. **(C)** Higher magnifications of transplanted Th^+/Dcx^+ cells (indicated by *white arrowheads*). **(D)** Quantification of EBC-derived DA neuroblasts in the intact and lesioned SNpc. GFP^+ cells positive for Th were manually counted; each *point* in graph represents the average differentiation efficiency of EBCs derived from an independent culture and transplanted to the brain of three rats. Note that most Th^+ cells derived from both lines were neuroblasts as indicated by the presence of Dcx. Color images are available online.

releasing dopamine without requiring the extension of long axons. In contrast, an approach based on transplantation to the SNpc requires cells for transplantation that not only produce dopamine but also are able to direct axons to the specific target neurons in the striatum.

We previously demonstrated that the intact adult SNpc can support efficient neuronal differentiation of non-neuralized EBCs, but DA neurons are not within the EBC-derived neurons [15]. Here we looked to find whether the inability of EBCs to derive DA neurons in the SNpc is limited by the capacity of transplanted cells or by the SNpc host environment that prevents specific differentiation or neuronal survival. For this purpose, we developed a traceable ESC line prompted to differentiate into DA neurons and

INFORME DE LABORES 2019

Downloaded by Sistemas Biblioinforma S.a De C.v. from www.liebertpub.com at 10/15/20. For personal use only.

evaluate its capacity to derive DA neurons in the intact and 6-OHDA-lesioned SNpc.

We confirmed that the introduction of *pNesE-Lmx1a* transgene into ESCs increases the production of DA neurons following the five-stage differentiation protocol in the presence of Shh and Fgf8 [19]. The analysis of these data allows to propose that Lmx1a increases DA differentiation by acting at two different steps of differentiation. Specifically, the higher number of groups containing Th^+ cells can be considered an indication of Lmx1a contribution to the initial specification of DA NPCs, whereas a larger number of Th^+ cells within a group might imply that, after the initial specification, Lmx1a also contributes to DA differentiation. In the context of the intact adult SNpc, Th^+ neuroblasts emerged only in the presence of exogenous Lmx1a and were detected since 6 dpt, but none remained by 15 dpt. Considering the above DA differentiation capacity of EBCs in vitro, this might indicate that the initial Lmx1a-induced specification is occurring in vivo but differentiation could not continue and neuroblasts lose DA identity or died.

Undifferentiated EBCs own the capacity to differentiate into neurons within certain regions of the adult brain. This neuronal differentiation capacity, rather than being a preferred default fate, is likely because of the presence of a permissive or an inductive neurogenic environment [15]. Accordingly, differentiation into neurons was poor in the striatum, although other neural cells (ie, astrocytes) were still among the major cell types derived. In particular, efficient neuronal differentiation of EBCs occurred in the adult SNpc, but DA neurons were not detected. Because EBCs are responsive to DA specification signals, these data are in agreement with the expected absence of specification signals in the intact adult SNpc, a deficit that was at least partially overcome by EBCs expressing an exogenous *Lmx1a* (ie, those derived from the R1B5/NesE-Lmx1a ESC line).

Brain damage creates a local condition that can critically determine the incorporation of new neurons into specific neuronal circuits. When NPCs are transplanted, not only it is necessary that they survive within the damaged area but also that the environment is proper for specific neurogenesis. Neurogenesis or a neurogenic environment sometimes arises upon damage [22–24]. In the 6-OHDA-lesioned SNpc, EBCs can still detect the preexisting neurogenic environment, but in contrast with the observations in the intact SNpc, exogenous Lmx1a for DA specification appeared superfluous and DA neuroblasts were also derived from wild-type EBCs. These data suggest that the lesion by 6-OHDA did not affect the neurogenic capacity of the SNpc and, rather generates a condition that favors DA differentiation. The possible specification molecules involved remain to be identified.

In contrast with the results presented here, significant survival and/or integration of DA neurons in the lesioned SNpc has been previously achieved with differentiating DA NPCs. For example, NPCs from mouse E12.5 developing mesencephalons transplanted to the lesioned SNpc produce a large number of DA neurons, in some cases showing the ability to project to the striatum [12,13]. However, it is relevant to mention that the NPCs transplanted in these cases include many NPCs already committed to differentiate into DA neurons, such that specific differentiation factors are no longer required. Accordingly, in a study in which NPCs at different stages of differentiation were selected and transplanted to the nonlesioned SNpc or lesioned striatum, DA neurons derived mainly from $Neurog2^+$ NPCs which, in the ventral mesencephalon, represent neuroblasts committed to become DA neurons [22,27].

Committed DA NPCs derived from human ESC in vitro might also be the source of projecting DA neurons emerging in the lesioned SNpc after transplantation [14]. Therefore, the inefficient differentiation and/or survival of DA neuroblasts in our study may be because of the inability of EBC-derived NPCs to reach the committed stage. In the lesioned SNpc this could not be determined because of the few cells surviving after 6 dpt, probably because of the adverse conditions within the damaged area. It will be interesting, however, to determine whether the addition of factors, such as Shh and Fgf8, needed for the progression of DA differentiation and absent in the unlesioned or lesioned SNpc can increase the differentiation efficiency of EBC into DA neurons after transplantation.

To increase the grafting efficiency, allotransplants and xenotransplants are commonly performed with immunosuppressed host animals. Here mouse EBCs were transplanted to the brain of immunocompetent rats, and the use of immunosuppressors such as cyclosporine and tacrolimus was avoided. This latter condition was taken because we noted that EBC growth and neurogenesis is reduced in the presence of these immunosuppressors (unpublished data), an effect that appears to be related to their antiangiogenic activity [28,29]. Although active immune response could affect grafting, this did not appear to be evident up to 15 dpt in the intact SNpc [15]. At 15 dpt, although DA neuroblasts were not detected, many neuroblasts derived from transplanted EBCs remained (Fig. 3D). Therefore, it is unlikely that a specific immune rejection is the cause of lack of EBC-derived DA neurons and, rather factors required for the establishment of committed DA NPC are missing in the SNpc, as mentioned previously.

Transplantation of undifferentiated NPCs for cell replacement therapies may favor their integration into specific neuronal circuits. Although the SNpc holds a strong neurogenic environment that, as shown here, was retained after 6-OHDA lesion, this was not sufficient to direct DA neuronal differentiation. Lmx1a and the 6-OHDA lesion contributed to promote the early DA specification stage of EBCs, but according to the observations presented, additional factors were required to reach terminal differentiation. Optimization of in vivo DA neuronal differentiation from non-neuralized EBCs will require the addition of intrinsic factors (eg, Foxa2) and/or extrinsic factors (eg, Shh and Fgf8), a protocol that needs to ponder also the tumorigenic potential of remaining undifferentiated EBCs.

Acknowledgments

The authors are grateful to Dr. Elisabet Andersson for the generous gift of pNesE-Lmx1a vector. The authors are also grateful to Claudia Rivera for the animal supply. The authors thank to Dr. Andrés Saraleguí and Dr. Arturo Pimentel at the Laboratorio Nacional de Microscopía Avanzada, and Dr. Miguel Tapia at the Unidad de Microscopía (Instituto de Investigaciones Biomédicas, UNAM) for their technical assistance in confocal images capturing. The authors also

INFORME DE LABORES 2019

thank to Marcela Palomero-Rivero, Concepción Valencia, Dr. Salvador Valencia-Sánchez, Francisco Pérez-Eugenio and Maria Escalante for their technical assistance along the present work. The authors are also grateful to Karla Cordova-Flores at Laboratorio Nacional de Recursos Genómicos for her assistance in the elaboration of this article. This study is a part of the requirements for the PhD degree in biomedical research at Programa de Doctorado en Ciencias Biomédicas of O.C.-N. at Universidad Nacional Autónoma de México supported by a fellowship from Consejo Nacional de Ciencia y Tecnología (CONACyT; No. 263466). This project was supported by grants from CONACyT CB-131031 and FOINS-1723, and from DGAPA-PAPIIT IN207116.

Author Disclosure Statement

No competing financial interests exist declared by authors.

Supplementary Material

Supplementary Figure S1
Supplementary Figure S2
Supplementary Table S1
Supplementary Table S2

References

1. Elbaz A, L Carcaillon, S Kab and F Moisan. (2016). Epidemiology of Parkinson's disease. Rev Neurol (Paris) 172: 14–26.
2. Cenci MA. (2017). Molecular mechanisms of L-DOPA-induced dyskinesia. In: *Handbook of Basal Ganglia Structure and Function*. H Steiner and KY Tseng, eds. Elsevier, Amsterdam, pp 857–871.
3. Kriks S, J-W Shim, J Piao, YM Ganat, DR Wakeman, Z Xie, L Carrillo-Reid, G Auyeung, C Antonacci, et al. (2011). Dopamine neurons derived from human ES cells efficiently engraft in animal models of Parkinson's disease. Nature 480:547–551.
4. Li W, E Englund, H Widner, B Mattsson, D van Westen, J Lätt, S Rehncrona, P Brundin, A Björklund, O Lindvall and J-Y Li. (2016). Extensive graft-derived dopaminergic innervation is maintained 24 years after transplantation in the degenerating parkinsonian brain. Proc Natl Acad Sci U S A 113:6544–6549.
5. Müller J, C Ossig, JFW Greiner, S Hauser, M Fauser, D Widera, C Kaltschmidt, A Storch and B Kaltschmidt. (2015). Intrastriatal transplantation of adult human neural crest-derived stem cells improves functional outcome in parkinsonian rats. Stem Cells Transl Med 4:31–43.
6. Meyer AK, M Maisel, A Hermann, K Stirl and A Storch. (2010). Restorative approaches in Parkinson's disease: which cell type wins the race? J Neurol Sci 289:93–103.
7. Lee SH, N Lumelsky, L Studer, JM Auerbach and RD McKay. (2000). Efficient generation of midbrain and hindbrain neurons from mouse embryonic stem cells. Nat Biotechnol 18:675–679.
8. Engel M, D Do-Ha, SS Muñoz and L Ooi. (2016). Common pitfalls of stem cell differentiation: a guide to improving protocols for neurodegenerative disease models and research. Cell Mol Life Sci 73:3693–3709.
9. Ying Q-L, M Stavridis, D Griffiths, M Li and A Smith. (2003). Conversion of embryonic stem cells into neuroectodermal precursors in adherent monoculture. Nat Biotechnol 21:183–186.
10. Kawasaki H, K Mizuseki, S Nishikawa, S Kaneko, Y Kuwana, S Nakanishi, SI Nishikawa and Y Sasai. (2000). Induction of midbrain dopaminergic neurons from ES cells by stromal cell-derived inducing activity. Neuron 28: 31–40.
11. Baizabal J-M and L Covarrubias. (2009). The embryonic midbrain directs neuronal specification of embryonic stem cells at early stages of differentiation. Dev Biol 325:49–59.
12. Gaillard A, M Decressac, I Frappé, PO Fernagut, L Prestoz, S Besnard and M Jaber. (2009). Anatomical and functional reconstruction of the nigrostriatal pathway by intranigral transplants. Neurobiol Dis 35:477–488.
13. Thompson LH, S Grealish, D Kirik and A Björklund. (2009). Reconstruction of the nigrostriatal dopamine pathway in the adult mouse brain. Eur J Neurosci 30: 625–638.
14. Grealish S, E Diguet, A Kirkeby, B Mattsson, A Heuer, Y Bramoulle, N Van Camp, AL Perrier, P Hantraye, A Björklund and M Parmar. (2014). Human ESC-derived dopamine neurons show similar preclinical efficacy and potency to fetal neurons when grafted in a rat model of Parkinson's disease. Cell Stem Cell 15: 653–665.
15. Maya-Espinosa G, O Collazo-Navarrete, D Millán-Aldaco, M Palomero-Rivero, G Guerrero-Flores, R Drucker-Colín, L Covarrubias and M Guerra-Crespo. (2014). Mouse embryonic stem cell-derived cells reveal niches that support neuronal differentiation in the adult rat brain. Stem Cells 33:491–502.
16. Paxinos G and C Watson. (2005). *The Rat Brain in Stereotaxic Coordinates*, 5th edn. Elsevier Academic Press, Amsterdam; Boston, MA.
17. Boronat-García A, M Palomero-Rivero, M Guerra-Crespo, D Millán-Aldaco and R Drucker-Colín. (2016). Intrastriatal grafting of chromospheres: survival and functional effects in the 6-OHDA rat model of Parkinson's disease. PLoS One 11:1–26.
18. Andersson E, U Tryggvason, Q Deng, S Friling, Z Alekseenko, B Robert, T Perlmann and J Ericson. (2006). Identification of intrinsic determinants of midbrain dopamine neurons. Cell 124:393–405.
19. Friling S, E Andersson, LH Thompson, ME Jönsson, JB Hebsgaard, E Nanou, Z Alekseenko, U Marklund, S Kjellander, et al. (2009). Efficient production of mesencephalic dopamine neurons by Lmx1a expression in embryonic stem cells. Proc Natl Acad Sci U S A 106: 7613–7618.
20. Sánchez-Danés A, A Consiglio, Y Richaud, I Rodríguez-Pizà, B Dehay, M Edel, J Bové, M Memo, M Vila, A Raya and JC Izpisua Belmonte. (2012). Efficient generation of A9 midbrain dopaminergic neurons by lentiviral delivery of LMX1A in human embryonic stem cells and induced pluripotent stem cells. Hum Gene Ther 23: 56–69.
21. Bayer SA, KV Wills, LC Triarhou and B Ghetti. (1995). Time of neuron origin and gradients of neurogenesis in midbrain dopaminergic neurons in the mouse. Exp Brain Res 105:191–199.
22. Guerrero-Flores G, A Bastidas-Ponce, O Collazo-Navarrete, M Guerra-Crespo and L Covarrubias. (2017). Functional determination of the differentiation potential of ventral

Downloaded by Sistemas Biblioinforma S.a De C.v. from www.liebertpub.com at 10/15/20. For personal use only.

INFORME DE LABORES 2019

mesencephalic neural precursor cells during dopaminergic neurogenesis. Dev Biol 429:56–70.
23. Arvidsson A, T Collin, D Kirik, Z Kokaia and O Lindvall. (2002). Neuronal replacement from endogenous precursors in the adult brain after stroke. Nat Med 8:963–970.
24. Jones KS and BJ Connor. (2016). The effect of pro-neurogenic gene expression on adult subventricular zone precursor cell recruitment and fate determination after excitotoxic brain injury. J Stem Cells Regen Med 12: P25–P35.
25. Saha B, S Peron, K Murray, M Jaber and A Gaillard. (2013). Cortical lesion stimulates adult subventricular zone neural progenitor cell proliferation and migration to the site of injury. Stem Cell Res 11:965–977.
26. Boronat-García A, M Guerra-Crespo and R Drucker-Colín. (2017). Historical perspective of cell transplantation in Parkinson's disease. World J Transplant 7:179–192.
27. Jönsson ME, Y Ono, A Björklund and LH Thompson. (2009). Identification of transplantable dopamine neuron precursors at different stages of midbrain neurogenesis. Exp Neurol 219:341–354.
28. Siamakpour-Reihani S, J Caster, DB Nepal, A Courtwright, E Hilliard, J Usary, D Ketelsen, D Darr, XJ Shen, C Patterson and N Klauber-DeMore. (2011). The role of calcineurin/NFAT in SFRP2 induced angiogenesis—a rationale for breast cancer treatment with the calcineurin inhibitor Tacrolimus. PLoS One 6(6):e20412.
29. Rafiee P, J Heidemann, H Ogawa, NA Johnson, PJ Fisher, MS Li, MF Otterson, CP Johnson and DG Binion. (2004). Cyclosporin A differentially inhibits multiple steps in VEGF induced angiogenesis in human microvascular endothelial cells through altered intracellular signaling. Cell Commun Signal 2(1), 3.

Address correspondence to:
Dr. Luis Covarrubias
Department of Developmental Genetics and Molecular Physiology
Instituto de Biotecnología
Universidad Nacional Autónoma de México
Av. Universidad 2001
Cuernavaca Mor. 62210
México

E-mail: covs@ibt.unam.mx

Dr. Magdalena Guerra-Crespo
Facultad de Medicina
Universidad Nacional Autónoma de México
Av. Universidad 3000, Coyoacán
Ciudad de México 04510
México

E-mail: magdagmx@hotmail.com

Received for publication November 8, 2018
Accepted after revision May 24, 2019
Prepublished on Liebert Instant Online May 29, 2019

Downloaded by Sistemas Biblioinforma S.a De C.v. from www.liebertpub.com at 10/15/20. For personal use only.

PLOS ONE

RESEARCH ARTICLE

The role of oxidant stress and gender in the erythrocyte arginine metabolism and ammonia management in patients with type 2 diabetes

Martha L. Contreras-Zentella[1], Lourdes Sánchez-Sevilla[1], Juan A. Suárez-Cuenca[2], Marisela Olguín-Martínez[1], Martha G. Alatriste-Contreras[3], Norberto García-García[1], Lorena Orozco[4], Rolando Hernández-Muñoz[1]*

1 Departamento de Biología Celular y Desarrollo, Instituto de Fisiología Celular; Universidad Nacional Autónoma de México (UNAM), Coyoacán, Mexico City, Mexico, **2** Departamento de Medicina Interna, Hospital General "Xoco", Secretaría de Salubridad, Coyoacàn, Mexico City, Mexico, **3** Departamento de Métodos Cuantitativos, División de Estudios Profesionales, Facultad de Economía, Universidad Nacional Autónoma de México (UNAM), Coyoacán, Mexico City, Mexico, **4** Laboratorio de Enfermedades Inmunogénicas y Metabólicas, Instituto Nacional de Medicina Genómica (INMEGEN), Tlalpan, Mexico City, Mexico

* rhernand@correo.ifc.unam.mx

Check for updates

OPEN ACCESS

Citation: Contreras-Zentella ML, Sánchez-Sevilla L, Suárez-Cuenca JA, Olguín-Martínez M, Alatriste-Contreras MG, García-García N, et al. (2019) The role of oxidant stress and gender in the erythrocyte arginine metabolism and ammonia management in patients with type 2 diabetes. PLoS ONE 14(7): e0219481. https://doi.org/10.1371/journal.pone.0219481

Editor: Jonathan M. Peterson, East Tennessee State University, UNITED STATES

Received: December 30, 2017

Accepted: June 25, 2019

Published: July 17, 2019

Copyright: © 2019 Contreras-Zentella et al. This is an open access article distributed under the terms of the Creative Commons Attribution License, which permits unrestricted use, distribution, and reproduction in any medium, provided the original author and source are credited.

Data Availability Statement: All relevant data are available in the Open Science Framework: https://osf.io/a6cd3/?view_only=90dfd426c06648f5bbb96470c689d106.

Funding: This work was supported by Consejo Nacional de Ciencia y Tecnología # 219710 and PAPIIT-DGAPA, UNAM # IN203217. The funders had no role in study design, data collection and

Abstract

Objectives

To study the differences in the levels of nitrogen metabolites, such as ammonia and nitric oxide and the correlations existing among them in both red blood cells (RBCs) and serum, as well as the possible differences by gender in healthy subjects and patients with type 2 Diabetes Mellitus (DM).

Design and methods

This cross-sectional study included 80 patients diagnosed with type 2 DM (40 female and 40 male patients) and their corresponding controls paired by gender (40 female and 40 male). We separated serum and RBC and determined metabolites mainly through colorimetric and spectrophotometric assays. We evaluated changes in the levels of the main catabolic by-products of blood nitrogen metabolism, nitric oxide (NO), and malondialdehyde (MDA).

Results

Healthy female and male controls showed a differential distribution of blood metabolites involved in NO metabolism and arginine metabolism for the ornithine and urea formation. Patients with DM had increased ammonia, citrulline, urea, uric acid, and ornithine, mainly in the RBCs, whereas the level of arginine was significantly lower in men with type 2 DM. These findings were associated with hyperglycemia, glycosylated hemoglobin (Hb A_{1C}), and levels of RBC's MDA. Furthermore, most of the DM-induced alterations in nitrogen-related metabolites appear to be associated with a difference in the RBC capacity for the

analysis, decision to publish, or preparation of the manuscript.

Competing interests: The authors have declared that no competing interests exist.

release of these metabolites, thereby causing an abrogation of the gender-related differential management of nitrogen metabolites in healthy subjects.

Conclusions

We found evidence of a putative role of RBC as an extra-hepatic mechanism for controlling serum levels of nitrogen-related metabolites, which differs according to gender in healthy subjects. Type 2 DM promotes higher ammonia, citrulline, and MDA blood levels, which culminate in a loss of the differential management of nitrogen-related metabolites seen in healthy women and men.

Introduction

Diabetes mellitus (DM) is a worldwide disease frequently associated with a high risk of atherosclerosis and renal, nervous system, and ocular damage [1]. Reactive oxygen species (ROS) have been implicated in the pathogenesis of DM [2], as well as in its complications [3,4]. Patients with type 2 DM frequently have vascular endothelium dysfunction, which is related to hypercholesterolemia, and nitric oxide (NO) deficiency, a major factor that contributes to endothelial dysfunction [5].

Another source of possible complications in DM patients could be derived from an altered nitrogen metabolism, even in the absence of evident liver disease and/or nephropathy. Certainly, experimentally induced diabetic rats have lower gut amino acids utilization, which can diminish alanine and ammonia release into the portal circulation [6]. Therefore, this type of experiments could provide a background for the understanding of why DM patients with hepatic encephalopathy have a lower liver glucose absorption and utilization [7]. Indeed, it has been reported that DM patients have severe hepatic encephalopathy at early stages of chronic liver disease, when compared with non-diabetic patients with hepatic dysfunction [8].

The red blood cells (RBC) play an important role in vascular function, delivering oxygen, minimizing NO scavenging, and further delivering NO bioactivity in hypoxia, through the compartmentalization of hemoglobin (Hb); therefore, RBC promote hemostasis through a well-regulated delivery of oxygen [9]. In fact, reduced levels of NO derived from arginine has been implicated in the vascular dysfunction of diabetic patients. This pathological process is characterized by an impaired endothelial cell production of the vasodilator and an anti-platelet adhesion factor, and/or a decreased NO bioavailability [10].

An increased activity and expression of arginase I is associated with diabetes-induced increase in oxidative stress. It also initiates the feed-forward cycle of diminished NO levels and oxidative stress [11]. Moreover, citrulline could promote NO production and endothelial function and improve peripheral insulin sensitivity [12], improving organ perfusion and the endothelial metabolism, which might involve an antioxidant property [13].

In this context, we have found that type 2 DM alters the metabolite distribution between serum and RBC. Results demonstrate that RBC regulate serum levels of nitrogen-related metabolites, not only by their transport but also by metabolizing amino acids such as arginine, probably through several enzyme-mediated metabolic pathways [14]. In fact, this extra-hepatic nitrogen metabolism, mediated by blood cells, could have a role in the specific physiopathology of type 2 DM. These findings indeed agree with proteomic profiling studies which showed that the mature human RBC have a lot of proteins related to metabolic function, which reveals

an unexpected level of complexity in the functional capabilities of human RBC metabolism [15].

Moreover, it has been reported that there are differences in the nitrogen metabolism in human subjects according to gender. Changes in vascular NO activity may contribute to changes in cardiovascular risk associated mainly with males, probably related to the α-adrenoceptor responsiveness, among other mechanisms [16]. The renal vasculature of men becomes more dependent on NO with age compared with that of women, suggesting that renal diseases progress could be related to gender [17]. Despite the fact that there is little information regarding the management of ammonia according to gender, it is noteworthy that hepatic myelopathy and blood ammonia elevation were found mainly among middle-aged Japanese men with chronic liver disease [18].

Based on the evidence above, we argue that patients with type 2 DM have an aggravated dysregulation of nitrogen metabolism and, therefore, the disturbed intermediary metabolism has more detrimental consequences in several organs. This altered nitrogen metabolism is influenced by gender and oxidant status. Consequently, this study improves our understanding of the relation between the disturbances in several metabolites reflecting nitrogen and nitric oxide (NO) metabolism, and abnormal levels of blood ammonia in the absence of evident nephropathy and liver disease.

Subjects and methods

Study population

We recruited patients with type 2 DM at different stages of the disease, from the outpatient clinics, mostly directly depending on the Ministry of Public Health (SSA, México), mainly from the Xoco General Hospital. The study group consisted of 40 female and 40 male patients with type 2 (non-insulin-dependent) DM. The patients were selected based upon the following criteria: All patients were not active alcoholics, non-smokers, and were on regular treatment for diabetes (with hypoglycemic agents). Patients were apparently free from any important secondary complications such as nephropathy or liver dysfunction. We studied in parallel a control group of healthy 40 female and 40 male who were non-smokers and non-alcoholics. Following a 12 h overnight fast, all individuals were subjected to blood sampling and all patients omitted their morning medication. This study was carried out in accordance with the Declaration of Helsinki (2000) of the World Medical Association and approved by the Ethics Committee of the General Hospital of Mexico (Ministry of Public Health), after written informed consent.

Clinical tests

We measured in serum, through standardized procedures with kits from SPINREACT (Spain), the following metabolites: glucose, cholesterol, triacylglycerols (TG), and the activities of "marker enzymes" of liver damage, namely alanine (ALT-GPT) and aspartate (AST-GOT) aminotransferases. Insulin level was measured with a kit from Ray Bio (USA) and Hb A_{1C} was measured with a kit from BioSys-Kovalent (Brasil) (Table 1).

Biochemical measurements

Whole blood was poured directly into ice-cold perchloric acid (8% w/v, final concentration). After centrifugation, we obtained acid-extracts of serum and RBC. We determined, using enzymatic methods, levels of ammonia [19] and free urea [20] in the neutralized perchloric extracts and assessed the uric acid using a commercial kit (SpinReact, Spain). In addition, we

Table 1. Clinical parameters in control subjects and in female and male patients with type 2 DM.

Subjects	Healthy volunteers		Patients with type 2 DM	
Parameter	Females	Males	Females	Males
BMI	25.6	24.8	27.1	26.5
Glucose (mg %)	88	94	149	142
Insulin (μUnits/ml)	6.4	4.6	8.34	10.1
HOMA-IR	1.7	1.5	3.6	3.5
Hb A_{1C} (%)	4.6	5.0	8.8	8.4
Hb A_{1C} (mmols/mol)	27	29	73	70
TG (mg/dL)	141	148	185	175
Cholesterol (mg/dL)	150	138	185	179
ALT-GPT (IU/L)	18	21	22	23
AST-GOT (IU/L)	19	17	22	25

The results are expressed as medians. Abbreviations: BMI, body mass index; TG, triacylglycerols; ALT, alanine aminotransferase, and AST, aspartate aminotransferase. Most of the distributions were best described by skewed distributions, thus the mean is no longer a good measure of central tendency. Consequently, we relied on the median to compare between sets of data (S1 and S2 Files).

https://doi.org/10.1371/journal.pone.0219481.t001

measured arginine, citrulline, ornithine, nitrites, and malondialdehyde (MDA), with the methods previously described in detail [14]. (dx.doi.org/10.17504/protocols.io.q5qdy5w).

Preparation of RBC for metabolites release assays

Another set of anti-coagulated blood samples was obtained from healthy subjects (40 female and 40 male) and diabetic patients (40 female and 40 male). The serum was rapidly separated and removed after centrifugation at 900 g and 4˚C for 5 min, the buffy coat was removed, and the erythrocyte pellet was washed four times with two volumes of cold (4˚C) buffered solution of 20 mmol/L HEPES (pH = 7.42) and containing 0.9% NaCl. Thereafter, RBC were gently suspended to a 33% hematocrit (Hct) with the same buffered solution and stored at 4˚C overnight, completing 24 h after washing. We obtained acid extracts from aliquots taken from all the washes, the overnight stored solution, and the remaining total RBC pellet. Then, we measured all the metabolites described above from them.

Arginase activity in RBC

The activity of arginase (EC 3.5.3.1) was determined in RBC lysates with 20 mmol/L arginine at pH = 9.5, essentially as described by Colombo and Konarska [21]. The results are expressed as nmol of ornithine • min^{-1} • mg^{-1} of Hb.

Calculations and statistical analysis

We calculated the concentration of serum and RBC metabolites as μmol • ml^{-1} or nmol • ml^{-1}, and the results are expressed as the mean ± SD for levels of metabolites showed. **Statistical analysis**. We have a total of 84 determinations according to metabolite, blood compartment, group, and gender. Each of these data sets has 40 values. We took several blood samples for each patient and each person in the control group, and we obtained determinations from clusters of samples (pooled samples for each individual). Consequently, all results and conclusions drawn out from the analysis should consider that results correspond to the clusters and not to individual patient's data. All data sets are available at the Data sets section of the open science

INFORME DE LABORES 2019

framework project (see https://osf.io/a6cd3/?view_only=90dfd426c06648f5bbb96470c689d106).

The statistical analysis described in this section was performed in the Python 2.7 language using the numpy and scipy libraries (see Statistical analysis code in open science framework project: https://osf.io/a6cd3/?view_only=90dfd426c06648f5bbb96470c689d106). We computed the following descriptive statistics for each set of data: mean, standard deviation, skewness, and medians (**S1 File**). To study differences according to gender we focused on comparing medians since most of the data is best described by skewed distributions and are not normally distributed. In this situation, medians are a better measure of central tendency than means.

Furthermore, to analyze statistical differences according to gender, we first fitted the data to different distributions of continuous variables using maximum likelihood estimation and then obtained estimators for shape, location, and scale parameters for the distributions. We fitted the data to the following distributions: beta, exponential, exponential-weibull, exponential-power law, Gilbrat, logistic, lognormal, normal, Pareto, power law, weibull minimum, and weibull maximum. Then with the maximum likelihood estimators (MLEs), we performed the Kolmogorov-Smirnov (KS) goodness of fit test to obtain the distribution that best described the data for each determination. We chose the best approximation as the distribution which had the smallest D-statistic among all distributions. The KS test for goodness of fit performs a test of the distribution of an observed random variable against a given distribution under the null hypothesis that the two distributions are identical. We report D-statistics and p-values of the KS tests, and MLEs for each determination (**S2 File**).

Finally, we computed Spearman correlation coefficients and their p-values. We use the Spearman correlation because it assesses monotonic relations and it does not assume a linear relation between two sets of data. With the Spearman correlations, we constructed a correlation matrix for all 84 determinations (see **S3 File**). Each row and each column corresponds to a data set of one determination. The cells of the matrix are the Spearman correlation coefficient between two sets of data and the p-value. The Spearman correlation coefficient can take values between -1 and 1, where 0 means no correlation.

Results

Clinical parameters

Most of the distributions were best described by skewed distributions, thus the mean is no longer a good measure of central tendency. Consequently, we relied on the median to compare between sets of data. The medians obtained for the values of the distributions for some clinical parameters (**S1 File**, **Table 1**). The medians for blood glucose, insulin, HbA_{1C} and HOMA-IR, obtained for the control subjects are within the established "normal ranges". In fact, insulin was lower in men, when compared to female healthy subjects. In the case of DM type 2 patients we observed a pronounced post fasting hyperglycemia (> 100 mg/dl), increased levels of Hb A_{1C} (>7%), and hyperinsulinemia (>8 μU/ml). These values are those expected for the two groups under study.

We performed the statistical analysis for each of these sets of values and compared the results. When comparing results for glucose between genders in the control subjects, we found that the best approximation shows different distributions (see **S2 File**, **Table 1**). The Spearman correlation coefficient was weak **S3 File**, **Table 1**).

In the case of patients with type 2 DM, the best approximation for glucose showed the same distribution in both genders, and interestingly, the same as in control men (logistic; **S2 File**, **Table 1**). Nevertheless, the Spearman correlation coefficient between genders for glucose in

diabetic patients indicate that the correlation between male and female is low (0.1581; p-value 0.3296; S3 File, Table 1). Indeed, the comparison between Spearman correlation coefficient of glucose levels in control subjects and in diabetic patients, strongly suggest that together with the difference in glucose management between genders, there is a significant difference between the control subjects and the diabetic patients.

When we compared the values for insulin in the control groups of men and women, the Spearman correlation coefficient suggested a low weak negative correlation according to gender (-0.219; p- value 0.1742) (S3 File, Table 1). In the case of DM type 2 patients, the distributions of insulin were also different according to gender; these distributions were as well different compared to those observed for glucose in the same group. When comparing the Spearman correlation coefficient for insulin in the same gender, between control subjects and diabetics, we found that for both men and women, there is a null correlation, but in the case of women, the distribution is in the opposite direction (S3 File, Table 1). These differences may indicate that the mechanisms involved are connected to other systems that work differently between genders.

With respect to triglycerides, the best approximation for men and women, both for control subjects and for diabetic patients, shows different distributions (see S2 File, Table 1), but the Spearman correlation coefficients (S3 File, Table 1), indicate a low correlation between genders. These differences in distributions suggest differences in the production and regulation of triglyceride synthesis between genders and also between both study groups. As to cholesterol, the best approximation of values in both genders of control subjects and in diabetic men, showed the same distribution (see S2 File, Table 1). Here, the Spearman correlation coefficient indicated a low correlation in the distribution of cholesterol between women and men in control subjects (S3 File, Table 1). The distribution in diabetic women was different and the Spearman correlation coefficient between genders of diabetic patients was close to zero, indicating a null correlation (See S3 File, Table 1).

When comparing the Spearman correlation coefficient for cholesterol in the same gender, between control subjects and diabetic patients, we found that, for both men and women, there is a low correlation between the groups studied (S3 File, Table 1). In the case of women, the distribution is in the opposite direction compared with men, in a manner similar to the distribution of insulin, which suggests important differences in the interconnections between genders.

Results of the statistical analysis of the data obtained for the transaminases enzymes ALT and AST indicated that best approximation for both determinations was different between men and women in control subjects as well as in DM type 2 patients (see S2 File, Table 1). In control subjects the Spearman correlation coefficient suggests a weak and positive correlation according to gender for ALT and AST (S3 File, Table 1), whereas in the case of DM type 2 patients, the relation between genders is null for ALT and weak negative for AST. These results suggest a change in the behavior of activities of both enzymes as a result of pathology. The analysis of the results of the clinical parameters in DM type 2 patients could indicate differences in their production or utilization according to gender. In general, results maintain the differences between genders and also show different effects in the handling of glucose and cholesterol between control subjects and DM type 2 patients.

Blood levels of ammonia, uric acid and urea in patients with type 2 DM

Ammonia, uric acid, and urea are products of the metabolism of proteins (nitrogen metabolism). The median values obtained for our control groups are those shown in the Fig 1. In the control groups, the "free" ammonia clearly predominated in the RBC over serum. Statistically,

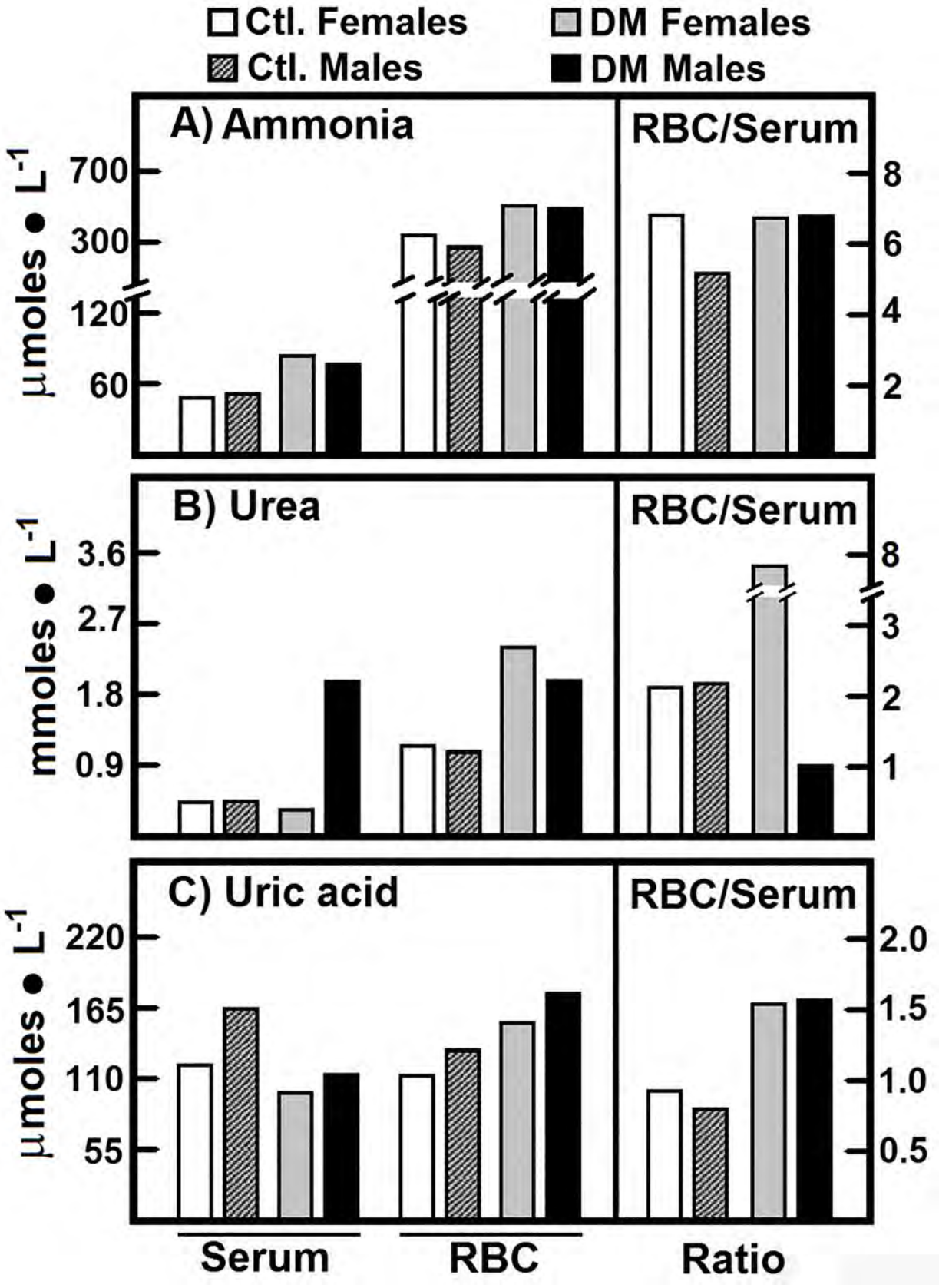
Ctl. Females
DM Females
Ctl. Males
DM Males
A) Ammonia
RBC/Serum
μmoles • L-1
700
300
120
60
8
6
4
2
B) Urea
RBC/Serum
mmoles • L-1
3.6
2.7
1.8
0.9
8
3
2
1
C) Uric acid
RBC/Serum
μmoles • L-1
220
165
110
55
2.0
1.5
1.0
0.5
Serum
RBC
Ratio

Fig 1. Metabolites participating in nitrogen metabolism quantified in serum and RBC from control subjects and in patients with type 2 DM. The results are expressed as the medians for levels of ammonia, urea, and uric acid, in healthy control female (n = 40) and male volunteers (n = 40), as well as in female patients with type 2 DM (n = 40) and male patients with type 2 DM (n = 40). Symbols for experimental groups at the top. Descriptive statistics: Most of the distributions were best described by skewed distributions, thus the mean is no longer a good measure of central tendency. Consequently, we relied on the median to compare between sets of data.

https://doi.org/10.1371/journal.pone.0219481.g001

we found that the ammonia values for the control subjects are best described by different distributions according to gender and blood compartment (see S2 File, Fig 1). The Spearman correlation coefficients for RBC-ammonia of the control subjects indicated a null correlation between genders (S3 File, Fig 1).

We found an accumulation of ammonia in RBC as well as a drastic enhancement of serum ammonia, in female and male patients with type 2 DM. Nevertheless, the RBC/serum ratio for ammonia was similar in the four groups (Fig 1A). The Spearman correlation coefficients indicate a low positive correlation between diabetic female and male ammonia levels in RBC (S3 File, Fig 1). These results give evidence in support of the differential regulation of ammonia according to gender.

The blood urea levels, in all subjects were within normal values (< 3.33 μmol• ml^{-1}). Urea predominated in the RBC fraction in a similar way to the ammonia levels. We noted that serum urea was lower in the male control group than the female control group, which led to an increased RBC/serum ratio of urea in the male control group (Fig 1B). The data obtained for the blood urea levels in the control groups showed different distributions depending on genders and blood compartment (S2 File, Fig 1). Here, we found a null correlation in RBC and a low positive correlation in serum levels (see S3 File, Fig 1), suggesting gender differences in blood urea levels in control subjects (Fig 1B).

The type 2DM patients had a drastic increase of urea in both blood compartments except for serum in women, also indicating clear gender differences for blood urea levels. Women patients had a significantly higher RBC/serum ratio for urea than the female controls, while DM male patients showed an opposite behavior (Fig 1B). These results show that in diabetic patients, RBCs accumulate both ammonia and urea, possibly to keep these metabolites in serum within normal levels, without gender differences. The statistical analysis pointed out of the data obtained for the urea in the DM type 2 patients (see S2 File, Fig 1). The Spearman correlation coefficient indicates a positive weak correlation between genders for urea levels in RBC and serum (see S3 File, Fig 1). These results, together with the above, provide strong evidence in favor of the differences in metabolic regulation according to gender.

The type 2 DM patients showed significantly lower serum levels for uric acid when compared to their respective controls, without modifying those in the RBC fraction. This resulted in higher RBC/serum ratios of uric acid in both genders with type 2 DM (Fig 1C). The statistical analysis for the uric acid determinations shows differences between genders. Nevertheless, uric acid in serum of control and diabetic males, and in RBC and serum of diabetic females, show the same distribution (see S2 File, Fig 1). The Spearman correlation coefficients indicate a positive low correlation between RBC values of control female and males, but a strong positive correlation between the control male and female serum values for uric acid (0.6439, p-value 0.0007). For DM type 2 patients the correlation was significant and positive in RBC (0.6247, p-value 0.0001) and positive but weak in serum (0.2407, p-value 0.1344) (S3 File, Fig 1).

We also measured arginase activity in RBC from control subjects and patients with type 2 DM. We did not find differences by gender in control subjects (2.17 vs. 2.62 nmol • min^{-1} • mg^{-1} of Hb, in women and men, respectively). On the contrary, in the DM type 2 patients indeed increased this enzyme activity. The female patients showed an activity of 3.84 nmol •

min-1 • mg-1 of Hb, which was even higher in diabetic men (6.06 nmol • min-1 • mg-1 of Hb). These significant increases of arginase activity in RBC from patients with type 2 DM could be explain the increased RBC urea amount in these patients (Fig 1B).

Upon comparing the Spearman correlation coefficients between arginase in RBC and urea in serum, we observed that for both genders in DM type 2 patients, the Spearman correlation coefficients indicate a moderate correlation between arginase in RBC and serum urea, although in inverse senses (S3 File, Fig 1).

Metabolites involved in the generation of NO in patients with type 2 DM

The arginine metabolism involving nitric oxide synthetase (NOS) results in the production of citrulline and NO [5]. We have shown that the human RBC in healthy subjects is capable to metabolize arginine into nitrites, citrulline, ornithine, and urea [14], we analyzed these metabolites in DM type 2 patients and compared the results. In the control group we observed that blood arginine was mostly present in RBC, compared to serum (Table 2). The statistical analysis of RBC-arginine values from control subjects showed that the behavior for both genders was best described by the same distribution (S2 File, Table 2), giving an evidence of a positive and significant relation between the values according to gender. Serum arginine levels in the same subjects were around 0.2 mmol • L^{-1} for both genders, and the Spearman correlation coefficient showed a positive and weak correlation (S3 File, Table 2), indicating differences according to gender and blood compartment.

We found an arginine RBC/serum ratio of 4.3 for control male subjects and 2.9 for control female subjects (Table 2). In male patients with type 2 DM, there were not significant differences in serum arginine levels compared to RBC (Table 2). On the opposite, women with DM had higher levels of RBC-arginine than male patients, with congruently higher RBC/serum ratio for this amino acid, when compared to the control group (Table 2).

The medians of the nitrites determinations show that levels in RBC in control subjects and diabetic patients were higher than in serum. We also found that nitrites determinations in RBC and serum of control male subjects were higher than those of control female. On the contrary in patients with DM type 2, the women showed an upper levels of RBC-nitrites (S1 File, Table 2). These results give evidence that type 2 DM reverted gender differences found for the nitrites blood distribution observed in the control groups (Table 2).

The statistical analysis of the nitrites determinations in control subjects shows that in the case of serum, the same distributions were obtained for control women and diabetic men. The distributions of the nitrites levels from RBC in control men and RBC and serum of diabetic women were also the same (S2 File, Table 2). There were positive weak and low correlations of values in RBC and in serum, respectively, between the both gender in control subjects. However, whereas that the Spearman correlation coefficients indicate a low correlation between levels of nitrites in RBC from female and male DM type 2 patients, (S3 File, Table 2), importantly a strong and positive correlation was obtained between levels of nitrites for diabetic men and women in serum (S3 File, Table 2). As previously found for other metabolites, the statistical distributions and the Spearman correlation coefficients indicate differences in nitrites levels according to gender and blood compartments.

Arginine is synthesized from citrulline by the sequential activities of the cytosolic enzymes argininosuccinate synthetase (ASS) and argininosuccinate lyase (ASL), and these proteins have already been identified in RBC [22]. While serum levels of ornithine showed no differences according to gender, the male control group showed higher RBC-ornithine than the control females (see S1 File, Table 2). Type 2 DM promoted higher ornithine content in RBC of female patients but not of men. This led to a significant increase the RBC/serum ratio for

INFORME DE LABORES 2019

Table 2. RBC and serum levels of nitrogen-related metabolites and their ratios in female and male patients with type 2 DM.

Subjects	Healthy volunteers		Patients with type 2 DM	
Parameter	Females	Males	Females	Males
Serum-Arginine	0.20	0.18	0.19	0.12
RBC-Arginine	0.47	0.77	0.89	0.67
RBC/serum ratio	2.9	4.3	4.7	5.6
Serum-Nitrites	0.010	0.017	0.056	0.040
RBC-Nitrites	0.094	0.117	0.074	0.068
RBC/serum ratio	9.4	6.9	1.3	1.7
Serum-Ornithine	0.062	0.064	0.060	0.069
RBC-Ornithine	0.127	0.176	0.207	0.177
RBC/serum ratio	2.0	2.8	3.5	2.6
Serum-Citrulline	0.233	0.245	0.606	0.577
RBC-Citrulline	0.179	0.151	0.364	0.311
RBC/serum ratio	0.77	0.62	0.60	0.54

The results are expressed as medians of the metabolites in μmol • ml^{-1}. Most of the distributions were best described by skewed distributions, thus the mean is no longer a good measure of central tendency. Consequently, we relied on the median to compare between sets of data (S1 and S2 Files).

https://doi.org/10.1371/journal.pone.0219481.t002

ornithine in the female patients, in contrast to the gender differences found in healthy subjects (Table 2).

On the contrary, blood citrulline was mainly found in serum, resulting in an RBC/serum ratio for citrulline below one. Here, control men presented a significantly lower level of RBC-citrulline than the healthy female group (Table 2). The onset of type 2 DM elicited an increase of citrulline in both blood compartments but maintained the RBC/serum ratios for this amino acid. Consequently, this pathology also annulled gender differences in the citrulline blood levels observed in control subjects (Table 2).

Relations between blood metabolites in serum and RBC in patients with type 2 DM

The aforementioned results allowed us to shed light on the possible metabolic paths followed in serum and RBC. The arginine/nitrites and citrulline/nitrites relations in serum were higher in healthy women compared to men (Table 3). However, the group of female patients with type 2 DM showed altered relations of these nitrogen compounds when compared to healthy women. The relations in serum of ammonia/urea, arginine/urea, and citrulline/ornithine were significantly higher, while that of arginine/ornithine did not change. On the contrary, the other relationships shown in Table 3 were found significantly lower in women with type 2 DM, when compared to the healthy female group. With respect to men, although the ammonia/urea was lower in men with type 2 DM, the other serum relationships among nitrogen compounds had the same pattern of behavior as that of type 2 DM women. However, the differences were even larger in men (Table 3).

The relations in RBC were significantly different according to the gender (Table 3). In this blood compartment, the relations arginine/ammonia, arginine/nitrites, and arginine/citrulline, were also higher in control men than those found in the healthy female group. On the contrary, the citrulline/nitrites as well as the citrulline/ornithine relations were lower in the male control group than in the healthy women (Table 3). These results, when related to the pattern of relationships in serum of control subjects, argue in favor of gender differences in the "management" of ammonia and nitrogen-related compound (Table 3). In addition, with the

Table 3. Nitrogen-related metabolites and their ratios in serum and RBC of patients with type 2 DM.

Subjects	Healthy volunteers		Patients with type 2 DM	
Serum ratios	Females	Males	Females	Males
Ammomia/urea	0.12	0.13	0.24	0.04
Arginine/ammonia	4.1	3.6	2.4	1.6
Arginine/urea	0.49	0.47	0.58	0.06
Arginine/nitrites	20.0	10.6	3.2	3.0
Arginine/ornithine	3.2	2.8	3.2	1.7
Arginine/citrulline	0.86	0.73	0.31	0.21
Citrulline/nitrites	23.3	14.4	10.8	14.4
Citrulline/ornithine	3.8	3.8	10.1	8.4
RBC ratios	Females	Males	Females	Males
Ammomia/urea	0.29	0.24	0.22	0.26
Arginine/ammonia	11.7	23.9	14.0	10.9
Arginine/urea	3.5	5.8	3.0	2.8
Arginine/nitrites	41.9	59.3	99.1	82.4
Arginine/ornithine	31.0	36.5	35.4	31.6
Arginine/citrulline	22.0	42.5	20.1	18.0
Citrulline/nitrites	1.9	1.3	4.9	4.6
Citrulline/ornithine	1.4	0.9	1.8	1.8

Descriptive statistics. We computed the arithmetic mean, the variance, the skewness, and median for each determination. Most of the distributions were best described by skewed distributions, thus the mean is no longer a good measure of central tendency. Consequently, we relied on the median to compare between sets of data.

https://doi.org/10.1371/journal.pone.0219481.t003

exception of the relationships of ammonia/urea and arginine/ammonia, the onset of type 2 DM in male patients readily neutralized gender differences in the blood distribution of these metabolites, seen in the healthy volunteers (Table 3).

Release of ammonia, urea, and arginine from RBC of patients with type 2 DM after washing and storage

Gender differences in amino acid concentrations in serum have been recorded in normal healthy Japanese people [23]. Therefore, to make an effort to explain the gender differences in healthy subjects and patients with DM we measured the metabolite "release" from the RBC of both experimental groups. The RBC from control female and male subjects showed an efflux of ammonia of 38.2% and 44.5% of total RBC content, respectively, after blood cells washing and storage (Fig 2A). In this context, patients with DM released even more ammonia (56.9% and 47.6% in women and men, respectively), which resulted in having a similar amount of ammonia, when compared to healthy subjects (Fig 2A).

Interestingly, RBC from healthy subjects had an efflux of urea of 58.4% and 47.7% of total RBC content in women and men, respectively. The patients with type 2 DM released a quite similar amount of urea than healthy subjects (63.0% and 53.9% in women and men, respectively, of the total RBC content) (Fig 2B). The RBC content of arginine showed a very small release of 11.5% and 11.1% of total RBC content in control women and men, respectively (Fig 2C). RBC from the patients with DM almost doubled the release of arginine (19.4 and 20.8% of total RBC content in women and men, respectively), even though the remaining RBC levels for arginine (Fig 2C) were almost the same as those found in non-washed blood cells, mainly in control preparations (Table 2).

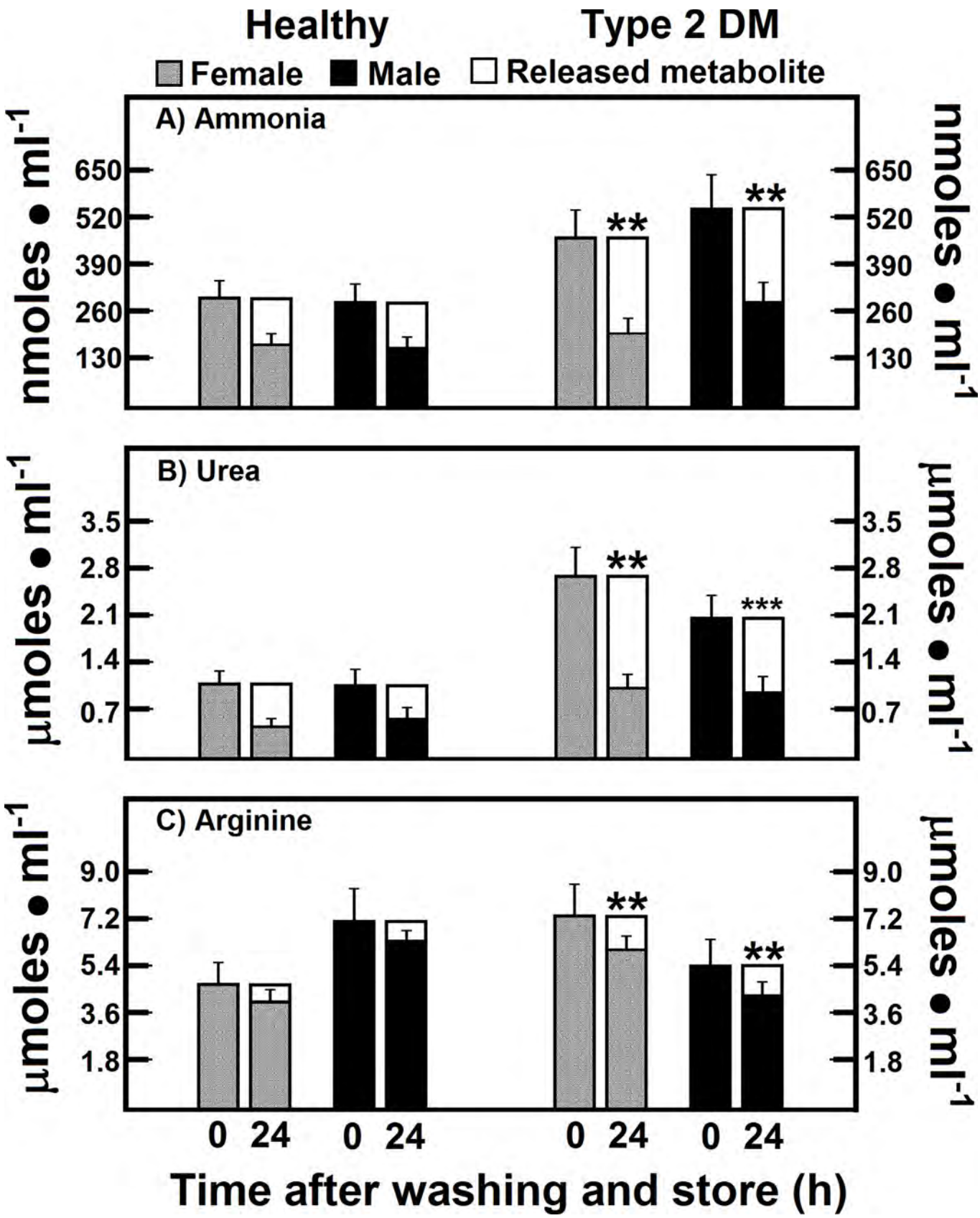

Fig 2. Release of ammonia, urea, and arginine from RBC of patients with type 2 DM after washing and storage. The results are expressed as the mean ± SD for levels of RBC ammonia, urea, and arginine, in healthy control female (n = 40) and male volunteers (n = 40), as well as in female (n = 40) and male DM type 2

patients (n = 40), at time 0. Empty bars represent the release rate for each metabolite 24 h after washing and storage (time 24). Symbols for experimental groups at the top. Statistical significance: *$p < 0.01$ against the control female group, and **$p < 0.01$ vs. the corresponding gender control group.

https://doi.org/10.1371/journal.pone.0219481.g002

Release of nitrites, ornithine, and citrulline from RBC of patients with type 2 DM after washing and store

The RBC content of nitrites, which are NO oxidation products, also showed changes after washing and storing the blood cells (Fig 3A). The efflux of nitrites from RBC in controls after washing and storing was 34.3% and 37.9% of total RBC content in women and men, respectively. On the contrary, RBC in patients with type 2 DM showed a lower release of nitrites (less than 10% of total RBC content) in both experimental groups (Fig 3A), which contrasted with the high levels of serum nitrites found in both, women and men DM patients (Table 2).

The efflux of ornithine in the RBC from DM patients, was closely similar to that of control cells after washing and storage (Fig 3B). We conclude that RBC do not release ornithine, since the rate of release of this amino acid was lower than 6% (Fig 3B). Interestingly, the citrulline that differs very little chemically from ornithine was readily released after washing and storage (more than 90% of the initial value) in female or male control subjects (Fig 3C). RBC-citrulline in type 2 DM patients also showed a reliable efflux under our experimental conditions; however, this release was proportionally lower in type 2 DM patients. Nevertheless, we also observed a gender difference, as men with type 2 DM retained more citrulline in their RBC than women (Fig 3C). Indeed, present data confirm the existence of a net efflux of by-products of RBC arginine metabolism in RBC of control and patients with type 2 DM, determined by radio-labeled tracing as previously reported under these experimental conditions [14].

Correlation between levels of ammonia and MDA and their release from RBC in patients with type 2 DM

For this section, we used the Pearson correlation coefficient and the mean and standard deviations to report results. When we calculated the area under the curve (AUC) for the progressive release of this ammonia from RBC of female subjects (6.4 ± 1.9 nmol • h^{-1} • ml^{-1} of RBC), this value was not statistically different when compared to male volunteers (AUC = 5.2 ± 1.6 nmol • h^{-1} • ml^{-1} of RBC; Fig 4A and 4B). Female patients with type 2 DM showed a significant increase of RBC ammonia release (AUC = 9.9 ± 2.5 nmol • h^{-1} • ml^{-1} of RBC) when compared with healthy women (Fig 4A and 4B). Interestingly, we also found a larger liberation of ammonia by RBC from diabetic male patients (AUC = 10.5 ± 2.9 nmol • h^{-1} • ml^{-1} of RBC), which is twice that of found in normal male subjects.

In women with type 2 DM the released RBC amount of MDA, a byproduct of membrane's lipid peroxidation (AUC = 0.55 ± 0.15 nmol • h^{-1} • ml^{-1} of RBC) was not significantly different from that found in healthy women (AUC = 0.58 ± 0.17 nmol • h^{-1} • ml^{-1} of RBC; Fig 4C). On the contrary, male patients with type 2 DM released more MDA from their isolated RBC when compared with healthy men (AUC = 0.60 ± 0.16 vs. 0.86 ± 0.25 nmol • h^{-1} • ml^{-1} of RBC, in diabetic patients; Fig 4D).

Correlations among nitrogen metabolites with serum glucose in patients with type 2 DM

In an attempt to define the specificity of the changes in blood nitrogen metabolism as a consequence of the alterations found in patients with type 2 DM, we investigated correlations among the different metabolites included in our experiments.

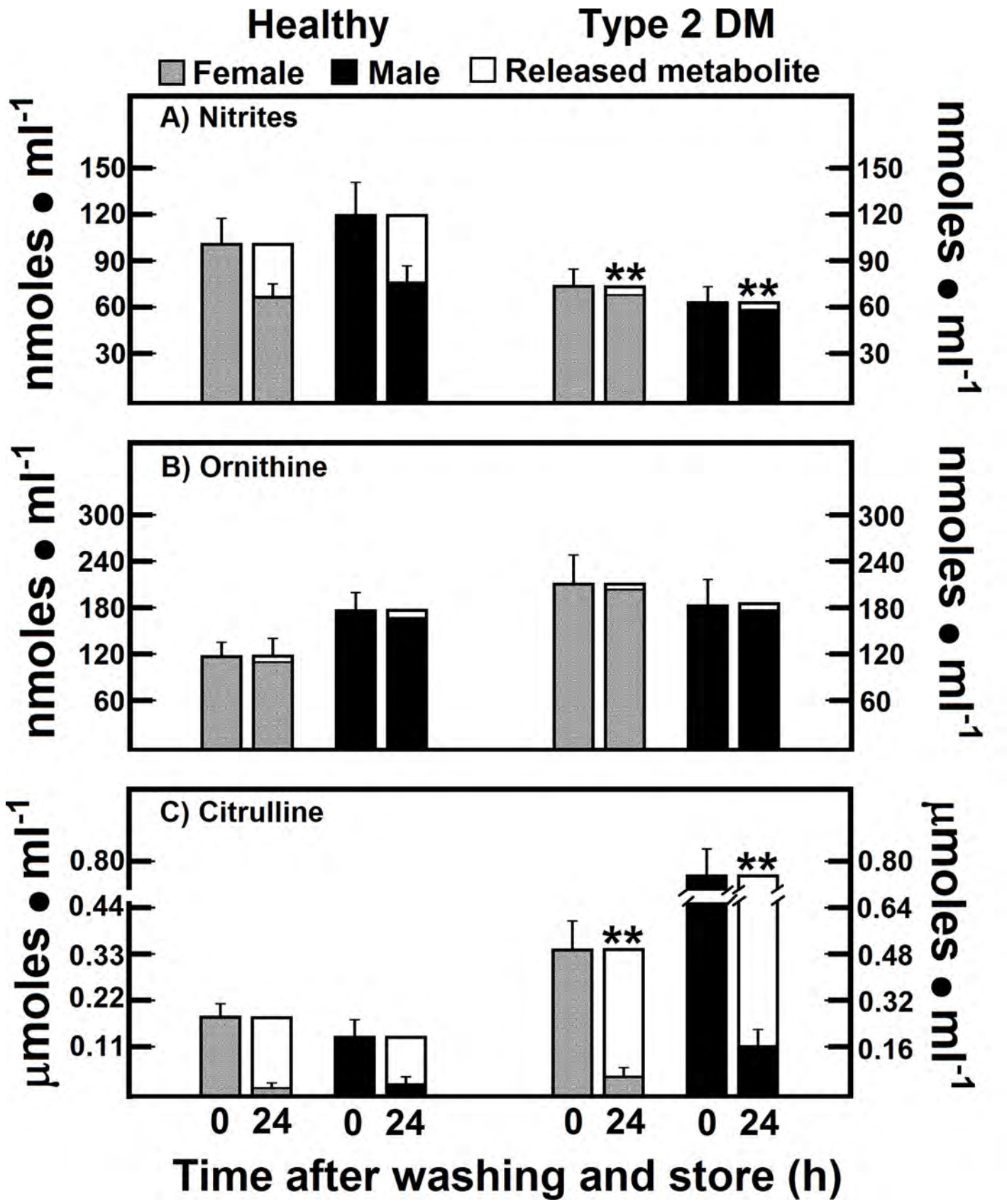
Healthy
Type 2 DM
Female
Male
Released metabolite
A) Nitrites
nmoles • ml-1
150
120
90
60
30
**
**
B) Ornithine
300
240
180
120
60
C) Citrulline
µmoles • ml-1
0.80
0.44
0.33
0.22
0.11
0.64
0.48
0.32
0.16
0 24 0 24 0 24 0 24
Time after washing and store (h)

INFORME DE LABORES 2019

Fig 3. Release of nitrites, ornithine, and citrulline from RBC of patients with type 2 DM after washing and storage. The results are expressed as the mean ± SD for levels of RBC nitrites, ornithine, and citrulline, in healthy control female (n = 40) and male volunteers (n = 40), as well as in females (n = 40) and males (n = 40) with type 2 DM at time 0. Empty bars represent the release rate for each metabolite 24 h after washing and store (Time 24). Symbols for experimental groups at the top. Statistical significance as pointed out in the Fig 2.

https://doi.org/10.1371/journal.pone.0219481.g003

There was a null Spearman correlation coefficient between RBC-arginine and glucose in male diabetics, indicating that these metabolites are not related in this blood compartment. When analyzing the correlations between arginine and glucose in serum we observed otherwise, the diabetic women have a null correlation coefficient (0.0146, p-value 0.9286), whereas

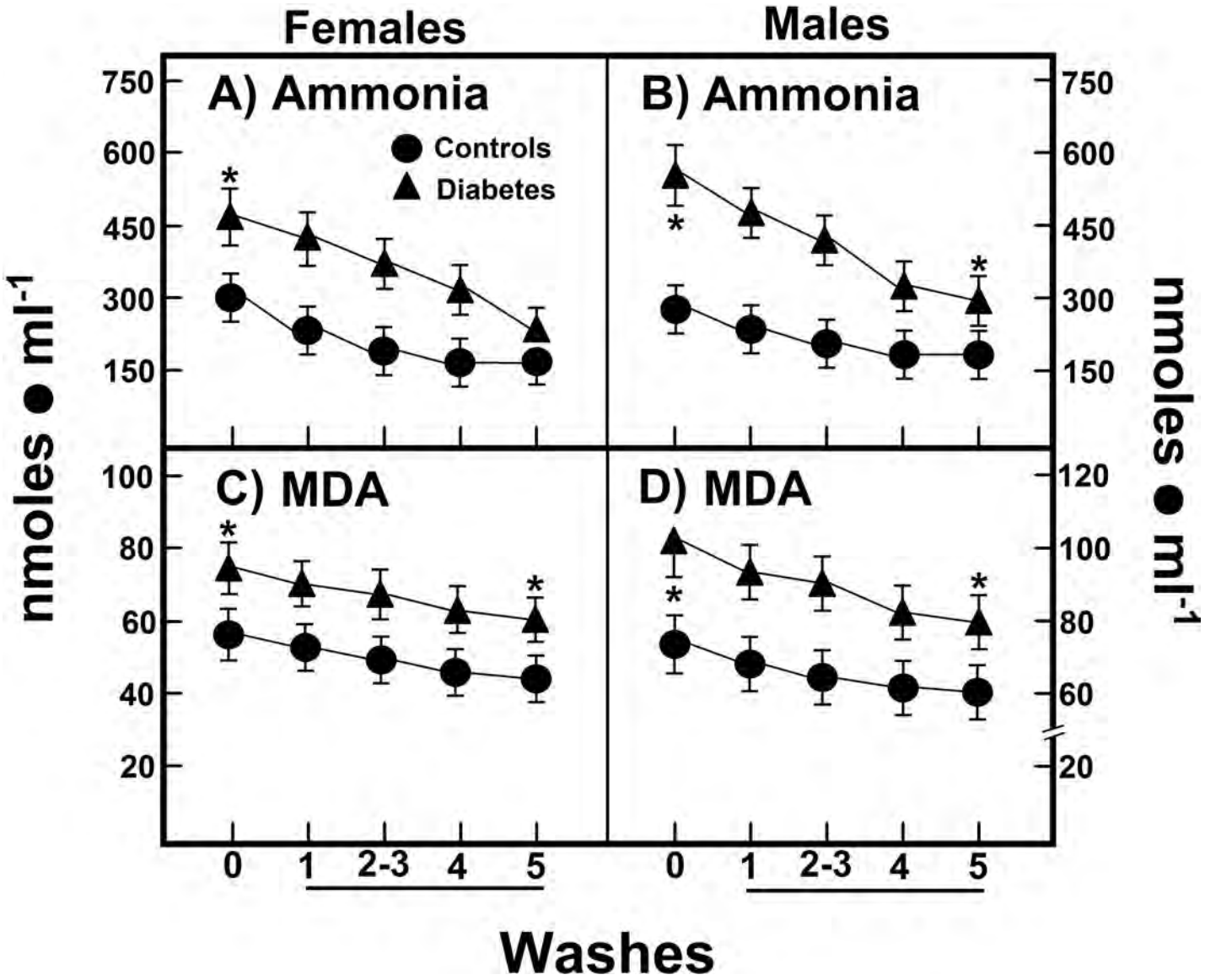

Fig 4. RBC amount and curves of release of ammonia and MDA from RBC of patients with type 2 DM after washing and storage. The results are expressed as the mean ± SD for levels of RBC ammonia (panels A and B), as well as of malondialdehyde (MDA; panels C and D), in healthy control female (n = 40) and male volunteers (n = 40), as well as in females (n = 40) and males (n = 40) with type 2 DM. The wash numbers 5 correspond to storage of RBC in the washing solution for 24 h. Symbols for experimental groups at the top of the figure, and statistical significance as indicated in the Fig 2.

https://doi.org/10.1371/journal.pone.0219481.g004

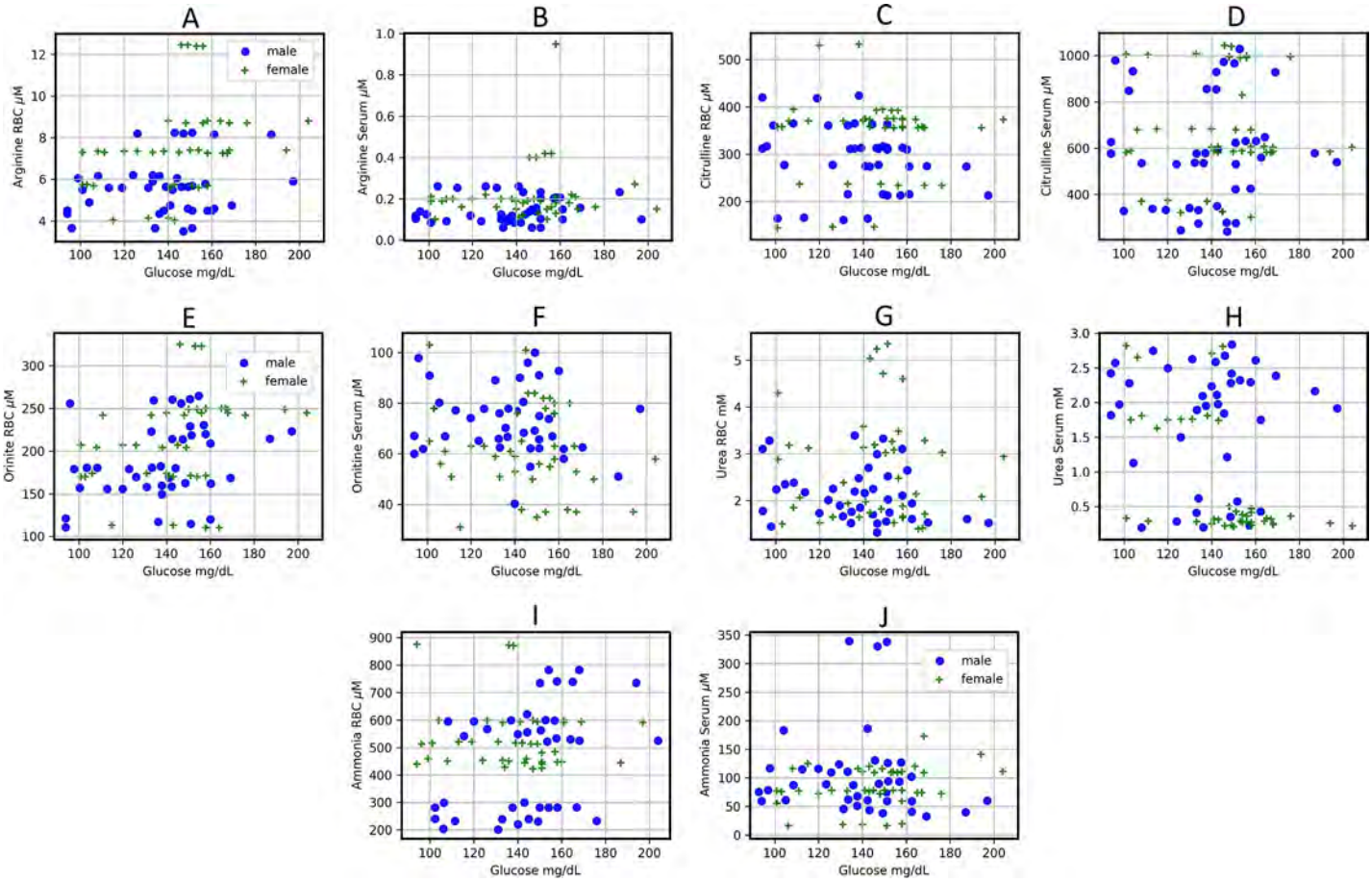

Fig 5. Scatter plots for different determinations according to gender (males are circles and females are stars) and RBC (A,C,E,G and I) or serum (B,D,F,H, and J) in DM type 2 patients. Scatter plots show the relation between two sets of data. This relation is summarized in the Spearman correlation coefficient (r) for each relation in each scatter plot:: A (rM = 0.08, rF = 0.39), B (rM = 0.14, rF = -0.014), C (rM = -0.301, rF = -0.086), D (rM = 0.113, rF = -0.044), E (rM = 0.299, rF = 0.425), F (rM = -0.133, rF = -0.163), G (rM = -0.227, rF = -0.04), H (rM = -0.013, rF = -0.559), I (rM = -0.132, rF = 0.322), and J (rM = -0.257, rF = 0.235). To see the p-values for each correlation, see the correlation matrix (S3 File).

https://doi.org/10.1371/journal.pone.0219481.g005

the diabetic men show a positive and low Spearman correlation coefficient (0.1420, p-value 0.3818; Fig 5B).

In diabetic males, the RBC-citrulline is inversely related with glucose, as evident from a weak negative Spearman correlation coefficient (Fig 5C). Also interestingly, serum levels of citrulline correlated directly with those of glucose in this patients with a low positive correlation for serum citrulline and glucose (Fig 5D). However, these correlations are lost in the case of diabetic women (Fig 5C and 5D).

The RBC levels of ornithine correlated weakly positive with serum glucose in both diabetic genders, although the Spearman correlation coefficient is higher in diabetic women (S3 File, Fig 5E). Conversely, Spearman correlation coefficient suggests a low negative relation between serum ornithine and glycaemia in both diabetic genders (S3 File, Fig 5F).

We found that when the glucose serum levels increase, the levels of urea decrease in RBC and serum in both genders. The Spearman correlation coefficient between urea in RBC and glucose in serum is low from diabetic men and females (Fig 5G). Interestingly, the comportment is opposite when we compared according to gender both compounds in serum (S3 File, Fig 5H). The RBC and serum levels of ammonia had a low and inverse correlation with serum

glucose in diabetic males (RBC: -0.132, p-value 0.1783; serum: -0.257, 0.1081. S3 File, Fig 5), while RBC and serum-ammonia had also a low but direct correlated with hyperglycemia in female patients with type 2 DM (S3 File, Fig 5I and 5J).

Correlations between serum nitrites with ammonia and urea in patients with type 2 DM

It has been speculated that facultative anaerobic bacteria might reduce nitrite to NO and possibly further to form ammonia [24]. Therefore, we searched relationships among the circulating amounts of nitrites, arginine, urea, and ammonia.

In relation to gender, the Spearman correlations coefficients show that the correlations between arginine and nitrites have an opposite behavior in control subjects, both in RBC and in serum. A weak negative correlation can be observed between arginine and nitrites in RBC of control men), whereas in RBC of control women the Spearman correlation coefficient indicates a weak positive correlation (S3 File). In the case of serum, correlation between nitrites and arginine showed an opposite pattern (S3 File, Fig 6A and 6B).

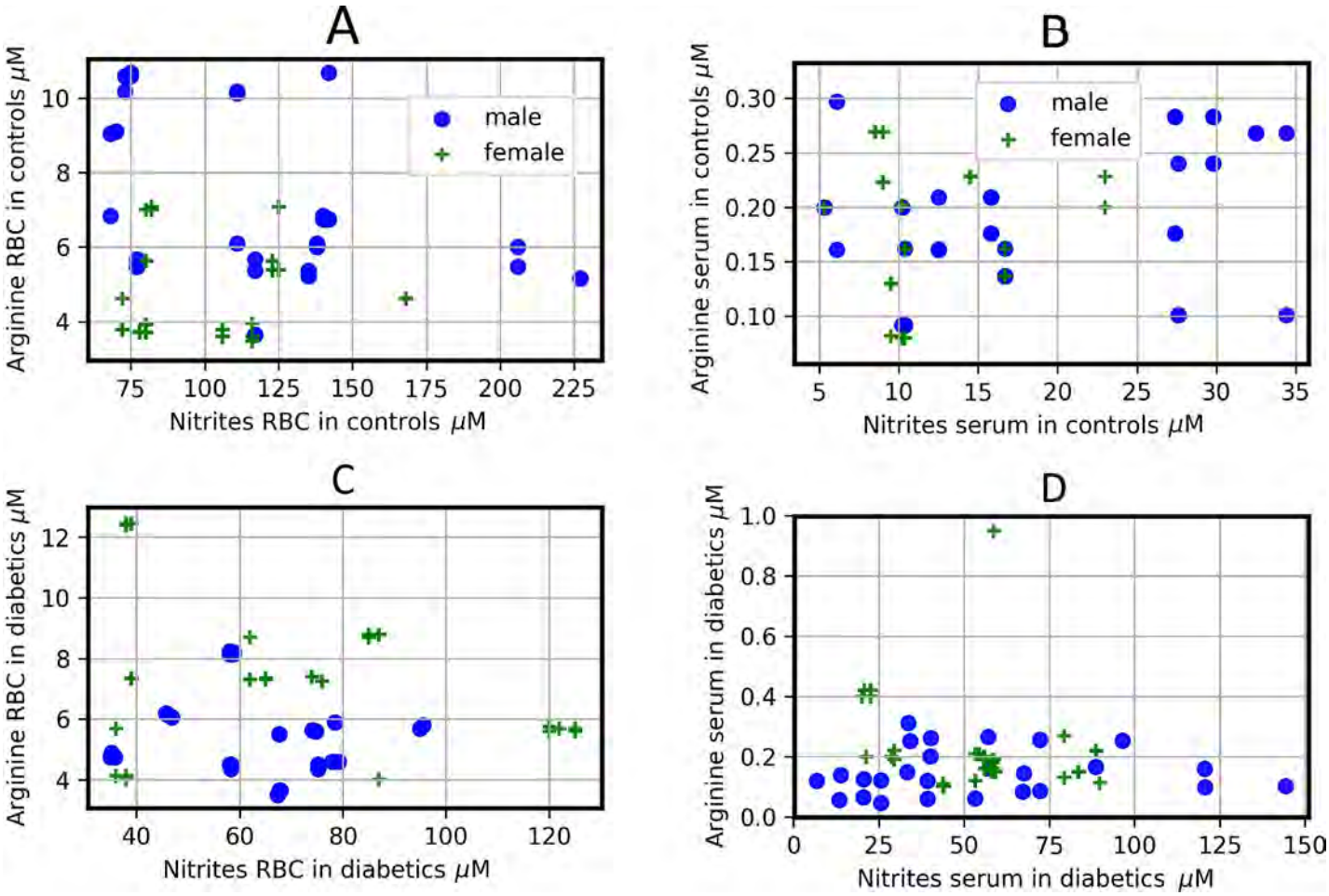

Fig 6. Scatter plots for different determinations for controls and diabetic patients according to gender (males are circles and females are stars) and RBC (left column) or serum (right column). Scatter plots show the relation between two sets of data; this relation is summarized in the Spearman correlation coefficients. These correlations are: A (rM = -0.439, rF = 0.269), B (rM = 0.276, rF = -0.22), C (rM = -0.2578, rF = -0.179), D (rM = 0.229, rF = -0.361). To see the p-values for each correlation, see the correlation matrix (S3 File).

https://doi.org/10.1371/journal.pone.0219481.g006

In serum of patients with DM type 2, the Spearman correlations coefficients between arginine and nitrites, showed a weak and inverse correlation pattern, while in RBC both correlations are weak and negative (S3 File, Fig 6C and 6D). If we compare the Spearman correlations coefficients between the levels of arginine and nitrites in both genders of control subjects with those of patients with type 2 DM, we observed that the pathology does not change the behavior of the correlations, neither in serum nor in RBC, with the exception of RBC of women, where the Spearman correlation coefficient goes from weak positive in control females to low negative in diabetics females (S3 File, Fig 6). Regarding the correlations between ammonia and nitrite, when comparing the Spearman correlations coefficients between RBC of control subjects and patients with type 2 DM of both genders, the pathology does not change the way in which they correlate (Fig 7A and 7C). Importantly, in serum the Spearman correlations coefficients between ammonia and nitrites change from null in control men to weak negative in diabetic men, whereas an inverse behavior is observed in women (Fig 7B and 7D). Control women have a weak positive correlation between ammonium and nitrites (S3 File, Fig 7), while DM type 2 women have a null correlation in this relation. Once again, the comparison of the Spearman correlations coefficients between genders shows us a different behavior in the correlations in both the groups studied.

Whereas we find null correlations between RBC or serum levels of nitrites and urea in control subjects (S3 File, Fig 7E and 7F), patients with DM type 2 exhibit different parameters. For instance, female patients had a low negative correlation between RBC-nitrites and those levels for urea (S3 File, Fig 7G), while in serum, the levels of nitrites and urea, both in male and in female patients with type 2 DM, showed weak correlation in these metabolites (Fig 7H). Therefore, results from **Figs 5, 6 and 7** strongly support the existence of a differential blood metabolism for nitrogen-related compounds by gender, which is largely disturbed by the presence of type 2 DM.

Discussion

The RBC are the most abundant cell in humans and their alterations are deeply involved in health and disease. Indeed, as a result of the metabolomic and proteomic analysis, it has been understood that they are very important in the physiology of the body; close to 2000 gene products have been reported [25]. Moreover, to our knowledge, this study provides the first documented evidence of a putative role of blood cells (mainly attributed to RBC) in the control of serum levels of diverse metabolites, such as those related to the nitrogen metabolism in humans, which is largely altered by pathologies such as type 2 DM. We highlight two main findings. Firstly, the distribution of these metabolites in human blood compartments (serum and RBC) is influenced by gender, probably affecting bi-directional transport through RBC membranes and its metabolism [14]. Secondly, onset of type 2 DM abrogates many of the gender-related differences found in healthy subjects.

The hyperglycemia and the increase in levels of HbA_{1C} found in patients with DM were closely associated with blood levels for either, ammonia or urea (Fig 5). These results suggested that abnormal levels of blood glucose might induce alterations in the nitrogen metabolism. The latter can be related to the fact that RBC may undergo suicidal death or eryptosis, which is characterized by cell shrinkage and cell membrane alterations triggered by oxidative stress [26]. Exposure of normal erythrocytes to high glucose concentrations *in vitro* intensified lipid peroxidation (LP) and the loss of RBC enzyme activities [27]. Moreover, high levels of HbA_{1c} are closely related to LP in RBC, which are also associated to a significant reduction in membrane Na+/K+-ATPase activity [28,29].

Type 2 DM is characterized by low-grade, chronic inflammation and an increased activity of IkB/NFkB seems to provide a molecular mechanism responsible for inflammation and

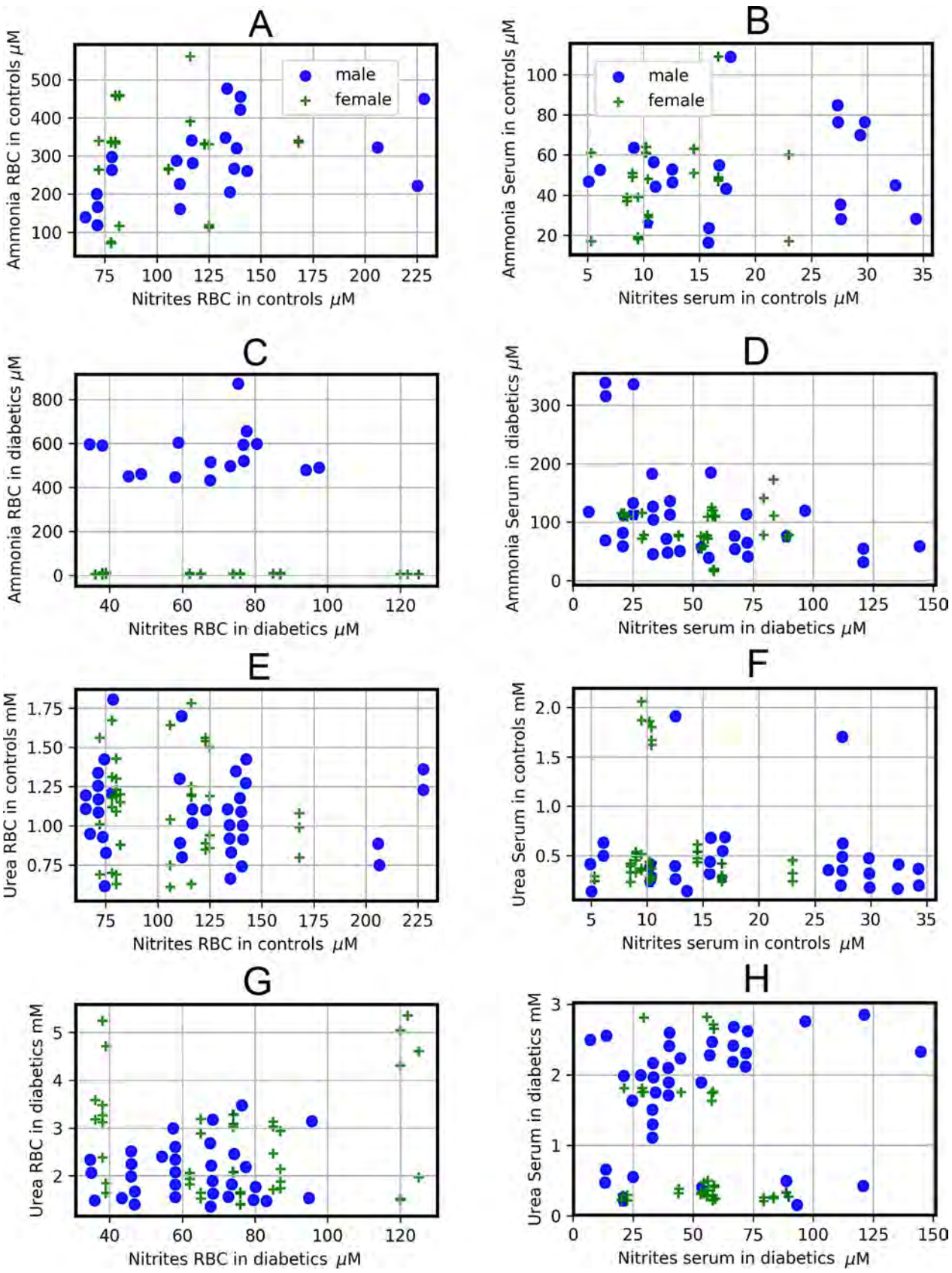
A
Ammonia RBC in controls μM
Nitrites RBC in controls μM
male
female
B
Ammonia Serum in controls μM
Nitrites serum in controls μM
male
female
C
Ammonia RBC in diabetics μM
Nitrites RBC in diabetics μM
D
Ammonia Serum in diabetics μM
Nitrites serum in diabetics μM
E
Urea RBC in controls mM
Nitrites RBC in controls μM
F
Urea Serum in controls mM
Nitrites serum in controls μM
G
Urea RBC in diabetics mM
Nitrites RBC in diabetics μM
H
Urea Serum in diabetics mM
Nitrites serum in diabetics μM

Fig 7. Scatter plots for different determinations for controls and diabetic patients according to gender (males are circles and females are stars) and RBC (left column) or serum (right column). Scatter plots show the relation between two sets of data; this relation is summarized in the Spearman correlation coefficients. These correlations are: A (rM = 0.562, rF = -0.0496), B (rM = -0.0388, rF = 0.3011), C (rM = 0.317, rF = -0.0588), D (rM = -0.4465, rF = -0.047). E (rM = -0.096, rF = -0.0636), F (rM = 0.0018, rF = -0.048), G (rM = -0.031, rF = - 0.1318), and H (rM = 0.3665, rF = -0.2506). To see the p-values for each correlation, see the correlation matrix (S3 File).

https://doi.org/10.1371/journal.pone.0219481.g007

insulin resistance in type 2 DM, associated with increased risk of cardiovascular diseases [30]. In endothelial cells, excess free fatty acids activate the pro-inflammatory IKKβ–NF-κB pathway causing cellular insulin resistance and impaired NO production [31]. In this scenario, structural and/or functional alterations of RBC could be playing a role in the endothelial dysfunction noticed in patients with type 2 DM.

Studies have suggested that when the liver capacity for removing ammonia is reduced, other organs interact to maintain ammonia levels [32]. Glutamine functions as a "trapper" for excess ammonia, through the reaction of glutamine synthetase, and this occurs in the skeletal muscle [33]. Indeed, blood patterns for these amino acids should be altered in patients with chronic liver damage [34]; but, what about the alterations in the nitrogen metabolism found in female and male patients in absence of liver failure?

The end-products of the nitrogen metabolism, ammonia and urea, were greatly elevated in blood in diabetic patients (**Fig 1**, **Table 2**). Urea drastically augmented in RBC, which could be accounted for by the blood cells capacity to uptake and transport these metabolites (**Fig 1**, **Table 2**). Despite the apparent high production of urea by the liver of DM patients, ammonia definitively increased. Increased serum ammonia and glutamic acid levels found in patients with type 2 DM could be associated with delayed gastrointestinal transit [35], as well as with the increased activity of monoamine oxidase DB [36]. Since the presence of high blood levels for ammonia was not related to liver dysfunction, this could indicate that other extra-hepatic cells, such as RBC, are participating in the control of nitrogen metabolism [25].

Ammonia toxicity may induce cell damage, as it occurs during neuro-degeneration in aging, and Alzheimer disease [37] and, in diabetic rats there was a marked increase in the Na +-dependent component of the L-glutamate transport, causing a higher intracellular concentration of glutamate [38]. Whether the same occurs within blood cells remains to be studied; however, our findings provide evidence that RBC from the patients with type 2 DM can transport potential toxic nitrogen-related molecules (ammonia, urea, glutamic acid), which constitutes an unexplored risk factor for further complications. In experimental models for DM, a differential susceptibility for the harmful effects of ammonia on female or male animals has been reported. A porta-caval shunt reduces growth and spontaneous motor activity in male but not in female rats [39].

On the other hand, an intra-portal load of L-glutamine in rat with experimentally-induced type 1 DM generates increased glucose output, accompanied by enhanced urea and ammonia production [40]. These might be providing a background to explain the enhanced blood levels for ammonia and urea found in our patients with type 2 DM (**Figs 1**, **2**, **4 and 5**). In this context, we have recently shown an association between oxidant stress and elevated levels of ammonia [41], where increased systemic free ammonia concentration was capable of mediating the deleterious effects of AZT on partial hepactectomy-Induced rat liver regeneration. Indeed, the AZT significantly increased blood levels of ammonia and of MDA; despite this nucleoside did not reduce the amount of urea in the whole blood, but rather did change its distribution in the blood compartments [41].

Hyperglycemia is associated with increasing levels of six amino acids (alanine, isoleucine, leucine, valine, phenylalanine, and tyrosine) and with decreasing levels of histidine and glutamine; these associations were explained by insulin sensitivity [42]. Plasma branched chain and

aromatic amino acids have been also associated with incident diabetes and underlying metabolic abnormalities [43], which could be a focus for identifying novel etiological mechanisms and treatment targets for DM.

An excess of ammonia can alter NO production; type 2 DM patients showed increased serum nitrites levels, as well as those of citrulline in both blood compartments, associated with a decreased blood arginine level, mainly observed in men with type 2 DM (**Table 2**). Interestingly, the existence of gender differences in the NO metabolism is currently known. Systemic NO production is higher in healthy premenopausal women than in men, paired by age, under ambulatory conditions. This variance could explain the differences in endothelial production of NO, and the differential vascular function observed in men and women [16,44]. Indeed, estrogens can play a role in modifying NO response in women. Estrogens can inhibit Ca^{2+} influx mediated by L-type Ca^{2+} channels, representing one way through which estrogen protects ischemic hearts [45].

The present study gives evidence that in healthy subjects exist significant gender differences in NO production and, for the first time, in arginine metabolism (**Tables 2 and 3, S2 and S3 Files**). The arginine/nitrites and arginine/citrulline ratios were bigger in RBC of healthy men than in women, suggesting a lower flow of arginine through putative nitric oxide synthase in men, and healthy men also seemed to use less arginine as substrate for arginase, i.e., the arginine/urea ratio (**Table 3**). These data agree with the aforementioned speculation that women seem to have a more active NO metabolism than men. Interestingly, serum arginine levels were maintained within a normal range in patients with DM; hence, the importance of maintaining normal serum arginine levels could be is related to its metabolic role as the ammonia detoxification product, and to production of L-citrulline and NO [5,46], improving RBC function and extending cell life span in old RBC [47]. So, it was noteworthy to find that onset of type 2 DM practically abrogates gender differences in nitrogen-related metabolites which are observed in controls (**S2 and S3 Files, Tables 2 and 3**).

We found significant relationships between serum nitrites levels with those of ammonia and urea, indicating the participation of NO metabolism in the management of blood ammonia and of urea (**Fig 6**). As to citrulline, what could cause its elevation in blood of patients with type 2 DM? Citrulline has beneficial effects such as the increased NO production and endothelial function through its conversion to arginine [48]. Therefore, it is attractive to speculate whether the massive outflow of citrulline from RBC is an attempt to reestablish NO metabolism, functioning as an antioxidant in RBC of type 2 DM patients.

Which mechanism is most probably involved in these unexpected results is left to be answered in future research. One possible explanation could be given by the role of RBC in handling molecules participating in the nitrogen metabolic pathways and the fact that these blood cells are altered by the occurrence of DM [14]. Indeed, we have shown that the RBC capacity for metabolizing arginine depends on the oxidant status and the lipid composition of RBC membranes, which are altered in patients with type 2 DM [49], and high glucose concentrations altered the content and distributions of three tubulin isotypes, reducing RBC deformability and osmotic resistance [50]. Moreover, the RBC abnormalities in the membrane lipid composition, associated with some perturbations, can significantly affect RBC receptor binding and enzyme activities, as it occurs in the diabetic retinopathy, where higher amounts of phosphatidyl-choline species have been found in RBC [51].

In conclusion, this study provides the first documented findings giving strong evidence of a putative role of RBC as an extra-hepatic mechanism for controlling serum levels of nitrogen-related metabolites, which differs according to gender in healthy subjects. Type 2 DM promotes a characteristic pattern of metabolic disturbances that culminates in a loss of the differential management of nitrogen-related metabolites seen in healthy women and men.

Therefore, it is not unlikely that these characteristic patterns of blood metabolites elicited by type 2 DM might be involved in the specific physiopathology of this disease, and changes in the oxidative status, i.e., increased lipid peroxidation in RBC membranes of diabetic patients, are playing a role in the metabolic alterations found in these blood cells.

Supporting information

S1 File. Descriptive statistics.
(XLS)

S2 File. Best fit distributions for all determinations. The table reports D-statistics and p-values of the KS goodness of fit test for each of the 84 data sets. The KS test for goodness of fit performs a test of the distribution of an observed random variable against a given distribution under the null hypothesis that the two distributions are identical. The table also reports the MLEs for shape, location and scale parameters obtained from the maximum likelihood estimation needed to perform the KS tests. We fitted the data to the following distributions: beta, exponential, exponential-Weibull, exponential-power law, Gilbrat, logistic, lognormal, normal, Pareto, power law, Weibull minimum, and Weibull maximum.
(PDF)

S3 File. Matrix containing the Spearman Rho and P values.
(XLS)

S4 File. Table 1 with "normal" statistics. Results are expressed as means ± SD. We used the Student's unpaired t-test and the Mann-Whitney test to compare a continous variable between the two groups. Thereafter, these differences were contrasted with t-test for paired data.
(TIF)

Acknowledgments

Authors acknowledge the expert aid from Biol. Gerardo Coello, Ing. Juan Manuel Barbosa, and Ivette Rosas, for designing figures and computational programs, as well as to Ing. Aurey Galván and Manuel Ortínez, for maintenance and supervision of the laboratory equipment. We also thank to Agustín Flores for his helpful assistance in the maintenance of the laboratory utilities.

Author Contributions

Conceptualization: Martha L. Contreras-Zentella, Rolando Hernández-Muñoz.

Data curation: Martha L. Contreras-Zentella, Lourdes Sánchez-Sevilla, Juan A. Suárez-Cuenca, Marisela Olguín-Martínez, Martha G. Alatriste-Contreras, Rolando Hernández-Muñoz.

Formal analysis: Martha L. Contreras-Zentella, Martha G. Alatriste-Contreras, Norberto García-García, Lorena Orozco, Rolando Hernández-Muñoz.

Funding acquisition: Martha L. Contreras-Zentella, Rolando Hernández-Muñoz.

Methodology: Martha L. Contreras-Zentella, Lourdes Sánchez-Sevilla, Juan A. Suárez-Cuenca, Marisela Olguín-Martínez, Rolando Hernández-Muñoz.

Supervision: Martha L. Contreras-Zentella, Juan A. Suárez-Cuenca, Lorena Orozco, Rolando Hernández-Muñoz.

Visualization: Martha L. Contreras-Zentella, Martha G. Alatriste-Contreras, Rolando Hernández-Muñoz.

Writing – original draft: Martha L. Contreras-Zentella, Lourdes Sánchez-Sevilla, Juan A. Suárez-Cuenca, Marisela Olguín-Martínez, Martha G. Alatriste-Contreras, Norberto García-García, Lorena Orozco, Rolando Hernández-Muñoz.

Writing – review & editing: Martha L. Contreras-Zentella, Lourdes Sánchez-Sevilla, Juan A. Suárez-Cuenca, Marisela Olguín-Martínez, Martha G. Alatriste-Contreras, Norberto García-García, Lorena Orozco, Rolando Hernández-Muñoz.

References

1. Zimmet P, Alberti KG, Shaw J. Metabolic syndrome—a new world-wide definition. A Consensus Statement from the International Diabetes Federation. Diabet Med. 2006 May; 23(5):469–480. https://doi.org/10.1111/j.1464-5491.2006.01858.x PMID: 16681555
2. Taysi S, Polat F, Gul M, Sari RA, Bakan E. Lipid peroxidation, some extracellular antioxidant enzymes in serum of patients with rheumatoid arthritis. Rheumatol Int 2002 Mar; 21(5):200–204. PMID: 11958437
3. Baynes JW. Role of oxidative stress in development of complications in diabetes. Diabetes 1991 Apr; 40(4):405–412. https://doi.org/10.2337/diab.40.4.405 PMID: 2010041
4. Hoeldtke RD, Bryner KD, McNeill DR, Warehime SS, Van Dyke K, Hobbs G. Oxidative stress and insulin requirements in patients with recent-onset type 1 diabetes. J Clin Endocrinol Metab 2003 Apr; 88 (4):1624–1628. https://doi.org/10.1210/jc.2002-021525 PMID: 12679448
5. Wu G, Meininger CJ. Arginine nutrition and cardiovascular function. J Nutr 2000 Nov; 130(11):2626–2629. https://doi.org/10.1093/jn/130.11.2626 PMID: 11053497
6. Ardawi MS. Glutamine and ketone-body metabolism in the gut of streptozotocin- diabetic rats. Biochem J 1988 Jan 15; 249(2):565–572. https://doi.org/10.1042/bj2490565 PMID: 2893606
7. Shimono J, Tsuji H, Azuma K, Hashiguchi M, Fujishima M. Recurring encephalopathy abolished by gastrorenal shunt ligation in a diabetic hemodialysis patient. Am J Gastroenterol 1998 Feb; 93(2):270–272. https://doi.org/10.1111/j.1572-0241.1998.270_2.x PMID: 9468259
8. Postic C, Girard J. Contribution of the novo fatty acid synthesis to hepatic steatosis and insulin resistance: lessons from genetically engineered mice. J Clin Invest 2008 Mar; 118(3):829–838. https://doi.org/10.1172/JCI34275 PMID: 18317565
9. Helms CC, Gladwin MT, Kim-Shapiro DB. Erythrocytes and vascular function: Oxygen and nitric oxide. Front Physiol 2018 Feb 22; 9:125. https://doi.org/10.3389/fphys.2018.00125 PMID: 29520238
10. Cosentino F, Luscher TF. Endothelial dysfunction in diabetes mellitus. J Cardiovasc Pharmacol 1998; 32 Suppl 3:S54–61. PMID: 9883749
11. Romero MJ, Platt DH, Tawfik HE, Labazi M, El-Remessy AB, Bartoli M, et al. Diabetes-induced coronary vascular dysfunction involves arginase activity. Circ Res 2008 Jan 4; 102(1):95–102. https://doi.org/10.1161/CIRCRESAHA.107.155028 PMID: 17967788
12. Wasserman DH, Kang L, Ayala JE, Fueger PT, Lee-Young RS. The physiological regulation of glucose flux into muscle in vivo. J Exp Biol 2011 Jan15; 214(Pt 2):254–262. https://doi.org/10.1242/jeb.048041 PMID: 21177945
13. Moinard C, Le Plenier S, Noirez P, Morio B, Bonnefont-Rousselot D, Kharchi C, et al. Citrulline supplementation induces changes in body composition and limits age-related metabolic changes in healthy male rats. J Nutr 2015 Jul; 145(7):1429–1437. https://doi.org/10.3945/jn.114.200626 PMID: 26019250
14. Ramírez-Zamora S, Méndez-Rodríguez ML, Olguín-Martínez M, Sánchez-Sevilla L, Quintana-Quintana M, García-García N, et al. Increased erythrocytes by-products of arginine catabolism are associated with hyperglycemia and could be involved in the pathogenesis of type 2 diabetes mellitus. *PLoS One* 2013;Jun24; 8(6):e66823. https://doi.org/10.1371/journal.pone.0066823 PMID: 23826148
15. Bordbar A, Jamshidi N, Palsson BO. iAB-RBC-283: A proteomically derived knowledge-base of erythrocyte metabolism that can be used to simulate its physiological and patho-physiological states. BMC Syst Biol 2011;Jul 12; 5:110. https://doi.org/10.1186/1752-0509-5-110 PMID: 21749716
16. Majmudar NG, Robson SC, Ford GA. Effects of the menopause, gender, and estrogen replacement therapy on vascular nitric oxide activity. J Clin Endocrinol Metab 2000 Apr; 85(4):1577–1583. https://doi.org/10.1210/jcem.85.4.6530 PMID: 10770200

17. Ahmed SB, Fisher ND, Hollenberg NK. Gender and the renal nitric oxide synthase system in healthy humans. Clin J Am Soc Nephrol 2007 Sep; 2(5):926–931. https://doi.org/10.2215/CJN.00110107 PMID: 17702739

18. Yin YH, Ma ZJ, Guan YH, Ren YD, Zhang ZL. Clinical features of hepatic myelopathy in patients with chronic liver disease. Postgrad Med J 2009 Feb; 85(1000):64–68. https://doi.org/10.1136/pgmj.2007.067371 PMID: 19329698

19. Bergmeyer HU, Beutler HO. Ammonia, in: Bergmeyer HU, Bergmeyer J, Grassl M, Eds. *Methods of Enzymatic Analysis*, Vol. VII. Deerfield Beach, Florida, Verlag Chemie, 1984:454–461.

20. Kerscher L, Ziegenhorn J. Urea, in: Bergmeyer HU, Bergmeyer J, Grassl M, Eds. *Methods of Enzymatic Analysis*, Vol. VII. Deerfield Beach, Florida, Verlag Chemie, 1984:444–453.

21. Colombo JP, Konarska L. Arginase, in: Bergmeyer HU, Bergmeyer J, Grassl M, Eds. *Methods of Enzymatic Analysis*, Vol. VII. Deerfield Beach, Florida, Verlag Chemie, 1984:285–294.

22. D'Alessandro A, Nemkov T, Sun K, Liu H, Song A, Monte AA, et al. AltitudeOmics: Red blood cell metabolic adaptation to high altitude hypoxia. J Proteome Res. 2016 Oct 7; 15(10):3883–3895. https://doi.org/10.1021/acs.jproteome.6b00733 PMID: 27646145

23. Kouchiwa T, Wada K, Uchiyama M, Kasezawa N, Niisato M, Murakami H, et al. Age-related changes in serum amino acids concentrations in healthy individuals. Clin Chem Lab Med 2012 Jan 4; 50(5):861–870. https://doi.org/10.1515/cclm-2011-0846 PMID: 22628330

24. Weitzberg E, Lundberg JO. Novel aspects of dietary nitrate and human health. Ann Rev Nutr 2013; 33:129–159. https://doi.org/10.1146/annurev-nutr-071812-161159 PMID: 23642194

25. D'Alessandro A, Zolla L. Proteomic analysis of red blood cells and the potential for the clinic: what have we learned so far? Expert Rev Proteomics 2017 Mar; 14(3):243–252. https://doi.org/10.1080/14789450.2017.1291347 PMID: 28162022

26. Lang E, Qadri SM, Lang F. Killing me softly—suicidal erythrocyte death. Int J Biochem Cell Biol 2012 Aug; 44(8):1236–1243. https://doi.org/10.1016/j.biocel.2012.04.019 PMID: 22561748

27. Viskupicova J, Blaskovic D, Galiniak S, Soszyński M, Bartosz G, Horakova L, et al. Effect of high glucose concentrations on human erythrocytes in vitro. Redox Biol 2015 Aug; 5:381–387. https://doi.org/10.1016/j.redox.2015.06.011 PMID: 26141922

28. Sompong W, Cheng H, Adisakwattana S. Protective effects of ferulic acid on high glucose-induced protein glycation, lipid peroxidation, and membrane ion pump activity in human erythrocytes. *PLoS One* 2015; 10(6):e0129495. https://doi.org/10.1371/journal.pone.0129495 PMID: 26053739

29. D'Alessandro A, Righetti PG, Zolla L. The red blood cell proteome and interactome: an update. J Proteome Res 2010 Jan; 9(1):144–163. https://doi.org/10.1021/pr900831f PMID: 19886704

30. Aljada A, Garg R, Ghanim H, Mohanty P, Kumbkarni Y, Assian E, et al. Suppression of nuclear factor-kappa β by troglitazone: evidence for an anti-inflammatory effect and a potential antiatherosclerotic effect in the obese. J Clin Endocrinol Metab 2001 Mar; 86(3):1306–1312. https://doi.org/10.1210/jcem.86.3.7309 PMID: 11238525

31. Kim F, Pham M, Luttrell I, Bannerman DD, Tupper J, Thaler J, et al. Toll-like receptor-4 mediates vascular inflammation and insulin resistance in diet-induced obesity. Circ Res 2007 Jun 8; 100(11):1589–1596. https://doi.org/10.1161/CIRCRESAHA.106.142851 PMID: 17478729

32. Olde Damink SW, Jalan R, Deutz NE, Redhead DN, Dejong CH, Hynd P, et al. The kidney plays a major role in the hyperammonemia seen after simulated or actual GI bleeding in patients with cirrhosis. Hepatology 2003 Jun; 37(6):1277–1285. https://doi.org/10.1053/jhep.2003.50221 PMID: 12774005

33. McFarlane Anderson N, Bennett FI, Alleyne GA. Ammonia production by the small intestine of the rat. Biochim Biophys Acta 1976 Jun 23; 437(1):238–243. https://doi.org/10.1016/0304-4165(76)90365-2 PMID: 7312

34. Davies NA, Wright G, Ytrebø LM, Stadlbauer V, Fuskevåg OM, Zwingmann C, et al. L-ornithine and phenylacetate synergistically produce sustained reduction in ammonia and brain water in cirrhotic rats. Hepatology 2009 Jul; 50(1):155–164. https://doi.org/10.1002/hep.22897 PMID: 19437490

35. Kalaitzakis E, Olsson R, Henfridsson P, Hugosson I, Bengtsson M, Jalan R, et al. Malnutrition and diabetes mellitus are related to hepatic encephalopathy in patients with liver cirrhosis. Liver Int 2007 Nov; 27(9):1194–1201. https://doi.org/10.1111/j.1478-3231.2007.01562.x PMID: 17919230

36. Yu PH, Zuo DM. Oxidative deamination of methylamine by semicarbazide-sensitive amino oxidase leads to cytotoxic damage in endothelial cells. Diabetes 1993 Apr; 42(4):594–603. https://doi.org/10.2337/diab.42.4.594 PMID: 8454111

37. Li JJ, Voisin D, Quiquerez AL, Bouras C. Differential expression of advanced glycosylation end-products in neurons of different species. Brain Res 1994 Apr 4; 641(2):285–288. https://doi.org/10.1016/0006-8993(94)90156-2 PMID: 8012830

38. Low SY, Taylor PM,Hundal HS, Pogson CI, Rennie MJ. Transport of L-glutamine and L-glutamate across sinusoidal membranes of rat liver. Biochem J 1992 Jun 1; 284 (Pt 2):333–340. https://doi.org/10.1042/bj2840333 PMID: 1350902

39. Conjeevaram HS, Mullen KD, May EJ, McCullough AJ. Gender-dependent reduction of spontaneous motor activity and growth in rats subjected to portacaval shunt. Hepatology 1994 Feb; 19(2):381–388. PMID: 8294095

40. Comar JF, de Oliveira DS, Bracht L, Kemmelmeier FS, Peralta RM, Bracht A. The metabolic responses to L-glutamine of livers from rats with diabetes types 1 and 2. *PLoS One* 2016 Aug 4; 11(8):e0160067. https://doi.org/10.1371/journal.pone.0160067 PMID: 27490892

41. Butanda-Ochoa A, Hernández-Espinosa DR, Olguín-Martínez M, Sánchez-Sevilla L, Rodríguez MR, Chávez-Rentería B, et al. A single zidovudine (AZT) administration delays hepatic cell proliferation by altering oxidative state in the regenerating rat liver. Oxid Med Cell Longev 2017; 2017:8356175. https://doi.org/10.1155/2017/8356175 PMID: 28479956

42. Stancáková A, Civelek M, Saleem NK, Soininen P, Kangas AJ, Cederberg H, et al. Hyperglycemia and a common variant of GCKR are associated with the levels of eight amino acids in 9,369 Finnish men. Diabetes 2012 Jul; 61(7):1895–1902. https://doi.org/10.2337/db11-1378 PMID: 22553379

43. Tillin T, Hughes AD, Wang Q, Würtz P, Ala-Korpela M, Sattar N, et al. Diabetes risk and amino acid profiles: cross-sectional and prospective analyses of ethnicity, amino acids and diabetes in a South Asian and European cohort from the SABRE (Southall And Brent REvisited) Study. Diabetologia 2015 May; 58(5):968–979. https://doi.org/10.1007/s00125-015-3517-8 PMID: 25693751

44. Forte P, KnealeJ BJ, Milne E, Chowienczyk PJ, Johnston A, Benjamin N, et al. Evidence for a difference in nitric oxide biosynthesis between healthy women and men. Hypertension 1998 Oct; 32(4):730–734. PMID: 9774371

45. Di Lisa F. A female way to protect the heart. Say NO to calcium. Circ Res 2006 Feb 17; 98(3):298–300. https://doi.org/10.1161/01.RES.0000208091.94643.6f PMID: 16484623

46. Moncada S, Higgs A. The L-arginine-nitric oxide pathway. New Engl J Med 1993 Dec 30; 329 (27):2002–2012. https://doi.org/10.1056/NEJM199312303292706 PMID: 7504210

47. Bizjak DA, Brinkmann C, Bloch W, Grau M. Increase in red blood cell-nitric oxide synthase dependent nitric oxide production during red blood cell aging in health and disease: A study on age dependent changes of rheologic and enzymatic properties in red blood cells. *PLoS One* 2015; 10(4):e0125206. https://doi.org/10.1371/journal.pone.0125206 PMID: 25902315

48. Jegatheesanm P, Bandt JP. Hepatic steatosis: a role for citrulline. Curr Opin Clin Nutr Metab Care 2016 19(1):360–365. https://doi.org/10.1097/MCO.0000000000000301 PMID: 27380311

49. Hernández-Muñoz R, Olguín-Martínez M, Aguilar-Delfín I, Sánchez-Sevilla L, García-García N, Díaz-Muñoz M. Oxidant status and lipid composition of erythrocyte membranes in patients with type 2 diabetes, chronic liver damage, and a combination of both pathologies. Oxid Med Cell Longev 2013; 2013:657387. https://doi.org/10.1155/2013/657387 PMID: 23840919

50. Nigra AD, Monesterolo NE, Rivelli JF, Amaiden MR, Campetelli AN, Casale CH, et al. Alterations of hemorheological parameters and tubulin content in erythrocytes from diabetic subjects. Int J Biochem Cell Biol 2016 May; 74:109–120. https://doi.org/10.1016/j.biocel.2016.02.016 PMID: 26923290

51. Koehrer P, Saab S, Berdeaux O, Isaïco R, Grégoire S, Cabaret S, et al. Erythrocyte phospholipid and polyunsaturated fatty acid composition in diabetic retinopathy. *PLoS One* 2014 Sep 4; 9(9):e106912. https://doi.org/10.1371/journal.pone.0106912 PMID: 25188352

Check for updates

Enhancer RNAs: Insights Into Their Biological Role

Josué Cortés-Fernández de Lara, Rodrigo G Arzate-Mejía and Félix Recillas-Targa

Departamento de Genética Molecular, Instituto de Fisiología Celular, Universidad Nacional Autónoma de México, Ciudad de México, México.

Epigenetics Insights
Volume 12: 1–7
© The Author(s) 2019
Article reuse guidelines:
sagepub.com/journals-permissions
DOI: 10.1177/2516865719846093

SAGE

ABSTRACT: Enhancers play a central role in the transcriptional regulation of metazoans. Almost a decade ago, the discovery of their pervasive transcription into noncoding RNAs, termed enhancer RNAs (eRNAs), opened a whole new field of study. The presence of eRNAs correlates with enhancer activity; however, whether they act as functional molecules remains controversial. Here we review direct experimental evidence supporting a functional role of eRNAs in transcription and provide a general pipeline that could help in the design of experimental approaches to investigate the function of eRNAs. We propose that induction of transcriptional activity at enhancers promotes an increase in its activity by an RNA-mediated titration of regulatory proteins that can impact different processes like chromatin accessibility or chromatin looping. In a few cases, transcripts originating from enhancers have acquired specific molecular functions to regulate gene expression. We speculate that these transcripts are either nonannotated long noncoding RNAs (lncRNAs) or are evolving toward functional lncRNAs. Further work will be needed to comprehend better the biological activity of these transcripts.

KEYWORDS: Enhancer, eRNAs, lncRNAs, chromatin loop, gene expression, chromatin

RECEIVED: April 2, 2019. **ACCEPTED:** April 4, 2019.

TYPE: Review

FUNDING: This work was supported by Dirección General de Asuntos del Personal Académico, Universidad Nacional Autónoma de México and Programa de Apoyo a Proyectos de Investigación e Innovación Tecnológica (DGAPA-PAPIIT IN201114 and IN203917), and by Consejo Nacional de Ciencia y Tecnología (CONACyT 220503) and Fronteras de la Ciencia 2015-290 to F.R-T.

DECLARATION OF CONFLICTING INTERESTS: J.C.F.L. and R.G.A.M. are PhD students from Programa de Doctorado en Ciencias Biomédicas, Universidad Nacional Autónoma de México. J.C-F.L. received fellowship 549543 from CONACyT, and R.G.A-M. received fellowships 288814 and 25590 from CONACyT.

CORRESPONDING AUTHOR: Félix Recillas-Targa, Departamento de Genética Molecular, Instituto de Fisiología Celular, Universidad Nacional Autónoma de México, Circuito Exterior S/N, Ciudad Universitaria, Ciudad de México, C.P. 04510, México. Email frecilla@ifc.unam.mx

General Features and Dynamics of eRNAs

One of the most intriguing questions in biology is how cells achieve transcriptional regulation. In the case of multicellular organisms, development and response to external stimuli are complex processes that require fine regulation of gene expression. At the heart of metazoan transcriptional regulation are found the enhancers,[1] which are DNA elements bound by cofactors and transcription factors (TFs) that are able to increase the transcription levels of their target genes by direct stimulation of their promoters often through chromatin looping.[2] At the chromatin level, enhancers are characterized by prominent accessibility to DNase I and high levels of histone H3K4me1,[3] as well as high levels of histone H3K27ac when active.[4] An interesting discovery in the biology of enhancers came in 2010 when 2 groups independently found that enhancers were transcribed genome-wide into noncoding RNAs termed enhancer RNAs (eRNAs).[5,6] This finding raised the question of the potential role that eRNAs could play in the regulation of gene expression, as several long noncoding RNAs (lncRNAs) have been shown to be functional molecules.[7]

eRNAs have been identified in diverse organisms like *Caenorhabditis elegans, Drosophila melanogaster*, and mouse, and in human cell lines, which suggest that transcription at enhancers is of ancient origin and might have an important role in enhancer activity.[8–11] eRNAs have been described as usually bidirectional, on average separated by 180 base pairs and transcribed at equal levels into nonpoly(A), unspliced molecules.[9] Most eRNAs are transcribed at lower levels than mRNAs and other noncoding RNAs such as lncRNAs and are rapidly degraded by the exosome.[9,12] Interestingly, it has been observed that eRNAs can be subject to methylation.[13,14] Recent single-cell genome-wide data of nascent transcription challenges some of the typical characteristics of eRNAs as it was shown that enhancer transcription is unidirectional, and therefore within a cellular population, some cells transcribe the sense strand and others the antisense strand.[15] In the cases where both strands of eRNAs were detected in the same cell, single-molecule fluorescence in situ hybridization (FISH) experiments showed that colocalization of both RNA molecules was rare. Because typical RNA expression methodologies show an average for total cells, that would explain why eRNAs have been described as bidirectional. Importantly, eRNAs were expressed at similar levels compared with gene promoters in single cells and were detected in just a subset of cells, ie, displaying transcriptional bursting.[15] More single-cell measurements of nascent transcription in different conditions are needed to clarify the real nature of transcripts originating from enhancers.

Active enhancers are the main source of eRNAs, and the transcription of enhancers into eRNAs has been correlated with increased transcription of nearby genes,[5,9,16] suggesting that transcription, the eRNAs themselves, or both, might be important for enhancer activity. In support of this, time course experiments evaluating the response of cells to different stimuli have provided strong evidence of specific timing of transcription of enhancers into eRNAs.[10,16] For example, in mammalian cells, upon stimulation with growth factors and exposure to pathogens, the eRNAs from active enhancers are transcribed first, then mRNAs that code for TFs, and finally non-TFs mRNAs. This suggests that upon stimuli, a concerted transcriptional response is established during which responsive enhancers are transcribed into eRNAs first and then genes coding for TFs which could ultimately lead to genome-wide changes in

Creative Commons Non Commercial CC BY-NC: This article is distributed under the terms of the Creative Commons Attribution-NonCommercial 4.0 License (http://www.creativecommons.org/licenses/by-nc/4.0/) which permits non-commercial use, reproduction and distribution of the work without further permission provided the original work is attributed as specified on the SAGE and Open Access pages (https://us.sagepub.com/en-us/nam/open-access-at-sage).

BOX 1. A toolbox to work with eRNAs.

Cap analysis gene expression (CAGE) and global nuclear run-on sequencing (GRO-seq)-based methods as well as other recently developed experimental strategies that target nascent unstable transcripts are the best approaches to start characterizing eRNAs.[9,19–22] The transcriptomic data can then be compared against ChIP-seq data for enhancer chromatin marks, as well as DNase I, and more recently, ATAC-seq data to annotate enhancers and in this way assign eRNAs to those genomic regions.

After identification of transcribed enhancers, the next desirable step is to assign enhancers to target genes. This can be done by assigning an enhancer to the closest gene; however, we find this undesirable and strongly suggest to use genome-wide 3C-based techniques like Hi-C,[23] Capture Hi-C,[24] ChIA-PET,[25] or HiChIP.[26] Alternative, expression has also been used to link enhancers with promoters,[9] and recent computational approaches have been developed to predict enhancer-promoter interactions.[27] Once enhancer-promoter relationships have been established, the next step is to characterize either both the enhancer and its eRNAs or just the function of the eRNAs in this case when the enhancer has already been tested for function. In the former scenario, genome editing tools such as CRISPR-Cas9 can be used to assess the importance of a given transcribed enhancer by direct deletion of the genomic sequence. Evaluation of the expression levels of its target gene by quantitative reverse transcription polymerase chain reaction (RT-qPCR) will inform on the transcriptional effect the enhancer has on that promoter while 3C or 4C-seq can inform on the contribution of that enhancer element on the topology of that locus.

To evaluate the functional contribution of eRNAs to enhancer activity and the regulation of the target promoter, several considerations should be taken. First, validate eRNAs presence by strand-specific RT-qPCR. If possible, perform a Northern blot analysis to identify large RNA molecules derived from the enhancer element. The data from CAGE, GRO-seq, strand-specific RT-qPCR, and Northern blot should provide critical information on the abundance of RNA species, if there is a strand that is particularly more abundant and on the size of the molecules. This information will be fundamental to design knockdown strategies to determine whether the RNA molecule itself is regulating expression. In this case, small interfering RNAs (siRNAs) or locked nucleic acid antisense oligonucleotides (LNAs) can be used to deplete eRNAs and should be preferentially designed against the most abundant RNA specie. However, it is important to notice that RNA interference machinery is found mainly in the cytoplasm, so techniques based on the use of antisense oligonucleotides might be better for loss of function assays to study eRNAs. In this regard, the efficiency of transfection can greatly affect the resulting knockdown efficiency and because of that a careful selection of a cell system remains fundamental.

To evaluate the effect of eRNA knockdown, we advise to measure transcription of target genes as well as possible changes in long-range interactions if it is the case. To further support a function of the mature eRNA, a dead-Cas9–based strategy can be used to bring an eRNA to an enhancer element and evaluate different features like changes in the chromatin organization, histone marks, DNA accessibility, and potency to increase transcription. Finally, to study the potential association of an eRNA with specific regulatory proteins, it is advisable to perform RNA immunoprecipitation against the protein of interest and evaluate enrichment of the eRNA. If there is no a priori knowledge of the involvement of a protein, pull down of the eRNA with nuclear or cytoplasmic extracts, protein purification, and mass-spectrometry of eluted proteins should inform on potential protein partners.

In some cases, it has been shown that the act of transcription rather than the RNA molecule itself can be important and therefore inserting early termination sites as poly(A) signals into the enhancer sequence could be useful to study the role of productive transcription on enhancer activity.

transcription by directly regulating transcription at target genes. A possibility is that early responsive enhancers might produce eRNAs that contribute to a robust transcriptional induction of TF coding genes. It would be interesting to knockdown eRNAs from active enhancers contacting early inducible TF-genes and to characterize if they are actually playing a functional role in transcriptional activation as it might be suggested by their timing of transcription. An intriguing observation in B-lymphocytes during an innate antiviral immune response is that a subset of active enhancers continues to be transcribed despite loss of expression of its target genes.[16] This is in contrast with the majority of cases where enhancer-promoter pairs are concordant in their transcriptional status, ie, enhancer is transcribed first, then its target gene and then loss of enhancer transcription correlates with loss of transcription of its target gene.[16]

Overall, these observations suggest that eRNA transcription at enhancers is a regulated and dynamic process. In many scenarios, stimulus-dependent transcription at enhancers precedes the transcription of associated genes. However, these are mostly correlative observations, and still little is known about the molecular function of eRNAs and how they can impact transcription.

Mechanisms of Action

In the past decade, loss and gain of function assays have been critical to characterize the function of many ncRNAs like the lncRNAs. Most of the described mechanisms involve the interaction of lncRNAs with key regulatory proteins, like Polycomb and Trithorax.[17,18] In many of these cases, the RNA acted as a decoy, a scaffold, a guide, or even as an enhancer.[7] In contrast to lncRNAs, assigning a molecular mechanism of action to eRNAs has been challenging mainly due to their unstable nature as well as their very low abundance (Box 1). However, over the past decade the function of some of these eRNAs, in very specific scenarios, has been characterized. We proceed to describe these examples and discuss their implications for eRNA functions and their impact in the control of transcription.

Stimulation of enzymatic activity

The strongest evidence for a common function of many eRNAs was the finding that eRNAs interact with CREB binding protein (CBP), an acetyltransferase that, alongside with p300, deposits the histone H3K27ac mark in chromatin.[28] Native RNA immunoprecipitation and PAR-CLIP (photoactivatable ribonucleoside-enhanced cross-linking and immunoprecipitation) experiments demonstrated a CBP-eRNAs interaction in vivo.[28] In vitro assays showed that CBP-eRNAs interactions were independent of sequence, which suggest that a particular secondary structure of these RNAs may influence binding to CBP, as has been suggested for lncRNAs interacting with other regulatory proteins.[29] Of note, CBP-eRNAs interactions are already detected at actively transcribed enhancers where CBP is already bound.[28] This could mean that the interaction between CBP and eRNAs is not required for CBP recruitment. In line

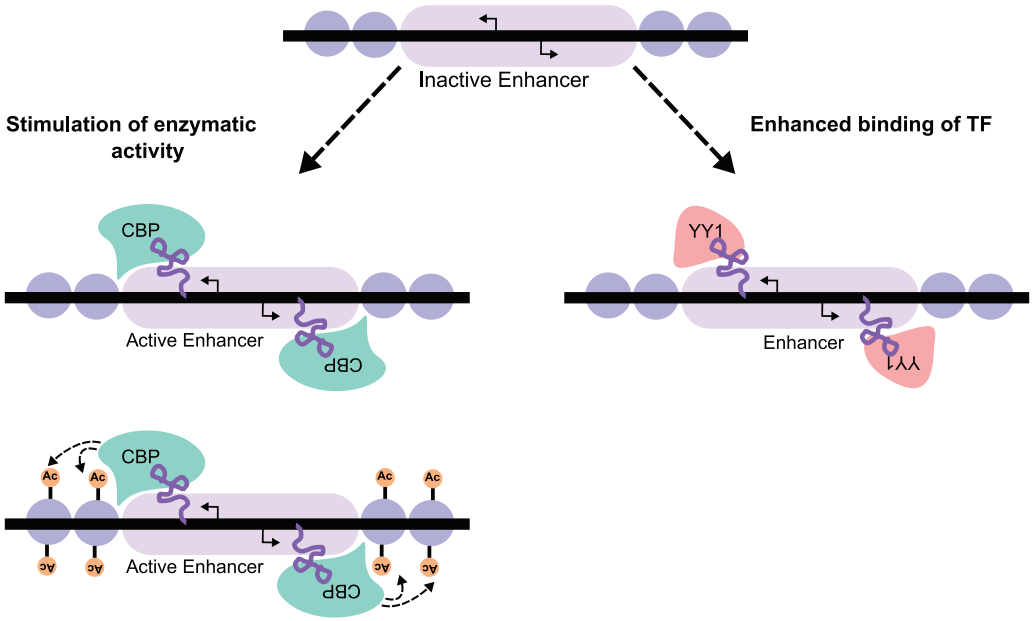

Figure 1. Enhancer RNAs (eRNAs) can influence catalytic activity of chromatin modifier proteins or act as traps for transcription factors. *Left*, eRNAs can directly interact with CBP, a histone acetyltransferase, and stimulate its enzymatic activity which results in a eRNA concentration dependent increase of H3K27ac as well acetylation in other amino acid residues of histones. *Right*, eRNAs at enhancers can trap transcription factors, like YY1, which results in an increase of signal for YY1 as evaluated by ChIP. This could mean that association with eRNAs increases residency time of TFs. CBP indicates CREB binding protein; TF, transcription factors.

with this, CBP-eRNA's interaction stimulates the histone acetyltransferase activity of CBP by increasing its affinity for a histone substrate which results in higher deposition of H3K27ac as well as H4K5ac histone marks[28] (Figure 1, *Left*). Knockdown of different eRNAs using antisense oligonucleotides resulted in a decrease in the histone H3K27ac level at the corresponding enhancer of origin and at the adjacent gene promoter with a concomitant reduction in the mRNA levels for target genes.[28] These data suggest that transcription of enhancers into eRNAs could enhance CBP acetyltransferase activity, which in turn might promote the acquisition of a chromatin environment permissive for enhancer function. In line with this, it has been shown that depletion of eRNAs during myogenesis results in a decrease in DNase I accessibility,[30] although the chromatin remodeling complex responsible for this effect remains elusive.

TFs trapping

lncRNAs can interact with different proteins involved in chromatin modification or organization, such as PRC2, MLL1, and CTCF.[17,18,31] Because enhancers are platforms for the binding of a variety of TFs, and Zinc Finger Domains of different TFs can interact with RNA[31–33]; therefore, eRNAs could interact with TFs, possibly influencing their residency time at enhancer elements. In line with this, YY1, a ubiquitously expressed TF in mammals, can interact in vivo with RNA when bound both at promoters and enhancers.[33] Inhibiting transcription or the exosome resulted in a decrease of YY1 recruitment at enhancers. This suggests that it is the nascent transcription of the eRNAs that is important for YY1 binding at enhancers. In line with this, tethering a specific eRNA in the vicinity of six enhancers bound by YY1 resulted in an increase in the binding of YY1 to those sites[33] (Figure 1, *Right*). Although the increase of YY1 binding to enhancers after eRNA tethering was modest, it supports a model where eRNAs might help to increase binding or residency time of YY1 at enhancers.

eRNAs can also interact with bromodomain-containing protein 4 (BRD4),[34] which is a member of the bromodomain and extraterminal domain (BET) family of proteins. It can bind to acetylated histones and stimulates elongation of protein-coding and noncoding RNAs. The interaction between eRNAs and BRD4 increases BRD4 binding to acetylated histones in vitro and to its target enhancers in vivo.[34] Knockdown of BRD4 interacting eRNAs results in loss of BRD4 and RNA polymerase II (RNA Pol II) binding at enhancer as well as loss of transcription of the target gene.[34]

Because other TFs have been shown to specifically interact with mRNAs and lncRNAs, like CTCF,[31] it remains to be determined if they can also interact with eRNAs as well. In addition, it is currently unclear what could be the effect of increasing the residency time of a TF at enhancer elements. An attractive possibility is that eRNAs could increase the binding of TFs to low affinity sites at enhancers; however, this remains to be elucidated.

Chromatin loop formation

Enhancer-promoter interactions through chromatin looping are important for tight control of gene expression either during development or cell differentiation, or in response to specific stimuli.[35,23] Defects in these interactions can have profound

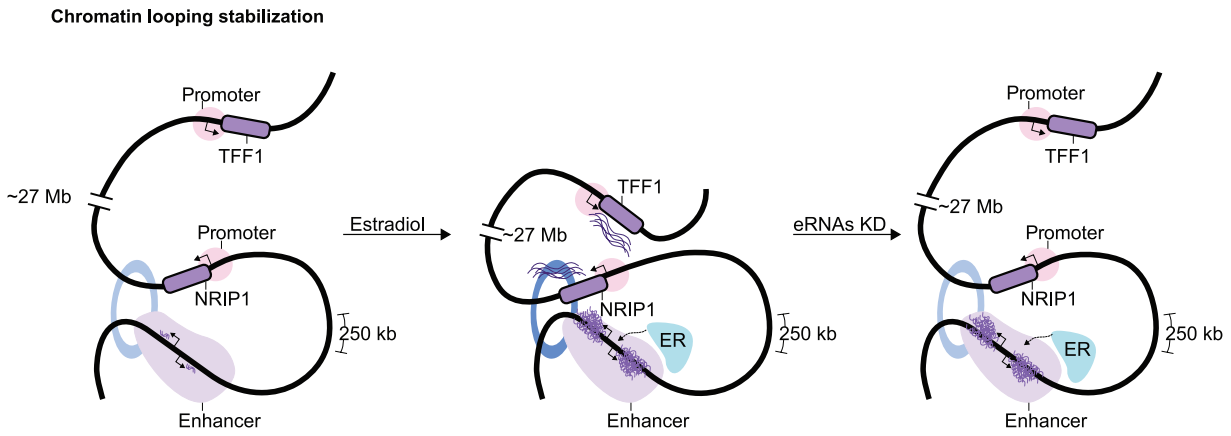

Figure 2. eRNAs can stabilize chromatin long-range interactions between transcribing enhancers and target promoters. The *NRIP1* promoter is in close proximity with an enhancer located ~250 kb upstream. Upon stimulation with estradiol, the transcription of both the enhancer and *NRIP1* is induced. This transcriptional effect is accompanied by increased deposition of the cohesin subunits Rad21 and SMC3 at the enhancer, as well as an increased frequency of interaction between the enhancer and the *NRIP1* promoter gene. This local reorganization is also accompanied by the gain of a novel interaction with *TFF1*, located 27 Mb away from *NRIP1* gene that is also transcriptionally induced during estradiol treatment. Depletion of *NRIP1*-associated eRNAs results in loss of *NRIP1* transcription, decreased deposition of cohesin subunits at the enhancer, and importantly, a decreased frequency of long-range interactions between the enhancer and the *NRIP1* promoter gene as evaluated by 3C and the loss of the 27 Mb interaction as evaluated by fluorescence in situ hybridization. Of note, eRNAs can directly interact with cohesin subunits. eRNA indicates enhancer RNAs; KD, knockdown; ER, Estrogen Receptor.

implications in development and disease generally due to changes in gene expression.[36–38] Different architectural proteins have shown to be important for promoting chromatin looping between regulatory elements, among them CTCF, YY1, and cohesin, as well as proteins involved in the general machinery of transcription like Mediator, RNA Pol II, Integrator, and cell-type-specific TFs.[23,39–44] These proteins can bind, for example, at enhancers and promoters and induce the establishment or the stability of long-range interactions. Because enhancers can be transcribed into eRNAs, it has been tempting to speculate that they might influence looping interactions between enhancers and promoters, which could ultimately result in regulated changes in gene expression. In line with this, several studies have reported a contribution of eRNAs to chromatin looping between selected activated enhancers and promoter elements.[12,16,40,45,46] In most of these studies, knockdown of eRNAs from selected enhancers either by small interfering RNAs (siRNAs) or locked nucleic acid antisense oligonucleotides (LNAs) results in quantitative and qualitative changes in looping contacts between transcribed enhancers and promoters which correlates with decreased transcription of their target genes.

In some cases, it has been shown that eRNAs can directly recruit architectural proteins like cohesin to their enhancer elements and this could directly contribute to changes in long-range interactions.[46] For example, in breast cancer cells the promoter of the *NRIP1* locus interacts in cis through chromatin looping with and enhancer located ~250 kb away. Upon stimulation with estradiol, the estrogen receptor binds to the enhancer. This results in strong transcription into eRNAs, increased binding of cohesin subunits, and higher frequency of long-range interaction with the *NRIP1* promoter which correlates with upregulation of the *NRIP1 mRNA* levels.[46] Importantly, reduction of eRNAs by the use of LNAs leads to the loss of looping interactions and transcription at *NRIP1* locus. These changes are also accompanied by decreased recruitment of cohesin subunits to the enhancer element. For this locus, the changes in long-range interactions are not just restricted to its enhancer element because depletion of eRNAs also results in loss of a ~27 Mb long-range interaction with the *TFF1* locus, which itself has an inducible enhancer transcribed upon estrogen stimulation (Figure 2).

Other proteins like Mediator, an important regulator of RNA Pol II activity, have been documented to play a role in promoting looping interactions between enhancers and promoters.[39,45,47] In regard to eRNAs, some reports have suggested that eRNAs interact with Mediator to promote long-range interactions between transcriptionally active enhancers and their target promoters.[45,47] However, a careful examination of current annotations for those locus suggest that those eRNAs are in fact lncRNAs that act in cis to regulate neighboring genes through direct interaction with Mediator and cell-type -specific TFs. Therefore, the role of Mediator in eRNA function requires further clarification.

The proper biogenesis of eRNAs is also important for stimulus-dependent enhancer activity and the establishment of long-range interaction between such enhancers and their target promoters. In this regard, it has been documented that Integrator, a multisubunit complex associated with RNA Pol II, is recruited to enhancers in a stimulus-dependent manner and is necessary for release of eRNA transcripts for elongating

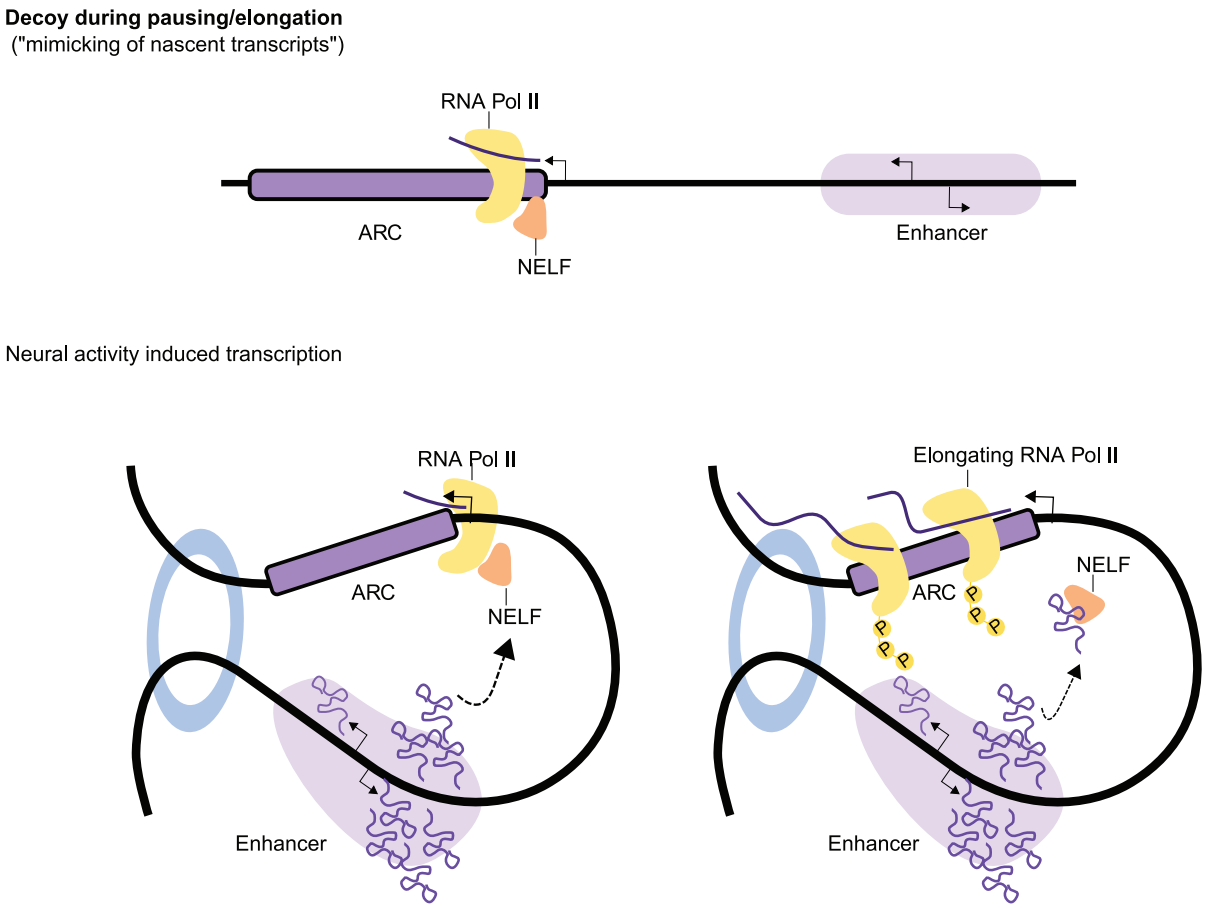

Figure 3. Enhancer RNAs (eRNAs) can promote exit of RNA Pol II pausing at promoters by mimicking nascent transcripts and interacting with NELF. The *ARC* locus is in physical proximity with an enhancer element throughout chromatin looping. Upon neuron stimulation, the transcription of both the enhancer and *ARC* gene is induced. Interestingly, transcription of one of the enhancer strands is more abundant. This eRNA can directly interact with NELF acting as a decoy for that protein. This results in loss of NELF at *ARC* promoter and the release of the paused RNA Pol II which engages in productive elongation. NELF indicates negative elongation factor; RNA Pol II, RNA polymerase II.

RNA Pol II.[40] Loss of Integrator results in accumulation of eRNAs primary transcripts. This effect compromises enhancer function, resulting in loss of chromatin looping between selected responsive enhancers and their target promoters with a corresponding loss of transcriptional induction. These data suggest that mature eRNAs, but not the transcription of enhancers, are required for long-range interactions between enhancers and promoters.

In this regard, it may be tempting to speculate that at stimulus-dependent enhancers, the induction of transcription by binding of specific TFs results in the generation of mature eRNAs by the Integrator complex. Then, these eRNAs in conjunction with boundary proteins like CTCF or YY1, could promote the stalling of loop-extrusion factors, like cohesin, through direct RNA-protein interactions.[48] Therefore, depletion of eRNAs could result in the loss of an RNA-dependent boundary that results in a decrease of specific long-range interactions between pairs of enhancer-promoter sequences. Interestingly, an RNA-dependent function of CTCF for chromatin looping has been recently reported.[49–51]

RNA Pol II productive elongation

eRNAs can regulate RNA Pol II elongation by interacting with proteins that either promote or inhibit elongation.[52,53] For example, eRNAs can promote exit of RNA Pol II pausing at activity-dependent neuronal promoters throughout direct interaction with the negative elongation factor (NELF), which promotes RNA Pol II pausing.[52] Knockdown of eRNAs associated with the enhancers of the neuronal genes *ARC* and *GADD45B* did not affect long-range interactions between the enhancers and promoters but resulted in an increase of the NELF at their promoters, which was accompanied by a decrease of the corresponding mRNA[52] (Figure 3). Because these eRNAs can interact with NELF via an RNA-binding domain, it was suggested that eRNAs could trap NELF, mimicking nascent transcription at target promoters. Therefore, eRNAs could promote RNA Pol II productive elongation by acting as a decoy for NELF, which in turn might be facilitated by the close physical proximity between the enhancers and promoters by means of chromatin looping.

eRNAs can also promote elongation by interaction with the positive transcription elongation factor b (p-TEFb) complex

which promotes RNA Pol II elongation by phosphorylation of different targets including NELF and Pol II-Ser2.[53–55] An eRNA transcribed from an enhancer that increases the expression of the target gene *PSA* can directly interact with the kinase CYCLIN T1 which is part of the p-TEFb complex.[53] Loss of this interaction correlates with a diminishment of Pol II-Ser2 phosphorylation and *PSA* expression. Interestingly, the interaction between CYCLIN T1 was achieved via an HIV-1 TAR RNA-like motif found in the eRNA. The motif present in the eRNA is also similar to the one found in the 7SK small nuclear RNA which can inhibit p-TEFb function. Therefore, this eRNA could favor elongation by RNA Pol II by competing with 7SK for the interaction with the p-TEFb complex thought CYCLIN T1. This is an example of a functional embedded structure in an eRNA and opens up the possibility that a subset of eRNAs act through specific sequence motifs. However, as we know that enhancers poorly conserved, this case might rather be an exception.

Concluding Remarks

The discovery of the pervasive transcription of the genome into ncRNAs has opened a whole new field of study. Enhancer transcription is of interest as these regulatory elements are at the heart of transcriptional regulation in processes as diverse as development, cell differentiation, and response to stimuli. One of the most important questions in the field is if eRNAs have a function. Even though it has been suggested that most eRNAs might be transcriptional noise,[56] for over almost a decade, different mechanisms of action have been characterized by which eRNAs could influence gene expression. Overall, eRNAs seem to exert their function by interacting with different regulatory proteins, similar to what has been discovered for lncRNAs. eRNAs can affect the chromatin environment of their enhancer, either by promoting chromatin accessibility, stimulating the histone acetyltransferase activity of CBP or enhancing the binding of TFs.

eRNAs can also stabilize chromatin looping contacts between enhancers and promoters by the recruitment of cohesin and can affect the transcriptional machinery already poised at promoters. In those cases, eRNAs can act as decoys for proteins like NELF, promoting elongation or influence the catalytic activity of other proteins associated with RNA Pol II.

Although progress has been made over the past years to uncover the potential molecular function of eRNAs, it should be pointed out that most of the examples covered here are restricted to a few loci. In many cases, although transcription of both strands of the enhancer is detected, one strand is prominently transcribed into an ncRNA that has a molecular function important for enhancer activity or gene transcription. This rise the concern of whether the molecular functions already reported for this subset of eRNAs could be a general feature of eRNAs or in fact they represent specific cases were eRNAs have acquired functions similar to lncRNAs or have been misannotated as eRNAs.[57] In this regard, a clear working definition that helps to distinguish eRNAs from lncRNAs might be of great help.

Based on current evidence, we propose that transcription of enhancers into eRNAs could be an RNA-based mechanism to trap proteins relevant for enhancer activity. In support of this, an increasing number of proteins with key regulatory functions like CTCF, YY1, and CBP have been shown to interact with RNA, and this association can have important consequences for their activity. In this regard, transcription at enhancers could be a means to increase the residency time of both DNA-binding proteins and cofactors.

For example, upon cell stimulation, specific TFs could bind to already CBP-bound enhancers and potentiate transcription. Those eRNAs could further stimulate the histone acetyltransferase activity of CBP which in turn could trigger BRD4 binding. Because eRNAs can also interact directly with BRD4 and increase the binding of this protein to the enhancer element, and BRD4 can promote elongation by recruitment of p-TEFb, Mediator, and RNA Pol II, these could lead to increased transcription of the enhancer into eRNAs.[34] All these can result in a net increase of RNA species at the enhancer that could lead to the establishment of a feed-forward loop where increasing eRNA molecules keep on promoting elongation at enhancer as well as acetylation of histones resulting in a chromatin structure that could boost enhancer activity over target promoters. Therefore, based on current evidence, we envision a general mechanism by which eRNAs favor the maintenance or reinforcement of a chromatin environment optimal for enhancer function. In some cases, these eRNAs could have evolved to acquire a specific molecular function and might be in a path toward becoming lncRNAs. Further work is needed, particularly on developing high-throughput genome-wide tools, to assess the functional role of eRNAs and clarify their relevance on transcriptional regulation.

Author Contributions

JC-FL, RGA-M and FR-T wrote and revised the manuscript.

REFERENCES

1. Bulger M, Groudine M. Functional and mechanistic diversity of distal transcription enhancers. *Cell*. 2011;144:327–339.
2. Shlyueva D, Stampfel G, Stark A. Transcriptional enhancers: from properties to genome-wide predictions. *Nat Rev Genet*. 2014;15:272–286.
3. Heintzman ND, Ren B. Finding distal regulatory elements in the human genome. *Curr Opin Genet Dev*. 2009;19:541–549.
4. Creyghton MP, Cheng AW, Welstead GG, et al. Histone H3K27ac separates active from poised enhancers and predicts developmental state. *Proc Natl Acad Sci U S A*. 2010;107:21931–21936.
5. De Santa F, Barozzi I, Mietton F, et al. A Large fraction of extragenic RNA Pol II transcription sites overlap enhancers. *PLoS Biol*. 2010;8:e1000384.
6. Kim T-K, Hemberg M, Gray JM, et al. Widespread transcription at neuronal activity-regulated enhancers. *Nature*. 2010;465:182–187.
7. Rinn JL, Chang HY. Genome regulation by long noncoding RNAs. *Annu Rev Biochem*. 2012;81:145–166.
8. Chen RA-J, Down TA, Stempor P, et al. The landscape of RNA polymerase II transcription initiation in ***C. elegans*** reveals promoter and enhancer architectures. *Genome Res*. 2013;23:1339–1347.

9. Andersson R, Gebhard C, Miguel-Escalada I, et al. An atlas of active enhancers across human cell types and tissues. *Nature*. 2015;507:455–461.
10. Arner E, Daub CO, Vitting-Seerup K, et al. Transcribed enhancers lead waves of coordinated transcription in transitioning mammalian cells. *Science*. 2015;347:1010–1014.
11. Mikhaylichenko O, Bondarenko V, Harnett D, et al. The degree of enhancer or promoter activity is reflected by the levels and directionality of eRNA transcription. *Genes Dev*. 2018;32:42–57.
12. Pefanis E, Wang J, Rothschild G, et al. RNA exosome-regulated long non -coding RNA transcription controls super-enhancer activity. *Cell*. 2015;161: 774–789.
13. Aguilo F, Li S, Balasubramaniyan N, et al. Deposition of 5-methylcytosine on enhancer RNAs enables the coactivator function of PGC-1α. *Cell Rep*. 2016;14:479–492.
14. Nachtergaele S, He C. The emerging biology of RNA post-transcriptional modifications. *RNA Biol*. 2017;14:156–163.
15. Kouno T, Moody J, Kwon AT-J, et al. C1 CAGE detects transcription start sites and enhancer activity at single-cell resolution. *Nat Commun*. 2019;10:360.
16. Kim YJ, Xie P, Cao L, Zhang MQ, Kim TH. Global transcriptional activity dynamics reveal functional enhancer RNAs. *Genome Res*. 2018;28:1799–1811.
17. Rinn JL, Kertesz M, Wang JK, et al. Functional demarcation of active and silent chromatin domains in human HOX loci by noncoding RNAs. *Cell*. 2007;129:1311–1323.
18. Wang KC, Yang YW, Liu B, et al. A long noncoding RNA maintains active chromatin to coordinate homeotic gene expression. *Nature*. 2011;472:120–124.
19. Core LJ, Waterfall JJ, Lis JT. Nascent RNA sequencing reveals widespread pausing and divergent initiation at human promoters. *Science*. 2008;322:1845–1848.
20. Kwak H, Fuda NJ, Core LJ, Lis JT. Precise maps of RNA polymerase reveal how promoters direct initiation and pausing. *Science*. 2013;339:950–953.
21. Lam MTY, Cho H, Lesch HP, et al. Rev-Erbs repress macrophage gene expression by inhibiting enhancer-directed transcription. *Nature*. 2013;498:511–515.
22. Mahat DB, Kwak H, Booth GT, et al. Base-pair-resolution genome-wide mapping of active RNA polymerases using precision nuclear run-on (PRO-seq). *Nat Protoc*. 2016;11:1455–1476.
23. Rao SSP, Huntley MH, Durand NC, et al. A 3D map of the human genome at kilobase resolution reveals principles of chromatin looping. *Cell*. 2014;159:1665–1680.
24. Schoenfelder S, Furlan-Magaril M, Mifsud B, et al. The pluripotent regulatory circuitry connecting promoters to their long-range interacting elements. *Genome Res*. 2015;25:582–597.
25. Fullwood MJ, Liu MH, Pan YF, et al. An oestrogen-receptor-α-bound human chromatin interactome. *Nature*. 2009;461:58–64.
26. Mumbach MR, Rubin AJ, Flynn RA, et al. HiChIP: efficient and sensitive analysis of protein-directed genome architecture. *Nat Methods*. 2016;13:919–922.
27. Rennie S, Dalby M, van Duin L, Andersson R. Transcriptional decomposition reveals active chromatin architectures and cell specific regulatory interactions. *Nat Commun*. 2018;9:487–416.
28. Bose DA, Donahue G, Reinberg D, Shiekhattar R, Bonasio R, Berger SL. RNA binding to CBP stimulates histone acetylation and transcription. *Cell*. 2017;168:135–149.e22.
29. Quinn JJ, Chang HY. Unique features of long non-coding RNA biogenesis and function. *Nat Rev Genet*. 2016;17:47–62.
30. Mousavi K, Zare H, Dell'orso S, et al. eRNAs promote transcription by establishing chromatin accessibility at defined genomic loci. *Mol Cell*. 2013;51:606–617.
31. Saldana-Meyer R, Gonzalez-Buendia E, Guerrero G, et al. CTCF regulates the human p53 gene through direct interaction with its natural antisense transcript, Wrap53. *Genes Dev*. 2014;28:723–734.
32. Font J, Mackay JP. Beyond DNA: Zinc finger domains as RNA-binding modules. In: Mackay, JP, Segal, DJ, eds. *Engineered Zinc Finger Proteins*. Vol 649. Totowa, NJ: Humana Press; 2010:479–491.
33. Sigova AA, Abraham BJ, Ji X, et al. Transcription factor trapping by RNA in gene regulatory elements. *Science*. 2015;350:978–981.
34. Lee JE, Park YK, Park S, et al. Brd4 binds to active enhancers to control cell identity gene induction in adipogenesis and myogenesis. *Nat Commun*. 2017;8:2217.
35. Jin F, Li Y, Dixon JR, et al. A high-resolution map of the three-dimensional chromatin interactome in human cells. *Nature*. 2013;503:290–294.
36. Franke M, Ibrahim DM, Andrey G, et al. Formation of new chromatin domains determines pathogenicity of genomic duplications. *Nature*. 2016;538:265–269.
37. Hnisz D, Weintraub AS, Day DS, et al. Activation of proto-oncogenes by disruption of chromosome neighborhoods. *Science*. 2016;351:1454–1458.
38. Lupianez DG, Kraft K, Heinrich V, et al. Disruptions of topological Chromatin domains cause pathogenic rewiring of gene-enhancer interactions. *Cell*. 2015;161:1012–1025.
39. Kagey MH, Newman JJ, Bilodeau S, et al. Mediator and cohesin connect gene expression and chromatin architecture. *Nature*. 2010;467:430–435.
40. Lai F, Gardini A, Zhang A, Shiekhattar R. Integrator mediates the biogenesis of enhancer RNAs. *Nature*. 2015;525:399–403.
41. Nora EP, Goloborodko A, Valton A-L, et al. Targeted degradation of CTCF decouples local insulation of chromosome domains from genomic compartmentalization. *Cell*. 2017;169:930–944.e22.
42. Rubin AJ, Barajas BC, Furlan-Magaril M, et al. Lineage-specific dynamic and pre-established enhancer–promoter contacts cooperate in terminal differentiation. *Nat Genet*. 2017;49:1522–1528.
43. Weintraub AS, Li CH, Zamudio AV, et al. YY1 is a structural regulator of enhancer-promoter loops. *Cell*. 2017;171:1573–1588.e28.
44. Tang Z, Luo OJ, Li X, et al. CTCF-mediated human 3D genome architecture reveals chromatin topology for transcription. *Cell*. 2015;163:1611–1627.
45. Hsieh C-L, Fei T, Chen Y, et al. Enhancer RNAs participate in androgen receptor-driven looping that selectively enhances gene activation. *Proc Natl Acad Sci U S A*. 2014;111:7319–7324.
46. Li W, Notani D, Ma Q,, et al. Functional roles of enhancer RNAs for oestrogen-dependent transcriptional activation. *Nature*. 2013;498:516–520.
47. Lai F, Orom UA, Cesaroni M, et al. Activating RNAs associate with mediator to enhance chromatin architecture and transcription. *Nature*. 2013;494:497–501.
48. Fudenberg G, Imakaev M, Lu C, Goloborodko A, Abdennur N, Mirny LA. Formation of chromosomal domains by loop extrusion. *Cell Rep*. 2016;15:2038–2049.
49. Hansen AS, Amitai A, Cattoglio C, et al. Guided nuclear exploration increases CTCF target search efficiency. bioRxiv, January 2018, 495457.
50. Hansen AS, Hsieh T-HS, Cattoglio C, et al. An RNA-binding region regulates CTCF clustering and chromatin looping. bioRxiv, January 2018, 495432.
51. Saldaña-Meyer R, Rodriguez-Hernaez J, Nishana M, et al. RNA interactions with CTCF are essential for its proper function. bioRxiv, January 2019, 530014.
52. Schaukowitch K, Joo J-Y, Liu X, Watts JK, Martinez C, Kim TK. Enhancer RNA facilitates NELF release from immediate early genes. *Mol Cell*. 2014;56:29–42.
53. Zhao Y, Wang L, Ren S, et al. Activation of P-TEFb by androgen receptor -regulated enhancer RNAs in castration-resistant prostate cancer. *Cell Rep*. 2016;15:599–610.
54. Peterlin BM, Price DH. Controlling the elongation phase of transcription with P-TEFb. *Mol Cell*. 2006;23:297–305.
55. Zhou Q,, Li T, Price DH. RNA polymerase II elongation control. *Annu Rev Biochem*. 2012;81:119–143.
56. Young RS, Kumar Y, Bickmore WA, Taylor MS. Bidirectional transcription initiation marks accessible chromatin and is not specific to enhancers. *Genome Biol*. 2017;18:242.
57. Orom UA, Derrien T, Beringer M, et al. Long noncoding RNAs with enhancer-like function in human cells. *Cell*. 2010;143:46–58.

Hindawi
Stem Cells International
Volume 2019, Article ID 7627148, 13 pages
https://doi.org/10.1155/2019/7627148

Research Article

Neuronal Transdifferentiation Potential of Human Mesenchymal Stem Cells from Neonatal and Adult Sources by a Small Molecule Cocktail

Lorena V. Cortés-Medina,[1] Herminia Pasantes-Morales,[1] Alejandro Aguilera-Castrejon,[2] Arturo Picones,[3] Cesar O. Lara-Figueroa,[3] Enoch Luis,[4] Juan Jose Montesinos,[5] Victor A. Cortés-Morales,[5] M. P. De la Rosa Ruiz,[5] Erika Hernández-Estévez,[5] Laura C. Bonifaz,[6] Marco Antonio Alvarez-Perez,[7] and Gerardo Ramos-Mandujano[1]

[1]*División de Neurociencias, Instituto de Fisiología Celular, Universidad Nacional Autónoma de México, Mexico City 04510, Mexico*
[2]*Department of Molecular Genetics, Weizmann Institute of Science, Rehovot 76100, Israel*
[3]*Laboratorio Nacional de Canalopatías, Instituto de Fisiología Celular, Universidad Nacional Autónoma de México, Mexico City 04510, Mexico*
[4]*Cátedras CONACyT Instituto de Fisiología Celular, Universidad Nacional Autónoma de México, Mexico City 04510, Mexico*
[5]*Mesenchymal Stem Cells Laboratory, Oncology Research Unit, Oncology Hospital, National Medical Center, IMSS, Mexico City 06720, Mexico*
[6]*Unidad de Investigación Médica en Inmunoquímica, Hospital de Especialidades, Centro Médico Nacional Siglo XXI, IMSS, Mexico City 06720, Mexico*
[7]*Tissue Bioengineering Laboratory, Division of Graduate Studies and Research of the Faculty of Dentistry, UNAM, Mexico City 04510, Mexico*

Correspondence should be addressed to Gerardo Ramos-Mandujano; gramos@ifc.unam.mx

Received 14 September 2018; Revised 22 December 2018; Accepted 30 December 2018; Published 1 April 2019

Academic Editor: Ludovic Zimmerlin

Copyright © 2019 Lorena V. Cortés-Medina et al. This is an open access article distributed under the Creative Commons Attribution License, which permits unrestricted use, distribution, and reproduction in any medium, provided the original work is properly cited.

Human mesenchymal stem cells (MSCs) are good candidates for brain cell replacement strategies and have already been used as adjuvant treatments in neurological disorders. MSCs can be obtained from many different sources, and the present study compares the potential of neuronal transdifferentiation in MSCs from adult and neonatal sources (Wharton's jelly (WhJ), dental pulp (DP), periodontal ligament (PDL), gingival tissue (GT), dermis (SK), placenta (PLAC), and umbilical cord blood (UCB)) with a protocol previously tested in bone marrow- (BM-) MSCs consisting of a cocktail of six small molecules: I-BET151, CHIR99021, forskolin, RepSox, Y-27632, and dbcAMP (ICFRYA). Neuronal morphology and the presence of cells positive for neuronal markers (TUJ1 and MAP2) were considered attributes of neuronal induction. The ICFRYA cocktail did not induce neuronal features in WhJ-MSCs, and these features were only partial in the MSCs from dental tissues, SK-MSCs, and PLAC-MSCs. The best response was found in UCB-MSCs, which was comparable to the response of BM-MSCs. The addition of neurotrophic factors to the ICFRYA cocktail significantly increased the number of cells with complex neuron-like morphology and increased the number of cells positive for mature neuronal markers in BM- and UCB-MSCs. The neuronal cells generated from UCB-MSCs and BM-MSCs showed increased reactivity of the neuronal genes TUJ1, MAP2, NF-H, NCAM, ND1, TAU, ENO2, GABA, and NeuN as well as down- and upregulation of MSC and neuronal genes, respectively. The present study showed marked differences between the MSCs from different sources in response to the transdifferentiation protocol used here. These results may contribute to identifying the best source of MSCs for potential cell replacement therapies.

1. Introduction

The *in vitro* generation of neuronal cells from neural (NSCs), embryonic (ESCs), and induced pluripotent stem cells (iPSCs), or by neuronal transdifferentiation of somatic cells by transcription factors (TF) has emerged as a useful strategy for cell replacement therapies in neurological disorders [1–3]; however, technical limitations, graft rejection, ethical issues, and/or tumorigenic risk are associated with the neurons derived from such processes [4–6]. Therefore, recent efforts have been focused on finding more suitable cell types or avoiding genetic manipulation for the generation of neurons [4, 7–11]. In this respect, mesenchymal stem cells (MSCs) offer some advantages over other cell types. MSCs are potentially able to differentiate into various cell lineages (including neurons), are easy to isolate and expand, have a low tumorigenic risk and low grafting rejection, and lack ethical issues [12–15]. These properties point to MSCs as suitable sources for cell replacement therapy in neurological disorders [16–19]; however, an optimal protocol to induce their conversion into neurons remains unestablished.

Chemical compounds known as small molecules have been shown to replace exogenous TF during cell reprogramming [7–9, 11]. Recent reports demonstrated the neuronal transdifferentiation of fibroblasts and astrocytes by small molecule cocktails [20–23]. These molecules act by modulating signaling pathways and epigenetic mechanisms implicated in cell reprogramming, neuronal specification, or neuronal survival [21], representing a convenient strategy to avoid the risks of genetic manipulation in the generation of induced neurons. In our previous report, after a small molecule screening assay, we found that a cocktail containing I-BET151, CHIR99021, forskolin, RepSox, Y-27632, and cAMP (ICFRYA) induced the formation of cells with neuron-like morphology and positive for TUJ1 and MAP2 from bone marrow- (BM-) MSCs [10].

MSCs can be isolated from many adult and neonatal tissues. However, comparative studies indicate that the MSCs from different tissues present differences in the efficiency of trilineage differentiation and other functional abilities, even though they meet the properties to be considered MSCs [24–27]. The present study is aimed at comparing the neuronal transdifferentiation potential of adult and neonatal MSCs obtained from different sources. To this end, we evaluated the neuronal-like morphology and neuronal markers induced by the ICFRYA cocktail in MSCs obtained from bone marrow (BM), skin (SK), dental pulp (DP), periodontal ligament (PDL), gingival tissue (GT), Wharton jelly (WhJ), placenta (PLAC), and umbilical cord blood (UCB). Neuronal induction was successful in the MSCs from some but not all sources. Strategies were selected to improve the induction of the MSC sources that showed neuronal properties. The presence of mature neuron markers, changes in global gene expression, and electrophysiological activity were examined in cells in which neuronal transdifferentiation was presumed.

2. Materials and Methods

2.1. Reagents and Antibodies. Neurobasal medium, α-MEM, RPMI medium, DMEM low glucose (DMEM-lg), DMEM/F-12, fetal bovine serum (FBS), L-glutamine, dispase II, Glutamax, antibiotics, trypsin/EDTA, human neurotrophic factors, N2, and B27 were all purchased from Gibco™ Thermo Fisher Scientific Inc. (MA, USA). Fibronectin, heparin, gelatin, nonessential amino acids, Hoechst 33258, and normal goat serum (NGT) were acquired from Sigma-Aldrich, Merck (St. Louis, MO, USA). The following primary antibodies were used: mouse anti-TUJ1 (SC-80016) and rabbit anti-MAP2 (SC-20172) obtained from Santa Cruz Biotechnology (CA, USA); rabbit anti-GABAB (SC-376282), ENO2 (GTX113428), TAU (GTX116044), and mouse anti-NF-H (GTX27795) from GeneTex Inc. (CA, USA); and rabbit anti-NeuN (MAB377) from Merck-Millipore (Darmstadt, Germany). Secondary antibodies against goat anti-mouse IgG conjugated to Alexa Fluor 488 and goat anti-rabbit IgG conjugated to Alexa Fluor 568 were obtained from Molecular Probes, Thermo Fisher Scientific Inc. (MA, USA). Small molecules I-BET151, CHIR99021, forskolin, RepSox, Y-27632, and dibutyryl cAMP were purchased from Sigma-Aldrich, Merck (St. Louis, MO, USA).

2.2. MSC Isolation and Characterization. All samples were isolated from healthy donors according to the Declaration of Helsinki. The bone marrow samples were obtained according to the Local Ethics Committee of the Villa Coapa Hospital, Mexican Institute for Social Security (IMSS, Mexico). The umbilical cord blood and placenta samples were collected according to the Local Ethics Committee of the Troncoso Hospital (IMSS, Mexico). The dental tissue samples were obtained according to the local Ethics Committee of the Orthodontics Clinic and the Faculty of Dentistry, National Autonomous University of Mexico. The skin samples were collected according to the Local Ethics Committee of the Dermatology Hospital, Health Secretary, Mexico City (SS, Mexico).

Mononuclear cells were isolated from bone marrow and umbilical cord blood samples by a Ficoll gradient, and cells from the internal area of the central placenta lobules were obtained using an enzymatic digestion procedure (Trypsin-EDTA). These cell samples were cultured in DMEM-lg plus 4 mM L-glutamine, 50 U/mL of penicillin, 50 μg/mL of streptomycin, and 50 μg/mL of gentamicin (DMEM-lg) and supplemented with FBS-10% [28]. The Wharton's jelly (membrane), gingival tissue, periodontal ligament, and dental pulp tissue samples were cut into small pieces and cultured as explants in α-MEM supplemented with FBS-15%. Finally, the skin samples were placed overnight in RPMI medium and dispase II, and then, the dermis was mechanically separated from the epidermis. Cells from the dermis were isolated by allowing them to migrate from the dermal segments placed in culture (DMEM-lg supplemented with FBS-10%). For all samples, the medium was changed every two days. The adherent cells were subcultured using trypsin/EDTA at 2×10^2 cells/cm^2 in DMEM-lg supplemented with FBS-10%. All experiments

were performed with MSCs between the fourth and sixth passages.

MSCs were characterized based on morphological, phenotypic, and differentiation parameters [28, 29]. FITC, PE, or APC-conjugated monoclonal antibodies against CD73, CD90, CD45 (BD Biosciences, San Diego, CA, USA), CD105, CD13, CD14, (Caltag, Buckingham, UK), HLA-ABC, HLA-DR, CD31, and CD34 (Invitrogen, Carlsbad, CA, USA) were used for immunophenotypic characterizations and analyzed on a FACSCanto II flow cytometer (BD Biosciences, Fullerton CA, USA). Adipogenic differentiation was determined by visualizing the presence of Oil Red O-stained (Sigma-Aldrich, Merck) lipid vacuoles. Osteogenic differentiation was assessed by alkaline phosphatase staining (FAST BCIP/NBT; Sigma-Aldrich, Merck). Chondrogenic differentiation was induced over 28 days with 10 ng/mL TGF-β (PeproTech). The resulting micromasses were fixed, embedded, and sliced, and cross-sections were stained with Alcian blue dye (Sigma-Aldrich, Merck).

2.3. Neuronal Induction by the ICFRYA Cocktail. Adult and neonatal MSCs were seeded onto fibronectin ($2\,\mu g/cm^2$)/0.1% gelatin-coated plates at a density of 2×10^4 cells/cm^2 and cultured in MSC growth medium for one day. For chemical induction, the cells were washed with serum-free medium and then cultured with neuronal induction medium (50% neurobasal medium, 50% DMEM/F12 with 1 × N2 and 1 × B27 with vitamin A, 1 × Glutamax, 1 × nonessential amino acids, and 20 ng/mL FGF2 plus 5 μg/mL heparin) plus the defined chemical cocktails for 8 or 4 days (as appropriate) at 37°C and 5% CO_2. The concentrations of the molecules in the ICFRYA cocktail were 1 μM I-BET151, 20 μM CHIR99021, 50 μM forskolin, 1 μM RepSox, 5 μM Y-27632, and 100 μM dbcAMP [10]. The neuronal induction medium was replaced on day 4. When indicated, the neuronal induction medium plus the ICFRYA cocktail was supplemented with human brain-derived neurotrophic factor (hBDNF), human glial cell-derived neurotrophic factor (hGDNF), and neurotrophin-3 (NT-3) at 20 ng/mL each.

2.4. In Situ Analysis of Cell Viability. Cells were incubated for 10 min with 1 μg/mL propidium iodide. Microphotographs were obtained using a direct epifluorescence microscope Olympus 1X71 with 10x magnification and the QCapture Pro 6.0 software.

2.5. Immunocytochemistry. After culture, the cells were fixed/permeabilized with cold methanol for 10 min and washed three times with PBS. The cells were blocked using PBS/0.1% BSA + 10% GS (goat serum) for 1 h. Then, the cells were incubated overnight at 4°C with primary antibodies: mouse anti-TUJ1 (1 : 1000), anti-NF-H (1 : 250), and anti-NeuN (1 : 200) and rabbit anti-MAP2 (1 : 500), anti-TAU (1 : 1000), anti-GABAB (1 : 250), and anti-ENO2 (1 : 250). Then, the cells were incubated for 1 h with goat anti-mouse Alexa 488 or goat anti-rabbit Alexa 568 as appropriate. The nuclei were counterstained with 1 μg/mL Hoechst 33258 diluted in PBS. Microphotographs were obtained by the direct epifluorescence microscope Olympus IX71 using the QCapture Pro 6.0 software, and data were analyzed with ImageJ software. At least 500 nuclei from five randomly selected fields were counted to calculate the percentage of positive cells.

2.6. Real-Time Quantitative PCR (qPCR). RNA samples from cultures were extracted with the GenElute Mammalian Total RNA Miniprep Kit (RTN70 Sigma-Aldrich, St. Louis, MO, USA) according to the manufacturer's instructions. The concentration of RNA samples was quantified by a NanoDrop spectrophotometer (Thermo Scientific). Complementary DNA (cDNA) was synthesized from 1 μg RNA with the iScript cDNA Synthesis Kit (Bio-Rad Laboratories Inc., CA, USA) and a Veriti® 96-Well Thermal Cycler (Applied Biosystems). PCR primers were designed using the last reference sequence (RefSeq) version of each gene with the PrimerBlast software; Supplementary Table 5 includes a list of primers used in this study. The qPCR reactions were conducted using a QuantiFast SYBR Green PCR Kit (Qiagen, MD, USA), according to the manufacturer's instructions, and run on a StepOnePlus Real-Time PCR system (Applied Biosystems). After amplification, the melting curves of the RT-PCR products were determined to demonstrate product specificity. PCR efficiency was optimal and ranged from 90% to 100% in the different target gene qPCR assays. For the selection of the best reference gene, a comparison of the transcriptional variation of different housekeeping genes in response to the conditions was performed. The gene with the least CT variation between treatments and control cultures was selected. Thus, gene expression was normalized to TATA-Box binding protein (TBP) mRNA. The relative quantification of mRNA levels was performed using the Pfaffl method [30].

2.7. Microarray Assay. Cells were incubated as described in the neuronal maturation protocol. The samples were then processed for RNA extraction. Total RNA (10 μg) was used for cDNA synthesis incorporating dUTP-Alexa 555 or dUTP-Alexa 647 and employing the CyScribe First-Strand cDNA labeling kit (Amersham). Equal quantities of labeled cDNA were hybridized using the hybridization solution HybIT2 (TeleChem International Inc.) on the collection of human arrays (10 K) for 14 h at 42°C. The acquisition and quantification of array images were performed in the ScanArray 4000 with its accompanying software from Packard BioChips. For each spot, the mean density, mean background, and mean normalized signal values were calculated with the Array-Pro Analyzer software from Media Cybernetics. Microarray data analysis was performed with the free software genArise, which was developed in the Computing Unit of the UNAM Cellular Physiology Institute (http://www.ifc.unam.mx/genarise/). The microarray data were deposited in the Gene Expression Omnibus database repository (GSE120681). The functional annotation gene analysis analyzed the up- and downregulated genes derived from the microarray assay using DAVID 2.0 (https://david.ncifcrf.gov/tools.jsp) and bioinformatics resources to obtain

the Gene Ontology functional annotation classification of the genes.

2.8. Electrophysiological Activity Recording. Whole-cell ion currents were experimentally recorded with an arrangement of Axopatch 200B/Digidata 1550/pCamp10 (amplifier/analog-digital converter/software, all from Molecular Devices, Sunnyvale, CA), analog filtered at 5 kHz and digitally sampled at 10 kHz. Patch-clamp pipettes were made of borosilicate glass (World Precision Instrument) using a P-97 puller (Sutter Instruments, Novato, CA). The intracellular pipette filling solution was composed of (in mM) 10 NaCl, 40 KCl, 10 HEPES, 5 EGTA, 3 $MgCl_2$, 95 K-gluconate, and 10 glucose (pH 7.2 adjusted with KOH). The extracellular solution contained (in mM) 140 NaCl, 4 KCl, 1 $MgCl_2$, 2 $CaCl_2$, 10 HEPES, and 5 glucose (pH 7.4 adjusted with NaOH). All solutions were perfused using a custom-made gravity-based perfusion system. The voltage-clamp protocol used in all experiments was 200 ms step pulses from -120 to +50 mV in 10 mV increments from a holding voltage of -70 mV.

2.9. Statistical Analysis. The results were expressed as the mean ± standard error (SEM) from three independent experiments of three biological samples or 4-6 independent experiments from one biological sample as indicated. The statistical analyses were performed using Student's t-test for between-group comparisons and a one-way ANOVA and the Tukey test for multiple comparisons. GraphPad Prism software for Windows version 6 (La Jolla, CA, USA) was used for all statistical procedures. Differences with $p < 0.05$ were considered statistically significant.

3. Results

3.1. MSC Characterization. Mesenchymal stem cells (MSCs) were isolated from human adult or neonatal sources (Supplementary Table 1) and characterized according to the criteria defining human MSCs proposed by the International Society for Cellular Therapy [31]. For all MSC samples, the cells adhered to the plastic exhibited fibroblastic morphology (Supplementary Figure 1), were positive for MSC markers (CD105, CD90, and CD73), were negative for hematopoietic markers and HLA-DR surface molecules (Supplementary Table 2), and were capable of differentiating into adipocytes, osteoblasts, and chondrocytes (Supplementary Table 3). The neuronal medium per se (NM: N2/B27/hFGF) did not induce neuronal morphology or reactivity to neuronal markers (Supplementary Figure 3); however, a weak reactivity against TUJ1 was observed in all MSC sources (Figures 1(b)–1(h) left picture).

3.2. Neuronal Induction by the ICFRYA Cocktail of Adult and Neonatal MSC Sources. Neuronal induction of all MSC sources was conducted using the ICFRYA small molecule cocktail protocol (Figure 1(a)) as previously reported for BM-MSCs [10]. In addition to neuronal properties, necrotic cell death was evaluated by propidium iodide staining. The neuronal induction effects of the ICFRYA cocktail on MSCs from different sources varied. Neuron-like cells with reactivity to TUJ1 were induced in DP-MSCs (50 ± 7.7%), PDL-MSCs (42 ± 7.1%), GT-MSCs (32 ± 1.9%), SK-MSCs (34 ± 9.1%), and PLAC-MSCs (67 ± 2.3%); however, very low percentages of $MAP2^+$ cells were found (0.7% to 5.9%) (Figures 1(b)–1(f), right pictures and graphs). In these MSC sources, the cocktail produced 48%-68% necrosis. In WhJ-MSCs, the chemical cocktail did not evoke cells with neuronal properties, but high levels of necrosis were present (Figure 1(g) right picture and graph). In UCB-MSCs, the ICFRYA cocktail induced neuronal properties, i.e., bipolar morphology with a high percentage of $TUJ1^+$ cells (57 ± 3.3%) and coexpression of MAP2 in 27 ± 3.9%; however, a very high rate of necrosis (84 ± 6.8%) was observed (Figure 1(h) right picture and graph). The removal of I-BET151 from the chemical cocktail reduced the necrotic cell death strongly in all MSC sources and also reduced the expression of neuronal properties (Figures 1(b)–1(h), no I-BET bars; Supplementary Table 4). It is noteworthy that I-BET alone did not exhibit any effects on the MSCs from any tissue (data not shown). I-BET151 and forskolin are considered key molecules for chemical-based neuronal transdifferentiation; in other reports, high concentrations of these molecules have been used for neuronal transdifferentiation [22]. However, increasing the concentration of I-BET151 (1 μM to 2 μM) and/or forskolin (50 μM to 75 μM) did not improve the expression of neuronal properties on WhJ-, DP-, PDL-, GT-, SK-, or PLAC-MSCs but did increase necrosis (Supplementary Table 4 and Supplementary Figure 2). As illustrated in Figures 2(a) and 2(e), very few cells from WhJ-MSCs presented a bipolar morphology and reactivity to TUJ1. In PDL-MSCs, although MAP2 reactivity was increased, the signal was not associated with cell protrusions, and almost all cells maintained the bipolar morphology (Figures 2(b) and (e)). On the other hand, in UCB-MSCs incubated with ICFRYA containing 2 μM I-BET151, neuronal morphology was observed after two days of induction (Figure 2(c)), notably reducing the induction time from 8 to 4 days. At this time, UCB-MSCs exhibited proper neuron-like induction with 77.6 ± 10.7% $TUJ1^+$ cells, protrusions with secondary ramifications, MAP2 reactivity associated with the branches, and only 25% necrotic death (Figures 2(c) and 2(d) and Supplementary Table 4). In our previous report, the ICFRYA cocktail containing 1 μM I-BET and 50 μM forskolin induced neuron-like cells from BM-MSCs with reactivity to TUJ1 and MAP2. BM-MSCs were added as the gold standard to compare neuronal induction with the other sources. Using different concentrations of the molecules, neuronal morphology was evident after 4 days (Figure 2(d)), and the original ICFRYA molecule concentration showed the best induction in BM-MSCs (Figures 2(d) and 2(e) and Supplementary Table 4).

3.3. Neurotrophic Factors Improve Neuronal Induction of BM- and UCB-MSCs by ICFRYA. To examine a possible effect of neurotrophic factors on the improvement of neuronal induction by the ICFRYA cocktail, BM- and UCB-MSCs were cocultured with astrocytes and/or in the presence of neurotrophic factors (BDNF, GDNF, and neurotrophin-3) and fetal bovine serum (FBS) 1%. Coculturing with astrocytes

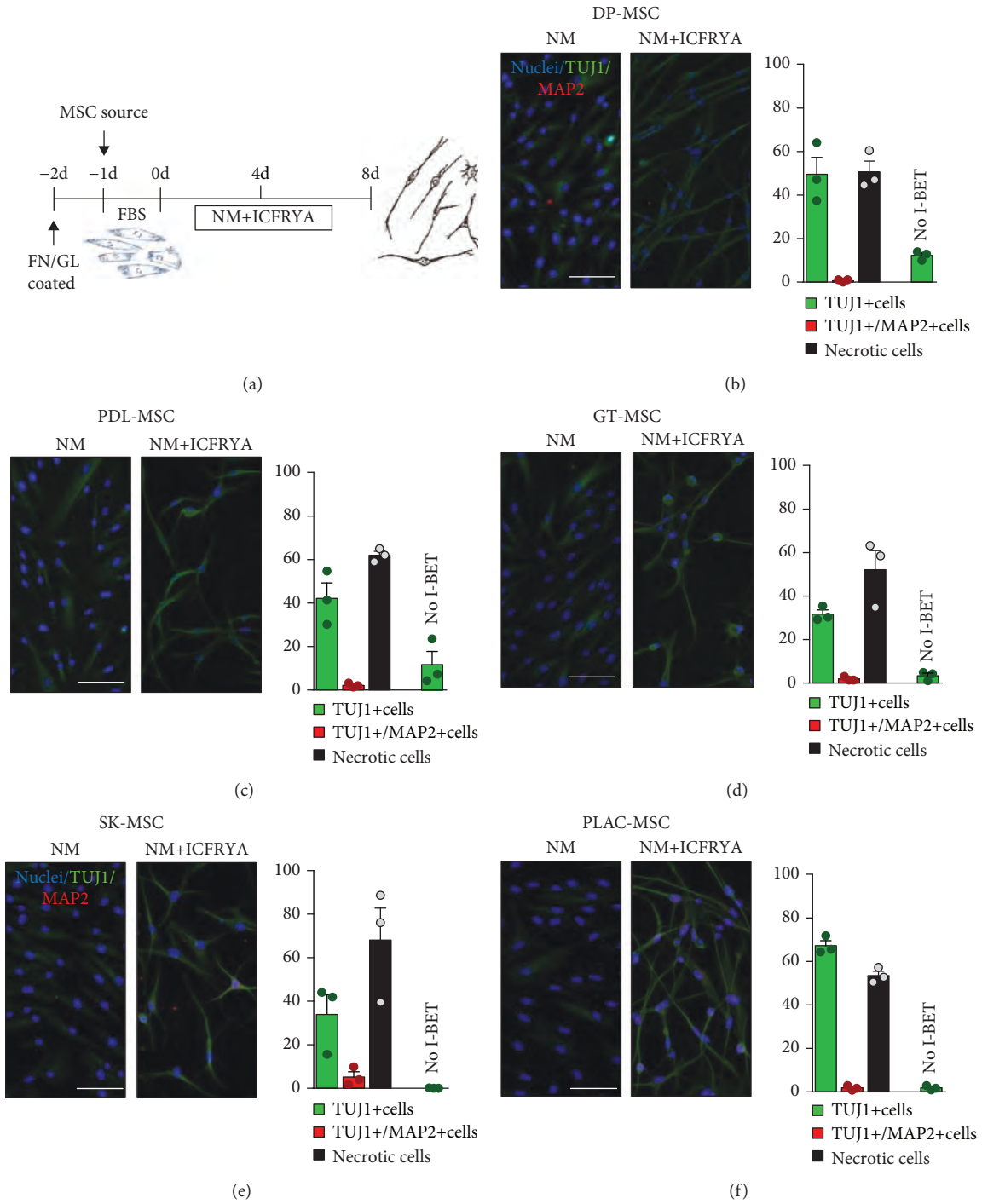

Figure 1: Continued.

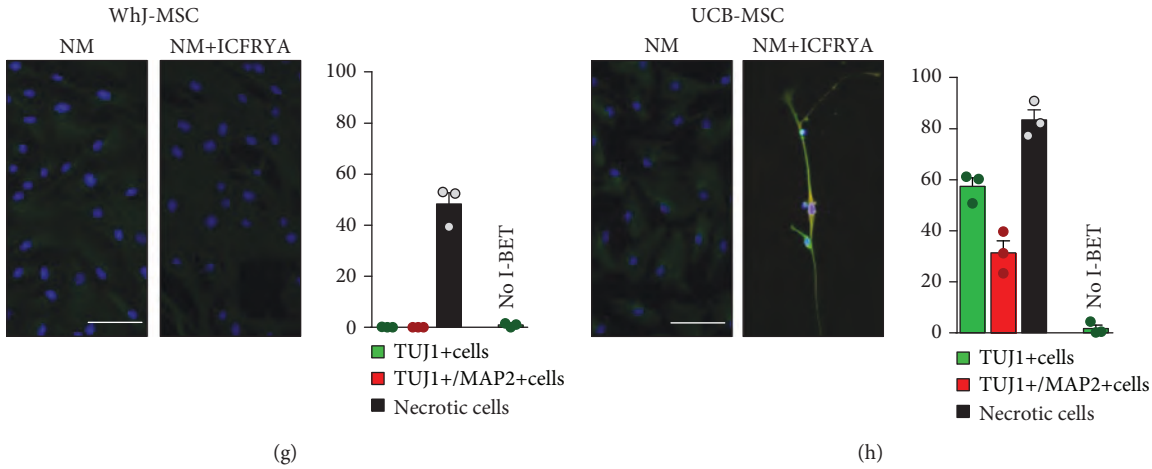

Figure 1: Neuronal properties induced by the ICFRYA small molecule cocktail in different sources of human mesenchymal stem cells (hMSCs). (a) Schematic diagram of the neuronal induction protocol. One day prior to the neuronal induction, MSCs were seeded on FN/GL-treated plates, and the medium was replaced with neuronal medium (NM: N2/B27/FGF/EGF) or NM containing the ICFRYA small molecule cocktail: I: I-BET151; C: CHIR99021; F: forskolin; R: RepSox; Y: Y27632; A: cAMP. NM or NM plus the ICFRYA cocktail was changed at day 4, and the neuronal properties and necrosis were evaluated on day 8. (b–h) Representative images and percentages of neuron-like morphology cells positive for TUJ1 (green bars), TUJ1/MAP2 (red bars), and necrotic cells (black bars). MSCs cultured with NM maintained fibroblastic morphology (panels (b–h) left picture) and acquired neuron-like morphology only under small molecule stimulation (panels (b–h) right picture). The presence of neuronal markers was estimated by immunostaining, and necrosis was evaluated in situ using propidium iodide (PI). In addition to marker reactivity, neuronal-like morphology was considered to define $TUJ1^+$ cells and $TUJ1^+/MAP2^+$ cells. The data are presented as the mean ± SEM of $n = 8$ from three biological replicates in three independent experiments. Scale bars represent 100 μm. FN/GL: fibronectin-gelatin; FBS: fetal bovine serum; NM: neuronal medium; ICFRYA: I-BET151, CHIR99021, forskolin, RepSox, Y27632, cAMP.

during chemical induction strongly decreased cell viability and did not improve the neuronal properties (data not shown). The ICFRYA cocktail plus neurotrophic factors and FBS was the best neuronal induction condition. In both BM- and UCB-MSCs, this condition generated neuron-like cells with multiple arborizing dendritic-like structures and high percentages of cells positive for MAP2, NF-H, TAU, and other mature neuron markers such as ENO2, GABA, and NeuN (Figures 3(a) and 3(b)). No significant differences were found between the positive neuron-like cells induced from BM- or UCB-MSCs (Figure 3(c)). BM-MSCs and UCB-MSCs in control conditions did not show reactivity to the neuronal markers, and no cells positive for the glial marker GFAP were detected in the control or induced cultures (Supplementary Figure 3).

Changes in the gene expression of neuronal, glial, and MSC markers as detected by qRT-PCR were analyzed after the induction process. The neuron-like cells derived from UCB-MSCs and BM-MSCs showed increased expression of neuronal genes, such as TUJ1, MAP2, NF-H, DCX, NCAM, ND1, NCAM, TAU, ENO2, GABA, and NeuN, and downregulated expression of the MSC markers CD90 and CD105 (Figure 4(a)). The fold change in expression of CD90, CD105, DCX, and ND1 was significantly higher in the cultures generated from UCB-MSCs than from BM-MSC cells.

To evaluate the transdifferentiation process, we conducted a global RNA expression analysis. In the presence of the ICFRYA cocktail, both UCB- and BM-MSC cells upregulated the expression of neuronal regulators and other genes associated with neurodevelopment and functional properties (Figure 4(b)). Among the genes implicated in functional differentiation, the potassium voltage-gated gene KCNC1 was upregulated in BMs, and the KCNC1 and KCNJ16 genes were upregulated in UCB-MSCs. The glial genes GFAP and S100B remained unchanged, and positive regulators of the cell cycle and genes associated with mesenchymal and fibroblastic lineages were downregulated (Figure 4(b)). Gene Ontology term analysis indicated enrichment in the genes related to processes such as small molecule metabolism, cell signal, cell differentiation, positive regulation of neurogenesis, neuronal differentiation, functional neuron activities, dendritic spine development, and action potentials (Figure 4(c)). Altogether, the results indicate that the neuron-like cells obtained can be considered induced neurons (iNs) generated from UCB-MSCs (UCB-iNs) or iNs generated from BM-MSCs (BM-iNs). Although the UCB-iNs and BM-iNs have similar neuronal features, there was a higher number of genes regulated in each Gene Ontology process and a higher p value in the UCB-iNs (Figure 4(c)).

3.4. Ion Currents in BM-iNs and UCB-iNs. Whole-cell ion currents were evaluated in control cells (UCB-MSCs and BM-MSCs) and in cells with complex neuron-like morphology from UCB-iNs and BM-iNs (Figures 5(a) and 5(b)). Fast inward sodium-like currents were not detected in the control nor treated conditions. Outward noninactivating ion potassium-like currents were also evaluated. Slight and irregular potassium-like currents were recorded in BM-iNs and no different to those in control BM-MSCs (Figures 5(c) and 5(d)). Potassium-like currents of high

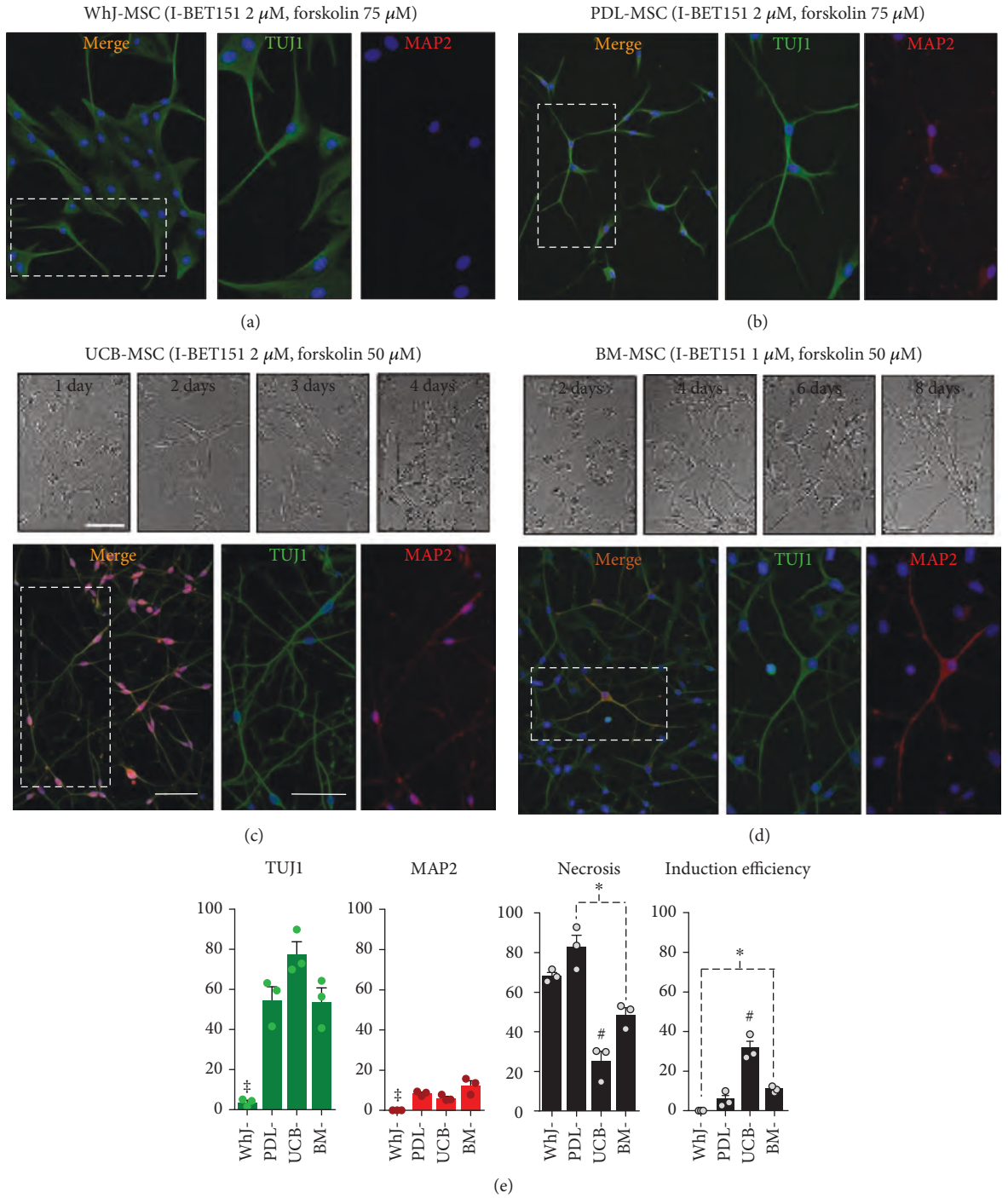

Figure 2: Effect of increasing I-BET151 and/or forskolin concentration on neuronal induction. Neuronal induction was conducted as in Figure 1, but the I-BET151 concentration was increased from 1 μM to 2 μM and/or forskolin concentration was increased from 50 μM to 75 μM. (a) Wharton's jelly cells did not show neuronal induction. (b) PDL-MSCs are shown as the representative source of an intermediate response (Supplementary Table 4), and (c, d) UCB and BM-MSCs show highly efficient neuronal induction. The morphological changes throughout culturing are shown in bright field pictures. UCB acquired neuron-like morphology after 2 days of induction, developing complex neuronal morphology at 4 days, while BM developed similar morphology after 8 days. Immunostaining shows that UCB- and BM-MSC developed complex TUJ1$^+$ and MAP2$^+$ neurite-like outgrowths. (e) Quantification of TUJ1$^+$ cells, MAP2$^+$ cells, and necrotic cells as in Figure 1. Induction efficiencies were calculated as the percentage of induced TUJ1$^+$ neuronal cells versus initial cell number at day 0. The data are presented as the mean ± SEM. Significant differences were determined using ANOVA and Tukey's test. $p < 0.05$: ‡WhJ-MSCs or $^#$UCB-MSCs vs. the other sources, and $^*p < 0.05$ between sources indicated with dotted lines. $n = 8$ from three independent biological replicates. Scale bars represent 100 μm.

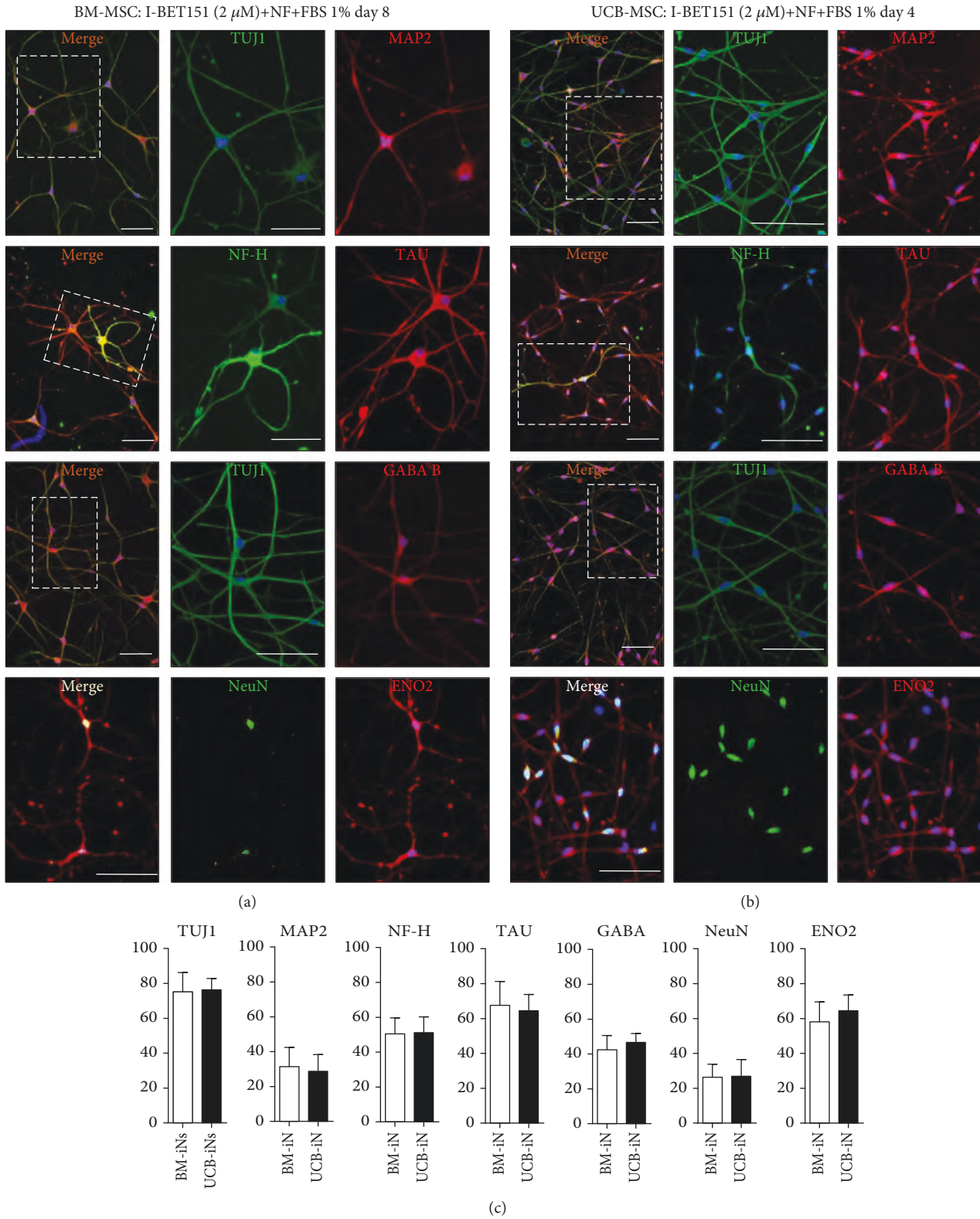

FIGURE 3: Presence of mature neuronal markers after induction with ICFRYA plus neurotrophic factors and FBS in UCB- and BM-MSCs. (a, b) Representative pictures of TUJ1, MAP2, TAU, NF-H, GABA B, ENO2, and NeuN positive cells after neuronal induction. The images on A show the merge, and the images on B and C show the individual signal for each antibody. (a) BM-MSCs after 8 days of induction and (b) UCB-MSCs after 4 days of induction. (c) Quantification of cells positive for the neuronal markers induced by the ICFRYA cocktail plus neurotrophic factors. The data are presented as the mean ± SEM ($^*p < 0.05$, Student's t-test) of $n = 8$ from three independent experiments. Scale bars represent 100 μm.

INFORME DE LABORES 2019

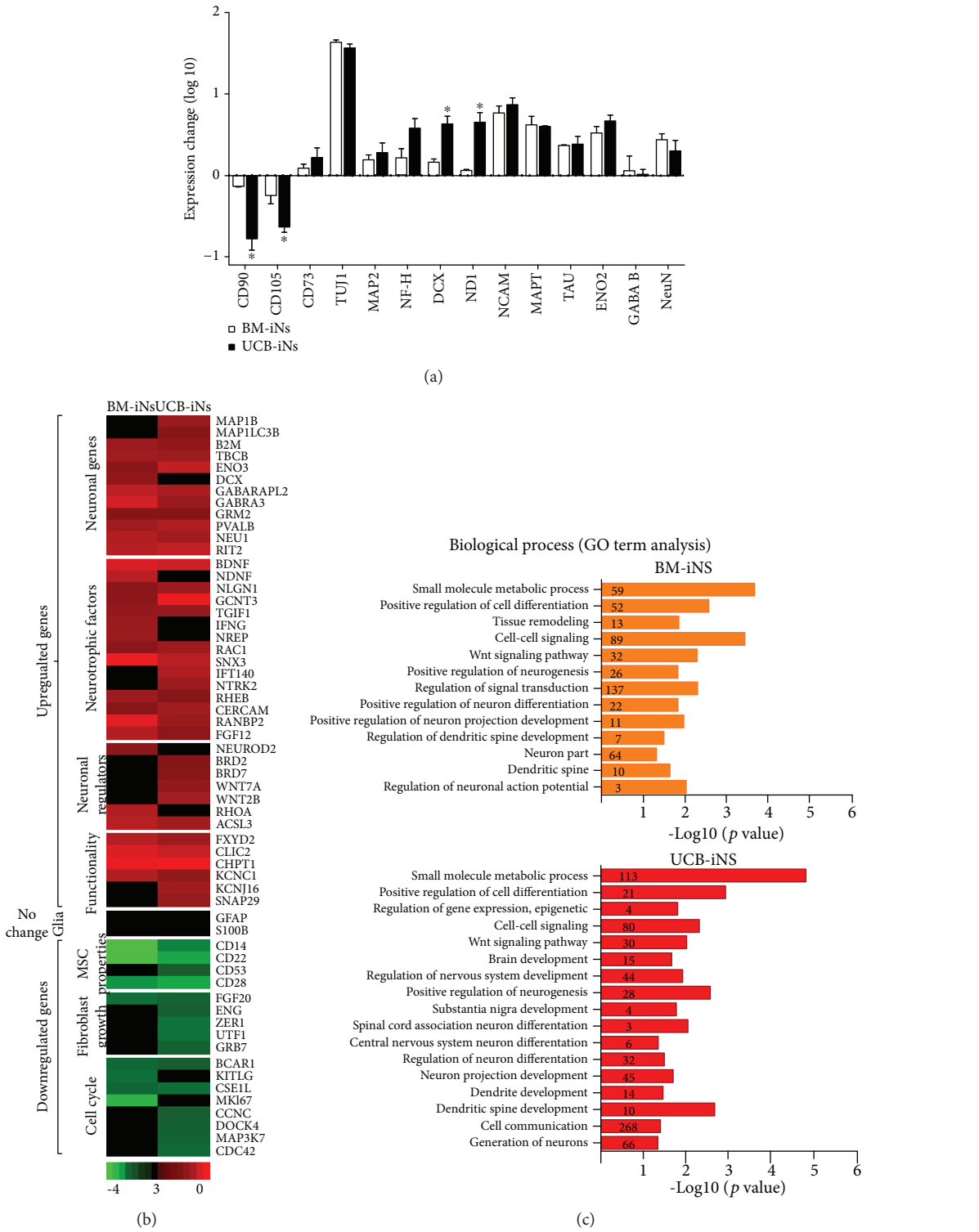

FIGURE 4: Gene expression analysis in neuron cells induced from UCB-MSCs (UCB-iNs) or BM-MSCs (BM-iNs). (a) Real-time qPCR evaluation of the expression of representative mesenchymal and neuronal genes. Data are shown as fold change versus noninduced MSCs (mean ± SEM, $n = 3$ independent experiments) ($^* p < 0.05$; Student's t-test). (b, c) Global gene expression analysis. (b) Heat map showing the change in expression of neuronal, glial, mesenchymal, and cell cycle genes from the microarray data after 8 and 4 days (BM-iNs and UCB-iNs, respectively) of induction by the ICFRYA cocktail plus neurotrophic factors. The fold change in expression was calculated by comparison with noninduced cells from the respective tissue source. Red color indicates increased gene expression while green indicates a decrease. (c) Gene Ontology (GO) analysis demonstrated that in BM-iNs and UCB-iNs, the genes with a ≥1.5-fold change in expression are implicated in the regulation of the neurogenic process. Highlighted in blue are the categories present in both BM- and UCB-INs. The number of genes implicated per category is indicated over the bars.

INFORME DE LABORES 2019

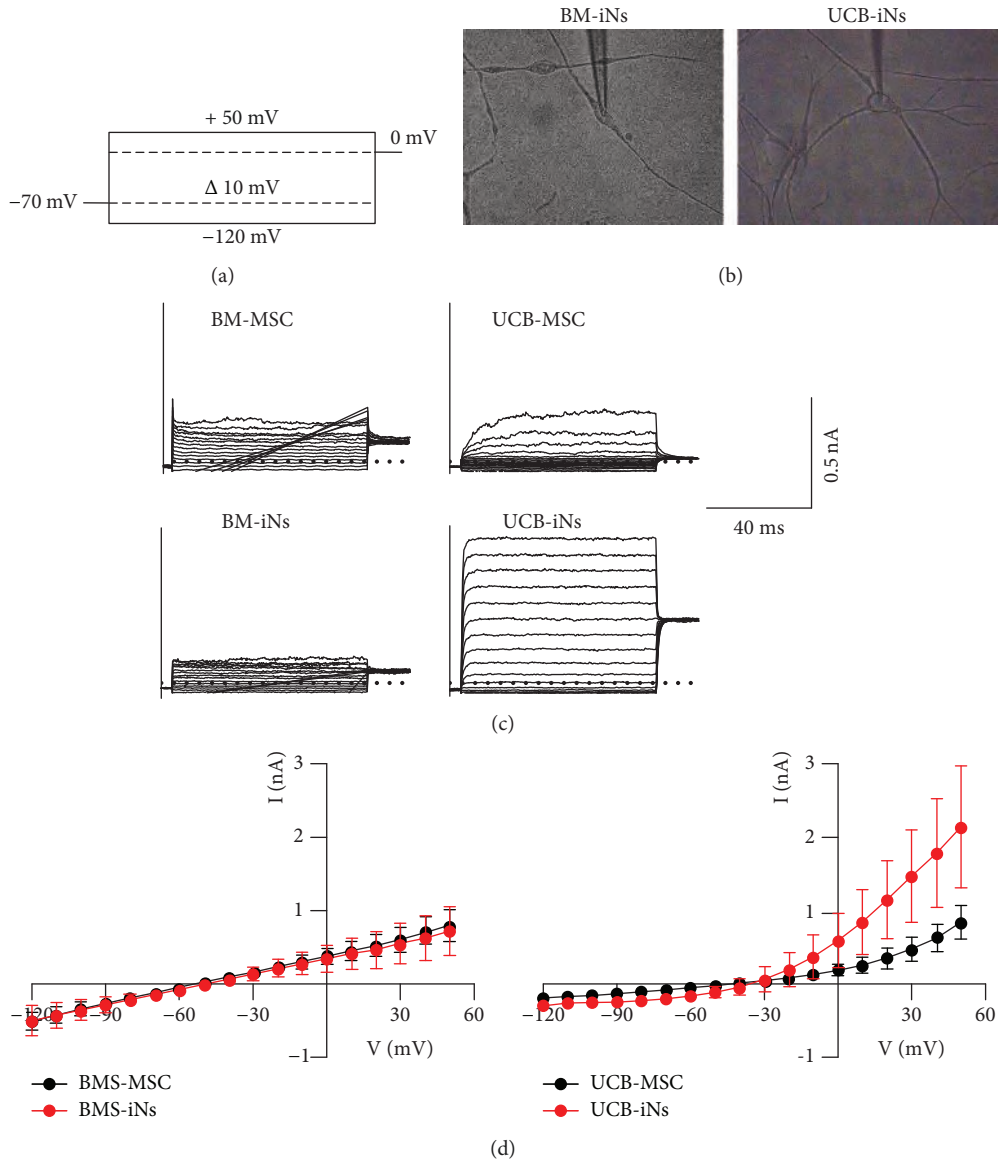

Figure 5: Ion currents in UCB-iNs and BM-iNs: (a) the voltage-clamp protocol used in all experiments (200 ms step pulses from -120 to +50 mV in 10 mV increments from a holding voltage of -70 mV); (b) iN-UCBs or iN-BMs with complex neuron-like morphology were selected for electrophysiological recordings; (c) representative traces of the currents recorded from the control or induced cells. UCB cells presented potassium-like currents, but Na^+-like currents were not detected. (d) Current-to-voltage relationships. The data are presented as the mean ± SEM.

magnitude were recorded in 6 of the 14 UCB-iNs, whereas in controls (UCB-MSCs), only small and irregular currents were recorded.

4. Discussion

Neuronal transdifferentiation without genetic manipulation from a suitable cell source is the most relevant cell replacement strategy in the brain. This strategy was approached in the present study by generating neuron-like cells from human MSCs with a small molecule cocktail.

The neuronal induction potential of neonatal and adult MSC sources was compared since some studies suggest that MSCs from neonatal sources may have greater plasticity and stemness than adult sources, possibly due to their lower degree of commitment [24, 32, 33]. This hypothesis was not confirmed in the protocol using the ICFRYA small molecule cocktail as the neuronal inductor because the best sources to generate cells with neuronal features were BM-MSCs and UCB-MSCs. In contrast, neuronal traits were not induced from WhJ-MSCs or were limited in the MSCs from dental tissues, SK-MSCs, and PLAC-MSCs.

In addition to the neuronal transdifferentiation potential, other studies have shown that MSCs from different tissues exhibit differences in other functional activities, such as cell proliferation, immune regulation properties, and trilineage differentiation potential [12, 26, 27]. The intrinsic properties of each MSC source or their tissue-specified functions may

explain the different responses; however, this has not been demonstrated. Each of the small molecules in the ICFRYA cocktail used to induce neuronal transdifferentiation regulates specific signaling pathways or epigenetic mechanisms [7, 9, 11, 34, 35]. By performing screening assays with small molecule combinations, it is possible to define whether the differences in the neuronal induction efficiency of each specific cocktail are related to the particular signaling pathway or epigenetic mechanism affected by the cocktail molecules in the different MSC sources.

Another relevant feature to be considered in the process of neuronal transdifferentiation is that cell death may function as a regulatory strategy *in vivo* to accomplish successful neurogenesis and neuronal connection in the neural network [36, 37]. During *in vitro* neuronal transdifferentiation, cell death could be a destabilization product of the process itself (activation/inhibition of metabolic pathways), resulting in the elimination of cells that could not adapt to changes. In other studies of neuronal transdifferentiation with small molecule cocktail protocols, cell viability was not examined or presented as a marker of induction efficiency [20, 21]. Here, we evaluated a possible correlation between necrosis and neuronal induction efficiency and found that the ICFRYA cocktail evoked high cell death without neuronal induction in WhJ-MSCs and high neuronal induction efficiency with low cell death in BM- and UCB-MSCs (Figure 2 and Supplement Table 4).

The relevant role of I-BET151 in the neuronal induction by small molecule cocktails has been reported for mouse fibroblasts [22], human astrocytes [20], and in our previous study on BM-MSCs [10]. This effect was extended for all the MSC sources studied here, since removing I-BET151 from the cocktail blocked the presence of neuronal properties regardless of the tissue source. I-BET151 is a regulator that disrupts the epigenetic memory of the original cell, thus favoring cell reprogramming [34, 38–40]. I-BET151 also arrests the cell cycle, a process that is associated with neuronal transdifferentiation [34, 41]; however, I-BET151 alone did not induce neuronal properties. The ICFRYA cocktail contains forskolin and dbcAMP, which increase the levels and synthesis of intracellular cAMP. CHIR99021 inhibits GSK3/beta catenin and promotes the expression of neuronal genes. RepSox is involved in the reprogramming processes that inhibit SMADS, and Y27632 inhibits ROCK to maintain cell viability [7, 35, 42]. Altogether, this suggests that the process of neuronal transdifferentiation requires the synergic regulation of pathways involved in neuronal transdifferentiation, neuronal specification, and survival.

During direct transdifferentiation, the original cells must first undergo partial dedifferentiation, allowing the repression of the lineage of origin and then differentiate into a new cell type [43, 44]; moreover, the cells have to arrest the cell cycle at the same time that the chromatin is modulated [41]. In BM-MSCs and UCB-MSCs, the ICFRYA cocktail enriched with neurotrophic factors (NT3, BDNF, and GDNF) favors the generation of cells with complex neuronal morphology, reactivity to mature neuronal markers, and upregulated neuronal genes and neuronal process. Moreover, mesenchymal markers were decreased, and genes related to mitosis, cell cycle, and mesenchymal lineage were downregulated. Considering all these criteria, the transdifferentiated cells were determined to be induced neurons generated from BM-MSCs (BM-iNs) and UCB-MSCs (UCB-iNs).

To be considered a functional iN, cells should exhibit electrophysiological activity, such as action potentials and synaptic transmission. To examine functional properties, the presence of voltage-gated potassium and sodium currents was evaluated in BM-iNs and UCB-iNs. Sodium currents were not detected, and potassium-like currents were present only in UCB-iNs. These results suggest that UCB-iNs may be in a transition phase towards functionally induced neurons. To obtain functional neurons, it is necessary to test other maturation strategies. Three-dimensional (3D) cultures have been shown to be an option to obtain functionally mature cells during the reprogramming or transdifferentiation processes of several cell types [45]. This option, together with the ICFRYA cocktail, may be a convenient strategy to generate functional iNs from MSCs.

It has been recognized that MSCs present advantages over other cell types and have a low tumorigenic risk in cell replacement therapies. Moreover, clinical studies in human and neurodegenerative animal models indicate that MSCs improve regeneration capacity and ameliorate brain injuries. Although BM-MSCs are commonly considered the "gold standard," other MSC sources are more accessible and raise fewer ethical issues. Therefore, identifying the most suitable cell type and cell source for neuronal conversion is an essential matter in cell therapy approaches for neurological disorders.

5. Conclusion

This study determines that human MSCs can be converted into transgene-free neuronal cells and establishes UCB-MSCs as the most suitable sources for undergoing neuronal transdifferentiation by a specific small molecule cocktail.

Data Availability

The microarray data used to support the findings of this study have been deposited in the GEO repository (GSE120681).

Conflicts of Interest

The authors declare that there is no conflict of interest regarding the publication of this article.

Authors' Contributions

L.V.C.M. worked on experiment design and conceptualization, experiment elaboration, collection and assembly of data, data analysis, design and organization of figures, writing of the manuscript, and final approval of the manuscript. H.P.M. worked on experiment design and conceptualization, project supervision, financial support writing of the manuscript, and final approval of the manuscript. A.A.C.

worked on experiment design and conceptualization, writing of the manuscript, and final approval of the manuscript. G.R.M. worked on experiment design and conceptualization, experiment elaboration, collection and assembly of data, data analysis, design and organization of figures, project supervision, financial support, writing of the manuscript, and final approval of the manuscript. A.P., C.O.L.F., and E.L. worked on electrophysiological assay performance. V.A.C.M., M.P.R.R., J.J.M., E.H.E., L.B., and M.A.A.P. worked on isolation and characterization of MSC sources.

Acknowledgments

L.V.C.M. acknowledges the financial support provided by the "Ayudante de Investigador Nacional Emérito" fellowship of CONACYT (Núm. Exp. 13982). We thank Dr. Jorge Ramírez Salcedo, Dr. José Luis Santillán Torres, M.I.B.B. Simón Guzmán León, and Q.B.P. Lorena Chávez Gonzáles from the microarray unit at the Instituto de Fisiología Celular UNAM, for their expert technical assistance in microarray protocols. This work was supported by the Dirección General de Asuntos del Personal Académico-Universidad Nacional Autónoma de México (DGAPA-UNAM) (H.P.M. and G.R.M., Grant No. IN205916).

Supplementary Materials

Supplemental information for this article includes three supplementary figures and five supplementary tables. Supplementary Figure 1, Supplementary Table 1, Supplementary Table 2, and Supplementary Table 3: mesenchymal stem cell isolation and characterization. Supplementary Figure 2 and Supplementary Table 4 are related to Figure 2. Supplementary Figure 3 and Supplementary Table 5 are related to Figure 3. *(Supplementary Materials)*

References

[1] S. Suksuphew and P. Noisa, "Neural stem cells could serve as a therapeutic material for age-related neurodegenerative diseases," *World Journal of Stem Cells*, vol. 7, no. 2, pp. 502–511, 2015.

[2] A. Trounson and C. McDonald, "Stem cell therapies in clinical trials: progress and challenges," *Cell Stem Cell*, vol. 17, no. 1, pp. 11–22, 2015.

[3] G. Martino and S. Pluchino, "The therapeutic potential of neural stem cells," *Nature Reviews. Neuroscience*, vol. 7, no. 5, pp. 395–406, 2006.

[4] S. A. Goldman, "Stem and progenitor cell-based therapy of the central nervous system: hopes, hype, and wishful thinking," *Cell Stem Cell*, vol. 18, no. 2, pp. 174–188, 2016.

[5] M. Kassem, "Stem cells: potential therapy for age-related diseases," *Annals of the New York Academy of Sciences*, vol. 1067, no. 1, pp. 436–442, 2006.

[6] K. Takahashi and S. Yamanaka, "A decade of transcription factor-mediated reprogramming to pluripotency," *Nature Reviews. Molecular Cell Biology*, vol. 17, no. 3, pp. 183–193, 2016.

[7] D. de, D. Halder, I. Shin, and K. K. Kim, "Small molecule-induced cellular conversion," *Chemical Society Reviews*, vol. 46, no. 20, pp. 6241–6254, 2017.

[8] D. W. Jung, W. H. Kim, and D. R. Williams, "Reprogram or reboot: small molecule approaches for the production of induced pluripotent stem cells and direct cell reprogramming," *ACS Chemical Biology*, vol. 9, no. 1, pp. 80–95, 2013.

[9] Y. Zhang, W. Li, T. Laurent, and S. Ding, "Small molecules, big roles – the chemical manipulation of stem cell fate and somatic cell reprogramming," *Journal of Cell Science*, vol. 125, no. 23, pp. 5609–5620, 2013.

[10] A. Aguilera-Castrejon, H. Pasantes-Morales, J. J. Montesinos et al., "Improved proliferative capacity of NP-like cells derived from human mesenchymal stromal cells and neuronal transdifferentiation by small molecules," *Neurochemical Research*, vol. 42, no. 2, pp. 415–427, 2017.

[11] K. Babos and J. K. Ichida, "Small molecules take a big step by converting fibroblasts into neurons," *Cell Stem Cell*, vol. 17, no. 2, pp. 127–129, 2015.

[12] G. Chamberlain, J. Fox, B. Ashton, and J. Middleton, "Concise review: mesenchymal stem cells: their phenotype, differentiation capacity, immunological features, and potential for homing," *Stem Cells*, vol. 25, no. 11, pp. 2739–2749, 2007.

[13] H. J. Kim and J. S. Park, "Usage of human mesenchymal stem cells in cell-based therapy: advantages and disadvantages," *Development & Reproduction*, vol. 21, no. 1, pp. 1–10, 2017.

[14] B. Parekkadan and J. M. Milwid, "Mesenchymal stem cells as therapeutics," *Annual Review of Biomedical Engineering*, vol. 12, no. 1, pp. 87–117, 2010.

[15] J. Zhang, X. Huang, H. Wang et al., "The challenges and promises of allogeneic mesenchymal stem cells for use as a cell-based therapy," *Stem Cell Research & Therapy*, vol. 6, no. 1, p. 234, 2015.

[16] G. D. Colpo, B. M. Ascoli, B. Wollenhaupt-Aguiar et al., "Mesenchymal stem cells for the treatment of neurodegenerative and psychiatric disorders," *Anais da Academia Brasileira de Ciências*, vol. 87, no. 2, pp. 1435–1449, 2015.

[17] J. Isern, A. García-García, A. M. Martín et al., "The neural crest is a source of mesenchymal stem cells with specialized hematopoietic stem cell niche function," *eLife*, vol. 3, article e03696, 2014.

[18] M. Tfilin, E. Sudai, A. Merenlender, I. Gispan, G. Yadid, and G. Turgeman, "Mesenchymal stem cells increase hippocampal neurogenesis and counteract depressive-like behavior," *Molecular Psychiatry*, vol. 15, no. 12, pp. 1164–1175, 2010.

[19] R. Volkman and D. Offen, "Concise review: mesenchymal stem cells in neurodegenerative diseases," *Stem Cells*, vol. 35, no. 8, pp. 1867–1880, 2017.

[20] L. Gao, W. Guan, M. Wang et al., "Direct generation of human neuronal cells from adult astrocytes by small molecules," *Stem Cell Reports*, vol. 8, no. 3, pp. 538–547, 2017.

[21] W. Hu, B. Qiu, W. Guan et al., "Direct conversion of normal and Alzheimer's disease human fibroblasts into neuronal cells by small molecules," *Cell Stem Cell*, vol. 17, no. 2, pp. 204–212, 2015.

[22] X. Li, X. Zuo, J. Jing et al., "Small-molecule-driven direct reprogramming of mouse fibroblasts into functional neurons," *Cell Stem Cell*, vol. 17, no. 2, pp. 195–203, 2015.

[23] L. Zhang, J. C. Yin, H. Yeh et al., "Small molecules efficiently reprogram human astroglial cells into functional neurons," *Cell Stem Cell*, vol. 17, no. 6, pp. 735–747, 2015.

[24] R. Hass, C. Kasper, S. Böhm, and R. Jacobs, "Different populations and sources of human mesenchymal stem cells (MSC): a comparison of adult and neonatal tissue-derived MSC," *Cell Communication and Signaling: CCS*, vol. 9, no. 1, p. 12, 2011.

[25] F. Rastegar, D. Shenaq, J. Huang et al., "Mesenchymal stem cells: molecular characteristics and clinical applications," *World Journal of Stem Cells*, vol. 2, no. 4, pp. 67–80, 2010.

[26] B. Sacchetti, A. Funari, C. Remoli et al., "No identical "mesenchymal stem cells" at different times and sites: human committed progenitors of distinct origin and differentiation potential are incorporated as adventitial cells in microvessels," *Stem Cell Reports*, vol. 6, no. 6, pp. 897–913, 2016.

[27] A. G. Via, A. Frizziero, and F. Oliva, "Biological properties of mesenchymal stem cells from different sources," *Muscles, Ligaments and Tendons Journal*, vol. 2, no. 3, pp. 154–162, 2012.

[28] J. J. Montesinos, E. Flores-Figueroa, S. Castillo-Medina et al., "Human mesenchymal stromal cells from adult and neonatal sources: comparative analysis of their morphology, immunophenotype, differentiation patterns and neural protein expression," *Cytotherapy*, vol. 11, no. 2, pp. 163–176, 2009.

[29] M. E. Castro-Manrreza and J. J. Montesinos, "Células troncales mesenquimales: potencial de terapia celular en trasplante de células troncales hematopoyéticas," *El Residente*, vol. 9, no. 2, pp. 66–73, 2014.

[30] M. W. Pfaffl, "A new mathematical model for relative quantification in real-time RT-PCR," *Nucleic Acids Research*, vol. 29, no. 9, pp. 45e–445, 2001.

[31] M. Dominici, K. le Blanc, I. Mueller et al., "Minimal criteria for defining multipotent mesenchymal stromal cells. The International Society for Cellular Therapy position statement," *Cytotherapy*, vol. 8, no. 4, pp. 315–317, 2006.

[32] F. A. Dąbrowski, A. Burdzinska, A. Kulesza, B. Kaleta, L. Pączek, and M. Wielgoś, "Premature fetal tissues are possible source of valuable mesenchymal stem cells," *Ginekologia Polska*, vol. 88, no. 4, pp. 191–197, 2017.

[33] C. H. Jo, O. S. Kim, E. Y. Park et al., "Fetal mesenchymal stem cells derived from human umbilical cord sustain primitive characteristics during extensive expansion," *Cell and Tissue Research*, vol. 334, no. 3, pp. 423–433, 2008.

[34] J. Li, J. Ma, G. Meng et al., "BET bromodomain inhibition promotes neurogenesis while inhibiting gliogenesis in neural progenitor cells," *Stem Cell Research*, vol. 17, no. 2, pp. 212–221, 2016.

[35] H. Qin, A. Zhao, and X. Fu, "Small molecules for reprogramming and transdifferentiation," *Cellular and Molecular Life Sciences*, vol. 74, no. 19, pp. 3553–3575, 2017.

[36] J. R. Ryu, C. J. Hong, J. Y. Kim, E. K. Kim, W. Sun, and S. W. Yu, "Control of adult neurogenesis by programmed cell death in the mammalian brain," *Molecular Brain*, vol. 9, no. 1, p. 43, 2016.

[37] W. Yeo and J. Gautier, "Early neural cell death: dying to become neurons," *Developmental Biology*, vol. 274, no. 2, pp. 233–244, 2004.

[38] Y. Taniguchi, "The Bromodomain and Extra-Terminal Domain (BET) family: functional anatomy of BET paralogous proteins," *International Journal of Molecular Sciences*, vol. 17, no. 11, 2016.

[39] S. C. Hsu, T. G. Gilgenast, C. R. Bartman et al., "The BET protein BRD2 cooperates with CTCF to enforce transcriptional and architectural boundaries," *Molecular Cell*, vol. 66, no. 1, pp. 102–116.e7, 2017.

[40] E. Korb, M. Herre, I. Zucker-Scharff, R. B. Darnell, and C. D. Allis, "BET protein Brd4 activates transcription in neurons and BET inhibitor Jq1 blocks memory in mice," *Nature Neuroscience*, vol. 18, no. 10, pp. 1464–1473, 2015.

[41] V. S. Fishman, T. A. Shnayder, K. E. Orishchenko, M. Bader, N. Alenina, and O. L. Serov, "Cell divisions are not essential for the direct conversion of fibroblasts into neuronal cells," *Cell Cycle*, vol. 14, no. 8, pp. 1188–1196, 2015.

[42] B. C. Feltes and D. Bonatto, "Combining small molecules for cell reprogramming through an interatomic analysis," *Molecular BioSystems*, vol. 9, no. 11, pp. 2741–2763, 2013.

[43] S. Sisakhtnezhad and M. M. Matin, "Transdifferentiation: a cell and molecular reprogramming process," *Cell and Tissue Research*, vol. 348, no. 3, pp. 379–396, 2012.

[44] N. Yang, Y. H. Ng, Z. P. Pang, T. C. Südhof, and M. Wernig, "Induced neuronal cells: how to make and define a neuron," *Cell Stem Cell*, vol. 9, no. 6, pp. 517–525, 2011.

[45] K. G. Chen, B. S. Mallon, K. Park et al., "Pluripotent stem cell platforms for drug discovery," *Trends in Molecular Medicine*, vol. 24, no. 9, pp. 805–820, 2018.





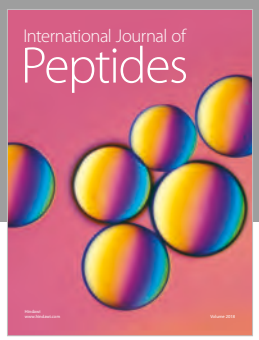



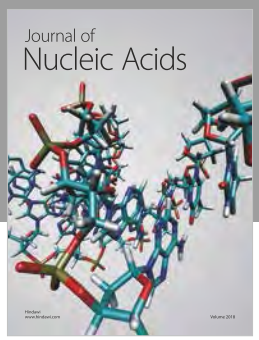

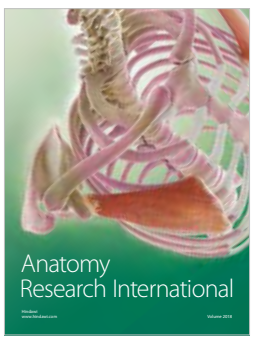



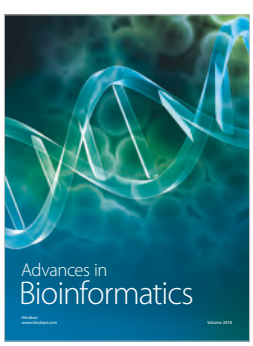

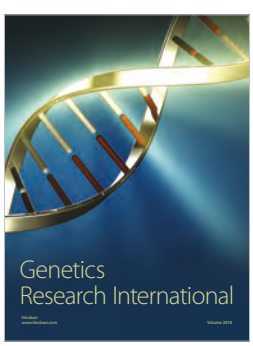



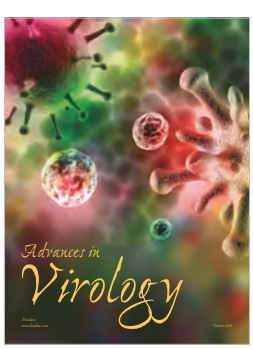

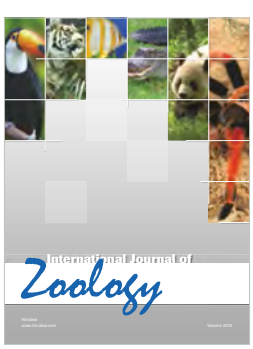

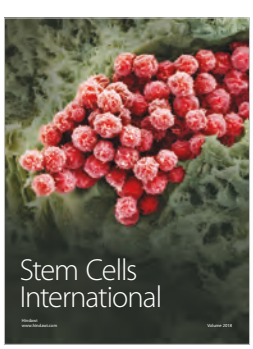



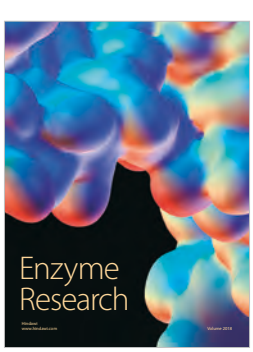







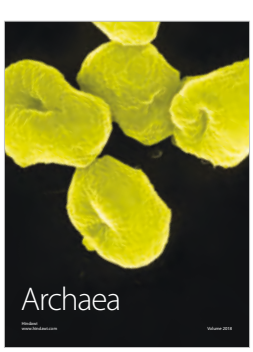

Hindawi

Submit your manuscripts at
www.hindawi.com

International Journal of Biochemistry and Cell Biology 107 (2019) 14–26

Contents lists available at ScienceDirect

International Journal of Biochemistry and Cell Biology

journal homepage: www.elsevier.com/locate/biocel

Non-muscle myosin IIA is post-translationally modified by interferon-stimulated gene 15 in breast cancer cells

Eduardo Cruz-Ramos[a], Marina Macías-Silva[b], Antonio Sandoval-Hernández[a], Angeles C. Tecalco-Cruz[a,*]

[a] Instituto de Investigaciones Biomédicas. Universidad Nacional Autónoma de México, Mexico City, 04510, Mexico
[b] Instituto de Fisiología Celular, Universidad Nacional Autónoma de México, Mexico City, 04510, Mexico

ARTICLE INFO

Keywords:
ISG15
ISGylation
Breast cancer
Non-muscle myosin IIA
Interferon gamma

ABSTRACT

ISG15 (interferon-stimulated gene 15) exists as free ISG15 or conjugated ISG15 modifying its target proteins via ISGylation. Few proteins have been identified and studied as ISGylation targets, and their relevance is not completely clear. Here, we isolated ISG15 from MDA-MB-231 breast cancer cells using immunoprecipitation and identified non-muscle myosin IIA (NMIIA) using mass spectrometry as endogenously associated with ISG15. The identification of NMIIA as an ISG15-interacting protein was important, because levels of NMIIA mRNA were not deregulated in all breast cancers, and because our *in silico* analysis indicated that NMIIA was the target of different posttranslational modifications and had an interactome associated with cytoskeletal remodeling. Furthermore, our experimental assays of co-immunoprecipitation and immunofluorescence confirmed that ISG15 was covalently associated with NMIIA in the cytoplasm of breast cancer cells and that interferon γ (IFN-γ) increased this association without alterations in the NMIIA levels. Thus, NMIIA ISGylation is regulated by IFN-γ, and this modification may modulate its interactions with proteins that remodel the cytoskeleton, participating in the growth and progression of mammary tumors.

1. Introduction

Interferon-stimulated gene 15 (*ISG15*) encodes a small l5 kDa protein made up of two ubiquitin-like domains and the amino acid sequence LRLRGG in the C-terminal domain. This sequence has been shown to covalently bind target proteins, resulting in ISGylation, a modification that requires a system similar to ubiquitination formed by the UBE1L (E1-activating), UBCH8 (E2-conjugating), and E3 ligase enzymes such as HERC5, EFP, and HHARI. Additionally, this ISGylation system contains an enzyme to remove ISGylation, the USP18 de-ISGylase enzyme, also named UBP43 (Basters et al., 2014; Dastur et al., 2006; Feng et al., 2008; Okumura et al., 2007; Wong et al., 2006; Zou and Zhang, 2006; Kim et al., 2004; Zhao et al., 2004). Nonetheless, ISG15 can be detected when it is not covalently bound to its target proteins, designated as free ISG15. The free ISG15 form can be secreted from lymphocytes and monocytes and can be recognized by the lymphocyte function-associated antigen 1 (LFA-1) receptor to induce interferon γ (IFN-γ) release from natural killer cells (D'Cunha et al., 1996; Knight and Cordova, 1991; Swaim et al., 2017). So far, it has been proposed that protein ISGylation can interfere or collaborate with the ubiquitination pathway and/or can affect the interactions between proteins. Moreover, the majority of ISGylated proteins seem to be monoISGylated (Burks et al., 2014; Desai et al., 2006; Fan et al., 2015; Huang and Bulavin, 2014; Jeon et al., 2009; Liu et al., 2003).

With respect to the regulation of ISGylation, ISG15 is upregulated in several cancer types (Chen et al., 2016; Mao et al., 2016; Padovan et al., 2002; Satake et al., 2010; Wan et al., 2013). Moreover, type I interferons (IFN-α and IFN-β) have been shown to be inducers of *ISG15* in several cell types, and, recently, we demonstrated that IFN-γ increased free ISG15 and ISGylation levels in ERα+ and ERα− breast cancer cells (Malakhova et al., 2003; Recht et al., 1991; Tecalco Cruz and Mejia-Barreto, 2017; Tecalco-Cruz and Cruz-Ramos, 2018). IFN-γ is a unique member of type II interferons that can transduce its signal via a specific heterotetrameric receptor that activates the Janus protein tyrosine kinase (JAK)/signal transducer and activator of transcription 1 (STAT1) system to modulate the transcription of its target genes. IFN-γ has immunoregulatory functions and dual roles in some cancer types. In breast cancer, IFN-γ seems to induce cycle arrest and apoptosis, and gene signatures for interferons have been associated with the resistance to chemotherapy or endocrine therapy (Gooch et al., 2000; Legrier

* Corresponding author.
E-mail address: atecalco@iibiomedicas.unam.mx (A.C. Tecalco-Cruz).

https://doi.org/10.1016/j.biocel.2018.12.002
Received 11 August 2018; Received in revised form 17 November 2018; Accepted 3 December 2018
Available online 05 December 2018
1357-2725/ © 2018 Elsevier Ltd. All rights reserved.

INFORME DE LABORES 2019

et al., 2016; Ning et al., 2010; Niu et al., 2015).

Hence, the effects of IFN-γ on breast cancer cells are important as mammary tumors are highly heterogeneous, able to present or develop resistance to treatments, and progress to invade other tissues because of several deregulated molecular pathways, including nuclear receptors signaling (Tecalco-Cruz, 2018; Tecalco-Cruz and Ramirez-Jarquin, 2017). Furthermore, it has been suggested that free ISG15 has anti-tumor functions *in vivo*; however, downregulation of ISG15 decreases proliferation and migration of breast cancer cell lines (Burks et al., 2014, 2015; Desai et al., 2012). Nevertheless, ISGylation functions have yet to be elucidated, as only a limited number of proteins modified by ISG15 are known. Likewise, IFN-γ signaling and its relationship with specific protein modification by ISGylation in breast cancer have not been studied. Here, we identified non-muscle myosin IIA (NMIIA) as a cytoplasmic protein that is modified via ISGylation and modulated by IFN-γ in breast cancer cells.

2. Results

2.1. NMIIA is an endogenous ISG15-interacting protein in breast cancer cells

In order to identify endogenous ISGylation target proteins in breast cancer cells, we decided to use MDA-MB-231 cells as they had higher levels of conjugated ISG15 than free, as shown by western blotting (WB) against ISG15 using total extracts of these cells (Fig. 1A). These cells acted as an adequate model to identify proteins covalently conjugated to ISG15. Next, we used the total extracts from these cells to carry out an immunoprecipitation assay using a specific monoclonal antibody for ISG15. The endogenous ISG15 was immunoprecipitated and separated using sodium dodecyl sulphate-polyacrylamide gel electrophoresis (SDS-PAGE) followed by Coomassie staining using IgG and a mock immunoprecipitation as negative controls. Among the detected bands, we selected one very dense band (approximately 250 kDa in size) to identify the ISG15-associated protein (Fig. 1B). Mass spectrometry (MS) revealed that this band corresponded to NMIIA (230 kDa in size) encoded by *MYH9*, a member of the non-muscle myosin family (NMII A, B, and C) (Fig. 1C and D). These proteins are comprised of a heavy chain encompassing a globular head domain that binds actin and adenosine triphosphate (ATP), a neck region that binds essential light chain (ELC), and a regulatory light chain (RLC) as well as a tail region that homodimerizes in a helical fashion. Light and heavy chains are conserved among NMII proteins; however, the end of the heavy chain tail is a sequence with considerable divergence between the NMII isoforms, as implicated in their regulation. NMII proteins associate with actin filaments, contracting them and forming the actomyosin complex that participates in cytoskeletal remodeling and regulation of shape, organization, polarity, and motility of the cell (Newell-Litwa et al., 2015; Ouderkirk and Krendel, 2014). Interestingly, our results indicate that only one of the NMII proteins described in humans, NMIIA, is endogenously associated with ISG15 in MDA-MB-231 breast cancer cells.

2.2. NMIIA mRNA is not deregulated in breast cancers, but NMIIA seems to be highly affected by posttranslational modifications and protein-protein interactions

Initially, we decided to explore the role of NMIIA expression in breast cancer and its regulation. We analyzed the expression of *MYH9* in normal mammary tissue and mammary tumors from patients. Using Oncomine, we selected the Curtis (2136 samples) database for this analysis and determined that *MYH9* expression was similar in breast cancers and normal conditions, as statistical analyses revealed that *MYH9* expression was not significantly different between breast cancer and normal mammary tissues (Fig. 2A). We also analyzed the reported and predicted posttranslational modifications for NMIIA using PhosphoSitePlus (PSP). Remarkably, NMIIA was a highly modified protein, mainly by phosphorylation but also through other modifications, including acetylation and ubiquitination (Fig. 2B). Using the Search Tool for the Retrieval of Interacting Genes (STRING) software, we also found proteins associated with cytoskeletal remodeling (RhoA, Ras, Cdc42, and ACTG1) in the interactome for NMIIA (Fig. 2C). Thus, *MYH9* expression was not deregulated in all mammary tumors from patients, suggesting that protein-protein interactions of NMIIA and its posttranslational modifications, including ISGylation, could be critical and interconnected in the regulation of the levels and functions of this protein.

2.3. Subcellular distribution of NMIIA and ISGylation mark in breast cancer cells

Because NMIIA has been reported as the central element of actomyosin, we first evaluated the subcellular distribution of this protein. We transfected the enhanced green fluorescent protein (EGFP)-NMIIA plasmid in AD293 cells (kidney cells with high transfection efficiency) and detected its localization in the cytoplasm using immunofluorescence (Fig. 3A). Next, we analyzed the localization of endogenous NMIIA protein in MDA-MB-231 and MCF-7 breast cancer cells using subcellular fractionation and immunofluorescence assays. NMIIA was detected mainly in the cytoplasmic fraction of these cells (Fig. 3B–D). Free ISG15 was localized in cytoplasm, and ISGylation was detected in both the nucleus and cytoplasm of these cells (Fig. 3B, C). We also performed immunofluorescence assays using anti-ISG15 and anti-NMIIA antibodies for the endogenous detection of these proteins in MDA-MB-231 and MCF-7 cells (Fig. 3D). Similarly, the results showed that NMIIA was mostly detected outside the nucleus, and ISG15 was detected in the cytoplasm and in the nucleus. Thus, NMIIA and ISG15 are principally co-localized in the cell cytoplasm as indicated by the merge of these images (Fig. 3D, E).

2.4. NMIIA is associated specifically with ISG15 in vivo

Based on our results, we evaluated whether ISG15 interacted specifically with NMIIA in *vivo*. We chose AD293 cells that had high levels of conjugated ISG15 and undetectable free ISG15 levels (Fig. 4A). Then, we used total extracts from AD293 cells transfected with EGFP-NMIIA and performed an immunoprecipitation assay to enrich endogenous conjugated ISG15 protein, followed by WB to detect EGFP-NMIIA. We determined that EGFP-NMIIA was contained in the immunoprecipitated ISG15 (Fig. 4B).

Similarly, AD293 cells were transfected with the EGFP-NMIIA plasmid. We performed an immunoprecipitation experiment for conjugated ISG15 and used anti-NMIIA antibody for the WB, resulting in detection of the exogenous (~260 kDa) and endogenous (~230 kDa) form of NMIIA in the transfected cells. Only endogenous NMIIA was observed in non-transfected cells, indicating a specific interaction between these proteins (Fig. 4C). Interestingly, ISG15-NMIIA interaction resulted in a shifted band compared to the band corresponding to NMIIA protein detected in total extracts by WB, suggesting that the association of these proteins occurred in a covalent manner.

2.5. NMIIA is an ISGylated protein in breast cancer cells

Based on the specific interaction between ISG15 and NMIIA, we verified this interaction in an endogenous context of breast cancer cells. We performed an immunoprecipitation assay using monoclonal antibody against ISG15 as well as IgG and/or mock immunoprecipitation as negative controls, followed by WB for NMIIA to demonstrate the specific endogenous binding between ISG15 and NMIIA in MDA-MB231 and MCF-7 cells (Fig. 5A). ISG15-NMIIA interaction (IP ISG15 WB NMIIA) resulted in a shifted band compared to the band of NMIIA protein detected by WB using total extracts (input) from breast cancer

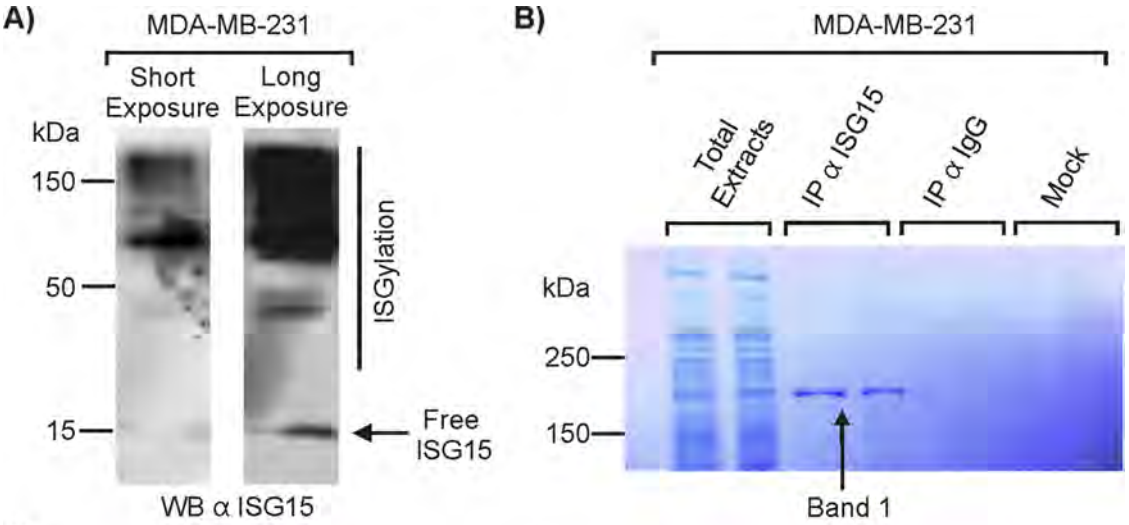

C)

MAQQAADKYLYVDKNFINNPLAQADWAAKKLVWVPSDKSGFEPASLKEEVGEEAIVELVENGKKVKVNKDDIQKMNPPKFSKVEDMAELTCLNEASVLHNLK
ERYYSGLIYTYSGLFCVVINPYKNLPIYSEEIVEMYKGKKRHEMPPHIYAITDTAYRSMMQDREDQSILCTGESGAGKTENTKKVIQYLAYVASSHKSKKDQGELE
RQLLQANPILEAFGNAKTVKNDNSSRFGKFIRINFDVNGYIVGANIETYLLEKSRAIRQAKEERTFHIFYYLLSGAGEHLKTDLLLEPYNKYRFLSNGHVTIPGQQD
KDMFQETMEAMRIMGIPEEEQMGLLRVISGVLQLGNIVFKKERNTDQASMPDNTAAQKVSHLLGINVTDFTRGILTPRIKVGRDYVQKAQTKEQADFAIEALAK
ATYERMFRWLVLRINKALDKTKRQGASFIGILDIAGFEIFDLNSFEQLCINYTNEKLQQLFNHTMFILEQEEYQREGIEWNFIDFGLDLQPCIDLIEKPAGPPGILALL
DEECWFPKATDKSFVEKVMQEQGTHPKFQKPKQLKDKADFCIIHYAGKVDYKADEWLMKNMDPLNDNIATLLHQSSDKFVSELWKDVDRIIGLDQVAGMSETA
LPGAFKTRKGMFRTVGQLYKEQLAKLMATLRNTNPNFVRCIIPNHEKKAGKLDPHLVLDQLRCNGVLEGIRICRQGFPNRVVFQEFRQRYEILTPNSIPKGFMD
GKQACVLMIKALELDSNLYRIGQSKVFFRAGVLAHLEEERDLKITDVIIGFQACCRGYLARKAFAKRQQQLTAMKVLQRNCAAYLKLRNWQWWRLFTKVKPLLQ
VSRQEEEMMAKEEELVKVREKQLAAENRLTEMETLQSQLMAEKLQLQEQLQAETELCAEAEELRARLTAKKQELEEICHDLEARVEEEEERCQHLQAEKKK
MQQNIQELEEQLEEEESARQKLQLEKVTTEAKLKKLEEEQIILEDQNCKLAKEKKLLEDRIAEFTTNLTEEEEKSKSLAKLKNKHEAMITDLEERLRREEKQRQE
LEKTRRKLEGDSTDLSDQIAELQAQIAELKMQLAKKEEELQAALARVEEEAAQKNMALKKIRELESQISELQEDLESERASRNKAEKQKRDLGEELEALKTELED
TLDSTAAQQELRSKREQEVNILKKTLEEEAKTHEAQIQEMRQKHSQAVEELAEQLEQTKRVKANLEKAKQTLENERGELANEVKVLLQGKGDSEHKRKKVEAQ
LQELQVKFNEGERVRTELADKVTKLQVELDNVTGLLSQSDSKSSKLTKDFSALESQLQDTQELLQEENRQKLSLSTKLKQVEDEKNSFREQLEEEEEAKHNLEK
QIATLHAQVADMKKKMEDSVGCLETAEEVKRKLQKDLEGLSQRHEEKVAAYDKLEKTKTRLQQELDDLLVDLDHQRQSACNLEKKQKKFDQLLAEEKTISAKYA
EERDRAEAEAREKETKALSLARALEEAMEQKAELERLNKQFRTEMEDLMSSKDDVGKSVHELEKSKRALEQQVEEMKTQLEELEDELQATEDAKLRLEVNLQ
AMKAQFERDLQGRDEQSEEKKKQLVRQVREMEAELEDERKQRSMAVAARKKLEMDLKDLEAHIDSANKNRDEAIKQLRKLQAQMKDCMRELDDTRASREEIL
AQAKENEKKLKSMEAEMIQLQEELAAAERAKRQAQQERDELADEIANSSGKGALALEEKRRLEARIAQLEEELEEEQGNTELINDRLKKANLQIDQINTDLNLE
RSHAQKNENARQQLERQNKELKVKLQEMEGTVKSKYKASITALEAKIAQLEEQLDNETKERQAACKQVRRTEKKLKDVLLQVDDERRNAEQYKDQADKASTR
LKQLKRQLEEAEEEAQRANASRRKLQRELEDATETADAMNREVSSLKNKLRRGDLPFVVPRRMARKGAGDGSDEEVDGKADGAEAKPAE

Band	Accession	Name	MW	Abbreviation
1	P35579	Myosin heavy chain, non-muscle type A	227 kDa	NMIIA

D)

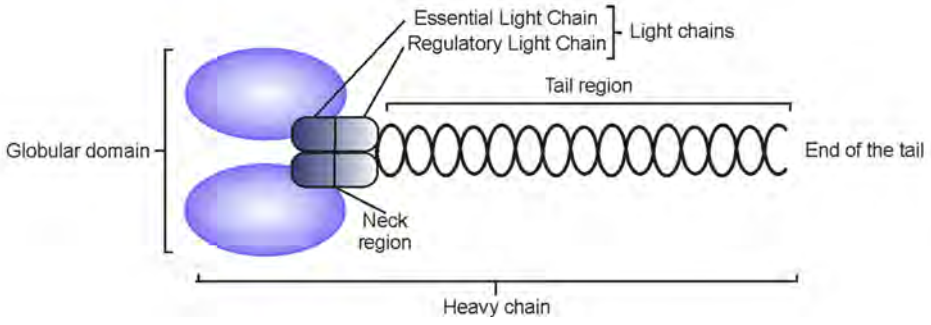

Fig. 1. Identification of non-muscle myosin IIA (NMIIA) as a putative interferon-stimulated gene 15 (ISG15)-associated protein.
A) Total extracts from MDA-MB-231 cells were analyzed by western blotting (WB) against interferon-stimulated gene 15 (ISG15). B) Coomassie staining of ISG15-immunoprecipitated complexes from MDA-MB-231 lysates. A band approximately 250 kDa in size was excised for analysis by mass spectrometry. Samples were analyzed in duplicate. C) ISG15-interacting protein identified by mass spectrometry is shown in the table. The identified peptides are indicated in green (bold) on non-muscle myosin IIA (NMIIA) protein sequence. NMIIA peptide coverage was 20%. D) Structural organization of NMIIA identified protein.

cells, indicating the covalent association between these proteins (Fig. 5A). The same assay was performed using cytoplasmic and nuclear extracts from these cells, and the interaction between ISG15 and NMIIA was strongly detected in the cytoplasm of these cells (Fig. 5B). Thus, we validated the endogenous interaction indicated by MS between ISG15 and NMIIA protein in breast cancer cells.

To discard the hypothesis of a non-covalent interaction between free ISG15 and NMIIA, we used MCF-7 cells, where both conjugated ISG15 and free ISG15 could be detected (Fig. 5C). We performed a reciprocal immunoprecipitation through the NMIIA protein immunoprecipitation, followed by a WB against ISG15 (Fig. 5D). Free ISG15 was detected in the total extracts (input); however, free ISG15 was not present in the immunoprecipitated NMIIA, suggesting that the interaction between ISG15 and NMIIA did not occur in a non-covalent manner but covalently via ISGylation. As control, the efficiency of NMIIA immunoprecipitation was tested, and the covalent interaction between ISG15 and NMIIA in these cells was confirmed (Fig. 5D bottom). These results indicate that ISG15 protein is covalently associated with NMIIA.

INFORME DE LABORES 2019

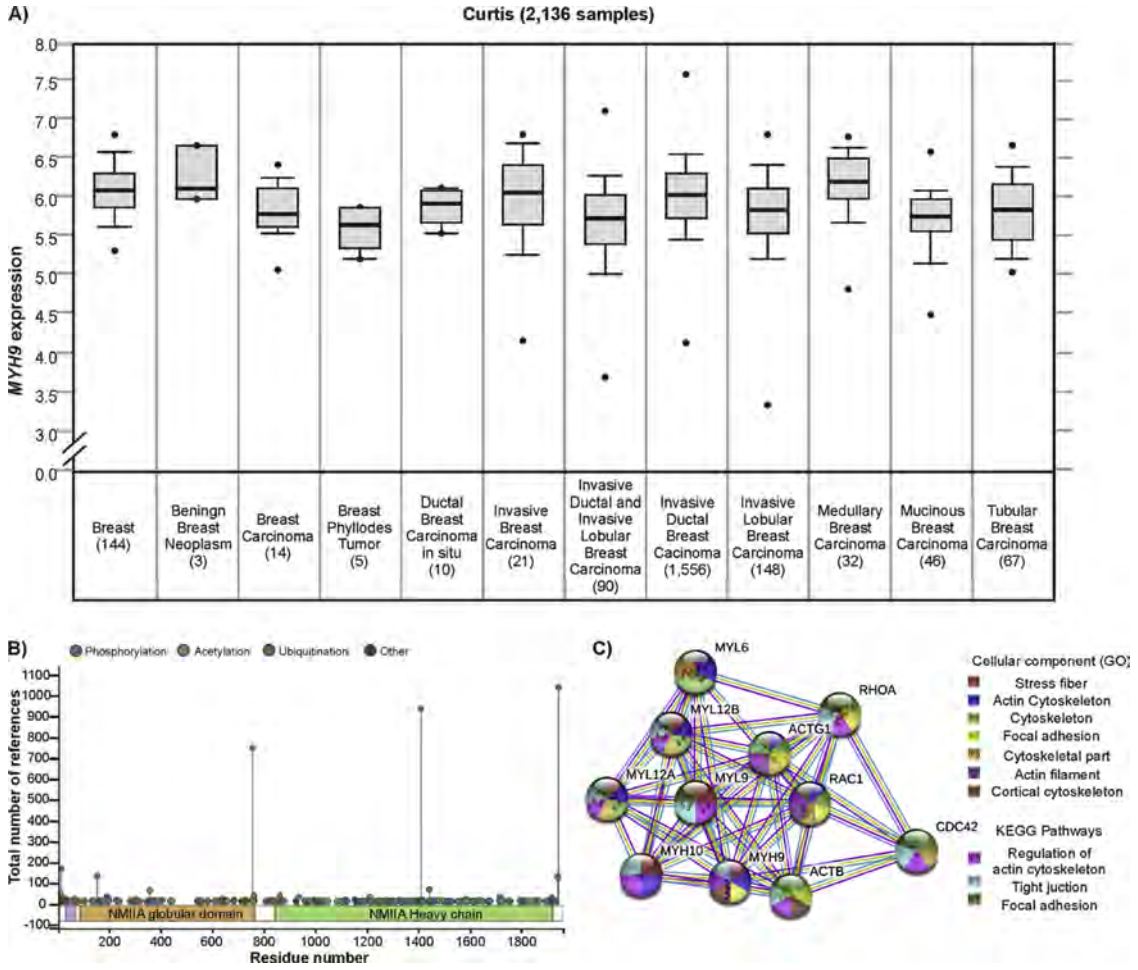

Fig. 2. Non-muscle myosin IIA (*MYH9*) mRNA levels in breast cancer and the modifications and protein-protein interactions for NMIIA.
A) Curtis datasets from Oncomine were analyzed to evaluate *MYH9* expression in human mammary tumors compared to normal tissue. B) Evaluation of sites target of posttranslational modification for non-muscle myosin IIA (NMIIA) using PhosphoSite. C) Analysis of NMIIA interactome using STRING. Known interactions from curated databases, text mining, experimental determination, and protein homology are indicated in blue, green, purple, and dark blue lines, respectively. Kyoto Encyclopedia of Genes and Genomes (KEGG). Gene Ontology (GO).

2.6. IFN-γ modulates NMIIA ISGylation in breast cancer cells

We previously showed that IFN-γ increased ISGylation levels in breast cancer cells; therefore, we sought to determine whether NMIIA ISGylation increased by treatment with IFN-γ. Using total extracts from MDA-MB-231 cells treated with IFN-γ or left untreated, we performed an ISG15 immunoprecipitation. The Coomassie staining showed that the band identified as NMIIA by MS was increased by IFN-γ treatment (Fig. 6A). Furthermore, we demonstrated that the specific interaction between ISG15 and NMIIA in MDA-MB-231 cells increased by IFN-γ treatment using WB with an anti-NMIIA antibody (Fig. 6B). This interaction was also enhanced by IFN-γ treatment in MCF-7 cells (Fig. 6C). Although IFN-γ enhanced the ISG15 and ISGylation levels after 24 h, no changes in the amount of NMIIA were detected in response to IFN-γ treatment in MDA-MB-231 and MCF-7 cells under these conditions (Fig. 6D and E)., suggesting that the availability of NMIIA was not affected by IFN-γ-induced ISGylation (Fig. 6F and G).

ISGylation has been reported to be associated with an increase or decrease in the protein stability and also in the protein-protein interactions. As NMIIA levels were not altered by IFN-γ-increased ISGylation, this modification could act affecting the interactions of NMIIA, many of them linked to cytoskeletal (Fig. 2C). For this reason, we performed an analysis using STRING software, evidencing an interconnection between the IFN-γ signaling pathway, ISGylation, and NMIIA, in which actin was the common protein that connected these pathways, similar to IQ motif containing GTPase activating protein 1 (IQGAP1), a cytoskeleton protein that has been reported to be a ISGylated target (Cerikan and Schiebel, 2017; Cerikan et al., 2016). Thus, our study demonstrated a new connection generated by the ISGylation of NMIIA modulated by IFN-γ. Moreover, our study suggests that IFN-γ may regulate the ISGylation of many other cytoskeleton proteins participating in the cytoskeletal dynamic in breast cancer cells (Fig. 7.

2.7. IFN-γ/ISG15-NMIIA-actin axis in cytoskeleton organization is important in modulation of the morphology of breast cancer cells

ISG15 conjugation to NMIIA had no effect on its stability (Fig. 6), but a functional interactome between NMIIA, cytoskeletal proteins and the IFN-γ/ISG15 route was suggested by our data (Fig. 7). Additionally, NMIIA interacts with F-actin to modulate cytoskeletal organization (Ouderkirk and Krendel, 2014). Based on these data, we considered that covalent interaction between ISG15 and NMIIA might have an effect on the cell morphology. Presently, immunofluorescence assays revealed greater elongation of MDA-MB-231 cells treated with IFN-γ, with an increasing co-localization of NMIIA with ISG15 in the cytoplasmic and perinuclear regions, in comparison with cells that were not treated with IFN-γ (Fig. 8A). Furthermore, co-localization of NMIIA and F-actin in the cytoplasm and at the edge of cells in response to IFN-γ was evident (Fig. 8B). Co-localization of NMIIA, ISG15, and F-actin occurred mainly in the cytoplasm of MDA-MB-231 cells treated with IFN-γ (Fig. 8C),

INFORME DE LABORES 2019

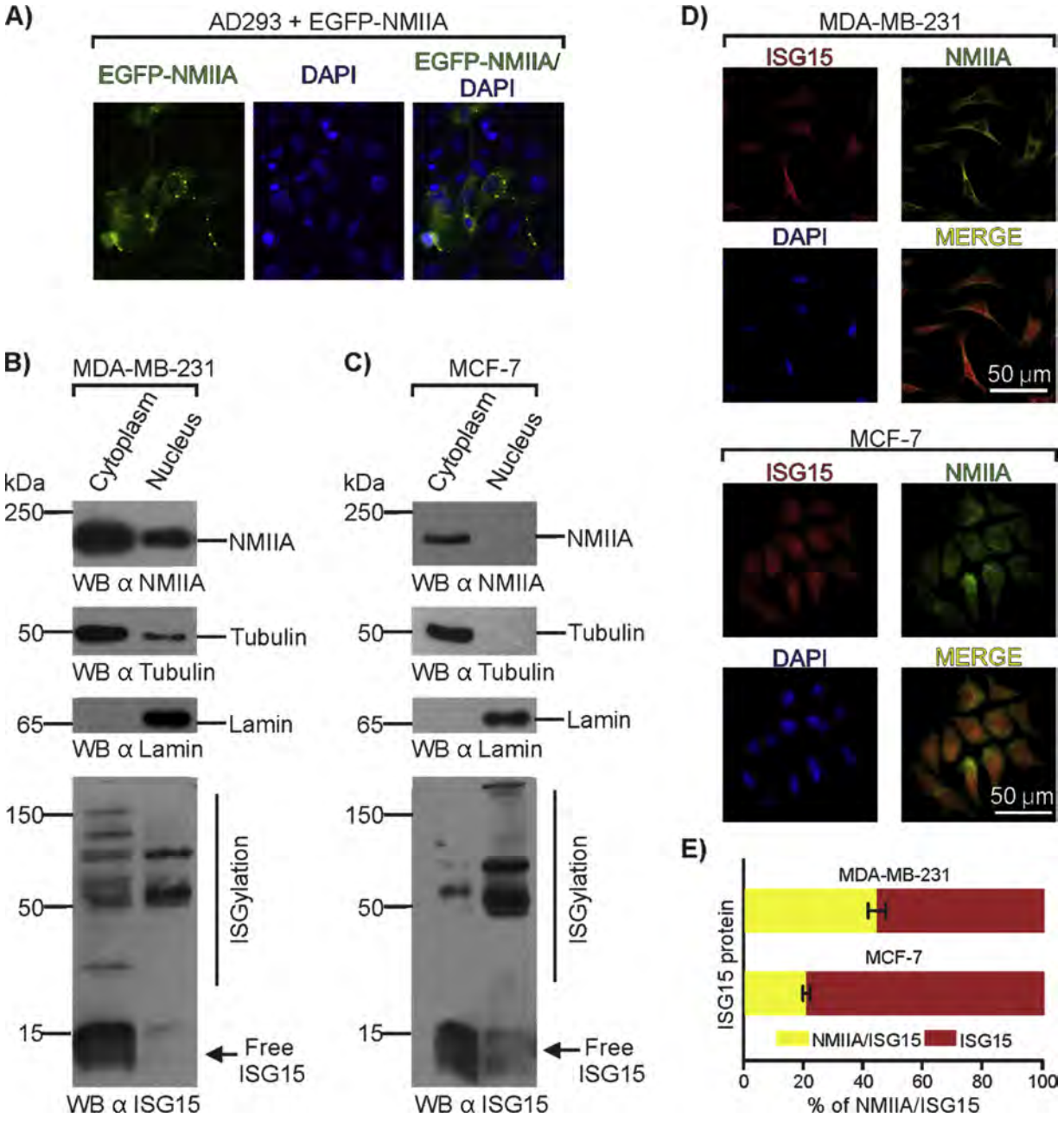

Fig. 3. Non-muscle myosin IIA (NMIIA) is a cytoplasmic protein associated with interferon-stimulated gene 15 (ISG15) in breast cancer cells.
A) Enhanced green fluorescent protein-non-muscle myosin IIA (EGFP-NMIIA) was detected in cytoplasm of AD293 cells. B) and C) Cytoplasmic and nuclear extracts from MDA-MB-231 and MCF-7 cells were analyzed by western blotting (WB) against NMIIA using tubulin and lamin as controls for cytoplasm and nucleus, respectively. D) Evaluation of subcellular distribution of interferon-stimulated gene 15 (ISG15) and NMIIA protein in MDA-MB-231 and MCF-7 using immunofluorescence assay. E) Analysis of co-localization for ISG15 and NMIIA in breast cancer cells.

suggesting that IFN-γ acting through ISG15 may be important to regulate the functional association of NMIIA and F-actin in the cytoplasm of breast cancer cells.

We decided to evaluate whether morphological changes induced by IFN-γ were associated with protein ISGylation (as ISGylated NMIIA), and whether this occurred in other breast cancer cell types. To this end, we examined MCF-7 cells, because they maintain an epithelial morphology, in contrast to MDA-MB-231 cells that present a mesenchymal-like morphology. Initially, we transfected these cells with EGFP-NMIIA or EGFP-NMIIA with ISG15, E1 (UBE1L), and E2 (UbcH8) ISGylation enzymes. ISGylation was increased when ISG15 and the ISGylation system was transfected (Fig. 8D). Under this condition, the immunoprecipitation of ISG15 and WB for NMIIA revealed the enhanced association of ISG15 with NMIIA, as well as EGFP-NMIIA (Fig. 8D bottom). Thus, ISG15-NMIIA interaction was increased when ISGylation enhanced, and MCF-7 cells displayed stress fibers with discrete morphological changes (Fig. 8E and 8F). Likewise, co-localization of NMIIA-ISG15 and NMIIA-F-actin was detected under the condition of ISGylation, in a manner similar to the co-localization of these proteins in MDA-MB-231 cells treated with IFN-γ (Fig. 8E and F). The results indicate that NMIIA ISGylation contributes to the changes in the morphology associated with F-actin organization in breast cancer cells.

2.8. NMIIA-ISG15 interaction occurs during spreading of breast cancer cells

Cell spreading is a critical event that involves actin polymerization

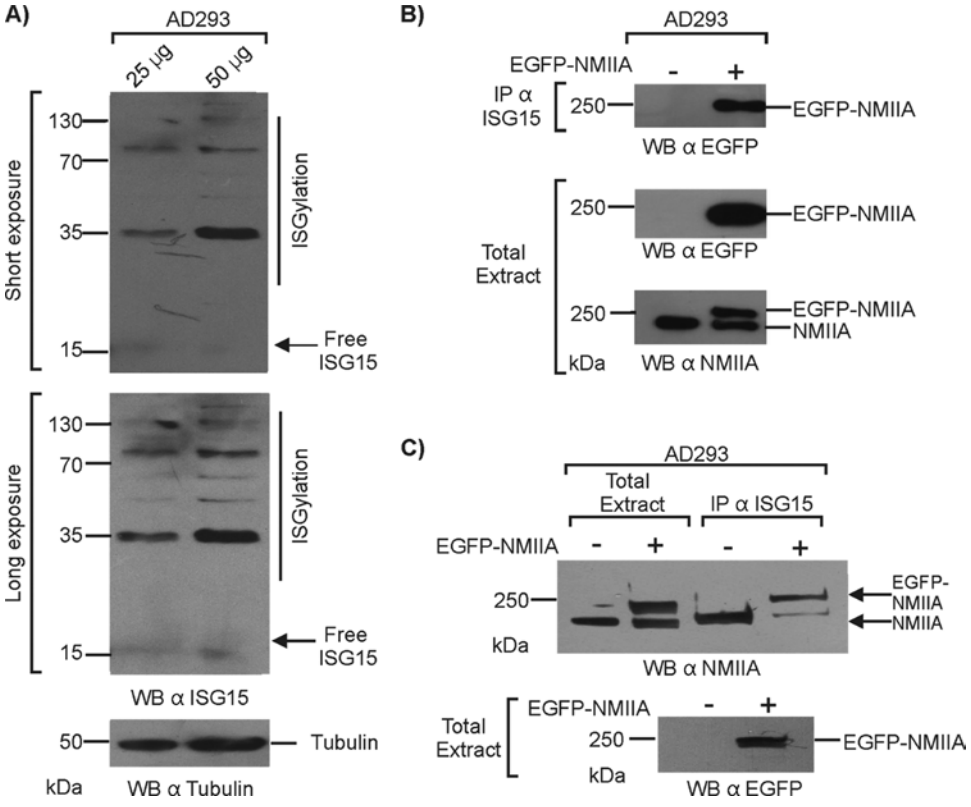

Fig. 4. Non-muscle myosin IIA (NMIIA) is specifically associated with interferon-stimulated gene 15 (ISG15).
A) Western blotting (WB) for interferon-stimulated gene 15 (ISG15) using 25 and 50 µg from AD293 cell total extracts. B) AD293 cells were transfected with or without enhanced green fluorescent protein-non-muscle myosin IIA (EGPF-NMIIA). After 48 h, the total extracts were used for ISG15 immunoprecipitation and WB for EGFP or C) WB for NMIIA.

to generate a cellular contact area with the extracellular matrix or substrate. NMII proteins participate differently in the generation of protrusive forces that regulate cell spreading for cell motility. NMIIA and NMIIB are recruited in the lamellar margin during the spreading of MDA-MB-231 breast cancer cells participating in the regulation of this process (Betapudi, 2010; Betapudi et al., 2006)

Since cell spreading is a fundamental NMII-regulated event, we examined whether NMIIA-ISG15 interaction can occur in the spreading

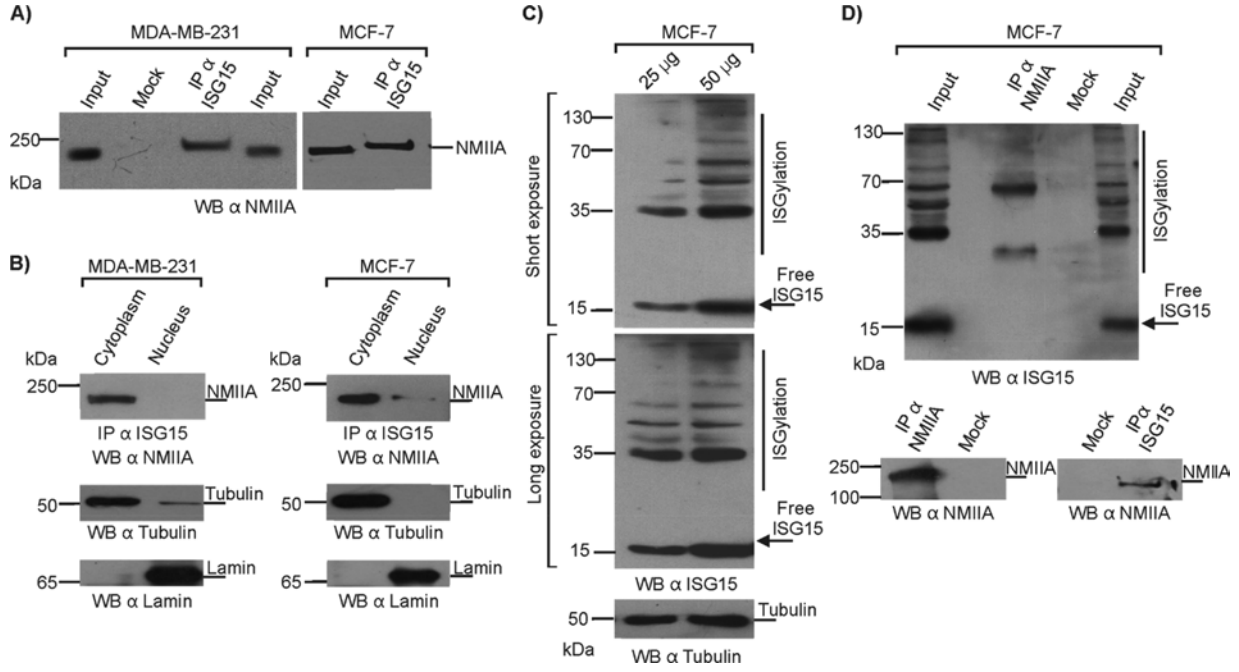

Fig. 5. Interferon-stimulated gene 15 (ISG15) is covalently associated with non-muscle myosin IIA (NMIIA) in breast cancer cells.
A) Interferon-stimulated gene 15 (ISG15) was immunoprecipitated from MDA-MB-231 and MCF-7 cell total extracts, and western blotting (WB) with anti-non-muscle myosin IIA (NMIIA) was performed. B) Cytoplasmic and nuclear fractions from MDA-MB-231 and MCF-7 cells were used for ISG15 immunoprecipitation followed by WB for NMIIA. Anti-tubulin and anti-lamin were used as controls for the cytoplasmic and nuclear extracts. C) WB for ISG15 using 25 and 50 µg from MCF-7 cell total extracts. D) Endogenous NMIIA immunoprecipitation from MCF-7 followed by WB for ISG15 was analyzed on 12% gels. Bottom: endogenous NMIIA and ISG15 immunoprecipitation followed by WB for NMIIA using total extract from MCF-7 cells.

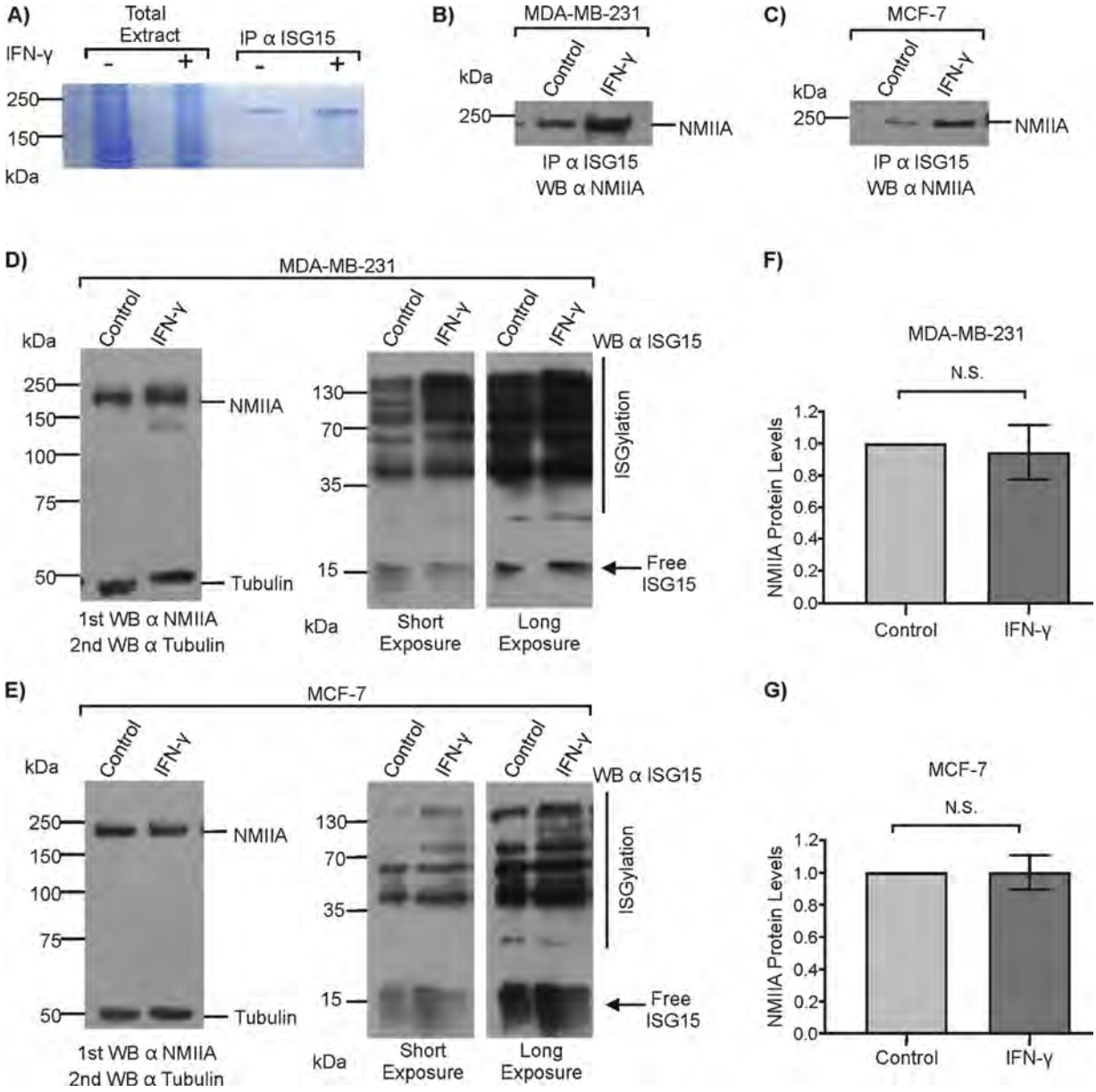

Fig. 6. Association between interferon-stimulated gene 15 (ISG15) and non-muscle myosin IIA (NMIIA) is increased by interferon γ (IFN-γ) treatment in breast cancer cells.

A) Coomassie staining of interferon-stimulated gene 15 (ISG15) immunoprecipitated complexes from MDA-MB-231 lysates treated or not treated with interferon γ (IFN-γ) (100 ng/mL) for 24 h. The band approximately 230 kDa in size that corresponds to NMIIA is enhanced in response to IFN-γ treatment. B) Endogenous ISG15 immunoprecipitation followed by western blotting (WB) for non-muscle myosin IIA (NMIIA), using total extract from MDA-MB-231 and C) MCF-7 cells treated or not treated with IFN-γ (100 ng/mL). D) and E) Total extract MDA-MB-231 and MCF-7 cells treated or not treated with IFN-γ (100 ng/mL) were analyzed by WB for NMIIA and ISG15, using tubulin as a loading control. F) and G) Densitometry of NMIIA protein levels in MDA-MB-231 and MCF-7 treated or not treated with IFN-γ. Not significant was indicated as N.S.

of MDA-MB-231 cells. We seeded cells in wells that were uncoated or coated with the fibronectin (FN) extracellular protein for 30 and 120 min. The early stage of spreading was detected at 30 min, whereas a well-defined spreading was observed at 120 min in the MDA-MB-231 cells seeded on FN in comparison with those seeded in uncoated wells (Fig. 9A and B). Since the later stages of cell spreading involve actin polymerization and myosin contraction, we analyzed the co-localization of NMIIA and ISG15, 120 min after seeding of MDA-MB-231 cells on glass treated with FN. ISG15 displayed mainly an extranuclear distribution that included its presence in lamellar margin, whereas NMIIA was detected completely as an extranuclear protein enriched in the lamellar margin. The collective results indicated that both proteins can co-localize during cell spreading, suggesting that ISG15-NMIIA association can occur in the marginal spreading lamellar region of MDA-MB-231 cells, as well as in more central regions in the cytoplasm of these cells during this event (Fig. 9C, arrowheads). Our results indicate that ISG15 and, NMIIA co-localize in the cytoplasm and lamellar region, and suggest that the association between these proteins may be critical in NMIIA-driven protrusive spreading events, in addition to the formation of focal adhesion complexes with the extracellular matrix.

3. Discussion

In contrast to other posttranslational modifications, ISGylation has not been extensively studied. This modification occurs when ISG15, an ubiquitin-like protein, is covalently bound to target proteins through an

INFORME DE LABORES 2019

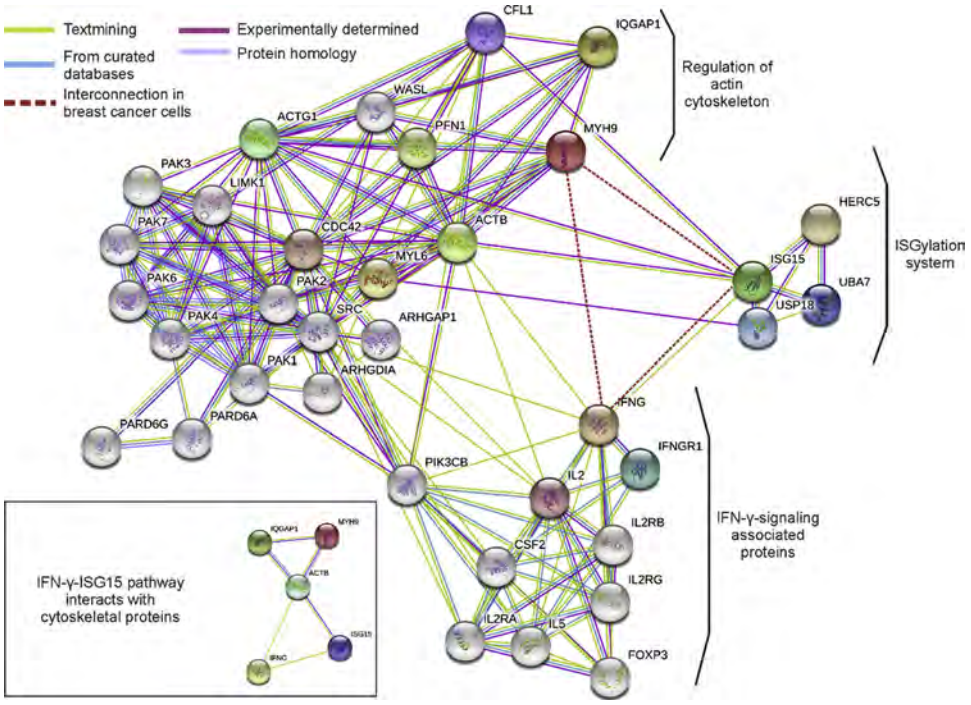

Fig. 7. Interconnection between interferon γ (IFN-γ) pathway, ISGylation system, and non-muscle myosin IIA (NMIIA).
Relationship between interferon γ (IFN-γ), interferon-stimulated gene 15 (ISG15), NMIIA. Analysis using STRING. Known interactions from curated databases, text mining, experimental determination, and protein homology are indicated in blue, green, purple, and dark blue lines, respectively. Connection of functional interactomes for IFN-γ, ISGylation system, NMIIA, and other proteins linked to cytoskeleton dynamic, is shown. Dashed red line indicates the interconnections suggested by our data.

enzymatic system similar to ubiquitination. A small number of candidate proteins have been proposed as ISGylation targets, and an even smaller number of ISGylated proteins have been studied mechanistically and functionally, including FILAMIN B, proliferating cell nuclear antigen (PCNA), IQGAP1, PARKIN, and C-terminus of Hsc70-interacting protein (CHIP). ISG15-dependent regulation of these proteins has important biological implications through modulating the stability and/or interactions of these proteins. Moreover, poly-ISGylation is not common as most proteins are mono or di-ISGylated (Jeon et al., 2009; Cerikan and Schiebel, 2017; Im et al., 2016; Park et al., 2014; Yoo et al., 2018).

ISG15 is upregulated in several cancer types, including breast cancer that has a characteristic profile of free ISG15 and ISGylation levels increased by IFN-γ (Tecalco Cruz and Mejia-Barreto, 2017; Tecalco-Cruz and Cruz-Ramos, 2018). However, proteins identified as ISGylation targets in this cancer are currently not studied. Here, we showed that NMIIA was endogenously associated with ISG15 in breast cancer cells using MS. This protein of high molecular weight (230 kDa) is important, as it is an element of actomyosin, participating in the cytoskeletal organization. Interestingly, our analysis indicated that *MHY9* expression was not altered in all mammary tumors compared to normal tissue, suggesting that posttranslational modifications might play a central role in regulating the NMIIA function. Bioinformatics analyses also showed many target sites in NMIIA for several different modifications that appeared to be critical in breast cancer. For example, NMIIA phosphorylation has been related to the contraction of actin filaments in the formation of protrusions and migration (Dulyaninova et al., 2007).

We identified NMIIA as an ISG15-interacting protein. This interaction occurred covalently in breast cancer cells. The results showed a migration for the band corresponding to ISG15-NMIIA interaction, revealing a band discretely higher than the detected band for NMIIA in total extracts. Our result was also validated by several co-immunoprecipitation assays using cell lines with high levels of conjugated ISG15. However, free ISG15 was not detectable, suggesting that proteins associated with ISG15 in these cells were ISGylated. In addition, our results are reinforced in part by a previous report that suggests that one of the several candidate proteins of ISGylation is NMIIA, confirming this covalent interaction in a non-endogenous system in 293T cells (Giannakopoulos et al., 2005). Thus, we showed an endogenous covalent association between ISG15 and NMIIA in breast cancer cells and demonstrated that this ISGylation of NMIIA was positively regulated by IFN-γ.

What is the function of ISGylation? It is a question not easily to understand so far, since this modification has been related to increased or decreased protein stability, and with stability-independent actions as the modulation of protein-protein interactions. Importantly, it has been reported that the NMIIA modification by monoubiquitination regulates its protein-protein interactions more than its stability or other functional aspects (Li et al., 2016). This is relevant because we show that the interaction between ISG15 ubiquitin-like protein and NMIIA in response to IFN-γ treatment has no effect on the abundance of this myosin but may affect its association with its protein partners. This observation is also supported by the fact that ISGylation alters some protein-protein interactions. For instance, FILAMIN B that binds actin and connects actin filaments to the cell membrane is also a scaffold for IFN-β signaling. Interestingly, IFN-β induces FILAMIN B ISGylation, and as a result, Ras-related C3 botulinum toxin substrate 1 (RAC1), MEKK1, and MKK4 are dissociated from FILAMIN B, thus blocking the activation of c-Jun N-terminal kinases (JNK) signaling. This occurs without any changes in FILAMIN B stability (Jeon et al., 2009). Moreover, ISGylation seems to be an important regulator of cytoskeleton dynamic as other proteins that participate in this process like IQGAP1 are modulated by this modification (Cerikan and Schiebel, 2017; Cerikan et al., 2016).

Hence, ISGylation is associated with stability and degradation of some proteins but also acts as a regulator of interactions between proteins. Therefore, NMIIA ISGylation may participate in modulating protein-protein interactions. The interactome analysis of NMIIA showed that many of its protein partners were related to cytoskeletal proteins and/or signaling and regulation of the actin cytoskeleton. Thus, NMIIA ISGylation induced by IFN-γ may affect the association between NMIIA and other cytoplasmic proteins involved in cytoskeletal remodeling. Furthermore, our data suggest that IFN-γ increases ISG15 levels and the ISGylation of its target proteins, including NMIIA. For this reason, the transfection of the ISGylation system also promoted an increase in the ISG15-NMIIA association. This association was apparent in the cytoplasm and perinuclear region of breast cancer cells. The increase of

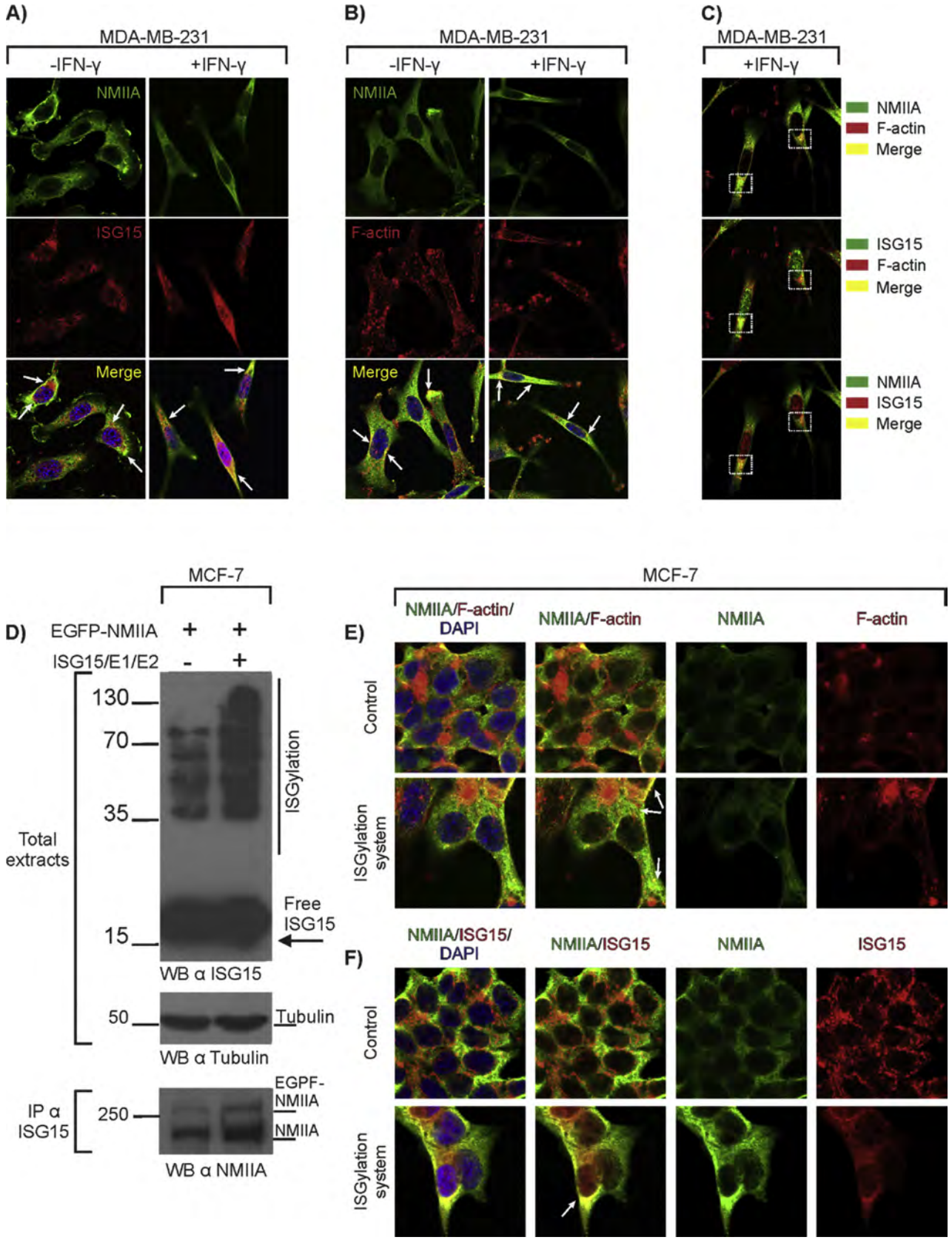

Fig. 8. Association induced by IFN-γ and the ISGylation system of non-muscle myosin IIA (NMIIA) and interferon-stimulated gene 15 (ISG15) is implicated in the morphology of breast cancer cells.

A-C) Evaluation of the subcellular distribution of NMIIA, and F-actin and/or interferon-stimulated gene 15 (ISG15) in MDA-MB-231 cells that were untreated or treated with IFN-γ using an immunofluorescence assay. D) Enhanced green fluorescent protein-non-muscle myosin IIA (EGFP-NMIIA) was expressed with or without ISG15 and E1 and E2 enzyme in MCF-7 cells. ISG15 and Tubulin were detected by western blotting (WB). Endogenous ISG15 immunoprecipitation was followed by WB for non-muscle myosin IIA (NMIIA), using total extract from MCF-7 cells. E and F) Immunofluorescence assay of the subcellular distribution of NMIIA and F-actin or interferon-stimulated gene 15 (ISG15) in control MCF-7 cells or cells expressing ISG15 and ISGylation system. Arrowheads, co-localization of NMIIA, ISG15 or F-

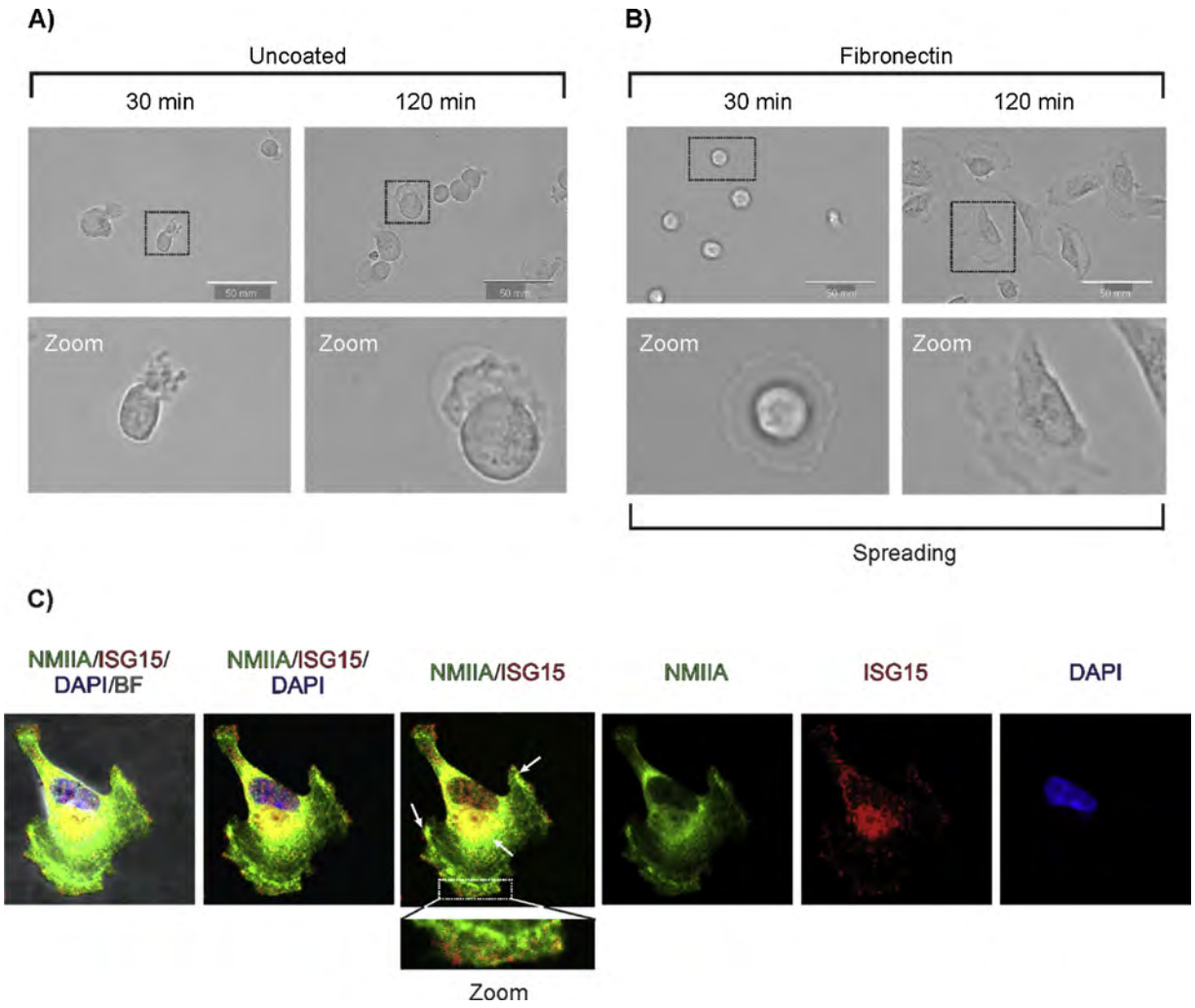

Fig. 9. Association of non-muscle myosin IIA (NMIIA) and interferon-stimulated gene 15 (ISG15) is implicated in the spreading of breast cancer cells induced by fibronectin (FN).

A and B) MDA-MB-231 cells were seeded in uncoated wells or wells coated with fibronectin (FN) and analyzed after 30 or 120 min. C) Immunofluorescence assay of the distribution and co-localization of NMIIA and ISG15 in MDA-MB-231 cells seeded in FN-coated wells after 120 min. Arrowheads and zoom image show co-localization regions.

ISG15-NMIIA association was accompanied by a more elongated morphology of the MDA-MB-231 cells (Fig. 8A–C), as well as with the formation of stress fibers of F-actin in MCF-7 cells (Fig. 8E). Thus, ISGylation of NMIIA may have implications in actin-cytoskeleton remodeling.

The dynamics of the cytoskeleton is also important in cell spreading, which is modulated by myosin proteins, and represents a critical step for the attachment and detachment of the cells with the substrate, a central event in cell migration. NMIIA and NMIIB are enriched in the lamellar margin. However, their functions are unclear. It has been suggested that they may have an opposite effect on spreading, with NMIIB promoting cell spreading (Betapudi, 2010; Betapudi et al., 2006; Cai et al., 2006). Interestingly, the ISG15-NMIIA association seems to occur in the spreading of breast cancer cells induced by FN, and this association is specific for NMIIA, but not for NMIIB. In addition, FN may induce *ISG15* expression and protein ISGylation via integrin-dependent signaling (Hermann et al., 2016).

Our findings are relevant since they open new avenues to understand ISG15 as a regulator of the NMIIA as a motor of the F-actin, and its effects in the spreading and migration of breast cancer cells, and its modulation by interferons and proteins of extracellular matrix as FN.

NMIIA has a high identity percentage with NMIIB and NMIIC isoforms (79% and 65%, respectively). Because NMIIA is a protein with high molecular weight, containing 10.56% lysine residues, there are many possible lysine residues for ISGylation. Our MS results identifying NMIIA suggest that lysines only in NMIIA but not in NMIIB and NMIIC may be involved in this covalent interaction. The generation of mutants of NMIIA to block its ISGylation may help to understand the function of this modification in NMIIA in breast cancer cells.

In conclusion, we have identified NMIIA as an endogenously and covalently ISG15-associated protein in the cytoplasm of breast cancer cells. NMIIA is modified by ISGylation, and this modification may regulate its protein-protein interactions, including its association with F-actin for cytoskeletal reorganization. IFN-γ treatment increases ISGylation of NMIIA and promotes changes in the morphology of breast cancer cells with the formation of stress fibers. The FN extracellular matrix protein may induce ISG15 expression and increases the ISGylation of NMIIA. This ISG15-NMIIA association seems also occur in the FN-induced and NMII-modulated spreading of MDA-MB-231 cells (Fig. 10). This new link between IFN-γ, ISGylation, and cytoskeletal proteins may be important in the progression of some cancers such as breast cancer.

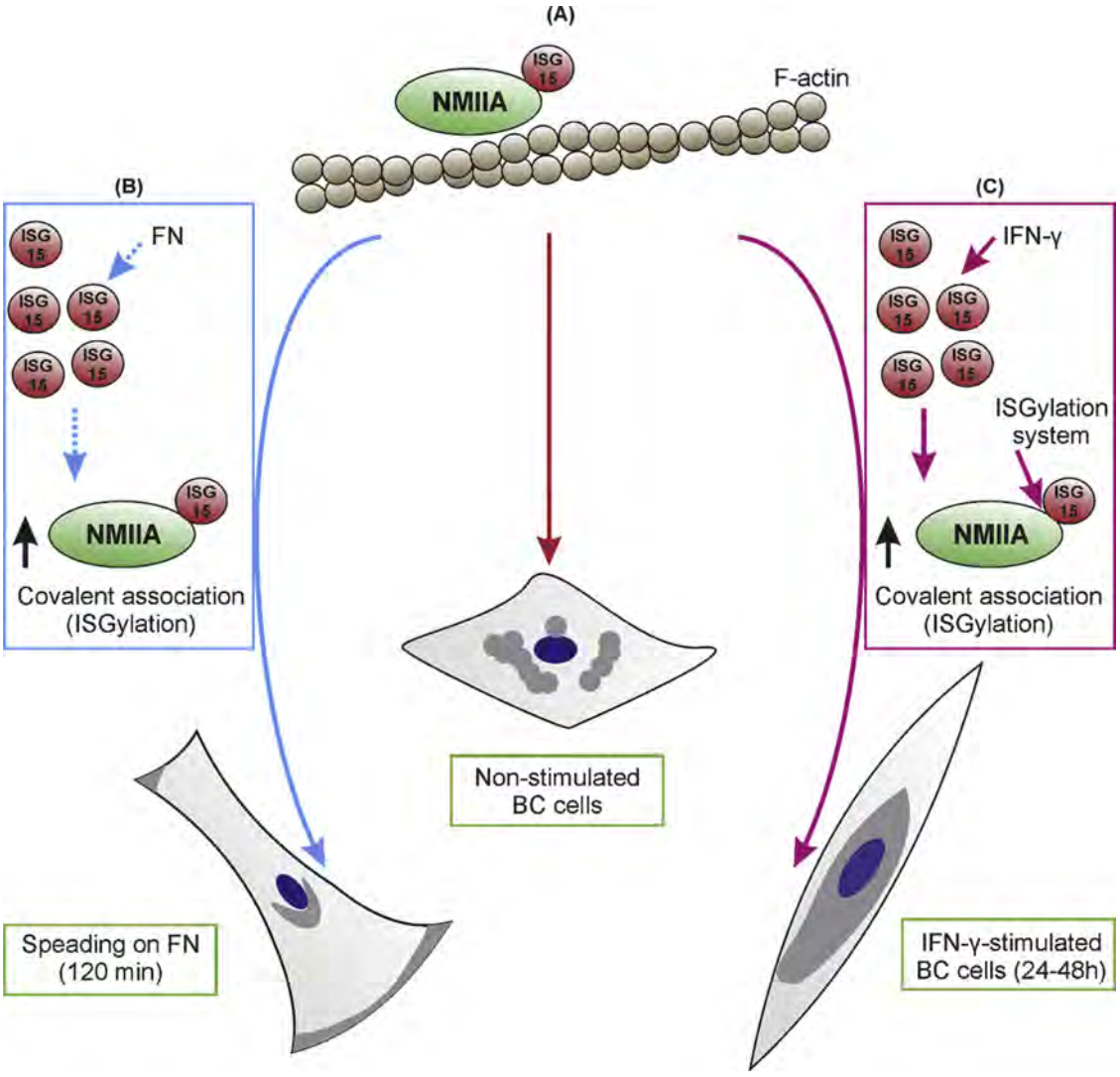

Fig. 10. Proposed model.
NMIIA is covalently associated with ISG15 in breast cancer cells. A) This modification of NMIIA by ISGylation may modulate the *actomyosin complex* (NMIIA-F-actin), which affects the reorganization of cytoskeleton and consequently the morphology of the cells. B) Extracellular matrix proteins like FN seem to induce *ISG15* expression, with subsequently increased NMIIA ISGylation. These events may be critical in FN-induced cell spreading, in which actomyosin activity is also required. C) In response to IFN-γ, *ISG15* expression and NMIIA ISGylation are increased, and changes in the cell morphology associated with F-actin organization are produced. These events are also generated by the overexpression of the ISGylation system. Thus, NMIIA ISGylation may have central implications in the proliferation and migration of mammary tumor cells. BC: breast cancer. In gray: ISG15, NMIIA and actin co-localization.

4. Materials and methods

4.1. Cell lines and reagents

The AD293 human embryonic kidney cell line and the MDA-MB-231 (ERα−, triple negative) and MCF-7 (ERα+) breast cancer cell lines were maintained in Dulbecco's modified Eagle's medium supplemented with 5% fetal bovine serum and penicillin/streptomycin. Recombinant human IFN-γ (285-IF-00) was obtained from R&D systems. Culture media were obtained from Invitrogen, and reagents were obtained from Sigma-Aldrich, AMRESCO-VWR, and Bio-Rad.

4.2. Plasmids and transfections

The pEGFPMIIAC3 plasmid was a gift from Dr. Anne R. Bresnick (Albert Einstein College of Medicine, USA) and plasmids pCAGGS-5HA-mISG15, pFlagCMV2-UbcH8, and pCAGGS-HA-hUBE1L were a gift from Dr. Dong-Er Zhang (Department of Pathology, Moores Cancer Center University of California, San Diego). AD293 or MCF-7 cells were seeded and grown to 80% confluence for transient transfection with plasmid DNA using the Lipofectamine 2000 system, according to the manufacturer's instructions (Invitrogen).

4.3. Total, cytoplasmic, and nuclear extract preparation

To obtain total extracts, cells were lysed with TNTE buffer (50 mM Tris−HCl, 150 mM NaCl, 5 mM ethylenediaminetetraacetic acid (EDTA), and 0.5% Triton-X-100) or radioimmunoprecipitation assay (RIPA) buffer (50 mM Tris−HCl pH 7.4, 150 mM NaCl, 1 mM EDTA, 0.5% deoxycholic acid, 1% NP-40, and 0.1% SDS) containing protease and phosphatase inhibitors. Subcellular fractionation was performed to obtain nuclear and cytoplasmic fractions, as described previously (Tecalco Cruz and Mejia-Barreto, 2017; Grewal et al., 2000). Briefly, cells were homogenized in homogenization buffer (250 mM sucrose, 3 mM imidazole, and protease and phosphatase inhibitors), passed through a 22−gauge needle 15 times for MDA-MB-231 cells and 12 times for MCF-7 cells, and then centrifuged at 700 × *g* for 10 min. The supernatant (cytoplasmic fraction) was separated from the pellet

INFORME DE LABORES 2019

(nuclear fraction). Both fractions were lysed with RIPA buffer at 4 °C for 1 h. Protein extracts were quantified using the Bradford method for the WB and immunoprecipitation assays.

4.4. Immunoprecipitation, Coomassie staining, and MS

Immunoprecipitation assays were performed with 0.6 or 1 µg of anti-ISG15 and anti-NMIIA antibodies, respectively. Immunoprecipitated complexes in Laemmli solution were separated by SDS-PAGE, followed by Coomassie Blue G staining for the selection of bands for MS analysis. The MS service from Instituto Nacional de Medicina Genómica (INMEGEN), Unidad de Proteómica, was utilized. The visible band was manually cut and reduced with dithiothreitol (DTT) 10 mM, alquilated with iodoacetamide 100 mM and destained with acetonitrile (ACN) (NH_4HCO_3 50 mM, 50:50 v/v). Protein digestion was carried out for 18 h at 37 °C with trypsin (Promega V528 A). The obtained peptides were extracted (ACN:H2O:formic acid, 50:45:5), the volume was reduced in a concentrator, and the sample was desalinated using a column C18 (ZipTipC18). The sample was loaded 6-fold using alpha-cyano as a matrix and analyzed using a MALDITOF/TOF 4800. A search was performed with the obtained MS/MS spectrums, using the Paragon algorithm from the software ProteinPilot.

4.5. Co-immunoprecipitation assays and WB

Cells were lysed using RIPA or TNTE lysis buffer as described previously (Tecalco-Cruz and Cruz-Ramos, 2018). Proteins were immunoprecipitated with specific anti–ISG15 (Santa Cruz Biotechnology), anti–NMIIA (Sigma-Aldrich), or anti–GFP (Clontech) antibodies. The immunoprecipitated proteins were separated by SDS-PAGE, followed by immunoblotting with specific primary antibodies (anti–GFP, anti-NMIIA, or anti-ISG15). The experiments were performed in triplicate, and representative images were shown. For analysis of total, cytoplasmic, and nuclear extracts, 25–100 µg of protein lysates were used. Protein lysates were separated by SDS-PAGE and then subjected to immunoblotting with anti-ISG15 (1:1000) (F-9, sc-166755), anti-α-tubulin (1:3000) (B7, sc-5286) obtained from Santa-Cruz Biotechnology, anti-lamin B1 (1:2000) obtained from Cell Signaling (D4Q4Z), anti-NMIIA (1:3000) (M8064), and anti-EGFP (1:3000) (632592) obtained from ClonTech. A secondary anti-rabbit IgG antibody was used (1:10,000 for anti-lamin and anti-GFP, 1:25,000 for anti-NMIIA) (sc-2004; Santa Cruz Biotechnology) as well as peroxidase AffiniPure goat anti-mouse (1:10,000 for anti-tubulin and anti-ISG15) (115-035-003, Jackson). Protein detection was performed using SuperSignal West Pico Chemiluminescent Substrates (Thermo Fisher Scientific) or Immobilon Western (Millipore). All experiments were performed in triplicate.

4.6. Immunofluorescence assay

Cells were seeded on glass coverslips coated with poly-L-lysine in 6-well plates. The cells were fixed in 4% paraformaldehyde for 10 min and then permeabilized with 0.1% Triton X-100 for 10 min. After blocking with 1% albumin for 1 h, cells were incubated overnight with anti-ISG15 (F-9, sc-166755; 1:100) and anti-NMIIA (M8064). After primary incubation, cells were washed and incubated with Alexa Fluor 647 anti-mouse IgG secondary antibody (ab150107, Abcam; 1:750) and Alexa Fluor 488 anti-rabbit IgG secondary antibody (ab150073, Abcam; 1:500) for 1 h in the dark. The slides were prepared with ProLong Diamond Antifade Mountant with 4′,6-diamidino-2-phenylindole (DAPI) (Invitrogen). For phalloidin assays (F-actin detection), after blocking, the cells were incubated for 1 h with phalloidin (1:40) and mounted with DAPI solution. An Olympus IX2 and FV10i confocal laser-scanning microscopes were used to visualize the cells, and ImageJ software was used for the imaging, processing, and analysis of results.

4.7. Spreading assays

MDA-MB-231 cells were seeded on wells or glass coverslips in 6-well plates treated with FN (25 mg/mL) for 1 h. After 30 or 120 min following seeding, cells were fixed and visualized, or were prepared for immunofluorescence assay. Cell morphology was evaluated using an Invitrogen EVOS FL Cell Imaging System. Co-localization was analyzed using an Olympus FV10i confocal laser scanning microscope.

4.8. Bioinformatics

The cancer microarray database Oncomine (www.oncomine.org) was consulted to analyze *MYH9* expression in patient-derived mammary tumors and normal mammary tissue. The analysis of post-translational modifications for NMIIA was performed with PhosphoSite (Hornbeck et al., 2015) (www.phosphosite.org), and analysis of protein-protein interactions for NMIIA was carried out using STRING 10.5 version (https://string-db.org/cgi/network.pl) (Szklarczyk et al., 2017).

4.9. Statistical analysis

Statistical analysis was performed with Student's *t*-test using GraphPad Prism 5 software (GraphPad). Densitometry for WB assays were performed using Fiji-ImageJ. Results were expressed as significant when $p < 0.05$ (*), $p < 0.01$ (**) and $p < 0.001$ (***). Not significant is described as N.S.

Author contributions

E.C.-R. performed the experiments and prepared some figures. M.M.-S. participated in the data analysis. A. S-H performed a colocalization analysis and prepared the figures. A.C.T.-C. designed research, the bioinformatics analysis, some WB, and wrote the manuscript.

Funding

This work was supported by the DGAPA-UNAM (grant numbers PAPIIT-IA200916 to A.C.T.-C.).

Acknowledgements

We appreciate the kind gift from Dr. Anne R. Bresnick (Albert Einstein College of Medicine, USA) of the NMIIA plasmid, as well as, the kind gifts from Dr. Dong-Er Zhang (Department of Pathology, Moores Cancer Center University of California, San Diego) of the ISGylation system plasmids used in this work. We thank Dr. Josué O. Ramírez Jarquín for his technical support (Instituto de Fisiología Celular, UNAM). We thank Dr. Miguel Tapia Rodríguez (Instituto de Investigaciones Biomédicas, Unidad de Microscopia, UNAM) for his technical support in analyzing the immunofluorescence. We also thank Dr. Sergio Agustín Román González (INMEGEN, Unidad de Proteómica) for mass spectrometry service. We thank Dr. Claudia Rivera Cerecedo for her comments (Instituto de Fisiología Celular, UNAM).

References

Basters, A., Geurink, P.P., El Oualid, F., Ketscher, L., Casutt, M.S., Krause, E., Ovaa, H., Knobeloch, K.P., Fritz, G., 2014. Molecular characterization of ubiquitin-specific protease 18 reveals substrate specificity for interferon-stimulated gene 15. FEBS J. 281 (7), 1918–1928.

Betapudi, V., 2010. Myosin II motor proteins with different functions determine the fate of lamellipodia extension during cell spreading. PLoS One 5 (1), e8560.

Betapudi, V., Licate, L.S., Egelhoff, T.T., 2006. Distinct roles of nonmuscle myosin II isoforms in the regulation of MDA-MB-231 breast cancer cell spreading and migration. Cancer Res. 66 (9), 4725–4733.

Burks, J., Reed, R.E., Desai, S.D., 2014. ISGylation governs the oncogenic function of Ki-Ras in breast cancer. Oncogene 33 (6), 794–803.

Burks, J., Reed, R.E., Desai, S.D., 2015. Free ISG15 triggers an antitumor immune response against breast cancer: a new perspective. Oncotarget 6 (9), 7221–7231.
Cai, Y., Biais, N., Giannone, G., Tanase, M., Jiang, G., Hofman, J.M., Wiggins, C.H., Silberzan, P., Buguin, A., Ladoux, B., Sheetz, M.P., 2006. Nonmuscle myosin IIA-dependent force inhibits cell spreading and drives F-actin flow. Biophys. J. 91 (10), 3907–3920.
Cerikan, B., Schiebel, E., 2017. DOCK6 inactivation highlights ISGylation as RHO-GTPase balancer. Cell Cycle 16 (4), 304–305.
Cerikan, B., Shaheen, R., Colo, G.P., Glasser, C., Hata, S., Knobeloch, K.P., Alkuraya, F.S., Fassler, R., Schiebel, E., 2016. Cell-intrinsic adaptation arising from chronic ablation of a key Rho GTPase regulator. Dev. Cell 39 (1), 28–43.
Chen, R.H., Du, Y., Han, P., Wang, H.B., Liang, F.Y., Feng, G.K., Zhou, A.J., Cai, M.Y., Zhong, Q., Zeng, M.S., Huang, X.M., 2016. ISG15 predicts poor prognosis and promotes cancer stem cell phenotype in nasopharyngeal carcinoma. Oncotarget 7 (13), 16910–16922.
D'Cunha, J., Knight Jr, E., Haas, A.L., Truitt, R.L., Borden, E.C., 1996. Immunoregulatory properties of ISG15, an interferon-induced cytokine. Proc. Natl. Acad. Sci. U. S. A. 93 (1), 211–215.
Dastur, A., Beaudenon, S., Kelley, M., Krug, R.M., Huibregtse, J.M., 2006. Herc5, an interferon-induced HECT E3 enzyme, is required for conjugation of ISG15 in human cells. J. Biol. Chem. 281 (7), 4334–4338.
Desai, S.D., Haas, A.L., Wood, L.M., Tsai, Y.C., Pestka, S., Rubin, E.H., Saleem, A., Nur, E.K.A., Liu, L.F., 2006. Elevated expression of ISG15 in tumor cells interferes with the ubiquitin/26S proteasome pathway. Cancer Res. 66 (2), 921–928.
Desai, S.D., Reed, R.E., Burks, J., Wood, L.M., Pullikuth, A.K., Haas, A.L., Liu, L.F., Breslin, J.W., Meiners, S., Sankar, S., 2012. ISG15 disrupts cytoskeletal architecture and promotes motility in human breast cancer cells. Exp. Biol. Med. 237 (1), 38–49.
Dulyaninova, N.G., House, R.P., Betapudi, V., Bresnick, A.R., 2007. Myosin-IIA heavy-chain phosphorylation regulates the motility of MDA-MB-231 carcinoma cells. Mol. Biol. Cell 18 (8), 3144–3155.
Fan, J.B., Arimoto, K., Motamedchaboki, K., Yan, M., Wolf, D.A., Zhang, D.E., 2015. Identification and characterization of a novel ISG15-ubiquitin mixed chain and its role in regulating protein homeostasis. Sci. Rep. 5, 12704.
Feng, Q., Sekula, D., Guo, Y., Liu, X., Black, C.C., Galimberti, F., Shah, S.J., Sempere, L.F., Memoli, V., Andersen, J.B., Hassel, B.A., Dragnev, K., Dmitrovsky, E., 2008. UBE1L causes lung cancer growth suppression by targeting cyclin D1. Mol. Cancer Ther. 7 (12), 3780–3788.
Giannakopoulos, N.V., Luo, J.K., Papov, V., Zou, W., Lenschow, D.J., Jacobs, B.S., Borden, E.C., Li, J., Virgin, H.W., Zhang, D.E., 2005. Proteomic identification of proteins conjugated to ISG15 in mouse and human cells. Biochem. Biophys. Res. Commun. 336 (2), 496–506.
Gooch, J.L., Herrera, R.E., Yee, D., 2000. The role of p21 in interferon gamma-mediated growth inhibition of human breast cancer cells. Cell Growth Different.: Mol. Biol. J. Am. Assoc. Cancer Res. 11 (6), 335–342.
Grewal, T., Heeren, J., Mewawala, D., Schnitgerhans, T., Wendt, D., Salomon, G., Enrich, C., Beisiegel, U., Jackle, S., 2000. Annexin VI stimulates endocytosis and is involved in the trafficking of low density lipoprotein to the prelysosomal compartment. J. Biol. Chem. 275 (43), 33806–33813.
Hermann, M.R., Jakobson, M., Colo, G.P., Rognoni, E., Jakobson, M., Kupatt, C., Posern, G., Fassler, R., 2016. Integrins synergise to induce expression of the MRTF-A-SRF target gene ISG15 for promoting cancer cell invasion. J. Cell. Sci. 129 (7), 1391–1403.
Hornbeck, P.V., Zhang, B., Murray, B., Kornhauser, J.M., Latham, V., Skrzypek, E., 2015. PhosphoSitePlus, 2014: mutations, PTMs and recalibrations. Nucleic Acids Res. 43, D512–20 (Database issue).
Huang, Y.F., Bulavin, D.V., 2014. Oncogene-mediated regulation of p53 ISGylation and functions. Oncotarget 5 (14), 5808–5818.
Im, E., Yoo, L., Hyun, M., Shin, W.H., Chung, K.C., 2016. Covalent ISG15 conjugation positively regulates the ubiquitin E3 ligase activity of parkin. Open Biol. 6 (8).
Jeon, Y.J., Choi, J.S., Lee, J.Y., Yu, K.R., Kim, S.M., Ka, S.H., Oh, K.H., Kim, K.I., Zhang, D.E., Bang, O.S., Chung, C.H., 2009. ISG15 modification of filamin B negatively regulates the type I interferon-induced JNK signalling pathway. EMBO Rep. 10 (4), 374–380.
Kim, K.I., Giannakopoulos, N.V., Virgin, H.W., Zhang, D.E., 2004. Interferon-inducible ubiquitin E2, Ubc8, is a conjugating enzyme for protein ISGylation. Mol. Cell. Biol. 24 (21), 9592–9600.
Knight Jr, E., Cordova, B., 1991. IFN-induced 15-kDa protein is released from human lymphocytes and monocytes. J. Immunol. 146 (7), 2280–2284.
Legrier, M.E., Bieche, I., Gaston, J., Beurdeley, A., Yvonnet, V., Deas, O., Thuleau, A., Chateau-Joubert, S., Servely, J.L., Vacher, S., Lassalle, M., Depil, S., Tucker, G.C., Fontaine, J.J., Poupon, M.F., Roman-Roman, S., Judde, J.G., Decaudin, D., Cairo, S., Marangoni, E., 2016. Activation of IFN/STAT1 signalling predicts response to chemotherapy in oestrogen receptor-negative breast cancer. Br. J. Cancer 114 (2), 177–187.
Li, T., Giagtzoglou, N., Eberl, D.F., Jaiswal, S.N., Cai, T., Godt, D., Groves, A.K., Bellen, H.J., 2016. The E3 ligase Ubr3 regulates Usher syndrome and MYH9 disorder proteins in the auditory organs of Drosophila and mammals. eLife 5.
Liu, M., Li, X.L., Hassel, B.A., 2003. Proteasomes modulate conjugation to the ubiquitin-like protein, ISG15. J. Biol. Chem. 278 (3), 1594–1602.
Malakhova, O.A., Yan, M., Malakhov, M.P., Yuan, Y., Ritchie, K.J., Kim, K.I., Peterson, L.F., Shuai, K., Zhang, D.E., 2003. Protein ISGylation modulates the JAK-STAT signaling pathway. Genes Dev. 17 (4), 455–460.
Mao, H., Wang, M., Cao, B., Zhou, H., Zhang, Z., Mao, X., 2016. Interferon-stimulated gene 15 induces cancer cell death by suppressing the NF-kappaB signaling pathway. Oncotarget 25 (7), 70143–70151 43.
Newell-Litwa, K.A., Horwitz, R., Lamers, M.L., 2015. Non-muscle myosin II in disease: mechanisms and therapeutic opportunities. Dis. Model. Mech. 8 (12), 1495–1515.
Ning, Y., Riggins, R.B., Mulla, J.E., Chung, H., Zwart, A., Clarke, R., 2010. IFNgamma restores breast cancer sensitivity to fulvestrant by regulating STAT1, IFN regulatory factor 1, NF-kappaB, BCL2 family members, and signaling to caspase-dependent apoptosis. Mol. Cancer Ther. 9 (5), 1274–1285.
Niu, X.L., Wang, Y., Yao, Z., Duan, H., Li, Z., Liu, W., Zhang, H., Deng, W.M., 2015. Autocrine interferon-gamma may affect malignant behavior and sensitivity to tamoxifen of MCF-7 via estrogen receptor beta subtype. Oncol. Rep. 34 (6), 3120–3130.
Okumura, F., Zou, W., Zhang, D.E., 2007. ISG15 modification of the eIF4E cognate 4EHP enhances cap structure-binding activity of 4EHP. Genes Dev. 21 (3), 255–260.
Ouderkirk, J.L., Krendel, M., 2014. Non-muscle myosins in tumor progression, cancer cell invasion, and metastasis. Cytoskeleton 71 (8), 447–463.
Padovan, E., Terracciano, L., Certa, U., Jacobs, B., Reschner, A., Bolli, M., Spagnoli, G.C., Borden, E.C., Heberer, M., 2002. Interferon stimulated gene 15 constitutively produced by melanoma cells induces e-cadherin expression on human dendritic cells. Cancer Res. 62 (12), 3453–3458.
Park, J.M., Yang, S.W., Yu, K.R., Ka, S.H., Lee, S.W., Seol, J.H., Jeon, Y.J., Chung, C.H., 2014. Modification of PCNA by ISG15 plays a crucial role in termination of error-prone translesion DNA synthesis. Mol. Cell 54 (4), 626–638.
Recht, M., Borden, E.C., Knight Jr, E., 1991. A human 15-kDa IFN-induced protein induces the secretion of IFN-gamma. J. Immunol. 147 (8), 2617–2623.
Satake, H., Tamura, K., Furihata, M., Anchi, T., Sakoda, H., Kawada, C., Iiyama, T., Ashida, S., Shuin, T., 2010. The ubiquitin-like molecule interferon-stimulated gene 15 is overexpressed in human prostate cancer. Oncol. Rep. 23 (1), 11–16.
Swaim, C.D., Scott, A.F., Canadeo, L.A., Huibregtse, J.M., 2017. Extracellular ISG15 signals cytokine secretion through the LFA-1 integrin receptor. Mol. Cell 68 (3), 581–590 e5.
Szklarczyk, D., Morris, J.H., Cook, H., Kuhn, M., Wyder, S., Simonovic, M., Santos, A., Doncheva, N.T., Roth, A., Bork, P., Jensen, L.J., von Mering, C., 2017. The STRING database in 2017: quality-controlled protein-protein association networks, made broadly accessible. Nucleic Acids Res. 45 (D1), D362–D368.
Tecalco Cruz, A.C., Mejia-Barreto, K., 2017. Cell type-dependent regulation of free ISG15 levels and ISGylation. J. Cell Commun. Signal. 11 (2), 127–135.
Tecalco-Cruz, A.C., 2018. Molecular pathways involved in the transport of nuclear receptors from the nucleus to cytoplasm. J. Steroid Biochem. Mol. Biol. 178, 36–44.
Tecalco-Cruz, A.C., Cruz-Ramos, E., 2018. Protein ISGylation and free ISG15 levels are increased by interferon gamma in breast cancer cells. Biochem. Biophys. Res. Commun. 499 (4), 973–978.
Tecalco-Cruz, A.C., Ramirez-Jarquin, J.O., 2017. Mechanisms that increase stability of estrogen receptor alpha in breast cancer. Clin. Breast Cancer 17 (1), 1–10.
Wan, X.X., Chen, H.C., Khan, M.A., Xu, A.H., Yang, F.L., Zhang, Y.Y., Zhang, D.Z., 2013. ISG15 inhibits IFN-alpha-resistant liver cancer cell growth. Biomed Res. Int.(2013), 570909.
Wong, J.J., Pung, Y.F., Sze, N.S., Chin, K.C., 2006. HERC5 is an IFN-induced HECT-type E3 protein ligase that mediates type I IFN-induced ISGylation of protein targets. Proc. Natl. Acad. Sci. U. S. A. 103 (28), 10735–10740.
Yoo, L., Yoon, A.R., Yun, C.O., Chung, K.C., 2018. Covalent ISG15 conjugation to CHIP promotes its ubiquitin E3 ligase activity and inhibits lung cancer cell growth in response to type I interferon. Cell Death Dis. 9 (2), 97.
Zhao, C., Beaudenon, S.L., Kelley, M.L., Waddell, M.B., Yuan, W., Schulman, B.A., Huibregtse, J.M., Krug, R.M., 2004. The UbcH8 ubiquitin E2 enzyme is also the E2 enzyme for ISG15, an IFN-alpha/beta-induced ubiquitin-like protein. Proc. Natl. Acad. Sci. U. S. A. 101 (20), 7578–7582.
Zou, W., Zhang, D.E., 2006. The interferon-inducible ubiquitin-protein isopeptide ligase (E3) EFP also functions as an ISG15 E3 ligase. J. Biol. Chem. 281 (7), 3989–3994.

INFORME DE LABORES 2019

Received: 30 June 2018 | Accepted: 4 September 2018

DOI: 10.1002/jcp.27474

Check for updates

ORIGINAL RESEARCH ARTICLE

WILEY Journal of Cellular Physiology

Cholesterol burden in the liver induces mitochondrial dynamic changes and resistance to apoptosis

Mayra Domínguez-Pérez[1,2,3] | Arturo Simoni-Nieves[1,2] | Patricia Rosales[2] | Natalia Nuño-Lámbarri[4] | Mónica Rosas-Lemus[5] | Verónica Souza[1,6] | Roxana U. Miranda[1,6] | Leticia Bucio[1,6] | Salvador Uribe Carvajal[5] | Jens U. Marquardt[7] | Daekwan Seo[8] | Luis E. Gomez-Quiroz[1,6] | María Concepción Gutiérrez-Ruiz[1,6]

[1]Laboratorio de Fisiología Celular, Departamento de Ciencias de la Salud, CBS Universidad Autónoma Metropolitana Iztapalapa, Mexico City, México

[2]Posgrado en Biología Experimental, DCBS, Universidad Autónoma Metropolitana Iztapalapa, Mexico City, México

[3]Laboratorio de Genómica de Enfermedades Cardiovasculares, Instituto Nacional de Medicina Genómica, Mexico City, México

[4]Unidad de Investigación Traslacional, Fundación Clínica Médica Sur, Mexico City, Mexico

[5]Departamento de Genética Molecular, Instituto de Fisiología Celular, UNAM, México City, Mexico

[6]Laboratorio de Medicina Experimental, Unidad de Medicina Translacional, Instituto de Investigaciones Biomédicas, UNAM/ Instituto Nacional de Cardiología Ignacio Chavez, Mexico City, Mexico

[7]First Department of Medicine, University Medical Center, Johannes Gutenberg University Mainz, Mainz, Germany

[8]Bioinformatics Department, Macrogen Corp, Rockville, Maryland,

Correspondence
María Concepción Gutiérrez-Ruiz, Departamento de Ciencias de la Salud, DCBS, Universidad Autónoma Metropolitana-Iztapalapa, Av. San Rafael Atlixco 186, Colonia Vicentina, Iztapalapa, D.F. 09340, México.
Email: mcgr@xanum.uam.mx

Funding information
Consejo Nacional de Ciencia y Tecnología, Grant/Award Numbers: CB-166042, CB252942; Universidad Autónoma Metropolitana Iztapalapa; SEP-PRODEP, Grant/Award Number: 913026-14612111

Abstract

Non-alcoholic fatty liver disease (NAFLD) encompasses a broad spectrum of histopathological changes ranging from non-inflammatory intracellular fat deposition to non-alcoholic steatohepatitis (NASH), which may progress into hepatic fibrosis, cirrhosis, or hepatocellular carcinoma. Recent data suggest that impaired hepatic cholesterol homeostasis and its accumulation are relevant to the pathogenesis of NAFLD/NASH. Despite a vital physiological function of cholesterol, mitochondrial dysfunction is an important consequence of dietary-induced hypercholesterolemia and was, subsequently, linked to many pathophysiological conditions. The aim in the current study was to evaluate the morphological and molecular changes of cholesterol overload in mouse liver and particularly, in mitochondria, induced by a high-cholesterol (HC) diet for one month. Histopathological studies revealed microvesicular hepatic steatosis and significantly elevated levels of liver cholesterol and triglycerides leading to impaired liver synthesis. Further, high levels of oxidative stress could be determined in liver tissue as well as primary hepatocyte culture. Transcriptomic changes induced by the HC diet involved disruption in key pathways related to cell death and oxidative stress as well as upregulation of genes related to glutathione homeostasis. Impaired liver function could be associated with a decrease in mitochondrial membrane potential and ATP content and significant alterations in mitochondrial dynamics. We demonstrate that cholesterol overload in the liver leads to mitochondrial changes which may render damaged hepatocytes proliferative and resistant to cell death whereby perpetuating liver damage.

KEYWORDS

apoptosis, cholesterol, mitochondrial dynamics, oxidative stress

 © 2018 Wiley Periodicals, Inc.

INFORME DE LABORES 2019

1 | INTRODUCTION

Non-alcoholic fatty liver disease (NAFLD) is the most common form of chronic liver disease (Lonardo et al., 2017). Patients with NAFLD are at high risk of developing inflammatory steatohepatitis (NASH) which can progress into fibrosis, cirrhosis, and ultimately, hepatocellular carcinoma (HCC; Calvisi et al., 2011). Several lines of evidence indicate that structural and functional alterations of mitochondria significantly contribute to changes of the cellular lipid metabolism as well as oxidant stress response. Consistently, mitochondrial dysfunction is frequently associated with the development of NAFLD (Auger, Alhasawi, Contavadoo, & Appanna, 2015; Serviddio & Sastre, 2010). Oxidative stress is one of the key mediators of hepatic damage and a major contributor to the progression from steatosis to NASH, particularly when mitochondria are compromised (Bellanti et al., 2018). Oxidative stress can result in various deleterious processes that stem from an imbalance between the excessive formation of pro-oxidants and the counteracting antioxidant mechanisms (Gomez-Quiroz, Gutierrez Ruiz, Marquardt, Factor, & Thorgeirsson, 2017). It is well known that mitochondrial dysfunction can be induced by dietary-induced hypercholesterolemia, leading to organ insufficiency or failure, particularly in the liver (Marí et al., 2006). Although mitochondria, particularly the inner membrane, only have low levels of cholesterol in the cell, cholesterol content is essential for the proper functionality of mitochondria (Garcia-Ruiz et al., 2009). Alterations in mitochondrial cholesterol have been associated with a wide range of pathological conditions, including steatosis and cancer (Enríquez-Cortina et al., 2017). Recently, it has been published that a high cholesterol (HC) diet (1.25% cholesterol) in combination with a high fat diet (60% cocoa butter) synergistically enables development and progression of NAFLD to NASH by a mechanism driven by cholesterol derivatives (oxysterols) in presence of free fatty acids with impact in mitochondrial function and dynamics (Bellanti et al., 2018), but the effects displayed by dietary cholesterol alone remains partially characterized. In the present work, we were aimed to figure out the effects of cholesterol overload in the liver, particularly in hepatocytes, and the influence on the transcriptome and in the cholesterol-overloaded mitochondria dynamic.

2 | MATERIAL AND METHODS

All chemicals and reagents were of the highest analytical grade, and most of them were purchased from Sigma (St. Louis, MO). Reagents obtained from other suppliers are detailed in the text.

2.1 | Animal model

C57BL/6 male mice (8–10 weeks old) were purchased from Jackson Laboratory (Bar Harbor, ME) and were maintained in pathogen-free conditions with controlled temperature and humidity on a 12 hr light–dark cycle in the animal facility at the Universidad Autonoma Metropolitana. The experimental protocols used were approved and performed in accordance with the Animal Care Committee of the Universidad Autonoma Metropolitana and the NIH Guide for the Care and Use of Laboratory Animals.

2.2 | Experimental design

Twenty mice were randomly divided in two groups, 10 animals were fed with an HC diet (2% cholesterol and 0.5% sodium cholate; Gomez-Quiroz et al., 2016; Nuño-Lámbarri et al., 2016) for 30 days, the second group was fed with control standard Chow diet (LabDiet #5001) for the same period. After 30 days, animals were killed. Liver weight was monitored, and liver tissue, as well as serum, was collected for subsequent analyzes.

2.3 | Histological analysis

Liver sections from all groups were fixed in absolute ethanol and embedded in paraffin for routine hematoxylin and eosin (H&E) staining, and both, morphometric and NAFLD activity score (NAS; Kleiner et al., 2005) studies were performed. For morphometric study five H&E slides, five random- view fields were selected, and 100 cells were counted in each field. Data are reported as cell percentage considering normal, regenerative, and death phenotypes (Enriquez-Cortina et al., 2013). Tissue for Oil Red O staining were fixed in 4% paraformaldehyde/phosphate-buffered saline (PBS) for 30 min and was stained with freshly diluted 0.2% Oil red O solution for 4 hr after that we proceeded to microphotography.

2.4 | Primary mouse hepatocytes isolation and culture

Hepatocytes were isolated from HC and Chow mice by the two-step collagenase perfusion, as we previously reported (Gómez-Quiroz et al., 2008). The viability was assessed by trypan blue exclusion and generally exceeded >90%. Hepatocytes were seeded at 2.5×10^5 cells per cm^2 either in Lab-Tek chambered slides or in 10-cm dishes (Nalge, Nunc) in Ham's F-12/Dulbecco's modified Eagle's basal hepatocyte growth medium supplemented with 10% fetal bovine serum. After 24 hr, cells were used for reactive oxygen species (ROS) determination, Oil Red O staining, cholesterol, and mitochondrial potential determination.

2.5 | Biochemical determinations and analysis of liver function

Blood samples were obtained from the orbital venous plexus under Avertin (2-2-2 tribromoethanol) anesthesia before sacrifice. Serum activity of aspartate aminotransferase (AST), alanine transferase (ALT), and alkaline phosphatase (ALP) were determined by an automated method using Reflovet Plus (Roche, Mannheim, Germany).

2.6 | Cholesterol determination

For total cholesterol determination, 10 mg of liver or mitochondrial protein was saponified with alcoholic KOH in a 60°C heating block for 30 min. After the mixture had cooled, 3 ml of hexane and 600 μl of distilled water were added and shaken to ensure complete mixing. Appropriate aliquots of the hexane layer were evaporated under nitrogen with vacuum (Speed Vac, Savant, Cranbury, NJ) and used for cholesterol measurement with O-phthalaldehyde dissolved in acetic acid (0.5 mg/ml). After that sulfuric acid (1 ml) was added and then read at 550 in a spectrophotometer (Rudel & Morris, 1973).

2.7 | Triglycerides determination

Triglycerides (TG) content was determined using the triglyceride determination kit (Sigma-Aldrich, St Louis, MO) following manufacturer's instructions.

2.8 | Oil red O staining

To detect intracellular neutral lipids accumulation, the cells were seeded into 24-well chambers. After treatments, cells were washed with ice-cold PBS and then fixed with 2.5% paraformaldehyde for 1 hr. The cells were stained with freshly diluted 0.2% Oil red O solution for 4 hr; after that, we proceeded to microphotography.

2.9 | In situ ROS determination

Animals were euthanized in parallel exclusively for in situ ROS determination. Fresh tissue was rapidly sectioned, frozen in liquid nitrogen, and embedded in optimum cutting temperature reagent (Sakura Finetec, Torrance, CA). Subsequently, 8-μm frozen sections were obtained in a cryostat (Leica CM-3050S) at −20°C and the slides were immediately incubated for 15 min, in the dark, at room temperature with either 2′,7′–dichlorofluorescin diacetate (DCFDA, 5 μM), a cell-permeable non-fluorescent probe that is intracellularly de-esterified and converted to the highly fluorescent 2′,7′-dichlorofluorescein (DCFH) upon oxidation by ROS, particularly peroxides, or with dihydroethidium (DHE, 1 μM) for determination of superoxide anion radical detecting ethidium fluorescence. Samples were covered and observed using a confocal microscope at excitation and emission wavelengths of 480 and 520 nm, respectively, for DCFDA; and excitation and emission wavelengths of 485 and 570 nm, respectively, for DHE-derived ethidium fluorescence, as we previously reported (Nuño-Lámbarri et al., 2016).

2.10 | Western blot

The whole liver homogenate was prepared in ice-cold PBS using dounce homogenizer. The cellular pellet was suspended in 200 μl of M-PER (Pierce Chemical, Rockford, IL); lysis buffer was supplemented with proteases and phosphatases inhibitors (Roche). Lysis was performed on ice for 15 min, and cell debris was removed by centrifugation at 13,000*g* at 4°C for 10 min and the supernatant was recovered (Hernández et al., 2015). Total protein concentration was determined using a bicinchoninic acid kit (Pierce Thermo Scientific, Rockford, IL), according to the manufacturer's instructions. Proteins were separated by electrophoresis using 10% gradient Duramide precast gels (Cambrex, Rockland, ME) and transferred to a polyvinylidene difluoride membranes (Invitrogen, Carlsbad, CA; Clavijo-Cornejo et al., 2013). Immunodetection was performed using antibodies listed in Supporting Information Table 1.

2.11 | Mitochondria isolation

Mitochondria were obtained by homogenization and differential centrifugation. Briefly, cells were suspended 50% w/v in mitochondrial buffer 0.22 M mannitol, 0.7 M sucrose, 2 mM HEPES, pH 7.4) plus 0.1% BSA and were homogenized. The homogenate was centrifuged in an F21- 8 × 50 y Sorvall rotor at 1017*g* for 5 min. Then the supernatant was recovered and centrifuged at 10,700*g* for 10 min. The pellet was suspended in mitochondrial buffer containing BSA and centrifuged at 3,600*g* for 5 min. The supernatant was recovered and centrifuged at 17,000*g* for 10 min. The resulting pellet was suspended in a small volume of mitochondrial buffer (without BSA), and protein was determined by Biuret (Rosas-Lemus, Uribe-Alvarez, Chiquete-Félix, & Uribe-Carvajal, 2014).

2.12 | Mitochondrial transmembrane potential ($\Delta\Psi$)

The $\Delta\psi$ was determined using 10 μM safranine-O, following the absorbance changes at 511–533 nm in a DW2000 Aminco spectrophotometer in dual mode (Åkerman & Wikström, 1976). At the end of each trace, $\Delta\psi$ was collapsed by adding 5 μM of the protonophoro m-chlorophenylhydrazone (CCCP). Additionally, changes in mitochondria membrane potential were addressed by using the rhodamine-based dye Mito Red, which upon mitochondria localization emits fluorescence in a membrane potential-dependent manner.

2.13 | ATP determination

Hepatic ATP concentration was determined colorimetrically in liver homogenates of Chow and HC mice using the Abcam ATP-assay kit (Abcam, MA) according to the manufacturer's instructions. Briefly, 30 mg of liver was lysed in the ATP assay buffer and centrifuged at 13,000*g* for 2 min to pellet-insoluble materials. Samples were deproteinized and neutralized with PCA-KOH. The supernatant was added to a 96-well plate and followed by the addition of 50 μl of the Reaction Mix to each well and was incubated at the room temperature in the dark for 30 min. Absorbance was read at 570 nm using a multimode detector DTX 880 (Beckman Coulter). The ATP content was calculated based on a standard curve generated at the same time.

INFORME DE LABORES 2019

2.14 | Electron microscopy

Tissues were fixed with 2% glutaraldehyde in 0.1 M phosphate buffer (pH 7.4) followed by 1% OsO_4. After dehydration, thin sections were stained with uranyl acetate and lead citrate for observation under an EOL JEM 12000 EII transmission electron microscope (TEM).

2.15 | Global transcriptomic analysis by microarray

Microarray analysis was performed as we previously described (Gomez-Quiroz et al., 2016). As input, 200 ng total RNA from liver tissue were used for the in vitro transcription reactions, which were incubated for 16 hr at 37°C. Hybridization, washing, detection (Cy3-streptavidin, Amersham Biosciences, GE Healthcare), and scanning were performed on an Illumina iScan system (Illumina) using reagents and protocols supplied by the manufacturer. The biotinylated cRNA (750 ng per sample) was hybridized on Sentrix whole genome beadchips mouse Ref-8v2 for 18 hr at 58°C while rocking (5 rpm). The beadchip covers ~24,000 RefSeq transcripts. Image analysis and data extraction were performed automatically using Illumina GenomeScan Software. Gene expression values were adjusted by subtracting background noises in each spot by GenomeStudio (Illumina) and normalized by quantile normalization method across all samples. A signal intensity with a detection *p*-value greater than 0.05 was treated as a missing value, and only genes with sufficient representation across the samples were included in further data analysis (presence in ≥2 replicates/group). Differentially expressed genes were identified by Bootstrap *t*-test with 10,000 repetitions (Neuhauser & Jockel, 2006). Genes with a Bootstrap *p*-value ≤ 0.01 were considered significantly different. Only genes with more than two fold differences and *p*-value ≤ 0.01 were included in further analyzes. Ingenuity Pathway Analysis tool (IPA, Ingenuity Systems Inc.) was used to explore the functional relationships among the differentially expressed genes. The significance of each network, function, and pathway was determined by the scoring system provided by IPA tool. The microarray datasets have been deposited to the Gene Expression Omnibus database (http://www.ncbi.nlm.nih.gov/geo, accession number GSE30651).

2.16 | Caspase 3 activity

Tissue was lysed in reaction buffer and incubated for 30 min on ice. For each reaction, caspase 3 synthetic tetrapeptide fluorogenic substrate (Ac-DEVD-AMC) was added (BD Pharmigen) and then the tissue lysate; after that, the samples were incubated for 1 hr. The amount of AMC released was measured by fluorometry at an excitation wavelength of 380 nm and an emission wavelength of 420 nm.

2.17 | Statistical analysis

The data are presented as mean ± standard error (*SE*). for at least three independent experiments. Comparisons between groups were made using Student's *T*-test follow post ad hoc by U Mann–Whitney using GraphPad Prism 6 for Mac OSX, a $p \leq 0.05$ was considered significant.

3 | RESULTS

3.1 | An HC diet consumption resulted in hepatic steatosis and liver damage

Livers of C57BL/6 mice fed with HC diet for 30 days showed hepatomegaly, the characteristic pale color of the fatty liver and increased liver to body weight ratio (Figure 1b,c). An increase in lipid content in the tissue was confirmed by Oil Red staining (Figure 1e). Further, total liver cholesterol increased 6.5-fold and triglycerides 5.2-fold compared with Chow diet fed mice (Figure 1f,g). Consistently, a steatotic phenotype and alterations of the liver architecture was present (Figure 1i), dispersed inflammation (white arrow) and hepatocyte ballooning (yellow arrow) were consistent with NASH according to the NAS (or Kleiner Scoring System, Supporting Information Table 2; Kleiner et al., 2005).

In addition, cellular hypertrophy with numerous hyperchromatic hepatocytes unveiling nuclear condensation were observed (Figure 1i, asterisks). The morphometric analysis confirmed significantly higher percentages of both, dead and proliferating cells, as well as a decrease in normal cells in liver from HC fed animals (Figure 1j). Mice fed with HC showed increased signs of liver injury, judged by an increased activity in ALT, AST, and ALP (Figure 1k).

In confirmation of the steatotic phenotype observed and the increment of neutral lipids in the liver of HC mice, oil red O staining, and filipin fluorescence further demonstrated that cultured primary hepatocytes isolated from HC mice maintained high levels neutral lipids (Supporting Information Figure 1b), and free cholesterol content (Supporting Information Figure 1d).

3.2 | Global transcriptomic analysis

Next, transcriptomic profiling of HC diet livers was performed. In comparison to Chow, a total of 938 differentially expressed genes (439 upregulated and 499 downregulated (Supporting Information Table 3) could be detected. These genes were highly efficient in separating the two different diets using unsupervised clustering analysis (Figure 2a). We found that a significant number of differentially expressed genes related to hepatic cell death and oxidative stress (Ccnd1, Cers2, E2F1, Sod2, Scd, Pon3, Hmox 1, Sod1, Plin5, App, Usp10, Adar, Casp7, Nr1i3, Gstz1, Gnmt, Irf5; Figure 2b–d). Interestingly, most of the genes related to glutathione homeostasis were upregulated (Gsta1, Gsta2, Gstm4, Gpx4, Gss), and many nuclear genes encoding mitochondrial proteins were downregulated (Abcb8, Abcb6, Mtif3, Shmt2, Slc25a23, Slc25a10, Hmgcs2, Gls2, Hsd17b10Bcat2) clearly indicating a compromise of mitochondrial functions.

INFORME DE LABORES 2019

Journal of Cellular Physiology — WILEY

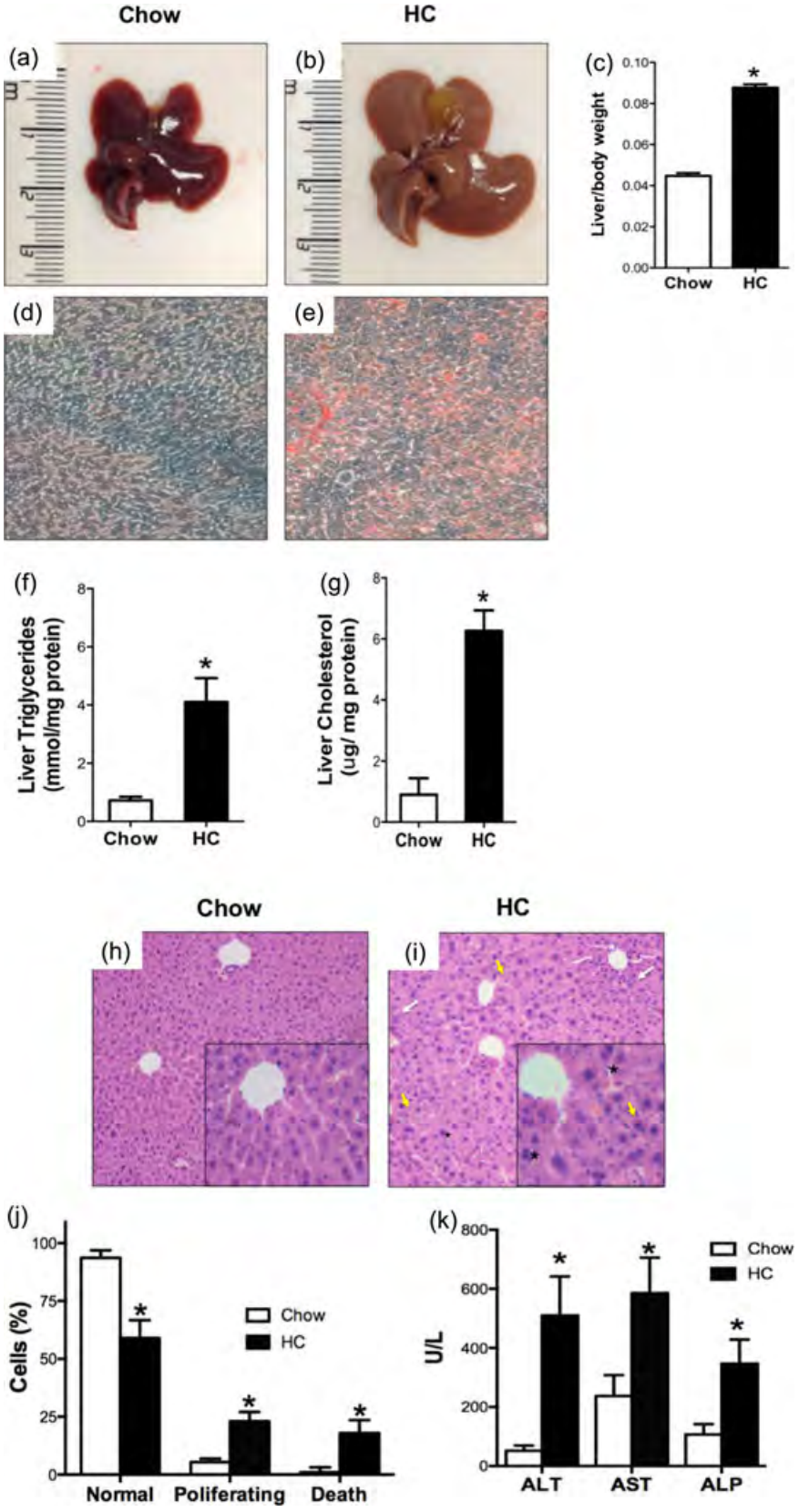

FIGURE 1 A high cholesterol diet consumption resulted in hepatic steatosis and liver damage. Gross inspection of the liver from mice fed with (a) chow control diet, (b) HC diet, (c) Liver to body weight ratio. Neutral lipid content determined by oil red O staining in liver tissue from animals fed with (d) chow control diet (e), HC diet. Biochemical determination of (f) triglycerides and, (g) cholesterol content in liver tissue. Histology analysis by H&E staining of liver tissue from mice fed with (i) HC diet or, (h) chow control diet. Original magnification 100 ×, (inset 200 ×), yellow arrow, hepatocyte ballooning; asterisk, nuclei condensation; white arrow inflammation. (h) Morphometric analysis of the H&E staining. (k) Liver function test. Each column represents the mean ± standard error of the mean (*SEM*) in at least four different mice. $^{*}p \leq 0.05$ versus Chow control mice. Images are representative of at least three independent experiments. ALT, alanine aminotransferase; AST, aspartate aminotransferase; ALP, alkaline phosphatase; HC: high cholesterol; H&E: hematoxylin and eosin

Consistently, affected toxicological functions were involved in liver cell death, steatosis, cholestasis, and HCC (Figure 2e), while top networks affected were cancer, organismal injury, metabolic diseases and lipid metabolism, among others (Figure 2f). Data clearly show an extensive impact in gene expression, indicating a profound adaptation of the cholesterol-overloaded liver.

INFORME DE LABORES 2019

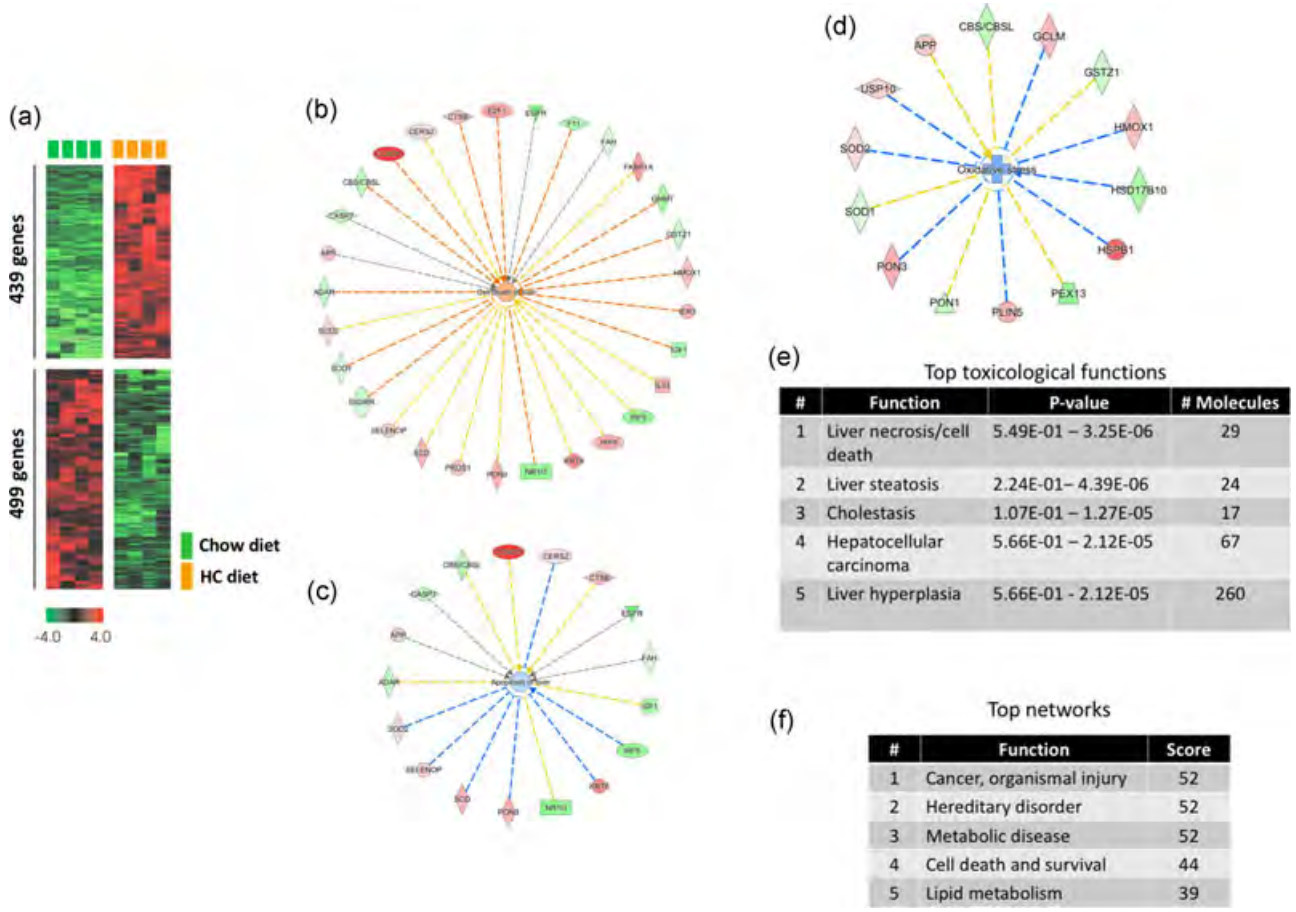

#	Function	P-value	# Molecules
1	Liver necrosis/cell death	5.49E-01 – 3.25E-06	29
2	Liver steatosis	2.24E-01– 4.39E-06	24
3	Cholestasis	1.07E-01 – 1.27E-05	17
4	Hepatocellular carcinoma	5.66E-01 – 2.12E-05	67
5	Liver hyperplasia	5.66E-01 - 2.12E-05	260

#	Function	Score
1	Cancer, organismal injury	52
2	Hereditary disorder	52
3	Metabolic disease	52
4	Cell death and survival	44
5	Lipid metabolism	39

FIGURE 2 Global transcriptomic analyzes by microarray. (a) Unsupervised hierarchical cluster analyses of liver tissue from mice fed with an HC diet or normal Chow diet for 30 days. A total of 938 differentially expressed genes were identified using bootstrap *t*-test with 10,000 repetitions (*p*-value 0.01). Gene regulatory networks associated with (b) cell death, (c) apoptosis and (d) oxidative stress in the liver overloaded with cholesterol, determined by IPA analysis. (e) Top toxicological functions and (f) top networks involved in cholesterol overload in the liver, determined by IPA analysis. HC: high cholesterol; IPA: ingenuity pathway analysis

3.3 | An HC diet induces increment of reactive oxygen species and oxidative stress

To evaluate the effect of cholesterol overload in the production of ROS, peroxides and superoxide were determined using specific probes for the superoxide anion (DHE) and peroxides (DCFH). Data show that lipid overload remarkably increased DHE fluorescence, showing that superoxide increased in both, liver tissue (Figure 3b,e) cultured primary hepatocytes (Supporting Information Figure 2b). Also, peroxides were considerably elevated, as shown by increased DCFH fluorescence (Figure 3d,e Supporting Information Figure 2d).

Next, we determined the content of the main enzymes responsible for peroxide and superoxide detoxification, as well as the levels of Nrf2, a key transcription factor involved in antioxidant response (Figure 3f). As expected, Nrf2 expression decreased dramatically in livers of animals fed with HC diet, whereas catalase content did not change. Further, while SOD1, a cytoplasmic enzyme responsible for converting superoxide radical to molecular oxygen and hydrogen peroxide, decreased in HC livers, SOD2, a mitochondrial manganese-dependent SOD increased dramatically. GST, an enzyme that conjugates xenobiotics, among them hydroperoxides to glutathione (GSH) and thereby detoxify cellular environments, markedly raised in lipid-overloaded tissue.

We also assessed the content of two intracellular GSH-dependent selenoperoxidases known to catalyze organoperoxides detoxification, GPx-1 and GPx-4. Consistent with our results from the gene expression profiling GPx-1 levels were significantly lower in HC livers, while GPx-4 significantly increased (Figure 3f). All Western blot results corroborate the data obtained by microarrays. Densitometric analysis of Western blots could be found in Supporting Information Figure 3.

3.4 | The development of hepatic steatosis and altered mitochondrial homeostasis in HC livers

Consistent with the hypercholesterolemic phenotype, cholesterol content in isolated mitochondria of HC livers revealed a two-fold increment compared to Chow (Figure 4a). To further characterize the influence of cholesterol overload in mitochondria functionality, we determined mitochondrial membrane potential using Mito Red. A significantly reduced fluorescence was observed in HC hepatocytes

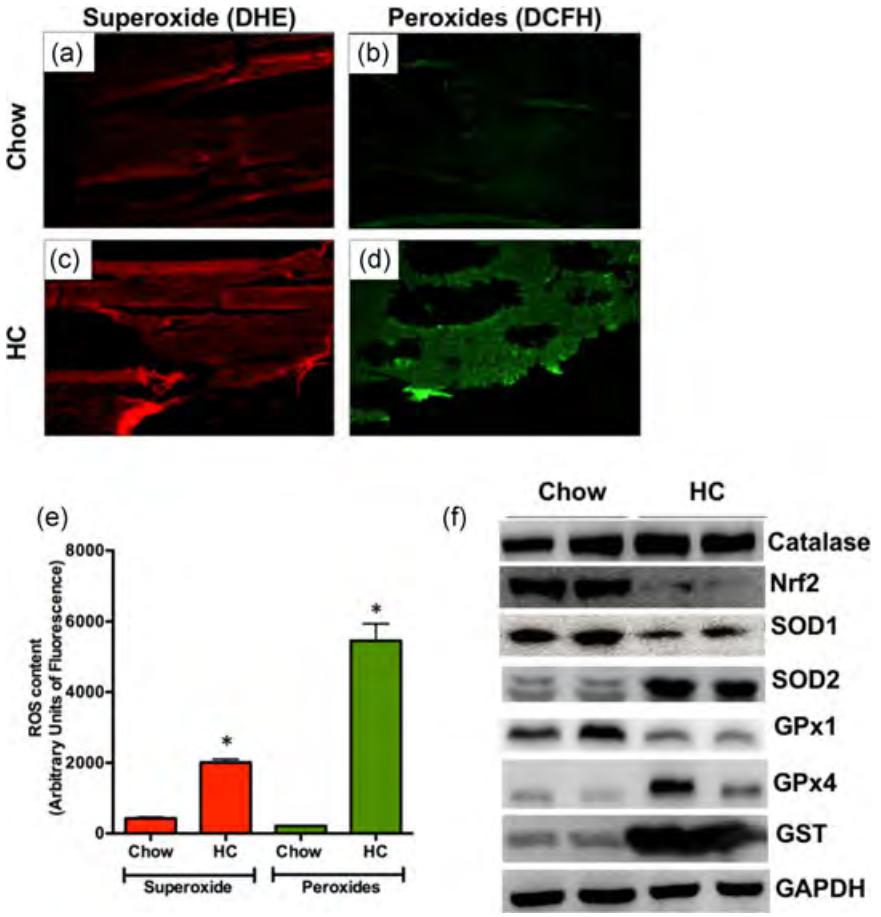

FIGURE 3 A high cholesterol diet induces increment of reactive oxygen species and oxidative stress. Reactive oxygen species content in liver tissue were determined by both, DHE (1 μM, in red) and DCFH (5 μM in green) fluorescence, in liver tissue from mice fed with Chow diet (a,c), and high cholesterol diet (b,d), representative images obtained by confocal microscopy. Original magnification ×100. (e) Fluorescence quantification. Each column represents the mean ± standard error of the mean (*SEM*) in at least four different mice. $^{*}p \leq 0.05$ versus Chow control mice. (f) Western blot analysis of the main antioxidant proteins using antibodies depicted in Supporting Information Figure 1. GAPDH was used as loading control. Images are representative of at least three independent experiments. DCFH: 2′,7′-dichlorofluorescein; DHE: dihydroethidium; GAPDH: glyceraldehyde-3-phosphate dehydrogenase

(Figure 4c), indicating that the membrane potential of mitochondria was decreased when compared cwith hepatocytes from Chow fed mice (Figure 4b). This result was corroborated in isolated mitochondria from mice under both diets. A significantly diminished membrane potential of liver mitochondria from HC fed mice determined by spectrophotometry using safranine was present (Figure 4d). HC mitochondria exhibited 50% of loss in membrane potential compared with those from Chow livers. In line with this, a 60% decrease in ATP content could be revealed for HC livers (Figure 4e), clearly suggesting impairment of mitochondrial functionality.

3.5 | HC diet causes imbalance of mitochondrial dynamics and fission

To estimate the structural impairment of mitochondria induced by HC diet, we performed TEM. HC diet led to abnormal mitochondria, with loss of cristae, rarefied matrix, and lipid droplet accumulation (Figure 5b). These signs of mitochondrial damage were not seen in cells from Chow fed mice (Figure 5a). Congruently, while the number of mitochondria was significantly increased the corresponding size in HC livers was reduced (Figure 5c). To evaluate the impact of HC diet on mitochondrial dysfunction, we studied the content of the main proteins involved in mitochondrial dynamic: PGC-1α, a central regulator of mitochondrial biogenesis through interactions with multiple transcription factors; Drp1, a main regulator in mitochondrial fission; OPA1, a mitochondrial dynamin like GTPase located at the inner membrane that regulates mitochondrial fusion and cristae remodeling alongside with mitofusin (Mfn) 1 and 2. Figure 5d, Supporting Information Figure 4, show an increase in the activation of Drp1 (Ser-616), and in the expression of PGC-1α, whereas OPA1, Mfn1, and Mtn2 all decreased significantly in the hepatocytes from HC mice. These results suggest that components regulating mitochondrial fission and biogenesis were increased by HC diet, contributing to the imbalance in mitochondrial dynamics.

3.6 | HC diet promotes cell survival

Compromised mitochondria homeostasis might affect cellular survival. Therefore, we evaluated the expression levels of the main mitochondrial survival-related proteins (Figure 6a, Supporting Information Figure 5). Interestingly, pro-apoptotic Bax protein was significantly increased and Bcl-2 was downregulated, but feasible compensatory antiapoptotic response was displayed by the increment of Bcl-X_L and, remarkably by Mcl-1.

The outstanding elevation in Mcl-1 was also associated with a strong activation of Stat3 in HC samples, its main transcription factor. As expected, apoptosis was unaffected, judged by caspase 3 activity, (Figure 6b), suggesting that cholesterol overload in mitochondrial

INFORME DE LABORES 2019

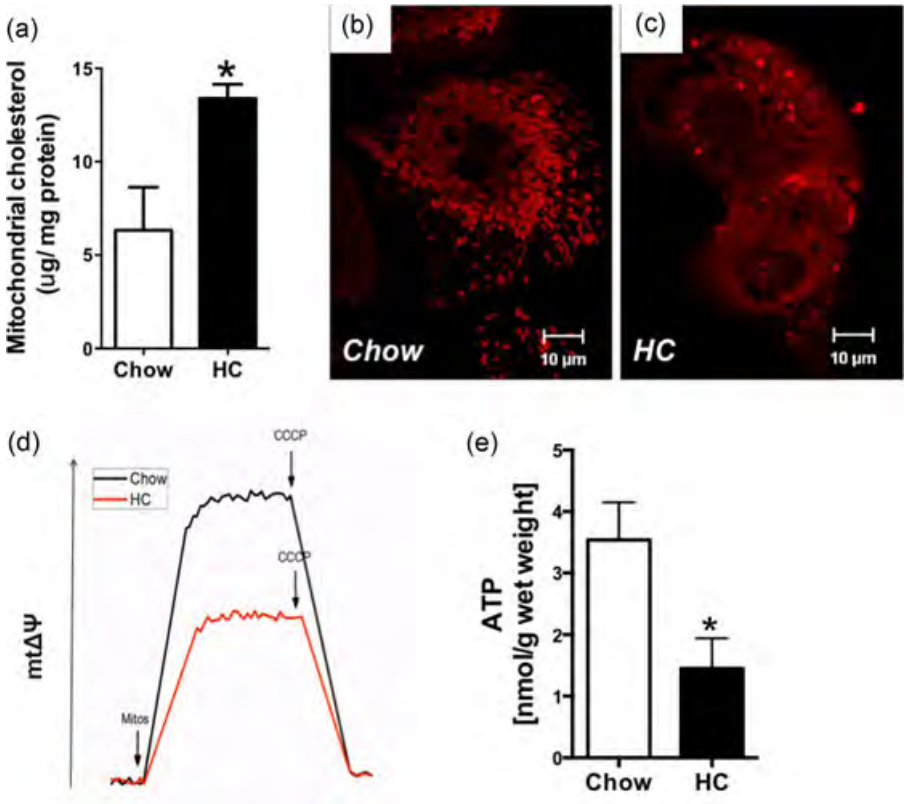

FIGURE 4 The high cholesterol diet induces mitochondria overload in mitochondria altering mitochondrial morphology and functionality. (a) Mitochondrial cholesterol content. Confocal Microscopy inspection of the mitochondrial transmembrane potential assayed by Mito Red fluorescence in cultured primary hepatocytes isolated from (b) HC diet fed mice and (c) Chow diet fed mice. (d) Mitochondrial transmembrane potential ($\Delta\Psi$) determined by using 10 μM safranine-O, following the absorbance changes at 511–533 nm. $\Delta\psi$ was collapsed by adding 5 μM of the protonophoro m-chlorophenylhydrazone (CCCP). Images are representative of at least three independent experiments. (e) ATP determination in liver homogenates from both HC and Chow diet fed mice. Each column represents the mean ± standard error of the mean (*SEM*), at least four independent experiments. $^{*}p \leq 0.05$ versus Chow

might yield to apoptosis resistance, despite ROS overproduction by a mechanism that could be mediated, particularly, by Mcl-1.

4 | DISCUSSION

We and others have reported that cholesterol overload in the liver promotes oxidative stress, liver damage and sensitizes to a more severe damage (Domínguez-Pérez et al., 2016; López-Islas et al., 2016; López-Reyes et al., 2015; Mari et al., 2006) in the context of relevant cytotoxic stimuli ultimately leading to advanced liver disease as well as cancer (Enríquez-Cortina et al., 2017). Moreover, mitochondrial dysfunction has been implicated in the progression of steatosis to NASH (Kim et al., 2017). Although mitochondria dysfunction has been frequently associated to chronic liver diseases and hepatocarcinogenesis, detailed molecular and functional characteristics remain partially characterized, in addition to the unknown effect in global gene expression signature.

In the current study, we aimed to dissect the effects of cholesterol overload in the mouse liver with emphasis on the mitochondria homeostasis and the relevance in the transcriptome.

An increased liver content of TG and cholesterol were observed, although HC mice maintained the same body weight as control, due to both experimental diets being isocaloric. Histopathological examination of the liver revealed microvesicular steatosis after 30 days of HC diet feeding (Figures 1i, and 5b), phenotype in agreement with that observed in rats under same diet (Marí et al., 2006). Liver function tests were elevated, and an increase in ROS content was found in tissue and in hepatocytes primary culture. Previous data from our group showed the ratio of reduced GSH to oxidized GSH (GSSG) was significantly decreased by the HC diet as compared to the corresponding Chow fed mice. HC mice also displayed a greater increase in lipid oxidation as measure by the rate of production of thiobarbituric acid-reactive substances (Gomez-Quiroz et al., 2016).

One of our main interest was to address the gene expression profile induced by cholesterol liver overload, HC diet induced dysregulation 938 genes, 493 were upregulated, and 499 downregulated, indicating a prominent impact in gene expression tending to an adaptive response, that could be related, among other physiological processes, to apoptosis resistance in a mechanism involving mitochondria homeostasis and function, narrowed linked to changes in mitochondria redox state, judged by the overexpression of SOD2 (Figures 2b and 3f) key regulator

INFORME DE LABORES 2019

Journal of Cellular Physiology — WILEY

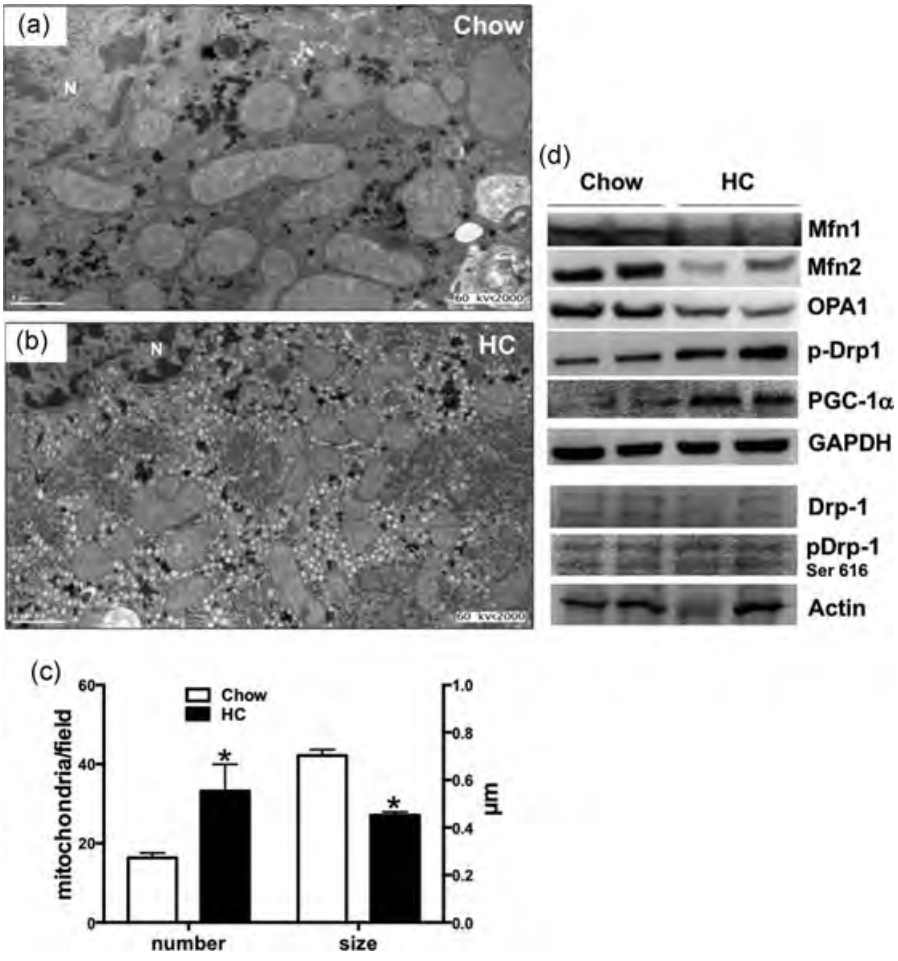

FIGURE 5 High cholesterol diet induces an imbalance in mitochondrial dynamics favoring the susceptibility to fission. TEM of primary hepatocytes isolated from mice fed with (a) Chow control diet, or (b) high cholesterol diet. (c) Morphometric analysis of TEM. Each column represents the mean ± standard error of the mean (*SEM*) in at least four independent experiments. $^{*}p \leq 0.05$ versus Chow. (d) Western blot analysis of the main mitochondria dynamics-related proteins using antibodies depicted in Supporting Information Table 1. GAPDH and actin were used as loading control. GAPDH: Glyceraldehyde-3-phosphate dehydrogenase; TEM: transmission electron microscopy

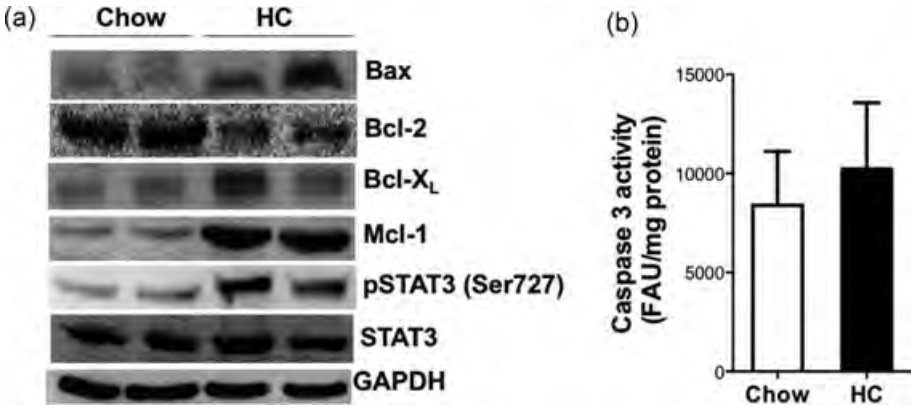

FIGURE 6 High cholesterol diet promotes cell survival. (a) Western blot analysis of the main apoptosis-related proteins using antibodies depicted in Supporting Information Figure 1. GAPDH was used as loading control. (b) Caspase 3 activity. Each column represents the mean ± standard error of the mean (*SEM*) in at least three independent experiments. GAPDH: glyceraldehyde-3-phosphate dehydrogenase

of the mitochondria redox status, and the selenoprotein (Selenop) another antioxidant protein particularly expressed in the liver. Figure 2e,f show that this gene expression signature favoring particularly hepathopaties such as cholestasis, HCC, and hyperplasia, consistent with our previous findings in a mice model of HCC (Enríquez-Cortina et al., 2017), previous work we have reported that under HC diet, and in the presence of a carcinogenic stimulus, mice develop an aggressive phenotype of HCC (Enríquez-Cortina et al., 2017), correlating with the present transcriptomic data; interestingly, we found the overexpression of Hspb1, a gene encoding the HSP 27, which has been reported to be associated with poor clinical outcome (Choi et al., 2017), in fact, we reported the finding of metastasis in lungs, and resistance to

INFORME DE LABORES 2019

cell death, but in the present work we are observing that this issue is related to cholesterol overload rather than N-diethylnitrosamine carcinogenic effect.

HC diet induced liver damage and dysfunction, associated with a decrease in mitochondrial membrane potential and ATP content. It has been reported that increased mitochondrial cholesterol content can lead to mitochondrial dysfunction (Balboa et al., 2017), including reduced fluidity of mitochondrial membranes (Garcia-Ruiz et al., 2009), reduced ATP generation (Yu et al., 2005), and decreased mitochondrial GSH import (Marí et al., 2006). Our data show decreased mitochondrial membrane potential, ATP production, and increased cholesterol levels in the organelle.

From the perspective of HC diet, we found that it induced several patterns of mitochondrial alteration: (a) increment in cholesterol content, which plays an important role in the change of membrane fluidity (Marí et al., 2006), (b) it induced sensitization to oxidative stress, leading to mitochondrial insufficiency and metabolic abnormality, (c) it impaired mitochondrial bioenergetics, and (d) it promoted steatohepatitis, leading to the retardation of mitochondrial function, as it has been recently reported (Bellanti et al., 2018). Mitochondria obtained from HC liver presented twice cholesterol content compared to control, and biogenesis and mitochondrial fission were observed. Mitochondrial cholesterol content is relevant for the transport of mitochondrial-reduced GSH. In fact, it has been found that cholesterol incorporation in isolated mitochondria decreases mGSH stores (Fernandez-Checa & Kaplowitz, 2005). Furthermore, we found alterations in mitochondrial dynamics in HC cells. Our study provides evidence of an increase in the activation of Drp1 related with increased fission (increased mitochondrial number), but not fusion, as suggested by the downregulation of Mfn1, Mfn2 and OPA-1 in addition, the increment of PGC-1α, strongly suggest mitochondrial biogenesis Both fission and fusion are critical mechanisms for the growth, redistribution, and maintenance of healthy mitochondria or disease-related processes, especially apoptosis and mitophagy. In the current study, HC diet induced the imbalance of fission and fusion proteins as shown by a high activation of Drp-1 and a low expression of OPA-1 and mitofusins.

An increased content of antiapoptotic proteins, particularly Mcl-1, in HC livers explains the result of caspase 3 activity which shows no changes despite Bax increment and Bcl-2 decrement.

Lucken-Ardjomande and coworkers (Lucken-Ardjomande, Montessuit, & Martinou, 2008) using the cationic sterol U18666A as a tool to increase mitochondrial cholesterol levels, reported that cholesterol prevents apoptosis impeding Bax activation after its insertion into the mitochondrial outer membrane. Mitochondria could sense stress to allow for cellular adaptation to the environment, with the flexibility to adapt. Our results show that mitochondria adapt to high levels of cholesterol content increasing fission. Also, a decrease in apoptosis was observed conferring cell survival in HC adverse condition. Thus, an increase in cholesterol could favor that damaged hepatocytes do not enter apoptosis and proliferate, perpetuating liver damage.

STAT3, a cell proliferation related transcription factor that modulates many genes related to apoptosis, cell cycle and epithelial to mesenchymal transition, was activated in HC hepatocytes.

All findings in this study, and the increase in p-STAT3 (Ser727) content and DNA oxidation (data not shown) in liver after one month HC diet could suggest that damaged hepatocytes could proliferate and perpetuate liver damage. NAFLD is an increasing cause HCC.

Recently, we have reported that an HC diet increases oxidative DNA damage and a rapid carcinogenic process, this was associated to an impairment in the activation of DNA repair enzymes, resulting in liver tumors with an aggressive phenotype in comparison with animals under Chow diet (Enríquez-Cortina et al., 2017), demonstrating that certainly, cholesterol could display tumor promoter properties. Even more, recently it was published that free fatty acids and cholesterol derivatives by autoxidation, synergically facilitates development and progression of NAFLD to NASH by impairing mitochondria function, supporting our findings particularly on cholesterol effects (Bellanti et al., 2018), although This study remarkably shows the relevance of cholesterol participation in NAFLD to NASH progression, our work focuses on the impact of cholesterol alone, providing evidence that mitochondria impairment is independent of free fatty acids overload.

In summary, cholesterol overload in the liver, and particularly in mitochondria, induces remarkably transcriptomic changes, mainly associated to mitochondria function and dynamic which favors oxidative stress, apoptosis resistance that could promote transformation, as we recently probed.

ACKNOWLEDGMENTS

This study was partially funded by a grant from CONACYT: Fronteras de la Ciencia #1320, CB-166042, CB252942, and SEP-PRODEP 913026-14612111, Universidad Autónoma Metropolitana Iztapalapa. We thank Roberto Lazzarini and the Confocal Core Unit of the DCBS-UAM-I for technical support and Jorge Sepúlveda for TEM.

CONFLICTS OF INTEREST

The authors declare that they have no conflicts of interest.

ORCID

María Concepción Gutiérrez-Ruiz http://orcid.org/0000-0003-0501-7226

REFERENCES

Auger, C., Alhasawi, A., Contavadoo, M., & Appanna, V. D. (2015). Dysfunctional mitochondrial bioenergetics and the pathogenesis of hepatic disorders. *Frontiers in Cell and Developmental Biology*, *3*, 40.

Balboa, E., Castro, J., Pinochet, M. J., Cancino, G. I., Matías, N., José sáez, P., … Zanlungo, S. (2017). MLN64 induces mitochondrial dysfunction

associated with increased mitochondrial cholesterol content. *Redox Biology*, *12*, 274–284.

Bellanti, F., Villani, R., Tamborra, R., Blonda, M., Iannelli, G., di Bello, G., … Serviddio, G. (2018). Synergistic interaction of fatty acids and oxysterols impairs mitochondrial function and limits liver adaptation during nafld progression. *Redox Biology*, *15*, 86–96.

Calvisi, D. F., Wang, C., Ho, C., Ladu, S., Lee, S. A., Mattu, S., … Evert, M. (2011). Increased lipogenesis, induced by AKT-mTORC1-RPS6 signaling, promotes development of human hepatocellular carcinoma. *Gastroenterology*, *140*(3), 1071–1083.

Choi, B., Choi, S. K., Park, Y. N., Kwak, S. Y., Lee, H. J., Kwon, Y., … Lee, Y. S. (2017). Sensitization of lung cancer cells by altered dimerization of HSP27. *Oncotarget*, *8*(62), 105372–105382.

Clavijo-Cornejo, D., Enriquez-Cortina, C., López-Reyes, A., Domínguez-Pérez, M., Nuño, N., Domínguez-Meraz, M., … Gómez-Quiroz, L. E. (2013). Biphasic regulation of the NADPH oxidase by HGF/c-Met signaling pathway in primary mouse hepatocytes. *Biochimie*, *95*(6), 1177–1184.

Domínguez-Pérez, M., Nuño-Lámbarri, N., Clavijo-Cornejo, D., Luna-López, A., Souza, V., Bucio, L., … Gutiérrez-Ruiz, M. C. (2016). Hepatocyte growth factor reduces free cholesterol-mediated lipotoxicity in primary hepatocytes by countering oxidative stress. *Oxidative Medicine and Cellular Longevity*, *2016*, 7960386–7960388.

Enriquez-Cortina, C., Almonte-Becerril, M., Clavijo-Cornejo, D., Palestino-Domínguez, M., Bello-Monroy, O., Nuño, N., … Gómez-Quiroz, L. E. (2013). Hepatocyte growth factor protects against isoniazid/rifampicin-induced oxidative liver damage. *Toxicological Sciences: An Official Journal of the Society of Toxicology*, *135*(1), 26–36.

Enríquez-Cortina, C., Bello-Monroy, O., Rosales-Cruz, P., Souza Arroyo, V., Miranda, R. U., Toledo-Pérez, R., … Gomez-Quiroz, L. (2017). Cholesterol overload in the liver aggravates oxidative stressmediated DNA damage and accelerates hepatocarcinogenesis. *Oncotarget*, *8*(61), 104136–104148.

Fernandez-Checa, J. C., & Kaplowitz, N. (2005). Hepatic mitochondrial glutathione: Transport and role in disease and toxicity. *Toxicology and Applied Pharmacology*, *204*(3), 263–273.

Garcia-Ruiz, C., Mari, M., Colell, A., Morales, A., Caballero, F., Montero, J., … Fernández-Checa, J. C. (2009). Mitochondrial cholesterol in health and disease. *Histology and Histopathology*, *24*(1), 117–132.

Gomez-Quiroz, L., Gutierrez Ruiz, M. C., Marquardt, J. U., Factor, V. M., & Thorgeirsson, S. S. (2017). Redox regulation by HGF/c-Met in liver disease. In Muriel, P. (Ed.), *Liver pathophysiology therapies and antioxidants*. USA: Academic Press

Gomez-Quiroz, L. E., Seo, D., Lee, Y. H., Kitade, M., Gaiser, T., Gillen, M., … Marquardt, J. U. (2016). Loss of c-Met signaling sensitizes hepatocytes to lipotoxicity and induces cholestatic liver damage by aggravating oxidative stress. *Toxicology*, *361-362*, 39–48.

Gómez-Quiroz, L. E., Factor, V. M., Kaposi-Novak, P., Coulouarn, C., Conner, E. A., & Thorgeirsson, S. S. (2008). Hepatocyte-specific c-Met deletion disrupts redox homeostasis and sensitizes to Fas-mediated apoptosis. *The Journal of Biological Chemistry*, *283*(21), 14581–14589.

Hernández, I., Domínguez-Pérez, M., Bucio, L., Souza, V., Miranda, R. U., Clemens, D. L., … Gutiérrez-Ruiz, M. C. (2015). Free fatty acids enhance the oxidative damage induced by ethanol metabolism in an in vitro model. *Food and Chemical Toxicology: An International Journal Published for the British Industrial Biological Research Association*, *76*, 109–115.

Kim, H. J., Han, Y. H., Na, H., Kim, J. Y., Kim, T., Kim, H. J., … Lee, M. O. (2017). Liver-specific deletion of RORalpha aggravates diet-induced nonalcoholic steatohepatitis by inducing mitochondrial dysfunction. *Scientific Reports*, *7*(1), 16041.

Kleiner, D. E., Brunt, E. M., Van Natta, M., Behling, C., Contos, M. J., Cummings, O. W., … Nonalcoholic Steatohepatitis Clinical Research, N. (2005). Design and validation of a histological scoring system for nonalcoholic fatty liver disease. *Hepatology*, *41*(6), 1313–1321.

Lonardo, A., Nascimbeni, F., Maurantonio, M., Marrazzo, A., Rinaldi, L., & Adinolfi, L. E. (2017). Nonalcoholic fatty liver disease: Evolving paradigms. *World Journal of Gastroenterology*, *23*(36), 6571–6592.

Lucken-Ardjomande, S., Montessuit, S., & Martinou, J. C. (2008). Bax activation and stress-induced apoptosis delayed by the accumulation of cholesterol in mitochondrial membranes. *Cell Death and Differentiation*, *15*(3), 484–493.

López-Islas, A., Chagoya-Hazas, V., Pérez-Aguilar, B., Palestino-Domínguez, M., Souza, V., Miranda, R. U., … Gutiérrez-Ruiz, M. C. (2016). Cholesterol enhances the toxic effect of ethanol and acetaldehyde in primary mouse hepatocytes. *Oxidative Medicine and Cellular Longevity*, *2016*, 9209825–9209829.

López-Reyes, A. G., Martínez-Flores, K., Clavijo-Cornejo, D., Nuño-Lámbarri, N., Palestino-Domínguez, M., Souza, V., … Gutiérrez-Ruiz, M. C. (2015). Cholesterol overload in hepatocytes affects nicotinamide adenine dinucleotide phosphate oxidase (NADPH) activity abrogating hepatocyte growth factor (HGF) induced cellular protection. *Gaceta Medica de Mexico*, *151*(4), 456–464.

Marí, M., Caballero, F., Colell, A., Morales, A., Caballeria, J., Fernandez, A., … García-Ruiz, C. (2006). Mitochondrial free cholesterol loading sensitizes to TNF- and Fas-mediated steatohepatitis. *Cell Metabolism*, *4*(3), 185–198.

Neuhauser, M., & Jockel, K. H. (2006). A bootstrap test for the analysis of microarray experiments with a very small number of replications. *Applied Bioinformatics*, *5*(3), 173–179.

Nuño-Lámbarri, N., Domínguez-Pérez, M., Baulies-Domenech, A., Monte, M. J., Marin, J. J., Rosales-Cruz, P., … Gomez-Quiroz, L. E. (2016). Liver Cholesterol overload aggravates obstructive cholestasis by inducing oxidative stress and premature death in mice. *Oxidative Medicine and Cellular Longevity*, *2016*, 9895176.

Rosas-Lemus, M., Uribe-Alvarez, C., Chiquete-Félix, N., & Uribe-Carvajal, S. (2014). In *Saccharomyces cerevisiae* fructose-1,6-bisphosphate contributes to the Crabtree effect through closure of the mitochondrial unspecific channel. *Archives of Biochemistry and Biophysics*, *555-556*, 66–70.

Rudel, L. L., & Morris, M. D. (1973). Determination of cholesterol using o-phthalaldehyde. *Journal of Lipid Research*, *14*(3), 364–366.

Serviddio, G., & Sastre, J. (2010). Measurement of mitochondrial membrane potential and proton leak. *Methods in Molecular Biology*, *594*, 107–121.

Yu, W., Gong, J. S., Ko, M., Garver, W. S., Yanagisawa, K., & Michikawa, M. (2005). Altered cholesterol metabolism in Niemann-Pick type C1 mouse brains affects mitochondrial function. *The Journal of Biological Chemistry*, *280*(12), 11731–11739.

Åkerman, K. E. O., & Wikström, M. K. F. (1976). Safranine as a probe of the mitochondrial membrane potential. *FEBS Letters*, *68*(2), 191–197.

SUPPORTING INFORMATION

Additional supporting information may be found online in the Supporting Information section at the end of the article.

How to cite this article: Domínguez-Pérez M, Simoni-Nieves A, Rosales P, et al. Cholesterol burden in the liver induces mitochondrial dynamic changes and resistance to apoptosis. *J Cell Physiol*. 2019;234:7213–7223. https://doi.org/10.1002/jcp.27474

Trends in Genetics

CellPress REVIEWS

Review

Whole-Genome Duplication and Yeast's Fruitful Way of Life

Ximena Escalera-Fanjul,[1] Héctor Quezada,[2] Lina Riego-Ruiz,[3] and Alicia González[1,*]

Studies on the fate of *Saccharomyces cerevisiae* paralogous gene pairs that arose through a whole-genome duplication event have shown diversification of retained duplicated genes. Paralogous functional specialization often results in improved function and/or novel function that could contribute to the adaptation of the organism to a new lifestyle. Here, we analyze and discuss particular case studies of paralogous functional diversification that could have played a role in the acquisition of yeast fermentative metabolism.

Highlights

S. cerevisiae genomic duplication resulting from an allopolyploidization event gave rise to a hybrid allotetraploid.

Retention and diversification of WGD paralogous genes allowed the establishment of fermentative metabolism.

Global analysis and case-specific studies are beginning to uncover the molecular mechanisms by which WGD paralogous diversification enabled the development and establishment of a 'new way of life'.

Origin and Significance of Yeast's Whole-Genome Duplication

Saccharomyces cerevisiae was the first eukaryote whose genome was fully sequenced. Genome analysis revealed the presence of duplicated gene blocks, indicating that this yeast lineage arose from a **whole-genome duplication** (**WGD**) (see Glossary) [1–3]. WGDs are a recurring phenomenon in evolution. Some fungi, most species of flowering plants, and vertebrates descend from ancestors that doubled their genomes. WGDs have been associated with the acquisition of novel traits as well as increased species richness [4].

It has been proposed that the selective conservation of duplicated genes in *S. cerevisiae* has been essential for the acquisition of a predominantly fermentative lifestyle, also termed the 'make-accumulate-consume' strategy (i.e., upon sugar availability, ethanol is produced, accumulated, and finally consumed). This strategy largely relies on the Crabtree effect (Box 1) that allows yeast to out-compete other microorganisms [5]. The retention of 551 WGD gene pairs involved in different cellular processes and the complexity of the Crabtree effect make it difficult to demonstrate whether the selective retention of WGD paralogous genes led to 'a new way of life'. *S. cerevisiae* is presently the best suited model to study this phenomenon due to the vast amount of technical resources and information available for this organism [6]. In addition, the advancement of whole-genome sequencing and phenotyping of 1011 *S. cerevisiae* isolates from diverse geographical locations has provided valuable information into the ecological and evolutive niche of this yeast [7]. This review examines evidence provided by different experimental approaches addressing the role of WGD in the acquisition of fermentative metabolism in *S. cerevisiae*.

Mapping the Beginning of the Fermentative Lifestyle

After the publication of the complete *S. cerevisiae* genome sequence in 1996, several studies focused on understanding its origins and evolution. While some groups supported the idea that the duplicated regions observed in this yeast's genome were the signatures of an ancient WGD [3,5], others proposed that these duplicated regions arose independently by local duplication events [8]. This controversy was not solved until 2004, when the genomic sequences of other yeast species were published and used for comparative genomic analyses. Independent studies revealed that the genome of *S. cerevisiae* mapped in 2:1 manner to non-WGD yeast genomes, supporting the WGD model [9–11]. Further scrutiny and the development of the

[1]Departamento de Bioquímica y Biología Estructural, Instituto de Fisiología Celular, Universidad Nacional Autónoma de México, Mexico City, Mexico
[2]Laboratorio de Investigación en Inmunología y Proteómica, Hospital Infantil de México Federico Gómez, Mexico City, Mexico
[3]División de Biología Molecular, Instituto Potosino de Investigación Científica y Tecnológica AC, San Luis Potosí, Mexico

*Correspondence: amanjarr@ifc.unam.mx (A. González).

© 2018 Elsevier Ltd. All rights reserved.

Box 1. *Saccharomyces cerevisiae* Fermentative Metabolism

The majority of cells only use fermentation when respiration is impaired, for example, when oxygen concentration is low (Pasteur effect). However, in the presence of high glucose concentrations and regardless of oxygen availability, *Saccharomyces cerevisiae* prefers to ferment glucose to ethanol. This physiological phenomenon is named the Crabtree effect [64]. In this metabolic state, the cytoplasmic pyruvate produced by glycolysis is transformed to acetaldehyde and then to ethanol, which diffuses to the extracellular medium [21].

During fermentation, the energy for growth is mainly provided by glycolysis and not by the oxidative respiration pathway. However, the amount of energy produced from a glucose molecule by fermentation is lower than that produced by its complete oxidation. Consequently, during fermentation *S. cerevisiae* displays a high glycolytic flux to match its growth requirements. The increased glycolytic rate under the fermentative regime helps yeasts grow much faster than when they grow in non-fermentable carbon sources, such as ethanol, where the oxidative respiration pathway is used to produce energy [65].

During fermentation, glucose repression reduces the mass and energy flux through the tricarboxylic acid (TCA) cycle, the respiratory chain, and the oxidative phosphorylation. However, the TCA cycle displays enough activity to provide the necessary precursors to produce the macromolecular components to sustain rapid growth rate [65,66]. Under these conditions, the TCA cycle does not work as a cycle, but rather in a branched manner, mainly because the succinate dehydrogenase complex does not operate under these conditions [67]. When glucose becomes limiting, cells undergo a so-called diauxic shift, a transient phase in which they switch to a fully respiratory metabolism, catabolizing the released ethanol via the TCA cycle [65].

S. cerevisiae response to sugar availability is dependent on different time scales and biological levels, from the reprogramming of gene expression to enzyme allosteric regulation, including post-transcriptional and post-translational regulatory mechanisms. It also involves a variety of cellular processes as different signal transduction pathways, energy and fatty acid metabolism, carbohydrate storage, and amino acid biosynthesis [68].

Yeast Gene Order Browser, an online tool for visualizing gene order context (synteny) of any gene from several yeast genomes [9,10,12], showed that the whole *S. cerevisiae* genome is duplicated [1–3,12]. Furthermore, it has now been confirmed that as well as *S. cerevisiae*, several other yeasts such as *Candida glabrata* arose from WGDs [13]. When WGD was initially proposed [3], it was not possible to tell whether it was the result of an **autopolyploidization** or an **allopolyploidization** event [14,15]. However, autopolyploidization constituted the most parsimonious hypothesis. Later, evidence was presented in favor of allopolyploidization, indicating that the *S. cerevisiae* lineage arose from an interspecies hybridization between a strain related to the *Kluyveromyces*, *Lachancea*, and *Eremothecium* (KLE) clade and another related to *Zygosaccharomyces rouxii* and *Torulaspora delbrueckii* (ZT) clade [9,16]. This proposal was extensively analyzed and accepted [2]. Therefore, the pair of **paralogous genes** that are observed today could have both originated from one of the parental species (ohnologous pairs), or each one of the parental species involved in the allopoliplodization event could have independently generated one member of the pair (homeologous genes) [16].

Even before the WGD controversy was settled (1996–2004), the fact that the WGD could have allowed *S. cerevisiae* to develop an oxygen-independent metabolism, through the retention and further specialization of duplicated genes/products, was considered for the first time [3,5] (Box 2). This proposition was based on the observation that the majority of yeasts were unable to grow in absence of oxygen [17].

The progress in comparative genomics in the 2000s allowed a better understanding of the evolution of the *S. cerevisiae* genome and a proper classification of the phylogenetic relationships among yeasts [13,18]. The new phylogenetic trees provided a framework to locate some major evolutionary events that could have contributed to the improved fermentation ability of

Glossary

Adaptive radiation: evolution of organisms into a wide variety of types adapted to specialized modes of life.
Allopolyploidization: a mechanism that generates an individual or strain with two complete sets of chromosomes, each one from a different species.
Autopolyploidization: in contrast to allopolyploidization, the two different sets of chromosomes are from the same species.
Biased fractionation: a phenomenon observed after WGDs where the ohnologues of a subgenome are preferentially lost.
Feedback inhibition: the phenomenon where the output of a process is used as an input to control the behavior of the process itself.
Genome dominance: a phenomenon observed after WGD where, in general, the ohnologues from one subgenome display higher transcriptional levels than their onhologous pair derived from the other subgenome.
Hetero-oligomers: a complex made of different protein subunits is called a hetero-oligomer; when only one type of protein subunit is used in the complex, it is called a homo-oligomer.
Moonlighting functions: protein moonlighting function is a phenomenon by which a protein can perform more than one biological role.
Orthologous: genes in different species that evolved from a common ancestral gene by speciation; orthologs retain the same function in the course of evolution.
Paralogous or ohnologous genes: duplicated genes in the same organism that were evolved from either a gene duplication, an autopolyploidization event, or an allopolyploidization event.
Robustness: the ability of a system to maintain its function despite a perturbation.
Small-scale duplication (SSD): doubling of a small-scale genomic regions involving one to a few genes.
Subgenome: set of genomic regions of a WGD species inherited from one of the parental species.

Box 2. Fate of Duplicated Genes

Gene duplicates, also called paralogs, are found in all three domains of life, suggesting that an important amount of genes were generated by gene duplication [69]. Although the immediate consequence of gene duplication is the doubling of the ancestral function (functional redundancy), after duplication genes can experience divergence that may result in the generation of new or specialized functions and thus shape evolution. This box summarizes the possible scenarios determining the fate of duplicated genes.

Loss of function: Loss of function occurs when functional redundancy is not advantageous and therefore one of the paralogous genes gradually becomes a pseudogene, through the accumulation of loss-of-function mutations [70]. Interestingly, soon after WGDs polyploids experience a rapid loss of genetic redundancy. The current hypothesis is that when WGDs result from an autopolyploidization, the loss of duplicated genes is randomly distributed between the two parental **subgenomes** (non-biased fractionation). By contrast, when the WGD derives from an allopoliploidization, loss of duplicated genes is biased towards a certain parental subgenome (**biased fractionation**), frequently towards the one displaying lower gene expression, a phenomenon called **genome dominance** [71,72].

Gene-dosage amplification: Gene-dosage amplification holds that after gene duplication, both gene copies are conserved since either incrementing the ancestral function represents a selective advantage or both copies are necessary to maintain the appropriate stoichiometry of higher complexes (e.g., protein complexes) [16,71,73,74]. However, it must be considered that increased gene copy number does not necessarily lead to an equivalent function increment, since function/product dosage can be negatively regulated [75–77]. Thus, the gene-dosage amplification requires that the increment in copy number produce an increase in the codified function.

Subfunctionalization: Subfunctionalization occurs when the ancestral function(s) is distributed between the two copies or is differentially specialized in each one, as a result of either the accumulation of degenerative mutations (duplication-degeneration-complementation model) or by positive selection (escape from adaptive conflict model). In both cases, both paralogs are necessary to perform the function that, in the ancestor, was carried out by a single gene [78–81].

Neofunctionalization: Neofunctionalization is the mechanism explaining the origin of novel functions through gene duplication. It considers that while one of the copies conserves the ancestral function, the other is free to acquire a new adaptative function through the accumulation of neutral mutations [82].

Whole-genome duplication (WGD): mechanism by which an organism doubles its chromosome number.

yeasts, such as the loss of the respiratory complex I, the horizontal transfer of the bacterial *URA1*, and the rewiring of rapid growth elements [19].

Starting in 2007, the role of the WGD in the acquisition of yeast fermentative metabolism began to be recognized, mainly through the characterization of the phenotypic responses of various representative species of the Saccharomycetaceae [19–21]. It was found that the Crabtree effect was present in several species of the above-mentioned family. However, yeasts closer to *Saccharomyces* in the phylogenetic tree displayed a more pronounced Crabtree effect, and with the exception of the *Tetrapisispora* group, were able to generate non-respiring mutants, while most of the non-WGD species could not [19,21]. As for the ability to grow under anaerobiosis, the post-WGD species were able to generate sufficient energy to grow under strictly anaerobic conditions, while non-WGD species showed a reduced Crabtree effect and ability to grow in the absence of oxygen [20]. These contributions support the proposition that yeasts' transition to a fermentative lifestyle began before the WGD in non-WGD yeasts in a rather multistep process. However, for Saccharomycetae, this metabolic trait was established after the WGD event [19]. This comparative physiological evidence, and the dating of both the WGD (from 150 to 100 Mya) and the **adaptive radiation** of flowering plants (from 101 to 66 Mya) in the Late Cretaceous [3,22,23], led to the hypothesis that the WGD allowed yeasts to compete for the increased amount of sugars present in fruits [19]. It could thus be expected that retained WGD genes could be enriched in cellular processes related to the make-accumulate-consume strategy.

WGD and Small-Scale Duplications Contribution to Fermentative Metabolism

The contribution of WGD to *S. cerevisiae* fermentative lifestyle could be assessed comparing WGD and **small-scale duplication** (SSD) gene sets in terms of genetic interactions and divergence in expression and functions. One of the first studies on this matter proposed that WGD, but not SSD, must have provided the raw material for conservation of dosage-sensitive genes and groups of genes expressed at a precise stoichiometric ratio, such as those encoding ribosomal proteins [24]. It has been proposed that such dosage and stoichiometric effects could have been involved in the conservation of glycolytic genes [25]. Consistent with this it was found that gene duplicates (combined WGD and SSD) were overrepresented in central carbon metabolism and hexose transport [26]. However, the separate analysis of the gene sets revealed that enrichment in genes involved in carbohydrate metabolism was higher for WGD than for SSD [27]. Divergence in the expression patterns between members of a pair has also been reported to be higher for the WGD than for the SSD set of paralogs [27]. It may be possible that divergent regulation between members of some duplicated pairs could have contributed to the specialization of one paralog for glycolysis-ethanol production and the other for gluconeogenesis-ethanol consumption phases. The impact of such differential regulation on the acquisition of fermentative metabolism could be estimated by comparing the rates of negative expression correlations between members of a pair during growth on glucose or ethanol as carbon sources. To explore this possibility, data from a quantitative proteomic study were used where the relative abundances of 3609 proteins were determined [28]. Comparison of the abundance of both paralogs during fermentation, diauxic shift, and glucose exhaustion phases indicated that 29% of WGD and 19% of SSD duplicates showed differential regulation during fermentative and respiratory metabolism. The same trend was observed using data from a transcriptomic study that determined the fold change in transcript levels for 5800 genes from cells cultured on rich media with glucose or ethanol as carbon sources [29]; the estimated percentage of divergent expression was 26% for the WGD and 14% for the SSD duplicates (for analysis details of proteomic and transcriptomic data, see the legend of Figure S1 in the supplemental information online). Interestingly, the enzyme-coding subset of genes with differential expression during fermentative and respiratory metabolism among WGD genes clustered around carbohydrate metabolism (Figure 1A; Figure S1A). By contrast, enzymes encoded by SSD paralogs seem to be randomly dispersed around various metabolic pathways (Figure 1B; Figure S1B) [28,29].

Comparison of gene ontology (GO) categories' fold enrichment between divergent and complete sets of genes (Figure 2) shows that for the WGD group, glucose metabolism GO terms are overrepresented (Figure 2A). Furthermore, the WGD divergent set displays a higher fold enrichment in glucose metabolism GO terms than that exhibited by the WGD complete set (Figure 1A; Figure S1A). Moreover, glucose metabolism is not represented in the SSD group (Figure 2B), which for divergent and complete categories is enriched in biosynthetic processes, suggesting a different evolutionary trend. Overall, these results indicate that the WGD set of genes display a more relevant contribution than those of SSD set to the acquisition of a fermentative lifestyle in the *S. cerevisiae* lineage.

Duplicated Genes Case Studies Uncover Molecular Mechanisms behind Subfunctionalization

Detailed analysis of subfunctionalization of particular paralogous pairs is necessary to identify the molecular mechanisms involved in functional diversification and the roles of specific duplicate genes in the acquisition of fermentative metabolism. We first analyze four examples

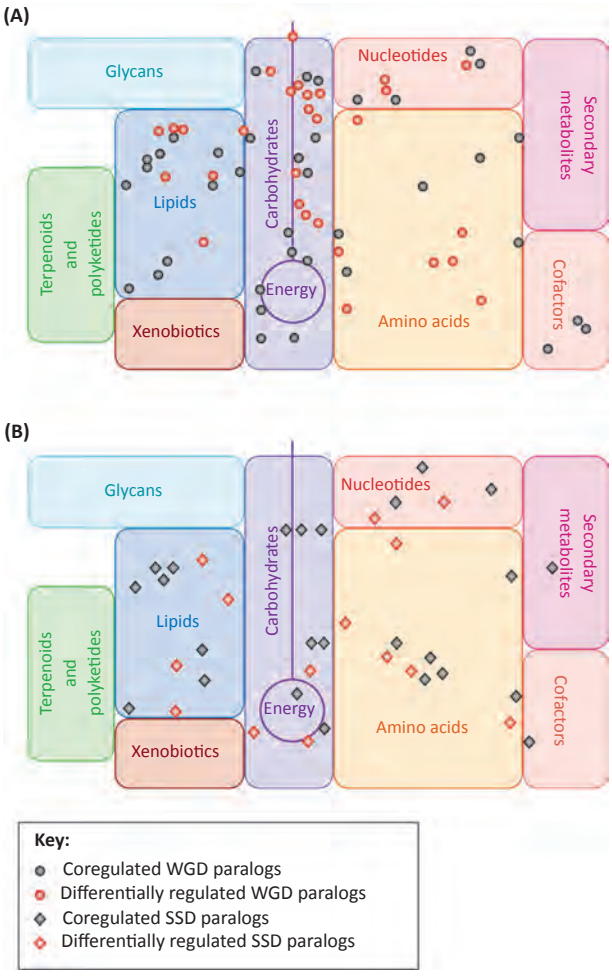

Figure 1. Duplicated Gene Pairs Originated from WGD Are Enriched for Genes Encoding Enzymes Involved in Carbohydrate Metabolism. Enzymes encoded by whole-genome duplication (WGD) (A) or small-scale duplication (SSD) (B) paralogs were mapped on the Kyoto Encyclopedia of Genes and Genomes refer pathway map (http://www.genome.jp/kegg/pathway/map/map01100.html) [84]. Coregulated or differentially regulated paralogs were selected according to their regulation pattern during fermentative or respiratory conditions from global studies [28,29]. For pathway details, gene identity, and analysis, please see Figure S1 in the supplemental information online.

of gene pairs that, according to the phylogeny-based prediction of PhylomeDB v4, could be proposed as ohnologous WGD pairs [30].

ENO1- and *ENO2*-encoded phosphopyruvate hydratases catalyze the reversible conversion of 2-phosphoglycerate to phosphoenolpyruvate. Under fermentative conditions, Eno2 constitutes the predominant form, while under respiratory conditions both polypeptides are present and contribute to gluconeogenesis [31]. Random assortment of Eno1/Eno2 monomers allows the formation of homo- and hetero-dimers: Eno1-Eno1, Eno2-Eno2, and Eno1-Eno2, whose peculiar organization could influence the opposed role these enzymes play in the glycolysis and gluconeogenesis [32] (Figure 3).

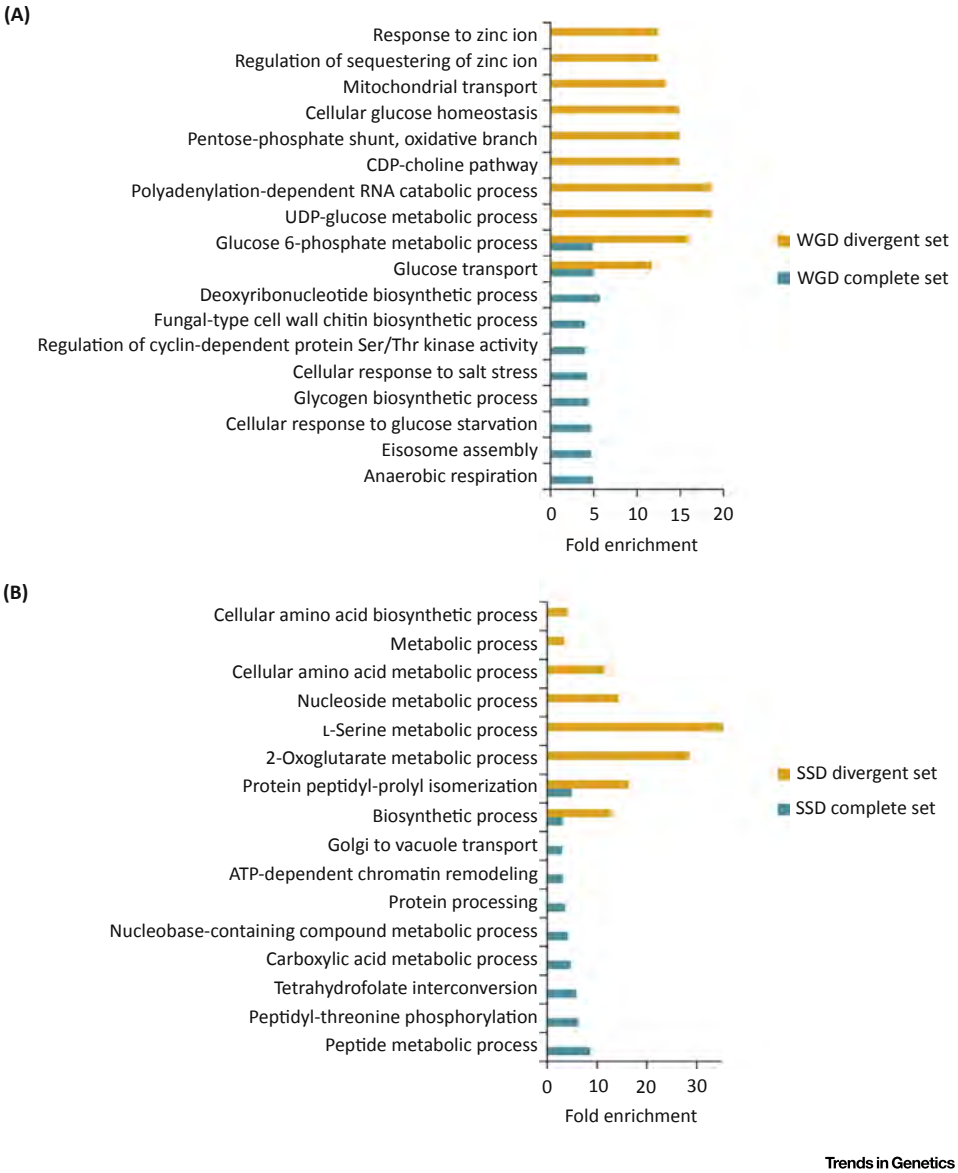

Figure 2. WGD and SSD Gene Sets Contribute to Different Cellular Processes during Fermentative and Respiratory Metabolism. Top ten GOTERM_BP_DIRECT categories with higher enrichment fold values among whole-genome duplication (WGD) (A) or small-scale duplication (SSD) (B) gene sets are shown ($P < 0.01$). The complete gene sets include 1094 and 674 genes for WGD and SSD, respectively. The sets with divergent expression patterns include 328 and 106 genes for WGD and SSD, respectively. Paralogs with divergent regulation between members of a pair were obtained from global studies [28,29] analyzed as described in Figure S1 in the supplemental information online. For the set of SSD paralogs with divergent regulation, only eight terms result with $P < 0.01$. Gene annotation enrichment analysis was made using the DAVID 6.7 website (https://david.ncifcrf.gov/) with default values. CDP, cytidine diphosphate; UDP, uridine diphosphate.

Formation of heteromeric isozymes plays a role in functional diversification of the two ohnologous WGD-pair [33] encoding cytosolic NADP-GDHs (*GDH1* and *GDH3*), catalyzing glutamate biosynthesis from ammonia and α-ketoglutarate (α-KG). While the homo-hexameric Gdh1 is the sole isoform present under fermentative conditions, the homo-hexameric Gdh3

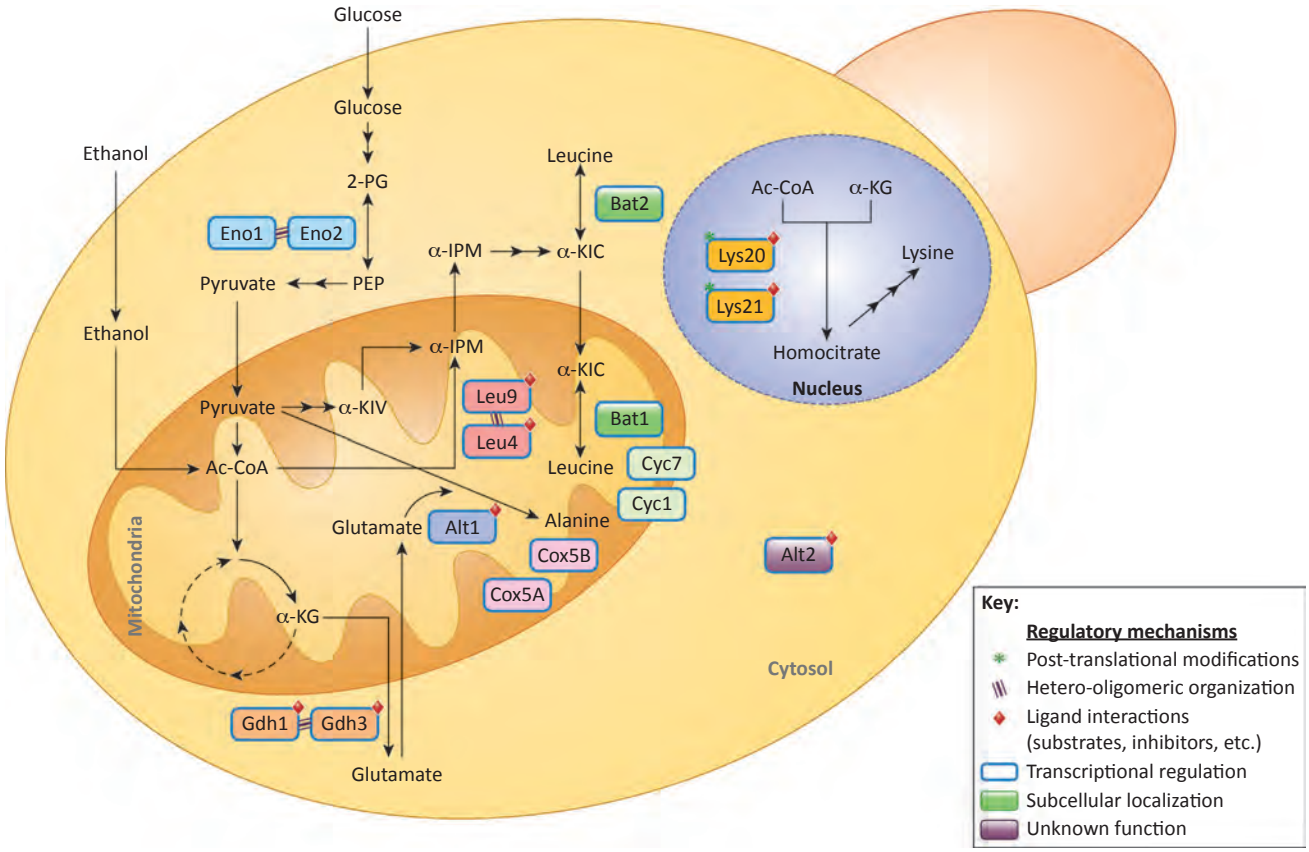

Trends in Genetics

Figure 3. Molecular Mechanisms of Paralog Subfunctionalization. Enzyme-coding whole-genome duplication paralogs can diverge and become specialized in different metabolic conditions. Illustrative examples and the corresponding mechanisms of subfunctionalization are shown. Ac-CoA, acetyl coenzyme A; α-IPM, alpha isopropylmalate α-KG, alpha ketoglutarate; α-KIC, alpha ketoisocaproate; KIV, alpha ketoisovalerate; PEP, phosphoenolpyruvate; 2-PG, 2-phosphoglycerate.

is only present in a *gdh1*Δ mutant grown on ethanol as sole carbon source and the Gdh1-Gdh3 hetero-hexameric isoform(s) prevail under respiratory conditions [34]. Accordingly, *GDH1* expression is maintained through the different growth phases, while that of *GDH3* is null during fermentation and due to chromatin remodeling increases 70-fold when cells enter diauxic shift and respiratory growth [35].

The affinity of the three isoforms towards α-KG (Gdh1-Gdh1 > Gdh1-Gdh3 > Gdh3-Gdh3) agrees with the idea that under fermentative growth, energy is provided by glycolysis; thus, the high rate activity of Gdh1 does not compromise energy yield. Under respiratory conditions when the tricarboxylic acid (TCA) cycle contributes to energy production, *GDH1* and *GDH3* are simultaneously expressed and a variety of isozymes can be built up depending on the Gdh1:Gdh3 ratio. Therefore, the modulable heteromeric isoforms constitute a pacemaker mechanism determining glutamate biosynthesis and balanced α-KG utilization [34,36] (Figure 3).

The kinetic properties of the NADP-*Lk*Gdh1 present in the non-WGD yeast *Lachancea kluyveri* are closer to those of Gdh1, while kinetics of the *Kluyveromyces lactis* NADP-*Kl*Gdh1 resemble those of Gdh3, suggesting there is a correlation between the NADP-GDHs kinetic properties

and the level of adaptation to the fermentative or respiratory lifestyle [33]. The above-mentioned results indicate that both *GDH1* and *GDH3* originated from the KLE lineage, supporting predictions obtained through PhylomeDB v4 [30].

Paralogous mitochondrial homo- and heteromeric isozymes were formed by the *LEU4*/*LEU9* ohnologous WGD-pair [30], encoding α-isopropylmalate synthases that synthesize α-isopropylmalate (α-IPM) from acetyl-coenzyme A (CoA) and α-ketoisovalerate, an intermediate of leucine biosynthesis and co-activator of the Leu3 transcriptional regulator [37]. Leu4-Leu4 and Leu9-Leu9 homodimers are leucine sensitive or resistant isoforms, respectively, while the heterodimeric isoform Leu4-Leu9 shows intermediate leucine sensitivity. On ethanol as carbon source, *LEU4* expression is 3-fold increased compared to that found in glucose, while that of *LEU9* is low on both carbon sources. Leu4-Leu9 and Leu4-Leu4 formation prevents leucine and α-IPM over-synthesis, mediating a more balanced distribution of pyruvate and acetyl-CoA to intermediary biosynthesis and energy yielding metabolism particularly under respiratory conditions. Exclusive expression of Leu9, in a *leu4Δ* genetic background, results in slow growth on either glucose or ethanol as carbon sources and leucine accumulation, indicating that Leu9-Leu9 resistance to leucine **feedback inhibition** impairs flux control through the biosynthetic pathway [37] (Figure 3).

Lys20 and Lys21 nuclear homocitrate synthases participate in lysine biosynthesis by catalyzing homocitrate production, condensing acetyl-CoA with α-KG [36]. Lysine is a strong inhibitor for Lys21, inducing positive cooperativity for α-KG binding. Under fermentative conditions, Lys20 and Lys21 play redundant roles, and even when *LYS20* and *LYS21* ohnologous WGD-pair are overexpressed, and lysine pools increase 4- to 10-fold, growth rate is not reduced, confirming the conclusion that α-KG drainage is not deleterious under fermentative conditions [36]. Lys21 activity is crucial for growth under respiratory conditions and can sustain wild-type growth by itself. Subfunctionalization includes differential *LYS20* and *LYS21* expression and a post-transcriptional mechanism that determines the abundance of each enzyme. Differential lysine inhibition, α-KG modulation, and the control of the intracellular amount of the two enzymes result in a regulatory mechanism determining the rate at which α-KG is diverted to either lysine biosynthesis or to other metabolic pathways (Figure 3) [38].

The above-mentioned presented cases show that the combined action of the formation of paralogous homo- and hetero-oligomeric isozymes with peculiar kinetic properties and contrasting gene expression results in functional diversification, providing a means to differentially control metabolic fluxes under fermentative or respiratory conditions.

The four next examples correspond to WGD-pairs that could be tentatively proposed as homeologous, according to PhylomeDB v4 prediction [30]. Bat1 and Bat2 branched chain aminotransferases are located in mitochondria and cytosol, respectively; thus, formation of **hetero-oligomers** is impeded. Diversification of the *BAT1* and *BAT2* relies on the acquisition of opposed expression profiles [39]. Bat1 has a biosynthetic character, since *BAT1* expression is privileged in the absence of branched chain amino acids, while Bat2 displays a catabolic role. *BAT2* expression is maximal in the presence of branched chain amino acids [39,40]. Acquisition of environmentally regulated expression profiles could allow operation of differential or redundant roles depending on the peculiar environments found in *S. cerevisiae* natural habitats [7,41,42].

In regard to the contribution of Bat1 and Bat2 adaptation to fermentative metabolism, *BAT1* decreased expression under respiratory conditions and resulted in diminished metabolic flow to

amino acid biosynthesis, favoring energy-yielding pathways (Figure 3) [40]. The *KlBAT1* **orthologous gene**, present in *K. lactis* non-WGD yeast, encodes an enzyme displaying the dual biosynthetic-catabolic character that was later specialized among the *S. cerevisiae BAT1/BAT2* paralogous pair [39].

Functional characterization of the *ALT1/ALT2* WGD-pair gene/products established that only Alt1 possessed the presumed role of alanine transaminase activity [43]. The analysis of the only orthologous gene/product present in *L. kluyveri* and *K. lactis* non-WGD type yeasts suggested that Alt2 functional diversification resulted in the loss of its alanine transaminase activity [44]. Probably, as the result of a structural change modifying the interaction with its cofactor pyridoxal 5-phosphate (PLP), allowing the formation of only one of the two tautomeric PLP isomers necessary for the transamination reaction. The fact that Alt2 forms a catalytically active Schiff base with PLP and is found in a phylogenetic branch with several *Saccharomyces* genera, which do not harbor Alt1, suggests this enzyme has a yet undiscovered function (Figure 3) [45].

Cytochrome *c* oxidase (COXC) is a complex composed of several proteins that transfer electrons from cytochrome *c* to molecular oxygen [46]. Cox5 is essential for complex assembly and has two paralogous isoforms: Cox5A and Cox5B. *CYC1* and *CYC7* encode paralogous isoforms of the electron carrier protein cytochrome *c*, promoting the final transfer of electrons to oxygen by COXC. Under aerobic conditions, *COX5A* and *CYC1* are expressed, whereas *COX5B* and *CYC7* are Rox repressed and are only expressed under hypoxia. Differential expression of these genes had been previously considered to be important in yeast evolutionary adaptation to anaerobic growth [3]. As for *BAT1* and *BAT2*, functional diversification is achieved through the acquisition of opposed transcriptional patterns [40].

For some cases, orthologous *K. lactis* and/or *L. kluyveri* counterparts have been analyzed; however, it would be important to study both a KLE and a ZT representative for each case. This is mandatory to clarify whether sub- or neofunctionalization has occurred.

WGD Paralogous Genes Impart Robustness and Phenotypic Plasticity

As mentioned above, duplicated genes allow *S. cerevisiae* to adjust its phenotype to properly respond to a changing environment. The role of paralogous homo- and hetero-oligomers as key players regulating metabolic fluxes leading to new phenotypes has also been highlighted. In this section, we discuss this evidence in terms of **robustness** and phenotypic plasticity (Box 3). Gene duplicates have been associated to genetic robustness [47–49]; however, a recent study found opposing evidence suggesting that in some cases gene duplication can impart fragility [50]. By analyzing the protein–protein interaction network of 56 pairs of duplicated genes (WGD or SSD), it was found that in one-third of the cases, upon deletion of a paralogous copy, the remaining copy conserved its capacity to interact with its native binding partners and increased its association with those of the deleted copy, thus compensating paralogous pair loss [50]. In a similar amount of cases, after deletion of its cognate pair, the remaining copy decreased interactions even with its own binding partners, demonstrating dependency on its paralogous copy. In these cases, the lower expressed copy of the homologous pair was the only one displaying the dependency phenotype, indicating asymmetry and showing a stronger decrease in fitness (fragility) than that displayed by the independent copies. Furthermore, in the absence of its pair, the protein concentration of the dependent copy decreased, although its mRNA showed wild-type levels, suggesting protein destabilization [50,51].

Considering that, in general, dependent pairs form paralogous hetero-oligomers, it was proposed that the different paralogous isoforms could be degraded at different rates

Box 3. Duplicated Genes Contribute to Genetic Robustness

Robustness is defined as the ability of a system to maintain its function upon a perturbation. In living systems, perturbations can either be environmental or genetic. Multiple mechanisms that confer robustness to biological systems have been described. (i) Distributed robustness. Upon a perturbation, specific biological functions can be accomplished by alternative pathways, as in signaling and metabolic routes [49,83]. (ii) Redundancy. Multiple functional copies of a given component of the biological system can compensate the failure of another highly similar component, for example, paralogous genes [49,83]. (iii) Feedback control. By sensing the output of a function, it is possible to modulate the input to either narrow the output function (negative feedback) or to amplify and maintain signals against noise (positive feedback). This type of control contributes to preservation of cellular function (homeostasis) [47–49]. (iv) Modularity. The confinement of functions minimize the effects of disturbances by containing perturbations and damage locally [47–49].

It is considered that duplicated genes contribute to genetic robustness since the paralogous copies maintain a certain degree of functional redundancy. Thus, when one of the gene duplicates is deleted, the remaining copy can provide enough function to compensate the deletion of its paralogous pair. In several cases, the wild-type function of the retained copy is enough to compensate the deleted pair (passive paralogous compensation). In many other cases, the remaining paralog needs to modify its performance, to avoid the phenotypic or fitness defects produced by the deletion of its pair (active paralogous compensation). Different molecular mechanisms of active paralogous compensation have been identified: (i) Transcriptional reprograming. Some paralogous genes are upregulated upon the genetic perturbation, functionally compensating the deleted copy. (ii) Protein relocalization. Even though there are limited examples, the remaining copy could experience relocalization to the subcellular compartment were the deleted copy used to reside. (iii) Protein interaction rewiring. Some paralogous genes can increase the association with the binding partners of the missing copy [51].

Another important attribute of biological systems is phenotypic plasticity. This plasticity is recognized as the ability of a single genotype to produce different phenotypes, allowing a best performance within changing environments. Often phenotypic plasticity is considered to be the opposite of robustness [54]. However, paralogous genes have also been associated with phenotypic plasticity [62].

(independent homo-oligomers < hetero-oligomers < dependent homo-oligomers < monomers) [52,53]. However, the above-mentioned analysis did not account for self-interactions [50]. Interestingly, for the paralogs proteins Leu4 and Leu9 the formation of the Leu4-Leu9 heterodimer is preferred over that of the homodimers, possibly as the result of a higher affinity between different monomers than between self-monomers. However, both paralogous copies can form homodimers; nevertheless, it cannot be ruled out that when the concentration of the independent form is too low, oligomer:monomer equilibrium may be displaced towards the monomeric forms, resulting in higher degradation [52]. Besides Leu4-Leu9 heterodimers, other paralogous genes are capable of forming hetero-oligomeric complexes such as Gdh1-Gdh3 and Eno1-Eno2. For Leu4/Leu9 and Gdh1/Gdh3, in all cases the three different isoforms show specific kinetic parameters [32,34,37]. The coexistence of more than one isoform allows coping with a wider range of metabolite concentrations (substrates, inhibitors, etc.) than when there is only one isoform, providing a buffering effect and thus contributing to robustness (feedback control).

Another important attribute of biological systems is the phenotypic plasticity. This plasticity is recognized as the ability of a single genotype to produce different phenotypes, allowing a best performance within changing environments. Often phenotypic plasticity is considered to be the opposite of robustness [54]. However, since different isozymes are used in distinct metabolic context [34,37], regulating carbon flux to biomass production. It is possible that the ability to form hetero-oligomers contribute to the acquisition of the Crabtree effect and thus to phenotypic plasticity. If this is the case, heteromeric forming paralogous proteins could be considered as major regulators of both robustness and phenotypic plasticity, providing optimal fitness within changing environments [55].

Concluding Remarks and Future Directions

Recent advances in entire genome sequencing have generated an increasing interest in understanding the role of polyploidy on ecological shifts. In particular, different approaches have been used to elucidate the relationship between WGD and the acquisition of fermentative metabolism in *S. cerevisiae*. By comparing some physiological traits among the Saccharomycetaceae, it was possible to determine the central role of the WGD in the establishment of a new way of life for *S. cerevisiae*. The localization of the origin of fermentative metabolism before the WGD [19] suggests the prior existence of a selection pressure towards an oxygen-independent metabolism. The evolutionary trends followed by paralogous genes originated from WGD, which were identified through global analyses, have unveiled the general strategies that favored the establishment of a new lifestyle [26,29]. Moreover, the detailed analysis of particular duplicated pairs has shown some of the mechanisms behind the functional diversification of paralogous genes. Although detailed studies are scarce, some general rules on how particular changes in paralogous pairs have contributed to the acquisition of fermentative metabolism are starting to emerge (Figure 3).

Particularly interesting has been the finding that formation of hetero-oligomeric complexes contributes to robustness and phenotypic plasticity by enhancing the role of paralogous enzymes influencing the intracellular concentration of key metabolites such as α-IPM controlling the Leu3 transcriptional network [40]; leucine influencing cell growth control [56,57]; lysine determining response to oxidative stress [58]; and α-KG playing a functional role in aging [59].

Although the neolocalization of a paralogous copy is frequently observed [60], the evolutionary and physiological role of diversification of subcellular localization remains to be fully addressed (see Outstanding Questions) and certainly constitutes an open pathway to understand functional diversification of paralogs. In this respect, the analysis of **moonlighting functions** could govern the diversification of subcellular localization.

Future studies of paralogous pairs diversification must imperatively include specific analyses to understand whether a particular pattern is the outcome of sub- or neofunctionalization. To this end, pertinent paralogous functional characterization will also have to be addressed in non-WGD yeasts.

The rapidly increasing amount of *S. cerevisiae* isolates and the availability of their entire genome sequences will promote the systematical study of WGD genes from yeast strains collected from natural habitats [7,41,42,61–63] that could lead to the understanding of the involvement of duplicated genes in other processes besides the fermentative metabolism observed in controlled environments.

Acknowledgments

We acknowledge Beatriz Aguirre-López for advice and productive discussions during the development of this review. Our research is supported by grant from Dirección de Asuntos del Personal Académico (IN204018) and Consejo Nacional de Ciencia y Tecnología (CB-2014-239492-B). This work was supported by the Deutsche Forschungsgemeinschaft (RTG1772 'Computational Systems Biology').

Supplemental Information

Supplemental information associated with this article can be found online at https://doi.org/10.1016/j.tig.2018.09.008.

Outstanding Questions

What is the role of subcellular localization in paralogues functional diversification? Although it has been '*a priori*' considered that subcellular localization could have an important influence in the physiological role of a protein, no experiments have been performed that result in re-localization or co-localization of paralogous enzymes.

Are moonligthing properties inherited from the ancestor or did they arise after WGD? Do moonlighting properties diversify between paralogs? There are several examples of paralogous genes generated through WGD in which one of the members of the paralogous pair has an identified additional function (moonlight). However detailed analysis of its counterpart is compelling to definitively establish whether the moonlighting property has been conserved in both paralogs. Differential localization of enzymes such as Bat1 and Bat2 placed in mitochondria and cytosol, respectively, could be considered as a mechanism preventing formation hetero-oligomers. However, since Bat1 has a moonlighting function forming a complex with aconitase, its mitochondrial localization could have an important role in TCA regulation and not in its aminotransferase function.

Mathematical models have proven useful in understanding complex system behavior. Models may help answer the following questions at a systemic level: How does gene duplication alter metabolic fluxes and transcriptional regulation? What are the underlying regulatory mechanisms that allowed yeasts to acquire a fermentative lifestyle? How do WGD homologous genes orchestrate energy metabolism and biomass production to sustain the rapid growth rate observed during the Crabtree effect?

What are the most appropriate culture conditions to address the role of duplicated genes?

What is the relative contribution of post-translational modifications to divergence in regulation of proteins encoded by duplicated genes?

References

1. Goffeau, A. *et al.* (1996) Life with 6000 genes. *Science* 274, 546, 563–567
2. Wolfe, K.H. (2015) Origin of the yeast whole-genome duplication. *PLoS Biol.* 13, 1–7
3. Wolfe, K.H. and Shields, D.C. (1997) Molecular evidence for an ancient duplication of the entire yeast genome. *Nature* 387, 708–713
4. Van De Peer, Y. *et al.* (2017) The evolutionary significance of polyploidy. *Nat. Rev. Genet.* 18, 411–424
5. Piškur, J. (2001) Origin of the duplicated regions in the yeast genomes. *Trends Genet.* 17, 302–303
6. Botstein, D. and Fink, G.R. (2011) Yeast: an experimental organism for 21st century biology. *Genetics* 189, 695–704
7. Peter, J. *et al.* (2018) Genome evolution across 1,011 *Saccharomyces cerevisiae* isolates. *Nature* 556, 339–344
8. Koszul, R. *et al.* (2004) Eucaryotic genome evolution through the spontaneous duplication of large chromosomal segments. *EMBO J.* 23, 234–243
9. Kellis, M. *et al.* (2004) Proof and evolutionary analysis of ancient genome duplication in the yeast *Saccharomyces cerevisiae*. *Nature* 428, 617–624
10. Dietrich, F.S. *et al.* (2004) The *Ashbya gossypii* genome as a tool for mapping the ancient *Saccharomyces cerevisiae* genome. *Science* 304, 304–307
11. Dujon, B. *et al.* (2004) Genome evolution in yeasts. *Nature* 430, 35–44
12. Byrne, K.P. and Wolfe, K.H. (2005) The yeast gene order browser: combining curated homology and syntenic context reveals gene fate in polyploid species. *Genome Res.* 15, 1456–1461
13. Kurtzman, C. (2003) Phylogenetic circumscription of *Saccharomyces*, *Kluyveromyces* and other members of the *Saccharomycetaceae*, and the proposal of the new genera *Lachancea*, *Nakaseomyces*, *Naumovia*, *Vanderwaltozyma* and *Zygotorulaspora*. *FEMS Yeast Res.* 4, 233–245
14. Gordon, J.L. *et al.* (2009) Additions, losses, and rearrangements on the evolutionary route from a reconstructed ancestor to the modern *Saccharomyces cerevisiae* genome. *PLoS Genet.* 5, 1–14
15. Gordon, J.L. *et al.* (2011) Mechanisms of chromosome number evolution in yeast. *PLoS Genet.* 7, 1–13
16. Marcet-Houben, M. and Gabaldón, T. (2015) Beyond the whole-genome duplication: phylogenetic evidence for an ancient interspecies hybridization in the baker's yeast lineage. *PLoS Biol.* 13, 1–26
17. Olsson, L. and Mo, K. (2001) Ability for anaerobic growth is not sufficient for development of the petite phenotype in *Saccharomyces kluyveri*. *J. Bacteriol.* 183, 2485–2489
18. Kurtzman, C. and Robnett, C. (2003) Phylogenetic relationships among yeasts of the "*Saccharomyces* complex" determined from multigene sequence analyses. *FEMS Yeast Res.* 3, 417–432
19. Hagman, A. *et al.* (2013) Yeast "make-accumulate-consume" life strategy evolved as a multi-step process that predates the whole genome duplication. *PLoS One* 8, 1–12
20. Merico, A. *et al.* (2007) Fermentative lifestyle in yeasts belonging to the *Saccharomyces* complex. *FEBS J.* 274, 976–989
21. Dashko, S. *et al.* (2014) Why, when, and how did yeast evolve alcoholic fermentation? *FEMS Yeast Res.* 14, 826–832
22. Augusto, L. *et al.* (2014) The enigma of the rise of angiosperms: can we untie the knot? *Ecol. Lett.* 17, 1326–1338
23. Lunau, K. (2004) Adaptive radiation and coevolution — pollination biology case studies. *Org. Divers. Evol.* 4, 207–224
24. Davis, J.C. and Petrov, D.A. (2005) Do disparate mechanisms of duplication add similar genes to the genome? *Trends Genet.* 21, 548–551
25. Conant, G.C. and Wolfe, K.H. (2007) Increased glycolytic flux as an outcome of whole-genome duplication in yeast. *Mol. Syst. Biol.* 3, 1–12
26. Kuepfer, L. *et al.* (2005) Metabolic functions of duplicate genes in *Saccharomyces cerevisiae*. *Genome* 15, 1421–1430
27. Guan, Y. *et al.* (2007) Functional analysis of gene duplications in *Saccharomyces cerevisiae*. *Genetics* 175, 933–943
28. Murphy, J.P. *et al.* (2015) Comprehensive temporal protein dynamics during the diauxic shift in *Saccharomyces cerevisiae*. *Mol. Cell. Proteomics* 14, 2454–2465
29. Mattenberger, F. *et al.* (2017) The phenotypic plasticity of duplicated genes in *Saccharomyces cerevisiae* and the origin of adaptations. *Genes Genomes Genet.* 7, 63–75
30. Huerta-Cepas, J. *et al.* (2014) PhylomeDB v4: zooming into the plurality of evolutionary histories of a genome. *Nucleic Acids Res.* 42, 897–902
31. Cohen, R. *et al.* (1987) Transcription of the constitutively expressed yeast enolase gene *ENO1* is mediated by positive and negative *cis*-acting regulatory sequences. *Mol. Cell. Biol.* 7, 2753–2761
32. Mcalister, L. and Holland, M.J. (1982) Targeted deletion of a yeast enolase structural gene. *J. Biol. Chem.* 257, 7181–7188
33. Campero-Basaldua, C. *et al.* (2017) Diversification of the kinetic properties of yeast NADP-glutamate-dehydrogenase isozymes proceeds independently of their evolutionary origin. *Microbiologyopen* 6, 1–18
34. DeLuna, A. *et al.* (2001) NADP-glutamate dehydrogenase isoenzymes of *Saccharomyces cerevisiae*. *J. Biol. Chem.* 276, 43775–43783
35. Avendaño, A. *et al.* (2005) Swi/SNF-GCN5-dependent chromatin remodelling determines induced expression of *GDH3*, one of the paralogous genes responsible for ammonium assimilation and glutamate biosynthesis in *Saccharomyces cerevisiae*. *Mol. Microbiol.* 57, 291–305
36. Quezada, H. *et al.* (2008) Specialization of the paralogue *LYS21* determines lysine biosynthesis under respiratory metabolism in *Saccharomyces cerevisiae*. *Microbiology* 154, 1656–1667
37. López, G. *et al.* (2015) Diversification of paralogous α-isopropylmalate synthases by modulation of feedback control and heterooligomerization in *Saccharomyces cerevisiae*. *Eukaryot. Cell* 14, 564–577
38. Quezada, H. *et al.* (2011) The Lys20 homocitrate synthase isoform exerts most of the flux control over the lysine synthesis pathway in *Saccharomyces cerevisiae*. *Mol. Microbiol.* 82, 578–590
39. Colón, M. *et al.* (2011) *Saccharomyces cerevisiae* Bat1 and Bat2 aminotransferases have functionally diverged from the ancestral-like *Kluyveromyces lactis* orthologous enzyme. *PLoS One* 6, 1–13
40. González, J. *et al.* (2017) Diversification of transcriptional regulation determines subfunctionalization of paralogous branched chain aminotransferases in the yeast *Saccharomyces cerevisiae*. *Genetics* 207, 975–991
41. Liti, G. *et al.* (2009) Population genomics of domestic and wild yeasts. *Nature* 458, 337–341
42. Naumov, G.I. *et al.* (2013) Molecular genetic diversity of the *Saccharomyces* yeasts in Taiwan: *Saccharomyces arboricola*, *Saccharomyces cerevisiae* and *Saccharomyces kudriavzevii*. *Antonie Van Leeuwenhoek* 103, 217–228
43. Peñalosa-Ruiz, G. *et al.* (2012) Paralogous *ALT1* and *ALT2* retention and diversification have generated catalytically active and inactive aminotransferases in *Saccharomyces cerevisiae*. *PLoS One* 7, 1–13
44. Escalera-Fanjul, X. *et al.* (2017) Evolutionary diversification of alanine transaminases in yeast: catabolic specialization and biosynthetic redundancy. *Front. Microbiol.* 8, 1–16
45. Rojas-Ortega, E. *et al.* (2018) *Saccharomyces cerevisiae* differential functionalization of presumed ScALT1 and ScALT2 alanine transaminases has been driven by diversification of pyridoxal phosphate interactions. *Front. Microbiol.* 9, 1–16
46. Dodia, R. *et al.* (2014) Comparisons of subunit 5A and 5B isoenzymes of yeast cytochrome c oxidase. *Biochem. J.* 464, 335–342

47. Stelling, J. *et al.* (2004) Robustness of cellular functions. *Cell* 118, 675–685
48. Kitano, H. (2004) Biological robustness. *Nat. Rev. Genet.* 5, 826–837
49. Frederik Nijhout, H. *et al.* (2017) Systems biology of phenotypic robustness and plasticity. *Integr. Comp. Biol.* 57, 171–184
50. Diss, G. *et al.* (2017) Gene duplication can impart fragility, not robustness, in the yeast protein interaction network. *Science* 355, 630–634
51. Diss, G. *et al.* (2014) Molecular mechanisms of paralogous compensation and the robustness of cellular networks. *J. Exp. Zool. Part B Mol. Dev. Evol.* 322, 488–499
52. Veitia, R.A. (2017) Gene duplicates: agents of robustness or fragility? *Trends Genet.* 33, 377–379
53. Veitia, R.A. (2017) Gene duplicates: agents of fragility? – a reply to Landry and Diss. *Trends Genet.* 33, 658–660
54. Padilla, D.K. *et al.* (2014) Addressing grand challenges in organismal biology: the need for synthesis. *Bioscience* 64, 1178–1187
55. Lachowiec, J. *et al.* (2016) Molecular mechanisms governing differential robustness of development and environmental responses in plants. *Ann. Bot.* 117, 795–809
56. Kingsbury, J.M. *et al.* (2015) Branched-chain aminotransferases control TORC1 signaling in *Saccharomyces cerevisiae*. *PLoS Genet.* 11, 1–24
57. Bonfils, G. *et al.* (2012) Leucyl-tRNA synthetase controls TORC1 via the EGO complex. *Mol. Cell* 46, 105–110
58. O'Doherty, P.J. *et al.* (2014) Transcriptomic and biochemical evidence for the role of lysine biosynthesis against linoleic acid hydroperoxide-induced stress in *Saccharomyces cerevisiae*. *Free Radic. Res.* 48, 1454–1461
59. Chin, R.M. *et al.* (2014) The metabolite α-ketoglutarate extends lifespan by inhibiting ATP synthase and TOR. *Nature* 510, 397–401
60. Marques, A.C. *et al.* (2008) Functional diversification of duplicate genes through subcellular adaptation of encoded proteins. *Genome Biol.* 9, 1–12
61. Stefanini, I. *et al.* (2016) Dynamic changes in microbiota and mycobiota during spontaneous 'Vino Santo Trentino' fermentation. *Microb. Biotechnol.* 9, 195–208
62. Legras, J.-L. *et al.* (2018) Adaptation of *S. cerevisiae* to fermented food environments reveals remarkable genome plasticity and the footprints of domestication. *Mol. Biol. Evol.* 35, 1712–1727
63. Liti, G. (2015) The fascinating and secret wild life of the budding yeast *S. cerevisiae*. *Elife* 4, 1–9
64. Kayikci, Ö. and Nielsen, J. (2015) Glucose repression in *Saccharomyces cerevisiae*. *FEMS Yeast Res.* 15, 1–8
65. Compagno, C. *et al.* (2014) Introduction to carbon metabolism in yeast. In *Molecular Mechanisms in Yeast Carbon Metabolism*, pp. 1–19, Springer
66. Sokolov, S.S. *et al.* (2015) Negative feedback of glycolysis and oxidative phosphorylation: mechanisms of and reasons for it. *Biochemistry* 80, 559–564
67. Gombert, A.K. and Moreira, M. (2001) Network identification and flux quantification in the central metabolism of *Saccharomyces cerevisiae* under different conditions of glucose repression. *J. Bacteriol.* 183, 1441–1451
68. Tripodi, F. *et al.* (2015) Post-translational modifications on yeast carbon metabolism: regulatory mechanisms beyond transcriptional control. *Biochim. Biophys. Acta Gen. Subj.* 1850, 620–627
69. Zhang, J. (2003) Evolution by gene duplication: an update. *Trends Ecol. Evol.* 18, 292–298
70. Conrad, B. and Antonarakis, S.E. (2007) Gene duplication: a drive for phenotypic diversity and cause of human disease. *Annu. Rev. Genomics Hum. Genet.* 8, 17–35
71. Emery, M. *et al.* (2018) Preferential retention of genes from one parental genome after polyploidy illustrates the nature and scope of the genomic conflicts induced by hybridization. *PLoS Genet.* 14, 1–24
72. Liang, Z. and Schnable, J.C. (2018) Functional divergence between subgenomes and gene pairs after whole genome duplications. *Mol. Plant* 11, 388–397
73. Birchler, J.A. and Veitia, R.A. (2007) The gene balance hypothesis: from classical genetics to modern genomics. *Plant Cell Online* 19, 395–402
74. Wapinski, I. *et al.* (2007) Natural history and evolutionary principles of gene duplication in fungi. *Nature* 449, 54–61
75. Kondrashov, F.A. (2012) Gene duplication as a mechanism of genomic adaptation to a changing environment. *Proc. R. Soc. B Biol. Sci.* 279, 5048–5057
76. Kondrashov, F.A. and Kondrashov, A.S. (2006) Role of selection in fixation of gene duplications. *J. Theor. Biol.* 239, 141–151
77. Tang, Y.C. and Amon, A. (2013) Gene copy-number alterations: a cost-benefit analysis. *Cell* 152, 394–405
78. Hughes, A.L. (1994) The evolution of functionally novel proteins after gene duplication. *Proc. Biol. Sci.* 256, 119–124
79. Innan, H. and Kondrashov, F. (2010) The evolution of gene duplications: classifying and distinguishing between models. *Nat. Rev. Genet.* 11, 97–108
80. Sikosek, T. *et al.* (2012) Escape from adaptive conflict follows from weak functional trade-offs and mutational robustness. *Proc. Natl. Acad. Sci. U. S. A.* 109, 14888–14893
81. Espinosa-Cantú, A. *et al.* (2015) Gene duplication and the evolution of moonlighting proteins. *Front. Genet.* 6, 1–7
82. Ohno, S. (1970) *Evolution by Gene Duplication,* Springer
83. Wagner, A. (2008) Robustness and evolvability: a paradox resolved. *Proc. R. Soc. B Biol. Sci.* 275, 91–100
84. Kanehisa, M. *et al.* (2016) KEGG as a reference resource for gene and protein annotation. *Nucleic Acids Res.* 44, D457–D462
85. Fares, M.A. *et al.* (2013) The roles of whole-genome and small-scale duplications in the functional specialization of *Saccharomyces cerevisiae* Genes. *PLoS Genet.* 9, 1–13

PCCP

PAPER

View Article Online
View Journal | View Issue

Check for updates

Cite this: *Phys. Chem. Chem. Phys.*, 2019, **21**, 15779

Unravelling the modus-operandi of chromenylium-cyanine fluorescent probes: a case study†

Ricardo Flores-Cruz,[a] Rafael López-Arteaga,[a] Lizbeth Ramírez-Vidal,[b] Fernando López-Casillas[b] and Arturo Jiménez-Sánchez *[a]

Received 10th June 2019,
Accepted 27th June 2019

DOI: 10.1039/c9cp03256h

rsc.li/pccp

Small-molecule fluorescent probes having optimized optical properties, such as high photostability and brightness, local microenvironment sensitivity and specific subcellular localizations, are increasingly available. Although the basis for designing efficient fluorophores for bioimaging applications is well established, implementing an improvement in a given photophysical characteristic always tends to compromise another optical property. This problem has enormous consequences for *in vivo* imaging, where ensuring a specific localization and precise control of the probe response is challenging. Herein we discuss a fluorescent probe, **CC334**, as a case study of the chromenylium-cyanine family that commonly exhibits highly complex photophysical schemes and highly interfered bioanalytical responses. By an exhaustive and concise analysis of the **CC334** optical responses including detailed spectroscopic calibrations, steady-state microenvironment effects, ultrafast photophysics analysis and computational studies, we elucidate a new strategy to apply the probe in the singlet oxygen reactive oxygen species ($^1O_2$-ROS) monitoring using *in vitro* and *in vivo* models. The probe provides a new avenue for designing fluorescent probes to understand the dynamic behavior of subcellular environments.

Published on 27 June 2019. Downloaded by FAC DE QUIMICA on 10/16/2020 6:26:22 AM.

Introduction

Chromenylium-cyanine (**CC**) probes are a well-studied family of fluorophores combining good photostability,[1] low cytotoxicity,[2] privileged structural diversity,[1–3] and low to moderate fluorescence quantum yields (QY_f),[4] expanding their applications from materials chemistry to fluorescence bioimaging.[1–5] Such properties, in part, are a consequence of their coumarin- and/or rhodamine-like identity, an intrinsic feature retained in their structure, exhibiting similar properties but lower QY_f. This brings the possibility to use these molecules as *fluorogens*, molecules able to activate their fluorescence in response to a given stimulus.[6] In fact, sacrificing QY_f to some extent enables different activation/deactivation pathways of the probe to be exploited in different stimuli-responsive scenarios. **CC** probes then comprise one of the most important examples of how existing fluorophores can be structurally modified to activate different response channels. However, the optical properties and the corresponding analytical responses of such 'recycled probes' are far from trivial. Activating a more versatile photophysical process in a fluorescent probe has several advantages, as mentioned, but the decrease in the QY_f and the signal-to-noise ratio are not the only disadvantages; in imaging microscopy more acquisition times are needed and unavoidable interference problems with the subcellular environment and misinterpretation of the output responses arise. For example, previously described **CC** probes are sensitive to acid–base,[7] oxidative,[8] local polarity,[9] ionic species,[10] temperature,[11] and reductant[12] stimuli, all of them however, present the same response scheme being extremely difficult to calibrate single-channel fluorescence profiles without no interference or cross-talk problems. Here we address the above-mentioned limitations using a **CC** probe having similar fluorescence responses upon exposure to different stimuli. Then, we describe a new strategy to analyse the multi-stimuli scenario of **CC** probes. The probe is derived from a chromenylium ion and coumarin 334, termed **CC334**. Finally, *in vivo* studies were implemented using Zebrafish models to draw a more robust conclusion.

Results and discussion

The chemical structures of **CC334** as well as some previously reported **CC** probes are presented in Fig. 1. To analyse their multistimuli-responsive profile, it is worth noticing that the

[a] *Instituto de Química, Universidad Nacional Autónoma de México, México D.F., No. 04510, Mexico. E-mail: arturo.jimenez@iquimica.unam.mx*
[b] *Instituto de Fisiología Celular, Universidad Nacional Autónoma de México, México D.F., No. 04510, Mexico*

† Electronic supplementary information (ESI) available. See DOI: 10.1039/c9cp03256h

Published on 27 June 2019. Downloaded by FAC DE QUIMICA on 10/16/2020 6:26:22 AM.

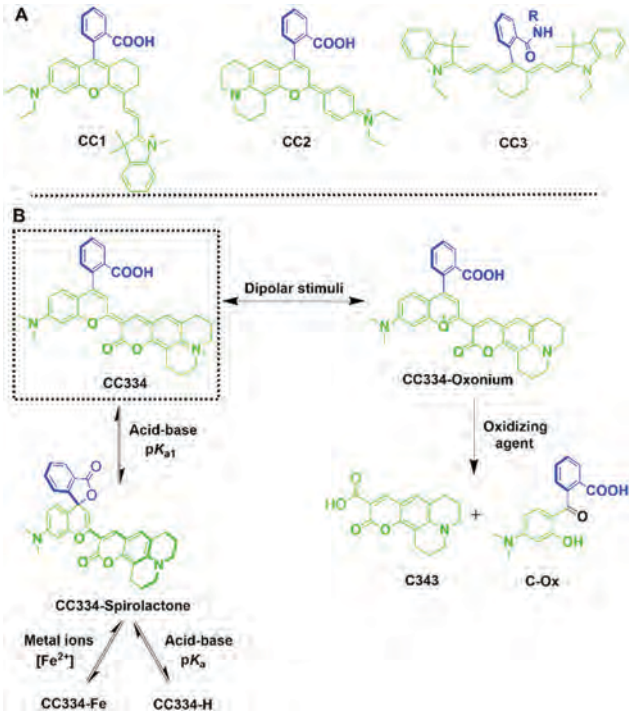

Fig. 1 Chemical structure of (A) three **CC** probes previously described[1–5] and (B) probe **CC334** upon exposure to different stimuli, *i.e.* dipolar: equilibrating the quinoline *vs.* oxonium cations, acid–base: promoting the closed spirolactone form *vs.* open acid form, oxidative: to release coumarin **C343** and a C-oxidation by-product. Further acid (**CC334-H**) or metal ion (Fe^{2+} ion, **CC334-Fe**) stimuli are also possible (see below).

probes exist in an equilibrium between the open-acid and closed-spirolactone forms. Previously reported **CC** structures suggest the spectroscopic features to be a consequence of this acid–base equilibrium. Such a general conception comes from the fact that the electronic conjugation between these forms is substantially different, favoring the open form to exhibit a near infrared (NIR) emission and the closed form to exhibit a visible (Vis) fluorescence. While the Vis-NIR emission pattern of **CC** probes can be modulated with acid–base stimuli, this dual-emission behaviour can also be tuned with redox, polarity (in terms of dielectric constant) variations and some environmental cues, Fig. 1.[13] The spectroscopic characterization of **CC334** is shown in Fig. 2. As can be seen, it is possible to calibrate the probe response to several stimuli which comprises an analytical problem of **CC** probes not described before. In panel A, although showing low fluorescence intensities, a clear dual-band pattern (λ_{em1} = 488 nm; λ_{em2} = 725 nm) is observed in methanol with a fluorescence quantum yield of 0.06 in this solvent. Panel B shows a quantitative interaction scheme for polarity using a continuous variation of dioxane:water volume fractions ($\phi_{dioxane}$), which is a suitable system to separate polarity from other solvent parameters.[14] As solvent polarity increased, both fluorescence intensities (I_{fl}) increased as well and the corresponding maximum wavelengths for the red-shifted emission at 720 nm and the blue one at 520 nm exhibited a remarkable hypsochromic shift to 655 nm and 485 nm, respectively. Notably, the blue-component showed a stronger intensity increment while the red-component showed a stronger wavelength shift. The position of I_{fl} and solvent polarity were used to construct calibration curves (Fig. 2B, inset) showing that altering the polarity of the surroundings is the major contributor to the observed changes in the blue- and red-components.

Then, the acid–base properties of **CC334** were studied in detail to know which species exist at a determined pH for imaging experiments, Fig. 2C. Proton dissociation constants were estimated by potentiometry. The obtained pK_a values were used to calculate the pH distribution of molar fractions for individual open forms (diprotic–dicationic and monoprotic–monocationic) and closed form (neutral) of **CC334**, Fig. S1 (ESI†). The first protonation at the dimethyl(amino) group has a pK_a = 2.21 ± 0.08, and the spirolactone cyclization reaches a pK_a = 10.74 ± 0.09. The pK_a assignment is corroborated by spectro-photometry. Thus, the acid form activates the NIR band where **CC334** is totally conjugated and planar in geometry, while the closed spirolactone form (non-planar with the electron conjugation dominating over the coumarin moiety) contributes more to the VIS band at 500 nm. Importantly for imaging experiments, the potentiometric data indicated a 100% molar fraction of the individual open-acid form at pH 5.5 to 8.5.

Once the pH properties were analysed and the possible species existing in a mitochondrial environment (pH ∼ 8.0) was determined, the oxidation interactions were studied since chromenylium ions are known to exhibit important reactivity for these analytes,[1,8] Fig. 2D–F. A strong binding interaction at pH 7.4 with the Fe^{2+} metal ion was only observed. However, the same result observed for Fe^{2+} was found for Fe^{3+} ions, which can be attributed to the fast oxidation of Fe^{2+} to Fe^{3+} ions upon ligand binding.[15,16] Then, the stability constant for Fe^{2+} ions determined at pH 7.4 showed a complex trend (Fig. 2D) probably because of simultaneous Fe^{2+}/Fe^{3+} oxidation and **CC334** ligand oxidation after one equivalent addition could be involved in this titration. The fitting of the titration results using the HypSpec program revealed the formation of a 1 : 1 complex with a logarithm of the observed stability constant K_{obs} of 5.01. This result highlights the ability of **CC** probes to interact with metal ions through oxygen functional groups.

Similarly, as shown in Fig. 2E and F, **CC334** also exhibits a strong fluorescence increment upon interaction with singlet oxygen ($^1O_2$), while competition experiments with common oxidizing agents revealed no significant interaction, Fig. S2 (ESI†). These results indicate that **CC334** is a specific $^1O_2$-ROS reporter providing the classical molecular probe scenario, *i.e.* oxidation of **CC334** to coumarin 343 (C343), a stronger green-fluorophore as confirmed by chemical characterization using high-resolution mass spectrometry and ^{1}H-NMR spectroscopy (see Fig. S3, ESI†). Note that such oxidation interactions make the fluorescence profiles of the red-shifted band disappear as **CC334** is fragmented to form coumarin 343. Fig. 2F shows the corresponding λ-ratiometric calibration plot for the **CC334**–$^1O_2$ interaction. A good linear fit was obtained at a wavelength ratio r (490/720) nm, such a fluorescence intensity variation is a consequence of the strong blue emission band increment with a simultaneous red emission deactivation.

This journal is © the Owner Societies 2019

INFORME DE LABORES 2019

Published on 27 June 2019. Downloaded by FAC DE QUIMICA on 10/16/2020 6:26:22 AM.

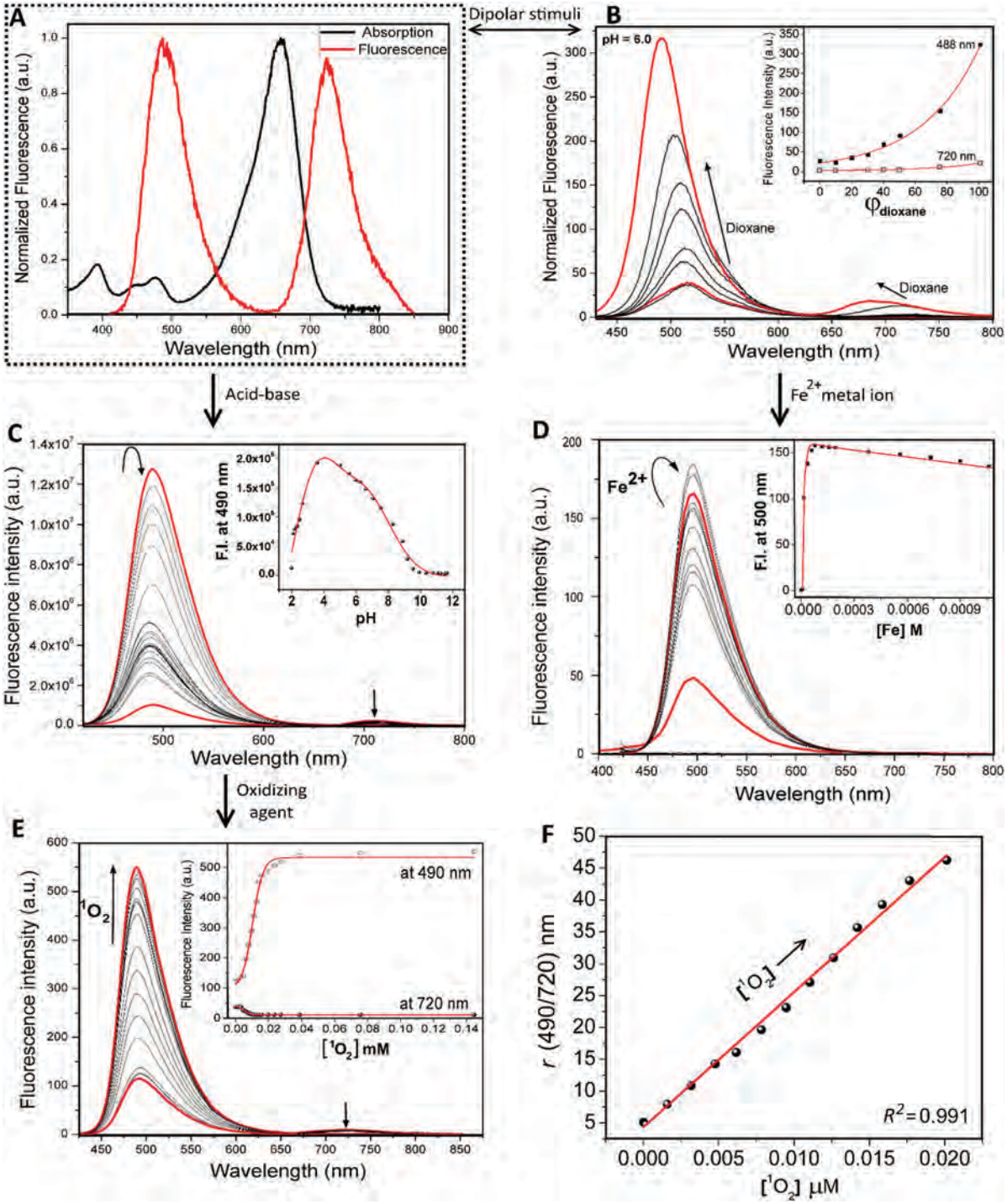

Fig. 2 Multistimuli-responsive scenario of **CC334** upon excitation at λ_{exc} = 400 nm. (A) UV-Vis and fluorescence spectra in methanol. (B) The dipolar stimuli titration using a dioxane:water system. (C) pH variation effect from 2.0 to 11.85. (D) Fe^{2+} ion titration profile. (E) Oxidation effect using singlet oxygen ($^1O_2$). (F) Corresponding λ-ratiometric calibration plot for the **CC334**–$^1O_2$ interaction. Insets: Titration profiles with their theoretical fittings: (B) fluorescence intensity at 488 and 720 nm; (C) the two-pK_a fitting; (D and E) the binding association constant (K_a) profiles: (F_0 + F_{inf}*K_a[**CC334**])/(1 + K_a[**CC334**]), where F = fluorescence intensity.

On the other hand, *in vitro* experiments were carried out to study the subcellular permeability and localization of the probe. Fig. 3 shows a highly specific mitochondrial localization in a human cell line. The mitochondrial localization is a consequence of the lipophilic and positive charge balance of **CC334**. In fact, octanol partitioning was measured, giving a log$P$ value of –0.51, reaching the lipophilic threshold for mitochondrial distribution.[17] This was corroborated by colocalization with the commercial dye MitoTracker Deep Red®, Fig. 3B. As discussed, **CC334** is an oxidizing-sensitive probe. Thus, mitochondrially generated ROS

INFORME DE LABORES 2019

Published on 27 June 2019. Downloaded by FAC DE QUIMICA on 10/16/2020 6:26:22 AM.

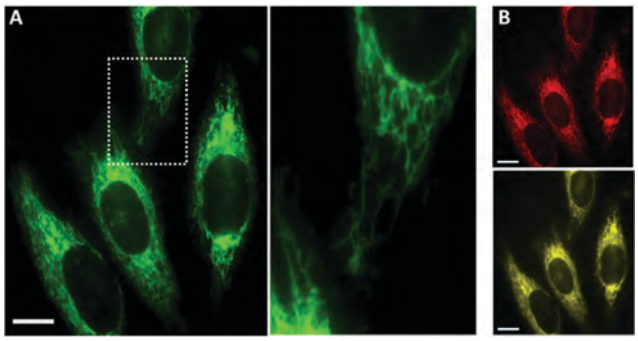

Fig. 3 (A) Intracellular localization of **CC334** in live HeLa cells. (B) Correlation of the **CC334** localization (green) with MitoTracker Deep Red® (red). The high level of overlap for the localization (yellow) of these two molecules indicates that **CC334** is mitochondria-specific. Scale bars represent 20 μm.

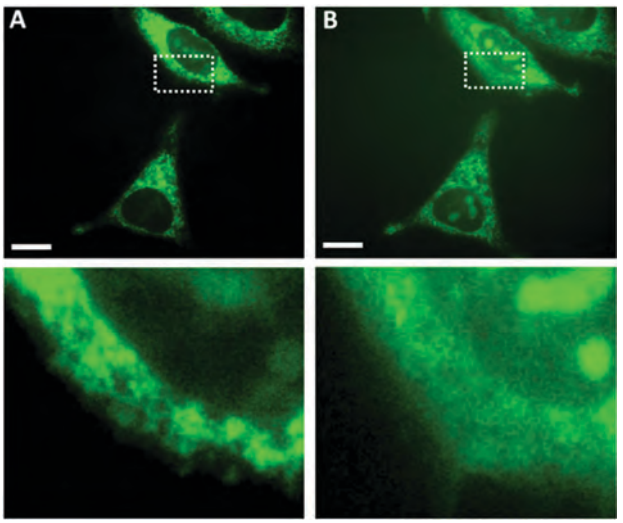

Fig. 4 Effect of low-dose singlet oxygen generation and 0.1 J cm^{-2} irradiation detected in the green (λ_{exc} = 488 nm) channel for HeLa cells. (A) Before and (B) after treatment. The image was manually focused, and excitation light was fully shielded between recordings to prevent artefacts and photobleaching. Scale bars represent 20 μm.

species can in principle be monitored using the fluorescence profile of **CC334**. Stimulating ROS formation in our *in vitro* studies by using low-dose singlet oxygen $^1O_2$ photodynamically generated under laser irradiation from 0.1 to 0.3 J cm^{-2} using 5-amino-levulinic acid (ALA), which is a common photosensitizer of intramitochondrial $^1O_2$ production,[18,19] resulted in a detectable fluorescence signal redistribution from mitochondria to cytosol and then into the nucleoli when recording with the confocal-green channel (λ_{exc} = 503 nm, λ_{em} = 512 nm), Fig. 4. This type of coumarin distribution in the nuclei has been described to occur because of DNA groove interactions.[20–22] Then, $^1O_2$–**CC334** interaction was analysed in more detail by UV-Vis and fluorescence spectrophotometry. However, to demonstrate that no signal interference or false positives are observed during such re-localization dynamics from mitochondria to nucleoli, the typical co-localization controls by staining those organelles with commercial co-localizers (in this case MitoTrackers® for the mitochondrion and DAPI or Hoechst® for the nuclei) and then probing that **CC334** moves from one organelle to the other are not enough and more precise structural information is required. Then, the confocal microscopies that are spectrally resolved provide continuous local information of the probe fluorescence profiles upon exposure to a given stimulus. We used a confocal array upgraded with a spectral detector unit having a 32-channel photomultiplier tube assembly. Thus, using a λ_{exc} = 488 nm, the mitochondria to nucleoli probe redistribution upon $^1O_2$–**CC334** interaction was spectrally-resolved, observing an important increment in the vis-emission band while a slight decrease in the NIR-emission band, Fig. S4 (ESI†), which is in full agreement with the $^1O_2$–**CC334** fluorescence profile discussed in Fig. 2E.

The observed *in vitro* fluorescence response of **CC334** and the unequivocal data interpretation can evidently be extremely difficult. The problem is that the photophysical properties of **CC** probes (including **CC334**) can be modulated by several inputs. One of the main disadvantages of **CC** probes is that they can be used as all, pH, metal ion, ROS, local polarity, local microviscosity sensors by using the same fluorescence response channel. Their Vis-NIR emission properties can originate from the combination of different activation pathways, *i.e.* acid–base equilibrium, intramolecular charge transfer, intramolecular proton transfer, photoacid generation, Kasha's rule breaking, chelation-enhanced fluorescence, site-specific-solvation, among others in such a way that either one or both Vis and NIR channels can be activated. To gain deep insight into the response scheme of **CC334** in highly heterogeneous media, the deactivation pathways present in the molecule were explored. Time-resolved fluorescence spectroscopy was carried out using the time correlated single-photon counting technique (TCSPC); solvents such as acetone and acetonitrile only favor the blue-shifted absorption band at 405 nm, although the emission spectra exhibit the characteristic dual-emission band pattern, λ_1 = 488 nm and λ_2 = 710 nm, see Fig. S5 (ESI†). Non-monoexponential decay life-times were mostly found, Fig. 5. BG40 and LPF 655 filters were used to isolate the emission from the blue and red bands, respectively. In acetone, the blue emission presented two life-times of τ_1 = 3.7 and a fast $\tau_2 < 1$ ns while the red band was short-lived and mono-exponential with 0.7 ns. One of the blue components can be attributed to the locally excited state while the red one is assigned to an ICT state. A similar scheme was found in acetonitrile, with lifetimes of τ_1 = 3.8 and $\tau_2 < 1$ ns in the blue emission and τ = 0.5 ns in the red emission. When testing a non-protic non-polar solvent such as cyclohexane the locally excited (LE) state was evidenced, finding a lifetime of τ = 2.9 ns in the blue emission band. However, in solvents such as methanol and water a more complex behaviour of **CC334** arises.

In methanol, the absorption spectrum exhibits a strong red-shifted band and a dual-emission band pattern as well. Being polar protic solvents, comparison with the polar non-protic features of acetone and acetonitrile the first hypothesis is that the red-shifted band comes from a proton transfer excited state. Thus, lifetimes of 3.8 and 0.5 ns were found for the blue component in methanol, while the red emission presented a

This journal is © the Owner Societies 2019

INFORME DE LABORES 2019

Published on 27 June 2019. Downloaded by FAC DE QUIMICA on 10/16/2020 6:26:22 AM.

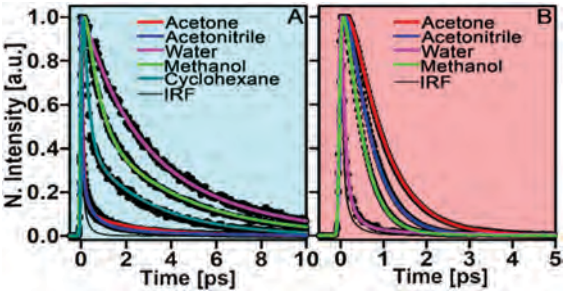

Fig. 5 Nanosecond fluorescence decay curves of **CC334** at the blue emission band (A); and at the red emission band (B) in different solvents, IRF: instrument response function.

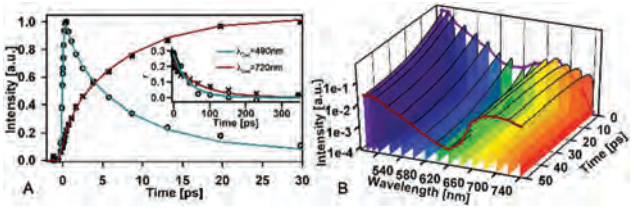

Fig. 6 (A) Normalized fluorescence up-conversion transients detected at 490 nm (blue) and 720 nm (red) for **CC334** in acetone; the inset shows the corresponding anisotropy decays. (B) Obtained ultrafast Time-Resolved Emission Spectra (TRES) in acetone.

0.3 ns lifetime, which in principle involves the closed-spirolactone and the open-acid forms, respectively. When changing from methanol to water the red band decreased, and the lifetimes were 4.3 and 0.9 ns for the blue emission and 2.9 and <0.1 ns for the red emission. Table S1 and Fig. S5 (ESI†) summarize the TCSPC results.

As noticed, the locally excited, charge transfer and proton transfer states can be activated by simple medium effects. However, those states define how much interference a **CC** probe will present *vs.* one specific analyte. Then, ultrafast time dynamics studies were implemented to study the excited state population of **CC334**, and femtosecond fluorescence up-conversion experiments were carried out in acetone and methanol. In acetone the probe only shows a blue absorption band at 438 nm and a dual emission band at 488 and 710 nm (Fig. S6A, ESI†), showing high Stokes shifts that are typical for photoinduced ICT states.[23] The formation of the ICT state is further supported since negligible absorption at longer wavelengths (>600 nm) is observed, and as can be seen in the excitation spectra (Fig. S6B, ESI†) the fluorescence of both the blue and red bands comes from the absorption band at 438 nm. As mentioned before, the dual-emission of **CC334** is a powerful tool in dual-channel confocal microscopies. Two representative results of the ultrafast photophysics for such emission patterns are presented in Fig. 6. There is a clear decay of 8 ps in the 490 nm transient and an accumulation with the same time constant is found at 720 nm, indicating that the locally excited state forms the ICT state in a kinetic scheme A $\rightarrow$ B with a rate constant of 1.25×10^{10} s^{-1}.

As mentioned, the molecular geometry in the excited state is crucial in the photophysical scheme of **CC** fluorophores and thus fundamental for the photophysical scheme to be properly interpreted. Then, to gain more insight into the molecular geometry dynamics at the excited state by means of the transition moment direction changes, we determined the fluorescence anisotropy $r(t)$ of **CC334**. The inset of Fig. 6A shows the anisotropy decays for the two detected states (bands). The blue band anisotropy presents an initial value of $r = 0.3$ and is lost in 40.5 ± 0.3 ps (Fig. S7, ESI†), which is typical for fluorescent probes that only have one emissive state. This indicates that the angle between the excited and the emissive transition dipole moments is around 24°, suggesting that the pumped state (locally excited) is the same as the one detected at 490 nm. The red band, however, presents an $r = 0.2$, which means that the angle between the excited and the ICT transition dipole moments is 35°. Overall this indicates the formation of a different molecular species in the excited state, probably, due to a conjugation and/or planarization of the whole molecule, which is further supported by a higher rotational diffusion constant in the ICT state. The ultrafast temporal evolution of the LE and the ICT states of the molecule is seen in the semi-logarithmic Time-Resolved Emission Spectrum (TRES), Fig. 6B.

In the blue region of the TRES, the LE state quickly decays (in 8 ps) to a relaxed state that lives 2.92 ns (obtained from the TCSPC experiments), while the red band accumulates also in 8 ps and reaches equilibrium between the two species; from the TCSPC results we obtained that the lifetime of this state is 0.69 ns. At 50 ps the temporal spectrum totally resembles the static emission spectrum (Fig. S6A, ESI†) indicating that the LE state relaxation is reached and ICT state is formed.

As mentioned before, the absorption spectrum of the molecule in methanol shows a maximum at 650 nm and some minor features at shorter wavelengths that correspond to higher singlet states (S_n) (Fig. S8A, ESI†). The emission spectrum presents a dual-band pattern when excited at these higher states, similar to the spectrum in acetone. Both bands come from different states as can be seen from the excitation spectra (Fig. S8B, ESI†), the red band corresponds to the S_1 state while the blue band corresponds to the emission from higher singlet excited states or to the coumarin moiety coming from the molecular population that can be found in the spirolactone form. These signatures are indicative that the kinetics of the excited state must be different. The ultrafast temporal behaviour (Fig. 7) indicates that S_n relaxes to S_1 in less than 500 fs, which is a typical time constant for an internal conversion process. This process is further confirmed since the red band is formed at the same time scale. The population of the S_n state that does not convert to the S_1 state reaches equilibrium as long as the pumped state lives (4.08 ns). The anisotropy value near $t = 0$ for the blue band ($r = 0.25$) indicates that the angle between the dipole moment of the pumped and the detected state is about 31° and the loss of the anisotropy occurs in 76.9 ± 0.4 ps (Fig. S9A, ESI†). The rotational diffusion presents a similar time constant to the photoinduced ICT state detected in acetone, which again suggests the extended conjugation of the **CC334** probe. On the other hand, the anisotropy of the S_1 state (Fig. S9B, ESI†) presents an initial value of -0.03, indicating that the angle between the dipole moments of

INFORME DE LABORES 2019

Published on 27 June 2019. Downloaded by FAC DE QUIMICA on 10/16/2020 6:26:22 AM.

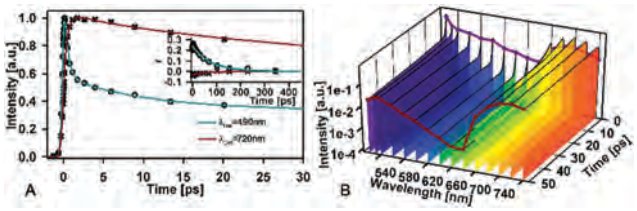

Fig. 7 (A) Normalized fluorescence up-conversion transients detected at 490 nm (blue) and 720 nm (red) for **CC334** in methanol. Inset: The corresponding anisotropy decays. (B) Obtained ultrafast Time-Resolved Emission Spectra (TRES) of **CC334** in methanol, obtained from the fluorescence up-conversion transient fits.

the higher singlet state and the S_1 states is around 58°. This strong variation in the angle indicates that the nature of the pumped state is completely different from the detected state, confirming that the initial state is a higher singlet excited state. Since this value of the anisotropy is very low, it remains difficult to extract the rotational diffusion constant from the experimental data. The TRES of the **CC334** probe in methanol at early times is presented in Fig. 7B. The molecule reaches the equilibrium between the S_n and the S_1 state in this time scale. The internal conversion process is nicely visualized as an ultrafast decay in the blue region and an accumulation in the red part of the spectrum. The long lifetimes of the bands were determined by the TCSPC technique described before: 4.08 ns and 0.32 ns for the blue and red bands, respectively. The different behaviour observed for the two bands in different environments is a clear indication of the highly complex and versatile molecular scenario that arises when using **CC334** as a fluorescent probe in cellular studies.

In order to schematize the photophysical dynamics of **CC334**, we optimized the molecular structures (open-acid and closed spirolactone forms, Fig. S10, ESI†) which were corroborated by a frequency analysis having no imaginary points at a PBE0/G-31+G(d,p)/IEF-PCM (water) level of theory. We analysed the electron density characteristics upon excitation[24] of the probe and the Natural Transition Orbital (NTO) analysis,[25] which provides a compact orbital representation of the electronic transition through a single configuration of a hole and electron interaction. Then, the NTO interactions show that the probe involves a different electronic distribution between open and closed forms when analysing the HONTO–LUNTO pair. The NTO eigenvalues (w) that represent the extent to which the electronic interaction can be written as a single excitation are 0.98 in both the open and closed forms. While the closed form has a non-planar conformation, which disrupts any electron communication in the conjugated molecular axis, the open form favours a highly planar conformation in this conjugated axis, enabling a pseudo-quadrupole moment with $\pi \rightarrow \pi^*$ charge transfer features, Fig. S10 (ESI†).

To study the effect of **CC334** probe incubation, *in vivo* imaging experiments in live Danio rerio (Zebrafish) embryos were performed. The localization studies were done in several stages of development. Fig. 8 shows 4 and 40 hpf (hours post fertilization) incubation with **CC334** before (panels A) and after (panels B) exposure to an oxidative stimulus induced by *in situ*

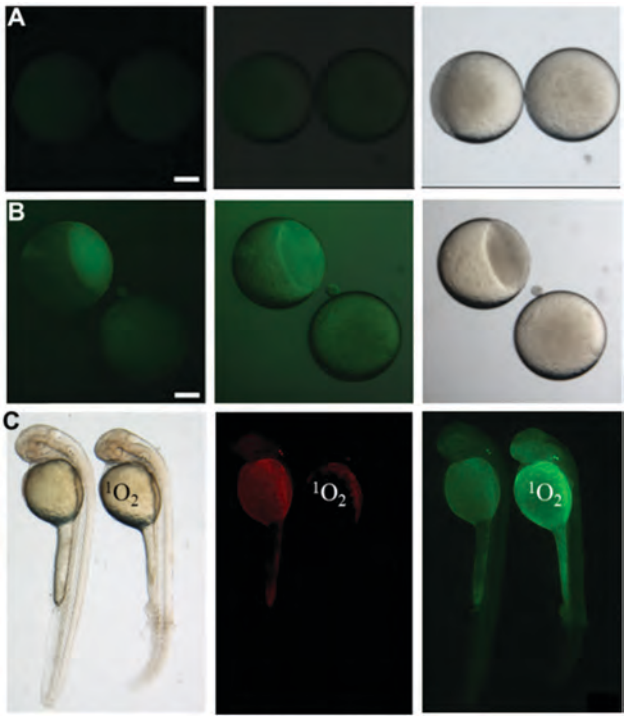

Fig. 8 Fluorescence microscopy of Zebrafish embryos at (A) sphere stage (4 hours post fertilization, hpf) incubated with **CC334** for 30 minutes followed by (B) *in situ* $^1O_2$ stimulation for 10 minutes. After washing excess **CC334** three times for 10 min, specimens were imaged. Left and middle panels show the green channel using 10 μM and 20 μM **CC334**, respectively. The right modules show the bright-field views. Panel C shows 40 hpf Zebrafish before (left) and after (right) $^1O_2$ stimulation in the bright, red and green channels. Scale bars represent 200 μm.

formed $^1O_2$ (preparation of $^1O_2$ and other ROS reagents is described in the ESI† file). These experiments revealed that **CC334** is a permeable fluorescent probe, which, due to the optical transparency of Zebrafish, makes it ideal for imaging single cell stages and subcellular dynamics *in vivo* and in real time.[26] Therefore, we tested whether the selective singlet oxygen **CC334** response could be observed in this model. Interestingly, the epidermis of the developing Zebrafish contains several specialized cell types that allow for the exchange of oxygen, ions and macromolecules, similar to mammalian bilayered epithelia.[27,28]

Stimulation by *in situ* $^1O_2$ generation for 10 minutes resulted in detectable changes of the **CC334** fluorescence, Fig. 8 and 9. The green-channel was enhanced after exposure to the oxidative stimuli, particularly in the embryonic cells composing the sphere, where the latter exhibited a high fluorescence distribution, Fig. 8. Then, confocal imaging of 72 hpf embryos allowed us to visualize the mitochondrial-nuclear redistribution observed in tissue culture cells after exposure to $^1O_2$ oxidative stimuli. Fig. 9 shows clear mitochondria to nucleoli re-localization, where the former was observed using the green and red confocal channels and the nucleoli were observed using the green-channel, indicating that **CC334** could be used in living epithelium to track mitochondrial nuclear redistribution dynamics during exposure to oxidative stimuli with $^1O_2$.

This journal is © the Owner Societies 2019

INFORME DE LABORES 2019

Published on 27 June 2019. Downloaded by FAC DE QUIMICA on 10/16/2020 6:26:22 AM.

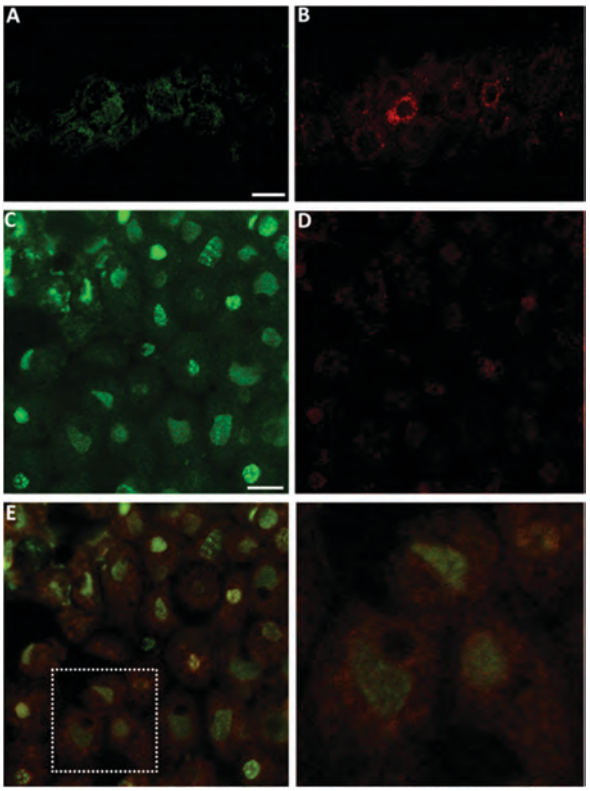

Fig. 9 Confocal imaging for the dorsal fin of the 40 hpf Zebrafish showing epithelial skin cells incubated with **CC334** before exposure to oxidative stimuli imaged in the green (A) and red (B) channels. $^1O_2$ stimulation for 10 minutes and washing excess **CC334** three times for 10 min, specimens were imaged in the green (C) and red (D) channels. (E) Merged image showing the nuclear distribution in the green channel. Scale bar represents 10 μm.

Conclusions

CC334 is a representative probe from the chromenylium-cyanine (**CC**) family of fluorophores. This versatile probe enables bioanalytical sensing and analysis of different species and local microenvironment parameters. Potential interfering factors present in living systems prevents **CC** probes to provide a selective recording of fluorescence. Here, singlet oxygen $^1O_2$, Fe^{2+} ions, pH and polarity/polarizability exert a strong influence on **CC334**, a common problem in the **CC** family. However, we demonstrate that understanding the **CC334** photophysics for all the possible excited-state dynamics (LE, ICT, and IPT) and how the change in molecular nature between the S_1 and S_n excited states governs its reactivity not only facilitates a correct and interference-free bioanalytical analysis but also allows the study of subcellular dynamics *in vivo*. With this study we also clarify that **CC** dual emission behaviour originates from a kinetic process involving the formation of the ICT state by the locally excited state. The dual emission is intrinsic to the **CC** probes regardless of whether the absorption bands have dual-absorption characteristics or not. This advantage is unique to **CC** probes and confers important properties in the analysis of living systems. Spectrally resolved confocal microscopy facilitated the interference-free analysis of $^1O_2$ providing continuous information of the probe emission during measurements. Using **CC** probes in different media inducing redox, pH, polarity and specific ionic interactions for super-resolution microscopy and upconversion luminescence imaging will provide a new avenue for the interference-free analysis of subcellular chemistry.

Conflicts of interest

The authors have no conflicts to declare.

Acknowledgements

We would like to thank Prof. Jorge Peón Peralta for fruitful discussions on ultrafast dynamics during this work and for the laser spectroscopy facility. The authors acknowledge financial support from PAPIIT IA201318. We acknowledge assistance of Miguel Tapia Rodríguez (PhD. IIBO, UNAM) and Ruth Rincón Heredia (PhD. Unidad de Imagenología, IFC-UNAM) in imaging microscopy and Salvador Ramírez Jiménez (Biol. IIBO, UNAM) in tissue culture, Everardo Tapia Mendoza (MS), Beatriz Quiroz García (NMR) from the LURMN at IQ-UNAM Project: 0224747.

References

1 H. Chen, B. Dong, Y. Tang and W. Lin, *Acc. Chem. Res.*, 2017, **50**, 1410–1422.
2 L. Yuan, W. Lin, Y. Yang and H. Chen, *J. Am. Chem. Soc.*, 2012, **134**, 1200–1211.
3 L. Wang, C. W. Barth, M. Sibrian-Vazquez, J. O. Escobedo, M. Lowry, J. Muschler, H. Li, S. L. Gibbs and R. M. Strongin, *ACS Omega*, 2017, **2**, 154–163.
4 X. Wu, M. Yu, B. Lin, H. Xing, J. Han and S. Han, *Chem. Sci.*, 2015, **6**, 798–803.
5 L. Zhou, Q. Wang, Y. Tan, M. J. Lang, H. Sun and X. Liu, *Chem. – Eur. J.*, 2017, **23**, 8736–8740.
6 H. Yang, C. Han, X. Zhu, Y. Liu, K. Y. Zhang, S. Liu, Q. Zhao, F. Li and W. Huang, *Adv. Funct. Mater.*, 2016, **26**, 1945–1953.
7 See ref. 4 and; Q. Wan, S. Chen, W. Shi, L. Li and H. Ma, *Angew. Chem.*, 2014, **126**, 11096–11100.
8 D.-Y. Zhou, Y. Li, W.-L. Jiang, Y. Tian, J. Fei and C.-Y. Li, *Chem. Commun.*, 2018, **54**, 11590–11593.
9 H. Xiao, C. Wu, P. Li, W. Gao, W. Zhang, W. Zhang, L. Tong and B. Tang, *Chem. Sci.*, 2017, **8**, 7025–7030.
10 See ref. 6 and; Y. Wei, D. Cheng, T. Ren, Y. Li, Z. Zeng and L. Yuan, *Anal. Chem.*, 2016, **88**, 1842–1849.
11 M. Homma, Y. Takei, A. Murata, T. Inoue and S. A. Takeoka, *Chem. Commun.*, 2015, **51**, 6194–6197.
12 Q. A. Best, A. E. Johnson, B. Prasai, A. Rouillere and R. L. McCarley, *ACS Chem. Biol.*, 2016, **11**, 231–240.
13 S. Kothavale, A. G. Jadhav and N. Sekar, *Dyes Pigm.*, 2017, **137**, 329.
14 B. R. Pujary, B. Barik and B. Behera, *Phys. Chem. Liq.*, 1998, **36**, 105–112.

INFORME DE LABORES 2019

15 V. A. Timoshnikova, V. I. Klimentieva, N. E. Polyakova and G. J. Kontoghiorghes, *J. Photochem. Photobiol., A*, 2014, **289**, 14.
16 E. Farkas, E. A. Enyedy, L. Zekany and G. Deak, *J. Inorg. Biochem.*, 2001, **83**, 107–114.
17 L. F. Yousif, K. M. Stewart, K. L. Horton and S. O. Kelley, *ChemBioChem*, 2009, **10**, 2081–2088.
18 A. Sparsa, S. Bellaton, T. Naves, M.-O. Jauberteau, J.-M. Bonnetblanc, V. Sol, M. Verdier and M.-H. Ratinaud, *Oncol. Rep.*, 2013, **29**, 1196–1200.
19 X. Zhou, Y. Wang, J. Si, R. Zhou, L. Gan, C. Di, Y. Xie and H. Zhang, *Sci. Rep.*, 2015, **5**, 16925, DOI: 10.1038/srep16925.
20 M. Mehiri, B. Jing, D. Ringhoff, V. Janout, L. Cassimeris and S. L. Regen, *Bioconjugate Chem.*, 2008, **19**, 1510–1513.
21 T. Umashankar, M. Govindappa, L. Yarappa, R. S. Padmalatha and R. Channabasava, *Metabolomics*, 2015, **5**, 1000158.
22 A. K. Saini, V. Sharma, P. Mathur and M. M. Shaikh, *Sci. Rep.*, 2016, **6**, 34807.
23 R. López-Arteaga, A. B. Stephansen, C. G. Guarin and T. I. Sølling, *J. Phys. Chem. B*, 2013, **117**, 9947–9955.
24 C. Adamo and D. Jacquemin, *Chem. Soc. Rev.*, 2013, **42**, 845–856.
25 R. L. Martin, *J. Chem. Phys.*, 2003, **118**, 4775–4777.
26 A. E. Webb and D. Kimelman, *Methods Mol. Biol.*, 2005, **289**, 137.
27 I. Jevtov, T. Samuelsson, G. Yao, A. Amsterdam and K. Ribbeck, *Sci. Rep.*, 2014, **4**, 6653, DOI: 10.1038/srep06653.
28 G. T. Eisenhoffer, G. Slattum, O. E. Ruiz, H. Otsuna, C. D. Bryan, J. Lopez, D. S. Wagner, J. L. Bonkowsky, C.-B. Chien, R. I. Dorsky and J. Rosenblatt, *J. Cell Sci.*, 2017, **130**, 269–277.

Published on 27 June 2019. Downloaded by FAC DE QUIMICA on 10/16/2020 6:26:22 AM.

This journal is © the Owner Societies 2019

Received: 17 August 2018 | Revised: 12 June 2019 | Accepted: 22 June 2019

DOI: 10.1111/acel.13002

Check for updates

ORIGINAL ARTICLE

Aging Cell WILEY

Enhanced nuclear protein export in premature aging and rescue of the progeria phenotype by modulation of CRM1 activity

Ian García-Aguirre[1] | Alma Alamillo-Iniesta[1] | Ruth Rodríguez-Pérez[1] | Griselda Vélez-Aguilera[1] | Elianeth Amaro-Encarnación[1] | Elizabeth Jiménez-Gutiérrez[1] | Alejandra Vásquez-Limeta[2] | Marco Samuel Laredo-Cisneros[1,3] | Sara L. Morales-Lázaro[4] | Reynaldo Tiburcio-Félix[5] | Arturo Ortega[5] | Jonathan J Magaña[6] | Steve J. Winder[3] | Bulmaro Cisneros[1]

[1]Department of Genetics and Molecular Biology, Center of Research and Advanced Studies (CINVESTAV-IPN), Mexico City, Mexico

[2]Laboratory of Protein Dynamics and Signaling, Center for Cancer Research-Frederick, National Cancer Institute, National Institutes of Health, Frederick, MD, USA

[3]Department of Biomedical Science, University of Sheffield, Sheffield, UK

[4]Department of Cognitive Neuroscience, Institute of Cellular Physiology, National Autonomous University of Mexico (UNAM), Mexico City, Mexico

[5]Department of Toxicology, Center of Research and Advanced Studies (CINVESTAV-IPN), Mexico City, Mexico

[6]Laboratory of Genomic Medicine, Department of Genetics, National Rehabilitation Institute, "Luis Guillermo Ibarra Ibarra", Mexico City, Mexico

Correspondence
Bulmaro Cisneros, Departamento de Genética y Biología Molecular, CINVESTAV. Av. IPN 2508, San Pedro Zacatenco, Gustavo A. Madero 07360, Ciudad de México, México.
Email: bcisnero@cinvestav.mx

Funding information
Bilateral Agreement CNR (Italy)/CINVESTAV (Mexico), Grant/Award Number: CNR2018/4; Consejo Nacional de Ciencia y Tecnología, Grant/Award Number: 237123; Geriatric national institute, Mexico, Grant/Award Number: INGER-DI-CRECITES-008-2018

Abstract

The study of Hutchinson–Gilford progeria syndrome (HGPS) has provided important clues to decipher mechanisms underlying aging. Progerin, a mutant lamin A, disrupts nuclear envelope structure/function, with further impairment of multiple processes that culminate in senescence. Here, we demonstrate that the nuclear protein export pathway is exacerbated in HGPS, due to progerin-driven overexpression of CRM1, thereby disturbing nucleocytoplasmic partitioning of CRM1-target proteins. Enhanced nuclear export is central in HGPS, since pharmacological inhibition of CRM1 alleviates all aging hallmarks analyzed, including senescent cellular morphology, lamin B1 downregulation, loss of heterochromatin, nuclear morphology defects, and expanded nucleoli. Exogenous overexpression of CRM1 on the other hand recapitulates the HGPS cellular phenotype in normal fibroblasts. CRM1 levels/activity increases with age in fibroblasts from healthy donors, indicating that altered nuclear export is a common hallmark of pathological and physiological aging. Collectively, our findings provide novel insights into HGPS pathophysiology, identifying CRM1 as potential therapeutic target in HGPS.

Ian García-Aguirre and Alma Alamillo-Iniesta contributed equally to this work.

This is an open access article under the terms of the Creative Commons Attribution License, which permits use, distribution and reproduction in any medium, provided the original work is properly cited.
© 2019 The Authors. *Aging Cell* published by the Anatomical Society and John Wiley & Sons Ltd.

KEYWORDS
aging, cellular senescence, exportin CRM1, Hutchinson-Gilford progeria syndrome, lamin B1, progerin

1 | INTRODUCTION

Aging is a universal process that occurs across all living species; in humans, aging is characterized by a gradual decline in physical and psychological capacities that in turn cause morphological, metabolic, and cognitive alterations that limit the quality of life and ultimately provoke death. Premature aging syndromes, a group of extremely rare but devastating disorders that mimic physiological aging, have been proposed as models to decipher the molecular mechanisms underlying aging (Kubben & Misteli, 2017).

Hutchinson–Gilford progeria syndrome (HGPS), the most well-studied progeroid syndrome, is typically caused by a silent point mutation (1824C > T) that activates a cryptic splicing site within exon 11 of the *LMNA* gene, resulting in the synthesis of a prelamin A mRNA that contains an internal deletion of 150 base pairs. Consequently, this leads to the translation of a mutant lamin A termed progerin, which harbors a deletion of 50 amino acids within its C-terminus. Progerin is permanently farnesylated because the deletion eliminates the cleavage site for Zmpste24, the enzyme that removes the C-terminal farnesyl group from prelamin A to render mature lamin A (Eriksson et al., 2003; De Sandre-Giovannoli et al., 2003).

Progerin acts in a dominant gain-of-function manner by anchoring to the nuclear envelope and perturbing nuclear lamin function, thereby inducing a plethora of cellular defects, including aberrant nuclear morphology, altered DNA repair and gene expression, and telomere instability (Gonzalo, Kreienkamp, & Askjaer, 2017). The complex network of downstream effects by which progerin exerts its toxicity is far from understood; it is thought that progerin impacts on central cellular process, which in turn triggers a cascade of noxious downstream effects that ultimately cause aging.

Owing to the deleterious effect exerted by progerin on nuclear envelope, we hypothesized that the nucleocytoplasmic transport of proteins through the nuclear pore complex (NPC) (Christie et al., 2016) could be a primary target of progerin. Supporting our hypothesis, perturbation in the Ran GTPase gradient affecting nuclear import of specific proteins, namely Ubc9, and nucleoporin TPR was previously reported in HGPS cells (Cobb et al., 2016; Snow, Dar, Dutta, Kehlenbach, & Paschal, 2013). Furthermore, the nonclassic transport pathway mediated by transportin-1 (TNPO1) is impaired in HGPS cells, due to cytoplasmic sequestration of TNPO1 by the microtubule network (Larrieu et al., 2018).

In this study, we aimed to analyze whether nuclear protein export is impaired in HGPS. Exportin-1 (XPO1), also known as chromosomal region maintenance 1 (CRM1), binds to cargo proteins through a leucine-rich nuclear export signal (NES) and transports the proteins across the NPC via a Ran-GTP gradient (Ishizawa, Kojima, Hail, Tabe, & Andreeff, 2015; Kirli et al., 2015). We show for the first time that the CRM1-driven nuclear protein export mechanism is abnormally enhanced in HGPS fibroblasts and that this novel hallmark is critically involved in the disease, because pharmacological inhibition of CRM1 rescues the HGPS cellular phenotype and exogenous overexpression of CRM1 recapitulates HGPS in normal fibroblasts.

2 | RESULTS

2.1 | Enhanced CRM1-driven nuclear protein export is a novel hallmark of HGPS cells

To ascertain whether the CRM1-mediated nuclear protein export mechanism is impaired in HGPS, we evaluated the subcellular distribution of six different proteins whose nuclear export depends on NES recognition by CRM1 (STAT3, B23, ZO-2, cyclin B1, Dp71, and HDAC1). Two different HGPS fibroblast cultures (HGPS-1 and HGPS-2) and a passage-matched fibroblast control culture (WT) were examined using confocal laser scanning microscopy (CLSM). There was a significant decrease in the nuclear localization with a concomitant increase in the cytoplasmic labeling for all the analyzed proteins in both HGPS cell cultures, with the exception of HDAC1 that was found to be mislocalized only in HGPS-2 cells (Figure 1a and Figure S1). Quantitative analysis of the fluorescence nuclear/cytoplasmic ratio (Fn/c) corroborated these observations (see graphs). Nuclear accumulation of NES-containing proteins was restored to a similar level to that of WT cells upon treatment of HGPS cells for 1 day with 1 nM leptomycin B (LMB), a specific CRM1 inhibitor (Figure 1a and Figure S1). This clearly indicates that their nuclear depletion is caused by enhanced nuclear export activity rather than nuclear import failure. Next, we analyzed the expression of NES-containing proteins in HGPS cells. The levels of STAT3 and B23 were similar between WT and HGPS cells, while an apparent increase for ZO-2 was observed only in HGPS-2 fibroblasts (Figure 1b).

2.2 | Enhanced nuclear protein export in HGPS cells is caused by progerin-induced CRM1 overexpression

We hypothesized that the exacerbated nuclear export activity of HGPS cells might be consequence of CRM1 overexpression. Consistent with this idea, elevated CRM1 protein levels were found in HGPS cells (Figure 1c,d), with qRT-PCR experiments showing a corresponding increase in CRM1 mRNA levels (Figure 1e). Given that CRM1 overexpression is primarily regulated at the transcriptional level, we next analyzed CRM1 promoter activity in HGPS cells by promoter reporter assays. An increase in CRM1 promoter activity was found in HGPS-2 but not HGPS-1 cells, compared with WT cells (Figure 1f).

INFORME DE LABORES 2019

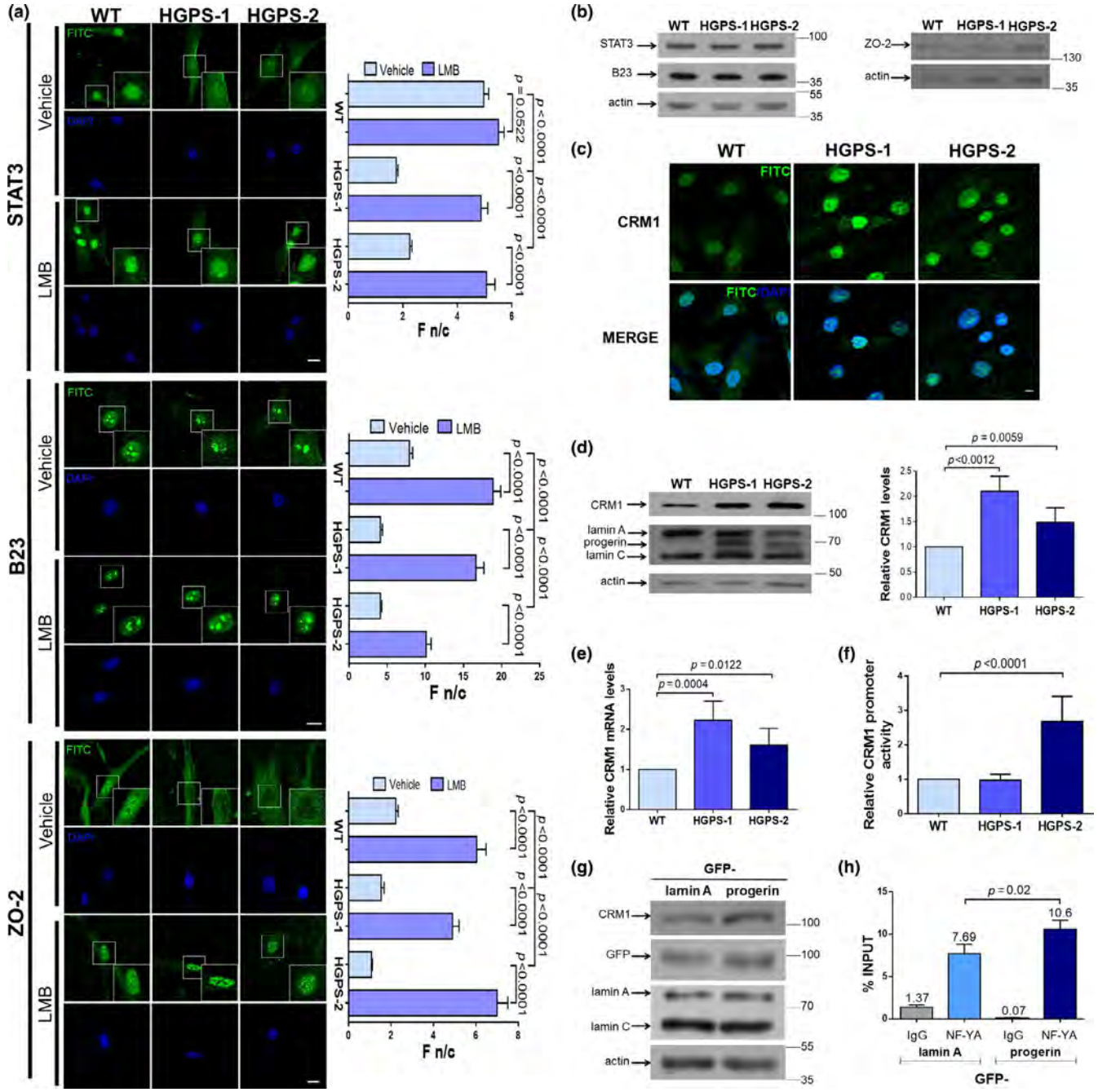

FIGURE 1 Mislocalization of NES-containing proteins is caused by progerin-mediated overexpression of CRM1. (a) Wild-type (WT) and HGPS cells, treated for 24 hr with 10 nM LMB or vehicle alone, were immunolabeled for the indicated proteins (bar, 10 μm). The Fn/c ratio was calculated (n = 50 cells), and significant differences were determined by Mann–Whitney U test (graphs). (b) Protein levels of STAT3, B23, ZO-2, and actin (loading control) were analyzed, and typical gels from two independent experiments are shown. (c) WT and HGPS cells were immunolabeled for CRM1 and analyzed by CLSM. Typical images from 3 independent assays are shown (bar 10 μm). (d) Lysates from WT and HGPS cells were subjected to Western blot using antibodies against CRM1, lamin A/C, or actin (loading control), and relative CRM1 levels were obtained (graph). (e) CRM1 messenger RNA expression was examined by qRT-PCR. (d-e) Significant differences were determined by unpaired t test. (f) WT and HGPS cells were transfected with both Luciferase reporter construct containing the human CRM1 promoter and Renilla luciferase vector, which was used to normalize transfection efficiency. Enzymatic activities were estimated after incubation for 48 hr as described in Methods. Data represent mean ± SEM of three independent experiments (unpaired t test). (g) Lysates from HeLa cells stably transfected to express GFP-lamin A or GFP-progerin were subjected to Western blotting using antibodies against CRM1, GFP, or actin (loading control). (h) HeLa cells expressing GFP-lamin A or GFP-progerin were subjected to chromatin immunoprecipitation (ChIP) with anti-NF-YA antibodies followed by PCR for the CRM1 promoter region. Data correspond to two independent experiments in triplicate

To ascertain whether CRM1 overexpression is causally linked to progerin, we evaluated whether exogenous expression of progerin is sufficient to elicit increased CRM1 levels in HeLa cells. Expression of GFP-progerin but not GFP-lamin A resulted in nuclear morphology aberrations (Figure S2a), decreased H3K9m3 levels (Figure S2b), and increased CRM1 levels (Figure 1g); the latter appears to provoke in turn cytoplasmic mislocalization of the NES-containing STAT3 (Figure S2c). We then evaluated whether exogenously expressed progerin induces CRM1 promoter activity, using ChIP-qPCR assays to assess binding activity of NF-YA, a transcription factor that positively regulates the CRM1 promoter (van der Watt & Leaner, 2011). The binding activity of NF-YA to the CRM1 promoter region was found to be augmented by ~30% in GFP-progerin-expressing cells, compared with those expressing GFP-lamin A (Figure 1h).

Because progerin toxicity is attributed at least in part to its farnesyl moiety, we next examined whether inhibition of progerin farnesylation using the farnesyltransferase inhibitor (FTI) lonafarnib would reduce overexpression of CRM1 in HGPS cells. As previously reported (Noda et al., 2015), treatment with 25 μM of lonafarnib for 3 days elicited a significant decrease in both nuclear blebbing (Figure S3a) and progerin levels (Figure S3b). Supporting our idea, the decrease in progerin levels resulted in CRM1 downregulation (Figure S3b).

2.3 | Pharmacological attenuation of CRM1 activity rescues premature senescence in HGPS cells by improving lamin B1 levels

We wondered whether enhanced CRM1 activity might be part of the molecular basis underlying HGPS. To address this, we evaluated whether amelioration of CRM1 activity through LMB treatment has an impact on cellular senescence. Remarkably, LMB treatment for 2 days resulted in a significant reduction of senescence cells in HGPS cultures, as determined by senescence-associated β-galactosidase (SA-β-gal) staining (Figure 2a). Consistent with this, the percentage of HGPS-1 and HGPS-2 cells arrested at G0/G1 phase of the cell cycle decreased upon treatment with LMB, as revealed by flow cytometry analysis (Figure S4a). We next analyzed the effect of LMB on cell proliferation. Treatment with LMB for 3 days resulted in significantly decreased cell growth in both WT and HGPS cells; however, it provoked only a slight increase in cell death by the third day, as shown by MTT and annexin V assays (Figure S4b,c, respectively). Since decreased lamin B1 expression is associated with senescence (Freund, Laberge, Demaria, & Campisi, 2012; Shimi et al., 2011), we were prompted to analyze whether treatment with LMB has a positive effect on lamin B1 levels. A ~80% decrease in lamin B1 levels was observed in HGPS cells incubated with vehicle alone. Nevertheless, partial restitution of lamin B1 expression was obtained after incubation of HGPS fibroblasts with LMB (50 nM) for 6 days, while no changes were found in WT cells upon treatment (Figure 2b). Redistribution of lamin B1 into distinct nucleoplasmic foci was observed in LMB-treated HGPS cells (Figure 2c). It is thought that nucleoplasmic foci of lamin B1 correspond to nascent lamin B1 incorporated in the nucleoplasmic reticulum in interphase nuclei (Drozdz, Jiang, Pytowski, Grovenor, & Vaux, 2017).

We considered that restoration of lamin B1 levels might consequently reduce those HGPS characteristics governed by lamin B1 (Camps et al., 2014). We then examined the impact of LMB treatment on heterochromatin organization using the heterochromatin marker H3K9me3. Supporting our idea, recovery of both nuclear staining and protein levels of H3K9me3 was evidenced in HGPS cells after LMB treatment (Figure 2d,e, respectively).

We next examined the effect of LMB on nuclear morphology, using nuclear morphometric analyses. Nuclear defects were commonly found in vehicle-treated HGPS fibroblasts immunostained for lamin A/C, compared with WT cells (Figure 3a and graphs). Remarkably, ovoid-shaped nuclei devoid of irregularities that resemble WT nuclei were evident after treatment of HGPS cells for 3 days with LMB (Figure 3a). Nuclear morphometric analyses confirmed significant differences between vehicle- and LMB-treated HGPS cells (right graphs). Collectively, these data indicate that mitigation of CRM1 activity through LMB treatment delayed the progression of HGPS cells to senescence by preventing lamin B1 downregulation.

2.4 | Pharmacological modulation of CRM1 activity ameliorates aging features of HGPS cells

To analyze in depth the effect of LMB-mediated CRM1 inhibition on senescence, two distinctive features of senescent cells, namely enlarged nucleolar morphology and senescent cellular morphology, were examined in HGPS fibroblasts. As reported previously, (Buchwalter & Hetzer, 2017), a single or two prominent nucleoli with increased nucleolar area were observed in most HGPS cells (Figure 3b). Notably, administration of LMB to HGPS cultures for 3 days resulted in increased number of nucleoli per cell (Figure 3b), with smaller nucleolar area (right graphs), which were comparable in size to wild-type nucleoli. Previously, the expansion of nucleoli was linked to elevated protein synthesis in HGPS cells (Buchwalter & Hetzer, 2017). Therefore, we were prompted to analyze whether alleviation of nucleolar expansion by LMB treatment has an effect on global protein synthesis by monitoring the phosphorylation state of the α subunit of eukaryotic initiation factor 2 (eIF2α), the p70 ribosomal protein S6 kinase (p70 S6K) and its substrate, and the ribosomal protein S6 (rpS6). Consistent with elevated protein synthesis, HGPS-1 cells treated with vehicle alone showed decreased p-eIF2a levels but elevated levels of p-p70 S6K and p-rpS6K (Figure 3c). By contrast, LMB treatment for 3 and 6 days resulted in increased p-eIF2α levels but reduced phosphorylated levels of both p70 S6K and rpS6 in HGPS-1 cells (Figure 3c), which is consistent with a translational repression effect mediated by LMB. With respect to the senescent cell morphology, LMB-mediated

INFORME DE LABORES 2019

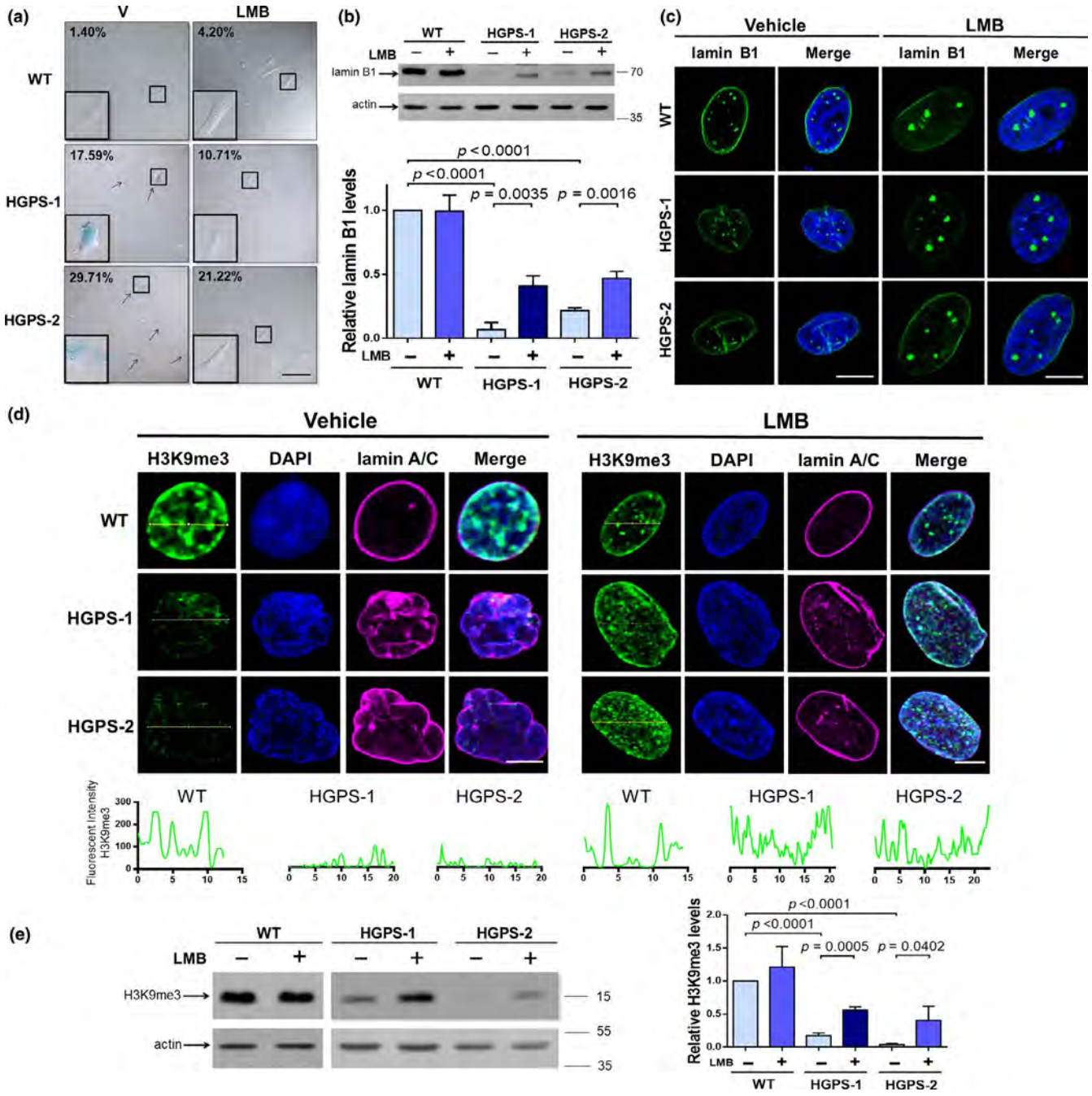

FIGURE 2 LMB-mediated inhibition of CRM1 prevents cellular senescence by improving lamin B1 levels. (a) WT and HGPS fibroblasts were treated for 2 days with 1 nM LMB or vehicle alone. The activity of β-galactosidase was assessed, and representative images are shown. Bar = 100 μM. The percentage of senescent cells was calculated from 3 separate experiments (n = 300 cells for each condition). (b) Lysates from WT and HGPS fibroblasts, previously treated for 6 days with 50 nM LMB or vehicle, were analyzed by Western blotting using antibodies against lamin B1 and actin (control). Lamin B1 levels were assessed (bottom panel). (c) WT and HGPS fibroblasts treated with 50 nM LMB or vehicle alone for 3 days were immunostaining for lamin B1, and typical images are shown. Bar, 10 μm. (d) WT and HGPS fibroblasts treated with 50 nM LMB or vehicle for 6 days were analyzed by CLSM, using antibodies against H3K9me3 and lamin A/C. Representative images are shown. B Bar, 10 μm. *Bottom*. Line profile analysis showing H3K9me3 fluorescence pattern. (e) Lysates from HGPS cells treated as peer C were analyzed by Western blotting using antibodies against H3K9me3 and actin (control). Relative H3K9me3 levels are shown (right graph). (b and e) Significant differences were determined by unpaired t test

inhibition of CRM1 activity shifted the flattened and expanded morphology of HGPS fibroblasts to the typical fusiform morphology of WT fibroblasts (Figure 3d), with a concomitant decrease in cell size (right graph).

Finally, we assessed whether treatment with LMB has an effect on progerin expression. Interestingly, progerin levels were found to significantly decrease in HGPS-2 cells but not HGPS-1 cells upon LMB treatment (Figure S4c).

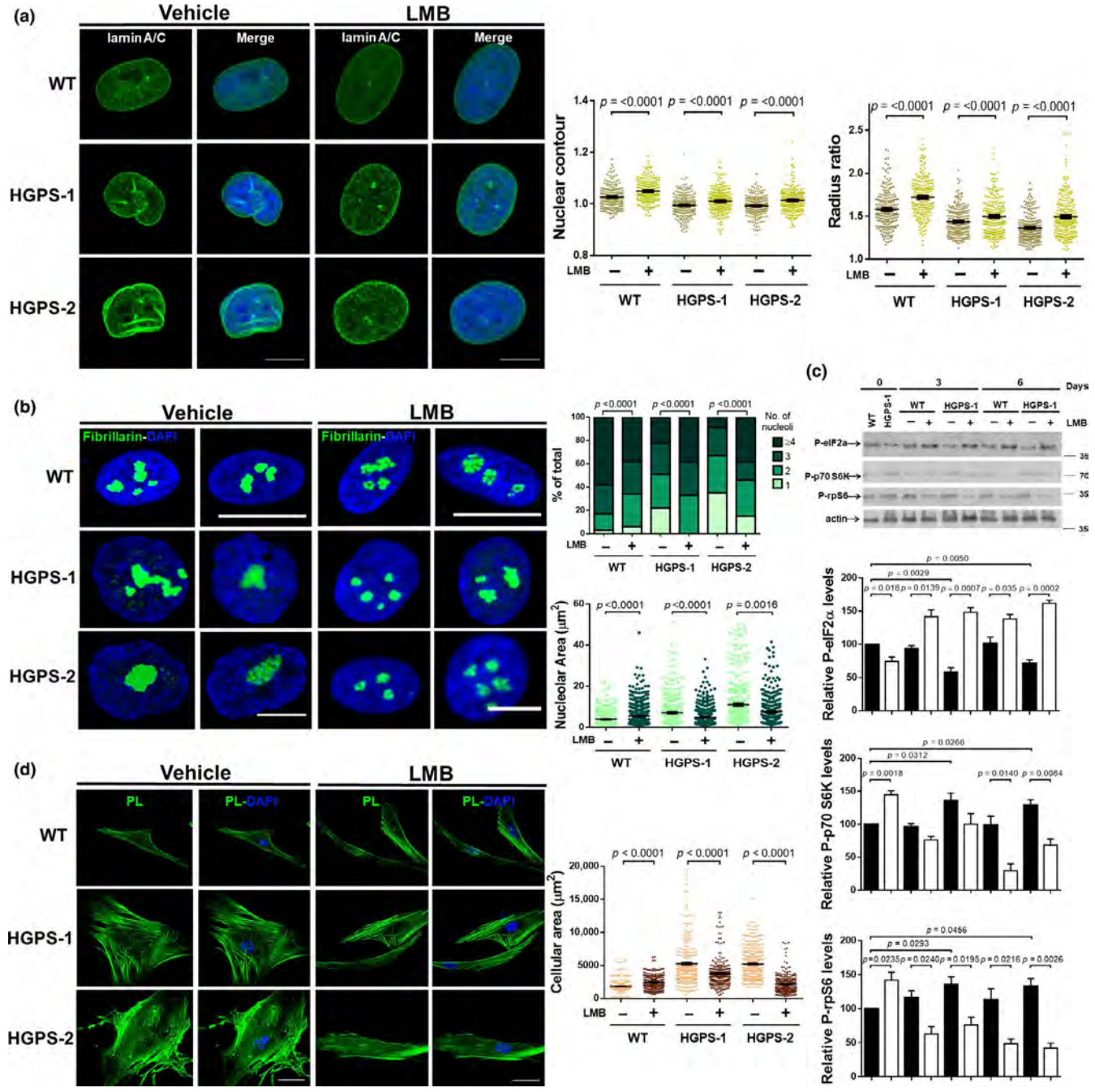

FIGURE 3 LMB-mediated inhibition of CRM1 alleviates aging features of HGPS cells. (a) WT and HGPS fibroblasts were treated for 3 days with 50 nM LMB or vehicle alone. Cells were immunolabeled for lamin A/C before being analyzed by CLSM, and representative images are shown. Bar, 10 μm. *Right*. Nuclear morphometric analysis was carried out as described in Methods (n = 200 nuclei for each condition), with significant differences determined by Mann–Whitney U test. (b) WT and HGPS fibroblasts, treated as peer A, were immunostained for fibrillarin to decorate nucleoli. Bar, 10 μm. *Right*. Nucleolar area was determined as described in Methods (n > 600 nucleoli per condition). Number of nucleoli per cell was estimated (bottom panel; n > 80 cells per sample), and significant differences were determined by Mann–Whitney U test. (c) Lysates from WT and HGPS-1 fibroblasts, previously treated for 0, 3, or 6 days with 1 nM LMB or vehicle, were analyzed by Western blotting using antibodies against the indicated proteins. Relative protein levels from three independent experiments are shown (bottom graphs), with significant differences determined by unpaired t test. (d) WT and HGPS fibroblasts were treated as peer A. Cells were labeled with phalloidin to visualize actin cytoskeleton. Bar, 50 μM. *Right*. The cellular area was estimated (n > 300 cells), with significant differences determined by Mann–Whitney U test

INFORME DE LABORES 2019

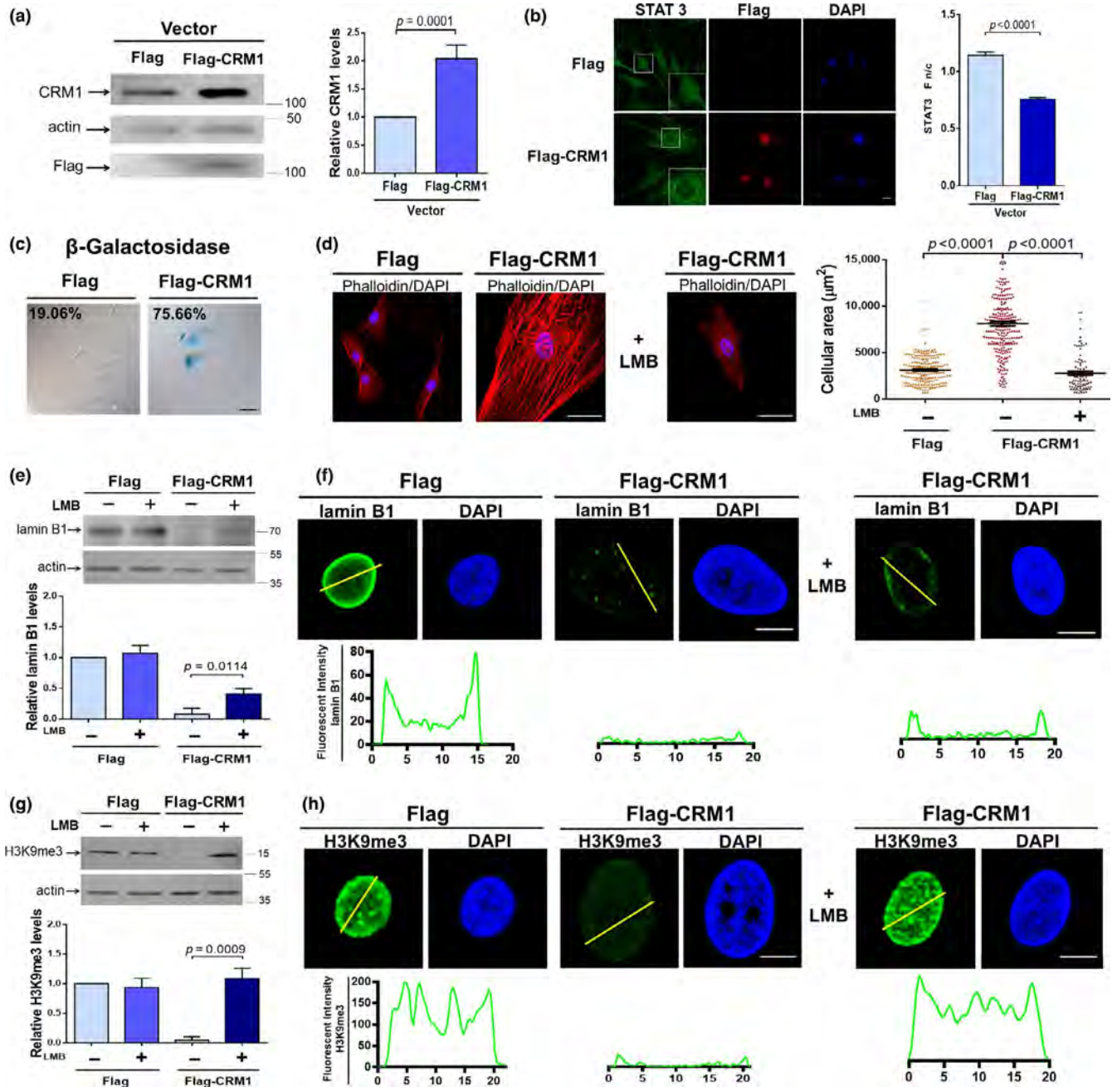

FIGURE 4 Ectopic overexpression of CRM1 induces premature aging phenotype in normal primary fibroblasts. Human primary fibroblasts derived from a healthy donor were stably transfected to express Flag-CRM1 or Flag alone. (a) Lysates were subjected to Western blotting using antibodies against CRM1, Flag, or actin (loading control). Relative CRM1 levels are shown (right panel). (b) Subcellular distribution of STAT3 was evaluated by CLSM and its n/c ratio estimated (graph). Bar, 10 μM. (c) The activity of β-galactosidase was measured, and the percentage of senescent cells was estimated from 3 independent experiments (n = 300 cells for condition). Bar, 100 μM. (a-c) Significant differences were determined by unpaired t test. (d) Transfected fibroblasts were labeled with phalloidin to visualize actin. *Right*. Flag-CRM1-expressing fibroblasts were treated with 50 nM LMB or vehicle alone for 3 days, prior to being stained with phalloidin and analyzed by CLSM. Bar, 50 μM. The cellular area was determined (n > 150 cells for condition), and significant differences were determined by Mann–Whitney U test. (e) Lysates from fibroblasts expressing Flag or Flag-CRM1, which were previously treated with 50 nM LMB or vehicle alone for six days, were analyzed by Western blotting with antibodies against lamin B1 and actin (control). *Bottom*. Relative lamin B1 levels are shown. Significant differences were determined by unpaired t test. (f) Transfected fibroblasts with or without LMB treatment were immunostained for lamin B1, and typical images are shown. Bar, 10 μm. *Bottom*. Line profile analysis showing lamin B1 fluorescence pattern. (g) WT fibroblasts stably expressing Flag or Flag-CRM1 were treated as peer (e) prior to be analyzed by Western blotting for H3K9me3. *Bottom*. Relative H3K9me3 levels are shown, and significant differences were determined by unpaired t test. (h) Nuclear distribution of H3K9me3 was analyzed in the indicated transfected fibroblasts with or without LMB treatment. *Bottom*. Line profile analysis showing the H3K9me3 fluorescence pattern

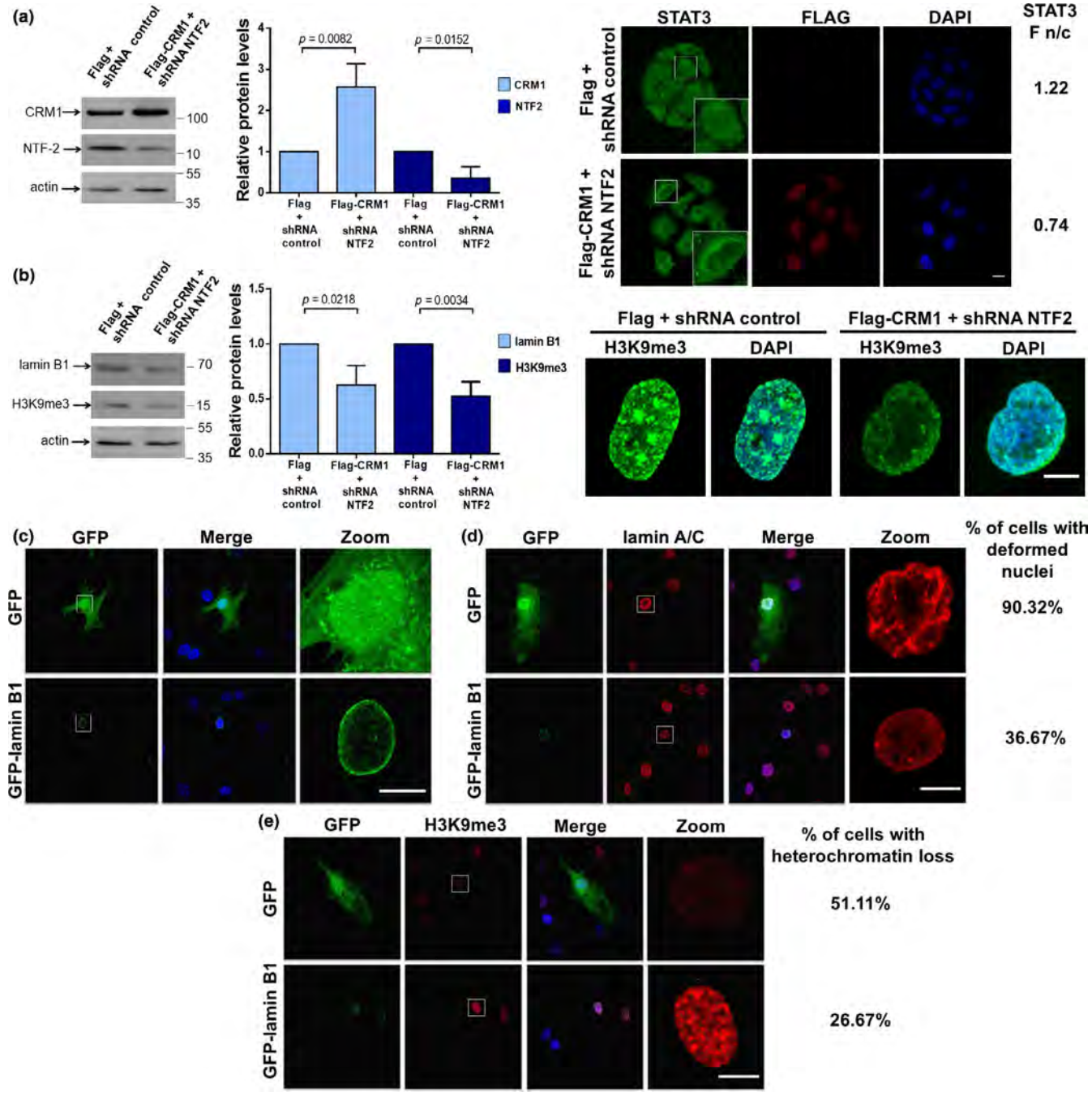

FIGURE 5 (a-b) Enhanced nuclear export activity due to CRM1 overexpression overcomes deficient Ran gradient in HeLa cells. Cells were double-transfected to stably expressed Flag-CRM1 or Flag alone, and a shRNA against NTF2 gene or a shRNA control. (a) Lysates from the transfected cells were analyzed by Western blotting using antibodies against CRM1, NTF2, and actin (control). *Middle*. Relative protein levels were assessed from three independent experiments (unpaired *t* test). *Right*. Distribution of STAT3 was analyzed in the indicated transfected cells. Bar, 20 μM. (b) Transfected cell lysates were analyzed by Western blotting with antibodies against lamin B1, H3K9me, and actin (control). *Middle*. Data correspond to 3 independent experiments (unpaired *t* test). *Right*. Distribution of H3K9me3 was analyzed in the indicated transfected cells. Bar, 20 μM. (c–e) Restoration of lamin B1 expression in HGPS cells (c) HGPS-1 cells were transiently transfected to express GFP-lamin B1 or GFP alone. Transfected cells were immunolabeled for lamin A/C (d) and H3K9m3 (e) to estimate the percentage of cells with aberrant nuclear morphology and heterochromatin loss, respectively. Bar, 10 μM

2.5 | Ectopic overexpression of CRM1 recreates the HGPS phenotype in normal human fibroblasts

Next, we ascertained whether exogenous overexpression of CRM1 is sufficient to mimic progeroid hallmarks in normal fibroblasts. A ~100% increase in CRM1 levels was observed after stable transfection of WT fibroblasts with a vector expressing FLAG-CRM1, compared to WT cells expressing FLAG alone (Figure 4a). Cytoplasmic mislocalization of the NES-containing protein STAT3 confirmed accelerated nuclear export activity in cells overexpressing CRM1

INFORME DE LABORES 2019

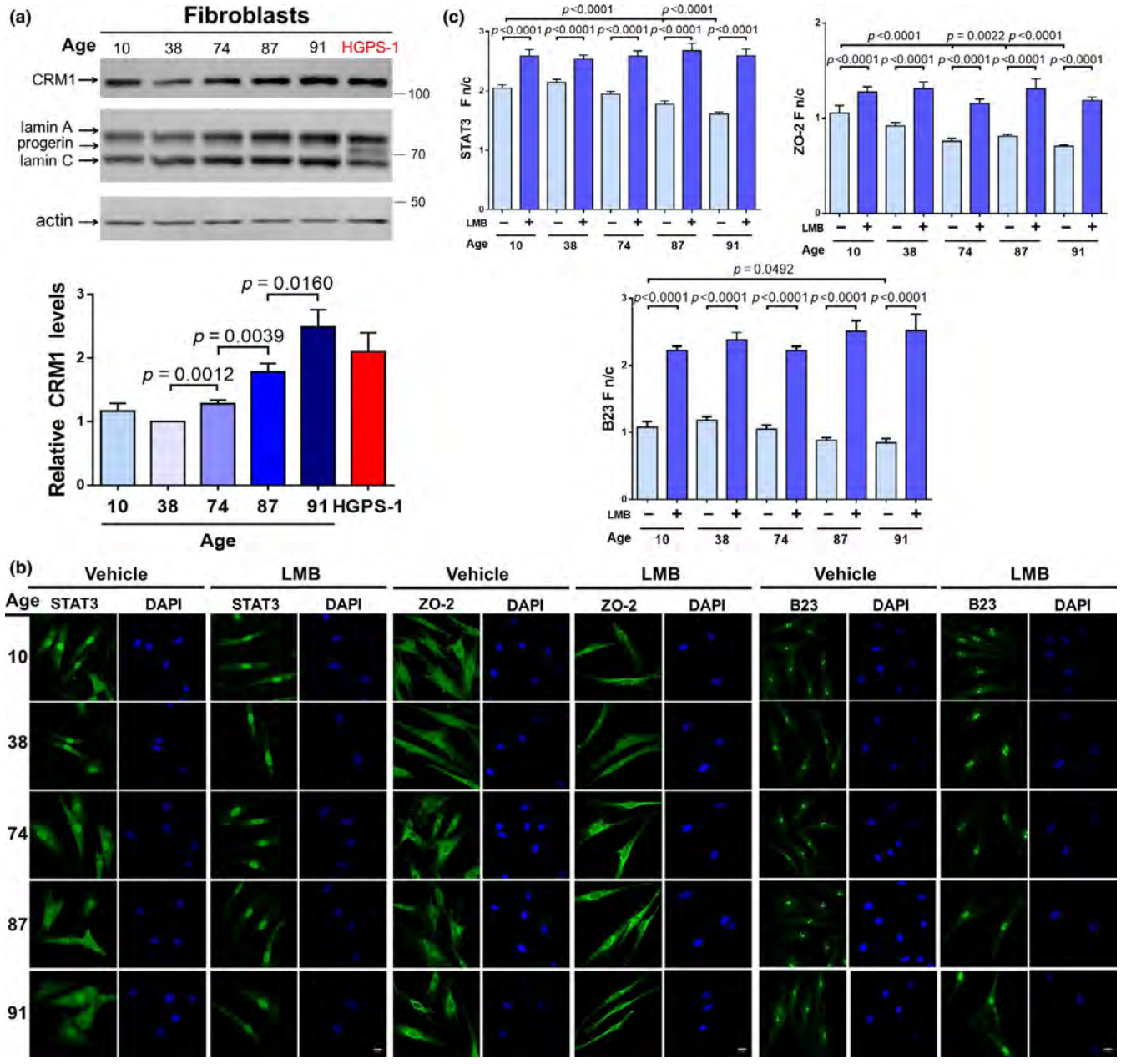

FIGURE 6 CRM1 expression and activity increased during normal aging. (a) Primary human fibroblast from healthy individuals of varying ages or HGPS-1 fibroblasts were analyzed by Western blotting using antibodies against CRM1, lamin A/C, and actin (control). CRM1 expression is shown (bottom panel; unpaired *t* test). (b) Localization of the NES-containing proteins STAT3, Z0-2, and B23 was evaluated in the indicated fibroblast cultures, treated with LMB or vehicle alone for 24 hr. Typical images are shown. Bar, 20 μM. (c) The n/c ratio of STAT3, Z0-2, and B23 was calculated as peer Methods (n = 50 cells; Mann–Whitney U test)

(Figure 4b). Remarkably, most of CRM1-overexpressing WT fibroblasts became senescent (75%), as shown by SA-β-gal staining and the acquisition of a flattened and extended cellular morphology (Figure 4c,d, respectively). Furthermore, forced overexpression of CRM1 in WT fibroblasts resulted in decreased lamin B1 levels (Figure 4e–f), with the consequent loss of H3k9m3 (Figure 4g–h). Interestingly, pharmacological inhibition of CRM1 in FLAG-CRM1-expressing fibroblasts alleviated the senescent morphology (Figure 4d) and prevented both lamin B1 downregulation (Figure 4e,f) and the loss of heterochromatin (Figure 4g,h).

The gradient of Ran, a key regulator of nucleocytoplasmic transport, was previously reported as disrupted in HGPS cells (Datta, Snow, & Paschal, 2014). We therefore investigated whether enhanced nuclear export activity via CRM1 overexpression can occur in cells with a deficient Ran gradient. Since depletion of the Ran import factor NTF2 (nuclear transport factor 2) is sufficient to disrupt the Ran gradient (Datta et al., 2014; Dworak et al., 2019), HeLa cells were double-transfected to express CRM1 and a shRNA against NTF2. Interestingly, stably transfected HeLa cells having both overexpressed levels of CRM1 and depleted levels of NTF2 (Figure 5a) still

showed elevated nuclear export activity, as shown by cytoplasmic mislocalization of the NES-containing protein STAT3 (right panel). Consequently, these cells acquired different aging marks, including depleted levels of lamin B1 and H3K9m3 (Figure 5b). Collectively, these data imply that enhancing CRM1 activity is necessary and sufficient to induce the cells to age prematurely.

2.6 | Exogenous restoration of lamin B1 levels partially alleviates the HGPS phenotype

To ascertain whether improvement of lamin B1 levels by LMB treatment is the basis of the HGPS phenotype rescue, the expression of lamin B1 was exogenously restored in HGPS-1 cells by stably transfecting a vector expressing GFP-lamin B1. GFP-lamin B1 was properly targeted to the nuclear envelope, while GFP alone was localized throughout all the cells (Figure 5c). Remarkably, HGPS cells expressing GFP-lamin B1 showed improved nuclear morphology (Figure 5d) and recovery of peripheral heterochromatin (Figure 5e), compared with HGPS-1 cells expressing GFP alone. However, restoration of lamin B1 expression failed to alleviate the senescent morphology (data not shown).

2.7 | The expression and activity of CRM1 increase during normal aging

We hypothesized that the CRM1-mediated nuclear export system could be dysregulated during normal aging as well. Thus, we analyzed expression and activity of CRM1 in a panel of primary human fibroblasts from healthy individuals ranging from 10 to 91 years of age. Interestingly, we found a significant and direct correlation between aging and increased CRM1 levels in individuals between 38 and 91 years of age (Figure 6a). Cytoplasmic mislocalization of the NES-containing proteins STAT3, Z0-2, and B23 was evident in fibroblasts from 74- to 91-year-old individuals (Figure 6b), with Fn/C analysis corroborating these observations (Figure 6c); further treatment with LMB restored predominant nuclear localization of NES-containing proteins, similar to that observed in fibroblasts from 10- to 38-year-old individuals (Figure 6b-c). Altogether, these data suggest that enhanced CRM1 activity is a hallmark of physiological aging.

3 | DISCUSSION

In this study, we show for the first time that the CRM1-driven nuclear protein export mechanism is abnormally enhanced in HGPS cells due to overexpression of CRM1. We revealed that upregulation of CRM1 in HGPS cells is controlled at the transcriptional level through induction of CRM1 promoter activity, at least for HGPS-2 cells. Furthermore, a causal link between progerin and CRM1 overexpression was demonstrated because ectopic expression of progerin in HeLa cells elicited elevated CRM1 levels, at least in part through enhancing the binding activity of NF-YA (a positive transcription factor) to the CRM1 promoter region, and because treatment of HGPS cells with FTI that decreased progerin levels resulted in turn in downregulation of CRM1. We speculated that exacerbated nuclear export activity might be part of the molecular basis underlying HGPS. As proof of concept, we evaluated whether inhibition of CRM1 activity by pharmacological treatment with LMB has a therapeutic effect on the HGPS phenotype. Remarkably, we found alleviation of virtually all HGPS hallmarks upon treatment with LMB, including reduced number of SA-β-gal positive cells, recovery of peripheral heterochromatin, and rescue of lamin B1 downregulation, nucleolar expansion, augmented protein synthesis, and the senescent cellular morphology. Furthermore, ectopic overexpression of CRM1 enabled normal fibroblasts to acquire all the aging marks aforementioned. Thus, CRM1 overexpression is sufficient to recapitulate an aging phenotype in the absence of progerin, which indicates that a dysregulated nuclear protein export is an early key event in the pathway leading to HGPS.

Most of the cellular processes rescued by LMB treatment are intimately related to lamin B1, including nuclear morphology (Vergnes, Peterfy, Bergo, Young, & Reue, 2004), organization of peripheral heterochromatin, nucleolar plasticity (Camps et al., 2014), and cellular senescence (Dreesen, Ong, Chojnowski, & Colman, 2013; Freund et al., 2012; Lukasova, Kovarik, & Kozubek, 2018; Shimi et al., 2011). Therefore, it is likely that rescue of the HGPS phenotype by treatment with LMB relies mainly on the improvement of lamin B1 levels. Consistent with this, exogenous expression of lamin B1 resulted in improved nuclear morphology and the recovery of peripheral heterochromatin, but failed to alleviate the senescent morphology of HGPS cells. Thus, alleviation of the HGPS aging marks appears to occur through more than one mechanism; further experiments are required to fully delineate pathways underlying the correction of aging marks in response to CRM1 inhibition.

A broad spectrum of treatments against HGPS has been tested in HGPS fibroblasts (Harhouri et al., 2018), and most of these are designed to target progerin. Blocking of progerin farnesylation by administration of farnesyltransferase inhibitors corrected nuclear structure but failed to alleviate other aging-associated marks (Glynn & Glover, 2005; Toth et al., 2005), while depletion of progeria via rapamycin-mediated activation of autophagy improved nuclear morphology and delayed the onset of senescence (Cao et al., 2011). In a similar manner, proteasome inhibitor MG132 enhanced proliferation and decreased cellular senescence by promoting progerin degradation (Harhouri et al., 2017). Finally, treatment with the chemical JH4 ameliorated nuclear defects and prevented premature senescence by interfering with the harmful interaction between progerin and lamin A (Lee et al., 2016). Alternative strategies aimed to repair downstream effects of progerin have been proposed as well; treatment with methylene blue rescued not only nuclear morphology and heterochromatin loss but also mitochondrial function (Xiong et al., 2016), while administration of the ROCK inhibitor Y-27632 ameliorated nuclear morphology defects and DNA double-strand breaks along with decreased ROS

INFORME DE LABORES 2019

TABLE 1 List of human dermal fibroblast cultures used in this study

Culture	Origin	LMNA mutation	Age of donor at biopsy	Gender
AG08469 (WT)	Coriell	None	38	M
AG11513 (HGPS−1)	Coriell	G608G	8	F
AG11498 (HGPS−2)	Coriell	G608G	14	M
AG08470	Coriell	None	10	F
AG06290	Coriell	None	74	M
AG10884	Coriell	None	87	M
AG07725	Coriell	None	91	M

levels and improvement of mitochondrial function (Kang et al., 2017). In this scenario, pharmacological modulation of CRM1 using selective inhibitors clearly provides a viable and promising therapy against HGPS, because this treatment specifically targets and corrects the nuclear export mechanism and, more importantly, because it alleviates the largest number of HGPS cellular characteristics (Graphical abstract), compared with the aforementioned treatments. Furthermore, synthetic selective inhibitors of CRM1 with pharmacological properties superior to LMB (selinexor/KPT-330), which have shown to be well-tolerated in human cancer clinical trials (Mahipal & Malafa, 2016), would facilitate future in vivo evaluation of this therapy in HGPS animal models.

Interestingly, we found increased CRM1 levels in primary fibroblast from healthy aged donors; however, no progerin was detected in these cell cultures. In analogy to the mechanism underlying CRM1 overexpression in cancer cells (van der Watt & Leaner, 2011), we hypothesized that upregulation of CRM1 in fibroblasts from aged individuals could be controlled by modulation of the binding activity of transcription factors involved in CRM1 promoter activity. Thus, enhanced CRM1-mediated nuclear export activity appears to be a key converging mechanism in both pathological and physiological aging. Consistent with this notion, silencing or pharmacological inhibition of CRM1 resulted in extended lifespan in *C. elegans* (Silvestrini et al., 2018).

In conclusion, we reveal that enhanced nuclear protein export is a new hallmark of both HGPS and normal aging. Furthermore, we provide evidence that pharmacological inhibition of CRM1 activity alleviates the progeroid cellular phenotype (Graphical abstract), which delineates CRM1 as potential therapeutic target for HGPS and other aging-related diseases.

4 | EXPERIMENTAL PROCEDURES

4.1 | Cell culture, treatments, and transfection

Primary human dermal fibroblasts from patients with HGPS and healthy donors (see Table 1) were cultured in MEM (Invitrogen) supplemented with 15% FBS (Invitrogen), nonessential amino acids, and antibiotics. All experiments were carried out with fibroblast cultures at passage numbers 12–16. Where indicated, fibroblasts were treated with 1 nM leptomycin B (LMB; Sigma-Aldrich) for 1, 3, or 6 days diluted in ethanol to a final concentration of 0.1% in the culture medium, or with 25 μM of the farnesyl transferase inhibitor (FTI) lonafarnib (Sigma-Aldrich) for three days. Fibroblasts were transfected with Lipofectamine 3,000 following manufacturer's protocol (Invitrogen). Stably transfected fibroblasts were obtained by culturing them for 12 days with 200 μg/ml G418 (Invitrogen). HeLa cells were double-transfected with pFlag-CRM1 vector and vector expressing either a short hairpin RNA (shRNA) specific for the human nuclear transport factor 2 gene (NUTF2) or a scrambled shRNA control (GeneCopoeia, Inc.), using Lipofectamine 2000 (Invitrogen). Stably transfected HeLa cells were obtained by culturing them for 6 days in the presence of 1 μg/ml puromycin and 800 μg/ml G418. Cloning strategies to obtain vectors pEGFP-C1-LB1, pFLAG-CRM1, and pCRM1 promoter are provided under request.

4.2 | Promoter reporter assays

WT, HGPS-1, and HGPS-2 fibroblasts were transfected as above with both the CRM1 promoter vector, which expresses Firefly luciferase under the control of human CRM1 promoter, and the Renilla luciferase vector as a control to normalize for differences in transfection efficiency. After 48 hr, the luciferase activity was measured using Dual Luciferase Assay kit (Promega).

4.3 | Quantitative chromatin immunoprecipitation (Q-ChIP) assays

Q-ChIP assays were performed as reported previously (Morales-Lazaro et al., 2010), using 7.8 μg of mouse anti-NF-YA antibodies or 7.8 μg of mouse IgG (irrelevant control). 20 ng of DNA was used to perform quantitative PCR (qPCR) using SYBR Green and primers specific to amplify the CRM1 promoter region (van der Watt & Leaner, 2011).

4.4 | Indirect immunofluorescence and confocal microscopy analysis

Immunostaining and CLSM analyses were carried out following standard techniques, using the appropriate primary antibodies (Table 2) and the corresponding secondary fluorochrome-conjugated antibodies (Jackson ImmunoResearch Laboratories). Images were acquired with the confocal laser system TCS-SP5, Leica. Quantification of nucleus/cytoplasm fluorescence intensity was performed as reported previously (Aguilar et al., 2015). Morphometric analysis of nuclei was performed with software

INFORME DE LABORES 2019

TABLE 2 List of antibodies and plasmids used in this study

Antibodies				
			Dilution	
Antibody target	Supplier	Host	WB	IF
STAT3	Santa Cruz Biotechnology (Cat: sc−482)	Rabbit polyclonal	1:3,000	1:50
B23	Santa Cruz Biotechnology (Cat: sc−6013-a)	Rabbit polyclonal	1:3,000	1:50
Cyclin B1	Santa Cruz Biotechnology (Cat: sc−752)	Rabbit polyclonal	N/A	1:100
GFP	Santa Cruz Biotechnology (Cat: sc−8334)	Rabbit polyclonal	1:1,500	N/A
CRM1	Novus Biologicals, (Cat: NB100−79802)	Rabbit polyclonal	1:4,000	1:250
Lamin B1	Abcam (Cat: ab16048)	Rabbit polyclonal	1:3,000	1:250
Fibrillarin	Abcam (Cat: ab5821)	Rabbit polyclonal	N/A	1:50
H3K9me3	Abcam (Cat: ab8898)	Rabbit polyclonal	1:3,000	1:1,500
ZO−2	Zymed Laboratories (Cat: 71−1400)	Rabbit polyclonal	1:1,000	1:200
FLAG	Cell Signaling Technology (Cat: 2368)	Rabbit polyclonal	1:1,000	N/A
Dp71	Genemed Synthesis (Cat: +78Dp71)	Rabbit polyclonal	N/A	1:100
Lamin A/C	Santa Cruz Biotechnology (Cat: sc−20681)	Rabbit polyclonal	1:4,000	N/A
Lamin A/C	Hybridoma Bank (Cat: MANLAC3(4C10))	Mouse monoclonal	N/A	1:10
HDAC	Santa Cruz Biotechnology (Cat: sc−7872)	Rabbit polyclonal	N/A	1:60
NTF2	Santa Cruz Biotechnology (Cat: sc−80008)	Mouse monoclonal	1:150	1:50
Phospho-p70 S6K	Santa Cruz Biotechnology (Cat: Sc230)	Rabbit polyclonal	1:300	N/A
Phospho-rpS6	Cell Signaling Technology (Cat: 4857)	Rabbit monoclonal	1:1,000	N/A
Phospho-eIF2α	Cell Signaling Technology (Cat: 9721)	Rabbit polyclonal	1:1,000	N/A
Actin	Dr. Manuel Hernández, CINVESTAV, Mexico	Mouse monoclonal	1:3,000	N/A
NF-YA	Santa Cruz Biotechnology (Cat: sc−17753 X)	Mouse monoclonal	N/A	N/A

Plasmids	
Name	Supplier
pBABE-puro-GFP-wt-lamin A	Addgene
pBABE-puro-GFP-progerin	Addgene
pFLAG-hCRM1	Addgene
p3xFLAG-CMV−10	Addgene
Flag-CRM1	This study
pSG5-LB1	MSc Paulina Azuara, CINVESTAV, Mexico
pEGFP-C1	Addgene
pEGFP-C1-LB1	This study
CSHCTR001-nH1	GeneCopoeia
CS-HSH090209-nH1−01a	GeneCopoeia
pCRM1promoter	This study

ImageJ 1.46j. Nucleolar area was quantified by measuring the cross-sectional area occupied by a mark corresponding to fibrillarin stain, with software ImageJ 1.46j.

4.5 | Senescence-Associated β-Galactosidase (SA-β-Gal) Assay

Fibroblasts seeded on coverslips were stained with SA-β-Gal following manufacturer's instructions (Senescent Cell Histochemical Staining Kit, Sigma-Aldrich). Blue-stained cells expressing β-galactosidase (senescent cells) were observed under bright-field microscopy.

4.6 | Western blotting

Immunoblotting analyses were carried out following standard protocol. Specific proteins were visualized using the Enhanced Chemiluminescence (ECL™) Western blotting detection system (Amersham Pharmacia, GE Healthcare), according to the manufacturer's instructions.

INFORME DE LABORES 2019

4.7 | Flow cytometry and cell proliferation assays

The analysis of cell cycle was carried out on a BD LSRFortessa flow cytometer (BD Biosciences), using the ModFit LT software (Verity Software House). Cell proliferation was assessed by the 3-(4,5-dimethylthiazole-2–5-diphenyl tetrazolium bromide (MTT) assay, as reported previously (Velez-Aguilera et al., 2018).

4.8 | Quantitative reverse transcription PCR (RT-qPCR)

Total RNA was isolated from fibroblasts using the Direct-zol™ RNA MiniPrep Kit (Zymo Research), according to the manufacturer's instructions. RT-qPCR was carried on the StepOnePlus Real-Time PCR System (Applied Biosystems), using the KAPA SYBR Fast One-Step qRT-PCR system (Kapa Biosystems) and following a standard protocol. The expression levels for *CRM1* mRNA were measured by the $2^{\Delta\Delta ct}$ method and normalized to *GAPDH* mRNA values. Primer sequences for CRM1 and GAPDH amplification will be provided under request.

4.9 | Statistical analysis

Statistical analyses were performed by the two-tailed unpaired Student's *t* test. Data represent the mean ± SEM from a series of three separate experiments, and *p* values < 0.05 are indicative of statistical significance. Where indicated, statistical analysis was carried out using exact nonparametric Mann–Whitney U test or unpaired *t* test and data were summarized by the mean ± SEM or the mean ± *SD* from a series of three separate experiments. *p* values < 0.05 were considered as significant. All statistical analyses were performed using GraphPad Prism 5 software (San Diego).

ACKNOWLEDGMENTS

We thank Gómez-Islas J. P. (CINVESTAV) for technical support. This project was supported by a grant from the Bilateral Agreement CNR (Italy)/CINVESTAV (Mexico) #CNR2018/4 to BC, and a grant from the Secretaria de Educación, Ciencia, Tecnología e Innovación de la Ciudad de México SECITI/042/2018 (INGER-DI-CRECITES-008-2018) "Red Colaborativa de Investigación Traslacional para el Envejecimiento Saludable de la Ciudad de México (RECITES)."

CONFLICT OF INTEREST

None declared.

AUTHOR CONTRIBUTIONS

IGA and AAI conceived and designed the study; acquired, analyzed, and interpreted the data; and drafted/revised the article. RP designed the study, and acquired and analyzed the data. GVA and AE participated in investigation, contributed to methodology, and acquired and interpreted the data. GEJG and AVL acquired the data. MSLC conceived and designed the study. JM reviewed the paper and collected the resources. SJW designed, wrote, reviewed, and edited the article. BC conceived and designed the study, collected the resources, performed formal analysis, supervised the study, acquired funding, wrote the original draft, administered the project, and reviewed and edited the article.

ORCID

Bulmaro Cisneros https://orcid.org/0000-0003-2802-1201

REFERENCES

Aguilar, A., Wagstaff, K. M., Suarez-Sanchez, R., Zinker, S., Jans, D. A., & Cisneros, B. (2015). Nuclear localization of the dystrophin-associated protein alpha-dystrobrevin through importin alpha2/beta1 is critical for interaction with the nuclear lamina/maintenance of nuclear integrity. *The FASEB Journal*, *29*(5), 1842–1858. https://doi.org/10.1096/fj.14-257147

Buchwalter, A., & Hetzer, M. W. (2017). Nucleolar expansion and elevated protein translation in premature aging. *Nature Communications*, *8*(1), 328. https://doi.org/10.1038/s41467-017-00322-z

Camps, J., Wangsa, D., Falke, M., Brown, M., Case, C. M., Erdos, M. R., & Ried, T. (2014). Loss of lamin B1 results in prolongation of S phase and decondensation of chromosome territories. *The FASEB Journal*, *28*(8), 3423–3434. https://doi.org/10.1096/fj.14-250456

Cao, K., Graziotto, J. J., Blair, C. D., Mazzulli, J. R., Erdos, M. R., Krainc, D., & Collins, F. S. (2011). Rapamycin reverses cellular phenotypes and enhances mutant protein clearance in Hutchinson-Gilford progeria syndrome cells. *Science Translational Medicine*, *3*(89), 89ra58. https://doi.org/10.1126/scitranslmed.3002346

Christie, M., Chang, C. W., Rona, G., Smith, K. M., Stewart, A. G., Takeda, A. A., Kobe, B. (2016). Structural biology and regulation of protein import into the nucleus. *Journal of Molecular Biology*, *428*(10), 2060–2090. https://doi.org/10.1016/j.jmb.2015.10.023

Cobb, A. M., Larrieu, D., Warren, D. T., Liu, Y., Srivastava, S., Smith, A. J. O., … Shanahan, C. M. (2016). Prelamin A impairs 53BP1 nuclear entry by mislocalizing NUP153 and disrupting the Ran gradient. *Aging Cell*, *15*(6), 1039–1050. https://doi.org/10.1111/acel.12506

Datta, S., Snow, C. J., & Paschal, B. M. (2014). A pathway linking oxidative stress and the Ran GTPase system in progeria. *Molecular Biology of the Cell*, *25*(8), 1202–1215. https://doi.org/10.1091/mbc.E13-07-0430

De Sandre-Giovannoli, A., Bernard, R., Cau, P., Navarro, C., Amiel, J., Boccaccio, I., … Levy, N. (2003). Lamin a truncation in Hutchinson-Gilford progeria. *Science*, *300*(5628), 2055. https://doi.org/10.1126/science.1084125

Dreesen, O., Ong, P. F., Chojnowski, A., & Colman, A. (2013). The contrasting roles of lamin B1 in cellular aging and human disease. *Nucleus*, *4*(4), 283–290. https://doi.org/10.4161/nucl.25808

Drozdz, M. M., Jiang, H., Pytowski, L., Grovenor, C., & Vaux, D. J. (2017). Formation of a nucleoplasmic reticulum requires de novo assembly of nascent phospholipids and shows preferential incorporation of nascent lamins. *Scientific Reports*, *7*(1), 7454. https://doi.org/10.1038/s41598-017-07614-w

Dworak, N., Makosa, D., Chatterjee, M., Jividen, K., Yang, C.-S., Snow, C., … Paschal, B. M. (2019). A nuclear lamina-chromatin-Ran GTPase axis modulates nuclear import and DNA damage signaling. *Aging Cell*, *18*(1), e12851. https://doi.org/10.1111/acel.12851

Eriksson, M., Brown, W. T., Gordon, L. B., Glynn, M. W., Singer, J., Scott, L., … Collins, F. S. (2003). Recurrent de novo point mutations in lamin

A cause Hutchinson-Gilford progeria syndrome. *Nature*, *423*(6937), 293–298. https://doi.org/10.1038/nature01629

Freund, A., Laberge, R. M., Demaria, M., & Campisi, J. (2012). Lamin B1 loss is a senescence-associated biomarker. *Molecular Biology of the Cell*, *23*(11), 2066–2075. https://doi.org/10.1091/mbc.E11-10-0884

Glynn, M. W., & Glover, T. W. (2005). Incomplete processing of mutant lamin A in Hutchinson-Gilford progeria leads to nuclear abnormalities, which are reversed by farnesyltransferase inhibition. *Human Molecular Genetics*, *14*(20), 2959–2969. https://doi.org/10.1093/hmg/ddi326

Gonzalo, S., Kreienkamp, R., & Askjaer, P. (2017). Hutchinson-gilford progeria syndrome: A premature aging disease caused by LMNA gene mutations. *Ageing Research Reviews*, *33*, 18–29. https://doi.org/10.1016/j.arr.2016.06.007

Harhouri, K., Frankel, D., Bartoli, C., Roll, P., De Sandre-Giovannoli, A., & Levy, N. (2018). An overview of treatment strategies for Hutchinson-Gilford Progeria syndrome. *Nucleus*, *9*(1), 246–257. https://doi.org/10.1080/19491034.2018.1460045

Harhouri, K., Navarro, C., Depetris, D., Mattei, M.-G., Nissan, X., Cau, P., … Lévy, N. (2017). MG132-induced progerin clearance is mediated by autophagy activation and splicing regulation. *EMBO Molecular Medicine*, *9*(9), 1294–1313. https://doi.org/10.15252/emmm.201607315

Ishizawa, J., Kojima, K., Hail, N. Jr, Tabe, Y., & Andreeff, M. (2015). Expression, function, and targeting of the nuclear exporter chromosome region maintenance 1 (CRM1) protein. *Pharmacology & Therapeutics*, *153*, 25–35. https://doi.org/10.1016/j.pharmthera.2015.06.001

Kang, H. T., Park, J. T., Choi, K., Choi, H. J. C., Jung, C. W., Kim, G. R., … Park, S. C. (2017). Chemical screening identifies ROCK as a target for recovering mitochondrial function in Hutchinson-Gilford progeria syndrome. *Aging Cell*, *16*(3), 541–550. https://doi.org/10.1111/acel.12584

Kırlı, K., Karaca, S., Dehne, H. J., Samwer, M., Pan, K. T., Lenz, C., … Görlich, D. (2015). A deep proteomics perspective on CRM1-mediated nuclear export and nucleocytoplasmic partitioning. *eLife*, *4*, e11466. https://doi.org/10.7554/eLife.11466

Kubben, N., & Misteli, T. (2017). Shared molecular and cellular mechanisms of premature ageing and ageing-associated diseases. *Nature Reviews Molecular Cell Biology*, *18*(10), 595–609. https://doi.org/10.1038/nrm.2017.68

Larrieu, D., Vire, E., Robson, S., Breusegem, S. Y., Kouzarides, T., & Jackson, S. P. (2018). Inhibition of the acetyltransferase NAT10 normalizes progeric and aging cells by rebalancing the Transportin-1 nuclear import pathway. *Science Signalling*, *11*(537), https://doi.org/10.1126/scisignal.aar5401

Lee, S.-J., Jung, Y.-S., Yoon, M.-H., Kang, S.-M., Oh, A.-Y., Lee, J.-H., … Park, B.-J. (2016). Interruption of progerin-lamin A/C binding ameliorates Hutchinson-Gilford progeria syndrome phenotype. *Journal of Clinical Investigation*, *126*(10), 3879–3893. https://doi.org/10.1172/jci84164

Lukasova, E., Kovarik, A., & Kozubek, S. (2018). Consequences of Lamin B1 and Lamin B receptor downregulation in senescence. *Cells*, *7*(2), 11. https://doi.org/10.3390/cells7020011

Mahipal, A., & Malafa, M. (2016). Importins and exportins as therapeutic targets in cancer. *Pharmacology & Therapeutics*, *164*, 135–143. https://doi.org/10.1016/j.pharmthera.2016.03.020

Morales-Lazaro, S. L., Gonzalez-Ramirez, R., Gomez, P., Tapia-Ramirez, V., de Leon, M. B., & Cisneros, B. (2010). Induction of dystrophin Dp71 expression during neuronal differentiation: Opposite roles of Sp1 and AP2alpha in Dp71 promoter activity. *Journal of Neurochemistry*, *112*(2), 474–485. https://doi.org/10.1111/j.1471-4159.2009.06467.x

Noda, A., Mishima, S., Hirai, Y., Hamasaki, K., Landes, R. D., Mitani, H., … Kodama, Y. (2015). Progerin, the protein responsible for the Hutchinson-Gilford progeria syndrome, increases the unrepaired DNA damages following exposure to ionizing radiation. *Genes and Environment*, *37*, 13. https://doi.org/10.1186/s41021-015-0018-4

Shimi, T., Butin-Israeli, V., Adam, S. A., Hamanaka, R. B., Goldman, A. E., Lucas, C. A., … Goldman, R. D. (2011). The role of nuclear lamin B1 in cell proliferation and senescence. *Genes & Development*, *25*(24), 2579–2593. https://doi.org/10.1101/gad.179515.111

Silvestrini, M. J., Johnson, J. R., Kumar, A. V., Thakurta, T. G., Blais, K., Neill, Z. A., … Lapierre, L. R. (2018). Nuclear export inhibition enhances HLH-30/TFEB activity, autophagy, and lifespan. *Cell Reports*, *23*(7), 1915–1921. https://doi.org/10.1016/j.celrep.2018.04.063

Snow, C. J., Dar, A., Dutta, A., Kehlenbach, R. H., & Paschal, B. M. (2013). Defective nuclear import of Tpr in Progeria reflects the Ran sensitivity of large cargo transport. *Journal of Cell Biology*, *201*(4), 541–557. https://doi.org/10.1083/jcb.201212117

Toth, J. I., Yang, S. H., Qiao, X., Beigneux, A. P., Gelb, M. H., Moulson, C. L., … Fong, L. G. (2005). Blocking protein farnesyltransferase improves nuclear shape in fibroblasts from humans with progeroid syndromes. *Proceedings of the National Academy of Sciences USA*, *102*(36), 12873–12878. https://doi.org/10.1073/pnas.0505767102

van der Watt, P. J., & Leaner, V. D. (2011). The nuclear exporter, Crm1, is regulated by NFY and Sp1 in cancer cells and repressed by p53 in response to DNA damage. *Biochimica Et Biophysica Acta*, *1809*(7), 316–326. https://doi.org/10.1016/j.bbagrm.2011.05.017

Velez-Aguilera, G., de Dios Gomez-Lopez, J., Jimenez-Gutierrez, G. E., Vasquez-Limeta, A., Laredo-Cisneros, M. S., Gomez, P., … Cisneros, B. (2018). Control of nuclear beta-dystroglycan content is crucial for the maintenance of nuclear envelope integrity and function. *Biochimica Et Biophysica Acta*, *1865*(2), 406–420. https://doi.org/10.1016/j.bbamcr.2017.11.013

Vergnes, L., Peterfy, M., Bergo, M. O., Young, S. G., & Reue, K. (2004). Lamin B1 is required for mouse development and nuclear integrity. *Proceedings of the National Academy of Sciences USA*, *101*(28), 10428–10433. https://doi.org/10.1073/pnas.0401424101

Xiong, Z.-M., Choi, J. Y., Wang, K., Zhang, H., Tariq, Z., Wu, D. I., … Cao, K. (2016). Methylene blue alleviates nuclear and mitochondrial abnormalities in progeria. *Aging Cell*, *15*(2), 279–290. https://doi.org/10.1111/acel.12434

SUPPORTING INFORMATION

Additional supporting information may be found online in the Supporting Information section at the end of the article.

How to cite this article: García-Aguirre I, Alamillo-Iniesta A, Rodríguez-Pérez R, et al. Enhanced nuclear protein export in premature aging and rescue of the progeria phenotype by modulation of CRM1 activity. *Aging Cell*. 2019;18:e13002. https://doi.org/10.1111/acel.13002

Molecular Neurobiology (2019) 56:4037–4050
https://doi.org/10.1007/s12035-018-1356-6

Genetic Knockdown of mGluR5 in Striatal D1R-Containing Neurons Attenuates L-DOPA-Induced Dyskinesia in Aphakia Mice

José-Rubén García-Montes[1,2] · Oscar Solís[1,2] · Juan Enríquez-Traba[1] · Irene Ruiz-DeDiego[1,2] · René Drucker-Colín[3] · Rosario Moratalla[1,2]

Received: 29 May 2018 / Accepted: 17 September 2018 / Published online: 27 September 2018
© Springer Science+Business Media, LLC, part of Springer Nature 2018

Abstract

L-DOPA is the main pharmacological therapy for Parkinson's disease. However, long-term exposure to L-DOPA induces involuntary movements termed dyskinesia. Clinical trials show that dyskinesia is attenuated by metabotropic glutamate receptor type 5 (mGluR5) antagonists. Further, the onset of dyskinesia is delayed by nicotine and mGluR5 expression is lower in smokers than in non-smokers. However, the mechanisms by which mGluR5 modulates dyskinesia and how mGluR5 and nicotine interact have not been established. To address these issues, we studied the role of mGluR5 in D1R-containing neurons in dyskinesia and examined whether nicotine reduces dyskinesia via mGluR5. In the aphakia mouse model of Parkinson's disease, we selectively knocked down mGluR5 in D1R-containing neurons (aphakia-mGluR5$^{KD\text{-}D1}$). We found that genetic downregulation of mGluR5 decreased dyskinesia in aphakia mice. Although chronic nicotine increased the therapeutic effect of L-DOPA in both aphakia and aphakia-mGluR5$^{KD\text{-}D1}$ mice, it caused a robust reduction in dyskinesia only in aphakia, and not in aphakia-mGluR5$^{KD\text{-}D1}$ mice. Downregulating mGluR5 or nicotine treatment after L-DOPA decreased ERK and histone 3 activation, and FosB expression. Combining nicotine and mGluR5 knockdown did not have an added antidyskinetic effect, indicating that the effect of nicotine might be mediated by downregulation of mGluR5 expression. Treatment of aphakia-mGluR5$^{KD\text{-}D1}$ mice with a negative allosteric modulator did not further modify dyskinesia, suggesting that mGluR5 in non-D1R-containing neurons does not play a role in its development. In conclusion, this work suggests that mGluR5 antagonists reduce dyskinesia by mainly affecting D1R-containing neurons and that the effect of nicotine on dyskinetic signs in aphakia mice is likely via mGluR5.

Keywords Basal ganglia · Dyskinesia · mGluR5 · Nicotine · Parkinson's disease

Introduction

Parkinson's disease (PD) is characterized by the loss of dopaminergic neurons in the *substantia nigra pars compacta* and is associated with a reduction of dopaminergic tone in the striatum that correlates with the motor symptomatology. The dopamine precursor L-3,4-dihydroxyphenylalanine (L-DOPA) provides the most effective symptomatic treatment for PD [1, 2]. However, chronic L-DOPA administration together with the progression of PD induces motor side effects, such as dyskinesia. Strong evidence demonstrates that the dopamine D1 receptor (D1R) is critical for the development of dyskinesia [3–5]. For instance, L-DOPA and D1R agonists induce dyskinesia [6], and increased activation of D1R is associated with enhanced expression of extracellular-signal-activated kinases (ERK), phospho-acetylated histone 3 (pAcH3) and FosB [7–12]. These findings indicate that reduction of D1R-dependent signaling may help to alleviate dyskinetic symptoms [8, 13, 14]. Previous evidence demonstrated that glutamatergic and cholinergic transmission modulate the D1R signaling pathway [15, 16]. In fact, glutamatergic transmission in the basal ganglia is increased in dyskinesia [17–20]. Interestingly, this overactivation could be reversed in animal

✉ José-Rubén García-Montes
jrgarcia@cajal.csic.es

✉ Rosario Moratalla
moratalla@cajal.csic.es

[1] Instituto Cajal, Consejo Superior de Investigaciones Científicas, Av. Dr. Arce 37, 28002 Madrid, Spain

[2] CIBERNED, Instituto de Salud Carlos III, Madrid, Spain

[3] Departamento de Neuropatología Molecular, Instituto de Fisiología Celular, Universidad Nacional Autónoma de México, Ciudad de México, Mexico

models by modulating the metabotropic glutamate receptor type 5 (mGluR5) [21].

The mGluR5 is highly expressed in striatal D1R- and D2R-containing neurons but also in cholinergic, parvalbumin, and somatostatinergic interneurons as well as in corticostriatal and thalamostriatal pathways [22, 23]. Several lines of evidence implicate mGluR5 in the development of dyskinesia [24–29]. First, L-DOPA treatment increases mGluR5 binding in the striatum of dyskinetic MPTP-treated monkeys and 6-OHDA-lesioned rats [28, 30]. Second, clinical and preclinical studies show that mGluR5 antagonists have moderate to mild antidyskinetic effects but at the expense of the therapeutic efficacy of L-DOPA [31–33]. Because mGluR5 is so widely distributed on striatal neurons, it is possible that these effects reside in different populations. Therefore, before dismissing mGluR5 as a potential therapeutic target for treatment or prevention of dyskinesia, it is important to determine if the antidyskinetic role of mGluR5 antagonists reside in a specific striatal population.

Previous studies have shown that dyskinesia is less frequent in PD patients who smoke compared to those who do not [34]. Although tobacco smoke contains many chemical components, it is possible that nicotine plays a role, since previous studies show that nicotine has antidyskinetic effects in rodents and non-human primates [35–38]. Nicotine actions are mediated by nicotinic acetylcholine receptors (nAChR) that are highly expressed in the striatum and modulate dopaminergic transmission. In the striatum, the two most abundant nicotine receptors are the β2* (α4β2*, α6β2*) and the α7 [39]. These receptors modulate the release of dopamine and glutamate in the striatum [3, 40]. Interestingly, previous studies showed that α7 receptor-specific binding is increased in the putamen of dyskinetic MPTP-treated monkeys and PD patients [41]. It is noteworthy that mGluR5 expression is downregulated in smokers, specifically in the caudate nucleus and putamen, suggesting that nicotine may be the cause of this downregulation [42]. Moreover, other previous studies suggest that the antidyskinetic effect of nicotine may be the result of targeting glutamatergic inputs [18, 43, 44].

Because D1R-containing neurons are strongly implicated in the development of dyskinesia, our aim in this study was to investigate the role of mGluR5, in direct pathway neurons, in dyskinesia. To produce a parkinsonian mouse model with D1R-specific reduction of mGluR5, we crossed transgenic mice, with a selective reduction of mGluR5 in D1R-containing neurons ($mGluR5^{KD\text{-}D1}$), with aphakia mice, a genetic model of PD [45, 46]. To understand the function of mGluR5 in direct pathway neurons in dyskinesia, we compared the effect of L-DOPA treatment in these mice to aphakia mice [46]. We also studied the dyskinetic effect of nicotine in these mice to determine if mGluR5 on D1R-containing neurons plays a role.

Methods

Mice

Female and male mice (22–30 g) were housed under 12-h light-dark cycle with food and water ad libitum, temperature 22 °C, and humidity 44%. $mGluR5^{KD\text{-}D1}$ mice were generated by homologous recombination and kindly provided by Dr. Bilbao and Dr. Spanagel, from the Central Institute of Mental Health, Manheim Germany [45]. Aphakia mice and C57BL/6J mice were obtained from our own facility. Aphakia mice with a selective knockdown of mGluR5 in D1R-containing neurons were created by crossing aphakia mice with $mGluR5^{KD\text{-}D1}$ mice. All mice were on a C57BL/6J background, and the genotype was determined by PCR analysis of tail-tip DNA as described previously [45, 46].

Drugs

L-DOPA, benserazide, and 1-methyl-3-(4-methylpyridin-3-yl)-6-(pyridin-2-ylmethoxy)-1H-pyrazolo-[3,4-b]pyrazine (PF470) were purchased from Sigma–Aldrich (Spain). (−)-Nicotine ditartrate was purchased from Tocris-Bioscience (UK).

Nicotine and L-DOPA Treatment

Half of the mice were randomly assigned to control (sweetened water) or nicotine groups. Nicotine was supplied in drinking water (300 μg/mL in 2% saccharine vehicle) for 8 weeks. This concentration corresponds to a level similar to that found in long-time smokers [3]. Chronic nicotine treatment in the drinking water was initiated a month before the chronic administration of L-DOPA. Mice received a daily injection of benserazide (10 mg/kg i.p.) followed, 20 min later, by L-DOPA (10 mg/kg i.p) (Fig. 1(a)) [47]. To assess the non-D1R role of mGluR5 in dyskinesia, a highly potent negative allosteric modulator, PF470 (1 mg/kg s.c.), was used (Ki = 0.9 nM vs MTEP Ki = 16 nM) together with benserazide.

Behavioral Analysis

Following injections, mice were placed individually in glass cylinders and were video-recorded for 4 min, beginning 30 min after L-DOPA or saline injection. Three and four paw dyskinesia (3–4 paw dyskinesia) was scored as described previously. Briefly, 3–4 paw dyskinesia was noted when mice stood on their hind paws and reared against the wall of the cylinder, moving both front paws and repeatedly lifting the hind paws up and down [47–49].

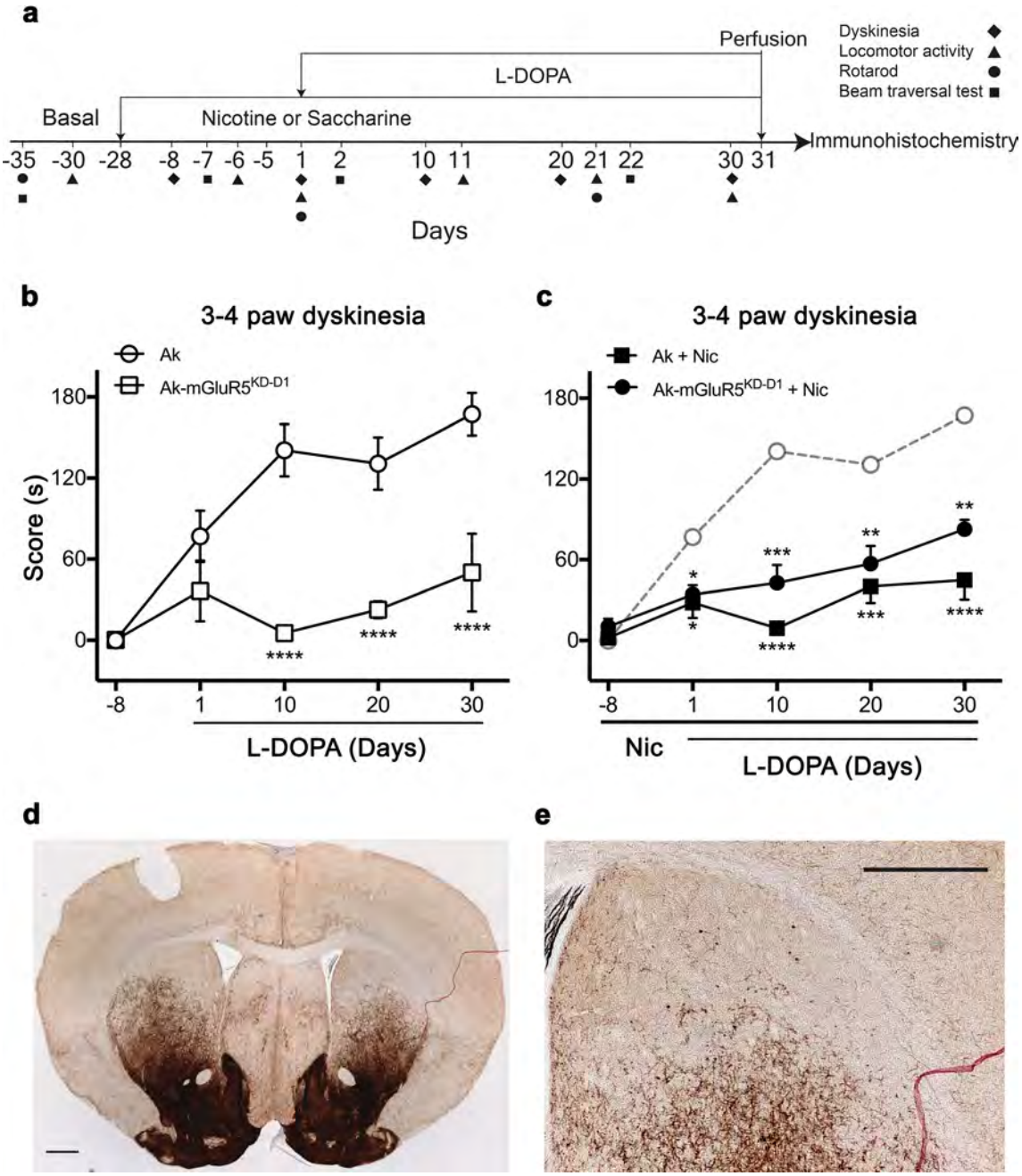

Fig. 1 Selective reduction of mGluR5 in D1R-containing neurons diminishes L-DOPA-induced dyskinesia in aphakia (Ak) mice. *a* Schematic view of the experimental timeline. *b*, *c* Scores of 3–4 paw dyskinesia in Ak and Ak-mGluR5^{KD-D1} mice treated with L-DOPA *b* and nicotine + L-DOPA *c*. *d* Coronal section from an Ak mouse immunostained for TH. *e* High magnification image from *d* showing a gradient of TH loss in dorsolateral striatum. Scale bar = 500 μm. Data are expressed as mean ± SEM, $n = 9–15$ per group. Two-way ANOVA followed by Bonferroni's post hoc test showed significant differences for *b* [genotype, $F_{1,102} = 48.95$, $p < 0.0001$; time, $F_{4,102} = 10.04$, $p < 0.0001$; interaction, $F_{4,102} = 5.21$, $p = 0.0007$] and for *c* [treatment, $F_{4,146} = 16.83$, $p < 0.0001$; time, $F_{2,146} = 40.3$, $p < 0.001$; interaction, $F_{8,146} = 4.35$, $p = 0.0001$]. $^{*}p < 0.05$, $^{**}p < 0.01$, $^{***}p < 0.001$, $^{****}p < 0.0001$ vs. L-DOPA-treated Ak (dotted line in *c*). Nic nicotine

Basal motor behavior was evaluated 1 to 2 weeks before L-DOPA administration. Locomotor activity was assessed in activity cages (AccuScan instruments, Inc.) as previously described [13]. We measured the total distance (cm) traveled during a 30-min period, beginning 30 min after L-DOPA injection. Motor coordination and balance were measured in the challenging beam traversal test as previously described [50]. Briefly, before treatments, mice were trained to cross the beam, and once trained, they were videotaped. We measured the total time it took the mice to cross the beam. The beam traversal test was evaluated 45 min after L-DOPA

INFORME DE LABORES 2019

injection, when dyskinesia is higher. Motor coordination was evaluated using the rotarod test (UgoBasile, Varese, Italy), following an accelerating protocol with increasing speed from 4 to 40 rpm over a 5-min period and measuring latency up to the first fall off the rod [47]. Mice were tested in six consecutive trials, 20 min apart. All behavioral experiments were assessed by observers who were blind to mouse genotypes and treatment.

Immunohistochemistry

One hour after the last L-DOPA injection, animals were anesthetized with an overdose of pentobarbital (Normon Labs, Madrid Spain) and perfused with saline solution, followed by 4% paraformaldehyde in phosphate-buffered saline. The brains were post-fixed overnight and transferred to a solution of 0.1 M phosphate buffer. The brains were cut into 30-μm coronal sections with a vibratome (Leica, Wetzlar, Germany), and immunohistochemistry was performed on free-floating sections. To stain sections of striatum, we used the standard avidin-biotin immunohistochemical protocol with the following primary antibodies: tyrosine hydroxylase (TH, 1:1000; Chemicon), FosB (1:15000; Santa Cruz Biotechnology), pERK (1:250; Cell Signaling Technology), and pAcH3 (1:10000; Millipore). For immunofluorescence, we used mGluR5 antibody (1:100; Alomone labs) revealed with Alexa fluor 647-conjugated secondary antibody (1:500; Invitrogen). Quantification of FosB, pAcH3, and pERK, TH and mGluR5 expression levels were carried out using ImageJ [51]. The number of immunolabeled cells were determined using two-three serial rostrocaudal sections (+ 1.10 to + 0.14 mm relative to bregma) per animal from the lesioned dorsolateral striatum as previously described. The digital images were obtained under a Leica microscope using a × 40 objective. The data are presented as the number of stained nuclei per square millimeter in the denervated striatum as previously reported [14]. We conducted fluorescence analyses of mGluR5 by using ImageJ to calculate the signal intensity contained in the double stained microphotographs obtained with confocal microscope using a × 60 objective as previously described [52]. Fluorescence intensity results are expressed as percentage of control (C57BL/6J mice).

Statistical Analysis

All values are given as mean ± SEM. Statistical analyses were performed using GraphPad Prism 6. Statistical analysis was assessed by using two-way ANOVA or repeated measures, followed by the appropriate post hoc comparisons. A level of $p < 0.05$ was considered statistically significant.

Results

Knockdown of mGluR5 in D1R-Containing Neurons Ameliorates L-DOPA-Induced Dyskinesia

The aphakia mice lack nigrostriatal innervation in both hemispheres (Fig. 1(d, e)) and, therefore, display bilateral dyskinetic symptoms after L-DOPA treatment as shown previously [46, 48]. To evaluate the role of mGluR5 in direct pathway neurons in dyskinesia, we used the aphakia-mGluR5$^{KD\text{-}D1}$. Aphakia-mGluR5$^{KD\text{-}D1}$ and aphakia mice were chronically treated with L-DOPA (10 mg/kg) for 31 days, (Fig. 1(a)), and 3–4 paw dyskinesia was evaluated at regular intervals by a researcher blinded to treatment and genotype [46, 47]. L-DOPA increased 3–4 paw dyskinesia in aphakia mice, while in aphakia-mGluR5$^{KD\text{-}D1}$ mice, dyskinetic scores were significantly lower ($p < 0.001$) (Fig. 1(b)). Because nicotine attenuates and delays the onset of dyskinetic symptoms [34–36, 53], and also reduces brain mGluR5 [42], we wanted to address if nicotine's effect on dyskinesia is related to reduced mGluR5 expression on D1R-containing neurons. Chronic treatment with nicotine robustly and significantly reduced dyskinesia in aphakia mice ($p < 0.01$), similar to its previously published effects in unilateral 6-OHDA-lesioned mice and in MPTP-treated monkeys [38, 40, 54]. In aphakia-mGluR5$^{KD\text{-}D1}$ mice, nicotine treatment did not further reduce dyskinetic symptoms. In fact, the aphakia-mGluR5$^{KD\text{-}D1}$ mice showed slightly higher dyskinetic scores compared with aphakia mice treated with nicotine (Fig. 1(c)).

Knockdown of mGluR5 in D1R-Containing Neurons Does Not Affect L-DOPA's Therapeutic Efficacy

To check that the antidyskinetic effects of mGluR5 knockdown were not due to a reduction in the therapeutic effect of L-DOPA, we compared motor behavior in L-DOPA-treated aphakia and aphakia-mGluR5$^{KD\text{-}D1}$ mice. In this experiment, we used activity cages that measure spontaneous locomotor activity as reflected by sequential horizontal beam breaks, computing the total distance traveled during each trial. We found no difference between aphakia and aphakia-mGluR5$^{KD\text{-}D1}$ mice in horizontal movements or the distance traveled under basal conditions or after chronic L-DOPA treatment (Fig. 2(a, b)). Chronic nicotine treatment also had no effect in motor activity in the L-DOPA-treated or naïve aphakia or aphakia-mGluR5$^{KD\text{-}D1}$ mice (Fig. 2(a', b')).

We then challenged the mice for finer motor coordination and activity using the beam traversal and rotarod tests before and after L-DOPA treatment. The time to cross the beam was similar in aphakia and aphakia-mGluR5$^{KD\text{-}D1}$ mice after saline. Chronic L-DOPA significantly reduced the time

INFORME DE LABORES 2019

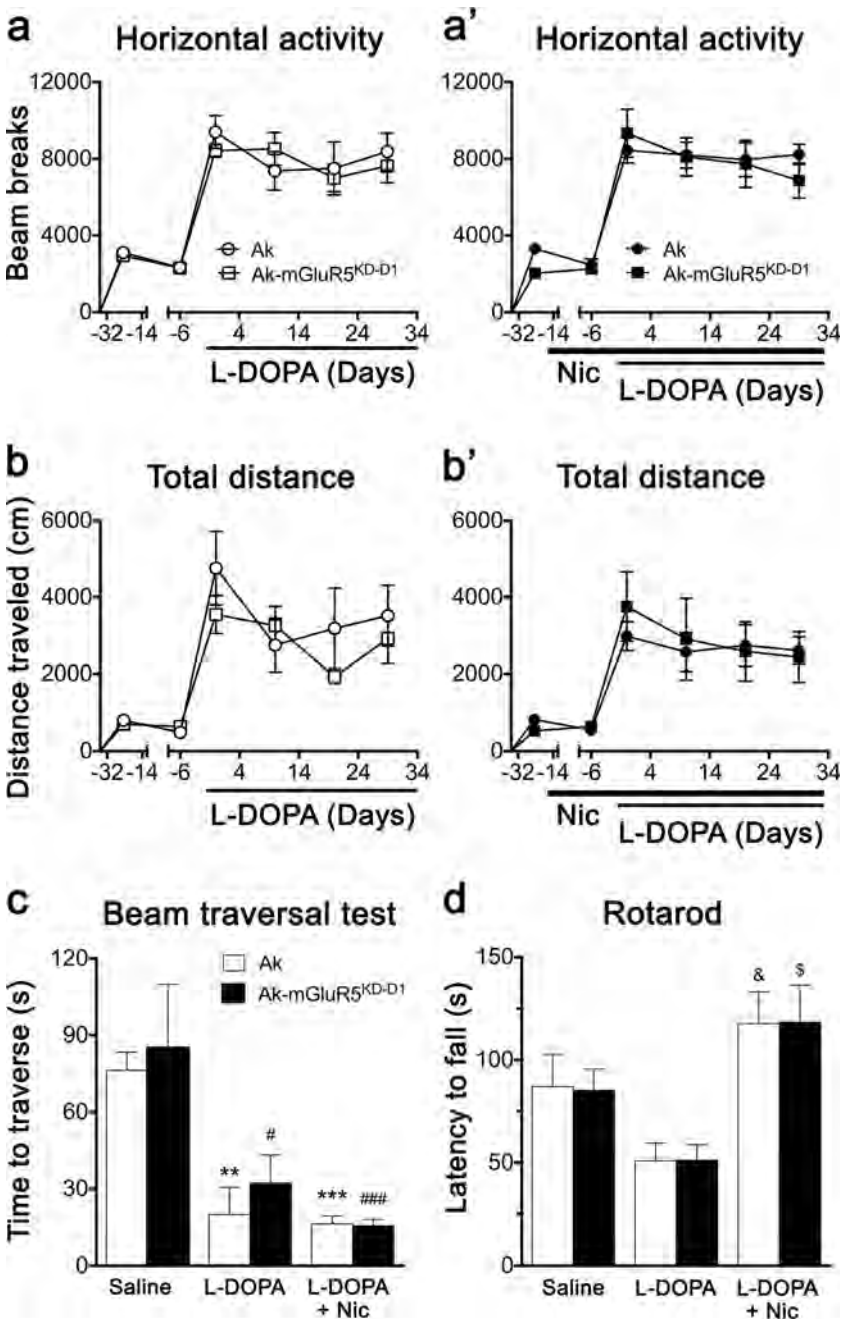

Fig. 2 Selective reduction of mGluR5 in D1R-containing neurons does not alter the therapeutic effect of L-DOPA. (a, a'). Horizontal locomotor activity and (b, b') total distance traveled were measured 30 min after L-DOPA administration for 30 min. Note that no differences were found between Ak and Ak-mGlur5^{KD-D1} neither in basal conditions nor with L-DOPA (a, b) or L-DOPA + nicotine (a', b'). Motor coordination and performance were measured in the beam traversal (c) and in the rotarod (d) tests at different time points: 5 weeks before any treatment (saline), or 45 min after L-DOPA administration (see timeline in Fig. 1(a)). Two-way ANOVA followed by Bonferroni's post hoc test showed significant differences for treatment [$F_{2,42} = 25.26$, $p < 0.001$ for (c); $F_{2,50} = 12.15$, $p = 0.0001$ for (*d*)]. $^{**}p < 0.01$, $^{***}p < 0.001$ vs. Ak saline, $^{\#}p < 0.05$, $^{\#\#\#}p < 0.001$ vs. Ak-mGlur5^{KD-D1} saline, $^{\&}p < 0.05$ vs. Ak L-DOPA, $^{\$}p < 0.05$ vs. Ak-mGlur5^{KD-D1} L-DOPA. Data are expressed as mean ± SEM, $n = 6$–11 per group. Nic nicotine

to cross beam in both groups of mice ($p < 0.01$), with no significant difference between genotypes. Chronic nicotine treatment did not further reduce the time to cross the beam (Fig. 2(c)). In terms of motor coordination, dyskinesia reduced the latency to fall from the rod in both aphakia and aphakia-mGluR5^{KD-D1} mice (Fig. 2(d)). Interestingly, chronic treatment with nicotine in addition to L-DOPA significantly potentiated L-DOPA's motor coordination effect in both aphakia and aphakia-mGluR5^{KD-D1} mice ($p < 0.01$) (Fig. 2(d)).

Molecular Markers as Cue in the Effect of Nicotine in Aphakia Mice Lacking mGluR5 in D1R-Containing Neurons

We then investigated whether the decrease in L-DOPA-induced dyskinesia in aphakia-mGluR5^{KD-D1} mice is accompanied by a reduction of molecular markers of L-DOPA-induced dyskinesia—pERK, pAcH3, and FosB. As expected, L-DOPA induced the expression of molecular markers selectively in the completely denervated striatal areas in both hemispheres (e.g. see FosB

inset in Fig. 3(c)). Chronic L-DOPA treatment significantly increased the expression of FosB, pAcH3, and pERK in aphakia mice compared to the saline- and nicotine-treated aphakia animals ($p < 0.001$) (Fig. 3). Interestingly, in aphakia-mGluR5^{KD-D1} mice, the number of neurons immunoreactive for pERK was reduced by 66% ($p < 0.01$), pAcH3 activation was reduced by 33% ($p < 0.05$, $p < 0.01$, $p < 0.001$), and FosB expression by 39% ($p < 0.05$) (Fig. 3(a'–c')) compared to aphakia mice. Consistent with its effect on dyskinesia signs, chronic treatment with nicotine resulted in a significant decrease of pERK- and pAcH3-induced by L-DOPA in aphakia ($p < 0.01$) (Fig. 3(a', b')) but not in aphakia-mGluR5^{KD-D1} mice. However, nicotine did not alter L-DOPA-induced FosB expression in either aphakia or aphakia-mGluR5^{KD-D1} mice (Fig. 3(c, c')).

The Antidyskinetic Effect of the mGluR5 Negative Allosteric Modulator Is Primarily Mediated by mGluR5 on D1R-Containing Neurons

Because mGluR5 is similarly expressed in D1R- and D2R-containing striatal neurons, and in most interneurons [22], we then tested if the antidyskinetic effects of the negative

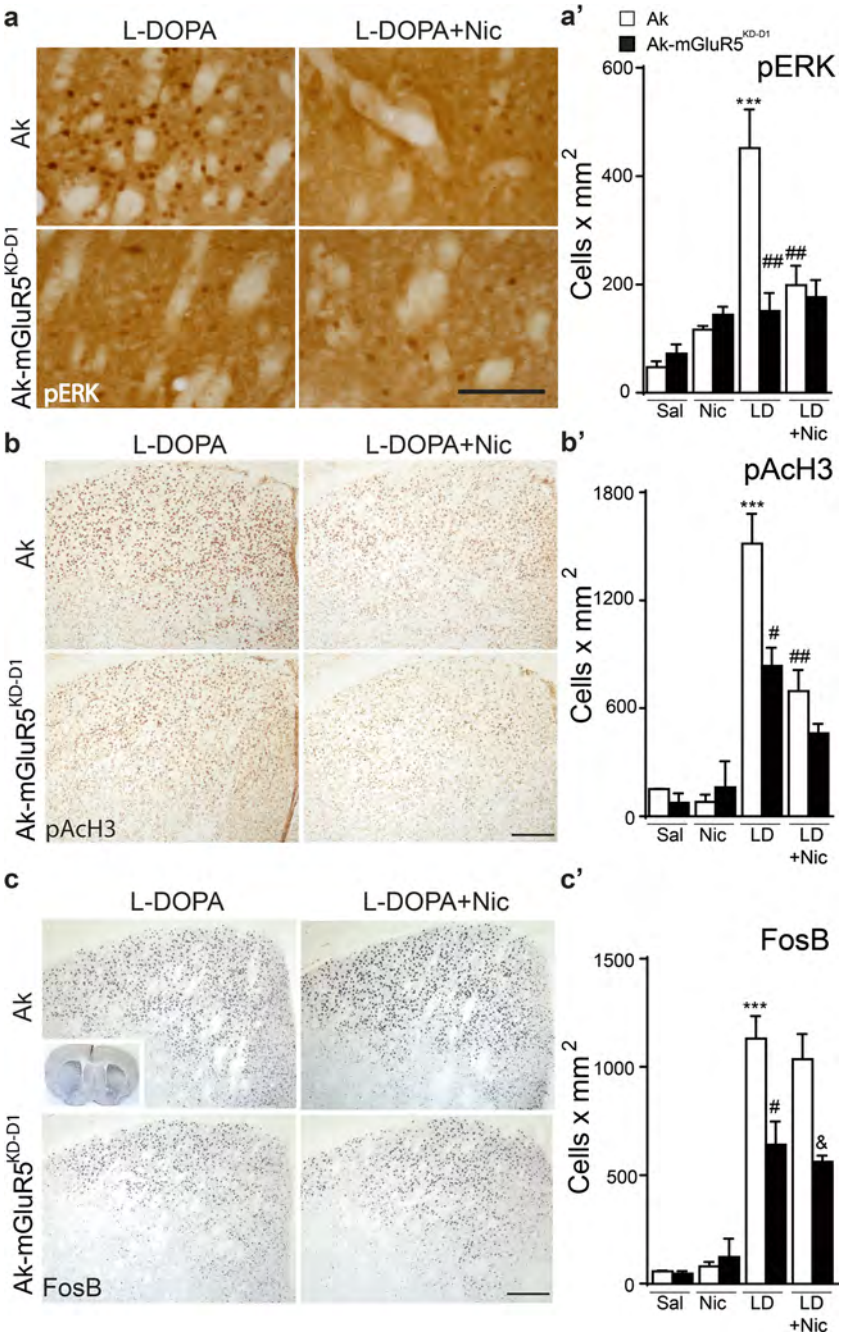

Fig. 3 Downregulation of mGluR5 in D1R neurons reduces L-DOPA-induced molecular markers of dyskinesia. (a, b, c) Microphotographs of striatal coronal sections from Ak and Ak-mGluR5^{KD-D1} mice sacrificed 1 h after the last L-DOPA injection, immunostained for pERK, pAcH3, and FosB. Scale bar = 100 μm, 200 μm. (a', b', c') Histograms represent the quantification of pERK, pAcH3, and FosB immunoreactive positive cells. Note that all molecular markers are expressed in the completely denervated striatal areas, see FosB image in (c). Two-way ANOVA followed by Bonferroni's post hoc test showed significant differences for genotype [$F_{1,26} = 4.49$, $p = 0.04$ for pERK; $F_{1,26} = 7.02$, $p = 0.01$ for FosB] and treatment [$F_{3,26} = 10.15$, $p = 0.0001$ for pERK; $F_{3,27} = 16.93$, $p = 0.0001$ for pAcH3; $F_{3,26} = 26.04$, $p = 0.0001$ for FosB]. ***$p < 0.001$ vs. Ak saline, $^{\#}p < 0.05$, $^{\#\#}p < 0.01$ vs. Ak L-DOPA. $^{\&} < 0.05$ vs. Ak-mGluR5^{KD-D1} L-DOPA + nicotine. Data are expressed as mean ± SEM, $n = 5–8$ per group, except in saline- and nicotine-treated groups, $n = 3$. Nic, nicotine; LD, L-DOPA

allosteric modulators in aphakia-mGluR5^{KD-D1} mice were mediated by the mGluR5 expressed in D1R-containing neurons. Previous studies showed a marked antidyskinetic effect of the highly selective and efficacious mGluR5 negative allosteric modulator, PF470 [55]. To assess the specific contribution of mGluR5 on D1R-containing neurons, we compared the effect of PF470 on L-DOPA-induced dyskinesia in aphakia and aphakia-mGluR5^{KD-D1} mice. We treated mice with PF470 20 min before the last dose of L-DOPA (Fig. 4(a)). Our results showed that a single dose (1 mg/kg, i.p.) of PF470 decreased dyskinetic behavior in aphakia mice by about 80% ($p < 0.05$), as expected [56]. However, acute PF470 had no significant effect on dyskinetic behavior in aphakia-mGluR5^{KD-D1} mice (Fig. 4(b)), suggesting that the effect of the mGluR5 antagonists on dyskinesia is primarily due to its action on mGluR5 located in D1R-containing neurons. Similarly, PF470 did not further reduce the antidyskinetic effects of nicotine in aphakia or aphakia-mGluR5^{KD-D1} mice (Fig. 4(b)).

We next compared the effect of PF470 on expression of molecular markers of dyskinesia in aphakia and aphakia-

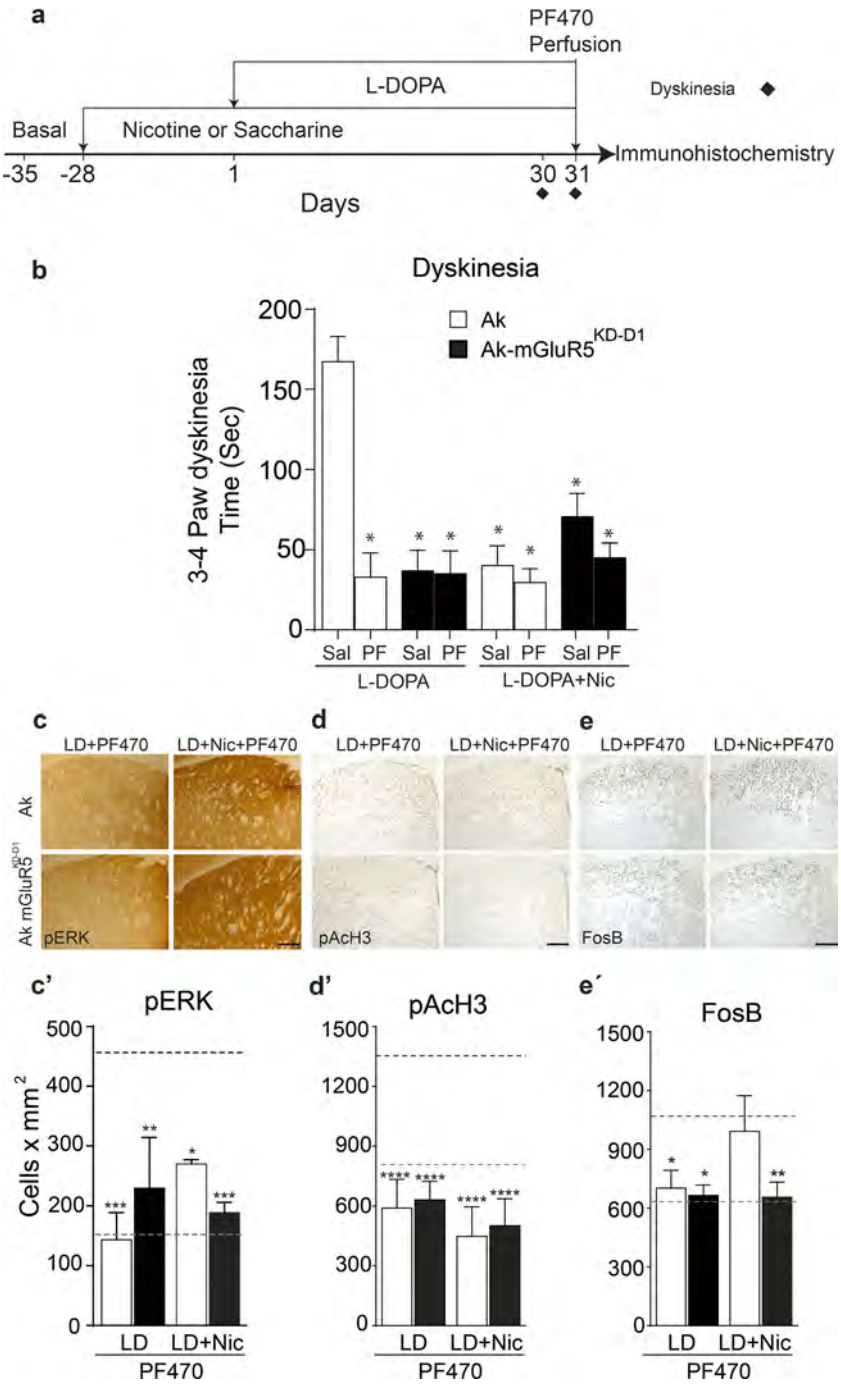

Fig. 4 The antidyskinetic effect of the mGluR5 negative allosteric modulator is mediated by mGluR5 on D1R-containing neurons. (a) Schematic view of the experimental timeline. (b) Acute administration of the mGluR5 negative allosteric modulator PF470 (PF) reduces already established L-DOPA-induced dyskinesia in Ak but not in Ak-mGluR5^{KD-D1} mice. One-way ANOVA followed by Bonferroni's post hoc test [$F_{7,71} = 15.23$, $p < 0.0001$]. *$p < 0.001$ vs. L-DOPA-treated Ak. (c–e') Immunohistochemical analysis illustrating that PF470 reduces L-DOPA-induced striatal pERK (c, c'), pAcH3 (d, d') and FosB (e, e') expression only in Ak mice. Black dotted line represents the expression levels induced by L-DOPA in Ak mice and the gray dotted line in Ak-mGluR5^{KD-D1} mice. Scale bar = 100 μm. Two-way ANOVA followed by Fisher's LSD post hoc test: genotype × treatment [$F_{2,19} = 6.58$, $p = 0.0067$ for pERK; $F_{2,19} = 8.65$, $p < 0.002$ for pAcH3; $F_{2,18} = 2.1$, $p = 0.15$ for FosB]. *$p < 0.05$, **$p < 0.01$, ***$p < 0.001$, ****$p < 0.0001$ vs. L-DOPA-treated Ak mice. Data are expressed as mean ± SEM. $n = 9$–14 per group in (b) and 3–4 per group in (c–e')

INFORME DE LABORES 2019

mGluR5$^{KD\text{-}D1}$ mice. PF470's effect on molecular markers of dyskinesia mirrored its effects in the behavioral assays of dyskinesia. Thus, PF470 decreased pERK and pAcH3 in both aphakia and aphakia-mGluR5$^{KD\text{-}D1}$ groups (Fig. 4(c, d')). In the mice chronically treated with nicotine, PF470 did not further alter pERK and pAcH3 in aphakia or aphakia-mGluR5$^{KD\text{-}D1}$ mice. Although PF470 treatment decreased FosB expression induced by L-DOPA in aphakia and aphakia-mGluR5$^{KD\text{-}D1}$ mice, as expected, in the nicotine-treated mice, this reduction occurred in the aphakia-mGluR5$^{KD\text{-}D1}$ mice only (Fig. 4(e, e')).

mGluR5 Expression in D1R-Containing Neurons

Previous studies showed that mGluR5 is downregulated in mGluR5$^{KD\text{-}D1}$ mice [15, 45]. Since aphakia mice express the tomato fluorescent protein in D1R-containing neurons, we were able to measure by immunofluorescence the expression of mGluR5. As expected, we found that saline-treated aphakia-mGluR5$^{KD\text{-}D1}$ mice display lower expression of the mGluR5 in D1R-containing neurons compared to aphakia mice ($p < 0.01$) in the denervated striatum. This pattern of expression was similar in the nicotine-treated animals. Next, we asked whether L-DOPA is able to increase the expression of mGluR5 in striatal D1R-containing neurons in the aphakia-mGluR5$^{KD\text{-}D1}$ mice, and second, if nicotine could further reduce mGluR5 in D1R-containing neurons. We found that L-DOPA increased the expression of mGluR5 in D1R-containing neurons in aphakia mice relative to saline-treated aphakia mice. This L-DOPA-induced increase in mGluR5 expression was prevented in aphakia-mGluR5$^{KD\text{-}D1}$ animals ($p < 0.01$), although the expression was slightly higher compared to saline aphakia-mGluR5$^{KD\text{-}D1}$ mice. Nicotine reduced mGluR5 fluorescence intensity in D1R-containing neurons in aphakia mice but not in aphakia-mGluR5$^{KD\text{-}D1}$ (Fig. 5).

Discussion

The present study demonstrates that selective knockdown of mGluR5 in D1R-containing neurons decreases L-DOPA-induced dyskinesia in aphakia mice, an established genetic mouse model of PD [46–49]. We observed that aphakia-mGluR5$^{KD\text{-}D1}$ mice, showed a robust decrease in dyskinesia but retained full therapeutic efficacy of L-DOPA compared to aphakia mice. Importantly, this reduction in behavioral indicators of dyskinesia was accompanied by reduced activation of the pERK/pAcH3/FosB signaling pathway, a known molecular cascade associated with L-DOPA-induced dyskinesia. Furthermore, administration of the highly selective mGluR5 negative allosteric modulator (PF470) reduced dyskinesia in aphakia but did not further modify dyskinetic behavior in apahakia-mGluR5$^{KD\text{-}D1}$ mice, suggesting that the effect of PF470 on dyskinesia is primarily mediated by its action on mGluR5 in D1R-containing neurons. Given that nicotine has been shown to regulate glutamate neurotransmission, we also asked whether nicotine was able to further reduce dyskinesia in aphakia-mGluR5$^{KD\text{-}D1}$ mice. Our results suggest that the effect of nicotine on dyskinesia is also mediated through mGluR5 in D1R direct pathway neurons. Chronic nicotine decreased dyskinesia in aphakia mice, but was unable to produce a further reduction of dyskinetic signs in aphakia-mGluR5$^{KD\text{-}D1}$. Interestingly, animals that received nicotine showed no reduction in the antiparkinsonian effect of L-DOPA and exhibited improvement in motor performance.

Previous research shows that striatal mGluR5 are increased when dyskinetic movements induced by L-DOPA appear [57]. In addition, it was demonstrated that there is a cross talk between D1R- and mGluR5-signaling pathways in direct pathway neurons that leads to ERK activation in the dopamine-depleted striatum [15], and it has been suggested that this modulation of the D1R signaling cascade mediates dyskinesia [8]. In our study, we found that aphakia-mGluR5$^{KD\text{-}D1}$ mice display fewer dyskinesia than aphakia mice (Fig. 1), but still exhibit the full therapeutic efficacy of L-DOPA (Fig. 2). This is in line with previous findings showing that mGluR5 antagonists such as MPEP, MTEP, fenobam, and MRZ-8676 reduce dyskinesia in 6-OHDA-lesioned rats and MPTP-lesioned non-human primates [6, 58, 59].

Chronic L-DOPA treatment causes long-term modification of synaptic activity in dyskinesia. For instance, there is an increase in D1R-mediated response, leading to enhanced activation of ERK, histone 3, and FosB expression in the dopamine-denervated striatum [60–62]. The exact mechanisms underlying the reduction of dyskinesia in aphakia-mGluR5$^{KD\text{-}D1}$ mice are not completely understood. One possible mechanism is that decreased levels of mGluR5 lead to a reduction in D1R signaling. A recent study demonstrated a cross talk between mGluR5 and D1R in the dopamine-depleted striatum by showing that mGluR5 modulates SKF38393-induced ERK activation [15]. Previous studies suggest at least two ways in which knocking down mGluR5 could affect D1R-dependent signaling pathway via ERK [15]: first, by decreasing diacylglycerol, which leads to lower activation of protein kinase C, which in turn reduces ERK signaling and second, by reducing intracellular calcium release, which reduces calcium calmodulin kinase II and ERK activation (Fig. 6) [63]. Here, we report that the reduced development of dyskinesia in aphakia-mGluR5$^{KD\text{-}D1}$ mice is associated with a decrease in the molecular markers pERK, pAcH3, and FosB (Fig. 3). These results are in agreement with previous studies showing that mGluR5 antagonist reduced L-DOPA-induced ERK activation and FosB expression in the 6-OHDA rat model of dyskinesia [26, 64]. The reduced pERK, pAcH3 activation, and FosB expression induced by L-DOPA in aphakia-mGluR5$^{KD\text{-}D1}$ mice suggests cooperation

INFORME DE LABORES 2019

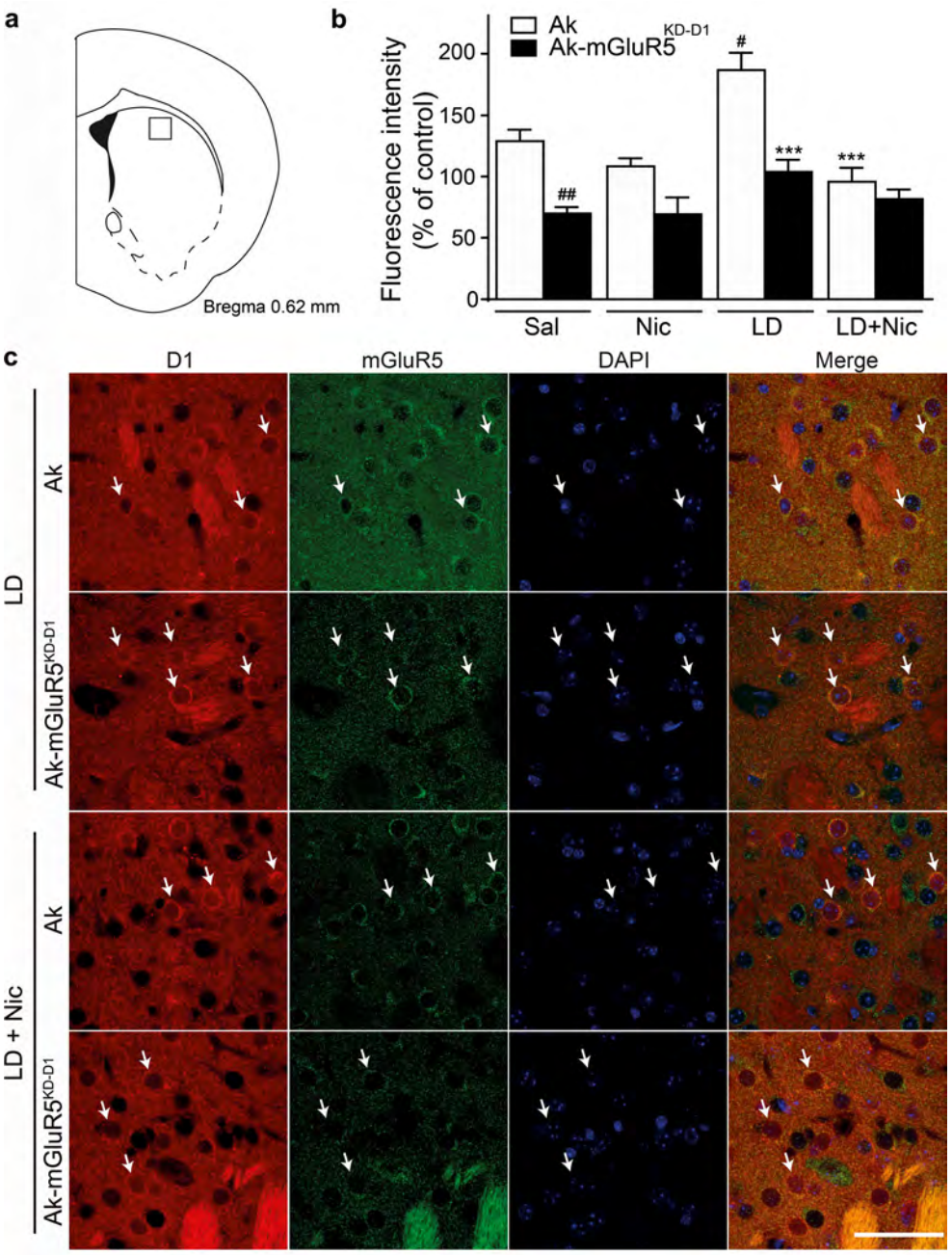

Fig. 5 Nicotine reduces mGluR5 expression in D1R-containing neurons. (a) Location of sampled areas is indicated by the black box in a schematic representation of a coronal section taken at 0.62 mm from bregma. (b) Graph represents mGluR5 expression in D1R-neurons expressed as the area under the curve (AUC) of fluorescence intensity. (c) Representative confocal images from L-DOPA-treated Ak and Ak-mGluR5^{KD-D1} mice without and with nicotine treatment illustrating D1R (red) and mGluR5 (green) coexpression. Nuclei are visualized via DAPI staining. Arrows indicate examples of dual D1R-positive and mGluR5-positive neurons. Scale bar = 100 μm. Two-way ANOVA followed by Bonferroni's post hoc test showed significant differences for genotype [$F_{1,46} = 43.9$, $p = 0.0001$] and treatment [$F_{3,46} = 13.2$, $p = 0.0001$]. $^{\#\#}p < 0.01$, $^{\#}p < 0.05$ vs. Ak saline, $^{***}p < 0.001$ vs. Ak L-DOPA. $n = 4$–8 per group

between D1R and mGluR5 in the D1R-dependent signaling pathway in dyskinesia. Our finding that PF470 does not further modify dyskinesia in aphakia-mGluR5^{KD-D1} mice (Fig. 4) rules out a role of mGluR5 in non-D1R-containing neurons in the development of dyskinesia.

Nicotinic receptors have recently emerged as a potential therapeutic target to treat dyskinesia. nAChR are ionotropic receptors widely expressed in the central nervous system. The striatum expresses two nAChR implicated in regulating the release of different neurotransmitters: the most abundant is the *β2 (α4β2*, α6β2*), which is implicated in dopamine release, while α7 is preferentially located in glutamatergic terminals [3, 37, 53]. The location of nicotinic receptor in striatal projection neurons remains controversial. For instance, electrophysiological recordings using the puff technique revealed that 32% of striatal projection neurons respond to nicotine. In this study, we tested whether nicotine could modulate dyskinesia via mGluR5 using the aphakia-mGluR5^{KD-D1} mice. We found that nicotine robustly reduced L-DOPA-induced dyskinesia in aphakia mice, but was unable to modify the already reduced dyskinetic signs in the aphakia-mGluR5^{KD-D1} mice. These results suggest that nicotine effects and mGluR5 blockade function via a similar mechanism.

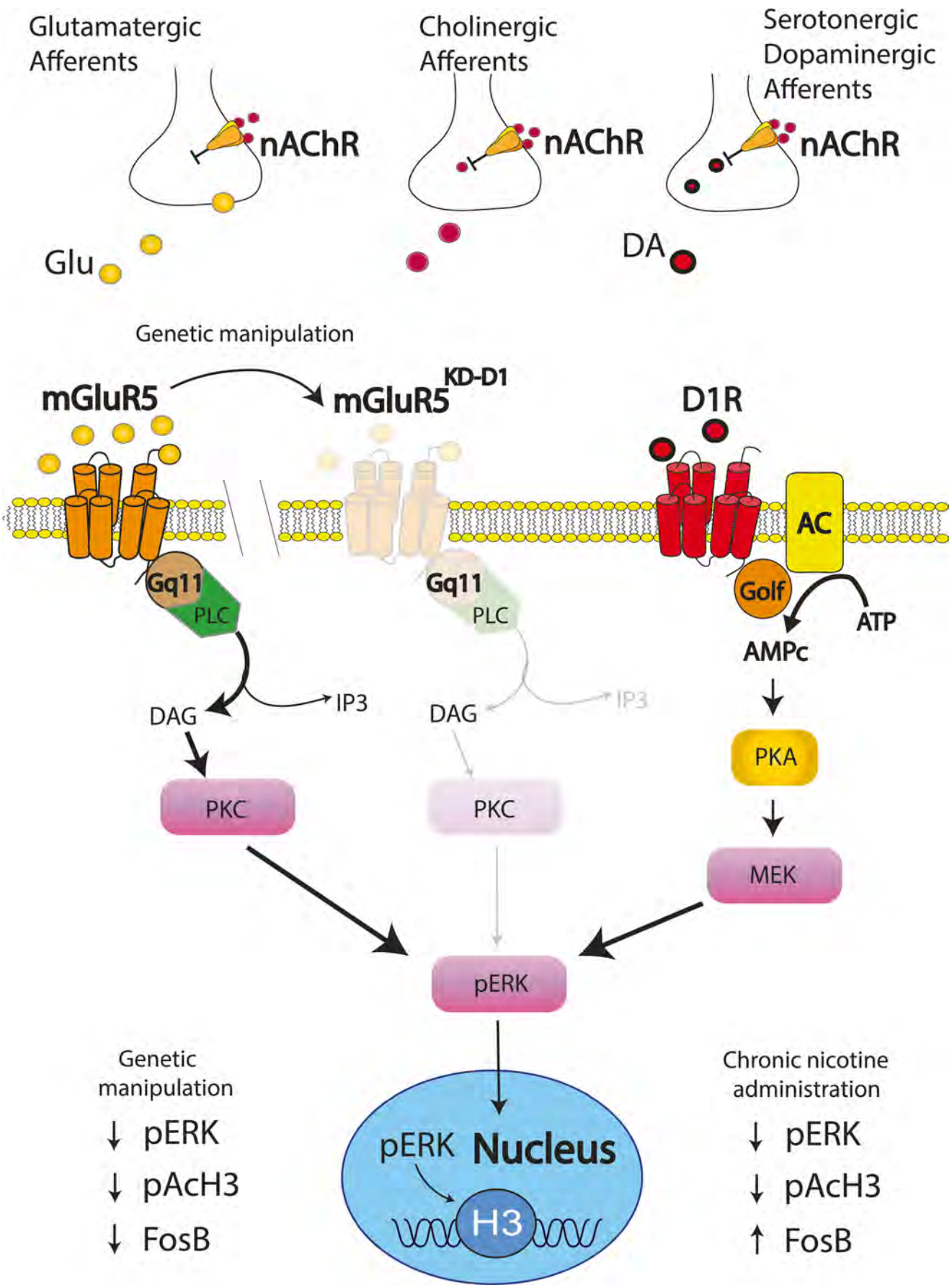
Glutamatergic Afferents
Cholinergic Afferents
Serotonergic Dopaminergic Afferents
nAChR
nAChR
nAChR
Glu
DA
Genetic manipulation
mGluR5
mGluR5 KD-D1
D1R
AC
Gq11
PLC
Gq11
PLC
Golf
ATP
AMPc
DAG
IP3
DAG
IP3
PKA
PKC
PKC
MEK
pERK
Genetic manipulation
↓ pERK
↓ pAcH3
↓ FosB
pERK Nucleus
H3
Chronic nicotine administration
↓ pERK
↓ pAcH3
↑ FosB

◀ **Fig. 6** Schematic diagram illustrating the molecular changes induced by L-DOPA and nicotine in aphakia and aphakia-mGluR5^{KD-D1} mice. Chronic nicotine treatment desensitizes presynaptic nAchR, decreasing L-DOPA-induced pERK and pAcH3 expression in dyskinetic Ak mice. mGluR5 genetic downregulation on D1R-containing neurons also reduces L-DOPA-induced pERK, pAcH3, and FosB expression in dyskinetic Ak mGluR5^{KD-D1} mice. Half-tones represent genetic manipulation in Ak mGluR5^{KD-D1} mice

The reduction of dyskinetic behavior in aphakia mice was accompanied with attenuation of the associated molecular markers pERK and pAcH3, but surprisingly not of FosB expression. A possible explanation for the unaltered FosB expression is that chronic nicotine treatment induces striatal FosB accumulation following dopamine receptor activation [16]. It is possible that in our nicotine-treated animals, FosB expression occurs, in part, independently of the ERK/pAcH3 pathway. However, future studies are needed to explore these possibilities.

The molecular mechanisms underlying the ability of nicotine to reduce dyskinesia in aphakia mice are not completely understood. There is evidence of pharmacological modulation of mGluR5 in the striatum by nicotine [18, 41, 42]. For instance, mGluR5 expression is downregulated in the caudate nucleus and putamen of smokers, suggesting an interaction between nicotine receptor and mGluR5 [42, 65]. This could be one of the reasons why we observed that nicotine did not further decrease the dyskinetic response to L-DOPA in aphakia-mGluR5^{KD-D1} mice. In fact, we found that nicotine treatment prevented the L-DOPA-induced mgluR5 expression in the denervated striatum (Fig. 5). Another possible explanation could involve the modulation of the nitrergic system by nicotine. Nicotine increases nitric oxide synthase expression in the striatum, which is involved in the development of dyskinesia [66–68]. We, and others, have shown that increasing nitric oxide signaling by administering a nitric oxide donor or a phosphodiesterase inhibitor decreases dyskinesia [47, 69, 70]. However, more studies are needed to clarify whether nicotine alleviates dyskinesia by modulating the nitrergic system. In addition, our results also showed that the antidyskinetic effect of nicotine is accompanied by a better performance of motor tasks, thus increasing the therapeutic effect of L-DOPA independently of mGluR5 in D1R-containing neurons.

In summary, the current study demonstrates the role of mGluR5 in D1R-containing neurons on dyskinesia. We found that the specific reduction of mGluR5 in direct pathway neurons reduces L-DOPA-induced dyskinesia in aphakia mice and the associated molecular markers. In support to this, we found that the antidyskinetic effect of a mGluR5 negative allosteric modulator is mainly due to the blockade of those receptors expressed in D1R-containing neurons. On the other hand, our results also indicate that the antidyskinetic effect of nicotine might be mediated by a downregulation of mGluR5 expression, because the combination of nicotine and reduction (or blockade) of mGluR5 did not have an added antidyskinetic effect. Further studies are needed to determine if combining subthreshold doses of these drugs might have an additive antidyskinetic effect. Our data suggest that therapies based on targeting mGluR5 (specifically expressed in D1R-containing neurons) or nicotine would be an efficient clinical approach to treat dyskinesia.

Acknowledgements *In memoriam* of Dr. René Drucker-Colín. JR acknowledges the Secretaría de Ciencia Tecnología e Innovación in México City, for fellowship and support. We acknowledge the priceless help of our expert technicians E. Rubio and B. Pro. We thank P. Garcia-Sanz, H. Escobar, S. Alberquilla, and N. Granado for their kind opinion and recommendations.

Funding Information This work was supported by grants from the Spanish Ministerios de Economía y Competitividad and of Sanidad Política Social e Igualdad, ISCIII: SAF2016-78207-R, CIBERNED ref. CB06/05/0055, PNSD 2016/33, and PCIN 2015-098; and Foundation Ramon Areces and Secretaria de Ciencia Tecnología e Innovación de la Ciudad de Mexico (037-2016) to RM.

Compliance with Ethical Standards

All experiments were conducted in accordance with the guidelines of the European Union Council Directive (86/609/EEC and 2003/65/CE). The protocol was approved by the Spanish Council ethics committee and the committee of ethics and animal experimentation of the Instituto Cajal (CSIC).

References

1. Cotzias GC, Van Woert MH, Schiffer LM (1967) Aromatic amino acids and modification of Parkinsonism. N Engl J Med 276:374–379. https://doi.org/10.1056/NEJM196702162760703
2. De Deurwaerdère P, Di Giovanni G, Millan MJ (2017) Expanding the repertoire of L-DOPA's actions: a comprehensive review of its functional neurochemistry. Prog Neurobiol 151:57–100. https://doi.org/10.1016/j.pneurobio.2016.07.002
3. García-Montes JR, Boronat-García A, López-Colomé AM et al (2012) Is nicotine protective against Parkinson's disease? An experimental analysis. CNS Neurol Disord Drug Targets 11:897–906
4. Heumann R, Moratalla R, Herrero MT, Chakrabarty K, Drucker-Colín R, Garcia-Montes JR, Simola N, Morelli M (2014) Dyskinesia in Parkinson's disease: mechanisms and current non-pharmacological interventions. J Neurochem 130:472–489. https://doi.org/10.1111/jnc.12751
5. Solís O, Moratalla R (2018) Dopamine receptors: homomeric and heteromeric complexes in L-DOPA-induced dyskinesia. J Neural Transm 125:1187–1194. https://doi.org/10.1007/s00702-018-1852-x
6. Rascol O, Nutt JG, Blin O, Goetz CG, Trugman JM, Soubrouillard C, Carter JH, Currie LJ et al (2001) Induction by dopamine D1 receptor agonist ABT-431 of dyskinesia similar to levodopa in patients with Parkinson disease. Arch Neurol 58:249–254
7. Guigoni C, Doudnikoff E, Li Q, Bloch B, Bezard E (2007) Altered D(1) dopamine receptor trafficking in parkinsonian and dyskinetic non-human primates. Neurobiol Dis 26:452–463. https://doi.org/10.1016/j.nbd.2007.02.001
8. Darmopil S, Martín AB, De Diego IR et al (2009) Genetic inactivation of dopamine D1 but not D2 receptors inhibits L-DOPA-

induced dyskinesia and histone activation. Biol Psychiatry 66:603–613. https://doi.org/10.1016/j.biopsych.2009.04.025
9. Lindgren HS, Rylander D, Iderberg H et al (2011) Putaminal up-regulation of FosB/ΔFosB-like immunoreactivity in Parkinson's disease patients with dyskinesia. J Parkinsons Dis 1:347–357. https://doi.org/10.3233/JPD-2011-11068
10. Espadas I, Darmopil S, Vergaño-Vera E, Ortiz O, Oliva I, Vicario-Abejón C, Martín ED, Moratalla R (2012) L-DOPA-induced increase in TH-immunoreactive striatal neurons in parkinsonian mice: insights into regulation and function. Neurobiol Dis 48:271–281. https://doi.org/10.1016/j.nbd.2012.07.012
11. Palafox-Sánchez V, Mendieta L, Ramírez-García G, Candalija A, Aguilera J, Limón ID (2016) Effect of the C-terminal domain of the heavy chain of tetanus toxin on dyskinesia caused by levodopa in 6-hydroxydopamine-lesioned rats. Pharmacol Biochem Behav 145: 33–44. https://doi.org/10.1016/j.pbb.2016.04.001
12. Solís O, García-Montes JR, Garcia-Sanz P, Herranz AS, Asensio MJ, Kang G, Hiroi N, Moratalla R (2017) Human COMT over-expression confers a heightened susceptibility to dyskinesia in mice. Neurobiol Dis 102:133–139. https://doi.org/10.1016/j.nbd.2017.03.006
13. Solís O, Garcia-Montes JR, González-Granillo A, Xu M, Moratalla R (2017) Dopamine D3 receptor modulates l-DOPA-induced dyskinesia by targeting D1 receptor-mediated striatal signaling. Cereb Cortex 27:435–446. https://doi.org/10.1093/cercor/bhv231
14. Ruiz-DeDiego I, Mellstrom B, Vallejo M, Naranjo JR, Moratalla R (2015) Activation of DREAM (downstream regulatory element antagonistic modulator), a calcium-binding protein, reduces L-DOPA-induced dyskinesias in mice. Biol Psychiatry 77:95–105. https://doi.org/10.1016/j.biopsych.2014.03.023
15. Fieblinger T, Sebastianutto I, Alcacer C, Bimpisidis Z, Maslava N, Sandberg S, Engblom D, Cenci MA (2014) Mechanisms of dopamine D1 receptor-mediated ERK1/2 activation in the parkinsonian striatum and their modulation by metabotropic glutamate receptor type 5. J Neurosci 34:4728–4740. https://doi.org/10.1523/JNEUROSCI.2702-13.2014
16. Levine A, Huang Y, Drisaldi B, Griffin EA, Pollak DD, Xu S, Yin D, Schaffran C et al (2011) Molecular mechanism for a gateway drug: epigenetic changes initiated by nicotine prime gene expression by cocaine. Sci Transl Med 3:107ra109. https://doi.org/10.1126/scitranslmed.3003062
17. Calabresi P, Mercuri NB, Sancesario G, Bernardi G (1993) Electrophysiology of dopamine-denervated striatal neurons. Implications for Parkinson's disease. Brain 116(Pt 2):433–452
18. Meshul CK, Kamel D, Moore C, Kay TS, Krentz L (2002) Nicotine alters striatal glutamate function and decreases the apomorphine-induced contralateral rotations in 6-OHDA-lesioned rats. Exp Neurol 175:257–274. https://doi.org/10.1006/exnr.2002.7900
19. Suarez LM, Solis O, Aguado C, Lujan R, Moratalla R (2016) L-DOPA oppositely regulates synaptic strength and spine morphology in D1 and D2 striatal projection neurons in dyskinesia. Cereb Cortex 26:4253–4264. https://doi.org/10.1093/cercor/bhw263
20. Solís O, García-Sanz P, Herranz AS, Asensio MJ, Moratalla R (2016) L-DOPA reverses the increased free amino acids tissue levels induced by dopamine depletion and rises GABA and tyrosine in the striatum. Neurotox Res 30:67–75. https://doi.org/10.1007/s12640-016-9612-x
21. Oueslati A, Breysse N, Amalric M, Kerkerian-le Goff L, Salin P (2005) Dysfunction of the cortico-basal ganglia-cortical loop in a rat model of early Parkinsonism is reversed by metabotropic glutamate receptor 5 antagonism. Eur J Neurosci 22:2765–2774. https://doi.org/10.1111/j.1460-9568.2005.04498.x
22. Testa CM, Standaert DG, Landwehrmeyer GB, Penney JB, Young AB (1995) Differential expression of mGluR5 metabotropic glutamate receptor mRNA by rat striatal neurons. J Comp Neurol 354: 241–252. https://doi.org/10.1002/cne.903540207
23. Conn PJ, Battaglia G, Marino MJ, Nicoletti F (2005) Metabotropic glutamate receptors in the basal ganglia motor circuit. Nat Rev Neurosci 6:787–798. https://doi.org/10.1038/nrn1763
24. Bezard E, Pioli EY, Li Q, Girard F, Mutel V, Keywood C, Tison F, Rascol O et al (2014) The mGluR5 negative allosteric modulator dipraglurant reduces dyskinesia in the MPTP macaque model. Mov Disord 29:1074–1079. https://doi.org/10.1002/mds.25920
25. Grégoire L, Morin N, Ouattara B, Gasparini F, Bilbe G, Johns D, Vranesic I, Sahasranaman S et al (2011) The acute antiparkinsonian and antidyskinetic effect of AFQ056, a novel metabotropic glutamate receptor type 5 antagonist, in L-Dopa-treated parkinsonian monkeys. Parkinsonism Relat Disord 17:270–276. https://doi.org/10.1016/j.parkreldis.2011.01.008
26. Levandis G, Bazzini E, Armentero MT, Nappi G, Blandini F (2008) Systemic administration of an mGluR5 antagonist, but not unilateral subthalamic lesion, counteracts l-DOPA-induced dyskinesias in a rodent model of Parkinson's disease. Neurobiol Dis 29:161–168. https://doi.org/10.1016/j.nbd.2007.08.011
27. Mela F, Marti M, Dekundy A, Danysz W, Morari M, Cenci MA (2007) Antagonism of metabotropic glutamate receptor type 5 attenuates L-DOPA-induced dyskinesia and its molecular and neurochemical correlates in a rat model of Parkinson's disease. J Neurochem 101:483–497. https://doi.org/10.1111/j.1471-4159.2007.04456.x
28. Ouattara B, Grégoire L, Morissette M, Gasparini F, Vranesic I, Bilbe G, Johns DR, Rajput A et al (2011) Metabotropic glutamate receptor type 5 in levodopa-induced motor complications. Neurobiol Aging 32:1286–1295. https://doi.org/10.1016/j.neurobiolaging.2009.07.014
29. Vranesic I, Ofner S, Flor PJ, Bilbe G, Bouhelal R, Enz A, Desrayaud S, McAllister K et al (2014) AFQ056/mavoglurant, a novel clinically effective mGluR5 antagonist: identification, SAR and pharmacological characterization. Bioorg Med Chem 22: 5790–5803. https://doi.org/10.1016/j.bmc.2014.09.033
30. Crabbé M, Van der Perren A, Weerasekera A et al (2018) Altered mGluR5 binding potential and glutamine concentration in the 6-OHDA rat model of acute Parkinson's disease and levodopa-induced dyskinesia. Neurobiol Aging 61:82–92. https://doi.org/10.1016/j.neurobiolaging.2017.09.006
31. Tison F, Keywood C, Wakefield M, Durif F, Corvol JC, Eggert K, Lew M, Isaacson S et al (2016) A phase 2A trial of the novel mGluR5-negative allosteric modulator dipraglurant for levodopa-induced dyskinesia in Parkinson's disease. Mov Disord 31:1373–1380. https://doi.org/10.1002/mds.26659
32. Trenkwalder C, Stocchi F, Poewe W, Dronamraju N, Kenney C, Shah A, von Raison F, Graf A (2016) Mavoglurant in Parkinson's patients with L-Dopa-induced dyskinesias: two randomized phase 2 studies. Mov Disord 31:1054–1058. https://doi.org/10.1002/mds.26585
33. Du JJ, Chen SD (2017) Current nondopaminergic therapeutic options for motor symptoms of Parkinson's disease. Chin Med J 130: 1856–1866. https://doi.org/10.4103/0366-6999.211555
34. De Reuck J, De Weweire M, Van Maele G, Santens P (2005) Comparison of age of onset and development of motor complications between smokers and non-smokers in Parkinson's disease. J Neurol Sci 231:35–39. https://doi.org/10.1016/j.jns.2004.12.003
35. Bordia T, Campos C, Huang L, Quik M (2008) Continuous and intermittent nicotine treatment reduces L-3,4-dihydroxyphenylalanine (L-DOPA)-induced dyskinesias in a rat model of Parkinson's disease. J Pharmacol Exp Ther 327:239–247. https://doi.org/10.1124/jpet.108.140897
36. Huang LZ, Grady SR, Quik M (2011) Nicotine reduces L-DOPA-induced dyskinesias by acting at beta2* nicotinic receptors. J Pharmacol Exp Ther 338:932–941. https://doi.org/10.1124/jpet.111.182949

37. Quik M, Campos C, Grady SR (2013) Multiple CNS nicotinic receptors mediate L-dopa-induced dyskinesias: studies with parkinsonian nicotinic receptor knockout mice. Biochem Pharmacol 86: 1153–1162. https://doi.org/10.1016/j.bcp.2013.06.027
38. Quik M, Mallela A, Ly J, Zhang D (2013) Nicotine reduces established levodopa-induced dyskinesias in a monkey model of Parkinson's disease. Mov Disord 28:1398–1406. https://doi.org/10.1002/mds.25594
39. Quik M, Zhang D, Perez XA, Bordia T (2014) Role for the nicotinic cholinergic system in movement disorders; therapeutic implications. Pharmacol Ther 144:50–59. https://doi.org/10.1016/j.pharmthera.2014.05.004
40. Quik M, Cox H, Parameswaran N, O'Leary K, Langston JW, di Monte D (2007) Nicotine reduces levodopa-induced dyskinesias in lesioned monkeys. Ann Neurol 62:588–596. https://doi.org/10.1002/ana.21203
41. Morissette M, Morin N, Grégoire L, Rajput A, Rajput AH, di Paolo T (2016) Brain α7 nicotinic acetylcholine receptors in MPTP-lesioned monkeys and parkinsonian patients. Biochem Pharmacol 109:62–69. https://doi.org/10.1016/j.bcp.2016.03.023
42. Akkus F, Ametamey SM, Treyer V, Burger C, Johayem A, Umbricht D, Gomez Mancilla B, Sovago J et al (2013) Marked global reduction in mGluR5 receptor binding in smokers and ex-smokers determined by [11C]ABP688 positron emission tomography. Proc Natl Acad Sci U S A 110:737–742. https://doi.org/10.1073/pnas.1210984110
43. de Aceves Buendia JJ, Tiroshi L, Chiu WH, Goldberg JA (2017) Selective remodeling of glutamatergic transmission to striatal cholinergic interneurons after dopamine depletion. Eur J Neurosci. https://doi.org/10.1111/ejn.13715
44. Dineley KT, Pandya AA, Yakel JL (2015) Nicotinic ACh receptors as therapeutic targets in CNS disorders. Trends Pharmacol Sci 36: 96–108. https://doi.org/10.1016/j.tips.2014.12.002
45. Novak M, Halbout B, O'Connor EC et al (2010) Incentive learning underlying cocaine-seeking requires mGluR5 receptors located on dopamine D1 receptor-expressing neurons. J Neurosci 30:11973–11982. https://doi.org/10.1523/JNEUROSCI.2550-10.2010
46. Suarez LM, Alberquilla S, García-Montes JR, Moratalla R (2018) Differential synaptic remodeling by dopamine in direct and indirect striatal projection neurons in Pitx3−/− mice, a genetic model of Parkinson's disease. J Neurosci 38:3619–3630. https://doi.org/10.1523/JNEUROSCI.3184-17.2018
47. Solís O, Espadas I, Del-Bel EA, Moratalla R (2015) Nitric oxide synthase inhibition decreases l-DOPA-induced dyskinesia and the expression of striatal molecular markers in Pitx3(−/−) aphakia mice. Neurobiol Dis 73:49–59. https://doi.org/10.1016/j.nbd.2014.09.010
48. Ding Y, Restrepo J, Won L, Hwang DY, Kim KS, Kang UJ (2007) Chronic 3,4-dihydroxyphenylalanine treatment induces dyskinesia in aphakia mice, a novel genetic model of Parkinson's disease. Neurobiol Dis 27:11–23. https://doi.org/10.1016/j.nbd.2007.03.013
49. Ding Y, Won L, Britt JP, Lim SAO, McGehee DS, Kang UJ (2011) Enhanced striatal cholinergic neuronal activity mediates L-DOPA-induced dyskinesia in parkinsonian mice. Proc Natl Acad Sci U S A 108:840–845. https://doi.org/10.1073/pnas.1006511108
50. Hwang D-Y, Fleming SM, Ardayfio P et al (2005) 3,4-dihydroxyphenylalanine reverses the motor deficits in Pitx3-deficient aphakia mice: behavioral characterization of a novel genetic model of Parkinson's disease. J Neurosci 25:2132–2137. https://doi.org/10.1523/JNEUROSCI.3718-04.2005
51. Collins TJ (2007) ImageJ for microscopy. BioTechniques 43:25–30. https://doi.org/10.2144/000112517
52. García-Sanz P, Orgaz L, Bueno-Gil G, Espadas I, Rodríguez-Traver E, Kulisevsky J, Gutierrez A, Dávila JC et al (2017) N370S-GBA1 mutation causes lysosomal cholesterol accumulation in Parkinson's disease. Mov Disord 32:1409–1422. https://doi.org/10.1002/mds.27119
53. Quik M, Campos C, Bordia T, Strachan JP, Zhang J, McIntosh JM, Letchworth S, Jordan K (2013) α4β2 nicotinic receptors play a role in the nAChR-mediated decline in L-dopa-induced dyskinesias in parkinsonian rats. Neuropharmacology 71:191–203. https://doi.org/10.1016/j.neuropharm.2013.03.038
54. Quik M, Park KM, Hrachova M, Mallela A, Huang LZ, McIntosh JM, Grady SR (2012) Role for α6 nicotinic receptors in l-dopa-induced dyskinesias in parkinsonian mice. Neuropharmacology 63:450–459. https://doi.org/10.1016/j.neuropharm.2012.04.029
55. Zhang L, Balan G, Barreiro G, Boscoe BP, Chenard LK, Cianfrogna J, Claffey MM, Chen L et al (2014) Discovery and preclinical characterization of 1-methyl-3-(4-methylpyridin-3-yl)-6-(pyridin-2-ylmethoxy)-1H-pyrazolo-[3,4-b]pyrazine (PF470): a highly potent, selective, and efficacious metabotropic glutamate receptor 5 (mGluR5) negative allosteric modulator. J Med Chem 57:861–877. https://doi.org/10.1021/jm401622k
56. Domenici MR, Potenza RL, Martire A, Coccurello R, Pèzzola A, Reggio R, Tebano MT, Popoli P (2005) Chronic treatment with the mGlu5R antagonist MPEP reduces the functional effects of the mGlu5R agonist CHPG in the striatum of 6-hydroxydopamine-lesioned rats: possible relevance to the effects of mGlu5R blockade in Parkinson's disease. J Neurosci Res 80:646–654. https://doi.org/10.1002/jnr.20489
57. Ouattara B, Gasparini F, Morissette M, Grégoire L, Samadi P, Gomez-Mancilla B, di Paolo T (2010) Effect of L-Dopa on metabotropic glutamate receptor 5 in the brain of parkinsonian monkeys. J Neurochem 113:715–724. https://doi.org/10.1111/j.1471-4159.2010.06635.x
58. Rascol O, Fox S, Gasparini F, Kenney C, di Paolo T, Gomez-Mancilla B (2014) Use of metabotropic glutamate 5-receptor antagonists for treatment of levodopa-induced dyskinesias. Parkinsonism Relat Disord 20:947–956. https://doi.org/10.1016/j.parkreldis.2014.05.003
59. Sebastianutto I, Cenci MA (2018) mGlu receptors in the treatment of Parkinson's disease and L-DOPA-induced dyskinesia. Curr Opin Pharmacol 38:81–89. https://doi.org/10.1016/j.coph.2018.03.003
60. Pavón N, Martín AB, Mendialdua A, Moratalla R (2006) ERK phosphorylation and FosB expression are associated with L-DOPA-induced dyskinesia in hemiparkinsonian mice. Biol Psychiatry 59: 64–74. https://doi.org/10.1016/j.biopsych.2005.05.044
61. Westin JE, Vercammen L, Strome EM, Konradi C, Cenci MA (2007) Spatiotemporal pattern of striatal ERK1/2 phosphorylation in a rat model of L-DOPA-induced dyskinesia and the role of dopamine D1 receptors. Biol Psychiatry 62:800–810. https://doi.org/10.1016/j.biopsych.2006.11.032
62. Suárez LM, Solís O, Caramés JM, Taravini IR, Solís JM, Murer MG, Moratalla R (2014) L-DOPA treatment selectively restores spine density in dopamine receptor D2-expressing projection neurons in dyskinetic mice. Biol Psychiatry 75:711–722. https://doi.org/10.1016/j.biopsych.2013.05.006
63. Jong Y-JI, Kumar V, O'Malley KL (2009) Intracellular metabotropic glutamate receptor 5 (mGluR5) activates signaling cascades distinct from cell surface counterparts. J Biol Chem 284:35827–35838. https://doi.org/10.1074/jbc.M109.046276
64. Rylander D, Iderberg H, Li Q, Dekundy A, Zhang J, Li H, Baishen R, Danysz W et al (2010) A mGluR5 antagonist under clinical development improves L-DOPA-induced dyskinesia in parkinsonian rats and monkeys. Neurobiol Dis 39:352–361. https://doi.org/10.1016/j.nbd.2010.05.001
65. Akkus F, Treyer V, Johayem A, Ametamey SM, Mancilla BG, Sovago J, Buck A, Hasler G (2016) Association of long-term nicotine abstinence with normal metabotropic glutamate receptor-5 binding. Biol Psychiatry 79:474–480. https://doi.org/10.1016/j.biopsych.2015.02.027

66. Shimohama S, Akaike A, Kimura J (1996) Nicotine-induced protection against glutamate cytotoxicity. Nicotinic cholinergic receptor-mediated inhibition of nitric oxide formation. Ann N Y Acad Sci 777:356–361
67. Tonnessen BH, Severson SR, Hurt RD, Miller VM (2000) Modulation of nitric-oxide synthase by nicotine. J Pharmacol Exp Ther 295:601–606
68. Weruaga E, Balkan B, Koylu EO, Pogun S, Alonso JR (2002) Effects of chronic nicotine administration on nitric oxide synthase expression and activity in rat brain. J Neurosci Res 67:689–697. https://doi.org/10.1002/jnr.10158
69. Giorgi M, D'Angelo V, Esposito Z, Nuccetelli V, Sorge R, Martorana A, Stefani A, Bernardi G et al (2008) Lowered cAMP and cGMP signalling in the brain during levodopa-induced dyskinesias in hemiparkinsonian rats: new aspects in the pathogenetic mechanisms. Eur J Neurosci 28:941–950. https://doi.org/10.1111/j.1460-9568.2008.06387.x
70. Picconi B, Bagetta V, Ghiglieri V, Paillè V, di Filippo M, Pendolino V, Tozzi A, Giampà C et al (2011) Inhibition of phosphodiesterases rescues striatal long-term depression and reduces levodopa-induced dyskinesia. Brain 134:375–387. https://doi.org/10.1093/brain/awq342

environmental microbiology

INFORME DE LABORES 2019

Environmental Microbiology (2019) **21**(8), 2964–2976 doi:10.1111/1462-2920.14692

Two *Pseudomonas aeruginosa* clonal groups belonging to the PA14 clade are indigenous to the Churince system in Cuatro Ciénegas Coahuila, México

Manuel García-Ulloa Il,[1] Gabriel-Yaxal Ponce-Soto,[2] Abigail González-Valdez,[3] Bertha González-Pedrajo,[4] Miguel Díaz-Guerrero,[4] Valeria Souza[1] and Gloria Soberón-Chávez[3*]

[1]*Departamento de Ecología Evolutiva, Instituto de Ecología, Universidad Nacional Autónoma de México, Ciudad Universitaria, 04510, CDMX, Mexico.*

[2]*Institute for Bio- and Geosciences (IBG-2: Plant Sciences), Forschungszentrum Jülich, Wilhelm Johnen Straße, Jülich, Germany.*

[3]*Departamento de Biología Molecular y Biotecnología, Instituto de Investigaciones Biomédicas, Universidad Nacional Autónoma de México, Ciudad Universitaria, 04510, CDMX, Mexico.*

[4]*Departamento de Genética Molecular, Instituto de Fisiología Celular, Universidad Nacional Autónoma de México, Ciudad Universitaria, 04510, CDMX, Mexico.*

Summary

***Pseudomonas aeruginosa* is a widely distributed environmental bacterium but is also an opportunistic pathogen that represents an important health hazard due to its high intrinsic antibiotic resistance and its production of virulence factors. The genetic structure of *P. aeruginosa* populations using whole genome sequences shows the existence of three clades, one of which (PA7 clade) has a higher genetic diversity. These three clades include clinical and environmental isolates that are very diverse in terms of geographical origins and isolation date. Here, we report the characterization of two distinct clonal *P. aeruginosa* groups that form a part of the PA14 clade (clade 2) sampled from the Churince system in Cuatro Ciénegas Basin (CCB). One of the clonal groups that we report here was isolated in 2011 (group 2A) and was displaced by the other clonal group (2B) in 2015. Both Churince groups are unable to produce pyoverdine but can produce other virulence-associated traits. The existence of these unique *P. aeruginosa* clonal groups in the Churince system is of ecological and evolutionary significance since the microbiota of this site is generally very distinct from other lineages, and this is the first time that a population of *P. aeruginosa* has been found in CCB.**

Received 27 January, 2019; revised 20 May, 2019; accepted 20 May, 2019. *For correspondence. E-mail gloria@biomedicas.unam.mx

© 2019 Society for Applied Microbiology and John Wiley & Sons Ltd.

Introduction

Pseudomonas aeruginosa is an environmental bacterium that has been considered ubiquitous since it is present in a wide range of environments, but it is also an opportunistic pathogen that represents an important health hazard due to its high intrinsic antibiotic resistance, the high frequency of multi-resistant strains (Castañeda-Montes *et al.*, 2018) and its production of virulence-associated traits (Gellatly and Hancock, 2013).

P. aeruginosa genomics has revealed the existence of three main clades (Freschi *et al.*, 2015) that include clinical and environmental isolates (Grosso-Becerra *et al.*, 2014; Stewart *et al.*, 2014; Diaz *et al.*, 2018). The geographical origin and date of isolation of the strains belonging to these three clades vary widely (Pirnay *et al.*, 2009; Castañeda-Montes *et al.*, 2018). One of the clades (the PA7 clade) presents a much higher genetic variability (Roy *et al.*, 2010), and a member of this clade (strain ATCC 9027) has been reported to produce low levels of virulence factors and to be non-virulent in a mouse model (Grosso-Becerra *et al.*, 2016).

The production of the siderophore pyoverdine is characteristic of all fluorescent *Pseudomonas*, including clinical and environmental *P. aeruginosa* isolates (Lamont and Martin, 2003; Ravel and Cornelis, 2003; Schalk and Guillon, 2013). The chemical structure of these siderophores consists of a dihydroxyquinoline chromophore attached to a 6 to 12 variable peptide chain with a sequence that is species- and even strain-specific (Meyer, 2000).

P. aeruginosa produces three types of pyoverdines, and their ferric ion specificity is around 10^{32} M^{-1}. These siderophores are also able to bind other metals, but with

a much lower affinity (Braud *et al.*, 2009). FpvA is the specific outer-membrane receptor for pyoverdine-iron complexes and is indispensable for its uptake (Schalk *et al.*, 2001). It has been reported that the production of pyoverdine is important for the pathogenesis of *P. aeruginosa*, but clinical isolates that do not produce this siderophore can be isolated (Tasake *et al.*, 2000; Visca *et al.*, 2006; Kirienko *et al.*, 2013; López-Medina *et al.*, 2015; Granato *et al.*, 2016).

P. aeruginosa is able to produce other non-fluorescent siderophores, such as piochelin that plays an ecological important role in the competition of this bacterium in environments where soluble iron is very low (Schiessi *et al.*, 2017).

Another conserved characteristic among the three described *P. aeruginosa* clades is the regulation at the transcriptional level of the production of most of the virulence factors by a complex regulatory network called quorum-sensing response (QSR) that depends on the production of autoinducers (AIs) that interact with transcriptional regulators (Williams and Cámara, 2009; Grosso-Becerra *et al.*, 2016).

P. aeruginosa QSR modulates the expression of several virulence factors such as pyocianin (PYO), elastase and rhamnolipids (RL) through the activity of two transcriptional regulators (LasR and RhlR) that interact with their cognate AIs 3-oxo-dodecanoyl-homoserine lactone (3O-C12-HSL) with LasR and butanoyl-homoserine lactone (C4-HSL) with RhlR. *P. aeruginosa* clades 1 and 2 share the secretion of toxins through the type III secretion system (T3SS), which is also an important virulence associated trait (Dacheaux *et al.*, 1999; Berube *et al.*, 2017). Strain PA14 and other members of clade 2 secrete ExoU and ExoT effectors through the T3SS (Miyata *et al.*, 2003).

P. aeruginosa is a very well-studied species, but in order to explore the possibility of isolating new *P. aeruginosa* lineages and to understand the origin of its pathogenic potential, we have characterized isolates from diverse environments (Grosso-Becerra *et al.*, 2014). In this work, we explore the Cuatro Ciénegas Basin (CCB) located in the Chihuahuan Desert in the Mexican State of Coahuila, a place previously referred as a lost world due to the presence of ancient bacterial lineages (Souza *et al.*, 2018). We have observed that in CCB microbial diversity is extremely high (Souza *et al.*, 2018) and a large portion of it seems to include direct descendants of marine organisms (Souza *et al.*, 2006; Alcaraz *et al.*, 2008) including marine virus (Desnues *et al.*, 2008; Taboada *et al.*, 2018), which is atypical for lagoons and springs outside CCB. We think that this is given in part by the ion composition of its water that is rich in sulphur and magnesium salts and poor in phosphorous and iron. Moreover, the extreme unbalanced nutrimental stoichiometry where the ratio of nitrogen/phosphorous is very high (Elser *et al.*, 2005; Lee *et al.*, 2015, 2017) can explain most of the endemicity due to extreme selective pressure. It has been proposed that within CCB, oligotrophy not only forces the collaboration within the community to optimize its nutrient cycling (Tapia-Torres *et al.*, 2016; Gomez-Lunar *et al.*, 2018; Rodríguez-Torres *et al.*, 2017), but it acts as an effective sieve against migration (Souza *et al.*, 2012, 2018).

Within the diverse and particular CCB water bodies, the most distinct site is the hydrological system of Churince, a particularly vulnerable site due to the overexploitation of its aquifer by alfalfa agriculture (Souza *et al.*, 2007; De Anda *et al.*, 2018; Souza *et al.*, 2018). Churince was composed of three interconnected sections: large lagoon, intermediate lagoon and a spring. In 2004, the lagoon farthest from the spring, the desiccation lagoon (large lagoon), began to shrink and completely dried in 2006 (Alcaraz *et al.*, 2008). Later, the intermediate lagoon began to shrink in 2011 and completely dried in 2017 (Souza *et al.*, 2018), now only the main spring maintains some water.

Given its cultivable nature, several studies at CCB water bodies have been focused in the genus *Pseudomonas* and hundreds of novel isolates have been identified (Escalante *et al.*, 2009; Toribio *et al.*, 2011; Bonilla-Rosso *et al.*, 2012; Rodríguez-Verdugo *et al.*, 2012; Ponce-Soto *et al.*, 2015). Twice each year for more than ten years, samples have been obtained from defined points in the Churince system to study the stability of different bacterial communities, and in the case of Pseudomonads it has also been determined the effect in their composition of fluctuations in temperature along the year (Rodríguez-Verdugo *et al.*, 2012), and of nutrient availability, for example (Ponce-Soto *et al.*, 2015). It is interesting that despite extensive sampling effort, only one *P. aeruginosa* strain (M10) was isolated from the Churince spring in 2008, which was very similar to the PAO1 type strain (Grosso-Becerra *et al.*, 2014). It is possible that strain M10 is an introduced *P. aeruginosa* clone and not a member of a CCB bacterial population.

However, as the system declined due to the severe overexploitation of the aquifer, both by superficial channels and deep wells, the community conditions changed and we started to isolate more *P. aeruginosa* strains. Herein, we report the isolation and phenotypic characterization of 49 *P. aeruginosa* isolates from the Churince system, 44 of them in October 2011 when intermediate lagoon started to dry, and 5 in October 2015 on an even more dry condition. The analysis of the genome sequence of 10 isolates from the 2011 sample and the 5 isolates from 2015 showed that they represent two novel *P. aeruginosa* clonal groups of the PA14 lineage that are indigenous to CCB. All the isolates studied in this

work were able to produce virulence-associated traits with the exception of pyoverdine and are virulent when tested in the *Galleria mellonella* model. The ecological significance of the existence of these new *P. aeruginosa* clonal groups that were native to CCB is discussed.

Results and discussion

Phylogenetic analysis of P. aeruginosa *strains isolated from intermediate lagoon in 2011 and 2015 using whole genome sequencing*

The water level of intermediate lagoon started to lower in October 2011 (date of the first sampling presented in this article) after a particularly hot summer where the diminishing water supply by the deep aquifer met with a larger evaporation. Due to the protected status of CCB (Área de Protección de Flora y Fauna) and the endangered lagoon, in coordination with federal authorities and with the local users, we were able to close for a year the canal located in La Becerra (an important spring close to Churince) from early 2013 to the fall of 2014, restoring, temporarily, the water levels of intermediate lagoon (de Anda *et al.*, 2018), therefore allowing the microbiota to recover, while the water levels increased. However, in our second sampling shown in this work in October 2015, the lagoon was dryer than in 2011.

In order to understand the evolutionary effect of the lowering water level on the population of aquatic microbes, we compared genomes of the 2011 sample with the genomes of bacteria isolated in a new survey of different *Pseudomonas* species in October 2015. Among the recovered strains 44 *P. aeruginosa* isolates were obtained in 2011 and only 5 in 2015. In order to study the population genetics of the two collections, we obtained the whole genome sequence of 10 strains isolated in 2011 and the 5 strains isolated in 2015 (Supporting Information Table S1) and their phylogeny was determined (Fig. 1).

Unexpectedly, we observed that the sequenced strains from each sampled year formed a distinct clonal group closely related to the PA14 clade 2: one contains the 10 strains isolated in 2011 (defined as *P. aeruginosa* group 2A) and the other contains the 5 strains isolated in 2015 (*P. aeruginosa* group 2B).

The result obtained (Fig. 1) through the phylogenetic analysis of the whole genome sequence of the 15 *P. aeruginosa* strains of clonal groups 2A and 2B, compared to 24 *P. aeruginosa* whole-genome sequences (5 members of PAO1 clade 1 including M10 strain; 17 belonging to the PA14 clade 2; and 2 to the PA7 clade 3), show that the 10 strains isolated in 2011 and the 5 strains isolated in 2015 form two distinct clonal groups (2A and 2B, respectively) within the PA14 clade 2 (Fig. 1).

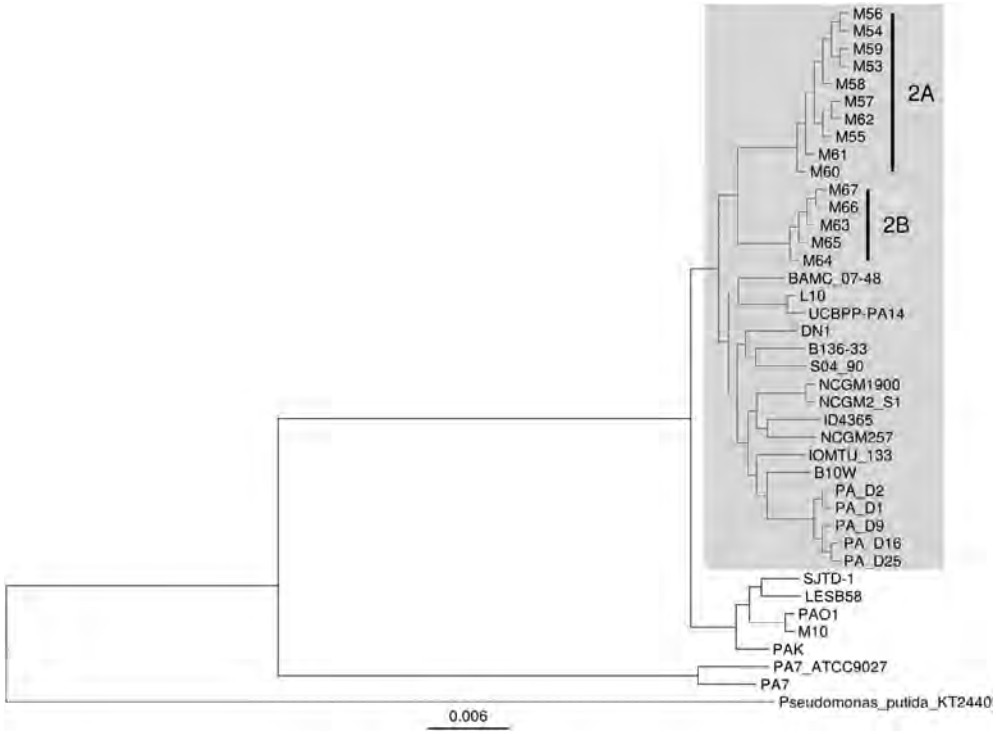

Fig. 1. Core genome phylogeny of the 15 sequenced *P. aeruginosa* strains isolated from the intermediate lagoon. The phylogeny was constructed with FastTree 2.0 (Price *et al.*, 2010) and annotated with the R package *ggtree* (Yu *et al.*, 2018). Clade 2 is highlighted in grey and clonal groups 2A and 2B are indicated with black bars. *Pseudomonas putida* KT2440 was used as outgroup.

The existence of two distinct clonal groups in Churince was further confirmed by the analysis of the phylogenetic tree constructed based on the MLST data of 2953 *P. aeruginosa* strains including the strains isolated in 2011 and 2015, and the M10 strain isolated previously, together with the data available on the PubMLST *Pseudomonas aeruginosa* database. This phylogenetic analysis of nearly 3000 strains confirmed the existence of the two indigenous CCB clonal groups (2A and 2B) in two distinct branches both presenting a 100% bootstrap support (Fig. 2). These results suggest that the wetland brief recovery in 2013 selected against the early *P. aeruginosa* clonal group 2A allowing the succession process of another, not previously seen group 2B in the drying lagoon.

The analysis of the genome assemblies of the 15 sequenced strains showed slight differences in genome size and GC content between the two clonal groups, but more interestingly, different number of CRISPR arrays, which can be used for differentiating *P. aeruginosa* strains (Van Belkum *et al.*, 2015); clonal group 2A has one CRISPR array, while group 2B has two (Supporting Information Table S1). In addition, we found that clonal group 2A has a genome size of 6.44–6.46 Mb with a GC content of 66.43%–66.46%, while group 2B has a slightly larger genome size (6.49–6.53 Mb) with a GC content of 66.31%–66.34% (Supporting Information Table S1). Thus, the two described clonal groups are indistinguishable using their size or GC content. However, the previously isolated M10 strain has more diverse genomic characteristics; it has a genome size of 6.20 Mb with a GC content of 66.56% and no CRISPR arrays (Supporting Information Table S1), features closer to those found on the PAO1 strain (Stover *et al.*, 2000; Grosso-Becerra *et al.*, 2014). Moreover, even though the novel strains that belong to each clonal group have a high genomic similarity and are closely related to PA14 clade 2 (Fig. 1), they are unique as can be concluded by the analysis of the structure of their *pvd* genes discussed below.

The finding of two Churince native clonal groups of *P. aeruginosa* was unexpected, since this is the first time

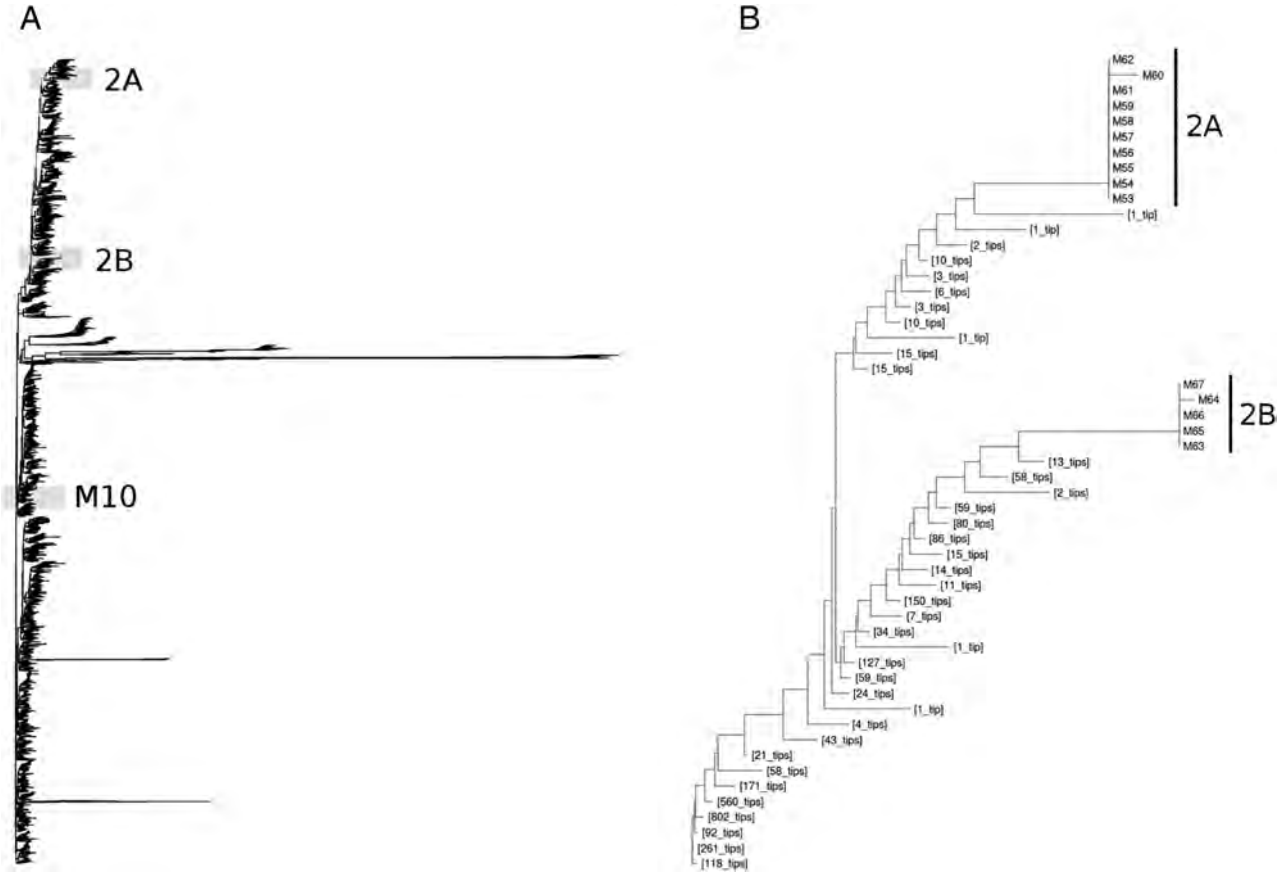

Fig. 2. MLST neighbour-joining phylogenetic reconstruction. 2953 *P. aeruginosa* concatenated MLST sequences from the PubMLST *Pseudomonas aeruginosa* Database alongside the 10 and 5 MLST from members of clonal groups 2A and 2B, respectively, and strain M10, whose positions are highlighted in grey, were used for the phylogenetic reconstruction shown in Fig. 2A. A total of 1000 bootstrap replicates were performed using MEGA7 (Kumar *et al.*, 2016); branches corresponding to clonal groups 2A and 2B are 100% supported. A summarized subtree of clonal groups 2A and 2B is shown in Fig. 2B and indicated with black bars was extracted from the complete phylogeny using the R package *ggtree* (Yu *et al.*, 2017).

© 2019 Society for Applied Microbiology and John Wiley & Sons Ltd.,

that lineages that are particular to a determined environment and time of isolation have been described in this well-studied species. All the previously reported collections contain clinical and environmental representatives and are in no way related to any specific environmental parameter (Freschi *et al.*, 2015; Mosquera-Rendón *et al.*, 2016; Castañeda-Montes *et al.*, 2018).

In agreement with the ubiquitous character of the three previously reported *P. aeruginosa* clades and the typical cosmopolitan way of life of this bacterial species, we isolated in 2008 from Churince spring, the M10 strain belonging to clade 1, which is very similar to the PAO1 strain (Grosso-Becerra *et al.*, 2014).

Nevertheless, the indigenous character of *P. aeruginosa* clonal groups 2A and 2B reported here was not surprising, since most of the microbiota studied in the Churince system seems to be unique (Souza *et al.*, 2018). We hypothesize that *P. aeruginosa* clonal groups 2A and 2B represent populations that belong to Churince communities, but that their population size was very small to be detected in previous samplings and that they were able to thrive in perturbed conditions. Our results suggest that the conditions found in the desiccating intermediate lagoon were favourable for *P. aeruginosa* clades 2A and 2B, and that the constant follow-up of Churince microbiota sampling, allowed us to pick up these rare inhabitants that could not be found before and not even in the 2016–2017 samplings.

Antibiotic resistance of P. aeruginosa *strains belonging to the 2A and 2B clonal groups*

It has been reported previously that the production and resistance to antibiotics are ecologically significant traits in the Churince system not only in sediment-associated *Bacillus* (Pérez-Gutiérrez *et al.*, 2012) but also in the water column Pseudomonads inhabitants (Aguirre-von-Wobeser *et al.*, 2014; Ponce-Soto *et al.*, 2015). Therefore, we determined the antibiotic resistant profile of the 15 strains studied in this work against carbenicillin (500 μg/ml), tetracycline (150 μg/ml), kanamycin (200 μg/ml), streptomycin (200 μg/ml), chloramphenicol (200 μg/ml), gentamycin (150 μg/ml), and apramycin (100 μg/ml). In agreement with previous results for *Pseudomonas* isolated from the intermediate lagoon (Ponce-Soto *et al.*, 2015), we found that the 15 analysed strains are resistant to carbenicillin and kanamycin and sensitive to the rest of the antibiotics tested. This, along with their unique phylogenetic position reinforces the idea of these two clonal groups being native to the Churince system. Meanwhile, strain M10, a typical environmental *P. aeruginosa*, is sensitive to all antibiotics tested, which is consistent with it being an introduced bacterium to the Churince system.

In addition, we determined the antibiotic resistance profile of these 15 strains to the antibiotics that are commonly used against *P. aeruginosa* infections and found that all of them are sensitive with only one exception (strain M58 has an intermediate resistance to aztreonam; supplementary information Table S2).

Virulence-factors production of P. aeruginosa *strains belonging to the 2A and 2B groups*

We carried out the phenotypic characterization of the *P. aeruginosa* strains belonging to clonal groups 2A and 2B with respect to the production of virulence factors

Table 1. Phenotypic characterization of *P. aeruginosa* CCB isolates analysed in this work compared to PAO1-type strain.

Strain	PYO (μg/ml)	RL (μg of rhamnose)	Elastase (Units)	3O-C12-HSL (Miller Units)	C4-HSL[a]	Virulence in *G. mellonella* model[a]
PAO1	3.46 ± 0.9	108.3 ± 5.24	1.41 ± 0.02	6658.7 ± 300	+	+
M53	3.19 ± 0.7	122.9 ± 1	1.72 ± 0.12	4240.7 ± 662	+	+
M54	3.84 ± 0.2	141.8 ± 3.42	2.57 ± 0.07	1226.6 ± 468	+	+
M55	0.84 ± 1.6	135.4 ± 8	2.05 ± 0.66	4714.8 ± 960	+	+
M56	0.84 ± 0.3	68.3 ± 7	1.40 ± 0.15	2594.5 ± 219	+	+
M57	2.03 ± 0.1	92.44 ± 8	1.57 ± 0.28	4898.8 ± 1219	+	+
M58	5.10 ± 0.8	83.8 ± 21.3	2.82 ± 0.07	3666.8 ± 101	+	+
M59	3.62 ± 1.7	179.2 ± 45.8	2.14 ± 0.12	5334.1 ± 134	+	+
M60	2.63 ± 0.2	151.8 ± 14.3	1.6 ± 0.12	5806.4 ± 1100	+	+
M61	0.99 ± 0.3	156.8 ± 3	1.49 ± 0.23	5537.8 ± 990	+	+
M62	0.51 ± 0.1	156 0.5 ± 15	1.96 ± 0.73	4052.79 ± 653	+	+
M63	3.19 ± 1.3	84.8 ± 1	1.57 ± 0.24	3917.3 ± 361	+	+
M64	2.74 ± 0.06	127.2 ± 1	1.42 ± 0.24	5389.4 ± 568	+	+
M65	1.55 ± 0.7	151.9 ± 12	2.03 ± 0.9	3053.1 ± 455	+	+
M66	35.72 ± 7.	110.2 ± 9	1.49 ± 0.18	519.2 ± 122	+	+
M67	5.12 ± 0.4	140.2 ± 3	1.46 ± 0.18	4475 ± 429	+	+

+ means that it was detected. A + sign in the virulence in the *G. mellonella* model means that the five tested larvae were dead at 24 h of injection of 10^5 CFU.

a. The production of C4-HSL was determined using the qualitative bioassay based on the production of violacein by *Chromobacterium violaceum* strain CV026.

regulated by the QSR and the production of the AIs C4-HSL and 3O-C12-HSL that participate in this complex regulatory network (Table 1).

We found that the production of the QSR-regulated virulence-factors (PYO, RL, and elastase) and the production of the AIs C4-HSL and 3O-C12-HSL of strains belonging to the *P. aeruginosa* 2A and 2B clonal groups (Table 1) are very similar to the QSR presented by strains belonging to clades 1 (including PAO1 strain), 2 (including PA14 strain) and 3 (including ATCC 9027 strain, analysed by Grosso-B*ecerra et al.*, 2016). The only strain with an atypical QSR is strain M66 of clonal group 2B, which has a high PYO production and a low production of the AI 3O-C12-HSL (Table 2). Strains with atypical QSR have been previously reported (Grosso-Becerra *et al.*, 2014; Morales *et al.*, 2017).

Furthermore, *P. aeruginosa* strains that belong to 2A and 2B clonal groups produce the two types of RL: mono-RL that contains one rhamnose moiety and di-RL, which contains two molecules of rhamnose (Supporting Information Fig. S1). Strains belonging to clade 3, as PA7 (Roy *et al.*, 2010) and ATCC 9027 (Grosso-Becerra *et al.*, 2016) only produce mono-RL.

We also found that all the strains belonging to clonal groups 2A and 2B secrete ExoU and ExoT effectors by the T3SS (Supporting Information Fig. S2), as has been reported for PA14 and other strains of clade 2. In addition we found that the two clonal groups studied here are pathogenic when tested in the *Galleria mellonellamodel* (Table 1), even though they are unable to produce pyoverdine as discuss below. These results suggest that these two lineages diverged from a clade 2 *P. aeruginosa* common ancestor that was able to establish pathogenic interactions.

Analysis of pyoverdine genes of P. aeruginosa *strains belonging to clonal groups 2A and 2B*

Many strains belonging to species of the fluorescent *Pseudomonas* isolated from the Churince system are unable to produce fluorescent siderophores even belonging to fluorescent *Pseudomonas* species (Escalante *et al.*, 2009; Toribio *et al.*, 2011; Bonilla-Rosso *et al.*, 2012; Rodríguez-Verdugo *et al.*, 2012; Ponce-Soto *et al.*, 2015), and the same is true for *P. aeruginosa* strains isolated in 2011 (44 strains) and 2015 (5 strains) analysed in this work.

In order to determine whether the lack of pyoverdine production reflected a specific arrangement of the *pvd* genes in the 15 *P. aeruginosa* isolates that were sequenced in this work, we analysed these loci and compared them with the *pvd* genes of the PAO1-type strain (Fig. 3).

Our results show that all the sequenced strains that belong to the 2A group contain a deletion spanning from the PA2403 ORF to the *pvdE* gene (including the gene encoding for the pyoverdine receptor FpvA), while the five strains belonging to clade 2B have deletions including the *pvdD* gene, but retaining *fpvA* (Fig. 3). In addition, strains M63 and M65 lack the *pvdI* gene and strain M65 also lacks *pvdJ* (Fig. 3). Thus among the five strains belonging to clonal group 2B, we found three different patterns of deletions affecting the *pvd* gene cluster (Fig. 3). The detected variability of the *pvd* gene cluster among the sequenced strains belonging to clonal groups 2A and 2B suggest that the lack of pyoverdine production is positively selected among *P. aeruginosa* isolates native to intermediate lagoon.

Furthermore, we analysed the *pvd* genes in strain M10 and as expected since it is a fluorescent isolate, we found that it has a very similar pattern of *pvd* genes to strain PAO1 (Fig. 3). These results reinforce the idea that strain M10 is an introduced bacterium to CCB and does not form part of a native *P. aeruginosa* population of the Churince system.

Structure of the pvd *locus among the strains isolated in October 2011 that were not sequenced*

To determine whether the remaining 34 strains isolated in 2011 that were not sequenced have the same structure of the ten 2A clonal group sequenced strains, we designed a series of oligonucleotides to amplify some of the deletions present in the 15 sequenced isolates, using as a positive control the region from *pvdE* to *fpvA* (which is present in the PAO1, M10 and the 5 strains belonging to the clonal group 2B) and oligonucleotides that specifically amplify the 16S rDNA (see Supporting Information Table S3 and Fig. S3).

Table 2. Characterization by PCR of the deletions present in 21 *P. aeruginosa* strains belonging to 2A clonal group that were not sequenced.

PCR product	Strains that present the PCR product	Type of deletion*
pvdE to PA2403	7 strains (they do not present the *pvdE* to *fpvA* PCR product)	Type 1, as in the 10 sequenced strains belonging to 2A clonal group (Fig. 3)
fpvA to *pvdJ*	2 strains (also have the *pvdE* to *fpvA* PCR product)	Type 2, as in strains: M63, M64, M66, M67, belonging to 2B clonal group (Fig. 3)
fpvA to PA2403	12 strains that also have the *pvdE* to *fpvA* PCR product.	Type 3, as strain M65 belonging to 2B clonal group (Fig. 3)

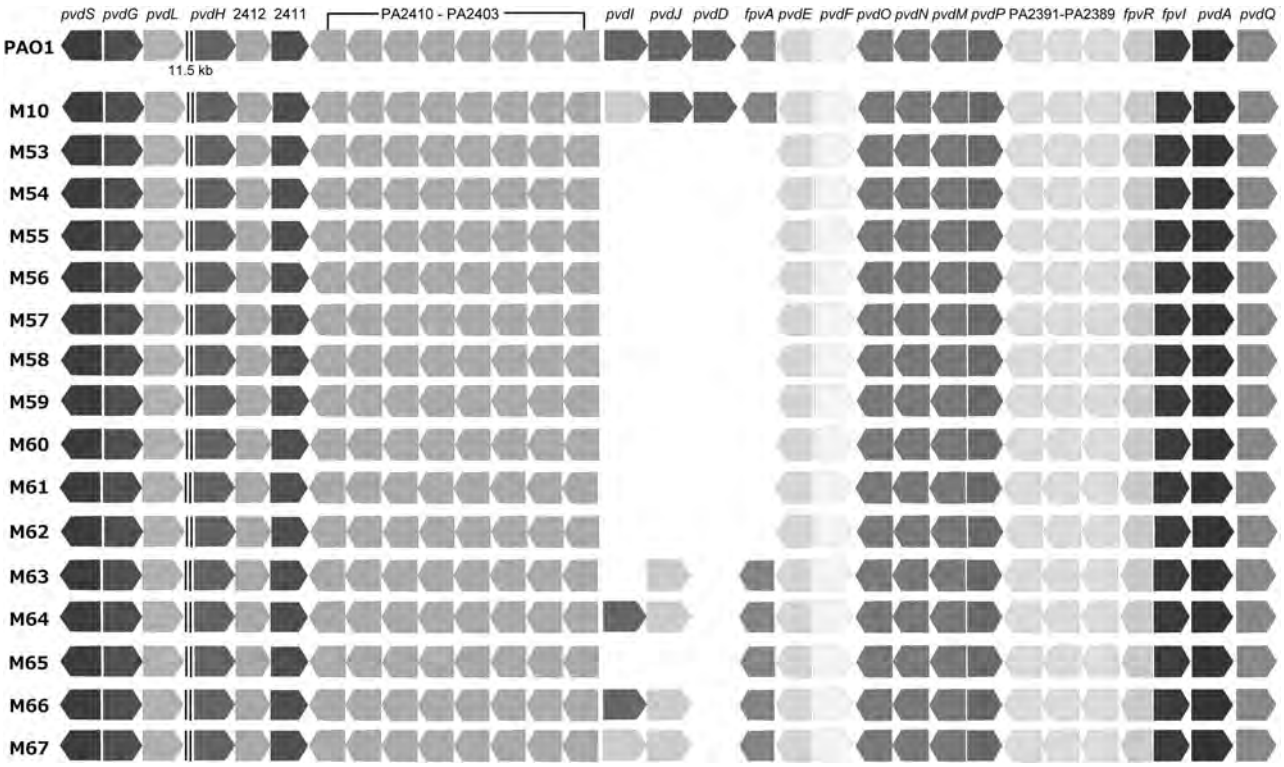

Fig. 3. Schematic representation of the *pvd* gene cluster. This chromosomal region is shown in the *P. aeruginosa* strains isolated from the Churince system compared with *P. aeruginosa* PAO1. Identification of the syntenic genes was done with progressive Mauve (Darling *et al.*, 2010).

Our results show that 13 of the 34 tested strains did not amplify the *pvdE* to *fpvA* region, nor the three types of *pvd* deletions that we screened by PCR (Table 2), even though we were able to amplify the gene encoding 16S rRNA in all of them. These results show that these 13 strains contain an uncharacterized deletion that is not equal to those found in the 10 sequenced strains belonging to 2A group, or to the deletions found in the 5 sequenced strains from clonal group 2B (Fig. 3).

Among the remaining 21 strains, only 7 have the type 1 deletion presented by the 10 sequenced strains belonging to clonal group 2A (Fig. 3 and Table 2). This was determined by the amplification of a PCR product using oligonucleotides from *pvdE* to PA2403 (Table 2; Supporting Information Fig. S3 and Table S3).

Interestingly, we detected among the bacteria that were collected in 2011, 2 strains that have the same deletion as strains M63, M64, M66 and M67 of the clonal group 2B, spanning from *fpvA* to *pvdJ* (type 2 deletion, Table 2), and 12 strains with a similar deletion as strain M65 (type 3 deletion, Table 2) that also belongs to the 2B group (Table 2).

The existence of 27 strains among the 44 strains collected in October 2011 that have a different structure of the deleted *pvd* locus as the 10 sequenced strains belonging to clonal group 2A (Fig. 3) shows that the 44 strains isolated in 2011 that presumably belong to clonal group 2A, are not the same individual that has been sampled twice and led us to the conclusion that the lack of pyoverdine production is positively selected among *P. aeruginosa* isolates indigenous to the intermediate lagoon.

It is possible that *P. aeruginosa* strains that were isolated in October 2011 that present a similar deletion to clonal group 2B strains, in fact belong to this phylogenetic group and not to the 2A group. So it is possible that clonal groups 2A and 2B coexisted in the Churince intermediate lagoon in 2011, but this possibility does not modify the conclusions attained in this work.

The results presented here strongly suggest that the lack of pyoverdine synthesis of *P. aeruginosa* strains endemic to CCB is of ecological significance. It is intriguing though, that pyoverdine deficient strains were selected in the Churince system, an environment with an extremely low iron concentration. A possible explanation for this apparent paradox is that FpvA might be used as the receptor of a common bacterial toxin in Churince, as has been shown in the case of pyocine S2 produced by *P. aeruginosa* (Denayer *et al.*, 2007). If this were the case, the *fpvA* gene present in some of the strains studied in this work (Fig. 3) would not be expressed. It has

been reported that antagonic interactions through diffusible molecules are common among Churince proteobacteria (Aguirre-von-Wobeser *et al.*, 2014).

In this scenario, the production of other siderophores as pyochelin will circumvent the problem of iron starvation, so we hypothesize that Churince *P. aeruginosa* strains belonging to the 2A and 2B clonal groups, that are deficient in pyoverdine production, can produce pyochelin, and possibly other siderophores. In support of this hypothesis, we found that the 15 sequenced *P. aeruginosa* strains have apparently functional *pchA, pchB, pchD, pchR* genes and in addition they present the *pfeA* gene encoding for the ferric enterobactin receptor that might enable them to capture iron coupled with this siderophore produced by other bacterial species.

Moreover, *P. aeruginosa* strains belonging to clonal groups 2A and 2B are pathogenic in the *Galleria mellonella* model (Table 1). These results suggest that pyoverdine deficiency is an ancient phenotype that has been counterbalanced by the production of other virulence-associated traits (Table 1, Supporting Information Fig. S2), since the production of pyoverdine has been reported to be indispensable for the establishment of pathogenic interactions when mutants lacking this siderophore were selected from pyoverdine proficient strains (Kirienko *et al.*, 2019). This rational has been used to select compounds that inhibit the production of this siderophore that block *P. aeruginosa* virulence (Kirienko *et al.*, 2019), but these molecules will not be effective for the treatment of infections caused by naturally occurring pyoverdine deficient strains such as those studied in this work.

Concluding remarks

In this study, we described the characterization of two novel *P. aeruginosa* clonal groups (2A and 2B) that are endemic to the Churince system in the CCB. This is the first time that *P. aeruginosa* isolates have been found to be limited to a particular environment and we think that this situation reflects that these clonal groups were part of this ecosystem, but they need perturbed conditions (low water levels) in order to outcompete the previously diverse bacterial community of Churince.

We have shown here that the two *P. aeruginosa* clonal groups isolated in CCB are virulent and thus capable of infecting the debilitating endemic fishes and turtles, so it is possible that the negative effect to these animals caused by the drought that started in 2011 gave them a proper niche to increase their population size.

Unfortunately the intermediate lagoon is been considered dead, since plants are growing on top of the stromatolites for the first time in the history of this site (Minckley *et al.*, 2019) since the Churince system had no previous record of plant occupation due to the long-term stability and presence of water in the site. Therefore, the 49 *P. aeruginosa* CCB isolates that we report in this work might be the only living representatives of the clonal groups described in this work. A similar fate has had all the bacterial isolates that have been collected over the years in what was a relict of the ancient ocean.

Experimental procedures

Sampling and isolation of P. aeruginosa *strains*

Samples were taken from surface water from all across intermediate lagoon (26°50′53.79″N, 102°08′30.29″W) using sterile BD Falcon vials (BD Biosciences, San Jose, CA). Bacterial colonies were obtained by plating 200 μl of each water sample on PIA medium agar plates, which were further incubated at 32 °C for 1 day. Individual colonies were transferred to new PIA plates and grown at 32 °C for 1 day. Each colony was stored in 30% glycerol solution at −80 °C.

Microbiological methods

The strains and plasmids used in this work are shown in Supporting Information Table S1. The strains were routinely cultured in LB broth (Miller, 1972), or in phosphate-limited peptone-protease, glucose, ammonium salts (PPGAS) medium (Zhang and Miller, 1992) using glucose as a main carbon source. For the analysis of phenotypic traits, the cultures were inoculated to start at the same optical density (0.05 at 600 nm) and were incubated 16 h in continuous shaking (225 rpm) at 37 °C.

Determination of the antibiotic resistance of P. aeruginosa *strains*

In order to compare the resistance profile of the 15 strains studied in this work to the antimicrobials that have been reported to be prevalent among *Pseudomonas* isolated from intermediate lagoon (Ponce-Soto *et al.*, 2015), we determine the antibiotic resistant profile of these isolates against carbenicillin (500 μg/ml), tetracycline (150 μg/ml), kanamycin (200 μg/ml), streptomycin (200 μg/ml), chloramphenicol (200 μg/ml), gentamicin (150 μg/ml) and apramycin (100 μg/ml).

The antibiotic resistance profile to antimicrobials commonly used to treat *P. aeruginosa* infections was done by micro dilution titre in 96-well plaques, according to the CLSI M100-ED28: 2018 Performance Standards for Antimicrobial Susceptibility Testing, 28th Edition. The antibiotics used were amikacin (AK), gentamicin (GN), aztreonam (AZT), ceftazidime (CAZ), cefepime (FEP), ciprofloxacin (CIP), levofloxacin (LVC), doripenem

(DORY), imipenem (IMP), meropenem (MRP), colistin (CL), piperacillin/tazobactam (TZP).

Determination of virulence-factors and autoinducers (AIs) production

PYO concentration was extracted and measured as reported previously (Essar *et al.*, 1990). Elastase activity was determined using Elastin Congo Red protocol (Beatson *et al.*, 2002) with some changes. Briefly, 50 μl of supernatant were added to 5 mg of Elastin Congo Red (Sigma) and 950 μl of a buffer solution containing 20 mM Tris–HCl (pH 7.5) and 1 mM $CaCl_2$. The reaction was incubated in continuous shaking at 37 °C for 30 min. After centrifugation, the absorbance at 495 nm of the supernatant was measured with a spectrophotometer zeroed with a control reaction using LB medium alone. RL were measured as reported (Chandrasekaran and Bemiller, 1980) and were visualized by thin layer chromatography (Matsuyama *et al.*, 1987).

The extracts to determine AIs production were prepared as previously reported (Grosso-Becerra *et al.*, 2014). To perform these determinations cells were grown in PPGAS medium at 37 °C for 24 h. Detection of C12-HSL was assessed by measuring β-galactosidase (β-gal) activity (Miller, 1972) in *E. coli* strain DH5α harbouring a plasmid expressing a *lasB´-lacZ* transcriptional fusion under the control of its transcriptional regulator LasR (plasmid pECP64, Pearson *et al.*, 1997).

Determination of virulence using the Galleria mellonella *assay*

Virulence in *Galleria mellonella* was evaluated according to the protocol described previously (Koch *et al.*, 2014). In brief five larvae with a size of 2.5 to 3 cm were injected with 10 μl of a 10 mM magnesium sulphate solution containing the inoculum of each strain at a concentration of 1×10^5 CFU/ml. As a positive virulence control, we used either PA14 or PAO1 strains (Table 1), and as a negative control, we used the non-virulent ATCC 9027 strain (Grosso-Becerra *et al.*, 2016), and 10 μl of sterile 10 mM magnesium sulphate was used as injection control. The larvae were incubated at 37 °C for 24, 48 or 72 h, and the dead and living organisms were quantified.

DNA extraction, whole genome sequencing and genome assembly

Strains were inoculated into 3 ml LB medium at 32 °C with 200 rpm shaking. Genomic DNA was extracted and purified from 1.5 ml of culture broth using the DNeasy Blood and Tissue Kit (Qiagen). Quality and quantity of purified genomic DNA was tested by using NanoDrop 2000 UV–Vis spectrophotometer (Thermo Scientific, MA). Whole genome sequencing for all 15 isolates was carried out by using the MiSeq 2x300 paired-end platform (Illumina, Inc.). *De novo* genome assembly was performed using MaSuRCa v3.2.2 assembler (Zimin *et al.*, 2013) followed by the *–trusted_contigs* option from SPAdes v.3.10.1 assembler (Bankevich *et al.*, 2012), which showed to improve the final result. Contigs with a length smaller than 600 bp and less than 10x coverage were removed. The quality of the assemblies was assessed with QUAST v4.5 (Gurevich *et al.*, 2013) and BUSCO v3.0.2 (Simão *et al.*, 2015; Waterhouse *et al.*, 2017). CRISPR arrays were detected with MinCED (Bland *et al.*, 2007) (Table 1).

Phylogenetic analysis

Genomic assemblies were aligned using progressiveMauve (Darling *et al.*, 2010), and core genomes were extracted with the stripSubsetsLCBs script. Core genome phylogenies were carried out by using FastTree 2.0 (Price *et al.*, 2010). MLST sequences were extracted from the genome assemblies with *blastdbcmd* command from BLAST+ software (Camacho *et al.*, 2008), concatenated manually and aligned alongside other 2953 MLST sequences from the PubMLST *Pseudomonas aeruginosa* Database with CLUSTAL W (Thompson *et al.*, 1994). The Neighbour Joining MLST phylogeny and 1000 bootstrap replicates were carried out by MEGA7 (Kumar *et al.*, 2016). Both core genome and MLST phylogenies were visualized with FigTree v.1.4.3.

PCR determination of deletions affecting the pvd *genes*

The oligonucleotides used to amplify the *pvd* genes deletion present in the 34 *P. aeruginosa* strains isolated in 2011 from intermediate lagoon (Supporting Information Table S2) were designed based on the alignment of flanking regions sequence present in the genomes of PAO1, M10 and the sequenced CCB isolates studied in this work. The conditions for the PCR assay were determined using one of the sequenced strains that contain each type of deletion.

Sequence accession numbers

The whole-genome sequences of members of 2A and 2B clonal groups and strain M10 were deposited at GenBank under the accession numbers NZ_SDVO00000000 (M10), NZ_SDVN00000000 (M53), NZ_SDVM00000000 (M54), NZ_SDVL00000000 (M55), NZ_SDVT00000000 (M56), NZ_SDVS00000000 (M57), NZ_SDVR00000000 (M58), NZ_SDVQ00000000 (M59), NZ_SDVK00000000

(M60), NZ_SDVJ00000000 (M61), NZ_SDVI00000000 (M62), NZ_SDVH00000000 (M63), NZ_SDVG00000000 (M64), NZ_SDVF00000000 (M65), NZ_SDVP00000000 (M66) and NZ_SDVE00000000 (M67). GenBank accession numbers of the reference strains used in the phylogenetic reconstruction are NC_002947 (*P. putida* KT2440), NC_020912 (*P. aeruginosa* B136-33), NZ_KE137323 (*P. aeruginosa* PAK), NC_011770 (*P. aeruginosa* LESB58), NC_017549 (*P. aeruginosa* NCGM2.S1), NC_009656 (*P. aeruginosa* PA7), NZ_LLKP01000001.1 (*P. aeruginosa* ATCC 9027), NZ_CP015377 (*P. aeruginosa* BAMC_07–48), NZ_CP017099 (*P aeruginosa* DN1), GCA_000647615 (*P. aeruginosa* ID4365), NZ_AP017302 (*P. aeruginosa* IOMTU_133), NZ_CP017969 (*P. aeruginosa* B10W), NZ_CP019338 (*P. aeruginosa* L10), NZ_AP014622 (*P. aeruginosa* NCGM1900), NZ_AP014651 (*P. aeruginosa* NCGM257), NZ_CP012585 (*P. aeruginosa* PA_D1), NZ_CP012581 (*P. aeruginosa* PA_D16), NZ_CP012578 (*P. aeruginosa* PA_D2), NZ_CP012584 (*P. aeruginosa* PA_D25), NZ_CP012580 (*P. aeruginosa* PA_D9), NZ_CP011369 (*P. aeruginosa* S04_90), NZ_CP015877 (*P. aeruginosa* SJTD-1), NC_008463 (*P. aeruginosa* UCBPP-PA14) and NC_002516 (*P. aeruginosa* PAO1).

Acknowledgements

This work represents part of the PhD thesis of Manuel García-Ulloa II in the Programa de Doctorado en Ciencias Biomédicas (PDCB), Universidad Nacional Autónoma de México (UNAM) and received fellowship from Consejo Nacional de Ciencia y Tecnología (CONACYT). We acknowledge Dra. Norma Espinosa Sánchez for technical assistance. This work was supported in part by grant PAPIIT IN201819 (DGAPA-UNAM) and from the 252269 CONACYT-grant. We are grateful to Dr. Rafael Franco Cendejas and M. C Melissa Hernández Durán of the Instituto Nacional de Rehabilitación Luis Guillermo Ibarra Ibarra for the determination of the antibiotic resistance of the Churince *P. aeruginosa* isolates as shown in Supporting Information Table S1.

Conflict of Interest

The authors declare that they do not have a conflict of interest.

References

Aguirre-von-Wobeser, E., Soberón-Chávez, G., Eguiarte, L.E., Ponce-Soto, G.Y., Vázquez-Rosas-Landa, M., and Souza, V. (2014) Two-role model of an interaction network of free-living Gama-proteobacteria from an oligotrophic environment. *Environ Microbiol* **16**: 1366–1377.

Alcaraz, L.D., Olmedo, G., Bonilla, G., Cerritos, R., Hernandez, G., Cruz, A., *et al.* (2008) The genome of *Bacillus coahuilensis* reveals adaptations essential for survival in the relic of an ancient marine environment. *Proc Nat Acad Sc USA* **105**: 5803–5808.

Bankevich, A., Nurk, S., Antipov, D., Gurevich, A.A., Dvorkin, M., Kulikov, A.S., *et al.* (2012) SPAdes: a new genome assembly algorithm and its applications to single-cell sequencing. *J Comput Biol* **19**: 455–477.

Beatson, S.A., Whitchurch, C.B., Sargent, J.L., Levesque, R.C., and Mattick, J.S. (2002) Differential regulation of twitching motility and elastase production by Vfr in *Pseudomonas aeruginosa*. *J Bacteriol* **184**: 3605–3613.

Berube, B.J., Murphy, K.R., Torhan, M.C., Bowlin, N.O., *et al.* (2017) Impact of type III secretion effectors and of phenoxyacetamide inhibitors of type III secretion on abscess formation in a mouse model of *Pseudomonas aeruginosa* infection. *Antimicrob Agents Chemother* **61**: e1202–e1217.

Bland, C., Ramsey, T.L., Sabree, F., Lowe, M., Brown, K., Kyrpides, N.C., and Hugenholtz, P. (2007) CRISPR recognition tool (CRT): a tool for automatic detection of clustered regularly interspaced palindromic repeats. *BMC-Bioinformatics* **8**: 209.

Bonilla-Rosso, G., Peimbert, M., Alcaraz, L.D., Hernández, I., Eguiarte, L.E., Olmedo-Alvarez, G., and Souza, V. (2012) Comparative metagenomics of two microbial mats at Cuatro Ciénegas Basin II: community structure and composition in oligotrophic environments. *Astrobiology* **12**: 659–673.

Braud, A., Hoegy, F., Jezequel, K., Lebau, T., and Schalk, I.J. (2009) New insights into the metal specificity of the *Pseudomonas aeruginosa* pyoverdine-iron uptake pathway. *Environ Microbiol* **11**: 1079–1091.

Camacho, C., Coulouris, G., Avagyan, V., Ma, N., *et al.* (2008) BLAST+: architecture and applications. *BMC Bioinformatics* **10**: 421.

Castañeda-Montes, F.J., Avitia, M., Sepúlveda-Robles, O., Cruz-Sánchez, V., Kameyama, L., Guarneros, G., and Escalante, A.E. (2018) Population structure of *Pseudomonas aeruginosa* through MLST approach and antibiotic resistance profile of a Mexican clinical collection. *Infect Genet Evol* **65**: 43–54.

Chandrasekaran, E.V., and Bemiller, J.N. (1980) Constituent analysis of glycosamynoglycans. *Methods Carbohydr Chem* **8**: 89–96.

Dacheaux, D., Altree, I., Schneider, C., and Toussaint, B. (1999) Cell death of human polymorphonuclear neutrophils induced by *Pseudomonas aeruginosa* cystic fibrosis isolate requires a functional type III secretion system Infect Immun. *Infect Immun* **67**: 6164–6167.

Darling, A.E., Mau, B., and Perna, N.T. (2010) progressiveMauve: multiple genome alignment with gene gain, loss and rearrangement. *PLoS One* **5**: e11147.

De Anda, V., Zapata-Peñasco, I., Eguiarte, L.E., and Souza, V. (2018) The sulfur cycle as the gear of the "clock of life": the point of convergence between geological and genomic data in the Cuatro Ciénegas Basin. In *Ecosystem Ecology and Geochemistry of Cuatro Ciénegas. Cuatro Ciénegas Basin: An Endangered Hyper Diverse Oasis*, García-Oliva, F., Elser, J., and Souza, V. (eds). Cham, Switzerland: Springer.

Denayer, S., Matthijs, S., and Cornelis, P. (2007) Pyocine S2 (Sa) kills *Pseudomonas aeruginosa* strains via the

FpvA type I ferripyoverdine receptor. *J Bacteriol* **189**: 7663–7668.

Desnues, C., Rodriguez-Brito, B., Rayhawk, S., Kelley, S., Tran, T., Haynes, M., *et al.* (2008) Biodiversity and biogeography of phages in modern stromatolites and thrombolites. *Nature* **452**: 340–343.

Diaz, K.E., Remold, S.K., Onyri, O., Bozeman, M., *et al.* (2018) Generalized growth of estuarine, household and clinical isolates of *Pseudomonas aeruginosa*. *Front Microbiol* **9**: 305.

Elser, J.J., Schampel, J.H., García-Pichel, F., Wade, B.D., *et al.* (2005) Effects of phosphorus enrichment and grazing snails on modern stromatolitic microbial communities. *Freshwater Biol* **50**: 1808–1825.

Escalante, A.E., Caballero-Mellado, J., Martínez-Aguilar, L., González-González, A., *et al.* (2009) *Pseudomonas cuatrocuenegasensis* sp. nov isolated from an evaporating lagoon in the Cuatro Ciénegas valley in Coahuila, México. *Int J Syst Evol Microbiol* **59**: 1416–1420.

Essar, D., Eberly, L., Hadero, A., and Crawford, I. (1990) Identification and characterization of genes for a second anthranilate synthase in *Pseudomonas aeruginosa*: interchangeability of the two anthranilate synthases and evolutionary implications. *J Bacteriol* **172**: 884–890.

Freschi, L., Jeukens, J., Kukavica-Ibrujl, I., Boyle, B., *et al.* (2015) Clinical utilization of genomics data produced by the *Pseudomonas aeruginosa* consortium. *Front Microbiol* **6**: 1036.

Gellatly, S.L., and Hancock, R.E.W. (2013) *Pseudomonas aeruginosa*: new insights into pathogenesis and host defenses. *Pathog Dis* **67**: 159–173.

Gomez-Lunar, Z., Vázquez-Rosas-Landa, M., Ponce-Soto, G.Y., Moreno-Letelier, A., Olmedo-Álvarez, G., Eguiarte, L.E., and Souza, V. (2018) How divergent is the Cuatro Ciénegas oasis? Genomic studies of microbial populations and niche differentiation. In *Cuatro Ciénegas Ecology, Natural History and Microbiology. Cuatro Ciénegas Basin: An Endangered Hyper Diverse Oasis*, Souza, V., Olmedo-Álvarez, G., and Eguiarte, L. (eds). Cham, Switzerland: Springer.

Granato, E.T., Harrison, F., Kümmerli, R., and Ros-Gilliespi, A. (2016) Do bacterial virulence factors always increases virulence? A meta-analysis of pyoverdine production as a test case. *Front Microbiol* **7**: 1952. https://doi.org/10.3389/fmicb.2016.01952.

Grosso-Becerra, M.V., Santos-Medellín, C., González-Valdez, A., Méndez, J.L., Delgado, G., Morales-Espinosa, R., *et al.* (2014) *Pseudomonas aeruginosa* clinical and environmental isolates constitute a single population with high phenotypic diversity. *BMC-Genomics* **15**: 318.

Grosso-Becerra, M.V., González-Valdez, A., Granados-Martínez, M.-J., Morales, E., Servín-González, L., Méndez, J.L., *et al.* (2016) *Pseudomonas aeruginosa* ATCC 9027 is a non-virulent strain suitable for mono-rhamnolipids production. *Appl Microbiol Biotech* **100**: 9995–10004.

Gurevich, A., Saveliev, V., Vyahhi, N., and Tesler, G. (2013) QUAST: quality assessment tool for genome assemblies. *Bioinformatics* **29**: 1072–1075.

Kirienko, N.V., Kirienko, D.R., Larkins-Ford, J., Wählby, C., Ruvkun, G., and Ausubel, F.M. (2013) *Pseudomonas aeruginosa* disrupts *Caenorhabditis elegans* iron homeostasis, causing a hypoxic response and death. *Cell Host Microbe* **13**: 406–416.

Kirienko, D.R., Kang, D., and Kirienko, N.V. (2019) Novel pyoverdine inhibitors mitigate *Pseudomonas aeruginosa* pathogenesis. *Front Microbiol* **9**: 3317. https://doi.org/10.3389/fmicb.2018.03317.

Koch, G., Nadal-Jiménez, P., Cool, R.H., and Quax, W.J. (2014) Assessing *Pseudomonas* virulence with non-mammalian hosts: *Galleria mellonella*. In Pseudomonas. *Methods and Protocols*, Filloux, A., and Ramos, J.L. (eds). New York: Springer, Humana Press, pp. 681–687.

Kumar, S., Stecher, G., and Tamura, K. (2016) MEGA7: molecular evolutionary genetics analysis version 7.0 for bigger datasets. *Mol Biol Evol* **33**: 1870–1874.

Lamont, I.L., and Martin, L.W. (2003) Identification and characterization of novel pyoverdine synthesis genes in *Pseudomonas aeruginosa*. *Microbiol* **149**: 833–842.

Lee, Z.M., Steger, L., Corman, J.R., Neveu, M., Poret-Peterson, A.T., Souza, V., and Elser, J.J. (2015) Response of a stoichiometrically imbalanced ecosystem to manipulation of nutrient supplies and ratios. *PLoS One* **10**: e0123949.

Lee, Z.M., Poret-Peterson, A.T., Siefert, J.L., Kaul, D., *et al.* (2017) Nutrient stoichiometry shapes microbial community structure in an evaporitic shallow pond. *Front Microbiol* **30**: 949.

López-Medina, E., Fan, D., Coughlin, L.A., Ho, E.X., *et al.* (2015) *Candida albicans* inhibits *Pseudomonas aeruginosa* virulence through suppression of pyochelin and pyoverdine biosynthesis. *PLoS Path* **11**: 1005129.

Matsuyama, T., Sogawa, M., and Yano, I. (1987) Direct colony thin-layer chromatography and rapid characterization of *Serratia marcescens* mutants defective in production of wetting agents. *Appl Environ Microbiol* **53**: 1186–1188.

Meyer, J.M. (2000) Pyoverdines: pigments, siderophores ans potential taxonomic markers of fluorescent pseudomonas species. *Arch Microbiol* **174**: 135–142.

Miller, J. (1972) *Experiments in Molecular Genetics*. New York: Cold Spring Harbor Laboratory, pp. 352–355.

Minckley, T.A., Felstead, N.J., and Gonzalez, S. (2019) Novel vegetation and establishment of Chihuahuan Desert communities in response to late Pleistocene moisture availability in the Cuatro Ciénegas Basin, NE Mexico. *The Holocene* **29**: 457–466. https://doi.org/10.1177/0959683618816490.

Miyata, S., Casey, M., Frank, D.W., Ausubel, F.M., and Drenkard, E. (2003) Use of the *Galleria mellonella* caterpillar as a model host to study the role of the type III secretion system in *Pseudomonas aeruginosa* pathogenesis. *Infect Immun* **71**: 2404–2413.

Morales, E., González-Valdez, A., Servín-González, L., and Soberón-Chávez, G. (2017) *Pseudomonas aeruginosa* quorum-sensing response in the absence of functional LasR and LasI proteins: the case of strain 148, a virulent dolphin isolate. *FEMS Microbiol Lett* **364**. https://doi.org/10.1093/femsle/fnx119 Thematic issue.

Mosquera-Rendón, J., Rada-Bravo, A.M., Cárdenas-Brito, S., Corredor, M., Restrepo-Pineda, E., and Benítez-Páez, A. (2016) Pangenome-wide and molecular evolution analysis of the *Pseudomonas aeruginosa* species. *BMC-Genomics* **17**: 45.

Pearson, J.P., Pesci, E.C., and Iglewski, B.H. (1997) Roles of *Pseudomonas aeruginosa las* and *rhl* quorum-sensing systems in control of elastase and rhamnolipid biosynthesis. *J Bacteriol* **179**: 5756–5767.

Pérez-Gutiérrez, R.A., López-Ramírez, V., Islas, A., Alcaraz, L.D., Hernández-González, I., Olivera, B.C., *et al.* (2012) Antagonism influences assembly of a bacillus guild in a local community and is depicted as a food-chain network. *ISME J* **7**: 487–497.

Pirnay, J.-P., Bilocq, F., Pot, B., Cornellis, P., *et al.* (2009) *Pseudomonas aeruginosa* population structure revisited. *PLoS One* **4**: e7740.

Ponce-Soto, G.Y., Aguirre von Wobeser, E., Eguiarte, L.E., Elser, J.J., *et al.* (2015) Enrichment experiment changes microbial interactions in an ultra-oligotrophic environment. *Front Microbiol* **6**: 246.

Price, M.N., Dehal, P.S., and Arkin, A.P. (2010) FastTree 2. Approximately maximum-likelihood trees for large alignments. *PLoS One* **5**: e9490.

Ravel, J., and Cornelis, P. (2003) Genomics of pyoverdine-mediated iron uptake in *Pseudomonads*. *Trends Microbiol* **11**: 195–200.

Rodríguez-Torres, M.D., Islas-Robles, A., Gómez-Lunar, Z., Delaye, L., *et al.* (2017) Phenotypic microdiversity and phylogenetic signal analysis of traits related to social interaction in *Bacillus spp.* from sediment communities. *Front Microbiol* **8**: 29.

Rodríguez-Verdugo, A., Souza, V., Eguiarte, L. E., Escalante, A. E. (2012) Diversity across seasons among cultivable *Pseudomonas* from a desiccation lagoon in Cuatro Ciénegas, Mexico. *Int J Microbiol* **2012**: 201389, 1, 10.

Roy, P.H., Tetu, S.G., Larouche, A., Elbourne, L., Tremblay, S., Ren, Q., *et al.* (2010) Complete genome sequence of the multiresistant taxonomic outlier *Pseudomonas aeruginosa* PA7. *PLoS One* **5**: e8842.

Schalk, I.J., and Guillon, L. (2013) Pyoverdine synthesis and secretion in *Pseudomonas aeruginosa*: implications for metal homeostasis. *Environ Microbiol* **15**: 1661–1673.

Schalk, I.J., Hennard, C., Dugave, C., Poole, K., Abdallah, M.A., and Pattus, F. (2001) Iron-free pyoverdine binds to its outer membrane receptor FpvA in *Pseudomonas aeruginosa*: a new mechanism for membrane iron transport. *Mol Microbiol* **39**: 351–360.

Schiessi, K.T., Janssen, E.M.L., Kraemer, S.M., McNeill, K., and Ackermann, M. (2017) Magnitude and mechanism of siderophore-mediated competition at low iron-solubility in the *Pseudomonas aeruginosa* piochelin synthesis. *Front Microbiol* **8**: 1964.

Simão, F.A., Waterhouse, R.M., Ioannidis, P., Kriventseva, E. V., and Zdobnov, E.M. (2015) BUSCO: assessing genome assembly and annotation completeness with single-copy orthologs. *Bioinformatics* **31**: 3210–3212.

Souza, V., Espinosa-Asuar, L., Escalante, A.E., Eguiarte, L. E., *et al.* (2006) An endangered oasis of aquatic microbial biodiversity in the Chihuahuan desert. *Proc Natl Acad Sci U S A* **113**: 6565–6570.

Souza, V., Siefert, J.L., Escalante, A.E., Elser, J.J., and Eguiarte, L.E. (2012) The Cuatro Ciénegas Basin in Coahuila, Mexico: an astrobiological Precambrian Park. *Astrobiology* **12**: 641–647.

Souza, V., Moreno-Letelier, A., Travisano, M., Alcaraz, L.D., *et al.* (2018) The lost world of Cuatro Ciénegas Basin, a relictual bacterial niche in a desert oasis. *eLife* **7**: e38278. https://doi.org/10.7554/eLife.38278.001.

Stewart, L., Ford, A., Sangal, V., Jeukens, J., Boyle, B., Kukavica-Ibrulj, I., *et al.* (2014) Draft genomes of 12 host-adapted and environmental isolates of *Pseudomonas aeruginosa* and their positions in the core genome phylogeny. *Pathog Dis* **71**: 20–25.

Stover, C.K., Pham, X.Q., Erwin, A.L., Mizoguchi, S.D., Warrener, P., Hickey, M.J., *et al.* (2000) Complete genome sequence of *Pseudomonas aeruginosa* PAO1, an opportunistic pathogen. *Nature* **406**: 959–964.

Taboada, B., Isa, P., Gutiérrez-Escolano, A.L., Del Ángel, R. M., Ludert, R.E., *et al.* (2018) The geographic structure of viruses in the Cuatro Ciénegas Basin, a unique oasis in northern Mexico, reveals a highly diverse population on a small geographic scale. *Appl Environ Microbiol* **84**: e00465–e00418.

Tapia-Torres, Y., Rodríguez-Torres, M.D., Elser, J.J., Islas, A., Souza, V., García-Oliva, F., and Olmedo-Álvarez, G. (2016) How to live with phosphorus scarcity in soil and sediment: lessons from bacteria. *Appl Environ Microbiol* **82**: 4652–4662.

Tasake, H., Nakanai, H., Hoshino, K., and Otani, T. (2000) Importance of siderophore production on *Pseudomonas aeruginosa* infections in immunosuppressed mice. *Infect Immun* **68**: 1834–1839.

Thompson, J.D., Higgins, D.G., and Gibson, T.J. (1994) CLUSTAL W: improving the sensitivity of progressive multiple sequence alignment through sequence weighting, position-specific gap penalties and weight matrix choice. *Nuc Acids Res* **22**: 4673–4680.

Toribio, J., Escalante, A.E., Caballero-Mellado, J., González-González, A., Zavala, S., Souza, V., and Soberón-Chávez, G. (2011) Characterization of a novel biosurfactant producing *Pseudomonas koreensis* lineage that is endemic to Cuatro Ciénegas Basin. *Syst Appl Microbiol* **34**: 531–535.

Van Belkum, A., Soriaga, L.B., LaFave, M.C., Akella, S., *et al.* (2015) Phylogenetic distribution of CRISPR-Cas Systems in Antibiotic-Resistant *Pseudomonas aeruginosa*. *MBio* **6**: e01796–e01715.

Visca, P., Imperi, F., and Lamont, I.L. (2006) Pyoverdine siderophores: from biogenesis to biosignificance. *Trends Microbiol* **15**: 22–30.

Waterhouse, R.M., Seppey, M., Simão, F.A., Manni, M., *et al.* (2017) BUSCO applications from quality assessments to gene prediction and phylogenomics. *Mol Biol Evol* **35**: 543–548.

Williams, P., and Cámara, M. (2009) Quorum sensing and environmental adaptation in *Pseudomonas aeruginosa*: a tale of regulatory networks and multifunctional signal molecules. *Curr Opin Microbiol* **12**: 182–191.

Yu, G., Lam, T.T.-Y., Zhu, H., and Guan, Y. (2018) Two methods for mapping and visualizing associated data on phylogeny using ggtree. *Mol Biol Evol* **35**: 3041–3043. https://doi.org/10.1093/molbev/msy194.

Zhang, Y., and Miller, R.M. (1992) Enhanced octadecane dispersion and biodegradation by a *Pseudomonas*

INFORME DE LABORES 2019

rhamnolipid surfactant (biosurfactant). *Appl Environ Microbiol* **58**: 3276–3282.

Zimin, A.V., Marçais, G., Puiu, D., Roberts, M., Salzberg, S.L., and Yorke, J.A. (2013) The MaSuRCA genome assembler. *Bioinformatics* **29**: 2669–2677.

Supporting Information

Additional Supporting Information may be found in the online version of this article at the publisher's web-site:

Appendix S1. Supplementary Information

Molecular Neurobiology (2019) 56:6594–6608
https://doi.org/10.1007/s12035-019-1546-x

Autophagy as a Homeostatic Mechanism in Response to Stress Conditions in the Central Nervous System

Cristian Gerónimo-Olvera [1,2] · Lourdes Massieu [1]

Received: 7 November 2018 / Accepted: 12 March 2019 / Published online: 23 March 2019
© Springer Science+Business Media, LLC, part of Springer Nature 2019

Abstract

Autophagy is considered a major bulk degradation system that helps cells to counteract different intracellular and extracellular stress signals. Several protein complexes integrate multiple signals in order to activate autophagy, which sequesters damaged cellular components and carries them to lysosomes for degradation. This active mechanism is essential to maintain cell homeostasis and particularly in neurons to sustain their viability. Because of their polarized morphology, neurons face special challenges to recycle cellular components through autophagy in dendrites and distal regions of axons. Thus, autophagy is critical in the remodeling of pre- and post-synaptic constituents to sustain neuronal functionality. Under stress conditions, autophagy may play either a cytotoxic or a cytoprotective role. This discrepancy is partly due to the lack of a full characterization of the autophagic process and conclusive evidence to support whether basal autophagy is stimulated or impaired in a particular condition. Moreover, in many studies, only pharmacologic tools have been used to modulate autophagy. Throughout the present review, we go over the literature revealing autophagy induction in the nervous system under diverse stressful conditions, the signaling pathways involved, and its consequences for neuronal homeostasis and survival. We have focused on five particular stress conditions that alter neuronal homeostasis and can induce neuronal death including, starvation, oxidative stress, endoplasmic reticulum (ER) stress, proteotoxic stress, and aging.

Keywords Autophagy · Neurons · Starvation · Oxidative stress · Endoplasmic reticulum stress · Aging

Introduction

Autophagy is an evolutionary conserved mechanism in eukaryotes, considered as the major bulk degradation system where damaged cytoplasmic components are delivered to the lysosome for degradation. Autophagy is also responsible for the turnover and recycling of cytoplasmic materials to produce building blocks and energy to maintain cellular homeostasis [1–3]. Several extracellular and intracellular stimuli promote autophagy representing an essential mechanism by which cells can adapt to stress conditions, particularly to starvation. However, basal levels of autophagy are present in all cells in order to maintain cellular homeostasis and energy balance [4].

✉ Cristian Gerónimo-Olvera
cgeronimo.olvera@gmail.com

[1] División de Neurociencias, Instituto de Fisiología Celular, Universidad Nacional Autónoma de México (UNAM), 04510 Ciudad de México, Mexico

[2] Present address: Center for Integrative Biology, Faculty of Sciences, Universidad Mayor, Santiago, Chile

Depending on how cytoplasmic material is delivered to the lysosome, autophagy is divided in three classes: macroautophagy, microautophagy, and chaperone-mediated autophagy. In macroautophagy, an isolation membrane (phagophore) sequesters portions of the cytoplasm, including proteins and organelles, to form a double- or multi-membrane structure named autophagosome. The autophagosome fuses with the lysosome to become an autolysosome and degrades its content. Microautophagy involves the engulfment of small portions of the cytoplasm directly by the lysosome membrane to be subsequently degraded [5]. Finally, chaperone-mediated autophagy is a specific type of autophagy, where substrate proteins are targeted one by one toward the lysosome and then translocated across the lysosomal membrane [6]. Macroautophagy has been mostly investigated and is considered as the major subtype of autophagy; thereby, we will refer to macroautophagy as autophagy.

The Autophagy Machinery

The process of autophagy involves the participation of autophagy-related (ATG) proteins, which are recruited to the

phagophore to form the autophagosome. The canonical formation of the autophagosome involves different steps including induction, autophagosome formation, fusion of the autophagosome with the lysosome, and cargo degradation, followed by the release of breakdown products into the cytosol. ATG proteins contribute to these steps and many of them are essential for a proper autophagy function.

A central inhibitor of autophagy is mTOR, a Ser/Thr protein kinase originally recognized as a target of rapamycin, which is involved in numerous cell processes such as protein synthesis, growth, sensing of environmental nutritional changes, and autophagy. mTOR integrates multiple upstream signals which control autophagic activity. Under nutrient-rich conditions, mTOR activation negatively regulates autophagy through inhibition of the ULK1 complex, composed by ULK1, ATG13, FIP200, and ATG101 [7, 8]. In contrast, upon starvation or rapamycin treatment, mTOR inactivation leads to a stable form of the ULK1 complex located at the phagophore to induce autophagy.

In cells undergoing autophagy, autophagosome formation initiates at phagophore assembly sites (PAS), where double-layered membrane elongates to form a phagophore and then an autophagosome [8]. Different organelles are considered as phagophore membrane sources such as endoplasmic reticulum (ER), mitochondria, and the Golgi complex, where multiple PAS can arise [9]. Phagophore formation initiates after ULK1 activation, which in turn targets class III PtdIns3K complex, containing VPS34, BECN1, ATG14, and VPS15, to produce PtdIns3P [7]. After the initiation of the phagophore formation, the elongation of the phagophore membrane that will ultimately become an autophagosome is regulated by two ubiquitin-like reactions. In the first reaction, ATG12 is activated by ATG7 (E1 ubiquitin-activating enzyme) and transferred to ATG10 (E2 ubiquitin-activating enzyme); after these two subsequent reactions, ATG12 is covalently bound to ATG5 to form the ATG12-ATG5 conjugate. This complex interacts with ATG16L1 resulting in a ternary complex ATG12-ATG5-ATG16L1 [8, 10], which localizes to the phagophore membrane and is essential for its elongation. This complex dissociates when the autophagosome is fully formed. The second ubiquitin-like reaction involves the conjugation of ATG8 family, which includes the microtubule-associated protein light chain 3 (MAP-LC3/ATG8/LC3), γ-amino-butyric acid receptor-associated protein (GABARAP), and Golgi-associated ATPase enhancer of 16 kDa (GATE-16), to phosphatidylethanolamine (PE). LC3, the best-characterized ATG8 member, is cleaved by ATG4B to produce the cytosolic form LC3-I [11]. LC3-I is conjugated to PE at the autophagosome membrane through two ubiquitin-like reactions involving ATG7 (E1 like) and ATG3 (E2 like), to form autophagosome-associated LC3-II. The ATG12-ATG5-ATG16L complex regulates the conjugation of LC3-I to PE acting as an E3-like enzyme, although it is not essential for conjugation to occur [8]. LC3-II is associated to both sides of the autophagosome and regulates its size due to its ability to determine membrane curvature.

Autophagosomes are mobilized toward lysosomes along microtubules through dynein-dependent transport; then, the outer membrane of the autophagosome fuses with the lysosome to form an autolysosome, a process that requires the lysosomal membrane protein LAMP-2 and the small GTPase Rab7 [12]. Soon after the fusion, LC3-II attached to the outer membrane is delipidated by ATG4B to recycle LC3-I [13]. Proper function and integrity of the lysosome are essential for successful fusion to occur. Degradation of the inner membrane and autophagosome content including LC3-II is dependent on lysosomal hydrolases such as cathepsin B, D, and L. Degraded autolysosome content is released into the cytosol for protein synthesis and maintenance of cellular homeostasis.

On the other hand, non-canonical pathways of autophagy have been discovered, whereby autophagosome formation occurs in the absence of some key autophagy proteins such as ATG7, ATG5, LC3, and BECN1. These non-canonical pathways have been identified under certain cellular circumstances and their role in cellular homeostasis is not completely clear [14]. For instance, BECN1-independent autophagy contributes to apoptosis in cortical neurons exposed to the pro-apoptotic agent staurosporine [15]. On the other hand, mouse embryonic fibroblast lacking ATG5 or ATG7 can undergo autophagy when exposed to certain stressors such as etoposide, staurosporine, and even nutrient deprivation. Interestingly, under these conditions, lipidation of LC3 does not occur, suggesting that ubiquitin-like proteins are not required for alternative autophagy. However, some conventional autophagy-related proteins including ULK1, BECN1, and VPS34 are required for alternative autophagy. These findings suggest that under certain stress conditions, an alternative autophagy can occur in order to overcome stress. Although, conventional autophagy is necessary for the clearance of protein aggregates in neurons [16].

Autophagy can be either nonselective or selective. Selectivity is mediated by autophagy receptors that recognize both, the tagged cargos with degradation signals and the autophagosome membrane through the LC3-interacting region [17]. The ubiquitin-binding protein p62/SQSTM1 is the best-characterized autophagy receptor and its degradation into the autolysosome has been widely used as a measure of the autophagic flux.

Autophagy in the CNS

In mammalian adult brain, neurogenesis is limited to selected regions, namely, the dentate gyrus of the hippocampus and the subventricular zone. Thus, there is no turnover of dysfunctional neurons and they ought to survive an entire lifetime. As

INFORME DE LABORES 2019

post-mitotic cells, neurons rely on autophagy for the maintenance of protein and organelle homeostasis and thus neuronal viability.

The relevance of autophagy as a quality control mechanism in the CNS is evidenced in animal models where essential autophagy genes are genetically suppressed. Mice lacking Atg5 [18], Atg7 [19], and FIP200 [20], specifically in the CNS, show neurological and behavioral defects, including abnormal limb-clasping reflexes, locomotor ataxia, and deficits in motor coordination that result in early death. Deficiency of these autophagy-related genes causes the accumulation of polyubiquitinated proteins in almost all brain regions, forming inclusion bodies that increase in size and number with age [18, 19]. Moreover, animals exhibit axonal degeneration and neuronal loss in the cerebral and cerebellar cortices. These findings highlight the importance of a continuous clearance of cytosolic proteins through basal autophagy, in order to prevent the accumulation of abnormal proteins, which might impair neuronal function.

Autophagy plays a housekeeping role degrading aggregate-prone proteins including polyglutamine-expanded huntingtin (mHTT) and mutant α-synuclein (PD) [21]. In agreement, autophagy dysfunction, leading to the accumulation of pathogenic proteins and autophagy vacuoles, has been reported in neurodegenerative disorders [22]. Conversely, stimulation of autophagy reduces the accumulation of mHTT and α-synuclein, protects against cell death, and reduces behavioral alterations in different animal models of neurodegenerative diseases [23–25].

Besides a housekeeping role, autophagy functions as an adaptive response exerting cytoprotective and anti-inflammatory actions under stress conditions [9]. Pharmacological or genetic inhibition of autophagy diminishes neuronal capacity to respond to nutritional, physical, and chemical insults, suggesting an adaptive role that contributes to reestablish physiological conditions [26]. In contrast, there is also evidence supporting that autophagy can lead to cell death, named autophagic cell death, under certain conditions such as starvation and hypoxia/ischemia [27]. Thus, autophagy may exert a cytotoxic rather than a cytoprotective action under some circumstances [28]. The differential role of autophagy as an adaptive response or a mechanism contributing to cell death is related to the intensity and the duration of the stress stimulus (Fig. 1).

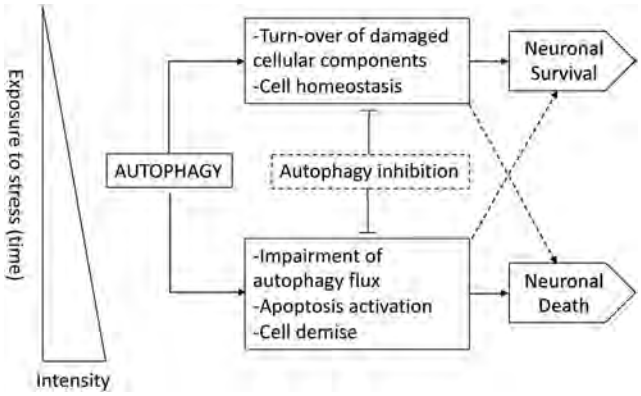

Fig. 1 Stress stimuli induce autophagy that depending on the duration and intensity can elicit different responses. Mild and short stress induce autophagy-dependent turnover of damaged cellular components to restore cell homeostasis that ultimately promote neuronal survival. Prolonged and intense stress induce autophagy dysfunction and apoptosis activation, which in turn causes neuronal death. Inhibition of neuroprotective autophagy leads to accumulation of damaged cellular components and cell homeostasis disruption. By contrast, inhibition of neurotoxic autophagy prevents apoptosis activation and autophagy-dependent cell demise

Autophagy Takes Place in Specific Neuronal Compartments

Neurons are polarized cells with unique morphology. The axon is a specialized compartment that can reach up long distances from the soma, the main site of protein degradation and synthesis. How autophagy regulates protein homeostasis along the different cell compartments is a challenging question [29]. Live-cell imaging studies indicate that autophagosomes are formed at the distal end of the axon. Autophagy core proteins are recruited to ER membranes present at the distal axon, where autophagosomes are generated [27, 28]. Then, autophagosomes travel by retrograde transport toward the soma and fuse with late endosomes or lysosomes, forming autolysosomes as they reach the soma [30, 31]. This process regulates axonal homeostasis and maintains the quality control of proteins present in nerve terminals. On the other hand, in the case of dendrites, it has been suggested that autophagosome biogenesis can occur locally or autophagy vesicles can be recruited to this compartment in a synaptic activity-dependent manner [32].

Synapses are critical neuronal compartments for brain function. Synaptic activity requires the participation of a large amount of proteins, which are highly susceptible to damage that leads to their accumulation and function impairment. Autophagy-recycling plays a crucial role in removing damaged proteins and maintaining homeostasis also in synapses [33]. In addition, autophagy regulates presynaptic structure and function. It has been reported that autophagy deficiency in dopaminergic neurons results in enhanced dopamine secretion in response to stimulation and accelerated presynaptic recovery due to the lack of the turnover of neurotransmitter vesicles [34]. Conversely, enhanced autophagy induced by rapamycin decreased dopaminergic synaptic vesicle density [35]. This suggests that autophagy regulates neurotransmission through the degradation of synaptic vesicles, altering synaptic terminal volume and the release of neurotransmitter. Also, autophagy is involved in synaptic plasticity. After chemical long-term depression, autophagosomes accumulate within dendrites and spines, and partially contribute to AMPA

receptor degradation. Under these conditions, ATG7 knockdown recovers AMPA protein levels only partially, suggesting the involvement of other degradation systems [36].

Starvation and Nutrient Deprivation

Neurons are highly metabolically active with a limited nutrient storage capacity; thereby, they are particularly sensitive to energy fluctuations. Glucose is the obligatory substrate for adult brain and a continuous supply of glucose and oxygen is required during development for normal brain function. Under prolonged fasting, which can lead to moderate hypoglycemia, or during pathological conditions such as ischemia and severe hypoglycemia, the brain is deprived from glucose. In these conditions, autophagy may be triggered in neurons in order to reestablish the energy status.

Metabolic stimuli that lead to autophagy activation are canonically integrated by the master regulator mTOR. However, depending on the stimuli, the upstream signaling can vary. For instance, growth factor deprivation, such as insulin, activates autophagy through PI3K/Akt signaling and subsequent inhibition of mTOR (reviewed in [37]). On the other hand, amino acid starvation is sensed by Rag GTPases that regulate the inhibition of mTOR and consequently ULK1/2 activation leading to autophagy [38]. Under these conditions, ablation of ULK1/2 completely abrogates autophagy activation [39]. Moreover, autophagy induced by glucose starvation also depends on mTOR-ULK1/2 but the upstream signaling involves AMPK activation [40]. Thus, cells can respond to a variety of metabolic challenges inducing autophagy in order to maintain the energy status. Nonetheless, severe conditions that lead to energy depletion result in autophagy impairment. This is because some autophagy steps are ATP-dependent such as lysosomal v-ATPase functioning, which is essential for the autophagosome-lysosome fusion and autolysosome degradation [41].

It is well known that food restriction induces autophagy in many organs. However, pioneer studies in mice exposed to food deprivation during 48 h showed no increase in brain autophagy [42]. The authors hypothesized that under these conditions, other organs could supply the brain with nutrients such as glucose and ketone bodies. However, more recent studies revealed that short-term fasting induces the upregulation of autophagy in cortical neurons and Purkinje cells, mediated by the decreased activation of neuronal mTOR in vivo [43]. In hypothalamic neurons, autophagy is induced by free fatty acids under fasting conditions in order to modulate food intake and long-term energy homeostasis [44]. Inhibition of hypothalamic autophagy alters energy balance and potentiates the development of metabolic diseases. Thus, autophagy within hypothalamic neurons is crucial for the control of food intake, energy and body weight balance [45].

Data on autophagy activation during nutrient stress in cultured neurons are still controversial. It has been observed that deprivation of growth factors and hormones in cortical cultures activates autophagy via mTOR inactivation [46]. In this condition, activation of autophagy protected neurons against proteotoxicity induced by polyQ-expanded huntingtin, suggesting an adaptive role. Conversely, in hippocampal-cultured neurons, nutrient or glucose deprivation markedly decreased mTOR signaling but it was not sufficient to activate autophagy. However, glucose deprivation attenuates retrograde transport of autophagosomes due to ATP depletion [47]. The authors hypothesized that autophagy has a key function regulating neuronal homeostasis, rather than providing amino acids in response to starvation. Likewise, we have recently demonstrated the impairment of the autophagy flux and the accumulation of autophagosomes in response to glucose deprivation in cortical-cultured neurons, due to lysosomal damage [48]. However, the autophagy flux can be restored upon glucose replenishment or when an alternative fuel such as the ketone body beta-hydroxybutyrate is added [49]. Similarly, long-term exposure to glucose deprivation during 18 h induces the accumulation of autophagy markers in the mouse neuroblastoma cell line Neuro2a suggesting the impairment of the autophagy flux [50].

Several molecules regulate autophagy under nutrient-deficient conditions, AMPK is one of the best characterized. AMPK monitors the energy homeostasis of the cells by sensing the AMP/ATP ratio. In addition, different upstream kinases can regulate AMPK activation including, LKB1 (liver kinase B1), CaMKKB (calcium/calmodulin kinase kinase B), and TAK-1 (TGFB-activated kinase-1) [51]. Autophagy is induced by AMPK-mediated mTOR inhibition, via phosphorylation of TSC2 and Raptor; however, AMPK can directly phosphorylate ULK1 and initiate autophagy [52] (Fig. 2a). Hypothalamic AMPK integrates diverse hormonal signals and plays an important role in the regulation of food intake. In hypothalamic cell lines exposed to low glucose or in animals treated with 2DG, autophagy is induced via AMPK activation, which increases the expression of NPY and decreases that of POMC stimulating food intake. Conversely, knockdown of AMPK within the hypothalamus induces the opposite changes in NPY and POMC expression leading to a reduction in food intake and body weight [53].

Under more severe conditions such as cerebral ischemia, morphological and biochemical markers of autophagy have been observed in several studies (reviewed [54]). However, whether autophagy plays a neuroprotective or neurotoxic role is still controversial [55]. Particularly, in ischemic injury, AMPK leads to autophagy activation, and inhibition of the AMPK-autophagy pathway confers protection against brain damage through the restoration of mTOR activity [56]. In contrast, it has been reported that metformin preconditioning

INFORME DE LABORES 2019

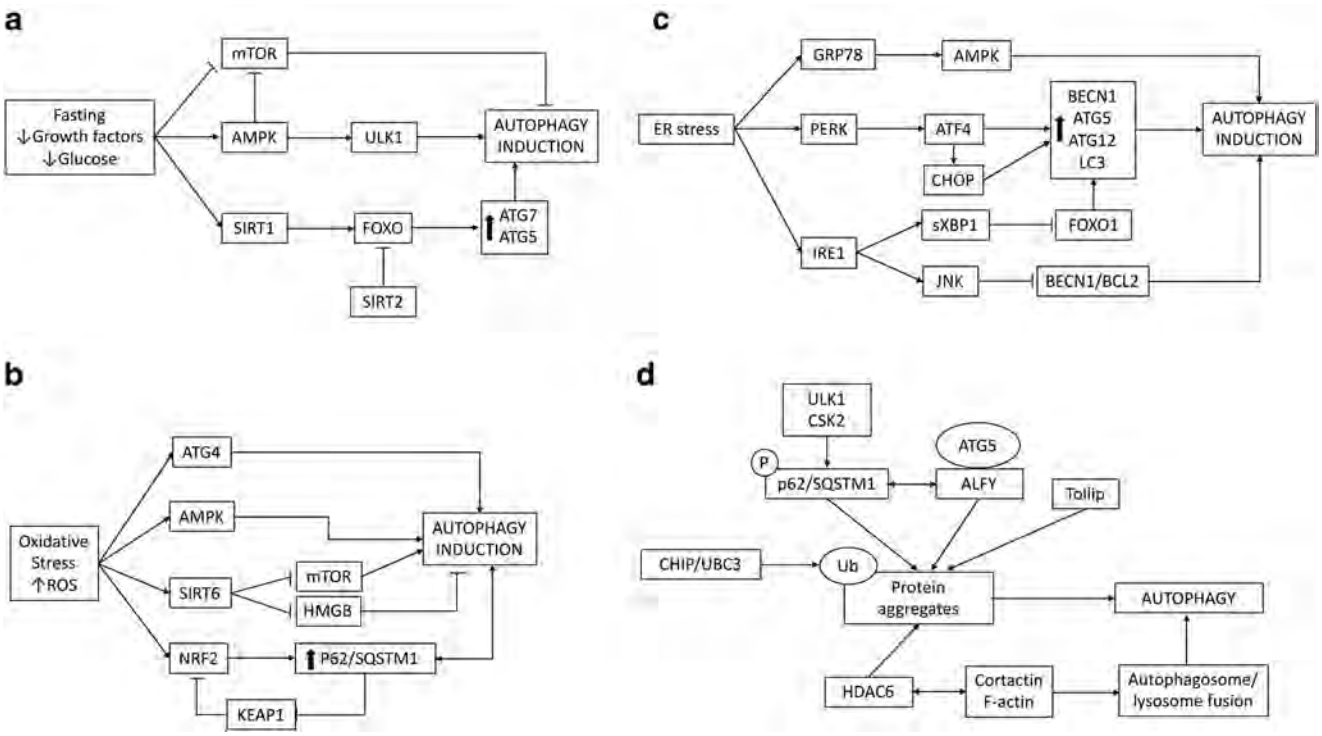

Fig. 2 Signal transduction pathways that regulate neuronal autophagy in response to **a** starvation and nutrient deprivation, **b** oxidative stress, **c** endoplasmic reticular stress, and **d** proteotoxic stress

protects against ischemia by activation of AMPK-dependent autophagy [57]. As mentioned before, autophagy plays an adaptive role in response to different types of stress; however, autophagy defects can compromise this adaptive response increasing the susceptibility to acute stress.

Manipulations that induce autophagy can elicit a hormetic effect increasing the resistance to several stressful conditions [28]. Autophagy induction during ischemic/hypoxic preconditioning exerts protection against a subsequent lethal hypoxic/ischemic insult. The mechanisms involved are not completely clear but some have been proposed. A recent study suggests that autophagy induction by hypoxic preconditioning (HPC) is mediated by the increased expression of HIF-1α and its downstream targets BECN1 and BNIP3, in SH-SY5Y cells exposed to oxygen and glucose deprivation exerting neuroprotection [58]. BNIP3 activates autophagy by mTOR inhibition and through the dissociation of BECN1 form Bcl-2 or Bcl-XL by competition with BECN1, favoring autophagosome formation [59]. Another recent study showed that HPC prevents neuronal damage in the hippocampus of rats exposed to transient global ischemia, through the restoration of the otherwise impaired autophagic flux. This effect involves the stimulation of autophagosome maturation by the activation of the small GTPase, Rab7, mediated by its interaction with UVRAG and Vps16, favoring the autophagosome-lysosome fusion [60].

On the other hand, autophagy activation by rapamycin increases the expression of p-PI3K, p-Akt1, and p-CREB, which correlates with decreased β-amyloid toxicity and improved cognitive decline in rats, suggesting that autophagy is part of a pro-survival response involving the activation of the pAkt1/CREB signaling pathway [61]. The molecular mechanisms involved in the activation of this survival pathway after autophagy induction have not been described. Additionally, rapamycin treatment prior to hypoxia-ischemia promotes neuroprotection through activation of either autophagy or Akt/CREB pathway [62].

Increased tolerance to lethal ischemic injury after ischemic preconditioning (IPC) has been shown to involve the increased expression of GRP78, an endoplasmic reticulum (ER) chaperone implicated in the unfolded protein response (UPR). GRP78 stimulates autophagy through the upregulation of AMPK in in vitro ischemia models, but the molecular mechanisms involved are still not clear [63, 64]. In addition, GRP78 can bind to p62/SQSTM1 to induce a conformational change which favors cargo degradation [65]. Conversely, autophagy activation during IPC upregulates GRP78, HSP60, and HSP70 and reduces the severity of ER stress triggered by lethal ischemia preventing ER-mediated apoptosis. Moreover, rapamycin administration before ischemia exerts similar effects, suggesting that protection elicited by IPC is mediated by the reduction of ER stress through autophagy activation [66]. From these studies, it can be concluded that moderate autophagy activation and mild ER stress induction are responsible at least in part of IPC protection against lethal ischemia.

Autophagy can be also regulated by Sirtuins, a family of NAD-dependent protein deacetylases that sense environmental stress. Sirt1 activity is necessary for the induction of autophagy by starvation, as it interacts and deacetylates autophagy-related proteins including ATG7, ATG5, and LC3 [67]. The lack of Sirt1 results in acetylated ATGs which associates with impaired autophagy, including the accumulation of p62/SQSTM1 and damaged organelles, disruption of energy homeostasis, and early death after birth [68]. Moreover, overexpression of Sirt1 is sufficient to stimulate autophagy even under nutrient-rich conditions. Increasing Sirt1 activity confers protection against axonopathy and neurodegeneration [69]. Furthermore, the sirtuin activator, resveratrol, rescues neuronal dysfunction induced by polyQ and β-amyloid toxicity through autophagy induction [70, 71]. Additionally, sirtuins can enhance the expression of autophagy proteins via deacetylation of FoxO, a well-known transcription factor regulating the expression of autophagy genes (Fig. 2a). Sirt1 promotes FoxO transcription activity, while Sirt2 prevents the interaction of acetylated FoxO with ATG7 preventing autophagy [67]. In addition, neurons lacking Sirt2 showed increased ATG5 acetylation and less recruitment of Parkin toward mitochondria resulting in mitophagy dysfunction [72], suggesting a crucial role of Sirt2 in mitochondrial homeostasis. In contrast, the overexpression of Sirt2 in cholinergic SN56 cells and neuroblastoma SH-SY5Y inhibits the autophagy flux leading to the accumulation of protein aggregates [73] by a mechanism that has not yet been elucidated.

Oxidative Stress and Autophagy

Due to its high metabolic energy requirements and rate of oxygen consumption, the brain is prone to reactive oxygen and nitrogen species (ROS/RNS) production and particularly vulnerable to oxidative stress. The antioxidant capacity of the brain to counteract ROS is limited compared to other organs. In addition, brain contains high levels of polyunsaturated fatty acids, which are targets for lipid peroxidation and act as pro-oxidants [74]. Oxidative stress has been implicated in the pathogenesis of neurodegenerative disorders, which are characterized by high levels of ROS [75]. Under these circumstances, autophagy reduces oxidative damage and ROS levels through the removal of pro-oxidant protein aggregates and damaged organelles [76].

ROS act as signaling molecules and modulate various pathways, including autophagy, through the redox regulation of proteins. Starvation triggers the accumulation of ROS, mainly H_2O_2, which leads to the inactivation of ATG4 ensuring the conjugation of LC3 with the autophagosome membrane, an essential step in autophagosome formation [77] (Fig. 2b). Given the role of ROS in autophagy induction, non-enzymatic and enzymatic antioxidants act as natural downregulators of this process.

Oxidative stress leads to autophagy activation and the accumulation of autophagosomes in different types of cells. Mitochondrial ROS, mainly $O_2^{\cdot-}$, induce autophagy mediated by AMPK activation during starvation [78, 79]. Likewise, in U87 glioblastoma cells, inhibitors of mitochondrial complexes I and II induce ROS-mediated autophagy, and SOD2 overexpression markedly reduces autophagosome formation [80]. Autophagy inhibition reduces the toxicity of mitochondrial electron transport chain inhibitors, suggesting that autophagy contributes to cell death. In normal mouse astrocytes, inhibition of mitochondrial complexes fails to produce ROS and to induce autophagy, possibly because of the lower energy requirements of this type of cells as compared to others such as cancer cells [80]. In contrast, in human neuroblastoma cells, SH-SY5Y rotenone (complex I inhibitor) treatment inhibits the autophagic flux and leads to cell death [81], while treatment with resveratrol, a well-known autophagy inducer, partially rescues SH-SY5Y cells from rotenone toxicity [82]. In the same cell line and in primary dopaminergic neurons, cell death induced by mitochondrial complex I inhibitor MPP+ is accompanied by the activation of autophagy mediated by the ERK/MAPK pathway. Under these circumstances, ablation of autophagy or inhibition of ERK signaling decreases MPP+ toxicity, suggesting the contribution of autophagy to cell death [83, 84]. However, manipulations that enhance autophagy and promote the autophagy flux, such as ischemic preconditioning or pharmacological pretreatments, protect against MPP+ toxicity [85–87], suggesting an adaptive role of autophagy under these circumstances.

On the other hand, oxidative stress caused by the direct exposure to H_2O_2 induces the accumulation of autophagosomes in primary cortical cultures and the genetic or pharmacological ablation of autophagy prevents neuronal death [88]. This result suggests that autophagy contributes to H_2O_2-induced oxidative stress and neuronal death. Furthermore, in SH-5YSY neuroblastoma cells, H_2O_2 exposure induces the activation of autophagy and the subsequent lysosome membrane permeabilization causing cell death [89, 90]. Inhibition of autophagy or prevention of lysosome membrane permeabilization protected cells against H_2O_2 damage. In contrast to H_2O_2 exposure, generation of $O_2^{\cdot-}$ by the xanthine + xanthine oxidase system causes neuronal death accompanied by autophagic features. Under these circumstances, ATG7 knockdown delays early cell death progression, suggesting the involvement of other cell death mechanisms in $O_2^{\cdot-}$-mediated oxidative stress damage [91].

Under acute stress such as traumatic brain injury, ischemia/reperfusion, and hypoxia, the excessive production of ROS leads to the loss of cellular homeostasis and autophagy induction [76]. Excessive production of ROS from NADPH oxidase and autophagy play an important role in neuronal death

INFORME DE LABORES 2019

induced by hypoxia-ischemia and ischemia/reperfusion in vitro and in vivo [92]. Treatment with the autophagy inhibitor 3-MA effectively reduces the abundance of autophagy markers and OGD-induced neuronal death. Moreover, inhibition of NADPH oxidase decreased autophagy in an OGD model, suggesting that oxidative stress-dependent autophagy, mediated by NADPH, contributes to brain injury [93]. On the other hand, during hypoxic conditions, autophagy can also be regulated by the hypoxia-inducible factor-1 (HIF1), a key player in the cellular response to hypoxia. HIF is stabilized by ROS and activates target genes such as BNIP3 and NIX [94]. In addition, BNIP3 and NIX are involved in mitophagy [95]. However, the direct activation of NIX-mediated mitophagy by ROS has not been explored.

The nuclear transcription factor NRF2 is considered as the master regulator of the antioxidant cell response [96]. NRF2 controls over 250 genes, including p62/SQSTM1, which in turn positively regulates NRF2. Under basal conditions, NRF2 is repressed by Keap1, which mediates its proteasomal degradation. However, ROS-induced autophagy leads to p62/SQSTM1 accumulation and sequestration of Keap1, leading to increased NRF2 signaling [97] (Fig. 2b).

Analysis of postmortem brain tissue from Alzheimer's patients supports the role of p62/SQSTM1 in NRF2 regulation during neurodegeneration. These samples show p62/SQSTM1 accumulation and co-localization with Keap1, suggesting that Keap1 is recruited to autophagosomes allowing NRF2 activity [98]. However, it is well known that autophagy is impaired in neurodegenerative diseases and thereby contributes to neuronal demise; thus, it is unknown to what extent autophagic degradation of Keap1 contributes to NRF2 transcriptional activity in Alzheimer's disease.

On the other hand, SIRT6, a NAD-dependent histone deacetylase, has been implicated in the regulation of metabolism, inflammation, and aging. SIRT6 deficiency leads to oxidative stress and mediates premature senescence-like phenotype, suggesting that disturbances in SIRT6 levels are involved in the aging process. Moreover, SIRT6 counteracts oxidative stress by transactivation of antioxidant genes like NRF2 [99]. SIRT6 stimulates the autophagy flux via attenuation of Akt/mTOR signaling under H_2O_2-induced oxidative stress (Fig. 2b). However, under these circumstances, inhibition of SIRT6 increases neuronal survival by suppressing autophagy [100].

On the other hand, SIRT6 can also modulate autophagy after cerebral ischemia. Reduced SIRT6 levels associate with the release of the high-mobility group box (HMGB1), a chromatin-associated nuclear protein that plays a pivotal function in inflammation and acts as autophagy effector [101]. HMGB1 interacts with BECN1 leading to its subsequent dissociation from Bcl-2 and autophagy activation under oxidative stress [102]. The mitochondrial inhibitor 3-nitropropionic acid (3-NP) induces oxidative stress, autophagy, and striatal neurodegeneration in vivo through HMGB1 activation. Pharmacological inhibition and shRNA targeting of HMGB1 reduces autophagy markers and striatal damage suggesting that HMGB1 is an important signaling molecule for autophagy in neurodegeneration induced by mitochondrial dysfunction [103]. During acute brain damage, HMGB1 is released from neurons and contributes to the inflammatory response. Particularly, after ischemia/reperfusion, HMGB1 mediates brain inflammatory injury and blocking HMGB1 function reverses the inflammatory response and brain damage [104]. Therefore, HMGB1 can be another mediator of oxidative stress-induced autophagy (Fig. 2b).

Altogether, the observations described above suggest that in response to ROS production and oxidative stress, autophagy plays a critical role in the maintenance of cellular homeostasis by degrading damaged proteins and organelles. Several molecules and proteins integrate ROS signals leading to autophagy activation. However, the correlation of autophagy markers with neuronal death under oxidative stress conditions suggests its contribution to neuronal damage, due to the impairment of this process, such as that resulting from the interruption of the autophagic flux. Therefore, genetic of pharmacologic ablation of autophagy confers protection against damage induced by oxidative stress. On the other hand, manipulations that enhance autophagy or stimulate the autophagy flux increase the resistance to oxidative stress conditions and promote cell survival.

ER Stress, UPR Activation, and Autophagy

The ER is an important organelle involved in cellular homeostasis and protein quality control. Several extracellular or intracellular stimuli can disturb ER homeostasis leading to ER stress. To counteract this condition, cells activate the UPR, which reestablishes ER function and ultimately cell homeostasis. Three ER transmembrane sensors, PERK (PKR-like ER kinase), IRE1 (Inositol-requiring enzyme 1), and ATF6 (activating transcription factor 6), orchestrate the UPR, which attenuates global protein translation, upregulates protein folding capacity, and executes programmed cell death. ER stress has been shown to induce autophagy through UPR signaling. Under these circumstances, autophagy functions as an adaptive response to alleviate ER stress.

The mechanisms involved in autophagy induction by activation of the UPR have not been completely elucidated but some reports have implicated GRP78/Bip. GRP78/Bip is an ER-resident chaperone that binds to and inhibits the three UPR sensors. Accumulation of unfolded proteins within the ER lumen recruits GRP78 releasing UPR sensors and allowing UPR activation. As mentioned above, GRP78 can regulate autophagy during ischemic preconditioning. Also, in primary cortical neurons, it has been reported that GRP78 can regulate autophagy. Exposure to cadmium produces ER stress,

which induces autophagy mediated by GRP78 upregulation. Conversely, GRP78 siRNA blocks the conversion of LC3-I to LC3-II and autophagosome formation. Furthermore, it is suggested that cadmium-induced GRP78 upregulation stimulates autophagy via AMPK activation [105] (Fig. 2c).

Under severe brain injury conditions such as hypoxia/ischemia, ER stress and UPR activation contribute to neuronal death [106]. In addition, the PERK and the IRE1 branches of the UPR can activate autophagy [107]. However, the role of autophagy in ischemic injury is still controversial. During ischemic preconditioning, mild ER stress induces autophagy and confers neuroprotection against the ischemic insult. Therefore, inhibition of ER stress and subsequent autophagy activation inhibits neuroprotection elicited by ischemic preconditioning [106]. Moreover, mild ER stress induced by tunicamycin triggers an autophagic response, which protects against 6-OHDA toxicity in mice [108]. On the other hand, it has been shown in in vitro and in vivo models of ischemia-reperfusion that autophagy is activated during the reperfusion phase contributing to the clearance of damaged mitochondria. In agreement, pharmacological or genetic inhibition of autophagy enhanced neuronal damage [109]. In accordance with these results, tunicamycin and thapsigargin administration during reperfusion confers protection against transient ischemia, enhancing autophagy, particularly mitophagy, through PERK-eIF2a-ATF4 signaling [110] (Fig. 2c).

ER stress and UPR dysfunction play an important role in the pathogenesis of neurodegenerative diseases and aging. In Huntington's disease models, upregulation of IRE1 kinase activity leads to impaired autophagic flux and thereby accumulation of mHTT, while reduction of IRE1 expression or inhibition of its kinase activity reduced the accumulation of mHTT [111]. However, how IRE1 inhibits the autophagy flux still remains to be elucidated.

IRE1 can induce autophagy by recruiting TRAF2/ASK and the activation of JNK, which phosphorylates Bcl-2, disrupting its interaction with BECN1, thereby activating autophagy [112] (Fig. 1c). This signaling depends on IRE1 kinase activity. In streptozotocin-induced diabetic mice, ER stress and UPR lead to cognitive decline. In this condition, autophagy activation through the JNK pathway counteracts ER stress-associated neuronal damage [113]. In addition, IRE1 RNAse activity can inhibit autophagy through the downregulation of FOXO1, a transcription factor that regulates autophagy through the upregulation of ATG5, LC3, and BECN1 transcription [114] (Fig. 2c). It has been shown in a transgenic mice model expressing mHTT that IRE1 RNAse activity leads to XBP-1 alternative splicing, which downregulates FOXO1 promoting its degradation by the proteasome. Thus, XBP1 deficiency enhances FOXO1 expression and autophagy reducing HD neurodegeneration [115]. These results suggest that IRE can induce opposite effects on autophagy activation through either its mRNAse or kinase activity.

The PERK branch of the UPR has been also implicated in autophagy. It has been reported that polyQ aggregates induce the activation of PERK/eIF2α-dependent autophagy, as defense mechanism against polyQ-induced cell death. PERK/eIF2α activates autophagy possibly through the upregulation of ATG12 mRNA and increased ATG5-dependent LC3 lipidation [116]. Furthermore, it is known that ATF4 and CHOP, the downstream transcription factors of the PERK pathway, induce the expression of autophagy genes such as ATG12, ATG5, LC3, and BECN1, connecting UPR signaling and autophagy (Fig. 2c) [117].

Proteotoxic Stress and Autophagy

Neurons are particularly vulnerable to the accumulation of misfolded proteins; due to their post-mitotic nature, protein aggregates cannot be dissipated by cell division. Additionally, the decline of degradation systems with advancing age further contributes to neuronal vulnerability. Approximately 30% of the newly synthetized proteins are misfolded and prone to form aggregates interfering with normal cellular function [118]. Therefore, quality control systems continuously operate to manage the flux of misfolded proteins and maintain proteostasis. This quality control machinery involves refolding (chaperones) and degradation (autophagy and ubiquitin proteasome system). The ubiquitin proteasome system (UPS) represents the first line of defense against misfolded proteins; however, aggregates or oligomeric forms of misfolded proteins are not efficiently degraded by the proteasome. Moreover, accumulation of protein aggregates leads to proteasome inhibition resulting in further accumulation of misfolded proteins [119]. Conversely, autophagy can target large protein complexes, aggregates, and organelles. Upon UPS inhibition, autophagy activity increases as a compensatory mechanism to alleviate subsequent proteotoxic stress [120]. Basal neuronal autophagy is critical to prevent the accumulation of ubiquitinated proteins and inclusion bodies, which can disrupt neuronal function [18, 19]. Thus, any genetic or pharmacologic manipulation that enhance autophagy results in the clearance of a variety of aggregate-prone disease proteins.

As we mentioned before, p62/SQSTM1 is the best-characterized autophagy receptor with a role in the clearance of ubiquitinated proteins, aggregates, and organelles [17]. Additionally, it has been identified as a common component of neuronal protein inclusions in several neurodegenerative diseases [121]. Phosphorylation of p62/SQSTM1 at serine 403 by casein kinase 2 (CSK2) increases the affinity of p62/SQSTM1 for polyubiquitinated proteins and the subsequent autophagy-mediated degradation. Overexpression of CSK2 reduces the formation of mutant huntingtin large inclusions [122]. Moreover, overexpression of mHTT induces the expression of p62/SQSTM1, suggesting that p62 plays an important role

in response to proteotoxicity [123]. Likewise, proteotoxic stress induced by proteasome inhibition or expression of polyQ-HTT causes ULK1-dependent phosphorylation of p62/SQSTM1 at S409. This phosphorylation increases binding affinity of p62 to ubiquitinated proteins. In contrast, phosphorylation of p62/SQSTM1 by ULK1 does not occur under amino acid or glucose deprivation, suggesting that ULK1-p62/SQSTM1 cascade is involved in the sensing of proteotoxic stress [124]. However, the upstream signaling pathway which activates ULK1-p62/SQSTM1 cascade remains unknown.

Another protein involved in the interplay between proteasome and autophagy is the histone deacetylase 6 (HDAC6), a microtubule-associated deacetylase that interacts with polyubiquitinated proteins. In Drosophila, HDAC6 activity is critical for autophagy in order to compensate UPS impairment. Furthermore, ectopic expression of HDAC6 is sufficient to prevent degeneration caused by proteasome inhibition and polyQ toxicity [125]. Additionally, HDAC6 controls the fusion of autophagosome with lysosomes in basal autophagy that targets protein aggregates. HDAC6 recruits and activates an actin-remodeling factor, cortactin, to the autophagy substrates and the subsequent assembly of F-actin network that facilitates the fusion of the autophagosome with the lysosome [126] (Fig. 2d). Interestingly, HDAC6 is not required for starvation-induced autophagy.

These two ubiquitin-binding proteins, p62/SQSTM1 and HDAC6, confer specificity to quality control by autophagy and distinguish aberrant protein aggregates and damaged organelles from normal ones. p62/SQSTM1 and HDAC6 bind preferentially lysine 63 (K63)-linked ubiquitinated proteins. Deletion of p62/SQSTM1 or HDAC6 induces a robust accumulation of K63-linked ubiquitin chains in mice brain and MEFs, respectively. This suggests that the specific type of ubiquitin chains added to misfolded proteins determines to which degradative pathway they are delivered [119]. On the other hand, CHIP, a chaperone-dependent ubiquitin E3 ligase, can form a complex with UBC3, which catalyzes the formation of ubiquitin chains in K63. Thus, this complex can direct the degradation of misfolded proteins via autophagy (Fig. 2d). In addition, CHIP colocalizes with α-synuclein and Hsp70 in Lewy bodies a hallmark of Parkinson disease, suggesting that CHIP plays a role in α-synuclein aggregation and degradation. Overexpression of CHIP promotes the degradation of α-synuclein by both proteasome- and autophagy-dependent mechanisms [127].

ALFY (autophagy-linked FYVE protein) has been shown to colocalize with ubiquitin and p62/SQSTM1-positive aggregates under stress conditions [128]. This protein acts as a scaffold which interacts with p62/SQSTM1 and ATG5 and recruits the autophagy machinery toward protein aggregates (Fig. 2d). ALFY is essential for selective autophagy under proteotoxic stress and its overexpression decreases the accumulation of polyQ-HTT and confers neuroprotection [129]. Conversely, ablation of ALFY in Drosophila results in the accelerated accumulation of ubiquitinated-positive inclusions and neuronal degeneration [130]. Tollip is another ubiquitin-binding protein with a role in the clearance of cytotoxic proteins such as polyQ-HTT. Tollip binds to polyubiquitinated proteins with high affinity compared to p62/SQSTM1 and may function cooperatively with p62/SQSTM1 in selective autophagy [131]. Interestingly, Tollip is downregulated in brain tissue samples from aged and Alzheimer's affected humans [132].

Besides protein aggregates, damaged organelles such as mitochondria are tagged with ubiquitin to trigger selective autophagy (mitophagy). Upon mitochondrial damage, the ubiquitin kinase PINK1 is translocated toward the outer membrane of mitochondria and phosphorylates ubiquitin. This activates the ubiquitin ligase Parkin, which builds ubiquitin chains to recruit autophagy receptors and subsequently the autophagy machinery. Under these conditions, PINK1 recruits the autophagy receptors NDP52 and optineurin but not p62/SQSTM1 [133]. Dysfunctional mitophagy is associated with degeneration in several neurodegenerative disorders (reviewed in [134, 135]).

Aging and Autophagy

Aging is associated with the loss of proteostasis, accumulation of altered macromolecules, and a decreased turnover of cellular components [136]. Reduced protein degradation can result from alterations in the autophagic/lysosomal system that finally contributes to the aging process [137]. In aged tissues, reduced expression of ATG proteins and other proteins required for autophagy induction has been reported. Particularly, in the human aged brain, key autophagy genes such as Atg5, Atg7, and BECN1 are downregulated, suggesting that normal aging is associated with decreased autophagy [138]. As previously mentioned, autophagy plays a protective role against neurodegenerative diseases; hence, its downregulation during aging might contribute to the predisposition to neurodegenerative diseases. Moreover, a decline in synaptic plasticity and deficient memory and cognitive function related to aging can be associated with the progressive transcriptional downregulation of autophagy genes [138, 139]. In addition, several autophagy proteins including ATG5-ATG12 and BECN1 complexes are highly reduced in old murine brains suggesting low levels of basal autophagy [140]. Furthermore, old brain tissue shows a significant increase in the protein level of mTOR, suggesting enhanced mTOR activity, which together with decreased autophagy machinery, may play an important role in the age-related impairment of autophagy [140].

A role of autophagy as an anti-aging mechanism has been suggested. Several interventions that modulate metabolism (augmenting ketone bodies), energy intake (caloric restriction), and energy expenditure (exercise) are shown to enhance

INFORME DE LABORES 2019

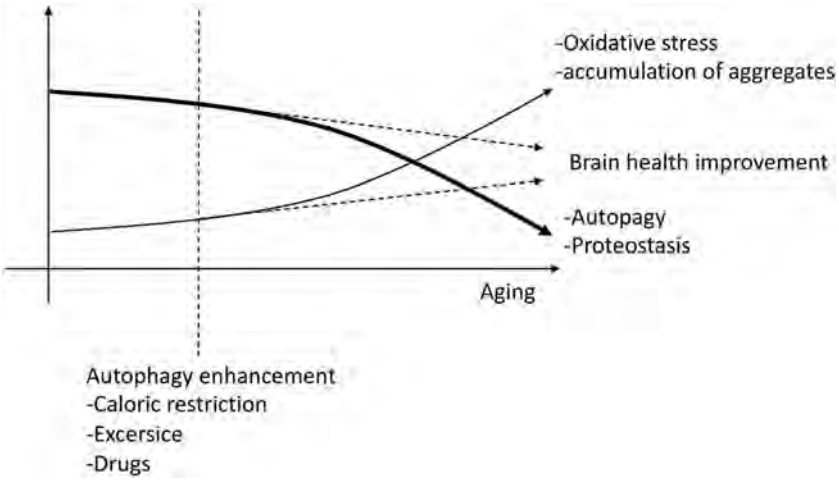

Fig. 3 Autophagy decreases with age leading to loss of proteostasis, accumulation of protein aggregates, and oxidative stress. Any intervention that enhances autophagy results in brain health improvement

autophagy and improve brain health. Inhibition of insulin-like growth factor promotes autophagy and shows an anti-aging effect extending the life span in some species such as the worm *C. elegans* [141]. Moreover, autophagy is required for dietary restriction to extend *C. elegans* life span [142]. Furthermore, caloric restriction delays the onset of age-associated pathologies including brain atrophy and extends life span in the rhesus monkey [143]. Likewise, in rodent models, caloric restriction extends the life span and reduces several age-associated process [144], although it is still not clear whether these effects are mediated by increased autophagy. Long-term exercise training ameliorates cognitive decline in aged rats and reduces oxidative stress. These effects are associated with the activation of autophagy in the hippocampus, which promotes mitochondrial recycling (mitophagy) [145]. Synaptic dysfunction is an early feature of aging that precedes neuronal loss and ultimately neurodegeneration. Therefore, restoration of synaptic homeostasis through the stimulation of autophagy has become a common strategy in order to help neurons to clear damaged proteins or aggregates [33]. Administration of spermidine increases the viability in an autophagy-dependent manner in several types of cells, including neurons [146]. Furthermore, this natural polyamine suppresses memory impairment by counteracting age-dependent synapse dysfunction in Drosophila. Conversely, memory improvement is impaired by deletion of Atg7 and Atg8 autophagy genes [147].

In addition to these findings, it has been observed that skeletal neuromuscular junctions of aged mice display a variety of alterations including axonal swelling and synaptic detachment, associated with autophagy impairment [148, 149]. Moreover, inhibition of autophagy exacerbates neuromuscular synaptic dysfunction and promotes the aging phenotype. Conversely, stimulation of autophagy by caloric restriction or exercise decreases pre- and post-synaptic abnormalities and reduces the loss of motor neurons in aged mice [148]. In agreement, it has been observed that metformin, an AMPK activator and a well-known autophagy inducer, mimics caloric restriction benefits in health. Long-term treatment with metformin counteracts oxidative stress augmenting the antioxidant defense and autophagy, suggesting that metformin promotes healthy aging in the brain [150]. Altogether, these observations lead to the suggestion that impaired autophagy contributes to brain aging and that pharmacologic or nutritional strategies to induce autophagy favor healthy brain aging (Fig. 3).

Conclusions

Autophagy is a major degradation system responsible for the turnover of cytoplasmic material in order to maintain cellular homeostasis. Particularly in neurons, autophagy plays a crucial role in the maintenance of protein and organelle

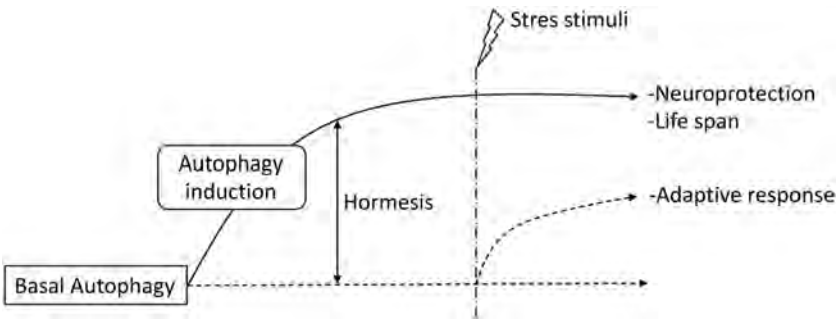

Fig. 4 Autophagy induction in the absence of stress stimuli leads to hormesis. Pharmacologic or nutritional manipulations that induce autophagy increase the resistance to stressful conditions resulting in neuroprotection or extended life span

homeostasis due to their post-mitotic nature. Besides its housekeeping role, autophagy is especially relevant as an adaptive mechanism in response to several stressful conditions to restore homeostasis and promote cell survival. However, autophagy has been implicated in neuronal damage, particularly that associated with acute injury, as autophagy markers correlate with cell death. Hence, ablation of autophagy elicits beneficial effects against brain injury. Nevertheless, in many reports, the lack of evidence to demonstrate whether the accumulation of autophagy markers (i.e., LC3-II, autophagosomes) results from the induction of autophagy or from the impairment of the autophagy flux has made it difficult to conclude about the role of autophagy. Therefore, in order to prove that autophagy is involved in cell death, it is essential to use both pharmacologic and genetic tools to inhibit autophagy components. On the other hand, under severe and prolonged stress insults, autophagy failure such as that induced by lysosome membrane permeabilization can trigger other cell death mechanisms, leading to the misconception that autophagy contributes to cell death. Finally, it is becoming clear that treatments that enhance autophagy (i.e., pharmacologic, nutritional, or preconditioning) or promote the autophagy flux increase resistance to acute stress and extend life span, supporting the idea of autophagy as an adaptive response (Fig. 4).

Funding LM was supported by PAPIIT IN205416 grant from Universidad Nacional Autónoma de México and CGO from Estímulos a Investigaciones Médicas Miguel Alemán Valdés.

Compliance with Ethical Standards

Conflict of Interest The authors declare that they have no conflict of interest.

References

1. Levine B, Klionsky DJ (2004) Development by self-digestion: molecular mechanisms and biological functions of autophagy. Dev Cell 6:463–477. https://doi.org/10.1016/S1534-5807(04)00099-1
2. He C, Klionsky DJ (2009) Regulation mechanisms and signaling pathways of autophagy. Annu Rev Genet 43:67–93. https://doi.org/10.1146/annurev-genet-102808-114910
3. Yang Z, Klionsky DJ (2010) Eaten alive: a history of macroautophagy. Nat Cell Biol 12:814–822. https://doi.org/10.1038/ncb0910-814
4. Høyer-Hansen M, Bastholm L, Szyniarowski P, Campanella M, Szabadkai G, Farkas T, Bianchi K, Fehrenbacher N et al (2007) Control of macroautophagy by calcium, calmodulin-dependent kinase kinase-β, and Bcl-2. Mol Cell 25:193–205. https://doi.org/10.1016/J.MOLCEL.2006.12.009
5. Li WW, Li J, Bao JK (2012) Microautophagy: lesser-known self-eating. Cell Mol Life Sci 69:1125–1136. https://doi.org/10.1007/s00018-011-0865-5
6. Arias E, Cuervo AM (2011) Chaperone-mediated autophagy in protein quality control. Curr Opin Cell Biol 23:184–189. https://doi.org/10.1016/j.ceb.2010.10.009
7. Weidberg H, Shvets E, Elazar Z (2011) Biogenesis and cargo selectivity of autophagosomes. Annu Rev Biochem 80:125–156. https://doi.org/10.1146/annurev-biochem-052709-094552
8. Rubinsztein DC, Shpilka T, Elazar Z (2012) Mechanisms of autophagosome biogenesis. Curr Biol 22:R29–R34. https://doi.org/10.1016/j.cub.2011.11.034
9. Kroemer G, Mariño G, Levine B (2010) Autophagy and the integrated stress response. Mol Cell 40:280–293. https://doi.org/10.1016/j.molcel.2010.09.023
10. Geng J, Klionsky DJ (2008) The Atg8 and Atg12 ubiquitin-like conjugation systems in macroautophagy. "Protein Modifications: Beyond the Usual Suspects" Review Series. EMBO Rep 9:859–864. https://doi.org/10.1038/embor.2008.163
11. Shpilka T, Weidberg H, Pietrokovski S, Elazar Z (2011) Atg8: an autophagy-related ubiquitin-like protein family. Genome Biol 12:226. https://doi.org/10.1186/gb-2011-12-7-226
12. Gutierrez MG, Munafó DB, Berón W, Colombo MI (2004) Rab7 is required for the normal progression of the autophagic pathway in mammalian cells. J Cell Sci 117:2687–2697
13. Tanida I (2011) Autophagy basics. Microbiol Immunol 55:1–11. https://doi.org/10.1111/j.1348-0421.2010.00271.x
14. Codogno P, Mehrpour M, Proikas-Cezanne T (2011) Canonical and non-canonical autophagy: variations on a common theme of self-eating? Nat Rev Mol Cell Biol 13:7–12
15. Grishchuk Y, Ginet V, Truttmann AC, Clarke PGH, Puyal J (2011) Beclin 1-independent autophagy contributes to apoptosis in cortical neurons. Autophagy 7:1115–1131. https://doi.org/10.4161/auto.7.10.16608
16. Nishida Y, Arakawa S, Fujitani K, Yamaguchi H, Mizuta T, Kanaseki T, Komatsu M, Otsu K et al (2009) Discovery of Atg5/Atg7-independent alternative macroautophagy. Nature 461:654–658
17. Stolz A, Ernst A, Dikic I (2014) Cargo recognition and trafficking in selective autophagy. Nat Cell Biol 16:495–501. https://doi.org/10.1038/ncb2979
18. Hara T, Nakamura K, Matsui M, Yamamoto A, Nakahara Y, Suzuki-Migishima R, Yokoyama M, Mishima K et al (2006) Suppression of basal autophagy in neural cells causes neurodegenerative disease in mice. Nature 441:885–889. https://doi.org/10.1038/nature04724
19. Komatsu M, Waguri S, Chiba T, Murata S, Iwata JI, Tanida I, Ueno T, Koike M et al (2006) Loss of autophagy in the central nervous system causes neurodegeneration in mice. Nature 441:880–884. https://doi.org/10.1038/nature04723
20. Liang CC, Wang C, Peng X, Gan B, Guan JL (2010) Neural-specific deletion of FIP200 leads to cerebellar degeneration caused by increased neuronal death and axon degeneration. J Biol Chem 285:3499–3509. https://doi.org/10.1074/jbc.M109.072389
21. Frake RA, Menzies FM, David C et al (2015) Autophagy and neurodegeneration. J Clin Invest 125:65–74. https://doi.org/10.1172/JCI73944
22. Nixon RA, Yang DS, Lee JH (2008) Neurodegenerative lysosomal disorders: a continuum from development to late age. Autophagy 4:590–599. https://doi.org/10.4161/auto.6259
23. Ravikumar B, Vacher C, Berger Z, Davies JE, Luo S, Oroz LG, Scaravilli F, Easton DF et al (2004) Inhibition of mTOR induces autophagy and reduces toxicity of polyglutamine expansions in fly and mouse models of Huntington disease. Nat Genet 36:585–595. https://doi.org/10.1038/ng1362

24. Tanaka M, Machida Y, Niu S, Ikeda T, Jana NR, Doi H, Kurosawa M, Nekooki M et al (2004) Trehalose alleviates polyglutamine-mediated pathology in a mouse model of Huntington disease. Nat Med 10:148–154. https://doi.org/10.1038/nm985
25. Sarkar S, Davies JE, Huang Z, Tunnacliffe A, Rubinsztein DC (2007) Trehalose, a novel mTOR-independent autophagy enhancer, accelerates the clearance of mutant huntingtin and α-synuclein. J Biol Chem 282:5641–5652. https://doi.org/10.1074/jbc.M609532200
26. Liu Y, Levine B (2015) Autosis and autophagic cell death: the dark side of autophagy. Cell Death Differ 22:367–376. https://doi.org/10.1038/cdd.2014.143
27. Liu Y, Shoji-Kawata S, Sumpter RM, Wei Y, Ginet V, Zhang L, Posner B, Tran KA et al (2013) Autosis is a Na+,K+-ATPase-regulated form of cell death triggered by autophagy-inducing peptides, starvation, and hypoxia-ischemia. Proc Natl Acad Sci U S A 110:20364–20371. https://doi.org/10.1073/pnas.1319661110
28. Galluzzi L, Bravo-San Pedro JM, Blomgren K, Kroemer G (2016) Autophagy in acute brain injury. Nat Rev Neurosci 17:467–484. https://doi.org/10.1038/nrn.2016.51
29. Kulkarni VV, Maday S (2018) Compartment-specific dynamics and functions of autophagy in neurons. Dev Neurobiol 78:298–310. https://doi.org/10.1002/dneu.22562
30. Maday S, Wallace KE, Holzbaur ELF (2012) Autophagosomes initiate distally and mature during transport toward the cell soma in primary neurons. J Cell Biol 196:407 LP–407417
31. Maday S, Holzbaur ELF (2014) Autophagosome biogenesis in primary neurons follows an ordered and spatially regulated pathway. Dev Cell 30:71–85. https://doi.org/10.1016/J.DEVCEL.2014.06.001
32. Goo MS, Sancho L, Slepak N et al (2017) Activity-dependent trafficking of lysosomes in dendrites and dendritic spines. J Cell Biol 16:2499–2513
33. Vijayan V, Verstreken P (2017) Autophagy in the presynaptic compartment in health and disease. J Cell Biol 216:1895–1906
34. Hernandez D, Torres CA, Setlik W, Cebrián C, Mosharov EV, Tang G, Cheng HC, Kholodilov N et al (2012) Regulation of presynaptic neurotransmission by macroautophagy. Neuron 74:277–284. https://doi.org/10.1016/J.NEURON.2012.02.020
35. Torres CA, Sulzer D (2012) Macroautophagy can press a brake on presynaptic neurotransmission. Autophagy 8:1540–1541. https://doi.org/10.4161/auto.21330
36. Shehata M, Matsumura H, Okubo-Suzuki R et al (2012) Neuronal stimulation induces autophagy in hippocampal neurons that is involved in AMPA receptor degradation after chemical long-term depression. J Neurosci 32:10413 LP–10410422
37. Baek KH, Park J, Shin I (2012) Autophagy-regulating small molecules and their therapeutic applications. Chem Soc Rev 41:3245–3263. https://doi.org/10.1039/c2cs15328a
38. Demetriades C, Doumpas N, Teleman AA (2014) Regulation of TORC1 in response to amino acid starvation via lysosomal recruitment of TSC2. Cell 156:786–799. https://doi.org/10.1016/j.cell.2014.01.024
39. McAlpine F, Williamson LE, Tooze SA, Chan EYW (2013) Regulation of nutrient-sensitive autophagy by uncoordinated 51-like kinases 1 and 2. Autophagy 9:361–373. https://doi.org/10.4161/auto.23066
40. Wong P-M, Puente C, Ganley IG, Jiang X (2013) The ULK1 complex. Autophagy 9:124–137. https://doi.org/10.4161/auto.23323
41. Plomp PJAM, Wolvetang EJ, Groen AK et al (1987) Energy dependence of autophagic protein degradation in isolated rat hepatocytes. Eur J Biochem 164:197–203. https://doi.org/10.1111/j.1432-1033.1987.tb11011.x
42. Mizushima N, Yamamoto A, Matsui M, Yoshimori T, Ohsumi Y (2004) In vivo analysis of autophagy in response to nutrient starvation using transgenic mice expressing a fluorescent autophagosome marker. Mol Biol Cell 15:1101–1111
43. Alirezaei M, Kemball CC, Flynn CT, Wood MR, Whitton JL, Kiosses WB (2010) Short-term fasting induces profound neuronal autophagy. Autophagy 6:702–710. https://doi.org/10.4161/auto.6.6.12376
44. Kaushik S, Rodriguez-Navarro JA, Arias E, Kiffin R, Sahu S, Schwartz GJ, Cuervo AM, Singh R (2011) Autophagy in hypothalamic AgRP neurons regulates food intake and energy balance. Cell Metab 14:173–183. https://doi.org/10.1016/J.CMET.2011.06.008
45. Meng Q, Cai D (2011) Defective hypothalamic autophagy directs the central pathogenesis of obesity via the IkappaB kinase beta (IKKbeta)/NF-kappaB pathway. J Biol Chem 286:32324–32332. https://doi.org/10.1074/jbc.M111.254417
46. Young JE, Martinez RA, La Spada AR (2009) Nutrient deprivation induces neuronal autophagy and implicates reduced insulin signaling in neuroprotective autophagy activation. J Biol Chem 284:2363–2373. https://doi.org/10.1074/jbc.M806088200
47. Maday S, Holzbaur ELF (2016) Compartment-specific regulation of autophagy in primary neurons. J Neurosci 36:5933 LP–5935945
48. Gerónimo-Olvera C, Montiel T, Rincon-Heredia R, Castro-Obregón S, Massieu L (2017) Autophagy fails to prevent glucose deprivation/glucose reintroduction-induced neuronal death due to calpain-mediated lysosomal dysfunction in cortical neurons. Cell Death Dis 8:e2911. https://doi.org/10.1038/cddis.2017.299
49. Camberos-Luna L, Gerónimo-Olvera C, Montiel T, Rincon-Heredia R, Massieu L (2016) The ketone body, β-hydroxybutyrate stimulates the autophagic flux and prevents neuronal death induced by glucose deprivation in cortical cultured neurons. Neurochem Res 41:600–609. https://doi.org/10.1007/s11064-015-1700-4
50. Jang BG, Choi BY, Kim JH et al (2013) Impairment of autophagic flux promotes glucose reperfusion-induced neuro2A cell death after glucose deprivation. PLoS One 8:e76466. https://doi.org/10.1371/journal.pone.0076466
51. Xu L, Ash JD (2016) The role of AMPK pathway in neuroprotection. In: Retinal degenerative diseases. Adv Exp Med Biol 854:425–430
52. Kim J, Kundu M, Viollet B, Guan K-L (2011) AMPK and mTOR regulate autophagy through direct phosphorylation of Ulk1. Nat Cell Biol 13:132–141
53. Oh TS, Cho H, Cho JH, Yu SW, Kim EK (2016) Hypothalamic AMPK-induced autophagy increases food intake by regulating NPY and POMC expression. Autophagy 12:2009–2025. https://doi.org/10.1080/15548627.2016.1215382
54. Wei K, Wang P, Miao C-Y (2012) A double-edged sword with therapeutic potential: an updated role of autophagy in ischemic cerebral injury. CNS Neurosci Ther 18:879–886. https://doi.org/10.1111/cns.12005
55. Wang P, Shao B-Z, Deng Z, Chen S, Yue Z, Miao CY (2018) Autophagy in ischemic stroke. Prog Neurobiol 163–164:98–117. https://doi.org/10.1016/J.PNEUROBIO.2018.01.001
56. Fu L, Huang L, Cao C, Yin Q, Liu J (2016) Inhibition of AMP-activated protein kinase alleviates focal cerebral ischemia injury in mice: interference with mTOR and autophagy. Brain Res 1650:103–111. https://doi.org/10.1016/J.BRAINRES.2016.08.035
57. Jiang T, Yu J-T, Zhu X-C, Wang HF, Tan MS, Cao L, Zhang QQ, Gao L et al (2014) Acute metformin preconditioning confers neuroprotection against focal cerebral ischaemia by pre-activation of AMPK-dependent autophagy. Br J Pharmacol 171:3146–3157. https://doi.org/10.1111/bph.12655
58. Lu N, Li X, Tan R, An J, Cai Z, Hu X, Wang F, Wang H et al (2018) HIF-1α/Beclin1-mediated autophagy is involved in

INFORME DE LABORES 2019

neuroprotection induced by hypoxic preconditioning. J Mol Neurosci 66:238–250. https://doi.org/10.1007/s12031-018-1162-7

59. Ney PA (2015) Mitochondrial autophagy: origins, significance, and role of BNIP3 and NIX. Biochim Biophys Acta 1853:2775–2783. https://doi.org/10.1016/J.BBAMCR.2015.02.022
60. Zhan L, Chen S, Li K et al (2017) Autophagosome maturation mediated by Rab7 contributes to neuroprotection of hypoxic preconditioning against global cerebral ischemia in rats. Cell Death Dis 8:e2949
61. Singh AK, Kashyap MP, Tripathi VK, Singh S, Garg G, Rizvi SI (2017) Neuroprotection through rapamycin-induced activation of autophagy and PI3K/Akt1/mTOR/CREB signaling against amyloid-β-induced oxidative stress, synaptic/neurotransmission dysfunction, and neurodegeneration in adult rats. Mol Neurobiol 54:5815–5828. https://doi.org/10.1007/s12035-016-0129-3
62. Carloni S, Girelli S, Scopa C, Buonocore G, Longini M, Balduini W (2010) Activation of autophagy and Akt/CREB signaling play an equivalent role in the neuroprotective effect of rapamycin in neonatal hypoxia-ischemia. Autophagy 6:366–377. https://doi.org/10.4161/auto.6.3.11261
63. Zhang X-Y, Zhang T-T, Song D-D, Zhou JH, Han R, Qin ZH, Sheng R (2015) Endoplasmic reticulum chaperone GRP78 is involved in autophagy activation induced by ischemic preconditioning in neural cells. Mol Brain 8:20. https://doi.org/10.1186/s13041-015-0112-3
64. Casas C (2017) GRP78 at the centre of the stage in cancer and neuroprotection. Front Neurosci 11:177. https://doi.org/10.3389/fnins.2017.00177
65. Cha-Molstad H, Yu JE, Lee SH, Kim JG, Sung KS, Hwang J, Yoo YD, Lee YJ et al (2016) Modulation of SQSTM1/p62 activity by N-terminal arginylation of the endoplasmic reticulum chaperone HSPA5/GRP78/BiP. Autophagy 12:426–428. https://doi.org/10.1080/15548627.2015.1126047
66. Sheng R, Liu X-Q, Zhang L-S, Gao B, Han R, Wu YQ, Zhang XY, Qin ZH (2012) Autophagy regulates endoplasmic reticulum stress in ischemic preconditioning. Autophagy 8:310–325. https://doi.org/10.4161/auto.18673
67. Ng F, Tang BL (2013) Sirtuins' modulation of autophagy. J Cell Physiol 228:2262–2270. https://doi.org/10.1002/jcp.24399
68. Lee IH, Cao L, Mostoslavsky R et al (2008) A role for the NAD-dependent deacetylase Sirt1 in the regulation of autophagy. Proc Natl Acad Sci 105:3374 LP–3373379
69. Araki T, Sasaki Y, Milbrandt J (2004) Increased nuclear NAD biosynthesis and SIRT1 activation prevent axonal degeneration. Science (80-) 305:1010 LP–1011013
70. Parker JA, Arango M, Abderrahmane S, Lambert E, Tourette C, Catoire H, Néri C (2005) Resveratrol rescues mutant polyglutamine cytotoxicity in nematode and mammalian neurons. Nat Genet 37:349–350
71. Deng H, Mi M (2016) Resveratrol attenuates Aβ25-35 caused neurotoxicity by inducing autophagy through the TyrRS-PARP1-SIRT1 signaling pathway. Neurochem Res 41:2367–2379. https://doi.org/10.1007/s11064-016-1950-9
72. Liu G, Park S-H, Imbesi M, Nathan WJ, Zou X, Zhu Y, Jiang H, Parisiadou L et al (2016) Loss of NAD-dependent protein deacetylase sirtuin-2 alters mitochondrial protein acetylation and dysregulates mitophagy. Antioxid Redox Signal 26:849–863. https://doi.org/10.1089/ars.2016.6662
73. Gal J, Bang Y, Choi HJ (2012) SIRT2 interferes with autophagy-mediated degradation of protein aggregates in neuronal cells under proteasome inhibition. Neurochem Int 61:992–1000. https://doi.org/10.1016/J.NEUINT.2012.07.010
74. Popa-Wagner A, Mitran S, Sivanesan S, Chang E, Buga AM (2013) ROS and brain diseases: the good, the bad, and the ugly. Oxidative Med Cell Longev 2013:963520–963514. https://doi.org/10.1155/2013/963520
75. Kim GH, Kim JE, Rhie SJ, Yoon S (2015) The role of oxidative stress in neurodegenerative diseases. Exp Neurobiol 24:325–340. https://doi.org/10.5607/en.2015.24.4.325
76. Li L, Tan J, Miao Y, Lei P, Zhang Q (2015) ROS and autophagy: interactions and molecular regulatory mechanisms. Cell Mol Neurobiol 35:615–621. https://doi.org/10.1007/s10571-015-0166-x
77. Scherz-Shouval R, Shvets E, Fass E, Shorer H, Gil L, Elazar Z (2007) Reactive oxygen species are essential for autophagy and specifically regulate the activity of Atg4. EMBO J 26:1749–1760
78. Li L, Chen Y, Gibson SB (2013) Starvation-induced autophagy is regulated by mitochondrial reactive oxygen species leading to AMPK activation. Cell Signal 25:50–65. https://doi.org/10.1016/J.CELLSIG.2012.09.020
79. Chen Y, Azad MB, Gibson SB (2009) Superoxide is the major reactive oxygen species regulating autophagy. Cell Death Differ 16:1040–1052
80. Chen Y, McMillan-Ward E, Kong J et al (2007) Mitochondrial electron-transport-chain inhibitors of complexes I and II induce autophagic cell death mediated by reactive oxygen species. J Cell Sci 120:4155 LP–4154166
81. Mader BJ, Pivtoraiko VN, Flippo HM, Klocke BJ, Roth KA, Mangieri LR, Shacka JJ (2012) Rotenone inhibits autophagic flux prior to inducing cell death. ACS Chem Neurosci 3:1063–1072. https://doi.org/10.1021/cn300145z
82. Lin TK, Der Chen S, Chuang YC et al (2014) Resveratrol partially prevents rotenone-induced neurotoxicity in dopaminergic SH-SY5Y cells through induction of heme oxygenase-1 dependent autophagy. Int J Mol Sci 15:1625–1646. https://doi.org/10.3390/ijms15011625
83. Zhu JH, Horbinski C, Guo F, Watkins S, Uchiyama Y, Chu CT (2007) Regulation of autophagy by extracellular signal-regulated protein kinases during 1-methyl-4-phenylpyridinium-induced cell death. Am J Pathol 170:75–86. https://doi.org/10.2353/ajpath.2007.060524
84. Garcia-garcia A, Anandhan A, Burns M et al (2018) Impairment of Atg5-dependent autophagic flux promotes paraquat- and MPP+-induced apoptosis but not rotenone or 6-hydroxydopamine toxicity. Toxicol Sci 136:166–182. https://doi.org/10.1093/toxsci/kft188
85. Tzeng YW, Lee LY, Chao PL, Lee HC, Wu RT, Lin AMY (2010) Role of autophagy in protection afforded by hypoxic preconditioning against MPP+-induced neurotoxicity in SH-SY5Y cells. Free Radic Biol Med 49:839–846. https://doi.org/10.1016/J.FREERADBIOMED.2010.06.004
86. Zhang Y, Wu JY, Weng LH, Li XX, Yu LJ, Xu Y (2017) Valproic acid protects against MPP+-mediated neurotoxicity in SH-SY5Y cells through autophagy. Neurosci Lett 638:60–68. https://doi.org/10.1016/J.NEULET.2016.12.017
87. Wu Y, Li X, Xie W, Jankovic J, le W, Pan T (2010) Neuroprotection of deferoxamine on rotenone-induced injury via accumulation of HIF-1α and induction of autophagy in SH-SY5Y cells. Neurochem Int 57:198–205. https://doi.org/10.1016/J.NEUINT.2010.05.008
88. Higgins GC, Devenish RJ, Beart PM, Nagley P (2011) Autophagic activity in cortical neurons under acute oxidative stress directly contributes to cell death. Cell Mol Life Sci 68:3725–3740. https://doi.org/10.1007/s00018-011-0667-9
89. Castino R, Bellio N, Follo C, Murphy D, Isidoro C (2010) Inhibition of Pi3k class III-dependent autophagy prevents apoptosis and necrosis by oxidative stress in dopaminergic neuroblastoma cells. Toxicol Sci 117:152–162. https://doi.org/10.1093/toxsci/kfq170

90. Castino R, Fiorentino I, Cagnin M, Giovia A, Isidoro C (2011) Chelation of lysosomal iron protects dopaminergic SH-SY5Y neuroblastoma cells from hydrogen peroxide toxicity by precluding autophagy and Akt dephosphorylation. Toxicol Sci 123:523–541. https://doi.org/10.1093/toxsci/kfr179
91. Higgins GC, Devenish RJ, Beart PM, Nagley P (2012) Transitory phases of autophagic death and programmed necrosis during superoxide-induced neuronal cell death. Free Radic Biol Med 53:1960–1967. https://doi.org/10.1016/J.FREERADBIOMED.2012.08.586
92. Uchiyama Y, Koike M, Shibata M (2008) Autophagic neuron death in neonatal brain ischemia/hypoxia. Autophagy 4:404–408. https://doi.org/10.4161/auto.5598
93. Lu Q, Harris VA, Kumar S, Mansour HM, Black SM (2015) Autophagy in neonatal hypoxia ischemic brain is associated with oxidative stress. Redox Biol 6:516–523. https://doi.org/10.1016/J.REDOX.2015.06.016
94. Scherz-Shouval R, Elazar Z (2011) Regulation of autophagy by ROS: physiology and pathology. Trends Biochem Sci 36:30–38. https://doi.org/10.1016/J.TIBS.2010.07.007
95. Schweers RL, Zhang J, Randall MS et al (2007) NIX is required for programmed mitochondrial clearance during reticulocyte maturation. Proc Natl Acad Sci 104:19500 LP–19519505
96. Pajares M, Cuadrado A, Rojo AI (2017) Modulation of proteostasis by transcription factor NRF2 and impact in neurodegenerative diseases. Redox Biol 11:543–553. https://doi.org/10.1016/j.redox.2017.01.006
97. Jiang T, Harder B, Rojo de la Vega M, Wong PK, Chapman E, Zhang DD (2015) p62 links autophagy and Nrf2 signaling. Free Radic Biol Med 88:199–204. https://doi.org/10.1016/J.FREERADBIOMED.2015.06.014
98. Yamazaki H, Tanji K, Wakabayashi K, Matsuura S, Itoh K (2015) Role of the Keap1/Nrf2 pathway in neurodegenerative diseases. Pathol Int 65:210–219. https://doi.org/10.1111/pin.12261
99. Ješko H, Wencel P, Strosznajder RP, Strosznajder JB (2017) Sirtuins and their roles in brain aging and neurodegenerative disorders. Neurochem Res 42:876–890. https://doi.org/10.1007/s11064-016-2110-y
100. Shao J, Yang X, Liu T, Zhang T, Xie QR, Xia W (2016) Autophagy induction by SIRT6 is involved in oxidative stress-induced neuronal damage. Protein Cell 7:281–290. https://doi.org/10.1007/s13238-016-0257-6
101. Lee O-H, Kim J, Kim J-M, Lee H, Kim EH, Bae SK, Choi Y, Nam HS et al (2013) Decreased expression of sirtuin 6 is associated with release of high mobility group box-1 after cerebral ischemia. Biochem Biophys Res Commun 438:388–394. https://doi.org/10.1016/J.BBRC.2013.07.085
102. Kang R, Livesey KM, Zeh HJ et al (2010) HMGB1: a novel Beclin 1-binding protein active in autophagy. Autophagy 6:1209–1211. https://doi.org/10.4161/auto.6.8.13651
103. Qi L, Sun X, Li FE, Zhu BS, Braun FK, Liu ZQ, Tang JL, Wu C et al (2015) Hmgb1 promotes mitochondrial dysfunction-triggered striatal neurodegeneration via autophagy and apoptosis activation. PLoS One 10:1–15. https://doi.org/10.1371/journal.pone.0142901
104. Wang C, Jiang J, Zhang X, Song L, Sun K, Xu R (2016) Inhibiting HMGB1 reduces cerebral ischemia reperfusion injury in diabetic mice. Inflammation 39:1862–1870. https://doi.org/10.1007/s10753-016-0418-z
105. Wang T, Yuan Y, Zou H, Yang J, Zhao S, Ma Y, Wang Y, Bian J et al (2016) The ER stress regulator Bip mediates cadmium-induced autophagy and neuronal senescence. Sci Rep 6:38091
106. Gao B, Zhang X, Han R, Zhang TT, Chen C, Qin ZH, Sheng R (2013) The endoplasmic reticulum stress inhibitor salubrinal inhibits the activation of autophagy and neuroprotection induced by brain ischemic preconditioning. Acta Pharmacol Sin 34:657–666
107. Feng D, Wang B, Wang L, Abraham N, Tao K, Huang L, Shi W, Dong Y et al (2017) Pre-ischemia melatonin treatment alleviated acute neuronal injury after ischemic stroke by inhibiting endoplasmic reticulum stress-dependent autophagy via PERK and IRE1 signalings. J Pineal Res 62:1–13. https://doi.org/10.1111/jpi.12395
108. Fouillet A, Levet C, Virgone A, Robin M, Dourlen P, Rieusset J, Belaidi E, Ovize M et al (2012) ER stress inhibits neuronal death by promoting autophagy. Autophagy 8:915–926. https://doi.org/10.4161/auto.19716
109. Zhang X, Yan H, Yuan Y, Gao J, Shen Z, Cheng Y, Shen Y, Wang RR et al (2013) Cerebral ischemia-reperfusion-induced autophagy protects against neuronal injury by mitochondrial clearance. Autophagy 9:1321–1333. https://doi.org/10.4161/auto.25132
110. Zhang X, Yuan Y, Jiang L, Zhang J, Gao J, Shen Z, Zheng Y, Deng T et al (2014) Endoplasmic reticulum stress induced by tunicamycin and thapsigargin protects against transient ischemic brain injury. Autophagy 10:1801–1813. https://doi.org/10.4161/auto.32136
111. Lee H, Noh J-Y, Oh Y, Kim Y, Chang JW, Chung CW, Lee ST, Kim M et al (2012) IRE1 plays an essential role in ER stress-mediated aggregation of mutant huntingtin via the inhibition of autophagy flux. Hum Mol Genet 21:101–114
112. Ogata M, Hino S-I, Saito A et al (2006) Autophagy is activated for cell survival after endoplasmic reticulum stress. Mol Cell Biol 26:9220–9231. https://doi.org/10.1128/MCB.01453-06
113. Kong F-J, Ma L-L, Guo J-J et al (2018) Endoplasmic reticulum stress/autophagy pathway is involved in diabetes-induced neuronal apoptosis and cognitive decline in mice. Clin Sci 132:111 LP–111125
114. Vidal RL, Hetz C (2012) Crosstalk between the UPR and autophagy pathway contributes to handling cellular stress in neurodegenerative disease. Autophagy 8:970–972. https://doi.org/10.4161/auto.20139
115. Vidal RL, Figueroa A, Court FA, Thielen P, Molina C, Wirth C, Caballero B, Kiffin R et al (2012) Targeting the UPR transcription factor XBP1 protects against Huntington's disease through the regulation of FoxO1 and autophagy. Hum Mol Genet 21:2245–2262. https://doi.org/10.1093/hmg/dds040
116. Kouroku Y, Fujita E, Tanida I, Ueno T, Isoai A, Kumagai H, Ogawa S, Kaufman RJ et al (2007) ER stress (PERK/eIF2α phosphorylation) mediates the polyglutamine-induced LC3 conversion, an essential step for autophagy formation. Cell Death Differ 14:230–239. https://doi.org/10.1038/sj.cdd.4401984
117. Rashid HO, Yadav RK, Kim HR, Chae HJ (2015) ER stress: autophagy induction, inhibition and selection. Autophagy 11:1956–1977. https://doi.org/10.1080/15548627.2015.1091141
118. Princiotta MF, Finzi D, Qian S-B, Gibbs J, Schuchmann S, Buttgereit F, Bennink JR, Yewdell JW (2003) Quantitating protein synthesis, degradation, and endogenous antigen processing. Immunity 18:343–354. https://doi.org/10.1016/S1074-7613(03)00051-7
119. Yao TP (2010) The role of ubiquitin in autophagy-dependent protein aggregate processing. Genes Cancer 1:779–786. https://doi.org/10.1177/1947601910383277
120. Kageyama S, Sou YS, Uemura T, Kametaka S, Saito T, Ishimura R, Kouno T, Bedford L et al (2014) Proteasome dysfunction activates autophagy and the Keap1-Nrf2 pathway. J Biol Chem 289:24944–24955. https://doi.org/10.1074/jbc.M114.580357
121. Zatloukal K, Stumptner C, Fuchsbichler A, Heid H, Schnoelzer M, Kenner L, Kleinert R, Prinz M et al (2002) p62 is a common component of cytoplasmic inclusions in protein aggregation diseases. Am J Pathol 160:255–263. https://doi.org/10.1016/S0002-9440(10)64369-6
122. Matsumoto G, Wada K, Okuno M, Kurosawa M, Nukina N (2011) Serine 403 phosphorylation of p62/SQSTM1 regulates selective

autophagic clearance of ubiquitinated proteins. Mol Cell 44:279–289. https://doi.org/10.1016/J.MOLCEL.2011.07.039
123. Nagaoka U, Kim K, Jana NR, Doi H, Maruyama M, Mitsui K, Oyama F, Nukina N (2004) Increased expression of p62 in expanded polyglutamine-expressing cells and its association with polyglutamine inclusions. J Neurochem 91:57–68. https://doi.org/10.1111/j.1471-4159.2004.02692.x
124. Lim J, Lachenmayer ML, Wu S, Liu W, Kundu M, Wang R, Komatsu M, Oh YJ et al (2015) Proteotoxic stress induces phosphorylation of p62/SQSTM1 by ULK1 to regulate selective autophagic clearance of protein aggregates. PLoS Genet 11: e1004987
125. Pandey UB, Nie Z, Batlevi Y, McCray BA, Ritson GP, Nedelsky NB, Schwartz SL, DiProspero NA et al (2007) HDAC6 rescues neurodegeneration and provides an essential link between autophagy and the UPS. Nature 447:860–864
126. Lee J, Koga H, Kawaguchi Y et al (2010) HDAC6 controls autophagosome maturation essential for ubiquitin-selective quality-control autophagy. EMBO J 29:969 LP–969980. https://doi.org/10.1038/emboj.2009.405
127. Shin Y, Klucken J, Patterson C, Hyman BT, McLean PJ (2005) The co-chaperone carboxyl terminus of Hsp70-interacting protein (CHIP) mediates α-synuclein degradation decisions between proteasomal and lysosomal pathways. J Biol Chem 280:23727–23734. https://doi.org/10.1074/jbc.M503326200
128. Simonsen A, Birkeland HCG, Gillooly DJ et al (2004) Alfy, a novel FYVE-domain-containing protein associated with protein granules and autophagic membranes. J Cell Sci 117:4239 LP–4234251. https://doi.org/10.1242/jcs.01287
129. Filimonenko M, Stuffers S, Raiborg C et al (2007) Functional multivesicular bodies are required for autophagic clearance of protein aggregates associated with neurodegenerative disease. J Cell Biol 179(3):485–500
130. Finley KD, Edeen PT, Cumming RC, Mardahl-Dumesnil MD, Taylor BJ, Rodriguez MH, Hwang CE, Benedetti M et al (2003) Blue cheese mutations define a novel, conserved gene involved in progressive neural degeneration. J Neurosci 23:1254–1264
131. Lu K, Psakhye I, Jentsch S (2014) Autophagic clearance of polyQ proteins mediated by ubiquitin-Atg8 adaptors of the conserved CUET protein family. Cell 158:549–563. https://doi.org/10.1016/j.cell.2014.05.048
132. Cribbs DH, Berchtold NC, Perreau V, Coleman PD, Rogers J, Tenner AJ, Cotman CW (2012) Extensive innate immune gene activation accompanies brain aging, increasing vulnerability to cognitive decline and neurodegeneration: a microarray study. J Neuroinflam 9:179. https://doi.org/10.1186/1742-2094-9-179
133. Lazarou M, Sliter DA, Kane LA, Sarraf SA, Wang C, Burman JL, Sideris DP, Fogel AI et al (2015) The ubiquitin kinase PINK1 recruits autophagy receptors to induce mitophagy. Nature 524: 309–314
134. Fivenson EM, Lautrup S, Sun N, Scheibye-Knudsen M, Stevnsner T, Nilsen H, Bohr VA, Fang EF (2017) Mitophagy in neurodegeneration and aging. Neurochem Int 109:202–209. https://doi.org/10.1016/J.NEUINT.2017.02.007
135. Pickles S, Vigié P, Youle RJ (2018) Mitophagy and quality control mechanisms in mitochondrial maintenance. Curr Biol 28:R170–R185. https://doi.org/10.1016/J.CUB.2018.01.004
136. Cuervo AM, Bergamini E, Brunk UT, Dröge W, Ffrench M, Terman A (2005) Autophagy and aging: the importance of maintaining "clean" cells. Autophagy 1:131–140. https://doi.org/10.4161/auto.1.3.2017
137. Rubinsztein DC, Mariño G, Kroemer G (2011) Autophagy and aging. Cell 146:682–695. https://doi.org/10.1016/J.CELL.2011.07.030
138. Lipinski MM, Zheng B, Lu T, Yan Z, Py BF, Ng A, Xavier RJ, Li C et al (2010) Genome-wide analysis reveals mechanisms modulating autophagy in normal brain aging and in Alzheimer's disease. Proc Natl Acad Sci 107:14164–14169. https://doi.org/10.1073/pnas.1009485107
139. Plaza-Zabala A, Sierra-Torre V, Sierra A (2017) Autophagy and microglia: novel partners in neurodegeneration and aging. Int J Mol Sci 18(3):E598
140. Ott C, König J, Höhn A, Jung T, Grune T (2016) Macroautophagy is impaired in old murine brain tissue as well as in senescent human fibroblasts. Redox Biol 10:266–273. https://doi.org/10.1016/J.REDOX.2016.10.015
141. Meléndez A, Tallóczy Z, Seaman M et al (2003) Autophagy genes are essential for dauer development and life-span extension in C. elegans. Science (80-) 301:1387–1391
142. Jia K, Levine B (2007) Autophagy is required for dietary restriction-mediated life span extension in C. elegans. Autophagy 3:597–599. https://doi.org/10.4161/auto.4989
143. Colman RJ, Anderson RM, Johnson SC et al (2009) Caloric restriction delays disease onset and mortality in rhesus monkeys. Science (80-) 325:201 LP–201204
144. Sohal RS, Forster MJ (2014) Caloric restriction and the aging process: a critique. Free Radic Biol Med 73:366–382. https://doi.org/10.1016/J.FREERADBIOMED.2014.05.015
145. Lu AM, Dai JR, Guo SS et al (2017) Lysosomal proteolysis is associated with exercise-induced improvement of mitochondrial quality control in aged hippocampus. J Gerontol Ser A 72:1342–1351. https://doi.org/10.1093/gerona/glw242
146. Bhukel A, Madeo F, Sigrist SJ (2017) Spermidine boosts autophagy to protect from synapse aging. Autophagy 13:444–445. https://doi.org/10.1080/15548627.2016.1265193
147. Gupta VK, Pech U, Bhukel A, Fulterer A, Ender A, Mauermann SF, Andlauer TFM, Antwi-Adjei E et al (2016) Spermidine suppresses age-associated memory impairment by preventing adverse increase of presynaptic active zone size and release. PLoS Biol 14: e1002563
148. Valdez G, Tapia JC, Kang H et al (2010) Attenuation of age-related changes in mouse neuromuscular synapses by caloric restriction and exercise. Proc Natl Acad Sci 107:14863 LP–14814868
149. Carnio S, LoVerso F, Baraibar MA, Longa E, Khan MM, Maffei M, Reischl M, Canepari M et al (2014) Autophagy impairment in muscle induces neuromuscular junction degeneration and precocious aging. Cell Rep 8:1509–1521. https://doi.org/10.1016/J.CELREP.2014.07.061
150. Garg G, Singh S, Singh AK, Rizvi SI (2016) Antiaging effect of metformin on brain in naturally aged and accelerated senescence model of rat. Rejuvenation Res 20:173–182. https://doi.org/10.1089/rej.2016.1883

Publisher's Note Springer Nature remains neutral with regard to jurisdictional claims in published maps and institutional affiliations.

ACS Pharmacology & Translational Science

Review

Cite This: ACS Pharmacol. Transl. Sci. 2019, 2, 66–91

pubs.acs.org/ptsci

Incretin Mimetics as Rational Candidates for the Treatment of Traumatic Brain Injury

Elliot J. Glotfelty,*[,†,⊥] Thomas E. Delgado,[†] Luis B. Tovar-y-Romo,[‡] Yu Luo,[§] Barry J. Hoffer,[∥] Lars Olson,[⊥] Tobias E. Karlsson,[⊥] Mark P. Mattson,[#] Brandon K. Harvey,[▽] David Tweedie,[†] Yazhou Li,[†] and Nigel H. Greig*[,†]

[†]Translational Gerontology Branch, and [#]Laboratory of Neurosciences, Intramural Research Program, National Institute on Aging, National Institutes of Health, Baltimore, Maryland 21224, United States

[‡]Division of Neuroscience, Institute of Cellular Physiology, Universidad Nacional Autónoma de México, Mexico City, Mexico

[§]Department of Molecular Genetics, University of Cincinnati, Cincinnati, Ohio 45221, United States

[∥]Department of Neurosurgery, Case Western Reserve University School of Medicine, Cleveland, Ohio 44106, United States

[⊥]Department of Neuroscience, Karolinska Institutet, Stockholm, Sweden

[▽]Molecular Mechanisms of Cellular Stress and Inflammation Unit, Integrative Neuroscience Department, National Institute on Drug Abuse, National Institutes of Health, Baltimore, Maryland 21224, United States

ABSTRACT: Traumatic brain injury (TBI) is becoming an increasing public health issue. With an annually estimated 1.7 million TBIs in the United States (U.S.) and nearly 70 million worldwide, the injury, isolated or compounded with others, is a major cause of short- and long-term disability and mortality. This, along with no specific treatment, has made exploration of TBI therapies a priority of the health system. Age and sex differences create a spectrum of vulnerability to TBI, with the highest prevalence among younger and older populations. Increased public interest in the long term effects and prevention of TBI have recently reached peaks, with media attention bringing heightened awareness to sport and war related head injuries. Along with short-term issues, TBI can increase the likelihood for development of long-term neurodegenerative disorders. A growing body of literature supports the use of glucagon-like peptide-1 (GLP-1), glucose-dependent insulinotropic peptide (GIP), and glucagon (Gcg) receptor (R) agonists, along with unimolecular combinations of these therapies, for their potent neurotrophic/neuroprotective activities across a variety of cellular and animal models of chronic neurodegenerative diseases (Alzheimer's and Parkinson's diseases) and acute cerebrovascular disorders (stroke). Mild or moderate TBI shares many of the hallmarks of these conditions; recent work provides evidence that use of these compounds is an effective strategy for its treatment. Safety and efficacy of many incretin-based therapies (GLP-1 and GIP) have been demonstrated in humans for the treatment of type 2 diabetes mellitus (T2DM), making these compounds ideal for rapid evaluation in clinical trials of mild and moderate TBI.

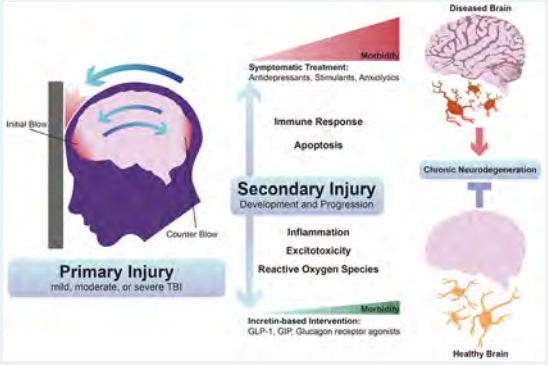

KEYWORDS: *TBI, incretins, GLP-1, GIP, Gcg, glucagon, exendin-4, neurodegeneration, microglia, brain trauma*

Downloaded via UNIV NACIONAL AUTONOMA MEXICO on October 16, 2020 at 05:28:11 (UTC).
See https://pubs.acs.org/sharingguidelines for options on how to legitimately share published articles.

INTRODUCTION

Incretin Based Therapies: A Well Supported Approach to Traumatic Brain Injury Treatment. Traumatic brain injury (TBI) constitutes a significant public health issue worldwide, increasing disability and mortality rates among all age groups.[1] TBI ranges from mild (mTBI) to severe and presents diverse acute symptoms; the heterogeneity of the initial injury remains a barrier to the development of effective therapeutic interventions and clinical trials.[2] The randomness of events leading to human head injuries requires a range of models that produce trauma analogous to that seen in incidents ranging from falls and sports related injuries to a severe car crash or explosion in war.[3]

The primary injury of TBI involves damage to brain tissue from direct trauma, typically in combination with inertial forces, with a secondary injury later emerging and characterized by widespread degeneration of neurons and glial cells.[4] Secondary injury manifestations are delayed and suggest a possible therapeutic window.[5] Pharmacologic intervention to reduce progression and severity of the secondary injury presents the greatest promise for counteracting a patient's long-term morbidity and improving quality of life. Currently, there are no Food and Drug Administration (FDA) approved treatments for the secondary TBI injury;[6] instead there is

Received: January 4, 2019
Published: February 11, 2019

© 2019 American Chemical Society

DOI: 10.1021/acsptsci.9b00003
ACS Pharmacol. Transl. Sci. 2019, 2, 66–91

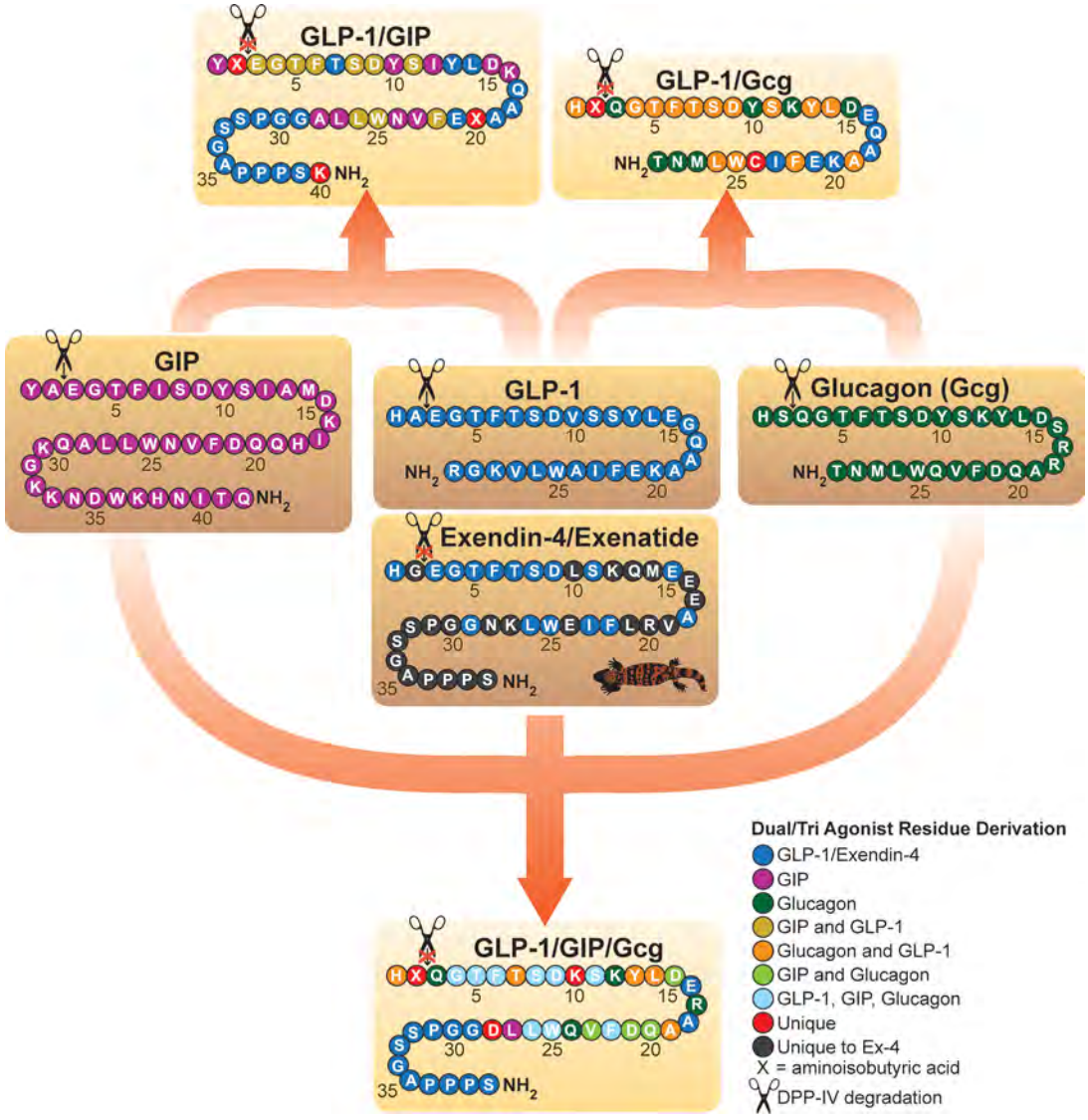

Figure 1. Amino acid sequences of incretins and glucagon and their mimetics. The discovery of the GLP-1 analogue exendin-4 (commercially known as Exenatide), in the saliva of the Gila monster has paved the way for DPP-IV resistant incretin mimetics. Residue derivations for the dual- and triagonist incretin-based therapies are highlighted as well as resistance to DPP-IV cleavage. All endogenous human peptides are susceptible to DPP-IV cleavage, while the mimetics display some form of resistance. For more detailed structures, see Tschöp et al. (2016) (ref 28).

much focus on symptomatic treatments of the condition, including those for headaches, sleep issues, fatigue, balance problems, and nausea.[7] Other common acute manifestations of TBI include cognitive deficits in attention, learning and memory, and higher-order executive functions. However, these consequences can remain long after the initial injury.[8,9] TBI can additionally lead to the development of chronic neurodegenerative disorders, including Alzheimer's disease (AD), Parkinson's disease (PD), frontotemporal dementia (FTD), and chronic traumatic encephalopathy (CTE).[10−12] As Masel and Dewitt (2010)[13] describe, TBI is "a disease process, not an event", referring to a common practice among insurance agencies to classify TBI as a singular injury. The long-term consequences of the injury need to be considered following initial treatment.

Understanding of the molecular mechanisms underpinning the secondary TBI injury are important for the development of effective therapies for the mitigation of long-term consequences. Pharmacological treatments focused on the secondary and long-term neurological effects of the condition are currently emerging.[14−20] Incretin mimetics are a particularly promising class of drugs for the treatment of mTBI and are based on the utilization of the endogenous incretin signaling system involving glucagon-like peptide 1 (GLP-1), glucose-dependent insulinotropic polypeptide (GIP), glucagon (Gcg), and their receptors (R). GLP-1 and GIP exert similar mechanisms of action,[21] and their long-acting drug analogues were originally developed for their insulinotropic and insulin-sensitizing actions for the treatment of type 2 diabetes mellitus (T2DM), characterized by insulin resistance[22,23] and blunted incretin effects.[24] Incretin effects account for up to 70% of insulin release and defects in this system are thought to be main contributors to the development of T2DM.[25] Endogenously, GLP-1 and GIP are chiefly produced in the small intestine and maintain low concentrations in the bloodstream[26] that are rapidly upregulated in response to food ingestion. Following upregulation, GLP-1 and GIP act in a glucose-dependent manner on pancreatic β-cells to stimulate

DOI: 10.1021/acsptsci.9b00003
ACS Pharmacol. Transl. Sci. 2019, 2, 66−91

Table 1. Incretin-Based Therapies in Animal Models of TBI[a]

Action	Study and TBI Model Used	Treatment Effects	Treatment Evaluated
GLP-1R agonist	1) *Heile et al., 2009*[m]: Controlled Cortical Impact (CCI) 2) *Rachmany et al., 2013*[b]: Concussive weight drop model (mTBI) 3) *Eakin et al., 2013*[c]: Fluid Percussion Injury (FPI) model (mTBI) 4) *DellaValle et al., 2014*[d]: Cold lesion model (severe TBI) 5) *Li et al., 2015*[e]: Concussive weight drop - 30 gram (mTBI) 6) *Hakon et al., 2015*[f]: CCI 7) *Tweedie et al., 2016*[g]: Blast induced mTBI 8) *Rachmany et al., 2017*[h]: Blast induced mTBI 9) *Bader et al., 2018*[i]: Concussive weight drop model- 30 gram (mTBI)	1) Attenuated hippocampal neuron loss and other histopathology associated with TBI. 2) Ameliorated H_2O_2- induced oxidative stress and glutamate toxicity in cell culture and deficits in novel object recognition 7 and 30 days post trauma. 3) Reduced cognitive impairments (Morris Water Maze), protection from glutamate toxicity, decreased Caspase-3 activity. 4) Reduced reactive oxygen species, reduced lesion volume ~50%, CREB-regulated cytoprotective and anti-neurodegenerative proteins increased. 5) Increased cellular proliferation via CREB phosphorylation, protection from glutamate toxicity, reduction in pro-apoptotic signaling. 6) Preservation of BBB and improved sensorimotor function 48 hours post TBI. Lesion size and cortical neuron death was reduced. 7) Hippocampal and lateral neurodegeneration reduced (pre- and post-treatment effects), increased preference for novel object (Novel Object Recognition test), attenuated upregulation of neurodegenerative disorder related genes sets. 8) Maintained synaptophysin reactivity, prevented injury induced impairment in spatial working memory, and showed neurotrophic activity in vitro. 9) Improved cognitive impairments, neuroprotection, decreased glial activation, inhibition of TNF-a generation	1) Encapsulated mesenchymal stem cell transplant (native and GLP-1 overexpressing cells). 2) Steady-state Exendin-4 (Ex-4, ***Liraglutide***) (3.5 pM/kg/min) over 7 days starting 48 hr prior to or 1 hr post- TBI 3) Subcutaneuous (SC) Ex-4 administration via Alzet mini-osmotic pump (model 2001) (3.5 pM/kg/min) post- TBI. 4) SC Ex-4 administration via Alzet mini-osmotic pump (model 1007D) (3.5 pM/kg/min), pre- and post- TBI. 5) ***Liraglutide*** once daily injection for 7 days (246.7μg/kg/day) 6) ***Liraglutide*** twice daily at doses of 75μg /kg or 200 μg/kg or 200 μg/kg post-TBI. 7) SC Ex-4 administration via Alzet mini-osmotic pump (model 1007D) (3.5 pM/kg/min), 48 hrs pre and 2 hrs post- TBI. Favorable comparison to ***Byetta®*** (AstraZeneca) administration in humans. 8) SC Ex-4 administration via Alzet mini-osmotic pump (model 1007D) (3.5 pM/kg/min), 48 hrs pre- and post- TBI. Mimicked use of Exenatide LAR (***Bydureon®***; AstraZeneca) in humans. 9) A single SC injection of Slow Release (SR) Exenatide ***PT302*** (Peptron) (0.6, 0.12, and 0.024 mg/kg) was administered and plasma Exenatide concentrations were time- dependently measured over 3 weeks.
GIPR Agonist	1) *Yu et al., 2016*[j]: CCI (mTBI)	1) Ameliorated mTBI-induced memory impairments, poor balance, and sensorimotor deficits after initiation in the post-injury period. Mitigation of mTBI induced changes in GFAP, APP, and BMX observed.	1) SC GIP administration using ALZET micro-osmotic pump at a rate of 21.58 or 38.85μg/kg/day.
GCGR Agonist	1) *Fanne et al., 2011*[k]: Concussive weight drop model – 35 gram (mTBI) 2) *Armstead et al., 2011*[l]; FPI	1) Pre-treatment significantly reduced the neurological severity score (NSS) and TBI lesion size. Post-treatment reduced free glutamate in the CSF compared to saline controls. 2) Blocked NMDA receptor mediated vasoconstriction and restored vasodilation response (via reduction of tissue plasminogen activator (tPA)). Increased cAMP levels with pre- or post- treatment.	1) Mice were IP injected with 25ug Gcg 10 minutes prior to receiving head injury. For glutamate studies, IP injection given 10 minutes after injury. 2) Newborn pigs were pre- or post-treated with 25 ug/kg Gcg 30 minutes before or after FPI.
GIPR-GcgR Dual Agonists	None to date	———	———
GLP-1R/GcgR Dual Agonist	None to date	———	———
GLP-1R/GIPR Dual Agonist	1) *Tamargo et al., 2017*[m]: Weight drop model- 30 gram (mTBI)	1) Neurotrophic activity, neuroprotection from glutamate/oxidative stress, increased pCREB, and dose dependent elevation of cAMP levels SH-SY5Y cells; neuroprotection from 6OHDA in primary neurons; increased neurotrophic activity compared to single incretin mimetics (GIP and GLP-1); prevention of deficits in visual and spatial memory in mice 7 and 30 days post TBI.	1) SC daily injection of 50μg/kg dual GLP-1R/GIPR agonist ("Twincretin") for 7 days, with first injection administered 30 min after injury.
GLP-1R/GIPR/GcgR Triagonist	None to date	———	———
DPP-IV Inhibition	1) *DellaValle et al., 2016*[n]: Cold lesion model (severe TBI)	1) Significant results: reduction in lesion volume, increased activation of CREB system (neurotrophic), and increased manganese superoxide dismutase (MnSOD) transcription.	1) Sitagliptin (***Januvia®***; Merck and Co.) administrated once-daily 50 mg/kg of sitagliptin in a 0.1 mL Nutella® ball or Nutella® alone throughout the study, beginning 2 days before TBI.

[a]Incretin-based therapies have been studied across a variety of TBI models of and have demonstrated efficacy in preventing apoptosis, oxidative stress, and inflammation, while providing neurotrophic support. GLP-1R agonism has been the most widely explored incretin-based therapy for TBI, though others have shown promise as well. FDA approved drugs and drugs in clinical trials are shown in red and blue respectively. SC = subcutaneous injection. Sources: (a) ref 80; (b) ref 81; (c) ref 82; (d) ref 83; (e) ref 84; (f) ref 85; (g) ref 86; (h) ref 87; (i) ref 74; (j) ref 88; (k) ref 89; (l) ref 90; (m) ref 75; (n) ref 91.

the production and secretion of insulin and potentiate absorption of glucose by the body.

In contrast to the incretins, Gcg is most well-known for its action on the liver, stimulating the process of glycogenolysis, or the breakdown of glycogen into glucose. This lends itself to the effective treatment of severe hypoglycemia, or low blood sugar. GcgR antagonism has been explored as a way to effectively manage hyperglycemia. However, effects of GcgR agonism appear to play a pivotal role in satiety, metabolic homeostasis, and glucose metabolism.[27] Clinically balancing combinatory levels of GLP-1, GIP, and Gcg in unimolecular incretin mimetics counteracts monotherapeutic problems, such as hyperglycemic liabilities of Gcg. Minor changes in peptide analogue sequences allow for longer acting pharmacological effects on receptors of interest.[28] Endogenously, GLP-1, GIP, and Gcg are cleaved and inactivated by dipeptidyl peptidase-4 (DPP-IV) within two and 8 min of their release.[29,30] Resistance to this degradation is essential for incretin-based mimetics to effectively treat T2DM and other metabolic conditions (Figure 1).[28,31]

Incretin mimetics used in T2DM treatment are based upon the amino acid sequence of human GLP-1 and the naturally occurring analogue exendin-4 (Ex-4), which was originally isolated from the saliva of the Gila monster (*Heloderma suspectum*)[32] and is resistant to degradation from DPP-IV consequent to a substitution of alanine (A) to glycine (G) in the 2-position of Ex-4 (Figure 1). These drugs have received increasing attention for their extrapancreatic effects, especially within the central and peripheral nervous system, as they have been shown to confer neurotrophic[33] and neuroprotective actions in both *in vivo* and *in vitro* models of neurogenerative disorders.[34−37] The recognition of a synergistic GLP-1/GIP or GLP-1/Gcg effect has led to the development of dual GLP-1/GIP and GLP-1/Gcg receptor coagonists with the potential for enhanced efficacy than either mimetic alone.[38−41] Recently, unimolecular combinations of GIP, GLP-1, and Gcg, have been shown to be a more physiologically balanced and amenable incretin combination for the diverse needs of human patients[42] and show promise in several models of neurodegeneration.[43] GLP-1 based polypharmacologic approaches to the treatment of metabolic diseases, and possibly neurological disorders, seem to hold much promise, as single therapeutics often have limited effectiveness.[44] Although all commercially available GLP-1R agonists are effective for

DOI: 10.1021/acsptsci.9b00003
ACS Pharmacol. Transl. Sci. 2019, 2, 66−91

Table 2. Incretin-Based Therapies Approved for Use or in Clinical Trials[a]

Mechanism of Action	Company	Drug Name		Administration	Uses	Other Notes
GLP-1R Agonist	AstraZeneca	Exenatide	*Bydureon®BCise™*	Once weekly SC	T2DM	Latest formulation of *Bydureon®*
			Bydureon®	Once weekly SC	T2DM	2 mg injection once each week, extended release formulation. Currently recruiting severely obese adolescents to participate in clinical trial (#NCT02496611). Phase 2 clinical trial (#NCT01971242) for PD patients completed (See a. *Athauda et al., 2017*)
			Byetta®	Twice daily SC	T2DM	Used any time within 1 hour before morning and evening meals (or before the two main meals of the day, approximately 6 hours or more apart). In clinical trial (#NCT02442791), neuroprotective effects of *Byetta®* administration following cardiac arrest showed no significant outcomes (See b. *Wiberg et al., 2016*). Phase 2 clinical trial (#NCT02838589) completed investigating effects on cerebral blood flow.
	Sanofi-Aventis	Lixisenatide	*Adlyxin®/ Lyxumia®*	Once daily SC	T2DM	10 mcg once daily injection for 14 days. On Day 15, dosage increased to 20 mcg once daily. Administered within one hour before the first meal of the day.
	Sanofi-Aventis/Hanmi Pharmaceuticals	Efpeglenatide	*HM 11260C*	Once weekly SC	T2DM	Currently recruiting patients for Phase 3 clinical trials (#NCT03353350, #NCT03496298)
	GlaxoSmithKline	Albiglutide	*Tanzeum®*	Once weekly SC	T2DM	Once weekly at any time of day, irrespective of meals. Dosage can be increased from 30 mg to 50 mg for those that need.
	Novo Nordisk	Liraglutide	*Victoza®*	Once daily SC	T2DM	Used at any time of day, independent of meals. Use 0.6 mg per day for one week then increase to 1.2 mg, which can be increased to 1.8 mg for additional glycemic control. Clinical trial in AD patients (#NCT01843933) completed in 2013 (See c. *Gejl et al., 2016*).
			Saxenda™	Once daily SC	Weight Loss	3 mg daily SC injection
		Semaglutide	*Ozempic®*	Once weekly SC	T2DM	0.25 mg (with or without meals). After 4 weeks, dose increased to 0.5 mg once weekly. Can be increased to 1 mg once weekly if needed.
			NASH	Daily SC	NASH/NAFLD	Currently in Phase 2 clinical trials (#NCT02970942). NASH measurements are primary outcome with NAFLD as secondary outcome measure.
		———	*NN9926, NN9927*	Oral	T2DM	Long acting, new molecular entities currently in development
	Eli Lilly	Dulaglutide	*Trulicity™*	Once weekly SC	T2DM	0.75 or 1.5 mg SC injection once weekly from single dose pen
	Peptron	Exenatide SR	*PT-302*	Biweekly SC	T2DM/ PD	Phase 2 clinical trials completed in South Korea for T2DM. Phase 1 clinical trial (#NCT00964262) completed for treatment of T2DM. Proprietary formulation allows for injection with smaller needle to reduce injection pain
	Intarcia	Exenatide	*ITCA 650*	Long term implant	T2DM	Implant with potential to offer 6 month exenatide delivery with 1 year delivery options in development. Phase 3 clinical trials have been completed with New Drug Application (NDA) submitted to the Food and Drug Administration (FDA) (pending approval)
	vTv Therapeutics	———	*TTP273*	Oral once or twice daily	T2DM	Non-peptide GLP-1R agonist. Has completed Phase 2 clinical trial (#NCT02653599).
	CSPC ZhongQi Pharmaceutical Technology Co., Ltd.	Recombinant Exenatide	*rExenatide-4*	SC twice daily	T2DM	Phase 3 Clinical trial (#NCT03239119) initiated, but not yet recruiting.
	Oramed	Exenatide Oral	*ORMD-0901*	Oral	T2DM	US FDA cleared Investigational New Drug (IND) application for trials in humans as of September 2018.
	Shanghai Biolaxy	Exenatide	*Nodaken*	Oral	T2DM	Nanoparticle oral delivery. Clinical trials ongoing in China.
	Jiangsu Hengrui Medicine Co. Ltd.	Loxenatide	*PEX168*	Once weekly SC	T2DM	Clinical trials in progress (#NCT02477969). This formulation is PEGylated.
	Neuraly Inc.	Exenatide	*NLY01*	Once weekly SC	PD/AD	Phase 1 clinical trial recruiting (#NCT03672604). This is a PEGylated formulation. See (d.) *Yun et al., 2018*
GIPR Agonist	———	GIP Peptide	———	———	T1DM	GIP peptide is currently recruiting for clinical trial (#NCT03556098) as a safeguard against hypoglycemia in patients with Type-1 diabetes mellitus (T1DM).
	Zealand Pharmaceuticals	———	*ZP4165*	Intra Venous (I.V.) or SC	T2DM	DPP-IV resistance and potentiates GLP-1 mediated weight loss and improved glycemic control in rats. See (e.) *Nørregaard et al., 2018*
GLP-1R/GcgR Dual Agonist	Hanmi Pharmaceuticals/ Janssen Research & Development, LLC	———	*HM12525A/ JNJ-64565111*	Once weekly SC	T2DM/Obesity	Currently recruiting for Phase 2 clinical trials (#NCT03586830).
	Zealand Pharmaceuticals/ Boehringer Ingelheim	———	*BI 456906*	Once weekly SC	Obesity	Long lasting analogue of amylin and partially builds on the effects of oxyntomodulin. Initiated Phase 1 clinical trial (#NCT03175211) in 2017 to assess safety, tolerability, and pharmacokinetics/pharmacodynamics. Phase 1 trials in Germany for obesity initiated.
	Astra Zeneca/ MedImmune	———	*MEDI0382*	Daily SC	T2DM	Completed Phase 2a clinical trials (see f. *Ambery et al., 2018*). Phase 2b clinical trials underway (#NCT03235050).
	Sanofi-Aventis	———	*SAR425899*	Daily SC	T2DM/Obesity	Clinical trials active (#NCT03414736). See (g.) *Gotfredi et al., 2018*
	Janssen Pharmaceuticals	———	*JNJ-54728518*	———	T2DM/Obesity	Phase I clinical trials initiated for obesity and T2DM in 2016. Pre-clinical trials for obesity also initiated in 2016.
	Novo Nordisk	———	*NNC9204-1177*	Once weekly SC	Obesity	Currently recruiting for Phase 1 clinical trial (#NCT03306721)
	Prolor/OPKO Biological	———	*OPK-88003*	Once weekly SC	T2DM	Currently recruiting for Phase 2 clinical trial (#NCT03406377)
	Spitfire Pharma	———	*SP-1373*	Once daily SC	NASH/T2DM/ Obesity	Clinical trial for T2DM and obesity planned for 2019.
	Boehringer Ingelheim	———	*BI 456906*	———	Obesity	Currently recruiting for Phase 1 clinical trials (#NCT03591718)
GLP-1R/GIPR Dual Agonist	Eli Lilly	———	*LY3298176*	Once weekly SC	T2DM	Completed Phase 2 clinical trials (#NCT03131687). See (h.) *Frias et al., 2018* for details.
	Novo Nordisk	———	*BG 7167/NNC0090-2746/ MAR709*	Once daily SC	T2DM	Completed Phase 2 clinical trial (#NCT02205528). See (i.) *Frias et al., 2017* for more details.
	Sanofi	———	*SAR438335*	Info not available	T2DM	Currently in Phase 1 clinical trials in France.
GLP-1R/GIPR/GcgR Triagonist	Novo Nordisk	———	*NNC9204-1706*	Once daily SC	Obesity	Current Phase I clinical trial (#NCT03661879) recruiting.
	Hanmi Pharmaceutical Co. Lmtd.	———	*HM15211*	SC	Obesity	Long acting formulation. Current Phase I clinical trial (#NCT03374241) recruiting. See (j.) *Kim et al., 2018* for latest research on compound
	Sanofi	———	*SAR441255*	SC	T2DM/Obesity/ NASH	Preclinical
DPP-IV Inhibition	Astra Zeneca	Saxagliptin	*Onglyza™*	Once daily oral	T2DM	2.5 or 5 mg regardless of meals
	Merck	Sitagliptin	*Januvia®*	Once daily oral	T2DM	25, 50, or 100 mg with or without food.
		Sitagliptin phosphate + metformin HCl	*Janumet®/ Janumet®XR*	Once daily oral (XR formula)/Twice daily	T2DM	Combination drug therapy with metformin. XR formulation is an extended release version. Max dosage 100 mg Sitagliptin and 2000 mg metformin.
		Omarigliptin	*Marizev®*	Oral once weekly	T2DM	Available in Japan. See (k.) *Goldenberg et al., 2017* for Phase 3 clinical trial information (#NCT01703221). Possible repositioning of drug for intranasal delivery for PD (l.) (*Ayoub et al., 2018*).
	Takeda	Trelagliptin	*Zafatek®*	Oral once weekly	T2DM	Approved for use in Japan. Phase 2 clinical trials abandoned in the USA because of costs.
		Alogliptin	*Nesina®*	Oral once daily	T2DM	25 mg with or without food
	Bristol-Myers Squib	Linagliptin	*Tradjenta®*	Oral once daily	T2DM	5 mg once daily
	Dong-A ST	Evogliptin	*Suganon®*	Oral once daily	T2DM	5 mg once daily. Approved for use in South Korea in 2015. Sold with extended release metformin.
	SatRx LLC	Gosogliptin	*Saxilin®*	Oral	T2DM	Approved for use in Russia. Completed Phase 3 clinical trial of safety alone or with metformin compared to Vildagliptin alone or with metformin (#NCT03088670.
	LG Life Sciences/ Sanofi	Gemigliptin	*Zemiglo™*	Oral once daily	T2DM	Long acting DPP-IV inhibitor. See (m.) *Kim et al., 2016* for characterization.
	Zealand Pharmaceuticals	Vildagliptin	*Galvus®*	Oral once daily	T2DM	50 mg in combination with metformin. See (n.) *Mathieu & Degronde, 2008*
	Mitsubishi Tanabe Pharma and Daiichi Sankyo	Teneligliptin	*Tenelia®*	Oral twice daily	T2DM	20 mg twice daily. See (o.) *Kishimoto, 2013*
	Zealand Pharmaceuticals	Anagliptin	*Suiny®*	Oral twice daily	T2DM	Approved for use in Japan, 200 mg daily. See (p.) *Nishio et al., 2015*

[a]There are currently a wide variety of incretin-based therapies approved for the treatment of metabolic diseases (shown in red and green if approved in the USA or elsewhere, respectively) and many more that are in clinical trials or development (shown in blue). Included in this table are the DPP-IV inhibitors which increase endogenous levels of GLP-1, GIP, and GCG. Formulations of incretin-based therapies in clinical trials focused on neurological diseases are highlighted in yellow. Bydureon and Victoza are the only FDA approved incretin analogues that have completed clinical trials for a neurological disease/disorder. There are currently no GIPR-GCGR antagonists under investigation. #: Clinical trials can be found at https://clinicaltrials.gov. NASH = nonalcoholic steatohepatitis; NAFLD = nonalcoholic fatty liver disease; SC = subcutaneous injection; T1DM = Type 1 Diabetes Mellitus. Sources: (a) ref 67; (b) ref 92; (c) ref 71; (d) ref 93; (e) ref 94; (f) ref 95; (g) ref 96; (h) ref 38; (i) ref 97; (j) ref 43; (k) ref 98; (l) ref 99; (m) ref 100; (n) ref 101; (o) ref 102; (p) ref 103.

diabetes treatment, head to head comparisons of clinical trials of each drug reveal differential ratios of reduced blood glucose and weight loss and the amount of adverse events associated with intake.[45] No systematic comparisons of the effectiveness of T2DM treatment using dual and triagonists have yet been explored, although there are also likely differences in efficacy across these compounds as well. Understanding the residue contributions to the efficacy of these unimolecular combinations is difficult to assess, although the use of genetically modified mice with receptors of interest removed is an avenue to explore these questions.[25] As Capozzi et. al (2018)[25] point out, genetic deletion of these receptors has limitations and can potentially confound findings, as these mice may genetically compensate for these deletions and present atypical physiologic responses to the compounds.[46] This leaves potential gaps in understanding of which mimetics to use in future clinical trials, especially for neurologic disorders. The amino acid

DOI: 10.1021/acsptsci.9b00003
ACS Pharmacol. Transl. Sci. 2019, 2, 66−91

A

	Mild	Moderate	Severe
Structural Imaging	Normal	Normal to Abnormal	Normal to Abnormal
Duration of lost consciousness	0-30 mins	>30 min and < 24 hours	>24 hours
Duration Confusion/Disorientation	0-24 hours	>24 hours + Additional criteria applied to these cases in determining severity.	
Duration of Memory Loss	0-24 hours	>1 Day and <7 Days	>7 Days

B

Glasgow Coma Scale

RESPONSE	SCALE	SCORE
Eye opening response	Spontaneously	4
	To speech	3
	To pressure	2
	No response	1
Verbal response	Oriented to time, place, and person	5
	Confused	4
	Inappropriate words	3
	Incomprehensible sounds	2
	No response	1
Motor response	Obeys commands	6
	Moves to localized pain	5
	Flexion withdrawal from pain	4
	Abnormal flexion	3
	Abnormal extension	2
	No response	1
Total score	Mild TBI	13-15
	Moderate TBI	9-12
	Severe TBI	3-8

Figure 2. Basic TBI diagnostic assessment in military and general clinical settings. Classifying the severity of a TBI is the first step in determining treatment options and trajectory. Basic diagnostic categorizations used in a military context are shown in panel A. With increasing use of blood-based biomarker surveillance, the use of brain imaging across each severity level will likely be highlighted less and perhaps deemed unnecessary for all cases. The Glasgow Coma Scale (GCS) (B) is a widely used diagnostic tool in assessing the severity of TBI, though the medical community is currently improving on less subjective readouts to better diagnose level of injury and needs of each patient. Panel A was adapted from Defense and Veterans Brain Injury Center (2015)[121] and panel B from Teasdale et al. (2014).[135]

sequences for GLP-1, GIP, Gcg, and their dual- or triagonist unimolecular combinations are shown in Figure 1.

Repurposing of the already well tested and tolerated incretin mimetics is promising for introduction to the general population for use in TBI treatment. Incretin mimetics have been shown to decrease neuroinflammation, excitotoxicity, oxidative stress, and apoptosis in animal models of a range of neurological maladies including autoimmune encephalomyelitis,[47] retinal neurodegeneration,[48,49] stroke,[50−53] AD,[54−57] PD,[58−63] and amyotrophic lateral sclerosis;[64] all of these processes are also implicated in the progression of secondary TBI injury.[65,66] Animal models of TBI have also demonstrated efficacy of incretin and Gcg based mechanisms; some of the treatments used in these studies are FDA approved or in clinical trials (Table 1). More promising, improved outcomes in human clinical trials for PD[67−70] and AD patients[71] following treatment with GLP-1 analogues provide additional evidence for the safe use of incretin mimetics for the treatment of neurodegenerative conditions. Only two of the FDA-approved incretin-based mimetics used for the treatment of metabolic diseases, *Bydureon* (AstraZeneca) and *Victoza* (Novo Nordisk), have entered into clinical trials for the treatment of a neurological disorder, although newer drugs are also currently being explored for similar trials (Table 2). Sustained release formulations of incretins are becoming available and have been used in human models of PD[67] and AD[71] and animal models of AD,[55] PD,[60,72,73] and TBI.[74] Recent studies of a unimolecular dual GLP-1/GIP receptor coagonist[41] have shown therapeutic promise in animal models of mTBI[75] (Table 1) and other neurodegenerative diseases.[39,40,76,77] The latest iterations of incretin-based analogues utilize unimolecular GLP-1/GIP/Gcg receptor triagonism[42] and have been shown to provide neuroprotection in models of AD.[78,79] These novel incretin mimetics likely provide similar neuroprotection and mitigation of neurodegeneration in models of TBI.

Traumatic Brain Injury: A Public Health Perspective.

The United States Center for Disease Control's (CDC) analysis of 2013 health care data finds that there were approximately 2.5 million TBI-related emergency department (ED) visits, 282 000 TBI related hospitalizations, and 56 000 TBI associated deaths,[104] all increases from previous estimates.[105] Although hospitalizations related to TBIs have remained consistent, TBI-related visits to the ED have escalated dramatically. Between 2007 and 2013 there was a 32% increase in overall TBI-related ED visits,[104] further corroborated by two other separate analyses showing significant upsurges in TBI related ED visits between 2006−2010[106] and 2007−2010.[107] The 2006−2010 analysis found a 56% rise in TBI-related hospitalizations, despite only a 3.6% increase in total ED visits. Increased public awareness of TBI, specifically of mild forms, has likely led to this rise in ED visits.[106] Increases in TBI-related ED visits include those associated with sports injuries, which saw a 65.9% rise in annual visits between 2006 and 2011 (65 516 to 105 384 annual visits).[108]

Epidemiological analyses of these trends is difficult to assess, although a similar conclusion can be made from them all: TBI remains a significant health issue for millions of people, both immediately following the injury and in the years and decades following. Estimates indicate approximately 3.2[109] to 5.3 million[110] Americans are currently living with a long-term disability associated with a TBI incident, albeit these estimates likely underestimate actual incidence due to underreporting from those sustaining a TBI and the lack of high quality monitoring data.[11,111] Long-term outcomes following a pediatric TBI are especially difficult to assess. Children, especially boys, are highly vulnerable to TBI.[112] Boys are less likely to wear head protection and are more likely to be injured deliberately causing much of the injury disparity compared to girls.[113] Whereas much of the general public's focus and interest in TBI stems from sports-related injuries, elderly individuals' falls are most associated with the increases in TBI-

DOI: 10.1021/acsptsci.9b00003
ACS Pharmacol. Transl. Sci. 2019, 2, 66−91

related ED visits.[104] The elderly population has lower thresholds of injury severity that result in higher mortality and worse functional outcomes than younger individuals.[114,115] This, combined with higher medication use and comorbid conditions, exacerbate poor outcomes in the elderly.[104] Globally, TBIs result in over 10 million deaths per year. It is not currently known how many individuals are living with a disease/disability resulting from a previous TBI, but approximately 60 million individuals worldwide have previously been hospitalized for TBI-related injuries.[110]

Military personnel remain at high risk for TBI. The Global War on Terrorism in the Middle East and ongoing military operations in Iraq and Afghanistan have spanned 16 years and have involved more than 2.7 million U.S. and coalition personnel.[116] TBI is referred to as the "signature wound" of the ongoing military conflict due to the higher rates of these injuries than in prior conflicts. United States personnel TBI cases are in addition to many more cases in enemy combatants and the unfortunate innocent citizens of the countries in which the combat has occurred. Blast injury is the main cause of casualties and TBI, resulting from enemy combatants' increased use of improvised explosive devices (IEDs), rocket-propelled grenades, and landmines. Estimates range from approximately 15%[117] to 19.5−22.8% of all returning deployed US troops[118,119] having suffered a blast exposure TBI, with total cases of military related TBI injuries between the years 2000 and 2018 reaching greater than 383 947.[120] For this assessment, only the highest severity injury was recorded for individuals who sustained more than one TBI. On the basis of the updated 2015 version of the International Classification of Diseases[121] (Figure 2A), roughly 82% of all military related TBIs between 2000 and 2018 can be classified as mild.[120]

Diagnosis of blast induced TBI is often delayed. Military personnel are 8.4 times more likely to be diagnosed with a TBI within 4 weeks following return from deployment than before entering combat.[122] Chances of a TBI diagnosis remain heightened for over a year, with reasons ranging from a lack of recognition or underreporting of experiencing high-risk events by those injured during combat to riskier behaviors upon return home.[122,123] Long-term outlook for military personnel diagnosed with an mTBI have shown increased risks for developing PD[124] and dementia[125] years after initial injuries. Commonly referred to as "shell shock" or "post-concussion syndrome" during World Wars I and II, closed head injuries related with proximity to explosions resulted in symptoms including amnesia, concentration issues, headache, and dizziness. During these wars, debate on whether these symptoms were of psychological or physical manifestation were unclear;[126] however, scientists now understand clear physical connections between injuries from blast exposure and many of the symptoms observed.[127]

Increasing evidence suggests that both single and repetitive TBI injuries can lead to the development of neurodegenerative diseases with possible dose- and frequency-dependent correlations;[11,128] however, genetic predisposition and environmental factors likely play a key role in the threshold for clinical manifestation.[129−133] Moderate and severe TBIs require high levels of monitored care, although mild injuries can also result in long-term deleterious health effects. In addition, cognitive deficits and behavioral or emotional changes such as irritability, poor memory, attention, and depression may manifest.[134] Whereas many symptoms of mTBI may resolve rapidly, deficits can be evident years later, often unattributed to the initial injury.

Although much of the mystery surrounding the long-term effects of TBI remain today, advances in diagnostic metrics and severity assessments have the potential to change disease outlook and treatment options. Since the 1970s, diagnosis of TBI severity has relied on using the Glasgow Coma Scale (GCS), which scores patients' ability to open eyes, respond verbally, and perform a motor response[135] (Figure 2B). Scores range from 3 to 15, with lower scores associated with the most severe TBIs and higher scores with injuries considered moderate or mild. Even though it is an easy to use tool for TBI diagnosis and potential prognosis, the GCS does not provide objective readouts underlying patient specific pathophysiological sequalae that underpin such diverse outcomes,[2] especially with regard to severe trauma in elderly patients.[136,137] New technologies in brain imaging[134] and blood biomarker surveillance[138−140] are in rapid development and will likely be standardized in the near future. This will be particularly helpful for long-term diagnoses and potentially be used for early identification of secondary disease manifestations such as the that of CTE.[141] Use of blood biomarkers remains in its relative infancy, with the FDA approving the first blood test for TBI patients in 2018.[142,143] A quick turnaround is clearly essential for these tests to be effective, and once standardization is achieved, this will represent a shift to biological readouts to diagnose TBI, instead of or in combination with the commonly used, and still useful, GCS. Moreover, simple blood tests may potentially decrease the costs of healthcare by decreasing the needed number of procedures such as head scans for many mTBIs.

Mechanisms of TBI Damage. Despite the diversity of TBI cases and their outcomes, all CNS trauma pathology is determined by primary and secondary phases of injury. Immediately following a contusion; primary injury includes mechanical force damage to the brain that can rapidly cause neuronal cell necrosis (limited to the epicenter in mild cases), axonal injury, disruption of the blood brain barrier (BBB), reactive oxygen species (ROS) release, and spreading excitatory neurotransmitter release and depolarization[65,144] (Figure 3A). A hallmark of diffuse TBI is axonal damage, with visible degeneration of white matter tracts, as evidenced in CT and magnetic resonance imaging (MRI) brain imaging studies.[145,146] Stretching and shearing of cell membranes from TBI cause rapid sodium and calcium ion influx into neurons, resulting in cell membrane depolarization.[147] Shortly after the primary TBI injury, neutrophils arrive to contain the damage by removing cellular debris and damaged cells, although their action can also have pathogenic effects, especially in more severe TBIs.[148] In events such as TBI, damaged neurons undergoing nonapoptotic death release danger-associated molecular patterns (DAMPs), including S-100 proteins and other alarmins,[149,150] into the extracellular space where they can activate cytokine and pattern-recognition receptors (Figure 3B). Activation of these receptors, including purinergic and toll-like receptors (TLRs), especially on astrocytes and microglia, initiates an inflammatory response.[151]

Microglia are the resident macrophages of the brain and are endowed with highly motile processes that survey the brain for damage and maintain homeostasis.[152] DAMPs inform an immune reaction that causes a phenotypic shift in microglia from a resting or "surveying" state in to an "activated" pro- or anti-inflammatory state, traditionally referred to as M1 and

DOI: 10.1021/acsptsci.9b00003
ACS Pharmacol. Transl. Sci. 2019, 2, 66−91

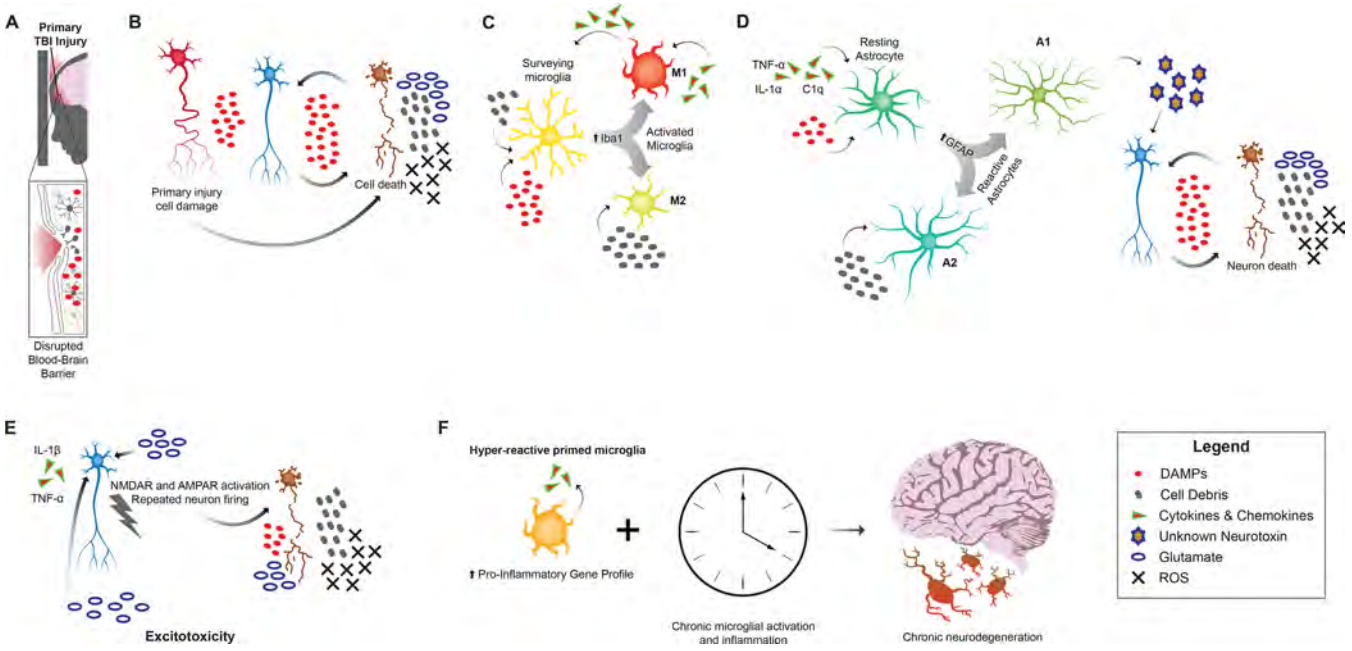

Figure 3. Mechanisms of TBI damage depend on severity. The primary TBI injury is scaled in the focal region and includes disruption of the blood-brain barrier (A) and direct injury to cells (B). This can result in cell death and release of intracellular contents including neurotransmitters, ROS, and other cell debris which act upon surrounding cells in a cascading fashion. Microglia phagocytize cell debris and detect damage signals that result in increased Iba1 expression, phenotypic shifts, and altering roles for microglia (C). M1 microglia act in a pro-inflammatory manner, releasing cytokines and chemokines that act in a paracrine and autocrine fashion alerting surrounding cells that damage has occurred. This initiates recruitment of other cells to respond. M2 microglia maintain a phagocytic role and continue to clear cell debris and release anti-inflammatory cytokines. DAMPs from damaged cells and cytokines released from M1 microglia, including Il-1α, C1q, and TNF-α, act upon resting astrocytes and initiate the formation of reactive astrocytes, most commonly characterized by increases in GFAP expression (D). A2 astrocytes are theorized to be reparative and maintain a phagocytic capability, clearing damage, while A1 astrocytes lose this ability and produce an unidentified neurotoxin that acts on surrounding neurons. Following TBI, astrocytes have decreased capability to transport free glutamate. This, compounded with cytokine, specifically TNF-α and IL-1β, initiated increases in glutamate production in neurons and the activation of glutamate receptors from excess interstitial glutamate, causes a classic excitotoxic response that damages healthy neurons and eventually can lead to cell death (E). Microglia affected during the TBI injury or secondary phase of the injury may become chronically activated with an overall increased pro-inflammatory profile (F). These cells are hyper-reactive to inflammatory stimuli (including subsequent TBIs) and have been implicated in the progression of long-term neurodegeneration and related diseases.

M2, respectively[153] (Figure 3C). However, this commonly used dichotomous nomenclature does not fully encompass the phenotypic diversity of microglia,[154] further supported by recent single cell RNA-sequencing of microglia throughout a mouse lifespan and following injury[155] as well as characterization of region-specific genetic diversity in mice[156] and rats.[157] Indeed, previous studies have shown varied activation states of microglia across a wide variety of models of TBI,[158] although a more thorough investigation of the diversity of microglia populations following this acute insult is needed. Markers of general microglia activation include antibodies to ionized calcium-binding adaptor molecule 1 (Iba-1) and/or some combination of others such as CD68 or CD11b.[159] A recent murine-based study found that following mTBI-induced disruption of the BBB, there is damage to the glial limitans—a barrier of astrocytic GFAP-positive endfeet tiling nearly all cerebrovascular basal lamina and that is central to the selective permeability of the BBB—resulting in a purinergic receptor-dependent recruitment of microglia to support or replace the damaged astrocytes. These microglia formed a phagocytic barrier, preventing further leakage into the brain parenchyma and provided neuroprotection early in the injury.[144] This is just one example of the many roles of microglia during a traumatic pathological event. Regardless of the current microglial heterogeneity debate, chronic activation of microglia is a hallmark of secondary TBI injury in humans. This has been demonstrated up to 17 years post-TBI *in vivo*[146] and in post-mortem tissues.[160] Inflammation can persist years after a single TBI event in humans,[160] and animal models of TBI show chronic microglial activation as a primary mechanism for TBI secondary injury and CNS deficits.[161,162] Chronic microglial activation in the thalamus, remote to the focal injury, is closely related to the amount of thalamocortical damage.[146] Preliminary evidence in human TBI patients indicates a correlation between increased chronic thalamic microglial activation and greater cognitive deficits.[146] Furthermore, diffusion tensor MRI studies in humans support the hypothesis that damage to thalamico-cortical fiber tracts is a key factor underpinning deficits in executive function following TBI.[163] Additional evidence comes from age-dependent upregulation of activated microglia in the thalamus in healthy individuals and in several cortical regions in humans with AD.[164]

Microglia in brains of people subjected to insult, injury, or disease, as well as microglia in aging, are often found to be in a "primed" state; that is, microglia that express a pro-inflammatory gene profile and exhibit a hyper-reactive inflammatory response to subsequent disturbances when compared to naïve cells.[165−167] Such priming of microglia is also thought to contribute to long-term effects of even a singular TBI event. Subsequent TBIs exacerbate the inflam-

DOI: 10.1021/acsptsci.9b00003
ACS Pharmacol. Transl. Sci. 2019, 2, 66−91

mation response in these cells[166,168] (Figure 3F). In addition, chronically activated microglia interact with neurons, removing excess synapses,[169,170] and release higher basal levels of cytokines.[168,171] In animal models of brain injury and aging, Kim Green and colleagues have experimented with "resetting" the microglial phenotypic profile by pharmacologically (via colony-stimulating factor 1 receptor inhibition) ablating primed microglia and repopulating them via drug withdrawal. Microglia-depleted mice experience no behavioral deficits,[172] and when repopulated following injury or in aging models, microglia are morphologically naive. These animals experience decreased inflammation profiles, rescued behavioral outcomes, and increased dendritic spine numbers.[173] Aged mice with repopulated microglia show similar microglial densities, morphologies, and overall gene expression profiles as those of young adults, with increased neuronal function and reversal of impairments in long-term potentiation (LTP).[170] Though responses to inflammatory stimuli remain unchanged in the repopulated microglia, these improvements are notable. Importantly, this reveals links to long-term deleterious implications of primed microglia involvement in chronic neurodegeneration and the aging process. Another recent study corroborates Elmore et al. (2018)[170] with findings that microglial repopulation in aged mice reverts microglial phenotypes but does not change responses to subsequent inflammatory stimuli; deleterious environmental cues such as astrocyte activation remain after repopulation and contribute to hyper-reactivity of the new microglia.[174] Microglia depletion and repopulation therapies have been tested successfully across a wide range of animal models.[175] Only recently has this therapy been utilized in a TBI model, reducing both inflammation-related gene profiles and astrogliosis following injury.[176] Future research is needed to show cognitive effects of microglia replacement following TBI.

Shortly after TBI, cytokine and chemokine protein expression are upregulated.[177] This orchestra of proteins includes CCL2, CCL20, CCL21, Il-1α, IL-1β, IL-6, IL-10, TNF-α, IL-8, iNOS, MHCII, IL-12p40[177−179] and the complement cascade (including C1q and complement component 3 (C3)).[180−182] These proteins facilitate a panoply of both deleterious and restorative processes[179] and can act in a paracrine or autocrine fashion. Increased C3 active fragments are observed in human TBI patients.[181,182] In mouse models, pharmacological inhibition of C3 active fragment formation[183] and C3 knock out (KO) mice[184] provide neuroprotection following TBI. Release of Il-1α, TNF-α, and C1q by activated microglia is sufficient to induce the formation of neurotoxic A1 astrocytes that produce a neurotoxin capable of inducing rapid death of subsets of neurons and oligodendrocytes[185] (Figure 3D). This so-called "A1" astrocyte profile, characterized by high C3 protein expression (among others), is prevalent in normal aging[186] and chronic neurodegenerative diseases such as PD, AD, ALS, and HD.[185] Normally aged triple-KO mice (mice that do not produce Il-1α, TNF-α, and C1q) have significantly reduced A1 gene profiles,[186] highlighting a role for primed microglia in the development of this cell phenotype in normal aging. Microglia depletion therapy in mice prevented TBI-induced increases of IL-1α and C1q and downstream astrogliosis.[176] There is increasing interest in the role of C3 and the complement cascade in the exacerbation of secondary injury and chronic neuroinflammation following TBI.[180] Recent work shows that targeted inhibition of C3 activation in a controlled cortical impact (CCI) TBI model improves cognitive recovery and inhibits chronic neuroinflammation and neurodegeneration.[187] Furthermore, aged C3 deficient mice lack age-related neuronal functional deficits in the hippocampus,[188] and pharmacologic or genetic inhibition of the complement pathway following TBI in aged mice prevents cognitive deficits.[189] The acute inflammatory environment immediately following a TBI and the long-term elevation of TNF-α from primed microglia may, likewise, be implicated in impaired memory via altered astrocyte activity and signaling,[190] again highlighting the importance of understanding the crosstalk between multiple cells types following brain trauma. It is important to note that the inflammatory response is not wholly adverse. For example, inflammatory mediators such as TNF-α also induce CNS repair. In a TBI model using transgenic mice that did not produce TNF-α, wild type mice recovered motor function faster and experienced less cortical tissue loss from the injury.[191]

Astrocytes respond to pro- and anti-inflammatory cytokines in a "context-dependent" manner that allows for a diverse range of phenotypic subtypes.[192] These "reactive astrocytes" have traditionally been characterized by increased GFAP expression;[193] however, increased GFAP expression is not limited to the A1 variety[194] (Figure 3D). Indeed, GFAP is an important marker for TBI pathology, as upregulated levels of astrocyte-derived GFAP in the blood serum of TBI patients is recognized as an accurate indicator of TBI severity.[143] Though not fully understood, GFAP serum levels in older patients may not be as accurate an indicator of TBI as in younger patients.[195] Although the biological role of the "neurotoxic" A1 astrocytes is not well-defined, this cell population is clearly involved in the neurodegenerative process. Importantly, such a role is not exclusive among astrocytic involvement in TBI. Participation of other inflammation-induced subtypes of astrocytes, such as the "A2" variety,[194] appear to play crucial roles in mitigating TBI pathology by providing neuroprotection via a variety of mechanisms.[192,196] In synopsis, glial cells appear to take on many different activities during pathological events, and it is the balance between these that ultimately defines the final outcome.

Excitotoxicity is a common pathological feature of secondary TBI injury arising from excess extracellular glutamate, the prominent excitatory neurotransmitter[171,197] (Figure 3E). Regional microdialysis studies have reported elevations of glutamate immediately following TBI that appear to depend on both injury severity, with a prolonged elevation in severe traumas, and the number of physiological variables involved.[198−200] Astrocytes are largely responsible for the uptake of extracellular glutamate via glutamate transporters[201] and following TBI, decreased expression of these transporters in astrocytes has been demonstrated in animal models[202] and in humans.[203,204] Astrocytes[205,206] and microglia[207,208] responded to TNF-α by amplifying glutamate release. TNF-α, together with Il-1β, increases neuronal production and release of glutamate, further escalating extracellular levels of the neurotransmitter[209] (Figure 3E). Research describing the role of TNF-α in mediating excess interstitial glutamate is growing, and there is extensive interest in using drugs to reduce this cytokine's activity across a wide variety of CNS conditions and injuries.[210,211] Excess glutamate leads to overstimulation of postsynaptic glutamatergic receptors, specifically the *N*-methyl-D-aspartate receptors (NMDARs) and 2-amino-3-[3-hydroxy-5-methylisoxazol-4-yl] proprionate receptors (AMPARs), which allow calcium entry into cells and causes neuron

DOI: 10.1021/acsptsci.9b00003
ACS Pharmacol. Transl. Sci. 2019, 2, 66−91

Table 3. Pharmacologic or Genetic Intervention of Cell Death Pathways in TBI[a]

Pharmacologic or Genetic Intervention	TBI Model/Outcome
Caspase-8 -/-	• *CCI*: Reduced injury size, apoptosis, reduced caspase-3 processing[a]
Caspase inhibitors	• *CCI* + secondary insult: Reduced contusion size, caspase-3 activity and DNA fragmentation but no functional benefit[b] • *FPI*: Improved motor and spatial learning[c] • *CCI*: Improved motor and cognitive function[d] • *CCI*: No improved functional or histological outcomes but reduced caspase-3 activity and cytochrome c expression[e]
Cyclin D1 -/-	• *CCI*: Reduced cell cycle activation, decreased lesion volume and microglial activation[f]
Cell Cycle inhibitors	• *FPI*: Decreased neuronal cell death, lesion size, glial activation, and improved cognitive recovery[g] • *FPI*: Decreased glial activation, oxidative stress, neuronal cell loss, and improvements in cognitive function[h]
p53 -/-	• Improved neuromotor function (cell loss not attenuated)[i]
p53 inhibitors	• *CCI*: Reduced lesion size and inhibition of NF-κB[j] • *CCI*: Decreased contusion volume, apoptosis, protection from glutamate excitotoxicity[k] • *CCI*: Improved motor deficits and memory and decreased apoptosis and apoptosis related gene expression[l] • *CCI*: Improved motor deficits and reduced oxidative damage, glial activation, inflammation, and apoptosis[m]
PARP -/-	• *CCI*: Improved motor and memory function but no effect on contusion volume[n]
PARP-1 inhibitor	• *FPI*: No effect on TUNEL-positive apoptotic cells but significantly reduced lesion size[o] • *CCI*: Decrease neuron death, microglial activation, and neurological deficits[p] • *CCI*: Reduced inflammation and glial cell activation[q]
AIF deficient (hq_{hom})	• *CCI*: Decreased neuronal cell death[r]
CypA -/-	• *CCI*: Reduced apoptotic cells and improved motor and cognitive recovery[s]
Bax Inhibitor-1 Tg	• *CCI*: Reduced brain lesion volumes and improved motor performance[t]
Bcl-2 Tg	• *CCI*: Reduced lesion volume in cortex and hippocampus with reduced glial cell activation[u] • *CCI*: Reduced lesion volume. No effect on composite motor scores or hippocampal death[v]
Bid -/-	• *CCI*: Decreased early cell death and tissue damage but no effect on functional outcome deficits[w]
Bax -/-	• *CCI*: Improved neurogenesis and increased neural progenitors[x]
TNFR -/-	• *CCI*: Reduced cortical lesion volume and improved BBB integrity[y]
MnSOD Tg	• *CCI*: Reduced cortical lesion volume and improved BBB integrity[y]

[a]Evidence for mechanisms of cell death in TBI are shown from pharmacologic (red) or genetic (green) disruption of these pathways. Included are transgenic (Tg) and knockout (−/−) animals of relevant cell death pathways. Effects of these interventions following TBI are shown on the right. Adapted from Schoch et al. (2012).[255] CCI = controlled cortical impact; FPI = fluid percussion injury; hq_{hom} = homozygous Harlequin mice. Sources: (a) 241; (b) 242; (c) 243; (d) 244; (e) 245; (f) 228; (g) 227; (h) 229; (i) 246; (j) 232; (k) 233; (l) 238; (m) 20; (n) 218; (o) 247; (p) 217; (q) 220; (r) 248; (s) 222; (t) 249; (u) 250; (v) 251; (w) 252; (x) 253; (y) 254.

depolarization and further glutamate release.[212] Overstimulation of these receptors leads to intracellular ionic imbalance, with excess calcium playing important roles initiating intracellular cascades and cell damage (Figure 3E). Altered calcium homeostasis can lead to calcium-dependent cysteine protease, or calpain, activation which amplifies pro-apoptotic signaling, including activation of BID, BAX, and p53, while decreasing antiapoptotic Bcl-2 protein. This leads to neuronal dysfunction and apoptosis,[213] and at very high levels of calpain activation, necrosis can result.[214]

In response to elevated levels of ROS and subsequent DNA damage during TBI, overactivation of poly(ADP-ribose) polymerase-1 (PARP-1) may result and is associated with depletion of cellular energy stores and necrosis.[215] PARP-1 inhibition shows improved outcomes in animal models of TBI[216−218] (Table 3) and increased expression of PARP-1 has been demonstrated following human TBI.[219] Along with its involvement in microglial activation,[217,220,221] PARP-1 promotes the mitochondrial release of apoptosis inducing factor (AIF) and its carrier protein cyclophilin A (CypA).[222,223] AIF is then translocated to the nucleus where it initiates chromatin condensation, DNA fragmentation, and ultimately cell death[223] (Table 3). Uniquely, this cell death pathway is caspase independent.[222] Additional cell death mechanisms can involve the initiation of cell-cycle activation (CSA). Neurons are postmitotic cells though CSA pathways may be reinitiated from oxidative stress and DNA damage induced from TBI or other insults.[224,225] This is supported by increased expression of the CSA markers cyclin D1, CDK4, E2F5, c-myc, and PCNA and downregulation of cell cycle inhibitors following TBI.[226] Genetic or pharmacologic inhibition of CSA in animal models of TBI show decreased cell death, glial activation, lesion size, and improved cognitive recovery[227−229] (Table 3).

Following even mild cases of TBI, apoptotic pathways rise acutely and are sustained in the long term.[230] Hyperactivity in neurons and decreased blood flow to the focal injury leads to increased metabolic stress and subsequent depletion of adenosine triphosphate (ATP) stores. This may cause high levels of ROS which can lead to cell death.[231] Within neurons, the transcription factor p53 is activated and results in delayed apoptotic cell death in the subacute period after TBI (as well as in response to oxidative stress, glutamate excitotoxicity, and other insults). In a CCI model of TBI in mice, p53 levels were found to be elevated in the brain as early as 15 min after the TBI procedure and time-dependently rose and was sustained over time.[232] At 5 h after TBI, a robust increase in p53-labeled

DOI: 10.1021/acsptsci.9b00003
ACS Pharmacol. Transl. Sci. 2019, 2, 66−91

cells was evident within the site of maximal CCI injury in the brain.[233] Stable inhibitors of p53 (Table 3), pifithrin-α (PFT-α) and analogues,[234,235] have been shown to minimize apoptotic cell death by inhibiting p53 transcriptional activity and preventing p53-dependent activation of apoptotic pathways.[236,237] This is also purported in rodents challenged with CCI-induced moderate TBI[20,232,233,238] as well as weight drop-induced mild TBI,[18] resulting in substantial mitigation of ensuing neuronal loss and cognitive deficits with a therapeutic window of 5 to 7 h after injury. These studies clearly demonstrate that the secondary TBI phase of cell death involves apoptosis and that post-TBI inhibition of apoptotic mechanisms can mitigate the associated deficits. Whereas PFT-α and analogues are pharmacological tools to inactivate p53-dependent pathways; importantly, approved classes of drugs can likewise prevent neuronal p53-dependent apoptosis *without* the potential concerns of globally blocking p53 activity. In addition to transactivation of multiple apoptotic gene pathways within the nucleus, p53 also mediates apoptosis by binding and inactivating the antiapoptotic proteins Bcl-xL and Bcl-2 on the mitochondrial surface and directly activating the apoptotic proteins Bak and Bax. Mitochondrial p53 translocation induces mitochondrial outer membrane permeabilization (MOMP) via Bak and Bax, release of mitochondrial proapoptotic factors (e.g., cytochrome *c*, Smac/DIABLO, PUMA, and AIF) into the cytosol, and subsequent activation of caspase 3-dependent apoptosis.[234,236,237,239,240] A thorough summary of the effects of various genetic and pharmacologic disruptions of cell death pathways following TBI is shown in Table 3.

Animal Models of TBI. Significant heterogeneity across the spectrum of clinical TBI subtypes necessitates a wide range of models to mimic aspects of human injury. Although similar GCS scores may indicate similar levels of injury, the appearances of those injuries can vary widely, including the presence of hematomas, cerebral contusions, pneumocephaly, hemorrhaging, and subdural hydromas,[256] or none of these at all. A wide range of models of TBI are necessary to evaluate the random nature of the injury. Although larger animals have been used in modeling TBI,[257] their expense and ethical concerns have shifted the scientific community to primarily use rodents for these studies. Arguments for the use of larger animals in these studies cite differences in the size and structure of rodent brain compared to human (lissencephalic versus gyrencephallic), clinically relevant monitoring ability (intracranial pressure, brain tissue oxygen content, and cerebral blood flow), and possible differences in mechanisms of repair.[257,258] The body of work using rodent models continues to grow due to the low cost, standardized methodologies, especially regarding behavioral testing, and ease of manipulating complex molecular cascades via pharmacologic or genetic means[255,259] (see Table 3). A focus on animal models that resemble mild human head injury is essential, as a majority (>70%) of human TBI's are classified as mild.[260]

The most commonly used models include the weight drop (WD) method, controlled cortical impact (CCI), and fluid percussion injury (FPI), and more recently models of blast injury to understand the large number of TBI cases from military personnel (all reviewed extensively).[3,259] Although rodents are primarily used in these models, they are amenable to larger species.[3] The CCI and FPI models require removal of a piece of skull (craniectomy in CCI and craniotomy in FPI) in a region of interest and are defined by a controlled pressure pulse initiated by either the tip of a rod attached to the CCI device or a pendulum striking a piston attached to a reservoir of fluid for the FPI device. Albeit the direct impact onto the dura and method of injury makes these models not completely analogous to common head injuries seen in humans, they are particularly effective at consistent and graded injuries.[3] The WD and blast models of TBI both utilize closed head injuries whereby a weight is dropped through a cylindrical tube of a predetermined height (such as 80 cm) and onto the head of an anesthetized mouse or the anesthetized mouse is exposed to some variation of blast waves from a controlled open-field explosion of TNT.[3] Due to the limitations and danger of explosives, increased use of "shock tubes" that use compressed gas to deliver shock waves are expanding the research of blast TBI.[261] These injury models closely resemble common clinical cases of TBI incurred through falls, sports injuries, traffic accidents,[262] or on the battlefield.[261]

The use of standard behavioral assays in rodent models are valuable for understanding cognitive deficits in human TBI, often considered a silent symptom of the condition. WD, CCI, FPI, and blast TBI models all demonstrate cognitive deficits (cited in Table 4). This is manifested in a neurological severity score (NSS), which combines behavioral and motor function performance tests (see ref 263), or in some cases, more simplified behavioral assays of memory such as the novel object recognition (NOR) or Y-Maze spontaneous alteration tests.[3] Previous WD-based studies confirm the visual memory deficits demonstrated by the NOR test at 7 and 30 days post-TBI,[81,84,264−266] although memory deficits demonstrated via the Y-maze are often evident but not as consistent across these same studies. This highlights the heterogeneity across mTBI injury and potential inconsistency in delivery of the TBI, which is in line with the human condition in which no two TBI events are identical. Depressive effects of mTBI are evaluated by the forced swim test and have been observed 7 days (for the 70 g WD) and 30 days (50 and 70 g WD) post-TBI. This is notable, as depression is a common symptom in human TBI patients.[267]

In addition to assessing behavioral and motor outcomes, WD, CCI, FPI, and blast models of TBI demonstrate a wide variety of pathophysiological sequelae similar to human TBI including (a) neuroinflammation, epitomized by increased cytokine production and microglial (increased Iba1 expression) and astrocyte (increased GFAP expression) activation; (b) apoptotic signaling and cell death/neurodegeneration indicated by increased TUNEL and BID positive cell staining, decreased neuronal nuclei (NeuN) staining, and increased protein expression of proapoptotic AIF, BAX, and caspases; (c) decreased synaptic plasticity and function shown by deficits observed in long-term potentiation (LTP) in brain slice preparations and decreased synaptic protein expression, such as synaptophysin; (d) blood-brain barrier degradation as evidenced by Evans blue dye or other blood-originating tracers entering into brain tissue following TBI; (e) oxidative stress shown by increased production of antioxidants, ROS, or remnants of oxidation such as malondialdehyde using thiobarbituric acid reactive species (TBARS) assays in brain tissue; and finally (f) glutamate regulation dysfunction shown by decreases in glutamate transporters, RNA sequencing data, or increases in free extracellular glutamate. A summary of the many studies demonstrating the effects observed in WD, blast, FPI, and CCI TBI models is shown in Table 4. Work demonstrating glutamate toxicity is lacking across all models

DOI: 10.1021/acsptsci.9b00003
ACS Pharmacol. Transl. Sci. 2019, 2, 66−91

Table 4. Observed Effects Following Animal Models of TBI[a]

	↑Iba1/microglial activation	↑GFAP/astrocyte activation	cytokine elevation	cognitive deficits	apoptotic signaling	cell death/ neurodegeneration	↓synaptic plasticity/ function	↓BBB integrity	oxidative stress	glutamate regulation
WD	74, 268−270	74, 265, 271, 272	74, 264, 265, 268, 270, 271, 273, 274	18, 19, 74, 84, 264, 265, 275−278	18, 232, 265, 276, 279	18, 74, 265, 280	281, 282	283, 284	19, 277	19, 285
Blast	286, 287	288−292	293, 294	86, 87, 293, 295	286, 292, 296	86, 286, 293	87, 297, 298	287, 296	287, 290, 292−294, 296	292
FPI	176, 229, 299, 300	176, 227, 229, 301−303	176, 299, 302, 304, 305	229, 299, 303, 305, 306	229, 299, 303, 305, 306	301, 306−309	310−312	302, 308, 313	229, 303, 312, 314	309, 315−318
CCI	161, 220, 319−324	20, 320, 323	20, 322, 324, 325	228, 244, 324	20, 242, 245, 249, 324	20, 228, 242, 244, 245, 249, 321, 326, 327	327, 328	85, 326, 329, 330	20, 321, 324, 326, 327, 331	198, 332−334

[a]The weight drop (WD), blast, fluid percussion injury (FPI), and closed cortical impact models of TBI effectively model pathophysiological sequalae of TBI in humans. Differences in reproducibility and applicability to human injury should be assessed before using one model over another, as each model has its own positive features and caveats. BBB = blood-brain barrier.

and generally relies on indirect indicators of glutamate regulation issues. Although rodent models of TBI are extremely useful, development of standardized models of TBI in larger animals should facilitate transfer to clinical trials.[258]

Incretin-Based Signaling To Counteract TBI Damage Mechanisms. GLP-1 and GIP are gastrointestinal peptide hormones with well-studied functions in glucose-dependent insulin secretion. Gcg has an opposing physiological effect, increasing glucose concentrations in the blood. As members of the glucagon peptide family, GLP-1 and Gcg are derived from the same proglucagon gene, while GIP originates from the GIP gene.[335] All three peptides are susceptible to cleavage and neutralization by the enzyme DPP-IV (Figure 1), reducing active endogenous levels of each within minutes after production and release.[29,30] Three forms of endogenous GLP-1 have been studied for their insulinotropic effects: the full-length form of GLP-1 (1−37), the truncated form of GLP-1 (7−37), and the truncated amide form (7−36 amide). Only the truncated forms have been found to stimulate glucose-dependent insulin secretion, while the full-length form appears inactive.[336] Most of the truncated GLP-1 that is produced undergoes amidation on its c-terminal glycine to form GLP-1 (7−36) amide. The benefit from amidation is unknown; it is thought that the amide form is more stable in the circulation, considering that GLP-1 (7−36) amide constitutes 70% or more of circulating GLP-1.[337]

The receptors for GLP-1, GIP, and Gcg are class B G-protein coupled receptors (GPCRs). Although the receptors for GIP and GLP-1 are predominantly expressed in the pancreatic islet cells[21,22] and those of Gcg in the liver,[338] all three are present in the CNS.[339−341] GLP-1R, GIPR, and GcgR mRNA are chiefly expressed in neurons,[342] and differential GLP-1R protein expression has been observed throughout the brain.[343,344] Under pathological conditions, such as in PD or TBI, expression of GLP-1R mRNA in affected brain regions and cells types can change drastically.[345] Observations in a mouse model of PD demonstrate decreased expression in neurons and 2-fold increases in microglia.[93] Additionally, human PD cases show 10-fold increases in GLP-1R expression in the substantia nigra.[93] These receptors have seven α-helical transmembrane domains (TMDs), a classic signature of all GPCRs, and an N-terminal extracellular domain (ECD) typical of class B GPCRs. The TMDs bind the N-terminal portion of the truncated GLP-1 peptide and the ECD binds the C-terminal portion of the peptide,[346] with multiple binding sites biasing activated intracellular cascades.[347−349] Unlike class A GPCRs, the class B ECD acts as more than an affinity trap, as both the ECD and TMD are responsible for class B GPCR activation.[350] All three receptors' activation can lead to neuroprotection and neurotrophic effects through multiple pathways.

Activated receptors interact with Gαs and dissociate the trimeric G protein to activate adenylyl cyclase and subsequent conversion of ATP to cAMP[27,335,351] (Figure 4). Upon GLP-1 addition, cAMP concentrations reach a peak at the 15 min time-point in PC12 cells,[33,51] neuroblastoma SH-SY5Y cells,[352] and rat hippocampal cells,[35] leading to cAMP-dependent protein kinase A (PKA) and exchange protein activated by cAMP (Epac) activation.[353−355] PKA directly activates the cAMP-responsive element binding protein (CREB) by phosphorylating Serine 133 on the protein.[356] CREB is a transcription factor with a well-studied role in neuronal plasticity and neuronal survival; it is regulated by multiple

DOI: 10.1021/acsptsci.9b00003
ACS Pharmacol. Transl. Sci. 2019, 2, 66−91

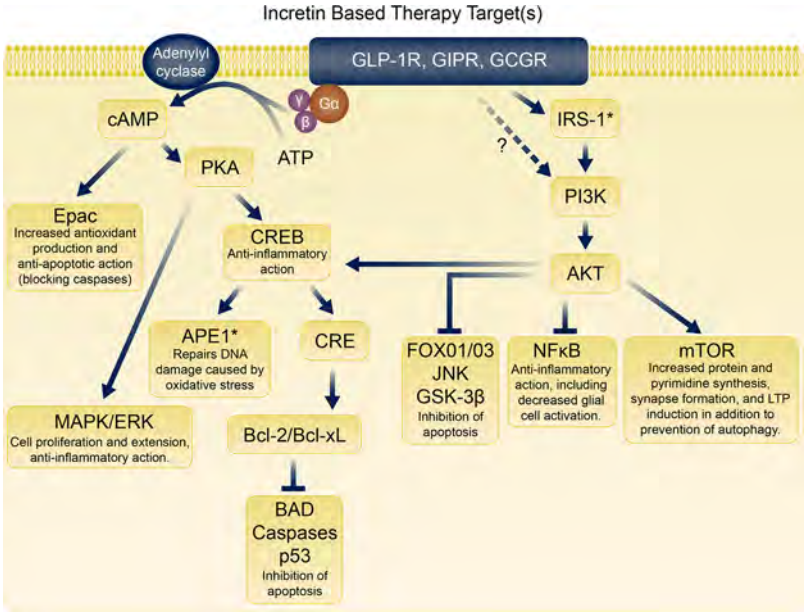

Figure 4. Incretin-based signaling to counteract TBI. Incretin based therapies target key cell signaling pathways that counteract TBI secondary phase injury. These include mechanisms to decrease apoptosis, inflammation, and oxidative stress, while also promoting repair. *Only demonstrated through GLP-1R agonism.

pathways in addition to the cAMP associated route, including the phosphatidylinositol-4,5-bisphosphate 3-kinase (PI3K)/AKT pathway.[357] Epac activation leads to similar downstream events.[354] Increasing circulation times of endogenous GLP-1, GIP, and Gcg via DPP-IV inhibition increases CREB activation.[91] Furthermore, Perry et al.[33] showed that activation of PKA nonessentially enhances GLP-1 mediated neuroplasticity in PC12 cells, and PI3K and ERK were found to play a role in neurite extension as a result of GLP-1R activation.[33]

The mechanism of GLP-1R/GIPR/GcgR activation of the PI3K pathway is unclear. However, GLP-1R appears to initiate this neurotrophic pathway near its beginning, as activation of the upstream protein, insulin receptor substrate-1 (IRS-1), was found to be markedly increased one hour after Ex-4 administration in hypothalamic neurons[358] (Figure 4). Downstream, the neuronal PI3K pathway branches to produce a variety of protective and neuroplastic effects. AKT, also known as Protein Kinase B (PKB), promotes cell survival by phosphorylating and thereby sequestering pro-apoptotic protein Bad, which normally heterodimerizes and neutralizes the mitochondria associated antiapoptotic protein, Bcl-2. In addition, AKT inhibits p53,[359] Forkhead box protein O1/03 (FOXO1/03), and subsequent production of pro-apoptotic proteins.[335,360] AKT also promotes the activation of mTOR which supports neuronal differentiation and growth by increasing protein synthesis, pyrimidine synthesis, and preventing autophagy.[360] Direct phosphorylation of CREB by AKT further promotes cell survival, possibly in part by inducing the expression of Bcl-2.[361] Numerous benefits of activation of CREB and downstream cAMP responsive element (CRE) by a GLP-1/GIP/Gcg receptor triagonist were recently described in a mouse model of AD.[79] Furthermore, in a secondary analysis of the recent successful 48-week Exenatide-PD trial,[67] researchers extracted neuronal derived exosomes from blood serum of human participants, and within these exosomes, found increased protein levels of IRS-1, AKT, and mTOR.[362] These findings present a clinical context for the positive outcomes of the Exenatide-PD trial, which noted improvements in motor scores for patients, and furthers understanding of GLP-1R agonism in the human CNS.

Following TBI, much of the oxidative stress, excitotoxicity and inflammation observed in the injured brain can be attenuated by incretin-based therapies. Such actions are a clear parallel to antiapoptotic effects provided by GLP-1 and analogues on pancreatic cells[21] and have been demonstrated in neuronal cell culture models[51] and recent mouse models of stroke and chronic cerebral hypofusion.[363,364] Pretreatment of β-cells with Ex-4 and subsequent induction of oxidative stress via hydrogen peroxide (H_2O_2) addition resulted in a 41.7% decrease in apoptosis. This was mediated by AKT inhibition of the c-Jun N-terminal kinase (JNK) and glycogen synthase kinase 3β (GSK3β)-mediated apoptosis pathway[365] (Figure 4). A GLP-1/GIP/Gcg triagonist was also shown to block activation of GSK3β and is thought to be a potential mechanism for rescue of neuronal plasticity deficits in a mouse model of AD.[79] Activation of caspase-9 and -3, two important mediators of apoptosis, was also reduced as a result of this pretreatment. Treatment with Ex-4 in similar H_2O_2-induced oxidative stress experiments resulted in Epac-dependent increases in β-cell production of prominent antioxidant enzymes, including catalase, glutathione peroxidase-1, and manganese superoxide dismutase (MnSOD).[353] Following oxidative stress, activation of PKA and induction of oxidative defense genes *HO-1* and *NQO1* via Ex-4 improved cell viability in human umbilical vein endothelial cells.[366] A recent report describes mitigation of oxidative DNA damage in a model of stroke through neuronal GLP-1R activation and subsequent enhancement of PI3K-AKT-induced expression of apurinic/apyrimidinic endonuclease 1 (APE1),[367] a protein key to amplifying base excision repair of oxidative DNA damage[368,369] (Figure 4). Further evidence for the antioxidant effects of incretin-based therapies comes from the use of the DPP-IV

DOI: 10.1021/acsptsci.9b00003
ACS Pharmacol. Transl. Sci. 2019, 2, 66−91

inhibitor sitagliptin in a mouse model of TBI, which resulted in increased MnSOD production and overall improved outcomes[91] (Table 1). In a model of stroke, GLP-1 analogues induced similar increases in MnSOD production.[363]

Another important neuroprotective effect of incretin-based therapies includes a strong anti-inflammatory component, namely the reduction of glial cell activation and related cytokine production. In a model of PD, the GLP-1 analogue NYLO1 (Table 2) blocked the formation of A1 astrocytes, indicated by decreased C3 immunoreactivity. Significant reduction in the number of activated microglia and subsequent production and release of Il-1α, TNF-α, and C1q was also observed.[93] In this model, blocking the formation of A1 astrocytes proved to be a major mechanism preventing neuronal loss, attributable to the attenuated microglial activation. Yun et al.[93] and Athauda and Foltynie[360] point out that reduction in microglial activation or activity by GLP-1R agonists may be the primary mechanism for neuroprotection in models of stroke,[53,58,370,371] PD,[372] ALS,[64] and other conditions.[49,373] GLP-1R agonism in microglia promotes an M2 phenotype induction[58,374] possibly via alternative CREB mediated pathways,[375] increasing the anti-inflammatory and reparative functions of these cells. In models of TBI and related *in vitro* studies, incretin-based therapies have shown efficacy in increasing CREB signaling[75,83,84,91] and anti-inflammatory effects, including reduced glial cell activation and cytokine production using independent administration of GIP[88] and the GLP-1 analogue PT-302[74] (Table 1). PARP-1 is involved in microglial activation[221] and its inhibited expression by GLP-1 and analogues, shown in models of stroke and chronic cerebral hypofusion,[363,364] may provide an additional anti-inflammatory mechanism for GLP-1 based therapies. Finally, inhibition of NF-κB downstream of PI3K and AKT is yet another possible mechanism of GLP-1R agonism for the mitigation of inflammation-related sequalae.[360] NF-κB inhibition is neuroprotective in models of PD[376] and TBI,[232] with DPP-IV inhibitors and GLP-1 analogues significantly suppressing the transcription factor and potentially increasing endogenous inhibitors.[93,360] Though NF-κB induction is neuroprotective when activated in neurons, blockage of glial cell NF-κB induction supersedes this potential benefit through mitigation of the release of inflammatory mediators and other neurotoxic proteins.[377]

In synopsis, incretin-based therapies present a multitude of beneficial signaling end points that can readily be applied to TBI pathophysiological sequalae (Table 4). Considering the strong neurotrophic/neuroprotective, antioxidant, and anti-inflammatory components that underlie the actions of incretin-based therapies, all of which are beneficial for TBI pathophysiological effects, these compounds appear to be ideally suited for introduction into clinical trials for TBI.

Targeting Specific Intracellular Pathways. As shown above, incretin-based mimetics affect a wide variety of intracellular pathways. Interest in the many signaling profiles of GPCRs is growing, including that of incretin receptors, and investigation of how these diverse pathways are activated is an increasingly important area of research for the development of more effective, disease-specific therapies.[378] Evidence of various biased activation sites of incretin receptors, specifically GLP-1R, adds an additional layer of complexity to their known pleiotropic signaling and provides possible opportunities for optimization of signaling pathways to best treat TBI or other neurological disorders with reduced side effects. Recent work has described specific binding sites of the GLP-1R receptor that preferentially activate intracellular calcium recruitment and cAMP and pERK1/2 signaling in insulinoma cells.[349] Adding to this knowledge, replacing the α-amino acids of the endogenous GLP-1 backbone with β-amino acids has helped characterize further nuances in these signaling paradigms.[379] Biased agonism is not exclusively a function of receptor binding sites and ligand structure, but can also depend on effector molecules and adapter proteins recruited to or allosteric modulation of the GPCR.[380] β-arrestin proteins are regulators of GPCR activity, including receptor desensitization.[381] Varying the amino acid backbone of GLP-1R agonists differentially promotes characteristic G-protein signaling (cAMP, etc.) and β-arrestin recruitment,[382] with the impacts of effector molecules or adapter proteins on downstream signaling and phenotypic responses varying.[383] In pancreatic β-cells, for example, β-arrestin 1, recruitment has been shown to help facilitate the antiapoptotic effects of GLP-1 through the phosphorylation of the pro-apoptotic protein, Bad.[384]

As yet, little to no information is available elucidating the occurrence of GLP-1R biased agonism in nervous system tissue or in relation to contributions of GIP or glucagon,[383] but this clearly appears to be a potentially fruitful avenue to evaluate. Furthermore, the differential expression patterns of incretin receptors in neurons or microglia also may add another level of intricacy to understanding the diverse pathways initiated by both endogenous and designer agonists. Interest in nonpeptide GLP-1R agonists is substantial and an example is the experimental diabetes drug TTP273 (Table 2). TTP273 appears to be a functionally biased ligand with a favorable tolerability and low incidence nausea and vomiting.[385] Interestingly, TTP273 lacks any β-arrestin 2 recruitment typical of endogenous GLP-1R agonists,[385] which promotes stereotypic GPCR signaling cascades.[386] β-arrestin 2 recruitment, however, can attenuate this normal signaling pattern, with the GLP-1R/β-arrestin 2 complex increasing the receptor's affinity for glucagon and internalization of the receptor.[386] The route of administration (e.g., oral, subcutaneous injection, or transdermal) can also impact a drug's time-dependent pharmacological actions as well as compliance.[387] Preliminary evidence shows that TTP273 has differential effects on food intake depending on its route of administration.[385] Delivery to target sites is also paramount to initial drug design and, for the treatment of neurological disorders a reasonable BBB penetration is vital to support therapeutic levels being achieved in brain. In the case of TTP273 that was designed for T2DM and likely not intended for neurological disorders, BBB permeability was probably not a key concern during the agent's initial design, with preliminary evidence showing that brain drug concentrations are only 2 to 3% of that of plasma's,[388] similar to Ex-4.[67,74] With these many considerations, understanding the mechanisms of biased agonist signaling may allow for the development of disease tailored drugs, particularly in relation to incretin receptor agonists.

CONCLUSION

In the present review, we have provided an overview of the current literature supporting the use of incretin-based therapies across a wide variety of nervous system disease and injury models, including TBI. The safety, availability, and demonstrated efficacy of incretin-based therapies make them ideal for rapid introduction into clinical trials to evaluate alternative

DOI: 10.1021/acsptsci.9b00003
ACS Pharmacol. Transl. Sci. 2019, 2, 66−91

uses to their already prescribed treatment of metabolic diseases. There is a great and immediate need for an effective drug therapy for treatment of secondary injury related to TBI, especially considering the long-term consequences of even a single TBI injury, including the development of conditions such as PD and AD that can be triggered by TBI. Considering the dangers of even just one TBI, it is encouraging that the general public is heeding current science and increasingly seeking medical attention for head injuries. Unfortunately, there are no treatments for secondary injuries associated with TBI. Incretin-based therapies can fill this pharmacological void, and there is sound and increasing scientific evidence of using translationally relevant doses across both cellular and animal models of brain injury to support trials of evaluating incretin-based mimetics in human TBI. Biased, designer incretin-receptor agonists are currently in development and further work needs to be done to tailor these compounds to neurological disorders. The next questions to consider are as follows: (a) Which of the available agents should be first appraised? (b) Which TBI subjects (mild, moderate or severe) should be evaluated in clinical trials? (c) When should treatment start and how should it be initiated to rapidly achieve and maintain therapeutic brain levels? (d) How long should treatment continue? (e) What biochemical and clinical outcome measures should be evaluated to define target engagement and response? With the use of the dose and route of administration approved and found effective for the treatment of T2DM, it is encouraging that several FDA approved incretin-based therapies and other emerging analogues are making their way into clinical trials for neurological diseases. A concerted effort is needed to effectively apply these safe and efficacious drugs to trials for TBI treatment.

AUTHOR INFORMATION

Corresponding Authors

*E-mail: Greign@grc.nia.nih.gov.
*E-mail: Elliot.glotfelty@nih.gov.

ORCID

Nigel H. Greig: 0000-0002-3032-1468

Notes

The authors declare the following competing financial interest(s): The National Institutes of Health holds issued and in process patents on the use of incretin mimetics for the treatment of neurodegenerative disorders through the work of NHG who has assigned all his rights to the National Institute on Aging. All other coauthors declare no conflicts of interest.

ACKNOWLEDGMENTS

We would like to thank Lauren Brick of the Visual Media core at the National Institute on Drug Abuse for artistic assistance and design on figures throughout the manuscript. Work described here was partially funded in part by the Intramural Research Programs of the National Institute on Aging and the National Institute on Drug Abuse, National Institutes of Health. L.O. and T.K. are supported by the Swedish Medical Research Council and Brain Foundation. L.B.T.Y.R. is supported by the Mexican Academy of Sciences and PAPIIT-DGAPA (IN226617). B.J.H. is funded by NIH grant 1R01 NS094152. Yu L. is funded by NIH grant R01NS091213. The content is solely the responsibility of the authors and does not necessarily represent the official views of the National Institutes of Health.

REFERENCES

(1) Harrison-Felix, C., Kolakowsky-Hayner, S. A., Hammond, F. M., Wang, R., Englander, J., Dams-O'Connor, K., Kreider, S. E. D., Novack, T. A., and Diaz-Arrastia, R. (2012) Mortality After Surviving Traumatic Brain Injury: Risks Based on Age Groups. *J. Head Trauma Rehabil. 27* (6), E45−E56.

(2) Saatman, K. E., Duhaime, A.-C., Bullock, R., Maas, A. I. R., Valadka, A., and Manley, G. T. (2008) Classification of Traumatic Brain Injury for Targeted Therapies. *J. Neurotrauma 25* (7), 719−738.

(3) Deselms, H., Maggio, N., Rubovitch, V., Chapman, J., Schreiber, S., Tweedie, D., Kim, D. S., Greig, N. H., and Pick, C. G. (2016) Novel Pharmaceutical Treatments for Minimal Traumatic Brain Injury and Evaluation of Animal Models and Methodologies Supporting Their Development. *J. Neurosci. Methods 272*, 69−76.

(4) Greve, M. W., and Zink, B. J. (2009) Pathophysiology of Traumatic Brain Injury. *Mt. Sinai J. Med. 76* (2), 97−104.

(5) Pearn, M. L., Niesman, I. R., Egawa, J., Sawada, A., Almenar-Queralt, A., Shah, S. B., Duckworth, J. L., and Head, B. P. (2017) Pathophysiology Associated with Traumatic Brain Injury: Current Treatments and Potential Novel Therapeutics. *Cell. Molec. Neurobiol.*, 571−585, DOI: 10.1007/s10571-016-0400-1.

(6) U.S. Food and Drug Administration. *Traumatic Brain Injury: FDA Actions and Research* https://www.fda.gov/ForConsumers/ConsumerUpdates/ucm519116.htm (accessed Oct 10, 2018).

(7) Paniak, C., Reynolds, S., Phillips, K., Toller-Lobe, G., Melnyk, A., and Nagy, J. (2002) Patient Complaints within 1 Month of Mild Traumatic Brain Injury: A Controlled Study. *Arch. Clin. Neuropsychol. 17* (4), 319−334.

(8) Rabinowitz, A. R., and Levin, H. S. (2014) Cognitive Sequelae of Traumatic Brain Injury. *Psychiatric Clinics of North America 37*, 1−11.

(9) Gareis, M., Bauer, J., Von Montgelas, A., and Gedek, B. (1984) Stimulation of Aflatoxin B'1 and T-2 Toxin Production by Sorbic Acid. *Appl. Environ. Microbiol. 47* (2), 416−418.

(10) Daneshvar, D. H., Riley, D. O., Nowinski, C. J., McKee, A. C., Stern, R. A., and Cantu, R. C. (2011) Long-Term Consequences: Effects on Normal Development Profile After Concussion. *Physical Medicine and Rehabilitation Clinics of North America 22*, 683−700.

(11) Gardner, R. C., and Yaffe, K. (2015) Epidemiology of Mild Traumatic Brain Injury and Neurodegenerative Disease. *Mol. Cell. Neurosci. 66*, 75−80.

(12) Kalkonde, Y. V., Jawaid, A., Qureshi, S. U., Shirani, P., Wheaton, M., Pinto-Patarroyo, G. P., and Schulz, P. E. (2012) Medical and Environmental Risk Factors Associated with Frontotemporal Dementia: A Case-Control Study in a Veteran Population. *Alzheimer's Dementia 8* (3), 204−210.

(13) Masel, B. E., and DeWitt, D. S. (2010) Traumatic Brain Injury: A Disease Process, Not an Event. *J. Neurotrauma 27* (8), 1529−1540.

(14) Greig, N. H., Tweedie, D., Rachmany, L., Li, Y., Rubovitch, V., Schreiber, S., Chiang, Y.-H., Hoffer, B. J., Miller, J., Lahiri, D. K., et al. (2014) Incretin Mimetics as Pharmacologic Tools to Elucidate and as a New Drug Strategy to Treat Traumatic Brain Injury. *Alzheimer's Dementia 10*, S62−75.

(15) Hoffer, B. J., Pick, C. G., Hoffer, M. E., Becker, R. E., Chiang, Y. H., and Greig, N. H. (2017) Repositioning Drugs for Traumatic Brain Injury - N-Acetyl Cysteine and Phenserine. *J. Biomed. Sci. 9*, 71.

(16) Wang, J.-Y., Huang, Y.-N., Chiu, C.-C., Tweedie, D., Luo, W., Pick, C. G., Chou, S.-Y., Luo, Y., Hoffer, B. J., Greig, N. H., et al. (2016) Pomalidomide Mitigates Neuronal Loss, Neuroinflammation, and Behavioral Impairments Induced by Traumatic Brain Injury in Rat. *J. Neuroinflammation 13* (1), 168.

(17) Hall, E. D., Wang, J. A., Miller, D. M., Cebak, J. E., and Hill, R. L. (2019) Newer Pharmacological Approaches for Antioxidant Neuroprotection in Traumatic Brain Injury. *Neuropharmacology 145*, 247.

(18) Rachmany, L., Tweedie, D., Rubovitch, V., Yu, Q.-S., Li, Y., Wang, J.-Y., Pick, C. G., and Greig, N. H. (2013) Cognitive

DOI: 10.1021/acsptsci.9b00003
ACS Pharmacol. Transl. Sci. 2019, 2, 66−91

Impairments Accompanying Rodent Mild Traumatic Brain Injury Involve P53-Dependent Neuronal Cell Death and Are Ameliorated by the Tetrahydrobenzothiazole PFT-α. *PLoS One 8* (11), No. e79837.
(19) Tweedie, D., Fukui, K., Li, Y., Yu, Q. S., Barak, S., Tamargo, I. A., Rubovitch, V., Holloway, H. W., Lehrmann, E., Wood, W. H., et al. (2016) Cognitive Impairments Induced by Concussive Mild Traumatic Brain Injury in Mouse Are Ameliorated by Treatment with Phenserine via Multiple Non-Cholinergic and Cholinergic Mechanisms. *PLoS One 11* (6), No. e0156493.
(20) Huang, Y.-N., Yang, L.-Y., Greig, N. H., Wang, Y.-C., Lai, C.-C., and Wang, J.-Y. (2018) Neuroprotective Effects of Pifithrin-α against Traumatic Brain Injury in the Striatum through Suppression of Neuroinflammation, Oxidative Stress, Autophagy, and Apoptosis. *Sci. Rep. 8* (1), 2368.
(21) Campbell, J. E., and Drucker, D. J. J. (2013) Pharmacology, Physiology, and Mechanisms of Incretin Hormone Action. *Cell Metab. 17* (6), 819−837.
(22) Lovshin, J. A., and Drucker, D. J. (2009) Incretin-Based Therapies for Type 2 Diabetes Mellitus. *Nat. Rev. Endocrinol. 5* (5), 262−269.
(23) Drucker, D. J., Buse, J. B., Taylor, K., Kendall, D. M., Trautmann, M., Zhuang, D., and Porter, L. (2008) Exenatide Once Weekly versus Twice Daily for the Treatment of Type 2 Diabetes: A Randomised, Open-Label, Non-Inferiority Study. *Lancet 372* (9645), 1240−1250.
(24) Nauck, M., Stöckmann, F., Ebert, R., and Creutzfeldt, W. (1986) Reduced Incretin Effect in Type 2 (Non-Insulin-Dependent) Diabetes. *Diabetologia 29* (1), 46−52.
(25) Capozzi, M. E., DiMarchi, R. D., Tschöp, M. H., Finan, B., and Campbell, J. E. (2018) Targeting the Incretin/Glucagon System With Triagonists to Treat Diabetes. *Endocr. Rev. 39* (5), 719−738.
(26) Vollmer, K., Holst, J. J., Baller, B., Ellrichmann, M., Nauck, M. A., Schmidt, W. E., and Meier, J. J. (2008) Predictors of Incretin Concentrations in Subjects with Normal, Impaired, and Diabetic Glucose Tolerance. *Diabetes 57* (3), 678−687.
(27) Müller, T. D., Finan, B., Clemmensen, C., DiMarchi, R. D., and Tschöp, M. H. (2017) The New Biology and Pharmacology of Glucagon. *Physiol. Rev. 97* (2), 721−766.
(28) Tschöp, M. H., Finan, B., Clemmensen, C., Gelfanov, V., Perez-Tilve, D., Müller, T. D., and DiMarchi, R. D. (2016) Unimolecular Polypharmacy for Treatment of Diabetes and Obesity. *Cell Metab. 24* (1), 51−62.
(29) Deacon, C. F. (2004) Circulation and Degradation of GIP and GLP-1. *Hormone and Metabolic Research*, pp 761−765, Georg Thieme Verlag KG Stuttgart, New York, DOI: 10.1055/s-2004-826160.
(30) Pospisilik, J. A., Hinke, S. A., Pederson, R. A., Hoffmann, T., Rosche, F., Schlenzig, D., Glund, K., Heiser, U., Mcintosh, C. H. S., and Demuth, H.-U. (2001) Metabolism of Glucagon by Dipeptidyl Peptidase IV (CD26). *Regul. Pept. 96*, 133−141.
(31) Brandt, S. J., Götz, A., Tschöp, M. H., and Müller, T. D. (2018) Gut Hormone Polyagonists for the Treatment of Type 2 Diabetes. *Peptides 100*, 190−201.
(32) Eng, J., Kleinman, W. A., Singh, L., Singh, G., and Raufman, J. P. (1992) Isolation and Characterization of Exendin-4, an Exendin-3 Analogue, from Heloderma Suspectum Venom: Further Evidence for an Exendin Receptor on Dispersed Acini from Guinea Pig Pancreas. *J. Biol. Chem. 267* (11), 7402−7405.
(33) Perry, T., Lahiri, D. K., Chen, D., Zhou, J., Shaw, K. T. Y., Egan, J. M., and Greig, N. H. (2002) A Novel Neurotrophic Property of Glucagon-like Peptide 1: A Promoter of Nerve Growth Factor-Mediated Differentiation in PC12 Cells. *J. Pharmacol. Exp. Ther. 300* (3), 958−966.
(34) Perry, T., Lahiri, D. K., Sambamurti, K., Chen, D., Mattson, M. P., Egan, J. M., and Greig, N. H. (2003) Glucagon-like Peptide-1 Decreases Endogenous Amyloid-Beta Peptide (Abeta) Levels and Protects Hippocampal Neurons from Death Induced by Abeta and Iron. *J. Neurosci. Res. 72* (5), 603−612.
(35) Perry, T. (2002) Protection and Reversal of Excitotoxic Neuronal Damage by Glucagon-Like Peptide-1 and Exendin-4. *J. Pharmacol. Exp. Ther. 302* (3), 881−888.
(36) Salcedo, I., Tweedie, D., Li, Y., and Greig, N. H. (2012) Neuroprotective and Neurotrophic Actions of Glucagon-like Peptide-1: An Emerging Opportunity to Treat Neurodegenerative and Cerebrovascular Disorders. *Br. J. Pharmacol.*, 1586−1599, DOI: 10.1111/j.1476-5381.2012.01971.x.
(37) Kim, D. S., Choi, H.-I., Wang, Y., Luo, Y., Hoffer, B. J., and Greig, N. H. (2017) A New Treatment Strategy for Parkinson's Disease through the Gut-Brain Axis: The Glucagon-Like Peptide-1 Receptor Pathway. *Cell Transplant 26* (9), 1560−1571.
(38) Frias, J. P., Nauck, M. A., Van, J., Kutner, M. E., Cui, X., Benson, C., Urva, S., Gimeno, R. E., Milicevic, Z., Robins, D., et al. (2018) Efficacy and Safety of LY3298176, a Novel Dual GIP and GLP-1 Receptor Agonist, in Patients with Type 2 Diabetes: A Randomised, Placebo-Controlled and Active Comparator-Controlled Phase 2 Trial. *Lancet 392*, 2180.
(39) Jalewa, J., Sharma, M. K., Gengler, S., and Hölscher, C. (2017) A Novel GLP-1/GIP Dual Receptor Agonist Protects from 6-OHDA Lesion in a Rat Model of Parkinson's Disease. *Neuropharmacology 117*, 238−248.
(40) Ji, C., Xue, G.-F., Lijun, C., Feng, P., Li, D., Li, L., Li, G., and Hölscher, C. (2016) A Novel Dual GLP-1 and GIP Receptor Agonist Is Neuroprotective in the MPTP Mouse Model of Parkinson's Disease by Increasing Expression of BNDF. *Brain Res. 1634*, 1−11.
(41) Finan, B., Ma, T., Ottaway, N., Müller, T. D., Habegger, K. M., Heppner, K. M., Kirchner, H., Holland, J., Hembree, J., and Raver, C. (2013) Unimolecular Dual Incretins Maximize Metabolic Benefits in Rodents, Monkeys, and Humans. *Sci. Transl. Med. 5* (209), 209ra151.
(42) Finan, B., Yang, B., Ottaway, N., Smiley, D. L., Ma, T., Clemmensen, C., Chabenne, J., Zhang, L., Habegger, K. M., Fischer, K., et al. (2015) A Rationally Designed Monomeric Peptide Triagonist Corrects Obesity and Diabetes in Rodents. *Nat. Med. 21* (1), 27−36.
(43) Kim, J. A., Lee, S., Lee, S. H., Jung, S. Y., Kim, Y. H., Choi, I. Y., and Kim, S. J. (2018) Neuroprotective Effects of HM15211, a Novel Long-Acting GLP-1/GIP/Glucagon Triple Agonist in the Neurodegenerative Disease Models. *Diabetes 67* (Suppl. 1), 1107.
(44) Sloop, K. W., Briere, D. A., Emmerson, P. J., and Willard, F. S. (2018) Beyond Glucagon-like Peptide-1: Is G-Protein Coupled Receptor Polypharmacology the Path Forward to Treating Metabolic Diseases? *ACS Pharmacol. Transl. Sci. 1* (1), 3−11.
(45) Trujillo, J. M., Nuffer, W., and Ellis, S. L. (2015) GLP-1 Receptor Agonists: A Review of Head-to-Head Clinical Studies. *Therapeutic Advances in Endocrinology and Metabolism*, pp 19−28, SAGE Publications, DOI: 10.1177/2042018814559725.
(46) Ali, S., Lamont, B. J., Charron, M. J., and Drucker, D. J. (2011) Dual Elimination of the Glucagon and GLP-1 Receptors in Mice Reveals Plasticity in the Incretin Axis. *J. Clin. Invest. 121* (5), 1917−1929.
(47) Lee, C.-H., Jeon, S. J., Cho, K. S., Moon, E., Sapkota, A., Jun, H. S., Ryu, J. H., and Choi, J. W. (2018) Activation of Glucagon-Like Peptide-1 Receptor Promotes Neuroprotection in Experimental Autoimmune Encephalomyelitis by Reducing Neuroinflammatory Responses. *Mol. Neurobiol. 55* (4), 3007−3020.
(48) Hernández, C., Bogdanov, P., Solà-Adell, C., Sampedro, J., Valeri, M., Genís, X., Simó-Servat, O., García-Ramírez, M., and Simó, R. (2017) Topical Administration of DPP-IV Inhibitors Prevents Retinal Neurodegeneration in Experimental Diabetes. *Diabetologia 60* (11), 2285−2298.
(49) Gonçalves, A., Lin, C.-M., Muthusamy, A., Fontes-Ribeiro, C., Ambrósio, A. F., Abcouwer, S. F., Fernandes, R., and Antonetti, D. A. (2016) Protective Effect of a GLP-1 Analog on Ischemia-Reperfusion Induced Blood-Retinal Barrier Breakdown and Inflammation. *Invest. Ophthalmol. Visual Sci. 57* (6), 2584−2592.
(50) Marlet, I. R., Ölmestig, J. N. E., Vilsbøll, T., Rungby, J., and Kruuse, C. (2018) Neuroprotective Mechanisms of Glucagon-like Peptide-1-Based Therapies in Ischaemic Stroke: A Systematic Review

Based on Pre-Clinical Studies. *Basic and Clinical Pharmacology and Toxicology* No. 10.1111, 559−569, DOI: 10.1111/bcpt.12974.
(51) Li, Y., Perry, T., Kindy, M. S., Harvey, B. K., Tweedie, D., Holloway, H. W., Powers, K., Shen, H., Egan, J. M., Sambamurti, K., et al. (2009) GLP-1 Receptor Stimulation Preserves Primary Cortical and Dopaminergic Neurons in Cellular and Rodent Models of Stroke and Parkinsonism. *Proc. Natl. Acad. Sci. U. S. A. 106* (4), 1285−1290.
(52) Zhang, H., Liu, Y., Guan, S., Qu, D., Wang, L., Wang, X., Li, X., Zhou, S., Zhou, Y., Wang, N., et al. (2016) An Orally Active Allosteric GLP-1 Receptor Agonist Is Neuroprotective in Cellular and Rodent Models of Stroke. *PLoS One 11* (2), No. e0148827.
(53) Teramoto, S., Miyamoto, N., Yatomi, K., Tanaka, Y., Oishi, H., Arai, H., Hattori, N., and Urabe, T. (2011) Exendin-4, a Glucagon-like Peptide-1 Receptor Agonist, Provides Neuroprotection in Mice Transient Focal Cerebral Ischemia. *J. Cereb. Blood Flow Metab. 31* (8), 1696−1705.
(54) Hölscher, C. (2018) Novel Dual GLP-1/GIP Receptor Agonists Show Neuroprotective Effects in Alzheimer's and Parkinson's Disease Models. *Neuropharmacology 136* (Pt B), 251−259.
(55) Cao, Y., Hölscher, C., Hu, M. M., Wang, T., Zhao, F., Bai, Y., Zhang, J., Wu, M. N., and Qi, J. S. (2018) DA5-CH, a Novel GLP-1/GIP Dual Agonist, Effectively Ameliorates the Cognitive Impairments and Pathology in the APP/PS1Mouse Model of Alzheimer's Disease. *Eur. J. Pharmacol. 827*, 215−226.
(56) Li, Y., Duffy, K. B., Ottinger, M. A., Ray, B., Bailey, J. A., Holloway, H. W., Tweedie, D., Perry, T., Mattson, M. P., Kapogiannis, D., et al. (2010) GLP-1 Receptor Stimulation Reduces Amyloid-β Peptide Accumulation and Cytotoxicity in Cellular and Animal Models of Alzheimer's Disease. *J. Alzheimer's Dis. 19* (4), 1205−1219.
(57) McClean, P. L., Parthsarathy, V., Faivre, E., and Holscher, C. (2011) The Diabetes Drug Liraglutide Prevents Degenerative Processes in a Mouse Model of Alzheimer's Disease. *J. Neurosci. 31* (17), 6587−6594.
(58) Darsalia, V., Hua, S., Larsson, M., Mallard, C., Nathanson, D., Nyström, T., Sjöholm, Å., Johansson, M. E., and Patrone, C. (2014) Exendin-4 Reduces Ischemic Brain Injury in Normal and Aged Type 2 Diabetic Mice and Promotes Microglial M2 Polarization. *PLoS One 9* (8), No. e103114.
(59) Liu, W., Jalewa, J., Sharma, M., Li, G., Li, L., and Hölscher, C. (2015) Neuroprotective Effects of Lixisenatide and Liraglutide in the 1-Methyl-4-Phenyl-1,2,3,6-Tetrahydropyridine Mouse Model of Parkinson's Disease. *Neuroscience 303*, 42−50.
(60) Sancandi, M., Schul, E. V., Economides, G., CONSTANTI, A., and Mercer, A. (2018) Structural Changes Observed in the Piriform Cortex in a Rat Model of Pre-Motor Parkinson's Disease. *Front. Cell. Neurosci. 12*, 479.
(61) Cao, L., Li, D., Feng, P., Li, L., Xue, G.-F., Li, G., and Hölscher, C. (2016) A Novel Dual GLP-1 and GIP Incretin Receptor Agonist Is Neuroprotective in a Mouse Model of Parkinson's Disease by Reducing Chronic Inflammation in the Brain. *NeuroReport 27* (6), 384−391.
(62) Harkavyi, A., Rampersaud, N., and Whitton, P. S. (2013) Neuroprotection by Exendin-4 Is GLP-1 Receptor Specific but DA D 3 Receptor Dependent, Causing Altered BrdU Incorporation in Subventricular Zone and Substantia Nigra. *J. Neurodegener. Dis. 2013*, 1−9.
(63) Zhang, Y. F., Chen, Y. M., Li, L., and Hölscher, C. (2015) Neuroprotective Effects of (Val8)GLP-1-Glu-PAL in the MPTP Parkinson's Disease Mouse Model. *Behav. Brain Res. 293*, 107−113.
(64) Li, Y., Chigurupati, S., Holloway, H. W., Mughal, M., Tweedie, D., Bruestle, D. A., Mattson, M. P., Wang, Y., Harvey, B. K., Ray, B., et al. (2012) Exendin-4 Ameliorates Motor Neuron Degeneration in Cellular and Animal Models of Amyotrophic Lateral Sclerosis. *PLoS One 7* (2), No. e32008.
(65) Bramlett, H. M., and Dietrich, W. D. (2015) Long-Term Consequences of Traumatic Brain Injury: Current Status of Potential Mechanisms of Injury and Neurological Outcomes. *J. Neurotrauma 32* (23), 1834−1848.
(66) Becker, R. E., Kapogiannis, D., and Greig, N. H. (2018) Does Traumatic Brain Injury Hold the Key to the Alzheimer's Disease Puzzle? *Alzheimer's Dementia 14* (4), 431−443.
(67) Athauda, D., Maclagan, K., Skene, S. S., Bajwa-Joseph, M., Letchford, D., Chowdhury, K., Hibbert, S., Budnik, N., Zampedri, L., Dickson, J., et al. (2017) Exenatide Once Weekly versus Placebo in Parkinson's Disease: A Randomised, Double-Blind, Placebo-Controlled Trial. *Lancet 390* (10103), 1664−1675.
(68) Athauda, D., MacLagan, K., Budnik, N., Zampedri, L., Hibbert, S., Skene, S. S., Chowdhury, K., Aviles-Olmos, I., Limousin, P., and Foltynie, T. (2018) What Effects Might Exenatide Have on Non-Motor Symptoms in Parkinson's Disease: A Post Hoc Analysis. *J. Parkinson's Dis. 8* (2), 247−258.
(69) Aviles-Olmos, I., Dickson, J., Kefalopoulou, Z., Djamshidian, A., Kahan, J., Ell, P., Whitton, P., Wyse, R., Isaacs, T., Lees, A., et al. (2015) Motor and Cognitive Advantages Persist 12 Months After Exenatide Exposure in Parkinson's Disease. *J. Parkinson's Dis. 4* (3), 337−344.
(70) Aviles-Olmos, I., Dickson, J., Kefalopoulou, Z., Djamshidian, A., Ell, P., Soderlund, T., Whitton, P., Wyse, R., Isaacs, T., Lees, A., et al. (2013) Exenatide and the Treatment of Patients with Parkinson's Disease. *J. Clin. Invest. 123* (6), 2730−2736.
(71) Gejl, M., Gjedde, A., Egefjord, L., Møller, A., Hansen, S. B., Vang, K., Rodell, A., Brændgaard, H., Gottrup, H., Schacht, A., et al. (2016) In Alzheimer's Disease, 6-Month Treatment with GLP-1 Analog Prevents Decline of Brain Glucose Metabolism: Randomized, Placebo-Controlled, Double-Blind Clinical Trial. *Front. Aging Neurosci. 8* (MAY), 108.
(72) Chen, S., Yu, S.-J., Li, Y., Lecca, D., Glotfelty, E., Kim, H. K., Choi, H.-I., Hoffer, B. J., Greig, N. H., Kim, D.-S., et al. (2018) Post-Treatment with PT302, a Long-Acting Exendin-4 Sustained Release Formulation, Reduces Dopaminergic Neurodegeneration in a 6-Hydroxydopamine Rat Model of Parkinson's Disease. *Sci. Rep. 8* (1), 10722.
(73) Zhang, L., Zhang, L., Li, L., and Hölscher, C. (2018) Neuroprotective Effects of the Novel GLP-1 Long Acting Analogue Semaglutide in the MPTP Parkinson's Disease Mouse Model. *Neuropeptides 71*, 70−80.
(74) Bader, M., Li, Y., Lecca, D., Rubovitch, V., Tweedie, D., Glotfelty, E., Rachmany, L., Kim, H. K., Choi, H.-I., Hoffer, B. J., et al. (2019) Pharmacokinetics and Efficacy of PT302, a Sustained-Release Exenatide Formulation, in a Murine Model of Mild Traumatic Brain Injury. *Neurobiol. Dis. 124*, 439−453.
(75) Tamargo, I. A., Bader, M., Li, Y., Yu, S.-J., Wang, Y., Talbot, K., DiMarchi, R. D., Pick, C. G., and Greig, N. H. (2017) Novel GLP-1R/GIPR Co-Agonist "Twincretin" Is Neuroprotective in Cell and Rodent Models of Mild Traumatic Brain Injury. *Exp. Neurol. 288*, 176−186.
(76) Kosaraju, J., Tam, K. Y., and Basavan, D. (2017) Novel Dual GLP-1 and GIP Receptor Analog Attenuates High-Fat Diet-Induced Disease Progression in 3XTg-AD Mice. *Alzheimer's Dementia 13* (7), P671.
(77) Feng, P., Zhang, X., Li, D., Ji, C., Yuan, Z., Wang, R., Xue, G., Li, G., and Hölscher, C. (2018) Two Novel Dual GLP-1/GIP Receptor Agonists Are Neuroprotective in the MPTP Mouse Model of Parkinson's Disease. *Neuropharmacology 133*, 385−394.
(78) Tai, J., Liu, W., Li, Y., Li, L., and Hölscher, C. (2018) Neuroprotective Effects of a Triple GLP-1/GIP/Glucagon Receptor Agonist in the APP/PS1 Transgenic Mouse Model of Alzheimer's Disease. *Brain Res. 1678*, 64−74.
(79) Li, T., Jiao, J. J., Hölscher, C., Wu, M. N., Zhang, J., Tong, J. Q., Dong, X. F., Qu, X. S., Cao, Y., Cai, H. Y., et al. (2018) A Novel GLP-1/GIP/Gcg Triagonist Reduces Cognitive Deficits and Pathology in the 3xTg Mouse Model of Alzheimer's Disease. *Hippocampus 28* (5), 358−372.
(80) Heile, A. M. B., Wallrapp, C., Klinge, P. M., Samii, A., Kassem, M., Silverberg, G., and Brinker, T. (2009) Cerebral Transplantation of Encapsulated Mesenchymal Stem Cells Improves Cellular Pathology

DOI: 10.1021/acsptsci.9b00003
ACS Pharmacol. Transl. Sci. 2019, 2, 66−91

after Experimental Traumatic Brain Injury. *Neurosci. Lett. 463* (3), 176−181.
(81) Rachmany, L., Tweedie, D., Li, Y., Rubovitch, V., Holloway, H. W., Miller, J., Hoffer, B. J., Greig, N. H., and Pick, C. G. (2013) Exendin-4 Induced Glucagon-like Peptide-1 Receptor Activation Reverses Behavioral Impairments of Mild Traumatic Brain Injury in Mice. *Age (Omaha). 35* (5), 1621−1636.
(82) Eakin, K., Li, Y., Chiang, Y. H., Hoffer, B. J., Rosenheim, H., Greig, N. H., and Miller, J. P. (2013) Exendin-4 Ameliorates Traumatic Brain Injury-Induced Cognitive Impairment in Rats. *PLoS One 8* (12), No. e82016.
(83) DellaValle, B., Hempel, C., Johansen, F. F., and Kurtzhals, J. A. L. (2014) GLP-1 Improves Neuropathology after Murine Cold Lesion Brain Trauma. *Ann. Clin. Transl. Neurol. 1* (9), 721−732.
(84) Li, Y., Bader, M., Tamargo, I., Rubovitch, V., Tweedie, D., Pick, C. G., and Greig, N. H. (2015) Liraglutide Is Neurotrophic and Neuroprotective in Neuronal Cultures and Mitigates Mild Traumatic Brain Injury in Mice. *J. Neurochem. 135* (6), 1203−1217.
(85) Hakon, J., Ruscher, K., Romner, B., and Tomasevic, G. (2015) Preservation of the Blood Brain Barrier and Cortical Neuronal Tissue by Liraglutide, a Long Acting Glucagon-like-1 Analogue, after Experimental Traumatic Brain Injury. *PLoS One 10* (3), No. e0120074.
(86) Tweedie, D., Rachmany, L., Rubovitch, V., Li, Y., Holloway, H. W., Lehrmann, E., Zhang, Y., Becker, K. G., Perez, E., Hoffer, B. J., et al. (2016) Blast Traumatic Brain Injury-Induced Cognitive Deficits Are Attenuated by Preinjury or Postinjury Treatment with the Glucagon-like Peptide-1 Receptor Agonist, Exendin-4. *Alzheimer's Dementia 12* (1), 34−48.
(87) Rachmany, L., Tweedie, D., Rubovitch, V., Li, Y., Holloway, H. W., Kim, D. S., Ratliff, W. A., Saykally, J. N., Citron, B. A., Hoffer, B. J., et al. (2017) Exendin-4 Attenuates Blast Traumatic Brain Injury Induced Cognitive Impairments, Losses of Synaptophysin and in Vitro TBI-Induced Hippocampal Cellular Degeneration. *Sci. Rep. 7* (1), 3735.
(88) Yu, Y.-W., Hsieh, T.-H., Chen, K.-Y., Wu, J. C.-C., Hoffer, B. J., Greig, N. H., Li, Y., Lai, J.-H., Chang, C.-F., Lin, J.-W., et al. (2016) Glucose-Dependent Insulinotropic Polypeptide Ameliorates Mild Traumatic Brain Injury-Induced Cognitive and Sensorimotor Deficits and Neuroinflammation in Rats. *J. Neurotrauma 33* (22), 2044−2054.
(89) Fanne, R. A., Nassar, T., Heyman, S. N., Hijazi, N., and Higazi, A. A.-R. (2011) Insulin and Glucagon Share the Same Mechanism of Neuroprotection in Diabetic Rats: Role of Glutamate. *AJP Regul. Integr. Comp. Physiol. 301* (3), R668−R673.
(90) Armstead, W. M., Kiessling, J. W., Cines, D. B., and Higazi, A. A.-R. (2011) Glucagon Protects Against Impaired NMDA-Mediated Cerebrovasodilation and Cerebral Autoregulation during Hypotension after Brain Injury by Activating CAMP Protein Kinase A and Inhibiting Upregulation of TPA. *J. Neurotrauma 28* (3), 451−457.
(91) DellaValle, B., Brix, G. S., Brock, B., Gejl, M., Rungby, J., and Larsen, A. (2016) Oral Administration of Sitagliptin Activates CREB and Is Neuroprotective in Murine Model of Brain Trauma. *Front. Pharmacol. 7*, 450.
(92) Wiberg, S., Hassager, C., Schmidt, H., Thomsen, J. H., Frydland, M., Lindholm, M. G., Høfsten, D. E., Engstrøm, T., Køber, L., Møller, J. E., et al. (2016) Neuroprotective Effects of the Glucagon-Like Peptide-1 Analog Exenatide after Out-of-Hospital Cardiac Arrest: A Randomized Controlled Trial. *Circulation 134* (25), 2115−2124.
(93) Yun, S. P., Kam, T. I., Panicker, N., Kim, S., Oh, Y., Park, J. S., Kwon, S. H., Park, Y. J., Karuppagounder, S. S., Park, H., et al. (2018) Block of A1 Astrocyte Conversion by Microglia Is Neuroprotective in Models of Parkinson's Disease. *Nat. Med. 24* (7), 931−938.
(94) Nørregaard, P. K., Deryabina, M. A., Tofteng Shelton, P., Fog, J. U., Daugaard, J. R., Eriksson, P. O., Larsen, L. F., and Jessen, L. (2018) A Novel GIP Analogue, ZP4165, Enhances Glucagon-like Peptide-1-Induced Body Weight Loss and Improves Glycaemic Control in Rodents. *Diabetes, Obes. Metab. 20* (1), 60−68.
(95) Ambery, P., Parker, V. E., Stumvoll, M., Posch, M. G., Heise, T., Plum-Moerschel, L., Tsai, L. F., Robertson, D., Jain, M., Petrone, M., et al. (2018) MEDI0382, a GLP-1 and Glucagon Receptor Dual Agonist, in Obese or Overweight Patients with Type 2 Diabetes: A Randomised, Controlled, Double-Blind, Ascending Dose and Phase 2a Study. *Lancet 391* (10140), 2607−2618.
(96) Goebel, B., Schiavon, M., Visentin, R., Riz, M., Man, C. D., Cobelli, C., and Klabunde, T. (2018) Effects of the Novel Dual GLP-1R/GCGR Agonist SAR425899 on Postprandial Glucose Metabolism in Overweight/Obese Subjects with Type 2 Diabetes. *Diabetes 67*, 72.
(97) Frias, J. P., Bastyr, E. J., Vignati, L., Tschöp, M. H., Schmitt, C., Owen, K., Christensen, R. H., and DiMarchi, R. D. (2017) The Sustained Effects of a Dual GIP/GLP-1 Receptor Agonist, NNC0090−2746, in Patients with Type 2 Diabetes. *Cell Metab. 26* (2), 343−352.e2.
(98) Goldenberg, R., Gantz, I., Andryuk, P. J., O'Neill, E. A., Kaufman, K. D., Lai, E., Wang, Y. N., Suryawanshi, S., and Engel, S. S. (2017) Randomized Clinical Trial Comparing the Efficacy and Safety of Treatment with the Once-Weekly Dipeptidyl Peptidase-4 (DPP-4) Inhibitor Omarigliptin or the Once-Daily DPP-4 Inhibitor Sitagliptin in Patients with Type 2 Diabetes Inadequately Controlled on M. *Diabetes. Diabetes, Obes. Metab. 19* (3), 394−400.
(99) Ayoub, B. M., Mowaka, S., Safar, M. M., Ashoush, N., Arafa, M. G., Michel, H. E., Tadros, M. M., Elmazar, M. M., and Mousa, S. A. (2018) Repositioning of Omarigliptin as a Once-Weekly Intranasal Anti-Parkinsonian Agent. *Sci. Rep. 8* (1), 8959.
(100) Kim, S. H., Yoo, J. H., Lee, W. J., and Park, C. Y. (2016) Gemigliptin: An Update of Its Clinical Use in the Management of Type 2 Diabetes Mellitus. *Diabetes Metab. J. 40* (5), 339−353.
(101) Mathieu, C., and Degrande, E. (2008) Vildagliptin: A New Oral Treatment for Type 2 Diabetes Mellitus. *Vascular Health and Risk Management*, pp 1349−1360, Dove Press.
(102) Kishimoto, M. (2013) Teneligliptin: A DPP-4 Inhibitor for the Treatment of Type 2 Diabetes. *Diabetes, Metab. Syndr. Obes.: Targets Ther. 6*, 187−195.
(103) Nishio, S., Abe, M., and Ito, H. (2015) Anagliptin in the Treatment of Type 2 Diabetes: Safety, Efficacy, and Patient Acceptability. *Diabetes, Metabolic Syndrome and Obesity: Targets and Therapy*, pp 163−171, Dove Press, DOI: 10.2147/DMSO.S54679.
(104) Taylor, C. A., Bell, J. M., Breiding, M. J., and Xu, L. (2017) Traumatic Brain Injury−Related Emergency Department Visits, Hospitalizations, and Deaths — United States, 2007 and 2013. *MMWR. Surveill. Summ. 66* (9), 1−16.
(105) Faul, M., Xu, L., Wald, M. M., and Coronado, V. G. (2010) *Traumatic Brain Injury in the United States: Emergency Department Visits, Hospitalizations and Deaths, 2002−2006*, CDC, Atlanta, GA.
(106) Marin, J. R., Weaver, M. D., Yealy, D. M., and Mannix, R. C. (2014) Trends in Visits for Traumatic Brain Injury to Emergency Departments in the United States. *JAMA 311* (18), 1917.
(107) Frieden, T. R., Houry, D., and Baldwin, G. (2015) *Report to Congress on Traumatic Brain Injury in the United States: Epidemiology and Rehabilitation*, CDC,Atlanta, GA.
(108) Haring, R. S., Canner, J. K., Asemota, A. O., George, B. P., Selvarajah, S., Haider, A. H., and Schneider, E. B. (2015) Trends in Incidence and Severity of Sports-Related Traumatic Brain Injury (TBI) in the Emergency Department 2006−2011. *Brain Inj 29* (7−8), 989−992.
(109) Zaloshnja, E., Miller, T., Langlois, J. A., and Selassie, A. W. (2008) Prevalence of Long-Term Disability from Traumatic Brain Injury in the Civilian Population of the United States, 2005. *J. Head Trauma Rehabil. 23* (6), 394−400.
(110) Langlois, J. A., Rutland-Brown, W., and Wald, M. M. (2006) The Epidemiology and Impact of Traumatic Brain Injury. *J. Head Trauma Rehabil 21* (5), 375−378.
(111) Roozenbeek, B., Maas, A. I. R., and Menon, D. K. (2013) Changing Patterns in the Epidemiology of Traumatic Brain Injury. *Nat. Rev. Neurol. 9* (4), 231−236.

DOI: 10.1021/acsptsci.9b00003
ACS Pharmacol. Transl. Sci. 2019, 2, 66−91

(112) Araki, T., Yokota, H., and Morita, A. (2017) Pediatric Traumatic Brain Injury: Characteristic Features, Diagnosis, and Management. *Neurol. Med. Chir. (Tokyo) 57* (2), 82−93.
(113) Collins, N. C., Molcho, M., Carney, P., McEvoy, L., Geoghegan, L., Phillips, J. P., and Nicholson, A. J. (2013) Are Boys and Girls That Different? An Analysis of Traumatic Brain Injury in Children. *Emerg. Med. J. 30* (8), 675−678.
(114) Susman, M., DiRusso, S. M., Sullivan, T., Risucci, D., Nealon, P., Cuff, S., and Benzil, D. (2002) Traumatic Brain Injury in the Elderly: Increased Mortality and Worse Functional Outcome at Discharge despite Lower Injury Severity. *J. Trauma 53* (2), 219−224.
(115) LeBlanc, J., Guise, E. de, Gosselin, N., and Feyz, M. (2006) Comparison of Functional Outcome Following Acute Care in Young, Middle-Aged and Elderly Patients with Traumatic Brain Injury. *Brain Inj 20* (8), 779−790.
(116) Hautzinger, S., Howell, A., Scandlyn, J., and Wool, Z. H. US Veterans & Military Families: Cost of War http://watson.brown.edu/costsofwar/costs/human/veterans (accessed Sep 22, 2017).
(117) Hoge, C. W., Castro, C. A., Yurgil, K. A., Barkauskas, D. A., Vasterling, J. J., Nievergelt, C. M., Larson, G. E., Schork, N. J., Litz, B. T., Nash, W. P., et al. (2014) Treatment of Generalized War-Related Health Concerns Placing TBI and PTSD in Context. *J. Am. Med. Assoc. 312*, 1685−1686.
(118) Terrio, H., Brenner, L. A., Ivins, B. J., Cho, J. M., Helmick, K., Schwab, K., Scally, K., Bretthauer, R., and Warden, D. (2009) Traumatic Brain Injury Screening: Preliminary Findings in a US Army Brigade Combat Team. *J. Head Trauma Rehabil. 24* (1), 14−23.
(119) Tanielian, T., and Jaycox, L. H., Eds. (2008) *Invisible Wounds of War: Psychological and Cognitive Injuries, Their Consequences, and Services to Assist Recovery*, RAND Corporation.
(120) Defense and Veterans Brain Injury Center. *DoD Worldwide Numbers for TBI* http://dvbic.dcoe.mil/dod-worldwide-numbers-tbi (accessed September 22, 2017).
(121) Defense and Veterans Brain Injury Center (2015) *Medical Provider Screening and Diagnostic Coding Rehabilitation Provider Diagnostic Coding ICD-10 Coding Guidance for Traumatic Brain Injury Severity of TBI.*
(122) Regasa, L. E., Michael Thomas, D., Gill, R. S., Marion, D. W., and Ivins, B. J. (2016) Military Deployment May Increase the Risk for Traumatic Brain Injury Following Deployment. *J. Head Trauma Rehabil. 31* (1), E28−E35.
(123) Williams, V. F., Stahlman, S., Hunt, D. J., and O'Donnell, F. L. (2017) Diagnoses of Traumatic Brain Injury Not Clearly Associated with Deployment, Active Component, U.S. Armed Forces, 2001−2016. *MSMR 24* (3), 2−8.
(124) Gardner, R. C., Byers, A., Barnes, D. E., Li, Y., Boscardin, J., and Yaffe, K. (2017) Mild Traumatic Brain Injury Is Associated with Increased Risk of Parkinson Disease in Military Veterans: A Chronic Effects of Neurotrauma Consortium Study. *Neurology 88* (16), No. P4.322.
(125) Barnes, D. E., Kaup, A., Kirby, K. A., Byers, A. L., Diaz-Arrastia, R., and Yaffe, K. (2014) Traumatic Brain Injury and Risk of Dementia in Older Veterans. *Neurology 83* (4), 312−319.
(126) Jones, E., Fear, N. T., and Wessely, S. (2007) Shell Shock and Mild Traumatic Brain Injury: A Historical Review. *Am. J. Psychiatry 1*, 1641−1645.
(127) Tsao, J. W., Stentz, L. A., Rouhanian, M., Howard, R. S., Perry, B. N., Haran, F. J., Pasquina, P. F., Wolde, M., Taylor, C. E., Lizardo, R., et al. (2017) Effect of Concussion and Blast Exposure on Symptoms after Military Deployment. *Neurology 89* (19), 2010−2016.
(128) Smith, D. H., Johnson, V. E., and Stewart, W. (2013) Chronic Neuropathologies of Single and Repetitive TBI: Substrates of Dementia? *Nat. Rev. Neurol. 9* (4), 211−221.
(129) Rosenfeld, J. V., McFarlane, A. C., Bragge, P., Armonda, R. A., Grimes, J. B., and Ling, G. S. (2013) Blast-Related Traumatic Brain Injury. *The Lancet Neurology*, 882−893, DOI: 10.1016/S1474-4422(13)70161-3.
(130) Duckworth, J. L., Grimes, J., and Ling, G. S. F. (2013) Pathophysiology of Battlefield Associated Traumatic Brain Injury. *Pathophysiology 20* (1), 23−30.
(131) McKee, A. C., and Robinson, M. E. (2014) Military-Related Traumatic Brain Injury and Neurodegeneration. *Alzheimer's Dementia 10*, S242−S253.
(132) Nemetz, P. N., Leibson, C., Naessens, J. M., Beard, M., Kokmen, E., Annegers, J. F., and Kurland, L. T. (1999) Traumatic Brain Injury and Time to Onset of Alzheimer's Disease: A Population-Based Study. *Am. J. Epidemiol. 149* (1), 32−40.
(133) Boussard, C. N., Holm, L. W., Cancelliere, C., Godbolt, A. K., Boyle, E., Stålnacke, B.-M., Hincapié, C. A., Cassidy, J. D., and Borg, J. (2014) Nonsurgical Interventions After Mild Traumatic Brain Injury: A Systematic Review. Results of the International Collaboration on Mild Traumatic Brain Injury Prognosis. *Arch. Phys. Med. Rehabil. 95* (3S), S257−S264.
(134) Levin, H. S., and Diaz-Arrastia, R. R. (2015) Diagnosis, Prognosis, and Clinical Management of Mild Traumatic Brain Injury. *Lancet Neurol. 14* (5), 506−517.
(135) Teasdale, G., Maas, A., Lecky, F., Manley, G., Stocchetti, N., and Murray, G. (2014) The Glasgow Coma Scale at 40 Years: Standing the Test of Time. *The Lancet Neurology*, 844−854, DOI: 10.1016/S1474-4422(14)70120-6.
(136) Salottolo, K., Stewart Levy, A., Slone, D. S., Mains, C. W., and Bar-Or, D. (2014) The Effect of Age on Glasgow Coma Scale Score in Patients with Traumatic Brain Injury. *JAMA Surg 149* (7), 727−734.
(137) Kehoe, A., Rennie, S., and Smith, J. E. (2015) Glasgow Coma Scale Is Unreliable for the Prediction of Severe Head Injury in Elderly Trauma Patients. *Emerg. Med. J. 32* (8), 613−615.
(138) Karnati, H. K., Garcia, J. H., Tweedie, D., Becker, R. E., Kapogiannis, D., and Greig, N. H. (2018) Neuronal Enriched Extracellular Vesicle Proteins as Biomarkers for Brain Traumatic Injury. *J. Neurotrauma*, 5898.
(139) Zetterberg, H., Smith, D. H., and Blennow, K. (2013) Biomarkers of Mild Traumatic Brain Injury in Cerebrospinal Fluid and Blood. *Nat. Rev. Neurol. 9* (4), 201−210.
(140) Podell, J., Korley, F., Yue, J., Wilson, D., Ferguson, A., Yuh, E., Mukherjee, P., Wang, K., Valadka, A., and Puccio, A. (2018) Acute Serum GFAP, NF-L, Tau, and UCH-L1 Predict CT Pathology and 3-Month Outcome in TBI (S42.004). *Neurology 90*, No. S42.004.
(141) Chen, S. T., Siddarth, P., Merrill, D. A., Martinez, J., Emerson, N. D., Liu, J., Wong, K.-P., Satyamurthy, N., Giza, C. C., Huang, S.-C., et al. (2018) FDDNP-PET Tau Brain Protein Binding Patterns in Military Personnel with Suspected Chronic Traumatic Encephalopathy. *J. Alzheimer's Dis. 65*, 79−88.
(142) Samson, K. (2018) In the Clinic-Traumatic Brain Injury: FDA Approves First Blood Test for Brain Bleeds After Mild TBI/Concussion. *Neurol. Today 18* (6), 12−18.
(143) Bazarian, J. J., Biberthaler, P., Welch, R. D., Lewis, L. M., Barzo, P., Bogner-Flatz, V., Gunnar Brolinson, P., Büki, A., Chen, J. Y., Christenson, R. H., et al. (2018) Serum GFAP and UCH-L1 for Prediction of Absence of Intracranial Injuries on Head CT (ALERT-TBI): A Multicentre Observational Study. *Lancet Neurol. 17* (9), 782−789.
(144) Corps, K. N., Roth, T. L., and McGavern, D. B. (2015) Inflammation and Neuroprotection in Traumatic Brain Injury. *JAMA Neurol 72* (3), 355−362.
(145) Bigler, E. D. (2013) Traumatic Brain Injury, Neuroimaging, and Neurodegeneration. *Front. Hum. Neurosci. 7*, 395.
(146) Ramlackhansingh, A. F., Brooks, D. J., Greenwood, R. J., Bose, S. K., Turkheimer, F. E., Kinnunen, K. M., Gentleman, S., Heckemann, R. A., Gunanayagam, K., Gelosa, G., et al. (2011) Inflammation after Trauma: Microglial Activation and Traumatic Brain Injury. *Ann. Neurol. 70* (3), 374−383.
(147) Andriessen, T. M. J. C., Jacobs, B., and Vos, P. E. (2010) Clinical Characteristics and Pathophysiological Mechanisms of Focal and Diffuse Traumatic Brain Injury. *J. Cell. Mol. Med. 14* (10), 2381−2392.

DOI: 10.1021/acsptsci.9b00003
ACS Pharmacol. Transl. Sci. 2019, 2, 66−91

(148) Mckee, C. A., and Lukens, J. R. (2016) Emerging Roles for the Immune System in Traumatic Brain Injury. *Front. Immunol. 7* (7), 556.
(149) Bianchi, M. E. (2007) DAMPs, PAMPs and Alarmins: All We Need to Know about Danger. *J. Leukocyte Biol. 81* (1), 1−5.
(150) Manson, J., Thiemermann, C., and Brohi, K. (2012) Trauma Alarmins as Activators of Damage-Induced Inflammation. *Br. J. Surg. 99*, 12−20.
(151) Jassam, Y. N., Izzy, S., Whalen, M., McGavern, D. B., and El Khoury, J. (2017) Neuroimmunology of Traumatic Brain Injury: Time for a Paradigm Shift. *Neuron 95*, 1246−1265.
(152) Nimmerjahn, A., Kirchhoff, F., and Helmchen, F. (2005) Resting Microglial Cells Are Highly Dynamic Surveillants of Brain Parenchyma in Vivo. *Science (Washington, DC, U. S.) 308* (5726), 1314−1318.
(153) Mosser, D. M., and Edwards, J. P. (2008) Exploring the Full Spectrum of Macrophage Activation. *Nat. Rev. Immunol. 8*, 958−969.
(154) Ransohoff, R. M. A. (2016) Polarizing Question: Do M1 and M2Microglia Exist. *Nat. Neurosci.*, 987−991, DOI: 10.1038/nn.4338.
(155) Hammond, T. R., Dufort, C., Dissing-Olesen, L., Giera, S., Young, A., Wysoker, A., Walker, A. J., Gergits, F., Segel, M., Nemesh, J., et al. (2019) Single-Cell RNA Sequencing of Microglia throughout the Mouse Lifespan and in the Injured Brain Reveals Complex Cell-State Changes. *Immunity 50*, 253.
(156) De Biase, L. M., Schuebel, K. E., Fusfeld, Z. H., Jair, K., Hawes, I. A., Cimbro, R., Zhang, H. Y., Liu, Q. R., Shen, H., Xi, Z. X., et al. (2017) Local Cues Establish and Maintain Region-Specific Phenotypes of Basal Ganglia Microglia. *Neuron 95* (2), 341−356.e6.
(157) Doorn, K. J., Breve, J. J. P., Drukarch, B., Boddeke, H. W., Huitinga, I., Lucassen, P. J., and van Dam, A.-M. (2015) Brain Region-Specific Gene Expression Profiles in Freshly Isolated Rat Microglia. *Front. Cell. Neurosci. 9*, 84.
(158) Donat, C. K., Scott, G., Gentleman, S. M., and Sastre, M. (2017) Microglial Activation in Traumatic Brain Injury. *Front. Aging Neurosci.*, 208 DOI: 10.3389/fnagi.2017.00208.
(159) Hoogland, I. C. M., Houbolt, C., van Westerloo, D. J., van Gool, W. A., and van de Beek, D. (2015) Systemic Inflammation and Microglial Activation: Systematic Review of Animal Experiments. *J. Neuroinflam.*, 114 DOI: 10.1186/s12974-015-0332-6.
(160) Johnson, V. E., Stewart, J. E., Begbie, F. D., Trojanowski, J. Q., Smith, D. H., and Stewart, W. (2013) Inflammation and White Matter Degeneration Persist for Years after a Single Traumatic Brain Injury. *Brain 136*, 28−42.
(161) Loane, D. J., Kumar, A., Stoica, B. A., Cabatbat, R., and Faden, A. I. (2014) Progressive Neurodegeneration after Experimental Brain Trauma: Association with Chronic Microglial Activation. *J. Neuropathol. Exp. Neurol. 73* (1), 14−29.
(162) Nagamoto-Combs, K., McNeal, D. W., Morecraft, R. J., and Combs, C. K. (2007) Prolonged Microgliosis in the Rhesus Monkey Central Nervous System after Traumatic Brain Injury. *J. Neurotrauma 24* (11), 1719−1742.
(163) Scott, G., Hellyer, P. J., Ramlackhansingh, A. F., Brooks, D. J., Matthews, P. M., and Sharp, D. J. (2015) Thalamic Inflammation after Brain Trauma Is Associated with Thalamo-Cortical White Matter Damage. *J. Neuroinflammation 12*, 224.
(164) Cagnin, A., Brooks, D. J., Kennedy, A. M., Gunn, R. N., Myers, R., Turkheimer, F. E., Jones, T., and Banati, R. B. (2001) In-Vivo Measurement of Activated Microglia in Dementia. *Lancet 358* (9280), 461−467.
(165) Perry, V. H., and Holmes, C. (2014) Microglial Priming in Neurodegenerative Disease. *Nat. Rev. Neurol.*, 217−224, DOI: 10.1038/nrneurol.2014.38.
(166) Norden, D. M., Muccigrosso, M. M., and Godbout, J. P. (2015) Microglial Priming and Enhanced Reactivity to Secondary Insult in Aging, and Traumatic CNS Injury, and Neurodegenerative Disease. *Neuropharmacology 96*, 29−41.
(167) Perry, V. H., Newman, T. A., and Cunningham, C. (2003) The Impact of Systemic Infection on the Progression of Neurodegenerative Disease. *Nat. Rev. Neurosci. 4* (2), 103−112.
(168) Witcher, K. G., Eiferman, D. S., and Godbout, J. P. (2015) Priming the Inflammatory Pump of the CNS after Traumatic Brain Injury. *Trends Neurosci. 38* (10), 609−620.
(169) Trapp, B. D., Wujek, J. R., Criste, G. A., Jalabi, W., Yin, X., Kidd, G. J., Stohlman, S., and Ransohoff, R. (2007) Evidence for Synaptic Stripping by Cortical Microglia. *Glia 55* (4), 360−368.
(170) Elmore, M. R. P., Hohsfield, L. A., Kramár, E. A., Soreq, L., Lee, R. J., Pham, S. T., Najafi, A. R., Spangenberg, E. E., Wood, M. A., and West, B. L. (2018) Replacement of Microglia in the Aged Brain Reverses Cognitive, Synaptic, and Neuronal Deficits in Mice. *Aging Cell*, No. e12832, DOI: 10.1111/acel.12832.
(171) Simon, D. W., McGeachy, M. J., Baylr, H., Clark, R. S. B., Loane, D. J., and Kochanek, P. M. (2017) The Far-Reaching Scope of Neuroinflammation after Traumatic Brain Injury. *Nat. Rev. Neurol.*, 171−191, DOI: 10.1038/nrneurol.2017.13.
(172) Elmore, M. R. P., Najafi, A. R., Koike, M. A., Dagher, N. N., Spangenberg, E. E., Rice, R. A., Kitazawa, M., Matusow, B., Nguyen, H., West, B. L., et al. (2014) Colony-Stimulating Factor 1 Receptor Signaling Is Necessary for Microglia Viability, Unmasking a Microglia Progenitor Cell in the Adult Brain. *Neuron 82* (2), 380−397.
(173) Rice, R. A., Pham, J., Lee, R. J., Najafi, A. R., West, B. L., and Green, K. N. (2017) Microglial Repopulation Resolves Inflammation and Promotes Brain Recovery after Injury. *Glia 65* (6), 931−944.
(174) O'Neil, S. M. O., Witcher, K. G., Mckim, D. B., and Godbout, J. P. (2018) Forced Turnover of Aged Microglia Induces an Intermediate Phenotype but Does Not Rebalance CNS Environmental Cues Driving Priming to Immune Challenge. *Acta Neuropathol. Commun. 8* (1), 1−20.
(175) Han, J., Zhu, K., Zhang, X. M., and Harris, R. A. (2019) Enforced Microglial Depletion and Repopulation as a Promising Strategy for the Treatment of Neurological Disorders. *Glia 1−15*, 217.
(176) Witcher, K. G., Bray, C. E., Dziabis, J. E., McKim, D. B., Benner, B. N., Rowe, R. K., Kokiko-Cochran, O. N., Popovich, P. G., Lifshitz, J., Eiferman, D. S., et al. (2018) Traumatic Brain Injury-Induced Neuronal Damage in the Somatosensory Cortex Causes Formation of Rod-Shaped Microglia That Promote Astrogliosis and Persistent Neuroinflammation. *Glia 66* (12), 2719−2736.
(177) Woodcock, T., and Morganti-Kossmann, M. C. (2013) The Role of Markers of Inflammation in Traumatic Brain Injury. *Front. Neurol. 4*, 18.
(178) Das, M., Mohapatra, S., and Mohapatra, S. S. (2012) New Perspectives on Central and Peripheral Immune Responses to Acute Traumatic Brain Injury. *J. Neuroinflam.*, 236 DOI: 10.1186/1742-2094-9-236.
(179) Loane, D. J., and Kumar, A. (2016) Microglia in the TBI Brain: The Good, the Bad, and the Dysregulated. *Exp. Neurol. 275*, 316−327.
(180) Hammad, A., Westacott, L., and Zaben, M. (2018) The Role of the Complement System in Traumatic Brain Injury: A Review. *J. Neuroinflam.*, 24 DOI: 10.1186/s12974-018-1066-z.
(181) Bellander, B.-M., Singhrao, S. K., Ohlsson, M., Mattsson, P., and Svensson, M. (2001) Complement Activation in the Human Brain after Traumatic Head Injury. *J. Neurotrauma 18* (12), 1295−1311.
(182) De Blasio, D., Fumagalli, S., Orsini, F., Neglia, L., Perego, C., Ortolano, F., Zanier, E. R., Picetti, E., Locatelli, M., and Stocchetti, N. (2018) Human Brain Trauma Severity Is Associated with Lectin Complement Pathway Activation. *J. Cereb. Blood Flow Metab.*, 58881.
(183) Leinhase, I., Schmidt, O. I., Thurman, J. M., Hossini, A. M., Rozanski, M., Taha, M. E., Scheffler, A., John, T., Smith, W. R., Holers, V. M., et al. (2006) Pharmacological Complement Inhibition at the C3 Convertase Level Promotes Neuronal Survival, Neuroprotective Intracerebral Gene Expression, and Neurological Outcome after Traumatic Brain Injury. *Exp. Neurol. 199* (2), 454−464.
(184) Sewell, D. L., Nacewicz, B., Liu, F., Macvilay, S., Erdei, A., Lambris, J. D., Sandor, M., and Fabry, Z. (2004) Complement C3 and C5 Play Critical Roles in Traumatic Brain Cryoinjury: Blocking Effects on Neutrophil Extravasation by C5a Receptor Antagonist. *J. Neuroimmunol. 155* (1−2), 55−63.

DOI: 10.1021/acsptsci.9b00003
ACS Pharmacol. Transl. Sci. 2019, 2, 66−91

(185) Liddelow, S. A., Guttenplan, K. A., Clarke, L. E., Bennett, F. C., Bohlen, C. J., Schirmer, L., Bennett, M. L., Münch, A. E., Chung, W. S., Peterson, T. C., et al. (2017) Neurotoxic Reactive Astrocytes Are Induced by Activated Microglia. *Nature 541* (7638), 481−487.
(186) Clarke, L. E., Liddelow, S. A., Chakraborty, C., Münch, A. E., Heiman, M., and Barres, B. A. (2018) Normal Aging Induces A1-like Astrocyte Reactivity. *Proc. Natl. Acad. Sci. U. S. A. 115* (8), E1896−E1905.
(187) Alawieh, A., Langley, E. F., Weber, S., Adkins, D., and Tomlinson, S. (2018) Identifying the Role of Complement in Triggering Neuroinflammation after Traumatic Brain Injury. *J. Neurosci. 38* (10), 2519−17.
(188) Shi, Q., Colodner, K. J., Matousek, S. B., Merry, K., Hong, S., Kenison, J. E., Frost, J. L., Le, K. X., Li, S., Dodart, J.-C., et al. (2015) Complement C3-Deficient Mice Fail to Display Age-Related Hippocampal Decline. *J. Neurosci. 35* (38), 13029−13042.
(189) Krukowski, K., Chou, A., Feng, X., Tiret, B., Paladini, M.-S., Riparip, L.-K., Chaumeil, M., Lemere, C., and Rosi, S. (2018) Traumatic Brain Injury in Aged Mice Induces Chronic Microglia Activation, Synapse Loss, and Complement-Dependent Memory Deficits. *Int. J. Mol. Sci. 19* (12), 3753.
(190) Habbas, S., Santello, M., Becker, D., Stubbe, H., Zappia, G., Liaudet, N., Klaus, F. R., Kollias, G., Fontana, A., Pryce, C. R., et al. (2015) Neuroinflammatory TNFα Impairs Memory via Astrocyte Signaling. *Cell 163* (7), 1730−1741.
(191) Scherbel, U., Raghupathi, R., Nakamura, M., Saatman, K. E., Trojanowski, J. Q., Neugebauer, E., Marino, M. W., and McIntosh, T. K. (1999) Differential Acute and Chronic Responses of Tumor Necrosis Factor-Deficient Mice to Experimental Brain Injury. *Proc. Natl. Acad. Sci. U. S. A. 96* (15), 8721−8726.
(192) Burda, J. E., Bernstein, A. M., and Sofroniew, M. V. (2016) Astrocyte Roles in Traumatic Brain Injury. *Exp. Neurol. 275*, 305−315.
(193) Hol, E. M., and Pekny, M. (2015) Glial Fibrillary Acidic Protein (GFAP) and the Astrocyte Intermediate Filament System in Diseases of the Central Nervous System. *Current Opinion in Cell Biology*, 121−130, DOI: 10.1016/j.ceb.2015.02.004.
(194) Liddelow, S. A., and Barres, B. A. (2017) Reactive Astrocytes: Production, Function, and Therapeutic Potential. *Immunity 46*, 957−967.
(195) Gardner, R. C., Rubenstein, R., Wang, K. K. W., Korley, F. K., Yue, J. K., Yuh, E. L., Mukherje, P., Valadka, A. B., Okonkwo, D. O., Diaz-Arrastia, R., and Manley, G. T. (2018) Age-Related Differences in Diagnostic Accuracy of Plasma Glial Fibrillary Acidic Protein and Tau for Identifying Acute Intracranial Trauma on Computed Tomography: A TRACK-TBI Study. *J. Neurotrauma 35* (20), 2341.
(196) Bush, T. G., Puvanachandra, N., Horner, C. H., Polito, A., Ostenfeld, T., Svendsen, C. N., Mucke, L., Johnson, M. H., and Sofroniew, M. V. (1999) Leukocyte Infiltration, Neuronal Degeneration, and Neurite Outgrowth after Ablation of Scar-Forming, Reactive Astrocytes in Adult Transgenic Mice. *Neuron 23* (2), 297−308.
(197) Werner, C., and Engelhard, K. (2007) Pathophysiology of Traumatic Brain Injury. *Br. J. Anaesth. 99* (1), 4−9.
(198) Palmer, A. M., Marion, D. W., Botscheller, M. L., Swedlow, P. E., Styren, S. D., and DeKosky, S. T. (1993) Traumatic Brain Injury-Induced Excitotoxicity Assessed in a Controlled Cortical Impact Model. *J. Neurochem. 61* (6), 2015−2024.
(199) Bullock, R., Zauner, A., Myseros, J. S., Marmarou, A., Woodward, J. J., and Young, H. F. (1995) Evidence for Prolonged Release of Excitatory Amino Acids in Severe Human Head Trauma: Relationship to Clinical Events. *Ann. N. Y. Acad. Sci. 765* (1), 290−297.
(200) Hutchinson, P. J. (2005) Microdialysis in Traumatic Brain Injury - Methodology and Pathophysiology. *Acta Neurochir. Suppl. 95*, 441−445.
(201) Chen, Y., and Swanson, R. A. (2003) Astrocytes and Brain Injury. *J. Cereb. Blood Flow Metab. 23*, 137−149.
(202) Raghavendra Rao, V. L., Başkaya, M. K., Doğan, A., Rothstein, J. D., and Dempsey, R. J. (1998) Traumatic Brain Injury Down-Regulates Glial Glutamate Transporter (GLT-1 and GLAST) Proteins in Rat Brain. *J. Neurochem. 70* (5), 2020−2027.
(203) Landeghem, F. K. H. V., Weiss, T., Oehmichen, M., and Deimling, A. V. (2006) Decreased Expression of Glutamate Transporters in Astrocytes after Human Traumatic Brain Injury. *J. Neurotrauma 23* (10), 1518−1528.
(204) Beschorner, R., Dietz, K., Schauer, N., Mittelbronn, M., Schluesener, H. J., Trautmann, K., Meyermann, R., and Simon, P. (2007) Expression of EAAT1 Reflects a Possible Neuroprotective Function of Reactive Astrocytes and Activated Microglia Following Human Traumatic Brain Injury. *Histol. Histopathol. 22* (4−6), 515−526.
(205) Bezzi, P., Domercq, M., Brambilla, L., Galli, R., Schols, D., De Clercq, E., Vescovi, A., Bagetta, G., Kollias, G., Meldolesi, J., et al. (2001) CXCR4-Activated Astrocyte Glutamate Release via TNFa: Amplification by Microglia Triggers Neurotoxicity. *Nat. Neurosci. 4* (7), 702−710.
(206) Santello, M., Bezzi, P., and Volterra, A. (2011) TNFα Controls Glutamatergic Gliotransmission in the Hippocampal Dentate Gyrus. *Neuron 69* (5), 988−1001.
(207) Takeuchi, H., Jin, S., Wang, J., Zhang, G., Kawanokuchi, J., Kuno, R., Sonobe, Y., Mizuno, T., and Suzumura, A. (2006) Tumor Necrosis Factor-α Induces Neurotoxicity via Glutamate Release from Hemichannels of Activated Microglia in an Autocrine Manner. *J. Biol. Chem. 281* (30), 21362−21368.
(208) Chen, C.-J., OU, Y.-C., Chang, C.-Y., Pan, H.-C., Liao, S.-L., Chen, S.-Y., Raung, S.-L., and Lai, C.-Y. (2012) Glutamate Released by Japanese Encephalitis Virus-Infected Microglia Involves TNF-α Signaling and Contributes to Neuronal Death. *Glia 60* (3), 487−501.
(209) Ye, L., Huang, Y., Zhao, L., Li, Y., Sun, L., Zhou, Y., Qian, G., and Zheng, J. C. (2013) IL-1β and TNF-α Induce Neurotoxicity through Glutamate Production: A Potential Role for Neuronal Glutaminase. *J. Neurochem. 125* (6), 897−908.
(210) Clark, I. A., and Vissel, B. (2016) Excess Cerebral TNF Causing Glutamate Excitotoxicity Rationalizes Treatment of Neurodegenerative Diseases and Neurogenic Pain by Anti-TNF Agents. *J. Neuroinflammation 13* (1), 236.
(211) Frankola, K. A., Greig, H. N., Luo, W., and Tweedie, D. (2011) Targeting TNF-Alpha to Elucidate and Ameliorate Neuroinflammation in Neurodegenerative Diseases. *CNS Neurol. Disord.: Drug Targets 10* (3), 391−403.
(212) Arundine, M., and Tymianski, M. (2003) Molecular Mechanisms of Calcium-Dependent Neurodegeneration in Excitotoxicity. *Cell Calcium*, 325−337, DOI: 10.1016/S0143-4160(03)00141-6.
(213) Fujikawa, D. G. (2015) The Role of Excitotoxic Programmed Necrosis in Acute Brain Injury. *Comput. Struct. Biotechnol. J.*, 212−221, DOI: 10.1016/j.csbj.2015.03.004.
(214) Nixon, R. A. (2003) The Calpains in Aging and Aging-Related Diseases. *Ageing Res. Rev.*, 407−418, DOI: 10.1016/S1568-1637(03)00029-1.
(215) Ha, H. C., and Snyder, S. H. (2000) Poly(ADP-Ribose) Polymerase-1 in the Nervous System. *Neurobiol. Disease*, 225−239, DOI: 10.1006/nbdi.2000.0324.
(216) Besson, V. C., Croci, N., Boulu, R. G., Plotkine, M., and Marchand-Verrecchia, C. (2003) Deleterious Poly(ADP-Ribose)-Polymerase-1 Pathway Activation in Traumatic Brain Injury in Rat. *Brain Res. 989* (1), 58−66.
(217) Stoica, B. A., Loane, D. J., Zhao, Z., Kabadi, S. V., Hanscom, M., Byrnes, K. R., and Faden, A. I. (2014) PARP-1 Inhibition Attenuates Neuronal Loss, Microglia Activation and Neurological Deficits after Traumatic Brain Injury. *J. Neurotrauma 31* (8), 758−772.
(218) Whalen, M. J., Clark, R. S. B., Dixon, C. E., Robichaud, P., Marion, D. W., Vagni, V., Graham, S. H., Virag, L., Hasko, G., Stachlewitz, R., et al. (1999) Reduction of Cognitive and Motor Deficits after Traumatic Brain Injury in Mice Deficient in Poly(ADP-Ribose) Polymerase. *J. Cereb. Blood Flow Metab. 19* (8), 835−842.

DOI: 10.1021/acsptsci.9b00003
ACS Pharmacol. Transl. Sci. 2019, 2, 66−91

(219) Ang, B. T., Yap, E., Lim, J., Tan, W. L., Ng, P. Y., Ng, I., and Yeo, T. T. (2003) Poly(Adenosine Diphosphate-Ribose) Polymerase Expression in Human Traumatic Brain Injury. *J. Neurosurg. 99* (1), 125−130.

(220) d'Avila, J. C., Lam, T. I., Bingham, D., Shi, J., Won, S. J., Kauppinen, T. M., Massa, S., Liu, J., and Swanson, R. A. (2012) Microglial Activation Induced by Brain Trauma Is Suppressed by Post-Injury Treatment with a PARP Inhibitor. *J. Neuroinflammation 9* (1), 521.

(221) Kauppinen, T. M., and Swanson, R. A. (2005) Poly(ADP-Ribose) Polymerase-1 Promotes Microglial Activation, Proliferation, and Matrix Metalloproteinase-9-Mediated Neuron Death. *J. Immunol. 174* (4), 2288−2296.

(222) Piao, C.-S., Loane, D. J., Stoica, B. A., Li, S., Hanscom, M., Cabatbat, R., Blomgren, K., and Faden, A. I. (2012) Combined Inhibition of Cell Death Induced by Apoptosis Inducing Factor and Caspases Provides Additive Neuroprotection in Experimental Traumatic Brain Injury. *Neurobiol. Dis. 46* (3), 745−758.

(223) Hong, S. J., Dawson, T. M., and Dawson, V. L. (2004) Nuclear and Mitochondrial Conversations in Cell Death: PARP-1 and AIF Signaling. *Trends Pharmacol. Sci.*, 259−264, DOI: 10.1016/j.tips.2004.03.005.

(224) Kruman, I. I. (2004) Why Do Neurons Enter the Cell Cycle? *Cell Cycle*, 769−773, DOI: 10.4161/cc.3.6.901.

(225) Kruman, I. I., Wersto, R. P., Cardozo-Pelaez, F., Smilenov, L., Chan, S. L., Chrest, F. J., Emokpae, R., Gorospe, M., and Mattson, M. P. (2004) Cell Cycle Activation Linked to Neuronal Cell Death Initiated by DNA Damage. *Neuron 41* (4), 549−561.

(226) Stoica, B. A., and Faden, A. I. (2010) Cell Death Mechanisms and Modulation in Traumatic Brain Injury. *Neurotherapeutics 7* (1), 3−12.

(227) Di Giovanni, S., Movsesyan, V., Ahmed, F., Cernak, I., Schinelli, S., Stoica, B., and Faden, A. I. (2005) Cell Cycle Inhibition Provides Neuroprotection and Reduces Glial Proliferation and Scar Formation after Traumatic Brain Injury. *Proc. Natl. Acad. Sci. U. S. A. 102* (23), 8333.

(228) Kabadi, S. V., Stoica, B. A., Loane, D. J., Byrnes, K. R., Hanscom, M., Cabatbat, R. M., Tan, M. T., and Faden, A. I. (2012) Cyclin D1 Gene Ablation Confers Neuroprotection in Traumatic Brain Injury. *J. Neurotrauma 29* (5), 813−827.

(229) Skovira, J. W., Wu, J., Matyas, J. J., Kumar, A., Hanscom, M., Kabadi, S. V., Fang, R., Faden, A. I., Di Giovanni, S., Movsesyan, V., et al. (2016) Cell Cycle Inhibition Reduces Inflammatory Responses, Neuronal Loss, and Cognitive Deficits Induced by Hypobaria Exposure Following Traumatic Brain Injury. *J. Neuroinflammation 13* (1), 299.

(230) Raghupathi, R., Graham, D. I., and McIntosh, T. K. (2000) Apoptosis After Traumatic Brain Injury. *J. Neurotrauma 17* (10), 927.

(231) Juurlink, B. H. J., and Paterson, P. G. (1998) Review of Oxidative Stress in Brain and Spinal Cord Injury: Suggestions for Pharmacological and Nutritional Management Strategies. *J. Spinal Cord Med. 21* (4), 309−334.

(232) Plesnila, N., von Baumgarten, L., Retiounskaia, M., Engel, D., Ardeshiri, A., Zimmermann, R., Hoffmann, F., Landshamer, S., Wagner, E., and Culmsee, C. (2007) Delayed Neuronal Death after Brain Trauma Involves P53-Dependent Inhibition of NF-KB Transcriptional Activity. *Cell Death Differ. 14* (8), 1529−1541.

(233) Yang, L.-Y., Chu, Y.-H., Tweedie, D., Yu, Q.-S., Pick, C. G., Hoffer, B. J., Greig, N. H., and Wang, J.-Y. (2015) Post-Trauma Administration of the Pifithrin-α Oxygen Analog Improves Histological and Functional Outcomes after Experimental Traumatic Brain Injury. *Exp. Neurol. 269*, 56−66.

(234) Greig, N. H., Mattson, M. P., Perry, T., Chan, S. L., Giordano, T., Sambamurti, K., Rogers, J. T., Ovadia, H., and Lahiri, D. K. (2004) New Therapeutic Strategies and Drug Candidates for Neurodegenerative Diseases: P53 and TNF-α Inhibitors, and GLP-1 Receptor Agonists. *Ann. N. Y. Acad. Sci. 1035* (1), 290−315.

(235) Zhu, X., Yu, Q. s., Cutler, R. G., Culmsee, C. W., Holloway, H. W., Lahiri, D. K., Mattson, M. P., and Greig, N. H. (2002) Novel P53 Inactivators with Neuroprotective Action: Syntheses and Pharmacological Evaluation of 2-Imino-2,3,4,5,6,7-Hexahydrobenzothiazole and 2-Imino-2,3,4,5,6,7-Hexahydrobenzoxazole Derivatives. *J. Med. Chem. 45* (23), 5090−5097.

(236) Gudkov, A. V., and Komarova, E. A. (2007) Dangerous Habits of a Security Guard: The Two Faces of P53 as a Drug Target. *Hum. Mol. Genet. 16*, R67−R72.

(237) Gudkov, A. V., and Komarova, E. A. (2016) P53 and the Carcinogenicity of Chronic Inflammation. *Cold Spring Harbor Perspect. Med. 6* (11), a026161.

(238) Yang, L.-Y., Greig, N. H., Huang, Y.-N., Hsieh, T.-H., Tweedie, D., Yu, Q.-S., Hoffer, B. J., Luo, Y., Kao, Y.-C., and Wang, J.-Y. (2016) Post-Traumatic Administration of the P53 Inactivator Pifithrin-α Oxygen Analogue Reduces Hippocampal Neuronal Loss and Improves Cognitive Deficits after Experimental Traumatic Brain Injury. *Neurobiol. Dis. 96*, 216−226.

(239) Mihara, M., Erster, S., Zaika, A., Petrenko, O., Chittenden, T., Pancoska, P., and Moll, U. M. (2003) P53 Has a Direct Apoptogenic Role at the Mitochondria. *Mol. Cell 11* (3), 577−590.

(240) Nakano, K., and Vousden, K. H. (2001) PUMA, a Novel Proapoptotic Gene, Is Induced by P53. *Mol. Cell 7* (3), 683−694.

(241) Krajewska, M., You, Z., Rong, J., Kress, C., Huang, X., Yang, J., Kyoda, T., Leyva, R., Banares, S., Hu, Y., et al. (2011) Neuronal Deletion of Caspase 8 Protects against Brain Injury in Mouse Models of Controlled Cortical Impact and Kainic Acid-Induced Excitotoxicity. *PLoS One 6* (9), No. e24341.

(242) Clark, R. S. B., Kochanek, P. M., Watkins, S. C., Chen, M., Dixon, C. E., Seidberg, N. A., Melick, J., Loeffert, J. E., Nathaniel, P. D., Jin, K. L., et al. (2000) Caspase-3 Mediated Neuronal Death after Traumatic Brain Injury in Rats. *J. Neurochem. 74* (2), 740−753.

(243) Knoblach, S. M., Nikolaeva, M., Huang, X., Fan, L., Krajewski, S., Reed, J. C., and Faden, A. I. (2002) Multiple Caspases Are Activated after Traumatic Brain Injury: Evidence for Involvement in Functional Outcome. *J. Neurotrauma 19* (10), 1155−1170.

(244) Knoblach, S. M., Alroy, D. A., Nikolaeva, M., Cernak, I., Stoica, B. A., and Faden, A. I. (2004) Caspase Inhibitor Z-DEVD-Fmk Attenuates Calpain and Necrotic Cell Death in Vitro and after Traumatic Brain Injury. *J. Cereb. Blood Flow Metab. 24* (10), 1119−1132.

(245) Clark, R. S., Nathaniel, P. D., Zhang, X., Dixon, C. E., Alber, S. M., Watkins, S. C., Melick, J. A., Kochanek, P. M., and Graham, S. H. (2007) Boc-Aspartyl(OMe)-Fluoromethylketone Attenuates Mitochondrial Release of Cytochrome C and Delays Brain Tissue Loss after Traumatic Brain Injury in Rats. *J. Cereb. Blood Flow Metab. 27* (2), 316−326.

(246) Tomasevic, G., Raghupathi, R., Scherbel, U., Wieloch, T., and McIntosh, T. K. (2010) Deletion of the P53 Tumor Suppressor Gene Improves Neuromotor Function but Does Not Attenuate Regional Neuronal Cell Loss Following Experimental Brain Trauma in Mice. *J. Neurosci. Res. 88* (15), 3414−3423.

(247) LaPlaca, M. C., Zhang, J., Raghupathi, R., Li, J. H., Smith, F., Bareyre, F. M., Snyder, S. H., Graham, D. I., and McIntosh, T. K. (2001) Pharmacologic Inhibition of Poly(ADP-Ribose) Polymerase Is Neuroprotective Following Traumatic Brain Injury in Rats. *J. Neurotrauma 18* (4), 369−376.

(248) Slemmer, J. E., Zhu, C., Landshamer, S., Trabold, R., Grohm, J., Ardeshiri, A., Wagner, E., Sweeney, M. I., Blomgren, K., Culmsee, C., et al. (2008) Causal Role of Apoptosis-Inducing Factor for Neuronal Cell Death Following Traumatic Brain Injury. *Am. J. Pathol. 173* (6), 1795−1805.

(249) Krajewska, M., Xu, L., Xu, W., Krajewski, S., Kress, C. L., Cui, J., Yang, L., Irie, F., Yamaguchi, Y., Lipton, S. A., et al. (2011) Endoplasmic Reticulum Protein BI-1 Modulates Unfolded Protein Response Signaling and Protects against Stroke and Traumatic Brain Injury. *Brain Res. 1370*, 227−237.

(250) Nakamura, M., Raghupathi, R., Merry, D. E., Scherbel, U., Saatman, K. E., and McIntosh, T. K. (1999) Overexpression of Bcl-2 Is Neuroprotective after Experimental Brain Injury in Transgenic Mice. *J. Comp. Neurol. 412* (4), 681−692.

DOI: 10.1021/acsptsci.9b00003
ACS Pharmacol. Transl. Sci. 2019, 2, 66−91

(251) Raghupathi, R., Fernandez, S. C., Murai, H., Trusko, S. P., Scott, R. W., Nishioka, W. K., and McIntosh, T. K. (1998) BCL-2 Overexpression Attenuates Cortical Cell Loss after Traumatic Brain Injury in Transgenic Mice. *J. Cereb. Blood Flow Metab. 18* (11), 1259−1269.
(252) Bermpohl, D., You, Z., Korsmeyer, S. J., Moskowitz, M. A., and Whalen, M. J. (2006) Traumatic Brain Injury in Mice Deficient in Bid: Effects on Histopathology and Functional Outcome. *J. Cereb. Blood Flow Metab. 26* (5), 625−633.
(253) Shi, J., Miles, D. K., Orr, B. A., Massa, S. M., and Kernie, S. G. (2007) Injury-Induced Neurogenesis in Bax-Deficient Mice: Evidence for Regulation by Voltage-Gated Potassium Channels. *Eur. J. Neurosci. 25* (12), 3499−3512.
(254) Sullivan, P. G., Bruce-Keller, A. J., Rabchevsky, A. G., Christakos, S., Clair, D. K., Mattson, M. P., and Scheff, S. W. (1999) Exacerbation of Damage and Altered NF-KappaB Activation in Mice Lacking Tumor Necrosis Factor Receptors after Traumatic Brain Injury. *J. Neurosci. 19*, 6248−6256.
(255) Schoch, K. M., Madathil, S. K., and Saatman, K. E. (2012) Genetic Manipulation of Cell Death and Neuroplasticity Pathways in Traumatic Brain Injury. *Neurotherapeutics*, 323−337, DOI: 10.1007/s13311-012-0107-z.
(256) Kim, J. J., and Gean, A. D. (2011) Imaging for the Diagnosis and Management of Traumatic Brain Injury. *Neurotherapeutics 8* (1), 39−53.
(257) Vink, R. (2018) Large Animal Models of Traumatic Brain Injury. *J. Neurosci. Res. 96* (4), 527−535.
(258) Sorby-Adams, A. J., Vink, R., and Turner, R. J. (2018) Large Animal Models of Stroke and Traumatic Brain Injury as Translational Tools. *Am. J. Physiol. Integr. Comp. Physiol. 315* (2), R165.
(259) Xiong, Y., Mahmood, A., and Chopp, M. (2013) Animal Models of Traumatic Brain Injury. *Nat. Rev. Neurosci. 14* (2), 128−142.
(260) Cassidy, J. D., Carroll, L. J., Peloso, P. M., Borg, J., von Holst, H., Holm, L., Kraus, J., and Coronado, V. G. (2004) Incidence, Risk Factors and Prevention of Mild Traumatic Brain Injury: Results of the WHO Collaborating Centre Task Force on Mild Traumatic Brain Injury. *J. Rehabil. Med. 43* (Suppl), 28−60.
(261) Kovacs, S. K., Leonessa, F., and Ling, G. S. F. (2014) Blast TBI Models, Neuropathology, and Implications for Seizure Risk. *Front. Neurol. 5*, 47.
(262) Milman, A., Rosenberg, A., Weizman, R., and Pick, C. G. (2005) Mild Traumatic Brain Injury Induces Persistent Cognitive Deficits and Behavioral Disturbances in Mice. *J. Neurotrauma 22* (9), 1003−1010.
(263) Chen, Y., Constantini, S., Trembovler, V., Weinstock, M., and Shohami, E. (1996) An Experimental Model of Closed Head Injury in Mice: Pathophysiology, Histopathology, and Cognitive Deficits. *J. Neurotrauma 13* (10), 557−568.
(264) Baratz, R., Tweedie, D., Rubovitch, V., Luo, W., Yoon, J. S., Hoffer, B. J., Greig, N. H., and Pick, C. G. (2011) Tumor Necrosis Factor-α Synthesis Inhibitor, 3,6′- Dithiothalidomide, Reverses Behavioral Impairments Induced by Minimal Traumatic Brain Injury in Mice. *J. Neurochem. 118* (6), 1032−1042.
(265) Baratz, R., Tweedie, D., Wang, J. Y., Rubovitch, V., Luo, W., Hoffer, B. J., Greig, N. H., and Pick, C. G. (2015) Transiently Lowering Tumor Necrosis Factor-Aα Synthesis Ameliorates Neuronal Cell Loss and Cognitive Impairments Induced by Minimal Traumatic Brain Injury in Mice. *J. Neuroinflammation 12* (1), 45.
(266) Tweedie, D., Rachmany, L., Rubovitch, V., Zhang, Y., Becker, K. G., Perez, E., Hoffer, B. J., Pick, C. G., and Greig, N. H. (2013) Changes in Mouse Cognition and Hippocampal Gene Expression Observed in a Mild Physical- and Blast-Traumatic Brain Injury. *Neurobiol. Dis. 54*, 1−11.
(267) Fann, J. R., Hart, T., and Schomer, K. G. (2009) Treatment for Depression after Traumatic Brain Injury: A Systematic Review. *J. Neurotrauma 26* (12), 2383−2402.
(268) Chhor, V., Moretti, R., Le Charpentier, T., Sigaut, S., Lebon, S., Schwendimann, L., Oré, M.-V., Zuiani, C., Milan, V., Josserand, J., et al. (2017) Role of Microglia in a Mouse Model of Paediatric Traumatic Brain Injury. *Brain, Behav., Immun. 63*, 197−209.
(269) Homsi, S., Piaggio, T., Croci, N., Noble, F., Plotkine, M., Marchand-Leroux, C., and Jafarian-Tehrani, M. (2010) Blockade of Acute Microglial Activation by Minocycline Promotes Neuroprotection and Reduces Locomotor Hyperactivity after Closed Head Injury in Mice: A Twelve-Week Follow-Up Study. *J. Neurotrauma 27* (5), 911−921.
(270) Bye, N., Habgood, M. D., Callaway, J. K., Malakooti, N., Potter, A., Kossmann, T., and Morganti-Kossmann, M. C. (2007) Transient Neuroprotection by Minocycline Following Traumatic Brain Injury Is Associated with Attenuated Microglial Activation but No Changes in Cell Apoptosis or Neutrophil Infiltration. *Exp. Neurol. 204* (1), 220−233.
(271) Singh, K., Trivedi, R., Devi, M. M., Tripathi, R. P., and Khushu, S. (2016) Longitudinal Changes in the DTI Measures, Anti-GFAP Expression and Levels of Serum Inflammatory Cytokines Following Mild Traumatic Brain Injury. *Exp. Neurol. 275*, 427−435.
(272) Kane, M. J., Pérez, M. A., Briggs, D. I., Viano, D. C., Kreipke, C. W., Kuhn, D. M., and Dingell, J. D. (2012) A Mouse Model of Human Repetitive Mild Traumatic Brain Injury. *J. Neurosci. Methods 15* (2031), 41−49.
(273) Shohami, E., Gallily, R., Mechoulam, R., Bass, R., and Ben-Hur, T. (1997) Cytokine Production in the Brain Following Closed Head Injury: Dexanabinol (HU-211) Is a Novel TNF-α Inhibitor and an Effective Neuroprotectant. *J. Neuroimmunol. 72* (2), 169−177.
(274) Shohami, E., Novikov, M., Bass, R., Yamin, A., and Gallily, R. (1994) Closed Head Injury Triggers Early Production of TNFα and IL-6 by Brain Tissue. *J. Cereb. Blood Flow Metab. 14* (4), 615−619.
(275) Tweedie, D., Rachmany, L., Rubovitch, V., Lehrmann, E., Zhang, Y., Becker, K. G., Perez, E., Miller, J., Hoffer, B. J., Greig, N. H., et al. (2013) Exendin-4, a Glucagon-like Peptide-1 Receptor Agonist Prevents MTBI-Induced Changes in Hippocampus Gene Expression and Memory Deficits in Mice. *Exp. Neurol. 239* (1), 170−182.
(276) Tweedie, D., Milman, A., Holloway, H. W., Li, Y., Harvey, B. K., Shen, H., Pistell, P. J., Lahiri, D. K., Hoffer, B. J., Wang, Y., et al. (2007) Apoptotic and Behavioral Sequelae of Mild Brain Trauma in Mice. *J. Neurosci. Res. 85* (4), 805−815.
(277) Schwarzbold, M. L., Rial, D., De Bem, T., Machado, D. G., Cunha, M. P., dos Santos, A. A., dos Santos, D. B., Figueiredo, C. P., Farina, M., Goldfeder, E. M., et al. (2010) Effects of Traumatic Brain Injury of Different Severities on Emotional, Cognitive, and Oxidative Stress-Related Parameters in Mice. *J. Neurotrauma 27* (10), 1883−1893.
(278) Lai, J.-H., Karlsson, T. E., Wu, J. C.-C., Huang, C.-Z., Chen, Y.-H., Kang, S.-J., Brodin, A. T. S., Hoffer, B. J., Olson, L., and Chiang, Y.-H. (2018) Role of Nogo Receptor-1 for Recovery of Balance, Cognition, and Emotion after Mild Traumatic Brain Injury in Mice. *J. Neurotrauma*, No. 5949, DOI: 10.1089/neu.2018.5949.
(279) Tashlykov, V., Katz, Y., Volkov, A., Gazit, V., Schreiber, S., Zohar, O., and Pick, C. G. (2009) Minimal Traumatic Brain Injury Induce Apoptotic Cell Death in Mice. *J. Mol. Neurosci. 37* (1), 16−24.
(280) Tashlykov, V., Katz, Y., Gazit, V., Zohar, O., Schreiber, S., and Pick, C. G. (2007) Apoptotic Changes in the Cortex and Hippocampus Following Minimal Brain Trauma in Mice. *Brain Res. 1130* (1), 197−205.
(281) Yaka, R., Biegon, A., Grigoriadis, N., Simeonidou, C., Grigoriadis, S., Alexandrovich, A. G., Matzner, H., Schumann, J., Trembovler, V., Tsenter, J., et al. (2007) D-Cycloserine Improves Functional Recovery and Reinstates Long-Term Potentiation (LTP) in a Mouse Model of Closed Head Injury. *FASEB J. 21* (9), 2033−2041.
(282) Shimon, M. B., Zeimer, T., Stein, E. S., Artan-Furman, A., Harnof, S., Chapman, J., Eisenkraft, A., Pick, C. G., and Maggio, N. (2017) Recovery from Trauma Induced Amnesia Correlates with Normalization of Thrombin Activity in the Mouse Hippocampus. *PLoS One 12* (11), No. e0188524.

DOI: 10.1021/acsptsci.9b00003
ACS Pharmacol. Transl. Sci. 2019, 2, 66−91

(283) Esen, F., Erdem, T., Aktan, D., Kalayci, R., Cakar, N., Kaya, M., and Telci, L. (2003) Effects of Magnesium Administration on Brain Edema and Blood-Brain Barrier Breakdown after Experimental Traumatic Brain Injury in Rats. *J. Neurosurg. Anesthesiol. 15* (2), 119−125.
(284) Habgood, M. D., Bye, N., Dziegielewska, K. M., Ek, C. J., Lane, M. A., Potter, A., Morganti-Kossmann, C., and Saunders, N. R. (2007) Changes in Blood-Brain Barrier Permeability to Large and Small Molecules Following Traumatic Brain Injury in Mice. *Eur. J. Neurosci. 25* (1), 231−238.
(285) Fanne, R. A., Nassar, T., Mazuz, A., Waked, O., Heyman, S. N., Hijazi, N., Goelman, G., and Higazi, A. A.-R. (2011) Neuroprotection by Glucagon: Role of Gluconeogenesis. *J. Neurosurg. 114* (1), 85−91.
(286) Kuehn, R., Simard, P. F., Driscoll, I., Keledjian, K., Ivanova, S., Tosun, C., Williams, A., Bochicchio, G., Gerzanich, V., and Simard, J. M. (2011) Rodent Model of Direct Cranial Blast Injury. *J. Neurotrauma 28* (10), 2155−2169.
(287) Readnower, R. D., Chavko, M., Adeeb, S., Conroy, M. D., Pauly, J. R., McCarron, R. M., and Sullivan, P. G. (2010) Increase in Blood-Brain Barrier Permeability, Oxidative Stress, and Activated Microglia in a Rat Model of Blast-Induced Traumatic Brain Injury. *J. Neurosci. Res. 88* (16), 3530−3539.
(288) Svetlov, S. I., Prima, V., Kirk, D. R., Gutierrez, H., Curley, K. C., Hayes, R. L., and Wang, K. K. W. (2010) Morphologic and Biochemical Characterization of Brain Injury in a Model of Controlled Blast Overpressure Exposure. *J. Trauma 69* (4), 795−804.
(289) Sajja, V. S. S. S., Galloway, M., Ghoddoussi, F., Kepsel, A., and Vandevord, P. (2013) Effects of Blast-Induced Neurotrauma on the Nucleus Accumbens. *J. Neurosci. Res. 91* (4), 593−601.
(290) Du, X., Ewert, D. L., Cheng, W., West, M. B., Lu, J., Li, W., Floyd, R. A., and Kopke, R. D. (2013) Effects of Antioxidant Treatment on Blast-Induced Brain Injury. *PLoS One 8* (11), No. e80138.
(291) Säljö, A., Bao, F., Hamberger, A., Haglid, K. G., and Hansson, H. A. (2001) Exposure to Short-Lasting Impulse Noise Causes Microglial and Astroglial Cell Activation in the Adult Rat Brain. *Pathophysiology 8* (2), 105−111.
(292) Sajja, V. S. S. S., Ereifej, E. S., and VandeVord, P. J. (2014) Hippocampal Vulnerability and Subacute Response Following Varied Blast Magnitudes. *Neurosci. Lett. 570*, 33−37.
(293) Cho, H. J., Sajja, V. S. S. S., VandeVord, P. J., and Lee, Y. W. (2013) Blast Induces Oxidative Stress, Inflammation, Neuronal Loss and Subsequent Short-Term Memory Impairment in Rats. *Neuroscience 253*, 9−20.
(294) Kochanek, P. M., Dixon, C. E., Shellington, D. K., Shin, S. S., Bayır, H., Jackson, E. K., Kagan, V. E., Yan, H. Q., Swauger, P. V., Parks, S. A., et al. (2013) Screening of Biochemical and Molecular Mechanisms of Secondary Injury and Repair in the Brain after Experimental Blast-Induced Traumatic Brain Injury in Rats. *J. Neurotrauma 30* (11), 920−937.
(295) Heim, L. R., Bader, M., Edut, S., Rachmany, L., Baratz-Goldstein, R., Lin, R., Elpaz, A., Qubty, D., Bikovski, L., and Rubovitch, V. (2017) The Invisibility of Mild Traumatic Brain Injury: Impaired Cognitive Performance as a Silent Symptom. *J. Neurotrauma 34* (17), 2518.
(296) Abdul-Muneer, P. M., Schuetz, H., Wang, F., Skotak, M., Jones, J., Gorantla, S., Zimmerman, M. C., Chandra, N., and Haorah, J. (2013) Induction of Oxidative and Nitrosative Damage Leads to Cerebrovascular Inflammation in an Animal Model of Mild Traumatic Brain Injury Induced by Primary Blast. *Free Radical Biol. Med. 60*, 282−291.
(297) Vogel, E. W., Effgen, G. B., Patel, T. P., Meaney, D. F., Bass, C. R. D., and Morrison, B. (2016) Isolated Primary Blast Inhibits Long-Term Potentiation in Organotypic Hippocampal Slice Cultures. *J. Neurotrauma 33* (7), 652−661.
(298) Goldstein, L. E., Fisher, A. M., Tagge, C. A., Zhang, X.-L., Velisek, L., Sullivan, J. A., Upreti, C., Kracht, J. M., Ericsson, M., and Wojnarowicz, M. W. (2012) Chronic Traumatic Encephalopathy in Blast-Exposed Military Veterans and a Blast Neurotrauma Mouse Model. *Sci. Transl. Med. 4* (134), 134ra60.
(299) Chio, C. C., Chang, C. H., Wang, C. C., Cheong, C. U., Chao, C. M., Cheng, B. C., Yang, C. Z., and Chang, C. P. (2013) Etanercept Attenuates Traumatic Brain Injury in Rats by Reducing Early Microglial Expression of Tumor Necrosis Factor-α. *BMC Neurosci. 14* (1), 33.
(300) Cao, T., Thomas, T. C., Ziebell, J. M., Pauly, J. R., and Lifshitz, J. (2012) Morphological and Genetic Activation of Microglia after Diffuse Traumatic Brain Injury in the Rat. *Neuroscience 225*, 65−75.
(301) Shojo, H., Borlongan, C. V., and Mabuchi, T. (2017) Genetic and Histological Alterations Reveal Key Role of Prostaglandin Synthase and Cyclooxygenase 1 and 2 in Traumatic Brain Injury−Induced Neuroinflammation in the Cerebral Cortex of Rats Exposed to Moderate Fluid Percussion Injury. *Cell Transplant 26* (7), 1301−1313.
(302) Gao, W., Zhao, Z., Yu, G., Zhou, Z., Zhou, Y., Hu, T., Jiang, R., and Zhang, J. (2015) VEGI Attenuates the Inflammatory Injury and Disruption of Blood-Brain Barrier Partly by Suppressing the TLR4/NF-KB Signaling Pathway in Experimental Traumatic Brain Injury. *Brain Res. 1622*, 230−239.
(303) Webster, K. M., Wright, D. K., Sun, M., Semple, B. D., Ozturk, E., Stein, D. G., O'Brien, T. J., and Shultz, S. R. (2015) Progesterone Treatment Reduces Neuroinflammation, Oxidative Stress and Brain Damage and Improves Long-Term Outcomes in a Rat Model of Repeated Mild Traumatic Brain Injury. *J. Neuroinflammation 12* (1), 238.
(304) Fan, L., Young, P. R., Barone, F. C., Feuerstein, G. Z., Smith, D. H., and McIntosh, T. K. (1996) Experimental Brain Injury Induces Differential Expression of Tumor Necrosis Factor-α MRNA in the CNS. *Mol. Brain Res. 36* (2), 287−291.
(305) Muccigrosso, M. M., Ford, J., Benner, B., Moussa, D., Burnsides, C., Fenn, A. M., Popovich, P. G., Lifshitz, J., Walker, F. R., Eiferman, D. S., et al. (2016) Cognitive Deficits Develop 1 Month after Diffuse Brain Injury and Are Exaggerated by Microglia-Associated Reactivity to Peripheral Immune Challenge. *Brain, Behav., Immun. 54*, 95−109.
(306) Spain, A., Daumas, S., Lifshitz, J., Rhodes, J., Andrews, P. J. D., Horsburgh, K., and Fowler, J. H. (2010) Mild Fluid Percussion Injury in Mice Produces Evolving Selective Axonal Pathology and Cognitive Deficits Relevant to Human Brain Injury. *J. Neurotrauma 27* (8), 1429−1438.
(307) Rink, A., Fung, K. M., Trojanowski, J. Q., Lee, V. M., Neugebauer, E., and McIntosh, T. K. (1995) Evidence of Apoptotic Cell Death after Experimental Traumatic Brain Injury in the Rat. *Am. J. Pathol. 147* (6), 1575−1583.
(308) Van Bregt, D. R., Thomas, T. C., Hinzman, J. M., Cao, T., Liu, M., Bing, G., Gerhardt, G. A., Pauly, J. R., and Lifshitz, J. (2012) Substantia Nigra Vulnerability after a Single Moderate Diffuse Brain Injury in the Rat. *Exp. Neurol. 234* (1), 8−19.
(309) Karklin Fontana, A. C., Fox, D. P., Zoubroulis, A., Valente Mortensen, O., and Raghupathi, R. (2016) Neuroprotective Effects of the Glutamate Transporter Activator (R)-(−)-5-Methyl-1-Nicotinoyl-2-Pyrazoline (MS-153) Following Traumatic Brain Injury in the Adult Rat. *J. Neurotrauma 33* (11), 1073−1083.
(310) Sanders, M. J., Sick, T. J., Perez-Pinzon, M. A., Dietrich, W. D., and Green, E. J. (2000) Chronic Failure in the Maintenance of Long-Term Potentiation Following Fluid Percussion Injury in the Rat. *Brain Res. 861* (1), 69−76.
(311) Chen, Y.-H., Kuo, T.-T., Huang, E. Y.-K., Hoffer, B. J., Chou, Y.-C., Chiang, Y.-H., Ma, H.-I., and Miller, J. P. (2018) Profound Deficits in Hippocampal Synaptic Plasticity after Traumatic Brain Injury and Seizure Is Ameliorated by Prophylactic Levetiracetam. *Oncotarget 9* (14), 11515−11527.
(312) Wu, A., Ying, Z., and Gomez-Pinilla, F. (2006) Dietary Curcumin Counteracts the Outcome of Traumatic Brain Injury on Oxidative Stress, Synaptic Plasticity, and Cognition. *Exp. Neurol. 197* (2), 309−317.

DOI: 10.1021/acsptsci.9b00003
ACS Pharmacol. Transl. Sci. 2019, 2, 66−91

(313) Tomura, S., Nawashiro, H., Otani, N., Uozumi, Y., Toyooka, T., Ohsumi, A., and Shima, K. (2011) Effect of Decompressive Craniectomy on Aquaporin-4 Expression after Lateral Fluid Percussion Injury in Rats. *J. Neurotrauma 28* (2), 237−243.

(314) Lima, F. D., Oliveira, M. S., Furian, A. F., Souza, M. A., Rambo, L. M., Ribeiro, L. R., Silva, L. F. A., Retamoso, L. T., Hoffmann, M. S., Magni, D. V., et al. (2009) Adaptation to Oxidative Challenge Induced by Chronic Physical Exercise Prevents Na+,K +-ATPase Activity Inhibition after Traumatic Brain Injury. *Brain Res. 1279*, 147−155.

(315) Hinzman, J. M., Thomas, T. C., Burmeister, J. J., Quintero, J. E., Huettl, P., Pomerleau, F., Gerhardt, G. A., and Lifshitz, J. (2010) Diffuse Brain Injury Elevates Tonic Glutamate Levels and Potassium-Evoked Glutamate Release in Discrete Brain Regions at Two Days Post-Injury: An Enzyme-Based Microelectrode Array Study. *J. Neurotrauma 27* (5), 889−899.

(316) Sun, F. Y., and Faden, A. I. (1995) Pretreatment with Antisense Oligodeoxynucleotides Directed against the NMDA-R1 Receptor Enhances Survival and Behavioral Recovery Following Traumatic Brain Injury in Rats. *Brain Res. 693* (1−2), 163−168.

(317) Okiyama, K., Smith, D. H., Gennarelli, T. A., Simon, R. P., Leach, M., and McIntosh, T. K. (1995) The Sodium Channel Blocker and Glutamate Release Inhibitor BW1003C87 and Magnesium Attenuate Regional Cerebral Edema Following Experimental Brain Injury in the Rat. *J. Neurochem. 64* (2), 802−809.

(318) Matsushita, Y., Shima, K., Nawashiro, H., and Wada, K. (2000) Real-Time Monitoring of Glutamate Following Fluid Percussion Brain Injury With Hypoxia in the Rat. *J. Neurotrauma 17* (2), 143−153.

(319) Shitaka, Y., Tran, H. T., Bennett, R. E., Sanchez, L., Levy, M. A., Dikranian, K., and Brody, D. L. (2011) Repetitive Closed-Skull Traumatic Brain Injury in Mice Causes Persistent Multifocal Axonal Injury and Microglial Reactivity. *J. Neuropathol. Exp. Neurol. 70* (7), 551−567.

(320) Sandhir, R., Onyszchuk, G., and Berman, N. E. J. (2008) Exacerbated Glial Response in the Aged Mouse Hippocampus Following Controlled Cortical Impact Injury. *Exp. Neurol. 213* (2), 372−380.

(321) Zhang, Q.-G., Laird, M. D., Han, D., Nguyen, K., Scott, E., Dong, Y., Dhandapani, K. M., and Brann, D. W. (2012) Critical Role of NADPH Oxidase in Neuronal Oxidative Damage and Microglia Activation Following Traumatic Brain Injury. *PLoS One 7* (4), No. e34504.

(322) Turtzo, L. C., Lescher, J., Janes, L., Dean, D. D., Budde, M. D., and Frank, J. A. (2014) Macrophagic and Microglial Responses after Focal Traumatic Brain Injury in the Female Rat. *J. Neuroinflammation 11*, 82.

(323) Isaksson, J., Hillered, L., and Olsson, Y. (2001) Cognitive and Histopathological Outcome after Weight-Drop Brain Injury in the Rat: Influence of Systemic Administration of Monoclonal Antibodies to ICAM-1. *Acta Neuropathol 102* (3), 246−256.

(324) Batsaikhan, B., Wang, J.-Y., Scerba, M., Tweedie, D., Greig, N., Miller, J., Hoffer, B., Lin, C.-T., Wang, J.-Y., et al. (2019) Post-Injury Neuroprotective Effects of the Thalidomide Analog 3,6′-Dithiothalidomide on Traumatic Brain Injury. *Int. J. Mol. Sci. 20* (3), 502.

(325) He, J., Evans, C.-O., Hoffman, S. W., Oyesiku, N. M., and Stein, D. G. (2004) Progesterone and Allopregnanolone Reduce Inflammatory Cytokines after Traumatic Brain Injury. *Exp. Neurol. 189* (2), 404−412.

(326) Choi, B. Y., Jang, B. G., Kim, J. H., Lee, B. E., Sohn, M., Song, H. K., and Suh, S. W. (2012) Prevention of Traumatic Brain Injury-Induced Neuronal Death by Inhibition of NADPH Oxidase Activation. *Brain Res. 1481*, 49−58.

(327) Ansari, M. A., Roberts, K. N., and Scheff, S. W. (2008) Oxidative Stress and Modification of Synaptic Proteins in Hippocampus after Traumatic Brain Injury. *Free Radical Biol. Med. 45* (4), 443−452.

(328) Albensi, B. C., Sullivan, P. G., Thompson, M. B., Scheff, S. W., and Mattson, M. P. (2000) Cyclosporin Ameliorates Traumatic Brain-Injury-Induced Alterations of Hippocampal Synaptic Plasticity. *Exp. Neurol. 162* (2), 385−389.

(329) Başkaya, M. K., Rao, A. M., Doğan, A., Donaldson, D., and Dempsey, R. J. (1997) The Biphasic Opening of the Blood-Brain Barrier in the Cortex and Hippocampus after Traumatic Brain Injury in Rats. *Neurosci. Lett. 226* (1), 33−36.

(330) Lopez, N. E., Krzyzaniak, M. J., Blow, C., Putnam, J., Ortiz-Pomales, Y., Hageny, A.-M., Eliceiri, B., Coimbra, R., and Bansal, V. (2012) Ghrelin Prevents Disruption of the Blood−Brain Barrier after Traumatic Brain Injury. *J. Neurotrauma 29* (2), 385−393.

(331) Marklund, N., Clausen, F., Lewander, T., and Hillered, L. (2001) Monitoring of Reactive Oxygen Species Production after Traumatic Brain Injury in Rats with Microdialysis and the 4-Hydroxybenzoic Acid Trapping Method. *J. Neurotrauma 18* (11), 1217−1227.

(332) Nilsson, P., Hillered, L., Ponten, U., and Ungerstedt, U. (1990) Changes in Cortical Extracellular Levels of Energy-Related Metabolites and Amino Acids Following Concussive Brain Injury in Rats. *J. Cereb. Blood Flow Metab. 10* (5), 631−637.

(333) Rose, M. E., Huerbin, M. B., Melick, J., Marion, D. W., Palmer, A. M., Schiding, J. K., Kochanek, P. M., and Graham, S. H. (2002) Regulation of Interstitial Excitatory Amino Acid Concentrations after Cortical Contusion Injury. *Brain Res. 943* (1), 15−22.

(334) Rao, V. L. R., Dogan, A., Bowen, K. K., Todd, K. G., and Dempsey, R. J. (2001) Antisense Knockdown of the Glial Glutamate Transporter GLT-1 Exacerbates Hippocampal Neuronal Damage Following Traumatic Injury to Rat Brain. *Eur. J. Neurosci. 13* (1), 119−128.

(335) Seino, Y., Fukushima, M., and Yabe, D. (2010) GIP and GLP-1, the Two Incretin Hormones: Similarities and Differences. *J. Diabetes Investig. 1* (1−2), 8−23.

(336) Holst, J. J., Ørskov, C., Vagn Nielsen, O., and Schwartz, T. W. (1987) Truncated Glucagon-like Peptide I, an Insulin-Releasing Hormone from the Distal Gut. *FEBS Lett. 211* (2), 169−174.

(337) Graaf, C. de, Donnelly, D., Wootten, D., Lau, J., Sexton, P. M., Miller, L. J., Ahn, J.-M., Liao, J., Fletcher, M. M., Yang, D., et al. (2016) Glucagon-Like Peptide-1 and Its Class B G Protein-Coupled Receptors: A Long March to Therapeutic Successes. *Pharmacol. Rev. 68* (4), 954−1013.

(338) Lee, Y. H., Wang, M.-Y., Yu, X.-X., and Unger, R. H. (2016) Glucagon Is the Key Factor in the Development of Diabetes. *Diabetologia 59* (7), 1372−1375.

(339) Abraham, M. A., and Lam, T. K. T. (2016) Glucagon Action in the Brain. *Diabetologia*, 1367−1371, DOI: 10.1007/s00125-016-3950-3.

(340) Campos, R. V., Lee, Y. C., and Drucker, D. J. (1994) Divergent Tissue-Specific and Developmental Expression of Receptors for Glucagon and Glucagon-like Peptide-1 in the Mouse. *Endocrinology 134* (5), 2156−2164.

(341) Nyberg, J., Anderson, M. F., Meister, B., Alborn, A.-M., Ström, A.-K., Brederlau, A., Illerskog, A.-C., Nilsson, O., Kieffer, T. J., Hietala, M. A., et al. (2005) Glucose-Dependent Insulinotropic Polypeptide Is Expressed in Adult Hippocampus and Induces Progenitor Cell Proliferation. *J. Neurosci. 25* (7), 1816−1825.

(342) Zhang, Y., Chen, K., Sloan, S. A., Bennett, M. L., Scholze, A. R., O'Keeffe, S., Phatnani, H. P., Guarnieri, P., Caneda, C., Ruderisch, N., et al. (2014) An RNA-Sequencing Transcriptome and Splicing Database of Glia, Neurons, and Vascular Cells of the Cerebral Cortex. *J. Neurosci. 34* (36), 11929−11947.

(343) Heppner, K. M., Kirigiti, M., Secher, A., Paulsen, S. J., Buckingham, R., Pyke, C., Knudsen, L. B., Vrang, N., and Grove, K. L. (2015) Expression and Distribution of Glucagon-like Peptide-1 Receptor MRNA, Protein and Binding in the Male Nonhuman Primate (Macaca Mulatta) Brain. *Endocrinology 156* (1), 255−267.

(344) Richards, P., Parker, H. E., Adriaenssens, A. E., Hodgson, J. M., Cork, S. C., Trapp, S., Gribble, F. M., and Reimann, F. (2014) Identification and Characterization of GLP-1 Receptor-Expressing Cells Using a New Transgenic Mouse Model. *Diabetes 63* (4), 1224−1233.

DOI: 10.1021/acsptsci.9b00003
ACS Pharmacol. Transl. Sci. 2019, 2, 66−91

(345) Chowen, J. A., Fonseca, F. R. De, Alvarez, E., Navarro, M., García-Segura, L. M., and Blázquez, E. (1999) Increased Glucagon-like Peptide-1 Receptor Expression in Glia after Mechanical Lesion of the Rat Brain. *Neuropeptides 33* (3), 212−215.

(346) Jazayeri, A., Rappas, M., Brown, A. J. H., Kean, J., Errey, J. C., Robertson, N. J., Fiez-Vandal, C., Andrews, S. P., Congreve, M., Bortolato, A., et al. (2017) Crystal Structure of the GLP-1 Receptor Bound to a Peptide Agonist. *Nature 546* (7657), 254−258.

(347) Koole, C., Wootten, D., Simms, J., Miller, L. J., Christopoulos, A., and Sexton, P. M. (2012) Second Extracellular Loop of Human Glucagon-like Peptide-1 Receptor (GLP-1R) Has a Critical Role in GLP-1 Peptide Binding and Receptor Activation. *J. Biol. Chem. 287* (6), 3642−3658.

(348) Lei, S., Clydesdale, L., Dai, A., Cai, X., Feng, Y., Yang, D., Liang, Y. L., Koole, C., Zhao, P., Coudrat, T., et al. (2018) Two Distinct Domains of the Glucagon-like Peptide-1 Receptor Control Peptide-Mediated Biased Agonism. *J. Biol. Chem. 293* (24), 9370−9387.

(349) Wootten, D., Reynolds, C. A., Smith, K. J., Mobarec, J. C., Koole, C., Savage, E. E., Pabreja, K., Simms, J., Sridhar, R., Furness, S. G. B., et al. (2016) The Extracellular Surface of the GLP-1 Receptor Is a Molecular Trigger for Biased Agonism. *Cell 165* (7), 1632−1643.

(350) Yin, Y., Zhou, X. E., Hou, L., Zhao, L. H., Liu, B., Wang, G., Jiang, Y., Melcher, K., and Xu, H. E. (2016) An Intrinsic Agonist Mechanism for Activation of Glucagon-like Peptide-1 Receptor by Its Extracellular Domain. *Cell Discov 2* (1), 16042.

(351) Tengholm, A., and Gylfe, E. (2017) CAMP Signalling in Insulin and Glucagon Secretion. *Diabetes, Obes. Metab. 19*, 42−53.

(352) Li, Y., Tweedie, D., Mattson, M. P., Holloway, H. W., and Greig, N. H. (2010) Enhancing the GLP-1 Receptor Signaling Pathway Leads to Proliferation and Neuroprotection in Human Neuroblastoma Cells. *J. Neurochem. 113* (6), 1621−1631.

(353) Mangmool, S., Hemplueksa, P., Parichatikanond, W., and Chattipakorn, N. (2015) Epac Is Required for GLP-1R-Mediated Inhibition of Oxidative Stress and Apoptosis in Cardiomyocytes. *Mol. Endocrinol. 29* (4), 583−596.

(354) Roscioni, S. S., Elzinga, C. R. S., and Schmidt, M. (2008) Epac: Effectors and Biological Functions. *Naunyn-Schmiedeberg's Archives of Pharmacology 377*, 345−357, DOI: 10.1007/s00210-007-0246-7.

(355) Rowlands, J., Heng, J., Newsholme, P., and Carlessi, R. (2018) Pleiotropic Effects of GLP-1 and Analogs on Cell Signaling, Metabolism, and Function. *Front. Endocrinol. (Lausanne, Switz.) 9*, 1−23.

(356) Parker, D., Montminy, M. R., Ferreri, K., Nakajima, T., LaMorte, V. J., Evans, R., Koerber, S. C., and Hoeger, C. (1996) Phosphorylation of CREB at Ser-133 Induces Complex Formation with CREB-Binding Protein via a Direct Mechanism. *Mol. Cell. Biol. 16* (2), 694−703.

(357) Ehrlich, D. E., and Josselyn, S. A. (2016) Plasticity-Related Genes in Brain Development and Amygdala-Dependent Learning. *Genes, Brain and Behavior 15*, 125−143.

(358) Yang, Y., Choi, P. P., Smith, W. W., Xu, W., Ma, D., Cordner, Z. A., Liang, N. C., and Moran, T. H. (2017) Exendin-4 Reduces Food Intake via the PI3K/AKT Signaling Pathway in the Hypothalamus. *Sci. Rep. 7* (1), 6936.

(359) Downward, J. (2004) PI 3-Kinase, Akt and Cell Survival. *Seminars in Cell and Developmental Biology*, 177−182, DOI: 10.1016/j.semcdb.2004.01.002.

(360) Athauda, D., and Foltynie, T. (2016) The Glucagon-like Peptide 1 (GLP) Receptor as a Therapeutic Target in Parkinson's Disease: Mechanisms of Action. *Drug Discovery Today 21* (5), 802−818.

(361) Pugazhenthi, S., Nesterova, A., Sable, C., Heidenreich, K. A., Boxer, L. M., Heasley, L. E., and Reusch, J. E. B. (2000) Akt/Protein Kinase B up-Regulates Bcl-2 Expression through CAMP-Response Element-Binding Protein. *J. Biol. Chem. 275* (15), 10761−10766.

(362) Athauda, D., Gulyani, S., Karnati, H., Li, Y., Tweedie, D., Mustapic, M., Chawla, S., Chowdhury, K., Skene, S. S., Greig, N. H., et al. (2019) Utility of Neuronal-Derived Exosomes to Examine Molecular Mechanisms That Affect Motor Function in Patients With Parkinson Disease. *JAMA Neurol*, DOI: 10.1001/jamaneurol.2018.4304.

(363) Li, P.-C., Liu, L.-F., Jou, M.-J., and Wang, H.-K. (2016) The GLP-1 Receptor Agonists Exendin-4 and Liraglutide Alleviate Oxidative Stress and Cognitive and Micturition Deficits Induced by Middle Cerebral Artery Occlusion in Diabetic Mice. *BMC Neurosci. 17* (1), 37.

(364) Tsai, T. H., Sun, C. K., Su, C. H., Sung, P. H., Chua, S., Zhen, Y. Y., Leu, S., Chang, H. W., Yang, J. L., and Yip, H. K. (2015) Sitagliptin Attenuated Brain Damage and Cognitive Impairment in Mice with Chronic Cerebral Hypo-Perfusion through Suppressing Oxidative Stress and Inflammatory Reaction. *J. Hypertens. 33* (5), 1001−1013.

(365) Kim, J. Y., Lim, D. M., Moon, C., Jo, K. J., Lee, S. K., Baik, H. W., Lee, K. H., Lee, K. W., Park, K. Y., and Kim, B. J. (2010) Exendin-4 Protects Oxidative Stress-Induced β-Cell Apoptosis through Reduced JNK and GSK3β Activity. *J. Korean Med. Sci. 25* (11), 1626−1632.

(366) Oeseburg, H., De Boer, R. A., Buikema, H., Van Der Harst, P., Van Gilst, W. H., and Silljé, H. H. W. (2010) Glucagon-like Peptide 1 Prevents Reactive Oxygen Species-Induced Endothelial Cell Senescence through the Activation of Protein Kinase A. *Arterioscler., Thromb., Vasc. Biol. 30* (7), 1407−1414.

(367) Yang, J.-L., Chen, W.-Y., Chen, Y.-P., Kuo, C.-Y., and Chen, S.-D. (2016) Activation of GLP-1 Receptor Enhances Neuronal Base Excision Repair via PI3K-AKT-Induced Expression of Apurinic/Apyrimidinic Endonuclease 1. *Theranostics 6* (12), 2015−2027.

(368) Yang, J. L., Tadokoro, T., Keijzers, G., Mattson, M. P., and Bohr, V. A. (2010) Neurons Efficiently Repair Glutamate-Induced Oxidative DNA Damage by a Process Involving CREB-Mediated up-Regulation of Apurinic Endonuclease 1. *J. Biol. Chem. 285* (36), 28191−28199.

(369) Yang, J. L., Lin, Y. T., Chuang, P. C., Bohr, V. A., and Mattson, M. P. (2014) BDNF and Exercise Enhance Neuronal DNA Repair by Stimulating CREB-Mediated Production of Apurinic/Apyrimidinic Endonuclease 1. *NeuroMol. Med. 16* (1), 161−174.

(370) Darsalia, V., Mansouri, S., Ortsäter, H., Olverling, A., Nozadze, N., Kappe, C., Iverfeldt, K., Tracy, L. M., Grankvist, N., Sjöholm, Å., et al. (2012) Glucagon-like Peptide-1 Receptor Activation Reduces Ischaemic Brain Damage Following Stroke in Type 2 Diabetic Rats. *Clin. Sci. 122* (10), 473−483.

(371) Hyun Lee, C., Yan, B., Yoo, K. Y., Choi, J. H., Kwon, S. H., Her, S., Sohn, Y., Hwang, I. K., Cho, J. H., Kim, Y. M., et al. (2011) Ischemia-Induced Changes in Glucagon-like Peptide-1 Receptor and Neuroprotective Effect of Its Agonist, Exendin-4, in Experimental Transient Cerebral Ischemia. *J. Neurosci. Res. 89* (7), 1103−1113.

(372) Kim, S., Moon, M., and Park, S. (2009) Exendin-4 Protects Dopaminergic Neurons by Inhibition of Microglial Activation and Matrix Metalloproteinase-3 Expression in an Animal Model of Parkinson's Disease. *J. Endocrinol. 202* (3), 431−439.

(373) Gullo, F., Ceriani, M., D'Aloia, A., Wanke, E., Constanti, A., Costa, B., and Lecchi, M. (2017) Plant Polyphenols and Exendin-4 Prevent Hyperactivity and TNF-α Release in LPS-Treated In Vitro Neuron/Astrocyte/Microglial Networks. *Front. Neurosci. 11*, 500.

(374) Shiraishi, D., Fujiwara, Y., Komohara, Y., Mizuta, H., and Takeya, M. (2012) Glucagon-like Peptide-1 (GLP-1) Induces M2 Polarization of Human Macrophages via STAT3 Activation. *Biochem. Biophys. Res. Commun. 425* (2), 304−308.

(375) Wu, H.-Y., Tang, X.-Q., Liu, H., Mao, X.-F., and Wang, Y.-X. (2018) Both Classic Gs-CAMP/PKA/CREB and Alternative Gs-CAMP/PKA/P38β/CREB Signal Pathways Mediate Exenatide-Stimulated Expression of M2Microglial Markers. *J. Neuroimmunol. 316*, 17−22.

(376) Ghosh, A., Roy, A., Liu, X., Kordower, J. H., Mufson, E. J., Hartley, D. M., Ghosh, S., Mosley, R. L., Gendelman, H. E., and Pahan, K. (2007) Selective Inhibition of NF-KappaB Activation Prevents Dopaminergic Neuronal Loss in a Mouse Model of

DOI: 10.1021/acsptsci.9b00003
ACS Pharmacol. Transl. Sci. 2019, 2, 66−91

Parkinson's Disease. *Proc. Natl. Acad. Sci. U. S. A. 104* (47), 18754−18759.
(377) Mattson, M. P., and Camandola, S. (2001) NF-KB in Neuronal Plasticity and Neurodegenerative Disorders. *J. Clin. Investig.*, 247−254, DOI: 10.1172/JCI11916.
(378) Kenakin, T., and Christopoulos, A. (2013) Signalling Bias in New Drug Discovery: Detection, Quantification and Therapeutic Impact. *Nat. Rev. Drug Discov. 15*, 205−216, DOI: 10.1038/nrd3954.
(379) Hager, M. V., Clydesdale, L., Gellman, S. H., Sexton, P. M., and Wootten, D. (2017) Characterization of Signal Bias at the GLP-1 Receptor Induced by Backbone Modification of GLP-1. *Biochem. Pharmacol. 136*, 99−108.
(380) Koole, C., Savage, E. E., Christopoulos, A., Miller, L. J., Sexton, P. M., and Wootten, D. (2013) Minireview: Signal Bias, Allosterism, and Polymorphic Variation at the GLP-1R: Implications for Drug Discovery. *Mol. Endocrinol. 27* (8), 1234−1244.
(381) Smith, J. S., and Rajagopal, S. (2016) The *β*-Arrestins: Multifunctional Regulators of G Protein-Coupled Receptors. *J. Biol. Chem. 291* (17), 8969−8977.
(382) Hager, M. V., Johnson, L. M., Wootten, D., Sexton, P. M., and Gellman, S. H. (2016) *β*-Arrestin-Biased Agonists of the GLP-1 Receptor from *β*-Amino Acid Residue Incorporation into GLP-1 Analogues. *J. Am. Chem. Soc. 138* (45), 14970−14979.
(383) Wootten, D., Miller, L. J., Koole, C., Christopoulos, A., and Sexton, P. M. (2017) Allostery and Biased Agonism at Class b g Protein-Coupled Receptors. *Chem. Rev. 117*, 111−138.
(384) Quoyer, J., Longuet, C., Broca, C., Linck, N., Costes, S., Varin, E., Bockaert, J. L., Bertrand, G., and Dalle, S. (2010) GLP-1 Mediates Antiapoptotic Effect by Phosphorylating Bad through a *β*-Arrestin 1-Mediated ERK1/2 Activation in Pancreatic *β*-Cells. *J. Biol. Chem. 285* (3), 1989−2002.
(385) Freeman, J. L. R., Dunn, I. M., and Valcarce, C. (2017) Beyond Topline Results for the Oral (Non-Peptide)GLP-1R Agonist TTP273 in Type 2 Diabetes: How Much and When? *Diabetol. Conf. 53rd Annu. Meet. Eur. Assoc. study diabetes, EASD 2017. Port. 60*, S51-S52.
(386) Jorgensen, R., Martini, L., Schwartz, T. W., and Elling, C. E. (2005) Characterization of Glucagon-Like Peptide-1 Receptor *β*-Arrestin 2 Interaction: A High-Affinity Receptor Phenotype. *Mol. Endocrinol. 19* (3), 812−823.
(387) Bruno, B. J., Miller, G. D., and Lim, C. S. (2013) Basics and Recent Advances in Peptide and Protein Drug Delivery. *Therapeutic Delivery*, 1443−1467, DOI: 10.4155/tde.13.104.
(388) Freeman, J. L., Agolory, J., and Valcarce, C. (2016) Preclinical Findings with Oral GLP-1 Receptor Agonist TTP273 Reinforce Importance of Neuro-Enteroendocrine Signaling. In *American Diabetes Association 76th Annual Scientific Session*, New Orleans.

DOI: 10.1021/acsptsci.9b00003
ACS Pharmacol. Transl. Sci. 2019, 2, 66−91

INFORME DE LABORES 2019
ResearchGate

See discussions, stats, and author profiles for this publication at: https://www.researchgate.net/publication/326564995

Network Pharmacology Uncovers Anticancer Activity of Mammea-Type Coumarins from Calophyllum brasiliense

Article *in* Planta Medica · January 2019
DOI: 10.1055/a-0660-0236

CITATIONS
4

READS
231

9 authors, including:


Juan Carlos Gomez-Verjan
Instituto Nacional De Geriatría
45 PUBLICATIONS **129** CITATIONS
SEE PROFILE


Nadia Alejandra Rivero-Segura
Instituto Nacional De Geriatría
20 PUBLICATIONS **161** CITATIONS
SEE PROFILE


edgar antonio estrella Parra
Universidad Nacional Autónoma de México
14 PUBLICATIONS **46** CITATIONS
SEE PROFILE


Ruth Rincón-Heredia
Universidad Nacional Autónoma de México
23 PUBLICATIONS **281** CITATIONS
SEE PROFILE

Some of the authors of this publication are also working on these related projects:


EGF regulates Cldn-2 and -4 expression through Src and STAT-3 in MDCK cells View project


Caveolin-1 knockout alters neural and myogenic functions in mouse small intestine View project

All content following this page was uploaded by Juan Carlos Gomez-Verjan on 08 May 2019.

The user has requested enhancement of the downloaded file.

INFORME DE LABORES 2019

Thieme

Network Pharmacology Uncovers Anticancer Activity of Mammea-Type Coumarins from *Calophyllum brasiliense*

Authors

Juan Carlos Gómez-Verjan[1]*, Nadia Alejandra Rivero-Segura[2]*, Edgar Estrella-Parra[3], Ruth Rincón-Heredia[4], Abraham Madariaga-Mazón[5], Edgar Flores-Soto[6], Mario González-Meljem[1], Marco Cerbón[2], Ricardo Reyes-Chilpa[5]

Affiliations

1 División de Investigación Básica, Instituto Nacional de Geriatría (InGer), Mexico City, Mexico
2 Unidad de Investigación en Reproducción Humana, Instituto de Perinatología/Lab. Biología Celular, Facultad de Química, Universidad Nacional Autónoma de México, Mexico City, Mexico
3 Laboratorio de Fitoquímica, Facultad de Estudios Superiores Iztacala, Universidad Nacional Autónoma de México, Tlalnepantla, Mexico
4 División de Neurociencias, Instituto de Fisiología Celular, Universidad Nacional Autónoma de México, Mexico City, Mexico
5 Instituto de Química, Universidad Nacional Autónoma de México, Mexico City, Mexico
6 Departamento de Farmacología, Facultad de Medicina, Universidad Nacional Autónoma de México, Mexico City, Mexico

Key words

network pharmacology, anticancer, mammea-type coumarins, *Calophyllum brasiliense*, cell death, autophagy, Clusiaceae

received April 13, 2018
revised July 2, 2018
accepted July 10, 2018

Bibliography

DOI https://doi.org/10.1055/a-0660-0236
Published online July 23, 2018 | Planta Med 2019; 85: 14–23
© Georg Thieme Verlag KG Stuttgart · New York |
ISSN 0032-0943

Correspondence

Dr. Ricardo Reyes-Chilpa
Instituto de Química, Universidad Nacional Autónoma de México, Circuito Exterior, Ciudad Universitaria
Del. Coyoacán S/N, C. P. 04510 Mexico City, Mexico
Phone: + 52 55 56 22 45 12, Fax: + 52 55 56 16 22 17
chilpa@unam.mx

Supporting information available online at http://www.thieme-connect.de/products

ABSTRACT

Mammea-type coumarins are a particular type of secondary metabolites biosynthesized by the tropical rainforest tree *Calophyllum Brasiliense*, which is distributed from South America to Mexico. Particularly, mammea A/BA and A/BB (alone or as a mixture) possess biological properties such as cytotoxic and antitumoral activities, however, most of its molecular targets remain unknown. In this context, novel bioinformatic approaches, such as network pharmacology analysis, have been successfully used in herbal medicine to accelerate research in this field, and the support of experimental validations has been shown to be quite robust. In the present study, we performed a network pharmacology analysis to assess the possible molecular biological networks that interact with mammea A/BA and A/BB. Moreover, we validated the most relevant networks experimentally *in vitro* on K562 cancer cells. The results of the network pharmacology analysis indicate that mammea A/BA and A/BB interacts with cell death, PI3K/AKT, MAPK, Ras, and cancer pathways. The *in vitro* model shows that mammea A/BA and A/BB induce apoptosis through the overexpression of the proapoptotic proteins Bax and Bak, disrupt the autophagic flux as seen by the cytosolic accumulation of LC3-II and p62, disrupting the mitochondria ultrastructure and concomitantly increase the intracellular calcium concentration. Additionally, docking analysis predicted a possible interaction with a rapamycin-binding domain of mTOR. In conclusion, we validated network pharmacology analysis and report, for the first time, that mammea A/BA and A/BB coumarins induce apoptosis through the inhibition of the autophagic flux, possibly interacting with mTOR.

* These two authors contributed equally to this work.

Downloaded by: Universidad de Barcelona. Copyrighted material.

ABBREVIATIONS

AO	acridine orange
BP	biological process
$[Ca^{2+}]i$	intracellular calcium concentration
CC	cellular component
CP	cisplatin
CQ	chloroquine
CTD	Comparative Toxicogenomics Database
FRB	FKBP-12 rapamycin-binding
iNOS	inducible nitric oxide synthase
KEGG	Kyoto Encyclopedia of Genes and Genomes
MABB	mammea A/BA and A/BB
MF	molecular function
NO	nitric oxide
NPr	network pharmacology analysis
OMIM	Online Mendelian Inheritance in Man
PDB	Protein Data Bank
PVDF	polyvinylidene difluoride
RMSD	root mean squared deviation

Introduction

Coumarins comprise a large class of secondary metabolites with phenolic structures, composed of fused benzene and α-pyrone rings, biosynthesized by several species of plants, fungi, and bacteria. Several studies have shown a wide range of pharmacological properties for these compounds, including anticoagulant, anti-inflammatory, antiparasitic, antibacterial, antiviral, and anticancer. These heterocyclic compounds represent the core structure for several molecules with pharmaceutical relevance already used in therapeutics, e.g., warfarin, coumermycin, and novobiocin, among others [1]. In this context, mammea-type coumarins, which are biosynthesized by plant species from *Mammea, Mesua*, and *Calophyllum* genera of the Calophyllaceae family, possess a 5,7-dihydroxycoumarin skeleton (▶ **Fig. 1**) and have different names, such as A/BA, A/BB, B/BB, A/AA, etc., according, to the type of substituent on C-4, C-6 and C-8 of the main chemical skeleton. In general, these compounds possess biological effects, such as antiparasitic [2, 3], anti-fimic [4], and cytotoxic [5]. For instance, mammea A/AA induces the release of the apoptotic-inducing factor to the cytoplasm in the HeLa cell line [6], and mammea E/BB plays an anionic protonophore [7] role that uncouples the mitochondrial electron transport in the cancer cell lines T47C and PC-3 [8]. On the other hand, mammeasin A, mammea A/AD, and kayeassamin G have shown an inhibitory effect on iNOS and, consequently, on the production of NO in lipopolysaccharide-activated RAW264.7 cells by an nuclear factor-kappa B-independent mechanism [9]. Particularly MABB (▶ **Fig. 1**), alone or as a mixture, displays antiparasitic effects against *Trypanosoma cruzi* [2] and *Leishmania amazonesis* [10], as well as cytotoxicity and antitumor properties *in vivo* [11]. These compounds have also been shown to be active against clinical isolates of *Mycobacterium tuberculosis*. Moreover, in a toxicogenomic analysis *in vivo* performed by our group, we describe that these compounds were not toxic over non-tumoral tissues from CD-1 mice [12]. Interestingly, in 2004, Reyes-Chilpa et al. [5] reported that mammea A/BA possess low cytotoxicity *in vitro* to normal human lymphocytes with an LC_{100} of 126.45 mg/mL.

NPr is a novel, exciting approach in herbal medicine and drug development that describes a field in systems biology to understand the role of how drugs interact with different targets, signaling pathways, organs, and diseases from a network point of view. This approach is used to discover novel mechanisms of actions and possible adverse effects of drugs through network analyses of multiple levels of biological complexity [13]. Altogether, these approaches combined with other chemoinformatic methods synergize the drug discovery process and help to rediscover the potential of already known compounds [13]. In recent years, several groups have used network pharmacology approaches to explore bioactive compounds, novel targets, and molecular mechanisms from different plants and fungi with known ethnobotanical uses [14–16], contained in different herbal preparations [17, 18], and to repurpose compounds in herbal remedies [19]. Therefore, in the present study, we used NPr to discover targets and pathways that could interact with MABB and performed an experimental *in vitro* validation of such paths on the K562 cancer cell line.

Results

We performed NPr on several databases. ▶ **Table 1** indicates the most enriched pathways, GO-Terms and diseases that interact with MABB (a set of the targets is shown in **Table 1S**, Supporting Information). Additionally, we performed the network construction for the first 50 targets to determine its potential relationships among them and its relation with pathways (▶ **Fig. 2**). Since the apoptotic process was the main enriched pathway, we evaluated the presence of the main proteins involved in such pathways as well as the mitochondrial ultrastructure morphology and intracellular calcium homeostasis ($[Ca2+]_i$).

As depicted in ▶ **Fig. 3**, MABB treatment increases the fluorescence of the proapoptotic proteins Bax (▶ **Fig. 3 A a, b**) and Bak (▶ **Fig. 3 B c, d**) in comparison to the vehicle (DMSO). Moreover, MABB treatment significantly decreases the fluorescence corresponding to Bcl-2 (▶ **Fig. 3 C e, f**), an antiapoptotic protein. These results suggest that MABB induces apoptosis through the overexpression of the proapoptotic proteins Bax and Bak, which are involved in the activation of the mitochondrial intrinsic apoptotic pathway in K562 cells.

We evaluated whether these compounds alter the $[Ca^{2+}]_i$. Interestingly, as seen in ▶ **Fig. 4 A–C**, MABB induces a slow rise in the $[Ca^{2+}]_i$, which reaches 600 nM. A plateau followed this increase a few minutes after MABB administration, however, the last seconds of the recording showed a burst in the $[Ca^{2+}]_i$, reaching 900 nM. These results suggest the possible activation of calcium-dependent pathways, since the $[Ca^{2+}]_i$ abruptly decreased once MABB was removed. Moreover, the $[Ca^{2+}]_i$ disruption, induced by MABB treatment, is accompanied by modifications in the ultrastructure of mitochondria of K562 cells. As seen in ▶ **Fig. 4 C**, MABB treatment induces mitochondria swelling. This morphology is typical in damaged mitochondria as depicted in the positive control, which was treated with rotenone, a specific inhibitor of the mitochondrial complex I (▶ **Fig. 4 C**). Interestingly, MABB in-

Downloaded by: Universidad de Barcelona. Copyrighted material.

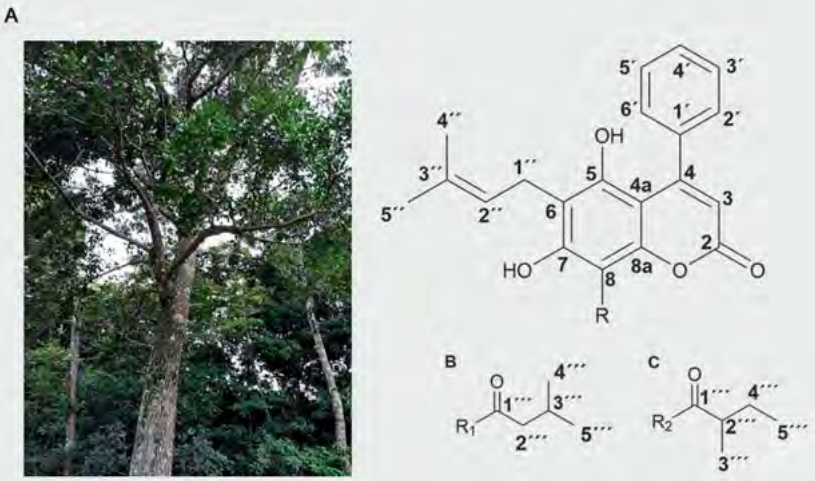

▶ **Fig. 1** *C. brasiliense* specimen. Ricardo Reyes-Chilpa took the image (**A**) at La Reserva de Los Tuxtlas, Veracruz, Mexico (May 2017). Chemical structures of mammea A/BA (**B**) and mammea A/BB (**C**).

▶ **Table 1** Enrichment analysis (GO and Pathway) of the targets of MABB.

Compound	Pathway or GO term	Count	Adjusted p value	DB
Mammea A/BA	Apoptotic process (GO-BP)	24	1.24e-16	CTD
	Protein kinase activity (GO-MF)	18	9.90e-19	CTD
	Cytosol (GO-CC)	34	1.43 e-20	CTD
	Erb signaling pathway (hsa 04012)	7	2.05e-07	KEGG
	PI3K-Akt signaling pathway (hsa 04151)	8	3.07e-05	KEGG
	MAPK signaling pathways (hsa 04919)	7	4.62e-05	KEGG
	Ras pathway (P04393)	5	8.76e-06	Panther
	Regulation of macromolecules metabolic process (GO-BP)	33	3.44e-16	CTD
	Diseases related with targets			
	Pathways in cancer (hsa05200)	9	6.36e-07	KEGG
	Prostate cancer (hsa05215)	7	2.68e-09	KEGG
	Angiogenesis (P00005)	5	1.95e-06	Panther
Mammea A/BB	Kinase activity (GO-MF)	22	2.45e-22	CTD
	Apoptotic process (GO-BP)	26	2.02e-23	CTD
	Cytoplasm (GO-CC)	45	6.03e-24	CTD
	PI3K-AKT signaling pathways (hsa 04151)	10	3.64e-07	KEGG
	ErbB signaling pathways (hsa 04012)	8	3.09e-09	KEGG
	MAPK signaling pathways (hsa 04919)	8	3.64e-07	KEGG
	Ras pathway (P04393)	6	3.11e-07	Panther
	Positive regulation of macromolecule metabolic process	27	5.49e-16	CTD
	Diseases related with targets			
	Prostate cancer (hsa05215)	8	3.09e-09	KEGG
	Pathways in cancer (hs05200)	10	3.64e-07	KEGG
	Colorectal cancer (hs05210)	5	4.58e-06	KEGG
	Pancreatic cancer (has 0512)	5	5.51e-06	KEGG

Downloaded by: Universidad de Barcelona. Copyrighted material.

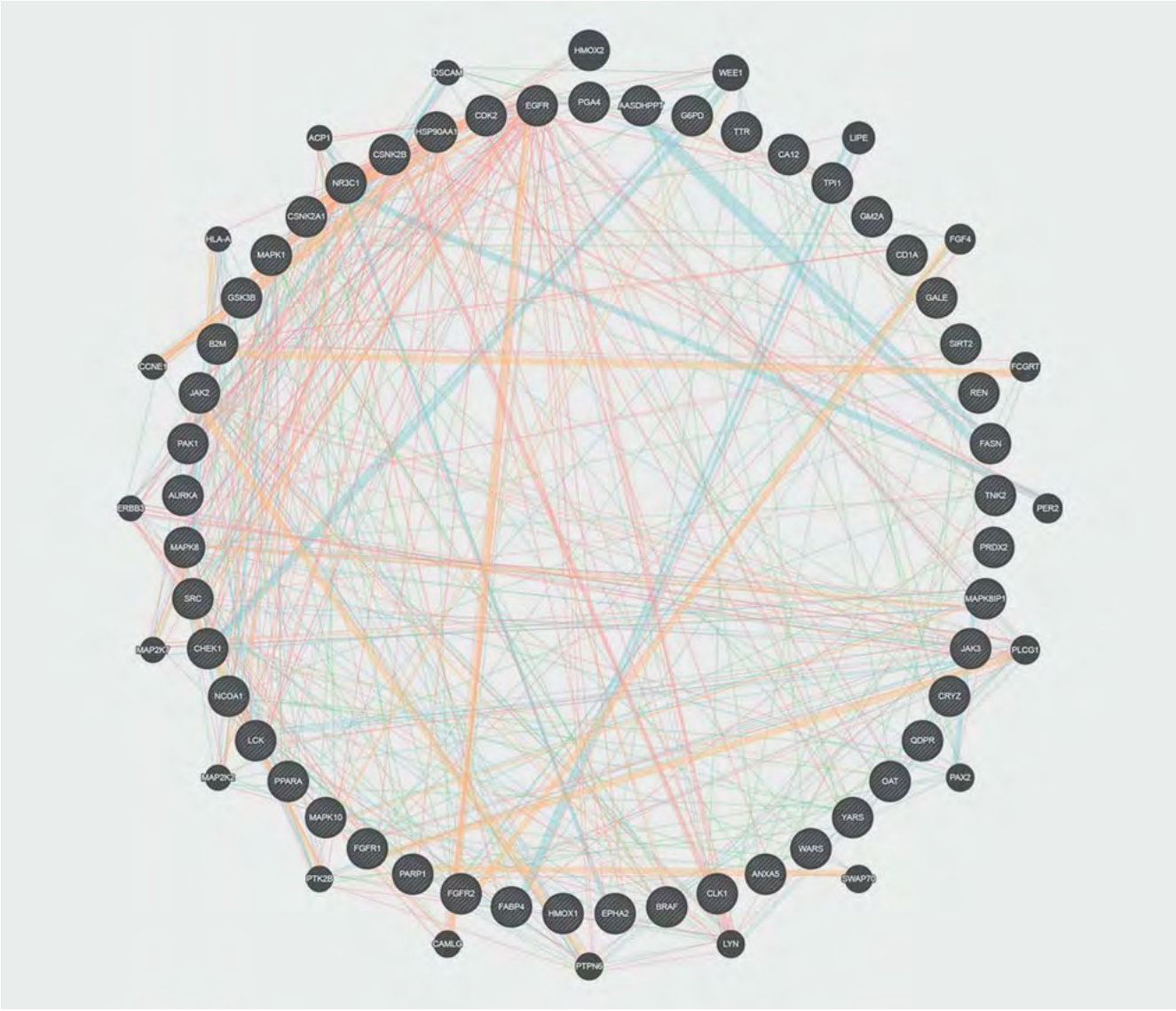

▶ **Fig. 2** Network of the interactions among the 50 primary targets predicted for mammea A/BA. The network interaction was predicted with GeneMania software. Red lines show physical interactions, yellow lines show predicted interactions, and blue lines show interactions shared by common signaling pathways.

duces cytoplasmic vesicles that surround the damaged mitochondria. This result is contrary to the negative control (DMSO) in which the cells showed mitochondrial ridges.

According to the NPr, PI3K-AKT and macromolecule metabolism were among the enriched pathways that correlate with the autophagy process. Therefore, we validated autophagy by the acidic vesicle formation and the quantification of autophagic markers, including the lipidated form of the microtubule-associated protein light chain 3 (LC3-II) and its receptor SQSTM1/p62 (p62). Finally, we evaluated the possible interaction between mTOR and MABB by a docking assay.

Autophagy induces the acidic vesicle aggregation, the decrease of LC3-I and p-62, and the increase of LC3-II [20]. As observed in ▶ **Fig. 5A**, MABB treatment induces acidic vesicle aggregation similar to that of the positive control CP (▶ **Fig. 5A** panels e and n, respectively). CQ prevented this effect, since the size of the vesicles is more significant than in MABB (▶ **Fig. 5A** panel k). Moreover, to evaluate the effect of MABB treatment on the autophagic flux, we determined the content of LC3-II and p62. Our results showed that MABB treatment increases the LC3-II protein content over 12 times (▶ **Fig. 5B**) in contrast to the vehicle (DMSO). However, MAAB treatment did not alter the content of p62 (▶ **Fig. 5C**), suggesting a disruption in the autophagic flux.

To predict whether coumarins may interact with mTOR, we performed an *in silico* study (docking), including binding sites, the ATP-binding domain, and the allosteric domain in the mTOR complex (▶ **Fig. 6**). We conducted a re-docking analysis of the co-crystallized ligands to validate our protocol. The docking of 17 G (PDB 4JSX) resulted in a similar conformation than the crystallized pose with an RMSD of 0.5789 and a docking score of

Downloaded by: Universidad de Barcelona. Copyrighted material.

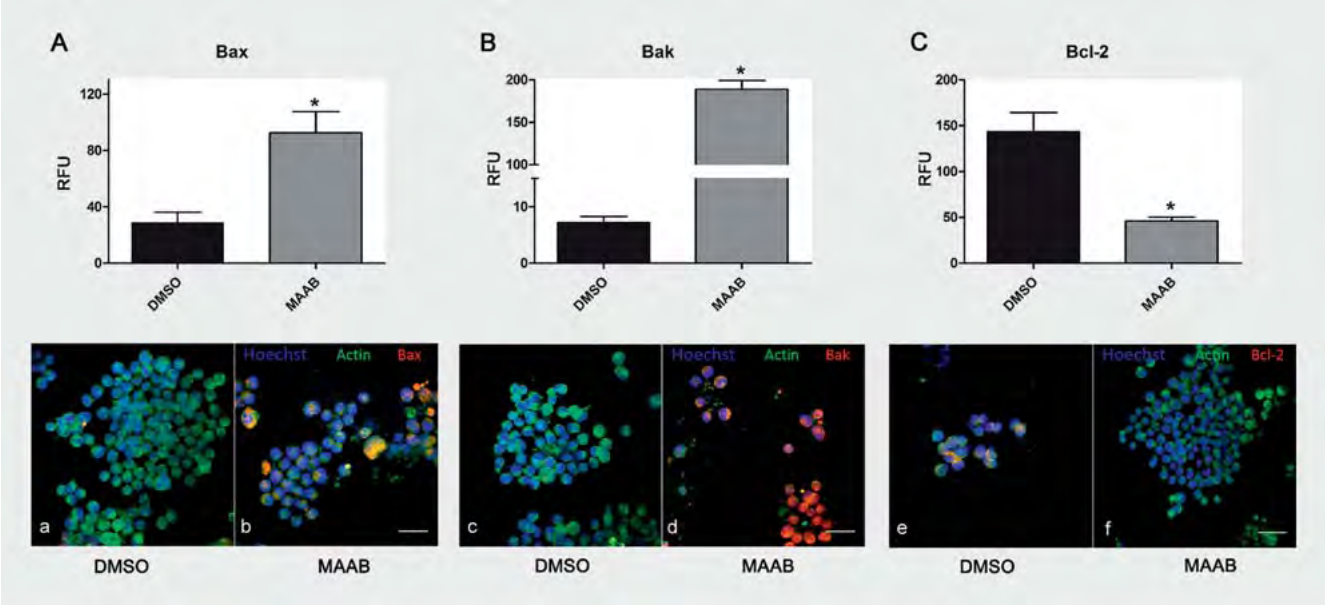

▶ **Fig. 3** MABB induce apoptosis in K562 cells. Immunofluorescence analysis and representative confocal images of triple immunofluorescence staining, showing the content, in red fluorescence, of Bax (**A**), Bak (**B**), and Bcl-2 (**C**) in K562 cells incubated with the vehicle (DMSO) (**a, c** and **e**) or with MABB (43.5 µM during 18 h) (**b, d** and **f**), respectively. Hoechst labeled nuclei in blue and phalloidin 488 labeled cytoskeleton in green. Bars represent the mean ± S. E. M. of the relative fluorescence units (RFU) from the red channel of five images from three independent experiments. Data were analyzed by Student's t-test followed by the Mann-Whitney test; $^{*}p \leq 0.05$ vs. vehicle. Scale bar: 50 nm.

− 33.07 kcal/mol. For the inhibitor ARD (PDB 3FAP), the RMSD was 2.0191 with a docking score of − 26.30 kcal/mol (**Fig. 3S A, B**, Supporting Information). These results suggest that the algorithm implemented in ICM Molsoft provides enough reproducibility and accuracy for the study. Based on the scoring function, the docking predicts that both coumarins may interact in the rapalogue-binding pocket (allosteric FRB domain), since docking scores for mammea A/BA were − 31.85 kcal/mol and − 21.13 kcal/mol for allosteric and ATP-binding domains, respectively. For mammea A/BB, the docking scores were − 31.98 kcal/mol and − 24.11 kcal/mol for allosteric and ATP-binding domains, respectively (**Table 2S**, Supporting Information). In the case of mammea A/BA, it's predicted to be stabilized by several hydrophobic interactions (Tyr26, Phe46, Glu54, Val55, Trp59) and a hydrogen bond with Ile56 of the FRB domain. According to the model, our results suggested hydrophobic interactions with the KD-N lobe, (Ser2036 and Phe2039) and a possible hydrogen bond with Tyr2105 for this analysis. In the same way, mammea A/BB appears to interact in a similar binding site as mammea A/BA, stacked in the pocket through hydrophobic interactions with Trp2101, Asp2102, Tyr2105, and Phe2039 of the KD-N lobe, and Phe36, Val55, and Ile91 of the FRB domain. Additionally, we predicted two hydrogen bonds with Ile56 and Tyr82 (FRB domain).

Discussion

As previously mentioned, MABB coumarins may be considered drug candidates since they present versatile pharmacological properties and have been shown to be safe [12]. Network pharmacology approaches have been used from two points of view: 1) to identify novel targets and 2) to determine which unknown signaling pathways interact with compounds [17, 21]. In this context, our data showed that MABB interacts with an apoptotic process and PI3K/AKT, MAPK, Ras, and Erb pathways. Interestingly, most of them possess tyrosine kinase properties [22] in this context, and the PI3K/AKT pathway is associated with the autophagy process [23]. Disease enrichment analysis indicates that MABB might be related with cancer pathways in general, suggesting its potential as an antitumoral compound.

First, we evaluated the effect of MABB in apoptosis through the fluorescence analysis of Bcl-2, Bax, and Bak proteins in K562 cells. Bax and Bak are two nuclear-encoded proteins that can pierce the mitochondrial outer membrane to mediate cell death by apoptosis, promoting permeabilization and the release of cytochrome C. Bcl-2 antiapoptotic protein also regulates this mitochondrial pathway. Our analyses showed that MABB treatment induces the overexpression of Bax and Bak. Meanwhile, the Bcl-2 signal was absent, suggesting that treatment induces apoptosis through the intrinsic mitochondrial pathway. These results are in concordance with another type of mammea coumarin that induces this type of cell death in another leukemia cell line [10].

Since we observed that MABB induces apoptosis through a previously mentioned pathway, we evaluated whether MABB could produce mitochondrial damage concomitantly. Transmission electron microscopy (TEM) images indicated the presence of mitochondrial damage, characterized by swelling and loss of the mitochondrial ridges, as well as cytoplasmic vacuolization surrounding damage. These results are consistent with previous studies in which similar coumarins induced mitochondrial uncoupling [6, 8]. Moreover, Brenzan et al. [10] demonstrated that

Downloaded by: Universidad de Barcelona. Copyrighted material.

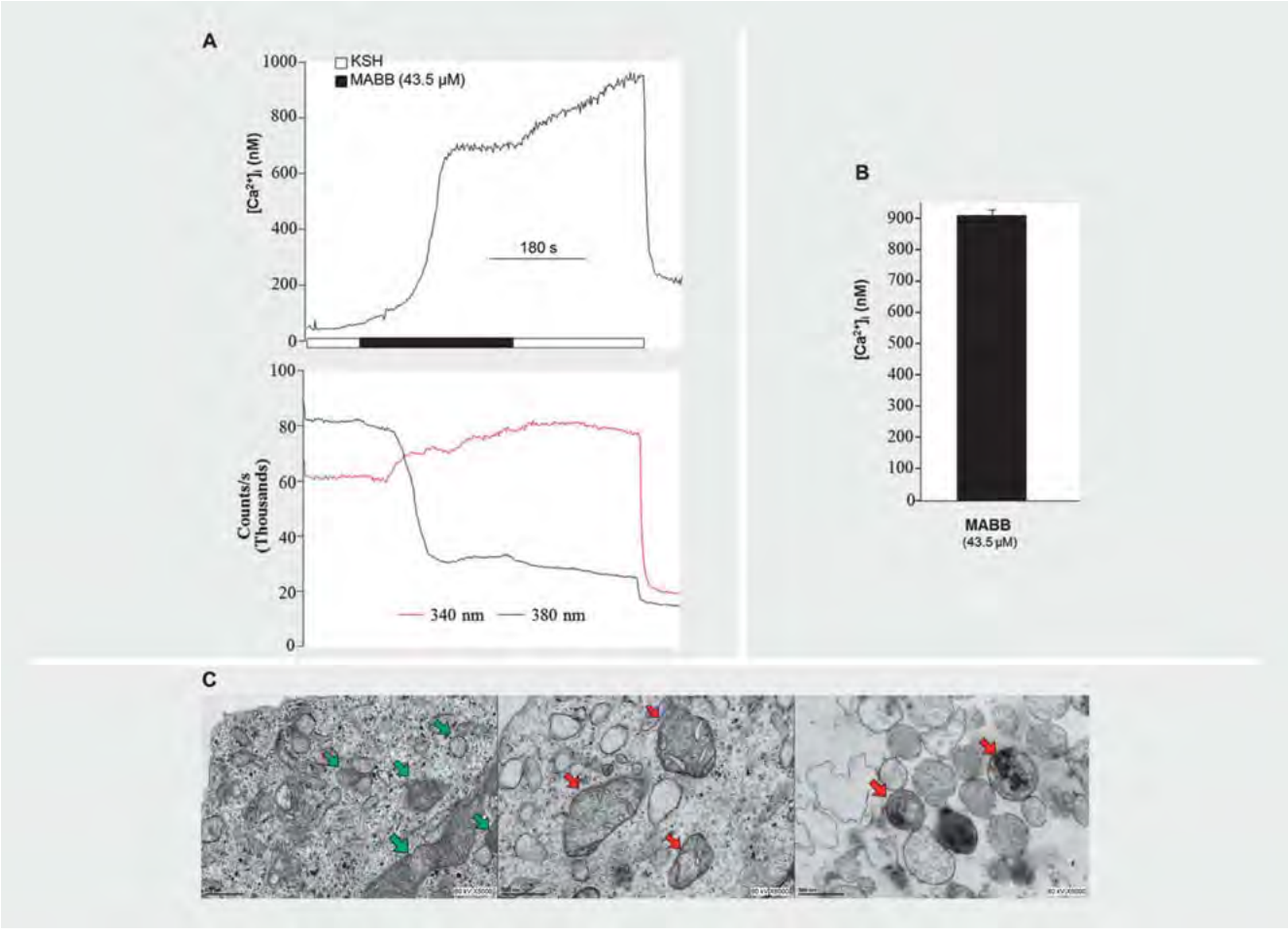

▶ **Fig. 4** MABB treatment induces $[Ca^{2+}]_i$ disruption and alters the mitochondria ultrastructure on K562 cells. **A** Representative recordings of the $[Ca^{2+}]_i$ measurements in cells treated with MABB (43.5 µM). Representative recording of Fura-2AM excitation at 340 nm and 380 nm. **B** The bar represents the $[Ca^{2+}]_i$ in MABB-treated cells (907 ± 14.71 nM, n = 5). **C** Representative images from TEM, respectively: negative control (DMSO), MABB (43.5 µM, 6 h), positive control (Rotenone, 13 µM, 6 h). Green arrows indicate normal mitochondrion and red arrows indicate damaged mitochondrion. Scale bar: 500 nm. Images represent three independent experiments.

mammea A/BB induces atypical cytoplasmic vacuolization and mitochondrial swelling in *Leishmani amazonensis*. Furthermore, our recordings indicate that 3 min after MABB administration, the $[Ca2+]_i$ rises to 900 nM, followed by an abrupt decrease, which suggests cell death. These results might explain the mitochondrial damage, the presence of acidic vesicles, and the eventual release of proapoptotic proteins that lead to cell death. Mitochondrion are active players in $[Ca^{2+}]_i$ homeostasis (chemiosmotic theory) and, as previously mentioned, the $[Ca^{2+}]_i$ overload induces the activation of several kinase-dependent proteins, such as PKC and ASK1, leading to apoptosis and mitochondrial damage [24, 25]. Our results are in accordance with other coumarins where the same effect was observed [26].

The second potential interaction, according to NPr, was PI3K/Akt, MAPK, and Ras pathways associated with autophagy. To validate this, we quantified the LC3-II and p62 protein content and the acidic vesicle aggregation, which are characteristics of such a process. Our results demonstrated that MABB treatment induces apoptosis through the disruption of the autophagic flux, since we observed acidic vesicle aggregation and autophagosome accumulation by LC3-II and p62. These results are in agreement with previous studies reporting that silver nanoparticles induce apoptosis through the cytoplasmic accumulation of LC3-II and p62 in NIH 3 T3 and HCT116 cells [27] and with those of spicatoside A, a steroidal saponin isolated from *Liriope platyphylla* that exerts antitumor activity through the modulation of both autophagy and apoptosis [28].

Finally, according to the literature, several synthetic coumarins have been found to possess potent anticancer properties through the inhibition of the PI3K-AKT-mTOR pathway [29] or as inhibitors of mTOR, a hub protein in this signaling pathway [30]. Moreover, some of these compounds are currently patented, such as CN103254203A. Hence, we decided to explore *in silico* whether MABB may interact with mTOR (since these types of approaches are a valuable low-cost tool). As reported in the literature, small molecules could inhibit the mTOR complex in two different ways [31]: 1) as competitive ligands in the ATP-binding pocket [32] or 2) as allosteric inhibitors interacting in the FRB domain [33]. The scoring function implemented in ICM software predicts that the coumarins interact in the allosteric binding site associated with

Downloaded by: Universidad de Barcelona. Copyrighted material.

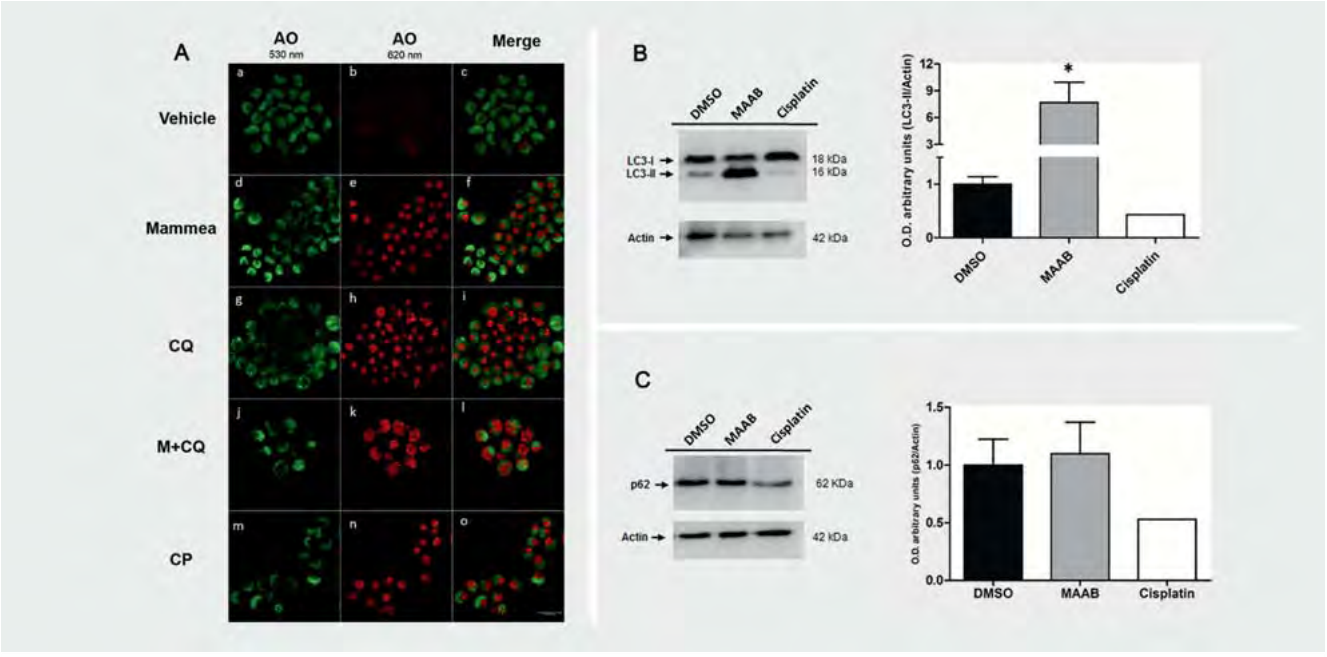

▶ **Fig. 5** MABB induce autophagy in K562 cells. Representative confocal images from K562 cells positive to acridine orange (AO) staining. When AO is incorporated into the acidic vesicles (during autophagy), it emits orange fluorescence. **A** Cells were exposed to vehicle (DMSO, panels a–c), mammea (MABB, 43.5 µM, 18 h, panels d–f), CQ (chloroquine, 20 µM, 18 h, panels g–i), M + CQ (MABB and CQ mixture, panels j–l), and CP (cisplatin, 20 µM, 18 h, panels m–o). Representative Western blots of LC3-II and p62 proteins. Densitometric analysis expresses the relative ratio of LC3-II/actin (**B**) or p62/actin (**C**). Bars represent the mean ± S. E. M. of four experiments. Data were analyzed by one-way ANOVA followed by Dunn's test; $^{*}p \leq 0.05$ vs. vehicle.

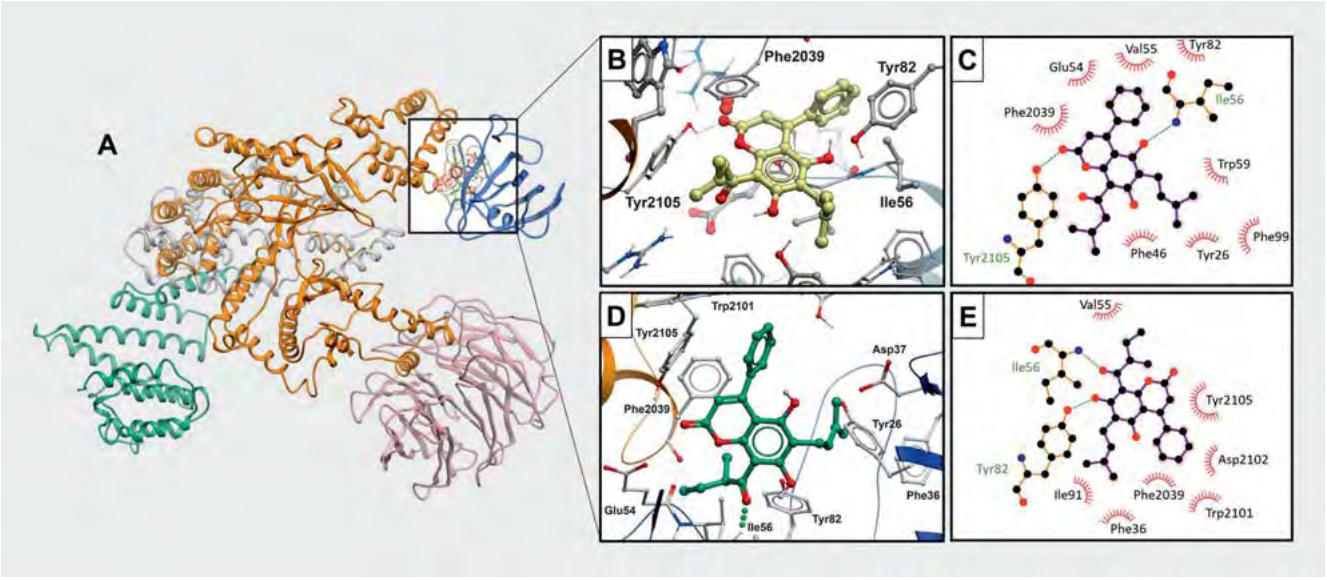

▶ **Fig. 6** MABB coumarins interact with mTOR. MABB and mTOR interaction complex. **A** Representation of the complex built from the superposition of two crystal structures of mTOR (PDB 4JSX: orange, gray, green, and pale pink; and PDB 3FAP: orange and blue). Details of the binding site for mammea A/BA (pale yellow sticks) in (**B**) 3D and (**C**) 2D representations, and mammea A/BB (green sticks) (**D**) 3D and (**E**) 2D representations (white sticks represent residues of mTOR involved in interactions). Green dotted lines represent hydrogen bonds. The figures were built with ICM-Molsoft and LogPlot Plus Softwares.

the analogs of rapamycin (rapalogues), which in turn could inhibit its activity. In both cases, the stabilization seems to be mainly by hydrophobic contacts, as expected for ligands that bind to the allosteric site [33]. According to a model proposed by Choi et al.

Downloaded by: Universidad de Barcelona. Copyrighted material.

[34], most of the interactions calculated for rapamycin and the FKBP12 domain (KD-N lobe) agree with the predicted ones for the MABB. These results predict that, as in the case of rapamycin, MABB may act as an inhibitor of the mTOR phosphorylation mechanism. Additionally, the prediction suggests that MABB may act as specific inhibitors of the complex, reducing the probability of side effects (by inhibiting other kinases).

In conclusion, NPr indicated that MABB is suitable for drug development of novel anticancer compounds since they interact with several targets related to cancer and induce apoptosis through the inhibition of the autophagic flux, possibly via an mTOR interaction. However, further experiments must be performed to experimentally validate the mTOR interaction with MABB to avoid false positives on the docking assay. Additionally, other possible targets and signaling pathways should be tested and experimentally confirmed since our results open possible novel applications and research for this type of compound.

Materials and Methods

Isolation and identification of mammea A/BA and A/BB

A mixture of coumarins, MABB, was isolated from *Calophyllum brasiliense* leaves (voucher 1523A-Instituto Mexicano del Seguro Social-Medicinal Herbarium), as previously described by [35], and identified by ^{1}H and ^{13}C NMR in comparison with previous reports [5]. For biological studies, we used a mixture of coumarins A/BA and A/BB, 75 to 25% (3:1) MABB. The content of each compound of the mixture was determined by ^{1}H NMR, assuming 100% for both compounds and using an integration of OH-7.

Network pharmacology

To identify if MABB could be repurposed or considered for treatment of other diseases, an NPr *in silico* approach was performed to identify novel target proteins and pathways that could interact with them. Predictive models were used, including DRAR-CPI [36], SEA [37], SwissTarget [38], and STITCH [39].

Enrichment analysis for targets

An analysis of network interactions related to the first 50 targets that interacted with each compound was performed using the CTD [40] and the GSEAPY package from Python. The main BP (GO:0008150), MF (GO:0003674), and CC (GO:0005575) were determined, as well as the main KEGG and Panther pathways along with OMIM-related diseases. The most significantly enriched terms in the BP, MF, and CC categories, KEGG, Panther, and OMIM ($p < 0.05$; p values were corrected using the Benjamini-Hochberg procedure) are listed in ▶ **Table 1** and separated accordingly with Pathways and Go-Terms and Diseases Related with Targets. We constructed the network of functional association of the targets with GeneMania (▶ **Fig. 2**) [41].

Cell culture

K562 cells were obtained from ATCC and cultured in RPMI (GIBCO) with 10% FBS (Mayimex) and 10000 IU/mL penicillin/streptomycin in humidified air at 37 °C with 5% CO_2. Cells used for confocal microscopy were cultured in 12-well plates, over rounded coverslips at 1×10^3 cells per well. For protein isolation, cells were cultured at 1×10^6 cells in 100 mm culture plates. The cultured cells were treated with MABB at 43.5 µM, CQ (20 µM, purity 98%; Sigma-Aldrich), CP (20 µM, purity 95%; Lemery Labs), or rotenone (13 µM, purity 95%; Sigma-Aldrich), as previously reported in [35]. DMSO (JT Baker) at a final concentration of 0.04% was used to dissolve the MABB, CQ, and rotenone compounds. CP was diluted in PBS 1X.

Immunofluorescence of BAK, BCL-2, and BAX

We performed the immunocytochemistry for all treatments according to the methodology of [42]. Briefly, K562 cells were cultured in round, glass coverslips and treated with MABB for 18 h and incubated with polyclonal antibodies of anti-Bax (1:100), anti-Bak (1:100), and anti-Bcl-2 (1:100) (Santa Cruz Biotechnology) overnight at 4 °C. Afterwards, cells were incubated with an anti-rabbit or anti-mouse secondary antibody conjugated with Alexa-Fluor 568 (1:500; Invitrogen). We used Alexa-Fluor 488 conjugated phalloidin (165 nM; Thermo Fisher Scientific) for cytoskeleton labeling and Hoechst 33342 (12 µg/mL; Thermo Fisher Scientific) for nucleus labeling. Confocal images were taken with an Olympus FV1000 microscope using a 60 x oil immersion objective and diode lasers (473 nm) at the USAII-Facultad de Química, UNAM, México. The fluorescence of Bax, Bak, and Bcl-2 was analyzed from five sections of three independent experiments using Image J software as previously described [43].

Transmission electron microscopy

K562 cells were treated with MABB at 43.5 µM for 6 h. DMSO 4% was used as a negative control (v/v) and rotenone (13 µM during 6 h) as a positive control. After 6 h of treatment, cells were fixed with 2.5% glutaraldehyde and postfixed in 1% OsO_4 and 0.8% $K_4Fe(CN)_6 \cdot 3H_2O$, and 5 mM calcium. Postfixed cells were dehydrated in acetone and embedded in Epon. Ultrathin sections were stained with uranyl acetate and lead citrate and examined under a JEOL JEM 12000 EII transmission electron microscope at the Unidad de Imagenología at the Instituto de Fisiología Celular (IFC) from UNAM, Mexico City, Mexico.

Microfluorometric Ca^{2+} measurements in K562 cells

K562 cells were plated at a density of 2×10^4 cells/cm^2 in round, 12 mm diameter coverslips and cultured for 24 h with supplemented DMEM. Cells were loaded with 2.5 Mm Fura 2-AM in low Ca^{2+} (0.1 mM) at room temperature and then treated according to [42]. Cells were stimulated with MABB (43.5 µM) for 3 min to determine the calcium response from 1 min to 1 h. Differences in the $[Ca^{2+}]$ response were evaluated through paired Student's t-test. Results presented as the mean ± SEM.

Lysosome membrane integrity assay

AO staining was performed as reported by [44]. Confocal images were taken with a Leica TCS SP5 using 63X water immersion objectives Arg 458/650 nm (red; acidic vacuoles) and Arg 488/525 nm (green; nuclei). Additionally, we used CP 20 µM for 18 h as a positive control for acidic vesicle formation since it is a well-known autophagy inductor, and CQ 20 µM for 12 h to disrupt the

Downloaded by: Universidad de Barcelona. Copyrighted material.

function of lysosomes and inhibit autophagy at the late stage due to its alkaline properties [45].

Western Blot

After cells were treated with MABB (43.5 µM for 18 h), we performed Western blot according to [42] with a few modifications as follows: Proteins were separated in 10 % (p62) or 18 % (LC3 and actin) SDS-PAGE and subsequently transferred to PVDF membranes. Membranes were incubated with anti-LC3 (1 : 1000; MBL international) and SQSTM1/p62 (1 : 1500; Cell Signaling Technology) overnight at 4 °C. The signal was detected by chemiluminescence using Immobilon Western Chemiluminescent HRP substrate (Millipore) with a blot scanner (LI-COR). We used Image Studio 3.1 to perform densitometry analysis. LC3-II and p62 contents were normalized against actin (1 : 7000; Millipore).

mTOR docking

Docking studies were performed using the Internal Coordinate System, ICM molecular modeling software (Molsoft). The crystal structures of the mTOR complex with an ATP-competitive inhibitor (PDB 4JSX) and an allosteric inhibitor (PDB 3FAP) were both retrieved from the PDB. We performed a validation protocol for the docking studies with the co-crystallized ligands in the original protein [9-(6-aminopyridine-3-yl)-1-[3-(trifluoromethyl)phenyl] benzo[*h*][1,6]naphthyridin-2(1*H*)-one, 17 G and C15-(*R*)-methylthienyl rapamycin for PDB 4JSX and 3FAP, respectively] structures removed, placed randomly outside the protein, and re-docked. The best poses were selected, according to the docking score, and the structural conformation was compared to that of the original pose in the crystal structure through their RMSD. Next, to determine the probable binding pocket of MABB coumarins, a 3D alignment of the protein structures was performed using the superimpose tool implemented in the ICM software, based on the KD-N lobe of the mTOR-mLST8 complex (**Fig. 3S**, Supporting Information). The receptor maps were calculated according to the pocket defined by the co-crystallized ligands (17 G and ARD). The grid box was built to cover both ATP and allosteric binding pockets entirely. The ICM software generates an internal docking score based on several energetic parameters, which include weighted van der Waals interactions, internal force field energy of the ligand, free energy of the conformational energy loss, solvation electrostatic energy upon ligand binding, hydrogen bonding, hydrogen donor, acceptor desolvation energy, hydrophobic free energy gain, and correction on the number of ligands. We built structures of MABB with Spartan v.10 software (Wavefunction) and the Monte Carlo protocol for energy minimization (MMFF98 force field) and conformer distribution. The structures of minimum energy were then geometrically optimized using density functional theory at the B3LYP/DGDZVP level of theory using Gaussian 09 software (Gaussian). The docking poses were analyzed and visualized in the ICM Molsoft software.

Statistical analysis

GraphPad Prism Software version 5.0 was used to process all statistic data. The Student's t-test analysis was used to examine the statistical difference between experimental data between groups. Significance was defined as $p < 0.05$.

Supporting information

A detailed scheme of NPr methodology (**Fig. 1S**), complete image for the Western blot of LC3 and P62 proteins (**Fig. 2S**), a complete list of the potential targets of MABB obtained by the NPr analysis (**Table 1S**), and the results for the validation of the docking protocol, which include resulting conformations of the validation protocol images (**Fig. 3S A, B**) and docking scores for MABB and ligands of co-crystallization for each mTOR studied (**Table 2S**), are available as Supporting Information.

Acknowledgements

This research was supported by grant IN210016 from DGAPA-PAPIIT, UNAM. The authors thank Lourdes Massieu, Ph.D. and Biol. Teresa Montiel from Instituto de Fisiología Celular, UNAM, for bringing the LC3 and p62 antibodies and for technical assistance during the Western blot. We also thank Karina Jiménez Duarte, Ph.D., for her technical support during the confocal sessions at Unidad de Servicio y Apoyo a la Industria e Investigación (USAII)-Facultad de Química, UNAM. The authors wish to thank Heidy Martínez-Pacheco for support with the docking assay.

Conflict of Interest

The authors declare no conflict of interest.

References

[1] Katsori AM, Hadjipavlou-Litina D. Coumarin derivatives: an updated patent review (2012–2014). Expert Opin Ther Pat 2014; 24: 1323–1347

[2] Reyes-Chilpa R, Estrada-Muñiz E, Vega-Avila E, Abe F, Kinjo J, Hernández-Ortega S. Trypanocidal constituents in plants: 7. Mammea-type coumarins. Mem Inst Oswaldo Cruz 2008; 103: 431–436

[3] Brenzan MA, Nakamura CV, Prado Dias Filho B, Ueda-Nakamura T, Young MCM, Aparício Garcia Cortez D. Antileishmanial activity of crude extract and coumarin from *Calophyllum brasiliense* leaves against *Leishmania amazonensis*. Parasitol Res 2007; 101: 715–722

[4] Pires CTA, de L Scodro RB, Brenzan MA, Cortez DAG, Siqueira VLD, Cardozo-Filho L, Goncalves RM, Caleffi-Ferracioli KR, Cardoso RF. Anti-mycobacterium tuberculosis activity of *Calophyllum brasiliense* extracts obtained by supercritical fluid extraction and conventional techniques. Curr Pharm Biotechnol 2016; 17: 532–539

[5] Reyes-Chilpa R, Estrada-Muñiz E, Apan TR, Amekraz B, Aumelas A, Jankowski CK, Vázquez-Torres M. Cytotoxic effects of mammea type coumarins from *Calophyllum brasiliense*. Life Sci 2004; 75: 1635–1647

[6] Álvarez-Delgado C, Reyes-Chilpa R, Estrada-Muñiz E, Mendoza-Rodríguez CA, Quintero-Ruiz A, Solano J, Cerbón MA. Coumarin A/AA induces apoptosis-like cell death in HeLa cells mediated by the release of apoptosis-inducing factor. J Biochem Mol Toxicol 2009; 23: 263–272

[7] Katsori AM, Hadjipavlou-Litina D. Coumarin derivatives: an updated patent review (2012–2014). Expert Opin Ther Pat 2014; 24: 1323–1347

[8] Du L, Mahdi F, Jekabsons MB, Nagle DG, Zhou YD. Mammea E/BB, an isoprenylated dihydroxycoumarin protonophore that potently uncouples mitochondrial electron transport, disrupts hypoxic signaling in tumor cells. J Nat Prod 2010; 73: 1868–1872

[9] Morikawa T, Sueyoshi M, Chaipech S, Matsuda H, Nomura Y, Yabe M, Matsumoto T, Ninomiya K, Yoshikawa M, Pongpiriyadacha Y, Hayakawa T, Muraoka O. Suppressive effects of coumarins from *Mammea siamensis* on inducible nitric oxide synthase expression in RAW264.7 cells. Bioorg Med Chem 2012; 20: 4968–4977

[10] Brenzan MA, Santos AO, Nakamura CV, Filho BPD, Ueda-Nakamura T, Young MCM, Côrrea AG, Júnior JA, Morgado-Díaz JA, Cortez DAG. Effects of (−) mammea A/BB isolated from *Calophyllum brasiliense* leaves and de-

Downloaded by: Universidad de Barcelona. Copyrighted material.

rivatives on the mitochondrial membrane of *Leishmania amazonensis*. Phytomedicine 2012; 19: 223–230

[11] Ruiz-Marcial C, Reyes Chilpa R, Estrada E, Reyes-Esparza J, Fariña GG, Rodríguez-Fragoso L. Antiproliferative, the cytotoxic and antitumor activity of coumarins isolated from *Calophyllum brasiliense*. J Pharm Pharmacol 2007; 59: 719–725

[12] Gomez-Verjan JC, Estrella-Parra E, Vazquez-Martinez ER, Gonzalez-Sanchez I, Guerrero-Magos G, Mendoza-Villanueva D, Isus L, Alfaro A, Cerbón-Cervantes M, Aloy P, Reyes-Chilpa R. Risk assessment of Soulatrolide and Mammea (A/BA+A/BB) coumarins from *Calophyllum brasiliense* by a toxicogenomic and toxicological approach. Food Chem Toxicol 2016; 91: 117–129

[13] Zhao S, Iyengar R. Systems pharmacology: network analysis to identify multiscale mechanisms of drug action. Annu Rev Pharmacol Toxicol 2012; 52: 505–521

[14] Huang J, Cheung F, Tan HY, Hong M, Wang N, Yang J, Feng Y, Zheng Q. Identification of the active compounds and significant pathways of yinchenhao decoction based on network pharmacology. Mol Med Rep 2017; 16: 4583–4592

[15] Pereira ASP, Bester MJ, Apostolides Z. Exploring the anti-proliferative activity of *Pelargonium sidoides* DC with *in silico* target identification and network pharmacology. Mol Divers 2017; 21: 809–820

[16] Zhao RL, He YM. Network pharmacology analysis of the anti-cancer pharmacological mechanisms of *Ganoderma lucidum* extract with experimental support using Hepa1-6-bearing C57 BL/6 mice. J Ethnopharmacol 2018; 210: 287–295

[17] Yue SJ, Liu J, Feng WW, Zhang FL, Chen JX, Xin LT, Peng C, Guan HS, Wang CY, Yan D. System pharmacology-based dissection of the synergistic mechanism of Huangqi and Huanglian for Diabetes mellitus. Front Pharmacol 2017; 8: 694

[18] Zhang Y, Mao X, Su J, Geng Y, Guo R, Tang S, Li J, Xiao X, Xu H, Yang H. A network pharmacology-based strategy deciphers the underlying molecular mechanisms of Qixuehe Capsule in the treatment of menstrual disorders. Chin Med 2017; 12: 23

[19] Tang HC, Huang HJ, Lee CC, Chen CYC. Network pharmacology-based approach of novel traditional Chinese medicine formula for the treatment of acute skin inflammation *in silico*. Comput Biol Chem 2017; 71: 70–81

[20] Camberos-Luna L, Gerónimo-Olvera C, Montiel T, Rincon-Heredia R, Massieu L. The ketone body, *β*-hydroxybutyrate stimulates the autophagic flux and prevents neuronal death induced by glucose deprivation in cortical cultured neurons. Neurochem Res 2016; 41: 600–609

[21] Gertsch J. Botanical drugs, synergy, and network pharmacology: forth and back to intelligent mixtures. Planta Med 2011; 77: 1086–1098

[22] Kidger AM, Sipthorp J, Cook SJ. ERK1/2 inhibitors: New weapons to inhibit the RAS-regulated RAF-MEK1/2-ERK1/2 pathway. Pharmacol Ther 2018; 187: 45–60

[23] Yang J, Pi C, Wang G. Inhibition of PI3K/Akt/mTOR pathway by apigenin induces apoptosis and autophagy in hepatocellular carcinoma cells. Biomed Pharmacother 2018; 103: 699–707

[24] Giorgi C, Missiroli S, Patergnani S, Duszynski J, Wieckowski MR, Pinton P. Mitochondria-associated membranes: composition, molecular mechanisms, and physiopathological implications. Antioxid Redox Signal 2015; 22: 995–1019

[25] Granatiero V, De Stefani D, Rizzuto R. Mitochondrial calcium handling in physiology and disease. Adv Exp Med Biol 2017; 982: 25–47

[26] Kim AD, Madduma Hewage SR, Piao MJ, Kang KA, Cho SJ, Hyun JW. Esculetin induces apoptosis in human colon cancer cells by inducing endoplasmic reticulum stress. Cell Biochem Funct 2015; 33: 487–494

[27] Lee YH, Cheng FY, Chiu HW, Tsai JC, Fang CY, Chen CW, Wang YJ. Cytotoxicity, oxidative stress, apoptosis and the autophagic effects of silver nanoparticles in mouse embryonic fibroblasts. Biomaterials 2014; 35: 4706–4715

[28] Kim WK, Pyee Y, Chung HJ, Park HJ, Hong JY, Son KH, Lee SK. Antitumor activity of spicatoside A by modulation of autophagy and apoptosis in human colorectal cancer cells. J Nat Prod 2016; 79: 1097–1104

[29] Liu H, Wang Y, Sharma A, Mao R, Jiang N, Dun B, She JX. Derivatives containing both coumarin and benzimidazole potently induce caspase-dependent apoptosis of cancer cells through inhibition of PI3K-AKT-mTOR signaling. Anticancer Drugs 2015; 26: 667–677

[30] Detsi A, Kontogiorgis C, Hadjipavlou-Litina D. Coumarin derivatives: an updated patent review (2015–2016), Expert Opin Ther Pat 2017, 27: 1201–1226

[31] Zhang YJ, Duan Y, Zheng XFS. Targeting the mTOR kinase domain: the second generation of mTOR inhibitors. Drug Discov Today 2011; 16: 325–331

[32] Park D, Jeong H, Lee MN, Koh A, Kwon O, Yang YR, Noh J, Suh PG, Park H, Ryu SH. Resveratrol induces autophagy by directly inhibiting mTOR through ATP competition. Sci Rep 2016; 6: 21772

[33] Kist R, Caceres RA. New potential inhibitors of mTOR: a computational investigation integrating molecular docking, virtual screening, and molecular dynamics simulation. J Biomol Struct Dyn 2017; 35: 3555–3558

[34] Choi J, Chen J, Schreiber SL, Clardy J. Structure of the FKBP12-rapamycin complex interacting with binding domain of human FRAP. Science 1996; 273: 239–242

[35] Gomez-Verjan JC, Estrella-Parra EA, González-Sánchez I, Vázquez-Martínez ER, Vergara-Castañeda E, Cerbón MA, Reyes-Chilpa R. Molecular mechanisms involved in the cytotoxicity induced by coumarins from *Calophyllum brasiliense* in K562 leukemia cells. J Pharm Pharmacol 2014; 66: 1189–1195

[36] Luo H, Chen J, Shi L, Mikailov M, Zhu H, Wang K, He L, Yang L. DRAR-CPI: a server for identifying drug repositioning potential and adverse drug reactions via the chemical-protein interactome. Nucleic Acids Res 2011; 39: W492–W498

[37] Wang Z, Liang L, Yin Z, Lin J. Improving chemical similarity ensemble approach in target prediction. J Cheminform 2016; 8: 20

[38] Gfeller D, Grosdidier A, Wirth M, Daina A, Michielin O, Zoete V. SwissTargetPrediction: a web server for target prediction of bioactive small molecules. Nucleic Acids Res 2014; 42: W32–W38

[39] Szklarczyk D, Santos A, von Mering C, Jensen LJ, Bork P, Kuhn M. STITCH 5: augmenting protein-chemical interaction networks with tissue and affinity data. Nucleic Acids Res 2015; 44: D380–D384

[40] Mattingly CJ, Colby GT, Forrest JN, Boyer JL. The Comparative Toxicogenomics Database (CTD). Environ Health Perspect 2003; 111: 793–795

[41] Zuberi K, Franz M, Rodriguez H, Montojo J, Lopes CT, Bader GD, Morris Q. GeneMANIA prediction server 2013 update. Nucleic Acids Res 2013; 41: W115–W122

[42] Rivero-Segura NA, Flores-Soto E, García de la Cadena S, Coronado-Mares I, Gomez-Verjan JC, Ferreira DG, Cabrera-Reyes EA, Lopes LV, Massieu L, Cerbón M. Prolactin-induced neuroprotection against glutamate excitotoxicity is mediated by the reduction of [Ca2+]i overload and NF-κB activation. PLoS One 2017; 12: e0176910

[43] Vanoye-Carlo A, Morales T, Ramos E, Mendoza-Rodríguez A, Cerbón M. Neuroprotective effects of lactation against kainic acid treatment in the dorsal hippocampus of the rat. Horm Behav 2008; 53: 112–123

[44] Gerónimo-Olvera C, Montiel T, Rincon-Heredia R, Castro-Obregón S, Massieu L. Autophagy fails to prevent glucose deprivation/glucose reintroduction-induced neuronal death due to calpain-mediated lysosomal dysfunction in cortical neurons. Cell Death Dis 2017; 8: e2911

[45] Han W, Sun J, Feng L, Wang K, Li D, Pan Q, Chen Y, Jin W, Wang X, Pan H, Jin H. Autophagy inhibition enhances daunorubicin-induced apoptosis in K562 cells. PLoS One 2011; 6: e28491

Downloaded by: Universidad de Barcelona. Copyrighted material.

View publication stats

INFORME DE LABORES 2019

Biochemical Pharmacology 168 (2019) 429–437

Contents lists available at ScienceDirect

Biochemical Pharmacology

journal homepage: www.elsevier.com/locate/biochempharm

Parkin is transcriptionally regulated by the aryl hydrocarbon receptor: Impact on α-synuclein protein levels

Emmanuel González-Barbosa[a], Rosario García-Aguilar[b], Libia Vega[b], María Asunción Cabañas-Cortés[a], Frank J. Gonzalez[c], José Segovia[d], Sara L. Morales-Lázaro[e], Bulmaro Cisneros[f], Guillermo Elizondo[a,*]

[a] Departamento de Biología Celular, CINVESTAV-IPN, Av. IPN 2508, C.P. 07360 Ciudad de México, Mexico
[b] Departamento de Toxicología, CINVESTAV-IPN, Av. IPN 2508, C.P. 07360 Ciudad de México, Mexico
[c] Laboratory of Metabolism, NCI, National Institutes of Health, Bethesda, MD 20892, USA
[d] Departamento de Fisiología, Biofísica y Neurociencias, CINVESTAV-IPN, Av. IPN 2508, C.P. 07360 Ciudad de México, Mexico
[e] Departamento de Neurociencia Cognitiva, Instituto de Fisiología Celular, Universidad Nacional Autónoma de México, 04510 Ciudad de México, Mexico
[f] Departamento de Genética y Biología Molecular, CINVESTAV-IPN, Av. IPN 2508, C.P. 07360 Ciudad de México, Mexico

ARTICLE INFO

Keywords:
Parkinson's disease
Aryl hydrocarbon receptor
Parkin
α-Synuclein
TCDD

ABSTRACT

Parkin (PRKN) is a ubiquitin E3 ligase that catalyzes the ubiquitination of several proteins. Mutations in the human Parkin gene, *PRKN,* leads to degeneration of dopaminergic (DA) neurons, resulting in autosomal recessive early-onset parkinsonism and the loss of PRKN function is linked to sporadic Parkinson's disease (PD). Additionally, several *in vitro* studies have shown that overexpression of exogenous PRKN protects against the neurotoxic effects induced by a wide range of cellular stressors, emphasizing the need to study the mechanism(s) governing PRKN expression and induction. Here, *Prkn* was identified as a novel target gene of the aryl hydrocarbon receptor (AhR), a ligand-activated transcription factor and member of the bHLH/PAS (basic helix-loop-helix/Per-Arnt-Sim) superfamily. AhR binds and transactivates the *Prkn* gene promoter. We also demonstrated that AhR is expressed in DA neurons and that its activation upregulates *Prkn* mRNA and protein levels in the mouse ventral midbrain. Additionally, the AhR-dependent increase in PRKN levels is associated with a decrease in the protein levels of its target substrate, α-synuclein, in an AhR-dependent manner, because this effect is not observed in *Ahr*-null mice. These results suggest that treatments designed to induce PRKN expression through the use of nontoxic AhR agonist ligands may be novel strategies to prevent and delay PD.

1. Introduction

Parkinson's disease (PD) is the second most common neurodegenerative disease and is clinically characterized by bradykinesia, resting tremor, and postural imbalance induced by the progressive loss of dopaminergic neurons in the substantia nigra pars compacta (SNc). Histopathologically, it is characterized by the presence of intracytoplasmic inclusions of α-synuclein called Lewy bodies [1].

Several reports support the role of Parkin (PRKN) in the development of PD. Parkin is ubiquitously expressed but predominantly in the brain and is an E3 ligase that catalyzes the ubiquitination of several proteins, including Pael-R, α-synuclein, synphilin-1, and Cdc-Rel. Parkin confers protection against several insults to neurons, and impairments in ubiquitination of some of its targets have been linked to the degeneration of dopamine (DA) neurons [2,3]. The neuroprotective effect of Parkin is also mediated by promoting the removal of damaged mitochondria via mitophagy [4] and by regulating the function and stability of excitatory glutamatergic synapses [5].

Mutations in the *PRKN* in humans are the most common cause of autosomal-recessive early-onset parkinsonism, and reduced Parkin expression has been linked to late-onset PD [6]. Moreover, *PRKN* haploinsufficiency is associated with an increased risk of developing the sporadic form of PD [7]. In addition to genetic factors, other conditions may alter Parkin function. Several cell stressors, such as hydrogen peroxide, S-nitrosylation, 1-methyl-4-phenylpyridine (MPP^+), 6-hydroxydopamine (6-OHDA), paraquat, and rotenone, induce Parkin aggregation [8], while the native structure of PRKN in the brain is modified with age [9]. Therefore, any condition leading to reduced Parkin levels or function compromises neuronal survival.

In agreement with these findings, the overexpression of exogenous

* Corresponding author at: P.O. Box 14-740, Ciudad de México 07000, Mexico.
E-mail address: gazuela@cinvestav.mx (G. Elizondo).

https://doi.org/10.1016/j.bcp.2019.08.002
Received 12 June 2019; Accepted 7 August 2019
Available online 09 August 2019
0006-2952/ © 2019 Elsevier Inc. All rights reserved.

INFORME DE LABORES 2019

Parkin confers protection against the neurotoxic effects induced by a wide range of cellular stressors [10–13], emphasizing the need to study the mechanism(s) governing *PRKN* gene expression and regulation. However, there is a lack of information regarding the transcription factors involved in *Prkn* gene regulation.

The aryl hydrocarbon receptor (AhR) mediates the expression of several genes encoding ubiquitin proteasome system proteins [14–16], in particular *Ubch7* (also known as *UBE2l3* in humans and *UbcM4* in mice), an E2 ubiquitin enzyme partner of PRKN. AhR is a ligand-activated transcription factor that mediates the toxicity of environmental pollutants, and its highest-affinity ligand is 2,3,7,8-tetrachlorodibenzo-*p*-dioxin (TCDD). Upon binding TCDD, AhR translocates to the nucleus, binds to xenobiotic-responsive elements (XREs), and upregulates the expression of a battery of genes that encode xenobiotic-metabolizing enzymes, including its canonical gene target, *Cyp1a1* [17].

On the other hand, it was reported that the promoter of the *D. melanogaster* homolog of human *PRKN* has a binding site for AhR [18], suggesting that AhR may be involved in the regulation of *Prkn* expression. Therefore, we initiated a study to determine whether AhR regulates *Prkn* expression in the mouse ventral midbrain and its effects on the protein levels of Parkin substrates, in particular α-synuclein (SNCA).

Our data showed that AhR is expressed in mouse DA neurons, and its activation by oral treatment with TCDD induces Parkin expression in the ventral midbrain and decreases the PRKN substrate α-synuclein.

2. Materials and methods

2.1. Materials

SH-SY5Y cells were obtained from the American Type Culture Collection (Manassas, VA, USA). 2,3,7,8-Tetrachlorodibenzo-*p*-dioxin (TCDD) was purchased from AccuStandard (New Haven, CT, USA). Phenylmethanesulfonyl fluoride (PMSF) and dimethyl sulfoxide (DMSO) were acquired from Sigma (St. Louis, MO, USA).

2.2. Animals and treatments

The development of *Ahr*-null mice was described previously [19]. Wild-type (WT) littermates on a C57BL/6J background were used as controls. The animals were housed in a pathogen-free facility and fed with autoclaved Purina rodent chow (St. Louis, MO, USA) with water available *ad libitum*. All animal procedures were performed according to the Guide for the Care and Use of Laboratory Animals, as adopted and enforced by the U.S. National Institutes of Health and the Mexican Regulation of Animal Care and Maintenance (NOM-062-ZOO-1999, 2001). The mice were distributed randomly into TCDD and vehicle treatment groups (N = 3, for each of the assay performed), and the treatments were carried out as described previously [20]. TCDD was dissolved in corn oil, and a single dose of TCDD (250 μg/kg) or corn oil alone (vehicle) was administered by gavage to 8- to 9-week-old male C57BL/6J wild-type (WT) and *Ahr*-null mice. Seven days later, the mice were anesthetized with pentobarbital and euthanized by decapitation. The brains were rapidly removed, and the ventral midbrain was dissected out as follow: the brain was removed, and the dorsal side was placed up. Using a thin blade, a coronal rostral cut was made at the level of the pineal recess, the junction between the caudal part of the interhemispheric scissure and the medial occipital lobe border. Next, a caudal coronal cut in the intercollicular sulcus was made. The midbrain was dissected, and the ventral midbrain section obtained.

Liver sections were also extracted. Brain and liver samples were snap frozen and stored at −70 °C.

2.3. Real-time quantitative polymerase chain reaction (qPCR)

Total RNA was prepared from mouse liver and ventral midbrain using TRIzol reagent according to the manufacturer's instructions (Invitrogen, Camarillo, CA, USA). RNA was quantified spectrophotometrically at an optical density of 260 nm. RNA integrity was evaluated by electrophoresis on 1% agarose gels. cDNA was prepared for quantitative PCR from 2 μg of total RNA using the SuperScript First-Strand Synthesis kit (Invitrogen, Camarillo, CA, USA) and oligo dTs. PCR was performed on a StepOne Real-Time PCR System (Applied Biosystems, Branchburg, NJ, USA), and the results were analyzed using the comparative threshold cycle (C_T) method. mRNAs encoding *Ahr, Cyp1a1 Prkn,* and 18S ribosomal RNA (rRNA, endogenous), were amplified in a single PCR to allow for the normalization of the mRNA data. The PCR mixture contained 2 μl of cDNA, 1x TaqMan Universal PCR Master Mix (Applied Biosystems, Branchburg, NJ, USA) and 0.9 and 0.25 μM primers and probes, respectively. The primer and probe sequences used for *Prkn* were 5′-CAAACAAGCAACCCTCACCTT-3′ (forward), 5′-ATCCGGTTTGGAATTAAGACATCGT-3′ (reverse), and CCCA GGGCCCATCTT (probe, FAM). The probes used for *Ahr*, *Cyp1a1* and 18S rRNA were obtained from Applied Biosystems (Branchburg, NJ, USA) with identification numbers Mm01291777_m1, Mm00487218_m1, and Mm00507222_s1, respectively.

2.4. Immunofluorescence

The localization of the AhR protein in the SNc of adult mouse brains was determined by immunofluorescence, and tyrosine hydroxylase (TH) was used to identify DA neurons. Mice were injected with an overdose of pentobarbital (80 mg/kg) and perfused intracardially with saline. Subsequently, the brains were fixed with 4% paraformaldehyde in phosphate-buffered saline (PBS), postfixed in the same solution for 48 h and then incubated in 20% sucrose in PBS. Coronal sections (30-μm-thick) were cut with a cryostat and used for immunohistochemical assays. Briefly, free-floating sections were incubated at room temperature for 1 h in 0.25% Triton X-100/PBS buffer and subsequently in 5% BSA and 0.25% Triton X-100/PBS buffer for 3 h. Then, the sections were incubated in 3% BSA and 0.25% Triton X-100/PBS solution containing AhR (1:500) and TH (1:1000) antibodies (Abcam, Cat. ab2770, CA, USA and Cell Signaling Technologies, Cat. 2792, MA, USA, respectively). After 48 h of incubation, the sections were incubated with secondary antibodies (1:400) (Alexa 594 anti-mouse IgG, Cat. A-21203 and Alexa 488 anti-rabbit, Cat. A-11008; Thermo Fisher Scientific, MA, USA) diluted in PBS with 0.25% Triton X-100. The sections were counterstained with DAPI to reveal the nuclei and observed by confocal microscopy. Triple-labeled images were obtained using a confocal laser-scanning microscope (Leica TCS-SPE, Wetzlar, Germany) in the XYZ (Z-stacks) mode using a 40x objective. The Z-stacks (3–4 optical slices) were then converted into three-dimensional projection images using the Leica LAS AF lite software.

2.5. Western blotting

Ventral midbrain sections were homogenized in buffer containing 20 mM HEPES, 350 mM NaCl, 1 mM $MgCl_2$, 0.5 mM EDTA, 0.1 mM EGTA, 1% Nonidet P40, 0.5 mM DTT, 0.1% PMSF and Mini cOmplete protease inhibitor cocktail (1 tablet/10 mL, Roche, Mannheim, Germany). The protein suspension was homogenized completely by sonication for 30 s. Protein concentrations were determined using the Bradford assay (Bio-Rad, Hercules, CA, USA). Aliquots (40 μg) were solubilized in sample buffer (60 mM Tris–HCl, pH 6.8, 2% sodium dodecyl sulfate (SDS), 20% glycerol, 2% mercaptoethanol, and 0.001% bromophenol blue) and subjected to 12% SDS polyacrylamide gel electrophoresis. The protein extracts were transferred to a nitrocellulose membrane using a mini trans-blot system (Bio-Rad, Hercules, CA, USA). The transfer was performed at a constant voltage of 80 V for 2 h in transfer buffer (48 mM Tris–HCl, 39 mM glycine, pH 8.3, and 20% methanol). Following the transfer, the membranes were blocked overnight at 4 °C in the presence of 2% nonfat dry milk and

INFORME DE LABORES 2019

0.5% bovine serum albumin (BSA) in blocking buffer (25 mM Tris–HCl, pH 7.5, and 150 mM NaCl) and subsequently incubated at 4 °C for 3 h with mouse monoclonal anti-Parkin (1:500; Thermo Fisher, Cat. 39-0900, Meridian Rock, IL, USA), rabbit polyclonal anti-Cyp1a1 (1:100, Santa Cruz Biotechnology, Cat. sc-20772, Visalia, CA, USA), and goat anti-β-actin (1:1000; Santa Cruz, Biotechnology, Cat. sc-1616, Visalia, CA, USA), and for 16 h at 4 °C for mouse monoclonal anti-α-synuclein (1:4000; Santa Cruz Biotechnology, Cat. Sc-12767, Visalia, CA, USA). The antibodies were diluted in buffer (25 mM Tris–HCl, pH 7.5, 150 mM NaCl, 0.1% Tween 20, 0.05% nonfat dry milk, and 0.05% BSA). After washing, the membranes were incubated with the relevant horseradish peroxidase (HRP)-conjugated goat anti-mouse IgG (Thermo Fisher, Cat. 62-6520, Meridian Rock, IL, USA), horse anti-mouse IgG (Vector laboratories, Cat. PI-2000, Burlingame, CA, USA), goat anti-rabbit IgG (Cell Signaling, Cat. 7074, Danvers, USA), and rabbit anti-goat IgG (Thermo Fisher, Cat. 31402, Meridian Rock, IL, USA) secondary antibodies for 2 h at 4 °C. The membranes were washed, and the immunoreactive proteins were detected using an ECL western blotting detection kit (Amersham, Arlington Heights, IL, USA). The integrated optical density of the bands was quantified using scanning densitometry (GS-800 Calibrated Densitometer, Bio-Rad, Hercules, CA, USA).

2.6. In silico analysis

The mouse *Prkn* promoter was analyzed using the web-based bioinformatics tool EPD (https://epd.epfl.ch//index.php). $P < 0.01$ was considered significant.

2.7. Chromatin immunoprecipitation (ChIP)

ChIP assays were performed according to the kit protocol (Santa Cruz Biotechnology, Visalia, CA, USA) with an anti-AhR antibody (Thermo Fisher Scientific, Cat. MA1-514, Rockland, IL, USA). The PCR product corresponding to the *Prkn* proximal gene promoter was generated from an aliquot of immunoprecipitated material. Brain homogenates from WT mice treated with a single oral dose of TCDD or vehicle (corn oil) were washed with PBS buffer and crosslinked with 1% formaldehyde. After chromatin isolation, the DNA was fragmented, and immunoprecipitation was performed. The crosslinking was reversed, the DNA was purified, and PCR amplification was performed as follows: initial denaturation at 94 °C for 3 min and 28 cycles of denaturation at 94 °C for 30 s, annealing at 65 °C for 30 s, and extension at 72 °C for 30 s. A final extension cycle at 72 °C for 10 min was added to the end of the program. The oligonucleotides used for PCR amplification were 5′-AGAAGTGAGCAGGGGGTCGGG-3′ (forward) and 5′-AAGGACCTAC GCGGGCACTG-3′ (reverse).

2.8. Plasmid

The reporter plasmid pGL4/-419-mPrkn, which includes the mouse *Prkn* gene promoter, was constructed as described. A −419/+1 fragment was generated by PCR amplification using mouse genomic DNA and oligonucleotides (forward: 5′-AGAAGTGAGCAGGGGGTCGGG-3′, reverse: 5′-AAGGACCTACGCGGGCACTG-3′). The fragment was then cloned into the pCR 2.1-TOPO transition vector (Invitrogen, Camarillo, CA, USA). To verify the amplicon orientation as well as its correct sequence, single and double restriction enzyme digestions and sequencing were performed. Then, the fragment was cloned into the KpnI/Xhol site of the pGL4.10 [luc2] reporter vector (Promega, Madison, WI, USA) containing the firefly luciferase gene. This plasmid was designated pGL4/-419_mPrkn.

2.9. Cell culture and transfections

SH-SY5Y cells were obtained from American Type Culture Collection (CRL-2266, Manassas, VA, USA). The cells were grown in 100-mm dishes with high-glucose DMEM (Gibco, Carlsbad, CA, USA) supplemented with 10% fetal bovine serum (Gibco, Logan, UT, USA) and 1% antibiotic/antimycotic (Invitrogen, Carlsbad, CA, USA) at 37 °C in a humidified incubator with a 5% CO_2 atmosphere. Transfections were performed using Escort IV (Sigma, Saint Louis, MO, USA). Each culture (1×10^6 cells/mL) was transfected with 1, 2.5, 5 or 10 μg of pGL4/-419-mPrkn and 1 μg of pRL-CMV as an internal control. The media was replaced with fresh media containing 10 nM TCDD for 48 h posttransfection. After 48 h, the cells were homogenized by incubation with Passive Lysis Buffer (Promega, Madison, WI, USA) for 15 min at room temperature. A luciferase activity assay was performed using the Dual-Glo Luciferase Reporter Assay System (Promega, Madison, WI, USA) according to the manufacturer's instructions with a Modulus luminometer (Turner Biosystems, Sunnyvale, CA, USA). Blanks were obtained by performing the luciferase activity assay on mock-transfected cells. Firefly luciferase activity levels were normalized by comparison to the activity levels of *Renilla* luciferase.

2.10. Electrophoretic mobility shift assay (EMSA)

Liver and brain tissues from C57BL/6J mouse strain were used to prepare nuclear extracts. Tissues and cells were homogenized in ice-cold buffer (10 mM HEPES, pH 7.9, 10 mM KCl, 0.1 mM EDTA, 0.1 mM EGTA, 1.0 mM DTT, and 0.5 mM PMSF) and incubated for 15 min on ice. Finally, the buffer was complemented with 0.5% IGEPAL CA-630 (Sigma-Aldrich), and the mixes were passed through a 22-gauge needle and centrifuged at 2000 × *g* for 5 min at 4 °C. The supernatant was removed, and the nuclear pellet was homogenized in 20 mM HEPES, pH 7.9, 0.4 M NaCl, 1 mM EDTA, 1 mM EGTA, 1 mM DTT, and 1.0 mM PMSF. Nuclear samples were mixed vigorously for 30 min at 4 °C. The nuclear homogenates were centrifuged at 3000 × *g* for 5 min at 4 °C, and the supernatant was recovered for protein quantification by bicinchoninic acid assay (Sigma-Aldrich).

EMSAs were carried out using a 3′ end-labeled biotin duplex and unlabeled probes. The biotin-labeled reactions were performed according to the manufacturer's instructions (LightShift Chemiluminescent EMSA kit, Thermo Scientific). The EMSA binding reactions contained 10 mM Tris, pH 8.0, 1 mM $MgCl_2$, 5 mM NaCl, 2.5 mM EDTA, 2.5 mM DTT, 4% glycerol, 1.5 μg nuclear protein extract, 10 mM salmon sperm DNA and 16 fmol of each labeled duplex probe. For competition assays, a 500-fold molar excess of the unlabeled duplex probe was added to the mixture. The samples were separated on pre-run native 5% polyacrylamide gels and transferred to nylon membranes (Amersham Hybond-N+, GE Healthcare). DNA crosslinking to the membranes was achieved by membrane exposure to a UV transilluminator (312 nM bulbs) for 15 min. Finally, the complexes were detected by chemiluminescence according to the manufacturer's instructions (LightShift Chemiluminescent EMSA kit, Thermo Scientific). The sequences of the primers used for duplex probes were as follows:

XRE1-forward: 5′-TGCGCCCGCCTGGCTCGC-3′, XRE1-reverse: 5′-GCGAGCCAGGCGGGCGCA-3′; XRE consensus-forward: 5′-CTCGAA CTCACGCAACTCCGT-3′, XRE consensus-reverse: 5′-CGGAGTTGCGTG AGTTCGAGC-3′; XRE consensus mut-forward: 5′-CTCGAACTCACTCA ACTCCGT-3′, and XRE consensus mut-reverse: 5′-CGGAGTTGAAGTGA GTTCGAGC-3′.

2.11. Statistical analysis

The results are presented as the mean values ± standard deviation (S.D.). The statistical significance of the data was evaluated using Student's *t*-test. In all cases, the differences between the groups were considered to be statistically significant when the *p* value was less than 0.05.

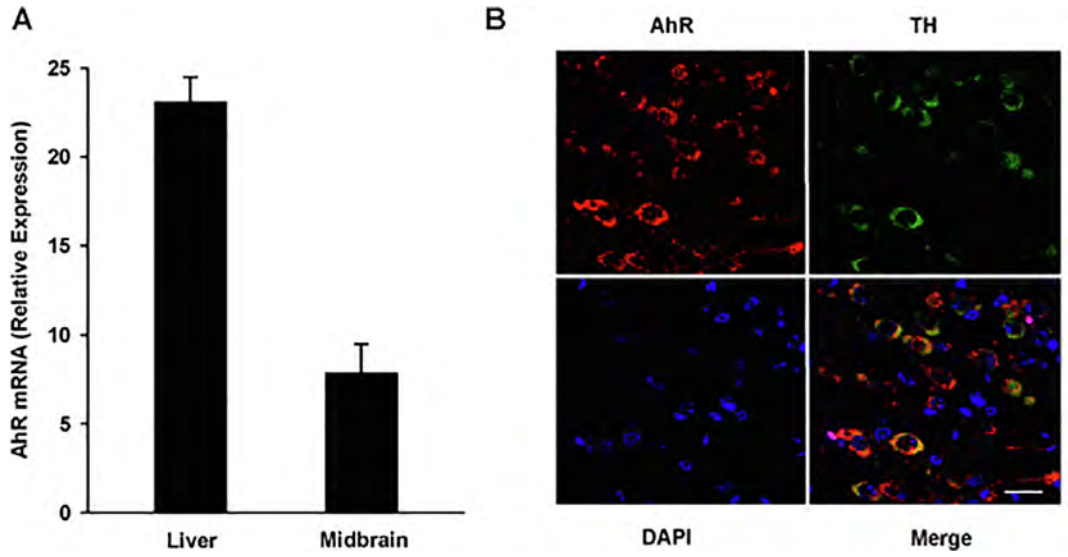

Fig. 1. AhR is expressed in the mouse ventral midbrain and DA neurons. A) Total RNA was extracted from the ventral midbrain region and liver of sacrificed mice. AhR mRNA levels were determined by qPCR and normalized to 18S ribosomal RNA. The results are expressed as the mean ± S.D. of samples from three different mice. B) Representative confocal microscopy images of AhR expression in the ventral midbrain region. AhR, TH and DAPI were visualized as red, green, and blue, respectively. Scale bar: 25 μM.

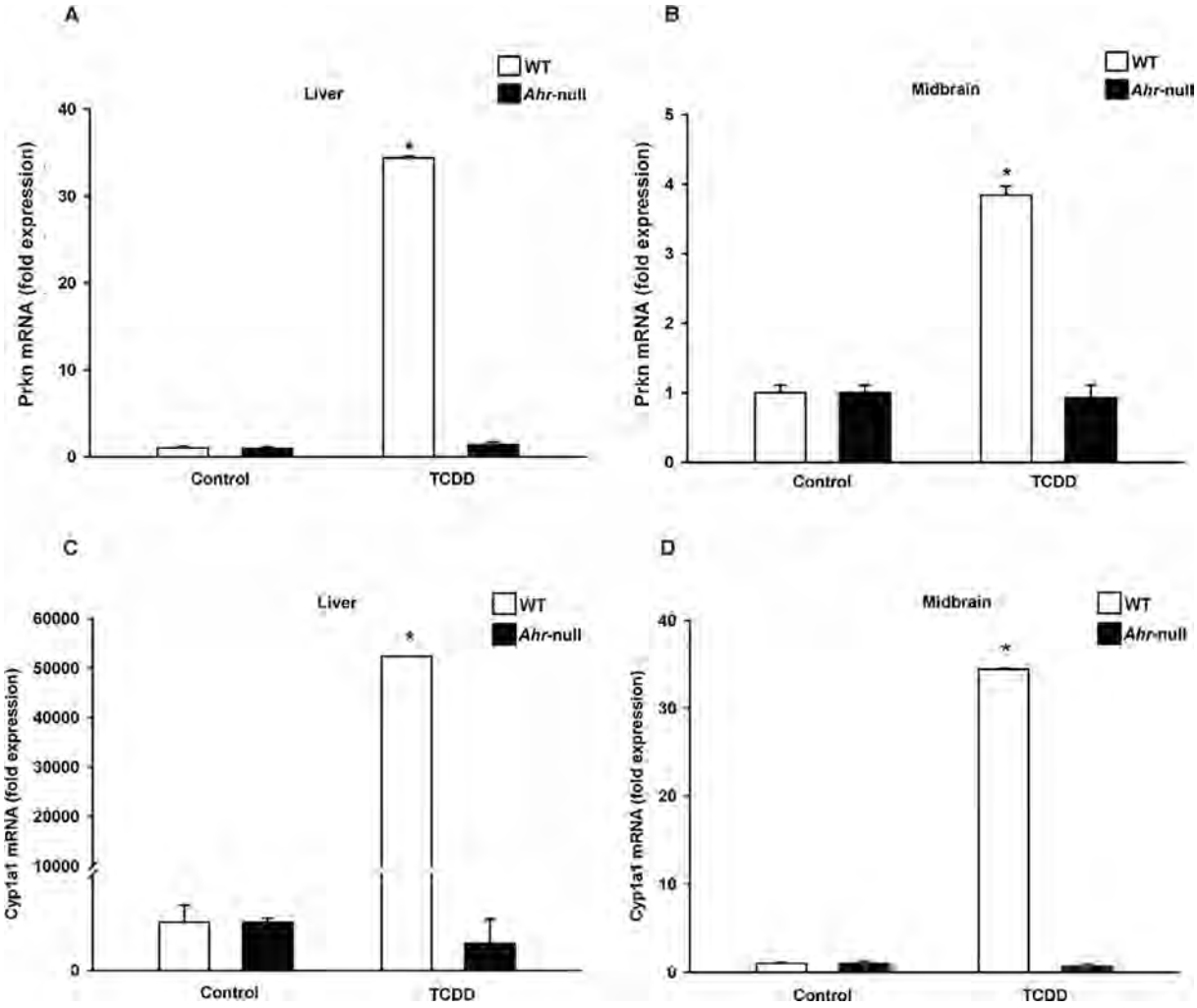

Fig. 2. AhR-dependent induction of *Cyp1a1* and *Prkn* mRNA in the ventral mouse liver and ventral midbrain. Wild-type (WT) and *Ahr*-null mice were treated with a single oral dose of TCDD or corn oil as vehicle. Total RNA was extracted from the liver and ventral midbrain region, and *Prkn* (A and B) and *Cyp1a1* (C and D) mRNA levels were determined by qPCR and normalized to 18S ribosomal RNA. The results are expressed as the mean ± S.D. of samples from three different mice. *$p < 0.05$, treatment *vs.* control.

INFORME DE LABORES 2019

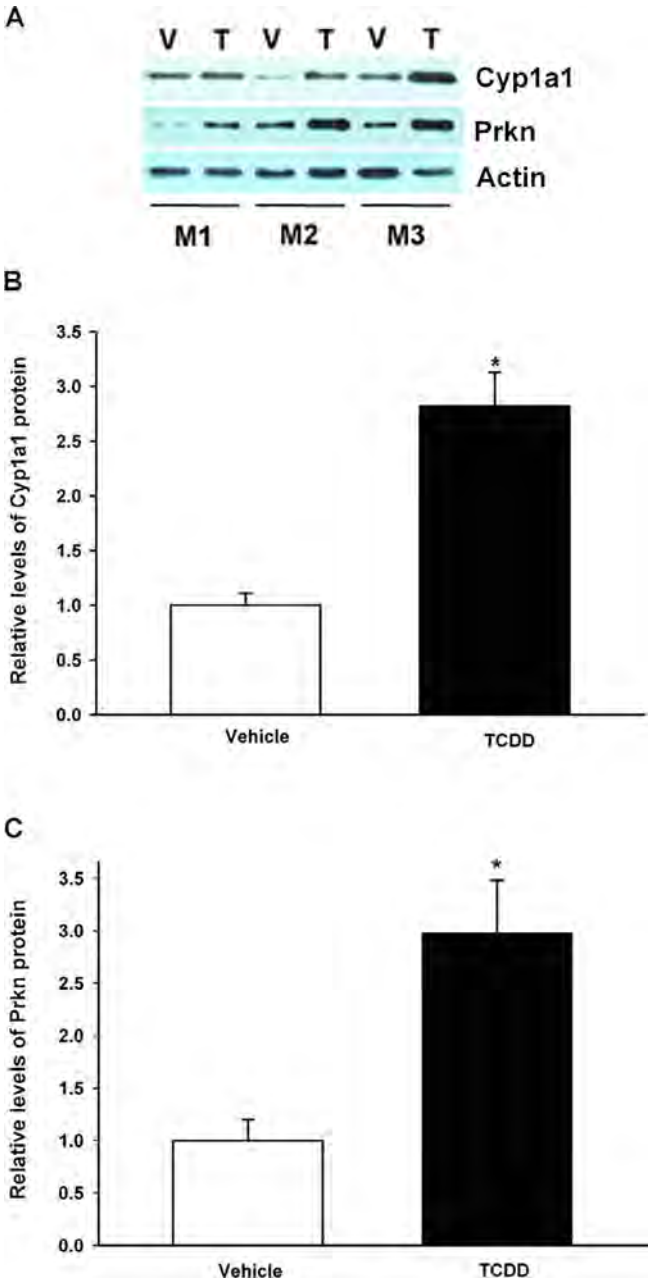

Fig. 3. TCDD treatment induced Cyp1a1 and Prkn protein levels in the mouse ventral midbrain. Wild-type mice were treated with a single oral dose of TCDD (T) or corn oil as vehicle (V), and Cyp1a1 and Parkin protein levels were determined by western blotting. Beta actin was used as a loading control (A). Relative Cyp1a1 (B) and Prkn (C) protein levels. The results are expressed as the mean ± S.D. of samples from three different mice (M1, M2, M3). *$p < 0.05$, treatment *vs.* control.

3. Results

Initially, AhR expression in the mouse ventral midbrain and DA neurons was evaluated. *AhR* mRNA was detected in the mouse ventral midbrain region at one-third of the level in the liver (Fig. 1A). Since the AhR expression is highest in the liver, the observed levels in the ventral midbrain are substantial. We then determined whether AhR protein is expressed in DA neurons. AhR protein was detected by immunofluorescence in the SNc of the adult mouse brain and the signal colocalized with that of tyrosine hydroxylase, a marker of dopaminergic neurons (Fig. 1B).

Compared to vehicle treatment, TCDD, an AhR agonist, induced 32- and 3.7-fold increases in the expression of *Prkn* mRNAs in the mouse liver and ventral midbrain, respectively (Fig. 2A and B). This induction was AhR-dependent, since no induction of *Prkn* mRNA was observed in TCDD-treated *Ahr*-null mouse liver and ventral midbrain. As expected, AhR activation induced expression of its canonical target gene, *Cyp1a1,* in both the liver and ventral midbrain region and the induction was also AhR-dependent (Fig. 2C and D).

Then, the Prkn and Cyp1a1 protein levels in the mouse ventral midbrain region were evaluated. Compared to vehicle treatment, TCDD treatment increased Prkn protein levels by approximately 3-fold (Fig. 3A and C). Similarly, a 3-fold increase in Cyp1a1 protein was observed (Fig. 3A and B).

The above studies confirm that AhR is expressed in the mouse ventral midbrain, particularly in DA neurons, and indicate that AhR activation upregulates *Prkn* mRNA and Prkn protein. These results prompted us to investigate and characterize the molecular mechanisms of AhR-dependent Parkin induction. *In silico* analysis of the mouse *Prkn* gene promoter was carried out (Fig. 4). Several response elements were identified. Of particular interest for the present study are the three putative concensus AhR binding sites, known as xenobiotic response elements (XREs), located −37, −54 and −349 bp from the *Prkn* transcription start site. ChIP revealed that AhR indeed binds to the *Prkn* gene promoter after TCDD treatment (Fig. 5A, lane 4). Moreover, a basal interaction between AhR and the *Prkn* gene promoter was also observed (Fig. 5A, lane 3), suggesting that this AhR may also be involved in the control of basal *Prkn* expression possibly through its activation by endogenous ligands.

To determine whether AhR binding to the *Prkn* promoter results in its transactivation, a luciferase reporter plasmid (pGL4/-419-mPrkn), driven by the mouse *Prkn* promoter, was constructed and transfected into SH-SY5Y human neuroblastoma cells. A dose response of increased luciferase expression from 1.0 to 10 µg of transfected plasmid was found after 10 nM TCDD treatment, up to a 3-fold increase with 10 µg of the reporter construct, relative to vehicle-treated cells (Fig. 5B).

According to the *in silico* study, among the three XREs identified, XRE1 exhibited the highest score. Therefore, the interaction between AhR and XRE1 was investigated by EMSAs. The addition of nuclear extracts from mouse livers and ventral midbrains treated with TCDD to the XRE1 motif resulted in the formation of a DNA-protein complex as represented by the shifted band (Fig. 6A-B, lane 2). This binding was specific since an excess of unlabeled XRE1 or consensus XRE probes blocked formation of this complex (Fig. 6A-B lanes 3 and 4), whereas an unlabeled mutated consensus XRE probe did not compete with the labeled XRE1 probe (Fig. 6A-B lane 5). Together, these results indicate that treatment with TCDD promotes AhR binding to XRE1, transactivates the *Prkn* gene promoter and induces *Prkn* mRNA and Prkn protein expression.

Next, we sought to determine whether the AhR-dependent increase in Parkin levels is associated with a decrease in the protein levels of their target substrates. For this purpose, WT and *Ahr*-null mice were treated with TCDD, and Snca protein levels in the ventral midbrain region were determined by western blot. After TCDD treatment, WT mice exhibited an approximately 10-fold decrease in α-synuclein protein levels compared to vehicle treatment (Fig. 7), and this change was significant. In contrast, this effect was not observed in *Ahr*-null samples.

4. Discussion

A deficit in Parkin levels and/or function have been associated with the etiology of several neurodegenerative disorders, including PD. Mutations in the human *PRKN* gene result in autosomal-recessive early-onset parkinsonism, and reduced Parkin expression has been linked to late-onset PD. Conversely, the overexpression of Parkin *in vitro* and *in vivo* protects DA neurons from a variety of cellular stressors that produce oxidative stress, excitotoxicity, mitochondrial dysfunction, endoplasmic reticular stress, apoptosis, and proteotoxicity [21,22]. Thus,

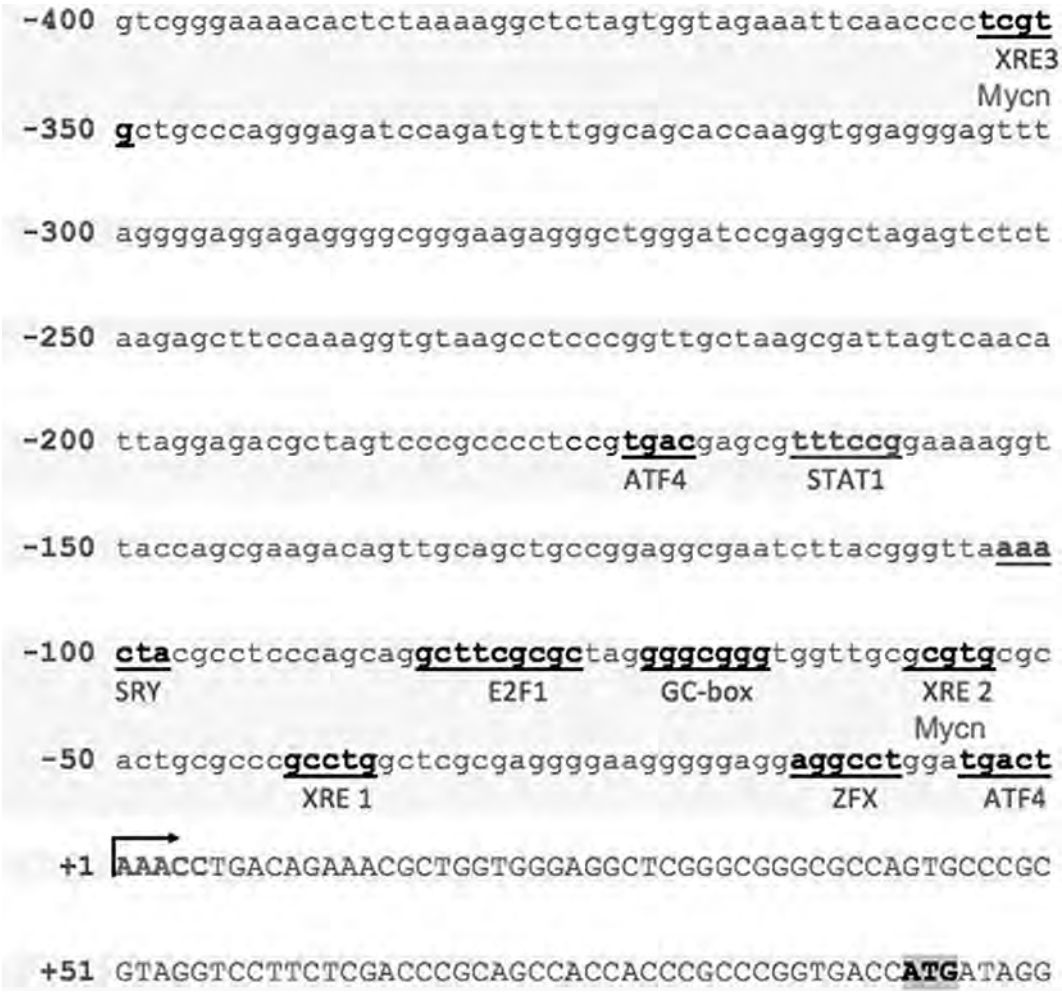

Fig. 4. Analysis of the 5′ region of the mouse *Prkn* gene. The 5′ region of the mouse *Prkn* gene was analyzed *in silico* to identify binding sites for known transcription factors (underlined). XRE: xenobiotic response element, Mycn: Mycn proto-oncogene neuroblastoma-derived response element, ATF4: activating transcription factor 4 response element, STAT1: signal transducer and activator of transcription 1 response element, SRY: sex-determining region Y factor response element, E2F: E2F transcription factor response element, GC box, and ZFX: zinc finger protein X-linked response element. The transcription start site is indicated by the arrow and the translation start site codon is indicated by shading.

gaining insight into the molecular mechanism that direct Parkin expression is crucial for the design of novel treatments based on the induction of Parkin levels.

Here, we show that Parkin is transcriptionally upregulated by TCDD via AhR activation. First, we demonstrated that this transcription factor is expressed in the mouse ventral midbrain, particularly in DA neurons. Considering that the liver is among the organs and tissues with the highest levels of AhR, the levels of its transcript in the mouse ventral midbrain were substantial; the levels in the ventral midbrain were one third of those observed in liver, suggesting that AhR has important functions in this brain region.

The induction of *Cyp1a1* mRNA in the ventral midbrain after TCDD treatment indicates that TCDD crosses the blood-brain barrier and reaches brain tissues to activate AhR. Similar to *Cyp1a1* but to a lesser extent, TCDD promotes the overexpression of Parkin. In both cases, the effect is AhR-dependent since no induction is observed in *Ahr*-null mice. At the protein level, compared to vehicle treatment, TCDD treatment results in a 3-fold induction in Prkn expression. These results clearly demonstrate that the activation of AhR upregulates *Prkn* gene expression.

The *in silico* analysis of the *Prkn* gene promoter identified 3 putative AhR binding sites, namely, XRE1, XRE2, and XRE3, which are located −37, −54 and −349 bp, respectively, from the transcription start site. The Prkn gene promoter in *Drosophila melanogaster* contains a binding site for AhR [18] and the human *PRKN* promoter contains 3 AhR binding sites, suggesting that the gene encoding Parkin may be under the control of AhR in several diverse species and thus this Ahr-driven signaling pathway must be of developmental and/or physiological consequence.

ChIP, EMSA, and transactivation studies confirmed that TCDD promotes AhR recruitment to the *Prkn* gene promoter, inducing Parkin expression. ChIP also showed an interaction between AhR and the promoter under control conditions, that is, without TCDD treatment. The above results suggest the possible presence of an endogenous ligand and that AhR may also control basal Parkin expression.

Prkn is transcriptionally regulated by the restriction of trophic factors and nutrients [23], p53 [24], activating transcription factor 4 (ATF4) [25], and N-myc (Mycn) [26]. Consistent with this, the *in silico* study identified the presence of ATF4 and Mycn binding sites. No p53 responsive elements were recognized because they are located in intron 1 and –3332 bp from the ATG site. Of particular interest is that Mycn and AhR share similar responsive elements within the *Prkn* promoter gene. In contrast to AhR, Mycn, a critical transcription factor involved in neural development [27], downregulates Parkin expression. The latter occurs in the context of differentiation when Parkin expression is observed in the latest stages of embryonic development and when Mycn expression is the lowest [26]. These data suggest that Mycn may negatively control Parkin expression by blocking AhR binding to Mycn/

INFORME DE LABORES 2019

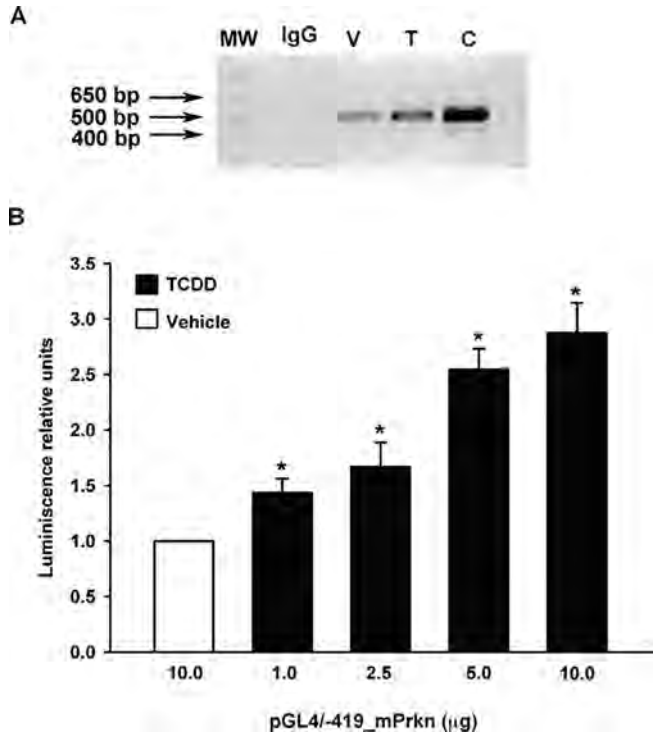

Fig. 5. AhR binds and transactivates the *Prkn* promoter gene. A) ChIP analysis of AhR binding to the mouse *Prkn* gene promoter region. Material for immunoprecipitation was obtained from the brain tissues of mice treated with corn oil as vehicle (V, lane 3) or a single oral dose of TCDD (T, lane 4). PCR products corresponding to the −407/+74 bp region of the *Prkn* gene promoter were generated. Genomic DNA was used as the positive control (C, lane 5) and IgG antibody was used as the negative control (IgG, lane 2). MW (lane 1) represents molecular weight markers. A representative gel of two independent experiments is shown. B) The luciferase activity of SH-SY5Y cells (1×10^6) transfected with 1, 2.5, 5 or 10 μg of the pGL4/-419_mPrkn vector containing the firefly luciferase open reading frame under the control of the mouse *Prkn* gene promoter and treated with 10 nM of TCDD or DMSO (vehicle) for 48 h was determined. The luciferase activity was normalized to *Renilla* luciferase activity and is expressed as the mean ± S.D. of three independent experiments. * $p < 0.05$, control *vs.* treatment.

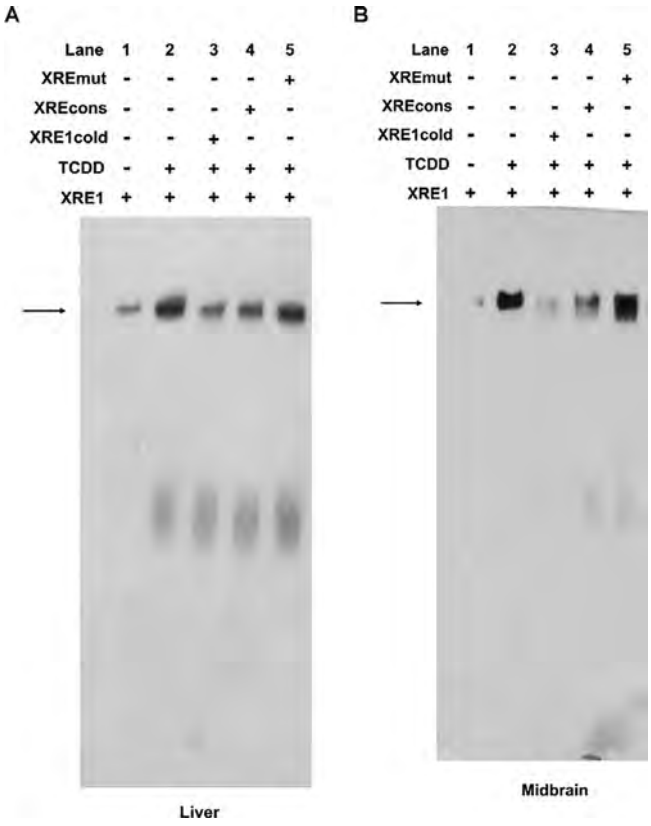

Fig. 6. EMSA analysis of protein binding to the putative XRE1 identified in the *Prkn* gene promoter. Nuclear extracts from the livers (A) or ventral midbrains (B) of mice treated with corn oil (lane 1) or 250 μg/kg TCDD (lanes 2–5) were incubated with a labeled putative XRE1 probe only (lane 2), with a labeled putative XRE1 probe plus a 500-fold molar excess of an unlabeled putative XRE1 probe (lane 3), with the putative XRE1 labeled probe plus an unlabeled consensus XRE probe characterized from the mouse *Cyp1a1* gene (lane 4), or with a labeled putative XRE1 probe plus an unlabeled mutated consensus XRE probe characterized from the mouse *Cyp1a1* gene (lane 5). The arrow indicates the shifted bands. The image is representative of 2 independent experiments. The nuclear extract was obtained from the ventral midbrain from 3 mice.

AhR responsive elements.

Additionally, a sex-determining region Y factor (SRY) response element located −98 bp from the transcription start site was identified. Immunohistochemical studies showed that SRY is expressed in DA neurons and that 6-OHDA induces its expression, while its knockdown exacerbates cell death produced by ROS [28]. It would not be unexpected for the reported SRY protective response to be mediated, at least in part, by the induction of Parkin expression. Similarly, the induction of ATF4 plays an important neuroprotection role against rotenone-induced DA neuronal death, presumably through the induction of Parkin levels [29].

TCDD treatment results in a significant decrease in the protein levels of α-synuclein (Snca) in the mouse ventral midbrain in an AhR-dependent manner. Snca function is not well understood, but it may play a role in synaptic functioning and neuroplasticity by regulating neurotransmitter release. It is present in several brain regions, including the SNc [30], and its progressive accumulation in cells leads to the degeneration of nigrostriatal circuits, resulting in several neurodegenerative diseases, such as PD. Cell stress, mutations, and posttranslational modifications disrupt the native Snca conformation exposing the central hydrophobic motif leading to its misfolding and aggregation. Particularly, phosphorylation at serine 129 (S129) has been associated with Snca fibrillation and the formation of cytoplasmic inclusions [31].

Snca clearance is carried out by the ubiquitin-proteosome system (UPS). However, there is no evidence indicating that S129-Snca is a parkin substrate. In contrast, in association with UbcH7, parkin ubiquitinate and promotes the proteasome degradation of *O*-linked glycosylated Snca [32]. Therefore, the decrease in Snca protein levels observed in the present study may be, in part, the result of the degradation of the *O*-linked glycosylated forms.

We previously reported that activation of AhR also results in UbcH7 induction together with a decrease in synphilin-1 (Sncaip) protein levels in the mouse ventral midbrain [16]. These data, together with those reported here, suggest that AhR-mediated increased Parkin and UbcH7 levels may be responsible for the decreased of both the *O*-linked glycosylated Snca and Sncaip protein levels. Snca degradation is also carried on by the autophagy-lysosomal pathway. We have reported recently that TCDD treatment, in an AhR-dependent way, induce the lysosome degradation of NFκB [33]. Thus, it is possible that the observed decrease in Snca is also due to lysosomal degradation.

The above may explain the parkinsonian effects derived from dieldrin exposure [34], a pesticide that has AhR antagonist properties [35]. On the other hand, AhR agonists such as beta-naphthoflavone and chemical mixtures containing AhR agonists such as cigarette smoke protect against MPP^+-induced dopamine depletion [36]. In fact, several epidemiological studies have reported a negative association between PD and cigarette smoking [37,38].

In addition to TCDD and beta-naphthoflavone, a highly toxic

INFORME DE LABORES 2019

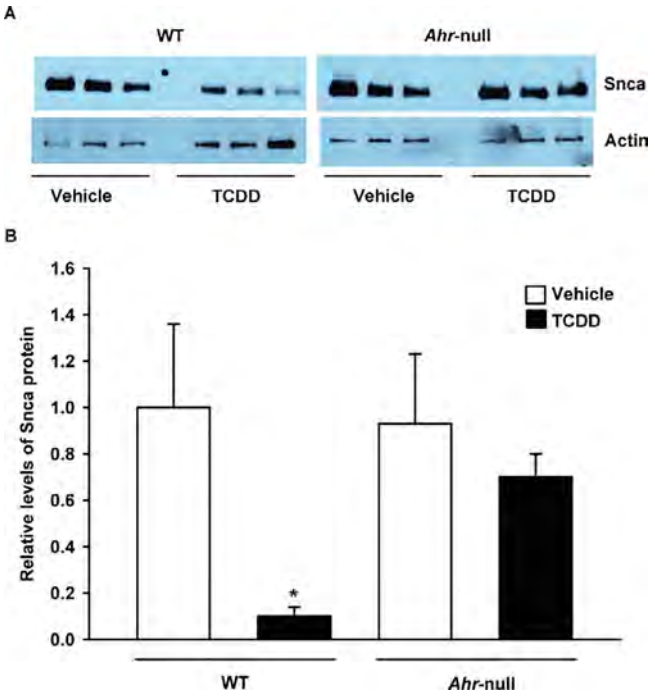

Fig. 7. AhR activation by TCDD results in a decrease in Snca protein levels in the mouse ventral midbrain. Wild-type (WT) and *Ahr*-null mice were treated with a single oral dose of TCDD or corn oil as vehicle, and Snca protein levels were determined by western blotting. Beta actin was used as a loading control (A). Relative Scna protein levels (B). The results are expressed as the mean ± S.D. of samples from three different mice. *p < 0.05, treatment *vs* control.

compounds, several endogenous or natural products such as kynurenine, FICZ (6-formylindolo (3,2b) carbazole), ITE (2-(1′H-indole-3′-carbonyl)-thiazole-4-carboxylic acid methyl ester) and I3C (indole-3-carbinol) act as AhR agonists. In particular, tangeritin, a citrus flavonoid with AhR agonistic activity [39], protects against parkinsonian effects induced by 6-OHDA in a rat model [40]. Similarly, carnosic acid, a diterpene with AhR agonist activity that is found in rosemary extract [41], protects SH-SY5Y cells from 6-OHDA-induced apoptosis [42].

Several investigations have shown that Parkin, in addition to playing a role in neuronal function, may act as a tumor suppressor gene. Mutations in the *PRKN* gene have been reported in colorectal and gastric cancer, lung carcinoma and breast cancer [43,44], while its overexpression inhibits the growth of colon [45], hepatocarcinoma [46], breast [47] and glioblastoma cancer cells [48]. Therefore, the induction of Parkin levels may have an effect on the development of carcinogenic processes.

Taken together, our findings provide *in vivo* and *in vitro* evidence suggesting that Parkin is transcriptionally upregulated by AhR, which is associated with reduced protein levels of Snca in the mouse ventral midbrain. The already established protective role of Parkin in DA neuron survival together with the present data strongly suggest that treatments designed to induce Parkin expression through the use of nontoxic AhR agonist ligands may prevent and delay the onset and progression of neurodegenerative disorders such as PD.

Acknowledgement

This work was supported by Consejo Nacional de Ciencia y Tecnología, México, grants 153377 and 280897.

References

[1] S.J. Kish, K. Shannak, O. Hornykiewicz, Uneven pattern of dopamine loss in the striatum of patients with idiopathic Parkinson's disease. Pathophysiologic and clinical implications, N. Engl. J. Med. 318 (14) (1988) 876–880.
[2] L. Petrucelli, C. O'Farrell, P.J. Lockhart, M. Baptista, K. Kehoe, L. Vink, P. Choi, B. Wolozin, M. Farrer, J. Hardy, M.R. Cookson, Parkin protects against the toxicity associated with mutant alpha-synuclein: proteasome dysfunction selectively affects catecholaminergic neurons, Neuron 36 (6) (2002) 1007–1019.
[3] Y. Yang, I. Nishimura, Y. Imai, R. Takahashi, B. Lu, Parkin suppresses dopaminergic neuron-selective neurotoxicity induced by Pael-R in Drosophila, Neuron 37 (6) (2003) 911–924.
[4] K.F. Winklhofer, Parkin and mitochondrial quality control: toward assembling the puzzle, Trends Cell Biol. 24 (6) (2014) 332–341.
[5] T.D. Helton, T. Otsuka, M.C. Lee, Y. Mu, M.D. Ehlers, Pruning and loss of excitatory synapses by the parkin ubiquitin ligase, Proc. Natl. Acad. Sci. U.S.A. 105 (49) (2008) 19492–19497.
[6] A.B. West, D. Maraganore, J. Crook, T. Lesnick, P.J. Lockhart, K.M. Wilkes, G. Kapatos, J.A. Hardy, M.J. Farrer, Functional association of the parkin gene promoter with idiopathic Parkinson's disease, Hum. Mol. Genet. 11 (22) (2002) 2787–2792.
[7] N. Pankratz, D.K. Kissell, M.W. Pauciulo, C.A. Halter, A. Rudolph, R.F. Pfeiffer, K.S. Marder, T. Foroud, W.C. Nichols, Parkin dosage mutations have greater pathogenicity in familial PD than simple sequence mutations, Neurology 73 (4) (2009) 279–286.
[8] C. Wang, H.S. Ko, B. Thomas, F. Tsang, K.C. Chew, S.P. Tay, M.W. Ho, T.M. Lim, T.W. Soong, O. Pletnikova, J. Troncoso, V.L. Dawson, T.M. Dawson, K.L. Lim, Stress-induced alterations in parkin solubility promote parkin aggregation and compromise parkin's protective function, Hum. Mol. Genet. 14 (24) (2005) 3885–3897.
[9] A.C. Pawlyk, B.I. Giasson, D.M. Sampathu, F.A. Perez, K.L. Lim, V.L. Dawson, T.M. Dawson, R.D. Palmiter, J.Q. Trojanowski, V.M. Lee, Novel monoclonal antibodies demonstrate biochemical variation of brain parkin with age, J. Biol. Chem. 278 (48) (2003) 48120–48128.
[10] C. Lo Bianco, B.L. Schneider, M. Bauer, A. Sajadi, A. Brice, T. Iwatsubo, P. Aebischer, Lentiviral vector delivery of parkin prevents dopaminergic degeneration in an alpha-synuclein rat model of Parkinson's disease, Proc. Natl. Acad. Sci. U.S.A. 101 (50) (2004) 17510–17515.
[11] H. Jiang, Y. Ren, J. Zhao, J. Feng, Parkin protects human dopaminergic neuroblastoma cells against dopamine-induced apoptosis, Hum. Mol. Genet. 13 (16) (2004) 1745–1754.
[12] Y. Ren, H. Jiang, F. Yang, K. Nakaso, J. Feng, Parkin protects dopaminergic neurons against microtubule-depolymerizing toxins by attenuating microtubule-associated protein kinase activation, J. Biol. Chem. 284 (6) (2009) 4009–4017.
[13] B. Liu, R. Traini, B. Killinger, B. Schneider, A. Moszczynska, Overexpression of parkin in the rat nigrostriatal dopamine system protects against methamphetamine neurotoxicity, Exp. Neurol. 247 (2013) 359–372.
[14] O.D. Reyes-Hernandez, A. Mejia-Garcia, E.M. Sanchez-Ocampo, M.A. Cabanas-Cortes, P. Ramirez, L. Chavez-Gonzalez, F.J. Gonzalez, G. Elizondo, Ube2l3 gene expression is modulated by activation of the aryl hydrocarbon receptor: implications for p53 ubiquitination, Biochem. Pharmacol. 80 (6) (2010) 932–940.
[15] A. Mejia-Garcia, E. Gonzalez-Barbosa, C. Martinez-Guzman, M.A. Torres-Ramos, M.S. Rodriguez, S. Guzman-Leon, G. Elizondo, Activation of AHR mediates the ubiquitination and proteasome degradation of c-Fos through the induction of Ubcm4 gene expression, Toxicology 337 (2015) 47–57.
[16] E. Gonzalez-Barbosa, A. Mejia-Garcia, E. Bautista, F.J. Gonzalez, J. Segovia, G. Elizondo, TCDD induces UbcH7 expression and synphilin-1 protein degradation in the mouse ventral midbrain, J. Biochem. Mol. Toxicol. 31 (10) (2017).
[17] J.C. Rowlands, J.A. Gustafsson, Aryl hydrocarbon receptor-mediated signal transduction, Crit. Rev. Toxicol. 27 (2) (1997) 109–134.
[18] Y.J. Bae, K.S. Park, S.J. Kang, Genomic organization and expression of parkin in Drosophila melanogaster, Exp. Mol. Med. 35 (5) (2003) 393–402.
[19] P. Fernandez-Salguero, T. Pineau, D.M. Hilbert, T. McPhail, S.S. Lee, S. Kimura, D.W. Nebert, S. Rudikoff, J.M. Ward, F.J. Gonzalez, Immune system impairment and hepatic fibrosis in mice lacking the dioxin-binding Ah receptor, Science 268 (5211) (1995) 722–726.
[20] P. Huang, S. Ceccatelli, P. Hoegberg, T.J. Sten Shi, H. Hakansson, A. Rannug, TCDD-induced expression of Ah receptor responsive genes in the pituitary and brain of cellular retinol-binding protein (CRBP-I) knockout mice, Toxicol. Appl. Pharmacol. 192 (3) (2003) 262–274.
[21] M.B. Feany, L.J. Pallanck, Parkin: a multipurpose neuroprotective agent? Neuron 38 (1) (2003) 13–16.
[22] K. Wahabi, A. Perwez, M.A. Rizvi, Parkin in Parkinson's disease and cancer: a double-edged sword, Mol. Neurobiol. 55 (8) (2018) 6788–6800.
[23] M. Klinkenberg, S. Gispert, J.A. Dominguez-Bautista, I. Braun, G. Auburger, M. Jendrach, Restriction of trophic factors and nutrients induces PARKIN expression, Neurogenetics 13 (1) (2012) 9–21.
[24] C. Zhang, M. Lin, R. Wu, X. Wang, B. Yang, A.J. Levine, W. Hu, Z. Feng, Parkin, a p53 target gene, mediates the role of p53 in glucose metabolism and the Warburg effect, Proc. Natl. Acad. Sci. U.S.A. 108 (39) (2011) 16259–16264.
[25] L. Bouman, A. Schlierf, A.K. Lutz, J. Shan, A. Deinlein, J. Kast, Z. Galehdar, V. Palmisano, N. Patenge, D. Berg, T. Gasser, R. Augustin, D. Trumbach, I. Irrcher, D.S. Park, W. Wurst, M.S. Kilberg, J. Tatzelt, K.F. Winklhofer, Parkin is transcriptionally regulated by ATF4: evidence for an interconnection between mitochondrial stress and ER stress, Cell Death Differ. 18 (5) (2011) 769–782.
[26] A.B. West, G. Kapatos, C. O'Farrell, F. Gonzalez-de-Chavez, K. Chiu, M.J. Farrer, N.T. Maidment, N-myc regulates parkin expression, J. Biol. Chem. 279 (28) (2004) 28896–28902.
[27] P.S. Knoepfler, P.F. Cheng, R.N. Eisenman, N-myc is essential during neurogenesis

for the rapid expansion of progenitor cell populations and the inhibition of neuronal differentiation, Genes Dev. 16 (20) (2002) 2699–2712.
[28] D.P. Czech, J. Lee, J. Correia, H. Loke, E.K. Moller, V.R. Harley, Transient neuroprotection by SRY upregulation in dopamine cells following injury in males, Endocrinology 155 (7) (2014) 2602–2612.
[29] L. Wu, N. Luo, H.R. Zhao, Q. Gao, J. Lu, Y. Pan, J.P. Shi, Y.Y. Tian, Y.D. Zhang, Salubrinal protects against rotenone-induced SH-SY5Y cell death via ATF4-parkin pathway, Brain Res. 1549 (2014) 52–62.
[30] H.A. Lashuel, C.R. Overk, A. Oueslati, E. Masliah, The many faces of alpha-synuclein: from structure and toxicity to therapeutic target, Nat. Rev. Neurosci. 14 (1) (2013) 38–48.
[31] W.W. Smith, R.L. Margolis, X. Li, J.C. Troncoso, M.K. Lee, V.L. Dawson, T.M. Dawson, T. Iwatsubo, C.A. Ross, Alpha-synuclein phosphorylation enhances eosinophilic cytoplasmic inclusion formation in SH-SY5Y cells, J. Neurosci. 25 (23) (2005) 5544–5552.
[32] H. Shimura, M.G. Schlossmacher, N. Hattori, M.P. Frosch, A. Trockenbacher, R. Schneider, Y. Mizuno, K.S. Kosik, D.J. Selkoe, Ubiquitination of a new form of alpha-synuclein by parkin from human brain: implications for Parkinson's disease, Science 293 (5528) (2001) 263–269.
[33] O. Dominguez-Acosta, L. Vega, E. Estrada-Muniz, M.S. Rodriguez, F.J. Gonzalez, G. Elizondo, Activation of aryl hydrocarbon receptor regulates the LPS/IFNgamma-induced inflammatory response by inducing ubiquitin-proteosomal and lysosomal degradation of RelA/p65, Biochem. Pharmacol. 155 (2018) 141–149.
[34] M.T. Baltazar, R.J. Dinis-Oliveira, M. de Lourdes Bastos, A.M. Tsatsakis, J.A. Duarte, F. Carvalho, Pesticides exposure as etiological factors of Parkinson's disease and other neurodegenerative diseases–a mechanistic approach, Toxicol. Lett. 230 (2) (2014) 85–103.
[35] M. Long, P. Laier, A.M. Vinggaard, H.R. Andersen, J. Lynggaard, E.C. Bonefeld-Jorgensen, Effects of currently used pesticides in the AhR-CALUX assay: comparison between the human TV101L and the rat H4IIE cell line, Toxicology 194 (1–2) (2003) 77–93.
[36] G.S. Shahi, N.P. Das, S.M. Moochhala, 1-Methyl-4-phenyl-1,2,3,6-tetrahydropyridine-induced neurotoxicity: partial protection against striato-nigral dopamine depletion in C57BL/6J mice by cigarette smoke exposure and by beta-naphthoflavone-pretreatment, Neurosci. Lett. 127 (2) (1991) 247–250.
[37] R.B. Godwin-Austen, P.N. Lee, M.G. Marmot, G.M. Stern, Smoking and Parkinson's disease, J. Neurol. Neurosurg. Psychiatry 45 (7) (1982) 577–581.
[38] V. Gallo, P. Vineis, M. Cancellieri, P. Chiodini, R.A. Barker, C. Brayne, N. Pearce, R. Vermeulen, S. Panico, B. Bueno-de-Mesquita, N. Vanacore, L. Forsgren, S. Ramat, E. Ardanaz, L. Arriola, J. Peterson, O. Hansson, D. Gavrila, C. Sacerdote, S. Sieri, T. Kuhn, V.A. Katzke, Y.T. van der Schouw, A. Kyrozis, G. Masala, A. Mattiello, R. Perneczky, L. Middleton, R. Saracci, E. Riboli, Exploring causality of the association between smoking and Parkinson's disease, Int. J. Epidemiol. (2018).
[39] P.B. Busbee, M. Rouse, M. Nagarkatti, P.S. Nagarkatti, Use of natural AhR ligands as potential therapeutic modalities against inflammatory disorders, Nutr. Rev. 71 (6) (2013) 353–369.
[40] K.P. Datla, M. Christidou, W.W. Widmer, H.K. Rooprai, D.T. Dexter, Tissue distribution and neuroprotective effects of citrus flavonoid tangeretin in a rat model of Parkinson's disease, NeuroReport 12 (17) (2001) 3871–3875.
[41] Y. Amakura, M. Yoshimura, M. Takaoka, H. Toda, T. Tsutsumi, R. Matsuda, R. Teshima, M. Nakamura, H. Handa, T. Yoshida, Characterization of natural aryl hydrocarbon receptor agonists from cassia seed and rosemary, Molecules 19 (4) (2014) 4956–4966.
[42] R.H. Fu, L.C. Huang, C.Y. Lin, C.W. Tsai, Modulation of ARTS and XIAP by Parkin is associated with carnosic acid protects SH-SY5Y cells against 6-hydroxydopamine-induced apoptosis, Mol. Neurobiol. 55 (2) (2018) 1786–1794.
[43] J. Liu, C. Zhang, Y. Zhao, X. Yue, H. Wu, S. Huang, J. Chen, K. Tomsky, H. Xie, C.A. Khella, M.L. Gatza, D. Xia, J. Gao, E. White, B.G. Haffty, W. Hu, Z. Feng, Parkin targets HIF-1alpha for ubiquitination and degradation to inhibit breast tumor progression, Nat. Commun. 8 (1) (2017) 1823.
[44] E. Cerami, J. Gao, U. Dogrusoz, B.E. Gross, S.O. Sumer, B.A. Aksoy, A. Jacobsen, C.J. Byrne, M.L. Heuer, E. Larsson, Y. Antipin, B. Reva, A.P. Goldberg, C. Sander, N. Schultz, The cBio cancer genomics portal: an open platform for exploring multidimensional cancer genomics data, Cancer Discov. 2 (5) (2012) 401–404.
[45] G. Poulogiannis, R.E. McIntyre, M. Dimitriadi, J.R. Apps, C.H. Wilson, K. Ichimura, F. Luo, L.C. Cantley, A.H. Wyllie, D.J. Adams, M.J. Arends, PARK2 deletions occur frequently in sporadic colorectal cancer and accelerate adenoma development in Apc mutant mice, Proc. Natl. Acad. Sci. U.S.A. 107 (34) (2010) 15145–15150.
[46] F. Wang, S. Denison, J.P. Lai, L.A. Philips, D. Montoya, N. Kock, B. Schule, C. Klein, V. Shridhar, L.R. Roberts, D.I. Smith, Parkin gene alterations in hepatocellular carcinoma, Genes Chromosom. Cancer 40 (2) (2004) 85–96.
[47] S.P. Tay, C.W. Yeo, C. Chai, P.J. Chua, H.M. Tan, A.X. Ang, D.L. Yip, J.X. Sung, P.H. Tan, B.H. Bay, S.H. Wong, C. Tang, J.M. Tan, K.L. Lim, Parkin enhances the expression of cyclin-dependent kinase 6 and negatively regulates the proliferation of breast cancer cells, J. Biol. Chem. 285 (38) (2010) 29231–29238.
[48] S. Veeriah, B.S. Taylor, S. Meng, F. Fang, E. Yilmaz, I. Vivanco, M. Janakiraman, N. Schultz, A.J. Hanrahan, W. Pao, M. Ladanyi, C. Sander, A. Heguy, E.C. Holland, P.B. Paty, P.S. Mischel, L. Liau, T.F. Cloughesy, I.K. Mellinghoff, D.B. Solit, T.A. Chan, Somatic mutations of the Parkinson's disease-associated gene PARK2 in glioblastoma and other human malignancies, Nat. Genet. 42 (1) (2010) 77–82.

Archives of Medical Research 49 (2018) 456–470

BIOMEDICAL

Therapeutic Intranasal Vaccine HB-ATV-8 Prevents Atherogenesis and Non-alcoholic Fatty Liver Disease in a Pig Model of Atherosclerosis

Roxana Gutiérrez-Vidal,[a] Blanca Delgado-Coello,[a] Kevin Manuel Méndez-Acevedo,[a,b] Sandra Calixto-Tlacomulco,[a] Salvador Damián-Zamacona,[c] and Jaime Mas-Oliva[a]

[a]*Departamento de Bioquímica y Biología Estructural, Instituto de Fisiología Celular, Universidad Nacional Autónoma de México, Ciudad de México, México*
[b]*Max Delbrück-Centrum für Molekulare Medizin, Berlin, Germany*
[c]*Bioextracto, S.A. de C.V., Ciudad de México, México*

Received for publication June 13, 2018; accepted January 22, 2019 (ARCMED_2018_143).

Background and Aims. Atherosclerosis as an inflammatory disease involved in the etiology of cardiovascular disease worldwide, in our days demands an array of different therapeutic approaches in order to soon be able to visualize an effective prevention. Based on an immunotherapeutic approach, we designed a non-invasive vaccine (HB-ATV-8), contained in a micellar nanoparticle composed of lipids and a peptide segment derived from the C-terminus of the cholesterol-ester transfer protein (CETP). Now we extend our successful proof of concept from the rabbit to a porcine model and investigated its effect in an attempt to undoubtedly establish the efficacy of vaccination in a model closer to the human.

Methods. A preclinical trial was designed to study the efficacy of vaccine HB-ATV-8 in pigs (Large White × Landrace). Male experimental animals were fed with standard diet (control), high fat diet (HFD) or the same HFD but treated with HB-ATV-8 (HFD + Vaccine) applied nasally for up to 7 months. All biochemical and enzymatic analyses were performed in peripheral venous blood and thoracic aorta and liver samples examined using conventional, two-photon excitation and second harmonic generation microscopy to identify atherosclerotic and hepatic lesions. mRNA concentrations for *KLF2*, *ACTA2*, *SOD1, COL1A1* genes and protein levels for PPARα and ABCA1 were quantified in aorta and liver respectively using qPCR and Western blot analysis.

Results. The administration of vaccine HB-ATV-8 induced anti-CETP IgG antibodies and reduced atherosclerotic and hepatic lesions promoted by the high fat diet. In addition, plasma triglyceride levels of vaccine treated pigs fed the HFD were similar to those of control group, in contrast to high concentrations reached with animals exclusively fed with HFD. Moreover, HFD promotes a tendency to decrease hepatic PPARα levels and increase in aorta gene expression of *KLF2*, *ACTA2*, *SOD1 and COL1A1*, while vaccine application promotes recovery close to control values.

Conclusions. Vaccine HB-ATV-8 administration constitutes a promissory preventive approach useful in the control of atherogenesis and fatty liver disease. The positive results obtained, the non-invasive characteristics of the vaccine, the simple design employed in its conception and its low production cost, support the novelty of this therapeutic strategy designed to prevent the process of atherogenesis and control the development of fatty liver disease.
© 2019 IMSS. Published by Elsevier Inc. This is an open access article under the CC BY-NC-ND license (http://creativecommons.org/licenses/by-nc-nd/4.0/).

Key Words: Atherogenesis, NAFLD, CETP, Nasal therapeutic vaccine, Porcine model.

Address reprint requests to: Jaime Mas-Oliva, Departamento de Bioquímica y Biología Estructural, Instituto de Fisiología Celular, Universidad Nacional Autónoma de México, Apartado Postal 70-243, 04510 Ciudad de México, México; Phone: (+52) (55) 5622-5584; FAX: (+52) (55) 5622-5611; E-mail: jmas@ifc.unam.mx

0188-4409/Copyright © 2019 IMSS. Published by Elsevier Inc. This is an open access article under the CC BY-NC-ND license (http://creativecommons.org/licenses/by-nc-nd/4.0/).
https://doi.org/10.1016/j.arcmed.2019.01.007

INFORME DE LABORES 2019

Introduction

Atherosclerosis is considered an inflammatory disease of the arterial wall that leads to cardiovascular disease (CVD), a common cause of death in the world according to WHO (1). Epidemiological studies have indicated that among the main risk factors associated with atherosclerosis there is an increased plasma level of low density lipoproteins cholesterol (LDL-C) associated to a decreased plasma concentration of high density lipoprotein cholesterol (HDL-C) (2−4). Nevertheless, the relationship between the concentration of the different plasma lipoproteins and its probability to develop atherosclerosis, is still unclear (5,6). Considering that a reduction of CVD nowadays should be directed towards prevention rather than treatment, there has been an important effort to reinforce measures mainly directed to a change in lifestyle and eating habits in order to impede the onset of atherosclerosis (7,8). Although this approach should be considered central in all prevention efforts, it has contributed little to the prevention of CVD in most countries of the western world (9,10).

From the pharmacologic point of view, although statins for years have offered a way to decrease the plasma concentration of LDL-C by acting upon the biosynthesis pathway of cholesterol, this approach has not been successful enough based on the fact that the number of deaths related to CVD associated with atherosclerosis continues to increase (11,12). Therefore, treatment of atherosclerosis exclusively based on a cholesterol lowering therapy still has to prove a significant efficacy in reducing CVD.

In consequence, considering this process is characterized by the accumulation of fat in the intima of arteries where innate and adaptive immunity play an important role in the process of atherogenesis (13,14), modulation of the immune response has attracted attention as a strategy for its prevention and treatment helping to restore the homeostasis of lipid metabolism and counteract an inflammatory state (15,16). In this sense, the study of several possibilities that contemplate potential proteins have been identified for their ability to decrease morbidity and mortality associated with the progression of atherosclerosis (17,18). Among the diverse strategies employed, the cholesteryl-ester transfer protein (CETP) has been studied as a potential therapeutic target (19−21). CETP promotes the mobilization of cholesteryl-esters, triglycerides and phospholipids between HDL and lipoproteins containing apolipoprotein B (ApoB) (LDL and VLDL) (22). Corresponds to a 66−74 kDa plasma glycoprotein that is mainly expressed in the liver and secreted into the bloodstream where it becomes associated to lipoproteins (23). Population studies have shown that a decreased concentration and/or reduced CETP activity are associated with increased HDL-C levels (23−25), and although several studies present a less clear correlation (26,27), most of them show that subjects presenting a low plasma CETP concentration show a lower probability to develop a cardiovascular event. In support of these findings, there are several reports indicating that a group of Japanese subjects while lacking CETP, present high HDL-C levels, low LDL-C levels and a low incidence of CVD (21,28).

The nasal administration of vaccine HB-ATV-8 composed of a micellar nanoparticle preparation has been designed as an immunotherapy to decrease CETP activity *in vivo*. Vaccine nanoparticles incorporate a 12 amino acid synthetic peptide corresponding to the C-terminal domain of CETP added of an N-terminal cysteine and a key mixture of lipids including caldarchaeol (29,30). As previously reported by us, the use of lysophosphatidylcholine allows the peptide to be kept in a key α-helical conformation (31,32), achieving at the same time structural stability and immunogenicity (33,34). Therefore, here we present an easy, cheap and efficient way to produce immunogenicity by applying a nanoparticulate preparation on the surface of the nasal mucosa.

Previous work from our group employing cholesterol-fed rabbits demonstrated that the nasal administration of vaccine HB-ATV-8 significantly reduces atherosclerotic lesions in the aorta, decreasing in parallel the presence of non-alcoholic fatty liver disease (NAFLD) in association with liver fibrotic lesions (16). This data might be considered important taking into account that CVD has been shown to be the leading cause of death in patients with NAFLD (35,36).

Now, before initiating the clinical phases for vaccine HB-ATV-8 to define safety and efficacy, we have extended our proof of concept to an animal model closer to human and studied the effect of therapeutic vaccine HB-ATV-8 in the pig as the experimental animal. Since the pig closely resembles the human in many traits including its anatomy, physiology, biochemistry and ultimately lifestyle (37−39), it has been considered for years an excellent non-primate model to study atherosclerosis. Therefore, the present study has been conducted for seven months employing pigs in an attempt to closely resemble conditions for the development of atherogenesis and fatty liver in the human.

Materials and Methods

Vaccine HB-ATV-8

Vaccine HB-ATV-8 (Patents US9539312, MX347400 B) contains as immunogen a synthetic peptide that corresponds to the carboxy-end amino acids H486−S496 of CETP (29,30). This peptide conjugated into a micellar nanoparticle system includes three of the four key residues that support lipid binding and transfer capacity (40). Micelles are composed of lipids derived from the cell membrane of *Thermus aquaticus*, mainly caldarchaeol. L-α-Phosphatidylcholine (PC) and 1-lauroyl-2-hydroxy-sn-glycero-3-phosphocholine (lyso-C_{12}PC) (31,32). These components

INFORME DE LABORES 2019

have been shown function as humoral adjuvants promoting a strong cytotoxic T-cell immune response characterized by a long-term memory (41–43).

Experimental Animal Procedures

The present study includes fifteen castrated male pigs (Large White x Landrace) housed at the Specific Pig facility (Barcelona, Spain). All animal procedures and experiments were performed in accordance with the Guide for the Care and Use of Laboratory Animals (NIH) and approved by the Deparment d'Agricultura, Ramaderia, Pesca, Alimentació i Medi Natural, de la Generalitat de Calalunya, and the Specific Pig Ethics Committee. The qualified staff of Specific Pig fed the animals, nasally administered the vaccine, collected blood samples, monitored their well-being, sacrificed the animals and collected tissues at the end of the experiment.

Pigs were housed at 10–24°C on a 12:12 h light/dark cycle in 3.32 m^2 pens (3–4 animals/pen) with a dry, non-toxic, absorbent and pathogen-free bed. The animals had free access to water and fed once daily. At the beginning of the protocol the average weight of animals corresponded to 40 kg. The study was based on three experimental groups: *Control group* (CT, $n = 3$) corresponds to pigs fed a standard diet (Porcs creixement 1, Pinallet) composed of 15.8% calories from protein, 3.5% from carbohydrates, and 3.7% from fat were kept for 4 ($n = 1$) and 7 months ($n = 2$). *High-Fat Diet group* (HFD, $n = 6$) corresponds to pigs fed a high-fat atherogenic diet (HFD) (SDS, 824100 Porcine Western, Dietex, France) for 4 ($n = 4$) and 7 months ($n = 2$). The diet contained 44% calories from fat (15% lard and 2% cholesterol), 16% calories from protein, and 40% calories from carbohydrates. *High-Fat Diet + Vaccine HB-ATV-8 group* (HFD + Vaccine, $n = 6$) corresponds to pigs fed the high-fat atherogenic diet that received vaccine HB-ATV-8 (300 µg) nasally administered twice a week for 4 ($n = 4$) and 7 months ($n = 2$). Blood samples from each experimental animal were taken every four weeks, and the experiment followed in two stages (4 and 7 months) as mentioned above where a certain number of animals at these specific times were anesthetized by intramuscular administration of ketamine (10–33 mg/kg) and midazolam (0.3–0.5 mg/kg), and euthanized with a sodium pentobarbital overdose (50–80 mg/kg, IV). Figure 1 summarizes the experimental protocol followed.

Plasma Lipid Profile and Enzyme Activity Measurements

Fifteen milliliters of peripheral venous blood were collected from the cranial vena cava at the beginning of the study and in a monthly basis till the end of the experiment. Serum and plasma-EDTA samples were used for biochemical and enzyme activity measurements, and the remaining biological material stored at –80°C until analysis. Zoologic Veterinaris laboratory (Barcelona, Spain) performed all lipid and enzymatic measurements. The lipid profile was measured by enzymatic methods following the manufacturers' instructions (Gernon platform, Ral, Spain). Plasma enzyme activity for aspartate aminotransferase, alanine aminotransferase, alkaline phosphatase and total protein concentration were measured by standardized and commercially available colorimetric assays (Gernon platform).

Histological Examination

At the time of euthanasia, the thoracic aorta and liver samples from the right lobule were collected and a portion of these samples fixed in 10% formaldehyde. Samples were embedded in paraffin and stained with hematoxylin-eosin (H&E) and Masson's trichrome stain. The remaining tissue was frozen in liquid nitrogen and stored at −80°C until further analysis. Histological results were obtained by reviewing five different optical fields of view where percentages represent the frequency of the characteristics observed within each group.

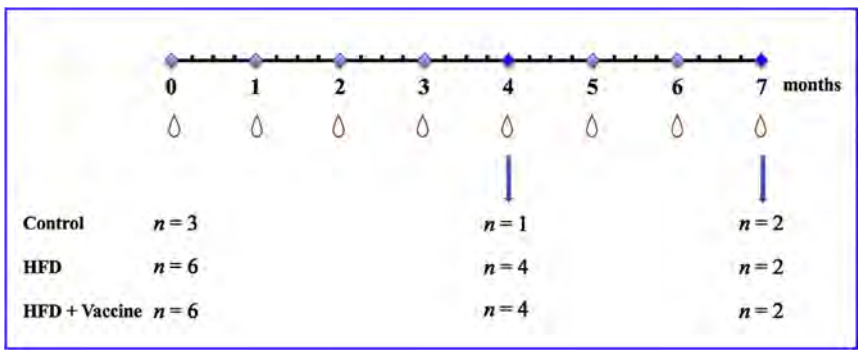

Figure 1. Experimental design. Control group (CT, $n = 3$); one animal from this group sacrificed at month 4 and the remaining two at month 7. High-fat diet group (HFD, $n = 6$); four animals from this group sacrificed at month 4 and the remaining two at month 7. High fat diet + vaccine treatment group (HFD + Vaccine, $n = 6$); four animals from this group sacrificed at month 4 and the remaining two at month 7. Blood samples were taken every month. HFD + vaccine group were administered with vaccine HB-ATV-8 twice a week.

INFORME DE LABORES 2019

Classification of atherosclerotic lesions was performed according to the guidelines of the American Heart Association (AHA) (44). The six aortic lesion types defined by the AHA are: (type I) isolated macrophage foam cells; (type II) intracellular lipid accumulation; (type III) type II changes and small extracellular lipid pools; (type IV) type III changes and presence of an extracellular lipid core; (type V) presence of a lipid core and a fibrotic layer or multiple lipid cores and fibrotic layers, areas of calcification; (type VI) all previous findings plus the presence of areas of hematoma/hemorrhage and thrombus.

Liver sections were evaluated considering histopathological characteristics for NAFLD: steatosis, inflammation, ballooning, and fibrosis (45,46) and data reported as presence or absence of these characteristics.

Two-photon Excitation Microscopy and Second-harmonic Generation Microscopy

Two-photon imaging was performed using a galvanometer-based scanning system LSM 710-Zeiss and a Ti: sapphire laser (Coherent) employing a wavelength of 850 nm (2.5% of laser power) for H&E stained aorta and liver slides. Second-harmonic generation imaging was performed using a wavelength of 900 nm (12% of laser power) and a BP 420−480 nm filter (Zeiss). Images were acquired using water immersion objectives; C-Apochromat 10x and W Plan-Apochromat 20x, with a 40x optical zoom for liver slices.

Anti-CETP Titer Determination

IgG antibody titer for CETP was measured by ELISA. Briefly, plates were coated with CETP synthetic peptide H486-S496, blocked and incubated with pig serum (1:100), a goat horseradish peroxidase-conjugate anti-pig IgG, and tetramethylbenzidine. OD was measured at 450 nm.

Protein Expression Analysis

Liver samples were homogenized in cold RIPA buffer (Thermo Fisher Scientific, MA, USA) supplemented with protease inhibitors (Roche, Rotkreuz, Switzerland). Total protein concentration (serum and liver extracts) was measured using the DC Protein Assay (Bio-Rad, CA, USA). Serum proteins were separated by SDS-PAGE using 8% gels and transferred to PVDF membranes (Immobilon-P, Millipore, MA, USA) to be analyzed by Western blot. Blots were incubated overnight with rabbit anti-CETP (Thermo Fisher Scientific, MA, USA) or mouse anti-ACTB antibodies (Santa Cruz Biotechnology, CA, USA). Also, membranes for liver extracts were incubated with mouse anti-PPARα, anti-ABCA1 and anti-GAPDH antibodies (Santa Cruz Biotechnology, CA, USA). Immunoreactive proteins were visualized with the Immobilon Western Chemiluminiscent HRP reagent (Millipore, MA, USA). Blots were quantified using the Image J software (http://rsb.info.nih.gov/ij/) and results presented as the CETP/ACTB (β-actin) ratio for serum protein and PPARα or ABCA1/GAPDH ratio for liver extracts.

Quantitative PCR Measurements

Total RNA was extracted from the thoracic aortas with Trizol reagent (Thermo Fisher Scientific, MA, USA). 1 μg of total RNA was used to synthesize cDNA using the iScript cDNA synthesis kit (Bio-Rad, CA, USA) and cDNA diluted to perform qPCR experiments. Expression of Krüppel-like factor-2 (*KLF2*), smooth muscle alpha (α)-2 actin (*ACTA2*), superoxide dismutase 1 (*SOD1*), collagen type I alpha 1 (*COL1A1*) and the housekeeping gene *ACTB* was determined by qPCR using the PowerUp Sybr Green Master Mix 2X (Applied Biosystems, CA, USA) on an ABI PRISM 7000 Sequence Detection cycler. Primer sequences are reported as supplementary material as well as relative levels of mRNA calculated as $2^{-\Delta\Delta Ct}$ (Supplementary Table 1).

Statistical Analysis

Data are expressed as mean±S.E.M. Statistical differences among study groups were calculated using ANOVA or Kruskal-Wallis tests, depending on the distribution of variables. p values ≤0.05 were considered significant. Analysis of data was performed with the SPSS v20 program (SPSS, Chicago, USA).

Results

The nasal administration of vaccine HB-ATV-8 induced the formation of anti-CETP IgG antibodies in the group of pigs fed a HFD where the rise in antibody titer became evident after the fourth month of treatment and remained at a high level until the end of the study (Figure 2A). Although the CETP serum concentration was kept at the same level throughout the study in the three groups of experimental animals (Figure 2B), the body weight of pigs fed a HFD was higher compared to those fed a standard diet regardless of whether they received the treatment or not (Figure 2C).

Since it is known that CETP is able to modify the serum level of the different types of lipoproteins by mobilizing cholesteryl-esters and triglycerides, we evaluated if the administration of vaccine HB-ATV-8 altered the serum level for these lipids. As expected, it was found that HFD fed pigs showed a steady increase of total cholesterol, LDL, HDL cholesterol and triglycerides (Figure 3). Interestingly, the only parameter that was significantly modified by the administration of vaccine HB-ATV-8 corresponds to triglycerides that remained at levels similar to the control group (Figure 3D). The serum level for total proteins and

INFORME DE LABORES 2019

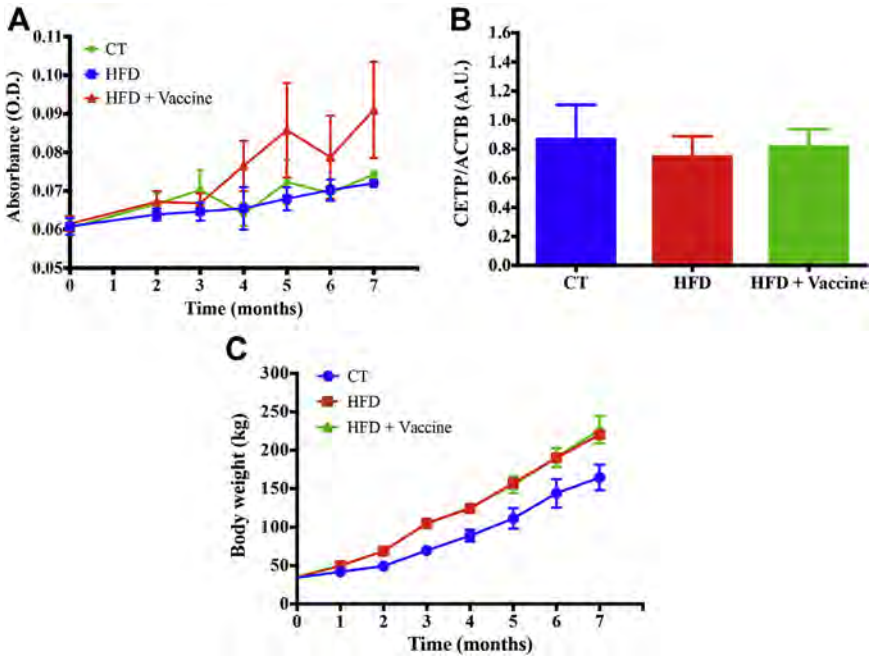

Figure 2. Effect of vaccine HB-ATV-8 administration on IgG anti-CETP antibody production and CETP plasma concentration. (A) Plasma IgG anti-CETP level of pigs from the three experimental groups. (B) Serum CETP concentration from the three experimental groups using Western blot analysis (data expressed as CETP/ACTB ratio). (A) and (B) Data represented as mean ± S.D. (C) Body weight. Control group (CT, $n = 3$); high-fat diet group (HFD, $n = 6$); and high-fat diet group + vaccine (HFD + Vaccine, $n = 6$). Data represented as mean ± S.E.

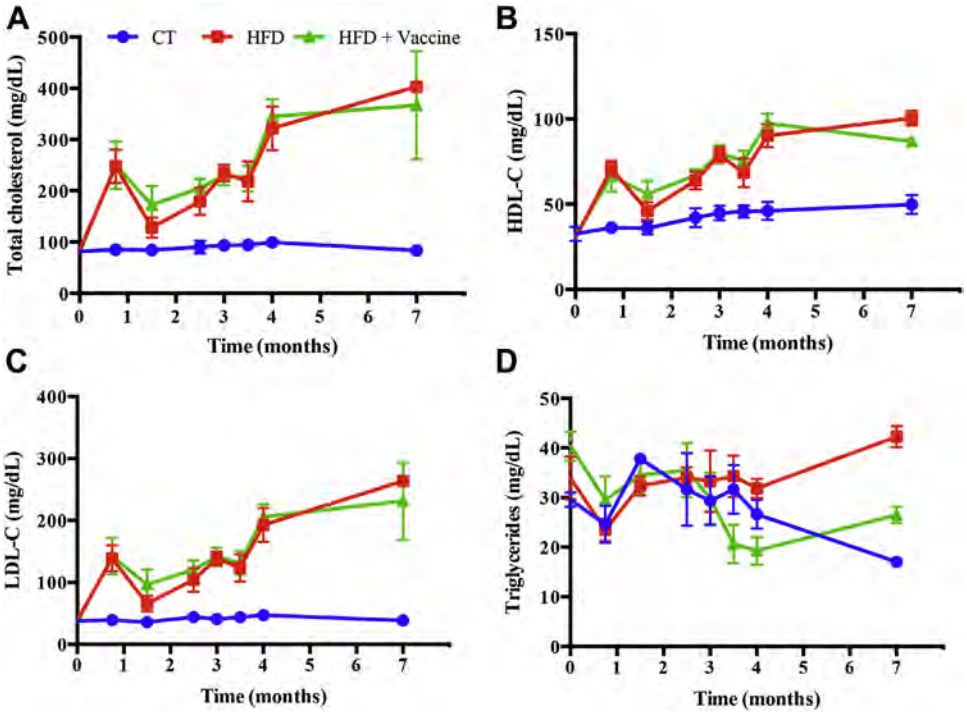

Figure 3. Effect of vaccine HB-ATV-8 administration on serum lipid profiles during the 7 months of treatment. (A) Total cholesterol; (B) HDL-C; (C) LDL-C, and (D) Triglycerides. Control group (CT, $n = 3$); one animal from this group sacrificed at month 4 and the remaining two at month 7. High fat diet group (HFD, $n = 6$); four animals from this group sacrificed at month 4 and the remaining two at month 7. High fat diet + vaccine treatment group (HFD + Vaccine, $n = 6$); four animals from this group sacrificed at month 4 and the remaining two at month 7. Data represented as mean ± S.E.

INFORME DE LABORES 2019

the activity for liver function enzymes such as transaminases and alkaline phosphatase remained stable without statistically significant differences among groups (Supplementary Table 2).

At the end of the experiment, thoracic aorta and liver samples were prepared and examined by conventional light microscopy together with two-photon excitation and second harmonic generation microscopy. Figure 4 shows representative images for samples of the thoracic aorta of pigs belonging to each one of the three experimental groups studied. As expected, aortas from pigs fed the standard diet showed a normal vessel structure. In contrast, pigs fed a HFD show lipid droplets and foam cells in the media and the intima layers of the aorta and an increase of vascular smooth muscle cells (VSMC) in the intima layer (Figure 4A and B) and present type II and III atherogenic

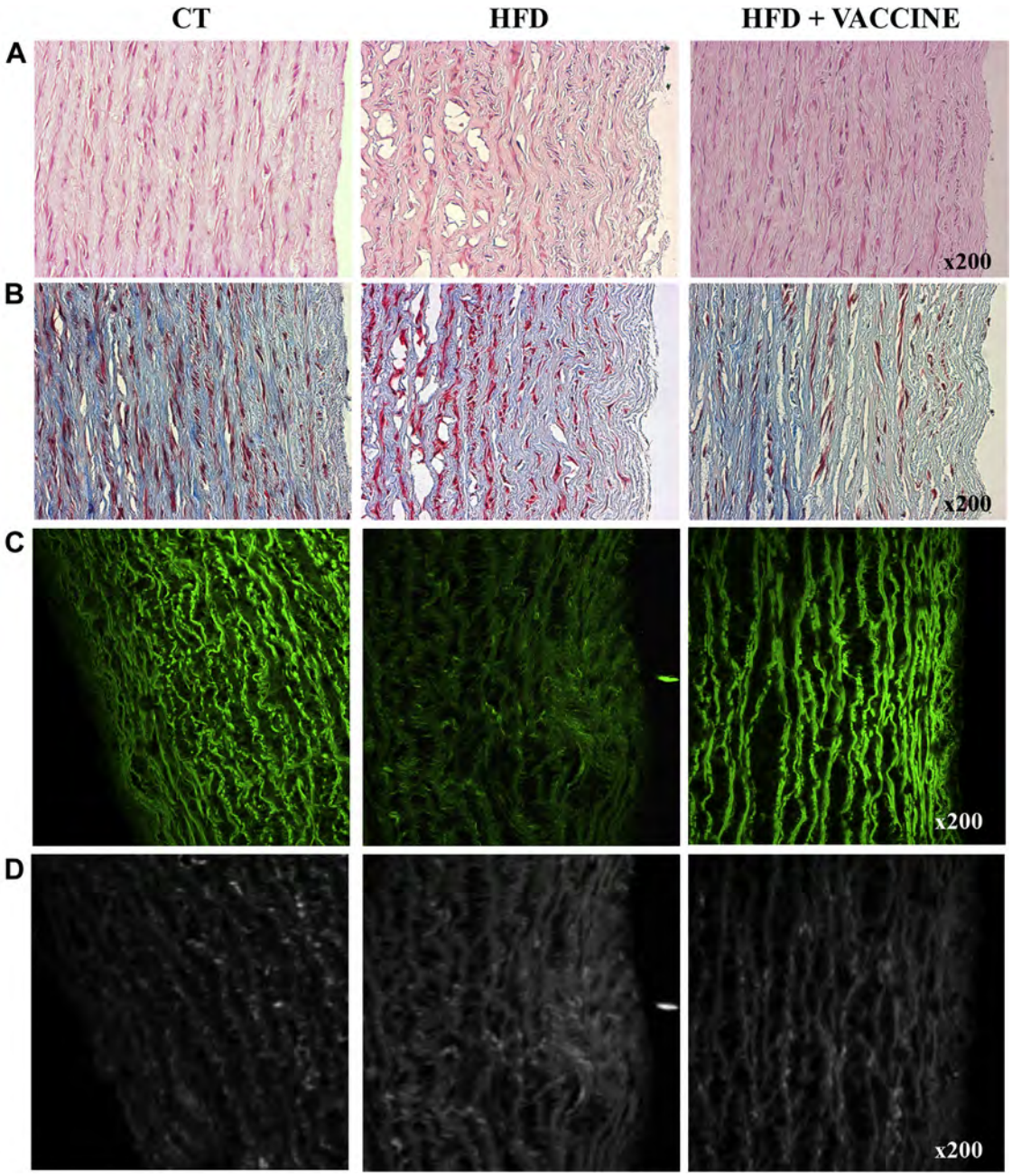

Figure 4. Vaccine HB-ATV-8 prevents the formation of atherosclerotic lesions induced by a HFD. Microscopic analysis of tissue sections from the thoracic aorta of a representative pig from each experimental group. Control group (CT), high fat diet group (HFD), and high fat diet + vaccine group (HFD + Vaccine). (A) Hematoxylin-eosin stain. (B) Masson's trichrome stain. (C) Two-photon excitation microscopy images. (D) Second-harmonic generation microscopy images.

INFORME DE LABORES 2019

lesions (Table 1). Moreover, collagen sheets observed in a widely distributed and spaced fashion, when studied with Masson's trichrome stain show a disordered and unevenly spaced arrangement. This can be clearly observed when the same samples are analyzed by two-photon excitation and second harmonic generation microscopy (Figure 4C and D). Using these imaging techniques, the connective fiber disorder found in aortas of pigs fed a HFD becomes evident denoting an important disarray among the different cell types that compose the vessel wall (Figure 4C and D). In contrast, the group of pigs that received the same HFD but was treated with vaccine HB-ATV-8 exhibit a decreased presence of lipid droplets and foam cells in the intima and media layers, and a smaller number of VSMC in the intima layer, similar to that shown in animals from the control group. More importantly, by two-photon excitation and second harmonic generation microscopy, a better ordered and a less spaced collagen fiber array together with a close to normal cellular architecture is observed (Figure 4C and D). Moreover, 50% of HB-ATV-8 treated pigs do not show any atherosclerotic lesions in their aortas and the remaining 50% only presented type I atherosclerotic lesions, in contrast to animals from the HFD group that showed type II or type III lesions (Table 1).

In order to obtain a better understanding at the molecular level of the histology changes observed with treatment, we analyzed the aortic expression of several genes known to be involved in vascular function such as the Krüppel-like factor-2 (*KLF2*), smooth muscle alpha-actin-2 (*ACTA2*), superoxide dismutase 1 (*SOD1*) and collagen type I alpha 1 (*COL1A1*) (Figure 5). KLF2 corresponds to an atheroprotective transcription factor that regulates expression of several vasoactive endothelial genes involved in the regulation of normal constriction/dilation of VSMCs (47), whereas SOD1 protects cells against cytotoxicity by scavenging superoxide radicals while being also involved in endothelial function by protecting nitric oxide release (48). *COL1A1* has been studied on the fact that corresponds to the most abundant protein associated to collagen fibrils (49). Furthermore, *ACTA2* has been employed as a cell marker for smooth muscle and associated to several occlussive diseases (50,51). So, consistent with tissue damage observed in our histology analysis associated to the HFD, there is a tendency for mRNA levels of these four genes to be upregulated in the aorta when compared to tissue from the control group (Figure 5). Interestingly, in all cases when gene expression is studied in the HFD group that received vaccine HB-ATV-8, the tendency is to go back to levels found associated to aortas from the control group (Figure 5).

We next assessed whether pigs fed a HFD present the typical hepatic alterations observed in NAFLD. Figure 6 shows sections of liver tissue from experimental animals of each group, displaying areas of hepatocytes around the central lobular vein. Hepatic tissue from control pigs presents the normal lobular histological characteristics. In contrast, hepatocytes from livers coming from pigs fed a HFD show microvesicular fat accumulation and signs of ballooning and inflammation. Interestingly, when the HFD + Vaccine group was examined, the frequency of these pathological features was considerably reduced (Table 2). It is important to mention that when compared to our previous findings employing a rabbit model (16), the current results show a less dramatic effect that might be related to the fact that the porcine model is considered refractory to develop not only fatty liver disease but also atherosclerosis in the same way as humans do (52). Nevertheless, when liver slides are studied by two-photon excitation and second harmonic generation microscopy, experimental animals from the HFD + Vaccine group, in comparison to the group that did not receive the vaccine, showed a decreased collagen deposition around the perisinusoidal and periportal areas and in general less fibrosis showing images close to the ones found in control tissue (Figure 6C and D).

Again, in order to initiate the exploration at the molecular of events that might be taking place with the administration of vaccine HB-ATV-8, we measured in liver tissue protein expression for the ATP-binding cassette transporter (ABCA1) defined as a cholesterol transporter that plays an important role in the homeostasis of cholesterol in the liver (53), and PPARα, reported to mediate fatty acid metabolism

Table 1. Effectiveness of vaccine HB-ATV-8 in decreasing aortic atherosclerotic lesions induced by a high fat diet measured at 4 and 7 months of treatment

	CT			HF			HF +VACCINE		
Lesion type	4 months (n = 1)	7 months (n = 2)	Total (n = 3)	4 months (n = 4)	7 months (n = 2)	Total (n = 6)	4 months (n = 4)	7 months (n = 2)	Total (n = 6)
TI	0	0	0	0	0	0	3 (75)	0	3 (50)
TII	0	0	0	3 (75)	1 (50)	4 (66.6)	0	0	0
TIII	0	0	0	1 (25)	0	1 (16.7)	0	0	0

CT, control group fed a standard diet; HFD, group fed a high fat diet; HFD + Vaccine, group fed a high fat diet + nasal administration of vaccine.
The histological classification of atherosclerotic lesions was carried out according to the American Heart Association guidelines (44).
Data in parenthesis represent percentage frequency within the specific number of experimental animals studied in each group.

INFORME DE LABORES 2019

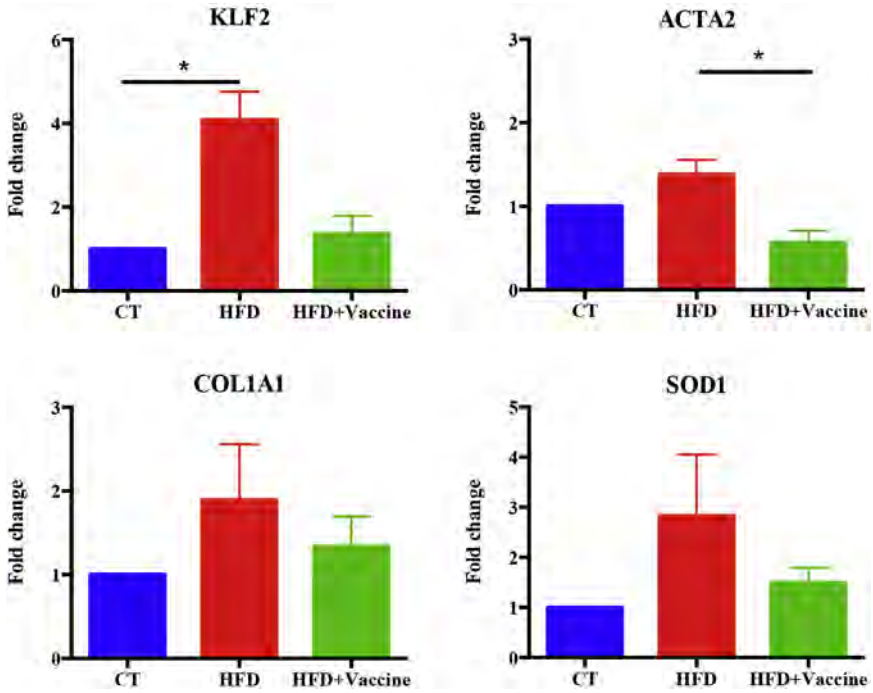

Figure 5. Vaccine HB-ATV-8 global effect on gene expression of *KLF2, ACTA2, COL1A1* and *SOD1* measured by qPCR in thoracic aorta samples. Control group (CT, $n = 3$), high fat diet group (HFD, $n = 6$), and high fat diet + vaccine treatment group (HFD + Vaccine, $n = 6$). Data presented as fold change with respect to actin expression. Data represented as mean ± S.E. $*p < 0.05$.

in the hepatocyte (54). Our analysis shows that although ABCA1 apparently is not significantly modified neither on animals fed with a HFD nor animals fed the HFD plus vaccine administration, there is a tendency for PPARα to increase in pigs fed a HFD that received the vaccine when compared to the HFD and control groups (Figure 7). These findings might support the possibility that a molecular compensatory effect at the cellular level might not only be carried out by the anti-CETP antibody but also by the peptide itself or one of the lipid components of vaccine HB-ATV-8.

Discussion

Since immunomodulation of key proteins that control the metabolism of cholesterol has been proposed as a prophylactic tool to treat atherosclerosis, vaccine HB-ATV-8 has been designed as a therapeutic strategy to reduce the development of atherosclerosis by generating autoantibodies against CETP. With support on our successful proof of concept carried out in the rabbit, vaccine HB-ATV-8 now has been tested in a porcine model. The pig as an experimental animal has gained interest in recent years since it has been shown that the evolutionary distance among many animal models used today, especially between rodents and humans, is a distant one (37). Preclinical studies performed in murine models can be useful in identifying new biochemical mechanisms or molecules and provide a platform for pharmacological development; nevertheless, as shown in the literature in many cases translation to a clinical setting has proven to be a difficult one. In contrast, the pig and the human share many characteristics, such as a similar anatomy and cardiovascular physiology, a situation that explains why cardiac output, mean arterial pressure and stroke volume are almost equivalent (55). Although the process of atherogenesis in pigs is difficult to develop given that many strains of farm pigs along time have been normally selected for an increase in protein deposition rather than fat accumulation (56), a HFD supplemented with cholesterol eventually promotes the development of artery lesions similar to those observed in the atherosclerotic disease in the human (5,57,58). Therefore, taking into account these considerations, the pig model can be considered an optimal model for the study of atherosclerosis and associated diseases such as NAFLD (59). Employing this experimental model and the use of a novel nanoparticle composition that serves as an immunogen when placed in the nasal mucosa, our study shows that modulation of the immune response continues to be a promising approach in the prevention of atherogenesis.

The present study shows that intranasal administration of vaccine HB-ATV-8 induces anti-CETP IgG antibodies, in turn reducing in parallel the presence of atherosclerotic lesions and hepatic damage in pigs fed a HFD. These results are also related to the fact that serum triglycerides remain at control values, in contrast to the not treated animal group fed a HFD. Even though triglycerides are not considered

INFORME DE LABORES 2019

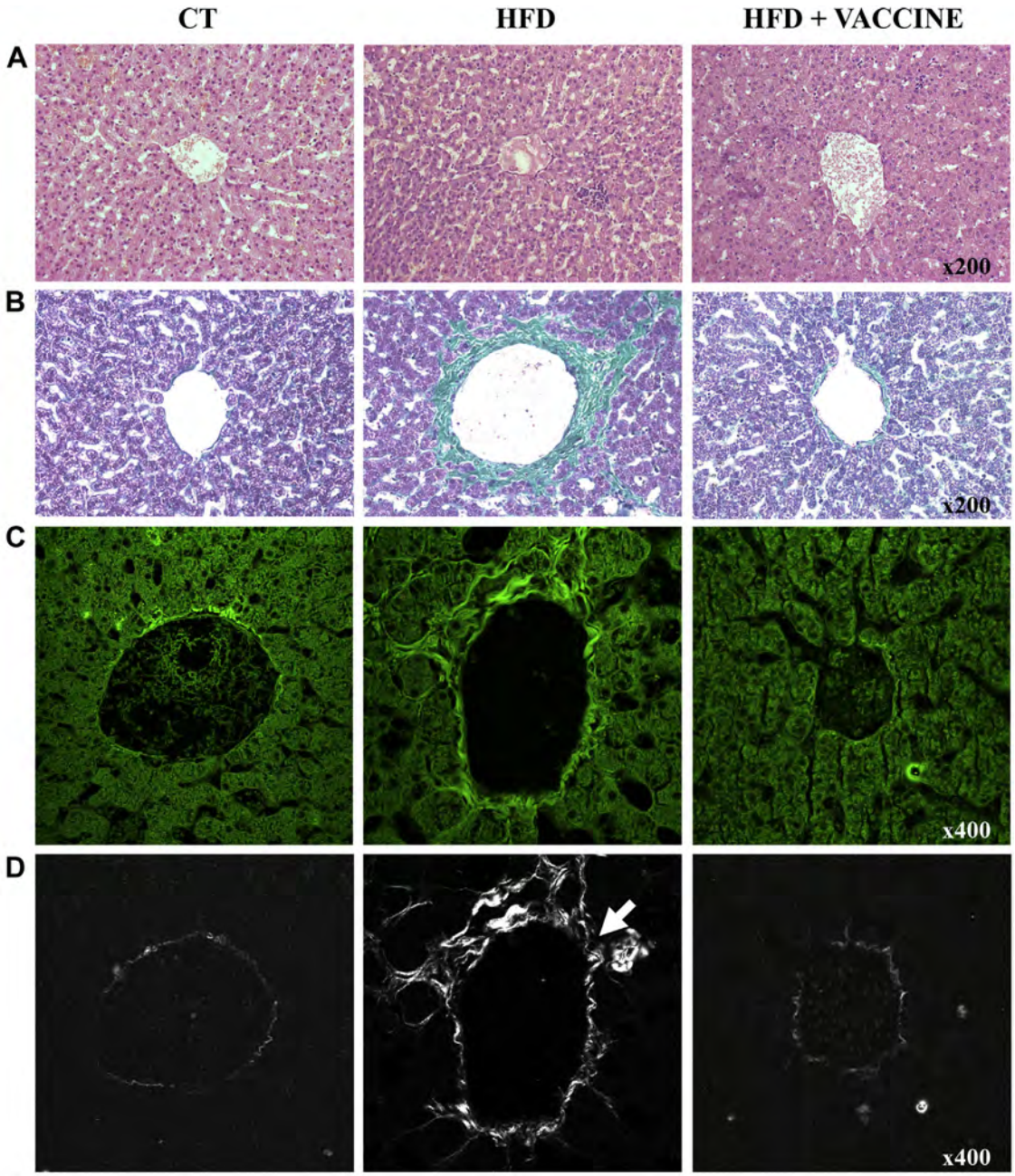

Figure 6. Vaccine HB-ATV-8 reduces hepatic inflammation and fibrosis induced by a HFD. Images show the central lobular vein from a liver sample of a representative pig from each experimental group. Control group (CT), high fat diet group (HFD), and high-fat diet + vaccine group (HFD + Vaccine). (A) Hematoxylin-eosin stain. (B) Masson's trichrome stain. (C) Two-photon excitation microscopy images. (D) Second-harmonic generation microscopy images. Arrow shows the presence of fibrosis.

atherogenic, it is well known that serum levels for this family of lipids are considered as a biomarker for CVD risk. This can be partially explained by their direct association with remnant lipoproteins and ApoCIII, a proinflammatory and proatherogenic apolipoprotein that inhibits the binding of ApoE and ApoB to proteoglycans and hepatic receptors, preventing clearance of these type of lipoproteins and therefore favoring their accumulation in the endothelium (60–63).

During an early stage of atherogenesis, cholesterol and other lipids penetrate the intima of arteries where their accumulation induce an inflammatory state and the activation of the immune system. As a consequence, macrophages infiltrate the tissue, start internalizing cholesterol and originate the formation of foam cells (44). Subsequently, foam cells are lysed, releasing lipids that further accumulate in the extracellular matrix. To decrease toxicity due to the extracellular deposition of lipids (64,65), VSMCs

INFORME DE LABORES 2019

Table 2. Vaccine HB-ATV-8 reduced hepatic inflammation and fibrosis induced by a high fat diet measured at 4 and 7 months of treatment

	CT			HF			HF + vaccine		
Histologic lesion	**4 months (n = 1)**	**7 months (n = 2)**	**Total (n = 3)**	**4 months (n = 4)**	**7 months (n = 2)**	**Total (n = 6)**	**4 months (n = 4)**	**7 months (n = 2)**	**Total (n = 6)**
Steatosis[a]	0	0	0	1 (25)	1 (50)	2 (33.3)	1 (25)	1 (50)	2 (33.3)
Ballooning	0	1	1 (33.3)	3 (75)	1 (50)	4 (66.7)	1 (25)	2 (50)	3 (50)
Inflammation	0	0	0	4 (100)	2 (100)	6 (100)	1 (25)	2 (100)	3 (50)
Fibrosis	0	0	0	4 (100)	2 (100)	6 (100)	2 (50)	1 (50)	3 (50)

CT, Control group fed a standard diet; HF, group fed a high-fat diet; HFD + Vaccine, group fed a high fat diet + nasal administration of vaccine.
Data represent number of cases by each category and data in parenthesis percentage frequencies.
Fibrosis reported in these samples was mainly portal or perisinusoidal and portal/periportal fibrosis.
[a]Microvesicular steatosis.

migrate and begin internalizing excess lipid in support of macrophage function. Although VSMCs are responsible for remodeling the arterial wall, a prolonged state of oxidative stress causes their trans-differentiation to macrophage-type cells (66). These cells are able to phagocytize and present antigens, favoring the inflammatory state (67,68). Moreover, the structure of the arterial wall specifically depends on a delicate equilibrium between the synthesis and degradation of extracellular matrix proteins such as collagen and elastin, where an acute change in this equilibrium might play an important role during the process of atherogenesis. In this sense, an uncontrolled degradation of proteins of the extracellular matrix carried out by proteases such as metalloproteinase-1 and -9, might induce further vascular damage. This in turn promotes atherogenesis through the trans-endothelial migration of leukocytes, migration and proliferation of VSMCs, neovascularization, vascular cell apoptosis, and finally the formation of a neointima that might progress until the rupture of the aortic wall takes place (69). Together with cells of the immune system involved in atherosclerosis such as monocytes converted into macrophages, new studies have pointed to mast cells and stellar cells as critical cell types important in collagen degradation and smooth muscle survival (70). Mast cells produce and release matrix metalloproteases together with proinflammatory molecules such as interferon and interleukin-6 inhibiting the proliferation of smooth muscle cells and also promoting the process of apoptosis (70–73).

Since the use of two-photon excitation and second harmonic generation microscopy has been extremely useful to study the extracellular matrix and to visualize collagen fibers in association to a classical light microscopy, the study of viable arteries *ex vivo* gives us a better understanding of the functionality and dynamic behavior of the artery wall (74,75). During the course of our study, we observed that vaccinated animals fed a HFD did not show the clear disarray of extracellular matrix observed in the aortas of

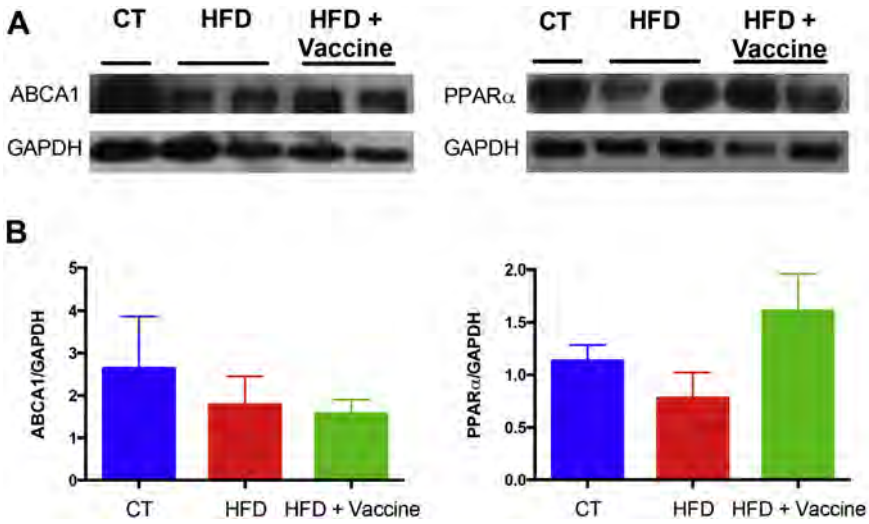

Figure 7. Vaccine HB-ATV-8 effect on hepatic PPARα and ABCA1 concentration. (A) Western blot analysis of samples obtained from one representative control animal and two representative samples from the HFD and HFD + vaccine groups. (B) Semicuantitative protein correlation between expression of ABCA1 and PPARα with GAPDH. Control group (CT, n = 3), high fat diet group (HFD, n = 6), and high fat diet + vaccine treatment group (HFD + Vaccine, n = 6). Data represented as mean ± S.E.

INFORME DE LABORES 2019

animals that were only fed a HFD without vaccination. This phenomenon is shown to be accompanied by an increased expression of *KLF2, ACTA2, COL1A1 and SOD1* mRNA's in the aortas of animals fed exclusively the HFD. Interestingly, this increase in mRNA levels is reversed close to control values in animals fed a normal diet when the HFD plus vaccination group is studied, suggesting that vaccine HV-ATV-8 might be also considered as a modulator of anti-atherosclerotic signals. It is well known that a HFD induces vascular dysfunction upregulating pathways associated to the production of reactive oxygen species (ROS), oxidative stress, and release of proinflammatory adipokynes/cytokynes (76–78). KLF2 inhibits both the expression of inflammatory cytokynes and the production of adhesion molecules such as VCAM-1 and E-selectin, known to be critical for leukocytes recruitment and extravasation (79,80). In addition, aortas from pigs fed a HFD show a disordered pattern of collagen fibrils, that to a certain extent, is less apparent in aortas isolated from animals fed the HFD plus vaccination, also in agreement with results showing a tendency to present a lower mRNA concentration and synthesis of type I collagen. Interestingly, during the development of an atherosclerotic plaque, the extracellular matrix composition of a vessel undergoes pronounced changes, where VSMCs initially showing a contractile phenotype are transformed to present a synthetic phenotype with the consequent increase in the deposit of types I and III collagen, elastin and fibronectin (49).

On the other hand, steatohepatitis and atherosclerosis share several characteristics such as lipid accumulation and the development of an inflammatory state (45,81). During the present study, pigs fed a HFD in addition to the presence of atherosclerotic changes, also developed hepatic disease characterized by microvesicular steatosis, ballooning, cellular inflammation, and fibrosis. Two-photon and second harmonic generation imaging clearly show the enormous difference in collagen deposition observed in liver tissue obtained from the group of animals exclusively fed the HFD and those treated simultaneously with vaccine HB-ATV-8. In general, experimental animals fed the HFD independently if they received or not the vaccine, do not show macrovesicular steatosis. This phenomenon is most probably due to the relatively short period of time used to carry out the study before animal sacrifice (56). Nevertheless, the presence of inflammation and fibrosis was less evident in the HFD + Vaccine group in comparison to HFD fed pigs.

The tendency for PPARα to increase in liver cells of animals fed a HFD that received the vaccine supports an explanation for the reduced level of plasma triglycerides found in this group of animals. PPARα considered a transcription factor that regulates the expression of genes involved in VLDL production, lipid trafficking and triglyceride-rich lipoprotein clearance, apparently helps suppress the acute-phase response and inflammation in the liver (82–84) and in conjunction with PPARβ/δ, shown to improve steatosis, inflammation and fibrosis in preclinical models of NAFLD (83,85).

Since our findings show that vaccine HB-ATV-8 decreases fat accumulation and most probably an inflammatory state in the artery wall and liver, it is important to point out that even though an auto-anti-CETP antibody titer was clearly detected around 4 months of treatment, at this time the effect was already observed. We also hypothesize that in addition to the regulation of lipid transport carried out by CETP due to the effect of the auto-anti-CETP antibody, there might be additional protective mechanisms that could be also related to a direct effect given by one of the components of the vaccine preparation, such as the peptide itself. This possibility is supported by studies of a series of peptides that promote the efflux of cholesterol from cells (86). Our group has also shown using cultured macrophages, a decrease in foam cell formation and down-regulation of CD36 and ACAT-1 when the peptide itself is tested (87,88). Evidence also shows that several other peptides interacting with endothelial cells, VSMCs, monocytes and/or macrophages, might be used for therapeutic purposes in the control of atherosclerosis (89–91). Since the HFD group independently if vaccinated or not maintain the same gain in body weight along the study, we speculate that vaccine HB-ATV-8 might also promote the accumulation of lipids in other tissues such as the adipose tissue. Current experiments are being carried out to establish this possibility.

Among the series of drugs offering to decrease the risk of cardiovascular disease by increasing the serum concentration of HDL-C, several CETP inhibitors obtained by chemical synthesis have been studied (92). Several other strategies include the use of fibrates (93) and antioxidants (94), but at the end also apparently ineffective to decrease the risk of CVD. Considering CETP as a plasma protein that transfers cholesteryl-esters among lipoproteins, specifically HDL to VLDL and LDL, it has been described as a molecule that promotes atherogenesis; therefore, the potential inhibition of its activity by new molecules has attracted attention in an effort to increase HDL-C and decrease coronary artery disease (95). Nevertheless, the use of these chemically synthesized compounds in the strategy to inhibit CETP has shown to be troublesome (92,95,96). Torcetrapib was the first CETP inhibitor to be tested in Phase 3 clinical trials, but had to be prematurely terminated due to a series of cardiovascular problems and mortality associated with non-cardiovascular events (97–100) such as infection and off-target aldosteronism as presented in the ILLUMINATE, RADIANCE and ILUSTRATE trials (97,100,101). These studies showed an increase in HDL-C and a decrease in LDL-C but no impact in the presence of atheroma lesions (100,102).

During the Phase 2 clinical trial of CETP inhibitor dalcetrapib, the study had to be stopped due to off-target side

INFORME DE LABORES 2019

effects and ineffectiveness shown by a non-significant effect on plasma LDL-C levels despite a moderate increase in HDL-C (103). Also, the OUTCOMES phase 3 trial had to be halted due to a lack of clinically meaningful efficacy (104). Although evacetrapib also improved lipoprotein biomarker distribution, treatment did not result in a lower rate of cardiovascular events among patients with high-risk vascular disease (105). So far, anacetrapib seems to show a better effect on various coronary events studying patients presenting atherosclerotic vascular disease but only under intensive statin therapy (106). Taken these data together, due to the presence of side effects and off-target activity, there seems that chemically synthesized CETP inhibitors need more time to be completely understood.

The example of torcetrapib could be considered a prototypical one since we now know that CETP binding sites for this molecule are shared with proteins of the Plunc family including an isoform of CETP named by our group as CETPI and identified as a lipopolysaccharide binding protein (107). According to our results, an non-specific binding phenomenon might have been directly related to sepsis and the mortality rate shown in the ILLUMINATE trial (108−110) since torcetrapib might have had an unknown secondary effect disabling the main function of CETPI directly related with the inactivation of LPS in plasma.

In contrast to the several strategies discussed in this study used to inhibit the function of CETP, the induction of an immune response by self-generating anti-CETP antibodies shows many advantages above other approaches to treat the process of atherogenesis (20,111−113). The present investigation studying a porcine model corroborates our previous reports showing that intranasal therapeutic vaccine HB-ATV-8 is effective in the control of the process of atherogenesis and the development of fatty liver disease, associated to important advantages such as simplicity of design and application combined to a low production cost.

Conclusion

Considering that for many years no new synthesis of lipid metabolism modulator molecules have been successfully introduced into clinical practice, the immunological approach using the generation of autoantibodies against key proteins involved in the physiopathology of atherosclerosis have come into play. Among the several immunological approaches used to inhibit CETP function, vaccine HB-ATV-8 seems to be the only one that offers non-invasive intranasal vaccination employing a micellar nanoparticle preparation composed of a mixture of common lipids and a peptide together with the use a simple delivery device. Since vaccination ameliorates atherosclerotic and hepatic lesions caused by a HFD improving triglyceride metabolism and promoting atheroprotective and anti-inflamatory signals, vaccine HB-ATV-8 offers a brand new approach to prevent the process of atherogenesis and associated NAFLD in the human.

Acknowledgments

This study was supported by grants from CONACyT, Mexico (255778) and PAPIIT-UNAM (IN205717), Mexico awarded to J.M-O. Support also came from CONACyT (grants 219327, 222227 and 233172) awarded to Bioextracto S.A. de C.V. and development grant HB08 received from Hamol Biosolutions LLC. R.G-V received a postdoctoral fellowship from UNAM. Authors thank Yazmín Ramiro-Cortés for expert advice with microscopy techniques, the Molecular Biology Unit at IFC, UNAM; members of the Oligonucleotide and DNA Sequencing Unit at IBT, UNAM; and Jorge Bravo-Martínez for fruitfull discussions and help with graphical art. We appreciate the generous donation of several monoclonal antibodies from Santa Cruz Biotechnology. This study is dedicated to the memory of Ale.

Supplementary Data

Supplementary data related to this article can be found at https://doi.org/10.1016/j.arcmed.2019.01.007.

References

1. Mozaffarian D, Benjamin EJ, Go AS, et al. Heart disease and stroke statistics-2016 update a report from the American Heart Association. Circulation 2016;133:e38−e48.
2. Sharrett AR, Ballantyne CM, Coady SA, et al. Coronary heart disease prediction from lipoprotein cholesterol levels, triglycerides, lipoprotein(a), apolipoproteins A-I and B, and HDL density subfractions: The atherosclerosis risk in communities (ARIC) study. Circulation 2001;104:1108−1113.
3. Goldbourt U, Yaari S, Medalie JH. Isolated low HDL cholesterol as a risk factor for coronary heart disease mortality: A 21-year follow-up of 8000 men. Arterioscler Thromb Vasc Biol 1997;17:107−113.
4. Franceschini G. Epidemiologic evidence for high-density lipoprotein cholesterol as a risk factor for coronary artery disease. Am J Cardiol 2001;88:9−13.
5. Padró T, Cubedo J, Camino S, et al. Detrimental effect of hypercholesterolemia on high-density lipoprotein particle remodeling in pigs. J Am Coll Cardiol 2017;70:165−178.
6. Niesor EJ. Different effects of compounds decreasing cholesteryl ester transfer protein activity on lipoprotein metabolism. Curr Opin Lipidol 2011;22:288−295.
7. Amy SM. Expanding the therapeutic frontier in atherosclerosis. J Cardiovasc Pharmacol 2013;62:237−238.
8. Thompson PD, Buchner D, Piña IL, et al. Exercise and Physical Activity in the Prevention and Treatment of Atherosclerotic Cardiovascular Disease: A Statement From the Council on Clinical Cardiology (Subcommittee on Exercise, Rehabilitation, and Prevention) and the Council on Nutrition, Physical Activity, and Metabolism (Subcommittee on Physical Activity). Circulation 2003;107:3109−3116.
9. Dalen JE, Devries S. Diets to prevent coronary heart disease 1957−2013: What have we learned? Am J Med 2014;127:364−369.
10. Pater C. The current status of primary prevention in coronary heart disease. Curr Control Trials Cardiovasc Med 2001;2:24−37.
11. Okuyama H, Langsjoen PH, Hamazaki T, et al. Statins stimulate atherosclerosis and heart failure: pharmacological mechanisms. Expert Rev Clin Pharmacol 2015;8:189−199.
12. Shapiro MD, Fazio S. From lipids to Inflammation: New approaches to reducing atherosclerotic risk. Circ Res 2016;118:732−749.

INFORME DE LABORES 2019

13. Witztum JL, Lichtman AH. The influence of innate and adaptive immune responses on atherosclerosis. Annu Rev Pathol 2014;9:73–102.
14. Libby P, Lichtman AH, Hansson GK. Immune effector mechanisms implicated in atherosclerosis: from mice to humans. Immunity 2013; 38:1092–1104.
15. Kimura T, Tse K, Sette A, et al. Vaccination to modulate atherosclerosis. Autoimmunity 2015;48:152–160.
16. García-González V, Delgado-Coello B, Pérez-Torres A, et al. Reality of a vaccine in the prevention and treatment of atherosclerosis. Arch Med Res 2015;46:427–437.
17. Chyu KY, Shah PK. Advances in immune-modulating therapies to treat atherosclerotic cardiovascular diseases. Ther Adv Vaccines 2014;2:56–66.
18. de Jager SCA, Kuiper J. Vaccination strategies in atherosclerosis. Thromb Haemost 2011;106:796–803.
19. Chyu KY, Dimayuga PC, Shah PK. Vaccine against arteriosclerosis: an update. Ther Adv Vaccines 2017;5:39–47.
20. Liaw YW, Lin CY, Lai YS, et al. A vaccine targeted at CETP alleviates high fat and high cholesterol diet-induced atherosclerosis and non-alcoholic steatohepatitis in rabbit. PLoS One 2014;9:e111529.
21. Mabuchi H, Nohara A, Inazu A. Cholesteryl ester transfer protein (CETP) deficiency and CETP inhibitors. Mol Cells 2014;37: 777–784.
22. Barter PJ, Rye K-A. Cholesteryl ester transfer protein inhibition as a strategy to reduce cardiovascular risk. J Lipid Res 2012;53: 1755–1766.
23. Barter PJ, Brewer HB, Chapman MJ, et al. Cholesteryl ester transfer protein: a novel target for raising HDL and inhibiting atherosclerosis. Arterioscler Thromb Vasc Biol 2003;23:160–167.
24. Inazu A, Brown ML, Hesler CB, et al. Increased high-density lipoprotein levels caused by a common cholesteryl-ester transfer protein gene mutation. N Engl J Med 1990;323:1234–1238.
25. Brown ML, Inazu A, Hesler CB, et al. Molecular basis of lipid transfer protein deficiency in a family with increased high-density lipoproteins. Nature 1989;342:448–451.
26. Ritsch A, Scharnagl H, Eller P, et al. Cholesteryl ester transfer protein and mortality in patients undergoing coronary angiography: the Ludwigshafen Risk and Cardiovascular Health study. Circulation 2010;121:366–374.
27. Vasan RS, Pencina MJ, Robins SJ, et al. Association of circulating cholesteryl ester transfer protein activity with incidence of cardiovascular disease in the community. Circulation 2009;120:2414–2420.
28. Inazu A, Mabuchi H. Therapeutic implications of cholesteryl ester transfer protein inhibitors in hyperlipidemia and low high-density lipoprotein-cholesterolemia. Curr Opin Investig Drugs 2003;4: 291–297.
29. Mas-Oliva J, Delgado-Coello BA, Gonzalez-García VG, et al, Inventors. Universidad Nacional Autónoma de México, assignee. Vacuna de aplicación nasal contra el desarrollo de la enfermedad aterosclerótica y el hígado graso. MX Patent 2017;347:400B.
30. Mas-Oliva J, Delgado-Coello BA, Gonzalez-García VG, et al, Inventors. Universidad Nacional Autónoma de México, assignee. Nasal vaccine against the development of atherosclerosis disease and fatty liver. US Patent 9 2017;539:312B2.
31. García-González V, Gutiérrez-Quintanar N, Mendoza-Espinosa P, et al. Key structural arrangements at the C-terminus domain of CETP suggest a potential mechanism for lipid-transfer activity. J Struct Biol 2014;186:19–27.
32. García-González V, Mas-Oliva J. Amyloid fibril formation of peptides derived from the C-terminus of CETP modulated by lipids. Biochem Biophys Res Commun 2013;434:54–59.
33. Kaur G, Garg T, Rath G, et al. Archaeosomes: an excellent carrier for drug and cell delivery. Drug Deliv 2016;23:2497–2512.
34. Benvegnu T, Lemiègre L, Cammas-Marion S. New generation of liposomes called archaeosomes based on natural or synthetic archaeal lipids as innovative formulations for drug delivery. Recent Pat Drug Deliv Formul 2009;3:206–220.
35. DeFilippis AP, Blaha MJ, Martin SS, et al. Nonalcoholic fatty liver disease and serum lipoproteins: the Multi-Ethnic Study of Atherosclerosis. Atherosclerosis 2013;227:429–436.
36. Fleischman MW, Budoff M, Zeb I, et al. NAFLD prevalence differs among hispanic subgroups: the Multi-Ethnic Study of Atherosclerosis. World J Gastroenterol 2014;20:4987–4993.
37. Getz GS, Reardon CA. Animal models of atherosclerosis. Arterioscler Thromb Vasc Biol 2012;32:1104–1115.
38. Davis SS, Illum L, Hinchcliffe M. Gastrointestinal transit of dosage forms in the pig. J Pharm Pharmacol 2001;53:33–39.
39. Kobayashi E, Hishikawa S, Teratani T, et al. The pig as a model for translational research: overview of porcine animal models at Jichi Medical University. Transplant Res 2012;1:8.
40. Alonso-García AL, Mas-Oliva J; Inventors. Universidad Nacional Autónoma de México; assignee. Immunoenzymatic method for cholesterol-ester transfer protein (CETP). US Patent 7,749,721.
41. Krishnan L, Sad S, Patel GB, et al. Archaeosomes induce long-term CD8+ cytotoxic T cell response to entrapped soluble protein by the exogenous cytosolic pathway, in the absence of CD4+ T cell help. J Immunol 2000;165:5177–5185.
42. Patel GB, Sprott GD. Archaeobacterial ether lipid liposomes (archaeosomes) as novel vaccine and drug delivery systems. Crit Rev Biotechnol 1999;19:317–357.
43. Sprott GD, Brisson J, Dicaire CJ, et al. A structural comparison of the total polar lipids from the human archaea Methanobrevibacter smithii and Methanosphaera stadtmanae and its relevance to the adjuvant activities of their liposomes. Biochim Biophys Acta 1999;1440: 275–288.
44. Stary HC, Chandler AB, Glagov S, et al. A definition of initial, fatty streak, and intermediate lesions of atherosclerosis. A report from the Committee on Vascular Lesions of the Council of arteriosclerosis. American Heart Association. Circulation 1994;89: 2462–2478.
45. Kleiner DE, Brunt EM, Van Natta M, et al. Design and validation of a histological scoring system for nonalcoholic fatty liver disease. Hepatology 2005;41:1313–1321.
46. Lee L, Alloosh M, Saxena R, et al. Nutritional model of steatohepatitis and metabolic syndrome in the Ossabaw miniature swine. Hepatology 2009;50:56–67.
47. Chistiakov DA, Orekhov AN, Bobryshev YV. Vascular smooth muscle cell in atherosclerosis. Acta Physiol 2015;214:33–50.
48. Fukai T, Ushio-Fukai M. Superoxide dismutases: role in redox signaling, vascular function, and diseases. Antioxid Redox Signal 2011;15:1583–1606.
49. Adiguzel E, Ahmad PJ, Franco C, et al. Collagens in the progression and complications of atherosclerosis. Vasc Med 2009;14:73–89.
50. Yuan SM. α-Smooth muscle actin and ACTA2 gene expressions in vasculopathies. Braz J Cardiovasc Surg 2015;30:644–649.
51. Azuma K, Ichimura K, Mita T, et al. Presence of alpha-smooth muscle actin-positive endothelial cells in the luminal surface of adult aorta. Biochem Biophys Res Commun 2009;380:620–626.
52. Lenfant C, Savage PJ. The early natural history of atherosclerosis and hypertension in the young: National Institutes of Health perspectives. Am J Med Sci 1995;310:S3–S7.
53. Basso F, Freeman L, Knapper CL, et al. Role of the hepatic ABCA1 transporter in modulating intrahepatic cholesterol and plasma HDL cholesterol concentrations. J Lipid Res 2003;44:296–302.
54. Mandard S, Müller M, Kersten S. Peroxisome proliferator-activated receptor alpha target genes. Cell Mol Life Sci 2004;61: 393–416.
55. Verma N, Rettenmeier AW, Schmitz-Spanke S. Recent advances in the use of Sus scrofa (pig) as a model system for proteomic studies. Proteomics 2011;11:776–793.

56. te Pas MFW, Visscher AH, de Greef KH. Molecular genetic and physiologic background of the growth hormone-IGF-I axis in relation to breeding for growth rate and leanness in pigs. Domest Anim Endocrinol 2004;27:287−301.
57. Reitman JS, Mahley RW, Fry DL. Yucatan miniature swine as a model for diet-induced atherosclerosis. Atherosclerosis 1982;43: 119−132.
58. Gerrity RG. The role of the monocyte in atherogenesis: I. Transition of blood-borne monocytes into foam cells in fatty lesions. Am J Pathol 1981;103:181−190.
59. Daugherty A, Tall AR, Daemen MJAP, et al. Recommendation on design, execution, and reporting of animal atherosclerosis studies: a scientific statement from the American Heart Association. Arterioscler Thromb Vasc Biol 2017;37:e131−e157.
60. Talayero BG, Sacks FM. The role of triglycerides in atherosclerosis. Curr Cardiol Rep 2011;13:544−552.
61. Rapp JH, Lespine A, Hamilton RL, et al. Triglyceride-rich lipoproteins isolated by selected-affinity anti-apolipoprotein B immunosorption from human atherosclerotic plaque. Arterioscler Thromb J Vasc Biol 1994;14:1767−1774.
62. Zheng C, Khoo C, Furtado J, et al. Apolipoprotein C-III and the metabolic basis for hypertriglyceridemia and the dense low-density lipoprotein phenotype. Circulation 2010;121:1722−1734.
63. Luo M, Peng D. The emerging role of apolipoprotein C-III: beyond effects on triglyceride metabolism. Lipids Health Dis 2016;15:184.
64. Louis SF, Zahradka P. Vascular smooth muscle cell motility: From migration to invasion. Exp Clin Cardiol 2010;15:e75−e85.
65. Ionita MG, Arslan F, de Kleijn DPV, et al. Endogenous inflammatory molecules engage Toll-like receptors in cardiovascular disease. J Innate Immun 2010;2:307−315.
66. Damián-Zamacona S, Toledo-Ibelles P, Ibarra-Abundis MZ, et al. Early Transcriptomic Response to LDL and oxLDL in Human Vascular Smooth Muscle Cells. PLoS One 2016;11:e0163924.
67. Feil S, Fehrenbacher B, Lukowski R, et al. Transdifferentiation of vascular smooth muscle cells to macrophage-like cells during atherogenesis. Circ Res 2014;115:662−667.
68. Bennett MR, Sinha S, Owens GK. Vascular smooth muscle cells in atherosclerosis. Circ Res 2016;118:692−702.
69. Xu J, Shi G-P. Vascular wall extracellular matrix proteins and vascular diseases. Biochim Biophys Acta 2014;1842:2106−2119.
70. Libby P, Shi G-P. Mast cells as mediators and modulators of atherogenesis. Circulation 2007;115:2471−2473.
71. Kovanen PT. Mast cells and degradation of pericellular and extracellular matrices: potential contributions to erosion, rupture and intraplaquehaemorrhage of atherosclerotic plaques. Biochem Soc Trans 2007;35:857−861.
72. Johnson JL, Jackson CL, Angelini GD, et al. Activation of matrix-degrading metalloproteinases by mast cell proteases in atherosclerotic plaques. Arterioscler Thromb Vasc Biol 1998;18:1707−1715.
73. Sun J, Sukhova GK, Wolters PJ, et al. Mast cells promote atherosclerosis by releasing proinflammatory cytokines. Nat Med 2007;13: 719−724.
74. Campagnola P. Second harmonic generation imaging microscopy: applications to diseases diagnostics. Anal Chem 2011;83: 3224−3231.
75. Zoumi A, Lu X, Kassab GS, et al. Imaging coronary artery microstructure using second-harmonic and two-photon fluorescence microscopy. Biophys J 2004;87:2778−2786.
76. Matsuzawa-Nagata N, Takamura T, Ando H, et al. Increased oxidative stress precedes the onset of high-fat diet-induced insulin resistance and obesity. Metabolism 2008;57:1071−1077.
77. Yida Z, Imam MU, Ismail M, et al. High fat diet-induced inflammation and oxidative stress are attenuated by N-acetylneuraminic acid in rats. J Biomed Sci 2015;22:96.
78. Alcalá M, Calderon-Dominguez M, et al. Increased inflammation, oxidative stress and mitochondrial respiration in brown adipose tissue from obese mice. Sci Rep 2017;7:16082.
79. Sweet DR, Fan L, Hsieh PN, et al. Krüppel-Like Factors in Vascular Inflammation: Mechanistic Insights and Therapeutic Potential. Front Cardiovasc Med 2018;5:6.
80. Bhattacharya R, Senbanerjee S, Lin Z, et al. Inhibition of vascular permeability factor/vascular endothelial growth factor-mediated angiogenesis by the Kruppel-like factor KLF2. J Biol Chem 2005; 280:28848−28851.
81. Fargion S, Porzio M, Fracanzani AL. Nonalcoholic fatty liver disease and vascular disease: State-of-the-art. World J Gastroenterol 2014; 20:13306−13324.
82. Cheng PTW, Mukherjee R. PPARs as targets for metabolic and cardiovascular diseases. Mini Rev Med Chem 2005;5:741−753.
83. Pawlak M, Lefebvre P, Staels B. Molecular mechanism of PPARα action and its impact on lipid metabolism, inflammation and fibrosis in non-alcoholic fatty liver disease. J Hepatol 2015;62: 720−733.
84. Kersten S, Stienstra R. The role and regulation of the peroxisome proliferator activated receptor alpha in human liver. Biochimie 2017;136:75−84.
85. Larter CZ, Yeh MM, Van Rooyen DM, et al. Peroxisome proliferator-activated receptor-α agonist, Wy 14,643, improves metabolic indices, steatosis and ballooning in diabetic mice with non-alcoholic steatohepatitis. J Gastroenterol Hepatol 2012;27:341−350.
86. Amar MJA, D'Souza W, Turner S, et al. 5A apolipoprotein mimetic peptide promotes cholesterol efflux and reduces atherosclerosis in mice. J Pharmacol Exp Ther 2010;334:634−641.
87. Nagashima M, Watanabe T, Terasaki M, et al. Native incretins prevent the development of atherosclerotic lesions in apolipoprotein E knockout mice. Diabetologia 2011;54:2649.
88. Mas-Oliva J, Delgado-Coello B, Méndez-Acevedo K, et al. Preclinical evidence studying intranasal HB-ATV-8 vaccine in a porcine model of atherosclerosis shows high efficiency in the prevention of atherogenesis and fatty liver disease. Atherosclerosis 2017;263:e52.
89. Chung EJ. Targeting and therapeutic peptides in nanomedicine for atherosclerosis. Exp Biol Med 2016;24:891−898.
90. McLeod O, Silveira A, Fredrikson GN, et al. Plasma autoantibodies against apolipoprotein B-100 peptide 210 in subclinical atherosclerosis. Atherosclerosis 2014;232:242−248.
91. Navab M, Anantharamaiah GM, Reddy ST, et al. Apolipoprotein A-I mimetic peptides and their role in atherosclerosis prevention. Nat Clin Pract Cardiovasc Med 2006;3:540−547.
92. Mohammadpour AH, Akhlaghi F. Future of cholesteryl ester transfer protein (CETP) inhibitors: a pharmacological perspective. Clin Pharmacokinet 2013;52:615−626.
93. Staels B, Dallongeville J, Auwerx J, et al. Mechanism of action of fibrates on lipid and lipoprotein metabolism. Circulation 1998;98: 2088−2093.
94. Toledo-Ibelles P, Mas-Oliva J. Antioxidants in the fight against atherosclerosis: is this a dead end? Curr Atheroscler Rep 2018;20:36.
95. Kosmas CE, DeJesus E, Rosario D, et al. CETP inhibition: past failures and future hopes. Clin Med Insights Cardiol 2016;10:37−42.
96. Di Bartolo BA, Duong M, Nicholls SJ. Clinical trials with cholesteryl ester transfer protein inhibitors. Curr Opin Lipidol 2016;27: 545−559.
97. Barter PJ, Caulfield M, Eriksson M, et al. Effects of torcetrapib in patients at high risk for coronary events. N Engl J Med 2007;357: 2109−2122.
98. Tanne JH. Pfizer stops clinical trials of heart drug. Brit Med J 2006; 333:1237.
99. Kastelein JJP, van Leuven SI, Burgess L, et al. Effect of torcetrapib on carotid atherosclerosis in familial hypercholesterolemia. N Engl J Med 2007;356:1620−1630.

INFORME DE LABORES 2019

100. Nissen SE, Tardif J-C, Nicholls SJ, et al. Effect of torcetrapib on the progression of coronary atherosclerosis. N Engl J Med 2007;356:1304–1316.
101. Bots ML, Visseren FL, Evans GW, et al. Torcetrapib and carotid intima-media thickness in mixed dyslipidaemia (RADIANCE 2 study): a randomised, double-blind trial. Lancet Lond 2007;370:153–160.
102. Joy TR, Hegele RA. The failure of torcetrapib: what have we learned? Br J Pharmacol 2008;154:1379–1381.
103. Lüscher TF, Taddei S, Kaski J-C, et al. Vascular effects and safety of dalcetrapib in patients with or at risk of coronary heart disease: the dal-VESSEL randomized clinical trial. Eur Heart J 2012;33:857–865.
104. Schwartz GG, Olsson AG, Abt M, et al. Effects of dalcetrapib in patients with a recent acute coronary syndrome. N Engl J Med 2012;367:2089–2099.
105. Lincoff AM, Nicholls SJ, Riesmeyer JS, et al. Evacetrapib and Cardiovascular Outcomes in High-Risk Vascular Disease. N Engl J Med 2017;376:1933–1942.
106. Group TH-RC. Effects of anacetrapib in patients with atherosclerotic vascular disease. N Engl J Med 2017;377:1217–1227.
107. Alonso-García AL, Zentella-Dehesa A, Mas-Oliva J. Characterization of a naturally occurring new version of the cholesterol ester transfer protein (CETP) from small intestine. Mol Cell Biochem 2003;245:173–182.
108. Barter P. Lessons learned from the investigation of lipid level management to understand its impact in atherosclerotic events (ILLUMINATE) trial. Am J Cardiol 2009;104:10E–15E.
109. Clark RW, Cunningham D, Cong Y, et al. Assessment of cholesteryl ester transfer protein inhibitors for interaction with proteins involved in the immune response to infection. J Lipid Res 2010;51:967–974.
110. García-González V, Gutiérrez-Quintanar N, Mas-Oliva J. The C-terminal Domain supports a novel function for CETPI as a new plasma lipopolysaccharide-binding protein. Sci Rep 2015;5:16091.
111. Rittershaus CW, Miller DP, Thomas LJ, et al. Vaccine-induced antibodies inhibit CETP activity in vivo and reduce aortic lesions in a rabbit model of atherosclerosis. Arterioscler Thromb Vasc Biol 2000;20:2106–2112.
112. Gaofu Q, Jun L, Xiuyun Z, et al. Antibody against cholesteryl ester transfer protein (CETP) elicited by a recombinant chimeric enzyme vaccine attenuated atherosclerosis in a rabbit model. Life Sci 2005;77:2690–2702.
113. Mao D, Kai G, Gaofu Q, et al. Intramuscular immunization with a DNA vaccine encoding a 26-amino acid CETP epitope displayed by HBc protein and containing CpG DNA inhibits atherosclerosis in a rabbit model of atherosclerosis. Vaccine 2006;24:4942–4950.

PLOS ONE

RESEARCH ARTICLE

Proteomic analysis of *Escherichia coli* detergent-resistant membranes (DRM)

José E. Guzmán-Flores[1], Lidia Steinemann-Hernández[1], Luis E. González de la Vara[2], Marina Gavilanes-Ruiz[3], Tony Romeo[4], Adrián F. Alvarez[1]*, Dimitris Georgellis[1]*

1 Departamento de Genética Molecular, Instituto de Fisiología Celular, Universidad Nacional Autónoma de México, México City, México, **2** Departamento de Biotecnología y Bioquímica, Unidad Irapuato, Cinvestav-IPN, Irapuato, Gto, México, **3** Departamento de Bioquímica, Facultad de Química, Universidad Nacional Autónoma de México, Mexico City, México, **4** Department of Microbiology and Cell Science, IFAS, University of Florida, Gainesville, Florida, United States of America

* dimitris@ifc.unam.mx (DG); aalvarez@ifc.unam.mx (AFA)

Check for updates

OPEN ACCESS

Citation: Guzmán-Flores JE, Steinemann-Hernández L, González de la Vara LE, Gavilanes-Ruiz M, Romeo T, Alvarez AF, et al. (2019) Proteomic analysis of *Escherichia coli* detergent-resistant membranes (DRM). PLoS ONE 14(10): e0223794. https://doi.org/10.1371/journal.pone.0223794

Editor: Fernando Navarro-Garcia, CINVESTAV-IPN, MEXICO

Received: June 7, 2019

Accepted: September 27, 2019

Published: October 11, 2019

Copyright: © 2019 Guzmán-Flores et al. This is an open access article distributed under the terms of the Creative Commons Attribution License, which permits unrestricted use, distribution, and reproduction in any medium, provided the original author and source are credited.

Data Availability Statement: All relevant data are within the manuscript and its Supporting Information files.

Funding: This work was supported by grants IN208718 (AFA) and IN209918 (DG) from Dirección General de Asuntos del Personal Académico (DGAPA), Universidad Nacional Autónoma de México (UNAM). The funders had no role in study design, data collection and analysis,

Abstract

Membrane microdomains or lipid rafts compartmentalize cellular processes by laterally organizing membrane components. Such sub-membrane structures were mainly described in eukaryotic cells, but, recently, also in bacteria. Here, the protein content of lipid rafts in *Escherichia coli* was explored by mass spectrometry analyses of Detergent Resistant Membranes (DRM). We report that at least three of the four *E. coli* flotillin homologous proteins were found to reside in DRM, along with 77 more proteins. Moreover, the proteomic data were validated by subcellular localization, using immunoblot assays and fluorescence microscopy of selected proteins. Our results confirm the existence of lipid raft-like microdomains in the inner membrane of *E. coli* and represent the first comprehensive profiling of proteins in these bacterial membrane platforms.

Introduction

Cell membranes not only confine the boundaries of cells, but also provide highly specialized lipid platforms involved in many cellular processes [1]. For instance, the most studied lipid assemblies of eukaryotic membranes are the lipid rafts, which are liquid-ordered (gel-like) lipid clusters enriched in sphingolipids and cholesterol. Lipid rafts are able to float and diffuse in the lateral plane of the cell membrane and fuse together forming larger aggregates [2]. They provide platforms for the assembly and proper functioning of many protein complexes, which are mainly involved in signal transduction, vesicle trafficking, cytoskeleton rearrangement, and ion channel regulation [3–6]. Cholesterol is known to increase the thickness and to regulate the fluidity of lipid bilayers, and it is considered as an essential lipid component of lipid rafts. Other common constituents of lipid rafts are the flotillins, which belong to a family of proteins that contain the Stomatin/Prohibitin/Flotillin/HflK/C (SPFH) domain. These proteins appear to be essential for the orchestration of processes related to lipid raft formation, and are used as lipid raft markers [4,5,7]. SPFH-domain containing proteins are widely distributed in most bacterial genera. In *Bacillus subtilis* they were found to act as the scaffold for

decision to publish, or preparation of the manuscript.

Competing interests: The authors have declared that no competing interests exist.

proteins that reside in raft-like membrane microdomains [8]. Moreover, the formation of such membrane microdomains in *B. subtillis* was found to be functionally associated with a signaling pathway involved in regulation of biofilm formation and with the Sec protein translocation apparatus [8–11]. However, the membrane *of B. subtillis*, like those of most bacteria, does not contain cholesterol, and it has been suggested that other lipids, such as farnesol or farnesol-derived polyisoprenoids, might promote an increased rigidity in the microdomains [12].

Lipid raft-like domains have been also identified in other bacteria, such as *Staphylococcus aureus*, *Borrelia burgdorferi*, *Bacillus anthracis*, *Helicobacter pylori* and *Escherichia coli* [9,13–17]. *B. burgdorferi* and *H. pylori* possess cholesterol as a membrane component, even though they do not carry out *de novo* sterol biosynthesis. Instead, both bacteria obtain cholesterol from the host epithelial cells to generate glyco-cholesterol derivatives, which are incorporated into the bacterial membranes. Interestingly, both bacterial species appear to form cholesterol-containing membrane microdomains that are assembled into the outer membrane [15,16].

The close packing of lipids in the liquid-ordered phases, typically found in lipid rafts, prevents its solubilization by cold non-ionic detergents. Therefore, the study of lipid rafts, in a variety of eukaryotic and prokaryotic organisms, has been based on the extraction of detergent resistant membranes (DRM). Although detergent resistance in itself does not necessarily reflect preexisting raft domains, results obtained from DRM analysis have often been consistent with those obtained by other approaches, such as direct imaging or functional analysis [18,19]. Thus, DRM isolation provides a useful tool for the study of potential protein-lipid raft associations.

In recent studies, proteomic analyses of DRMs have been carried out in *B. subtilis*, *S. aureus*, *B. burgdorferi* and *H. pylori*, and the results suggest that bacterial membrane microdomains, like eukaryotic lipid rafts, play important roles in various cellular processes, such as membrane transport, secretion and virulence [9,16,20–23]. Nevertheless, even though several proteomic analyses of *E. coli* membranes have been carried out [24–28], there are no data regarding the composition or protein content of raft-like microdomains from this model bacterium. Here, we report that some 80 proteins, involved in transport, protein secretion, energy metabolism, cell maintenance and signaling, were found to be enriched in DRM. Among these proteins were HflC, HflK, and YbbK (QmcA), three of the four SPFH-containing proteins encoded by the *E. coli* genome, that are generally used as lipid raft markers. Thus, the first comprehensive proteomic profile of DRMs from *E. coli* is reported, providing information about the cellular processes that may be associated with lipid rafts in this organism.

Materials and methods

Bacterial strains, plasmids, and growth conditions

E. coli strain MG1655 was chosen as the genetic background of all created strains because it is a reference *E. coli* strain, and because we recently reported a DRM isolation protocol using this strain [17]. Chromosomal tagging of *hflC*, *hflK*, *qmcA*, *yqiK* and *yidC* genes was achieved by PCR and homologous recombination of the amplification products using the lambda red recombinase system [29,30], resulting in strains IFC5019 (*hflC*::*ha*-Cm^r) [17], IFC5021 (*hflK*::*ha*-Cm^r), IFC5022 (*qmcA*::*3xFLAG*-Kn^r), IFC5023 (*yqiK*::*3xFLAG*-Kn^r) and IFC5024 (*yidC*::*3xFLAG*-Kn^r). All oligonucleotides used in PCR amplification reactions are shown in S1 Table. Strain IFC5025 (*hflC*::*ha qmcA*::*3xFLAG yqiK*::*3xFLAG*-Kn^r) was constructed by two successive transfer steps of the *qmcA*::*3xFLAG*-Kan^r and *yqiK*::*3xFLAG*-Kan^r alleles from strains IFC5022 and IFC5023 into strain IFC5019 by P1*vir* transduction. In some cases, antibiotic resistance marker was eliminated by expressing the FLP recombinase from plasmid pCP20 [29]. Similarly, strains IFC5026 (*qmcA*::*mCherry*-Kn^r) and IFC5027 (*yidC*::*mCherry*-

Cm^r) were generated by lambda red recombinase-facilitated homologous recombination of PCR amplified products using primers pair pFluor-ybbK-Fw / pKD-ybbK-Rv and plasmid pMXFL1 [17] as template or yidC-Fluor-Fw / pKD-yidC-Rv and pMXFL2 [17] as template, respectively.

To construct plasmid pMX549, expressing a *glnP-mCherry* fusion under the control of the L-arabinose-inducible promoter *ara*, the *glnP* and *mCherry*, coding sequences were PCR amplified using the primer pair Glnp-EcoRI-Fw / Glnp-SacI-Rv and chromosomal DNA from MG1655 as the template, and the primer pair YfpcfSacI / YfPcr1HindIII and plasmid pCHYC-4 [31] as the template, respectively. The two amplified DNA fragments were SacI digested and ligated together, and the product was used as template in a PCR reaction with primers Glnp-EcoRI-Fw and YfPcr1HindIII. Then, purified PCR product was digested with EcoRI and HindIII and cloned into the same restriction sites of pMX020 [32], resulting in plasmid pMX549. To construct plasmid pMX550 (*glnP-mCherry*), a 2.7 Kb DNA fragment containing the *ara* promoter and the *glnP-mCherry* fusion, obtained from plasmid pMX549 by ClaI and HindIII digestion, was cloned into NruI and HindIII restriction sites of plasmid pACT3 [33]. To construct plasmids pMX551 (*acrA-mCherry*), pMX552 (*aas-mCherry*) and pMX553 (*rbbA-mCherry*), the *acrA*, *aas* and *rbbA* coding DNA sequences were PCR amplified, using the primer pairs Acra-NdeI-Fw / Acra-SacI-Rv, Aas-NdeI-Fw / Aas-SacI-Rv, and Rbba-NdeI-Fw / Rbba-SacI-Rv, respectively, and chromosomal DNA from MG1655 as template, and cloned into NdeI and SacI sites of plasmid pMX550. To construct plasmids pMX554 (*acrA-3xFLAG*), pMX555 (*aas-3xFLAG*) and pMX556 (*rbbA-3xFLAG*), a DNA fragment carrying the 3xFLAG coding sequence upstream the kanamycin resistance cassette was amplified by PCR using primers 3xFLAG-SacI-Fw and 3xFLAG-HindIII-Rv, and plasmid pSUB11 [30] as template. Then, purified PCR product was digested with SacI and HindIII and cloned into the same restriction sites of plasmids pMX551, pMX552 or pMX553, respectively. A schematic work-flow of the above constructed plasmids is presented in S1 Fig. All DNA fragments cloned from PCR-amplified material were sequenced to check that no undesired base changes had been introduced. DNA sequence analysis was performed by the "Unidad de Biologia Molecular" at IFC, UNAM.

E. coli strains were routinely grown in LB medium at 37˚C. When necessary, ampicillin, kanamycin, or chloramphenicol was used at a final concentration of 100, 50 or 25 μg/ml, respectively.

DRM isolation

DRM fractions were obtained as described previously [17]. Briefly, exponential phase growing *E. coli* cells were treated with 10 μg/ml ampicillin to generate filamented cells that were harvested, resuspended in buffer A (1 M sucrose, 0.2 M Tris-HCl [pH 8.0]), and treated with 2 mM EDTA and 12.5 μg/ml lysozyme for 10 min. Next, spheroplasts were obtained by adding sterile water to reach a sucrose concentration of 0.1 M. Spheroplasts, whose formation was confirmed by phase-contrast microscopy, were harvested, resuspended in ice-cold buffer B (20 mM Tris-HCl [pH 7.2], 50 mM NaCl, 5 mM EDTA) containing 20% w/w sucrose, and passed through a French pressure cell. Inner membrane (IM) vesicles were isolated from the spheroplast lysate by ultracentrifugation (~113,000xg) in a discontinuous sucrose gradient (20–50% w/w). IM-containing fractions were pooled and recovered by ultracentrifugation, and 500 μg of protein was mixed with ice-cold Triton X-100 (Pierce, Rockford, IL, USA), resulting in a final detergent concentration of 1% w/v and in a detergent:protein ratio of 8:1, and incubated for 30 min on ice. The DRM fraction were obtained by flotation in a continuous OptiPrep (Axis-Shield, Oslo, Norway) gradient after ultracentrifugation (~173,000xg), concentrated by ultracentrifugation (~106,000xg), and stored at -80˚C.

Protein digestion with trypsin

Proteins in IM or DRM samples were precipitated with trichloroacetic acid (TCA) by adding 100 μl of 10X TE buffer (100 mM Tris-HCl, 10 mM disodium EDTA, pH 8.0) and 100 μl of 72% TCA to samples with 20 μg of total protein. After 2 h of incubation on ice, proteins were pelleted by centrifugation at 14,000 rpm at 4 ˚C for 10 min, washed with 1 ml of cold acetone and dried at room temperature for 20 min. Precipitated proteins were solubilized in 10 μL of 6 M urea, reduced by with 2.5 μL of reduction buffer (45 mM DTT, 100 mM ammonium bicarbonate) for 30 min at 37 ˚C, and alkylated by adding 2.5 μL of alkylation buffer (100 mM iodoacetamide, 100 mM ammonium bicarbonate) for 20 min at 24 ˚C in the dark. Before trypsin digestion, 20 μL of water was added to reduce the urea concentration to 2 M. Protein digestion was performed by adding 10 μL of trypsin solution (5 ng/μL of trypsin sequencing grade from Promega, 50 mM ammonium bicarbonate), samples were incubated at 37 ˚C for 18 h, and the reaction was stopped by adding 5 μL of 5% formic acid. Protein digests were dried down by vacuum centrifugation and stored at -20 ˚C.

LC-MS/MS analysis

Prior to LC-MS/MS analysis, protein digests were resolubilized under agitation in 10 μL of 0.2% formic acid for 15 min. Desalting and cleanup of the samples was done by using C18 ZipTip pipette tips (Millipore, Billerica, MA). Eluates were dried down in a vacuum centrifuge and then resolubilized under agitation in 10 μL of 2% ACN and 1% formic acid for 15 min. The peptide mixture was separated by LC using C18 reversed phase column with a high-pressure packing. A 75 μm i.d. Self-Pack PicoFrit fused silica capillary column (New Objective, Woburn, MA) was packed with the C18 Jupiter 5 μm 300 Å reverse-phase material (Phenomenex, Torrance, CA), and this column was installed on the Easy-nLC II system (Proxeon Biosystems, Odense, Denmark). The separated peptides were directly electrosprayed into a Linear Trap Quadropole (LTQ) Orbitrap Velos (ThermoFisher Scientific, Bremen, Germany) equipped with a Proxeon nanoelectrospray ion source. The solutions used for chromatography were 0.2% formic acid (Solvent A) and 100% ACN/0.2% formic acid (Solvent B). Samples were loaded on-column at a flowrate of 600 nL/min and eluted with a 2-slope gradient at a flowrate of 250 nL/min. Solvent B first increased from 2 to 40% in 100 min and then from 40 to 80% B in 20 min.

LC-MS/MS data acquisition was accomplished using a seventeen-scan event cycle comprised of a full scan MS for scan event 1 acquired in the Orbitrap. The mass resolution for MS was set to 60,000 (at m/z 400) and used to trigger the sixteen additional MS/MS events acquired in parallel in the linear ion trap for the top sixteen most intense ions. Mass over charge ratio range was from 360 to 1700 for MS scanning with a target value of 1,000,000 charges and from ~1/3 of parent m/z ratio to 2000 for MS/MS scanning with a target value of 10,000 charges. The data dependent scan events used a maximum ion fill time of 100 ms and 1 microscan. Target ions already selected for MS/MS were dynamically excluded for 31 s after 2 counts. Nanospray and S-lens voltages were set to 1.3–1.8 kV and 50 V, respectively. Capillary temperature was set to 250 ˚C. MS/MS conditions were: normalized collision energy, 35 V; activation q, 0.25; activation time, 10 ms.

Database search

Raw data files of fragmentation spectra were converted to *mzXML* files by RawConverter software tool [34] and compared against the MG1655 *E. coli* strain sequence (4,306 entries) of the UniProt database (downloaded on August 18, 2017; Proteome ID: UP000000625), using the Comet search engine in the Trans Proteome Pipeline (TPP) suite [35] with the following

parameters: The ion-mass tolerances of monoisotopic peptide precursor and fragmentation products were 3 Da and 1 Da respectively, without correcting for isotope errors. Oxidation of methionines (+16) was considered as the only variable modification, and two missed cleavages were allowed. Peptide assignations were validated with PeptideProphet, filtering out peptides with a probability under 0.7. A protein was considered to be positively identified when ProteinProphet probability was >0.99, and at least three unique peptides were assigned (S2 Table). The spectra count for each inner membrane protein from an IM sample and the average value from two biological replica of DRM fraction were analyzed and used to determine which proteins were enriched in lipid rafts (S3 Table).

In silico analyses

Prediction of number of the transmembrane (TM) domains and signal peptides was carried out using the TOPCONS server (http://topcons.cbr.su.se/) [36]. Lipoprotein signal sequences and lipoprotein inner or outer membrane association were predicted using the LipoP 1.0 Server (http://www.cbs.dtu.dk/services/LipoP/) [37]. Amphipathic in-plane membrane anchor was predicted using Amphipaseek tool of NPS@ server [38].

Immunoblotting

Equal volumes (10 μl) of representative fractions from OptiPrep gradients were separated by SDS-PAGE (10% polyacrylamide gel), and the proteins were transferred to a Hybond-ECL filter (Amersham Bio-sciences). The filter was equilibrated in TTBS buffer (25 mM Tris, 150 mM NaCl, and 0.1% Tween-20) for 10 min and incubated in blocking buffer (5% w/v milk in TTBS) for 1 h at room temperature. Monoclonal antibodies against HA or 3XFLAG epitope were added at a dilution of 1:10,000 and incubated for 1 h at room temperature. The bound antibody was detected by using anti-mouse IgG antibody conjugated to horseradish peroxidase (Sigma Aldrich) and the Immobilon Western detection system (Millipore). It has to be mentioned that immunodetection of HflC-HA and YbbK-3Flag was carried out on all independently generated membrane fractions, including the ones used for proteomics. Immunodetection of all other protein markers was carried out on at least three independently generated membrane fractions, but not the ones used for proteomic analysis.

Fluorescence microscopy

E. coli cells carrying either AcrA-mCherry, YidC-mCherry, HflC-mCherry, QmcA-mCherry, Aas-mCherry or RbbA-mCherry fusion, were grown in LB medium at 37 ˚C to an optical density at 600 nm (OD_{600}) of 1.5, and aliquots of the cell cultures (2 μl) were immobilized on glass slides previously covered with freshly made M9 medium 1% agarose pads [39]. Cells were observed under an upright microscope (Eclipse E600, Nikon) equipped with an oil-immersion objective lens microscope (100x, NA 1.47). mCherry fluorescence was exited with an X-Cite 120 light source system, using a Chroma filter 39010, and images were acquired with a Hamamatsu ORCA-ER cooled-CCD camera controlled with QCapture Pro (version 6.0) software (QImages). Phase contrast and mCherry fluorescence images were taken at 40 ms and 500 ms exposure, respectively, and processed with ImageJ software [40]. Fluorescence images were subjected to background subtraction using a rolling ball radius of 20 pixels, and fluorescence signals were colored in red, before copying the relevant selections to an image editor software.

Results

Preparation of DRM fractions from *E. coli* membranes

In a recent study, we reported the existence of lipid raft-like microdomains within the plasma membrane of the Gram-negative bacteria *E. coli* [17]. The composition and protein cargo of these lipid platforms, however, remain elusive. In order to explore the proteome of these membrane microdomains, we isolated detergent-resistant membranes (DRM), which is the procedure that is typically used for the analysis of lipid rafts of both eukaryotic and prokaryotic cells [19,41]. Because Gram-negative bacteria, such as *E. coli*, in addition to the cytoplasmic or inner membrane (IM) are surrounded by an outer membrane (OM), which is naturally resistant to solubilization by detergents [42,43], the use of OM-free IM as the starting material is required if pure DRM are to be obtained [17]. A schematic illustration for DRM isolation is presented in Fig 1A. Briefly, giant spheroplasts of strains IFC5025 and IFC5021, harboring chromosomal HA- or FLAG-tagged hybrids of the four known SPFH-domain proteins of *E. coli*, namely HflC, HflK, YqiK and QmcA (YbbK), were generated and lysed by passing them through a French Press. IMs were isolated by ultracentrifugation in discontinuous sucrose gradients, and treated with cold Triton X-100 at a detergent:protein ratio of 8:1. Finally, detergent treated IMs were separated by ultracentrifugation in OptiPrep gradients. DRMs, because of their low density, are able to float on density gradients [44], and, therefore, the visible opaque band settled in the upper part of the gradient (Fig 1A), containing the DRM fraction, was recovered and stored for further analysis. It is worth mentioning that the DRM protein content represented approximately 10% of the initial protein in IM. Proteins in detergent-sensitive membranes (DSM), present in the lower fractions of the gradient were also recovered for immunoblotting assays.

Subsequently, the above collected fractions were probed for their content of the SPFH-domain proteins, namely HflK, HflC, QmcA and YqiK. This was performed because proteins containing the SPFH-domain have been shown to be associated with DRMs in both eukaryotic and bacterial membranes, and are therefore used as lipid raft markers [3,9]. Immunoblot analysis revealed that HflC, HflK and QmcA were partitioned principally into the DRM fraction (Fig 1B), whereas YqiK, which was marginally detected in IM, was not detected along the OptiPrep gradient (not shown). It is likely that the low *yqiK* expression results in not-detectable amounts of YqiK protein in DRM fractions. Interestingly, QmcA, and at a lesser extent HflK, were also detected in DSM fractions, suggesting that the conditions used to obtain DRMs were stringent enough to avoid false positives. Alternatively, populations of membrane rafts with different rigidity may exist, such that these proteins partition into both raft and non-raft membrane regions, depending on the cell physiology, as previously reported [45]. Nevertheless, the presence of the three membrane raft-marker proteins in the DRM fraction corroborates the suitability of our procedures for DRM isolation.

Proteomic analysis of DRM fraction from *E. coli*

To identify proteins residing in DRM fractions, LC-MS/MS analyses of the obtained IMs and DRMs were conducted. The obtained results were filtered by excluding proteins represented by less than three unique peptides, resulting in the identification of 785 proteins. These proteins were grouped depending on their subcellular localization according to the Uniprot database (S2 Table). Even though the IMs were separated from the OMs and cytosolic proteins, the portion of proteins annotated as IM residents was only 52.23% (420 proteins) of the identified proteins (Fig 2A). On the other hand, 5.73% (45 proteins) corresponded to OM proteins, whereas 12.72% (100 proteins) and 4.45% (35 proteins) represented cytosolic and periplasmic

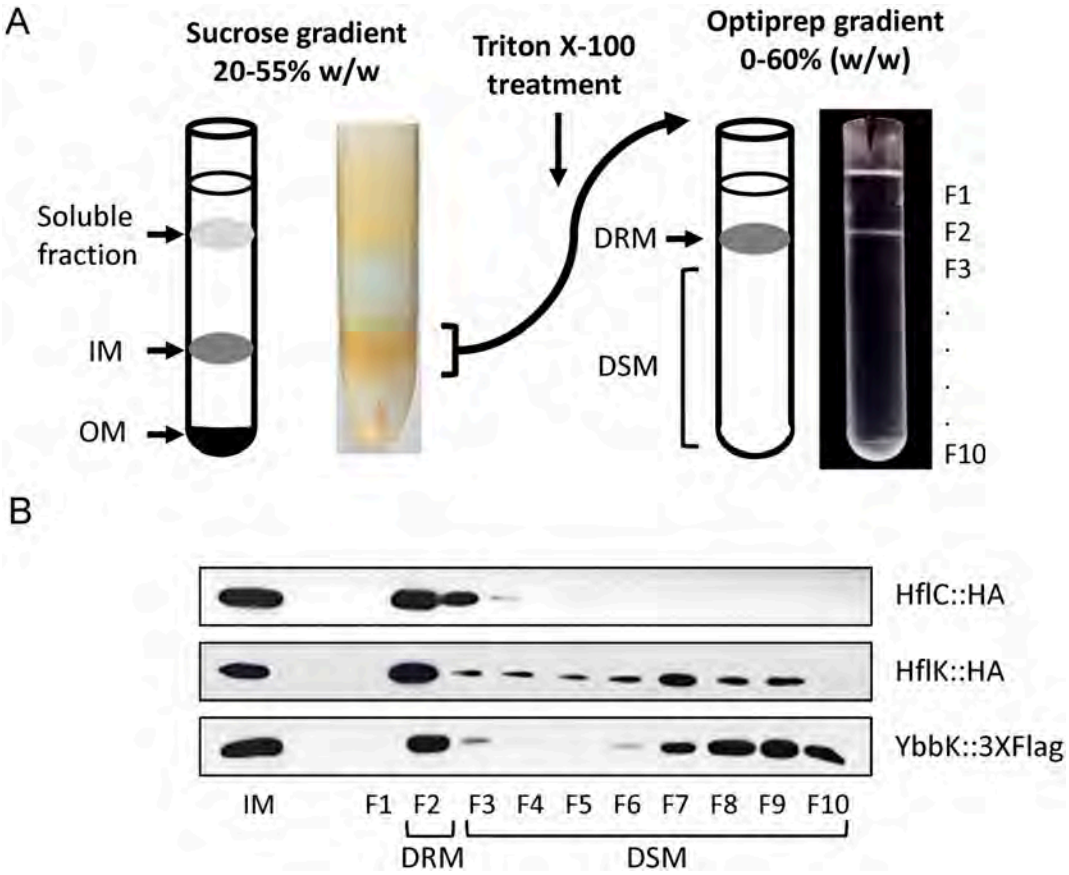

Fig 1. DRM preparation. (A) Schematic illustration of inner-membrane separation by density gradient ultracentrifugation. A spheroplast lysate was loaded on a discontinuous sucrose gradient (20–50% w/w) (cartoon on the left and photography of gradient on the right). The fraction matching to approximately 45% w/w sucrose, corresponding to IM, was separated and treated with ice-cold Triton X-100. The mixture was then loaded on an OptiPrep gradient and ultracentrifuged (cartoon on the left and photography of OptiPrep gradient on the right). Ten 1ml fractions were collected from the top to the bottom of the tube (F1 to F10). DRMs were recovered from F2 whereas DSMs were recovered from lower fractions. (B) IM sample and OptiPrep gradient collected fractions were analyzed by Western blot using specific antibodies against HflC-HA, HflK-HA or QcmA-3xFLAG as described in Materials and Methods section. A representative immunoblot from at least three entirely independent experiments is shown for each protein.

https://doi.org/10.1371/journal.pone.0223794.g001

proteins, respectively. The remaining 23.54% (185 proteins) represented proteins with unknown localization (Fig 2A). Inspection of the relative abundance of spectra indicated that the number of peptides corresponding to IM proteins in DRM were slightly higher than in the IM sample (66.76% and 62.36%, respectively), whereas peptides corresponding to OM proteins were greatly enriched (~ 5 times) in DRM in comparison to the IM (24.46% and 5.40%, respectively) (Fig 2B and 2C). This is expected because of the intrinsic detergent-resistance of OMs. In contrast, the amount of peptides corresponding to proteins with cytosolic or periplasmic localization diminished significantly in DRM as compared to the IM (1.22% and 9.14%, respectively for the cytosolic proteins and 1.22 and 3.89%, respectively for the periplasmic proteins) (Fig 2B and 2C). It is probable that some cytosolic or periplasmic proteins could weakly associate with the IM, and were released after detergent treatment. It has to be mentioned that approximately 19% and 5% of the identified peptides in IM and DRM, respectively, corresponded to proteins with unknown localization, and therefore the above mentioned relative abundance of proteins may vary.

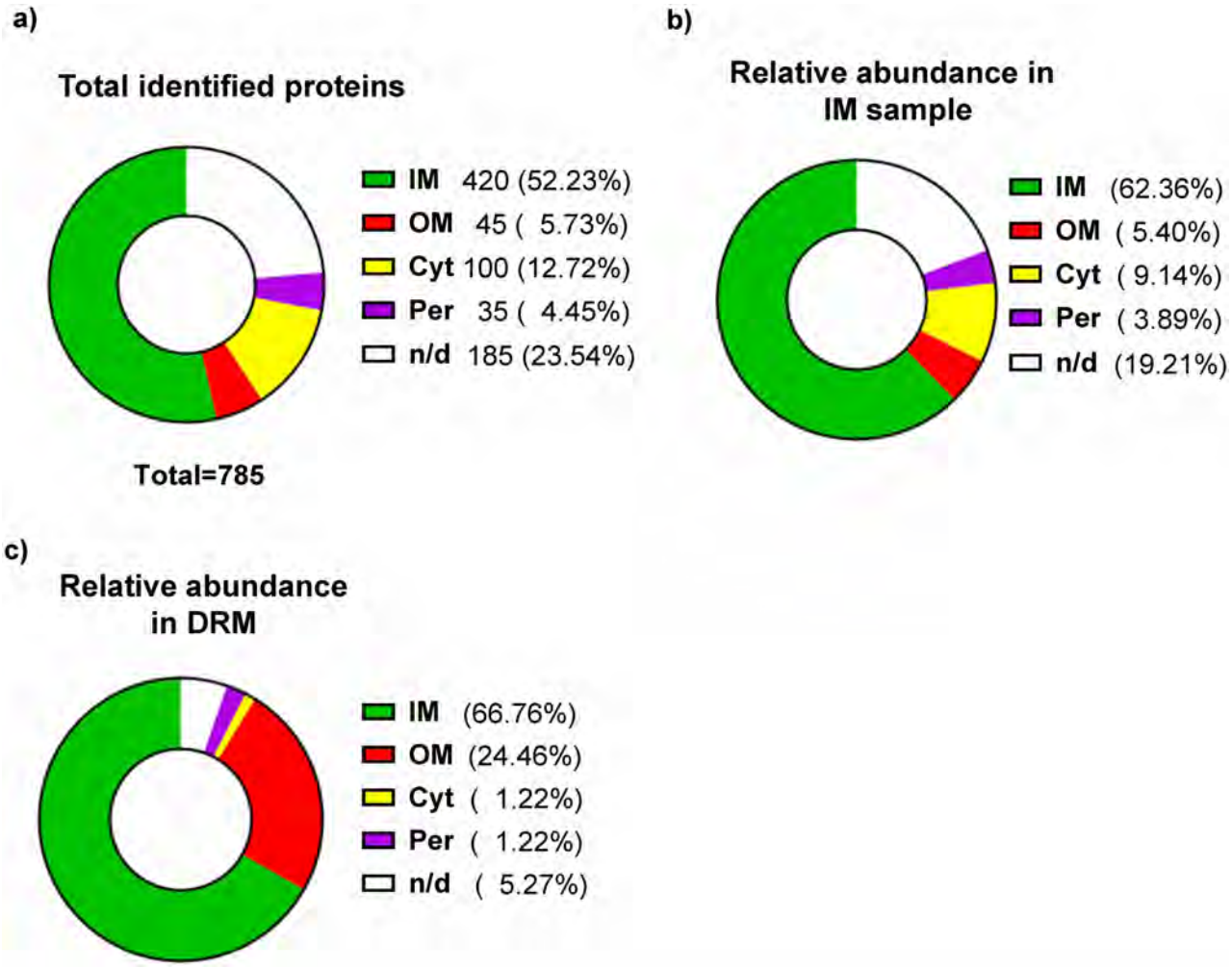

Fig 2. Distribution of identified proteins according to subcellular location. (A) Total proteins identified in inner membrane and DRM samples. (B) Relative abundance of peptides in IM sample. (C) Relative abundance of peptides in DRM samples. IM: Inner membrane proteins, OM: outer membrane proteins, Cyt: cytosolic proteins, Per: periplasmic proteins, n/d: proteins without localization data.

https://doi.org/10.1371/journal.pone.0223794.g002

Next, we examined which of the identified proteins were enriched in DRM, suggesting that they may be components of lipid raft-like membrane microdomains. To this end, the spectral counts obtained from the IM sample were subtracted from the ones obtained from the DRM sample, for each of the 420 IM identified proteins. We argued that if, for a given protein, the difference is positive, this protein may reside in a membrane with higher resistance to the detergent treatment, and, therefore, could be considered as a possible resident of membrane microdomains. On the other hand, if the difference is negative, it would suggest that the protein is located in a membrane sensitive to detergent treatment and, therefore, would not be considered as DRM resident. The distribution of the spectra differences for the 420 IM-proteins is shown in Fig 3 and the values in S3 Table. Subsequently, proteins with a difference of less than 10 were excluded and only proteins with a difference of 10 or higher were considered as putative lipid raft components, permitting us to identify 80 proteins (Tables 1–7). As expected, among these proteins were found the SPFH-containing proteins HflK, HflC and QmcA. A functional classification of the identified proteins shows that the *E.*

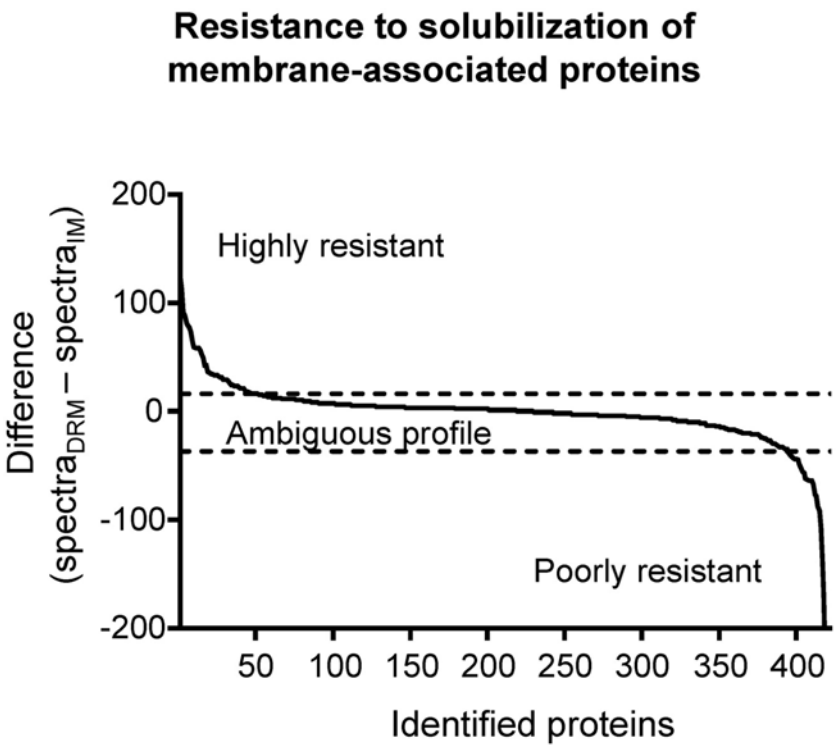

Fig 3. Distribution of identified IM associated proteins according to their detergent solubilization resistance profile. The resistance profile of each protein was determined by calculating the difference between spectra counts obtained from DRM and IM samples. A cut-off of at least 10 positive difference spectra (+10) was used to identify a potential lipid raft associated protein, resulting in 80 selected proteins.

https://doi.org/10.1371/journal.pone.0223794.g003

coli membrane rafts were mainly enriched in proteins involved in membrane transport, energy metabolism, cell wall metabolism, secretion, and, to a lesser extent, in signaling and scaffolding, reminiscent to those observed for other bacterial membrane microdomains [9,16,20–23]. Noteworthy, among the 80 DRM-enriched proteins, 17 lacked an apparent transmembrane segment. This could be due to their association with membrane-anchored proteins, as is the case for AcrA, which interacts with AcrB on its periplasmic face, forming a multidrug efflux pump complex. Alternatively, periplasmic proteins carrying a lipoprotein signal peptide (SPII) can be covalent linked to membrane lipids by their N-terminal. Our prediction indicates that 8 of the 17 soluble proteins harbor this lipoprotein signal peptide. Finally, proteins could be attached to the membrane by amphipathic helices (in-plane membrane helices, or IPM), which appear to be present in almost half of the total DRM-enriched proteins (Tables 1–7).

DRM-enriched proteins localize in membrane foci in *E. coli* cells

To investigate whether the DRM-enriched proteins displayed expected localization patterns within membrane foci, C-terminal mCherry fusions of 6 proteins, 4 of which exhibited a high detergent resistant profile (AcrA, YidC, QmcA and HflC) and 2 not identified in DRM fractions (Aas and RbbA), were generated, and their localization in live cells were detected by epifluorescence microscopy. HflC was used as a control because it contains the SPFH-domain (lipid raft-marker) and its polar localization was previously determined [17]. It was observed that AcrA-mCherry and YidC-mCherry accumulated on the poles of cells, similarly to HflC-

Table 1. Transporter proteins.

Protein name	Uniprot entry name	Max coverage	IM	DRM	Diff.	Ratio	TM	SP	IPM
Multidrug efflux pump subunit AcrB	ACRB	48.30%	68	191	123	2.81	12	No	Yes
Multidrug efflux pump subunit AcrA	ACRA	81.40%	132	220	88	1.66	0	SPII (IM)	No
PTS system mannitol-specific EIICBA component	PTM3C	67.20%	70	161	91	2.30	7	No	Yes
Multidrug resistance protein MdtF	MDTF	38.10%	25	83	58	3.32	12	No	No
Alpha-ketoglutarate permease	KGTP	30.80%	9	40	31	4.44	12	No	Yes
Paraquat-inducible protein B	PQIB	62.80%	21	52	31	2.45	1	No	Yes
Lipid A export ATP-binding/permease protein MsbA	MSBA	45.00%	38	67	29	1.76	6	No	No
L-cystine transport system ATP-binding protein YecC	YECC	60.40%	4	33	29	8.13	0	No	No
PTS system glucose-specific EIICB component	PTGCB	54.70%	46	75	29	1.62	10	No	Yes
Magnesium transport protein CorA	CORA	74.70%	37	61	24	1.65	2	No	Yes
Nitrate/nitrite transporter NarK	NARK	33.00%	11	35	24	3.14	12	No	No
Multidrug resistance protein MdtE	MDTE	76.40%	41	64	23	1.56	0	SPII (IM)	No
PTS system glucitol/sorbitol-specific EIIB component	PTHB	42.30%	4	23	19	5.63	5	No	Yes
PTS system N-acetylglucosamine-specific EIICBA component	PTW3C	50.20%	58	76	18	1.31	12	No	Yes
Probable glutamate/gamma-aminobutyrate antiporter	GADC	18.20%	11	27	16	2.41	12	No	Yes
D-methionine-binding lipoprotein MetQ	METQ	84.10%	125	140	15	1.12	0	SPII (OM)	No
Glycerol-3-phosphate transporter	GLPT	29.20%	35	49	14	1.39	12	No	No
Lipoprotein 28	NLPA	56.20%	12	25	13	2.08	0	SPII (IM)	No
Probable aminoglycoside efflux pump	ACRD	12.30%	4	16	12	4.00	12	No	No
Macrolide export protein MacA	MACA	41.50%	10	22	12	2.15	1	No	Yes
Putative cation/proton antiporter YbaL	YBAL	24.70%	7	19	12	2.64	13	No	Yes
Serine transporter	SDAC	32.90%	14	25	11	1.79	11	No	No
Proline/betaine transporter (Proline porter II) (PPII)	PROP	17.80%	24	35	11	1.46	12	No	Yes
Carbon starvation protein A	CSTA	15.70%	3	14	11	4.67	16	No	No
Low-affinity inorganic phosphate transporter 1	PITA	27.70%	13	24	11	1.81	10	No	Yes

Max coverage, maximum percentage of coverage of identified protein; **IM**, spectra from inner membrane sample; **DRM**, average spectra obtained from DRM samples; **Diff**, average difference between spectra counts in DRM and in IM samples; **Ratio**, average ratio between spectra counts in DRM and in IM samples; **TM**, Predicted transmembrane domains; **SP**, predicted signal peptide [SPI, signal peptide; SPII (IM), lipoprotein signal peptide (predicted inner membrane–specific lipoprotein); SPII (OM), lipoprotein signal peptide (predicted outer membrane–specific lipoprotein); **IPM**, predicted amphipathic in-plane membrane helices.

https://doi.org/10.1371/journal.pone.0223794.t001

mCherry (Fig 4), indicating that these proteins are lipid raft residents. Also, the mCherry fusion of QmcA, another lipid raft-marker protein that was enriched in DRM fractions, appeared as discrete foci with both polar and lateral localization. In contrast, both Aas-mCherry and RbbA-mCherry, which were not identified in DRM fractions, were distributed throughout the membrane, reinforcing the suggestion that these proteins were not associated with lipid raft microdomains. Then, we examined the detergent resistance profile of the membranes in which the above selected proteins are located. To this end, cells carrying 3xFLAG-fusions were obtained and used for IM isolation and Triton X-100 treatment. After separation in OptiPrep gradients, fractions were analyzed by Western blot analysis using anti-Flag antibodies. As expected, AcrA-3xFLAG, YidC-3xFLAG, QmcA-3xFLAG and HflC-3xFLAG were mainly found in the floating DRM fractions, whereas Aas-3xFLAG and RbbA-3xFLAG were present in the soluble fractions at the bottom of gradients. Thus, these results indicate that proteins with higher differences in the number of spectra counts between DRM and IM could be associated to lipid raft-like membrane microdomains in *E. coli*, validating our proteomic analysis and their identification as membrane microdomain-residents.

Table 2. Energy biosynthesis related proteins.

Protein name	Uniprot entry name	Max coverage	IM	DRM	Diff.	Ratio	TM	SP	IPM
Cytochrome bo(3) ubiquinol oxidase subunit 2	CYOA	67.60%	36	148	112	4.11	2	No	No
NAD(P) transhydrogenase subunit beta	PNTB	40.00%	25	102	77	4.06	9	No	Yes
NAD(P) transhydrogenase subunit alpha	PNTA	70.00%	145	208	63	1.43	5	No	No
Respiratory nitrate reductase 1 beta chain	NARH	83.60%	120	178	58	1.48	0	No	Yes
Respiratory nitrate reductase 1 alpha chain	NARG	70.70%	313	365	52	1.17	0	No	Yes
Cytochrome bd-I ubiquinol oxidase subunit 1	CYDA	45.00%	108	143	35	1.32	9	No	Yes
Hydrogenase-2 large chain (HYD2)	MBHM	80.60%	107	141	34	1.31	0	No	Yes
Cytochrome bo(3) ubiquinol oxidase subunit 1	CYOB	15.50%	23	45	22	1.93	15	No	Yes
Hydrogenase-2 small chain (HYD2)	MBHT	76.30%	44	65	21	1.48	1	SPI	No
Respiratory nitrate reductase 2 beta chain	NARY	23.00%	6	24	18	4.00	0	No	No
Thiol:disulfide interchange protein DsbD	DSBD	32.00%	8	25	17	3.06	8	SPI	Yes
Electron transport complex subunit RsxG	RSXG	52.40%	4	17	13	4.13	0	SPI	No
Cytochrome c biogenesis ATP-binding export protein CcmA	CCMA	66.70%	3	15	12	4.83	0	No	No
Cytochrome bd-I ubiquinol oxidase subunit 2	CYDB	27.40%	9	21	12	2.28	9	No	Yes
Cytochrome bo(3) ubiquinol oxidase subunit 3	CYOC	20.60%	2	13	11	6.25	5	No	Yes

Max coverage, maximum percentage of coverage of identified protein; **IM**, spectra from inner membrane sample; **DRM**, average spectra obtained from DRM samples; **Diff**, average difference between spectra counts in DRM and in IM samples; **Ratio**, average ratio between spectra counts in DRM and in IM samples; **TM**, Predicted transmembrane domains; **SP**, predicted signal peptide [SPI, signal peptide; SPII (IM), lipoprotein signal peptide (predicted inner membrane–specific lipoprotein); SPII (OM), lipoprotein signal peptide (predicted outer membrane–specific lipoprotein); **IPM**, predicted amphipathic in-plane membrane helices.

https://doi.org/10.1371/journal.pone.0223794.t002

Table 3. Lipid modification and metabolism proteins.

Protein name	Uniprot entry name	Max coverage	IM	DRM	Diff.	Ratio	TM	SP	IPM
Probable phospholipid ABC transporter-binding protein MlaD	MLAD	95.10%	70	119	49	1.69	1	No	No
Phosphoethanolamine transferase EptC	EPTC	45.80%	25	58	33	2.32	5	No	Yes
Uncharacterized lipoprotein YfhM	YFHM	41.70%	35	68	33	1.93	0	SPII (IM)	No

Max coverage, maximum percentage of coverage of identified protein; **IM**, spectra from inner membrane sample; **DRM**, average spectra obtained from DRM samples; **Diff**, average difference between spectra counts in DRM and in IM samples; **Ratio**, average ratio between spectra counts in DRM and in IM samples; **TM**, Predicted transmembrane domains; **SP**, predicted signal peptide [SPI, signal peptide; SPII (IM), lipoprotein signal peptide (predicted inner membrane–specific lipoprotein); SPII (OM), lipoprotein signal peptide (predicted outer membrane–specific lipoprotein); **IPM**, predicted amphipathic in-plane membrane helices.

https://doi.org/10.1371/journal.pone.0223794.t003

Table 4. Response to stimulus proteins.

Protein name	Uniprot entry name	Max coverage	IM	DRM	Diff.	Ratio	TM	SP	IPM
Modulator of FtsH protease HflK	HFLK	75.20%	40	96	56	2.39	1	No	Yes
Modulator of FtsH protease HflC	HFLC	62.90%	80	122	42	1.53	1	No	Yes
Prophage lipoprotein Bor homolog	BORD	58.80%	4	32	28	8.00	0	SPII (OM)	No
Transcriptional activator CadC	CADC	49.60%	2	18	16	9.00	1	No	Yes
Protein QmcA	QMCA	49.50%	8	22	14	2.75	1	No	Yes
Sensor kinase CusS	CUSS	25.20%	5	15	10	2.90	2	No	Yes

Max coverage, maximum percentage of coverage of identified protein; **IM**, spectra from inner membrane sample; **DRM**, average spectra obtained from DRM samples; **Diff**, average difference between spectra counts in DRM and in IM samples; **Ratio**, average ratio between spectra counts in DRM and in IM samples; **TM**, Predicted transmembrane domains; **SP**, predicted signal peptide [SPI, signal peptide; SPII (IM), lipoprotein signal peptide (predicted inner membrane–specific lipoprotein); SPII (OM), lipoprotein signal peptide (predicted outer membrane–specific lipoprotein); **IPM**, predicted amphipathic in-plane membrane helices.

https://doi.org/10.1371/journal.pone.0223794.t004

Table 5. Cell maintaining proteins.

Protein name	Uniprot entry name	Max coverage	IM	DRM	Diff.	Ratio	TM	SP	IPM
Cell division protein DamX	DAMX	81.10%	65	138	73	2.12	1	No	No
Mechanosensitive channel MscK	MSCK	42.60%	50	108	58	2.15	11	SPI	Yes
Peptidoglycan D,D-transpeptidase FtsI	FTSI	59.50%	33	75	42	2.27	1	No	No
Penicillin-binding protein 1B	PBPB	45.10%	32	68	36	2.11	1	No	Yes
Peptidoglycan D,D-transpeptidase MrdA	MRDA	42.80%	17	43	26	2.53	1	No	No
Serine endoprotease DegS	DEGS	62.80%	23	46	23	1.98	0	SPI	No
Cell division protein FtsN	FTSN	73.40%	29	50	21	1.71	1	No	Yes
ECA polysaccharide chain length modulation protein	WZZE	65.80%	17	38	21	2.21	2	No	Yes
3-deoxy-D-manno-octulosonic acid transferase	KDTA	54.80%	17	33	16	1.91	3	No	Yes
Lipopolysaccharide export system permease protein LptG	LPTG	48.10%	5	21	16	4.10	6	No	Yes
Cell division protein FtsQ	FTSQ	61.60%	17	32	15	1.85	1	No	No
Lipopolysaccharide export system protein LptC	LPTC	54.50%	10	23	13	2.30	0	SPI	No
Co-chaperone protein DjlA (DnaJ-like protein DjlA)	DJLA	47.20%	12	23	11	1.92	2	No	Yes
Protein TolQ	TOLQ	44.30%	29	40	11	1.38	3	No	Yes
Protein TolR	TOLR	31.70%	8	19	11	2.31	1	No	No
Cytoskeleton protein RodZ	RODZ	39.20%	22	32	10	1.43	1	No	Yes

Max coverage, maximum percentage of coverage of identified protein; **IM**, spectra from inner membrane sample; **DRM**, average spectra obtained from DRM samples; **Diff**, average difference between spectra counts in DRM and in IM samples; **Ratio**, average ratio between spectra counts in DRM and in IM samples; **TM**, Predicted transmembrane domains; **SP**, predicted signal peptide [SPI, signal peptide; SPII (IM), lipoprotein signal peptide (predicted inner membrane–specific lipoprotein); SPII (OM), lipoprotein signal peptide (predicted outer membrane–specific lipoprotein); **IPM**, predicted amphipathic in-plane membrane helices.

https://doi.org/10.1371/journal.pone.0223794.t005

Discussion

During the past 10 years increasing attention has been drawn to the study of lipid raft-like structures in bacterial membranes. Such membrane microdomains have been identified in *B. subtilis*, *S. aureus*, *B. burgdorferi*, *H. pylori* and *E. coli* [9,13,15–17]. The herein presented results provide the first comprehensive profile of the lipid raft proteome of *E. coli*, providing information on membrane protein organization in this important model bacterium. An important step in our approach was the isolation of *E. coli* inner membranes prior to detergent treatment, in order to minimize the contamination of outer membrane proteins. This is because OMs resist detergent treatment and coincide at the same floatation density in Opti-Prep gradients. In fact, a ~ 5% of OM-protein contaminants in the isolated IMs were still found in our proteomic analysis, similarly to that reported in previous studies [24,25,28]. As

Table 6. Secretion system proteins.

Protein name	Uniprot entry name	Max coverage	IM	DRM	Diff.	Ratio	TM	SP	IPM
Sec translocon accessory complex subunit YajC	YAJC	87.30%	207	286	79	1.38	1	No	No
Membrane protein insertase YidC	YIDC	58.40%	56	115	59	2.04	5	SPI	Yes
Apolipoprotein N-acyltransferase	LNT	46.70%	9	41	32	4.56	8	No	Yes
Protein-export membrane protein SecG	SECG	55.50%	17	31	14	1.82	2	No	No
Protein translocase subunit SecY	SECY	45.80%	19	31	12	1.61	10	No	No

Max coverage, maximum percentage of coverage of identified protein; **IM**, spectra from inner membrane sample; **DRM**, average spectra obtained from DRM samples; **Diff**, average difference between spectra counts in DRM and in IM samples; **Ratio**, average ratio between spectra counts in DRM and in IM samples; **TM**, Predicted transmembrane domains; **SP**, predicted signal peptide [SPI, signal peptide; SPII (IM), lipoprotein signal peptide (predicted inner membrane–specific lipoprotein); SPII (OM), lipoprotein signal peptide (predicted outer membrane–specific lipoprotein); **IPM**, predicted amphipathic in-plane membrane helices.

https://doi.org/10.1371/journal.pone.0223794.t006

Table 7. Unknown function proteins.

Protein name	Uniprot entry name	Max coverage	IM	DRM	Diff.	Ratio	TM	SP	IPM
Uncharacterized protein YebT	YEBT	69.90%	20	101	81	5.03	1	No	No
Inner membrane protein YejM	YEJM	49.30%	24	58	34	2.40	5	No	Yes
Putative membrane protein IgaA	IGAA	33.80%	9	42	33	4.67	5	No	No
Inner membrane protein YhcB	YHCB	68.90%	35	58	23	1.66	1	No	No
Uncharacterized lipoprotein YbjP	YBJP	65.50%	4	20	16	4.88	0	SPII (OM)	No
Uncharacterized lipoprotein YajG	YAJG	51.00%	4	19	15	4.63	0	SPII (OM)	Yes
Chain length determinant protein	WZZB	77.00%	55	66	11	1.19	2	No	No
Probable inner membrane protein Smp	SMP	46.30%	6	16	10	2.67	1	SPI	No
Low conductance mechanosensitive channel YnaI	YNAI	40.20%	11	21	10	1.91	5	No	Yes
Putative transport protein YbjL	YBJL	29.60%	4	14	10	3.50	11	No	Yes

Max coverage, maximum percentage of coverage of identified protein; **IM**, spectra from inner membrane sample; **DRM**, average spectra obtained from DRM samples; **Diff**, average difference between spectra counts in DRM and in IM samples; **Ratio**, average ratio between spectra counts in DRM and in IM samples; **TM**, Predicted transmembrane domains; **SP**, predicted signal peptide [SPI, signal peptide; SPII (IM), lipoprotein signal peptide (predicted inner membrane–specific lipoprotein); SPII (OM), lipoprotein signal peptide (predicted outer membrane–specific lipoprotein); **IPM**, predicted amphipathic in-plane membrane helices.

https://doi.org/10.1371/journal.pone.0223794.t007

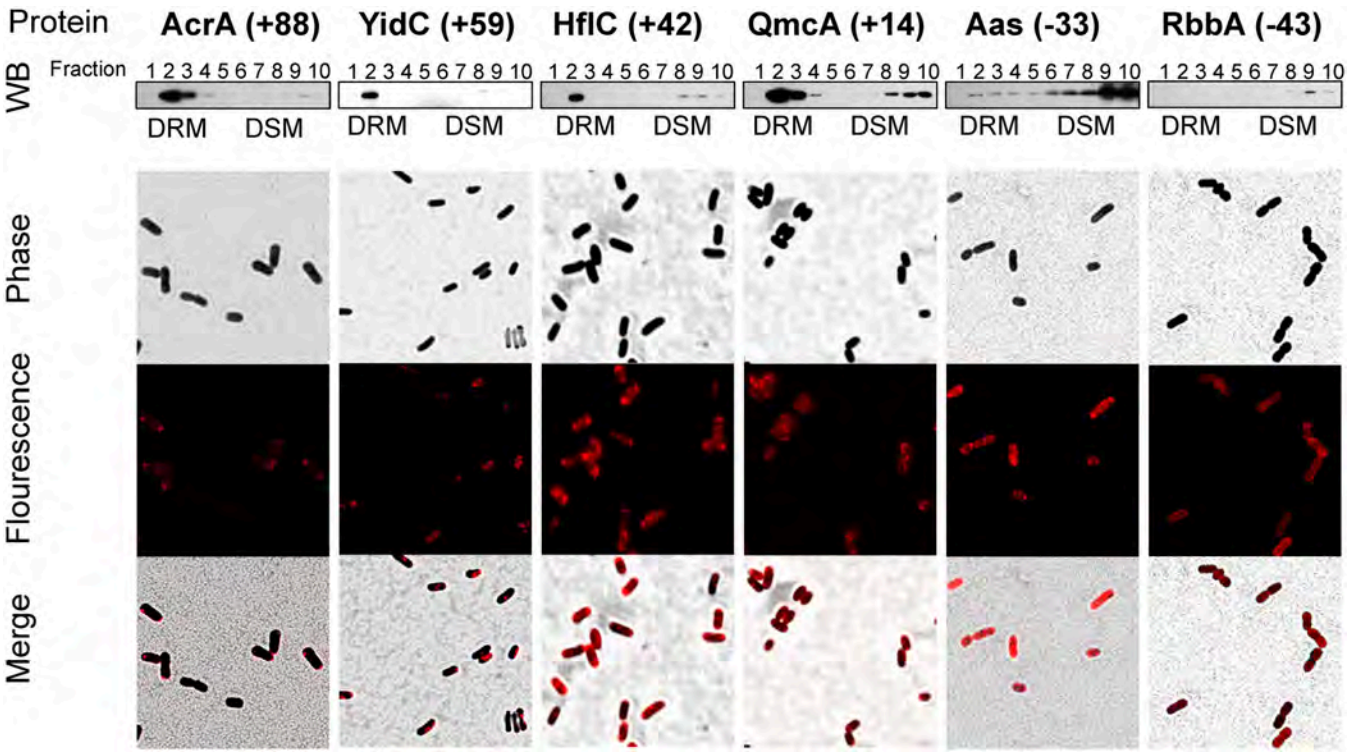

Fig 4. Distribution in OptiPrep gradients and *in vivo* localization of selected lipid raft associated proteins. Top panels: Western blot analysis of DRM (F2) and DSM fractions (F3 to F10), obtained from strains carrying either the AcrA-3xFLAG, YidC-3xFLAG, HflC-HA, QcmA-3xFLAG, Aas-3xFLAG or RbbA-3xFLAG coding sequence allele. A representative immunoblot from at least three entirely independent experiments is shown for each protein. Bottom panels: phase contrast microscopy (top), fluorescence microscopy (middle) and merge (bottom) of living *E. coli* cells carrying either AcrA-mCherry, YidC-mCherry, HflC-mCherry, QmcA-mCherry, Aas-mCherry or RbbA-mCherry are shown. Values in parentheses are differences in spectra counts between DRM and IM samples.

https://doi.org/10.1371/journal.pone.0223794.g004

expected, these contaminants were notably enriched in the DRM fractions. For interpreting our mass-spectrometry data, a difference of 10 or higher between spectra obtained from DRM and IM samples (spectraDRM—spectra$_{IM} \geq 10$) was used to assign lipid raft residency to each protein. In total, 80 proteins were identified as DRM components, and among them were found three of the four *E. coli* SPFH-containing proteins that are typically used as lipid raft markers. Using the above criterion, the location in DRM of proteins producing many spectra (*i.e.* most abundant proteins) is emphasized, whereas proteins poorly represented in the proteomic analysis, although important, may be neglected. An alternative approach could be the use of the ratio between peptide counts in DRM and IM samples. For instance, a ratio of 1.5 or higher (spectra$_{DRM}$ / spectra$_{IM} \geq 1.5$) could be used as a criterion to determine enrichment of a protein in DRM. In this case, several proteins (>75) that were discarded in the above analysis could qualify as possible microdomain components, while only 14 of the previously deemed DRM-located proteins failed to meet this criterion. However, proteins with few peptides identified in IM could mislead the interpretation of the proteomic analysis. Taking this into account, 17 additional proteins could be designated as putative lipid raft components if values of spectra$_{DRM}$ / spectra$_{IM} \geq 1.5$ and spectraDRM—spectra$_{IM} > 5$ were considered (S4 Table). Interestingly, YqiK, the only SPFH-containing protein that was not identified by our proteomic analysis, belongs to a group of membrane proteins that has been shown to be particularly elusive to identification by mass spectrometry [25].

In addition to the SPFH-domain containing proteins (lipid raft markers), proteins committed to protein secretion and membrane insertion (e.g. SecY, SecG, YajC, YidC) were identified as putative raft constituents, comparable to those reported for *B. subtilis*, *B. burgdorferi*, S. *aureus* [20–22]. Likewise, proteins with transport functions were well represented in DRM fractions. These include members of the superfamily of ATP-binding cassette (ABC) transporters, multidrug efflux complexes, and members of the family of phosphoenolpyruvate-dependent sugar phosphotransferase systems (sugar-PTS). This is consistent with previous studies that have identified transporters as common components of lipid microdomains in *B. subtilis*, *B. burgdorferi* [20,21]. Moreover, the location and function of several eukaryotic ABC transporters, involved in multidrug resistance, have been found to be controlled by their presence in lipid rafts from tumor cells [46]. Interestingly, the ABC transporter MsbA, an essential protein involved in the translocation of lipid A-core from the inner leaflet to the outer leaflet of the IM [47], exhibits a high similarity to mammalian multidrug resistance proteins (MDR) [48]. MDR-1, a member from the latter, which shares a 30% amino acid sequence identity and 46% similarity to MsbA, was also found to be structurally and functionally associated with lipid rafts [49]. Thus, the association of MsbA and other ABC transporters with raft-like microdomains in *E. coli* could highlight the co-evolution of transporter complexes and lipid rafts, establishing a suitable microenvironment for proper transport functions.

On the other hand, *E. coli* complexes involved in energy metabolism exhibited differential resistance detergent profiles. For instance, all identified components of cytochrome bo_3 and cytochrome *bd* terminal oxidases were enriched in DRM, indicating that these complexes are lipid raft residents. In contrast, NADH-quinone oxidoreductase I components (NuoJ, NuoA, NuoM, NuoH, NuoN, NuoL, NuoB and NuoI), the NADH-quinone oxidoreductase II (Ndh), and components of the ATP-synthase complex, which are functionally associated with terminal oxidases in the electron transport chain, were not enriched in DRM fractions, suggesting that components of a given metabolic pathway could be differentially partitioned into lipid rafts in a point of time.

In spite of the widely established idea that the lipid rafts are implicated in the orchestration of processes related to signal transduction in both eukaryotes and prokaryotes [9,19,50], the only two bacterial histidine kinases associated with lipid rafts, so far, are KinC and WalK from

B. subtilis and *S. aureus*, respectively [9]. Here, we identified the sensor kinase of the CusSR two-component system, which regulates the expression of genes involved in copper uptake, as a lipid raft resident. Also, the histidine kinase DcuS, which participates in the control of expression of genes involved in the C4 dicarboxylates catabolism, was found to be enriched 7.5-fold in DRM in comparison with IM. However, this protein was not selected as a raft resident due to its low spectra representation, which was only 1 and 7.5 peptides from IM and DRM, respectively. The absence of bacterial sensor kinases in proteomic analyses of lipid rafts may be due to their very low expression, hampering their identification in membrane samples [25]. Thus, the organization of signaling pathways involving sensor kinases into membrane microdomains remains to be determined.

Although the proteomic analysis of DRMs may provide important data regarding the characteristics of lipid rafts, it is important to emphasize that proteins whose localization in DRM fractions was not validated by experimental approaches must be interpreted with caution. For instance, to support the results of our proteomic analysis, we probed the distribution of selected proteins in live cells, by fluorescence microscopy. As expected, proteins that were enriched in DRM were observed as discrete foci, principally in cell poles, whereas proteins not identified in DRM were widely distributed in the cell membrane. Moreover, the results of immunodetection assays of the selected proteins were in agreement with the proteomic and microscopy analyses. While localization of proteins within foci does not necessarily involve active recruitment to lipid rafts and could implicate other elements such as the bacterial cytoskeleton, the combination of the identification of a given protein, by proteomic analysis, immunodetection, and fluorescence microscopy localization, strongly suggests that such protein could be a *bona fide* lipid raft resident. Nevertheless, the mechanism by which proteins are partitioned into membrane microdomains, as well as the functional consequences of this recruitment remains unclear and in need of further investigation.

Finally, an attracting issue in the study of bacterial lipid rafts is their lipid composition. In eukaryotic membranes, cholesterol increases membrane thickness and reduces its fluidity by improving the close packing of the longer and saturated acyl chains of sphingolipids. This promotes the segregation of sphingolipids from glycerophospholipids and leads to raft formation. However, most bacteria lack sterols and sphingolipids, and other specialized lipid species, such as farnesol [12], polyisoprenoid lipids (carotenoids) [9], or cyclic polyisoprenoid lipids (hopanoids) [51] have been proposed to functionally and structurally replace cholesterol in ordered membrane microdomains. Nevertheless, neither of these lipid species has been found to be present in *E. coli* membranes. Thus, a comparative lipidomic analysis between DRM and DSM fractions obtained from *E. coli* inner membrane is of foremost interest.

Supporting information

S1 Fig. Schematic work-flow for plasmids construction.
(TIFF)

S1 Table. DNA oligonucleotides used in this work.
(XLSX)

S2 Table. Total spectra counts obtained by LC/MS/MS and protein assignment.
(XLSX)

S3 Table. Relative abundance of inner membrane proteins in IM and DRM samples.
(XLSX)

S4 Table. Additional DRM enriched proteins and putative lipid raft-resident.
(XLSX)

Acknowledgments

We thank Claudia Rodríguez Rangel for technical assistance. LC-MS/MS were performed at the Mass spectrometry facility at the Institut de Recherches Cliniques de Montréal (IRCM).

Author Contributions

Conceptualization: Marina Gavilanes-Ruiz, Tony Romeo, Adrián F. Alvarez, Dimitris Georgellis.

Data curation: José E. Guzmán-Flores, Luis E. González de la Vara.

Funding acquisition: Adrián F. Alvarez, Dimitris Georgellis.

Investigation: José E. Guzmán-Flores, Lidia Steinemann-Hernández, Luis E. González de la Vara.

Project administration: Adrián F. Alvarez, Dimitris Georgellis.

Supervision: Adrián F. Alvarez, Dimitris Georgellis.

Writing – original draft: José E. Guzmán-Flores, Adrián F. Alvarez, Dimitris Georgellis.

Writing – review & editing: José E. Guzmán-Flores, Lidia Steinemann-Hernández, Luis E. González de la Vara, Marina Gavilanes-Ruiz, Tony Romeo, Adrián F. Alvarez, Dimitris Georgellis.

References

1. Astro V, de Curtis I. Plasma membrane-associated platforms: dynamic scaffolds that organize membrane-associated events. Sci Signal. 2015; 8: re1. https://doi.org/10.1126/scisignal.aaa3312 PMID: 25759479
2. Lingwood D, Simons K. Lipid rafts as a membrane-organizing principle. Science. 2010; 327: 46–50. https://doi.org/10.1126/science.1174621 PMID: 20044567
3. Browman DT, Hoegg MB, Robbins SM. The SPFH domain-containing proteins: more than lipid raft markers. Trends Cell Biol. 2007; 17: 394–402. https://doi.org/10.1016/j.tcb.2007.06.005 PMID: 17766116
4. Langhorst MF, Reuter A, Stuermer CAO. Scaffolding microdomains and beyond: the function of reggie/flotillin proteins. Cell Mol Life Sci. 2005; 62: 2228–2240. https://doi.org/10.1007/s00018-005-5166-4 PMID: 16091845
5. Morrow IC, Parton RG. Flotillins and the PHB domain protein family: rafts, worms and anaesthetics. Traffic. 2005; 6: 725–740. https://doi.org/10.1111/j.1600-0854.2005.00318.x PMID: 16101677
6. Kato N, Nakanishi M, Hirashima N. Flotillin-1 regulates IgE receptor-mediated signaling in rat basophilic leukemia (RBL-2H3) cells. J Immunol. 2006; 177: 147–154. https://doi.org/10.4049/jimmunol.177.1.147 PMID: 16785509
7. Langhorst MF, Solis GP, Hannbeck S, Plattner H, Stuermer CAO. Linking membrane microdomains to the cytoskeleton: Regulation of the lateral mobility of reggie-1/flotillin-2 by interaction with actin. FEBS Lett. 2007; 581: 4697–4703. https://doi.org/10.1016/j.febslet.2007.08.074 PMID: 17854803
8. Bach JN, Bramkamp M. Flotillins functionally organize the bacterial membrane. Mol Microbiol. 2013; 88: 1205–1217. https://doi.org/10.1111/mmi.12252 PMID: 23651456
9. López D, Kolter R. Functional microdomains in bacterial membranes. Genes Dev. 2010; 24: 1893–1902. https://doi.org/10.1101/gad.1945010 PMID: 20713508
10. Schneider J, Mielich-Süss B, Böhme R, Lopez D. *In vivo* characterization of the scaffold activity of flotillin on the membrane kinase KinC of *Bacillus subtilis*. Microbiology. 2015; 161: 1871–1887. https://doi.org/10.1099/mic.0.000137 PMID: 26297017

11. Schneider J, Klein T, Mielich-Süss B, Koch G, Franke C, Kuipers OP, et al. Spatio-temporal Remodeling of Functional Membrane Microdomains Organizes the Signaling Networks of a Bacterium. Casadesús J, editor. PLOS Genet. 2015; 11: e1005140. https://doi.org/10.1371/journal.pgen.1005140 PMID: 25909364

12. Feng X, Hu Y, Zheng Y, Zhu W, Li K, Huang C-H, et al. Structural and functional analysis of *Bacillus subtilis* YisP reveals a role of its product in biofilm production. Chem Biol. 2014; 21: 1557–1563. https://doi.org/10.1016/j.chembiol.2014.08.018 PMID: 25308276

13. Mielich-Süss B, Wagner RM, Mietrach N, Hertlein T, Marincola G, Ohlsen K, et al. Flotillin scaffold activity contributes to type VII secretion system assembly in *Staphylococcus aureus*. PLOS Pathog. 2017; 13: e1006728. https://doi.org/10.1371/journal.ppat.1006728 PMID: 29166667

14. Somani VK, Aggarwal S, Singh D, Prasad T, Bhatnagar R. Identification of novel raft marker protein, FlotP in *Bacillus anthracis*. Front Microbiol. 2016; 7: 169. https://doi.org/10.3389/fmicb.2016.00169 PMID: 26925042

15. LaRocca TJ, Pathak P, Chiantia S, Toledo A, Silvius JR, Benach JL, et al. Proving lipid rafts exist: membrane domains in the prokaryote *Borrelia burgdorferi* have the same properties as eukaryotic lipid rafts. PLOS Pathog. 2013; 9: e1003353. https://doi.org/10.1371/journal.ppat.1003353 PMID: 23696733

16. Hutton ML, D'Costa K, Rossiter AE, Wang L, Turner L, Steer DL, et al. A *Helicobacter pylori* homolog of eukaryotic flotillin is involved in cholesterol accumulation, epithelial cell responses and host colonization. Front Cell Infect Microbiol. 2017; 7: 219. https://doi.org/10.3389/fcimb.2017.00219 PMID: 28634572

17. Guzmán-Flores JE, Alvarez AF, Poggio S, Gavilanes-Ruiz M, Georgellis D. Isolation of detergent-resistant membranes (DRMs) from *Escherichia coli*. Anal Biochem. 2017; 518: 1–8. https://doi.org/10.1016/j.ab.2016.10.025 PMID: 27984012

18. Staneva G, Seigneuret M, Koumanov K, Trugnan G, Angelova MI. Detergents induce raft-like domains budding and fission from giant unilamellar heterogeneous vesicles: A direct microscopy observation. Chem Phys Lipids. 2005; 136: 55–66. https://doi.org/10.1016/j.chemphyslip.2005.03.007 PMID: 15927174

19. Brown DA. Lipid rafts, detergent-resistant membranes, and raft targeting signals. Physiology (Bethesda). 2006; 21: 430–439. https://doi.org/10.1152/physiol.00032.2006 PMID: 17119156

20. Yepes A, Schneider J, Mielich B, Koch G, García-Betancur J-C, Ramamurthi KS, et al. The biofilm formation defect of a *Bacillus subtilis* flotillin-defective mutant involves the protease FtsH. Mol Microbiol. 2012; 86: 457–471. https://doi.org/10.1111/j.1365-2958.2012.08205.x PMID: 22882210

21. Toledo A, Pérez A, Coleman JL, Benach JL. The lipid raft proteome of *Borrelia burgdorferi*. Proteomics. 2015; 15: 3662–3675. https://doi.org/10.1002/pmic.201500093 PMID: 26256460

22. García-Fernández E, Koch G, Wagner RM, Fekete A, Stengel ST, Schneider J, et al. Membrane Microdomain Disassembly Inhibits MRSA Antibiotic Resistance. Cell. 2017; https://doi.org/10.1016/j.cell.2017.10.012 PMID: 29103614

23. Toledo A, Huang Z, Coleman JL, London E, Benach JL. Lipid rafts can form in the inner and outer membranes of *Borrelia burgdorferi* and have different properties and associated proteins. Mol Microbiol. 2018; 108: 63–76. https://doi.org/10.1111/mmi.13914 PMID: 29377398

24. Zhang N, Chen R, Young N, Wishart D, Winter P, Weiner JH, et al. Comparison of SDS- and methanol-assisted protein solubilization and digestion methods for *Escherichia coli* membrane proteome analysis by 2-D LC-MS/MS. Proteomics. 2007; 7: 484–493. https://doi.org/10.1002/pmic.200600518 PMID: 17309111

25. Bernsel A, Daley DO. Exploring the inner membrane proteome of *Escherichia coli*: which proteins are eluding detection and why? Trends Microbiol. 2009; 17: 444–449. https://doi.org/10.1016/j.tim.2009.07.005 PMID: 19766000

26. Masuda T, Saito N, Tomita M, Ishihama Y. Unbiased quantitation of *Escherichia coli* membrane proteome using phase transfer surfactants. Mol Cell Proteomics. 2009; 8: 2770–7. https://doi.org/10.1074/mcp.M900240-MCP200 PMID: 19767571

27. Papanastasiou M, Orfanoudaki G, Koukaki M, Kountourakis N, Sardis MF, Aivaliotis M, et al. The *Escherichia coli* peripheral inner membrane proteome. Mol Cell Proteomics. 2013; 12: 599–610. https://doi.org/10.1074/mcp.M112.024711 PMID: 23230279

28. Lee H-L, Chiang I-C, Liang S-Y, Lee D-Y, Chang G-D, Wang K-Y, et al. Quantitative Proteomics Analysis Reveals the Min System of *Escherichia coli* Modulates Reversible Protein Association with the Inner Membrane. Mol Cell Proteomics. 2016; 15: 1572–83. https://doi.org/10.1074/mcp.M115.053603 PMID: 26889046

29. Datsenko KA, Wanner BL. One-step inactivation of chromosomal genes in *Escherichia coli* K-12 using PCR products. Proc Natl Acad Sci U S A. 2000; 97: 6640–6645. https://doi.org/10.1073/pnas.120163297 PMID: 10829079

30. Uzzau S, Figueroa-Bossi N, Rubino S, Bossi L. Epitope tagging of chromosomal genes in *Salmonella*. Proc Natl Acad Sci U S A. 2001; 98: 15264–15269. https://doi.org/10.1073/pnas.261348198 PMID: 11742086

31. Thanbichler M, Iniesta AA, Shapiro L. A comprehensive set of plasmids for vanillate- and xylose-inducible gene expression in *Caulobacter crescentus*. Nucleic Acids Res. 2007; 35: e137. https://doi.org/10.1093/nar/gkm818 PMID: 17959646

32. Peña-Sandoval GR, Kwon O, Georgellis D. Requirement of the receiver and phosphotransfer domains of ArcB for efficient dephosphorylation of phosphorylated ArcA *in vivo*. J Bacteriol. 2005; 187: 3267–3272. https://doi.org/10.1128/JB.187.9.3267-3272.2005 PMID: 15838055

33. Dykxhoorn DM, St Pierre R, Linn T. A set of compatible *tac* promoter expression vectors. Gene. 1996; 177: 133–136. Available: http://www.ncbi.nlm.nih.gov/entrez/query.fcgi?cmd=Retrieve&db=PubMed&dopt=Citation&list_uids=8921858 PMID: 8921858

34. He L, Diedrich J, Chu YY, Yates JR. Extracting Accurate Precursor Information for Tandem Mass Spectra by RawConverter. Anal Chem. 2015; 87: 11361–11367. https://doi.org/10.1021/acs.analchem.5b02721 PMID: 26499134

35. Deutsch EW, Mendoza L, Shteynberg D, Farrah T, Lam H, Tasman N, et al. A guided tour of the Trans-Proteomic Pipeline [Internet]. Proteomics. WILEY-VCH Verlag; 2010. pp. 1150–1159.

36. Tsirigos KD, Peters C, Shu N, All L, Elofsson A. The TOPCONS web server for consensus prediction of membrane protein topology and signal peptides. Nucleic Acids Res. 2015; 43. https://doi.org/10.1093/nar/gkv485 PMID: 25969446

37. Juncker AS, Willenbrock H, von Heijne G, Brunak S, Nielsen H, Krogh A. Prediction of lipoprotein signal peptides in Gram-negative bacteria. Protein Sci. 2003; 12: 1652–1662. https://doi.org/10.1110/ps.0303703 PMID: 12876315

38. Combet C, Blanchet C, Geourjon C, Deléage G. NPS@: Network protein sequence analysis. Trends Biochem Sci. 2000; 25: 147–150. https://doi.org/10.1016/s0968-0004(99)01540-6 PMID: 10694887

39. Sambrook J, Russell DW. Molecular cloning: a Laboratory Manual. 3rd ed. NY: Cold Spring Harbor Laboratory: Cold Spring Harbor; 2001.

40. Schneider CA, Rasband WS, Eliceiri KW. NIH Image to ImageJ: 25 years of image analysis. Nat Methods. 2012; 9: 671–675. https://doi.org/10.1038/nmeth.2089 PMID: 22930834

41. Lopez D, Koch G. Exploring functional membrane microdomains in bacteria: an overview. Curr Opin Microbiol. 2017; 36: 76–84. https://doi.org/10.1016/j.mib.2017.02.001 PMID: 28237903

42. Thein M, Sauer G, Paramasivam N, Grin I, Linke D. Efficient subfractionation of gram-negative bacteria for proteomics studies. J Proteome Res. 2010; 9: 6135–6147. https://doi.org/10.1021/pr1002438 PMID: 20932056

43. Emiola A, Andrews SS, Heller C, George J. Crosstalk between the lipopolysaccharide and phospholipid pathways during outer membrane biogenesis in *Escherichia coli*. Proc Natl Acad Sci. 2016; 113: 3108–3113. https://doi.org/10.1073/pnas.1521168113 PMID: 26929331

44. Lai EC. Lipid rafts make for slippery platforms. J Cell Biol. 2003; 162: 365–370. https://doi.org/10.1083/jcb.200307087 PMID: 12885764

45. Kenworthy AK, Nichols BJ, Remmert CL, Hendrix GM, Kumar M, Zimmerberg J, et al. Dynamics of putative raft-associated proteins at the cell surface. J Cell Biol. 2004; 165: 735–746. https://doi.org/10.1083/jcb.200312170 PMID: 15173190

46. Klappe K, Hummel I, Hoekstra D, Kok JW. Lipid dependence of ABC transporter localization and function. Chem Phys Lipids. 2009; 161: 57–64. https://doi.org/10.1016/j.chemphyslip.2009.07.004 PMID: 19651114

47. Zhou Z, White KA, Polissi A, Georgopoulos C, Raetz CRH. Function of *Escherichia coli* MsbA, an essential ABC family transporter, in lipid A and phospholipid biosynthesis. J Biol Chem. 1998; 273: 12466–12475. https://doi.org/10.1074/jbc.273.20.12466 PMID: 9575204

48. Karow M, Georgopoulos C. The essential *Escherichia coli msbA* gene, a multicopy suppressor of null mutations in the *htrB* gene, is related to the universally conserved family of ATP-dependent translocators. Mol Microbiol. 1993; 7: 69–79. https://doi.org/10.1111/j.1365-2958.1993.tb01098.x PMID: 8094880

49. Yun UJ, Lee JH, Koo KH, Ye SK, Kim SY, Lee CH, et al. Lipid raft modulation by Rp1 reverses multidrug resistance via inactivating MDR-1 and Src inhibition. Biochem Pharmacol. 2013; 85: 1441–1453. https://doi.org/10.1016/j.bcp.2013.02.025 PMID: 23473805

50. Allen JA, Halverson-Tamboli RA, Rasenick MM. Lipid raft microdomains and neurotransmitter signalling. Nat Rev Neurosci. 2007; 8: 128–140. https://doi.org/10.1038/nrn2059 PMID: 17195035

51. Sáenz JP, Grosser D, Bradley AS, Lagny TJ, Lavrynenko O, Broda M, et al. Hopanoids as functional analogues of cholesterol in bacterial membranes. Proc Natl Acad Sci U S A. 2015; 112: 11971–6. https://doi.org/10.1073/pnas.1515607112 PMID: 26351677

INFORME DE LABORES 2019
ResearchGate

See discussions, stats, and author profiles for this publication at: https://www.researchgate.net/publication/336444769

Caracterización cognitiva y conductual de una muestra de adolescentes consumidores de inhalables de la Ciudad de México

Article *in* Salud y drogas · August 2019
DOI: 10.21134/haaj.v19i2.429

CITATIONS
0

READS
188

5 authors, including:



Jessica Zapata Téllez
Instituto Nacional de Psiquiatría "Ramón de la Fuente Muñiz"
5 PUBLICATIONS **0** CITATIONS

SEE PROFILE

Some of the authors of this publication are also working on these related projects:



Teoría de la Mente y Reconocimiento Facial de Emociones en el Trastorno Bipolar. View project



Psychometric properties of the spanish version of the Mindfulness Attention Awareness Scale (MAAS) in a Mexican clinical sample. View project

All content following this page was uploaded by Jessica Zapata Téllez on 11 October 2019.

The user has requested enhancement of the downloaded file.

Health and Addictions salud y drogas

© He
ISSN 1578-5319 ISSNe 1988-205X
Vol. 19, No.2, 19-28
Recibido: Noviembre 2018 - Aceptado: Enero 2019

CARACTERIZACIÓN COGNITIVA Y CONDUCTUAL DE UNA MUESTRA DE ADOLESCENTES CONSUMIDORES DE INHALABLES DE LA CIUDAD DE MÉXICO

COGNITIVE AND BEHAVIORAL CHARACTERIZATION OF A SAMPLE OF INHALANTS-CONSUMING ADOLESCENTS FROM MEXICO CITY

Dailett María Hernández Álvarez[1], Carmen Fernández Cáceres[2], Jessica Zapata Tellez[2], Minerva Crespo Ramírez[1] y Nadia González García[3]

[1]Universidad Nacional Autónoma de México

[2]Centros de Integración Juvenil, México

[3]Hospital Infantil Federico Gómez, México

Abstract

Inhalants are one of the drugs of choice for young people in Mexico City. Its consumption usually begins in a critical period of brain development, associated with processes of myelination and synaptic refinement. There is insufficient information on the cognitive, behavioral and emotional characteristics of inhalants-consuming adolescents. The objective of this study was to determine the neuropsychological profile of the executive functioning of a group of adolescents having Inhalant Use Disorder and to explore the presence of concomitant mental health risk behaviors. Thirty-one adolescents with Inhalant Use Disorder were evaluated through a large test battery for the exploration of executive functioning and a scale on mental health risk behavior. The results show the coexistence of important cognitive and behavioral alterations that are of great relevance for therapeutic treatment of this disorder.

Keywords: Inhalants, adolescence, executive cognitive functioning, mental health.

Resumen

Los inhalables constituyen una de las drogas de preferencia de los jóvenes de la Ciudad de México. Su consumo inicia generalmente en un período crítico de desarrollo cerebral asociado a procesos de mielinización y refinamiento sináptico. Hay sin embargo, insuficiente información sobre las características cognitivas, conductuales y emocionales de los adolescentes que consumen esta droga. El objetivo de este estudio fue determinar el perfil neuropsicológico del funcionamiento ejecutivo de un grupo de adolescentes con trastorno por consumo de inhalables y explorar la presencia de conductas de riesgo para la salud mental. Treinta y un adolescentes con trastorno por consumo de inhalables se evaluaron mediante una amplia batería de pruebas para la exploración del funcionamiento ejecutivo y una escala sobre conductas de riesgo para la salud mental. Los resultados muestran la coexistencia de alteraciones cognitivas y conductuales de gran relevancia para el manejo terapéutico de este trastorno.

Palabras clave: Inhalables, adolescencia, funciones ejecutivas, salud mental.

Correspondencia: Dra. Nadia García González
nadiag.him@gmail.com

El consumo de inhalables se identificó en la década de 1960 como un problema de salud en la población marginada o en situación de calle en México. Con los años ha ocurrido una propagación importante en el país de su uso intencional para conseguir efectos psicoactivos y en la actualidad se observa entre personas de todos los estratos socioeconómicos (Medina-Mora et al., 2015).

Estudios epidemiológicos recientes describen que el 71% de los consumidores de inhalables iniciaron su consumo antes de los 17 años, es decir, durante la adolescencia (Villatoro-Velázquez et al., 2017), período crítico por las transformaciones importantes que acontecen en las estructuras cerebrales (Casey et al., 2005). Los principales cambios en la arquitectura neuronal durante esta etapa de vida ocurren en áreas prefrontales y en la compleja conectividad de éstas con otras regiones cerebrales, asociadas a funciones de regulación y control conductual, cognitivo y emocional (Blakemore & Choudhury, 2006; Lozano & Ostrosky, 2011). Se ha sugerido que el principal beneficio de estos procesos de maduración cerebral durante la adolescencia es brindar oportunidad para la conformación de conexiones sinápticas funcionales con base a las necesidades conductuales y ambientales del sujeto (Flores, 2012) y que esta remodelación cerebral si bien permite una mayor eficiencia de la actividad neural y funcionamiento cognitivo, es la que hace a los adolescentes más vulnerables a las adicciones y los desórdenes psiquiátricos (Crews & Boettinger, 2009; Hackman & Farah, 2008).

Los inhalables contienen una gran variedad de sustancias químicas, entre sus compuestos orgánicos principales se encuentra el tolueno, compuesto altamente neurotóxico, con efectos sumamente negativos sobre la mielina y la transmisión sináptica. La mayoría de las investigaciones se han realizado en consumidores adultos crónicos y describen síndromes cerebrales difusos, desmielinización, y atrofia asociados a deterioro cognitivo (Rosenberg et al., 2002; Takagi et al., 2008). Algunas investigaciones realizadas en población adolescente muestran que hay presencia de daños en la arquitectura cerebral desde edades tempranas, por ejemplo Aydin et al. (2009) reporta menor volumen en diversas regiones bilaterales de la corteza prefrontal en adolescentes expuestos a altas concentraciones de tolueno respecto a un grupo control y Yücel et al. (2010) describe una menor anisotropía fraccional en las regiones del hipocampo y el esplenio del cuerpo calloso.

El abordaje de la problemática del consumo de inhalables en la población adolescente desde una perspectiva neuropsicológica ha sido pobre a pesar de que algunas investigaciones han informado la presencia de deficiencias significativas en el funcionamiento cognitivo en estos usuarios con respecto a grupos controles y a usuarios de otras drogas (Scott & Scott, 2013; Takagi et al., 2011). De acuerdo a los datos reportados por dichas investigaciones, los daños cognitivos se caracterizan principalmente por deterioro de la memoria, la atención y una disminución en la velocidad de procesamiento de información. Por otra parte, también son insuficientes los estudios que investigan la coexistencia de alteraciones mentales en la drogodependencia a inhalables en individuos menores de edad, pese a que se ha señalado la existencia de una alta prevalencia de comorbilidad psiquiátrica en la población general de consumidores de esta sustancia (Perron & Howard, 2009; Wu & Howard, 2007).

En la presente investigación se tiene como sujetos de estudio una muestra de adolescentes cuyo uso intencional y problemático de inhalables es considerado de acuerdo al Manual Diagnóstico y Estadístico de los Trastornos Mentales DSM-5 como un trastorno por consumo de inhalables. Este trastorno se caracteriza por un deterioro clínico significativo manifestado por un período no menor a doce meses, en el cual el consumo recurrente lleva al individuo a problemas sociales, a la reducción de sus actividades diarias e incluso al riesgo físico (APA, 2013). Las principales directrices que guían esta investigación son determinar el perfil neuropsicológico del funcionamiento ejecutivo de un grupo de adolescentes con trastorno por consumo de inhalables y explorar la presencia de conductas de riesgo para la salud mental concomitante. En este estudio partimos del supuesto, de acuerdo a la literatura científica precedente, que los adolescentes consumidores de inhalables presentan alteraciones significativas en el funcionamiento ejecutivo y una alta tasa de comorbilidad psiquiátrica. Ambos aspectos repercuten significativamente en el proceso de la drogodependencia y en la respuesta del individuo al tratamiento (Robles-Martínez et al., 2017), por lo que una caracterización detallada del estado cognitivo y conductual de esta población puede contribuir al

desarrollo de estrategias específicas de intervención que eleven la efectividad en los tratamientos.

MÉTODO

Participantes

Los adolescentes fueron reclutados por conveniencia en seis Centros de Integración Juvenil (CIJ) para la atención de jóvenes consumidores de drogas distribuidos en la Ciudad de México. Se invitó a participar en el estudio a todos los adolescentes que acudieron a estos CIJ durante el período de mayo de 2016 a Diciembre de 2017 que cumplían con los siguientes criterios de inclusión: edad entre 10 y 17 años de edad, duración del consumo de inhalables igual o mayor a un año, frecuencia de consumo mínima de varias veces a la semana, escolaridad mayor a cuarto grado de primaria y vivir en un entorno familiar. Se excluyeron del estudio a los individuos con diagnóstico de trastorno psicótico actual, discapacidad intelectual, trastorno por consumo de otras sustancias adictivas y antecedentes patológicos prenatales y perinatales.

Instrumentos

Entrevista estructurada

La entrevista fue elaborada en función de tres objetivos: a) obtener datos sociodemográficos de interés de los participantes, b) conocer la historia del consumo de drogas: edad de inicio, duración, frecuencia, drogas utilizadas y c) reunir información cualitativa sobre las motivaciones del consumo de los inhalables y percepción del impacto de éste en la salud mental.

Evaluación de las funciones ejecutivas

La evaluación de las funciones ejecutivas se realizó a través de la Batería de Funciones Ejecutivas y Lóbulos Frontales, BANFE-2 (Flores, Ostrosky-Solís & Lozano, 2014). Está batería evalúa diversos procesos cognitivos y cuenta con datos normativos en población mexicana de acuerdo a la edad y la escolaridad. A continuación se enlistan las pruebas empleadas y las funciones principales que evalúan.

- Laberintos: Planeación de la conducta viso-espacial y respeto de reglas.
- Señalamiento autodirigido: Memoria de trabajo viso-espacial en una tarea autodirigida.
- Ordenamiento alfabético de palabras: Memoria de trabajo verbal.
- Resta consecutiva: Capacidad para desarrollar operaciones mentales consecutivas e inversas.
- Clasificación de cartas: Capacidad para generar una hipótesis de clasificación, cambiar de forma flexible el criterio de clasificación (flexibilidad mental) y mantener una conducta en relación a reforzamiento positivo.
- Generación de clasificaciones semánticas: Capacidad de abstracción y nivel de productividad en relación al número de categorías producidas.
- Efecto Stroop (dos modalidades o tareas): Inhibición de una respuesta automatizada.
- Fluidez verbal: Capacidad de producir fluidamente verbos en un lapso corto de tiempo.
- Juego de cartas: Toma de decisiones que implican evaluación de relaciones de riesgo – beneficio.
- Selección de refranes: Abstracción del significado, comprensión del sentido figurado.
- Torre de Hanoi: Planeación secuencial. Implica la realización de pasos intermedios para llegar a una meta.
- Metamemoria: Capacidad para realizar juicios predictivos sobre la capacidad de memoria y ajustes del juicio de acuerdo al desempeño (monitoreo y control).
- Memoria de trabajo viso-espacial: Capacidad de memoria de trabajo viso-espacial para seguir un orden específico.

Evaluación conductual

Para la descripción de las conductas de riesgo para la salud mental se empleó la traducción y adaptación mexicana (Albores-Gallo et al., 2007) de la versión más reciente del Cuestionario sobre la Conducta Infantil CBCL

elaborado por Achenbach & Rescorla (2007) la cual tiene una confiabilidad test-retest de .84 y confiabilidad interna para el total de problemas de .97. Este cuestionario para padres está constituido por 113 ítems que se clasifican en escalas comparables con los criterios diagnósticos del DSM-IV. El cuestionario abarca conductas infantiles asociadas a problemas de ansiedad, depresión, trastorno por déficit de atención e hiperactividad, quejas somáticas, conductas oposicionistas desafiantes y conductas agresivas y delictivas. Cada uno de estos ítems se encuentra configurado con tres opciones de respuesta: falso (0), algunas veces (1), y muy cierto (2).

Procedimiento

Los adolescentes fueron reclutados por trabajadores profesionales de los CIJ con experiencia en los trastornos de conductas adictivas tomando en cuenta los objetivos del estudio y los criterios de elegibilidad. Posteriormente, los sujetos interesados en compañía de algún familiar pasaron por un proceso de consentimiento donde el entrevistador proporcionaba información más detallada relativa a la confidencialidad del estudio, los riesgos y beneficios, las pruebas psicométricas, la duración del estudio, etc. y recababa información relevante por medio de una entrevista estructurada sobre la historia del consumo de sustancias adictivas. En ese encuentro se les aplicaba la Escala de Inteligencia para Niños, WISC-IV (Wechsler, 2007) o la Escala de Inteligencia para Adultos WAIS-IV (Wechsler, 2013), en dependencia de la edad del sujeto, para descartar la presencia de discapacidad intelectual, mientras que sus familiares respondían preguntas sobre el neurodesarrollo y la Escala sobre Conducta Infantil CBCL. A los voluntarios que cumplían con todos los criterios de investigación, se les administró en una segunda sesión la Batería de Funciones Ejecutivas y Lóbulos Frontales BANFE-2. Todos los procedimientos del estudio fueron llevados a cabo individualmente y se realizaron en un lugar privado y sin distractores proporcionados por las instituciones involucradas. La aplicación de las pruebas se realizó por profesionales de la psicología con experiencia en el uso de éstas. El tiempo promedio de contacto con los participantes fue de una hora y media por sesión. Todos los procedimientos del protocolo fueron aprobados por el Comité de Investigación Científica del Centro de Integración Juvenil. El procesamiento y tratamiento estadístico de los datos se realizó mediante el programa SPSS versión 21.0.

RESULTADOS

Análisis descriptivo de la muestra

La muestra quedó constituida por 31 adolescentes con una edad media de 15 años, que incluía 25 hombres y 6 mujeres. Dos individuos fueron excluidos del estudio debido a puntuaciones del cociente intelectual inferiores a 70 que indicaba la presencia de discapacidad intelectual y uno por interrupción voluntaria de la evaluación. El 81% de los sujetos reportó inhalar más de tres veces a la semana productos rebajadores de pintura, acetona y gasolina y un 19% reportó hacer uso además de pinturas, desodorantes y pegamentos. La edad media del inicio del consumo fue de 13.02 (*DT* = 1.7). El tiempo de consumo promedio fue de 24 meses, el tiempo mínimo fue de 12 meses y el máximo de 60 meses.

El 61% de la muestra reportó consumo de otras drogas aunque en menor frecuencia que los inhalables. En la Tabla 1 se pueden observar las características del policonsumo. El 53.3% de la muestra reportó cese del consumo de drogas apenas unos días atrás y el 20% abandono de éstas desde hacía un mes. El 10% de la muestra reportó no consumir drogas desde hacía tres meses, mientras que el 16.6% de los participantes mencionó no haber logrado suspender su uso. El 66% de la muestra describió uno o dos intentos fallidos por abandonar la droga antes de solicitar ayuda profesional.

Tabla 1. Reporte sobre el consumo de drogas

	Número de sujetos
Solo inhalables	12
Inhalables y alcohol	5
Inhalables y mariguana	6
Inhalables, alcohol y mariguana	2
Inhalables y cocaína	1
Inhalables, mariguana y cocaína	2
Inhalables, alcohol, mariguana y cocaína	3

Nota: Drogas usadas sistemáticamente (de varias veces por semana a casi diario).

El nivel educativo promedio de los participantes fue de 8.1 (*DT* = 1.1) años. Las principales motivaciones descritas que dieron al inicio del consumo de inhalables fueron mitigar malestares emocionales (63% de los entrevistados), la mayoría de los cuales se vinculaban con problemas familiares así como fines recreativos (curiosidad y diversión con amigos). A la pregunta ¿a qué problemas le ha llevado su consumo? la respuesta más frecuente fue: a conflictos en el ámbito familiar (63%) seguida de peleas en la escuela y en la calle (20%). Los problemas cognitivos autoreportados por los voluntarios fueron: fallos en la memoria en el 77% de ellos, problemas de atención en el 70%, pobre control de los impulsos en el 64%, alteraciones en el lenguaje expresivo en el 48%, dificultades en la toma de decisiones en el 48% y lentitud en el pensamiento también en el 48%. Respecto a su estado emocional el 70% de los participantes autoreportó sentir ansiedad y el 48% mencionó sentimientos de depresión.

Análisis del funcionamiento ejecutivo

La batería neuropsicológica de funciones ejecutivas y lóbulos frontales BANFE-2, permite obtener un perfil individual, que describe las habilidades e inhabilidades del evaluado. Las puntuaciones naturales de las pruebas se transforman en puntuaciones normalizadas con una media de 10 y una desviación estándar de 3. A partir de estos parámetros la prueba permite determinar si el individuo tiene un funcionamiento ejecutivo normal alto, normal, con alteraciones leves a moderadas o con alteraciones severas para cada una de las subpruebas. En la Tabla 2 se muestra por cada subprueba el porcentaje de participantes que puntuó en los cuatro grados de clasificación del funcionamiento ejecutivo y la clasificación de acuerdo a las puntuaciones promedios de la muestra.

De acuerdo a los resultados en la batería BANFE-2 hubo una gran variabilidad en el funcionamiento ejecutivo de los participantes. Los resultados obtenidos mostraron la presencia de adolescentes con puntuaciones dentro del rango de alteraciones leves a moderadas así como dentro del rango de alteraciones severas en todas las pruebas, sin embargo, tomando en cuenta las puntuaciones medias del grupo, el perfil cognitivo tiende a la normalidad en la mayoría de éstas.

Las puntuaciones medias evidencian por otra parte, algunos déficits importantes en el funcionamiento ejecutivo. El bajo rendimiento en la prueba de laberintos, específicamente las dificultades para acatar la regla de no atravesar o tocar las paredes al resolver el ejercicio, pudiera indicar un pobre control de los impulsos. En la tarea de ordenamiento alfabético en el nivel de mayor dificultad (nivel 3), la puntuación media de los participantes se situó dentro del perfil de alteraciones leves a moderadas. Esta tarea está dirigida a evaluar la capacidad de memoria de trabajo verbal y la puntuación media obtenida apunta hacia una pobre retención y dificultad para la manipulación mental de palabras en esta muestra de adolescentes. También se encontraron déficits en los participantes en la capacidad de inhibición de una respuesta automática, pues los puntajes medios en la cantidad de errores Stroop se situaron en el perfil de alteraciones leves a moderadas. Las funciones cognitivas menos afectadas de acuerdo al perfil general de funcionamiento ejecutivo de la muestra fueron la fluidez verbal y la memoria de trabajo visoespacial.

Se realizó un análisis de correlación de Pearson para analizar si la edad de inicio del consumo, el tiempo y la frecuencia del mismo, se relacionan con el rendimiento de los participantes en las tres tareas en las cuales se observó un perfil de desempeño promedio de alteraciones leves a moderadas. Los valores de la *p* de Pearson se pueden observar en la Tabla 3. No se halló correlación entre las variables del consumo y el número de errores cometidos por atravesar paredes en la prueba de laberintos. Tampoco se halló vínculo entre éstas y los errores de inhibición en la prueba Stroop, pero se observó asociación entre la edad de inicio del consumo de inhalables y la frecuencia del mismo con el desempeño en el nivel máximo de la prueba ordenamiento alfabético. Una menor edad de inicio del consumo y el uso más frecuente de esta droga, se asocia con un menor rendimiento en esta tarea. Estos resultados apuntan a que la frecuencia y la edad de inicio del consumo de inhalables influyen en el desarrollo de la memoria de trabajo verbal.

Al correlacionar de manera cualitativa los datos arrojados por la BANFE-2 con el autoreporte de los participantes sobre los efectos percibidos del consumo de inhalables en el funcionamiento cognitivo, observamos congruencia entre ambos datos, pues como ya habíamos descrito, más del 50% de los participantes mencionó tener problemas en la memoria y pobre

control de impulsos lo cual fue confirmado a través de la evaluación neuropsicológica.

Tabla 2. Perfil neuropsicológico de las funciones ejecutivas

	Clasificación del funcionamiento ejecutivo				
	Normal alto %	Normal %	Alteración Leve-Moderada %	Alteración severa %	Clasificación del FE de acuerdo a la puntuación media de la muestra
Laberintos					
Errores –planeación	0	77	10	13	Normal
Atravesar bordes	0	42	6	52	Alteraciones leve- Moderadas
Tiempo de ejecución	0	81	13	6	Normal
Señalamiento autodirigido					
Aciertos	9	61	16	14	Normal
Tiempo	0	71	9	20	Normal
Ordenamiento alfabético					
Nivel 1	0	52	22	26	Normal
Nivel 2	3	64	7	26	Normal
Nivel 3	0	22	61	17	Alteraciones leve- Moderadas
Resta consecutiva					
Aciertos	0	61	22	17	Normal
Tiempo de ejecución	0	71	9	20	Normal
Clasificación de cartas					
Aciertos	0	58	23	19	Normal
Errores de mantenimiento	0	64	16	20	Normal
Clasificación semántica					
Total de categorías	0	61	35	4	Normal
Categorías abstractas	0	61	20	19	Normal
Stroop A					
Errores stroop	0	41	9	40	Alteraciones leve- Moderadas
Tiempo de ejecución	7	64	7	22	Normal
Stroop B					
Errores stroop	0	61	8	21	Alteraciones leve- Moderadas
Tiempo de ejecución	4	61	19	16	Normal
Fluidez verbal					
Total de palabras	9	66	22	3	Normal
Juego de cartas					
% de cartas de riesgo	16	58	22	4	Normal
Puntuación total	4	58	22	16	Normal
Refranes					
Aciertos	5	87	4	4	Normal
Torre de Hanoi- 1					
Total de movimientos	0	84	13	3	Normal
Tiempo de ejecución	0	74	9	17	Normal
Torre de Hanoi 2					
Total de movimientos	0	52	26	22	Normal
Tiempo de ejecución	0	52	26	22	normal
Metamemoria					
Errores positivos	0	77	9	14	Normal
Errores negativos	1	71	6	13	Normal
Memoria de trabajo visoespacial					
Nivel máximo	0	64	19	1	Normal

Nota: FE = Funcionamiento ejecutivo

Tabla 3. Correlación de Pearson entre variables sobre el consumo de inhalables y variables neuropsicológicas

	Edad de inicio del consumo	Tiempo de consumo	Frecuencia de consumo
Laberintos			
Atravesar bordes	-.12	-.11	- .10
Ordenamiento alfabético			
Nivel 3	.62**	-.22	-.42*
Stroop A			
Errores stroop	.15	-.02	-.09
Stroop B			
Errores stroop	-.01	-.04	-.03

Nota: * p < .05, ** p < .01

Resultados de la evaluación conductual

El Cuestionario sobre la Conducta Infantil CBCL (Achenbach, 2001) permite obtener valores numéricos para cada una de las siguientes escalas o subdominios: problemas afectivos, ansiedad, problemas somáticos, trastorno por déficit de atención e hiperactividad, conducta oposicionista desafiante y problemas de conducta. El puntaje obtenido para cada una de las escalas queda ubicado en uno de 3 rangos posibles: menor del percentil 93, entre el percentil 93 y el 97 y mayor al percentil 97. Los datos clínicamente significativos son los dos últimos, entre el percentil 93 y 97, que se considera un rango límite en el cual los sujetos tienen un riesgo medio de presentar los problemas a los que hace referencia la escala en comparación con otros niños/as de su edad. Un percentil superior a 97 indica un riesgo alto de presentar el problema. En la figura 1 se muestra el porcentaje de sujetos en cada rango por cada una de las escalas.

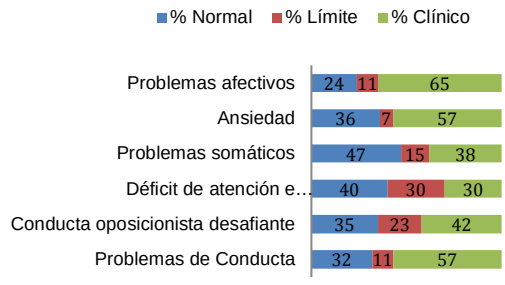

Figura 1. Porcentaje de sujetos en los rangos normal, límite y clínico en cada una de las escalas del CBCL

Al analizar las escalas se observó que más del 50% de los evaluados presentaban conductas clínicas asociadas a problemas afectivos, ansiedad y problemas de conducta. La puntuación media del grupo en la escala de problemas afectivos fue superior al percentil 97 equivalente a un rango clínico que indica un alto riesgo de padecer tal psicopatología. En el resto de las escalas las puntuaciones se ubicaron entre los percentiles 93 y 97 correspondiente con un rango límite o un riesgo medio de padecer los problemas de salud mental explorados. En ninguna de las escalas se obtuvo un percentil medio inferior a 93 mostrando una gran prevalencia de alteraciones conductuales en la muestra evaluada de adolescentes consumidores de inhalables. Cualitativamente se puede distinguir que la alta prevalencia de problemas afectivos y ansiedad detectada a través de las subescalas correspondientes del cuestionario del CBCL, coincide con el autoreporte de los participantes en la entrevista estructurada quienes en su mayoría mencionaron presentar ansiedad y síntomas depresivos.

Se analizó la relación entre las variables sobre el consumo de inhalables y las escalas del cuestionario CBCL. Se encontró poca relación entre dichas medidas (tabla 4). La edad de inicio, el tiempo y la frecuencia de consumo no mostraron asociación con los problemas afectivos, el Trastorno por déficit de atención e hiperactividad y las conductas oposicionistas desafiantes. Se halló una asociación significativa pero moderada entre la edad de inicio del consumo de inhalables y la ansiedad y el tiempo de consumo y la presencia de problemas somáticos y problemas de la conducta. A menor edad de inicio del consumo de inhalables mayor sintomatología ansiosa y a mayor tiempo de consumo mayor número de problemas somáticos y de conducta.

Tabla 4. Correlación de Pearson entre variables sobre el consumo de inhalables y las escalas del CBCL

	Edad de inicio del consumo	Tiempo de consumo	Frecuencia de consumo
Problemas afectivos	-.11	.10	.04
Ansiedad	-.40*	.29	.27
Problemas somáticos	-.23	.42*	.35
Déficit de atención e hiperactividad	-.01	.18	-.03
Conducta oposicionista desafiante	-.28	.30	.00
Problemas de conducta	-.29	.46*	.10

Nota: * p < .05

DISCUSIÓN

El presente estudio estuvo dirigido a la determinación del perfil neuropsicológico del funcionamiento ejecutivo de un grupo de adolescentes con trastorno por consumo de inhalables y la exploración de la presencia concomitante de conductas de riesgo para la salud mental. Nuestros resultados no muestran la presencia de un déficit generalizado en el funcionamiento ejecutivo en los adolescentes y apuntan más bien hacia alteraciones neuropsicológicas específicas. Concretamente se observaron alteraciones en los procesos de control de impulsos, en la capacidad para inhibir una respuesta cognitiva automática y en la memoria de trabajo verbal. Esta última afectada por la edad de inicio del consumo y la frecuencia de uso de la droga. La memoria de trabajo verbal y el control inhibitorio son funciones cognitivas importantes para la toma de decisiones en la vida cotidiana y para el procesamiento e interiorización de los contenidos terapéuticos (Khurana et al, 2017; Wanmaker Yucel et al., 2008). Estos resultados ayudan a comprender los retos del tratamiento de la adicción a inhalables, pues investigaciones con drogodependientes han señalado que dichos déficits en el funcionamiento ejecutivo se asocian con el abandono del proceso terapéutico y aumentan el riesgo a las recaídas (Lorea et al., 2010; Madoz & Ochoa, 2012).

Pese a que a que el perfil promedio de la muestra apunta hacia déficits cognitivos concretos, hay que destacar que algunos participantes mostraron un perfil más generalizado de deterioro en el funcionamiento ejecutivo. Esta variabilidad en el desempeño neuropsicológico puede deberse a diversos factores como la variabilidad en la historia y patrón de consumo, el período de abstinencia, el consumo de otras drogas además de los inhalables, las diferencias en factores psicosociales como la calidad de la educación e instrucción recibida, etc. cuyo análisis estuvo limitado por el tamaño de la muestra. De manera general nuestros datos señalan la necesidad de una evaluación neuropsicológica como parte del diagnóstico clínico en los adolescentes con trastorno por consumo de inhalables.

El diseño transversal de nuestra investigación es una limitación para conocer si los déficits cognitivos detectados en nuestra muestra existían antes del inicio del consumo. Investigaciones longitudinales en adolescentes describen la presencia de una memoria de trabajo débil y un pobre control de impulsos asociados con el uso progresivo de alcohol y mariguana (Khurana et al., 2013; 2017). Las debilidades cognitivas predictoras del consumo progresivo de alcohol y mariguana reportadas por estas investigaciones coinciden con el deterioro ejecutivo encontrado en nuestra muestra de adolescentes consumidores de inhalables, por lo que es probable que los déficits cognitivos detectados en los participantes existieran antes del trastorno. Se necesitan estudios longitudinales que permitan entender si la presencia de déficits en el funcionamiento cognitivo influye en el desarrollo de la conducta adictiva de inhalables durante la adolescencia

El segundo aspecto a destacar en nuestros resultados fue que encontramos una alta presencia de conductas que indican un alto riesgo a padecer trastornos mentales. Más del 50 % de la muestra presenta indicadores conductuales clínicos asociados a trastornos de la afectividad, ansiedad y problemas de conducta y un porcentaje no menos importante mostró indicadores clínicos de trastorno por déficit de atención y trastorno oposicionista desafiante. Si bien nuestro análisis se basa en medidas de tamizaje y no en un diagnóstico clínico psicopatológico, nuestros datos apuntan hacia una elevada frecuencia de alteraciones mentales en los adolescentes con trastorno por consumo de inhalables. Nuestros datos son coherentes con investigaciones previas que reportan gran comorbilidad psiquiátrica en la población general de consumidores de estas sustancias (Martín-Navarrete et al., 2018; Perron & Howard, 2009; Wu & Howard, 2007) y llaman la atención hacia la gran presencia de ésta en los consumidores más jóvenes.

Al igual que se discutió la posibilidad de que los déficits en el funcionamiento ejecutivo existiesen antes e influyeran en el desarrollo del trastorno por consumo de inhalables, también queda la duda sobre la contribución de las alteraciones detectadas en la salud mental de los participantes en el inicio y curso del trastorno. La mayoría de los participantes expresó que el inicio del consumo de inhalables estuvo motivado por la necesidad de mitigar malestares emocionales pero no se cuenta con información clínica sobre el estado previo de su salud mental para analizar la posible contribución de este factor. Esperamos que investigaciones futuras

longitudinales puedan dar respuesta a estos interrogantes.

Conclusiones

En los adolescentes con trastorno por consumo de inhalables coexisten alteraciones emocionales, conductuales y cognitivas, lo que da muestra de la complejidad de la drogodependencia. Las alteraciones en el funcionamiento ejecutivo y las conductas de riesgo para la salud mental detectadas tienen implicaciones importantes para la prevención, diagnóstico y tratamiento ya que pueden causar la progresión negativa del curso clínico, afectar el mantenimiento de la abstinencia o propiciar la reincidencia en el consumo. La detección y atención temprana de estos aspectos puede ayudar a reducir las implicaciones del consumo a largo plazo, pues la adolescencia brinda una ventana de oportunidad para la recuperación de las funciones dado la gran plasticidad cerebral que la caracteriza. Los resultados obtenidos proporcionan evidencia clara de la necesidad de hacer un diagnóstico individualizado oportuno que incluya no solo factores relacionados con el abuso de la sustancia, sino también del estado cognitivo y la salud mental del adolescente.

Agradecimientos

Los autores agradecen la financiación recibida por el Consejo Nacional de Ciencia y Tecnología CONACYT (CVU 264242, No de becario 222482, No de apoyo 412003) sin la cual no se hubiera podido llevar a cabo el estudio.

REFERENCIAS

Achenbach, T., & Rescorla, L. (2007). *Multicultural guide for the ASEBA School-Age form & profiles*. Burlington, VT: University of Vermont. Research Center for Children, Youth and Families.

Albores-Gallo, L., Lara-Munoz, C., Esperon-Vargas, C., Cárdenas, J. A., Pérez, A., & Villanueva, G. (2007). Validez y fiabilidad del CBCL/6-18. *Actas Españolas de Psiquiatría, 35* (6), 393-399.

American Psychiatric Association. (2013). *Diagnostic and statistical manual of mental disorders* (5th ed.). Arlington, VA: American Psychiatric Publishing.

Aydin, K., Sencer, S., Demir, T., Ogel, K., Tunaci, A., & Minareci, O. (2002). Cranial MR findings in chronic toluene abuse by inhalation. *American Journal of Neuroradiology*, *23*(7), 1173–1179.

Blakemore, S. J., & Choudhury, S. (2006). Development of the adolescent brain: Implications for executive function and social cognition. *Journal of Child Psychology and Psychiatry and Allied Disciplines*, *47* (3–4), 296–312. doi: 10.1111/j.1469-7610.2006.01611.x

Casey, B. J., Tottenham, N., Liston, C., & Durston, S. (2005). Imaging the developing brain : what have we learned about cognitive development ?, *9*(3). doi:10.1016/j.tics.2005.01.011

Crews, F. T., & Boettiger, C. A. (2009). Impulsivity, frontal lobes and risk for addiction. *Pharmacology, Biochemistry and Behavior, 93*, 237-247. doi: 10.1016/j.pbb.2009.04.018

Flores, J. (2006). *Neuropsicología de los Lóbulos Frontales.* México: Universidad Juárez Autónoma de Tabasco, División Académica de Ciencias de la Salud.

Flores, J., Ostrosky, F., & Lozano, A. (2014). *Batería neuropsicológica de funciones ejecutivas y lóbulos frontales BANFE-2.* México: El Manual Moderno.

Hackman, D. A., & Farah, M.J. (2008). Socioeconomic status and the developing brain. *Trends in Cognitive Sciences, 13*, 65- 73. doi: 10.1016/j.tics.2008.11.003

Khurana, A., Romer, D., Betancourt, LM., Brodsky, NL., Giannetta, JM., Hurt, H. (2013). Working memory ability predicts trajectories of early alcohol use in adolescents: the mediational role of impulsivity. *Addiction, 108*(3), 506-15. doi: 10.1111/add.12001

Khurana, A., Romer, D., Betancourt, L., & Hurt, H. (2017). Working Memory Ability and Early Drug Use Progression as Predictors of Adolescent Substance Use Disorders . *Addiction*, *112*(7), 1220-1228. doi: 10.1111/add.13792

Lorea, I., Fernández, J., Tirapu., J., Landa, N., & López, J. (2010). Rendimiento neuropsicológico en la adicción a la cocaína: una revisión crítica. *Revista de Neurología, 51*(7), 412- 426.

Lozano, A., & Ostrosky, F. (2011). Desarrollo de las funciones ejecutivas y la corteza prefrontal. *Revista Neuropsicología, Neuropsiquiatría y Neurociencias, 1* (1), 159-172

Madoz, A., & Ochoa, A. (2012). Alteraciones de funciones cognitivas y ejecutivas en pacientes dependientes de cocaína: estudio de casos y controles. *Revista de Neurología, 54*(4) ,199-208.

Medina-Mora, M., Rafful, C., Villatoro, J.,Oliva, N., Bustos, M., & Moreno, M. (2015). Diferencias sociodemográficas entre usuarios de otras drogas y adolescentes no consumidores en una muestra mexicana de estudiantes. *Revista Internacional de Investigación en Adicciones, 1*(1), 6-15. doi: 10.28931/riiad.2015.1.02

Perron, B., & Howard, M. (2009). Adolescent inhalant use, abuse and dependence. *Addiction*, *104*, 1185–1192. doi:10.1111/j.1360-0443.2009.02557.

Robles-Martínez, M., García-Carretero, M., Rahola, G., Palma-Álvarez, R., Abad, A., & Roncero, Carlos. (2017). Comorbilidad médica y psiquiátrica en pacientes con dependencia alcohólica en tratamiento ambulatorio: un estudio descriptivo. *Revista de Patología Dual, 4*(3-4), 1-9. doi:10.17579/Revpatdual.04.11

Rosenberg, N. L., Grigsby, J., Dreisbach, J., Busenbark, D., Rosenberg, N. L., Grigsby, J., et al. (2002). Neuropsychologic Impairment and MRI Abnormalities Associated with Chronic Solvent *Journal of Toxicology: Clinical Toxicology, 40*(1), 21-34. doi:10.1081/CLT-120002883

Scott, K., & Scott, A. (2013). Adolescent inhalant use and executive cognitive functioning. *Child: Care, Health, and Development*, *40*(1), 20-28. doi:10.1111/cch.12052

Takagi, M. J., Lubman, D. I., & Yücel, M. (2008). Interpreting neuropsychological impairment among adolescent inhalant users: Two case reports. *Acta Neuropsychiatrica*, *20*(1), 41–43. doi:10.1111/j.1601-5215.2007.00236

Takagi, M., Yücel, M., Cotton, SM., & Baliz, Y. (2011). Verbal memory, learning, and executive functioning among adolescent inhalant and cannabis users. *Journal of Studies on Alcohol and Drugs, 72*(1), 96-105.

Villatoro-Velázquez JA., Reséndiz-Escobar, E., Mujica-Salazar, A., Bretón-Cirett, M., Gutiérrez-Reyes, J., Franco-Núñez, A., … Mendoza-Alvarado, L. (2017). *Encuesta Nacional de Consumo de Drogas, Alcohol y Tabaco 2016-2017: Reporte de Drogas.* México: Instituto Nacional de Psiquiatría Ramón de la Fuente Muñiz

Wanmaker, W., Jorinde S., Geraerts, E., van de Wetering, B., Renkema, P., & Franken, I. (2018). The efficacy of a working memory training in substance use patients: A randomized double-blind placebo-controlled clinical trial. *Journal of Clinical and Experimental Neuropsychology, 40*(5), 473-486. doi:10.1080/13803395.2017.1372367

Wechsler, D. (2007). *Escala Wechsler de inteligencia para niños WISC- IV.* México: El Manual Moderno.

Wechsler, D. (2013). *Escala Wechsler de inteligencia para adultos WAIS- IV.* México: El Manual Moderno.

Wu, L., & Howard, M. (2007). Psychiatric disorders in inhalant users: Results from The National Epidemiologic Survey on Alcohol and Related Conditions. *Drug & Alcohol Dependence , 88*(2) 146 – 155. doi:10.1016/j.drugalcdep.2006.10.012

Yücel, M., Zalesky, A., Takagi, MJ., Bora, E., Fornito, A., Ditchfield, M., … Lubman, Ph. (2010). White-matter abnormalities in adolescents whit long-term inhalant and cannabis use: a diffusion magnetic resonance imaging study. *Journal of Psychiatry & Neuroscience*, *35*(6), 409-12. doi: 10.1503/jpn.090177

View publication stats

cells

MDPI

Article

Tunicamycin Sensitivity-Suppression by High Gene Dosage Reveals New Functions of the Yeast Hog1 MAP Kinase

Mariana Hernández-Elvira [1], Ricardo Martínez-Gómez [1], Eunice Domínguez-Martin [1], Akram Méndez [1], Laura Kawasaki [1], Laura Ongay-Larios [2] and Roberto Coria [1,*]

[1] Departamento de Genética Molecular, Instituto de Fisiología Celular, Universidad Nacional Autónoma de México, CP 04510 Cd., Mexico

[2] Unidad de Biología Molecular, Instituto de Fisiología Celular, Universidad Nacional Autónoma de México, CP 04510 Cd., Mexico

* Correspondence: rcoria@ifc.unam.mx; Tel.: +52-55-56-22-56-52

Received: 8 April 2019; Accepted: 9 July 2019; Published: 12 July 2019



Abstract: In the yeast *Saccharomyces cerevisiae*, components of the High Osmolarity Glycerol (HOG) pathway are important for the response to diverse stresses including response to endoplasmic reticulum stress (ER stress), which is produced by the accumulation of unfolded proteins in the lumen of this organelle. Accumulation of unfolded proteins may be due to the inhibition of protein *N*-glycosylation, which can be achieved by treatment with the antibiotic tunicamycin (Tn). In this work we were interested in finding proteins involved in the ER stress response regulated by Hog1, the mitogen activated protein kinase (MAPK) of the HOG pathway. A high gene dosage suppression screening allowed us to identify genes that suppressed the sensitivity to Tn shown by a *hog1*Δ mutant. The suppressors participate in a limited number of cellular processes, including lipid/carbohydrate biosynthesis and protein glycosylation, vesicle-mediated transport and exocytosis, cell wall organization and biogenesis, and cell detoxification processes. The finding of suppressors Rer2 and Srt1, which participate in the dolichol biosynthesis pathway revealed that the *hog1*Δ strain has a defective polyprenol metabolism. This work uncovers new genetic and functional interactors of Hog1 and contributes to a better understanding of the participation of this MAPK in the ER stress response.

Keywords: yeast; Hog1; MAP kinase; endoplasmic reticulum; stress; suppression; unfolded protein response (UPR)

1. Introduction

The synthesis of transmembrane and secreted proteins occurs in ribosomes attached to the endoplasmic reticulum (ER) membrane. In the ER lumen such proteins are subjected to different modifications such as *N*-glycosylation, formation of disulphur bonds and protein folding. Properly processed proteins continue through the secretion pathway in order to be transported to their final location. All organisms are exposed to adverse conditions that decrease the capacity of the ER to fulfill these processes, leading to the production and accumulation of misfolded proteins, inducing a condition known as endoplasmic reticulum stress (ER stress). ER stress triggers a cellular response that includes the unfolded protein response (UPR), which is a conserved signaling pathway present in all eukaryotic cells, including yeast [1], *Dictyostelium discoideum* [2], plants [3], and mammals [4]. In the yeast *Saccharomyces cerevisiae* the UPR consists of an endoplasmic reticulum membrane sensor named Ire1 [5], which in the presence of misfolded proteins oligomerises and autophosphorylates [6,7]; this in turn triggers its cytoplasmic endonuclease activity, which processes the *HAC1* pre-mRNA [8].

INFORME DE LABORES 2019

The spliced mRNA is efficiently translated to produce the transcription factor Hac1 [8,9], which regulates transcription of several target genes, such as those encoding chaperones, glycosylation enzymes and proteases among others [10] in order to alleviate the accumulation of unfolded proteins.

It has been proposed that the UPR is not the only cellular pathway needed to cope with the ER stress [11]. Components of other pathways appear to be required to produce a full cellular response to ER stress inducers; particularly, some components of the high osmolarity glycerol (HOG) pathway have been implicated in the response to ER stress induced by the antibiotic tunicamycin (Tn). This antibiotic is a nucleoside structurally similar to the UDP-*N*-acetylglucosamine and blocks the first step of the *N*-glycosylation catalyzed by the Glucosamine-*N*-acetil phosphotransferase enzyme [12,13]. The HOG pathway is a signaling system involved in survival under hyperosmotic conditions and it consists of two mechanistically different branches connected to a MAPK module, the SLN1 branch and the SHO1 branch, which converge on the scaffold MAPKK Pbs2, which in turn activates the MAPK Hog1 [14–16]. Once activated, Hog1 is translocated into the nucleus [17,18] where it regulates expression of genes whose products are involved in cell cycle arrest and adaptation to high osmolarity conditions.

In order to respond to ER stress induced by Tn, the cell requires the presence of both Pbs2 and Hog1. Additionally, Ssk1, the phosphorelay response regulator of the SLN1 branch, appears to be required for Tn response; however, components of the SHO1 branch seem to be dispensable [12,13]. As mentioned above, the presence of Hog1 is required for a proper response to Tn, but it appears that it does not need to be phosphorylated in order to produce resistance to the ER stress inducer. Indeed, a strain expressing an unphosphorylated form of Hog1 is able to grow in Tn, although not at the wild type level, but clearly above the growth shown by the *HOG1* null mutant [13]. Additionally, treatment with high Tn concentrations for an extended period of time only produces a very weak level of Hog1 phosphorylation that does not trigger its nuclear import [13]. Interestingly, a full cellular response to Tn requires the kinase activity of Hog1, since a point mutation that eliminates its kinase activity produces high sensitivity to Tn [13]. In addition to its participation in the ER stress response, several reports suggest that Hog1 has cytoplasmic activities, for example in the general stress response system [19,20] and in regulation of mitophagy [21,22].

With the aim of increasing knowledge regarding the participation of Hog1 in the ER stress response, we searched for genes whose products can suppress the sensitivity to Tn displayed by a Hog1-deficient strain but not its sensitivity to hyperosmotic stress. With this screening, we not only detected genes that were able to specifically suppress the Tn sensitivity of the *hog1*Δ mutant, but we also found genes that reverted the sensitivity shown by the *hog1*Δ mutant and by the *hac1*Δ mutant.

2. Materials and Methods

2.1. Yeast Strains, Gene Disruptions, and Culture Conditions

The *S. cerevisiae* strains used in this work are shown in Supplementary Table S1. All of them are isogenic to BY4742 or BY4741. The wild type and the single null mutants were obtained from the EUROSCARF collection. Double mutants were constructed by integration of the *NATMX4* cassette (which provides nourseothricin resistance) into the *HOG1* locus of single mutants. The integrating cassette was constructed by PCR using the oligonucleotides DHOG1F and DHOG1R (Supplementary Table S2) and contained the *NATMX4* gene flanked by *HOG1* 5′ and 3′ UTR fragments of 40 base pairs respectively. Integrations of the cassette were performed by homologous recombination. All deletions were confirmed by PCR.

Yeast cells were grown at 30 °C in YPD medium (1% yeast extract, 2% peptone, and 2% glucose) or SD medium (0.67% yeast nitrogen base without amino acids and 2% glucose, supplemented with the required amino acids for plasmid selection). Glucose was substituted by 2% raffinose (Sraf) or 2% galactose (Sgal) according to the requirements of the experiments. When needed, nourseothricin (100 µg/mL) was added to the media. YPGAL was the same as YPD except for the substitution of glucose by galactose.

INFORME DE LABORES 2019

Escherichia coli DH5α strain was used to propagate plasmids. Bacteria were grown at 37 °C in LB medium (1% tryptone, 0.5% yeast extract, and 0.5% NaCl) containing 100 μg/mL ampicillin or 50 μg/mL kanamycin (for library-plasmid selection).

2.2. Stress Assays

Stress sensitivity assays were done by dropping aliquots of 10-fold serial dilutions of early-logarithmic YPD-cell cultures (OD_{600} adjusted to 0.05) on Tn and KCl plates. Plates were incubated at 30 °C for 72 h and scanned. For liquid cultures, cells with the same density were inoculated in triplicate in Honeycomb 2 plates (100 wells). Density readings were recorded every hour during 48 h of incubation at 30 °C in a BioScreen C microplate spectrophotometer (Oy Growth Curves Ab Ltd, Helsinki, Finland). The relative growth rate is the slope value of the linear regression of three independent liquid cultures.

2.3. High Dosage Suppression Screening

A diagram representing the suppression-screening assay is shown in Figure 1. The *hog1*Δ mutant was transformed with a genomic library constructed to specifically perform overexpression screenings in *S. cerevisiae* [23]. The library contains a collection of more than 1000 overlapping genome fragments from the FY4 *S. cerevisiae* strain, cloned into the multicopy pGP564 plasmid. Transformants were plated in selective medium containing 1 μg/mL Tn. Tn resistant clones were streaked on 1 M KCl and those sensitive to high osmolarity were selected. Plasmids from Tn resistant/KCl sensitive cells were extracted and propagated in *E. coli*. The selected plasmids were re-introduced into *hog1*Δ yeast cells for a second round of selection. Ends of the yeast genome inserts were sequenced in order to map the Tn suppressor genome fragments. Standard yeast genetics protocols were used [24].

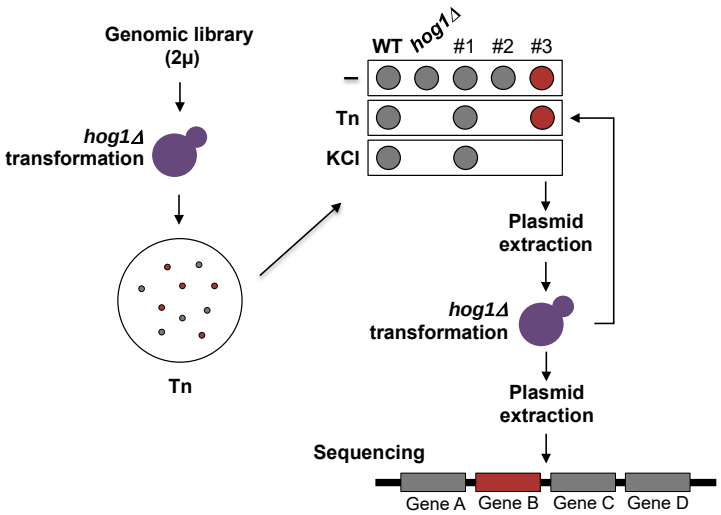

Figure 1. Dosage suppression screening protocol. The *hog1*Δ strain was transformed with a genomic library constructed in a 2 μ plasmid. Yeast cells were plated on selective medium (SD + 25 μg/mL of the required amino acids and nitrogen bases) containing 1 μg/mL Tn. Plates were incubated for 48 h at 30 °C. Colonies that appeared were grown to early-logarithmic phase in liquid selective medium and adjusted to 0.5 OD_{600}. An aliquot of each transformant was dropped onto selective medium containing either 0.5 μg/mL Tn or 1M KCl. Plasmids were purified from the Tn-resistant and KCl-sensitive clones and reintroduced into the *hog1*Δ strain for a second round of selection. Suppressor plasmids were extracted, and the genomic inserts were sequenced.

2.4. Gene Expression

Each ORF contained in the suppression plasmids was cloned with its respective promoter in order to be expressed in yeast cells. Subcloning was done by PCR using oligonucleotides shown in

INFORME DE LABORES 2019

Supplementary Table S2 (only the oligonucleotides for suppressor genes are shown). The PCR products were obtained using genomic DNA of the BY4742 wild type strain as template. The PCR products were cloned into the pGEM-T-Easy vector and then subcloned into the yeast YEp352 vector [25]. The YEp352 clones were used for yeast transformation. All PCR products were sequenced in full.

2.5. Physical Interactions and Construction of the Interaction Network

Physical protein interactions between Hog1 and suppressor proteins were determined by the Bimolecular Fluorescence Complementation (BiFC) assay [26]. Proteins fused to the amino-end (VN) of the fluorescent protein Venus were obtained from the VN-fusion library (Bioneer, Daejeon, Republic of Corea) that is constructed in the BY4741 (*Mata*) strain. Hog1-VC (carboxyl-end of the Venus protein) was constructed by fusing the *HOG1* ORF in frame with the gene encoding VC. The fused gene was integrated into the *HOG1* locus of the BY4742 (*Matα*) strain by homologous recombination. Co-expression of VN and VC fusion constructs was achieved in diploid cells after mating BY4741 and BY4742 recombinant strains. Protein interactions were detected by flow cytometry using the Attune Acoustic Focusing Cytometer. Fluorescence statistics were calculated with the Attune software (version 2.1) and the statistical significance was determined with a Welch *t*-test.

Data of the known interactors for each suppressor gene and *HOG1* were obtained from the BioGRID database (https://thebiogrid.org/) (version 3.4.144), which is a repository of available physical and genetic interactions determined by different low- and high-throughput experimental assays and compiled through comprehensive curation [27]. The physical interaction data were extracted and visualized with Cytoscape [28] according to the protocol previously described [29]. The output interactors, i.e., the proteins that interact with only one node of the network, were eliminated in order to select the proteins connected with at least two other interactors. The network obtained after this reduction was clustered with the force directed layout with default parameters in Cytoscape and the visualization (separation of the nodes) was improved manually. The edges were colored according to the experimental assay that supports each interaction in the database.

2.6. Polyprenol Determination

Yeast cells were grown to mid-logarithmic phase in YPGAL (OD_{600} adjusted to 0.5) and incubated during 2 h with either 1µg/mL Tn or DMSO (Tn dissolvent). Yeast cells were centrifuged and the pellet was washed with water. Polyprenols extraction was performed as previously described [30] with modifications. Yeast cells were resuspended in water and disrupted with glass beads. The lipids were extracted by shaking during 2 h with chloroform/methanol (2:1 *v*/*v*) at RT. The organic phase was collected washed three times with 1/5 volume of 10mM EDTA in 0.9% NaCl and evaporated to dryness. Lipids were resuspended in methanol/water (10:1 *v*/*v*) containing 15% KOH and alkaline hydrolysis was performed during 2 h at 95 °C. Lipophylic products were extracted twice with diethyl ether and evaporated to dryness. The lipids obtained were dissolved in hexane and applied to a silica column equilibrated with hexane. The column was washed with 3% diethyl ether in hexane and the polyprenol fraction was eluted with 17% diethyl ether in hexane. The fraction was evaporated to dryness, resuspended in hexane and subjected to HPLC analysis. Polyprenols detection was performed with a reverse phase Symmetry C18 Waters column (3.5 µm, 4.6 × 75 mm) using a HPLC Waters Alliance e2695/2489/2414 equipment (Milford, MA, USA). Samples were run at 25 °C at a flow rate of 1.2 mL/min in isocratic elution with 55% methanol, 23% isopropanol, and 22% hexane and detected with UV light (210 nm). We used 1 µg/µL of C-90 Dolichol (Dolichol-18) from Larodan Research Grade Lipids (Solna, Sweden) as a standard. Polyprenol concentration corresponded to the area under the curve of each peak, referred to the area under the curve of the internal standard peak and expressed by mg of protein. Mean values, standard deviation, and significance were graphed and analyzed from three independent experiments. Statistical significance was tested with Student *t* test.

INFORME DE LABORES 2019

3. Results

3.1. Isolation of High Dosage-Gene Suppressors of Hog1Δ Tunicamycin Sensitivity

In order to shed light onto the way in which Hog1 participates in the response to ER stress inducers, we designed a dosage-suppression screening to identify genes required for the Hog1-Tn response. For the screening the *hog1*Δ mutant was transformed with a genome library constructed in a high copy plasmid [23] selecting clones resistant to Tn but sensitive to KCl. To this end, yeast transformants were plated in medium containing Tn to isolate cells resistant to the antibiotic; then, the transformants were dropped on plates containing KCl in order to identify the clones that were sensitive to hyperosmotic stress (Figure 1). The suppressor plasmids were extracted from the selected transformants and were reintroduced into the *hog1*Δ mutant to confirm Tn resistance and KCl sensitivity (Figure 1).

With this strategy, we isolated 40 plasmids that conferred resistance to Tn but not to hyperosmotic stress. These plasmids were sequenced to determine the chromosomal region responsible for the suppression. Among these 40 plasmids only 8 different regions were represented (Figure 2A). The regions are distributed in 6 different chromosomes and their size range is from 9 Kb to 12 Kb. Figure 2A summarizes the characteristics of the 40 suppressor plasmids; suppressor 8 was the most represented (14 times), while suppressors 70, 86, and 87 were isolated only one time. The level of Tn sensitivity suppression varied between strains. Sup 11 showed the weakest suppressor level while suppressors 8, 39, and 70 showed the strongest (Figure 2A,B). In our assays we included as a control the *hac1*Δ mutant, which lacks the basic leucine zipper (b-Zip) transcription factor, which regulates the gene transcription in the UPR pathway. This mutant is highly sensitive to Tn (Figure 2B).

Since each chromosomal region contained several ORFs (Figure 2A), we subcloned each of them independently in order to identify the ORF responsible for the suppression. From this assay we identified 8 genes (colored in brown in Figure 2A) that conferred resistance to Tn but not to hyperosmotic stress upon the *hog1*Δ mutant (Figure 2C). The level of suppression varied among the genes. We found differences in sensitivity to Tn and therefore in the growth rate of the *hog1*Δ mutant transformed with the different genes (Figure 2C). The highest growth rate of the *hog1*Δ mutant in Tn was observed with *ALG7*, while the lowest was obtained with *ECM13*. Although *KIN1* was not found as a suppressor in this screening, it was included in this study since it has been reported to be paralogous to *KIN2* [31]. As can be observed, *KIN1* and *KIN2* had the same level of suppression (Figure 2C).

Name	Chromosome coordinates	Size (bp)	Chromosome region	No. of times isolated	Relative suppression level*
Sup8	II 702,406-712,203	9797	YBR241C YBR242C ALG7 GPX2 ISW1 RRT2	14	+++++
Sup39	XI 238,339-250,650	12311	AAT1 SEG2 GFA1 APE1 YKL102C HSL1	13	+++++
Sup47	VII 1,050,372-1,061,331	10959	PXR1 YOR1 BGL2 YGR283C ERV29	3	++++
Sup11	XIII 28,455-38,857	10402	NDI1 YML119W NGL3 YWL116W-A NAB6 ATR1	5	++
Sup31	XII 330,854-341,765	10911	IOC2 KIN2 HRT3 CHA4 ICT1 MIM2	2	++++
Sup70	II 239,720-249,439	9719	NTH2 RER2 COQ1 GPI18 RCR1 UGA2 DSF2	1	+++++
Sup86	II 133,290-141,740	8450	PSY4 COR1 YBL004W ECM13 FUI1 PRE7	1	+++
Sup87	III 111,555-122,059	10504	YCL002C RER1 YCL001W-A YCL001W-B YCR001W CDC10 MRPL32 YCP4 CIT2	1	++++

Figure 2. *Cont.*

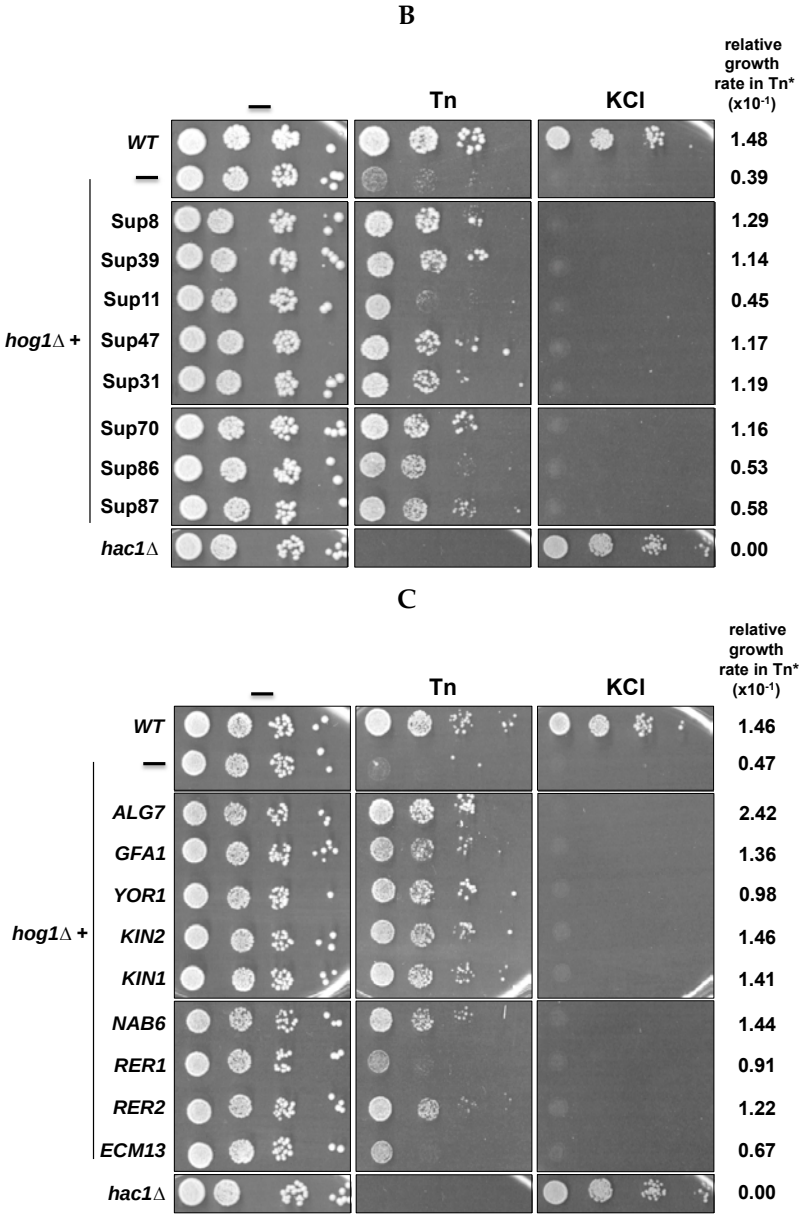

Figure 2. Suppression of the *hog1*Δ Tn sensitivity. (**A**) Schematic representation of the genomic region contained in each suppressor plasmid. Chromosome number and insert coordinates and size are shown. Number of isolated times that each suppressor plasmid was isolated along with its relative suppression level (according to Figure 2B) are indicated. ORF orientation is depicted by the colored arrows. ORFs that show suppressor activity are marked in brown. (**B**) Serial dilution dropping assay of the *hog1*Δ strain transformed with suppressor plasmids. Yeast cells were grown in YPD to early-logarithmic phase and adjusted to 0.5 OD_{600} in fresh YPD. 10-fold serial dilutions were spotted on selective medium (see legend of Figure 1) containing either 0.5 µg/mL Tn or 1 M KCl. The *hac1*Δ mutant was used as Tn sensitivity control. Plates were incubated at 30 °C for 72 h and scanned. (**C**) Genes colored in brown in Figure 2A were subcloned into the multicopy plasmid YEp352 and expressed in the *hog1*Δ strain under the control of their own promoter. A serial dilution assay was performed as described in Figure legend 2B. (*) The relative growth rate is the slope value of the linear regression of liquid cultures made in triplicate and grown in YPD containing 0.5 µg/mL Tn. Liquid cultures were performed in a microplate spectrophotometer at 30 °C with constant shaking. The OD_{600} readings were determined at 1 h intervals during 48 h. *KIN1*, which was not detected in the screening was included in this assay since it is paralogous to *KIN2* (see text).

INFORME DE LABORES 2019

3.2. Genes Can Be Divided into General and HOG-Specific Suppressors of Tn Sensitivity

In order to determine whether the isolated genes were specific suppressors of the Tn-sensitivity observed in the *hog1*Δ mutant, we tested their suppressor activity in mutants of other components of the HOG pathway that have been implicated in the response to ER stress induced by Tn, specifically *PBS2* and *SSK1* [13]. We also introduced the suppressor genes in the *hac1*Δ in order to ascertain whether suppression is or is not restricted to the components of the HOG pathway. We observed that all suppressor genes did confer resistance, to different degrees, upon the *pbs2*Δ and *ssk1*Δ mutants. Interestingly, three genes, *ALG7*, *GFA1* and *YOR1*, also conferred resistance upon the *hac1*Δ mutant (Figure 3). This indicates that *ALG7*, *GFA1* and *YOR1* are general suppressors of Tn sensitivity, while *NAB6*, *KIN1*, *KIN2*, *RER1*, *RER2* and *ECM13* can be considered specific suppressors of the deficiency shown by the mutants of the HOG pathway. The general suppressors were the most represented in the isolated plasmids (30 of 40) (Figure 2B). In contrast, the specific suppressors were represented in only 10 of 40 isolated plasmids (excluding *KIN1*), suggesting that these suppressors can be found more rarely in this kind of screening. Table 1 summarizes the main characteristics of the general and specific suppressors including the proved or putative cellular process where they can be participating (Saccharomyces Genome Database (SGD): www.yeastgenome.org; Gene Ontology (GO) database: www.geneontology.org). Regarding the general suppressors, *ALG7* encodes the UDP-*N*-acetyl-glucosamine-1-P-transferase which catalyzes the first step of *N*-glycosylation and is a direct target of Tn [32,33]; *GFA1* encodes the glutamine-fructose-6-phosphate amidotransferase which participates in the synthesis of chitin, a constituent of the yeast cell wall, and in the synthesis of *N*-acetylglucosamine [34,35]; and *YOR1* codes for an ATP-binding cassette (ABC) transporter located in the plasma membrane [36,37] which participates in cell detoxification processes. Regarding the specific *hog1*Δ suppressors, these include genes that code for proteins with a variety of functions. *NAB6* encodes a protein that binds polyadenylated RNAs which mainly encode proteins destined to the cell wall [38]; *KIN2* and its paralogous *KIN1* encode serine/threonine protein kinases that have been implicated in exocytosis and may also play a role in septin cytoskeleton and cell wall organization [39,40]; *RER2* encodes the *cis*-prenyltransferase involved in the production of dolichol from the isoprenoid lipid farnesyl diphosphate [41]. Dolichol is the acceptor and carrier of oligosaccharides that are transferred to proteins during the folding process. *RER1* encodes a protein known as Retention in the Endoplasmic Reticulum which participates in protein retention in the ER lumen and in retrograde vesicle-mediated transport from Golgi to ER [42,43]; and *ECM13* encodes a protein of unknown function that is upregulated by cell wall damage and appears to be involved in cell wall biosynthesis and architecture [44,45].

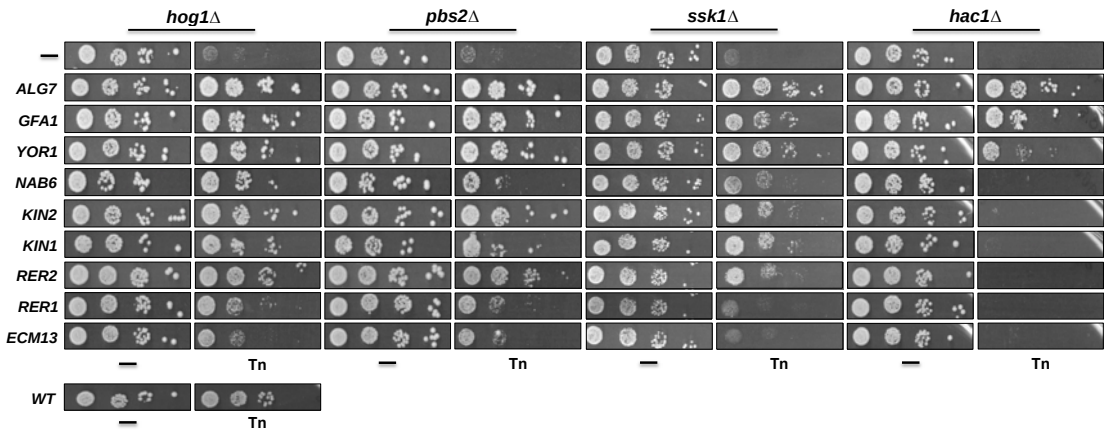

Figure 3. Effect of expression of suppressor genes in the Tn sensitivity of different strains. The suppressor genes were overexpressed in the indicated strains as described in Figure legend 2C. A serial dilution assay was performed as described (Figure legend 2B). Plates were incubated at 30 °C for 72 h and scanned.

INFORME DE LABORES 2019

Table 1. General and specific suppressors and the cellular process where they participate.

Gene	Protein Name	Biological Process	Cellular Component
ALG7	UDP-*N*-acetyl-glycosamine-1-P-transferase	Protein N-linked glycosylation	Endoplasmic reticulum
GFA1	Glutamine-fructose-6-phosphate amidotransferase	Cell wall biosynthesis	Unknown
YOR1	Plasma membrane ATP-binding cassette (ABC) transporter	Xenobiotic transport	Plasma membrane
NAB6	Putative RNA binding protein	Binds to poliA RNAs	Cytoplasm
KIN2	Serine/threonine protein kinase	Exocytosis	Plasma membrane
KIN1	Serine/threonine protein kinase	Exocytosis	Plasma membrane
RER2	Cis-prenyltranferase	ER to Golgi vesicle-mediated transport. Protein glycosilation	Endoplasmic reticulum
RER1	Retention in the endoplasmic reticulum	ER to Golgi vesicle-mediated transport. Protein retention in the ER lumen. Retrograde vesiclemediated transport, Golgi to ER	COPI-coated vesicle vacuole
ECM13	Protein induced by traetment with methoxypsoralen and UVA irradation	Cell wall biosynthesis?	Unknown

3.3. Inactivation of Some Suppressor Genes Confers Sensitivity to Tn

We next evaluated whether the inactivation of some of the suppressor genes affects cell growth in Tn and KCl. In this assay we did not include *ALG7*, *GFA1*, and *RER2* null mutants since *ALG7* and *GFA1* are essential genes and the *rer2*Δ mutant has a severe growth impairment. It was evident that disruption of *YOR1*, *NAB6*, and *KIN2* induced sensitivity to Tn at the highest concentration tested (1 µg/mL), while sensitivity was barely detected at lower concentrations (Figure 4). Disruption of *RER1* also induced sensitivity to Tn but to a lesser extent compared to disruption of *YOR1, NAB6*, and *KIN2*, while inactivation of the *ECM13* gene did not affect growth in Tn. In contrast to the *kin2*Δ mutant, the *kin1*Δ mutant showed very low sensitivity to Tn. As expected, none of the null mutants of the suppressor genes showed growth defects when they were plated on 1M KCl (Figure 4). Additionally, we detected that inactivation of *YOR1*, *NAB6*, *KIN2*, and *KIN1* in a *hog1*Δ background increased the sensitivity to Tn shown by the *hog1*Δ mutant (Figure 4), suggesting that they might participate in Hog1 independent pathways during the Tn response. In contrast, inactivation of *RER1* and *ECM13* did not affect the Tn sensitivity of the *hog1*Δ mutant, suggesting that they may be components of the same pathway.

INFORME DE LABORES 2019

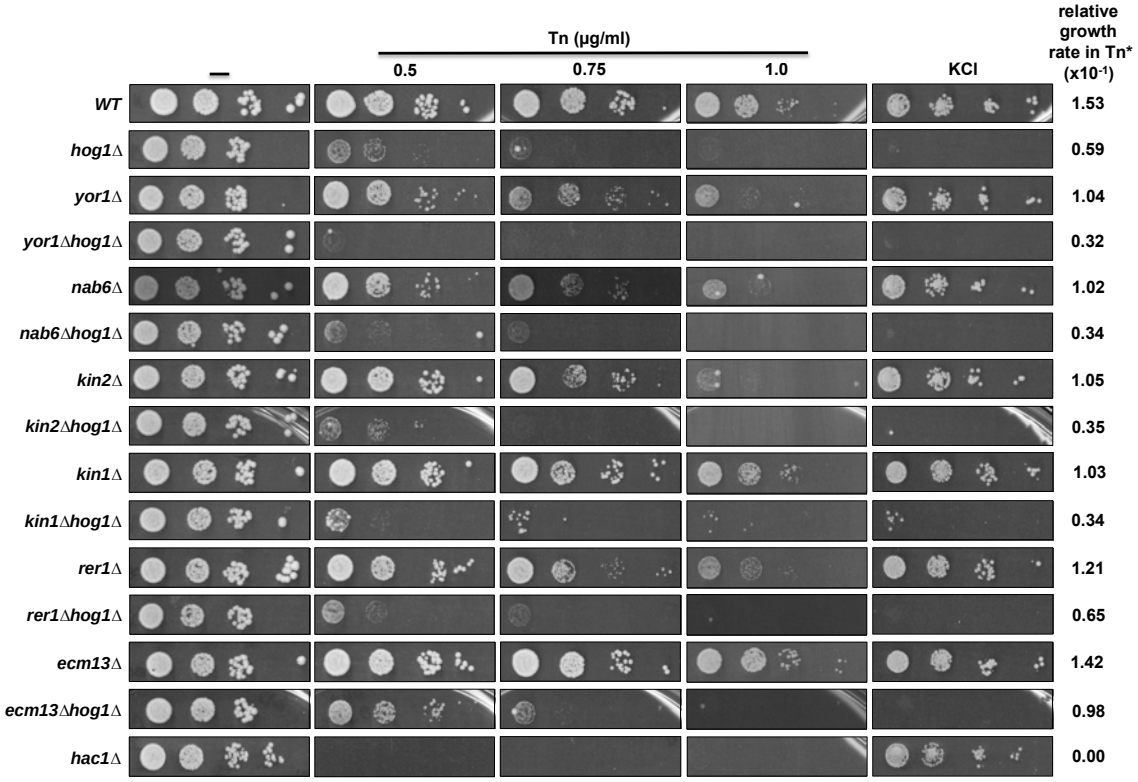

Figure 4. Effect of the inactivation of the suppressor genes on Tn sensitivity and their epistatic interaction with *HOG1*. Single mutants of each suppressor ORF (obtained from the EUROSCARF collection) and the double mutants (constructed as described in the methods section), were tested in different concentrations of Tn or 1M KCl. Yeast cells were grown in YPD and plated as described in Figure legend 2B. Plates were incubated at 30 °C for 72 h and scanned. (*) Relative growth rate was determined from growth at 0.5 µg/mL Tn as described in Figure legend 2.

3.4. Suppressor Genes may Form an Interaction Network with HOG1

The genes that suppress the Tn sensitivity of the *hog1*Δ strain do not appear to encode canonical interactors of Hog1. However, it could be that a putative interaction with one or more suppressor proteins would occur in conditions that induce ER stress. Therefore, we looked for physical interactions between Hog1 and the specific suppressor proteins in the presence of Tn. Using Hog1 as bait and the specific suppressor proteins Nab6, Kin1, Kin2, Rer1, Rer2, and Ecm13 as prays we performed a Bimolecular Fluorescence Complementation (BiFC) assay to detect physical interactions. As expected, none of the suppressor proteins tested appeared to interact physically with Hog1 with and without Tn exposure (Supplementary Table S3), although the fluorescence displayed by the Kin2-Hog1 and Rer2-Hog1 pairs under un-induced conditions was slightly higher than the negative control (Supplementary Table S3). This observation suggests that the suppressors could require one or more intermediates to associate physically with Hog1.

In order to determine whether or not the suppressor genes could participate in functional processes required to cope with the ER stress induced by Tn, we constructed a physical interaction network based on available data from the BioGRID database (Figure 5). This analysis showed that five suppressors, namely Kin1, Kin2, Rer2, Gfa1, and Nab6 may indeed interact with Hog1 through one intermediate. For Kin1, Rer2, and Gfa1, the intermediate protein is Ssb2, a cytoplasmic chaperon of the Hsp70 family that is involved in protein folding processes [46]. Interestingly, Rer2 may also have a physical interaction with Hog1 through Gis2, a RNA binding protein present in processing bodies and stress granules, which contain translationally repressed RNAs [47]. Although the suppression mechanism cannot be deducted from the structure of the interaction network, it provides relevant information

INFORME DE LABORES 2019

regarding proteins that belong to pathways linked with the ER stress response and not previously associated with Hog1.

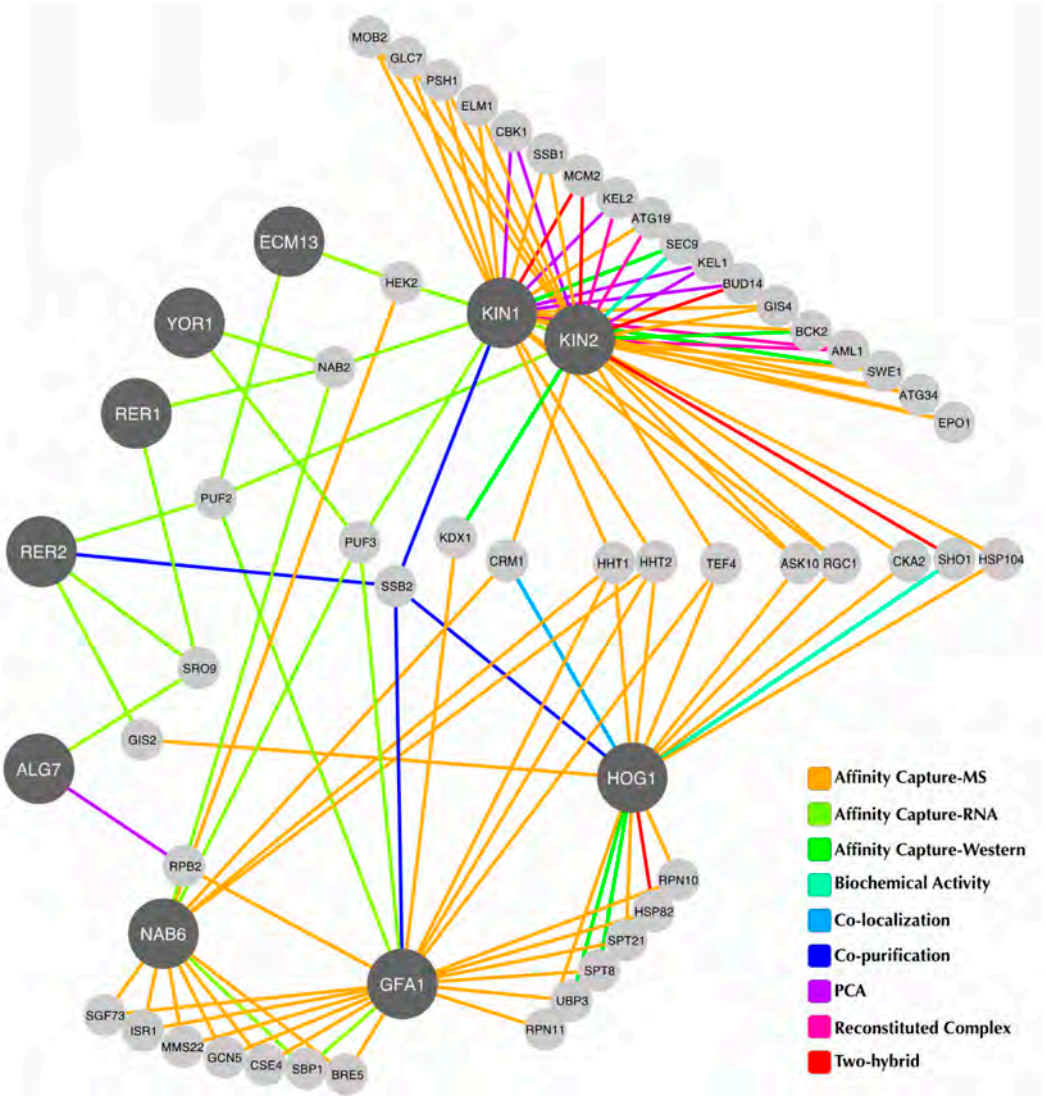

Figure 5. Physical interaction network. Physical interactions of suppressor proteins and Hog1 as deduced from the BioGRID database and visualised with Cytoscape. The network was constructed according to the criteria described in the methods section. Hog1 and suppressor proteins are depicted with dark grey circles. The connecting lines represent the physical interactions and are colored according to the experimental assay that supports each interaction. Known interactors found in the database are colored in light grey.

Since *SSB2* encodes a chaperon of the Hsp70 family that participates in protein folding and appears to be an important interaction node for Rer2 and Kin1 we evaluated its involvement in the ER stress response. We observed that the mutant lacking Ssb2 showed resistance to Tn at the same level as the wild type strain (Figure 6), however overexpression of *RER2*, *KIN1*, and its paralog *KIN2* in the *ssb2*Δ mutant increased its resistance to Tn, while overexpression of *RER1* and *ECM13* did not (Figure 6). This observation indicates that *RER2*, *KIN1*, and *KIN2* interact genetically with *SSB2*, and also validates the proposed physical interaction network.

INFORME DE LABORES 2019

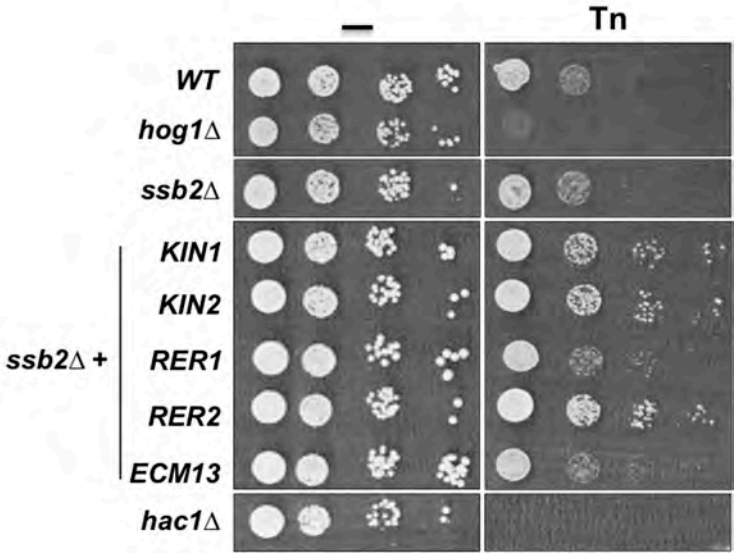

Figure 6. Effect of the inactivation of *SSB2* and overexpression of suppressor genes on Tn sensitivity. The single *ssb2*Δ mutant and transformants carrying the indicated genes were tested in 1.0 μg/mL of Tn as indicated in figure legend 2B. Overexpression was achieved by cloning the indicated genes in the multicopy plasmid YEp352 under the control of their own promoter. Serial dilution assay was performed as indicated in figure legend 2B. Plates were incubated at 30 °C for 72 h and scanned.

*3.5. The Cis-Prenyltransferase Srt1 also Suppresses the Tn Sensitivity of the Hog1*Δ *Mutant*

Tn is a protein glycosylation inhibitor that blocks the activity of the UDP-*N*-acetylglucosamine phosphate transferase (Alg7). This enzyme catalyzes the addition of *N*-acetylglucosamine to dolichol-phosphate, located in the ER membrane. Production of dolichol from farnesyl diphosphate is dependent on the activity of the *cis*-prenyltransferase Rer2 which synthesizes dolichols of 14–18 isoprene units. Yeast cells express a second *cis*-prenyltransferase known as Srt1 (Figure 7A), located mainly in lipid droplets, which synthesizes dolichols of 18–23 isoprene units [41,48]. We tested whether overexpression of *SRT1* would suppress the Tn sensitivity displayed by the *hog1*Δ mutant. We found that *hog1*Δ cells overexpressing *SRT1* grow as well as those expressing *RER2* in a medium containing 0.75 μg/mL Tn (Figure 7B). Accordingly, overexpression of *SRT1* was able to revert the sensitivity of a *pbs2*Δ mutant but not that of the *hac1*Δ mutant, indicating that the suppression process is specific to the HOG1 pathway (not shown). These results suggest that an increase in the cellular concentration of dolichol may revert the Tn sensitivity displayed by the *hog1*Δ mutant.

INFORME DE LABORES 2019

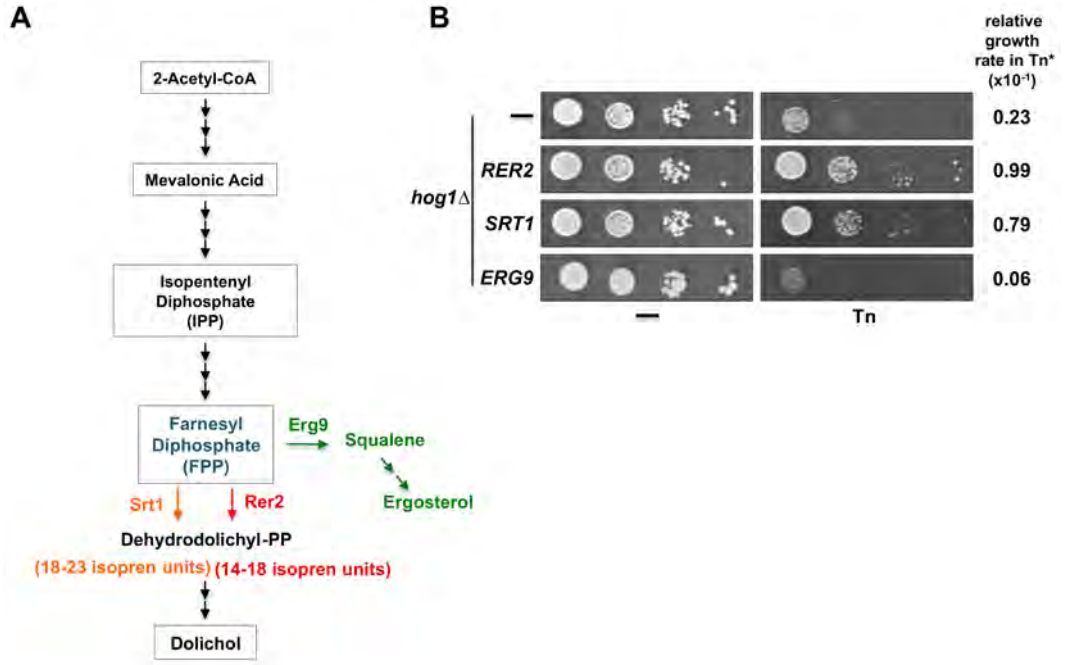

Figure 7. Effects of overexpression of proteins involved in the dolichol and ergosterol synthesis pathways on *hog1*Δ Tn sensitivity. (**A**) Schematic representation of the dolichol and ergosterol synthesis pathways. Farnesyl diphosphate (FPP) is synthesized from 2-Acetyl-CoA through the mevalonic acid pathway. FPP is a shared substrate of Rer2 (and Srt1) and Erg9 to synthesize either dolichol or ergosterol respectively. (**B**) Serial dilution assay of the *hog1*Δ strain transformed with the pYES2 vector or with pYES2 carrying *RER2*, *SRT1*, or *ERG9* genes. A spot dilution assay was performed as described above (Figure legend 2B) except that the cells were grown in SRaf medium and then spotted onto SGal or SGal containing 0.5 µg/mL Tn. Plates were incubated at 30 °C for 72 h and scanned. (*) The growth rate in Tn was measured as described in Figure legend 2C.

3.6. Hog1-Tn Sensitivity Is Enhanced by Overexpression of ERG9

Farnesyl diphosphate (FPP) is not only a precursor of dolichol but also of ergosterol through a series of reactions initiated by the farnesyl-diphosphate farnesyl transferase encoded by the essential *ERG9* gene (Figure 7A). We set out to determine whether the over-utilization of farnesyl diphosphate for the production of ergosterol would affect growth of the *hog1*Δ mutant in Tn. We found that the sensitivity to 0.5 µg/mL Tn of the *hog1*Δ mutant was enhanced when *ERG9* was overexpressed (Figure 7B). Taking this result together with the observation of the effect of *RER2* and *SRT1* overexpression indicated that the effect of Tn on the *hog1*Δ mutant may in part be dependent on the cellular concentration of dolichol.

3.7. The hog1Δ *Strain Has Reduced Polyprenols Concentration*

Based on the previous observations, we hypothesized that the deficient growth of the *hog1*Δ mutant in media containing Tn could be due to an impairment in the dolichol synthesis. We determined the polyprenol content by liquid chromatography (HPLC) in wild type, *hog1*Δ, and the *hog1*Δ overexpressing *RER2* strains treated or not treated with Tn. It was possible to detect in the three strains an enriched polyprenol that may range from 12 to 15 isopren units (Figure 8A). In the wild type strain, the Tn treatment induced approximately a two-fold increase in dolichol concentration (Figure 8B). The same treatment however was unable to induce an increment of dolichol in the *hog1*Δ strain. Overexpression of *RER2* in the *hog1*Δ mutant produced an increment of dolichol, which was statistically significant in both treatments (Figure 8B). Taking together, these results suggest that the *hog1*Δ strain has a strong defect in the polyprenol metabolism under stressful conditions and that this defect is partially compensated with the *RER2* overexpression.

INFORME DE LABORES 2019

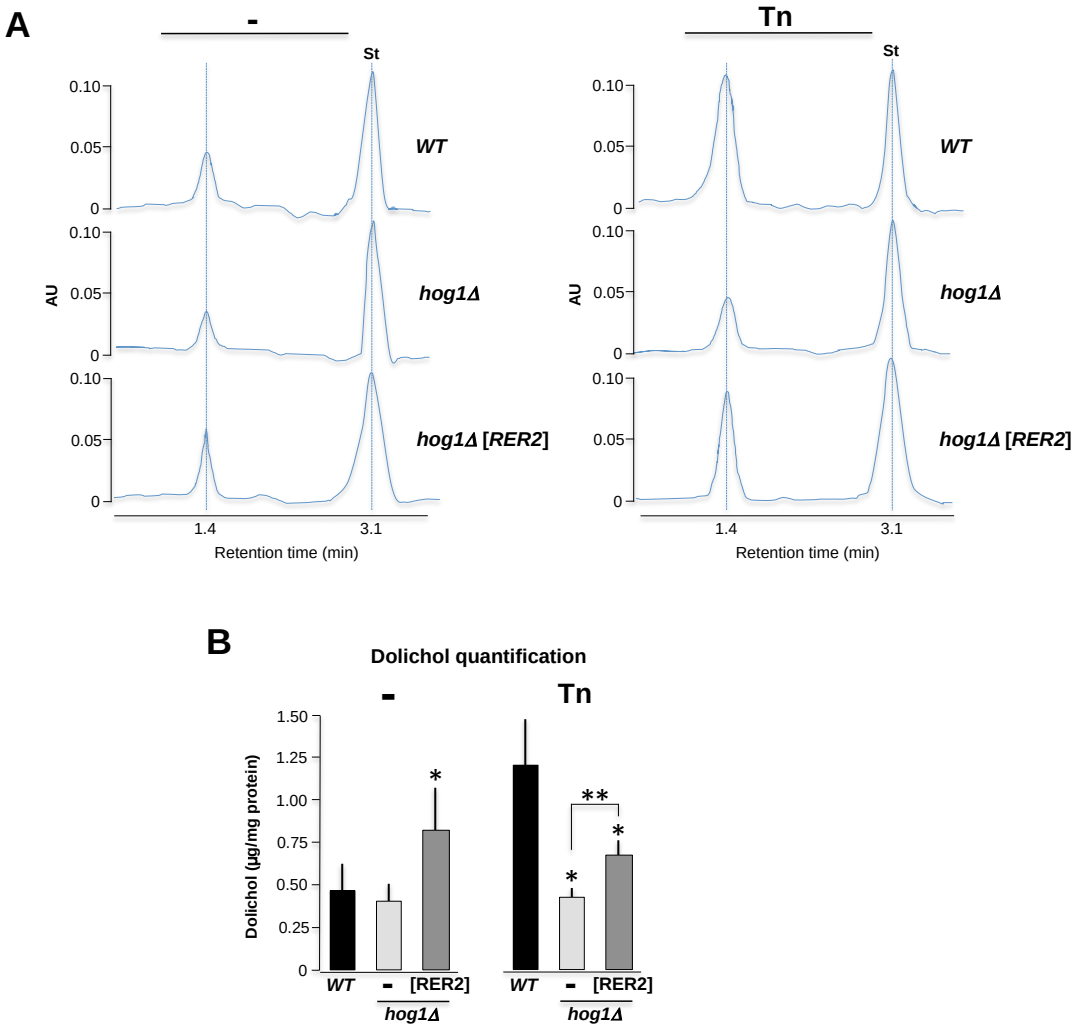

Figure 8. Effect of Hog1 inactivation and Tn treatment on the polyprenols concentration. (**A**) HPLC analysis of dolichols isolated from the wild type, *hog1*Δ and *hog1*Δ[*RER2*] strains, with or without 1 µg/mL Tn. Dolichol detection was performed by reverse phase HPLC analysis. One representative profile out of three is depicted. 1 µg/µL of standard dolichol (18 isoprene units) was included as internal control (St). (**B**) Dolichol concentration was calculated by determining the area under the curve of the dolichol peak relative to the area under the curve of the standard peak (St) and adjusted by protein concentration (See supplemental Table S4). Mean values (± SD) were calculated from three independent experiments. One asterisk indicates statistical significance regarding the WT strain. Two asterisks indicate statistical significance between *hog1*Δ and *hog1*Δ[*RER2*] strains.

4. Discussion

The isolated suppressors of Hog1 Tn sensitivity allowed us to identify genes whose products participate in a restricted number of cellular processes. According to the SGD and GO geneontology databases, these include protein glycosylation (Rer2 and Alg7); vesicle transport and exocytosis (Rer1, Rer2, Kin1, and Kin2); cell wall organization or biogenesis (Gfa1, Nab6, and Ecm13); and cell detoxification processes (Yor1). The limited number of specific suppressors that were detected indicates that the mechanisms by which Hog1 participates in a protective response to ER stress may be limited to very few pathways. It is interesting that with this screening we did not detect proven physical interactors of Hog1. This can be explained by the fact that most interaction assays with Hog1 are carried out under hyperosmotic conditions. This observation suggests that the suppressor proteins may not be phosphorylation targets of Hog1 and that Hog1 may play a regulatory role in the Tn response through one or more intermediates with the suppressor proteins. Several of these intermediates participate

INFORME DE LABORES 2019

in cellular processes related to stress conditions. However, it has been demonstrated that the kinase activity of Hog1 is essential to trigger a protective response to ER stress inducers [13,49]. Accordingly, we found putative Hog1 phosphorylation motifs (S/T-P) [50,51] in some suppressor proteins except Rer1, Rer2, and Alg7. Kin1 and Kin2 have 3 and 5 putative S/T-P phosphorylation sites respectively, while Nab6, Yor1 and Gfa1 contain one site each [52] (https://phosphogrid.org/). Although we cannot rule out that Hog1 may phosphorylate some suppressor proteins our interaction assay disregard this possibility, however a more extensive interaction study would be suitable.

It is interesting that none of the suppressors found plays a role in gene transcription and that all of them have extra-nuclear activities, which is in agreement with the observation that Hog1 is not transported into the nucleus in response to Tn stress [13,49]. Additionally, the specific suppressors found in this study were able to revert the Tn sensitivity shown by the *pbs2*Δ and the *ssk1*Δ mutants. This indicates that these suppressors may participate in one or several pathways made up of extra-nuclear proteins, including components of the phosphorelay pathway. Accordingly, a version of Hog1 that has been anchored to the plasma membrane by means of a CAAX motif was able to provide full ER stress protection [49]. All these observations support a model in which Hog1 shows regulatory cytoplasmic activity in order to counteract the stress caused by Tn.

The functions that Alg7, Gfa1 and Yor1 have in the cell make them logical candidates to provide cellular protection against Tn. In fact, they revert the Tn sensitivity not only of the *hog1*Δ mutant but also that of the *hac1* mutant. The increased concentration of Alg7, the UDP-*N*-acetylglucosamine phosphate transferase that catalyzes the addition of *N*-acetylglucosamine to dolichyl-phosphate [32], would titer the drug due to the fact that Tn and the enzyme substrate UDP-GlcNAc have a similar structure and compete for the enzyme's active site. Similarly, the overexpression of Gfa1, an amidotransferase that participates in the formation of glucosamine 6-P, which is a precursor of UDP-GlcNAc [34], would increase the concentration of UDP-GlcNAc, counteracting the inhibitory effect of Tn on Alg7. Finally, the overactivity of the ABC transporter Yor1 would help to eliminate the Tn from the cell as it does with different organic compounds and xenobiotics [36,53]. The finding of these suppressors is an indication that the screening has been performed properly since their function is related to the action mode of Tn.

Within the specific suppressors, *KIN1* and *KIN2* encode serine/threonine kinases. They are part of the Snf1 kinase family of the Ca^{2+}/calmodulin-dependent kinase II (CaMK), involved in the regulation of cell polarity and exocytosis, as well as in the regulation of the septin cytoskeleton and cell wall [39,40]. Their *hog1*Δ-suppression activity may be related to one of those functions; however, it has been recently assigned a new role for the Kin kinases. It appears that Kin1 and Kin2 may have a role in the Ire1-mediated targeting and processing of *HAC1* mRNA, thus positively regulating the UPR [54]. Interestingly, as detected by Anshu et al. [54] and in our assays, Kin1 and Kin2 are not totally redundant since a lack of Kin2 produced high sensitivity to Tn; in contrast, a lack of Kin1 barely affected the cellular response to Tn. Since the *HAC1* processing appears to be normal in a *hog1*Δ mutant [13], it is interesting to have found Kin1 and Kin2 as specific suppressors of Hog1. Our epistatic experiments suggest that Hog1 and at least Kin2 act in parallel pathways regarding ER stress. Taken together, these observations suggest that the suppression activity of Kin2 (and perhaps that of Kin1) is more closely related to its function in cell wall regulation and exocytosis, than to its role in regulating the UPR [40,54].

Rer1 and Rer2 were also found as specific Hog1-suppressors. Unlike Kin1 and Kin2, these proteins do not contain putative Hog1 phosphorylation motifs. Rer1 is localized in the early region of the Golgi apparatus and is involved in the retrieval of proteins from the Golgi and is also essential for the proper localization of proteins in the ER [42,43]. Its suppressor activity could be related to its participation in the ER localization of type II membrane proteins, including Mns1, which is the alpha-1,2-mannosidase that catalyzes the last step in glycoprotein maturation in the ER and is required for the ER-associated protein degradation [55–57]. In our assays, disruption of *RER1* moderately impaired the cell in its response to Tn and apparently it is not additive to *HOG1*. The functional relationship between the two proteins in the Tn response requires a more detailed study.

INFORME DE LABORES 2019

RER2 encodes the *cis*-prenyltransferase enzyme, which catalyzes the conversion of farnesyl diphosphate (FPP) to dehydrodolichyl diphosphate, the precursor of dolichol, which is the ER lipid where the oligosaccharide required for the *N*-glycosylation is assembled [41]. The suppression activity of Rer2 could be related mainly to its role in increasing dolichol concentration. This observation is supported by the fact that the *cis*-prenyltransferase Srt1, which catalyzes the same reaction, also suppresses the Tn sensitivity of a *hog1*Δ mutant. Rer2 is localized in dots associated with the ER and in lipid particles, while Srt1 appears to be localized only in lipid particles [48,58]. Nevertheless, Rer2 is expressed in early logarithmic phase and Srt1 is expressed in stationary phase, and the products of Srt1 are apparently not converted totally to dolichol and dolichyl phosphate; Srt1 behaves as a multicopy suppressor of *rer2*Δ mutant [48] indicating that in the absence of Rer2, Srt1 may adequately supplement the dolichol pool. The *rer2*Δ mutant has a severe growth defect while the *srt1*Δ mutant grows normally [41]. All of these characteristics imply that Rer2 and Srt1 are not redundant, and that they play different roles in the cell physiology; interestingly, they suppress the Tn sensitivity of the *hog1*Δ mutant almost to the same level. Here we found evidence that in the presence of Tn the dolichol content in a wild type strain increases significantly. This suggests that one mechanism to partially counteract the Tn effect is by overproducing dolichol. This protective mechanism is defective in the absence of Hog1 and is partially compensated by the overexpression of *RER2*. For the *hog1*Δ mutant the increased production of dolichol by *RER2* overexpression will partially suppress the Tn sensitivity. This finding is interesting since it has been observed that a *Trypanosoma brucei* mutant with defects in the *N*-glycosylation pathway accumulates larger amounts of polyprenols compared to its parental strain [59]. The involvement of Hog1 in lipid metabolism has been observed previously, for example, inhibition of sphingolipids and ergosterol biosynthesis activates the Hog1 pathway [60] and stress-mediated activation of Hog1 represses the synthesis of ergosterol [61]. An alternative approach to test that the suppression activity of Rer2 (and Srt1) is related to its function in the synthesis of dolichol was by overexpressing, in the *hog1*Δ mutant, the *ERG*9 gene, which encodes the farnesyl-diphosphate farnesyl transferase [62]. FPP is precursor of squalene, which is eventually converted to ergosterol [63,64]. Indeed, here we found that Erg9 may act as a diverter, converting FPP into squalene and enhancing the Tn sensitivity of the *hog1*Δ mutant. All these evidences indicate that the Hog1 role in the ER stress response could be related in part to its involvement in lipid metabolism including the polyprenol pathway.

The Nab6 and Ecm13 suppression mechanism is at present difficult to deduce since their function remains undefined. Nab6 appears to bind RNAs that encode proteins for the cell wall [38]. It is present in stress granules and co-purifies with Cap-binding proteins and other translation factors [38,65]. It could be that Nab6 regulates translation of this sort of mRNA in response to stress conditions since we detected that the *nab6*Δ mutant is moderately sensitive to Tn. *ECM13* encodes a protein of unknown function that is upregulated by cell wall damage and it may be involved in cell wall biosynthesis and architecture [44,45]; however the null mutant is as resistant to Tn as the wild type strain.

In summary, the screening of high dosage gene suppressors allowed us to conclude that Hog1 may be performing pleiotropic functions in order to regulate the cellular response to ER stress inducers. To counteract the effects of tunicamycin, the cell requires a number of cellular proteins to act in concert with Hog1. It is of the highest interest to study in detail the functional relationship between the suppressor proteins and Hog1. This study opens the field to the investigation of new functions of this MAP kinase in yeast.

Supplementary Materials: The following are available online at http://www.mdpi.com/2073-4409/8/7/710/s1, Table S1: Yeast strains used in this work, Table S2: List of oligonucleotides used in this work; Table S3: Relative interaction of Hog1 with suppressor proteins, Table S4: Dolichol concentration determined from HPLC profiles.

Author Contributions: Investigation, M.H.-E., R.M.-G., and E.D.-M.; Methodology, M.H.-E. and A.M.; Writing—original draft, M.H.-E., E.D.-M., A.M., L.K., L.O.-L., and R.C.; Writing—review and editing, M.H.-E., L.K., L.O.-L., and R.C.

INFORME DE LABORES 2019

Funding: This work was supported by grant numbers CONACyT: CB-254078; and PAPIIT, DAGAPA, UNAM: IN210616.

Acknowledgments: M.H.-E. is a PhD student in the Doctorate program in Biochemical Sciences, Universidad Nacional Autónoma de México (UNAM), and received fellowship 366635 from CONACYT; E.D.-M. is a PhD candidate in the Doctorate program in Biomedical Sciences, Universidad Nacional Autónoma de México (UNAM), and received fellowship 380127 from CONACYT. We wish to acknowledge the technical support provided by the Molecular Biology and Computer Facilities, IFC, UNAM. We acknowledge David Eduardo Meza Sánchez from the Metabolic and Proteomic Unit (RAI) for his technical assistance in the HPLC analysis. We also acknowledge the technical assistance of Ma. Teresa Lara Ortiz, Francisco Torres-Quiroz, Georgina Garza, Juliana Rojo, Norma Sánchez and Martha Calahorra. We acknowledge Patrick Weill for the revision of the English language.

Conflicts of Interest: The authors declare no conflict of interest.

References

1. Hernández-Elvira, M.; Torres-Quiroz, F.; Escamilla-Ayala, A.; Domínguez-Martin, E.; Escalante, R.; Kawasaki, L.; Ongay-Larios, L.; Coria, R. The unfolded protein response pathway in the yeast *Kluyveromyces lactis*. A comparative view among yeast species. *Cells* **2018**, *7*, 106. [CrossRef] [PubMed]
2. Domínguez-Martín, E.; Hernández-Elvira, M.; Vincent, O.; Coria, R.; Escalante, R. Unfolding the endoplasmic reticulum of a social amoeba: *Dictyostelium discoideum* as a new model for the study of endoplasmic reticulum stress. *Cells* **2018**, *7*, 56. [CrossRef] [PubMed]
3. Fanata, W.I.D.; Lee, S.Y.; Lee, K.O. The unfolded protein response in plants: A fundamental adaptive cellular response to internal and external stresses. *J. Proteom.* **2013**, *93*, 356–368. [CrossRef] [PubMed]
4. Chakrabarti, A.; Chen, A.W.; Varner, J.D. A review of the mammalian unfolded protein response. *Biotechnol. Bioeng.* **2011**, *108*, 2777–2793. [CrossRef] [PubMed]
5. Cox, J.S.; Shamu, C.E.; Walter, P. Transcriptional induction of genes encoding endoplasmic reticulum resident proteins requires a transmembrane protein kinase. *Cell* **1993**, *73*, 1197–1206. [CrossRef]
6. Shamu, C.E.; Walter, P. Oligomerization and phosphorylation of the Ire1p kinase during intracellular signaling from the endoplasmic reticulum to the nucleus. *EMBO J.* **1996**, *15*, 3028–3039. [CrossRef] [PubMed]
7. Welihinda, A.A.; Kaufman, R.J. The Unfolded Protein Response Pathway in *Saccharomyces cerevisiae*: Oligomerization and trans-phosphorylation of Ire1p (Ern1p) are required for kinase activation. *J. Biol. Chem.* **1996**, *271*, 18181–18187. [CrossRef] [PubMed]
8. Sidrauski, C. The unfolded protein response: An intracellular signaling pathway with many surprising features. *Trends Cell Biol.* **1998**, *8*, 245–249. [CrossRef]
9. Cox, J.S.; Walter, P. A novel mechanism for regulating activity of a transcription factor that controls the unfolded protein response. *Cell* **1996**, *87*, 391–404. [CrossRef]
10. Mori, K.; Ogawa, N.; Kawahara, T.; Yanagi, H.; Yura, T. Palindrome with spacer of one nucleotide is characteristic of the *cis*-acting unfolded protein response element in *Saccharomyces cerevisiae*. *J. Biol. Chem.* **1998**, *273*, 9912–9920. [CrossRef]
11. Chen, Y.; Feldman, D.E.; Deng, C.; Brown, J.A.; De Giacomo, A.F.; Gaw, A.F.; Shi, G.; Le, Q.T.; Brown, J.M.; Koong, A.C. Identification of mitogen-activated protein kinase signaling pathways that confer resistance to endoplasmic reticulum stress in *Saccharomyces cerevisiae*. *Mol. Cancer Res.* **2005**, *3*, 669–677. [CrossRef] [PubMed]
12. Bicknell, A.A.; Tourtellotte, J.; Niwa, M. Late phase of the endoplasmic reticulum stress response pathway is regulated by Hog1 MAP kinase. *J. Biol. Chem.* **2010**, *285*, 17545–17555. [CrossRef] [PubMed]
13. Torres-Quiroz, F.; García-Marqués, S.; Coria, R.; Randez-Gil, F.; Prieto, J.A. The activity of yeast Hog1 MAPK is required during endoplasmic reticulum stress induced by tunicamycin exposure. *J. Biol. Chem.* **2010**, *285*, 20088–20096. [CrossRef] [PubMed]
14. Brewster, J.; de Valoir, T.; Dwyer, N.; Winter, E.; Gustin, M. An osmosensing signal transduction pathway in yeast. *Science* **1993**, *259*, 1760–1763. [CrossRef] [PubMed]
15. Maeda, T.; Wurgler-Murphy, S.M.; Saito, H. A two-component system that regulates an osmosensing MAP kinase cascade in yeast. *Nature* **1994**, *369*, 242–245. [CrossRef] [PubMed]
16. Posas, F. Osmotic activation of the HOG MAPK pathway via Ste11p MAPKKK: Scaffold role of Pbs2p MAPKK. *Science* **1997**, *276*, 1702–1705. [CrossRef]

INFORME DE LABORES 2019

17. Ferrigno, P. Regulated nucleo/cytoplasmic exchange of HOG1 MAPK requires the importin beta homologs NMD5 and XPO1. *EMBO J.* **1998**, *17*, 5606–5614. [CrossRef]
18. Reiser, V.; Salah, S.M.; Ammerer, G. Polarized localization of yeast Pbs2 depends on osmostress, the membrane protein Sho1 and Cdc42. *Nat. Cell Biol.* **2000**, *2*, 620–627. [CrossRef]
19. de Nadal, E.; Posas, F. Multilayered control of gene expression by stress-activated protein kinases. *EMBO J.* **2010**, *29*, 4–13. [CrossRef]
20. Martínez-Montañés, F.; Pascual-Ahuir, A.; Proft, M. Toward a genomic view of the gene expression program regulated by osmostress in yeast. *OMICS J. Integr. Biol.* **2010**, *14*, 619–627. [CrossRef]
21. Aoki, Y.; Kanki, T.; Hirota, Y.; Kurihara, Y.; Saigusa, T.; Uchiumi, T.; Kang, D. Phosphorylation of Serine 114 on Atg32 mediates mitophagy. *Mol. Biol. Cell* **2011**, *22*, 3206–3217. [CrossRef] [PubMed]
22. Mao, K.; Klionsky, D.J. MAPKs regulate mitophagy in *Saccharomyces cerevisiae*. *Autophagy* **2011**, *7*, 1564–1565. [CrossRef] [PubMed]
23. Jones, G.M.; Stalker, J.; Humphray, S.; West, A.; Cox, T.; Rogers, J.; Dunham, I.; Prelich, G. A systematic library for comprehensive overexpression screens in *Saccharomyces cerevisiae*. *Nat. Methods* **2008**, *5*, 239–241. [CrossRef] [PubMed]
24. Amberg, D.C.; Burke, D.; Strathern, J.N.; Burke, D. *Methods in Yeast Genetics: A Cold Spring Harbor Laboratory Course Manual*, 2005 ed.; Cold Spring Harbor Laboratory Press: Cold Spring Harbor, NY, USA, 2005; ISBN 978-0-87969-728-0.
25. Hill, J.E.; Myers, A.M.; Koerner, T.J.; Tzagoloff, A. Yeast/*E. coli* shuttle vectors with multiple unique restriction sites. *Yeast* **1986**, *2*, 163–167. [CrossRef] [PubMed]
26. Sung, M.-K.; Huh, W.-K. Bimolecular fluorescence complementation analysis system forin vivo detection of protein-protein interaction in *Saccharomyces cerevisiae*. *Yeast* **2007**, *24*, 767–775. [CrossRef]
27. Stark, C. BioGRID: A general repository for interaction datasets. *Nucleic Acids Res.* **2006**, *34*, D535–D539. [CrossRef]
28. Shannon, P. Cytoscape: A software environment for integrated models of biomolecular interaction networks. *Genome Res.* **2003**, *13*, 2498–2504. [CrossRef]
29. Baryshnikova, A. Exploratory analysis of biological networks through visualization, clustering, and functional annotation in cytoscape. *Cold Spring Harb. Protoc.* **2016**, *2016*. [CrossRef]
30. Grabińska, K.; Sosińska, G.; Orłowski, J.; Swiezewska, E.; Berges, T.; Karst, F.; Palamarczyk, G. Functional relationships between the *Saccharomyces cerevisiae* cis-prenyltransferases required for dolichol biosynthesis. *Acta Biochim. Pol.* **2005**, *52*, 221–232.
31. Levin, D.E.; Hammond, C.I.; Ralston, R.O.; Bishop, J.M. Two yeast genes that encode unusual protein kinases. *Proc. Natl. Acad. Sci. USA* **1987**, *84*, 6035–6039. [CrossRef]
32. Rine, J.; Hansen, W.; Hardeman, E.; Davis, R.W. Targeted selection of recombinant clones through gene dosage effects. *Proc. Natl. Acad. Sci. USA* **1983**, *80*, 6750–6754. [CrossRef] [PubMed]
33. Barnes, G.; Hansen, W.J.; Holcomb, C.L.; Rine, J. Asparagine-linked glycosylation in *Saccharomyces cerevisiae*: Genetic analysis of an early step. *Mol. Cell. Biol.* **1984**, *4*, 2381–2388. [CrossRef] [PubMed]
34. Watzele, G.; Tanner, W. Cloning of the glutamine: Fructose-6-phosphate amidotransferase gene from yeast. Pheromonal regulation of its transcription. *J. Biol. Chem.* **1989**, *264*, 8753–8758. [PubMed]
35. Bowman, S.M.; Free, S.J. The structure and synthesis of the fungal cell wall. *BioEssays* **2006**, *28*, 799–808. [CrossRef] [PubMed]
36. Katzmann, D.J.; Hallstrom, T.C.; Voet, M.; Wysock, W.; Golin, J.; Volckaert, G.; Moye-Rowley, W.S. Expression of an ATP-binding cassette transporter-encoding gene (YOR1) is required for oligomycin resistance in *Saccharomyces cerevisiae*. *Mol. Cell. Biol.* **1995**, *15*, 6875–6883. [CrossRef] [PubMed]
37. Rogers, B.; Decottignies, A.; Kolaczkowski, M.; Carvajal, E.; Balzi, E.; Goffeau, A. The pleitropic drug ABC transporters from *Saccharomyces cerevisiae*. *J. Mol. Microbiol. Biotechnol.* **2001**, *3*, 207–214. [PubMed]
38. Abruzzi, K.; Denome, S.; Olsen, J.R.; Assenholt, J.; Haaning, L.L.; Jensen, T.H.; Rosbash, M. A novel plasmid-based microarray screen identifies suppressors of rrp6 in *Saccharomyces cerevisiae*. *Mol. Cell. Biol.* **2007**, *27*, 1044–1055. [CrossRef]
39. Elbert, M.; Rossi, G.; Brennwald, P. The yeast Par-1 homologs Kin1 and Kin2 show genetic and physical interactions with components of the exocytic machinery. *Mol. Biol. Cell* **2005**, *16*, 532–549. [CrossRef]

40. Yuan, S.-M.; Nie, W.-C.; He, F.; Jia, Z.-W.; Gao, X.-D. Kin2, the budding yeast ortholog of animal MARK/PAR-1 kinases, localizes to the sites of polarized growth and may regulate septin organization and the cell wall. *PLoS ONE* **2016**, *11*, e0153992. [CrossRef]
41. Sato, M.; Sato, K.; Nishikawa, S.; Hirata, A.; Kato, J.; Nakano, A. The yeast *RER2* gene, identified by endoplasmic reticulum protein localization mutations, encodes *cis*-Prenyltransferase, a key enzyme in dolichol synthesis. *Mol. Cell. Biol.* **1999**, *19*, 471–483. [CrossRef]
42. Nishikawa, S.; Nakano, A. Identification of a gene required for membrane protein retention in the early secretory pathway. *Proc. Natl. Acad. Sci. USA* **1993**, *90*, 8179–8183. [CrossRef] [PubMed]
43. Sato, K.; Sato, M.; Nakano, A. Rer1p as common machinery for the endoplasmic reticulum localization of membrane proteins. *Proc. Natl. Acad. Sci. USA* **1997**, *94*, 9693–9698. [CrossRef] [PubMed]
44. Lussier, M.; White, A.M.; Sheraton, J.; di Paolo, T.; Treadwell, J.; Southard, S.B.; Horenstein, C.I.; Chen-Weiner, J.; Ram, A.F.; Kapteyn, J.C.; et al. Large scale identification of genes involved in cell surface biosynthesis and architecture in *Saccharomyces cerevisiae*. *Genetics* **1997**, *147*, 435–450.
45. García, R.; Bermejo, C.; Grau, C.; Pérez, R.; Rodríguez-Peña, J.M.; Francois, J.; Nombela, C.; Arroyo, J. The global transcriptional response to transient cell wall damage in *Saccharomyces cerevisiae* and its regulation by the cell integrity signaling pathway. *J. Biol. Chem.* **2004**, *279*, 15183–15195. [CrossRef]
46. Pfund, C.; Lopez-Hoyo, N.; Ziegelhoffer, T.; Schilke, B.A.; Lopez-Buesa, P.; Walter, W.A.; Wiedmann, M.; Craig, E.A. The molecular chaperone Ssb from *Saccharomyces cerevisiae* is a component of the ribosome—Nascent chain complex. *EMBO J.* **1998**, *17*, 3981–3989. [CrossRef] [PubMed]
47. Rojas, M.; Farr, G.W.; Fernandez, C.F.; Lauden, L.; McCormack, J.C.; Wolin, S.L. Yeast Gis2 and its human ortholog CNBP are novel components of stress-induced RNP granules. *PLoS ONE* **2012**, *7*, e52824. [CrossRef] [PubMed]
48. Sato, M.; Fujisaki, S.; Sato, K.; Nishimura, Y.; Nakano, A. Yeast *Saccharomyces cerevisiae* has two cis-prenyltransferases with different properties and localizations. Implication for their distinct physiological roles in dolichol synthesis. *Genes Cells* **2001**, *6*, 495–506. [CrossRef]
49. García-Marqués, S.; Randez-Gil, F.; Prieto, J.A. Nuclear versus cytosolic activity of the yeast Hog1 MAP kinase in response to osmotic and tunicamycin-induced ER stress. *FEBS Lett.* **2015**, *589*, 2163–2168. [CrossRef]
50. Songyang, Z.; Lu, K.P.; Kwon, Y.T.; Tsai, L.H.; Filhol, O.; Cochet, C.; Brickey, D.A.; Soderling, T.R.; Bartleson, C.; Graves, D.J.; et al. A structural basis for substrate specificities of protein Ser/Thr kinases: Primary sequence preference of casein kinases I and II, NIMA, phosphorylase kinase, calmodulin-dependent kinase II, CDK5, and Erk1. *Mol. Cell. Biol.* **1996**, *16*, 6486–6493. [CrossRef]
51. Bardwell, L. Mechanisms of MAPK signaling specificity. *Biochem. Soc. Trans.* **2006**, *34*, 837–841. [CrossRef]
52. Ledesma, L.; Sandoval, E.; Cruz-Martínez, U.; Escalante, A.M.; Mejía, S.; Moreno-Álvarez, P.; Ávila, E.; García, E.; Coello, G.; Torres-Quiroz, F. YAAM: Yeast Amino Acid Modifications Database. *Database* **2018**, *2018*. [CrossRef] [PubMed]
53. Cui, Z.; Hirata, D.; Tsuchiya, E.; Osada, H.; Miyakawa, T. The Multidrug Resistance-associated Protein (MRP) Subfamily (Yrs1/Yor1) of *Saccharomyces cerevisiae* is important for the tolerance to a broad range of organic anions. *J. Biol. Chem.* **1996**, *271*, 14712–14716. [CrossRef] [PubMed]
54. Anshu, A.; Mannan, M.A.; Chakraborty, A.; Chakrabarti, S.; Dey, M. A novel role for protein kinase Kin2 in regulating *HAC1* mRNA translocation, splicing, and translation. *Mol. Cell. Biol.* **2015**, *35*, 199–210. [CrossRef] [PubMed]
55. Camirand, A.; Heysen, A.; Grondin, B.; Herscovics, A. Glycoprotein biosynthesis in *Saccharomyces cerevisiae*. Isolation and characterization of the gene encoding a specific processing alpha-mannosidase. *J. Biol. Chem.* **1991**, *266*, 15120–15127. [PubMed]
56. Massaad, M.J.; Franzusoff, A.; Herscovics, A. The processing α1,2-mannosidase of *Saccharomyces cerevisiae* depends on Rer1p for its localization in the endoplasmic reticulum. *Eur. J. Cell Biol.* **1999**, *78*, 435–440. [CrossRef]
57. Sato, K.; Sato, M.; Nakano, A. Rer1p, a retrieval receptor for ER membrane proteins, recognizes transmembrane domains in multiple modes. *Mol. Biol. Cell* **2003**, *14*, 3605–3616. [CrossRef] [PubMed]
58. Currie, E.; Guo, X.; Christiano, R.; Chitraju, C.; Kory, N.; Harrison, K.; Haas, J.; Walther, T.C.; Farese, R.V. High confidence proteomic analysis of yeast LDs identifies additional droplet proteins and reveals connections to dolichol synthesis and sterol acetylation. *J. Lipid Res.* **2014**, *55*, 1465–1477. [CrossRef] [PubMed]

59. Acosta-Serrano, A.; O'Rear, J.; Quellhorst, G.; Lee, S.H.; Hwa, K.-Y.; Krag, S.S.; Englund, P.T. Defects in the N-linked oligosaccharide biosynthetic pathway in a *Trypanosoma brucei* glycosylation mutant. *Eukaryot. Cell* **2004**, *3*, 255–263. [CrossRef] [PubMed]
60. Tanigawa, M.; Kihara, A.; Terashima, M.; Takahara, T.; Maeda, T. Sphingolipids regulate the yeast high-osmolarity glycerol response pathway. *Mol. Cell. Biol.* **2012**, *32*, 2861–2870. [CrossRef]
61. Montañés, F.M.; Pascual-Ahuir, A.; Proft, M. Repression of ergosterol biosynthesis is essential for stress resistance and is mediated by the Hog1 MAP kinase and the Mot3 and Rox1 transcription factors. *Mol. Microbiol.* **2011**, *79*, 1008–1023. [CrossRef]
62. Jennings, S.M.; Tsay, Y.H.; Fisch, T.M.; Robinson, G.W. Molecular cloning and characterization of the yeast gene for squalene synthetase. *Proc. Natl. Acad. Sci. USA* **1991**, *88*, 6038–6042. [CrossRef] [PubMed]
63. Janik, A.; Juchimiuk, M.; Kruszewska, J.; Orowski, J.; Pasikowska, M.; Palamarczyk, G. Impact of yeast glycosylation pathway on cell integrity and morphology. In *Glycosylation*; Petrescu, S., Ed.; InTech: London, UK, 2012; ISBN 978-953-51-0771-2.
64. Ma, B.-X.; Ke, X.; Tang, X.-L.; Zheng, R.-C.; Zheng, Y.-G. Rate-limiting steps in the *Saccharomyces cerevisiae* ergosterol pathway: Towards improved ergosta-5,7-dien-3β-ol accumulation by metabolic engineering. *World J. Microbiol. Biotechnol.* **2018**, *34*, 55. [CrossRef] [PubMed]
65. Mitchell, S.F.; Jain, S.; She, M.; Parker, R. Global analysis of yeast mRNPs. *Nat. Struct. Mol. Biol.* **2013**, *20*, 127–133. [CrossRef] [PubMed]



© 2019 by the authors. Licensee MDPI, Basel, Switzerland. This article is an open access article distributed under the terms and conditions of the Creative Commons Attribution (CC BY) license (http://creativecommons.org/licenses/by/4.0/).

Trends in Biochemical Sciences

CellPress
REVIEWS

Opinion

Conservation and Variability of the AUG Initiation Codon Context in Eukaryotes

Greco Hernández,[1,*] Vincent G. Osnaya,[1] and Xochitl Pérez-Martínez[2]

Selection of the translation initiation site (TIS) is a crucial step during translation. In the 1980s Marylin Kozak performed key studies on vertebrate mRNAs to characterize the optimal TIS consensus sequence, the Kozak motif. Within this motif, conservation of nucleotides in crucial positions, namely a purine at −3 and a G at +4 (where the A of the AUG is numbered +1), is essential for TIS recognition. Ever since its characterization the Kozak motif has been regarded as the optimal sequence to initiate translation in all eukaryotes. We revisit here published *in silico* data on TIS consensus sequences, as well as experimental studies from diverse eukaryotic lineages, and propose that, while the −3A/G position is universally conserved, the remaining variability of the consensus sequences enables their classification as optimal, strong, and moderate TIS sequences.

Highlights

The Kozak sequence has been characterized as a conserved TIS in eukaryotes.

Sequencing of mRNAs from diverse species coupled to functional studies will continue to contribute to understanding the impact of sequence context on TISs with cognate or non-cognate initiation codons.

The 3D resolution of both translational initiation factors and ribosomes on mRNA will enable better understanding of their conservation, as well as the conservation of the TIS sequences.

Ongoing sequencing projects, such as the Earth BioGenome Project, will help to determine the conservation of the Kozak sequence between eukaryotes such as vertebrates, plants, and fungi.

Conservation and Variability of the Kozak Motif

Translation, namely the synthesis of proteins by the ribosome and translation factors using mRNA as the template, is a fundamental process for all forms of life because proteins catalyze the vast majority of reactions sustaining life and play structural, transport, and regulatory roles in all living organisms. In eukaryotes, regulating gene expression at the level of translation is crucial for tissues or developmental stages where transcription is quiescent or limited, as well as for the differential spatial distribution of proteins in cells and tissues [1]. Regulating translation also gives cells the potential to elicit rapid and reversible responses to sudden environmental changes and stresses without invoking mRNA transcription, processing, or transport [1]. Thus, translational control plays a significant role in determining both protein abundance and proteome composition, and, accordingly, a myriad of mechanisms to regulate translation have evolved throughout eukaryotic evolution [2,3]. Recognition of the mRNA AUG **codon** (see Glossary) that initiates translation, termed the **translation initiation site** (TIS), is subject to tight control because this step establishes the correct open reading frame for mRNA decoding (Box 1).

In the decades following 1980, Marylin Kozak analyzed the frequency of nucleotides around the TIS of vertebrate **coding sequences** (CDSs) in mRNAs [4–6]. She established that the sequence GCC*R*CCAUG*G* (where R at −3, in italic font, is A or G; and the AUG **initiation codon** is underlined) is both the consensus sequence flanking the TIS and the one most optimal for translation in vertebrate lineages; this sequence is termed the **Kozak motif** [7]. Interestingly, many new TIS sequences of phylogenetically distant, non-vertebrate phyla have been analyzed with the advent of the genomic era and high-throughput technologies, as well as with the development of different systems in which to study translation (discussed below). Even so, there is a lack of a comprehensive view of TIS consensus sequences across eukaryotes. We revisit here published data with a primary focus on vertebrates, unicellular fungi, insects, flowering land plants, and some protists to explore these data and evaluate whether the Kozak motif is also the TIS consensus sequence in different taxa. Remarkably, we observe that the −3R position is universally conserved among all eukaryotes scrutinized here, but that there is variation in the +4 position, particularly in single-celled fungi and some protists. Surprisingly, we observed that A/C at the −2 position is universally conserved as well. We also noticed that there are differences between eukaryotic lineages, and therefore propose that TIS consensus sequences can be categorized as Kozak optimal, strong, and moderate motifs.

The Kozak Motif: Optimal, Strong, and Moderate Beginnings

During translation initiation, the small (40S) ribosomal subunit binds to the mRNA at the **5′-untranslated region** (5′-UTR) and **scans** in the 5′ to 3′ direction to reach the CDS start codon, most usually an

[1]Translation and Cancer Laboratory, Unit of Biomedical Research on Cancer, National Institute of Cancer (Instituto Nacional de Cancerología, INCan), 22 San Fernando Avenue, Tlalpan, 14080 Mexico City, Mexico

[2]Department of Molecular Genetics, Cell Physiology Institute (Instituto de Fisiología Celular), Universidad Nacional Autónoma de México (UNAM), 04510 Mexico City, Mexico

*Correspondence: ghernandezr@incan.edu.mx

© 2019 The Author(s). Published by Elsevier Ltd. This is an open access article under the CC BY-NC-ND license (http://creativecommons.org/licenses/by-nc-nd/4.0/).

Trends in Biochemical Sciences

CellPress
REVIEWS

Box 1. Translation Initiation in Eukaryotes

Translational control primarily occurs at the initiation step in which mRNA is recruited to the ribosome (reviewed in [1,25,92,93] and references therein). Translation begins with the recognition of the cap structure (m^7GpppN, where N is any nucleotide) located at the 5′ end of the mRNA by eIF4E. A 40S ribosomal subunit bound to eIF1, eIF1A, eIF3, and eIF5 then promotes recruitment of a **ternary complex** (TC), consisting of eIF2 attached to GTP and an initiator Met-tRNA$_i^{Met}$, to form a 43S **preinitiation complex** (PIC). This step positions the initiator Met-tRNA$_i^{Met}$ in the peptidyl (P) site of the ribosome. In a parallel set of interactions, the scaffold protein eIF4G interacts with the poly(A)-binding protein (PABP), the RNA helicase eIF4A, the ribosome-bound eIF3, and the cap-bound eIF4E to coordinate recruitment of the 43S PIC to the mRNA 5′-UTR. eIF4A unwinds secondary structures of 5′-UTR, allowing the 43S PIC to scan base-by-base the 5′-UTR in the search for an AUG initiation codon to start translation [1,25,92,93].

eIF1 and eIF1A drive selection of the correct start codon. They cooperatively promote the adoption of an **open conformation** of the 43S PIC that is compatible with scanning. Such conformation features the Met-tRNA$_i^{Met}$ loosely engaged in the P-site, and allows eIF1 and eIF1A to discriminate against codon–**anticodon** mismatches. 5′-UTR scanning proceeds until an authentic initiator codon, most often an AUG codon, is reached and establishes correct codon–anticodon basepairing. This event arrests scanning and promotes transition of the 43S PIC to a **closed conformation** in which Met-tRNA$_i^{Met}$ and eIF1A become tightly positioned within the P-site. Together, these actions result in the formation of a 48S PIC. Then, GTP–eIF5B promotes the release of eIF1 and eIF5B, facilitating binding of a 60S subunit to the 48S PIC to assemble an 80S initiation complex [1,25,92,93].

AUG [8,9]. The scanning model predicts that translation initiates at the AUG codon closest to the 5′ end of the mRNA, which is termed the 'first-AUG rule' [8,9]. Landmark studies to understand the role of the flanking sequence in TIS recognition by the ribosome led Kozak to analyze 153 cellular and viral mRNAs from vertebrates, observing that 'the sequences flanking the TIS are not random' [4]. She initially found that *R*NNAUG*G* (where N is any base) is the consensus sequence surrounding the AUG initiator codon, and that the two positions which show the most significant conservation, −3R and +4G, function to generate the most efficient initiation signal [4]. She later analyzed 211 cellular mRNAs, mostly from vertebrates but also from some insects, sea urchins, and flowering land plants, and observed that CC*R*CCAUG*G* was the consensus sequence around the TIS [5]. Kozak then analyzed 699 vertebrate mRNAs, and from this study an expanded consensus for the TIS context emerged, namely (GCC)GCC*R*CCAUG*G* in which 97% of mRNAs have a purine, most often an A (61%), at the −3 position [6].

Site-directed mutagenesis experiments to analyze the functional contribution of every nucleotide at positions −1 to −10 and the G at +4 position showed that translation decreases five to tenfold when either −3A or the +4G is replaced by C or U, and 20-fold when pyrimidines are substituted at both of those positions ([4,7,8] and references therein, [10]). These studies also demonstrated that the −3R position plays a key role in TIS recognition and that, in its absence, the +4G position also significantly contributes to promoting translation [7,10,11]. Lütcke *et al*. also demonstrated that, in a vertebrate system, the translational efficiency of an mRNA was 100, 85, 61, and 38% for A, G, U, and C at position −3, respectively [12]. By contrast, positions −1C, −2C, −4C, −5C, and −6G slightly contributed to promoting translation only in the absence of both −3R and +4G. Nucleotides in positions −7 to −10 showed essentially no influence on translation [7,10,11]. Likewise, the +5 and +6 positions also had no impact on translation [11].

Additional experiments showed that changing −3R and/or +4G caused some 40S ribosomal subunits to bypass the first AUG and instead initiate at the next AUG [7,13] in a mechanism termed 'leaky scanning' [8,14]. However, because recognizing the TIS position is crucial, ribosomes may initiate at AUG codons even if they lie in a weak context (i.e., lacking the −3R and/or +4G). Indeed, a −3A is usually sufficient for ribosomes to recognize the first AUG irrespective of the other nucleotides in the context [8,14]. It has also been shown that stem-loop structures ~14 nt downstream of a suboptimal AUG context improve its recognition by the 40S ribosome, possibly by slowing the scanning process. This facilitation is most significant when the ribosome stalls directly over the AUG [15].

Glossary

Aminoacyl (A) site: the site on the 40S ribosomal subunit that holds the incoming aminoacyl-tRNA.
Anticodon: the triplet of a tRNA that is complementary to an mRNA codon.
Biosphere: layer of Earth where life exists. The biosphere is one of the four layers that surround the Earth, together with the lithosphere (soil and rock), hydrosphere (water), and atmosphere (air), and the biosphere is the sum of all the ecosystems and communities on a global scale.
Coding sequences (CDSs): usually start with an AUG codon and end with any of the stop codons. In a few examples, non-cognate codons such as GUG, CUG, ACG, or AUU are used to start the coding sequences.
Closed conformation: a ribosomal state of codon–anticodon base pairing that results in displacement of eIF1s from the P-site; also called the 'in' conformation.
Codon: a sequence of three RNA nucleotides that encodes a specific amino acid (or stop signal) during protein synthesis.
Eukaryotic initiation factors (eIFs): soluble proteins that drive the initiation phase of eukaryotic translation, in other words the mRNA recruitment to the ribosome and the further formation of a ribosomal preinitiation complex at an initiation codon.
Initiation codon: mRNA triplet that opens a reading frame for protein synthesis. The majority of peptides initiate with an AUG codon which encodes methionine. Some open reading frames start with non-AUG codons (also termed 'near-cognate'), which may be GUG, CUG, ACG, and, very rarely, AUU.
Kozak motif: a consensus sequence surrounding the mRNA translation initiation site (TIS, usually the codon AUG) that was discovered by Marilyn Kozak in the 1980s in vertebrate mRNAs.
Microbial dark matter: microbial world composed of genes, genomes, bacteria, archaea, protists, and viruses of unknown identity, as well as their processes and communities. The term is by analogy to the dark matter of the cosmos studied by astronomers.

Table 1. Interactions between Factors, Ribosome, and mRNA during TIS Recognition

Species	Protein	Amino acid	Contacts	Refs
Saccharomyces cerevisiae (budding yeast)	eIF1	Arg36	Codon/anticodon duplex	[19]
Yeast	eIF1	Asp71, Glu73, Glu76	D stem backbone of Met-tRNA$_i$	[19]
Tetrahymena thermophila	eIF1	Arg26, Arg27, Gly28, Arg29, and Lys30	Codon/anticodon duplex	[20]
Oryctolagus cuniculus (Rabbit)	eIF1	Arg38–Lys42	+4 of mRNA, codon/anticodon duplex	[21]
Rabbit	eIF1	Pro77–Gly80	D stem of tRNA$_i^{Met}$	[21]
Tetrahymena thermophila	eIF1A	Asn43, Arg45, Trp69, Lys87	rRNA	[22]
Yeast	eIF1A	Gly8, Gly9, Lys10	Codon/anticodon duplex	[19]
Yeast	eIF1A	Lys16	+5 of mRNA	[19]
Yeast	eIF1A	Trp70	AUG and +4 of mRNA	[19]
Rabbit	eIF1A	Amino terminal	+4 and antisense loop of tRNA$_i$	[21]
Yeast	eIF2α	Arg55	−3 of mRNA	[18,19]
Yeast	eIF2α	Arg57	−2 of mRNA	[18,19]
Rabbit	eIF2α		−3 of mRNA	[17,24]
Rabbit	rpS26e	Val83	−3 of mRNA	[21]
Rabbit	rpS5		−3 and −4 of mRNA	[17,24]
Rabbit	rpS15		+4 and +5 of mRNA	[17,24,26]

Overall, these experiments showed that the context sequence strongly influences TIS recognition by the ribosome in vertebrate mRNAs. Mainly, positions −3R (most often A) and +4G are both the most conserved nucleotides and exert the most critical influence on translational efficiency. Thus, the Kozak motif GCC*R*CCAUG*G* was established as the optimal context for TIS recognition in vertebrate mRNAs [8]. Further, depending on the presence of the two crucial nucleotides (i.e., −3*R* and +4*G*), sequences surrounding the TIS have been classified as 'optimal', GCC*R*CCAUG*G*; 'strong', NNN*R*NNAUG*G* (only the two important nucleotides are present); 'adequate', NNN*R*NNAUG(A/C/U) or NNN(C/U)NNAUG*G* (only one of these nucleotides is present); and 'weak', NNN(C/U)NNAUG(A/C/U) (any sequence lacking both key nucleotides) Kozak motifs [16].

Consistent with the importance of a purine at the −3 and +4 positions, Pisarev *et al.* showed an interaction between these nucleotides and the translational machinery [17]. They observed interactions between −3A and the **eukaryotic initiation factor** (eIF) 2α subunit, and of +4G with ribosomal protein S9 (rpS9) and 18S ribosomal RNA (rRNA). Further biochemical, genetic, and structural studies in yeast, rabbit, and *Tetrahymena thermophila* have recently led to a full understanding of the mRNA TIS recognition by the 40S ribosome **peptidyl (P) site**, eIF1, eIF1A, eIF2α, and rpS26e at the atomic level (Table 1 and Box 2) [18–27].

Open conformation: a complete ribosomal complex in which initiation factors eIF1, eIF1A, eIF2, and eIF4F, together with the 40S subunit, establish a state that promotes scanning; also called the 'out' conformation.
Peptidyl (P) site: ribosomal tRNA-binding site that holds the peptidyl-tRNA.
Preinitiation complex (PIC): a macromolecular complex containing the 40S small ribosomal subunit (bound to eIF1A, eIF1, and eIF3) and the ternary complex. This complex requires the cooperative action of eIF4F to attach to the mRNA.
Scanning: ribosomal movement in a 5′ to 3′ direction along the 5′-UTR of an mRNA to unwind secondary structures (promoted by RNA helicases) to reach an initiation codon.
Ternary complex (TC): molecular complex comprising eIF2, a molecule of GTP, and an initiator Met-tRNA (Met-tRNA$_i$). It binds the 40S ribosomal subunit to promote 43S complex formation during translation initiation.
Translation initiation site (TIS): mRNA triplet that opens the reading frame for protein synthesis. TIS triplets are most frequently AUG (encoding methionine), but other non-cognate codons such as GUG (encoding valine) and CUG (encoding leucine) may sometimes act as a TIS.
5′-Untranslated region (5′-UTR): the mRNA 5′-UTR is located upstream of the AUG start codon. It does not contain a protein coding sequence but is crucial for regulating translation by a variety of mechanisms.

Trends in Biochemical Sciences

CellPress
REVIEWS

The TIS Consensus Context in Disparate Lineages

Sequence Analyses of TIS Consensus Sequences

More recently, the TIS context of CDSs from many species belonging to phylogenetically distant taxa, namely single-celled fungi, insects, vertebrate, flowering land plants, and some protists, have been analyzed *in silico* by different research groups to identify TIS consensus sequences (Tables S1–S5 in the supplemental information online). The universe of published consensus motifs prompted us to determine their distribution across the tree of life [28,29], and to ask whether or not the optimal vertebrate Kozak motif GCC*R*CCAUG*G* is also the TIS consensus sequence in non-vertebrate species.

In analyzing these data, different authors have used various criteria to select a 'consensus' sequence. Many of them used the most common procedure in the field, namely the Cavener consensus rule [30,31]. According to this rule, a particular nucleotide at a specific position is given a consensus status indicated by a capital letter if its frequency is greater than 50% and greater than twice the frequency of the second most frequent nucleotide at that position. When no single nucleotide satisfies these criteria, a pair of bases are assigned co-consensus status and indicated by capital letters if the sum of their frequencies is greater than 75%. If no single nucleotide or pair of nucleotides meet these criteria, the most frequent nucleotide is denoted by a lower-case letter.

Thus, by using the Cavener consensus rule, we recalculated the published consensus sequences of those reports that did not use it. We observed only slight variations between the recalculated sequences and the original sequences (Tables S1–S5). We then categorized all consensus sequences according to the Kozak motifs defined above [16]. We choose to use the term 'moderate' instead of 'adequate' for those TIS contexts that possess only one of the key nucleotides. We did not recalculate the sequences of Nakagawa *at al.* [32], Pesole *et al.* [33], and Acevedo *et al.* [34] because the raw data were not provided. Figure 1 (Key Figure) depicts a global view of the distribution of the consensus sequences surrounding the CDSs TIS across the tree of life, according to the current classification of eukaryotes [28,29].

Over the years, many studies have corroborated that the optimal Kozak motif GCC*R*CCAUG*G*, or a slight variation of it, GCM*R*NCAUG*G* (where M is an A or C), is actually the consensus sequences around the TIS in vertebrate (phylum Chordata) mRNAs, demonstrating the highly predictive power of Kozak's findings (Table S1) [31,32,35–37]. However, some of the species analyzed, such as cattle, pig, red junglefowl, and the fish *Danio rerio*, possess strong motifs NNN*R*NCAUG*G* as the consensus

Box 2. Recognition of the AUG Start Codon

To date, recognition of the correct AUG start codon by initiation factors in eukaryotes is well known at the ultrastructural level (Figure I) [9,18–22,92]. During the initiation of translation, eIF1 and eIF1A attach to the 40S subunit near the P-site and the **aminoacyl (A) site**, respectively. For mRNA scanning to proceed, eIF1 and the eIF1A C-terminal tail (CTT) act together to discriminate against non-AUG codons. When non-AUG codons are detected, the Arg38–Lys42 stretch of rabbit eIF1 spatially interferes with the anticodon stem-loop of $tRNA_i^{Met}$ and nucleotide +4 of mRNA [21]. The Pro77–Gly80 region of rabbit eIF1 also obstructs interaction with the D stem of $tRNA_i^{Met}$ [21]. These steric clashes destabilize mismatches between codon–anticodon duplexes and result in the open conformation that promotes scanning (Figure IA). In brief, the open conformation does not allow full accommodation of $tRNA_i^{Met}$ in the P-site owing to clashes with eIF1 and eIF1A-CTT [18–25,92].

Upon recognition of an AUG codon by correct basepairing with the anticodon of Met-$tRNA_i^{Met}$, yeast eIF1A N-terminal tail (NTT) residues Gly8, Gly9, and Lys10 interact with the codon–anticodon duplex and stabilize it, while yeast eIF1A Lys16 and Trp70 contact nucleotides +4 and +5 of the mRNA [19,21]. These interactions inhibit scanning, stabilize codon–anticodon duplex formation, and promote a transition to the closed conformation that displays tight accommodation of $tRNA_i^{Met}$ within the P-site. AUG recognition also drives conversion of GTP–eIF2 to GDP–eIF2, liberating phosphate (Pi), as well as dissociation of eIF1, GDP–eIF2, and eIF1A-CTT from the P-site. Transition to the closed conformation (Figure IB) brings rabbit Arg55 and Arg57 of eIF2α D1 loop in contact with mRNA nucleotides −2 and −3, and Val83 of rabbit rpS26e to contact nucleotide −3. These interactions promote the initiation of translation from an AUG in an appropriate context [18–25,92].

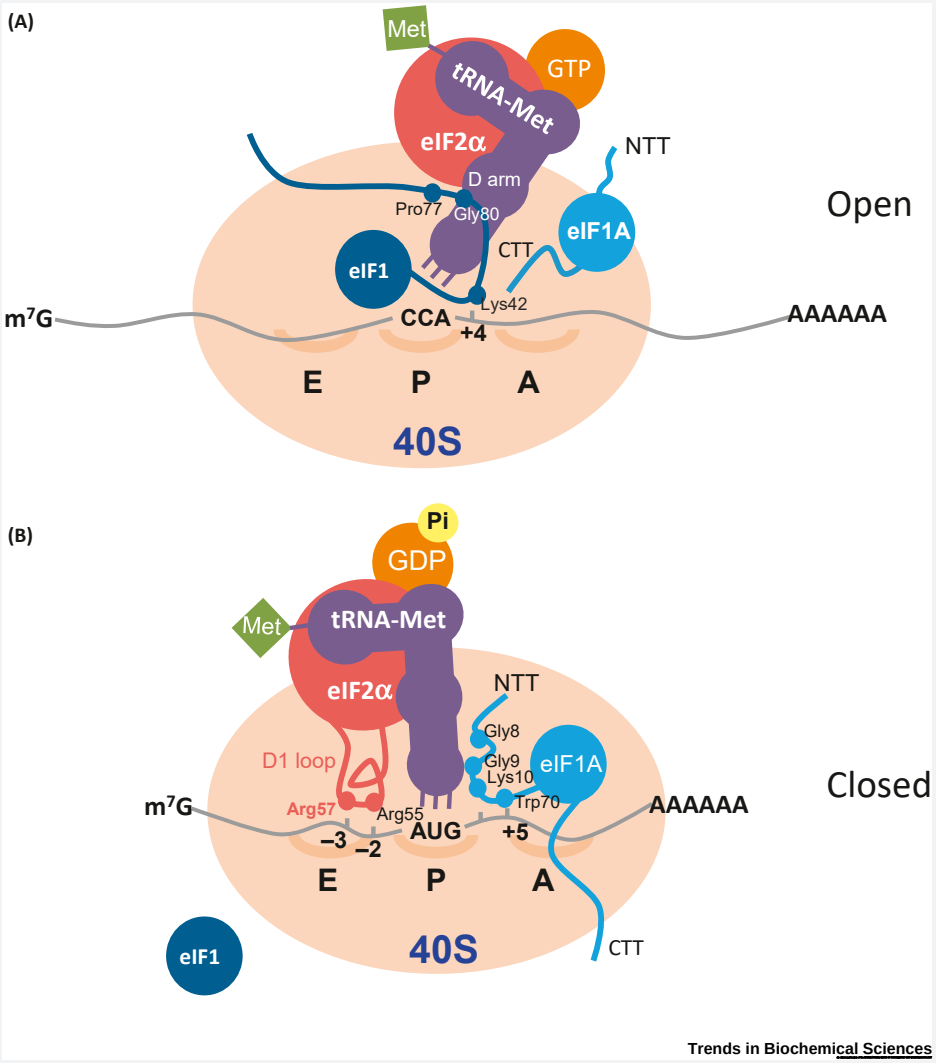

Figure I. Recognition of the mRNA AUG Start Codon by the Ribosome.

(A) Ribosome open conformation during scanning. (B) Once a TIS is recognized, that ribosome changes to a closed conformation that is incompatible with the scanning process.

context instead of an optimal motif [32,37]. Indeed, the −6G, −5C, and −1C positions are relatively well conserved across vertebrate consensus sequences (Table S1 and Table 2). Further, tunicates (phylum Chordata), the closest living relatives of vertebrates, occupy the most basal position in the chordate phylogeny and have been extensively studied to understand the evolutionary origin of vertebrates [38]. Within this lineage, the sea squirt *Ciona intestinalis* possesses a moderate Kozak motif with a K at the +4 position (where K is a G or U) as the preferred TIS consensus sequence [32] (Table S1). This observation could suggest that the optimal Kozak motif for vertebrates appeared at the emergence of the chordates. It would be exiting to study whether or not this motif is also the TIS consensus motif in other tunicate species. We also noticed that the –2M position is highly conserved among the consensus sequences of the vertebrates and the tunicate studied (Table 2).

Trends in Biochemical Sciences

CellPress REVIEWS

Key Figure

The Consensus Translation Initiation Site (TIS) Kozak Motif Varies among Different Eukaryotes

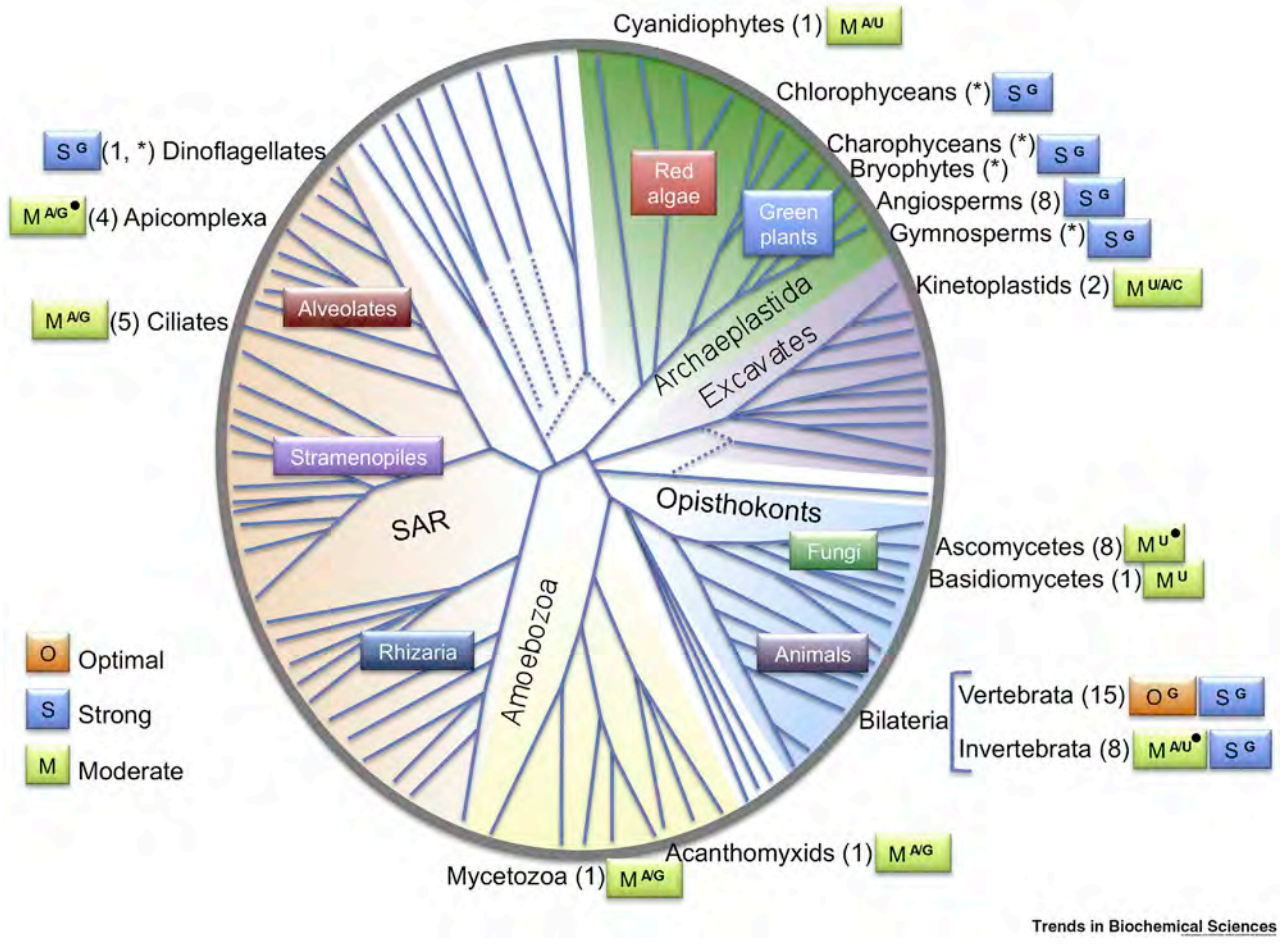

Figure 1. The A or G at the −3 position is conserved in all lineages studied. Other positions (including the functionally key +4 nucleotide) of the consensus Kozak motif vary among different eukaryotes. As a preferred sequence, the optimal Kozak motif is restricted to vertebrates and some angiosperm (monocotyledon) plants. Strong Kozak motifs are present in some vertebrates, flowering land plants (supergroup Archaeoplastida), and Dinoflagellates (supergroup Alveolates). Moderate Kozak motifs are the prevalent TIS consensus in fungi, invertebrates, apicomplexans, ciliates, mycetozoans, and acanthomyxidans. Numbers in brackets indicate the number of species analyzed in each lineage, an asterisk (*) indicates cases where the number was not specified by the authors. (●) Indicates lineages that generally use moderate Kozak motifs but contain a few species that use strong Kozak motifs (Tables S1–S5 for details). The preferentially used nucleotide(s) at the +4 position are indicated as superscripts. Classification of eukaryotes is according to [28,29]. Kozak motifs are defined according to [16]: O, optimal GCC*R*CCAUG*G*; S, strong NNN*R*NNAUG*G*; M, moderate NNN*R*NNAUG(A/C/U) or NNN(C/U)NNAUG*G*. Abbreviations: N, any nucleotide; R, purine (A or G); SAR, stramenopiles, alveolates, and rhizaria. Scheme adapted from Burky [28] with permission from Cold Spring Harbor Laboratory Press.

Among invertebrate species, several insects (phylum Arthropoda) have been analyzed (Table S2) [31,32,34,37,39]. Whereas the fruit fly *Drosophila melanogaster* possesses a strong motif [31,34,37], species from different orders, including *Apis mellifera*, *Bombyx mori*, and *Tribolium castaneum* on the one hand, and *Anopheles gambiae* on the other, contain moderate consensus motifs of the type NNM*R*MMAUGK and NNN*R*NNAUGW (where W is A or U), respectively [32,39]. Further,

invertebrate from other phyla, such as the roundworm *Caenorhabditis elegans* (phylum Nematoda) and the blood fluke *Schistosoma japonicum* (phylum Platyhelminthes), also possess moderate motifs as TIS consensus flanking sequences [31,32]. More specifically, *A. mellifera*, *B. mori*, *T. castaneum*, and *S. japonicum* have moderate consensus motifs with a K at the +4 position [31,32,39]. Interestingly, the −4M and −2M positions appear to be relatively well conserved in the consensus sequences of the invertebrates mentioned here (Table 2).

Within the supergroup Archaeplastida (Plantae), several species of green plants (land plants and green algae) have been analyzed (Table S3). They possess strong Kozak motifs as the consensus TIS context [31–33,36,40–43]. The frequencies of TISs containing guanine at positions −3 and +4 were observed to be different between monocotyledon and dicotyledon mRNAs. Whereas monocot mRNAs contain higher frequencies of −3G/+4G nucleotides, −3A/+4G are more frequent in dicot mRNAs. It should be pointed out that the 5′-UTRs of monocot mRNAs are GC-rich, whereas those of dicots are AU-rich sequences [31–33,40,41,43]. Moreover, we have noticed that, among the consensus sequences of the plant species here scrutinized, the −2M position is well conserved (Table 2). A single species of red algae has also been analyzed, namely *Cyanidioschyzn merolae* [32], which possesses a moderate consensus motif.

All fungi (supergroup Opisthokonts) analyzed have been unicellular species, including *Saccharomyces cerevisiae*, *Aspergillus fumigatus*, *Deberyomyces hansenii*, *Yarrowia lipolytica*, *Eremothecium gossypii*, *Kluyveromyces lacti*, *Candida glabrata*, *Schizosaccharomyces pombe* (phylum Ascomycetes), and *Cryptococcus neoformans* (phylum Basidiomycetes) (Table S4). In contrast to the animals and plants mentioned above, these unicellular fungi mainly have moderate Kozak motifs with a bias towards U at the +4 position [31–33,44,45] (Figure 1). Moreover, the −2M and −4M positions also appear to be relatively well conserved (Table 2). It would be interesting to analyze whether or not this is also the case in multicellular fungi.

Table S5 shows protist species from diverse phyla of the supergroups Amebozoa and Excavates, and the group Alveolates. Among them, different species of dinoflagellates (Alveolates), such as *Symbiodinium kawatii*, use strong Kozak motifs as TIS consensus sequences [46,47]. By contrast,

Table 2. Most Conserved Positions among TIS Consensus Sequences from Coding Sequences in Different Groups of Eukaryotes[a]

Group	Sequence[b]							
	−6	−5	−4	−3	−2	−1	AUG	+4
Vertebrates	G	C		*R*	M	C	———	*G*
Tunicata			M	*A*	M		———	G/U
Invertebrates			M	*R*	M		———	G/A/U
Green plants				*R*	M		———	*G*
Red algae				*A*	M	C	———	A/U
Fungi			M	*R*	M		———	U
Amoebozoa (Mycetozoa, Acanthomyxids)				*R*	M		———	R
Alveolates (Dinoflagellates, Apicomplexa, and Ciliates)								
Excavata (Kinetoplastids)				*R*	M		———	C/A/U
Universally conserved				*R*	M		———	

[a]Owing to its key functional importance, the +4 position is also shown despite its lack of conservation.
[b]Key: ———, AUG; M is A or C; R is A or G.

apicomplexan species (Alveolates) such as *Theileria* spp., *Cryptosporidim parvum*, and *Plasmodium falciparum* [32,48], the kinetoplastids (Excavata) *Leishmania major* and *Trypanosome brucei* [32], the mycetozoan (Amebozoa) *Dictyostelium* spp. and *Acanthamoeba castellanii* [31,32,49], and the ciliates *Paramecium* spp., *Tetrahymena* spp., *Euplotes* spp., *Oxytricha* spp., and *Stylonyclia lemnae* [49], prefer moderate Kozak motifs with different nucleotides (namely G, A, U, or C) at the +4 position as the consensus TIS context. Interestingly, although the −2M position is well conserved in all protist consensus sequences included here, M at the −4 position is also conserved among apicomplexan, dinoflagellate, and mycetozoan species (Table 2).

Recently, a myriad of giant, novel viruses have been discovered that contain substantial sets of translational factors, including eIF1 and eIF2α [50,51]. It would be exciting to investigate whether or not those factors are involved in the host TIS context recognition.

Experimentally Tested TIS Consensus Sequences

Despite the high value of *in silico* analyses, the functional importance of most TIS consensus sequences remains to be experimentally evaluated. Indeed, only some sequences from a few species have been tested in the laboratory (Table S6). As mentioned, the optimal Kozak motif has experimentally been shown *in vitro* to be the best sequence for promoting translation in vertebrates, in particular, rat and rabbit [7,10,11]. Despite these findings, for other vertebrates such as the model organism zebrafish (*Danio rerio*), the optimal Kozak sequence was found to be a poor predictor of translation efficiency [37]. In this case, the investigators found that, although the optimal Kozak sequence efficiently promoted translation *in vivo*, it is neither the most frequent nor the most efficient sequence for initiating translation. Instead, the most frequent sequence is almost twice as efficient at promoting translation as the optimal Kozak motif [37]. Thus, the capacity of the sequences to promote translation may vary among different species, and therefore should be experimentally tested in the specific organism of interest.

Experimental studies of invertebrate species are scarce. Only two insects have been analyzed, namely *D. melanogaster* [34] and *B. mori* [39]. According to what has been observed *in silico*, strong Kozak motifs have the most influence on promoting translation in *Drosophila* [34]. In the case of *B. mori*, a difference was observed between the *in silico*-obtained consensus TIS sequence [32,39] and the most efficient sequence determined experimentally [39]. In particular, the +4 position appears to be different. This apparent discrepancy might be explained by the significant dissimilarity between the number of analyzed sequences in both approaches, namely 14 sequences *in vitro* [39] versus 50 [39] and 875 sequences [32] *in silico*.

Regarding plants, the influence of the TIS context on translation initiation has been experimentally examined in some flowering species (Table S6). *In vitro* translation assays observed no differences in translation efficiency in the wheat system when −3A was changed for G, U, or C [12]. Other *in vitro* assays with 21 sequences did find that −3A/G and +4G are the most efficient nucleotides for translation initiation [4]. Later, *in vivo* experiments in tobacco (16 sequences) [43], *Arabidopsis thaliana* and *Oryza sativa* (64 sequences) [52], and *Picea abies* and *Zea mays* (both 16 sequences) [43] have shown that −3A/G and +4G indeed confer the best translational efficiency.

Among fungi, only *S. cerevisiae* has been experimentally studied, although some discrepancies have been observed. Early studies by Looman and Kuivenhoven (1993) of 47 sequences showed that this yeast prefers the moderate Kozak motif AAUUANNAUGUCU for optimal mRNA translation [53], in agreement with different *in silico* analyses of genomic sequences that also established a moderate sequence with a +4U as the TIS consensus context [31,32,44,45]. Among these studies, Nakagawa *et al.* [32] analyzed 5980 CDSs. By contrast, Pesole *et al.* inspected 1378 CDSs *in silico* [33], obtaining the strong Kozak motif CAMMAUGG as the TIS consensus context. In agreement with this result, ribosome profiling experiments (also termed Ribo-Seq) enabled the analysis of 1735 mRNAs and observed that both core nucleotides (−3A and +4G) are widely used in yeast [54]. The different results between the genomic and the Ribo-Seq observations might reflect incorrect annotation of the main

Trends in Biochemical Sciences

CellPress REVIEWS

CDS AUGs in the earliest studies because we now know that there may be considerable use of upstream AUGs or non-AUG codons of CDSs. We could also explain these differences by the fact that the genomic studies analyzed all annotated genes, whereas the second approach investigated the set of mRNAs being translated at a specific moment under specific growth conditions. More studies will be necessary to better understand the optimal TIS Kozak motif in *S. cerevisiae*. So far, apart from *S. cerevisiae*, no other unicellular organisms have been experimentally analyzed in this regard.

Conservation and Variability among Eukaryotes

Overall, the *in silico* and experimental studies show that, across taxa, the most highly conserved position in the consensus TIS context and the nucleotide that influences translation the most is the purine at position −3 (most frequently A). The conservation of the initiation factors involved in TIS recognition, together with the fact that all taxa here examined possess identical preferences for the crucial −3 position, is an indication of the mechanistic similarities in translation initiation.

Interestingly, the −2A/C position appeared to be the second most conserved position in those lineages scrutinized here (Table 2). This observation is in agreement with early studies by Nakagawa *et al.* who reported a strong bias towards A/C at position −2 in 47 genomes of diverse species of animals, fungi, plants, and protists [32]. They found that genes with higher expression levels showed stronger signals, suggesting that nucleotides at these positions are involved in the regulation of translation initiation [32]. Accordingly, a contact between yeast eIF2α and the −2 position has been observed during TIS recognition by the translation machinery [18,19]. Position −2A/C is present in chordates, the invertebrate, plants, single-celled fungi, and protist TIS consensus sequences. This observation means that the translation machinery that recognizes the start codon is highly conserved. In the line with this idea, sequence comparisons of the translational machinery factors driving recognition of the TIS consensus sequence, namely eIF1, eIF1A, eIF2α, and ribosomal protein S26 (rpS26), showed no significant differences in the amino acids involved in TIS and Kozak motif recognition among the species reviewed here (Figures S1–S4). Indeed, the percentage of identity among these factors is in the same range of identity of other initiation factors such as eIF4E and eIF4A from the same lineages (Figure S5), suggesting that the variations in those factors causing a context preference are subtle, or that more mechanistic details of context recognition remain to be uncovered.

Early studies of genomic sequences of 47 species from different taxa by Nakagawa *et al.* [32] showed that the diversity of TIS consensus motifs can be arranged into two distinct general patterns, namely GCCGCCAUG and AAAAAAAUG. By reviewing a much broader spectrum of species from different taxa, we have observed significant variability of Kozak motifs among different species (Figure 1 and Table 2). The experimental and *in silico* studies described here agree with *in silico* analyses that optimal and strong Kozak motifs (i.e., with a +4G) appear to be the best sequences to promote translation in vertebrates [5,6,31–33,35]. In *Drosophila*, land plants, and dinoflagellates, strong Kozak motifs (with a +4G) are also the preferred sequence surrounding the CDS TIS [31–34,36,40–43,46,47]. Interestingly, the consensus sequence flanking the AUG initiator codon appears to have diverged in other eukaryotes. In particularly, nucleotides at positions −6, −5, −4, and −1, as well as the key position +4, in single-celled fungi (Ascomycetes) [31–33,44,45] and some protists (for instance some ciliates, kinetoplastids, apicomplexans, and mycetozoans [31,32,48,49] show a preference for moderate Kozak motifs with a bias towards a +4U (Ascomycetes) and +4A/C/U for the aforementioned protists. Thus, the optimal Kozak motif does not appear to be the optimal sequence to initiate translation in all lineages. Finally, we noticed that –3U/C and –2U/G are universally absent nucleotides in the consensus TIS motif for CDSs. Because 18S rRNA is also involved in TIS recognition, differences in this rRNA among species might also contribute to differential TIS context recognition. It would be interesting to experimentally study the sequences flanking the TISs in a larger number of species of different phyla to better understand the distribution of Kozak motifs across the tree of eukaryotes.

Strong Initiation at Non-AUG Initiator Codons

Despite the predominant use of the AUG codon to start CDS translation across eukaryotic lineages, decoding in some mRNAs initiates at codons different from AUG. Although translation starting at non-AUG codons is much less efficient than canonical initiation, CUG, GUG, ACG, and UUG are the most commonly used near-cognate codons [55]; codons AUU, AUC, AUA, and AGG may also be used, albeit very rarely [55].

Recent advances in ribosome profiling aiming to precisely map TISs genome-wide in different systems, particularly human, mouse, and *S. saccharomyces*, have revealed thousands of alternative translation initiation events at non-AUG codons [56,57]. These approaches are based on the action of antibiotics such as lactimidomycin, harringtonine, puromycin, and cycloheximide which block ribosome activity at different steps of translation. However, there is ongoing debate on the value of some of these data because it remains unknown what proportion of these ribosomal footprints are due to experimental artifacts and how many represent actual translation initiation events [55,58,59]. It is noteworthy that a computational analysis found a weak correlation between context strength and TIS efficiency for the non-AUGs codons obtained in several Ribo-Seq datasets [60]. By contrast, the use of genetically engineered reporters in mammals indicates that translation from non-AUGs is more dependent on their TIS context than is translation from AUG codons, although sequence context affects each non-AUG start codon differently [61].

We reviewed studies that experimentally addressed the translation of non-AUG codons in their natural contexts (Table S7). In vertebrate mRNAs (*H. sapiens*, *M. musculus*, *O. cuniculus*, *Ratus norvegicus*, and the monkey *Chlorocebus aethiops*) there is a sharp bias to use either strong or moderate Kozak motifs around non-AUG TISs to achieve the most efficient translation [13,62–77]. This context usage contrasts with the AUG TIS of vertebrate CDSs which prevalently prefers an optimal Kozak motif as the consensus context [5,6,32,33,36]. The flowering land plants *N. plumbaginifolia*, *Orychophragmus violaceus* [69], wheat [70], and *A. thaliana* [71], as well as the fungi *N. crassa* [78] and *S. cerevisiae* [72,74], also prefer either optimal or strong Kozak motifs flanking non-AUGs TISs in different transcripts. In the case of the ascomycetes *S. cerevisiae* [73] and *Candida albicans* [75], the galactokinase and CARP2A mRNAs, respectively, possess moderate contexts with an A at the +4 position. Among protists, *P. falciparum* uses the moderate Kozak context and start codon UUUUUUUUAGG in aldolase mRNA (interestingly, UAG is a stop codon in the canonical genetic code) [76].

In Table S8 we have reviewed the influence of context on the translation of non-AUG TISs in experimentally tested human [79] and *S. cerevisiae* [80–82] transcripts. Although human non-AUGs prefer strong Kozak motifs (NNN*R*NNAUG*G*) for most efficient translation, *S. cerevisiae* may prefer moderate (NNN*A*NNAUGA or NNN*A*NNAUGR) Kozak motifs for efficient translation. Again, more sequences and species should be tested to understand in more depth the influence of context on non-AUG TIS recognition.

Concluding Remarks

The evolution of eukaryotes towards a myriad of different lineages has resulted in large-scale changes and significant innovations at many levels. At the molecular level, this includes the translation process. Emerging evidence suggests that the fundamental mechanisms of translation are well conserved in all eukaryotes, even though the initiation step has undergone substantial increases in sophistication upon the emergence of eukaryotes [2,83,84]. Likewise, the studies reviewed here show that the TIS consensus context also has diverged to some extent during eukaryotic evolution, and that this diversity includes the crucial nucleotide at the +4 position; thus, some lineages appear to possess optimal Kozak consensus sequences, some have moderate to strong TIS consensus sequences, and others may utilize various TIS consensus sequences. Near-cognate start codon TISs from the few species analyzed to date, including vertebrates, show a strong preference for a strong, but not optimal, TIS consensus context. It is remarkable that, despite these changes, for both AUG and non-AUG initiator codons, A or G (most frequently A) at the −3 position is a universal feature of all taxa analyzed so

far. The second most conserved position across the lineages scrutinized here appears to be A/C at the −2 position, and U/C and U/G at the –3 and –2 positions are universally absent in the consensus Kozak motif for CDSs.

In the near future we believe that several recently launched and highly ambitious global sequencing initiatives will unlock a wealth of highly valuable novel information on the **biosphere**. These projects include the Earth BioGenome Project that aims to sequence the genomes of all of eukaryotic species on Earth over a period of 10 years [85], metagenomics projects that plan to publish the genomes of over 100 000 species of the **microbial dark matter** within the next 5 years [86–89], and projects that will extensively study the spectrum of viruses in thousands of geographically diverse samples to uncover the so-called 'virome of Earth' [90,91]. Undoubtedly, the field of translation will benefit from these ground-breaking projects (see Outstanding Questions).

Outstanding Questions

Is the Kozak motif of monophyletic origin, meaning that it appeared in the last ancestor of all eukaryotes, or it did appear several times during eukaryotic evolution?

From the data discussed herein, the −3 position is the most conserved base in the TIS sequence. Is the purine at the −3 position conserved across all eukaryotes?

After the publication of global sequencing initiatives such as the Earth BioGenome Project, will we find further diversity in TIS consensus sequences across eukaryotes?

It is well documented that translational control plays a key role in cancer onset and progression. Is the prevalence of translation of mRNAs containing specific Kozak motifs (i.e., weak, moderate, strong, or optimal) altered during cancer development?

Acknowledgments

G.H. was financed by internal funding of the National Institute for Cancer (INCan, Mexico). V.G.O. was supported by a Master in Sciences Scholarship from the Consejo Nacional de Ciencia y Tecnologia (CONACyT; grant 355715), Mexico. X.P-M. was supported by CONACyT (grant 284514) and the Programa de Apoyo a Proyectos de Investigación e Innovación Tecnológica (PAPIIT)–UNAM (IN209217). We thank Cold Spring Harbor Laboratory Press for permission to adapt Figure 1 (permission 186208/1156417P). We also appreciate valuable criticism and comments from anonymous reviewers and the editors that significantly improved the manuscript.

Supplemental Information

Supplemental information associated with this article can be found online at https://doi.org/10.1016/j.tibs.2019.07.001.

References

1. Hershey, J.W.B. *et al.* (2018) Principles of translational control. *Cold Spring Harb. Perspect. Biol.* a032607
2. Hernández, G. *et al.* (2016) On the origin and early evolution of translation in eukaryotes. In *Evolution of the Protein Synthesis Machinery and Its Regulation* (Hernández, G. and Jagus, R. eds), pp. 81–108, Springer
3. Hernández, G. *et al.* (2010) Origins and evolution of the mechanisms regulating translation initiation in eukaryotes. *Trends Biochem. Sci.* 35, 63–73
4. Kozak, M. (1981) Possible role of flanking nucleotides in recognition of the AUG initiator codon by eukaryotic ribosomes. *Nucleic Acids Res.* 9, 5233–5252
5. Kozak, M. (1984) Compilation and analysis of sequences upstream from the translational start site in eukaryotic mRNAs. *Nucleic Acids Res.* 12, 857–872
6. Kozak, M. (1987) An analysis of 5′-noncoding sequences from 699 vertebrate messenger RNAs. *Nucleic Acids Res.* 15, 8125–8148
7. Kozak, M. (1986) Point mutations define a sequence flanking the AUG initiator codon that modulates translation by eukaryotic ribosomes. *Cell* 44, 283–292
8. Kozak, M. (2002) Pushing the limits of the scanning mechanism for initiation of translation. *Gene* 299, 1–34
9. Hinnebusch, A.G. (2014) The scanning mechanism of eukaryotic translation initiation. *Annu. Rev. Biochem.* 83, 779–812
10. Kozak, M. (1987) At least six nucleotides preceding the AUG initiator codon enhance translation in mammalian cells. *J. Mol. Biol.* 196, 947–950
11. Kozak, M. (1997) Recognition of AUG and alternative inititator codons is augmented by G in position +4 but is not generally affected by nucleotides in position +5 and + 6. *EMBO J.* 16, 2482–2492
12. Lütcke, H.A. *et al.* (1987) Selection of AUG initiation codons differs in plants and animals. *EMBO J.* 6, 43–48
13. Kozak, M. (1989) Context effects and inefficient initiation at non-AUG codons in eucaryotic cell-free translation systems. *Mol. Cell. Biol.* 9, 5073–5080
14. Kozak, M. (1991) Structural features in eukaryotic mRNAs that modulate the initiation of translation. *J. Biol. Chem.* 266, 19867–19870
15. Kozak, M. (1990) Downstream secondary structure facilitates recognition of initiator codons by eukaryotic ribosomes. *Proc. Natl. Acad. Sci. U. S. A.* 87, 8301–8305
16. Meijer, H.A. and Thoma, A.A.M. (2002) Control of eukaryotic protein synthesis by upstream open reading frames in 5′-untranslated region of an mRNA. *Biochem. J.* 367, 1–11
17. Pisarev, A. *et al.* (2006) Specific functional interactions of nucleotides at key −3 and +4 positions flanking the initiation codon with components of the mammalian 48S translation initiation complex. *Genes Dev.* 20, 624–636
18. Llacer, J.L. *et al.* (2015) Conformational differences between open and closed states of the eukaryotic translation initiation complex. *Mol. Cell* 59, 1–14
19. Hussain, T. *et al.* (2014) Structural changes enable start codon recognition by the eukaryotic translation initiation complex. *Cell* 159, 597–607
20. Rabl, J. *et al.* (2011) Crystal structure of the eukaryotic 40S ribosomal subunit in complex with initiation factor 1. *Science* 331, 730–736
21. Lomakin, I.B. and Steitz, T.A. (2013) The initiation of mammalian protein synthesis and mRNA scanning mechanism. *Nature* 500, 307–311

22. Weisser, M. *et al.* (2013) The crystal structure of the eukaryotic 40S ribosomal subunit in complex with eIF1 and eIF1A. *Nat. Struct. Mol. Biol.* 20, 1015–1017
23. Pestova, T.V. and Kolupaeva, V.G. (2002) The roles of individual eukaryotic translation initiation factors in ribosomal scanning and initiation codon selection. *Genes Dev.* 16, 2906–2922
24. Pisarev, A.V. *et al.* (2008) Ribosomal position and contacts of mRNA in eukaryotic translation initiation complexes. *EMBO J.* 27, 1609–1621
25. Lind, C. and Åqvist, J. (2016) Principles of start codon recognition in eukaryotic translation initiation. *Nucleic Acids Res.* 44, 8425–8432
26. Bulygin, K. *et al.* (2005) The first position of a codon placed in the A site of the human 80S ribosome contacts nucleotide C1696 of the 18S rRNA as well as proteins S2, S3, S3a, S30, and S15. *Biochemistry* 44, 2153–2162
27. Martin-Marcos, P. *et al.* (2011) Functional elements in initiation factors 1, 1A, and 2β discriminate against poor AUG context and non-AUG start codons. *Mol. Cell. Biol.* 31, 4814–4831
28. Burki, F. (2014) The eukaryotic tree of life from a global phylogenomic perspective. *Cold Spring Harb. Perspect. Biol.* 6, a016147
29. Adi, S.M. *et al.* (2019) Revisions to the classification, nomenclature, and diversity of eularyotes. *J. Eukaryot. Microbiol.* 66, 4–119
30. Cavener, D.R. (1987) Comparison of the consensus sequence flanking translational start sites in *Drosophila* and vertebrates. *Nucleic Acids Res.* 15, 1353–1361
31. Cavener, D.R. and Ray, S.C. (1991) Eukaryotic start and stop translation sites. *Nucleic Acids Res.* 19, 3185–3192
32. Nakagawa, S. *et al.* (2008) Diversity of preferred nucleotide sequences around the translation initiation codon in eukaryote genomes. *Nucleic Acids Res.* 36, 861–871
33. Pesole, G. *et al.* (2000) Analysis of oligonucleotide AUG start codon context in eukariotic mRNAs. *Gene* 261, 85–91
34. Acevedo, J.M. *et al.* (2018) Changes in global translation elongation or initiation rates shape the proteome via the Kozak sequence. *Sci. Rep.* 8, 4018
35. Kochetov, A.V. *et al.* (1998) Eukaryotic mRNAs encoding abundant and scarce proteins are statistically dissimilar in many structural features. *FEBS Lett.* 440, 351–355
36. Rangan, L. *et al.* (2008) Analysis of context sequence surrounding translation initiation site from complete genome of model plants. *Mol. Biotechnol.* 39, 207–213
37. Grzegorski, S.J. *et al.* (2014) Natural variability of Kozak sequences correlates with function in a zebrafish model. *PLoS One* 9, e108475
38. Kourakis, M.J. and Smith, W.C. (2015) An organismal perspective on *C. intestinalis* development, origins and diversification. *eLife* 4, e06024
39. Tatematsu, K. *et al.* (2014) Effect of ATG initiation codon context motifs on the efficiency of translation of mRNA derived from exogenous genes in the transgenic silkworm, *Bombyx mori*. *Springerplus* 3, 136
40. Gupta, P. *et al.* (2016) Comparative analysis of contextual bias around the translation initiation sites in plant genomes. *J. Theoret. Biol.* 404, 303–311
41. Joshi, C.P. *et al.* (1997) Context sequences of translation initiation codon in plants. *Plant Mol. Biol.* 35, 993–1001
42. Kawaguchi, R. and Bailey-Serres, J. (2005) mRNA sequence features that contribute to translational regulation in *Arabidopsis*. *Nucleic Acids Res.* 33, 955–965
43. Lukaszewicz, M. *et al.* (2000) *In vivo* evaluation of the context sequence of the translation initiation codon in plants. *Plant Sci.* 154, 89–98
44. Hamilton, R. *et al.* (1987) Compilation and comparison of the sequence context around the AUG startcodons in *Saccharomyces cerevisiae* mRNAs. *Nucleic Acids Res.* 15, 3581–3593
45. Cigan, A.M. and Donahue, T.F. (1987) Sequence and structural features associated with translational initiator regions in yeast. *Gene* 59, 1–18
46. Zhang, H. *et al.* (2013) Proof that dinoflagellate spliced leader (DinoSL) is a useful hook for fishing dinoflagellate transcripts from mixed microbial samples: *Symbiodinium kawagutii* as a case study. *Protist* 164, 510–527
47. Bodył, A. and Mackiewicz, P. (2007) Analysis of the targeting sequences of an iron-containing superoxide dismutase (SOD) of the dinoflagellate *Lingulodinium polyedrum* suggests function in multiple cellular compartments. *Arch. Microbiol.* 187, 281–296
48. Saul, A. and Battistutta, D. (1990) Analysis of the sequences flanking the translational start sites of *Plasmodium falciparum*. *Mol. Biochem. Parasitol.* 42, 55–62
49. Yamauchi, K. (1991) The sequence flanking translational initiation site in protozoa. *Nucleic Acids Res.* 19, 2715–2720
50. Abrahão, J. *et al.* (2018) Tailed giant Tupanvirus possesses the most complete translational apparatus of the known virosphere. *Nat. Comm.* 9, 749
51. Abrahão, J. *et al.* (2017) The analysis of translation-related gene set boosts debates around origin and evolution of mimiviruses. *PLoS Genet.* 13, e1006532
52. Sugio, T. *et al.* (2010) Effect of the sequence context of the AUG initiation codon on the rate of translation in dicotyledonous and monocotyledonous plant cells. *J. Biosci. Bioeng.* 109, 170–173
53. Looman, A.C. and Kuivenhoven, J.A. (1993) Influence of the three nucleotides upstream of the initiation codon on expression of the *Escherichia coli* lacZ gene in *Saccharomyces cerevisiae*. *Nucleic Acids Res.* 21, 4268–4271
54. Robbins-Pianka, A. *et al.* (2010) The mRNA landscape at yeast translation initiation sites. *Bioinformatics* 26, 2651–2655
55. Kearse, M.G. and Wilusz, J.E. (2017) Non-AUG translation: a new start for protein synthesis in eukaryotes. *Genes Dev.* 31, 1717–1731
56. Ingolia, N.T. *et al.* (2018) Ribosome profiling: global views of translation. *Cold Spring Harb. Perspect. Biol.* 11, a032698
57. Ingolia, N.T. (2014) Ribosome profiling: new views of translation, from single codons to genome scale. *Nat. Rev. Genet.* 15, 205–213
58. Andreev, D.E. *et al.* (2017) Insights into the mechanisms of eukaryotic translation gained with ribosome profiling. *Nucleic Acids Res.* 45, 513–526
59. Guttman, M. *et al.* (2013) Ribosome profiling provides evidence that large noncoding RNAs do not encode proteins. *Cell* 154, 240–251
60. Andreev, D.E. and Baranov, P.V. (2014) Computational approach for calculating the probability of eukaryotic translation initiation from ribo-seq data that takes into account leaky scanning. *BMC Bioinformatics* 15, 380
61. Diaz de Arce, A.J. *et al.* (2018) Complete motif analysis of sequence requirements for translation initiation at non-AUG start codons. *Nucleic Acids Res.* 46, 985–994
62. Florkiewicz, R.Z. and Sommer, A. (1989) Human basic fibroblast growth factor gene encodes four polypeptides: three initiate translation from non-AUG codons. *Proc. Natl. Acad. Sci. U. S. A.* 86, 3978–3981

63. Arnaud, E. *et al.* (1999) A new 34-kilodalton isoform of human fibroblast growth factor 2 is cap dependently synthesized by using a non-AUG start codon and behaves as a survival factor. *Mol. Cell. Biol.* 19, 505–514
64. Huez, I. *et al.* (2001) New vascular endothelial growth factor isoform generated by internal ribosome entry site-driven CUG translation initiation. *Mol. Endocrinol.* 15, 2197–2210
65. Fuxe, J. *et al.* (2000) Translation of p15.5INK4B, an N-terminally extended and fully active form of p15INK4B, is initiated from an upstream GUG codon. *Oncogene* 19, 1724–1728
66. Tikole, S. and Sankararamakrishnan, R. (2000) A survey of mRNA sequences with a non-AUG start codon in RefSeq database. *J. Biomol. Struct. Dyn.* 24, 33–42
67. Acland, P. *et al.* (1990) Subcellular fate of the int-2 oncoprotein is determined by choice of initiation codon. *Nature* 343, 662–665
68. Bruening, W. and Pelletier, J. (1996) A non-AUG translational initiation event generates novel WT1 isoforms. *J. Biol. Chem.* 271, 8646–8654
69. Gordon, K. *et al.* (1992) Efficient initiation of translation at non-AUG triplets in plant cells. *Plant J.* 2, 809–813
70. Peabody, D.S. (1989) Translation initiation at non-AUG triplets in mammalian cells. *J. Biol. Chem.* 264, 5031–5035
71. Christensen, A.C. *et al.* (2005) Dual-domain, dual-targeting organellar protein presequences in *Arabidopsis* can use non-AUG start codons. *Plant Cell* 17, 2805–2816
72. Clements, J.M. *et al.* (1988) Efficiency of translation initiation by non-AUG codons in *Saccharomyces cerevisiae*. *Mol. Cell. Biol.* 8, 4533–4536
73. Zitomer, R.S. *et al.* (1984) *Saccharomyces cerevisiae* ribosomes recognize non-AUG initiation codons. *Mol. Cell. Biol.* 4, 1191–1197
74. Donahue, T.F. and Cigan, A.M. (1988) Genetic selection for mutations that reduce or abolish ribosomal recognition of the HIS4 translational initiator region. *Mol. Cell. Biol.* 8, 2955–2963
75. Abramczyk, D. *et al.* (2003) Non-AUG translation initiation of mRNA encoding acidic ribosomal P2A protein in *Candida albicans*. *Yeast* 20, 1045–1052
76. Ghersa, P. *et al.* (1990) Initiation of translation at a UAG stop codon in the aldolase gene of *Plasmodium falciparum*. *EMBO J.* 9, 1645–1649
77. Prats, H. *et al.* (1989) High molecular mass forms of basic fibroblast growth factor are initiated by alternative CUG codons. *Proc. Natl. Acad. Sci. U. S. A.* 86, 1836–1840
78. Wei, J. *et al.* (2013) The stringency of start codon selection in the filamentous fungus *Neurospora crassa*. *J. Biol. Chem.* 288, 9549–9562
79. Mehdi, H. *et al.* (1990) Initiation of translation at CUG, GUG, and ACG codons in mammalian cells. *Gene* 91, 173–178
80. Chen, S.J. *et al.* (2008) Translational efficiency of a non-AUG initiation codon is significantly affected by its sequence context in yeast. *J. Biol. Chem.* 283, 3173–3180
81. Chen, S.J. *et al.* (2009) Translational efficiency of redundant ACG initiator codons is enhanced by a favorable sequence context and remedial initiation. *J. Biol. Chem.* 248, 818–827
82. Chang, C.P. *et al.* (2010) A single sequence context cannot satisfy all non-AUG initiator codons in yeast. *BMC Microbiol.* 10, 188
83. Hernández, G. (2009) On the origin of the cap-dependent initiation of translation in eukaryotes. *Trends Biochem. Sci.* 34, 166–175
84. Hernández, G. *et al.* (2012) On the diversification of the translational apparatus across eukaryotes. *Comp. Funct. Genomics* 2012, 256848
85. Lewin, H.A. *et al.* (2018) Earth BioGenome Project: sequencing life for the future of life. *Proc. Natl. Acad. Sci. U. S. A.* 115, 4325–4333
86. Parks, D.H. *et al.* (2017) Recovery of nearly 8,000 metagenome-assembled genomes substantially expands the tree of life. *Nat. Microbiol.* 2, 1533–1542
87. Solden, L. *et al.* (2016) The bright side of microbial dark matter: lessons learned from the uncultivated majority. *Curr. Opin. Microbiol.* 31, 217–226
88. Hugenholtz, P. *et al.* (2016) Genome-based microbial taxonomy coming of age. *Cold Spring Harb. Perspect. Biol.* 8, a018085
89. Kyrpides, N.C. *et al.* (2016) Microbiome data science: understanding our microbial planet. *Trends Microbiol.* 24, 425–427
90. Paez-Espino, D. *et al.* (2016) Uncovering Earth's virome. *Nature* 25, 425–430
91. Khalil, J. *et al.* (2016) Updating strategies for isolating and discovering giant viruses. *Curr. Opin. Microbiol.* 31, 80–87
92. Hinnebusch, A.G. (2017) Structural insights into the mechanism of scanning and start codon recognition in eukaryotic translation initiation. *Trends Biochem. Sci.* 42, 589–611
93. Pelletier, J. and Sonenberg, N. (2019) The organizing principles of eukaryotic ribosome recruitment. *Annu. Rev. Biochem.* 88, 307–335

INFORME DE LABORES 2019

BBA - Molecular Cell Research 1866 (2019) 1509–1519

Contents lists available at ScienceDirect

BBA - Molecular Cell Research

journal homepage: www.elsevier.com/locate/bbamcr

Sites phosphorylated in human α_{1B}-adrenoceptors in response to noradrenaline and phorbol myristate acetate

David A. Hernández-Espinosa, Gabriel Carmona-Rosas, Marco A. Alfonzo-Méndez, Rocío Alcántara-Hernández, J. Adolfo García-Sáinz*

Departamento de Biología Celular y Desarrollo, Instituto de Fisiología Celular, Universidad Nacional Autónoma de México, Ap. Postal 70-248, Ciudad de México CP 04510, Mexico

ARTICLE INFO

Keywords:
Adrenergic receptor
Mass spectrometry
Receptor phosphorylation
Calcium
Extracellular-signal-regulated kinase
Receptor internalization
Receptor desensitization

ABSTRACT

Phosphorylation of the human α_{1B}-adrenergic receptor (fused with the green fluorescent protein) was studied employing the inducible Flp-In HEK293 T-Rex system for expression. Serine/alanine substitutions were performed in five sites corresponding to those previously identified as phosphorylation targets in the hamster ortholog. Desensitization was decreased in these mutants but receptor phosphorylation was still clearly detected. The protein phosphorylation of the wild-type receptor (fused to the green fluorescent protein) was studied, using mass spectrometry, under baseline and stimulated conditions (noradrenaline or phorbol myristate acetate). Basal phosphorylation was detected at sites located at the intracellular loop 3 and carboxyl terminus, and the number of sites detected increased under agonist activation and stimulation of protein kinase C. The phosphorylation patterns differed under the distinct conditions. Three of the phosphorylation sites detected in this work corresponded to those observed in the hamster receptor. The phosphorylation sites detected included the following: a) at the intracellular loop 3: serines 246, 248, 257, 267, and 277; and threonines 252, 264, and 268, and b) at the carboxyl terminus: serines 396, 400, 402, 406, 423, 425, 427, 455, and 470, and threonines 387, 392, 420, and 475. Our data indicate that complex phosphorylation patterns exist and suggest the possibility that such differences could be relevant in receptor function and subcellular localization.

1. Introduction

G protein-coupled receptors (GPCR) are involved in a plethora of actions that maintain homeostasis, mediating the physiological action of a large variety of hormones, local hormones (autacoids), neurotransmitters and growth factors and also participate in the pathogenesis of many diseases. As indicated by their name, GPCR interact with G proteins, which modulate the activity of enzymes and ionic channels to exert their actions [1,2]. These receptors exhibit a characteristic structure constituted of an extracellular amino terminus, an intracellular carboxyl terminus (Ctail), and seven transmembrane domains joined by intracellular and extracellular loops [1,2].

GPCR phosphorylation appears to be a very early event that regulates the function of this large family of receptors and it is associated with the attenuation of receptor activity (desensitization) and internalization [3–5]. However, there is evidence of desensitization in the absence of receptor phosphorylation [3,6], and recent data indicate a role of GPCR phosphorylation in membrane targeting/localization [7,8]. In addition, there is clear evidence indicating that desensitization is not limited to a decrease in GPCR signaling through a particular pathway but that in fact it represents a “switch” in which a pathway is attenuated while another (others) is (are) activated [4,9]. Frequently, such a switch involves the decrease of G protein-mediated signaling and the triggering of additional molecular events including, in addition to post-translational modifications of receptors and the resulting conformational changes, interaction with other molecular entities, such as β-arrestins [9,10].

Current data also indicate that the sites at which the phosphorylation of GPCR takes place is of great importance, since these might vary depending on the cell type in which they are expressed or on the agents that lead to a such covalent modification and, more importantly, that phosphorylation at different sites can lead to distinct functional outcomes and receptor localizations [11,12]. These general proposals have been denominated the “phosphorylation barcode hypothesis” [11,12].

Abbreviations: α_1-AR, α_1-adrenergic receptor; ERK, extracellular signal-regulated kinase; NA, noradrenaline; PMA, phorbol 12-myristate, 13-acetate; PKC, protein kinase C; GPCR, G protein-coupled receptor; GRK, GPCR kinase; IL3, intracellular loop 3; Ctail, carboxyl terminus; eGFP, enhanced green fluorescent protein

* Corresponding author at: Inst. Fisiología Celular, UNAM, Ap. Postal 248, Ciudad de México CP 04510, Mexico.
E-mail address: agarcia@ifc.unam.mx (J.A. García-Sáinz).

https://doi.org/10.1016/j.bbamcr.2019.07.006
Received 26 April 2019; Received in revised form 27 June 2019; Accepted 14 July 2019
Available online 17 July 2019
0167-4889/ © 2019 Elsevier B.V. All rights reserved.

INFORME DE LABORES 2019

In many cases, this involves receptor's phosphorylation at both Ctail and intracellular loop 3 (IL3) residues (see for example [7,13–21]).

α_1-Adrenergic receptors (α_1-AR) constitute a subfamily of GPCR composed of three members, the α_{1A}-, the α_{1B}-, and the α_{1D}-AR [22–24]. All of these couple to Gq and exert their actions mainly through the inositol trisphosphate/diacylglycerol/calcium signaling pathway [22,23], although other signaling processes also appear to participate in their actions [25]. It is well-known that the three receptor subtypes are phosphorylated in response to agonists and the pharmacological or physiological activation of protein kinase C (PKC) [7,19,20,23,26–33]. The α_{1B}-AR subtype was the first receptor of this subfamily to be cloned [34] and it has been extensively studied. Pioneer contributions by Cotecchia and coworkers, using receptor mutants with deletions and mutagenesis of specific sites, together with functional studies, identified that relevant phosphorylation sites for hamster α_{1B}-AR are located in a cluster at the Ctail, which seem to be targeted by G protein-coupled receptor kinases (GRK) and PKC [30,32]. In addition, the group of Toews [35,36] has observed that, in the hamster receptor, two domains play key roles in receptor internalization/down regulation. Using deletions and site-directed mutagenesis, these authors observed that some mutated receptors internalize but do not down-regulate, other mutants that down-regulate without internalization, and that there are also receptors defective in both internalization and down-regulation [35].

Using mass spectrometry of purified receptors, we recently reported phosphorylation sites detected in human α_{1A}- [19] and α_{1D}-AR [7,20]. Interestingly, we observed differential phosphorylation of these receptor subtypes under distinct conditions (baseline, agonist stimulation, and activation of PKC) and detected that phosphorylation sites were present both at the Ctail and at the intracellular loop 3 (IL3) [7,19,20]. In the present work, again utilizing mass spectrometry, we examined the phosphorylation sites of the α_{1B}-AR subtype human ortholog and observed the following: 1) a large amount of phosphorylation sites located at both the Ctail and IL3 and 2) that the phosphorylation pattern varies under the different conditions employed. Our data suggest that the regulation of this receptor subtype is likely more complex than anticipated.

2. Materials and methods

2.1. Materials

(−)-Noradrenaline (NA), phorbol 12-myristate 13-acetate (PMA), phentolamine, and propranolol were obtained from Sigma-Aldrich Chemical. [^{32}P]Pi (8500–9120 Ci/mmol) was obtained from Perkin-Elmer Life Sciences. Dulbecco's modified Eagle's medium, fetal bovine serum, trypsin, streptomycin, penicillin, amphotericin B, blasticidin, hygromycin B, doxycycline hyclate and Fura-2AM were purchased from Invitrogen-Life Technologies. Polyethyleneimine was obtained from PolyScience and GenJet was obtained from SignaGen Laboratories. Nitrocellulose membranes were from BioRad, and SuperSignal West Pico Chemiluminescence kits were from Thermo Fisher Scientific. Agarose-coupled protein A was obtained from Merck-Millipore. Anti-phospho-ERK 1/2 (Thre202/Tyr204) (catalog number 9101S, lot: 30) and anti-total ERK (p42/44) antibodies (catalog number 4695S, lot: 21) were obtained from Cell Signaling Technology; monoclonal anti-GFP was from Clontech (catalog number 632381, lot A5033481) and polyclonal anti-GFP was generated in our laboratory [37]. Secondary antibodies were purchased from Zymed (Thermo Fisher Scientific) or Jackson ImmunoResearch, including the peroxidase affiniPure Goat anti-mouse IgG light chain antibody. Antibody dilutions were 1:1000 for primary antibodies and 1:10,000 for secondary antibodies. Parental Flp-In T-Rex HEK293 cells and the plasmid, pOG44, were obtained from Invitrogen.

2.2. Receptor mutants, cells, and transfections

The plasmid for the expression of the human α_{1B}-AR fused at the Ctail with the enhanced green fluorescent protein (eGFP) was previously described [38]. The receptor construct was subcloned into pCDNA5/FRT/TO to employ the inducible Flp-ln T-Rex expression system (Invitrogen), and the construct is referred as wild-type α_{1B}-AR. This was used as a template to generate the different mutants used; mutagenesis was commercially performed by Mutagenex, Inc. and proper changes were confirmed by sequencing (Mutagenex, Inc.).

To generate inducible receptor-expressing cells, parental Flp-In T-Rex HEK293 cells were transfected with pCDNA5/FRT/TO, containing the cDNA coding for the desired mutant, and pOG44 using GenJet following the manufacturer's instructions. Transfected cells were subjected to selection with 5 μg/ml blasticidin and 100 μg/ml hygromycin B, as previously described [39,40]. Experiments were performed after inducing receptor expression with 1 μg/ml doxycycline hyclate for 14–24 h. Cells were routinely grown in Dulbecco's modified Eagle's medium supplemented with 10% fetal bovine serum, 100 μg/ml streptomycin, 100 U/ml penicillin, and 0.25 μg/ml amphotericin B. In all experiments using NA, 1 μM propranolol was also added to avoid any β-adrenergic action; the β-blocker did not alter baseline parameters by itself (data not shown).

2.3. Intracellular calcium determinations

Intracellular calcium concentrations were assessed as previously described [41,42]. Briefly, cells were serum-starved for 2 h, and then loaded with 2.5 μM Fura-2/AM for 1 h at 37 °C, and cells were washed to eliminate unincorporated dye. Fluorescence measurements were performed at 340- and 380-nm excitation wavelengths and at a 510-nm emission wavelength, with a chopper interval set to 0.5 s, using an Aminco-Bowman Series 2 Luminescence Spectrometer. Intracellular calcium levels were calculated as described by Grynkiewicz et al. [43].

2.4. Receptor phosphorylation

Receptor phosphorylation was performed as previously described [42]. In brief, cells cultured in six-well plates were incubated for 3 h in phosphate-free Dulbecco's Modified Eagle's media supplemented with 50 μCi/ml [^{32}P]Pi. Labeled cells were stimulated as indicated, washed with ice-cold phosphate-buffered saline (137.9 mM NaCl, 2.7 mM KCl, Na_2HPO_4 10 mM; pH 7.4) (PBS) and solubilized for 1 h in the lysis buffer described previously. The extracts were centrifuged and supernatants were incubated overnight with protein A-agarose and anti-eGFP antiserum generated in our laboratory [37]. Samples were subjected to SDS-PAGE, transferred onto nitrocellulose membranes, and exposed for 18–24 h. The amount of phosphorylated receptor was assessed by PhosphorImager analysis, using the ImageQuant program. The average of the baseline values obtained in these experiments was considered as 100% and the error bar of the baselines corresponds to the dispersion of these values. Western blotting for loading controls was performed using a commercial monoclonal anti-eGFP antibody.

2.5. ERK 1/2 phosphorylation

Cells were serum-starved for 2 h. After stimulation with the indicated agents, cells were washed with ice-cold phosphate-buffered saline and lysed with Laemmli sample buffer [44]. Lysates were centrifuged at 12,700 × *g* for 5 min, and proteins in supernatants were separated by SDS-PAGE. Proteins were electrotransferred onto nitrocellulose membranes and immunoblotting was performed. Duplicate samples were run in parallel to determine total- and phospho-ERK 1/2 levels. For data normalization, maximal response was considered as 100%.

INFORME DE LABORES 2019

2.6. α_{1B}-AR purification and mass spectrometry analysis

The procedure employed was similar to those employed for α_{1A}- and α_{1D}-AR [7,19,20]. Ten 10 cm-diameter dishes (90% confluence) of HEK 293 cells expressing the wild-type α_{1B}-AR-eGFP construct, per condition, were used in each experiment. Control experiments employing non-induced HEK 293 cells were also performed. Cells were stimulated as indicated, washed twice with ice-cold PBS and solubilized for 1 h at 4 °C with ice-cold lysis buffer (10 mM Tris HCl, 150 mM NaCl, 1% sodium cholate, 1% Nonidet P40, 10% SDS, 5 mM EDTA, pH 7.4, 10 mM NaF, 10 mM sodium pyrophosphate, leupeptin 20 mg/ml, phenylmethylsulfonyl fluoride 100 mg/ml, bacitracin 500 mg/ml, soybean trypsin inhibitor 50 mg/ml, 1 mM p-serine, 1 mM p-threonine, and 1 mM p-tyrosine). The solubilized extracts were centrifuged at 12,700 ×*g* for 15 min. Pre-cleaning of the supernatants was performed using 100 µl of protein A-agarose with constant agitation for 1 h at 4 °C. After 5000 ×*g* centrifugation, the supernatants were incubated overnight under constant agitation with 30 µl anti-GFP serum and 30 µl of protein A-agarose. Pellets were washed five times with lysis buffer and solubilized with Laemmli sample buffer [44] containing 20 mg/ml dithiothreitol, 10% SDS, and 8 M urea. The samples were resolved by SDS-PAGE by running two 10% gels in parallel, one containing > 95% of the sample and the other with the remaining amount. The first gel was stained with colloidal Coomassie Blue and the bands of interest were excised and sent for mass spectrometry analysis to the Taplin Mass Spectrometry Facility (Harvard Medical School. Cambridge, MA, USA). The second gel was used to confirm the presence of eGFP-tagged receptors by Western blotting. Four different purification-mass spectrometry experiments were performed. Ascore [45], a probability-based score, was employed. The program measures the probability of correct phosphorylation site localization, based on the presence and intensity of site-determining ions in the mass spectrometry spectra. Two considerations were made: a) Ascore values > 19 were considered as the limit for reliable phosphorylation sites, and b) when two sites were detected in the same peptide, the different Ascore values were considered [45].

2.7. In silico analysis

Receptor sequences were obtained from the UniProt Knowledgebase [46]. Sequence alignments were performed using the blast-protein suite (protein-protein BLAST (http://www.uniprot.org/blast/). The possible phosphorylation sites were obtained from analysis performed using NetPhos 3.0 (http://www.cbs.dtu.dk/services/NetPhos) [47] and the Group-based Prediction System, GPS 2.1 (http://gps.biocuckoo.org/) [48] on-line services, employing cut-off values of 0.75 and 4, respectively. Prediction of the probable protein kinases involved was obtained using GPS 2.1 [48].

2.8. Statistical analysis

Statistical comparisons between groups were performed employing a parametric analysis of variance with Bonferroni's post-test, assuming Gaussian data distribution (http://www.graphpad.com/guides/prism/7/statistics/index.htm). We used the software included in the GraphPad Prism 6 software to perform these analyses. A p value of < 0.05 was considered statistically significant.

3. Results and discussion

As previously indicated, in the experiments of Cottechia and coworkers [30,32] the hamster α_{1B}-AR was studied. We centered our work on the human ortholog, mainly for its medical interest and also in order to compare the findings with what has been observed in the phosphorylation of human α_{1A}- and α_{1D}-AR [7,19,20]. Human α_{1B}-AR are phosphorylated in response to agonists and activation of PKC in a comparable way to what has been observed with the hamster receptor, and the functional consequences of such phosphorylations are also alike [26]. This is hardly surprising considering that these orthologs are remarkably similar; i.e. overall identity is ~94.6%, with the human ortholog five amino acids larger than that of the hamster (520 amino acids vs. 515 in the hamster receptor). Amino acids 1–351, which comprise the main cores of these receptors (amino termini, the seven transmembrane domains, and the intracellular and extracellular loops) show notable similarity, exhibiting only three conservative and two semi-conservative substitutions (Supplementary Fig. S1). The Ctail domains of these receptors have more differences: i.e., five additional residues are present in the human ortholog as compared to the hamster, and conservative (10), semi-conservative (3) and non-conservative (5) substitutions are present (Supplementary Fig. S2; please note that alternative alignments are possible). However, the phosphorylation sites detected in the hamster receptor [30] are all conserved in the human ortholog (S396, 402,406, 410, and 412) (Supplementary Fig. S2).

As an initial step in our work, we examined the possible roles of the sites of the human α_{1B}-AR, equivalent to those observed as phosphorylated in the hamster ortholog [30]. To achieve this goal, mutations of the putative phosphorylation sites were performed to the wild-type human α_{1B}-AR, as depicted in Supplementary Fig. S3, as well as receptor phosphorylation and functional studies (intracellular calcium determination and ERK 1/2 phosphorylation). The following receptors were generated: a) wild-type (no modification other than fusion to the eGFP). b) S396,402A (altering putative PKC sites, named PKC-m), c) S406,410,412A (altering putative GRK sites; named GRK-m), and d) S396,402,406,410,412A, altering these five sites (named PKC + GRK-m). Receptor expression was similar as reflected by fluorescence confocal microscopy (Supplementary Fig. S4) and Western blotting (see later).

β_2-AR are known to be endogenously expressed in HEK 293 cells and their activation mobilizes intracellular calcium [49]; therefore, in all experiments in which NA was employed, the cells were also incubated in the presence of 10 µM propranolol. As shown in Fig. 1A, cells expressing the wild-type receptor or any of the mutants studied increased intracellular calcium in response to NA in concentration-dependent fashion. This effect was blocked by 10 µM phentolamine, as anticipated (data not shown; prazosin was not used due to its intrinsic fluorescence). The efficacy of the different receptors was similar (i.e., an increase in intracellular calcium of ~150–200 nM was observed), with the exception of the PKC + GRK-m mutant, which was in some of the experiments less responsive to NA (statistically insignificant); the potencies of NA were also similar (EC_{50} ~ 20–60 nM). In Fig. 1B, calcium transients in response to 10 µM NA are presented. As can be observed the calcium response peaks were very similar (see also Fig. 1C); however, return to baseline was considerably slower in mutants with the putative GRK sites mutated, which resulted in significantly higher residual intracellular calcium values (determined at 100 s after agonist addition) (Fig. 1, panels B and C). These data are consistent with the idea that the receptor mutants are less susceptible to desensitization than the wild-type; i.e., the mutant receptors did not appear to desensitize as fast as the wild-type, which is in accordance with the data of Diviani et al. [30]. It has been suggested that α_{1B}-AR internalization diminish calcium signaling [50]. To what extent this plays a role in our experiments is unknown; however, vanishing of the NA-induced free calcium increases occurs within seconds, and changes in receptor internalization are hard to detect in this time frame.

The ability of PKC activation with PMA to desensitize α_{1B}-AR action was also tested with the different mutants. As shown in Fig. 2A, NA-induced increase in intracellular calcium was reduced (~50%) by preincubation for 5, 10, or 15 min with 1 µM PMA in cells expressing the wild-type receptor. A similar effect was observed in the receptor mutant in which the putative sites for this kinase family were mutated to alanine (PKC-m) but the effect of PMA decreased with the incubation time (Fig. 2B). Interestingly, cells expressing receptors in which the

INFORME DE LABORES 2019

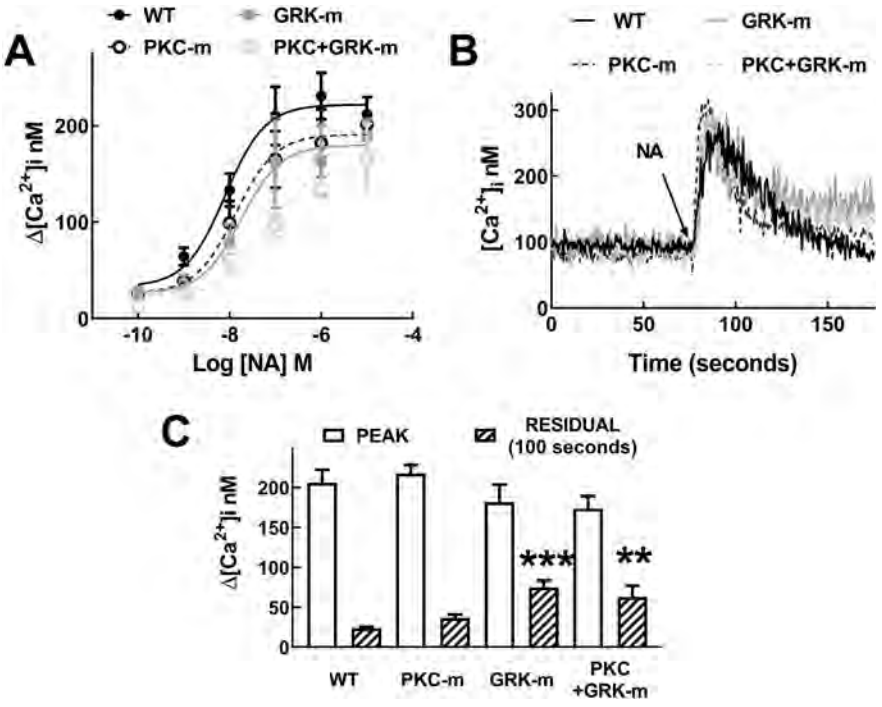

Fig. 1. NA-induced calcium response in cells expressing α_{1B}-AR mutants. Panel A. Cells expressing the different α_{1B}-AR-eGFP constructs were stimulated with the indicated concentrations of NA (in the presence of propranolol) and intracellular free calcium concentration was quantified. Wild-type (WT) receptor and the following mutants with the indicated substitutions in parenthesis: (S396,402A), PKC-m; (S406,410,412A), GRK-m; and (S396,402,406,410,412A), PKC-GRK-m. Plotted are the maximal increases as the means ± S.E.M. of 7–9 experiments using different cell preparations (where no error bar is shown, it is within the symbol). Panel B. Representative free calcium tracings using the different mutants. Panel C. Bars indicate the maximal increases (PEAK, open bars) and the remaining increase over baseline observed 100 s after NA addition (RESIDUAL, dashed bars). Plotted are the means ± S.E.M. of 7–9 experiments using different cell preparations. ***$p < 0.001$ vs. Residual WT; **$p < 0.005$ vs. Residual WT.

putative GRK sites were changed to alanine (GRK-m and PKC + GRK-m) were not significantly affected by the treatment with PMA (Fig. 2, panels C and D). Attempts to study NA-induced desensitization (intracellular calcium response or inositol phosphate production) were unsuccessful due to that the action of the catecholamine decreased the general response of the cells even after extensive washing. This might involve depletion of calcium stores and/or changes in the metabolic pools of the phosphoinositides.

We examined receptor phosphorylation and observed that all of the receptors studied (wild-type α_{1B}-AR and the different mutants) were phosphorylated under baseline conditions and that this estate increased in response to NA (Fig. 3) and PMA (Fig. 4). Western blotting of the immunoprecipitated receptors was performed and, in all cases, two bands were identified; a major band of ~110 kD and another of ~100 kD. Phosphorylation was mainly detected in the band with the higher Mr, although some radioactivity was also present in the lower Mr band. Signal in both bands was quantified together (the lower Mr band might represent the receptor being processed (glycosylated) or partially degraded). In cells expressing the wild-type receptor, 1 μM NA rapidly increased receptor phosphorylation (at 2 and 5 min), which decreased at longer incubation times (15–60 min). The different mutants also augmented their phosphorylation state rapidly in response to

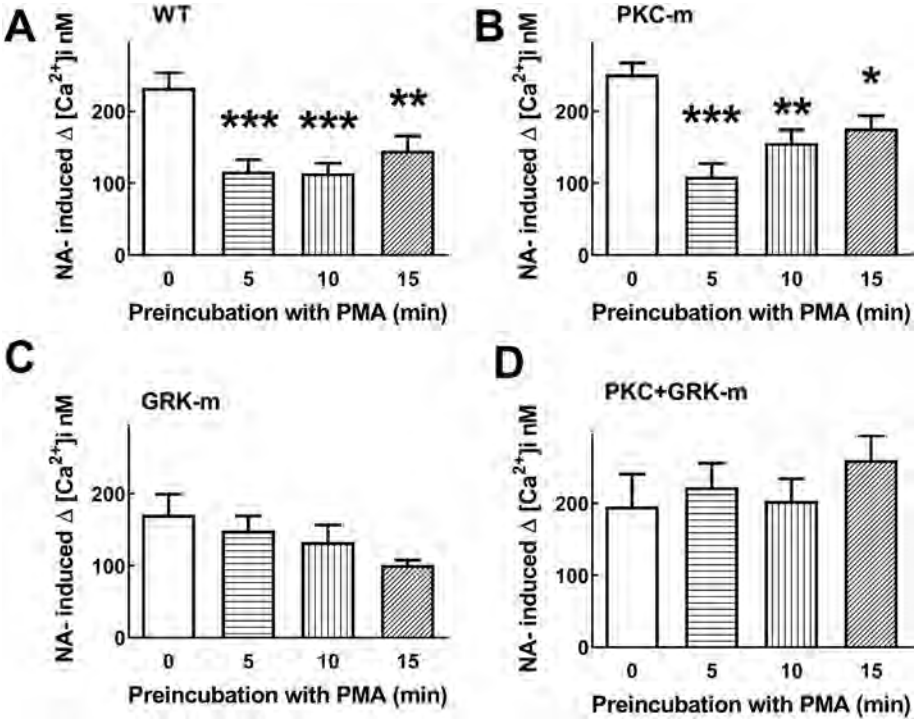

Fig. 2. Effect of PMA on NA-induced calcium response in cells expressing α_{1B}-AR mutants. Cells were preincubated for the times indicated in the presence of 1 μM PMA and then they were challenged with 10 μM NA (in the presence of propranolol). Plotted are the maximal increases in free calcium concentration as the means ± S.E.M. of 6–7 experiments using different cell preparations. ***$p < 0.001$ vs. respective time 0; **$p < 0.005$ vs. respective time 0; *$p < 0.05$ vs. respective time 0. Other indications as in Fig. 1.

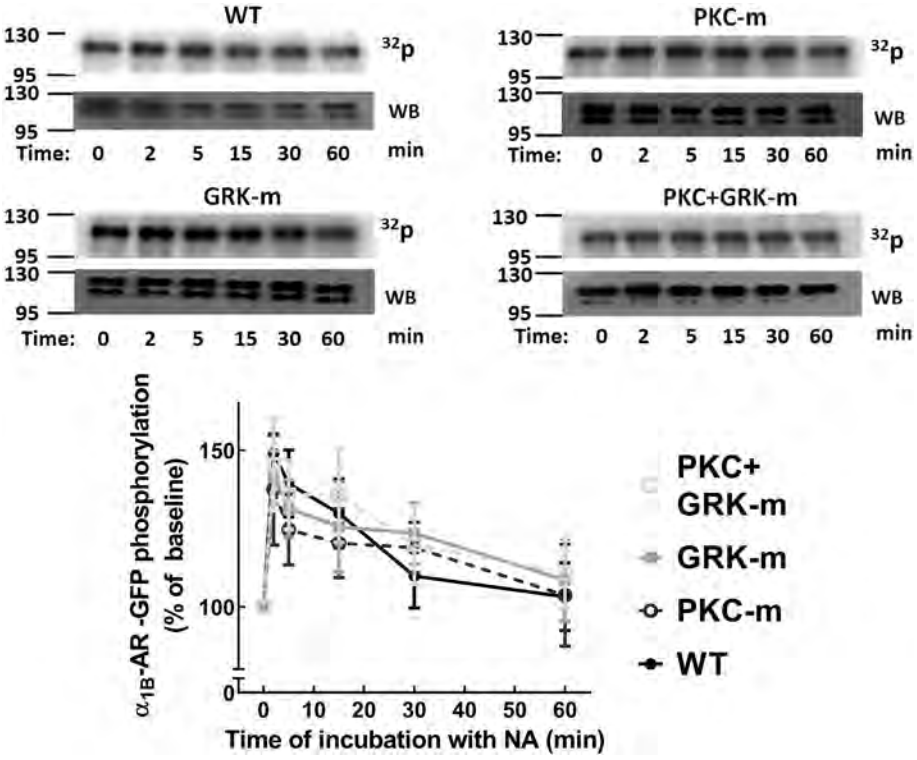

Fig. 3. Effect of NA on α_{1B}-AR phosphorylation. Cells were challenged with 10 μM NA (in the presence of propranolol) for the times indicated and receptor phosphorylation was determined. Plotted are the means ± S.E.M. of 6–9 experiments using different cell preparations. Above the graph, representative autoradiographs (^{32}P) and Western blots (WB) are shown. Other indications as in Fig. 1.

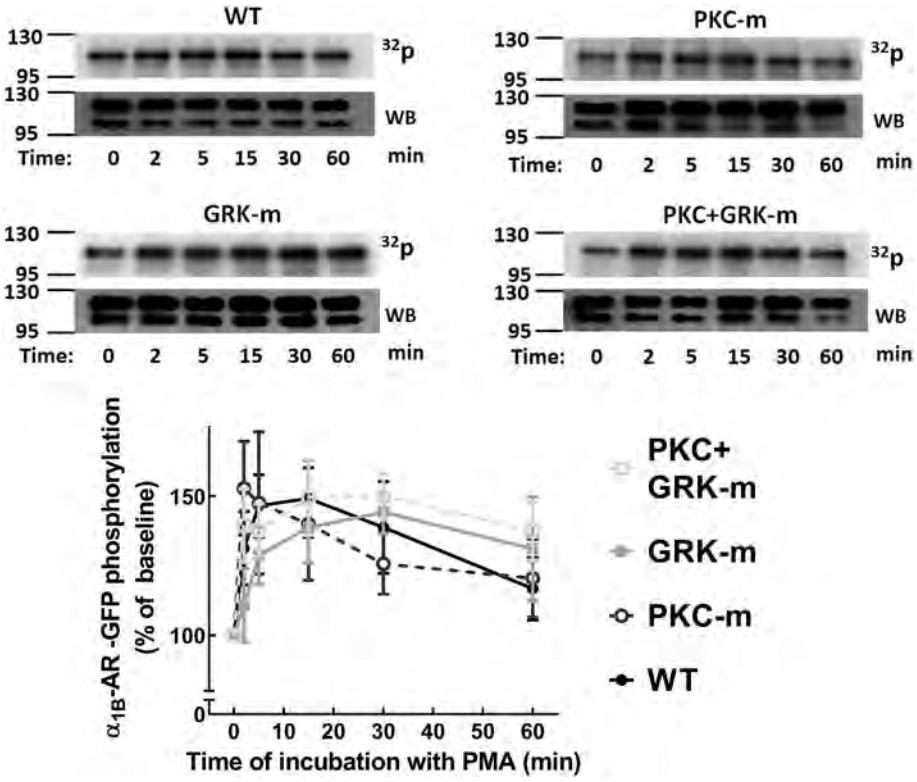

Fig. 4. Effect of PMA on α_{1B}-AR phosphorylation. Cells were challenged with 1 μM PMA for the times indicated and receptor phosphorylation was determined. Plotted are the means ± S.E.M. of 6–9 experiments using different cell preparations. Above the graph, representative autoradiographs (^{32}P) and Western blots (WB) are shown. Other indications as in Fig. 1.

NA and the effect diminished similarly (Fig. 3). In the presence of 1 μM PMA, the receptors studied, increased their phosphorylation state at 2 and 5 min, which was maintained up to 30 min, decreasing slightly afterward (60 min); when the wild-type receptor and the different mutants were compared, no statistically significant difference, was observed (Fig. 4). Nevertheless, it should be emphasized that, in these experiments, data were always normalized to the baseline phosphorylation of the receptor studied. In order to obtain a direct comparative view of the actions, cells expressing the different receptors were cultured and treated simultaneously, and samples were run using the same gels and analyzed using the baseline of the wild-type receptor as a reference (Fig. 5). These experiments evidenced that baseline phosphorylation was reduced in cells expressing the mutant receptors as compared to the wild-type even considering the relative expression,

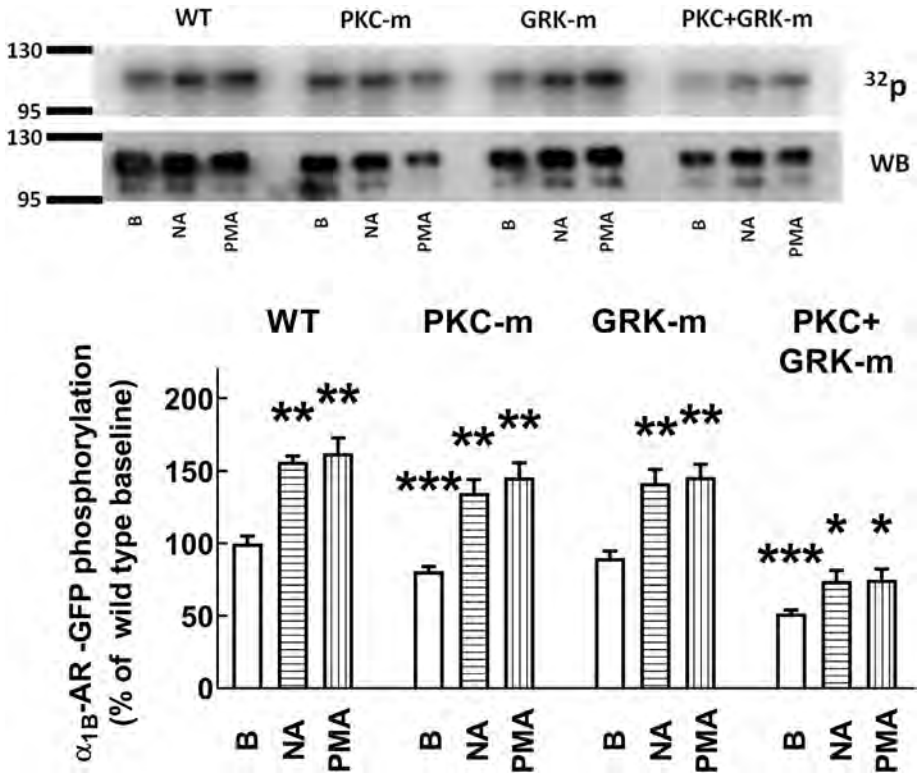

Fig. 5. Comparative α_{1B}-AR phosphorylation of the different mutants. Cells were challenged with no agent (B, baseline), 10 μM NA (plus propranolol) for 2 min, or 1 μM PMA for 15 min and receptor phosphorylation was determined. Data were normalized to the baseline phosphorylation observed in cell expressing the wild-type receptor. Plotted are the means ± S.E.M. of 10–12 experiments using different cell preparations. ***$p < 0.001$ vs. wild-type baseline (B); **$p < 0.001$ vs. respective baseline (B); *$p < 0.05$ vs. respective baseline (B). Above the graph, representative autoradiographs (^{32}P) and Western blots (WB) are shown. Other indications as in Fig. 1.

as evidenced by Western blotting, i.e., the PKC-m receptor to ~80%, the GRK-m to ~90%, and the PCK-GRK-m to ~50% of the wild-type receptor phosphorylation. These differences were reproducible and statistically significant. Similarly, decreases in phosphorylation were observed by Diviani et al. [30], which reported diminutions of 13–30% as compared to the wild-type receptor. In addition, our experiments showed that baseline and both NA- and PMA-induced phosphorylation, was present in these receptors. i.e. these mutations reduced but did not completely blocked receptor phosphorylation. Nevertheless, it should be emphasized that the phosphorylation state of the PKC + GRK-m receptor was markedly decreased, as compared to the wild-type, and that the effects of NA and PMA were reduced and were only marginally statistically significant. Work by Cotecchia and coworkers has shown that truncation of the hamster α_{1B}-AR Ctail (i.e., lacking the last 147 amino acids) nearly abolished NA- or PMA-induced receptor phosphorylation [32] as did truncation of the domain where the phosphorylation sites were detected (sites 393–414 of the hamster ortholog) [30]. The differences between our present work and those of Cottechia and coworkers [30,32] could be due to the receptor orthologs studied or to differences in the experimental conditions employed including, but not limited to, the cellular models in which the receptors were expressed, the receptor densities, and/or the conformational changes induced by the receptor modifications performed.

The effect of NA on ERK 1/2 phosphorylation was also studied. It can be observed in Fig. 6, that when cells expressing the wild-type human α_{1B}-AR were stimulated by the agonist, ERK phosphorylation increased very rapidly (i.e., maximal phosphorylation was observed at 2 min; the earliest time of determination), which progressively decreased after 15, 30 and 60 min of incubation with the agonist (Fig. 6). Interestingly, the initial response was nearly identical in cells expressing the different receptors; however, ERK 1/2 phosphorylation decreased at a much slower rate in cells with the different mutants as compared to those expressing the wild-type receptor (Fig. 6). This difference was statistically significant (at 30 and 60 min), when the response of cells with the distinct mutants were compared to those expressing the wild-type receptor. These flatter decreases are consistent with the idea that the different mutants reduce receptor turn off. It is possible that such differences could be related to changes in receptor trafficking/internalization [50]. A similar pattern was observed in cell expressing α_{1D}-AR mutants; i.e., NA-induced ERK phosphorylation decreased at a slower rate in cells expressing receptors with Ctail S/A substitutions than in those with unmodified carboxyl terminus [7,20].

The former data revealed that the modifications made to the human α_{1B}-AR mimicked some of the functional effects observed with the mutated hamster ortholog [30], but that remaining baseline, NA- and PMA-stimulated human α_{1B}-AR phosphorylation continued to be observed. Some remaining phosphorylation was also detected in the experiments using the hamster receptor [30]. Therefore, as a second step in our research, we decided to directly explore the phosphorylation sites directly present in human α_{1B}-AR under three different conditions: baseline, activation with 10 μM NA (in the presence of propranolol), or 1 μM PMA; cells were stimulated for 15 min on the basis of the previous experiments. To accomplish this, we performed receptor immunopurification experiments using a protocol similar to those employed previously to study the α_{1A}- and α_{1D}-AR [7,19,20], as described in Materials and Methods. In immunopurification studies for mass spectrometry analysis, two bands in the 110–100 kDa region were present in the Coomassie blue-stained gels which were identified as the α_{1B}-AR-eGFP construct by Western blotting using a primary antibody against the eGFP (Fig. 7). This is consistent with what was observed in the receptor phosphorylation experiments, using metabolic labeling with [^{32}P]Pi.

Mass spectrometry analysis of the immunopurified bands, obtained from four independent experiments, revealed peptides corresponding to 67% of the IL3 and 74% of the Ctail α_{1B}-AR sequences (Supplementary Fig. S5). The detected α_{1B}-AR phosphorylation sites present, under the different experimental conditions, are shown in Fig. 8, which includes the following: prediction in silico, amino acid number and peptide sequence in which it was detected, and domain localization. α_{1B}-AR phosphorylation is quite strong under baseline conditions [23,29–32,51–53] and a large number of amino acid residues present at the IL3 and also at the Ctail were phosphorylated under baseline/

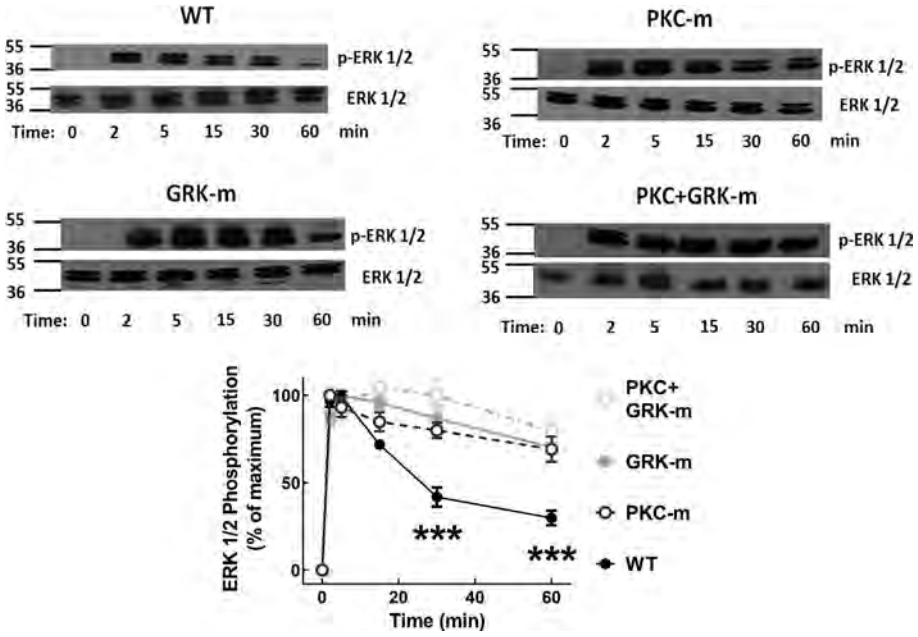

Fig. 6. Effect of NA on ERK 1/2 phosphorylation. Cells were challenged with 10 μM NA (in the presence of propranolol) for the times indicated and ERK 1/2 phosphorylation was determined. Plotted are the means ± S.E.M. of 6–8 experiments using different cell preparations. Above the graph, representative phospho-ERK 1/2 (p-ERK 1/2) and total ERK 1/2 (ERK 1/2) Western blots are shown. ***$p < 0.001$ vs. the different mutants. Other indications as in Fig. 1.

unstimulated conditions (Fig. 8, panels A and B). Interestingly, some of these residues were not found phosphorylated under stimulation by NA or PMA; these include S248, S268, T420, and T475 (Fig. 8, panels A and B). Some amino acids were detected phosphorylated only in response to NA and include: S246, S277, S396, S400, S402, and S406. Residues phosphorylated in response to PMA include T387 and T392 whereas S267 and S425 were found phosphorylated under both baseline and PMA-stimulated conditions (Fig. 8, panels A and B). Other residues were detected phosphorylated under all studied conditions (baseline, NA- and PMA-stimulated) including: T252, S257, T264, S423, S427, S455, and S470 (Fig. 8, panel A and B). Other phosphorylation sites were detected but their Ascore value [45] was low. It should be mentioned, that the mass spectrometry method employed in this study is only qualitative and therefore, we cannot estimate the proportion/relative magnitude of receptors phosphorylated in a given residue. Phospho-amino acid analysis of experiment using the hamster ortholog have not detected p-tyrosine and either only p-serine (COS-7 cells) [30] or marked signal of phospho-serine with clear traces of p-threonine (Rat-1 fibroblasts) [29]. This latter finding is consistent with our present data, in which some threonine residues were detected phosphorylated. This difference could be due to the cell system model employed for receptor expression, as this has been shown with muscarinic receptors and which seems to be of great importance in defining the so-called phosphorylation bar-code and its functional consequences [12].

The putative protein kinases involved in these phosphorylations were explored using the Group-based Prediction System, GPS 2.0. As it could have been anticipated on the bases of the previous work on this receptor [30,31], in many cases, several kinases, including members of the GRK and PKC families, were able to phosphorylate these sites (Supplementary Table 1); other protein kinases, such as PKA, AKT, GSK3, PDK-1, and p38, were also identified in the protein kinase prediction analysis (Supplementary Table S1).

Sequence alignment of the IL3 and Ctail domains of the α_{1B}-ARs of different species was subsequently performed (Supplementary Fig. S6). All of the phosphorylation sites were conserved among these orthologs. In contrast, when these domains of human α_{1A}-, α_{1B}- and α_{1D}-AR subtypes, were aligned, none of the identified phosphorylation sites were conserved among these three different subtypes and only a few

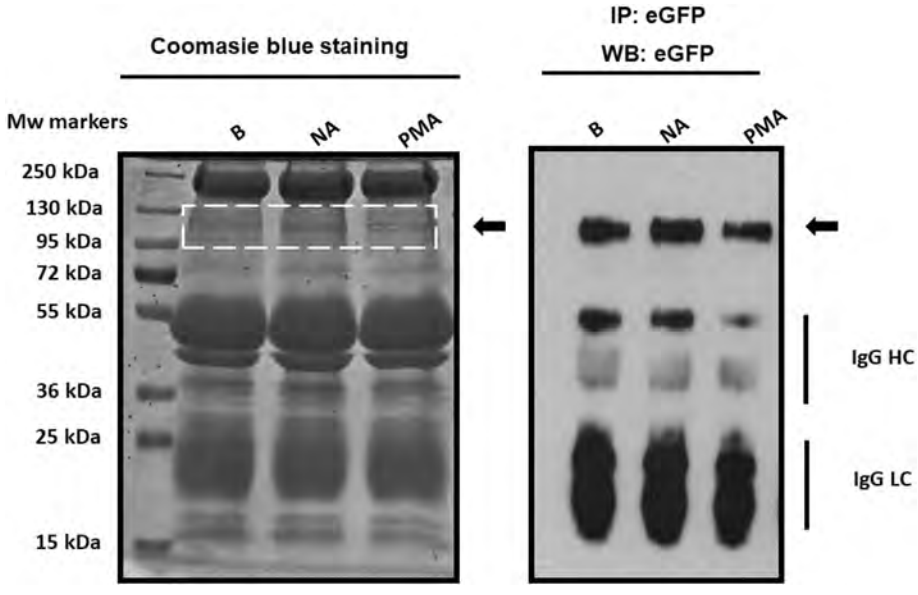

Fig. 7. Representative α_{1B}-AR immunopurification samples employed for the mass spectrometry studies. Cells expressing the α_{1B}-AR-eGFP construct were treated with: no agent (baseline, B), 10 μM NA (and propranolol), or 1 μM PMA, for 15 min; subsequently were lysed and subjected to immunopurification as described under Material and Methods. Samples were separated by SDS-polyacrylamide gel electrophoresis and stained with Coomassie blue (left image); molecular weight markers are shown in the first lane and their Mr is indicated. A small aliquot was also subjected to electrophoresis, and the gel was electrotransferred onto a nitrocellulose membrane. Western blotting was performed using anti-GPF antibodies. The arrows indicate α_{1B}-AR-eGFP localization. Bands corresponding to IgG HC (heavy chains) and LC (light chains) are also indicated.

A

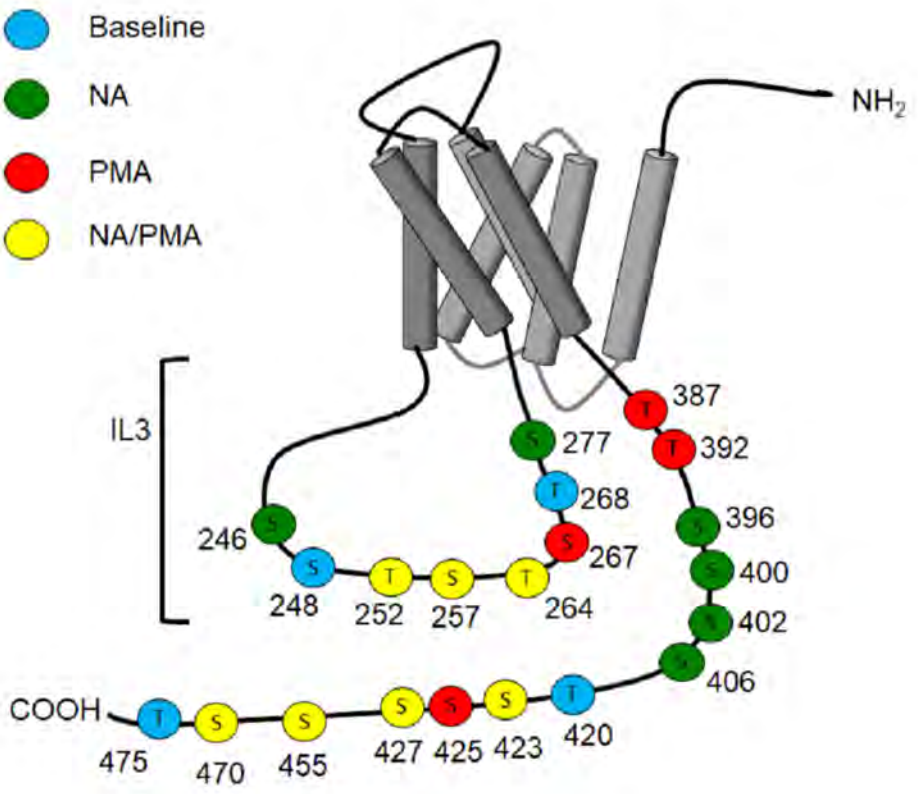

B

In silico	#	Residue	Sequence	Location	Baseline	NA	PMA	NA/PMA
X	246	S	EMSNSKELTLR	IL-3				
X	248	S	EMSNSKELTLR	IL-3				
✓	252	T	EMSNSKELTLR	IL-3				
✓	257	S	IHSKNFHEDTLSSTK	IL-3				
✓	264	T	IHSKNFHEDTLSSTKAK	IL-3				
✓	267	S	NFHEDTLSSTKAK	IL-3				
✓	268	T	NFHEDTLSSTKAK	IL-3				
X	277	S	GHNPRSSIAVK	IL-3				
✓	387	T	LGGCAYTYRPWTR	Ctail				
X	392	T	LGGCAYTYRPWTR	Ctail				
✓	396	S	GGSLERSQSR	Ctail				
✓	400	S	GGSLERSQSR	Ctail				
✓	402	S	SQSRKDSLDDSGSCLSGSQR	Ctail				
✓	406	S	KDSLDDSGSCLSGSQR	Ctail				
✓	420	T	TLPSASPSPGYLGR	Ctail				
✓	423	S	TLPSASPSPGYLGR	Ctail				
X	425	S	TLPSASPSPGYLGR	Ctail				
X	427	S	TLPSASPSPGYLGR	Ctail				
X	455	S	APGALLSLPAPEPPGRR	Ctail				
X	470	S	GRHDSGPLFTFK	Ctail				
X	475	T	RGRHDSGPLFTFK	Ctail				

(caption on next page)

INFORME DE LABORES 2019

Fig. 8. Phosphorylation sites detected by mass spectrometry in samples of the wild-type α_{1B}-AR-eGFP construct. Panel A. Diagram of the wild-type α_{1B}-AR indicating the observed phosphorylation sites under the different conditions employed. Numbers indicate the residue sequence position, and letters identify the amino acid. Blue (B, baseline); green (NA + propranolol) sites only observed phosphorylated in samples from cells incubated with noradrenaline; red (PMA) sites only observed in samples from cells incubated with phorbol myristate acetate; and yellow (NA/PMA) sites observed phosphorylated in cells incubated with either NA or PMA. IL3, intracellular loop 3. Panel B, α_{1B}-AR phosphorylated peptides detected by mass spectrometry. The first column indicates whether the site phosphorylated was or was not predicted by in silico analysis. The second and third columns indicate the amino acid detected and its position in the receptor's sequence. The next columns show the phosphopeptides detected and their domain location. The last column shows the cell-incubation conditions under which the modifications were detected, marked with the same color code employed in panel A.

were conserved between two of them (Supplementary Fig. S7).

Supplementary Fig. S8 presents comparative models of the human α_{1B}-AR putative phosphorylation sites (extrapolated from the mutational/functional data obtained with the human ortholog [30]) and the actual phosphorylation sites detected by mass spectroscopy. As can be observed, three of the sites were confirmed by the present data and a much more complex phosphorylation pattern was detected. Supplementary Fig. S9, presents models of the three human α_1-AR with the phosphorylation patterns observed by mass spectrometry; these were obtained using the same cell-expression model and similar receptor constructions (i.e., receptors fused at the Ctail with the eGFP).

The pioneer work of Diviani, Lattion and Cotecchia [30] performed > 20 years ago, using mutagenesis and deletions in parallel with functional studies, defined a cluster of five serines as the major phosphorylation sites of the hamster α_{1B}-AR. Methodological advances over the past years allow now direct identification of phosphorylated sites. In the present work, we detected S396, S402 and S406 as phosphorylated, which correspond to three of the sites detected in the hamster receptor (Supplementary Fig. S8). The former two correspond to residues assigned as targets for PKC [30] and the kinase prediction performed is consistent with such an assignment (Supplementary Table S1). The third site, S406, was assigned as a GRK target [30]; however, kinase prediction failed to detect it as such, despite its being surrounded by acidic residues, suggesting the possible roles of other kinases (Supplementary Table S1). The remaining two serines, defined for hamster α_{1B}-AR (i.e., S410 and S412 in the human receptor), were covered by the mass spectrometry analysis (Supplementary Fig. S5) but no phosphorylation was detected. A series of possibilities might explain this, as follows: it could due to the conformation of the human receptor ortholog, as due to availability or accessibility to GRK (namely GRK2 and GRK3 [30]); restrictions imposed by the eGFP tag, and/or the possibility that those (phospho)-ester bonds could be unstable during the mass spectrometry analysis, among others. In any case, the data obtained with the hamster receptor and the present findings define S396, S402, and S406 as major phosphorylation targets in the α_{1B}-AR of humans, hamsters, and likely, other species (Supplementary Fig. S6).

It is noteworthy that it has been observed that at least two domains at the hamster α_{1B}-AR Ctail of the, one including amino acids 403–425 and another in the 367–380 region, appear to play roles in internalization/down-regulation [35]. No phosphorylation was detected in the region corresponding to amino acids 367–380 of hamster α_{1B}-AR. However, in the region corresponding to the first domain, we detected phosphorylated S406, T420, S423, and S425. We have previously observed that human α_{1B}-AR internalize through different processes, i.e., processes involving interaction with different Rab proteins when stimulated by NA, or through the physiological or pharmacological activation of PKC [54,55]. It is possible that the phosphorylated sites might play a role in internalization/down-regulation, but this remains to be experimentally tested.

Detection of phosphorylated residues at the human α_{1B}-AR IL3 was unexpected, because it has been observed that deletion of the hamster Ctail or of the serine cluster (Δ 393–413) in this domain, nearly abolished receptor phosphorylation [30]. Consistent with this, work from our laboratory has shown, using Rat-1 fibroblast as expression model, that hamster α_{1B}-AR are markedly phosphorylated under baseline, NA- or PMA-stimulated conditions, whereas bovine α_{1A}-AR is also phosphorylated, but to a much lesser degree [53]. Swapping the Ctail of these receptors demonstrated that this domain of the α_{1B}-AR comprises the main phosphorylation target, and that the intense phosphorylation pattern can be transplanted to the α_{1A}-AR [53,56] (although little correlation between receptor phosphorylation and function was detected [56]). It is possible that the three phosphorylated sites detected are those predominantly phosphorylated but that overexpression and strong stimulation, required to obtain significant signal in the mass spectrometry experiments, might permit detection of residues that under other conditions might be phosphorylated to a much lesser extent. However, significant α_{1B}-AR phosphorylation was observed in mutants with S/A substitutions (Figs. 3–6). It is also of interest that our studies on the three human α_1-AR ([7,19,20] and the present work) showed phosphorylation at both the IL3 and Ctail domains (Supplementary Fig. S9), although such sites were poorly conserved (Supplementary Fig. S7).

The complexity of the phosphorylation patterns of the human α_1-AR hampers the possibility of studying the functional significance of the different sites. Recently we obtained evidence that sites at the human α_{1D}-AR Ctail might control the plasma membrane location of this receptor subtype [7]. Similarly, in a recent and elegant study, Strakova and coworkers [8] reported that casein kinase 1-mediated phosphorylation of the Frizzled 6 receptor is required for its plasma membrane localization and that this contributes to its asymmetric distribution in epithelial cells. Our present work provides further evidence that three serine residues are important in human α_{1B}-AR phosphorylation and suggests that phosphorylation patterns are much more complex than previously anticipated. Receptor phosphorylation is an intricate process that takes place within space-temporal dimensions and, very likely, our phosphorylation data represent just a “frame” within the large “picture”. The fact that some sites were detected phosphorylated under baseline conditions, but not when stimulated (Fig. 8), suggest to us that, during cell activation, the action of different protein kinases and phosphatases might take place, and this could occur in a very dynamic manner, with different receptor phosphorylation patterns, coexisting at distinct times and receptor's cellular localizations. In addition, there is evidence showing that phosphorylated β_2-adrenoceptor subpopulations (i.e., receptors phosphorylated at different sites) could be present simultaneously in a single cell; these might be present in different subcellular compartments and subserve in different functions [57]. It is likely, therefore, that the phosphorylation pattern we observed might be the addition of a series of different states present in the cells.

Funding information

This research was supported by grants from Consejo Nacional de Ciencia y Tecnología (CONACYT) [grant number 253156] and Dirección General de Personal Académico-UNAM [PAPIIT, grant number IN200718].

Author contribution statement

Conceived and designed the experiments: DAH-E, GR-C, MAA-M, and JAG-S. Performed the experiments: DAH-E, GR-C, and RA-H. Analyzed the data: DAH-E, GR-C, MAA-M, RA-H, and JAG-S. Wrote the paper: DAH-E and JAG-S. All authors reviewed, corrected, and

INFORME DE LABORES 2019

approved the final manuscript.

Transparency document

The Transparency document associated this article can be found, in online version.

Declaration of Competing Interest

All authors declare no conflict of interest.

Acknowledgments

The authors thank Dr. Myron L. Toews for reading and commenting on the manuscript. They also thank Drs. Steven C. Prinster and Myron L. Toews for allowing us access to unpublished data on internalization and down-regulation of α_{1B}-AR. The advice of Ross Tomaino, Associate Director of the Taplin Mass Spectrometry Facility (Harvard Medical School, USA) was very important for the development of this work, and it is gratefully acknowledged. The authors express their gratitude for advice and technical support to Dr. Maria Teresa Romero-Ávila from our laboratory and the following members of the indicated Service Units of our Institute: Dr. Héctor Malagón and Dr. Claudia Rivera (Bioterio); Juan Barbosa and Gerardo Coello (Cómputo); and Aurey Hernández and Manuel Ortín (Taller) for their advice and technical support. David A. Hernández-Espinosa is a doctoral student from Programa de Doctorado en Ciencias Bioquímicas, Universidad Nacional Autónoma de México, and was the recipient of a doctoral fellowship (CVU: 706381) from Consejo Nacional de Ciencia y Tecnología (CONACyT).

Appendix A. Supplementary data

Supplementary data to this article can be found online at https://doi.org/10.1016/j.bbamcr.2019.07.006.

References

[1] B. Kobilka, The structural basis of G-protein-coupled receptor signaling (nobel lecture), Angew Chem. Int. Ed. Engl. 52 (2013) 6380–6388.
[2] R.J. Lefkowitz, A brief history of G-protein coupled receptors (nobel lecture), Angew Chem. Int. Ed. Engl. 52 (2013) 6366–6378.
[3] S.S. Ferguson, Evolving concepts in G protein-coupled receptor endocytosis: the role in receptor desensitization and signaling, Pharmacol. Rev. 53 (2001) 1–24.
[4] R.J. Lefkowitz, G protein-coupled receptors. III. New roles for receptor kinases and beta-arrestins in receptor signaling and desensitization, J. Biol. Chem., 273 (1998) 18677–18680.
[5] S. Rajagopal, S.K. Shenoy, GPCR desensitization: acute and prolonged phases, Cell. Signal. 41 (2018) 9–16.
[6] S.S. Ferguson, Phosphorylation-independent attenuation of GPCR signalling, Trends Pharmacol. Sci. 28 (2007) 173–179.
[7] G. Carmona-Rosas, D.A. Hernández-Espinosa, R. Alcántara-Hernández, M.A. Alfonzo-Méndez, J.A. García-Sáinz, Distinct phosphorylation sites/clusters in the carboxyl terminus regulate alpha1D-adrenergic receptor subcellular localization and signaling, Cell. Signal. 53 (2019) 374–389.
[8] K. Strakova, M. Kowalski-Jahn, T. Gybel, J. Valnohova, V.M. Dhople, J. Harnos, O. Bernatik, R.S. Ganji, Z. Zdrahal, J. Mulder, C. Lindskog, V. Bryja, G. Schulte, Dishevelled enables casein kinase 1-mediated phosphorylation of Frizzled 6 required for cell membrane localization, J. Biol. Chem. 293 (2018) 18477–18493.
[9] S.K. Shenoy, R.J. Lefkowitz, Seven-transmembrane receptor signaling through beta-arrestin, Science's STKE: signal transduction knowledge environment, 2005 (2005) cm10.
[10] L.M. Luttrell, R.J. Lefkowitz, The role of beta-arrestins in the termination and transduction of G-protein-coupled receptor signals, J. Cell Sci. 115 (2002) 455–465.
[11] A.B. Tobin, G-protein-coupled receptor phosphorylation: where, when and by whom, Br. J. Pharmacol. 153 (Suppl. 1) (2008) S167–S176.
[12] A.B. Tobin, A.J. Butcher, K.C. Kong, Location, location, location…site-specific GPCR phosphorylation offers a mechanism for cell-type-specific signalling, Trends Pharmacol. Sci., 29 (2008) 413–420.
[13] E. Alvarez-Curto, A. Inoue, L. Jenkins, S.Z. Raihan, R. Prihandoko, A.B. Tobin, G. Milligan, Targeted elimination of G proteins and arrestins defines their specific contributions to both intensity and duration of G protein-coupled receptor signaling, J. Biol. Chem. 291 (2016) 27147–27159.
[14] M. Bouzo-Lorenzo, I. Santo-Zas, M. Lodeiro, R. Nogueiras, F.F. Casanueva, M. Castro, Y. Pazos, A.B. Tobin, A.J. Butcher, J.P. Camina, Distinct phosphorylation sites on the ghrelin receptor, GHSR1a, establish a code that determines the functions of ss-arrestins, Sci. Rep. 6 (2016) 22495.
[15] S.J. Bradley, C.H. Wiegman, M.M. Iglesias, K.C. Kong, A.J. Butcher, B. Plouffe, E. Goupil, J.M. Bourgognon, T. Macedo-Hatch, C. LeGouill, K. Russell, S.A. Laporte, G.M. Konig, E. Kostenis, M. Bouvier, K.F. Chung, Y. Amrani, A.B. Tobin, Mapping physiological G protein-coupled receptor signaling pathways reveals a role for receptor phosphorylation in airway contraction, Proc. Natl. Acad. Sci. U. S. A. 113 (2016) 4524–4529.
[16] A.J. Butcher, B.D. Hudson, B. Shimpukade, E. Alvarez-Curto, R. Prihandoko, T. Ulven, G. Milligan, A.B. Tobin, Concomitant action of structural elements and receptor phosphorylation determine arrestin-3 interaction with the free fatty acid receptor FFA4, J. Biol. Chem. 289 (2014) 18451–18465.
[17] R. Prihandoko, E. Alvarez-Curto, B.D. Hudson, A.J. Butcher, T. Ulven, A.M. Miller, A.B. Tobin, G. Milligan, Distinct phosphorylation clusters determine the signaling outcome of free fatty acid receptor 4/G protein-coupled receptor 120, Mol. Pharmacol. 89 (2016) 505–520.
[18] D. Zindel, S. Engel, A.R. Bottrill, J.P. Pin, L. Prezeau, A.B. Tobin, M. Bunemann, C. Krasel, A.J. Butcher, Identification of key phosphorylation sites in PTH1R that determine arrestin3 binding and fine-tune receptor signaling, Biochem. J. 473 (2016) 4173–4192.
[19] R. Alcántara-Hernández, A. Hernández-Méndez, M.T. Romero-Ávila, M.A. Alfonzo-Méndez, A.S. Pupo, J.A. García-Sáinz, Noradrenaline, oxymetazoline and phorbol myristate acetate induce distinct functional actions and phosphorylation patterns of alpha1A-adrenergic receptors, Biochim. Biophys. Acta 1864 (2017) 2378–2388.
[20] M.A. Alfonzo-Méndez, G. Carmona-Rosas, D.A. Hernández-Espinosa, M.T. Romero-Ávila, J.A. García-Sáinz, Different phosphorylation patterns regulate alpha1D-adrenoceptor signaling and desensitization, Biochim. Biophys. Acta 1865 (2018) 842–854.
[21] M.A. Alfonzo-Méndez, R. Alcántara Hernández, J.A. García-Sáinz, Novel structural approaches to study GPCR regulation, Int. J. Mol. Sci. 18 (2017) 27.
[22] J.A. García-Sáinz, J. Vázquez-Prado, R. Villalobos-Molina, Alpha 1-adrenoceptors: subtypes, signaling, and roles in health and disease, Arch. Med. Res. 30 (1999) 449–458.
[23] J.A. García-Sáinz, J. Vázquez-Prado, L.C. Medina, Alpha 1-adrenoceptors: function and phosphorylation, Eur. J. Pharmacol. 389 (2000) 1–12.
[24] J.P. Hieble, D.B. Bylund, D.E. Clarke, D.C. Eikenburg, S.Z. Langer, R.J. Lefkowitz, K. P. Minneman, R.R. Ruffolo, Jr., International Union of Pharmacology. X. Recommendation for nomenclature of alpha 1-adrenoceptors: consensus update, Pharmacol. Rev., 47 (1995) 267–270.
[25] D.M. Perez, M.B. DeYoung, R.M. Graham, Coupling of expressed alpha 1B- and alpha 1D-adrenergic receptor to multiple signaling pathways is both G protein and cell type specific, Mol. Pharmacol. 44 (1993) 784–795.
[26] J.A. García-Sáinz, A. Gottfried-Blackmore, J. Vázquez-Prado, M.T. Romero-Ávila, Protein kinase C-mediated phosphorylation and desensitization of human alpha (1b)-adrenoceptors, Eur. J. Pharmacol. 385 (1999) 263–271.
[27] J.A. García-Sáinz, C.E. Rodríguez-Pérez, M.T. Romero-Ávila, Human alpha-1D adrenoceptor phosphorylation and desensitization, Biochem. Pharmacol. 67 (2004) 1853–1858.
[28] J. Vázquez-Prado, J.A. García-Sáinz, Effect of phorbol myristate acetate on alpha 1-adrenergic action in cells expressing recombinant alpha 1-adrenoceptor subtypes, Mol. Pharmacol. 50 (1996) 17–22.
[29] J. Vázquez-Prado, L.C. Medina, J.A. García-Sáinz, Activation of endothelin ETA receptors induces phosphorylation of alpha1b-adrenoreceptors in Rat-1 fibroblasts, J. Biol. Chem. 272 (1997) 27330–27337.
[30] D. Diviani, A.L. Lattion, S. Cotecchia, Characterization of the phosphorylation sites involved in G protein-coupled receptor kinase- and protein kinase C-mediated desensitization of the alpha1B-adrenergic receptor, J. Biol. Chem. 272 (1997) 28712–28719.
[31] D. Diviani, A.L. Lattion, N. Larbi, P. Kunapuli, A. Pronin, J.L. Benovic, S. Cotecchia, Effect of different G protein-coupled receptor kinases on phosphorylation and desensitization of the alpha1B-adrenergic receptor, J. Biol. Chem. 271 (1996) 5049–5058.
[32] A.L. Lattion, D. Diviani, S. Cotecchia, Truncation of the receptor carboxyl terminus impairs agonist-dependent phosphorylation and desensitization of the alpha 1B-adrenergic receptor, J. Biol. Chem. 269 (1994) 22887–22893.
[33] R.R. Price, D.P. Morris, G. Biswas, M.P. Smith, D.A. Schwinn, Acute agonist-mediated desensitization of the human alpha 1a-adrenergic receptor is primarily independent of carboxyl terminus regulation: implications for regulation of alpha 1aAR splice variants, J. Biol. Chem. 277 (2002) 9570–9579.
[34] S. Cotecchia, D.A. Schwinn, R.R. Randall, R.J. Lefkowitz, M.G. Caron, B.K. Kobilka, Molecular cloning and expression of the cDNA for the hamster alpha 1-adrenergic receptor, Proc. Natl. Acad. Sci. U. S. A. 85 (1988) 7159–7163.
[35] J. Wang, L. Wang, J. Zheng, J.L. Anderson, M.L. Toews, Identification of distinct carboxyl-terminal domains mediating internalization and down-regulation of the hamster alpha(1B)- adrenergic receptor, Mol. Pharmacol. 57 (2000) 687–694.
[36] M.L. Toews, S.C. Prinster, N.A. Schulte, Regulation of alpha-1B adrenergic receptor localization, trafficking, function, and stability, Life Sci. 74 (2003) 379–389.
[37] S.E. Avendaño-Vázquez, A. García-Caballero, J.A. García-Sáinz, Phosphorylation and desensitization of the lysophosphatidic acid receptor LPA1, Biochem. J. 385 (2005) 677–684.
[38] T. Molina-Muñoz, M.T. Romero-Ávila, S.E. Avendaño-Vázquez, J.A. García-Sáinz, Phosphorylation, desensitization and internalization of human alpha(1B)-adrenoceptors induced by insulin-like growth factor-I, Eur. J. Pharmacol. 578 (2008) 1–10.
[39] R.J. Ward, E. Alvarez-Curto, G. Milligan, Using the Flp-In T-Rex system to regulate GPCR expression, Methods Mol. Biol. 746 (2011) 21–37.

[40] O.B. Sánchez-Reyes, M.T. Romero-Ávila, J.A. Castillo-Badillo, Y. Takei, A. Hirasawa, G. Tsujimoto, R. Villalobos-Molina, J.A. García-Sáinz, Free fatty acids and protein kinase C activation induce GPR120 (free fatty acid receptor 4) phosphorylation, Eur. J. Pharmacol. 723 (2014) 368–374.
[41] C.E. Rodríguez-Pérez, E. Calvo-Ochoa, E.V. Kalashnikova, G. Reyes-Cruz, M.T. Romero-Ávila, J.A. García-Sáinz, Receptor tyrosine kinases regulate alpha1D-adrenoceptor signaling properties: phosphorylation and desensitization, Int. J. Biochem. Cell Biol. 41 (2009) 1276–1283.
[42] C.E. Rodríguez-Pérez, M.T. Romero-Ávila, G. Reyes-Cruz, J.A. García-Sáinz, Signaling properties of human alpha(1D)-adrenoceptors lacking the carboxyl terminus: intrinsic activity, agonist-mediated activation, and desensitization, Naunyn Schmiedeberg's Arch. Pharmacol. 380 (2009) 99–107.
[43] G. Grynkiewicz, M. Poenie, R.Y. Tsien, A new generation of Ca2+ indicators with greatly improved fluorescence properties, J. Biol. Chem. 260 (1985) 3440–3450.
[44] U.K. Laemmli, Cleavage of structural proteins during the assembly of the head of bacteriophage T4, Nature 227 (1970) 680–685.
[45] S.A. Beausoleil, J. Villen, S.A. Gerber, J. Rush, S.P. Gygi, A probability-based approach for high-throughput protein phosphorylation analysis and site localization, Nat. Biotechnol. 24 (2006) 1285–1292.
[46] C. UniProt, Activities at the Universal Protein Resource (UniProt), Nucleic Acids Res. 42 (2014) D191–D198.
[47] N. Blom, S. Gammeltoft, S. Brunak, Sequence and structure-based prediction of eukaryotic protein phosphorylation sites, J. Mol. Biol. 294 (1999) 1351–1362.
[48] Y. Xue, J. Ren, X. Gao, C. Jin, L. Wen, X. Yao, GPS 2.0, a tool to predict kinase-specific phosphorylation sites in hierarchy, Mol. Cell. Proteomics 7 (2008) 1598–1608.
[49] M. Galaz-Montoya, S.J. Wright, G.J. Rodriguez, O. Lichtarge, T.G. Wensel, Beta2-adrenergic receptor activation mobilizes intracellular calcium via a non-canonical cAMP-independent signaling pathway, J. Biol. Chem., 292 (2017) 9967–9974.
[50] V. Segura, M. Perez-Aso, F. Monto, E. Carceller, M.A. Noguera, J. Pediani, G. Milligan, I.C. McGrath, P. D'Ocon, Differences in the signaling pathways of alpha (1A)- and alpha(1B)-adrenoceptors are related to different endosomal targeting, PLoS One 8 (2013) e64996.
[51] L.M. Leeb-Lundberg, S. Cotecchia, J.W. Lomasney, J.F. DeBernardis, R.J. Lefkowitz, M.G. Caron, Phorbol esters promote alpha 1-adrenergic receptor phosphorylation and receptor uncoupling from inositol phospholipid metabolism, Proc. Natl. Acad. Sci. U. S. A. 82 (1985) 5651–5655.
[52] L.C. Medina, J. Vázquez-Prado, M.E. Torres-Padilla, A. Mendoza-Mendoza, M.E. Cruz Muñoz, J.A. García-Sáinz, Crosstalk: phosphorylation of alpha1b-adrenoceptors induced through activation of bradykinin B2 receptors, FEBS Lett. 422 (1998) 141–145.
[53] J. Vázquez-Prado, L.C. Medina, M.T. Romero-Ávila, C. González-Espinosa, J.A. García-Sáinz, Norepinephrine- and phorbol ester-induced phosphorylation of alpha (1a)-adrenergic receptors. Functional aspects, J. Biol. Chem., 275 (2000) 6553–6559.
[54] M.A. Alfonzo-Méndez, D.A. Hernández-Espinosa, G. Carmona-Rosas, M.T. Romero-Ávila, G. Reyes-Cruz, J.A. García-Sáinz, Protein kinase C activation promotes alpha1B-adrenoceptor internalization and late endosome trafficking through Rab9 interaction. Role in heterologous desensitization, Mol. Pharmacol., 91 (2017) 296–306.
[55] J.A. Castillo-Badillo, O.B. Sánchez-Reyes, M.A. Alfonzo-Méndez, M.T. Romero-Ávila, G. Reyes-Cruz, J.A. García-Sáinz, Alpha1b-adrenergic receptors differentially associate with Rab proteins during homologous and heterologous desensitization, PLoS One, 10 (2015) e0121165.
[56] A. Cabrera-Wrooman, M.T. Romero-Ávila, J.A. García-Sáinz, Roles of the alpha1A-adrenergic receptor carboxyl tail in protein kinase C-induced phosphorylation and desensitization, Naunyn Schmiedeberg's Arch. Pharmacol. 382 (2010) 499–510.
[57] A. Shen, M. Nieves-Cintron, Y. Deng, Q. Shi, D. Chowdhury, J. Qi, J.W. Hell, M.F. Navedo, Y.K. Xiang, Functionally distinct and selectively phosphorylated GPCR subpopulations co-exist in a single cell, Nat Commun, 9 (2018) 1050, 1051–1012.

Hernández-Espinosa et al. Journal of Neuroinflammation (2019) 16:91
https://doi.org/10.1186/s12974-019-1478-4

Journal of Neuroinflammation

RESEARCH Open Access

Role of NADPH oxidase-2 in the progression of the inflammatory response secondary to striatum excitotoxic damage

Diego Rolando Hernández-Espinosa, Lourdes Massieu, Teresa Montiel and Julio Morán*

Abstract

Background: During excitotoxic damage, neuronal death results from the increase in intracellular calcium, the induction of oxidative stress, and a subsequent inflammatory response. NADPH oxidases (NOX) are relevant sources of reactive oxygen species (ROS) during excitotoxic damage. NADPH oxidase-2 (NOX-2) has been particularly related to neuronal damage and death, as well as to the resolution of the subsequent inflammatory response. As ROS are crucial components of the regulation of inflammatory response, in this work, we evaluated the role of NOX-2 in the progression of inflammation resulting from glutamate-induced excitotoxic damage of the striatum in an in vivo model.

Methods: The striata of wild-type C57BL/6 J and NOX-2 KO mice (gp91$^{Cybbtm1Din/J}$) were stereotactically injected with monosodium glutamate either alone or in combination with IL-4 or IL-10. The damage was evaluated in histological sections stained with cresyl violet and Fluoro-Jade B. The enzymatic activity of caspase-3 and NOX were also measured. Additionally, the cytokine profile was identified by ELISA and motor activity was verified by the tests of the cylinder, the adhesive tape removal, and the inverted grid.

Results: Our results show a neuroprotective effect in mice with a genetic inhibition of NOX-2, which is partially due to a differential response to excitotoxic damage, characterized by the production of anti-inflammatory cytokines. In NOX-2 KO animals, the excitotoxic condition increased the production of interleukin-4, which could contribute to the production of interleukin-10 that decreased neuronal apoptotic death and the magnitude of striatal injury. Treatment with interleukin-4 and interleukin-10 protected from excitotoxic damage in wild-type animals.

Conclusions: The release of proinflammatory cytokines during the excitotoxic event promotes an additional apoptotic death of neurons that survived the initial damage. During the subsequent inflammatory response to excitotoxic damage, ROS generated by NOX-2 play a decisive role in the extension of the lesion and consequently in the severity of the functional compromise, probably by regulating the anti-inflammatory cytokines production.

Keywords: NADPH oxidase, NOX-2, Glutamate, Excitotoxicity, Striatum, Caspase-3, Neuroinflammation, Interleukin-4, Interleukin-10

* Correspondence: jmoran@ifc.unam.mx
Instituto de Fisiología Celular, División de Neurociencias, Universidad Nacional Autónoma de México (UNAM), Apartado Postal 70-253, 04510 Ciudad de México, Mexico

© The Author(s). 2019 **Open Access** This article is distributed under the terms of the Creative Commons Attribution 4.0 International License (http://creativecommons.org/licenses/by/4.0/), which permits unrestricted use, distribution, and reproduction in any medium, provided you give appropriate credit to the original author(s) and the source, provide a link to the Creative Commons license, and indicate if changes were made. The Creative Commons Public Domain Dedication waiver (http://creativecommons.org/publicdomain/zero/1.0/) applies to the data made available in this article, unless otherwise stated.

Background

During excitotoxic damage, neuronal death produced by the overstimulation of the glutamate receptors is determined by several factors, including the increase of intracellular calcium [1], reactive oxygen species (ROS) production [2], microglia activation, and inflammatory responses [3]. Among these factors, the increase in ROS contributes significantly to the subsequent inflammatory process [4]. This condition has implications not only at the onset of damage, but also during the progression of the neuronal death [5].

Although the mitochondria have been classically considered as the main source of ROS [6], the relevance of other sources of ROS such as the NADPH oxidases family (NOX), which are widely distributed in all the studied species and are present in basically all the cell types evaluated, has gained great importance as mediators of excitotoxic damage [7]. In this regard, the genetic or pharmacological inhibition of NOX activity constitutes a neuroprotective condition in several pathologies involving excitotoxicity, such as hypoxia, hypoglycemia, and neuroinflammation [8–10]. Among the homologs of the NOX family, NOX-2 seems to be the main responsible for the observed neuronal death in numerous models of excitotoxic damage [11, 12]. The specific inhibition of NOX-2 in neurons, astrocytes, and microglia prevents neuronal death in different experimental conditions [13, 14]. In a previous study, we observed in genetically deficient NOX-2 mice and wild-type animals treated with a NOX inhibitor that ROS production, lesion size, and microglial reactivity were markedly decreased during excitotoxic damage [13].

A large body of evidence points to neuroinflammation as a main component of most of the central nervous system (CNS) disorders, including those involving excitotoxic damage [15]. Local immune cells orchestrate a series of events in order to stimulate tissue reparation in response to cell damage [16]. Microglia activation constitutes the first line of defense against brain tissue injury [17], through the induction of a range of phenotypes from resting ramified cells to motile amoeboid microglial cells [18]. At the molecular level, a variety of pro- and anti-inflammatory mediators, including interleukins, as well as ROS, nitric oxide, and eicosanoids are produced [19]. In contrast to proinflammatory mediators that participate in neuronal death, the anti-inflammatory mediators can contribute to neuroprotective actions [20, 21].

Cytokines are pleiotropic molecules that define the characteristics and the resolution of the immune response [22]. The characteristics of the response are subordinated to the sum of the proinflammatory and anti-inflammatory stimuli in the microenvironment. TNF-α, IL-1β, IL-6, IL-8, and IL-12, among others, are considered as classic proinflammatory molecules [23–25], while TGF-β, IL-4, and IL-10 are classified as anti-inflammatory cytokines [26, 27].

A simplified classification of the polarization of microglia has been developed, and two phenotypes were proposed based on functional characteristics, the type of cytokines released, and the presence of some molecular markers [28]. The M1 phenotype refers to the classically activated macrophages, which is characterized by the expression of proinflammatory cytokines [29] and the M2 phenotype designates the alternatively activated macrophages that are related to the production of anti-inflammatory cytokines and the resolution of the process [30–32].

Although the M1/M2 concept is widely accepted, it should be noted that the new technologies and the recent data in the field have led to reconsider this classification. For example, both “M1” and “M2” markers can be simultaneously expressed in the same microglial cells or macrophages [33] and M2 cells show a wide range of functional and biochemical features [34]. Thus, the microglial/macrophage polarization seems to be a more complex process than originally described and the M1/M2 phenotypic classification has been reviewed [35, 36], and different intermediate phenotypes have been described on the basis of their functionality and the molecular markers expressed under different physiological states [35, 37].

The mechanisms mediating the inflammatory response of macrophages/microglia are not completely understood, but evidence has provided a framework to propose that ROS may shape the inflammatory response [38, 39], as well as the regulation of microglial activation [40, 41]. This is in line with the association between ROS and several microglia-driven neuropathologies [38]. On the other hand, experimental evidence suggests that microglial NOX2 is involved in neurotoxicity by both producing extracellular ROS [41] and by participating in the redox signal involved in the inflammatory response [42, 43]. For example, NOX activation by interferon and LPS results in microglial expression of iNOS and cytokines mediated by the activation of MAP kinases, NFκB, and STAT1 phosphorylation [44, 45].

It has been suggested that NOX2 plays a key role in the expression of the M1 phenotype by a mechanism mediated by IL10 and STAT3 [37, 46]. Furthermore, the lack of NOX2 leads to a M2 phenotype mediated by a downregulation of NFκB nuclear translocation in a model of TBI and diabetes [46, 47]. Thus, ROS derived from glial cells and from different sources, including NOX2, participate in the microglial activation and play a key action by defining the microglial phenotype, which may have a central role in neurotoxicity and neurodegenerative diseases [43, 45].

In this study, we evaluated the time course of cell damage, NOX activity, and production of cytokines, as well as the functional sequelae, resulting from the excitotoxic damage in an in vivo model. We also tested the

protective action of two exogenous anti-inflammatory cytokines in this model. We propose that NOX-2, besides participating in the neuronal excitotoxic damage, also regulate the production of pro- and anti-inflammatory cytokines, which results critical for the progression of the cell death.

Methods

Animals

All animals were handled according to the National Institutes of Health Guide for the Care and Use of laboratory animals (NIH Publication No. 8023, revised 1978) and the local Committee for the Care and Use of Laboratory Animals (CICUAL protocol JMA72-15). All efforts were made to minimize pain, as well as the number of animals used. Wild-type (WT) adult mice C57BL/6 (8 weeks old) were obtained from the bioterium of the Instituto de Fisiología Celular, Universidad Nacional Autónoma de México. The NOX-2 KO (gp91$^{Cybbtm1Din/J}$) adult mice generated on a C57BL/6 background were purchased from the Jackson Laboratory (Bar Harbor, ME), and the colony was established at the vivarium of the Instituto de Fisiología Celular, Universidad Nacional Autónoma de México. Mice were housed and kept under controlled temperature (20–22 °C) with a regulated 12-h light-dark cycle, with water and food ad libitum. The mice used for this study were divided as follows: 40 animals were used for histological analyses, 30 for immunoblot and enzyme activity determinations (NOX and caspase-3), and 30 for cytokine analysis.

Intrastriatal glutamate injection

C57BL/6 WT and NOX-2 KO mice were anesthetized with 3% isoflurane in a 95% O2/5% CO2 mixture and placed on a stereotaxic frame (David Kopf Instruments, Tujunga, CA). A stainless steel needle was positioned in the right striatum according to the following coordinates: anterior-posterior + 0.8 mm from bregma, lateral + 2.2 mm from midline, and vertical 3.2 mm from dura [35]. With the aid of an injection pump (model 55; Harvard, South Natick, MA), 0.5 μL of a solution of monosodium glutamate (1 M) or saline solution (0.9%) was injected (0.175 μL/min). A second (25 WT animals) and a third group (25 WT animals) of mice were treated with 0.7 ng/mL of interleukin-4 (cell signaling #5208) or 0.4 ng/mL of interleukin-10 (cell signaling #5261), respectively, in the same monosodium glutamate solution (Fig. 1). Five minutes after the injection, the needle was gently withdrawn, and the skin was sutured with nylon [48]. Mice recovered from anesthesia in a temperature-controlled chamber and were placed in individual cages with water and food ad libitum.

At different times after the surgery, animals received a lethal dose of sodium pentobarbital to subsequently extract the brain. For biochemical analyses, some animals were killed by cervical dislocation at different times (1, 6, 12, and 24 h) and striata were dissected and homogenized. To that, the olfactory bulb and cerebellum were removed from the brain and a sagittal section was made on the midline to separate the hemispheres and dissect the striate, which can be delimited as tissue slightly more transparent than the surrounding cortex [49]. The tissue obtained (15–20 mg) was homogenized in lysis buffer and protease inhibitors at 4 °C (OMNI TC homogenizer). The homogenate was centrifuged at 5000 g for 5 min to remove the cellular debris and subsequently the amount of protein was quantified [50].

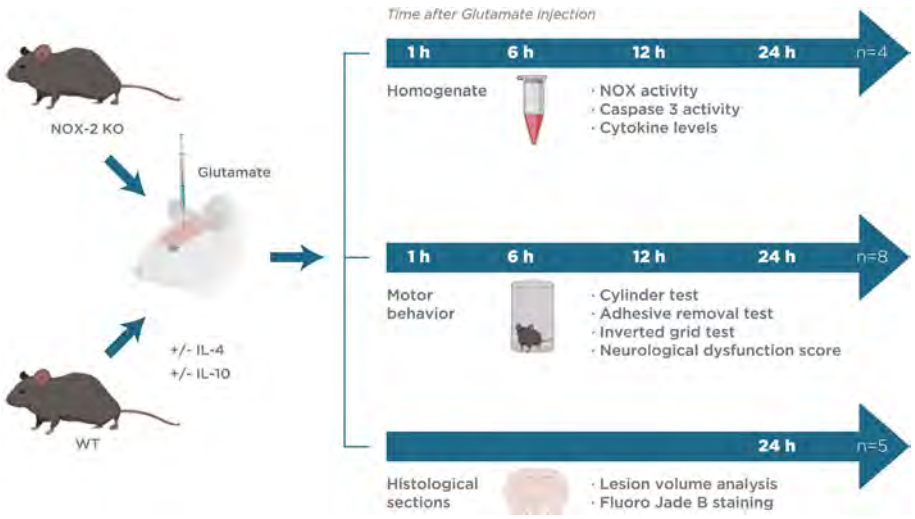

Fig. 1 Illustration of the timeline experimental design. Wild mice (WT, without treatment and treated with interleukins 4 or 10) and NOX-2 KO were administered with monosodium glutamate (1 M). Subsequently, they were sacrificed at 24 h to obtain histological sections ($n = 5$). Some animals were sacrificed at 1, 6, 12, and 24 h to obtain striatum homogenate ($n = 4$). Motor behavior tests were performed at 1, 6, 12, and 24 h in animals of both groups ($n = 8$)

Lesion volume analysis

Glutamate-induced lesions were evaluated 24 h after the surgery (Fig. 1). Mice were deeply anesthetized with sodium pentobarbital and were transcardially perfused with 30 mL of 0.9% saline solution followed by 35 mL of 4% paraformaldehyde solution in 0.1 mM phosphate buffer at pH 7.4. Brains were removed and placed in the same fixative solution at 4 °C. Consecutive series of striatal coronal sections (40 μm thick) for cresyl violet and Fluoro-Jade B (FJB; Chemicon, Temecula, CA) staining were obtained in a cryostat (1510s, Leica, Microsystems Nussloch GmbH, Heidelberger Nussloch, Germany). After staining with cresyl violet, all sections where a lesion was visible (pale cresyl violet stain) were selected for quantification of the lesion volume. The damaged areas were delineated manually and measured using an image analyzer (ImageJ 1.48v analyzer program; Wayne Rasband, NIH, USA) by an experimenter blinded to the treatments. Total lesion volume was obtained from the sum of all damaged areas multiplied by the width of the sections (40 μm).

Fluoro-Jade B staining

Briefly, one drop of 1% NaOH solution diluted in 80% ethanol was added to coronal sections mounted on slides, and after 2 min, it was replaced by a 70% ethanol solution. Slides were covered with 0.06% potassium permanganate for 10 min, and then brain sections were washed and incubated for 10 min with a 0.0004% Fluoro-Jade B (FJB) solution prepared in 0.1% acetic acid. Finally, the sections were washed, dried at 50 °C, dehydrated with xylol, and covered with Permount (Fisher Scientific, Fair Lawn, NJ). Slices were observed under an epi-fluorescence microscope (Eclipse Ti-S, Nikon instruments Inc.) using a U-MNB2 filter (395–590 nm). Total FJB-positive cells were counted as previously described using the ImageJ.1.48v analyzer program (Wayne Rasband, NIH, USA) in the entire striatum in three sections per mouse, namely, the section containing the needle tract (middle section) and the adjacent anterior and posterior sections located 160 μm away from the middle section [48].

NOX activity

NOX activity was determined in striatal homogenates at different times (0.5, 1, 3, 6, 12, and 24 h) after glutamate administration (Fig. 1). NOX activity was estimated as the oxidation of dihydroethidium (DHE) to ethidium (Et) [48]. Briefly, tissue homogenates were incubated with 0.02 mM DHE, 0.5 mg/mL salmon DNA, and 0.2 mM NADPH as substrate. Et fluorescence was measured during 30 min at an excitation wavelength of 480 nm and emission of 610 nm using a Synergy HT Multi-Detection fluorescence microplate reader (Biotek Instruments, Colchester, VT). Duplicate samples were prepared, and NOX activity was expressed as the change in Et fluorescence per milligram protein per minute versus control (saline). Some samples were incubated in the presence of 1 μM of the NOX inhibitor diphenyleneiodonium (DPI; Sigma) or 15 UI of superoxide dismutase (SOD, Sigma) to corroborate the specificity of the assay.

Immunoblot

Tissue homogenates (50 μg protein per lane) were subjected to SDS–PAGE. The resolved proteins were transferred to PVDF membranes at 120 V for 1 h. The membranes were blocked overnight with 5% nonfat dry milk in TBS and treated, overnight at 4 °C, with anti-NOX2/gp91phox (1:500; ab80508, Abcam, USA) and anti-GAPDH (1:3000; 14C10, Cell signaling, USA) antibodies. After further washing, the blots were incubated with alkaline phosphatase-conjugated secondary antibody (1:10000) for 1 h at room temperature. Bands were visualized by using the enhanced chemiluminescence system according to the manufacturer's recommendations (Bio-Rad Laboratories, Hercules, CA) and exposed to Kodak XAR-5 film.

Caspase-3 activity

Caspase-3 activity was determined in striatal homogenates at different times (1, 3, 6, 12, and 24 h) after glutamate administration (Fig. 1). Caspase-3 activity was assayed by a fluorogenic technique [51] in a luminescence spectrometer (Shimadzu, RF-5301PC), using the peptide Ac-VDVAD-AMC as a substrate to detect the proteolytic activity. Caspase activity was followed 30 min after addition of substrate (80 μM) and tissue homogenate (50 μg/mL) in a standard solution. Results depicting caspase activity were calculated as the change in fluorescence intensity per milligram protein per minute and expressed as fold change versus control (saline).

Cytokine levels

Cytokine levels were measured using the mouse ultrasensitive ELISA kit assay for IL-1β (ab100704), IL-4 (ab100710), IL-6 (Abcam, ab100712), IL-10 (ab46103), IL-12 p40/70 (100699), TNF-α (100747), and TGF-β (119557). The tissue samples, corresponding to 100 μg of striatal protein (diluted 1:10), were obtained after different times (1, 3, 6, 12, and 24 h) of glutamate administration (Fig. 1) and were used for cytokines measurement according to the manufacturer's protocol (Abcam, MA, USA). Assays were carried out in a colorimetric spectrometer (Shimadzu, RF-5301PC). The results were calculated based on a concentration curve provided by the manufacturer and were expressed as picograms of cytokine per milligrams of protein.

Cylinder test of forelimb asymmetry

Animals were examined for preferential use of the unilateral forelimb during upright postural support before and after glutamate administration (Fig. 1). Briefly, mice were placed in a pyro-glass cylinder (10 cm in diameter) on a tabletop and video-recorded for 3 min. The number of unilateral and bilateral wall contacts was recorded. The percentage of bilateral contacts was assessed on each test using the formula 100 × bilateral contacts/total forelimb wall contacts, whereas the percentage of unilateral contacts was assessed using the formula 100 × unilateral contacts/total forelimb wall contacts. The results are expressed as the percent of unilateral exploration [52].

Adhesive removal test

The animal cage was placed in the testing room at least 30 min before starting the experiment to allow habituation to the new environment. Animals were gently removed from the testing box and an adhesive tape strip (0.2-in. square) was placed on the snout (dorsal portion). Animals were returned to the testing cage and a timer was set. Conduct was observed and recorded for 60 s or until the piece of tape was removed with the forelimb. Training consisted of five trials (one per day), and testing after glutamate administration at different times (1, 3, 6, 12, and 24 h) was carried out (Fig. 1). Result indicated the latency to adhesive tape removal in seconds [53].

Inverted grid test

The inverted grid test was used to assess coordination and limbs muscular strength, especially related to distal musculature and digit manipulations. Mice were placed in the center of a horizontal square (15 cm^2) grid consisting of a wire mesh (0.5 cm^2) surrounded by wooden walls. The grid was placed 20 cm above a tabletop and was rotated upside down allowing mice to move freely. Each mouse was recorded for 60 s. The time the mice remained and moved upside down was recorded. If a mouse fell from the mesh grid within 10 s, additional trials were allowed (max three trials) within an interval of 1 min, in this case, latencies before falling were measured. The means ± standard error of the mean (SEM) of three trials were calculated. No pretraining was performed, but a pretest of 30 s before the day of the experiment was carried out for habituation [53].

Neurological dysfunction score

All behavioral tests were conducted by the same experimenter in a quiet and low-lit room with white noise background. Pretests were conducted to exclude abnormally behaving animals. A combination score from a battery of three behavioral tests (adhesive test, inverted grip test, and cylinder test) was used to measure the neurological functional deficits (ND). We determined the grand NDs score (NDS) by combining all the tests, assuming an equal weight of each of the tests and assigning a value of 15 points to the maximum performance [53, 54].

Statistical analysis

Data were analyzed as means ± SEM. The data were evaluated statistically by the two-way analysis of variance (ANOVA) for biochemical and histological tests and repeated measures ANOVA for behavioral tests, followed by Tukey's test for pairwise comparisons by using GraphPad Prism v6.0 and SigmaPlot 12.3 software. In the case of significance, a further ad hoc two-tailed Student's t test was applied. Significance was considered when $p < 0.05$.

Results

Striatal excitotoxic lesion and neuronal degeneration are minor in NOX-2 KO mice

To determine the impact of excitotoxic damage, both lesion volume and neuronal degeneration were evaluated in WT and NOX-2 KO mice as detailed in the "Methods" section. Representative tissue sections from WT and NOX-2 KO animals stained with cresyl violet are shown in Fig. 2a. WT and NOX2 KO mice treatment with saline, as a control of the procedure, developed a small lesion similar in both groups (0.05 ± 0.02 mm^3 and 0.03 ± 0.01 mm^3, respectively). As it was expected, in the groups treated with glutamate, NOX-2 KO mice showed only 38% of the lesion observed in WT mice (WT, 1.2 ± 0.14 mm^3 vs NOX-2 KO, 0.45 ± 0.10 mm^3 $p < 0.05$; Fig. 2b).

The FJB-positive cells were counted in tissue sections 24 h after glutamate injection (Fig. 2c). Again, a higher number of degenerated cells were found in WT mice injected with glutamate (82.3 ± 11.1 cells/mm^2) than in saline-injected animals (3.06 ± 0.6 cells/mm^2; $p < 0.05$). In accordance to the tissue lesion measurements, the number of FJB-positive cells in NOX-2 KO mice (35.9 ± 7.5 cells/mm^2; $p < 0.05$) were about half of that observed in WT mice treated with glutamate. Representative tissue sections from WT and NOX-2 KO animals showing FJB-labeled cells are shown in Fig. 2a. Together, these results confirm that NOX-2 participates in the tissue injury and neuronal degeneration induced by glutamate.

NOX-2 activity increases during excitotoxic damage

In the present study, we measured NOX activity in striatal homogenates of WT and NOX-2 KO mice at different times after glutamate injection (0.5, 1, 3, 6, 12, and 24 h). An increase in the enzyme activity over saline (control) levels was detected at 1 h after glutamate administration in WT mice (225 ± 27% vs control, $p < 0.05$;

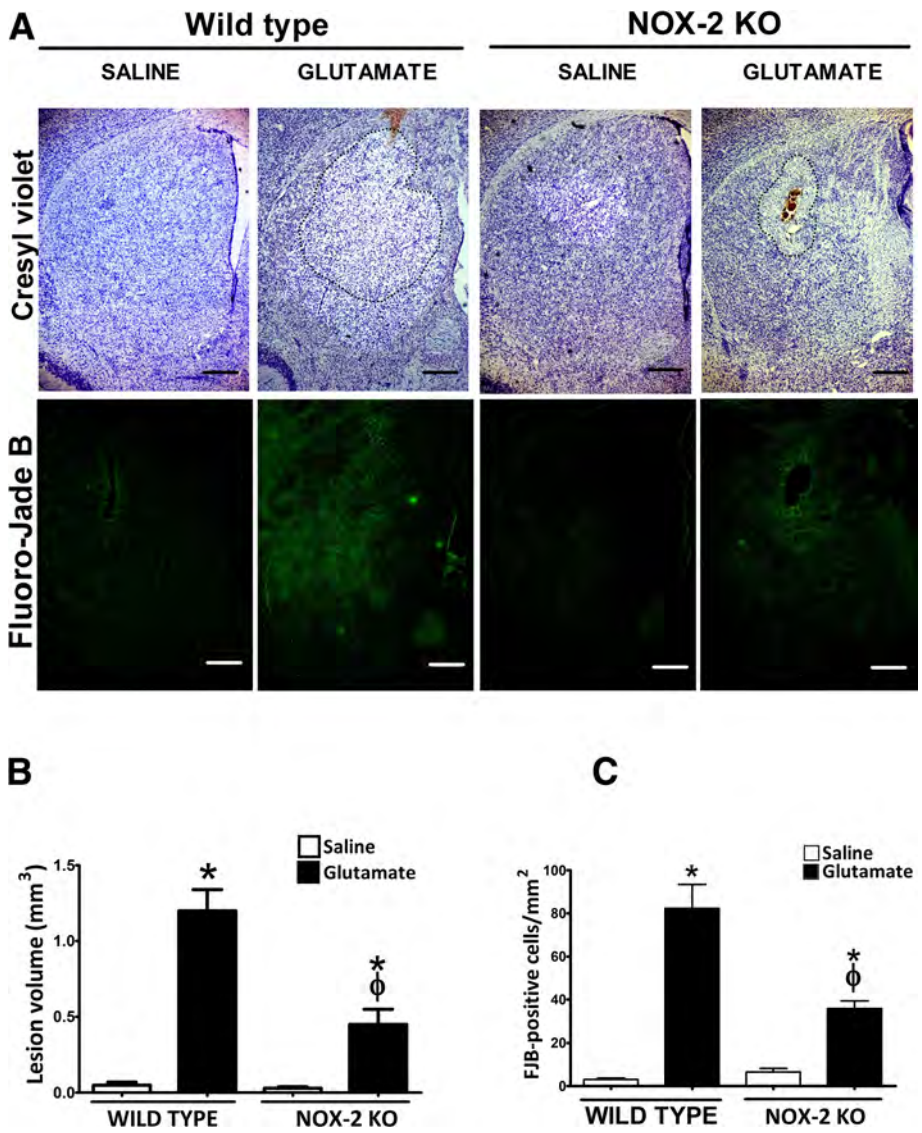

Fig. 2 Lesion area and neuronal degeneration in wild-type and NOX-2 KO mice injected with glutamate in the striatum. Histological sections were obtained after 24 h of intracerebral administration of saline (NaCl 0.9%) or glutamate (1 M) as detailed in the "Methods" section. **a** Representative micrographs of coronal striatal sections showing striatal lesions stained with cresyl violet and damaged cells positive to Fluoro-Jade B. The dotted line delimits the area of lesion of mice treated with glutamate. The scale bars represent 200 μm. **b** Quantification of the lesion volume 24 h after saline or glutamate injection is expressed in cubic millimeters. **c** Total number of FJB-positive cells counted in three slices per mice. Data are expressed as means ± SEM of five independent experiments. *$p < 0.05$ vs the corresponding saline control; $^{\varphi}p < 0.05$ vs wild-type mouse (WT) treated with glutamate

Fig. 3). Although the NOX activity remained increased during 24 h, we observed two peaks of activation, the first 1 h after glutamate injection (130 ± 15% vs control) and the second after 12 h (195 ± 10% vs control). The increase of NOX activity in NOX-2 KO mice after glutamate administration was more discrete and about half of that in WT mice at 12 and 24 h ($p < 0.05$). These results indicate that the administration of glutamate leads to an early and a late activation of NOX during the excitotoxic damage and that this activation is attenuated in NOX-2 KO animals.

We found that NOX2 protein was upregulated by glutamate treatment in a time-dependent manner. The protein levels increased from 6 h and continued increasing after 12 and 24 h (Additional file 1: Figure S1). The observed changes in protein levels did not correlate with the observed changes in NOX activity. For example, at 1 h no change in the protein was observed, while a large increase in NOX activity occurred (Fig. 3 and Additional file 1: Figure S1). This suggests that the observed changes in NOX activity are regulated by other conditions than protein enrichment.

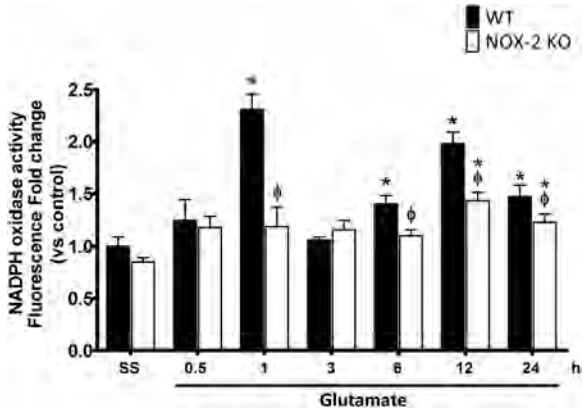

Fig. 3 NOX-2 activity during excitotoxic damage in wild-type and NOX-2 KO mice. NOX activity was evaluated as the change of fluorescence intensity resulting from dihydroethidium (DHE) oxidation to ethidium (Et) in striatum homogenates of WT and NOX-2 KO mice treated with glutamate (1 M) 0.5, 1, 3, 6, 12, and 24 h after glutamate administration. Data are expressed as fold change of Et fluorescence relative to WT saline. Values are means ± SEM of four independent experiments. *$p < 0.05$ vs the corresponding saline control; $^{\varphi}p < 0.05$ vs the corresponding wild-type mouse (WT) treated with glutamate

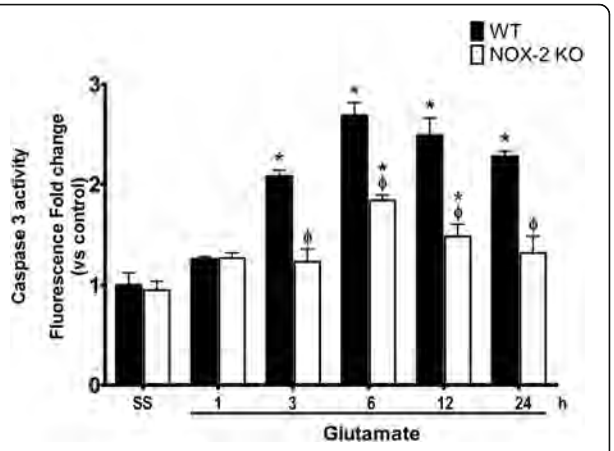

Fig. 4 Caspase-3 activity in wild-type mice and NOX-2 KO after administration of glutamate. Active caspase-3 was measured in striatum homogenates after 1, 3, 6, 12, and 24 h of glutamate (1 M) administration in WT and NOX-2 KO mice. Fluorescence produced by the cleavage of the specific substrate for caspase-3 was quantified in relative units of fluorescence (FRU) and the results are expressed as the fluorescence fold change relative to WT saline. Values are mean ± SEM of three independent experiments. *$p < 0.05$ vs the corresponding saline control; $^{\varphi}p < 0.05$ vs corresponding wild-type mouse (WT) treated with glutamate

NOX-2 KO mice resistance to excitotoxic damage involves a decrease in caspase-3 activation

Intrastriatal injection of glutamate causes an increase of caspase-3 activation at 3 h after glutamate administration in WT (208 ± 9% vs control) and after 6 h in NOX-2 KO mice (197 ± 16% vs control). We found that after 6 h, caspase-3 activation was lower in NOX-2 KO ($p < 0.05$) as compared to WT mice (NOX-2 KO 180 ± 10% vs WT 280 ± 25%, $p < 0.05$), and the same effect is observed during the following 24 h (NOX-2 KO 57 ± 15% vs WT 128 ± 9%, $p < 0.05$; Fig. 4). Thus, NOX-2 KO mice exhibit a lower activation of caspase-3 during excitotoxic injury induced by the administration of glutamate.

NOX-2 KO mice exhibit better motor recovery than wild-type mice after excitotoxic damage

Striatum lesions lead to alterations in the control of voluntary movements and muscle tone, predominantly in the forelimbs [53]. We therefore explored the degree of functional compromise resulting from the excitotoxic damage as an index of striatal injury. To assign a neurological deficit score (NDS), we evaluated three tests in WT and NOX-2 KO mice to obtain a motor score (Fig. 5).

The cylinder test indicates the latency of forelimb asymmetry (Fig. 5a). Prior to glutamate administration, WT and NOX-2 KO mice tended to preferentially make bilateral wall contacts in the cylinder before glutamate administration (WT 10 ± 3% and NOX-2 KO 8 ± 2% of unilateral contacts). Excitotoxic damage in WT mice resulted in an early and sustained decrease in bilateral contacts from 1 h (90 ± 5% unilateral contacts) to 24 h (50 ± 4% unilateral contacts). NOX-2 KO mice show a similar compromised motor function that WT mice at 1 h (78 ± 6% unilateral contacts; $p < 0.05$), but despite the fact that they exhibited a severe decline at short time, they managed to recover at 24 h (18 ± 8% unilateral contacts), unlike the WT, which do not reach control levels ($p > 0.05$; Fig. 5a).

The adhesive removal test evaluates the control of voluntary movements (Fig. 5b). Prior to administration of glutamate, both WT and NOX-2 KO mice took a maximum of 14 s to remove the adhesive (WT 12 ± 2 s and NOX-2 KO 10 ± 2 s). After 1 h of glutamate administration, WT mice were unable to remove the label before 60 s. After 24 h, WT mice showed an improvement in the ability to remove the label; however, the time to removal was markedly higher than that shown by the saline controls (WT + GLU 37 ± 5 s vs WT + SS 11 ± 3 s, $p < 0.05$). NOX-2 KO mice had a similar performance to that shown by the WT mice after 1 h (WT 55 ± 5 s vs NOX-2 KO 50 ± 7 s, $p > 0.05$). However, at 6 h, the NOX-2 KO mice showed a marked recovery as compared to WT mice (WT 44 ± 5 s vs NOX-2 KO 22 ± 4 s; $p < 0.05$). It reaches control levels after 12 h, a situation that did not occur in WT mice (WT 37 ± 5 s vs NOX-2 KO 12 ± 3 s, $p < 0.05$; Fig. 5b).

Finally, the inverted grid test indirectly allows evaluation of the muscle tone of the mice extremities (Fig. 5c).

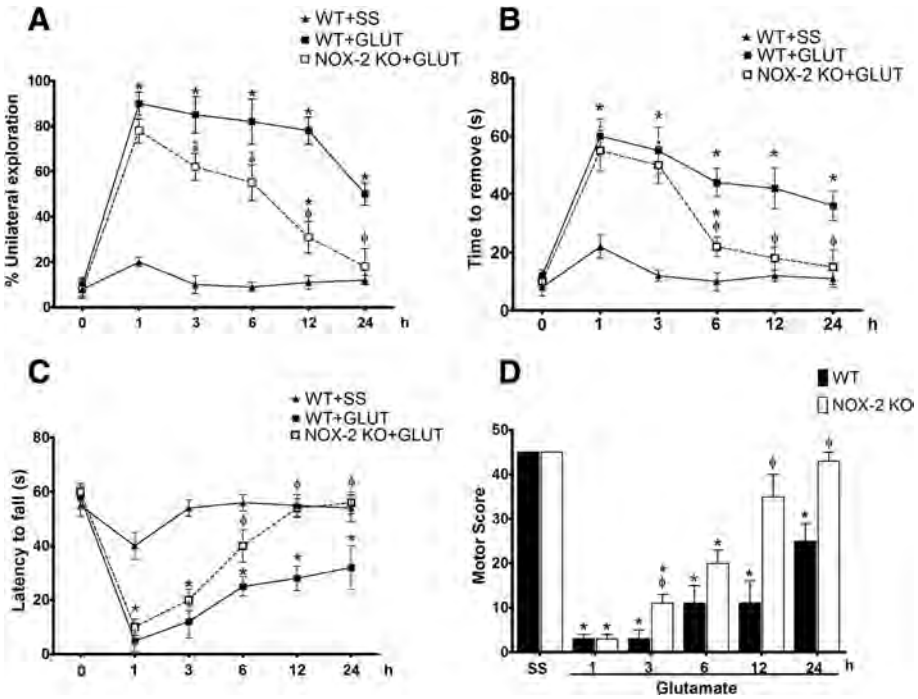

Fig. 5 Motor activity recovery after glutamate administration in NOX-2 KO mice. Performance of wild-type (WT + SS) animals and WT or NOX-2 KO mice injected with glutamate (WT + GLUT; NOX-2 KO + GLUT) was evaluated in three tests of motor behavior at 1, 3, 6, 12, and 24 h after glutamate intracerebral injection. These tests were later integrated to obtain a motor score that reflects functional deterioration. **a** Cylinder test in which each mouse obtained a percentage based on the ratio of unilateral and bilateral explorations performed in three trials, of 3 min each; the percentage was expressed as mean ± SEM of eight independent tests. **b** Adhesive removal test that quantifies the time in which the animals remove a label previously placed by the examiner. The time of removal was quantified in seconds and was expressed as means ± SEM of six independent animals. **c** The tone and muscle strength of the four limbs was evaluated by exposing the mice to the inverted grid test in which the decay time was quantified for three non-consecutive opportunities of a maximum of 60 s of duration. The results are expressed as means ± SEM of the latency to fall of six independent tests. **d** To integrate the three previous tests, an arbitrary score was assigned to the performance of each animal, giving the highest score to the performance of the mice injected with saline (45 points). The results are expressed in arbitrary units of motor score as the mean ± SEM of the latency to fall of six independent tests. *$p < 0.05$ vs the corresponding saline control; $^{\Phi}p < 0.05$ vs the corresponding wild-type (WT) mouse treated with glutamate

Control mice remained attached to the inverted grid for about a minute (56 ± 4 s), which is considered an adequate performance and is established as the baseline. After 1 hour of glutamate administration, both the WT and NOX-2 KO mice were unable to remain attached for long time to the grid (WT 5 ± 4 s and NOX-2 KO 10 ± 3 s). In comparison to WT mice, the NOX-2 KO mice showed a better functional recovery from 6 h after the event (WT 25 ± 4 vs NOX-2 KO 40 ± 6 s $p < 0.05$) reaching a performance similar to control animals from 12 h, which is not observed in WT mice (WT 32 ± 8 vs NOX-2 KO 54 ± 4 s $p > 0.05$; Fig. 5c).

Motor function parameters were integrated into a NDS (Fig. 5d). To that, each test was given an equivalent weight in the score, assigning an arbitrary value of 15 points (for each test) to the control animals treated with saline solution. Therefore, a poor performance during the test corresponded to a decrease in the points awarded [55]. The WT mice treated with glutamate showed a poor score in the first 3 h (3 ± 1 points), which improved at 12 h (11 ± 5 points) and 24 h (25 ± 4 points). NOX-2 KO mice treated with glutamate obtained a poor score in the first hour (3 ± 1 points), reaching a marked improvement at 24 h with a performance similar to the control animals (43 ± 2 points, $p > 0.05$; Fig. 5d). As we observed in the previous tests, the functional recovery of the NOX-2 KO mice surpasses that observed in WT mice after 12 h of glutamate administration (WT 11 ± 5 vs NOX-2 KO 35 ± 4 s $p < 0.05$). Based on these findings, we suggest that NOX-2 activity is associated with a worst functional motor recovery after glutamate administration.

The pattern of cytokine production in response to excitotoxic damage depends on NOX-2

The resolution of the excitotoxic damage depends on the inflammatory response, which aims to remove damaged tissue and recover functions [56]. We characterized the inflammatory response to excitotoxic damage and evaluated the involvement of NOX-2 in the production

of cytokines associated with the inflammatory response in the CNS (Fig. 6a).

Regarding the inflammatory cytokines, we observed an increase of IL-1β in the WT (701 ± 30 pg/mg^{-1} protein) after 6 h of glutamate administration, when compared with the saline control (298 ± 41 pg/mg^{-1} protein). In a similar manner, the NOX-2 KO mice depicted and increased value for this interleukin (682 ± 24 pg/mg^{-1} protein). At 12 h, the IL-1β levels were markedly reduced in both conditions, but still above the control (WT + GLU 400.7 ± 22 vs. NOX-2 KO + GLU 420 ± 15 pg/mg^{-1} protein, $p < 0.05$), returning to control levels at 24 h (WT + GLU, 380 ± 58 and NOX-2 KO + GLU, 401 ± 63 pg/mg protein; Fig. 6a). No differences were found between WT mice and NOX-2 KO in the production of IL-1β.

Excitotoxic damage also caused a similar increase of the inflammatory cytokine IL-6 in both groups at 6 h and 12 h (WT + GLU, 650 ± 85 and NOX-2 KO + GLU, 553 ± 91 pg/mg^{-1} protein). Unexpectedly, after 24 h of glutamate administration, NOX-2 KO maintained high levels of IL-6 compared to WT mice (WT 381 ± 41 vs NOX-2 KO 581 ± 43 pg /mg^{-1} protein, $p < 0.05$; Fig. 6c).

IL-12 levels increased at the first hour after glutamate treatment in both WT (423 ± 52 pg /mg^{-1} protein) and NOX-2 KO (475 ± 74 pg /mg^{-1} protein) mice as compared to the saline control (WT 282 ± 28) and saline NOX-2 KO (321 ± 31 pg /mg^{-1} protein, $p < 0.05$), respectively. After 6 h, WT mice treated with glutamate showed a maximum increase, which was significantly higher than that observed in NOX-2 KO mice (WT 673 ± 39 vs NOX-2 KO 385 ± 35 pg /mg^{-1} protein, $p < 0.05$).

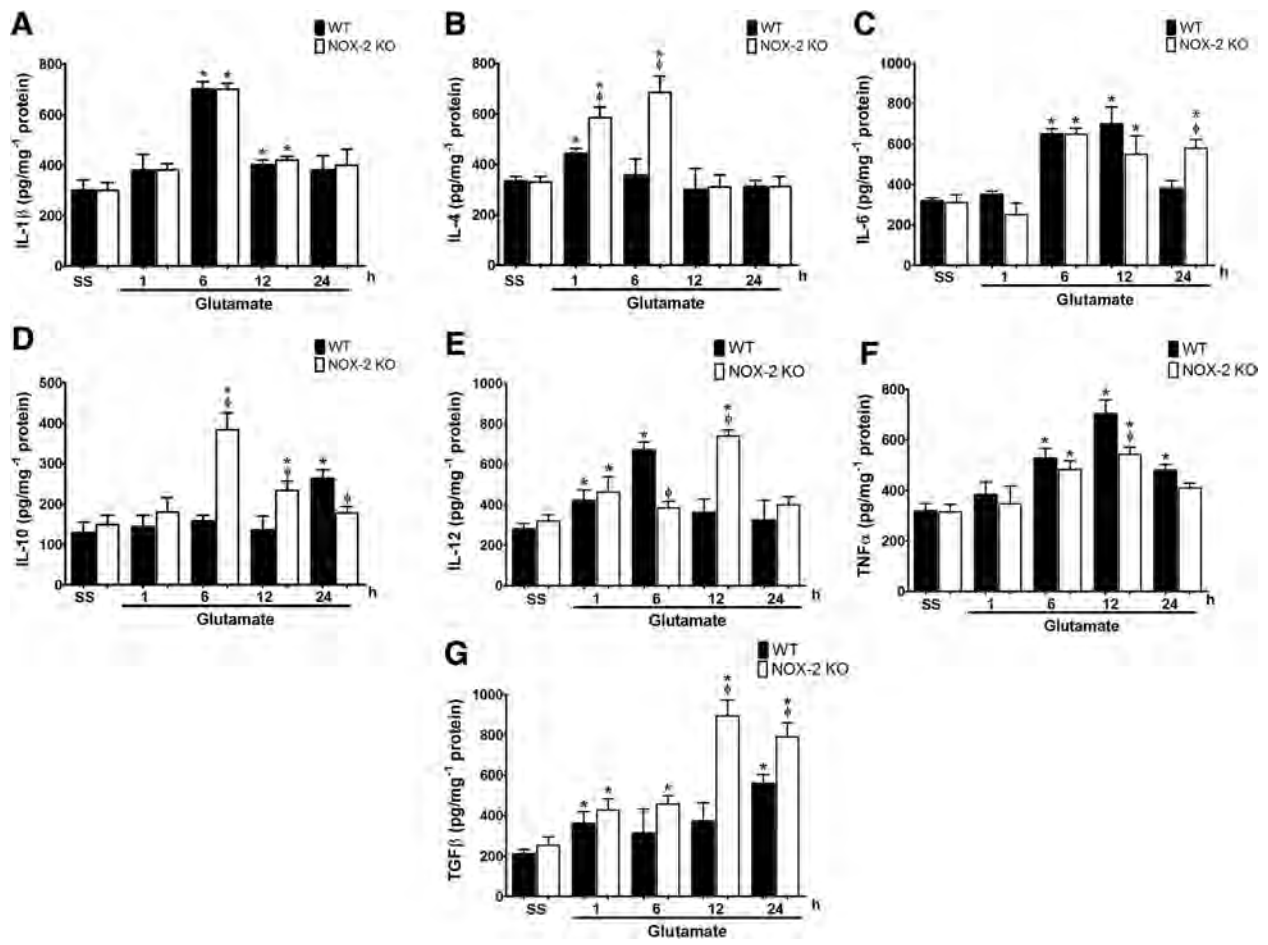

Fig. 6 Pattern of cytokine production in wild-type and NOX-2 KO mice after the striatal injection of glutamate. Characterization of the inflammatory response was carried out by determination of cytokines concentration in striatum homogenates of wild-type (WT) and NOX-2 KO mice determined by enzyme-linked immunosorbent assays (ELISA) at 1, 6, 12, and 24 h after administration of saline (SS) or glutamate (1 M) as detailed in the "Methods" section. **a** Interleukin-1β (IL-1β), **b** interleukin-4 (IL-4), **c** interleukin-6 (IL-6), **d** interleukin-10 (IL-10), **e** interleukin-12 (IL-12), **f** tumor necrosis factor α (TNF-α), and **g** transforming growth factor β (TGF-β). Data are expressed as picograms per milligram of protein and are means ± SEM of three independent experiments. *$p < 0.05$ vs the corresponding saline control; $^{\Phi}p < 0.05$ vs the corresponding WT mouse treated with glutamate

At 12 h, this pattern was inverse since IL-12 levels were much higher in NOX-2 KO than in WT mice (WT 363 ± 67 vs NOX-2 KO 743 ± 29 pg /mg^{-1} protein, $p < 0.05$; Fig. 6e).

We observed an increase of TNF-α induced by glutamate in both WT (528 ± 39 pg /mg^{-1} protein) and NOX-2 KO mice at 6 h (483 ± 35 pg /mg^{-1} protein) and 12 h (WT 704 ± 54; NOX-2 KO 542 ± 29 pg /mg^{-1} protein). The production of TNF-α in NOX-2 KO mice was always lower than in WT, particularly at 6 and 12 h. After 24 h, the observed increase was reduced in both WT (482 ± 22 pg/mg protein) and NOX-2 KO mice (410 ± 20 pg/mg^{-1} protein, $p > 0.05$; Fig. 6f).

Regarding the production of anti-inflammatory cytokines, we measured the concentration of some of the anti-inflammatory cytokines previously reported in the CNS, such as IL-4, IL-10, and TGF-β [21, 22]. One hour after glutamate administration, NOX-2 KO mice showed an almost twofold increase in the production of IL-4 as compared to control (saline) (NOX-2 KO 586 ± 42 vs NOX-2 KO + SS 330 ± 32 pg/mg^{-1} protein; $p < 0.05$), while in WT mice, glutamate induced an increase of 125% with respect to the saline control (WT + GLU 443 ± 20 vs WT + SS 335 ± 18 pg/mg^{-1} protein; $p < 0.05$). The observed difference between WT and NOX-2 KO was markedly increased at 6 h (WT 357 ± 54 vs NOX-2 KO 685 ± 65 pg/mg protein, $p < 0.05$; Fig. 6b). At 12 and 24, no difference was observed between groups and values returned to control values.

The administration of glutamate to NOX-2 KO mice caused an increase of IL-10 more than double respect to WT mice at 6 h (WT 158 ± 14 vs NOX-2 KO 384 ± 42 pg/mg^{-1} protein, $p < 0.05$) and this increase was maintained only in NOX-2 KO group until 12 h (WT 136 ± 34 vs NOX-2 KO 234 ± 24 pg/mg^{-1} protein, $p < 0.05$). However, at 24 h, we observe an increase of IL-10 in WT, while values in NOX-2 KO continued decreasing (WT 263 ± 21 vs NOX-2 KO 178 ± 18 pg/mg^{-1} protein, $p < 0.05$; Fig. 6d).

Regarding the production of TGF-β (Fig. 6g), a negative regulatory cytokine, we observed a similar increase both in WT as NOX-2 KO mice treated with glutamate at 1 h (WT 360 ± 59 vs NOX-2 KO 427 ± 56 pg/mg^{-1} protein, $p < 0.05$). This increase was maintained only in the NOX-2 KO group, until 24 h, reaching a maximum concentration at 12 h (WT 372 ± 91 vs NOX-2 KO 893 ± 79 pg/mg^{-1} protein, $p < 0.05$). At this time, it reaches more than double than that found in WT mice. In contrast, WT mice showed only a second increase at 24 h, which was lower than that observed in NOX-2 KO (WT 557 ± 45 vs NOX-2 KO 789 ± 69 pg/mg^{-1} protein, $p < 0.05$). These results suggest that the change in the cytokines profile in NOX-2 KO mice is characterized by an increase in the production of anti-inflammatory cytokines and that this increase occurs preferentially at early times during the excitotoxic event.

Administration of IL-4 partially prevents the excitotoxic lesion

One of the most evident differences in the response of the NOX-2 KO mice to the excitotoxic damage was the increase in the production of anti-inflammatory cytokines; therefore, we treated animals with exogenous IL-4 or IL-10 simultaneously to glutamate administration and evaluated neuronal degeneration and lesion volume. Representative tissue sections from WT and NOX-2 KO animals stained with cresyl violet and Fluoro-Jade B are shown in Fig. 7a. In the case of WT mice treated with IL-4, we observed a significant decrease in the lesion volume (WT 1.2 ± 0.14 vs WT + IL-4 0.72 ± 0.05 $p < 0.05$; Fig. 7b), as well as a decrease in degenerating cells (WT 82.3 ± 11.1 vs WT + IL-4 35.4 ± 4.7 cells/mm^2 $p < 0.05$) as compared to mice administered only with glutamate (Fig. 7c).

NOX activity and caspase-3 activation are regulated by IL-4 in the excitotoxic process

Since the NOX-2 KO mice showed an increased production of IL-4, we explored the possibility of reciprocal regulation through the determination of NOX activity in WT mice treated with IL-4 (Fig. 8). Under these conditions, WT mice treated with IL-4 showed a 50% reduction in NOX activity induced by glutamate only at 12 h (GLU 85 ± 12% and GLU + IL-4 vs 44 ± 12% above control $p < 0.05$; Fig. 8). Concordantly, mice treated with IL-4 also showed a significant reduction in the activation of caspase-3 after 12 h (GLU 249 ± 10% vs GLU + IL-4 187 ± 9% compared with controls, $p < 0.05$) that was maintained at 24 h (GLU 229 ± 9% vs GLU + IL-4 172 ± 10% compared with the control $p < 0.05$; Fig. 9).

The administration of IL-10 reduces the lesion induced by excitotoxic damage

After glutamate administration, we found that the lesion volume was also markedly reduced in mice treated with IL-10. Representative tissue sections from WT and NOX-2 KO animals stained with cresyl violet and Fluoro-Jade B are shown in Fig. 10a. Animals treated with IL-10 showed a decrease of more than 60% in the lesion volume as compared to the untreated mice (GLU 1.2 ± 1.14 vs GLU + L-10 0.45 ± 0.05 mm^3 $p < 0.05$; Fig. 10b). As for the degenerating cells, the administration of IL-10 also decreased the number of positive cells to Fluoro-Jade B by 60% (GLU 83.4 ± 11.3 vs GLU + IL-10 32.3 ± 4.6 mm^3 $p < 0.05$; Fig. 10c).

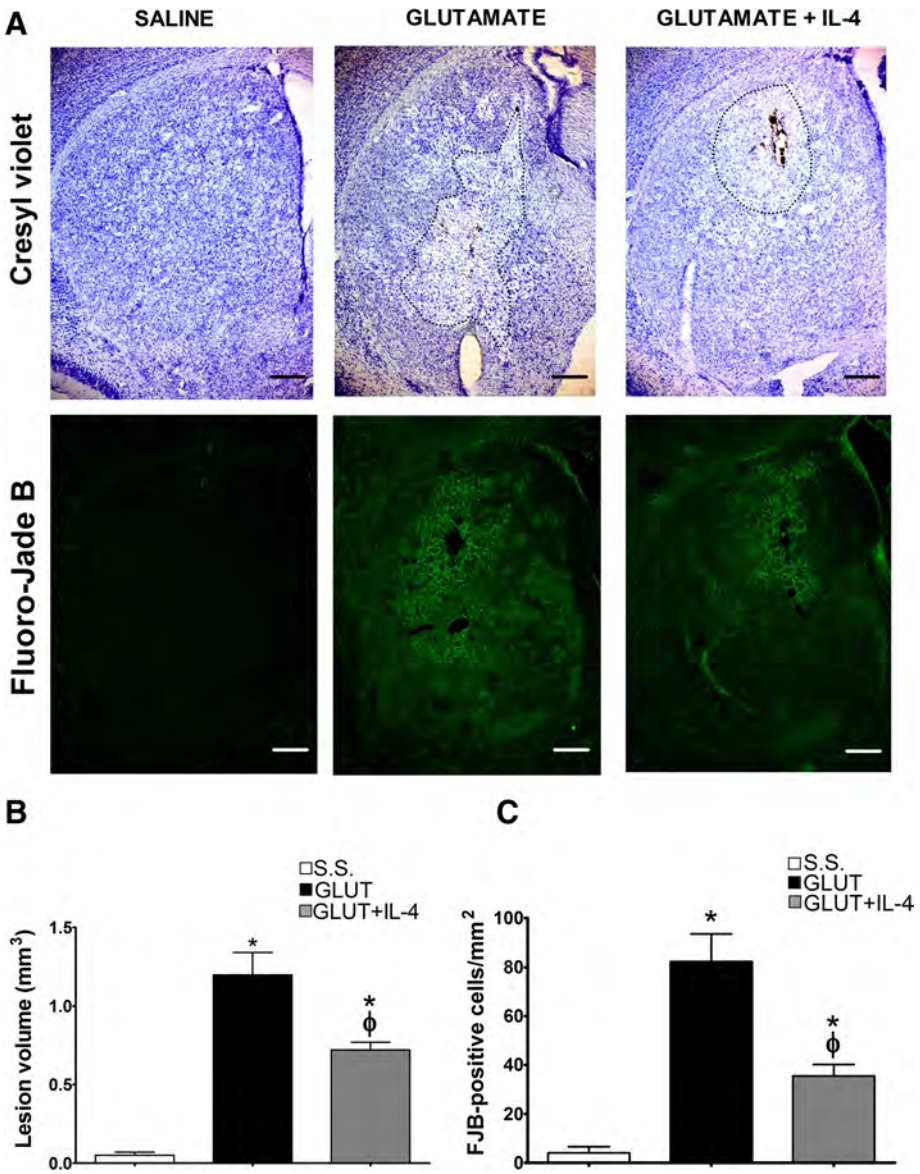

Fig. 7 Effect IL-4 on the striatal lesion and neuronal degeneration in wild-type mice treated with glutamate. Histological sections of wild-type (WT) mice were obtained after 24 h of intracerebral administration of NaCl 0.9% (S.S.), only glutamate (GLUT) or glutamate + 0.7 ng/mL of IL-4 (GLUT + IL4) as detailed in the "Methods" section. **a** Representative micrographs of coronal striatal sections showing lesions stained with cresyl violet and damaged cells positive to Fluoro-Jade B. The dotted line delimits the area of lesion of mice treated with glutamate. The scale bars represent 200 μm. **b** Quantification of the lesion volume 24 h after saline or glutamate injection is expressed in cubic millimeters. **c** Total number of FJB-positive cells were counted in three slices per mice. Data are expressed as mean ± SEM of six independent experiments. *$p < 0.05$ vs saline control (S.S.); $^{\varphi}p < 0.05$ vs the corresponding mouse treated only with glutamate (GLUT)

The NOX activity and caspase-3 activation are regulated negatively by IL-10

When WT animals were simultaneously treated with glutamate and IL-10, NOX activity was markedly reduced at 1 h (GLU 231 ± 25% vs GLU + IL-10 108 ± 7% of the control, $p < 0.05$); 6 h (GLU 141 ± 5% vs GLU + IL-10 115 ± 4% compared with controls, $p < 0.05$); and 12 h (GLU 195 ± 12% vs GLU + IL-10 132 ± 7% of the control, $p < 0.05$), as compared to mice injected only with glutamate. Nevertheless, 24 h after the excitotoxic insult, both groups showed similar levels of catalytic activity (GLU 147 ± 4% vs GLU + IL-10 134 ± 5% $p > 0.05$; Fig. 11).

Under these conditions, IL-10 also decreased the activity of caspase-3. As we showed previously, the administration of glutamate promotes the increase of active caspase-3 from 3 to up 24 h after the injection. The co-administration of IL-10 reduced caspase-3 activation

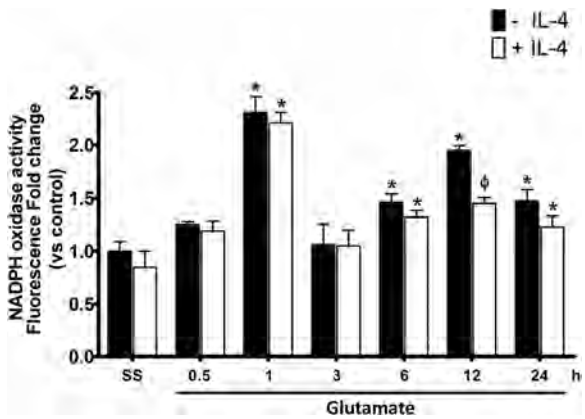

Fig. 8 NOX activity in wild type mice treated with IL-4 after glutamate administration. NOX activity was evaluated in WT mice treated with NaCl 0.9% (S.S.), only glutamate (– IL-4) or glutamate + 0.7 ng/mL of interleukin-4 (+IL4); the determination of NOX activity was measured by the fluorescence resulting from the dihydroethidium (DHE) oxidation in striatal homogenates of mice from 0.5 to 24 h (0.5, 1, 3, 6, 12, and 24 h) after glutamate administration. Data are expressed as fold change of fluorescence relative to saline without IL-4. Values are means ± SEM of three independent experiments. *$p < 0.05$ vs the corresponding saline control; $^{\Phi}p < 0.05$ vs the corresponding time of mice treated with glutamate alone

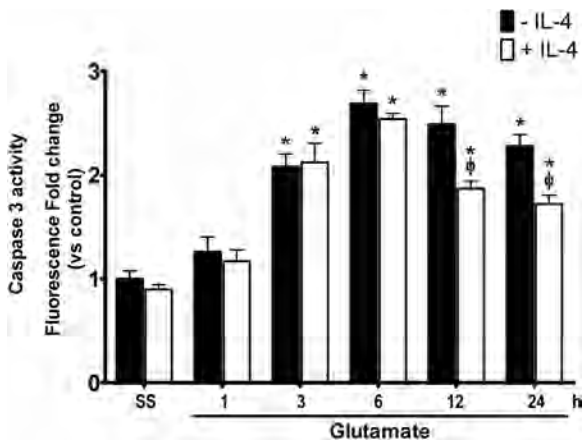

Fig. 9 Caspase-3 activity in wild-type mice treated with IL-4 after glutamate administration. Active caspase-3 was measured in striatal homogenates of wild-type (WT) mice treated with NaCl 0.9% (S.S.), only glutamate (– IL-4) or glutamate + 0.7 ng/mL of interleukin-4 (+IL4) after 1, 3, 6, 12, and 24 h. Fluorescence produced by the cleavage of the specific substrate for caspase-3 was quantified as relative units of fluorescence (FRU). Data are expressed as fold change of fluorescence relative to saline without IL-4. Values are means ± SEM of three independent experiments. *$p < 0.05$ vs the corresponding saline control; $^{\Phi}p < 0.05$ vs the corresponding time of mice treated with glutamate alone

by 90% at 3 h (GLU 201 ± 18% vs GLU + IL-10 112 ± 4% above control, $p < 0.05$) and 24 h (GLU 228 ± 27% vs GLU + IL-10 118 ± 6% above control, $p < 0.05$) after the injection. At 6 h and 12 h, it decreased approximately 50% (GLU 270 ± 30% vs GLU + IL-10 194 ± 15% of the controls, $p < 0.05$; GLU 249 ± 10% vs GLU + IL-10 177 ± 6% compared with controls, $p < 0.05$; Fig. 12).

IL-10 administration improves motor recovery in mice after excitotoxic damage

Mice treated with IL-10 had a better performance in tests of motor behavior after glutamate administration (Fig. 13). In the cylinder test, although mice treated with IL-10 showed a performance similar to those that did not receive treatment, at 1 h (GLU 10 ± 3% vs GLU + IL-10 8 ± 2 unilateral contacts $p < 0.05$) they were able to recover the control level at 6 h (GLU 82 ± 5% vs GLU + IL-10 20 ± 4% unilateral contacts, $p < 0.05$), while this did not happen in the untreated mice (Fig. 13a). In the adhesive test, mice treated with IL-10 were also able to recover baseline performance at 3 h (GLU 55 ± 8 s and GLU + IL-10 20 ± 6.5 s, $p < 0.05$), while those not treated did not reach these recovery levels in 24 h (GLU 36 ± 5 s vs GLU + IL-10 15 ± 5 s, $p < 0.05$; Fig. 13b). In the inverted grid test, mice treated with IL-10 had a better performance than the untreated mice from the first hour after glutamate treatment (GLU 5 ± 4 s vs GLU + IL-10 26 ± 3 s $p < 0.05$). In contrast to the animals treated with glutamate alone, these animals recovered to values similar to the control group after 12 h (SS 58 ± 2 s vs GLU + IL-10 50 ± 4 s, $p > 0.05$) and 24 h (Fig. 13c).

The improvements by IL-10 treatment observed in the individual tests were reflected in the NDS (Fig. 13d). We observed a significant high score in mice treated with IL-10 at 3 h (GLU 3 ± 2 points and GLU + IL-10 22 ± 4 points $p < 0.05$), which progressively improved and reached values similar to those observed in control group at 24 h (GLU 11 ± 5 points and GLU + IL-10 40 ± 3 points $p < 0.05$; Fig. 13d). Mice injected only with glutamate also showed a progressive increase in the motor score, but it was significantly lower of the control values at all times.

Discussion

In ischemia and brain trauma, neurons lose the ability to control ion homeostasis minutes after the primary injury, resulting in the accumulation of intracellular calcium, cell depolarization, release of glutamate, impaired mitochondrial function, energy failure, and elevated reactive oxygen species production [57–59]. This occurs during the first few minutes-hours after the event and will determine the course of brain damage, including neuroinflammation. For example, the use of NMDA receptor blockers in experimental models of ischemia and

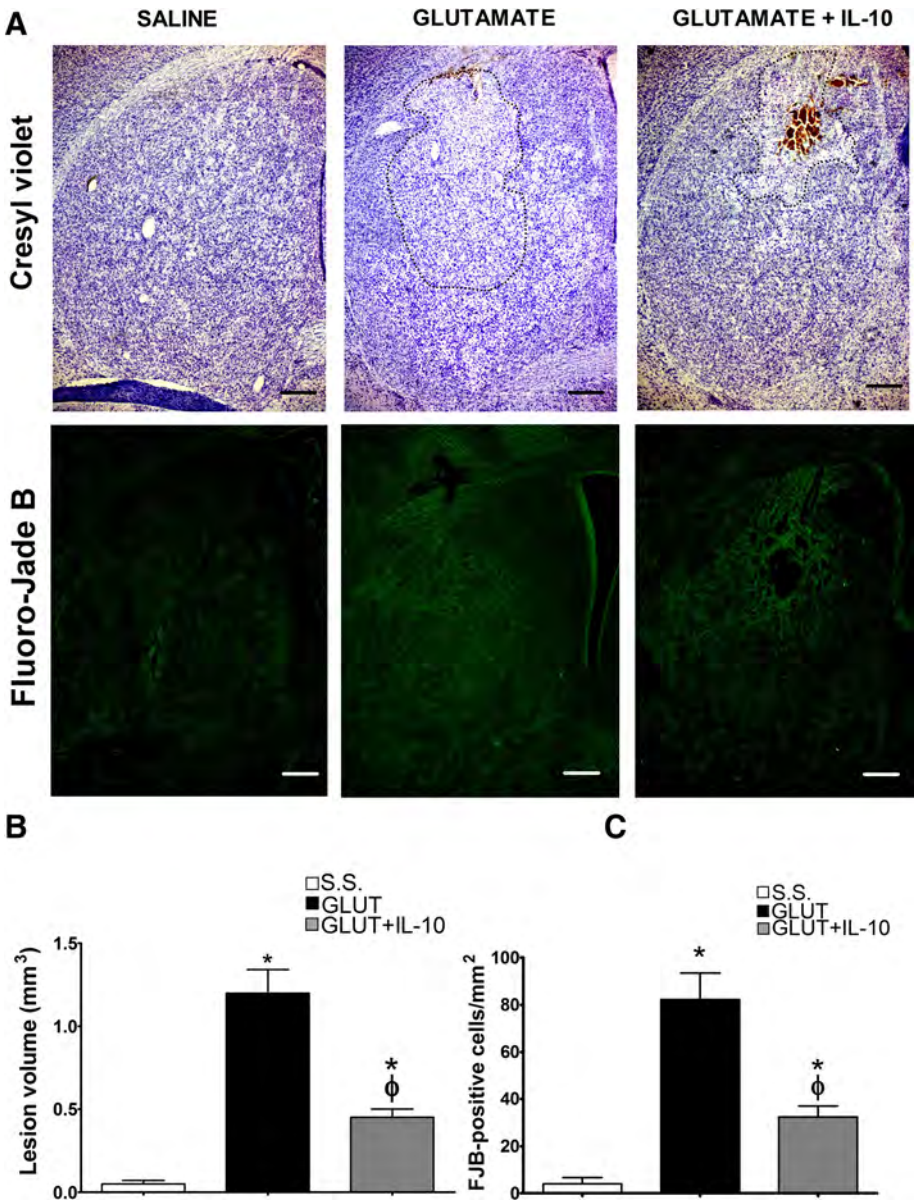

Fig. 10 Effect of IL-10 on the lesion area and neuronal degeneration in wild-type mice treated with glutamate. Histological sections of wild-type (WT) mice were obtained after 24 h of intracerebral administration of NaCl 0.9% (S.S.), only glutamate 1 M (GLUT) or glutamate + 0.4 ng/mL of interleukin-10 (GLUT+IL-10) as detailed in the "Methods" section. **a** Representative micrographs of coronal striatal sections showing lesions stained with cresyl violet and damaged cells positive for Fluoro-Jade B. The dotted line delimits the area of lesion of mice treated with glutamate. The scale bars represent 200 μm. **b** Quantification of the lesion volume 24 h after saline or glutamate injection is expressed in cubic millimeters. **c** Total number of FJB-positive cells counted in three slices per mice. Data are expressed as mean ± SEM of six independent experiments. $*p < 0.05$ vs saline control (S.S.); $^{\Phi}p < 0.05$ vs the corresponding mouse treated only with glutamate (GLUT)

trauma markedly reduces neuronal damage and neuroinflammation when administered during the first minutes-hours of insult [60, 61]. Diverse studies postulate that the magnitude of the primary response is associated with the severity of the inflammatory response that can last for months or even years [62, 63]. Therefore, it is necessary to evaluate the processes taking place during the early stages of brain injury, as we did in this study. This could help to define the early clinical intervention that can be decisive in the prognosis.

In animal models, the exogenous administration of glutamate produces an overstimulation of synaptic receptor that leads to oxidative stress and neuronal death. Besides, the excitotoxic damage is closely associated with an inflammatory response [64]. During this process, ROS are key pieces since they participate directly in

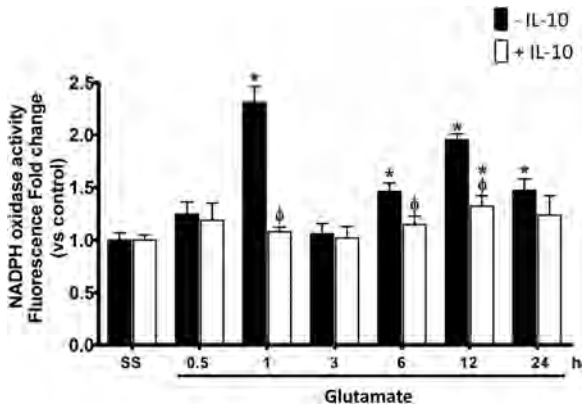

Fig. 11 NOX activity in wild-type mice treated with IL-10 after glutamate administration. NOX activity was evaluated in wild-type mice (WT) treated with NaCl 0.9%(S.S.), only glutamate 1 M (– IL-10) or glutamate + 0.4 ng/mL of IL-10 (+ IL-10) as detailed in the "Methods" section. The determination of NOX activity was measured as the change in fluorescence intensity resulting from the dihydroethidium (DHE) oxidation to ethidium (Et) in striatal homogenates after 0.5, 1, 3, 6, 12, and 24 h after glutamate administration. Data are expressed as fold change of Et fluorescence relative to saline without IL-4. Values are means ± SEM of three independent experiments. *$p < 0.05$ vs the corresponding saline control; $^{\Phi}p < 0.05$ vs the corresponding time of mice treated with glutamate alone

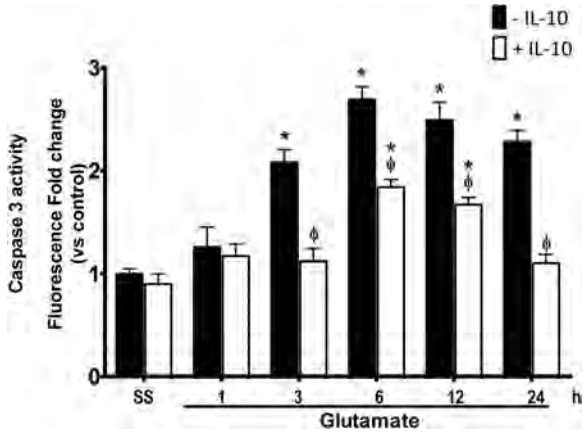

Fig. 12 Active caspase-3 in mice treated with IL-10 after glutamate administration. Active caspase-3 was measured in striatal homogenates of wild-type (WT) mice treated with NaCl 0.9% (S.S.), only glutamate 1 M (– IL-10) or glutamate + 0.4 ng/mL of IL-10 (+ IL-10) at 1, 3, 6, 12, and 24 h after glutamate administration. Fluorescence produced by the cleavage of the specific substrate was quantified in relative units of fluorescence (FRU). Data are expressed as fold change of fluorescence relative to saline without IL-4. Values are means ± SEM of three independent experiments. *$p < 0.05$ vs the corresponding saline control; $^{\Phi}p < 0.05$ vs the corresponding time of mice treated with glutamate alone

neuronal death and other parallel physiological processes that are also affected by the excitotoxicity [65, 66].

Several sources of cellular ROS have been involved in the excitotoxic damage; one of the most interesting is the NOX family, whose only known function is ROS production [64, 67]. The seven homologs (NOX-1 to NOX-5 and DUOX-1 and DUOX-2) have different subcellular localizations, and their activation is associated with various signaling pathways of the cell physiology [25, 48]. Particularly, NOX-2 seem to be involved in cell death, since its inhibition markedly reduces neuronal damage in several pathological processes such as ischemia, hypoglycemia, and brain trauma [8, 9, 14], where excitotoxicity is a main component.

In previous studies, we demonstrated that pharmacological inhibition of NOX in primary cultures of cerebellar granule neurons decreases apoptotic death caused by different conditions [67, 68]. Using an animal model of genetic inhibition of NOX-2 or with the administration of NOX inhibitors, we have confirmed the involvement of NOX-2 in excitotoxic neuronal death [13], which correlated with findings of other groups that report that the increase of NOX-2 activity promotes apoptotic death [69].

In the present study, we corroborated that NOX-2 KO mice are less susceptible to excitotoxic damage than WT mice, evidenced by a smaller lesion and less number of positive cells to Fluoro-Jade B in NOX-2 KO mice treated with glutamate (Fig. 2). In this model, we corroborated that NOX-2 is involved in excitotoxic damage since an increase of NOX activity was observed in response to the administration of glutamate. This increase occurred in a biphasic manner (1 and 12 h after glutamate administration). Since both peaks of NOX activity occurred within 12 h of difference (Fig. 3), we suggest that this feature is part of two separate phenomena. We hypothesize that the first increase in ROS participates in a direct response to the extracellular increase of glutamate, while the increase observed at 12 h probably corresponds to the cellular response for the recovery of homeostasis; however, more studies are required to test this possibility.

Our results indicated that the lack of NOX-2 is associated with a minor activation of caspase-3 (Fig. 4), probably resulting from a decrease in apoptotic signaling pathways. It is likely that the neuroprotective effect observed in NOX-2 KO mice results from a decrease of the initial damage and reduced activation of subsequent death signaling pathways. These findings correlate with reports in showing that the increase of NOX-2 activity is associated with the activation of caspase-3 and apoptotic death [68, 69]. It is important to emphasize that the excitotoxic damage includes other mechanisms of cell death (necrosis and autophagy) and that the lack of NOX-2 activity does not completely prevent cell death.

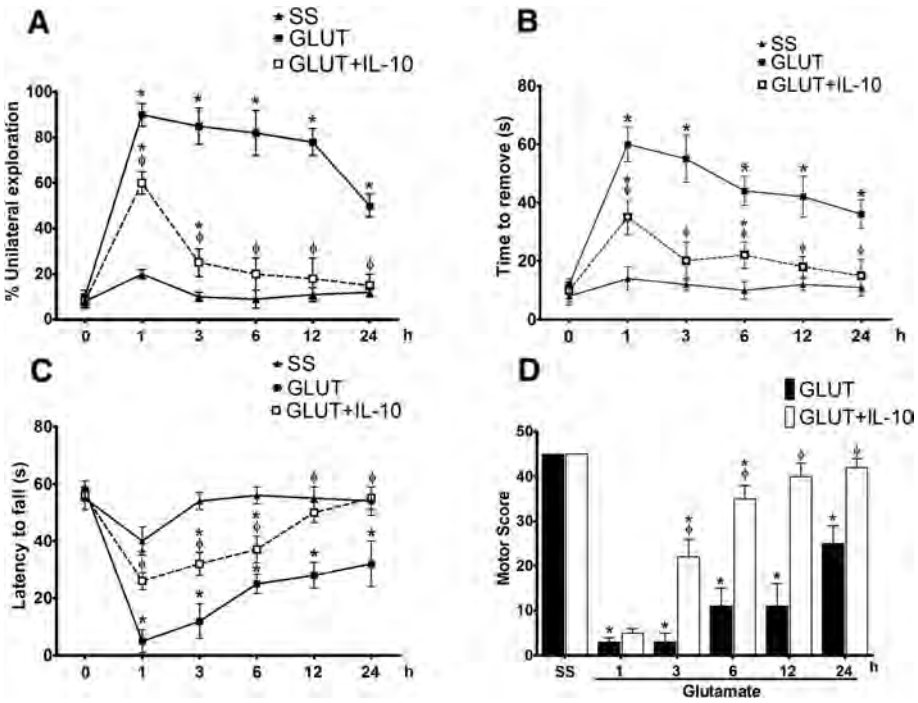

Fig. 13 IL-10 improves motor recovery in wild-type mice after glutamate administration. Motor behavior of wild-type mice injected with NaCl 0.9% (SS), 1 M glutamate (GLUT) and glutamate + 0.4 ng/mL of IL-10 (GLUT + IL-10), was evaluated in three tests of motor behavior at 1, 3, 6, 12, and 24 h after glutamate intracerebral injection. **a** Cylinder test, in which each mouse obtained a percentage based on the ratio of unilateral and bilateral explorations performed in three trials, of 3 min each; the percentage was expressed as mean ± SEM of six independent tests. **b** Adhesive removal test quantifies the time in which the animals remove a label previously placed by the examiner. The time of removal was quantified in seconds and was expressed as means ± SEM of six independent tests. **c** Inverted grid test was evaluated by exposing the mice to the inverted grid test in which the decay time was quantified for three non-consecutive opportunities of a maximum of 60 s of duration. The results are expressed as means ± SEM of the latency to fall of six independent tests. **d** Integration of behavioral performance of three previous tests was carried out by assigned an arbitrary score to the performance of each animal, giving the highest score to the performance of the mice injected with saline (45 points). The results are expressed in arbitrary units of motor score as the mean ± SEM of the latency to fall of six independent tests. *$p < 0.05$ vs the corresponding saline control; $^{\varphi}p < 0.05$ vs corresponding mouse treated with glutamate alone

Striatal injuries usually result in impaired sensorimotor function and movement execution [70]. The present results show a clear positive correlation between a reduction of the lesion size and a better recovery of motor function. In both WT and NOX-2 KO mice treated with glutamate, the initial motor function was similarly affected, probably due to the action of glutamate on striatal neuronal circuits. However, this condition improves much faster for the NOX-2 KO animals (Fig. 5) according to the damage observed in both animals (Fig. 2).

The increase in NOX-2 activity is relevant for excitotoxic damage and the inflammatory process. It has been suggested that it contributes, along with various cytokines, to the function impairment and secondary damage orchestrated by microglia [71, 72]. Persistent inflammation can promote secondary tissue injury through excess production of proinflammatory factors, such as TNF-α, IL-1β, and IL-6. These factors promote the polarization of the resident microglia to the M1 phenotype, which in turn causes neuronal death; the sum of these events results in the aggravation of the initial injury and a poor resolution of damage.

In a previous study, we observed that during the excitotoxic damage, the activated microglia in NOX-2 KO mice showed different morphological characteristics as compared to WT animals [13]. In the present work, we observed that NOX-2 mice have a different profile of cytokines production. The major change in the pattern of cytokine production corresponded to the increase in anti-inflammatory cytokines such as IL-4, IL-10, and TGF-β, just a few hours after the initiation of the injury (Fig. 6).

As expected, we observed an increase in the production of IL-1β after 6 and 12 h of glutamate treatment. However, we did not observe any differences between the WT and NOX2-KO mice at any time after glutamate treatment (Fig. 6). This contrasts with the observed results in a model of TBI, where NOX2 deficiency induced a lower expression of IL-1β after the trauma [46]. In addition to NOX2, it has been suggested that mitochondrial ROS also play a key role in the inflammatory

process through the NLRP3 inflammasome activation [73]. It is known that the production of IL-1β is regulated enzymatically by the NLRP3 inflammasome [74, 75] and a lower IL-1β secretion is observed in macrophages treated with mitochondrial ROS scavengers [42]. The NLRP3 inflammasome is stimulated by ROS [76], and NOX-derived ROS were initially suggested to be necessary for NLRP3 inflammasome activation [77]. However, in mouse macrophages deficient in NOX, IL-1β production is unaffected [78]. This observation suggests that the mechanisms involved in NLRP3 activation and IL-1β production are dependent on the source of ROS production and the type of insult. Possibly in the present experimental conditions, other sources of ROS rather than NOX are necessary for IL-1β production.

One of the most remarkable findings in this study is that in the NOX-2 KO mice, IL-4 production increases very early during the excitotoxic process, which correlates with previous reports, suggesting that IL-4 contributes to the polarization of the microglia to an M2 phenotype promoting an anti-inflammatory response. Recent evidence shows that neurons that survive a noxious stimulus (i.e., ischemia) respond by increasing the production and release of IL-4 [20]. Although the effects of IL-4 on neuronal survival have not been extensively described, it is known that its increase may promote the release of neurotrophic factors that favor axonal repair and neuronal survival.

The increase of IL-4 in NOX-2 KO mice suggests that NOX-2 participates in the negative regulation of this interleukin. This can directly influence the inflammatory response dynamics, since IL-4 contributes decisively to the acquisition of a microglial anti-inflammatory phenotype producer of IL-10. During excitotoxic damage, the increase of NOX-2 activity correlated temporarily with the decrease of anti-inflammatory cytokines and the increase in inflammatory mediators, which agrees with that reported by other groups who postulate that NOX regulates the production and release of anti-inflammatory cytokines [79, 80].

Similarly, the production of IL-10 is also markedly increased, probably induced by IL-4 [21]. The stimulation of IL-4Rα microglial receptors promotes the activation of several signaling pathways, including the activation of Janus kinase 3/transcription 6 (JAK3/STAT6) and insulin receptor substrate 2 (IRS2). This situation promotes the expression of IL-10 by the nuclear factor kappa-light-chain-enhancer of activated B cells (NFκB) and negatively regulates the production of inflammatory interleukins by the suppressor of cytokine signaling 1 (CS1) [80].

It is known that the binding of IL-10 to its neuronal receptors (IL-10R) activates the JAK2/STAT3 pathway, which reduces oxidative stress and promotes neuronal survival [81]. It is possible that part of the observed decrease in caspase-3 activation and cell death in NOX-2 KO animals could be a consequence of a decreased ROS production, by activation of IL-10R during excitotoxicity.

In our model, a single intracerebral dose of recombinant IL-10 decreased caspase-3 activation in WT mice subjected to excitotoxic damage (Fig. 12), and it is important to note that the concentration of IL-10 administered was similar to that found in the NOX-2 KO mice subjected to the excitotoxic event. Our results showed that the treatment with IL-10 negatively regulates NOX activity (Fig. 11), which could also be associated with the reduction of oxidative stress and therefore less neuronal death.

Interestingly, in contrast to what we observed in NOX-2 KO mice (Fig. 4), the administration of IL-10 did not decrease active caspase-3 induced by glutamate treatment in the initial phase (3 and 6 h), but late in the process (12 and 24 h) (Fig. 9). This suggests that IL-10 could promote neuronal survival only during the secondary phase, being the inflammatory process a probable target. This is in line with the finding that the administration of a single dose of IL-4 markedly reduced the lesion volume (Fig. 7), but the decrease in NOX activity (Fig. 8) and caspase-3 activity (Fig. 9) occurred after 12 and 24 h of glutamate administration.

Based on our findings, including the time course of the different parameters evaluated, we can delimit two phases in the progression of neuronal damage induced by glutamate administration: an initial response, from the onset of administration to the subsequent 6 h and a secondary response, from 6 h and up to 24 h post administration. In WT mice, the initial phase is characterized by an increase in NOX activity and IL-12 production, which promotes a proinflammatory state and severe motor deterioration. During the secondary response, a proinflammatory environment predominates (increased IL-1β, IL-6, and TNF-α production and NOX activity), which promotes apoptotic neuronal death. In contrast, in NOX-2 KO mice, the initial response is characterized by an increased production of IL-4 and IL-10, which probably contributes to a decreased apoptotic death and an improved functional recovery.

Interestingly, when IL-4 was administered to WT mice treated with glutamate, NOX activity and caspase-3 activation were reduced only during the secondary response, probably because its effect depends on the increase of other factors. In support of this, when IL-10 was administered to these animals, NOX activity and caspase-3 activation decreased in both the early and the late phase after glutamate administration.

Altogether, these results lead us to propose that the neuroprotection resulting from the genetic inhibition of NOX-2 could be due, at least partially, to a differential response to excitotoxic damage, which is characterized

by an early increased production of anti-inflammatory cytokines. We have shown that the inhibition of NOX-2 activity facilitates the production of anti-inflammatory cytokines, which in turn decreases the injury secondary to excitotoxic damage and improves functional recovery.

Conclusions

The release of proinflammatory cytokines during the excitotoxic cascade promotes a secondary apoptotic death of neurons that survived the damage. During the excitotoxic process and the subsequent inflammatory response, ROS generated by NOX-2 play a decisive role in the extension of the lesion and consequently in the severity of the functional compromise.

We propose that the neuroprotection resulting from a lack of NOX-2 activity could be due, at least partially, to a differential response against excitotoxic damage, characterized by an increased production of anti-inflammatory cytokines. Although it is necessary to determine the exact mechanism by which NOX-2 participates in the regulation of these cytokines, we suggest that the inhibition of NOX-2 activity facilitates the production of IL-4, which contributes to the production of IL-10.

Additional file

Additional file 1: Figure S1. Expression of gp91phox (NOX-2) in the striatum of wild-type and NOX-2 KO mice after glutamate treatment. (A) Levels of gp91phox (NOX-2) at 1, 6, 12, and 24 h after the intracerebral administration of glutamate (1 M). The results are expressed as fold over the relative intensity in relation to the load control (GAPDH), against time in hours (h). Values represent the average ± SEM of four independent tests. *$p < 0.05$ vs the corresponding saline control. (B) Western blot of gp91phox (band size 65 kDa) and GAPDH (band size 37 kDa) representative images. (TIF 121140 kb)

Abbreviations

ANOVA: Analysis of variance; CNS: Central nervous system; DHE: Dihydroethidium; DPI: Diphenyleneiodonium; DUOX: Dual oxidases; ELISA: Enzyme-linked immunosorbent assay; Et: Ethidium; FJB: Fluoro-Jade B; GLU: Glutamate; IL: Interleukin; IL-R: Interleukin receptor; JAK: Janus kinase; NDS: Neurological dysfunction score; NOX: NADPH oxidases; NOX-2: NADPH oxidase-2; ROS: Reactive oxygen species; SEM: Standard error of the mean; SOD: Superoxide dismutase; TGF-β: Transforming growth factor beta; TNF-α: Tumor necrosis factor-α; WT: Wild-type

Acknowledgements

The authors are grateful to María Guadalupe Domínguez Macouzet for her excellent technical assistance. The authors thank Héctor Alfonso Malagón Rivero and Claudia V. Rivera Cerecedo for mice care at the Bioterio, as well as to Daniela Rodríguez for processing the tissue sections in the Histology Unit.

Funding

This work was supported by DGAPA-UNAM (IN210716 and IN212019) and CONACYT (285184). Diego R. Hernández Espinosa is a doctoral student from the Programa de Doctorado en Ciencias Biomédicas, Universidad Nacional Autónoma de México (UNAM), and he was a recipient of fellowship from CONACYT (290121).

Availability of data and materials

The datasets used and/or analyzed during the current study are available from the corresponding author on reasonable request.

Authors' contributions

DRHE carried out the work, data analysis, and the writing of the manuscript and participated in the design of the study. LM and TM contributed to the planning of the model and the revision of the data and the images. JM conceived the study and participated in the analysis of the data, the feedback, and the draft of the manuscript. All authors read and approved the final manuscript.

Ethics approval and consent to participate

All animals were handled according to the National Institutes of Health Guide for the Care and Use of laboratory animals (NIH Publication No. 8023, revised 1978) and the local Committee for the Care and Use of Laboratory Animals (protocol JMA72-15).

Consent for publication

Not applicable

Competing interests

The authors declare that they have no competing interests.

Publisher's Note

Springer Nature remains neutral with regard to jurisdictional claims in published maps and institutional affiliations.

Received: 21 January 2019 Accepted: 3 April 2019
Published online: 17 April 2019

References

1. MacDermott AB, Mayer ML, Westbrook GL, Smith SJ, Barker JL. NMDA-receptor activation increases cytoplasmic calcium concentration in cultured spinal cord neurones. Nature. 1986;1986(321):519–22. https://doi.org/10.1038/321519a0.
2. Lai TW, Zhang S, Wang YT. Excitotoxicity and stroke: identifying novel targets for neuroprotection. Prog Neurobiol. 2014;115:157–88. https://doi.org/10.1016/j.pneurobio.2013.11.006.
3. Brown GC. Mechanisms of inflammatory neurodegeneration: iNOS and NADPH oxidase. Biochem. Soc. Trans. 2007;35(Pt 5):1119–21. https://doi.org/10.1042/BST0351119.
4. Cooney SJ, Zhao Y, Byrnes KR. Characterization of the expression and inflammatory activity of NADPH oxidase after spinal cord injury. Free Radic Res. 2014;48(8):929–39. https://doi.org/10.3109/10715762.2014.927578.
5. Hoffmann MH, Griffiths HR. The dual role of ROS in autoimmune and inflammatory diseases: evidence from preclinical models. Free Radic Biol Med. 2018;125:62–71. https://doi.org/10.1016/j.freeradbiomed.2018.03.016.
6. Nicholls DG, Johnson-Cadwell L, Vesce S, Jekabsons M, Yadava N. Bioenergetics of mitochondria in cultured neurons and their role in glutamate excitotoxicity. J Neurosci Res. 2007;85(15):3206–12. https://doi.org/10.1002/jnr.21290.
7. Kahles T, Brandes RP. NADPH oxidases as therapeutic targets in ischemic stroke. Cell Mol Life Sci. 2012;69(14):2345–63. https://doi.org/10.1007/s00018-012-1011-8.
8. Páramo B, Montiel T, Rivera-Martínez M, Morán J, Massieu L. Calpain activation induced by glucose deprivation is mediated by oxidative stress and contributes to neuronal damage. Int J Biochem Cell Biol. 2013;45(11):2596–604. https://doi.org/10.1016/j.biocel.2013.08.013.
9. Hirano K, Chen WS, Chueng AL, Dunne AA, Seredenina T, Filippova A, Ramachandran S, Bridges A, Chaudry L, Pettman G, Allan C, Duncan S, Lee KC, Lim J, Ma MT, Ong AB, Ye NY, Nasir S, Mulyanidewi S, Aw CC, Oon PP, Liao S, Li D, Johns DG, Miller ND, Davies CH, Browne ER, Matsuoka Y, Chen DW, Jaquet V, Rutter AR. Discovery of GSK2795039, a novel small molecule NADPH oxidase 2 inhibitor. Antioxid Redox Signal. 2015;23(5):358–74. https://doi.org/10.1089/ars.2014.6202.
10. Ma MW, Wang J, Dhandapani KM, Brann DW. NADPH oxidase 2 regulates NLRP3 inflammasome activation in the brain after traumatic brain injury. Oxidative Med Cell Longev. 2017;2017:6057609. https://doi.org/10.1155/2017/6057609.

11. Wang Z, Wei X, Liu K, Zhang X, Yang F, Zhang H, He Y, Zhu T, Li F, Shi W, Zhang Y, Xu H, Liu J, Yi F. NOX2 deficiency ameliorates cerebral injury through reduction of complexin II-mediated glutamate excitotoxicity in experimental stroke. Free Radic Biol Med. 2013;65:942–51. https://doi.org/10.1016/j.freeradbiomed.2013.08.166.
12. Zhang L, Li Z, Feng D, Shen H, Tian X, Li H, Wang Z, Chen G. Involvement of Nox2 and Nox4 NADPH oxidases in early brain injury after subarachnoid hemorrhage. Free Radic Res. 2017;51(3):316–28. https://doi.org/10.1080/10715762.2017.1311015.
13. Guemez-Gamboa A, Estrada-Sánchez AM, Montiel T, Páramo B, Massieu L, Morán J. Activation of NOX2 by the stimulation of ionotropic and metabotropic glutamate receptors contributes to glutamate neurotoxicity in vivo through the production of reactive oxygen species and calpain activation. J Neuropathol Exp Neurol. 2011;70(11):1020–35. https://doi.org/10.1097/NEN.0b013e3182358e4e.
14. Chandran R, Kim T, Mehta SL, Udho E, Chanana V, Cengiz P, Kim H, Kim C, Vemuganti R. A combination antioxidant therapy to inhibit NOX2 and activate Nrf2 decreases secondary brain damage and improves functional recovery after traumatic brain injury. J Cereb Blood Flow Metab. 2017:271678X17738701. https://doi.org/10.1177/0271678X17738701.
15. Lyman M, Lloyd DG, Ji X, Vizcaychipi MP, Ma D. Neuroinflammation: the role and consequences. Neurosci Res. 2014;79:1–12. https://doi.org/10.1016/j.neures.2013.10.004.
16. Hong H, Kim BS, Im HI. Pathophysiological role of neuroinflammation in neurodegenerative diseases and psychiatric disorders. Int Neurourol J. 2016;20(Suppl 1):S2–7. https://doi.org/10.5213/inj.1632604.302.
17. Vinet J, Weering HR, Heinrich A, Kälin RE, Wegner A, Brouwer N, Heppner FL, Rooijen N, Boddeke HW, Biber K. Neuroprotective function for ramified microglia in hippocampal excitotoxicity. J Neuroinflammation. 2012;9:27. https://doi.org/10.1186/1742-2094-9-27.
18. Kreutzberg GW. Microglia: a sensor for pathological events in the CNS. Trends Neurosci. 1996;19(8):312–8 https://doi.org/10.1016/0166-2236(96)10049-7.
19. Nakajima M, Nito C, Sowa K, Suda S, Nishiyama Y, Nakamura-Takahashi A, Nitahara-Kasahara Y, Imagawa K, Hirato T, Ueda M, Kimura K, Okada T. Mesenchymal stem cells overexpressing interleukin-10 promote neuroprotection in experimental acute ischemic stroke. Mol Ther Methods Clin Dev. 2017;6:102–11. https://doi.org/10.1016/j.omtm.2017.06.005.
20. Kim DW, Lee JC, Cho JH, Park JH, Ahn JH, Chen BH, Shin BN, Tae HJ, Seo JY, Cho JH, Kang IJ, Hong S, Kim YM, Won MH, Kim IH. Neuroprotection of ischemic preconditioning is mediated by anti-inflammatory, not pro-inflammatory, cytokines in the gerbil hippocampus induced by a subsequent lethal transient cerebral ischemia. Neurochem. Res. 2015;40(9):1984–95. https://doi.org/10.1007/s11064-015-1694-y.
21. Lobo-Silva D, Carriche GM, Castro AG, Roque S, Saraiva M. Balancing the immune response in the brain: IL-10 and its regulation. J Neuroinflammation. 2016;13(1):297. https://doi.org/10.1186/s12974-016-0763-8.
22. Dinarello C. Historical review of cytokines. Eur J Immunol. 2007;37(Suppl 1):S34–45. https://doi.org/10.1002/eji.200737772.
23. Patel RK, Prasad N, Kuwar R, Haldar D, Abdul-Muneer PM. Transforming growth factor-beta 1 signaling regulates neuroinflammation and apoptosis in mild traumatic brain injury. Brain Behav Immun. 2017;64:244–58. https://doi.org/10.1016/j.bbi.2017.04.012.
24. Dong Y, Kalueff AV, Song C. N-methyl-d-aspartate receptor-mediated calcium overload and endoplasmic reticulum stress are involved in interleukin-1beta-induced neuronal apoptosis in rat hippocampus. J Neuroimmunol. 2017;307:7–13. https://doi.org/10.1016/j.jneuroim.2017.03.005.
25. Dai Y, Zhang H, Zhang J, Yan M. Isoquercetin attenuates oxidative stress and neuronal apoptosis after ischemia/reperfusion injury via Nrf2-mediated inhibition of the NOX4/ROS/NF-κB pathway. Chem Biol Interact. 2018;284:32–40. https://doi.org/10.1016/j.cbi.2018.02.017.
26. Park KW, Lee DY, Joe EH, Kim SU, Jin BK. Neuroprotective role of microglia expressing interleukin-4. J Neurosci Res. 2005;81(3):397–402. https://doi.org/10.1002/jnr.20483.
27. Garcia JM, Stillings SA, Leclerc J, Phillips H, Edwards NJ, Robicsek S, Hoh BL, Blackburn S, Doré S. Role of interleukin-10 in acute brain injuries. Front Neurol. 2017;8:244. https://doi.org/10.3389/fneur.2017.00244.
28. Mills CD, Kincaid K, Alt JM, Heilman MJ, Hill AM. M-1/M-2 macrophages and the Th1/Th2 paradigm. J Immunol. 2000;164(12):6166–73.
29. Mikita J, Dubourdieu-Cassagno N, Deloire MS, Vekris A, Biran M, Raffard G, Brochet B, Canron MH, Franconi JM, Boiziau C, Petry KG. Altered M1/M2 activation patterns of monocytes in severe relapsing experimental rat model of multiple sclerosis. Amelioration of clinical status by M2 activated monocyte administration. Mult Scler. 2011;17(1):2–15. https://doi.org/10.1177/1352458510379243.
30. Loke P, Nair MG, Parkinson J, Guiliano D, Blaxter M, Allen JE. IL-4 dependent alternatively-activated macrophages have a distinctive in vivo gene expression phenotype. BMC Immunol. 2002;3:7.
31. Xia CY, Zhang S, Gao Y, Wang ZZ, Chen NH. Selective modulation of microglia polarization to M2 phenotype for stroke treatment. Int Immunopharmacol. 2015;25(2):377–82. https://doi.org/10.1016/j.intimp.2015.02.019.
32. Gordon S, Martinez FO. Alternative activation of macrophages: mechanism and functions. Immunity. 2010;32(5):593–604. https://doi.org/10.1016/j.immuni.2010.05.007.
33. Morganti JM, Riparip LK, Rosi. Call off the dog(ma): M1/M2 polarization is concurrent following traumatic brain injury. PLoS One. 2016;11(1):e0148001. https://doi.org/10.1371/journal.pone.0148001.
34. Edwards JP, Zhang X, Frauwirth KA, Mosser DM. Biochemical and functional characterization of three activated macrophage populations. J Leukoc Biol. 2006;80(6):1298–307.
35. Franco R, Fernández-Suárez D. Alternatively, activated microglia and macrophages in the central nervous system. Prog Neurobiol. 2015;131:65–86. https://doi.org/10.1016/j.pneurobio.2015.05.003.
36. Ransohoff RM. A polarizing question: do M1 and M2 microglia exist? Nat Neurosci. 2016;19(8):987–91. https://doi.org/10.1038/nn.4338.
37. Mosser DM, Edwards JP. Exploring the full spectrum of macrophage activation. Nat Rev Immunol. 2008;8(12):958–69. https://doi.org/10.1038/nri2448.
38. Chhor V, Le Charpentier T, Lebon S, Ore M, Celador I, Josserand J, Degos V, Jacotot E, Hagberg H, Savman K, Mallard C, Gressens P, Fleiss B. Characterization of phenotype markers and neuronotoxic potential of polarized primary microglia in vitro. Brain Behav Immun. 2013;32:70–85. https://doi.org/10.1016/j.bbi.2013.02.005.
39. Sironi M, Martinez FO, D'Ambrosio D, Gattorno M, Polentarutti N, Locati M, Gregorio A, Iellem A, Cassatella MA, Van Damme J, Sozzani S, Martini A, Sinigaglia F, Vecchi A, Mantovani A. Differential regulation of chemokine production by Fcgamma receptor engagement in human monocytes: association of CCL1 with a distinct form of M2 monocyte activation (M2b, type 2). J Leukoc Biol. 2006;80(2):342–9.
40. Liao B, Zhao W, Beers DR, Henkel JS, Appel SH. Transformation from a neuroprotective to a neurotoxic microglial phenotype in a mouse model of ALS. Exp Neurol. 2012;237(1):147–52. https://doi.org/10.1016/j.expneurol.2012.06.011.
41. Qin L, Liu Y, Wang T, Wei SJ, Block ML, Wilson B, Liu B, Hong JS. NADPH oxidase mediates lipopolysaccharide-induced neurotoxicity and proinflammatory gene expression in activated microglia. J Biol Chem. 2004;279(2):1415–21. https://doi.org/10.1074/jbc.M307657200.
42. Brüne B, Dehne N, Grossmann N, Jung M, Namgaladze D, Schmid T, von Knethen A, Weigert A. Redox control of inflammation in macrophages. Antioxid Redox Signal. 2013;19(6):595–637. https://doi.org/10.1089/ars.2012.4785.
43. Rojo AI, McBean G, Cindric M, Egea J, López MG, Rada P, Zarkovic N, Cuadrado A. Redox control of microglial function: molecular mechanisms and functional significance. Antioxid Redox Signal. 2014;21(12):1766–801. https://doi.org/10.1089/ars.2013.5745.
44. Mander P, Brown GC. Activation of microglial NADPH oxidase is synergistic with glial iNOS expression in inducing neuronal death: a dual-key mechanism of inflammatory neurodegeneration. J Neuroinflammation. 2005;2:20. https://doi.org/10.1186/1742-2094-2-20.
45. Lee SH, Suk K. Identification of glia phenotype modulators based on select glial function regulatory signaling pathways. Expert Opin Drug Discov. 2018;13(7):627–41. https://doi.org/10.1080/17460441.2018.1465925.
46. Pawate S, Shen Q, Fan F, Bhat NR. Redox regulation of glial inflammatory response to lipopolysaccharide and interferon gamma. J Neurosci Res. 2004;77(4):540–51. https://doi.org/10.1002/jnr.20180.
47. Kumar A, Barrett JP, Alvarez-Croda DM, Stoica BA, Faden AI, Loane DJ. NOX2 drives M1-like microglial/macrophage activation and neurodegeneration following experimental traumatic brain injury. Brain Behav Immun. 2016;58:291–309. https://doi.org/10.1016/j.bbi.2016.07.158.

48. Padgett LE, Burg AR, Lei W, Tse HM. Loss of NADPH oxidase-derived superoxide skews macrophage phenotypes to delay type 1 diabetes. Diabetes. 2015;64(3):937–46. https://doi.org/10.2337/db14-0929.
49. Estrada-Sánchez AM, Montiel T, Segovia J. Glutamate toxicity in the R6/2 Huntington's disease transgenic mice is age-dependent and correlates with decreased levels of glutamate transporters. Neurobiol Dis. 2009;34:78–86. https://doi.org/10.1016/j.nbd.2008.12.017.
50. Schmidt E, Morello F, Pasterkamp R. Dissection and culture of mouse dopaminergic and striatal explants in three-dimensional collagen matrix assays. J Vis Exp. 2012;61:3691. https://doi.org/10.3791/3691.
51. Liu X, Miller B, Rebec G, David E. Protein expression in the striatum and cortex regions of the brain for a mouse model of Huntington's disease. J Proteome Res. 2007;6(8):3134–42. https://doi.org/10.1021/pr070092s.
52. Thornberry NA, Rano TA, Peterson EP, Rasper DM, Timkey T, Garcia-Calvo M. A combinatorial approach defines specificities of members of the caspase family and granzyme B. functional relationships established for key mediators of apoptosis. J Biol Chem. 1997;272:17907–11.
53. Fleming SM, Zhu C, Fernagut PO, Mehta A, DiCarlo CD, Seaman RL, Chesselet MF. Behavioral and immunohistochemical effects of chronic intravenous and subcutaneous infusions of varying doses of rotenone. Exp Neurol. 2004;187:418–29. https://doi.org/10.1016/j.expneurol.2004.01.023.
54. Bouet V, Boulouard M, Toutain J, Divoux D, Bernaudin M, Schumann-Bard P, Freret T. The adhesive removal test: a sensitive method to assess sensorimotor deficits in mice. Nat Protoc. 2009;4(10):1560–4. https://doi.org/10.1038/nprot.2009.125.
55. Wells J, Biernaskie J, Szymanska A, Larsen P, Yong VW, Corbett D. Matrix metalloproteinase (MMP)-12 expression has a negative impact on sensorimotor function following intracerebral hemorrhage in mice. Eur J Neurosci. 2005;21(1):187–96. https://doi.org/10.1111/j.1460-9568.2004.03829.
56. Barrett JP, Henry RJ, Villapol S, Stoica BA, Kumar A, Burns MP, Faden AI, Loane DJ. NOX2 deficiency alters macrophage phenotype through an IL-10/STAT3 dependent mechanism: implications for traumatic brain injury. J Neuroinflammation. 2017;14(1):65. https://doi.org/10.1186/s12974-017-0843-4.
57. Satoh M, Fujimoto S, Haruna Y. NAD(P)H oxidase and uncoupled nitric oxide synthase are major sources of glomerular superoxide in rats with experimental diabetic nephropathy. Am J Physiol Renal Physiol. 2005;288:F1144–52. https://doi.org/10.1152/ajprenal.00221.2004.
58. Zhao X, Zhang Y, Strong R, James C, Grotta A, Jaroslaw A. 15d-Prostaglandin J (2) activates peroxisome proliferator-activated receptor-gamma, promotes expression of catalase, and reduces inflammation, behavioral dysfunction, and neuronal loss after intracerebral hemorrhage in rats. J Cereb Blood Flow Metab. 2006;26. https://doi.org/10.1038/sj.jcbfm.9600233.
59. Guerriero R, Giza C, Rotenberg A. Glutamate and GABA imbalance following traumatic brain injury. Curr Neurol Neurosci Rep. 2015;15:27. https://doi.org/10.1007/s11910-015-0545-1.
60. Hill R, Singh I, Wang J, Hall E. Time courses of post-injury mitochondrial oxidative damage and respiratory dysfunction and neuronal cytoskeletal degradation in a rat model of focal traumatic brain injury. Neurochem Int. 2017;111:45–56. https://doi.org/10.1016/j.neuint.2017.03.015.
61. Hinson H, Rowell S, Schreiber M. Clinical evidence of inflammation driving secondary brain injury: a systematic review. J Trauma Acute Care Surg. 2015;78:184–91. https://doi.org/10.1097/TA.0000000000000468.
62. Diaz-Arrastia R, Kochanek P, Bergold P, Kenney K, Marx C, Grimes C. Pharmacotherapy of traumatic brain injury: state of the science and the road forward: report of the department of defense neurotrauma pharmacology workgroup. J Neurotrauma. 2014;31:135–58. https://doi.org/10.1089/neu.2013.301.
63. Rich M, Keene C, Neher M, Johnson K, Yu Z, Ganivet A, Holers V, Stahel P. Site-targeted complement inhibition by a complement receptor 2-conjugated inhibitor (mTT30) ameliorates post-injury neuropathology in mouse brains. Neurosci Lett. 2016;617:188–94. https://doi.org/10.1016/j.neulet.2016.02.025.
64. Maycotte P, Guemez-Gamboa A, Moran J. Apoptosis and autophagy in rat cerebellar granule neuron death: role of reactive oxygen species. J Neurosci Res. 2010;88(1):73–85. https://doi.org/10.1002/jnr.22168.
65. Batlle M, Ferri L, Andrade C, Ortega F, Vidal-Taboada J, Pugliese M, Mahy N, Rodríguez M. Astroglia-microglia cross talk during neurodegeneration in the rat hippocampus. Biomed Res Int. 2015;2015:102419. https://doi.org/10.1155/2015/102419.
66. Choi HS, Park JH, Ahn JH, Hong S, Cho JH, Won MH, Lee CH. The anti-inflammatory activity of duloxetine, a serotonin/norepinephrine reuptake inhibitor, prevents kainic acid-induced hippocampal neuronal death in mice. J Neurol Sci. 2015;358(1–2):390–7. https://doi.org/10.1016/j.jns.2015.10.001.
67. Coyoy A, Valencia A, Guemez-Gamboa A, Morán J. Role of NADPH oxidase in the apoptotic death of cultured cerebellar granule neurons. Free Radic Biol Med. 2008;45(8):1056–64. https://doi.org/10.1016/j.freeradbiomed.2008.06.027.
68. Guemez-Gamboa A, Morán J. NOX2 mediates apoptotic death induced by staurosporine but not by potassium deprivation in cerebellar granule neurons. J Neurosci Res. 2009;87(11):2531–40. https://doi.org/10.1002/jnr.22079.
69. Altenhöfer S, Kleikers PW, Radermacher KA, Scheurer P, Rob Hermans J, Schiffers P, Ho H, Wingler K, Schmidt HH. The NOX toolbox: validating the role of NADPH oxidases in physiology and disease. Cell Mol Life Sci. 2012;69(14):2327–43. https://doi.org/10.1007/s00018-012-1010-9.
70. Gensel JC, Zhang B. Macrophage activation and its role in repair and pathology after spinal cord injury. Brain Res. 2015;1619:1–11. https://doi.org/10.1016/j.brainres.2014.12.045.
71. Pepe G, De Maglie M, Minoli L, Villa A, Maggi A, Vegeto E. Selective proliferative response of microglia to alternative polarization signals. J Neuroinflammation. 2017;14(1):236. https://doi.org/10.1186/s12974-017-1011-6.
72. Lawrence CB, Allan SM, Rothwell NJ. Interleukin-1beta and the interleukin-1 receptor antagonist act in the striatum to modify excitotoxic brain damage in the rat. Eur J Neurosci. 1998;10(3):1188–95.
73. Meissner F, Seger RA, Moshous D, Fischer A, Reichenbach J, Zychlinsky A. Inflammasome activation in NADPH oxidase defective mononuclear phagocytes from patients with chronic granulomatous disease. Blood. 2010;116(9):1570–3. https://doi.org/10.1182/blood-2010-01-264218.
74. Heid ME, Keyel PA, Kamga C, Shiva S, Watkins SC, Salter RD. Mitochondrial reactive oxygen species induces NLRP3-dependent lysosomal damage and inflammasome activation. J Immunol. 2013;191(10):5230–8. https://doi.org/10.4049/jimmunol.1301490.
75. Dostert C, Pétrilli V, Van Bruggen R, Steele C, Mossman BT, Tschopp J. Innate immune activation through Nalp3 inflammasome sensing of asbestos and silica. Science. 2008;320(5876):674–7. https://doi.org/10.1126/science.1156995.
76. Codolo G, Plotegher N, Pozzobon T, Brucale M, Tessari I, Bubacco L, de Bernard M. Triggering of inflammasome by aggregated α-synuclein, an inflammatory response in synucleinopathies. PLoS One. 2013;8(1):e55375. https://doi.org/10.1371/journal.pone.0055375.
77. Hornung V, Bauernfeind F, Halle A, Samstad EO, Kono H, Rock KL, Fitzgerald KA, Latz E. Silica crystals and aluminum salts activate the NALP3 inflammasome through phagosomal destabilization. Nat Immunol. 2008;9(8):847–56. https://doi.org/10.1038/ni.1631.
78. Pal R, Bajaj L, Sharma J, Palmieri M, Di Ronza A, Lotfi P, Chaudhury A, Neilson J, Sardiello M, Rodney GG. NADPH oxidase promotes Parkinsonian phenotypes by impairing autophagic flux in an mTORC1-independent fashion in a cellular model of Parkinson's disease. Sci Rep. 2016;6:22866. https://doi.org/10.1038/srep22866.
79. Lou Z, Wang AP, Duan XM, Hu GH, Song GL, Zuo ML, Yang ZB. Upregulation of NOX2 and NOX4 mediated by TGF-β signaling pathway exacerbates cerebral ischemia/reperfusion oxidative stress injury. Cell Physiol Biochem. 2018;46(5):2103–13. https://doi.org/10.1159/000489450.
80. Ferreira R, Lively S, Schlichter LC. IL-4 type 1 receptor signaling up-regulates KCNN4 expression and increases the KCa3.1 current and its contribution to migration of alternative-activated microglia. Front Cell Neurosci. 2014;8:183. https://doi.org/10.3389/fncel.2014.00183.
81. Zhu Y, Liu Z, Peng YP, Qiu YH. Interleukin-10 inhibits neuroinflammation-mediated apoptosis of ventral mesencephalic neurons via JAK-STAT3 pathway. Int Immunopharmacol. 2017;50:353–60. https://doi.org/10.1016/j.intimp.2017.07.017.

INFORME DE LABORES 2019

Biochemical Pharmacology 161 (2019) 63–72

Contents lists available at ScienceDirect

Biochemical Pharmacology

journal homepage: www.elsevier.com/locate/biochempharm

Involvement of cell oxidant status and redox state in the increased non-enzymatic ethanol oxidation by the regenerating rat liver

Rolando Hernández-Muñoz*, Martha Lucinda Contreras-Zentella

Departamento de Biología Celular y Desarrollo, Instituto de Fisiología Celular, Universidad Nacional Autónoma de México (UNAM), Apdo. Postal 70-245, Mexico City 04510, Mexico

ARTICLE INFO

Keywords:
Acetaldehyde
Cell redox state
Alcohol dehydrogenase
Lipid peroxidation
Malate-aspartate shuttle

ABSTRACT

Ethanol administration is capable of inhibiting or delaying the partial hepatectomy (PH)-induced liver regeneration, probably altering liver metabolism by means of its oxidative metabolism. Since the regenerating liver has increased capacity for oxidizing ethanol, the present study was aimed to address the contribution of the ethanol-oxidizing metabolic pathways in the regenerating liver cells. Isolated hepatocytes were prepared from control livers and from animals subjected to two-thirds PH. In both preparations, ethanol oxidation was largely increased by incubation with glucose and was highly sensitive to inhibitors of ethanol-oxidizing enzymatic pathways (alcohol dehydrogenase, catalase and cytochrome P-4502E1 activities). The latter led to a total blockade of ethanol disposal by control hepatocytes, while liver cells from PH-rats only showed an early 70–75% inhibition of ethanol catabolism with the inhibitors used. In regenerating hepatocytes, the enhanced ethanol oxidation was blocked by scavengers of reactive oxygen species, an effect that correlated with enhanced cytoplasmic lipid peroxidation by-products. Both cell preparations showed similar sensitivity to inhibitors for the malate-aspartate shuttle and mitochondrial electron transport chain; the shift of the cytoplasmic redox state was also quite similar after ethanol oxidation. A more oxidized mitochondrial redox state was found in hepatocytes from PH-rats and more shifted to the reduced state during ethanol oxidation this effect was not abolished by inhibiting alcohol dehydrogenase activity. In conclusion, data clearly show that an important fraction of ethanol is metabolized through a non-enzymatic-mediated oxidative event, which could largely contribute to the deleterious effect of ethanol on the proliferating liver.

1. Introduction

The etiology of alcoholic liver disease (ALD) is highly complex involving different disease stages, such as steatosis, steatohepatitis, fibrosis, and cirrhosis, as well as disruptions in multiple liver cell types, metabolic and signaling pathways, and sub-cellular organelle function. Alcohol consumption depresses hepatic mitochondrial bioenergetics, increasing mitochondrial reactive oxygen species (ROS) production, and promotes an increased sensitivity of the mitochondrial permeability transition (MPT) pore [1]. Indeed, patients with ALD are not good candidates for replacement of their own liver by a donor organ, despite that patient and organ survival is excellent after liver transplantation in this patient's population. Interestingly, ALD patients returning to consume alcohol may consume greater amounts of ethanol [2]. This could be indicating that the transplanted organ, probably promoted to somehow proliferate, could have a distinct handling of the consumed ethanol.

In this context, although the mechanisms of its inhibitory effect are not defined, it is well known that acute and chronic ethanol treatment inhibits DNA synthesis in the regenerating rat liver after partial hepatectomy (PH), induced by a toxic injury, as well as in cultured hepatocytes [3–5]. However, evidence suggests that acute and chronic ethanol inhibits hepatocyte proliferation through different mechanisms. A single oral ethanol administration is capable of inhibiting or delaying the PH-induced liver regeneration [6,7]. Here, it is likely that liver metabolism of exogenous ethanol could alter the overall metabolism of the regenerating liver, i.e., causing disturbances in the cell redox state, energy charge, and the mitochondrial metabolism in the regenerating organ [8].

The ability of the regenerating organ to oxidize the administered ethanol could participate in the deleterious alcohol effects on liver cell proliferation. After PH, the remnant liver shows very enhanced

* Corresponding author at: Depto. de Biología Celular, Instituto de Fisiología Celular, Universidad Nacional Autónoma de México (UNAM), Apdo. Postal 70-243, Mexico 04510, Mexico.
E-mail address: rhernand@correo.ifc.unam.mx (R. Hernández-Muñoz).

https://doi.org/10.1016/j.bcp.2019.01.003
Received 12 November 2018; Accepted 2 January 2019
Available online 06 January 2019
0006-2952/ © 2019 Published by Elsevier Inc.

INFORME DE LABORES 2019

metabolism of ethanol, which constitutes the main factor affecting ethanol pharmacokinetics in hepatectomized rats [9]. Moreover, ethanol blocks the PH-induced changes in the liver cell redox state, minimizing the metabolic adjustments mediated by redox potentials and affecting preparative events that culminate in the compensatory liver growth [10]. Despite having demonstrated that the regenerating liver oxidizes ethanol faster in vivo, the underlying mechanisms remain to be elucidated.

Isolated hepatocytes have been proved to be a useful system for studying regulatory events in ethanol oxidation. Despite that isolated liver cells do not oxidize ethanol at rates comparable to those in vivo [11], rate-determining factors on ethanol oxidation have been identified [12,13]. As other metabolic pathways, there is not a single rate-determining step for the ethanol metabolism pathway, and control is shared among several steps [14]. However, factors such as liver alcohol dehydrogenase (ADH) activity, translocation of cytosolic reducing equivalents into mitochondria, and their further oxidation through the mitochondrial electron transport [15,16] could become rate-limiting for ethanol oxidation, depending on the experimental conditions.

Little is known about ethanol metabolism at the onset of liver cells proliferation; however, some interesting findings have been reported. For instance, neonatal liver cells have a higher capacity of NADH generation and, thereby, ethanol oxidation by these cells induces a more reduced cytoplasmic redox state [17]. In addition, cells from malignant hepatomas showed decreased ADH-mediated ethanol oxidation, and ADH-independent enzyme pathways are also dramatically reduced. Indeed, the content of mitochondrial protein and oxygen consumption are reduced in liver tumors; hence, cytosolic re-oxidation of NADH becomes the limiting factor during ethanol metabolism by tumoral liver cells [18]. In actively ethanol-metabolizing hepatoma cells, accumulation of acetaldehyde and increased mitochondrial NADH/NAD ratio lead to a dramatic ethanol-induced reduction in cell number [19], which strengthens the relationship between ethanol metabolism and liver cell proliferation.

Since there are no reports evaluating the main ethanol-oxidizing metabolic pathways in the rat regenerating liver, induced by PH, the present study was aimed at addressing the underlying mechanism in the stimulated ethanol oxidation, which is found in the PH-induced proliferating liver. Results clearly show that an important fraction of ethanol is metabolized through non-enzymatic mediating oxidative events that can largely contribute to the deleterious effect of ethanol on the proliferating liver.

2. Material and methods

2.1. Materials

4-Methylpyrazole (4-MP), 3-amino 1,2,4-triazole (3-AT), diallyl sulfone, amino-oxyacetate, rotenone, and other reagents were purchased from Sigma Chemical Co. (St. Louis, MO). Collagenase (type CS II) was obtained from Worthington Biochemicals (Freehold, NJ).

2.2. Animal treatments

Male Wistar rats (240–270 g, body weight, n = 70 in total) obtained from the certified bioterium of the Instituto de Fisiología Celular, UNAM, were housed under a 12:12 h light/dark cycle with free access to food (diet chow 500I, LabDiet Co.) and water. Two-thirds PH was performed according to the technique of Higgins and Anderson [20]: in rats intraperitoneally anesthetized with ketamine (40 mg • kg^{-1}), the liver central and left lateral lobes were removed in order to achieve a two-thirds hepatectomy, while controls were sham-operated rats. Abdominal wall and skin were sutured by planes and animals were allowed to recover. At indicated times post-treatment animals were euthanized by decapitation, after an overdose with sodium pentobarbital. Another set of control animals was fasted overnight before euthanasia. Animal procedures were conducted according to the Federal Regulations for Animal Experimentation (Ministry of Agriculture, SAGARPA, Mexico).

2.3. Ethanol bioavailability in rats subjected to PH and treated with 4-MP

In a set of fed animals (n = 20) grouped according to their surgical status (sham-operated or with PH), ethanol only (1.5 g • kg^{-1}b.w. in 40% w/v solution) was administered by intragastric intubation immediately after surgery, or concomitantly with a single dose of 4-MP (200 mg • kg^{-1}b.w.) intraperitoneally administered. Either, ethanol and 4-MP concentrations administered in vivo, were selected to accomplish an adequate estimation of blood ethanol clearance, as well as to achieve a maximal inhibition of liver ADH [9,21]. After treatments, animals were placed in restriction cages, without further access to water and food, and blood samples were collected from the wound of the excised tips of the tail with heparinized 50-μL capillary pipettes. Blood sampling was scheduled every 15 min during the first 2 h, every 30 min for the next 2 h, and every hour thereafter for a total of 10 h post-administration of ethanol only [9]. In the animals treated with 4-MP, sampling was done every 2 h until 12 to 16 h post-administration (not shown). Blood ethanol was quantified in neutralized acid extracts by an enzymatic method, recording reduction of NAD^+ [22]. The area under the curve (AUC) for ethanol elimination from the blood was calculated by a trapezoidal method, from the beginning of ethanol administration to the time it was no longer detected [23].

2.4. Hepatocyte incubations

In another set of animals (n = 25) and at the indicated times after surgical treatment, animals were anesthetized with ketamine (30 mg • kg^{-1}) in the morning, and liver cells were prepared essentially by the collagenase method of Berry and Friend [24], as modified by Seglen [25]. The liver was perfused with a calcium-free buffer prior to the perfusion with a collagenase (0.03%) and calcium-containing buffer (pH 7.4), previously oxygenated by bubbling carbogen (95% O_2 −5% CO_2). After separation from non-parenchymal cells by centrifugation, viability of hepatocytes was 90–95% as judged by trypan blue exclusion for all preparations. The hepatocytes were suspended in the same buffer containing 10 mmoles • L^{-1} glucose and 2.0% (w/v) fatty acid-free bovine serum albumin [26]. Typical assays were done usually with 100 mg (wet wt.) of liver cells in 2 mL of the described incubation medium plus 1 mL of buffer, containing 10 mmoles • L^{-1} of ethanol and agents, such as (in mmoles • L^{-1}, final concentration): 5.0 4-MP, 1.0 3-AT, 1.0 diallyl sulfone, 0.005 rotenone, 0.2 amino-oxyacetate, 0.5 thiourea, and 0.4 butylated hydroxytoluene; all these compounds were added 5 min before adding ethanol. Hepatocytes were incubated in rubber-stoppered 25-mL plastic flasks for 60 min at 37 °C, and the reaction was ended with 1 mL of 3 mol • L^{-1} perchloric acid.

2.5. Analytical procedures

In neutralized samples from perchloric acid-extracts, ethanol and glucose concentrations were determined enzymatically as previously described [9,22]. The cytosolic and mitochondrial fractions were obtained from whole liver by differential centrifugation, as described previously in detail [27]. The activities of alcohol dehydrogenase (ADH; EC 1.1.1.1), aldehyde dehydrogenase (ALDH; EC 1.2.1.3), and catalase (EC 1.11.1.6) were measured as described elsewhere [4]. The “supplemented” activities of the malate-aspartate and of the α-glycerophosphate shuttles were essentially determined using the assay previously described by Hernández-Muñoz et al. [28]. Mitochondrial and cytosolic activities of aspartate aminotransferase (AST; EC 2.6.1.1), as well as that of malate dehydrogenase (MDH; EC 1.1.1.27), were determined as described elsewhere [28]. In the same acid extracts, neutralized with 4 mol • L^{-1} K2CO3, the redox-pair metabolites: lactate,

pyruvate, α-glycerophosphate, dihydroxyacetone phosphate, β-hydroxybutyrate, and acetoacetate, were enzymatically determined, as described before [29,30]. The amount of aldehydic products generated by lipid peroxidation was quantified in the cytosolic fraction through the technique using the thiobarbituric acid reaction (TBARS), as previously modified [31].

2.6. Calculations and Statistics

Cytoplasmic and mitochondrial NAD/NADH ratios were calculated as follows: NAD/NADH = [oxidized substrate]/[reduced substrate] × $1/K_{eq}$, taking into account equilibrium constants for lactate, α-glycerophosphate, and β-hydroxybutyrate dehydrogenases [32]. Areas under curves were calculated by a trapezoidal method. All data were analyzed with the GraphPad Prism software, using an ordinary one-way ANOVA and a post hoc Newman-Keuls analysis, considering $p < 0.01$ as significant.

3. Results

3.1. Blood ethanol clearance in rats subjected to PH and treated with 4-MP

After intragastric administration of a single ethanol dose (1.5 g/kg b.w.), sham-operated rats reached a maximum blood alcohol concentration (BAC) of 21.2 ± 3.9 mM, associated with an area under the curve (AUC) of 11.7 ± 1.1 mM • h^{-1} (Fig. 1A). As previously found [9], animals subjected to PH (24 h after surgery) showed a much lower peak during the first 4 h after ethanol administration (BAC = 12.6 ± 2.5 mM, $p < 0.01$ against controls) without significantly modifying the AUC (15.8 ± 2.2 mM • h^{-1}; Fig. 1A). These data indicate that the regenerating liver has a very enhanced ethanol metabolism, particularly at 24 h post-surgery (Fig. 1A). Under conditions of inhibiting in vivo liver ADH activity, such as the main ethanol-metabolizing enzyme in the liver, 4-MP administration significantly changed AUCs and BACs in both sham operated and animals subjected to PH (Fig. 1B). Whereas in vivo 4-MP administration did not significantly change maximal BAC in control animals (22.6 ± 3.9 mM), and an expected prolongation of the AUC was noted (39.4 ± 4.1 mM • h^{-1}; Fig. 1B).

Also expected, rats undergoing PH and administered ethanol plus 4-MP showed a delayed maximal BAC of 30.8 ± 2.8 mM, significantly higher than that in controls ($p < 0.01$), and the AUC was largely increased (51.8 ± 5.6 vs. 39.4 ± 4.1 mM • h^{-1} in controls, $p < 0.01$; Fig. 1B). Hence, in vivo treatment with 4-MP readily delayed blood ethanol clearance in both experimental groups; however, since the magnitude of the inhibitory effect of 4-MP was differential (Fig. 1B), data suggest that ADH activity in the regenerating rat liver could have a lower participation in ethanol oxidation.

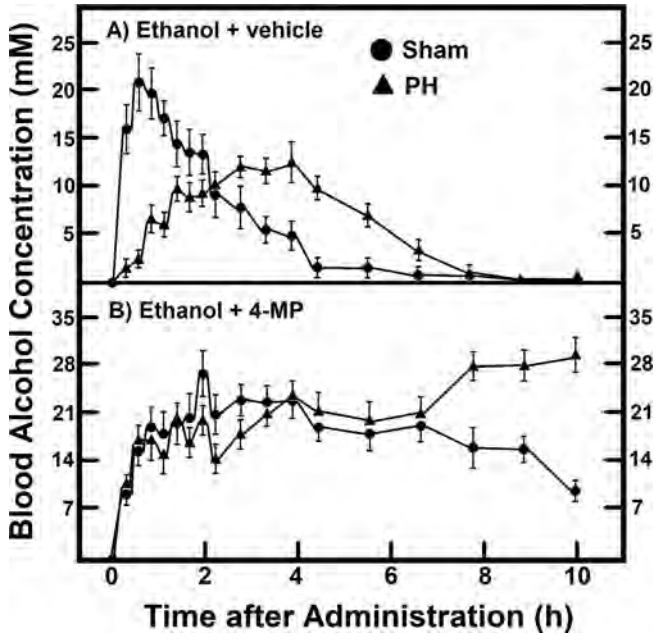

Fig. 1. Effect of in vivo 4-MP administration on blood alcohol concentrations in sham-operated and rats subjected to PH. Results are expressed as mean ± SE of 5 animals per experimental group. Panel A shows BACs and AUCs for ethanol metabolism in control and PH-rats (24 h after surgery) after intra-gastric alcohol administration (1.5 g • kg^{-1}b.w.). Panel B, control and partially hepatectomized rats additionally treated with 200 mg • kg^{-1}b.w. of 4-MP. Note the participation of first-pass metabolism of ethanol (panel A) without 4-MP treatment. Symbols for the experimental groups at the top of panel A.

3.2. Glucose utilization and ethanol oxidation by hepatocytes isolated from normal animals and from regenerating livers

To test the participation of possible metabolic pathways involved in ethanol oxidation, we used fresh isolated liver cells. Firstly, since ethanol oxidation largely depends on the metabolic status of isolated hepatocytes, the rates of glucose and ethanol utilization in liver cells obtained from normal fed or fasted animals were determined. Hepatocytes obtained from overnight fasted rats consumed more actively glucose than those from fed animals, an effect found to be constant up to 60 min of cell incubation (Fig. 2A). Despite that ethanol did not significantly modify glucose utilization in both cell preparations (fasted and fed animals) its oxidation was practically doubled in hepatocytes also incubated with glucose (Fig. 2B). Once tested the metabolic conditions for glucose utilization and ethanol oxidation in the hepatocyte's preparations, ethanol oxidation by hepatocytes obtained at different times post-surgery was measured (Fig. 2C). In the presence

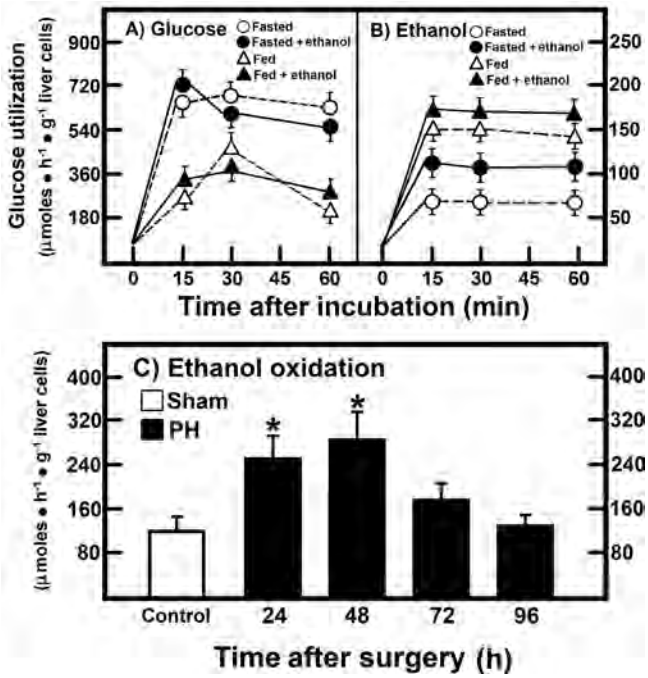

Fig. 2. Glucose and ethanol consumption by hepatocytes isolated from normal starved or fed rats, and the increased ethanol oxidation after PH. Results are the mean ± SE of five individual determinations made in duplicate per each experimental group. Panel A, glucose (10 mmoles • L^{-1}) consumption and, in panel B, ethanol (10 mmoles • L^{-1}) clearance by control hepatocytes from fed and starved rats. Panel C depicts the rate of ethanol oxidation by control hepatocytes and those isolated from PH-rats after several times post-surgery. Symbols at the top of each panel. Statistics as follows: *$p < 0.01$ against the control group.

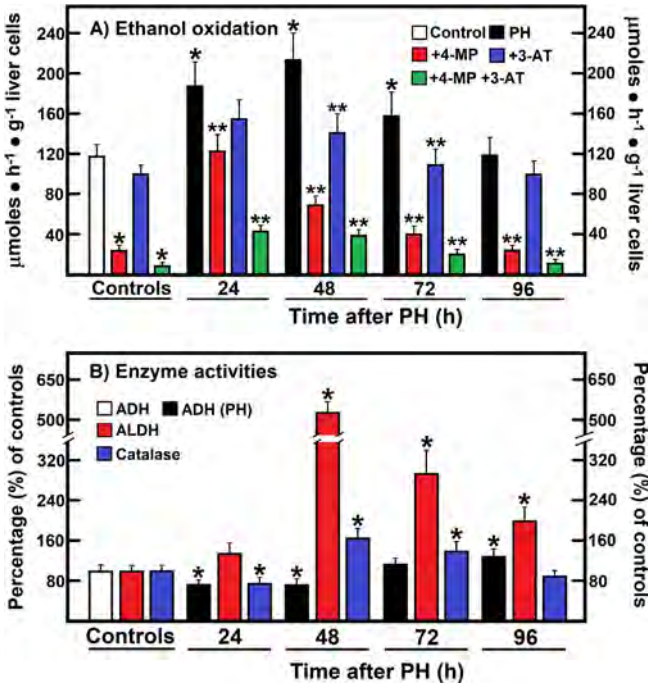

Fig. 3. Effect of inhibitors of ethanol-oxidizing enzyme pathways on ethanol catabolism by control and regenerating liver cells, and cytosolic activities of ADH, ALDH, and catalase. Results are expressed as mean ± SE of five individual observations per experimental point. Rates of ethanol oxidation were 120 ± 11, and 265 ± 24 µmoles • h^{-1} • g^{-1} of liver cells for control and hepatocytes from regenerating livers, respectively (panel A). In panel B, enzyme activities are expressed as percentage of the control values (22 ± 3 nmoles • min^{-1} • mg^{-1} of protein for ADH, 10 ± 2 nmoles • min^{-1} • mg^{-1} of protein for ALDH, and 310 ± 45 kcat • g^{-1} of total protein for catalase. Symbols at the top of each panel. Statistics: *$p < 0.01$ vs. the control group, and **$p < 0.01$ vs. the group with PH.

of glucose (5 mmoles • L^{-1}), isolated cells from regenerating livers showed a pronounced increase in ethanol oxidation (mainly during the first 48 h after surgery). At 96 h after PH, these liver cells oxidized ethanol at a similar magnitude to that found in hepatocytes from sham-operated controls (Fig. 2C).

3.3. Ethanol oxidation by hepatocytes isolated from proliferating livers and the participation of the main ethanol-oxidizing pathways

The relative contribution of the main enzymatic pathways for ethanol oxidation in hepatocytes was examined using "specific inhibitors" for ADH, catalase, and cytochrome P-4502E1 (Fig. 3). In "quiescent" liver cells, addition of 4-MP (the ADH inhibitor) decreased ethanol oxidation up to 80–85%, whereas the catalase-inhibitor (3-AT) only caused a 10–15% inhibition of ethanol disappearance. Diallyl sulfone, inhibitor of cytochrome P-450 2E1 (CYP2E1), accounted for only < 5% of the overall ethanol oxidation by control hepatocytes; moreover, the relative contribution of CYP2E1 in ethanol oxidation by hepatocytes from PH-rats was of 5, 4, 5, and 5%, at 24, 48, 72, and 96 h after surgery.

Control hepatocytes incubated in the presence of 4-MP and 3-AT showed about a 95% inhibition of ethanol catabolism (Fig. 3A). In isolated hepatocytes from proliferating livers, the contribution of the ADH pathway, as the main ethanol-oxidizing system, was much lower. The 4-MP only inhibited 45% of ethanol oxidation (at 24 h after surgery; Fig. 3A), while the magnitude of inhibition on ethanol consumption elicited by 3-AT and that of diallyl sulfone was quite similar in these cells, when compared to control hepatocytes. Indeed, addition of both, 4-MP and 3-AT, was only capable of inhibiting up to 70% of the increased ethanol oxidation found in liver cells from proliferating livers (Fig. 3A). Two days after surgery, the contribution of ADH to ethanol oxidation started to increase in proliferating liver cells, and a higher inhibitory effect of 3-AT was noted. Thus, the combination of both inhibitors of the ethanol-oxidizing pathway blocked ethanol metabolism at up to 90% at this time post-surgery (Fig. 3A). Hepatocytes, obtained 96 h after PH, oxidized ethanol and responded to the used inhibitors at the same magnitude as those from control animals (Fig. 3A).

Activities of the two main oxidizing-systems for ethanol largely contrasted with the rate of ethanol oxidation found in hepatocytes from regenerating livers (Fig. 3B). Cytosolic ADH activity was diminished as early as 24 h after PH remaining decreased up to 48 h post-surgery, and returned to the control value, thereafter (Fig. 3B). On the contrary, total activity of catalase (cytosolic and peroxisome activities) showed a mirror image in relation to that of ADH. Despite that catalase was also inhibited at 24 h after PH, it sharply augmented 48 h after surgery, returning to the control values within 3 to 4 days after PH (Fig. 3B). Moreover, ALDH activity, which removes acetaldehyde from the cytoplasm (low-affinity ALDH), showed changes evoking a mirror-image with respect to ADH (Fig. 3B). For instance, a maximum increase in ALDH activity was noted at 48 h after surgery, the time at which ADH was significantly lower as compared to controls. Thereafter, the augmented ALDH activity decreased progressively (72 to 96 h post-PH), whereas ADH increased now as compared to control livers (Fig. 3B).

3.4. Ethanol oxidation after inhibition of mitochondrial electron transport chain and the activity of the malate-aspartate shuttle

Rotenone, an inhibitor of site I of the mitochondrial electron chain, induced the same percentage of inhibition on ethanol oxidation in both normal and proliferating hepatocytes along the first 48 h after surgery (Fig. 4A). Unexpectedly, rotenone was less effective in inhibiting ethanol oxidation in cells isolated from PH-rats 96 h after surgery. Inhibition of AST activity by amino-oxyacetate (reduced activity of malate-aspartate shuttle) exerted a very small effect on hepatocyte's ethanol oxidation in control and at 24 after PH (Fig. 4A). However, apparent participation of the malate-aspartate shuttle in ethanol oxidation by proliferating hepatocytes (48 to 96 h after PH) was substantially increased (Fig. 4A).

3.5. Liver mitochondrial activities of hydrogen translocating shuttles and their involved enzyme activities

In the same context, the supplemented (reconstituted with missing cytosolic metabolites and enzymes) activities of malate-aspartate and α-glycerophosphate shuttles were determined in mitochondrial preparations (Fig. 4B). The activities of both mitochondrial shuttles were similar in control and PH-animals during the first 3 days after surgery; however, in PH-rats (4 days post-surgery), mitochondria preparations depicted enhanced activity of both pathways, mainly that of the α-glycerophosphate shuttle (Fig. 4B). The lack of early changes in the activity of the malate-aspartate shuttle in the regenerating liver (24 h after PH) contrasted with the measured activities of the participating enzymes, namely AST and MDH (Table 1). For instance, whereas the cytosolic activities of AST and MDH were not significantly modified by PH during the first 24 h after surgery, both AST and MDH activities were decreased in mitochondria from PH-animals (12–24 h after surgery; Table 1). Thereafter, mitochondrial AST and MDH activities were normalized (data not shown).

3.6. Participation of ROS and LP By-products in the rate of ethanol oxidation by hepatocytes from control and PH-rats

Since a remnant 25 to 30% of ethanol oxidation did not seem to be mediated by the main ethanol-oxidizing enzymes present in the proliferating hepatocytes (at early post-surgery times), probable non-

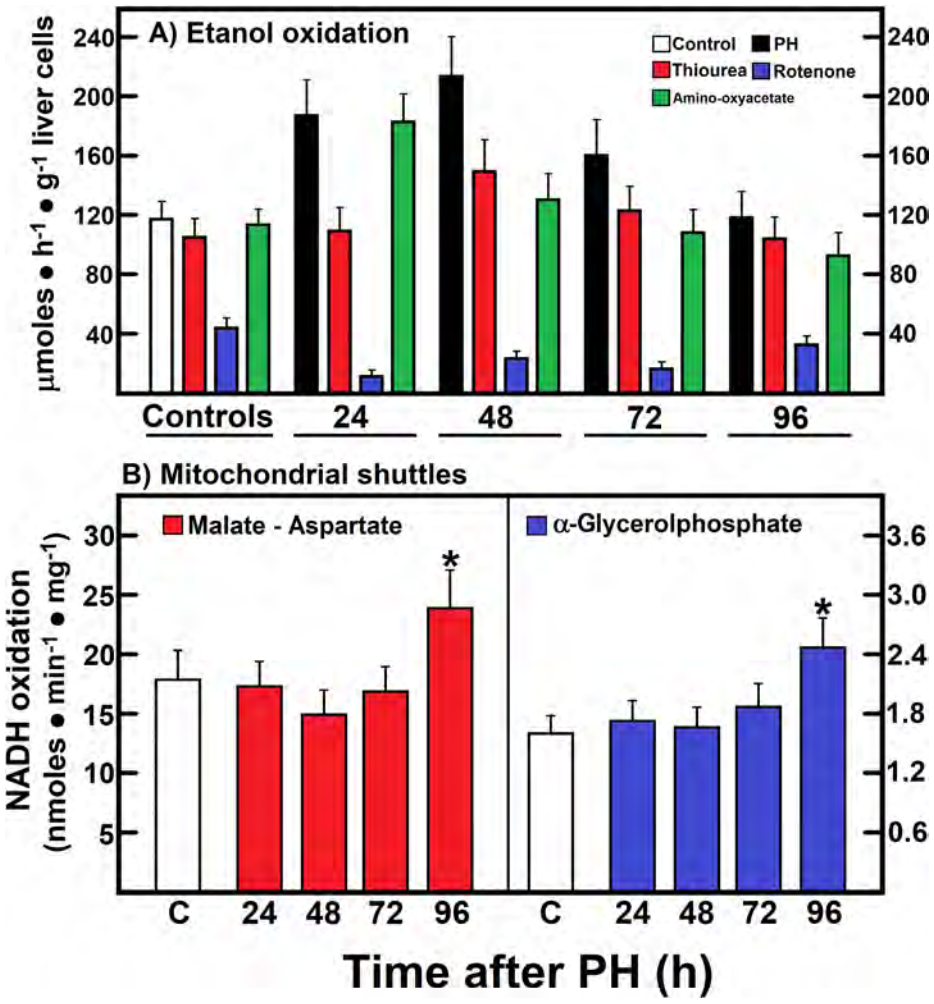

Fig. 4. Effects of inhibitors of the mitochondrial malate-aspartate shuttle, electron transport chain, and of scavengers for oxygen radicals on ethanol oxidation in control and regenerating liver cells. Results are expressed as mean ± SE of five individual observations per experimental point. Rates of ethanol oxidation in control liver cells and hepatocytes obtained from PH-rats are indicated in previous figures (panel A). Panel B, NADH oxidizing activity of the reconstituted mitochondrial shuttles for malate-aspartate, as well as that of α-glycerophosphate by the addition of the missing cytoplasmic components, in isolated mitochondria from livers of control and PH-rats. Symbols at the top of each panel. Statistical significance as indicated in Fig. 3.

Table 1
Aspartate aminotransferase (AST) and malate dehydrogenase (MDH) activities in cytosolic and mitochondrial fractions from sham-operated and PH-rats.

Cell fraction Enzyme activity	Time after surgery			
	0 h (control)	6 h	12 h	24 h
Cytosolic fraction				
A S T	0.55 ± 0.03	0.59 ± 0.05	0.60 ± 0.06	0.64 ± 0.06
M D H	0.46 ± 0.03	0.44 ± 0.03	0.50 ± 0.04	0.51 ± 0.05
Mitochondrial fraction				
A S T	1.15 ± 0.08	0.75 ± 0.07*	0.58 ± 0.06*	0.58 ± 0.07*
M D H	0.68 ± 0.03	0.52 ± 0.04*	0.38 ± 0.04*	0.48 ± 0.05*

Results are the mean ± SE of five individual determinations per each experimental group. Liver cytosolic and mitochondrial fractions were obtained by differential centrifugation from control and PH-animals. Statistics: *$p < 0.01$ against the control group.

enzymatic routes were searched for; focusing especially on the hydroxyl radicals-mediated ethanol oxidation, which is thought to play a minor role in in vivo ethanol catabolism [33]. Addition of thiourea, a scavenger for hydroxyl radicals, did have a slight inhibitory effect on ethanol oxidation by control hepatocytes, but elicited up to 30–42% inhibition of the stimulated ethanol catabolism in proliferating livers (24 h after PH). Nonetheless, the inhibitory effect of thiourea rapidly declined, reaching the control value at 4 days after PH (Fig. 4A).

Since data support that an important fraction of ethanol catabolism could be mediated by a non-enzymatic pathway, depending on the generation of free oxygen radicals, liver sub-cellular levels of lipid peroxidation by-products (TBARS) were determined. Fig. 5B reveals that whole homogenate levels of aldehydic products derived from LP events were greatly enhanced in fractions obtained from hepatocytes at different times post-PH. This significant increase was mainly accounted for by augmented TBARS levels in the cytosolic and plasma membrane fractions (Fig. 5B). A maximum peak of cytosolic LP was found at 24 h after PH and was still significantly higher 48 h after surgery; thereafter, this parameter was promptly normalized (Fig. 5B). Indeed, increased amount of LP by-products coincided with the enhanced ethanol oxidation by hepatocytes from animals subjected to PH, which was sensitive to inhibition by thiourea (Fig. 4A).

When animals subjected to PH where in vivo administered with ethanol, the subcellular patterns for TBARS content was significantly modified (Fig. 5). During the first 48 h after PH, ethanol administration indeed promoted an unexpected diminution in either cytosol or plasma membrane fractions, when compared with PH-animals treated with the ethanol vehicle (Fig. 5B and C). On the contrary, ethanol treatment to rats undergoing PH elicited a sustained increase of liver microsomal LP (24 to 72 h after surgery; Fig. 5D), which could be related somehow to endoplasmic reticulum stress.

3.7. Changes in hepatocyte's redox states after ethanol oxidation

As previously mentioned, hepatocyte's capacity for oxidizing ethanol is accompanied by changes mainly in the cytoplasmic redox state. Therefore, the levels of lactate/pyruvate and α-glycerophosphate/dihydroxyacetone phosphate, as markers of cytoplasmic redox state, were measured in isolated hepatocytes during ethanol oxidation.

INFORME DE LABORES 2019

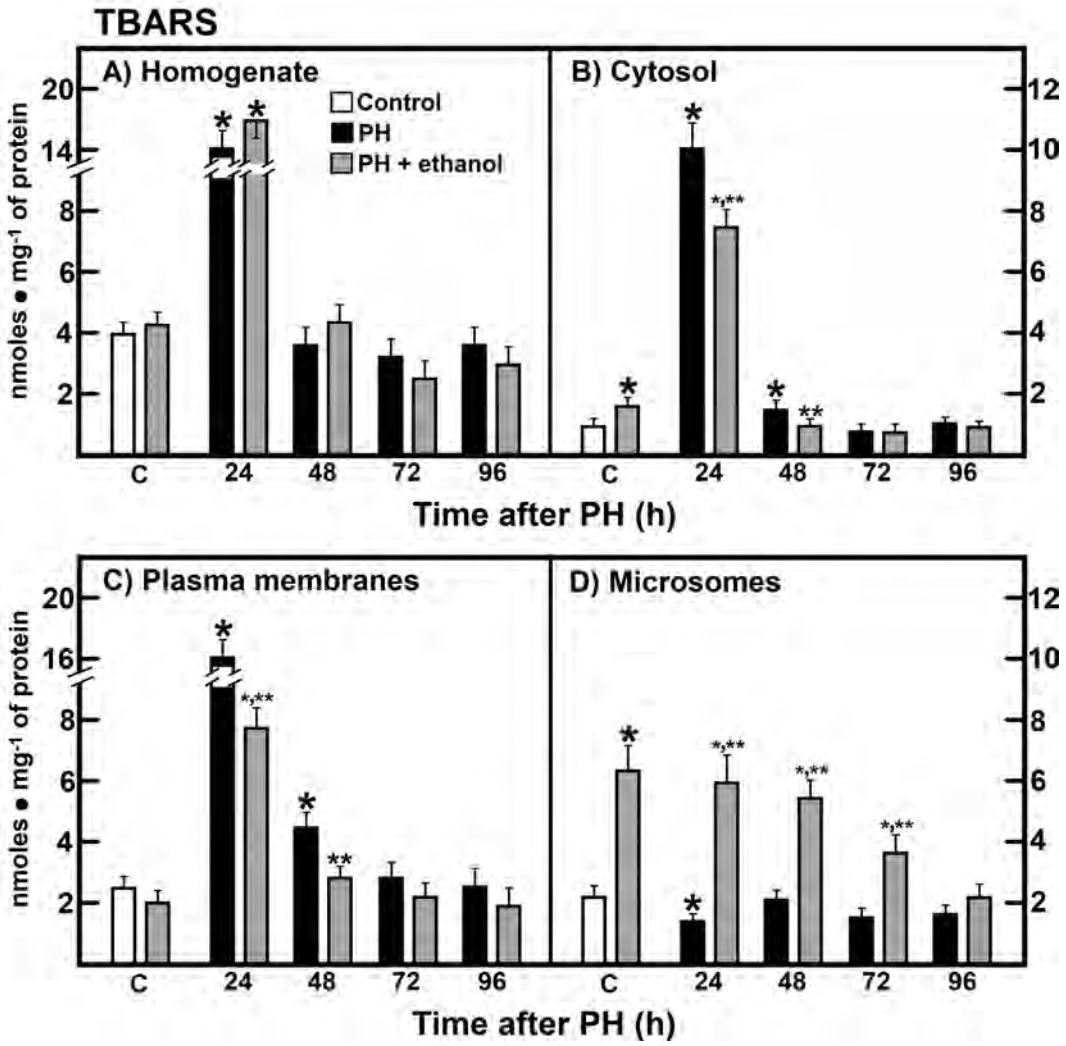

Fig. 5. Levels of TBARS in subcellular fractions from sham-operated and PH-rats, after in vivo ethanol administration. Results are expressed as mean ± SE of five individual observations per experimental point. Levels of lipid peroxidation by-products, mainly malondialdehyde, are expressed as thiobarbituric acid reactive substances (TBARS), determined in whole liver homogenate (panel A), cytosol (panel B), mitochondrial fraction (panel C), and those in microsomes (panel D). Symbols at the top of panel A. Statistical significance as pointed out in Fig. 3.

Determination of ß-hydroxybutyrate and acetoacetate were also done to calculate the mitochondrial redox state (Fig. 6). In control liver cells, ethanol oxidation diminished pyruvate and dihydroxyacetone phosphate levels whereas it increased those of α-glycerophosphate (not shown). The latter led to increases in the lactate/pyruvate and α-glycerophosphate/ dihydroxyacetone phosphate ratios (Fig. 6A). Consequently, the cytoplasmic NAD/NADH was strongly decreased when calculated by means of the equilibrium constants for lactate and α-glycerophosphate dehydrogenases (Fig. 6B). When ADH activity was inhibited by 4-MP, the ethanol-induced shift of cytoplasmic NAD/NADH ratio was largely prevented in control hepatocytes (Fig. 6A and B). Despite that ethanol did not significantly decrease mitochondrial NAD/NADH redox state (Fig. 6A), addition of 4-MP promoted a shift of mitochondrial NAD/NADH to a more oxidized state (Fig. 6A and B).

In cell preparations obtained from regenerating livers, 24 h after PH, ethanol oxidation induced smaller increases of the lactate/pyruvate and α-glycerophosphate/ dihydroxyacetone phosphate ratios (Fig. 6A), as well as a lower reduction of the cytoplasmic NAD/NADH ratio (Fig. 6B). The 4-MP also afforded protection against the ethanol-induced shift of the cytoplasmic NAD/NADH ratio, but at a much lesser magnitude. Interestingly, proliferating hepatocytes showed a more oxidized mitochondrial NAD/NADH, which was readily reduced by ethanol oxidation (Fig. 6B). Here, 4-MP failed to restore the mitochondrial NAD/NADH redox potential in the presence of ethanol (Fig. 6B).

4. Discussion

To our knowledge, the present constitutes the first study focused on investigating the participation of the known metabolic pathways to oxidize exogenous ethanol, in proliferating rat liver cells, induced by in vivo two-thirds PH. Having demonstrated that the regenerating liver shows a much enhanced metabolism of ethanol in vivo [9], the present work is an attempt to elucidate the main hepatic factors involved in the increased ethanol utilization by proliferating liver cells, as well as by subcellular fractions (mitochondria). The latter is particularly important, because we have previously shown an early decrease in the activities of the main liver ethanol-oxidizing enzymatic systems, at the onset of PH-induced liver regeneration [5]. First, we found in the in vivo experiments that removal of an important fraction of liver mass clearly influenced ethanol bioavailability in PH rats (Fig. 1). The present study shows that during the first 24 h after PH, ethanol reaching the systemic circulation, after its intragastric administration, varied in PH animals. After PH, ethanol administration elicited lower BACs than sham-operated rats (Fig. 1), which was mainly due a decreased gastric absorption for ethanol or to an increased gastric first-pass metabolism for ethanol [9]. Our results clearly show that the capacity of the

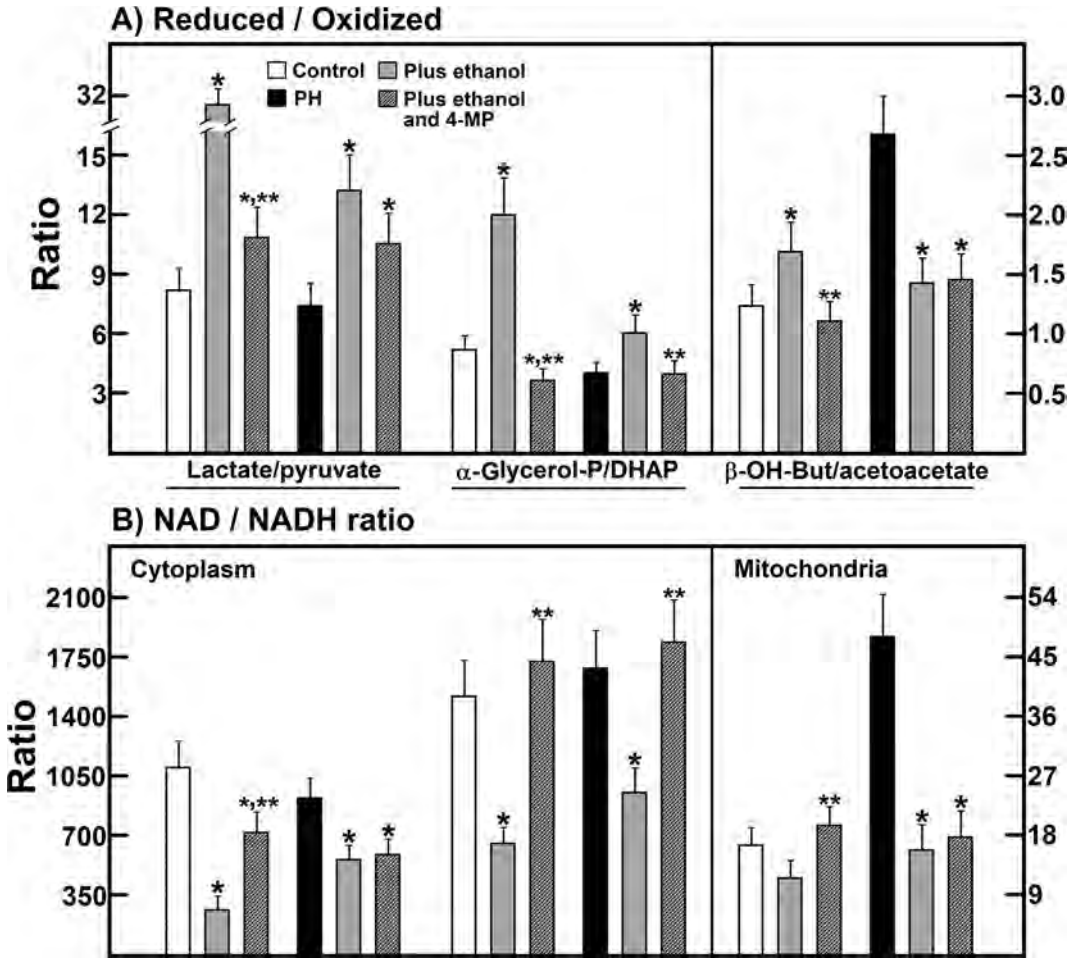

Fig. 6. Changes in cytoplasmic and mitochondrial redox state induced by ethanol oxidation in control and regenerating hepatocytes. Hepatic levels of redox-pair metabolites were determined enzymatically; the cytoplasmic and mitochondrial redox potentials (NAD/NADH ratios) were calculated from the reduced/oxidized metabolite ratios, as described under Methods. Results are expressed as mean ± SE of five individual observations per experimental point. Symbols for each experimental condition at the top of the Figure. Statistical significance as indicated in Fig. 3.

remnant liver (after 24 h of surgery; Fig. 1) to oxidize ethanol, was largely increased, which might potentiate the deleterious effect that ethanol exerts on liver regeneration.

Proliferating rat liver cells, such as those induced by PH, showed particular features in oxidizing ethanol in vitro: 1) Either in the presence or absence of glucose, isolated liver cells from animals subjected to PH had increased ethanol oxidation, despite that the main enzymatic pathways were initially decreased in these cells; 2) addition of inhibitors for ADH, catalase, and the CYP2E1 blunted ethanol oxidation in more than 90% in normal cells, whereas they only inhibited ethanol disposal at around 70% in proliferating liver cells; 3) scavengers of ROS did not significantly affect ethanol oxidation in control cells, but inhibited up to 30% of ethanol catabolism by proliferating hepatocytes; 4) inhibition of the ADH (by 4-MP) abolished ethanol-induced shifts in cytoplasmic and mitochondrial redox potentials in normal hepatocytes, while a more reduced mitochondrial redox state persisted in liver cells from proliferating livers.

Liver regeneration constitutes a unique model to study signal transduction and cell cycle events in a synchronized manner in vivo, and the extent and timing of liver regeneration are well known even to use interventional modifiers. After PH, stars the pre-replicative phase (G0 to G1), reaching the first peak of DNA synthesis 24 h post-surgery, and many participating factors lead cells to replicate (G2 cells) entering into mitosis (at 48 h post-PH). Thereafter, a second peak of DNA synthesis (72 h) is recorded, and at 96 h post-PH, many liver cells are returning to G1. In this time period (24 to 48 post-PH), we have proposed that ADH and, probably, ALDH could be actively using endogenous substrates involved in PH-induced rat liver regeneration [21]. Therefore, the diminished ADH-mediated ethanol oxidation might promote the participation of alternative pathways for the liver elimination of ethanol.

There are at least two hypotheses concerning the liver metabolic control in ethanol oxidation. The first states that this event is limited by the rate at which NADH can be re-oxidized to NAD [34], and the second hypothesis proposes that the rate of ethanol metabolism is regulated by the amount of ADH in the liver [11]. Although ADH activity is the major rate-determining enzyme, metabolic control is shared among several steps, including aldehydes dehydrogenase. Enzyme activities of the hydrogen shuttles for the transfer of cytosolic NADH into mitochondria and the electron transport chain, which are involved in the re-oxidation of the NADH that is formed during reactions driving to dehydrogenation, are also primary liver sites for the control of ethanol utilization [14,35].

Despite that ADH activity in the remnant liver after PH does not significantly change after surgery, the rate of ethanol removal is significantly faster in PH-rats [36]. In this context, Fig. 1 shows that the regenerating liver (24 h after PH) has a much enhanced capacity to metabolize ethanol, which seemed to be the main factor affecting ethanol pharmacokinetics in these animals. Here, in vivo treatment with 4-MP, a specific inhibitor of ADH, demonstrated that liver ADH was the main via oxidizing ethanol in both controls and PH-rats. However, the differential inhibitory effect of 4-MP observed in both

experimental groups could indicate that other ethanol-metabolizing systems are actively participating in removing ethanol from the systemic circulation (Fig. 1). Similarly, hepatocytes isolated from PH-rats had an enhanced in vitro oxidation of ethanol (Fig. 2).

In the liver, there is a second system located in hepatic cell peroxisomes, where ethanol oxidation is simultaneously coupled to decomposition of a H_2O_2 molecule through the catalase reaction [37]. In addition, a third enzymatic pathway for ethanol oxidation to acetaldehyde is constituted by the microsomal ethanol oxidizing system (MEOS), which requires the participation of a cytochrome P-450 isozyme (namely CYP2E1) and NADPH, reacting with an oxygen molecule and forming H_2O_2 [38]. The contribution of each enzymatic pathway to ethanol oxidation has been subjected to debate, but it is widely accepted that liver ADH plays a pivotal role in ethanol metabolism. Compared to ADH, the MEOS requires higher ethanol levels for full saturation and maximal velocity; hence, with high ethanol concentrations or after chronic ethanol consumption, the contribution of this non-ADH pathway is increased [39]. Moreover, it has been claimed that the physiological rate of H_2O_2 generation largely limits peroxidation by catalase [37].

The present results, using specific inhibitors for each enzymatic pathway, pointed toward ADH as the quantitatively most important pathway for the oxidation of ethanol to acetaldehyde, in the hepatocytes obtained from rats subjected to PH. In addition, the relative contribution of the non-ADH enzyme pathways (catalase and MEOS) was not modified in these cells (Fig. 3A). Since inhibitors used here can potentially block more than one enzymatic pathway for ethanol oxidation [40,41], this could complicate assessment of the relative participation of the main enzymatic pathways for ethanol oxidation. However, while a total blockade of ethanol oxidation was achieved when the main enzymatic systems were inhibited in normal liver cells, a remaining 30% of ethanol catabolism seemed to be carried out by a non-enzymatic mechanism in proliferating liver cells. As regard to the CYP2E1, this metabolizes and activates many toxicological substrates, including ethanol, generating in turn, ROS, such as superoxide, hydrogen peroxide and even hydroxyl radical [42]. Using Western blot analysis, it was found a significantly decreased expression of CYP 2El apoprotein as well as the dependent monooxygenase activities, after PH in rats [43], or not a significant change on CYP2E1 apoprotein expression has been also reported [44]. In this context, it is though that a close relationship between the periodicities of thymidine kinase activity and a decreased microsomal LP has some role in modulating the cell division process [27]. Whereas, an enhanced expression of CYP 2R1 and CYP 26A1 is important in the differentiation of oval cells into hepatoblast-like cells in the injured mice liver [45], an imputable role of the CYP 2E1 in the proliferating liver is still unknown.

On the other hand, the putative non-enzymatic pathways, here reported, required the presence of ROS (presumably hydroxyl radicals), which were readily inhibited by free radical scavengers (Fig. 4A), and closely correlated with cytoplasmic levels of lipid peroxidation by-products found in PH-rats (Fig. 5B). This non-enzymatic system has been previously shown to be functional in vitro and depends on iron chelation, through the Fenton reaction, which drives a spontaneous reaction given between the hydroxyl radical and ethanol [32,46]. The latter could well explain the enhanced ethanol oxidation shown by regenerating hepatocytes and, in turn, largely contribute to the deleterious action of ethanol on the regenerating liver, probably through perturbations in the cellular redox state and the production of acetaldehyde.

Some of the well-recognized effects of ethanol on hepatic metabolism are due to a substantial reduction of cytoplasm NAD (increased lactate/pyruvate ratio), promoted by a steep decline in pyruvate levels [47]. Thus, re-oxidation of cytosolic NADH partly limits the rate of ethanol oxidation and would cause several of the metabolic effects of ethanol [48]. During ethanol oxidation, fluxes through various dehydrogenases are sufficient to equilibrate both hydrogen atoms of cytosolic NADH [49]. For instance, activity of malate dehydrogenase, connected via the malate-aspartate shuttle to mitochondria [50], is high enough to account for the near-equilibrium of the hydrogen atoms of NADH. The generated cytoplasmic reducing equivalents are transferred to mitochondria by both the malate-aspartate and α-glycerophosphate shuttles [51] and, in combination with the activity on the mitochondrial respiratory chain, affect ethanol oxidation [18,37].

Using amino-oxyacetate, which inhibits both cytoplasmic and mitochondrial AST activities [52], the rates of gluconeogenesis and ureagenesis, and the oxidation of ethanol by hepatocytes are decreased, due to limitation of re-oxidation of cytosolic NADH generated by the ADH reaction [53]. In the same context, rotenone inhibits ethanol oxidation even in the presence of largely supplemented shuttles for reducing equivalents transport [54]. In both, normal and regenerating liver cells (at early times post-surgery), inhibition of the malate-aspartate shuttle had little effect on the rate of ethanol oxidation, whereas blocking the mitochondrial electron transport chain (by rotenone) induced an almost complete inhibition of ethanol oxidation (Fig. 4A). However, hepatocytes taken from PH-rats at later times post-surgery were more sensitive to the inhibition of the malate-aspartate shuttle and, surprisingly, a less inhibition was achieved with rotenone. These data correlated well with the changes previously reported in the liver cytoplasmic and mitochondrial redox states after PH [10], and found in hepatocytes obtained from regenerating livers (Fig. 6A and B). Despite that the activity of the malate-aspartate shuttle was not significantly modified by PH (Fig. 4B), mitochondrial oxidative capacity seemed to closely correlate with the ability of regenerating livers to oxidize ethanol. Indeed, our group reported that mitochondrial function, LP, and the onset of MPT are tightly regulated during progression of PH-induced liver regeneration [55].

Despite that acetaldehyde accumulates scarcely during alcohol oxidation because of its rapid conversion to acetate by aldehyde dehydrogenase, a number of ethanol-related complications may be explained by acetaldehyde production. Decreased mitochondrial NAD/NADH ratio caused by ethanol oxidation is attributable to acetaldehyde oxidation [56], as well as increased lipid peroxidation and microtubular alterations with its adverse effects on various cellular activities, including disturbances of cell division [57]. This is particularly important in view that acetaldehyde produced by the non-ADH pathways is degraded more slowly, which would contribute, indeed, to the alcoholic liver disease [58].

The LP might be the most important reaction involved in alcohol-induced liver damage [59,60] by the formation of toxic aldehydes, including MDA and 4-hydroxynonenal (4-HNE). These products, in a similar fashion to acetaldehyde, are able to react with the DNA to form exocyclic DNA adducts [61], which could be exacerbated by high concentrations of lactate during ethanol oxidation. Indeed, data indicated that early alcohol ingestion in rats subjected to PH promotes a significant change in the PH-induced LP, mainly in the microsomal fraction, probably suggesting the onset of endoplasmic reticulum stress.

It is well documented that ethanol metabolism impairs the regenerative capacity of the liver [1,3,4], and an accumulation of acetaldehyde and increased mitochondrial NADH/NAD ratio has led to an important ethanol-induced reduction in cell numbers or growth of a rat hepatic tumor cell line [19]. In fact, replenishing NAD + reduces oxidative stress and activates sirtuin-1 PGC-1α-induced mitochondrial biosynthesis, therefore, protecting against liver lipid accumulation, mitochondrial dysfunction, and promoting liver regeneration [62].

In conclusion, present results clearly show that regenerating adult liver cells (after PH) had an enhanced ethanol oxidation, largely attributable to a non-enzymatic mechanism for ethanol oxidation. This oxidative mechanism for ethanol acted mainly during the first 2 days after surgery, and involved acetaldehyde production and a consequent shift of mitochondrial NAD/NADH ratio to a more reduced state, which was not blocked by 4-MP (Fig. 3). Results suggest that an unusual ethanol metabolism, by the regenerating liver, could partly be

responsible for the deleterious actions of ethanol on liver regeneration induced by PH in rats, especially due to a “desynchronized” LP dependent on subcellular localization and temporal bases. The finding that an ADH and catalase-independent mechanism is readily oxidizing ethanol in the regenerating rat liver could have significant clinical implications.

Authors disclosure statement

Authors declare that we do not have any conflict of interests.

Acknowledgements

We thank Dr. José Gutiérrez-Salinas for his technical assistance in the preparation of the liver cells.

References

[1] A.L. King, S.K. Mantena, K.K. Andringa, T. Millender-Swain, K.J. Dunham-Snary, C.R. Oliva, et al., The methyl donor S-adenosylmethionine prevents liver hypoxia and dysregulation of mitochondrial bioenergetic function in a rat model of alcohol-induced fatty liver disease, Redox Biol. 9 (2016) 188–197.
[2] I. Bergheim, C.J. McClain, G.E. Arteel, Treatment of alcoholic liver disease, Dig. Dis. 23 (2005) 275–284.
[3] C.M. Leevy, T. Chen, Ethanol inhibition of liver regeneration, Gastroenterology 77 (1979) 1151–1153.
[4] L. Duguay, D. Coutu, C. Hetu, J.G. Joly, Inhibition of liver regeneration by chronic alcohol administration, Gut 23 (1982) 8–13.
[5] J. Gutiérrez-Salinas, A. Aranda-Fraustro, R. Paredes-Díaz, R. Hernández-Muñoz, Sucrose administration to partially hepatectomized rats: a possible model to study ethanol-induced inhibition of liver regeneration, Int. J. Biochem. Cell. Biol. 28 (1996) 1007–1016.
[6] W.O. Frank, A.M. Rayyes, A. Washington, P.R. Holt, Effect of acute ethanol administration upon hepatic regeneration, J. Lab. Clin. Med. 93 (1979) 402–413.
[7] J.R. Wands, E.A. Carter, N.L.R. Bucher, K.J. Isselbacher, Inhibition of hepatic regeneration in rats by acute and chronic ethanol intoxication, Gastroenterology 77 (1979) 528–531.
[8] A.R. Pösö, H. Pösö, Relationship between the phosphorylation state and the rate of ethanol elimination in regenerating rat liver, FEBS Lett. 100 (1979) 272–275.
[9] J.A. Morales-González, J. Gutiérrez-Salinas, R. Hernández-Muñoz, Pharmacokinetics of the ethanol bioavailability in the regenerating rat liver induced by partial hepatectomy, Alcohol. Clin. Exp. Res. 22 (1998) 1557–1563.
[10] J. Gutiérrez-Salinas, L. Miranda-Garduño, E. Trejo-Izquierdo, M. Díaz-Muñoz, J.A. Morales-González, R. Hernández-Muñoz, Redox state and energy metabolism during liver regeneration. Alterations produced by acute ethanol administration, Biochem. Pharmacol. 58 (1999) 1831–1839.
[11] K.E. Crow, N.W. Cornell, R.L. Veech, The rate of ethanol metabolism in isolated rat hepatocytes, Alcohol. Clin. Exp. Res. 1 (1977) 43–47.
[12] A.I. Cederbaum, E. Dicker, C.S. Lieber, E. Rubin, Ethanol oxidation by isolated hepatocytes from ethanol-treated and control rats; factors contributing to the metabolic adaptation after chronic ethanol consumption, Biochem. Pharmacol. 27 (1978) 7–15.
[13] K.E. Crow, N.W. Cornell, R.L. Veech, Lactate-stimulated ethanol oxidation in isolated rat hepatocytes, Biochem. J. 172 (1978) 29–36.
[14] R.A. Page, K.E. Kitson, M.J. Hardman, The importance of alcohol dehydrogenase in regulation of ethanol metabolism in rat liver cells, Biochem. J. 278 (1991) 659–665.
[15] A.J. Meijer, G.M. van Woerkom, J.R. Williamson, J.M. Tager, Rate-limiting factors in the oxidation of ethanol by isolated rat liver cells, Biochem. J. 150 (1975) 205–209.
[16] R.G. Thurman, Hepatic alcohol oxidation and its metabolic liability, Fed. Proc. 36 (1977) 1640–1646.
[17] M.R. Sly, D.G. Walker, A comparison of lipid metabolism in hepatocytes isolated from fed and starved neonatal and adult rats, Comp. Biochem. Physiol. 61B (1978) 471–477.
[18] A.I. Cederbaum, F.F. Becker, E. Rubin, Ethanol metabolism by a transplantable hepatocellular carcinoma. Role of microsomes and mitochondria, J. Biol. Chem. 251 (1976) 5366–5374.
[19] D.L. Clemens, A. Forman, T.R. Jerrells, M.F. Sorrell, D.J. Tuma, Relationship between acetaldehyde levels and cell survival in ethanol-metabolizing hepatoma cells, Hepatology 35 (2002) 1196–1204.
[20] G.M. Higgins, R.M. Anderson, Experimental pathology of the liver. Restoration of the liver of the white rat following partial surgical removal, Arch. Pathol. 12 (1931) 186–202.
[21] V. López-Valencia, P. Rangel, S. Rodríguez, R. Hernández-Muñoz, Involvement of alcohol and aldehyde dehydrogenase activities on hepatic retinoid metabolism and its possible participation in the progression of rat liver regeneration, Biochem. Pharmacol. 73 (2007) 586–596.
[22] D. Villalobos-García, R. Hernández-Muñoz, Catalase increases ethanol oxidation through the purine catabolism in rat liver, Biochem. Pharmacol. 137 (2017) 107–112.
[23] R.E. Rangno, J.H. Kreeft, D.S. Sitar, Ethanol 'dose-dependent' elimination: Michaelis-Menten v classical kinetic analysis, Br. J. Clin. Pharmacol. 12 (1981) 667–673.
[24] M.N. Berry, D.S. Friend, High-yield preparation of isolated rat liver parenchymal cells: a biochemical and fine structural study, J. Cell. Biol. 43 (1969) 506–520.
[25] P.O. Seglen, Preparation of rat liver cells. 3. Enzymatic requirements for tissue dispersion, Exp. Cell. Res. 82 (1973) 391–398.
[26] M. Díaz-Muñoz, R. Cañedo-Merino, J. Gutiérrez-Salinas, R. Hernández-Muñoz, Modifications of intracellular calcium release channels and calcium mobilization following 70% hepatectomy, Arch. Biochem. Biophys. 349 (1998) 105–112.
[27] I. Aguilar-Delfín, F. López-Barrera, R. Hernández-Muñoz, Selective enhancement of lipid peroxidation in plasma membrane in two experimental models of liver regeneration: partial hepatectomy and acute CCl_4 administration, Hepatology 24 (1996) 657–662.
[28] R. Hernández-Muñoz, M. Díaz-Muñoz, V. Chagoya de Sánchez, In vivo and in vitro adenosine stimulation of ethanol oxidation by hepatocytes, and the role of the malate-aspartate shuttle, Biochim. Biophys. Acta 930 (1987) 254–263.
[29] R. Hernández-Muñoz, A. Santamaría, J.A. García-Sáinz, E. Piña, V. Chagoya de Sánchez, On the mechanism of etanol-induced fatty liver and its reversibility by adenosine, Arch. Biochem. Biophys. 190 (1978) 155–162.
[30] R. Hernández-Muñoz, M. Díaz-Muñoz, V. Chagoya de Sánchez, Possible role of cell redox state on collagen metabolism in carbon tetrachloride-induced cirrhosis as evidenced by adenosine administration to rats, Biochim. Biophys. Acta 1200 (1994) 93–99.
[31] R. Hernández-Muñoz, W. Glender, M. Díaz-Muñoz, J.A. García-Sáinz, V. Chagoya de Sánchez, Effects of adenosine on liver cell damage induced by carbon tetrachloride, Biochem. Pharmacol. 33 (1984) 2599–2604.
[32] E.L. Christensen, J.J. Higgins, Effect of acute and chronic administration of ethanol on the redox states of brain and liver, in: E. Majchrowicz, E.P. Noble (Eds.), Pharmacology of Ethanol, Vol. 1 Plenum Press, New York, 1978, pp. 191–247.
[33] M. Ingelman-Sundberg, I. Johansson, Mechanisms of hydroxyl radical formation and ethanol oxidation by ethanol-inducible and other forms of rabbit liver microsomal cytochromes P-450, J. Biol. Chem. 259 (1984) 6447–6458.
[34] J.M. Khanna, Y. Israel, Ethanol metabolism, Int. Rev. Physiol. 21 (1980) 275–315.
[35] R. Rognstad, Control of ethanol utilization by rat hepatocytes, Biochim. Biophys. Acta 676 (1981) 270–273.
[36] H. Pösö, A.R. Pösö, Ethanol elimination in regenerating liver: the roles of alcohol dehydrogenase and acetaldehyde, Acta Chem. Scand. B. 33 (1979) 249–255.
[37] C.S. Lieber, E. Baraona, M.A. Leo, A.I. Garro, Metabolism and metabolic effects of ethanol, including interaction with drugs, carcinogens and nutrition, Mutation Res. 186 (1987) 201–233.
[38] D.R. Koop, J.P. Casazza, Identification of ethanol-inducible P-450 isozyme 3a as the acetone and acetol monooxygenase of rabbit microsomes, J. Biol. Chem. 260 (1985) 13607–13612.
[39] T. Takagi, J. Alderman, C.S. Lieber, In vivo roles of alcohol dehydrogenase (ADH), catalase and the microsomal ethanol oxidizing system (MEOS) in deermice, Alcohol 2 (1985) 9–12.
[40] S. Puntarulo, A.I. Cederbaum, Oxidation of pyrazole to 4-hydroxypyrazole by intact rat hepatocytes, Biochem. Pharmacol. 37 (1988) 1555–1561.
[41] K.S. Salmela, I.G. Kessova, I.B. Tsyrlov, C.S. Lieber, Respective roles of human cytochrome P-4502E1, 1A2, and 3A4 in the hepatic microsomal ethanol oxidizing system, Alcohol. Clin. Exp. Res. 22 (1998) 2125–2132.
[42] Y. Lu, A.I. Cederbaum, CYP2E1 and oxidative liver injury by alcohol, Free Radic Biol. Med. 44 (2008) 723–748.
[43] C. Trautwein, T. Rakemann, P. Obermayer-Straub, M. Niehof, M.P. Manns, Differences in the regulation of cytochrome P450 family members during liver regeneration, J. Hepatol. 26 (1997) 48–54.
[44] M. Ishizuka, S. Yoshino, Y. Yamamoto, H. Yamamoto, S. Imaoka, Y. Funae, et al., Isozyme selective alterations of the expression of cytochrome P450 during regeneration of male rat liver following partial hepatectomy, Xenobiotica. 27 (1997) 923–931.
[45] A. Hirose, W. Ochiai, Y. Yamamoto, M. Fukaya, H. Iwasaki, N. Wakui, et al., Analysis of CYP2R1 and CYP26A1 expression patterns in regeneration in mice with liver injury, Biol. Pharm. Bull. 39 (2016) 1955–1960.
[46] H. Riveros-Rosas, A. Julián-Sánchez, E. Piña, Enzymology of ethanol and acetaldehyde metabolism in mammals, Arch. Med. Res. 28 (1997) 453–471.
[47] M.A. Efthivoulou, J.W. Phillips, M.N. Berry, Abolition of the inhibitory effect of ethanol oxidation on gluconeogenesis from lactate by asparagine or low concentrations of ammonia, Biochim. Biophys. Acta 1244 (1995) 303–310.
[48] J. Mørland, A. Bessenen, L. Svendsen, The role of alcohol metabolism in the effect of ethanol on protein synthesis in isolated rat hepatocytes, Alcohol. Clin. Exp. Res. 4 (1980) 313–321.
[49] C. Vind, A. Hunding, N. Grunnet, Pathways of reducing equivalents in hepatocytes from rats. Estimation of cytosolic fluxes by means of ^{3}H-labelled substrates from either A- or B-specific dehydrogenases, Biochem. J. 243 (1987) 625–630.
[50] T. Cronholm, Incorporation of the 1-pro-R and 1-pro-S hydrogen atoms of ethanol in the reduction of acids in the liver of intact rats and in isolated hepatocytes, Biochem. J. 229 (1985) 323–331.
[51] T. Sugano, T. Ohta, A. Tarui, Y. Miyamae, Effects of alanine on malate-aspartate shuttle in perfused libres from cold-exposed rats, Am. J. Physiol. 251 (1986) E385–E392.
[52] A.J. Meijer, J.A. Gimpel, G. Deleeuw, M.E. Tischler, J.M. Tager, J.R. Williamson, Interrelationships between gluconeogenesis and ureogenesis in isolated hepatocytes, J. Biol. Chem. 253 (1978) 2308–2320.
[53] A.I. Cederbaum, E. Dicker, E. Rubin, Transfer and reoxidation of reducing equivalents as the rate-limiting steps in the oxidation of ethanol by liver cells isolated from

fed and fasted rats, Arch. Biochem. Biophys. 183 (1977) 638–646.
[54] R.N. Zahlten, M.E. Nejtek, J.C. Jacobsen, Ethanol metabolism in guinea pig: ethanol oxidation and its effect on NAD/NADH ratios, oxygen consumption, and ketogenesis in isolated hepatocytes of fed and fasted animals, Arch. Biochem. Biophys. 213 (1982) 200–231.
[55] R. Hernández-Muñoz, L. Sánchez-Sevilla, A. Martínez-Gómez, M.A.R. Dent, Changes in mitochondrial adenine nucleotides and in permeability transition in two models of rat liver regeneration, Hepatology 37 (2003) 842–851.
[56] E. Mezey, J.J. Potter, S. Sharma, B.E. Akinshola, Effect of epinephrine on ethanol metabolism by isolated rat hepatocytes, Biochem. Pharmacol. 40 (1990) 2473–2478.
[57] Y. Matsuda, E. Baraona, M. Salaspuro, C.S. Lieber, Effects of ethanol on liver microtubules and Golgi apparatus. Possible role in altered hepatic secretion of plasma proteins, Lab. Invest. 41 (1979) 455–463.
[58] Y. Matsuda, A. Takada, M. Yasuhara, S. Takase, Degradation of acetaldehyde by the non-alcohol dehydrogenase pathway, Alcohol Alcohol. 1 (1988) 77–80.
[59] E. Albano, Free radical mechanisms in immune reactions associated with alcoholic liver disease, Free Radic. Biol. Med. 32 (2002) 110–114.
[60] K. Nagata, H. Suzuki, S. Sakaguchi, Common pathogenic mechanism in development progression of liver injury caused by non-alcoholic or alcoholic steatohepatitis, J. Toxicol. Sci. 32 (2007) 453–468.
[61] E. Ceni, T. Mello, A. Galli, Pathogenesis of alcoholic liver disease: role of oxidative metabolism, World J. Gastroenterol. 20 (2014) 17756–17772.
[62] S. Wang, T. Wan, M. Ye, Y. Qiu, L. Pei, R. Jiang, et al., Nicotinamide riboside attenuates alcohol induced liver injuries via activation of SirT1/PGC-1α/mitochondrial biosynthesis pathway, Redox Biol. 17 (2018) 89–98.

INFORME DE LABORES 2019

Received: 20 June 2018 | Revised: 1 December 2018 | Accepted: 14 December 2018

DOI: 10.1111/crj.12987

Check for updates

WILEY

ORIGINAL ARTICLE

Identification of genomic copy number variations in lung benign metastasizing leiomyomatosis

Everardo Hernández-Plata[1,2] | **Ana Claudia Velázquez-Wong**[1] | **Carmina Jiménez-Ramírez**[3] | **Fernando Fernández-Ramírez**[4] | **Luz María Galicia-Sánchez**[5] | **César Antonio Flores-García**[6] | **José Manuel Hernández-Hernández**[1] | **Haydeé Rosas-Vargas**[1] | **Juan Carlos Huicochea-Montiel**[7] | **Eliseo Espinosa-Poblano**[8]

[1]Unidad de Investigación Médica en Genética Humana, UMAE Hospital de Pediatría, Centro Médico Nacional Siglo XXI, Instituto Mexicano del Seguro Social IMSS, Ciudad de México, México

[2]Departamento de Neuropatología Molecular, Instituto de Fisiología Celular, UNAM, Ciudad de México, México

[3]Unidad Médica de Alta Especialidad, Hospital de traumatología, Dr. Victorio de la Fuente Narváez Instituto Mexicano del Seguro Social IMSS, Ciudad de México, México

[4]Unidad de Genética, Hospital General de México Dr. Eduardo Liceaga, Ciudad de México, México

[5]Servicio de Neumología, Hospital de Cardiología, Centro Médico Nacional Siglo XXI, IMSS, Ciudad de México, México

[6]Departamento de Patología, Unidad Médica de Alta Especialidad, Hospital de Cardiología del Centro Médico Nacional, Siglo XXI, IMSS, Ciudad de México, México

[7]Departamento Clínico de Genética Médica, Hospital de Pediatría, Centro Médico Nacional Siglo XXI, Instituto Mexicano del Seguro Social, Ciudad de México, México

[8]Servicio de Neumología, Unidad Médica de Alta Especialidad, Hospital de Especialidades del Centro Médico Nacional, Siglo XXI, IMSS, Ciudad de México, México

Correspondence
Everardo Hernández-Plata, Unidad de Investigación Médica en Genética Humana, UMAE Hospital de Pediatría, Centro Médico Nacional Siglo XXI, Instituto Mexicano del Seguro Social IMSS, Avenida Cuauhtémoc 330, Doctores, 06720 Cuauhtémoc, Ciudad de México, México.
Email: ehplata@ifc.unam.mx

Funding information
Instituto Mexicano del Seguro Social, Grant/Award Number: R-2011-785-066.

Abstract

Objectives: Lung metastasizing leiomyomatosis (LML) is an infrequently diagnosed pathology developed after sexual maturation, commonly preceded by uterine myomas. Symptoms can include difficulties to breathe, cough, dyspnea and pain, because of mechanical obstruction exerted by expanding local growing leiomyomas. Lung leiomyomas are normally detected by imaging studies, but nowadays the precise diagnosis demands histological characterization of biopsies obtained from the affected tissues. The purpose of the present study was to determine the presence of genomic alterations in circulating cells of LML.

Methods: Immunohistochemical characterization of a lung biopsy extracted by thoracoscopy was performed. Pathologic proliferative smooth muscle cells were observed in a major lung metastasizing nodule, with a growing pattern similar to a uterine myoma. The presence of cellular linages different to smooth muscle cells was discarded by testing the presence of a battery of molecular markers. Also, a normal karyotype was determine by GTG-banding cytogenetic study, but a high density microarray analysis revealed six submicroscopic chromosomal regions displaying

All the authors contribute importantly to this work.

 © 2018 John Wiley & Sons Ltd

INFORME DE LABORES 2019

genomic abnormalities: microduplications were detected on chromosomes 4, 14, 17 and 22; and microdeletions on chromosomes 8 and 10.

Conclusion: This study remarks the relevance of submicroscopic chromosomal analysis of unusual pathologic conditions such as Benign Metastasizing Leiomyomatosis. This propitiate a better understanding of the molecular basis on the development of the pathology, in order to reckon on minimally invasive diagnostic methods, and to design appropriate treatments.

KEYWORDS

benign metastasizing leiomyomatosis, copy number variations, lung metastasizing leiomyomas, uterine myomas

1 | INTRODUCTION

Benign Metastasizing Leiomyomatosis (BML) is characterized by abnormal proliferation of smooth muscle cells presented as secondary neoplasms in women, appearing from several months up to 26 years after presenting uterine myomas.[1] Uterine leiomyomas constitute the most frequent neoplasms in women, affecting up to 20%-30% of the female population over 30 years old.[2] Infrequently leiomyomatosis is detected outside the uterus, this condition is represented by peritoneal disseminated, intravenous, parasitic, retroperitoneal and BML.[3]

Among the sites where secondary leiomyomas can grow up, lungs are the most frequent organ presenting metastasis, although other tissues, such as mesentery, mediastinum, heart, or even dorsal spine and bones can also be affected.[4] In many cases, the lesions are indolent and discovered rather incidentally; the clinical signs vary depending on the location of metastasizing leiomyomas. When lungs are affected, multiple well-defined pulmonary nodules sizing from millimetres to some centimetres in diameter can be detected by imaging routine chest examinations.[5] The symptoms can include cough, pain, or dyspnea and sometimes these are associated with conditions, such as pneumonia or bronchitis. The precise diagnosis of the disease currently demands analysis of affected pulmonary nodules by histopathological characterization of a thoracic biopsy.

Metastasizing leiomyomatosis constitutes a big diagnostic challenge; because of their appearance and distribution, benign leiomyomas could be misidentified. The most useful modalities for detecting extrauterine leiomyomas are ultrasonography, computed tomography, magnetic resonance imaging and positron emission tomography (PET). Typically, X-ray imaging appearance of pulmonary nodules in BML varies from solitary millimetric lesions to multiple lesions.[6]

Hysterectomy is typically accomplished as a common treatment for symptomatic uterine leiomyomatosis-affected patients,[7] but several secondary effects, such as urinary incontinence, cardiovascular diseases[8] or cognitive disorders are related to this procedure.[9] Hence, less invasive procedures as myomectomy or hysteroscopy are effective surgical alternatives for benign uterine leiomyomatosis.[10,11] The clinical course of the pathology inside and outside the uterus is hormone-dependent, so when surgery is not carried out, recommended pharmacological alternative treatments include the aromatase inhibition, selective progesterone-receptor modulators and GnRH agonists.[12]

Aetiology and risk factors of BML remain unclear but several reports have provided evidences of intravenous leiomyomatosis dissemination, embolism of benign leiomyoma cells from myometrium, or independent and multifocal proliferation of smooth-muscle cells depending on oestrogenic hormones.[13,14] Cytogenetic reports of the BML tumours are non-convergent; the clonality between primary and secondary neoplasms still remains in controversy. The present study was focused on the immunohistological characterization of uterine and lung leiomyomas which appeared several years after first myomas detection and a hormone treatment. Additionally, it was investigated the presence of chromosomal abnormalities and genomic copy number variations (CNVs) in peripheral blood cells.

2 | MATERIALS AND METHODS

2.1 | Case history

The patient presented menarche at 10 years old, and consumed oral oestrogens between 17 and 24 years old because of dysmenorrhea. Uterine leiomyomas and ovarian cysts were detected for the first time at 32 years old; they were resected. The histological characterization of two excised myomas, sizing 8 and 14 cm, showed a smooth muscle cellular conformation, so they were diagnosed as benign leiomyomas. At the age of 41 years old, with a referred history as a passive smoker, the patient entered to the hospital referring shoulder and pleural chest pain, and dyspnea.

INFORME DE LABORES 2019

Laboratory studies at the hospitalization moment included blood chemistry, tumour markers and hormonal profile; all of them reflected normal parameters (CA 15-3 antigen: 11.3 U/mL; CA 19-9 antigen: 12.96 U/mL; CA 125 antigen: 20.6 U/mL; carcinoembryonic antigen: 0.49 ng/mL; estradiol: 77 pg/mL; luteinizing hormone: 8.0 mUI/mL; gonadotrophin chorionic fraction beta 0.3 mUI/mL; progesterone: 0.2 ng/mL). She had never been pregnant and reported a negative family record of cancer. Imaging studies were performed for detection of possible abnormalities in chest and lungs at the moment of hospitalization, and PET was developed after treatment to discard any derivative abnormality.

2.2 | Immunohistochemistry

Biopsies of lung and uterine nodules were fixed in paraformaldehyde solution after resection by surgery, and paraffin imbibed for later characterization by immunohistochemical assays. Briefly, slices sizing 4 μm in thick were obtained from each tissue and deparaffinized in xylene; then, slices were hydrated in ethanol decreasing concentration series. Tissues-morphology was tested firstly in hematoxylin-eosin stained sections. Antigen epitopes retrieval was performed by boiling citrate-buffered (pH 6.0) slices in a pressure cooker. The endogenous peroxidase activity was blocked by incubating in a 3% H_2O_2/methanol solution during 10 minutes at room temperature, and rinsed in phosphates buffered solution for 5 minutes. Afterward, tissue sections were incubated with the corresponding primary antibody, as specified below, for 40 minutes; then, phosphate buffered saline rinses were carried out twice followed by incubation with the secondary antibody conjugated with peroxidase enzyme for 30 minutes. Peroxidase activity was revealed by incubation with diaminobenzidine/H_2O_2 for 5 minutes. Appropriate immunoreactive tissue samples were stained in parallel as positive controls for each antibody. Slices were subsequently washed in water, counterstained with hematoxylin, dehydrated and mounted. The primary antibodies employed for the characterization of tissue slices were: Bcl-2 (BioSb, mouse monoclonal; 1:100 dilution); calretinin (BioSb, rabbit monoclonal; 1:250 dilution); cytokeratin AE1/AE3 (Cell Marque, mouse monoclonal; 1:200 dilution), desmin (Bio Genex, mouse monoclonal; 1:200 dilution). Smooth muscle actin (Cell Marque, mouse monoclonal; 1:1000 dilution), and S-100 protein (Cell Marque Mouse monoclonal; 1:120 dilution).

2.3 | GTG-bands and karyotype

A fresh peripheral blood sample was taken from the patient. Lymphocytes were isolated, cultured and harvested using standard methods. Chromosome preparations were banded with Wright-Giemsa and observed under microscope. To determine the karyotype a minimum of 50 metaphases were analysed.

2.4 | Microarray CytoScan HD

A fresh peripheral blood sample was centrifuged at 4500 rpm during 10 minutes at room temperature. 200 μL of the buffy coat fraction was processed to isolate genomic DNA (gDNA) using the QIAamp DNA Mini Kit, according to the manufacturer's protocol (Qiagen, Gaithersburg, Maryland). Concentration and purity of the extracted DNA was determined by spectrophotometry in a NanoDrop 1000 (Thermo Fisher Scientific, Waltham, Maryland). Then, the DNA was processed to determine CNVs and loss of heterozygosity (LOH) with an Affymetrix CytoScan HD array (Thermo Fisher Scientific), following the manufacturer's instructions.

Briefly, 250 ng of gDNA were digested with Nsp I. Then, DNA fragments were joined to Adaptors using T4 DNA ligase. The mix was used as template for DNA amplification. The PCR reaction was developed using the Titanium® DNA amplification kit (Takara, Clontech. Mountain View, California). DNA amplification was corroborated by electrophoresis in a 2% agarose gel, where ~150-2000 bp DNA fragments were observed. Concentration of purified DNA was determined by spectrophotometry. Then DNA was enzymatically fragmented using the case reagents. Fragmentation was verified by electrophoresis in a 4% agarose gel. Latter, DNA was labelled, and then mixed with the hybridization buffer. All the thermal varying programs were run in a thermo cycler Gene Amp PCR System 9700 (Applied Biosystems, Foster City, California). The DNA was injected into an Affymetrix CytoScan HD array. The covered array was incubated into a GeneChip Hybridization Oven 645. The array was washed and stained into a Gene Chip Fluidics Station 450 (Affymetrix), operated by means of the AGCC software (Thermo Fisher Scientific). Finally, the array was scanned using a GeneChip®3000 Scanner. The corresponding batch registration file was created in the Affymetrix GeneChip Command Console Portal. The array contains ~2.6 million copy number markers. Chromosome Analysis Suite (ChAS) software v3.2 (Thermo Fisher Scientific) was used after procedure for data analysis, where a minimum length of 100 000 base pairs (bp) was fixed to determine gains and losses; and 3 Mbp for LOH.

2.5 | Epigenetic *in silico* analysis

Epigenetic consequences involving deleted genomic regions were analysed based on available data from the Broad Institute, ID numbers 30003 and 30004, containing ChIP-Seq mapping of H3K4me1, H3K4me3, H3K27me3, H3K9me3 and CTCF binding profile in HUVEC cells. Human smooth muscle Hi-C data was loaded and analysed in the 3D genome

browser suite (http://promoter.bx.psu.edu/hi-c/) using the hg19 human reference sequence.

3 | RESULTS

3.1 | Imaging

Computed tomography and X-ray studies showed lungs with multiple irregular, bilateral nodular lesions suggesting a metastatic disease (Figure 1). Pleural effusion and an acute unspecific inflammatory process were noticed. No signs of malignancy or infections were detected.

One month after thoracoscopy, a PET of high resolution was accomplished to discard the presence of malignant tumours in the whole body of the patient. Intravenous non-ionic iodized contrast and 370 MBq of ^{18}F-FDG was administrated. After 60 minutes of rest, reconstruction images were taken from skull to the proximal third of thighs. It was observed a minimum focal increase in the glycolytic metabolism in lungs with multiple hypodense lesions, one of them with 35 mm in the major axis, localized in the lower left lobe. A 19 mm cyst was also detected in the same segment, possibly caused by postsurgical effects. Two cysts <5 mm were observed in segment 4 of liver. No focal lesions were detected in the rest of the body.

3.2 | Immunohistochemistry

Immunohistochemical characterization of an open thoracoscopy biopsy revealed benign proliferative smooth muscle fibres in lung nodules (Figure 2). The pathological growing pattern of the major lung metastasizing nodule was similar to the uterine leiomyoma, as revealed by hematoxylin and eosin staining (Figure 2A and H). Positive and specific reactivity was detected in the pulmonary nodule for smooth-muscle actin and desmin (Figure 2F and G). The neoplasic nature of the tissue was proved by positive staining for Bcl-2 (Figure 2E).

The negative cytokeratins staining excluded the epithelial nature of this neoplasm (Figure 2B); positive expression was detected in pneumocytes, as control (not showed). Likewise, negative expression for S-100 protein (Figure 2C), and calretinin (Figure 2D) allowed us to reject the presence of other tumour cells linages, such as schwannoma, melanoma or mesothelioma. Importantly, only several smooth muscle cells in the lung nodule were present as reveled by smooth muscle actin staining (Figure 2F), this indicates the migration of metastatic cells from uterus into lungs, probably throughout lymph vessels.

3.3 | Karyotype and molecular cytogenetics

The conventional GTG-banding cytogenetic analysis revealed a normal karyotype 46,XX in at least 50 well-defined metaphases.

The submicroscopic copy-number changes detected across the genome in the BML sample were: arr[GRCh37] 4q22.3(98593089_98768685)x3, 8p11.22(39247097_39386952)x1, 10q11.22(46981355_47147301)x1, 14q32.33(106207204_106736911)x3, 17q21.31(44212823_44784639)x3, 22q11.22(23146338_23258369)x3.

The microarray analysis identified six regions displaying CNVs: microduplications on chromosomes 4, 14, 17 and 22; and microdeletions on chromosomes 8 and 10 (Figure 3). Five of these CNVs correspond to rare alterations whose role on pathogenicity has not been well established (Table 1). Importantly, genes contained in the chromosome 10 (q11.22 deletion) modulate neurite outgrowth and branching[15]; as well as the gut–brain axis including neural, immune and endocrine signalling pathways implicated in anxiety and depression.[16]

The duplication in chromosome 17q21.31 includes the genes *ARL17A, ARL17B* and *NSF* encoding for molecular elements required for protein trafficking and intracellular vesicle-mediated transport.[17] Interestingly in the same segment, *KANSL1* was also duplicated; this gene encodes for a nuclear protein that is a subunit of two histone acetyltransferase complexes,[18] and therefore may be involved in chromatin remodelling and transcription regulation of several genes. Segments in chromosomes 14 and 22 encoding for a long non-coding RNA (lncRNA), and several microRNAs (miRNAs), were also amplified.

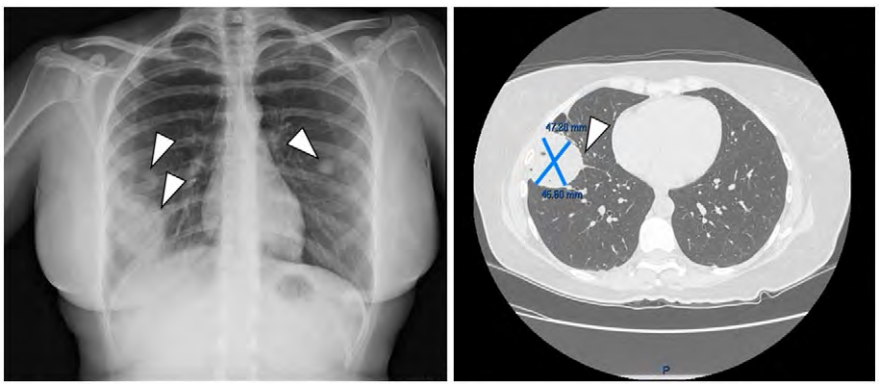

FIGURE 1 Chest radiography (left) presenting bilateral nodular lesions in lungs, indicated by arrowheads. Computed tomography scan (right) showing a well distinguished unilateral nodule sizing 47.20 × 45.60 mm (indicated by arrowhead), and several smaller nodules distributed bilaterally in lungs

INFORME DE LABORES 2019

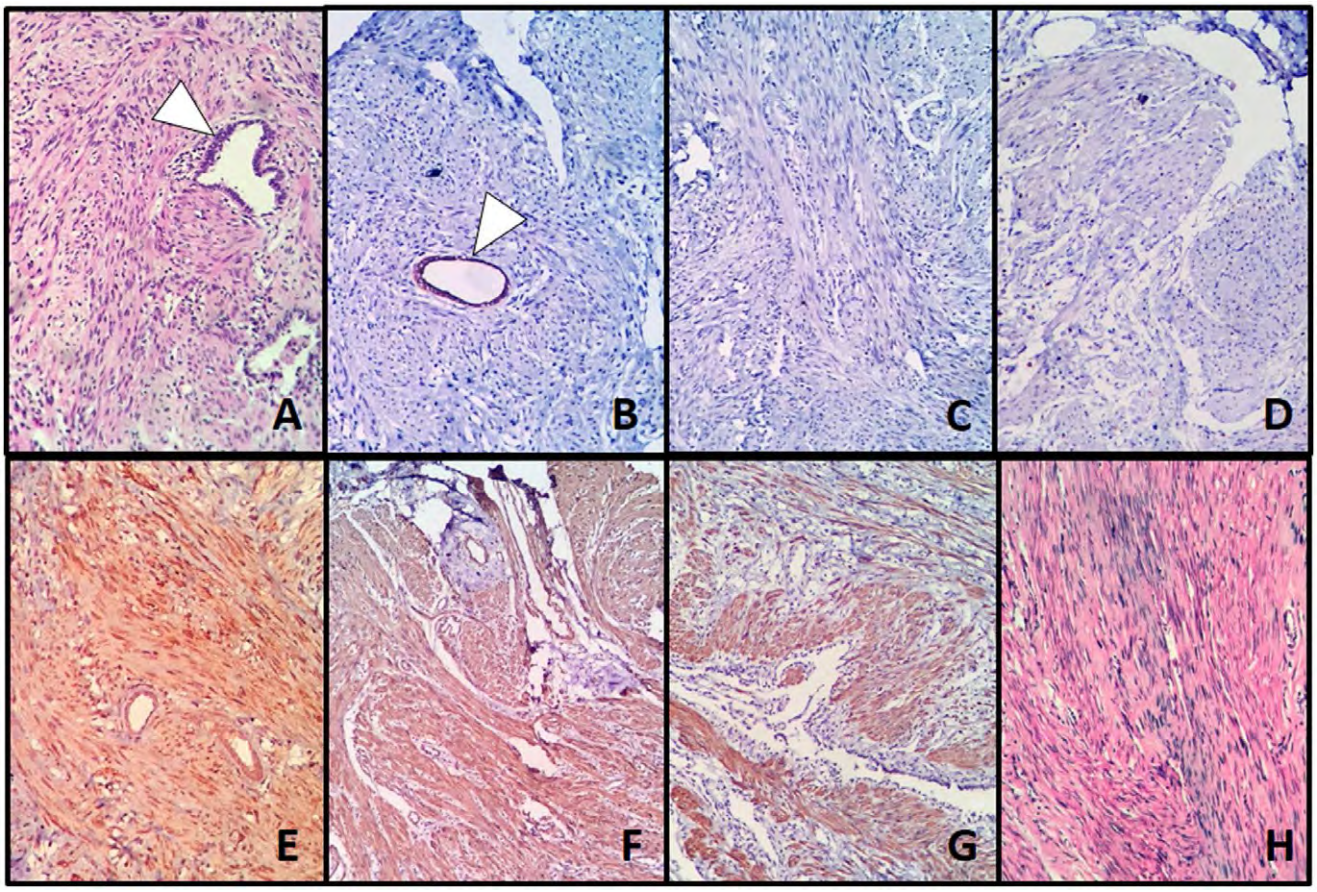

FIGURE 2 Immunohistochemical analysis of a lung metastasizing leiomyoma (LML). A, Hematoxylin and eosin staining of an LML section revealed proliferative spindle cells in random fascicles pattern; alveolar trapping is indicated with the arrowhead. Immunohistochemistry for B, cytokeratin was negative in lesion; positive signal was detected in the alveolar epithelium, as indicated by the arrowhead. No staining was observed for C, protein S-100, and D, calretinin. Positive and strong expression was detected with a diffuse cellular distribution pattern for E, Bcl-2, F, smooth muscle actin, and G, desmin. In H, a section of a uterine leiomyoma stained with hematoxylin and eosin showed similar cellular characteristics as the pulmonary lesion. Total magnification for all shown images is 100X

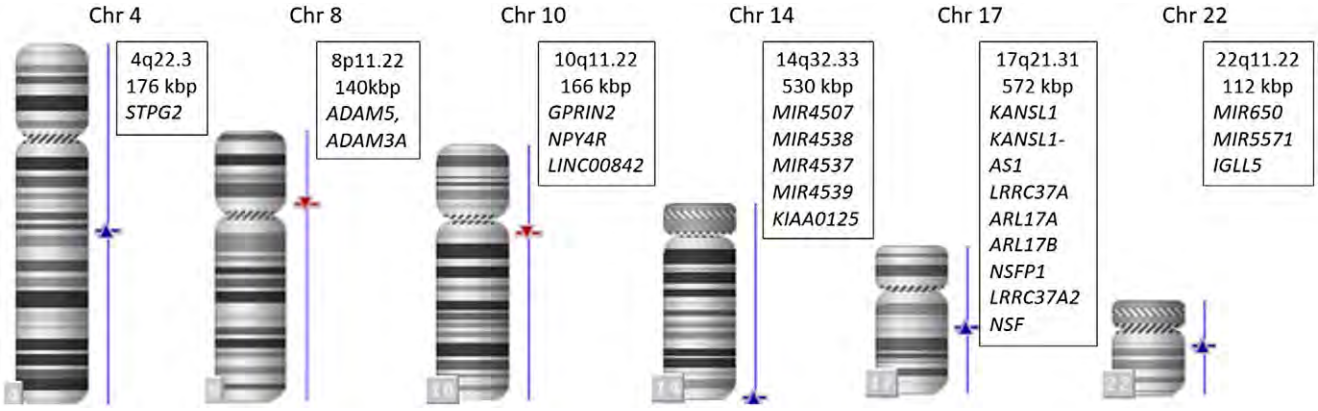

FIGURE 3 Genomic copy number variations (CNVs) observed in DNA from peripheral blood lymphocytes. ▲ represents microduplications, and ▼ represents microdeletions, which are mapped at the corresponding chromosomal band position. In each case, the size of the CNV and the gene content are indicated. Data files were generated using GeneChip Command Console Software, version 1.2, and analysed with the Chromosome Analysis Suite v3.2 using the human genome assembly GRCh 37/hg19 (July 2017), high resolution parameters, and the built-in reference model

INFORME DE LABORES 2019

TABLE 1 Copy number variations (CNVs) detected in lung metastasizing leiomyomatosis (LML)

Chromosome	Alteration	Localization	Size (kbp)	Genes
4	Gain	q22.3	176	STPG2
10	Loss	q11.22	166	GPRIN2, NPY4R, CH17-360D5.1, LINC00842, HNRNPA1P33
14	Gain	q32.33	530	MIR4507, MIR4538, MIR4537, MIR4539, KIAA0125, ADAM6
17	Gain	q21.31	572	KANSL1, KANSL1-AS1, LRRC37A, ARL17A, ARL17B, NSFP1, LRRC37A2, NSF
22	Gain	q11.22	112	MIR650, MIR5571, IGLL5

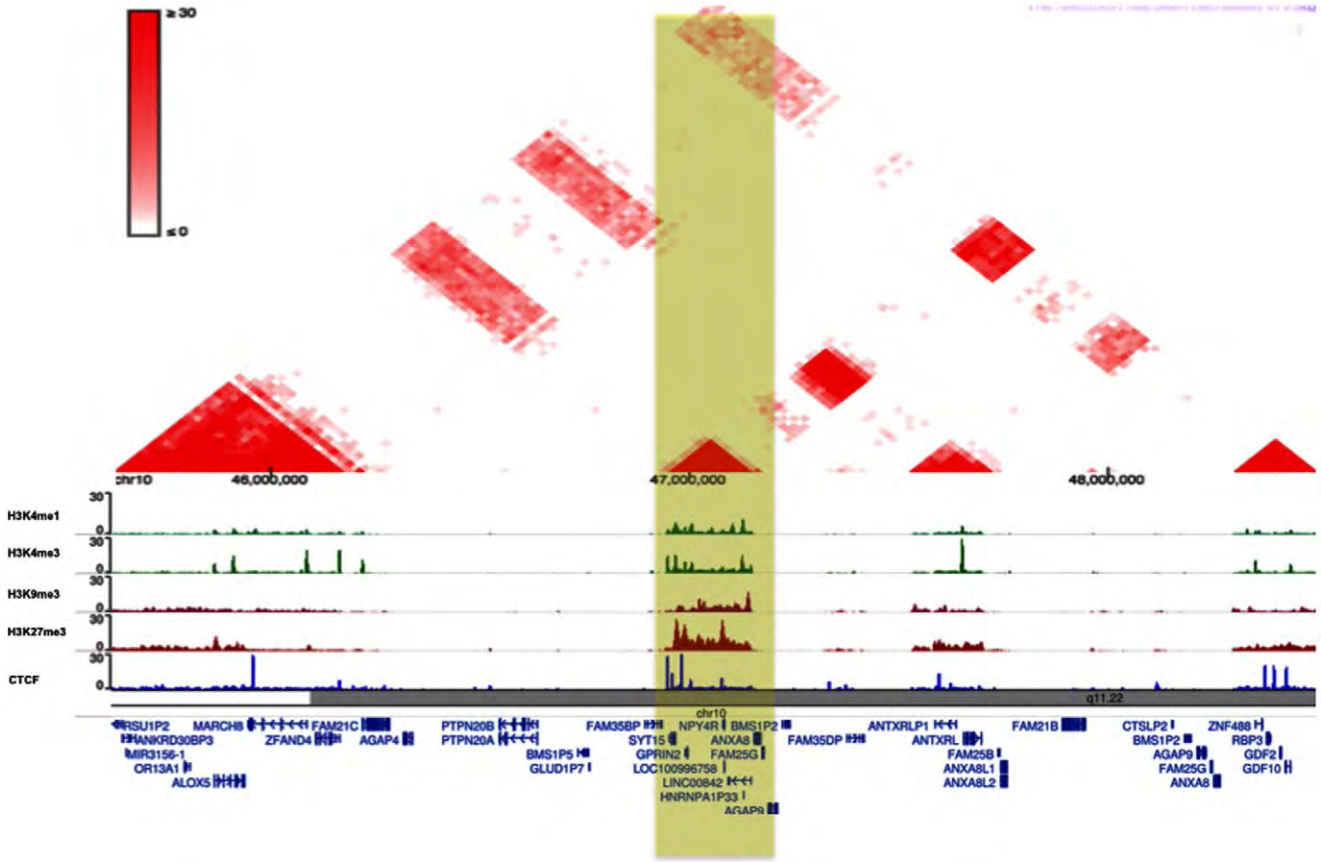

FIGURE 4 Epigenetic analysis of the 10q11.22 deleted region. The eliminated region (vertical shadowed-yellow bar) indicates the deleted genes, where dense histone modifications that mediate gene activation are enriched. Furthermore, the sequence contained in this locus corresponds to a stable domain (red triangle) that delimitates the region from the transcriptional effect of surrounding chromatin. Analysis was performed using available data from the Broad Institute, ID numbers 30003 and 30004, containing ChIP-Seq mapping of H3K4me1, H3K4me3, H3K27me3, H3K9me3 and CTCF binding profile in HUVEC cells. Human smooth muscle Hi-C data was loaded and analysed in the 3D genome browser suite (http://promoter.bx.psu.edu/hi-c/) using the hg19 human reference sequence

3.4 | Epigenetic *in silico* analysis

In addition, we performed an epigenetic in silico analysis to detect possible conformation changes that could modify the chromatin organization, and therefore, the expression of genes which may contribute to the BML development.

To determine whether the deleted region at chromosome 10 might have a role in chromatin remodelling, an epigenetic analysis was performed based on public data sets of ChIP-seq for histone marks and the transcription factor CTCF (CCCTC-binding factor). Additionally, the presence of topologically associated domains in this region was analysed using Hi-C public data for smooth muscle cells (Figure 4). The fragment where the deletion occurs is enriched by very dense histone modifications that mediate gene activation, and the lost sequence corresponds to a stable domain that

delimitates the region from the transcriptional effect of surrounding chromatin.

4 | DISCUSSION

BML is a pathology infrequently diagnosed, and normally detected by imaging techniques as a consequence of complications derived from the growing secondary myomas. The pathogenesis of the disease is not well defined. In this study, we report for the first time, submicroscopic chromosomal abnormalities detected in a patient with a history of benign uterine leiomyomas metastasized to lungs.

The smooth muscle cellular lineage of the primary and secondary neoplasms was determined by immunohistochemical assays. Leiomyomas consisted of spindle-shaped cells growing in a trabecular pattern and creating a whorled appearance (Figure 2). Conforming the major lung nodule, the presence of some smooth muscle cells positive for Bcl-2 protein (Figure 2E), suggests the infiltration of metastatic cells from uterus into the lungs, probably via lymph vessels as the most probable origin for the lung metastasizing leiomyomas.

In this case of BML an apparently normal karyotype was firstly observed with standard GTG-banding cytogenetic analysis. Similar results for this kind of alterations have been published by other groups,[14] however our study shows the relevance of chromosomal microarray analysis to identify submicroscopic genomic alterations in rare conditions such as BML.

Genomic CNVs, either amplifications or deletions, have a high impact on predisposition to human diseases.[19,20] In this study, six chromosomes presented CNVs involving genes encoding for proteins, miRNAs (short no-coding RNAs conformed by 20-25 nucleotides), or lncRNAs (long no-coding RNAs constituted by ~200 nucleotides) involved in the regulation of gene expression. The potential of these both kind of RNAs to modulate gene expression is being extensively described.[21,22] These molecules regulate gene expression finely, but their perturbed activity can disturb the normal genome behaviour and promote pathological conditions.[23]

The gain presented at 14q32.33 contains the coding sequence for miRNA4507, miRNA4537, miRNA4538, miRNA4539 and lncRNA *KIAA0125*. miRNAs 4538 and 4539 are over-expressed in Duchenne Muscular Dystrophy, where they could modulate muscular functions such as locomotion and motor motility. miR4539 is over-expressed in both colon and rectal carcinoma; and it has been proposed as a molecular tool to differentiate between carcinoma and normal mucosa. In highly metastatic gallbladder cancer cells, migration and invasion have been inhibited by means of the down-regulation of lncRNA *KIAA0125*.[24]

The duplicated DNA segment at chromosome 22q11.22 harbours the microRNA-650, whose deregulated activity promotes the epithelial-mesenchymal transition through the down-regulation of tumour suppressor genes conferring an invasive and metastasizing phenotype.[25,26] Also, there is experimental evidence showing that miR-650 is involved in lymphatic and distant metastasis in human gastric cancer. This miRNA targets the inhibitor of cellular growth 4, so its ectopic expression promotes tumourigenesis and proliferation of gastric cancer cells,[27] and modify the biology of melanoma,[28] as well as chronic lymphocytic leukaemia.[29]

The fragment in chromosome 10 where the deletion occurs is enriched by very dense histone modifications that mediate gene activation; the lost sequence corresponds to a stable domain that delimitates the region from the transcriptional effect of surrounding chromatin (Figure 4).

Therefore, we suggest that the genomic loss at 10q11.22 region creates a perturbed transcriptional environment that may affect other genes in the vicinity, promoting deregulation of pathways that could exacerbate the phenotype of BML, as occurs in other pathological conditions. A previous report showed the presence of the translocation t(10;17)(q22;q21) as the sole chromosomal abnormality in a benign retroperitoneal smooth muscle tumour detected in a woman.[30] The translocation produced the fusion gene *KAT6B-KANSL1* that could regulate transcription with affinity for chromatin. The region in chromosome 17 harbouring *KANSL1* was detected amplified in the present study, no translocations were detected, but the expression of its normally targeted genes could be modified.

Among specialists it is hypothesized that many BML cases are underdiagnosed, meanly because the pathology is detected only when the metastasizing nodules interfere importantly with physiological functions in the body; nevertheless, the symptoms vary in each case, and are linked to the affected organ or tissue. In consequence, symptomatology cannot be generalized, and specific tests based on histological analysis of biopsies could be unviable depending on the localization of the metastasizing nodules.

In order to determine if the presence of the submicroscopic genomic abnormalities reported here are the same in other patients, more studies are needed. Additionally, future analysis sampling leiomyomas in uterus comparing to early metastatic tumours; as well as metastasizing nodules compared to case-control samples, would clarify characteristic genetic abnormalities and the molecular signs of BML. This could bring to light molecular markers useful in the appropriated and timely diagnosis of the pathology, as well as the identification of molecular targets for safe treatments.

ACKNOWLEDGEMENTS

The authors thank the patient and her family for their participation in this study.

INFORME DE LABORES 2019

CONFLICT OF INTEREST

The authors declared that they have no conflict of interests with the contents of this article.

AUTHOR CONTRIBUTIONS

All the authors contribute importantly to this work. EHP collected data, analysed microarray results and wrote the paper. ACVW performed the microarray assay, collected data and participated in writing the manuscript. CJR collected data and contributed to achieve the manuscript. FFR analysed data and contributed to achieve the manuscript. LMGS realized the clinical follow-up of the patient and discussed the organization of the manuscript. CAFG performed and interpreted the histopathological characterization of the tissues. JMHH performed the in silico epigenetic analysis. HRV reviewed and provided critical comments to the manuscript. JCHM reviewed and validated the cytogenetic test reported. EEP started the clinical care of the patient, and participated in the design of the study.

ETHICS

This study was approved by the Institutional ethics committees, and the corresponding informed consent was obtained and signed by the patient.

ORCID

Everardo Hernández-Plata https://orcid.org/0000-0002-8057-3604

REFERENCES

1. Lin J, Song X, Liu C. Pelvic intravascular leiomyomatosis associated with benign pulmonary metastasizing leiomyoma: clinicopathologic, clonality, and copy number variance analysis. *Int J Gynecol Pathol*. 2014;33(2):140-145.
2. Szklaruk J, Tamm EP, Choi H, Varavithya V. MR imaging of common and uncommon large pelvic masses. *Radiographics*. 2003;23(2):403-424.
3. Fasih N, Prasad Shanbhogue AK, Macdonald DB, et al. Leiomyomas beyond the uterus: unusual locations, rare manifestations. *Radiographics*. 2008;28(7):1931-1948.
4. Nucci MR, Drapkin R, Dal Cin P, Fletcher CD, Fletcher JA. Distinctive cytogenetic profile in benign metastasizing leiomyoma: pathogenetic implications. *Am J Surg Pathol*. 2007;31(5):737-743.
5. Thomas EO, Gordon J, Smith-Thomas S, Cramer SF. Diffuse uterine leiomyomatosis with uterine rupture and benign metastatic lesions of the bone. *Obstet Gynecol*. 2007;109(2 Pt2):528-530.
6. Pacheco-Rodriguez G, Taveira-DaSilva AM, Moss J. Benign metastasizing leiomyoma. *Clin Chest Med*. 2016;37(3):589-595.
7. Gante I, Medeiros-Borges C, Aguas F. Hysterectomies in Portugal (2000–2014): What has changed? *Eur J Obstet Gynecol Reprod Biol*. 2017;208:97-102.
8. Ingelsson E, Lundholm C, Johansson AL, Altman D. Hysterectomy and risk of cardiovascular disease: a population-based cohort study. *Eur Heart J*. 2011;32(6):745-750.
9. Rocca WA, Grossardt BR, Shuster LT, Stewart EA. Hysterectomy, oophorectomy, estrogen, and the risk of dementia. *Neurodegener Dis*. 2012;10(1-4):175-178.
10. Corona LE, Swenson CW, Sheetz KH, et al. Use of other treatments before hysterectomy for benign conditions in a statewide hospital collaborative. *Am J Obstet Gynecol*. 2015;212(3): 304e1-e7.
11. Olejek A, Olszak-Wasik K, Czerwinska-Bednarska A. Long-term intermittent pharmacological therapy of uterine fibroids - a possibility to avoid hysterectomy and its negative consequences. *Prz Menopauzalny*. 2016;15(1):48-51.
12. Lewis EI, Chason RJ, DeCherney AH, Armstrong A, Elkas J, Venkatesan AM. Novel hormone treatment of benign metastasizing leiomyoma: an analysis of five cases and literature review. *Fertil Steril*. 2013;99(7):2017-2024.
13. Kayser K, Zink S, Schneider T, et al. Benign metastasizing leiomyoma of the uterus: documentation of clinical, immunohistochemical and lectin-histochemical data of ten cases. *Virchows Arch*. 2000;437(3):284-292.
14. Tietze L, Gunther K, Horbe A, et al. Benign metastasizing leiomyoma: a cytogenetically balanced but clonal disease. *Hum Pathol*. 2000;31(1):126-128.
15. Iida N, Kozasa T. Identification and biochemical analysis of GRIN1 and GRIN2. *Methods Enzymol*. 2004;390:475-483.
16. Holzer P, Reichmann F, Farzi A, Neuropeptide Y. peptide YY and pancreatic polypeptide in the gut-brain axis. *Neuropeptides*. 2012;46(6):261-274.
17. Rothman JE. Mechanisms of intracellular protein transport. *Nature*. 1994;372(6501):55-63.
18. Smith ER, Cayrou C, Huang R, Lane WS, Cote J, Lucchesi JC. A human protein complex homologous to the Drosophila MSL complex is responsible for the majority of histone H4 acetylation at lysine 16. *Mol Cell Biol*. 2005;25(21):9175-9188.
19. Perry GH, Ben-Dor A, Tsalenko A, et al. The fine-scale and complex architecture of human copy-number variation. *Am J Hum Genet*. 2008;82(3):685-695.
20. Kidd JM, Sampas N, Antonacci F, et al. Characterization of missing human genome sequences and copy-number polymorphic insertions. *Nat Methods*. 2010;7(5):365-371.
21. Delsin L, Roberto GM, Fedatto PF, et al. Downregulated Adhesion-associated microRNAs as prognostic predictors in childhood osteosarcoma. *Pathol Oncol Res*. 2017;25:1-10.
22. Bhat NS, Colden M, Dar AA, et al. MicroRNA-720 regulates E-cadherin-alphaE-catenin complex and promotes renal cell carcinoma. *Mol Cancer Ther*. 2017;16(12):2840-2848.
23. Sannigrahi MK, Sharma R, Panda NK, Khullar M. Role of noncoding RNAs in head and neck squamous cell carcinoma: a narrative review. *Oral Dis*. 2017;24(8):1417-1427.
24. Lv W, Wang L, Lu J, Mu J, Liu Y, Dong P. Long noncoding RNA KIAA0125 potentiates cell migration and invasion in gallbladder cancer. *Biomed Res Int*. 2015;2015:108458.
25. Zeng ZL, Li FJ, Gao F, Sun DS, Yao L. Upregulation of miR-650 is correlated with down-regulation of ING4 and progression of hepatocellular carcinoma. *J Surg Oncol*. 2013;107(2):105-110.
26. Zuo ZH, Yu YP, Ding Y, et al. Oncogenic activity of miR-650 in prostate cancer is mediated by suppression of CSR1 expression. *Am J Pathol*. 2015;185(7):1991-1999.

INFORME DE LABORES 2019

27. Zhang X, Zhu W, Zhang J, et al. MicroRNA-650 targets ING4 to promote gastric cancer tumorigenicity. *Biochem Biophys Res Commun*. 2010;395(2):275-280.
28. Chan E, Patel R, Nallur S, et al. MicroRNA signatures differentiate melanoma subtypes. *Cell Cycle*. 2011;10(11): 1845-1852.
29. Mraz M, Dolezalova D, Plevova K, et al. MicroRNA-650 expression is influenced by immunoglobulin gene rearrangement and affects the biology of chronic lymphocytic leukemia. *Blood*. 2012;119(9):2110-2113.
30. Panagopoulos I, Gorunova L, Bjerkehagen B, Heim S. Novel KAT6B-KANSL1 fusion gene identified by RNA sequencing in retroperitoneal leiomyoma with t(10;17)(q22;q21). *PLoS ONE*. 2015;10(1):e0117010.

How to cite this article: Hernández-Plata E, Velázquez-Wong AC, Jiménez-Ramírez C, et al. Identification of genomic copy number variations in lung benign metastasizing leiomyomatosis. *Clin Respir J*. 2019;13:105–113. https://doi.org/10.1111/crj.12987

Hazardous alcohol consumption and risk of alcohol dependence present different neurophysiological correlates

Wendy V. Herrera-Morales, Leticia Ramírez-Lugo, Efraín Santiago-Rodríguez, Julián V. Reyes-López, Luis Núñez-Jaramillo

Introduction. Hazardous alcohol consumption (HAC) is a pattern of alcohol use that may result in harm for the user and/or for those around them. Prior research has suggested that HAC and alcohol dependence share some neurophysiological features but differ in others.

Aim. To determine whether HAC and alcohol dependence presented different neurophysiological correlates.

Subjects and methods. Two hundred subjects were screened for HAC or alcohol dependence. A quantitative electroencephalographic analysis of delta, theta, alpha and beta absolute power, relative power and mean frequency in subjects with HAC but not alcohol dependence, subjects with risk of alcohol dependence and controls was performed.

Results. One hundred and fourteen subjects met inclusion criteria. The HAC group presented with higher beta absolute power and relative power, as well as a lower beta mean frequency than the control group, while the group with risk of alcohol dependence presented lower delta absolute power than controls.

Conclusions. HAC and risk of alcohol dependence present different neurophysiological correlates. There is an important effect of the severity of alcohol dependence on neurophysiological correlates of this condition. Our results support the existence of two different types of behavioral disinhibition.

Key words. Alcohol dependence. Behavioral disinhibition. Beta activity. Delta activity. Hazardous alcohol consumption. Quantitative EEG.

División de Ciencias de la Salud; Universidad de Quintana Roo; Chetumal, Quintana Roo (W.V. Herrera-Morales, L. Núñez-Jaramillo). División de Neurociencias; Instituto de Fisiología Celular; Universidad Nacional Autónoma de México; Ciudad de México (L. Ramírez-Lugo). Diagnóstico, Tratamiento e Investigación Neurológica S.C.; Querétaro (E. Santiago-Rodríguez). Clínica del Sistema Nervioso; Facultad de Medicina; Universidad Autónoma de Querétaro; Querétaro, México (J.V. Reyes-López).

Corresponding author:
Luis Núñez-Jaramillo, PhD. División de Ciencias de la Salud. Universidad de Quintana Roo. Avda. Erick Paolo Martínez, s/n, esq. Avda. 4 de Marzo. Colonia Magisterial. CP 77039. Chetumal, Quintana Roo, México.

E-mail:
lnunez@uqroo.edu.mx

Funding:
Programa de Fortalecimiento de la Calidad en Instituciones Educativas, LNJ (P/PFCE-2016-23MSU0140Z-08).

Accepted:
02.10.18.

How to cite this paper:
Herrera-Morales WV, Ramírez-Lugo L, Santiago-Rodríguez E, Reyes-López JV, Núñez-Jaramillo L. Hazardous alcohol consumption and risk of alcohol dependence present different neurophysiological correlates. Rev Neurol 2019; 68: 137-46.

Versión española disponible en www.neurologia.com

© 2019 Revista de Neurología

Introduction

Alcohol is a psychoactive substance with abuse rates among the five top risk factors for disease, disability and death worldwide. A global study revealed that alcohol use disorders (AUDs) represent 9.6% of mental and substance disorders, which in turn are responsible for 7.4% of disability-adjusted life years [1].

The most frequently studied AUD is alcohol dependence, however, hazardous alcohol consumption (HAC), 'a pattern of alcohol consumption that increases the risk of harmful consequences for the user or others', which is not necessarily accompanied by alcohol dependence [2], is another AUD that strongly impacts society. Research has shown that HAC is strongly correlated with alcohol-related injuries [3,4]. HAC is frequent among college students and leads to risky behavior such as drunk-driving and the use of other substances, as well as risky sexual practices [5-7].

Quantitative electroencephalography (qEEG) has been used to study AUDs. qEEG is an affordable and non-invasive technique that allows the study of brain electrical activity both at resting state and associated with cognitive processes [8]. An increase in theta [9], and beta absolute power (AP) [10,11] are the main resting qEEG correlates consistently found in alcohol dependent subjects. Regarding delta frequency band in alcohol dependent patients, there are reports for both increased and decreased delta activity, thus remaining inconclusive at the moment [8]. Different reports have addressed alpha activity in relation with familiar history of alcohol consumption and ethnicity [12,13]. Some reports have described a decrease in alpha activity in alcoholics, but other studies have failed to replicate this result [8].

An increase in beta and theta AP has been implicated as a homeostatic imbalance in cortical excitability [8] and as such, it has been proposed that subjects with a genetic predisposition towards developing alcohol dependence present a homeostatic imbalance leading to disinhibition/hyperexcitability in the central nervous system [8]. Behavioral disinhibition is found not only in alcohol dependence, but also in other disorders such as HAC [14], implying a deficit in impulse control [15].

Prior research on binge drinkers has found deficits in white matter integrity, cortical thickness and neurocognitive markers that are similar to that observed in alcoholic patients, suggesting that binge drinking may be the predecessor to alcoholism [16]. A study addressing basal qEEG activity found that binge drinking is associated with high delta and fast beta (20-35 Hz) activity in the eyes open condition [17].

Alcohol dependence produces important plastic changes within the central nervous system [18] and as such, it is important to rule out alcohol dependence when investigating the neurophysiological correlates of patients with HAC. We have previously reported that subjects with HAC, in the absence of alcohol dependence, present with a decrease in beta mean frequency (MF) in frontal and centro-parietal areas, as well as an increase in beta AP in centro-parietal areas [19] compared to controls. Previous reports of qEEG analyses in alcohol dependent subjects revealed increased beta and theta AP [9,11]. Thus, subjects with HAC present with some similar neurophysiological correlates observed in alcohol dependent subjects (increased beta AP) but differ in others. As mentioned earlier, both HAC and alcohol dependence are associated with behavioral disinhibition. However, alcohol dependence includes neurophysiological mechanisms underlying substance dependence, while HAC does not share this set of mechanisms. Since it has been suggested that beta activity is involved in the regulation of cortical excitability [15,20], it is important to determine whether the decrease in beta MF observed in subjects with HAC [19] represents a neurophysiological feature unique to HAC and not shared with subjects with alcohol dependence. Moreover, since no conclusive results have been obtained on delta and alpha activity in AUDs we will study these frequency bands in HAC and risk of alcohol dependence in the same population.

Subjects and methods

Participants

Participants were first year health sciences students and were verbally invited during class to participate in the study. All procedures and data management were carried out in accordance with the Declaration of Helsinki, and the protocol was approved by the Committee of Ethics in Research of the Health Sciences Division of the university. All participants signed an informed consent.

Clinical evaluation

The Spanish version of the Alcohol Use Disorders Identification Test (AUDIT) was used to assess HAC and risk of alcohol dependence. The AUDIT consists of 10 items that explore the frequency, amount of consumption, negative consequences, and associated psychosocial problems related to alcohol consumption [2]. Different cut-points in the AUDIT have been used in college students, but a study comparing four different alcohol screening tests in adolescents, found that for this age group a cut-point of two was optimal for detecting alcohol problem use and a cut-point of 3 for identifying risk of abuse or dependence [21]. In order to avoid false positives we confirmed the results analyzing specific sections of the AUDIT test. A score of 1 or above on items 2 and 3 met criteria for HAC, while a score over 0 on items 4, 5 and 6 met criteria for risk of alcohol dependence [2]. Subjects rating 3 or more in total AUDIT score, but who did not fulfill the criteria for the section assessing risk of alcohol dependence, were included in the HAC group. Thus, subjects rating positive for HAC presented a total AUDIT score of 2 or more, a score of 1 or above on items 2 and 3, and a score of 0 on items 4, 5 and 6; while subjects rating positive for risk of alcohol dependence presented a total AUDIT score of 3 or more, and a score over 0 on items 4, 5 and 6 of this test. While the AUDIT has been validated in different countries such as México, Brazil and Venezuela [2,22,23], no further clinical evaluation was performed for alcohol dependence in this work, thus subjects rating positive for alcohol dependence are considered as 'at risk'.

All participants were non-smokers. Consumption of other drugs was not determined for the subjects in this study.

Participants completed a self-reported questionnaire (ASRS v. 1.1) to test for attention deficit hyperactivity disorder (ADHD) [24,25], and the Plutchick Suicide Risk test. These instruments were selected based on our previous study [19] and are conditions related to AUDs and present in the population [26-28]. Participants had no current or previous history of neurological illness and were not taking any medication that could affect EEG activity.

Quantitative electroencephalography

EEG recording

Subjects were comfortably seated in a dimly lit room, were awake, and had their eyes closed. EEGs were recorded with a 19-channel Medicid Fenix

electroencephalograph. Amplifier was set with a low frequency filter of 0.5 Hz, a high frequency filter of 30 Hz, and a 50/60 Hz notch filter. A sampling frequency of 240 Hz, with a 16-bit resolution was used. The signal was collected through 19 electrodes from the international 10/20 system (FP1, FP2, F7, F8, F3, F4, T3, T4, C3, C4, T5, T6, P3, P4, O1, O2, FZ, CZ and PZ), fitted in an electrode cap, and linked mastoids were used as references. All EEG recordings were rigorously analyzed by a clinical neurophysiologist (E.S.R).

Quantitative analysis

Quantitative analysis was performed on EEG segments of at least 2.56 s. The segments were manually selected until summing to at least one minute. Only segments during which the subject was awake and presented alpha activity were included. Segments with muscular activity and blinking were also eliminated.

Quantitative EEG analysis software was used to calculate the AP, relative power (RP) and MF for delta (1.56-3.52 Hz), theta (3.91-7.42 Hz), alpha (7.81-12.5 Hz) and beta (12.89-19.14 Hz) frequency bands [29] using a fast Fourier transform algorithm. In order to decrease non-physiological variability, subtraction of the global scale factor (GSF) was applied to AP measures in all frequency bands. The mathematical model used to obtain GSF can be summarized as a logarithmic transformation applied to the brain electrical signal. This equation is $V_i\,(e,t) = \gamma_1\beta_1\,(e,t)$, where the brain electrical activity obtained in the EEG may be represented by a matrix where $V\,(e,t)$, V being the potential recorded at electrode e at the moment t. A global factor scale is represented by γ. The mathematical model used to obtain it is described in detail in the work published by Hernández et al [30]. The subtraction of GSF has been incorporated into some EEG software analysis, such as the one used in this study, and many papers have been published since then. EEG recordings were reformatted to the average reference for quantitative analysis [31].

Statistical analysis

For the analysis of AUDIT, suicide risk and ADHD raw scores, as well as age, we performed ANOVA's tests followed by Bonferroni's post hoc test.

For qEEG analysis a mixed design analysis of variance (mixed ANOVA) with electrode as a within-subject variable and group as between-subject variable was performed. Greenhouse-Geisser corrected degrees of freedom were used to assess the significance of the corresponding *F*-value when necessary. Partial eta squared (η^2_p) was used to determine effect size. The AP, RP and MF for delta, theta, alpha and beta frequency bands were analyzed through separated mixed ANOVAs. Where an effect of group was found, pairwise comparison revealed specific inter-group differences, and an ANOVA test was carried out to determine in which electrodes this effect was found. *P*-values were adjusted for multiple comparisons using a Bonferroni correction (Table I).

Table I. Outcomes of mixed ANOVAs performed for absolute power, relative power and mean frequency values of delta, theta, alpha and beta frequency bands. Specification of the groups differing is indicated in those measures where an effect of group was found.

	Absolute power	Relative power	Mean frequency
Delta	DEP < control ($p < 0.05$)	Non-significant	Non-significant
Theta	Non-significant	Non-significant	Non-significant
Alpha	Non-significant	Non-significant	Non-significant
Beta	HAC > control ($p < 0.01$)	HAC > control ($p < 0.01$)	HAC < control ($p < 0.05$)

DEP: risk of alcohol dependence; HAC: hazardous alcohol consumption.

Results

A total of 200 students participated in the study (106 females, age 19.6 ± 0.25, and 94 males, age 19.8 ± 0.35). Subjects older than 22 years, with a present or previous history of neurological disorders, and those in which EEG visual analysis revealed abnormalities were excluded from the analysis.

Only 114 subjects were included in the statistical analysis. Of the 114 subjects, 48 subjects scored negatively for all clinical conditions evaluated (HAC, risk of alcohol dependence, suicide risk and ADHD) and were included in the control group; 45 subjects scored positive for HAC but negatively for risk of alcohol dependence, as well as negative for all other tests (suicide risk, ADHD) and were included in the HAC group; and 21 subjects scored positively for risk of alcohol dependence and were included in the risk of alcohol dependence group (DEP). The majority of subjects within the DEP group presented comorbidities; 18 rated positive for HAC, 6 rated positive for suicide risk and 8 rated positive for ADHD. Age and gender composition of each group is depicted in table II.

Figure 1. Site where ANOVA revealed an effect of group on delta AP (mean ± standard error). Differences revealed by Bonferroni post hoc test are shown. [a] $p < 0.05$ (DEP vs control). Electrode in grey indicate lower value in DEP when compared with controls. HAC: hazardous alcohol consumption; DEP: risk of alcohol dependence.

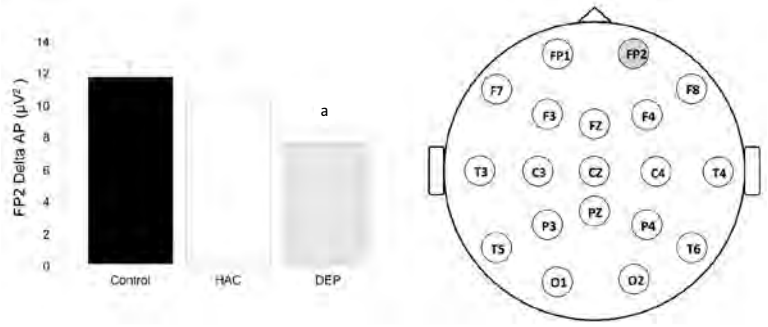

There was no difference in age between groups. ANOVA performed on raw scores for the tests applied revealed a difference in total scores for ADHD ($F_{2,111}$ = 11.59; $p < 0.0001$) and suicide risk ($F_{2,111}$ = 16.49; $p < 0.0001$) tests. For suicide risk, DEP group presented higher scores than control (DEP 4.434 ± 0.6; control 2.0 ± 0.17; $p < 0.0001$) and HAC (2.33 ± 0.21; $p < 0.0001$) groups, while in the ADHD test DEP group scored higher than control (DEP 2.67 ± 0.37; control 1.39 ± 0.16; $p < 0.01$) and HAC (0.18 ± 0.15; $p < 0.0001$). The three groups also differed in AUDIT total score ($F_{2,111}$ = 57.11; $p < 0.0001$), as well as in the score analyzed for HAC ($F_{2,111}$ = 240.66; $p < 0.0001$) and DEP ($F_{2,111}$ = 70.86; $p < 0.0001$). In AUDIT total score DEP group presented higher scores than HAC (DEP 5.24 ± 0.62; HAC 2.89 ± 0.33; $p < 0.0001$) and control (control 0.208 ± 0.09; $p < 0.0001$) groups, while HAC presented a higher score than control group ($p < 0.0001$). In the AUDIT section analyzed for HAC, Bonferroni's post hoc test revealed that control group presented lower scores than HAC (control 0.0 ± 0.0; HAC 1.11 ± 0.47; $p < 0.0001$) and DEP (DEP 0.86 ± 0.078; $p < 0.0001$) groups, while DEP and HAC also differed from each other ($p < 0.01$). In the section evaluated to determine risk of alcohol dependence, Bonferroni's post hoc test showed that DEP group presented higher scores than HAC (DEP 1.48 ± 0.26; HAC 0.0 ± 0.0; $p < 0.0001$) and control (control 0.0 ± 0.0; $p < 0.0001$) groups, while no difference was found between control and HAC groups.

Delta activity

There was an effect of the electrode studied on delta AP ($F_{4.71,\ 522.35}$ = 57.98; $p < 0.001$; η^2_p = 0.343), as well as an effect of group ($F_{2,\ 111\ =}$ 3.25; $p < 0.05$; η^2_p = 0.055). Pairwise comparison revealed a difference between control and DEP groups ($p < 0.05$). ANOVA revealed an effect of group at Fp2 ($F_{2,11}$ = 3.12; $p < 0.05$) (Fig. 1).

There was an effect of electrode on delta RP ($F_{7.45,\ 827.84}$ = 153.91; $p < 0.001$; η^2_p = 0.581) and MF ($F_{10.67,\ 1185.15}$ = 28.83; $p < 0.001$; η^2_p = 0.206). No effect of group or electrode × group interaction was found for these measures.

Table II. Age and gender composition of control, hazardous alcohol consumption (HAC) and risk of alcohol dependence (DEP) groups.

	Female (mean age)	Male (mean age)
Control	26 (19.15 ± 0.21 years)	22 (19.08 ± 0.13 years)
HAC	17 (19.11 ± 0.21 years)	28 (19.30 ± 0.19 years)
DEP	16 (19.05 ± 0.23 years)	5 (18.90 ± 0.18 years)

Theta activity

There was an effect of the electrode on theta AP ($F_{5.08,\ 563.4}$ = 50.99; $p < 0.001$; η^2_p = 0.315), RP ($F_{8.6,\ 954.38}$ = 92.58; $p < 0.001$; η^2_p = 0.455) and MF ($F_{8.97,\ 995.58}$ = 32.95; $p < 0.001$; η^2_p = 0.229). There was no effect of group or electrode × group interaction on any measure of theta activity.

Alpha activity

Mixed ANOVA revealed an effect of electrode on alpha AP ($F_{3.73,\ 374.42}$ = 90.35; $p < 0.001$; η^2_p = 0.449), RP ($F_{70.9,\ 787.19}$ = 149.73; $p < 0.001$; η^2_p = 0.574) and MF ($F_{7.72,\ 856.61}$ = 28.39; $p < 0.001$; η^2_p = 0.204). However, no effect of group or electrode × group interaction was found for any of them.

Beta activity

Mixed ANOVA on beta AP values revealed an effect of electrode ($F_{6.89,\ 764.42}$ = 60.59; $p < 0.001$; η^2_p = 0.353) and an effect of group ($F_{2,111}$ = 5.81; p = 0.004; η^2_p = 0.095). There was no electrode × group interaction. Pairwise comparison revealed a difference between control and HAC groups (p = 0.003). Figure 2 shows the sites in which a difference between these groups was found.

There was an effect of electrode ($F_{60.3,\ 669.2}$ = 29.78; $p < 0.001$; η^2_p = 0.212) and an effect of group ($F_{2,111}$

Figure 2. Sites where ANOVA revealed an effect of group on beta AP (mean ± standard error). Differences revealed by Bonferroni post hoc test are shown. [a] $p < 0.05$; [b] $p < 0.01$. Electrodes in grey indicate higher values in HAC when compared with controls. HAC: hazardous alcohol consumption; DEP: risk of alcohol dependence.

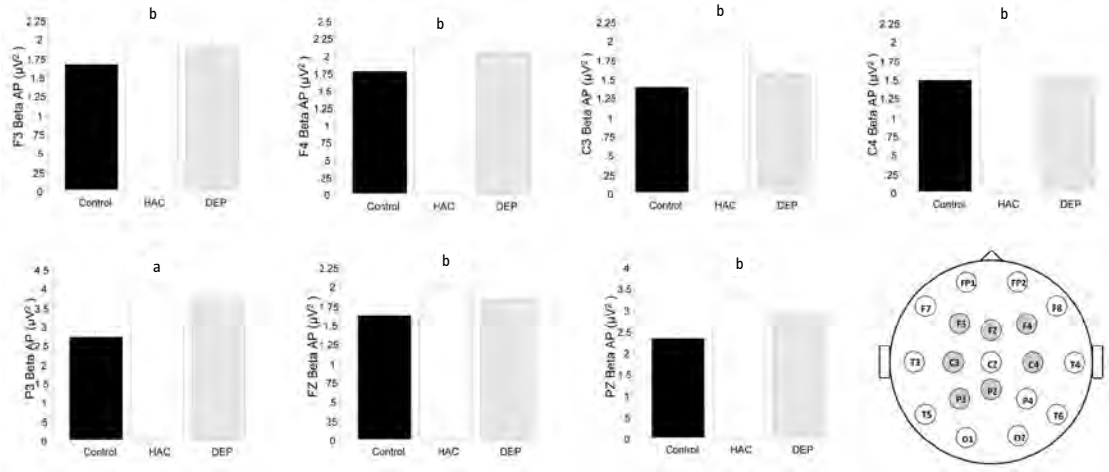

= 6.08; $p = 0.003$; $\eta^2_p = 0.099$) on beta RP. There was no electrode × group interaction. Pairwise comparison showed a difference between control and HAC groups ($p = 0.002$). Figure 3 shows the sites in which a difference between these groups was found.

There was an effect of electrode ($F_{8.18,\ 908.19} = 27.34$; $p < 0.001$, $\eta^2_p = 0.198$) and an effect of group ($F_{2,111} = 4.26$; $p = 0.017$; $\eta^2_p = 0.071$) on beta MF. However, there was no electrode × group interaction. Pairwise comparison showed a difference between control and HAC groups ($p = 0.004$). Figure 4 shows the sites in which a difference between these groups was found.

Discussion

The current study explored qEEG activity between subjects with HAC and risk of alcohol dependence along with a control population without an alcohol-related disorder. Subjects with HAC presented higher beta AP, higher beta RP, and lower beta MF when compared with controls. Subjects with risk of alcohol dependence presented lower delta AP when compared with controls.

Beta activity has been linked with activity of cortical GABAergic interneurons, and as such has been related to inhibition/excitability homeostasis in the cortex. Changes in beta activity have therefore been associated with a homeostatic imbalance leading to central nervous system disinhibition/hyperexcitability [8], and this association has been supported by electrophysiological and genetic analyses [15]. Both HAC and alcohol dependence are manifestations of behavioral disinhibition [8,14,15], and prior research has proposed that behavioral and central nervous system disinhibition share common neurophysiological markers [8,15]. Thus, the higher beta AP and RP, as well as the lower beta MF present in the HAC group suggest an imbalance in central nervous system disinhibition/hyperexcitability.

As mentioned earlier, available data on delta activity in alcoholics is non-conclusive, while earlier works point to an increase in delta activity, more recent works reveal an decrease in delta activity in these patients [8]. A very interesting study performed on alcohol dependent subjects identified two different profiles within the same population based on qEEG analysis, one with increased delta and theta activity, and another with decreased delta and theta activity. Both groups presented a delay in P300 and impairments in attention and memory, although these effects were stronger in the first group (increased delta and theta activity). Authors suggest that this could be reflecting different stages of alcohol dependence [32], although other factors (different types of alcohol dependence, ethnic influence, etc.) cannot be discarded.

Thus, decreased delta AP is present only in some patients with alcohol dependence. We believe that

Figure 3. Sites where ANOVA revealed an effect of group on beta RP (mean ± standard error). Differences revealed by Bonferroni post hoc test are shown. [a] $p < 0.05$; [b] $p < 0.01$; [c] $p < 0.0001$ (HAC vs control); [d] $p < 0.01$ (HAC vs DEP). Electrodes in grey indicate higher values in HAC when compared with controls. HAC: hazardous alcohol consumption; DEP: risk of alcohol dependence.

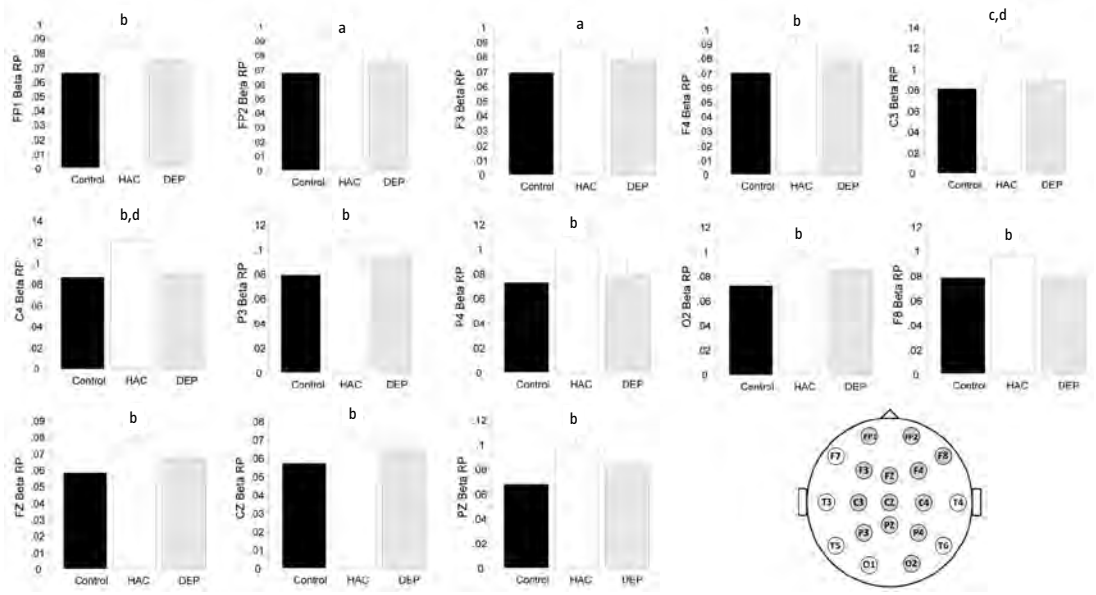

this might represent variations in the type of alcohol dependence. One of the studies showing a decrease in delta activity in alcohol dependent patients shed some light about the possible relevance of this finding, since decreased slow-wave activity (decreased delta and theta activity) correlated with cortical atrophy and onset age of alcohol consumption below 20 years [33]. While cortical atrophy and decreased delta activity might be the result of prolonged alcohol abuse, it might also be possible that decreased delta activity be found primarily in subjects beginning alcohol consumption at an early age, which would also be the case of our study. The implications of this requires further studies characterizing the two subtypes of alcohol dependent subjects, since variation in delta activity probably is not the only neurophysiological difference.

In this work we found statistically significant differences revealed by the ANOVA, but small effect sizes. It is noteworthy that effect size and statistical significance serve different purposes, while statistical significance test reveals the probability of obtaining the between groups difference by chance, effect size provides information about the magnitude of that difference and its possible practical implications [34]. Different works have assessed the importance of small changes on qEEG activity. For example, carbamazepine treatment produces impairment in neuropsychological performance in those patients whose alpha mean frequency in the occipital region slows 0.5-0.6 Hz after treatment, and has been used to determine possible outcome of different antiepileptic drugs [35]. Even though effect size is not always reported along with statistical significance in qEEG studies, previous reports have revealed important findings in studies of alcohol use disorders with small (but significant) differences between groups in different qEEG parameters such as P300 [32,36,37], AP [38] and event related oscillations [39,40].

Gender composition was not equal in all groups, particularly in the DEP group we had a small number of males. Previous reports addressing possible gender differences in neurophysiological correlates of alcohol dependence have found that males present with higher theta AP at central and parietal regions, while females present with higher theta AP at parietal regions only [9]. Another study found that both males and females with alcohol dependence had an increase in beta AP, although for fe-

Figure 4. Sites where ANOVA revealed an effect of group on beta MF (mean ± standard error). Differences revealed by Bonferroni post hoc test are shown. [a] $p < 0.05$; [b] $p < 0.01$ (HAC vs control). Electrodes in grey indicate lower values in HAC when compared with controls. HAC: hazardous alcohol consumption; DEP: risk of alcohol dependence.

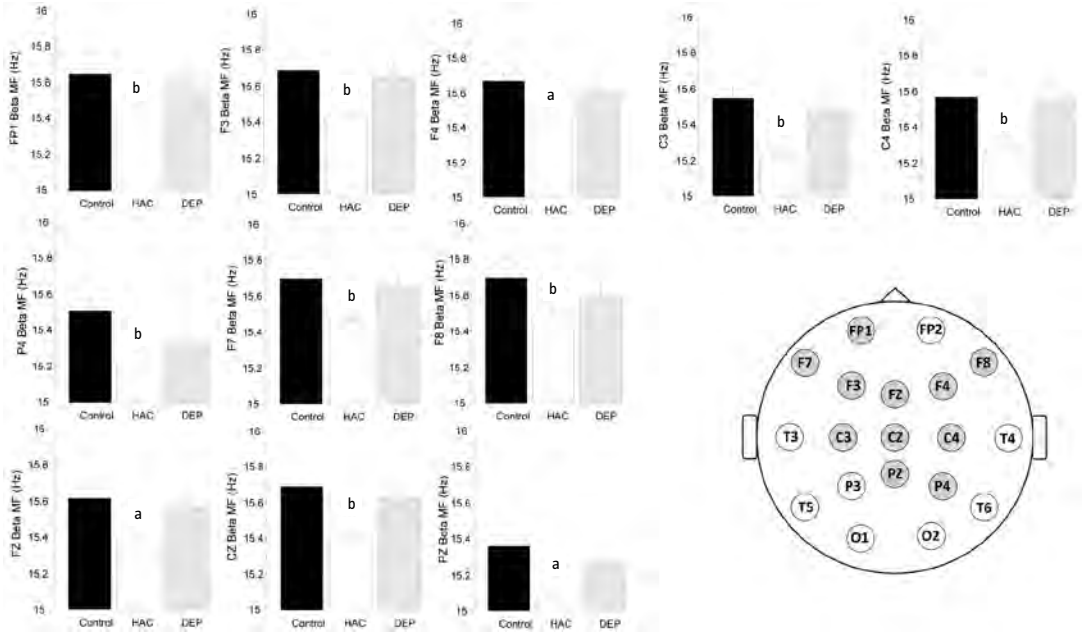

males this increase did not reach statistical significance [11]. However, a more recent study performed on only women with alcohol use disorders found that alcohol dependent women presented a significant increase in beta AP and RP [10]. Thus, previous studies addressing gender influence on the neurophysiological correlates of alcohol use disorders suggest a mild influence, mostly in regard to the particular distribution of qEEG changes in both genders. However, further studies are warranted to fully confirm the precise influence of gender.

The majority of studies on the neurophysiological correlates of alcohol dependence to date have been carried out in adult populations of medically treated alcohol dependent subjects, which by definition have a more severe alcoholism than the population in the current study. However, studies performed with adult treatment-naïve alcohol dependent subjects have revealed a mild non-significant ($p = 0.05$) decrease in P300 [37], and treatment-naïve adolescents with alcohol dependence do not present any reduction in P300 [41], while studies on adult treated population revealed a significant decrease in P300 amplitude [8]. P300 signifies brain activity during cognitive functioning, and as such, it is a very different type of neurophysiological marker than the resting EEG activity reported herein. However, taken together the results allow us to have a better understanding of the differences in brain electrical activity in subjects with early and more severe alcohol dependence.

Although the subjects in the current study presented with alcohol use disorders, they had not yet sought medical treatment, and therefore, it is not surprising that our neurophysiological results differ from those that studied participants with a more severe alcoholism who had sought treatment or were already in treatment [37,41]. The results from resting qEEGs of subjects with risk of alcohol dependence in the current study were inconsistent with features previously described in alcoholic patients, namely, increased theta and beta AP [9-11]. The participants in the current study were young (age 17 to 22 years old) and treatment-naïve, meaning that their alcohol use disorder was not yet severe enough to seek for medical help. All subjects were first-year university students, and attended classes and other academic activities on a regular basis. Therefore, the risk of alcohol dependence had not yet caused a serious impairment in daily activi-

ties, suggesting an early stage of alcohol addiction [42]. Thus, we believe that a low addiction severity may account for the lack of differences in theta and beta activity between subjects with risk of alcohol dependence and control subjects in the current study. However, we found a lower delta AP, significant at Fp2, in the group with risk of alcohol dependence when compared versus controls, indicating a differential qEEG activity associated with risk of alcohol dependence. Moreover, in this work we did not analyze other EEG parameters reported to be altered in association with alcohol dependence such as event related potentials, thus differences in these measures cannot be ruled out.

Despite the fact that most of the subjects with risk of alcohol dependence in the current study also presented with HAC (82.6%); high beta AP and RP, as well as low beta MF, were found only in subjects with HAC, but not alcohol dependence. One possible interpretation suggests the existence of a different etiology for HAC in the two groups (HAC only and DEP).

There is some controversy on whether HAC is a prelude of alcohol dependence or if HAC and alcohol dependence are two separate conditions [16]. If these two conditions are not linked, then alcohol dependence is not a 'higher level' of HAC, allowing the existence of neurophysiological correlates exclusive to HAC, as may be the case for the lower beta MF. However, the question remains as to why differences in neurophysiological correlates differ between the HAC and DEP groups when most of the DEP group also presents with HAC.

HAC can be present in an individual with or without alcohol dependence [2] since alcohol dependence includes factors associated with addiction. The possibility exists that HAC that is associated with alcohol dependence has a different etiology than HAC not associated with addiction. Interestingly, a previous study among cocaine abusers with and without comorbid personality disorders, found that subjects with cocaine dependence and comorbid personality disorders reported higher behavioral disinhibition than those without comorbid personality disorders and this disinhibition was present prior to the development of cocaine dependence. Comparatively, while cocaine dependent subjects without comorbidities also presented increased disinhibition, this behavior developed along with cocaine dependence, suggesting a difference in disinhibition trajectory between these two groups [43]. These results suggest the existence of at least two subtypes of disinhibition: one resulting from the development of addiction and another that precedes addictive behavior. The current results suggest that these two types of disinhibition may have different neurophysiological correlates. Applied to our results, this theory implies that HAC observed in individuals in the DEP group would be secondary to an addiction process, while in the HAC group this condition would not be related with the development of alcohol dependence.

While HAC and DEP are manifestation of behavioral disinhibition [8,14,15], it is reasonable that they differ in their neurophysiological correlates, since alcohol dependence implies neurophysiological mechanisms associated with addiction. However, if higher beta activity is related with cortical and behavioral disinhibition [8], why is it present only in the HAC group, and not in the DEP group? In the work of Albein-Urios et al [43] they report two different types of disinhibition, one preceding addiction and the other developing along with addiction. We believe that our subjects in the HAC group have the first type and our subjects in the DEP group the second. According to this, and given that we are observing the first stages of alcohol dependence, the increase in beta activity associated with disinhibition would be under development in these subjects. In agreement with this proposal we can observe that, although DEP group does not differ from controls in beta AP, RP and MF, it does not differ from the HAC group either in most of the cases observed in this study. However, further studies on subjects with more advanced alcohol dependence are necessary in order to prove this idea.

References

1. Whiteford HA, Degenhardt L, Rehm J, Baxter AJ, Ferrari AJ, Erskine HE, et al. Global burden of disease attributable to mental and substance use disorders: findings from the Global Burden of Disease Study 2010. Lancet 2013; 382: 1575-86.
2. Babor T, Higgins-Biddle J, Saunders J, Monteiro M. The Alcohol Use Disorders Identification Test. Guidelines for use in primary care. Geneva: World Health Organization; 2001.
3. Martin RJ, Brechbiel K, Chaney BH, Cremeens-Matthews J, Vail-Smith K. Alcohol-related injuries, hazardous drinking, and BrAC levels among a sample of bar patrons. Am J Addict 2016; 25: 132-7.
4. Cherpitel CJ, Ye Y, Bond J, Rehm J, Poznyak V, Macdonald S, et al. Multi-level analysis of alcohol-related injury among emergency department patients: a cross-national study. Addiction 2005; 100: 1840-50.
5. Connor J, Psutka R, Cousins K, Gray A, Kypri K. Risky drinking, risky sex: a national study of New Zealand university students. Alcohol Clin Exp Res 2013; 37: 1971-8.
6. Brett EI, Leavens EL, Miller MB, Lombardi N, Leffingwell TR. Normative perceptions of alcohol-related consequences among college students. Addict Behav 2016; 58: 16-20.
7. Chaney BH, Vail-Smith K, Martin RJ, Cremeens-Matthews J. Alcohol use, risky sexual behavior, and condom possession among bar patrons. Addict Behav 2016; 60: 32-6.
8. Kamarajan C, Porjesz B Advances in electrophysiological research. Alcohol Res 2015; 37: 53-87.

9. Rangaswamy M, Porjesz B, Chorlian DB, Choi K, Jones KA, Wang K, et al. Theta power in the EEG of alcoholics. Alcohol Clin Exp Res 2003; 27: 607-15.
10. Herrera-Díaz A, Mendoza-Quiñones R, Melie-García L, Martínez-Montes E, Sanabria-Díaz G, Romero-Quintana Y, et al. Functional connectivity and quantitative EEG in women with alcohol use disorders: a resting-state study. Brain Topogr 2016; 29: 368-81.
11. Rangaswamy M, Porjesz B, Chorlian DB, Wang K, Jones KA, Bauer LO, et al. Beta power in the EEG of alcoholics. Biol Psychiatry 2002; 52: 831-42.
12. Ehlers CL, Phillips E, Schuckit MA. EEG alpha variants and alpha power in Hispanic American and white non-Hispanic American young adults with a family history of alcohol dependence. Alcohol 2004; 33: 99-106.
13. Ehlers CL, Phillips E, Wall TL, Wilhelmsen K, Schuckit MA. EEG alpha and level of response to alcohol in Hispanic- and non-Hispanic-American young adults with a family history of alcoholism. J Stud Alcohol 2004; 65: 301-8.
14. Hamilton KR, Sinha R, Potenza MN. Hazardous drinking and dimensions of impulsivity, behavioral approach, and inhibition in adult men and women. Alcohol Clin Exp Res 2012; 36: 958-66.
15. Porjesz B, Rangaswamy M. Neurophysiological endophenotypes, CNS disinhibition, and risk for alcohol dependence and related disorders. Sci World J 2007; 7: 131-41.
16. Petit G, Maurage P, Kornreich C, Verbanck P, Campanella S. Binge drinking in adolescents: a review of neurophysiological and neuroimaging research. Alcohol Alcohol 2014; 49: 198-206.
17. Courtney KE, Polich J. Binge drinking effects on EEG in young adult humans. Int J Environ Res Public Health 2010; 7: 2325-36.
18. Buhler M, Mann K. Alcohol and the human brain: a systematic review of different neuroimaging methods. Alcohol Clin Exp Res 2011; 35: 1771-93.
19. Núñez-Jaramillo L, Vega-Perera P, Ramírez-Lugo L, Reyes-López JV, Santiago-Rodríguez E, Herrera-Morales WV. Quantitative electroencephalography analysis in university students with hazardous alcohol consumption, but not alcohol dependence. Neuroreport 2015; 26: 555-60.
20. Whittington MA, Traub RD, Kopell N, Ermentrout B, Buhl EH. Inhibition-based rhythms: experimental and mathematical observations on network dynamics. Int J Psychophysiol 2000; 38: 315-36.
21. Knight JR, Sherritt L, Harris SK, Gates EC, Chang G. Validity of brief alcohol screening tests among adolescents: a comparison of the AUDIT, POSIT, CAGE, and CRAFFT. Alcohol Clin Exp Res 2003; 27: 67-73.
22. Puig-Nolasco A, Cortaza-Ramírez L, Pillon SC. Consumo de alcohol entre estudiantes mexicanos de medicina. Rev Lat Am Enfermagem 2011; 19: 714-21.
23. Guzmán-Facundo FR, Pedrão LJ, Rodríguez-Aguilar L, López-García KS, Esparza-Almanza SE. Alcohol consumption disorder (AUDIT) for marginal adolescents and youth from juvenile gangs of Mexico. Esc Anna Nery Rev Enferm 2007; 11: 611-8.
24. Reyes-Zamorano E, García-Vargas KL, Palacios-Cruz L. Concurrent validity in Mexican college population of the adult ADHD self report scale. Rev Invest Clin 2013; 65: 30-8.
25. Ramos-Quiroga JA, Daigre C, Valero S, Bosch R, Gómez-Barros N, Nogueira M, et al. Validación al español de la escala de cribado del trastorno por déficit de atención/hiperactividad en adultos (ASRS v. 1.1): una nueva estrategia de puntuación. Rev Neurol 2009; 48: 449-52.
26. Rooney M, Chronis-Tuscano A, Yoon Y. Substance use in college students with ADHD. J Atten Disord 2012; 16: 221-34.
27. SINAIS, Indicadores Básicos de Salud 2000-2008. Indicadores de mortalidad. México DF: Secretaría de Salud; 2008.
28. Fergusson DM, Boden JM, Horwood LJ. Alcohol misuse and psychosocial outcomes in young adulthood: results from a longitudinal birth cohort studied to age 30. Drug Alcohol Depend 2013; 133: 513-9.
29. John ER, Prichep LS, Easton P. Normative data banks and neurometrics: basic concepts, methods and results of norm construction. In Remond A, ed. Handbook of electroencephalography and clinical neurophysiology. Vol. III. Amsterdam: Elsevier; 1987. p. 449-95.
30. Hernández JL, Valdés P, Biscay R, Virues T, Szava S, Bosch J, et al. A global scale factor in brain topography. Int J Neurosci 1994; 76: 267-78.
31. Gudmundsson S, Runarsson TP, Sigurdsson S, Eiriksdottir G, Johnsen K. Reliability of quantitative EEG features. Clin Neurophysiol 2007; 118: 2162-71.
32. De Quesada-Martínez ME, Díaz-Pérez GF, Herrera-Ramos A, Tamayo-Porras M, Rubio-López R. Características del electroencefalograma cuantitativo y trastornos cognitivos en pacientes alcohólicos. Rev Neurol 2007; 44: 81-8.
33. Coutin-Churchman P, Moreno R, Anez Y, Vergara F. Clinical correlates of quantitative EEG alterations in alcoholic patients. Clin Neurophysiol 2006; 117: 740-51.
34. Fan X, Konold TR. Statistical significance versus effect size. In Peterson P, Baker E, McGaw B, eds. International encyclopedia of education. New York: Elsevier; 2010. p. 444-50.
35. Clemens B, Menes A, Piros P, Bessenyei M, Altmann A, Jerney J, et al. Quantitative EEG effects of carbamazepine, oxcarbazepine, valproate, lamotrigine, and possible clinical relevance of the findings. Epilepsy Res 2006; 70: 190-9.
36. Ehlers CL, Phillips E, Finnerman G, Gilder D, Lau P, Criado J. P3 components and adolescent binge drinking in Southwest California Indians. Neurotoxicol Teratol 2007; 29: 153-63.
37. Fein G, Andrew C. Event-related potentials during visual target detection in treatment-naive active alcoholics. Alcohol Clin Exp Res 2011; 35: 1171-9.
38. Bjork MH, Sand T, Brathen G, Linaker OM, Morken G, Nilsen BM, et al. Quantitative EEG findings in patients with acute, brief depression combined with other fluctuating psychiatric symptoms: a controlled study from an acute psychiatric department. BMC Psychiatry 2008; 8: 89.
39. Chen AC, Tang Y, Rangaswamy M, Wang JC, Almasy L, Foroud T, et al. Association of single nucleotide polymorphisms in a glutamate receptor gene (GRM8) with theta power of event-related oscillations and alcohol dependence. Am J Med Genet B Neuropsychiatr Genet 2009; 150B: 359-68.
40. Rangaswamy M, Jones KA, Porjesz B, Chorlian DB, Padmanabhapillai A, Kamarajan C, et al. Delta and theta oscillations as risk markers in adolescent offspring of alcoholics. Int J Psychophysiol 2007; 63: 3-15.
41. Cuzen NL, Andrew C, Thomas KG, Stein DJ, Fein G. Absence of P300 reduction in South African treatment-naive adolescents with alcohol dependence. Alcohol Clin Exp Res 2013; 37: 40-8.
42. Koob GF, Le Moal M. Neurobiology of addiction. London: Academic Press; 2006.
43. Albein-Urios N, Martínez-González JM, Lozano O, Verdejo-García A. Frontal systems related symptoms in cocaine dependent patients with comorbid personality disorders. Psychopharmacology (Berl) 2013; 228: 367-73.

El consumo de riesgo de alcohol y el riesgo de dependencia al alcohol presentan correlatos neurofisiológicos diferentes

Introducción. El consumo de riesgo de alcohol (CRA) es un patrón de consumo que puede resultar dañino para el usuario o para los demás. Investigaciones previas sugieren que el CRA y la dependencia al alcohol comparten algunas características neurofisiológicas, pero difieren en otras.

Objetivo. Determinar si el CRA y la dependencia al alcohol presentan correlatos neurofisiológicos diferentes.

Sujetos y métodos. Doscientos sujetos realizaron la prueba de detección de CRA y riesgo de dependencia al alcohol (DEP). Se realizó un estudio de electroencefalografía cuantitativa para determinar la potencia absoluta, la potencia relativa y la frecuencia media de las bandas delta, theta, alfa y beta en sujetos con CRA, con DEP y controles.

Resultados. Un total de 114 sujetos cumplió los criterios de inclusión. El grupo con CRA presentó mayor potencia absoluta, mayor potencia relativa y menor frecuencia media de la banda beta en comparación con los controles, mientras que el grupo con DEP presentó menor potencia absoluta de la banda delta que los controles.

Conclusiones. El DEP y el CRA presentan diferentes correlatos neurofisiológicos. Hay un efecto importante de la gravedad de la dependencia al alcohol sobre sus correlatos neurofisiológicos. Nuestros resultados apoyan la existencia de dos tipos distintos de desinhibición conductual.

Palabras clave. Actividad beta. Actividad delta. Consumo de riesgo de alcohol. Dependencia al alcohol. Desinhibición conductual. EEG cuantitativo.

Check for updates

Development-Dependent Changes in the NR2 Subtype of the N-Methyl-D-Aspartate Receptor in the Suprachiasmatic Nucleus of the Rat

J. Manuel Herrera-Zamora,* Luis A. Castro-Sánchez,*,† Miriam Reyes-Mendez,* Irving Aguilar-Martinez,* Fernando Osuna-López,* Eloy G. Moreno-Galindo,* Ricardo A. Navarro-Polanco,* Raul A. Aguilar-Roblero,‡ Enrique Sánchez-Pastor,* and Javier Alamilla*,†,1

*Centro Universitario de Investigaciones Biomédicas "CUIB", Universidad de Colima, Colima, Col, Mexico, †Consejo Nacional de Ciencia y Tecnología (CONACYT), Universidad de Colima, Colima, Col, Mexico, and ‡División de Neurociencias, Instituto de Fisiología Celular, Universidad Nacional Autónoma de México

Abstract The suprachiasmatic nucleus (SCN) is the main brain clock that regulates circadian rhythms in mammals. The SCN synchronizes to the LD cycle through the retinohypothalamic tract (RHT), which projects to ventral SCN neurons via glutamatergic synapses. Released glutamate activates N-methyl-D-aspartate (NMDA) receptors, which play a critical role in the activation of signaling cascades to enable phase shifts. Previous evidence indicates that presynaptic changes during postnatal development consist of an increase in RHT fibers impinging on SCN neurons between postnatal day (P) 1 to 4 and P15. The aim of this study was to evaluate postsynaptic developmental changes in the NR2 subunits that determine the pharmacological and biophysical properties of the neuronal NMDA receptors in the ventral SCN. To identify the expression of NR2 subtypes, we utilized RT-PCR, immunohistochemical fluorescence, and electrophysiological recordings of synaptic activity. We identified development-dependent changes in NR2A, C, and D subtypes in mRNA and protein expression, whereas NR2B protein was equally present at all analyzed postnatal ages. The NR2A antagonist PEAQX (100 nM) reduced the frequency of NMDA excitatory postsynaptic currents (EPSCs) at P8 significantly more than at P34, but the antagonists for NR2B (3 μM Ro 25-6981) and NR2C/D (150 nM PPDA) did not influence NMDA EPSCs differently at the 2 analyzed postnatal ages. Our results point to P8 as the earliest analyzed postnatal age that shows mRNA and protein expression similar to those found at the juvenile stage P34. Taken together, our findings indicate that postsynaptic development-dependent modifications in the NR2 subtypes of the NMDA receptor could be important for the synchronization of ventral SCN neurons to the LD cycle at adult stages.

Keywords SCN, NMDA, NR2, development, retinohypothalamic tract, glutamate

1. To whom all correspondence should be addressed: Javier Alamilla, Centro Universitario de Investigaciones Biomédicas, Av. 25 de Julio # 965, Col. Villas de San Sebastián, Col, Col. CP 28045, Mexico; e-mail: jfalamillago@conacyt.mx; alamilla78@gmail.com.

JOURNAL OF BIOLOGICAL RHYTHMS, Vol. 34 No. 1, February 2019 39–50
DOI: 10.1177/0748730418824198
© 2019 The Author(s)
Article reuse guidelines: sagepub.com/journals-permissions

The hypothalamic suprachiasmatic nucleus (SCN) is the main clock responsible for the regulation of circadian rhythms. The SCN synchronizes with the environmental LD cycle through the retinohypothalamic tract (RHT). Ablation of the RHT abolishes the synchronization of circadian rhythms to the LD cycle, allowing its free-running expression (Johnson et al., 1988). The RHT originates from a population of melanopsin-containing photosensitive ganglion cells in the retina (Hankins et al., 2008) and projects its fibers to various hypothalamic nuclei, including the SCN. The RHT releases glutamate and the pituitary adenylate cyclase-activating polypeptide (Hannibal, 2006; You et al., 2012) to the ventrolateral part of the SCN, which receives its principal innervation from the retina (Abrahamson and Moore, 2001). Glutamate released from the RHT activates ionotropic glutamatergic α-amino-3-hydroxy-5-methyl-4-isoxazolepropionic acid (AMPA)/kainate and N-methyl-D-Aspartate (NMDA) receptors (Kim and Dudek, 1991). Activation of NMDA receptors is a crucial step in phase shifts induced by light (Colwell and Menaker, 1992), which subsequently activate signaling pathways to achieve phase advances or delays (Ding et al., 1994; Ding et al., 1997).

The NMDA receptor is a heteromeric protein principally composed of 2 NR1 and 2 NR2 subunits. The 4 known types of subunits are termed NR2A to NR2D. The 2 NR2 subunits of the NMDA receptor can comprise the same or different types, thus providing diversity to the biophysical and pharmacological properties of NMDA receptors (see Cull-Candy and Leszkiewicz, 2004). Several reports indicate that the NR2B subtype plays an important role in the synchronization to light. In SCN neurons, Clark and Kofuji (2010) found that the NMDA current is reduced to about 50% by the NR2B antagonist ifenprodil. It was furthermore shown in mice that ifenprodil microinjected into the SCN region significantly reduces light-induced phase shifts in wheel running activity and that the phosphorylated form of this NR2 subtype varies in the ventral SCN according to circadian rhythms (Wang et al., 2008).

When NR2A and NR2C are individually knocked out in the whole animal, they do not seem to play a role in the synchronization of SCN neurons to light, even though there is biophysical and pharmacological evidence of their presence in NMDA currents of SCN neurons. Clark and Kofuji (2010) showed that the remaining NMDA current after NR2B inhibition with ifenprodil presents pharmacological characteristics of the NR2A subtype, even though they exhibit a $Mg^{2}+$ sensitivity similar to that of NR2C and NR2D subunits. Thus, these authors suggest that a subpopulation of NMDA receptors in SCN neurons consists of NR2A and NR2C/D heteromers. Moriya and colleagues (2000) showed that synchronization to light was slower in NR2A-knockout animals under low-intensity light conditions, indicating that NR2A indeed plays a role in synchronization. However, no effects were found in NR2C-knockout animals, and the role of the NR2D subunit in the synchronization of SCN neurons to light has not been reported yet.

Pre- and postsynaptic changes during development are critical for all sensory systems to prepare them for an optimal performance at adult stages, and the photic circadian system is no exception. It has been reported that RHT fibers start the SCN innervation at an early stage, i.e., postnatal days (P) 1 to 4 (Mason et al., 1977; Munoz Llamosas et al., 2000; Speh and Moore, 1993; Stanfield and Cowan, 1976); although, functional Fos immunoreactivity is already found at P0 (Hannibal and Fahrenkrug, 2004; Sekaran et al., 2005). The RHT achieves an adult appearance at P10 to P15 (Frost et al., 1979; Guldner, 1978; Mason et al., 1977; Munoz Llamosas et al., 2000; Speh and Moore, 1993). At the behavioral level, neonatal rats synchronize to LD cycles by P7 (Duncan et al., 1986), when the maternal influence wanes (Reppert and Schwartz, 1986) and the RHT synaptic terminals innervate the SCN neurons. Anatomical and behavioral evidence of the maturation in RHT - SCN connections may imply pre- and postsynaptic changes during this development that help to prepare the circadian system to correctly synchronize to light. To further understand these processes, this study was aimed to determine the postsynaptic changes in NR2 subunit expression (both at the mRNA and protein levels) in rats during development and determine their influence on synaptic activity.

MATERIALS AND METHODS

All studies were performed in accordance with the Guide for the Care and Use of Laboratory Animals published by the US National Institutes of Health (NIH Publication No. 85-23, revised 1996). All procedures were approved by the Institutional Bioethics Committee of the University Center for Biomedical Research of the University of Colima. Experiments were carried out in Wistar rat pups (n = 111) bred in our animal facilities from parents supplied by Harlan (Mexico). We analyzed postnatal developmental changes in the ventral SCN of animals at the ages of P4, P8, P12, and P34. For tissue sampling, animals were euthanized (between ZT 3 and 6) with sodium pentobarbital (125 mg/kg, i.p.).

INFORME DE LABORES 2019

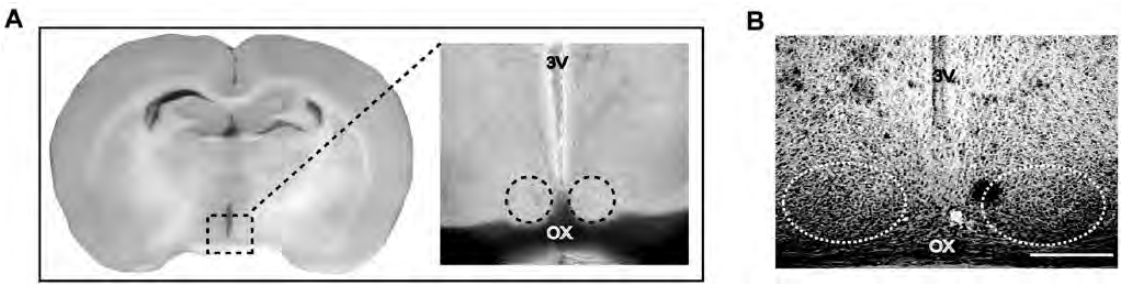

Figure 1. Coronal brain slices containing the SCN used in the different methodological approaches of this study. (A) Slice corresponding to a P12 animal, illustrating the sectioned area where RT-PCR assays were performed. (B) Ventral and medial SCN examined for immunofluorescence experiments. Coronal slice of a P8 animal imaged with transmitted light containing the ventral SCN and reference structures such as the third ventricle (3V) and optic chiasm (OX). Circles indicate the ventral parts of the SCN analyzed in confocal microscopy. Scale bar, 150 µm.

Table 1. Primers used to identify genes that code for NR2 subtypes and housekeeping genes.

Gene	Forward	Reverse
Grin2a	5′-ACACCACCTGAGGACGTTTG-3′	5′-TGGAAGAACGTGGATGTCGG-3′
Grin2b	5′-AATACAGTCCCGTGCCAGAA-3′	5′-CACCGATCATGCCATTCCAG-3′
Grin2c	5′-CCCTACCTCCCGTTATTCCC-3′	5′-CAGAGGGTTGGATCGAGTGA-3′
Grin2d	5′-CCACCTCTGAAGTTTGGCAC-3′	5′-GATGAAGGCGTCCAGTTTCC-3′
Gapdh	5′-AGTCTACTGGCGTCTTCACC-3′	5′-CCACGATGCCAAAGTTGTCA-3′
Actb	5′-CCGCGAGTACAACCTTCTTG-3′	5′-CAGTTGGTGACAATGCCGTG-3′

RNA Extraction and Quantitative Real-Time PCR Analysis

Coronal brain slices (300 µm) containing the hypothalamus were obtained with a VT1000 microtome (Leica Microsystems; Wetzlar, Germany). Brain slices were maintained in artificial cerebrospinal fluid (ACSF) containing 124 mM NaCl, 1 mM $MgSO_4$, 5 mM KCl, 1.25 mM KH_2PO_4, 10 mM dextrose, 26 mM $NaHCO_3$, 2 mM $CaCl_2$; bubbled with 95% O_2/5% CO_2; pH 7.4. Tissue from the SCN was microdissected from 8 animals belonging to each of the above-mentioned postnatal ages (Fig. 1A). Total RNA was extracted from the pool (20 mg) of SCN samples using the Aurum Total RNA Mini Kit (Bio-Rad; Hercules, CA). RNA (500 ng) was reverse transcribed using an iScript cDNA Synthesis Kit (Bio-Rad). The cDNA was used as a template for real-time PCR experiments using the iQ SYBR Green Supermix (Bio-Rad) with the primers for the following genes that code for the different NR2 subtypes *Grin2a* (NR2A), *Grin2b* (NR2B), *Grin2c* (NR2C), and *Grin2d* (NR2D) in addition to the housekeeping genes *Gapdh* (glyceraldehyde-3-phosphate dehydrogenase) and *Actb* (β-actin) (Table 1). Specific primers were purchased from Invitrogen (Carlsbad, CA). Real-time PCR was performed using a CFX96 detection system (Bio-Rad). The thermal cycling parameters were 95°C for 3 min, 40 cycles of 95°C for 15 s, followed by 60°C for 1 min. The experiment for each postnatal age was run in triplicate and normalized to *Gapdh* and *Actb* mRNA levels. We used *Actb* as an additional housekeeping gene because it has been shown that the mRNA levels remain very steady throughout the development of the whole brain in Wistar rats (Fedoseeva et al., 2014). Three replicates of measurements from the same pool were then averaged, and the fold induction was determined in a $\Delta\Delta C_T$-based fold-change calculation. Furthermore, raw data (not normalized to P4) were obtained with the ΔC_T method (Schmittgen and Livak, 2008). A melting curve analysis was performed to confirm the specificity of the PCR products.

Immunohistochemistry

A total of 47 rat pups were used at different postnatal ages: 15 animals for P4, 14 animals for P8, 11 for P12, and 7 for P34. After the animals were euthanized with sodium pentobarbital (125 mg/kg), the brain was perfused transcardially with 0.1 M phosphate-buffered saline (PBS; pH 7.4), followed by cold (4°C) 4% paraformaldehyde diluted in 0.1 M phosphate buffer (PB; pH 7.4). Thereafter, the brain was extracted and post-fixed in 4% paraformaldehyde for 1 h before being transferred to 10% sucrose (overnight), 20% sucrose (24 h),

INFORME DE LABORES 2019

Table 2. Specifications of antibodies used in this research.

Antigen	Immunogen	Manufacturer, Species, Type, Catalog number, Test performed	Dilution Tested (Used •)	Reference
NR2A	Synthetic peptide within Human NMDA2A aa 850-900.	Abcam, rabbit, polyclonal, # ab203197, IHC.	1:50 1:100• 1:200	-
NR2B (phospho Y1252)	Synthetic peptide conjugated to LKH derived from within residues 1200-1300 of mouse NMDAR2B.	Abcam, rabbit, polyclonal, # ab18532, IHC.	1:50 1:100• 1:200	Delint et al., (2010)
NR2C	Antibody raised against 21-100 amino acids mapping near the human N-terminus of NMDAR2C.	Santa Cruz Biotechnology (Dallas, TX, USA), rabbit, polyclonal, # sc-50437, IHC.	1:50 1:250• 1:500	Liu and Wong-Riley (2010)
NR2D	Synthetic peptide corresponding to 661-710 amino acids of NMDAR2D of human.	Thermo Fisher Scientific (Rockford, IL, USA), rabbit, polyclonal, # PA5-36539, IHC.	1:50, 1:100• 1:200	-
PSD-95	Recombinant full length protein corresponding to PSD-95	Abcam, mouse, monoclonal, # ab2723, IHC.	1:1000 1:2000 1:3000 1:4000•	Zhao et al., (2016)

and finally 30% sucrose (48 h). Consecutive frozen coronal sections (40 µm) containing the hypothalamus were obtained with an SM2010R microtome (Leica) and collected into 0.1 M PBS. Brain sections belonging to the different postnatal ages were stained for the antibodies listed below and imaged at the same time for consistency between runs. On average, 4 consecutive sections (per brain) were carefully chosen with the help of a stereomicroscope (MicroscoSB; Commack, NY). They contained the medial SCN and were immunostained for protein pairs consisting of 1 of the 4 NR2 subunit subtypes of the NMDA receptor (A to D) and the scaffolding protein PSD-95; i.e., NR2A and PSD-95, NR2B and PSD-95, NR2C and PSD-95, NR2D and PSD-95. Immunofluorescence labeling was performed with free-floating sections at 4°C for 72 h in 1% normal donkey serum and 0.03% Triton X-100 in 0.1 M PBS (PBSDT). Secondary antibodies were incubated in PBSDT for 2 h at room temperature in black tubes protected from light. Slices were then washed in PBS (3 times, 10 min each), mounted, and coverslipped with 97% 2,2′-thiodiethanol (Staudt et al., 2007).

Antibodies

All antibodies used in this study (Table 2) were tested and characterized by the supplier companies. Negative control experiments were performed by incubation with only the secondary antibody, and no unspecific immunolabeling was observed (Suppl. Fig. S1A). Dilution-fluorescence curves were carried out for primary antibodies (Table 2, Suppl. Fig. S1B). Secondary antibodies (anti-rabbit Alexa Fluor 488 and anti-mouse Alexa Fluor 647; both from Abcam, Cambridge, UK) were used at a 1:500 dilution.

Image Acquisition and Analysis

SCNs were imaged with an LSM-700 confocal microscope (Carl Zeiss; Oberkochen, Baden-Württemberg, Germany). The best mounted and coverslipped brain slices containing the medial SCN were chosen for imaging by confocal microscopy (1 or 2 slices were selected from each animal at every stage of postnatal development) using the Zen software (Carl Zeiss) for image acquisition. A 10× objective (NA 0.3) was used to obtain a panoramic view of the SCN and adjacent structures. Then, 40× (NA 1.3) and 63× (NA 1.4) objectives were used to visualize the ventral SCN (Abrahamson and Moore, 2001) (Fig. 1B), and optical slices were obtained at 1 µm steps (on average, we obtained more than 20 optical slices per image). Two images (medial and lateral) were taken for each ventral SCN (left and right) for a total of 4 images for each slice. For intensity fluorescence measurements, PMT gain, laser intensity, and all other parameters (e.g., acquisition and exposure time) were adjusted for each age to show the highest brightness without saturation and were maintained constant for all subsequent images obtained within the same run.

Images were 3D blind deconvoluted using the AutoQuant X3 (Media Cybernetics Inc., Rockville, MD) and then analyzed using the ImageJ software (National Institutes of Health, Bethesda, MD). The signals were separated into 2 channels, and the mean pixel immunofluorescence intensity was measured in the entire image, i.e., the stack of optical slices (at least 20). A stack of optical slices was obtained with the maximum intensity projection function of the Zen software. Immunofluorescence intensity measurement obtained from medial and lateral images were pooled. Co-localization was analyzed on the entire image using the Zen software, and this co-localization

analysis was performed on a pixel by pixel basis. Each pixel was plotted in a scatter diagram based on its intensity level from each channel. Thereafter, the Pearson correlation coefficient was calculated with a value of 1 indicating a perfect co-localization.

Electrophysiological Recordings

Spontaneous postsynaptic currents from ventral SCN neurons of slices obtained at P8 and P34 were recorded at room temperature (22°C to 24°C) in the whole-cell configuration of the patch-clamp technique using an Axopatch 200B amplifier (Molecular Devices; Sunnyvale, CA). Neurons were visualized with an upright Axioexaminer A1 microscope (Carl Zeiss). Data acquisition and command potentials were carried out with a Digidata 1322A interface controlled by the pClamp 8.2 software (Molecular Devices). Recording electrodes of 2 to 4 MΩ were made in a P97 puller (Sutter Instrument Co., Novato, CA) and filled with intracellular solution containing 64 mM D-gluconic acid, 64 mM CsOH, 11 mM EGTA, 56 mM CsCl, 1 mM $MgCl_2$, 1 mM $CaCl_2$, 10 mM HEPES, and 5 mM QX-314. Series resistance was compensated (~80%), and the seal was monitored throughout the whole experiment. ACSF Mg^2+-free solution (124 mM NaCl, 1 mM K_2SO_4, 5 mM KCl, 1.25 mM KH_2PO_4, 10 mM dextrose, 26 mM $NaHCO_3$, 2 mM $CaCl_2$; bubbled with 95% O_2/5% CO_2; pH 7.4) was used as the external recording solution. Cells were discarded if the input resistance was less than 150 MΩ or the access resistance greater than 15 MΩ, or changed more than 15%. Currents were low-pass filtered at 2 kHz and sampled at 10 kHz.

Contribution of NR2 Subtypes to the Frequency and Amplitude of NMDA EPSCs

To analyze the contribution of NR2 subtypes to isolated spontaneous NMDA excitatory postsynaptic currents (EPSCs), 50 µM picrotoxin (a GABA-A receptor antagonist) and 5 µM 6-cyano-7-nitroquinoxaline-2,3-dione (CNQX, an antagonist of AMPA/kainate receptors) were added to the external recording solution (ACSF Mg^2+-free solution). After 5 min of recording basal NMDA isolated currents, each of the selective NR2 subtype antagonists were applied in a random sequence; for NR2A, 100 nM [[[(1*S*)-1-(4-Bromophenyl) ethyl]amino] (1,2,3,4-tetrahydro-2,3-dioxo-5-quinoxalinyl)methyl] phosphonic acid tetrasodium salt (PEAQX); for NR2B, 3 µM (α*R*,β*S*)-α-(4-Hydroxyphenyl)-β-methyl-4-(phenylmethyl)-1-piperidinepropanol maleate (Ro 25-6981); or for NR2C/D, 150 nM (2*S**,3*R**)-1-(Phenanthren-2-carbonyl)piperazine-2,3-dicarboxylic acid (PPDA). PEAQX has an IC_{50} of 8 nM on NMDA receptors containing the NR2A subunit. PEAQX is over 100-fold more selective to NR2A than NR2B subunits (Auberson et al., 2002). Thus, we chose a concentration of 100 nM, according to previous reports demonstrating the highest specificity for NR2A (Tackenberg et al., 2013). By contrast, Ro 25-6981 exhibits a higher affinity for NR2B over the NR2A subtype, since its IC_{50} values are 0.009 and 52 µM, respectively (Fischer et al., 1997). Hence, we used 3 µM Ro 25-6981 to detect the presence of NR2B subunits, which agrees with previous studies (Alamilla and Gillespie, 2011). Likewise, PPDA exhibits a K_i of 0.096, 0.125, 0.31, and 0.55 µM for the NR2C, D, B, and A subtypes, respectively (Morley et al., 2005). Based on this information, we assumed that 150 nM would be sufficient to distinguish between NR2C/D and NR2B/A subunits. The effects of these NR2 subtype blockers on the frequency and amplitude of NMDA EPSCs were analyzed, and the percentages of NR2A, NR2B, and NR2C/D subunit contributions were calculated for each recorded neuron.

Drugs and Reagents

Picrotoxin, CNQX, PEAQX, PPDA, and Ro 25-6981 were obtained from Tocris Bioscience (Ellisville, MO), and all other reagents were purchased from Sigma-Aldrich (St. Louis, MO).

Data Analysis

Data are reported as the mean ± SEM. GraphPad Prism 5 (GraphPad Software; La Jolla, CA) was used to perform statistical analyses. Where appropriate, the unpaired *t*-test or one-way ANOVA with Dunnett's post-hoc test were used to evaluate statistical differences. The non-parametric Kruskal–Wallis test with Dunn's post-hoc test was used to analyze the fold-change in mRNA expression (Hoang et al., 2009). A two-tailed alpha value of 0.05 ($P < 0.05$) was considered statistically significant.

RESULTS

mRNA Expression of NR2 Subunits during Postnatal Development in the SCN

As mRNA expression of NR2 subtypes must be normalized to that of housekeeping genes according to the $\Delta\Delta C_T$ method, we first sought to validate that the mRNA levels of the housekeeping genes

INFORME DE LABORES 2019

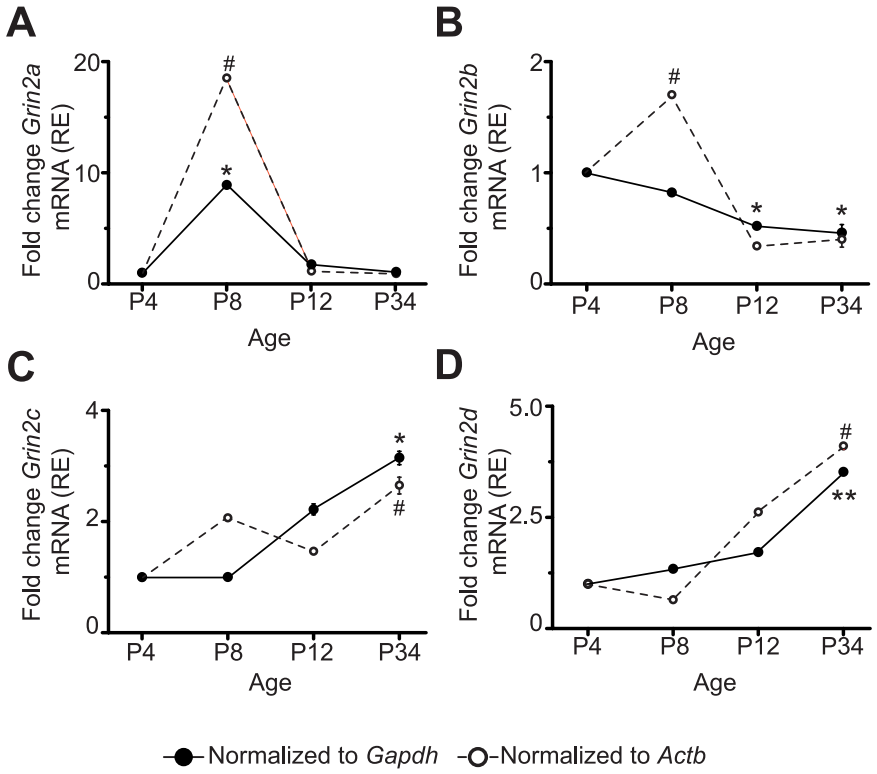

Figure 2. mRNA expression relative (RE) to P4 of the different NR2 subunits during the postnatal development of the rat. mRNA of *Grin2a* that encodes for NR2A (A), *Grin2b* for NR2B (B), *Grin2c* for NR2C (C), and *Grin2d* for NR2D (D) at postnatal ages 4, 8, 12, and 34. Data correspond to triplicate experiments of the same mRNA pool from 8 animals belonging to each analyzed postnatal age. *$P < 0.05$, **$P < 0.01$ vs. P4 normalized to *Gapdh*; #$P < 0.05$ normalized to *Actb*.

displayed no development-dependent variation. Although there was a statistically significant *Gapdh* variation between P8 and P12, we did not find a significant difference in C_T between the control age P4 and any other analyzed age (Suppl. Fig. S2). Likewise, *Actb* did not show a development-dependent variation in C_T at all analyzed ages (Suppl. Fig. S2).

Next, the mRNA expression levels of NMDAR2 subtypes in the SCN were analyzed at different postnatal ages (Fig. 1A), using P4 as a reference (Fig. 2). Normalized to both housekeeping genes, *Grin2a* (NR2A subtype) mRNA expression levels only peaked at P8 (Fig. 2A). When normalized to *Gapdh*, *Grin2b* (NR2B) showed a decrease in mRNA expression at P12 and P34, whereas when normalized to *Actb*, mRNA levels significantly increased at P8 (Fig. 2B). The mRNA levels of *Grin2c* (NR2C) were elevated at P34 with respect to those at P4 (Fig. 2C) with a similar result for *Grin2d* (NR2D), which also displayed a significant increase in mRNA expression at P34 (Fig. 2D). Similar tendencies were found when data were not normalized to P4 (ΔC_T) (Suppl. Fig. S3). These results indicate that mRNA levels of NR2 subtypes in SCN neurons are differentially expressed during postnatal development.

Developmental Expression of NR2 Subtypes and Scaffolding Protein PSD-95 in the Ventral SCN

Immunofluorescence intensities of NR2 subtypes were analyzed at different ages of postnatal development (Figs. 3A, 4A, 5A, and 6A). For NR2A, a higher fluorescence intensity was observed at P8 (79 ± 7 arbitrary units [a.u.]) and P34 (72 ± 8 a.u.) compared with P4 (49 ± 4 a.u.; $F_{[3,56]} = 5$, $P = 0.010$; Fig. 3B). No significant differences in immunofluorescence were found for the NR2B subtype among all postnatal ages investigated (54 ± 6 a.u., 68 ± 13 a.u., 68 ± 15 a.u., and 63.4 ± 10 a.u. at P4, P8, P12, and P34, respectively; $F_{[3,56]} = 0.34$, $P = 0.8$; Fig. 4B). The immunofluorescence intensities of the NR2C subunit were significantly increased at all time points (70 ± 5 a.u., 64 ± 3 a.u., and 69 ± 3 a.u. at P8, P12, and P34, respectively) compared with P4 (52 ± 3 a.u.; $F_{[3,50]} = 6.0$, $P = 0.0013$; Fig. 5B). For the NR2D subtype, the immunofluorescence intensities were increased at all analyzed ages compared with that at P4 (47 ± 3 a.u., 71 ± 4 a.u., 67 ± 3 a.u., and 67 ± 2 a.u. at P4, P8, P12, and P34, respectively; $F_{[3,60]} = 3.7$, $P = 0.017$; Fig. 6B). Similarly, the protein PSD-95 showed a development-dependent expression that was significantly

INFORME DE LABORES 2019

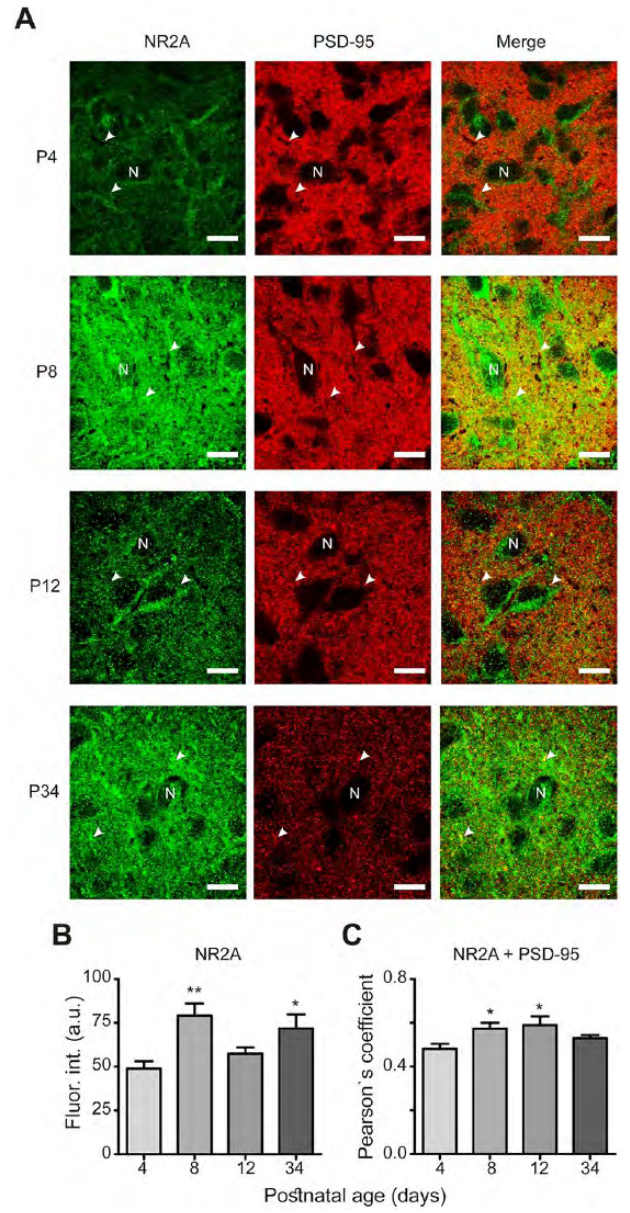

Figure 3. Developmental expression of the NR2A subtype. (A) For this and subsequent graphs in A panels from Figs. 3-6: green channel (first column) shows NR2 expression, NR2A in this case; red channel (second column) gives evidence for its corresponding PSD-95 immunoreactivity and the third column illustrates the merge of the two mentioned channels. A white letter *N* indicates a putative neuronal soma, and arrowheads depict co-localization dots of the NR2 subtype with PSD-95. Scale bars, 10 μm. (B) Fluorescence intensity (Fluor. int) in arbitrary units (a.u.) of the NR2A subtype at the 4 examined postnatal ages. (C) Co-localization of NR2A and PSD-95 denoted by Pearson's coefficient. *$P < 0.05$, **$P < 0.01$ vs. P4.

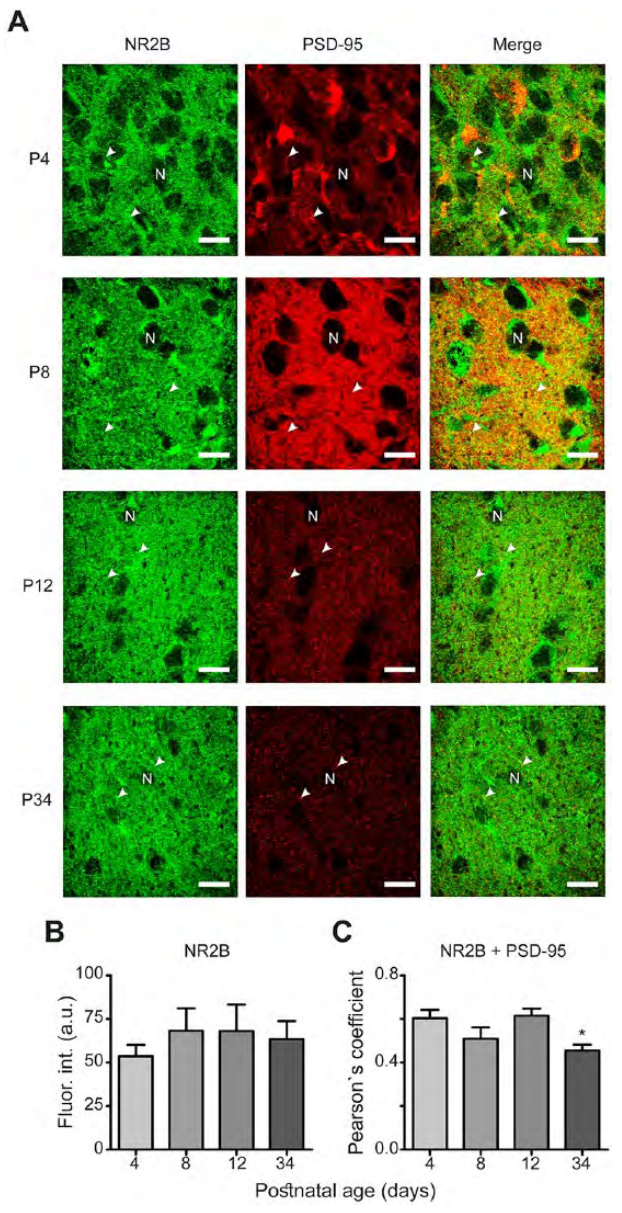

Figure 4. Expression of the NR2B subtype during postnatal development. (A) Similar micrographs as described for Fig. 3A (scale bars, 10 μm). (B) The fluorescence intensity of the NR2B subtype does not exhibit developmental changes at the analyzed postnatal ages. (C) Data from co-localization analyses of NR2B with the PSD-95 protein.

higher at P8 and P12; although, the mean intensity at P34 did not differ compared with that at P4 (66 ± 4 a.u., 97 ± 4 a.u., 113 ± 8 a.u., and 78 ± 5 a.u. at P4, P8, P12, and P34, respectively; $F_{[3,150]} = 12$, $P < 0.0001$; Fig. 7). Overall, these results suggest a differential developmental pattern of the protein expression of NMDA-NR2 subtypes as well as that of the NMDA scaffolding protein PSD-95.

Co-Localization of NR2 Subunits and PSD-95 Protein

PSD-95 functions as a platform for NMDA receptors, and it is therefore expected that NR2 subtypes and PSD-95 are co-localized. We analyzed the degree

INFORME DE LABORES 2019

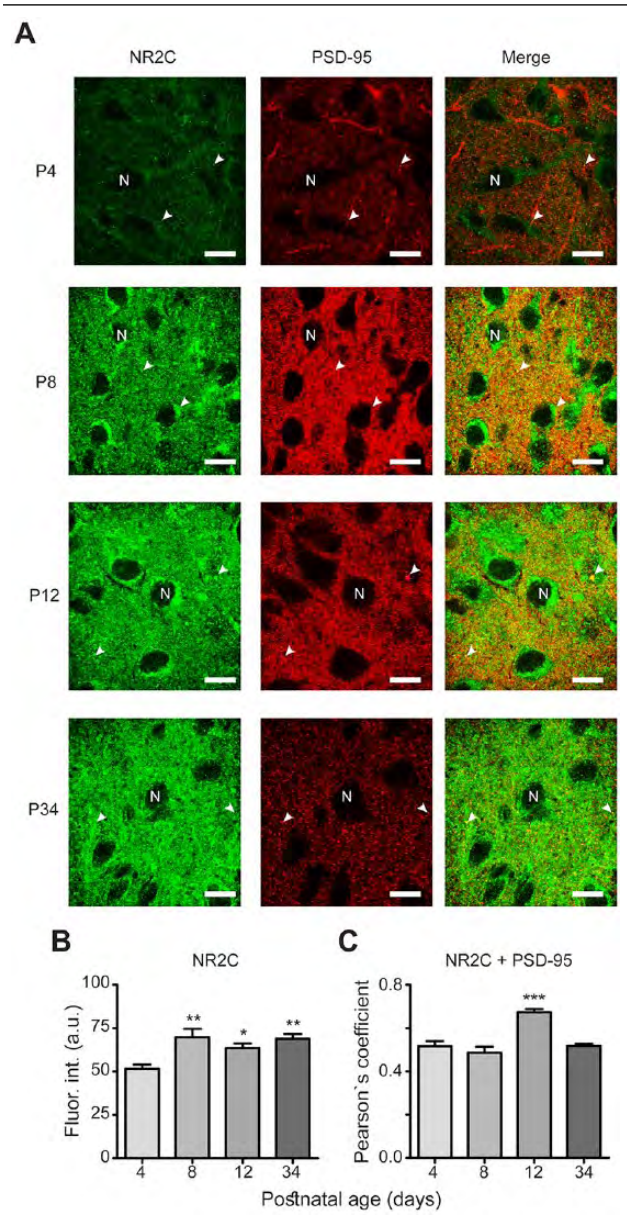

Figure 5. Development-dependent expression of the NR2C subtype. (A) Similar micrographs as described for Fig. 3A (scale bars, 10 μm). (B) Significant increase in NR2C immunofluorescence intensity at P8, P12, and P34. (C) Significantly augmented co-localization of NR2C and PSD-95 at P12. *$P < 0.05$, **$P < 0.01$, ***$P < 0.001$ vs. P4.

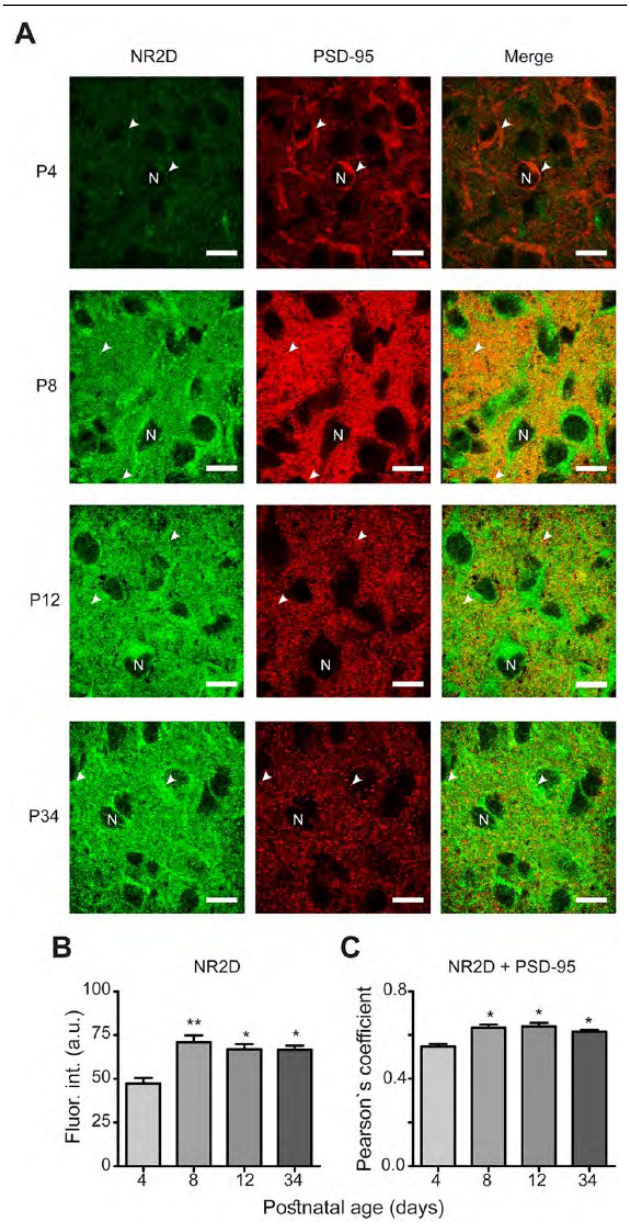

Figure 6. NR2D subtype expression during postnatal development. (A) Similar micrographs as described for Fig. 3A (scale bars, 10 μm). Immunofluorescence intensity is significantly increased after P8 (B), and similar situation in co-localization analyses (C). *$P < 0.05$, **$P < 0.01$ vs. P4.

of this co-localization, and our results revealed high co-localization between NR2 subtypes and PSD-95 (0.6 Pearson's coefficient on average; Figs. 3-6, merge panels). Particularly, NR2A and PSD-95 showed an increased co-localization index at P8 and P12 (Pearson's coefficient of 0.57 ± 0.02 and 0.59 ± 0.03, respectively) compared with that at P4 (0.48 ± 0.02) (Fig. 3C). NR2B showed a reduction at P34 (0.45 ± 0.02) compared with P4 (0.6 ± 0.04), whereas NR2C increased at P12 (0.67 ± 0.01) relative to P4 (0.51 ± 0.02). Similarly, co-localization of NR2D and PSD-95 was larger at all studied postnatal ages (0.63 ± 0.01, 0.64 ± 0.01, and 0.61 ± 0.01 at P8, P12, and P34, respectively) compared with P4 (0.54 ± 0.01) (Fig. 6C). These results suggest that NR2 subunits co-localize with PSD-95 in the developing ventral SCN, and the higher co-localization index at specific postnatal ages may imply that NR2 subtypes are recruited into postsynaptic densities.

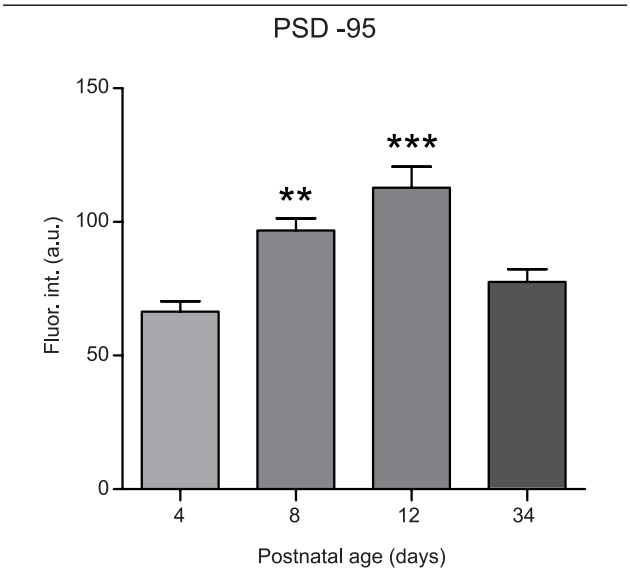

Figure 7. Postnatal expression of PSD-95. Significant changes in this scaffolding protein at P8 and P12. PSD-95 expression (illustrated in the middle columns of Figs. 3A, 4A, 5A, and 6A) supports a development-dependent expression. **$P < 0.01$, ***$P < 0.001$ vs. P4.

Electrophysiological Changes of NR2 Subtypes during Development

Because we found developmental changes in mRNA and protein expression of the diverse NR2 subtypes, we hypothesized that these changes have an impact on the physiology of SCN ventral neurons receiving glutamatergic RHT inputs. Consequently, we analyzed the effects of a selective antagonist for the different NR2 subtypes and determined their contributions to the frequency and amplitude of spontaneous NMDA EPSCs recorded in ventral SCN neurons at the 2 developmental ages, P8 and P34. We selected these 2 postnatal ages because we wanted to elucidate if there are changes in the physiology of NMDA receptors between the age where the initial synchronization to light starts (P8) (Duncan et al., 1986) and an older juvenile age (P34). The NR2A subtype had a larger contribution at P8 compared with that at P34, with reductions in EPSC frequencies by PEAQX of 57% ± 11% and 18% ± 10%, respectively ($t = 2.6$, $df = 15$, $P = 0.01$, unpaired t-test) (Fig. 8A). No statistically significant differences in antagonist-induced changes were found in the frequencies of NMDA EPSCs attributable to the NR2B subunit at the 2 analyzed ages. The reductions in EPSC frequencies by Ro 25-6981 were 33% ± 11% and 51% ± 12% at P8 and P34, respectively ($t = 1$, $df = 15$, $P = 0.3$, unpaired t-test) (Fig. 8B). Similar results were found in NMDA EPSC frequencies attainable to the NR2C/D subtype participation because the PPDA-induced reductions in EPSC frequencies were 19% ± 10% at P8 and 34% ± 10% at P34 ($t = 1$, $df = 12$, $P = 0.1$, unpaired t-test; Fig. 8C).

The analysis of the NMDA EPSC amplitudes indicated no developmental changes in NR2 subtype contributions at the examined time points P8 and P34 (Table 3). NR2A showed a similar participation at the 2 analyzed ages (30% ± 6% and 41% ± 14% at P8 and P34, respectively; $t = 1.2$, $P = 0.11$, unpaired t-test) (Table 3). The NR2B subtype displayed an age-independent performance (22% ± 7% and 31% ± 7% at P8 and P34, respectively; $t = 0.9$, $P = 0.2$, unpaired t-test; Table 3). Comparable results were also obtained for the NR2C/D subtypes (25% ± 11% and 24% ± 7% at P8 and P34, respectively; $t = 0.1$, $P = 0.44$, unpaired t-test; Table 3).

To investigate the effects of the 2 variables (drug administration and developmental ages) on NMDA EPSCs, a 2-way ANOVA test was carried out to analyze the contribution of NR2 subtypes on the frequency and amplitude of NMDA EPSCs. The interaction test indicated that the participation of NR2 subtypes on the reduction in EPSC frequency was dependent on age (P8 vs. P34; $F_{[2, 90]} = 4.6$, $p = 0.01$; data not shown). Regarding the amplitude of EPSCs, the interaction test showed that the contribution of NR2 subtypes did not depend on the developmental age ($F_{[2,90]} = 0.43$, $p = 0.64$; data not shown).

Taken together, our results indicate that NR2 subtypes, at least NR2A, exhibit a development-dependent contribution to the EPSC frequency of SCN neurons at P8 and P34.

DISCUSSION

The main result of this study is that we found developmental changes in the expression of the NR2 subtypes of glutamatergic NMDA receptors both in mRNA content and protein expression, which were consistent with the findings in experiments measuring the postsynaptic electrical activity. To our knowledge, this is the first study focused on an investigation of postsynaptic changes in SCN neurons related to light synchronization that occurs at adult stages. Previous studies were aimed at analyzing presynaptic changes by examining the innervations connecting the retina with SCN neurons during postnatal development (Speh and Moore, 1993).

In the current study, we found that the NR2A subtype had a stronger influence on the frequency of NMDA EPSCs at P8, just when the pup starts synchronizing to light via its RHT, whereas the NR2A contribution is decreased afterwards at age P34. Behavioral studies performed in adult animals implicate the NR2A subtype in the synchronization to light, with knockout animals taking longer to synchronize to damped light conditions (Moriya et al., 2000). The NR2B subtype did not show developmental changes

INFORME DE LABORES 2019

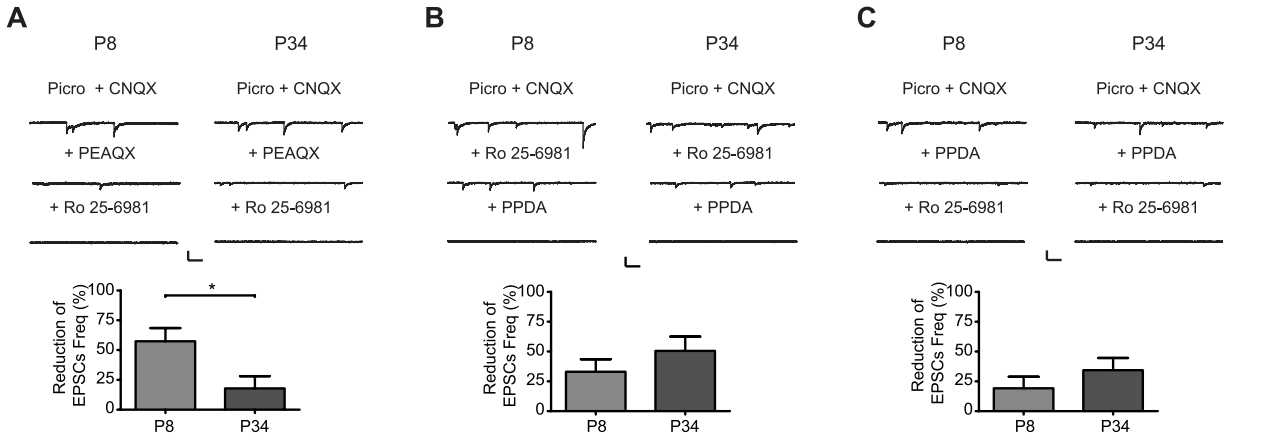

Figure 8. Contribution of the different NR2 subtypes on EPSC frequency (Freq) at 2 postnatal ages (P8 and P34). NMDA EPSCs recorded before (Control = Picro + CNQX) and after application of the NR2A antagonist PEAQX (A), the NR2B antagonist Ro 25-6981 (B), and the NR2C/D antagonist PPDA (C) at the 2 analyzed developmental ages. Scale bars: 40 pA, 200 ms. Bar graphs show the reduction in NMDA EPSC frequency induced by the respective NR2 antagonist. *$P < 0.05$.

Table 3. Amplitude of spontaneous NMDA EPSCs after the addition of selective antagonists for the different NR2 subtypes.

P8			P34		
Control	PEAQX	*n*	Control	PEAQX	*n*
13.5 ± 1 pA	9.4 ± 1 pA	10	23.7 ± 3 pA	14 ± 1 pA	6
Control	Ro-25	*n*	Control	Ro-25	*n*
15.5 ± 2 pA	12 ± 1 pA	7	19 ± 2 pA	13 ± 1 pA	9
Control	PPDA	*n*	Control	PPDA	*n*
17 ± 1 pA	12.7 ± 2 pA	6	23.7 ± 3 pA	18 ± 1 pA	7

in protein expression at all of the examined postnatal ages; although, its mRNA expression progressively decreased with age when normalized to *Gapdh.* However, it peaked at P8 when normalized to *Actb*. The latter result is probably more reliable since the levels of this housekeeping gene remain very steady throughout development. The data regarding the expression of the NR2B protein and its co-localization with PSD-95 are consistent with our electrophysiological results. Several lines of evidence indicate that the NR2B subunit is already present at pre- and early postnatal ages (see Cull-Candy et al., 2001). NR2B plays an important role in the synaptic communication of the RHT–SCN pathway at adult stages (Clark and Kofuji, 2010). We believe that the presence of NR2B at all analyzed ages supports the notion of the main influence of this subtype on RHT–SCN synaptic transmission, from early postnatal ages until a young stage. Wang and colleagues (2008) elicited phase-shift reductions in animals by ifenprodil administration but not their complete abolition, which indicates that other NR2 subtypes could participate in the synchronization of SCN neurons to light.

As shown in knockout animals, the NR2C subtype does not seem to be involved in the synchronization to light at adult ages (Moriya et al., 2000). In the present study, we found larger mRNA levels and protein expression of NR2C at juvenile ages; i.e., P34, in which synchronization to light is completed. Similar results (major mRNA content and protein expression) were obtained for the NR2D subtype at the same age. The electrophysiological experiments measuring the EPSC frequencies did not show developmental changes between P8 and P34 according to the effects of an NR2C/D antagonist, which is in agreement with the immunohistochemical experiments because the protein expression of the NR2D subtype was increased at P8 and afterwards. To date, there are no specific antagonists for NR2C and NR2D subtypes, and thus there are no functional studies focused on the contribution of the NR2D subtype to the light synchronization of SCN neurons. Although there are reports indicating that NR2D is not present at the synapses (in a diheteromeric form) (see Cull-Candy, 2001), our co-localization analyses of NR2D and PSD-95 suggest that this subtype is present in the postsynaptic membrane. Clark and Kofuji (2010) proposed that, in SCN neurons, there is a subpopulation of triheteromeric NMDA receptors formed by NR2A and NR2C/D proteins, because the NMDA current remaining after application of the NR2B antagonist ifenprodil shows pharmacological properties of the NR2A subtype with a Mg^2+ sensitivity more similar to that of the NR2C/D than the NR2A subtype.

Even though the developmental expression of NR2 subtypes in the brain indicates that NR2B/C and D are mainly expressed at early postnatal ages (P0-P12) while NR2A predominates at later developmental stages (Monyer et al., 1994), our results indicate that the NR2 subtypes of the NMDA receptors in ventral SCN neurons do not follow this pattern. In fact, the functional performance of NR2A showed a reduction

at later postnatal ages, NR2B did not present any developmental modification regarding electrophysiology and protein expression, and NR2C and D expressions were not reduced but rather increased at more advanced developmental stages compared with the earlier postnatal age, P4.

PSD-95 has been described as a scaffolding protein for NMDA receptors, localized specifically at the postsynaptic membrane of glutamatergic synapses (Hunt et al., 1996). The increased number of synapses could explain the increase in PSD-95 expression that we found at P8 and P12. Moore and Bernstein (1989) have shown an increase in synaptogenesis between P6 and P10, which is in accordance with our results. Additionally, our analysis of the PSD-95 co-localization with the NR2 subtypes resulted in values higher than 0.5, suggesting that at least half of the immunofluorescence signal is found in the postsynaptic membrane, whereas the remaining fluorescence could be due to NR2 subtypes present in the presynaptic membrane or other cellular structures, such as glial cells (Bouvier et al., 2015; Steinhäuser and Gallo, 1996).

Moreover, our results point to P8 as the developmental stage where NMDA receptors, specifically the NR2 subunit, have reached an adequate level of maturation to allow SCN neuron synchronization to light, which is consistent with a pioneering study that shows that around P7 the rat pup is able to synchronize to the LD cycle without maternal influence (Duncan et al., 1986).

In conclusion, our results indicate that ventral SCN neurons present a development-dependent change in the mRNA content, protein expression, and postsynaptic electrical activity of NR2 subtypes of glutamatergic NMDA receptors that may be important for the synchronization to light at adult stages.

ACKNOWLEDGMENTS

This work was supported by Consejo Nacional de Ciencia y Tecnología (CONACYT): CB-2015-01- 254887 to JA.

CONFLICT OF INTEREST STATEMENT

The author(s) have no potential conflicts of interest with respect to the research, authorship, and/or publication of this article.

ORCID IDs

Raul A. Aguilar-Roblero https://orcid.org/0000-0001-6213-9313
Javier Alamilla https://orcid.org/0000-0002-9666-5490

NOTE

Supplemental material for this article is available online.

REFERENCES

Abrahamson EE and Moore RY (2001) Suprachiasmatic nucleus in the mouse: retinal innervation, intrinsic organization and efferent projections. Brain Res 916: 172-191.

Alamilla J and Gillespie DC (2011) Glutamatergic inputs and glutamate-releasing immature inhibitory inputs activate a shared postsynaptic receptor population in lateral superior olive. Neuroscience 196:285-296.

Auberson YP, Allgeier H, Bischoff S, Lingenhoehl K, Moretti R, and Schmutz M (2002) 5-Phosphonomethylquinoxalinediones as competitive NMDA receptor antagonists with a preference for the human 1A/2A, rather than 1A/2B receptor composition. Bioorg Med Chem Lett 12:1099-1102.

Bouvier G, Bidoret C, Casado M, and Paoletti P (2015) Presynaptic NMDA receptors: Roles and rules. Neuroscience 311:322-340.

Clark JP 3rd and Kofuji P (2010) Stoichiometry of N-methyl-D-aspartate receptors within the suprachiasmatic nucleus. J Neurophysiol 103:3448-3464.

Colwell CS and Menaker M (1992) NMDA as well as non-NMDA receptor antagonists can prevent the phase-shifting effects of light on the circadian system of the golden hamster. J Biol Rhythms 7:125-136.

Cull-Candy S, Brickley S, and Farrant M (2001) NMDA receptor subunits: diversity, development and disease. Curr Opin Neurobiol 11:327-335.

Cull-Candy SG and Leszkiewicz DN (2004) Role of distinct NMDA receptor subtypes at central synapses. Sci STKE 2004:re16.

Delint-Ramirez I, Fernandez E, Bayes A, Kicsi E, Komiyama NH, and Grant SG (2010) In vivo composition of NMDA receptor signaling complexes differs between membrane subdomains and is modulated by PSD-95 and PSD-93. J Neurosci 30:8162-8170.

Ding JM, Chen D, Weber ET, Faiman LE, Rea MA, and Gillette MU (1994) Resetting the biological clock: mediation of nocturnal circadian shifts by glutamate and NO. Science 266:1713-1717.

Ding JM, Faiman LE, Hurst WJ, Kuriashkina LR, and Gillette MU (1997) Resetting the biological clock: mediation of nocturnal CREB phosphorylation via light, glutamate, and nitric oxide. The J Neurosci 17:667-675.

Duncan MJ, Banister MJ, and Reppert SM (1986) Developmental appearance of light-dark entrainment in the rat. Brain Res 369:326-330.

Frost DO, So KF, and Schneider GE (1979) Postnatal development of retinal projections in Syrian hamsters: a

study using autoradiographic and anterograde degeneration techniques. Neuroscience 4:1649-1677.

Fedoseeva LA, Shevelev OB, Kolosova NG, and Dymshits GM (2014) MS2 phage ribonucleoproteins as exogenous internal control for RT_qPCR data normalization in gene expression study of developing rat brain. Biochemistry (Moscow) 79:706-716.

Fischer G, Mutel V, Trube G, Malherbe P, Kew JN, Mohacsi E, Heitz MP, and Kemp JA (1997) Ro 25-6981, a highly potent and selective blocker of N-methyl-D-aspartate receptors containing the NR2B subunit. Characterization in vitro. J Pharmacol Exp Ther 283:1285-1292.

Guldner FH (1978) Synapses of optic nerve afferents in the rat suprachiasmatic nucleus. II. Structural variability as revealed by morphometric examination. Cell Tissue Res 194:37-54.

Hankins MW, Peirson SN, and Foster RG (2008) Melanopsin: an exciting photopigment. Trends Neurosci 31:27-36.

Hannibal J and Fahrenkrug J (2004) Melanopsin containing retinal ganglion cells are light responsive from birth. Neuroreport 15:2317-2320.

Hannibal J (2006) Roles of PACAP-containing retinal ganglion cells in circadian timing. Int Rev Cytol 251:1-39.

Hoang KN, Dinh CT, Bas E, Chen S, Eshraghi AA, and Van De Water TR (2009) Dexamethasone treatment of naïve organ of Corti explants alters the expression pattern of apoptosis-related genes. Brain Res 1301:1-8.

Hunt CA, Schenker LJ, and Kennedy MB (1996) PSD-95 is associated with the postsynaptic density and not with the presynaptic membrane at forebrain synapses. J Neurosci 16:1380-1388.

Johnson RF, Moore RY, and Morin LP (1988) Loss of entrainment and anatomical plasticity after lesions of the hamster retinohypothalamic tract. Brain Res 460:297-313.

Kim YI and Dudek FE (1991) Intracellular electrophysiological study of suprachiasmatic nucleus neurons in rodents: excitatory synaptic mechanisms. J Physiol 444:269-287.

Liu Q and Wong-Riley MT (2010) Postnatal development of N-methyl-D-aspartate receptor subunits 2A, 2B, 2C, 2D, and 3B immunoreactivity in brain stem respiratory nuclei of the rat. Neuroscience 171:637-654.

Mason CA, Sparrow N, and Lincoln DW (1977) Structural features of the retinohypothalamic projection in the rat during normal development. Brain Res 132:141-148.

Moore RY and Bernstein ME (1989) Synaptogenesis in the rat suprachiasmatic nucleus demonstrated by electron microscopy and synapsin I immunoreactivity. J Neurosci 9:2151-2162.

Moriya T, Takahashi S, Ikeda M, Suzuki-Yamashita K, Asai M, Kadotani H, Okamura H, Yoshioka T, and Shibata S (2000) N-methyl-D-aspartate receptor subtype 2C is not involved in circadian oscillation or photoic entrainment of the biological clock in mice. J Neurosci Res 61:663-673.

Monyer H, Burnashev N, Laurie DJ, Sakmann B, and Seeburg PH (1994) Developmental and regional expression in the rat brain and functional properties of four NMDA receptors. Neuron 12:529-540.

Morley RM, Tse HW, Feng B, Miller JC, Monaghan DT, and Jane DE (2005) Synthesis and pharmacology of N1-substituted piperazine-2,3-dicarboxylic acid derivatives acting as NMDA receptor antagonists. J Med Chem 48:2627-37.

Munoz Llamosas M, Huerta JJ, Cernuda-Cernuda R, and Garcia-Fernandez JM (2000) Ontogeny of a photic response in the retina and suprachiasmatic nucleus in the mouse. Brain Res Dev Brain Res 120:1-6.

Reppert SM and Schwartz WJ (1986) Maternal suprachiasmatic nuclei are necessary for maternal coordination of the developing circadian system. J Neurosci 6:2724-2729.

Schmittgen and Livak (2008) Analyzing real-time PCR data by the comparative Ct method. Nat Protoc 3:1101-1108.

Sekaran S, Lupi D, Jones SL, Sheely CJ, Hattar S, Yau K-W, Lucas RJ, Foster RG, and Hankins MW (2005) Melanopsin-dependent photoreception provides earliest light detection in the mammalian retina. Curr Biol 15:1099-1107.

Speh JC and Moore RY (1993) Retinohypothalamic tract development in the hamster and rat. Brain Res Dev Brain Res 76:171-181.

Stanfield B and Cowan WM (1976) Evidence for a change in the retino-hypothalamic projection in the rat following early removal of one eye. Brain Res 104:129-136.

Staudt T, Lang MC, Medda R, Engelhardt J, and Hell SW (2007) 2,2′-thiodiethanol: a new water soluble mounting medium for high resolution optical microscopy. Microsc Res Tech 70:1-9.

Steinhäuser C and Gallo V (1996) News on glutamate receptors in glial cells. Trends Neurosci 19:339-345.

Tackenberg C, Grinschgl S, Trutzel A, Santuccione AC, Frey MC, Konietzko U, Grimm J, Brandt R, and Nitsch RM (2013) NMDA receptor subunit composition determines beta-amyloid-induced neurodegeneration and synaptic loss. Cell Death Dis 4:e608

Wang LM, Schroeder A, Loh D, Smith D, Lin K, Han JH, Michel S, Hummer DL, Ehlen JC, Albers HE, et al (2008) Role for the NR2B subunit of the N-methyl-D-aspartate receptor in mediating light input to the circadian system. Eur J Neurosci 27:1771-1779.

You IJ, Jung YH, Kim MJ, Kwon SH, Hong SI, Lee SY, and Jang CG (2012) Alterations in the emotional and memory behavioral phenotypes of transient receptor potential vanilloid type 1-deficient mice are mediated by changes in expression of 5-HT(1)A, GABA(A), and NMDA receptors. Neuropharmacology 62:1034-1043.

Zhao X, Kotilinek LA, Smith B, Hlynialuk C, Zahs K, Ramsden M, Cleary J, and Ashe KH (2016) Caspase-2 cleavage of tau reversibly impairs memory. Nat Med 22:1268-1276.

Biochemistry

Article

Cite This: *Biochemistry* 2019, 58, 1679−1688

pubs.acs.org/biochemistry

Specific and Selective Inhibitors of Proprotein Convertases Engineered by Transferring Serpin B8 Reactive-Site and Exosite Determinants of Reactivity to the Serpin α1PDX

Gonzalo Izaguirre,*[,†] Marcelino Arciniega,[‡] and Andrea G. Quezada[‡]

[†]Department of Periodontics, College of Dentistry, University of Illinois at Chicago, Chicago, Illinois 60612, United States

[‡]Department of Biochemistry and Structural Biology, Institute of Cellular Physiology, National Autonomous University of Mexico, Mexico City 04510, Mexico

Supporting Information

ABSTRACT: The molecular determinants of substrate specificity and selectivity in the proprotein convertase (PC) family of proteases are poorly understood. Here we demonstrate that the natural serpin family inhibitor, serpin B8, is a specific and selective inhibitor of furin relative to the other PCs of the constitutive protein secretion pathway, PC4, PC5, PACE4, and PC7 (PC4−PC7, respectively), and identify reactive-site (P6−P5′ residues) and exosite elements of the serpin that contribute to this specificity and selectivity through studies of chimeras of serpin B8 and α1PDX, an engineered serpin inhibitor of furin. Kinetic studies revealed that the specificity and selectivity of the serpin chimeras for inhibiting PCs were determined by P6−P5 and P3−P2 residue-dependent recognition of the P4Arg-X-X-P1Arg PC consensus sequence and exosite-dependent recognition of the reactive loop P2′ residue of the chimeras by the PCs. Both productive and nonproductive binding of the chimeras to PC4−PC7 but not to furin contributed to a decreased specificity for inhibiting PC4−PC7 and an increased selectivity for inhibiting furin. Molecular dynamics simulations suggested that nonproductive binding of the chimeras to the PCs was correlated with a greater conformational variability of the catalytic sites of PC4−PC7 relative to that of furin. Our findings suggest a new approach for designing selective inhibitors of PCs using α1PDX as a scaffold, as evidenced by our ability to engineer highly specific and selective inhibitors of furin and PC4−PC7.

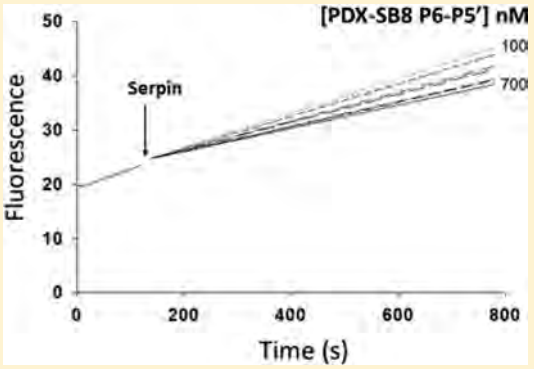

Proprotein convertases (PCs) are ubiquitous calcium-dependent serine proteases of the subtilisin fold. In mammals, PCs are complex multidomain proteins that carry out the proteolytic posttranslational modification of many secreted peptides and proteins and regulate central cellular processes like growth and proliferation.[1,2] The PCs of the Kexin-like subtype, furin, PC4, PC5, PACE4, and PC7, localize to the trans-Golgi network and endosomes of the constitutive protein secretion pathway and cleave precursors of a large diversity of proteins at polybasic sites consisting of the general P4Arg-X-X-P1Arg PC substrate specificity motif. Many important viral and bacterial pathogens exploit these PCs to promote and regulate their own growth. For this reason, specific PC inhibitors are sought as potential therapeutic agents.[3]

Furin reactivity is regulated by changes in pH and calcium concentration to impact enzymatic activity and autocatalytic activation.[4,5] Protein crystallography and molecular dynamics simulations (MDS) revealed that the furin catalytic site is in equilibrium between active and inactive conformations.[6,7] Given the similarities at the catalytic site among PCs,[8] it is predictable that furin shares with PC4, PC5, PACE4 (PC6), and PC7 (PC4−PC7, respectively) similar mechanisms for regulating reactivity.

The assignment of natural substrates to individual PCs has been speculative due to the great deal of cross-reactivity among these proteases, and substrate preferences have been assumed to depend mainly on differences in expression and cell-type distribution among PCs. Efforts to identify amino acid residue preferences at the substrate cleavage site by individual PCs have been attempted with the use of peptide libraries with limited success.[9] We developed a more robust approach in which the serpin-type protease inhibitor, α1-antitrypsin, was used as a model PC substrate to engineer changes in its reactive center loop (RCL) site of cleavage.[10] The validity of this approach is supported by the fact that serpin B8 is the only mammalian natural furin inhibitor known so far, and PCs from a variety of organisms are regulated by serpins.[10−14] Here, we found that serpin B8 is a selective furin inhibitor and used the serpin α1-antitrypsin as a scaffold to graft serpin B8 RCL and

Received: December 19, 2018
Revised: February 9, 2019
Published: March 8, 2019

Downloaded via UNIV NACIONAL AUTONOMA MEXICO on October 16, 2020 at 05:36:54 (UTC).
See https://pubs.acs.org/sharingguidelines for options on how to legitimately share published articles.

© 2019 American Chemical Society

DOI: 10.1021/acs.biochem.8b01295
Biochemistry 2019, 58, 1679−1688

exosite amino acid residues to elucidate the basis for this selectivity. α1-Antitrypsin is known to inhibit furin efficiently when arginine residues are engineered at its RCL P4 and P1 positions (α1PDX).[15,16] This approach is supported by our previous study showing that RCL and exosite determinants of serpin B8 reactivity, when substituted into their homologous regions in α1-antitrypsin, regulate reactivity with furin.[10] The same approach was here extended to the other PCs of the constitutive secretion pathway to identify the serpin B8 determinants responsible for the specific and selective inhibition of furin compared to PC4−PC7. Knowledge of these determinants enabled us to engineer α1PDX derivatives that were highly specific and selective inhibitors of furin and PC4−PC7.

MATERIALS AND METHODS

Production of PCs. Recombinant proprotein convertases were produced in truncated form as described for furin.[10] They included the first 579 residues of furin (UniProtKB entry P09958), 584 of PC4 (UniProtKB entry Q6UW60), 605 of PC5 (UniProtKB entry Q92824), 638 of PACE4 (UniProtKB entry P29122), and 621 of PC7 (UniProtKB entry Q16549), up to the end of their P domains. The gene constructs were synthesized (Integrated DNA Technologies) with a 10-His tag extension at the C-terminus. The proteins were expressed for 24 h in 1 L of Hi5 or sf9 insect cells using the baculovirus expression system. The PCs were purified from secreted proteins to homogeneity using nickel-affinity and size exclusion chromatography as shown previously for furin.[10] Protein yields were between 100 μg and 1 mg of purified protein. PC4−PC7 were expressed less abundantly than furin, especially PC7.

Production and Engineering of α1-Antitrypsin Mutants. The serpin α1-antitrypsin (UniProtKB entry P01009) was expressed in bacteria, refolded from inclusion bodies, and purified by ion exchange chromatography as described previously.[10] Mutagenesis of the serpin was achieved by polymerase chain reaction using specifically designed oligonucleotides (Integrated DNA Technologies) and *Pfu* Ultra II HF DNA polymerases (Agilent Technologies).

Production of Serpin B8. Recombinant serpin B8 (UniProtKB entry P50452) was produced in insect cells using the baculovirus system as described previously.[10] Five of its cysteine residues were mutated into serine and five into alanine (serpin B8-5S5A) to improve stability.

Protease Activity Assay. Protease activity assays and determinations of Michaelis−Menten enzyme kinetic parameters (K_m and k_{cat}) with the fluorogenic substrates, Boc-Arg-Val-Arg-Arg-7-amido-methylcoumarin and pyr-Arg-Thr-Lys-Arg-amido-methylcoumarin (Bachem), were performed in 100 mM Hepes (pH 7.5), 1 mM $CaCl_2$, 1 mM β-mercaptoethanol, 0.5% Triton X-100, and 0.1% polyethylene glycol 8000 at 25 °C employing the same methodology as described previously for furin.[10] The same conditions were used with all PCs to compare their activities.

Protease Active-Site Titrations. Concentrations of active enzymes and turnover numbers were determined from titrations of fixed enzyme concentrations with the inhibitor dec-Arg-Val-Lys-Arg-chloromethyl ketone (Bachem) to reach end points of zero activity at pH 5.5, as described previously.[10] The stoichiometric inhibition of PCs can be achieved only under acidic conditions. At the commonly used neutral pH of the enzyme activity assay, the competing hydrolysis of the inhibitor results in a curved line instead of a straight line, stoichiometric titrations, due to depletion of the inhibitor. Specific activity values of 6.4, 1.9, 1.8, 1.3, and 1.5 $\Delta F\ min^{-1}\ (nM\ PC)^{-1}$ were measured for furin, PC4, PC5, PACE4, and PC7, respectively, with 10 μM pyr-Arg-Thr-Lys-Arg-amido-methylcoumarin under protease activity assay conditions and used to calculate the concentration of the enzyme from changes in fluorescence.

Protease Inhibition Assays. The second-order association rate constant (k_a) values for the reaction of PCs with serpin B8 and α1-antitrypsin variants were determined from the kinetics of protease inhibition by the serpins as described previously.[10] All reactions were performed under protease activity assay conditions and under pseudo-first-order reaction conditions in which the inhibitor concentrations exceeded that of the enzyme by at least 10-fold. Measurements of fast reactions (k_a in the range of $10^5-10^7\ M^{-1}\ s^{-1}$) were obtained from the continuous exponential loss of enzyme activity observed under protease assay conditions that consumed minimal amounts of the 10 μM fluorogenic substrate pyr-Arg-Thr-Lys-Arg-amido-methylcoumarin present in the assay. The observed first-order rate constants (k_{obs}) were obtained by fitting the time-dependent increase in the observed fluorescence (ΔF_{obs}) in reaction progress curves to the exponential rise equation $\Delta F = \Delta F_{max}[1 - \exp(-k_{obs}t)]$, where ΔF_{max} is the maximum fluorescence change at the end point. Apparent association rate constant values were derived from slopes of the linear dependency of the k_{obs} values versus inhibitor concentrations that were corrected for the competitive effect of the substrate by dividing by the factor $1 + [S]_o/K_m$. For slower reactions (k_a values of $<10^5\ M^{-1}\ s^{-1}$), longer time assays of discontinuous protease inhibition were performed and residual activities determined from aliquots removed from the inhibition reaction mixtures. Plots of time-dependent residual protease activity (A_{obs}) were fitted to exponential decay equation $A_{obs} = A_o \times \exp(-k_{obs}t)$ to obtain k_{obs} values. Apparent association rate constant values were derived from slopes of the linear dependency of the k_{obs} values on inhibitor concentration. For those reactions in which the initial Michaelis encounter complex was formed rapidly and the subsequent chemical step was comparatively slow, association rate constant (k_a) values were determined from k_{cat}/K_d ratios (equal to k_{cat}/K_m), where $k_{cat} = k_{obs}/$(fractional occupation of the Michaelis complex). Apparent association rate constant values were corrected by factoring the stoichiometry of protease inhibition (SI) to yield the true association rate constant (k_a) value. The stoichiometry for protease inhibition was determined under protease assay conditions as the serpin:protease molar ratio that yielded zero enzyme activity and was obtained from the linear decrease in enzyme activity as a function of the increasing inhibitor concentration.

PC−Serpin Binding Affinity. The reaction of some of the α1-antitrypsin variants with PCs yielded fast enzyme activity decreases that were dependent on the concentration of the inhibitor in a manner that reflected equilibrium formation of the Michaelis complex. The rapid loss of reactivity was followed by a slower loss of the remaining activity that reflected acylation of the Michaelis complex to form the conformationally trapped covalent serpin−enzyme complex. Equilibrium binding dissociation constants for the Michaelis complex (K_d) were determined from nonlinear least-squares computer fits of plots of the dependency of residual PC activity, calculated from the initial linear segment of residual activity, to inhibitor concentration to the tight binding

DOI: 10.1021/acs.biochem.8b01295
Biochemistry 2019, 58, 1679−1688

Table 1. Michaelis–Menten Kinetic Constant Values for the Hydrolysis of Two Tetrapeptide Fluorogenic Substrates by PCs[a]

	Boc-Arg-Val-Arg-Arg-AMC			pyr-Arg-Thr-Lys-Arg-AMC		
	K_m	k_{cat} (s^{-1})	k_{cat}/K_m (M^{-1} s^{-1})	K_m (μM)	k_{cat} (s^{-1})	k_{cat}/K_m (M^{-1} s^{-1})
furin	28 ± 1	0.27 ± 0.01	(9.2 ± 1.0) × 10^3	4.7 ± 0.5	0.16 ± 0.00	(3.4 ± 0.7) × 10^4
PC4	51 ± 4	0.040 ± 0.001	(7.9 ± 1.0) × 10^2	2.6 ± 0.2	0.041 ± 0.00	(1.6 ± 0.1) × 10^4
PC5	40 ± 2	0.031 ± 0.001	(7.6 ± 0.5) × 10^2	2.0 ± 0.1	0.038 ± 0.001	(1.9 ± 0.1) × 10^4
PACE4	45 ± 3	0.021 ± 0.001	(4.6 ± 0.4) × 10^2	2.6 ± 0.2	0.028 ± 0.001	(1.1 ± 0.1) × 10^4
PC7	27 ± 3	0.018 ± 0.001	(6.8 ± 1.0) × 10^2	2.2 ± 0.3	0.032 ± 0.002	(1.5 ± 0.3) × 10^4

[a]Michaelis–Menten constant (K_m and k_{cat}) values were determined from initial velocities of product formation from the catalyzed hydrolysis of two fluorogenic peptide substrates. Reactions were carried out under protease activity assay conditions as described in Materials and Methods. Errors represent the standard error from linear regression fits of data. Fixed concentrations of active-site-titrated PCs were used in reactions with substrate concentrations ranging from 0.2 to 5 times the K_m values. Parameters defining the dependence of initial velocities on substrate concentrations were obtained from fits of data to the Michaelis–Menten equation.

Table 2. Rate Constant Values for the Reaction of PCs with Serpin B8 and α1PDX[a]

	serpin B8		α1PDX	
	k_a (M^{-1} s^{-1})	SI	k_a (M^{-1} s^{-1})	SI
furin	(2.3 ± 0.2) × 10^5	2.2 ± 0.1	(1.1 ± 0.1) × 10^6	1.1 ± 0.1
PC4	(1.4 ± 0.2) × 10^4	1.2 ± 0.1	(1.6 ± 0.3) × 10^6	1.2 ± 0.2
PC5	(1.1 ± 0.2) × 10^4	0.9 ± 0.1	(2.0 ± 0.1) × 10^6	1.3 ± 0.1
PACE4	(1.1 ± 0.3) × 10^4	0.9 ± 0.1	(1.2 ± 0.3) × 10^6	1.0 ± 0.2
PC7	(1.2 ± 0.2) × 10^4	1.0 ± 0.1	(2.3 ± 0.8) × 10^6	1.4 ± 0.2

[a]Second-order association rate constant (k_a) values for the reaction of PCs with serpin B8 and α1PDX and their stoichiometry of inhibition (SI) were measured under protease activity assay conditions as described in Materials and Methods. SI measures the partition between the inhibitory and substrate pathways of the serpin mechanism of protease inhibition. A value of 1 corresponds to an efficient inhibition (Figure S1). Errors represent the standard error from linear regression fits of data. The k_a and SI values for furin were taken from ref 10.

Serpin variant	RCL amino acid sequence (residue #)										
Serpin B8	334	335	336	337	338	339	340	341	342	343	344
α1-antitrypsin	353	354	355	356	357	358	359	360	361	362	363
	P6	P5	P4	P3	P2	P1	P1′	P2′	P3′	P4′	P5′
α1-antitrypsin	L	E	A	I	P	M	S	I	P	P	E
α1-antitrypsin Pittsburgh	L	E	A	I	P	R	S	I	P	P	E
α1-antitrypsin Portland (α1-PDX)	L	E	R	I	P	R	S	I	P	P	E
Serpin B8-5S5A	V	V	R	N	S	R	S	S	R	M	E
α1-PDX-Serpin B8 P6-P5′ chimera α1-antitrypsin Chicago 1 (α1-ORD)	V	V	R	N	S	R	S	S	R	M	E
α1-PDX-Serpin B8 P6-P1 chimera	V	V	R	N	S	R	S	I	P	P	E
α1-PDX+YE exosites (K222Y + L224E) α1-antitrypsin Chicago 2 (α1-MDW)	L	E	R	I	P	R	S	I	P	P	E

Figure 1. Amino acid residue sequences at the RCL of α1-antitrypsin derivatives and serpin B8. The amino acid residue sequences from the RCL of α1-antitrypsin variants and of serpin B8 were aligned on the basis of the location of the protease cleavage site between residues P1 and P1′. A natural mutant of α1-antitrypsin, the Pittsburgh variant, has an arginine substitution at the P1 residue that changes the serpin specificity to inhibit trypsin-type proteases.[20] The α1-antitrypsin Portland variant (α1PDX) was engineered with arginine residues at the P4 and P1 positions to inhibit furin.[15,16] The serpin B8-5S5A variant is a stabilized form of serpin B8 in which cysteine residues were mutated, five to serine and five to alanine, including the one at the P1′ position.[10] The α1PDX–serpin B8 P6–P5′ chimera is now designated the Chicago 1 derivative (α1ORD) due to its high furin selectivity. The α1PDX+YE exosite variant is now designated the Chicago 2 derivative (α1MDW) due to its high selectivity for PC4, PC5, PACE4, and PC7 over furin.

quadratic equation of Morrison, $[E]/[E]_o = 1 - \{[E]_o + [I]_o + K_d - [([E]_o + [I]_o + K_d)^2 - 4[E]_o[I]_o]^{0.5}\}/(2[E]_o)$, where $[E]$ and $[E]_o$ are the residual active and total PC concentrations, respectively, and $[I]_o$ is the total inhibitor concentration.[21] Inhibitor concentrations were corrected for the competitive effect of the substrate by dividing by the factor $1 + [S]_o/K_m$.

Molecular Dynamic Simulations. Principal component analyses on two furin crystal structures and models of the catalytic domain of PC4–PC7 were carried out as described previously.[7] MDS were performed using the GROMACS (version 5.0.3) molecular simulation package as described previously.[7] Models of the catalytic domain of PC4, PC5, PACE4, and PC7 were obtained using the SWISS-MODEL tool for protein homology modeling and on the basis of the X-ray crystal structures of the ligand-free form (Protein Data

DOI: 10.1021/acs.biochem.8b01295
Biochemistry 2019, 58, 1679–1688

Table 3. Rate Constant Values for the Reaction of PCs with α1PDX−Serpin B8 RCL Chimeras[a]

α1PDX−serpin B8 RCL chimera	second-order association rate, k_a (M^{-1} s^{-1})				
	furin	PC4	PC5	PACE4	PC7
α1PDX	$(1.1 \pm 0.1) \times 10^6$	$(1.6 \pm 0.3) \times 10^6$	$(2.0 \pm 0.1) \times 10^6$	$(1.2 \pm 0.3) \times 10^6$	$(2.3 \pm 0.8) \times 10^6$
P6−P5′[b]	$(1.1 \pm 0.1) \times 10^5$	$(7.1 \pm 1.0) \times 10^2$	$(6.0 \pm 0.2) \times 10^2$	$(2.9 \pm 0.1) \times 10^2$	$(7.7 \pm 2.2) \times 10^2$
P6−P1[b]	$(2.5 \pm 0.3) \times 10^6$	$<10^3$	$<10^3$	$(7.5 \pm 0.8) \times 10^3$	$(1.5 \pm 0.2) \times 10^3$
P6−P5[b]	$(2.2 \pm 0.2) \times 10^6$	$(7.9 \pm 1.8) \times 10^5$	$(2.0 \pm 0.3) \times 10^6$	$(4.7 \pm 0.8) \times 10^5$	$(3.3 \pm 1.2) \times 10^6$
P3−P2	$(1.3 \pm 0.1) \times 10^5$	$>2 \times 10^3$[c]	$>2 \times 10^3$[c]	$>9 \times 10^2$[c]	$>4 \times 10^2$[c]
P1′−P5′	$(5.5 \pm 0.8) \times 10^4$	$(3.1 \pm 0.9) \times 10^4$	$(4.9 \pm 1.3) \times 10^4$	$(1.5 \pm 0.3) \times 10^4$	$(4.8 \pm 2.0) \times 10^4$
P2′	$(6.4 \pm 0.8) \times 10^4$	$(2.5 \pm 0.6) \times 10^4$	$(3.3 \pm 0.6) \times 10^4$	$(1.0 \pm 0.2) \times 10^4$	$(2.4 \pm 0.3) \times 10^4$
P3′	$(4.7 \pm 0.2) \times 10^6$	$(3.8 \pm 0.5) \times 10^6$	$(1.8 \pm 0.4) \times 10^6$	$(8.6 \pm 1.3) \times 10^5$	$(4.8 \pm 2.4) \times 10^6$
P4′	$(7.9 \pm 0.5) \times 10^5$	$(3.9 \pm 0.6) \times 10^5$	$(5.8 \pm 0.6) \times 10^5$	$(1.9 \pm 0.5) \times 10^5$	$(4.0 \pm 0.1) \times 10^5$

[a]Amino acid sequences in the RCL of α1PDX were substituted with the homologous sequences from the RCL of serpin B8. Second-order association rate constant (k_a) values for the reaction of PCs with α1PDX−serpin B8 chimeras were determined as described in Materials and Methods. Errors represent the standard error from linear regression fits of data. The k_a values for the reaction of furin with α1PDX and the P6−P5′, P6−P1, and P1′−P5′ chimeras were taken from ref 10. [b]k_a values for PC4−PC7 were determined from k_{cat}/K_d ratios as described in Materials and Methods. The reactions with furin were monophasic; therefore, the effects of K_d and k_{cat} on reactivity were not separated. [c]Unstable covalent complexes prevented the SI from being determined, so the rate constant values are larger than those reported here.

Bank entry 5JXG) and the ligand-bound form (Protein Data Bank entry 5JXH) of human furin as templates.

RESULTS

Furin Hydrolyzes Two Small Peptide Substrates at a Chemical Conversion Rate That Is Faster Than Those of PC4, PC5, PACE4, and PC7. Recombinant furin, PC4, PC5, PACE4, and PC7, consisting of only their catalytic and P domains, were produced in a fully active and highly purified form.[10] To determine the relative specificity and selectivity of these PCs for two of the most commonly used PC substrates, we measured the Michaelis−Menten kinetic parameters for the PC-catalyzed hydrolysis of the substrates (Table 1). This comparative study showed that furin is 2−20-fold more reactive than PC4−PC7 primarily because of the faster chemical conversion step (k_{cat}).

Serpin B8 Is a Specific and Selective Furin Inhibitor. We have previously determined that serpin B8 inhibits furin at a physiologically relevant rate.[10] If serpin B8 is a specific and selective natural furin inhibitor, then it should react much more rapidly with furin than with PC4−PC7. To test this hypothesis, the rate of inhibition of PC4, PC5, PACE4, and PC7 by serpin B8 was measured using our stabilized recombinant form of serpin B8 that we previously described,[10] in which five external or internal cysteine residues were mutated to serine or alanine, respectively (Table 2). Serpin B8 reacted ∼20-fold slower with PC4−PC7 ($k_a = 1 \times 10^4$ M^{-1} s^{-1}) than with furin ($k_a = 2 \times 10^5$ M^{-1} s^{-1}). Serpin B8 is thus significantly more selective for inhibiting furin over PC4−PC7.

The Serpin B8 P6−P5′ RCL Segment Confers Greater Furin Selectivity in α1PDX Than in Serpin B8. We previously determined that the primed and nonprimed regions of the serpin B8 RCL, when grafted onto the RCL of the serpin α1PDX, play critical roles in influencing reactivity with furin.[10] The same analysis was applied here to investigate the role that these two serpin B8 RCL regions play in determining the differential reactivity between furin and PC4−PC7. Serpins share the same general structure and a suicide substrate mechanism of inhibition of proteases that results in the formation of a conformationally trapped serpin−protease covalent complex (Figure S1).[17] α1PDX is a derivative of the serpin α1-antitrypsin that was developed as a specific furin inhibitor by grafting the P4Arg-X-X-P1Arg PC recognition sequence onto the RCL.[18] We found that α1PDX is equally reactive with furin, PC4, PC5, PACE4, and PC7, all of the PCs being inhibited efficiently by α1PDX at similar rates (10^6 M^{-1} s^{-1}) and with stoichiometries of inhibition of 1:1 (Table 2). A previous report[16] found differences in α1PDX reactivity with some of these PCs based on an erroneous characterization of serpin reactivity by K_i values instead of k_a values.[19] The serpin B8 RCL P6−P5′ segment (Figure 1), when placed at its homologous location in the RCL of α1PDX, resulted in a chimera that reacted with furin 10-fold slower (10^5 M^{-1} s^{-1}) than α1PDX, similar to serpin B8 (Table 3). However, the P6−P5′ chimera reacted with PC4−PC7 much slower than serpin B8 and in a biphasic manner distinct from the monophasic reaction with furin (Figure 2A). The P6−P5′ chimera thus caused an immediate inhibition of a fraction of the protease activity followed by a slower exponential inhibition of the remaining activity (Figure 2C). This behavior suggested that an initial rapid equilibrium binding of the serpin and protease to form a Michaelis complex was kinetically separated from the slower acylation of the Michaelis complex to form the conformationally trapped serpin−protease covalent complex. Indeed, the serpin concentration dependence of the initial rapid inhibition phase was consistent with K_d values of ∼1 μM for formation of the Michaelis complex (Figure 2B and Table 4), whereas the subsequent exponential reaction phase indicated first-order rates of acylation of the Michaelis complex ($k_{obs} \sim 10^{-4}$ s^{-1}) that were ∼100-fold slower than k_{cat} values measured for the hydrolysis of the tetrapeptide fluorogenic substrates by PC4−PC7 (Table 5). Because of the kinetic separation, the contributions to overall reactivity ($k_a = k_{cat}/K_m$) by the binding (K_m) and chemical (k_{cat}) steps can be calculated separately. The K_m equals the K_d for the rapid equilibrium formation of the Michaelis complex, and the k_{cat} can be calculated by dividing k_{obs} for formation of the covalent complex by the fractional saturation of the Michaelis complex (Figure 2C and Table 5). Values of k_a calculated from k_{cat}/K_d ratios (10^2 M^{-1} s^{-1}) were several thousand-fold lower than k_a values for reactions of α1PDX with PC4−PC7 (Table 3). The serpin B8 P6−P5′ segment when grafted onto α1PDX thus amplified the differences in reactivity observed for serpin B8 with furin and PC4−PC7.

The Serpin B8 P6−P1 RCL Segment Determines PC Selectivity. To define the origin of the large difference in

DOI: 10.1021/acs.biochem.8b01295
Biochemistry 2019, 58, 1679−1688

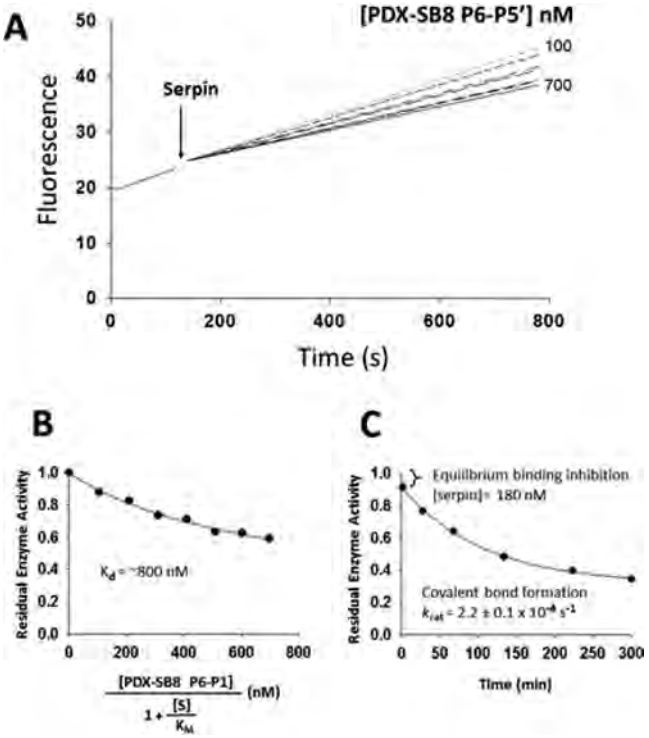

Figure 2. Reaction of the α1PDX−serpin B8 P6−P5′ chimera with PACE4. (A) Plots of PACE4 residual activity at increasing concentrations of the α1PDX−serpin B8 P6−P5′ chimera. Progressive reactions of 2 nM PACE4 activity with 10 μM fluorogenic substrate pyr-Arg-Thr-Lys-Arg-amido-methylcoumarin under protease activity assay conditions were performed as described in Materials and Methods. (B) Fitted plot of the dependence of residual PACE4 activity on increasing concentrations of the serpin chimera that were corrected for the fluorogenic substrate concentration [S]. The plot was fitted to the quadratic tight binding equation of Morrison.[21] Similar results were obtained with PC4, PC5, and PC7, and K_d values are listed in Table 4. (C) Plot of residual PACE4 activity for the inhibition of 50 nM PACE4 by 1.4 μM serpin chimera. The initial decrease in activity reflects the fast equilibrium binding for the formation of the Michaelis complex that precedes slow covalent complex formation.

reactivity between furin and PC4−PC7 observed with the P6−P5′ chimera, the serpin B8 P6−P1 segment was alone grafted onto the RCL of α1PDX. In contrast to the P6−P5′ segment, the P6−P1 segment resulted in a 2-fold increase in reactivity with furin (2×10^6 M^{-1} s^{-1}) (Table 3). However, the P6−P1 chimera reacted with PC4−PC7 like the P6−P5′ chimera did, i.e., with a greatly reduced overall reactivity relative to α1PDX and biphasic kinetics of inhibition (Figure 3A). Surprisingly, the chimera formed Michaelis complexes in an initial rapid equilibrium binding step that exhibited affinities ∼100-fold stronger than those of the P6−P5′ chimera (K_d values of 7−15 nM) (Figure 3B and Table 4). Moreover, the subsequent slower exponential phase reflecting conversion of the noncovalent Michaelis complex to the covalent inhibitory complex (Figure 3C) exhibited k_{cat} values minimally 10-fold slower than those observed with the P6−P5′ chimera ($\leq 10^{-5}$ s^{-1}) (Table 5). This slow reactivity was confirmed by electrophoresis analysis of the serpin chimera−PC reaction that showed minimal reaction of the serpin to form a covalent complex or to be cleaved as a substrate over the time frame in which covalent complexes formed with the P6−P5′ chimera. Calculated k_a values for PACE4 and PC7, for which k_{cat} values were measurable, were determined from the k_{cat}/K_d ratios (10^3 M^{-1} s^{-1}) to be 100−1000-fold lower than those for the reaction of α1PDX with PC4−PC7 (Table 3).

Further reducing the size of the grafted serpin B8 RCL to only the P6−P5 segment produced a chimera with PC reactivity that resembled that of the P6−P1 chimera. This chimera thus increased the reactivity with furin 2-fold and reduced the reactivity with PC4−PC7 relative to α1PDX (Figure 4A). Moreover, the kinetics of PC inhibition was monophasic for furin and biphasic for PC4−PC7. However, unlike the immediate equilibrium formation of the Michaelis complex observed for the P6−P1 chimera reaction, the P6−P5 chimera showed a slower approach to the Michaelis complex binding equilibrium (Figure 4A). Notably, Michaelis complex affinities for the interaction of the P6−P5 chimera with PC4−PC7 were 10−30-fold greater than those for the P6−P1 chimera (K_d values of 0.4−1 nM) (Figure 4B and Table 4). Moreover, the conversion of the Michaelis complex to the covalent complex in the subsequent slow exponential phase indicated that k_{cat} values were 3−12-fold faster for the P6−P5 chimera than for the P6−P1 chimera ($1-3 \times 10^{-4}$ s^{-1}) (Figure 4C and Table 5). As a result, k_a values calculated from k_{cat}/K_d ratios were larger for the P6−P5 chimera than for the P6−P1 chimera (10^5-10^6 M^{-1} s^{-1}) and approached those for the reactions of α1PDX with PC4−PC7 (Table 3). Like the P6−P5′ and P6−P1 chimeras, the serpin B8 P6−P5 substitution in α1PDX thus resulted in the formation of stable high-affinity Michaelis complexes with PC4−PC7 that were poorly reactive in forming a conformationally trapped covalent complex.

The grafting of the serpin B8 RCL P3−P2 segment led to losses of α1PDX reactivity of ∼10-fold with furin (10^5 M^{-1} s^{-1}) and ∼1000-fold with PC4−PC7 (∼10^3 M^{-1} s^{-1}) (Table 3). In contrast to the reaction of the P6−P5 chimera, the reaction of the P3−P2 chimera with PC4−PC7 showed an initial equilibrium binding of low affinity that was not measurable at the inhibitor concentrations used. The serpin B8 P3−P2 segment thus decreased the reactivity of α1PDX with all PCs, but especially with PC4−PC7.

Together, these results suggest that the RCL P6−P1 segment contributes to the enhanced substrate selectivity

Table 4. Dissociation Constant Values for the Binding of PCs to α1PDX−Serpin B8 RCL Chimeras[a]

	equilibrium binding dissociation constant, K_d (nM)				
α1PDX−serpin B8 chimera	furin	PC4	PC5	PACE4	PC7
P6−P5′	–	∼1400	∼1000	∼800	∼1500
P6−P1	–	13 ± 1	7.8 ± 0.8	9.1 ± 0.7	15 ± 0.9
P6−P5	–	0.52 ± 0.01	0.62 ± 0.01	1.0 ± 0.1	0.41 ± 0.06

[a]Equilibrium binding dissociation constant (K_d) values were determined from the fittings of plots of the dependence of residual PC activity on inhibitor concentration described in panels B of Figures 2−4. Errors represent the standard error from linear regression fits of data.

DOI: 10.1021/acs.biochem.8b01295
Biochemistry 2019, 58, 1679−1688

Table 5. Rate Constant Values for the Catalytic Chemical Step in the Reaction of PCs with α1PDX−Serpin B8 RCL Chimeras and Tetrapeptide Substrates[a]

	chemical reaction step, k_{cat} (s^{-1})				
	furin	PC4	PC5	PACE4	PC7
peptide substrates	0.27−0.16	0.040−0.041	0.031−0.038	0.021−0.028	0.018−0.032
P6−P5′	–	0.00029	0.00029	0.00022	0.00034
P6−P1	–	nonmeasurable	nonmeasurable	0.000068	0.000023
P6−P5	–	0.00011	0.00035	0.00024	0.00029

[a]Comparison of k_{cat} values for the catalyzed hydrolysis of two tetrapeptide fluorogenic substrates by PCs (taken from Table 1) against the k_{cat} values obtained from the reaction of PCs with three α1PDX−serpin B8 RCL chimeras. These reactions, which are described in Figures 2−4, occur on the basis of initial rapid formation of high-affinity Michaelis complexes followed by slower chemical step reactivity leading to covalent complex formation. The k_{cat} values for the chemical step were obtained from the equation $k_{obs} = k_{cat} \times$ fractional occupation. The reactions of furin with serpins were monophasic; therefore, the value of k_{cat} could not be determined.

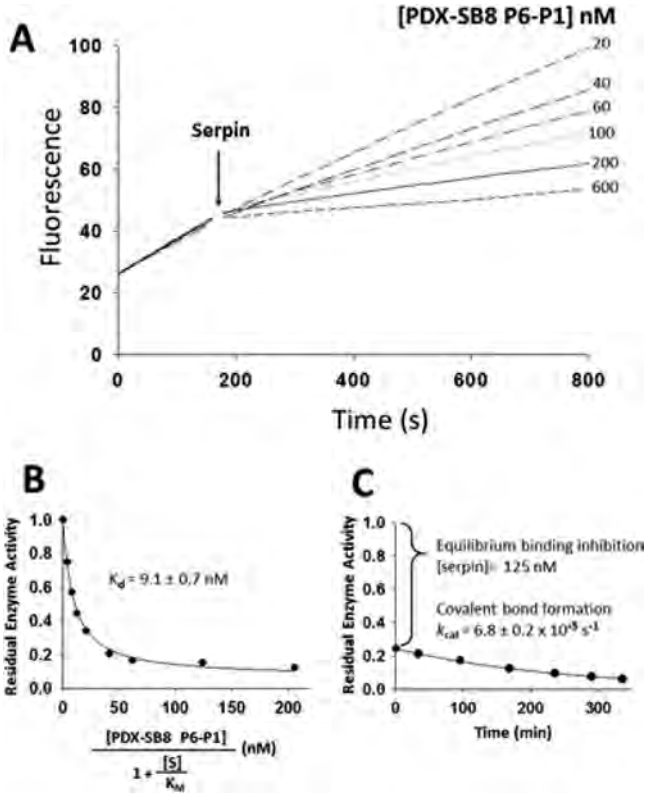

Figure 3. Reaction of the α1PDX−serpin B8 P6−P1 chimera with PACE4. (A) Plots of PACE4 residual activity at increasing concentrations of the α1PDX−serpin B8 P6−P1 chimera. Progressive reactions of 5 nM PACE4 were performed as described in the legend of Figure 2. (B) Fitted plot of the dependence of residual PACE4 activity on increasing concentrations of the serpin chimera as described in the legend of Figure 2. Similar results were obtained with PC4, PC5, and PC7, and K_d values are listed in Table 4. (C) Plot of residual PACE4 activity for the time course of inhibition of 50 nM PACE4 by 1.0 μM chimera. The large initial decrease in activity reflects the fast equilibrium binding for the formation of the Michaelis complex that precedes slow covalent complex formation.

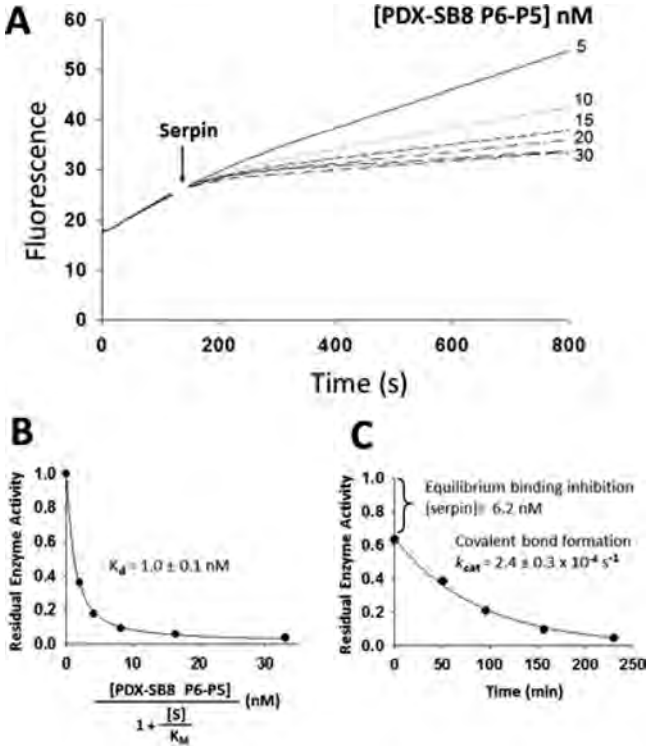

Figure 4. Reaction of the α1PDX−serpin B8 P6−P5 chimera with PACE4. (A) Plots of PACE4 residual activity at increasing concentrations of the α1PDX−serpin B8 P6−P5 chimera. Progressive reactions of 3 nM PACE4 were performed as described in the legend to Figure 2. (B) Fitted plot of the dependence of residual PACE4 activity on increasing concentrations of the serpin chimera as described in the legend of Figure 2. Similar results were obtained with PC4, PC5, and PC7, and K_d values are listed in Table 4. (C) Plot of residual PACE4 activity for the time course of inhibition of 2 nM PACE4 by 50 nM chimera. The large initial decrease in activity reflects the fast equilibrium binding for the formation of the Michaelis complex that precedes slow covalent complex formation.

between furin and PC4−PC7 observed with the P6−P5′ chimera.

The P2′ Residue Determines PC Reaction Specificity. In contrast to the effect of the P6−P1 segment, the serpin B8 RCL P1′−P5′ segment decreased α1PDX reactivity with furin, 20-fold, and PC4−PC7, 40−80 fold (10^4 M^{-1} s^{-1}) (Table 3). No kinetic separation of the formation of the Michaelis and covalent complexes was observed for this chimera. Single-residue substitutions within the P2′−P4′ region identified the P2′ substitution as the most detrimental to reactivity as it reduced α1PDX reactivity 17-fold with furin and 60−120-fold with PC4−PC7 (10^4 M^{-1} s^{-1}), similar to the effect produced by substituting the full P1′−P5′ region (Table 3). The effect of the P3′ and P4′ serpin B8 residue substitutions on α1PDX reactivity with all PCs was comparatively modest (10^5−10^6 M^{-1} s^{-1}). The lack of importance of the P1′ residue in terms of PC substrate specificity and selectivity was shown by a serine

DOI: 10.1021/acs.biochem.8b01295
Biochemistry 2019, 58, 1679−1688

Table 6. Second-Order Association Rate Constant Values for the Reaction of PCs with α1PDX RCL Non-Serpin B8 Substitutions[a]

	second-order association rate, k_a (M^{-1} s^{-1})				
α1PDX variant	furin	PC4	PC5	PACE4	PC7
P4A (Pittsburgh)	(3.2 ± 0.1) × 10	(6.7 ± 0.1) × 10	not determined	(6.7 ± 0.2) × 10	not determined
P3E	(1.5 ± 0.2) × 10^4	(4.6 ± 0.3) × 10^2	(4.6 ± 0.7) × 10^2	(5.6 ± 0.3) × 10^2	(2.2 ± 0.5) × 10^2
P2G	(1.5 ± 0.3) × 10^6	>4 × 10^3[b]	(1.2 ± 0.3) × 10^5	(5.3 ± 0.4) × 10^4	>7 × 10^3[b]
P1′D	(2.3 ± 0.6) × 10^5	(4.5 ± 1.0) × 10^5	(3.4 ± 0.5) × 10^5	(9.5 ± 3.1) × 10^4	(2.8 ± 0.4) × 10^5

[a]The amino acid sequence in the RCL of α1PDX was mutated at single amino acid positions to nonserpin B8 residues. Second order association rate constant (k_a) values for the reaction of PCs with α1PDX mutants were determined as described in Table 3. Errors represent the standard error from linear regression fits of data. [b]Unstable covalent complexes prevented the SI from being determined, so the rate values are larger than here reported.

Table 7. Effect of the YE Exosite Residues on PC Reactivity with α1PDX and the α1PDX−Serpin B8 RCL P6−P5′ Chimera[a]

	second-order association rate, k_a (M^{-1} s^{-1})				
α1PDX-Serpin B8 chimera	furin	PC4	PC5	PACE4	PC7
P6−P5′	(1.1 ± 0.1) × 10^5	(7.1 ± 1.0) × 10^2	(6.0 ± 0.2) × 10^2	(2.9 ± 0.1) × 10^2	(7.7 ± 2.2) × 10^2
P6−P5′+YE exosites	(1.5 ± 0.2) × 10^3	(9.1 ± 0.1) × 10	(6.9 ± 0.4) × 10	(8.1 ± 0.2) × 10	(2.2 ± 0.1) × 10
α1PDX	(1.1 ± 0.1) × 10^6	(1.6 ± 0.3) × 10^6	(2.0 ± 0.1) × 10^6	(1.2 ± 0.3) × 10^6	(2.3 ± 0.8) × 10^6
α1PDX+YE exosites	(2.1 ± 0.3) × 10^5	(1.4 ± 0.4) × 10^7	(8.6 ± 2.9) × 10^6	(4.4 ± 1.0) × 10^6	(6.7 ± 2.0) × 10^6

[a]The tyrosine (Y) and glutamic acid (E) exosite residues were grafted at their homologous location in strand 3 of sheet C of α1PDX and the P6−P5′ chimera. Serpin B8 has the conserved residue phenylalanine at the position of the tyrosine residue. Second-order association rate constant (k_a) values for the reaction of PCs with the chimeras α1PDX+YE exosites and the α1PDX−serpin B8 RCL P6−P5′+YE exosites were determined as described in Table 3. Errors represent the standard error from linear regression fits of data. The k_a values for the reaction of furin with both chimeras were taken from ref 10. The k_a values for the reaction of α1PDX and the P6−P5′ chimera with all PCs were taken from Tables 2 and 3 and included for comparison.

to aspartic acid mutation that had a <10-fold detrimental effect on α1PDX reactivity with all PCs (Table 6).

Exosites Selectively Regulate Reactivity with PCs. We have previously shown that the homologous grafting of the serpin B8 strand 3C exosite residues onto α1PDX or the α1PDX−serpin B8 P6−P5′ chimera leads to losses of reactivity with furin of 5-fold (10^5 M^{-1} s^{-1}) or 70-fold (10^3 M^{-1} s^{-1}), respectively.[10] In stark contrast, the serpin B8 exosite residues increased α1PDX reactivity with PC4−PC7 by 3−9-fold (10^6−10^7 M^{-1} s^{-1}) but reduced reactivity of the α1PDX−serpin B8 P6−P5′ chimera with PC4−PC7 by 8−30-fold (10 M^{-1} s^{-1}) (Table 7).

The Catalytic-Site Conformations of Furin and PC4−PC7 Differ. Protein crystallography and MDS studies have shown that the catalytic site of furin adopts active and inactive conformations and have suggested that substrates preferentially bind to the active conformation through conformational selection or induced fit binding mechanisms.[7,8] The kinetic studies described above show that unlike furin, the catalytic site of PC4−PC7 may adopt inactive conformations that preferentially bind substrate nonproductively. To investigate the basis for such differences, we compared the catalytic-site conformations of furin and PC4−PC7 by MDS. Homology models of the whole catalytic domain for PC4−PC7 were built on the basis of the X-ray crystal structures of the ligand-free and ligand-bound forms of furin. Although the amino acid sequence is 50−65% conserved between furin and PC4−PC7, the structures are expected to be highly conserved.[8] MDS were performed on 10 simulated systems of five proteins and two different conditions: (1) ligand-free form associated with active and inactive configurations and (2) ligand-bound form associated with only active configurations. A principal component analysis (PCA), constructed on a common structural core of 313 Cα atoms in the catalytic domain, was performed employing MDS trajectories for a global evaluation of the structures (Figure 5A). The analysis showed well-resolved and distinct active and inactive furin conformations in agreement with previous studies.[7] PC4−PC7 showed the most pronounced differences in PACE4 and, especially, in PC7 for the ligand-free forms. The ligand-bound forms were more consistent with furin, except for PC7. A second PCA was performed on five Cα atoms located in the catalytic site. Again, furin produced two clearly distinguishable sets of conformations corresponding to active and inactive states (Figure 5B). In agreement, PC4−PC7 also produced clearly differentiated active and inactive conformations. Only the ligand-free conformations of PC4−PC7 showed more variability compared to furin, especially that of PC7.

DISCUSSION

Despite the large body of information regarding how PCs regulate the growth, proliferation, and differentiation of cells in numerous physiological and pathological processes, a molecular understanding of how PCs perform their specific regulatory functions has remained elusive.[22] Because PCs are co-expressed and overlap at their cellular location, significant cross-reactivity seems to be unavoidable, and the significance of the redundant targeting of substrates by PCs is unclear. However, examples of PCs with opposite regulatory effects imply that PCs should be able to target their substrates selectively.[23] A recurrent theme is that of furin and PC4−PC7 playing opposite roles by targeting the same protein but in a selective manner involving different recognition sites.[24,25] The basis for this PC selectivity has not been well characterized. In this study, serpin B8 was demonstrated to react with furin selectively on the basis of a 20-fold faster reactivity with furin than with PC4, PC5, PACE4, and PC7 (Table 2). In addition, it was shown that furin catalyzes the hydrolysis of two

DOI: 10.1021/acs.biochem.8b01295
Biochemistry 2019, 58, 1679−1688

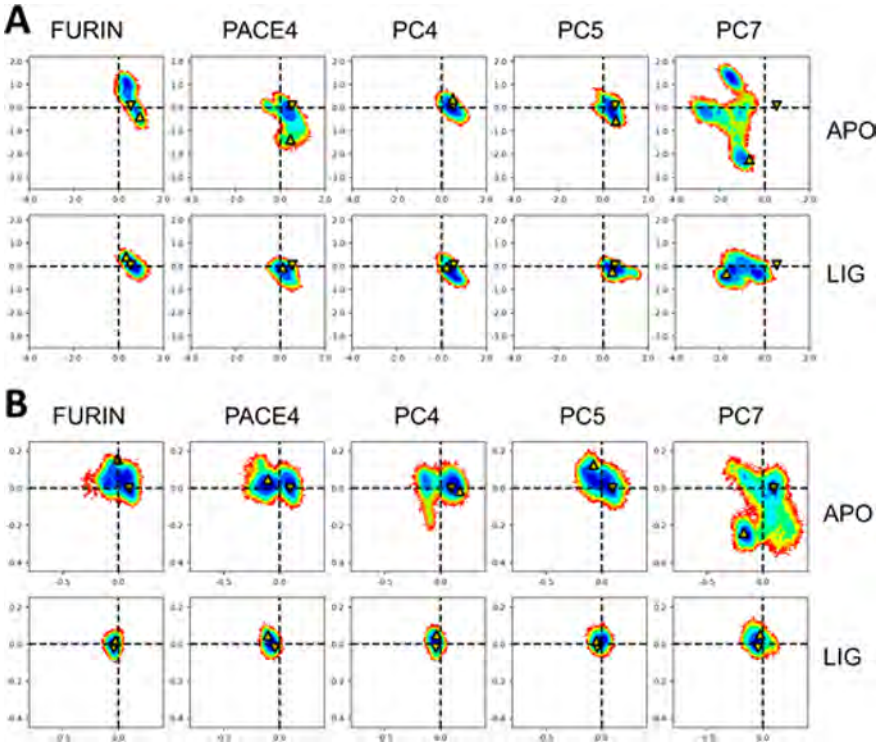

Figure 5. Molecular dynamics simulation analysis of the structure of PCs. The configuration of amino acid residues in the catalytic domain of furin, PC4, PC5, PACE4, and PC7 was simulated employing furin crystal structures and molecular models of the catalytic domain of PC4−PC7 based on the X-ray crystal structure of the ligand-free and ligand-bound furin, as described in Materials and Methods. Two different starting structure conditions were employed: (i) ligand-free form, which is associated with active and inactive configurations, and (ii) ligand-bound form, which is associated with only active configurations. Shown are molecular dynamics trajectories from the simulated systems projected on the first two principal components (nanometers). These projections are presented as heat maps where blue represents highly populated states. The maps derived from scenario i are labeled as APO, and the ones from scenario ii as LIG. The arrows pointing down correspond to the starting frame, which is the furin crystal structure. The arrows pointing upward correspond to the last frame of the analysis. (A) Comparative MDS analysis of the PC catalytic domain. PCA performed over 313 Cα atoms of amino acid residues. (B) Comparative MDS analysis of the PC catalytic site. PCA performed over five Cα atoms of catalytic-site amino acid residues (Asp153, His194, Gly255, Asn295, and Ser368).

tetrapeptide substrates at a faster catalytic rate, especially with the substrate Boc-Arg-Val-Arg-Arg-AMC (20-fold), than PC4−PC7 (Table 1). These observations suggested that furin and PC4−PC7 differ in substrate specificity and selectivity. Following the same rationale that we used to study the reactive-site and exosite elements of serpin B8 that determine reactivity with furin,[10] we used α1PDX as a model substrate to determine the basis for the differences in serpin B8 reactivity between furin and PC4−PC7 by the homologous transferring of RCL and exosite amino acid residues from serpin B8 to α1PDX.

Notably, the serpin B8 P6−P5′ RCL segment induced a difference in reactivity between furin and PC4−PC7 that was significantly larger within α1PDX (140−400-fold) than within serpin B8 (20-fold) (Tables 2 and 3). This disparity argues that the conformation that the serpin B8 RCL P6−P5′ segment adopts in the α1PDX context accentuates the difference in reactivity between furin and PC4−PC7. Unexpectedly, the α1PDX−serpin B8 P6−P5′ chimera reacted with furin with monophasic kinetics but reacted with PC4−PC7 with biphasic kinetics. The serpin thus bound rapidly to PC4−PC7 to form a Michaelis complex in the first kinetic phase, and this complex then slowly underwent acylation to form the trapped covalent serpin−enzyme complex in the second phase. The marked reduction in the rate of the second catalytic step therefore accounted for the biphasic kinetics and large reduction in overall reactivity of the chimera with PC4−PC7. The chimera thus by binding to the more variable catalytic site of PC4−PC7 than furin, as shown by the MDS experiments (Figure 5), may be favoring nonproductive conformations of the catalytic site.

The grafting of smaller segments of the RCL showed the P6−P1 segment and, in particular, the P6−P5 residues were responsible for the marked difference in reactivity between furin and PC4−PC7. By contrast, the serpin B8 P3−P2 residues did not produce biphasic reaction kinetics with PC4−PC7 but did result in marked reductions in reactivity with both furin (10-fold) and PC4−PC7 (1000-fold). The effects of other mutations of the P3 and P2 residues in α1PDX are also consistent with such mutations affecting reactivity more with PC4−PC7 than with furin (Table 6).

The major effects of the P6−P5 and P3−P2 residues, which flank the P4 Arg residue, on the reactivity of the P6−P1 chimera with PC4−PC7 suggest that the conformation of the P6−P1 segment plays a key role in regulating the productive insertion of the P4 arginine side chain into the S4 pocket of the enzyme catalytic site. Consistent with this idea, the level of PC reactivity of the P6−P1 chimera ($10-10^2$ M^{-1} s^{-1}) is comparable to that of α1-antitrypsin Pittsburgh (10 M^{-1} s^{-1}) (Table 6), a natural mutant of α1-antitrypsin,[20] which has an arginine for methionine substitution at the P1 position but lacks the P4 arginine (Figure 1).

The P1′−P5′ chimera led to significant losses of reactivity with all PCs (Table 3). The finding that the P2′ chimera

DOI: 10.1021/acs.biochem.8b01295
Biochemistry 2019, 58, 1679−1688

largely accounted for the losses in reactivity indicated that the P2′ residue was principally responsible for the detrimental effect of the serpin B8 primed region on α1PDX reactivity. Like α1PDX, the P1′−P5′ and P2′ α1PDX chimeras showed little selectivity in their reaction with furin and PC4−PC7. This region thus contributes to general PC specificity but not to selectivity.

The contribution of the primed region of the RCL to PC reactivity was also shown to be influenced by exosite interactions. In our previous study of furin reactivity, we showed that of the four furin active-site loops, only the 298−300 loop is involved in the exosite regulation of furin reactivity.[10] We also demonstrated that the 298−300 furin loop, of which Arg298 forms part of the S2′ pocket in the catalytic site,[8] mediates the interactions of the exosite residues in strand 3C of the serpin with the primed region of the RCL (Figure S2). In this study, we further advanced this notion by establishing that the exosite residues selectively affected PC reactivity depending on the RCL primed region amino acid sequence. While the serpin B8 exosite residues were detrimental to reactivity with all of the PCs in the presence of the serpin B8 primed region, they negatively affected furin reactivity but promoted reactivity with PC4−PC7 in the context of the α1PDX primed region (Table 7). These observations strongly suggest that the exosite residues modulate the insertion of the P2′ residue into the S2′ pocket and can regulate substrate selectivity between furin and PC4−PC7. Thus, the P1′−P5′ segment serves as a determinant of general PC substrate specificity that can be modulated by exosites.[10,25]

Our demonstration of differences in substrate specificity and selectivity between furin and PC4−PC7 significantly advances our understanding of the molecular determinants of specificity and selectivity in the PC family of proteases. Our findings thus clearly establish the ability of PCs to differentiate target substrates on the basis of the recognition of different preferred substrate cleavage sequences. Moreover, our findings underscore the importance of the structural context of such recognition sequences and the ability of exosites to influence this context.[26] Finally, they establish that substrate recognition can be favored or disfavored by differential abilities of furin and PC4−PC7 to bind their substrates productively versus nonproductively, due to differences in catalytic-site conformational states of PCs. Interestingly, such differences may be exploited to engineer selective inhibitors of PC4−PC7 as shown by the nanomolar Michaelis complex affinities observed for P6−P1 and P6−P5 chimera interactions with these PCs (Table 4).

Serpins are the only known natural PC inhibitors.[10−14] Protein-based inhibitors have an advantage over small molecule inhibitors in that they can be expressed by the targeted cell and directed to specific subcellular locations.[18,27] We have demonstrated that serpin B8 is a specific and selective furin inhibitor and shown that introducing serpin B8 reactivity determinants into the engineered general PC inhibitor, α1PDX, results in added selectivity for furin or for PC4−PC7 (Figure 1). The P6−P5′ chimera (now named α1ORD) achieves a 140−400-fold higher reactivity with furin than with PC4−PC7 (Table 3). Although this chimera forms inhibitory Michaelis complexes with PC4−PC7, the binding affinity is weak (K_d = 1 μM) and minimal inhibition is expected at concentrations of <1 μM. The α1PDX+YE derivative (now named α1MDW) is selective for PC4−PC7 with 20−60-fold higher reactivity with these PCs than with furin (Table 7). These inhibitors, and their future improved derivatives, should become useful tools in efforts to understand the regulatory role of PCs and to discover new therapeutic drugs.

■ ASSOCIATED CONTENT

Supporting Information

The Supporting Information is available free of charge on the ACS Publications website at DOI: 10.1021/acs.biochem.8b01295.

Figures S1 and S2 (PDF)

■ AUTHOR INFORMATION

Corresponding Author

*Department of Periodontics, College of Dentistry, University of Illinois at Chicago, Chicago, IL 60612. E-mail: goniza@uic.edu. Telephone: (312) 355-0573.

ORCID

Gonzalo Izaguirre: 0000-0002-6648-981X

Funding

This work was supported by the National Institutes of Health (R37 HL 39888) and Dirección General de Asuntos del Personal Académico at Universidad Nacional Autónoma de México (PAPIIT-IA202917).

Notes

The authors declare no competing financial interest.

■ ACKNOWLEDGMENTS

The authors thank Dirección General de Cómputo y de Tecnologías de Información y Comunicación at Universidad Nacional Autónoma de México for granting the use of the supercomputer Miztli (LANCAD-UNAM-DGTIC-320) and Dr. Steve Olson, from the University of Illinois at Chicago, for helpful discussions and critical comments on the manuscript.

■ REFERENCES

(1) Seidah, N. G., and Prat, A. (2012) The biology and therapeutic targeting of the proprotein convertases. *Nat. Rev. Drug Discovery 11*, 367−383.

(2) Seidah, N. G., Mayer, G., Zaid, A., Rousselet, E., Nassoury, N., Poirier, S., Essalmani, R., and Prat, A. (2008) The activation and physiological functions of the proprotein convertases. *Int. J. Biochem. Cell Biol. 40*, 1111−1125.

(3) Shiryaev, S. A., Remacle, A. G., Ratnikov, B. I., Nelson, N. A., Savinov, A. Y., Wei, G., Bottini, M., Rega, M. F., Parent, A., Desjardins, R., Fugere, M., Day, R., Sabet, M., Pellecchia, M., Liddington, R. C., Smith, J. W., Mustelin, T., Guiney, D. G., Lebl, M., and Strongin, A. Y. (2007) Targeting host cell furin proprotein convertases as a therapeutic strategy against bacterial toxins and viral pathogens. *J. Biol. Chem. 282*, 20847−20853.

(4) Feliciangeli, S. F., Thomas, L., Scott, G. K., Subbian, E., Hung, C. H., Molloy, S. S., Jean, F., Shinde, U., and Thomas, G. (2006) Identification of a pH sensor in the furin propeptide that regulates enzyme activation. *J. Biol. Chem. 281*, 16108−16116.

(5) Williamson, D. M., Elferich, J., Ramakrishnan, P., Thomas, G., and Shinde, U. (2013) The mechanism by which a propeptide-encoded pH sensor regulates spatiotemporal activation of furin. *J. Biol. Chem. 288*, 19154−19165.

(6) Omotuyi, I. O. (2015) Ebola virus envelope grycoprotein derived peptide in human furin-bound state: computational studies. *J. Biomol. Struct. Dyn. 33*, 461−470.

(7) Dahms, S. O., Arciniega, M., Steinmetzer, T., Huber, R., and Than, M. E. (2016) Structure of the unliganded form of the

DOI: 10.1021/acs.biochem.8b01295
Biochemistry 2019, 58, 1679−1688

proprotein convertase furin suggests activation by a substrate-induced mechanism. *Proc. Natl. Acad. Sci. U. S. A. 113*, 11196−11201.
(8) Henrich, S., Lindberg, I., Bode, W., and Than, M. E. (2005) Proprotein convertase models based on the crystal structures of furin and kexin: explanation of their specificity. *J. Mol. Biol. 345*, 211−227.
(9) Remacle, A. G., Shiryaev, S. A., Oh, E. S., Cieplak, P., Srinivasan, A., Wei, G., Liddington, R. C., Ratnikov, B. I., Parent, A., Desjardins, R., Day, R., Smith, J. W., Lebl, M., and Strongin, A. Y. (2008) Substrate cleavage analysis of furin and related proprotein convertases. A comparative study. *J. Biol. Chem. 283*, 20897−20906.
(10) Izaguirre, G., Qi, L., Lima, M., and Olson, S. T. (2013) Identification of serpin determinants of specificity and selectivity for furin inhibition through studies of α1PDX (α1-protease inhibitor Portland)-serpin B8 and furin active-site loop chimeras. *J. Biol. Chem. 288*, 21802−21814.
(11) Leblond, J., Laprise, M. H., Gaudreau, S., Grondin, F., Kisiel, W., and Dubois, C. M. (2006) The serpin proteinase inhibitor 8: an endogenous furin inhibitor released from human platelets. *Thromb. Haemostasis 95*, 243−252.
(12) Osterwalder, T., Kuhnen, A., Leiserson, W. M., Kim, Y. S., and Keshishian, H. (2004) Drosophila serpin 4 functions as a neuroserpin-like inhibitor of subtilisin-like proprotein convertases. *J. Neurosci. 24*, 5482−5491.
(13) Richer, M. J., Keays, C. A., Waterhouse, J., Minhas, J., Hashimoto, C., and Jean, F. (2004) The Spn4 gene of Drosophila encodes a potent furin-directed secretory pathway serpin. *Proc. Natl. Acad. Sci. U. S. A. 101*, 10560−10565.
(14) Bentele, C., Krüger, O., Tödtmann, U., Oley, M., and Ragg, H. (2006) A proprotein convertase-inhibiting serpin with an endoplasmic reticulum targeting signal from Branchiostoma lanceolatum, a close relative of vertebrates. *Biochem. J. 395*, 449−456.
(15) Anderson, E. D., Thomas, L., Hayflick, J. S., and Thomas, G. (1993) Inhibition of HIV-1 gp160-dependent membrane fusion by a furin-directed α1-antitrypsin variant. *J. Biol. Chem. 268*, 24887−24891.
(16) Jean, F., Stella, K., Thomas, L., Liu, G., Xiang, Y., Reason, A. J., and Thomas, G. (1998) α1-Antitrypsin Portland, a bioengineered serpin highly selective for furin: Application as an antipathogenic agent. *Proc. Natl. Acad. Sci. U. S. A. 95*, 7293−7298.
(17) Silverman, G. A., Bird, P. I., Carrell, R. W., Church, F. C., Coughlin, P. B., Gettins, P. G., Irving, J. A., Lomas, D. A., Luke, C. J., Moyer, R. W., Pemberton, P. A., Remold-O'Donnell, E., Salvesen, G. S., Travis, J., and Whisstock, J. C. (2001) The serpins are an expanding superfamily of structurally similar but functionally diverse proteins. Evolution, mechanism of inhibition, novel functions, and a revised nomenclature. *J. Biol. Chem. 276*, 33293−33296.
(18) Benjannet, S., Savaria, D., Laslop, A., Munzer, J. S., Chrétien, M., Marcinkiewicz, M., and Seidah, N. G. (1997) Alpha1-antitrypsin Portland inhibits processing of precursors mediated by proprotein convertases primarily within the constitutive secretory pathway. *J. Biol. Chem. 272*, 26210−26218.
(19) Gettins, P. G. (2002) Serpin structure, mechanism, and function. *Chem. Rev. 102*, 4751−4804.
(20) Vidaud, D., Emmerich, J., Alhenc-Gelas, M., Yvart, J., Fiessinger, J. N., and Aiach, M. (1992) Met 358 to Arg mutation of alpha 1-antitrypsin associated with protein C deficiency in a patient with mild bleeding tendency. *J. Clin. Invest. 89*, 1537−1543.
(21) Morrison, J. F. (1969) Kinetics of the reversible inhibition of enzyme-catalyzed reactions by tight binding inhibitors. *Biochim. Biophys. Acta 185*, 269−286.
(22) Scamuffa, N., Calvo, F., Chrétien, M., Seidah, N. G., and Khatib, A. M. (2006) Prorpotein convertases: lessons from knockouts. *FASEB J. 20*, 1954−1963.
(23) Seidah, N. G., Sadr, M. S., Chrétien, M., and Mbikay, M. (2013) The multifaceted proprotein convertases: their unique, redundant, complementary, and opposite functions. *J. Biol. Chem. 288*, 21473−21481.
(24) Lapierre, M., Siegfried, G., Scamuffa, N., Bontemps, Y., Calvo, F., Seidah, N. G., and Khatib, A. M. (2007) Opposing function of the proprotein convertases furin and PACE4 on breast cancer cells' malignant phenotypes: role of tissue inhibitors of metalloproteinase-1. *Cancer Res. 67*, 9030−9034.
(25) Maret, D., Sadr, M. S., Sadr, E. S., Colman, D. R., Del Maestro, R. F., and Seidah, N. G. (2012) Opposite roles of furin and PC5A in N-cadherin processing. *Neoplasia 14*, 880−892.
(26) Komiyama, T., and Fuller, R. S. (2000) Engineered eglin c variants inhibit yeast and human proprotein processing proteases, Kex2 and furin. *Biochemistry 39*, 15156−15165.
(27) Richer, M. J., Juliano, L., Hashimoto, C., and Jean, F. (2004) Serpin mechanism of hepatitis C virus nonstructural 3 (NS3) protease inhibition: induced fit as a mechanism for narrow specificity. *J. Biol. Chem. 279*, 10222−10227.

DOI: 10.1021/acs.biochem.8b01295
Biochemistry 2019, 58, 1679−1688

INFORME DE LABORES 2019

Received: 24 July 2018 | Revised: 17 December 2018 | Accepted: 25 December 2018

DOI: 10.1111/ejn.14344

RESEARCH REPORT

WILEY EJN European Journal of Neuroscience FENS

Synchronized activation of striatal direct and indirect pathways underlies the behavior in unilateral dopamine-depleted mice

Omar Jáidar | **Luis Carrillo-Reid** | **Yoko Nakano** | **Violeta Gisselle Lopez-Huerta** | **Arturo Hernandez-Cruz** | **José Bargas** | **Marianela Garcia-Munoz** | **Gordon William Arbuthnott**

Okinawa Institute of Science and Technology Graduate University, Okinawa, Japan

Correspondence
Gordon W. Arbuthnott, Okinawa Institute of Science and Technology Graduate University, Okinawa, Japan.
Email: gordon@oist.jp

Funding information
This research was supported by the Government of Japan.

Abstract

For more than three decades it has been known, that striatal neurons become hyperactive after the loss of dopamine input, but the involvement of dopamine (DA) D1- or D2-receptor-expressing neurons has only been demonstrated indirectly. By recording neuronal activity using fluorescent calcium indicators in D1 or D2 eGFP-expressing mice, we showed that following dopamine depletion, both types of striatal output neurons are involved in the large increase in neuronal activity generating a characteristic cell assembly of particular neurons that dominate the pattern. When we expressed channelrhodopsin in all the output neurons, light activation in freely moving animals, caused turning like that following dopamine loss. However, if the light stimulation was patterned in pulses the animals circled in the other direction. To explore the neuronal participation during this stimulation we infected normal mice with channelrhodopsin and calcium indicator in striatal output neurons. In slices made from these animals, continuous light stimulation for 15 s induced many cells to be active together and a particular dominant group of neurons, whereas light in patterned pulses activated fewer cells in more variable groups. These results suggest that the simultaneous activity of a large dominant group of striatal output neurons is intimately associated with parkinsonian symptoms.

KEYWORDS

assemblies, basal ganglia, calcium imaging, optogenetics, Parkinson's disease

Abbreviations: 6-OHDA, 6-hydroxydopamine; AAV, adeno-associated viruses; ANOVA, Analysis of variance; BAC, bacterial artificial chromosome; CCD, cooled charge-coupled device; ChR2, channelrhodopsin variant 2; D1, DA receptor 1; D2, DA receptor 2; DA, Dopamine; EF1a, elongation factor-1 alpha; eGFP, enhanced fluorescent protein; Fluo-#, calcium indicator; hSyn, human promoter of synapsin 1; LED, light-emitting diode; PBS, phosphate-buffered saline; PD, Parkinson disease; RCaMP1h, red calcium indicator; SPNs, spiny projection neurons.

Edited by Paul Bolam. Reviewed by Anthony West and Nicolas Mallet.

All peer review communications can be found with the online version of the article.

This is an open access article under the terms of the Creative Commons Attribution-NonCommercial License, which permits use, distribution and reproduction in any medium, provided the original work is properly cited and is not used for commercial purposes.
© 2019 The Authors. *European Journal of Neuroscience* published by Federation of European Neuroscience Societies and John Wiley & Sons Ltd.

INFORME DE LABORES 2019

1 | INTRODUCTION

Since pioneering work in the 1970s we know that unilateral destruction of dopamine (DA) neurons in the rodent mesencephalon induces unilateral hypokinesia, deviated posture, and spontaneous circling or turning behavior toward the lesion side (Ungerstedt & Arbuthnott, 1970). This experimental model of Parkinson's disease (PD) was initially useful in pharmacological studies and it is still useful in the characterization of function of basal ganglia outputs (Greco et al., 2008). However, one of the most striking initial findings using this model is that unilateral destruction of striatal DA input is accompanied by an increase in activity of striatal neuronal activity on the ipsilateral side (Arbuthnott, 1974; Hull, Levine, Buchwald, Heller, & Browning, 1974; Ohye, Bouchard, Boucher, & Poirier, 1970; Schultz, 1982; Schultz & Ungerstedt, 1978).

It is characteristic of striatal projection neurons (SPNs), in anaesthetized animals, that in spite of a correlation between cortical rhythmic activity and membrane potential fluctuations (up and down states) they do not fire rhythmically or synchronously in the presence of DA. However, in the absence of DA, the cortically induced rhythmicity is dramatically increased from less than 1 burst/min to more than 2.5 bursts/min as seen in anesthetized (Arbuthnott, 1974; Nisenbaum, Stricker, Zigmond, & Berger, 1986; Schultz & Ungerstedt, 1978) and awake animals (Chen, Morales, Woodward, Hoffer, & Janak, 2001; Kish, Palmer, & Gerhardt, 1999; Ohye et al., 1970) as well as in vitro (Calabresi, Mercuri, Sancesario, & Bernardi, 1993; Galarraga, Bargas, Martinez-Fong, & Aceves, 1987). Rhythmic bursting of SPN output targets in the absence DA is a consistent finding (Bergman, Wichmann, Karmon, & DeLong, 1994; MacLeod, Ryman, & Arbuthnott, 1990; Murer, Riquelme, Tseng, & Pazo, 1997; Murer, Tseng, Kasanetz, Belluscio, & Riquelme, 2002; Ni, Bouali-Benazzouz, Gao, Benabid, & Benazzouz, 2000; Nini, Feingold, Slovin, & Bergman, 1995; Pan & Walters, 1988; Rohlfs et al., 1997; Sanderson, Mavoungou, & Albe-Fessard, 1986; Wichmann et al., 1999).

Concurrent pharmacological blockade of DA receptor 1 (D1) and DA receptor 2 (D2) SPNs produces an akinesia (often mischaracterized as catalepsy) similar to a DA lesion, but specific blockade of D1 or D2 SPNs indicates that synchronous activity is affected in greater extent by D1 compared to D2 receptor antagonists (Burkhardt, Jin, & Costa, 2009).

In order to understand the role of DA in specific subpopulations of SPNs we used calcium imaging of individual D1- or D2-expressing enhanced eGFP to visualize their activity and study their characteristic patterns of activation in cell assemblies. Moreover, we used calcium imaging and optogenetics to illustrate the specific contribution of both D1 and D2 microcircuits in the generation of the pathological circling behavior characteristic of the animal model of PD.

2 | MATERIAL AND METHODS

2.1 | Ethical standards

We used a total of 64 of 78 (14 discarded as failures in procedure or stereotaxic coordinates) Swiss Webster bacterial artificial chromosome (BAC) transgenic mice D1- enhanced fluorescent protein (eGFP) and D2-eGFP (postnatal 21–25 days, males) or C57BL/6J control mice were used. Animals were bred in the university's animal facilities. In general, we adjust the number of animals in our experiments according to the mortality rates after surgeries, the success rate of stereotaxic placement of viral injections and the general success of the experiments considering the expertise of trainees. Our experiments complied with the Guide for the care and use of laboratory animals of the US National Institutes of Health; the Society for Neuroscience Policy on the Use of Animals in Neuroscience Research and the Guiding Policies and Principles for Experimental Procedures endorsed by the government of Japan and supervised by the local Animal Care and Use Committee, approved protocol number 2018-212-2.

2.2 | Stereotaxic surgeries

Surgeries were performed under aseptic conditions in a small animal stereotaxic instrument (Leica Angle Two, Leica Biosystems, Wetzlar, Germany). Isoflorane inhalation (IsoFlo, Abbot, 1.0%–1.5% in medical O_2) was used as anesthetic and the respiratory rate, heart rate, and hindpaw withdrawal reflexes were monitored throughout the procedure to maintain an adequate anesthetic level as stably as possible. Animals were fixed with atraumatic earbars, the cornea protected with mycochlorin ointment 2% and the skin rubbed with anesthetic gel (10% ketoprofen and lidocaine). Post-operative care measures to control hypothermia, dehydration and pain included keeping mice warm until they came out of anesthesia (<15 min) by placing them on a disposable heating pad, administering sterile saline (0.5 ml, s.c.) immediately after surgery and leaving available, during the first 72 hr after surgery, a can of diet gel with carprofen (e.g., MediGel CPF, Portland, ME, USA). One-to-two weeks after surgery, animals were tested or the brain extracted.

For the intracerebral unilateral administration of the neurotoxin 6-hydroxydopamine (6-OHDA, Sigma), mice were premedicated 1 hr before surgery with desipramine HCl (25 mg/kg base, in 0.9% sterile saline, subcutaneous). The 6-OHDA (0.5 µl of 4 mg/ml in 0.9% NaCl and 0.5% ascorbate)

INFORME DE LABORES 2019

was slowly injected (0.01 µl/min) at stereotaxic coordinates (Franklin & Paxinos, 2008) aimed to the left substantia nigra pars compacta (bregma: AP, −2.3 mm; L, 0.7 mm and from dura: V, −4.3 mm). These animals were challenged with apomorphine (Sigma, 0.01 mg/kg, subcutaneous) 1 week after surgery and turning behavior was automatically evaluated by protocols written under Ethovision XT 11 animal tracking system (Noldus, Wageningen, The Netherlands). Behavioral measurements were counted for 5 min after being placed in the recording environment. Only animals showing robust turning (>5 turns/min) were considered to have adequate DA depletion.

To induce viral infection in SPNs, adeno-associated viruses (AAV) were intracerebrally delivered D1-eGFP and D2-eGFP BAC mice. The AAV10 under the human origin elongation factor-1 alpha (EF1a) promoter was used to drive expression of channelrhodopsin variant 2 (ChR2) and the fluorescent protein 2mCherry. The AAV1 under the human promoter of synapsin 1 (hSyn) was used for the expression of the genetically engineered red calcium indicator (RCaMP1h, Penn Vector Core, AV-1-PV3010). Either a single AAV (0.3 µl) or a combination of both (0.15 µl each) was unilaterally injected in the left dorsal striatum of D1-eGFP and D2-eGFP BAC mice (AP, 0.98 mm; L, 1.89 mm; V −3.45 mm) (Franklin & Paxinos, 2008).

Animals that received AAV1 RCaMP1h were left for at least 2 weeks to recover and allow viral expression before in vitro recording experiments. Animals that received AAV-10 ChR2-2mCherry injection had a longer surgery since a 3 mm stainless steel guide cannula (25 gauge) was inserted above the injection site and fixed to the skull with a small amount of dental cement (Super-Bond C&B, Sun Medical) followed by a 5-mm-long optic fiber (diameter: 260 µm, length 5.45 mm, Teleopto, Nagoya, Japan) placement into the injection site. A device containing the optic fiber, the high-intensity light-emitting diode (LED; 470 nm) and a connector to plug the wireless receiver was also fixed to the skull with more dental cement.

2.3 | Behavioral observations

To allow viral expression, animals were housed for at least 2 weeks before any recording or behavioral observation was performed. A couple of days before the experiments, animals were first trained for 20 min to carry a mock receiver (12 × 18 × 7 mm, 2 g) plugged to the wireless stimulation system in their home cage. On the experiment day, the infrared receiver (Teleopto, Nagoya, Japan) with the same dimensions and weight, replaced the mock receiver and animals were placed in a rectangular (45 × 20 × 15 cm) or circular (15 cm diameter × 20 cm high) testing chamber.

The stimulation device (Teleopto, Nagoya, Japan) triggered a LED of 470 nm (blue light) with intensity at the tip of 1.0 mW. Behavioral procedures consisted of a period of habituation (≈5 min) followed by a sequence of three periods repeated 10 times: 20 s pre-stimulation, 15 s of light stimulation either delivered continuously or in patterned pulses (6 ms pulses at 14 Hz) and a 30–60 s post-stimulation period. Turning behavior was measured and evaluated automatically by protocols written under Ethovision XT 11 animal tracking system (Noldus, Wageningen, The Netherlands).

2.4 | Corticostriatal slice preparation

Mice were anesthetized with isoflorane inhalation and perfused transcardially using cold saline containing (in mM): 124 choline chloride, 2.5 KCL, 1.3 $MgCl_2$, 26 $NaHCO_3$, 1.2 NaH_2PO_4–H_2O, 1 $CaCl_2$ and 10 glucose saturated with 95% O_2 and 5% CO_2, pH = 7.4, 298 mOsm/L. Sagittal corticostriatal slices (200–250 µm) were cut (Leica VT1200S, Nussloch, Germany) and transferred to regular artificial cerebral spinal fluid containing the following in mM: 123 NaCl, 3.5 KCl, 1 $MgCl_2$, 1 $CaCl_2$, 26 $NaHCO_3$, and 11 glucose, saturated with 95% O_2 and 5% CO_2, where they remained at room temperature (21–25°C) for at least 1 hr before recording.

2.5 | In vitro recordings of neuronal activity

For recordings of neuronal calcium activity Fluo-4 or RCaMP1h, corticostriatal slices (210–250 µm) of D1-eGFP or D2-eGFP BAC mice were visualized using an upright microscope (Olympus BX51W1F, Japan, 100W halogen lamp) fitted with brightfield (UM Plan FL 10×) and water immersion (10× Olympus) objective. The microscope was also equipped with a cooled charge-coupled device (CCD) camera (PCO.EDGE, Kelheim, Germany) with a field view of 800 × 600 µm; acquisition of images was set to 5–6 images/s. At the beginning of each experiment coordinates and landmarks of the displayed image were stored for reference and subsequent analysis. Experimental data were recorded using the CCD camera with acquisition protocols written in camware software. Short movies (180 s, 50–100 ms exposure, 250–500 ms/frames) were taken at time intervals of 5–20 min during 1–2 hr). At the end of the experiment potassium depolarization (mM): 50 KCl, 120 NaCl, 10 HEPES-Na, and 2 $CaCl_2$ pH7.4, was applied for 5 s to validate slice integrity, slices with small numbers of responsive cells (<10) were discarded from the analysis.

When a cell-permeant calcium indicator was used, slices were incubated in the dark at 38°C for 20–30 min with Fluo-4 (Fluo-5AM in few occasions) in 0.1% dimethyl sulfoxide diluted to a final concentration of 10 µM, pH 7.4 (95%O_2 and 5%CO_2). Once loaded with the calcium indicator, slices were transferred back to the microscope's recording chamber perfused with artificial cerebrospinal fluid.

The pair ChR2 and RCaMP provided independent addressable spectral channels. For neuronal activation with

INFORME DE LABORES 2019

ChR2 and imaging via the genetically encoded red calcium indicator RCaMP1h and RCaMP1 h activation was achieved using excitation pulses at 580 nm delivered by a xenon-arc lamp of (Lambda LS Sutter Instruments) and a bandpass filter (FB580-10, ThorLabs, Newton, NJ, USA). A combined non-overlapping calcium imaging/optogenetics was possible since light of 580 nm—the peak activation for RCaMP1h—does not activate ChR2 (Glock, Nagpal, & Gottschalk, 2015). The emitted RCaMP1h fluorescence was passed through a long pass filter (550 nm, FEL0550, ThorLabs, Newton, NJ, USA) (Akerboom et al., 2013). Optogenetic stimulation (488 nm) was achieved using a fiber-coupled LED light source (DC2100, OGKR2 Thorlabs. Newton, NJ, USA). The same optogenetic stimulation parameters (continuous or in 14 Hz pulses) were used in slices and behaving animals.

For depolarization block assessment electrical neuronal activity of ChR2-/RCaMp1h- expressing neurons was recorded during 30 s of continuous light stimulation emitted from the fiber-coupled LED with the same intensity at the tip than the in vivo configuration (1 mW). Electrical neuronal activity was recorded using borosilicate glass micropipettes (Harvard Apparatus 30-0057, Holliston, MA, USA) heat polished to obtain direct current resistances of ~4–6 MΩ. Micropipettes were filled with an internal solution containing in mM: 115 KH_2PO_4, 2 $MgCl_2$, 10 HEPES, 0.5 EGTA, 0.2 Na_2ATP, and 0.2 Na_3GTP. The recordings were made with a microelectrode amplifier with bridge and voltage clamp modes of operation (BVC-700A, Dagan Co, Minneapolis, MN, USA). Conventional characterization of neurons was made in voltage and current clamp configurations. Access resistances were continuously monitored to be less than 20 MΩ, experiments with changes over 20% were interrupted and terminated. Software designed in LabVIEW environment (National Instruments, Austin, Texas, USA) was used for data acquisition and we performed analysis with Origin (version 8.6, Microcal, Northampton, MA, USA).

During recordings of calcium or electrical activity, slices received a constant flow of artificial cerebral spinal fluid of 2.5 ml/min.

2.6 | Processing of neuronal calcium images

For this processing we used the methods previously described (Carrillo-Reid et al., 2008; Jaidar et al., 2010). Briefly, Image J (v.1.45s, National Institutes of Health, WA), MATLAB (Math-Works, Inc., Natick, MA, USA) and programs written in IDL (Exelis-Harris software version 8.2) (Cossart, Aronov, & Yuste, 2003; Mao, Hamzei-Sichani, Aronov, Froemke, & Yuste, 2001; Schwartz et al., 1998) were used to analyze the movies acquired during the recordings (see above). For each movie frame neurons were identified, their contours defined and the mean fluorescence measured as a function of time. Changes in fluorescence were computed as (Fi–Fo)/Fo, where Fi = fluorescence intensity and Fo = resting fluorescence, that is, median fluorescence of the first four frames of the movie. The calcium signals elicited by action potentials were detected based on a threshold value given by their first derivative over time (2.5× standard deviation of the noise). Images were inspected one by one to remove artifacts and slow calcium transients, most likely from glial cells (Carrillo-Reid et al., 2008; Cossart et al., 2003; Jaidar et al., 2010; Sasaki, Matsuki, & Ikegaya, 2007). As previously described (Miller, Ayzenshtat, Carrillo-Reid, & Yuste, 2014) to determine whether peaks of synchrony were significant (number of coactive neurons per peak), binary activity from recorded calcium imaging (calcium spikes) were shuffled 1,000 times by randomly transposing intervals of activity within each cell. We then set a threshold corresponding to a significance level of $p < 0.05$ for peak detection.

2.7 | Visualization of network states

The vectorization of all recorded activity was performed to express network activity as a function of time. Active and inactive elements were therefore represented within a 250 ms time bin. With this analysis, association of bursting activity of synchronized cells occurring at a particular time can be easily identified (Carrillo-Reid et al., 2008, 2009; Sasaki, Kimura, Tsukamoto, Matsuki, & Ikegaya, 2006; Sasaki et al., 2007). The inner product of all possible vector pairs (equivalent to the cosine of the angle between the vectors) was used to construct a similarity matrix of all neurons firing in synchrony. This process graphically reveals whether vectors have same or similar components (Sasaki et al., 2006, 2007). To follow network dynamics within the neuronal microcircuits and determine how neuronal activity travels among the different network states in the field of observation, we analyzed the data using multidimensional reduction techniques previously described (Carrillo-Reid et al., 2008, 2009; Jaidar et al., 2010). Briefly, (a) To reduce the dimensionality of population vectors representing network states, we applied locally linear embedding (LLE), a technique that preserves the structure of nonlinear multidimensional data (Brown, Joseph, & Stopfer, 2005; Carrillo-Reid et al., 2008; Roweis & Saul, 2000). (b) To choose the optimal number of network states, we used hard and fuzzy clustering algorithms and the Dunn's index as a validity function (Bezdek & Pal, 1998; Carrillo-Reid et al., 2008, 2009; Sasaki et al., 2007). (c) To visualize clusters of data points representing similar population vectors (i.e., network states) following activity sequences or closed cycles we projected vectors into a two-dimensional space (Jaidar et al., 2010; Liu, Khalil, & Oweiss, 2011; Sasaki et al., 2007; Schreiber, Fellous, Whitmer, Tiesinga, & Sejnowski,

2003). (d) The position of all cells involved in each state was plotted onto the original image of the slice containing the defined neuronal contours (see previous paragraph).

2.8 | Statistical analyses

Experimental and control sample size was chosen based on previous literature (Lee et al., 2016). The Shapiro–Wilk test was applied to all original data to assess normality in data distribution. Data withdrawn from a normal distribution were analyzed with the parametric statistical significance test one-way ANOVA followed by post hoc Tukey honestly significant difference (HSD). When necessary, a paired-*t* test was also used. Results were expressed as M = mean, SD = standard deviation and n = number of cases; statistical probability values were expressed in the results and figure legends. A simple randomization (i.e., heads-continuous; tail-pulses) was applied when the same slices were activated with pulsed or continuous light.

2.9 | Histology

Following a brief rinse in phosphate buffer 0.01 M, mice were perfused with 4% paraformaldehyde and 14% picric acid; brains were post-fixed for at least 2 hr and then cryoprotected in a 50/50 mixture of fixative and 20% sucrose in 0.01 M phosphate-buffered saline (PBS) for at least 24 hr. Sections were cut at 60 μm on a sledge microtome with a freezing stage (Yamato REM-710 electrofreeze MC-802A), washed in PBS and incubated in 20% normal goat serum. Primary antibodies to tyrosine hydroxylase (rabbit polyclonal 1:5,000, Enzo Life Sciences) or glial fibrillary acid protein (GFAP, rabbit polyclonal, Dako; 1:500) were incubated overnight at 4°C and stained with secondary goat antirabbit antibodies (Life Technologies; 1:200). At least 2 hr were allowed for binding before rinsing in PBS. Sections were mounted on slides; Vectamount AQ (Vector) or occasionally Santa Cruz mountant with DAPI was used to fix the coverslips. A spinning disk confocal microscope (Olympus BX-DSU) was used and pictures were taken using Neurolucida software and a Hammatsu (EM-CCD C91) camera.

3 | RESULTS

3.1 | Spontaneous calcium activity in corticostriatal slices of intact or DA-depleted mice

The proposed involvement of DA in the generation of striatal neuronal assemblies (Burke, Rotstein, & Alvarez, 2017; Nicola, Surmeier, & Malenka, 2000; O'Donnell, 2003) became testable through calcium imaging that allows simultaneous measurement of many individual neurons (Carrillo-Reid et al., 2008; Jaidar et al., 2010). With the use of population calcium imaging that allows the indirect measurement of neuronal spiking in striatal networks in vitro (Carrillo-Reid et al., 2008; Jaidar et al., 2010; Lopez-Huerta et al., 2013) we characterized the population activity of SPNs in slices obtained from naïve controls and mice depleted of DA for at least 9 days. Examples of simultaneous recordings of fluo-4 calcium signals and analysis of large numbers of D1eGFP$^+$ and D2eGFP$^+$ SPNs are shown for naïve and DA-depleted mice in Figure 1 and Supporting Information Video S1. Spontaneous activity of both D1 and D2 SPNs from non-lesioned mice slices is characterized by sparse events without significant coactivity episodes (Figure 1a), and following DA depletion, a significant increase in the number of D1 and D2 active SPNs relative to controls is observed (one-way ANOVA $(3,28) = 27.12$, $p < 0.0001$), accompanied by the presence of significant coactivity peaks absent in non-lesioned controls (Figure 1b). As indicated in the graphs of coactive cells (Figure 1c), we counted calcium fluorescent signals not only on eGFP-positive neurons (D1-green dots- or D2-red dots-) but also in SPNs with negative eGFP expression (black dots) that represent the other half of SPNs (D1 or D2) and the interneurons. Group analyses of the number of active SPNs and the number of calcium events of DA-depleted and control slices revealed as that slices from DA-depleted slices showed increases of active SPNs for D1eGFP$^+$- and D2eGFP$^+$-expressing groups, D1 (green): $M = 37.7$, $SD = 5.33$, $n = 11$ mice, and D2 (red): $M = 30.18$, $SD = 7.01$, $n = 11$ mice, whereas control animals exhibited very few active D1 or D2 neurons for the duration of the measurements (3 min), D1: $M = 4.8$, $SD = 1.3$, $n = 5$ mice and D2: $M = 4.4$, $SD = 1.94$, $n = 5$ mice. The coactivity histograms (Figure 1d) are consistent with an increase in activity in both populations (green and red boxes), and also with significant increases in cell activity and peaks of coactivity in the eGFP-negative neurons (gray boxes). This is a corroboration that most SPNs and possibly interneurons become active in the absence of DA.

Similar results were obtained from neurons with negative eGFP expression (black dots) (Figure 1b1): a low number of active neurons in the control group (Figure 1a) (D1: $M = 11.8$, $SD = 4.96$, $n = 5$ mice and D2: $M = 9.6$, $SD = 4.03$, $n = 5$ mice) and high number of active neurons in the DA-depleted slices (Figure 1b) (D1: $M = 59.6$, $SD = 5.33$, $n = 11$ mice and D2: $M = 30.18$, $SD = 7.01$, $n = 11$ mice). The increase in the number of active neurons was statistically significant when compared to controls (Figure 1d). DA depletion was corroborated with immunohistochemistry (Figure 2) and turning behavior (see Section 3). Animals depleted of DA displayed spontaneous turning toward the side of the lesion ($M = 1.77$ turns/15 s, $SD = 1.35$, $n = 11$ mice) (Figure 1d).

To continue with the analysis of cell activity and peaks of coactivity as illustrated in Figure 1c, we compared network

INFORME DE LABORES 2019

EJN European Journal of Neuroscience FENS WILEY

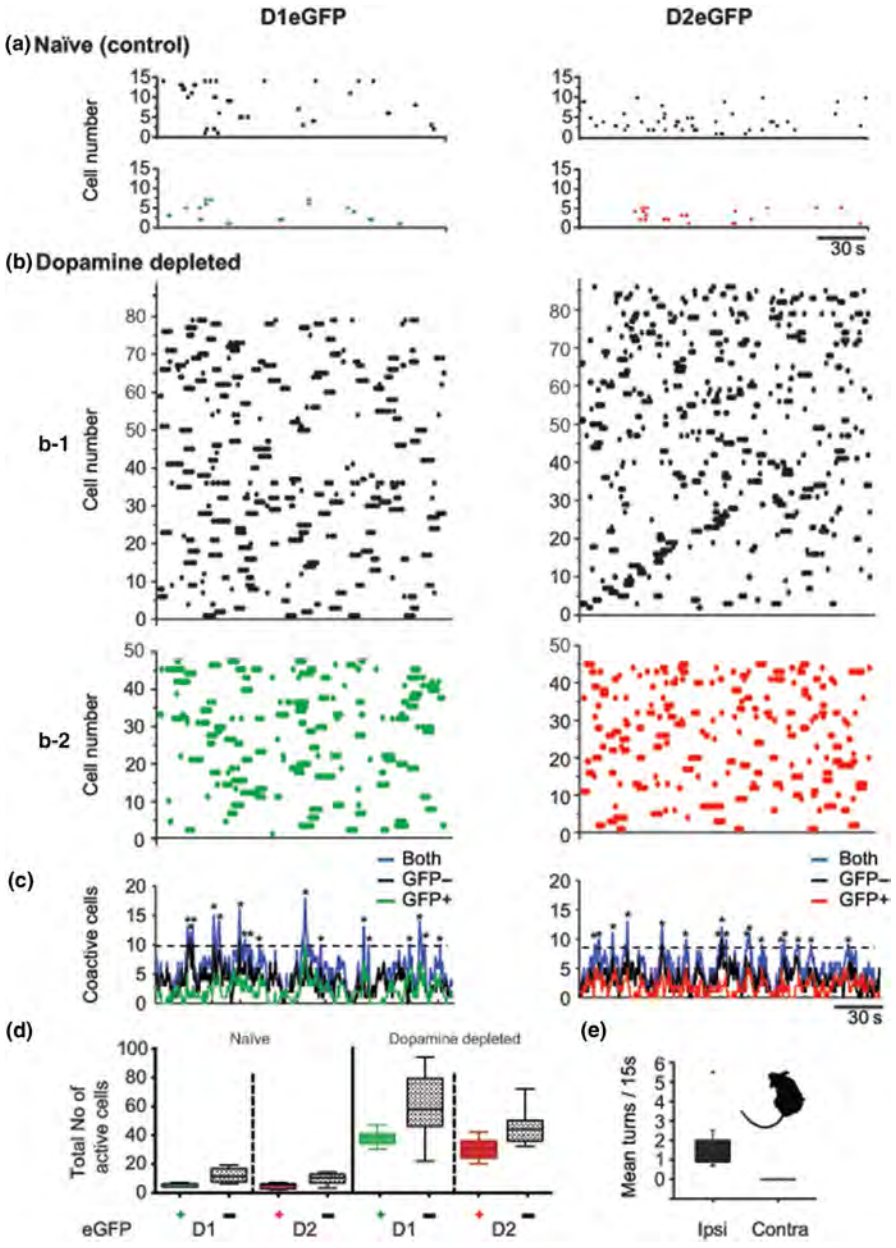

FIGURE 1 SPNs of the direct or indirect output pathways (D1-dSPN or D2-iSPN) contribute to the synchronized network activity after DA depletion. Data are displayed in raster plots where every dot at any given time along the *x* axis represents an active neuron identified by its unique number in the *Y* axis. (a) Representative raster plots of spontaneous striatal activity from D1eGFP (left) and D2 eGFP (right) unlesioned mice. (b) Representative raster plots (top) of D1eGFP (left) and D2eGFP (right) from DA-depleted animals. (b1) Raster plots of eGPP-negative neurons, that is, interneurons and the unlabeled SPNs (black dots), (b2) Raster plots of eGPP-positive neurons of D1 (green) and D2 (red) mice. The increment of neuronal activity after DA depletion compared to controls was statistically significant (one-way ANOVA (3,28) = 27.12, $p < 0.0001$). (c) Plots of coincidently firing cells (identified by colors: black: eGFP$^-$ negative; green: D1eGFP positive; red: D2eGFPpositive; blue: all recorded neurons, that is, eGFP positive and eGFP negative$^-$ together). (d) Box plots of total number of spontaneous active neurons recorded in periods of 180s. (e) Box plot of spontaneous mean rotations recorded on separate experiments. Rotation was toward the side depleted of DA ($M = 1.77$ turns/15 s, SD 1.35, $n = 10$ mice). For later comparisons with turns obtained with optogenetic stimulation, turns in DA-depleted mice were also recorded for 15 s after a 5–10 min period. A contour detection snapshot of a recorded mouse illustrates the deviated posture typical of an ipsilateral DA depletion

responses induced by DA depletion (Figure 3) using multi-dimensional reduction techniques as described (see Section 2.7). A previous description of the striatal microcircuit of un-identified SPNs of rats deprived of DA, was characterized by a dominant network state (Jaidar et al., 2010). Similarly, as previously observed in rats (Jaidar et al., 2010) we observed that D1- or D2-eGFP-expressing neurons formed three sets that generated sequential activity states. Moreover, as

INFORME DE LABORES 2019

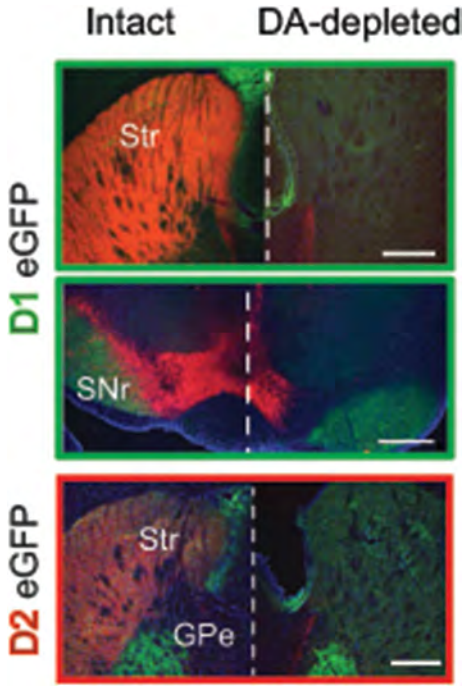

FIGURE 2 Immunohistochemistry of control and dopamine-depleted brains. Coronal brain slices of intact and DA-depleted D1eGFP+ and D2eGFP+ mice illustrate DA neurons and axons by tyrosine hydroxylase (TH) staining (red); positive expression of fluorescent protein (green) and the presence of cell bodies stained with 4,6-diamidino-2phenylindole, dihydrochloride (DAPI) (blue). GPe: external globus pallidus; Scale bars: 1 mm; Str: striatum; SNr: substantia nigra pars reticulata

observed in rats (Jaidar et al., 2010), one state that comprised the largest number of active neurons became dominant (refer to Figure 3a,b,d,e orange dots). Importantly, the dominant state was formed by SPNs belonging to both striatal output pathways as illustrated by the presence and absence of the plus sign in active neurons (Figure 3c,f).

3.2 | Simultaneous photoactivation of direct and indirect pathway SPNs

Consistent with the coordinated synchronous activation of indirect and direct SPNs necessary for the selection, initiation and performance of a particular movement, it has been reported that when the animal is not moving, SPNs remain inactive, but become coactive during movement initiation (Cui et al., 2013; Klaus et al., 2017). With the increase in the number of active cells and peaks of synchrony observed in DA-depleted tissue, we hypothesized that in the absence of DA, the observed increase in synchronous activation of large sets of striatal neurons could be responsible for the animal's motor impairments, such as deviated posture and persistent spontaneous turning (Costall, Marsden, Naylor, & Pycock, 1976; Dunnett & Iversen, 1982), Figure 1e.

To examine the relationship between the increment of neuronal activity and behavior, animals expressing AAV10 ChR2-mCherry (EF-1promoter) were used for the unilateral optogenetic activation through an optic probe implanted into the dorsolateral striatum (Figure 4a). We delivered to our behaving animals stimulation at the same intensity (470 nm; 1.0 mW at the tip) for 15 s in two modes as reported by others, for example, a single continuous 15 s pulse (Kravitz et al., 2010) or patterned pulses at 14 Hz (210 pulses of 6 ms each: (Jin, Tecuapetla, & Costa, 2014). When stimulation was delivered in pulses (14 Hz, 6 ms) it induced turning toward the opposite side characteristic of the activation of striatal cell assemblies (Ossowska & Wolfarth, 1995) (M 1.73 turns, SD 0.99, $n = 7$ mice) (Figure 4b right panel and Supporting Information Video S3). Interestingly, when light was delivered continuously in control animals, behavior changed drastically, mice turned toward the stimulated side (M 1.92 turns, SD 0.35, $n = 9$; Figure 4b, left panel). This turning behavior is compelling since it is similar to the one observed in DA-depleted animals ($M = 1.77$ turns, $SD = 1.35$, $n = 11$; Figure 1e). Optogenetically induced turning to the two types of stimulation was statistically significantly different (one-tail ANOVA $F(3,28) = 97.14$, $p < 0.001$, $n = 9$, 7 continuous vs. patterned pulses), Figure 4b.

Our results demonstrate that in the absence of DA, spontaneous synchronous patterns of SPN activation are observed in both D1 and D2 SPNs, and that when similar large synchronous patterns of activity are induced in both D1 or D2 SPNs by continuous optogenetic stimulation, normal mice turn in circles as do animals with a DA depletion.

3.3 | Visualization in vitro of striatal dynamics under optogenetic stimulation

To further visualize how the striatal network elements behaved under optogenetic stimulations we used electrophysiology, calcium imaging, and optogenetics (Figure 5). We combined AAV10 ChR2-mCherry (EF-1promoter) with genetically encoded calcium indicator RCaMP1h (hSyn promoter) delivered by AAV1 viral infection. It is relevant to mention that AAV10 ChR2-mCherry labels the majority of SPNs, but excludes the population of SPN contained in the striosomes (less than 20%) (Lopez-Huerta et al., 2016).

Neuronal calcium responses were recorded and their amplitude of the responsive cells was normalized by considering the brightest recorded neuronal fluorescence as 100% for each tissue slice. This analysis showed that the normalized calcium response amplitude elicited with continuous stimulation ($M = 0.77$, $\Delta F/F$, $SD = 0.1$, $n = 17$ slices) was significantly larger than the response observed with stimulation in patterned pulses ($M = 0.37$, $\Delta F/F$, $SD = 0.1$, $n = 17$ slices; paired t (16) = 16.22, $p = 2.33504^{-11}$; Figure 5 and Supporting Information Video S2).

INFORME DE LABORES 2019

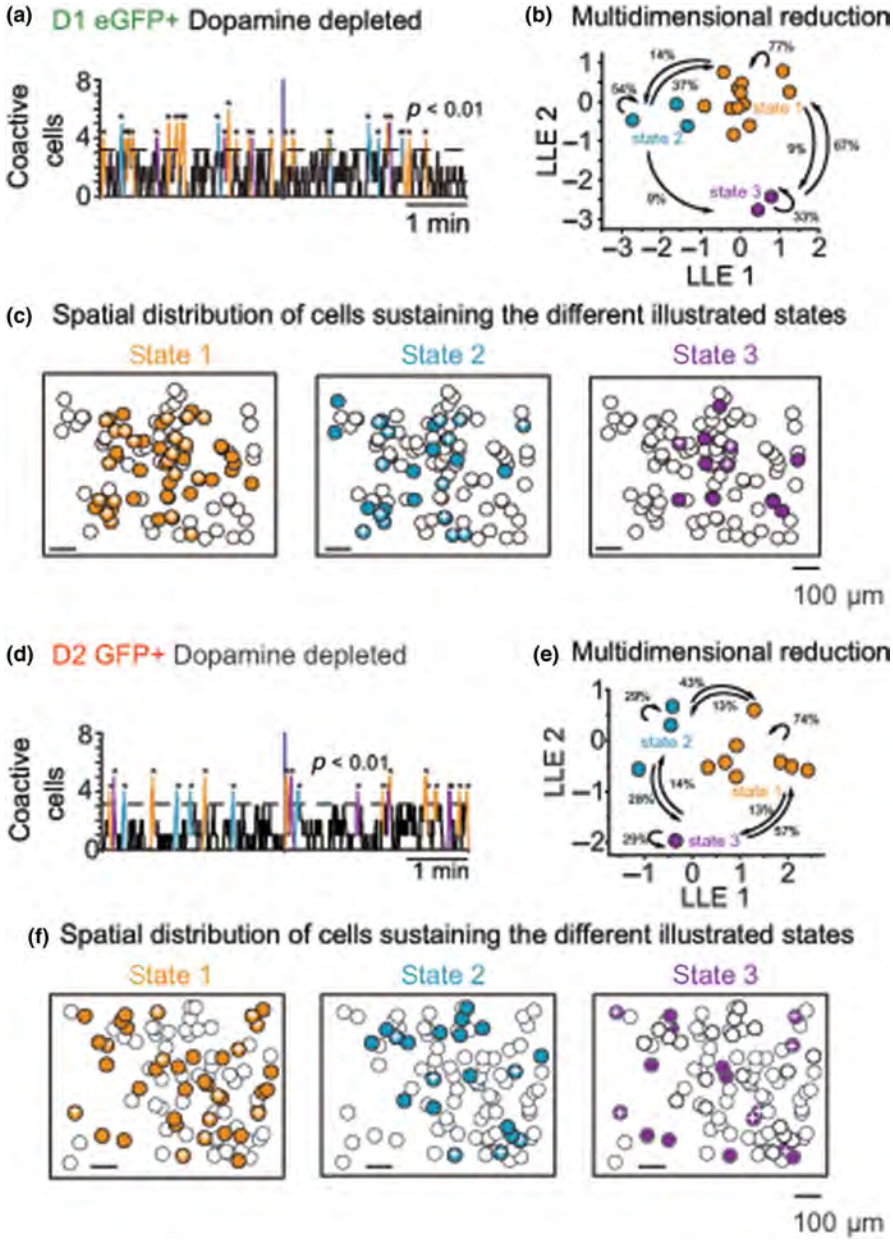

FIGURE 3 D1 or D2eGFP expressing neurons formed three sets that generated sequential activity states with one predominant set. (a and d) Analyses of coactive cells with significant peaks of synchrony (above the dotted line) also seen in Figure 1c were used for multidimensional reduction (see 2.7). (b and e). The network states reconstructed from the raster plots show that D1 or D2SPNs generate three sequential activity states (one color per state). The numbers indicate the percentage of transitions between states in the direction of the arrows. The "orange" state clearly dominates. (c and f). Superimposed onto the ROI or map of all observed active neurons, the spatial location of active SPNs can be observed for each one of the states. Colored circles represent active neurons that belong to the same state, circles with no color represent active neurons that do not belong to that particular state, and the plus sign inside the colored circles represents positive eGFPs, that is, represented as red green dots in the raster plots of Figure 1

Similarly, when the same tissue slices from 11 animals were activated with stimulation delivered at random either continuously or in patterned pulses, the total number of neurons activated by continuous stimulation was significantly larger ($M = 108$ active neurons, $SD = 32.63$, $n = 11$) than the number of neurons activated by patterned pulses ($M = 61.54$ active neurons, $SD = 29.65$, $n = 11$; paired t (20) $= 3.5$, $p = 0.005$, Figure 5d).

Since prolonged electrical stimulation often induces adaptation of SPN discharge (Kita, Kita, & Kitai, 1985) and strong (10–40 mW/mm^2) prolonged light activation of ChR-2 can silence instead of activating neurons by depolarization block, particularly interneurons (Herman, Huang, Murphey, Garcia, & Arenkiel, 2014), we first determined in vitro, the firing characteristics of our ChR2-RCaMP1h-expressing neurons by stimulating with 470 nm (blue light), 1.0 mW at the tip, for 30 s (see Section 3). A total of 14 SPNs ($n = 7$ for each D1 or D2 neurons) responded in similar proportions of activation/adaptation. During depolarization block assessment neurons were exposed to a continuous light pulse for 30 s, the duration of response of activated neurons before undergoing to depolarization block was: D1: $M = 17.5$ s, $SD = 6.38$, $n = 3$ and D2: $M = 18.25$s, $SD = 11.02$, $n = 4$. The other neurons continued firing for the whole exposure time. To our behaving animals stimulation at the same intensity (470 nm; 1.0 mW at the tip) for 15 s in two modes as reported by others, for example, (Jin et al., 2014; Kravitz et al., 2010): a single continuous 15s pulse or patterned pulses at 14 Hz (210 pulses of 6 ms each), all the experimental stimulations were therefore shorter than the average time to cease firing in both groups of

INFORME DE LABORES 2019

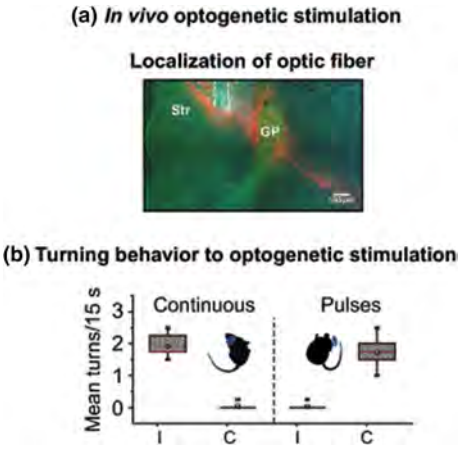

FIGURE 4 Photostimulation. (a) Photomicrograph illustrating the location of the stimulation optic fiber fixed in the dorsolateral striatum as delineated by dashed white line. (b) Box plots summarizing all behavioral sessions during optostimulation. With continuous light (15 s) (left) animals displayed turning behavior similar to 6-OHDA treated animals, that is, toward the side stimulated. With stimulation in patterned pulses (14 Hz) animals displayed turning behavior opposite to the stimulated side (right). Behavioral sessions lasted approximately 10–15 min divided as follows: a period of habituation (≈5 min) followed by three sequences repeated 10 times: 1–20 s pre-stimulation, 2–15 s of light stimulation either delivered continuously or in pulses and 3–30–60 s post-stimulation. As described in Section 2.3, a tracking system was used to automatically measure turning. A contour detection snapshot of a recorded mouse illustrates the deviated posture typical of an ipsilateral DA depletion, but in this case in an intact mouse during optogenetic stimulation

cells. Although depolarization block is likely induced in up to half the stimulated cells, the obtained pattern of activation of larger calcium transients was indication that most of the striatal cells were not blocked from firing impulses. The activation was clearly sufficient to induce behavioral changes, in vivo, suggesting that the cells excited did influence behavior and so a large recruitment of output neurons is the likeliest explanation of the outcome of the optogenetic stimulation.

We studied striatal responses from both direct and indirect pathway (D1eGFP and D2eGFP mice) from the same slices (Figure 6). Light stimulation induced synchronous activation in similar proportions, in both positive and negative eGFP neurons regardless of stimulation delivered continuously or in patterned pulses (D1–D2: range 47–54 synchronous neurons; one-way ANOVA $F(7,36) = 1.2$, $p = 0.32$, $n = 5,6$; Figure 5a–e), however, it is important to underline that continuous stimulation activated a larger number of both direct and indirect SPNs, whereas patterned pulsed stimulation recruited a smaller number of neurons (continuous D1–D2: $M = 54.0$, $SD = 27.8$, $n = 24$; $M = 82.6$, $SD = 28.47$, $n = 24$; patterned pulses D1–D2: $M = 19.79$, $SD = 10.13$, $n = 24$; $M = 26.3$, $SD = 11.43$, $n = 24$; one-way ANOVA $F(3,92) = 43.56$, $p \leq 0.0001$, $n = 24$; Figure 6a–d,f).

To visualize the differences in population activity evoked by continuous or patterned optogenetic stimulation we created similarity maps (Carrillo-Reid, Hernandez-Lopez, Tapia, Galarraga, & Bargas, 2011; Carrillo-Reid et al., 2008, 2009; Jaidar et al., 2010) (Figure 7a,b). We found that similarity index between synchronized neurons was significantly higher with continuous stimulation compared to responses following patterned pulses, in other words, continuous stimulation not only activates a larger population of neurons, but it has the tendency of recruit the same neurons across stimuli, whereas patterned pulses recruits fewer and more alternated neurons. Network dynamic between DA-depleted and pharmacological-activated striatal cell assemblies, were mimicked by the two forms of light stimulation. That is, pathologically engaged under continuous stimulation and flexible or alternating under patterned stimulation (continuous: $M = 0.52$, $SD = 0.19$ $n = 12$ mice; pulsed: $M = 0.4$, $SD = 0.23$ $n = 12$; paired $t(11) = 4.24$, $p < 0.001$; Figure 7c).

DA modulates short and long-term SPN function (Gerfen & Surmeier, 2011; Wickens, 2009), modulates its own release (Shen, Flajolet, Greengard, & Surmeier, 2008), presynaptically modulates GABA release at recurrent collateral synapses (Guzmaan et al., 2003; Tecuapetla, Carrillo-Reid, Bargas, & Galarraga, 2007; Tecuapetla, Koos, Tepper, Kabbani, & Yeckel, 2009), tonically inhibits D2-SPNs and possibly interneurons too all variables that affect SPN excitability. (Flores-Barrera, Vizcarra-Chacon, Tapia, Bargas, & Galarraga, 2010). However, in the unilateral absence of DA, striatal neurons increase their activity and animals display persistent spontaneous ipsilateral turning.

4 | DISCUSSION

Early studies of striatal cells after DA damage were unanimous in finding the striatal cells more active in anaesthetized animals for example (Arbuthnott, 1974; Hull et al., 1974; Ohye et al., 1970; Schultz, 1982; Schultz & Ungerstedt, 1978). Then came the formulation that made a clear prediction that in PD the direct pathway SPNs should be less active, whereas the indirect pathway SPNs were more active (Albin, Young, & Penney, 1989). This formulation had its origin in changes in genetic activity in the two groups of cells (Gerfen & Young, 1988; Gerfen et al., 1990). The idea was very powerful and led to new therapies including globus pallidus lesions (Laitinen, Bergenheim, & Hariz, 1992), then to subthalamic nucleus deep brain stimulation (Bergman, Wichmann, & DeLong, 1990) and thence to deep brain stimulation (Polack et al., 2007). However, there were difficulties in relating this success to the electrophysiology of individual cells of the two types once they became identifiable by transgenesis. Some laboratories did find differences in the expected direction (Flores-Barrera, Vizcarra-Chacon,

INFORME DE LABORES 2019

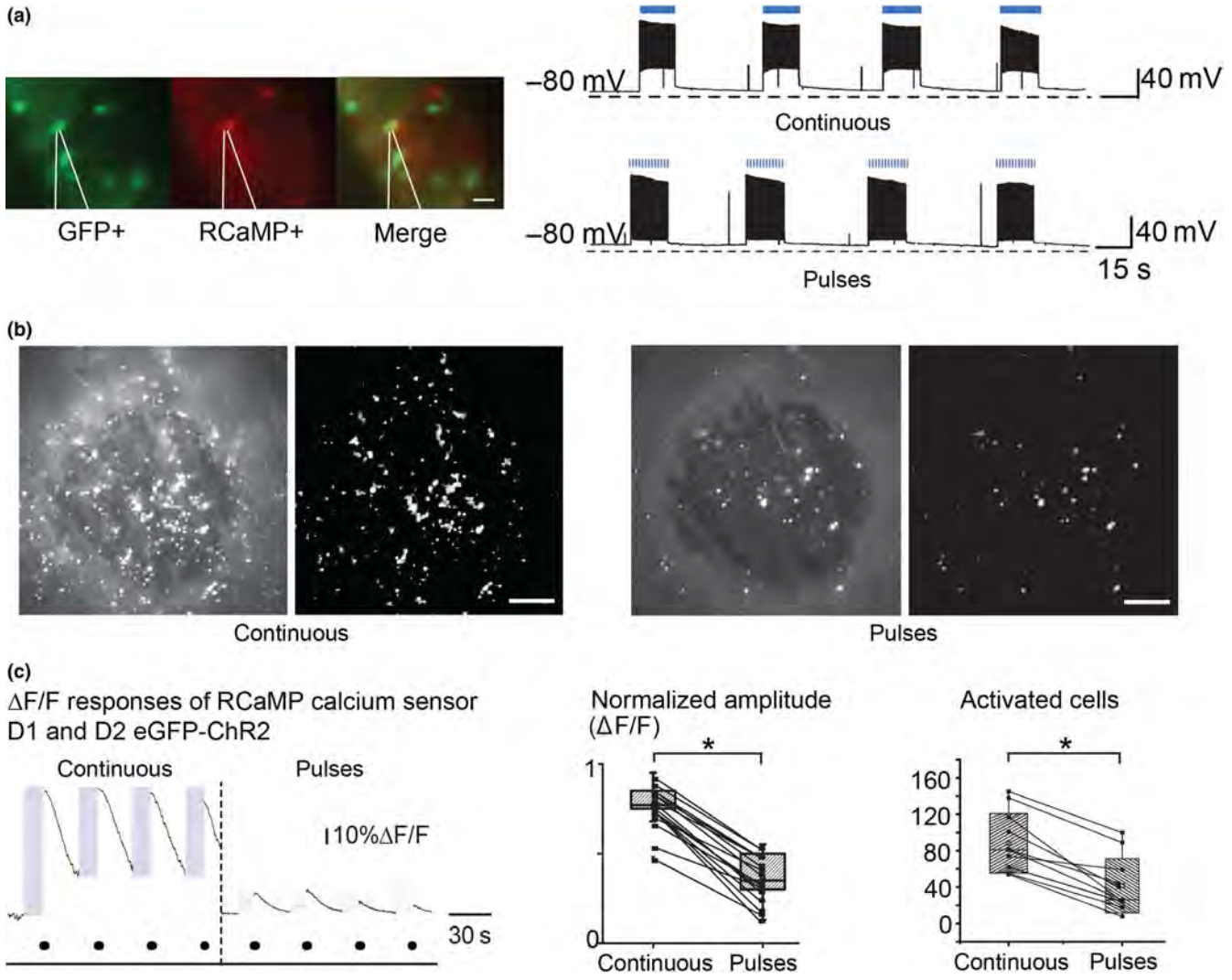

FIGURE 5 Comparison of responses to in vitro optogenetic stimulation delivered continuously or in patterned pulses. (a) Patch clamp recordings of SPNs expressing ChR2-RCaMP1 h show normal passive and active membrane properties to 15 s stimulation delivered continuously (top) or in pulses at 14 Hz (bottom). (b) Example of in vitro recorded neuronal response of calcium indicator (RCaMP1 hr) from ChR2-expressing SPNs with continuous (left) and pulsed (right) light stimulation. (c) Left and middle—Normalized amplitudes of calcium traces from cells activated by continuous stimulation were larger ($M = 0.77$, $SD = 0.12$, $n17$) than those produced by stimulation in patterned pulses ($M = 0.37$, $SD = 0.13$, $n = 17$); paired $t\,(16) = 16.22$, $p = 2.33504^{-11}$). Right— Total number of activated cells from same recorded fields during continuous ($M = 108$, $SD = 32.63$, $n = 11$) and stimulation in patterned pulses ($M = 61.54$, $SD = 29.65$, $n = 11$) paired $t\,(20) = 3.5$, $p = 0.00221$. Parameters of stimulation were: 15 s of LED of 470 nm blue light stimulation either delivered continuously or in patterned pulses (6 ms pulses at 14 Hz), with intensity at the tip of 1.0 mW

Bargas, Tapia, & Galarraga, 2011; Shen et al., 2008; Warre et al., 2011) but as the methodology became more sophisticated, the obvious interactions of both cell types with cortical activity and the beta power increase in the electrocorticogram, common in PD, has changed the emphasis from "faster or slower firing" to changes in the intrastriatal dynamics which result from the interactions of the many effects of DA removal on functional relationships within the striatal network (Cui et al., 2013; Klaus et al., 2017; Lindahl & Hellgren Kotaleski, 2016; Parker, Kim, Alberico, Emmons, & Narayanan, 2016; Parker et al., 2018; Perez-Ortega et al., 2016; da Silva, Tecuapetla, Paixao, & Costa, 2018).

Analyses of many cells at a time have revealed that such neuronal activation is characterized by an increased number of coactive neuronal discharges that involve both types of SPNs (Jaidar, Carrillo-Reid, & Bargas, 2012; Jaidar et al., 2010). Using calcium imaging in eGFP transgenic animals, we first confirmed the characteristics of SPN activity in the absence of DA, and revealed that both populations of SPNs equally participate in this abnormal microcircuit activity. In our in vitro recordings of spontaneous activity in DA deprived animals, both populations of D1 and D2 SPNs to some extent increased their activity. Therefore, although electrophysiological and anatomical evidence indicates that D2, but not

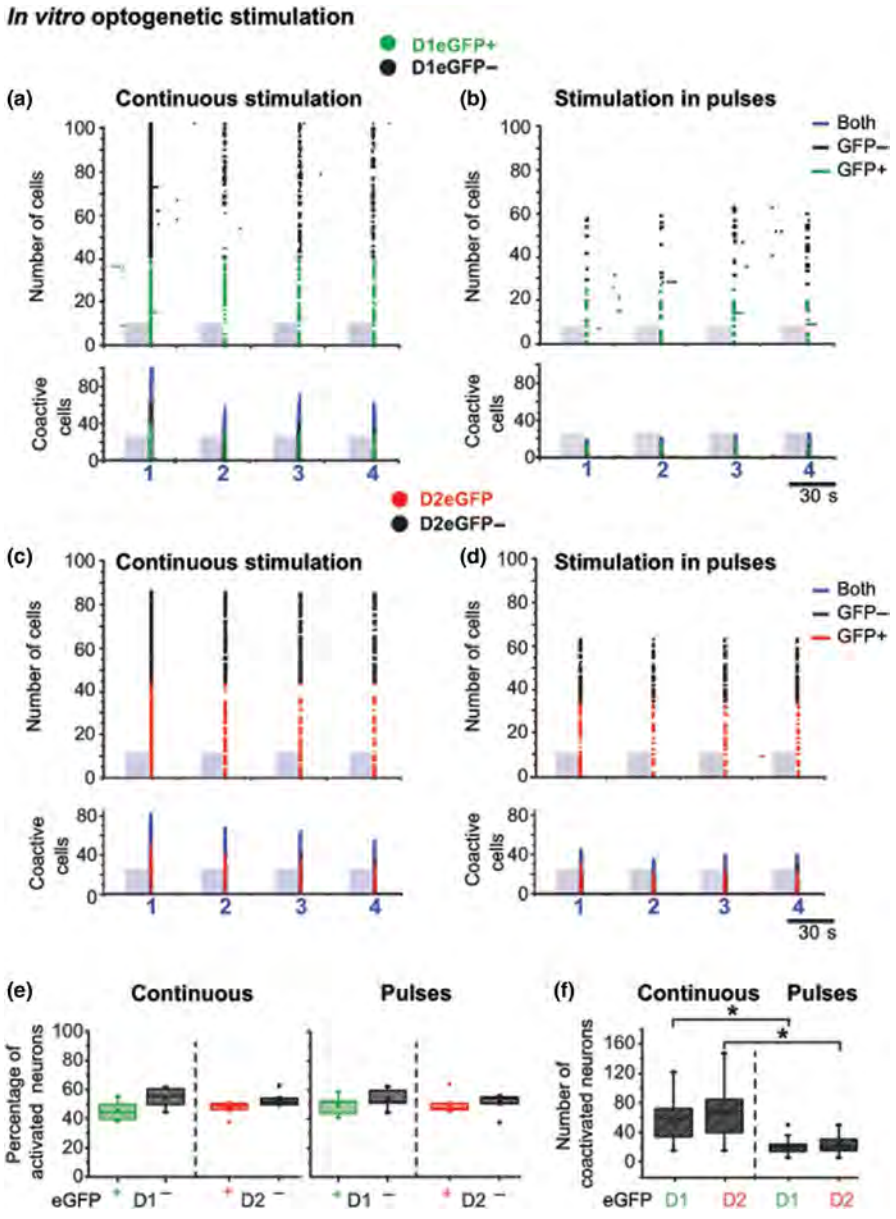

FIGURE 6 Comparison of SPN activity of synchronous striatal calcium signals induced by continuous and pulsed patterned optogenetic stimulation. Data are represented in sets of two graphs of striatal activity induced by a blue-light-emitting diode (470 nm;1.0 mW at the tip) delivered continuously for 15 s or in patterned pulses (14 Hz/15 s). Top traces: illustrate representative examples of raster plots of ChR2-induced SPN calcium activity reported by RCaMP1 hr. Bottom traces: illustrate histograms of number of coactivated neurons from continuous (a, c, and e left) or patterned pulsed stimulations (b, d, and e right). Blue rectangles represent the light stimulus artifact (see Figure 4a); colors representing individual active neurons and coactivity are, black: all eGFP negative; green: D1eGFP^{+}; red D2eGFP^{+}. (e) In spite of a differential neuronal activation induced by stimulation delivered continuously or in patterned pulses, the percentage of activated SPNs within groups of positive or negative D1 or D2eGFP neurons remains around 50%, as expected. No preferential neuronal activation was observed. (f) Total number of coactivated neurons from both D1 or D2 neurons with positive eGFP expression. Note that both cell types showed higher synchronization to optogenetic stimulation delivered continuously than in patterned pulses (one-way ANOVA $F(3,92) = 43.56$, $p \leq 0.0001$)

D1 neurons suffer a loss of dendritic spines (Day et al., 2006) but see (Suarez, Solis, Aguado, Lujan, & Moratalla, 2016) and an increase in excitability (Day, Wokosin, Plotkin, Tian, & Surmeier, 2008), in the absence of DA, perhaps the increase in excitability could somewhat compensate the loss of dendritic spines. A recent electrophysiological study in anesthetized rats by Sharott and collaborators claimed that only D2 cells were changed in firing rate but their laborious methodology meant a very small fraction of identified D1 cells in the lesioned animals ($n = 5$ in Figure 3 and $n = 8$ in figure 8) (Sharott, Vinciati, Nakamura, & Magill, 2017). Our method, although in vitro, samples at least 50 cells per slice of both genotypes, the calcium signals are not single action potentials like those of the electrophysiological studies but the likeliest

INFORME DE LABORES 2019

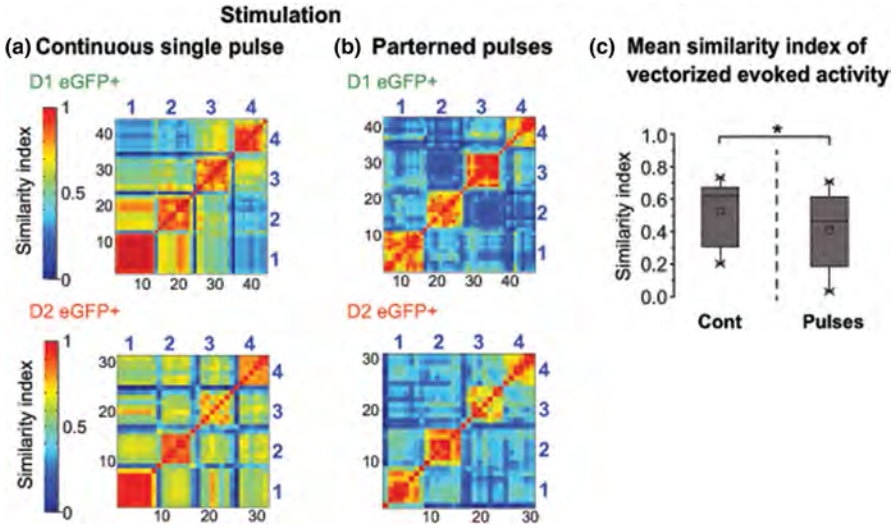

FIGURE 7 Analysis of network dynamics of D1 and D2 SPNs. The similarity index matrices of the stimulation induced by continuous (a) and stimulation in patterned pulses (b) show that continuous delivery of light activated sets of neurons with higher similarity index across stimulations, than stimulation delivered in patterned pulses. (c) Summary box plots to illustrate the significantly higher mean similarity index of vectorized activity observed with continuous versus patterned stimulation (paired $t\,(11) = 4.24$, $p < 0.001$, $n = 12$ mice). Black numbers: vector numbers; blue numbers: responses from one of the four stimulations

explanation for the transients we measure is a burst of at least three spikes (Carrillo-Reid et al., 2008). The synchronization of striatal cells is common to both studies, with the Sharott et al. (2017) having correlated the synchronous discharges of D2 cells with beta frequencies in the EEG in their anaesthetized animals; an effect we could not test in vitro. Parker et al. (2018) reported on calcium transients in freely moving animals with a miniature camera and implanted GRIN lens. Although they too see reductions in D1 cell activity, they also see a dislocation of the response of (particularly D2) cells to the initiation of movements after 6-OHDA injections. During normal movement both D1 and D2 cells are tuned to movements but the rate changes obliterate the movement relations in D2 cells. These different results reflect the within animal control that we lose in our ex vivo models, but we do find a similar disruption of patterned activity in "clusters" of cells that they report.

The effect of bilateral SPN activation using optogenetic techniques has been studied (Parker et al., 2016), but only a few have explored unilateral effects of SPN manipulations (Cui et al., 2013; Jin et al., 2014; Lee et al., 2016). We observed similar results following stimulation in patterned pulses. This suggests that stimulation in patterned pulses is sufficient to stimulate striatal SPNs of either type. Consistently, network analyses revealed that stimulation delivered in patterned pulses (14 Hz/15 s), compared to continuous stimulation, was less efficient in recruiting neurons, but obviously sufficient to induce contralateral turning. The smaller number of coactivated neurons by pulses (14 Hz) induced contralateral turning characteristic of tonic activation of striatal cell assemblies (Carrillo-Reid et al., 2008; Ossowska & Wolfarth, 1995). Reminiscent of the patterning of responses in striatal cells (independent of output class) observed in the awake mice (Parker et al., 2018). In contrast, from the analyses of network dynamics, it is clear that continuous stimulation induces a significantly higher similarity index compared to patterned stimulation, as also seen in dopamine-depleted rats (Jaidar et al., 2010).

Therefore, it seems plausible that continuous stimulation induces a dominant recurrent pattern of network activity sufficiently pronounced to induce ipsilateral turning like the spontaneous turning observed in DA-depleted animals. Such largely synchronous activity patterns would perhaps look "unstructured" if viewed with the small field of view in the in vivo camera, but in our study is obviously a very dispersed concurrent activation. *Pulsed* patterned stimulation could induce a restorative neuronal activity by recruiting fewer coactive neurons. This is a speculative functional relationship obtained from the observed in vitro neuronal network activation by the two stimulation parameters, that remains to be proven with in vivo recordings of neural networks, once technical advances allow such striatal recordings of hundreds of cells, without removal of the overlying cortical tissue.

The reasons for the differences in neuronal recruitment between patterned and continuous stimulation, although interesting, are not the focus of this paper; methodological aspects perhaps involving a ChR2-activated calcium conductance; reciprocal multisynaptic influences between direct and indirect SPNs and motor cortex (Burke et al., 2017; Freeze, Kravitz, Hammack, Berke, & Kreitzer, 2013; O'Hare et al., 2016; Oldenburg & Sabatini, 2015; Shipp, 2017), intrastriatal

INFORME DE LABORES 2019

influences on SPNs (Planert, Szydlowski, Hjorth, Grillner, & Silberberg, 2010; Taverna, Ilijic, & Surmeier, 2008) and or the participation of interneurons (Damodaran, Evans, & Blackwell, 2014; Dehorter et al., 2009) should be considered in further analyses. Modulation of neuronal assemblies by specific patterns of neuronal stimulation may represent a modified animal model to study the pathogenesis in basal ganglia.

Our purposes were to optogenetically activate selective groups containing both D1- and D2-eGFP-expressing neurons enough to induce the striatal network activity that presumably supports the spontaneous turning in dopamine-depleted animals. Therefore, it may be possible that the larger synchronization of the striatal circuit (via continuous stimulation) more closely reproduced the effects of DA depletion. Consequently, the abnormal turning observed in the 6-hydroxydopamine animal model of PD may result from the pathological striatal synchronous activity that follows DA depletion.

It may be meaningful that to reproduce the pathological state, strong neuronal activation is necessary. It is clear that the stronger continuous stimulation of both D1 and D2 SPNs was required to induce the ipsilateral turning, as it is also the case for the bilateral excitation of D2 SPNs to elicit parkinsonian bradykinesia (Kravitz et al., 2010). A robust inhibition and excitation of different subsets of substantia nigra reticulata neurons has been reported following bilateral striatal optogenetic stimulation of D1 or D2 SPNs, for 1,000 ms but not for 100 ms (Freeze et al., 2013).

Recently, in freely moving animals, it was reported that both SPN populations become active in localized compact groups of synchronized neurons, that alternate their activity over time (Barbera et al., 2016; Klaus et al., 2017; London et al., 2018), these results are similar to previous slice recordings treated with NMDA (Carrillo-Reid et al., 2008). In contrast, slices from DA-depleted animals report neuronal activity locked into a dominant network state with reduced alternations between the assemblies (Jaidar et al., 2010; Lopez-Huerta et al., 2013). Normal striatal motor control requires activation of both direct and indirect SPNs population in a "complementary" and "coordinate" network dynamic (Jin et al., 2014; Klaus et al., 2017; Tecuapetla, Jin, Lima, & Costa, 2016; Vicente, Galvao-Ferreira, Tecuapetla, & Costa, 2016). Very recent results from a modeling study suggest that for planned movements both output pathways need to be engaged (Bahuguna, Weidel, & Morrison, 2018).

We conclude that the concept of neural networks has provided neuroscientists with an important tool not only to study their properties and capabilities (Blaeser, Connors, & Nurmikko, 2017; Carrillo-Reid, Lopez-Huerta, Garcia-Munoz, Theiss, & Arbuthnott, 2015; Carrillo-Reid et al., 2009, 2011; Liu et al., 2011), but to activate different functional processes and the related behavior. Fear memories and freezing behavior have been induced by optically stimulating dentate gyrus neurons whose activity during passive avoidance was previously identified (Liu et al., 2012; Ramirez et al., 2013); for review see (Carrillo-Reid, Yang, Kang Miller, Peterka, & Yuste, 2017).

Here we have used neural network manipulation to demonstrate that: (a) DA depletion caused simultaneous activation of both types of identified D1 and D2 SPNs, (b) the contralateral turning behavior, characteristic of unilateral activated striatal neurons, was induced by patterned pulsed optogenetic stimulation of both types of SPNs, (c) ipsilateral turning behavior, as observed in DA-depleted animals, was induced in normal animals by continuous optogenetic stimulation that mimics the pathological microcircuit dynamics that accompany this animal model of PD. Our experiments confirm that large, unilateral and synchronous discharges of SPNs can simulate the ipsilateral turning model of PD in intact animals, and suggest that dopamine degeneration causes circling due to a similar large increase in unilateral SPNs discharge. The clinical relevance of this finding is supported by past studies using turning behavior as a model for PD. Resent results implicating glutamate receptors in the hyperexcitability of SPNs in monkeys (Singh et al., 2018) only add to the idea that this striatal pathological activity is close to the symptom development in PD.

ACKNOWLEDGMENTS

We thank Dr. Michael Lazarus University of Tsukuba, Ibaraki, 305-0006, Japan for the generous gifts AAV-10 ChR2-2mCherry, and Looger lab. and HHMI for the use of RCaMPh1.

CONFLICT OF INTEREST

There are no conflicts of interest.

DATA ACCESSIBILITY

All raw data are stored in the Information Technology section of the Okinawa Institute of Technology Graduate University, Japan and are available upon request to the corresponding author.

AUTHOR CONTRIBUTIONS

Although with particular predominant and stronger contributions, all authors complied with the criteria for authorship of the European Journal of Neurocience.

ORCID

José Bargas https://orcid.org/0000-0002-8205-8163
Gordon William Arbuthnott https://orcid.org/0000-0002-3386-8362

INFORME DE LABORES 2019

REFERENCES

Akerboom, J., Carreras Calderon, N., Tian, L., Wabnig, S., Prigge, M., Tolo, J., … Looger, L. L. (2013). Genetically encoded calcium indicators for multi-color neural activity imaging and combination with optogenetics. *Frontiers in Molecular Neuroscience*, *6*, 2.

Albin, R. L., Young, A. B., & Penney, J. B. (1989). The functional anatomy of basal ganglia disorders. *Trends in Neurosciences*, *12*, 366–375. https://doi.org/10.1016/0166-2236(89)90074-X

Arbuthnott, G. W. (1974). Spontaneous activity of single units in the striatum after unilateral destruction of the dopamine input. *Journal of Physiology*, *239*, 121P–122P.

Bahuguna, J., Weidel, P., & Morrison, A. (2018). Exploring the role of striatal D1 and D2 medium spiny neurons in action selection using a virtual robotic framework. *The European Journal of Neuroscience*. https://doi.org/10.1111/ejn.14021

Barbera, G., Liang, B., Zhang, L., Gerfen, Charles R., Culurciello, E., Chen, R., … Lin, D.-T. (2016). Spatially compact neural clusters in the dorsal striatum encode locomotion relevant information. *Neuron*, *92*, 1–12.

Bergman, H., Wichmann, T., & DeLong, M. R. (1990). Reversal of experimental parkinsonism by lesions of the subthalamic nucleus. *Science*, *249*, 1436–1438. https://doi.org/10.1126/science.2402638

Bergman, H., Wichmann, T., Karmon, B., & DeLong, M. R. (1994). The primate subthalamic nucleus. II. Neuronal activity in the MPTP model of parkinsonism. *Journal of Neurophysiology*, *72*, 507–520. https://doi.org/10.1152/jn.1994.72.2.507

Bezdek, J. C., & Pal, N. R. (1998). Some new indexes of cluster validity. *IEEE Transactions on Systems, Man, and Cybernetics. Part B, Cybernetics*, *28*, 301–315. https://doi.org/10.1109/3477.678624

Blaeser, A. S., Connors, B. W., & Nurmikko, A. V. (2017). Spontaneous dynamics of neural networks in deep layers of prefrontal cortex. *Journal of Neurophysiology*, *117*, 1581–1594. https://doi.org/10.1152/jn.00295.2016

Brown, S. L., Joseph, J., & Stopfer, M. (2005). Encoding a temporally structured stimulus with a temporally structured neural representation. *Nature Neuroscience*, *8*, 1568–1576. https://doi.org/10.1038/nn1559

Burke, D. A., Rotstein, H. G., & Alvarez, V. A. (2017). Striatal local circuitry: A new framework for lateral inhibition. *Neuron*, *96*, 267–284. https://doi.org/10.1016/j.neuron.2017.09.019

Burkhardt, J. M., Jin, X., & Costa, R. M. (2009). Dissociable effects of dopamine on neuronal firing rate and synchrony in the dorsal striatum. *Frontiers in Integrative Neuroscience*, *3*, 28.

Calabresi, P., Mercuri, N. B., Sancesario, G., & Bernardi, G. (1993). Electrophysiology of dopamine-denervated striatal neurons. Implications for Parkinson's disease. *Brain*, *116*, 433–452.

Carrillo-Reid, L., Hernandez-Lopez, S., Tapia, D., Galarraga, E., & Bargas, J. (2011). Dopaminergic modulation of the striatal microcircuit: Receptor-specific configuration of cell assemblies. *Journal of Neuroscience*, *31*, 14972–14983. https://doi.org/10.1523/JNEUROSCI.3226-11.2011

Carrillo-Reid, L., Lopez-Huerta, V. G., Garcia-Munoz, M., Theiss, S., & Arbuthnott, G. W. (2015). Cell assembly signatures defined by short-term synaptic plasticity in cortical networks. *International Journal of Neural Systems*, *25*, 1550018–1550021.

Carrillo-Reid, L., Tecuapetla, F., Ibanez-Sandoval, O., Hernandez-Cruz, A., Galarraga, E., & Bargas, J. (2009). Activation of the cholinergic system endows compositional properties to striatal cell assemblies. *Journal of Neurophysiology*, *101*, 737–749. https://doi.org/10.1152/jn.90975.2008

Carrillo-Reid, L., Tecuapetla, F., Tapia, D., Hernandez-Cruz, A., Galarraga, E., Drucker-Colin, R., & Bargas, J. (2008). Encoding network states by striatal cell assemblies. *Journal of Neurophysiology*, *99*, 1435–1450. https://doi.org/10.1152/jn.01131.2007

Carrillo-Reid, L., Yang, W., Kang Miller, J. E., Peterka, D. S., & Yuste, R. (2017). Imaging and optically manipulating neuronal ensembles. *Annual Review of Biophysics*, *46*, 271–293. https://doi.org/10.1146/annurev-biophys-070816-033647

Chen, M. T., Morales, M., Woodward, D. J., Hoffer, B. J., & Janak, P. H. (2001). In vivo extracellular recording of striatal neurons in the awake rat following unilateral 6-hydroxydopamine lesions. *Experimental Neurology*, *171*, 72–83. https://doi.org/10.1006/exnr.2001.7730

Cossart, R., Aronov, D., & Yuste, R. (2003). Attractor dynamics of network UP states in the neocortex. *Nature*, *423*, 283–288. https://doi.org/10.1038/nature01614

Costall, B., Marsden, C. D., Naylor, R. J., & Pycock, C. J. (1976). The relationship between striatal and mesolimbic dopamine dysfunction and the nature of circling responses following 6-hydroxydopamine and electrolytic lesions of the ascending dopamine systems of rat brain. *Brain Research*, *118*, 87–113. https://doi.org/10.1016/0006-8993(76)90843-X

Cui, G., Jun, S. B., Jin, X., Pham, M. D., Vogel, S. S., Lovinger, D. M., & Costa, R. M. (2013). Concurrent activation of striatal direct and indirect pathways during action initiation. *Nature*, *494*, 238–242. https://doi.org/10.1038/nature11846

Damodaran, S., Evans, R. C., & Blackwell, K. T. (2014). Synchronized firing of fast-spiking interneurons is critical to maintain balanced firing between direct and indirect pathway neurons of the striatum. *Journal of Neurophysiology*, *111*, 836–848. https://doi.org/10.1152/jn.00382.2013

da Silva, J. A., Tecuapetla, F., Paixao, V., & Costa, R. M. (2018). Dopamine neuron activity before action initiation gates and invigorates future movements. *Nature*, *554*, 244–248. https://doi.org/10.1038/nature25457

Day, M., Wang, Z., Ding, J., An, X., Ingham, C. A., Shering, A. F., … Surmeier, D. J. (2006). Selective elimination of glutamatergic synapses on striatopallidal neurons in Parkinson disease models. *Nature Neuroscience*, *9*, 251–259. https://doi.org/10.1038/nn1632

Day, M., Wokosin, D., Plotkin, J. L., Tian, X., & Surmeier, D. J. (2008). Differential excitability and modulation of striatal medium spiny neuron dendrites. *Journal of Neuroscience*, *28*, 11603–11614. https://doi.org/10.1523/JNEUROSCI.1840-08.2008

Dehorter, N., Guigoni, C., Lopez, C., Hirsch, J., Eusebio, A., Ben-Ari, Y., & Hammond, C. (2009). Dopamine-deprived striatal GABAergic interneurons burst and generate repetitive gigantic IPSCs in medium spiny neurons. *Journal of Neuroscience*, *29*, 7776–7787. https://doi.org/10.1523/JNEUROSCI.1527-09.2009

Dunnett, S. B., & Iversen, S. D. (1982). Spontaneous and drug-induced rotation following localized 6-hydroxydopamine and kainic acid-induced lesions of the neostriatum. *Neuropharmacology*, *21*, 899–908. https://doi.org/10.1016/0028-3908(82)90082-X

Flores-Barrera, E., Vizcarra-Chacon, B. J., Bargas, J., Tapia, D., & Galarraga, E. (2011). Dopaminergic modulation of corticostriatal responses in medium spiny projection neurons from direct and indirect pathways. *Frontiers in Systems Neuroscience*, *5*, 15.

Flores-Barrera, E., Vizcarra-Chacon, B. J., Tapia, D., Bargas, J., & Galarraga, E. (2010). Different corticostriatal integration in spiny projection neurons from direct and indirect pathways. *Frontiers in Systems Neuroscience*, *4*, 15.

Franklin, K. B. J., & Paxinos, G. (2008). *The mouse brain in stereotaxic coordinates*. New York, NY: Elsevier.

Freeze, B. S., Kravitz, A. V., Hammack, N., Berke, J. D., & Kreitzer, A. C. (2013). Control of basal ganglia output by direct and indirect pathway projection neurons. *Journal of Neuroscience*, *33*, 18531–18539. https://doi.org/10.1523/JNEUROSCI.1278-13.2013

Galarraga, E., Bargas, J., Martinez-Fong, D., & Aceves, J. (1987). Spontaneous synaptic potentials in dopamine-denervated neostriatal neurons. *Neuroscience Letters*, *81*, 351–355. https://doi.org/10.1016/0304-3940(87)90409-5

Gerfen, C. R., Engber, T. M., Mahan, L. C., Susel, Z., Chase, T. N., Monsma, F. J. Jr, & Sibley, D. R. (1990). D1 and D2 dopamine receptor-regulated gene expression of striatonigral and striatopallidal neurons. *Science*, *250*, 1429–1432. https://doi.org/10.1126/science.2147780

Gerfen, C. R., & Surmeier, D. J. (2011). Modulation of striatal projection systems by dopamine. *Annual Review of Neuroscience*, *34*, 441–466. https://doi.org/10.1146/annurev-neuro-061010-113641

Gerfen, C. R., & Young, W. S. 3rd (1988). Distribution of striatonigral and striatopallidal peptidergic neurons in both patch and matrix compartments: An in situ hybridization histochemistry and fluorescent retrograde tracing study. *Brain Research*, *460*, 161–167. https://doi.org/10.1016/0006-8993(88)91217-6

Glock, C., Nagpal, J., & Gottschalk, A. (2015). Microbial Rhodopsin Optogenetic Tools: Application for analyses of synaptic transmission and of neuronal network activity in behavior. *Methods in Molecular Biology*, *1327*, 87–103. https://doi.org/10.1007/978-1-4939-2842-2

Greco, R., Tassorelli, C., Armentero, M. T., Sandrini, G., Nappi, G., & Blandini, F. (2008). Role of central dopaminergic circuitry in pain processing and nitroglycerin-induced hyperalgesia. *Brain Research*, *1238*, 215–223. https://doi.org/10.1016/j.brainres.2008.08.022

Guzmaan, J. N., Hernandez, A., Galarraga, E., Tapia, D., Laville, A., Vergara, R., … Bargas, J. (2003). Dopaminergic modulation of axon collaterals interconnecting spiny neurons of the rat striatum. *Journal of Neuroscience*, *23*, 8931–8940. https://doi.org/10.1523/JNEUROSCI.23-26-08931.2003

Herman, A. M., Huang, L., Murphey, D. K., Garcia, I., & Arenkiel, B. R. (2014). Cell type-specific and time-dependent light exposure contribute to silencing in neurons expressing Channelrhodopsin-2. *Elife*, *3*, e01481. https://doi.org/10.7554/eLife.01481

Hull, C. D., Levine, M. S., Buchwald, N. A., Heller, A., & Browning, R. A. (1974). The spontaneous firing pattern of forebrain neurons. I. The effects of dopamine and non-dopamine depleting lesions on caudate unit firing patterns. *Brain Research*, *73*, 241–262. https://doi.org/10.1016/0006-8993(74)91047-6

Jaidar, O., Carrillo-Reid, L., & Bargas, J. (2012). Comparison of normal and Parkinsonian microcircuit dynamics in the rodent striatum, mechanisms in Parkinson's disease – Models and treatments. In J. Dushanova (Ed.), *Mechanisms in Parkinson's disease- models and treatments*. London, UK: InTech.

Jaidar, O., Carrillo-Reid, L., Hernandez, A., Drucker-Colin, R., Bargas, J., & Hernandez-Cruz, A. (2010). Dynamics of the Parkinsonian striatal microcircuit: Entrainment into a dominant network state. *Journal of Neuroscience*, *30*, 11326–11336. https://doi.org/10.1523/JNEUROSCI.1380-10.2010

Jin, X., Tecuapetla, F., & Costa, R. M. (2014). Basal ganglia subcircuits distinctively encode the parsing and concatenation of action sequences. *Nature Neuroscience*, *17*, 423–430. https://doi.org/10.1038/nn.3632

Kish, L. J., Palmer, M. R., & Gerhardt, G. A. (1999). Multiple single-unit recordings in the striatum of freely moving animals: Effects of apomorphine and D-amphetamine in normal and unilateral 6-hydroxydopamine-lesioned rats. *Brain Research*, *833*, 58–70. https://doi.org/10.1016/S0006-8993(99)01496-1

Kita, H., Kita, T., & Kitai, S. T. (1985). Active membrane properties of rat neostriatal neurons in an in vitro slice preparation. *Experimental Brain Research. Experimentelle Hirnforschung*, *60*, 54–62.

Klaus, A., Martins, G. J., Paixao, V. B., Zhou, P., Paninski, L., & Costa, R. M. (2017). The spatiotemporal organization of the striatum encodes action space. *Neuron*, *95*(1171–1180), e1177.

Kravitz, A. V., Freeze, B. S., Parker, P. R., Kay, K., Thwin, M. T., Deisseroth, K., & Kreitzer, A. C. (2010). Regulation of Parkinsonian motor behaviours by optogenetic control of basal ganglia circuitry. *Nature*, *466*, 622–626. https://doi.org/10.1038/nature09159

Laitinen, L. V., Bergenheim, A. T., & Hariz, M. I. (1992). Leksell's posteroventral pallidotomy in the treatment of Parkinson's disease. *Journal of Neurosurgery*, *76*, 53–61. https://doi.org/10.3171/jns.1992.76.1.0053

Lee, H. J., Weitz, A. J., Bernal-Casas, D., Duffy, B. A., Choy, M., Kravitz, A. V., … Lee, J. H. (2016). Activation of direct and indirect pathway medium spiny neurons drives distinct brain-wide responses. *Neuron*, *91*, 412–424. https://doi.org/10.1016/j.neuron.2016.06.010

Lindahl, M., & Hellgren Kotaleski, J. (2016). Untangling basal ganglia network dynamics and function: Role of dopamine depletion and inhibition investigated in a spiking network model. *eNeuro*, *3*. https://doi.org/10.1523/ENEURO.0156-16.2016

Liu, J., Khalil, H. K., & Oweiss, K. G. (2011). Model-based analysis and control of a network of basal ganglia spiking neurons in the normal and Parkinsonian states. *Journal of Neural Engineering*, *8*, 045002. https://doi.org/10.1088/1741-2560/8/4/045002

Liu, X., Ramirez, S., Pang, P. T., Puryear, C. B., Govindarajan, A., Deisseroth, K., & Tonegawa, S. (2012). Optogenetic stimulation of a hippocampal engram activates fear memory recall. *Nature*, *484*, 381–385.

London, T. D., Licholai, J. A., Szczot, I., Ali, M. A., LeBlanc, K. H., Fobbs, W. C., & Kravitz, A. V. (2018). Coordinated ramping of dorsal striatal pathways preceding food approach and consumption. *Journal of Neuroscience*, *38*, 3547–3558. https://doi.org/10.1523/JNEUROSCI.2693-17.2018

Lopez-Huerta, V. G., Carrillo-Reid, L., Galarraga, E., Tapia, D., Fiordelisio, T., Drucker-Colin, R., & Bargas, J. (2013). The balance of striatal feedback transmission is disrupted in a model of parkinsonism. *Journal of Neuroscience*, *33*, 4964–4975. https://doi.org/10.1523/JNEUROSCI.4721-12.2013

Lopez-Huerta, V. G., Nakano, Y., Bausenwein, J., Jaidar, O., Lazarus, M., Cherassse, Y., … Arbuthnott, G. (2016). The neostriatum: Two entities, one structure? *Brain Structure & Function*, *221*, 1737–1749. https://doi.org/10.1007/s00429-015-1000-4

MacLeod, N. K., Ryman, A., & Arbuthnott, G. W. (1990). Electrophysiological properties of nigrothalamic neurons after 6-hydroxydopamine lesions in the rat. *Neuroscience*, *38*, 447–456. https://doi.org/10.1016/0306-4522(90)90041-2

Mao, B. Q., Hamzei-Sichani, F., Aronov, D., Froemke, R. C., & Yuste, R. (2001). Dynamics of spontaneous activity in

INFORME DE LABORES 2019

neocortical slices. *Neuron*, *32*, 883–898. https://doi.org/10.1016/S0896-6273(01)00518-9

Miller, J. E., Ayzenshtat, I., Carrillo-Reid, L., & Yuste, R. (2014). Visual stimuli recruit intrinsically generated cortical ensembles. *Proceedings of the National Academy of Sciences of the United States of America*, *111*, E4053–E4061. https://doi.org/10.1073/pnas.1406077111

Murer, M. G., Riquelme, L. A., Tseng, K. Y., & Pazo, J. H. (1997). Substantia nigra pars reticulata single unit activity in normal and 60HDA-lesioned rats: Effects of intrastriatal apomorphine and subthalamic lesions. *Synapse*, *27*, 278–293. https://doi.org/10.1002/(ISSN)1098-2396

Murer, M. G., Tseng, K. Y., Kasanetz, F., Belluscio, M., & Riquelme, L. A. (2002). Brain oscillations, medium spiny neurons, and dopamine. *Cellular and Molecular Neurobiology*, *22*, 611–632. https://doi.org/10.1023/A:1021840504342

Ni, Z., Bouali-Benazzouz, R., Gao, D., Benabid, A. L., & Benazzouz, A. (2000). Changes in the firing pattern of globus pallidus neurons after the degeneration of nigrostriatal pathway are mediated by the subthalamic nucleus in the rat. *The European Journal of Neuroscience*, *12*, 4338–4344.

Nicola, S. M., Surmeier, J., & Malenka, R. C. (2000). Dopaminergic modulation of neuronal excitability in the striatum and nucleus accumbens. *Annual Review of Neuroscience*, *23*, 185–215. https://doi.org/10.1146/annurev.neuro.23.1.185

Nini, A., Feingold, A., Slovin, H., & Bergman, H. (1995). Neurons in the globus pallidus do not show correlated activity in the normal monkey, but phase-locked oscillations appear in the MPTP model of parkinsonism. *Journal of Neurophysiology*, *74*, 1800–1805. https://doi.org/10.1152/jn.1995.74.4.1800

Nisenbaum, E. S., Stricker, E. M., Zigmond, M. J., & Berger, T. W. (1986). Long-term effects of dopamine-depleting brain lesions on spontaneous activity of type II striatal neurons: Relation to behavioral recovery. *Brain Research*, *398*, 221–230. https://doi.org/10.1016/0006-8993(86)91481-2

O'Donnell, P. (2003). Dopamine gating of forebrain neural ensembles. *The European Journal of Neuroscience*, *17*, 429–435. https://doi.org/10.1046/j.1460-9568.2003.02463.x

O'Hare, J. K., Ade, K. K., Sukharnikova, T., Van Hooser, S. D., Palmeri, M. L., Yin, H. H., & Calakos, N. (2016). Pathway-specific striatal substrates for habitual behavior. *Neuron*, *89*, 472–479. https://doi.org/10.1016/j.neuron.2015.12.032

Ohye, C., Bouchard, R., Boucher, R., & Poirier, L. J. (1970). Spontaneous activity of the putamen after chronic interruption of the dopaminergic pathway: Effect of L-dopa. *The Journal of Pharmacology and Experimental Therapeutics*, *175*, 700–708.

Oldenburg, I. A., & Sabatini, B. L. (2015). Antagonistic but not symmetric regulation of primary motor cortex by basal ganglia direct and indirect pathways. *Neuron*, *86*, 1174–1181. https://doi.org/10.1016/j.neuron.2015.05.008

Ossowska, K., & Wolfarth, S. (1995). Stimulation of glutamate receptors in the intermediate/caudal striatum induces contralateral turning. *European Journal of Pharmacology*, *273*, 89–97. https://doi.org/10.1016/0014-2999(94)00671-S

Pan, H. S., & Walters, J. R. (1988). Unilateral lesion of the nigrostriatal pathway decreases the firing rate and alters the firing pattern of globus pallidus neurons in the rat. *Synapse*, *2*, 650–656. https://doi.org/10.1002/(ISSN)1098-2396

Parker, K. L., Kim, Y., Alberico, S. L., Emmons, E. B., & Narayanan, N. S. (2016). Optogenetic approaches to evaluate striatal function in animal models of Parkinson disease. *Dialogues in Clinical Neuroscience*, *18*, 99–107.

Parker, J. G., Marshall, J. D., Ahanonu, B., Wu, Y. W., Kim, T. H., Grewe, B. F., … Schnitzer, M. J. (2018). Diametric neural ensemble dynamics in Parkinsonian and dyskinetic states. *Nature*, *557*, 177–182. https://doi.org/10.1038/s41586-018-0090-6

Perez-Ortega, J., Duhne, M., Lara-Gonzalez, E., Plata, V., Gasca, D., Galarraga, E., … Bargas, J. (2016). Pathophysiological signatures of functional connectomics in Parkinsonian and dyskinetic striatal microcircuits. *Neurobiology of Diseases*, *91*, 347–361. https://doi.org/10.1016/j.nbd.2016.02.023

Planert, H., Szydlowski, S. N., Hjorth, J. J., Grillner, S., & Silberberg, G. (2010). Dynamics of synaptic transmission between fast-spiking interneurons and striatal projection neurons of the direct and indirect pathways. *Journal of Neuroscience*, *30*, 3499–3507. https://doi.org/10.1523/JNEUROSCI.5139-09.2010

Polack, P. O., Guillemain, I., Hu, E., Deransart, C., Depaulis, A., & Charpier, S. (2007). Deep layer somatosensory cortical neurons initiate spike-and-wave discharges in a genetic model of absence seizures. *Journal of Neuroscience*, *27*, 6590–6599. https://doi.org/10.1523/JNEUROSCI.0753-07.2007

Ramirez, S., Liu, X., Lin, P. A., Suh, J., Pignatelli, M., Redondo, R. L., … Tonegawa, S. (2013). Creating a false memory in the hippocampus. *Science*, *341*, 387–391. https://doi.org/10.1126/science.1239073

Rohlfs, A., Nikkhah, G., Rosenthal, C., Rundfeldt, C., Brandis, A., Samii, M., & Loscher, W. (1997). Hemispheric asymmetries in spontaneous firing characteristics of substantia nigra pars reticulata neurons following a unilateral 6-hydroxydopamine lesion of the rat nigrostriatal pathway. *Brain Research*, *761*, 352–356. https://doi.org/10.1016/S0006-8993(97)00475-7

Roweis, S. T., & Saul, L. K. (2000). Nonlinear dimensionality reduction by locally linear embedding. *Science*, *290*, 2323–2326. https://doi.org/10.1126/science.290.5500.2323

Sanderson, P., Mavoungou, R., & Albe-Fessard, D. (1986). Changes in substantia nigra pars reticulata activity following lesions of the substantia nigra pars compacta. *Neuroscience Letters*, *67*, 25–30. https://doi.org/10.1016/0304-3940(86)90202-8

Sasaki, T., Kimura, R., Tsukamoto, M., Matsuki, N., & Ikegaya, Y. (2006). Integrative spike dynamics of rat CA1 neurons: A multineuronal imaging study. *Journal of Physiology*, *574*, 195–208. https://doi.org/10.1113/jphysiol.2006.108480

Sasaki, T., Matsuki, N., & Ikegaya, Y. (2007). Metastability of active CA3 networks. *Journal of Neuroscience*, *27*, 517–528. https://doi.org/10.1523/JNEUROSCI.4514-06.2007

Schreiber, S., Fellous, J. M., Whitmer, D., Tiesinga, P., & Sejnowski, T. J. (2003). A new correlation-based measure of spike timing reliability. *Neurocomputing*, *52–54*, 925–931. https://doi.org/10.1016/S0925-2312(02)00838-X

Schultz, W. (1982). Depletion of dopamine in the striatum as an experimental model of Parkinsonism: Direct effects and adaptive mechanisms. *Progress in Neurobiology*, *18*, 121–166. https://doi.org/10.1016/0301-0082(82)90015-6

Schultz, W., & Ungerstedt, U. (1978). Short-term increase and long-term reversion of striatal cell activity after degeneration of the nigrostriatal dopamine system. *Experimental Brain Research. Experimentelle Hirnforschung*, *33*, 159–171.

INFORME DE LABORES 2019

Schwartz, T. H., Rabinowitz, D., Unni, V., Kumar, V. S., Smetters, D. K., Tsiola, A., & Yuste, R. (1998). Networks of coactive neurons in developing layer 1. *Neuron*, *20*, 541–552. https://doi.org/10.1016/S0896-6273(00)80993-9

Sharott, A., Vinciati, F., Nakamura, K. C., & Magill, P. J. (2017). A population of indirect pathway striatal projection neurons is selectively entrained to parkinsonian beta oscillations. *Journal of Neuroscience*, *37*, 9977–9998. https://doi.org/10.1523/JNEUROSCI.0658-17.2017

Shen, W., Flajolet, M., Greengard, P., & Surmeier, D. J. (2008). Dichotomous dopaminergic control of striatal synaptic plasticity. *Science*, *321*, 848–851. https://doi.org/10.1126/science.1160575

Shipp, S. (2017). The functional logic of corticostriatal connections. *Brain Structure & Function*, *222*, 669–706. https://doi.org/10.1007/s00429-016-1250-9

Singh, A., Jenkins, M. A., Burke, K. J. Jr, Beck, G., Jenkins, A., Scimemi, A., … Papa, S. M. (2018). Glutamatergic tuning of hyperactive striatal projection neurons controls the motor response to dopamine replacement in Parkinsonian primates. *Cell Reports*, *22*, 941–952. https://doi.org/10.1016/j.celrep.2017.12.095

Suarez, L. M., Solis, O., Aguado, C., Lujan, R., & Moratalla, R. (2016). L-DOPA oppositely regulates synaptic strength and spine morphology in D1 and D2 striatal projection neurons in dyskinesia. *Cerebral Cortex*, *26*, 4253–4264. https://doi.org/10.1093/cercor/bhw263

Taverna, S., Ilijic, E., & Surmeier, D. J. (2008). Recurrent collateral connections of striatal medium spiny neurons are disrupted in models of Parkinson's disease. *Journal of Neuroscience*, *28*, 5504–5512. https://doi.org/10.1523/JNEUROSCI.5493-07.2008

Tecuapetla, F., Carrillo-Reid, L., Bargas, J., & Galarraga, E. (2007). Dopaminergic modulation of short-term synaptic plasticity at striatal inhibitory synapses. *Proceedings of the National Academy of Sciences of the United States of America*, *104*, 10258–10263. https://doi.org/10.1073/pnas.0703813104

Tecuapetla, F., Jin, X., Lima, S. Q., & Costa, R. M. (2016). Complementary contributions of striatal projection pathways to action initiation and execution. *Cell*, *166*, 703–715. https://doi.org/10.1016/j.cell.2016.06.032

Tecuapetla, F., Koos, T., Tepper, J. M., Kabbani, N., & Yeckel, M. F. (2009). Differential dopaminergic modulation of neostriatal synaptic connections of striatopallidal axon collaterals. *Journal of Neuroscience*, *29*, 8977–8990. https://doi.org/10.1523/JNEUROSCI.6145-08.2009

Ungerstedt, U., & Arbuthnott, G. W. (1970). Quantitative recording of rotational behavior in rats after 6-hydroxy-dopamine lesions of the nigrostriatal dopamine system. *Brain Research*, *24*, 485–493. https://doi.org/10.1016/0006-8993(70)90187-3

Vicente, A. M., Galvao-Ferreira, P., Tecuapetla, F., & Costa, R. M. (2016). Direct and indirect dorsolateral striatum pathways reinforce different action strategies. *Current Biology*, *26*, R267–R269. https://doi.org/10.1016/j.cub.2016.02.036

Warre, R., Thiele, S., Talwar, S., Kamal, M., Johnston, T. H., Wang, S., … Nash, J. E. (2011). Altered function of glutamatergic corticostriatal synapses causes output pathway abnormalities in a chronic model of parkinsonism. *Neurobiology of Diseases*, *41*, 591–604. https://doi.org/10.1016/j.nbd.2010.10.013

Wichmann, T., Bergman, H., Starr, P. A., Subramanian, T., Watts, R. L., & DeLong, M. R. (1999). Comparison of MPTP-induced changes in spontaneous neuronal discharge in the internal pallidal segment and in the substantia nigra pars reticulata in primates. *Experimental Brain Research. Experimentelle Hirnforschung*, *125*, 397–409. https://doi.org/10.1007/s002210050696

Wickens, J. R. (2009). Synaptic plasticity in the basal ganglia. *Behavioural Brain Research*, *199*, 119–128. https://doi.org/10.1016/j.bbr.2008.10.030

SUPPORTING INFORMATION

Additional supporting information may be found online in the Supporting Information section at the end of the article.

How to cite this article: Jáidar O, Carrillo-Reid L, Nakano Y, et al. Synchronized activation of striatal direct and indirect pathways underlies the behavior in unilateral dopamine-depleted mice. *Eur J Neurosci*. 2019;49:1512–1528. https://doi.org/10.1111/ejn.14344

INFORME DE LABORES 2019



Plant Signaling & Behavior

ISSN: (Print) 1559-2324 (Online) Journal homepage: https://www.tandfonline.com/loi/kpsb20

Emerging roles of tetraspanins in plant inter-cellular and inter-kingdom communication

Saul Jimenez-Jimenez, Kenji Hashimoto, Olivia Santana, Jesús Aguirre, Kazuyuki Kuchitsu & Luis Cárdenas

To cite this article: Saul Jimenez-Jimenez, Kenji Hashimoto, Olivia Santana, Jesús Aguirre, Kazuyuki Kuchitsu & Luis Cárdenas (2019) Emerging roles of tetraspanins in plant inter-cellular and inter-kingdom communication, Plant Signaling & Behavior, 14:4, e1581559, DOI: 10.1080/15592324.2019.1581559

To link to this article: https://doi.org/10.1080/15592324.2019.1581559

Published online: 04 Mar 2019.

Submit your article to this journal

Article views: 904

View related articles

View Crossmark data

Citing articles: 3 View citing articles

Full Terms & Conditions of access and use can be found at
https://www.tandfonline.com/action/journalInformation?journalCode=kpsb20

PLANT SIGNALING & BEHAVIOR
2019, VOL. 14, NO. 4, e1581559 (11 pages)
https://doi.org/10.1080/15592324.2019.1581559

Taylor & Francis
Taylor & Francis Group

REVIEW

Check for updates

Emerging roles of tetraspanins in plant inter-cellular and inter-kingdom communication

Saul Jimenez-Jimenez[a], Kenji Hashimoto[b], Olivia Santana [a], Jesús Aguirre [c], Kazuyuki Kuchitsu [b], and Luis Cárdenas[a]

[a]Departamento de Biología Molecular de Plantas, Instituto de Biotecnología, Universidad Nacional Autónoma de México, Cuernavaca, México; [b]Department of Applied Biological Science, Tokyo University of Science, Noda, Japan; [c]Instituto de Fisiología Celular, Universidad Nacional Autónoma de México, Ciudad de México

ABSTRACT

Inter-cellular and inter-kingdom signaling systems of various levels of complexity regulate pathogenic and mutualistic interactions between bacteria, parasites, and fungi and animal and plant hosts. Inter-kingdom interactions between mutualistic bacteria such as rhizobia and legumes during nodulation and between fungi and plants during mycorrhizal associations, are characterized by the extensive exchange of molecular signals, which allow nitrogen and phosphate assimilation, respectively. A novel aspect of this signaling exchange is the existence of specific structures, the exosomes, that carry important molecules that shape the plant–pathogen interactions. Exosomes contain a wide array of molecules, such as lipids, proteins, messenger RNA, and microRNAs, that play important roles in cell-to-cell communication in animal and plant cells by affecting gene expression and other physiological activity in distant cells within the same organism (e.g., during cancer metastases and neuron injuries). In plant cells, it has been recently reported that exosomes go beyond organism boundaries and inhibit a pathogenic interaction in plants. Plant produce and send exosomes loaded with specific small miRNA which inhibit the pathogen infection, but the pathogen can also produce exosomes carrying pro-pathogenic proteins and microRNAs. Therefore, exosomes are the important bridge regulating the signal exchange. Exosomes are small membrane-bound vesicles derived from multivesicular bodies (MVBs), which carries selected cargos from the cytoplasm (protein, lipids, and microRNAs) and under certain circumstances, they fuse with the plasma membrane, releasing the small vesicles as cargo-carrying exosomes into the extracellular space during intercellular and inter-kingdom communication. Animal and plant proteomic studies have demonstrated that tetraspanin proteins are an integral part of exosome membranes, positioning tetraspanins as essential components for endosome organization, with key roles in membrane fusion, cell trafficking, and membrane recognition. We discuss the similarities and differences between animal tetraspanins and plant tetraspanins formed during plant–microbe interactions and their potential role in mutualistic communication.

ARTICLE HISTORY
Received 7 January 2019
Revised 28 January 2019
Accepted 1 February 2019

KEYWORDS
Tetraspanin; exosomes; plant-microbe interaction; multivesicular bodies; nodulation; mycorrhization

Introduction

The multiple functions of tetraspanins

Tetraspanins constitute a diverse superfamily of transmembrane proteins, with 33 members identified in mammals and 17 in the model plant *Arabidopsis thaliana*. Although tetraspanin homologues have not yet been reported in yeast, bacteria, and archae, they are ubiquitous in eukaryotic cells and the first member of this family likely appeared around 570 million years ago.[1,2] Several tetraspanin isoforms exist in deuterostomata, including fruitfly (*Drosophila melanogaster*), zebrafish (*Danio rerio*), and humans.[3–5] Tetraspanins are involved in basic cell functions such as motility, fusion, and membrane and vesicular trafficking, and play key roles in diverse physiological processes including sperm–egg fusion, antigen presentation, and tissue differentiation.[2,6–8] While knockout of the tetraspanins CD9- and CD81 in mice (*Mus musculus*) results in a clear defect in egg–sperm fusion, other tetraspanins are involved in virus and parasite interactions.[2,6–10] More recently it has been reported that a single point mutation, L31S substitution in the third amino acid of TM1 has been associated with field-evolved resistance of cotton bollworm to transgenic Bt cotton.[11]Tetraspanins also regulate cellular invasiveness or metastases through associating with peptidases, matrix metalloproteinases, and urokinase plasminogen activator surface receptors in animal cells.[12] In animals and plants, some tetraspanins have a broad tissue distribution, while others show a restricted expression; for instance, in plant cells, different tetraspanins are expressed in specialized tissues such as the reproductive tissue and meristems, during embryo development, and in specific cell niches, such as the quiescent center or the early initial cells that give rise to lateral roots.[13–15]

Tetraspanins appear to act as molecular organizers by forming homo- or heterodimers that localize to microdomains known as tetraspanin-enriched microdomains (TEMs). As components of TEMs, both animal and plant tetraspanins maintain a network of interactions with other membrane proteins, such as integrins, and signaling molecules, such as receptors, allowing the assembly of multi-molecular signaling platforms.[12] Therefore, tetraspanins are dynamic master organizers within membranes that control the

CONTACT Luis Cárdenas luisc@ibt.unam.mx Departamento de Biología Molecular de Plantas, Instituto de Biotecnología, Universidad Nacional Autónoma de México, Cuernavaca, México

© 2019 Taylor & Francis Group, LLC

distribution and clustering of associated partner-proteins and thereby regulate cellular functions, such as signaling and adhesion.[14,16] Their role in vesicular trafficking and as a component of exosomes, which mediate the transport of protein, lipids, and microRNAs during intercellular and interkingdom communication, open a new avenue of research in pathogenic and mutualistic interactions in plant and animal hosts.[17]

Tetraspanin structure

As its name implies, tetraspanins are proteins with four membrane-spanning domains. The amino- and carboxy-terminal tails and a small loop between transmembrane regions 2 (TM2) and 3 (TM3) are localized in the cytoplasmic compartment. Two loops, a small one (ECL1) located between TM1 and TM2, and a large one (ECL2) between TM3 and TM4, are extracellular (Figure 1).[6,18] ECL2 can be subdivided into a conserved and variable region. The conserved region mediates dimerization, whereas the variable region is required for interactions with non-tetraspanin partner molecules. The highly conserved cysteine residues in the large ECL2 are essential tetraspanin signatures, and the polar residues conserved in the TM regions stabilize the tertiary structure.[12]

Palmitoylation of intracellular and juxta-membrane cysteines might be required for initiating tetraspanin–tetraspanin web formation. This chemical modification also protects tetraspanins from lysosomal degradation, provides a link to cholesterol and gangliosides, and promotes cell–cell contact.[6,19] In animal cells, palmitoylation of specific integrins also contributes to tetraspanin complex formation.[20] Although *bona fide* integrins have not been identified in plant cells, other proteins such as NDR1 play similar functions.[21] In plant cells, some tetraspanins possess a tyrosine-based sorting motif (Yxxφ, with φ representing an amino acid with a bulky hydrophobic side chain) at the carboxyl end that delivers the tetraspanin to a specific intracellular compartment.[17,22] However, internalization can also proceed through association with proteins with a sorting motif or by additional, not yet defined domains.[12] The major extracellular loop ECL2 is a key region for tetraspanin function in animal and plant cells. Disulfide bonding between conserved cysteines in ECL2 produces a sub-loop structure in this region, which shows the greatest variability between tetraspanins.[15,23] Some tetraspanins have an additional two-to-four cysteines within this sub-loop, which may also participate in disulfide bonding. The remainder of the ECL2 region is highly conserved and contains three alpha helices.[2] The ECL2 loop appears to determine tetraspanin functional specificity and most specific monoclonal antibodies (mAb) bind to this region.[2]

Conservation of a single Cys residue at a specific point in the small loop is a unique feature of plant cell tetraspanins, suggesting that it plays a particular role that has not yet been determined. For instance, disulfide bonding between the big and small loops, which is important for tetraspanin–tetraspanin interactions, could stabilize the interaction in a redox-dependent fashion or affect the affinity for cholesterol or gangliosides present in the plasma membrane.[24] In contrast to animal tetraspanins, plant tetraspanins

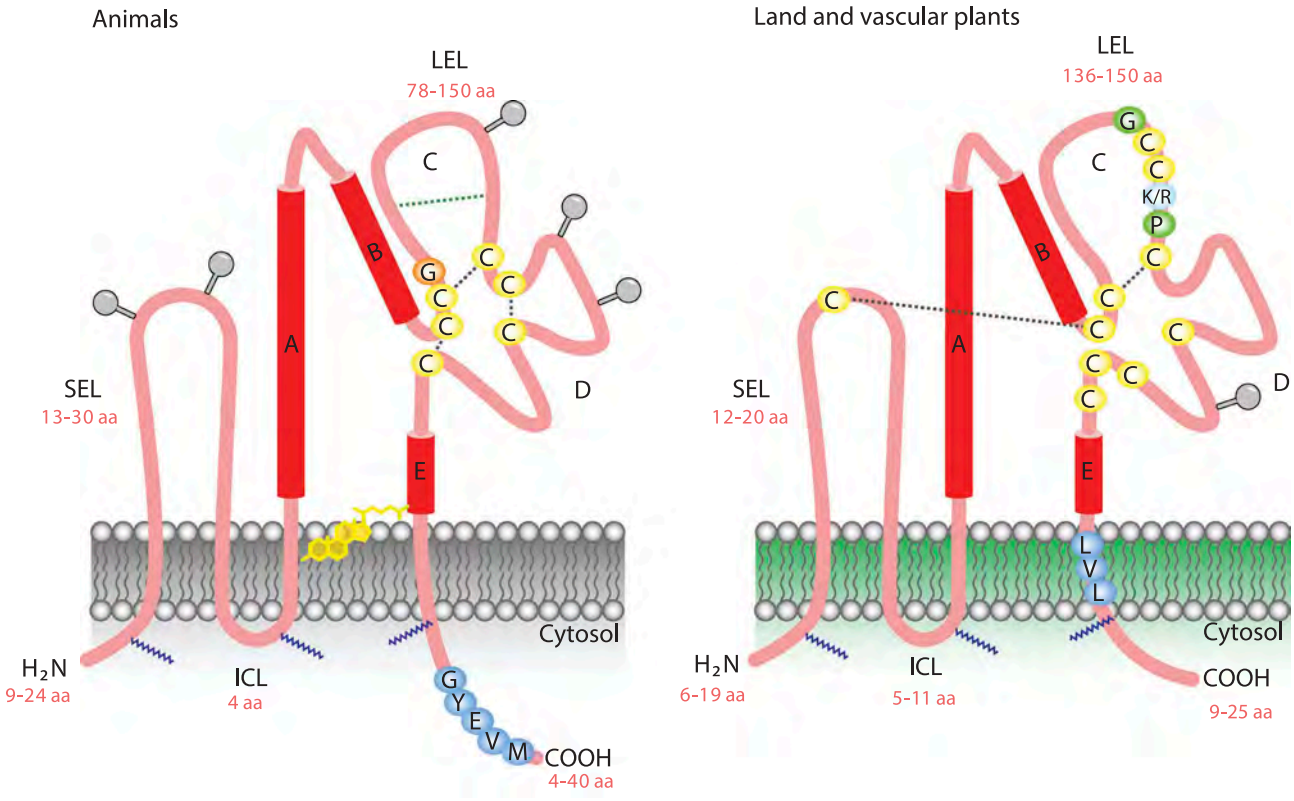

Figure 1. A general model describing the tetraspanin organization in the plasma membrane. Note the similarity and differences in the two extracellular loops. Plant tetraspanins contain a conserved cysteine that is not present in animal tetraspanin. (SEL) small extracellular loop, (LEL) large extracellular loop, (ICL) intracellular cytoplasmic loop, (GYEVM) endosome signal peptide, (GCCK/RPC) conserved sequence in plants, (LVL) putative plasmodesmata sorting.

have nine, rather than four, six, or eight, completely conserved Cys residues.[14] In plants, missense mutations in these Cys residues in *trn2–2* and *trn2–3* alleles, or the exchange of an uncharged amino acid (Pro-164 in *trn2–2* and Gly-177 in *trn2–3*) with a charged amino acid (Gluc) within the conserved EC2 region containing three Cys residues, could affect folding due a defect in disulfide bridges and thereby inhibit tetraspanin function.[25] This is intriguing, as crystallographic data and an analysis of the molecular dynamics of tetraspanin CD81 ECL2, showed the conformational plasticity of the EC2 region under different pH values and redox environments, suggesting that it acts as a molecular sensor of environmental change.[15,26] It is possible that plant tetraspanins could have a similar response under pH and redox changes. Little is known about the C-terminal tail of tetraspanins, a divergent and short region (4 to 40 amino acids) in animals and plants that is longer in fungi.[14,15,27] However, the C-terminal tail has been implicated in trafficking, as discussed below.[28–30]

Tetraspanin interactors: what we have learned from the animal field and how little is known in plant cells

In animal cells, the most prominent tetraspanin interactors are the integrins, growth factor receptors, G-protein-coupled receptors (GPCRs), several peptidases, transmembrane proteins associated with tumor progression (CD44), epithelial cell adhesion molecule (EPCAM), immunoglobulin (Ig), protein kinase C PKC), phosphatidylinositol 4-kinase (PI4KII), and phospholipase Cγ (PLCγ).[12] By contrast, the interactors of plant tetraspanins are unknown and the literature is limited to the expression and subcellular localization of plant tetraspanins in a few cell models,[4,14,15,31] and their role in recruiting ROS generating enzymes.[32–34]

In animal cells, TEM components have been dissociated using various detergents to examine interactions between tetraspanins and other molecules in the TEM. Different levels of interactions, ranging from strong associations to much weaker associations that are stable only in less hydrophobic detergents, such as Brij97, have been observed.[23] Three types of primary tetraspanin interactions, types I–III, exist. Type I interactions involve direct protein–protein interactions, such as those occurring in tetraspanin homodimers, homotrimers, homotetramers, and some heterointeractions.[23,35] Most tetraspanin–integrin and tetraspanin–tetraspanin interactions are type II interactions, which are less strong. Palmitoylation of tetraspanins, and possibly of their associating proteins, is essential for this type of interaction, which may be initiated in the Golgi apparatus.[36] Weak type III interactions, such as those occurring between tetraspanin and several kinases, are also stabilized by palmitoylation. In addition to primary interactions, the functional activity of tetraspanins also depends on cholesterol and gangliosides, which enable higher-order tetraspanin complexes to form, which constitute the TEM.[37] TEMs provide a signaling platform that recruits tetraspanin and its interactors. The palmitoylation of juxta-membrane cysteine residues of tetraspanins (Figure 1) is critical for the assembly of TEMs and is necessary for tetraspanin/tetraspanin interactions. Some integrins are also palmitoylated, and this modification appears to promote TEM formation. Cholesterol embedded in the membrane of the endosome is thought to stabilize TEMs.

Although TEMs share features with lipid rafts, they are independent and distinct from these structures. For instance, lipid rafts, but not TEMs, are disrupted by Triton X-100 at 4° C and the signature molecules of classical rafts, such as the glycosylphosphatidylinositol-anchored proteins and caveolin, do not associate with tetraspanins.[12] Furthermore, TEMs can be purified in low-density sucrose gradient fractions and are enriched in certain lipids (e.g., cholesterol and ganglioside GM3), while lipid rafts have different biophysical properties, are more sensitive to cholesterol depletion, and contain different arrays of membrane proteins.[6,7] Visualization of TEMs by fluorescence microscopy suggested that they are confined in discrete units at the nanometric scale for each class of tetraspanin. Recent single-molecule analyses of tetraspanin CD9 in animal cells shed light on tetraspanin dynamics in TEMs and the plasma membrane, redefining the tetraspanin web.[7,38,39] These studies indicate that tetraspanins form stable interaction platforms that are distinct from lipid rafts and in permanent exchange with the rest of the cell membrane. In addition, CD9 mobility and partitioning into these platforms depends on palmitoylation and cholesterol.[2]

Although no direct interaction partners of tetraspanins have been identified in plant cells, the cellular distribution of tetraspanin in reproductive tissues has been described.[15] Genetic data indicate that AtTET1 functions in a common pathway with TORNADO1 (TRN1), a leucine-rich-repeat protein that regulates patterning processes during *Arabidopsis thaliana* development, and double mutant analysis showed that these proteins are required for related, overlapping signaling events.[14] Furthermore, AtTET1 functions together with WINDHOSE1 and 2 (WIH1/WIH2), two small peptides, to promote megasporogenesis.[25,40,41] The short and divergent C-terminal tail of both animal and plant tetraspanins has been linked to targeting to intracellular locations and interaction with cytoskeletal or signaling molecules, including protein kinase C, integrins, and mu3A subunit AP-3.[14,15,19] The phenotype of the Arabidopsis mutant *trn2-4*, which lacks 10 of 14 amino acids of the tetraspanin C-terminal tail, is as dramatic as that of the other *trn2* alleles, suggesting that this region of plant tetraspanins is as critical as that described for animal tetraspanins.[25] The C-terminal tail of the fungal tetraspanin Tps3 is larger than that of plant and animal tetraspanins and its specific interactors are unknown.[27]

Tetraspanins are key players in cancer development, with multiple antagonistic effects.[42] For example, the tetraspanin CD82 is downregulated, while tetraspanins CD151 and tetraspanin 8 are induced during metastases and support tumor progression.[12] Not all activities of tetraspanin rely on primary interactions with associating molecules; some biological phenomena can only be explained by considering the higher organization of tetraspanin complexes, which can interfere with the capacity of tetraspanins to recruit other molecules that negatively regulate a cellular event, such as the activation of a tyrosine phosphatase.[43] However, recruitment of specific partner molecules in TEMs such as gangliosides could contribute to CD82-mediated metastasis-inhibiting activity.[12] Tetraspanin CD9 also hampers the migration of metastasizing cells by interacting with the cytoskeleton. Indeed, overexpression of CD9 downregulates WAVE2 by a yet unknown mechanism,[44] since WAVE is part of the ARP2 and ARP3

complex in actin polymerization, it links upstream signals to activation of the ARP2 and ARP3 complex (e.g., during lamellipodium and filipodium formation). Some tetraspanins have a Yxxφ sorting motif, located close to the transmembrane region, that can disrupt the binding of the μ subunit of the AP2 adaptor complex, resulting in another cytoskeleton key regulatory component.[12,17] Therefore, tetraspanins exert their function by modulating, stabilizing, or preventing the activities of their associated molecules, depending on the composition of the TEM.[12,44,45]

Role of tetraspanin in cell trafficking

Although tetraspanins were first identified as cell surface markers, it is now clear that some associate with the endosomal pathway, i.e., in early and late endosomes, multivesicular bodies [MVBs], clathrin-coated vesicles, lysosomes, and various types of secretory vesicles.[46] Tetraspanins on the plasma membrane can be internalized via endocytosis and traffic to intracellular vesicles.[47,48] Conversely, on cell stimulation, secretory vesicles containing tetraspanins fuse with the plasma membrane.[46] Late endosomes and MVBs also fuse with the plasma membrane and release vesicles containing microRNA, proteins, and lipids known as exosomes that are enriched in certain tetraspanin proteins.[49] Exosomes released from cells infected with intracellular pathogens, including mycobacteria, are potent stimulators of inflammation in uninfected cells.[50] Thirteen of the 33 mammalian tetraspanins contain potential tyrosine-based sorting motifs, which have also been described in plants. However, in plants, additional motifs have been identified in tetraspanins, and the coat protein clathrin is necessary and sufficient for the uptake of cargo into clathrin-coated vesicles (CCVs). These motifs in the tetraspanins are based on the sequences YXXØ [D/E]XXXL[L/I] and FXNPXY, which are recognized by a family of adaptor protein (AP) complexes that determine the cellular localization of interacting proteins.[2,17] The intracellular trafficking of tetraspanin CD63 has been well described.[17,22] CD63 has a conserved GYEVM motif at its C-terminus, which interacts primarily with AP-2 complexes, linking tetraspanins to clathrin-mediated endocytosis pathways, and with AP-3 complexes for trafficking from endosomes to lysosomes. Furthermore, CD63 is also targeted to lysosomes directly from the trans-Golgi network.[22] Tetraspanin CD63 interacts directly through its C-terminus with syntenin, which may compete with AP-2 and AP-3 to alter the trafficking of syntenin and therefore link its spatial localization with actual function.[17,22] It has also been recently suggested that CD63 in animal cells is internalized from the plasma membrane by endocytosis of a specialized type of lipid raft known as caveolae, linking tetraspanin to the regulation of endocytosis.[2,17,22]

Tetraspanins as key players in pathogenic interactions in animal and plant cells

Several infectious agents evolved mechanisms to exploit tetraspanins for pathogen entry, subsequent intracellular trafficking, replication, and even exit from the host cell. Tetraspanins have been associated with or shown to mediate infection by human hepatitis C (HCV), HIV, *Plasmodium* species that cause malaria, certain types of bacteria, and even prions.[2] Some viruses (e.g., HIV, human T-cell leukemia virus [HTLV]) induce cell–cell fusion in a tetraspanin-dependent manner, resulting in the formation of giant cells or viral syncytia that contribute to spread of infection.[2,51] In some cases, tetraspanins act as pathogen receptors; however, they can also work as 'molecular organizers', forming TEMs by the lateral association of tetraspanins with other tetraspanin and non-tetraspanin membrane proteins.[2]

In T cells themselves, tetraspanins in TEMs promote actin cytoskeleton associations that may lead to more efficient signaling or contribute to the formation of the immune synapse in T cells and it has been suggested that tetraspanins facilitate antigen presentation or antigen signaling.[2] The localization of tetraspanins in TEMs has made it challenging to define the functions of individual family members, mainly because the antibodies that cross-link specific tetraspanins also perturb the organization and functions of interacting molecules, giving misleading information.[23,43] However, the soluble recombinant EC2 domain is an alternative tool to investigate the role of specific tetraspanins.[52] Recombinant EC2s appear to fold correctly and have biological activity in a number of systems.[2,52] Nonetheless, knockouts clearly demonstrate that particular cellular functions (e.g., T-cell proliferation, sperm–egg fusion) can be affected by the modulation of a specific tetraspanin. Targeting of individual tetraspanins may provide a therapeutic means to modulate cellular processes without global detrimental effects on the organism, including plant cells.[2]

Plants have the capability to respond to abiotic and biotic stresses, including fungal pathogens. Fungi are responsible for major diseases of agriculturally important plants. For example, *Magnaporthe grisea* is the causative agent of the most devastating fungal disease (blast) of rice (*Oryza sativa*) worldwide, *Botrytis cinerea* is a necrotrophic pathogen affecting more than 200 different host plants, and *Colletotrichum lindemuthianum* is responsible for anthracnose diseases in a wide range of crops and ornamental plants. The ability of plant pathogenic fungi to infect their host plants depends on successful penetration into plant tissues. During the infection process, these fungi differentiate a specialized cell called the appressorium, in a process involving arrest of polarized growth, apex swelling, and cell wall reinforcement[27,53,54] (Figure 2). Appressorium-mediated penetration occurs through the formation of a penetration peg at the base of the appressorium lying against the plant substratum, a region called the 'appressorium pore'. The narrow penetration peg is able to perforate the host surface, which includes the plant cuticle and cell wall, allowing the fungus to penetrate into host tissues.[27,53,54] The penetration peg emerges at a certain point of the base of the appressorium and requires spatial and temporal coordination of cellular functions, including reorganization of cytoskeletal elements; vesicular trafficking; exocytosis, including membrane and synthesis; assembly and remodeling of the cell wall.[53,55,56] Fungal tetraspanins have emerged as key coordinators of the infection process in several pathogenic fungi (*M. grisea, B. cinerea*, and *C. lindemuthianum*).[32,54,57,58] In these phytopathogenic fungi, Pls1 is essential for appressorium-mediated penetration into the host plant, since Pls1 null mutations result in appressoria that are unable to form functional

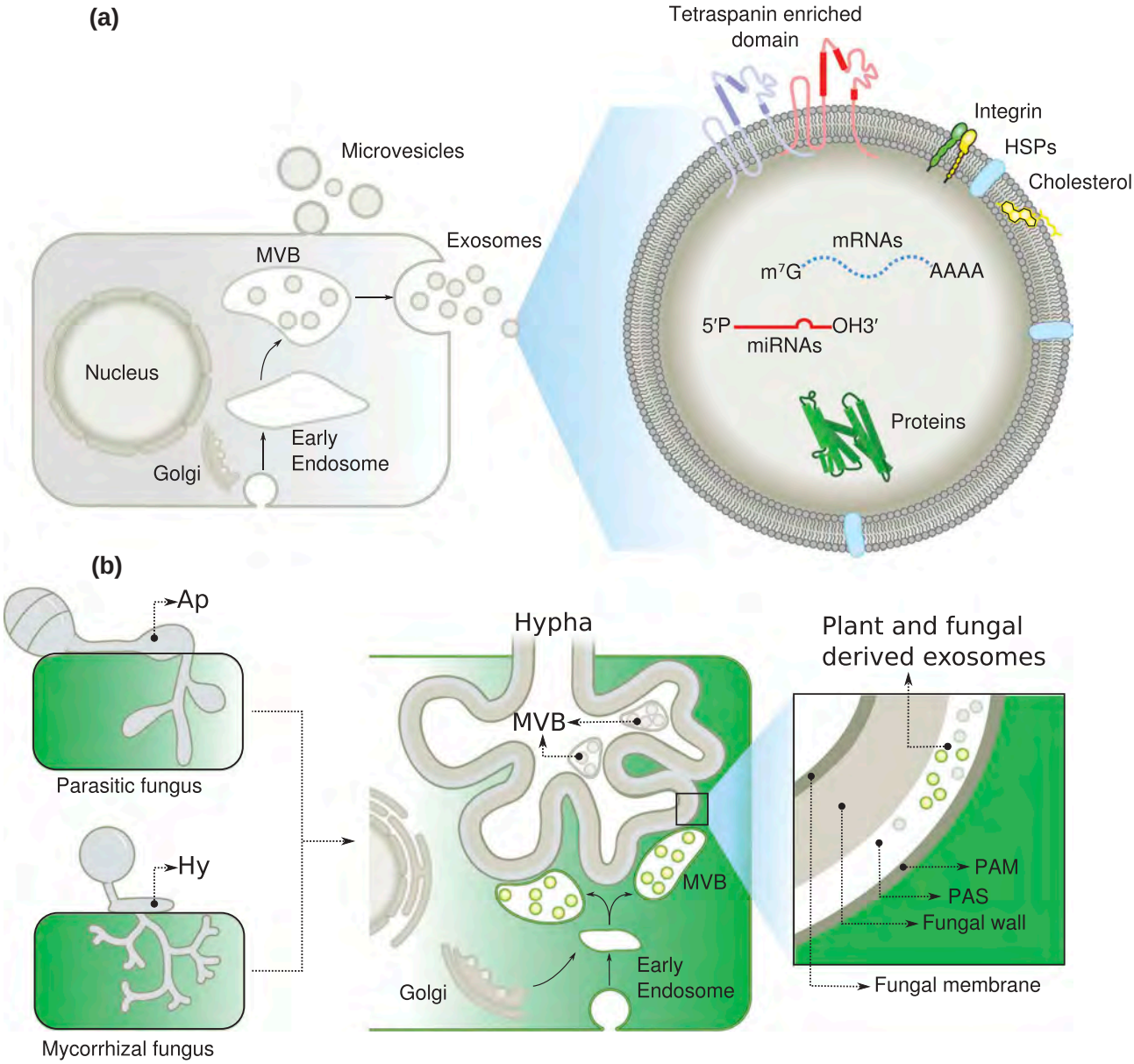

Figure 2. A model describing the role of exosomes in inter-kingdom communication. (a), Note the key role of exosomes in transporting molecules and tetraspanin in the exosome membranes as a marker. (b) Putative role of exosomes in mutualistic interactions. (MVB) multivesicular bodies, (Ap) appressorium, (Hy) hyphae, (PAM) periarbuscular membrane, (PAS) periarbuscular space, (HSPs) heat shock proteins.

penetration pegs.[27,53,58] Using a transcriptional fusion between the *PLS1* promoter and an eGFP reporter gene, clear expression is observed during the penetration of *B. cinerea*.[54] These results suggest that processes involved in appressorium-mediated penetration are conserved among taxonomically unrelated fungal species.[27,54] Since peg formation and penetration require the re-establishment of cell polarity at a focal point localized at the base of the appressorium, Pls1 tetraspanins might be required for the correct localization of the emergence site of the penetration peg. The finding that penetration peg was aborted or mislocalized in *C. lindemuthianum clpls1* null mutants supports this interpretation.[58] Therefore, functional studies of Pls1 tetraspanins in pathogenic fungi may reveal more general functions such as the generation of positional information during specific stages of fungal morphogenesis.

Tetraspanins as regulators of localized ROS generation by NADPH oxidases (NOX)

The wide distribution of tetraspanins in eukaryotes and their notable absence in unicellular fungi suggest that tetraspanins co-emerged with multi-cellular organisms during evolution, and are thus associated with multicellularity.[4] It is largely unknown how tetraspanins engage in multi-faceted functions at the cellular level. However, there is an emerging co-occurrence between tetraspanins and the mechanisms of ROS generation.[33] In the nematode *C. elegans*, the rigid and flexible cuticular exoskeleton, which is composed of collagen, protects the internal tissues. Once secreted, this collagen is tyrosine cross-linked in a ROS-dependent manner, in a process assisted by BLI-3, a DUOX NADPH oxidase.[59] This process also requires the participation

of tetraspanin TSP-15, which recruits the NADPH oxidase.[33,34,60] Inactivation of this tetraspanin or of BLI-3 produces similar phenotypes. This finding suggests a connection between the mechanism generating ROS and the tetraspanins. In fungi, tetraspanins have been related to NOX function based on the fact that mutants lacking either of these proteins show the same phenotypes. Furthermore, during plant infection with the pathogenic fungus *M. grisea* or *B. cinerea*, the tetraspanin PLS1 specify the infection sites, and the tetraspanin and ROS generated by NADPH oxidase coordinate ROS production at the infection site. Furthermore, in the pathogenic *C. lindemuthianum*, a tetraspanin is required in the appressorium, which is a swollen not growing structure, but in order to progress the fungal infection a re-initiation of the polarity is required.[32–34,58,61] Furthermore, in *Claviceps purpurea*, Nox2 and Pls1 are also important for host–pathogen interaction.[62]

These data point to a strong connection between tetraspanins and the ROS generating machinery, both in animal and plant cells, suggesting that tetraspanins regulate localized ROS production.[33,34,60,63] Localized ROS production is also required during Casparian strip lignification in plants, where CASP, a protein that recruits NADPH oxidase, plays a role similar to tetraspanin, by bringing together NADPH oxidase and peroxidase and ensuring the localized activation of the oxidase.[64] Tetraspanins have also been found at the tip of growing pollen tubes, a region that requires NADPH oxidase activity for the generation of ROS, key players in the regulation of polar growth.[65,66] Moreover, tetraspanins accumulate at the site of female gametophyte differentiation, suggesting an active role during pollen fertilization, a well-described ROS-dependent process that regulates programmed cell death.[15] It is tempting to speculate that tetraspanins recruit the ROS-generating machinery in a site-localized manner.

Exosomes as signaling shuttles, from inter-cellular communication to inter-kingdom communication

Inter-cellular and inter-kingdom signaling require specific molecules that can diffuse and be recognized by a different cell. Exosomes have emerged as a ubiquitous mechanism for transferring information between cells and organisms across all three kingdoms of life.[67,68] Initially described in animal cells as a general signaling pathway that allows communication between tumor and distal tissue during metastases, exosomes have also been shown to function in immune surveillance in plant cells during host–pathogen interactions,[69–72] and we propose that exosomes could also contribute to the regulation of mutualistic interactions.

Exosomes containing proteins, lipids, and RNAs produced by fungal pathogens can promote plant infection by transmitting pathogen-related molecules that could escape the host immune system or inhibit immune responses by favoring immune cell apoptosis. Furthermore, exosomes secreted by the plant host can have anti-infection roles by inducing immune responses that inhibit pathogen proliferation or infection. Therefore, exosomes might act as regulatory "bridges" during plant–pathogen interactions.[70]

How are exosomes produced and how are they related to tetraspanins? The general view is that exosomes are derived from multivesicular bodies (MVBs), which form when the endosomal membrane undergoes invagination, taking up proteins, lipids, inhibitors of apoptosis, and microRNAs from the cytosol.[73,74] The resulting vesicles inside the endosomes are termed MVBs. MVB either fuse with lysosomes or the plasma membrane, releasing their intraluminal vesicles as exosomes. There are other similar structures such as the ectosomes and microvesicles, which are assembled and released directly from the plasma membrane and therefore represent a different size and origin. The molecular composition of exosomes reflects their origin from intraluminal vesicles and includes several tetraspanins both in animals and plants.[71] It is important to note that exosomal proteins maintain their activity. Another notable feature is phosphatidylserine content on the outer membrane leaflet of the exosome in animal cells, which facilitates or triggers exosome uptake by phosphatidylserine-binding proteins (such as scavenger receptors, integrins, and complement receptors). The finding that exosomes can contain mRNAs and microRNAs that can be transferred to target cells where they can be translated or mediate RNA silencing, is a critical aspect of intercellular communication during the immune response, cell-to-cell spread of infectious agents, and tumor progression.[75–79] This process is specific to the target cell, such that RNA is transcribed in one cell, but travels long distances to affect another cell. Notably, the relative abundance of proteins, mRNA, and microRNA differs between exosomes and the cytoplasm of donor cells, suggesting a certain degree of specificity in the segregation of these components and therefore in the specificity of this type of communication. This implies that cargo is actively sorted into multivesicular bodies, through mechanisms such as monoubiquitylation, localization in cholesterol-rich membrane microdomains, or higher-order oligomerization. Although the contribution of tetraspanins to the composition of exosomes is well established, their impact on the functions of exosomes is unknown. However, it seems likely that tetraspanins are involved in the cross-talk between distant cells.[12] Specific tetraspanins and their interacting proteins, might contribute to exosome function and define the target cell.[80] Future studies providing the molecular mechanism to select the cargo and target cells by the exosomes will provide important information to manipulate the formation and targeting of exosomes.[2,81,82]

Exosomes in inter-kingdom communication during plant–pathogen interactions and future directions in mutualistic interactions

Eukaryotic regulatory small RNAs (sRNAs) that induce RNA interference (RNAi) are involved in a plethora of biological processes, including host immunity and pathogen virulence for successful infection.[83–85] In plants, diverse classes of sRNAs contribute to the regulation of host innate immunity. These immune-regulatory sRNAs operate through distinct RNAi pathways that trigger transcriptional or post-transcriptional gene silencing. Remarkably, the influence of regulatory sRNAs is not limited to the individual organism in which they are generated and it can sometimes extend to interacting species from different kingdoms.[71,86] Similarly, many pathogen-derived sRNAs regulate pathogen virulence, where they trigger gene silencing in the interacting organism, a phenomenon called cross-kingdom RNAi.[85,86] Aggressive

fungal pathogens such as *Botrytis* and *Verticillium* spp. that cause severe crop losses worldwide secrete effector proteins that suppress host immune responses.[86] Notably, the plant fungal pathogen *Botrytis cinerea* delivers and translocates small RNA effectors into host cells, where they hijack the plant RNAi machinery and suppress host immunity.[85,86] Upon *B. cinerea* infection, expression of the microRNA Bc-siR37 is specifically induced in the fungus, downregulating at least eight predicted Arabidopsis target genes and thereby enhancing disease susceptibility to *B. cinerea*.[86] Furthermore, knockout of the target genes of Bc-siR37 enhances disease susceptibility, further indicating that these genes promote plant defense against *B. cinerea*.[86] In summary, by regulating the expression of specific target genes in the plant host, it is possible to control multiple fungal diseases simultaneously. Therefore, cross-kingdom RNAi opens up a vastly unexplored area of research on mobile sRNAs in the host–pathogen interactions.[71,78,85] The big question is how is cross-kingdom communication carried out? Exosomes are produced in all domains of life, but little is known about exosomes in plants despite their implication in plant defense.[71,87–89] This work lays the foundation for the concept of cell-to-cell communication through exosomes in plants.[79] This idea is also supported in sunflower (*Helianthus annuus*), where exosomes in extracellular fluids of seedlings are enriched in cell wall remodeling enzymes and defense proteins which can be taken up by the phytopathogenic fungus *Sclerotinia sclerotiorum*, and affect fungal growth and even killing fungal cells.[88]

In animal cells, sRNAs can be transported by extracellular vesicles, specific transmembrane proteins, high-density lipoprotein complexes, or gap junctions.[90] The gastrointestinal parasite *Heligmosomoides polygyrus* also secretes exosomes, thereby transporting microRNAs (miRNAs) into mammalian cells and suppressing host immunity.[76] By contrast, the mechanism by which sRNAs are transported from hosts to interacting pathogens is unknown. In plant cells, it is well known that sRNAs travel through plasmodesmata, and thus systemically through the vasculature; however, cross-kingdom/organism RNA interference (RNAi) mediated by exosomes opens up a new area of research.[71] Because exosomes transfer miRNAs between animal cells as part of a long-distance signaling system and also in parasites interacting with mammalian host cells, the recent finding that plants and pathogenic fungi employ a similar mechanism involving exosome-mediated sRNA transfer indicates that exosomes constitute a general mechanism for intercellular and inter-kingdom signaling. This is a bi-directional communication with exosomes generated in the host to control the pathogen, but also with exosomes generated in the pathogen to promote the infection. Thus, studies should examine how exosomes travel across the boundaries between organisms of different taxonomic kingdoms.[71] In Arabidopsis, the cuticle is an important barrier against pathogens. However, in cuticle mutants, higher ROS production is able to sustain constitutive resistance against *B. cinerea* due to an increase in the cuticle permeability, which facilitates the diffusion and recognition of the cuticle monomers that induce the innate response. However, increased cuticle permeability could also facilitate exosome transport and diffusion in the permeable cuticle, allowing for neutralization of the pathogen through the exchange of miRNAs.[91–93]

Mammalian tetraspanins, such as CD63, are specific exosome markers.[77] Arabidopsis has 17 *TETRASPANIN* (*TET*)-like genes, but only closely related *TET8* and *TET9*, which are structurally similar to mammalian CD63, are induced by *B. cinerea* infection, at the fungal infection sites and as part of the exosomes.[15,94] Since mammalian exosomes are derived from MVBs, it is not surprising that the *Arabidopsis thaliana* MVB marker Rab5-like GTPase ARA6[95] is also enriched at infection sites, and is partially co-localized with TET8, suggesting that TET8-associated vesicles are likely derived from MVBs. Electron microscopy studies revealed in Arabidopsis that MVBs fuse with the plasma membrane and release extracellular vesicles at infection sites. Furthermore, TET8-associated vesicles have been visualized with*TET8-GFP*, but not ARA6, because ARA6 localizes to MVB outer membranes that fused to and remained on plasma membranes.[71] Thus, TET8-labeled extracellular vesicles can be considered as a specific marker for plant exosomes. The observations that TET8-GFP-labeled exosomes can be taken up by fungal cells under *in vitro* conditions[71] and that exosome-carried sRNAs can be translocated to fungal cells supports the involvement of a shuttle mechanism in inter-kingdom communication.

Animal tetraspanin proteins can induce the formation of specific TEMs; therefore, the finding that TET8-CFP and TET9-YFP are co-localized at fungal infection sites suggests that a particular TEM exists in those regions where hetero-tetraspanin organization is required. Such a TEM could play a key role in exosome biogenesis and translocation since the *tet8* T-DNA knock-out mutant and two independent *tet9* CRISPR frame-shift lines resulted in a weak, but consistently enhanced susceptibility to *B. cinerea*, as compared to the wild type.[71] Moreover, *tet8tet9* double mutants showed pronounced enhanced susceptibility, suggesting that TET8 and TET9 have partially redundant functions, and supporting the idea that TET8- and TET9-associated exosomes contribute to plant immunity against fungal infection by transferring host sRNAs into fungal cells.[71] The transferred sRNAs are thought to suppress fungal pathogenicity by targeting fungal virulence genes. Most Arabidopsis sRNAs transferred to *B. cinerea* have predicted target genes, such as those involved in trafficking pathways, that are downregulated after infection. When such target genes were mutated in *B. cinerea*, the resulting strains showed reduced virulence on Arabidopsis, supporting the idea that vesicle trafficking pathways are important for fungal virulence.[71,86] Furthermore, transgenic Arabidopsis lines overexpressing those sRNAs displayed a reduced susceptibility to *B. cinerea* and the pathogen showed reduced expression of the target genes.[71] Therefore, exosomes play an essential role in cross-kingdom sRNA trafficking between Arabidopsis and the fungal pathogen *B. cinerea*.

An interesting parallel has been reported in humans: cross-kingdom trafficking of human miRNAs into the parasite *Plasmodium falciparum* inhibits expression of its pathogenicity genes, which explains why sickle cell anemia patients, who have elevated levels of these transferred miRNAs, are more resistant to malaria.[71,96] It is unclear whether human exosomes are also responsible for sRNA delivery, and how ubiquitous such sRNA trafficking-mediated defense mechanisms are in animals and plants. Functional studies of host-transferred sRNAs may reveal

INFORME DE LABORES 2019

important virulence genes in pathogens and pests. Knowledge of tetraspanin activity during exosome biogenesis, cargo loading, and cross-kingdom RNAi may suggest a strategy to develop effective delivery methods of pathogen-targeting artificial RNAs with the goal of controlling plant diseases during pre- and post-harvesting of crops.

MVBs proliferate in susceptible and resistant barley (*Hordeum vulgare*) leaves in response to infection by the biotrophic powdery mildew fungus *Blumeria graminis* f. sp. *hordei*, and this response is associated with the cell wall defense response.[97,98] This response is also exacerbated in the cytoplasm of haustorium-containing epidermal cells, where MVBs proliferate in the vicinity of the cell wall-associated oxidative microburst.[99] Since MVBs are related to exosome biogenesis, this could explain the exosome production observed at infection sites.

The successful establishment of the arbuscular mycorrhizal (AM) symbiosis relies on the formation of arbuscules in the inner cortex of the root, which mediates a nutrient exchange between the plant and fungus (Figure 2). A variety of transporter proteins on the peri-arbuscular membrane facilitate nutrient exchange and communication. Arbuscule formation depends on fungal recognition by the host plant, which requires the tight coordination of several cellular processes ranging from the formation of the pre-penetration apparatus to initial fungal colonization and development of arbuscules. During the early stages of infection, mycorrhizal associations also require cross-talk between the host and the beneficial fungus, and this signaling can occur before the hyphae have come into contact with the host. Plants secrete strigolactones, which induce hyphal branching, and stimulate the production and secretion of Myc factors, which allow the colonization process.[100,101] It would be interesting to determine if MVBs proliferate at the arbuscule region and to determine at which stages of the mutualistic interaction exosomes are produced. So far, there is clear evidence that the secretory pathway of the plant host plays a critical role in the arbuscule formation, but it is unclear how this pathway is redirected during arbuscule development. It is attractive to speculate that exosomes coordinate the exchange of proteins, lipids, and sRNA during the establishment of AM symbiosis. Transcription factors are known to function in the transcriptional reprogramming of cortical cells during arbuscule development, and it is possible that they are modulated by exosomes released from fungi and the plant host. Studies involving the silencing and overexpression of key proteins involved in exosome biogenesis and function, such as the tetraspanins, will provide further insight into exosome biogenesis and the possible reprogramming of hyphal polarity in the hyphopodium structure which requires a further re-initiation of polarity to infect the host cells and generates the arbuscule formation.

Proteomic analyses of exosome cargo components formed during the AM symbiosis will be instrumental in determining their composition relative to those reported in pathogenic interactions.[71,102] Recently, H_2O_2 has been described as an important component of axonal regeneration after acute injury.[103] However, the injured neurons do not express the NADPH oxidase required for ROS generation. Instead, macrophages recruited to the vicinity secrete exosomes carrying NOX enzymes, which are taken up by the injured neuron via endocytosis and promote axonal growth in a ROS-dependent manner.[103–105] This is the first report describing the role of exosomes in NADPH oxidase translocation in injured neurons. This is an interesting finding since NOX enzymes also function in the injury response of the fungus *Trichoderma atroviride*.[106] It remains to be determined whether an exosome shuttle system carrying ROS generating enzymes contributes to localized ROS production in mutualistic and pathogenic interactions, at the infection thread or during arbuscule formation. Since the arbuscules and the infected cells require an intense vesicular trafficking, it will be important to decipher the role of tetraspanins and the exosomes in the exchange of key proteins, miRNA and mRNA, required for the mutualistic interaction (Figure 2). It could be involved in hyphal colonization during mycorrhizal association and arbuscular formation. During the legume–rhizobia interaction, the infection thread allows migration of the rhizobium through the root hairs until they reach the cortical cells. It is not clear how root hairs are inverted during infection thread formation, but this process clearly involves a complete change in root hair polarity. Given the involvement of tetraspanins in membrane fusion and endocytosis, we anticipate that tetraspanins might be key players in the regulation of root hair or fungal hypha polarity and in the exocytosis and endocytosis occurring at the tip of migrating infection threads. It is clear that the exosome role is just emerging in the plant biology field, but the parallelism between the pathogenesis and mutualism, and the different strategies used by the host, pathogen or symbiont to modulate the interaction, point out to the exosomes as a key player for tuning the interaction by exchanging important components required for a successful interaction. In this scenery, specific tetraspanin such as AtTET8, which are specific markers for exosomes, will open the door for the manipulating the number of exosomes and understand the role of exosomes in pathogenic and mutualistic interaction.

Acknowledgments

We greatly appreciate the technical support from Juan E. Olivares Grajales and the National Advanced Microscopy Laboratory (LNMA).

Funding

We acknowledge the funding support from Conacyt for grants 240595, 132155, 253247 and Investigación en Fronteras de la Ciencia 2015-I-319, and DGAPA-UNAM for grants PAPIIT IV200519 and IN209118. Saúl Jiménez Jiménez was supported by Conacyt PhD Scholarship number 314168.

ORCID

Olivia Santana http://orcid.org/0000-0001-9299-3385
Jesús Aguirre http://orcid.org/0000-0002-7847-9379
Kazuyuki Kuchitsu http://orcid.org/0000-0001-8854-0375

References

1. Garcia-Espana, A, Chung, P-J, Sarkar, IN, Stiner, E, Sun, T-T, Desalle, R. Appearance of new tetraspanin genes during vertebrate evolution. Genom. 2008;91(4):326–334. doi:10.1016/j.ygeno.2007.12.005.
2. Hassuna, N, Monk, PN, Moseley, GW, Partridge, LJ. Strategies for targeting tetraspanin proteins. BioDrugs. 2009;23(6):341–359. doi:10.2165/11315650-000000000-00000.
3. Zhang, X, Muto, A, Van de Velde, J, Neyt, P, Himanen, K, Vandepoele, K. Van Lijsebettens, M, Molecular cloning, expression pattern, and phylogenetic analysis of a tetraspanin CD82-like molecule in lamprey Lampetra japonica. Dev Genes Evol. 2016;226(2):87–98. doi:10.1007/s00427-016-0530-y.
4. Wang F, Vandepoele K, Van Lijsebettens M. Tetraspanin genes in plants. Plant Sci. 2012;190:9–15. doi:10.1016/j.plantsci.2012.03.005.
5. Garcia-Espana, A, Chung, PJ, Zhao, X, Lee, A, Pellicer, A, Yu, J, Sun, TT, DeSalle, R. Origin of the tetraspanin uroplakins and their co-evolution with associated proteins: implications for uroplakin structure and function. Mol Phylogenet Evol. 2006;41(2):355–367. doi:10.1016/j.ympev.2006.04.023.
6. Hemler ME. Tetraspanin functions and associated microdomains. Nat Rev Mol Cell Biol. 2005;6(10):801–811. doi:10.1038/nrm1736.
7. Levy S, Shoham T. Protein-protein interactions in the tetraspanin web. Physiol (Bethesda). 2005;20:218–224. doi:10.1152/physiol.00015.2005.
8. Rubinstein, E, Ziyyat, A, Wolf, J-P, Le Naour, F, Boucheix, C. The molecular players of sperm-egg fusion in mammals. Semin Cell Dev Biol. 2006;17(2):254–263. doi:10.1016/j.semcdb.2006.02.012.
9. Harada, Y, Yoshida, K, Kawano, N, Miyado, K. Critical role of exosomes in sperm-egg fusion and virus-induced cell-cell fusion. Reprod Med Biol. 2013;12(4):117–126. doi:10.1007/s12522-013-0152-2.
10. Jankovicova, J, Simon, M, Antalíková, J, Cupperová, P, Michalková, K. Role of tetraspanin CD9 molecule in fertilization of mammals. Physiol Res. 2015;64(3):279–293.
11. Jin, L, Wang, J, Guan, F, Zhang, J, Yu, S, Liu, S, Xue, Y, Li, L, Wu, S, Wang, X, Yang, Y. Dominant point mutation in a tetraspanin gene associated with field-evolved resistance of cotton bollworm to transgenic Bt cotton. Proc Natl Acad Sci USA. 2018;115(46):11760–11765. doi:10.1073/pnas.1812138115.
12. Zöller M. Tetraspanins: push and pull in suppressing and promoting metastasis. Nat Rev Cancer. 2009;9(1):40. doi:10.1038/nrc2543.
13. Wang, F, Muto, A, Van de Velde, J, Neyt, P, Himanen, K, Vandepoele, K, Van Lijsebettens, M. Functional analysis of the Arabidopsis tetraspanin gene family in plant growth and development. Plant Physiol. 2015;169(3):2200–2214. doi:10.1104/pp.15.01310.
14. Reimann R, Kost B, Dettmer J. Tetraspanins in plants. Front Plant Sci. 2017;8:545. doi:10.3389/fpls.2017.00545.
15. Boavida, LC, Qin, P., Broz, M., Becker, JD, McCormick, S. Arabidopsis tetraspanins are confined to discrete expression domains and cell types in reproductive tissues and form homo- and heterodimers when expressed in yeast. Plant Physiol. 2013;163(2):696–712. doi:10.1104/pp.113.216598.
16. Berditchevski F, Odintsova E. Characterization of integrin-tetraspanin adhesion complexes: role of tetraspanins in integrin signaling. J Cell Biol. 1999;146:477–492.
17. Berditchevski F, Odintsova E. Tetraspanins as regulators of protein trafficking. Traffic. 2007;8(2):89–96. doi:10.1111/j.1600-0854.2006.00515.x.
18. Kovalenko, OV, Metcalf, DG, DeGrado, WF, Hemler, ME. Structural organization and interactions of transmembrane domains in tetraspanin proteins. BMC Struct Biol. 2005;5:11. doi:10.1186/1472-6807-5-11.
19. Stipp CS, Kolesnikova TV, Hemler ME. Functional domains in tetraspanin proteins. Trends Biochem Sci. 2003;28(2):106–112. doi:10.1016/S0968-0004(02)00014-2.
20. Termini CM, Gillette JM. Tetraspanins function as regulators of cellular signaling. Front Cell Dev Biol. 2017;5:34. doi:10.3389/fcell.2017.00034.
21. Knepper C, Savory EA, Day B. Arabidopsis NDR1 is an integrin-like protein with a role in fluid loss and plasma membrane-cell wall adhesion. Plant Physiol. 2011;156(1):286–300. doi:10.1104/pp.110.169656.
22. Pols MS, Klumperman J. Trafficking and function of the tetraspanin CD63. Exp Cell Res. 2009;315(9):1584–1592. doi:10.1016/j.yexcr.2008.09.020.
23. van Deventer SJ, Dunlock VE, van Spriel AB. Molecular interactions shaping the tetraspanin web. Biochem Soc Trans. 2017;45(3):741–750. doi:10.1042/BST20160284.
24. Zimmerman, B., Kelly, B., McMillan, BJ, Seegar, TC, Dror, RO, Kruse, AC, Blacklow, SC. Crystal structure of a full-length human tetraspanin reveals a cholesterol-binding pocket. Cell. 2016;167(4):1041–1051. e11. doi:10.1016/j.cell.2016.09.056.
25. Cnops, G, Neyt, P, Raes, J, Petrarulo, M, Nelissen, H, Malenica, N, Luschnig, C, Tietz, O, Ditengou, F, Palme, K, Azmi, A. The TORNADO1 and TORNADO2 genes function in several patterning processes during early leaf development in Arabidopsis thaliana. Plant Cell. 2006;18(4):852–866. doi:10.1105/tpc.105.040568.
26. Cunha, ES, Sfriso, P, Rojas, AL, Roversi, P, Hospital, A, Orozco, M, Abrescia, NG. Mechanism of structural tuning of the Hepatitis C Virus Human Cellular Receptor CD81 large extracellular loop. Structure. 2018;26(1):181. doi:10.1016/j.str.2018.06.013.
27. Lambou, K, Tharreau, D, Kohler, A, Sirven, C, Marguerettaz, M, Barbisan, C, Sexton, AC, Kellner, EM, Martin, F, Howlett, BJ and Orbach, MJ. Fungi have three tetraspanin families with distinct functions. BMC Genomics. 2008;9:63. doi:10.1186/1471-2164-9-63.
28. Rous, BA, Reaves, BJ, Ihrke, G, Briggs, JAG, Gray, SR, Stephens, DJ, Banting, G, Luzio, JP. Role of adaptor complex AP-3 in targeting wild-type and mutated CD63 to lysosomes. Mol Biol Cell. 2002;13(3):1071–1082. doi:10.1091/mbc.01-08-0409.
29. Latysheva, N, Muratov, G, Rajesh, S, Padgett, M, Hotchin, NA, Overduin, M, Berditchevski, F. Syntenin-1 is a new component of tetraspanin-enriched microdomains: mechanisms and consequences of the interaction of syntenin-1 with CD63. Mol Cell Biol. 2006;26(20):7707–7718. doi:10.1128/MCB.00849-06.
30. Sala-Valdes, M, Ursa, A, Charrin, S, Rubinstein, E, Hemler, ME, Sánchez-Madrid, F, Yáñez-Mó, M. EWI-2 and EWI-F link the tetraspanin web to the actin cytoskeleton through their direct association with ezrin-radixin-moesin proteins. J Biol Chem. 2006;281(28):19665–19675. doi:10.1074/jbc.M602116200.
31. Olmos E, Reiss B, Dekker K. The ekeko mutant demonstrates a role for tetraspanin-like protein in plant development. Biochem Biophys Res Commun. 2003;310:1054–1061.
32. Clergeot, PH, Gourgues, M, Cots, J, Laurans, F, Latorse, MP, Pepin, R, Tharreau, D, Notteghem, JL, Lebrun, MH. PLS1, a gene encoding a tetraspanin-like protein, is required for penetration of rice leaf by the fungal pathogen Magnaporthe grisea. Proc Natl Acad Sci USA. 2001;98(12):6963–6968. doi:10.1073/pnas.111132998.
33. Moribe H, Mekada E. Co-occurrence of tetraspanin and ROS generators: conservation in protein cross-linking and other developmental processes. Worm. 2013;2(2):e23415. doi:10.4161/worm.23415.
34. Moribe, H, Konakawa, R, Koga, D, Ushiki, T, Nakamura, K, Mekada, E, Chisholm, AD. Tetraspanin is required for generation of reactive oxygen species by the dual oxidase system in Caenorhabditis elegans. PLoS Genet. 2012;8(9):e1002957. doi:10.1371/journal.pgen.1002957.
35. Charrin, S, Manié, S, Billard, M, Ashman, L, Gerlier, D, Boucheix, C, Rubinstein, E. Multiple levels of interactions within the tetraspanin web. Biochem Biophys Res Commun. 2003;304(1):107–112.
36. Charrin, S, Manié, S, Oualid, M, Billard, M, Boucheix, C, Rubinstein, E. Differential stability of tetraspanin/tetraspanin

interactions: role of palmitoylation. FEBS Lett. 2002;516 (1–3):139–144.
37. Zuidscherwoude, M, et al. Tetraspanin microdomains control localized protein kinase C signaling in B cells. Sci Signal. 2017;10(478):1–15.
38. Espenel, C, Margeat, E, Dosset, P, Arduise, C, Le Grimellec, C, Royer, CA, Boucheix, C, Rubinstein, E, Milhiet, P-E. Single-molecule analysis of CD9 dynamics and partitioning reveals multiple modes of interaction in the tetraspanin web. J Cell Biol. 2008;182(4):765–776. doi:10.1083/jcb.200803010.
39. Zuidscherwoude, M, Göttfert, F, Dunlock, VME, Figdor, CG, Van Den Bogaart, G, Van Spriel, AB. The tetraspanin web revisited by super-resolution microscopy. Sci Rep. 2015;5:12201. doi:10.1038/srep12201.
40. Cnops, G, Wang, X, Linstead, P, Van Montagu, M, Van Lijsebettens, M, Dolan, L. Tornado1 and tornado2 are required for the specification of radial and circumferential pattern in the Arabidopsis root. Development. 2000;127(15):3385–3394.
41. Lieber, D, Lora, J, Schrempp, S, Lenhard, M, Laux, T. Arabidopsis WIH1 and WIH2 genes act in the transition from somatic to reproductive cell fate. Curr Biol. 2011;21(12):1009–1017. doi:10.1016/j.cub.2011.05.015.
42. Couto, N, Caja, S, Maia, J, Strano Moraes, MC, Costa-Silva, B. Exosomes as emerging players in cancer biology. Biochimie. 2018. doi:10.1016/j.biochi.2018.03.006.
43. Tucci, M, Mannavola, F, Passarelli, A, Stucci, LS, Cives, M, Silvestris, F. Exosomes in melanoma: a role in tumor progression, metastasis and impaired immune system activity. Oncotarget. 2018;9(29):20826–20837. doi:10.18632/oncotarget.24846.
44. Huang, CL, Ueno, M., Liu, D, Masuya, D, Nakano, J, Yokomise, H, Nakagawa, T, Miyake, M. MRP-1/CD9 gene transduction regulates the actin cytoskeleton through the downregulation of WAVE2. Oncogene. 2006;25(49):6480–6488. doi:10.1038/sj.onc.1209654.
45. Maecker HT, Todd SC, Levy S. The tetraspanin superfamily: molecular facilitators. FASEB J. 1997;11:428–442.
46. Murk, JL, Humbel, BM, Ziese, U, Griffith, JM, Posthuma, G, Slot, JW, Koster, AJ, Verkleij, AJ, Geuze, HJ, Kleijmeer, MJ. Endosomal compartmentalization in three dimensions: implications for membrane fusion. Proc Natl Acad Sci USA. 2003;100 (23):13332–13337. doi:10.1073/pnas.2232379100.
47. Duffield, A, Kamsteeg, E-J, Brown, AN, Pagel, P, Caplan, MJ. The tetraspanin CD63 enhances the internalization of the H,K-ATPase beta-subunit. Proc Natl Acad Sci USA. 2003;100(26):15560–15565.
48. Spoden, G, Freitag, K, Husmann, M, Boller, K, Sapp, M, Lambert, C, Florin, L, Sommer, P. Clathrin- and caveolin-independent entry of human papillomavirus type 16–involvement of tetraspanin-enriched microdomains (TEMs). PLoS One. 2008;3 (10):e3313. doi:10.1371/journal.pone.0003313.
49. Guix, FX, et al. Tetraspanin 6: a pivotal protein of the multiple vesicular body determining exosome release and lysosomal degradation of amyloid precursor protein fragments. Mol Neurodegener. 2017;12(1):25. doi:10.1186/s13024-017-0165-0.
50. Schorey JS, Bhatnagar S. Exosome function: from tumor immunology to pathogen biology. Traffic. 2008;9(6):871–881. doi:10.1111/j.1600-0854.2008.00734.x.
51. Martin, F, Roth, DM, Jans, DA, Pouton, CW, Partridge, LJ, Monk, PN, Moseley, GW. Tetraspanins in viral infections: a fundamental role in viral biology? J Virol. 2005;79 (17):10839–10851. doi:10.1128/JVI.79.17.10839-10851.2005.
52. Grove, J, Hu, K, Farquhar, MJ, Goodall, M, Walker, L, Jamshad, M, Drummer, HE, Bill, RM, Balfe, P, McKeating, JA. A new panel of epitope mapped monoclonal antibodies recognising the prototypical tetraspanin CD81. Wellcome Open Res. 2017;2:82. doi:10.12688/wellcomeopenres.12058.1.
53. Veneault-Fourrey C, Lambou K, Lebrun MH. Fungal Pls1 tetraspanins as key factors of penetration into host plants: a role in re-establishing polarized growth in the appressorium? FEMS Microbiol Lett. 2006;256 (2):179–184. doi:10.1111/j.1574-6968.2006.00128.x.
54. Gourgues, M, Brunet-Simon, A, Lebrun, M-H, Levis, C. The tetraspanin BcPls1 is required for appressorium-mediated penetration of Botrytis cinerea into host plant leaves. Mol Microbiol. 2004;51(3):619–629.
55. Bourett TM, Howard RJ. Actin in penetration pegs of the fungal rice blast pathogen, Magnaporthe grisea. Protoplasma. 1992;168:20–26. doi:10.1007/BF01332647.
56. Park, G, Bruno, KS, Staiger, CJ, Talbot, NJ, Xu, J-R. Independent genetic mechanisms mediate turgor generation and penetration peg formation during plant infection in the rice blast fungus. Mol Microbiol. 2004;53(6):1695–1707. doi:10.1111/j.1365-2958.2004.04220.x.
57. Gourgues, M, Clergeot, PH, Veneault, C, Cots, J, Sibuet, S, Brunet-Simon, A, Levis, C, Langin, T, Lebrun, MH. A new class of tetraspanins in fungi. Biochem Biophys Res Commun. 2002;297 (5):1197–1204.
58. Veneault-Fourrey, C, Parisot, D, Gourgues, M, Laugé, R, Lebrun, M-H, Langin, T. The tetraspanin gene ClPLS1 is essential for appressorium-mediated penetration of the fungal pathogen Colletotrichum lindemuthianum. Fungal Genet Biol. 2005;42 (4):306–318. doi:10.1016/j.fgb.2005.01.009.
59. Edens, WA, et al. Tyrosine cross-linking of extracellular matrix is catalyzed by Duox, a multidomain oxidase/peroxidase with homology to the phagocyte oxidase subunit gp91phox. J Cell Biol. 2001;154(4):879–891. doi:10.1083/jcb.200103132.
60. Moribe, H, Yochem, J, Yamada, H, Tabuse, Yo, Fujimoto, T, Mekada, E. Tetraspanin protein (TSP-15) is required for epidermal integrity in Caenorhabditis elegans. J Cell Sci. 2004;117(Pt 22):5209–5220. doi:10.1242/jcs.01403.
61. Siegmund, U, Heller, J, van Kann, JAL, Tudzynski, P, Schmidt, HH. The NADPH oxidase complexes in Botrytis cinerea: evidence for a close association with the ER and the tetraspanin Pls1. PLoS One. 2013;8(2):e55879. doi:10.1371/journal.pone.0055879.
62. Schurmann, J, Buttermann, D, Herrmann, A, Giesbert, S, Tudzynski, P. Molecular characterization of the NADPH oxidase complex in the ergot fungus Claviceps purpurea: cpNox2 and CpPls1 are important for a balanced host-pathogen interaction. Mol Plant Microbe Interact. 2013;26(10):1151–1164. doi:10.1094/MPMI-03-13-0064-R.
63. Charrin, S, Jouannet, S, Boucheix, C, Rubinstein, E. Tetraspanins at a glance. J Cell Sci. 2014;127(Pt 17):3641–3648. doi:10.1242/jcs.154906.
64. Lee, Y, Rubio, MC, Alassimone, J, Geldner, N. A mechanism for localized lignin deposition in the endodermis. Cell. 2013;153 (2):402–412. doi:10.1016/j.cell.2013.02.045.
65. Foreman, J, et al. Reactive oxygen species produced by NADPH oxidase regulate plant cell growth. Nature. 2003;422 (6930):442–446. doi:10.1038/nature01485.
66. Takeda, S, Gapper, C, Kaya, H, Bell, E, Kuchitsu, K, Dolan, L. Local positive feedback regulation determines cell shape in root hair cells. Science. 2008;319(5867):1241–1244. doi:10.1126/science.1152505.
67. Coakley G, Maizels RM, Buck AH. Exosomes and other extracellular vesicles: the new communicators in parasite infections. Trends Parasitol. 2015;31(10):477–489. doi:10.1016/j.pt.2015.06.009.
68. Li, Y, Liu, Y, Xiu, F, Wang, J, Cong, H, He, S, Shi, Y, Wang, X, Li, X, Zhou, H. Characterization of exosomes derived from Toxoplasma gondii and their functions in modulating immune responses. Int J Nanomedicine. 2018;13:467–477. doi:10.2147/IJN.S151110.
69. Weidle, UH, Birzele, F, Kollmorgen, G, Rueger, R. The multiple roles of exosomes in metastasis. Cancer Genom Proteom. 2017;14 (1):1–15. doi:10.21873/cgp.20015.
70. Zhang, W, Jiang, X, Bao, J, Wang, Y, Liu, H, Tang, L. Exosomes in pathogen infections: A bridge to deliver molecules and link functions. Front Immunol. 2018;9:90. doi:10.3389/fimmu.2018.00090.
71. Cai, Q, Qiao, L, Wang, M, He, B, Lin, FM, Palmquist, J, Huang, SD, Jin, H. Plants send small RNAs in extracellular vesicles to fungal pathogen to silence virulence genes. Science. 2018;360(6393):1126–1129. doi:10.1126/science.aar4142.

72. Li, Y, Xiu, F, Mou, Z, Xue, Z, Du, H, Zhou, C, Li, Y, Shi, Y, He, S, Zhou, H. Exosomes derived from Toxoplasma gondii stimulate an inflammatory response through JNK signaling pathway. Nanomedicine (Lond). 2018;13(10):1157–1168. doi:10.2217/nnm-2018-0035.
73. Valenzuela, MM, Bennit, HRF, Gonda, A, Osterman, CJD, Hibma, A, Khan, S, Wall, NR. Exosomes secreted from human cancer cell lines contain Inhibitors of Apoptosis (IAP). Cancer Microenviron. 2015;8(2):65–73. doi:10.1007/s12307-015-0167-9.
74. Stahl PD, Raposo G. Exosomes and extracellular vesicles: the path forward. Essays Biochem. 2018;62(2):119–124. doi:10.1042/EBC20170088.
75. Cai, ZY, Xiao, M, Quazi, SH, Ke, ZY. Exosomes: a novel therapeutic target for Alzheimer's disease? Neural Regen Res. 2018;13(5):930–935. doi:10.4103/1673-5374.232490.
76. Buck, AH, et al. Exosomes secreted by nematode parasites transfer small RNAs to mammalian cells and modulate innate immunity. Nat Commun. 2014;5:5488. doi:10.1038/ncomms5972.
77. Mathivanan S, Ji H, Simpson RJ. Exosomes: extracellular organelles important in intercellular communication. J Proteomics. 2010;73(10):1907–1920. doi:10.1016/j.jprot.2010.06.006.
78. Gonzalez JF, Venturi V. A novel widespread interkingdom signaling circuit. Trends Plant Sci. 2013;18(3):167–174. doi:10.1016/j.tplants.2012.09.007.
79. Yoon YJ, Kim OY, Gho YS. Extracellular vesicles as emerging intercellular communicasomes. BMB Rep. 2014;47(10):531. doi:10.5483/BMBRep.2014.47.10.164.
80. Lakkaraju A, Rodriguez-Boulan E. Itinerant exosomes: emerging roles in cell and tissue polarity. Trends Cell Biol. 2008;18(5):199–209. doi:10.1016/j.tcb.2008.03.002.
81. Hassuna, N, Monk, PN, Moseley, GW, Partridge, LJ. Strategies for targeting tetraspanin proteins: potential therapeutic applications in microbial infections. BioDrugs. 2009;23(6):341–359. doi:10.2165/11315650-000000000-00000.
82. Bellavia, D, Raimondi, L, Costa, V, De Luca, A, Carina, V, Maglio, M, Fini, M, Alessandro, R, Giavaresi, G. Engineered exosomes: A new promise for the management of musculoskeletal diseases. Biochim Biophys Acta. 2018;1862:1893–1901.
83. Wang, M, Weiberg, A, Lin, FM, Thomma, BP, Huang, HD, Jin, H. Bidirectional cross-kingdom RNAi and fungal uptake of external RNAs confer plant protection. Nature Plants. 2016;2(10):16151. doi:10.1038/nplants.2016.151.
84. Weiberg, A, Wang, M, Lin, FM, Zhao, H, Zhang, Z, Kaloshian, I, Huang, HD, Jin, H. Fungal small RNAs suppress plant immunity by hijacking host RNA interference pathways. Science. 2013;342(6154):118–123. doi:10.1126/science.1239705.
85. Weiberg A, Jin HL. Small RNAs - the secret agents in the plant-pathogen interactions. Curr Opin Plant Biol. 2015;26:87–94. doi:10.1016/j.pbi.2015.05.033.
86. Wang, M, Weiberg, A, Dellota Jr, E, Yamane, D, Jin, H. Botrytis small RNA Bc-siR37 suppresses plant defense genes by cross-kingdom RNAi. RNA Biol. 2017;14(4):421–428. doi:10.1080/15476286.2017.1291112.
87. Gangoda, L, Boukouris, S, Liem, M, Kalra, H, Mathivanan, S. Extracellular vesicles including exosomes are mediators of signal transduction: are they protective or pathogenic? Proteomics. 2015;15(2–3):260–271. doi:10.1002/pmic.201400234.
88. Regente, M, Pinedo, M, San Clemente, H, Balliau, T, Jamet, E, de la Canal, L. Plant extracellular vesicles are incorporated by a fungal pathogen and inhibit its growth. J Exp Bot. 2017;68(20):5485–5495. doi:10.1093/jxb/erx355.
89. Rutter BD, Innes RW. Extracellular vesicles isolated from the leaf apoplast carry stress-response proteins. Plant Physiol. 2017;173(1):728–741. doi:10.1104/pp.16.01253.
90. Mittelbrunn M, Sanchez-Madrid F. Intercellular communication: diverse structures for exchange of genetic information. Nat Rev Mol Cell Biol. 2012;13(5):328–335. doi:10.1038/nrm3335.
91. Blanc, C, et al. The cuticle mutant eca2 modifies plant defense responses to biotrophic and necrotrophic pathogens and herbivory insects. Mol Plant Microbe Interact. 2018;31(3):344–355. doi:10.1094/MPMI-07-17-0181-R.
92. Serrano, M, Coluccia, F, Torres, M, L'Haridon, F, Métraux, JP. The cuticle and plant defense to pathogens. Front Plant Sci. 2014;5:274. doi:10.3389/fpls.2014.00274.
93. L'Haridon, F, Besson-Bard, A, Binda, M, Serrano, M, Abou-Mansour, E, Balet, F, Schoonbeek, HJ, Hess, S, Mir, R, Léon, J, Lamotte, O. A permeable cuticle is associated with the release of reactive oxygen species and induction of innate immunity. PLoS Pathog. 2011;7(7):e1002148. doi:10.1371/journal.ppat.1002148.
94. Ferrari, S, Galletti, R, Denoux, C, De Lorenzo, G, Ausubel, FM, Dewdney, J. Resistance to Botrytis cinerea induced in Arabidopsis by elicitors is independent of salicylic acid, ethylene, or jasmonate signaling but requires PHYTOALEXIN DEFICIENT3. Plant Physiol. 2007;144(1):367–379. doi:10.1104/pp.107.095596.
95. Ebine, K, et al. A membrane trafficking pathway regulated by the plant-specific RAB GTPase ARA6. Nat Cell Biol. 2011;13(7):853–859. doi:10.1038/ncb2270.
96. LaMonte, G, et al. Translocation of sickle cell erythrocyte microRNAs into Plasmodium falciparum inhibits parasite translation and contributes to malaria resistance. Cell Host Microbe. 2012;12(2):187–199. doi:10.1016/j.chom.2012.06.007.
97. An, Q, Ehlers, K, Kogel, KH, Van Bel, AJ, Hückelhoven, R. Multivesicular compartments proliferate in susceptible and resistant MLA12-barley leaves in response to infection by the biotrophic powdery mildew fungus. New Phytol. 2006;172(3):563–576. doi:10.1111/j.1469-8137.2006.01844.x.
98. An, Q, Hückelhoven, R, Kogel, KH, Van Bel, AJ. Multivesicular bodies participate in a cell wall-associated defence response in barley leaves attacked by the pathogenic powdery mildew fungus. Cell Microbiol. 2006;8(6):1009–1019. doi:10.1111/j.1462-5822.2006.00683.x.
99. An Q, van Bel AJ, Huckelhoven R. Do plant cells secrete exosomes derived from multivesicular bodies? Plant Signal Behav. 2007;2:4–7.
100. Luginbuehl LH, Oldroyd GED. Understanding the Arbuscule at the Heart of endomycorrhizal symbioses in plants. Curr Biol. 2017;27(17):R952–R963. doi:10.1016/j.cub.2017.06.042.
101. Luginbuehl, LH, Menard, GN, Kurup, S, Van Erp, H, Radhakrishnan, GV, Breakspear, A, Oldroyd, GED, Eastmond, PJ. Fatty acids in arbuscular mycorrhizal fungi are synthesized by the host plant. Science. 2017;356(6343):1175–1178. doi:10.1126/science.aan0081.
102. Choi, D-S, Yang, JS, Choi, EJ, Jang, SC, Park, S., Kim, OY, Hwang, D., Kim, KP, Kim, YK, Kim, S., Gho, YS. The protein interaction network of extracellular vesicles derived from human colorectal cancer cells. J Proteome Res. 2012;11(2):1144–1151. doi:10.1021/pr200842h.
103. Hervera, A, Hervera, A, De Virgiliis, F, Palmisano, I, Zhou, L, Tantardini, E, Kong, G, Hutson, T, Danzi, MC., Perry, RBT, Santos, CX, Kapustin, AN. Reactive oxygen species regulate axonal regeneration through the release of exosomal NADPH oxidase 2 complexes into injured axons. Nat Cell Biol. 2018;20(3):307–319. doi:10.1038/s41556-018-0039-x.
104. Krishnamoorthy L, Chang CJ. Exosomal NADPH Oxidase: delivering Redox Signaling for Healing. Biochemistry. 2018. doi:10.1021/acs.biochem.8b00429.
105. Morelli, AE, Larregina, AT, Shufesky, WJ, Sullivan, ML, Stolz, DB, Papworth, GD, Zahorchak, AF, Logar, AJ, Wang, Z, Watkins, SC, Falo, LD. Endocytosis, intracellular sorting, and processing of exosomes by dendritic cells. Blood. 2004;104(10):3257–3266. doi:10.1182/blood-2004-03-0824.
106. Hernandez-Onate, MA, Esquivel-Naranjo, EU, Mendoza-Mendoza, A, Stewart, A, Herrera-Estrella, AH. An injury-response mechanism conserved across kingdoms determines entry of the fungus Trichoderma atroviride into development. Proc Natl Acad Sci USA. 2012;109(37):14918–14923. doi:10.1073/pnas.1209396109.

PLOS ONE

RESEARCH ARTICLE

Differential tetraspanin genes expression and subcellular localization during mutualistic interactions in *Phaseolus vulgaris*

Saul Jimenez-Jimenez[1], Olivia Santana[1], Fernando Lara-Rojas[1], Manoj-Kumar Arthikala[2], Elisabeth Armada[1], Kenji Hashimoto[3], Kazuyuki Kuchitsu[3], Sandra Salgado[1], Jesús Aguirre[4], Carmen Quinto[1], Luis Cárdenas[1]*

1 Departamento de Biología Molecular de Plantas, Instituto de Biotecnología, Universidad Nacional Autónoma de México, Cuernavaca, Morelos, México, **2** Ciencias Agrogenómicas, Escuela Nacional de Estudios Superiores Unidad León-Universidad Nacional Autónoma de México, León, Guanajuato, México, **3** Department of Applied Biological Science, Tokyo University of Science, Yamazaki, Noda, Chiba, Japan, **4** Instituto de Fisiología Celular, Universidad Nacional Autónoma de México, Ciudad de México, México

* luisc@ibt.unam.mx

Check for updates

OPEN ACCESS

Citation: Jimenez-Jimenez S, Santana O, Lara-Rojas F, Arthikala M-K, Armada E, Hashimoto K, et al. (2019) Differential tetraspanin genes expression and subcellular localization during mutualistic interactions in *Phaseolus vulgaris*. PLoS ONE 14 (8): e0219765. https://doi.org/10.1371/journal.pone.0219765

Editor: Ricardo Aroca, Estacion Experimental del Zaidin, SPAIN

Received: January 31, 2019

Accepted: July 1, 2019

Published: August 22, 2019

Copyright: © 2019 Jimenez-Jimenez et al. This is an open access article distributed under the terms of the Creative Commons Attribution License, which permits unrestricted use, distribution, and reproduction in any medium, provided the original author and source are credited.

Data Availability Statement: All data needed to replicate all of the figures, graphs, tables, statistics, and other values are provided within the paper.

Funding: We acknowledge the funding support from Conacyt for grants 240595, 132155, and 253247 (to LC), Investigación en Fronteras de la Ciencia 2015-I-319 (to JA), and DGAPA-UNAM for grants PAPIIT IV200519 (to JA) and IN209118 (to LC). SJ was supported by Conacyt PhD Scholarship number 314168. The funders had no

Abstract

Arbuscular mycorrhizal fungi and rhizobia association with plants are two of the most successful plant-microbe associations that allow the assimilation of P and N by plants, respectively. These mutualistic interactions require a molecular dialogue, i.e., legume roots exude flavonoids or strigolactones which induce the Nod factors or Myc factors synthesis and secretion from the rhizobia or fungi, respectively. These Nod or Myc factors trigger several responses in the plant root, including calcium oscillations, and reactive oxygen species (ROS). Furthermore, superoxide and H_2O_2 have emerged as key components that regulate the transitions from proliferation to differentiation in the plant meristems. Similar to the root meristem, the nodule meristem accumulates superoxide and H_2O_2. Tetraspanins are transmembrane proteins that organize into tetraspanin web regions, where they recruit specific proteins into platforms required for signal transduction, membrane fusion, cell trafficking and ROS generation. Plant tetraspanins are scaffolding proteins associated with root radial patterning, biotic and abiotic stress responses, cell fate determination, and hormonal regulation and recently have been reported as a specific marker of exosomes in animal and plant cells and key players at the site of plant fungal infection. In this study, we conducted transcriptional profiling of the tetraspanin family in common bean (*Phaseolus vulgaris L*. var. Negro Jamapa) to determine the specific expression patterns and subcellular localization of tetraspanins during nodulation or under mycorrhizal association. Our results demonstrate that the tetraspanins are transcriptionally modulated during the mycorrhizal association, but are also expressed in the infection thread and nodule meristem development. Subcellular localization indicates that tetraspanins have a key role in vesicular trafficking, cell division, and root hair polar growth.

role in study design, data collection and analysis, decision to publish, or preparation of the manuscript.

Competing interests: The authors have declared that no competing interests exist.

Introduction

The symbiotic interaction between rhizobia and legumes requires a molecular dialogue that involves the exchange of specific signaling molecules. Legumes secrete particular flavonoids or strigolactones that are specifically recognized by rhizobia or mycorrhizal fungi [1]. These compounds induce the expression of specific genes, which encode proteins involved in the synthesis and secretion of Nod factors (NFs) from rhizobia, which are lipochitin-oligosaccharides or the Myc factor from the mycorrhizal fungi [2, 3]. Thereafter, NFs or Myc factors are specifically recognized by the plant root and induce several responses, including ionic changes, membrane depolarization, cytoskeleton rearrangements, reactive oxygen species (ROS) generation, and gene expression [4–7]. Soon after the rhizobia reach the root hair, microfilament structures and Ca^{2+} gradients undergo dramatic changes in the tip region of root hair cells in response to NFs [8–11]. In *Arabidopsis thaliana* root hairs, ROS-mediated Ca^{2+} channel activity supports polar growth [12–14]. Therefore, ionic responses, ROS production, and cytoskeletal rearrangements have been suggested as key players in reprogramming root hair growth, which allows the root hair tip curling response during the establishment of symbiotic interactions in legume plants. Then, a tunnel-like infection thread (IT) forms through invagination of the plasma membrane and the cell wall [2]. While the bacteria travel inside the IT through the root hair, the cortical cells divide in a NF-dependent manner to form the nodule primordia that the rhizobia colonize in structures named symbiosome. Once mature, the nodule is able to fix atmospheric nitrogen [15]. On the other hand, the arbuscular mycorrhizal association induces the hypopodium and the further invasion of the cortical cells, which end up with the arbuscule formation. Both processes, the bacterial colonization trough the infection thread and arbuscule formation, require an active vesicular trafficking, endocytosis and exocytosis in order to increase the membranal surface required for symbiosome and arbuscule formation [16, 17].

Given their wide distribution in mammals, insects, fungi, mosses, and plants, tetraspanins likely coemerged in multicellular organisms during evolution [18]. In animal cells, tetraspanins are typically localized at the cell–cell interface in tetraspanin-enriched microdomains (TEMs), where they associate with each other and with other membrane-bound molecules and build important molecular platforms or cell–cell interactions [19, 20]. Tetraspanins get their name from their four transmembrane domains. The N and C tails of tetraspanins are localized on the cytoplasmic side of the membrane, and four transmembrane domains allow for the formation of two extracellular loops, one small and one large. The large loop has highly conserved cysteine residues, which could act as redox and pH sensors or promote protein–protein interactions. The small loop in plant tetraspanins contains a cysteine residue that is absent in animal tetraspanins [21]. Although tetraspanins in animal cells have been involved in various biological functions, such as cell motility, morphology, signaling, plasma membrane dynamics, and protein trafficking, how tetraspanins engage in plant cells functions at the cellular level is largely unknown [18]. Furthermore, tetraspanin have been described in animal and recently in plant cells as key components and specific markers of the exosomes, which are vesicles derived from the exocytic multivesicular bodies (MVB) that carry important molecules such as lipids, proteins, messenger RNA, and microRNAs, that play important roles in cell-to-cell communication in animal [22]. In plant cells it has been recently reported that exosomes go beyond organism boundaries and inhibit a pathogenic interaction in plants [23]. There is also an emerging idea that tetraspanins are part of a mechanism that generates ROS [24, 25]. In animal cells, H_2O_2 has been described as an important component of axonal regeneration after acute injury [26]. However, the injured neurons do not express the NADPH oxidase required for ROS generation. Instead, macrophages recruited to the vicinity secrete exosomes carrying NOX enzymes, which are taken up by the injured neuron via endocytosis and promote axonal

growth in a ROS-dependent manner with a key participation of exosomes [26–28]. On the other hand, the cuticle exoskeleton of the nematode *Caenorhabditis elegans*, in a similar way to the cell wall in plant cells, requires the ROS-dependent cross-linking of tyrosine residues, in a process assisted by BLI-3, which is a DUOX NADPH oxidase, and tetraspanin TSP-15 [24, 25, 29, 30]. When plants are infected with the pathogenic fungus *Magnaporthe grisea*, the fungal tetraspanin Pls1 and an NADPH oxidase are localized at the infection sites or appressorium structure to generate a ROS accumulation response that is required to reestablish the appressorium polarity [24, 25, 31–33]. Therefore, accumulating evidence links tetraspanin with ROS and polarity. Furthermore, tetraspanins have been identified at the tip of growing pollen tubes, a region that requires NADPH oxidase activity for the generation of ROS, a key player regulating polar growth [34]. However, we do not know if tetraspanins also function in pollen tube or even root hair polar growth [35].

Tetraspanins also accumulate in the female gametophyte, suggesting that they have an active role during gametophyte development or fertilization, a well-described ROS-dependent process. Furthermore, tetraspanins function during the transition from the floral meristem to the gynoecium as well as during the somatic-to-reproductive cell fate transition during megasporogenesis, suggesting that these proteins are regulators of cell fate determination [35–37]. As tetraspanins are also expressed in specialized tissues, such as the the quiescent center or the early initial cells that give rise to lateral roots meristems, these proteins may function in specific tissues or contribute to cell fate determination [18, 35, 38]. The meristematic distribution of some tetraspanins suggests that these proteins might be involved in regulating meristematic activity, which is highly dependent on ROS accumulation generated by NADPH oxidase activity, with superoxide-promoting meristematic activity and H_2O_2-promoting cell differentiation [39, 40].

On the other hand, NADPH-oxidase-derived ROS is a key component during nodule development and mycorhizal formation [41–43]. Since superoxide and H_2O_2 are produced during nodulation [43], it is possible that the molecular mechanism that maintains meristematic activity in the root is conserved during nodule meristem development [38]. Therefore, it is plausible that the ROS requirement for meristematic activity in the plant root is conserved during primordium development during nodule organogenesis and that tetraspanins have similar functions during the early stages of nodule development, as described in lateral root formation in *Arabidopsis* [38].

Here, we report the differential expression profile of the tetraspanin family in *P. vulgaris* in response to rhizobia or NF inoculation in several specific plant cells, such as root primordia, root hairs, and nodules at several developmental stages. *PvTET8*, *PvTET4* and *PvTET3* were highly expressed in the root meristematic region and during the early stages of primordium nodule development. Since PvTET8 was highly induced during nodulation, but not during mycorrhizal association, we suggest that this tetraspanin plays a particular role during nodulation, including the infection thread formation. Furthermore, the subcellular localization of some tetraspanins at the apical plasma membrane of *P. vulgaris* root hairs and in cytoplasmic vesicles suggests that these proteins function in polar growth, a central process during infection thread formation and migration. Our findings suggest that tetraspanins may also contribute to the vesicular trafficking required for localized exocytosis during the infection process or contribute to the exosome biogenesis as described during the pathogenic responses.

Materials and methods

Phylogenetic analysis

Using the methodology described by Huang et al. (2010), tetraspanin sequences containing four transmembrane domains were database screened, including a small and large extracellular loop,

using bioinformatics tools. The sequences were aligned in ClustalW. To avoid subjective bias, manual alignment editing was minimized. A phylogenetic tree was built using MEGA version 6.0.6 with 1000 bootstrap tests and pairwise deletion.

Vector construction for analyzing the activity promoter and subcellular localization

To evaluate promoter activity, the *pPvTET1A*::*GFP-GUS*, *pPvTET8*::*GFP-GUS and pPvTET3*::*GFP-GUS* construct, which includes the 1000-bp fragment upstream of the initiation codon of TET1A, TET8 and TET3 respectively, was created by PCR using *P. vulgaris* cv *Negro Jamapa* genomic DNA as template and gene-specific primers (S1 Fig). Each product of PCR was cloned into the pENTR/D-TOPO vector (Invitrogen) and recombined into the destination binary vector pBGWFS7.0 using Gateway LR Clonase II Enzyme Mix (Invitrogen) [44]. In each step, the presence of the insert was confirmed by Sanger sequencing and PCR. All constructed plasmids were introduced by electroporation into *Agrobacterium rhizogenes* strain K599. To design constructs for overexpressing *PvTET10*, *PvTET6* and *PvTET3*, the open reading frame of each gene was isolated from *P. vulgaris* cDNA and inserted into the pH7WG2D.1 binary vector under the control of the constitutive 35S promoter [45]. Empty pH7WG2D.1 vector, which constitutively expresses GFP, was used as the control in the overexpression system. All constructed plasmids were introduced by electroporation into *A. rhizogenes* strain K599 and used for further generation of transgenic roots or *Agrobacterium tumefaciens* strain AGL1 for transient expression in *N. benthamiana* leaves.

Bean hairy root transformation

Common bean seeds (*Phaseolus vulgaris cv* Negro Jamapa) were used for *A. rhizogenes* K599-mediated transformation to generate hairy roots harboring a construct of interest in composite plants using a previously described method [46].

Treatment with Nod factors by nebulization

Common bean seedlings were incubated with Nod factors at 48 h post germination (hpg) by nebulization with the Omron ComAir Nebulizer System Model NE-C801 according to the manufacturer's instructions. The Nod factors were purified according to our reported method [47]. A kinetic of transcript accumulation was conducted in roots incubated with Nod factors at 12, 24, and 36 h post inoculation for each tetraspanin. Nebulization with 1% CHAPS (w/v) was used as a control.

Nodulation assays

Rhizobium tropici CIAT899 bacteria were grown in 250-mL flasks containing 100 mL of PY broth supplemented with 7 mM $CaCl_2$, 50 μg/mL rifampicin, and 20 μg/mL nalidixic acid, in a shaking incubator (250 rpm) at 30˚C until the suspension reached an OD_{600} of 0.8. For nodulation assays, transgenic composite plants were transplanted under hydroponic conditions in glass tubes containing Fahreus medium and inoculated with 1 mL of a *R. tropici* CIAT899 suspension diluted to an OD_{600} of 0.05 in 10 mM $MgSO_4$ and grown in a controlled environment chamber (16 h light/8 h darkness, at 26˚C). At the indicated time points after inoculation, inoculated roots were frozen in liquid nitrogen and stored at −80˚C. At 5 and 7 days post infection (dpi), the root region close to the tail that is most susceptible to nodule formation was selected, and at 10, 14, and 18 dpi, only nodules were selected. In all cases, the equivalent root region of uninoculated roots was collected as a control.

Mycorrhizal spore inoculation and mycorrhization

Common bean seedlings at 48 hpg were transferred into pots (20-cm diameter) with vermiculite that was previously well inoculated in the pot with 1 gr of *Rhizophagus irregularis* substrate containing on average 800 spores homogeneously distributed. Inoculated plants were irrigated twice weekly with half-strength B&D solution containing a low concentration of potassium phosphate (50 μM; a 95% reduction compared with the control (500μM) to potentiate AM colonization [48]). As controls, two conditions without spores of *R. irregularis* were used: one set of plants were irrigated with 50 μM potassium phosphate (scarcity phosphate) and the other with 500 μM potassium phosphate (standard condition). AM fungal colonization status was determined by light and confocal microscopy, as indicated. Root samples were collected at 1, 2, 3, and 6 wpi and frozen in liquid nitrogen. All samples were stored at −80˚C.

Quantification of transcript levels by RT-qPCR analysis

Total RNA was extracted from frozen tissues using TRIzol reagent (Life Technologies) according to the manufacturer's instructions. To eliminate contaminating genomic DNA, total RNA samples (1 μg in 20 μL) were treated with 1 unit of DNaseI (RNase-free; Invitrogen) at 37˚C for 30 min and then at 65˚C for 10 min. Two-step RT-qPCR was performed using Maxima SYBR Green qPCR Master Mix (2X; Thermo Fisher Scientific), following the manufacturer's instructions. Each reaction was set up using 100 ng of cDNA as template in a 20-μL final volume. Gene-specific primers used in RT-qPCR reactions are listed in S1 Fig. qPCRs were performed in a LightCycler 480 real-time PCR system (Roche). Relative transcript abundance was calculated using the formulae reported by Schmitteng et al. [49]. *P. vulgaris* Elongation Factor 1α (Pv-EF1α) was used as a reference gene, as previously described. RT-qPCR data are averages of three independent experiments or biological replicates with two technical replicates.

Root hair and root isolation

The roots of *P. vulgaris* seedlings were divided and separated at 48 hpg. First, the region of the primary root that contained root hairs was cut into three equal segments named zones I, II, and III. Zone I contained the tip of the root that contained the initial or bulging out root hairs, zone II contained the rapidly growing root hairs, and zone III contained the mature or full-grown root hairs. Each fraction was collected in different containers in liquid nitrogen. Samples were stirred vigorously to separate the root hairs from the roots. Root hairs were isolated by pouring the liquid nitrogen mixture through a metal strainer. At the end, the root hairs were separated from the root (now shaved root) using a strainer. The shaved roots corresponding to regions I, II, and III were collected for tetraspanin transcript analysis. Fractions were stored at −80˚C until use. In each biological replicate, in order to confirm the different developmental stage of root hairs, the level of *RabA2* transcript was measured to assess the differential expression of this gene in each enriched tissue fraction.

Subcellular localization of common bean tetraspanins

Transient expression assays were conducted in *Nicotiana benthamiana* leaves to determine the subcellular localization of PvTET3 and PvTET6 proteins. The molecular construction carrying 35S:PvTET3-GFP and 35S:PvTET6-GFP was transferred to *A. tumefaciens* AGL1. For transient assays, leaves from 4- to 6-week-old wild-type *N. benthamiana* plants were coinfiltrated with the agrobacterium suspension harboring 35S:PvTETx-GFP. The infiltrated plants were marked and kept in a growth room at 16 h light/8 h darkness at 25 ± 2˚C. Plasmolysis was

INFORME DE LABORES 2019

induced using a 1M NaCl hypertonic solution. Fluorescence was visualized 48–72 h after infiltration using a spinning disk confocal microscope (Yokogawa, Japan) as described below.

Microscopy imaging and analysis

Transgenic roots were mounted in chambers adapted from large Petri dishes with a hole in the center. The hole was covered with a large glass coverslip. The chamber contained a layer of solid Fahreus medium (with Phytagel at 0.8%) and cellophane paper to prevent root movement. Roots were visualized under the inverted microscope (Nikon Eclipse Ti-E, Japan) with a 40x/1.25 NA water immersion lens (Nikon). For confocal images, we used a spinning disk confocal system (Intelligent Imaging Innovations /3i, USA) consisting of a CSU-W1 confocal head (Yokogawa, Japan) and a modular solid-state laser stack; Slidebook software was used to control the system and capture images (Intelligent Imaging Innovations /3i, USA). Images were recorded with a digital camera (Andor-IXON 3; Andor^{TM} Technology) for 1–2 min at 512-nm resolution and with frame rates of 100–300 ms. GFP fluorescence was obtained by exciting with an argon/2 ion laser (488 nm), and emitted fluorescence was collected using an emission filter (500 to 530 nm).

Statistical analysis

Data processing and statistical analysis were performed using GraphPad Prism version 6.00 for Windows (GraphPad Software). An unpaired two-tailed Student's *t*-test was used to determine whether data from two different groups were significantly different, Double, or triple asterisks above the columns indicate differences that are statistically significant (p-value < 0.05).

Results

Plant tetraspanins have a unique cysteine residue in the small extracellular loop

To determine the number of tetraspanin members in common bean (*Phaseolus vulgaris L*. var. Negro Jamapa), we searched the database of nonredundant protein sequences in NCBI using BLASTP (Protein-protein BLAST) using AtTET10 as query. AtTET10 and OsTET14 from *O. sativa* can be considered the founders of the tetraspanin family in their respective species [35, 50]. We identified 13 putative tetraspanin sequences in *P. vulgaris*, 25 in *Glycine max*, 9 in *Medicago truncatula*, and 5 in *Lotus japonicus* (Fig 1 and S2 Fig). Seventeen tetraspanins have been described in the model plant *Arabidopsis* and 15 in *Oryza sativa* [35, 50]. PvTET10, and other orthologs of AtTET10 and OsTET14, have between 10 and 12 introns in all reported genomes, including *Marchantia polymorpha* and *Physcomitrella patens*.

The amino acid sequences and functional motifs previously described in *Arabidopsis* allowed us to select tetraspanin members in *P. vulgaris* and compare them to other tetraspanins in the legume genome database reported in Phytozome (https://phytozome.jgi.doe.gov/pz/portal.html). Next, we conducted a bioinformatic screen based on several sequences, including the transmembrane domains, the cysteine pattern in the large extracellular loop (LEL), the single cysteine residue located exclusively in plant tetraspanins in the small extracellular loop (SEL), and the GCC(K/R)P signature in the large extracellular loop. Multiple sequence alignment and motif analyses revealed that common bean tetraspanins maintain the general features described for plant tetraspanins, with high conservation in specific motifs. For instance, in *P. vulgaris*, these proteins share an average of 38% identity and 42% similarity, which is comparable to that observed for *O. sativa* and *Arabidopsis*.

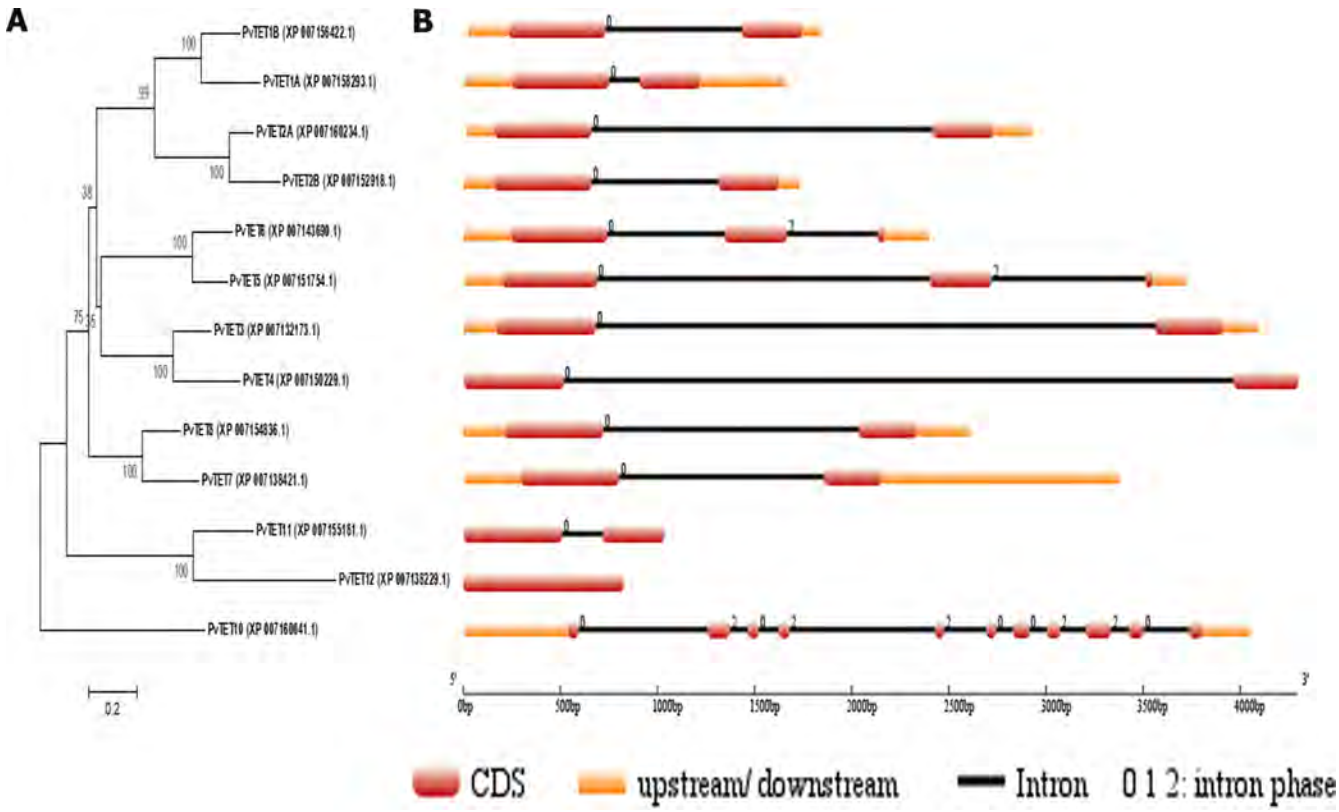

Fig 1. A rooted neighbor-joining phylogenetic tree of common bean tetraspanin. (A) On the left shown is the phylogenetic tree constructed using MEGA6.06, with amino acidic sequences from phytozome.org. Numbers above branches indicate bootstrap percentage values. PvTET proteins were clustered based on a significant bootstrap value of ≥50%. (B) On the right using an online tool, Gene Structure Display Server (GSDS; http://gsds.cbi.pku.edu.cn/), was used to draw the tetraspanin gene structure. Red boxes indicate exons, black lines depict introns, upstream/downstream sequences are shown as oranges boxes. Intron phases are indicated at exon–intron junctions.

https://doi.org/10.1371/journal.pone.0219765.g001

Based on these data, we generated an unrooted phylogenetic three using PvTET10 as a query from *Arabidopsis* (S2 Fig and S3 Fig). In our analysis, PvTET10 clustered with AtTET10 and OsTET14, whereas PvTET1A and PvTET1B clustered with AtTET1 (TORNADO) and AtTET2, and PvTET8 clustered with OsTET7-9 and AtTET8-9. We did not find a homolog of AtTET13 in the *P. vulgaris* genome or in any other legume genome. This could suggest the presence of a particular clade in *Arabidopsis* or in the Brassicaceae that does not exist in other plants, at least not in *P. vulgaris* or in legumes. In our molecular tree, we identified 7 groups, each of which contained at least two members, except the group that contained PvTET10 alone. Sequence identity and similarity analysis coupled with the number of introns supported the idea that PvTET10 is a common ancestor of tetraspanin in common bean, as described for its homologs in *Arabidopsis* (Fig 1). By contrast, PvTET12, which has no introns, is the most recent tetraspanin member and arose by functional divergence and loss of introns [51, 52].

GmTET12A (accession number XP_003551251.1) and GmTET12B (accession number XP_003547633.1) are homologs of PvTET12 (accession number XM_007138229.1). In *M. truncatula*, we identified one homologue of TET12 (accession number XP_013463988.1); however, we did not find a corresponding homolog in *L. japonicus*. The cytoplasmic N and C termini of plant tetraspanins each have 6–10 aa, making them shorter than animal tetraspanins, which contain between 9 and 40 aa, and even shorter than fungal ones, which contain between 4 and 100 aa.

In addition, we conducted an exhaustive *in silico* characterization of tetraspanins in common bean to predict disulfide bond formation. We used a bioinformatic tool for disulfide connectivity prediction named DiANNA (clavius.bc.edu/~clotelab/DiANNA/) and found that disulfide bonds form between the single cysteine located in the SEL and the cysteine residues found in the LEL of all common bean tetraspanins, as previously suggested for tetraspanins in *Arabidopsis* [35].

Tetraspanins PvTET3 and PvTET1A are highly expressed in root and root hair cells

To establish the transcript accumulation for the different tetraspanin genes in *P. vulgaris* roots, we selected root tissues and sectioned different regions with different developmental stages according to the experimental requirements (described in Materials and methods). In our experiments with *P. vulgaris*, we considered the three developmental root hair zones, which were evident by 48 h post germination (hpg). As depicted in Fig 2C we sectioned the three different root zones and separated the root hair cells from the root tissue, generating the enriched root hair fraction from the three developmental stages (zones I, II, and III) and the corresponding shaved root (Fig 2C). Transcript accumulation for all tetraspanin genes, except *PvTET2B* due to the lack of specific regions for primers design for amplification (accession number XP 007152918.1), was determined in each one of the generated samples (root hairs and shaved root); this analysis was conducted by selecting each tetraspanin family member and determining its accumulation in root hairs at different developmental stages (Fig 2B).

The monomeric GTPase PvRabA2 is a good marker of the different developmental stages of root hairs due to its key role in root hair tip growth (S4 Fig), although it is also expressed in root tissue [53, 54]. We observed that RabA2 transcript accumulated in root hairs; as expected, the transcript accumulation was higher in zones II and III, where the cells are rapidly expanding or reaching full length, compared with zone I, where root hairs are just bulging out (S4 Fig). As expected, the shaved root section that lacked root hairs also had increased *PvRabA2* transcript accumulation in zones I, II, and III, again with higher accumulation in zones II and III (S4 Fig). Therefore, these root sections were used to determine the transcript accumulation for selected tetraspanin members in *P. vulgaris*. We found that *PvTET3* and *PvTET1A* are more abundant in shaved roots or root hairs from zones II and III than from zone I (Fig 2A and 2B). However, *PvTET1A* present a very low expression in root hairs from zone II, but it is expressed in those from zone III (Fig 2B). This differential expression contrasts with shaved roots, where *PvTET1A* transcript accumulation increases gradually beginning from zone I to zone II and from zone II to zone III (Fig 2A). Furthermore, an analysis of the reported expression atlas of *P. vulgaris* [55] indicates that *PvTET3* is ubiquitously expressed during the different root developmental stages, while *PvTET1A* is constitutively expressed in all root tissue, but with higher expression in some stages of root development (S5 Fig).

PvTET1A, *PvTET8*, *PvTET3* and *PvTET4* are induced in response to NFs or rhizobia inoculation

We then evaluated the transcript accumulation of some tetraspanin genes in response to nanomolar concentration of NFs (10^{-9} M), which can reprogram polar growth and nodule primordia development [6]. In agreement with previous observations [6], treatment with 10^{-9} M NFs caused root hairs to swell and undergo morphological changes (S6B Fig). As expected, no morphological responses were observed when chitosan was used as a negative control (S6A Fig).

We initially considered to evaluate the transcript accumulation in response to NFs or rhizobia for *PvTET1A and PvTET3* since these genes were the most highly expressed in shaved root

INFORME DE LABORES 2019

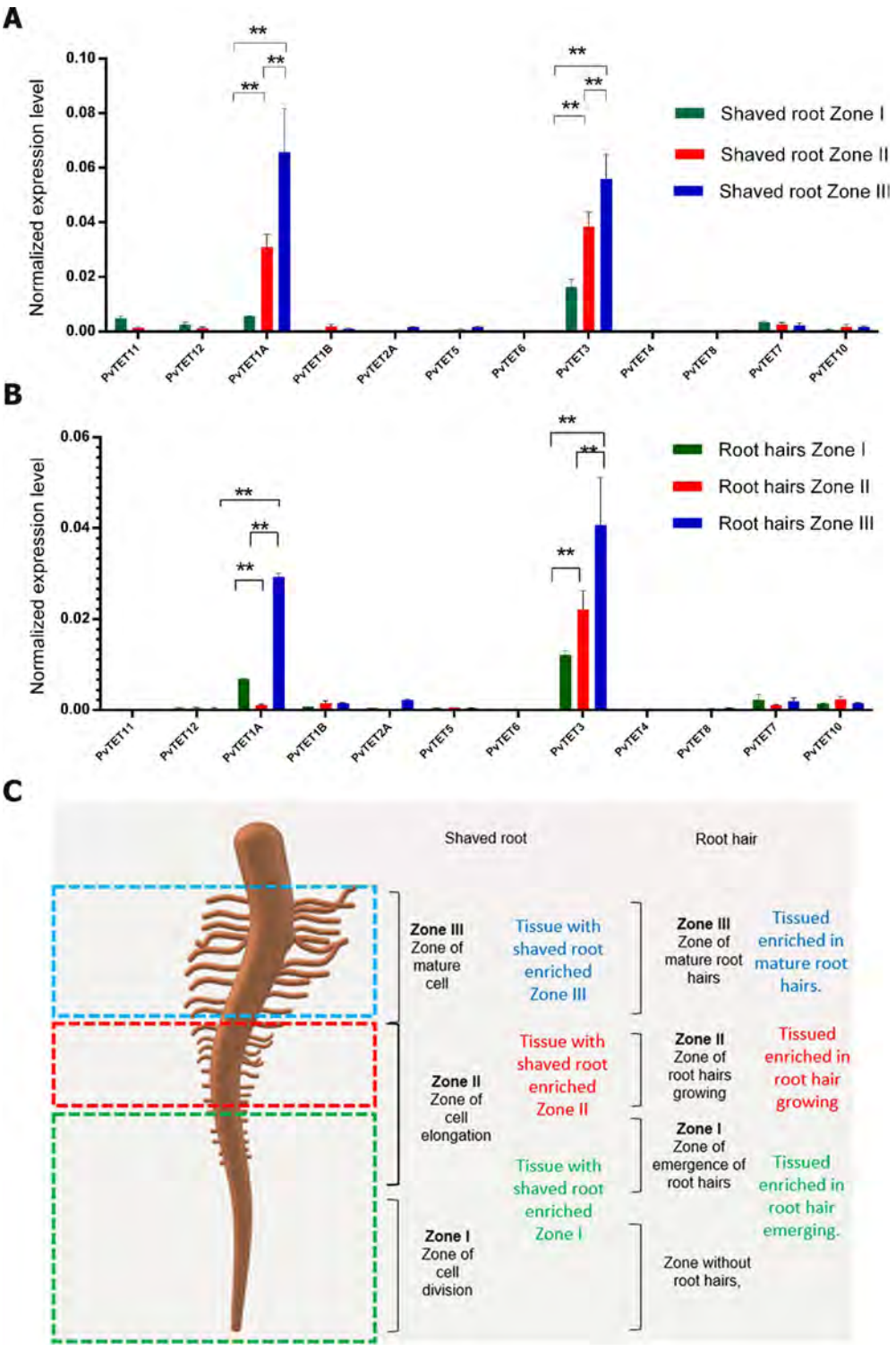

Fig 2. Tetraspanin gene expression profile in *P. vulgaris* root or root hairs from different developmental stages. The relative expression of each *PvTET* gene was evaluated by qRT–PCR in three different sections of root at 48 h post germination (hpg). Mature zone or Zone III (blue), elongation zone or Zone II (red), and meristematic, elongating and differentiating region or Zone I (green). Transcript accumulation was normalized to the expression of *EF1a*, which was used as a reference gene. Bars represent means ± SEM from at least three independent biological replicates with three technical repeats. (A) Tetraspanin (TET) gene expression in shaved root and (B) root hairs at different development stages at 48 hpg. Tissues enriched with emerging or bulging root hairs from Zone I (green bar), tissues enriched with

INFORME DE LABORES 2019

growing root hairs (red bar) and tissues enriched with mature root hairs (blue bar). Transcript accumulation was normalized to the expression of *EF1a*, which was used as a reference gene. Bars represent means ± SEM from at least three independent biological replicates with three technical repeats. P-values <0.05 are marked with two asterisks (Student's t-test). (C) Cartoon depicting the different root and root hairs zones analyzed.

https://doi.org/10.1371/journal.pone.0219765.g002

and root hairs under normal conditions, other tetraspanin genes were also tested, under NFs or Rhizobia inoculation, but the one that did not respond were not considered for further analysis (S7 Fig). *PvTET1A* was downregulated in *P. vulgaris* roots in the first 36 h days after inoculation with NFs, but we detected a response at 5–10 days post inoculation with rhizobia (Fig 3A). By contrast, *PvTET3* expression did not change within the first 24 h following inoculation with NFs, but a significative decrease was observed at 36 h after treatment. On the other hand, when inoculated with *R. tropici*, a further decrease was observed at 5 and 14–18 dpi (Fig 3B). Thus, some tetraspanin transcript levels respond to NF treatment or bacterial inoculation depending of the developmental stage, i.e at 5 dai, *PvTET1A* increases while *PvTET3* decreases. To confirm that *P. vulgaris* roots respond to rhizobia inoculation, we assessed the transcript accumulation of *PvENOD40*, an early nodulin gene induced during nodule development. *PvENOD40* is clearly induced after rhizobia inoculation, indicating that the nodule program is induced under our experimental conditions (Fig 3C).

We then further analyzed the transcript accumulation of *PvTET4* and *PvTET8* in roots treated with NFs and rhizobia. *PvTET4* was upregulated after *R. tropici* inoculation (Fig 3D), whereas *PvTET8* did not increase in response to NFs within the first 6 days, but it was specifically induced in response to rhizobia inoculation after 7 days (Fig 3E). Therefore, we selected *PvTET8* to examine whether transcript accumulation was correlated with promoter activity. We cloned the promoter and generated the *pPvTET8*::*GUS-GFP* construct, which revealed that *pPvTET8* was induced during nodule primordium development as well as in the meristematic region of the apical root, including the lateral root primordium (Fig 3F and 3G). We also observed clear promoter activity during the emergence of lateral root primordium, which originates from the pericycle (Fig 4B–4E), and this promoter activity remained in the root primordium (Fig 4F). Whereas the nodule primordium arises in the outer cells of the cortex (Figs 3G and 5D), the lateral root originates from the internal pericycle cells (Fig 3F). We examined promoter activity by assessing GUS activity (Fig 4B–4E) and fluorescence from the pPvTET8::GUS-GFP fusion. Both approaches yielded the same results (Fig 4G) including the pPvTET10::GUS-GFP (Fig 4I).

Next, we assessed *PvTET8* promoter activity during nodule development, from infection thread formation to fully grown nodules, and we found that the *pPvTET8*::*GUS-GFP* promoter is highly active during the early stages of nodule development, which includes infection thread formation in the root hairs (Fig 5A and 5B). Thereafter, when the cortical cells started to divide, forming cells that will give rise to the nodule primordium, clear promoter activity was observed in the outer cells that form the primordium (Fig 5C–5E). The fully developed nodule also depicts a clear and specific promoter activity in the infected zone of the nodule (Fig 5E). We also evaluated the promotor activity for *pPvTET1A*::*GUS-GFP* (Fig 5F and 5G) and *pPvTET3*::*GUS-GFP* (Fig 5H) the two most highly expressed gene in *P. vulgaris* root. Although these genes do not seem to have a strong increase during nodulation, when the promotor activity was assayed, there is a clear evidence that apart from the vascular bundle, the expression in the nodule is very clear.

Since *pPvTET8* was specifically induced in response to rhizobia inoculation, we analyzed the promoter sequence from *PvTET8* up to 1.0 kb upstream of the translation start site of *PvTET8* using PlantCARE (database) to identify putative *cis*-acting regulatory elements. In

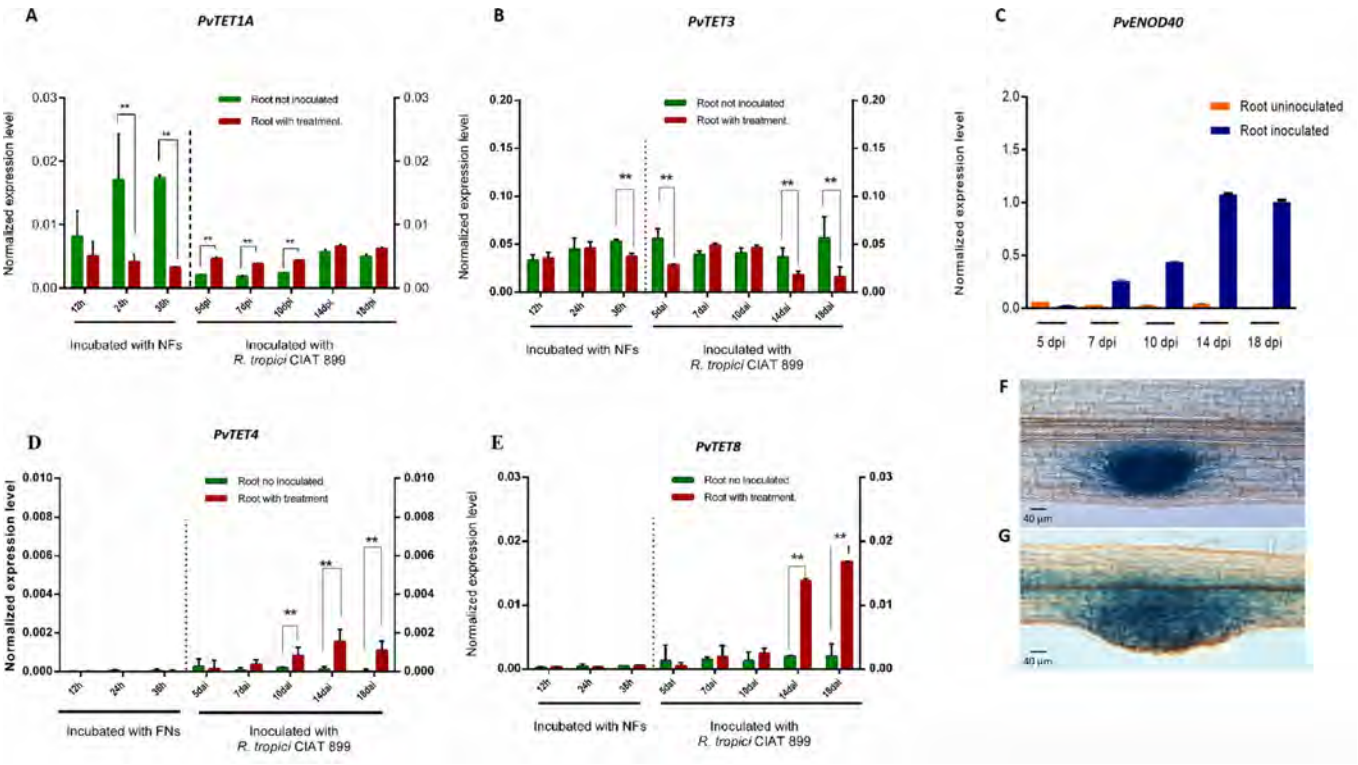

Fig 3. Expression of *PvTET1A*, *PvTET3*, *PvTET4*, and *PvTET8* in *P. vulgaris* during nodule development. Transcript accumulation is observed during nodule development under rhizobia colonization. (A) *PvTET1A*, (B) *PvTET3* and (C) *PvENOD40* transcript accumulation after Nod factor (NF) treatment or inoculation with *R. Tropici* CIAT 899 are depicted. *PvTET4* (D) and *PvTET8* (E) specifically respond to rhizobia inoculation. These results are compared with uninoculated roots harvested at the same time (green bars). Expression values were normalized with those of *EF1a*. Bars represent means ± SEM of at least three independent biological replicates with three technical repeats. P-values <0.05 are marked with two asterisks (Student's t-test). Promotor activity of *PvTET8* in lateral root primordia (F) and nodule primordia development (G).

https://doi.org/10.1371/journal.pone.0219765.g003

this analysis, we identified at least 14 different regulatory elements with a length of between 4 and 11 bp. Some *cis*-elements are represented in Fig 4A. The *cis*-regulatory elements TATA and CAAT were highly repeated in the promoter sequences. In addition, several putative *cis*-elements involved in the light, heat, and drought stress response, circadian control, defense, and anaerobic induction were present, as was one box associated with the YABBY transcription factor. Thus, *cis*-elements associated with defense and stress responsiveness and cell fate were well represented in this promoter region, as represented in Fig 4A.

Since *pPvTET3*::*GUS-GFP* was highly expressed in the root (Fig 5H), we prompted to explore if there is promotor activity during different stages of nodule development. We found that pPvTET3::*GUS-GFP* is expressed in the root meristematic region and vascular bundles (Fig 6A and 6B), including a low promotor activity during the early cell divisions in the nodule primordium (Fig 6C and 6D) and during the early nodule development (Fig 6E), again with higher activity in the vascular bundles, however, a clear localization in the nodule was found, although at latter stages of development in fully developed nodules (Fig 6F and 6G). Furthermore, the *pPvTET3* seems to be more localized in the cortex of the nodule, as compared to the *pPvTET8*, which seems more localized in the central region (Fig 5E) and most related to the infected region. These results suggest that both, *pPvTET8* and *pPvTET3* could be differentially expressed in the same organ, but in different region.

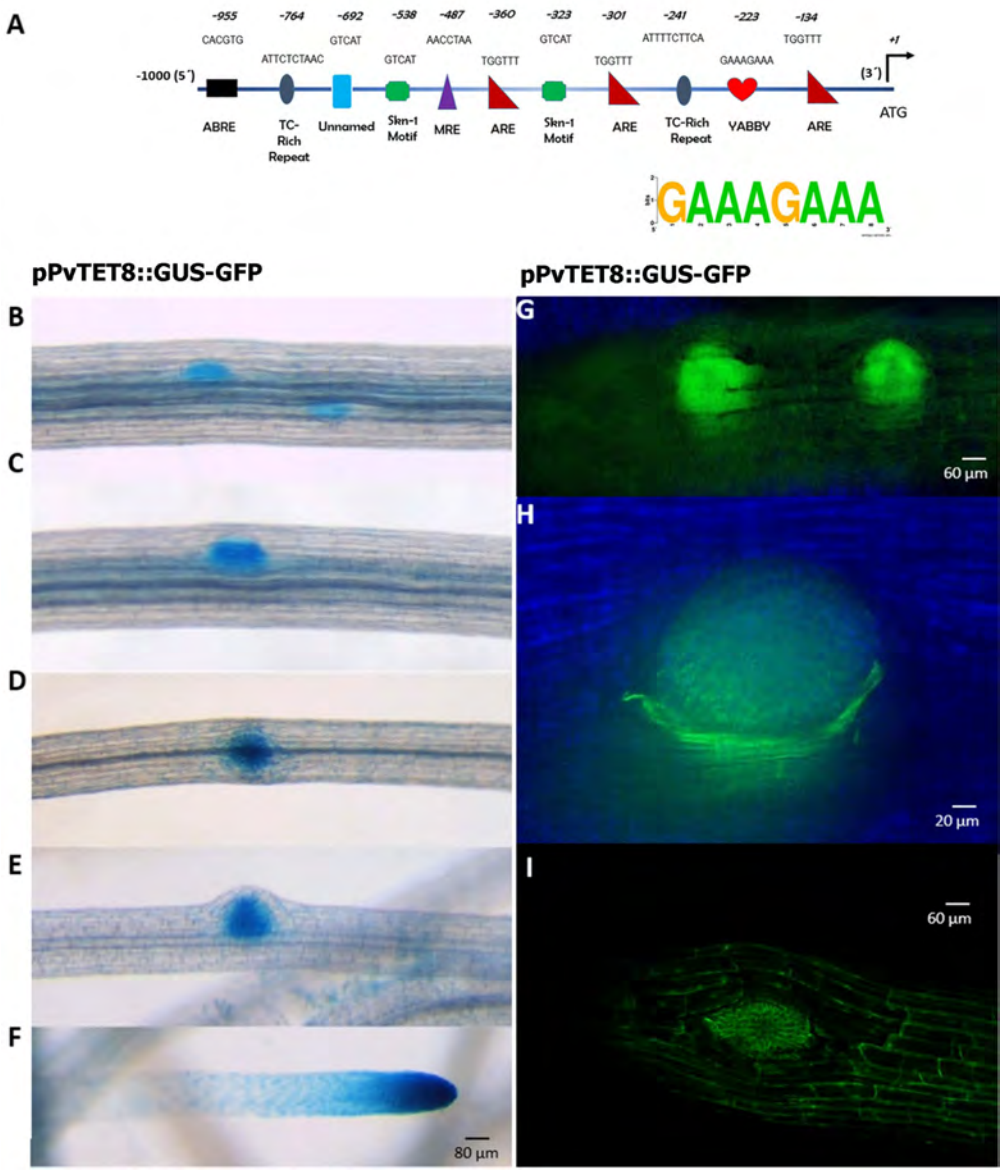

Fig 4. *PvTET8* transcript accumulation and promotor activity during lateral root and nodule primordia development. (A) Analysis of putative cis-regulatory elements in the promoter region of *PvTET8*. (B-F), *pPvTET8*::*GUS-GFP* promotor activity in *P. vulgaris* root during lateral root emergence. (G and H) show the promoter activity during the onset of lateral root development and the meristematic region of the emerging lateral root as depicted by fluorescence. (I), Subcellular localization of 35S:PvTET10-GFP during lateral root formation. Transgenic composite plants from *P. vulgaris* were generated by the *A. rhizogenes* method.

https://doi.org/10.1371/journal.pone.0219765.g004

Mycorrhizal association downregulates *PvTET3*, while phosphate scarcity upregulates *PvTET12* and downregulates *PvTET3*

Since the nodulation process recruited many genes from the mycorrhizal association, we also explored if the tetraspanin genes could be modulated in response and mycorrhizal association and low phosphate. Therefore, we determined the effect of mycorrhizal interaction with *P. vulgaris* on the accumulation of different TET transcripts. We inoculated *P. vulgaris* seedlings with *R. irregularis* and included two controls, one in which plants were uninoculated and

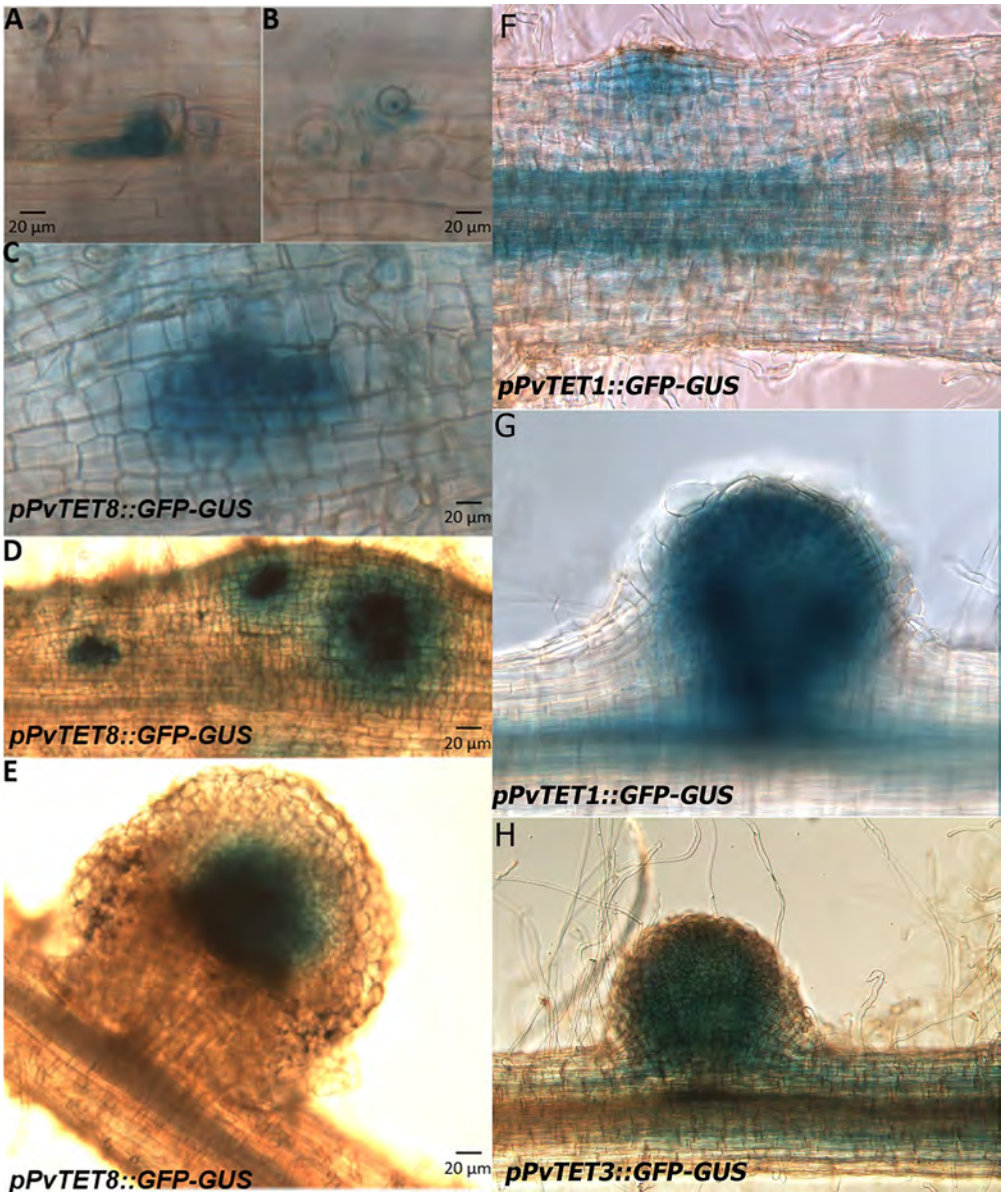

Fig 5. Promotor activity of *PvTET8* during nodule development and subcelular localization of PvTET6 in *P. vulgaris* during the infection process with rhizobia. (A-C) *pPvTET8*::*GUS-GFP* promotor activity at the early stages of infection thread formation in root hairs. (C and D) Promotor activity of *pPvTET8*::*GUS-GFP* during the early stages of cell division during primordia development and (E) in fully developed mature nodule, as depicted the promotor is highly expressed in the infection zone of the nodule. (F-G) Promotor activity for *pPvTET1A*::*GUS-GFP* and (H) promotor activity for *pPvTET3*::*GUS-GFP*. Transgenic composite plants were generated with *A. rhizogenes* and promotor expression analyzed by GUS activity. Bars represent 20 µm in all images.

https://doi.org/10.1371/journal.pone.0219765.g005

irrigated with a standard concentration of phosphate (500 µM) and another in which plants were uninoculated and irrigated with medium deficient in phosphate (phosphate scarcity at 50 µM), which is expected to induce the plant root response to phosphate scarcity, such as lateral root formation and root hair proliferation. Both controls were included to show the specific effect of mycorrhization on different tetraspanin transcript accumulation as a result of root hair proliferation and lateral root formation. While *PvTET8*, *PvTET4*, and *PvTET3* expression was modulated during nodule formation (Fig 3A and 3B and Fig 4A), inoculation

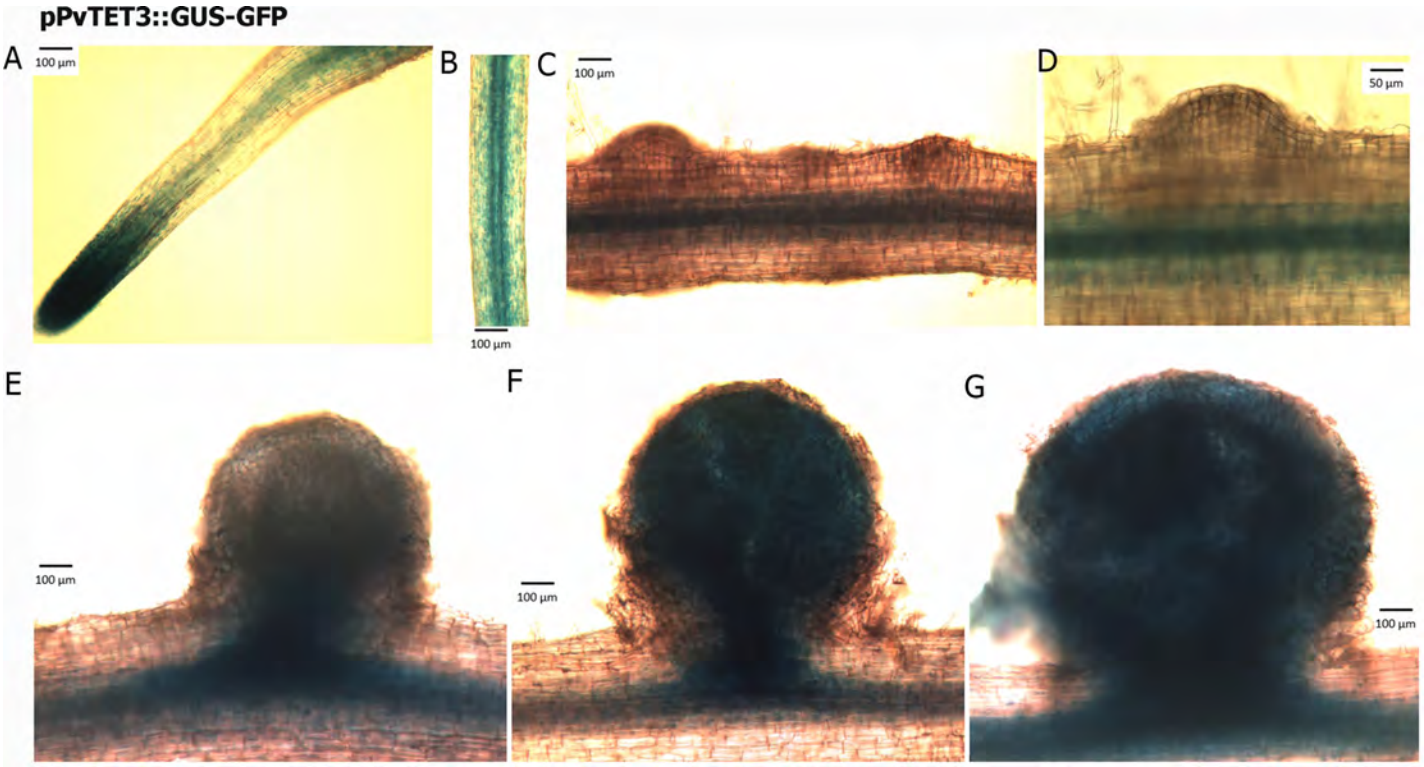

Fig 6. Promotor activity of *PvTET3* in the root and during nodule development in *P. vulgaris* during symbiotic conditions. (A and B) *pPvTET3*::*GUS-GFP* promotor activity in the apical root and vascular bundles. (C and D) *PvTET3* promotor activity at the early stages of nodule primordium formation. (E- G) Promotor activity during the nodule development. Transgenic composite plants were generated with *A. rhizogenes* and promotor expression analyzed by GUS activity.

https://doi.org/10.1371/journal.pone.0219765.g006

with *R. irregularis* only affected *PvTET3* expression during the mycorrhizal association (see Fig 7A). As expected, the expression of the phosphate transporter PT4 which is induced during the mycorrhizal association, was found to be induced under our experimental condition (Fig 7C).

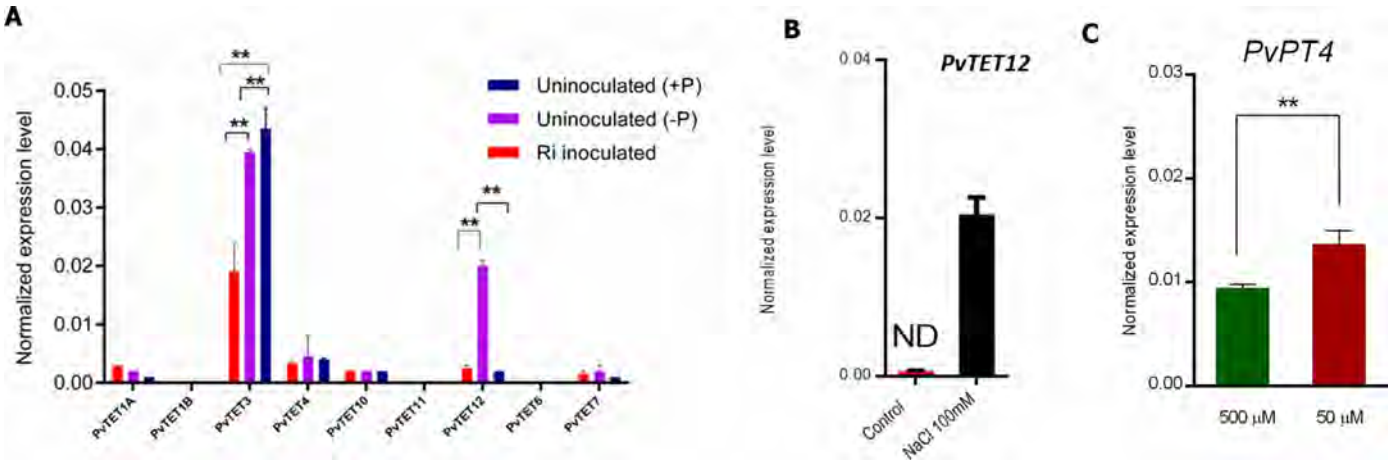

Fig 7. Tetraspanin transcript accumulation profile in *P. vulgaris* under *R. irregularis* colonization. (A) Tetraspanin transcript accumulation in *P. vulgaris* roots colonized with *R. irregularis* in the symbiotic stage at 6 wpi as compared with uninoculated plants under phosphate scarcity with potassium phosphate at 50 µM. Transcript accumulation was normalized to the expression of *Ef1a*, which was used as a reference gene. (B) Expression of tetraspanin *PvTET12* in *P. vulgaris* roots during abiotic stress induced by NaCl conditions at 100 mM at 24 hpi. (C) Phosphate transporter PT4 transcript accumulation under mycorrhizal condition. Data are the means ± SEM of two biological experiments (three roots collected from each biological experiment and for each period were used).

https://doi.org/10.1371/journal.pone.0219765.g007

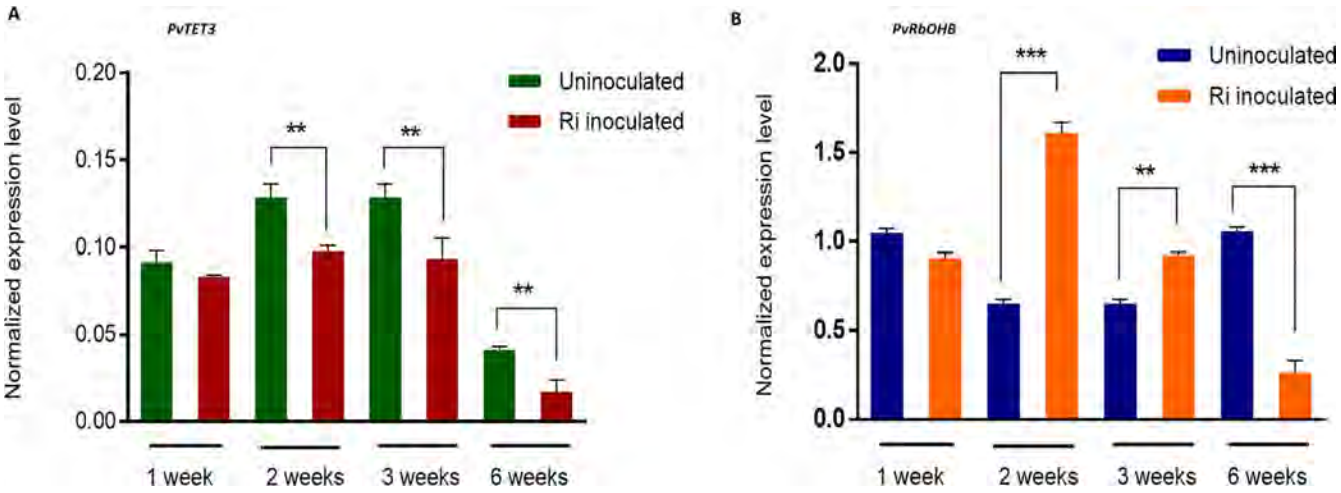

Fig 8. *PvTET3* and *PvRbohB* expression during mycorrhiza formation. (A) Quantitative RT-PCR analysis of relative expression levels of *PvTET3* in roots (wild type) inoculated with *R. irregularis* and under un-inoculated condition at the indicated number of weeks post-inoculation (wpi). Transcript accumulation was normalized to the expression of *Ef1a*, which was used as a reference gene. Data are the means ± SEM of two biological experiments (three roots collected from each biological experiment and for each period were used). (B) Expression of *PvRbohB* in *P. vulgaris* roots colonized by *R. irregularis*. Quantitative RT-PCR analysis of relative expression levels of *PvRbohB* in roots (wild type) inoculated with *R. irregularis* compared with expression in uninoculated roots of *P. vulgaris* at different weeks post-inoculation (wpi). Transcript accumulation was normalized to the expression of *Ef1a*, as a reference gene. The data are the means ± SEM of two biological experiments (three roots collected from each biological experiment and for each period).

https://doi.org/10.1371/journal.pone.0219765.g008

A temporal analysis of *PvTET3* transcript accumulation under mycorrhization confirmed that *PvTET3* transcript levels were lower at 2, 3, and 6 weeks after mycorrhization compared with the control (Fig 8A). This suggests that *PvTET3* was downregulated during mycorrhization (Fig 7A and Fig 8A). It has been reported that transcript accumulation of *PvRbOHB* decreases during mycorrhizal association [56]. Therefore, we evaluated the accumulation of *PvRbOHB* transcript at 1, 2, 3, and 6 weeks post inoculation (wpi) to define its temporal response and correlate it with that of *PvTET3* (Fig 8B). *PvRbOHB* was not induced during the first week post inoculation, during which its expression was comparable to that of the control condition (Fig 8B). However, after 2–3 weeks, a clear increase in *PvRbOHB* transcript accumulation was observed, but a decreased *PvTET3* expression was found. However, at 6 weeks, a clear decrease in both *PvRbOHB* and *PvTET3* was observed, and thus confirming the previously reported data for *PvRbOHB* under mycorrhizal association [56].

We found no significant differences at the transcriptional level for the other tetraspanins under our experimental conditions (S7 Fig). However, we identified a clear *PvTET12* upregulation under phosphate scarcity (Fig 7A). It is interesting that under normal growth conditions, we did not observe significant *PvTET12* expression in root hairs at different developmental stages or even in the shaved roots (Fig 2A and 2B), even though its homolog, *AtTET12*, has been identified as a transcriptional signature in root hairs and pollen tubes [57]. To determine if another different stress, such as osmotic or saline treatment, could modify the *PvTET12* transcript level, we treated the *P. vulgaris* root with 100 mM NaCl; which is known to induce a saline response [58–60]. Under saline stress conditions, we found that *PvTET12* expression was also upregulated (Fig 7B).

P. vulgaris tetraspanins localize to the apical plasma membrane, intracellular vesicles, and meristematic regions

Tetraspanin proteins in general have been described to be plasma membrane proteins and component of cytoplasmic vesicles. However, TET3 in Arabidopsis has been found in

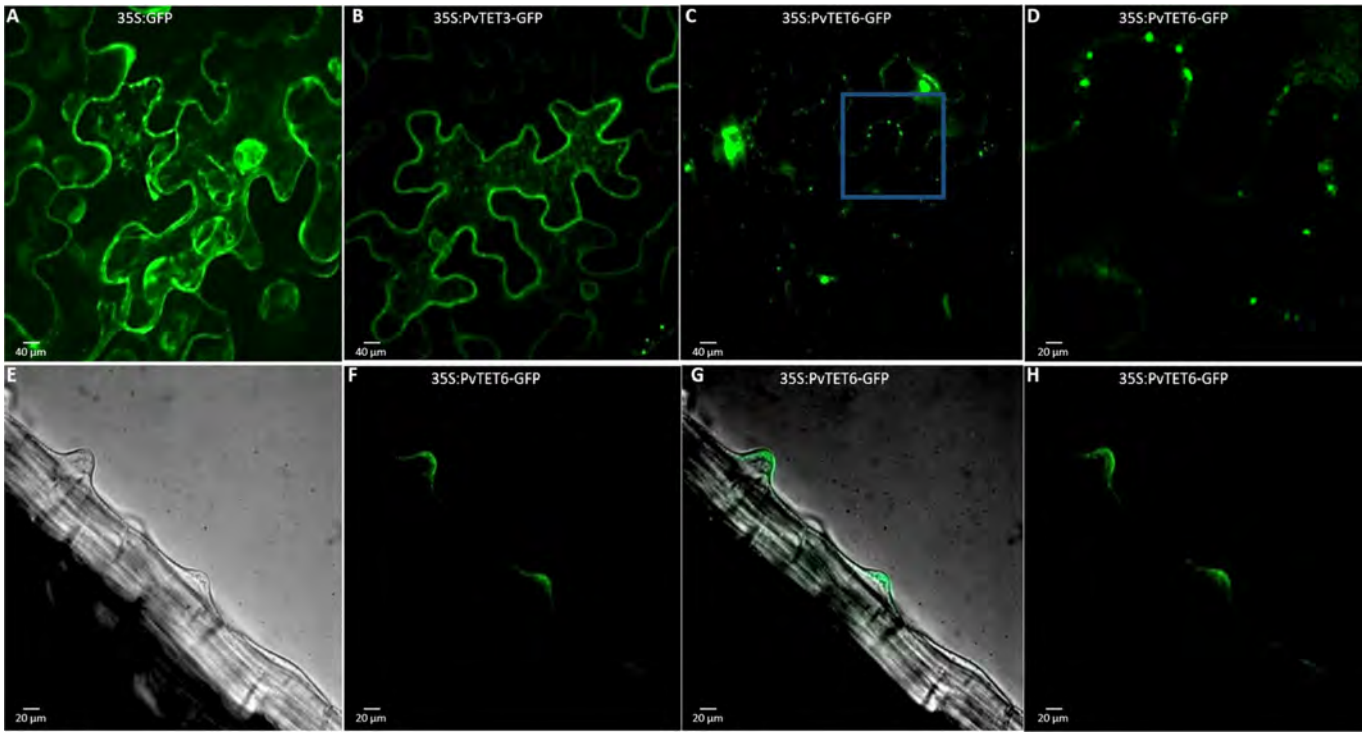

Fig 9. Subcellular localization of PvTET6 and PvTET3 in *Nicotiana benthamiana* leaves and growing root hairs of *P. vulgaris*. (A) Confocal analysis of GFP expression in the leaves of transgenic *N. benthamiana* plants. (B) 35S:PvTET3-GFP. (C) 35S:PvTET6-GFP. (D) 35S:PvTET6-GFP (close-up of region indicated in C). (E-H) 35S:PvTET6-GFP subcellular localization in transgenic living *P. vulgaris* root hairs. Images in bright field (E), Merge (G), GFP signal (F), Z-projection (H). Bars = 20 μm.

https://doi.org/10.1371/journal.pone.0219765.g009

proteomic analysis of plasmodesmata. Therefore, we determined the subcellular localization of *PvTET3* and *PvTET6* by generating GFP fusions of their encoding genes and transiently expressing these constructs in *N. benthamiana* leaves (Fig 9A–9D). An analysis of leaves expressing the 35S:PvTET3-GFP and 35S:PvTET6-GFP constructs under the control of a constitutive promoter (CaMV35S) showed that these proteins examined in this study accumulated at the periphery of *N. benthamiana* epidermal cells, indicating a membrane localization (Fig 9B and S8 Fig), and clearly differentiated from the cytoplasmic localization of GFP in control agroinfiltrated cells (Fig 9A). Furthermore, some of the tetraspanins localized to fluorescent spots in the plasma membrane, suggesting plasmodesmata localization (Fig 9C, inset). We also generated transgenic *P. vulgaris* composite plants expressing 35S:PvTET6-GFP using *A. rhizogenes* and found that some tetraspanins are expressed in vesicular structures that are swept along by cytoplasmic flux in growing root hairs, but are also localized in the apical plasma membrane of these cells (Fig 9E–9H, S1 Movie and S2 Movie). In order to determine the plasma membrane localization, we generated agroinfiltrated *N. benthamiana* epidermal cells expressing the tetraspanin and subjected to NaCl treatment for plasmolysis. These results suggest that the signal remains associated to the plasma membrane (S8 Fig).

We then evaluated 35S:PvTET10-GFP expression in composite plants. TET10 exhibited similar localization to TET6, namely, apical localization in the plasma membrane and dynamic vesicles in the cytoplasm of growing root hair cells in a pattern that sometimes follows the cytoplasmic streaming with higher ambulation at the tip dome (Fig 10A–10C). Furthermore, in *P. vulgaris* composite plants expressing 35S:PvTET10-GFP under nodulation conditions, the cortical cells that enter the division process that will generate the nodule primordium are

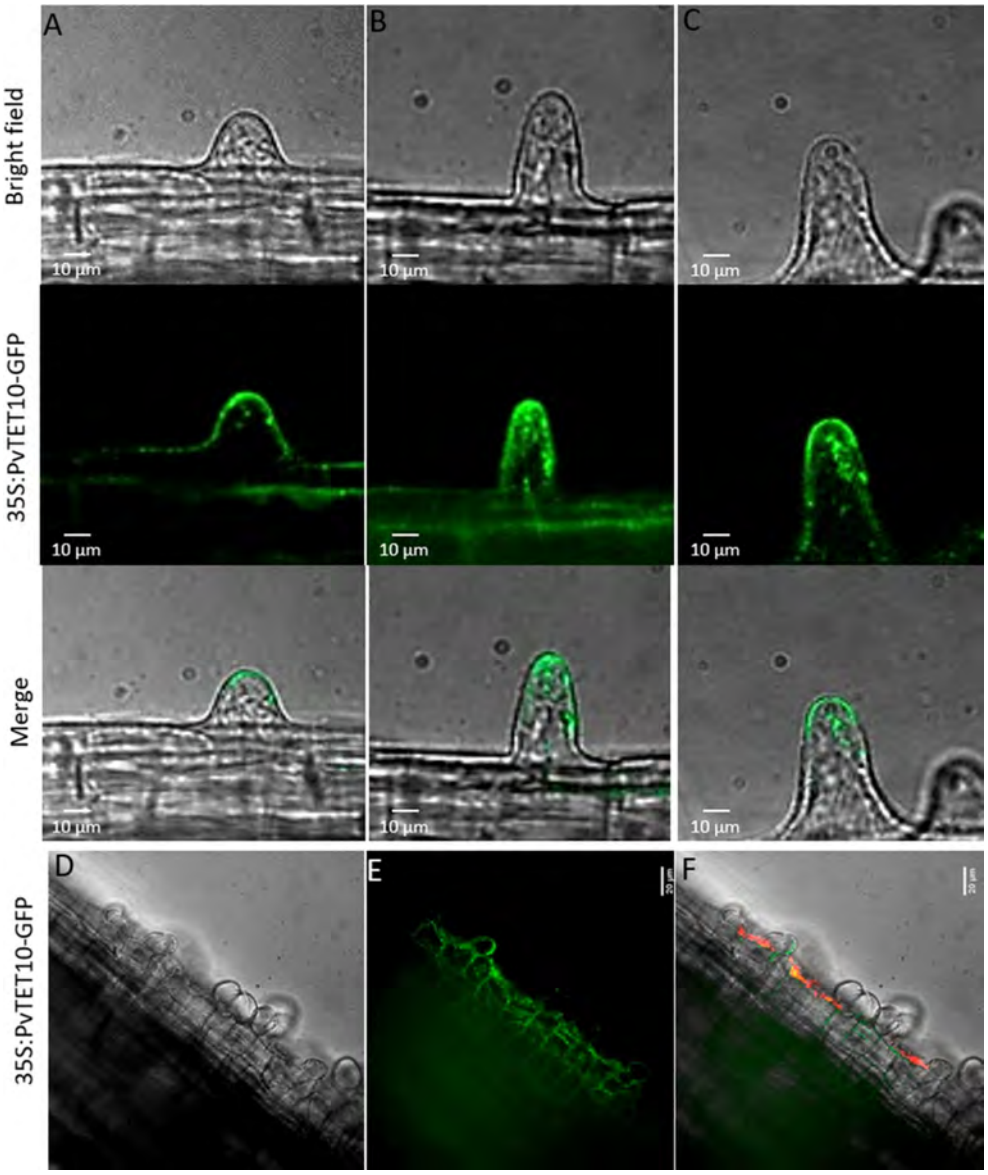

Fig 10. Subcellular localization of PVTET10 in growing root hairs from *P. vulgaris*. (A, B and C) Apical membrane localization of 35S:PvTET10-GFP at different developmental stages of the growing root hair. (D, E and F) Cytoplasmic vesicle localization for PvTET10, and its accumulation in the infection site where the infection thread and nodule primordia are induced. *P. vulgaris* plants were transformed by *A. rhizogenes* in order to generate the composite plants. Bacterial colonization is in red and the subcellular localization of PvTET10 is in green.

https://doi.org/10.1371/journal.pone.0219765.g010

enriched in these cytoplasmic vesicles (Fig 10D–10F). Since TET3, TET6, and TET10 localized to moving vesicles, we further examined the dynamics and behavior of these vesicles.

We selected PvTET3, which we know localizes to vesicular structures in *N. benthamiana* (Fig 11A and 11B) and *P. vulgaris* composite plants (Fig 11C–11J), to determine the dynamics and shapes of these vesicles. In *P. vulgaris* epidermal cells, these vesicles were tracked in a time lapse of 1.6 seconds for 3 min in transgenic roots overexpressing 35S:PvTET3-GFP. We observed fusion events that resulted in larger vesicles, with amorphous shapes that resemble protrusions (Fig 11C–11J).

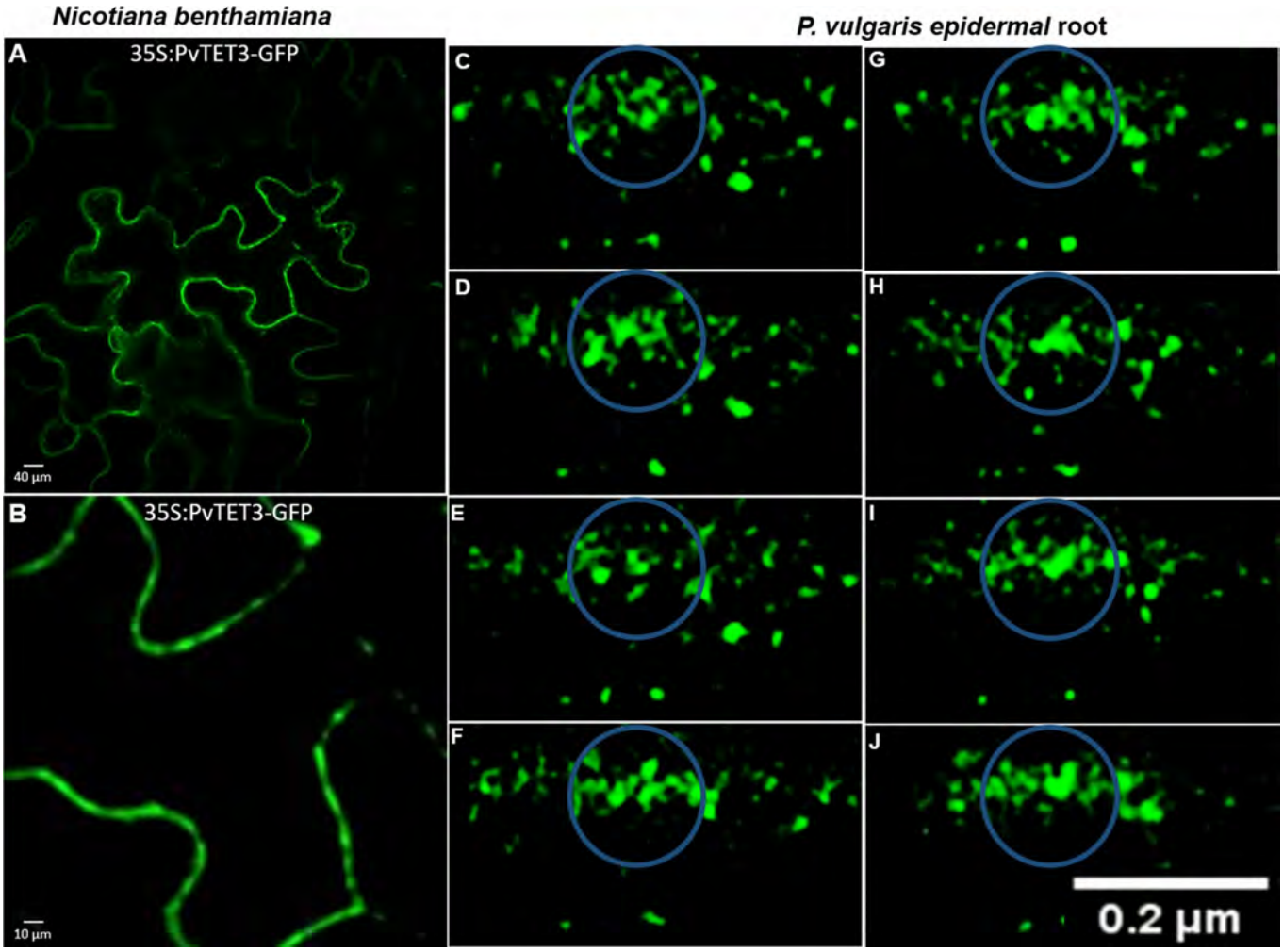

Fig 11. Subcellular localization of PvTET3 in *N. benthamiana* leaves and *P. vulgaris* roots. (A and B) 35S:PvTET3-GFP localization in cytoplasmic vesicles in agroinfiltrated *N. benthamiana* leaves. (C-J) Subcellular localization of 35S:PvTET3:GFP in *P. vulgaris* composite epidermal root cells. Cytoplasmic vesicles were tracked over time in order to show the fusion and morphological changes resembling protrusions during the cytoplasmic streaming. Vesicles were tracked in a time lapse of 1.6 seconds for 3 min in transgenic roots expressing 35S:PvTET3-GFP.

https://doi.org/10.1371/journal.pone.0219765.g011

Discussion

We found that *PvTET1A*, *PvTET3*, *PvTET4* and *PvTET8* are induced and differentially expressed during early nodule development, as depicted by transcript accumulation and promoter activity and in the fully grown and mature nodule, but with different timing and strength. Furthermore, these expression patterns resemble those found in primordia during lateral root formation which also requires a new program that involves cell division and ROS production. The finding that some tetraspanin presents a clear membrane localization at the tip of the root hairs and some others in what appears to be associated with plasmodesmata (PD), and cytoplasmic vesicles, suggest a role in symplastic communication trough regulation of PD or in cell trafficking as described in animal cells [18].

We identified the tetraspanin family in *P. vulgaris* and found *PvTET10* to be a conserved tetraspanin with at least one representative in each legume species examined, except for soybean, which contained more members due to a genome duplication event [61]. *PvTET10* clusters with *AtTET10* and *OsTET14*, which contain similar structural features of introns/exons,

INFORME DE LABORES 2019

suggesting that *PvTET10* is the ancestral tetraspanin gene, as is AtTET10 in the Brassicaceae and *OsTET14* in *O. sativa* [35, 50]. These structural intron/exon patterns indicate a similar origin as suggested for deuterostomes, in which tetraspanins are the product of a divergent evolutionary process and originated from at least one common ancestor [51, 62]. In our unrooted phylogenetic tree, *PvTET1A* and *PvTET1B* grouped with *AtTET1* (*TORNADO*) and *AtTET2*, while *PvTET8*, *OsTET7-9*, and *AtTET8-9* clustered together (S2 Fig and S3 Fig).

We found that *PvTET3* and *PvTET1A* transcripts are more abundant and ubiquitously expressed during root and root hair development (Fig 2A and 2B). In angiosperms plants such as *Arabidopsis* and *P. vulgaris*, primary root formation takes place during embryogenesis, whereas lateral roots form post-embryonically from pericycle founder cells, and both of these processes are mediated by changes in hormone levels [63, 64]. *PvTET1A* is expressed post-embryonically, between 2 and 4 dpg, in the seedling when root growth begins and before lateral roots emerge [38]. According with our phylogenetic data, *PvTET1A* is the homolog of *TORNADO* in *Arabidopsis* (*AtTET1* or *AtTRN1*), which regulates cell specification in the root epidermis during radial pattern formation and thus in agreement with our transcriptional profile for *PvTET1A* with a high expression in root [65]. However, our transcriptional profile does not correspond with the reported higher *TRN1* promoter activity in the meristematic zone in the root tip. This discrepancy with higher expression in root zone II and III and lower in zone I that correspond to the meristematic region could be due to the fact that the promoter region of *PvTET1A* does not contain a putative cis-regulatory element, GCCACT, that exists in *Arabidopsis TRN1*, and associated with meristematic expression and auxin dependency [65, 66]. Therefore, *PvTET1A* could have a different regulation, or its expression pattern could differ from that reported in *Arabidopsis*.

The finding that *PvTET3* transcript accumulation was downregulated under nodulation and mycorrhizal conditions in *P. vulgaris* roots and that the encoded protein localizes to the PM and PD, suggests that PD could be a regulated structure during the mutualistic interactions. We also found that *PvTET6* is specifically targeted to the PM and PD, in agreement with the subcellular localization of some homologous tetraspanins identified in *Arabidopsis*, such as *AtTET3* and *AtTET5* [35, 67–71]. PD are connections between cells that mediate symplastic communication from single cells to tissue domains, these structures have essential roles in cell-to-cell communication [72]. Both the density and aperture size of PD are developmentally regulated through the deposition or solubilization of callose by callose synthases or glucanases, allowing the formation of spatial symplastic domains that establish tissue-specific developmental programs [73]. Numerous non-cell-autonomous proteins (NCAPs) and small RNAs travel through the PD and play crucial roles in cell fate determination and organ patterning during plant development. In vascular plants, it has been suggested that PD networks are associated with shoot apical meristem (SAM) organization in *Arabidopsis* and maize (*Zea mays*) [74–76]. Typical PD proteins, such as AtPDLP1, have a specific signal peptide, LVL, located in a transmembrane domain [67], which was also found in PvTET6 and PvTET3. Transmembrane domains in tetraspanin have turned to play important roles. For instance, a single point mutation, L31S substitution in the third amino acid of TM1 has been associated with field-evolved resistance of cotton bollworm to transgenic Bt cotton [77].

In rice, blast disease caused by the hemibiotrophic fungus *Magnaporthe oryzae* grow from one cell to the next through PD. This response is coordinated by chitin perception that requires a receptor kinase (CERK1) and a chitin elicitor binding protein (CEBiP), which sense the chitin and induce a reduction in the cell-to-cell connectivity via PD [80, 81]. During the nodulation process it has been recently described that PD connection between the phloem-early primordium-epidermal cell forming the infection thread is a key step for the infection process [82, 83]. Again, it seems that PD are key components of the photogenic and

mutualistic response and PD localized tetraspanins could be important modulators of the intercellular flux regulating the symplastic continuity and molecular flux between cells. It could involve ROS to regulate PD permeability by facilitating the cross-linking process of callose [84]. Therefore, the observed downregulation or upregulation of *PvTET3* could affect PD composition by modulating the capability of tetraspanin to recruit some additional molecular components required to modify the callose composition in PD during mycorrhizal or rhizobia association. This may also facilitate the hypha or infection thread to move cell-to-cell through the PD connections or facilitate the diffusion of some proteins, such as transcription factors or metabolites, required to fine-tune the regulation of cortical and cortex responses.

Nodulation involves substantial crosstalk between NFs and auxin signaling in *Medicago truncatula*, with a high accumulation of auxin at the site of nodule meristem formation [85]. Indeed, there is a large overlap between genes induced in response to NFs and auxin, including two tetraspanin genes with homology to *PvTET3* (Medtr4g061010) and *PvTET1A* (Medtr8g101600) [85]. In addition, a previous report showed that *PIN1* expression was reduced in the *Arabidopsis trn2-1* mutant, which has compromised auxin transport activity during the transition from floral meristem termination to gynoecium development, which suggests a link between tetraspanin and auxin homeostasis [86]. Therefore, in addition to altering auxin transport, Nod factors could modulate the expression of specific tetraspanins that influence hormone levels, which could regulate cell division, a well-described process during nodulation [87]. If *PvTET1A* and *PvTET3* are downregulated during the interaction with NFs, this response could be associated with the disruption of auxin transport or the stimulation of auxin biosynthesis [88]. We suggest that NFs signaling has a profound impact on *PvTET1A* and *PvTET3* expression by affecting auxin levels and thereby coordinates nodule primordium development. Indeed, it is well known that NFs interfere with auxin transport, biosynthesis, and homeostasis [87, 89].

The finding that *PvTET4* and *PvTET8* are induced during early nodule development with different timing and localization, as depicted by transcript accumulation and promoter activity and in the fully grown and mature nodule. Our results indicate that *PvTET8* could be involved at different developmental stages of nodule primordia formation and in the infected thread region, and *PvTET3* although we did not find a high transcript accumulation, the promotor activity indicates that is expressed in root and mature nodule, suggesting a role in the mature nodule or later on during senescence. Furthermore, these expression patterns resemble those found during lateral root formation. Both lateral root primordium and nodule primordium formation require differentiated cells to become dedifferentiated and then to enter a new program that involves cell division. Therefore, this tetraspanin could be involved in the molecular mechanism that maintains meristem activity.

Furthermore, the roles of tetraspanin have been expanded beyond intercellular boundaries. It has been reported recently that *Arabidopsis* cells secrete exosome-like extracellular vesicles that are derived from the multivesicular bodies (MVBs), which contain cytoplasmic material, such as proteins, miRNA, and lipids [23, 90]. Under certain circumstances, these MVBs fuse to the plasma membrane and release the internal vesicles into the extracellular space. It has been demonstrated recently that tetraspanins are key components and specific markers for animal (CD63) and plant exosomes (*AtTET8* and *AtTET9*) [23]. In *Arabidopsis*, exosomes transport key miRNAs that induce silencing of fungal genes critical for pathogenicity in *Botrytis cinerea*, defining a role for tetraspanin and exosome biogenesis in intercellular and inter-kingdom communication [23]. This could explain why *AtTET8* expression is upregulated upon treatment with pathogen elicitors [38] and why, during our experimental conditions, *PvTET8* is induced when plants are infected with rhizobia. It is possible that exosomes could play an important role during the mutualistic interaction. Furthermore, tetraspanin genes are among

the induced genes in the reported legume transcriptome of wild peanut (*Arachis spp*) roots infected with nematodes, suggesting that the pathogenic response in legumes also involves tetraspanins [91].

The upregulation of *PvTET8* during the defense response also can be explained by the enrichment of defense response cis-regulatory elements in its promoter region. Indeed, it has been widely suggested that the molecular mechanism underlying mutualism was derived from that underlying pathogenic interactions, but suppression of the immune response allows the symbiont to colonize the plant host [92]. It will be interesting to determine the specific role of *PvTET8* during nodulation and mycorrhization and explore the role that vesicles and exosomes could play in recruiting proteins or membrane-associated proteins that are required in the plasma membrane during mutualistic interactions.

Our data showing that *PvTET12* is upregulated under phosphate scarcity, but not under mycorrhizal association, suggest that *PvTET12* expression is highly dependent on environmental nutrition conditions. In *Arabidopsis*, *AtTET12* has been identified in root hairs and in the pollen tube [57]. Furthermore, the microarray data of *Glycine max* reported on the Soybean Efb Browser website shows a differential expression of *GmTET12* in roots and root hairs at 24 h after inoculation with bacteria [35, 57, 93]. These data suggest a role for *PvTET12* in the massive proliferation of root hairs as a response to phosphate acquisition [94–96].

In animal cells, tetraspanins have multiple antagonistic effects. For example, the tetraspanin CD82 is downregulated during metastases, while the tetraspanin CD151 and tetraspanin 8 are induced and able to support tumor progression [21, 22]. It has been reported that the CD63 tetraspanin in animal cells recruits a H^+-ATPase beta-subunit in parietal cells that affects its trafficking. Also, saline stress has been used to induce changes in the H^+-ATPase localization mediated by tetraspanin [97, 98]. Here, we also found that NaCl could upregulate *PvTET12*. Furthermore, in *Arabidopsis*, a mutant of one isoform of PM H^+-ATPase, *AHA7*, exhibited reduced root hair density and lower H^+ density efflux in the root hair zone, while the transcript was upregulated under low-phosphate conditions [99]. Since phosphate scarcity affects *PvTET12* expression, it could affect the recruitment of protein related to the change in H^+ efflux, and it is tempting to think that tetraspanins are somehow related to the regulation or trafficking of H^+-ATPase. Furthermore, a PT4/PT11 H^+-ATPase has been found to be important for arbuscule maintenance and AM-mediated phosphate uptake [100, 101]. Plants have developed several strategies to increase phosphate acquisition, including changes to root architecture and the formation of root hairs [95, 102]. However, the finding that other TETs, such as tetraspanin-1, are also related to changes in root hair regulation suggests the existence of a more complex regulation [65].

There is an emerging association between tetraspanins and the mechanisms of ROS generation [24]. In the nematode *C. elegans*, the exoskeleton, the cuticle composed of collagen, is tyrosine cross-linked in a ROS-dependent manner, in a process assisted by BLI-3, a DUOX NADPH oxidase [29]. This process also requires the participation of tetraspanin TSP-15, which allows recruitment of the NADPH oxidase [24, 25, 30]. Inactivation of this tetraspanin or BLI-3 produces similar phenotypes. Furthermore, during plant infection with the pathogenic fungus *M. grisea* or *B. cinerea*, the tetraspanin PLS1 is required for infection site formation. Therefore, the tetraspanin and ROS generated by a NADPH oxidase is needed to coordinate ROS production at the infection site. In pathogenic *C. lindemuthianum*, a tetraspanin is also required to reestablish appressorium polarity [24, 25, 31–33]. Furthermore, in *Claviceps purpurea*, Nox2 and Pls1 are important for a balanced host–pathogen interaction, while in HeLa cells, the cotransfection of tetraspanin CD82 and GTPase Cdc42 induces apoptosis by generating ROS [103, 104]. These data add weight to the strong connection between tetraspanins and the ROS-generating machinery, both in animal and plant cells, to coordinate localized ROS production [24, 25, 30, 105].

During the mycorrhizal association of *P. vulgaris* with *R. irregularis*, only *PvTET3* was downregulated. This response coincides with previous reports in which a decrease in ROS production induced by RNAi of *PvRbOHB* enhanced colonization by *R. irregularis* [56]. Thus, a coordinated decrease in ROS production and *PvTET3* expression could be required for mycorrhizal colonization, as previously suggested [56, 78, 79].

This spatial ROS requirement is also observed during the Casparian strip lignification that occurs in plants, where CASP, a protein recruiting the NADPH oxidase, plays a role similar to tetraspanin, bringing together NADPH oxidase and peroxidase and ensuring localized activation of the oxidase [106]. Tetraspanins have also been localized to the tip of growing pollen tubes and root hairs (this work), and it is well known that the tip regions require NADPH oxidase activity for the generation of ROS, key players in the regulation of polar growth [12, 13]. The subcellular localization of some tetraspanins at the apical plasma membrane suggests that tetraspanins may play a key role during polar growth. Furthermore, the particular expression of *PvTET8* in root hairs in which an infection thread forms during early cell division in cortical cells could be related to the NADPH-oxidase-mediated ROS generation that is required for meristematic activity. Therefore, it is tempting to speculate that tetraspanins also play a role in recruiting the ROS-generating machinery to a specific cellular location. Moreover, tetraspanin also accumulates at the site of female gametophyte differentiation, a well-described ROS-dependent process [35].

Finally, the site-specific localization of *PvTET8* in root and nodule meristematic regions points to a role in meristem maintenance. The well-described role of $O_2^{\cdot-}$ accumulation in the root apical meristem (RAM) and shoot apical meristem (SAM) in inhibiting the transition from proliferation to differentiation suggests a key role for tetraspanins in undifferentiated cells to inhibit differentiation in plant. Indeed, the balance of $O_2^{\cdot-}/H_2O_2$ levels in undifferentiated and differentiated cells is crucial for WUSCHEL (WUS) activation to promote stem cell differentiation. For instance, ROS can activate *WUS* and thereby repress expression of the TF YABBY, which regulates the tetraspanin *TORNADO* at the transcriptional level. Therefore, the tetraspanin *TORNADO* could be involved in processes that regulate ROS production, both at the temporal and spatial level. It is interesting that the WUS-RELATED HOMEOBOX (*WOX*) family transcription factor *WOX5* like *PvTET8*, *PvTET3* (this work), are also highly expressed during nodule organogenesis, suggesting that *WOX* genes are common regulators of cell proliferation in different systems, such as the SAM, RAM, and nodule primordium, including in megasporogenesis [36, 40, 86, 107].

Calcium and ROS are important cellular messengers and key players during mutualistic interactions [9, 108]. ROS, and therefore the enzymes that generate ROS (e.g., NADPH oxidases), play a key role in root hair tip growth, both in the presence and absence of pathogenic or mutualistic interactions, and in the growth of other tip-growing cells such as pollen tubes [12]. The observation that FNs from rhizobia have a different effect on ROS accumulation than do pathogenic signals, such as elicitors, suggests that plant cells differentiate symbiotic from pathogenic signals [6, 14, 109]. We previously reported that *P. vulgaris* produces 9 NADPH oxidases (Rboh), some of which are mainly expressed in roots, root hairs, or nodules [43]. The overexpression of one, *RbohB*, results in increased nodulation, but with a reduced mycorrhizal association [56], suggesting that ROS are important players in mutualistic interactions [42, 43, 56]. We suggest that the co-occurrence of tetraspanin and NADPH oxidase in the apical root hair cells or the early infection thread, and nodule primordia, could be related to the ROS-generating machinery. The role of tetraspanins in regulating the plasma membrane by recruiting the required proteins to specific membrane microdomains enriched in tetraspanins (tetraspanin web) or by affecting its vesicular trafficking have been well described. It is important to bear in mind that the release of the rhizobia from the infection thread or the

INFORME DE LABORES 2019

arbuscule formation requires a complete coordination with the secretory system from the host plant cells for symbiont accommodation. This involves a high rate of exocytosis of specific components required for cell wall remodeling, including the extra membrane required to form the peribacteroideal membrane. In this scenery, tetraspanins could also play a central role organizing those membrane domains, but also facilitating the required vesicular trafficking to specific places as those reported for photogenic interactions that involves the specific exosomes secretion.

Supporting information

S1 Fig. Oligonucleotides used in this study.
(DOCX)

S2 Fig. Phylogenetic tree of TET family proteins from *Arabidopsis* and *P. vulgaris*. The phylogenetic tree was generated from the alignment of tetraspanin proteins with $n = 1000$ bootstrap replicates. The TET proteins were classified into clades based on phylogenetic analysis using the neighbor-joining (NJ) method. We used as query all tetraspanins reported by Boavida et al., 2013.
(TIF)

S3 Fig. An unrooted neighbor-joining three phylogenetic tree was constructed based on the amino acid sequences alignment of some legumes tetraspanins using the neighbor-joining method (NJ)(Saitou and Nei, 1987, Takata et al., 2013). We selected amino acid sequences from *Medicago truncatula*, *Phaseolus vulgaris*, *Glycine max*, and *Lotus japonicus*. In this phylogenetic tree we schematize seven groups formed with legumes tetraspanin and are represented by different color branch. We selected a bootstrapping method to build the phylogenetic tree with 1000 replicates using MEGA Version 6.0.6 (Tamura et al., 2013)
(TIF)

S4 Fig. Rab2A transcript levels during root hair development. Transcript levels were quantified by reverse transcription and real-time PCR (RT-qPCR) and calculated using the expression levels of *Elongation Factor 1α* as reference. Measures were performed in each enriched tissues and different zones in root of common bean at 48 hpg. The number of biological replicates ($n = 3$) is indicated. Error bars indicate mean and SEM (±SEM).
(TIF)

S5 Fig. Expression level reported in transcriptomic atlas of common bean. FY- Young flowers, collected prior to floral emergence; **LF**- Leaf tissue from fertilized plants collected at the same time of LE and LI; **L5**- Leaf tissue collected 5 days after plants were inoculated with effective rhizobium; **LE**- Leaf tissue collected 21 days after plants were inoculated with effective rhizobium; **LI**- Leaf tissue collected 21 days after plants were inoculated with ineffective rhizobium; **N5**- Pre-fixing (effective) nodules collected 5 days after inoculation; **NE**- Effectively fixing nodules collected 21 days after inoculation; **NI**- Ineffectively fixing nodules collected 21 days after inoculation; **P1**- Pods between 10 and 11 cm long, associated with stage 1 seeds (pod only); **P2**- Pods between 12 and 13 cm long associated with stage 2 seeds (pod only); **PH**- Pods approximately 9cm long, associated with seeds at heart stage (pod only); **PY**- Young pods, collected 1 to 4 days after floral senescence. Samples contain developing embryos at globular stage; **R**- Whole roots from fertilized plants collected at the same time as RE and RI; **R5**- Whole roots separated from 5 day old pre-fixing nodules; **RE**- Whole roots separated from fix+ nodules collected 21 days after inoculation; **RI**- Whole roots separated from fix- nodules collected 21 days after inoculation; **RT**- Root tips, 0.5 cm of tissue, collected from

fertilized plants at 2nd trifoliate stage of development.; **S1**- Stage 1 seeds, between 6 and 7 mm across and approximately 50 mg; **S2**- Stage 2 seeds, between 8 and 10 mm across and between 140 and 150 mg; **SH**- Heart stage seeds, between 3 and 4 mm across and approximately 7 mg; **ST**- Shoot tip, including the apical meristem, collected at the 2nd trifoliate stage; **YL**- Fully expanded 2nd trifoliate leaf tissue from plants provided with fertilizer; **YR**- Whole roots, including root tips, collected at the 2nd trifoliate stage of development; **YS**- All stem internodes above the cotyledon collected at the 2nd trifoliate stage. Common bean atlas source (https://plantgrn.noble.org/PvGEA/blastprotein.jsp).
(TIF)

S6 Fig. Common bean root responses to NFs treatment. (A) Representative image of root hairs of roots of common bean under control condition treated with chitosan 10^{-9} M and **(B)** root hair subjected to a treatment with 10^{-9} M of NFs for 4 h (Scale = 100 μm).
(TIF)

S7 Fig. Expression of the other of tetraspanin members in *P. vulgaris* during nodule formation. Different transcript abundance under two treatments: incubated with Nod Factor or inoculated with *R. Tropici* CIAT 899 (separated with a dotted line). The experiment included uninoculated roots harvested as control at the same time (green bars). Expression values were normalized with EF1a. Bars represent means ± SEM from at least three independent biological replicates with three technical repeats. P-values <0.05 are marked with two asterisks, respectively (Student's t-test).
(TIF)

S8 Fig. Subcellular localization of 35S:PvTET3-GFP, 35S:PvTET6-GFP after plasmolysis. Agroinfiltrated cells from *N. benthamiana* leaves under plasmolysis induced by NaCl. **A**, **B** and **C**, 35S:GFP, 35S:PvTET3-GFP, 35S:PvTET6-GFP respectively, showing the regular cytoplasmic protein localization under control condition (left panel) and under plasmolysis (right small panels). Arrows in **B** and **C** indicates the 35S:PvTET3-GFP and 35S:PvTET6-GFP fluorescence associated with the retracted plasma membrane, while the 35S:GFP remains in the cytoplasm in **A**.
(TIF)

S1 Movie. Composite plants from *P. vulgaris* expressing the fusion protein 35S: PvTET6-GFP. Images were acquired with a spinning disk confocal system (Intelligent Imaging Innovations /3i, USA) consisting of a CSU-W1 confocal head (Yokogawa, Japan) and a modular solid-state laser stack; Slidebook software was used to control the system and capture images (Intelligent Imaging Innovations /3i, USA). Movie represent 40 images taken 15 seconds apart. Note the apical membrane localization and the cytoplasmic localization in vesicular structures that follows the cytoplasmic streaming.
(WMV)

S2 Movie. Composite plants from *P. vulgaris* expressing the fusion protein 35S: PvTET6-GFP in epidermal cells. Images were acquired with a spinning disk confocal system (Intelligent Imaging Innovations /3i, USA) consisting of a CSU-W1 confocal head (Yokogawa, Japan) and a modular solid-state laser stack; Slidebook software was used to control the system and capture images (Intelligent Imaging Innovations /3i, USA). Movie represent 40 images taken 15 seconds apart. Note the apical membrane localization and the cytoplasmic localization in vesicular structures that follows the cytoplasmic streaming.
(AVI)

Acknowledgments

We acknowledge the technical support from Noreide Nava, Juan E. Olivares Grajales, Rosana Sánchez, Georgina Estrada, the facility for Oligonucleotides synthesis, and the National Advanced Microscopy Laboratory (LNMA).

Author Contributions

Conceptualization: Luis Cárdenas.

Funding acquisition: Kazuyuki Kuchitsu, Jesús Aguirre, Carmen Quinto, Luis Cárdenas.

Investigation: Saul Jimenez-Jimenez, Olivia Santana, Fernando Lara-Rojas, Manoj-Kumar Arthikala, Elisabeth Armada, Kenji Hashimoto, Sandra Salgado, Luis Cárdenas.

Methodology: Saul Jimenez-Jimenez, Kenji Hashimoto, Kazuyuki Kuchitsu, Jesús Aguirre, Carmen Quinto.

Supervision: Luis Cárdenas.

Writing – original draft: Saul Jimenez-Jimenez, Luis Cárdenas.

Writing – review & editing: Kenji Hashimoto, Kazuyuki Kuchitsu.

References

1. Fisher RF, Long SR. Rhizobium—plant signal exchange. Nature. 1992; 357(6380):655–60. https://doi.org/10.1038/357655a0 PMID: 1614514.
2. Oldroyd GE. Speak, friend, and enter: signalling systems that promote beneficial symbiotic associations in plants. Nature reviews Microbiology. 2013; 11(4):252–63. https://doi.org/10.1038/nrmicro2990 PMID: 23493145.
3. Ferguson BJ, Mens C, Hastwell AH, Zhang M, Su H, Jones CH, et al. Legume nodulation: The host controls the party. Plant, cell & environment. 2019; 42(1):41–51. https://doi.org/10.1111/pce.13348 PMID: 29808564.
4. Zepeda I, Sanchez-Lopez R, Kunkel JG, Banuelos LA, Hernandez-Barrera A, Sanchez F, et al. Visualization of highly dynamic F-actin plus ends in growing phaseolus vulgaris root hair cells and their responses to Rhizobium etli nod factors. Plant & cell physiology. 2014; 55(3):580–92. https://doi.org/10.1093/pcp/pct202 PMID: 24399235.
5. Denarie J, Debelle F, Prome JC. Rhizobium lipo-chitooligosaccharide nodulation factors: signaling molecules mediating recognition and morphogenesis. Annual review of biochemistry. 1996; 65:503–35. https://doi.org/10.1146/annurev.bi.65.070196.002443 PMID: 8811188.
6. Cárdenas L, Quinto C. Reactive oxygen species (ROS) as early signals in root hair cells responding to rhizobial nodulation factors. Plant Signaling & Behavior. 2008; 3:1–3.
7. Cardenas L, Holdaway-Clarke TL, Sanchez F, Quinto C, Feijo JA, Kunkel JG, et al. Ion changes in legume root hairs responding to Nod factors. Plant physiology. 2000; 123(2):443–52. https://doi.org/10.1104/pp.123.2.443 PMID: 10859175; Central PMCID: PMC1539257.
8. Cárdenas L, Feijó JA, Kunkel JG, Sánchez F, Holdaway-Clarke T, Hepler PK, et al. *Rhizobium* Nod factors induce increases in intracellular free calcium and extracellular calcium influxes in bean root hairs. Plant J. 1999; 19(12657):347–52.
9. Shaw SL, Long SR. Nod factor elicits two separable calcium responses in Medicago truncatula root hair cells. Plant physiology. 2003; 131(3):976–84. https://doi.org/10.1104/pp.005546 PMID: 12644650; Central PMCID: PMC166863.
10. Miller DD, de Ruijter NCA, Bisseling T, Emons AM. The role of actin in root hair morphogenesis: studies with lipochito-oligosaccharide as a growth stimulator and cytochalasin as an actin perturbing drug. Plant J. 1999; 17(12336):141–54.
11. Yokota K, Fukai E, Madsen LH, Jurkiewicz A, Rueda P, Radutoiu S, et al. Rearrangement of Actin Cytoskeleton Mediates Invasion of Lotus japonicus Roots by Mesorhizobium loti. The Plant cell. 2009; 21(1):267–84. https://doi.org/10.1105/tpc.108.063693 PMID: 19136645.

12. Foreman J, Demidchik V, Bothwell JH, Mylona P, Miedema H, Torres MA, et al. Reactive oxygen species produced by NADPH oxidase regulate plant cell growth. Nature. 2003; 422(6930):442–6. https://doi.org/10.1038/nature01485 PMID: 12660786.

13. Takeda S, Gapper C, Kaya H, Bell E, Kuchitsu K, Dolan L. Local positive feedback regulation determines cell shape in root hair cells. Science. 2008; 319(5867):1241–4. https://doi.org/10.1126/science.1152505 PMID: 18309082.

14. Cardenas L. New findings in the mechanisms regulating polar growth in root hair cells. Plant signaling & behavior. 2009; 4(1):4–8. https://doi.org/10.4161/psb.4.1.7341 PMID: 19568333; Central PMCID: PMC2634060.

15. Oldroyd GE, Murray JD, Poole PS, Downie JA. The rules of engagement in the legume-rhizobial symbiosis. Annual review of genetics. 2011; 45:119–44. https://doi.org/10.1146/annurev-genet-110410-132549 PMID: 21838550.

16. Russo G, Carotenuto G, Fiorilli V, Volpe V, Chiapello M, Van Damme D, et al. Ectopic activation of cortical cell division during the accommodation of arbuscular mycorrhizal fungi. The New phytologist. 2019; 221(2):1036–48. https://doi.org/10.1111/nph.15398 PMID: 30152051.

17. Heck C, Kuhn H, Heidt S, Walter S, Rieger N, Requena N. Symbiotic Fungi Control Plant Root Cortex Development through the Novel GRAS Transcription Factor MIG1. Current biology: CB. 2016; 26(20):2770–8. https://doi.org/10.1016/j.cub.2016.07.059 PMID: 27641773.

18. Reimann R, Kost B, Dettmer J. TETRASPANINs in Plants. Frontiers in plant science. 2017; 8:545. https://doi.org/10.3389/fpls.2017.00545 PMID: 28458676

19. Wang F, Vandepoele K, Van Lijsebettens M. Tetraspanin genes in plants. Plant science: an international journal of experimental plant biology. 2012; 190:9–15. https://doi.org/10.1016/j.plantsci.2012.03.005 PMID: 22608515.

20. Huang C, Fu C, Wren JD, Wang X, Zhang F, Zhang YH, et al. Tetraspanin-enriched microdomains regulate digitation junctions. Cellular and molecular life sciences: CMLS. 2018. https://doi.org/10.1007/s00018-018-2803-2 PMID: 29589089.

21. Zöller M. Tetraspanins: push and pull in suppressing and promoting metastasis. Nature Reviews Cancer. 2009; 9(1):40. https://doi.org/10.1038/nrc2543 PMID: 19078974

22. Couto N, Caja S, Maia J, Strano Moraes MC, Costa-Silva B. Exosomes as emerging players in cancer biology. Biochimie. 2018. https://doi.org/10.1016/j.biochi.2018.03.006 PMID: 29555374.

23. Cai Q, Qiao L, Wang M, He B, Lin F-M, Palmquist J, et al. Plants send small RNAs in extracellular vesicles to fungal pathogen to silence virulence genes. Science. 2018; 360(6393):1126–9. https://doi.org/10.1126/science.aar4142 PMID: 29773668

24. Moribe H, Mekada E. Co-occurrence of tetraspanin and ROS generators: Conservation in protein cross-linking and other developmental processes. Worm. 2013; 2(2):e23415. https://doi.org/10.4161/worm.23415 PMID: 24058871; Central PMCID: PMC3704445.

25. Moribe H, Konakawa R, Koga D, Ushiki T, Nakamura K, Mekada E. Tetraspanin is required for generation of reactive oxygen species by the dual oxidase system in Caenorhabditis elegans. PLoS genetics. 2012; 8(9):e1002957. https://doi.org/10.1371/journal.pgen.1002957 PMID: 23028364; Central PMCID: PMC3447965.

26. Hervera A, De Virgiliis F, Palmisano I, Zhou L, Tantardini E, Kong G, et al. Reactive oxygen species regulate axonal regeneration through the release of exosomal NADPH oxidase 2 complexes into injured axons. Nature cell biology. 2018; 20(3):307–19. https://doi.org/10.1038/s41556-018-0039-x PMID: 29434374.

27. Krishnamoorthy L, Chang CJ. Exosomal NADPH Oxidase: Delivering Redox Signaling for Healing. Biochemistry. 2018. https://doi.org/10.1021/acs.biochem.8b00429 29889508. PMID: 29889508

28. Morelli AE, Larregina AT, Shufesky WJ, Sullivan ML, Stolz DB, Papworth GD, et al. Endocytosis, intracellular sorting, and processing of exosomes by dendritic cells. Blood. 2004; 104(10):3257–66. https://doi.org/10.1182/blood-2004-03-0824 PMID: 15284116.

29. Edens WA, Sharling L, Cheng G, Shapira R, Kinkade JM, Lee T, et al. Tyrosine cross-linking of extracellular matrix is catalyzed by Duox, a multidomain oxidase/peroxidase with homology to the phagocyte oxidase subunit gp91phox. The Journal of cell biology. 2001; 154(4):879–91. https://doi.org/10.1083/jcb.200103132 PMID: 11514595.

30. Moribe H, Yochem J, Yamada H, Tabuse Y, Fujimoto T, Mekada E. Tetraspanin protein (TSP-15) is required for epidermal integrity in Caenorhabditis elegans. Journal of cell science. 2004; 117(Pt 22):5209–20. https://doi.org/10.1242/jcs.01403 PMID: 15454573.

31. Clergeot PH, Gourgues M, Cots J, Laurans F, Latorse MP, Pepin R, et al. PLS1, a gene encoding a tetraspanin-like protein, is required for penetration of rice leaf by the fungal pathogen Magnaporthe

grisea. Proceedings of the National Academy of Sciences of the United States of America. 2001; 98 (12):6963–8. https://doi.org/10.1073/pnas.111132998 PMID: 11391010; Central PMCID: PMC34461.

32. Veneault-Fourrey C, Parisot D, Gourgues M, Lauge R, Lebrun MH, Langin T. The tetraspanin gene ClPLS1 is essential for appressorium-mediated penetration of the fungal pathogen Colletotrichum lindemuthianum. Fungal genetics and biology: FG & B. 2005; 42(4):306–18. https://doi.org/10.1016/j.fgb.2005.01.009 PMID: 15749050.

33. Siegmund U, Heller J, van Kan JA, Tudzynski P. The NADPH oxidase complexes in Botrytis cinerea: evidence for a close association with the ER and the tetraspanin Pls1. PloS one. 2013; 8(2):e55879. https://doi.org/10.1371/journal.pone.0055879 PMID: 23418468; Central PMCID: PMC3572182.

34. Damiani I, Pauly N, Puppo A, Brouquisse R, Boscari A. Reactive Oxygen Species and Nitric Oxide Control Early Steps of the Legume—Rhizobium Symbiotic Interaction. Frontiers in plant science. 2016; 7:454. https://doi.org/10.3389/fpls.2016.00454 PMID: 27092165; Central PMCID: PMC4824774.

35. Boavida LC, Qin P, Broz M, Becker JD, McCormick S. Arabidopsis tetraspanins are confined to discrete expression domains and cell types in reproductive tissues and form homo- and heterodimers when expressed in yeast. Plant physiology. 2013; 163(2):696–712. https://doi.org/10.1104/pp.113.216598 PMID: 23946353; Central PMCID: PMC3793051.

36. Lieber D, Lora J, Schrempp S, Lenhard M, Laux T. Arabidopsis WIH1 and WIH2 genes act in the transition from somatic to reproductive cell fate. Current biology: CB. 2011; 21(12):1009–17. https://doi.org/10.1016/j.cub.2011.05.015 PMID: 21658947.

37. Yamaguchi H, Kawaguchi K, Sagawa T. Dynamical crossover in a stochastic model of cell fate decision. Physical review E. 2017; 96(1–1):012401. https://doi.org/10.1103/PhysRevE.96.012401 PMID: 29347197.

38. Wang F, Muto A, Van de Velde J, Neyt P, Himanen K, Vandepoele K, et al. Functional Analysis of the Arabidopsis TETRASPANIN Gene Family in Plant Growth and Development. Plant physiology. 2015; 169(3):2200–14. https://doi.org/10.1104/pp.15.01310 PMID: 26417009; Central PMCID: PMC4634101.

39. Tsukagoshi H, Busch W, Benfey PN. Transcriptional regulation of ROS controls transition from proliferation to differentiation in the root. Cell. 2010; 143(4):606–16. https://doi.org/10.1016/j.cell.2010.10.020 PMID: 21074051.

40. Zeng J, Dong Z, Wu H, Tian Z, Zhao Z. Redox regulation of plant stem cell fate. The EMBO journal. 2017; 36(19):2844–55. https://doi.org/10.15252/embj.201695955 PMID: 28838936; Central PMCID: PMC5623875.

41. Montiel J, Arthikala MK, Cardenas L, Quinto C. Legume NADPH Oxidases Have Crucial Roles at Different Stages of Nodulation. International journal of molecular sciences. 2016; 17(5). https://doi.org/10.3390/ijms17050680 PMID: 27213330; Central PMCID: PMC4881506.

42. Arthikala MK, Sanchez-Lopez R, Nava N, Santana O, Cardenas L, Quinto C. RbohB, a Phaseolus vulgaris NADPH oxidase gene, enhances symbiosome number, bacteroid size, and nitrogen fixation in nodules and impairs mycorrhizal colonization. The New phytologist. 2014; 202(3):886–900. https://doi.org/10.1111/nph.12714 PMID: 24571730.

43. Montiel J, Nava N, Cardenas L, Sanchez-Lopez R, Arthikala MK, Santana O, et al. A Phaseolus vulgaris NADPH oxidase gene is required for root infection by Rhizobia. Plant & cell physiology. 2012; 53 (10):1751–67. https://doi.org/10.1093/pcp/pcs120 PMID: 22942250.

44. Karimi M, Inze D, Depicker A. GATEWAY vectors for Agrobacterium-mediated plant transformation. Trends in plant science. 2002; 7(5):193–5. PMID: 11992820.

45. Rezaie J, Ajezi S, Avci CB, Karimipour M, Geranmayeh MH, Nourazarian A, et al. Exosomes and their Application in Biomedical Field: Difficulties and Advantages. Molecular neurobiology. 2018; 55 (4):3372–93. https://doi.org/10.1007/s12035-017-0582-7 PMID: 28497202.

46. Estrada-Navarrete G, Alvarado-Affantranger X, Olivares JE, Guillen G, Diaz-Camino C, Campos F, et al. Fast, efficient and reproducible genetic transformation of Phaseolus spp. by Agrobacterium rhizogenes. Nature protocols. 2007; 2(7):1819–24. https://doi.org/10.1038/nprot.2007.259 PMID: 17641650.

47. Cardenas L, Dominguez J, Quinto C, Lopez-Lara IM, Lugtenberg BJ, Spaink HP, et al. Isolation, chemical structures and biological activity of the lipo-chitin oligosaccharide nodulation signals from Rhizobium etli. Plant molecular biology. 1995; 29(3):453–64. PMID: 8534845.

48. Smith SE, Smith FA, Jakobsen I. Mycorrhizal fungi can dominate phosphate supply to plants irrespective of growth responses. Plant physiology. 2003; 133(1):16–20. https://doi.org/10.1104/pp.103.024380 PMID: 12970469; Central PMCID: PMC1540331.

49. Schmittgen TD, Livak KJ. Analyzing real-time PCR data by the comparative C(T) method. Nature protocols. 2008; 3(6):1101–8. PMID: 18546601.

50. Mani B, Agarwal M, Katiyar-Agarwal S. Comprehensive Expression Profiling of Rice Tetraspanin Genes Reveals Diverse Roles During Development and Abiotic Stress. Frontiers in plant science. 2015; 6:1088. https://doi.org/10.3389/fpls.2015.01088 PMID: 26697042; Central PMCID: PMC4675852.

51. Garcia-Espana A, Chung PJ, Sarkar IN, Stiner E, Sun TT, Desalle R. Appearance of new tetraspanin genes during vertebrate evolution. Genomics. 2008; 91(4):326–34. https://doi.org/10.1016/j.ygeno.2007.12.005 PMID: 18291621.

52. Garcia-España A, Mares R, Mung-Tien S, DeSalle R. Intron Evolution: Testing Hypotheses of Intron Evolution Using the Phylogenomics of Tetraspanins. PloS one. 2009; 4(3):1–12.

53. Blanco FA, Meschini EP, Zanetti ME, Aguilar OM. A small GTPase of the Rab family is required for root hair formation and preinfection stages of the common bean-Rhizobium symbiotic association. The Plant cell. 2009; 21(9):2797–810. https://doi.org/10.1105/tpc.108.063420 PMID: 19749154; Central PMCID: PMC2768941.

54. Dalla Via V, Traubenik S, Rivero C, Aguilar OM, Zanetti ME, Blanco FA. The monomeric GTPase RabA2 is required for progression and maintenance of membrane integrity of infection threads during root nodule symbiosis. Plant molecular biology. 2017; 93(6):549–62. https://doi.org/10.1007/s11103-016-0581-5 PMID: 28074430.

55. O'Rourke JA, Iniguez LP, Fu F, Bucciarelli B, Miller SS, Jackson SA, et al. An RNA-Seq based gene expression atlas of the common bean. BMC genomics. 2014; 15:866. https://doi.org/10.1186/1471-2164-15-866 PMID: 25283805; Central PMCID: PMC4195886.

56. Arthikala MK, Montiel J, Nava N, Santana O, Sanchez-Lopez R, Cardenas L, et al. PvRbohB negatively regulates Rhizophagus irregularis colonization in Phaseolus vulgaris. Plant & cell physiology. 2013; 54(8):1391–402. https://doi.org/10.1093/pcp/pct089 PMID: 23788647.

57. Becker JD, Takeda S, Borges F, Dolan L, Feijo JA. Transcriptional profiling of Arabidopsis root hairs and pollen defines an apical cell growth signature. BMC plant biology. 2014; 14:197. https://doi.org/10.1186/s12870-014-0197-3 PMID: 25080170; Central PMCID: PMC4236730.

58. Borges A, Tsai SM, Caldas DG. Validation of reference genes for RT-qPCR normalization in common bean during biotic and abiotic stresses. Plant cell reports. 2012; 31(5):827–38. https://doi.org/10.1007/s00299-011-1204-x PMID: 22193338.

59. Delgado MJ, Ligero F, Lluch C. Effects of salt stress on growth and nitrogen fixation by pea, faba-bean, common bean and soybean plants. Soil Biology and Biochemistry. 1994;(26(3)):371–6.

60. Kaymakanova M, N. Stoeva N. Physiological hystological reaction of bean plants (Phaseolus Vulg. L.) to salt stress. Gen Appl Plant Physiology. 2008; 34(3–4):177–88.

61. Schmutz J, Cannon SB, Schlueter J, Ma J, Mitros T, Nelson W, et al. Genome sequence of the palaeopolyploid soybean. Nature. 2010; 463(7278):178–83. https://doi.org/10.1038/nature08670 PMID: 20075913.

62. Garcia-Espana A, Chung PJ, Zhao X, Lee A, Pellicer A, Yu J, et al. Origin of the tetraspanin uroplakins and their co-evolution with associated proteins: implications for uroplakin structure and function. Molecular phylogenetics and evolution. 2006; 41(2):355–67. https://doi.org/10.1016/j.ympev.2006.04.023 PMID: 16814572.

63. Malamy JE, Benfey PN. Organization and cell differentiation in lateral roots of Arabidopsis thaliana. Development. 1997; 124(1):33–44. PMID: 9006065.

64. Dubrovsky JG, Sauer M, Napsucialy-Mendivil S, Ivanchenko MG, Friml J, Shishkova S, et al. Auxin acts as a local morphogenetic trigger to specify lateral root founder cells. Proceedings of the National Academy of Sciences of the United States of America. 2008; 105(25):8790–4. https://doi.org/10.1073/pnas.0712307105 PMID: 18559858; Central PMCID: PMC2438385.

65. Cnops G, Wang X, Linstead P, Van Montagu M, Van Lijsebettens M, Dolan L. Tornado1 and tornado2 are required for the specification of radial and circumferential pattern in the Arabidopsis root. Development. 2000; 127(15):3385–94. PMID: 10887093.

66. Chaubet N, Flenet M, Clement B, Brignon P, Gigot C. Identification of cis-elements regulating the expression of an Arabidopsis histone H4 gene. The Plant journal: for cell and molecular biology. 1996; 10(3):425–35. PMID: 8811858.

67. Thomas CL, Bayer EM, Ritzenthaler C, Fernandez-Calvino L, Maule AJ. Specific targeting of a plasmodesmal protein affecting cell-to-cell communication. PLoS biology. 2008; 6(1):e7. https://doi.org/10.1371/journal.pbio.0060007 PMID: 18215111; Central PMCID: PMC2211546.

68. Fernandez-Calvino L, Faulkner C, Walshaw J, Saalbach G, Bayer E, Benitez-Alfonso Y, et al. Arabidopsis plasmodesmal proteome. PloS one. 2011; 6(4):e18880. https://doi.org/10.1371/journal.pone.0018880 PMID: 21533090; Central PMCID: PMC3080382.

69. Ehlers K, Kollmann R. Primary and secondary plasmodesmata: structure, origin, and functioning. Protoplasma. 2001; 216(1–2):1–30. PMID: 11732191.

70. AJ vB. Interaction between sieve element and companion cell and the consequences for photoassimilate distribution. Two structural hardware frames with associated physiological software packages in dicotyledons. Journal of experimental botany. 1996; 47(1129):1129–40.

71. Salmon MS, Bayer EM. Dissecting plasmodesmata molecular composition by mass spectrometry-based proteomics. Frontiers in plant science. 2012; 3:307. https://doi.org/10.3389/fpls.2012.00307 PMID: 23335932; Central PMCID: PMC3542633.

72. Maule A, Faulkner C, Benitez-Alfonso Y. Plasmodesmata "in Communicado". Frontiers in plant science. 2012; 3:30. https://doi.org/10.3389/fpls.2012.00030 PMID: 22645579; Central PMCID: PMC3355775.

73. Sevilem I, Yadav SR, Helariutta Y. Plasmodesmata: channels for intercellular signaling during plant growth and development. Methods in molecular biology. 2015; 1217:3–24. https://doi.org/10.1007/978-1-4939-1523-1_1 PMID: 25287193.

74. Juniper BE, Barlow PW. The distribution of plasmodesmata in the root tip of maize. Planta. 1969; 89 (4):352–60. https://doi.org/10.1007/BF00387235 PMID: 24504513.

75. Imaichi R, Hiratsuka R. Evolution of shoot apical meristem structures in vascular plants with respect to plasmodesmatal network. American journal of botany. 2007; 94(12):1911–21. https://doi.org/10.3732/ajb.94.12.1911 PMID: 21636385.

76. Zhu T, Lucas WJ, Rost TL. Directional cell-to-cell communication in theArabidopsis root apical meristem I. An ultrastructural and functional analysis. Protoplasma. 1998; 203:35–47.

77. Jin L, Wang J, Guan F, Zhang J, Yu S, Liu S, et al. Dominant point mutation in a tetraspanin gene associated with field-evolved resistance of cotton bollworm to transgenic Bt cotton. Proceedings of the National Academy of Sciences of the United States of America. 2018; 115(46):11760–5. https://doi.org/10.1073/pnas.1812138115 PMID: 30381456; Central PMCID: PMC6243265.

78. Genre A, Chabaud M, Faccio A, Barker DG, Bonfante P. Prepenetration apparatus assembly precedes and predicts the colonization patterns of arbuscular mycorrhizal fungi within the root cortex of both Medicago truncatula and Daucus carota. The Plant cell. 2008; 20(5):1407–20. https://doi.org/10.1105/tpc.108.059014 PMID: 18515499; Central PMCID: PMC2438458.

79. Murakami E, Cheng J, Gysel K, Bozsoki Z, Kawaharada Y, Hjuler CT, et al. Epidermal LysM receptor ensures robust symbiotic signalling in Lotus japonicus. eLife. 2018; 7. https://doi.org/10.7554/eLife.33506 PMID: 29957177; Central PMCID: PMC6025957.

80. Faulkner C, Petutschnig E, Benitez-Alfonso Y, Beck M, Robatzek S, Lipka V, et al. LYM2-dependent chitin perception limits molecular flux via plasmodesmata. Proceedings of the National Academy of Sciences of the United States of America. 2013; 110(22):9166–70. https://doi.org/10.1073/pnas.1203458110 PMID: 23674687; Central PMCID: PMC3670346.

81. Kankanala P, Czymmek K, Valent B. Roles for rice membrane dynamics and plasmodesmata during biotrophic invasion by the blast fungus. The Plant cell. 2007; 19(2):706–24. https://doi.org/10.1105/tpc.106.046300 PMID: 17322409; Central PMCID: PMC1867340.

82. Complainville A, Brocard L, Roberts I, Dax E, Sever N, Sauer N, et al. Nodule initiation involves the creation of a new symplasmic field in specific root cells of medicago species. The Plant cell. 2003; 15 (12):2778–91. https://doi.org/10.1105/tpc.017020 PMID: 14615602; Central PMCID: PMC282798.

83. Gaudioso-Pedraza R, Beck M, Frances L, Kirk P, Ripodas C, Niebel A, et al. Callose-Regulated Symplastic Communication Coordinates Symbiotic Root Nodule Development. Current biology: CB. 2018; 28(22):3562–77 e6. https://doi.org/10.1016/j.cub.2018.09.031 PMID: 30416059.

84. Benitez-Alfonso Y, Cilia M, San Roman A, Thomas C, Maule A, Hearn S, et al. Control of Arabidopsis meristem development by thioredoxin-dependent regulation of intercellular transport. Proceedings of the National Academy of Sciences of the United States of America. 2009; 106(9):3615–20. https://doi.org/10.1073/pnas.0808717106 PMID: 19218459; Central PMCID: PMC2651306.

85. Herrbach V, Chirinos X, Rengel D, Agbevenou K, Vincent R, Pateyron S, et al. Nod factors potentiate auxin signaling for transcriptional regulation and lateral root formation in Medicago truncatula. Journal of experimental botany. 2017; 68(3):569–83. https://doi.org/10.1093/jxb/erw474 PMID: 28073951; Central PMCID: PMC6055581.

86. Yamaguchi N, Huang J, Xu Y, Tanoi K, Ito T. Fine-tuning of auxin homeostasis governs the transition from floral stem cell maintenance to gynoecium formation. Nature communications. 2017; 8(1):1125. https://doi.org/10.1038/s41467-017-01252-6 PMID: 29066759; Central PMCID: PMC5654772.

87. Larrainzar E, Riely BK, Kim SC, Carrasquilla-Garcia N, Yu HJ, Hwang HJ, et al. Deep Sequencing of the Medicago truncatula Root Transcriptome Reveals a Massive and Early Interaction between Nodulation Factor and Ethylene Signals. Plant physiology. 2015; 169(1):233–65. https://doi.org/10.1104/pp.15.00350 PMID: 26175514; Central PMCID: PMC4577383.

88. Finet C, Jaillais Y. Auxology: when auxin meets plant evo-devo. Developmental biology. 2012; 369 (1):19–31. https://doi.org/10.1016/j.ydbio.2012.05.039 PMID: 22687750.

89. Mathesius U, Schlaman HR, Spaink HP, Of Sautter C, Rolfe BG, Djordjevic MA. Auxin transport inhibition precedes root nodule formation in white clover roots and is regulated by flavonoids and derivatives of chitin oligosaccharides. The Plant journal: for cell and molecular biology. 1998; 14(1):23–34. https://doi.org/10.1046/j.1365-313X.1998.00090.x PMID: 15494052.

90. Rutter BD, Innes RW. Extracellular Vesicles Isolated from the Leaf Apoplast Carry Stress-Response Proteins. Plant physiology. 2017; 173(1):728–41. https://doi.org/10.1104/pp.16.01253 PMID: 27837092; Central PMCID: PMC5210723.

91. Guimaraes PM, Guimaraes LA, Morgante CV, Silva OB Jr., Araujo AC, Martins AC, et al. Root Transcriptome Analysis of Wild Peanut Reveals Candidate Genes for Nematode Resistance. PloS one. 2015; 10(10):e0140937. https://doi.org/10.1371/journal.pone.0140937 PMID: 26488731; Central PMCID: PMC4619257.

92. Chen T, Duan L, Zhou B, Yu H, Zhu H, Cao Y, et al. Interplay of Pathogen-Induced Defense Responses and Symbiotic Establishment in Medicago truncatula. Frontiers in microbiology. 2017; 8:973. https://doi.org/10.3389/fmicb.2017.00973 PMID: 28611764; Central PMCID: PMC5447765.

93. Libault M, Farmer A, Brechenmacher L, Drnevich J, Langley RJ, Bilgin DD, et al. Complete transcriptome of the soybean root hair cell, a single-cell model, and its alteration in response to Bradyrhizobium japonicum infection. Plant physiology. 2010; 152(2):541–52. https://doi.org/10.1104/pp.109.148379 PMID: 19933387; Central PMCID: PMC2815892.

94. Foehse D, Jungk A. Influence of phosphate and nitrate supply on root hair formation of rape, spinach and tomato plants. Plant and soil. 1983; 74 (3):359–68.

95. Bates TR, Lynch JP. Stimulation of root hair elongation in Arabidopsis thaliana by low phosphorus availability. Plant, cell & environment. 1996; 19(5):529–38.

96. Bhosale R, Giri J, Pandey BK, Giehl RFH, Hartmann A, Traini R, et al. A mechanistic framework for auxin dependent Arabidopsis root hair elongation to low external phosphate. Nature communications. 2018; 9(1):1409. https://doi.org/10.1038/s41467-018-03851-3 PMID: 29651114; Central PMCID: PMC5897496.

97. Duffield A, Kamsteeg EJ, Brown AN, Pagel P, Caplan MJ. The tetraspanin CD63 enhances the internalization of the H,K-ATPase beta-subunit. Proceedings of the National Academy of Sciences of the United States of America. 2003; 100(26):15560–5. https://doi.org/10.1073/pnas.2536699100 PMID: 14660791; Central PMCID: PMC307607.

98. Hager A. Role of the plasma membrane H+-ATPase in auxin-induced elongation growth: historical and new aspects. Journal of plant research. 2003; 116(6):483–505. https://doi.org/10.1007/s10265-003-0110-x PMID: 12937999.

99. Yuan W, Zhang D, Song T, Xu F, Lin S, Xu W, et al. Arabidopsis plasma membrane H+-ATPase genes AHA2 and AHA7 have distinct and overlapping roles in the modulation of root tip H+ efflux in response to low-phosphorus stress. Journal of experimental botany. 2017; 68(7):1731–41. https://doi.org/10.1093/jxb/erx040 PMID: 28369625; Central PMCID: PMC5441905.

100. Krajinski F, Courty PE, Sieh D, Franken P, Zhang H, Bucher M, et al. The H+-ATPase HA1 of Medicago truncatula Is Essential for Phosphate Transport and Plant Growth during Arbuscular Mycorrhizal Symbiosis. The Plant cell. 2014; 26(4):1808–17. https://doi.org/10.1105/tpc.113.120436 PMID: 24781114; Central PMCID: PMC4036587.

101. Wang E, Yu N, Bano SA, Liu C, Miller AJ, Cousins D, et al. A H+-ATPase That Energizes Nutrient Uptake during Mycorrhizal Symbioses in Rice and Medicago truncatula. The Plant cell. 2014; 26 (4):1818–30. https://doi.org/10.1105/tpc.113.120527 PMID: 24781115; Central PMCID: PMC4036588.

102. Lopez-Bucio J, Hernandez-Abreu E, Sanchez-Calderon L, Nieto-Jacobo MF, Simpson J, Herrera-Estrella L. Phosphate availability alters architecture and causes changes in hormone sensitivity in the Arabidopsis root system. Plant physiology. 2002; 129(1):244–56. https://doi.org/10.1104/pp.010934 PMID: 12011355; Central PMCID: PMC155888.

103. Schurmann J, Buttermann D, Herrmann A, Giesbert S, Tudzynski P. Molecular characterization of the NADPH oxidase complex in the ergot fungus Claviceps purpurea: CpNox2 and CpPls1 are important for a balanced host-pathogen interaction. Molecular plant-microbe interactions: MPMI. 2013; 26 (10):1151–64. https://doi.org/10.1094/MPMI-03-13-0064-R PMID: 23777432.

104. Schoenfeld N, Bauer MK, Grimm S. The metastasis suppressor gene C33/CD82/KAI1 induces apoptosis through reactive oxygen intermediates. FASEB journal: official publication of the Federation of American Societies for Experimental Biology. 2004; 18(1):158–60. https://doi.org/10.1096/fj.03-0420fje PMID: 14597553.

105. Charrin S, Jouannet S, Boucheix C, Rubinstein E. Tetraspanins at a glance. Journal of cell science. 2014; 127(Pt 17):3641–8. https://doi.org/10.1242/jcs.154906 PMID: 25128561.

106. Lee Y, Rubio MC, Alassimone J, Geldner N. A mechanism for localized lignin deposition in the endodermis. Cell. 2013; 153(2):402–12. https://doi.org/10.1016/j.cell.2013.02.045 PMID: 23541512.

107. Osipova MA, Mortier V, Demchenko KN, Tsyganov VE, Tikhonovich IA, Lutova LA, et al. Wuschel-related homeobox5 gene expression and interaction of CLE peptides with components of the systemic control add two pieces to the puzzle of autoregulation of nodulation. Plant physiology. 2012; 158 (3):1329–41. https://doi.org/10.1104/pp.111.188078 PMID: 22232385; Central PMCID: PMC3291250.

108. Cardenas L, Feijo JA, Kunkel JG, Sanchez F, Holdaway-Clarke T, Hepler PK, et al. Rhizobium nod factors induce increases in intracellular free calcium and extracellular calcium influxes in bean root hairs. The Plant journal: for cell and molecular biology. 1999; 19(3):347–52. PMID: 10476081.

109. Cardenas L, Martinez A, Sanchez F, Quinto C. Fast, transient and specific intracellular ROS changes in living root hair cells responding to Nod factors (NFs). The Plant journal: for cell and molecular biology. 2008; 56(5):802–13. https://doi.org/10.1111/j.1365-313X.2008.03644.x PMID: 18680562.

SCIENTIFIC REPORTS

OPEN

The crystal structure of the chitinase ChiA74 of *Bacillus thuringiensis* has a multidomain assembly

Received: 20 June 2018
Accepted: 24 January 2019
Published online: 22 February 2019

Estefania O. Juárez-Hernández[1], Luz E. Casados-Vázquez[1,2], Luis G. Brieba[3], Alfredo Torres-Larios[4], Pedro Jimenez-Sandoval[3] & José E. Barboza-Corona[1,2]

There is no structural information about any chitinase synthesized by *Bacillus thuringiensis*, the most successful microbial insect larvicide used worldwide. In this study, we solved the 3D structure of the chitinase ChiA74 at 2.26 Å. The crystal structure shows that ChiA74 is composed of a modular arrangement formed by (i) a catalytic region (CD), (ii) a chitinase insertion domain (CID), (iii) a fibronectin type III domain (FnIII), and (iv) a chitin binding domain (CBD). The location of the CBD with respect to the CD has no structural similarity to other chitinases with known structures. The activity of a ChiA74 lacking its secretion signal peptide (ChiA74ΔSp) and a truncated version lacking its CBD/FnIII domains (ChiA74ΔSp-50) did not have statistical differences in activity against colloidal chitin. However, ChiA74ΔSp exhibits 4.5 and 2.0 higher activity than versions lacking the CBD (ChiA74ΔSp-60) and CBD/FnIII domains (ChiA74ΔSp-50), respectively, when crystalline chitin was used as substrate. Our data suggest that the CBD might plays a significant role in crystalline chitin hydrolysis. We also demonstrated the importance of the catalytic E211 in the CD, as mutants ChiA74ΔSp$_{E211N}$ and ChiA74ΔSp$_{D207N, E211N}$ were inactive against colloidal and crystalline chitins, chitosan and 4-MU-GlcNAc$_3$. ChiA74 has a processive activity producing oligosaccharides with degree of polymerization (DP) of 1 (GlcNAc) and 2 (GlcNAc$_2$).

Chitinases are secreted by many prokaryotes and eukaryotes and are utilized for hydrolysis of chitin (a homopolymer of N-acetyl-D-glucosamine, GlcNAc), a rich ubiquitous nutrient resource[1]. According with the CAZy database (http://www.cazy.org/Glycoside-Hydrolases.html), chitinolytic enzymes are classified as chitinases (EC 3.2.1.14) and β-*N*-acetylhexosaminidases (EC 3.2.1.52), formerly called endochitinases and exochitinases, respectively. The first type of enzyme cleaves the chitin chain at internal sites randomly, whereas the second one hydrolyzes chitin from the nonreducing end of chitin by removing GlcNAc residues. Chitinases and β-*N*-acetylhexosaminidases are classified into four (18, 19, 23 and 48) and six (3, 5, 18, 20, 84, 116) glycoside hydrolases (GH) families, respectively, based on their amino acid sequence similarities[2]. Most bacterial chitinases belong to the GH 18 family (GH-18), and share a TIM-barrel fold in their catalytic subunit, have a conserved DxDxE motif, and employ a substrate-assisted catalytic mechanism[3]. Structural studies of different chitinases show that subsites +1 and +2 of the enzyme interacts with the reducing end of the chitin, and the hydrolysis occurs in the binding cleft between subsites −1 and +1[4]. Family 18 chitinases are classified into three subfamilies (A, B, C), based on the amino acid sequence similarity. Chitinases from subfamily A have a modular structure composed of the catalytic domain (CD), a fibronectin type III domain (FnIII), and a chitin binding domain

[1]Universidad de Guanajuato Campus Irapuato-Salamanca, División de Ciencias de la Vida, Posgrado en Biociencias, Irapuato, Guanajuato, 36500, México. [2]Universidad de Guanajuato Campus Irapuato-Salamanca, División de Ciencias de la Vida, Departamento de Alimentos, Irapuato, Guanajuato, 36500, México. [3]Laboratorio Nacional de Genómica para la Biodiversidad, Centro de Investigación y de Estudios Avanzados del Instituto Politécnico Nacional (LANGEBIO-CINVESTAV), Apartado Postal 629, Irapuato, Guanajuato, 36824, México. [4]Departamento de Bioquímica y Biología Estructural, Instituto de Fisiología Celular, Universidad Nacional Autónoma de México, Circuito Exterior s/n, Ciudad Universitaria, Apartado Postal 70–243, Ciudad de México, 04510, México. Correspondence and requests for materials should be addressed to P.J.-S. (email: pedro.jimenez@cinvestav.mx) or J.E.B.-C. (email: josebar@ugto.mx)

(CBD). One of the main structural differences between the three subfamilies is that subfamily A has a small $\alpha+\beta$ domain (chitinase insertion domain, CID) inserted into the TIM barrel catalytic domain, which is absent in the subfamily B. Also, the substrate-binding cleft of chitinases from subfamily A is deeper than that observed in subfamilies B and C[5–10]. Although the definitive role of the CID has not been completely understood, it seems that its insertion into the TIM domain facilitate the orientation and strong association of the enzyme to the substrates[10]. CIDs have been reported in chitinases from *Vibrio harveyi*, the human cartilage glycoprotein-39, *Bacillus thuringiensis* and *Serratia marcescens*[7,11–13]. When the CID of *S. marcescens chiA* was deleted, the truncated enzyme showed a shallower tunnel in the catalytic domain than that of the intact enzyme, and also had reduction in thermal stability, specific activity and the substrate/product specificities[13]. A multiple sequence and structural alignment of twenty-seven CIDs shows the conservation of two motifs, YxR and [E/D]xx[V/I]. These conserved amino acids are predicted to be important for the interaction with the substrate through salt bridge and hydrogen bonds. Also five residues were identified into the CID that might be implicated in the formation of the hydrophobic core, as well as the stabilization of the domain[10].

B. thuringiensis is the most successful microbial insect larvicide used worldwide. Its toxic effect is primarily due to Cry (crystal) and Cyt (cytotoxic) proteins that aggregate into stable crystalline inclusions during sporulation[14,15]. Although *B. thuringiensis* is most known for the plethora of Cry and Cyt proteins it produces, strains of this microbe produces other proteins that have applied biotechnological value, including chitinases, vegetative insecticidal proteins (Vip) and enhancing-like proteins, antimicrobial peptides and parasporins which can be used to synergize the activity of Cry proteins, to control lepidopteran and coleopteran pests, to inhibit food-borne pathogenic bacteria and to kill human cancer cells of various origins, respectively[1,14,16]. In particular, ChiA74, a chitinase synthesized by a Mexican strain of *B. thuringiensis* subsp. *kenyae*, has been shown to synergize the insecticidal activity of Cry proteins, and to generate chitin-oligosaccharides with antimicrobial activity[17–19]. This chitinase has a molecular mass of ~74 kDa, and its bioinformatic analysis predicts that it is composed of four domains: TIM-barrel, chitinase insertion (CID), fibronectin type III (FnIII) and chitin binding domains (CBD)[12]. The presence of a putative CID in a chitinase of *B. thuringiensis* was first reported by Juárez-Hernández *et al.*[12,20,21]. It has been shown that when ChiA74 is secreted, a protein of ~70 kDa and two truncated versions of ~60 and 50 kDa, which are processed from the C-terminal end are generated by an unknown mechanism[12,22]. Biochemical data demonstrated that the 50 kDa containing the $(\alpha/\beta)_8$-TIM-barrel plus the CID is the minimum version of the enzyme that possesses similar activity and catalytic efficiencies (kcat/Km) that ChiA74 lacking its secretion signal peptide (i.e. ChiA74Δsp) when colloidal chitin is used as substrate[12].

To date, the three-dimensional (3D) structures for several proteins of biotechnological interest synthesized by *B. thuringiensis* have been elucidated[15,23–27]. However, there is no report about the tertiary structure of a chitinase synthesized by this bacterium. In this study, we solved the 3D structure of chitinase ChiA74 and demonstrated the importance of the conserved motif in the catalytic domain by site-directed mutagenesis. Our data demonstrate that this enzyme has a modular arrangement formed by four domains: (i) the catalytic region with an $(\alpha/\beta)_8$-TIM-barrel as a core structure, (ii) the chitinase insertion domain as a barrel insertion, (iii) the fibronectin type III and (iv) a chitin binding domain.

Results

Overall structure of ChiA74. Recombinant ChiA74 contains 676 amino acids including a N-terminal His-tag. ChiA74 crystallized in space group P 1 21 1 (Table 1). The cell content analysis in CCP4 suggest two copies of the molecule in the asymmetric unit. A molecular replacement solution was found with Phaser-MR using an alanine truncated model of the chitinase A1 from *B. circulans* (PDB ID 1ITX) as the search model. Side chains were completed from the initial MR solution in Coot as supported by electron density. The rest of the model was built manually in Coot (including the FnIII and the CBD) and several cycles of refinement in REFMAC5 were performed. The structure was refined to 2.26 Å resolution with a final R_{work} and R_{free} of 23.9% and 25.3%, respectively (Table 1). No electron density was observed for the N-terminal His-tag, residues 572 to 581 and residues 675 to 676, and were not included in the final model. Residues from the CBD showed poor electron density that may indicate its high flexibility. However, most of the CBD was modeled as alanines due to the poor electron density maps.

The crystal structure of the ChiA74 consists of an $(\alpha/\beta)_8$-TIM-barrel, a CID, a FnIII and a C-terminal CBD (Fig. 1). Chitinases from family 18 share a common active site shape, which is often called "tunnel shaped"[28]. The catalytic region is composed of 442 residues and forms a substrate binding cleft and a semi-closed tunnel-shaped active site, with both the $(\alpha/\beta)_8$-TIM-barrel and the CID, similar to other chitinases with CID, the substrate binding groove is partially closed[29]. Three disulfide bonds between residues C78-C100, C140-C146, and C453-C461 are located in the TIM-barrel, with an additional one formed between residues C348-C359 in the CID domain. Structural comparison of the catalityc region of ChiA74 with other chitinases shows structural differences (Fig. S1) Although the catalytic region of chitinase A1 of *B. circulans* WL-12 shows high similarity with ChiA74 (~60% of identity), ChiA74 differs mainly in a loop (residues 454 to 465) that is close to the CID (Fig. S1, loop in magenta) and in two segments of the CID-loop 1 defined as l′ and l″ (Fig. S1, regions of the CID-loop 1 are indicated in yellow and red, and corresponds to residue range 361 to 366 and 375 to 380, respectively). The two regions of the CID-loop 1 (l′ and l″), the loops of the TIM-barrel harboring the CID (Fig. S1, loops showed in magenta and orange), and the TIM-barrel loop 2 (Fig. S1, showed in green) are the main structural differences of ChiA74 with chitinase A from *S. marcescens*, chitinase A from *V. harveyi* and ChiW from *Paenibacillus sp.* str. FPU-7 (Fig. S2, PDB code 1FFR, 3B9A and 5GZT, respectively). ChiW from *Paenibacillus sp.* str. FPU-7 differs even more on its TIM-barrel loop 2, which is considerable smaller to the rest of the chitinases showed in Fig. S1.

In our structure, the FnIII-like domain is linked to the TIM-barrel through residues 476 to 484 at the opposite site of the catalytic region, defined as FnIII linker loop. A calcium ion is highly coordinated by residues D483 and E485 (witin the FnIII linker loop), residues D512 and N513 (within the FnIII loop 2 which harbors residues 508

PDB code	6BT9
Data collection	
Space group	P 1 21 1
Cell dimensions	
a, *b*, *c* (Å)	85.8 82.4 101.6
α, β, γ (°)	90, 108.1, 90
Resolution (Å)	62.76-2.26 (2.31–2.26)*
R_{merge}	0.155 (0.712)
Mean I/σ(I)	8.9 (1.9)
$CC_{1/2}$	0.965 (0.847)
Completeness (%)	99.7 (99.1)
Redundancy	5.4 (4.9)
Refinement	
Resolution (Å)	62.76-2.26
No. reflections	63155
R_{work}/R_{free}	23.9%/25.3%
No. non-hydrogen atoms	9450
Protein	9370
Water	78
B-factors	
Protein	24.32
Ligands	15.46
Water	11.79
Root mean squared deviations	
Bond lengths (Å)	0.0103
Bond angles (°)	1.354

Table 1. Data collection and refinement statistics of ChiA74. *Values in parentheses are for the highest resolution shell.

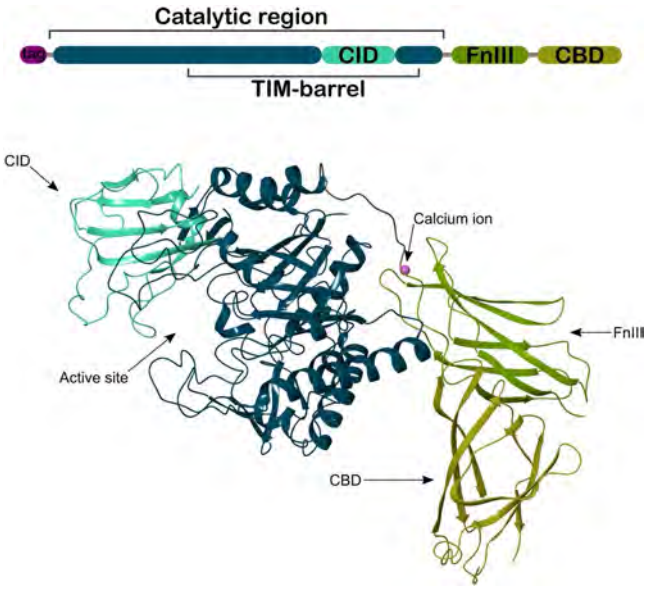

Figure 1. Overall structure of ChiA74. The scheme of the multidomain enzyme is shown at the top of the image. The catalytic region is composed of the characteristic $(\alpha/\beta)_8$-TIM-barrel and the chitinase insertion domain (CID), in dark blue and cyan, respectively. The fibronectin type III (FnIII) and the chitin binding domain (CBD), in green and lemon colors, respectively, are located at the C-terminal region. The rest of the image shows the active site into the cavity formed between the CID and the $(\alpha/\beta)_8$-TIM-barrel, indicated with an arrow. Two loops of the FnIII domain (green) and the linker loop to the $(\alpha/\beta)_8$-TIM-barrel keeps a highly coordinated calcium ion. The CBD at the C-terminal is shows in lemon color. The image only shows one molecule, for clarity, of two contained in the asymmetric unit.

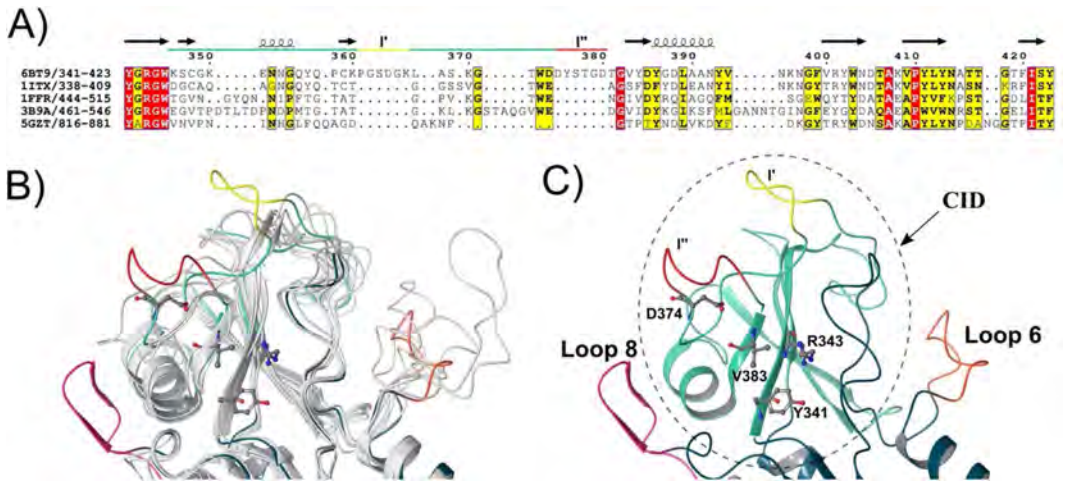

Figure 2. Structure-based sequence alignment of ChiA74 with other chitinases. The image shows the structure-based sequence alignment of the catalytic cleft of ChiA74 and others CID containing chitinases. Similar and conserved residues are indicated in yellow and red, respectively, according with ENDScript server[35]. UCSF Chimera[34] for structures superimposing. (**A**) Structure-based sequence alignment, only the region of the CID is shown. Main difference with other CIDs is the CID-loop 1 long. Regions l′ and 1″ are indicated in yellow and red, respectively. The PDB ID are the following: 6BT9 (chitinase ChiA74 from *B. thuringiensis*); 1ITX (catalytic domain of chitinase A1 from *B. circulans* WL-12); 1FFR (chitinase of mutant Y390F complexed with hexa-N-acetylchitohexaose from *S. marcescens*); 3B9A (*V. harveyi* chitinase A complexed with hexasaccharide) and 5GZT (chitinase ChiW from *Paenibacillus* sp. str. FPU-7). (**B**) Structural superimposition of ChiA74 with other chitinases where the differences between structures are shown with color. PDB codes of the superimposed structures are the same used in A. (**C**) CID in ChiA74 (dashed line) protrudes from Loops 6 and 8 of the TIM-barrel. Residues that would be interacting with substrate are indicated. Region 1′ of the CID-loop1 closes the substrate binding groove ″ of the active cleft (yellow).

to 516) and D554 (within the FnIII loop 6, residues 554 to 562); these loops are the linkers between β strands of the domain, i. e. loop 2 links β strand 2 to 3, and loop 6 links β strand 6 to 7. Other contacts of the N-terminal region of the FnIII occur with residues E248 to K251 of the TIM-barrel. FnIII does not form an extended substrate binding surface with the catalytic cleft as has been observed in other chitinases, for instance, chitinase ChiA of *Serratia marcescens*, and ChiA of *V. harveyi*, where this domain has multiple sites for substrate binding along the surface towards the active site, and which functions in enhancing binding and hydrolyzing activities against natural chitin[30,31]. The crystal structure of ChiA74 and the catalytic parameters of the truncated FnIII version of the enzyme[12], shows that FnIII (i) lacks exposed aromatic residues, and (ii) acts as a stable linker between the catalytic region and the CBD. A similar role of a FnIII domain has been suggested in chitinase ChiW from *Paenibacillus* sp. str. FPU-7[32], and other multimodular carbohydrate-interacting proteins containing FnIII domains[33]. Additionally, CBD shares interfaces between both FnIII and the $(\alpha/\beta)_8$-TIM-barrel. Briefly, N664 to E667 form hydrophobic and electrostatic interactions with the β-sheet 7of the FnIII (residues 563 to 568), and its loop 1 interacts with the α -helix 4 of the TIM-barrel (Figs 1 and S2).

Structure of the CID of ChiA74. The CID is located between the seventh alpha-helix and the seventh beta-strand of the $(\alpha/\beta)_8$-TIM-barrel. Residues in this loop assemble the "half active site wall" of the entire catalytic region. The CID consists of 82 residues, constrained between residues 341 and 423. In ChiA74 this domain is composed by five antiparallel beta-strands, one α -helix and one loop of 38 residues long between its first and the second β-strand of the CID, defined as CID-loop 1. A structure-based sequence alignment and a structural comparison with other chitinases (Fig. 2) carried out by the structure comparison tool MatchMaker of the UCSF Chimera program[34] showed that the CID-loop 1 is longer in ChiA74, with two segments that extend and closes the catalytic cleft, named as l′ and l″. CID-loop 1 is the less conserved region compared with similar chitinases of known structure. PDB codes indicated in Fig. 2A, and similar, conserved residues are indicated in yellow and red, respectively, according with ENDScript[35]. Those segments are considerably long when compared with other structures (Fig. 2B). PDB codes of the superimposed structures are the same that are indicated in Fig. 2A, ribbon representation images were rendered in Maestro program[36]. The CID-loop 1 together with the TIM-barrel loop 2 (residues 74 to 147) (Fig. S1) assemble into a structure that partially closes the substrate binding groove. This assembling is characteristic of exo-acting processive enzymes during the degradation of non-soluble polysaccharides[37], since processive chitinases possess partially closed tunnels at the active site and conserved aromatic residues that bind the substrate and allows substrate translocation and processivity[38], and is also an important structural element for endo-acting chitinases on soluble substrates[28,32]. Additionally, four residues in the CID are suggested to interact with the substrate at the catalytic cleft[10]; in ChiA74 these residues are Y341, R343, V383 and D374 (Fig. 2C).

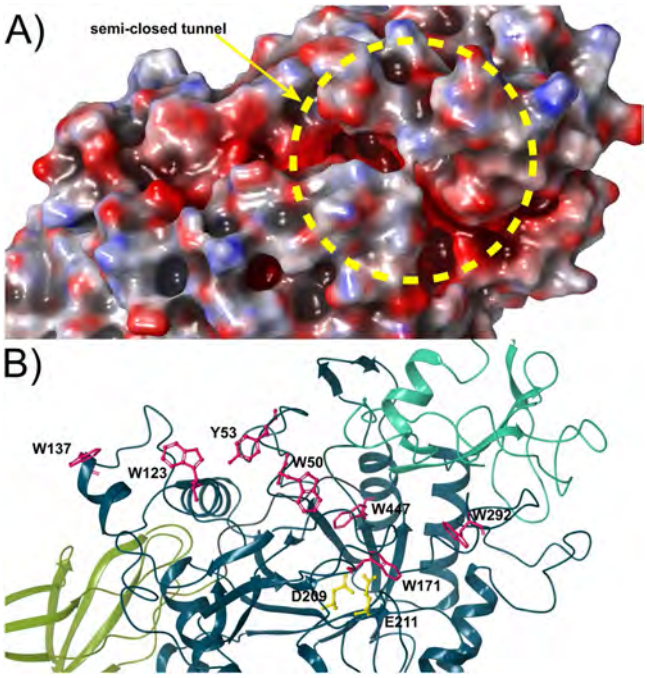

Figure 3. Structural details of the catalytic cleft in ChiA74. (**A**) Electrostatic surface potential of the semiclosed tunnel active site of ChiA74. Red and blue color indicate negative and positive charges, respectively, generated using Poisson-Boltzmann (APBS) method for the solvated molecule. The binding and catalytic area displays an extended negatively charged surface. The discontinued circle in yellow is indicating the semi-closed tunel. (**B**) A series of aromatic residues for substrate stabilization and binding are shown in magenta. Residues W137, W123, Y53, W50 and W447 form an extended surface towards the catalytic site (only D209 and E211 are shown, in yellow). Images are superimposables.

Structural details of the catalytic cleft of ChiA74. The catalytic semi-closed tunnel of ChiA74 formed by the TIM-barrel and CID displays a negatively charged surface (Fig. 3A). The $(\alpha/\beta)_8$-TIM-barrel harbors a series of aromatic residues through its molecular surface, that control substrate binding near the active site, subsites −5 to +2. The subsites −1 and +1 are between the cut-off site of the enzyme, the positive subsites (e.g.+2) toward the reducing end, and the negative subsites (−2, −3, −4, −5…) in the direction to the non-reducing end (Figs S3, S4B). Several studies in model enzymes from subfamily A of the family 18 chitinases[30,39] indicate that conserved exposed aromatic residues at the entrance of the catalytic cleft play a key role in hydrolyzing the chitin chain, when using crystalline chitin as a substrate, by guiding the entrance of the substrate into the active site. In ChiA74, the aromatic residues at the entrance of the catalytic cleft correspond to W123 and W137 which are similarly located as in chitinase from *B. circulans, S. marcescens* and *V. harveyi*, and may play the same role as substrate guiding residues (Figs 3B, S3). Residues Y53 and W50 are also conserved and they may be involved in extending from −5 to −3. These amino acids are structurally superimposable to Y56 and W53 of ChiA1 from *B. circulans*, and appear to be essential for crystalline chitin hydrolysis[30,40]. Due to their structural resemblance, residues Y53 and W50 may have the same function in hydrolyzing crystalline chitin. Residues W137, W123, Y53, and W50 are located on the extended surface at the entrance to the catalytic cleft in ChiA74, suggesting that this chitinase works as processive chitinases towards the non-reducing end of chitin[41] predominantly releasing disaccharides and also monosaccharides at +1 and +2 subsites, as it was recently observed with purified ChiA74[22]. For ChiA74, residues stacking in subsites +1 and +2 are W171 and W292, respectively (Fig. S3).

The catalytic domain harbors the motif (DxDxE) which is conserved in most family 18 chitinases, and whose role in the catalytic process has been demonstrated in other bacterial chitinases[21,34–43]. In the current accepted model, the second Asp within the DxDxE motif turns towards the Glu after substrate binding, enabling hydrogen bond interactions with the substrate and Glu, then the glycosidic oxygen acts as a nucleophile and the second Asp deprotonates the N-acetamido nitrogen during oxazolinium ion formation. Finally the Glu protonates the glycosidic oxygen and deprotonates the nucleophilic water, giving the hydrolysis of the oxazolinium ion[44]. In ChiA74 this motif harbors the following amino acids: D207, D209, and the catalytic E211[21] (Figs 3B, S3).

Chitinase activity of truncated versions and catalytic motif mutants against different substrates. ChiA74Δsp and its versions lacking the chitin binding domain (ChiA74Δsp-60) and chitin binding-fibronectin type III domains (ChiA74Δsp-50) were assayed against three natural substrates (crystalline chitin, colloidal chitin, chitosan) and one synthetic compound, i.e. 4-MU-$(GlcNAc)_3$ (Table 2). Also, mutants of ChiA74Δsp with one (ChiA74Δsp_{E211N}) and two (ChiA74$\Delta sp_{mD207N, E211N}$) amino acid replacements in the catalytic motif were generated, substituting D207 and the catalytic E211 (negative amino acids) with asparagines (N, uncharged amino acid). The importance of those amino acids in catalysis has been demonstrated in chitinase A1 of *B.*

Enzymes	crystalline-chitin*	Colloidal chitin*	Chitosan*	4-MU-GlcNAc$_3$**
ChiA74Δsp	$97.46 \pm 6^{a***}$	187.15 ± 13^{a}	48.73 ± 23^{a}	13093.16 ± 635^{a}
ChiA74Δsp-60	21.54 ± 1^{b}	60.53 ± 4^{b}	28.52 ± 14^{a}	10313.68 ± 500^{b}
ChiA74Δsp-50	47.76 ± 3^{c}	170.44 ± 12^{a}	51.28 ± 25^{a}	8846.54 ± 429^{c}
ChiA74Δsp$_{E211N}$	0.71 ± 0.0^{c}	0.71 ± 0.05^{c}	1.41 ± 0.7^{b}	64.97 ± 3^{d}
ChiA74Δsp$_{D207N, E211N}$	1.77 ± 0.1^{d}	3.53 ± 0.25^{d}	2.82 ± 1^{b}	51.55 ± 2^{e}

Table 2. Chitinase activity (U/μmol) of different versions of ChiA74 against several substrates. *One Unit of chitinase activity was defined as the amount of enzyme required to release 1 μmol of NAG in 1 h. **One Unit of chitinase activity was defined as the amount of enzyme required to release 1 μmol of MU in 1 h. ***Different letter in the same column (a, b, c) indicate significant difference at $P < 0.05$ determined by the Tukey multiple range test.

circulans and *S. marcescens*, primarily the glutamic acid which is directly involved in the hydrolysis of the oxazolinium ion intermediate[42,44]. In general, the highest activity with natural substrates was observed with colloidal chitin rather than crystalline chitin and chitosan in a time reaction of 12 h at 37 °C. As was previously reported[12], we confirmed that ChiA74Δsp and ChiA74Δsp-50 show the highest activity with colloidal chitin, without statistical difference. With crystalline chitin, ChiA74Δsp showed 4.5 and 2.0 higher activity than ChiA74Δsp-60 and ChiA74Δsp-50, respectively, but with chitosan the highest activity was detected with ChiA74Δsp-50. Using 4-MU-(GlcNAc)$_3$, truncated versions showed differences in the activity against this substrate. When mutants (ChiA74Δsp$_{E211N}$) and ChiA74Δsp$_{D207N, E211N}$ were assayed with crystalline chitin, colloidal chitin, chitosan and 4-MU-(GlcNAc)$_3$, no enzymatic activity was observed, demonstrating the importance of the catalytic E211 in the chitinase activity[42,44] of ChiA74Δsp.

On the other hand, TLC (Fig. S4) was carried out with colloidal chitin and crystalline chitin, the natural substrates that were most susceptible to the hydrolytic activity of purified ChiA74Δsp and ChiA74Δsp-50. Chitin-oligosaccharide derivatives with degree of polymerization of 1 and 2 were detected, as previously reported[22], which suggest a processive activity in substrate degradation. Similar results were reported with BthChi74, a chitinase that shares 98% identity with ChiA74[45].

Discussion

The crystal structure of ChiA74 shows that this enzyme has a modular structure formed by four domains: (i) the catalytic region with an (α/β)8-TIM-barrel as a core structure, (ii) the chitinase insertion domain as a barrel insertion, (iii) the fibronectin type III and (iv) a chitin binding domain, as previously hypothesized by Juárez-Hernández *et al.*[12].

The modular organization of ChiA74 has similarities, but it is not identical to the structure reported for other bacterial chitinases (e.g. ChiA1 from *B. circulans*, ChiA from *S. marcescens*, ChiA from *V. harveyi*, ChiW from *Paenibacillus* sp. str. FPU-7[30-32,40]. Some chitinases have immunoglobulin-like fold domains (FnIII, CBD or both), but ChiA74 differ from those enzymes mainly at the structural arrangement level, because of the very closed substrate binding groove of the catalytic cleft and in the multimodular assembly (Figs 1, 2). The TIM-barrel/CID catalytic domain of ChiA74 harbors the conserved motif in most family 18 chitinase involved in chitin hydrolysis (i.e. DxDxE), where E211 plays an important role as the catalytic amino acid initiator of the oxazolinium ion intermediate hydrolysis[42,44]. We demonstrated the importance of residues present in the conserved motif of the catalytic domain by site-directed mutagenesis, in particular, the significance of the catalytic E211 in ChiA74, as mutants ChiA74Δsp$_{E211N}$, ChiA74Δsp$_{D207N, E211N}$ were inactive against two natural polysaccharides (i.e. chitin, chitosan) and one short synthetic substrate (4-MU-GlcNAc$_3$) (Table 2), similar as reported for other chitinases[42]. The catalytic domain of ChiA74 from *B. thuringiensis* shows high identity with ChiA of *S. marcescens*, suggesting that ChiA74 might has similar catalytic mechanism. In the proposed mechanism for ChiA74, D209 interacts with D207, after binding of substrate D209 flips to its alternative position where it interacts with E211 forcing the substrate acetamido group of −1 sugar to rotate around the C2-N2 bond (Fig. S5)[29].

As ChiA74 contains a CID inserted into the TIM barrel catalytic domain, this enzyme can be classified in the subfamily A of the family 18 chitinases[10]. The location of the FnIII and CBD in ChiA74 is different with respect to other chitinases of the family 18, in which the FnIII domain is often located along the catalytic region and functions as a chitin binding module[29,46]. In ChiA74, the FnIII might act as a stable linker between the catalytic regions and the CBD in a similar way as has been proposed in ChiAW fom *Paenibacillus* sp. str. FPU-7 and *Microbacterium aurum* B8[32,33]. The modular arrangement of ChiA74 represents the first report of a full version chitinase structure with a CBD located slightly distal from the catalytic region linked by a FnIII domain, and suggests a different role (substrate binding and guiding to the active site) for the CBD. The location of the CBD with respect to the catalytic region has no structural similarity with other chitinases of known structure, and to date, represents the first report of this particular multimodular assembly. The structural arrangement of this domain remains unclear, but our data indicates that this domain could be important for crystalline chitin hydrolysis. For example, the activity of the truncated version against crystalline chitin is lower (from 0.22 X to 0.49X) than ChiA74Δsp, suggesting that CBD is necessary for crystalline chitin hydrolysis. We do not have experimental evidence, but as crystalline chitin has a fibrillar structure with high degree of crystallinity and polymorphism, and the chitin binding domain surface might facilitate the movement of the chitin chain toward the catalytic region, as suggested previously[7] or prevent dissociation from the crystalline substrate. In general, we observed a higher chitinase activity when using colloidal chitin as a substrate than using chitin in its crystalline form. It is likely

that colloidal chitin might interact more easily with the enzyme because the crystalline structure maintained by hydrogen bonds is disrupted due to the acid treatment, thus facilitating the interaction of the sugar chains of the colloidal chitin with ChiA74. Similar results have been observed with a chitinase from *V. harveyi*[7]. Our data confirmed that ChiA74Δsp and the truncated version ChiA74Δsp-50 (i.e., the enzyme version with the CD and CID) have the same activity against colloidal chitin, indicating the CBD and FnIII are not necessary for the chitinase activity against this substrate[12]. When crystalline and colloidal chitin were treated with ChiA74Δsp and analyzed by TLC, oligosaccharides of DP of 1 (GlcNAc) and DP of two ($GlcNAc_2$) were obtained, indicating that ChiA74Δsp has an exo-acting processive activity which is congruent with the presence of a partially closed substrate binding groove formed by the CID-loop 1 and the TIM-barrel loop 2, characteristics of enzymes with this activity[37]. Similar results were obtained previously in our laboratory using purified ChiA74Δsp and colloidal chitin[22]. The crystal structure and TLC data suggest that ChiA74 probably hydrolyses chitin chains from reducing toward non-reducing end, similar to ChiA by *S. marcescens*[47]. We previously reported that ChiA74 has an endo-chitinase activity which was determined using crude extracts and synthetic fluorescent substrates[21]. However, the putative endochitinase activity reported in that work might be erroneous considering the fact that ChiA74 was mixed with other proteins in the crude extract and the substrate was not a chitin polymer. In this regard, in future studies it is very important to confirm or discard, experimentally, whether ChiA74 cleaves the chitin chain at internal sites or hydrolyzes chitin from the end in a processive mode, or both, using more sensitive techniques than TLC (e.g. HPLC)[44,47].

Finally, we report for the first time the three-dimensional structure of a chitinase synthesized by *B. thuringiensis*, the most important microbial insecticide worldwide. The elucidation of the crystal structure of ChiA74 is an important advancement in the study of metabolites of *B. thuringiensis* and provides a foundation for future studies of chitinases synthesized by this bacterium, including protein engineering or directed evolution to enhance the applied versatility of these enzymes.

Materials and Methods

Bacterial strains and culture conditions. The recombinant plasmid, *pColdI-chiA74Δsp*, harbors *chiA74* lacking sequences coding for the secretion signal peptide, and its N-terminal end is fused to a heterologous sequence of 28 amino acids that includes the 6x-histidine tag and Factor Xa cleavage sites[12,22]. *Escherichia coli* TOP10 (Invitrogen, Carlsbad CA, EE.UU.) and *E. coli* BL21 Rosetta 2 (Merck Millipore, MA) were used as host cells for propagation or protein production, respectively. All bacteria were cultured at 37 °C in Luria-Bertani (LB) liquid medium (Invitrogen, Carlsbad CA, USA), supplemented with ampicillin (100 mg/ml) or chloramphenicol (34 mg/ml).

Expression and purification of ChiA74Δsp. *E. coli* BL21 Rosetta 2/*pColdI-chiA74Δsp* was grown overnight in 10 ml of LB broth supplemented with ampicillin and chloramphenicol, and then transferred to 1000 ml fresh medium supplemented with the same antibiotics. Culture was grown at 37 °C/200 rpm to reach an OD_{600} of 0.5, and then incubated at 4 °C for 15 min. Bacterial culture was incubated with agitation at 15 °C for 30 min, and IPTG was added to a final concentration of 0.5 mM. The culture was incubated for 24 h at 16 °C, 200 rpm, and then centrifuged, the supernatant was discarded, and the pellet was resuspended and incubated on ice for 30 min in 25 ml of buffer A (100 mM Tris-HCl, pH 7; 500 mM NaCl, 10 mM imidazole) supplemented with lysozyme (1 mg/ml). Samples were sonicated 10x, 30 s each, at an amplitude of 30 Hz using a 20 kHz ultrasonic processor (Sonic and Materials, Inc., New-town, CT 06470-1614 USA). The extract was centrifuged 30 min at 13,000 *g* and the supernatant was passed through a HisTrap HP column (GE Healthcare Bio-Sciences AB, Upsala Sweden) pre-equilibrated with buffer A. Unbound protein was removed with 15 ml of buffer A, 15 ml of buffer A-20 mM imidazole, 15 ml of buffer A-40 mM imidazole, and finally samples were eluted with 3 ml of buffer A-500 mM imidazole. Eluted samples were dialyzed at 4 °C in buffer E (100 mM Tris-HCl, pH 7; 150 mM NaCl) without imidazole. Collected fractions were analyzed by 10% SDS–polyacrylamide gel (SDS–PAGE) and zymogram. Samples, purified with the HisTrap HP column were loaded onto a Superdex 200 10/300 GL (GE Healthcare life science) column previously equilibrated with buffer A (100 mM Tris–HCl pH 7.0, 25 mM NaCl) and ChiA74Δsp was separated by fast protein liquid chromatography (FPLC) (Biologic Duo-Flow Pathfinder 20 System BioRad, Hercules CA, USA). Fractions of 1 ml were collected at a rate of 0.5 ml/min using buffer A and monitored at 280 nm. Fractions in the peak were collected and analyzed by 10% SDS–PAGE and zymograms. Protein concentration was determined at 595 nm using the Quick Start Bradford 1 x Dye reagent (BioRad, HerculesCA, USA) in a Synergy HTX Biotek (Winooski, VT).

SDS-PAGE and zymograms. Fractions containing ChiA74Δsp were monitored by SDS-PAGE and zymogram to corroborate the presence and activity of the purified recombinant protein. Portions of each fraction were treated with Laemmli's disruption buffer supplemented with β-mercaptoethanol. Identical samples were fractionated by electrophoresis in a 10% SDS–PAGE. One gel was stained with coomassie blue and the second was washed with casein-EDTA buffer [1% (w/v) casein, 2 mM EDTA, 40 mM Tris–HCl, pH 9], and activity detected with 25 μM of the fluorogenic substrate 4-MU-$(GlcNAc)_3$ (Sigma, St. Louis, MO), as previously described[21].

Protein crystallization and data collection. Initial crystallization tests were performed by using a Crystal Gryphon robot (Art Robbins Instruments, Sunnyvale CA, USA) using MRC 3 well crystallization plates (Jena Bioscience, Jena, Germany). Approximately 300 conditions were tested for crystallization at 292 K and crystals were formed in 30 conditions after two weeks using protein at 15 mg/ml, whereby a selection of the most appropriate crystals was made to improve their size. New drops were set in VDX plates (Hampton Research, Aliso Viejo CA, USA) using hanging-drop vapor diffusion technique by mixing equal volumes of the pure protein with selected precipitants from a sparse matrix screen. All the crystals were grown as a sheet clusters; no individual

crystals were obtained even after crystal seeding. Crystals were selected for diffraction from a condition containing 25% (w/v) PEG 6000, 100 mM HEPES/NaOH pH 7.0 and 200 mM NaCl. A single sheet crystal was obtained by breakage and cryoprotected in a similar solution containing 20% (w/v) of glycerol prior to flash cooling in liquid nitrogen. Two crystals were used to collect diffraction data at 100 K using a MarMosaic 225 CCD detector at APS beam line LS-CAT 21-ID-F with 1° rotation per image.

Structure determination and refinement. Diffraction intensities were integrated and scaled as monoclinic P 1 21 1 lattice symmetry with DIALS using xia2[48] and AIMLESS[49] from the CCP4 software suite, respectively. The program MATTHEWS_COEF[50], through the cell content analysis task in CCP4 suggests two copies of ChiA74 in the asymmetric unit. A molecular replacement solution was found with Phaser-MR[51], using a poly alanine model of the chitinase A1 structure from *B. circulans* (PDB ID 1ITX) as the search template. Residues of the catalytic region were modeled in Coot according with sequence as they were supported by electron density. Crystallographic refinement was performed with REFMAC5[52]. A total of 3145 reflections (5.0%) were used as the test set. Simulated annealing, individual atomic coordinate and individual atom isotropic displacement parameter refinement strategies were performed with non-crystallographic symmetry (NCS) restraints. The model was adjusted to improve the fit to likelihood weighted electron density maps using Coot[53], and the rest of the model corresponding to the fibronectin type III and carbohydrate binding domains were constructed manually in agreement with electron density maps, in Coot. Some solvent molecules were added where they were supported by both chemistry and geometry. The quality and stereochemistry of the model were evaluated using Coot validation tools, Molprobity and the wwPDB Validation Server[54].

Construction of ChiA74 mutant. Mutations in the catalytic domain were carried out by site-directed mutagenesis using pCold-*chiA74*Δsp as template[22]. This recombinant plasmid was amplified with the Phusion high-fidelity DNA polymerase (Thermo Scientific, MA, USA) using 5′ phosphorylated oligonucleotides allowing the plasmid's re-ligation. Two *chiA74*Δsp mutants, encoding proteins with one (E211N) or two (D207N, E211N) amino acids changes in the catalytic motif were obtained. The following primers were used, respectively: Fw E211N: 5′-CGTAGATTTAGACTGGAACTATCCGGGCGTTGAAA-3′, Rv E211N: 5′-TTTCAACGCCCGGATAGTTCCAGTCTAAATCTACG-3′, and Fw D207N,E211N: 5′-GATGGCGTAAACTTAGACTGGAACTATCCGGGCGTT-3′, Rv D207N,E211N: 5′-AACGCCCGGATAGTTCCAGTCTAAGTTTACGCCATC-3′. Amplicons were treated with DpnI to eliminate DNA templates and then visualized in 0.8% agarose. Samples were purified with the agarose gel extraction kit (Jena Biosciences, Jena, Germany) and dialyzed. *E. coli* Top10 was transformed with the purified amplicons by electroporation at 2.5 kV and transformants were selected on LB agar with ampicillin at 37 °C. The presence of point mutations was corroborated by sequencing and analyzed with the program LALING (https://embnet.vital-it.ch/software/LALIGN_form.html).

Enzymatic activity. Chitinase activity was determined in triplicate assays at 37 °C in 20 mM phosphate buffer, pH 7, using the substrate 4-methylumbelliferyl β-D-N,N′,N″-triacetylchitotrioside (4-MU-GlcNAc$_3$) (Sigma, St. Louis, MO) and purified recombinant enzymes at final concentrations of 100 µg/ml. The amount of 4-MU released from the substrate was calculated spectrofluorometrically (excitation at 360 nm and emission at 455 nm) with a Synergy HTX Biotek (Winooski, VT) instrument using a 4-MU standard curve. One unit (U) of chitinolytic activity was defined as the amount of enzyme required to release 1 µmol of 4-methylumbelliferone in 1 h. To determine chitinase activity with crystalline chitin (Sigma-Aldrich, St. Louis MO, USA), colloidal chitin (Sigma-Aldrich, St. Louis MO, USA) and chitosan, a suspension containing 0.5% of these substrates was mixed with 0.036 mg/ml of purified enzyme to reach a final volume of 0.5 ml using 20 mM phosphate buffer, pH 7, and then incubated at 37 °C with gentle agitation. Aliquots of 40 µL were taken after 12 h of incubation and mixed with 40 µL of 3,5-dinitrosalicylic acid. The samples were boiled for 5 min, allowed to cool and water was added to a final volume of 200 µl, then the absorbance was measured at 540 nm to determine the concentration of reducing sugars[19,21].

Analysis of chitin hydrolysis with ChiA74Δsp using thin layer chromatography. Mixtures containing 0.036 mg/ml of ChiA74Δsp, 0.5% (w/v) colloidal chitin, and 20 mM phosphate buffer (pH 7.0) were incubated at 37 °C, 200 rpm for 12 h to generate chitin-derived oligosaccharides (OGS). Reaction was terminated by heating at 100 °C for 5 min. Samples were centrifuged, supernatants were collected and concentrated in a DNA120 SpeedVac (ThermoSavant), then pellets were resuspended in 10 µl of double distilled water and 10 µl of methanol. OGS were analyzed by silica gel (Merk) thin layer chromatography (TLC) using 5:4:3 (v/v/v) n-butanol: methanol:16% aqueous ammonia as the mobile phase. Samples were visualized by staining with 20% (v/v) sulfuric acid in ethanol and incubated at 80 °C until chitin-derived oligosaccharides signals were developed. Molecular markers (Sigma, St. Louis, MO) *N*-acetyl-D-glucosamine (GlcNAc) and *N,N′*-diacetylchitobiose (GlcNAc$_2$) were used to determine the degree of polymerization (DP)[22].

Data Availability

All reagents and data described in this manuscript are available upon request. The coordinates and structure factors of ChiA74 have been deposited in the PDB under Accession code 6BT9.

References

1. Nagpure, A., Choudhary, B. & Gupta, R. K. Chitinases: in agriculture and human healthcare. *Crit. Rev. Biotechnol.* **34**, 215–232 (2014).
2. Adrangi, S. & Faramarzi, M. A. From bacteria to human: A journey into the world of chitinases. *Biotechnol. Adv.* **31**, 1786–1795 (2013).

3. Van Aalten, D. M. *et al*. Structural insights into the the catalytic mechanism of a family 18 exochitinase. *Proc. Natl. Acad. Sci. USA* **98**, 8979–84 (2001).
4. Brameld, K. A. & Goddard, W. A. Substrate distortion to a boat conformation at subsite -1 is critical in the mechanism of family 18 chitinases. *J. Am. Chem. Soc.* **120**, 3571–3580 (1998).
5. Aronson, N. N. *et al*. Family 18 chitinase-oligosaccharide substrate interaction: subsite preference and anomer selectivity of *Serratia marcescens* chitinase. *A. Biochem. J.* **376**, 87–95 (2003).
6. Watanabe, T. *et al*. The roles of the C-terminal domain and type III domains of chitinase A1 from *Bacillus circulans* WL-12 in chitin degradation. *J. Bacteriol.* **176**, 4465–4472 (1994).
7. Suginta, W., Sirimontree, P., Sritho, N., Ohnuma, T. & Fukamizo, T. The chitin-binding domain of a GH-18 chitinase from *Vibrio harveyi* is crucial for chitin-chitinase interactions. *Int. J. Biol. Macromol.* **93**(PtA), 1111–1117 (2016).
8. Hsieh, Y. C. *et al*. Crystal Structures of *Bacillus cereus* NCTU2 chitinase complexes with chitooligomers reveal novel substrate binding for catalysis: A chitinase without chitin binding and insertion domains. *J. Biol. Chem.* **285**, 31603–31615 (2010).
9. Kuo, C. Y. *et al*. Purification, crystallization and preliminary X-ray crystallographic analysis of chitinase from *Bacillus cereus* NCTU2. *Acta Crystallogr Sect. F. Struct. Biol. Cryst. Commun.* **62**(Pt9), 916–919 (2006).
10. Li, H. & Greene, L. H. Sequence and structural analysis of the chitinase insertion domain reveals two conserved motifs involved in chitin-binding. *PLoS One* **5**, e8654 (2010).
11. Fusetti, F., Pijning, T., Kalk, K. H., Bos, E. & Dijkstra, B. W. Crystal structure and carbohydrate-binding properties of the cartilage glycoprotein-39. *J. Biol. Chem.* **278**, 37753–37760 (2003).
12. Juárez-Hernández, E. O., Casados-Vázquez, L. E., Bideshi, D. K., Salcedo-Hernández, R. & Barboza-Corona, J. E. Role of the C-terminal and chitin insertion domains on enzymatic activity of endochitinase ChiA74 of *Bacillus thuringiensis*. *Int. J. Biol. Macromol.* **102**, 52–59 (2017).
13. Zees, A. C., Pyrpassopoulos, S. & Vorgias, C. E. Insights into the role of the (alpha + beta) insertion in the TIM-barrel catalytic domain, regarding the stability and the enzymatic activity of chitinase A from *Serratia marcescens*. *Biochim. Biophys. Acta* **1794**, 23–31 (2009).
14. Lacey, L. A. *et al*. Insect pathogens as biological control agents: Back to the future. *J. Invertebr. Pathol.* **132**, 1–41 (2015).
15. Evdokimov, A. G. *et al*. Structure of the full-length insecticidal protein Cry1Ac reveals intriguing details of toxin packaging into *in vivo* formed crystals. *Protein Sci.* **23**, 1491–1497 (2014).
16. Palma, L., Muñoz, D., Berry, C., Murillo, J. & Caballero, P. *Bacillus thuringiensis* toxins: an overview of their biocidal activity. *Toxins* **6**, 3296–3325 (2014).
17. Juárez-Hernández, E. O. *et al*. *Bacillus thuringiensis* subsp. *israelensis* producing endochitinase ChiA74Δsp inclusion and its improved activity against. *Aedes aegypti. J. Appl. Microbiol.* **119**, 1692–1699 (2015).
18. Barboza-Corona, J. E. *et al*. *Bacillus thuringiensis* subsp. *kurstaki* HD1 as a factory to synthesize alkali-labile ChiA74Δsp chitinase inclusions, Cry crystals and spores for applied use. *Microb. Cell Fact.* **13**, 15 (2014).
19. Ortiz-Rodríguez, T., de la Fuente-Salcido, N., Bideshi, D. K., Salcedo-Hernández, R. & Barboza-Corona, J. E. Generation of chitin-derived oligosaccharides toxic to pathogenic bacteria using ChiA74, an endochitinase native to *Bacillus thuringiensis. Lett. Appl. Microbiol.* **51**, 184–190 (2010).
20. Sha, L., Shao, S., Guan, X. & Huang, Z. Purification and partial characterization of intact and truncated chitinase from *Bacillus thuringiensis* HZP7 expressed in *Escherichia coli*. *Biotechnol. Lett.* **38**, 279–284 (2016).
21. Barboza-Corona, J. E. *et al*. Cloning, sequencing and expression of the chitinase gene *chiA74* from *Bacillus thuringiensis*. *Appl. Environ. Microbiol.* **69**, 1023–1029 (2003).
22. Casados-Vazquez, L. E., Avila-Cabrera, S., Bideshi, D. K. & Barboza-Corona, J. E. Heterologous expression, purification and biochemical characterization of endochitinase ChiA74 from. *Bacillus thuringiensis. Protein Expr. Purif.* **109**, 99–105 (2015).
23. Li, J. D., Carrol, J. & Ellar, D. J. Crystal structure of insecticidal delta endotoxin from *Bacillus thuringiensis* at 2.5. *Nature* **353**, 815–821 (1991).
24. Akiba, T. *et al*. Structure of parasporin-1, a novel bacterial cytotoxin against human cancer cells. *Acta Cryst.* **A61**, C250 (2005).
25. Cohen, S. *et al*. Cyt1Aa toxin: Crystal structure reveals implications for its membrane-perforating function. *J. Mol. Biol.* **413**, 804–814 (2011).
26. Sit, C. S., McKay, R. T., Hill, C., Ross, R. P. & Vederas, J. C. The 3D Structure of Thuricin CD, a two-component bacteriocin with cysteine sulfur to α-carbon cross-links. *J. Am. Chem. Soc.* **133**, 7680–7683 (2011).
27. Sit, C. S., van Belkum, M. J., McKay, R. T., Worobo, R. W. & Vederas, J. C. The 3D solution structure of Thurincin H, a bacteriocins with four sulfur to α-carbon crosslinks. *Angew Chem. Int. Ed. Engl.* **50**, 8718–8721 (2011).
28. Sikorski, P., Sørbotten, A., Horn, S. J., Eijsink, V. G. & Vårum, K. M. *Serratia marcescens* chitinases with tunnel-shaped substrate-binding grooves show endo activity and different degrees of processivity during enzymatic hydrolysis of chitosan. *Biochem.* **45**, 9566–9574 (2006).
29. Papanikolau, Y. *et al*. High resolution structural analyses of mutant chitinase A complexes with substrates provide new insight into the mechanism of catalysis. *Biochem.* **40**, 11338–11343 (2001).
30. Uchiyama, T. *et al*. Roles of the exposed aromatic residues in crystalline chitin hydrolysis by chitinase A from *Serratia marcescens* 2170. *J. Biol. Chem.* **276**, 41343–41349 (2001).
31. Katouno, F. *et al*. Importance of exposed aromatic residues in chitinase B from *Serratia marcescens* 2170 for crystalline chitin hydrolysis. *J. Biochem.* **136**(2), 163–168 (2004).
32. Itoh, T. *et al*. Crystal structure of chitinase ChiW from *Paenibacillus* sp. str. FPU-7 reveals a novel type of bacterial cell-surface-expressed multi-modular enzyme machinery. *PloS One,* **11**(12), e0167310 (2016).
33. Valk, V., van der Kaaij, R. M. & Dijkhuizen, L. The evolutionary origin and possible functional roles of FNIII domains in two *Microbacterium aurum* B8. A granular starch degrading enzymes, and in other carbohydrate acting enzymes. *Amylase* **1**, 1–11 (2017).
34. Pettersen, E. F. *et al*. UCSF Chimera- a visualization system for exploratory research and analysis. *J. Comput. Chem.* **25**, 1605–1612 (2004).
35. Robert, X. & Gouet, P. Deciphering key features in protein structures with the new ENDscript server. *Nucleic Acids Res.* **42**, W320–W324 (2014).
36. Schrödinger Release 2018-3: Maestro, Schrödinger, LLC, New York, NY, (2018).
37. Varrot, A., Hastrup, S., Schülein, M. & Davies, G. J. Crystal structure of the catalytic core domain of the family 6 cellobiohydrolase II, Cel6A, from Humicola insolens, at 1.92 Å resolution. *Biochem. J.* **337**, 297–304 (1999).
38. Payne, C. M. *et al*. Hallmarks of processivity in glycoside hydrolases from crystallographic and computational studies of the *Serratia marcescens* chitinases. *J. Biol. Chem.* **287**, 36322–36330 (2012).
39. Zakariassen, H. *et al*. Aromatic residues in the catalytic center of chitinase A from *Serratia marcescens* affect processivity, enzyme activity, and biomass converting efficiency. *J. Biol. Chem.* **284**, 10610–10617 (2009).
40. Matsumoto, T., Nonaka, T., Hashimoto, M., Watanabe, T. & Mitsui, Y. Three-dimensional structure of the catalytic domain of chitinase Al from *Bacillus circulans* WL-12 at a very high resolution. *Proc. Japan Acad.* **75**, 269–274 (1999).
41. Horn, S. J., Sørlie, M., Vårum, K. M., Väljamäe, P. & Eijsink, V. G. Measuring processivity. *Methods Enzymol.* **510**, 69–95 (2012).
42. Watanabe, T. *et al*. Identification of glutamic acid 204 and aspartic 200 in chitinase A1 of *Bacillus circulans* WL-12 as essential residues for chitinase activity. *J. Biol. Chem.* **268**, 18567–18572 (1993).

43. Vaaje-Kolstad, G. *et al*. Structure of the D142N mutant of the family 18 chitinase ChiB from *Serratia marcescens* and its complex with allosaminid. *Biochim Biophys Acta* **1696**, 103–111 (2004).
44. Van Aalten, D. M. *et al*. Structural insights into the catalytic mechanism of a family 18 exo-chitinase. *Proc. Natl. Acad. Sci. USA* **98**, 8979–8984 (2001).
45. Honda, S. *et al*. Characterization of a *Bacillus thuringiensis* chitinase that binds to cellulose and chitin. *AMB Expr.* **7**, 51 (2017).
46. Vaaje-Kolstad, G., Horn, S. J., Sørlie, M. & Eijsink, V. G. The chitinolytic machinery of *Serratia marcescens*-a model system for enzymatic degradation of recalcitrant polysaccharides. *FEBS J.* **280**, 3028–3049 (2013).
47. Horn, S. V. *et al*. Endo/exo mechanism and processivity of family 18 chitinase produced by *Serratia marcescens*. *FEBS J*. **273**, 491–503 (2006).
48. Waterman, D. G. *et al*. Diffraction-geometry refinement in the DIALS framework. *Acta Crystallogr. D Struc. Biol.* **72**, 558–575 (2016).
49. Evans, P. R. & Murshudov, G. N. How good are my data and what is the resolution? *Acta Crystallogr. D Biol. Crystallogr.* **69**, 1204–1214 (2013).
50. Kantardjieff, K. A. & Rupp, B. Matthews coefficient probabilities: improved estimates for unit cell contents of proteins, DNA, and protein-nucleic acid complex crystals. *Protein Sci.* **12**, 1865–1871 (2003).
51. McCoy, A. J. *et al*. Phaser crystallographic software. *J. Appl. Crystallogr.* **40**, 658–674 (2007).
52. Vagin, A. A. *et al*. REFMAC5 dictionary: organization of prior chemical knowledge and guidelines for its use. *Acta Crystallogr. D Biol. Crystallogr.* **60**, 2184–2195 (2004).
53. Emsley, P. & Cowtan, K. Coot: model-building tools for molecular graphics. *Acta Crystallogr. D Biol. Crystallogr.* **60**, 2126–2132 (2004).
54. Chen, V. B. *et al*. MolProbity: all-atom structure validation for macromolecular crystallography. *Acta Crystallogr. D Biol. Crystallogr.* **66**, 12–21 (2010).

Acknowledgements

This research was supported by Grant SEP-CONACYT (258220), México to J.E. B.-C and Fronteras de la Ciencia-CONACYT(11) to L.G.B. E.O. J.-H. is a doctoral student in the graduate program in BioSciences in the University of Guanajuato, México. L.E. C.-V is an Associate Researcher supported by Grant 2069 from Cátedras-CONACYT, México. E.O.J.-H and P.J.-S. thank CONACYT for their doctoral studies fellowship. This research used resources provided by the Advanced Photon Source, a U.S. Department of Energy (DOE) Office of Science User Facility operated for the DOE Office of Science by Argonne National Laboratory under Contract No. DE-AC02-06CH11357. Use of the LS-CAT Sector 21 was supported by the Michigan Economic Development Corporation and the Michigan Technology Tri-Corridor (Grant 085P1000817). We appreciate the critical review of the manuscript by Dr. Dennis K. Bideshi, California Baptist University, Riverside, California USA.

Author Contributions

E.O. J.-H. performed ChiA74 purification, crystallization and mutant analyses. L.E. C.-V. assisted with the experiments. A.T.-L. assisted in crystal evaluation and data collection. P.J.-S. contributed to the crystallization and structure solution of ChiA74. E.O. J.-H., P.J.-S. and J.E. B.-C. interpreted the results and wrote the paper with the assistance from L.-G.B.

Additional Information

Supplementary information accompanies this paper at https://doi.org/10.1038/s41598-019-39464-z.

Competing Interests: The authors declare no competing interests.

Publisher's note: Springer Nature remains neutral with regard to jurisdictional claims in published maps and institutional affiliations.

Open Access This article is licensed under a Creative Commons Attribution 4.0 International License, which permits use, sharing, adaptation, distribution and reproduction in any medium or format, as long as you give appropriate credit to the original author(s) and the source, provide a link to the Creative Commons license, and indicate if changes were made. The images or other third party material in this article are included in the article's Creative Commons license, unless indicated otherwise in a credit line to the material. If material is not included in the article's Creative Commons license and your intended use is not permitted by statutory regulation or exceeds the permitted use, you will need to obtain permission directly from the copyright holder. To view a copy of this license, visit http://creativecommons.org/licenses/by/4.0/.

© The Author(s) 2019

Article

Structure

Structural Adaptation in Its Orphan Domain Engenders Betaglycan with an Alternate Mode of Growth Factor Binding Relative to Endoglin

Graphical Abstract

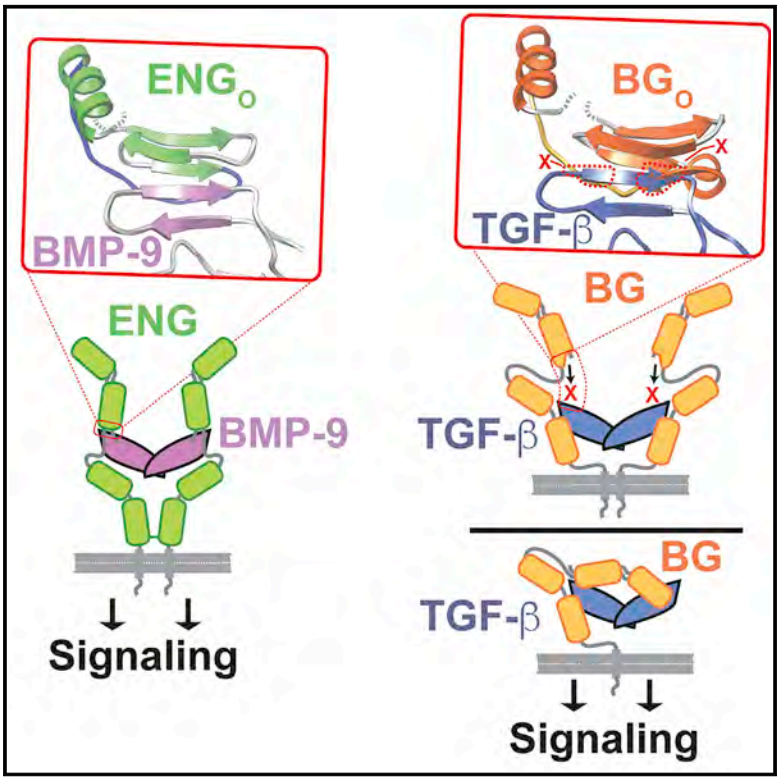

Authors

Sun Kyung Kim, Matthew J. Whitley, Troy C. Krzysiak, ..., Fernando López-Casillas, William Furey, Andrew P. Hinck

Correspondence

ahinck@pitt.edu

In Brief

Kim et al. determine the structure of the betaglycan orphan domain (BG_O) and show that the edge β strand that endoglin uses to bind its cognate growth factor is blocked by an insertion. Binding studies and SAXS show that BG_O binds its cognate growth factor differently compared with endoglin.

Highlights

- Structure of the betaglycan orphan domain (BG_O) was determined by crystallography
- Structure reveals an insertion compared with the endoglin orphan domain (ENG_O)
- Insertion blocks the edge β strand used in the ENG_O to bind BMP-9 or BMP-10
- BG_O binds TGF-β in a different manner than ENG_O binds BMP-9 or BMP-10

Kim et al., 2019, Structure 27, 1427–1442
September 3, 2019 © 2019 Elsevier Ltd.
https://doi.org/10.1016/j.str.2019.06.010

CellPress

Structure
Article

CellPress

Structural Adaptation in Its Orphan Domain Engenders Betaglycan with an Alternate Mode of Growth Factor Binding Relative to Endoglin

Sun Kyung Kim,[1,3,6] Matthew J. Whitley,[1,2] Troy C. Krzysiak,[1] Cynthia S. Hinck,[1] Alexander B. Taylor,[3,4] Christian Zwieb,[3] Chang-Hyeock Byeon,[1] Xiaohong Zhou,[1] Valentín Mendoza,[5] Fernando López-Casillas,[5] William Furey,[2] and Andrew P. Hinck[1,7,*]

[1]Department of Structural Biology, University of Pittsburgh School of Medicine, Biomedical Science Tower 3, Room 2051, 3501 Fifth Avenue, Pittsburgh, PA 15260, USA
[2]Department of Pharmacology and Chemical Biology, University of Pittsburgh School of Medicine, Pittsburgh, PA 15260, USA
[3]Department of Biochemistry and Structural Biology, University of Texas Health Science Center at San Antonio, San Antonio, TX 78229-3900, USA
[4]X-ray Crystallography Core Laboratory, University of Texas Health Science Center at San Antonio, San Antonio, TX 78229-3900, USA
[5]Instituto de Fisiología Celular, Universidad Nacional Autónoma de México, Ciudad de México 04510, México
[6]Present address: Department of Biochemistry and Biophysics, University of California San Francisco, San Francisco, CA, 94158, USA
[7]Lead Contact
*Correspondence: ahinck@pitt.edu
https://doi.org/10.1016/j.str.2019.06.010

SUMMARY

Betaglycan (BG) and endoglin (ENG), homologous co-receptors of the TGF-β family, potentiate the signaling activity of TGF-β2 and inhibin A, and BMP-9 and BMP-10, respectively. BG exists as monomer and forms 1:1 growth factor (GF) complexes, while ENG exists as a dimer and forms 2:1 GF complexes. Herein, the structure of the BG orphan domain (BG_O) reveals an insertion that blocks the region that the endoglin orphan domain (ENG_O) uses to bind BMP-9, preventing it from binding in the same manner. Using binding studies with domain-deleted forms of TGF-β and BG_O, as well as small-angle X-ray scattering data, BG_O is shown to bind its cognate GF in an entirely different manner compared with ENG_O. The alternative interfaces likely engender BG and ENG with the ability to selectively bind and target their cognate GFs in a unique temporal-spatial manner, without interfering with one another or other TGF-β family GFs.

INTRODUCTION

Temporal and spatial control of cell signaling is critical for normal development of embryos and for tissue maintenance in adults. The signaling molecules that regulate temporal-spatial control include those of the Wnt and Notch families, but also those of the transforming growth factor β (TGF-β) family, which have essential roles in patterning (Bier and De Robertis, 2015; Zinski et al., 2018) organogenesis (Mullen and Wrana, 2017) in embryos, and maintenance of the heart (Goumans and Ten Dijke, 2018), vasculature (Goumans et al., 2018; Roman and Hinck, 2017), and musculoskeletal system (Walker et al., 2016) in adults. TGF-β family signaling proteins have greatly diversified, with more than 30 family members in humans. The proteins of the family can be classified as belonging either to the ancestral bone morphogenetic protein (BMP)/growth and differentiation factor (GDF) branch of the family, or the more recently evolved TGF-β/activin branch (Hinck et al., 2016). The proteins of both branches bind and bring together two type I and two type II receptors to initiate a transphosphorylation cascade and intracellular Smad signaling (Hata and Chen, 2016; Wrana et al., 1994). TGF-β family signaling proteins are well-suited to enable temporal-spatial control because multiple mechanisms exist for targeting them with high spatial and temporal resolution. These range from cell- and tissue-specific expression of receptors, co-receptors, or soluble antagonists specific for a subset of TGF-β family growth factors (GFs), to proteolytic release of the mature signaling GF dimers from their inhibitory pro-domains (Brazil et al., 2015; Hinck et al., 2016; Nolan and Thompson, 2014; Robertson and Rifkin, 2013).

The membrane-anchored co-receptors of the TGF-β family, betaglycan (BG) and endoglin (ENG), do not directly participate in the transphosphorylation cascade that leads intracellular Smad signaling, but have essential roles in promoting receptor binding and signaling by select family members (Brown et al., 2005; Lewis et al., 2000; Lopez-Casillas et al., 1993; Nickel et al., 2018; Scharpfenecker et al., 2007). The co-receptor BG has been shown to promote binding of low-affinity TGF-β2 to the TGF-β type II receptor, TβRII ($K_D \sim 20$ μM for binding to the monomeric TβRII ectodomain [Baardsnes et al., 2009]), and to restore cellular sensitivity to concentrations comparable with that of high-affinity TGF-β1 and TGF-β3 ($K_D \sim$ 50–150 nM for binding to the monomeric TβRII ectodomain [Cheifetz et al., 1990; Lopez-Casillas et al., 1993; Radaev et al., 2010]). TGF-β2 is essential for transformation of endothelial progenitor cells required for normal development and maintenance of the heart and liver, and knockout of either TGF-β2 or BG in mice leads to similar defects in heart and liver development (Sanford et al.,

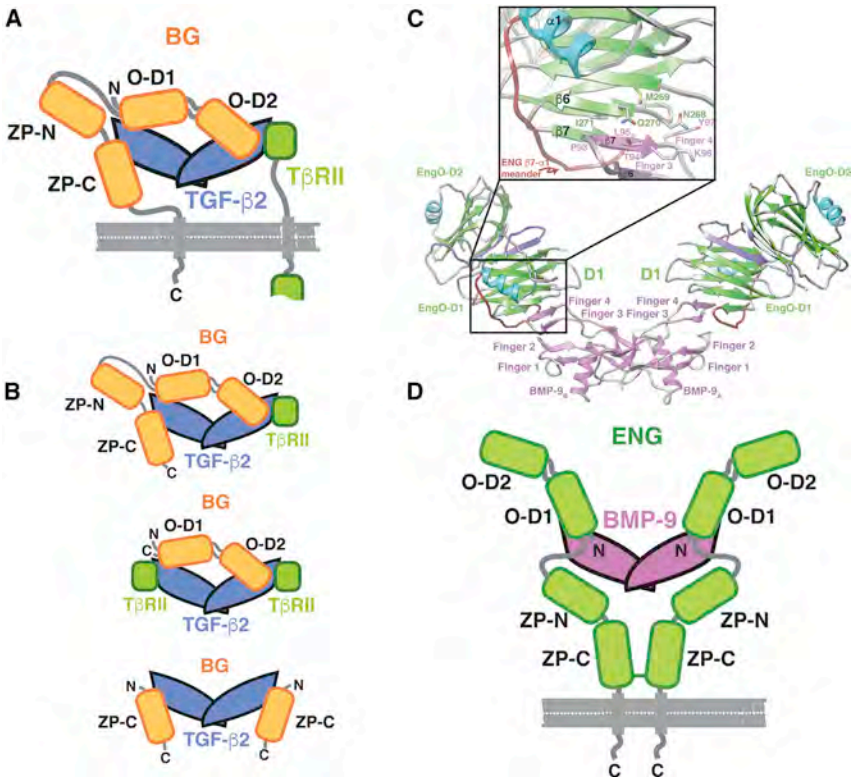

Figure 1. Schematic of BG and ENG Binding to their Cognate GFs

(A) Proposed model for BG binding of TGF-β2 homodimer with 1:1 stoichiometry (Villarreal et al., 2016). The orphan domain binds around the center of the dimer without interfering with either TβRII site, while the ZP-C domain binds in one of the TβRII sites, leaving one TβRII site accessible for binding.

(B) Complexes and subcomplexes shown by SEC, SEC-MALS, and SPR that led to the model shown in (A).

(C) Structure of the 2:1 $hENG_O$:BMP-9 complex determined by crystallography (Saito et al., 2017). The super β sheet formed by finger 4 of BMP-9 and β6 of O-D1 of $hENG_O$ is shown in the inset.

(D) Schematic of the 2:1 ENG:BMP-9 complex, in which the orphan domain binds symmetrically, and only through orphan domain (O-D1), to finger 4 of the growth factor (GF). The ZP domain, which is covalently dimerized by formation of a disulfide bond in its ZP-C domain, does not directly contact the GF and is connected to the orphan domain by a flexible linker.

1997; Stenvers et al., 2003). TGF-β2 and BG therefore function together to enable signaling essential for the proper development and maintenance of these organs. BG is also expressed by gonadotropic cells in the anterior pituitary and binds the TGF-β family heterodimer inhibin A (inhA) to promote activin type II/IIB receptor (ActRII or ActRIIB) binding, which is essential for inhibiting activin-stimulated follicle-stimulating hormone β secretion by gonadotropic cells in the anterior pituitary (Lewis et al., 2000; Li et al., 2018; Wiater et al., 2006). The co-receptor ENG is expressed on the surface of vascular endothelial cells and selectively binds BMP-9 and BMP-10 to promote binding of the type I receptor, activin-like kinase 1 (Alk1), and signaling (Alt et al., 2012; Castonguay et al., 2011; Scharpfenecker et al., 2007). This signaling stimulates migration of the endothelial cells and is essential for normal development and maintenance of the vasculature, as shown by vascular abnormalities known as arteriovenous malformations, which are the result of germline mutations in either Alk1 or ENG (Goumans et al., 2018; Roman and Hinck, 2017).

The extracellular domains of BG and ENG are comprised of two subdomains, the N-terminal membrane-distal orphan domain and the membrane-proximal zona pellucida (ZP) domain (Figures 1A and 1D) (Alt et al., 2012; Esparza-Lopez et al., 2001; Mendoza et al., 2009). The structure of the BG orphan domain, BG_O, is not known, but is likely a tandem β sandwich, designated orphan domain 1 (O-D1) and O-D2, similar to the ENG orphan domain (ENG_O), whose structure was recently reported (Saito et al., 2017). The BG ZP (BG_{ZP}) domain is likely comprised of tandem immunoglobulin-like domains, designated $BG_{ZP\text{-}N}$ and $BG_{ZP\text{-}C}$, based on available structures of $BG_{ZP\text{-}C}$ from rat (Lin et al., 2011) and mouse (Diestel et al., 2013) and homology to the ENG ZP (ENG_{ZP}) domain, whose structure was also recently reported (Saito et al., 2017). Through biochemical studies, rat BG, which has 5 cysteines within its orphan domain and 10 in its ZP domain, is found on cells as a monomer (Lopez-Casillas et al., 1993) and binds TGF-β homodimers asymmetrically with an overall 1:1 stoichiometry (Villarreal et al., 2016) using both its orphan domain and the C-terminal portion of its ZP domain, $BG_{ZP\text{-}C}$ (Henen et al., 2019; Mendoza et al., 2009; Villarreal et al., 2016) (Figure 1A). Human ENG (hENG), on the other hand, which has 5 cysteines in its orphan domain and 11 in its ZP domain, is found on cells as a disulfide-linked dimer and binds BMP-9 and BMP-10 using only its orphan domain (Alt et al., 2012). Recent structural studies revealed that ENG_O binds BMP-9 homodimers with 2:1 stoichiometry by forming a super β sheet with finger 4 of the GF through an exposed β strand, β6, in domain 1 (O-D1) (Figure 1C) (Saito et al., 2017). ENG's ZP domain is known to form a disulfide-linked dimer (Alt et al., 2012) and thus ENG binds BMP-9/-10 dimers in an antibody-like manner, in which the disulfide-linked ZP domain forms the F_c domain and the orphan domain the "antigen-binding" F_{ab} domain (Saito et al., 2017) (Figure 1D).

The objective of this study was to identify the structural basis for the different modes of GF binding by BG and ENG. Toward this end, the high-resolution structure of zebrafish BG_O ($zfBG_O$) was determined. This showed that BG_O has the same two-domain architecture as ENG_O, but differs in that the loop connecting β strand 7 to α helix 1 in O-D1 includes an additional α helix and β strand. The additional strand, β8, pairs with putative O-D1 GF-interacting β6, sequestering β6 and likely preventing it from pairing with finger 4 of the GF, as does ENG_O. To investigate if this modification engendered BG_O with an alternative manner of binding, binding studies were carried out with BG_O

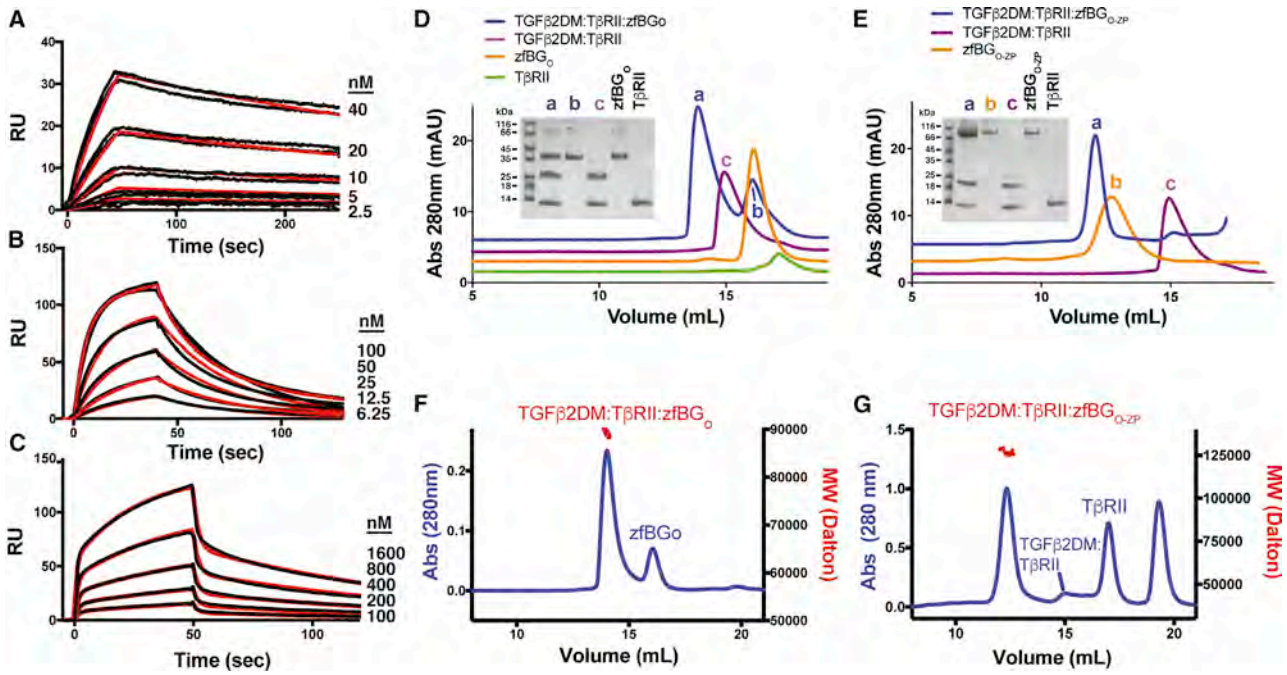

Figure 2. Characterization of zfBG Binding

(A–C) SPR sensorgrams of zfBG$_{O-ZP}$ (A), zfBG$_O$ (B), and zfBG$_{ZP-C}$ (C) binding to immobilized TGF-β2. Kinetic fits are shown in red over duplicate experimental curves in black.

(D and E) Complexes formed between zfBG$_O$ (D) and zfBG$_{O-ZP}$ (E) with TGF-β2DM and TβRII in solution as assessed using SEC. Shown in the insets are non-reducing SDS-PAGE gels of the major peaks that eluted.

(F and G) SEC-MALS analysis of the TGF-β2DM:TβRII:zfBG$_O$ (F) and TGF-β2DM:TβRII:zfBG$_{O-ZP}$ (G) complexes, with the blue trace corresponding to the UV absorbance and the red data points the molecular mass. Observed/anticipated masses for the TGF-β2DM:TβRII:zfBG$_O$ and TGF-β2DM:TβRII:zfBG$_{O-ZP}$ complexes are 89.6 ± 1.8/88.2 and 127 ± 1/121 kDa, respectively.

See also Figure S2.

O-D1 and O-D2 and an engineered TGF-β monomer. These studies, together with accompanying small-angle X-ray scattering (SAXS) measurements, supported an alternative 1:1 manner of binding in which BG$_O$ recognizes more than just the finger region and does so by utilizing both O-D1 and O-D2 to bind the GF. The alternative interfaces between BG and TGF-β and ENG and BMP-9 likely engender these otherwise structurally similar co-receptors with the ability to selectively bind their cognate GFs, enabling them to selectively target the heart, liver, and anterior pituitary and vasculature, respectively, without interference from one another or TGF-β family GFs.

RESULTS

Zebrafish and Rat BG Bind Human TGF-β2 in the Same Overall Manner

Previous surface plasmon resonance (SPR), size-exclusion chromatography (SEC), and isothermal titration calorimetry (ITC) binding studies showed that the full-length rat BG (rBG) ectodomain (rBG$_{O-ZP}$) bound TGF-β2 dimers with 1:1 stoichiometry, with the orphan and ZP-C domain (rBG$_O$ and rBG$_{ZP-C}$, respectively), both directly binding the GF (Mendoza et al., 2009; Villarreal et al., 2016) (Figure 1A). SPR, ITC, and SEC showed that this asymmetric manner of binding, which blocked one of the TβRII binding sites, but left the other accessible, was driven by the orphan domain, which alone bound TGF-β dimers with 1:1 stoichiometry and did not interfere with TβRII binding (Villarreal et al., 2016) (Figure 1B). SPR, SEC, and structural studies, showed in contrast, that the hENG ectodomain (hENG$_{O-ZP}$) bound BMP-9 dimers symmetrically with 2:1 stoichiometry, with only the orphan domain (hENG$_O$) bound to the GF (Alt et al., 2012; Saito et al., 2017) (Figures 1C and 1D). To decipher the origins of these disparate modes of binding, crystallization of rBG$_O$ was pursued. Although unsuccessful, parallel efforts with the zfBG orphan domain (zfBG$_O$), which has 54% identity with rBG$_O$ (Figure S1A), succeeded.

Previously, zfBG had been shown to bind TGF-β, but, when knocked down in zebrafish embryos, it had effects on blood vessel development (Kamaid et al., 2015), a phenotype not seen in BG null mice (Stenvers et al., 2003), raising questions as to whether zfBG was a true ortholog of mammalian BG. SPR experiments with the full-length zfBG ectodomain (zfBG$_{O-ZP}$) and its component domains, zfBG$_O$ and zfBG$_{ZP-C}$, and immobilized human TGF-β2 (hTGF-β2), were therefore performed to determine whether zfBG possessed the same binding properties as rBG (Figures 2A–2C). Similar experiments with rBG$_{O-ZP}$, rBG$_O$, and rBG$_{ZP-C}$ were also performed to enable a direct comparison (Figures S2A–S2C). In accord with previous results (Kamaid et al., 2015; Mendoza et al., 2009; Villarreal et al., 2016), the rat and zebrafish full-length BG ectodomain bound hTGF-β2, but in contrast to either the

Table 1. SPR Binding Constants for zfBG and rBG, and their Subdomains, to TGF-β2

Surface	Analyte	k_{a1} (M^{-1} s^{-1})	k_{d1} (s^{-1})	K_{D1} (nM)	k_{a2} (M^{-1} s^{-1})	k_{d2} (s^{-1})	K_{D2} (nM)	R_{max1} (RU)	R_{max2} (RU)	k_m (m/s)[a]
TGF-β2	$zfBG_{O\text{-}ZP}$	$3.50 \pm 0.05 \times 10^5$	0.00173 ± 0.00002	4.95 ± 0.13	ND[b]	ND	ND	69.1 ± 0.3	ND	$5.0 \pm 0.9 \times 10^9$
TGF-β2	$zfBG_O$	$1.066 \pm 0.007 \times 10^6$	0.0288 ± 0.0002	27.0 ± 0.4	ND	ND	ND	144.8 ± 0.5	ND	$1.5 \pm 0.1 \times 10^9$
TGF-β2	$zfBG_{ZP\text{-}C}$	$4.8 \pm 0.7 \times 10^5$	0.51 ± 0.01	1,100 ± 200	$2.0 \pm 0.3 \times 10^4$	$9.3 \pm 0.4 \times 10^3$	480 ± 80	93 ± 9	105 ± 2	ND
TGF-β2	$rBG_{O\text{-}ZP}$	$1.478 \pm 0.006 \times 10^6$	0.000755 ± 0.000001	0.511 ± 0.002	ND	ND	ND	83.5 ± 0.2	ND	$1.0 \pm 0.3 \times 10^{10}$
TGF-β2	rBG_O	$6.03 \pm 0.02 \times 10^5$	0.00596 ± 0.00002	9.88 ± 0.04	ND	ND	ND	176.0 ± 0.4	ND	$1.0 \pm 0.4 \times 10^{10}$
TGF-β2	$rBG_{ZP\text{-}C}$	$3.25 \pm 0.20 \times 10^4$	0.0029 ± 0.0001	90.0 ± 0.8	$2.60 \pm 0.04 \times 10^5$	$1.57 \pm 0.20 \times 10^{-1}$	610 ± 70	150 ± 9	60 ± 9	ND

[a]k_m, mass transfer rate constant.
[b]ND, not determined.

orphan or ZP-C domain alone, both of which also bound hTGF-β2, the full-length ectodomains dissociated more slowly, presumably due to bivalent binding. Kinetic analysis of the sensorgrams showed that the K_D values were 5 nM for $zfBG_{O\text{-}ZP}$, 27 nM for $zfBG_O$, and 480–1,100 nM for $zfBG_{ZP\text{-}C}$, 3- to 10-fold weaker compared with $rBG_{O\text{-}ZP}$, rBG_O, and $rBG_{ZP\text{-}C}$, which bound with K_D values of 0.5, 10, and 90–610 nM (Table 1). Human and rat TGF-β2 differ at three positions, while human and zebrafish TGF-β2 differ at ten positions (Figure S1B), which may account for the lower affinities of the zfBG constructs compared with rat.

Binding stoichiometry and effects on TβRII binding were assessed by combining $zfBG_{O\text{-}ZP}$ or $zfBG_O$ with the TGF-β:TβRII binary complex and analyzing the complexes that formed by SEC and SEC-multiangle light scattering (SEC-MALS). To enable a direct comparison, the same experiments were also performed with $rBG_{O\text{-}ZP}$ and rBG_O; to minimize disassociation of TβRII, TGF-β2 K25R K94R or TGF-β2DM was used, which binds TβRII with high affinity (Baardsnes et al., 2009; De Crescenzo et al., 2006). In accord with previous findings with rBG (Villarreal et al., 2016), the orphan and full-length ectodomains of both zebrafish and rat BG formed ternary complexes, as shown by a peak in the SEC profiles (labeled a) that eluted earlier than either the corresponding BG domain (labeled b) or the TGF-β2DM:TβRII binary complex (labeled c) (Figures 2D, 2E, S2D, and S2E). In accord with previous findings with rBG (Villarreal et al., 2016), the apparent molecular weights of ternary complexes were consistent with the 1:1:1 TGF-β2DM:TβRII:$BG_{O\text{-}ZP}$ complex anticipated for the full-length ectodomain (127 ± 1 and 129 ± 2 kDa observed, versus 121 and 123 kDa anticipated, for zfBG and rBG, respectively) and the 1:2:1 TGF-β2DM:TβRII:BG_O complex anticipated for the orphan domain (89.6 ± 1.8 and 94.9 ± 2.0 kDa observed, versus 88.2 and 91.1 kDa anticipated, for zfBG and rBG, respectively) (Figures 2F, 2G, S2F, and S2G). In summary, the binding data show that zfBG binds TGF-β2 in the same overall manner as rBG (Villarreal et al., 2016), indicating that it is a true ortholog of mammalian BG and justifying it as a model system for deciphering the function of mammalian BG.

Structure of $zfBG_O$

The crystal structure of $zfBG_O$ was determined to 2.10 and 2.38 Å from orthorhombic ($P2_12_12_1$) and tetragonal ($P4_1$) crystal forms, respectively (Table 2). The initial efforts to determine the structure focused on the tetragonal form, but these were unfruitful as molecular replacement with $hENG_O$, which has 20% sequence identity with $zfBG_O$ (Figure S3A), proved unsuccessful, as did phasing with heavy atoms, primarily due to difficulty reproducing the crystals. To overcome these obstacles, we reasoned that $zfBG_O$, which has six cysteines in its orphan domain (Figure S1A), has two free cysteines, which might be forming disulfide-linked aggregates. This hypothesis is based on the observation that four of the six cysteines of $zfBG_O$ are conserved with the four cysteines in $hENG_O$, which form two disulfide bonds, while the other two cysteines are at positions expected to be far apart in the three-dimensional structure (Figure S3A). Therefore, $zfBG_O$ was pre-treated with iodoacetamide before SEC and final purification. This led to more consistent crystal formation, in an orthorhombic space group, and enabled

Table 2. X-Ray Data Collection and Refinement

Crystal Form	Tetragonal (Native)	Orthorhomic (Native)	Orthorhombic (Pt)	Orthorhombic (I)
Data Collection				
X-ray source	Advanced Photon Source SER-CAT 22-ID	Advanced Photon Source SER-CAT 22-ID	Advanced Photon Source SER-CAT 22-ID	Rigaku FR-E generator and RAXIS HTC image plate detector
Space group	$P4_1$	$P2_12_12_1$	$P2_12_12_1$	$P2_12_12_1$
Cell dimensions				
a, *b*, *c* (Å)	62.9, 62.9, 114.3	63.5, 107.3, 113.2	64.0, 106.5, 113.7	63.1, 107.5, 113.4
α, β, γ (°)	90, 90, 90	90, 90, 90	90, 90, 90	90, 90, 90
Wavelength (Å)	1.0000	0.9692	0.9795	1.5418
Resolution (Å)	35.11–2.38 (2.47–2.38)[a]	40.98–2.10 (2.16–2.10)[a]	54.87–3.00 (3.18–3.00)[a]	22.18–3.20 (3.46–3.20)[a]
R_{merge}	0.080 (1.784)	0.126 (2.49)	0.118 (0.586)	0.159 (0.510)
R_{pim}	0.046 (1.100)	0.053 (1.069)	0.069 (0.341)	0.059 (0.193)
CC½	0.998 (0.520)	0.998 (0.565)	0.992 (0.932)	0.998 (0.967)
$I/\sigma I$	10.6 (1.1)	10.8 (1.3)	8.5 (2.4)	16.0 (5.4)
Completeness (%)	99.4 (99.8)	99.9 (99.6)	100.0 (100.0)	99.7 (99.9)
Redundancy	7.5 (6.8)	11.6 (11.2)	7.3 (7.3)	14.5 (14.7)
Phasing				
No. of sites			7	20
Resolution			33.2–2.80	33.2–2.80
Phasing power[b] (acentric/centric)				
Isomorphous			0.558/0.614	0.721/0.712
Anomalous			0.566/–	0.349/–
Cullis R factor[c] (acentric/centric)				
Isomorphous			0.777/0.788	0.936/0.875
Anomalous			0.698/–	0.940/–
Overall figure of merit (acentric/centric)			0.52/0.49	
Refinement				
Molecules/ASU	1	2		
No. of reflections	17,730	45,850		
R_{work}/R_{free}	0.198/0.229	0.233/0.258		
No. of atoms				
Protein	2,442	4,803		
Water	8	79		
B factor (Å^2)				
Chain A backbone/overall	101.3/105.4	58.5/62.7		
Chain B backbone/overall		79.9/83.9		
RMSD				
Bond lengths (Å)	0.010	0.010		
Bond angles (°)	1.27	1.17		
Ramachandran statistics (%)				
Favored	98.0	98.0		
Allowed	2.0	1.4		
Outliers	0.0	0.6		
PDB	6MZN	6MZP		

ASU, asymmetric unit; RMSD, root-mean-square deviation.

[a]Highest-resolution shell is shown in parentheses.

[b]Phasing power = < [|Fh(calc)|/E]>, where Fh(calc) is the calculated heavy atom structure factor amplitude and E is the phase-integrated lack of closure error.

[c]Cullis R factor = <E>/<| Fph − Fp |>, where E is the phase-integrated lack of closure error, Fph is structure factor amplitude of the derivative, and Fp structure factor amplitude of the native.

preparation of two derivatives, one platinum and one iodide. Using multiple isomorphous replacement with anomalous scattering phasing (Table 2), this led to an interpretable map, a portion of which is shown in Figure S4. This map enabled building of a nearly complete model, which in turn enabled solution of the tetragonal form by molecular replacement. The asymmetric unit of the tetragonal and orthorhombic forms contained one and two molecules, respectively. The tetragonal form and one of the chains in the orthorhombic form, chain A, were well ordered, with weak electron density in only a few loop regions (Table S3). The other chain in the orthorhombic form, chain B, had overall weaker density and higher B factors (Table 2), especially in domain 2 and was difficult to model, with additional regions of weak density compared with chain A (Table S3). The weak density in this region appears to be because the nature of the lattice packing, which, as shown in Figure S5, places domain 2 of chain B in a solvent void without lattice contacts to either domain of either chain (Figure S5).

The structure of $zfBG_O$ is comprised of two β sandwich domains arranged in an arch-like manner (Figure 3A). The two β sandwich domains are each comprised of 10 β strands and share the same fold (Figures 3B, 3D, and 3E). They are decorated with two α helices, one in the loop following β7 (α1), and the other packed against the convex surface of the arch-like structure formed by the two β sandwiches (α2) (Figures 3A, 3D, and 3E). One of the unusual features is that the N terminus of the protein is comprised of two extended segments, each approximately 10 amino acids in length, connected by a bend: the N-terminal half is tethered to the N-terminal β strand (β1) of O-D1 by a disulfide bond (C31-C225), while the C-terminal half is paired with the C-terminal β strand of O-D1 (β10) and extends into O-D2 (Figures 3A, 3C, and 3D). A similarly structured extended "exit" segment is present in O-D2, where, after exiting the C-terminal β strand of O-D2 (β10), it is tethered to the N-terminal β strand (β1) by a disulfide bond (C55-C201), paired with the C-terminal β strand (β10), and extends into O-D1 (Figures 3A, 3C, and 3E). One further point is that a sequence alignment of the repeating element present in $zfBG_O$, that is the O-D1 exit sequence followed by the O-D2 β sandwich and the O-D2 exit sequence followed by the O-D1 β sandwich, shows that these share significant (20%) sequence identity (Figure S1C), and thus are likely the result of gene duplication. One important consequence is that, similar to $hENG_O$ (Saito et al., 2017), $zfBG_O$ is pseudosymmetric, not only in terms of its architecture, but also its sequence.

The paired antiparallel β strands that connect O-D1 and O-D2, seen previously in $hENG_O$ (Saito et al., 2017), represent another unique structural feature and might be important in restricting the orientation of O-D1 and O-D2. To gauge the extent of this restriction, the two $zfBG_O$ orthorhombic structures and one $zfBG_O$ tetragonal structure were aligned by minimizing coordinate differences for one domain, but not the other. This showed that the structures of individual domains were, on the one hand, very consistently determined, with root-mean-square deviation (RMSD) well under 1.0 Å for both O-D1 and O-D2 when all three structures were compared (Figure S6A). The relative domain orientations in the three structures, on the other hand, were more variable, with displacements ranging from 1.3 Å at the centroid of unaligned domain when the orthorhombic chain A and tetragonal structures were compared, to 3.7 Å, when orthorhombic chain A and chain B were compared (Figures S6B and S6D). This suggests some degree of hinge bending, although evidently this must be limited, as solution-based SAXS measurements with $zfBG_O$ showed that the experimental scattering curves, as well as P(r) function and calculated electron density, correlated well with the three $zfBG_O$ structures or parameters calculated from them (Figures S7A–S7C, S7G, and S7H). The rat BG orphan domain also appeared to have an overall structure similar to the zebrafish orphan domain because the experimental SAXS data for rBG_O also correlated very well with the three $zfBG_O$ structures or parameters calculated from them (Figures S7D–S7F, S7I, and S7J).

Structural Comparison of $zfBG_O$ and $hEng_O$

The overall architecture and domain structures of $zfBG_O$ and $hENG_O$ are similar (Figures 4A–4C), despite only 20% sequence identity (Figure S3A). There are nonetheless differences, the most prominent of which is a shift of O-D2 downward and toward the concave surface of O-D1 in $zfBG_O$ (Figure 4A). This shift, which corresponds to a 17.6-Å displacement in the centroid of the zfBG O-D2 relative to hENG O-D2 when the residues of O-D1 are aligned, results in an arch-like structure in $zfBG_O$, but not in $hENG_O$ (Figure 4A). The primary reason for the more arch-like structure in $zfBG_O$ compared with $hENG_O$ is the O-D1 exit sequence. In zfBG O-D1, after exiting the domain, the β strand of the exit sequence bends upward before extending into the N-terminal β strand of O-D2 (Figure S8). In contrast, in hENG O-D1, the exit sequence is shorter and has a sharp bend downward before it leads into the N-terminal β strand of O-D2 (Figure S8). Importantly the lengthening of the exit sequence and opposite direction of the bend as it exits the domain leads to very different positioning of the N-terminal β strand of O-D2 in $hENG_O$ and $zfBG_O$, and thus relative positioning of O-D1 and O-D2 (Figure S8). To accommodate the difference in domain orientation, the β strand of the O-D2 exit sequence of $zfBG_O$ pairs mostly with the O-D1 exit sequence, while that of $hENG_O$ pairs with the C-terminal β strand of O-D2 and the O-D1 exit sequence (Figure S8).

Although more subtle, another difference pertains to the loop region following OD-1 β7. In hENG O-D1, immediately after β7 there is a sharp bend followed by an extended meander that leads into the three-turn α helix (α1) packed against the convex surface of the sandwich (Figure 4B). In zfBG O-D1, after β7 there is an insertion of a one-turn helix (α1) that traverses the gap between the concave and convex surfaces of the sandwich (Figure 4B). Immediately following α1, there is an insertion of a β strand (β8), which pairs with β6 on the convex surface, followed by an extended meander that connects into three-turn α2 packed against the convex surface (Figure 4B). Importantly, in $hENG_O$, the absence of β8 and altered positioning of the meander leaves O-D1 edge β strand 6 accessible on the convex surface, while, in $zfBG_O$, the O-D1 α1-β8 insertion sequesters β6, making it inaccessible.

The structure of the 2:1 $hENG_O$:BMP-9 complex shows that BMP-9 and $hENG_O$ bind through a super β sheet formed between the exposed finger region of BMP-9, specifically finger 4 β7 and the exposed edge β strand, β6, of hENG O-D1 (Figures 1C and 4D). Through positioning of the $zfBG_O$

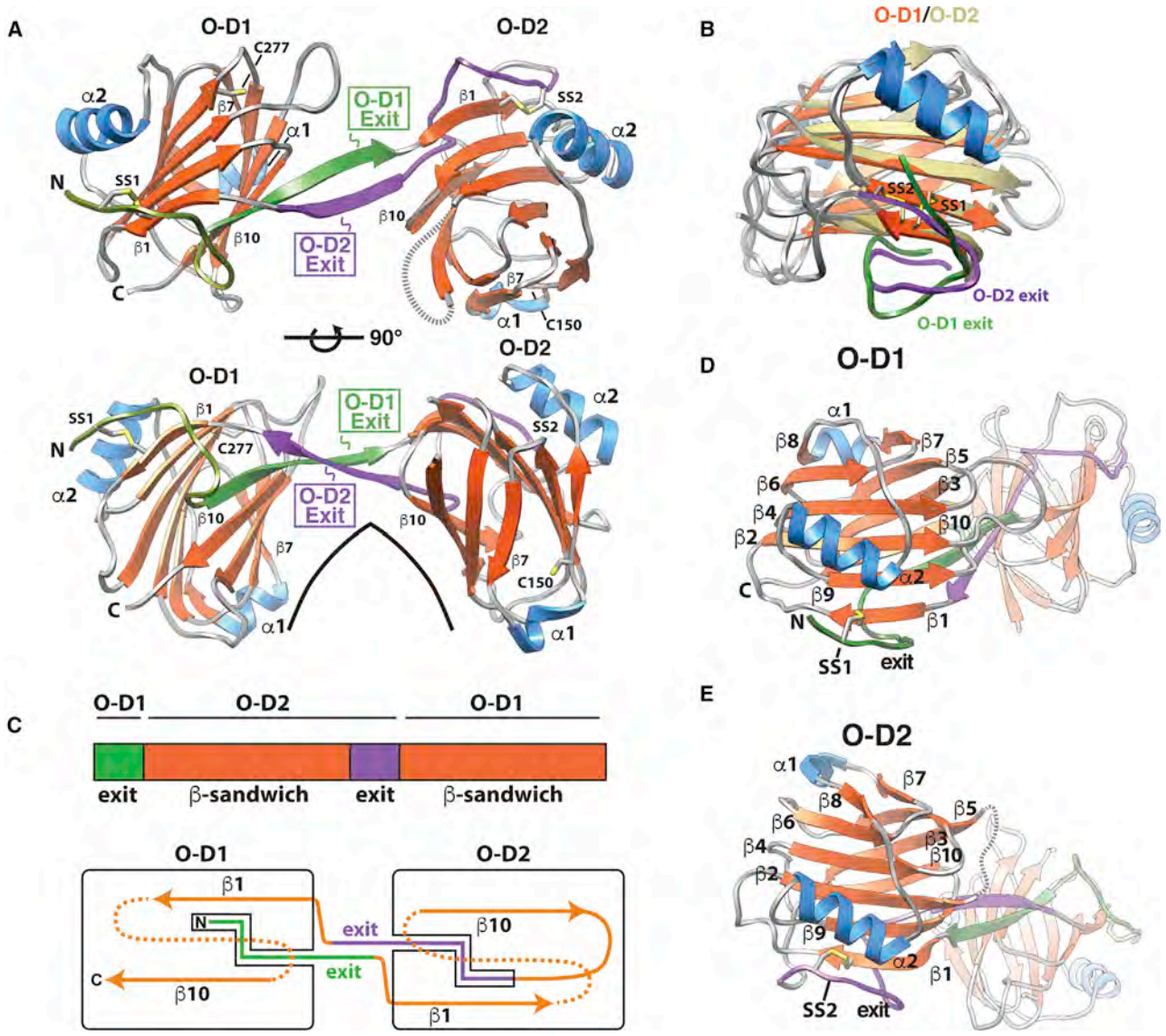

Figure 3. Structure of zfBG$_O$

(A) Structure of zfBG$_O$ with "exit" sequences for O-D1 and O-D2 in green and lavender, respectively. Positionally conserved disulfide in the O-D1 and O-D2 subdomains, C31-C225 and C55-C201, are labeled SS1 and SS2, respectively. Single free cysteines in O-D1 and O-D2, C277 and C150, respectively, are also shown. Residue numbering can be deduced by reference to the secondary structure/residue numbering shown for zfBG$_O$ in Figure S3.

(B) Overlay of zfBG$_O$ O-D1 and O-D2 with the β strands of O-D1 depicted in orange, the β strands of O-D2 depicted in tan, the α helices of O-D1 and O-D2 in blue, and the exit sequences of O-D1 and O-D2 in green and lavender, respectively.

(C) Schematic showing the overall architecture of zfBG$_O$.

(D and E) Similar orientations of the zfBG$_O$ O-D1 (D) and O-D2 (E) subdomains, illustrating the conservation of their folds and secondary structure.

See also Figures S1 and S4–S7, and Table S3.

structure onto the hENG$_O$ structure at the hENG$_O$:BMP-9 interface, zfBG$_O$ O- D1 β8 is shown to sterically clash with BMP-9 finger 4 β7 (Figure 4E). The region corresponding to β6-β7-α1-β8 in zfBG O-D1 is consistently determined by the three zfBG$_O$ structures (Figure 4F) and is well-defined by the electron density in zfBG$_O$ (Figure 4G); it is, therefore, unlikely that β8 would be displaced by GF binding. Thus, zfBG$_O$ is unlikely to use β6 to bind its cognate GF, TGF-β2, in an hENG$_O$-like manner.

Binding of zfBG$_O$ to the TGF-β Mini Monomer

Using previous functional and structural studies, mmTGF-β2-7M, an engineered form of TGF-β that includes the finger region and cystine knot, but not the heel helix, was shown to maintain the same high affinity for TβRII as TGF-β1 and TGF-β3, and to have a structure, both alone and as bound to TβRII, essentially indistinguishable from that of TGF-β1 and TGF-β3 (Figure S9A) (Kim et al., 2017). The intact finger region in mmTGF-β2-7M can therefore be used to determine

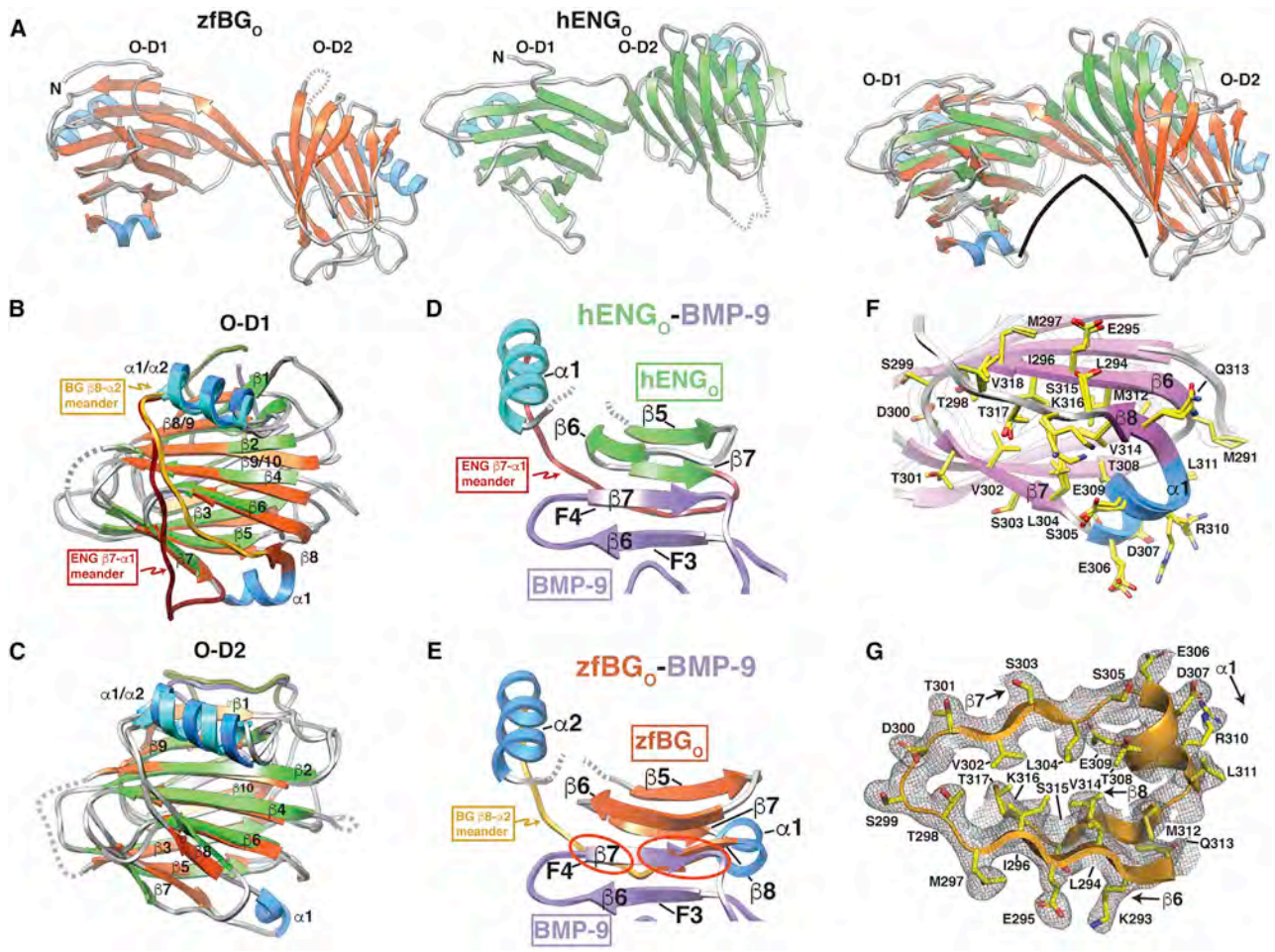

Figure 4. Structural Comparison of zfBG$_O$ and hENG$_O$

(A) Comparison of the overall structures of zfBG$_O$ and hENG$_O$, whose strands and helices are shaded orange and blue and green and blue, respectively. Changes in the relative domain orientation of zfBG$_O$ and human ENG$_O$ (green, β strands; cyan, helices) is shown in the right-most subpanel in which only the backbone atoms of O-D1 have been superposed.

(B and C) Superposition of zfBG$_O$ and hENG$_O$ O-D1 (B) or O-D2 (C). Distinct orientation of the O-D1 "meander" loop connecting β8-α2 in zfBG$_O$ and β7-α1 in hEng$_O$ is highlighted. Structures are shaded as in (A), with additional shading of the β8-α2 meander in zfBG$_{O\text{-}D1}$ and β7-α1 meander in hENG$_{O\text{-}D1}$ in gold and dark red, respectively.

(D) Region of super β sheet formation in the hENG$_O$:BMP-9 complex, but only with the β strands corresponding to fingers 3 and 4 (F3 and F4) of BMP-9 shown, and the segment of hENG$_O$ extending from β5 to α1 shown.

(E) The same as that shown in (D), but with zfBG$_O$ in place of hENG$_O$; the structure shown was generated by superimposing zfBG$_O$ onto hENG$_O$ in the structure of the hENG$_O$:BMP-9 complex and then by undisplaying hENG$_O$. The superposition highlights clashes (red ovals) between zfBG$_O$ β8 and finger 4 of BMP-9 for this mode of binding.

(F) Overlay of the two $P2_12_12_1$ zfBG$_O$ models and one $P4_1$ zfBG$_O$ model in the region including an additional α helix (α1) and β strand (β8) compared with hENG$_O$.

(G) $2mF_o - DF_c$ electron density for $P2_12_12_1$ zfBG$_O$ (chain A) extending from β6 to α2; the map shown was calculated with phenix.maps with a bulk solvent correction and anisotropic scaling and was contoured at 1σ.

See also Figures S1, S3, and S8.

if zfBG$_O$ recognizes and binds the finger region of TGF-β2, similar to hENG$_O$, or whether it recognizes and binds features beyond those in mmTGF-β2-7M. To test this, zfBG$_O$ was combined with equimolar amounts of the mmTGF-β2-7M:TβRII binary complex and analyzed by SEC. The mmTGF-β2-7M:TβRII binary complex was used for these experiments, rather than mmTGF-β2-7M alone, because it has improved solubility compared with mmTGF-β2-7M alone and because models showed that TβRII should not interfere with binding of zfBG$_O$ to mmTGF-β2-7M (Figure S9B). The SEC chromatogram of the ternary mixture corresponded to that of zfBG$_O$ alone, and the mmTGF-β2-7M:TβRII binary complex alone (Figure 5A), which indicated that zfBG$_O$ binds mmTGF-β2-7M:TβRII weakly. To further assess binding, the SPR response was measured as increasing concentrations of zfBG$_O$ were injected over immobilized mmTGF-β2-7M (Figure 5B). This led to a barely detectable response, consistent with the weak binding detected by SEC. There were, however, robust responses in control experiments in which TβRII was injected over mmTGF-β2-7M (Figure 5E) or zfBG$_O$ was injected over

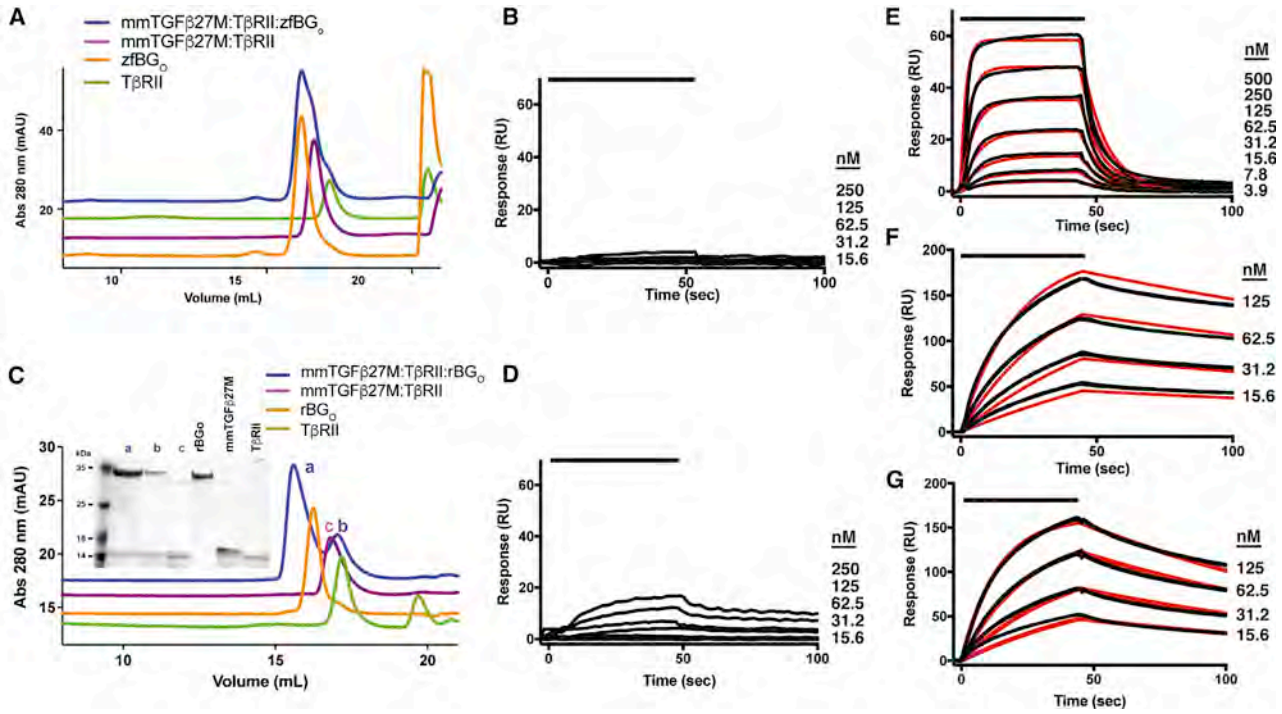

Figure 5. Binding of Monomeric TGF-β by BG$_O$

(A and C) SEC chromatograms to assess binding of zfBG$_O$ (A) or rBG$_O$ (C) to the mmTGF-β2-7M:TβRII binary complex. Chromatograms of the mmTGF-β2-7M:TβRII:BG$_O$ ternary complex, the mmTGF-β2-7M:TβRII binary complex, TβRII, and BG$_O$ are shown in blue, magenta, green, and orange, respectively. Shown in the inset in (C) is a non-reducing SDS-PAGE gel of the major peaks that eluted.

(B and D) SPR sensorgrams for binding of zfBG$_O$ (B) or rBG$_O$ (D) to immobilized mmTGF-β2-7M.

(E) SPR sensorgrams for binding of TβRII to mmTGF-β2-7M. Kinetic fit is shown in red over the experimental data shown in black.

(F and G) SPR sensorgrams for binding of zfBG$_O$ (F) or rBG$_O$ (G) to immobilized TGF-β2. Kinetic fit is shown in red over the experimental data shown in black. SPR experiments shown in (B, D, and E) were performed using the same neutravidin-coupled CM5 sensor chip with captured biotinylated avi-mmTGF-β2-7M.

See also Figure S9.

immobilized TGF-β2 (Figure 5F). The fitted disassociation constants for TβRII:mmTGF-β2-7M and zfBG$_O$:TGF-β2 interactions were 63 and 15 nM, respectively (Table 3), comparable with the previously reported values (Table 1) (Kim et al., 2017). These results show that zfBG$_O$ binds mmTGF-β2-7M weakly and must therefore attain its high affinity for TGF-β2 by recognizing more than just finger 4 of the GF.

To determine if this property was also shared with rBG$_O$, the same experiments were performed, but using rBG$_O$ rather than zfBG$_O$. The SEC experiments showed that, unlike zfBG$_O$, rBG$_O$ was able to form a detectable ternary complex with mmTGF-β2-7M and TβRII because these three proteins were each present in a peak (labeled a) that eluted before either rBG$_O$ or the mmTGFβ2-7M:TβRII binary complex alone (Figure 5C). The formation of this complex is, however, evidently a result of weak binding, because SPR experiments showed that, when rBG$_O$ was injected over immobilized mmTGFβ2-7M, only a very weak response was obtained relative to that of TβRII, which itself is only one-third of the mass of rBG$_O$ (Figures 5D and 5E). The weak response when rBG$_O$ was injected over immobilized mmTGFβ2-7M, which could not be fitted to derive a reliable binding constant, stood in contrast the robust response when rBG$_O$ was injected over TGF-β2 (Figure 5G), which could be readily fitted to derive a binding constant (Table 3). The fact that rBG$_O$ did form a detectable complex with mmTGF-β2-7M and TβRII by SEC, while zfBG$_O$ did not, may be because of the higher overall affinity of rBG$_O$ for TGF-β2 relative to zfBG$_O$ (Figures 2 and S2; Table 1).

Binding of zfBG$_{O\text{-}D1}$ and zfBG$_{O\text{-}D2}$ to TGF-β2

The structural differences relative to hENG$_O$ revealed by the zfBG$_O$ crystal structure, together with impaired binding of zfBG$_O$ to the TGF-β mini monomer, suggest that zfBG$_O$ binds TGF-β2 in a manner different to that by which hENG$_O$ binds BMP-9. To determine whether zfBG$_O$ uses both of its subdomains to contact TGF-β2, SEC and SPR binding experiments were performed using the zfBG$_{O\text{-}D1}$ and zfBG$_{O\text{-}D2}$ subdomains. zfBG$_{O\text{-}D2}$ was made as a secreted protein in HEK-293 cells, similar to the full-length zfBG$_O$, by expressing a construct that began a few residues before it entered O-D2 and ended a few residues after it exited (Table S2). zfBG$_{O\text{-}D1}$ was made similarly by expressing a construct that included most of the N-terminal exit sequence, an artificial two-residue Thr-Asp dipeptide, the C-terminal part of the O-D2 exit sequence, and the O-D1 β sandwich fused C-terminally to human serum albumin and an engineered thrombin cleavage site (Table S2). Before the final purification step for zfBG$_{O\text{-}D1}$, the fusion protein

Table 3. SPR Binding Constants for Receptor Binding to TGF-β2 or mmTGF-β2-7M

Surface	Analyte	k_{a1} (M^{-1} s^{-1})	k_{d1} (s^{-1})	K_{D1} (μM)	k_{a2} (M^{-1} s^{-1})	k_{d2} (s^{-1})	K_{D2} (μM)	R_{max1} (RU)	R_{max2} (RU)	k_m (m/s)[a]
TGF-β2	$zfBG_O$	5.28 ± 0.04 × 10^5	7.72 ± 0.08 × 10^{-3}	0.015 ± 0.002	ND[b]	ND	ND	181 ± 9	ND	ND
TGF-β2	rBG_O	3.74 ± 0.07 × 10^3	3.45 ± 0.05 × 10^{-3}	0.009 ± 0.002	ND	ND	ND	212 ± 6	ND	ND
mmTGF-β2-7m	TβRII	2.03 ± 0.03 × 10^6	1.28 ± 0.03 × 10^{-1}	0.063 ± 0.001	ND	ND	ND	71 ± 5	ND	ND
TGF-β2	$zfBG_{O\text{-}D1}$	9.3 ± 0.3 × 10^3	0.114 ± 0.004	12.3 ± 0.4	ND	ND	ND	20.8 ± 0.4	ND	1.2 ± 0.3 × 10^6
TGF-β2	$zfBG_{O\text{-}D2}$	5.2 ± 0.3 × 10^3	0.0064 ± 0.0017	1.2 ± 0.3	2.8 ± 0.7 × 10^5	2.7 ± 3.9 × 10^3	0.0083 ± 0.0100	18 ± 0.3	1.8 ± 0.3	ND

[a]k_m, mass transfer rate constant.
[b]ND, not determined.

was treated with thrombin, which enabled separation of $zfBG_{O\text{-}D1}$ from albumin.

To assess binding, TGF-β2DM:TβRII binary complex was combined with $zfBG_O$, $zfBG_{O\text{-}D1}$, or $zfBG_{O\text{-}D2}$ and analyzed by SEC. The results showed that, in contrast to full-length $zfBG_O$, $zfBG_{O\text{-}D1}$ and $zfBG_{O\text{-}D2}$ both failed to form a peak that eluted earlier than the TGF-β2DM:TβRII binary complex or $zfBG_{O\text{-}D1}$/$zfBG_{O\text{-}D2}$ alone (Figures 6A and 6B). To further investigate, SPR experiments were performed in which $zfBG_{O\text{-}D1}$ and $zfBG_{O\text{-}D2}$ were injected over the same immobilized TGF-β2 used for the experiments shown in Figures 2 and S2. Although the concentrations of $zfBG_{O\text{-}D1}$ and $zfBG_{O\text{-}D2}$ injected were the same as those used for $zfBG_O$, the maximal responses obtained were nonetheless only 10%–20% of that compared with $zfBG_O$ (Figures 6C, 6D, and 2B). Using kinetic analysis, the data for O-D1 could be fitted to a 1:1 model, with a K_D of 12 μM, while the data for O-D2 could only be fit to a heterogeneous ligand 1:1 model, with K_D values of 0.008 and 1.2 μM (Figures 6C and 6D; Table 3). The K_D of 0.008 μM for $zfBG_{O\text{-}D2}$ is not likely meaningful, as the response attained upon injection of $zfBG_{O\text{-}D2}$ over TGF-β2 (Figure 6D) was significantly lower compared with that of $zfBG_O$ when injected at the same concentrations over the same TGF-β2 surface (Figure 2B). Thus, both $zfBG_O$ subdomains bind TGF-β2 weakly, suggesting that both simultaneously engage TGF-β2 to enable high-affinity binding (K_D = 27 nM) of TGF-β2 by full-length $zfBG_O$ (Figure 2B; Table 1). To rule out the possibility that the weak binding of TGF-β2 by $zfBG_{O\text{-}D1}$ or $zfBG_{O\text{-}D2}$ was due to misfolding of the domains, NMR natural abundance ^1H-^{13}C shift correlation spectra of the methyl resonances were recorded. These spectra both revealed a well-dispersed pattern of peaks, with several resonances upfield of 0.0 ppm ^1H (Figures 6E and 6F), indicating that both were natively folded.

Structural Modeling of the Complex of BG_O with TGF-β2 and TβRII

The finding that BG_O bound TGF-β dimers with 1:1 stoichiometry, together with the results above that BG_O binds more than just the finger region and does so by contacting the GF with both O-D1 and O-D2, suggests an entirely different manner of GF binding compared with ENG_O. To determine, at low resolution, how BG_O might bind TGF-β, 1:2:1 TGF-β2TM:TβRII:BG_O complexes formed with both $zfBG_O$ and rBG_O were isolated by SEC and analyzed by SAXS over a range of concentrations (1, 2, and 4 mg mL^{-1} and 2 and 4 mg mL^{-1}, respectively) (Figures 7A and 7B). The overall shape of the scattering curves of the two complexes were similar, consistent with the SEC and SEC-MALS results (Figures 2D–2G and S2D–S2G), which showed that $zfBG_O$ and rBG_O form similar complexes in solution. There was, however, a concentration-dependent increase in scattering in the low-q region for the zebrafish complex, which indicates aggregation (Figure 7A). Thus, all subsequent modeling was performed with the scattering data for the rat protein, which was almost perfectly behaved (Figure 7B).

To determine whether an alternative manner of binding was required, a model was constructed with rBG_O placed onto the 1:2 TGF-β3:TβRII complex (Hart et al., 2002) in the same 2:1 manner that $hENG_O$ binds BMP-9 (the structure of rBG_O was obtained by building a $zfBG_O$-based homology model) (Figure 7D).

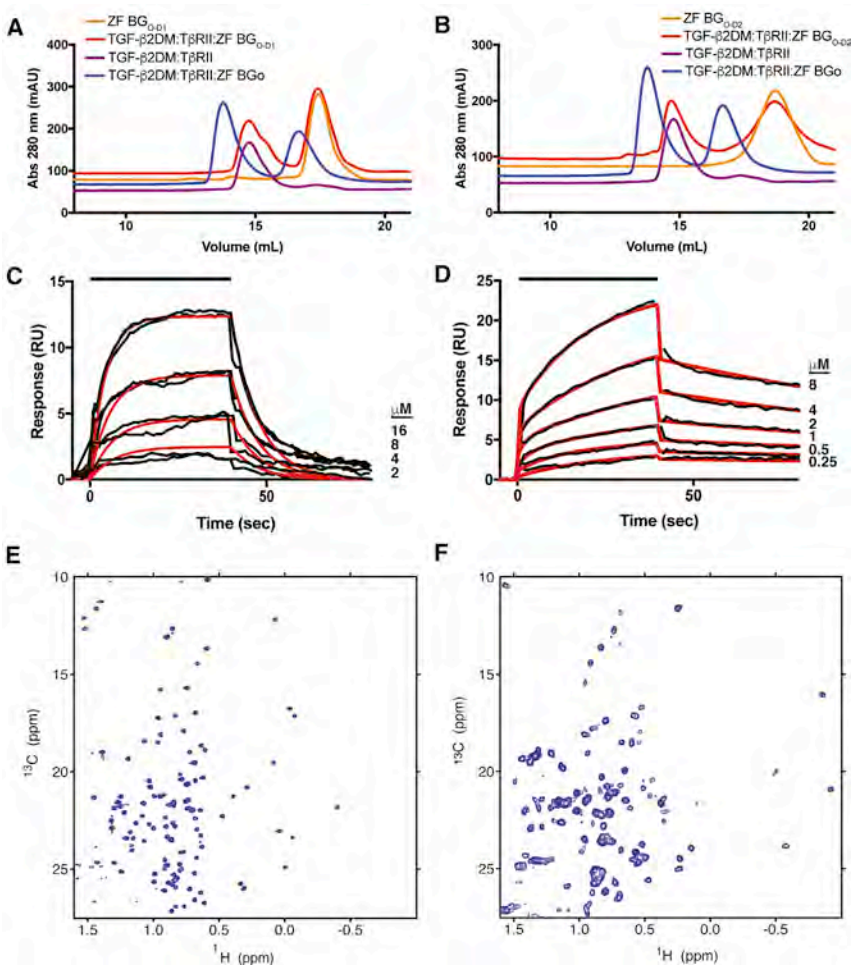

Figure 6. Binding of zfBG$_{O-D1}$ and zfBG$_{O-D2}$ to TGF-β2

(A and B) SEC chromatograms of complexes between zfBG$_O$ and zfBG$_{O-D1}$ (A) and zfBG$_O$ and zfBG$_{O-D2}$ (B) with TGF-β2DM and TβRII are depicted in blue and red, respectively. Chromatograms of the TGF-β2DM:TβRII binary complex and zfBG$_{O-D1}$/zfBG$_{O-D2}$ alone are shown in purple and orange curves, respectively.

(C and D) SPR sensorgrams for binding of zfBG$_{O-D1}$ (C) and zfBG$_{O-D2}$ (D) to immobilized TGF-β2. Kinetic fit is shown in red over the experimental data shown in black. The SPR sensor chip with immobilized TGF-β2 is the same as that used for the experiments shown in Figures 2 and S2.

(E and F) Methyl region of natural abundance ^{1}H-^{13}C HSQC spectra of BG$_{O-D1}$ (E) and BG$_{O-D2}$ (F).

The scattering curve was then calculated from this model and compared with the experimentally measured scattering curve for the rat complex. This revealed large systematic deviations over the entire scattering curve and a very high χ^2 value (65.2) (Figure 7C), indicating that this model poorly describes the structure of the TGF-β:TβRII:rBG$_O$ ternary complex in solution. This model was also poorly described by the electron density calculated from the experimental scattering data, with a significant portion of both molecules of rBG$_O$ protruding from the density (Figure 7E).

To determine whether models with an altered stoichiometry (1:1 BG$_O$:TGF-β) and manner of binding (direct binding by O-D1 and O-D2 at sites beyond the fingertip region) might be more consistent with the experimental data, the program pyDockSAXS (Jimenez-Garcia et al., 2015) was used to construct 1:2:1 TGF-β2:TβRII:rBG$_O$ models that optimized favorable van der Waals, H-bonding, and electrostatic contacts at the interface, and consistency with the experimental SAXS data. The complex that best met these criteria, shown in Figures 7G and 7H, had the orphan domain straddling the TGF-β dimer, with O-D1 and O-D2 in contact with residues protruding from the C-terminal end of the TGF-β N-terminal helix, α1, and the heel helix, α3, within each monomer. This manner of binding, which had the pseudosymmetry axis of rBG$_O$ near, but not coincident with the symmetry axis of TGF-β2, agreed well with the experimental scattering data (χ^2 = 1.38) and resulted in no significant protrusions of the structure from the calculated electron density (Figures 7F and 7I). The manner of binding described above was well-represented within the ensemble of the ten best scoring structures, with the first six best scoring structures having an overall RMSD within 1.0 Å of that shown in Figures 7G and 7H. The next two best scoring structures had a similar staggered positioning of the orphan domain, but were rotated by approximately 100° around an axis connecting the centroid of O-D1 and O-D2. The next two structures within the ensemble were bound closer to the fingertips in a manner that would enable two molecules of the orphan domain to bind, which based on the SEC-MALS data shown in Figures 2F and S2F, is not feasible. The experimental SAXS data are therefore sufficient to rule out a 2:1 ENG$_O$-like manner of binding, and while it suggests and is consistent with a pseudo-symmetric 1:1 manner of binding, it is not sufficient to unambiguously determine the structure of such a complex.

DISCUSSION

The TGF-β pathway has expanded and diversified as organisms have diversified, with 3 family members in nematodes, 7 in flies, and more than 30 in vertebrates (Hinck, 2012). Although the type I and type II receptors have also similarly expanded, there are consistently fewer signaling receptors than GFs—flies, for example, have three type I and two type II receptors for 7 family GFs (Upadhyay et al., 2017), while humans have seven type I and five type II receptors for 33 family GFs (Hinck, 2012). The type I receptors of the family also couple to and activate just two classes of R-Smads: the GFs of the TGF-β/activin branch of the pathway bind type I receptors that activate R-Smads 2 and 3, while those of the BMP/GDF branch bind type I receptors that activate R-Smads 1, 5, and 8 (Chen et al., 1998; Hinck, 2012). The functional diversity that can be attained through intrinsic

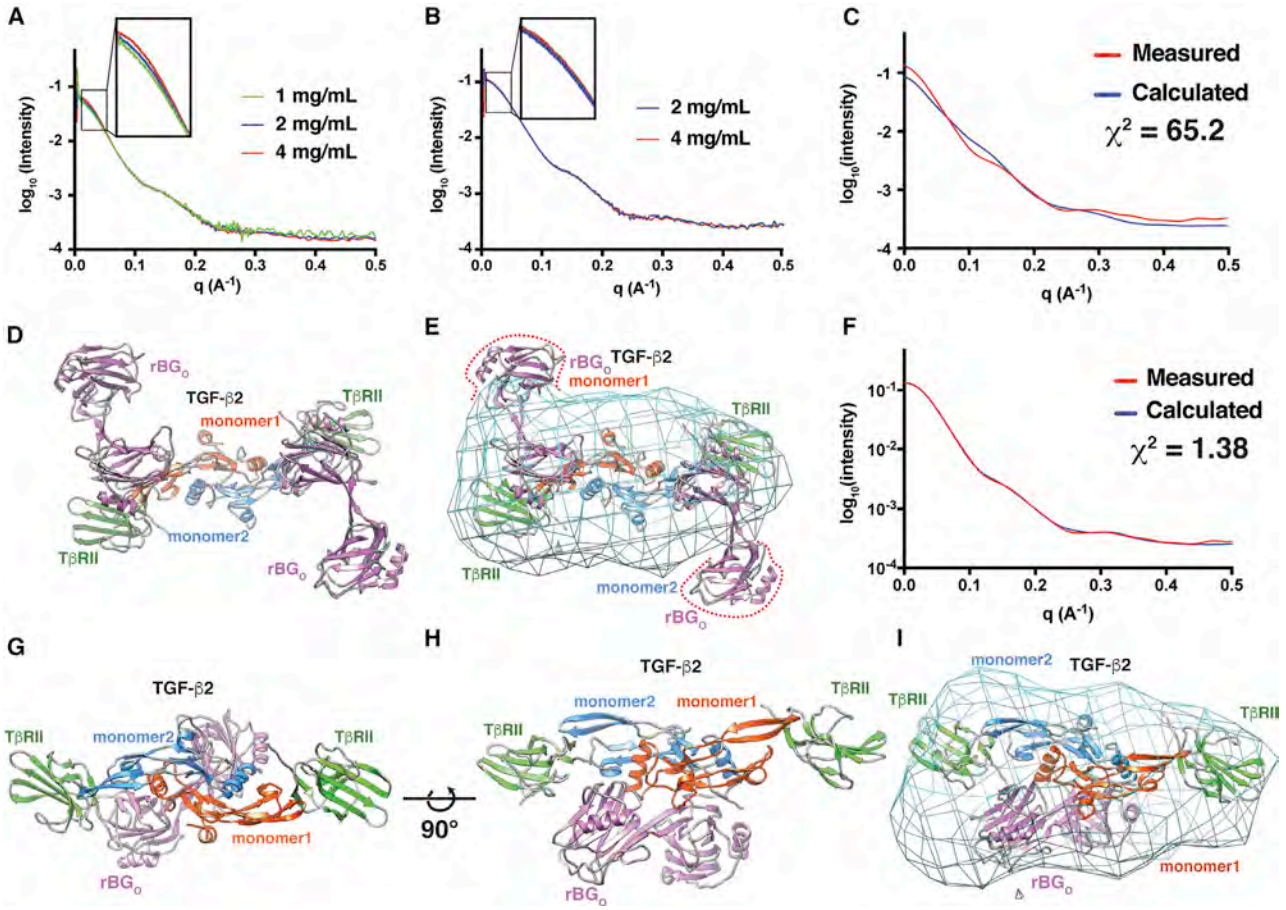

Figure 7. Structural Modeling of the Complex of BG_O with TGF-β2 and TβRII

(A and B) SAXS data for 1:2:1 TGF-β2TM:TβRII:zfBG_O (A) or 1:2:1 TGF-β3:TβRII:rBG_O (B) complexes at the concentrations shown (scattering curves are scaled by the expected dilution factor). Insets highlight concentration-dependent changes in the low-q region.

(C–E) Comparison of the experimental SAXS data for the 1:2:1 TGF-β3:TβRII:rBG_O complex (red) with the scattering curve calculated (blue) (C) from a 1:2:2 TGF-β3:TβRII:rBG_O model with rBG_O positioned in an hENG_O-like manner (D). Calculated electron density map for the 1:2:1 TGF-β3:TβRII:rBG_O complex contoured at 1.5 σ with the hENG_O-like 1:2:2 TGF-β3:TβRII:rBG_O model fitted into the density.

(F–I) Comparison of the experimental SAXS data for the 1:2:1 TGF-β3:TβRII:rBG_O complex (red) with the calculated scattering curve (blue) (F) from the best scoring 1:2:1 TGF-β3:TβRII:rBG_O model derived from positioning rBG_O onto the 1:2 TGF-β3:TβRII binary complex using pyDockSAXS (G and H). Calculated electron density map for the 1:2:1 TGF-β3:TβRII:rBG_O complex contoured at 1.5 σ with the pyDockSAXS 1:2:1 TGF-β3:TβRII:rBG_O model fitted into the density (I). Estimated resolution of the electron density map shown in (E and I) from Fourier shell correlation analysis is 30.9 Å.

See also Figure S10.

differences in signaling is therefore limited and cannot account for the functional diversity of the 33 TGF-β family GFs in humans.

The membrane-anchored co-receptors of the TGF-β family, BG and ENG, have essential roles potentiating the signaling activity of TGF-β2 and inhA and BMP-9 and BMP-10, respectively (Lewis et al., 2000; Lopez-Casillas et al., 1993; Nickel et al., 2018; Scharpfenecker et al., 2007). The selectivity with which BG and ENG recognize these GFs (Castonguay et al., 2011; Henen et al., 2019), together with the restricted pattern of their expression, is vital in enabling unique temporal-spatial patterns of signaling that underlie the unique functions of these GFs *in vivo*—for TGF-β2, morphogenetic transformation of endothelial progenitors in the developing heart and liver (Brown et al., 1999; Stenvers et al., 2003), for inhA antagonism of activin A and B in the anterior pituitary (Bernard et al., 2002; Lewis et al., 2000), and for endoglin activation of BMP-9 and BMP-10 signaling on endothelial cells required for normal development and maintenance of the vasculature (Roman and Hinck, 2017).

The previous studies aimed at uncovering how BG and ENG recognize their cognate GFs, and potentiate assembly of their signaling complexes showed that they differ in terms of the overall manner with which they engage their respective GFs: ENG exists as a covalent dimer and uses only its orphan domain to engage the GF dimer with 2:1 stoichiometry (Alt et al., 2012; Castonguay et al., 2011), while BG, which exists as a monomer, uses both its orphan and ZP-C domains to engage the GF dimer with 1:1 stoichiometry (Esparza-Lopez et al., 2001; Mendoza et al., 2009; Villarreal et al., 2016). The two co-receptors also have different effects on the binding of the signaling receptors, with ENG_O competing against type II receptors that BMP-9 and BMP-10 bind, such as ActRII and ActRIIB, but not the type I receptor Alk1 (Alt et al., 2012; Castonguay et al., 2011), while BG_O

potentiates the binding of the TGF-β type II receptor, TβRII, but competes against the TGF-β type I receptor, TβRI (Villarreal et al., 2016).

The recent structural studies of the human ENG ZP domain alone, and human ENG_O, both alone and bound to its cognate GF BMP-9, showed that ENG binds the GF dimer with 2:1 stoichiometry in an antibody-like manner, with the covalently dimerized ZP domain homologous to the F_c region, and the orphan domain, bound to the GF by formation of a super β sheet with the extended finger region, homologous to the F_{ab} region (Figures 1C and 4D) (Saito et al., 2017). If BG_O were to bind TGF-β2 in the same manner as the ENG_O, it would on the one hand be consistent with the observed effects of ENG and BG on type II receptor binding, because structural studies show that ActRII/ActRIIB and TβRII bind their cognate GFs differently: ActRII/ActRIIB bind the knuckle in a way that would directly overlap with the co-receptor (Greenwald et al., 2003; Thompson et al., 2003; Townson et al., 2012), while TβRII binds the fingertips in a way that would not directly overlap with the co-receptor (Figure S9B) (Groppe et al., 2008; Hart et al., 2002; Radaev et al., 2010). On the other hand, this manner of binding, in addition to being inconsistent with the observed 1:1 binding of BG_O to TGF-β dimers (Villarreal et al., 2016), would also be inconsistent with effects on type I receptor binding, because previous structural studies showed that Alk1 and TβRI both bind in a similar, although not identical, manner, on the underside of the fingers of one monomer and the heel helix of the other monomer in a way that would not directly overlap with that of the co-receptor (Groppe et al., 2008; Radaev et al., 2010; Townson et al., 2012).

The structure of $zfBG_O$ shows that, while it shares the same tandem β sandwich architecture as $hENG_O$, it nonetheless differs in that there is an additional helix (α1) and β strand (β8) following β7 within subdomain 1 (O-D1). The additional β strand, β8, is shown to pair with β6. This would block BG O-D1 from pairing and forming a super β sheet with finger 4 of TGF-β, as does β6 of ENG O-D1. Three observations consistent with the α1-β8 insertion fulfilling this "blocking" role are as follows: (1) the electron density for BG_O α1 and β8, as well as most of the meandering loop that follows, is well-defined (Figure 4G). (2) The backbone conformation, and even the conformation of many of the side chains in the region spanning from β6 to α2, are consistently determined in the orthorhombic and tetragonal $zfBG_O$ structures, indicating that this region is relatively rigid and would not likely be displaced by binding of the GF (Figure 4F). (3) Residues involved in the formation of the additional α helix (α1) and β strand (β8) in BG O-D1 are either conserved or invariant in species ranging from fish to mammals (Figure S3B), consistent with these fulfilling the same role in blocking β6 as they do in $zfBG_O$.

The structural modification above, together with the absence of any additional edge β strands that could possibly form a super β sheet with the GF, suggest that BG_O engages TGF-β2 in an entirely different manner than ENG_O engages BMP-9. To test this, binding studies were performed with full-length $zfBG_O$ and rBG_O and an engineered TGF-β monomer that had the finger region and base of the fingers with the cystine knot intact, but lacked the heel helix as well as all of the second monomer. To further test this, binding studies were also performed with $zfBG_O$ constructs that included only subdomain 1, O-D1, or subdomain 2 O-D2, and intact TGF-β2 dimers. The results demonstrated weak binding, both for intact $zfBG_O$ and rBG_O to the engineered TGF-β monomer, and both of the orphan subdomains to intact TGF-β2. This suggested that the orphan domain recognizes and binds to features beyond those present in the engineered monomer and that the BG orphan domain gains its high affinity by utilizing both of its subdomains to contact TGF-β2 dimers. This sets BG_O apart from ENG_O as the latter recognizes only the finger region of the GF and does so by utilizing only subdomain 1, O-D1. The alternative explanation, that weak binding is a consequence of an altered conformation or misfolding of the domain-deleted constructs, is unlikely because the engineered monomer was shown to bind TβRII through the fingertips with the same affinities as native TGF-β dimers, and NMR spectra clearly showed that both zfBG O-D1 and O-D2 were natively folded. Thus, binding studies with domain-deleted constructs are consistent with the structure-based hypothesis that BG_O will be unable to bind to TGF-β by formation of a super β sheet as does ENG_O, and, as a consequence, must bind in an alternative manner.

The observations above, together with the previous observations that the orphan domain binds TGF-β dimers with 1:1 stoichiometry and in a manner that partially blocks binding of TβRI, but not TβRII, suggested that the orphan domain binds across the TGF-β dimer interface with at least one of its subdomains protruding into the TβRI site, but neither subdomain protruding into the TβRII site. This is supported by the SAXS data for the 1:2:1 TGF-β2DM:TβRII:rBG_O complex, which was most consistent with models of the complex in which the orphan domain straddled the dimer interface and subdomains 1 and 2 both contacted the N-terminal and heel helices (α1 and α3, respectively). This manner of binding, in addition to accounting for the lack of competition against TβRII binding and competition against TβRI binding, had the pseudosymmetry axis of the orphan domain near the symmetry axis of TGF-β, but not exactly coincident. This accounts for the 1:1 stoichiometry with which BG_O binds TGF-β dimers, because positioning of a second symmetry-related molecule is impossible due to steric overlap. There were notably alternative models that were nearly as consistent with the SAXS data, but were rotated around an axis passing through the centroid of orphan subdomains 1 and 2. To determine if the predicted modes of binding might involve regions of BG_O with a high density of conserved surface-exposed residues, the product of an amino acid conservation index and the solvent accessible surface (SAS) area was calculated and smoothed over a 10-residue window (Figure S10). This highlighted three regions with a high conservation/SAS index, residues 199–211, 249–255, and 308–322, the first and second of which had close contact with TGF-β in the first and second class of models. This provides further, albeit indirect, support for the SAX-derived models; however, even with this additional information, there is insufficient information to uniquely determine the positioning of the orphan domain on TGF-β2. There is, however, ample evidence to rule out 2:1 models with an ENG_O-like manner of binding, because these are inconsistent with the SEC and SEC-MALS data, the analysis of the domain-deleted forms of TGF-β and BG_O, and the experimental SAXS data. Thus, it is concluded that BG_O binds its cognate GF, TGF-β2, in a

completely different manner compared with ENG_O, and that the general features of the complex are likely similar to those shown in Figures 7G and 7H. However, because the docking algorithm used does not allow for flexibility of the backbone and because no effort was made to validate the interfaces, the actual structure, which must await the direct determination of the TGF-β:BG_O complex using crystallography, could certainly differ from that presented in Figures 7G and 7H.

The alternative manner by which evolutionary latecomers to the family, such as the TGF-β family, bind their type II receptor, TβRII, compared with other more ancestral GFs of the family, such as BMPs, GDFs, and activins (Allendorph et al., 2006; Greenwald et al., 2003; Groppe et al., 2008; Hart et al., 2002; Hinck, 2012; Kirsch et al., 2000; Radaev et al., 2010; Weber et al., 2007), has already shown how structurally homologous proteins of the TGF-β family can diverge from one another in terms of the interfaces they use to assemble into functional complexes. The alternative interfaces expand the range of receptor binding specificity and provide an effective means of segregating the binding, and thus function, of different subclasses of TGF-β family GFs from one another. The different modes of GF binding for BG and ENG are therefore not unprecedented. The different modes likely engender BG and ENG with the ability to selectively bind their cognate GFs, imparting them with the ability to selectively target the heart, liver, and anterior pituitary and vasculature, respectively, without interfering with one another or TGF-β family GFs.

STAR★METHODS

Detailed methods are provided in the online version of this paper and include the following:

- KEY RESOURCES TABLE
- LEAD CONTACT AND MATERIALS AVAILABILITY
- EXPERIMENTAL MODEL AND SUBJECT DETAILS
- METHOD DETAILS
  - Protein Preparation
  - SPR Measurements
  - SEC and SEC-MALS
  - Crystallization, Structure Determination, and Refinement
  - NMR Spectroscopy
  - Small Angle X-Ray Scattering
- QUANTIFICATION AND STATISTICAL ANALYSIS
- DATA AND CODE AVAILABILITY

SUPPLEMENTAL INFORMATION

Supplemental Information can be found online at https://doi.org/10.1016/j.str.2019.06.010.

ACKNOWLEDGMENTS

The authors would like to thank Doowon Lee for assistance with the X-ray instrumentation, Mike Delk for assistance with the NMR instrumentation, Drs. Lixin Fan and Xiaobing Zuo for assistance with SAXS data collection, Drs. Christopher Barnes and Guillermo Calero for their assistance with structure determination of rBG_O, and Dr. Łukasz Wieteska for providing valuable comments on the manuscript. This research was supported by the NIH (GM58670 and CA172886), the US Department of Defense (DoD W81XWH-17-1-0429), and the University of Pittsburgh Vascular Medicine Institute. S.K.K. was supported by training grants provided by CPRIT (RP1450105) and the AHA (15PRE25550015), and F.L.-C. is supported by CONACYT (254046). X-ray diffraction data were collected at the SER-CAT 22-ID beamline at the Advanced Photon Source (APS), Argonne National Laboratory (ANL). SER-CAT is supported by its member institutions and equipment grants (RR25528 and RR028976) from the NIH. SAXS data were collected through the SAXS core facility of Center for Cancer Research, National Cancer Institute (NCI), which utilized ANL APS beamline 12-ID-B under PUP-24152. Molecular graphics and analyses were performed with UCSF Chimera, which is developed by the Resource for Biocomputing, Visualization, and Informatics at the University of California, San Francisco, and supported by NIGMS P41-GM103311. The X-ray Crystallography Core Laboratory at UT Health Science Center at San Antonio is supported by the Office of the Vice President for Research and the Mays Cancer Center, the center home to the UT Health San Antonio MD Anderson Cancer Center (NIH P30 CA054174).

AUTHOR CONTRIBUTIONS

S.K.K. crystallized $zfBG_O$ and collected and analyzed the X-ray data, with assistance from M.J.W., W.F., X.Z., A.B.T., and A.P.H. S.K.K. performed the accompanying functional studies, with assistance from C.-H.B. S.K.K. produced all the coding constructs and expressed and purified the protein, with assistance from C.S.H., T.C.K., C.Z., C.-H.B., V.M., F.L.-C., and A.P.H. S.K.K. and A.P.H. wrote the manuscript.

DECLARATION OF INTERESTS

The authors declare no competing interests.

Received: March 6, 2019
Revised: June 11, 2019
Accepted: June 28, 2019
Published: July 18, 2019

REFERENCES

Adams, P.D., Afonine, P.V., Bunkoczi, G., Chen, V.B., Davis, I.W., Echols, N., Headd, J.J., Hung, L.W., Kapral, G.J., Grosse-Kunstleve, R.W., et al. (2010). PHENIX: a comprehensive Python-based system for macromolecular structure solution. Acta Crystallogr. D Biol. Crystallogr. *66*, 213–221.

Allendorph, G.P., Vale, W.W., and Choe, S. (2006). Structure of the ternary signaling complex of a TGF-beta superfamily member. Proc. Natl. Acad. Sci. U S A *103*, 7643–7648.

Alt, A., Miguel-Romero, L., Donderis, J., Aristorena, M., Blanco, F.J., Round, A., Rubio, V., Bernabeu, C., and Marina, A. (2012). Structural and functional insights into endoglin ligand recognition and binding. PLoS One *7*, e29948.

Baardsnes, J., Hinck, C.S., Hinck, A.P., and O'Connor-McCourt, M.D. (2009). TbetaR-II discriminates the high- and low-affinity TGF-beta isoforms via two hydrogen-bonded ion pairs. Biochemistry *48*, 2146–2155.

Battye, T.G., Kontogiannis, L., Johnson, O., Powell, H.R., and Leslie, A.G. (2011). iMOSFLM: a new graphical interface for diffraction-image processing with MOSFLM. Acta Crystallogr. D Biol. Crystallogr. *67*, 271–281.

Bernard, D.J., Chapman, S.C., and Woodruff, T.K. (2002). Inhibin binding protein (InhBP/p120), betaglycan, and the continuing search for the inhibin receptor. Mol. Endocrinol. *16*, 207–212.

Bier, E., and De Robertis, E.M. (2015). EMBRYO DEVELOPMENT. BMP gradients: a paradigm for morphogen-mediated developmental patterning. Science *348*, aaa5838.

Brazil, D.P., Church, R.H., Surae, S., Godson, C., and Martin, F. (2015). BMP signalling: agony and antagony in the family. Trends Cell Biol. *25*, 249–264.

Bricogne, G., Vonrhein, C., Flensburg, C., Schiltz, M., and Paciorek, W. (2003). Generation, representation and flow of phase information in structure determination: recent developments in and around SHARP 2.0. Acta Crystallogr. D Biol. Crystallogr. *59*, 2023–2030.

Bricogne, G., Blanc, E., Brandl, M., Flensburg, C., Keller, P., Paciorek, W., Roversi, P., Sharff, A., Smart, O.S., Vonrhein, C., and Womack, T.O. (2018). BUSTER Version 2.10.2 (Global Phasing Ltd.).

Brown, C.B., Boyer, A.S., Runyan, R.B., and Barnett, J.V. (1999). Requirement of type III TGF-beta receptor for endocardial cell transformation in the heart. Science *283*, 2080–2082.

Brown, M.A., Zhao, Q., Baker, K.A., Naik, C., Chen, C., Pukac, L., Singh, M., Tsareva, T., Parice, Y., Mahoney, A., et al. (2005). Crystal structure of BMP-9 and functional interactions with pro-region and receptors. J. Biol. Chem. *280*, 25111–25118.

Castonguay, R., Werner, E.D., Matthews, R.G., Presman, E., Mulivor, A.W., Solban, N., Sako, D., Pearsall, R.S., Underwood, K.W., Seehra, J., et al. (2011). Soluble endoglin specifically binds bone morphogenetic proteins 9 and 10 via its orphan domain, inhibits blood vessel formation, and suppresses tumor growth. J. Biol. Chem. *286*, 30034–30046.

Cheifetz, S., Hernandez, H., Laiho, M., ten Dijke, P., Iwata, K.K., and Massague, J. (1990). Distinct transforming growth factor-beta (TGF-beta) receptor subsets as determinants of cellular responsiveness to three TGF-beta isoforms. J. Biol. Chem. *265*, 20533–20538.

Chen, Y.G., Hata, A., Lo, R.S., Wotton, D., Shi, Y., Pavletich, N., and Massague, J. (1998). Determinants of specificity in TGF-beta signal transduction. Genes Dev. *12*, 2144–2152.

Collaborative Computational Project, Number 4 (1994). The CCP4 suite: programs for protein crystallography. Acta Crystallogr. D Biol. Crystallogr. *50*, 760–763.

De Crescenzo, G., Hinck, C.S., Shu, Z., Zuniga, J., Yang, J., Tang, Y., Baardsnes, J., Mendoza, V., Sun, L., Lopez-Casillas, F., et al. (2006). Three key residues underlie the differential affinity of the TGFbeta isoforms for the TGFbeta type II receptor. J. Mol. Biol. *355*, 47–62.

DeLano, W.L. (2019). The PyMOL Molecular Graphics System, Version 2.0 (Schrödinger, LLC.).

Diestel, U., Resch, M., Meinhardt, K., Weiler, S., Hellmann, T.V., Mueller, T.D., Nickel, J., Eichler, J., and Muller, Y.A. (2013). Identification of a novel TGF-beta-binding site in the zona pellucida C-terminal (ZP-C) domain of TGF-beta-receptor-3 (TGFR-3). PLoS One *8*, e67214.

Emsley, P., Lohkamp, B., Scott, W.G., and Cowtan, K. (2010). Features and development of Coot. Acta Crystallogr. D Biol. Crystallogr. *66*, 486–501.

Esparza-Lopez, J., Montiel, J.L., Vilchis-Landeros, M.M., Okadome, T., Miyazono, K., and Lopez-Casillas, F. (2001). Ligand binding and functional properties of betaglycan, a co-receptor of the transforming growth factor-beta superfamily. Specialized binding regions for transforming growth factor-beta and inhibin A. J. Biol. Chem. *276*, 14588–14596.

Evans, P. (2006). Scaling and assessment of data quality. Acta Crystallogr. D Biol. Crystallogr. *62*, 72–82.

Evans, P. (2011). An introduction to data reduction: space-group determination, scaling and intensity statistics. Acta Crystallogr. D Biol. Crystallogr. *67*, 282–292.

Goumans, M.J., and Ten Dijke, P. (2018). TGF-beta signaling in control of cardiovascular function. Cold Spring Harb. Perspect. Biol. *10*, https://doi.org/10.1101/cshperspect.a022210.

Goumans, M.J., Zwijsen, A., Ten Dijke, P., and Bailly, S. (2018). Bone morphogenetic proteins in vascular homeostasis and disease. Cold Spring Harb. Perspect. Biol. *10*, https://doi.org/10.1101/cshperspect.a031989.

Grant, T.D. (2018). Ab initio electron density determination directly from solution scattering data. Nat. Methods *15*, 191–193.

Greenwald, J., Groppe, J., Gray, P., Wiater, E., Kwiatkowski, W., Vale, W., and Choe, S. (2003). The BMP7/ActRII extracellular domain complex provides new insights into the cooperative nature of receptor assembly. Mol. Cell *11*, 605–617.

Groppe, J., Hinck, C.S., Samavarchi-Tehrani, P., Zubieta, C., Schuermann, J.P., Taylor, A.B., Schwarz, P.M., Wrana, J.L., and Hinck, A.P. (2008). Cooperative assembly of TGF-beta superfamily signaling complexes is mediated by two disparate mechanisms and distinct modes of receptor binding. Mol. Cell *29*, 157–168.

Hart, P.J., Deep, S., Taylor, A.B., Shu, Z., Hinck, C.S., and Hinck, A.P. (2002). Crystal structure of the human TbetaR2 ectodomain–TGF-beta3 complex. Nat. Struct. Biol. *9*, 203–208.

Hata, A., and Chen, Y.G. (2016). TGF-beta signaling from receptors to Smads. Cold Spring Harb. Perspect. Biol. *8*, https://doi.org/10.1101/cshperspect.a022061.

Henen, M.A., Mahlawat, P., Zwieb, C., Kodali, R.B., Hinck, C.S., Hanna, R.D., Krzysiak, T.C., Ilangovan, U., Cano, K.E., Hinck, G., et al. (2019). TGF-beta2 uses the concave surface of its extended finger region to bind betaglycan's ZP domain via three residues specific to TGF-beta and inhibin-alpha. J. Biol. Chem. *294*, 3065–3080.

Hinck, A.P. (2012). Structural studies of the TGF-betas and their receptors - insights into evolution of the TGF-beta superfamily. FEBS Lett. *586*, 1860–1870.

Hinck, A.P., Mueller, T.D., and Springer, T.A. (2016). Structural biology and evolution of the TGF-beta family. Cold Spring Harb. Perspect. Biol. *8*, https://doi.org/10.1101/cshperspect.a022103.

Hinck, A.P., Walker, K.P., 3rd, Martin, N.R., Deep, S., Hinck, C.S., and Freedberg, D.I. (2000). Sequential resonance assignments of the extracellular ligand binding domain of the human TGF-beta type II receptor. J. Biomol. NMR *18*, 369–370.

Huang, T., and Hinck, A.P. (2016). Production, isolation, and structural analysis of ligands and receptors of the TGF-beta superfamily. Methods Mol. Biol. *1344*, 63–92.

Jimenez-Garcia, B., Pons, C., Svergun, D.I., Bernado, P., and Fernandez-Recio, J. (2015). pyDockSAXS: protein-protein complex structure by SAXS and computational docking. Nucleic Acids Res. *43*, W356–W361.

Kabsch, W. (2010). Xds. Acta Crystallogr. D Biol. Crystallogr. *66*, 125–132.

Kamaid, A., Molina-Villa, T., Mendoza, V., Pujades, C., Maldonado, E., Ispizua Belmonte, J.C., and Lopez-Casillas, F. (2015). Betaglycan knock-down causes embryonic angiogenesis defects in zebrafish. Genesis *53*, 583–603.

Kim, S.K., Barron, L., Hinck, C.S., Petrunak, E.M., Cano, K.E., Thangirala, A., Iskra, B., Brothers, M., Vonberg, M., Leal, B., et al. (2017). An engineered transforming growth factor beta (TGF-beta) monomer that functions as a dominant negative to block TGF-beta signaling. J. Biol. Chem. *292*, 7173–7188.

Kirsch, T., Sebald, W., and Dreyer, M.K. (2000). Crystal structure of the BMP-2-BRIA ectodomain complex. Nat. Struct. Biol. *7*, 492–496.

Konarev, P.V., Volkov, V.V., Sokolova, A.V., Koch, M.H.J., and Svergun, D.I. (2003). PRIMUS: a Windows PC-based system for small-angle scattering data analysis. J. Appl. Crystallogr. *36*, 1277–1282.

Krissinel, E., and Henrick, K. (2007). Inference of macromolecular assemblies from crystalline state. J. Mol. Biol. *372*, 774–797.

Lewis, K.A., Gray, P.C., Blount, A.L., MacConell, L.A., Wiater, E., Bilezikjian, L.M., and Vale, W. (2000). Betaglycan binds inhibin and can mediate functional antagonism of activin signalling. Nature *404*, 411–414.

Li, Y., Fortin, J., Ongaro, L., Zhou, X., Boehm, U., Schneyer, A., Bernard, D.J., and Lin, H.Y. (2018). Betaglycan (TGFBR3) functions as an inhibin A, but not inhibin B, coreceptor in pituitary gonadotrope cells in mice. Endocrinology *159*, 4077–4091.

Lin, S.J., Hu, Y., Zhu, J., Woodruff, T.K., and Jardetzky, T.S. (2011). Structure of betaglycan zona pellucida (ZP)-C domain provides insights into ZP-mediated protein polymerization and TGF-beta binding. Proc. Natl. Acad. Sci. U S A *108*, 5232–5236.

Lopez-Casillas, F., Wrana, J.L., and Massague, J. (1993). Betaglycan presents ligand to the TGF beta signaling receptor. Cell *73*, 1435–1444.

Mendoza, V., Vilchis-Landeros, M.M., Mendoza-Hernandez, G., Huang, T., Villarreal, M.M., Hinck, A.P., Lopez-Casillas, F., and Montiel, J.L. (2009). Betaglycan has two independent domains required for high affinity TGF-beta binding: proteolytic cleavage separates the domains and inactivates the neutralizing activity of the soluble receptor. Biochemistry *48*, 11755–11765.

Mullen, A.C., and Wrana, J.L. (2017). TGF-beta family signaling in embryonic and somatic stem-cell renewal and differentiation. Cold Spring Harb Perspect. Biol. *9*, https://doi.org/10.1101/cshperspect.a022186.

Nickel, J., Ten Dijke, P., and Mueller, T.D. (2018). TGF-beta family co-receptor function and signaling. Acta Biochim. Biophys. Sin. (Shanghai) *50*, 12–36.

Nolan, K., and Thompson, T.B. (2014). The DAN family: modulators of TGF-beta signaling and beyond. Protein Sci. *23*, 999–1012.

Painter, J., and Merritt, E.A. (2006). Optimal description of a protein structure in terms of multiple groups undergoing TLS motion. Acta Crystallogr. D Biol. Crystallogr. *62*, 439–450.

Pettersen, E.F., Goddard, T.D., Huang, C.C., Couch, G.S., Greenblatt, D.M., Meng, E.C., and Ferrin, T.E. (2004). UCSF Chimera–a visualization system for exploratory research and analysis. J. Comput. Chem. *25*, 1605–1612.

Qin, T., Barron, L., Xia, L., Huang, H., Villarreal, M.M., Zwaagstra, J., Collins, C., Yang, J., Zwieb, C., Kodali, R., et al. (2016). A novel highly potent trivalent TGF-beta receptor trap inhibits early-stage tumorigenesis and tumor cell invasion in murine Pten-deficient prostate glands. Oncotarget *7*, 86087–86102.

Radaev, S., Zou, Z., Huang, T., Lafer, E.M., Hinck, A.P., and Sun, P.D. (2010). Ternary complex of transforming growth factor-beta1 reveals isoform-specific ligand recognition and receptor recruitment in the superfamily. J. Biol. Chem. *285*, 14806–14814.

Robertson, I.B., and Rifkin, D.B. (2013). Unchaining the beast; insights from structural and evolutionary studies on TGFbeta secretion, sequestration, and activation. Cytokine Growth Factor Rev. *24*, 355–372.

Roman, B.L., and Hinck, A.P. (2017). ALK1 signaling in development and disease: new paradigms. Cell. Mol. Life Sci. *74*, 4539–4560.

Saito, T., Bokhove, M., Croci, R., Zamora-Caballero, S., Han, L., Letarte, M., de Sanctis, D., and Jovine, L. (2017). Structural basis of the human endoglin-BMP9 interaction: insights into BMP signaling and HHT1. Cell Rep. *19*, 1917–1928.

Sanford, L.P., Ormsby, I., Gittenberger-de Groot, A.C., Sariola, H., Friedman, R., Boivin, G.P., Cardell, E.L., and Doetschman, T. (1997). TGFbeta2 knockout mice have multiple developmental defects that are non-overlapping with other TGFbeta knockout phenotypes. Development *124*, 2659–2670.

Scharpfenecker, M., van Dinther, M., Liu, Z., van Bezooijen, R.L., Zhao, Q., Pukac, L., Lowik, C.W., and ten Dijke, P. (2007). BMP-9 signals via ALK1 and inhibits bFGF-induced endothelial cell proliferation and VEGF-stimulated angiogenesis. J. Cell Sci. *120*, 964–972.

Schomaker, V., and Trueblood, K.N. (1968). On the rigid-body motion of molecules in crystals. Acta Crystallogr. *B24*, 63–76.

Sievers, F., Wilm, A., Dineen, D., Gibson, T.J., Karplus, K., Li, W., Lopez, R., McWilliam, H., Remmert, M., Soding, J., et al. (2011). Fast, scalable generation of high-quality protein multiple sequence alignments using Clustal Omega. Mol. Syst. Biol. *7*, 539.

Stenvers, K.L., Tursky, M.L., Harder, K.W., Kountouri, N., Amatayakul-Chantler, S., Grail, D., Small, C., Weinberg, R.A., Sizeland, A.M., and Zhu, H.J. (2003). Heart and liver defects and reduced transforming growth factor beta2 sensitivity in transforming growth factor beta type III receptor-deficient embryos. Mol. Cell Biol. *23*, 4371–4385.

Svergun, D., Barberato, C., and Koch, M.H.J. (1995). CRYSOL - a program to evaluate X-ray solution scattering of biological macromolecules from atomic coordinates. J. Appl. Crystallogr. *28*, 768–773.

Ten Eyck, L.F. (1973). Crystallographic fast Fourier transforms. Acta Crystallogr. *A29*, 183–191.

Terwilliger, T.C., Grosse-Kunstleve, R.W., Afonine, P.V., Moriarty, N.W., Adams, P.D., Read, R.J., Zwart, P.H., and Hung, L.W. (2008). Iterative-build OMIT maps: map improvement by iterative model building and refinement without model bias. Acta Crystallogr. D Biol. Crystallogr. *64*, 515–524.

Thompson, T.B., Woodruff, T.K., and Jardetzky, T.S. (2003). Structures of an ActRIIB:activin A complex reveal a novel binding mode for TGF-beta ligand:receptor interactions. EMBO J. *22*, 1555–1566.

Townson, S.A., Martinez-Hackert, E., Greppi, C., Lowden, P., Sako, D., Liu, J., Ucran, J.A., Liharska, K., Underwood, K.W., Seehra, J., et al. (2012). Specificity and structure of a high affinity activin receptor-like kinase 1 (ALK1) signaling complex. J. Biol. Chem. *287*, 27313–27325.

Upadhyay, A., Moss-Taylor, L., Kim, M.J., Ghosh, A.C., and O'Connor, M.B. (2017). TGF-beta family signaling in *Drosophila*. Cold Spring Harb. Perspect. Biol. *9*, https://doi.org/10.1101/cshperspect.a022152.

Vagin, A., and Teplyakov, A. (2010). Molecular replacement with MOLREP. Acta Crystallogr. D Biol. Crystallogr. *66*, 22–25.

Villarreal, M.M., Kim, S.K., Barron, L., Kodali, R., Baardsnes, J., Hinck, C.S., Krzysiak, T.C., Henen, M.A., Pakhomova, O., Mendoza, V., et al. (2016). Binding properties of the transforming growth factor-beta coreceptor betaglycan: proposed mechanism for potentiation of receptor complex assembly and signaling. Biochemistry *55*, 6880–6896.

Walker, R.G., Poggioli, T., Katsimpardi, L., Buchanan, S.M., Oh, J., Wattrus, S., Heidecker, B., Fong, Y.W., Rubin, L.L., Ganz, P., et al. (2016). Biochemistry and biology of GDF11 and myostatin: similarities, differences, and questions for future investigation. Circ. Res. *118*, 1125–1141, discussion 1142.

Waterhouse, A.M., Procter, J.B., Martin, D.M., Clamp, M., and Barton, G.J. (2009). Jalview Version 2–a multiple sequence alignment editor and analysis workbench. Bioinformatics *25*, 1189–1191.

Weber, D., Kotzsch, A., Nickel, J., Harth, S., Seher, A., Mueller, U., Sebald, W., and Mueller, T.D. (2007). A silent H-bond can be mutationally activated for high-affinity interaction of BMP-2 and activin type IIB receptor. BMC Struct. Biol. *7*, 6.

Wiater, E., Harrison, C.A., Lewis, K.A., Gray, P.C., and Vale, W.W. (2006). Identification of distinct inhibin and transforming growth factor beta-binding sites on betaglycan: functional separation of betaglycan co-receptor actions. J. Biol. Chem. *281*, 17011–17022.

Winn, M.D., Ballard, C.C., Cowtan, K.D., Dodson, E.J., Emsley, P., Evans, P.R., Keegan, R.M., Krissinel, E.B., Leslie, A.G., McCoy, A., et al. (2011). Overview of the CCP4 suite and current developments. Acta Crystallogr. D Biol. Crystallogr. *67*, 235–242.

Wrana, J.L., Attisano, L., Wieser, R., Ventura, F., and Massague, J. (1994). Mechanism of activation of the TGF-beta receptor. Nature *370*, 341–347.

Zinski, J., Tajer, B., and Mullins, M.C. (2018). TGF-beta family signaling in early vertebrate development. Cold Spring Harb. Perspect. Biol. *10*, https://doi.org/10.1101/cshperspect.a033274.

STAR★METHODS

KEY RESOURCES TABLE

REAGENT or RESOURCE	SOURCE	IDENTIFIER
Bacterial and Virus Strains		
E. coli BL21(DE3)	EMD-Millipore	Cat# 69450-3
Chemicals, Peptides, and Recombinant Proteins		
sulfo-N-hydroxysulfosuccinimide	Thermo	Cat# 24510
Ethyl-3-[3- dimethylaminopropyl]carbodiimide hydrochloride	Thermo	Cat# 22980
(+)- biotinyl-3,6,9,- trioxaundecanediamine	Thermo	Cat# 21347
Deposited Data		
Structure of TGF-β3:TβRII:TβRI	Groppe et al., 2008	PDB:2PJY
Structure of mmTGF-β27M:TβRII	Kim et al., 2017	PDB:5TX4
Structure of ENG_O	Saito et al., 2017	PDB:5I04
Structure of ENG_O:BMP-9	Saito et al., 2017	PDB:5HZW
Structure of zfBGO (orthorhombic form)	This study	PDB: 6MZP
Structure of zfBGO (tetragonal form)	This study	PDB: 6MZN
Experimental Models: Cell Lines		
Human: Expi293F	Invitrogen	Cat# A14527
Recombinant DNA		
pET32a-TGF-β2	De Crescenzo et al., 2006	Hincklab #225
pET32a-TGF-β2DM	Baardsnes et al., 2009	Hincklab #253
pET32a-TGF-β2TM	De Crescenzo et al., 2006	Hincklab #225
pET32a-mmTGF-β27M	Kim et al., 2017	Hincklab #267
pET32a-avi-mmTGF-β27M	Kim et al., 2017	Hincklab #273
pET32a-TGF-β3	Groppe et al., 2008	Hincklab #27
pET32a-TβRII	Hinck et al., 2000	Hincklab #249
pcDNA3.1+- $zfBG_{O\text{-}ZP}$	This study	Hincklab #305
pcDNA3.1+- $zfBG_O$	This study	Hincklab #309
pcDNA3.1+- $zfBG_{ZP\text{-}C}$	This study	Hincklab #310
pcDNA3.1+- $zfBG_{O\text{-}D1}$	This study	Hincklab #391
pcDNA3.1+- $zfBG_{O\text{-}D2}$	This study	Hincklab #392
pcDNA3.1+- $rBG_{O\text{-}ZP}$	Villarreal et al., 2016	Hincklab #276
pcDNA3.1+- rBG_O	Villarreal et al., 2016	Hincklab #281
pcDNA3.1+- $rBG_{ZP\text{-}C}$	Villarreal et al., 2016	Hincklab #282
Software and Algorithms		
XDS	Kabsch, 2010	https://strucbio.biologie.uni-konstanz.de/xdswiki/index.php/Main_Page
iMOSFLM	Battye et al., 2011	https://www.mrc-lmb.cam.ac.uk/harry/imosflm/ver722/introduction.html
Pointless	Evans, 2006, 2011	http://www.ccp4.ac.uk/dist/html/pointless.html
Aimless	Evans, 2006, 2011	http://www.ccp4.ac.uk/dist/html/aimless.html
Ctruncate	Evans, 2006, 2011	http://www.ccp4.ac.uk/html/ctruncate.html
MolRep	Vagin and Teplyakov, 2010	http://www.ccp4.ac.uk/html/molrep.html
autoSHARP	Bricogne et al., 2003	https://www.globalphasing.com/sharp/
Phenix.autobuild	Adams et al., 2010	https://www.phenix-online.org/documentation/reference/autobuild.html
COOT	Emsley et al., 2010	https://www2.mrc-lmb.cam.ac.uk/personal/pemsley/coot/

(*Continued on next page*)

Continued

REAGENT or RESOURCE	SOURCE	IDENTIFIER
Buster	Bricogne et al., 2018	https://www.globalphasing.com/buster/
FFT	Ten Eyck, 1973	http://www.ccp4.ac.uk/dist/html/fft.html
TLSMD	Painter and Merritt, 2006	http://skuld.bmsc.washington.edu/~tlsmd/
PDBePISA	Krissinel and Henrick, 2007	https://www.ebi.ac.uk/pdbe/pisa/
UCSF Chimera	Pettersen et al., 2004	https://www.cgl.ucsf.edu/chimera/
Pymol	Schrodinger LLC	http://www.pymol.org
PRIMUS	Konarev et al., 2003	https://www.embl-hamburg.de/biosaxs/primus.html
CRYSOL	Svergun et al., 1995	https://www.embl-hamburg.de/biosaxs/crysol.html
DENSS	Grant, 2018	https://denss.ccr.buffalo.edu
pyDockSAXS	Jimenez-Garcia et al., 2015	https://life.bsc.es/pid/pydocksaxs
Scrubber	BioLogic Software	http://www.biologic.com.au/scrubber.html
BiaEval	Biacore	https://www.biacore.com/lifesciences/index.html
ASTRA 6.0	Wyatt Technology	https://www.wyatt.com/products/software/astra.html
Jalview	Waterhouse et al., 2009	http://www.jalview.org
Clustal Omega	Sievers et al., 2011	http://www.clustal.org
Other		
CM-5 SPR sensor chip	GE Lifesciences	Cat# 29149604
Ni-NTA agarose	Qiagen	Cat# 30210
Superdex 200 16/60 SEC Column	GE Lifesciences	Cat# 17-1069-01
Superdex 200 Increase 10/300 GL SEC Column	GE Lifesciences	Cat# 28-9909-44

LEAD CONTACT AND MATERIALS AVAILABILITY

Further information and requests for resources and reagents should be directed to and will be fulfilled by the Lead Contact, Andrew P. Hinck (ahinck@pitt.edu).

EXPERIMENTAL MODEL AND SUBJECT DETAILS

The BL21(DE3) strain of *E. coli* was purchased from EMD-Millipore (Cat# 69450-3) and plasmids of interest used for protein expression that encode β-lactamase for antibiotic resistance were directly transformed into the competent cells provided and plated onto LB plates with 50 μg/mL carbenicillin. The resistant cells were cultured at 37°C, both before and after the induction of protein expression, on liquid medium containing 50 μg/mL carbenicillin with shaking at 250 rpm in baffled 2.8 L Fernbach flasks.

The expi293 strain of HEK-293F (female) cells (Cat# A14527) and the corresponding expi293 growth medium (Cat# A14351-01) were purchased from Invitrogen. Cells were grown in baffled flasks with shaking (125 rpm) at 37°C with 8% CO_2. Cells are passaged every 3-4 days when the cells reach 5 x 10^6 cells/mL by diluting the cells in fresh media to 5 x 10^5 cells mL^{-1}. Low passage stocks of 1 x 10^7 cells mL^{-1} were frozen back with 10% DMSO. For protein expression, the day before transfection cells were diluted to 2.5 x 10^6 cells mL^{-1} and allowed to continue growing for 20 – 24 h. The transfection solution was prepared in 1/10th the volume of the total desired expression growth. For the transfection solution, CsCl purified DNA (1.5 μg per mL total culture volume) was diluted with media to 1/20th the culture volume. Linear polyethylenimine MW 2500 (Polysciences Cat# 23966-1) (4.5 ug per mL total volume) was diluted with media to 1/20th the culture volume. These two components were then combined and gently agitated. The transfection solution was allowed to incubate at room temperature for 30 min before being added to enough of the overnight cell culture to make 2.5 x 10^6 cells mL^{-1} of the desired volume. Medium was then added to adjust the volume to the desired amount. Cells were grown in the presence of the transfection solution for 14-16 hrs before protein production was stimulated by the addition of 2.2 mM valproic acid (Alfa Aesar Cat# A12962-18). Cells were allowed to continue to grow for 4 days and the conditioned media containing the desired protein was harvested.

METHOD DETAILS

Protein Preparation

Recombinant human TβRII extracellular domain and TGF-βs, including TGF-β2, TGF-β2DM, TGF-β2TM, mmTGF-β2-7M, avi-mmTGF-β2-7M, and TGF-β3, were expressed in *E. coli* at 37°C in the form of insoluble inclusion bodies, refolded, and purified as described (Hinck et al., 2000; Huang and Hinck, 2016; Kim et al., 2017). Zebrafish and rat betaglycan constructs were expressed in transiently transfected suspension cultured human embryonic kidney (HEK) 293 expi cells (Invitrogen, Carlsbad, CA) and purified

by metal affinity chromatography (NiNTA) and size exclusion chromatography (SEC) as described (Qin et al., 2016). Iodoacetamide treated $zfBG_O$ for crystallization was prepared by dialyzing NiNTA-purified protein into 25 mM sodium carbonate, 50 mM NaCl, pH 8.0, followed by the addition of freshly prepared iodoacetamide to a concentration of 20 mM. Following a 1 hr incubation at 25°C, the reaction was quenched with ethanolamine and the protein was purified by SEC. Sequences, along with database references and short descriptions, are provided in Supplemental Information (Tables S1 and S2).

SPR Measurements

Minimally biotinylated TGF-β2 for SPR was prepared by reaction of 5 nmol TGF-β2 in 40% DMSO with 60 nmol ethyl-3-[3- dimethylaminopropyl]carbodiimide hydrochloride (EDC, Pierce, Rockford, IL), 120 nmol sulfo-N-hydroxysulfosuccinimide (Sulfo-NHS, Pierce, Rockford, IL), and 480 nmol (+)- biotinyl-3,6,9,- trioxaundecanediamine (EZ-Link Amine-PEG3-Biotin, Pierce, Rockford, IL) for 1 h at 25°C at pH 6.0. Electrospray ionization time of flight mass spectrometry showed that roughly 10% of the growth factor was singly modified, while the remaining 90% was unmodified. Biotinylated avi-tagged mmTGF-β2-7m for SPR was prepared by enzymatic biotinylation with BirA biotin ligase as previously described (Kim et al., 2017).

SPR binding studies were performed with a BIAcore X100 instrument (GE Lifesciences, Piscataway, NJ) with biotinylated GFs captured onto neutravidin-coated CM-5 sensor chips (GE Lifesciences, Piscataway, NJ) at a density of 50 – 150 RU. Kinetic binding assays were performed by duplicate injections of the analytes in 20 mM HEPES, pH 7.0, 150 mM NaCl, 0.05% surfactant P20 (Pierce, Rockford, IL) at 100 uL min^{-1}. Regeneration of the surface was achieved by a 30 sec injection of 4 M guanidine hydrochloride. Baseline correction was performed by subtracting the response both from the reference surface with no immobilized ligand and 5 – 10 blank buffer injections. Kinetic analyses were performed by fitting the results to either a simple 1:1 model with a single set of kinetic constants (k_a, k_d) using the program Scrubber (BioLogic Software, Canberra, Australia) or a 1:1 model with high and low affinity classes of immobilized ligands and two sets of kinetic constants (k_{a1}, k_{d1} for binding to one class of immobilized ligand and k_{a2}, k_{d2} for binding to the other class of immobilized ligand) using the program BIAevaluation (GE Lifesciences, Piscataway, NJ). Importantly the latter model was used only if the data could not be satisfactorily fit to the simpler model and was needed only in three instances, binding of $zfBG_{ZP\text{-}C}$, $rBG_{ZP\text{-}C}$, or $zfBG_{O\text{-}D2}$ to TGF-β2.

SEC and SEC-MALS

Protein complexes were prepared by combining 1:2.5 TGF-β2DM:TβRII binary complex with a concentrated stock of full-length betaglycan or its component subdomain at the desired ratio. Samples for SEC and SEC-MALS were prepared in 25 mM HEPES, 150 mM arginine, pH 7.4, concentrated to 100 μL, and loaded onto a Superdex 200 Increase 10/300 GL column (GE Lifesciences, Piscataway, NJ) equilibrated in the same buffer. SEC measurements were made using an Akta FPLC (GE Lifesciences, Piscataway, NJ), while SEC-MALS measurements were made using a Waters high-performance liquid chromatography system (Waters, Milford, MA) and a Wyatt DAWN HELEOS-II multiangle light scattering detector and Optilab T-rEX refractive index detector (Wyatt, Santa Barbara, CA). SEC-MALS instrument control and data analyses were performed with the ASTRA software package (Wyatt, Santa Barbara, CA).

Crystallization, Structure Determination, and Refinement

Native orthorhombic crystals were grown using hanging-drop vapor diffusion at 25°C with drops consisting of 2.0 μL 9.2% v/v PEG 5K mono methyl ether, 4.6% w/v PEG 20K, 0.1M MES pH 6.2, 1.6 μL 20 mg mL^{-1} iodoacetamide-treated $zfBG_O$ in 10 mM MES pH 6.0, and 0.4 μL crushed $zfBG_O$ crystals (formed from non-iodoacetamide treated protein) as micro-seeds. For data collection, harvested crystals were mounted in nylon loops, cryo-protected in well solution containing 10% ethylene glycol, and flash-cooled in liquid nitrogen. Data were acquired at the Advanced Photon Source (APS) SER-CAT 22-ID and integrated and scaled using XDS (Kabsch, 2010). For phasing, platinum and iodide derivatized crystals were prepared by soaking the native crystals in crystallization well buffer with 5 mM K_2PtCl_4 or 4% saturated KI for 20 min and 20 s, respectively. For the platinum-derivatized crystals, data were collected at the APS SER-CAT 22-ID with the X-ray wavelength optimized for platinum anomalous scattering. Iodide-derivatized crystal data were collected at the Cu K-α wavelength with a Rigaku FR-E generator and RAXIS HTC image plate detector at the University of Pittsburgh Department of Structural Biology X-ray facility. Data reduction and processing of the derivative data sets were performed using iMOSFLM (Battye et al., 2011) and Pointless, Aimless, and Ctruncate (Collaborative Computational Project; Number 4, 1994; Winn et al., 2011). MIRAS phasing to 2.80 Å in autoSHARP (Bricogne et al., 2003) yielded an overall figure of merit of 0.52 for acentric reflections and 0.49 for centric reflections. Solvent flattening yielded interpretable electron density, which after autobuilding with phenix.autobuild (Adams et al., 2010) and manual adjustment with COOT (Emsley et al., 2010), could be traced to build nearly the complete model for Chain A except for four loop regions with weak density (Table S3). Chain B had weaker density and additional breaks, especially in domain 2 (Table S3).

Native tetragonal crystals were grown using hanging-drop vapor diffusion at 25°C with drops consisting of 2 μL 8% v/v PEG 5K mono methyl ether, 4% w/v PEG 20K, 0.1M MES pH 6.5, 1.6 μL 20 mg mL^{-1} non-iodoacetamide treated protein, and 0.4 μL micro-seeds (formed from non-iodoacetamide treated protein). For data collection, harvested crystals were mounted in nylon loops, cryo-protected in well solution containing 10% ethylene glycol, and flash-cooled in liquid nitrogen. Data were acquired at the Advanced Photon Source (APS) SER-CAT 22-ID and integrated and scaled using XDS (Kabsch, 2010). For phasing, structure model A from the asymmetric unit of the orthorhombic crystal form was used as a search model for molecular replacement in Molrep (Vagin and Teplyakov, 2010).

Coordinates were refined using Buster (Bricogne G. and Roversi P, 2018) with TLS (Schomaker and Trueblood, 1968), alternated with manual rebuilding in COOT (Emsley et al., 2010). TLS groups were identified with the TLSMD server (Painter and Merritt, 2006) and corresponded to most of domain 1 (residues 233-360), all of domain 2 (residues 58-215), and the extended segments that exit (residues 29-48) and re-enter domain 1 (residues 216-232) from domain 2. The refinement procedure was supported/accompanied by analysis of composite omit maps (Terwilliger et al., 2008). X-ray sources, data collection and refinement statistics are provided in Table 2. Figures were prepared using UCSF Chimera (Pettersen et al., 2004), except for Figures 4G and S4 which was prepared using PyMOL (DeLano, 2019).

NMR Spectroscopy

Natural abundance ^{1}H-^{13}C HSQC spectra of the methyl bearing residues of $BG_{O\text{-}D1}$ and $BG_{O\text{-}D2}$ were collected by preparing samples at 3 - 4 mg mL^{-1} in 25 mM sodium phosphate, 50 mM NaCl, pH 7.0 and by recording spectra at 30°C using a Bruker AVI 700 or AV-II 900 MHz spectrometer equipped with a 5 mm $^{1}H\{^{13}C,^{15}N\}$ TCI cryogenically cooled probe (Bruker Biospin, Billerica, MA).

Small Angle X-Ray Scattering

Experimental SAXS data of $zfBG_O$ and rBG_O, both alone and as SEC-purified complexes with either TβRII:TGF-β2TM or TβRII:TGF-β3, were collected at APS beamline 12-ID-B. Samples were prepared at 1.0, 2.0, and 4.0 mg mL^{-1} in 20 mM CHES, 100 mM NaCl, pH 9.5. Scattering data was recorded with sample oscillation as 30 2 sec exposures with a 1 sec delay between exposures. Raw scattering data were radially averaged, and after removing outliers, the data were averaged and subtracted from a buffer alone reference using the program PRIMUS (Konarev et al., 2003). Data corresponding to different concentrations were scaled, and if shown to not exhibit any systematic deviation over the $0 < q < 0.5$ range, were merged using PRIMUS (Konarev et al., 2003). Solution scattering curves were calculated from PDB coordinate files and fit to the concentration merged curves using the program CRYSOL (Svergun et al., 1995). Electron density envelopes were calculated from the merged scattering curves using the program DENSS (Grant, 2018). Models of $ratBG_O$ bound to the 1:2 TGF-β3:TβRII complex were generated using the program pyDockSAXS (Jimenez-Garcia et al., 2015), with the merged scattering curve for the 1:2:1 TGF-β3:TβRII:rBG_O complex, the structure of the 1:2 TGF-β3:TβRII complex (extracted from the structure of the TGF-β3:TβRII:TβRI complex, PDB 2PJY (Groppe et al., 2008)), and a homology model of rBG_O (built based on the $zfBG_O$ structure) as input.

QUANTIFICATION AND STATISTICAL ANALYSIS

The statistics of the X-ray crystallographic data processing, phasing, refinement, and structure validation are summarized in Table 2. The quality of the fit of the experimental SAXS data to that calculated from the corresponding structures was determined using the program CRYSOL, and the molecular weights and corresponding errors estimated from the SEC-MALS measurements were determined using the ASTRA software package (Wyatt, Santa Barbara, CA). The quality of the fit of the experimental SPR data to the kinetic constants and R_{max} was determined using either Scrubber (for data fit to a 1:1 binding model) or Biaeval (for data fit to a 1:1 heterogenous ligand model).

DATA AND CODE AVAILABILITY

The accession number for the structure factor and coordinate files of zfBGO reported in this paper are Protein Data Bank (PDB) 6MZP and 6MZN (orthorhombic and tetragonal forms, respectively).

frontiers in Neural Circuits

ORIGINAL RESEARCH
published: 01 February 2019
doi: 10.3389/fncir.2019.00004

Two eARCHT3.0 Lines for Optogenetic Silencing of Dopaminergic and Serotonergic Neurons

Alexandra Krol[1†], Violeta G. Lopez-Huerta[1,2,3†], Taylor E. C. Corey[1], Karl Deisseroth[4,5,6], Jonathan T. Ting[1,7] and Guoping Feng[1,2*]*

[1]McGovern Institute for Brain Research, Department of Brain and Cognitive Sciences, Massachusetts Institute of Technology, Cambridge, MA, United States, [2]Stanley Center for Psychiatric Research, Broad Institute of Massachusetts Institute of Technology (MIT) and Harvard, Cambridge, MA, United States, [3]Institute of Cellular Physiology, Department of Neurodevelopment and Physiology, National Autonomous University of Mexico, Mexico City, Mexico, [4]Department of Bioengineering, Stanford University, Stanford, CA, United States, [5]Department of Psychiatry and Behavioral Sciences, Stanford University, Stanford, CA, United States, [6]Howard Hughes Medical Institute, Stanford University, Stanford, CA, United States, [7]Human Cell Types, Allen Institute for Brain Science, Seattle, WA, United States

Dopaminergic and serotonergic neurons modulate and control processes ranging from reward signaling to regulation of motor outputs. Further, dysfunction of these neurons is involved in both degenerative and psychiatric disorders. Elucidating the roles of these neurons has been greatly facilitated by bacterial artificial chromosome (BAC) transgenic mouse lines expressing channelrhodopsin to readily enable cell-type specific activation. However, corresponding lines to silence these monoaminergic neurons have been lacking. We have generated two BAC transgenic mouse lines expressing the outward proton pump, enhanced ArchT3.0 (eArchT3.0), and GFP under control of the regulatory elements of either the dopamine transporter (DAT; Jax# 031663) or the tryptophan hydroxylase 2 (TPH2; Jax# 031662) gene locus. We demonstrate highly faithful and specific expression of these lines in dopaminergic and serotonergic neurons respectively. Additionally we validate effective and sensitive eArchT3.0-mediated silencing of these neurons using slice electrophysiology as well as with a well-established behavioral assay. These new transgenic tools will help expedite the study of dopaminergic and serotonergic system function in normal behavior and disease.

Keywords: opsin, inhibitory, serotonergic, dopaminergic, mouse, eArchT3.0

OPEN ACCESS

Edited by:
Seung-Hee Lee, Korea Advanced Institute of Science & Technology (KAIST), South Korea

Reviewed by:
Nicola Berretta, Fondazione Santa Lucia (IRCCS), Italy
Stephen Rayport, Columbia University, United States

***Correspondence:**
Jonathan T. Ting
jonathant@alleninstitute.org
Guoping Feng
fengg@mit.edu

†Co-first authors

Received: *03 August 2018*
Accepted: *14 January 2019*
Published: *01 February 2019*

Citation:
Krol A, Lopez-Huerta VG, Corey TEC, Deisseroth K, Ting JT and Feng G (2019) Two eARCHT3.0 Lines for Optogenetic Silencing of Dopaminergic and Serotonergic Neurons. Front. Neural Circuits 13:4. doi: 10.3389/fncir.2019.00004

INTRODUCTION

Neuroscience research has been revolutionized by cell-type specific access to neurons, by optical control of neuronal firing, and particularly by the intersection of the two. Since initial reports of optically gated ion channels and pumps, many new varieties and variants with increased sensitivity, kinetics, and various improved properties have been generated (Fenno et al., 2011; Mattis et al., 2011). Previously we generated a suite of cell type-specific bacterial artificial chromosome (BAC) transgenic lines to drive channelrhodopsin-2 (ChR2) expression in parvalbumin, serotonergic, cholinergic and GABAergic neurons (JAX# 012355, 014555, 014548, 014545, 014546; Zhao et al., 2011), which have been used widely in the field (Herde et al., 2013; Nelson et al., 2014; Van Dort et al., 2015; Li et al., 2016b; Latchoumane et al., 2017; Zhang et al., 2018).

However, a complementary suite of silencing lines has been lacking. Here, we present two mouse lines expressing enhanced ArchT3.0 (eArchT3.0) that allow efficient optogenetic silencing of dopaminergic and serotonergic cells. By brightly co-expressing GFP, these lines are also useful for visualization of these neurons. ArchT is an outward proton pump from *Halorubrum sodomense* strain TP009 (Han et al., 2011). In eArchT3.0, the addition of endoplasmic reticulum export and neurite trafficking sequences produces enhanced membrane localization with correspondingly reduced intracellular accumulation, leading to subsequently much larger photocurrents. eArchT3.0 has a two-fold increase in photocurrent compared to unoptimized ArchT or Arch, measured *in vitro*, and double the current of the enhanced halorhodopsin chloride pump (eNpH3.0; Mattis et al., 2011).

Dopaminergic and serotonergic neurons control many diverse processes in the brain. Classically the main dopaminergic centers in the midbrain, the ventral tegmental area (VTA) and substantia nigra pars compacta (SNc), are mostly associated with reward processing in varied contexts (Wise, 2004). In particular, these neurons fire for reward prediction error (Schultz et al., 1997; Bayer and Glimcher, 2005; Cohen et al., 2015). In the clinic, dysregulation of dopamine leads to both motivational changes, for instance with drug abuse (Everitt and Robbins, 2005), and to movement disorders, such as difficulties initiating movement seen in Parkinson's disease due to dopaminergic neuron degeneration in the sNC (Redgrave et al., 2010). The serotonergic system, in particular the raphe nuclei in the brainstem, the largest of which is the dorsal raphe nucleus (DRN), has also been associated with reward learning (Liu et al., 2014; Cohen et al., 2015). In the clinic, serotonin misregulation has been particularly implicated in depression, impulsivity, and anxiety in psychiatric disorders (Ansorge et al., 2004; Michelsen et al., 2007). Indeed, both dopaminergic and serotonergic signaling are key targets of some of the most widely used antipsychotic and antidepressant drugs (Li et al., 2016a; Yohn et al., 2017). However, our understanding of the functional roles of these circuits remains far from complete and a much more detailed and nuanced understanding is required to design better medications. The complexity and wide-ranging roles of these systems is beginning to be revealed using tools such as optogenetics which allow cell-type specific manipulations and fine temporal control. For example, the use of optogenetics has identified causal roles of VTA dopaminergic neurons in mediating depression symptoms from chronic stress (Tye et al., 2013), chronic defeat (Chaudhury et al., 2013), social interaction reward (Gunaydin et al., 2014) and dissected the dynamics of prediction error learning (Steinberg et al., 2013). For the serotonergic system, optogenetics has helped elaborate a complex role in reward-related behavior on multiple time scales (Liu et al., 2014; Miyazaki et al., 2014; Cohen et al., 2015) as well as diverse roles from signal processing in the olfactory system (Kapoor et al., 2016; Lottem et al., 2016) to regulating respiration and body temperature (Ray et al., 2011).

Here, we present two mouse lines with sensitive eArchT3.0-mediated silencing and high fidelity of expression in dopaminergic and serotonergic neurons. We characterize the specificity of the lines and their electrophysiology and validate the effectiveness of one of the lines in a well-established behavioral assay.

MATERIALS AND METHODS

Vector Construction

To construct the targeting vectors, a pBlueScript-derived vector iTV1-WPRE was used to generate BAC targeting vectors, as previously described (Ting and Feng, 2014). BAC specific homology arms [dopamine transporter (DAT) box A and B or tryptophan hydroxylase 2 (TPH2) box A and B] were PCR amplified from template BAC DNA and cloned into iTV1-WPRE. In a separate mammalian expression vector, eArchT3.0 [ArchT (Han et al., 2011) but with a trafficking sequence and ER export motif added to the C-terminus similar to Mattis et al. (2011)] and enhanced green fluorescent protein cDNAs were combined using the P2A linker. We selected P2A with a C-terminal GSG linker because this combination was shown to be the most efficiently processed of all viral 2A elements (Kim et al., 2011) and thus was the most likely to enable a complete physical uncoupling of the opsin and fluorophore with no significant unprocessed protein fraction. Verification of proper expression and functionality were performed by transient transfection of the eArchT3.0-P2A-EGFP plasmid DNA into HEK293 cells and primary rat hippocampal neurons, followed by epifluorescent imaging and patch clamp recording. The eArchT3.0-P2A-EGFP cassette was then sub-cloned into the multiple cloning site of iTV1-A/B-WPRE to complete the BAC targeting vectors. In this final cloning step great care was taken to ensure minimal disruptions to the junction between 5′ homology arm and the start of the eArchT3.0 sequence, except for addition of a Kozak consensus sequence. BAC recombineering steps, including trimming of the DAT BAC clone, have been described previously (Ting and Feng, 2014).

Animals

All experiments were done in accordance with NIH guidelines and approved by the MIT Institutional Animal Care and Use Committee. Mice were housed with a standard 12 h light/12 h-dark cycle (lights on at 07:00, lights off at 19:00) and given food and water *ad libitum*. eArchT3.0+ and eArchT3.0− mice of both genders from the same litters were used for experiments. Only heterozygous eArchT3.0+ mice were used for all experiments.

Surgery

Five- to six-month-old mice were anesthetized with isoflurane and placed in a small animal stereotax (David Kopf Instruments, St. Tujunga, CA, USA). They were implanted with a manually-constructed optic fiber [200 um core, NA = 0.22 (FG200UCC, Thorlabs, Newton, NJ, USA)] held in a ceramic ferrule (CF270-10, Thorlabs, Newton, NJ, USA). Measurements were made relative to Bregma, coordinates: −3.1, 0.35–0.37, −4.3. The fiber was held in place to the skull with adhesive cement (C&B Metabond; Parkell Inc., Brentwood, NY, USA). The incision was

closed with vetbond and mice were recovered on a heat pad in a clean cage. Mice were group housed pre and post surgery. Fiber placement was confirmed after behavior with serial coronal sections, anti-TH staining to identify the VTA and epifluorescent imaging (**Supplementary Figure S1**).

Conditioned and Real-Time Place Aversion

Behavioral testing was performed 3.5 weeks post-surgery, allowing time for recovery. Mice were tested between 7 am and 7 pm during their light cycle. Pre-testing, mice were habituated at least 1 h in the behavioral testing room. For testing, single mice were place in a clear plexiglass open top chamber with equally sized left and right chambers (22 × 22 cm) and a smaller central chamber (9 × 22 cm) separated by dividers leaving a gap (9 cm) between the center chamber and the side chambers. Each trial began with placement of the mouse in a corner of the central chamber. Between each trial, the chamber was cleaned with 70% ethanol. On the 1st day mice were allowed to freely explore the chamber for 15 min with the light turned off. On the 2nd and 3rd days mice were allowed to freely move between the compartments for 30 min. Entry into one of the side chambers was paired with photostimulation (532 nm light, GL532T3-100 mW Shanghai Laser and Optics Century Co.). Laser power was approximately 5 mW at tip of fiber, but substantial ramping up of the laser seen upon turn on could have led to approximately ±1 mW during stimulation. To avoid overheating, optical stimulation was paused for 30 s if the mouse stayed in the stimulated zone over 30 s. The stimulated side was counterbalanced between animals and genotypes but kept constant for each individual animal between days. On the 4th day mice were allowed, as on the 1st day, to explore freely for 15 min with the laser turned off. Mouse movement was tracked and paired with photostimulation control using a video camera and EthoVision software (EthoVision XT, Noldus, Wageningen, Netherlands) through a Master-9 Pulse Stimulator (A.M.P.I, Jerusalem, Israel). For analysis, tracks were edited for the correct start and end times blind to condition. Dwell time in each predefined area was calculated automatically using EthoVision software.

Immunohistochemistry and Image Quantification

Mice were deeply anesthetized with isoflurane, transcardially perfused with ice-cold PBS solution followed by fresh ice-cold 4% paraformaldehyde (PFA) in PBS. Brains were dissected out and postfixed overnight with 4% PFA at 4°C, and stored in PBS at 4°C. Sixty to hundred microgram sections were cut on a vibratome (Leica VT100S). Floating brain slices were permeabilized with 1.2% Triton X-100 in PBS for 15 min, washed 3 × 5 min in PBS and blocked 1 h in 5% normal goat serum, 2% BSA, 0.2% Triton X-100 in PBS (blocking buffer) for 1 h at room temperature. Sections were incubated with primary antibodies in blocking solution 1–3 overnights at 4°C. Slices were then washed three times with PBS for 20 min, incubated with secondary antibodies for 1–2 h at room temperature, washed 1× with DAPI (1:10,000) in PBS for 20 min then 2× with PBS for 20 min. Slice were mounted with 50% glycerol in Tris Buffer. Primary antibodies used were ms anti-TPH2 (1:500, Sigma, St. Louis, MO, USA to678), ms IgG1 anti-TH (1:1,000, immunostar 22941), rb anti p2A (1:1,000 Millipore, Burlington, MA, USA ABS31), and rat anti-DAT (1:1,000 Millipore, Burlington, MA, USA MAB369). Widefield epifluorescent images were capture using a 4× lens on a Olympus BX61 microscope with a PRIOR ProScan III motorized stage (Prior Scientific Instruments, UK) and CellSens Dimension 1.11 stitching software (Olympus). To quantify overlap, images were captured using Olympus Fluoview FV1000 confocal microscope, 20× lens. Three mice were imaged per condition, three sections per mouse. DAT sections, since they were coronal, were imaged bilaterally. Cells were counted manually using the ImageJ Cell Counter plugin (Schindelin et al., 2012). To quantify cell number and TPH2 and DAT expression levels in old animals over 1 year old, serial 60 um sagittal sections were collected from TPH2 and DAT-eArchT3.0 BAC transgenic animals and immunostained with TPH2, DAT or TH. Every third section from three animals was confocal imaged as described above; sections were matched referenced to the midline. Cells were counted automatically with CellProfiler (Lamprecht et al., 2007) using primary object detection and the Otsu global thresholding method. For the DAT-eArchT3.0 transgenic line, DAT immunostaining did not clearly distinguish individual dopaminergic cell bodies, so TH staining was used. To quantify DAT expression levels, DAT staining in the striatum was used to take advantage of relatively uniform coverage by dopaminergic terminals. To correct for absence of terminals around nuclei and fibers of passage, a mask was used to remove those areas from quantification. For the TPH2 transgenic line, TPH2 immunostaining was used both to quantify cell number and to assess expression levels. To correct for variable cell number between sections and animals, intensity levels were only measured from detected cells and normalized to total cell area per image.

Slice Preparation for Electrophysiological Recordings

Sagittal or coronal slices (250 μm) were obtained from DAT-eArchT3.0 or TPH2- eArchT3.0 expressing mice at 30–40 p.n. days. Mice were anesthetized *via* isoflurane inhalation and perfused transcardially using cold saline containing (in mM): 194 sucrose, 30 NaCl, 4.5 KCl, 1.2 NaH_2PO_4, 0.2 $CaCl_2$, 2 $MgCl_2$, 26 $NaHCO_3$, and 10 D-(+)-glucose saturated with 95% O_2 and 5% CO_2, pH = 7.4, 320–340 mOsm/L. Slices were cut using a slicer (VT1200 S, Leica Microsystems In., Grove, IL, USA) and then incubated for 10–15 min in a holding chamber (BSK4, Scientific System Design Inc., Little Ferry, NJ, USA) at 32°C with regular artificial cerebral spinal fluid containing the following in mM: 136 NaCl, 3.5 KCl, 1 $MgCl_2$, 2.5 $CaCl_2$, 26 $NaHCO_3$ and 11 glucose saturated with 95% O_2 and 5% CO_2, followed by at least 1 h recovery at room temperature (21–25°C) before recording.

Electrophysiological Recordings

We performed whole cell patch-clamp recordings with borosilicate glass pipettes (KG33, King Precision Glass) heat polished to obtain direct current resistances of ∼4–6 MΩ.

Pipettes were filled with an internal solution containing in mM: 120 K-Gluconate, 2 $MgCl_2$, 10 HEPES, 0.5 EGTA, 0.2 Na_2ATP, and 0.2 Na_3GTP. The recordings were made with a microelectrode amplifier with bridge and voltage clamp modes of operation (Multiclamp 700B, Molecular Devices, San Jose, CA, USA). Cell membrane potential was held at −60 mV, unless specified otherwise. Signals were low-pass filtered at 2 kHz and sampled at 10–20 kHz with a Digidata 1440A (Molecular Devices, San Jose, CA, USA), and data were stored on a computer for subsequent off-line analysis. Cells in which the series resistance (Rs, typically 8–12 MΩ) changed by >20% were excluded for data analysis. In addition, cells with Rs more than 20 MΩ at any time during the recordings were discarded. In some cases conventional characterization of neurons was made in voltage and current clamp configurations.

DAT+ or TPH+ neurons were identified for recordings on the basis of GFP expression visualized with a microscope equipped with a GFP filter (BX-51WI, Olympus). We also targeted GFP negative (−) neurons to confirm the specificity of eArchT3.0 effects in neurons. Photo stimulation parameters were 532 nm and 1–4 mW per mm^2 (GL532T3-100 mW Shanghai Laser and Optics Century Co.). Neurons were held at −70 mV during photocurrent measurements. To confirm the ability of photo stimulation to inhibit action potential firing, action potentials were induced by continuous positive current injection until tonic firing was reached.

Statistics

All data were transferred to GraphPad Prism for analysis and graphing. Electrophysiological data are presented as mean ± SEM, and with the values given for each experiment referring to the number of cells analyzed unless noted otherwise. All error bars indicate SEM. The significance level for all tests was $p < 0.05$. Group results were compared by using an unpaired Student's *t*-test. Quantification of cell immunohistochemistry results are presented as mean ± SD. Cell number quantification in old animals is presented as a scatter plot showing the number of cells across three sections per animal with mean ± SD overlaid. For immunofluorescent intensity the median intensity of each section from three animals is shown and for TPH2 staining the intensity is normalized to the cell area coverage in each section. Immunohistochemistry results were compared using an unpaired Student's *t*-test; the significance level for all tests was $p < 0.05$. Behavioral testing data is presented as a scatter plot with individual animal's performance with mean and SEM error bars overlaid. Results were compared using one-way analyses of variance (ANOVA) and adjusted *P* values were calculated using Sidak's multiple comparison.

RESULTS

Generation of eArchT3.0 BAC Transgenic Lines

Two eArchT3.0 lines were generated, the first to silence dopaminergic neurons and the second to silence serotonergic neurons using an optimized archeorhodopsin, eArchT3.0 (Han et al., 2011; Mattis et al., 2011). Both lines were generated using an improved BAC-transgenic approach that avoids overexpression of endogenous genes (Ting and Feng, 2014). In both cases, the eArchT3.0 cDNA was inserted into the BAC clone followed by the self-cleaving peptide p2A and GFP. This allows both bright visualization of expressing neurons, including in fresh tissue, through cytoplasmic GFP expression as well as localization of the Arch protein by immunochemical detection of the P2A fragment remaining at the eArchT3.0 C-terminus. To improve RNA stability, and hence protein expression levels, a woodchuck hepatitis virus posttranscriptional regulatory element (WPRE) and a bovine growth hormone polyadenylation signal (BGHpA) were added. For dopaminergic expression, this engineered cDNA was placed after the translation initiation codon, ATG, of the DAT gene in a BAC clone. DAT is present in dopaminergic neurons to reuptake dopamine from the synaptic cleft to be repackaged into synaptic vesicles and is selective for dopaminergic neurons (Augood et al., 1993; Lammel et al., 2015). For serotonergic expression, a TPH2 BAC clone was used. TPH2 is an enzyme that catalyzes the first and rate limiting step in serotonin production and is specific for serotonergic neurons (Walther et al., 2003).

eArchT3.0 Expression in Dopaminergic Neurons of DAT-eArchT3.0 BAC Transgenic Mice

Accurate expression of GFP and eArchT3.0 protein in dopaminergic neurons was found in neurons of the VTA and SNc with excellent overlap between tyrosine hydroxylase (TH) staining, the rate-limiting enzyme for dopamine synthesis, and GFP expression (**Figure 1**). Quantification shows very high overlap between GFP and TH with both high specificity of GFP expression, most GFP positive cells were also TH positive (**Figure 1C**; 96 ± 2%, VTA, **Figure 1D**; 96 ± 3%, SNc) and high coverage of GFP expression, most TH positive cells were also GFP positive (**Figure 1C**; 95 ± 3% VTA, **Figure 1D**; 98 ± 2% SNc). These neurons were also DAT positive (**Supplementary Figure S2**). Although TH is specific for dopaminergic neurons of the midbrain, because TH catalyzes the first step in catecholamine biosynthesis, TH is also expressed in some neurons that are not dopaminergic or DAT positive, such as the catecholamine neurons of the locus coeruleus (Augood et al., 1993; Lorang et al., 1994). Highlighting the specificity of this line, the locus coeruleus (**Figure 1A″**) though labeled by TH is not correspondingly labeled by GFP (**Figure 1A′**). GFP expression was also present in dopaminergic neurons of the olfactory bulbs (Pignatelli and Belluzzi, 2017; **Supplementary Figure S2**) as well as small TH-positive interneurons in the striatum (Ibáñez-Sandoval et al., 2010; Xenias et al., 2015; **Supplementary Figure S3F**). Notably, the GFP signal was bright enough to be seen and quantified without enhancement. This indicated a high level of eArchT3.0 expression since production of the two was stoichiometric at the mRNA level and likely protein level. Bright GFP expression also makes these mice a useful tool for targeting dopaminergic neurons in slice recordings. To determine possible effects of long-term eArchT3.0 expression

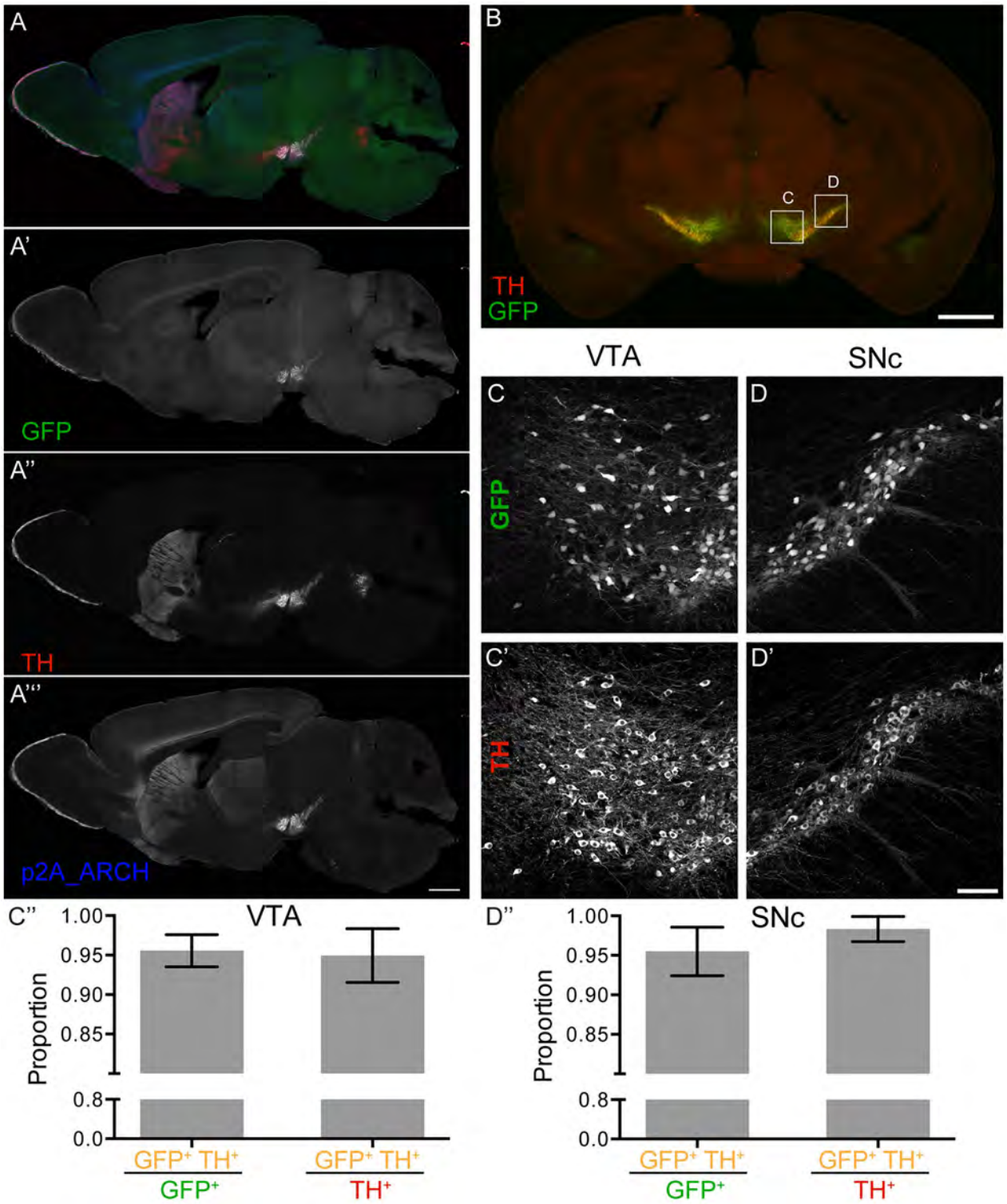

FIGURE 1 | Dopamine transporter (DAT)-enhanced ArchT3.0 (eArchT3.0) expression pattern. **(A)** Merged image **(A′–A‴)** of a sagittal section highlighting the ventral tegmental area (VTA), substantia nigra pars compacta (SNc) and striatum. **(A′)** Native GFP expression labeling targeted neurons. **(A″)** Tyrosine hydroxylase (TH) staining labeling dopaminergic neurons. (**A‴**) P2A staining labeling P2A-tagged- eArchT3.0 protein, localizing both to cell bodies in the VTA and SNc, and neuronal terminals in the striatum. Scale bar 1 mm. **(B)** Example section used for quantification of overlap between TH and GFP. Scale bar 1 mm. **(C–C″)** Quantification in the VTA of GFP and TH overlap. **(C–C′)** Example image used for quantification. **(C)** GFP fluorescence. **(C′)** TH staining. **(C″)** Specificity of GFP expression (left hand

(*Continued*)

FIGURE 1 | Continued
side): the proportion of cells labeled for both TH and GFP out of all GFP positive cells (96 ± 2%). Coverage of TH positive cells by GFP expression (right hand side): the proportion of cells labeled for both TH and GFP out of all TH positive cells (95 ± 3%). **(D–D″)** Quantification in the SNc of GFP and TH overlap. **(D–D′)** Example images used for quantification. **(D)** GFP fluorescence. **(D′)** TH staining. Scale bar 100 um. **(D″)** Specificity of GFP expression (left hand side): the proportion of cells labeled for both TH and GFP out of all GFP positive cells (96 ± 3%). Coverage of TH positive cells by GFP expression (right hand side): the proportion of cells labeled for both TH and GFP out of all TH positive cells (98 ± 2%; quantification: mean ± SD, bilateral images from eight sections from three animals).

or the transgenic approach on dopaminergic neuronal number or DAT gene expression levels, cell number in the midbrain (**Supplementary Figures S4A,D**) and DAT intensity levels in the striatum (**Supplementary Figures S4B,E**) in old animals over 1 year old were quantified. There was no difference in cell number (689 ± 201, 793 ± 189, n.s. unpaired *t*-test, $n = 3$ animals, **Supplementary Figure S4D**) or protein levels (0.014 ± 0.006, 0.015 ± 0.004, n.s. unpaired *t*-test, $n = 12$ sections, **Supplementary Figure S4E**) between the controls and DAT-eArchT3.0 animals.

We observed some off-target expression of eArchT3.0-GFP in subplate neurons and subiculum (**Supplementary Figure S3F**). A low level of expression was also seen sparsely in cells of the cortex (**Supplementary Figure S3E**). However, these neurons are spatially distinct from the VTA and SNc. Thus, separable control of these two populations should be easily achieved with optic fiber placement.

eArchT3.0 Expression in Serotonergic Neurons of TPH2-ArchT3.0 BAC Transgenic Mice

Serotonergic neurons in both the DRN and the ventral brainstem, which contains multiple more sparsely distributed serotonergic nuclei, all faithfully expressed eArchT3.0-GFP (**Figure 2**). Expression of GFP was as bright as in the DAT-eArchT3.0 line as was the excellent fidelity of expression. Quantification confirmed high overlap between GFP expression and TPH2; assessing specificity of GFP expression determined most GFP positive cells were also TPH2 positive (**Figure 2C**, 96 ± 1% in DRN, **Figure 2D**, 86 ± 8%, ventral brainstem) and assessing coverage of GFP expression determined most TPH2 positive cells were GFP positive (88 ± 4% in DRN, **Figure 2D**, 89 ± 4% ventral brainstem). TPH2 immunostaining was sometimes faint so overlap may be underestimated. Altogether this indicates faithful and robust expression of eArchT3.0 in serotonergic neurons in the brain. As for the DAT line, we determined possible long-term effects of the transgene in old animals over 1 year old by quantifying serotonergic neuronal number and TPH2 intensity levels in the DRN (**Supplementary Figures S4C,F,G**). There was no difference in cell number (1,032 ± 159, 728 ± 224, n.s. unpaired *t*-test, $n = 3$ animals, **Supplementary Figure S4F**) or protein levels (0.006 ± 0.005, 0.004 ± 0.004, n.s. unpaired *t*-test, $n = 9$ sections, **Supplementary Figure S4G**) between the controls and TPH2-eArchT3.0 animals.

Off-target expression of eArchT3.0-GFP at a lower level of expression was present in granule cells of the cerebellum (**Supplementary Figures S5A′,B′**), as well as sparse scattered cells in the cortex (**Supplementary Figures S5A‴,B‴**).

Electrophysiological Characterization of eArchT3.0-Expressing Dopaminergic Neurons

To analyze the ability of genetically encoded eArchT3.0 to enable reversible silencing of neuronal activity, we recorded from GFP-positive neurons in the VTA ($n = 10$, from five mice; **Figure 3A**). These neurons had characteristic properties of TH cells including: presence of a depolarized resting membrane potential (RMP; −52 ± 8 mV), wide action potentials (1.7 ± 0.16 ms half width) and Ih current (sag amplitude 34.9 ± 5.2 mV; **Figure 3B**; Chieng et al., 2011; Krashia et al., 2017). We demonstrated that GFP-positive neurons were sensitive to 532 nm light which led to eArchT3.0 mediated-hyperpolarization and evoked photocurrent with similar kinetics as reported previously (**Figures 3C–E**; Han et al., 2011; Mattis et al., 2011). A roughly linear relationship between photocurrent and light intensity was found as shown by the input-output curve (**Figure 3E**). At −45 ± 4.1 mV neurons had spontaneous tonic firing around 2.5 ± 0.9 Hz and application of 532 nm light (1–4 mW) for 10 s was highly effective at silencing firing precisely during light exposure (**Figure 3D**, paired *t*-test, $p = 0.01$). We repeated this manipulation 3–5 times on each neuron recorded and all cells showed inhibition. Lastly, to confirm the specificity of GFP-eArchT3.0 expression we also targeted GFP negative (−) cells in the VTA (**Supplementary Figures S6A–C**). We did not observe any evoked photocurrent in neurons recorded in VTA, or any significant changes in the RMP (light OFF −52.4 ± 2.2 mV and light ON −53.2 ± 2.1 mV, n.s. unpaired *t*-test, $n = 9$) or firing rate when there was spontaneous spiking (light OFF 5.9 ± 2 Hz and light ON 6.1 ± 2.2, n.s. unpaired *t*-test, $n = 5$; **Supplementary Figure S6C**). These results give us confidence that neurons that do not express GFP do not express eArchT3.0 and they are not affected by photo stimulation.

Electrophysiological Characterization of eArchT3.0-Expressing Serotonergic Neurons

The same characterization was carried out in DRN neurons. Recordings from GFP-positive cells ($n = 11$, from four mice) showed typical characteristics of serotonergic neurons (**Figure 4A**) with a RMP of −59 ± 2.5 mV and action potential threshold of −40.5 ± 0.9 mV (**Figure 4B**; Mlinar et al., 2016; Asaoka et al., 2017). As reported before for eArchT3.0 activation and found in the dopaminergic neurons, 532 nm light led to neuron hyperpolarization and sustained evoked photocurrent (**Figure 4C**; Han et al., 2011; Mattis et al., 2011). Similarly, a linear relationship between photocurrent and light intensity was found (**Figure 4E**). At −45 mV neurons had spontaneous tonic or irregular firing patterns at 0.96 ± 0.3 Hz and application of 532 nm light (1–4 mW) for 10 s was highly

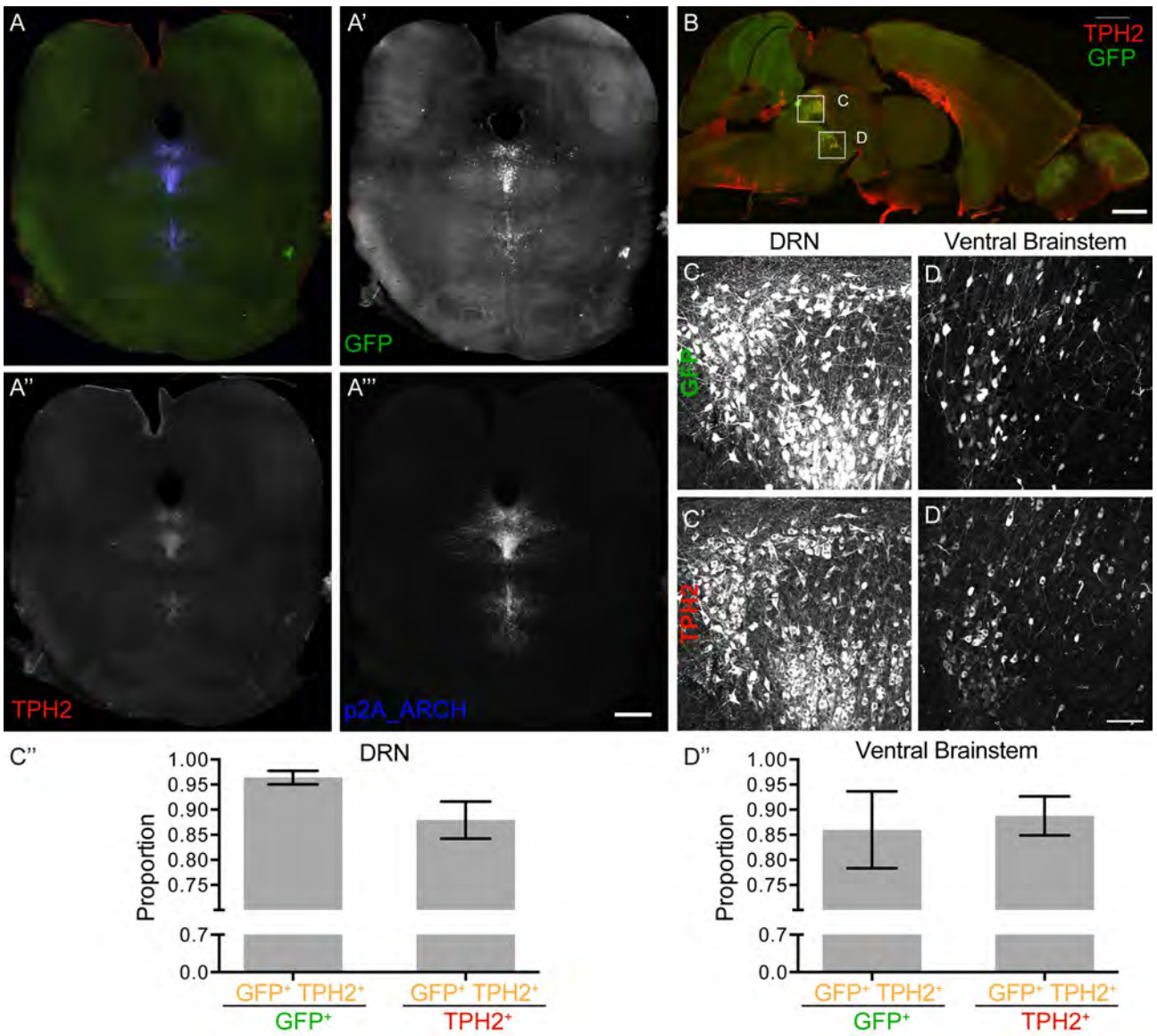

FIGURE 2 | Tryptophan hydroxylase 2 (TPH2)- eArchT3.0 expression pattern. **(A)** Merged image **(A′–A‴)** of a coronal section, highlighting the dorsal raphe nucleus (DRN). **(A′)** Native GFP expression labeling targeted neurons. **(A″)** TPH2 staining labeling serotonergic neurons. **(A‴)** P2A staining labeling P2A-tagged-eArchT3.0 protein. Scale bar 1 mm. **(B)** Example section used for quantification of overlap between TPH2 and GFP. Scale bar 1 mm. **(C–C″)** Quantification in the dorsal raphe nucleus (DRN) of GFP and TPH2 overlap. **(C–C′)** Example image used for quantification. **(C)** GFP fluorescence. **(C′)** TPH2 staining. **(C″)** Specificity of GFP expression (left hand side): the proportion of cells labeled for both TPH2 and GFP out of all GFP positive cells (96 ± 1%). Coverage of TPH2 positive cells by GFP expression (right hand side): the proportion of cells labeled for both TPH2 and GFP out of all TPH2 positive cells (88 ± 4%). **(D–D″)** Quantification in the ventral brainstem of GFP and TH overlap. **(D–D′)** Example image used for quantification. **(D)** GFP fluorescence. **(D′)** TH staining. Scale bar 100 um. **(D″)** Specificity of GFP expression (left hand side): the proportion of cells labeled for both TPH2 and GFP out of all GFP positive cells (86 ± 8%). Coverage of TPH2 positive cells by GFP expression (right hand side): the proportion of cells labeled for both TPH2 and GFP out of all TPH2 positive cells (89 ± 4%; quantification: mean ± SD, bilateral images from eight sections from three animals).

effective at silencing neuronal activity (**Figure 4D**, paired *t*-test, $p = 0.014$). We repeated this manipulation 3–5 times on each neuron recorded and all cells showed inhibition. Again, to confirm the specificity of GFP-eArchT3.0 expression we also targeted GFP (−) cells in the DRN (**Supplementary Figures S6D–F**). We observed that GFP (−) neurons did not show any current when stimulated with light and only showed a slight change in the firing frequency (light OFF 0.85 ± 0.26 Hz and light ON 0.81 ± 0.35 Hz, n.s. unpaired *t*-test, $n = 8$) likely due to changes in the surrounding inhibited neurons (**Supplementary Figure S6F**). These results give us confidence that neurons that do not express GFP do not express eArchT3.0 and they are not affected by photo stimulation.

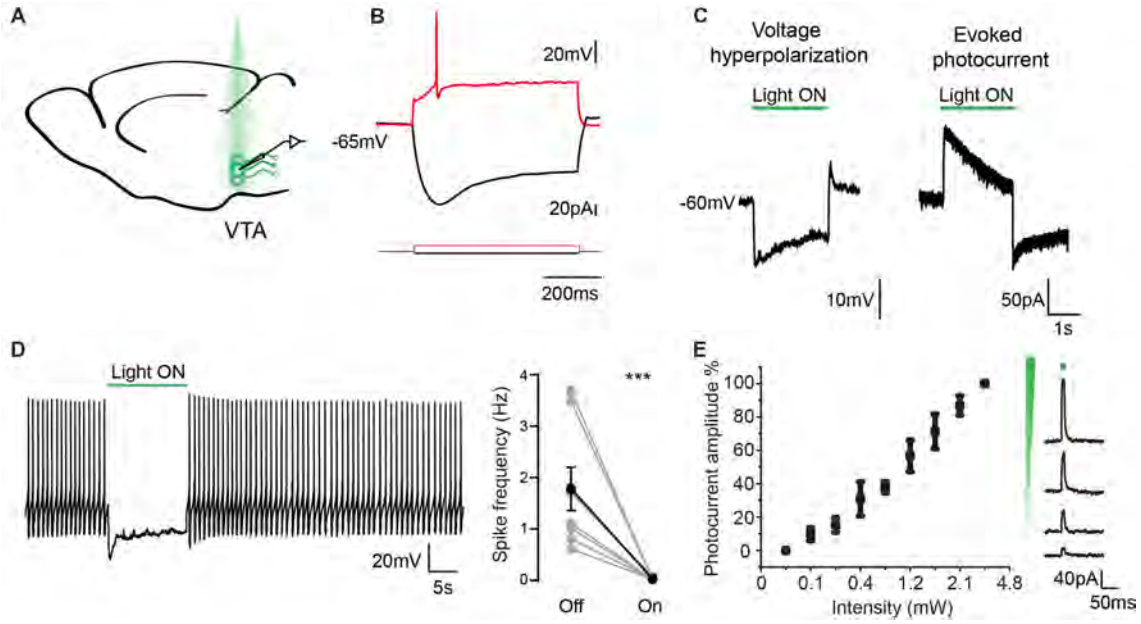

FIGURE 3 | Electrophysiological characterization of eArchT3.0 in dopaminergic neurons. **(A)** Schematic representation of the recording and stimulation preparation. **(B)** Typical VTA neuron response to hyperpolarizing and depolarizing current steps. **(C)** Whole cell recording in current (left) and voltage clamp (right) of the photoresponse in an example eArchT3.0-GFP expressing neuron from DAT-eArchT3.0 transgenic mouse (green bar, 532 nm light). **(D)** Sample trace of light-induced inhibition of spikes generated by current injection (left). During 10-s of photo stimulation (green bar), action potentials are suppressed. Population summary (right). Total spike rate before and during 10 s of photo stimulation (n = 10 neurons, mean ± SEM paired two-tailed t-test, ***p = 0.01, all cells showed inhibition). **(E)** Intensity response curve, data represents mean ± SEM (n = 8, left). Sample traces for evoked photocurrent at different light intensities (right).

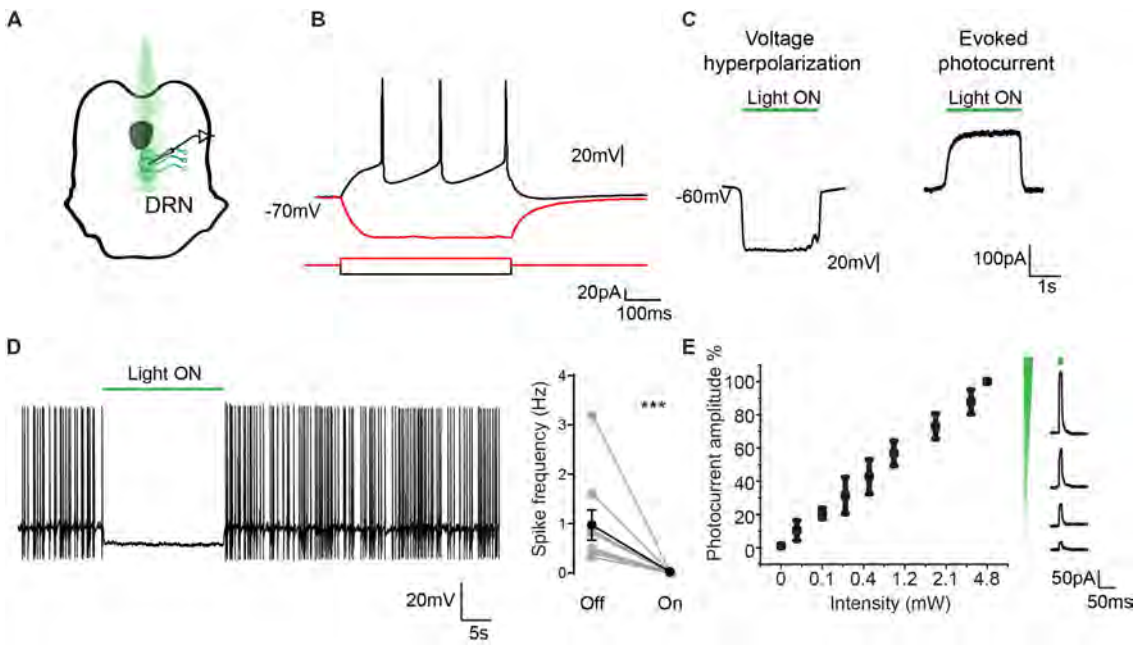

FIGURE 4 | Electrophysiological characterization of eArchT3.0 in serotonergic neurons. **(A)** Schematic representation of the recording and stimulation preparation. **(B)** Typical DRN neuron response to hyperpolarizing and depolarizing current steps. **(C)** Whole cell recording in current (left) and voltage clamp (right) of the photoresponse in an example eArchT3.0-GFP expressing neuron from TPH2- eArchT3.0 transgenic mouse (green bar, 532 nm light). **(D)** Sample trace of light-induced inhibition of spikes generated by current injection (left). During 10-s of photostimulation (green bar), action potentials are suppressed. Population summary (right). Total spike rate before and during 10 s of photostimulation. (n = 12 neurons, mean ± SEM paired two-tailed t-test, ***p = 0.014, all cells showed inhibition). **(E)** Intensity response curve, data represents mean ± SEM (n = 9, left). Sample traces for evoked photocurrent at different light intensities (right).

Optogenetic Activation of eArchT3.0 in VTA Is Sufficient to Drive Conditioned Place Aversion

Our slice experiments determined that eArchT3.0 expression was effective at silencing dopaminergic and serotonergic neurons. To determine whether eArchT3.0 was effective in a behavioral assay we used the dopaminergic eArchT3.0 line. Inhibition of dopaminergic neurons has been shown to be sufficient to mediate place aversion (Tan et al., 2012; Danjo et al., 2014). In place aversion, a location in an arena is paired with either an aversive condition, such as a foot shock, or a neuronal signal, such as inhibition of the VTA, over several conditioning days. In conditioned place aversion, aversive conditioning is delivered to an animal restrained to the location. In real-time place aversion, aversive conditioning is delivered to a freely exploring animal upon entry into the location. In both assays, animals avoid the aversive conditioned-location in a post-conditioning test day. In real-time place aversion, a decreased dwell time in the conditioned location can also be observed during conditioning days. Both conditioned place aversion and real-time place aversion have been reported previously upon inhibition of dopaminergic neurons *via* optogenetic activation of local inhibitory neurons in the VTA (Tan et al., 2012) or by direct optogenetic inactivation of the VTA with viral-driven expression of eNpH3.0 (Tan et al., 2012) or eArchT3.0 in a TH Cre mouse (Danjo et al., 2014).

To validate our DAT eArchT3.0 line in a similar assay, we used a three chamber arena with two equivalent larger chambers connected by a smaller third one (**Figure 5A"**), allowing mice to explore freely between the chambers, performing the assay over 4 days (**Figure 5A'**). On the first, pretest, day mice were allowed to explore with the laser turned off. On the next two, conditioning, days, the laser was triggered when mice entered the designated conditioning side, leading to unilateral eArchT3.0-mediated inhibition of the VTA. On the 4th day, mice were tested as on day one without light delivery. As expected, on the 1st day at pretest, mice showed no preference for one chamber vs. the other (**Figures 5B,D**). Following conditioning using eArchT3.0-mediated inhibition of DAT^{+} VTA neurons, aversion to the conditioned side was seen upon the fourth test day (**Figures 5B,D**). Mice spent significantly less time in the conditioned side (**Figure 5C**) both in the fraction of time spent (**Figure 5B**) and in net time (**Figure 5D**). Real-time place aversion during training was also observed with less time spent in the conditioned area each conditioning day (**Figure 5B**). These changes were not seen for the control, wildtype, littermate mice, which were implanted and stimulated the same way but did not express eArchT3.0. Overall this demonstrates that the DAT-eArchT3.0 line is a sensitive tool for effectively inducing inhibition of dopaminergic neurons *in vivo*.

DISCUSSION

We have generated and characterized two new lines of transgenic mice for optogenetically silencing dopaminergic or serotonergic neurons robustly and reproducibly. These two mouse lines will be shared with the community *via* Jackson Laboratory: DAT-eArchT3.0-GFP (Jax# 031663) and Tph2-eArchT3.0-GFP

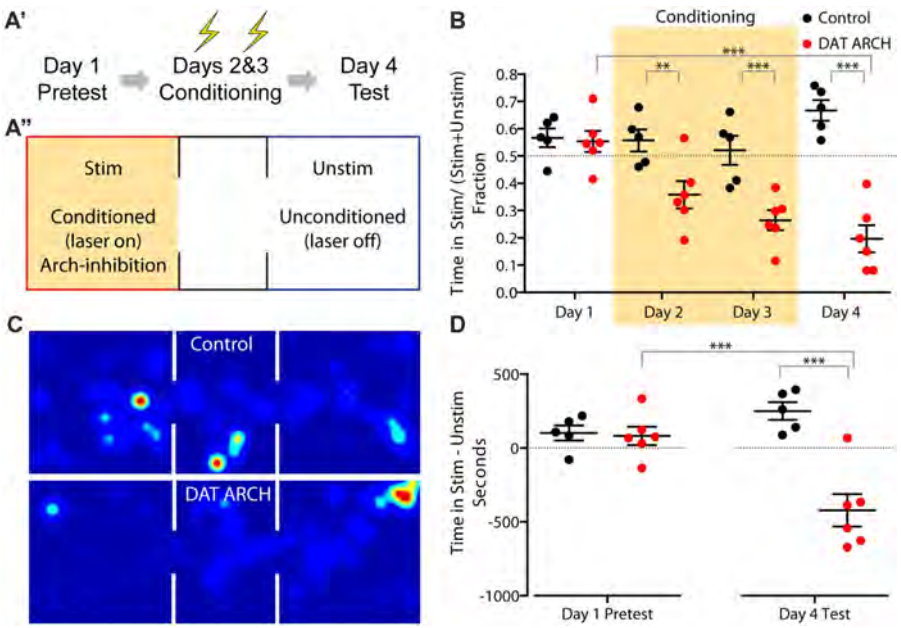

FIGURE 5 | Place aversion induced by DAT-eArchT3.0 mediated VTA inhibition. **(A)** Experimental timeline **(A')** and schematic of arena **(A")**. Mice were stimulated unilaterally when in the stimulated (stim) zone during conditioning days. **(B)** Fraction of time spent in the stimulated zone on each day. **(C)** Heatmap of time spent in each area (schematized above) on day 4 by example control or DAT-eArchT3.0 animal. **(D)** The difference in time spent in the stimulated zone vs. the unstimulated zone before and after conditioning. Data are plotted mean ± SEM, n = 5–6. Analysis uses one-way analyses of variance (ANOVA) and reports Sidak's multiple comparison adjusted P values, $^{**}P < 0.01$, $^{***}P < 0.001$.

(Jax# 031662). Generating these lines using optimized trimmed BACs avoided unwanted overexpression of other genes in the BAC clones, a concern with previous lines such as Chat-ChR2 (Kolisnyk et al., 2013; Ting and Feng, 2014). Reassuringly quantification of cell number and DAT or TPH2 intensity levels in old animals showed little long-term effects in transgenic animals. Additionally, the characteristic electrophysiological properties of both dopaminergic and serotonergic neurons expressing eArchT3.0 were consistent with the published literature for non-eArchT3.0 expressing neurons. Both lines also showed good fidelity and coverage for dopaminergic and serotonergic neurons. The co-expressed GFP fluorescence is also clearly visible without immunostaining amplification and can be used both to target cells for *in vitro* recordings and for morphological studies, making these lines useful for a range of eArchT3.0-independent applications. Both lines show excellent and sensitive silencing *in vitro*, although it is worth noting that the same level of photostimulation may not completely bock firing *in vivo*, where neurons can display higher firing rates and have additional extrinsic drives. Nonetheless our robust behavioral results in the conditioned place aversion assay using the DAT line indicate a substantial reduction in neuronal activity.

Compared to the original ArchT pump (Han et al., 2011), eArchT3.0 has an added endoplasmic reticulum export sequence and neurite trafficking sequencing, enhancing localization of the pump at the membrane (Mattis et al., 2011). Further, in our lines, GFP is not fused to the pump and instead is produced ratiometrically through a P2A self-cleaving peptide. Compared to the other widely used pumps, eNpHR3.0 (Gradinaru et al., 2010), unmodified Arch (Chow et al., 2010) and unmodified ArchT (Han et al., 2011), eArchT3.0 has much greater photocurrent and this difference is greater with increased light power density (Mattis et al., 2011). Both enhanced Arch (eArch3.0) and enhanced ArchT (eArchT3.0) proteins pass significantly more current than the original variants and this difference increases as the light power density increases (Mattis et al., 2011). Of consideration for certain applications, the maximum wavelength sensitivity of eArchT3.0 is between 520–560 nm. This is green shifted compared to eNPHr3.0 which is 560–590 and Jaws, which is further red shifted, with more photocurrent at 632 nm compared to eNpHR3.0 (Gradinaru et al., 2010; Mattis et al., 2011; Chuong et al., 2014). With all of these pumps caution is warranted (Wiegert et al., 2017); all three for instance exhibit comparable post-illumination rebound spiking (Chuong et al., 2014; Mahn et al., 2016) which can be avoided using a gradual off-ramp of illumination (Chuong et al., 2014; Mahn et al., 2016). Additional challenges can arise from use of these inhibitors at axon terminals. In such small cellular compartments, ionic changes can be exacerbated. In particular, prolonged activation of terminals on the 2–5 minute timescale using eArchT3.0 can cause significant increase in spontaneous activity, due to alkalinization of the boutons and the subsequence pH-dependent increase in intracellular calcium (Mahn et al., 2016; Wiegert et al., 2017).

The use of transgenic lines for targeted opsin expression presents several advantages compared to expressing opsins virally in combination with a Cre-line. Unlike virally mediated opsin expression, these lines will have less variable levels of expression from mouse to mouse which can result from variable viral injection and neuronal uptake and will eliminate the need to wait for viral expression post surgery. The ability to drive earlier eArchT3.0 expression could also facilitate future studies of the developmental roles of serotonergic and dopaminergic signaling. Admittedly, the need to implant fibers to optically silence the neurons may still limit developmental questions to acute experiments, up to an age when mice are not rapidly growing and when they are not still dependent on maternal care. Additionally, by dissociating eArchT3.0 expression from Cre expression, crossed in Cre lines can be used to target additional tools or neuronal populations of interest, for instance either for gene knockout or other opsin expression. By expressing eArchT3.0 in one cell population and channelrhodopsin in another, either using Cre-mediated recombination or a different transgenic line, different populations of neurons could be stimulated and inhibited in the same animal. Such a combination of tools could prove particularly powerful when exploring the effects of neuromodulatory neurons on other circuits on both the short and long timescales at which they act. We hope that these two new DAT and TPH2-eArchT3.0 lines will help facilitate a refined understanding of the roles of dopaminergic and serotonergic systems.

AUTHOR CONTRIBUTIONS

AK, JT and GF conceived the study and oversaw the project. AK screened the founder mouse lines for successful transgenics, performed the staining, imaging and quantification to characterize transgene expression as well as surgeries and place aversion behavior. VL-H performed the electrophysiology and analysis. TC helped screen the founder lines, performed quantification and mapped fiber placement. KD provided the original eArchT3.0 construct. JT created and tested the BAC constructs and generated the mice. AK and GF wrote the manuscript with input from all authors.

FUNDING

Research related to this work in the laboratory of GF is supported by the Poitras Center for Affective Disorders Research at MIT, Stanley Center for Psychiatric Research at Broad Institute of MIT and Harvard, National Institute of Neurological Disorders and Stroke (R01NS098505, R21NS079992), Nancy Lurie Marks Family Foundation, Simons Foundation Autism Research Initiative (SFARI Grant No. 307913), and Simons Center for the Social Brain at MIT. AK is supported by a fellowship from the Simons Foundation to the Simons Center for the Social Brain at MIT. KD is supported by National Institute of Mental Health (NIMH; R01MH099647), National Institute on Drug Abuse (NIDA; P50DA042012), the Defense Sciences Office, DARPA NeuroFAST program W911NF-14-2-0013, the NSF NeuroNex program, the Gatsby Foundation, the AE Foundation, the NOMIS Foundation, the Fresenius Foundation, the Wiegers Family Fund, the James Grosfeld Foundation, the Sam and Betsy Reeves Foundation, and the HL Snyder Foundation.

ACKNOWLEDGMENTS

We thank Morgan Fleishman for superb animal husbandry and technical assistance. Kirsten Levandowski for help with surgeries and Cailey Talbot for help in quantification.

SUPPLEMENTARY MATERIAL

The Supplementary Material for this article can be found online at: https://www.frontiersin.org/articles/10.3389/fncir.2019.00004/full#supplementary-material

REFERENCES

Ansorge, M. S., Zhou, M., Lira, A., Hen, R., and Gingrich, J. A. (2004). Early-life blockade of the 5-HT transporter alters emotional behavior in adult mice. *Science* 306, 879–881. doi: 10.1126/science.1101678

Asaoka, N., Nishitani, N., Kinoshita, H., Kawai, H., Shibui, N., Nagayasu, K., et al. (2017). Chronic antidepressant potentiates spontaneous activity of dorsal raphe serotonergic neurons by decreasing $GABA_B$ receptor-mediated inhibition of L-type calcium channels. *Sci. Rep.* 7:13609. doi: 10.1038/s41598-017-13599-3

Augood, S. J., Westmore, K., McKenna, P. J., and Emson, P. C. (1993). Co-expression of dopamine transporter mRNA and tyrosine hydroxylase mRNA in ventral mesencephalic neurones. *Mol. Brain Res.* 20, 328–334. doi: 10.1016/0169-328x(93)90059-x

Bayer, H. M., and Glimcher, P. W. (2005). Midbrain dopamine neurons encode a quantitative reward prediction error signal. *Neuron* 47, 129–141. doi: 10.1016/j.neuron.2005.05.020

Chaudhury, D., Walsh, J. J., Friedman, A. K., Juarez, B., Ku, S. M., Koo, J. W., et al. (2013). Rapid regulation of depression-related behaviours by control of midbrain dopamine neurons. *Nature* 493, 532–536. doi: 10.1038/nature11713

Chieng, B., Azriel, Y., Mohammadi, S., and Christie, M. J. (2011). Distinct cellular properties of identified dopaminergic and GABAergic neurons in the mouse ventral tegmental area. *J. Physiol.* 589, 3775–3787. doi: 10.1113/jphysiol.2011.210807

Chow, B. Y., Han, X., Dobry, A. S., Qian, X., Chuong, A. S., Li, M., et al. (2010). High-performance genetically targetable optical neural silencing by light-driven proton pumps. *Nature* 463, 98–102. doi: 10.1038/nature08652

Chuong, A. S., Miri, M. L., Busskamp, V., Matthews, G. A. C., Acker, L. C., Sorensen, A. T., et al. (2014). Noninvasive optical inhibition with a red-shifted microbial rhodopsin. *Nat. Neurosci.* 17, 1123–1129. doi: 10.1038/nn.3752

Cohen, J. Y., Amoroso, M. W., and Uchida, N. (2015). Serotonergic neurons signal reward and punishment on multiple timescales. *Elife* 4:06346. doi: 10.7554/eLife.06346

Danjo, T., Yoshimi, K., Funabiki, K., Yawata, S., and Nakanishi, S. (2014). Aversive behavior induced by optogenetic inactivation of ventral tegmental area dopamine neurons is mediated by dopamine D2 receptors in the nucleus accumbens. *Proc. Natl. Acad. Sci. U S A* 111, 6455–6460. doi: 10.1073/pnas.1404323111

Everitt, B. J., and Robbins, T. W. (2005). Neural systems of reinforcement for drug addiction: from actions to habits to compulsion. *Nat. Neurosci.* 8, 1481–1489. doi: 10.1038/nn1579

Fenno, L., Yizhar, O., and Deisseroth, K. (2011). The development and application of optogenetics. *Annu. Rev. Neurosci.* 34, 389–412. doi: 10.1146/annurev-neuro-061010-113817

Gradinaru, V., Zhang, F., Ramakrishnan, C., Mattis, J., Prakash, R., Diester, I., et al. (2010). Molecular and cellular approaches for diversifying and extending optogenetics. *Cell* 141, 154–165. doi: 10.1016/j.cell.2010.02.037

Gunaydin, L. A., Grosenick, L., Finkelstein, J. C., Kauvar, I. V., Fenno, L. E., Adhikari, A., et al. (2014). Natural neural projection dynamics underlying social behavior. *Cell* 157, 1535–1551. doi: 10.1016/j.cell.2014.05.017

Han, X., Chow, B. Y., Zhou, H., Klapoetke, N. C., Chuong, A., Rajimehr, R., et al. (2011). A high-light sensitivity optical neural silencer: development and application to optogenetic control of non-human primate cortex. *Front. Syst. Neurosci.* 5:18. doi: 10.3389/fnsys.2011.00018

Herde, M. K., Iremonger, K. J., Constantin, S., and Herbison, A. E. (2013). GnRH neurons elaborate a long-range projection with shared axonal and dendritic functions. *J. Neurosci.* 33, 12689–12697. doi: 10.1523/jneurosci.0579-13.2013

Ibáñez-Sandoval, O., Tecuapetla, F., Unal, B., Shah, F., Koós, T., and Tepper, J. M. (2010). Electrophysiological and morphological characteristics and synaptic connectivity of tyrosine hydroxylase-expressing neurons in adult mouse striatum. *J. Neurosci.* 30, 6999–7016. doi: 10.1523/jneurosci.5996-09.2010

Kapoor, V., Provost, A. C., Agarwal, P., and Murthy, V. N. (2016). Activation of raphe nuclei triggers rapid and distinct effects on parallel olfactory bulb output channels. *Nat. Neurosci.* 19, 271–282. doi: 10.1038/nn.4219

Kim, J. H., Lee, S.-R., Li, L.-H., Park, H.-J., Park, J.-H., Lee, K. Y., et al. (2011). High cleavage efficiency of a 2A peptide derived from porcine Teschovirus-1 in human cell lines, zebrafish and mice. *PLoS One* 6:e18556. doi: 10.1371/journal.pone.0018556

Kolisnyk, B., Guzman, M. S., Raulic, S., Fan, J., Magalhaes, A. C., Feng, G., et al. (2013). ChAT-ChR2-EYFP mice have enhanced motor endurance but show deficits in attention and several additional cognitive domains. *J. Neurosci.* 33, 10427–10438. doi: 10.1523/JNEUROSCI.0395-13.2013

Krashia, P., Martini, A., Nobili, A., Aversa, D., D'Amelio, M., Berretta, N., et al. (2017). On the properties of identified dopaminergic neurons in the mouse substantia nigra and ventral tegmental area. *Eur. J. Neurosci.* 45, 92–105. doi: 10.1111/ejn.13364

Lammel, S., Steinberg, E. E., Földy, C., Wall, N. R., Beier, K., Luo, L., et al. (2015). Diversity of transgenic mouse models for selective targeting of midbrain dopamine neurons. *Neuron* 85, 429–438. doi: 10.1016/j.neuron.2014.12.036

Lamprecht, M. R., Sabatini, D. M., and Carpenter, A. E. (2007). CellProfiler: free, versatile software for automated biological image analysis. *Biotechniques* 42, 71–75. doi: 10.2144/000112257

Latchoumane, C.-F. V., Ngo, H.-V. V., Born, J., and Shin, H.-S. (2017). Thalamic spindles promote memory formation during sleep through triple phase-locking of cortical, thalamic and hippocampal rhythms. *Neuron* 95, 424.e6–435.e6. doi: 10.1016/j.neuron.2017.06.025

Li, P., Snyder, G. L., and Vanover, K. E. (2016a). Dopamine targeting drugs for the treatment of schizophrenia: past, present and future. *Curr. Top. Med. Chem.* 16, 3385–3403. doi: 10.2174/1568026616666160608084834

Li, Y., Zhong, W., Wang, D., Feng, Q., Liu, Z., Zhou, J., et al. (2016b). Serotonin neurons in the dorsal raphe nucleus encode reward signals. *Nat. Commun.* 7:10503. doi: 10.1038/ncomms10503

Liu, Z., Zhou, J., Li, Y., Hu, F., Lu, Y., Ma, M., et al. (2014). Dorsal raphe neurons signal reward through 5-HT and glutamate. *Neuron* 81, 1360–1374. doi: 10.1016/j.neuron.2014.02.010

Lorang, D., Amara, S. G., and Simerly, R. B. (1994). Cell-type-specific expression of catecholamine transporters in the rat brain. *J. Neurosci.* 14, 4903–4914. doi: 10.1523/jneurosci.14-08-04903.1994

Lottem, E., Lörincz, M. L., and Mainen, Z. F. (2016). Optogenetic activation of dorsal raphe serotonin neurons rapidly inhibits spontaneous but not odor-evoked activity in olfactory cortex. *J. Neurosci.* 36, 7–18. doi: 10.1523/jneurosci.3008-15.2016

Mahn, M., Prigge, M., Ron, S., Levy, R., and Yizhar, O. (2016). Biophysical constraints of optogenetic inhibition at presynaptic terminals. *Nat. Neurosci.* 19, 554–556. doi: 10.1038/nn.4266

Mattis, J., Tye, K. M., Ferenczi, E. A., Ramakrishnan, C., O'Shea, D. J., Prakash, R., et al. (2011). Principles for applying optogenetic tools derived from direct comparative analysis of microbial opsins. *Nat. Methods* 9, 159–172. doi: 10.1038/nmeth.1808

Michelsen, K. A., Schmitz, C., and Steinbusch, H. W. M. (2007). The dorsal raphe nucleus—from silver stainings to a role in depression. *Brain Res. Rev.* 55, 329–342. doi: 10.1016/j.brainresrev.2007.01.002

Miyazaki, K. W., Miyazaki, K., Tanaka, K. F., Yamanaka, A., Takahashi, A., Tabuchi, S., et al. (2014). Optogenetic activation of dorsal raphe serotonin neurons enhances patience for future rewards. *Curr. Biol.* 24, 2033–2040. doi: 10.1016/j.cub.2014.07.041

Mlinar, B., Montalbano, A., Piszczek, L., Gross, C., and Corradetti, R. (2016). Firing properties of genetically identified dorsal raphe serotonergic neurons in brain slices. *Front. Cell. Neurosci.* 10:195. doi: 10.3389/fncel.2016.00195

Nelson, A. B., Hammack, N., Yang, C. F., Shah, N. M., Seal, R. P., and Kreitzer, A. C. (2014). Striatal cholinergic interneurons drive GABA release

from dopamine terminals. *Neuron* 82, 63–70. doi: 10.1016/j.neuron.2014.01.023

Pignatelli, A., and Belluzzi, O. (2017). Dopaminergic neurones in the main olfactory bulb: an overview from an electrophysiological perspective. *Front. Neuroanat.* 11:7. doi: 10.3389/fnana.2017.00007

Ray, R. S., Corcoran, A. E., Brust, R. D., Kim, J. C., Richerson, G. B., Nattie, E., et al. (2011). Impaired respiratory and body temperature control upon acute serotonergic neuron inhibition. *Science* 333, 637–642. doi: 10.1126/science.1205295

Redgrave, P., Rodriguez, M., Smith, Y., Rodriguez-Oroz, M. C., Lehericy, S., Bergman, H., et al. (2010). Goal-directed and habitual control in the basal ganglia: implications for Parkinson's disease. *Nat. Rev. Neurosci.* 11, 760–772. doi: 10.1038/nrn2915

Schindelin, J., Arganda-Carreras, I., Frise, E., Kaynig, V., Longair, M., Pietzsch, T., et al. (2012). Fiji: an open-source platform for biological-image analysis. *Nat. Methods* 9, 676–682. doi: 10.1038/nmeth.2019

Schultz, W., Dayan, P., and Montague, P. R. (1997). A neural substrate of prediction and reward. *Science* 275, 1593–1599. doi: 10.1126/science.275.5306.1593

Steinberg, E. E., Keiflin, R., Boivin, J. R., Witten, I. B., Deisseroth, K., and Janak, P. H. (2013). A causal link between prediction errors, dopamine neurons and learning. *Nat. Neurosci.* 16, 966–973. doi: 10.1038/nn.3413

Tan, K. R., Yvon, C., Turiault, M., Mirzabekov, J. J., Doehner, J., Labouèbe, G., et al. (2012). GABA neurons of the VTA drive conditioned place aversion. *Neuron* 73, 1173–1183. doi: 10.1016/j.neuron.2012.02.015

Ting, J. T., and Feng, G. (2014). Recombineering strategies for developing next generation BAC transgenic tools for optogenetics and beyond. *Front. Behav. Neurosci.* 8:111. doi: 10.3389/fnbeh.2014.00111

Tye, K. M., Mirzabekov, J. J., Warden, M. R., Ferenczi, E. A., Tsai, H.-C., Finkelstein, J., et al. (2013). Dopamine neurons modulate neural encoding and expression of depression-related behaviour. *Nature* 493, 537–541. doi: 10.1038/nature11740

Van Dort, C. J., Zachs, D. P., Kenny, J. D., Zheng, S., Goldblum, R. R., Gelwan, N. A., et al. (2015). Optogenetic activation of cholinergic neurons in the PPT or LDT induces REM sleep. *Proc. Natl. Acad. Sci. U S A* 112, 584–589. doi: 10.1073/pnas.1423136112

Walther, D. J., Peter, J.-U., Bashammakh, S., Hortnagl, H., Voits, M., Fink, H., et al. (2003). Synthesis of serotonin by a second tryptophan hydroxylase isoform. *Science* 299:76. doi: 10.1126/science.1078197

Wiegert, J. S., Mahn, M., Prigge, M., Printz, Y., and Yizhar, O. (2017). Silencing neurons: tools, applications and experimental constraints. *Neuron* 95, 504–529. doi: 10.1016/j.neuron.2017.06.050

Wise, R. A. (2004). Dopamine, learning and motivation. *Nat. Rev. Neurosci.* 5, 483–494. doi: 10.1038/nrn1406

Xenias, H. S., Ibáñez-Sandoval, O., Koós, T., and Tepper, J. M. (2015). Are striatal tyrosine hydroxylase interneurons dopaminergic? *J. Neurosci.* 35, 6584–6599. doi: 10.1523/jneurosci.0195-15.2015

Yohn, C. N., Gergues, M. M., and Samuels, B. A. (2017). The role of 5-HT receptors in depression. *Mol. Brain* 10:28. doi: 10.1186/s13041-017-0306-y

Zhang, H., Zhao, H., Zeng, C., Van Dort, C., Faingold, C. L., Taylor, N. E., et al. (2018). Optogenetic activation of 5-HT neurons in the dorsal raphe suppresses seizure-induced respiratory arrest and produces anticonvulsant effect in the DBA/1 mouse SUDEP model. *Neurobiol. Dis.* 110, 47–58. doi: 10.1016/j.nbd.2017.11.003

Zhao, S., Ting, J. T., Atallah, H. E., Qiu, L., Tan, J., Gloss, B., et al. (2011). Cell type-specific channelrhodopsin-2 transgenic mice for optogenetic dissection of neural circuitry function. *Nat. Methods* 8, 745–752. doi: 10.1038/nmeth.1668

Conflict of Interest Statement: The authors declare that the research was conducted in the absence of any commercial or financial relationships that could be construed as a potential conflict of interest.

Copyright © 2019 Krol, Lopez-Huerta, Corey, Deisseroth, Ting and Feng. This is an open-access article distributed under the terms of the Creative Commons Attribution License (CC BY). The use, distribution or reproduction in other forums is permitted, provided the original author(s) and the copyright owner(s) are credited and that the original publication in this journal is cited, in accordance with accepted academic practice. No use, distribution or reproduction is permitted which does not comply with these terms.

Check for updates

Original Article

JCBFM

Journal of Cerebral Blood Flow & Metabolism
2019, Vol. 39(5) 808–821
© Author(s) 2017
Article reuse guidelines:
sagepub.com/journals-permissions
DOI: 10.1177/0271678X17733640
journals.sagepub.com/home/jcbfm
SAGE

Recurrent moderate hypoglycemia exacerbates oxidative damage and neuronal death leading to cognitive dysfunction after the hypoglycemic coma

Gabriela Languren, Teresa Montiel, Leticia Ramírez-Lugo, Israela Balderas, Gustavo Sánchez-Chávez, Francisco Sotres-Bayón, Federico Bermúdez-Rattoni and Lourdes Massieu

Abstract

Moderate recurrent hypoglycemia (RH) is frequent in Type 1 diabetes mellitus (TIDM) patients who are under intensive insulin therapy increasing the risk for severe hypoglycemia (SH). The consequences of RH are not well understood and its repercussions on neuronal damage and cognitive function after a subsequent episode of SH have been poorly investigated. In the current study, we have addressed this question and observed that previous RH during seven consecutive days exacerbated oxidative damage and neuronal death induced by a subsequent episode of SH accompanied by a short period of coma, in the parietal cortex, the striatum and mainly in the hippocampus. These changes correlated with a severe decrease in reduced glutathione content (GSH), and a significant spatial and contextual memory deficit. Administration of the antioxidant, N-acetyl-L-cysteine, (NAC) reduced neuronal death and prevented cognitive impairment. These results demonstrate that previous RH enhances brain vulnerability to acute hypoglycemia and suggests that this effect is mediated by the decline in the antioxidant defense and oxidative damage. The present results highlight the importance of an adequate control of moderate hypoglycemic episodes in TIDM.

Keywords

Diabetes, antioxidants, cognitive impairment/decline, glucose, hippocampus, hypoglycemia, risk factors, selective neuronal death

Received 3 March 2017; Revised 17 August 2017; Accepted 1 September 2017

Introduction

Glucose is the major metabolic substrate in brain and its continuous supply from blood is mandatory for its correct functioning. Repeated episodes of moderate hypoglycemia are frequently observed in 70–80% of Type-1 (T1DM) and 40% of Type-2 (T2DM) diabetes mellitus patients due to insulin therapy.[1,2] Recurrent moderate hypoglycemia (RH; $<70->55$ mg/dl blood glucose) increases the risk for severe hypoglycemia (SH; <55 mg/dl), which has been reported in 36% and 7% of TIDM and T2DM patients, respectively, with an incidence of one episode per patient per year.[3–5] Hypoglycemia is alleviated by the hormonal autonomic counter-regulatory response, which stimulates glycogenolysis and glyconeogenesis.[6,7] This response is blunted in T1DM patients, who are unable to respond to the autonomic signs of hypoglycemia (hypoglycemia unawareness).[4,7,8] A single episode of hypoglycemia induces defective glucose counter-regulation, favoring recurrent hypoglycemia (RH) and increasing the patient's vulnerability to SH.[6,9] Conversely, patients

División de Neurociencias, Instituto de Fisiología Celular, Universidad Nacional Autónoma de México (UNAM), Ciudad Universitaria, Ciudad de México, México

Corresponding author:
Lourdes Massieu, Departamento de Neuropatología Molecular, División de Neurociencias, Instituto de Fisiología Celular, Universidad Nacional Autónoma de México (UNAM), Ciudad de México CP 04510, México.
Email: lmassieu@ifc.unam.mx

INFORME DE LABORES 2019

treated for SH are at risk for RH.[10] SH can progress to seizures and the hypoglycemic coma in approximately 25% of the episodes.[11] A prolonged period of hypoglycemic coma induces oxidative stress and neuronal death[12,13] and associates with cognitive dysfunction in rodents and humans.[10,14–16] However, the effect of previous episodes of RH on brain damage induced by SH, is poorly understood.

Moderate hypoglycemia is more common than SH in T1DM patients, particularly in children and adolescents. Although not an immediate threat, a repeated history of RH might cause cognitive dysfunction.[17,18] Studies show that RH in healthy animals induces synaptic alterations, oxidative stress and limited neuronal death in the cerebral cortex[13,19,20] and even improvement of spatial memory.[20–22] In diabetic animals, RH associates with increased cognitive deficit and oxidative damage, suggesting that diabetes exacerbates the damaging effects of hypoglycemia.[13,23–25] Conversely, diabetes is associated with oxidative stress[26,27] and cognitive decline, which might be enhanced by hypoglycemia.[28–31]

The repercussions of RH on brain function after a subsequent episode of SH are not well understood. In the present study, we have addressed this question in healthy animals, precluding the influence of diabetic pathology. Results indicate that animals exposed to RH do not show neuronal death, oxidative damage or cognitive decline despite a partial decrease in the content of reduced glutathione (GSH) and increased lipoperoxidation (LPO). However, RH notably augmented oxidative damage and the number of dead cells in the cortex, the striatum and mainly in the hippocampus of animals exposed to a subsequent short period of hypoglycemic coma. These animals showed a large decrease in GSH content and severe cognitive impairment. Treatment with the antioxidant, N-acetyl-L-cysteine (NAC), significantly reduced neuronal death and prevented cognitive decline. The present results demonstrate that in non-diabetic animals, previous RH can enhance brain vulnerability to SH and suggest that this effect is mediated by a decrease in the antioxidant defense and oxidative damage.

Material and methods

Three-month-old male Wistar rats (280–300 g) obtained from Instituto de Fisiología Celular (IFC), Universidad Nacional Autónoma de México were treated according to The National Institute of Health Guide for the care and use of laboratory animals (NIH publication No.80-23 revised 1996), and experimental protocols were approved by the Committee for the Care and Use of Laboratory Animals (CICUAL) of the IFC (LMT101-16). All efforts were made to minimize the number of animals used. Animals were housed in individual cages under standard dark/light cycle and temperature conditions with food and water at libitum. Experiments are reported in compliance with the ARRIVE guidelines (Animal Research: Reporting in Vivo Experiments). A sample size of six to seven animals per group was used to achieve reliable statistical power and minimize the number of animals used.

Induction of recurrent moderate hypoglycemia

RH was induced (in the home cage) in non-anesthetized non-fasted animals receiving a daily intraperitoneal (i.p.) injection of 6.5 insulin units (IU, Humulin 70/30, Eli Lilly, Indianapolis, USA) between 11 and 12:00 a.m. during seven consecutive days, while control animals were injected with vehicle solution (0.1% acetic acid) (Supplementary Figure 1(a)). Moderate hypoglycemia was defined as blood glucose between 40 and 55 mg/dl, without loss of consciousness or seizures. Blood glucose was measured from the tail vein using a One Touch Ultra meter, every 60 min after insulin injection, and was maintained at 2.2–3.0 mM (40–55 mg/dl) for 2.5–3 h (Supplementary Figure 1(a)). Rats spontaneously recovered euglycemia after food addition. Twenty-four hours after the last hypoglycemic episode, animals were euthanized under pentobarbital overdose anesthesia and brains were prepared for histology (see below). Independent groups were used for behavioral tests (see below).

Induction of hypoglycemic coma (SH)

One week before the induction of hypoglycemia, animals were implanted with epidural electrodes under 2.5–3.0% isofluorane anesthesia for two channel (right and left hemispheres) electroencephalographic recordings (EEG). Meloxicam (1 mg/kg i.p) was used as post-surgery anesthesia. Before SH induction, food was restricted to four pellets overnight. For EEG recording, animals were maintained in acrylic special cages. The experimental animals were randomly distributed among the different experimental groups as follows: (1) SH: animals received an i.p injection of 32 IU (Humulin 70/30, Eli Lilly, Indianapolis, USA) and after 2–3 h of SH (blood glucose levels <1.0 mM), they lost their righting reflex and hypoglycemia was left to progresses to EEG isoelectricity (coma) for 7–10 min. Animals were immediately rescued with an i.p. (300 µl) bolus of 25% glucose in Krebs-Henseleit Buffer followed by a continuous intravenous perfusion at a rate of 1.5 ml/h during 3 h through the tail vein using a perfusion pump (Harvard Apparatus 22, South Natik, MA, USA) (Supplementary Figure 1(b)). (2) RH/SH: animals were treated with moderate

INFORME DE LABORES 2019

RH during seven days and 24 h after the last episode SH was induced and left to progress to 7–10 min coma. Immediately afterwards, rats were rescued with glucose as described above (Supplementary Figure 1(c)). (3) NAC: animals were identically treated to those of the RH/SH group, except that they received one subcutaneous administrations of 100 mg/kg NAC in distilled water (Sigma–Aldrich St. Louis MO, USA) 1 h after glucose reperfusion and one daily injection during the following four days (five total administrations at 2:00 p.m.). Experimental protocols are described in Supplementary Figure 1. Twenty-four hours after all treatments, animals were anesthetized (pentobarbital overdose) and intracardially perfused with 0.9% saline solution followed by 4% paraformaldehyde in 0.1 mol/L phosphate buffer, pH 7.3; brains were extracted and fixed during 24 h in paraformaldehyde and transferred to a 20–30% sucrose gradient (24 and 72 h, respectively) and 25 µm coronal slides were obtained in a cryostat for histological analysis. Independent groups were treated and randomly distributed for behavioral tests; they were euthanized at the indicated times. Animals showing seizures (less than 10%) were discarded. One animal from the NAC group was discarded due to the lack of exploratory activity in the open field test.

Evaluation of neuronal death

Neuronal death ($n = 68$ total animals, distributed as follows: $n = 7$ per group evaluated at 24 h; $n = 6$ per group evaluated at 5 days and $n = 7$ per group evaluated at 16 days after the different treatments) was evaluated using Fluoro Jade B (FJB) for the identification of degenerating neurons, as described.[32] Sections were imaged under a fluorescence microscope (Leica DM1000) using a FITC filter (395–590 nm). The total number of FJB-positive cells in the parietal cortex and the striatum was quantified in 18 coronal sections of 25 µm (3.20 to −4.20 from bregma), while 4 sections were used for the hippocampus. In this case, cells were counted in an area of 200 μm^2 of the different hippocampal subregions (CA1, CA3, dentate gyrus (DG) and hilus) using the Image J program. Data are expressed as the total number of degenerating cells in these four sections. Cell damage was confirmed by Nissl staining at 24 h ($n = 7$ per group) and five days ($n = 4$ per group), and the number of condensed darkly stained cells or pyknotic nuclei were counted in consecutive brain sections to those labeled with FJB. In the case of the NAC experiment, FJB and Nissl-positive cells were counted in three areas of 200 μm^2 of the DG comprising the inferior and superior blades and the crest of the DG. To monitor DNA fragmentation, the TUNEL Roche In Situ Cell Death Detection Kit was used following the manufacturer instructions (Roche Applied Science, USA). Briefly, adjacent sections were blocked with 3% peroxide in methanol for 10 min at room temperature. Slides were incubated in a mixture containing sodium citrate 0.1%/triton 0.1% for 10 min followed by TUNEL reaction mixture (5 µl TdT enzyme, 5 µl Biotin-dUTP, 90 µl TdT buffer) for 90 min at 37°C. Slides were washed and counterstained with Hoechst (0.001% in PBS) for 10 min at room temperature to facilitate the identification of TUNEL-positive cells.

Immunohistochemistry

Twenty-four hours after the treatments ($n = 7$ per group), oxidative protein modification was detected using polyclonal anti-4-2-hydroxy-2-nonenal (4-HNE) (Alpha Diagnostic International, San Antonio, Texas, USA) and monoclonal anti-3-Nitrotyrosine (Cayman Company, Ann Arbor Michigan, USA) antibodies. Coronal 25 µm sections were incubated with anti-4-HNE or anti-3-NT antibodies (1:200 dilution) for 72 h at 4°C and anti-mouse DyLight 594 or anti-rabbit DyLight 488 (Jackson ImmunoResearch Lab. Inc. West Grove, Pennsylvania, USA, 1:250 dilution) secondary antibodies, for 2 h at room temperature. Three sections per animal were examined and representative images were obtained by confocal microscopy (Leica TCS SP5) using a scanning mode for lasser 488 and 546 nm. As a control for antibody specificity, brain sections were incubated with the secondary antibody in the absence of the primary antibody and immunoreactivity was observed.

LPO levels

Twenty-four hours after the treatments ($n = 7$ per experimental group and $n = 10$ control group), brain homogenates from parietal cortex, hippocampus and striatum were obtained to determine malondialdehyde (MDA) levels using the thiobarbituric acid-reactive substances (TBARS) method as described in Haces et al.[33] Briefly brain tissues were homogenized in 0.5 ml of 1.15% KCL/0.4 mM sodium azide and incubated at 37°C for 20 min. Suspensions were centrifuged at 14,000 rpm, mixed with thiobarbituric acid at 0.75% (Merck, Darmstadt Germany) and incubated at 50°C for 20 min. The protein concentration was determined by Bradford's method and data are expressed as nmol MDA/mg of protein.

Reduced GSH determination

Reduced GSH ($n = 3$–7) was determined using the fluorometric o-phthalaldehyde (OPA) method as

INFORME DE LABORES 2019

described by Senft et al.[34] 12 and 24 h after the treatments. Briefly, parietal cortex, hippocampus and striatum were dissected, weighed and homogenized in detection buffer containing 20 mM HCl, 5 mM DTPA and 10 mM ascorbic acid; samples were rapidly centrifuged at 20,000 rpm for 20 min. For GSH determination, 5% trichloroacetic acid, 7.5 mM N-ethylmaleimide (Sigma-Aldrich, Steinheim, Germany) and 100 µl o-phthaldialdehyde (Sigma-Aldrich, Steinheim, Germany) (used as derivatizing agent to react with GSH) were added to 5 µl supernatant. After mixing, samples were incubated at room temperature for 30 min. Fluorescence was read at 365 nm excitation and 430 nm emission. GSH concentrations were calculated and expressed as nmol/mg tissue based on standard curve.

Behavioral tests

Water maze

Forty-eight hours after the treatments, animals were habituated in an isolated testing room for 30 min. Rats ($n = 7$ per group, 28 total animals) were trained (9:00 a.m.) during five days (five trials per day) in a circular pool divided in four quadrants where a platform was hidden 1 cm under the water at constant temperature (21°C) as described in Delint-Ramírez et al.[35] Twenty-four hours after the last day of training (7 days and 15 days after the SH), the memory test was performed. The platform was removed and animals were allowed to swim during 60 s. The latency and number of crossings through the quadrant where the platform was initially placed were recorded with the Ethovision video tracking.

Contextual fear conditioning

At 48 h after the treatments, different series of animals (treated and non-treated with NAC, $n = 6$–9 per group, 33 total animals) were trained for contextual fear conditioning (9:00 a.m.) and they were tested 24 h later. This was carried out in standard operant chambers (Coulbourn Instruments) located inside sound-attenuating boxes (Med Associates) in an isolated testing room. The floor of the chambers consisted of stainless steel bars that delivered scrambled electric footshock. Between experiments, shock grids and floor trays were cleaned with soap and water, and the walls with wet paper towels as described in Sotres-Bayon et al.[36] On day 1, rats habituated during 5 min to the chamber were immediately followed by fear conditioning to the context consisting of five 2 s, 0.8 mA foot shocks. The interval between successive foot shocks was variable with an average of 2 min. The next day (day 2), rats were tested for contextual fear conditioning memory during 10 min. Behavior was recorded with digital video cameras. Freezing was used as a measure of conditioned fear. Freezing was defined as the absence of all movement except for those related to breathing. The amount of time spent freezing to the context was expressed as a percentage of the total time in the chamber.

Open field

Twenty-four hours after contextual fear conditioning memory test (10:00 a.m.), rats were placed at the center of a wooden open arena (90 cm length × 90 cm width × 60 cm height) with a textured floor illuminated by 22 lux of intensity. Grid lines drawn on the floor of the arena (30 × 30 cm) divided it into a peripheral region (within 60 cm of the walls) and a central region (30 × 30 cm) of approximately equal area. Behavior was recorded for 10 min with a digital video camera and analyzed with commercially available video tracking software (ANY-maze, Stoelting). The total distance traveled (cm) was taken as an index of the locomotor activity and the number of entries to the center of open field as an anxiety index.

Statistical analysis

Data are expressed as mean ± SEM (Standard Error of the mean) and analyzed by one-way ANOVA followed by a Fisher's least multiple comparison test, except for neuronal damage comparisons between NAC-treated and non-treated groups, which were compared by Student's t test. Behavioral tests were analyzed by the Kruskal–Wallis non-parametric test for Water Maze and Tukey for fear conditioning.

Results

Changes in blood glucose and EEG recordings

No significant differences were found in mean basal blood glucose concentration (99.66 ± 1.20 mg/dl) among the different animal groups. In animals exposed to RH blood, glucose declined to 40 mg/dl 30 min after insulin administration and remained between 40 and 45 mg/dl during the following 3 h. Glucose was recovered after food addition (Supplementary Figure 2(a)). The daily mean blood glucose concentration reached during the 3-h period of moderate hypoglycemia was 40 mg/dl (Supplementary Figure 2(b)). In animals exposed to SH alone and to RH/SH, glucose concentration rapidly declined after 30 min insulin administration and remained ≤ 20 mg/dl during the next 2.5–3.0 h up to isoelectricity. It partially recovered 1 h after glucose reperfusion and at 24 h it reached control values in

INFORME DE LABORES 2019

all animals groups (Supplementary Figure 2(a)). Basal cerebral activity was recorded for 30 min before insulin administration and no differences were observed between the groups. After 2–3 h, the EEG characteristic changes of hypoglycemia reported in previous studies were observed.[33] When glucose was close to 20 mg/dl, electrical brain activity slowed and was completely absent during the coma period. Normal brain activity was recovered 1 h after glucose reperfusion (Supplementary Figure 2(c)).

Neuronal death induced by the hypoglycemic coma is exacerbated by previous RH

Figures 1 to 2 show the number of degenerating cells at 24 h and 16 days after the induction of coma. No degenerating cells were observed in animals from the control and RH groups in any of the regions studied (Figures 1(a) and (c) and 2(a)). Twenty-four hours after the animals were exposed to the hypoglycemic coma (9.5 ± 0.54 min) alone (SH), degenerating cells were observed in the parietal cortex and the dorsolateral striatum (Figure 1), while in the hippocampus, degenerating cells were observed only in the crest of DG in 50% of these animals (Figure 2(a), (b) and (d)). Animals examined 16 days after the coma (8.0 ± 0.36 min), showed a lower number of FJB-positive cells in the parietal cortex and the striatum (Figure 1(b) and (d)), while in the crest of the DG, FJB-positive cells were no longer visible (Figure 2(c)).

Animals exposed to coma (9.5 ± 0.20 min) and previously treated with RH (RH/SH), exhibited a significant increase in the number of degenerating cells in the parietal cortex and the striatum as compared to those treated with SH alone at 24 h. This increase was also observed when animals were examined 16 days after RH/SH (7.28 ± 0.42 min of coma) (Figure 1(b) and (d)). Representative micrographs showing FJB-positive

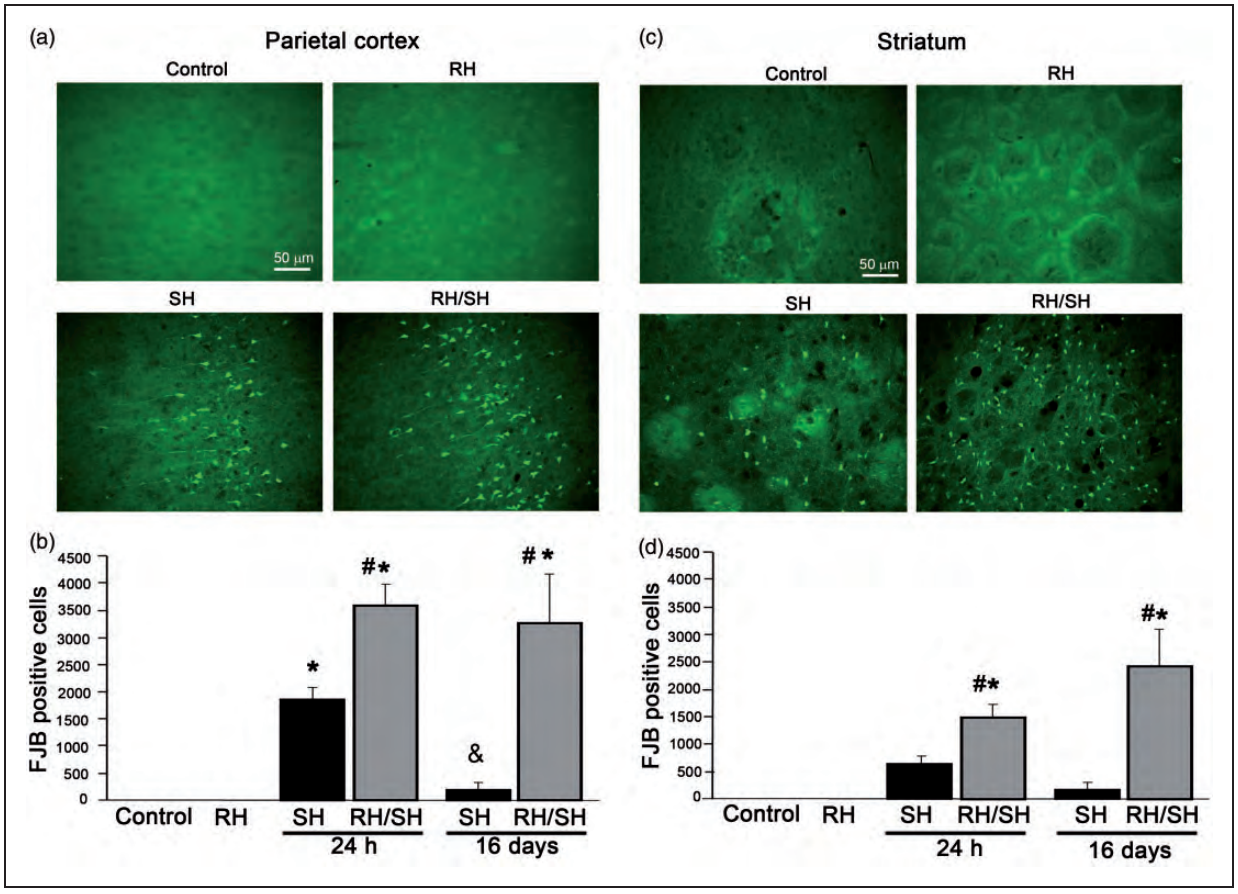

Figure 1. Neuronal death induced by the hypoglycemic coma in the parietal cortex and the striatum is exacerbated by antecedent RH. Neuronal death was evaluated 24 h and 16 days after the treatments and the number of FJB-positive cells was counted. Representative micrographs showing no FJB-positive in control and RH-treated animals and degenerating cells in the parietal cortex (a) and the striatum (c) of animals exposed to SH and RH/SH. (b–d) Cell death was exacerbated in animals exposed to RH/SH at 24 h and 16 days after the treatments. Data are expressed as mean ± SEM from seven animals per group. $^{*}p < 0.0001$ relative to control and RH, $^{\#}p < 0.0001$ relative to SH.

INFORME DE LABORES 2019

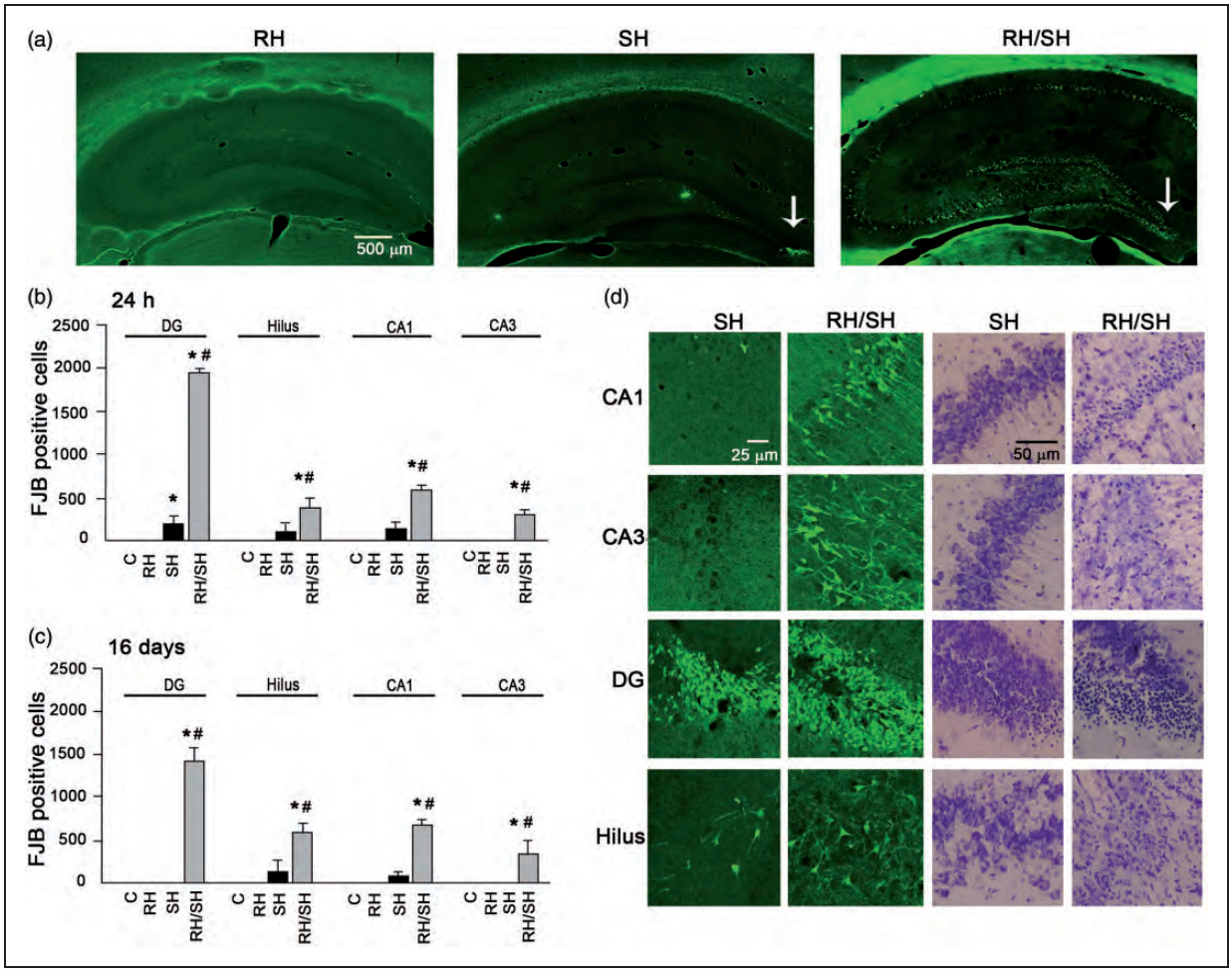

Figure 2. Neuronal death induced by the hypoglycemic coma in the hippocampus is exacerbated by antecedent RH. Neuronal death was evaluated 24 h or 16 days after the different treatments in brain sections stained with Nissl or FJB. (a) Representative micrographs showing degenerating cells only in the crest of the DG of animals exposed to SH and extensive neuronal death in animals from the RH/SH group. (b–c) Quantitative data showing exacerbated neuronal death in animals exposed to RH/SH at 24 h or 16 days. (d) Representative micrographs showing FJB-positive and pyknotic cells in the different hippocampal subregions of rats exposed to the different treatments. Data are expressed as mean ± SEM from seven animals per group. $^{*}p < 0.0001$ relative to control and RH, $^{\#}p < 0.0001$ relative to SH.

cells of animals exposed to the different treatments are shown in Figure 1(a) and (c). Similarly, the hippocampus showed a dramatic elevation in the number of degenerating neurons, which were present not only in the crest of the DG but also in the superior and inferior blades of the DG, the hilus, CA1 and CA3 (Figure 2(a)). This increase was statistically different relative to the SH group at 24 h and 16 days in all hippocampal regions (Figure 2(b) and (c)). These results were corroborated by the quantification of pyknotic cells in Nissl-stained sections (Supplementary Figure 3). Representative micrographs showing degenerating neurons in animals exposed to the different treatments are shown in Figure 2(a) and (d). The presence of pyknotic cells correlated with FJB labeling in the parietal cortex, the striatum (not shown) and the hippocampus (Figure 2(d)). Similarly, TUNEL-positive nuclei, indicative of DNA fragmentation were found in the parietal cortex, the striatum (Supplementary Figure 4) and the hippocampus (Figure 3(a)) of animals of the RH/SH group, while in animals exposed to coma alone, TUNEL-positive nuclei were observed only in the DG (Figure 3(b)). In control and RH groups, no TUNEL-positive nuclei were observed in any region (Supplementary Figure 4). Altogether, these observations indicate that RH increases the vulnerability to neuronal death in the parietal cortex, the striatum and mainly in the hippocampus of animals exposed to a subsequent short period of coma.

INFORME DE LABORES 2019

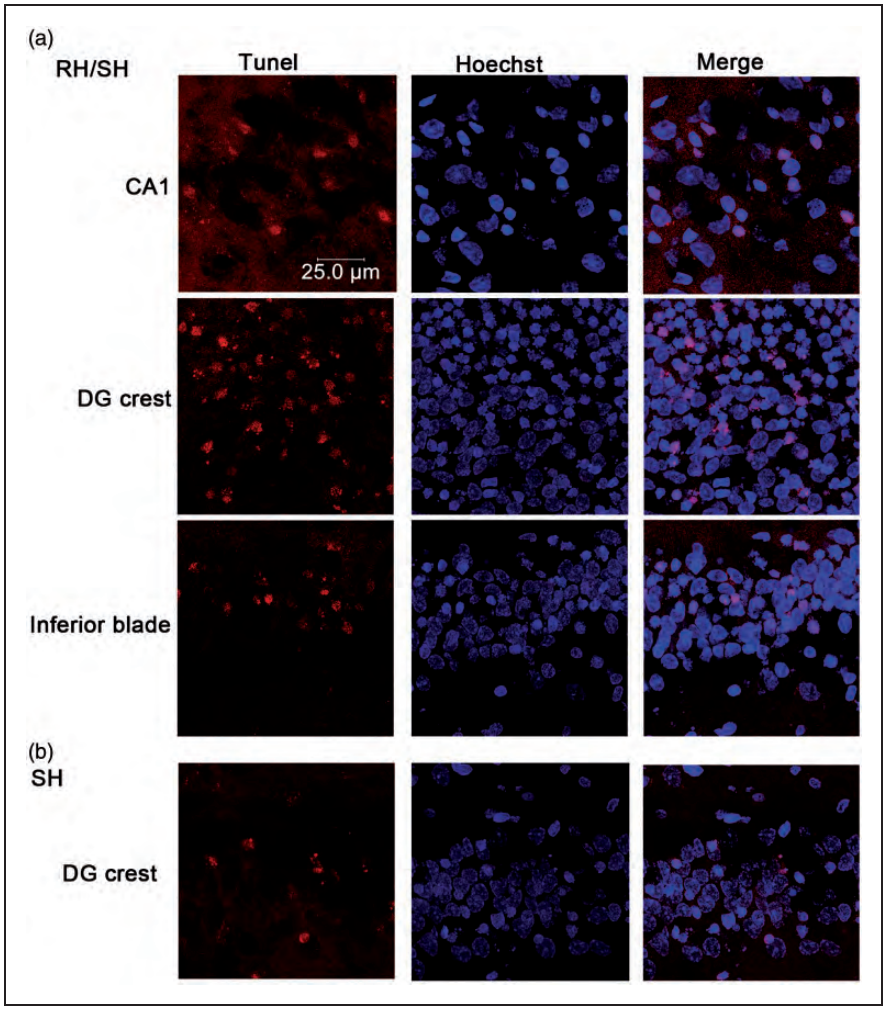

Figure 3. DNA fragmentation induced by the hypoglycemic coma is exacerbated by RH. The presence of DNA fragmentation was examined by the TUNEL assay and Hoechst was used as counterstain. (a) Representative micrographs showing TUNEL-positive cells in CA1 and the DG of rats treated with RH/SH. (b) In rats exposed to SH alone TUNEL-positive were detected only in the crest of the DG.

RH aggravates cognitive impairment induced by the hypoglycemic coma

According to the above-described results, RH notably enhanced neuronal death induced by the hypoglycemic coma in the hippocampus. Therefore, we aimed to test whether animals exposed to RH/SH showed memory impairment using two hippocampal-dependent memory tests. Figure 4(a) shows that during the five days of training in the water maze, the latency to locate the platform decreased similarly in all experimental groups indicating no difference in learning acquisition. At seven days after the coma, the SH and the RH/SH groups exhibited a significant decrease in number of crossings relative to controls, while animals exposed to RH alone showed no significant decrease (Figure 4(b)). At 15 days after the coma, only animals from the RH/SH showed a significant decrease in the number of crossings suggesting a long-term change in spatial memory (Figure 4(c)).

Figure 4(d) shows the performance of animals on the contextual fear conditioning. No statistical differences were found during contextual fear acquisition (day 1) since a similar percent freezing was observed in all groups. In the retrieval test (day 2), only the RH/SH group showed a significant decrease in the percent freezing relative to the control and the RH groups (Figure 4(d) right panel). No changes in locomotor activity and anxiety were found in any of the groups (Figure 4(e) and (f)). These data are in agreement with the spatial memory test and suggest that RH preceding the hypoglycemic coma exacerbates cognitive decline, which correlates with the presence of degenerating neurons in the hippocampus.

INFORME DE LABORES 2019

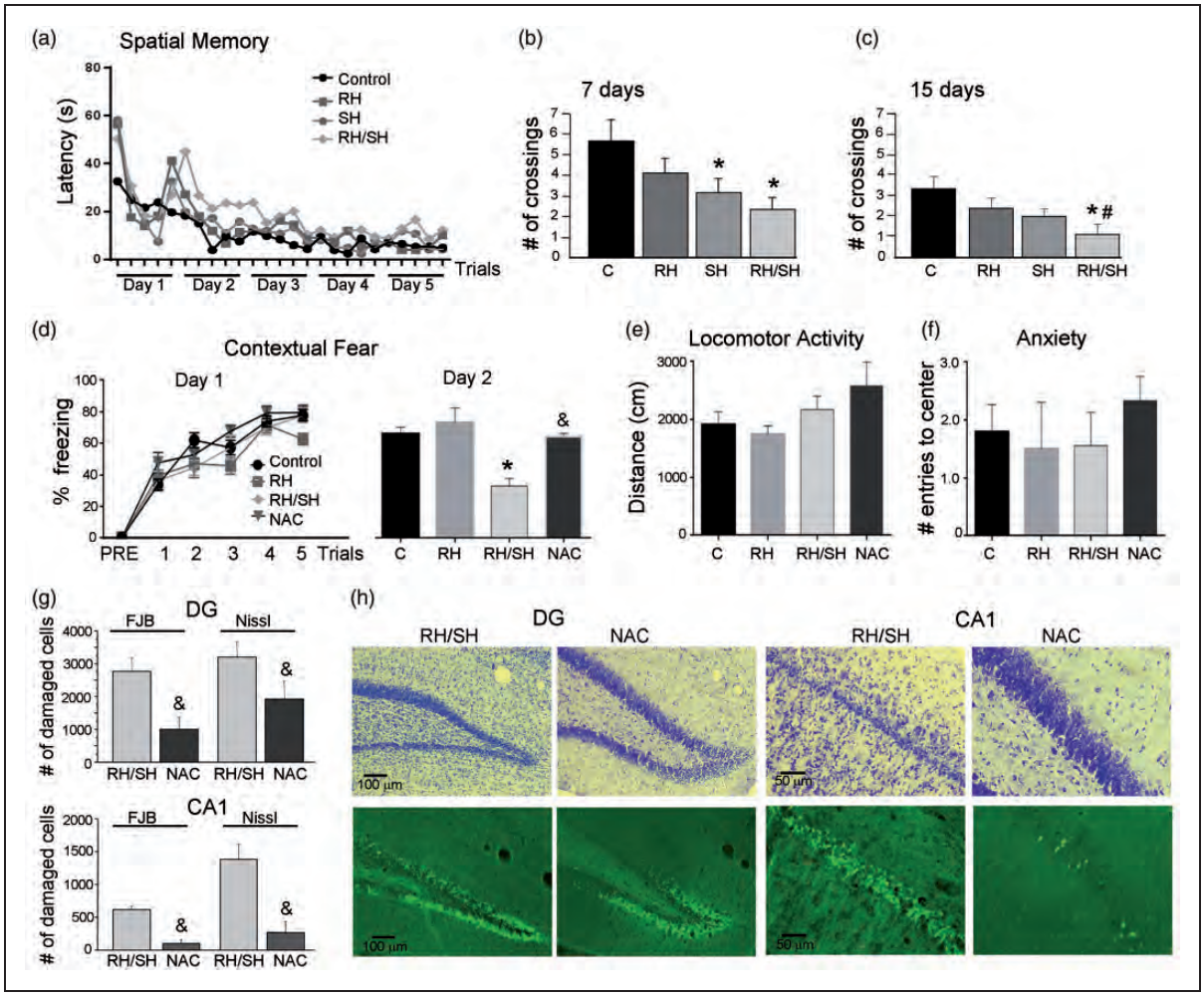

Figure 4. Previous RH aggravates cognitive impairment induced by the hypoglycemic coma. Spatial memory test (Water maze) was performed 7 and 15 days after the treatments. (a) Learning curve of animals exposed to the different treatments. (b) At day 7, animals of the SH and RH/SH groups showed a decrease in the number of crossings. (c) At 15 days, only animals of the RH/SH group showed a significant decrease in the number of crossings. Data are expressed as mean ± SEM from seven animals per group. $^{*}p < 0.01$ relative to control $^{\#}p < 0.05$ relative to SH. Contextual fear conditioning test was performed 48 h after the treatments. (d) No statistical differences between the groups were observed in the acquisition phase (day 1). The RH/SH group showed a significant decrease, while the NAC group showed no change in the percent freezing relative to control and RH groups during retrieval (day 2). Data are expressed as mean ± SEM from six to nine animals per group. $^{*}p < 0.0001$ relative to control and RH $^{\&}p < 0.05$ relative RH/SH. (e) No significant changes were observed between groups in (e) locomotor activity and (f) anxiety tests. (g) Number of damaged cells (FJB-positive group and pyknotic Nissl stained) in the dentate gyrus (DG) and CA1 of animals of the RS/SH and the NAC groups, 24 h after the fear-conditioning test. Data are expressed as mean ± SEM from four to six animals per group. $^{\&}p < 0.002$ relative to RH/SH). (h) Representative images showing the protective effect induced by NAC administration against cell damage (FJB-positive cell and pyknotic cells in Nissl stained section) induced in the DG and CA1 after exposure to RH/SH.

RH preceding the hypoglycemic coma induces oxidative damage

Oxidative stress has been highly implicated in neuronal death induced by the hypoglycemic coma.[12,32,33,37] Therefore, we aimed to evaluate the presence of the LPO product 4-HNE and 3-NT residues in proteins by immunohistochemistry. 4-HNE positive cells were observed in the parietal cortex, the striatum and all hippocampal subregions of animals of the RH/SH group, while in the control, RH and SH groups, 4-HNE inmmunoreactivity was not observed (Figure 5). As shown in the Figure 6, 3-NT-positive cells were observed mainly in the parietal cortex, DG and hilus of animals exposed to RH/SH. In contrast, no 3-NT immunoreactivity was observed in control, and RH groups, and only a few cells were observed in the parietal cortex of some animals of the SH group (Figure 6).

INFORME DE LABORES 2019

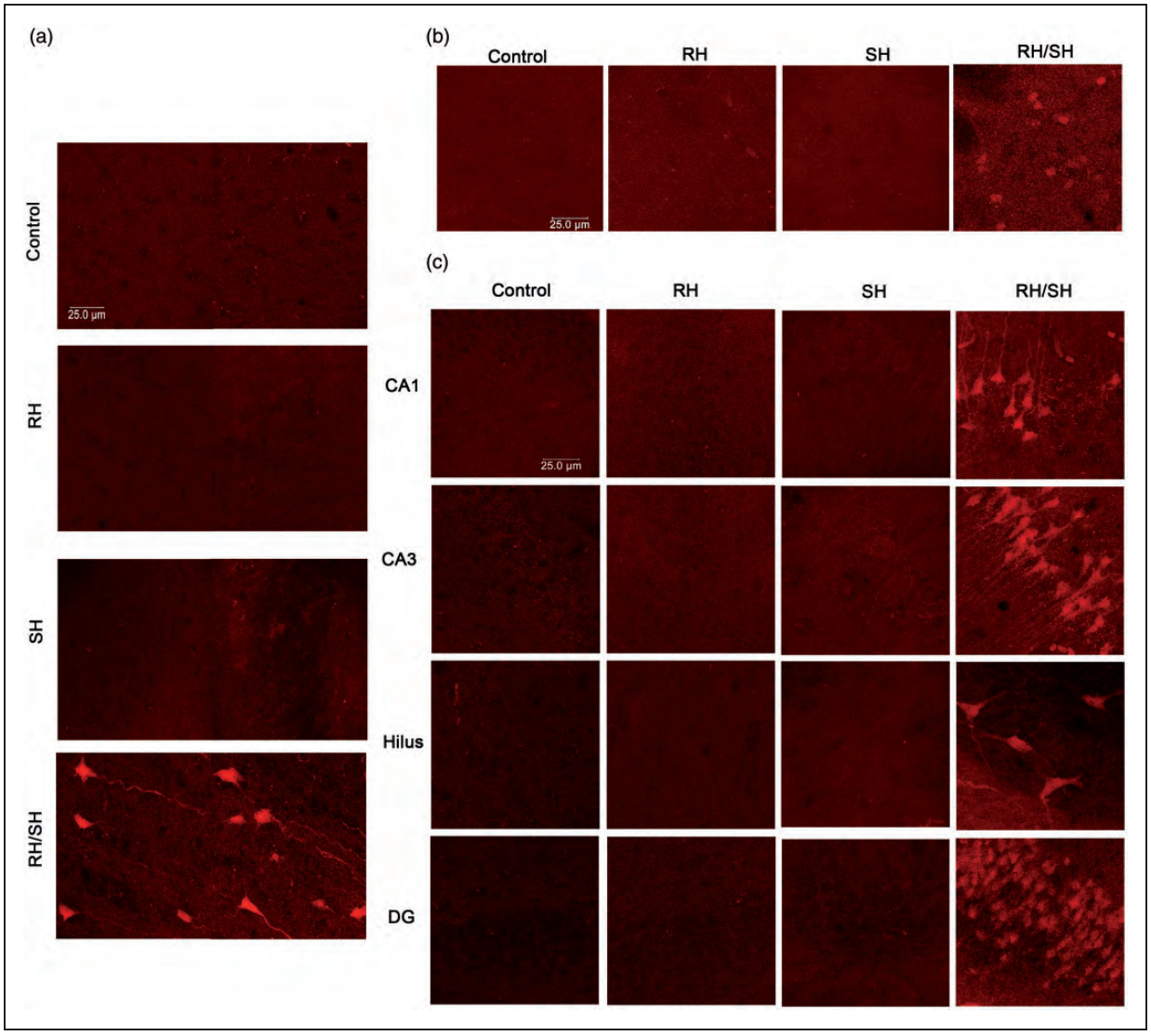

Figure 5. Immunoreactivity to 4-HNE in the brain of animals exposed to RH/SH. Representative fluorescent images showing the presence of 4-HNE-positive cells in (a) parietal cortex, (b) striatum and (c) hippocampus of animals treated with RH/SH. No 4-HNE-positive cells were detected in control, RH and SH groups.

Results suggest that RH facilitates oxidative damage to proteins in animals exposed to a subsequent short period of coma, which correlates with the presence of cell death.

Then we aimed to investigate whether a decrease in reduced GSH, the major antioxidant defense in brain, was involved in oxidative damage observed in animals treated with RH/SH. As observed in Figure 7, RH induced a partial (from 23 to 30%) but significant decrease in GSH, while animals of the RH/SH group showed a further decrease (from 49 to 58%) in GSH in all brain regions, the largest change was observed in the hippocampus (58%). The changes in GSH content were observed at 12 h after the end of treatments and were maintained at 24 h in all regions. These results suggest that a reduction in GSH contributes to enhanced oxidative damage in animals from the RH/SH group. Supporting this hypothesis, we observed that treatment with the antioxidant NAC, completely prevented cognitive decline in the contextual fear conditioning test (Figure 4(d)) and reduced hippocampal neuronal damage (Figure 4(g) and (h)). The number of pyknotic neurons and neurons positive to FJB was significantly reduced in the DG, CA1 (Figure 4(g) and (h)), CA3 and hilus (not shown). In the RH group, a significant increase in LPO was observed in all brain regions studied (Supplementary Figure 5); however, as in the case of GSH, increased LPO did not correlate with oxidative damage in these animals.

INFORME DE LABORES 2019

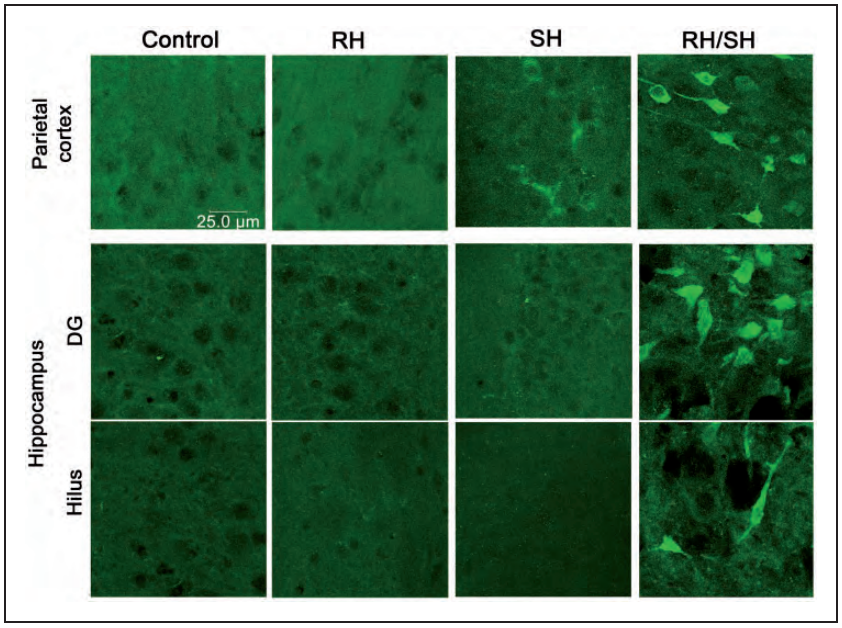

Figure 6. Immunoreactivity to 3-NT in the brain of animals exposed to RH/SH. Representative fluorescent images showing the presence of 3-NT-positive cells in the parietal cortex and the hippocampus of animals treated with RH/SH. No 3-NT-positive cells were detected in control and RH groups and only a few cells were observed in the parietal cortex of animals of the SH groups.

Discussion

TIDM is a long-term disease frequently diagnosed during infancy and a 3–4% annual increase rate in children and adolescents has been estimated in Europe.[3,18] TIDM patients under strict insulin treatment can show one to two episodes per week of moderate hypoglycemia, which increases the risk for SH (one episode per year) due to a blunted counter-regulatory hormonal response and hypoglycemia unawareness.[1–5] Mild to moderate hypoglycemia has been described as blood glucose < 70 mg/dl and > 55 mg/dl without loss of consciousness, while SH is considered when blood glucose falls below 50 mg/dl, is accompanied by seizures, altered consciousness or coma and requires external assistance for treatment with carbohydrates or glucagon.[3,37,38] Hypoglycemic episodes can last for several hours (from 1 to 5 h), as those reported during nocturnal hypoglycemia.[39] TIDM patients are exposed to mild RH for a life-time, and although at moderate levels, hypoglycemia has not been considered a potential threat, its consequences on brain function either alone or when it is followed by an episode of SH, are unknown so far. In the present study, we have addressed this question in a short-term period and as such, the frequency of moderate hypoglycemia was increased to seven consecutive episodes. To mimic T1DM patient's condition, moderate hypoglycemia periods were induced by decreasing blood glucose to 55–40 mg/dl during 2.5–3 h, without loss of consciousness or seizures and spontaneous recovery of euglycemia after food addition. SH was induced by the fall in blood glucose to 20 mg/dl or below accompanied by 7–10 min of EEG isoelectricity (coma state).

The most important finding of the present study is that previous RH exacerbates oxidative damage and neuronal death, leading to memory impairment in animals subsequently exposed to a short period of coma. In previous studies, we have demonstrated that short 5–10 min coma episodes induce neuronal death mainly in the parietal cortex but not in the hippocampus except for the crest of the DG.[32,33] In the present study, we demonstrate that animals exposed to a brief period of coma, which were previously treated with RH, show enhanced neuronal death in the parietal cortex and the striatum, but notably in the hippocampus, where degenerating and pyknotic cells are present in all hippocampal subregions. Degenerating neurons were observed even 16 days after the coma and correlated with deficient spatial memory. Cognitive decline was confirmed by defective performance in the contextual fear-conditioning retrieval test and interestingly we observed that in both spatial and contextual memory tests, mainly the consolidation of memory was impaired. When animals were exposed to coma alone (SH), only a transitory memory decline was present, consistent with the lack of degenerating neurons in the hippocampus, except for a small population of cells in the crest of the DG. Previous studies have implicated oxidative stress in neuronal death after

INFORME DE LABORES 2019

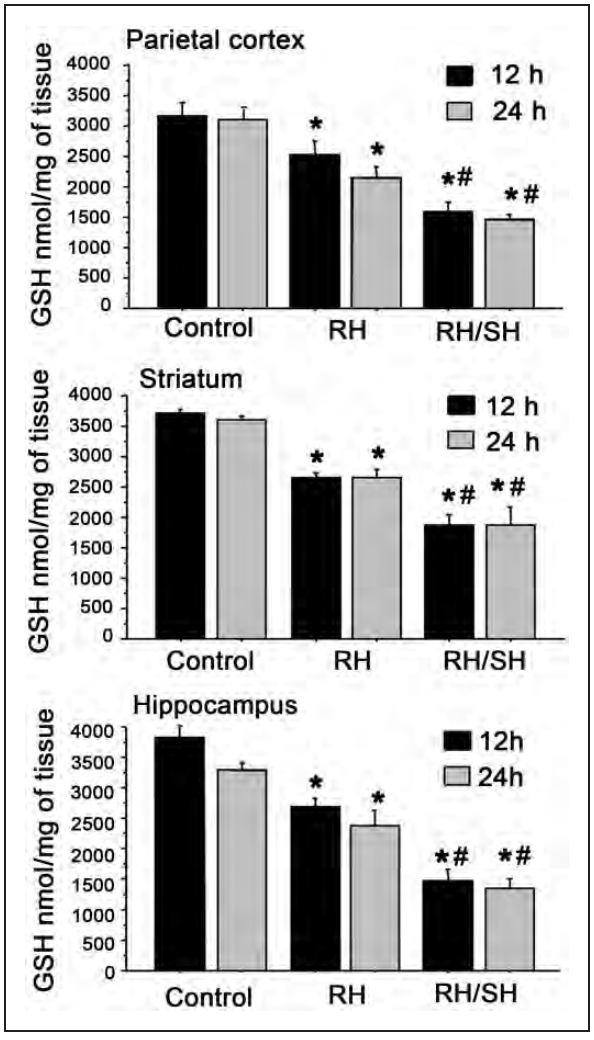

Figure 7. Changes in GSH content after RH and RH/SH. Animals were exposed to the different treatments and 12 and 24 h later reduced GSH levels were measured in different brain regions. Animals exposed to RH show a significant moderate decrease in reduced GSH in all brain regions, which is further decreased in animals from the RH/SH group ($n = 3$–7 animals per group). Data are expressed in means ± SEM. $^{*}p < 0.01$ relative to control; $^{\#}p < 0.01$ relative to RH.

a prolonged period of hypoglycemic coma.[12,13,40,41] In agreement, we observed immunoreactive cells to 4-HNE and 3-NT in brain regions showing dead cells in animals treated with RH/SH. 4-HNE and 3-NT react with proteins altering their function.[42,43] Thus, neuronal death correlates with oxidative alteration of proteins, which might be caused by a deficient antioxidant defense, based on the significant reduction in GSH content in all brain regions. Supporting this conclusion, it was observed that animals treated with NAC showed a significant reduction in the number of degenerating neurons and pyknotic cells in the hippocampus and no memory deficit in the contextual fear-conditioning test. GSH is the main antioxidant defense in the nervous system and its decrease is associated with oxidative stress and cell damage.[44,45] In addition, NAC has been demonstrated to have antioxidant actions and to restore GSH levels in rodents' brain after systemic administration.[46] Furthermore, it was recently reported that treatment with NAC prevents neuronal damage induced by a prolonged period of hypoglycemic coma.[41] Besides a deficient antioxidant defense, decreased glucose brain metabolism might also contribute to exacerbated hypoglycemic neuronal death induced by antecedent RH. A previous study has shown that three consecutive episodes of antecedent hypoglycemia result in decreased glucose oxidation in the brain of animals tested under acute hypoglycemia.[47]

The observed enhancement of hypoglycemic neuronal damage induced by antecedent RH, is in agreement with previous studies showing that exposure to RH in diabetic rats exacerbates brain injury induced by a short period of acute ischemia. This effect correlates with mitochondrial superoxide production implicating oxidative stress.[48] In contrast, a previous study showed that previous RH during three days elicited a preconditioning effect, reducing the number of degenerating neurons and preventing cognitive impairment induced by acute hypoglycemia in non-diabetic animals.[49] However, in that study, the presence of seizures possibly highly contributed to neuronal death, masking the effect of RH on hypoglycemic damage. In addition, a lower number of moderate hypoglycemic periods was used.

Rats treated with RH alone showed a partial decrease in GSH, which correlated with increased LPO but no oxidative damage, cell death or cognitive decline. The absence of neuronal death in this group of animals might result from the lack of glucose infusion since they were allowed to recover euglycemia after food addition. It is well known that glucose reperfusion plays a major role in neuronal death, mainly when blood glucose exceeds physiological levels resulting in hyperglycemia.[40,50,51] Previous data have reported a decrease in GSH content even after a single episode of moderate hypoglycemia,[52] and some studies have shown that RH in healthy animals produces an increase in LPO and 4-HNE immunoreactivity, without leading to significant neuronal death or cognitive decline.[13,19,25] Furthermore, studies have reported that RH in healthy animals can even improve cognitive performance due to synaptic changes and brain metabolic adaptations.[20,21,22,53]

In summary, the present results demonstrate that previous RH can have an adverse effect on subsequent SH in healthy animals, and suggests that this effect is mediated by the decline in the antioxidant defense and oxidative damage. It is expected that the consequences of RH treatment used in the present conditions could

INFORME DE LABORES 2019

be aggravated under diabetic conditions. Recent studies have demonstrated that the effects of RH on oxidative stress and the antioxidant defense are exacerbated in diabetic animals, enhancing cognitive decline.[13,24,25,54] Furthermore, depletion of Nrf2, a major transcription factor regulating the antioxidant defense, exacerbates RH-induced oxidative damage to proteins and cognitive decline in control and diabetic animals.[25]

The present observations demonstrate that RH renders the brain and particularly the hippocampus, more vulnerable to oxidative damage and neuronal death induced by a subsequent episode of hypoglycemic coma, ultimately leading to cognitive dysfunction. These observations highlight the relevance of the history of hypoglycemic episodes in TIDM patients and help us to estimate the consequences of RH on a subsequent episode of SH.

Funding

The author(s) disclosed receipt of the following financial support for the research, authorship, and/or publication of this article: This study was supported by CB239607 CONACYT grant to LM, CB250870 and 176639 CONACYT grants to FB-R and FS-B. GL was supported by CONACYT fellowship 363968.

Acknowledgements

The authors thank Dr. Ruth Rincón-Heredia for her valuable help in confocal imaging, Gianfranco Chávez Marchetta for his help in Water Maze assays and Francisco Pérez Eugenio for computer facilities. GL performed this study in partial fulfillment of the requirements of the Programa de Doctorado en Psicología at the Universidad Nacional Autónoma de México (UNAM).

Declaration of conflicting interests

The author(s) declared no potential conflicts of interest with respect to the research, authorship, and/or publication of this article.

Authors' contributions

LM and GL conceived the study, analyzed all data and wrote the manuscript. GL performed all experiments; TM performed all hypoglycemic treatments, contributed to data analysis and provided technical assistance; LR-L and FS-B participated in the contextual fear-conditioning experiments, data analysis and results interpretation; IB and FB-R participated in water maze experiments, data analysis and results interpretations; GS-C provided technical assistance and participated in manuscript revision. All authors participated in discussions and critically reviewed the manuscript.

Supplementary material

Supplementary material for this paper can be found at the journal website: http://journals.sagepub.com/home/jcb

References

1. Donelly LA, Morris AD, Frier BM, et al. Frequency and predictors of hypoglycaemia in Type 1 and insulin-treated type 2 diabetes: a population-based study. *Diab Med* 2005; 22: 749–755.
2. Heller S, Colagiuri S, Vaaler S, et al. Hypoglycaemia with insulin aspart: a doubleblind randomised, crossover trial in subjects with Type 1 diabetes. *Diab Med* 2004; 21: 769–775.
3. Blasetti A, Di Giulio C, Tocco AM, et al. Variables associated with severe hypoglycemia in children and adolescents with Type 1 diabetes: a population-based study. *Pediatr Diab* 2011; 12: 4–10.
4. Frier BM. Hypoglycaemia in diabetes mellitus: epidemiology and clinical implications. *Nat Rev Endocrinol* 2014; 10: 711–722.
5. Languren G, Montiel T, Julio-Amilpas A, et al. Neuronal damage and cognitive impairment associated with hypoglycemia: an integrated view. *Neurochem Int* 2013; 63: 331–343.
6. Cryer PE. Mechanisms of sympathoadrenal failure and hypoglycemia in diabetes. *J Clin Invest* 2006; 116: 1470–1473.
7. Tesfaye N and Seaquist ER. Neuroendocrine responses to hypoglycemia. *Ann Acad Sci* 2010; 1212: 12–28.
8. Beall C, Michael L, McCrimmon A, et al. The physiology and pathophysiology of the neural control of the counterregulatory response. *Am J Physiol Regul Integr Comp Physiol* 2012; 202: 215–223.
9. Jensen VF, Bogh IV and Lykesfeldt J. Effect of insulin–induced hypoglycemia on the central nervous system: evidence from experimental studies. *J Neuroendocrinol* 2014; 26: 123–150.
10. Lin YY, Hsu CW, Sheu W, et al. Risk factors for recurrent hypoglycemia induced in hospitalized diabetic patients admitted for severe hypoglycemia. *Yonsei Med J* 2010; 51: 367–374.
11. Strachan MWJ. Frequency, causes and risk factors for hypoglycaemia in type 1 diabetes. In: Frier BM, Heller SR and McCrimmon R (eds) *Hypoglycaemia in clinical diabetes*, 3rd ed. eBook. Chichester: John Wiley & Sons Ltd, 2014, pp.63–95.
12. Suh SW, Hamby AM, Gum ET, et al. Sequential release of nitric oxide, zinc and superoxide in hypoglycemic neuronal death. *J Cereb Blood Flow Metab* 2008; 28: 1697–1706.
13. Won SJ, Yoo BH, Kauppinen TM, et al. Recurrent/moderate hypoglycemia induces hippocampal dendritic injury, microglial activation, and cognitive impairment in diabetic rats. *J Neuroinflammation* 2012; 9: 1–45.
14. Suh S, Aoyama K, Matsumori Y, et al. Pyruvate administered after severe hypoglycemia reduces neuronal death and cognitive impairment. *Diabetes* 2005; 54: 1452–1458.
15. Fujioka M, Okuchi K, Hiramatsu K, et al. Specific changes in human brain after hypoglycemic injury. *Stroke* 1997; 28: 584–587.
16. Xu C, Yogaratman J, Lua R, et al. Persistent, severe hypoglycemia–induced organic brain syndrome with neurological sequelae: a case report. *Gen Hosp Psichiatr* 2011; 33: 411–412.

INFORME DE LABORES 2019

17. Perantie DC, Lim A, Wu J, et al. Effects of prior hypoglycemia and hyperglycemia on cognition in children with type 1 diabetes mellitus. *Pediatr Diab* 2008; 9: 87–95.
18. Franchini S, Comegna L, Prezioso G, et al. Hypoglycemia in children with type 1 diabetes: unawareness is a concrete risk. *Curr Med Res Opin* 2016; 32: 1487–1491.
19. Yamada KA, Rensing N, Izumi Y, et al. Repetitive hypoglycemia in young rats impairs hippocampal long-term potentiation. *Pediatr Res* 2004; 55: 372–379.
20. McNay EC, Williamson A, McCrimmon R, et al. Cognitive and neural hippocampal effects of long-term moderate recurrent hypoglycemia. *Diabetes* 2006; 55: 1088–1095.
21. McNay EC and Sherwin RS. Effect of recurrent hypoglycemia on spatial cognition and cognitive metabolism in normal and diabetic rats. *Diabetes* 2004; 53: 418–425.
22. Osborne DM, ÓLeary KE, Fitzgerald DP, et al. Context-dependent memory following recurrent hypoglycaemia in non-diabetic rats is mediated via glucocorticoid signaling in the dorsal hippocampus. *Diabetologia* 2016; 60: 182–191.
23. Bree AJ, Puente EC, Daphna-Iken D, et al. Diabetes increases brain damage caused by severe hypoglycemia. *Am J Physiol Endocrinol Metab* 2009; 297: 194–201.
24. Cardoso S, Santos RX, Correia SC, et al. Insulin-induced recurrent hypoglycemia exacerbates diabetic brain mitochondrial dysfunction and oxidative imbalance. *Neurobiol Dis* 2012; 49: 1–12.
25. McNeilly AD, Gallagher JR, Dinkova-Kostova AT, et al. Nrf2-mediated neuroprotection against recurrent hypoglycemia is insufficient to prevent cognitive impairment in a rodent model of Type 1 diabetes. *Diabetes* 2016; 65: 3151–3160.
26. McGrowder DA, Anderson-Jackson L and Crawford T. Biochemical evaluation of oxidative stress. In: Escher AP and Li A (eds) *Type 1 diabetes*. Rijeka, Croatia: InTech Open Accsess Publisher, 2013; pp.223–248. http:dx.doi.org/10.5772/45927.
27. Kumar P, Rao N, Bhusan Pal B, et al. Hyperglycemia-induced oxidative stress induces apoptosis by inhibiting PI3-kinase/Akt and ERK 1/2 MAPK mediated signaling pathway causing downregulation of 8-oxoG-DNA glycosylase levels in glial cells. *Int J Biochem Cell Biol* 2014; 53: 302–319.
28. Gold A, Macleod K, Deary I, et al. Hypoglycemia-induced cognitive dysfunction in diabetes mellitus: effect of hypoglycemia unawareness. *Physiol Behav* 1995; 58: 501–511.
29. Kirchhoff BA, Lugar HM, Smith SE, et al. Hypoglycemia-induced changes in regional brain volume and memory function. *Diab Med* 2013; 30: 151–156.
30. Moheet A, Mangia S and Seaquist ER. Impact of diabetes on cognitive function and brain structure. *Ann N Y Acad Sci* 2015; 1353: 60–71.
31. Kirchhoff BA, Jundt DK, Doty T, et al. A longitudinal investigation of cognitive function in children and adolescents with type 1 diabetes mellitus. *Pediatr Diab* 2016; 12414: 1–7.
32. Julio Amilpas A, Montiel T, Soto-Tinoco E, et al. Protection of hypoglycemia-induced neuronal death by ß-hydroxybutyrate involves the preservation of energy levels and decreased production of reactive oxygen species. *J Cereb Blood Flow Metab* 2015; 35: 851–860.
33. Haces ML, Montiel T and Massieu L. Selective vulnerability of brain regions to oxidative stress in a non-coma model of insulin-induced hypoglycemia. *Neurosci* 2010; 165: 28–38.
34. Senft AP, Dalton TP and Shertzer HG. Determining glutathione and glutathione disulfide using the fluorescence probe o-Phthalaldehyde. *Anal Biocehem* 2000; 280: 80–86.
35. Delint-Ramírez I, Salcedo-Tello P and Bermúdez-Rattoni F. Spatial memory formation induced recruitment of NMDA receptor and PSD-95 to synaptic lipid rafts. *J Neurochem* 2008; 106: 1658–1668.
36. Sotres-Bayón F, Sierra-Mercado D, Pardilla-Delgado, et al. Gating of fear in prelimbic cortex by hippocampal and amygdala inputs. *Neuron* 2012; 76: 804–812.
37. Ryan C, Gurtunca N and Becker D. Hypoglycemia: a complication of diabetes therapy in children. *Pediatr Clin N Am* 2005; 52: 1705–1733.
38. Festa A, Heller S, Seaquist E, et al. Association between mild and severe hypoglycemia in people with type 2 diabetes initiating insulin. *J Diab Complicat* 2017; 31: 1047–1052.
39. Yale J. Nocturnal hypoglycemia in patients with insulin-treated diabetes. *Diab Res Clin Pract* 2004; 65S: S41–S46.
40. Suh SW, Gum ET, Hamby AM, et al. Hypoglycemic neuronal death is triggered by glucose reperfusion and activation of neuronal NADPH oxidase. *J Clin Invest* 2007; 117: 910–918.
41. Kho AR, Choi BY, Kim JH, et al. Prevention of hypoglycemia-induced hippocampal neuronal death by N-acetil-L- Cysteine (NAC). *Amino Acids* 2016; 49: 367–378.
42. Ullery C and Marnett LJ. Protein modification by oxidized phospholipids and hydrolytically released lipid electrophiles: investigating cellular response. *Biochim Biophys Acta* 2012; 1818: 2424–2442.
43. Radi R. Protein tyrosine nitration: biochemical mechanisms and structural basis of functional effects. *Acc Chem Res* 2013; 46: 550–559.
44. Dringen R, Gutterer JM and Hirrlinger J. Glutathione metabolism in brain. Metabolic interaction between astrocytes and neurons in the defense against reactive oxygen species. *Eur J Biochem* 2000; 16: 4912–4916.
45. Baxter PS and Hardingham PE. Adaptative regulation of the brain's antioxidant defenses by neurons and astrocytes. *Free Radic Biol Med* 2016; 100: 147–152.
46. Reyes R, Cittolin-Santos G, Kim J, et al. Neuronal glutathione content and antioxidant capacity can be normalized *In Situ* by N-acetyl Cysteine concentrations attained in human cerebrospinal fluid. *Neurotherapeutics* 2016; 13: 217–225.
47. Jiang L, Herzog RI, Mason GF, et al. Recurrent antecedent hypoglycemia alters neuronal oxidative metabolism in vivo. *Diabetes* 2009; 58: 1266–1274.

INFORME DE LABORES 2019

48. Dave KR, Tamariz J, Desai KM, et al. Recurrent hypoglycemia exacerbates cerebral ischemic damage in streptozotocin-induced diabetic rats. *Stroke* 2011; 42: 1404–1411.
49. Puente EC, Silverstein J, Bree AJ, et al. Recurrent moderate hypoglycemia ameliorates brain damage and cognitive dysfunction induced by severe hypoglycemia. *Diabetes* 2010; 59: 1055–1062.
50. Ennis K, Dotterman H, Stein A, et al. Hyperglycemia accentuates and ketonemia attenuates hypoglycemia-induced neuronal injury in the developing rat brain. *Pediatr Res* 2015; 77: 84–90.
51. Rao R, Ennis K, Mitchell P, et al. Recurrent moderate hypoglycemia suppresses brain-derived neurotrophic factor expression in the prefrontal cortex and impairs sensoriomotor gating in the post-hypoglycemia period in young rats. *Dev Neurosci* 2016; 38: 74–82.
52. Rao A, Quach H, Smith E, et al. Changes in ascorbate, glutathione and α-tocopherol concentrations in the brain regions during normal development and moderate hypolgycemia in rats. *Neurosci Lett* 2014; 568: 67–71.
53. Canada S, Weaver S, Sharpe S, et al. Brain glycogen supercompensation in the mouse after recovery from insulin-induced hypoglycemia. *J Neurosci Res* 2011; 4: 585–591.
54. Choi BY, Kim JH, Kim HJ, et al. Pyruvate administration reduces recurrent/moderate hypoglycemia-induced cortical neuron death in diabetic rats. *PLoS One* 2013; 8: 1–15.

NEUROSCIENCE
RESEARCH ARTICLE

Esther Lara-González et al. / Neuroscience 410 (2019) 76–96

Comparison of Actions between L-DOPA and Different Dopamine Agonists in Striatal DA-Depleted Microcircuits In Vitro: Pre-Clinical Insights

Esther Lara-González,[ab] Mariana Duhne,[a] Fátima Ávila-Cascajares,[a] Silvia Cruz[a] and José Bargas[a]*

[a]*División Neurociencias, Instituto de Fisiología Celular, Universidad Nacional Autónoma de México, México City 04510, Mexico*

[b]*Facultad de Ciencias Químicas, Benemérita Universidad Autónoma de Puebla, Puebla City 72000, Mexico*

Abstract—Parkinson's disease (PD) is a neurodegenerative illness presenting motor and non-motor symptoms due to the loss of dopaminergic terminals in basal ganglia, most importantly, the striatum. L-DOPA relieves many motor signs. Unfortunately, in the long term, L-DOPA use causes motor disabilities by itself and does not act in comorbid conditions such as depression. These deficiencies have led to search for drugs such as dopamine (DA) receptor agonists (DA-agonists) that allow the reduction of L-DOPA dose. Previously, we have identified the attributes of non-stimulated (resting) and cortical stimulated (active) striatal microcircuits following the activity of dozens of neurons simultaneously using calcium imaging in brain slices. We also have characterized the changes that take place in DA-depleted microcircuits in vitro. In control conditions, there is *low* spontaneous activity. After cortical stimulation (CtxS) sequences and alternation of neuronal ensembles activity occur, including reverberations. In contrast, DA-deprived circuits exhibit *high* spontaneous activity at rest, and a highly recurrent ensemble curtails alternation. Interestingly, CtxS briefly relieves these Parkinsonian signs in DA-depleted tissue. Here we compare the actions of some DA-agonists used in PD therapeutics on the pathological dynamics of DA-depleted microcircuits at rest and with CtxS; taking L-DOPA as reference. D_2-class agonists better reduce the excessive spontaneous activity of DA-depleted microcircuits. All DA-agonists tend to maintain ensemble alternation seen in control circuits after CtxS. However, quantitative analyses suggest differences in their actions: in general, DA-agonists only approximate L-DOPA actions. Nonetheless no treatment, including L-DOPA, completely restores microcircuit dynamics to control conditions. **© 2019 IBRO. Published by Elsevier Ltd. All rights reserved.**

Key words: Parkinson's Disease, Dopaminergic agonists, 6-OHDA, Calcium imaging, L-DOPA, Microcircuit analysis.

INTRODUCTION

Parkinson's disease (PD) is a neurodegenerative disorder characterized by motor deficits such as tremor, postural instability, rigidity and bradykinesia (Lees et al., 2009; Obeso et al., 2017). Motor signs correlate with the loss of 50–70% of the dopaminergic terminals in the striatum (Burke and O'Malley, 2013). Terminals loss causes alterations on both the direct and indirect pathways of the basal ganglia (Kravitz et al., 2010; Gerfen and Surmeier, 2011; Calabresi et al., 2014; Parker et al., 2018). Even though L-DOPA, as dopamine (DA) replacement therapy, has been the gold standard for PD treatment (Carlsson et al., 1957; Foley, 2000; Mercuri and Bernardi, 2005; Lees et al., 2015; De Deurwaerdère et al., 2017) in the long-term its usage generates motor secondary effects such as dyskinesia (L-DOPA induced dyskinesia), wearing-off and on–off phenomena (Ahlskog and Muenter, 2001; Aquino and Fox, 2015; Sharma et al., 2015; Picconi et al., 2017). In addition, L-DOPA does not improve non-motor conditions of the disease such as depression and cognitive deficits (Millan, 2010). Therefore, there has been a search for adjuvant therapies, including dopaminergic receptor agonists (DA-agonists) whose use has been associated with lower L-DOPA dosage and a lower incidence of motor complications (Sprenger and Poewe, 2013; Jimenez-Shahed, 2016). There are two main classes of DA-agonists: the less selective $D_{1,2}$ receptors agonists such as rotigotine (Jenner and Katzenschlager, 2016; Chen et al., 2017) and the more selective D_2-class receptor agonists such as pramipexole (Mizuno et al., 2014; Shen et al., 2017).

The neurotoxic-based animal models of Parkinsonism have been used for many years, since they mimic many of the pathological and behavioral features of PD in humans, which make them convenient for the development of new therapies (Dunnet and Lelos, 2010; Morissette and Di Paolo, 2018). Recently, calcium imaging in 6-OHDA injured rodents allowed us to compare network activity of dopamine

*Corresponding author.
E-mail address: jbargas@ifc.unam.mx (José Bargas).

Abbreviations: Ctr, control; CtxS, Cortical Stimulation; DA, dopamine; FDR, False Discovery Rate; CDF, Cumulative distribution function; PD, Parkinson's Disease; L-DOPA, levodopa.

https://doi.org/10.1016/j.neuroscience.2019.04.058
0306-4522/© 2019 IBRO. Published by Elsevier Ltd. All rights reserved.

depleted (DA-depleted) and control microcircuits (Pérez-Ortega et al., 2016; Aparicio-Juárez et al., 2019) with single cell resolution, opening the possibility of in vitro drug testing in brain slice preparations of histological scale to observe changes in microcircuit dynamics. The present study is an initial attempt to do that, using reproducible circuitry properties, easy to observe.

In control non-stimulated resting microcircuits, there is little spontaneous neuronal activity. But after cortical stimulation (CtxS), control microcircuits activity is enhanced showing transient neuronal groups firing together. These neuronal assemblies can alternate with other groups forming sequences or closed cycles (Hebb, 1949; Edelman, 1993; Carillo-Reid et al., 2009; Buzsaki, 2010; Pérez-Ortega et al., 2016). In contrast, non-stimulated DA-depleted microcircuits exhibit enhanced spontaneous activity with respect to the controls and become particularly engaged into a highly recurrent network state with increased synchronization (Liang et al., 2008; Jáidar et al., 2010, 2019; Lemaire et al., 2012; Pérez-Ortega et al., 2016). This state may have a surplus activity of D_2-receptor expressing striatal projection neurons although D_1-receptor expressing striatal projection neurons activity remains important (Parker et al., 2018; Jáidar et al., 2019). The highly recurrent state is dissolved by the action of D_1-agonists, but the enhancement of spontaneous activity is not reversed (Jáidar et al., 2010), in contrast to L-DOPA, which restores spontaneous activity to resting-like conditions (Lemaire et al., 2012; Plata et al., 2013). Interestingly, CtxS in DA-depleted striatal microcircuits, though briefly, also relieves the network from the excessive pathological activity. Addition of L-DOPA to the stimulated microcircuit prolongs this restoration (Aparicio-Juárez et al., 2019).

D_2-class agonist have been used as mono-therapy in the initial stages of PD (Baker et al., 2009) and co-applied with L-DOPA in more advanced phases of the disease (Brooks, 2000; Linazasoro and Spanish Dopamine Agonists Study Group, 2004; Stocchi, 2009; Millan, 2010). D_2-agonists restore the balance between direct and indirect pathways (Ballion et al., 2009), decreasing pathological activity. Here we want to correlate these findings in vitro using the activity of neuronal networks of histological scale. We compare the actions of less selective $D_{1,2}$- agonists with those of more selective D_2-agonists (Hu and Wang, 1988; Wang and Zhou, 2017) under two different conditions pertaining the pathophysiological signatures of parkinsonism (Pérez-Ortega et al., 2016): First, how agonists decrease excessive spontaneous neuronal activity in non-stimulated DA-depleted striatum. Secondly, how they act during network dynamics restoration induced by CtxS (Aparicio-Juárez et al., 2019). The results of this work show that both classes of DA-agonists exhibit subtle differences in spontaneous and stimulated network activity when compared with different metrics during circuit dynamics, a finding that may have clinical relevance. In vitro preparations appear to be potential bioassays to test combinations of adjuvant therapies and new drugs, in addition to cellular, behavioral and clinical tests. Their cost is low and the actions of several drugs can be tested and correlated with other assays.

EXPERIMENTAL PROCEDURES

Research subjects

Protocols were designed and performed as approved by the Institutional Committee for Laboratory Animals Care and Use of the Instituto de Fisiología Celular (IFC), UNAM (NOM-062-Z00–1999; laboratory protocols JBD-59-15) in accordance with the international norms for the ethical use of experimental animals established in the National Institutes of Health Guide for Care and Use of Laboratory Animals Eighth Edition (NIH, 2010). Male and female C57BL/6 mice breaded in the animal facilities of the IFC were used in all experiments. Mice were housed in a temperature controlled, pathogen-free room, on a 12:12 light: dark cycle and allowed food and water ad libitum.

Drugs

6-OHDA (6-Hydroxydopamine hydrochloride, Sigma-Aldrich H4381-100MG) was dissolved in saline solution and injected intracranially (0.1 mg/ml) to obtain hemi-parkinsonian mice. Apomorphine (R-(−)-apomorphine hydrochloride hemihydrate Sigma-Aldrich A4393-250MG) was diluted in saline vehicle and administered via subcutaneous injection to measure rotational behavior in 6-OHDA injected animals. Calcium Orange 8.2 μM (Molecular Probes®, Life technologies, Mexico City, MX) was diluted in dimethyl sulfoxide (DMSO) solution, 0.1% DMSO, 0.67% Pluronic Acid (Pluronic TM F-127, Life Technologies Corporation, Oregon USA, P3000MP) and dissolved in artificial cerebral spinal fluid (ACSF) to be applied to brain slices at 36 °C for 40 min for calcium imaging. NMDA (N-Methyl-D-aspartic acid, Sigma-Aldrich M3262), L-DOPA (3,4-Dihydroxy-L-phenylalanine, Sigma-Aldrich D9628), apomorphine (R-(−)-apomorphine hydrochloride hemihydrate, Sigma-Aldrich A4393), quinelorane (quinelorane hydrochloride, Tocris Bioscience. CAS97548–97-5), pramipexole (pramipexole dihydrochloride, Sigma-Aldrich A1237), ropinirole (ropinirole dihydrochloride, Sigma-Aldrich R2530) and rotigotine (rotigotine hydrochloride, Sigma-Aldrich R9281) were dissolved in ACSF and applied to the bath saline during calcium imaging. Saturating concentrations were employed in all cases reported.

6-OHDA model

The hemi-parkinsonian mouse obtained by 6-OHDA unilateral injections is the most common Parkinsonian rodent model used in research (Ungerstedt and Arbuthnott, 1970). For that purpose 125 mice 25–30 days old were anesthetized intraperitoneally with ketamine (85 mg/kg)-xylacine (15 mg/kg) for stereotaxic surgery. 0.8 μL of 6-OHDA (0.1 mg/ml) were injected intracranially at a 0.2 μL/min rate in −2.6 mm AP, −1.5 mm LM y − 4.7 mm DV from Bregma, targeting the edge of SNc and MFB. Immediately after surgery animals were placed on a heating pad until fully awaken. After 15–30 days recovery period (Postnatal day 45–60), DA-depletion was measured by rotational behavior test, during this period mice received chocolate pellets ad libitum and subcutaneous 100 μL glucose 2% in

saline solution daily injections were administered if more than 20% weight loss was detected. 80% of the injected mice survived (100 mice) until rotational evaluation. For turning behavior evaluation, apomorphine was injected subcutaneously (0.5 mg/kg in saline vehicle with 0.02% ascorbate). Ipsilateral and contralateral rotations to the lesion site were counted with the program RotaCount 2.0 (Omni-Tech, Sioux Falls SD) for at least 50 min. The ratio of contralateral vs ipsilateral rotations was used to identify unilateral DA-depleted mice. Whenever mice presented more contralateral rotations than ipsilateral rotations (ratio ≥ 2) and total contralateral rotations were at least 50 (1 per minute) mice were considered as successfully DA-depleted. Lesion efficacy was 65% as measured by this test (for rotation data see Fig. 1E). This test has previously been reported as effective in detecting about 80% dopamine depletion (Heuer et al., 2012). The lesioned hemisphere used for in vitro experiments is referred to as dopamine depleted (DA-depleted) in the present paper. Not every DA-depleted mouse resulted in experiments reported here since slices with less than 80% cell survival were discarded; this was quantified based on videos with 20 mM KCl application at the end of each experiment. In total, slices from 50 mice were used for calcium imaging experiments.

Immunohistochemistry

Tyrosine Hydroxylase (TH) immunohistochemistry staining was performed as previously reported (Aparicio-Juárez et al., 2019) to confirm DA depletion in some 6-OHDA lesioned mice (Fig.1A-D). Briefly, 8 days after behavioral evaluation, lesioned mice were anesthetized and perfused with phosphate buffer solution 0.1 M (PBS) (NaH_2PO_4 15 mM, Na_2HPO_4 80 mM, NaCl 50 mM, pH 7.4) and 4% paraformaldehyde fixative (PFA) in PBS 0.1 M, pH 8). After brain extraction, 50 µm coronal slices were obtained in a vibratome (PELCO easiSlicer Ted Pella, Redding, CA) and stored in PBS. Slices were blocked with 1% bovine serum albumin (BSA) in PBS and 0.1 M- Tritón 3% for 40 min at room temperature and washed three times in PBS 0.1 M. Primary antibody (Rabbit, anti-Tyrosine Hydroxylase, Chemicon International, 1:500 in PBS 0.1 M- Tritón 3%) was incubated at room temperature for 12 h and washed three times with PBS 0.1 M. Slices were incubated with secondary antibody (Cy3-conjugated Affini Pure Donkey anti-Rabbit, Jackson Immuno Research, Inc. 711–165-152 1:250 in PBS 0.1 M- Tritón 3%) at room temperature for 2 h and washed three times with PBS 0.1 M. Finally, slices were cover slipped with DAPI (Vecta Shield, Vector Laboratories, Inc. H-1200) and images were obtained by confocal microscopy (Zeiss LSM-710, objective: C-Apochromat 10X N.A. 0.45, laser 543 nm). DA fibers in the striatum were quantified as fluorescence intensity compared to the intact side using ImageJ®, while DA somata were manually counted from confocal micrographies. In both cases DA depletion was confirmed to be at least 80%, as illustrated in Fig. 1C-D, across 17 slices taken from different animals. Stereoscopic images were obtained on a Nikon SMZ1500 (HR objective, Apo 1x WD 54).

Calcium imaging

Both controls and DA-depleted mice were anesthetized intraperitoneally with ketamine-xylacine (85 mg/kg-15 mg/kg) and perfused intracardially with chilled sucrose solution (234 mM sucrose, 28 mM $NaHCO_3$, 7 mM dextrose, 4.54 mM pyruvate, 0.28 mM ascorbic acid, 2.5 mM KCl, 7 mM $MgCl_2$, 1.44 mM NaH_2PO_4, 0.4 mM $CaCl_2$, 4 °C). For DA-depleted mice, there was a 14 days delay between rotational behavioral tests and calcium imaging experiments. Once brains were extracted, 300 µm thick para-horizontal slices with a 30° angle were taken (Fig. 1F). in a vibratome (PELCO easiSlicer Ted Pella, Redding, CA) and kept in ACSF (126 mM NaCl, 15 mM dextrose, 26 mM $NaHCO_3$, 0.2 mM thiourea, 0.2 mM ascorbic acid, 2.5 mM KCl, 1.3 mM $MgCl_2$, 1.2 mM NaH_2PO_4 and 2.0 mM $CaCl_2$; pH = 7.4; 300 ± 5 mOsm/L) continually perfused with 95% O_2 and 5% CO_2. Slices from control (Ctr) and lesioned (DA-depleted) animals were used. Since long-term data acquisition was required, a low photobleaching fluorophore (Thomas et al., 2000), Calcium Orange, was chosen. Slices were incubated in a Calcium Orange solution (Calcium Orange 8.2 µM, 0.1% DMSO, 0.67% Pluronic Acid in ACSF) at 36 °C for 40 min and later located in a perfusion chamber with constant ACSF flow under a 20X immersion objective (Olympus XLUMPLFLN Objective, 1.00 NA, 2.0 mm WD). Observation field was 750 × 750 µm. Fluorophore stimulation was carried out with a Lambda LS Illuminator (Sutter Instruments, Petaluma, CA, USA) and a 570/30 nm light filter. Im-Patch© an open source software designed in the LabView environment (National Instruments, Mexico City, Mexico; available at http://Impatch.ifc.unam.mx) was used for fluorescence recordings controlling a CoolSnap K4 camera (Photometrics, Tucson, AZ, USA). Videos were 720–2160 frames long and acquisition rate was 6 frames/ s. To cover long periods, 7–10 videos were taken per experiment, making up to 90 min per experiment.

In order to confirm calcium fluorescence reliability as activity reporter simultaneous calcium and electrophysiological recordings were obtained using whole cell current-clamp configuration. Patch pipettes (3–6 MΩ) were filled with a solution that contains in mM: 115 KH_2PO_4, 2 $MgCl_2$, 10 HEPES, 0.5 EGTA,10 NaCl, 0.2 ATP, 0.2 GTP and 0.03 Calcium Orange salt, the pH was 7.24. As shown in Fig. 1G, the positive derivative $d(\Delta F/F)/dt$ of fluorescence transients coincide in time and duration with cell activity.

Data acquisition

Control striatum slices were compared in two main conditions: spontaneous activity and stimulation-evoked activity. Two stimuli were compared, the previously used pharmacological stimulation consisting in the application of 2 µM NMDA (Carrillo-Reid et al., 2008) and CtxS (Aparicio-Juárez et al., 2019) consisting in 10 pulses, at 40 Hz, 1.1–1.3 mA through a bipolar concentric electrode 50 µm at the tip (FHC, #CBCFE75, Bowdoin, ME, USA) inserted in primary motor cortex (M1) layer V as shown in Fig. 1F. Recordings were obtained in the adjacent dorsal, mostly dorsolateral, striatum in every case. DA-depleted striatum slices were also compared in two conditions: activity altered solely by dopaminergic agonists application (10 µM L-

INFORME DE LABORES 2019

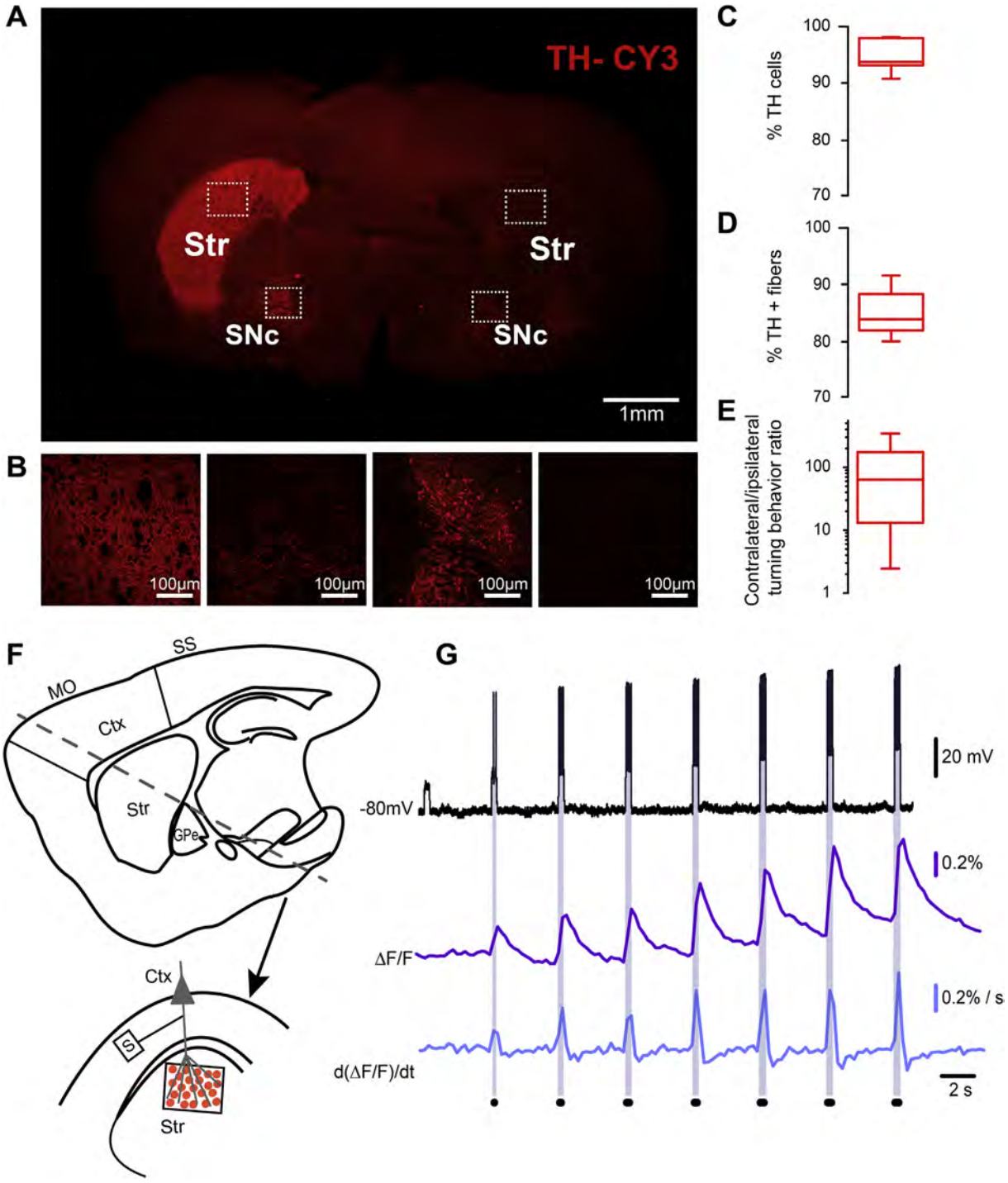

Fig. 1. (A) Stereoscopic fluorescence microscopy showing decreased TH-CY3 on the lesioned hemisphere (right) compared to the intact hemisphere (left) both on striatum (Str) and Substantia nigra compacta (SNc). (B) Confocal microscopy of chosen areas of the Str and SNc from both hemispheres. (C) Percentage reduction of TH+ cells somata in the SNc as compared to the non-lesioned side (n = 17 mice). (D) Percentage reduction of TH-immunoreactive (TH+) fibers (n = 17 mice; fluorescence intensity compared to the non-lesioned side). (E) Box plot showing unbalance in turning behavior evaluated in a sample of experimental animals (n = 65 mice; apomorphine 0.5 mg/Kg). Note variability. (F) Diagram of a sagittal mouse brain slice showing (dotted line) the orientation of a para-horizontal (30°) brain slice (top). Diagram of stimulation and recording sites: mostly motor cortex and dorsolateral striatum, respectively (bottom). (G) Simultaneous electrophysiological (top signal) and calcium imaging recordings (middle) are shown. An intracellular current step of increasing strength was applied to evoke increasing numbers of action potentials and corresponding increases in calcium entry seen as changes in the fluorescence signal (ΔF/F). The positive phase of the time derivative of the calcium transient, d(ΔF/F)/dt, reports the duration of electrophysiological activity (bottom). These durations are denoted with dots in raster plots (bottom).

DOPA, 20 μM apomorphine, 10 μM rotigotine, 10 μM pramipexole, 10 μM ropinirole, 10 μM quinelorane) and activity evoked by cortical stimulation (CtxS) in the presence of one DA-agonist. Spontaneous activity of DA-depleted tissue was always recorded before the addition of any drug to the superfusion system.

Data analysis

Videos were processed with ImPatch©, as previoulsy reported (Aparicio-Juárez et al., 2019). Briefly, cell activity was extracted and transformed into activity matrices were 1 denotes an active frame and 0 an inactive frame for each cell. Whole experiments can be contained in these matrices and expressed as raster plots, where each dot stands for a cell firing in that frame and each row represents the activity of a cell along time (Fig. 1G). The activity of all cells per frame was added to build coactivity histograms. Significant coactivity peaks were determined using several variants of Montecarlo simulations with 10,000 iterations each (see Pérez-Ortega et al., 2016). The significant coactivity peaks were built from the frames in which the threshold was overcome, 12 to 18 frames time bins were used. Coactivity peaks were compared based on a similarity index calculated as the cosine of the angle between vectors obtained with the dot product of each pair of column vectors (Carrillo-Reid et al., 2008), and were associated using hierarchical cluster analysis into groups of neurons that fire together in a time bin, thus defining neuronal ensembles as neurons that transiently fire together and can alternate their activity forming sequences (Carillo-Reid et al., 2009; Buzsaki, 2010; Pérez-Ortega et al., 2016). Ensemble sequences comprise network dynamics (Buzsaki, 2010) which was compared under different conditions: non-stimulated control (Ctr), cortical stimulated controls (Ctr + CtxS or Ctr + NMDA), non-stimulated DA-depleted microcircuits (DA-depleted) and cortical stimulated DA-depleted microcircuits: DA-depleted + CtxS.

Activity of neurons forming ensembles defined by similarity (see above) are colored differently in raster plots and are symbolized as colored circles in temporal network sequences, allowing to see circuit activity as the transitions between distinct network states. In control conditions these sequences may exhibit closed cycles or reverberations as previously reported (Pérez-Ortega et al., 2016). A reverberation occurs when the transitions between network states generate a closed loop, meaning that every state appeared at least once and the initial state is equal to the last state. To assess significance of coactivity peaks/min, the number of frames in which the coactivity histogram value was greater than the threshold determined by Montecarlo simulations was divided by the total length (min) of the experiment. Numbers of coactivity peaks/min were compared with Wilcoxon matched-paired signed rank tests (Wilcoxon T tests).

Amount of activity per experiment was quantified by cumulative activity plots, which were built by adding activity along time. To consider samples of experiments in the same condition, a linear fit was approximated to cumulative activity plots. Slopes of these fits from samples of neurons were then represented as Tukey box plots. This method was used to compare cell activity in both spontaneous and stimulated conditions. Cumulative activity was compared with Kruskal-Wallis ANOVA corrected for multiple comparisons using the Benjamini-Hochberg procedure (Benjamini et al., 2006) with a false-discovery rate (FDR) of 0.05. To compare individual cells activity trough different sections of a single experiment, activity of each cell was defined as the total number of active frames over the total number of frames. This value was used to compare cellular activity between different microcircuit conditions (see above), with or without a dopamine agonist (+ L-DOPA, + apomorphine, + rotigotine, + pramipexole, + ropinirole, + quinelorane). Cumulative distribution functions (CDFs) were performed for each condition using all neurons of a given sample. CDFs were compared with Kolmogorov–Smirnov tests corrected for multiple comparisons using the Benjamini-Hochberg procedure with a 0.05 FDR.

The DA-depleted microcircuit is characterized by enhanced spontaneous activity with a highly recurrent ensemble (Jáidar et al., 2010; Pérez-Ortega et al., 2016). To quantify its appearance in DA-depleted conditions and in the presence of CtxS and DA-agonists (+ L-DOPA, + rotigotine, + pramipexole, + ropinirole), we calculated a recurrence index for every state with respect to the other states as previously reported. Recurrence is the consecutive repetition of a network state instead of alternation of activity with another state. It is calculated as the total sum of such events whose minimum value is 1 for one state appearance. The recurrence index is the recurrence of a single state divided by the sum of the recurrence of all the other states (Aparicio-Juárez et al., 2019). Network states recurrence was compared using the O'Brien Homogeneity of variance test. Another characteristic of DA-depleted microcircuits is the almost complete absence of closed cycles (recurrence impedes alternation and closed cycles). To measure this, we quantified the number of transitions required to accomplish a closed loop between network states. If a closed loop was not observed during the experiment, the value “infinity” was assigned. The distribution of the number of transitions required to close a loop was presented in pie plots and their underlying distributions were compared with Kolmogorov–Smirnov tests. To assess the transitions required to close a loop, sequences that never closed were excluded and the number of transitions before closure were compared using Kruskal-Wallis tests. All multiple comparisons were corrected using a Benjamini-Hochberg procedure with a 0.05 FDR.

Statistics

The determination of a significance threshold for coactivity peaks has been described previously (see Pérez-Ortega et al., 2016) using custom programs in MATLAB (The Math Works, Inc. Natick, MA). Some statistical tests were run in Graph Prism (GraphPad Software, Inc. La Jolla, CA) for the following purposes: Mann–Whitney tests to compare between samples, Wilcoxon's T test to compare conditions in the same sample, Kruskal-Wallis ANOVA test to compare cumulative activity and transitions to reach closed-loops, and Kolmogorov–Smirnov test to compare distributions of data sets. All multiple comparisons were corrected using a

Benjamini-Hochberg procedure with a 0.05 FDR and recurrence index among different pharmacological conditions were compared using O'Brian Homogeneity of variance test.

RESULTS

DA-depleted microcircuits differ from control striatal microcircuits

Microcircuit activity can be accurately recorded by calcium entry during neuronal firing (see Experimental Procedures and Pérez-Ortega et al., 2016), the positive time derivative of a calcium transient corresponds in time and magnitude with action potentials firing (Fig. 1G). Microcircuit activity can be illustrated in the form of raster plots where rows in the y-axis represent the activity of each neuron in the microcircuit along time, and each dot the activity of a cell in one frame (Fig. 1G). Every raster plot in this work corresponds to a single brain slice taken from a single animal, there are no different experiments coming from the same slice or animal (Videos using calcium orange can be seen in Aparicio-Juárez et al., 2019 and in Video A of the present work).

As previously reported (Carrillo-Reid et al., 2008; Jáidar et al., 2010; Pérez-Ortega et al., 2016), the non-stimulated

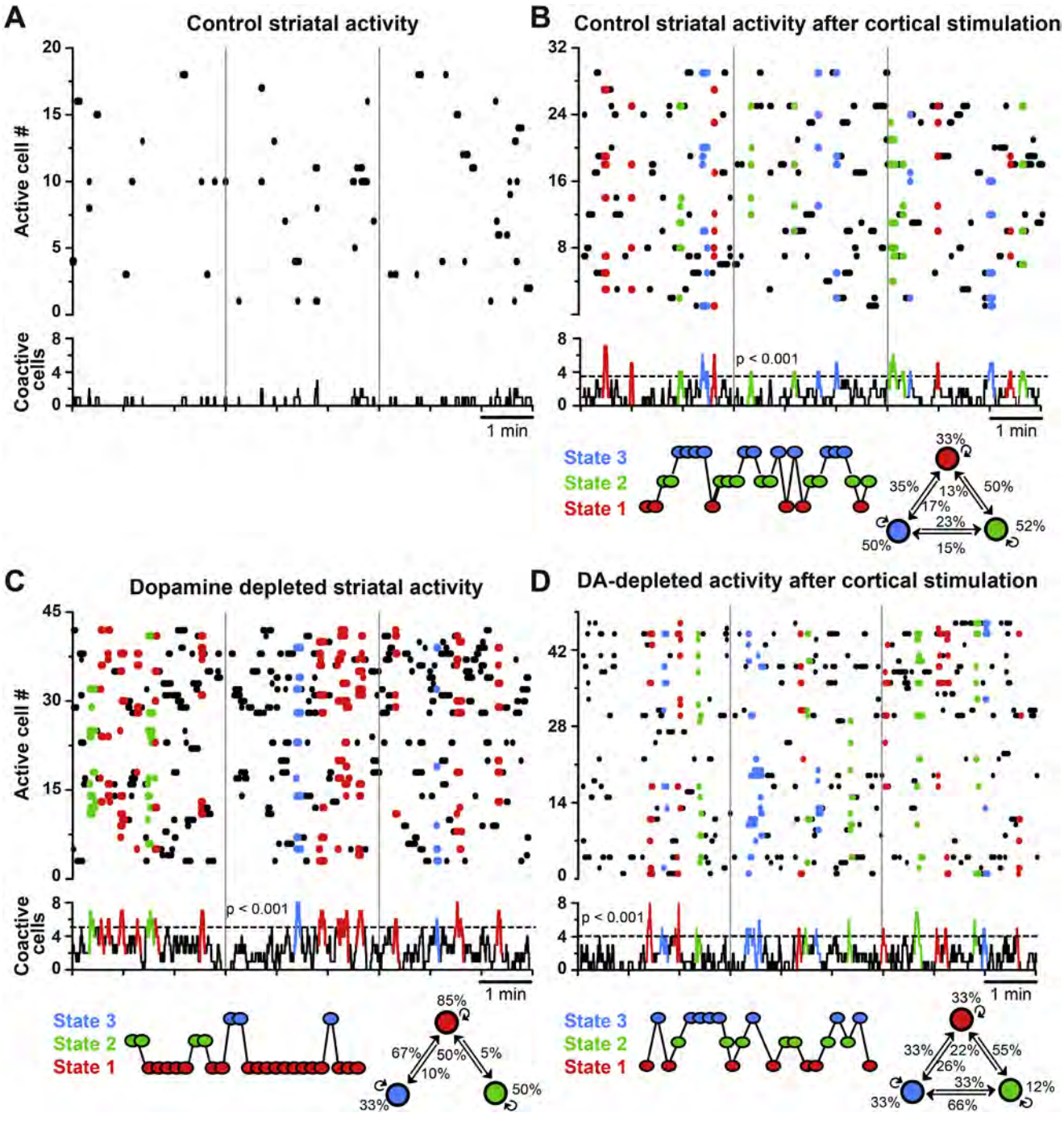

control (Ctr) striatal microcircuit has little spontaneous activity (Fig. 2A), similar to that recorded in a resting subject in vivo (Mink, 2003; Parker et al., 2018). In contrast, after cortical stimulation (CtxS; 10 pulses at 40 Hz in cortex layer V see Experimental Procedures), the striatal microcircuit exhibits enhanced activity that may be recorded for a long time after the stimulus (Fig. 2B; see also Aparicio-Juárez et al., 2019), resembling that recorded during motor activity in vivo (Mink, 2003; Cacace et al., 2017; Parker et al., 2018). A similar increase in network activity and motor behavior may be recorded during the administration of NMDA (2 μM), a glutamatergic receptor agonist, into the striatum (data not shown); see also Ossowska and Wolfarth, 1995; Carrillo-Reid et al., 2008). Both cortical stimulation and NMDA generate network dynamics characterized by the alternation or transitions between network states activity.

Histograms of cellular coactivity at the bottom of raster plots show the sum of neuronal activity per frame in each panel (Fig. 2A-D). The threshold to consider a significant peak of coactivity is represented by a dotted line ($P < 0.001$). In control conditions there are no significant peaks of coactivity (Fig. 2A; n = 12 experiments) due to low spontaneous activity; frames with no activity can be recorded. In contrast, after delivering a cortical stimulus (CtxS; Fig. 2B; n = 5; see Aparicio-Juárez et al., 2019), network activity is enhanced and displays significant peaks of neuronal coactivity (Fig. 2B) as compared to non-stimulated controls (cf., Fig. 2A). Similarly, the non-stimulated DA-depleted striatal microcircuit (Fig. 2C; n = 33) exhibits significant spontaneous activity as compared to the non-stimulated controls (cf., Fig. 2A) accompanied by several significant coactivity peaks (histogram below raster plot in Fig. 2C) without any electrical or chemical stimulus. Significant coactivity peaks in a stimulated control (Fig. 2B), non-stimulated DA-depleted microcircuit (Fig. 2C) and stimulated DA-depleted microcircuits (Fig. 2D) are illustrated as colored circles below the histograms (network states). Note that in stimulated control and DA-depleted microcircuits (Fig. 2B and D) network states form chain-like sequences with alternation of activity between network states (Buzsaki, 2010; Pérez-Ortega et al., 2016) including closed ring-like cycles, or reverberations. In contrast, the non-stimulated DA-depleted microcircuit exhibits a sequence of network states in which a highly recurrent state greatly curtails the alternation with other states (Fig. 2C bottom, dominant state colored in red; n = 33), as previously described in rats and mice (Jáidar et al., 2010; Pérez-Ortega et al., 2016; Aparicio-Juárez et al., 2019; Jáidar et al., 2019).

We then compared network activity in these microcircuits. The cumulative activity of every neuron, that is, the area obtained under the histograms of summed activity, was calculated for each experiment, and representative examples are shown in Fig. 3A. Straight lines were fitted to these data and the slope values for each neuron representing activity of each cell along time (active / non-active frames) were graphed as box plots (Fig. 3B). The non-stimulated Ctr microcircuit had significantly less activity than all the other conditions ($P < 0.001$; Kruskal-Wallis ANOVA, FDR correction: Ctr + CtxS, *P = 0.008; Ctr + NMDA, **P = 0.002; non-stimulated DA-depleted striatum, ***P < 0.0001; DA-depleted + CtxS striatum, ** P = 0.0015). Activity levels between stimulated controls ($P = 0.74$) and DA-depleted stimulated microcircuits (Ctr + CtxS, P = 0.96; Ctr + NMDA, P = 0.74) and non-stimulated DA-depleted microcircuits to stimulated conditions (Ctr + CtxS, P = 0.5; Ctr + NMDA, P = 0.8; DA + depleted + CtxS, P = 0.43) showed no significant differences using this test. We conclude that differences between stimulated and non-stimulated DA-depleted microcircuits are not based on the number of active neurons but the dynamics represented by the sequences of network states (Fig. 2, see also Aparicio-Juárez et al., 2019).

We next calculated cumulative distribution functions (CDFs) for cell activity by adding up the cells from all experiments in each condition (Fig. 3C). Extremes of the CDFs are non-stimulated Ctr (n = 449 cells, black trace) and non-stimulated DA-depleted (n = 1258 cells, gray trace). Stimulated controls and stimulated DA-depleted cases stand between both extreme conditions (Ctr + CtxS, n = 173 cells and DA-depleted + CtxS, n = 287 cells). Ctr + CtxS vs. DA-depleted + CtxS were not significantly different, suggesting that stimulation relieves the pathologic state found in the DA-depleted microcircuit (Pérez-Ortega et al., 2016;

Fig. 2. Striatal microcircuit activity in vitro: comparing spontaneous, stimulated, DA-depleted and DA-depleted stimulated conditions. (A-D top) Representative raster plots showing neuronal activity in single experiments of Ca^{2+} imaging recording with single cell resolution (each row in the y-axis shows the activity of a single cell - numbered; x-axis is time in min, in this and other related figures). Each dot in the plot represents firing as the first time derivative of the somatic Ca^{2+} transient from a single cell (Pérez-Ortega et al., 2016). Histograms at the middle in panels A to D show cellular coactivity and significant neuronal coactivity peaks (dotted line denotes significance level). Neurons belonging to the same neuronal ensembles are presented by different colors in their respective coactivity peaks. (A) Control striatal activity without stimulation shows little spontaneous activity (top), intervals without activity, and no significant coactive events (bottom). (B) Administration of an adequate cortical stimulus (CtxS; see Experimental Procedures and Aparicio-Juárez et al., 2019) increases overall activity in the circuit (top) reflected by significant peaks of coactivity (middle) made by different neuronal groups (colored). Each significant coactivity peak is represented by a colored circle at the bottom showing a sequence of activation of network states. The sequence of activation shows alternation between states which may reach closed cycles or reverberations (triangle at bottom right). (C) In contrast to control (panel A), non-stimulated dopamine (DA) depleted striatum shows high overall spontaneous activity (top), without applying any electrical or chemical stimuli. Significant coactivity peaks are also present (middle). However, sequences of network states show that most activity is due to a highly recurrent state (red). This behavior disrupts alternation and reverberations during the time shown (bottom right). (D) Administration of a cortical stimulus in a DA-depleted striatum dissolves the highly recurrent state and more diverse neuronal ensembles reappear as significant peaks of coactivity (middle). The sequence of network states shows again alternation (bottom) and reverberation (bottom right) between network states. Raster-plots are representative examples of samples in each condition (non-stimulated control, n = 12 experiments; Ctr + CtxS, n = 5 experiments; non-stimulated DA-depleted striatum, n = 33 experiments; DA-depleted +CtxS, n = 7 experiments).

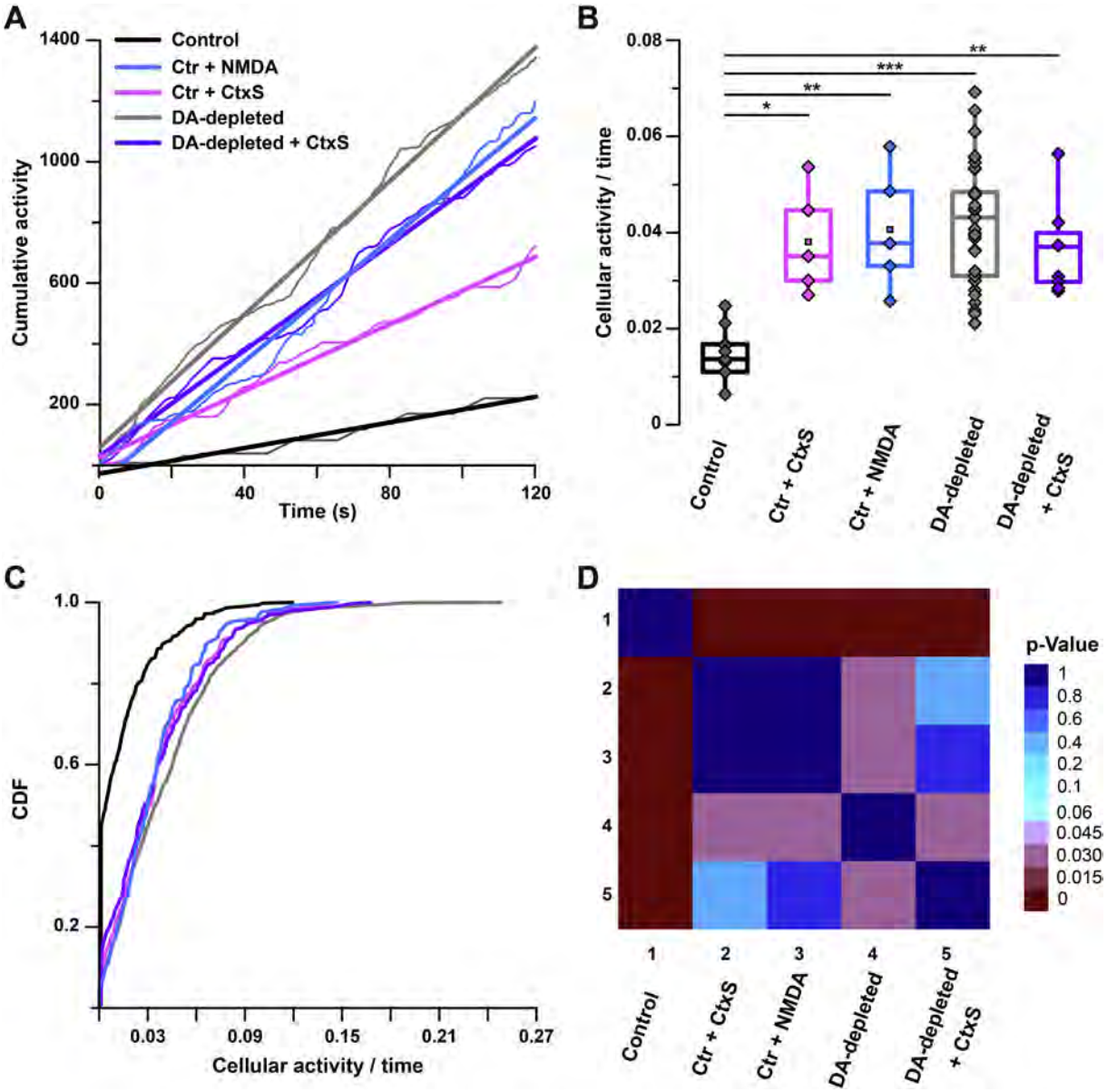

Fig. 3. Measurements of microcircuit activity in different conditions: control (Ctr) without any stimulus, control plus cortical stimulation (Ctr + CtxS), control plus NMDA administration (Ctr + NMDA), non-stimulated DA-depleted tissue (DA-depleted) and cortically stimulated DA-depleted microcircuits (DA-depleted + CtxS). (A) Cumulative activity graphs from single representative experiments as those in Fig. 2 were built adding the areas under activity histograms along time. Straight lines are fitted to the data and the slopes of fitted lines denote cellular activity along time (activity/time). (B) Box and density plots of cellular activity along time in samples of different conditions, each point is a slope obtained as in (A). All conditions are significantly different to the control (Kruskal-Wallis test with post-hoc FDR test; $P < 0.001$) but there are no differences between Ctr + CtxS, Ctr + NMDA and DA-depleted + CtxS with or without stimulation, suggesting that the level of activity is equivalent (Ctr, n = 12 experiments; Ctr + CtxS, n = 5 experiments; Ctr + NMDA, n = 5 experiments; non-stimulated DA-depleted, n = 33 experiments; DA-depleted + CtxS, n = 7 experiments), implying that differences between control and DA-depleted circuits reside in the dynamics and not the level of activity. (C) Still, we built Cumulative distribution functions (CDFs) using all cells from the different experimental samples in each condition: (Ctr, n = 449 cells; Ctr + CtxS, n = 173 cells; Ctr + NMDA, n = 127 cells; DA-depleted, n = 1258 cells; DA-depleted + CtxS, n = 287 cells). For these data, Kolmogorov Smirnov test (with post hoc pair-wise comparisons using FDR (Benjamini et al., 2006)) yielded significant differences between the non-stimulated DA-depleted circuit and stimulated Ctr and DA-depleted circuits. (D) A matrix of the significant P values confirms that control non-stimulated microcircuit differs from all four conditions. The non-stimulated DA-depleted condition shows activity significantly higher to that from Ctr + CtxS, Ctr + NMDA and DA-depleted + CtxS microcircuits. No significant differences between Ctr + CtxS, Ctr + NMDA and DA-depleted + CtxS conditions were found. *denotes statistical significance in this and other figures. FDR stands for false discovery rate correction.

Aparicio-Juárez et al., 2019). A difference with non-stimulated DA-depleted microcircuits and Ctr stimulated circuits was revealed ($P < 0.03$; Kolmogorov Smirnov tests, FDR correction test). A color matrix with post hoc FDR corrected test P-values is shown in Fig. 3D. Note that there are no significant differences between Ctr + NMDA and Ctr + CtxS

INFORME DE LABORES 2019

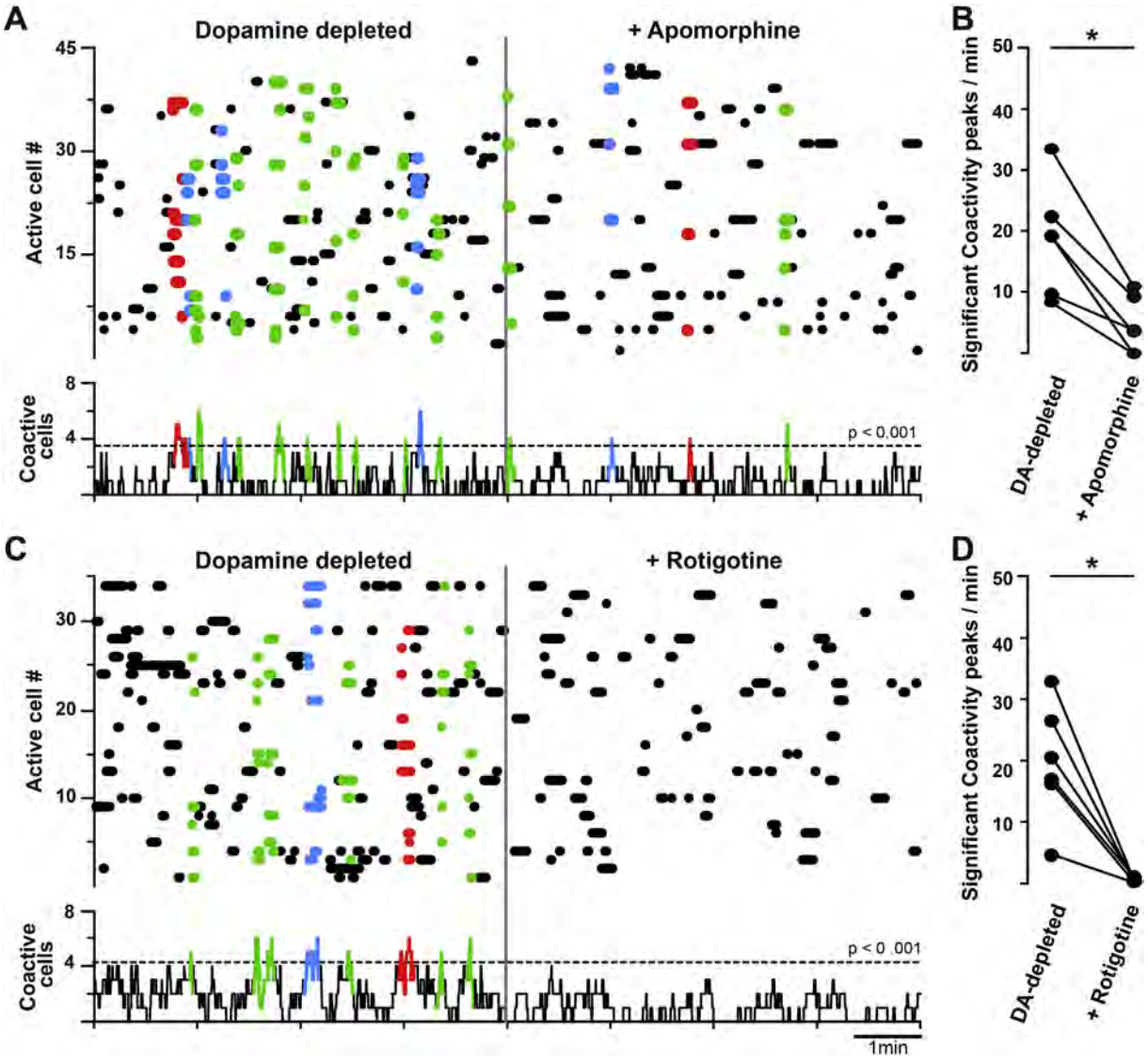

Fig. 4. $D_{1,2}$-class of DA-agonists decrease the spontaneous activity of DA-depleted microcircuits in vitro. Left sections of the raster plots (A and C) show representative non-stimulated DA-depleted microcircuit activity. Notice that in both cases peaks of significant coactivity and a highly recurrent ensemble are evident (green) prior to DA-agonists administration as shown in the histograms bellow. DA-agonists were added after the vertical line. (A) Addition of apomorphine (20 μM) reduces the number of significant coactivity peaks. (B) The reduction of coactivity peaks per minute significantly decreased after apomorphine administration compared with DA-depleted microcircuit without treatment (n = 6 experiments; Wilcoxon matched pairs signed rank test or Wilcoxon T test, P = 0.0313). (C) Addition of rotigotine (10 μM) not only decreased overall activity but also eliminated most significant peaks of coactivity (bottom). (D) This is clear when comparing significant peaks of coactivity per minute before and after rotigotine administration (n = 6 experiments; P = 0.0313; Wilcoxon T test).

conditions, suggesting that both ways to activate striatal microcircuits are equivalent.

Dopamine receptor agonists reduce enhanced spontaneous activity in the DA-depleted microcircuit

Typically, the DA-depleted microcircuit exhibits an excess of activity compared to non-stimulated controls (cf., Fig. 2A and C). Previously, we demonstrated that the application of L-DOPA reduces spontaneous activity of the DA-depleted microcircuit to control-like levels and that this action is reversible upon washing off L-DOPA (Plata et al., 2013). Now, we compare dopamine receptor agonists (DA-agonists) in the absence of stimulus. First, we tested less selective DA-agonists (Fig. 4), that is, agonists with considerable actions on both D_1 and D_2 receptor classes. The most used in PD treatment are apomorphine and rotigotine, which bind to both D_1- and D_2-class receptors with different affinities.

$D_{1,2}$-class agonists reduced the enhanced spontaneous activity of DA-depleted microcircuits. Both 20 μM apomorphine (Fig. 4A; representative raster; the gray line divides activity before and after administering the drug) and 10 μM rotigotine (Fig. 4B, representative) showed similar effects by reducing microcircuit activity significantly. Coactivity peaks per minute were compared before and after drug administration (Wilcoxon T test), and their reduction was demonstrated

in samples of both apomorphine (Fig.4B, n = 6 experiments; P = 0.0313) and rotigotine (Fig. 4D; n = 6 experiments; P = 0.0313). The assay shows that at therapeutic but saturating concentrations rotigotine performance is better than that of apomorphine.

More selective D_2-class ($D_{2/3}$) receptor agonists are also used for the early treatment of PD (Stocchi et al., 2016). To explore the effects of these agonists on the enhanced spontaneous activity of DA-depleted microcircuits, 10 μM pramipexole (Fig. 5A; n = 6 experiments), 10 μM ropinirole (Fig. 5C;

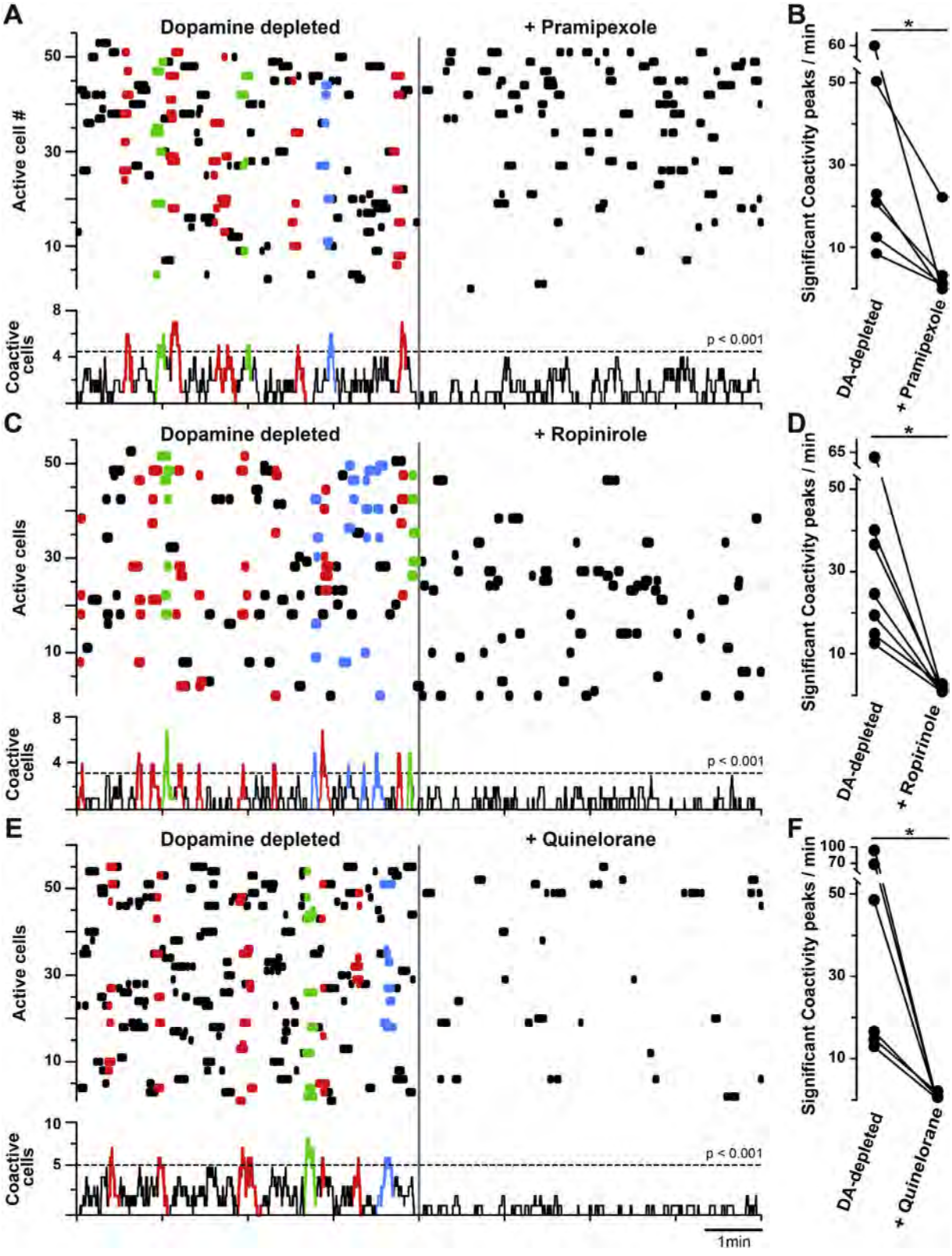

n = 7 experiments) and 10 μM quinelorane (Fig. 5E; n = 6 experiments) were applied. All of them reduced the excess in spontaneous activity of DA-depleted microcircuits (pramipexole: Fig. 5B, P = 0.0313; ropinirole: Fig. 5D; P = 0.0156; quinelorane: Fig. 5F; P = 0.0313; Wilcoxon T tests). To conclude, all DA-agonists tested reduced the pathological spontaneous activity of DA-depleted microcircuits.

D_2-class receptor agonists were more effective in decreasing the spontaneous activity of DA-depleted microcircuits

All DA-agonists reduced the excess in pathological spontaneous activity of non-stimulated DA-depleted microcircuits (see previous section). To better evaluate whether there were differences between the different DA-agonists, a Kruskal-Wallis ANOVA analysis with FDR post hoc correction test between the cumulative cellular activity was made (Fig. 6A). As previously mentioned, spontaneous neuronal activity of the non-stimulated DA-depleted microcircuit was significantly enhanced in comparison with non-stimulated Ctr microcircuit (P < 0.0001; control: n = 12 experiments; DA-depleted microcircuit: n = 33 experiments). Then we compared the activity of DA-depleted microcircuits after a DA-agonist was added with that of non-stimulated DA-depleted microcircuits (Kruskal-Wallis ANOVA, P < 0.0001, post hoc FDR correction test). Activity in non-stimulated DA-depleted circuits was significantly larger than the activity in DA-depleted microcircuits plus L-DOPA (Fig. 6A; P = 0.0004; n = 7 experiments), confirming previous studies (Plata et al., 2013). Surprisingly, however, DA-depleted microcircuits treated with apomorphine or rotigotine were not significantly different from the non-stimulated DA-depleted microcircuits (Fig. 6A; P = 0.99; n = 6 experiments and Fig. 6A; P = 0.5; n = 6 experiments), suggesting that less selective agonists have a more limited action on the spontaneous activity of DA-depleted microcircuits (Jáidar et al., 2010). Nonetheless, when adding more selective D_2-agonists to DA-depleted microcircuits, activity was significantly less than that found in untreated DA-depleted microcircuits, namely: pramipexole (Fig. 6A; P = 0.00015; n = 6 experiments), ropinirole (Fig. 6A; P = 0.0001; n = 8 experiments) and quinelorane (Fig. 6A; P = 0.0001; n = 6 experiments). These results suggest that more selective D_2-class agonists were better than less selective $D_{1,2}$-class agonists in reducing the excess of spontaneous activity observed in non-stimulated DA-depleted microcircuits.

An even more stringent test was performed by comparing cumulative probability distribution functions (CDFs) for each condition using all cells from each experiment (Fig. 6B-D). First, we compared non-stimulated control CDF (n = 449 cells, black trace; Fig. 6B) with that of the non-stimulated DA-depleted microcircuit (n = 1258 cells, gray trace; Fig. 6B), and with the DA-depleted + L-DOPA (n = 232 cells, red trace; Fig. 6B). There was no significant difference between control microcircuit activity and DA-depleted microcircuit plus L-DOPA (P = 0.15; Kolmogorov–Smirnov test with FDR correction), suggesting that in this stage of experimental early Parkinsonism (i.e., "L-DOPA honey moon"), L-DOPA tends to return the microcircuit dynamics to control conditions. As expected, the CDF of the non-stimulated DA-depleted microcircuit was significantly different from these two conditions, its CDF was far right to control and L-DOPA CDFs (Fig. 6B; see graded pseudocolored matrix of paired P-values in Fig. 6E).

Using this stringent test, most DA-agonists employed could not match L-DOPA actions (Fig. 6C and D; see graded pseudocolored matrix of paired P-values in Fig. 6E Kolmogorov–Smirnov test with FDR corrections). However, quinelorane was not significantly different from the non-stimulated control (207 cells, P = 0.06). Every other CDF was significantly different from control CDF: apomorphine = 262 cells, $P = 6.6 \times 10^{-12}$; rotigotine = 139 cells, $P = 5.0 \times 10^{-6}$; pramipexole = 255 cells, P = 0.004; ropinirole = 249 cells, P = 0.006. This analysis showed that apomorphine and rotigotine CDFs were to the right of the control and L-DOPA CDFs (Fig. 6C), while D_2-agonists CDFs superimpose in part with control and L-DOPA CDFs (Fig. 6D). We conclude that D_2-agonists better reduce the excess of spontaneous activity of non-stimulated DA-depleted microcircuits, but no agonist completely emulates L-DOPA actions in this respect. Up to now, we have compared non-stimulated DA-depleted microcircuits before and after addition of L-DOPA or DA-agonists: all DA-agonists reduced spontaneous resting pathological activity when compared one by one. Though, only L-DOPA (and to a minor extent quinelorane) approached the activity of non-stimulated controls. Activity remained significantly different from control microcircuit after the reduction of pathological activity by any of the DA-agonists. It has been previously demonstrated (Aparicio-Juárez et al., 2019, Fig. 2D) that cortical stimulation reduces overall activity restoring neural ensembles sequences similar to control for a limited period of time. Therefore, we asked how DA agonists would interact with this action, perhaps prolonging it. In addition, a comparison between DA agonists actions may suggest which are the more effective.

DA-agonists actions on cortical stimulated DA-depleted microcircuits

To answer the previous questions CtxS was applied to DA-depleted microcircuits previously infused with L-DOPA or other DA-agonists. First, a representative raster plot of L-DOPA is shown in Fig. 7A (top) divided into three different epochs separated by vertical lines. Left epoch shows the

Fig. 5. Comparison of D_2-class receptor agonists effects on DA-depleted microcircuits in vitro. Panels: representative raster plots of spontaneously active DA-depleted microcircuits before and after addition of a dopamine D_2-class receptor agonist (separated by a vertical line). Histograms at bottom show significant peaks of coactive neurons in the same frame. Dotted lines on the histograms show the significance coactivity threshold to record a neuronal ensemble. (A) Representative experiment showing DA-depleted microcircuit spontaneous activity and the reduction of this activity after addition of 10 μM pramipexole. (B) Pramipexole reduced the number of significant peaks of coactivity per min (n = 6 experiments; P = 0.0313; Wilcoxon T test). (C) After the vertical line 10 μM ropinirole was added to the DA-depleted microcircuit. (D) Reduction of coactivity peaks is obvious (n = 7 experiments; P = 0.0156; Wilcoxon T test). (E) When adding 10 μM quinelorane reduction of activity was evident and (F) coactivity peaks were virtually abolished (n = 6 experiments; P = 0.0313; Wilcoxon T test).

typical spontaneous activity of a DA-depleted microcircuit. Middle epoch shows the decrease of this spontaneous activity due to L-DOPA administration. Right epoch illustrates network activity after cortical stimulation (CtxS) in the continuous presence of L-DOPA, showing that activity is enhanced again. Coactivity histograms and sequences of transitions between network states (below the raster plots) show significant coactivity peaks in the DA-depleted microcircuit both before and after CtxS + L-DOPA. However, a difference is evident: the untreated DA-depleted microcircuit exhibits a highly recurrent network state that impedes reverberation (bottom), while the stimulated DA-depleted microcircuit in the presence of L-DOPA shows a variety of coactivity peaks and alternation between network states including reverberation (bottom; n = 4 experiments, see also Aparicio-Juárez et al., 2019) resembling control activity (see Fig. 2A). In the presence of L-DOPA the DA-depleted microcircuit is able respond to a

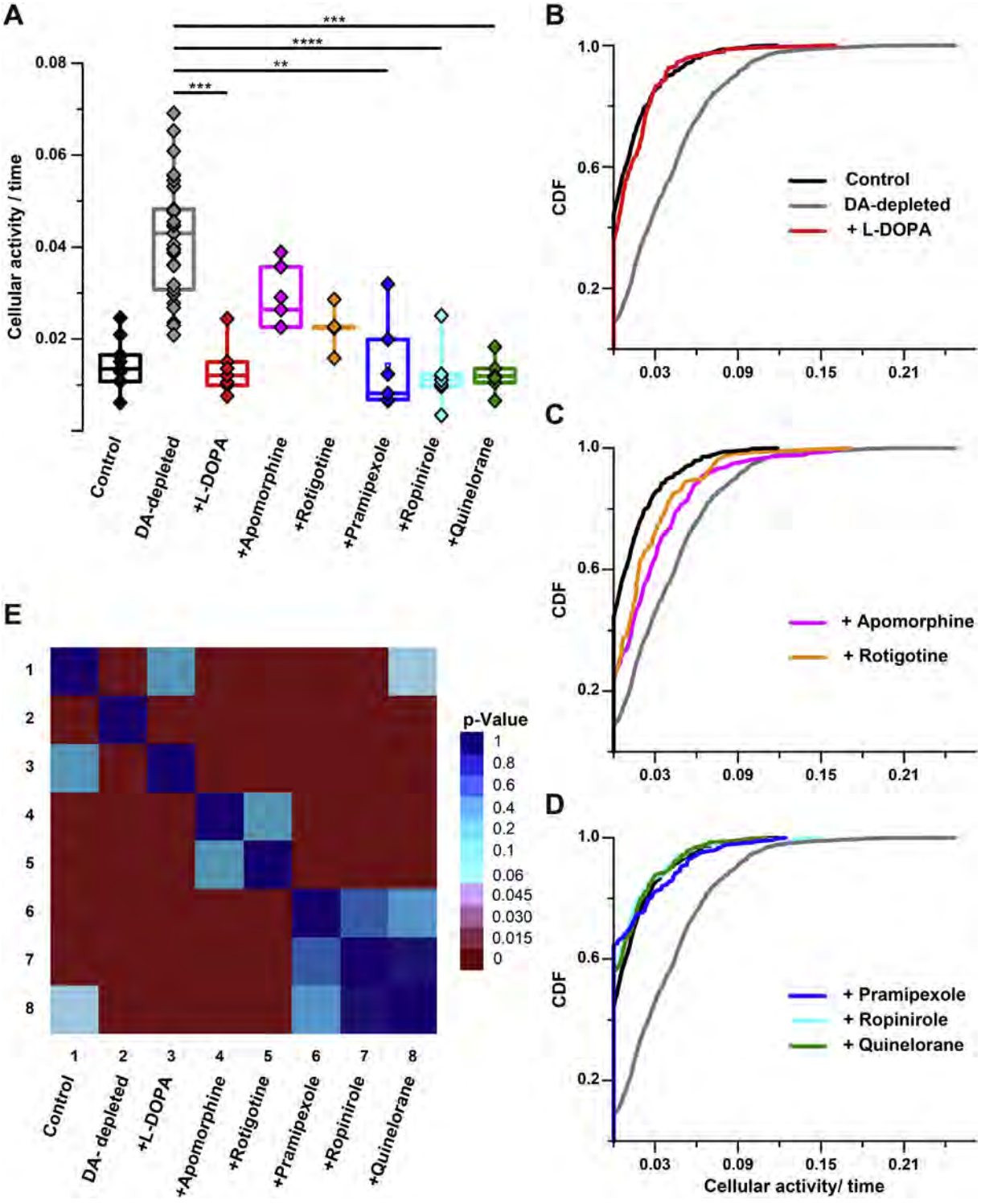

cortical command with near control-like dynamics: a sequence of network states. This experimental protocol was then applied to DA-depleted microcircuits when administering rotigotine, a representative $D_{1,2}$-agonist (Fig. 7B), pramipexole, a more selective D_2-agonist ($D_{2,3}$; Fig. 8A) and ropinirole, another D_2-agonist (Fig. 8B). Similar results to the sole administration of L-DOPA were obtained: prior to stimulation a highly recurrent state is impeding alternation and DA-agonists application have a silencing effect. When CtxS was delivered in the continuous presence of DA-agonists, network dynamics became a sequence of alternating network states.

Specifically, rotigotine induced less peaks of coactivity than L-DOPA (Mann–Whitney T test, P = 0.02), although it restored alternation between network states and closed cycles. On the other hand, pramipexole induced a more balanced alternation between network states, although in the experiment shown, closed cycles did not appear (see statistics below). Ropinirole did not restore alternation completely during the sequence of network states, but closed cycles could be present in some cases.

Performance comparison of DA-agonists on cortical activated DA-depleted microcircuits

As shown in Fig. 2, CtxS briefly and transiently recovers control stimulated network dynamics in DA-depleted microcircuits by inducing a sequence of network states activity, similar to that induced in Ctr circuits. However, this change towards control dynamics only lasts approximately 30 min (Fig. 9A top), unless L-DOPA is administered (see Aparicio-Juárez et al., 2019). In that case, a DA-depleted circuit activated by CtxS maintains the alternation of network states for a longer period of time, e.g., 60 min. Therefore, here we compare the actions of CtxS plus the presence of L-DOPA or other DA-agonists (after 60 min), and solely CtxS (30 min), over DA-depleted circuits. First, we used the number of transitions between network states to achieve a closed cycle, a measure of how much alternation between network states is allowed by the circuit (Pérez-Ortega et al., 2016), presented in pie plots (Fig. 9A). A colored scale (at the bottom) shows the number of transitions required to reach a closed cycle, where black color indicates the cases in which a closed cycle was not reached during the time of recording. Even in control conditions (Ctr + CtxS) sequences of neuronal ensembles may not reach a closed cycle during the course of the experiment (12%). When DA-depleted microcircuits receive a cortical stimulus (DA-depleted + CtxS) the highly recurrent state is transiently abolished and microcircuit dynamics resembles that of the Ctr + CtxS microcircuits (Fig. 9A top): where only a minority of sequences do not reach closed cycles (18%; P = 0.206; Kolmogorov–Smirnov test with post hoc FDR correction). This confirms that cortical stimulation briefly (30 min) relieves the microcircuit from the highly recurrent state as previously reported (Aparicio-Juárez et al., 2019). The maintenance of control-like network dynamics in stimulated DA-depleted microcircuits for longer time, e.g., 60 min, requires the action of L-DOPA (Aparicio-Juárez et al., 2019). Therefore, here we compared to what extent different DA-agonist could prolong the action of CtxS in terms of network alternation sequences and closed cycles (Pérez-Ortega et al., 2016).

It was found that, even if L-DOPA induces alternation of network states in the stimulated condition, a higher percentage of non-closed cycles, 36%, is revealed as compared with Ctr + CtxS (P = 0.007; n = 4 experiments; Kolmogorov–Smirnov test with post hoc FDR correction in this and next comparisons of this section). Still, most sequences had closed cycles. Using the same test other agonists yield: rotigotine (P = 0.002, n = 4 experiments), pramipexole (P = 0.016, n = 4 experiments) and ropinirole (P = $1X10^{-9}$, n = 4 experiments). The results suggest that even when active DA-depleted circuits exhibit sequences of network states. However, no DA-agonist, including L-DOPA, is capable of completely resembling the Ctr + CtxS circuit.

Since all active DA-depleted circuits exhibit several closed cycles we asked how many transitions between network states were needed to reach them, excluding the instances in which there were no closed cycles during recording time. Fig. 9B shows this comparison with density plots: Ctr + CtxS distribution was compared (Kruskal-Wallis

Fig. 6. D_2-class receptor agonists were more effective in decreasing the excess of spontaneous activity in DA-depleted microcircuits. (A) As in Fig. 3B, cellular activity over time was compared among the different experimental conditions (experiments/condition: non-stimulated control (Ctr) = 12, non-stimulated DA-depleted = 33, non-stimulated DA-depleted + L-DOPA = 7, + apomorphine = 6, + rotigotine = 6, + pramipexole = 6, + ropinirole = 8, + quinelorane = 6). As previously mentioned, activity over time of the non-stimulated DA-depleted microcircuit is significantly larger than that of the non-stimulated control microcircuit (P < 0.0001). DA-depleted microcircuit activity significantly decreased (Kruskal-Wallis ANOVA, P < 0.0001, with FDR correction) after administration of L-DOPA (P < 0.0004), and D2-class agonists, namely: pramipexole (P = 0.00015), ropinirole (P = 0.0001) and quinelorane (P = 0.0001). However, $D_{1,2}$-class agonists: apomorphine (P = 0.99) and rotigotine (P = 0.5) failed to differ from the DA-depleted microcircuit. (B) Cumulative distribution functions (CDFs) of cell activity from: non-stimulated control (n = 449 cells; black trace); non-stimulated DA-depleted (n = 1258 cells; gray trace) and DA-depleted + L-DOPA (n = 232 cells; red trace) microcircuits. Note that when adding L-DOPA to the DA-depleted microcircuit its CDF greatly resembles the one from control microcircuit (P = 0.15; Kolmogorov–Smirnov test with FDR correction). Non-significant differences with non-stimulated controls predicts a good therapeutic effect. (C) In this respect, CDFs from DA-depleted microcircuits after the addition of apomorphine (n = 262 cells; P = $6.6X10^{-12}$) and rotigotine (n = 139 cells; P = $5.0X10^{-6}$) showed significant differences with non-stimulated controls, that is, less selective DA-agonists did not approach the control; these DA-agonists stay in between non-stimulated Ctr and non-stimulated DA-depleted circuits. (D) In addition, compared to control CDF, CDFs from DA-depleted microcircuits after the addition of D_2-class selective DA-agonist were also significantly different to non-stimulated Ctr: pramipexole (n = 255 cells; P = 0.004), ropinirole (n = 249 cells; P = 0.006) and quinelorane (n = 207 cells; P = 0.06). However, the CDFs of these DA-agonists are nearer to control CDF (black line). (E) A matrix of P-values from pairwise comparisons, based on CDFs (Kolmogorov–Smirnov test with FDR corrections) shows that only the action of L-DOPA was not statistically different from control activity. All DA-agonists statistically differ from the control using this stringent test. D_2-agonists do not differ much among them.

ANOVA with post hoc FDR correction) with: DA-depleted microcircuits plus CtxS at 30 min (P = 0.149), and with DA-depleted microcircuits plus CtxS and DA-agonists at 60 min: L-DOPA (P = 0.736), rotigotine (**P = 0.003), pramipexole (P = 0.199) and ropinirole (***P = 0.001). These results suggest that L-DOPA and pramipexole have a better performance than rotigotine and ropinirole in DA-depleted microcircuit dynamics.

In order to unveil drugs' efficacy while making a hierarchical scale between them we used the recurrence index test

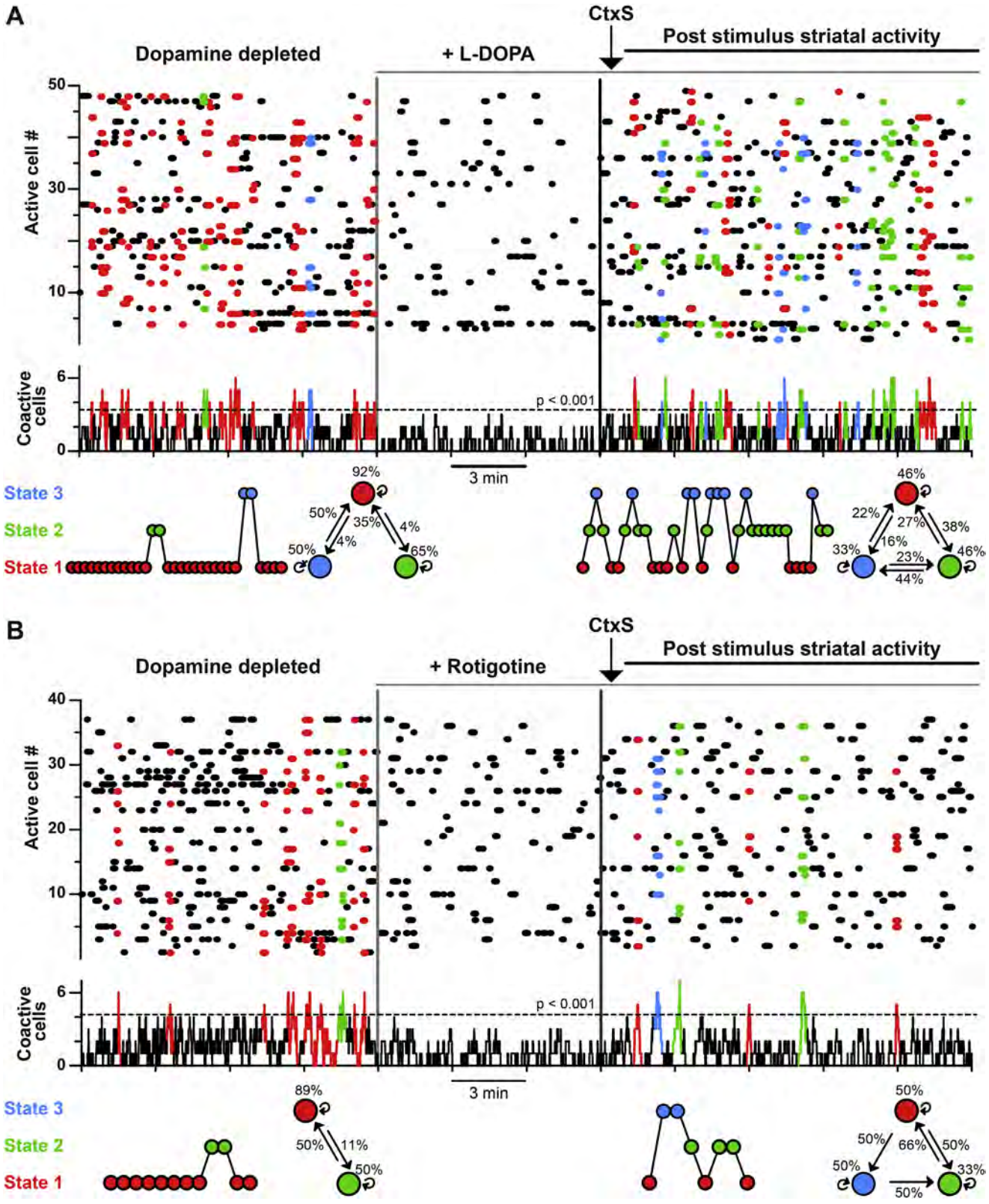

(Aparicio-Juárez et al., 2019), a measure of how much a pathological microcircuit has a highly recurrent network state that curtails alternation between neuron groups. Using this metric, all DA-agonists were significantly similar to control stimulated circuits (O'Brien homogeneity of variance test): DA-depleted + CtxS (30 min) P = 0.073, and at 60 min: L-DOPA + CtxS (P = 0.186); rotigotine + CtxS (P = 0.079); pramipexole + CtxS (P = 0.214); ropinirole + CtxS, P = 0.071). These results suggest that clinically available DA-agonists help maintaining microcircuit dynamics away from the typically highly recurrent dominant state network seen in DA-depleted conditions, even if they fail to completely preserve CtxS effects along time.

DISCUSSION

Previously, we have described some properties of the striatal microcircuit at histological scale (dozens of neurons) in vitro, to compare controls with DA-depleted microcircuits (Carrillo-Reid et al., 2008; Jáidar et al., 2010; Carrillo-Reid et al., 2011; López-Huerta et al., 2013; Pérez-Ortega et al., 2016). Because between molecular-cellular studies (Millan, 2010) and in vivo animal models (Liang et al., 2008; Dunnet and Lelos (2010) or clinical studies (Lam, 2000), there is a gap: pharmacological tools or studies at the microcircuit level in vitro, where drug concentrations can be controlled. The present work intends to use some previously described striatal microcircuit properties in vitro to compare antiparkinsonian agents used in PD therapeutics.

Spontaneous striatal activity

As seen in vitro, non-stimulated control striatal microcircuits at a histological scale show little activity (Plata et al., 2013; Aparicio-Juárez et al., 2019), similar to the activity seen in resting subjects in vivo (Mink, 2003; Parker et al., 2018). In contrast, striatal microcircuits depleted of dopamine show a significantly enhanced spontaneous activity, mainly consisting of a highly recurrent network state (Liang et al., 2008; Jáidar et al., 2010; Pérez-Ortega et al., 2016; Jáidar et al., 2019), with both indirect and direct pathway striatal projection neurons (Parker et al., 2018; Jáidar et al., 2019). Because the non-stimulated microcircuit behaves differently in control and after DA-depletion, exhibiting different functional network architectures (Pérez-Ortega et al., 2016), here we considered the non-stimulated and stimulated microcircuits separately.

The present results show that pramipexole, ropinirole and quinelorane, more selective D_2-class DA-receptor agonists ($D_{2,3}$-types), greatly decrease the enhanced spontaneous activity of non-stimulated DA-depleted microcircuits. Less selective $D_{1,2}$-agonists such as apomorphine and rotigotine were not that good in decreasing this enhanced spontaneous activity. L-DOPA was better in suppressing this enhanced spontaneous activity than any other DA-receptor agonist, suggesting that when a Parkinsonian subject is at rest, D_2-class DA-agonists signaling would better control rigidity and resting tremor, the clinical correlates of this enhanced activity.

Cortical stimulated striatal microcircuits

Striatal microcircuit activity in vitro can be elicited in control conditions by chemical or electrical stimulus. Low concentrations of NMDA (2 μM in mice) maintains in vitro microcircuits activated for long periods of time (Fig. 3, see also Carrillo-Reid et al., 2008), as well as, electrical cortical stimulation (Control + CtxS). Activation of control microcircuits significantly above spontaneous activity can last about half an hour or more (Fig. 2B, Aparicio-Juárez et al., 2019), resembling in vivo microcircuits during movement (Mink, 2003; Cui et al., 2014; Parker et al., 2018). The mechanism by which the striatal microcircuit remains active long after the stimulus is unknown. A working hypothesis is that spontaneously active excitatory interneurons, such as cholinergic interneurons (Goldberg and Wilson, 2005; Tepper et al., 2018; Surmeier et al., 2011) may ignite microcircuit activation.

Once activated, striatal microcircuits are characterized by sequences of significant and transient coactivity peaks, given by different neuronal groups or ensembles (Hebb, 1949; Edelman, 1993; Carrillo-Reid et al., 2008; Buzsaki, 2010; Carrillo-Reid et al., 2017; Klaus et al., 2017), composed of functionally connected neurons (Buzsaki, 2010; Carrillo-Reid et al., 2015). Different neuronal groups show alternation between them (Carrillo-Reid et al., 2008, 2009; 2017), reflecting behavioral stages in vivo (Klaus et al., 2017; Owen et al., 2018; Parker et al., 2018). In contrast, alternation between ensembles is restricted in DA-depleted microcircuits in which a highly recurrent network state which correlates with in vivo locked or disturbed locomotion, and reduced encoding specificity (Parker et al., 2018). Changes in synaptic plasticity after DA-depletion have been reported (e.g., Calabresi et al., 2006; Gerfen and Surmeier, 2011; Barroso-Flores et al., 2015; Deffains and Bergman, 2015) and those might underlie the lack of alternation between ensembles.

Interestingly, in CtxS DA-depleted microcircuits, the highly recurrent state disappears temporarily, mitigating

Fig. 7. Cortical stimulation activates DA-depleted microcircuits similarly to control stimulated circuits when $D_{1,2}$-class dopamine receptor agonists are present. Representative raster-plots are divided by vertical lines into three epochs. 1) Non-stimulated DA-depleted spontaneous activity, 2) Addition of 10 μM L-DOPA (A) or 10 μM rotigotine (B) to the microcircuit, and 3) Activity after cortical stimulation (CtxS) in the presence of DA-agonists. Histograms bellow each raster plot show significant coactivity events, which are colored according to network states. In both cases (A and B) non-stimulated DA-depleted microcircuits show a highly recurrent state (colored in red) and less alternation, confirmed by the sequence of network states which fail to form closed loops. Both L-DOPA (A) and rotigotine (B) eliminate significant coactivity peaks and decrease spontaneous activity. In that condition, cortical stimulation reignites activity in the DA-depleted circuit in the presence of the DA-agonists. Microcircuits exhibit several and alternating significant peaks of coactivity (histogram and sequences at bottom). Activation sequences now allow reverberations during recording time. At glance, peaks of coactivity are less likely to occur after cortical stimulation in the presence of rotigotine as compared to L-DOPA.

pathological network dynamics (Figs. 2, 3). There are no significant differences when comparing Ctr + CtxS with DA-depleted + CtxS circuits within 30 min of stimulation (in early Parkinsonism). However, after 30 min the highly recurrent state is reestablished. L-DOPA administration prolongs the improvement (e.g., 60 min), which in in vitro activated circuits is seen as a recovery of network states alternations (Aparicio-Juárez et al., 2019). We used different statistical analyses to compare the actions of different DA-agonists in DA-depleted + CtxS microcircuits 60 min

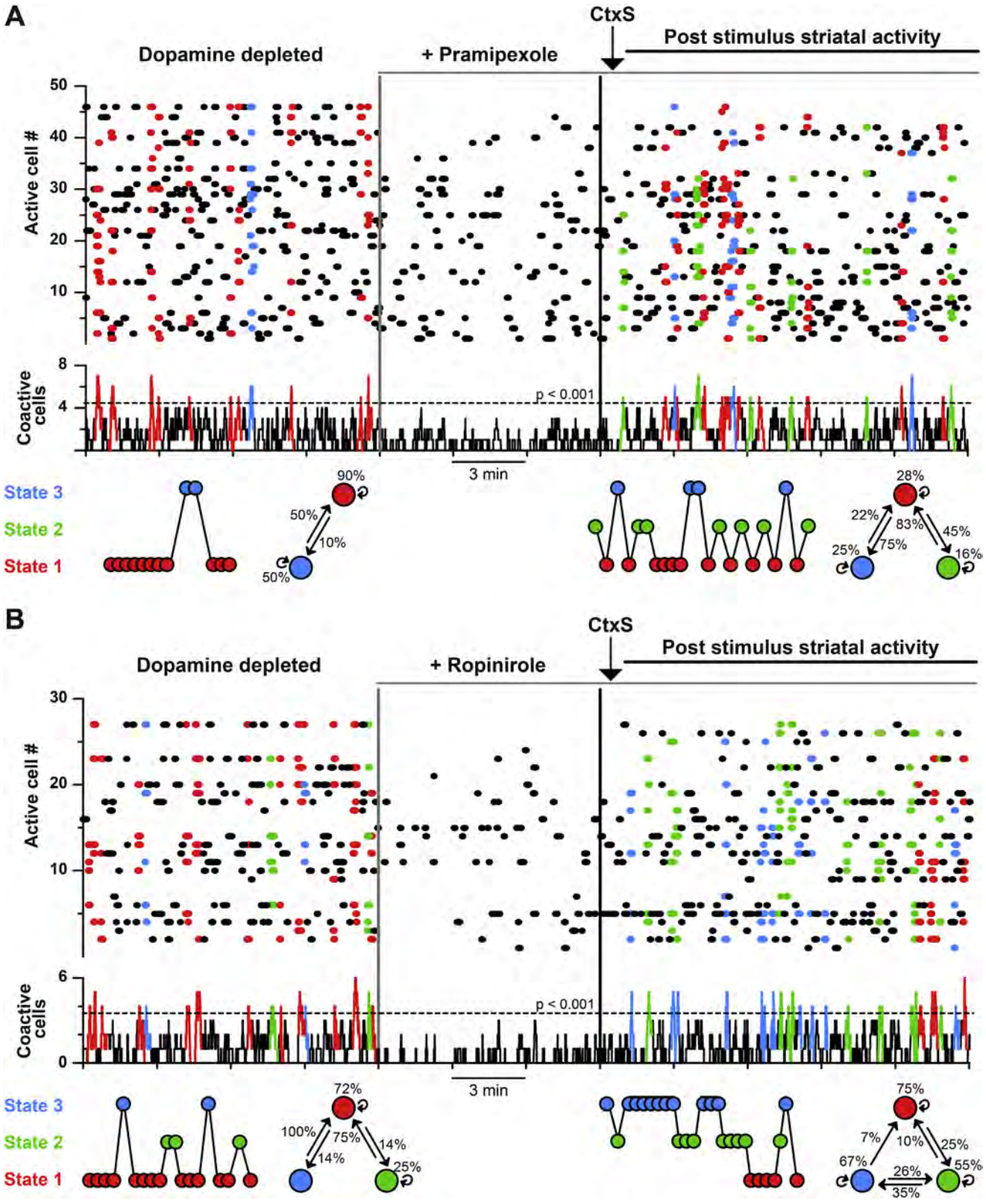

INFORME DE LABORES 2019

after the stimulus, using the property of alternation between ensembles activity. We focused on the actions of the most used DA-agonists in PD therapeutics (Blandini and Armentero, 2014; Stocchi et al., 2016). Future work will test other drugs (Millan, 2010).

Dopamine receptor agonists actions on cortical stimulated striatal microcircuits

At a first glance (see statistical comparisons below), all DA-agonists had an action similar to that of L-DOPA on DA-depleted + CtxS microcircuits (Figs. 7, 8): alternation between network states and closed cycles during the time of recording were recovered. The highly recurrent network state was dissolved (Jáidar et al., 2010; Aparicio-Juárez et al., 2019).

However, we quantitatively compared the actions of DA-agonists with different metrics. First, distributions of the number of transitions required to close a cycle were compared (pie plots in Fig. 9A black color indicates that no cycle was closed during recording time; Kolmogorov–Smirnov tests with post hoc FDR corrections). Within the first 30 min after the stimulus, DA-depleted + CtxS circuits yielded a distribution that was not significantly different than that from Ctr + CtxS circuits ($P = 0.206$). In contrast, all DA-agonists tested 60 min after CtxS in DA-depleted circuits had distributions of the number of transitions required to close a cycle significantly different than Ctr + CtxS circuits, suggesting that no DA-agonist, including L-DOPA, is capable of maintaining CtxS effects.

Thereafter, we excluded the cases with unclosed cycles. The measurements showed that L-DOPA and pramipexole produce a better performance than rotigotine and ropinirole, suggesting that L-DOPA and pramipexole will better improve movement in Parkinsonian subjects.

Finally, the presence of a highly recurrent network state is another signature of in vitro DA-depleted microcircuits. The presence of this condition may be measured with a recurrence index (Aparicio-Juárez et al., 2019). This is shown in box plots as increased variance (Fig. 9C; O'Brien homogeneity of variance test). A comparison of DA-agonists in DA-depleted + CtxS circuits after 60 min of stimulation showed that all DA-agonists have some benefit on stimulated DA-depleted circuits.

Correlations

The present work aims to show that the use of behavioral tests in animal models of PD (Liang et al., 2008; Dunnet and Lelos, 2010) as well as molecular and cellular studies (Millan, 2010) to investigate neurological therapies may be assisted with in vitro bio-assays that record several neurons during microcircuit dynamics. The theoretical framework to find circuit features to measure quantitatively posits that vertebrate neurons work together forming neuronal ensembles or groups (e.g., motoneurons pools) and that a microcircuit of histological scale can be seen as a temporal sequence of neuronal ensembles (Hebb, 1949; Edelman, 1993; Carrillo-Reid et al., 2008; Buzsaki, 2010; Carrillo-Reid et al., 2017; Klaus et al., 2017). In addition, synaptic plasticity abnormalities during PD have been described (Calabresi et al., 2006; Gerfen and Surmeier, 2011), as well as the connections within an ensemble (Carrillo-Reid et al., 2017) and closed cycles or reverberations (Carrillo-Reid et al., 2008). Moreover, sequences of neuronal ensembles have been correlated with motor actions in vivo (Klaus et al., 2017; Owen et al., 2018; Parker et al., 2018), showing the crucial role of interneurons (Owen et al., 2018).

By using this framework, we provide circuitry correlates to the usefulness of D_2-class agonists as initial mono-therapy in early PD, evidencing insufficient performance in the case of ropinirole, and supporting L-DOPA as the leading option in advanced PD (Rascol et al., 1998; Reichmann, 2000; Radad et al., 2005; UK PD MED Collaborative Group, 2014; Zesiewicz et al., 2017). Further, we show a poorer performance of the less selective $D_{1,2}$ DA-agonists. Not expected in the logic that occupancy of both receptors may be thought to prevent the disarray in their signaling, but consistent with previous results showing that bath application of a selective D_1-agonist (SKF81297) does not revert the enhanced spontaneous activity in non-stimulated DA-depleted microcircuits (Jáidar et al., 2010). Microcircuit results support previous multivariate binding analyses that show that these two classes of agonists belong to different pharmacological families (Millan, 2010). In addition, a subtle difference between pramipexole and ropinirole was disguised. In the present bio-assay the chosen DA-agonists were administered continuously and for a short period of time, in contrast to a pulsatile activation for a very long time (Fabbrini et al., 1988). Long-lasting and dramatic reduction in motor complications have been observed in advanced PD patients when the treatment is not pulsatile (Nutt et al., 2000; Devos and DUOPOPA Study Group, 2009). Therefore, our results support the development of an oral long-acting form of L-DOPA (Olanow and Stocchi, 2017) since all DA-agonists were below L-DOPA performance. At the

Fig. 8. Cortical stimulation activates DA-depleted microcircuits similarly to the control stimulated circuit when D_2-class dopamine receptor agonists are present. Representative raster-plots are divided by vertical lines into three epochs. 1) Non-stimulated DA-depleted spontaneous activity, 2) Addition of 10 μM pramipexole (A) or 10 μM ropinirole (B) to the microcircuit, and 3) activity after cortical stimulation (CtxS) in the presence of DA-agonists. Histograms bellow each raster plot show coactivity events, and significant peaks are colored according to network states. In both cases (A and B) non-stimulated DA-depleted microcircuits show a highly recurrent state (colored in red) and less alternation, confirmed by the sequence of network states which fail to form closed loops. Both pramipexole (A) and ropinirole (B) are sufficient to abolish significant coactivity peaks. Finally, cortical stimulation reignites activity in the DA-depleted circuit in the presence of DA-agonists. Stimulated network activity now exhibits different significant coactivity peaks (histogram and sequences at bottom) that alternate their activity forming sequences. In these cases, pramipexole better reduced activity of the highly recurrent network state, however, in this case closed cycles did not appear during recording time (A), on the other hand, ropinirole shows less alternation between network states but closed cycles or reverberations were commonly completed.

INFORME DE LABORES 2019

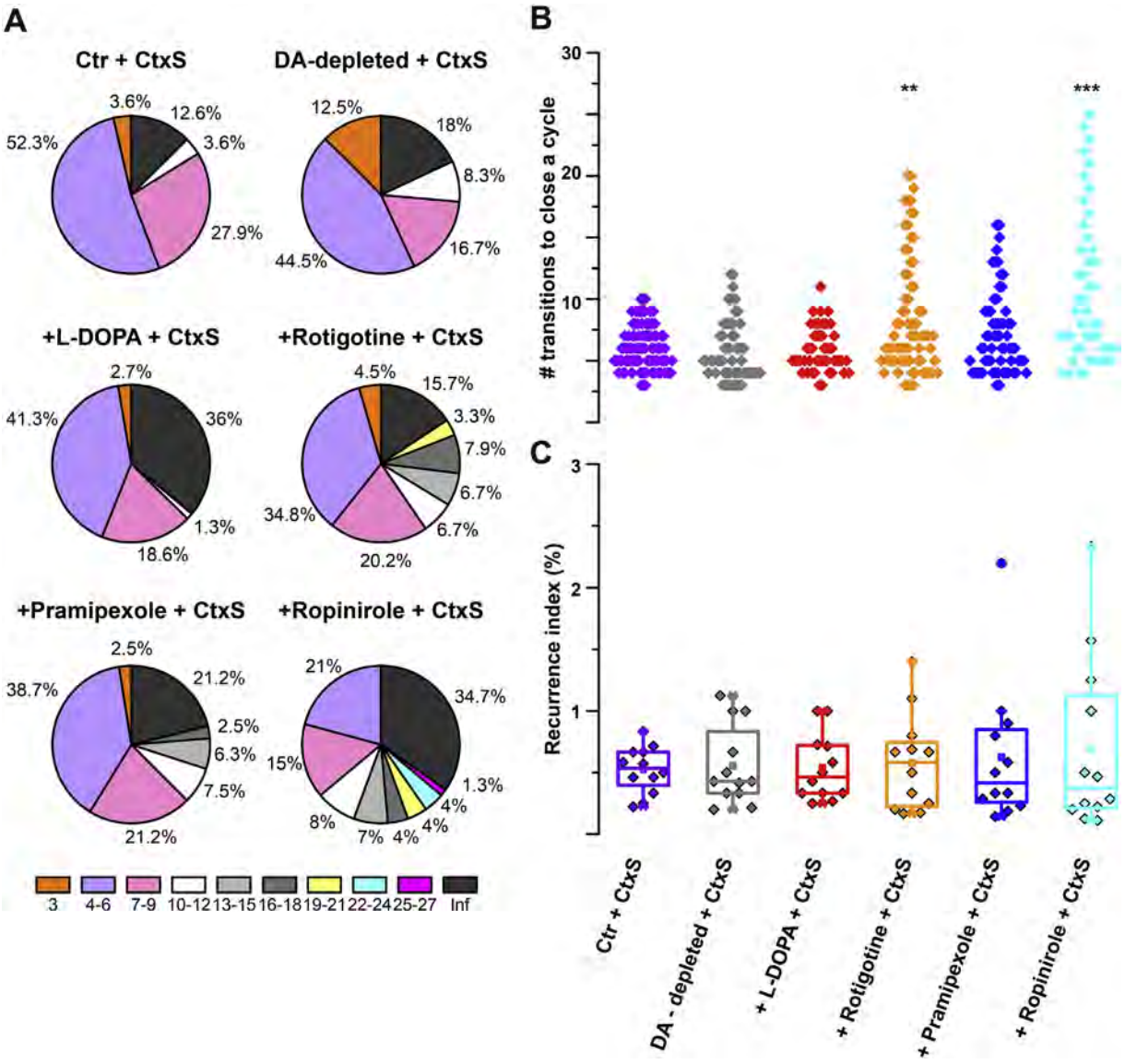

Fig. 9. Performance comparisons of DA-agonists on cortical activated DA-depleted microcircuits. (A) Pie plots show number of network state transitions necessary to close a cycle (see color scale below), including the cases in which there were no closed cycles during recording (in black). Top: the first 30 min after cortical stimulation of the DA-depleted microcircuit in absence of any drug (n = 4 experiments) was compared with control stimulated microcircuits (n = 5 experiments): there is no significant difference (Kolmogorov–Smirnov test with post hoc FDR correction, P = 0.206). Then, actions of DA-agonists on DA-depleted + CtxS circuits were compared with CtxS control circuits 60 min after stimulation (Aparicio-Juárez et al., 2019). In this condition, we compared different DA-agonists to find which one was not statistically different (resembled more) to control activated circuits: L-DOPA (P = 0.007, n = 4 experiments), rotigotine (P = 0.002, n = 4 experiments), pramipexole (P = 0.016, n = 4 experiments) and ropinirole ($P = 1X10^{-9}$, n = 4 experiments). The results of this stringent test were that no DA-agonist, including L-DOPA, is capable to completely resemble the control activated (Ctr + CtxS) circuit. (B) To see if these results were due to the number of incomplete cycles, we excluded them from the analyses and simply looked at the number of transitions required to close a cycle (when they could be closed during recording time). These data are displayed in density plots: Ctr + CtxS distribution was compared (Kruskal-Wallis ANOVA with post hoc FDR correction) with: DA-depleted + CtxS at 30 min (P = 0.149) and with CtxS plus a given DA-agonist at 60 min: L-DOPA + CtxS (P = 0.736), rotigotine + CtxS (**P = 0.003), pramipexole + CtxS (P = 0.199) and ropinirole + CtxS (***P = 0.001). This metric shows that L-DOPA and pramipexole produce a better microcircuit performance than rotigotine and ropinirole after CtxS. (C) A third metric was the recurrence index (Aparicio-Juárez et al., 2019) which indicates the appearance of a highly recurrent network state, shown in Tukey box plots as increased variance, and compared with the O'Brien homogeneity of variance test. In this perspective, DA-depleted + CtxS (30 min) P = 0.073 was not significantly different. While DA-agonists + CTxS compared at 60 min yield: L-DOPA + CtxS (P = 0.186); rotigotine + CtxS (P = 0.079); pramipexole + CtxS (P = 0.214); ropinirole + CtxS, P = 0.071), showing that all DA-agonists have some positive effect on active stimulated DA-depleted circuits, maintaining them out of a complete Parkinsonian dynamics after being activated by CtxS.

same time we confirm that no drug, including L-DOPA, completely restores circuitry function. However, new drugs and drug combinations (Millan, 2010) can also be tested with the present preparation. In addition, the action of CtxS to the DA-depleted circuit suggests that a combination of electrical plus pharmacologic stimulation may be helpful.

In conclusion, the present results show that microcircuit properties can be used to compare different drugs used in

neurological disorders, in particular, Parkinson's disease. By using calcium imaging with single cell resolution and recording dozens of cells simultaneously we found different effectiveness of DA-agonists in reversing pathological network dynamics in both, the resting non-stimulated tissue and the active stimulated one. A hierarchy in agonists performance was found: L-DOPA > selective D_2-class agonists > less selective $D_{1,2}$-class agonists. Paralleling cellular, behavioral and clinical studies (Baker et al., 2009; Bello et al., 2017; Blandini and Armentero, 2014; UK PD MED Collaborative Group, 2014).

Supplementary data to this article can be found online at https://doi.org/10.1016/j.neuroscience.2019.04.058.

ACKNOWLEDGEMENTS

Authors thank Antonio Laville, Dagoberto Tapia and Ariadna Aparicio-Juárez for technical support, Claudia Rivera and Héctor Malagón for their help at the animal facility. This work was supported by public grants CONACYT Frontera 57 y FON.INS. 29-10 and DGAPA-UNAM: IN201603 to J.B. Esther Lara-González is student from the Programa de Doctorado en Ciencias Biomedicas, Universidad Nacional Autónoma de México (UNAM), and received doctoral fellowship 218676 from CONACYT. Data in this work are part of her doctoral dissertation.

AUTHOR CONTRIBUTIONS

Esther Lara-González: Study conception and design, Acquisition of data, Analysis and interpretation of data, Drafting of manuscript. Mariana Duhne: Study conception and design, Acquisition of data, Analysis and interpretation of data. Fátima Ávila-Cascajares: Acquisition of data, Drafting of manuscript, Critical revision. Silvia Cruz: Acquisition of data. and José Bargas: Study conception and design, Critical revision.

DECLARATIONS OF INTEREST

None.

REFERENCES

Ahlskog JE, Muenter MD. (2001) Frequency of levodopa-related dyskinesias and motor fluctuations as estimated from the cumulative literature. Mov Disord 16:448-458, https://doi.org/10.1002/mds.1090.

Aparicio-Juárez A, Duhne M, Lara-González E, Ávila-Cascajares F, Calderón V, Galarraga E, Bargas J. (2019) Cortical stimulation relieves parkinsonian pathological activity in vitro. Eur J Neurosci 49:834-848, https://doi.org/10.1111/ejn.13806.

Aquino CC, Fox SH. (2015) Clinical spectrum of levodopa-induced complications. Mov Disord 30:80-89, https://doi.org/10.1002/mds.26125.

Baker WL, Silver D, White CM, Kluger J, Aberle J, Patel AA, Coleman CI. (2009) Dopamine agonists in the treatment of early Parkinson's disease: a meta-analysis. Parkinsonism Relat Disord 15:287-294, https://doi.org/10.1016/j.parkreldis.2008.07.004.

Ballion B, Frenois F, Zold CL, Chetrit J, Murer MG, Gonon F. (2009) D2 receptor stimulation, but not D1, restores striatal equilibrium in a rat model of parkinsonism. Neurobiol Dis 35:376-384, https://doi.org/10.1016/j.nbd.2009.05.019.

Barroso-Flores J, Herrera-Valdez MA, Lopez-Huerta VG, Galarraga E, Bargas J. (2015) Diverse short-term dynamics of inhibitory synapses converging on striatal projection neurons: differential changes in a rodent model of Parkinson's disease. Neural Plast 573543, https://doi.org/10.1155/2015/573543.

Bello EP, Casas-Cordero R, Galiñanes GL, Casey E, Belluscio MA, Rodríguez V, Noaín D, Murer MG, Rubinstein M. (2017) Inducible ablation of dopamine D2 receptors in adult mice impairs locomotion, motor skill learning and leads to severe parkinsonism. Mol Psychiatry 22:595-604, https://doi.org/10.1038/mp.2016.105.

Benjamini Y, Krieger AM, Yekutieli D. (2006) Adaptive linear step-up procedures that control the false discovery rate. Biometrika 93:491-507, https://doi.org/10.1093/biomet/93.3.49.

Blandini F, Armentero M-T. (2014) Dopamine receptor agonists for Parkinson's disease. Expert Opin Investig Drugs 23(3):387-410, https://doi.org/10.1517/13543784.2014.869209.

Brooks DJ. (2000) Dopamine agonists: their role in the treatment of Parkinson's disease. J Neurol Neurosurg Psychiatry 68:685-690, https://doi.org/10.1136/jnnp.68.6.685.

Burke RE, O'Malley K. (2013) Axon degeneration in Parkinson's disease. Exp Neurol 246:72-83, https://doi.org/10.1016/j.expneurol.2012.01.011.

Buzsaki G. (2010) Neural syntax: cell assemblies, synapsembles, and readers. Neuron 68:362-385, https://doi.org/10.1016/j.neuron.2010.09.023.

Cacace F, Mineo D, Viscomi MT, Latagliata EC, Mancini M, Sasso V, Vannelli A, Pascucci T, Pendolino V, Marcello E, Pelucchi S, Puglisi-Allegra S, Molinari M, Picconi B, Calabresi P, Ghiglieri V. (2017) Intermittent theta-burst stimulation rescues dopamine-dependent corticostriatal synaptic plasticity and motor behavior in experimental parkinsonism: possible role of glial activity. Mov Disord 32:1035-1046, https://doi.org/10.1002/mds.26982.

Calabresi P, Picconi B, Parnetti L, Di Filippo M. (2006) A convergent model for cognitive dysfunctions in Parkinson's disease: the critical dopamine-acetylcholine synaptic balance. Lancet Neurol 5:974-983, https://doi.org/10.1016/S1474-4422(06)70600-7.

Calabresi P, Picconi B, Tozzi A, Ghiglieri V, Di Filippo M. (2014) Direct and indirect pathways of basal ganglia: a critical reappraisal. Nat Neurosci 17:1022-1030, https://doi.org/10.1038/nn.3743.

Carillo-Reid L, Tecuapetla F, Ibanez-Sandoval O, HernandezCruz A, Galarraga E, Bargas J. (2009) Activation of the cholinergic system endows compositional properties to striatal cell assemblies. J Neurophysiol 101:737-749, https://doi.org/10.1152/jn.90975.2008.

Carlsson A, Lindqvist M, Magnusson TOR. (1957) 3, 4-Dihydroxyphenylalanine and 5-hydroxytryptophan as reserpine antagonists. Nature 180(4596):1200.

Carrillo-Reid L, Hernández-López S, Tapia D, Galarraga E, Bargas J. (2011) Dopaminergic modulation of the striatal microcircuit: receptor-specific configuration of cell assemblies. J Neurosci 31:14972-14983, https://doi.org/10.1523/JNEUROSCI.3226-11.2011.

Carrillo-Reid L, Lopez-Huerta VG, Garcia-Munoz M, Theiss S, Arbuthnott GW. (2015) Cell assembly signatures defined by short-term synaptic plasticity in cortical networks. Int J Neural Syst 251550026, https://doi.org/10.1142/S0129065715500264.

Carrillo-Reid L, Tecuapetla F, Tapia D, Hernández-Cruz A, Galarraga E, Drucker-Colin R, Bargas J. (2008) Encoding network states by striatal cell assemblies. J Neurophysiol 99:1435-1450, https://doi.org/10.1152/jn.01131.2007.

Carrillo-Reid L., Tecuapetla F., Ibáñez-Sandoval O., Hernández-Cruz A., Galarraga E., Bargas J.. (2009) Activation of the cholinergic system endows compositional properties to striatal cell assemblies. J Neurophysiol 101:737-749, https://doi.org/10.1152/jn.90975.2008.

Carrillo-Reid L, Yang W, Bando Y, Peterka DS, Yuste R. (2017) Imprinting and recalling cortical ensembles. Science 353:691-694, https://doi.org/10.1126/science.aaf7560.

Chen F, Jin L, Nie Z. (2017) Safety and efficacy of Rotigotine for treating Parkinson's disease: a meta-analysis of randomised controlled trials. J Pharm Pharm Sci 20:285-294, https://doi.org/10.18433/J3Q35D.

Cui G, Jun SB, Jin X, Luo G, Pham MD, Lovinger DM, Vogel SS, Costa RM. (2014) Deep brain optical measurements of cell type-specific neural activity in behaving mice. Nat Protoc 9:1213-1228, https://doi.org/10.1038/nprot.2014.080.

De Deurwaerdère P, Di Giovanni G, Millan MJ. (2017) Expanding the repertoire of L-DOPA's actions: a comprehensive review of its functional neurochemistry. Prog Neurobiol 151:57-100, https://doi.org/10.1016/j.pneurobio.2016.07.002.

Deffains M, Bergman H. (2015) Striatal cholinergic interneurons and cortico-striatal synaptic plasticity in health and disease. Mov Disord 30:1014-1025, https://doi.org/10.1002/mds.26300.

Devos D, French DUODOPA Study Group . (2009) Patient profile, indications, efficacy and safety of duodenal levodopa infusion in advanced Parkinson's disease. Mov Disord 24:993-1000, https://doi.org/10.1002/mds.22450.

Dunnet SB, Lelos M. (2010) Behavioral analysis of motor and non-motor symptoms in rodent models of Parkinson's disease. Prog. Brain Res 184:35-51, https://doi.org/10.1016/S0079-6123(10)84003–8.

Edelman GM. (1993) Neural Darwinism: selection and reentrant signaling in higher brain function. Neuron 10:115-125.

Fabbrini G, Mouradian MM, Juncos JL, Schlegel J, Mohr E, Chase TN. (1988) Motor fluctuations in Parkinson's disease: central pathophysiological mechanisms, part I. Ann Neurol 24:366-371, https://doi.org/10.1002/ana.410240303.

Foley P. (2000) The L-DOPA story revisited. Further surprises to be expected? J Neural Transm Suppl 2000:1-20.

Gerfen CR, Surmeier DJ. (2011) Modulation of striatal projection systems by dopamine. Annu Rev Neurosci 34:441-466, https://doi.org/10.1146/annurev-neuro-061010-113641.

Goldberg J.A., Wilson C.J.. (2005) Control of spontaneous firing patterns by the selective coupling of calcium currents to calcium-activated potassium currents in striatal cholinergic interneurons. J Neurosci 25:10230-10238, https://doi.org/10.1523/JNEUROSCI.2734-05.2005.

Hebb DO. (1949) The Organization of Behavior. New York: Wiley, 1949.

Heuer A, Smith GA, Lelos MJ, Lane EL, Dunnett SB. (2012) Unilateral nigrostriatal 6-hydroxydopamine lesions in mice: motor impairments identify extent of dopamine depletion at three different lesion sites. Behav Brain Res 228:30-43, https://doi.org/10.1016/j.bbr.2011.11.027.

Hu X-T, Wang RY. (1988) Comparison of effects of D-l and D-2 dopamine receptor agonists on neurons in the rat caudate putamen: an electrophysiological study. J Neurosci 8:4340-4348.

Jáidar O, Carrillo-Reid L, Hernández A, Drucker-Colín R, Bargas J, Hernández-Cruz A. (2010) Dynamics of the parkinsonian striatal microcircuit: entrainment into a dominant network state. J Neurosci 30:11326-11336, https://doi.org/10.1523/JNEUROSCI.1380-10.2010.

Jáidar O, Carrillo-Reid L, Nakano Y, Lopez-Huerta VG, Hernandez-Cruz A, Bargas J, Garcia-Munoz M, Arbuthnott GM. (2019) Synchronized activation of striatal direct and indirect pathways underlies the behavior in unilateral dopamine-depleted mice. Eur J Neurosci , https://doi.org/10.1111/ejn.14344.

Jenner P, Katzenschlager R. (2016) Apomorphine - pharmacological properties and clinical trials in Parkinson's disease. Parkinsonism Relat Disord 33(1):S13-S21, https://doi.org/10.1016/j.parkreldis.2016.12.003.

Jimenez-Shahed J. (2016) A review of current and novel levodopa formulations for the treatment of Parkinson's disease. Ther Deliv 7:179-191, https://doi.org/10.4155/tde.15.96.

Klaus A, Martins GJ, Paixao VB, Zhou P, Paninski L, Costa RM. (2017) The spatiotemporal Organization of the Striatum Encodes Action Space. Neuron 95:1171-1180, https://doi.org/10.1016/j.neuron.2017.08.015.

Kravitz AV, Freeze BS, Parker PR, Kay K, Thwin MT, Deisseroth K, Kreitzer AC. (2010) Regulation of parkinsonian motor behaviours by optogenetic control of basal ganglia circuitry. Nature 466:622-626https://doihttps://doi.org/10.1038/nature09159.

Lam YW. (2000) Clinical pharmacology of dopamine agonists. Pharmacotherapy 20:17S-25S.

Lees AJ, Hardy J, Revesz T. (2009) Parkinson's disease. Lancet 373:2055-2066, https://doi.org/10.1016/S0140-6736(09)60492-X.

Lees AJ, Tolosa E, Olanow CW. (2015) Four pioneers of L-dopa treatment: Arvid Carlsson, Oleh Hornykiewicz, George Cotzias, and Melvin Yahr. Mov Disord 30:19-36, https://doi.org/10.1002/mds.26120.

Lemaire N, Hernandez LF, Hu D, Kubota Y, Howe MW, Graybiel AM. (2012) Effects of dopamine depletion on LFP oscillations in striatum are task- and learning-dependent and selectively reversed by L-DOPA. Proc Natl Acad Sci U S A 109:18126-18131, https://doi.org/10.1073/pnas.1216403109.

Liang L, DeLong MR, Papa SM. (2008) Inversion of dopamine responses in striatal medium spiny neurons and involuntary movements. J Neurosci 28:7537-7547, https://doi.org/10.1523/JNEUROSCI.1176-08.2008.

Linazasoro G, Spanish Dopamine Agonists Study Group . (2004) Conversion from dopamine agonists to pramipexole. An open-label trial in 227 patients with advanced Parkinson's disease. J Neurol 251:335-339, https://doi.org/10.1097/wnf.0b013e318067bcc4.

López-Huerta VG, Carrillo-Reid L, Galarraga E, Tapia D, Fiordelisio T, Drucker-Colin R, Bargas J. (2013) The balance of striatal feedback transmission is disrupted in a model of parkinsonism. J Neurosci 33:4964-4975, https://doi.org/10.1523/JNEUROSCI.4721-12.2013.

Mercuri NB, Bernardi G. (2005) The 'magic' of L-dopa: why is it the gold standard Parkinson's disease therapy? Trends Pharmacol Sci 26:341-344, https://doi.org/10.1016/j.tips.2005.05.002.

Millan MJ. (2010) From the cell to the clinic: a comparative review of the partial D2/D3 receptor agonist and α2-adrenoceptor antagonist, piribedil, in the treatment of Parkinson's disease. Pharmacol Ther 128:229-273, https://doi.org/10.1016/j.pharmthera.2010.06.002.

Mink JW. (2003) The basal ganglia. In: Squire LR, Bloom FE, McConnell SK, Roberts JM, Spitzer NC, & Zigmon MJ, editors. Fundamental Neuroscience. Amsterdam: Academic Press. p. 815-839.

Mizuno Y, Nomoto M, Hasegawa K, Hattori N, Kondo T, Murata M, Takeuchi M, Takahashi M, Tomida T, Rotigotine Trial Group . (2014) Rotigotine vs ropinirole in advanced stage Parkinson's disease: a double-blind study. Parkinsonism Relat Disord 20:1388-1393, https://doi.org/10.1016/j.parkreldis.2014.10.005.

Morissette M, Di Paolo T. (2018) Non-human primate models of PD to test novel therapies. J Neural Transm (Vienna) 125:291-324, https://doi.org/10.1007/s00702-017-1722-y.

Nutt JG, Obeso JA, Stocchi F. (2000) Continuous dopamine-receptor stimulation in advanced Parkinson's disease. Trends Neurosci 23: S109-S115.

Obeso JA, Stamelou M, Goetz CG, Poewe W, Lang AE, Weintraub D, Burn D, Halliday GM, Bezard E, Przedborski S, Lehericy S, Brooks DJ, Rothwell JC, Hallett M, DeLong MR, Marras C, Tanner CM, Ross GW, Langston JW, Klein C, Bonifati V, Jankovic J, Lozano AM, Deuschl G, Bergman H, Tolosa E, Rodriguez-Violante M, Fahn S, Postuma RB, Berg D, Marek K, Standaert DG, Surmeier DJ, Olanow CW, Kordower JH, Calabresi P, Schapira AHV, Stoessl AJ. (2017) Past, present, and future of Parkinson's disease: a special essay on the 200th anniversary of the shaking palsy. Mov Disord 32:1264-1310, https://doi.org/10.1002/mds.27115.

Olanow CW, Stocchi F. (2017) Levodopa: a new look at an old friend. Mov Disord , https://doi.org/10.1002/mds.27216.

Ossowska K, Wolfarth S. (1995) Stimulation of glutamate receptors in the intermediate/caudal striatum induces contralateral turning. Eur J Pharmacol 273:89-975.

Owen SF, Berke JD, Kreitzer AC. (2018) Fast-spiking interneurons supply feedforward control of bursting, calcium, and plasticity for efficient learning. Cell. 172:683-695, https://doi.org/10.1016/j.cell.2018.01.005.

Parker JG, Marshall JD, Ahanonu B, Wu YW, Kim TH, Grewe BF, Zhang Y, Li JZ, Ding JB, Ehlers MD, Schnitzer MJ. (2018) Diametric neural ensemble dynamics in parkinsonian and dyskinetic states. Nature, https://doi.org/10.1038/s41586-018-0090-6 Epub ahead of print.

Pérez-Ortega J, Duhne M, Lara-González E, Plata V, Gasca D, Galarraga E, Hernández-Cruz A, Bargas J. (2016) Pathophysiological signatures of functional connectomics in parkinsonian and dyskinetic striatal microcircuits. Neurobiol Dis 91:347-361, https://doi.org/10.1016/j.nbd.2016.02.023.

Picconi B, Hernández LF, Obeso JA, Calabresi P. (2017) Motor complications in Parkinson's disease: striatal molecular and electrophysiological mechanisms of dyskinesias. Mov Disord , https://doi.org/10.1002/mds.27261.

Plata V, Duhne M, Pérez-Ortega JE, Barroso-Flores J, Galarraga E, Bargas J. (2013) Direct evaluation of L-DOPA actions on neuronal activity of parkinsonian tissue in vitro. Biomed Res Int 2013519184, https://doi.org/10.1155/2013/519184.

INFORME DE LABORES 2019

Radad K, Gille G, Rausch WD. (2005) Short review on dopamine agonists: insight into clinical and research studies relevant to Parkinson's disease. Pharmacol Rep 57:701-712.

Rascol O, Brooks DJ, Brunt ER, Korczyn AD, Poewe WH, Stocchi F. (1998) Ropinirole in the treatment of early Parkinson's disease: a 6-month interim report of a 5-year levodopa-controlled study. 056 study group. Mov Disord 13:39-45, https://doi.org/10.1002/mds.870130111.

Reichmann H. (2000) Long-term treatment with dopamine agonists in idiopathic Parkinson's disease. J Neurol 247:17-19, https://doi.org/10.1007/PL00007768 Suppl 4.

Sharma S, Singh S, Sharma V, Singh VP, Deshmukh R. (2015) Neurobiology of l-DOPA induced dyskinesia and the novel therapeutic strategies. Biomed Pharmacother 70:283-293, https://doi.org/10.1016/j.biopha.2015.01.029.

Shen T, Ye R, Zhang B. (2017) Efficacy and safety of pramipexole extended-release in Parkinson's disease: a review based on meta-analysis of randomized controlled trials. Eur J Neurol 24:835-843, https://doi.org/10.1111/ene.13303.

Sprenger F, Poewe W. (2013) Management of motor and non-motor symptoms in Parkinson's disease. CNS Drugs 27:259-272, https://doi.org/10.1007/s40263-013-0053-2.

Stocchi F. (2009) Dopamine receptor agonists in the treatment of advanced Parkinson's disease. Parkinsonism Relat Disord 15: S54-S57, https://doi.org/10.1016/S1353-8020(09)70836-3.

Stocchi F, Torti M, Fossati C. (2016) Advances in dopamine receptor agonists for the treatment of Parkinson's disease. Expert Opin Pharmacother 17:1889-1902, https://doi.org/10.1080/14656566.2016.1219337.

Surmeier DJ, Carrillo-Reid L, Bargas J. (2011) Dopaminergic modulation of striatal neurons, circuits, and assemblies. Neuroscience 198:3-18, https://doi.org/10.1016/j.neuroscience.2011.08.051.

Tepper J.M., Koós T., Ibanez-Sandoval O., Tecuapetla F., Faust T.W., Assous M.. (2018) Heterogeneity and Diversity of Striatal GABAergic Interneurons: Update 2018. Front Neuroanat 12:91, https://doi.org/10.3389/fnana.2018.00091. eCollection 2018.

Thomas D, Tovey SC, Collins TJ, Bootman MD, Berridge MJ, Lipp P. (2000) A comparison of fluorescent Ca^{2+} indicator properties and their use in measuring elementary and global Ca^{2+} signals. Cell Calcium 28:213-223.

UK PD MED Collaborative Group. (2014) Long-term effectiveness of dopamine agonists and monoamine oxidase B inhibitors compared with levodopa as initial treatment for Parkinson's disease (PD MED): a large, open-label, pragmatic randomised trial. Lancet 384:1196-1205, https://doi.org/10.1016/S0140-6736(14)60683-8.

Ungerstedt U, Arbuthnott GW. (1970) Quantitative recording of rotational behavior in rats after 6-hydroxy-dopamine lesions of the nigrostriatal dopamine system. Brain Res 24:485-493.

Wang Y, Zhou FM. (2017) Striatal but not Extrastriatal dopamine receptors are critical to dopaminergic motor stimulation. Front Pharmacol 8(935), https://doi.org/10.3389/fphar.2017.00935.

Zesiewicz TA, Chriscoe S, Jimenez T, Upward J, Davy M, VanMeter S. (2017) A randomized, fixed-dose, dose-response study of ropinirole prolonged release in advanced Parkinson's disease. Neurodegener Dis Manag 7:61-72, https://doi.org/10.2217/nmt-2016-0038.

(Received 5 February 2019, Accepted 30 April 2019)
(Available online 9 May 2019)

International Journal of
Molecular Sciences

MDPI

Article

Novel Potassium Channels in Kidney Mitochondria: The Hyperpolarization-Activated and Cyclic Nucleotide-Gated HCN Channels

Daniel León-Aparicio [1], Carolina Salvador [1], Omar Emiliano Aparicio-Trejo [2], Alfredo Briones-Herrera [2], José Pedraza-Chaverri [2], Luis Vaca [3], Alicia Sampieri [3], Teresa Padilla-Flores [1], Zinaeli López-González [1], Juan C León-Contreras [4], Rogelio Hernández-Pando [4] and Laura I Escobar [1,*]

1 Departamento de Fisiología, Facultad de Medicina, Universidad Nacional Autónoma de México (UNAM), Mexico City 04510, Mexico; dalebx4@gmail.com (D.L.-A.); caro.unam@gmail.com (C.S.); mhaytte@hotmail.com (T.P.-F.); zinaeli_lopezglz@hotmail.com (Z.L.-G.)
2 Departamento de Biología, Facultad de Química, Universidad Nacional Autónoma de México (UNAM), Mexico City 04510, Mexico; emilianoaparicio91@gmail.com (O.E.A.-T.); bhalfredo@gmail.com (A.B.-H.); pedraza@unam.mx (J.P.-C.)
3 Departamento de Biología Celular y del Desarrollo, Instituto de Fisiología Celular, Universidad Nacional Autónoma de México (UNAM), Mexico City 04510, Mexico; lvaca@ifc.unam.mx (L.V.); asampieri@ifc.unam.mx (A.S.)
4 Departamento de Patología, Instituto Nacional de Ciencias Médicas y Nutrición Salvador Zubirán, Mexico City 14080, Mexico; jcleonc@hotmail.com (J.C.L.-C.); rhdezpando@hotmail.com (R.H.-P.)
* Correspondence: laurae@unam.mx

Received: 17 August 2019; Accepted: 6 October 2019; Published: 9 October 2019



Abstract: Hyperpolarization-activated cationic HCN channels comprise four members (HCN1–4) that control dendritic integration, synaptic transmission and action potential firing. In the kidney, HCN1, HCN2 and HCN3 are differentially expressed and contribute to the transport of sodium, potassium (K^+) and ammonium into the nephrons. HCN3 is regulated by K^+ diets in the kidney. In this work we performed a proteomic analysis of HCN3 expressed in human embryonic kidney cells (HEK293 cells). More than 50% of the interacting proteins belonged to mitochondria. Therefore, we explored the presence of HCN channels in kidney mitochondria. By immunoblotting and immunogold electron microscopy HCN3 protein expression was found in rat kidney mitochondria; it was also confirmed in human kidney. Patch-clamp recordings of renal mitochondria and mitochondria from HEK293 cells overexpressing HCN1, HCN2 and HCN3 channels, stained with MitoTracker Green FM, indicated that only HCN3 could produce inwardly K^+ currents that were inhibited by ZD7288, a specific blocker of HCN channels. Furthermore, ZD7288 caused inhibition of the oxygen consumption coupled to ATP synthesis and hyperpolarization of the inner mitochondrial membrane. In conclusion, we show for the first time that pacemaker HCN channels contribute to K^+ transport in mitochondria facilitating the activity of the respiratory chain and ATP synthesis by controlling the inner mitochondrial membrane potential.

Keywords: mitochondria; kidney; mitochondrial potassium channel; hyperpolarization-activated cyclic nucleotide-gated cationic HCN channels in mitochondria; potassium transport in mitochondria; mitochondria uncoupling

1. Introduction

The large number of mitochondria in the kidney provides the energy required to remove waste products and maintain electrolyte balance. Mitochondria are important organelles for cell viability,

INFORME DE LABORES 2019

since they produce ATP via oxidative phosphorylation (OXPHOS) and play an active role in calcium homeostasis, reactive oxygen species (ROS) production and apoptosis. The electron transport system (ETS) and the ATP synthase are located in the inner mitochondrial membrane (IMM) and are essential components for the generation and preservation of energy metabolism [1]. The high negative value of the IMM potential ($\Delta\Psi m$) required for oxidative phosphorylation is a powerful driving force for potassium (K^+) uptake. Therefore, dynamic regulation of mitochondrial K^+ flux in vivo is necessary to maintain the structural and functional membrane integrity for oxidative phosphorylation. To avoid swelling and lysis, the ion leakage in the mitochondria has to be balanced by extrusion of ions against the electrical gradient and this mechanism is accomplished by the mitochondrial K^+ cycle [2].

The electrogenic transport of K^+ into the mitochondrial matrix is strictly ion-channel-dependent. Activation of mitochondrial K^+ channels is a hallmark of cell death and plays a central role in cardiomyocytes and neuron protection [3–5]. Mitochondrial K^+ channels, such as the ATP-regulated (mitoKATP) channel, the Ca^{2+}-activated K^+ (mitoKCa) channel, the voltage-gated Kv1.3 (mitoKv1.3) channel and the two-pore domain TASK-3 (mitoTASK) channel, have been documented at the IMM of different organs, tissues or glioma cell lines. IMM K^+ channels contribute to the regulation of the matrix volume, to establish $\Delta\Psi$ and ΔpH, to calcium influx and to ROS production [6,7]. Activation of IMM K^+ channels favors an uncoupling effect that could in turn decrease energetic efficiency [8]. So far only an ATP-sensitive K^+ transport pathway has been documented in the rat kidney mitochondria [9].

The hyperpolarization-activated cyclic nucleotide-gated cationic (HCN) channels comprise four members termed HCN1–4 [10]; they have a pacemaker activity in excitable tissues controlling excitability, establishment of the resting membrane potential, dendritic integration, synaptic transmission and action potential firing [11,12]. Previously, we found that HCN channels transport ammonium (NH_4^+) in addition to Na^+/K^+ in the acid-secretory type-A intercalated cells of distal nephron segments of the kidney [13], contributing to the acid-base balance. Among HCN channel subtypes only HCN1, HCN2 and HCN3 are expressed and differentially distributed in the proximal convoluted tubule, the thick ascending limb of Henle, connecting tubule and collecting ducts of the rat kidney [14]. Due to the wide and abundant distribution of HCN3 in the kidney, in this work we performed a proteomic analysis of HCN3 overexpressed in HEK293 cells. Analysis of the proteomic data revealed interaction of HCN3 with mitochondria proteins. By immunoblotting, immunogold electron microscopy, patch-clamp recordings, oximetry and $\Delta\Psi$ measurements, we confirmed this prediction and determined that HCN channels behave as open K^+ channels in the kidney mitochondria, contributing to oxygen consumption, ATP synthesis and $\Delta\Psi$ establishment.

2. Results

2.1. Proteomic Analysis of HCN3 Channel

HCN3 is differentially expressed in the rat kidney: proximal tubules and thick ascending limb of Henle and its protein abundance is regulated by K^+ metabolism [14]. In this study, proteomics and bioinformatics analyses were performed to establish a protein-protein interaction network (interactome) associated with HCN3. For this purpose, HCN3 protein was immunoprecipitated from transfected HEK293, electrophoretically separated and analyzed by mass spectrometry. Mitochondrial proteins were the most prominent protein family identified (Table 1).

INFORME DE LABORES 2019

Table 1. List of HCN3 channel-interacting proteins identified by LC/MS/MS during mass spectrometry.

Protein Name	UniProt Accession	UniProt Entry Name	Gene Name	Molecular Mass (kDa)
40S ribosomal protein S3 *	E9PPU1	E9PPU1_HUMAN	*RPS3*	17.4
ATP synthase subunit alpha_ mitochondrial *	P25705	ATPA_HUMAN	*ATP5F1A*	59.9
ATP synthase subunit beta_ mitochondrial *	P06576	ATPB_HUMAN	*ATP5F1B*	56.6
ATP-dependent RNA helicase DDX3X *	A0A2R8Y5G6	A0A2R8Y5G6_HUMAN	*DDX3X*	69.4
C-1-tetrahydrofolate synthase_ cytoplasmic *	P11586	C1TC_HUMAN	*MTHFD1*	102.2
Clathrin heavy chain 2	A0A087WX41	A0A087WX41_HUMAN	*CLTCL1*	144.1
Elongation factor Tu_ mitochondrial *	P49411	EFTU_HUMAN	*TUFM*	49.9
Eukaryotic translation initiation factor 4 gamma 1	Q04637	IF4G1_HUMAN	*EIF4G1*	176.2
Fatty acid synthase	A0A0U1RQF0	A0A0U1RQF0_HUMAN	*FASN*	275.8
Filamin-A	A0A087WWY3	A0A087WWY3_HUMAN	*FLNA*	248.3
Golgin subfamily B member 1	Q14789	GOGB1_HUMAN	*GOLGB1*	377.4
Heat shock 70 kDa protein 1A *	P0DMV8	HS71A_HUMAN	*HSPA1A*	70.3
Heat shock-related 70 kDa protein 2	P54652	HSP72_HUMAN	*HSPA2*	70.3
Isoform 2 of Clathrin heavy chain 1	Q00610-2	CLH1_HUMAN	*CLTC*	189.7
Isoform 2 of Glyceraldehyde-3-phosphate dehydrogenase	P04406-2	G3P_HUMAN	*GAPDH*	31.7
Isoform 2 of Heat shock protein 75 kDa_ mitochondrial *	Q12931-2	TRAP1_HUMAN	*TRAP1*	74.5
Isoform 3 of Pyruvate kinase PKM	P14618-3	KPYM_HUMAN	*PKM*	56.9
Isoform 3 of Vacuolar protein sorting-associated protein 13C	Q709C8-3	VP13C_HUMAN	*VPS13C*	419.6
Isoform MBP-1 of Alpha-enolase	P06733-2	ENOA_HUMAN	*ENO1*	37.3
Isoform Short of Delta-1-pyrroline-5-carboxylate synthase *	P54886-2	P5CS_HUMAN	*ALDH18A1*	87.8
Matrix-remodeling-associated protein 5	Q9NR99	MXRA5_HUMAN	*MXRA5*	314.3
Polyadenylate-binding protein 4	Q13310	PABP4_HUMAN	*PABPC4*	71.1
Polyubiquitin-B (Fragment) *	J3QS39	J3QS39_HUMAN	*UBB*	10.5
Prohibitin (Fragment) *	C9JZ20	C9JZ20_HUMAN	*PHB*	22.3
Prohibitin-2 *	Q99623	PHB2_HUMAN	*PHB2*	33.3
Receptor of activated protein C kinase 1	P63244	RACK1_HUMAN	*RACK1*	35.5
RuvB-like 2	Q9Y230	RUVB2_HUMAN	*RUVBL2*	51.3
Tubulin beta chain	Q5JP53	Q5JP53_HUMAN	*TUBB*	48.2
Tubulin beta-4B chain	P68371	TBB4B_HUMAN	*TUBB4B*	50.3
Vimentin	P08670	VIME_HUMAN	*VIM*	53.7

The resulting candidate proteins had a percentage ≥95% of reliability (Protein AutoCurate green), highlighting the robustness of the analytical method. * Proteins identified with at least one Gene Ontology (GO) term related with mitochondria (www.geneontology.org, www.pantherdb.org and www.string-db.org) and these proteins are listed in the actual version of the MitoProteome database (www.mitoproteome.org).

2.2. Identification of HCN Potassium Channels in Kidney Mitochondria

To investigate HCN3 expression in mitochondria, we performed immunoblot analysis with mitochondria isolated from the renal cortex. Immunoblotting of all HCN subtypes revealed very low amounts of HCN2 and abundant expression of HCN3 in kidney mitochondria. α-tubulin and VDAC were used as negative and positive controls of mitochondria abundance, respectively (Figure 1a). Therefore, we proceeded to study HCN3 protein expression in HEK293 cells. Before the transfection

INFORME DE LABORES 2019

assay with each member of the HCN family (HCN1–4) in HEK293 ells, we analyzed and confirmed the expression of endogenous HCN1, HCN2 and HCN3 (Figure 1b). However, only HCN3 was detected in the mitochondrial fraction. In contrast, overexpression of HCN1–4 channels in HEK293 cells showed that HCN3 and HCN4 could be trafficked to mitochondria (Figure 1b,c).

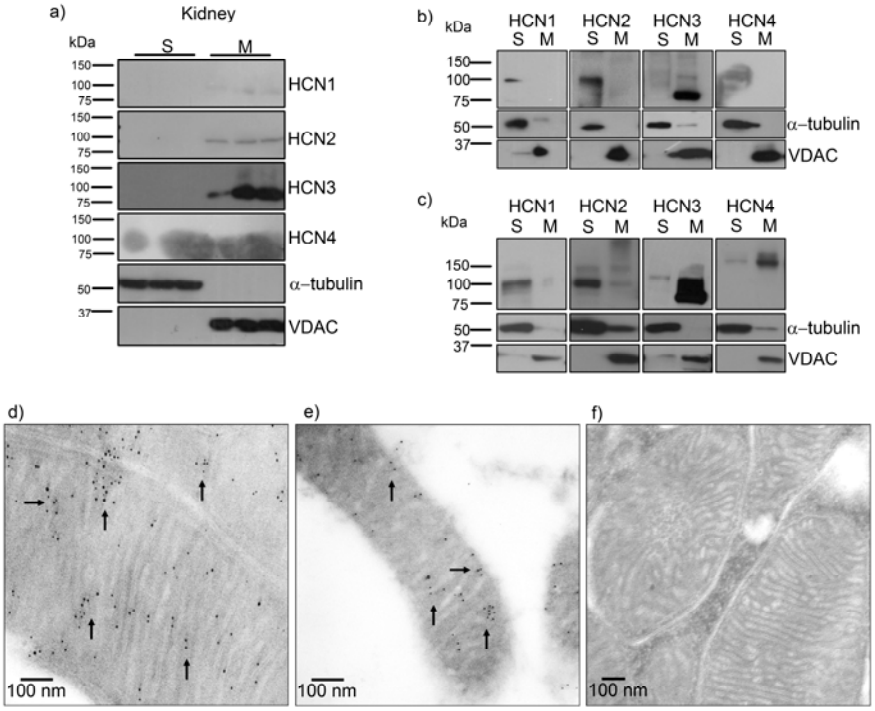

Figure 1. HCN3 channel expression in mitochondria isolated from renal cortex and HEK293 cells. (**a**) Immunoblotting of HCN1, HCN2, HCN3 and HCN4 with polyclonal antibodies detected only HCN2 (~94 kDa) and HCN3 (~86 kDa) in renal mitochondria. α-tubulin (~50 kDa) and voltage dependent anion channel (VDAC, ~31 kDa) were used as negative and positive controls of mitochondria abundance, respectively. (**b**) Immunoblotting of HCN1, HCN2, HCN3 and HCN4 in supernatant (S) and mitochondria (M) of control HEK293 cells. (**c**) Immunoblotting of HEK293 cells transfected with HCN1, HCN2, HCN3 and HCN4 in supernatant (S) and mitochondria (M). Only HCN3 (86 kDa) and HCN4 (160 kDa) were observed in HEK293 mitochondria. Immunogold electron microscopy localization of HCN3 (arrows) in the inner mitochondrial membrane of mitochondria from (**d**) rat (renal cortex) and (**e**) human kidney. (**f**) Negative control was performed in the absence of the primary antibody.

HCN3 immunogold labeling was developed in rat and human renal tissue and examined by electron microscopy. HCN3 was localized specifically in the IMM in rat and human (Figure 1d,e). Human mitochondria looked smaller than rat mitochondria since they were recovered from formalin-fixed paraffin-embedded tissues.

2.3. Functional Characterization of HCN Channels in Mitochondria

We aimed to study HCN3 functional expression in mitochondria isolated from the renal cortex (Figure 2a–c). To identify clearly mitochondria and separate them from cell debris, we incubated the isolated mitochondria with the mitochondria-selective fluorescent label MitoTracker Green FM (Figure 2a). Patch clamp recordings obtained from isolated mitochondria (whole-mitochondria recordings) evidenced the presence of hyperpolarization-activated K^+ currents (Figure 2b,c) that were inhibited by the HCN-specific inhibitor, ZD7288 (Figure 2b,c). Based on immunoblotting assays (Figure 1a) and the time constant of activation (τ) at −100 mV of 1120 ± 450 ms (n = 17), the currents observed in kidney mitochondria were produced mostly by HCN3 channels (Figure 1a) since HCN2 displays a fast activation (τ = 562 ± 198) [15].

INFORME DE LABORES 2019

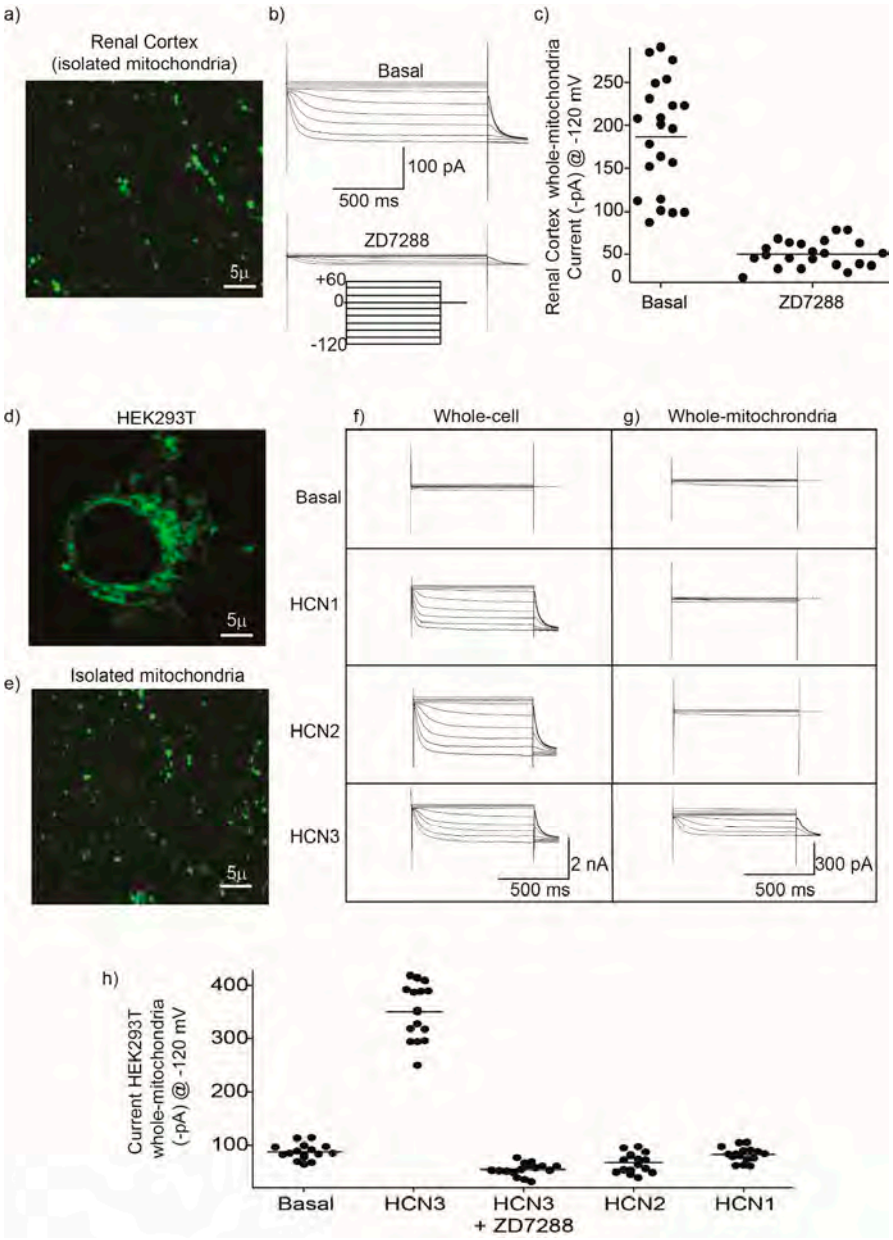

Figure 2. Inwardly potassium (K^+) currents recorded in isolated mitochondria from the renal cortex and HEK293 cells correspond to HCN3. (**a**) Fluorescence microscopy imaging from isolated mitochondria obtained from the renal cortex. Mitochondria were incubated for 10 min with 5 µM of the fluorescent indicator MitoTracker Green FM. Excitation was 490 nm and emission collected at 525 nm. By fluorescence microscopy it was possible to separate mitochondria from debris during patch clamp experiments. (**b**) Whole-mitochondria voltage clamp currents were recorded with 20 mV steps from −120 mV to +60 mV and a holding potential of 0 mV. Basal shows a representative family of HCN currents obtained from a single mitochondrion and the same family of currents after 2 min of incubation with 50 µM of the inhibitor ZD7288. (**c**) Currents obtained at −120 mV from different independent mitochondria under basal conditions and after addition of ZD7288. Each filled circle represents a single measurement and the horizontal line indicates the mean value. (**d**) HEK293T cells labeled with the fluorescent indicator MitoTracker Green FM. (**e**) Isolated mitochondria from HEK293 cells labeled with MitoTracker Green FM. (**f**) Family of currents obtained in whole-cell configuration and (**g**) in whole-mitochondria, under basal conditions and from cells overexpressing HCN1, HCN2 and HCN3. (**h**) Currents recorded at −120 mV from mitochondria isolated from HEK293 control cells (Basal) and cells overexpressing HCN1, HCN2, HCN3 and HCN3 + ZD7288. Each filled circle represents a single measurement and the horizontal line indicates the mean value.

INFORME DE LABORES 2019

We proceeded next to explore the presence of HCN currents in HEK293 cells comparing whole-cell currents with currents from isolated mitochondria (whole-mitochondria recordings). Firstly, we labeled mitochondria with MitoTracker Green FM in intact living HEK293 cells (Figure 2d) and isolated mitochondria (Figure 2e). As illustrated in the Figure, MitoTracker Green FM labeled selectively mitochondria in culture cells and also in isolated mitochondria. Transfecting of all HCN1–3 plasmids resulted in whole-cell currents associated with each channel (Figure 2f). These results indicated that although each HCN channel subtype is expressed and localized at the plasma membrane of HEK293 cells (therefore identified by whole-cell recordings), only HCN3 produced functional currents in isolated mitochondria (Figure 2g,h).

2.4. ZD7288 Decreased the Mitochondrial Respiratory Control Index and ΔΨm

To elucidate the functional role of HCN3 in mitochondria, the effect of ZD7288 was evaluated on isolated mitochondria from the renal cortex and HEK293 cells transfected with HCN3. It is well established that activation of NADH quinone oxidoreductase (Complex I) in respiratory state 2 (S2), increases hyperpolarization of the IMM by the electron transport chain proton pumping. Also, the addition of ADP or state 3 (S3) stimulates oxygen consumption due to ATP synthesis; this effect is inhibited by oligomycin (S4o). ZD7288 did not affect S2 and S4o. In contrast, ZD7288 drastically reduced oxygen consumption in S3 from 1202 ± 166.6 pmol O_2 s^{-1} mg^{-1} to 330.4 ± 29.72 pmol O_2 s^{-1} mg^{-1} (Figure 3a). As a consequence, mitochondrial coupling decreased: the respiratory control index (RCI) changed from 6.71 ± 0.70 to 2.09 ± 0.27 with ZD7288 (Figure 3b). Therefore, ZD7288 reduced the mitochondrial OXPHOS capacity. Interestingly, ΔΨm measured with safranin O diminished progressively from S2 to S3 to S4 with ZD7288. This effect was exacerbated in S3. Furthermore, ΔΨ in S4o also diminished with respect to the control group (Figure 3c).

Cationic dyes preferentially accumulate in the mitochondrial matrix because of the higher ΔΨ (−120 to −160 mV) with respect to plasma membrane ΔΨ (−60 to −90 mV) [16]. To further estimate the contribution of HCN3 to ΔΨm, JC-1 assays were performed in control and transfected HEK293 cells with HCN3. As expected, ΔΨm was significantly lower in cells transfected with HCN3 than in control cells, which is consistent with the reduction in both routine and leak respiration observed in HEK293 transfected cells. Strikingly, addition of CCCP did not further diminish ΔΨ of the transfected cells, confirming the strong uncoupling effect of recombinant HCN3 K^+ channel in the mitochondria (Figure 4a,b).

Each merge image of Figure 4a corresponds to one representative experiment captured during four to eight independent assays performed for each experimental condition. Therefore, conclusions were extracted from the statistical analysis of the values plotted in Figure 4b.

It is well known that not all potential energy in mitochondria is transformed into ATP, as some processes like substrate transport and thermogenesis also depend on ΔΨm. Therefore, cell respiration in vitro is regulated by aerobic ATP demand but also by mitochondria processes that are required for cell growth, such as mitochondrial anabolism, and by processes that reduce mitochondrial coupling such as proton leak, electron leak and electron slip. So, cells incubated in the corresponding culture medium maintain this "basal (or routine) respiration". The oxygen consumption of all mitochondrial processes that do not produce ATP can be evaluated by the oligomycin induction of the non-phosphorylating resting state (an uncoupled state) known as "leak respiration". According to our results, endogenous HCN3 in kidney mitochondria and in mitochondria from HEK292 cells reduce ΔΨm. In fact, a stronger ΔΨm reduction effect was observed by overexpressing HCN3 in HEK293 cells (Figure 4b). Therefore, we performed an additional experiment in an attempt to explain the origin of this effect. In general, overexpression of HCN3 lowers "routine respiration" but also reduces "leak respiration" (Figure 5a,b). Although the value of respiration attributable to oxidative phosphorylation (P) decreased (Figure 5c), recombinant HCN3 did not change the respiratory control (RCI) (Figure 5d). Together these findings indicated that although mitochondrial ATP production decreased with channel overexpression, this was not due to a lower efficiency of mitochondrial function, but rather to a lower activity of all

INFORME DE LABORES 2019

mitochondrial processes in the HCN3 group. A possible explanation could be a decrease in the mitochondrial mass since both groups produced ATP with equal efficiency (RCI did not change). In summary, the fact that both routine and leak respiration decreased with HCN3 overexpression seems to indicate fewer mitochondria. This hypothesis should be confirmed in the future.

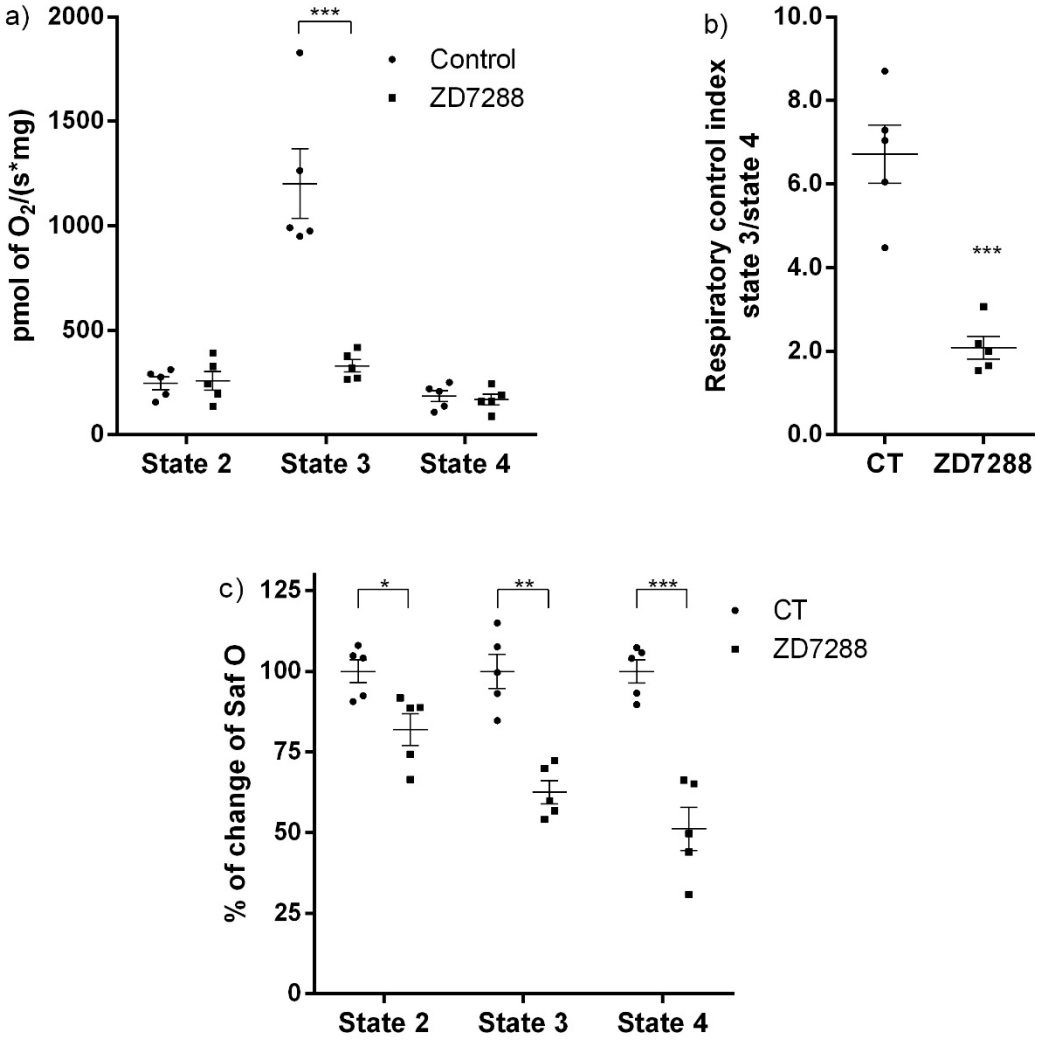

Figure 3. Effect of ZD7288 on the mitochondrial respiration rate and mitochondrial membrane potential (ΔΨm) on isolated mitochondria from renal cortex. (**a**) Respiratory parameters: state 2 (S2), state 3 (S3) and state 4 induced by oligomycin (S4o) and (**b**) respiratory control index (RCI). (**c**) Δψm in S2, S3 and S4o. Data are mean ± SEM, $n = 5$. *** $p < 0.001$, ** $p < 0.01$ and * $p < 0.05$.

INFORME DE LABORES 2019

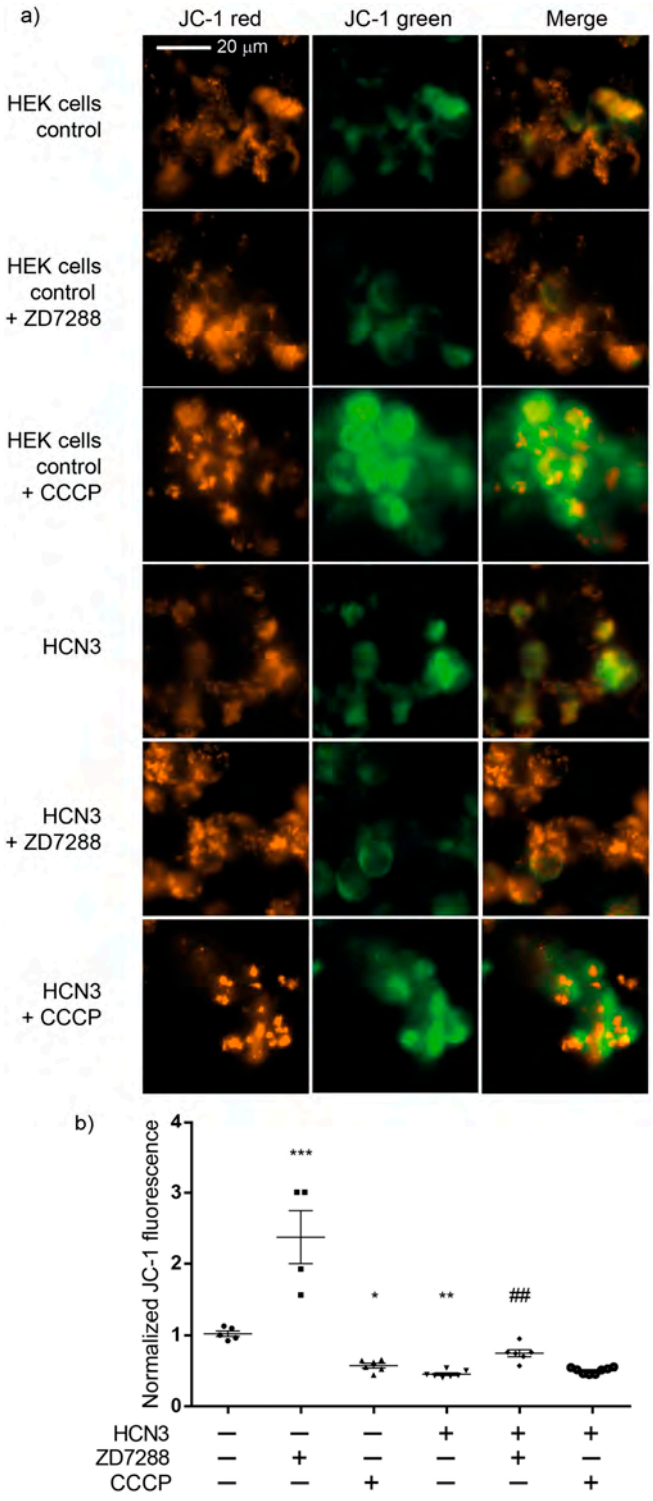

Figure 4. Effect of ZD7288 and carbonyl cyanide m-chlorophenylhydrazone (CCCP) on mitochondrial membrane potential (ΔΨm) in HEK293 cells (control) and HEK293 cells transfected with HCN3. (**a**) Visualization by Cytation 5 showing JC-1 red, JC-1 green and merge images of HEK293 cells. (**b**) The JC-1 fluorescence was quantified as the ratio of the red fluorescence (590 nm) to green fluorescence (525 nm) using Cytation 5 and the fluorescence was normalized with HEK293 cells (control) without inhibitor. ZD7288 (50 µM), CCCP (50 µM). Data are mean ± SEM, n = 4–8. *** $p < 0.001$, ** $p < 0.01$ and * $p < 0.05$ vs. HEK293 cells control. ### $p < 0.001$ vs. HCN3 without inhibitor. JC-1 = 5,5′,6,6′-tetrachloro-1,1′,3,3′-tetraethylbenzimidazolylcarbocyanine iodide.

INFORME DE LABORES 2019

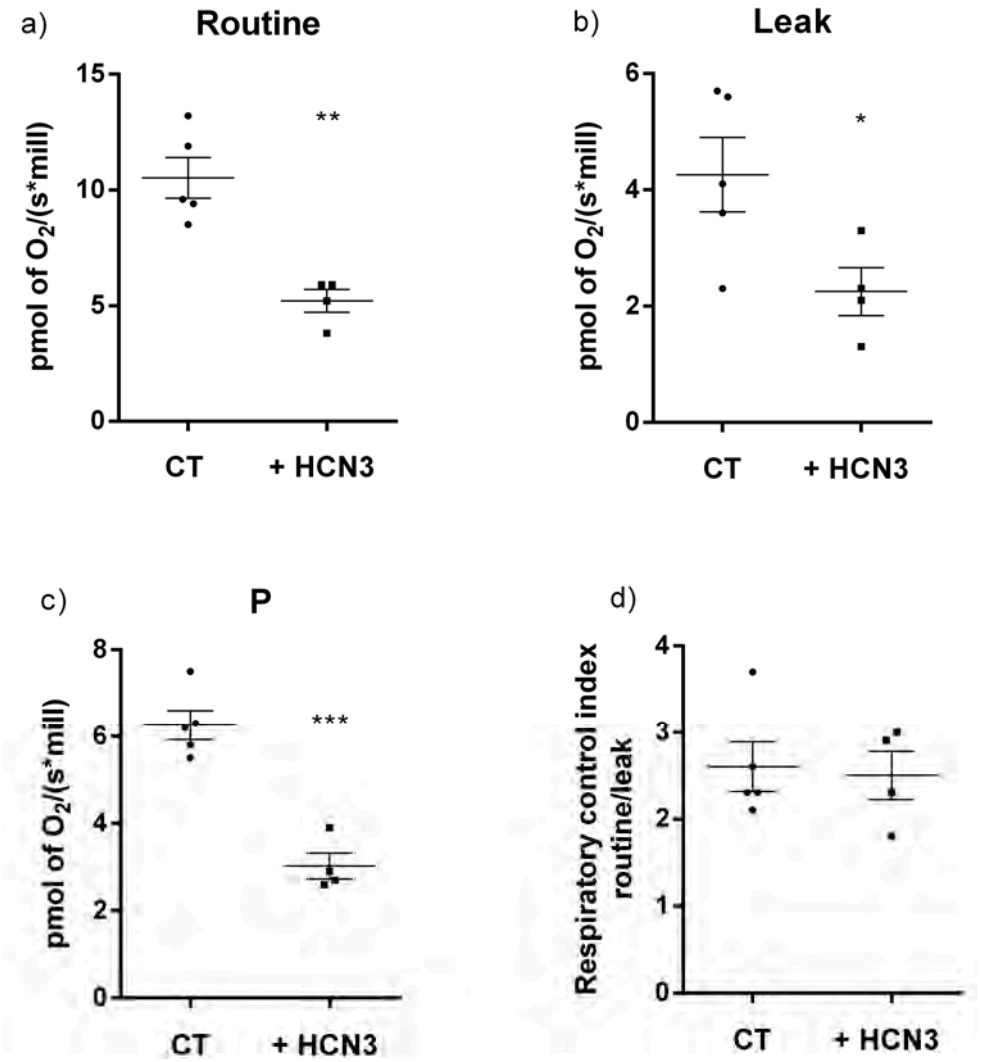

Figure 5. Respiratory parameters for control and HCN3 overexpressed in HEK293 cells. (**a**) Cellular routine respiration; (**b**) leak of respiration; (**c**) respiration associated to oxidative phosphorylation (P); (**d**) respiratory control index (RCI). Data is presented as mean ± SEM, n = 4–5. Unpaired t-test. *** $p < 0.001$, ** $p < 0.01$ and * $p < 0.05$ vs. control (CT).

3. Discussion

The kidney is, after the heart, the organ with the highest resting metabolic rates, mitochondrial content and oxygen consumption. The kidney contains abundant mitochondria to provide the energy necessary to recover or eliminate nutrients from the filtrated blood (amino acids, glucose, urea, electrolytes) and maintain the acid-base balance. Furthermore, healthy mitochondria are essential for the Na^+-K^+-ATPase activity and to generate the electrochemical gradients across the plasma membrane of epithelial cells.

The development of quantitative high-throughput assays for identification of candidate proteins that interact with membrane proteins represents a powerful approach for biomarker discovery. In this work, targeted proteomics provided a sensitive assay to develop the hypothesis of the presence of the HCN3 channel in the kidney mitochondria.

The HCN family has been widely studied in the brain and heart, where they play a key role in the initiation and regulation of the electrical rhythmic activity [17,18]. In the mammalian heart and nervous system HCN channels contribute to spontaneous beating in pacemaker cells [17]. In nonpacing cells, inward cationic currents carried by HCN channels facilitate the establishment of the resting membrane properties by limiting the fluctuation of membrane potentials [18]. Although HCN channels form

cationic non-selective channels, they display a higher selectivity for K^+ over NH_4^+ and Na^+. Our assays of ΔΨm helped to determine that HCN channels are K^+ channels in the IMM and that their topology seems to be a mirror of the HCN channels in the plasma membrane but facing the cytosol instead of the extracellular side.

Previously we found that HCN channels are differentially distributed along the rat nephron. In particular HCN3 is observed near luminal membranes and the cytosol in the proximal convoluted tubule and towards basolateral membranes of the medullary thick ascending limb of Henle [14]. HCN3 has been found in the bladder and the junction of renal pelvis and has been implicated in ureteral peristaltic activity [19,20].

In this work we demonstrated for the first time and through several approaches that HCN channels, mostly HCN3, are located in mitochondria of the rat and human kidney by immunogold-labeling. Remarkably, by transfecting each HCN subtype in HEK293 cells, we observed that only HCN3 and HCN4 subtypes could be trafficked to mitochondria. In fact, we predicted these finding by proteomic analysis of HCN3 in HEK293 cells (Table 1).

Mitochondria HCN3 functional expression was confirmed by patch-clamp recordings in rat kidney and HEK293 mitochondria. The magnitude of HCN inward K^+ currents (100–300 pA) that were recorded by patch-clamp (Figure 2) should correspond to the electrical activity of several fused mitochondria. This experiment confirmed not only the presence of HCN K^+ currents in the kidney mitochondria but, by HCN1–3 subtype transfection in HEK293T cells, that only HCN3 could be trafficked to these organelles. In the distal NH_2 and COOH termini exist multiple regions specific to each of the four vertebrate HCN paralogs. These multiple regions of variable length and sequence confer isoform-specific properties. For example, in the COOH terminus of the HCN1, HCN2 and HCN4 isoforms, there is a block of residues conserved immediately downstream of the cyclic nucleotide binding domain [21,22]. Even when HCN3 subtype lacks this conserved block of residues, this would not explain HCN3 targeting to mitochondria since HCN4 is also trafficked to this organelle (Figure 1c). Further experiments should be performed to identify the targeting signals of HCN3 and HCN4 to mitochondria that have not been identified for other mammalian mitochondrial K^+ channels.

Since patch-clamp recordings of HCN channels in the whole mitochondria does not allow to distinguish between the outer and the IMM, we evaluated the effect of the HCN channel blocker ZD7288 on the mitochondrial oxygen consumption and ΔΨm on isolated renal mitochondria. Oxygen consumption by the respiratory chain in S2 or when ATP synthesis was inhibited with oligomycin in S4o was not affected by ZD7288. In contrast, oxygen consumption during ATP synthesis in S3 decreased to basal conditions with ZD7288. These results suggested that HCN3 K^+ channel participates in the respiratory chain activity, especially during ATP synthesis. The effect of ZD7288 on the respiratory control index (RCI) confirmed this conclusion. It is important to underline that the control group is defined as the assay in the absence of ZD7288. States 2 and 4o (induced by oligomycin) must not be considered as basal respiration; these states are bioenergetic parameters determined according to the protocol followed in oxygraphic experiments with isolated mitochondria. Briefly, state 2 corresponds to the respiration due to the added substrates: sodium pyruvate, malate and glutamate in the absence of exogenous ADP. Later, ADP is added to achieve a stationary state of maximum oxygen flux triggered by oxidative phosphorylation (OXPHOS) or state 3. Finally, oligomycin is added to inhibit ATP synthase developing a non-phosphorylating stationary state (state 4o) when oxygen flux is maintained to compensate proton leak [1,3]. The difference between state 2 and state 4o is that in state 2 an ATPase residual activity may cause a recycling of ATP to ADP and, therefore, a residual activation of respiration. In contrast, in state 4o oligomycin inhibition of ATP synthase eliminates this contribution. Oxygen consumption in S3 is mostly determined by OXPHOS and depends highly on changes in ΔΨm [1]. Therefore, small changes in ΔΨm more severely affect the respiration rate in S3 than in S2 or S4o, where OXPHOS is not present. In conclusion, our results support that inhibition by ZD7288 affects OXPHOS more than it does leak states of respiration.

Regarding ΔΨm, changes in safranine O fluorescence were more sensitive to inhibition of HCN3 by ZD7288 than oximetry assays: safranine O fluorescence in states 2, 3 and 4o diminished by about 20%, 40% and 50%, respectively, with respect to basal conditions (Figure 3c). These results supported that HCN3 is an open K^+ channel and its blockade by ZD7288 provoked a higher IMM polarization (i.e., a more negative ΔΨm). Therefore, HCN3 represents a K^+ leak towards the mitochondrial matrix in resting conditions.

To further confirm the effect of HCN3 channel on the polarization of the IMM, assays were carried out with culture control HEK293T cells and HEK293T cells transfected with HCN3, using the lipophilic cationic dye JC-1. JC-1 forms aggregates with intense red fluorescence in healthy mitochondria with high ΔΨm (hyperpolarization) and monomers with green fluorescence when ΔΨm diminishes (depolarization). The higher the ratio of red to green fluorescence, the higher the polarization of the IMM [23]. The red to green fluorescence intensity ratio is not dependent on the mitochondrial size, density and shape. Therefore, JC-1 can be used both as qualitative and quantitative measure of ΔΨm. ZD7288 more than doubled JC-1 the fluorescence ratio with respect to control cells, supporting that endogenous expression of HCN3 enhances mitochondrial K^+ fluxes with a mild uncoupling effect. Moreover, enrichment of mitochondria with HCN3 revealed a stronger uncoupling effect similar to that obtained with CCCP. In these circumstances, 50 μM ZD7288 reverses partially the uncoupling effect of overexpression of mitochondrial HCN3 since most probably not all HCN3 channels were blocked.

The fact that recombinant HCN3 did not change the respiratory control (RCI) indicated that, although mitochondrial ATP production decreased with channel overexpression, this was not due to a lower efficiency of mitochondrial function. A decrement in the mitochondrial mass might be implied since mitochondria of both groups were equally efficient producing ATP. Furthermore, these results help to explain why ΔΨm is lower with HCN3 overexpression compared to ΔΨm in control HEK293 cells.

Only an ATP-sensitive K^+ transport has been identified in kidney mitochondria [9]. In contrast to this ATP-K^+ channel (KATP), which is inhibited by ATP, HCN channels are constitutively open in the mitochondria. Interestingly, voltage-gated mitochondrial K^+ channels documented so far are closed in physiological conditions, for example: the maxi-conductance K^+ channel (BKCa) and voltage-gated Kv1.3 channel. TWIK-related acid-sensitive K^+ channel 2 (TASK3) regulates mitochondrial morphology, membrane potential and aldosterone production in adrenal cortex [24]. All K^+ channels have been involved in the regulation of mitochondrial respiration, ΔΨm and ROS production within mitochondria. Opening of mitochondrial K^+ channels has been associated with cytoprotection, while closed K^+ channels may facilitate cell death [6,7]. The IMM K^+ channels identified so far comprise BKCa [25], intermediate-conductance K^+ channel (IKCa) [26], small-conductance K^+ channel (SKCa) [27], Kv1.3 [28], KATP channel [29], two-pore TASK-3 [30], Kv1.5 [31], ROMK2 and Kv7.4 [32].

The proton pumps of the respiratory chain maintain ΔΨm in the range of −150 to −180 mV in the IMM. While Δp (combination of both ΔΨm and the mitochondrial pH gradient, ΔpH_m) provides the bioenergetic driving force for and regulates ATP production, ΔΨm provides the charge gradient required for mitochondrial Ca^{2+} sequestration and production of reactive oxygen species (ROS) [33]. The opening of K^+ channels provokes depolarization (uncoupling effect) while their blocking induces hyperpolarization in the IMM [34].

The mitochondrial electrochemical equilibrium is continuously maintained by the coupling of K^+ channels and K^+ efflux mediated by exchangers [35]. Mitochondrial swelling occurs after continuous K^+ entry, caused by osmotic entrance of water through aquaporins and triggers the blockade of mitochondrial functions, favoring the release of cytochrome c. To avoid osmotic volume changes and mitochondrial depolarization, the positive K^+ influx is counterbalanced by the efflux of protons (H^+) through the activities of the respiratory chain complexes and by the K^+/H^+ antiporter (i.e., K^+ "futile cycle") [36].

4. Materials and Methods

4.1. Reactives, Antibodies and Plasmids

Antimycin A, adenosine diphosphate (ADP), (4-(2-hydroxyethyl)-1-piperazineethanesulfonic acid) (HEPES), fat-free bovine serum albumin (BSA), carbonyl cyanide m-chlorophenylhydrazone (CCCP), D-sucrose, ethylenediaminetetraacetic acid (EDTA), ethylene glycol-bis(2-aminoethylether)-N,N,N′,N′-tetraacetic acid (EGTA), K-lactobionate acid, mannitol, magnesium chloride ($MgCl_2$) tetrahydrate, oligomycin, rotenone, safranin O, sodium phosphate dibasic (Na_2HPO_4), sodium phosphate monobasic (NaH_2PO_4), sodium glutamate, sodium malate, sodium pyruvate, taurine, polylysine, mannitol and anti-α-tubulin (t9026) were purchased from Sigma-Aldrich (St. Louis, MO, USA). Dulbecco's Modified Eagle Medium (DMEM, 31600-083) Optimem (22600-134) were purchased from Gibco, Life Technologies. Dynabeads protein G (10003D), MitoTracker Green FM, NuPAGE® LDS buffer 4×, NuPAGE (NP0007) 10% Bis-Tris protein gels, MOPS sodium dodecyl sulfate (SDS) buffer, 5,5′,6,6′-tetrachloro-1,1′,3,3′-tetraethylbenzimidazolylcarbocyanine iodide (JC-1, T3168), anti-green fluorescent protein (GFP, clone 3E6) HindIII and kpnI were purchased from Invitrogen by Thermo Fisher Scientific. Fetal Bovine Serum was purchased from Biowest (S1650). Normal mouse IgG (sc-2025) and polyethyleneimine (PEI, sc360988A) were purchased from Santa Cruz Biotechnology (Dallas, TX, USA). Bio-safe Coomassie G250 was purchased from Bio-Rad (Hercules, CA, USA). Polyclonal voltage-dependent anion channel (VDAC, ab34726) was purchased from Abcam (Cambridge, UK) and Immobilon Western Chemiluminescent horseradish peroxidase (HRP) substrate was from Millipore (Mexico City, México). Anti-HCN1, anti-HCN2, anti-HCN3 and anti-HCN4 were purchased from Alomone (Jerusalem, Israel). cOmplete™ Protease Inhibitor Cocktail Roche, Mexico. ZD7288 was purchased from Tocris (Minneapolis, MN, USA). pcDNA3-mHCN1, pcDNA3-mHCN2, pcDNA3-hHCN4 and pEGFP·C3 were provided by Luis Vaca. pcDNA3-mHCN3 was provided by Andreas Ludwig.

4.2. DNA Constructs

pcDNA3-mHCN3 was subcloned into eukaryotic expression vector pEGFP·C3 using HindIII and KpnI. After subcloning, the sequence was confirmed by restriction assay and DNA sequencing analysis using an automated DNA sequencing technique.

4.3. Cultures and Transfection of HEK293 Cells

Human embryonic kidney cells (HEK293T cells) were grown in DMEM supplemented with 100 U/mL penicillin, 100 mg/mL streptomycin and 10% fetal bovine serum at 37 °C in a humidified atmosphere with 5% CO_2. HEK293T cells were grown in tissue culture and transfected at 80% confluence using 1 mg/mL PEI and Optimem. Briefly, 1 μg of each plasmid pcDNA3-mHCN1, pcDNA3-mHCN2, pcDNA3-mHCN3 and pcDNA3-hHCN4 were diluted in low serum medium Optimem and mixed with the transfection reagent PEI, incubated at room temperature for 20–25 min and added to cultures. HEK293 cells were washed with cold phosphate buffer saline (PBS). For IP, 5 μg of GFP-HCN3 was transfected in HEK cells.

4.4. Proteomic Assays

For GFP-HCN3 immunoprecipitation from HEK293T cells lysate, 5 μg of anti-GFP and 50 μL of Dynabeads protein G were mixed and incubated at 4 °C for 2 h. Then, 2 mg/mL of sample was added to the antibody-beads complex and incubated at 4 °C for 2 h. As control we used 2 μg/mL normal mouse IgG. Sample was extensively washed with radioimmunoprecipitation (RIPA) buffer with Protease Inhibitor Cocktail. NuPAGE LDS buffer was added and boiled for 7 min to separate the beads. The supernatant (30 μL) was loaded on NuPAGE 10% Bis-Tris protein gels in MOPS SDS buffer. Electrophoresis was run at 150 V for 20 min and the gel was stained with Bio-safe Coomassie G250. Samples from gel were enzymatically digested according to the modified protocol from [37]. Then, 4 μL

per sample were loaded into Symmetry C18 Trap V/M precolumn (Waters, MA, USA); 180 µm × 20 mm, 100 Å pore size, 5 µm particle size desalted using as a mobile phase A, 0.1% formic acid (FA) in H_2O; and mobile phase B, 0.1% FA in acetonitrile; under the followed isocratic gradient: 99.9% mobile phase A and 0.1% of mobile phase B at a flow of 5 µL min^{-1} for 3 min. After, peptides were loaded and separated on a HSS T3 C18 Column 75 µm × 150 mm (Waters); 100 Å pore size, 1.8 µm particle size; using an UPLC ACQUITY M-Class (Waters) with the same mobile phases under the following gradient: 0 min 7% B, 30.37 min 40% B, 32.03–35.34 min 85% B, 37–47 min 7% B at a flow of 400 nL min^{-1} and 45 °C. The spectral data were acquired in a mass spectrometer with electrospray ionization (ESI) and ion mobility separation (IMS) Synapt G2-Si (Waters) using data-independent acquisition (DIA) approach by $HDMS^E$ mode (Waters). The tune page for the ionization source was set with the following parameters: 2.60 kV in the sampler capillary, 30 V in the sampling cone, 30 V in the source offset, 70 °C for the source temperature, 0.6 bar for the nano flow gas and 120 L h^{-1} for the purge gas flow. Two chromatograms were acquired (low- and high-energy chromatograms) in positive mode in a range of m/z 50–2000 with a velocity of 0.5 scans s^{-1}. No collision energy was applied to obtain the low-energy chromatogram, while for the high-energy chromatograms, the precursor ions were fragmented in the transfer using a collision energy ramp of 19–55 V. Generated raw files containing MS and MS/MS spectra were deconvoluted and compared using ProteinLynx Global SERVER (PLGS) v3.0.3 software Waters [38] against a reversed *Homo sapiens* database (downloaded from Uniprot, 71,785 protein sequences, last modification 1 December 2017). Workflow parameters were as follows: trypsin as a cut enzyme and one missed cleavage allowed; carbamidometh©(C) as a fixed modification and amidation (N-term), deamidation (N,Q), oxidation (M), Phosphoryl (S,T,Y) as variable modifications. Automatic peptide and fragment tolerance, two minimum fragment ion matches per peptide, five minimum fragment ion matches per protein, one minimum peptide match per protein and a false discovery rate (FDR) ≤4%. All identifications had a percentage of reliability ≥95% (Protein AutoCurate green). Synapt G2-Si was calibrated with [Glu^1]-Fibrinopeptide, $[M + 2H]^{2+}$ = 785.84261 at ≤ 1 ppm.

4.5. Isolation of Kidney and HEK293 Cell Mitochondria

Male Wistar rats (200–250 g) were anesthetized by intraperitoneal administration of pentobarbital sodium (50 mg/Kg). Kidney cortex was excised and cooled by immersion in isolation buffer (225 mM D-mannitol, 75 mM sucrose, 1 mM EDTA, 5 mM HEPES, 0.1% fatty acid-free BSA, pH = 7.4) at 4 °C and then cut in small pieces. The isolation procedure was performed at 4 °C. The kidney capsule was removed; tissues were washed with isolation buffer to remove blood, were cut and homogenized with three up/down strokes in a glass Potter-Elvehjem homogenizer with a Teflon@ pestle with 2 mL of isolation buffer. The homogenates were centrifuged at 4000× *g* for 5 min to precipitate debris and unbroken tissue. The supernatant was transferred to new tubes and centrifuged at 12,500× *g* for 15 min without centrifuge brake. The supernatant was recovered as control and the mitochondrial-enriched fraction (bottom) was gently resuspended in 1 mL of BSA-free isolation buffer and centrifuged at 10,000× *g* for 10 min. Finally, the pellet was gently resuspended in 180 µL of BSA-free isolation buffer. Isolation of HEK293 cells mitochondria for immunoblotting was prepared as previously described [39] with minor modifications. Briefly, HEK293 were collected in cold PBS and centrifuged at 700× *g* for 10 min at 4 °C. The cell pellet was resuspended and homogenized in a mitochondrial isolation buffer (MIB; 200 mM sucrose, 10 mM Tris/MOPS pH 7.4, 1 mM EGTA/Tris), using a Teflon pestle attached to a drill at medium speed for three passes. Homogenized cells were passed through two syringes (18 gauge 1 $\frac{1}{2}$ inch and 27 gauge $\frac{1}{2}$ inch). To isolate the mitochondria, the homogenate was centrifuged at 600× *g* for 10 min at 4 °C. The supernatant was transferred to a new tube and centrifuged at 10,000× *g* for 10 min at 4 °C. The mitochondrial pellet was washed 2× with MIB, centrifuged at 10,000× *g* for 10 min at 4 °C, and resuspended with RIPA buffer. For purification of mitochondria for patch-clamp assays, the supernatant obtained from either HEK293T cells or renal cortex was mixed with Percoll to form an 8% (v/v) solution that was stratified with a 15% (v/v) Percoll solution carefully added through the walls. Tubes were centrifuged at 12,500× *g* for 10 min without centrifuge brake. The supernatant

INFORME DE LABORES 2019

was discarded and the mitochondrial-enriched fraction (bottom) was gently resuspended in 1 mL of BSA-free isolation buffer and centrifuged at 10,000× *g* for 10 min. Finally, the pellet was resuspended in 100 µL of BSA-free isolation buffer. All procedures were performed at 4 °C. The protein content was measured by the Lowry method.

4.6. Immunoblotting

For SDS-PAGE electrophoresis, the samples were mixed with loading buffer and boiled for 5–8 min. Proteins were separated in 10% acrylamide gels and transferred to 0.2 mm PVDF membrane. Blots were blocked for 1 h at room temperature (RT) in Tris-buffered saline with 0.1% Tween-20 (TBST) containing 5% blotting-grade dry milk, incubated overnight with primary antibody diluted in blocking buffer at 4 °C and washed 3× for 10 min in TBST. Then were incubated with secondary antibody horseradish peroxidase-conjugated for 1h at RT and washed 3× for 10 min in TBST. Dilution of primary antibodies applied to blots from transfected HEK293T cells and isolated mitochondria was 1:1000 for anti-HCN1–3, and 1:1200 for anti-HCN4. As positive control of mitochondrial purification we used polyclonal anti-VDAC and as negative control, anti-α-tubulin. Immunoreactivity was detected using Immobilon Western Chemiluminescent HRP Substrate.

4.7. Immunogold Electron Microscopy

For immunogold labeling, adult Wistar rats were euthanized with intraperitoneal Pentothal, both kidneys were immediately removed, thin tissue slices were obtained and immersed into Karnovsky fixer solution (4% paraformaldehyde and 1.5% glutaraldehyde). Animals were treated in accordance to "Technical specifications for the production, use and care of laboratory animals" (NOM-062-ZOO-1999), and experiments approved by the School of Medicine UNAM, Committee on Animal Research and Ethics (86-2008, date of approval 8 September 2008). The kidney cortex was selected and sectioned in small tissue fragments that were deposited into glass tubes and fixed by immersion in the same fixer solution during 4 h at 20 °C, dehydrated and infiltrated with LR-White hydrosoluble resin. Ultrathin sections of 60–70 nm were placed on nickel grids and incubated overnight at 4 °C with specific anti-HCN-3 (1:100) rabbit antibodies followed by a 2-h incubation at room temperature with goat anti-rabbit IgG conjugated to 5-nm gold particles. The grids were contrasted with uranyl acetate and examined with FEI Tecnai G2 Spirit transmission electron microscope (Hillsboro, OR, USA). The human sample was from a transplant donor and was recovered from formalin-fixed paraffin-embedded tissues; later it was fixed for a day in formaldehyde at 10% in PBS buffer. These conditions did not help to preserve the sample for electron microscopy.

4.8. Patch-Clamp Recordings of Whole-Cell and Whole-Mitochondria

HEK293T cells expressing the different constructs described in Figure 2 were placed on coverslips coated with polylysine. Cells were studied between 24–48 h post-transfection. Coverslips were mounted on an open perfusion chamber (TIRF Labs, Cary, NC, USA). The patch clamp amplifier used for whole-cell recordings was the EPC-10 (HEKA Electroniks, Lambrecht Germany). The patch clamp pipettes were prepared from Corning 7052 glass and had a resistance of 5–10 MΩ when filled with the pipette solution (see below). Pipette tip diameter under these conditions was smaller than 1 micron which was sufficiently small to patch large mitochondrion. An Ag/AgCl electrode was utilized to attain electrical continuity and was connected to the bath solution via a KCl-agar bridge. Whole-cell currents were studied in the whole-cell mode with cells expressing the different constructs carrying HCN channels. The pipette solution was: KCl 150 mM, EGTA 5 mM, HEPES 10 mM, pH 7.2. The bath solution contained: KCl 150 mM, glucose 30 mM and HEPES 10 mM, pH adjusted to 7.2. Osmolarity of both solutions was adjusted to 310 mOsm with mannitol. The voltage protocol consisted of 20 mV steps from −120 mV to +60 mV with a holding potential of 0 mV with a duration of 2 s.

For whole-mitochondria currents, mitochondria were isolated either from HEK293 cells expressing the different HCN channels indicated in Figure 2, or from the renal cortex. Isolated mitochondria were

identified using fluorescence microscopy to separate mitochondria from cellular debris. Mitochondria were incubated for 3 min with 5 μM of the fluorescent indicator MitoTracker Green FM. Mitochondria were identified under fluorescence microscopy using the emission filter 525/50 nm (peak emission for MitoTracker Green FM is 516 nm). Excitation was produced using a 490 nm, 205 mW LED from Thorlabs (excitation peak for MitoTracker Green FM is 490 nm). Whole-cell and whole-mitochondria currents were imported into Igor pro v. 7 (Wavemetrics, Tigard, OR, USA) for further analysis and plotting. Final figures were created with Adobe Illustrator (Adobe Systems).

4.9. Mitochondrial Oxygen Consumption

Mitochondrial oxygen consumption rates were evaluated with a high resolution respirometry (oxygraph O2k, OROBOROS, Innsbruck, Austria) at 37 °C. Isolated mitochondria were loaded into the chamber with 2 mL of MiR05 respiration buffer (0.5 mM EGTA, 3 mM $MgCl_2$, 60 mM K-lactobionate, 20 mM taurine, 10 mM KH_2PO_4, 20 mM HEPES, 110 mM sucrose and 1 g/L essentially fatty acid free BSA). The mitochondrial electron transfer system (ETS) was started by addition of complex I (CI) linked substrates: 5 mM sodium pyruvate, 2 mM malate and 10 mM glutamate. After stabilization, the corresponding inhibitor (100 μM ZD7288) or vehicle (water) was added and respiration in state 2 (S2) was determined. Respiration in state 3 (S3) was stimulated by the addition of 2.5 mM ADP, later 2.5 μM oligomycin was used to induced state 4 (S4o) respiration. All the above parameters were corrected by residual respiration (ROX), which was obtained by addition of 0.5 μM rotenone (complex I inhibitor) and 2.5 μM antimycin A (complex III inhibitor). The respiratory control index (RCI) was defined as the S3/S4o ratio. All values were normalized by total protein content measured by the Lowry method.

Oxygen consumption in HEK293 cells was performed using 2 mL of culture medium. Each experiment was initiated by addition of the cells. The respiratory parameters were: 1. Routine respiration defined as oxygen consumption by the cells; 2. Leak of the respiration, corresponding to oxygen consumption in the presence of 5 μM oligomycin; 3. Respiratory control index (RCI) corresponding to the ratio basal/leak; 4. Respiration attributable to oxidative phosphorylation (P) was calculated by the formula: Routine minus Leak. All parameters were corrected by subtracting the non-mitochondrial respiration, obtained by the addition of 1 μM rotenone, 5 μM antimycin A, and normalized by the number of cells determined by trypan blue.

4.10. Mitochondrial Membrane Potential (ΔΨm) Monitored by Safranin O and JC-1 Staining

ΔΨm was determined in tandem with the oxygen consumption assays using an O2k-Fluorometer module (OROBOROS). Briefly, the changes in safranin O fluorescence (3 μM) in MiR05 medium were used to monitor changes in ΔΨm. To stimulate complex I linked respiration, 5 mM sodium pyruvate, 2 mM malate and 10 mM glutamate were added. ΔΨm in S2 was obtained after addition of the corresponding inhibitor or vehicle (see above); ΔΨm in S3 was estimated by addition of 2.5 mM ADP and in S4o 2.5 μM oligomycin was added. Finally, 0.5 μM rotenone and 2.5 μM antimycin A were used to completely dissipate ΔΨm and correct by non-specific interactions. Calibration curves of safranin O were employed to ensure the linearity of the assay and the ΔΨm sensibility to CCCP was employed to confirm the veracity of the assay. Results were expressed as the percent of changes in the measurable concentration of safranin O of the sample with respect to the control change. To measure ΔΨm potential by JC-1, 7000 cells were cultured into wells of 96-well plate. Cells were transfected with pcDNA3 (control) or pcDNA3-HCN3 (see above, transfection of HEK cells). After transfection, cells were incubated with 8 μg/mL JC-1 for 60 min on non-supplemented medium. To remove excess probe, cells were washed three times with PBS; fresh supplemented medium was placed on cultures. Depolarized-related (green) fluorescence was measured at 525 nm and polarized-related (red) signal was read at 590 nm, both emissions were obtained at 488 nm excitation. ZD7288 and CCCP were used at 50 μM. Data and representative images were obtained with a Cytation 5 Cell Imaging Multi-Mode reader (BioTek Instruments, Winooski, VT, USA), with GFP and RFP filters. JC-1 fluorescence was

calculated as the ratio of red fluorescence and green fluorescence and were normalized with HEK cells (control) without inhibitor.

5. Conclusions

HCN3 constitutes a novel mitochondrial K^+ channel in the kidney that is coupled to the respiratory chain and ATP synthesis. HCN3 produces a mild uncoupling effect in renal mitochondria and therefore would alter the rate of ROS production and be protective in the kidney. HCN pacemaker channels in the kidney mitochondria contribute importantly to the bioenergetic field and open a new route to the understanding of mitochondrial diseases and new therapeutic avenues. Finally, our study predicts that mitochondria from other organs like heart, brain and liver should also express HCN3 and HCN4 channels.

Author Contributions: Conceptualization, L.I.E., J.P.-C., L.V., R.H.-P., D.L.-A., O.E.A.-T.; Methodology, D.L.-A., C.S., O.E.A.-T., A.B.-H., A.S., T.P.-F., Z.L.-G., J.C.L.-C.; Validation and Data Curation, D.L.-A., O.E.A.-T., A.B.-H., L.V.; Funding Acquisition, L.I.E., J.P.-C., L.V.; Supervision, L.I.E.; Writing-Original Draft Preparation, L.I.E.; Writing-Review and Editing, L.I.E.

Funding: This research was funded by PAPIIT, UNAM, Mexico, DGAPA grants IN214316 and IN224919 (L.I.E.) and IN202219 (J.P.-C.); Post Doctoral Scholarship Program DGAPA at UNAM (D.L.-A.). Fulbright-Garcia Robles (L.V.).

Acknowledgments: We thank Emmanuel Ríos Castro, "Unidad de Genómica, Proteómica y Metabolómica LaNSE-CINVESTAV" for his technical assistance.

Conflicts of Interest: The authors disclose no conflicts of interest.

Abbreviations

IMM	inner mitochondrial membrane
$\Delta\Psi m$	mitochondrial membrane potential

References

1. Bernardi, P. Mitochondrial Transport of Cations: Channels, Exchangers, and Permeability Transition. *Physiol. Rev.* **1999**, *79*, 1127–1155. [CrossRef] [PubMed]
2. Garlid, K.D. On the Mechanism of Regulation of the Mitochondrial K+/H+ Exchanger. *J. Biol. Chem.* **1980**, *255*, 11273–11279. [PubMed]
3. Szewczyk, A.; Marbán, E. Mitochondria: A new target for K+ channel openers? *Trends Pharmacol. Sci.* **1999**, *20*, 157–161. [CrossRef]
4. Busija, D.W.; Lacza, Z.; Rajapakse, N.; Shimizu, K.; Kis, B.; Bari, F.; Domoki, F.; Horiguchi, T. Targeting mitochondrial ATP-sensitive potassium channels—A novel approach to neuroprotection. *Brain Res. Rev.* **2004**, *46*, 282–294. [CrossRef] [PubMed]
5. O'Rourke, B. Evidence for Mitochondrial K^+ Channels and Their Role in Cardioprotection. *Circ. Res.* **2004**, *94*, 420–432. [CrossRef] [PubMed]
6. Szabo, I.; Zoratti, M. Mitochondrial Channels: Ion Fluxes and More. *Physiol. Rev.* **2014**, *94*, 519–608. [CrossRef] [PubMed]
7. Laskowski, M.; Augustynek, B.; Kulawiak, B.; Koprowski, P.; Bednarczyk, P.; Jarmuszkiewicz, W.; Szewczyk, A. What do we not know about mitochondrial potassium channels? *Biochim. Biophys. Acta* **2016**, *1857*, 1247–1257. [CrossRef] [PubMed]
8. Cardoso, A.R.; Cabral-Costa, J.V.; Kowaltowski, A.J. Effects of a high fat diet on liver mitochondria: Increased ATP-sensitive K+ channel activity and reactive oxygen species generation. *J. Bioenerg. Biomembr.* **2010**, *42*, 245–253. [CrossRef] [PubMed]
9. Cancherini, D.V.; Trabuco, L.G.; Rebouças, N.A.; Kowaltowski, A.J. ATP-sensitive K^+ channels in renal mitochondria. *Am. J. Physiol. Renal Physiol.* **2003**, *285*, F1291–F1296. [CrossRef] [PubMed]
10. Ludwig, A.; Zong, X.; Hofmann, F.; Biel, M. Structure and Function of Cardiac Pacemaker Channels. *Cell. Physiol. Biochem.* **1999**, *9*, 179–186. [CrossRef] [PubMed]
11. Santoro, B.; Tibbs, G.R. The HCN Gene Family: Molecular Basis of the Hyperpolarization-Activated Pacemaker Channels. *Ann. N. Y. Acad. Sci.* **1999**, *868*, 741–764. [CrossRef] [PubMed]

INFORME DE LABORES 2019

12. Biel, M.; Wahl-Schott, C.; Michalakis, S.; Zong, X. Hyperpolarization-Activated Cation Channels: From Genes to Function. *Physiol. Rev.* **2009**, *89*, 847–885. [CrossRef] [PubMed]
13. Carrisoza-Gaytán, R.; Rangel, C.; Salvador, C.; Saldaña-Meyer, R.; Escalona, C.; Satlin, L.M.; Liu, W.; Zavilowitz, B.; Trujillo, J.; Bobadilla, N.A.; et al. The hyperpolarization-activated cyclic nucleotide-gated HCN2 channel transports ammonium in the distal nephron. *Kidney Int.* **2011**, *80*, 832–840. [CrossRef] [PubMed]
14. López-González, Z.; Ayala-Aguilera, C.; Martinez-Morales, F.; Galicia-Cruz, O.; Salvador-Hernández, C.; Pedraza-Chaverri, J.; Medeiros, M.; Hernández, A.M.; Escobar, L.I. Immunolocalization of hyperpolarization-activated cationic HCN1 and HCN3 channels in the rat nephron: Regulation of HCN3 by potassium diets. *Histochem. Cell Biol.* **2016**, *145*, 25–40. [CrossRef] [PubMed]
15. Stieber, J.; Stöckl, G.; Herrmann, S.; Hassfurth, B.; Hofmann, F. Functional expression of the human HCN3 channel. *J. Biol. Chem.* **2005**, *280*, 34635–34643. [CrossRef] [PubMed]
16. Yousif, L.F.; Stewart, K.M.; Kelley, S.O. Targeting Mitochondria with Organelle-Specific Compounds: Strategies and Applications. *ChemBioChem* **2009**, *10*, 1939–1950. [CrossRef] [PubMed]
17. DiFrancesco, D. Pacemaker Mechanisms in Cardiac Tissue. *Annu. Rev. Physiol.* **1993**, *55*, 455–472. [CrossRef] [PubMed]
18. Pape, H.-C. Queer Current and Pacemaker: The Hyperpolarization-Activated Cation Current in Neurons. *Annu. Rev. Physiol.* **1996**, *58*, 299–327. [CrossRef] [PubMed]
19. Hurtado, R.; Bub, G.; Herzlinger, D. The pelvis–kidney junction contains HCN3, a hyperpolarization-activated cation channel that triggers ureter peristalsis. *Kidney Int.* **2010**, *77*, 500–508. [CrossRef]
20. Xue, L.; Li, Y.; Han, X.; Yao, L.; Yuan, J.; Qin, W.; Liu, F.; Wang, H. Investigation of Hyperpolarization-activated Cyclic Nucleotide-gated Channels in Interstitial Cells of Cajal of Human Bladder. *Urology* **2012**, *80*, e13–e224. [CrossRef]
21. Proenza, C.; Tran, N.; Angoli, D.; Zahynacz, K.; Balcar, P.; Accili, E.A. Different roles for the cyclic nucleotide binding domain and amino terminus in assembly and expression of hyperpolarization-activated, cyclic nucleotide-gated channels. *J. Biol. Chem.* **2002**, *277*, 29634–29642. [CrossRef] [PubMed]
22. Wainger, B.J.; DeGennaro, M.; Santoro, B.; Siegelbaum, S.A.; Tibbs, G.R. Molecular mechanism of cAMP modulation of HCN pacemaker channels. *Nature* **2001**, *411*, 805–810. [CrossRef] [PubMed]
23. Reers, M.; Smith, T.W.; Chen, L.B. J-Aggregate Formation of a Carbocyanine as a Quantitative Fluorescent Indicator of Membrane Potential. *Biochemistry* **1991**, *30*, 4480–4486. [CrossRef] [PubMed]
24. Yao, J.; McHedlishvili, D.; McIntire, W.E.; Guagliardo, N.A.; Erisir, A.; Coburn, C.A.; Santarelli, V.P.; Bayliss, D.A.; Barrett, P.Q. Functional TASK-3–Like Channels in Mitochondria of Aldosterone-Producing Zona Glomerulosa Cells. *Hypertension* **2017**, *70*, 347–356. [CrossRef] [PubMed]
25. Singh, H.; Stefani, E.; Toro, L. Intracellular BK_{Ca} (iBK_{Ca}) channels. *J. Physiol.* **2012**, *590*, 5937–5947. [CrossRef] [PubMed]
26. De Marchi, U.; Sassi, N.; Fioretti, B.; Catacuzzeno, L.; Cereghetti, G.M.; Szabò, I.; Zoratti, M. Intermediate conductance Ca2+-activated potassium channel (KCa3.1) in the inner mitochondrial membrane of human colon cancer cells. *Cell Calcium* **2009**, *45*, 509–516. [CrossRef]
27. Dolga, A.M.; Netter, M.F.; Perocchi, F.; Doti, N.; Meissner, L.; Tobaben, S.; Grohm, J.; Zischka, H.; Plesnila, N.; Decher, N.; et al. Mitochondrial small conductance SK2 channels prevent glutamate-induced oxytosis and mitochondrial dysfunction. *J. Biol. Chem.* **2013**, *288*, 10792–10804. [CrossRef]
28. Szabò, I.; Bock, J.; Jekle, A.; Soddemann, M.; Adams, C.; Lang, F.; Zoratti, M.; Gulbins, E. A novel potassium channel in lymphocyte mitochondria. *J. Biol. Chem.* **2005**, *280*, 12790–12798. [CrossRef]
29. Inoue, I.; Nagase, H.; Kishi, K.; Higuti, T. ATP-sensitive K+ channel in the mitochondrial inner membrane. *Nature* **1991**, *352*, 244–247. [CrossRef]
30. Pocsai, K.; Kosztka, L.; Bakondi, G.; Gönczi, M.; Fodor, J.; Dienes, B.; Szentesi, P.; Kovács, I.; Feniger-Barish, R.; Kopf, E.; et al. Melanoma cells exhibit strong intracellular TASK-3-specific immunopositivity in both tissue sections and cell culture. *Cell. Mol. Life Sci.* **2006**, *63*, 2364–2376. [CrossRef]
31. Leanza, L.; Zoratti, M.; Gulbins, E.; Szabo, I. Induction of Apoptosis in Macrophages via Kv1.3 and Kv1.5 Potassium Channels. *Curr. Med. Chem.* **2012**, *19*, 5394–5404. [CrossRef]
32. Testai, L.; Barrese, V.; Soldovieri, M.V.; Ambrosino, P.; Martelli, A.; Vinciguerra, I.; Miceli, F.; Greenwood, I.A.; Curtis, M.J.; Breschi, M.C.; et al. Expression and function of Kv7.4 channels in rat cardiac mitochondria: Possible targets for cardioprotection. *Cardiovasc. Res.* **2016**, *110*, 40–50. [CrossRef] [PubMed]

33. Szabadkai, G.; Duchen, M.R. Mitochondria: The Hub of Cellular Ca $^{2+}$ Signaling. *Physiology* **2008**, *23*, 84–94. [CrossRef] [PubMed]
34. Leanza, L.; Venturini, E.; Kadow, S.; Carpinteiro, A.; Gulbins, E.; Becker, K.A. Targeting a mitochondrial potassium channel to fight cancer. *Cell Calcium* **2015**, *58*, 131–138. [CrossRef] [PubMed]
35. Massari, S.; Balboni, E.; Azzone, G.F. Distribution of permeant cations in rat liver mitochondria under steady-state conditions. *Biochim. Biophys. Acta* **1972**, *283*, 16–22. [CrossRef]
36. Beavis, A.D.; Lu, Y.; Garlid, K.D. On the Regulation of K+ Uniport in Intact Mitochondria by Adenine Nucleotides and Nucleotide Analogs. *J. Biol. Chem.* **1993**, *268*, 997–1004. [PubMed]
37. Shevchenko, A.; Tomas, H.; Havli, J.; Olsen, J.V.; Mann, M. In-gel digestion for mass spectrometric characterization of proteins and proteomes. *Nat. Protoc.* **2006**, *1*, 2856–2860. [CrossRef] [PubMed]
38. Li, G.-Z.; Vissers, J.P.-C.; Silva, J.C.; Golick, D.; Gorenstein, M.V.; Geromanos, S.J. Database searching and accounting of multiplexed precursor and product ion spectra from the data independent analysis of simple and complex peptide mixtures. *Proteomics* **2009**, *9*, 1696–1719. [CrossRef]
39. Lampl, T.; Crum, J.A.; Davis, T.A.; Milligan, C.; Del, V.; Moore, G. Isolation and Functional Analysis of Mitochondria from Cultured Cells and Mouse Tissue. *J. Vis. Exp.* **2015**, *97*, 1–9. [CrossRef] [PubMed]



© 2019 by the authors. Licensee MDPI, Basel, Switzerland. This article is an open access article distributed under the terms and conditions of the Creative Commons Attribution (CC BY) license (http://creativecommons.org/licenses/by/4.0/).

Molecular Vision 2019; 25:546-558 <http://www.molvis.org/molvis/v25/546>
Received 26 February 2019 | Accepted 3 October 2019 | Published 5 October 2019

© 2019 Molecular Vision

Thrombin induces Ca^{2+}-dependent glutamate release from RPE cells mediated by PLC/PKC and reverse Na^{+}/Ca^{2+} exchange

Edith López, Irene Lee-Rivera, Alejandro Alvarez-Arce, Ana María López-Colomé

Department of Molecular Neuropathology, Instituto de Fisiología Celular, UNAM, Ciudad Universitaria, México City, CdMx, Mexico

Purpose: We analyzed the molecular mechanisms leading to glutamate release from rat primary cultures of RPE cells, under isosmotic conditions. Thrombin has been shown to stimulate glutamate release from astrocytes and retinal glia; however, the effect of thrombin on glutamate release from RPE cells has not been examined. Our previous work showed that upon the alteration of the blood–retina barrier, the serine protease thrombin could contribute to the transformation, proliferation, and migration of RPE cells. In this condition, elevated extracellular glutamate causes neuronal loss in many retinal disorders, including glaucoma, ischemia, diabetic retinopathy, and inherited photoreceptor degeneration.
Methods: Primary cultures of rat RPE cells were preloaded with 1 µCi/ml ^{3}H-glutamate in Krebs Ringer Bicarbonate (KRB) buffer for 30 min at 37 °C. Cells were rinsed and super-perfused with 1 ml/min KRB for 15 min. Stable release was reached at the 7th minute, and on the 8th minute, fresh KRB containing stimuli was added.
Results: This study showed for the first time that thrombin promotes specific, dose-dependent glutamate release from RPE cells, induced by the activation of protease-activated receptor 1 (PAR-1). This effect was found to depend on the Ca^{2+} increase mediated by the phospholipase C-β (PLC-β) and protein kinase C (PKC) pathways, as well as by the reverse activity of the Na^{+}/Ca^{2+} exchanger.
Conclusions: Given the intimate contact of the RPE with the photoreceptor outer segments, diffusion of RPE-released glutamate could contribute to the excitotoxic death of retinal neurons, and the development of thrombin-induced eye pathologies.

The RPE is the predominant component of the outer blood–retina barrier (BRB), and plays an essential role in the maintenance of the functional and structural integrity of the neural retina required for visual function. The RPE is involved in the trans-epithelial transport of nutrients, the storage and metabolism of vitamin A derivatives, the renewal of photoreceptor outer segments, and the release of trophic compounds, cytokines, chemokines, and growth factors required for the proper function of the neural retina [1,2].

As a main component of the epithelium that separates the inner eye from the bloodstream, the RPE also contributes to establishing the immune privilege of the eye. Under pathological conditions, which alter the BRB, such as rhegmatogenous retinal detachment, contact with blood-contained thrombin may contribute to the induction of the epithelial-mesenchymal transition (EMT) of RPE cells [3-5], which, in turn, results in the death of retinal neurons and the loss of vision [6-8]. Within the eye, several pathological insults which disrupt the BRB may induce RPE cells to undergo EMT, which has been identified in several proliferative ocular diseases [9]. Among these ailments, the pathogenesis of proliferative vitreoretinopathy (PVR), a major cause of failure in retinal surgery aimed to the correction of retinal detachment or severe ocular trauma, includes a fibrotic reaction leading to the formation of contractile membranes on both retinal surfaces formed mainly by transformed RPE and glial cells [9]. This process involves EMT through which RPE cells become fibroblastic, proliferate, and acquire the ability to migrate [10].

In addition to the well-known role in hemostasis, the proinflammatory serine protease thrombin, activated upon tissue injury, is involved in the regulation of cell proliferation, invasiveness, and tumor growth [11]. Through the activation of distinct signaling cascades, thrombin may provide cytoprotective effects or lead to cell degeneration [12,13]. Thrombin is present in the brain during primary cerebral hemorrhage, ischemia, or after trauma episodes which disrupt the blood–brain barrier [14,15]. Thrombin also seems to be involved in neurologic complications in HIV [16], and it is accumulated in Alzheimer senile plaques [17]. Despite this evidence, information concerning the signaling mechanisms mediating thrombin actions in the retina is scarce.

Cell responses to thrombin occur via the protease-activated receptors 1, 3, and 4 (PARs) [18], coupled to members of the G-protein families, particularly Gq, Gi,

Correspondence to: Ana María López-Colomé, Department of Molecular Neuropathology, Instituto de Fisiología Celular, UNAM, Apartado Postal 70-253, Ciudad Universitaria, México City, CdMx, Mexico; Phone: +52 55 56 22 5527; FAX: +52 55 56225607; email: acolome@ifc.unam.mx

INFORME DE LABORES 2019

and $G_{12/13}$. Through this interaction, thrombin elicits various downstream signaling cascades [12,19]. Thrombin effects are direct, mediated by the activation of PAR signaling, or indirect, triggered by the release of chemokines, growth factors, neurotransmitters, and angiogenic factors [20]. In RPE cells, thrombin activation of PAR-1 induces the release of epidermal growth factor (EGF) [21] and the stimulation of monocyte chemoattractant protein 1 (MCP1) and GRO chemokine expression and release [22].

Glutamate (Glu) has been shown to regulate the proliferation, migration, and survival of several cell types within the nervous system [23,24], and to play a key role in synaptic plasticity and gene expression [25]. However, the excessive release of glutamate is an early and critical event in the Ca^{2+}-mediated death of neurons implicated in neurodegenerative processes associated with ischemia, epilepsy, and other neuropathological conditions [26,27].

Glutamate is the main excitatory neurotransmitter in the radial signaling pathway of the vertebrate retina from photoreceptors to ganglion cells, acting at ionotropic and metabotropic glutamate receptors (GluRs) [28]. Stimulation of GluRs has been shown to induce the release of glutamate from the retina [29], and to promote the excitotoxic death of retinal neurons [30]. In such a system, any additional factor enhancing glutamate efflux from retinal cells will exacerbate the excitotoxic damage.

Retinal photoreceptors lie between the inner retina and the RPE. Efficient photoreceptor function depends on short- and long-term support from the RPE [31]. The apical membrane of the RPE is separated from the plasma membrane of the photoreceptor outer segments by an extracellular space of only 10–20 nm [32]. Thus, glutamate released by RPE cells may influence synaptic transmission at the main signaling pathway of the retina. Although glutamate release from photoreceptors to inner retinal neurons has been extensively documented, the role of glutamate in communicating the RPE with the neural retina is largely unexplored. Thrombin has been shown to stimulate glutamate release from astrocytes and retinal glia in response to ATP and osmotic stress [33-35]. In turn, glutamate promotes ATP release and RPE cell proliferation acting through N-Methyl-D-aspartic acid (NMDA) and metabotropic receptors [31,36,37]. Thus, the autoactivation of glutamate receptors may contribute to the induction of RPE cell transformation and the development of PVR. However, the effect of thrombin on glutamate release from RPE cells is unexplored. We demonstrated that thrombin-induced activation of PAR-1 glutamate release from RPE is protein kinase C (PKC)-regulated and calcium-dependent.

METHODS

Reagents: All reagents used were cell culture grade. Dulbecco's modified Eagle's medium (DMEM), Opti-MEM, Hanks' balanced salt solution (HBSS), trypsin-EDTA, fetal bovine serum (FBS), penicillin, streptomycin, and dispase were obtained from Invitrogen (Carlsbad, CA). Bovine serum albumin (BSA) was from Equitech-Bio Inc. (Kerrville, TX). Thrombin, hirudin, KN-93, and Ro-32–0432 were from EMD Millipore (Burlington, MA). Ser-Phe-Leu-Leu-Arg-Asn-amide trifluoroacetate salt (SFLLRN), aminooxyacetic acid (AAOA), L-methionine sulfoximine, EGTA, ryanodine, dantrolene, and wortmannin were obtained from Merck KGaA (Darmstadt, Germany). L-trans-2, 4-L-trans-Pyrrolidine-2,4-dicarboxylic acid (PDC), U73122, U0126, and KB-R7943 were from Tocris Bioscience (Bristol, UK). 1,2-Bis(2-aminophenoxy)ethane-N,N,N',N'-tetraacetic acid tetrakis(acetoxymethyl ester) (BAPTA AM) was obtained from Molecular Probes (Eugene, OR). D-Phenylalanyl-prolyl-arginyl Chloromethyl Ketone (PPACK) was from Enzo Life Sciences (New York, NY).

Cell culture: RPE cells were isolated as previously described [36]. Briefly, 8- to 10-day-old Long Evans rats (RRID:RGD_2308852) were anesthetized with pentobarbital (100 mg/kg) and euthanized following the Animal Care and the Guidelines for Animal Care of the ARVO Statement for the Use of Animals in Ophthalmic and Vision Research and Mexican NOM-062-ZOO-1999. Eyes were enucleated, rinsed in DMEM, containing 100 U/ml penicillin and streptomycin, and incubated in DMEM containing 1% v/v dispase for 30 min at 37 °C. The RPE was detached from the neural retina, the choroid, and the sclera in calcium- and magnesium-free HBSS. The tissue was then incubated in the presence of 0.1% trypsin–EDTA, for 5 min at 37 °C. The cells were mechanically dissociated using a Pasteur pipette. Trypsin digestion was stopped with the addition of 4% FBS. Cells were separated with centrifugation at 195 ×g for 5 min, suspended in Opti-MEM containing 4% FBS, and seeded onto six-well culture plates at 2×10^5 cells/cm^2 density. After 4 days in the presence of FBS, the medium was replaced with serum-free Opti-MEM for 24 h to synchronize the cells. All experiments were performed in confluent, passage 1 cultures 2 weeks after seeding.

Immunocytochemistry: RPE cells from the primary cultures were seeded on 22 mm glass coverslips and allowed to reach confluence for 2 weeks with the medium (Opti-MEM containing 4% FBS) changed every 4 days. Cells were fixed in 4% paraformaldehyde for 10 min, washed with PBS (137 mM NaCl, 2.7 mM KCl, 10 mM Na_2HPO_4, 2 mM KH_2PO_4, pH 7.4), and permeabilized with 0.1% Triton X-100 for 5 min,

Molecular Vision 2019; 25:546-558 <http://www.molvis.org/molvis/v25/546> © 2019 Molecular Vision

and then blocked for 1 h with either PBS-Tween-0.05%, FBS 10% (for zonula occludens 1 [ZO-1]), PBS-Tween-0.05%, FBS 10%, 1% BSA (for RPE), and PBS-casein 0.5%-saponin 0.1% (for CRALPB). Primary antibody was incubated overnight at 4 °C in blocking buffer. For ZO-1 (Santa Cruz, Santa Cruz, CA, Cat No sc33725), the antibody was diluted 1:50, RPE65 (Novus Biologicals, Centennial, CO, Cat No NB100355) 1:250, and CRALPB (Abcam, Cambridge, UK, Cat No 15051), 1:50. Fluorescein isothiocyanate (FITC)-labeled secondary antibodies were incubated in blocking buffer 1:100 for ZO-1 and cellular retinaldehyde-binding protein (CRALBP); 1:500 for RPE65. The cells were washed three times with PBS for 5 min. Samples were mounted with Dako Fluorescence Mounting Medium (Dako North America, Inc., Carpinteria, CA), and visualized using a microscope Eclipse TE 2000-U. Images were acquired with a DXM1200F camera and 40X objective (0.6 NA) using ACT-1 software (All from Nikon, Tokyo, Japan).

Release experiments: Cultures of rat RPE cells were incubated in the presence of the glutamate decarboxylase inhibitor amino-oxyacetic acid (1 mM), methionine sulfoximine (0.5 mM), and reuptake inhibitor 1-transpyrrolidine-2,-4-dicarboxylic acid (trans-PDC) 50 µM for 30 min before loading with 1 µCi/ml ^{3}H-glutamate in Krebs Ringer Bicarbonate (KRB; 118 mM NaCI, 4.7 mM KCI, 2.5 mM $CaCl_2$, 1.2 mM KH_2PO_4, 1.17 mM $MgSO_4$, 25 mM $NaHCO_3$, 5.6 mM glucose, pH 7.4) solution for 30 min at 37 °C. Cells were rinsed and superfused with KRB, and samples of 1 ml were collected every minute for 10–15 min. Once stable release was attained, stimulus was applied in fresh KRB. The values in the bar graphs represent the percentage of ^{3}H-Glu released on the first minute following stimulation, compared to the value in an unstimulated control. The results in the line graphs represent the percentage of ^{3}H-Glu released each minute compared to the total ^{3}H-Glu incorporated in the cells. When inhibitors were used, they were included 30 min before thrombin or SFLLRN stimulation.

Statistical analysis: The paired Student *t* test was applied for statistical analysis, using the Prism V7.0 program (GraphPad Prism, RRID:SCR_002798). Results are expressed as the mean ± standard error of the mean (SEM) of at least three independent experiments.

RESULTS

RPE cell morphology and identity: RPE cells in culture are considered a suitable model in which dedifferentiation and proliferation of these cells can be studied [38]. Previous studies conducted by our group showed some of the biochemical features of cultured RPE cells in response to thrombin and the glutamate receptors expressed by these cells [22,36]. To confirm the identity of the cultured cells, we tested the expression of RPE65. RPE-specific 65 kDa protein (RPE65) is a critical enzyme in the vertebrate visual cycle that catalyzes the conversion of all-trans-retinyl esters to 11-cis-retinol during phototransduction. RPE65 expression is considered a hallmark of RPE cells [39], and as shown in Figure 1A, it is widely expressed in these cultures. CRALBP also plays an important role in the visual cycle, and it is considered a marker for RPE cells [39]. As shown in Figure 1E, CRALBP was negative in these cells, suggesting that they were not mature RPE cells. However, the RPE cultures showed a typical epithelial morphology, with the presence of melanosomes (Figure 1B,D,E). The tight junction (TJ) protein ZO-1 is a membrane-associated TJ adaptor protein that plays a key role in cell-cell adhesion and epithelial function, particularly in BRB function. Figure 1C shows that ZO-1 expression is restricted to the cell membrane, and reveals a polygonal structure characteristic of differentiated RPE. However, it is noticeable that not all cells express ZO-1. These results suggested that although these cultures have many features of differentiated RPE cells, they are probably not fully mature cells, and could resemble RPE cells transitioning into PVR cells.

Thrombin induces ^{3}H-glutamate release from RPE cells: Our previous work showed that thrombin activation of PAR-1 signaling promotes RPE cell transformation, proliferation, and migration, characteristic of fibroproliferative eye pathologies [22]. In addition to these effects directly derived from PAR signaling, Glu release from RPE may induce RPE proliferation by stimulating Glu receptors on the same RPE cells [36], which may contribute to excitotoxicity through diffusion to the inner retina [29]. To assess this possibility, we tested the effect of thrombin (2 U/ml) on the release of ^{3}H-glutamate from rat RPE cells in primary culture, and showed that the inclusion of 2 U/ml thrombin stimulated Glu release by about 40% over control, which was increased to 60% upon preincubation with the glutamate metabolism inhibitor AAOA and the Glu reuptake inhibitor PDC (Figure 2A). Thrombin-induced Glu release was fast, attained 1 min after the addition of thrombin. Glu release was shown to be specifically prevented by the thrombin inhibitors hirudin (4 U/ml) and PPACK (10 µM; Figure 2B).

Thrombin-induced Glu release is dose-dependent, mediated by the activation of PAR-1: The dose–response curve for thrombin stimulation of glutamate release from 1 pM to 20 nM concentration showed that glutamate release was evident from 100 pM, and reached a saturation value at 10 nM thrombin (Figure 3A). These results indicated that thrombin

INFORME DE LABORES 2019

concentration in plasma [40] suffices for the induction of glutamate release upon RPE exposure to blood due to disruption of the BRB.

To determine if the thrombin effect is mediated by the activation of PAR-1, RPE cells were stimulated with the highly specific PAR-1 agonist peptide SFLLRN. Figure 3B shows that PAR-1 activation induces the dose-dependent release of glutamate, with the maximum effect (100% stimulation over control) attained at 10 µM SFLLRN concentration. This result demonstrated that thrombin-induced Glu release is mediated by activation of PAR-1.

PAR-1-induced glutamate release requires calcium increase from intra- and extracellular stores: Thrombin has been shown to increase intracellular calcium through PAR-1 activation. To investigate if PAR-1-mediated Glu release is calcium-dependent, RPE cells were stimulated with 10 µM SFLLRN in nominally calcium-free medium. As shown in Figure 4A, SFLLRN-induced release was decreased by

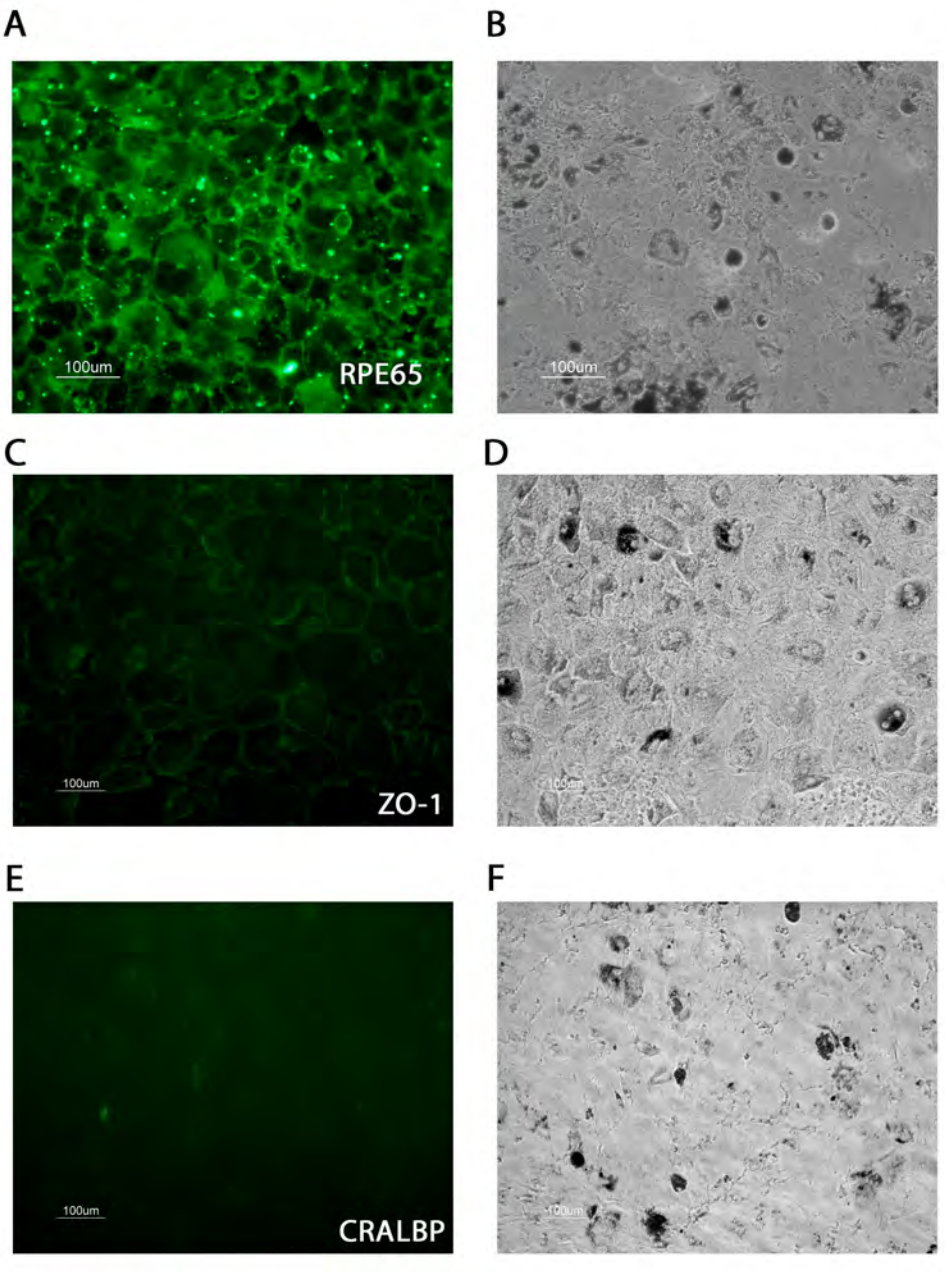

Figure 1. RPE cell morphology and identity. RPE cultures without any treatment were stained with antibodies against RPE65 (**A**), zonula occludens 1 (ZO-1) (**C**), and cellular retinaldehyde-binding protein (CRALBP) (**E**), as described in the experimental procedure section. The corresponding bright-field images are shown in the right column (**B**, **D**, **F**).

Molecular Vision 2019; 25:546-558 <http://www.molvis.org/molvis/v25/546> © 2019 Molecular Vision

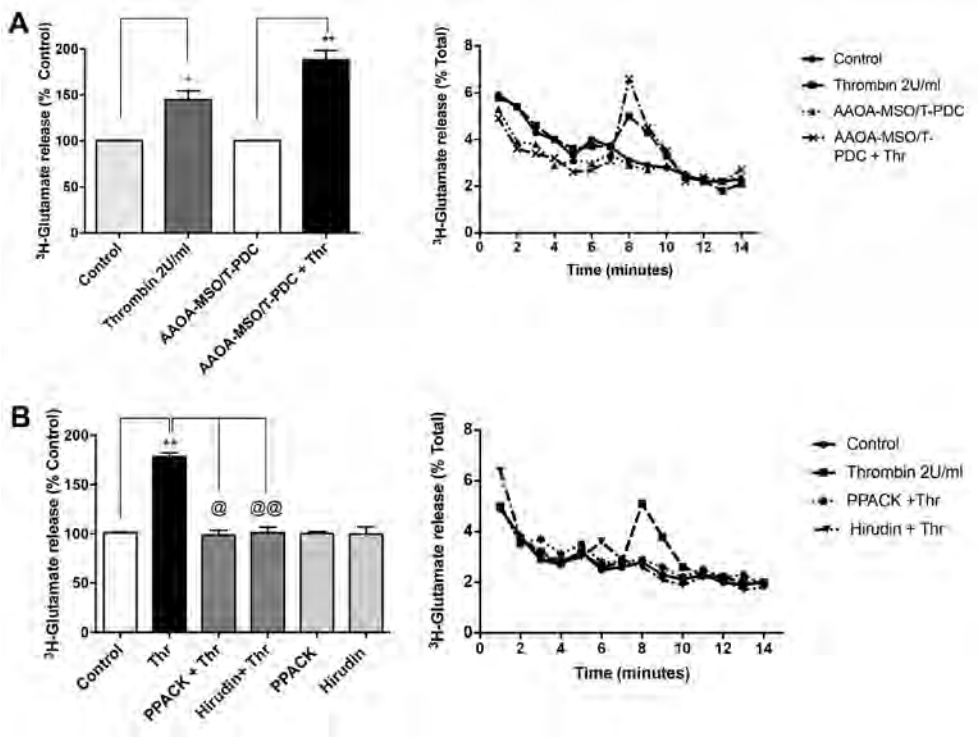

Figure 2. Thrombin induces glutamate release from rat RPE cells. Primary cultures of rat RPE cells were incubated for 30 min with 1 mM amino-oxyacetic acid and 0.5 mM methionine sulfoximine (AAOA-MSO) before loading with ^{3}H-glutamate in Krebs ringer bicarbonate (KRB; 1 µCi/ml 30 min). Cultures were superfused with KRB containing 50 µM 1-trans-pyrrolidine-2,4-dicarboxylic acid (trans-PDC) and stimulated with 2 U/ml thrombin. One milliliter samples were collected at 1 min intervals. Results are expressed as % of total ^{3}H-Glu incorporation or as a % of unstimulated control. **A**: Thrombin stimulates glutamate release. Thrombin-induced ^{3}H-Glu release was increased by the inhibition of glutamate (Glu) metabolism and reuptake. Values are the mean ± standard error of the mean (SEM) of three independent experiments. The Student *t* test with respect to negative control was statistically significant (*p<0.05; ** p<0.005). **B**: Specificity of the thrombin effect. Thrombin-induced Glu release was prevented by the inclusion of thrombin inhibitors hirudin (4 U/ml) and D-Phenylalanyl-Prolyl-Arginyl Chloromethyl Ketone (PPACK; 10 µM) during superfusion. Values are the mean ± SEM of three independent experiments. The Student *t* test with respect to negative control was statistically significant (**p<0.005); the Student *t* test with respect to thrombin stimulation was statistically significant (@p<0.05; @@p<0.005).

about 40% in this condition. Furthermore, the removal of extracellular calcium by the inclusion of 1 mM EGTA inhibited PAR-1 stimulation of Glu release to the same extent as calcium-free medium (about 40%). In contrast, preloading of the cells with the permeable calcium chelator BAPTA-AM completely prevented SFLLRN-induced ^{3}H-glutamate release; this effect was not modified by the joint inclusion of BAPTA-AM plus EGTA. These results indicated that thrombin induction of Glu release from RPE cells depends primarily on intracellular calcium increase, although extracellular calcium is required to attain the maximum effect. To further confirm the requirement of calcium from intracellular stores for glutamate release, RPE cells were treated with 5 µM ionomycin, known to promote the release of calcium from the endoplasmic reticulum (ER) to the cytosol, and showed a highly significant increase in thrombin-stimulated glutamate release in this condition (Figure 4B).

Additional mechanisms promoting Ca^{2+} entry into RPE cells, such as the reverse activity of the Na^{+}/Ca^{2+} exchanger (NCX) [41] and the L-type calcium channels, have been identified [42]. We tested the effect of the NCX inhibitors KB-R7943 (75 µM) and SEA0400 (50 µM), and that of the L-type channel blocker nifedipine, on thrombin-induced Glu release. Figure 4C shows that the inhibition of NCX by both tested inhibitors completely prevented the release of Glu, whereas nifedipine had no effect on thrombin-induced glutamate release Figure 4D, supporting the requirement of extracellular Ca^{2+} entry through NCX activity for a thrombin-induced effect.

Signaling pathways involved in thrombin-induced glutamate release: Thrombin promotion of phospholipase C-β (PLC-β) activity and the consequent release of calcium from the ER through IP3 receptors, has been reported [43]. To analyze this pathway, cells were stimulated with 10 µM SFLLRN in the presence of the PLC-β inhibitor U73122 (2.5 µM). Figure 5A shows that the inhibition of PLC-β decreases PAR-1-mediated Glu release by about 50%, suggesting the participation of ER-IP3 calcium channels in SFLLRN-induced Glu release. Moreover, the inhibition of ryanodine receptor by 10 µM ryanodine or 30 µM dantrolene did not modify thrombin-induced Glu release (data not shown).

PLC-β activity generates diacyl-glycerol (DAG), a known activator of c/n PKC. Figure 5B shows that preincubation of

Molecular Vision 2019; 25:546-558 <http://www.molvis.org/molvis/v25/546> © 2019 Molecular Vision

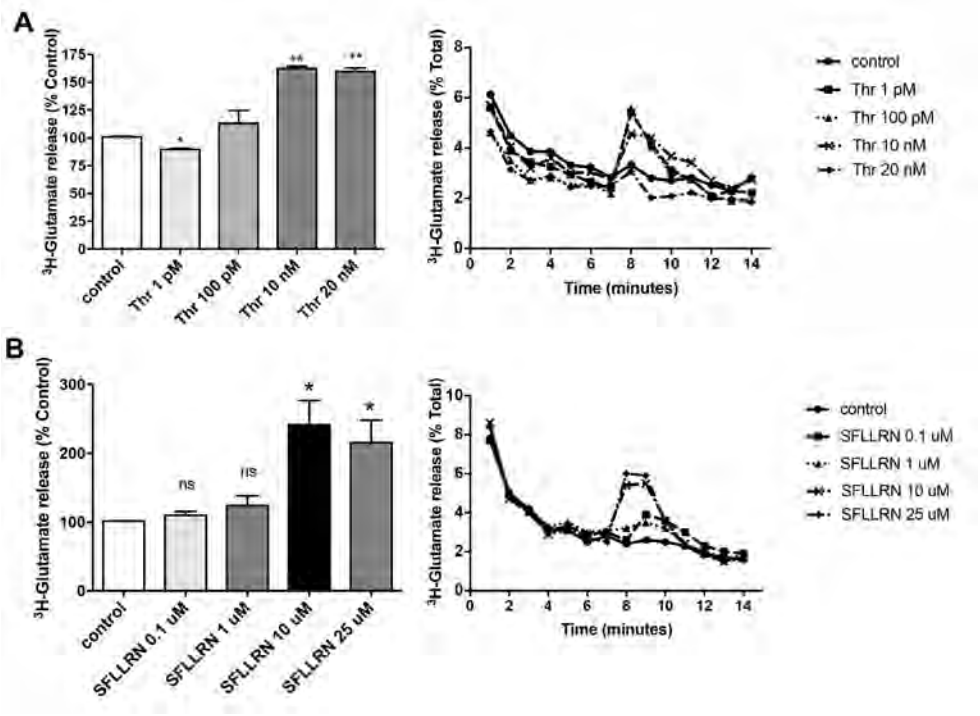

Figure 3. Thrombin-induced glutamate release is mediated by PAR-1. Primary cultures of rat RPE cells were loaded with 1 µCi/ml ^{3}H-glutamate and superfused with Krebs ringer bicarbonate (KRB; negative control) as described in Methods. Stimulation was carried in KRB containing increasing concentrations of thrombin (**A**) or of the specific protease-activated receptor 1 (PAR-1) agonist peptide Ser-Phe-Leu-Leu-Arg-Asn-amide trifluoroacetate salt (SFLLRN) (**B**), as described for Figure 2. Values are the mean ± standard error of the mean (SEM) of three independent experiments. The Student *t* test with respect to negative control was statistically significant (*p<0.05).

RPE cells with 20 µM of the c/n PKC-specific inhibitor Ro 32–0432 inhibits PAR-1 stimulation of glutamate release by about 80%. This result further confirmed the participation of the PLC-β/DAG/c/n PKC signaling pathway in thrombin-induced Glu release.

We previously demonstrated that thrombin activates $G_{12/13}$, known to activate phosphoinositide-3 kinase (PI3K) via the dissociated G-protein βγ subunit in a Ca^{2+}-independent manner [44,45]. In turn, PI3K may lead to the stimulation of mitogen-activated protein kinases pathway (MEK/ERK) [44,46]. We tested the effect of the PI3K inhibitor wortmannin (2.5 µM) and of the MEK inhibitor U0126 (20 µM) on PAR-1-stimulated Glu release, and showed that neither the inhibition of PI3K nor that of MEK prevented PAR-1-induced Glu release. This result indicated that activation of the Gβγ signaling pathway is not involved in thrombin-induced glutamate release.

PAR-1-induced glutamate release is not mediated by vesicular transport or the reverse activity of GLAST: Control of the extracellular glutamate concentration is a crucial mechanism in the prevention of excitotoxic cell death. Among the mechanisms involved in this process, Glu released by the reverse activity of the reverse activity of the Glutamate Aspartate Transporter (GLAST) or through Ca^{2+}-dependent vesicular release in a neurotransmitter-like mode could contribute to the thrombin effect. To test this possibility, we used the vesicular release inhibitor bafilomycin (Figure 6A) and the reverse transport inhibitor DL-threo-β-Benzyloxyaspartic acid (TBOA; Figure 6B). Neither had an effect on PAR-1-induced glutamate release.

DISCUSSION

Glutamate is the excitatory transmitter in the main signaling pathway of the retina from photoreceptors to ganglion cells. Because the elevation of the Glu concentration in pathological conditions has been shown to induce the excitotoxic death of retinal neurons, the extracellular Glu concentration must be tightly regulated [47]. Glutamate has also been shown to promote RPE cell proliferation by activating distinct signaling pathways linked to selective glutamate receptor subtypes [46,48,49]; thus, Glu release induced by thrombin may autoactivate Glu receptors on RPE cells, resulting in the alteration of RPE physiology, and the consequent death of retinal neurons.

The RPE is separated from the photoreceptor outer segments by the sub-retinal space. Although the actual volume of this space is minimal, the communication that occurs across this microenvironment is important to the visual process. In pathological conditions that alter the BRB, exposure of RPE cells to blood-contained thrombin promotes the EMT of RPE cells, including the transformation, increased proliferation, and migration to the vitreous which ultimately

Molecular Vision 2019; 25:546-558 <http://www.molvis.org/molvis/v25/546> © 2019 Molecular Vision

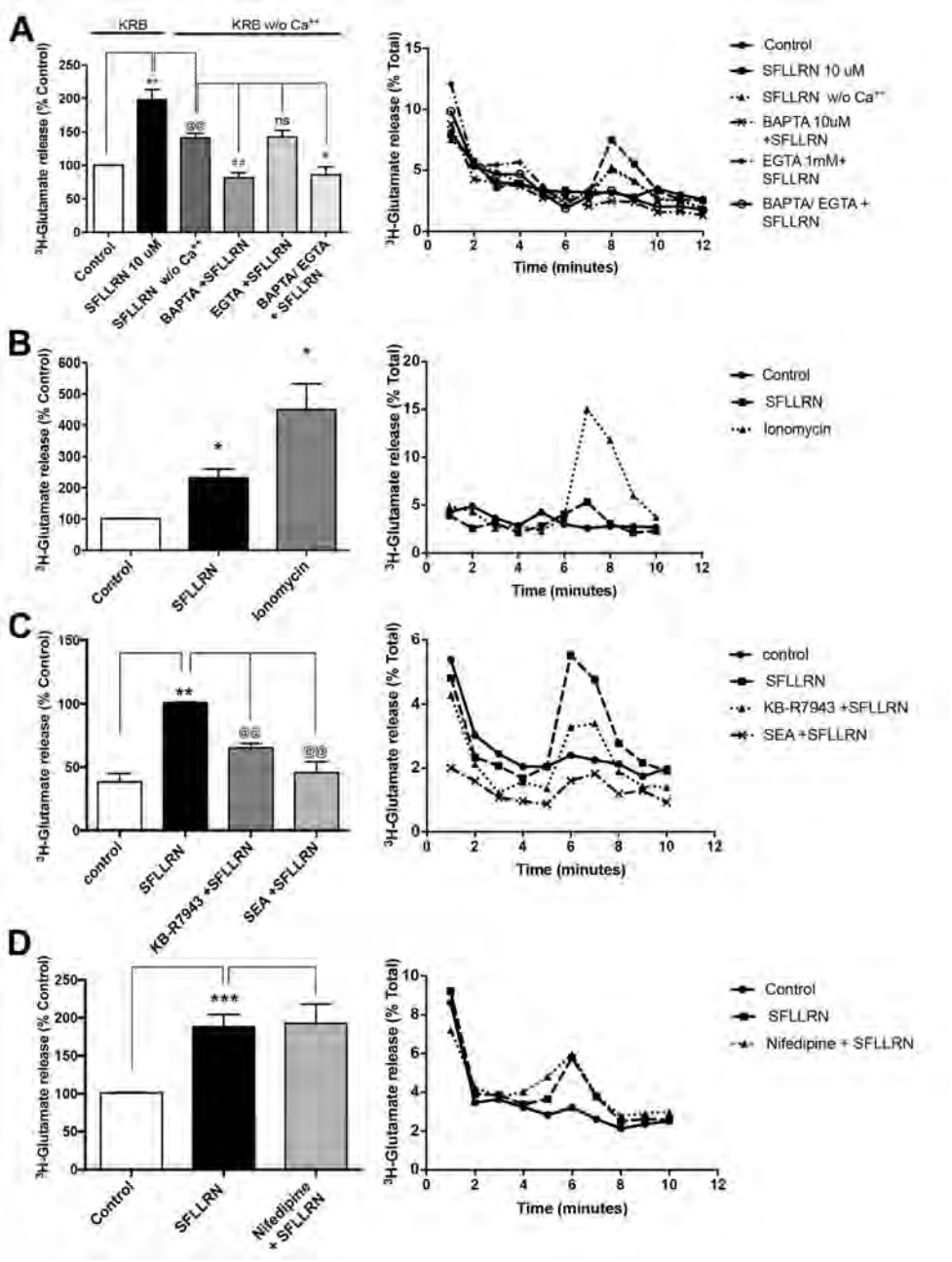

Figure 4. SFLLRN-induced glutamate release is calcium-dependent. Primary cultures of rat RPE cells loaded with 1 µCi/ml ^{3}H-glutamate in Krebs ringer bicarbonate (KRB) for 30 min and stimulated with 10 µM protease-activated receptor 1 (PAR-1) AP (Ser-Phe-Leu-Leu-Arg-Asn-amide trifluoroacetate salt [SFLLRN]). **A**: SFLLRN-induced glutamate release is calcium-dependent. 1,2-Bis(2-aminophenoxy)ethane-N,N,N',N'-tetraacetic acid tetrakis(acetoxymethyl ester) (BAPTA AM) and/or EGTA were included in Ca^{2+}-free KRB for 15 min in the presence or absence of the Ca^{2+} chelators BAPTA-AM (10 µM) and/or EGTA (1 mM) before stimulation. Values are the mean ± standard error of the mean (SEM) of three independent experiments. The Student *t* test with respect to negative control was statistically significant (**p<0.005); the Student *t* test with respect to SFLLRN w/ Ca^{2+} was statistically significant (@@p<0.005); the Student *t* test with respect to SFLLRN w/o Ca^{2+} was statistically significant (#p<0.05, ##p<0.005). **B**: Ca^{2+} release from intracellular stores is the main contributor to PAR-1 induced glutamate release. Cells were stimulated with 5 µM ionomycin to further demonstrate the requirement for intracellular Ca^{2+}. Values are the mean ± SEM of three independent experiments. The Student *t* test with respect to negative control was statistically significant (*p<0.05). **C**: Extracellular Ca^{2+} contributes to PAR-1-induced glutamate release. Cells were incubated with the Na^{+}/Ca^{2+} exchanger (NCX) inhibitor SEA 0400 (50 µM), and of the inhibitor of the exchanger reverse activity KB-R7943 (75 µM) before stimulation with 10 µM of the PAR-1 agonist peptide SFLLRN. Results showed that PAR-1-induced release was statistically significantly decreased by these compounds. Data are the mean of three independent experiments. The Student *t* test with respect to negative control was statistically significant (**p<0.005); the Student *t* test with respect to SFLLRN was statistically significant (@@p<0.005). **D**: PAR-1-induced glutamate release is independent of L-type calcium channel activation. Thrombin stimulation in the presence of the L-type calcium channel blocker nifedipine (5 µM) showed that Glu release is unrelated to L-calcium channel activity. Values are the mean ± SEM of three independent experiments. The Student *t* test with respect to negative control was statistically significant (***p<0.005). The Student *t* test with respect to SFLLRN was not statistically significant.

Molecular Vision 2019; 25:546-558 <http://www.molvis.org/molvis/v25/546> © 2019 Molecular Vision

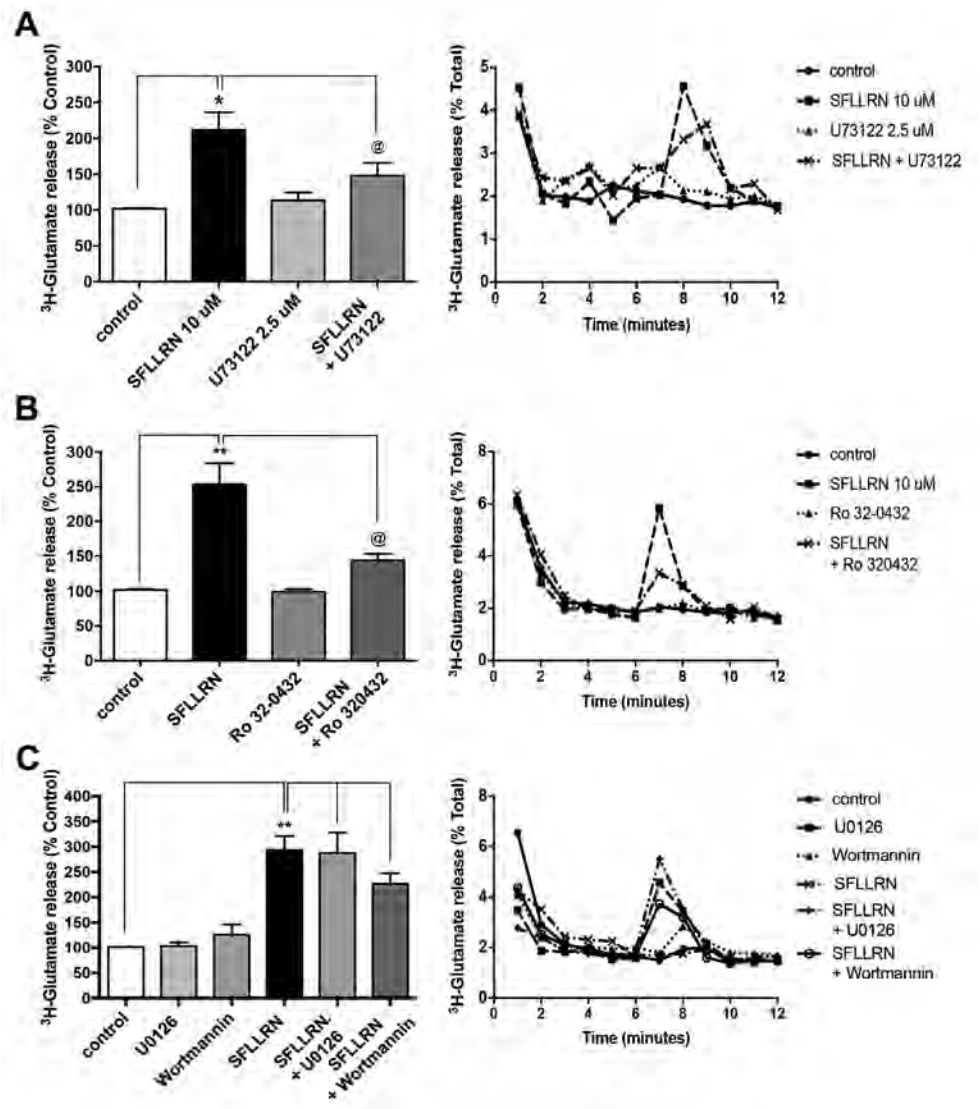

Figure 5. Signaling pathways involved in thrombin-induced glutamate release. **A**: Protease-activated receptor 1 (PAR-1)-induced glutamate (Glu) release requires phospholipase C-β (PLC-β) activity. Cells were incubated in the presence of the PLC-β inhibitor U73122 (2.5 μM) for 30 min. The inhibitor was removed before stimulation with 10 μM PAR-1 AP. Results showed that Ser-Phe-Leu-Leu-Arg-Asn-amide trifluoroacetate salt (SFLLRN) induced Glu release which was prevented by the inhibition of PLC-β. Results are the mean of three independent experiments. The Student *t* test with respect to negative control was statistically significant (*p<0.05). The Student *t* test with respect to SFLLRN was statistically significant (@ p<0.05). **B**: Inhibition of c/n protein kinase C (PKC) isoforms prevents SFLLRN-induced Glu release. Cells were incubated with the c/n PKC inhibitor Ro 32–0432 (20μM) for 30 min, and removed before stimulation with 10 μM PAR-1 AP. Data are the mean ± standard error of the mean (SEM) of three independent experiments. The Student *t* test with respect to negative control was statistically significant (**p<0.005). The Student *t* test with respect to SFLLRN was statistically significant (@ p<0.05). **C**: Thrombin-induced Glu release is independent of phosphoinositide 3-kinase (PI3K) and mitogen-activated protein kinase kinase (MEK) activity. The MEK inhibitor U0126 (20 μM) and the PI3K inhibitor wortmannin (1 μM) were included in KRB for 30 min and removed, before stimulation. Data are the mean ± SEM of three independent experiments. The Student *t* test with respect to negative control was statistically significant (**p<0.005). The Student *t* test with respect to SFLLRN was not statistically significant.

contributes to neuronal death and the development of blindness. Despite the close apposition of the photoreceptors and RPE cells, the possible release and diffusion of glutamate from RPE, and its influence on retinal signaling, have not been examined. The present results showed that thrombin induces the fast, specific, dose-dependent release of Glu from RPE cells, suggesting that under pathological conditions or surgical procedures in which the BRB is compromised, the elevation of extracellular Glu induced by thrombin activation of PAR-1 may contribute to the long-term increase in RPE cell proliferation, a main feature in the development of fibroproliferative eye diseases.

Numerous factors seem to be involved in the proliferation and transformation of RPE cells in PVR [50,51]. Although the glutamate concentration in PVR tissue has not been determined, an increase in glutamate levels in the vitreous cavity of patients is increased by retinal detachment and hypoxia [52], due to a decrease in the expression of glutamate transporters in retinal glia [35,53-55]. Additionally, glutamate from serum or from damaged retinal cells which

Molecular Vision 2019; 25:546-558 <http://www.molvis.org/molvis/v25/546> © 2019 Molecular Vision

contain millimolar concentrations may reach the RPE [56]. Thus, under pathologic conditions in vivo, elevation of glutamate could contribute to the development of PVR through the activation of specific receptors on RPE cells.

Activation of PAR-1 by endogenous agonists, including thrombin and plasmin, or by specific agonist peptides (TFLLR and SFLLRN) has been shown to elevate intracellular Ca^{2+} in RPE cells [57,58] and astrocytes [59]. Consistent with these data, the present results showed that removal of intracellular calcium by BAPTA-AM completely prevents PAR-1-induced Glu release, clearly indicating that downstream pathways associated with Ca^{2+} release from internal stores are involved. This was further confirmed by the robust induction of Glu release by ionomycin (Figure 4B), known to deplete ER Ca^{2+} pools. Because EGTA modestly decreased PAR-1-induced Glu release, a contribution of extracellular calcium is also required, possibly aimed to the refilling of ER intracellular calcium stores. Therefore, it is tempting to speculate that the thrombin-triggered rise in $[Ca^{2+}]i$ primes cells for glutamate release, as it has been shown for the release of ATP [37].

There are several mechanisms that trigger the elevation of intracellular Ca^{2+} levels. One mechanism for Ca^{2+} release from internal stores involves the activation of inositol 1,4, 5-trisphosphate (IP3)-sensitive Ca^{2+} channels on the ER membrane. PAR-1 coupling to the GPCR $G_{q11}\alpha$ subunit activates PLC-β, which catalyzes the formation of inositol 1,4,5-trisphosphate (IP_3) and DAG, leading to an increase in the intracellular Ca^{2+} concentration and DAG activation of c/n PKC isoforms [2]. We examined the contribution of this pathway to thrombin/PAR-1-induced Ca^{2+}-dependent glutamate release from RPE cells, and demonstrated that the pharmacologic inhibition of PLC-β by U73122, or that of its downstream target c/n PKC by Ro-32–0432, statistically significantly decreased PAR-1-induced Glu release, further confirming that the intracellular Ca^{2+} increase required for glutamate release is induced by activation of this pathway. Although PAR-1 is coupled to Gβγ subunits, essential for glutamate efflux from cultured astrocytes [34], inhibition of PI3K by wortmannin and of MEK/Erk by U0126 (Figure 5C) had no effect on PAR-1 evoked glutamate release, indicating that signaling through Gβγ subunits is not involved in this process.

Additionally, we examined the contribution of the caffeine/ryanodine-sensitive ER Ca^{2+} store to thrombin-induced Ca^{2+}-dependent glutamate release. Unexpectedly, the results showed that neither the pharmacological blockage of these pathways nor the inhibition of the thapsigargin-sensitive ER Ca^{2+} ATPase had an effect on thrombin-induced Glu release (data not shown). On this matter, RPE cells and

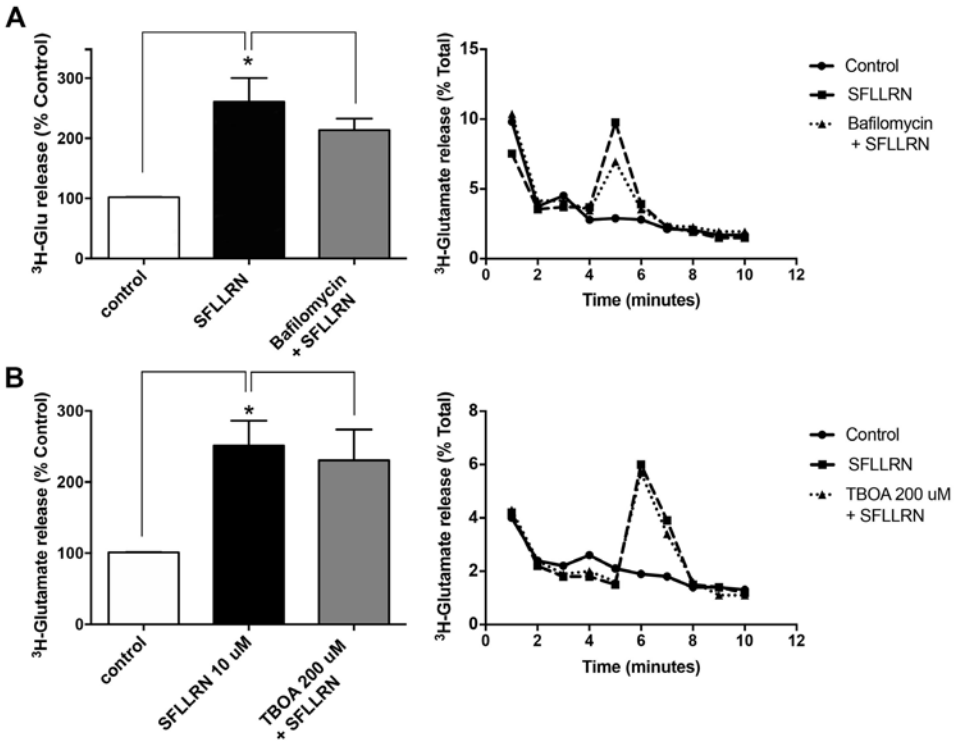

Figure 6. Thrombin induces glutamate release in a non-vesicular mode. The participation of vesicular mechanisms (Figure 6A) or reverse activity of Glutamate Aspartate Transporter (GLAST; Figure 6B) in thrombin induction of glutamate (Glu) release was tested. Results showed that neither GLAST inhibition by DL-threo-β-Benzyloxyaspartic acid (TBOA) nor that of vesicular release by bafilomycin prevented thrombin induction of Glu release. Data are the mean ± standard error of the mean (SEM) of three independent experiments. The Student *t* test with respect to negative control was statistically significant (*p<0.05). The Student *t* test with respect to Ser-Phe-Leu-Leu-Arg-Asn-amide trifluoroacetate salt (SFLLRN) was not statistically significant.

Molecular Vision 2019; 25:546-558 <http://www.molvis.org/molvis/v25/546> © 2019 Molecular Vision

astrocytes express several types of transient receptor potential (TRP) channels [60,61] which contribute to modulate Ca^{2+}-dependent vesicular glutamate release by the promotion of store-operated Ca^{2+} entry (SOCE) [62,63]. However, bafilomycin, a macrolide that specifically targets vacuolar-type H^+-ATPase (V-ATPase), therefore inhibiting vesicular release, had no effect on thrombin-induced Glu release (Figure 6A).

Interestingly, recent evidence suggested that L-type calcium channels present in RPE are linked to intracellular signaling pathways by protein kinase-dependent regulation. RPE L-type Ca^{2+} channels can be activated by protein kinase C, protein tyrosine kinases of the Src-subtype [64,65], and receptor tyrosine kinases [66]. Although we tested this possibility, the lack of effect of nifedipine indicates that these channels are not involved in thrombin-induced release of glutamate.

The deregulation of the thrombin-PAR system in pathological conditions results in the loss of barrier function [67]. Thrombin is capable of modifying endothelial cell permeability [12], and it has been suggested to play a role in retinal disease [67,68]. Recent reports on this matter showed that the ion transporter NCX operating in the Ca^{2+}-influx (reverse) mode promotes endothelial barrier dysfunction in response to thrombin, which is prevented by the reverse-mode NCX inhibitor (KB-R7943) or NCX1 knockdown in vitro [69]. Ca^{2+} entry by this exchanger has been identified as a mechanism for inducing amplification of Ca^{2+} signals that occur during conditions of agonist activation. Thus, we investigated whether Ca^{2+} influx through NCX was involved in Glu release in response to thrombin, and showed that the specific inhibition of this process by KB-R7943 completely blocked thrombin-induced glutamate release.

In conclusion, the present study demonstrated that contact of RPE cells with thrombin, which may be present in pathological conditions, promotes the release of glutamate in a dose-dependent-specific manner. This effect is mediated by an increase in the intracellular Ca^{2+} concentration induced by the activation of the PLC-β/PKC pathways, and by the reverse activity of the Na^+/Ca^{2+} exchanger. Therefore, the deregulation of this system may allow glutamate diffusion to the inner retina, thus promoting the excitotoxic death of neurons.

ACKNOWLEDGMENTS

The authors thank A. Ortega (CINVESTAV-IPN, Mexico) for the donation of KB-R7943 and SEA0400. FUNDING: This work was supported by CONACyT [254,333 to AMLC]; and PAPIIT/UNAM [IN205317 to AMLC].

REFERENCES

1. Mund M, Rodrigues M. (2006) The retinal pigment epithelium. In: Zinn K, Marmar M (eds) The Retinal Pigment Epithelium. Harvard University Press, London, pp 45–52.
2. Strauss O. The retinal pigment epithelium in visual function. Physiol Rev 2005; 85:845-81. [PMID: 15987797].
3. Bastiaans J, van Meurs JC, van Holten-Neelen C, Nagtzaam NMA, van Hagen PM, Chambers RC, Hooijkaas H, Dik WA. Thrombin Induces Epithelial-Mesenchymal Transition and Collagen Production by Retinal Pigment Epithelial Cells via Autocrine PDGF-Receptor Signaling. Investig Opthalmology Vis Sci 2013; 54:8306-[PMID: 24302586].
4. Kim IK, Arroyo JG. Mechanisms in proliferative vitreoretinopathy. Ophthalmol Clin North Am 2002; 15:81-6. [PMID: 12064085].
5. Palma-Nicolás JP, López-Colomé AM. Thrombin induces slug-mediated E-cadherin transcriptional repression and the parallel Up-regulation of N-cadherin by a transcription-independent mechanism in RPE cells. J Cell Physiol 2013; 228:581-9. [PMID: 22833386].
6. Iwano M, Plieth D, Danoff T, Xue C, Okada H, Neilson E. Evidence that fibroblasts derive from epithelium during tissue fibrosis. J Clin Invest 2002; 110:341-50. [PMID: 12163453].
7. Kiemer AK, Takeuchi K, Quinlan MP. Identification of genes involved in epithelial-mesenchymal transition and tumor progression. Oncogene 2001; 20:6679-88. [PMID: 11709702].
8. Nagasaki H, Shinagawa K, Mochizuki M. Risk factors for proliferative vitreoretinopathy. Prog Retin Eye Res 1998; 17:77-98. [PMID: 9537796].
9. Pastor JC, de la Rua ER, Martin F. Proliferative vitreoretinopathy: risk factors and pathobiology. Prog Retin Eye Res 2002; 21:127-44. [PMID: 11906814].
10. Grisanti S, Guidry C. Transdifferentiation of retinal pigment epithelial cells from epithelial to mesenchymal phenotype. Invest Ophthalmol Vis Sci 1995; 36:391-405. [PMID: 7531185].
11. Wojtukiewicz MZ, Hempel D, Sierko E, Tucker SC, Honn KV. Protease-activated receptors (PARs)—biology and role in cancer invasion and metastasis. Cancer Metastasis Rev 2015; 34:775-96. [PMID: 26573921].
12. Coughlin SR. Thrombin signalling and protease-activated receptors. Nature 2000; 407:258-64. [PMID: 11001069].
13. Noorbakhsh F, Vergnolle N, Hollenberg MD, Power C. Proteinase-activated receptors in the nervous system. Nat Rev Neurosci 2003; 4:981-90. [PMID: 14682360].
14. de Castro Ribeiro M, Badaut J, Price M, Meins M, Bogousslavsky J, Monard D, Hirt L. Thrombin in ischemic neuronal death. Exp Neurol 2006; 198:199-203. [PMID: 16427045].
15. Xi G, Reiser G, Keep RF. The role of thrombin and thrombin receptors in ischemic, hemorrhagic and traumatic brain

Molecular Vision 2019; 25:546-558 <http://www.molvis.org/molvis/v25/546> © 2019 Molecular Vision

injury: deleterious or protective? J Neurochem 2003; 84:3-9. [PMID: 12485396].

16. Boven LA, Vergnolle N, Henry SD, Silva C, Imai Y, Holden J, Warren K, Hollenberg MD, Power C. Up-regulation of proteinase-activated receptor 1 expression in astrocytes during HIV encephalitis. J Immunol 2003; 170:2638-46. [PMID: 12594292].

17. Akiyama H, Ikeda K, Kondo H, McGeer PL. Thrombin accumulation in brains of patients with Alzheimer's disease. Neurosci Lett 1992; 146:152-4. [PMID: 1491781].

18. Trejo J. Protease-activated receptors: new concepts in regulation of G protein-coupled receptor signaling and trafficking. J Pharmacol Exp Ther 2003; 307:437-42. [PMID: 12966163].

19. Macfarlane SR, Seatter MJ, Kanke T, Hunter GD, Plevin R. Proteinase-activated receptors. Pharmacol Rev 2001; 53:245-82. [PMID: 11356985].

20. Bian ZM, Elner SG, Elner VM. Thrombin-induced VEGF expression in human retinal pigment epithelial cells. Invest Ophthalmol Vis Sci 2007; 48:2738-46. [PMID: 17525207].

21. Parrales A, Lopez E, Lopez-Colome AM. Thrombin activation of PI3K/PDK1/Akt signaling promotes cyclin D1 upregulation and RPE cell proliferation. Biochim Biophys Acta 2011; 1813:1758-66. [PMID: 21736902].

22. Palma-Nicolas JP, Lopez E, Lopez-Colome AM. Thrombin stimulates RPE cell motility by PKC-zeta- and NF-kappaB-dependent gene expression of MCP-1 and CINC-1/GRO chemokines. J Cell Biochem 2010; 110:948-67. [PMID: 20564194].

23. Guerrini L, Blasi F, Denis-Donini S. Synaptic activation of NF-kappa B by glutamate in cerebellar granule neurons in vitro. Proc Natl Acad Sci U A 1995; 92:9077-81. [PMID: 7568076].

24. Komuro H, Rakic P. Modulation of neuronal migration by NMDA receptors. Science 1993; 260:95-7. [PMID: 8096653].

25. Thomas GM, Huganir RL. MAPK cascade signalling and synaptic plasticity. Nat Rev Neurosci 2004; 5:173-83. [PMID: 14976517].

26. Chapman AG. Glutamate and epilepsy. J Nutr 2000; 130:1043S-5S. [PMID: 10736378].

27. Nicholls D, Attwell D. The release and uptake of excitatory amino acids. Trends Pharmacol Sci 1990; 11:462-8. [PMID: 1980041].

28. Daw NW, Brunken WJ, Parkinson D. The function of synaptic transmitters in the retina. Annu Rev Neurosci 1989; 12:205-25. [PMID: 2564755].

29. Lopez-Colome AM, Roberts PJ. Effect of excitatory amino acid analogues on the release of D-[3H]aspartate from chick retina. Eur J Pharmacol 1987; 142:409-17. [PMID: 3428354].

30. Lopez-Colome AM, Somohano F. Effect of selective kainate lesions on the release of glutamate and aspartate from chick retina. J Neurosci Res 1986; 15:205-16. [PMID: 2870197].

31. Mitchell CH, Reigada D. Purinergic signalling in the subretinal space: a role in the communication between the retina and the RPE. Purinergic Signal 2008; 4:101-7. [PMID: 18368526].

32. Steinberg RH, Wood I. Pigment epithelial cell ensheathment of cone outer segments in the retina of the domestic cat. Proc R Soc Lond B Biol Sci 1974; 187:461-78. [PMID: 4155505].

33. Mongin AA, Kimelberg HK. ATP regulates anion channel-mediated organic osmolyte release from cultured rat astrocytes via multiple Ca2+-sensitive mechanisms. Am J Physiol Cell Physiol 2005; 288:C204-13. [PMID: 15371260].

34. Ramos-Mandujano G, Vazquez-Juarez E, Hernandez-Benitez R, Pasantes-Morales H. Thrombin potently enhances swelling-sensitive glutamate efflux from cultured astrocytes. Glia 2007; 55:917-25. [PMID: 17437307].

35. Takano T, Kang J, Jaiswal JK, Simon SM, Lin JH, Yu Y, Li Y, Yang J, Dienel G, Zielke HR, Nedergaard M. Receptor-mediated glutamate release from volume sensitive channels in astrocytes. Proc Natl Acad Sci U A 2005; 102:16466-71. [PMID: 16254051].

36. Pacheco-Dominguez RL, Palma-Nicolas JP, Lopez E, Lopez-Colome AM. The activation of MEK-ERK1/2 by glutamate receptor-stimulation is involved in the regulation of RPE proliferation and morphologic transformation. Exp Eye Res 2008; 86:207-19. [PMID: 18061165].

37. Reigada D, Lu W, Mitchell CH. Glutamate acts at NMDA receptors on fresh bovine and on cultured human retinal pigment epithelial cells to trigger release of ATP. J Physiol 2006; 575:707-20. [PMID: 16809361].

38. Abe T, Durlu YK, Tamai M. The Properties of Retinal Pigment Epithelial Cells in Proliferative Vitreoretinopathy Compared with Cultured Retinal Pigment Epithelial Cells. Exp Eye Res 1996; 63:201-10. [PMID: 8983978].

39. Brandl C, Zimmermann SJ, Milenkovic VM, Rosendahl SMG, Grassmann F, Milenkovic A, Hehr U, Federlin M, Wetzel CH, Helbig H, Weber BHF. In-Depth Characterisation of Retinal Pigment Epithelium (RPE) Cells Derived from Human Induced Pluripotent Stem Cells (hiPSC). Neuromolecular Med 2014; 16:551-64. [PMID: 24801942].

40. Andrew M, Paes B, Milner R, Johnston M, Mitchell L, Tollefsen DM, Powers P. Development of the human coagulation system in the full-term infant. Blood 1987; 70:165-72. [PMID: 3593964].

41. Mangini NJ, Haugh-Scheidt L, Valle JE, Cragoe EJ Jr, Ripps H, Kennedy BG. Sodium-calcium exchanger in cultured human retinal pigment epithelium. Exp Eye Res 1997; 65:821-34. [PMID: 9441706].

42. Ueda Y, Steinberg RH. Voltage-operated calcium channels in fresh and cultured rat retinal pigment epithelial cells. Invest Ophthalmol Vis Sci 1993; 34:3408-18. [PMID: 8225876].

43. Vaidyula VR, Rao AK. Role of Galphaq and phospholipase C-beta2 in human platelets activation by thrombin receptors PAR1 and PAR4: studies in human platelets deficient in Galphaq and phospholipase C-beta2. Br J Haematol 2003; 121:491-6. [PMID: 12716374].

Molecular Vision 2019; 25:546-558 <http://www.molvis.org/molvis/v25/546> © 2019 Molecular Vision

44. Parrales A, Lopez E, Lee-Rivera I, Lopez-Colome AM. ERK1/2-dependent activation of mTOR/mTORC1/p70S6K regulates thrombin-induced RPE cell proliferation. Cell Signal 2013; 25:829-38. [PMID: 23291002].

45. Ruiz-Loredo AY, Lopez E, Lopez-Colome AM. Thrombin promotes actin stress fiber formation in RPE through Rho/ROCK-mediated MLC phosphorylation. J Cell Physiol 2011; 226:414-23. [PMID: 20672289].

46. Garcia S, Lopez E, Lopez-Colome AM. Glutamate accelerates RPE cell proliferation through ERK1/2 activation via distinct receptor-specific mechanisms. J Cell Biochem 2008; 104:377-90. [PMID: 18022816].

47. Sherry DM, Townes-Anderson E. Rapid glutamatergic alterations in the neural retina induced by retinal detachment. Invest Ophthalmol Vis Sci 2000; 41:2779-90. [PMID: 10937598].

48. Nedergaard M, Takano T, Hansen AJ. Beyond the role of glutamate as a neurotransmitter. Nat Rev Neurosci 2002; 3:748-55. [PMID: 12209123].

49. Uchida N, Kiuchi Y, Miyamoto K, Uchida J, Tobe T, Tomita M, Shioda S, Nakai Y, Koide R, Oguchi K. Glutamate-stimulated proliferation of rat retinal pigment epithelial cells. Eur J Pharmacol 1998; 343:265-73. [PMID: 9570476].

50. Hecquet C, Lefevre G, Valtink M, Engelmann K, Mascarelli F. Activation and role of MAP kinase-dependent pathways in retinal pigment epithelial cells: ERK and RPE cell proliferation. Invest Ophthalmol Vis Sci 2002; 43:3091-8. [PMID: 12202534].

51. Holtkamp GM, Kijlstra A, Peek R, de Vos AF. Retinal pigment epithelium-immune system interactions: cytokine production and cytokine-induced changes. Prog Retin Eye Res 2001; 20:29-48. [PMID: 11070367].

52. Diederen RM, La Heij EC, Deutz NE, Kijlstra A, Kessels AG, van Eijk HM, Liem AT, Dieudonne S, Hendrikse F. Increased glutamate levels in the vitreous of patients with retinal detachment. Exp Eye Res 2006; 83:45-50. [PMID: 16530753].

53. Gadea A, Lopez E, Lopez-Colome AM. Glutamate-induced inhibition of D-aspartate uptake in Muller glia from the retina. Neurochem Res 2004; 29:295-304. [PMID: 14992289].

54. Lewis GP, Erickson PA, Guerin CJ, Anderson DH, Fisher SK. Changes in the expression of specific Muller cell proteins during long-term retinal detachment. Exp Eye Res 1989; 49:93-111. [PMID: 2503391].

55. Li Q, Puro DG. Diabetes-induced dysfunction of the glutamate transporter in retinal Muller cells. Invest Ophthalmol Vis Sci 2002; 43:3109-16. [PMID: 12202536].

56. Castillo J, Davalos A, Noya M. Progression of ischaemic stroke and excitotoxic aminoacids. Lancet 1997; 349:79-83. [PMID: 8996418].

57. Alvarez-Arce A, Lee-Rivera I, Lopez E, Hernandez-Cruz A, Lopez-Colome AM. Thrombin-Induced Calpain Activation Promotes Protease-Activated Receptor 1 Internalization. Int J Cell Biol 2017; 1908310:[PMID: 29250115].

58. Puro DG, Stuenkel EL. Thrombin-induced inhibition of potassium currents in human retinal glial (Muller) cells. J Physiol 1995; 485:337-48. [PMID: 7666362].

59. Wang H, Ubl JJ, Stricker R, Reiser G. Thrombin (PAR-1)-induced proliferation in astrocytes via MAPK involves multiple signaling pathways. Am J Physiol Cell Physiol 2002; 283:C1351-64. [PMID: 12372796].

60. Verkhratsky A, Reyes RC, Parpura V. TRP channels coordinate ion signalling in astroglia. Rev Physiol Biochem Pharmacol 2014; 166:1-22. [PMID: 23784619].

61. Wimmers S, Strauss O. Basal calcium entry in retinal pigment epithelial cells is mediated by TRPC channels. Invest Ophthalmol Vis Sci 2007; 48:5767-72. [PMID: 18055830].

62. Jin YH, Yamaki F, Takemura M, Koike Y, Furuyama A, Yonehara N. Capsaicin-induced glutamate release is implicated in nociceptive processing through activation of ionotropic glutamate receptors and group I metabotropic glutamate receptor in primary afferent fibers. J Pharmacol Sci 2009; 109:233-41. [PMID: 19202316].

63. Parpura V, Grubisic V, Verkhratsky A. Ca(2+) sources for the exocytotic release of glutamate from astrocytes. Biochim Biophys Acta 2011; 1813:984-91. [PMID: 21118669].

64. Strauss O, Buss F, Rosenthal R, Fischer D, Mergler S, Stumpff F, Thieme H. Activation of neuroendocrine L-type channels (alpha1D subunits) in retinal pigment epithelial cells and brain neurons by pp60(c-src). Biochem Biophys Res Commun 2000; 270:806-10. [PMID: 10772906].

65. Strauss O, Mergler S, Wiederholt M. Regulation of L-type calcium channels by protein tyrosine kinase and protein kinase C in cultured rat and human retinal pigment epithelial cells. FASEB J 1997; 11:859-67. [PMID: 9285484].

66. Rosenthal R, Thieme H, Strauss O. Fibroblast growth factor receptor 2 (FGFR2) in brain neurons and retinal pigment epithelial cells act via stimulation of neuroendocrine L-type channels (Ca(v)1.3). FASEB J 2001; 15:970-7. [PMID: 11292657].

67. Terasaki H, Shirasawa M, Otsuka H, Yamashita T, Uchino E, Hisatomi T, Sonoda S, Sakamoto T. Different Effects of Thrombin on VEGF Secretion, Proliferation, and Permeability in Polarized and Non-polarized Retinal Pigment Epithelial Cells. Curr Eye Res 2015; 40:936-45. [PMID: 25310246].

68. Klaassen I, Noorden CJFV, Schlingemann RO. Molecular basis of the inner blood-retinal barrier and its breakdown in diabetic macular edema and other pathological conditions. Prog Retin Eye Res 2013; 34:19-48. [PMID: 23416119].

69. Andrikopoulos P, Kieswich J, Harwood SM, Baba A, Matsuda T, Barbeau O, Jones K, Eccles SA, Yaqoob MM. Endothelial Angiogenesis and Barrier Function in Response to Thrombin Require Ca2+ Influx through the Na+/Ca2+ Exchanger. J Biol Chem 2015; 290:18412-28. [PMID: 25979335].

INFORME DE LABORES 2019

Articles are provided courtesy of Emory University and the Zhongshan Ophthalmic Center, Sun Yat-sen University, P.R. China. The print version of this article was created on 5 October 2019. This reflects all typographical corrections and errata to the article through that date. Details of any changes may be found in the online version of the article.

INFORME DE LABORES 2019

Available online at www.sciencedirect.com

ScienceDirect

Current Opinion in Pharmacology

The race between drug introduction and appearance of microbial resistance. Current balance and alternative approaches

Esaú López-Jácome[1,2], Rafael Franco-Cendejas[2], Héctor Quezada[3], Rosario Morales-Espinosa[1], Israel Castillo-Juárez[4], Bertha González-Pedrajo[5], Ana María Fernández-Presas[1], Arturo Tovar-García[1,6], Vanesa Angarita-Zapata[7], Paula Licona-Limón[5], Mariano Martínez-Vázquez[8] and Rodolfo García-Contreras[1]

As current levels of antimicrobial resistance are alarming, the World Health Organization urged the development of new antimicrobials to fight infections produced by multidrug resistant bacteria. Antibiotics impose severe selective pressure for the development of resistance, and currently bacteria resistant to all of them exist. In this review, we discuss the release and development of new antibacterial drugs and their properties as well as the current advances in the development of alternative approaches to combat bacterial infections, including the repurposing of drugs, anti-virulence therapies, the use of photosensitizers, phage therapy, and immunotherapies, with an emphasis on what is currently known about the possible development of bacterial resistance against them.

Addresses
[1] Departamento de Microbiología y Parasitología, Facultad de Medicina, Universidad Nacional Autónoma de México, Mexico City, Mexico
[2] Laboratorio de Infectología, Instituto Nacional de Rehabilitación Luis Guillermo Ibarra Ibarra, Mexico City, Mexico
[3] Laboratorio de Investigación en Inmunología y Proteómica, Hospital Infantil de México Federico Gómez, Mexico City, Mexico
[4] Colegio de Postgraduados, Campus Montecillo, Texcoco, Mexico
[5] Instituto de Fisiología Celular, Universidad Nacional Autónoma de México, Mexico City, Mexico
[6] Hospital General de Zona 8 San Ángel, IMSS, Mexico City, Mexico
[7] Escuela de Ingeniería Química, Universidad Industrial de Santander, Bucaramanga, Colombia
[8] Instituto de Química, Universidad Nacional Autónoma de México, Mexico City, Mexico

Corresponding author: García-Contreras, Rodolfo (rgarc@bq.unam.mx)

Current Opinion in Pharmacology 2019, **48**:48–56

This review comes from a themed issue on **Anti-infectives**

Edited by **Sergio Sánchez Esquivel** and **Arnold L Demain**

For a complete overview see the Issue and the Editorial

Available online 26th May 2019

https://doi.org/10.1016/j.coph.2019.04.016

1471-4892/© 2019 Elsevier Ltd. All rights reserved.

Introduction

Current levels of antimicrobial resistance are alarming [1] and the projections indicate that if no new effective antimicrobials are introduced, by the year 2050 there will be more deaths caused by multidrug resistant (MDR) bacteria (MDR) than by current leading causes of death including cancer [2]. The most recent World Health Organization's (WHO) review about antibiotic resistance announced a global priority pathogens list, classifying the bacteria depending on priority in critical, high and medium. The majority of infections in hospitals are caused by 'ESKAPE' pathogens (*Enterococcus faecium*, *Staphylococcus aureus*, *Klebsiella pneumoniae*, *Acinetobacter baumannii*, *Pseudomonas aeruginosa* and *Enterobacter* spp.) [3,4]. Antibiotics interfere with essential bacterial processes such as cell wall, protein, and nucleic acid synthesis, interrupting DNA replication, disrupting membrane integrity and important metabolic pathways, either killing or arresting bacterial growth, therefore exerting an intense selection pressure for the development of resistance. Since the introduction of penicillin in the early 1940's, the selection of resistant bacteria is typical and the percentage of resistant strains against multiple antibiotics and even to all is increasing. Antibiotic resistance can be achieved by modifications in the antibiotic targets, expression of alternative ones, expression of efflux pumps that expel several groups of antibiotics, decrease in antibiotic permeability or antibiotic inactivation by enzymes (e.g. β-lactams by β-lactamases [5•]). Other less well characterized mechanisms are the sequestration of antibiotics such as in *P. aeruginosa* biofilms via glucans that sequester aminoglycosides [6], and the protection of the antibiotic's target (protection of the fluoroquinolone target site by a protein designated Qnr or ribosomal protection proteins that confer resistance against tetracycline [7–9]).

In general, resistance against antibiotics that had single protein targets such as β-lactams (penicillin binding proteins), quinolones (topoisomerases) or rRNA targets, like macrolides and aminoglycosides, is readily achieved by mutations. In contrast, antibiotics like polymyxins that

target the non-protein components of the cell membrane such as LPS, often require the accumulation of multiple gene mutations that encode the enzymes used for their biosynthesis, (e.g. *lpx* lipid A biosynthesis genes) or in regulators of their modification, like *pmrAB* that influence the expression of the lipid A modification genes in response to pH and cation levels [10], and hence the appearance of resistance against these kind of antibiotics arises slowly. In the last decades, polymyxins have been reused worldwide as a last therapy resource for Gram negative infections, regardless their complex pharmacokinetic knowledge and potential serious adverse events. Nevertheless, in 2016 plasmid mediated colistin resistance was reported for the first time, in commensal *Escherichia coli* isolated from pigs, the resistance was mediated by the *mcr*-1 gene, encoding a phosphoethanolamine transferase that adds phosphoethanolamine to lipid A [11]. Another old antibiotic used in Gram negative severe infections is fosfomycin that, although it has a unique mechanism of action at earlier bacterial cell biosynthesis, it is not recommended to be used as monotherapy because of its faster and higher resistance appearance [12].

Resistance is the ability to proliferate in the presence of an antimicrobial that previously inhibited growth; however, bacteria survive antibiotics also through tolerance and persistence. Tolerance is the ability to survive a transient exposure to antibiotic, unlike resistance, which is only observed against bactericidal antibiotics and can be acquired through a genetic mutation or conferred by environmental conditions [13]. Tolerance may evolve more rapidly than resistance and it may extend to other classes of antibiotics [13]. Persistence is the survival of a small proportion of antibiotic susceptible cells after the exposure against high antibiotic concentrations [14]. Persisters have strong clinical implications in several infectious diseases, such as tuberculosis, syphilis and typhoid fever and unlike resistance, which is genetically acquired and passed on to subsequent generations, persistence is a transient phenotype, which could spontaneously switch to fast growth and generate a population that is susceptible to the antibiotic with a small proportion of tolerant antibiotic cells [15•]. Factors like the presence of toxin–antitoxin (TA) loci promote persistence, since overproduction of toxin arrests bacterial growth [16]. A better understanding of the mechanisms behind bacterial persistence may lead to the design of drugs to combat chronic and recurrent infections. This review provides an overview of the current state of antimicrobials, then discusses the development of new antibiotics and finally presents a series of promising alternatives for the future combat of bacterial infections.

Current balance of antimicrobial utilization

Around one-half of the antibiotics used today were found between 1950 and 1960, mainly from soil bacteria. After this period, several factors such as the saturation of the screening approaches, the inability to culture most soil bacterial species, and the lack of interest among the pharmaceutical companies [17]; had severely decreased the rate of antibiotic discovery and their introduction into the clinic. Moreover, new antimicrobials under development often fail, among other reasons since their targets readily mutate, therefore, selecting for resistance rapidly [18]. Also many active molecules against bacteria are not selective and damage the host, hence new antibiotics are frequently reserved as a last resort for MDR infections [18]. Nevertheless from 2010 at least a dozen of new antimicrobial agents and combinations have been approved for the treatment of infectious diseases (Table 1). However, these molecules are improved versions of previous antibiotics namely β-lactams, aminoglycosides, glycopeptides, tetracyclines, and so on, that although are less susceptible to current resistance mechanisms, are not impervious to them; in fact, for all of them, except omadacycline, resistant strains have already been found. Therefore, if the same approaches are repeated, the introduction of new antibiotics likely will be almost simultaneous to the appearance of resistance. Hence, the discovery of novel antibiotics with new structures, action mechanisms, and targets, as well as the implementation of alternative strategies less prone to the development of resistance, is highly advisable (Table 2).

Development of new antibiotics

New promising antimicrobials under development include oxadiazoles, heterocyclic aromatic compounds of the azole family, that have anticancer, anti-inflammatory, antiretroviral, analgesic, anticonvulsant, and antibacterial activities. Recently, several new compounds were tested as antimicrobials, being F6 (Figure 1A) the only one with antibacterial activity, and the basis for the synthesis of analogs with improved activity. From all the analogs only F6-5 (Figure 1B) was slightly better than the original compound and in contrast with ciprofloxacin did not select resistance after several culture passes. This molecule is a bacteriostatic agent active only against Gram positive bacteria [19]. Other novel molecules such as 4(3*H*)-quinazolinone derivatives are present in agents with antibacterial application as first generation cephalosporins such as cefatrizine. Moreover, 2,3-triazole linked 4(3*H*)-quinazolinone derivatives (3-chlorophenyl; 4-chlorophenyl; 3-tolluoyl; phenyl; 3-bromophenyl; 4-methoxyphenyl and 4-nitrophenyl) (Figure 1C–I) were non cytotoxic against Vero cells and showed activity against *S. aureus* but not against Gram negatives, probably due to the presence of the external membrane; however, resistance development was not tested for these molecules [20]. Since 2014, new compounds from thiazole and its derivatives have been synthesized. Alkoxyphenylthiazoles, analogs of phenylthiazole, showed activity against Gram positive bacteria. In comparison with vancomycin, these phenylthiazoles showed good activity and shorter

DE LABORES 2019

Table 1

New antimicrobials that have been approved in the last decade to be used in the clinical field against MDR bacterial infections

Antibiotic	Kind	Year approved	Target	Clinical uses	Year of resistance emergence
Ceftaroline (Figure 1S)	Fifth-generation cephalosporin	2010	Penicillin-binding protein (PBPs) β-lactamase inhibitor	Community-acquired bacterial pneumonia (CAP) and acute bacterial skin infections (ABSSSI)	2014 [65]
Ceftolozane/tazobactam (Figure 1T/1U)	Cephalosporin plus β-lactamase inhibitor	2014	Penicillin-binding proteins (PBPs)/inhibits the action of bacterial ß-lactamases	Complicated intra-abdominal infections (cIAIs) complicated urinary tract infections (cUTI)	2014 [66]
Ceftazidime/avibactam (Figure 1V/1M)	Third-generation cephalosporin and the novel, non-β-lactam β-lactamase inhibitor avibactam (bicyclic diazabicyclooctane)	2015	Penicillin binding protein 3 (PBP3)/β-lactamase inhibitor	Complicated urinary tract infections (cUTIs), complicated intra-abdominal infections (cIAIs), hospital-acquired pneumonia (HAP) including ventilator-associated pneumonia (VAP)	2015 [67]
Meropenem/vaborbactam (Figure 1W/1X)	Carbapenem and non-β-lactam, cyclic, boronic acid-based, β-lactamase inhibitor	2017	Penicillin-binding-protein (PBP)/β-lactamase inhibitor	Complicated urinary tract infections	2017 [69]
Tedizolid (Figure 1Y)	2-Oxazolidone	2014	Protein synthesis, inhibits the binding of fMet-tRNA to 70S ribosomes	Acute bacterial skin and skin structure infections (ABSSSI)	2015 [70]
Oritavancin (Figure 1Z)	Lipoglycopeptides antibiotic	2014	Inhibits cell wall biosynthesis by binding noncovalently to the D-alanyl-D-alanine terminal ends of the peptidoglycan chain and pentaglycine bridge, thereby inhibiting transglycosylation and transpeptidation	Acute bacterial skin and skin structure infections (ABSSSI)	2016 [71]
Dalbavancin (Figure 1A1)	Second-generation lipoglycopeptide antibiotic	2014	Inhibition of cell-wall biosynthesis, prevents incorporation of *N*-acetylmuramic acid (NAM)-peptide and *N*-acetylglucosamine (NAG)-peptide subunits from being incorporated into the peptidoglycan matrix	Acute bacterial skin and skin structure infections (ABSSSI)	2018 [72]
Delafloxacin (Figure 1B1)	Fluoroquinolone	2017	Bacterial DNA topoisomerase IV and DNA gyrase (topoisomerase II)	Acute bacterial skin and skin structure infections (ABSSSI)	2012 [73]
Omadacycline (Figure 1C1)	Tetracycline	2018	30S ribosomal subunit	Community acquired bacterial pneumonia (CABP) and acute skin and skin structure infections (ABSSSI)	Not yet [8]
Eravacycline (Figure 1D1)	Tetracycline	2018	30S ribosomal subunit	Complicated intra-abdominal infections (cIAIs) in adults	2018 [74]
Plazomicin (Figure 1E1)	Next-generation aminoglycoside	2018	30S ribosomal subunit	Complicated urinary tract infections	2013 [75]

INFORME DE LABORES 2019

Table 2

Alternative approaches to the use of antibiotics

Approach	Function	Target	Susceptible bacteria
Gallium nitrate (Figure 1F1)	Disrupts iron acquisition and iron-dependent processes	Iron transport by siderophores, iron containing enzymes	*P. aeruginosa, A. baumannii*
QS inhibition	Disruption of bacterial cel–cell communication and virulence	QS receptors, signal disruption, inhibition of signal synthesis	Gram negative including *P. aeruginosa*, Vibrio spp., *A. baumannii* Gram positive including *S. aureus*
Inhibition of T3SS	Disrupts T3SS blocking the secretion of toxins	T3SS	Gram negative bacteria including *E. coli* and *P. aeruginosa*
5-Fluorouracil (Figure 1G1)	Quorum sensing/biofilm inhibitor	QS systems, inhibition of uridine synthesis	Gram negative such as *E. coli* and *P. aeruginosa* Gram positive such as *S. mutants*
Mitomycin C (Figure 1H1)	Crosslinks DNA promoting damage	DNA	*A. baumannii* and *E. coli, P. aeruginosa, S. aureus* (regular and persister cells)
Cisplatin (Figure 1 I1)	Crosslinks DNA promoting damage	DNA	*E. coli, P. aeruginosa, S. aureus* (regular and persister cells)
Photosensitizers	Promoting DNA damage	DNA	Gram negative bacteria *E. coli* and Gram positive *S. aureus*
Far-UVC light	Promoting DNA damage	DNA	*S. aureus*
Adjuvants	Restore antibiotic efficacy	β-Lactamases, efflux pumps, membrane permiability	Gram negative bacteria such as *A. baumannii*, *P. aeruginosa* and Enterobacteria
Antibodies	Bind and neutralize bacterial toxins or cells. Promote destruction of bacterial cells	Toxins, surface proteins, LPS, components of cell wall	Gram negative such as *E. coli* and *P. aeruginosa* Gram positive such as *S. aureus, S. mutants, C. difficile*
Cytokines and other immunomodulatory agents	Adjunctive immunostimulation during sepsis	Host immune cells	Gram negative such as *Pseudomonas* spp., *Enterobacteriacae* spp., Gram positive such as *S. aureus*
Vaccination	Elicit an immune response against an antigen	Host immune cells	*M. tuberculosis*, *S. typhi*, *S. aureus*, *C. difficile*, *E. coli*, *P. aeruginosa*, and so on
Phage therapy	Elicit cell lysis	Bacterial enzymes and cofactors to replicate phages	Gram negative such as *P. aeruginosa,* Gram positive such as *C. difficile*

killing times, and also good antimicrobial activity against antibiotic resistant Gram positive cocci [21]. In 2015, teixobactin, a novel depsipeptide antibiotic that inhibits cell wall synthesis in Gram positive bacteria by binding to conserved motifs of lipid II and lipid III was discovered using a novel culture technique that allowed growth of soil bacteria *in situ* [22]. Interestingly, no resistance to *S. aureus* was found upon 27 daily serial passes in the presence of teixobactin (Figure 1L) [22], suggesting that the presence of multiple simultaneous mutations are needed to achieve resistance, and that if eventually this experimental drug reaches the clinic, resistance against it will be slowly developed. Although several new antibiotics have been developed against Gram positives, MDR Gram negative bacteria represent a higher risk because of lack of treatment possibilities. *A. baumannii*, *P. aeruginosa* and Enterobacteriacea resistant to carbapenems have several resistance mechanisms limiting the use of new antibiotics or antibiotics/adjuvants mixtures such as ceftazidime/avibactam which is active against KPC (*K. pneumoniae* carbapenemase), OXA-48 (oxacillin) and AMPc ß-lactamases producing bacteria, but not against metallo β-lactamases or other OXA like enzymes [23]. Moreover, ceftolozane/tazobactam is active against ESBL (Extended Spectrum ß-Lactamases) but not against carbapenemases, including metallo β-lactamases [24]. Nevertheless a new molecule, cefiderocol (Figure 1K), a combination of a cephalosporin and a catechol group present in siderophores, that allows its internalization, is effective against bacteria expressing metallo β-lactamases, KPC's and OXA members [25••], including non-fermenter bacteria such as *P. aeruginosa*, *A. baumannii* and *Stenotrophomonas maltophilia* [26].

Alternative approaches to the use of antibiotics

An alternative to antibiotics is the use of metals with antimicrobial properties such as silver and copper that are actually used in the clinic [27]. One metal with promising antibacterial activity is gallium, which is a non-redox iron (III) mimetic able to inhibit growth of the majority of MDR isolates of *P. aeruginosa* [28] and *A. baumannii* [29]. Gallium replaces iron in enzymes such as respiratory complexes, anti-oxidant enzymes (catalase), ribonucleotide reductase, and so on, inactivating them. It also disrupts iron transport via the siderophore pyoverdine in *P. aeruginosa* and promotes the generation of oxygen reactive species [28,30,31]. Since it has multiple targets, it was postulated that resistance would be not likely to arise. Indeed, studies in the *P. aeruginosa* reference strains PA14 and PAO1 indicate that either no selection of resistance [32] or only mild selection against it, is achieved by

Figure 1

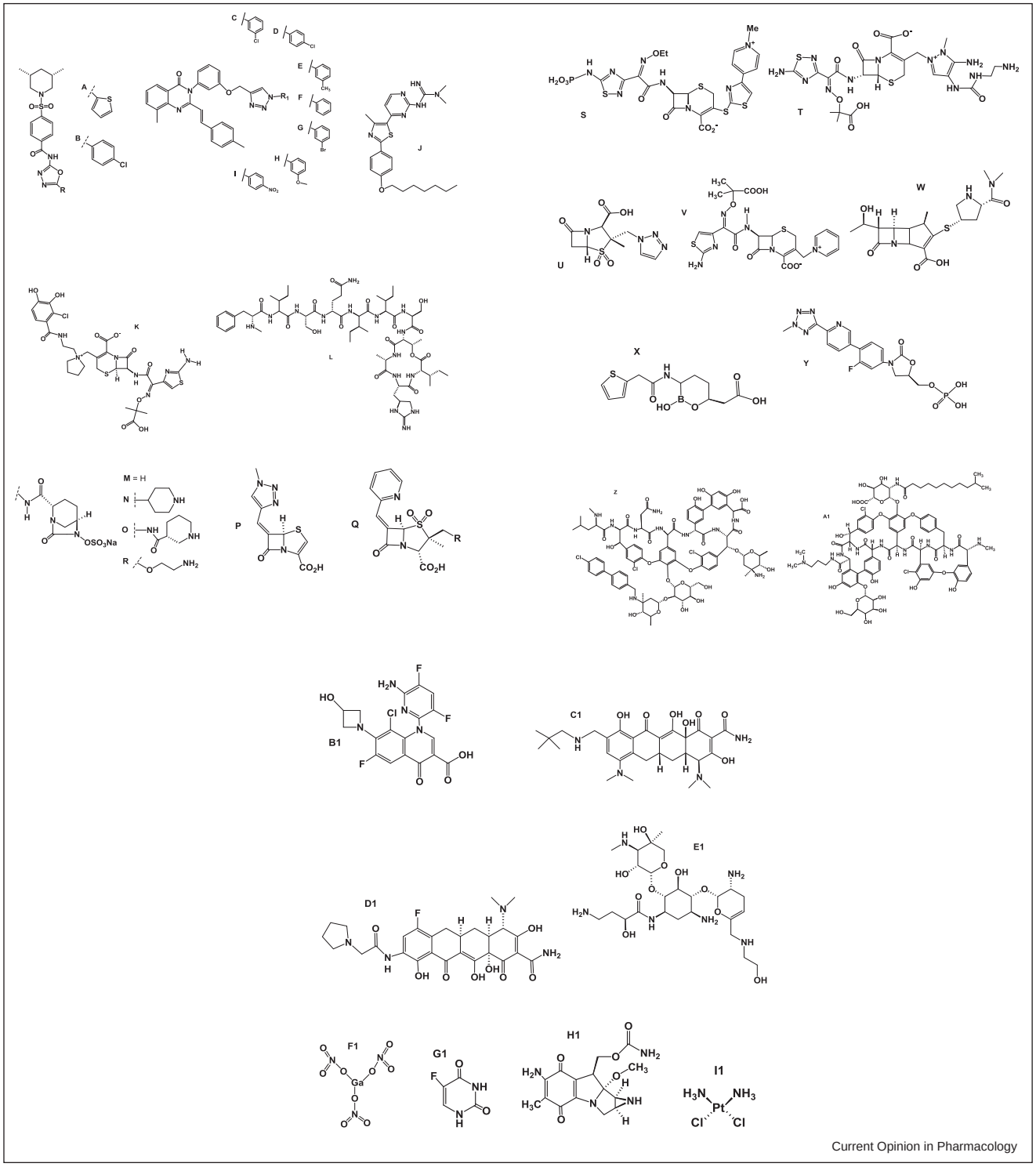

A: Oxadiazol-derived F6 and **B:** F6-5. **C:** 3-chlorophenyl. **D:** 4-chlorophenyl. **E:** 3-tolluoyl. **F:** phenyl. **G:** 3-bromophenyl. **H:** 4-methoxyphenyl. **I:** 4-nitrophenyl. **J:** alkoxyphenylthiazol. **K:** cefiderocol. **L:** teixobactin. **M:** avibactam. **N:** relebactam. **O:** zidebactam. **P:** BRL 4271O. **Q:** LN-1-255. **R:** OP0595. **S:** ceftaroline. **T:** ceftolozane. **U:** tazobactam. **V:** ceftazidime. **W:** meropenem. **X:** vaborbactam. **Y:** tedizolid. **Z:** oritavancin. **A1:** dalbavancin. **B1:** delafloxacin. **C1:** omadacycline. **D1:** oravacycline. **E1:** plazomicin. **F1**: gallium nitrate. **G1**: 5-fluorouracil. **H1**: mitomycin C. **I1**: cisplatin.

INFORME DE LABORES 2019

decreasing its uptake via the iron transporter HitAB or by increasing the production of the redox active phenazine pyocyanin [30,33,34]. In addition, gallium is effective in treating murine lung infections and improved the respiratory function of patients with cystic fibrosis infected with *P. aeruginosa* [30]. Moreover, one recent report demonstrated that gallium maltolate is active not only against *P. aeruginosa* and *A. baumannii* but also against some strains of *K. pneumoniae* [35].

A different approach for the treatment of infections is based on the inhibition of virulence, arguing that this would not exert a strong selective pressure for the development of resistance (expression of virulence factors in the presence of the virulence inhibitors [36]). To date, anti-virulence therapies have been focused in the inhibition of quorum sensing (QS) [37]; however, experimental evidence shows that selection of resistance against anti-virulence therapies is possible [38,39]. Recent preclinical studies show that it is possible to attenuate bacterial infections with quorum quenching (QQ) enzymes. In the mouse model of pulmonary infection with *P. aeruginosa*, administration of the acylase PvdQ decreased inflammation and bacterial load, and prolonged mice survival [40•]. Also, flavones reduce bacterial load and damage in a murine model of dermonecrosis with methicillin-resistance *S. aureus* [41]. Nevertheless, it has not been possible to demonstrate that QQ therapies have the capacity to eliminate the damage and clear infections and recent studies indicate that QS inhibition is not sufficient to completely block bacterial virulence in *P. aeruginosa* since this does not block the expression of important virulence factors such as the type three secretion system (T3SS) [42•]. The T3SS is used by many Gram negative pathogenic bacteria including enterohemorrhagic *E. coli*, *Shigella flexneri*, *Salmonella enterica* and *P. aeruginosa*, to inject effector proteins into the cytoplasm of host cells [43]. The importance of the T3SS has been demonstrated in animal models [44]. It has also been shown that cystic fibrosis patients infected with *P. aeruginosa* strains carrying a T3SS were more prompt to develop severe acute infections [45]. In contrast to conventional antibiotics, inhibiting the T3SS would not affect the resident microbiota, avoiding opportunistic infections. Moreover, even though resistance to T3SS inhibition could arise, this would likely not be a resistance mechanism that would be horizontally transferred to non-pathogenic bacteria. Therapeutic strategies against the T3SS include antibodies, small molecules, natural compounds and peptides that inhibit its function [46].

Potential sources of antimicrobial and anti-virulence molecules ready to be used are drugs currently in use in the clinical setting for other purposes, since their implementation will be much faster compared to antimicrobials developed *de novo*, examples are 5-fluorouracil, gallium nitrate, and anticancer drugs such as cisplatin and mitomycin C that are able to kill MDR bacteria and persister cells [47,48]. Nevertheless, more studies aiming to evaluate the development of bacterial resistance against these molecules are necessary.

Another promising strategy to combat MDR bacteria is the administration of photosensitizers, which generate reactive oxygen species upon illumination killing bacteria without promoting the selection of resistance [49], or the utilization far-UVC light, which kills MDR bacteria, without damaging cells in tissues [50]. Nevertheless, the potential for the development of resistance against these treatments is still unexplored.

Recently phage therapy has regained attention to be used as an alternative or complement to antibiotics. The potential effectiveness of phage therapy could be of great use especially in patients with chronic MDR infections. Successful phage therapy in humans was demonstrated in two recent case reports, one concerning a patient with *P. aeruginosa* septicaemia [51] and the other a patient with *P. aeruginosa* aortic graft infection [52], aiming a favorable outcome. Some issues such as bacteriophage choice, isolation, preparation, purification, storage, and pharmacology must be considered, as well as regulations for their production.

A way to circumvent bacterial resistance is the use of adjuvants (that administered simultaneously with antibiotics), rescue the antimicrobial action via the disruption of bacterial resistance pathways. To date three main types of adjuvants exist: β-lactamase inhibitors, efflux pumps and external membrane permeabilizers. The β-lactamase inhibitors are widely used, among them clavulanic acid, sulbactam and tazobactam are in clinical use and act as covalent inhibitors, although they are not effective against class C and D β-lactamases. Compounds such as avibactam (Figure 1M) a diazabicyclooctane (DBO) have high inhibitory activity in the majority of β-lactamases of class A and C, as mentioned above. Other DBO compounds in clinical trials are relebactam (Figure 1N), zidebactam (Figure 1O), BRL 42715 (Figure 1P, LN-1-255 (Figure 1Q) and OP0595 (Figure 1R); however, to date there are no inhibitors for class B β-lactamases [5•].

Although several efflux pump inhibitors such as piperidines, quinolines, pyridopyrimidines and arylpiperazines, have been discovered they are still not in use in the clinic [5•,53]. Alternatively, the external membrane permeabilizers could be useful for the treatment of Gram negative bacteria by facilitating the entry of antibiotics as they destabilize the outer layer of the membrane interacting with polyanionic lipopolysaccharides or trapping cations of the outer layer, among them some cationic peptides and polyamines, had shown promising results [5•].

Other clever strategies recently developed to combat bacterial infections include cytotoxic pore-forming toxins secreted by Gram positive bacteria sequestered by

artificial liposomes [54]. The use of an extracorporeal device that cleanses circulating blood using magnetic nanobeads coated with an engineered human mannose binding lectin that reduce the load of circulating bacterial cells and toxins [55], and immunotherapies with antibodies, cytokines or vaccines [56,57,58•]. Antibodies bind and neutralize bacterial toxins or cells promoting their phagocytosis and destruction by macrophages and neutrophils; additionally, opsonization promotes bacterial lysis via complement [57]. Currently, 78 therapeutic antibodies are FDA-approved and hundreds more are in clinical trials [IMGTDB]. Although only 2 targeting bacterial epitopes are in the market (bezlotoxumab and raxibacumab), about 20 more are currently in clinical trials [IMGTDB]. Antibodies targeting MDR bacteria could be used therapeutically or for prophylaxis, if the epitope is highly conserved or is involved in pathogenesis, the probability of resistance is low [57]. Although one of the concerns is their narrow spectrum [58•], specificity is one of their strengths [59]. Moreover, antibodies that target host antigens can correct exacerbated inflammation or reverse immunosuppression [56].

The use of cytokines as immunostimulators has been proved useful during sepsis (IFNg, IL-7, GM-CSF, thymosin-a1, IL-15, FLT3L) and tuberculosis (IFNg, TNF, IL-1) [56,60], and some are in clinical trials [56]. However, in-depth knowledge of host–pathogen interactions is necessary to design effective immunotherapies as overdoses of cytokines may lead to hyper inflammation and death of immune cells [56].

Vaccination has the potential to prevent infections by MDR bacteria [58•]. Among the recent technologies in vaccine development are reverse vaccinology, new adjuvants, structural vaccinology, glycoconjugate vaccines, live vaccines, and engineered outer membrane vesicles [58•].

An additional important aspect to consider related to immunotherapies is that MDR acquisition is closely related to modifications in bacterial structures that modulate the host immune system [61–64], so the host–pathogen interactions might not be equivalent in susceptible versus resistant bacterial strains. Hence, to develop effective immunotherapies to control and eradicate this health problem, it will be critical to use MDR clinical isolates to assure its efficacy *in vivo*.

Concluding remarks

Although the current situation regarding MDR resistance is alarming, there are several approaches to fight drug-resistant bacteria. The interest in the development of new antimicrobials, open several research avenues and bring hope for the development of effective and robust therapies against bacterial infections that eventually could give us an advantage in the race between antimicrobial

Conflict of interest statement

Nothing declared.

Acknowledgements

R G-C research is supported by the grant PAPIIT-UNAM number IN214218. PLL was supported by grants PAPIIT-UNAM number IA202116 and CONACYT CB 255287. B G-P was supported by grants PAPIIT-UNAM number IN209617 and CONACYT 284081.

References and recommended reading

Papers of particular interest, published within the period of review, have been highlighted as:

- • of special interest
- •• of outstanding interest

1. Zaman SB, Hussain MA, Nye R, Mehta V, Mamun KT, Hossain N: **A review on antibiotic resistance: alarm bells are ringing**. *Cureus* 2017, **9**:e1403.

2. de Kraker ME, Stewardson AJ, Harbarth S: **Will 10 million people die a year due to antimicrobial resistance by 2050?** *PLoS Med* 2016, **13**:e1002184.

3. Renwick MJ, Simpkin V, Mossialos E: *Targeting Innovation in Antibiotic Drug Discovery and Development: The Need for a One Health – One Europe – One World Framework*. European Observatory Health Policy Series; 2016.

4. Tillotson G: **A crucial list of pathogens**. *Lancet Infect Dis* 2018, **18**:234-236.

5. • Gonzalez-Bello C: **Antibiotic adjuvants—a strategy to unlock bacterial resistance to antibiotics**. *Bioorg Med Chem Lett* 2017, **27**:4221-4228.
Comprehensive review about antibiotic adjuvants currently in use and under development, presenting them as a suitable way to overcome bacterial tolerance and resistance.

6. Sadovskaya I, Vinogradov E, Li J, Hachani A, Kowalska K, Filloux A: **High-level antibiotic resistance in *Pseudomonas aeruginosa* biofilm: the ndvB gene is involved in the production of highly glycerol-phosphorylated beta-(1->3)-glucans, which bind aminoglycosides**. *Glycobiology* 2010, **20**:895-904.

7. Munita JM, Arias CA: **Mechanisms of antibiotic resistance**. *Microbiol Spectr* 2016, **4**.

8. Villano S, Steenbergen J, Loh E: **Omadacycline: development of a novel aminomethylcycline antibiotic for treating drug-resistant bacterial infections**. *Future Microbiol* 2016, **11**:1421-1434.

9. Honeyman L, Ismail M, Nelson ML, Bhatia B, Bowser TE, Chen J, Mechiche R, Ohemeng K, Verma AK, Cannon EP *et al.*: **Structure-activity relationship of the aminomethylcyclines and the discovery of omadacycline**. *Antimicrob Agents Chemother* 2015, **59**:7044-7053.

10. Thi Khanh Nhu N, Riordan DW, Do Hoang Nhu T, Thanh DP, Thwaites G, Huong Lan NP, Wren BW, Baker S, Stabler RA: **The induction and identification of novel Colistin resistance mutations in *Acinetobacter baumannii* and their implications**. *Sci Rep* 2016, **6**:28291.

11. Liu YY, Wang Y, Walsh TR, Yi LX, Zhang R, Spencer J, Doi Y, Tian G, Dong B, Huang X *et al.*: **Emergence of plasmid-mediated colistin resistance mechanism MCR-1 in animals and human beings in China: a microbiological and molecular biological study**. *Lancet Infect Dis* 2016, **16**:161-168.

12. Dijkmans AC, Zacarias NVO, Burggraaf J, Mouton JW, Wilms EB, van Nieuwkoop C, Touw DJ, Stevens J, Kamerling IMC: **Fosfomycin: pharmacological, clinical and future perspectives**. *Antibiotics (Basel)* 2017, **6**.

13. Brauner A, Fridman O, Gefen O, Balaban NQ: **Distinguishing between resistance, tolerance and persistence to antibiotic treatment**. *Nat Rev Microbiol* 2016, **14**:320-330.

14. Rocco A, Kierzek AM, McFadden J: **Slow protein fluctuations explain the emergence of growth phenotypes and persistence in clonal bacterial populations**. *PLoS One* 2013, **8**:e54272.

15. • Van den Bergh B, Fauvart M, Michiels J: **Formation, physiology, ecology, evolution and clinical importance of bacterial persisters**. *FEMS Microbiol Rev* 2017, **41**:219-251.
In this review article several aspect of bacterial persistence, from the molecular mechanisms leading to it, to their physiology and ecology are discussed, in addition the role of persisters in chronic infections is also analyzed.

16. Ramisetty BC, Santhosh RS: **Horizontal gene transfer of chromosomal type II toxin-antitoxin systems of *Escherichia coli***. *FEMS Microbiol Lett* 2016, **363**.

17. Davies J: **Where have all the antibiotics gone?** *Can J Infect Dis Med Microbiol* 2006, **17**:287-290.

18. Fernandes P: **Antibacterial discovery and development—the failure of success?** *Nat Biotechnol* 2006, **24**:1497-1503.

19. Opoku-Temeng C, Naclerio GA, Mohammad H, Dayal N, Abutaleb NS, Seleem MN, Sintim HO: **N-(1,3,4-oxadiazol-2-yl) benzamide analogs, bacteriostatic agents against methicillin- and vancomycin-resistant bacteria**. *Eur J Med Chem* 2018, **155**:797-805.

20. Gatadi S, Gour J, Shukla M, Kaul G, Das S, Dasgupta A, Malasala S, Borra RS, Madhavi YV, Chopra S *et al.*: **Synthesis of 1,2,3-triazole linked 4(3H)-quinazolinones as potent antibacterial agents against multidrug-resistant *Staphylococcus aureus***. *Eur J Med Chem* 2018, **157**:1056-1067.

21. ElAwamy M, Mohammad H, Hussien A, Abutaleb NS, Hagras M, Serya RAT, Taher AT, Abouzid KA, Seleem MN, Mayhoub AS: **Alkoxyphenylthiazoles with broad-spectrum activity against multidrug-resistant gram-positive bacterial pathogens**. *Eur J Med Chem* 2018, **152**:318-328.

22. Ling LL, Schneider T, Peoples AJ, Spoering AL, Engels I, Conlon BP, Mueller A, Schaberle TF, Hughes DE, Epstein S *et al.*: **A new antibiotic kills pathogens without detectable resistance**. *Nature* 2015, **517**:455-459.

23. Tuon FF, Rocha JL, Formigoni-Pinto MR: **Pharmacological aspects and spectrum of action of ceftazidime-avibactam: a systematic review**. *Infection* 2018, **46**:165-181.

24. Cluck D, Lewis P, Stayer B, Spivey J, Moorman J: **Ceftolozane-tazobactam: a new-generation cephalosporin**. *Am J Health Syst Pharm* 2015, **72**:2135-2146.

25. •• Aoki T, Yoshizawa H, Yamawaki K, Yokoo K, Sato J, Hisakawa S, Hasegawa Y, Kusano H, Sano M, Sugimoto H *et al.*: **Cefiderocol (S-649266), a new siderophore cephalosporin exhibiting potent activities against *Pseudomonas aeruginosa* and other gram-negative pathogens including multi-drug resistant bacteria: structure activity relationship**. *Eur J Med Chem* 2018, **155**:847-868.
In this paper, the authors present a novel antibacterial agent, a combination of a b-lactam and a siderophore, that is able to inhibit growth of MDR *Pseudomonas aeruginosa*, expressing several b-lactamase classes.

26. Hsueh SC, Lee YJ, Huang YT, Liao CH, Tsuji M, Hsueh PR: **In vitro activities of cefiderocol, ceftolozane/tazobactam, ceftazidime/avibactam and other comparative drugs against imipenem-resistant *Pseudomonas aeruginosa* and *Acinetobacter baumannii*, and *Stenotrophomonas maltophilia*, all associated with bloodstream infections in Taiwan**. *J Antimicrob Chemother* 2019, **74**:380-386.

27. Lemire JA, Harrison JJ, Turner RJ: **Antimicrobial activity of metals: mechanisms, molecular targets and applications**. *Nat Rev Microbiol* 2013, **11**:371-384.

28. Kaneko Y, Thoendel M, Olakanmi O, Britigan BE, Singh PK: **The transition metal gallium disrupts *Pseudomonas aeruginosa* iron metabolism and has antimicrobial and antibiofilm activity**. *J Clin Invest* 2007, **117**:877-888.

29. Antunes LC, Imperi F, Minandri F, Visca P: **In vitro and in vivo antimicrobial activities of gallium nitrate against multidrug-resistant *Acinetobacter baumannii***. *Antimicrob Agents Chemother* 2012, **56**:5961-5970.

30. Goss CH, Kaneko Y, Khuu L, Anderson GD, Ravishankar S, Aitken ML, Lechtzin N, Zhou G, Czyz DM, McLean K *et al.*: **Gallium disrupts bacterial iron metabolism and has therapeutic effects in mice and humans with lung infections**. *Sci Transl Med* 2018, **10**.

31. Beriault R, Hamel R, Chenier D, Mailloux RJ, Joly H, Appanna VD: **The overexpression of NADPH-producing enzymes counters the oxidative stress evoked by gallium, an iron mimetic**. *Biometals* 2007, **20**:165-176.

32. Ross-Gillespie A, Weigert M, Brown SP, Kummerli R: **Gallium-mediated siderophore quenching as an evolutionarily robust antibacterial treatment**. *Evol Med Public Health* 2014, **2014**:18-29.

33. Garcia-Contreras R, Lira-Silva E, Jasso-Chavez R, Hernandez-Gonzalez IL, Maeda T, Hashimoto T, Boogerd FC, Sheng L, Wood TK, Moreno-Sanchez R: **Isolation and characterization of gallium resistant *Pseudomonas aeruginosa* mutants**. *Int J Med Microbiol* 2013, **303**:574-582.

34. Rezzoagli C, Wilson D, Weigert M, Wyder S, Kummerli R: **Probing the evolutionary robustness of two repurposed drugs targeting iron uptake in *Pseudomonas aeruginosa***. *Evol Med Public Health* 2018, **2018**:246-259.

35. Hijazi S, Visaggio D, Pirolo M, Frangipani E, Bernstein L, Visca P: **Antimicrobial activity of gallium compounds on ESKAPE pathogens**. *Front Cell Infect Microbiol* 2018, **8**:316.

36. Allen RC, Popat R, Diggle SP, Brown SP: **Targeting virulence: can we make evolution-proof drugs?** *Nat Rev Microbiol* 2014, **12**:300-308.

37. Castillo-Juarez I, Maeda T, Mandujano-Tinoco EA, Tomas M, Perez-Eretza B, Garcia-Contreras SJ, Wood TK, Garcia-Contreras R: **Role of quorum sensing in bacterial infections**. *World J Clin Cases* 2015, **3**:575-598.

38. Maeda T, Garcia-Contreras R, Pu M, Sheng L, Garcia LR, Tomas M, Wood TK: **Quorum quenching quandary: resistance to antivirulence compounds**. *ISME J* 2012, **6**:493-501.

39. Garcia-Contreras R, Nunez-Lopez L, Jasso-Chavez R, Kwan BW, Belmont JA, Rangel-Vega A, Maeda T, Wood TK: **Quorum sensing enhancement of the stress response promotes resistance to quorum quenching and prevents social cheating**. *ISME J* 2015, **9**:115-125.

40. • Utari PD, Setroikromo R, Melgert BN, Quax WJ: **PvdQ quorum quenching acylase attenuates *Pseudomonas aeruginosa* virulence in a mouse model of pulmonary infection**. *Front Cell Infect Microbiol* 2018, **8**:119.
In vivo demonstration of the effectivity of quorum quenching via enzymatic degradation of the autoinducers to alleviate pulmonary infections.

41. Muhs A, Lyles JT, Parlet CP, Nelson K, Kavanaugh JS, Horswill AR, Quave CL: **Virulence inhibitors from *Brazilian peppertree* block quorum sensing and abate dermonecrosis in skin infection models**. *Sci Rep* 2017, **7**:42275.

42. • Soto-Aceves MP, Cocotl-Yanez M, Merino E, Castillo-Juarez I, Cortes-Lopez H, Gonzalez-Pedrajo B, Diaz-Guerrero M, Servin-Gonzalez L, Soberon-Chavez G: **Inactivation of the quorum-sensing transcriptional regulators LasR or RhlR does not suppress the expression of virulence factors and the virulence of *Pseudomonas aeruginosa* PAO1**. *Microbiology* 2019, **165**:425-432.
First experimental demonstration that either inhibiting one of the two main quorum sensing systems of *Pseudomonas aeruginosa* is not enough to attenuate its virulence and that even the suppression of both is not enough likely because the expression of type III system remains unchanged, suggesting that effective anti-virulence therapies against these bacteria should be multi-target.

43. Coburn B, Sekirov I, Finlay BB: **Type III secretion systems and disease**. *Clin Microbiol Rev* 2007, **20**:535-549.

44. Coombes BK, Coburn BA, Potter AA, Gomis S, Mirakhur K, Li Y, Finlay BB: **Analysis of the contribution of Salmonella pathogenicity islands 1 and 2 to enteric disease progression using a novel bovine ileal loop model and a murine model of infectious enterocolitis**. *Infect Immun* 2005, **73**:7161-7169.

45. Roy-Burman A, Savel RH, Racine S, Swanson BL, Revadigar NS, Fujimoto J, Sawa T, Frank DW, Wiener-Kronish JP: **Type III protein secretion is associated with death in lower respiratory and systemic *Pseudomonas aeruginosa* infections**. *J Infect Dis* 2001, **183**:1767-1774.

46. Fasciano AC, Shaban L, Mecsas J: **Promises and challenges of the type three secretion system injectisome as an antivirulence target**. *EcoSal Plus* 2019, **8**.

47. Rangel-Vega A, Bernstein LR, Mandujano-Tinoco EA, Garcia-Contreras SJ, Garcia-Contreras R: **Drug repurposing as an alternative for the treatment of recalcitrant bacterial infections**. *Front Microbiol* 2015, **6**:282.

48. Soo VW, Kwan BW, Quezada H, Castillo-Juarez I, Perez-Eretza B, Garcia-Contreras SJ, Martinez-Vazquez M, Wood TK, Garcia-Contreras R: **Repurposing of anticancer drugs for the treatment of bacterial infections**. *Curr Top Med Chem* 2017, **17**:1157-1176.

49. Al-Mutairi R, Tovmasyan A, Batinic-Haberle I, Benov L: **Sublethal photodynamic treatment does not lead to development of resistance**. *Front Microbiol* 2018, **9**:1699.

50. Buonanno M, Ponnaiya B, Welch D, Stanislauskas M, Randers-Pehrson G, Smilenov L, Lowy FD, Owens DM, Brenner DJ: **Germicidal efficacy and mammalian skin safety of 222-nm UV light**. *Radiat Res* 2017, **187**:483-491.

51. Jennes S, Merabishvili M, Soentjens P, Pang KW, Rose T, Keersebilck E, Soete O, Francois PM, Teodorescu S, Verween G *et al.*: **Use of bacteriophages in the treatment of colistin-only-sensitive *Pseudomonas aeruginosa* septicaemia in a patient with acute kidney injury–a case report**. *Crit Care* 2017, **21**:129.

52. Chan BK, Turner PE, Kim S, Mojibian HR, Elefteriades JA, Narayan D: **Phage treatment of an aortic graft infected with *Pseudomonas aeruginosa***. *Evol Med Public Health* 2018:60-66.

53. Lomovskaya O, Bostian KA: **Practical applications and feasibility of efflux pump inhibitors in the clinic—a vision for applied use**. *Biochem Pharmacol* 2006, **71**:910-918.

54. Henry BD, Neill DR, Becker KA, Gore S, Bricio-Moreno L, Ziobro R, Edwards MJ, Muhlemann K, Steinmann J, Kleuser B *et al.*: **Engineered liposomes sequester bacterial exotoxins and protect from severe invasive infections in mice**. *Nat Biotechnol* 2015, **33**:81-88.

55. Kang JH, Super M, Yung CW, Cooper RM, Domansky K, Graveline AR, Mammoto T, Berthet JB, Tobin H, Cartwright MJ *et al.*: **An extracorporeal blood-cleansing device for sepsis therapy**. *Nat Med* 2014, **20**:1211-1216.

56. Kaufmann SHE, Dorhoi A, Hotchkiss RS, Bartenschlager R: **Host-directed therapies for bacterial and viral infections**. *Nat Rev Drug Discov* 2018, **17**:35-56.

57. Irani V, Guy AJ, Andrew D, Beeson JG, Ramsland PA, Richards JS: **Molecular properties of human IgG subclasses and their implications for designing therapeutic monoclonal antibodies against infectious diseases**. *Mol Immunol* 2015, **67**:171-182.

58. • Baker SJ, Payne DJ, Rappuoli R, De Gregorio E: **Technologies to address antimicrobial resistance**. *Proc Natl Acad Sci U S A* 2018, **115**:12887-12895.
A comprehensive review of new strategies and approaches for combating multi drug resistant bacteria, with emphasis in vaccine development.

59. Silver JN, Ashbaugh CD, Miles JJ, Wu H, Marecki GT, Hwang JK, Jiao JA, Abrams M, Sullivan EJ, Wesemann DR: **Deployment of transchromosomal bovine for personalized antimicrobial therapy**. *Clin Infect Dis* 2018, **66**:1116-1119.

60. Thampy LK, Remy KE, Walton AH, Hong Z, Liu K, Liu R, Yi V, Burnham CD, Hotchkiss RS: **Restoration of T cell function in multi-drug resistant bacterial sepsis after interleukin-7, anti-PD-L1, and OX-40 administration**. *PLoS One* 2018, **13**: e0199497.

61. Smani Y, Fabrega A, Roca I, Sanchez-Encinales V, Vila J, Pachon J: **Role of OmpA in the multidrug resistance phenotype of *Acinetobacter baumannii***. *Antimicrob Agents Chemother* 2014, **58**:1806-1808.

62. Zhai MX, Chen F, Zhao YY, Wu YH, Li GD, Gao YF, Qi YM: **Novel epitopes identified from efflux pumps of *Mycobacterium tuberculosis* could induce cytotoxic T lymphocyte response**. *PeerJ* 2015, **3**:e1229.

63. Hill M, Deghmane AE, Segovia M, Zarantonelli ML, Tilly G, Blancou P, Beriou G, Josien R, Anegon I, Hong E *et al.*: **Penicillin binding proteins as danger signals: meningococcal penicillin binding protein 2 activates dendritic cells through toll-like receptor 4**. *PLoS One* 2011, **6**:e23995.

64. Dupont M, Pages JM, Lafitte D, Siroy A, Bollet C: **Identification of an OprD homologue in *Acinetobacter baumannii***. *J Proteome Res* 2005, **4**:2386-2390.

65. Long SW, Olsen RJ, Mehta SC, Palzkill T, Cernoch PL, Perez KK, Musick WL, Rosato AE, Musser JM: **PBP2a mutations causing high-level ceftaroline resistance in clinical methicillin-resistant *Staphylococcus aureus* isolates**. *Antimicrob Agents Chemother* 2014, **58**:6668-6674.

66. Cabot G, Bruchmann S, Mulet X, Zamorano L, Moya B, Juan C, Haussler S, Oliver A: ***Pseudomonas aeruginosa* ceftolozane-tazobactam resistance development requires multiple mutations leading to overexpression and structural modification of AmpC**. *Antimicrob Agents Chemother* 2014, **58**:3091-3099.

67. Humphries RM, Yang S, Hemarajata P, Ward KW, Hindler JA, Miller SA, Gregson A: **First report of ceftazidime-avibactam resistance in a KPC-3-expressing *Klebsiella pneumoniae* isolate**. *Antimicrob Agents Chemother* 2015, **59**:6605-6607.

69. Sun D, Rubio-Aparicio D, Nelson K, Dudley MN, Lomovskaya O: **Meropenem-vaborbactam resistance selection, resistance prevention, and molecular mechanisms in mutants of KPC-producing *Klebsiella pneumoniae***. *Antimicrob Agents Chemother* 2017, **61**.

70. Sahm DF, Deane J, Bien PA, Locke JB, Zuill DE, Shaw KJ, Bartizal KF: **Results of the surveillance of Tedizolid activity and resistance program: in vitro susceptibility of gram-positive pathogens collected in 2011 and 2012 from the United States and Europe**. *Diagn Microbiol Infect Dis* 2015, **81**:112-118.

71. Jones RN, Moeck G, Arhin FF, Dudley MN, Rhomberg PR, Mendes RE: **Results from oritavancin resistance surveillance programs (2011 to 2014): clarification for using vancomycin as a surrogate to infer oritavancin susceptibility**. *Antimicrob Agents Chemother* 2016, **60**:3174-3177.

72. Werth BJ, Jain R, Hahn A, Cummings L, Weaver T, Waalkes A, Sengupta D, Salipante SJ, Rakita RM, Butler-Wu SM: **Emergence of dalbavancin non-susceptible, vancomycin-intermediate *Staphylococcus aureus* (VISA) after treatment of MRSA central line-associated bloodstream infection with a dalbavancin- and vancomycin-containing regimen**. *Clin Microbiol Infect* 2018, **24**:429 e421-429 e425.

73. Remy JM, Tow-Keogh CA, McConnell TS, Dalton JM, Devito JA: **Activity of delafloxacin against methicillin-resistant *Staphylococcus aureus*: resistance selection and characterization**. *J Antimicrob Chemother* 2012, **67**:2814-2820.

74. Zheng JX, Lin ZW, Sun X, Lin WH, Chen Z, Wu Y, Qi GB, Deng QW, Qu D, Yu ZJ: **Overexpression of OqxAB and MacAB efflux pumps contributes to eravacycline resistance and heteroresistance in clinical isolates of *Klebsiella pneumoniae***. *Emerg Microbes Infect* 2018, **7**:139.

75. Hidalgo L, Hopkins KL, Gutierrez B, Ovejero CM, Shukla S, Douthwaite S, Prasad KN, Woodford N, Gonzalez-Zorn B: **Association of the novel aminoglycoside resistance determinant RmtF with NDM carbapenemase in Enterobacteriaceae isolated in India and the UK**. *J Antimicrob Chemother* 2013, **68**:1543-1550.

frontiers in Microbiology

ORIGINAL RESEARCH
published: 14 November 2019
doi: 10.3389/fmicb.2019.02657

AiiM Lactonase Strongly Reduces Quorum Sensing Controlled Virulence Factors in Clinical Strains of *Pseudomonas aeruginosa* Isolated From Burned Patients

*Luis Esaú López-Jácome[1,2], Georgina Garza-Ramos[3], Melissa Hernández-Durán[2], Rafael Franco-Cendejas[2], Daniel Loarca[1], Daniel Romero-Martínez[3], Phuong Thi Dong Nguyen[4], Toshinari Maeda[4], Bertha González-Pedrajo[5], Miguel Díaz-Guerrero[5], Jorge Luis Sánchez-Reyes[1], Dánae Díaz-Ramírez[1] and Rodolfo García-Contreras[1]**

[1] Laboratorio de Bacteriología, Departamento de Microbiología y Parasitología, Facultad de Medicina, Universidad Nacional Autónoma de México, Mexico City, Mexico, [2] Laboratorio de Infectología, Centro Nacional de Investigación y Atención de Quemados, Instituto Nacional de Rehabilitación, Mexico City, Mexico, [3] Laboratorio de Fisicoquímica e Ingeniería de Proteínas, Departamento de Bioquímica, Universidad Nacional Autónoma de México, Mexico City, Mexico, [4] Department of Biological Functions Engineering, Gradute School of Life Sciences and System Engineering, Kyushu Institute of Technology, Kitakyushu, Japan, [5] Departamento de Genética Molecular, Instituto de Fisiología Celular, Universidad Nacional Autónoma de México, Mexico City, Mexico

OPEN ACCESS

Edited by:
Ana Maria Otero, University of Santiago de Compostela, Spain

Reviewed by:
Giordano Rampioni, Roma Tre University, Italy
Wim J. Quax, University of Groningen, Netherlands

***Correspondence:**
Rodolfo García-Contreras
rgarc@bq.unam.mx

Specialty section:
This article was submitted to Microbial Physiology and Metabolism, a section of the journal Frontiers in Microbiology

Received: *15 May 2019*
Accepted: *31 October 2019*
Published: *14 November 2019*

Citation:
López-Jácome LE, Garza-Ramos G, Hernández-Durán M, Franco-Cendejas R, Loarca D, Romero-Martínez D, Nguyen PTD, Maeda T, González-Pedrajo B, Díaz-Guerrero M, Sánchez-Reyes JL, Díaz-Ramírez D and García-Contreras R (2019) AiiM Lactonase Strongly Reduces Quorum Sensing Controlled Virulence Factors in Clinical Strains of Pseudomonas aeruginosa Isolated From Burned Patients. Front. Microbiol. 10:2657. doi: 10.3389/fmicb.2019.02657

Pseudomonas aeruginosa is an opportunistic bacterium associated with healthcare infections in intensive care units (ICUs), ventilator-associated pneumonia (VAP), surgical site infections, and burns. This bacterium causes 75% of death in burned patients, since it can develop a persistent biofilm associated with infections, express several virulence factors, and antibiotic-resistance mechanisms. Some of these virulence factors are proteases such as elastase and alkaline protease, or toxic metabolites such as pyocyanin and is one of the few microorganisms able to produce cyanide, which inhibits the cytochrome oxidase of host cells. These virulence factors are controlled by quorum sensing (QS). In this work, 30 *P. aeruginosa* clinical strains isolated from burned patients from a tertiary hospital in Mexico City were studied. Antibiotic susceptibility tests were done, and virulence factors (elastase, alkaline protease, HCN, and pyocyanin) were determined in presence of an N-acylhomoserine lactonase, AiiM able to hydrolyze a wide range of acyl homoserine lactones. The treatment reduced significantly the activities of elastase and alkaline protease, and the production of pyocyanin and HCN in all producer strains but not the secretion of toxins through the type III secretion system. Our work suggests that AiiM treatment may be an effective therapy to combat *P. aeruginosa* infection in burn patients.

Keywords: AiiM lactonase, virulence factors, *Pseudomonas aeruginosa*, quorum quenching, burned patients, anti-virulence therapy

INTRODUCTION

Pseudomonas aeruginosa is an opportunistic bacteria associated with healthcare infections in intensive care units (ICUs), ventilator-associated pneumonia (VAP), central line-associated blood stream infections, surgical site infections (Cohen et al., 2017), burnt wounds (Fournier et al., 2016), and urinary tract infections, otitis media, and keratitis (Chatterjee et al., 2016; Olivares et al., 2016). In the United States, according to the Centers for Disease Control and Prevention, in 2013 it was estimated that every year around 51,000 health-care infections are associated to *P. aeruginosa,* of which 6,700 are multidrug resistant, causing 440 deaths per year (Centers for Disease Control and Prevention, 2018)[1]. Both *P. aeruginosa* and *Acinetobacter baumannii* complex are the most important, resistant and dangerous microorganisms infecting burnt patients (Tredget et al., 1992; Estahbanati et al., 2002; Turner et al., 2014; Centers for Disease Control and Prevention, 2019). Despite medicine advances, these sorts of complications are still a huge problem to solve, and as a consequence, around 75% of burned infected patients die. Burn infections related to *P. aeruginosa* often promote a faster deterioration allowing the spread of bacteria causing death in weeks and even in days (Mcmanus et al., 1985; Turner et al., 2014). *P. aeruginosa* has a wide arsenal of virulence factors that enable it to colonize and cause infections in the host, the relevance of these virulence factors has been demonstrated using *P. aeruginosa* strains with deficiencies in their production, leading to a reduced ability of colonizing and a lower dissemination in the host (Pavlovskis and Wretlind, 1979; Rumbaugh et al., 2009; Jimenez et al., 2012; Castillo-Juarez et al., 2015). Elastase is a metalloprotease that disrupts several proteins such as: collagen, elastin, immunoglobulins (IgA and IgG), complement components, and cytokines like interferon gamma and tumor necrosis factor alpha (Pavlovskis and Wretlind, 1979; Lyczak et al., 2000; Ben Haj Khalifa et al., 2011). Alkaline protease is also a zinc metalloprotease that inhibits phagocytosis, killing through neutrophils, opsonization, the action of the complement cascade by degrading C3b and is as well related to corneal damage (Howe and Iglewski, 1984; Ben Haj Khalifa et al., 2011; Laarman et al., 2012; Lee and Zhang, 2015). *P. aeruginosa* is one of the few microorganisms that can synthesize cyanide through the oxidative decarboxylation of glycine by hydrogen cyanide synthase enzyme, under micro-aerobic conditions (O_2 < 5%). HCN is a poison that inhibits respiration by inactivating cytochrome oxidase C (Huber et al., 2016). Another important virulence factor is pyocyanin, a blue phenazine, that promotes oxidative stress, which inhibits ciliary movement and delays inflammatory response due to the damage of neutrophils and apoptosis induction (Ben Haj Khalifa et al., 2011; Lee and Zhang, 2015). In burn injuries, pyocyanin plays an important role because it stimulates colonization, damage of surrounding tissue and promotes dissemination. Furthermore, *P. aeruginosa* strains are often multi-drug resistant, limiting treatment options in healthcare settings around the globe, owing this the World Health Organization classified *P. aeruginosa* as the second more threatening bacterium. Moreover, although new antibiotics are available, each time, resistance against those new drugs quickly appears (Fournier et al., 2016; Shortridge et al., 2017; Karampatakis et al., 2018; Shields et al., 2018). In many pathogenic bacteria, virulence factors are controlled by cell to cell communication known as quorum sensing (QS). *P. aeruginosa* has two QS systems mediated by N-acyl homoserine lactones, Las and Rhl, each one is constituted by three elements, a synthase, a signal receptor and an autoinducer signal. The Las system is formed by LasI which is the synthase, the receptor is LasR and the autoinducer is N-3-oxo-dodecanoyl-L-homoserine lactone, meanwhile the Rhl system is formed by the synthase RhlI, RhlR as receptor and the auto-inducer is N-butyryl-homoserine lactone. These two systems are hierarchically organized and each one of them controls several virulence factors. The Las system regulates the Rhl system and virulence factors such as elastase, protease, exotoxin A, alkaline protease and type II secretion system; while the Rhl system enhances the production of rhamnolipids, hydrogen cyanide, and pyocyanin (Van Delden and Iglewski, 1998; Douzi et al., 2011; Lee and Zhang, 2015). Due to the fast increase in bacterial resistance, alternative strategies such as quorum quenching (QQ) have been proposed. QQ consists of blocking or inhibiting cell to cell communication by obstructing the autoinducer synthases, the signal receptors or by degrading the autoinducers via two enzymatic strategies: disrupting the lactone ring through a lactonase or through the cleavage of the acylic tail by acylases (Defoirdt et al., 2013; Defoirdt, 2018). The aim of this work is to evaluate the activity of AiiM, a lactonase enzyme, in *P. aeruginosa* clinical bacterial strains isolated from burnt patients in a third level center of Mexico City, in order to find out if its utilization could eventually be proposed to treat infected burnt patients.

MATERIALS AND METHODS

Clinical Strains

Randomly 200 strains were selected[2] from the collection belonging to Infectious Diseases Laboratory at Centro Nacional de Investigación y Atención de Quemados at Instituto Nacional de Rehabilitación Luis Guillermo Ibarra, to avoid genomic redundancy pulsed field, gel electrophoresis was performed and only one strain per clonal group was selected for further experiments. Clinical strains were identified with Vitek 2 Compact® (Biomerieux, France) with Gram negative card identification, some biochemical tests included were oxidase, indole production, growth at 42°C, arginine dihydrolase and glucose oxidation/fermentation. The origin of each clinical isolate is shown in **Supplementary Table S1**.

Minimal Inhibitory Concentrations

Minimal inhibitory concentrations were determined according to Clinical and Laboratory Standards Institute® (CLSI) M07-A10 (CLSI, 2015) in 96-well plates. Breakpoints interpretation were made according to the M100 Performance Standards for

[1]https://www.cdc.gov/hai/organisms/pseudomonas.html

[2]www.randomization.com

Antimicrobial susceptibility testing 28th edition (CLSI, 2019). Antibiotics included were amikacin (Sigma Aldrich A1774), gentamicin (Sigma Aldrich G3632), aztreonam (Sigma Aldrich PZ0038), ceftazidime (Sigma Aldrich C3809), cefepime (Sigma Aldrich PHR1763), ciprofloxacin (Sigma Aldrich 17850), levofloxacin (Sigma Aldrich 28266), doripenem (Sigma Aldrich 32138), imipenem (Sigma Aldrich I0160), meropenem (Sigma Aldrich M2574), colistin (Sigma Aldrich C4461), and piperacillin/tazobactam (Sigma Aldrich P8396/T2820). *P. aeruginosa* ATCC® 27853 was used as control as according to CLSI (**Supplementary Table S1**).

las/rhl Genes Detection

DNA Extraction

Pseudomonas aeruginosa strains were cultured in 5% sheep blood agar during 18 h at 37°C, and then one single colony was taken and lysed in an Eppendorf tube with 500 μL of TE buffer (10 mM Tris–HCl, 1 mM EDTA, pH 7.5) and were set into a heat block at 95°C for 5 min. Tubes were centrifuged, and the supernatant was added into a new tube.

Genes related to Las and Rhl systems were amplified (**Table 1**) in a final volume of 25 μL of buffer 1X, 3 mM $MgCl_2$, 200 μM dNTP′s, 0.2 μM primer forward and reverse, 0.026 U/μL Taq polymerase (Amplitaq Gold® DNA Polymerase, Applied Biosystems N808-0241, United States). The amplification conditions used were: 95°C 10 min, 95°C 30 s, 58°C 45 s and 72°C 50 s during 35 cycles, 72°C 5 min and finally 4°C (Veriti 96 Well thermal cycler, Applied Biosystems, United States). Amplification products were loaded into a 1% agarose gel stained with SYBR® green I (S7567, Life Technologies, United States) and visualized with Gel DOC™ XR + with Image Lab™ software (Bio-Rad, United States). *P. aeruginosa* PAO1 was used as positive control in each one of the systems and Δ *lasR/rhlR* PAO1 as negative control of transcriptional regulators.

AiiM Purification

AiiM construction was provided by Dr. Toshinari Maeda (Nguyen et al., 2019). Briefly 50 mL *Escherichia coli* M15/pQE30 AiiM was grown overnight (ON) in Luria Bertani broth with 100 μg/mL of carbenicillin (Sigma Aldrich C1389) and 50 μg/mL of kanamycin (Sigma Aldrich K1876), afterward, 10 mL of the ON cultures were taken and inoculated into 1 L of terrific broth with carbenicillin and kanamycin as above described, cultures were incubated at 37°C 220 rpm, optical density (OD) at 600 nm was measured until the culture reached an OD of 0.5 and immediately after, it was induced with 500 μM IPTG. The cultures were incubated at 37°C 220 rpm for 6 h and centrifuged at 10,000 rpm for 40 min. Pellets were resuspended in 40 mL of purification buffer (50 mM NaH_2PO_4, 300 mM NaCl and 10% glycerol, pH adjusted to 8.0) and 500 μM PMSF (Sigma Aldrich P7626), sonicated (45% amplitude for 45 s and 2 min of rest, all this 10 times; Ultrasonic processor, Cole Parmer) and centrifuged at 10,000 rpm during 40 min. The supernatants were passed through a 0.2 nm filter and loaded onto Protino® Ni-TED resin (Macherey-Nagel, 745200.600) for purification of His-tagged proteins previously equilibrated with 3 column volumes (CV) of 20 mL of purification buffer, then filtered protein extracts were passed through the column, after that, 2 additional CV of purification buffer were passed. Protein was eluted with 150 mM imidazole (Sigma Aldrich I5513) in 2 CV of purification buffer. AiiM fractions with higher purity were selected, concentrated with polyethylene glycol 35 KDa (Sigma Aldrich 946-46) into dialysis tubing cellulose membrane (Sigma Aldrich D9777). Afterward, dialysis was done to remove imidazole using dialysis buffer (50 mM Tris, 300 mM NaCl adjusted at pH 7.5). SDS-PAGE was done to estimate the amount and purity of AiiM. Protein was quantified by its absorbance at 280 nm with NanoDrop 2000 (Thermo Fisher Scientific, United States), using an extinction coefficient (Abs 0.1%) of 1.08. Aliquots of protein were made and stored at −20°C until they were used.

TABLE 1 | Primers used in this study.

Primer	Tm (°C)	Size (bp)
lasI-F 5′-CGCGAAGAGTTCGATAAA-3′	59.7	531
lasI-R 5′-GGTCTTGGCATTGAGTTC-3′	58.7	
lasR-F 5′-ATGGCCTTGGTTGACGGT-3′	65.9	706
lasR-R 5′-GACCCAAATTAACGGCCA-3′	63.7	
rhlI-F 5′-TTGCTCTCTGAATCGCTG-3′	61	590
rhlI-R 5′-GCCATCGACAGCGGTACG-3′	68.3	
rhlR-F 5′-ATGAGGAATGACGGAGGC-3′	63.2	675
rhlR-R 5′-CGCGTCGAACTTCTTCTG-3′	62.9	

AiiM Activity Against N-acyl Homoserine Lactones

To evaluate the HSL lytic activity of the purified AiiM, an analytical assay was developed in an Alliance HPLC system (Waters, United States) with a Symmetry (Waters, United States) C18 Column (75 mm, 3.5 mm). Both short and long acylated chains were included, 1 mM *N*-butyryl-DL-homoserine lactone (C4-HSL; Sigma Aldrich 09945), 1 mM *N*-(3-oxooctanoyl)-L-homoserine lactone (3OC8-HSL;Sigma Aldrich O1764), 1 mM *N*-decanoyl-DL-homoserine lactone (C10-HSL; Sigma Aldrich 17248), 1 mM *N*-(3-oxodecanoyl)-L-homoserine lactone (3OC10-HSL; Sigma Aldrich O9014), and *N*-(3-oxododecanoyl) homoserine lactone (3OC12-HSL; Sigma Aldrich O9139). 60 mM NaOH was used as positive control since it can hydrolyze HSL molecules and the reaction was stopped with the addition of 2N HCl. Several concentrations, from 250, 100, 50, 25, 10, and 5 μg/mL of purified AiiM were tested. Time exposition was also varied; 24 h, 2 h, 1 h, 30 min, 20 min, 10 min, and 5 min. All experiments were performed in triplicate. Chromatographic conditions were: column temperature 25°C, sample temperature 25°C, injection volume 10 μL, flow rate 1 mL/min, detection 205 nm. Elution mixture was made with 50 mM phosphates buffer pH 2.9:acetonitrile. For C4-HSL the relation was 90:10, 3OC8-HSL 60:40, C10-HSL 60:40, 3OC10-HSL 60:40, and 3OC12-HSL 50:50.

Bacterial Growth With and Without AiiM

Grow curves were analyzed to test the effect of AiiM on *P. aeruginosa* PAO1 and Δ *lasR/rhlR* PAO1 growth kinetics.

A 50 mL flask with 5 mL of LB was inoculated with each one of the strains at an initial OD_{600nm} of 0.05 with and without 5 μg/mL of AiiM, samples were taken each hour for 12 h.

Virulence Factors Determination

Elastase was determined for clinical strains and *P. aeruginosa* PAO1 Δ*lasR/rhlR* and Δ*lasI/rhlI* PAO1 mutants according to methods previously described (Ohman et al., 1980), with some modifications. ON of each clinical strain and control strains were cultured in LB at 37°C 220 rpm and were inoculated at an initial OD_{600nm} of 0.05 in 5 mL of LB with and without AiiM (5 μg/mL), samples were incubated for 18 h at 37°C and 220 rpm, and centrifuged at 14,000 rpm for 2 min. 50 μL of the supernatant were taken and set into 950 μL of elastase buffer (100 mM Tris–HCl, 1 mM $CaCl_2$, pH 7.5) with 2.5 mg of elastin-congo red (Sigma Aldrich reference E0502) as substrate. Tubes were incubated at 37°C, 220 rpm for 2 h, centrifuged at 14,000 rpm for 5 min and the released die in the supernatant was measured at 495 nm with a spectrophotometer SmartSpec Plus (Bio-Rad, United States). All determinations were performed by triplicate.

Alkaline Protease

Alkaline protease was determined according to methods previously described (Howe and Iglewski, 1984), with some modifications. ON of each strains were cultured into LB at 37°C 220 rpm and were inoculated in 5 mL of LB at an initial OD_{600nm} of 0.05 with and without AiiM (5 μg/mL). AiiM protein was added at the beginning of the cultures, samples were incubated for 18 h at 37°C and 220 rpm, and centrifuged at 14,000 rpm for 2 min. 50 μL of supernatant were taken and added into 950 μL of protease buffer with 2.5 mg of Hide-Remazol brilliant blue R (Sigma Aldrich reference H6268) as substrate. Tubes were incubated at 37°C, 220 rpm for 20 min centrifuged at 14,000 rpm 5 min and the supernatant was measured at 595 nm with a spectrophotometer SmartSpec Plus (Bio-Rad, United States).

Pyocyanin

For pyocyanin production ON of each clinical and control strains were cultured in LB at 37°C at 220 rpm and inoculated into 5 mL of LB at an initial OD_{600nm} 0.05 with and without AiiM (5 μg/mL). AiiM protein was added at the beginning, samples were incubated 18 h at 37°C and 220 rpm. One milliliter of supernatant was taken, centrifuged at 14,000 rpm for 5 min, and then 800 μL of supernatant were set into new 1.5 mL conic tube and 400 μL of chloroform was added, each tube was mixed in vortex for 2 min. Tubes were centrifuged for 5 min at 14,000 rpm, 300 μL of the organic phase were taken and deposited into a new tube, 800 μL of 0.2 N HCl were added and mixed for 2 min in vortex then samples were read at 520 nm (Maeda et al., 2012). *P. aeruginosa* PAO1, Δ*lasR/rhlR* PAO1 and Δ*lasI/rhlI* PAO1 were used as positive and negative controls, respectively.

HCN Determination

For HCN determination, bacteria were cultured in 3 mL of LB medium in flasks with rubber stoppers at 37°C and 200 rpm for 18 h, after the incubation two needles were inserted in the rubber stopper, one of them was used for pumping air for 1 h and the other to collect the outflow in 5 mL of 4 M NaOH. HCN concentrations were determined as described by Gallagher and Manoil (2001), briefly, samples were mixed with a 1:1 fresh mixture of 0.1 M *o*-dinitrobenzene and 0.2 M *p*-nitrobenzaldehyde both dissolved in 2-methoxyethanol, and following 20 min of incubation at room temperature, the absorbance at 578 nm was determined and compared with a calibration curve made with KCN standards.

AiiM Dose Response Curve and Suppression of Its Activity by Exogenous Addition of 3OC12-HSL

For these control experiments, the PAO1 reference strain and the clinical isolate P809 were used. Three independent cultures per strain were inoculated in LB medium at an initial OD_{600nm} of 0.05 without and with AiiM at 0.5, 1, 2.5, and 5 μg/mL, and incubated 37°C at 220 rpm, supernatants were then obtained and used for the determination of pyocyanin concentration and elastase activity (as described before). In addition another 3 cultures per strain with AiiM 0.5 μg/mL were grown to an OD_{600nm} of ∼ 1.0, supplemented with a final concentration of 30 μM of 3OC12-HSL, and incubated until 18 h of incubation were completed, supernatants were collected and pyocyanin concentration and elastase activity determined.

Long Chain HSL Autoinducer Detection and Its Inactivation by AiiM

To identify autoinducer production and its inactivation by AiiM, each one of the 30 clinical strains were grew up onto MacConkey agar plates, then one colony was taken and inoculated into 5 mL of LB for ON growth. After that, new cultures were inoculated at an initial OD_{600nm} 0.05 in 5 mL of LB and grown at 37°C, with 220 rpm shaking during 18 h, with AiiM 5 μg/mL and without AiiM enzyme. LB cultures then were centrifuged 14,000 rpm for 5 min. Supernatants were separated in new tubes. For long chain HSL detection *Agrobacterium tumefaciens* NT1 pZLR4 (Shaw et al., 1997) was used as a biosensor strain. Previously the biosensor strain was grown in one liter of M9 medium and incubated at 37°C and 220 rpm for 18 h. Bacteria were concentrated by centrifugation at 12,000 rpm during 5 min to a final volume of 15 mL, then aliquots of 1 mL of concentrated bacteria were separated. M9 agar plates were prepared and before solidification 1 mL of the concentrated biosensor plus Xgal at a final concentration of 40 μg/mL (5-bromo-4-chloro-3-indolyl- ß-D-galactopyranoside, USB corporation, Cleveland, OH, United States) were added for 100 mL of M9 agar. 15 μL of each supernatant (with and without AiiM) were then added onto 6 mm filter paper sterile disk on the M9 agar. All experiments were done by triplicate. 1 mM *N*-decanoyl-DL-homoserine lactone (C10-HSL; Sigma Aldrich 17248), 1 mM *N*-(3-oxodecanoyl)-L-homoserine lactone (3OC10-HSL; Sigma Aldrich O9014) and *N*-(3-oxododecanoyl) homoserine lactone (3OC12-HSL; Sigma Aldrich O9139) were used as positive controls and the molecules treated with AiiM 5 μg/mL as negative controls. Plates were incubated at 28°C and results were observed, a positive reaction associated to the production of long chain HSL was observed as a green halo and inactivation of the signals when the halo was absent.

Type III Protein Secretion Profiles

For type III secretion assays *P. aeruginosa* strains (PAO1, PA14, and the clinical isolates H015 and P729) were grown overnight in LB medium. Bacteria were diluted 1:200 into 4 mL of a modified LB medium supplemented with 10 mM $MgCl_2$, 0.5 mM $CaCl_2$ and 5 mM EGTA (pH 7.4) in the presence or absence of 5 μg/mL of AiiM, and grown at 37°C to an OD_{600nm} of 0.8 to 1.0. 1 mL of each culture was collected into a microcentrifuge tube and bacteria were pelleted by centrifugation. The resulting pellet was resuspended in 200 μl of 1× Laemmli SDS sample buffer normalized for OD_{600nm}. The supernatant was centrifuged once again and the resulting supernatant was transferred into a clean tube. Supernatant proteins were precipitated overnight at 4°C by adding trichloroacetic acid to a final concentration of 10%, pelleted by centrifugation and resuspended in 20 μL of 1x Laemmli SDS sample buffer containing 10% saturated Tris base normalized for OD_{600nm}. Samples were separated by 15% SDS-PAGE, transferred onto a nitrocellulose membrane and probed for the presence of the effectors ExoS and ExoU by immunoblotting. Detection was performed using the Immobilon Western chemiluminescent HRP substrate (Millipore), and bands were visualized on X-ray films (Carestream MXB Film).

ß-Lactams Inactivation

As ß-lactams have a lactone ring, we performed the inactivation disk method to determine whether AiiM would be able to inactivate this kind of antibiotics. Briefly, 2 mL of 0.8% isotonic saline solution (ISS) was added into sterile 12 mm × 75 mm tube, disks of 30 μg ceftazidime (Becton Dickinson, United States), 30 μg cefepime (Becton Dickinson, United States), 10 μg imipenem (Becton Dickinson, United States), and 10 μg meropenem (Becton Dickinson, United States). One set of disks containing ISS was used as negative control, another set of all antibiotics above mentioned with 5 μg/mL of AiiM, and finally, since NaOH can break the lactone ring another set of all antibiotics was used as positive control with 60 mM NaOH. *Escherichia coli* ATCC® 25922 was used as a pansusceptible strain. Disks were incubated for 1 and 10 min, 2 and 24 h. A suspension of 0.5 McFarland was made with *E. coli* ATCC® 25922 and was plated onto Müller Hinton agar (Becton Dickinson, United States), tubes were incubated at 37°C until their use. All experiments were made by triplicate; the inhibition diameter was measured using a Vernier device.

RESULTS

All clinical isolates were obtained from burned patients infected with *P. aeruginosa*. The most common burn etiology was fire (66.7%) followed by scalds (23.3%) and electrical burns (10%). Medians of hospital length of stay were 53 days (8-303), the mean total body surface area was 40% (10-85%) with a mortality rate of 26.6% ($n = 8$). *P. aeruginosa* strains were isolated from urine ($n = 8$), quantitative biopsies ($n = 8$), blood ($n = 6$), endotracheal aspirates ($n = 3$), bronchoalveolar lavage fluid ($n = 2$), catheter tips ($n = 2$), and qualitative biopsy ($n = 1$).

Pseudomonas aeruginosa Antibiotic Susceptibility Patterns

Susceptibility tests were carried out for all clinical isolates with different antibiotic families including aminoglycosides, monobactams, cephalosporins, fluoroquinolones, carbapenems, lipopeptides, and ß-lactam combination agents. The strains were resistant to almost all antibiotics except colistin (**Figure 1**), resistance rates against all antibiotics families were over 50%. The highest resistance rates were for carbapenems which, until recent decades, were the most potent antibiotics against *P. aeruginosa* and other non-fermentative Gram negative rods; therefore colistin represents the last treatment option for these types of infections (**Supplementary Table S1**).

Gene Amplification

In order to determine if Las/Rhl systems were present in *P. aeruginosa* isolated from burned patients, PCR was performed using the primers described in **Table 1**. Results showed that the genes encoding the Las system (*lasI* and *lasR*) and Rhl system (*rhlI* and *rhlR*) were found in all the clinical strains. *P. aeruginosa* PAO1 was used as positive control and Δ*lasR/rhlR* PAO1 was used as negative control (data not shown).

AiiM Purification

AiiM protein was obtained at a purity of >90% as judged by SDS-PAGE. After elution with 150 mM imidazole, fractions were collected, and those in which AiiM was present were concentrated into dialysis tubing cellulose membrane with polyethylene glycol, then protein concentration was determined and kept at −20°C until used. The purified protein consists of a single band of ≈ 27 kDa, compared with a theoretical molecular mass of 27.2 kDa (**Supplementary Figure S1**).

AiiM Activity Against Homoserine Lactones

In order to prove AiiM activity against acylated chains of diverse HSL, cleavage was determined by HPLC. Five HSL autoinducers with both short and long chains were tested (C4-HSL, 3OC8-HSL, C10-HSL, 3OC10-HSL, and 3OC12-HSL). First HSL alone was run to identify retention times (**Supplementary Table S2**), later the same HSL were treated with 60 mM NaOH to disrupt the lactone ring and finally HSL molecules were treated with AiiM and HPLC experiments were performed under the same conditions. Several AiiM concentrations (250 μg/mL, 100 μg/mL, 50 μg/mL, 25 μg/mL, 10 μg/mL, and 5 μg/mL) were used, in order to identify the lowest one suitable for inhibiting the expression of virulence factors. Each HSL was used at 1 mM. The lowest concentration of AiiM tested (5 μg/mL) was enough to cleave all the HSLs in 5 min (**Figure 2** and **Supplementary Figure S2**) and therefore, this concentration was used for all subsequent experiments.

AiiM Does Not Affect *Pseudomonas aeruginosa* Growth

Growth curves of *P. aeruginosa* with and without AiiM were done to determine if its addition had any effect in the growth rates.

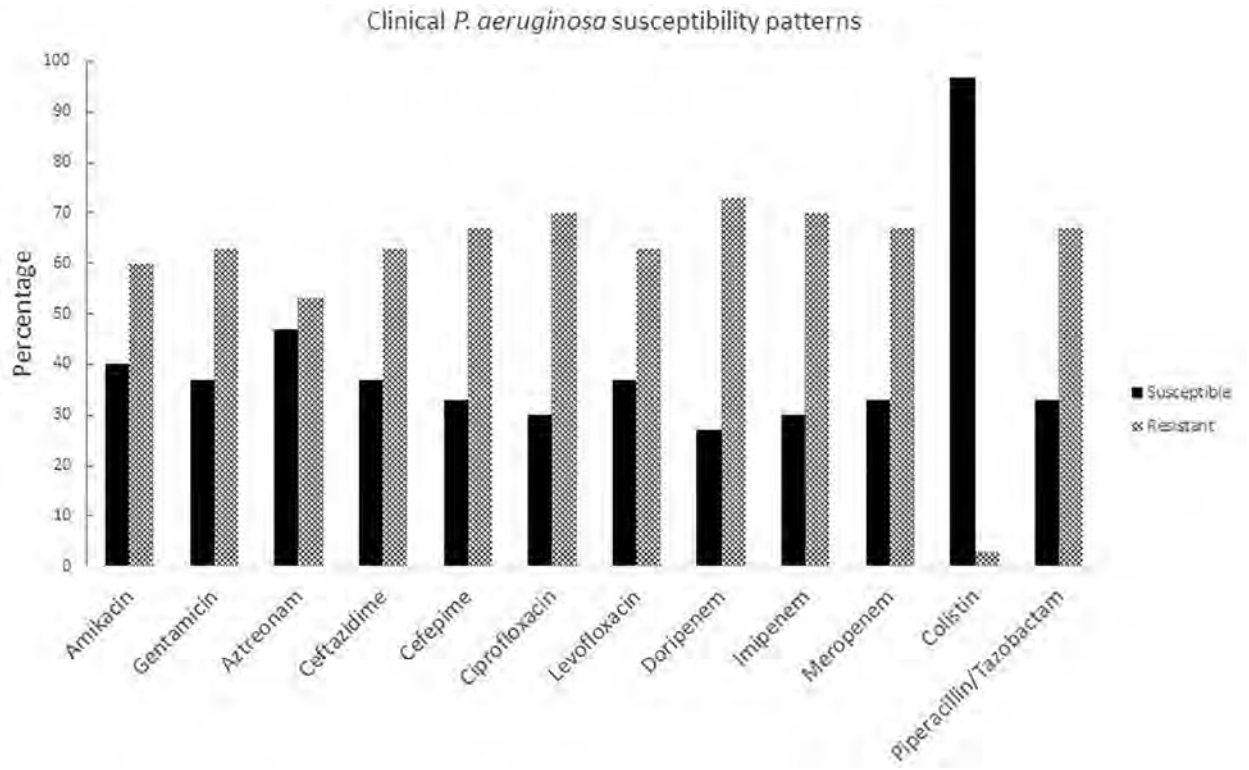

FIGURE 1 | Susceptibility patterns of clinical *P. aeruginosa* strains isolated from burned patients.

As expected, there was no difference in the growing dynamics between these cultures (**Supplementary Figure S3**). PAO1 and Δ *lasR/rhlR* strains were used as controls.

QS-Controlled Virulence Factors Inhibition

Once it was confirmed that AiiM did not affect *P. aeruginosa* growth, its effect over the expression of the QS-controlled virulence factors was determined. Experiments were classified in two groups, one without AiiM addition, and the other with 5 μg/mL addition of AiiM. For elastolytic activity (**Figure 3A**), activity was found in 29 clinical samples, while for alkaline protease activity (**Figure 3B**) there were 27 producing strains; only 12 strains produced pyocyanin (**Figure 3C**), and seven strains were HCN producers (**Figure 3D**). At the same time, experiments with AiiM addition were carried out and the same virulence factors were measured. A significant decrease in the production of each virulence factor was found (elastase $p = 0.000002$, protease $p = 0.000004$, pyocyanin $p = 0.001$ and $p = 0.008$ for HCN).

In addition, AiiM dose response experiments using it at 0.5, 1, 2.5 and 5 μg/mL were performed with the reference strain PAO1 and the clinical isolate P809 measuring pyocyanin production and elastase activity, as expected the degree of inhibition of both phenotypes was dependent in the concentration of AiiM for both virulence factors (**Supplementary Figure S4**). Moreover the effect of 0.5 μg/mL was partially reversed by the addition of 30 μM of 3OC12-HSL (**Supplementary Figure S4**). In order to verify that the clinical strains had active QS systems and that the inhibitory effect in the expression of QS-dependent virulence factors exerted by AiiM was mediated by the degradation of QS signals. Identification of long chain HSL for each strain was done using the biosensor strain *Agrobacterium tumefaciens* NT1 pZLR4 (Shaw et al., 1997), as expected all strains were long chain HSL producers, moreover also for all strains AiiM at 5 μg/mL was enough to degrade the long chain HSL of all strains as determined with the biosensor strain (**Supplementary Figure S5**).

AiiM Does Not Inhibit the Type III Secretion System

Despite its strong inhibitory activity against QS-controlled virulence factors, AiiM had no effect on the secretion of T3SS effectors in both PA14 and PAO1 type strains as well as in the clinical strains P729 and H015 at 5 μg/mL (**Supplementary Figure S6**) and even using 20 μg/mL (data not shown). These two clinical strains were selected as representative examples of a secretion profile similar to strains PAO1 or PA14, respectively.

AiiM Does Not Inactivate ß-Lactam Antibiotics

Wang et al. (2010) defined AiiM as a member of the superfamily of alpha/beta hydrolases, this may represent a problem if it has the ability to inactivate the broad spectrum of ß-lactam antibiotics

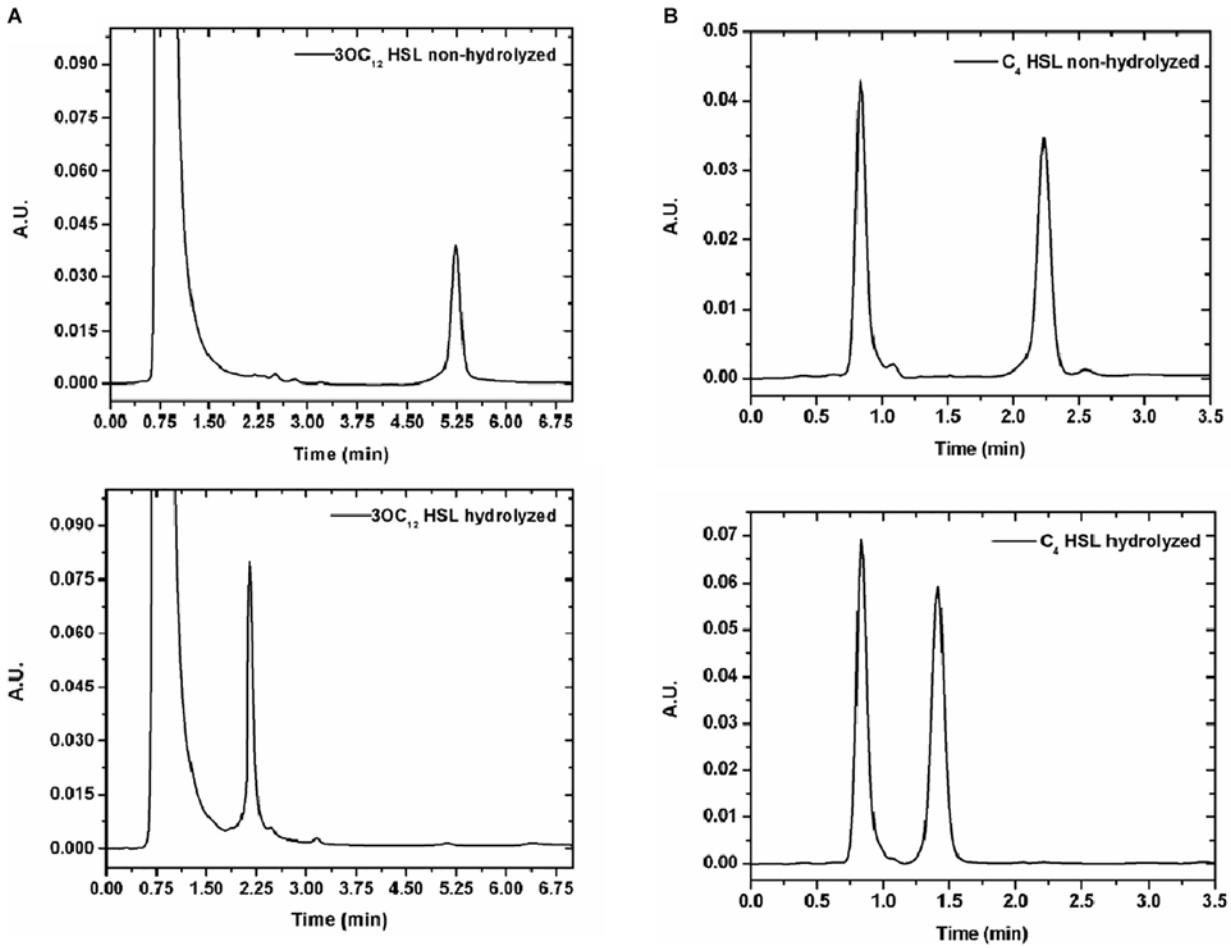

FIGURE 2 | (A) HPLC of HSL without (above) and with 5 μg/mL of AiiM (below) after 5 min of exposition. 2A *N*-(3-oxododecanoyl) homoserine lactone. Retention time for non-hydrolyzed HSL is 5.3 min whereas for hydrolyzed is 2.24 min. **(B)** 2B *N*-butyryl-DL-homoserine lactone. Retention time for non-hydrolyzed is 2.29 min whereas for hydrolyzed is 1.42 min.

as other carbapenem enzymes do, such as NDM, IMP or VIM. In order to test this, we exposed anti *Pseudomonas* ß-lactam antibiotics to 5 μg/mL of AiiM (**Supplementary Figures S7, S8**). Nevertheless, AiiM did not degrade any anti *Pseudomonas* ß-lactam antibiotics.

DISCUSSION

Pseudomonas aeruginosa is one of the main bacteria that causes hospital acquired infections in immunocompromised patients and vulnerable ones (Azam and Khan, 2018). *P. aeruginosa* is one of the 12 priority multi-drug resistant bacteria according to the WHO list published in 2017 (WHO, 2017) and belongs to the ESKAPE group, together with *Enterococcus faecium, Staphylococcus aureus, Klebsiella pneumoniae, A. baumannii,* and *Enterobacter* species (Chen et al., 2018). In addition to acquired resistance mechanisms such as carbapenemases (Carmeli et al., 2016), *P. aeruginosa* has many intrinsic antibiotic tolerance mechanisms, for instance low permeability in its external membrane, and expression of several efflux pumps (Malhotra et al., 2018; Ferrer-Espada et al., 2019).

Burn injuries are one of the most common and devastating forms of trauma and patients with serious thermal injury require immediate specialized care in order to minimize morbidity and mortality (Church et al., 2006). *P. aeruginosa* is one of the most frequent bacteria associated to infection in burn patients together with *A. baumannii* (Li et al., 2018). In a recent Mexican study (Garza-Gonzalez et al., 2019), *P. aeruginosa* had around 27% of resistance to carbapenems, in a global context it was one of the main bacteria in 47 Mexican health centers in 20 states, 175/1995 strains were multi-drug-resistant, 165/1995 were possible extreme drug resistant and 87/1995 possible pandrug resistant. In our 30 isolates we had more than 60% of resistance to cephalosporins (ceftazidime and cefepime), carbapenems (dorypenem, imipenem, and meropenem), aminoglycosides (amikacin and gentamicin), fluoroquinolones (ciprofloxacin and levofloxacin), and piperacillin/tazobactam. Moreover, one strain was resistant to colistin, which is the last antibiotic resource.

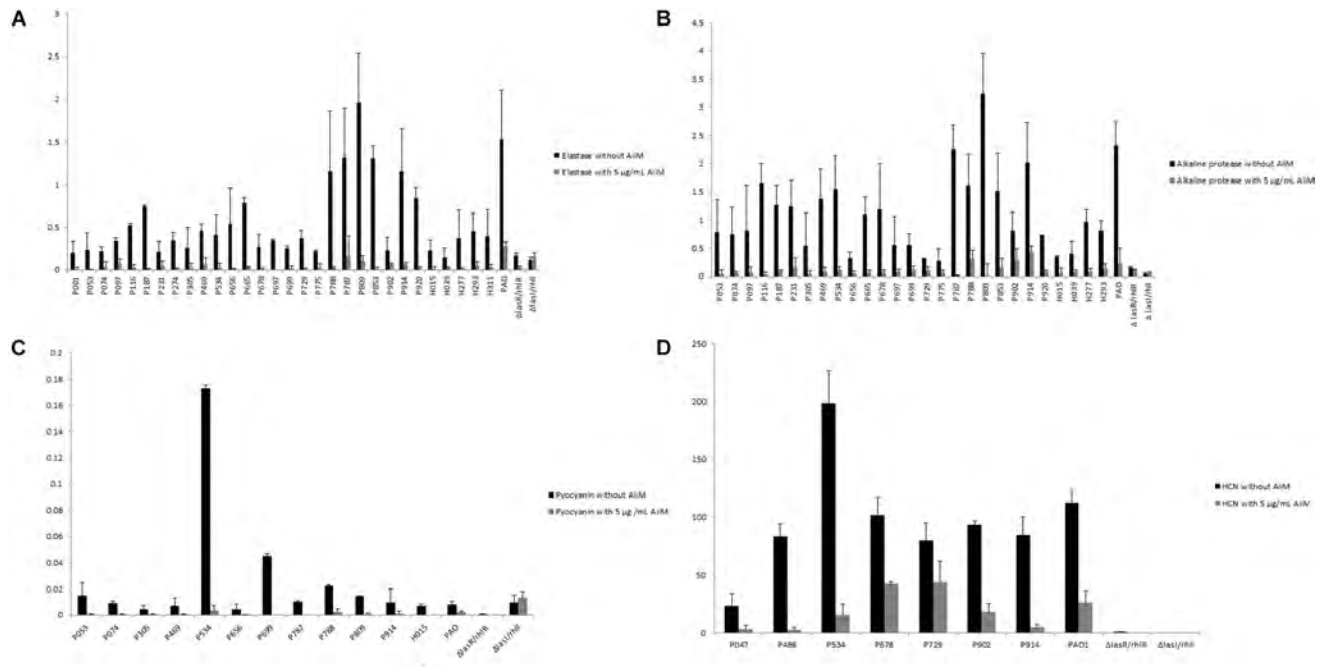

FIGURE 3 | (A) Elastase activity, black bars correspond to clinical strains determination without addition of AiiM, gray bars correspond to clinical strains with 5 μg/mL of AiiM with $p = 0.000002$. **(B)** Alkaline protease activity, black bars correspond to clinical strains without AiiM addition while gray bars correspond to strains with the addition of 5 μg/mL of AiiM with $p = 0.000004$. **(C)** Pyocyanin production, black bars correspond to clinical strains without AiiM addition, whereas gray bars correspond to clinical strains with AiiM 5 μg/mL with $p = 0.001$. **(D)** HCN production, black bars correspond to clinical strains without AiiM addition while gray bars correspond to clinical strains with AiiM 5 μg/mL having a $p = 0.008$.

AiiM showed a wide activity and was able to cut all HSL molecules tested, consistent with a previous report by Wang et al. (2010). Even though we did not analyze it in a quantitative form, we infer a strong activity of AiiM due to its ability to degrade all HSL tested within 5 min of exposition, moreover in our study 5 μg/mL were enough to break down these molecules. One of the main characteristics that a quorum quencher must fulfill is that it should not inhibit bacterial growth (Defoirdt et al., 2013; Defoirdt, 2018) and as expected, AiiM treatment did not affect *P. aeruginosa* growth kinetic.

In contrast, AiiM significantly reduced the four QS-dependent virulence factors tested in our study following a dose response pattern; moreover, others have demonstrated that AiiM had very good activity in a mouse model of acute pneumonia (Migiyama et al., 2013) and reduces methane production in waste sewage sludge (Nguyen et al., 2018). Although to date, the majority of studies with QQ enzymes have been performed only in type strains like PAO1, PA14 (Fetzner, 2015), recently, Guendouze et al. (2017) did the first investigation with *P. aeruginosa* clinical strains isolated from diabetic foot using the lactonase *Sso*Pox with a substitution in the amino acid 263 changing a tryptophan to isoleucine, in order to increase the enzymatic activity, using 0.5 mg/mL of protein, they found some strains with certain tolerance to the *Sso*Pox addition. In our study, AiiM reduced elastase and alkaline protease activities, pyocyanin and HCN concentrations, and we did not find any strain with tolerance against AiiM treatment, in spite that AiiM was used at a 100 times lower concentration than SsoPox. Moreover, AiiM effectivity is much higher than the effectivity of small molecule QS inhibitors such as brominated furanones and 5-fluorouracil, that cannot inhibit QS-virulence factor production of several of the clinical strains tested, and that are very toxic to some of them (García-Contreras et al., 2013, 2015; García-Contreras, 2016; García-Contreras et al., 2016; Guendouze et al., 2017).

Nevertheless, for type III secretion, no inhibition by AiiM was found, which is consistent with recent findings showing that in a Δ*lasR/rhlR* mutant of *P. aeruginosa* PAO1, T3SS effector toxins are secreted at the same levels than in the wild-type strain, demonstrating that this virulence factor is not positively regulated by QS (Soto-Aceves et al., 2019), instead it may be used at low cell densities to establish infections in the host (Hauser, 2009). These highlights the importance of targeting both QS and T3SS to develop robust anti-virulence therapies (García-Contreras, 2016). Moreover, other results indicate that the inhibition of QS systems and T3SS by molecules such as coumarin (Zhang et al., 2018) must be due to independent effects over the QS systems and T3SS.

One possible limitation of the utilization of AiiM and other QQ enzymes for treating *P. aeruginosa* infections is the fact that *lasR* defective mutants are often found in infections and although in principle these mutants will produce low levels of QS-dependent virulence factors, this is not always the case due to a rewiring of the virulence factor regulation

(Morales et al., 2017). And these strains could be tolerant against the effect of QQ enzymes.

Since AiiM is a member of the alpha/beta hydrolases superfamily and several antibiotics are inactivated by metallo ß-lactamases, reducing clinical options to treat infections (Hong et al., 2015), we tested if AiiM could cleave these ß-lactamase antibiotics, however, AiiM did not inactivate those tested, and hence it could be safely used in combination with them.

Although *in vivo* tests in burn infection models are lacking, our work suggests that AiiM treatment may be an effective addition for the treatment of *P. aeruginosa* infections, and since research by other groups had shown also the utility of the lactonase *Sso*Pox against clinical isolates from diabetic foot patients *in vitro* (Guendouze et al., 2017) and *in vivo* using an amoeba model (Mion et al., 2019), and in rat pneumonia against the PAO1 strain (Hraiech et al., 2014) lactonase utilization became an strong candidate for its eventual application in the clinical practice, moreover although *in vivo* studies using acylases are scarce, recently it was shown the PvdQ in addition to their inhibitory properties *in vitro* (Sio et al., 2006) and in *Caenorhabditis elegans* model was also able to increase survival, reduce damage and decrease bacterial loads in a pulmonary infection mice model (Papaioannou et al., 2009; Utari et al., 2018). Hence QQ enzymes may be beneficial for the treatment of burn and lung infections as well.

CONCLUSION

AiiM showed a strong activity against C4-HSL, 3OC8-HSL, C10-HSL, 3OC10-HSL, and 3OC12-HSL. It reduced elastase and alkaline protease activities as well as pyocyanin and HCN concentrations in all tested clinical strains of *P. aeruginosa* isolated from burned patients and no AiiM tolerant strain was found. However, it had no inhibitory effect against the T3SS.

DATA AVAILABILITY STATEMENT

All datasets generated for this study are included in the article/**Supplementary Material**.

ETHICS STATEMENT

Pseudomonas aeruginosa clinical strains used in this study were isolated as part of routine clinical hospital procedures to diagnose infection and hence ethical approval was not required, according to the National Institute of Rehabilitation ethical committee. All bacterial isolates were stored as part of laboratory and epidemiology necessities.

AUTHOR CONTRIBUTIONS

LL-J, GG-R, MH-D, DR-M, PN, MD-G, DL, JS-R, and DD-R performed the experiments. RF-C, TM, BG-P, GG-R, LL-J, and RG-C designed the study, supervised the project and discussed the results. LL-J wrote the manuscript with input from all authors.

FUNDING

This work was supported by Grants from the Programa de Apoyo a Proyectos de Investigación e Innovación Tecnológica (PAPIIT), the Universidad Nacional Autónoma de México number IN214218, the Consejo Nacional de Ciencia y Tecnología number SEP-CONACYT CB-A1-S-8530, and the CONACYT INFR-2015-252140 grant.

ACKNOWLEDGMENTS

RG-C is grateful to Beatriz Meráz Rios for her assistance with some experiments. We acknowledge Dr. Norma Espinosa Sánchez and Eugenia Flores Robles for technical assistance. LL-J is a doctoral student from the Programa de Doctorado en Ciencias Biomédicas, Universidad Nacional Autónoma de México.

SUPPLEMENTARY MATERIAL

The Supplementary Material for this article can be found online at: https://www.frontiersin.org/articles/10.3389/fmicb.2019.02657/full#supplementary-material

REFERENCES

Azam, M. W., and Khan, A. U. (2018). Updates on the pathogenicity status of *Pseudomonas aeruginosa*. *Drug. Discov. Today* 24, 350–359. doi: 10.1016/j.drudis.2018.07.003

Ben Haj Khalifa, A., Moissenet, D., Vu Thien, H., and Khedher, M. (2011). Virulence factors in *Pseudomonas aeruginosa*: mechanisms and modes of regulation. *Ann. Biol. Clin.* 69, 393–403. doi: 10.1684/abc.2011.0589

Carmeli, Y., Armstrong, J., Laud, P. J., Newell, P., Stone, G., Wardman, A., et al. (2016). Ceftazidime-avibactam or best available therapy in patients with ceftazidime-resistant *Enterobacteriaceae* and *Pseudomonas aeruginosa* complicated urinary tract infections or complicated intra-abdominal infections (REPRISE): a randomised, pathogen-directed, phase 3 study. *Lancet Infect. Dis.* 16, 661–673. doi: 10.1016/S1473-3099(16)30004-4

Castillo-Juarez, I., Maeda, T., Mandujano-Tinoco, E. A., Tomas, M., Perez-Eretza, B., Garcia-Contreras, S. J., et al. (2015). Role of quorum sensing in bacterial infections. *World J Clin Cases* 3, 575–598. doi: 10.12998/wjcc.v3.i7.575

Centers for Disease Control and Prevention, (2018). *Pseudomonas* aeruginosa in Healthcare Settings. Available at: https://www.cdc.gov/hai/organisms/pseudomonas.html (accessed March 9, 2018).

Centers for Disease Control and Prevention, (2019). *Diseases and Organisms in Healthcare Settings*. Atlanta GA: Centers for Disease Control and Prevention.

Chatterjee, M., Anju, C. P., Biswas, L., Anil Kumar, V., Gopi Mohan, C., and Biswas, R. (2016). Antibiotic resistance in *Pseudomonas aeruginosa* and alternative therapeutic options. *Int. J. Med. Microbiol.* 306, 48–58. doi: 10.1016/j.ijmm.2015.11.004

Chen, J. W., Lau, Y. Y., Krishnan, T., Chan, K. G., and Chang, C. Y. (2018). Recent advances in molecular diagnosis of *Pseudomonas aeruginosa* infection

by state-of-the-art genotyping techniques. *Front. Microbiol* 9:1104. doi: 10.3389/fmicb.2018.01104

Church, D., Elsayed, S., Reid, O., Winston, B., and Lindsay, R. (2006). Burn wound infections. *Clin. Microbiol. Rev* 19, 403–434.

CLSI, (2015). *M07-A10 Methods for Dilution Antimicrobial Susceptibility Test for Bacteria that Grow Aerobically; Approved Standard*, 10th Edn. Wayne, PA: Clinical and Laboratory Standards Institute.

CLSI, (2019). *M100 Performance Standards for Antimicrobial Susceptibility Testing*, 29th Edn. Wayne, PA: Clinical and Laboratory Standards Institute.

Cohen, R., Babushkin, F., Cohen, S., Afraimov, M., Shapiro, M., Uda, M., et al. (2017). A prospective survey of *Pseudomonas aeruginosa* colonization and infection in the intensive care unit. *Antimicrob. Resist. Infect. Control* 6:7.

Defoirdt, T. (2018). Quorum-sensing systems as targets for antivirulence therapy. *Trends Microbiol.* 26, 313–328. doi: 10.1016/j.tim.2017.10.005

Defoirdt, T., Brackman, G., and Coenye, T. (2013). Quorum sensing inhibitors: how strong is the evidence? *Trends Microbiol* 21, 619–624. doi: 10.1016/j.tim.2013.09.006

Douzi, B., Ball, G., Cambillau, C., Tegoni, M., and Voulhoux, R. (2011). Deciphering the Xcp *Pseudomonas aeruginosa* type II secretion machinery through multiple interactions with substrates. *J. Biol. Chem.* 286, 40792–40801. doi: 10.1074/jbc.M111.294843

Estahbanati, H. K., Kashani, P. P., and Ghanaatpisheh, F. (2002). Frequency of *Pseudomonas aeruginosa* serotypes in burn wound infections and their resistance to antibiotics. *Burns* 28, 340–348. doi: 10.1016/s0305-4179(02)00024-4

Ferrer-Espada, R., Shahrour, H., Pitts, B., Stewart, P. S., Sanchez-Gomez, S., and Martinez-De-Tejada, G. (2019). A permeability-increasing drug synergizes with bacterial efflux pump inhibitors and restores susceptibility to antibiotics in multi-drug resistant *Pseudomonas aeruginosa* strains. *Sci. Rep.* 9:3452. doi: 10.1038/s41598-019-39659-4

Fetzner, S. (2015). Quorum quenching enzymes. *J. Biotechnol.* 201, 2–14. doi: 10.1016/j.jbiotec.2014.09.001

Fournier, A., Voirol, P., Krahenbuhl, M., Bonnemain, C. L., Fournier, C., Pantet, O., et al. (2016). Antibiotic consumption to detect epidemics of *Pseudomonas aeruginosa* in a burn centre: a paradigm shift in the epidemiological surveillance of *Pseudomonas aeruginosa* nosocomial infections. *Burns* 42, 564–570. doi: 10.1016/j.burns.2015.10.030

Gallagher, L. A., and Manoil, C. (2001). *Pseudomonas aeruginosa* PAO1 kills *Caenorhabditis elegans* by cyanide poisoning. *J. Bacteriol.* 183, 6207–6214. doi: 10.1128/jb.183.21.6207-6214.2001

García-Contreras, R. (2016). Is quorum sensing interference a viable alternative to treat *Pseudomonas aeruginosa* infections? *Front. Microbiol.* 7:1454. doi: 10.3389/fmicb.2016.01454

García-Contreras, R., Maeda, T., and Wood, T. K. (2016). Can resistance against quorum-sensing interference be selected? *ISME J.* 10, 4–10. doi: 10.1038/ismej.2015.84

García-Contreras, R., Martinez-Vazquez, M., Velazquez Guadarrama, N., Villegas Paneda, A. G., Hashimoto, T., Maeda, T., et al. (2013). Resistance to the quorum-quenching compounds brominated furanone C-30 and 5-fluorouracil in *Pseudomonas aeruginosa* clinical isolates. *Pathog. Dis.* 68, 8–11. doi: 10.1111/2049-632X.12039

García-Contreras, R., Perez-Eretza, B., Jasso-Chavez, R., Lira-Silva, E., Roldan-Sanchez, J. A., Gonzalez-Valdez, A., et al. (2015). High variability in quorum quenching and growth inhibition by furanone C-30 in *Pseudomonas aeruginosa* clinical isolates from cystic fibrosis patients. *Pathog. Dis.* 73:ftv040. doi: 10.1093/femspd/ftv040

Garza-Gonzalez, E., Morfin-Otero, R., Mendoza-Olazaran, S., Bocanegra-Ibarias, P., Flores-Trevino, S., Rodriguez-Noriega, E., et al. (2019). A snapshot of antimicrobial resistance in Mexico. Results from 47 centers from 20 states during a six-month period. *PLoS One* 14:e0209865. doi: 10.1371/journal.pone.0209865

Guendouze, A., Plener, L., Bzdrenga, J., Jacquet, P., Remy, B., Elias, M., et al. (2017). Effect of quorum quenching lactonase in clinical isolates of *Pseudomonas aeruginosa* and comparison with quorum sensing inhibitors. *Front. Microbiol.* 8:227. doi: 10.3389/fmicb.2017.00227

Hauser, A. R. (2009). The type III secretion system of *Pseudomonas aeruginosa*: infection by injection. *Nat. Rev. Microbiol.* 7, 654–665. doi: 10.1038/nrmicro2199

Hong, D. J., Bae, I. K., Jang, I. H., Jeong, S. H., Kang, H. K., and Lee, K. (2015). Epidemiology and characteristics of metallo-beta-lactamase-producing *Pseudomonas aeruginosa*. *Infect. Chemother.* 47, 81–97. doi: 10.3947/ic.2015.47.2.81

Howe, T. R., and Iglewski, B. H. (1984). Isolation and characterization of alkaline protease-deficient mutants of *Pseudomonas aeruginosa* in vitro and in a mouse eye model. *Infect. Immun.* 43, 1058–1063.

Hraiech, S., Hiblot, J., Lafleur, J., Lepidi, H., Papazian, L., Rolain, J. M., et al. (2014). Inhaled lactonase reduces *Pseudomonas aeruginosa* quorum sensing and mortality in rat pneumonia. *PLoS One* 9:e107125. doi: 10.1371/journal.pone.0107125

Huber, P., Basso, P., Reboud, E., and Attree, I. (2016). *Pseudomonas aeruginosa* renews its virulence factors. *Environ. Microbiol. Rep.* 8, 564–571. doi: 10.1111/1758-2229.12443

Jimenez, P. N., Koch, G., Thompson, J. A., Xavier, K. B., Cool, R. H., and Quax, W. J. (2012). The multiple signaling systems regulating virulence in *Pseudomonas aeruginosa*. *Microbiol. Mol. Biol. Rev.* 76, 46–65. doi: 10.1128/MMBR.05007-11

Karampatakis, T., Antachopoulos, C., Tsakris, A., and Roilides, E. (2018). Molecular epidemiology of carbapenem-resistant *Pseudomonas aeruginosa* in an endemic area: comparison with global data. *Eur. J. Clin. Microbiol. Infect. Dis.* 37, 1211–1220. doi: 10.1007/s10096-018-3244-4

Laarman, A. J., Bardoel, B. W., Ruyken, M., Fernie, J., Milder, F. J., Van Strijp, J. A., et al. (2012). *Pseudomonas aeruginosa* alkaline protease blocks complement activation via the classical and lectin pathways. *J. Immunol.* 188, 386–393. doi: 10.4049/jimmunol.1102162

Lee, J., and Zhang, L. (2015). The hierarchy quorum sensing network in *Pseudomonas aeruginosa*. *Protein Cell* 6, 26–41. doi: 10.1007/s13238-014-0100-x

Li, L., Dai, J. X., Xu, L., Chen, Z. H., Li, X. Y., Liu, M., et al. (2018). Antimicrobial resistance and pathogen distribution in hospitalized burn patients: a multicenter study in Southeast China. *Medicine* 97:e11977. doi: 10.1097/MD.0000000000011977

Lyczak, J. B., Cannon, C. L., and Pier, G. B. (2000). Establishment of *Pseudomonas aeruginosa* infection: lessons from a versatile opportunist. *Microbes Infect.* 2, 1051–1060. doi: 10.1016/s1286-4579(00)01259-4

Maeda, T., Garcia-Contreras, R., Pu, M., Sheng, L., Garcia, L. R., Tomas, M., et al. (2012). Quorum quenching quandary: resistance to antivirulence compounds. *ISME J.* 6, 493–501. doi: 10.1038/ismej.2011.122

Malhotra, S., Limoli, D. H., English, A. E., Parsek, M. R., and Wozniak, D. J. (2018). Mixed communities of mucoid and nonmucoid *Pseudomonas aeruginosa* exhibit enhanced resistance to host antimicrobials. *mBio* 9:e275-18. doi: 10.1128/mBio.00275-18

Mcmanus, A. T., Mason, A. D., Mcmanus, W. F., and Pruitt, B. A. (1985). Twenty-five year review of *Pseudomonas aeruginosa* bacteremia in a burn center. *Eur. J. Clin. Microbiol.* 4, 219–223. doi: 10.1007/bf02013601

Migiyama, Y., Kaneko, Y., Yanagihara, K., Morohoshi, T., Morinaga, Y., Nakamura, S., et al. (2013). Efficacy of AiiM, an N-acylhomoserine lactonase, against *Pseudomonas aeruginosa* in a mouse model of acute pneumonia. *Antimicrob. Agents Chemother.* 57, 3653–3658. doi: 10.1128/AAC.00456-13

Mion, S., Remy, B., Plener, L., Bregeon, F., Chabriere, E., and Daude, D. (2019). Quorum quenching lactonase strengthens bacteriophage and antibiotic arsenal against *Pseudomonas aeruginosa* clinical isolates. *Front. Microbiol.* 10:2049. doi: 10.3389/fmicb.2019.02049

Morales, E., Gonzalez-Valdez, A., Servin-Gonzalez, L., and Soberon-Chavez, G. (2017). *Pseudomonas aeruginosa* quorum-sensing response in the absence of functional LasR and LasI proteins: the case of strain 148, a virulent dolphin isolate. *FEMS Microbiol. Lett.* 364:fnx119. doi: 10.1093/femsle/fnx119

Nguyen, P. D. T., Mustapha, N. A., Kadokami, K., Garcia-Contreras, R., Wood, T. K., and Maeda, T. (2018). Quorum sensing between Gram-negative bacteria responsible for methane production in a complex waste sewage sludge consortium. *Appl. Microbiol. Biotechnol.* 103, 1485–1495. doi: 10.1007/s00253-018-9553-9

Nguyen, P. D. T., Mustapha, N. A., Kadokami, K., Garcia-Contreras, R., Wood, T. K., and Maeda, T. (2019). Quorum sensing between Gram-negative bacteria responsible for methane production in a complex waste sewage sludge consortium. *Appl. Microbiol. Biotechnol.* 103, 1485–1495. doi: 10.1007/s00253-018-9553-9

Ohman, D. E., Cryz, S. J., and Iglewski, B. H. (1980). Isolation and characterization of *Pseudomonas aeruginosa* PAO mutant that produces altered elastase. *J. Bacteriol.* 142, 836–842.

Olivares, E., Badel-Berchoux, S., Provot, C., Jaulhac, B., Prevost, G., Bernardi, T., et al. (2016). The biofilm ring test: a rapid method for routine analysis of *Pseudomonas aeruginosa* biofilm formation kinetics. *J. Clin. Microbiol.* 54, 657–661. doi: 10.1128/JCM.02938-15

Papaioannou, E., Wahjudi, M., Nadal-Jimenez, P., Koch, G., Setroikromo, R., and Quax, W. J. (2009). Quorum-quenching acylase reduces the virulence of *Pseudomonas aeruginosa* in a *Caenorhabditis elegans* infection model. *Antimicrob. Agents Chemother.* 53, 4891–4897. doi: 10.1128/AAC.00380-09

Pavlovskis, O. R., and Wretlind, B. (1979). Assessment of protease (elastase) as a *Pseudomonas aeruginosa* virulence factor in experimental mouse burn infection. *Infect. Immun.* 24, 181–187.

Rumbaugh, K. P., Diggle, S. P., Watters, C. M., Ross-Gillespie, A., Griffin, A. S., and West, S. A. (2009). Quorum sensing and the social evolution of bacterial virulence. *Curr. Biol.* 19, 341–345. doi: 10.1016/j.cub.2009.01.050

Shaw, P. D., Ping, G., Daly, S. L., Cha, C., Cronan, J. E. Jr., Rinehart, K. L., et al. (1997). Detecting and characterizing N-acyl-homoserine lactone signal molecules by thin-layer chromatography. *Proc. Natl. Acad. Sci. U.S.A.* 94, 6036–6041. doi: 10.1073/pnas.94.12.6036

Shields, R. K., Clancy, C. J., Pasculle, A. W., Press, E. G., Haidar, G., Hao, B., et al. (2018). Verification of ceftazidime-avibactam and ceftolozane-tazobactam susceptibility testing methods against carbapenem-resistant *Enterobacteriaceae* and *Pseudomonas aeruginosa*. *J. Clin. Microbiol.* 56:e1093-17. doi: 10.1128/JCM.01093-17

Shortridge, D., Castanheira, M., Pfaller, M. A., and Flamm, R. K. (2017). Ceftolozane-tazobactam activity against *Pseudomonas aeruginosa* clinical isolates from U.S. Hospitals: report from the PACTS antimicrobial surveillance program, 2012 to 2015. *Antimicrob. Agents Chemother.* 61:e465-17. doi: 10.1128/AAC.00465-17

Sio, C. F., Otten, L. G., Cool, R. H., Diggle, S. P., Braun, P. G., Bos, R., et al. (2006). Quorum quenching by an N-acyl-homoserine lactone acylase from *Pseudomonas aeruginosa* PAO1. *Infect. Immun.* 74, 1673–1682. doi: 10.1128/iai.74.3.1673-1682.2006

Soto-Aceves, M. P., Cocotl-Yanez, M., Merino, E., Castillo-Juarez, I., Cortes-Lopez, H., Gonzalez-Pedrajo, B., et al. (2019). Inactivation of the quorum-sensing transcriptional regulators LasR or RhlR does not suppress the expression of virulence factors and the virulence of *Pseudomonas aeruginosa* PAO1. *Microbiology* 165, 425–432. doi: 10.1099/mic.0.000778

Tredget, E. E., Shankowsky, H. A., Joffe, A. M., Inkson, T. I., Volpel, K., Paranchych, W., et al. (1992). Epidemiology of infections with *Pseudomonas aeruginosa* in burn patients: the role of hydrotherapy. *Clin. Infect. Dis* 15, 941–949. doi: 10.1093/clind/15.6.941

Turner, K. H., Everett, J., Trivedi, U., Rumbaugh, K. P., and Whiteley, M. (2014). Requirements for *Pseudomonas aeruginosa* acute burn and chronic surgical wound infection. *PLoS Genet.* 10:e1004518. doi: 10.1371/journal.pgen.1004518

Utari, P. D., Setroikromo, R., Melgert, B. N., and Quax, W. J. (2018). PvdQ quorum quenching acylase attenuates *Pseudomonas aeruginosa* virulence in a mouse model of pulmonary infection. *Front. Cell Infect. Microbiol.* 8:119. doi: 10.3389/fcimb.2018.00119

Van Delden, C., and Iglewski, B. H. (1998). Cell-to-cell signaling and *Pseudomonas aeruginosa* infections. *Emerg. Infect. Dis* 4, 551–560.

Wang, W. Z., Morohoshi, T., Ikenoya, M., Someya, N., and Ikeda, T. (2010). AiiM, a novel class of N-acylhomoserine lactonase from the leaf-associated bacterium *Microbacterium testaceum*. *Appl. Environ. Microbiol.* 76, 2524–2530. doi: 10.1128/AEM.02738-09

WHO, (2017). *WHO Publishes List of Bacteria for Which New Antibiotics are Urgently Needed*. Available at: https://www.who.int/en/news-room/detail/27-02-2017-who-publishes-list-of-bacteria-for-which-new-antibiotics-are-urgently-needed (accessed February 2, 2018).

Zhang, Y., Sass, A., Van Acker, H., Wille, J., Verhasselt, B., Van Nieuwerburgh, F., et al. (2018). Coumarin reduces virulence and biofilm formation in *Pseudomonas aeruginosa* by affecting quorum sensing, type III secretion and C-di-GMP levels. *Front. Microbiol.* 9:1952. doi: 10.3389/fmicb.2018.01952

Conflict of Interest: The authors declare that the research was conducted in the absence of any commercial or financial relationships that could be construed as a potential conflict of interest.

Copyright © 2019 López-Jácome, Garza-Ramos, Hernández-Durán, Franco-Cendejas, Loarca, Romero-Martínez, Nguyen, Maeda, González-Pedrajo, Díaz-Guerrero, Sánchez-Reyes, Díaz-Ramírez and García-Contreras. This is an open-access article distributed under the terms of the Creative Commons Attribution License (CC BY). The use, distribution or reproduction in other forums is permitted, provided the original author(s) and the copyright owner(s) are credited and that the original publication in this journal is cited, in accordance with accepted academic practice. No use, distribution or reproduction is permitted which does not comply with these terms.

INFORME DE LABORES 2019



Channels

ISSN: 1933-6950 (Print) 1933-6969 (Online) Journal homepage: https://www.tandfonline.com/loi/kchl20

TRP ion channels: Proteins with conformational flexibility

Ana Elena López-Romero, Ileana Hernández-Araiza, Francisco Torres-Quiroz, Luis B. Tovar-Y-Romo, León D. Islas & Tamara Rosenbaum

To cite this article: Ana Elena López-Romero, Ileana Hernández-Araiza, Francisco Torres-Quiroz, Luis B. Tovar-Y-Romo, León D. Islas & Tamara Rosenbaum (2019) TRP ion channels: Proteins with conformational flexibility, Channels, 13:1, 207-226, DOI: 10.1080/19336950.2019.1626793

To link to this article: https://doi.org/10.1080/19336950.2019.1626793

© 2019 The Author(s). Published by Informa UK Limited, trading as Taylor & Francis Group.

Published online: 11 Jun 2019.

Submit your article to this journal

Article views: 1865

View related articles

View Crossmark data

Citing articles: 4 View citing articles

Full Terms & Conditions of access and use can be found at
https://www.tandfonline.com/action/journalInformation?journalCode=kchl20

CHANNELS
2019, VOL. 13, NO. 1, 207–226
https://doi.org/10.1080/19336950.2019.1626793

Taylor & Francis
Taylor & Francis Group

REVIEW

OPEN ACCESS Check for updates

TRP ion channels: Proteins with conformational flexibility

Ana Elena López-Romero[a,&], Ileana Hernández-Araiza[a,&], Francisco Torres-Quiroz[b], Luis B. Tovar-Y-Romo[c], León D. Islas[d], and Tamara Rosenbaum[a]

[a]Departamento de Neurociencia Cognitiva, División Neurociencias, Instituto de Fisiología Celular, Universidad Nacional Autónoma de México, Mexico, Mexico; [b]Departamento de Bioquímica y Biología Estructural, División Investigación Básica, Instituto de Fisiología Celular, Universidad Nacional Autónoma de México, Mexico City, Mexico; [c]Departamento de Neuropatología Molecular, División Neurociencias, Instituto de Fisiología Celular, Universidad Nacional Autónoma de México, Mexico City, Mexico.; [d]Departamento de Fisiología, Facultad de Medicina, Universidad Nacional Autónoma de México, Mexico City, Mexico

ABSTRACT

Ion channels display conformational changes in response to binding of their agonists and antagonists. The study of the relationships between the structure and the function of these proteins has witnessed considerable advances in the last two decades using a combination of techniques, which include electrophysiology, optical approaches (i.e. patch clamp fluorometry, incorporation of non-canonic amino acids, etc.), molecular biology (mutations in different regions of ion channels to determine their role in function) and those that have permitted the resolution of their structures in detail (X-ray crystallography and cryo-electron microscopy). The possibility of making correlations among structural components and functional traits in ion channels has allowed for more refined conclusions on how these proteins work at the molecular level. With the cloning and description of the family of Transient Receptor Potential (TRP) channels, our understanding of several sensory-related processes has also greatly moved forward. The response of these proteins to several agonists, their regulation by signaling pathways as well as by protein-protein and lipid-protein interactions and, in some cases, their biophysical characteristics have been studied thoroughly and, recently, with the resolution of their structures, the field has experienced a new boom. This review article focuses on the conformational changes in the pores, concentrating on some members of the TRP family of ion channels (TRPV and TRPA subfamilies) that result in changes in their single-channel conductances, a phenomenon that may lead to fine-tuning the electrical response to a given agonist in a cell.

ARTICLE HISTORY
Received 10 April 2019
Revised 17 May 2019
Accepted 21 May 2019

KEYWORDS
TRP Channels; structure-function; Ion channels; lipid-protein interactions

Introduction

The appearance of the plasma membranes of cells constituted a key event for life during evolution. These structures represent boundaries of the units of life, achieving pivotal functions for the cell, including transport of molecules, communication with the environment, and metabolic functions. The intrinsic hydrophobic nature of these structures renders them impermeable to the flux of charged molecules, a process necessary for cell-cell communication, activation of signaling pathways, as well as for the ability to respond to endogenous and exogenous signals. This issue is resolved by the presence of certain types of proteins in plasma membranes, called ion channels that allow for the passage of ions from one side to the other. The specific structure of one ion channel may differ substantially from another; however, all these proteins contain a pore that opens and closes to permit the flow of ions, mediating ionic currents that, in turn, result in the generation of signals with distinct physiological consequences.

There is an intimate relationship between the structures and the functions of ion channels, with their different component regions serving a specific role in the activity of these proteins. In the 1980s, when the patch-clamp recording technique was developed, it became possible to study the behavior of single ion channels in real time[1]. Furthermore, with the advances seen in the areas of molecular biology, cloning and generation of knockout animal models, we have been provided with valuable methods[1] to carefully determine the roles of ion channels in normal and under pathophysiological conditions. A large variety of ion channels have been cloned and biophysically characterized and, in the past three decades,

CONTACT Tamara Rosenbaum trosenba@ifc.unam.mx
[&]These authors contributed equally to this work

© 2019 The Author(s). Published by Informa UK Limited, trading as Taylor & Francis Group.
This is an Open Access article distributed under the terms of the Creative Commons Attribution License (http://creativecommons.org/licenses/by/4.0/), which permits unrestricted use, distribution, and reproduction in any medium, provided the original work is properly cited.

INFORME DE LABORES 2019

research-oriented towards determining the structure of ion channels has witnessed remarkable progress.

The Nobel Prize in Chemistry was awarded to Roderick MacKinnon and Peter Agre in 2003, for advancing the field by resolving the molecular structures K^+ channels [2–5] and aquaporins [6,7], allowing us to further understand their functional features.

The present review focuses on a family of proteins named Transient Receptor Potential (TRP) ion channels, which has fundamentally reshaped our knowledge of sensory physiology and their importance is illustrated by their pivotal roles in smell, taste, vision, touch and our ability to detect changes in temperature. Originally, the first *trp* gene was identified in a *Drosophila* mutant with altered vision [8]; however, it was not until it was cloned that the deduced amino acid sequence led to the suggestion that *trp* encoded for a cation channel [9]. Electrophysiological studies later showed that *trp* indeed was an ion channel and that its selectivity could be modified by inserting mutations in the amino acid region that formed the pore loop [10].

The field of study of TRP channels witnessed a boom when mammalian homologs of the *Drosophila trp* channel were cloned and when some of these were identified as temperature sensors [11,12]. A feature of these proteins is that several of these channels are polymodal, that is, being activated by several distinct physical stimuli and more than one ligand. In some cases, different biophysical properties as well as distinct conformational changes in their pores, associated with interactions with different ligands, have been demonstrated.

We will discuss a few examples of ion channels where conformational changes are associated with different ion conductance states. However, we will mainly focus on TRPV1 and other TRP ion channels for which structures have been solved, making emphasis on the conformational changes produced by various ligands and on their effects in the functional properties of these proteins.

Rearrangements in the outer pore of kv2.1 lead to changes in ion conductance

For voltage-gated ion channels, modulation of macroscopic current magnitude archetypically is thought to occur through an effect on the gating (opening and closing properties) of these proteins. In this sense, most studies of gating have concentrated on the voltage-dependent gate at the cytoplasmic entrance to the pore. Moreover, there is a large body of evidence that also supports an important role for the selectivity filter in gating activation [13,14]. It has been suggested that some form of voltage-dependent gating can exist at the selectivity filter (the region that discriminates among types of ions passing through the pore) [15–17], although the main closed-open transition is controlled by the S6 bundle-crossing intracellular gate [18].

These aspects have been explored in Kv2.1 potassium channels, which are slowly inactivating delayed rectifiers present in non-neuronal excitable cells and several neurons. In these channels, the current magnitude is modulated by the external K^+ concentration, making outward currents through Kv2.1 channels become larger when the extracellular K^+ concentration is increased [19]. Kv2.1 channels exhibit two distinct pharmacological profiles as a function of the K^+ concentration since they can either be sensitive to external tetraethylammonium (TEA; $IC_{50} \sim 3–5$ mM), or completely insensitive to this blocker [20]. The underlying mechanism of these effects encompasses the opening of Kv2.1 channels into one of two different outer vestibule conformations with different sensitivities to TEA. It has been shown that the channels that open into a TEA-sensitive conformation produce larger macroscopic currents [19]. In contrast, channels that open into a TEA-insensitive conformation, a phenomenon that occurs in the presence of higher potassium concentrations, yield smaller macroscopic currents [19].

Trapani and collaborators examined the mechanism by which conformational changes in Kv2.1 channels produced changes in current magnitude. By using a combination of single-channel, macroscopic recordings, and hidden Markov modeling they proposed a model in which an outer vestibule lysine residue in position 356 (pore turret region) interferes with the flux of K^+ through the channel [19]. This led to the suggestion that the K^+ concentration-dependent change in orientation of that specific K356 can modify single channel conductance through a change in the level of such an interference [19].

In summary, in the conformation where currents are smaller in magnitude, K356 would be oriented towards the center of the ion conduction pathway, not easily allowing the flux of K^+ ions and resulting in a change in the single-channel conductance. In contrast, when K356 is oriented away from the conduction pathway, it readily allows the passage of ions. Thus, these results obtained by Trapani et al., not only provided evidence where Kv2.1 single-channel conductance is modulated by the outer end of the conduction pathway through the occupancy of open states with different outer vestibule conformations, but they also showed that these occur under physiologically-relevant K^+ concentrations [19].

Hence, in a physiological scenario, it is important to consider that with rising extracellular K^+ concentrations, the current magnitude of K^+ channels in most neuronal cells is reduced as a result of a decrease in electrochemical driving force. However, Kv2.1 counteracts this reduction in net outward current in the presence of higher K^+ concentrations and, as suggested by the authors, this would provide the cells where these channels are expressed with a mechanism that maintains action potential integrity when high-frequency firing conditions are present [19].

The validity of the pore dilation phenomenon to explain changes in ion channel conductance

Ion channels exhibit different permeability and selectivity to various ions. Potassium, sodium, and calcium channels contain ion binding sites in their selectivity filters that enable them to finely discriminate among the ions that will flow through their pores[5][21],. Nonetheless, some ion channels have been shown to exhibit dynamic changes in their ion selectivity in response to agonist activation that could, in theory, allow for changes in their conductance. Examples of these ion channels are P2X receptor channels [22,23], acid-sensing ion channels (ASIC) [24,25] and TRPV1 channels [26,27]. This phenomenon has been called pore dilation and it will be next discussed for P2X receptors, a well-studied example of this process, and for TRPV1 in a later section.

P2X receptors are ion channels gated by extracellular ATP [28] and it was originally thought that the pore first opened rapidly to a conducting state selective for small cations such as Na^+, K^+ and Ca [2]+ (I_1 current) and gradually increased in size or dilated over time, rendering the channel permeable to large organic cations such as N-methyl-D-glucamine ($NMDG^+$) or I_2 current, as well as to large fluorophores and dyes (i.e. YO-PRO1) [22,23]. However, based on the original assumption that P2X receptors experience a slow, time- and agonist-dependent pore dilation, three mechanisms have been suggested to explain this phenomenon: (1) it represents an intrinsic gating property of the functional P2XR channel, where ATP exposure results in the widening of the pore and a change from a state that conducts Na^+, K^+, Ca^{2+} (I_1) to one that conducts $NMDG^+$ and YO-PRO 1, a large propidium dye. Such a switch has been proposed to be modulated by phosphorylation or dephosphorylation events [22,23]; (2) macropores are formed as a result of an agonist-dependent redistribution and oligomerization of P2XRs. The fusion of two or more trimeric P2XRs, as well as an enlargement of the channel pore, or the formation of a separate but larger pore among aggregating trimeric assemblies, could underly macropore formation. This hypothesis has been ruled out by some research groups since no clustering or redistribution of channels expected during oligomerization has been found to occur [23,29], but some others still support it [30]; (3) the permeability to large cations is facilitated by a structurally separate transport pathway downstream of P2XR activation [22].

Although the phenomenon of pore dilation has been extensively explored, accumulating evidence suggests that it may be an artifact of the experimental conditions used, as will be detailed in the Discussion section.

Next, we will discuss some structural characteristics of TRP ion channels that shed light into why these proteins represent an example of conformational flexibility in response to agonists that may result in changes in cellular excitability.

The structures of thermotrp channels reveal conformational flexibility

The TRPV1 channel was the first mammalian TRP channel to be cloned. In 1997, it was shown that

TRPV1 is the receptor for capsaicin [11,12]. In this groundbreaking study, the laboratory of David Julius isolated a cDNA clone that reconstituted the response to capsaicin in non-neuronal cells. By examining the amino acid sequence of this clone, they demonstrated TRPV1 is an integral membrane protein, homologous to a family of putative store-operated calcium channels and that it is expressed by small-diameter neurons within sensory ganglia such as the dorsal root (DRG) and trigeminal (TG). Moreover, these authors showed that TRPV1 is also a thermal sensor, activated in response to temperatures in a range known to elicit pain-associated behaviors in animals and pain in humans [11]. It was later shown, in 1998, that TRPV1 is also activated by low extracellular pH (pH ≤ 5.9) [12].

Continued work on the study of the function of TRPV1, one of the best studied TRP channels, has led to the identification of several other agonists and modulators including resiniferatoxin (RTx) [12], diacylglycerol [31], hydroperoxyeicosatetraenoic acid (HPETE) [32], anandamide [33], *N*-acyl ethanolamines (NAEs) [34], n-acyl-dopamines [35], nitric oxide [36], cations [37,38], hydrogen sulphide (H_2S) [39], the double-knot toxin (DkTx) from the Earth Tiger tarantula [40] and lysophosphatidic acid (LPA) [41].

TRP channels are all tetrameric structures. The structure of TRPV1 had been initially solved in the year of 2008 by the group of Vera Moiseenkova-Bell. These authors obtained a 19 Å resolution cryo-EM structure that showed that TRPV1 exhibits a four-fold symmetry with a large open basket-like domain, formed by the N- and C-termini of the channel as well as a compact transmembrane region [42]. In this first solved structure of TRPV1, the authors described a 150 Å tall ion channel which is divided into a "small" compact region (30% of the total volume) and into a "large" region or the "basket-like" domain (70% of the total mass).

This seminal study was followed by the higher resolution structures for TRPV1 obtained by the research groups of Yifan Cheng and David Julius. Two, back-to-back reports, described structures of 3.4–4.2 Å resolution obtained by cryo-EM [43,44]. They confirmed that TRPV1 has a four-fold symmetry with a central ion pathway that is formed by transmembrane segments S5 and S6 and a pore-loop, all of which are surrounded by the S1-S4 domains with a domain-swapped geometry [43,44]. The pore region was described as one containing a wide extracellular mouth and a short selectivity filter. The important TRP domain, which is a region conserved in these family of ion channels and that is thought to play an important role in their allosteric modulation, was shown to interact with the S4-S5 intracellular linker. Each of four subunits in TRPV1 contains six ankyrin repeats that form the ankyrin repeat domain (ARD) localized to their N-termini [43,44] (Figure 1).

These research groups also described the structures of TRPV1 obtained in the presence of different agonists, providing insight into the mechanisms that allow the polymodal activation of this channel. One of these structures was obtained in the presence of RTx (which also binds to the vanilloid pocket where capsaicin binds through residues Y511 and S512 in S3 and M547 and T550 in S4) and DkTx together. The authors showed that DkTx was bound to the extracellular loops of the outer pore region and defined contacts of the toxin with residues at the top of the pore helix of one subunit and the outer pore loop in the proximal S6 region of another nearby subunit [43,45] (Figure 2).

The structures of TRPV1 obtained in the presence of both agonists display evident rearrangements in the ion conduction pathway and the outer pore region. With RTx and DkTx bound to the channel, the ion conduction pathway appears completely eased of constrictions. This is in contrast to the structure obtained only in the presence of capsaicin, where the lower gate I679 is extended, but the selectivity filter G643 remains unaltered [45] (Figure 2).

When TRPV1 has RTx and DkTx bound, a shift or tilt of the S6 helix 1.9 Å away from the central axis of the channel is produced, as compared to the apo or unliganded state. Moreover, an increase in the distance between the carbonyl oxygens of G643, which constitutes the narrowest point of the selectivity filter, is also observed when both ligands are present: it goes from 4.6 Å in apo (PDB 3J5P) to 7.6 Å in RTx/DkTx (PDB 3J5Q) [45].

As mentioned above, G643 (at the upper gate) remains unaltered between the apo structure (PDB 3J5P) and in the structure in complex with

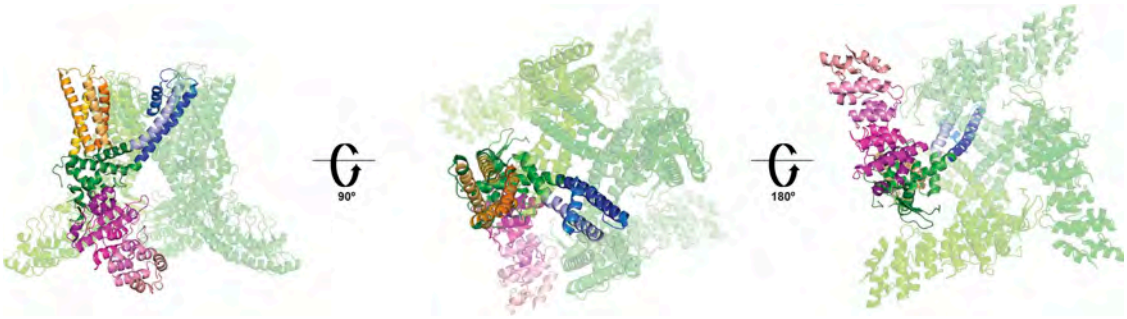

Figure 1. Structure of the TRPV1 channel. Only one of the subunits is highlighted for clarity.
The ankyrin repeat domain is shown in purple, the S1- S4 domain in orange, the pore forming S5-P-S6 is shown in blue. The pre-S1, S4-S5 linker, and TRP domain, which participate in the allosteric modulation of the channel, are shown in green. The left panel is a lateral view, the central and right panels are extracellular and intracellular views, respectively. (PDB 3J5P).

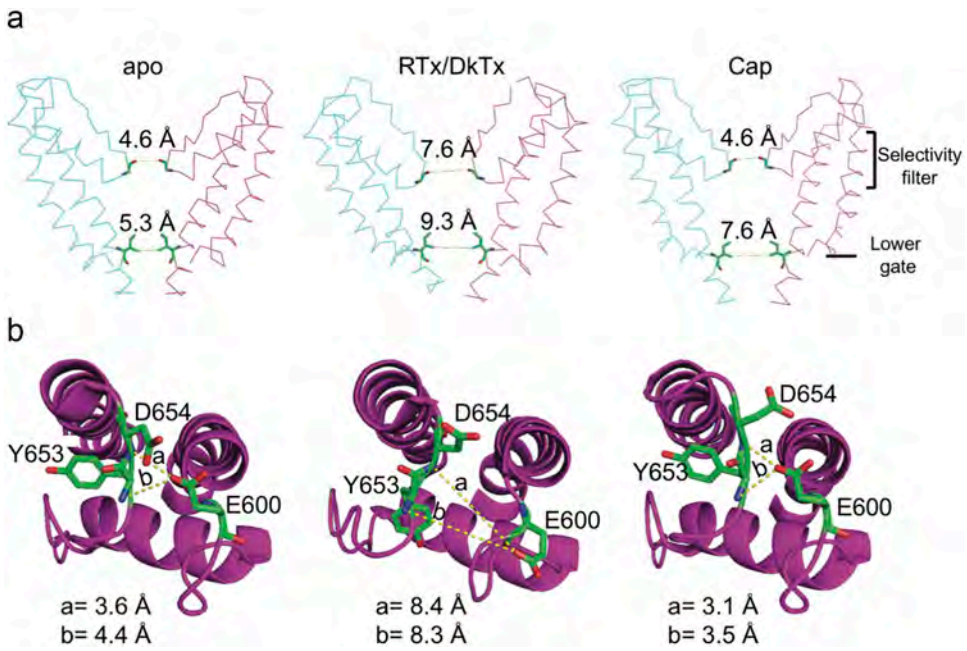

Figure 2. Relative movements of the selectivity filter and lower gate of TRPV1 in the presence of different agonists.
A. Distances between G643 (at the selectivity filter) and I679 (lower gate) in the apo (left, PDB 3J5P), RTx/DkTx (middle, PDB 3J5Q) and capsaicin (right, PDB 3J5R) structures. Compared to the apo structure, in the presence of both RTk and DkTx the selectivity filter and the lower gate expanded. In the structure with capsaicin only (Cap), the outer pore region remains unaltered in comparison with the apo structure, while the lower gate widens. **B**. Interactions among residues in the outer pore that stabilize the closed conformation of TRPV1. The hydrogen-bonds between E600 side chain with the main-chain nitrogen atoms of Y653 and D654 are broken in the structure with RTk/DkTx but maintained with capsaicin only.

capsaicin, and this could be explained because, in the absence of DkTx, the channel could be undergoing transitions to closed states. However, the distance between the I679 residues (lower gate) in the apo state is 5.3 Å (PDB 3J5P) and, when in complex with RTx/DkTx (PDB 3J5Q), it shifts to 9.3 Å, while it is at 7.6 Å with capsaicin only (PDB 3J5R). Therefore, the authors concluded that the structure obtained with capsaicin is likely only a partially activated state of TRPV1 [45].

When TRPV1 is in the presence of capsaicin only, the structure can be superimposed to that of the apo state in the outer pore region. Hydrogen bond interactions among side chains of the E600 residues and main-chain nitrogen atoms of the Y653 and D654 amino acids in the outer pore loops thought to stabilize the ion channel in the closed state, are broken when the distances among them are increased in response to the binding of DkTx and RTx. The distances between residues

that stabilize the closed state change when the channel is in the apo state or in the presence of RTx/DkTx: D654-E600 goes from 3.6 Å to 8.4 Å, while for Y653-E600 it goes from 4.4Å to 8.3Å, respectively [45] (Figure 2).

In summary, this ion channel displays extraordinary flexibility of movement in response to the presence of different agonists.

Another example of conformational changes that may allow for "superactivated" states is that of TRPV2. This channel is activated by temperatures near 52°C [46] and by membrane stretch [47]. Although structurally similar to TRPV1, TRPV2 is not activated by vanilloid compounds. However, the laboratory of Kenton Swartz produced a TRPV2 channel with four-point mutations to form a vanilloid-binding site located in the S4-S5 linker and the base of S5 [48], rendering this channel sensitive to RTx. These results were also confirmed by Yang et al., who used a TRPV2-Quad channel (with the same point mutations in mouse), where capsaicin competed for the same site as RTx [49]. This TRPV2_Quad channel was found to bind RTx, and that leads the channel to an unstable open state through a mechanism that bridges the S4-S5 linker to the S1-domain [49].

A couple of years later, Zubcevic and collaborators obtained the crystal structure of a minimal construct of the rabbit TRPV2 channel (miTRPV2) in the absence of agonist and compared it with that of the vanilloid-sensitive miTRPV2 (F470S, L505M, L508T, and Q528E, in the rabbit TRPV2) in complex with RTx [50].

Interestingly, in the structure in complex with RTx, they found that two subunits adopt distinct orientations between the S4-S5 linker and the S5, as compared to the other two subunits. In other words, while two subunits (A and C) are found to spread away from each other, the other two (B and D) get closer. This rearrangement results in an asymmetric pore that adopts a wider conformation at the selectivity filter when compared to the structure without RTx (Figure 3).

The authors determined that with RTx the distance between the G604 carbonyl oxygens in contracted subunits was ~7.1 Å, and in the widened subunits the distance between the I603 carbonyls was ~12.3 Å, while in the structure with only Ca^{2+} the distances between G604 carbonyl oxygens are 6.1–6.4 Å [50,51]. The conclusion was that, when RTx binds to the channel, it pushes the base of S5 downwards and produces a bend in the S4-S5 linker producing a different conformation that leads to rotation and widening of the entire involved subunit (Figure 3).

The authors also suggested that this wider conformation of the pore could allow for the permeation of larger cations since they performed experiments where it is observed that, upon activation of the vanilloid-sensitive TRPV2 with RTx (250 nM), uptake of the large fluorescent molecule YO-PRO-1 (376 Da) could be attained. With this experiment, they confirmed the functionality of this conformation, and suggested that it was either a fully open state or an intermediate state that occurred before a symmetric open state capable of permeating large organic cations [50].

Just as in TRPV2, a vanilloid-binding site can be introduced into the TRPV3 channel upon the insertion of six residues in the putative vanilloid-pocket: W521Y, H523E, F522S, L557M, A560T, and Q580E, as shown for the mouse TRPV3 channel by Zhang and collaborators [52]. Nonetheless, the insertion of this vanilloid-binding site is not enough to achieve activation of TRPV3 by RTx and the presence of other agonists, such as 2-APB (aminoethoxydiphenyl borate) or heat, is required [52]. These results demonstrate that gating pathways are conserved among the TRPV channels, but they also show that the energetics for activation can dictate their sensitivity to certain stimuli since adding a binding site for an agonist does not necessarily result in the activation of the ion channel [52].

Structurally, the sensitized state of the human TRPV3 undergoes an α-helix to π-helix transition in the S6 which, in turn, disrupts the S4-S5 linker and S6 and the latter bends ~9° away from the pore [53]. In a previous report, the open conformation of the mouse TRPV3 obtained with 2-APB only shows a π-helix in the S6 [54], leading the authors to suggest that the secondary structure transition could be a hallmark for a sensitized channel, in other words, a state that requires less energy to activate [53].

Additionally, Zubcevic and collaborators also observed that during the activation of TRPV3

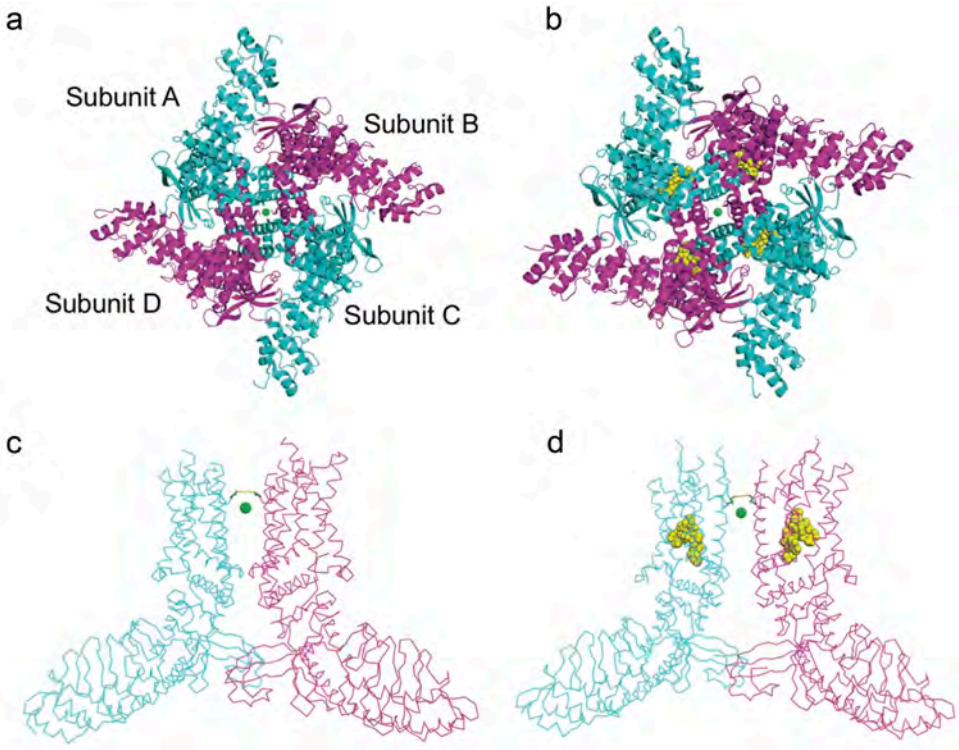

Figure 3. Comparison of open and closed states of TRPV2.
Extracellular views of A) a closed miTRPV2 channel (PDB 6BWM) and B) vanilloid-sensitive miTRPV2 (PDB 6BWJ) in complex with RTx shown as yellow spheres, representing the open state. On the lower panel are side views of the closed (C) and open (D) channel. Only two subunits are shown for simplicity. The green sphere is Ca^{2+} trapped in the pore which is notably wider in the open configuration, its also visible the rearrangement of the intracellular domain. The side chains of G604 are also depicted.

with 2-APB, the intermediate states display asymmetrical rearrangements that are not present in the apo or sensitized states. The differently observed deviations for the subunits are caused because theπ-helices in the S4-S5 linkers begin at different residues. This is interesting because it accounts for a similar phenomenon as the one described above for the activation of TRPV2 with RTx, which also originates at the S4-S5 linker [50]. Together, these results further support the hypothesis that the gating mechanisms of TRPV channels are conserved and a break in symmetry may be characteristic to these channel's gating.

The TRPV4 channel was first described as an osmosensor, capable of activating after exposure to extracellular hypotonic conditions [55,56]. Subsequent reports demonstrated that, like other members of the TRPV subfamily, TRPV4 is a heat-sensitive channel activated by temperatures above 27°C [57] and chemical agonists such as phorbol derivates [58] and 5,6-epoxyeicosatrienoic acid, a metabolite of arachidonic acid [59,60].

Deng and collaborators obtained the first high-resolution cryo-EM structure (3.8 Å) of the TRPV4 channel [61]. These authors determined that the channel was in a closed conformation, that the narrowest diameter in the pore (5.3 Å) was located at residue M714, which impeded the permeation of ions. Even in the closed state, TRPV4 displayed a particularly wide selectivity filter: the diameter at G675 in TRPV4 was 10.6 Å, while the diameter at G643 in TRPV1 in complex with RTx/DkTx was 7.6 Å[45]. This evidence suggested that unlike TRPV1, the TRPV4 channel lacks an upper gate [61].

The single-channel conductance of TRPV4, when stimulated with hypotonic solutions, has been reported to be around 310 pS, at positive voltages [55]. However, reports for its single-channel conductance during spontaneous activity is near 88 pS [56], which is near the value (around 98 pS) obtained with other agonists such as 4α-Phorbol 12,13-didecanoate (4αPDD) and with heat (around 105 pS) [58]. Altogether these results

suggest that the channel can adopt a different functional state when it is stimulated under hypotonic conditions vs. heat or phorbol, and that differences in the conductance of TRPV4 may be observed with other agonists, but further studies must be performed.

TRPA1 is a channel mainly expressed in nociceptive neurons which responds to multiple noxious stimuli, including pungent chemicals present in garlic, mustard oil, cinnamon or wasabi [62,63]. Moreover, TRPA1 was initially described as a channel activated by noxious cold temperatures [64,65], but there has been controversy around this topic since this channel functions as a temperature receptor in a species-specific fashion [66–68]. Chemical agonists of TRPA1 have been divided based on their mechanism of action into electrophilic and non-electrophilic agonists. Examples of the first are allyl isothiocyanate (AITC) [69] or allicin [62] that activate the channel through covalent modification of cysteines at the N-terminal domain. In fact, allicin can also activate TRPV1 through the same mechanism [70–72]. The non-electrophilic agonists include carvacrol, oleocanthal, Δ9-tetrahydrocannabinol (THC) and acidic pH, which activate TRPA1 by mechanisms not associated with cysteine modifications and which remain mostly unclarified [73–75].

Cavanaugh et al., determined, in excised TRPA1-expressing membrane patches, that the channel needs to be exposed to polyphosphates (PPPi) [76] in order to be activated by AITC, but in this AITC-insensitive conformation (in the absence of PPPi) it can be activated by THC [77]. This result indicates that the channel shifts to a different functional conformation unresponsive to cysteine modification but responsive to activation by a different mechanism [77], each with a distinguishable function and agonist dependence.

The different functional states described by Cavanaugh et al., have not been structurally compared. Unlike TRPV1, the cryo-EM structure for TRPA1 was not obtained in the presence of different agonists, but only with AITC (PDB 3J9P). Nonetheless, it was possible to determine that the pre-S1 helix, linker S4-S5, and TRP-like domain are bound by hydrophobic interactions and represent an important site for allosteric modulation, similar to what happens with TRPV1 [45,78].

Nevertheless, recent studies have compared the structural rearrangements of TRPA1 in the presence of different agonists using techniques such as limited proteolysis combined with mass spectrometry [75]or circular dichroism spectroscopy only for the N- and C- terminal domains [79]. These robust methodologies show important interactions between cytoplasmatic domains involved in the gating of the channel [79], as well as differences between the activation with electrophilic and non-electrophilic agonists [75].

TRPV5 and TRPV6 display limited structural rearrengements in their pores

Both TRPV5 and TRPV6 ion channels are expressed mainly in the epithelial tissue of the digestive tract and kidney, where they play roles in the reabsorption and transcellular transport of Ca^{2+} [80]. Unlike other members of the TRPV family, TRPV6 and TRPV5 show inward rectification and these highly Ca^{2+}-selective proteins are constitutively active under physiological conditions [81]. Despite the high ion selectivity, in the absence of extracellular divalent cations, they can permeate monovalent cations [80].

TRPV5 and TRPV6 channels share structural traits that differentiate them from the other known TRPV channels. Three phenylalanine residues in S6 give rigidity to the pore, and a ring of aspartates in the selectivity filter confers its high Ca^{2+} selectivity [82]. Neutralization mutation of the negative aspartate charge not only affects Ca^{2+} selectivity but reduces inward rectification [80].

Functionally, both channels can be inhibited by endogenous calmodulin (CaM) [83] or by econazole, an antifungal [84], while PIP_2 helps stabilize their open state [85]. The conformational changes between open and closed states of these channels have been explored by comparing the cryo-EM structures of econazole-bound TRPV5 and of both channels in the presence of either PIP_2 or CaM [86,87].

One of the main findings of this comparison is that the selectivity filter remains mostly the same regardless of the molecule that binds the channel. The lower gate identified in TRPV5 is formed by F574, M578, and H582 that constrict the pore to a diameter between 4.5 and 5.9 Å in the same bundle crossing configuration observed in other TRP channels. The closing seems to involve a change in the position of the S4-S5 linker and the loop connecting S6 with the TRP domain [86,87].

The binding of PIP_2, induce a change in the orientation of the lateral chain of the aspartate in the selectivity filter. This change may be explained by an interaction of the head group of PIP_2 with R584 in the S6 helix, analogous to what has been observed in TRPV1, which rotates and pulls away from the center of the pore accompanied by movement of the S4-S5 linker [87]. The main difference in the response of TRPV5 and TRPV6 was observed in the CaM-bound structures. Both channels bind to a single CaM-molecule which is capable of physically blocking the pore from the intracellular side, but while TRPV5 shows no conformational changes, TRPV6 shows an α- to a π-helical transition of S6 which tilts the helix toward the center, so I575 becomes an inactivation gate [87], which has also been observed in TRPV3 [53].

Analysis of the pores of TRPV5 and TRPV6 points to rigid structures that contrast with the more flexible pores of TRPV1-4. To date, there is no physiological evidence of changes in their single-channel conductances in response to different stimuli, but it has been suggested that their activity might be regulated by the formation of TRPV5/V6 heterotetramers, as they are co-expressed in several tissues. Hoenderop et al. used *Xenopus laevis* oocytes to express such heterotetramers and found that they have Ca [2]+ -dependent inactivation and block by ruthenium red with features intermediate to those of TRPV5 and TRPV6 [88]. Although this is an interesting possibility, they have not been identified *in vivo*, and their biophysical properties at the level of single-channels have not been investigated.

Lysophosphatidic acid: A pain-producing phospholipid

Another activator of TRPV1 shown by our group to directly interact with this ion channel is lysophosphatidic acid (LPA) [41]. This is the only example for which a change in single channel conductance in a TRP channel has been shown to depend upon the presence of different agonists; thus, we will discuss this phenomenon in detail.

LPA has been extensively linked to the generation of chronic neuropathic pain through its interactions with G protein-coupled receptors (GPCRs) [89–92] and to modulate the activity of several ion channels [93–97]. Regulation of the activity of TRPV1 by molecules of a lipidic nature has been explored, and it has been described that PIP_2 [98–106], polyunsaturated fatty acids (PUFAs) [107], monounsaturated fatty acids [108] and cholesterol [109–111] can modulate the activity of TRPV1, either directly or indirectly. However, reports of direct interactions of LPA with ion channels, in general, are scarce [95,112,113].

LPA is a phospholipid constituted by an acyl chain of saturated or unsaturated fatty acids associated with a glycerol backbone by ester links, and that contains a phosphate head group [114]. LPA can be naturally found as different species that vary in their acyl-chain length as well as in their saturation (16:0; 18:0; 16:1, 18:1; 18:2 and 20:4).

Our group studied whether LPA could produce acute pain in mice and showed that it is considerably dependent upon TRPV1. These results led us to determine that LPA could, in fact, produce currents and action potentials in DRG neurons from wild-type mice but not in DRG neurons from $Trpv1^{-/-}$animals. Using a heterologous expression system of HEK293 cells transfected with TRPV1, we found that currents could be induced when LPA was applied to the intracellular or extracellular faces of the ion channels and that the responses were dose-dependent [41].

In our studies, we ruled out the participation of GPCR-related signaling pathways on TRPV1 activation by LPA and identified a site of interaction for this phospholipid, residue K710 in the C-terminus of TRPV1 [41]. Confirmation of these results was obtained later by another group in a study where TRPV1 was expressed in lipid bilayers and activated by LPA [115].

Hence, we extended the aforementioned study and determined that, for fatty acids to activate TRPV1, the following features had to be met by these molecules: the presence of a charged phosphate group, a length of, at least 18 carbons of the acyl chain and a mono unsaturation [116].

LPA produces a different open conformational state to that of capsaicin

Our first study on the effects of LPA on TRPV1 was published in 2011 [41], and since then, we have been studying the specifics of how this molecule regulates the activity of TRPV1. Our most recent study on this subject provides functional

evidence that LPA produces a different open conformational state of TRPV1 that has a larger conductance.

In preliminary experiments, we had found that addition of LPA (5 μM) to excised membrane patches of TRPV1-expressing HEK293 cells resulted in larger magnitude macroscopic currents, as compared to those obtained in the presence of saturating capsaicin concentrations (4 μM). We had also observed that LPA (5 μM) produced activation of TRPV1 single-channel currents with an open probability (Po is 0.8) similar to that of capsaicin (4 μM).

These data could be explained as 1) LPA either producing an increase in the number of ion channels in the excised membrane patches (which was highly improbable); 2) An increase in the membrane negative surface charge near the channel leading to an accumulation of positively-charged ions near the pore mouth of TRPV1, 3) Producing a phenomenon termed "pore-dilation" in which the permeability to large ions occurs in the presence of prolonged exposures to agonists and that had only been described for activation with capsaicin [26] and/or 4) a change in the single-channel conductance.

In this last study, we performed a set of experiments in order to discern among all of these possibilities. We started by studying how LPA affected the unitary TRPV1 currents by first applying capsaicin (4 μM), washing off the agonist and then applying LPA (5 μM) to the same membrane patch. The results showed that LPA produced a 41% increase in the magnitude of single-channel currents at a single voltage (60 mV), which was also observed at other voltages (Figure 4).

Furthermore, our experiments ruled out all of the other possibilities enlisted above and showed that coapplication of subsaturating concentrations of both agonists together resulted in two different types of openings in a single channel, with conductances corresponding to those achieved either by adding capsaicin or LPA alone [117]. This was the strongest indication of these two agonists producing distinct open conformations that varied in their conductance. Finally, we defined that the presence of K710, the residue that is pivotal for the activation of TRPV1 by LPA, was also necessary for the generation of the higher-conductance open state [117].

TRPC and TRPM channels

Until just recently, finely defined structural characteristics of TRPC channels have remained elusive, mainly because of the lack of high-resolution structures. The cryo-EM structures obtained to date are those for the TRPC3, TRPC4, TRPC5 and TRPC6 channels [118–123]. However, no functional studies reporting changes in the conductance of these channels in response to different agonists are available.

These channels exhibit four ankyrin repeats and linker helices at their N-terminal domains and at the C-terminal domains they possess a TRP domain that connects a helix and a coiled-coil domain. Inside the pore, all TRPC members have a conserved "LFW" motif that maintains the structure of the pore [124].

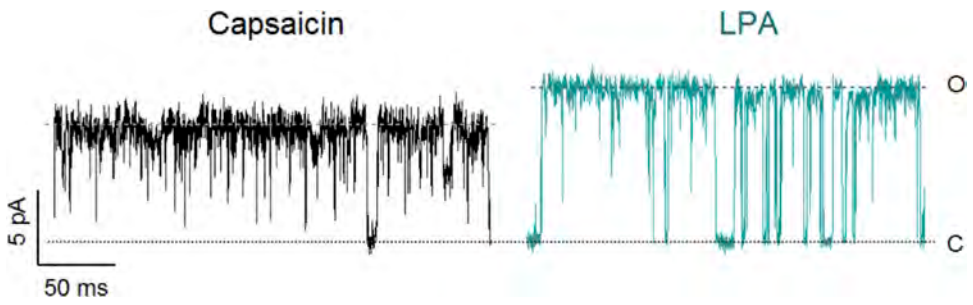

Figure 4. LPA increases single channel currents.
Current amplitude for a TRPV1-expressing membrane patch in the presence of capsaicin (4 μM; left) and in the presence of LPA (5 μM; right). Traces were obtained at +60 mV.

The TRPC subfamily can be divided into two groups that share some distinctive characteristics. The first group is constituted by the TRPC3/C6/C7 channels are activated by DAG. Structurally, both TRPC3 and TRPC6 display a pre-S1 elbow, a TRP re-entrant helix embedded in the membrane bilayer after the TRP domain, and an unusually long S3 that forms a "pseudo" extra cellular domain (ECD) [121,122,124]. Furthermore, unlike most TRP channels, TRPC3 channels possess a linker that connects the TRP domain to the S6. This results in a more flexible TRP domain that exhibits a higher coupling with the S4-S5 linker and a lipid binding site near the pre-S1. All of these peculiar interplays of domains may provide a molecular basis for TRPC3 lipid gating [121].

The second group includes the TRPC4/C5 channels that are modulated by G_q, $G_{i/o}$ GPCRs, membrane lipids, and intracellular Ca^{2+} [119,125]. These channels share the common feature of a disulfide bond between two cysteines at the loop linking S5 and the pore domain that maintains the residue E555 in proper position and thus stabilize the upper region of their selectivity filters [119,120,123,124]. As in other TRP channels, the TRP domain of TRPC4 is an important molecular effector for gating in this protein since it interacts with the S4-S5 linker and other proteins [123].

The structures of TRPC3/C6 and TRPC4 (both human and mouse) show a closed pore conformation. For TRPC3 the lower gate is located at residues I658 and L654 where they present a radius of less than 1 Å [121]. As for the human TRPC4, the residues I617 and N621 were identified as the lower gate where the constriction of the diameter was around 1.6 and 0.7 Å (defined by opposing van der Waals surfaces) [123], and for the mouse TRPC4 the narrowest point is located at N621 (3.6 Å) and constitutes the lower gate along with I617 and Q625 [119].

However, the TRPC5 is considered at least partially open since the constriction at the lower gate formed by the residues I621, N625 and Q629 was around 4.9 Å [120]. Comparing this structure with the closed TRPC4, Duan and collaborators suggest that the extracellular disulfide bond is a transducer of conformational changes. Nonetheless, more structures of TRPC channels at their open conformation will help to elucidate if there are differences in the pore during their gating [120].

The TRPM subfamily is composed of eight members with diverse features and functions [126]. The TRPM members for which cryo-EM structures have been solved in the closed or partially open conformations are TRPM2, TRPM4, TRPM7 and TRPM8 [127–135]. Their subunits are composed of six transmembranal segments, but at their N-terminal domains, they present four TRPM homology regions (MHR) and a C-terminal coiled-coil domain [127–135].

The C-termini of TRPM2, TRPM6, and TRPM7 channels possess enzymatic domains and have been named "chanzymes" [136–139]. Similar to TRPC4/C5 channels, TRPM channels possess disulfide bonds at their extracellular pore that stabilize the pore domain, but these disulfide-bonds form between cysteines at the pore loop and the pore helix S6 [119].

TRPM2 is a non-selective cation channel sensitive to temperature [140] that is activated when ADP-Ribose (ADPR) and Ca^{2+} are co-applied [141]. Wang and collaborators obtained the structures of human apo-, ADPR-bound, and ADPR-Ca^{2+}-bound TRPM2 channels. They observed that the binding of ADPR alone produced a closed conformation, considering it a "primed state" [128].

The lower gate was identified at residues I1045 and Q1053 in the pore and shown to be enlarged in the ADPR/Ca^{2+} structure. Although a change distance of the residues that form the gate was observed, it was not considered large enough to allow passage of Ca^{2+} (~4 Å radius) [128].

For zebrafish TRPM2 channels it was shown that, once ADPR binds to the MHR1/2 domain, a displacement of MHR4 is transmitted to the TRP helix, pushing it towards the S4-S5 linker. Consequently, the S4-S5 relocates the S5 and S6 and finally produces the opening of the channel. Again, as for other TRP channels, the TRP helix is shown to act as a transducer between the intracellular and transmembranal domains during gating [129]. Moreover, the authors propose putative binding sites for Ca^{2+} in the S3, leading them to speculate that Ca^{2+} facilitates the opening due to the movement of the S3 upon the binding of this ion which allows for the relocation of the S4-S5 linker [129].

TRPM4 and TRPM5 channels are among the only TRP members that are not permeable to

divalent cations [132,142,143]. Despite their ion selectivity, TRPM4/5 channels are activated upon intracellular Ca^{2+} increases [144] and can be modulated by $PI(4,5)P_2$ [145,146]. However, TRPM4 is inhibited by intracellular ATP and nucleotides, while TRPM5 is insensitive to these molecules [147,148].

The pore of TRPM4 has two gates: one located at the selectivity filter and another formed by the intracellular portion of the S6. In the human channel, the selectivity filter gate is formed by residues 975-FGQ-977 [130–132]. Likewise, the intracellular gate is formed by the I1040 residue [131,132].

Strikingly, both gates remain unchanged in all reported Ca^{2+}-bound structures, and it has been suggested that Ca^{2+}- binding is required for the opening of the channel in response to voltage [131].

In the structure obtained in complex with ATP, Guo and collaborators located a nucleotide binding domain along with twelve helices and two ankyrin repeats in the N-terminal [149]. The ATP-bound structure is an inhibited state of TRPM4, and there were no overall changes in the pore compared to the apo structure. The TRP domain forms hydrophobic interactions with the S4-S5 linker and forms a cavity between the S1-S4 domain, which harbors a potential Ca^{2+} -binding site [149].

The protein kinase domain in TRPM7 induces phosphorylation of receptor tyrosine kinase (RTK)-signaling intermediates and chromatin modifications [150,151]. TRPM7 is permeable to Mg^{2+}, Zn^{2+} and Ca^{2+} [152], and the cryo-EM structure of TRPM7 was obtained in the presence and absence of Mg^{2+} [133].

There were no notable changes on the pore domain of TRPM7 under different ionic conditions. Interestingly, the selectivity filter identified in TRPM7 (1045-FGE-1047), varies only on one residue to the selectivity filter described in TRPM4 (971-FGQ-973 in mouse TRPM4 channel), which is crucial to confer the monovalent selectivity of the latter. The lower gate was determined to be formed by I1093 and N1097 residues [133].

The TRP domain of TRPM7 interacts with different regions of the channel, highlighting the importance of this region for gating in this protein. For example, the TRP domain interacts with the N-terminal residues S744 and Q740, with the S4-S5 linker by forming hydrogen bonds between W1111 and R1115 (both located to the TRP domain) and with A981 and V982 (in the S4-S5 linker) [133]. Additionally, it establishes π-π stacking (Phe1118/Tyr1122) and cation- π interactions (Arg1115/Trp1111) among its α-helical structure [133]. However, unlike what has been observed in other TRP structures, the TRP domain of TRPM7 does not contact the pre-S1 helix [133].

Another region that may produce important conformational rearrangements in TRPM7 is the pore helix. It has been shown that a disulfide-bond established between residues C1056 and C1066, is only formed in the presence of Mg^{2+}. Thus, it has been proposed that this cation could stabilize the bond and impact directly on the structure of the pore [133].

Finally, the TRPM8 is a non-selective cationic channel permeable to Ca^{2+} and activated by cold temperatures (below 25°C) and menthol [153]. The channel is modulated by $PI(4,5)P_2$ [153,154].

In the same report, the cryo-EM structures for TRPM8 have been obtained in complex with PIP_2, $Ca^{2+,}$ and icilin, and with WS-12 (a menthol analog) together with PIP_2 [134]. These structures demonstrate that both, icilin and WS-12, bind to a cavity formed between S1-S4 and the TRP domain [134].

The structures reveal a different binding site of PIP_2, as compared to other TRP channels. This site is formed by the pre-S1 domain, the S4-S5 junction, the TRP domain and the MHR4 of an adjacent subunit. Interestingly, upon the binding of PIP_2, the S4 undergoes a change from a complete α-helical to a 3_{10} helical conformation [134]. This produces the movement of the TRP domain and the S5 toward the cavity. At the same time, it disrupts the interaction among the S1-S4 domain and the S6-pore domain, enabling gating [134]. Additionally, during gating, the S1-S4 domain of TRPM8 suffers a rigid rotation away from the pore [134], unlike what happens to the S1-S4 domain in TRPV1 which remains static [45].

The lower gate of TRPM8 is formed by L973 where the tightest constriction along the pore was found in a previous structure[134135], Yin and collaborators determined that both structures (PIP_2-Ca^{2+}-icilin and WS-12-PIP_2) were non-conducting states. Although, in the icilin-PIP_2-Ca^{2+} structure the S6 is curved, which

suggested that there may be a π helical turn along the S6 as previously described for the sensitized state of TRPV3[53]. Therefore, the structures may represent sensitized or presensitized states of TRPM8 [134].

Although conformational changes in TRPM channels in response to agonists or modulators of their activities have been clarified, changes in their conductance levels in response to these molecules have not been reported.

Discussion

Here we have summarized some phenomena that could potentially lead to changes in the conductance of single ion channels. For example, pore dilation is a phenomenon suggested to occur in TRPV1 [26,155] and other channels such as the P2X receptors, and it is characterized by a change in the permeability of the ion channel to larger ions, induced by long times in the presence of the agonist. However, the results that we have obtained, as well as those of other groups, suggest that permeability changes may result from changes in the cytoskeleton organization or from time-dependent local changes in the concentrations of ions in the vicinity of the channel, a phenomenon known as ion accumulation, that is at play in whole-cell experiments [156] and is further discussed below.

Li and collaborators have examined this carefully and have shown that P2X receptors readily activate and do not display a slow phase of activation under symmetrical ionic conditions [156]. These authors also show that changes in the equilibrium potential are observed with $NMDG^+$ in the external solution during sustained activation and that this prolonged activation in bi-ionic solutions primes the depletion of internal Na^+ and accumulation of $NMDG^+$ in the cell. Li et al., also discuss that P2X receptors are exceptional in that they demonstrate significant permeability to large cations such as $NMDG^+$ and that, even in the absence of pore dilation, would allow the conduction of relatively large molecules to enter or exit cells [156]. Finally, and most importantly, these authors point out that changes in ion concentration, produced by ion accumulation and revealed during experiments with P2X receptors, are an inherent problem in voltage-clamp recordings, where the flow of ionic currents across the membrane may alter the concentrations of intracellular ions [157,158]. In other words, when symmetrical ionic conditions are used, ion concentrations can be maintained by working under conditions in which current amplitudes are moderate and current measurements will always be equal to or greater than the flux of any individual ionic species. This is in contrast to experiments performed with asymmetric ionic conditions, which require a membrane conductance of an order of magnitude smaller than the access conductance to adequately control ion concentrations.

These results are prompting a reexamination of the concepts of pore dilation and dynamic ion selectivity for all ion channels [156], and highlight the importance of further studying the molecular mechanisms underlying different conformational changes induced by ligands in these proteins.

TRPV1 has been shown to contribute to several physiological and pathophysiological processes, importantly. Among these, the participation of TRPV1 in pain-related processes is an aspect that has attracted the attention of several research groups. Understanding cellular mechanisms leading to the generation of pain constitutes the basis for designing tools in order to attack them. Hence, research directedtoward defining the molecular mechanisms that underlie the production of pain is of invaluable importance. This requires a great effort from many researchers and from several points of view, including that of understanding various particularities of the modulation of the effectors involved in pain processes.

As for changes in the conductance of TRPV1 due to the actions of agonists, it is interesting to note that, it has been recently reported that DkTx diminishes the unitary conductance by 32% of TRPV1, as compared to that observed with capsaicin [159]. DkTx is a molecule composed of two moieties joined by a short linker, which bind in the outer pore region of the channel so that each motif sits at a subunit interface [45]. Moreover, the effect was eliminated when the linker of DkTx was either absent or elongated and also when the pore turret of TRPV1 was removed. The lack of pore turret in the construct used for the cryo-EM of TRPV1 explains why the structure with DkTx/RTx is observed to be fully open. In fact, the unitary

conductance of the construct used to obtain the TRPV1 structure with bound DkTx was similar to that obtained with capsaicin [159].

With this, Geron et al. confirmed that DkTx and capsaicin elicit distinct gating mechanisms that are dependent upon the pore turret of TRPV1. They argued that the binding of DkTx directly restricts the movement of the pore helix and consequently the conductance.

In terms of the physiological relevance of LPA's actions on the conductance of the TRPV1 channel, one can only hypothesize that in the presence of this agonist, as compared to capsaicin, depolarization of the neuron where it is expressed will occur more efficiently. Since the change in the conductance of the channel also occurs at subsaturating concentrations of LPA (i.e., 1 μM), this would mean that such an efficient depolarization could also occur even when lower levels of the phospholipid are present.

TRP channels share conserved sequences of amino acids in some regions of their structures. One such region is the TRP box (Figure 5), the region where the K710 residue that interacts with LPA lies. We have tested the effects of LPA on some TRP ion channels and have found that TRPV2, TRPV3, or TRPA1 channels are not activated by this phospholipid [41]. Although TRPV3 and TRPA1 have a lysine in this position, just as TRPV1, LPA is not capable of activating these channels. Thus, this phospholipid seems incapable of providing the energy necessary to drive the transition from the closed to the open state in this particular ion channels and the question of why this occurs remains open. Moreover, since other members of the TRPV subfamily of ion channels exhibit a lysine in the corresponding position to that of K710, it will be interesting to test whether their activities can be modulated by LPA. If so, this would constitute the identification of an agonist for these other ion channels for which there are few endogenous activators known (i.e., TRPV4, TRPV5, and TRPV6).

Since achieving different conductance states can modulate the response of the cell where ion channels are expressed, not only will it be interesting to determine if LPA activates these other TRP channels, but also whether it can produce different conformational changes as what happens with TRPV1.

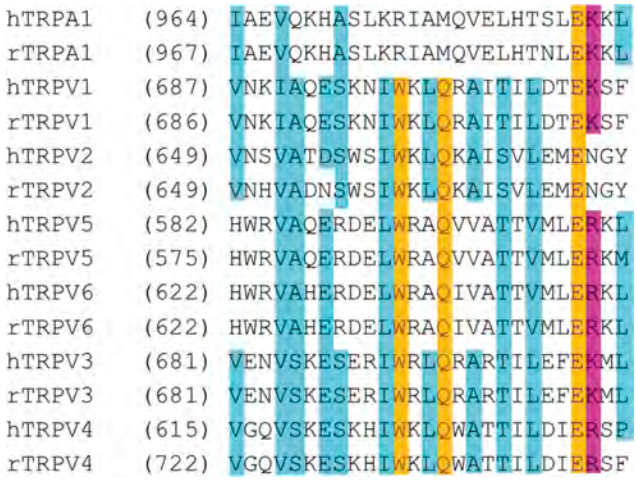

Figure 5. Sequence alignment corresponding to the trp box in rat and human TRPV and TRPA1 channels.

Identical residues are highlighted in yellow and similar residues in blue. Tryptophan and glutamine residues in the middle of the trp box are only present in TRPV channels. The residue K710 in hTRPV1 and the corresponding residue in other TRP channels is highlighted in pink, notice that most channels, including TRPA1 have a positively charged residue in that position.

This would further demonstrate the conformational versatility of this family of ion channels.

Several ion channels have been studied at great detail with respect to their responses to different agonists. In particular, the idea that LPA produces a conformational change that results in a different conductance of TRPV1 at the single-channel level compared to capsaicin challenges the notion in the field of study of ion channels in general.

Here we have discussed that LPA leads the TRPV1 ion channel to open with a single-channel conductance level that is higher than that attained with capsaicin. Both ligands promote nearly maximal open probabilities [117]; hence, this is most probably not a mechanism in which different subconductance levels can be attained in the presence of partial and full agonists.

Thus, it will be interesting to reflect upon and determine what mechanisms or structural rearrangements allow TRPV1, and maybe other TRP channels, to exhibit a higher conductance level in the presence of one agonist or another.

Acknowledgments

This work was supported by grants from Dirección General de Asuntos del Personal Académico (DGAPA)-Programa de Apoyo a Proyectos de Investigación e Innovación

Tecnológica (PAPIIT) IN200717 and Consejo Nacional de Ciencia y Tecnología (CONACyT) A1-S-8760 to T.R.

Disclosure statement

No potential conflict of interest was reported by the authors.

Funding

This work was supported by the Consejo Nacional de Ciencia y Tecnología [A1-S-8760];Dirección General de Asuntos del Personal Académico, Universidad Nacional Autónoma de México [IN200717];

ORCID

Ileana Hernández-Araiza http://orcid.org/0000-0003-4102-5282
Francisco Torres-Quiroz http://orcid.org/0000-0002-3073-8546
Luis B. Tovar-Y-Romo http://orcid.org/0000-0003-2605-1378
León D. Islas http://orcid.org/0000-0002-7461-5214
Tamara Rosenbaum http://orcid.org/0000-0002-4791-3195

References

[1] Hamill OP, Marty A, Neher E, et al. Improved patch-clamp techniques for high-resolution current recording from cells and cell-free membrane patches. Pflugers Arch. 1981;391(2):85–100.
[2] MacKinnon R. New insights into the structure and function of potassium channels. Curr Opin Neurobiol. 1991;1(1):14–19.
[3] Pore Loops: MR. An emerging theme in ion channel structure. Neuron. 1995;14(5):889–892.
[4] Potassium MR. Channels and the atomic basis of selective ion conduction (nobel Lecture). Angew Chem Int Ed Engl. 2004;43(33):4265–4277.
[5] Doyle DA, Morais Cabral J, Pfuetzner RA, et al. The structure of the potassium channel: molecular basis of K+ conduction and selectivity. Science. 1998;280(5360):69–77.
[6] Agre P. Aquaporin water channels (nobel lecture). Angew Chem Int Ed Engl. 2004;43(33):4278–4290.
[7] Yasui M, Kwon TH, Knepper MA, et al. Aquaporin-6: an intracellular vesicle water channel protein in renal epithelia. Proc Natl Acad Sci U S A. 1999;96(10):5808–5813.
[8] Cosens DJ, Manning A. Abnormal electroretinogram from a drosophila mutant. Nature. 1969;224(5216):285–287.
[9] Montell C, Rubin GM. Molecular characterization of the drosophila trp locus: A putative integral membrane protein required for phototransduction. Neuron. 1989;2(4):1313–1323.
[10] Hardie RC, Minke B. The Trp gene is essential for a light-activated Ca2+ channel in drosophila photoreceptors. Neuron. 1992;8(4):643–651.
[11] Caterina MJ, Schumacher MA, Tominaga M, et al. The capsaicin receptor: A heat-activated ion channel in the pain pathway. Nature. 1997;389(6653):816–824.
[12] Tominaga M, Caterina MJ, Malmberg AB, et al. The cloned capsaicin receptor integrates multiple pain-producing stimuli. Neuron. 1998;21(3):531–543.
[13] Perozo E, Cortes DM, Cuello LG. Structural rearrangements underlying K+-channel activation gating. Science. 1999;285(5424):73–78.
[14] VanDongen AMJ. K channel gating by an affinity-switching selectivity filter. Proc Natl Acad Sci U S A. 2004;101(9):3248–3252.
[15] Schoppa NE, Sigworth FJ. Activation of shaker potassium channels iii. An activation gating model for wild-type and V2 mutant channels. J Gen Physiol. 1998;111(2):313–342.
[16] Zheng J, Sigworth FJ. Intermediate conductances during deactivation of heteromultimeric shaker potassium channels. J Gen Physiol. 1998;112(4):457–474.
[17] Bao H, Hakeem A, Henteleff M, et al. Voltage-insensitive gating after charge-neutralizing mutations in the S4 segment of shaker channels. J Gen Physiol. 1999;113(1):139–151.
[18] Yifrach O, MacKinnon R. Energetics of pore opening in a voltage-gated K(+) channel. Cell. 2002;111(2):231–239.
[19] Trapani JG, Andalib P, Consiglio JF, et al. Control of single channel conductance in the outer vestibule of the Kv2.1 potassium channel. J Gen Physiol. 2006;128(2):231–246.
[20] Immke D, Korn SJ. Ion-ion interactions at the selectivity filter evidence from K(+)-dependent modulation of tetraethylammonium efficacy in Kv2.1 potassium channels. J Gen Physiol. 2000;115(4):509–518.
[21] Tang L, Gamal El-Din TM, Payandeh J, et al. Structural basis for Ca2+ Selectivity of a voltage-gated calcium channel. Nature. 2014;505(7481):56–61.
[22] Virginio C, MacKenzie A, Rassendren FA, et al. Pore dilation of neuronal P2X receptor channels. Nat Neurosci. 1999;2(4):315–321.
[23] Khakh BS, Lester HA. Dynamic selectivity filters in ion channels. Neuron. 1999;23(4):653–658.
[24] Lingueglia E, de Weille JR, Bassilana F, et al. A modulatory subunit of acid sensing ion channels in brain and dorsal root ganglion cells. J Biol Chem. 1997;272(47):29778–29783.
[25] de Weille JR, Bassilana F, Lazdunski M, et al. Identification, functional expression and chromosomal localisation of a sustained human proton-gated cation channel. FEBS Lett. 1998;433(3):257–260.
[26] Chung M-K, Güler AD, Caterina MJ. TRPV1 shows dynamic ionic selectivity during agonist stimulation. Nat Neurosci. 2008;11(5):555–564.

[27] Munns CH, Chung M-K, Sanchez YE, et al. Role of the outer pore domain in transient receptor potential vanilloid 1 dynamic permeability to large cations. J Biol Chem. 2015;290(9):5707–5724.
[28] Brake AJ, Wagenbach MJ, Julius D. New structural motif for ligand-gated ion channels defined by an ionotropic ATP receptor. Nature. 1994;371(6497):519–523.
[29] Khakh BS, Egan TM. Contribution of transmembrane regions to ATP-gated P2X2 channel permeability dynamics. J Biol Chem. 2005;280(7):6118–6129.
[30] Di Virgilio F, Schmalzing G, Markwardt F. The elusive P2X7 macropore. Trends Cell Biol. 2018;28(5):392–404.
[31] Woo DH, Jung SJ, Zhu MH, et al. Direct activation of transient receptor potential vanilloid 1(TRPV1) by diacylglycerol (DAG). Mol Pain. 2008;4:42.
[32] Wen H, Östman J, Bubb KJ, et al. 20-hydroxyeicosatetraenoic acid (20-HETE) is a novel activator of transient receptor potential vanilloid 1 (TRPV1) channel. J Biol Chem. 2012;287(17):13868–13876.
[33] Smart D, Gunthorpe MJ, Jerman JC, et al. The endogenous lipid anandamide is a full agonist at the human vanilloid receptor (HVR1). Br J Pharmacol. 2000;129 (2):227–230.
[34] Movahed P, Jönsson BAG, Birnir B, et al. Endogenous unsaturated C18 N-acylethanolamines are vanilloid receptor (TRPV1) agonists. J Biol Chem. 2005;280 (46):38496–38504.
[35] Chu CJ, Huang SM, De Petrocellis L, et al. N-oleoyldopamine, a novel endogenous capsaicin-like lipid that produces hyperalgesia. J Biol Chem. 2003;278 (16):13633–13639.
[36] Yoshida T, Inoue R, Morii T, et al. Nitric oxide activates TRP channels by cysteine s-nitrosylation. Nat Chem Biol. 2006;2(11):596–607.
[37] Yang F, Ma L, Cao X, et al. Divalent cations activate TRPV1 through promoting conformational change of the extracellular region. J Gen Physiol. 2014;143(1):91–103.
[38] Jara-Oseguera A, Bae C, Swartz KJ. An external sodium ion binding site controls allosteric gating in TRPV1 channels. eLife. 2016;5. DOI:10.7554/eLife.13356.
[39] Patacchini R, Santicioli P, Giuliani S, et al. Pharmacological investigation of hydrogen sulfide (H2S) contractile activity in rat detrusor muscle. Eur J Pharmacol. 2005;509(2–3):171–177.
[40] Bohlen CJ, Priel A, Zhou S, et al. A bivalent tarantula toxin activates the capsaicin receptor, TRPV1, by targeting the outer pore domain. Cell. 2010;141(5):834–845.
[41] Nieto-Posadas A, Picazo-Juárez G, Llorente I, et al. Lysophosphatidic acid directly activates TRPV1 through a C-terminal binding site. Nat Chem Biol. 2011;8(1):78–85.
[42] Moiseenkova-Bell VY, Stanciu LA, Serysheva II, et al. Structure of TRPV1 channel revealed by electron cryo-microscopy. Proc Natl Acad Sci U S A. 2008;105 (21):7451–7455.
[43] Liao M, Cao E, Julius D, et al. Structure of the TRPV1 ion channel determined by electron cryo-microscopy. Nature. 2013;504(7478):107–112.
[44] Lishko PV, Procko E, Jin X, et al. The ankyrin repeats of TRPV1 bind multiple ligands and modulate channel sensitivity. Neuron. 2007;54(6):905–918.
[45] Cao E, Liao M, Cheng Y, et al. TRPV1 structures in distinct conformations reveal activation mechanisms. Nature. 2013;504(7478):113–118.
[46] Caterina MJ, Rosen TA, Tominaga M, et al. A capsaicin-receptor homologue with a high threshold for noxious heat. Nature. 1999;398(6726):436–441.
[47] Shibasaki K. Physiological Significance of TRPV2 as a mechanosensor, thermosensor and lipid sensor. J Physiol Sci JPS. 2016;66(5):359–365.
[48] Zhang F, Hanson SM, Jara-Oseguera A, et al. Engineering vanilloid-sensitivity into the rat TRPV2 channel. eLife. 2016;5. DOI:10.7554/eLife.16409.
[49] Yang F, Vu S, Yarov-Yarovoy V, et al. Rational design and validation of a vanilloid-sensitive TRPV2 ion channel. Proc Natl Acad Sci U S A. 2016;113(26): E3657–3666.
[50] Zubcevic L, Le S, Yang H, et al. Conformational Plasticity in the Selectivity Filter of the TRPV2 Ion Channel. Nat Struct Mol Biol. 2018;25(5):405–415.
[51] Zubcevic L, Herzik MA, Chung BC, et al. Cryo-Electron Microscopy Structure of the TRPV2 Ion Channel. Nat Struct Mol Biol. 2016;23(2):180–186.
[52] Zhang F, Swartz KJ, Jara-Oseguera A. Conserved allosteric pathways for activation of TRPV3 revealed through engineering vanilloid-sensitivity. eLife. 2019;8. DOI:10.7554/eLife.42756.
[53] Zubcevic L, Herzik MA, Wu M, et al. Conformational ensemble of the human TRPV3 ion channel. Nat Commun. 2018;9(1):4773.
[54] Singh AK, McGoldrick LL, Sobolevsky AI. Structure and gating mechanism of the transient receptor potential channel TRPV3. Nat Struct Mol Biol. 2018;25 (9):805–813.
[55] Liedtke W, Choe Y, Martí-Renom MA, et al. Vanilloid receptor-related osmotically activated channel (VR-OAC), a candidate vertebrate osmoreceptor. Cell. 2000;103(3):525–535.
[56] Strotmann R, Harteneck C, Nunnenmacher K, et al. OTRPC4, a nonselective cation channel that confers sensitivity to extracellular osmolarity. Nat Cell Bio. 2000;2(10):695–702.
[57] Güler AD, Lee H, Iida T, et al. Heat-evoked activation of the ion channel, TRPV4. J Neurosci Off J Soc Neurosci. 2002;22(15): 6408–6414. 20026679.

[58] Watanabe H, Davis JB, Smart D, et al. Activation of TRPV4 Channels (HVRL-2/MTRP12) by Phorbol Derivatives. J Biol Chem. 2002;277(16):13569–13577.
[59] Watanabe H, Vriens J, Prenen J, et al. Anandamide and arachidonic acid use epoxyeicosatrienoic acids to activate TRPV4 channels. Nature. 2003;424 (6947):434–438.
[60] Vriens J, Watanabe H, Janssens A, et al. Cell swelling, heat, and chemical agonists use distinct pathways for the activation of the cation channel TRPV4. Proc Natl Acad Sci U S A. 2004;101(1):396–401.
[61] Deng Z, Paknejad N, Maksaev G, et al. Cryo-EM and X-ray structures of TRPV4 Reveal Insight into Ion Permeation and Gating Mechanisms. Nat Struct Mol Biol. 2018;25(3):252–260.
[62] Macpherson LJ, Geierstanger BH, Viswanath V, et al. The pungency of garlic: activation of TRPA1 and TRPV1 in response to allicin. Curr Biol CB. 2005;15(10):929–934.
[63] Bautista DM, Movahed P, Hinman A, et al. Pungent products from garlic activate the sensory ion channel TRPA1. Proc Natl Acad Sci U S A. 2005;102 (34):12248–12252.
[64] Story GM, Peier AM, Reeve AJ, et al. ANKTM1, a TRP-like channel expressed in nociceptive neurons, is activated by cold temperatures. Cell. 2003;112(6):819–829.
[65] Viswanath V, Story GM, Peier AM, et al. Opposite thermosensor in fruitfly and mouse. Nature. 2003;423 (6942):822–823.
[66] Caspani O, Heppenstall PA. TRPA1 and cold transduction: an unresolved issue?. J Gen Physiol. 2009;133(3):245–249.
[67] Karashima Y, Talavera K, Everaerts W, et al. TRPA1 acts as a cold sensor in vitro and in vivo. Proc Natl Acad Sci U S A. 2009;106(4):1273–1278.
[68] Vandewauw I, De Clercq K, Mulier M, et al. A TRP channel trio mediates acute noxious heat sensing. Nature. 2018;555(7698):662–666.
[69] Bandell M, Story GM, Hwang SW, et al. Noxious cold ion channel TRPA1 is activated by pungent compounds and bradykinin. Neuron. 2004;41(6):849–857.
[70] Hinman A, Chuang -H-H, Bautista DM, et al. TRP channel activation by reversible covalent modification. Proc Natl Acad Sci U S A. 2006;103(51):19564–19568.
[71] Salazar H, Llorente I, Jara-Oseguera A, et al. A single n-terminal cysteine in trpv1 determines activation by pungent compounds from onion and garlic. Nat Neurosci. 2008;11(3):255–261.
[72] Salazar H, Jara-Oseguera A, Hernández-García E, et al. Structural determinants of gating in the TRPV1 channel. Nat Struct Mol Biol. 2009;16(7):704–710.
[73] Peyrot Des Gachons C, Uchida K, Bryant B, et al. Unusual pungency from extra-virgin olive oil is attributable to restricted spatial expression of the receptor of oleocanthal. J Neurosci Off J Soc Neurosci. 2011;31(3):999–1009.
[74] Laursen WJ, Bagriantsev SN, Gracheva EO. TRPA1 channels: chemical and temperature sensitivity. Curr Top Membr. 2014;74:89–112.
[75] Samanta A, Kiselar J, Pumroy RA, et al. Structural insights into the molecular mechanism of mouse TRPA1 Activation and inhibition. J Gen Physiol. 2018;150(5):751–762.
[76] Jordt S-E, Bautista DM, Chuang -H-H, et al. Mustard oils and cannabinoids excite sensory nerve fibres through the TRP channel ANKTM1. Nature. 2004;427(6971):260–265.
[77] Cavanaugh EJ, Simkin D, Kim D. Activation of transient receptor potential a1 channels by mustard oil, tetrahydrocannabinol and Ca2+ reveals different functional channel states. Neuroscience. 2008;154(4):1467–1476.
[78] Paulsen CE, Armache J-P, Gao Y, et al. Structure of the TRPA1 ion channel suggests regulatory mechanisms. Nature. 2015;525(7570):552.
[79] Martinez GQ, Gordon SE. Multimerization of homo sapiens TRPA1 ion channel cytoplasmic domains. PloS One. 2019;14(2):e0207835.
[80] Voets T, Janssens A, Prenen J, et al. Mg2+-dependent gating and strong inward rectification of the cation channel TRPV6. J Gen Physiol. 2003;121(3):245–260.
[81] Den Dekker E, Hoenderop JGJ, Nilius B, et al. The epithelial calcium channels, TRPV5 & TRPV6: from identification towards regulation. Cell Calcium. 2003;33(5–6):497–507.
[82] McGoldrick LL, Singh AK, Saotome K, et al. Opening of the human epithelial calcium channel TRPV6. Nature. 2018;553(7687):233–237.
[83] Kovalevskaya NV, Bokhovchuk FM, Vuister GW. The TRPV5/6 calcium channels contain multiple calmodulin binding sites with differential binding properties. J Struct Funct Genomics. 2012;13(2):91–100.
[84] Nilius B, Prenen J, Vennekens R, et al. Pharmacological modulation of monovalent cation currents through the epithelial Ca2+ channel ECaC1. BrJ Pharmacol. 2001;134(3):453–462.
[85] van Goor MKC, Hoenderop JGJ, van der Wijst J. TRP channels in calcium homeostasis: from hormonal control to structure-function relationship of TRPV5 and TRPV6. Biochim Biophys Acta Mol Cell Res. 2017;1864(6):883–893.
[86] Hughes TET, Lodowski DT, Huynh KW, et al. Structural basis of TRPV5 channel inhibition by econazole revealed by Cryo-EM. Nat Struct Mol Biol. 2018;25(1):53–60.
[87] Hughes TET, Pumroy RA, Yazici AT, et al. Structural insights on TRPV5 gating by endogenous modulators. Nat Commun. 2018;9(1):4198.
[88] Hoenderop JGJ, Voets T, Hoefs S, et al. Homo- and heterotetrameric architecture of the epithelial Ca2+ channels TRPV5 and TRPV6. Embo J. 2003;22 (4):776–785.
[89] Ohsawa M, Miyabe Y, Katsu H, et al. Identification of the sensory nerve fiber responsible for lysophosphatidic acid-induced allodynia in mice. Neuroscience. 2013;247:65–74.

[90] Ueda H, Matsunaga H, Olaposi OI, et al. Chemical signature of neuropathic pain. Biochim Biophys Acta. 2013;1831(1):61–73.
[91] Inoue M, Rashid MH, Fujita R, et al. Initiation of neuropathic pain requires lysophosphatidic acid receptor signaling. Nat Med. 2004;10(7):712–718.
[92] Inoue M, Ma L, Aoki J, et al. Autotaxin, a synthetic enzyme of lysophosphatidic acid (LPA), mediates the induction of nerve-injured neuropathic pain. Mol Pain. 2008;4:6.
[93] Chemin J, Patel A, Duprat F, et al. Lysophosphatidic Acid-Operated K+ Channels. J Biol Chem. 2005;280 (6):4415–4421.
[94] Stirling L, Williams MR, Morielli AD. Dual Roles for RHOA/RHO-kinase in the regulated trafficking of a voltage-sensitive potassium channel. Mol Biol Cell. 2009;20(12):2991–3002.
[95] Kittaka H, Uchida K, Fukuta N, et al. Lysophosphatidic acid-induced itch is mediated by signalling of LPA5 receptor, phospholipase D and TRPA1/TRPV1. J Physiol. 2017;595(8):2681–2698.
[96] Hernández-Araiza I, Morales-Lázaro SL, Canul-Sánchez JA, et al. Role of lysophosphatidic acid in ion channel function and disease. J Neurophysiol. 2018;120(3):1198–1211.
[97] Czirják G, Tóth ZE, Enyedi P. The two-pore domain K + channel, TRESK, is activated by the cytoplasmic calcium signal through calcineurin. J Biol Chem. 2004;279(18):18550–18558.
[98] Chuang HH, Prescott ED, Kong H, et al. Bradykinin and nerve growth factor release the capsaicin receptor from PtdIns(4,5)P2-mediated inhibition. Nature. 2001;411(6840):957–962.
[99] Prescott ED, Julius D. A modular PIP2 binding site as a determinant of capsaicin receptor sensitivity. Science. 2003;300(5623):1284–1288.
[100] Klein RM, Ufret-Vincenty CA, Hua L, et al. Determinants of molecular specificity in phosphoinositide regulation. phosphatidylinositol (4,5)-Bisphosphate (PI(4,5)P2) is the endogenous lipid regulating TRPV1. J Biol Chem. 2008;283(38):26208–26216.
[101] Rosasco MG, Gordon SE, Bajjalieh SM. Characterization of the functional domains of a mammalian voltage-sensitive phosphatase. Biophys J. 2015;109(12):2480–2491.
[102] Senning EN, Collins MD, Stratiievska A, et al. Regulation of TRPV1 ion channel by phosphoinositide (4,5)-bisphosphate: the role of membrane asymmetry. J Biol Chem. 2014;289(16):10999–11006.
[103] Stein AT, Ufret-Vincenty CA, Hua L, et al. Phosphoinositide 3-kinase binds to TRPV1 and mediates NGF-stimulated TRPV1 trafficking to the plasma membrane. J Gen Physiol. 2006;128(5):509–522.
[104] Stratiievska A, Nelson S, Senning EN, et al. Reciprocal regulation among TRPV1 channels and phosphoinositide 3-kinase in response to nerve growth factor. eLife. 2018;7. DOI:10.7554/eLife.38869.
[105] Ufret-Vincenty CA, Klein RM, Collins MD, et al. Mechanism for phosphoinositide selectivity and activation of TRPV1 Ion Channels. J Gen Physiol. 2015;145(5):431–442.
[106] Ufret-Vincenty CA, Klein RM, Hua L, et al. Localization of the PIP2 Sensor of TRPV1 Ion Channels. J Biol Chem. 2011;286(11):9688–9698.
[107] Matta JA, Miyares RL, Ahern GP. TRPV1 Is a Novel Target for Omega-3 Polyunsaturated Fatty Acids. J Physiol. 2007;578(Pt 2):397–411.
[108] Morales-Lázaro SL, Llorente I, Sierra-Ramírez F, et al. Inhibition of TRPV1 channels by a naturally occurring omega-9 fatty acid reduces pain and itch. Nat Commun. 2016;7:13092.
[109] Picazo-Juárez G, Romero-Suárez S, Nieto-Posadas A, et al. Identification of a binding motif in the S5 helix that confers cholesterol sensitivity to the TRPV1 Ion Channel. J Biol Chem. 2011;286(28):24966–24976.
[110] Liu M, Huang W, Wu D, et al. TRPV1, but not P2X, requires cholesterol for its function and membrane expression in rat nociceptors. Eur J Neurosci. 2006;24 (1):1–6.
[111] Szoke E, Börzsei R, Tóth DM, et al. Effect of lipid raft disruption on TRPV1 receptor activation of trigeminal sensory neurons and transfected cell line. Eur J Pharmacol. 2010;628(1–3):67–74.
[112] Telezhkin V, Reilly JM, Thomas AM, et al. Structural requirements of membrane phospholipids for M-Type potassium channel activation and binding. J Biol Chem. 2012;287(13):10001–10012.
[113] Jang Y, Lee MH, Lee J, et al. TRPM2 Mediates the Lysophosphatidic Acid-Induced Neurite Retraction in the Developing Brain. Pflugers Arch. 2014;466 (10):1987–1998.
[114] Yung YC, Stoddard NC, Chun J, et al. Pathophysiology. J Lipid Res. 2014;55(7):1192–1214.
[115] Cao E, Cordero-Morales JF, Liu B, et al. TRPV1 channels are intrinsically heat sensitive and negatively regulated by phosphoinositide lipids. Neuron. 2013;77 (4):667–679.
[116] Morales-Lázaro SL, Serrano-Flores B, Llorente I, et al. Structural determinants of the transient receptor potential 1 (TRPV1) channel activation by phospholipid analogs. J Biol Chem. 2014;289(35):24079–24090.
[117] Canul-Sánchez JA, Hernández-Araiza I, Hernández-García E, et al. Different agonists induce distinct single-channel conductance states in TRPV1 channels. J Gen Physiol. 2018;150(12):1735–1746.
[118] Madej MG, Ziegler CM. Dawning of a new era in TRP channel structural biology by cryo-electron microscopy. Pflugers Arch. 2018;470(2):213–225.
[119] Duan J, Li J, Zeng B, et al. Structure of the mouse TRPC4 ion channel. Nat Commun. 2018;9(1):3102.
[120] Duan J, Li J, Chen G-L, et al. Cryo-EM structure of the receptor-activated TRPC5 ion channel at 2.9 angstrom

resolution. bioRxiv. 2018;467969. DOI:10.1101/467969.
[121] Fan C, Choi W, Sun W, et al. Structure of the human lipid-gated cation channel TRPC3. eLife. 2018;7. DOI:10.7554/eLife.36852.
[122] Tang Q, Guo W, Zheng L, et al. Structure of the receptor-activated human TRPC6 and TRPC3 ion channels. Cell Res. 2018;28(7):746–755.
[123] Vinayagam D, Mager T, Apelbaum A, et al. Electron cryo-microscopy structure of the canonical TRPC4 ion channel. eLife. 2018;7. DOI:10.7554/eLife.36615.
[124] Li J, Zhang X, Song X, et al. The structure of TRPC ion channels. Cell Calcium. 2019;80:25–28.
[125] Thakur DP, Tian J, Jeon J, et al. Critical roles of Gi/o proteins and phospholipase C-Δ1 in the activation of receptor-operated TRPC4 channels. Proc Natl Acad Sci U S A. 2016;113(4):1092–1097.
[126] Kraft R, Harteneck C. The mammalian melastatin-related transient receptor potential cation channels: an overview. Pflugers Arch. 2005;451(1):204–211.
[127] Zhang Z, Tóth B, Szollosi A, et al. Structure of a TRPM2 channel in complex with Ca2+ explains unique gating regulation. eLife. 2018;7. DOI:10.7554/eLife.36409.
[128] Wang L, Fu T-M, Zhou Y, et al. Structures and gating mechanism of human TRPM2. Science. 2018;362:6421.
[129] Huang Y, Winkler PA, Sun W, et al. Architecture of the TRPM2 channel and its activation mechanism by ADP-ribose and calcium. Nature. 2018;562(7725):145–149.
[130] Duan J, Li Z, Li J, et al. Structure of full-length human TRPM4. Proc Natl Acad Sci U S A. 2018;115(10):2377–2382.
[131] Autzen HE, Myasnikov AG, Campbell MG, et al. Structure of the human TRPM4 ion channel in a lipid nanodisc. Science. 2018;359(6372):228–232.
[132] Winkler PA, Huang Y, Sun W, et al. Electron cryo-microscopy structure of a human TRPM4 channel. Nature. 2017;552(7684):200–204.
[133] Duan J, Li Z, Li J, et al. Structure of the mammalian TRPM7, a magnesium channel required during embryonic development. Proc Natl Acad Sci U S A. 2018;115(35):E8201–E8210.
[134] Yin Y, Le SC, Hsu AL, et al. Structural basis of cooling agent and lipid sensing by the cold-activated TRPM8 channel. Science. 2019;363(6430):eaav9334.
[135] Yin Y, Wu M, Zubcevic L, et al. Structure of the cold- and menthol-sensing ion channel TRPM8. Science. 2018;359(6372):237–241.
[136] Perraud AL, Fleig A, Dunn CA, et al. ADP-ribose gating of the calcium-permeable LTRPC2 channel revealed by nudix motif homology. Nature. 2001;411(6837):595–599.
[137] Runnels LW, Yue L, Clapham DE. TRP-PLIK, a bifunctional protein with kinase and ion channel activities. Science. 2001;291(5506):1043–1047.
[138] Tóth B, Iordanov I, Csanády L. Putative chanzyme activity of TRPM2 cation channel is unrelated to pore gating. Proc Natl Acad Sci U S A. 2014;111(47):16949–16954.
[139] Iordanov I, Tóth B, Szollosi A, et al. Enzyme activity and selectivity filter stability of ancient TRPM2 channels were simultaneously lost in early vertebrates. eLife. 2019;8. DOI:10.7554/eLife.44556.
[140] Tan C-H, McNaughton PA. The TRPM2 ion channel is required for sensitivity to warmth. Nature. 2016;536(7617):460–463.
[141] Csanády L, Törocsik B. Four Ca2+ ions activate TRPM2 Channels by binding in deep crevices near the pore but intracellularly of the gate. J Gen Physiol. 2009;133(2):189–203.
[142] Launay P, Fleig A, Perraud AL, et al. TRPM4 is a Ca2+-activated nonselective cation channel mediating cell membrane depolarization. Cell. 2002;109(3):397–407.
[143] Hofmann T, Chubanov V, Gudermann T, et al. TRPM5 is a voltage-modulated and Ca(2+)-activated monovalent selective cation channel. Curr Biol CB. 2003;13(13):1153–1158.
[144] Ullrich ND, Voets T, Prenen J, et al. Comparison of functional properties of the Ca2+-activated cation channels TRPM4 and TRPM5 from mice. Cell Calcium. 2005;37(3):267–278.
[145] Liu D, Liman ER. Intracellular Ca2+ and the phospholipid PIP2 regulate the taste transduction ion channel TRPM5. Proc Natl Acad Sci U S A. 2003;100(25):15160–15165.
[146] Zhang Z, Okawa H, Wang Y, et al. Phosphatidylinositol 4,5-bisphosphate rescues TRPM4 channels from desensitization. J Biol Chem. 2005;280(47):39185–39192.
[147] Nilius B, Prenen J, Voets T, et al. Intracellular nucleotides and polyamines inhibit the Ca2+-activated cation channel TRPM4b. Pflugers Arch. 2004;448(1):70–75.
[148] Liman ER. The Ca2+-Activated TRP Channels: TRPM4 and TRPM5. In: Liedtke WB, Heller S, editors. *TRP ion channel function in sensory* transduction *and* cellular signaling cascades. Boca Raton (FL): Frontiers in Neuroscience; CRC Press/Taylor & Francis; 2007:203–211.
[149] Guo J, She J, Zeng W, et al. Structures of the calcium-activated, non-selective cation channel TRPM4. Nature. 2017;552(7684):205–209.
[150] Krapivinsky G, Krapivinsky L, Manasian Y, et al. The TRPM7 chanzyme is cleaved to release a chromatin-modifying kinase. Cell. 2014;157(5):1061–1072.
[151] Zou Z-G, Rios FJ, Montezano AC, et al. TRPM7, Magnesium, and Signaling. Int J Mol Sci. 2019;20(8). DOI:10.3390/ijms20081877
[152] Numata T, Okada Y. Molecular determinants of sensitivity and conductivity of human TRPM7 to Mg2+ and Ca2+. Channels Austin Tex. 2008;2(4):283–286.

[153] Yudin Y, Rohacs T. Regulation of TRPM8 Channel Activity. Mol Cell Endocrinol. 2012;353(1–2):68–74.
[154] Rohács T, Lopes CMB, Michailidis I, et al. PI(4,5)P2 regulates the activation and desensitization of trpm8 channels through the TRP domain. Nat Neurosci. 2005;8(5):626–634.
[155] Bautista D, Julius D. Fire in the hole: pore dilation of the capsaicin receptor TRPV1. Nat Neurosci. 2008;11(5):528–529.
[156] Li M, Toombes GES, Silberberg SD, et al. Physical basis of apparent pore dilation of ATP-activated P2X receptor channels. Nat Neurosci. 2015;18(11):1577–1583.
[157] Mathias RT, Cohen IS, Oliva C. Limitations of the whole cell patch clamp technique in the control of intracellular concentrations. Biophys J. 1990;58(3):759–770.
[158] Frazier CJ, George EG, Jones SW. Apparent change in ion selectivity caused by changes in intracellular K(+) during whole-cell recording. Biophys J. 2000;78(4):1872–1880.
[159] Geron M, Kumar R, Zhou W, et al. TRPV1 pore turret dictates distinct DKTX and capsaicin gating. Proc Natl Acad Sci U S A. 2018;115(50):E11837–E11846.

INFORME DE LABORES 2019



Cancer Biology & Therapy

ISSN: 1538-4047 (Print) 1555-8576 (Online) Journal homepage: https://www.tandfonline.com/loi/kcbt20

Diminished S-adenosylmethionine biosynthesis and its metabolism in a model of hepatocellular carcinoma is recuperated by an adenosine derivative

María Guadalupe Lozano-Rosas, Enrique Chávez, Gabriela Velasco-Loyden, Mariana Domínguez-López, Lidia Martínez-Pérez & Victoria Chagoya De Sánchez

To cite this article: María Guadalupe Lozano-Rosas, Enrique Chávez, Gabriela Velasco-Loyden, Mariana Domínguez-López, Lidia Martínez-Pérez & Victoria Chagoya De Sánchez (2020) Diminished S-adenosylmethionine biosynthesis and its metabolism in a model of hepatocellular carcinoma is recuperated by an adenosine derivative, Cancer Biology & Therapy, 21:1, 81-94, DOI: 10.1080/15384047.2019.1665954

To link to this article: https://doi.org/10.1080/15384047.2019.1665954

View supplementary material

Published online: 25 Sep 2019.

Submit your article to this journal

Article views: 265

View related articles

View Crossmark data

Citing articles: 4 View citing articles

Full Terms & Conditions of access and use can be found at
https://www.tandfonline.com/action/journalInformation?journalCode=kcbt20

CANCER BIOLOGY & THERAPY
2020, VOL. 21, NO. 1, 81–94
https://doi.org/10.1080/15384047.2019.1665954

Taylor & Francis
Taylor & Francis Group

RESEARCH PAPER

Check for updates

Diminished S-adenosylmethionine biosynthesis and its metabolism in a model of hepatocellular carcinoma is recuperated by an adenosine derivative

María Guadalupe Lozano-Rosas, Enrique Chávez, Gabriela Velasco-Loyden, Mariana Domínguez-López, Lidia Martínez-Pérez, and Victoria Chagoya De Sánchez

Departamento de Biología Celular y Desarrollo, Instituto de Fisiología Celular, Universidad Nacional Autónoma de México, Mexico City, Mexico

ABSTRACT

S-adenosylmethionine (SAM), biosynthesis from methionine and ATP, is markedly decreased in hepatocellularular carcinoma (HCC) for a diminution in ATP levels, and the down regulation of the liver specific MAT1a enzyme. Its metabolic activity is very important in the transmethylation reactions, the methionine cycle, the biosynthesis of glutathione (GSH) and the polyamine pathway, which are markedly affected in the HCC. The chemo-preventive effect of IFC305 in HCC induced by DEN, and the increase of ATP and SAM in CCl_4-induced cirrhosis have been previously demonstrated. The aim of this work was to test whether this chemo-preventive effect is mediated by the induction of SAM biosynthesis and its metabolic flow. SAM hepatic levels and the methionine cycle were recovered with IFC305 treatment, restoring transmethylation and transsulfuration activities. IFC305 treatment, increased MAT1a levels and decrease MAT2a levels through modulation of their post-transcriptional regulation. This occurred through the binding of the AUF1 (binding factor 1 AU-rich sites) and HuR (human antigen R) ribonucleoproteins to *Mat1a* and *Mat2a* messenger RNAs, which maintained their nuclear localization. Finally, the compound inhibited the polyamine pathway favoring the recuperation of the normal methionine and one carbon cycle recuperating the metabolic flow of methionine, which probably facilitated its HCC chemo-preventive effect.

ARTICLE HISTORY
Received 11 January 2019
Revised 19 June 2019
Accepted 1 September 2019

KEYWORDS
Hepatocellular carcinoma; S-adenosylmethionine; IFC305; *Mat1a*; *Mat2a*; methionine cycle; glutathione

1. Introduction

Liver cancer, mainly hepatocellular carcinoma (HCC), is the fourth leading cause of cancer-related deaths globally.[1] Risk factors for HCC include chronic infection with hepatitis B and C viruses (HBV and HCV), dietary aflatoxin, excessive alcohol intake, and cigarette smoking, as well as diabetes and obesity, which play a prominent role in HCC development.[2,3] Mortality is high due to difficulties in early detection and a lack of available treatment therapies.[4] HCC is characterized by epigenetic alterations that contribute to preneoplastic and neoplastic lesions. Among them, DNA and protein methylation that induce genomic instability result in a hepatocarcinogenic effect in methyl-deficient conditions with a decrease in S-adenosylmethionine (SAM) in the liver. SAM is an ubiquitous methyl donor that was reported to have chemoprotective activity against liver cancer.[5–8] Several authors have studied the chemopreventive effects of SAM administration in HCC.[5,6]

SAM is synthesized in all mammalian cells but is most abundant in the liver. It is synthesized from L-methionine and adenosine triphosphate (ATP), and this reaction is catalyzed by the enzyme methionine adenosyltransferase (MAT; E.C. 2.5.6.1).[7,8] In mammals, two distinct genes encode MAT enzymes (MAT1A and MAT2A). *Mat1a* is predominantly expressed in the adult liver, while *Mat2a* is ubiquitously expressed in all extrahepatic tissues. MAT2A is found predominantly in the liver during the fetal period and is progressively replaced by MAT1A during development.[7,9]

Chronic liver damage initiates a switch in MAT protein expression due to a decrease in MAT1A activity that occurs concomitantly with MAT2A upregulation.[7,10,11] The kinetics of MAT1A and MAT2A are different since MAT2A is inhibited by its product, which consequently results in lower levels of SAM.[7,12]

SAM is mostly used in the transmethylation pathway to produce S-adenosylhomocysteine (SAH), which is transformed by SAH-hydrolase into homocysteine and adenosine.[7,13] SAH is a potent and competitive inhibitor of transmethylation reactions and must be quickly removed.[7] The SAM/SAH ratio is considered an indicator of methylation activity and liver injury sensitivity.[9,14] Therefore, low SAM levels and high SAH levels are characteristics of the development of liver cancer.[15,16]

Previous studies described the effect of the RNA binding proteins (RBPs) HuR (human antigen R) and AUF1 (binding factor 1 AU-rich sites) on the posttranscriptional regulation of the *Mat2a* and *Mat1a* transcripts, for a review, see ref.[17] Both RBPs are nuclear proteins that are translocated to the cytoplasm to regulate MAT mRNA stability through their association with the 3′ UTR of specific mRNAs. The translocation of the RBPs is related to various processes, including fetal liver dedifferentiation, apoptosis, hepatic proliferation, and HCC progression, and consequently, diminishes the biosynthesis of SAM.[18–21]

CONTACT Victoria Chagoya de Sánchez vchagoya@ifc.unam.mx Departamento de Biología Celular y Desarrollo, Instituto de Fisiología Celular, Universidad Nacional Autónoma de México. Ciudad de México, Mexico City, C.P. 04510, Mexico
Supplemental data for this article can be accessed on the publisher's website.
© 2019 Taylor & Francis Group, LLC

Previously, we demonstrated that an increased adenosine level coincided with a rise in SAM levels and a decline in SAH levels, suggesting flux in the methylation pathway and phospholipid methylation.[14,22] In addition, an important circadian change in SAM and adenosine in the rat liver coincides with changes in ATP levels, for a review, see ref.[23] Thus, these findings suggested a correlation between energetic metabolism and SAM formation.

SAM regulates a number of methionine cycle pathways that are perturbed in liver cancer, including the generation of glutathione (GSH) from homocysteine, which can be converted to cysteine via the transsulfuration pathway that utilizes methionine for GSH synthesis.[24–26]

In addition, SAM also donates an aminopropyl group to putrescine to produce spermidine and 5′methylthioadenosine (MTA) through the polyamine pathway. MTA is used to regenerate methionine by the salvation pathway.[9,27] Cancer cells have enhanced polyamine biosynthesis and uptake resulting in high intracellular polyamine concentrations. This increase is coupled with different tumors, such as breast, colon, prostate and liver cancer.[28,29] The high polyamine levels are essential for the rapidly growing cancer cells.[9,30] In fact, a decline in SAM and MTA levels is necessary for the development of liver cancer.[9,28,30] However, many other mechanisms are related to decreases in SAM levels and MAT proteins switching.

It has been shown that adenosine administration induces increased SAM and phospholipid methylation, for a review, see ref.[14]

Recently, we showed HCC chemoprevention by IFC305 in a sequential model of cirrhosis-HCC induced by diethylnitrosamine (DEN) in rats. DEN is a carcinogen used in different experimental models of HCC. To exert its carcinogenic effects, DEN needs to be bio activated by CYP2E1.[31] Once bio activated, DEN can generate DNA adducts through alkylation mechanisms. Moreover, the importance of oxidative stress in the development of hepatocarcinogenesis induced by DEN has been suggested because there is a correlation between the induction of lipid peroxidation and preneoplastic lesions, and it has been further shown that the addition of an antioxidant prevents this effect.[32] IFC305 induces the down-regulation of thymidylate synthase and hepatocyte growth factor (HGF), along with augmented protein levels of the cell cycle inhibitor p27, resulting in the inhibition of cell proliferation, for a review, see ref.[33] In addition, we demonstrated that IFC305 promotes increases in ATP levels and the normalization of mitochondrial function in the cirrhosis-HCC model studied here, for a review, see ref.[34]

As described above, the development of HCC is promoted by a decrease in hepatic SAM. Therefore, the aim of this work was to test whether the chemopreventive effect of IFC305 is mediated by the recovery of the metabolic flow of SAM, the regulation of the SAM/SAH ratio and the inhibition of the polyamine pathway, thereby avoiding cell proliferation.

2. Results

The sequential model of cirrhosis-HCC previously described by Schiffer was histologically corroborated using Masson's trichrome stain. Cirrhosis was detected at week 12, when nodules surrounded by collagen fibers were observed. HCC was established at week 16 when preneoplastic nodules were observed, which were maintained until week 22 (Figure 1 and Supplementary Figure 1). After having ensured the reproducibility of the model, we proceeded to study the effect of IFC305 on SAM synthesis and metabolism.

2.1 IFC305 treatment recovered decreased SAM levels and the SAM/SAH ratio in a sequential model of cirrhosis-hepatocellular carcinoma

A drop in the biosynthesis of SAM affects hepatic function since it regulates cell differentiation and proliferation and thus sensitivity to liver injury. SAM and SAH levels and the SAM/SAH ratio were quantified in this chronic damage model induced by DEN (Figure 2a). Our results showed

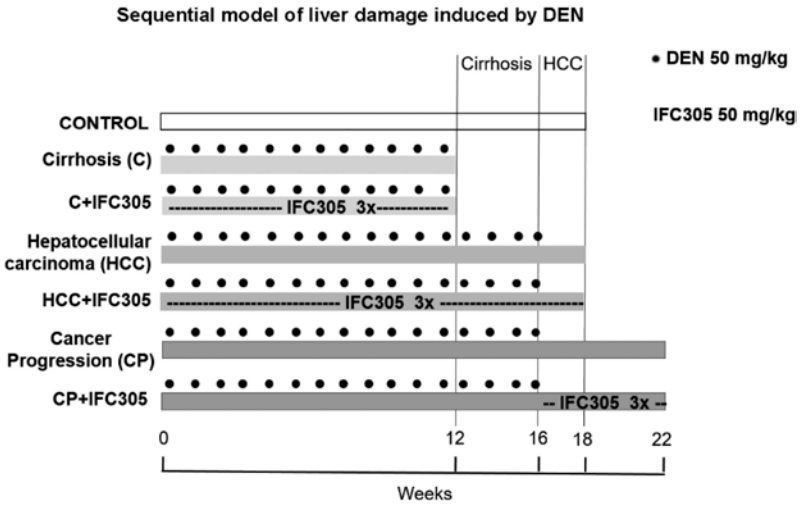

Figure 1. Sequential model of liver damage induced by DEN.

Rats received DEN for 12 weeks to induce cirrhosis (C) and for 16 weeks to induce HCC development. IFC305 was injected in parallel with DEN as a prevention scheme (C+ IFC305 and HCC+IFC305). After suspending DEN treatment, IFC305 was administered from week 16 to week 22 in the cancer progression scheme (CP+IFC305). Rats received DEN dissolved in saline solution once a week, and IFC305 was administered three times per week (IFC305 3X).

a significant diminution in SAM levels in the HCC and CP groups, which were increased with IFC305 treatment in both groups. Once the transmethylation reaction occurs, the product of the reaction is SAH, which is a potent inhibitor of methylation reactions. There were no significant changes in SAH levels in the HCC and CP groups compared to the control group; however, SAH levels diminished significantly in the HCC+IFC305 group and slightly in the CP+IFC305 group (Figure 2b). The SAM/SAH ratio controls the activity of methylation reactions; this calculated ratio indicated a decrease in methylation activity in the HCC and CP groups but a significant increase in the presence of IFC305 (Figure 2c). Similar results in the cirrhosis stage were obtained (Supplementary Figure 2A, 2B, and 2C), in which decreased SAM levels were obtained upon DEN treatment, and IFC305 increased the SAM/SAH ratio.

2.2 IFC305 treatment differentially regulated MAT genes implicated in methionine synthesis in a hepatocellular carcinoma model

We next evaluated the transcriptional changes in the *Mat1α* and *Mat2α* genes in our experimental groups with and without IFC305 treatment. We found that *Mat1a* expression was significantly diminished in DEN-treated samples in both the HCC and CP groups, while treatment with IFC305 increased *Mat1a* expression (Figure 3a). Although *Mat2a* did not show a change in the HCC group, its expression was upregulated in the CP group and downregulated in IFC305-treated rats (Figure 3b).

Next, we analyzed MAT1A protein content. We found that upon DEN treatment, MAT1A protein content was significantly diminished in the HCC group and slightly decreased in the CP group. Our analysis showed a significant increase in

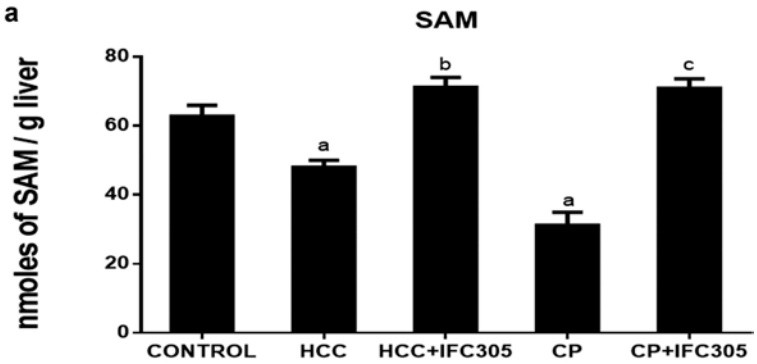

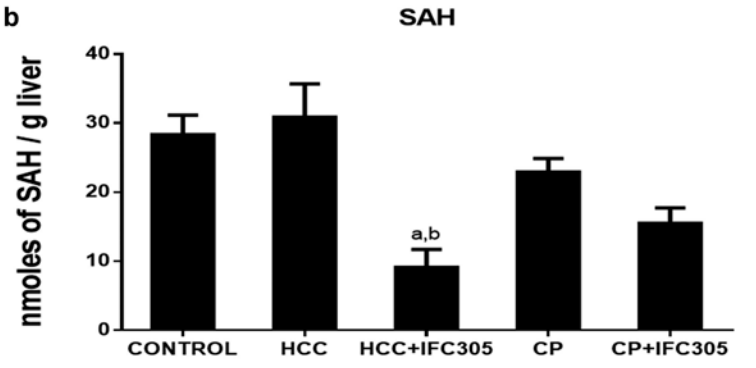

C

SAM/SAH Ratio	2.2	1.6	7.8	1.4	4.6
Groups	CONTROL	HCC	HCC+IFC305	CP	CP+IFC305

Figure 2. SAM, SAH and SAM/SAH ratio.

A Knauer HPLC system, a UV monitor operating at 254 nm, and a C18 column were used to quantify SAM and SAH in perchloric extracts. A) SAM; B) SAH; C) The SAM/SAH ratio was calculated from the mean of the SAM and SAH quantifications. Values are expressed as the mean ± standard error (SE) (n = 7 rats/group); [a] indicates a significant difference vs. the control group; [b] indicates a significant difference vs. the HCC group; [c] indicates a significant difference vs. the CP group; $P < .05$.

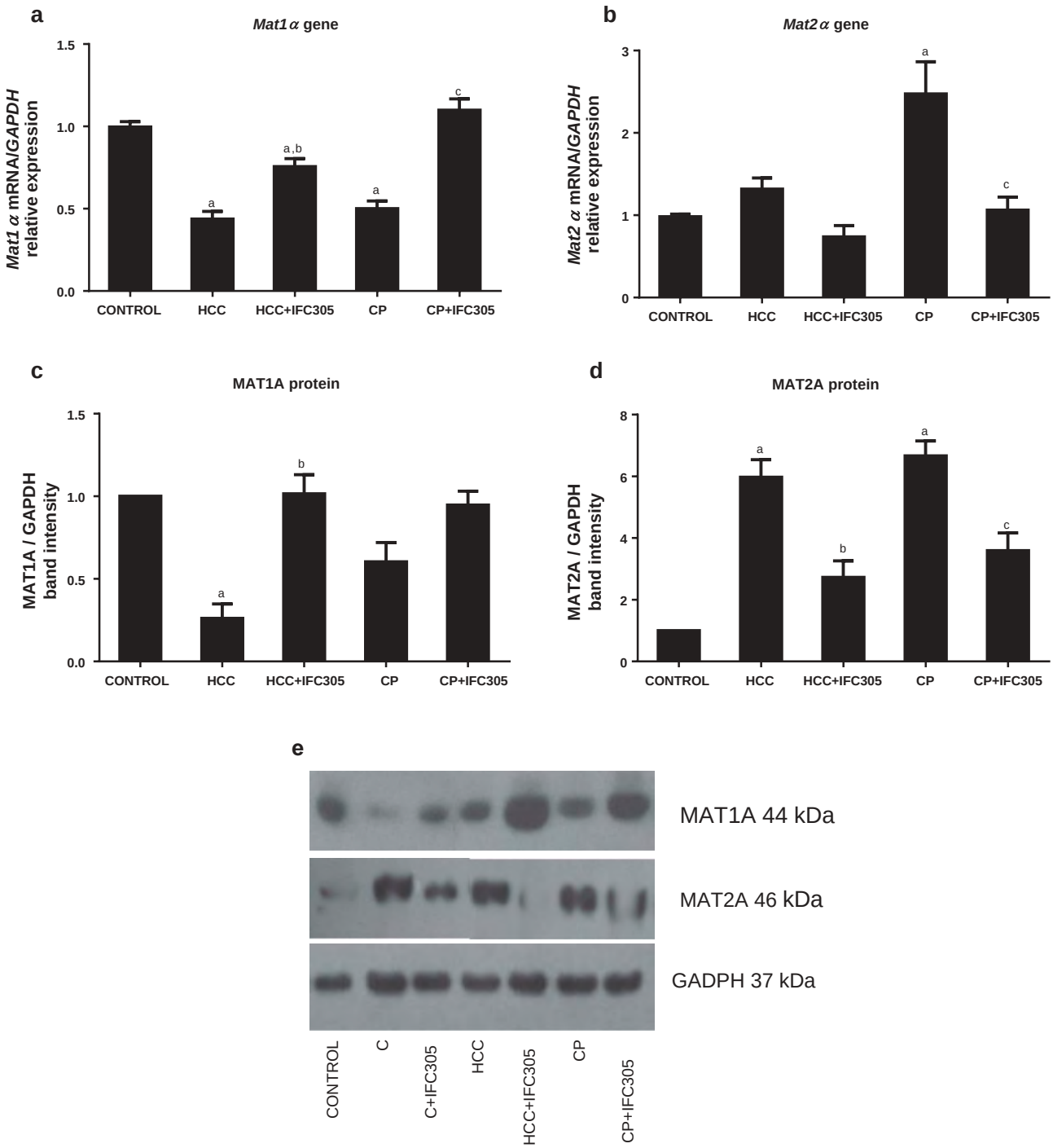

Figure 3. *Mat1a* and *Mat2a* mRNA quantification by qRT-PCR and protein quantification by Western blot.

A) Expression level of the *Mat1a* gene; B) Expression level of the *Mat2a* gene; C) Determination of MAT1A protein level; D) Determination of MAT2A protein level; E) Representative blot showing each experimental group of this model including cirrhosis stage. Values are expressed as the mean ± SE (n = 7 rats/group). [a] indicates a significant difference vs. the control group; [b] indicates a significant difference vs. the HCC group; [c] indicates a significant difference vs. the CP group; $P < .05$.

MAT1A protein upon IFC305 treatment (Figure 3c,e). Compared with the control group, the amount of MAT2A protein increased in both the HCC and CP groups, whereas MAT2A protein levels were significantly diminished in the IFC305-treated groups (Figure 3d,e).

We also determined the levels of MAT genes and proteins in the cirrhosis stage. We observed a switch in protein level with a decreased level of MAT1A and an increased level of MAT2A; these changes were prevented by IFC305 treatment (Supplementary Figure 3). Interestingly, the MAT protein switch that was reversed by IFC305 treatment is strongly implicated in liver cancer progression and prognosis.

2.3 IFC305 treatment changed the status of the cellular distribution of RBPs in a hepatocarcinogenesis rat model

The MAT expression pattern in chronic damage can occur through different mechanisms, such as post transcriptionally

through RBPs. For this reason, the levels of the RBPs, HuR and AUF1 were determined in both cellular compartments (nuclei and cytosol). There is a great interest in understanding how the mature *Mat2a* gene transcript is targeted for upregulation by HuR.

Figure 4a shows that the *HuR* expression level was significantly reduced in the HCC group but did not change in the CP group with respect to the control group. The *HuR* expression level was significantly reduced in the HCC+IFC305 group with

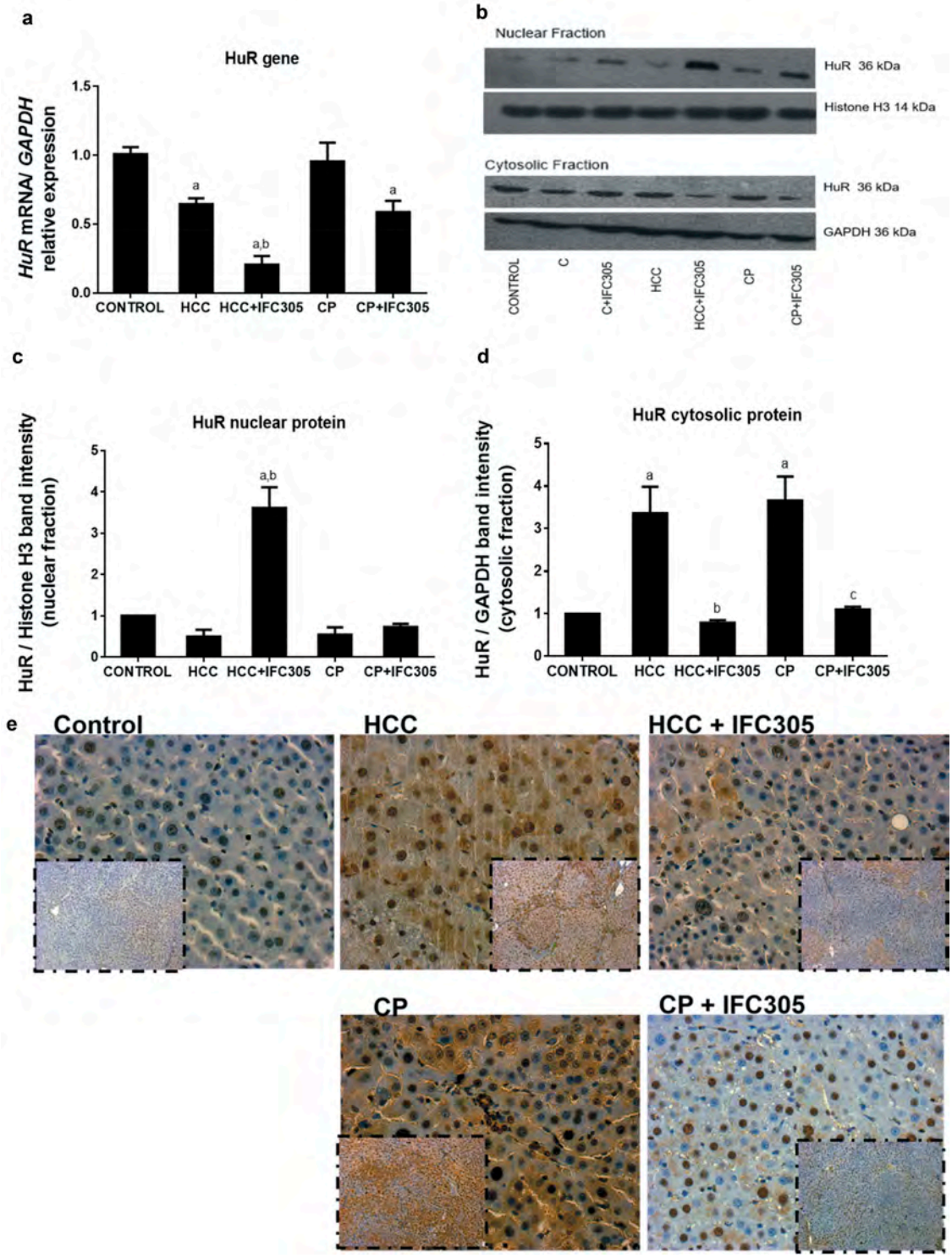

Figure 4. HuR expression, protein level, and immunohistochemical localization.

A) *HuR* mRNA quantification by qRT-PCR; B) Representative blot showing each experimental group of this model including cirrhosis stage; C) Amount of HuR protein in the nuclear compartment; D) Amount of HuR protein in the cytosolic compartment; E) Immunohistochemical localization of HuR at 40X amplification. Values are expressed as the mean ± SE (n = 5 rats/group). [a] indicates a significant difference vs. the control group; [b] indicates a significant difference vs. the HCC group; $P < .05$.

respect to the control and HCC groups, and CP+IFC305 samples was reduced only with respect to the control group.

Next, we analyzed the changes in HuR subcellular localization by Western blot and immunohistochemical analysis. Nuclear HuR levels in the HCC and CP groups decreased slightly compared to the control group, but nuclear levels were increased with IFC305 treatment (HCC+IFC305). By contrast, the CP+IFC305 group did not show a change in the amount of nuclear HuR with respect to the control group (Figure 4b,c). However, we also determined the amount of cytoplasmic HuR protein. This assay showed an important increase in this protein in DEN-treated samples in comparison to the control group, while the IFC305-treated groups maintained and restored cytosolic HuR levels (Figure 4b,d). As shown by the representative images of the control, DEN and IFC305-treated samples in Figure 4e, we observed significantly reduced staining of these proteins in IFC305-treated samples compared to DEN-treated control groups.

The alteration in the subcellular localization of HuR in our sequential hepatic damage model in response to DEN and the IFC305-induced translocation of this protein from the cytosol to the nucleus were also documented at the cirrhosis stage. In addition, the level of the HuR protein in a total liver extract was also measured (Supplementary Figure 4).

There is a great interest in understanding how the mature *Mat1a* gene transcript is targeted for downregulation by AUF1. For this reason, we also evaluated changes in the levels of AUF1 in the nuclear and cytoplasmic compartments.

As shown in Figure 5a, the expression level of the *Auf1* gene was increased in the DEN-treated groups and diminished by IFC305 administration. Furthermore, the amount of AUF1 protein detected in the nuclear fraction was enhanced by IFC305 (Figure 5c). In the cytoplasm, the hepatoprotective IFC305 treatment dramatically reduced AUF1 levels compared with the augmented content in the HCC and CP groups (Figure 5d). The immunohistochemical analysis corroborated these results (Figure 5e).

In cirrhosis, the nuclear AUF1 protein content was reduced in the cirrhosis group, and consequently, the AUF1 cytoplasmic protein content was enriched. This effect was prevented by IFC305 treatment. In addition, the level of the AUF1 protein in a total liver extract was also measured (Supplementary Figure 5).

Additionally, the effect of the IFC305 compound on the level of the MAT proteins and RBPs were evaluated in the HUH7 cell line; we found an increment of MAT2A, HuR and AUF1 after 4 h of IFC305 (5mM) treatment and after this time, a diminution was observed. In the case of MAT1A a diminution was observed at 4 and 6 h after IFC305 (5mM) treatment but a recuperation to the level of the not treated cells was detected. Thus, we observed that IFC305 also modulates the levels of these proteins in the human HuH7 cell line and that supports the data obtained in tissue (data not show).

2.4 The hepatoprotective IFC305 treatment aided in recovering the interactions of RBPs and MAT genes that are altered by DEN

The cytoplasmic stability of eukaryotic mRNA is an important checkpoint in the control of gene expression. In fact, AUF1 and HuR are also involved in liver dedifferentiation and the development and progression of HCC. We next examined the effect of IFC305 on RNP (ribonucleoprotein) complexes.

As shown in Figure 6a, RNP complexes (HuR-*Mat2a* mRNA) were increased markedly in the HCC group, whereas RNP complex formation was reduced in the HCC+IFC305 group. However, in the CP and CP+IFC305 groups, the number of HuR-*Mat2a* mRNA complexes was not modified with respect to the control group.

We found that the AUF1-*Mat1a* mRNA complex was reduced in both the HCC and CP groups, however, only a slight increase in complex formation was observed with IFC305 treatment compared to DEN treatment (Figure 6b).

2.5 IFC305 treatment stimulated GSH biosynthesis and reduced spermidine synthetase expression that is altered by DEN

In hepatocytes, methionine can be generated by the one carbon cycle (Figure 8), and HCyst can be converted to cysteine to generate GSH. We determined the effect of the IFC305 adenosine derivative on the GSH pool and its contribution to protection against hepatic damage. Our results showed that DEN administration for 16 weeks did not induce significant changes in the levels of GSH seen in the HCC group; however, treatment with IFC305 increased GSH levels significantly compared to the control group. No significative diminution was observed in the CP or CP+IFC305 group (Figure 7a). A significant increase in the levels of GSSG were observed in the HCC group (Figure 7b), whereas no changes were observed in the HCC+IFC305 group compared to the control group. A significant decrease in the GSSG content in the CP and CP+IFC305 groups was observed compared to the HCC group. The GSH/GSSG ratio is a useful parameter as an indicator of the redox state. Despite the changes described in GSH and GSSG, no changes in the GSH/GSSG ratio were observed, except in the CP +IFC305 group, where a significant increase was observed compared with the control, HCC and CP groups (Figure 7c). The total glutathione content (GSH+GSSG) is shown in Figure 7d. An increased glutathione content in the HCC and HCC+IFC305 groups compared to the control group was seen. No significant changes in the CP and CP+IFC305 groups compared to the control group were found. Our results from the experimental HCC group treated with IFC305 suggest that this adenosine derivative salt also mediates the GSH biosynthesis in the cirrhosis stage, and the effect of IFC305 on the GSH pool is not significant (Supplementary Figure 6A-D).

It is well known that GSH is the most abundant non-protein thiol in mammalian cells and it protects against oxidative stress. As such, we next assessed the antioxidant potential of IFC305 treatment.

MDA (malondialdehyde) is one of the products of lipid peroxidation and has been related to carcinogenesis induced by DEN; thus, measuring MDA levels is a useful approach to assess lipid peroxidation. A significant increase in lipid peroxidation in the HCC group was observed, which was prevented by IFC305 treatment (HCC+IFC305 group). MDA levels were diminished in the CP group, and there was no change in the CP+IFC305

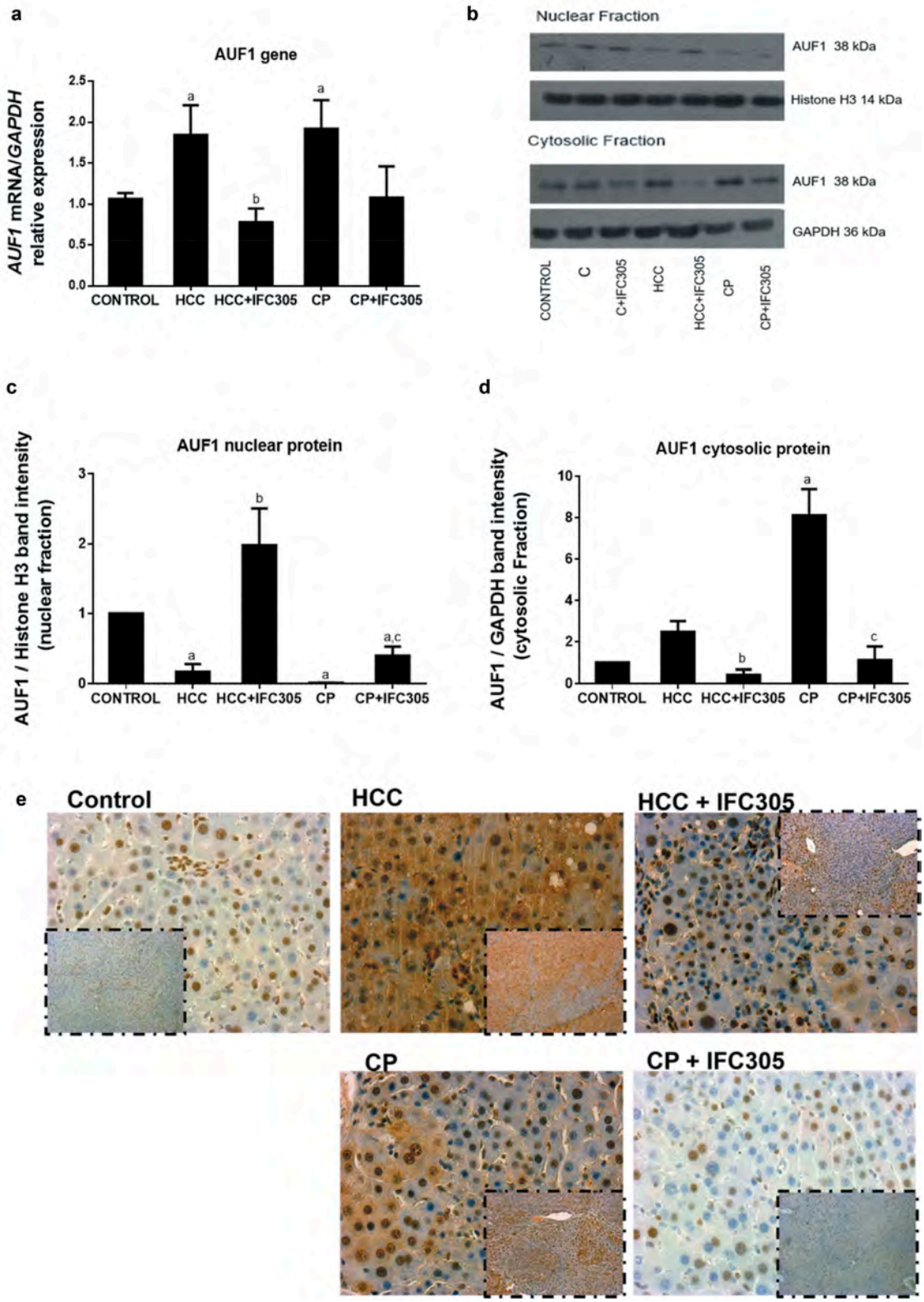

Figure 5. AUF1 expression, protein level, and immunohistochemical localization.

A) AUF1 mRNA quantification by qRT-PCR; B) Representative blot showing each experimental group of this model including cirrhosis stage; C) Amount of AUF1 protein in the nuclear compartment; D) Amount of AUF1 protein in the cytosolic compartment; E) Immunohistochemical localization of AUF1 at 40X amplification. Values are expressed as the mean ± SE (n = 5 rats/group). [a] indicates a significant difference vs. the control group; [b] indicates a significant difference vs. the HCC group; [c] indicates a significant difference vs. the CP group; $P < .05$.

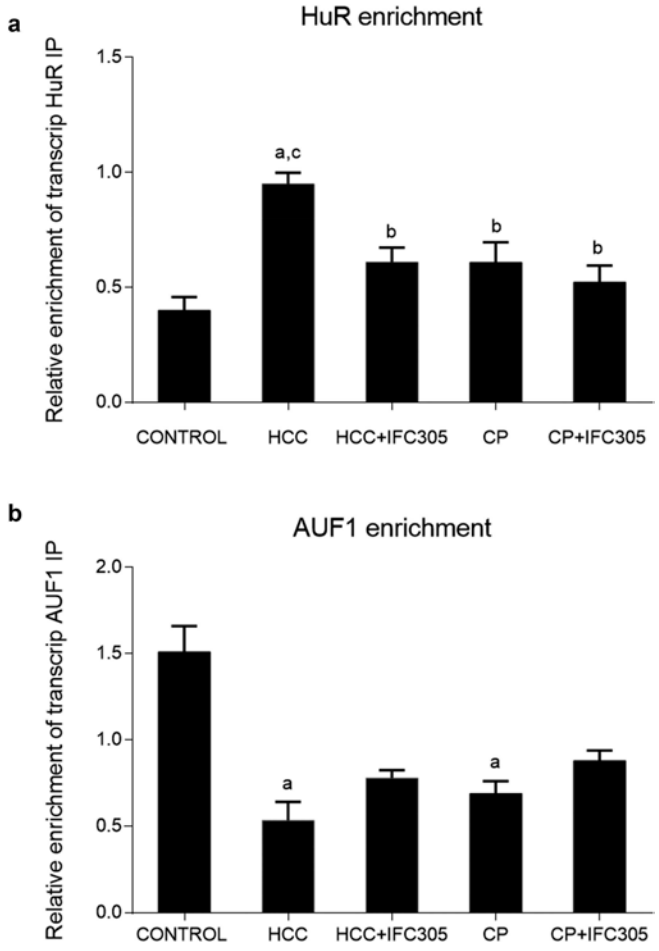

Figure 6. A) Enrichment of IP AUF-1 transcript; B) Enrichment of IP HuR-1 transcript.

Values are expressed as the mean ± SE (n = 5 rats/group). [a] indicates a significant difference vs. the control group; [b] indicates a significant difference vs. the HCC group; $P < .05$.

group (Figure 7e). No significant changes in the cirrhotic stage were observed (Supplementary Figure 6E).

As mentioned above, polyamine levels increase in different types of cancer through a pathway derived from SAM. We next measured *Sms* gene expression since it is part of the polyamine pathway. A significant increase in *Sms* expression in the HCC group was observed compared to the control group, and a slight decrease in *Sms* expression was observed in the CP group compared to the HCC group. *Sms* expression was diminished markedly with IFC305 treatment (Figure 7f), which probably decreased the activity of the polyamine pathway. This effect was evaluated in the cirrhosis stage (Supplementary Figure 6F), where diminished *Sms* expression (C group) and a slight effect of IFC305 were observed (C+ IFC305 group).

3. Discussion

S-adenosylmethionine deficiency strongly favors HCC development, which can be inhibited by reconstitution of normal levels by exogenous administration of SAM.[6,35] SAM biosynthesis requires methionine and ATP as substrates for the enzyme MAT1A. Nevertheless, methionine is not synthetized de novo, but it can be recovered from homocysteine remethylation by methionine synthetase or betaine/homocysteine methyltransferase through the one carbon cycle (Figure 8). ATP is an energetic substrate generated through oxidative phosphorylation in mitochondria. Previous studies in hepatotoxicity induced with ethanol or carbon tetrachloride showed that decreased ATP levels generated an energetic unbalance that was recuperated by adenosine treatment.[23,36,37] Similar effects of increasing ATP in hepatocytes[38] and in the blood by adenosine treatment[39] have been reported. At the time of publication, the mechanism of the effect was not clear, but we have recently described an important effect of adenosine

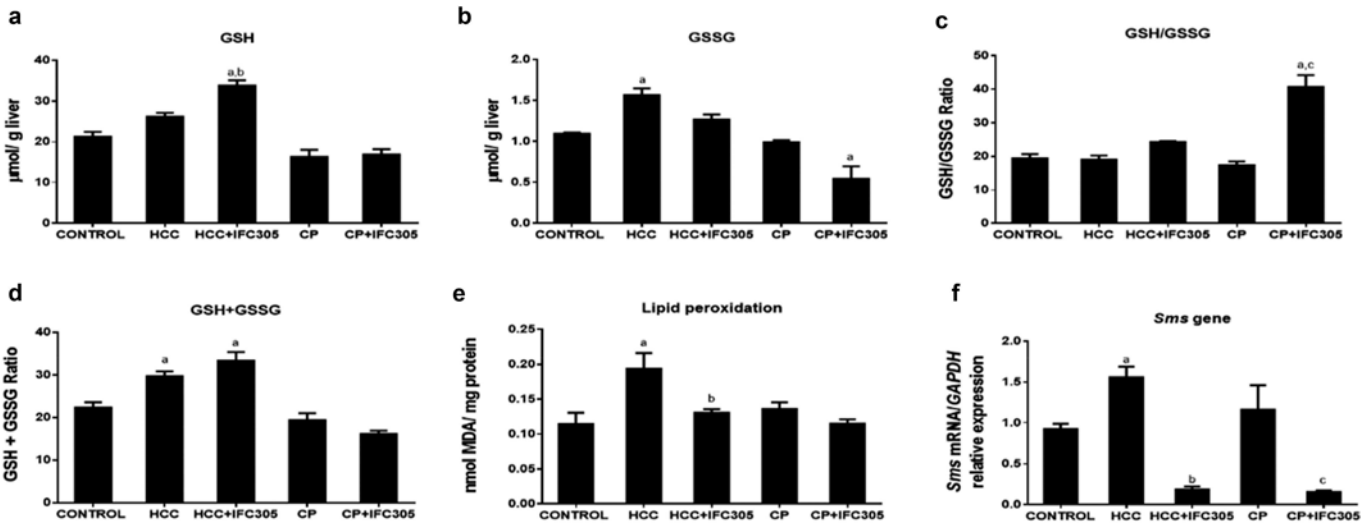

Figure 7. Oxidative stress determined through lipid peroxidation and glutathione content and *Sms* gene expression in the HCC and CP groups and the effect of IFC305.

A) Lipid peroxidation as determined by malondialdehyde (MDA) content; B) Reduced glutathione (GSH) content; C) Oxidized glutathione (GSSG) content; D) GSH/GSSG ratio; E) Total glutathione (GSH+GSSG) content; F) *Sms* gene expression. Values are expressed as the mean ± standard error (SE) (n = 5 rats/group). [a] indicates a significant difference vs. the control group; [b] indicates a significant difference vs. the HCC group; [c] indicates a significant difference vs. the CP group; $P < .05$.

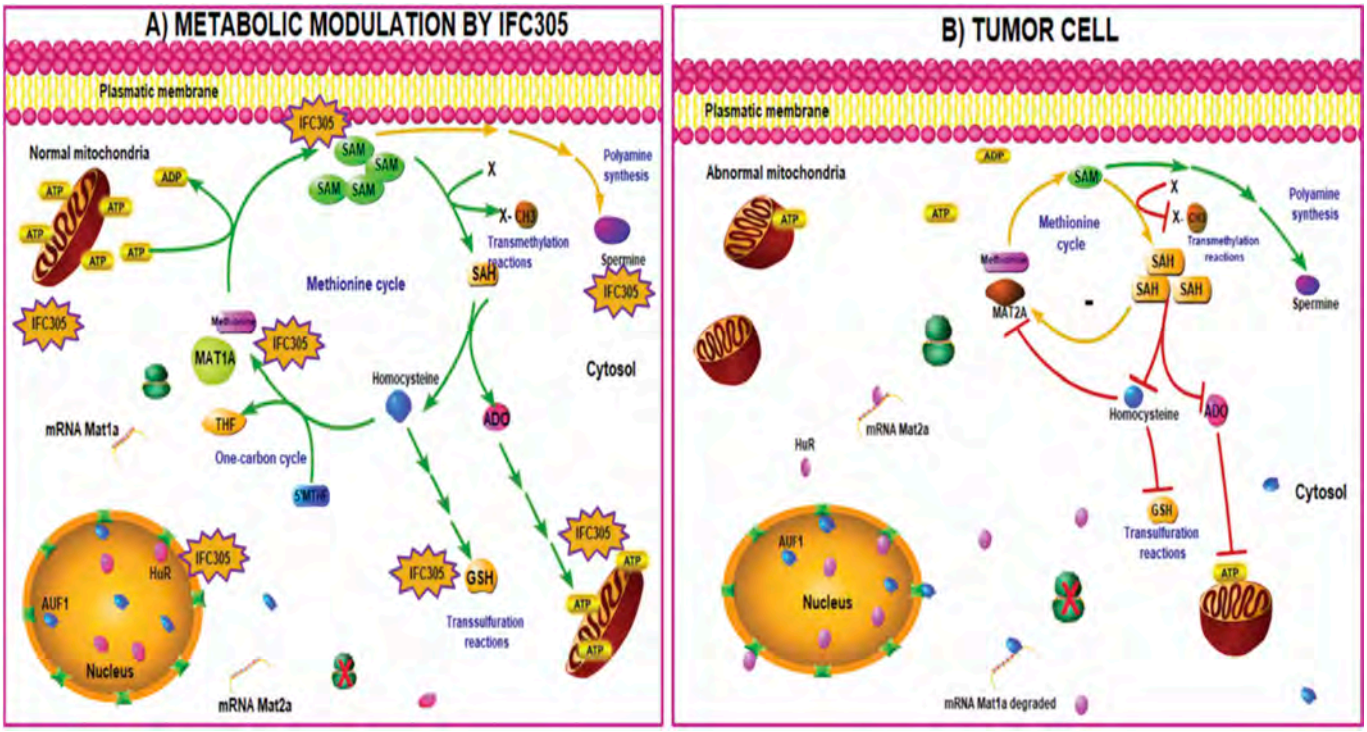

Figure 8. SAM metabolic deficiency in liver cancer and its recovery induced by a hepatoprotective agent derived from adenosine.

A) In tumor cells, SAM synthesis is low due to mitochondrial dysfunction and the consequent decrease in ATP levels. Additionally, biosynthesis catalyzed by MAT2A, which is only expressed in chronic liver damage such as cirrhosis or hepatocellular carcinoma, is limited. This is supported by the RNA-binding proteins HuR and AUF1. HuR positively regulates *Mat2a* mRNA stability, promoting its cytosolic translation and consequently altering the methionine cycle and SAM levels. *Mat1a* mRNA is rapidly destabilized and degraded due to the specific binding of AUF1, which is translocated to the cytosol during the tumor process. B) The hepatoprotective agent IFC305 normalizes mitochondrial function, recuperating ATP levels and SAM biosynthesis, which is also favored by the normalization of MAT1A expression. The IFC305 compound promotes *Mat1a* mRNA translation, avoiding AUF1 translocation to the cytosol, whereas *Mat2a* mRNA is not stabilized by HuR and its translation is not carried out. As a consequence of the recovery of mitochondrial function and SAM levels, the methylation index and the metabolic flow of the methionine cycle are recuperated, which facilitate glutathione biosynthesis, thereby preventing the oxidative imbalance in the tumor.

derivatives in recovering and maintaining ATP synthesis in the HCC and CP groups induced by DEN. We have shown that this occurs through a recuperation of the functional, metabolic and dynamic mitochondrial changes observed in this model.[34] There is much evidence that MAT protein switching and RBPs play an important role in the transcriptional regulation of liver cancer.[20,40,41] The results of this study showed a cytoplasmic increase in HuR and AUF1 in the HCC and CP groups; the presence of IFC305 administration increased the nuclear levels of these RBPs, with a consequent reduction in the cytoplasmic levels favoring the increase in MAT1A and the recuperation of SAM biosynthesis.

Pioneering observations have demonstrated that hepatocyte growth factor (HGF) induces the phosphorylation and activation of LKB1 and, consequently, AMPK.[19,42] AMPK phosphorylation then induces HuR translocation to cytoplasm, promoting an increase in the half-life of MAT2A mRNA, which further contributes to decreasing SAM synthesis. Although a clear mechanism is not described for AUF1, a similar regulation is likely to occur since both RBPs are preferably nuclear and respond to various cell stresses through cytoplasmic translocation. We observed that the hepatoprotective agent IFC305 reduced AMPK protein phosphorylation in our sequential model induced by DEN (data not shown) preventing such translocation.

In chronic liver damage, the nuclear membrane becomes permeable due to the high levels of reactive oxygen species (ROS). Previously, we demonstrated that adenosine and IFC305 have antioxidant properties that repair the mitochondria and prevent the main ROS source from diminishing lipid peroxidation.[34,37] Therefore, the probable mechanism by which IFC305 blocks the cytoplasmic translocation of HuR and AUF1 could be through repairing mitochondrial function and reducing the cellular energy stress and ROS formation. However, other possibilities must be explored, for example, a decrease in proteins that favor subcellular translocation, such as nucleolin 5, or perhaps increased RBP degradation by the proteasome. Once IFC305 is able to maintain the AUF1 protein in the nucleus, MAT1A-mRNA can be translated freely and normally in the cytosol. The MAT1A enzyme is ubiquitously expressed in normal hepatocytes and is downregulated in HCC. In the case of MAT2A mRNA and HuR protein, IFC305 promotes a reduction in the level of these RBPs in the cytosol, and consequently MAT2A protein levels were reduced to control levels. This in vivo study suggests that the IFC305 hepatoprotective compound can reduce the interaction of HuR-MAT2A mRNA in preneoplastic or neoplastic stages of HCC. Furthermore, we found a significant decrease in nuclear AUF1 content, favoring the decrease in Mat1a mRNA expression and consequently SAM content, starting

in the cirrhosis stage and maintained until HCC in this sequential model. Because the exact mechanism of the progression from cirrhosis to HCC is not yet known, this result suggests a potential role for the MAT protein switch in the promotion and evolution of damage.

Once the substrate levels and MAT1A activity recuperated, there was an increase in the SAM level in the HCC and CP groups and in cirrhosis. We calculated the methylation activity through the SAM/SAH ratio, obtaining a high ratio in the HCC and CP groups treated with IFC305. Specific studies are in progress, but previous epigenetic studies in a cirrhotic model induced with CCl_4 showed that IFC305 induced an increase in total DNA methylation, as well as an increase in specific genes, such as the *Col1a1* gene.[43] The low methylation ratio in the HCC and CP groups results from the accumulation of SAH, which is an inhibitor of the methylation reaction and is not degraded by S-adenosylhomocysteine hydrolase, thereby preventing the progression of the methionine cycle. Our results showed that IFC305 helped to maintain the methionine cycle through the activity of SAH-hydrolase, which generates adenosine and homocysteine that can be converted to cysteine, and the transsulfuration pathway, which contributed to maintaining a high GSH pool in the liver in HCC. No changes were observed in glutathione content in the cancer progression groups (CP and CP+IFC305), probably due to the absence of DEN and the fact that IFC305 recovers mitochondrial function and, therefore, decreases ROS generation.

Chemical carcinogenesis is strongly associated with the formation of ROS, and DEN, which was used in this model, generates ROS during its metabolism.[44] In this study, we assessed its participation through lipid peroxidation as evaluated by liver MDA levels. The results showed an important increase in the HCC group that was normalized in the presence of IFC305, possibly by the effect that the compound has on GSH formation and the reduction of damage from free radicals.

Hepatocarcinogenesis is also associated with marked increases in polyamine synthesis, which is also modulated by SAM.[45] This process was evaluated by measuring the expression of the *Sms* gene of the spermine synthase pathway, which was increased in the HCC and CP groups. IFC305 decreased the expression of *Sms* markedly, resulting in the decrease in polyamines and representing another anticarcinogenic effect of the compound. The results of this study reflect the differential effects of IFC305 in a sequential model of hepatocarcinogenesis induced by DEN. These effects include the increase in antioxidant reactions and an inhibition of polyamine synthesis that is related to cell growth, proliferation and the promotion of liver cancer. Furthermore, it was previously demonstrated that this compound induces the downregulation of hepatocyte growth factor and thymidylate synthase, which together with the augmentation of the cell cycle inhibitor p27, resulted in proliferation inhibition,[33] confirming the chemopreventive effect of IFC305.

A schematic representation of the changes observed in the present work and their modulation by the chemopreventive compound IFC305 is shown in Figure 8.

4. Concluding remarks

Cirrhosis-hepatocellular carcinoma induced by chronic DEN intoxication results in SAM diminution, modifies the activity of MAT proteins, induces the posttranscriptional modification of MAT mRNAs, causes abnormalities in the methionine cycle and favors cellular proliferation. Our studies indicated that IFC305 could prevent DEN-induced liver injury by increasing ATP levels, SAM biosynthesis, normalizing MAT protein activities, inducing MAT protein switching and RBP localization to the nucleus, normalizing the methionine cycle that regulates GSH and polyamines in the liver, and reducing proliferation pathways.

The changes in methionine and SAM metabolism induced by DEN strongly contribute to HCC. However, IFC305-induced changes maintain physiological SAM levels, metabolism and function, which could be therapeutic targets in preneoplastic liver lesions and liver tumors.

5. Materials and methods

5.1 Chemicals

IFC305 is the aspartate salt of adenosine, and it was prepared with adenosine free base (MP Biomedicals, (100199)) and L-aspartic acid (MP Biomedicals, (100809)) as described previously (Patent No. MX220780; MX 207422; US 8,507,459 B2).[46–48] N-Diethylnitrosamine (DEN, N0756), SAM (A4377), SAH (A9384), and 1-heptanosulfonic acid sodium salt (PH015877) were purchased from Sigma-Aldrich. $NH_4H_2PO_4$ and $HClO_4$ (109065) solutions (at a 0.4 N concentration) were from Merck (Darmstad, Germany), and methanol (HPLC grade, 822283) was obtained from Merck.

5.2 Study design

Male Wistar rats weighing 200–250 g were obtained from and housed at the Animal Facility of the *Universidad Nacional Autónoma de México (UNAM)*. The animals were fed *ad libitum* and housed under controlled conditions (22 ± 2°C, 50-60% relative humidity, and 12 h light-dark cycles).

The rats received DEN (0.05 g kg^{-1} of body weight, i.p) dissolved in saline solution once a week, and IFC305 was administered (0.05 g kg^{-1} of body weight, i.p) three times per week (IFC305 3X). The sequential model induced by DEN was divided into two main groups: hepatocellular carcinoma (HCC) and cancer progression (CP) (Figure 1).

The HCC group was treated over 16 weeks with DEN, followed by a 2-week wash-out period for multifocal HCC development. The HCC plus IFC305 group (HCC+IFC305) was treated for 16 continuous weeks with both compounds. The cancer progression group (CP) received DEN for 16 weeks, followed by saline solution for 6 weeks. Finally, the cancer progression plus IFC305 group (CP+IFC305) received DEN for 16 weeks and then IFC305 for 6 weeks after DEN was suspended (Figure 1).[49] Age-matched normal rats were used as controls; these animals received only saline solution. Animals were euthanized by sodium pentobarbital (Pisa, Mexico) anesthesia, after which the liver was recovered,

and the cirrhotic area and tumor foci were frozen in liquid nitrogen for the determinations described later. An additional fraction was fixed with paraformaldehyde.

Animals received humane care and were used according to institutional guidelines, and the protocol was approved by the *Comité Institucional para el Cuidado y Uso de Animales de Laboratorio del Instituto de Fisiología Celular (VCHH53-14)* and the Mexican Official Norm (NORM-062-ZOO-1999).

5.3 Total protein extraction

Liver samples were homogenized with RIPA buffer (0.1 g of tissue per milliliter of buffer) supplemented with protease and phosphatase inhibitors (Roche Diagnostics Corp, 116974498001). The homogenate was centrifuged at 15,965 *g* for 10 min at 4°C, and the supernatant was utilized as the total liver homogenate.

5.4 Nuclear protein extraction

The isolation of intact and stable nuclei was accomplished through an isosmotic lysis procedure, as reported previously.[50] The nuclear envelope remained intact even during further manipulations of washing, freezing, and ultracentrifugation. Briefly, 0.8 g of liver tissue was homogenized in 1.6 ml of buffer containing 0.25 M sucrose (S9378, Sigma), 0.05 M Tris-Cl (T1503, Sigma), and 0.005 M KCl (3040–01 JT Baker). The homogenate was filtered and supplemented with 3 ml of a 2.3 M sucrose solution to increase the homogenate's density. Then, a sucrose gradient was created by adding 1.5 ml of a 2.3 M sucrose solution to the bottom of the tube. The nucleus was isolated by centrifugation at 255,000 *g* for 30 min at 4°C. After isolation, nuclear lysis was achieved by incubation and stirring with hypotonic and hypertonic solutions.

5.5 Western blot

Volumes equivalent to 30 µg of protein (determined using a Bradford assay, 500–0114, Biorad) were separated by 12% SDS-PAGE, transferred to a PVDF membrane (IPVH00010, Merck) and blotted using the following antibodies: HuR (sc-20694), MATIA (sc-13142), and MATIIA (H-48) (Santa Cruz Biotechnology); AUF1 (Abcam, ab61193), histone H3 (SC56616, Santa Cruz Biotechnology) and GAPDH (Ab2302, Millipore Corp).[51] Densitometric analyzes of bands were performed with Quantity-One software (Bio-Rad Laboratories, Hercules, CA).

5.6 Assessment of lipid peroxidation

The extent of lipid peroxidation was determined by measuring the formation of malondialdehyde (MDA) using the thiobarbituric acid method as previously described by Okawa et al.[52]

5.7 Determination of GSH and GSSG levels

Liver samples were homogenized on ice in a solution consisting of 3.75 ml of phosphate-EDTA (E5134, Sigma) and 1 ml of 25% H_3PO_4. The total homogenate was centrifuged at 17,700 *g* at 4°C for 30 min, and the supernatant was used in the assay. Determination of the GSH level was performed according to Hissin and Hilf.[53] To dilute the supernatant, 0.01 ml of the supernatant and 4.9 ml of phosphate-EDTA buffer, pH 8.0, were mixed. The assay mixture (2.0 ml) contained 100 µl of the diluted supernatant, 1.8 ml of phosphate-EDTA buffer, and 100 µl of o-phthalaldehyde (1 µg/µl, PO6576 Sigma). After incubation at room temperature for 15 min, the solution was transferred to a quartz cuvette. To determine the GSSG content,[53] 0.5 ml of the supernatant was incubated at room temperature with 200 µl of 0.04 M N-ethylmaleimide (E3876, Sigma) for 30 min to interact with the GSH in the tissue. Then, 4.3 ml of 0.1 N NaOH (S8045, Sigma) was added. This mixture was used to measure GSSG using the assay for GSH, but 0.1 N NaOH was used as the diluent rather than phosphate-EDTA buffer. Fluorescence at 420 nm was determined with excitation at 350 nm.

5.8 RT-PCR

Total RNA was obtained using an RNA isolation kit (Direct-Trizol RNA mini Prep R205S, Zymo Research, The Epigenetics Company). RNA quantity and purity were determined spectrophotometrically at 260/280 nm with a Nanodrop®. RNA quality was verified by agarose-gel electrophoresis. cDNA synthesis was performed with 2 µg of total RNA using the High-Capacity cDNA Archive Kit (Applied Biosystems, Inc., Foster City, CA) following the manufacturer's protocol. The mRNA determinations of *Mat1a* (Rn00563454_m1), *Mat2a* (Rn01643368_g1), *HuR* (Rn01403240_m1), *AUF1* (Rn01450137_g1), *Sms* (Rn01770794_g1), and *Gapdh* (Rn01775763_g1) were carried out with a TaqMan® Gene expression assay using a FAM™ dye-labeled probe for rats (Applied Biosystems, Inc.). *Mat1a, Mat2a, HuR, AUF1* and *Sms* expression was normalized against *Gapdh* expression with the comparative Ct method. All reactions were performed in the Step One Real-Time PCR System (Applied Biosystems).

5.9 HPLC

Liver tissue (0.250 g) was homogenized in ice-cold 0.4 M perchloric acid (500 µl). Then, it was centrifuged at 8380 *g* for 10 min. The supernatant was divided into aliquots and frozen until quantification was done. The method was performed according to She *et al.*[54] Briefly, aliquots of the acid extracts (50 µl) were directly subjected to HPLC analysis.

A Knauer HPLC system (UV detector Model 2500, Isocratic Pump Model 1000 and Manager Model 5000), a UV monitor operating at 254 nm, and a C18 150 × 4.6 mm × 5 µm column (ACE-Generix, Scotland) were used. The mobile phase was chosen according to She et al.,[54] filtered through a 0.45 µm RC membrane filter and degassed under vacuum. The isocratic elution was carried out at a flow-rate of 1 ml/min at 25°C. During HPLC analysis, the SAM and SAH standards and biological samples were identified according to their retention times.

The standards were dissolved in Milli-Q^R grade water at a concentration of 10 mM and then diluted with 0.4 N $HClO_4$ to the final concentration used in the HPLC system (14 µM SAM and 41.5 µM SAH). Aliquots of a standard solution (50 µl) were injected into the column.

5.10 RNA-binding protein immunoprecipitation (RIP)

Liver tissue (200 mg) was finely fragmented, resuspended in 1 ml PBS plus protease and phosphatase inhibitors (freshly prepared) and 37% formaldehyde (F8775, Sigma, 27 µl) and kept at room temperature for 10 min with frequent mixing. Glycine was added (G8898, Sigma, 75 µl), and samples were kept at room temperature for 10 min with frequent mixing, after which they were subsequently centrifuged (1,397.5 *g*, 5 min, 4°C).

The pellet was resuspended in 1 ml PBS plus protease and phosphatase inhibitors (freshly prepared), followed by centrifugation (1,397.5 *g*, 5 min, 4°C).

The pellet was then resuspended in freshly prepared RIP buffer (1.5 ml; 150 mM KCl, 25 mM Tris-HCl pH 7.4, 5 mM EDTA, 0.5 mM DTT (D0632, Sigma), 0.5% IGEPAL I3021, Sigma), 100 U/mL RNase Inhibitor and protease and phosphatase inhibitors).

Samples were homogenized with a Teflon rod with 15–-30 strokes. The nuclear pellet and debris were separated by centrifugation (9,447.1 *g*, 10 min, 4°C).

Next, the supernatant was divided into three fractions of 500 µl (for Input, IgG, and IP). The input fraction was kept at 4°C until use.

Antibody (5 µg for HuR and AUF1) was added to the protein of interest, and IgG (5 µg) was added to the supernatant (500 µg of protein, previously quantified), followed by incubation overnight at 4°C with gentle rotation. A/G beads (40 µl, Chip-Grade Protein A/G Magnetic Beads, Thermo Scientific) were then added, followed by a 2 h incubation at 4°C with gentle rotation. The beads were then pelleted by centrifugation (349.3 *g*, 30 s), the supernatant was removed, and the beads were resuspended in RIP buffer (500 µl). This was repeated for a total three RIP washes, followed by one wash in PBS, and finally centrifugation at 349.3 *g* for 1 min.

For purification of RNA bound to immunoprecipitated RBPs, the coprecipitated RNAs were isolated by resuspending beads in Tripure RNA extraction reagent (1166716S001, Roche; 1 ml, according to the manufacturer´s instructions). An INPUT sample was also included.

The RNA was eluted with nuclease-free water (20 µl). The RNA was reverse transcribed into DNA according to the manufacturer´s instructions (Applied Biosystems High Capacity cDNA Reverse Transcription Kit), and qRT-PCR analyses were performed as described above.

5.11 Tissue preparation, histology and immunohistochemistry

Liver samples were taken from all the animals and fixed with 10% paraformaldehyde in phosphate-buffered saline for 24 h and transferred to 70% ethanol. Fixed tissues were embedded in paraffin, sectioned to a thickness 4 µm and stained for primary antibodies at 1:100, anti-HuR and anti-AUF1; and 1:50 anti-Mat1a and anti-MAT2A with the DakoEnVision®+ System-HRP (DAB) (Dako, Carpinteria, CA) as previously described.[51] Histological slides were analyzed with the MBF ImageJ processing software for microscopy.

5.12 Statistical analysis

Data are expressed as the mean ± standard error of the mean (SE). Statistical significance was evaluated by Tukey's test using Graph Pad Prism 5.0 (Graph Pad Software Inc., La Jolla, CA). Differences were considered statistically significant when $P \leq 0.1$.

Acknowledgments

We are grateful for the Histology unit and the Bioterium technical collaboration of the Instituto de Fisiología Celular. We thank Dr. Julio Isael Pérez-Carreón for the donation of the *SMS* Taqman probe.

Disclosure of potential conflicts of interest

The authors report no conflict of interest

Funding

This work was supported by Consejo Nacional de Ciencia y Tecnología (CONACYT) under grant [240315] and Dirección General de Asuntos del Personal Académico–Programa de Apoyo a Proyectos de Investigación e Innovación Tecnológica (DGAPA-PAPIIT) under grant [IN208915].

Authorship contributions

Participated in the research design: María Guadalupe Lozano-Rosas, Enrique Chávez, Mariana Domínguez-López, Gabriela Velasco-Loyden and Victoria Chagoya de Sánchez.

Conducted experiments: María Guadalupe Lozano-Rosas, Enrique Chávez, Gabriela Velasco-Loyden, Mariana Domínguez-López and Lidia Martínez-Pérez.

Performed data analysis: María Guadalupe Lozano-Rosas, Enrique Chávez, and Victoria Chagoya de Sánchez.

Contributed to the writing of the manuscript: María Guadalupe Lozano-Rosas, Enrique Chávez, Mariana Domínguez-López, Gabriela Velasco-Loyden and Victoria Chagoya de Sánchez.

References

1. IARC. 2018. Available from: www.iarc.fr/wp-content/uploads/2018/09/pr263_E.pdf
2. Gan L, Liu Z, Sun C. Obesity linking to hepatocellular carcinoma: A global view. Biochim Biophys Acta. 2018;1869:97–102.
3. Yeh FS, Yu MC, Mo CC, Luo S, Tong MJ, Henderson BE. Hepatitis B virus, aflatoxins, and hepatocellular carcinoma in southern Guangxi, China. Cancer Res. 1989;49:2506–2509.
4. Ferlay J, Shin HR, Bray F, Forman D, Mathers C, Parkin DM. Estimates of worldwide burden of cancer in 2008: GLOBOCAN 2008. Int J Cancer J Int Du Cancer. 2010;127:2893–2917. doi:10.1002/ijc.25516.
5. Wang Y, Sun Z, Szyf M. S-adenosyl-methionine (SAM) alters the transcriptome and methylome and specifically blocks growth and invasiveness of liver cancer cells. Oncotarget. 2017;8:111866–-111881. doi:10.18632/oncotarget.22942.
6. Pascale RM, Simile MM, De Miglio MR, Feo F. Chemoprevention of hepatocarcinogenesis: S-adenosyl-L-methionine. Alcohol. 2002;27:193–198.
7. Lu SC, Mato JM. S-adenosylmethionine in liver health, injury, and cancer. Physiol Rev. 2012;92:1515–1542. doi:10.1152/physrev.00047.2011.
8. Li TW, Yang H, Peng H, Xia M, Mato JM, Lu SC. Effects of S-adenosylmethionine and methylthioadenosine on

inflammation-induced colon cancer in mice. Carcinogenesis. 2012;33:427–435. doi:10.1093/carcin/bgr295.
9. Pascale RM, Feo CF, Calvisi DF, Feo F. Deregulation of methionine metabolism as determinant of progression and prognosis of hepatocellular carcinoma. Transl Gastroenterol Hepatol. 2018;3:36. doi:10.21037/tgh.
10. Mato JM, Corrales FJ, Lu SC, Avila MA. S-Adenosylmethionine: a control switch that regulates liver function. Faseb J. 2002;16:15–26. doi:10.1096/fj.01-0401rev.
11. Anstee QM, Day CP. S-adenosylmethionine (SAMe) therapy in liver disease: a review of current evidence and clinical utility. J Hepatol. 2012;57:1097–1109. doi:10.1016/j.jhep.2012.04.041.
12. Ramani K, Mato JM, Lu SC. Role of methionine adenosyltransferase genes in hepatocarcinogenesis. Cancers (Basel). 2011;3:1480–1497. doi:10.3390/cancers3021480.
13. Kotb M, Mudd SH, Mato JM, Geller AM, Kredich NM, Chou JY, Cantoni GL. Consensus nomenclature for the mammalian methionine adenosyltransferase genes and gene products. Trends in Genet. 1997;13:51–52.
14. Chagoya de Sanchez V, Hernandez-Munoz R, Sanchez L, Vidrio S, Yanez L, Suarez J. Twenty-four-hour changes of S-adenosylmethionine, S-adenosylhomocysteine adenosine and their metabolizing enzymes in rat liver; possible physiological significance in phospholipid methylation. Int J Biochem. 1991;23:1439–1443. doi:10.1016/0020-711x(91)90287-w.
15. Lu SC. Glutathione synthesis. Biochim Biophys Acta. 2013;1830:3143–3153. doi:10.1016/j.bbagen.2012.09.008.
16. Mosharov E, Cranford MR, Banerjee R. The quantitatively important relationship between homocysteine metabolism and glutathione synthesis by the transsulfuration pathway and its regulation by redox changes. Biochemistry. 2000;39:13005–13011. doi:10.1021/bi001088w.
17. Vazquez-Chantada M, Fernandez-Ramos D, Embade N, Martinez-Lopez N, Varela-Rey M, Woodhoo A, Luka Z, Wagner C, Anglim PP, Finnell RH, et al. HuR/methyl-HuR and AUF1 regulate the MAT expressed during liver proliferation, differentiation, and carcinogenesis. Gastroenterology. 2010;138:1943–1953. doi:10.1053/j.gastro.2010.01.032.
18. Zucal C, D'Agostino V, Loffredo R, Mantelli B, NatthakanThongon LP, Lal P, Latorre E, Provenzani A. Targeting the multifaceted HuR protein, benefits and caveats. Curr Drug Targets. 2015;16:499–515.
19. Gomez-Santos L, Vazquez-Chantada M, Mato JM, Martinez-Chantar ML. SAMe and HuR in liver physiology: usefulness of stem cells in hepatic differentiation research. Methods Mol Biol. 2012;826:133–149. doi:10.1007/978-1-61779-468-1_12.
20. Frau M, Tomasi ML, Simile MM, Demartis MI, Salis F, Latte G, Calvisi DF, Seddaiu MA, Daino L, Feo CF, et al. Role of transcriptional and posttranscriptional regulation of methionine adenosyltransferases in liver cancer progression. Hepatology. 2012;56:165–175. doi:10.1002/hep.25643.
21. Trojanowicz B, Dralle H, Hoang-Vu C. AUF1 and HuR: possible implications of mRNA stability in thyroid function and disorders. Thyroid Res. 2011;4(Suppl 1):S5. doi:10.1186/1756-6614-4-S1-S5.
22. Chagoya de Sanchez V. Circadian variations of adenosine and of its metabolism. Could adenosine be a molecular oscillator for circadian rhythms? Can J Physiol Pharmacol. 1995;73:339–355. doi:10.1139/y95-044.
23. Chagoya de Sanchez V, Brunner A, Pina E. In vivo modification of the energy charge in the liver cell. Biochem Biophys Res Commun. 1972;46:1441–1445. doi:10.1016/s0006-291x(72)80138-4.
24. Ishii I, Akahoshi N, Yamada H, Nakano S, Izumi T, Suematsu M. Cystathionine gamma-Lyase-deficient mice require dietary cysteine to protect against acute lethal myopathy and oxidative injury. J Biol Chem. 2010;285:26358–26368. doi:10.1074/jbc.M110.147439.
25. Meredith MJ, Cusick CL, Soltaninassab S, Sekhar KS, Lu S, Freeman ML. Expression of Bcl-2 increases intracellular glutathione by inhibiting methionine-dependent GSH efflux. Biochem Biophys Res Commun. 1998;248:458–463. doi:10.1006/bbrc.1998.8998.
26. Tsukamoto H, Lu SC. Current concepts in the pathogenesis of alcoholic liver injury. Faseb J. 2001;15:1335–1349. doi:10.1096/fj.00-0650rev.
27. Mato JM, Martinez-Chantar ML, Lu SC. S-adenosylmethionine metabolism and liver disease. Ann Hepatol. 2013;12:183–189.
28. Cervelli M, Pietropaoli S, Signore F, Amendola R, Mariottini P. Polyamines metabolism and breast cancer: state of the art and perspectives. Breast Cancer Res Treat. 2014;148:233–248. doi:10.1007/s10549-014-3156-7.
29. Bae DH, Lane DJR, Jansson PJ, Richardson DR. The old and new biochemistry of polyamines. Biochim Biophys Acta. 2018;1862:2053–2068. doi:10.1016/j.bbagen.2018.06.004.
30. Olsen RR, Chung I, Zetter BR. Knockdown of antizyme inhibitor decreases prostate tumor growth in vivo. Amino Acids. 2012;42:549–558. doi:10.1007/s00726-011-1032-x.
31. Verna L, Whysner J, Williams GM. N-nitrosodiethylamine mechanistic data and risk assessment: bioactivation, DNA-adduct formation, mutagenicity, and tumor initiation. Pharmacol Ther. 1996;71:57–81.
32. Sanchez-Perez Y, Carrasco-Legleu C, Garcia-Cuellar C, Perez-Carreon J, Hernandez-Garcia S, Salcido-Neyoy M, Alemán-Lazarini L, Villa-Treviño S. Oxidative stress in carcinogenesis. Correlation between lipid peroxidation and induction of preneoplastic lesions in rat hepatocarcinogenesis. Cancer Lett. 2005;217:25–32. doi:10.1016/j.canlet.2004.07.019.
33. Velasco-Loyden G, Perez-Martinez L, Vidrio-Gomez S, Perez-Carreon JI, Chagoya de Sanchez V. Cancer chemoprevention by an adenosine derivative in a model of cirrhosis-hepatocellular carcinoma induced by diethylnitrosamine in rats. Tumour Biol. 2017;39:1010428317691190. doi:10.1177/1010428317691190.
34. Chavez E, Lozano-Rosas MG, Dominguez-Lopez M, Velasco-Loyden G, Rodriguez-Aguilera JR, Jose-Nunez C, Tuena de Gómez-Puyou M, Chagoya de Sánchez V. Functional, metabolic, and dynamic mitochondrial changes in the rat cirrhosis-hepatocellular carcinoma model and the protective effect of IFC-305. J Pharmacol Exp Ther. 2017;361:292–302. doi:10.1124/jpet.116.239301.
35. Yang HP, Zheng YH, Li TWH, Peng H, Fernandez-Ramos D, Martinez-Chantar ML, Rojas AL, Mato JM, Lu SC. Methionine adenosyltransferase 2B, HuR, and sirtuin 1 protein cross-talk impacts on the effect of resveratrol on apoptosis and growth in liver cancer cells (vol 288, pg 23161, 2013). J Biol Chem. 2014;289:696. doi:10.1074/jbc.A113.487157.
36. Garcia-Sainz JA, Hernandez-Munoz R, Glender W, Pina E, Chagoya de Sanchez V. Effects of adenosine on ethanol-induced modifications of liver metabolism. Role of hepatic redox state, purine and fatty acid metabolism. Biochem Pharmacol. 1980;29:1709–1714. doi:10.1016/0006-2952(80)90129-x.
37. Chagoya de Sanchez V, Hernandez-Munoz R, Yanez L, Vidrio S, Diaz-Munoz M. Possible mechanism of adenosine protection in carbon tetrachloride acute hepatotoxicity. Role of adenosine by-products and glutathione peroxidase. J Biochem Toxicol. 1995;10:41–50.
38. Lund P, Cornell NW, Krebs HA. Effect of adenosine on the adenine nucleotide content and metabolism of hepatocytes. Biochem J. 1975;152:593–599. doi:10.1042/bj1520593.
39. Lerner MH, Rubinstein D. The role of adenine and adenosine as precursors for adenine nucleotide synthesis by fresh and preserved human erythrocytes. Biochim Biophys Acta. 1970;224:301–310. doi:10.1016/0005-2787(70)90563-0.
40. Lu SC, Mato JM. S-Adenosylmethionine in cell growth, apoptosis and liver cancer. J Gastroenterol Hepatol. 2008;23(Suppl 1):S73–7. doi:10.1111/j.1440-1746.2007.05289.x.
41. Xu R, Wang D, Wang C, Zhang G, Wei G. Improved S-adenosylmethionine and glutathione biosynthesis by heterologous expression of an ATP6 gene in Candida utilis. J Basic Microbiol. 2018;58:875–882. doi:10.1002/jobm.201800151.

42. Martinez-Chantar ML, Vazquez-Chantada M, Garnacho M, Latasa MU, Varela-Rey M, Dotor J, Santamaria M, Martínez-Cruz LA, Parada LA, Lu SC, et al. S-adenosylmethionine regulates cytoplasmic HuR via AMP-activated kinase. Gastroenterology. 2006;131:223–232. doi:10.1053/j.gastro.2006.04.019.
43. Rodriguez-Aguilera JR, Guerrero-Hernandez C, Perez-Molina R, Cadena-Del-Castillo CE, de Vaca RP, Guerrero-Celis N, Domínguez-López M, Murillo-de-Ozores AR, Arzate-Mejía R, Recillas-Targa F, et al. Epigenetic effects of an adenosine derivative in a Wistar rat model of liver cirrhosis. J Cell Biochem. 2018;119(1):401–413. doi:10.1002/jcb.26192.
44. Aparicio-Bautista DI, Perez-Carreon JI, Gutierrez-Najera N, Reyes-Grajeda JP, Arellanes-Robledo J, Vasquez-Garzon VR, Jiménez-García MN, Villa-Treviño S. Comparative proteomic analysis of thiol proteins in the liver after oxidative stress induced by diethylnitrosamine. Biochim Biophys Acta. 2013;1834:2528–2538. doi:10.1016/j.bbapap.2013.08.005.
45. Damiani E, Wallace HM. Polyamines and Cancer. Methods Mol Biol. 2018;1694:469–488. doi:10.1007/978-1-4939-7398-9_39.
46. Chagoya de Sánchez V, Hernández-Muñoz R inventors. Uso de la adenosina para preparar medicamentos para el tratamiento de enfermedades hepáticas fibrosantes. Patent N° 220780. Mexico City: Instituto Mexicano de la Propiedad Intelectual; 2004.
47. Chagoya-Hazas V, Hernandez Munoz R, Villa-Trevino S inventors. Use of Adenosine Aspartate for the preparation of pharmaceutical products for the treatment of liver cancer. EE.UU. Patent Nº. 8,507,459 B2. Washington (DC): U.S. Patent and Trademark Office; 2013.
48. Chagoya de Sanchez V, Hernández-Muñoz R. Método para preparar aspartato de adenosina a partir de la adenosina, composición farmacéutica que las contiene y uso de las mismas en el tratamiento de enfermedades hepáticas fibrosantes. Patent N° 207422. Mexico City: Instituto Mexicano de la Propiedad Intelectual; 2002.
49. Schiffer E, Housset C, Cacheux W, Wendum D, Desbois-Mouthon C, Rey C, Clergue F, Poupon R, Barbu V, Rosmorduc O. Gefitinib, an EGFR inhibitor, prevents hepatocellular carcinoma development in the rat liver with cirrhosis. Hepatology. 2005;41:307–314. doi:10.1002/hep.20538.
50. Dyer RB, Herzog NK. Isolation of intact nuclei for nuclear extract preparation from a fragile B-lymphocyte cell line. Biotechniques. 1995;19:192–195.
51. Chagoya de Sanchez V, Martinez-Perez L, Hernandez-Munoz R, Velasco-Loyden G, McVicker BL, Tuma DJ, Wisecarver JL, Bailey SM. Recovery of the cell cycle inhibition in CCl(4)-induced cirrhosis by the adenosine derivative IFC-305. Int J Hepatol. 2012;2012:212530. doi:10.1155/2012/962183.
52. Ohkawa H, Ohishi N, Yagi K. Assay for lipid peroxides in animal tissues by thiobarbituric acid reaction. Anal Biochem. 1979;95:351–358. doi:10.1016/0003-2697(79)90738-3.
53. Hissin PJ, Hilf R. A fluorometric method for determination of oxidized and reduced glutathione in tissues. Anal Biochem. 1976;74:214–226. doi:10.1016/0003-2697(76)90326-2.
54. She QB, Nagao I, Hayakawa T, Tsuge H. A simple HPLC method for the determination of S-adenosylmethionine and S-adenosylhomocysteine in rat tissues: the effect of vitamin B6 deficiency on these concentrations in rat liver. Biochem Biophys Res Commun. 1994;205:1748–1754. doi:10.1006/bbrc.1994.2871.

INFORME DE LABORES 2019

Acta Histochemica 121 (2019) 151440

Contents lists available at ScienceDirect

Acta Histochemica

journal homepage: www.elsevier.com/locate/acthis

Differential expression and immunoreactivity of thyroid hormone transporters MCT8 and OATP1C1 in rat ovary

Enoch Luis[a,b], Yesenia Fernández[c], Mayvi Alvarado[d], Libertad Juárez-Santacruz[e], Edelmira García-Nieto[e], Arely Anaya-Hernández[c,e,*]

[a] Cátedra CONACYT – Laboratorio Nacional de Canalopatías, Instituto de Fisiología Celular, Universidad Autónoma de México, CDMX, Mexico
[b] Laboratorio Nacional de Canalopatías, Universidad Nacional Autónoma de México, CDMX, Mexico
[c] PE en Química Clínica, Facultad de Ciencias de la Salud, Universidad Autónoma de Tlaxcala, Tlaxcala, Mexico
[d] Departamento de Neurofisiología, Instituto de Neuroetología, Universidad Veracruzana, Xalapa, Veracruz, Mexico
[e] Centro de Investigación en Genética y Ambiente, Universidad Autónoma de Tlaxcala, Tlaxcala, Mexico

ARTICLE INFO

Keywords:
Monocarboxylate transporter
Organic anion transporting polypeptide
Thyroid hormone transporter
Ovary
Female reproduction

ABSTRACT

Thyroid hormones (THs) regulate several physiological processes in female mammals, many of which are related to reproduction such as steroidogenesis in the ovary, oocyte and granulosa cells maturation, follicular development and differentiation, and ovulation. THs actions require the presence of THs transporters to facilitate their cellular uptake and efflux. MCT8 and OATP1C1 are the principal THs transporters. The aim of the present study was to determine the gene expression and cellular localization of MCT8 and OATP1C1 in the rat ovary during the diestrus-II cycle phase. Ovaries of virgin adult rats were histologically processed. Reverse Transcription-PCR and immunohistochemistry analyses for MCT8 and OATP1C1 were done. MCT8 gene expression level was significantly higher ($P \leq 0.01$) than that of OATP1C1 in the rat ovary. MCT8 and OATP1C1 were found in all types of ovarian cells but with different immunoreactivity. MCT8 showed stronger immunoreactivity in tertiary and Graafian follicles, corpus luteum and blood vessels, whereas OATP1C1's immunoreactivity was stronger in stroma cells, tunica albuginea, and blood vessels. Our results provide evidence that THs and their transporters are both necessary for ovarian function and that any alteration in these transporters could interfere with reproductive processes such as ovulation and steroidogenesis, compromising fertility.

1. Introduction

There is substantial evidence in human and in animals that the hypothalamic-pituitary-thyroid axis plays a key role in female reproduction (Chen et al., 2015; Krassas et al., 2015; Vissenberg et al., 2015; Yoshimura, 2013). In the ovary, thyroid hormones (THs), triiodothyronine (T3) and thyroxine (T4), through their thyroid receptors (TRs), act as modulators of several physiological processes such as steroidogenesis, oocyte and granulosa cells maturation, follicular development and differentiation, and ovulation (Cecconi et al., 1999; Kobayashi et al., 2009; Maruo et al., 1987; Zheng et al., 2015). These receptors have been found in the ovarian surface epithelium, all ovarian follicles, the corpus luteum and corpus albicans indicating a relationship between the THs and the ovary (Aghajanova et al., 2009; Rodríguez-Castelán et al., 2017a; Wakim et al., 1994). Moreover, thyroid dysfunctions have been associated with disturbed folliculogenesis, impaired ovulation and fertilization rate, and in severe cases complete ovarian failure or cancer (Fedail et al., 2014; Hsieh et al., 2017; Meng et al., 2017; Rodríguez-Castelán et al., 2017b; Shinderman-Maman et al., 2016). These effects might be associated with altered levels of THs in the target cell, which depends on various factors. These factors include the concentration of the circulating THs, the activity of the iodothyronine deiodinases D1 and D2 which convert T4 into T3, D3 that converts T4 into T3 reverse (rT3) and T3 into diiodothyronine (T2); the presence of transporters in the plasma membrane is also a related factor (Friesema et al., 2005). In addition, the activity of THs requires the presence of THs transporters to facilitate their cellular uptake and efflux. Therefore, the deficiency of THs transporters can greatly compromise tissue THs homeostasis (Friesema et al., 2005; Müller and Heuer, 2014).

Several proteins are capable to transport THs across cell membranes. These proteins include some members of the monocarboxylate

* Corresponding author at: Centro de Investigación en Genética y Ambiente, Universidad Autónoma de Tlaxcala, México. Autopista Tlaxcala-San Martín, Km 10.5, C.P. 90120, Ixtacuixtla, Tlaxcala Mexico.
E-mail address: arely.anaya.h@uatx.mx (A. Anaya-Hernández).

https://doi.org/10.1016/j.acthis.2019.151440
Received 12 April 2019; Received in revised form 2 August 2019; Accepted 3 September 2019
0065-1281/ © 2019 Elsevier GmbH. All rights reserved.

INFORME DE LABORES 2019

transporters (MCT), organic anion transporter polypeptides (OATP), large neutral amino acid transporters (LAT) and the sodium/taurocholate cotransporting polypeptide (NTCP) families (Friesema et al., 2003, 2001, 1999; Hagenbuch, 2007; Pizzagalli et al., 2002; Visser et al., 2010). Interestingly, the identification of pathogenic mutations of THs transporters or their inactivation in animal models, indicate that only MCT8 and OATP1C1 have a pathophysiological role in thyroid hormone transport (Dumitrescu et al., 2006, 2004; Friesema et al., 2004; Mayerl et al., 2014; Schwartz et al., 2005; Trajkovic et al., 2007; Van Der Deure et al., 2008).

MCT8 (also known as MOT8 or XPCT) is a protein of about 67 kDa with 12 transmembrane domains (both N and C terminus have a cytoplasmic localization) encoded by the *SLC16A2* gene located on the human chromosome Xq13.2. MCT8 is a specific THs transporter that facilitates the uptake of T4, T3, rT3 and T2, but not of sulfated and sulfamated iodothyronines or aromatic amino acids (Phe, Leu, Tyr, and Trp) (Friesema et al., 2003; Lafrenière et al., 1994; Visser et al., 2011).

On the other hand, OATP1C1 (also known as OATP14 or OATP-F) is a protein with 12 transmembrane domains encoded by the *SLCO1C1* gene. OATP1C1 contributes to the membrane transport of THs (T3, T4, rT3, and T4 sulfate) (Pizzagalli et al., 2002; Sugiyama et al., 2003).

Both MCT8 and OATP1C1 are expressed in most tissues including the brain, liver, kidney, heart, thyroid, gastrointestinal tract, and testes (Cheng et al., 2005; Friesema et al., 2003; Kirat et al., 2013; Muzzio et al., 2014; Nishimura and Naito, 2008). Nevertheless, there is limited information about the expression of THs transporters in the mammal ovary and the cellular localization of MCT8 or OATP1C1 in the rat ovary remains unclear. Therefore, the aim of this study was to determine the expression, cellular localization, and immunoreactivity of MCT8 and OATP1C1 in the ovary of adult virgin rats.

2. Materials and methods

2.1. Animals and tissue preparation

Six adult virgin female Wistar rats (150–200 g) were maintained under a 14:10 h light/dark cycle (lights on 06:00 h) with food and water available *ad libitum* for this study. Their estrous cycle was determined by vaginal smears and after two regular consecutive cycles were chosen during the diestrus-II phase. Ovaries from rats were collected immediately after euthanized with an overdose of sodium pentobarbital (50 mg/kg, i.p., Pisa). Samples from ovaries for Reverse Transcription-PCR were frozen in liquid nitrogen and stored at −80 °C. For their use in immunohistochemistry, the samples were fixed in 4% paraformaldehyde in phosphate buffered saline (PBS) for 24 h, dehydrated, embedded in paraffin, serially sectioned at 7 µm and mounted on poly-L-lysine-coated slides. All procedures were conducted in accordance with the Mexican Law for Production, Care and Use of Laboratory Animals (NOM-062-ZOO-1999) under the approval and supervision of Universidad Autónoma de Tlaxcala, whose internal Bioethical Committee carefully reviewed and approved this research protocol.

2.2. RNA isolation and reverse Transcription-PCR

Total RNA was extracted from the right ovaries (n = 6) using TRI reagent (Sigma-Aldrich) followed by DNase treatment (RQ1 RNase-Free DNase; Promega), according to the manufacturer´s instructions. The RNA concentration was determined spectrophotometrically at 260 nm (6715 UV/Vis; Jenway), purity was assessed from the 260/280 absorbance ratio, where ratios obtained were between 1.9 and 2.0. The RNA integrity was electrophoretically evaluated on 1% agarose gel staining with ethidium bromide.

For each sample, cDNA was synthesized from 2 µg total RNA using 1 µl M-MLV Reverse Transcriptase (Promega, USA) mixed with 1 µl Oligo (dT) 10 µM (Sigma-Aldrich, USA), 1 µl dNTP Mix10 mM (Promega, USA) and RNase-free water (Sigma-Aldrich, USA) in a total volume of 20 µl according to the manufacturer's instructions. The reverse transcription reaction was performed, in a single run, in a Verity Thermal Cycler (Applied Biosystems) for 5 min at 70 °C followed for 60 min at 42 °C and finally for 15 min at 70 °C.

Table 1
Primers for PCR used in this study.

Gen /# Accession	Primer sequences (5´- 3´)	Length bp
SLC16A2 (MCT8)	F: CCCAAGCAAGAGAGGCGCCC	94
NM_147216.1	R: CGGTAGGTGCGCTGGCGAAA	
SLCO1C1 (OATP1C1)	F: GGATCCCCAGTGGGTCGGGG	82
NM_053441.1	R: ACCAGAAAGGCACGGCTGCA	
PPIA (CYCLOPHILIN A)	F: CCGCTGTCTCTTTTCGCC	128
NM_017101.1	R: GCTGTCTTTGGAACTTTGTCTG	

To investigate the mRNA expression of MCT8 and OATP1C1, PCR analysis was performed in triplicate and in different runs for each sample. Primers sequences for amplification of THs transporters were obtained from the literature (MCT8 and OATP1C1: de Souza et al., 2017; and PPIA, housekeeping gene: de Souza et al., 2015), and purchased from Sigma-Aldrich (USA). Details of the primers used in this study are shown in Table 1. PCR was performed with 1 µg of cDNA incubated with 1 µl of *Taq* DNA polymerase (Sigma-Aldrich, USA) and 1 µl of 10 µM specific primers. Thermal cycling conditions were established as follows: 94 °C for 3 min for initial denaturation; followed by 35 cycles of 94 °C for 30 s, with an annealing temperature of 55 °C for 30 s and 72 °C for 30 s; the final elongation step was set at 72 °C for 10 min. The cDNA was omitted for the negative control. PCR end products were detected by electrophoresis on 3% agarose gels stained with ethidium bromide and visualized on an UV-transilluminator (UVP). The relative levels of expression of MCT8, OATP1C1 and PPIA were analyzed by densitometry, determining the intensity of the bands by the area under its intensity profile curve using ImageJ software (NIH, USA). The results are expressed as the relative expression (average of three repetitions for each sample) and all results were normalized to the expression of the PPIA.

2.3. Immunohistochemical analysis

The avidin-biotin-peroxidase (ABC) method was performed on tissue sections to localize the THs transporters MCT8 and OATP1C1. We previously reported the immunostaining procedure (Anaya-Hernández et al., 2014), briefly, one slide per ovary and per rat was deparaffinized and incubated in a microwave oven in 10 mM sodium citrate (pH 6) to retrieve antigens. Endogenous peroxidase was quenched with 3% hydrogen peroxide at room temperature, and endogenous binding sites were blocked with 5% normal goat serum diluted in PBS with 0.3% Triton X-100 (PBST). The slides were incubated with the primary antibody (rabbit polyclonal anti-MOT8, Abcam, Cat. ab136980, 1:200; or rabbit polyclonal anti-SLCO1C1, ThermoFisher Scientific, Cat. PA5-42469, 1:200) diluted with PBST in a humidified chamber for 24 h at 4 °C. Subsequently, they were rinsed with PBST and incubated with the secondary antibody (biotinylated goat anti-rabbit IgG, ThermoFisher Scientific, Cat. 65–6140, 1:200) diluted in PBST for 2 h at room temperature in the humidified chamber, and then washed with PBS. Negative controls were done omitting the primary antibodies and incubated only with the secondary antibody. Immunostaining was developed using Vectastain ABC kit (Vector Labs, Burlingame, CA, USA), and 0.05% 3,3-diaminobenzidine with 0.03% H_2O_2 until a brown color was observed. Slides were counterstained with Mayer's hematoxylin, dehydrated, and were covered with the mounting medium and a coverslip. The preparations were examined under light microscope (Leica DM750), and images were acquired with 4×, 10×, 40× or 100× objectives (Camera Leica ICC50E, 5 M P). A semi-quantitative analysis of immunoreactivity to THs transporters in ovary cells was scored independently by 3 observers. Immunoreactivity to MCT8 and

INFORME DE LABORES 2019

OATP1C1 (separately) was done based on the intensity of brown color. Thus, dark-brown was considered as strong immunoreactivity (+++), light-brown was considered as weak immunoreactivity (+), and an intermediate color between dark-brown and light-brown was considered as moderate immunoreactivity (++) (Thongrod et al., 2019).

2.4. Statical analysis

All data of the relative gene expression were tested for normality (Kolmogorov-Smirnov), and analyzed by a *T*-test. Data are presented as mean ± SEM values (of three experiments). GraphPad Prism version 5.01 software (La Jolla, CA, USA) was used and differences were considered statistically significant at $P \leq 0.05$.

3. Results

3.1. Expression of MCT8 and OATP1C1

In the ovarian tissue, Reverse Transcription-PCR detected mRNA amplification products for MCT8 and OATP1C1. In this tissue, MCT8 gene expression level was significantly higher than that of OATP1C1 ($P < 0.01$; Fig. 1). No PCR products were detected in samples without mRNA (negative control).

3.2. Cellular immunolocalization of MCT8

All ovarian cell types showed immunoreactivity to MCT8 (Fig.1A; Table 2). Oocyte and follicular epithelium of primordial (Fig.1B), oocytes, theca and granulosa cells of primary (Fig.1C) and secondary follicles (Fig.1D, E), as well as stroma cells (Fig.1L) and tunica albuginea (Fig.1K) showed moderate labeling to MCT8; while in tertiary (Fig.1F, G) and Graafian follicles (Fig.1H, I) the intensity of immunoreaction in oocytes, theca, and granulosa cells was very high. In addition, the cells from corpus luteum (Fig.1J), the germinal epithelium (Fig.1K), blood vessels (Fig.1L), and adipose tissue (Fig.1M) showed very strong immunoreactivity. No immunoreactivity was seen in negative control ovary sections (Fig.1N).

Table 2
Immunoreactivity of MCT8 and OATP1C1 in the different ovarian cells of the virgin rat. Strong (+++), moderate (++) and weak (+) immunoreactivity.

	Cell type	MCT8	OATP1C1
Follicles	Primordial		
	oocyte	++	++
	follicular epithelium	++	++
	Primary		
	oocyte	++	+
	granulosa	++	+
	Secundary		
	oocyte	++	+
	granulosa	++	++
	theca	++	++
	Tertiary		
	oocyte	+++	+
	granulosa	+++	++
	theca	+++	++
	Graafian		
	oocyte	+++	+
	corona radiata	+++	++
	cumulous oophorus	+++	++
	granulosa	+++	++
	theca	+++	++
	Corpus luteum	+++	+
	Stroma	++	+++
	Tunica albuginea	++	+++
	Germinal epithelium	+++	+
	Blood vessels	+++	+++
	Adipose tissue	+++	+++

All ovarian cell types showed immunoreactivity to MCT8 (Fig. 2A; Table 2). Oocyte and follicular epithelium of primordial (Fig. 2B), oocytes, theca and granulosa cells of primary (Fig. 2C) and secondary follicles (Fig. 2D, E), as well as stroma cells (Fig. 2L) and tunica albuginea (Fig. 2K) showed moderate labeling to MCT8; while in tertiary (Fig. 2F, G) and Graafian follicles (Fig. 2H, I) the intensity of immunoreaction in oocytes, theca, and granulosa cells was very high. In addition, the cells from corpus luteum (Fig. 2J), the germinal epithelium (Fig. 2K), blood vessels (Fig. 2L), and adipose tissue (Fig. 2M) showed very strong immunoreactivity. No immunoreactivity was seen in negative control ovary sections (Fig.2N)

3.3. Cellular immunolocalization of OATP1C1

Ovarian cell types showed variable immunoreactivity to OATP1C1 (Fig. 3A; Table 2). Very weak immunoreactivity was observed in oocytes of primary (Fig. 3C), secondary (Fig.3D, E) and tertiary follicles (Fig.3F), and granulosa cells of primary (Fig. 3D), corpus luteum (Fig. 3J), and germinal epithelium (Fig.3K). Oocytes of primordial (Fig. 3B) and Graafian follicles (Fig. 3H), as well as granulosa and theca cells of secondary (Fig. 3G), tertiary and Graafian follicles showed moderate immunoreactivity. Cells from stroma (Fig. 3B), tunica albuginea (Fig. 3K), blood vessels (Fig.3L), and adipose tissue (Fig. 3M) showed very strong immunoreactivity. No immunoreactivity to OATP1C1 was seen in negative control ovary sections (Fig. 3N).

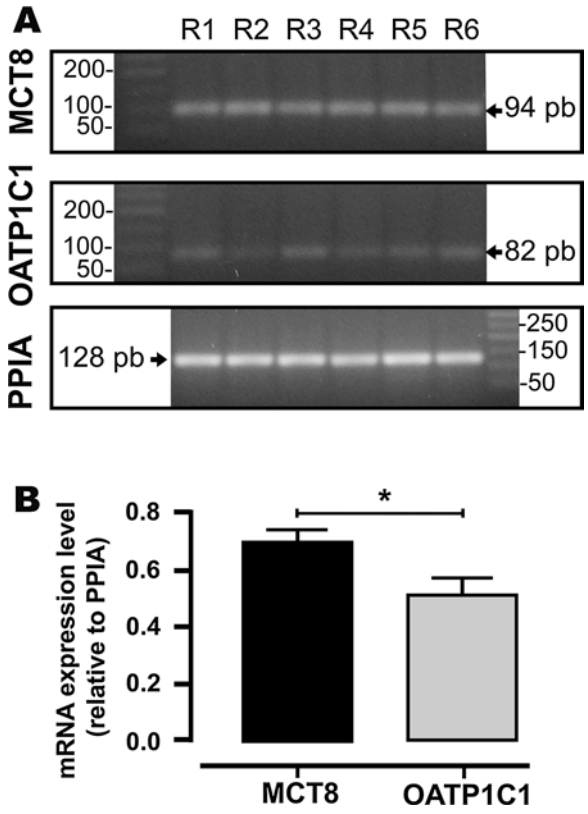

Fig. 1. Relative mRNA expression of MCT8 and OATP1C1 in the ovary from six rats (R1–R6). A) Representative PCR-amplified products in agarose gel stained with ethidium bromide. B) Densitometry analysis of gene expression, the results were normalized with the reference gene PPIA. Each bar represents the mean ± SEM of each gen (*$p \leq 0.01$).

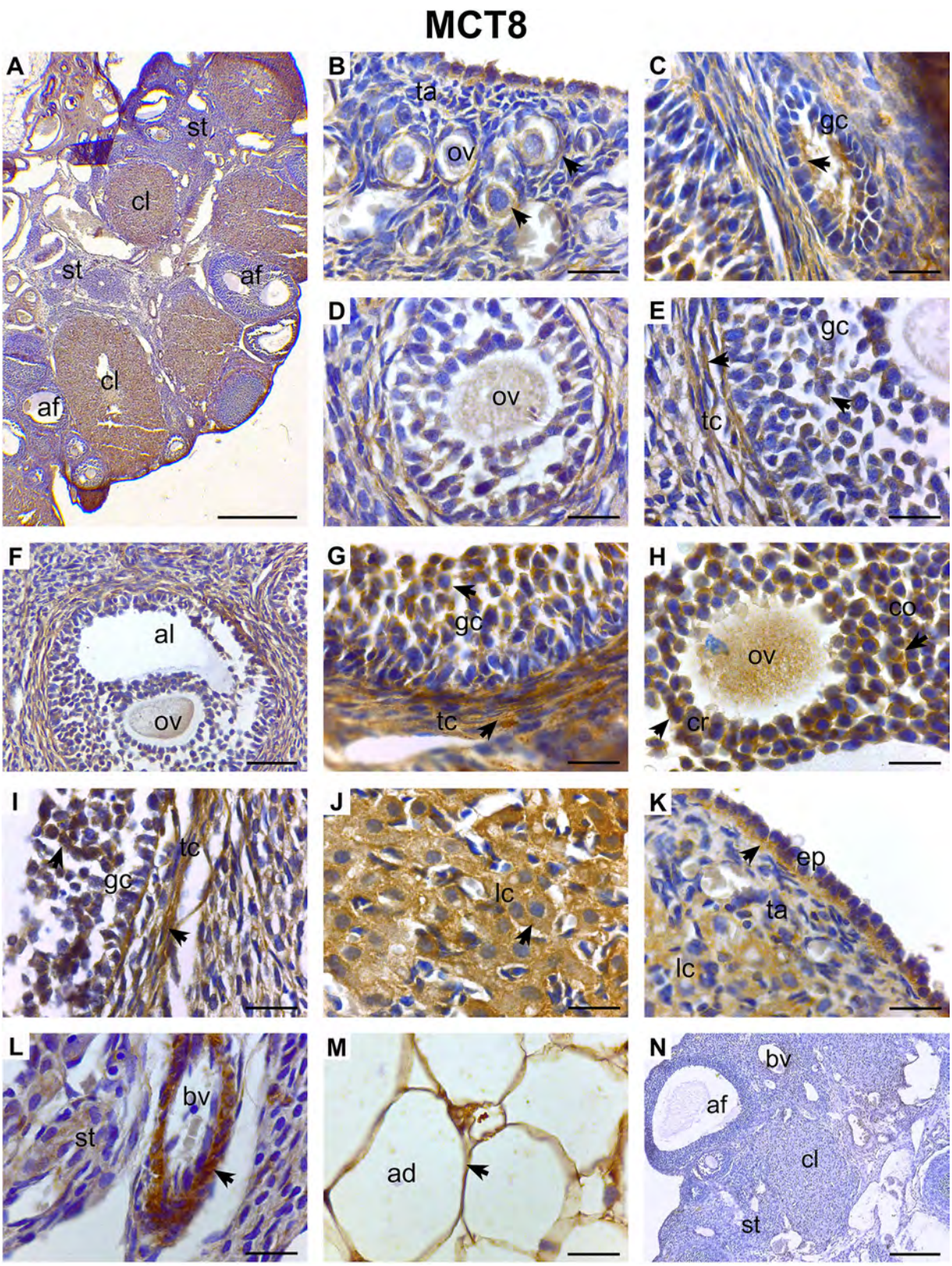

Fig. 2. Immunohistochemical localization of MCT8 in the ovary of virgin adult rat (A, K). Ovarian follicles (B–I), corpus luteum (J), blood vessel (L) and adipose tissue (M). Negative control (N). Abbreviations: af, antral follicle; cl, corpus luteum; st, stroma cells, ta, tunica albuginea; ov, oocito; gc, granulosa cells; tc, theca cells; cr, corona radiata; co, cumulus oophorus; lc, luteal cells; ep, epithelium germinal; bv, blood vessel; ad, adipose tissue. Scale bars: 500 μm in A; 500 μm in N; 50 μm in F; 20 μm in.B–E,G–M.

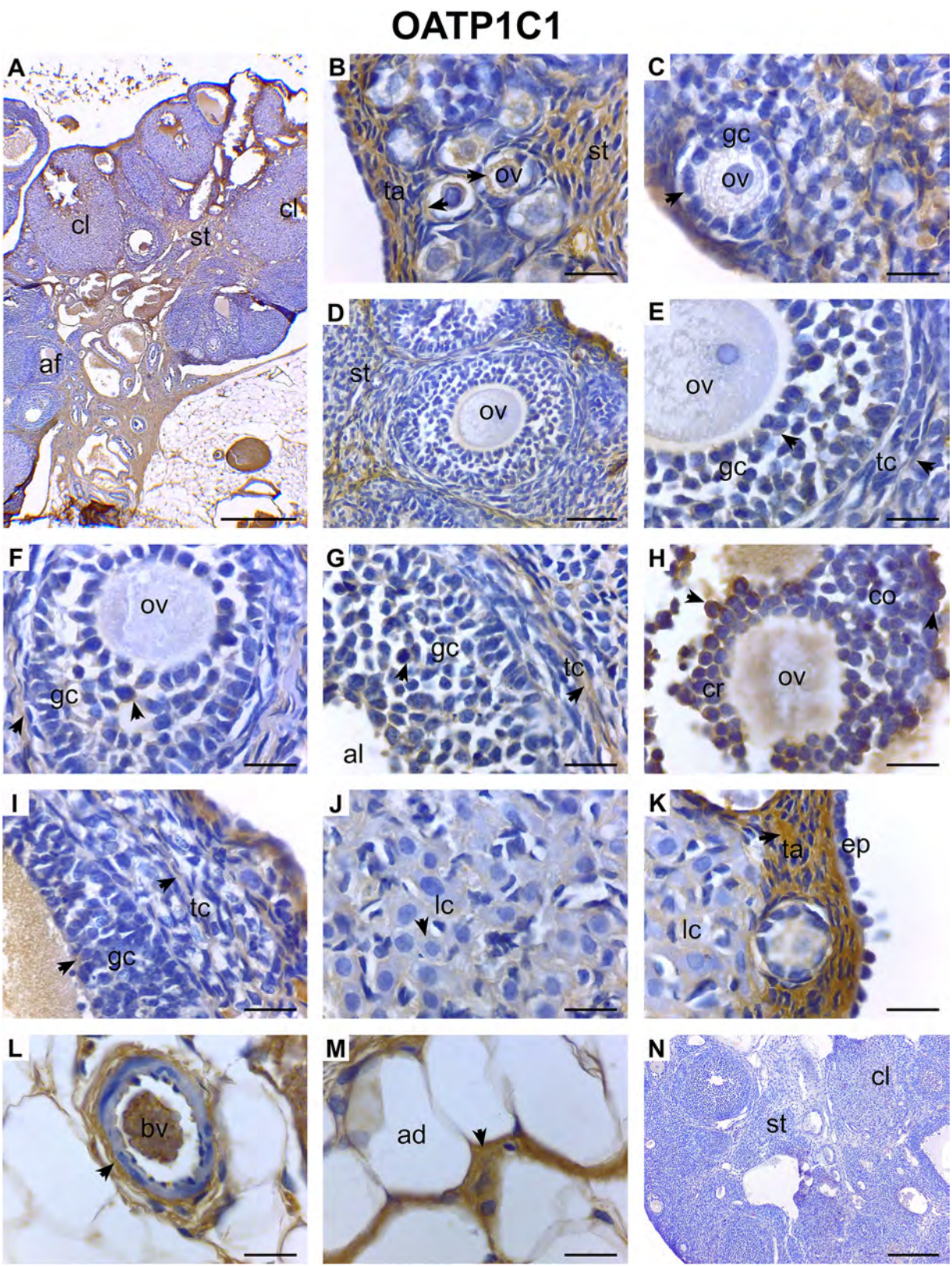

Fig. 3. Immunohistochemical localization of OATP1C1 in the ovary of virgin adult rat (A, K). Ovarian follicles (B–I), corpus luteum (*J*), blood vessel (L) and adipose tissue (M). Negative control (N). Abbreviations: af, antral follicle; cl, corpus luteum; st, stroma cells, ta, tunica albuginea; ov, oocito; gc, granulosa cells; tc, theca cells; cr, corona radiata; co, cumulus oophorus; lc, luteal cells; ep, epithelium germinal; bv, blood vessel; ad, adipose tissue. Scale bars: 500 μm in A; 200 μm in N; 20 μm in B–M.

INFORME DE LABORES 2019

4. Discussion

4.1. Expression of MCT8 and OATP1C1

This study shows that the ovary of the rat expresses the THs transporters MCT8 and OATP1C1. This is in accordance to the results reported for the ovary of other species (zebrafish, fathead minnow, mouse and human) where the presence of MCT8 mRNA (Arjona et al., 2011; Muzzio et al., 2014; Nishimura and Naito, 2008) and mRNA of OATP1C1 (Cheng et al., 2005; Muzzio et al., 2014) has been proved. In this study, we found that the MCT8 gene expression level was higher than that of OATP1C1, in contrast to what was reported in the ovary of teleost fish, fathead minnow (Muzzio et al., 2014). No data are available on the comparison of the expression of MCT8 and OATP1C1 in mammalian ovaries. In other reproductive tissue, such as the placenta of the Wistar rat, the expression of MCT8 is also higher than the expression of OATP1C1 (Sun et al., 2014).

Although MCT8 is part of the family of the MCTs, it has been characterized as an exclusive transporter of THs, specifically T3 and T4 (Bernal et al., 2015; Friesema et al., 2003). This suggests that the expression of MCT8 shown by the ovarian tissue is given as a function of the thyroid status as seen in other tissues (Engels et al., 2015). On the other hand, OATP1C1 has an average affinity for transporting THs, and sulfated T3 and T4 (Bernal et al., 2015; Visser et al., 2011). In addition to transporting THs, OATP1C1 can also transport sulfated estrone-3-sulfate and estradiol-17β-glucuronide (Visser et al., 2011). In this case, the functional role of the OATP1C1 transporter is very important, allowing not only the efflux of THs but also of metabolites of steroid hormones.

This study is the first to show the cellular localization and the differential immunoreactivity of both THs transporters in all ovarian cell types of the adult virgin rat.

4.2. Cellular immunolocalization of MCT8

The immunoreactivity of MCT8 was found in all ovarian structures. The fact that antral follicles, as well as the corpus luteum, show an abundant immunoreactivity of MCT8 may be related to the function of THs in these structures. The ovarian follicles (primordial, primary, secondary, tertiary and Graaf) are susceptible to the action of THs. Therefore, by synergizing with follicle-stimulating hormone (FSH), THs regulate the development and maturation of granulosa, theca and oocyte cells, as well as the regulation of steroidogenesis (Fedail et al., 2014; Liu et al., 2017; Zhang et al., 2013). Due to this, both the oocyte and the granulosa cells (including the radiated corona and the oophorous cumulus) and the theca express the TRα and TRβ (Aghajanova et al., 2009; Rodríguez-Castelán et al., 2017a; Wakim et al., 1994). In this study, we found an abundant immunoreactivity of MCT8 in tertiary and Graafian follicles, which could be related to the degree of maturity from several processes mediated by developmental thyroid hormone signal. Since this work is the first to demonstrate the cellular immunoreactivity of MCT8, comparison with previous studies is not possible. Nevertheless, research shows that in other mammal tissues the expression of MCT8 is also differentially influenced by cellular type, physiological condition and thyroid status (Alkemade et al., 2011; Alvarez-Salas et al., 2016; Arjona et al., 2011; Engels et al., 2015; Kirat et al., 2013).

It has been described that in the corpus luteum of mammals, THs have different functions, including regulating proliferation, apoptosis, and angiogenesis for luteal cells maintenance, and secretion of progesterone (Macchiarelli et al., 2013; Navas et al., 2014; Silva et al., 2013). In addition, the corpus luteum expresses the TRα and TRβ that help the THs carry out the functions described above (Aghajanova et al., 2009; Rodríguez-Castelán et al., 2017a; Wakim et al., 1994). The abundant immunoreactivity of the MCT8 transporter found in the corpus luteum of the rat demonstrates the importance of the THs in this structure. Adipose tissue also shows an abundant immunoreactivity of MCT8, this is because THs regulates adipogenesis, mobilization, and storage of lipids, inflammation and insulin sensitivity (Obregon, 2014; Panveloski-Costa et al., 2018).

4.3. Cellular immunolocalization of OATP1C1

The ovarian cells of the virgin adult rat show immunoreactivity to the OATP1C1 transporter. The ovarian structures that exhibit the highest immunoreactivity to OATP1C1 are the tertiary and Graafian follicles, as well as the stroma and tunica albuginea. This could be because these structures are targets of THs (Fedail et al., 2014; Zhang et al., 2013).

Likewise, the adipose tissue also has an abundant immunoreactivity to OATP1C1, possibly because adipocytes, like the ovary, secrete estrone and store it as sulfated estrone, which requires OATP1C1 to enter and leave the cell (Bernal et al., 2015; Ihunnah et al., 2014).

The higher immunoreactivity to MCT8 and OATP1C1 observed in the blood vessels can be explained by the fact that the molecules that transport these proteins (T4, T3, T2, T3S, T4S, rT3) must pass through the bloodstream to reach the cells that require them (Bernal et al., 2015; Visser et al., 2011).

In conclusion, our results provide evidence that the rat ovary expresses the THs transporters MCT8 and OATP1C1, which could play a key role in ovary responses to circulating THs. Furthermore, the results indicate that some alteration in these transporters could interfere with reproductive processes, such as ovulation and steroidogenesis, compromising the fertility of the female. In addition, our findings in the ovarian tissue provide a basis to the study of the THs transporters on different physiological conditions.

Author contributions

EL, YF, MA, AAH carried out the experiment. EL, MA, LJS, EGN contributed with reagents, materials, analysis tools, as well as to the interpretation of the results and helped supervise the project. EL and AAH contributed to the conception and design of the study and drafting the article. All authors discussed the results, contributed, and approved to the final manuscript.

CRediT authorship contribution statement

Enoch Luis: Conceptualization, Investigation, Resources, Supervision, Validation, Writing - review & editing. **Yesenia Fernández:** Investigation, Validation, Visualization, Writing - review & editing. **Mayvi Alvarado:** Investigation, Resources, Supervision, Validation, Writing - review & editing. **Libertad Juárez-Santacruz:** Resources, Supervision, Validation, Writing - review & editing. **Edelmira García-Nieto:** Resources, Supervision, Validation, Writing - review & editing. **Arely Anaya-Hernández:** Conceptualization, Formal analysis, Investigation, Methodology, Project administration, Supervision, Validation, Visualization, Writing - original draft, Conceptualization.

Declaration of Competing Interest

The authors declare no conflicts of interest.

Acknowledgments

Authors thank LANISAF (UACh-UATx) project. AAH, thanks to the postdoctoral fellowship PRODEP (511-6/17-3560) and to Fis. César Oliver Lara Figueroa (from Laboratorio Nacional de Canalopatías) for the excellent technical assistance. The language revision of Pamela Robles Martínez is also acknowledged.

INFORME DE LABORES 2019

References

Aghajanova, L., Lindeberg, M., Carlsson, I.B., Stavreus-Evers, A., Zhang, P., Scott, J.E., Hovatta, O., Skjöldebrand-Sparre, L., 2009. Receptors for thyroid-stimulating hormone and thyroid hormones in human ovarian tissue. Reprod. Biomed. Online 18, 337–347. https://doi.org/10.1016/S1472-6483(10)60091-0.

Alkemade, A., Friesema, E.C., Kalsbeek, A., Swaab, D.F., Visser, T.J., Fliers, E., 2011. Expression of thyroid hormone transporters in the human hypothalamus. J. Clin. Endocrinol. Metab. 96, E967–E971. https://doi.org/10.1210/jc.2010-2750.

Alvarez-Salas, E., Mengod, G., García-Luna, C., Soberanes-Chávez, P., Matamoros-Trejo, G., de Gortari, P., 2016. Mct8 and trh co-expression throughout the hypothalamic paraventricular nucleus is modified by dehydration-induced anorexia in rats. Neuropeptides 56, 33–40. https://doi.org/10.1016/j.npep.2015.11.001.

Anaya-Hernández, A., Méndez-Tepepa, M., Hernández-Aragón, L.G., Pacheco, P., Martínez-Gómez, M., Castelán, F., Cuevas, E., 2014. Farnesoid X receptor immunolocalization in reproductive tissues of adult female rabbits. Acta Histochem. 116, 1068–1074. https://doi.org/10.1016/j.acthis.2014.05.003.

Arjona, F.J., de Vrieze, E., Visser, T.J., Flik, G., Klaren, P.H., 2011. Identification and functional characterization of zebrafish solute carrier Slc16a2 (Mct8) as a thyroid hormone membrane transporter. Endocrinology 152, 5065–5073. https://doi.org/10.1210/en.2011-1166.

Bernal, J., Guadaño-Ferraz, A., Morte, B., 2015. Thyroid hormone transporters-functions and clinical implications. Nat. Rev. Endocrinol. 11, 406–417. https://doi.org/10.1038/nrendo.2015.66.

Cecconi, S., Rucci, N., Scaldaferri, M.L., Masciulli, M.P., Rossi, G., Moretti, C., D'Armiento, M., Ulisse, S., 1999. Thyroid hormone effects on mouse oocyte maturation and granulosa cell aromatase activity. Endocrinology 140, 1783–1788. https://doi.org/10.1210/endo.140.4.6635.

Chen, C.Y., Chen, C.P., Lin, K.H., 2015. Biological functions of thyroid hormone in placenta. Int. J. Mol. Sci. 16, 4161–4179. https://doi.org/10.3390/ijms16024161.

Cheng, X., Maher, J., Chen, C., Klaassen, C.D., 2005. Tissue distribution and ontogeny of mouse organic anion transporting polypeptides (Oatps). Drug Metab. Dispos. 33, 1062–1063. https://doi.org/10.1124/dmd.105.003640.

de Souza, E.C., Dias, G.R., Cardoso, R.C., Lima, L.P., Fortunato, R.S., Visser, T.J., Vaisman, M., Ferreira, A.C., Carvalho, D.P., 2015. MCT8 is downregulated by short time iodine overload in the thyroid gland of rats. Horm. Metab. Res. 47, 910–915. https://doi.org/10.1055/s-0035-1550008.

de Souza, J.S., Kizys, M.M., da Conceição, R.R., Glebocki, G., Romano, R.M., Ortiga-Carvalho, T.M., Giannocco, G., da Silva, I.D., Dias da Silva, M.R., Romano, M.A., Chiamolera, M.I., 2017. Perinatal exposure to glyphosate-based herbicide alters the thyrotrophic axis and causes thyroid hormone homeostasis imbalance in male rats. Toxicology 377, 25–37. https://doi.org/10.1016/j.tox.2016.11.005.

Dumitrescu, A.M., Liao, X.H., Best, T.B., Brockmann, K., Refetoff, S., 2004. A novel syndrome combining thyroid and neurological abnormalities is associated with mutations in a monocarboxylate transporter gene. Am. J. Hum. Genet. 74, 168–175. https://doi.org/10.1086/380999.

Dumitrescu, A.M., Liao, X.H., Weiss, R.E., Millen, K., Refetoff, S., 2006. Tissue-specific thyroid hormone deprivation and excess in monocarboxylate transporter (mct) 8-deficient mice. Endocrinology 147, 4036–4043. https://doi.org/10.1210/en.2006-0390.

Engels, K., Rakov, H., Zwanziger, D., Moeller, L.C., Homuth, G., Köhrle, J., Brix, K., Führer, D., 2015. Differences in mouse hepatic thyroid hormone transporter expression with age and hyperthyroidism. Eur. Thyroid J. 4, 81–86. https://doi.org/10.1159/000381020.

Fedail, J.S., Zheng, K., Wei, Q., Kong, L., Shi, F., 2014. Roles of thyroid hormones in follicular development in the ovary of neonatal and immature rats. Endocrine 46, 594–604. https://doi.org/10.1007/s12020-013-0092-y.

Friesema, E.C., Docter, R., Moerings, E.P., Stieger, B., Hagenbuch, B., Meier, P.J., Krenning, E.P., Hennemann, G., Visser, T.J., 1999. Identification of thyroid hormone transporters. Biochem. Biophys. Res. Commun. 254, 497–501. https://doi.org/10.1006/bbrc.1998.9974.

Friesema, E.C., Docter, R., Moerings, E.P., Verrey, F., Krenning, E.P., Hennemann, G., Visser, T.J., 2001. Thyroid hormone transport by the heterodimeric human system L amino acid transporter. Endocrinology 142, 4339–4348. https://doi.org/10.1210/endo.142.10.8418.

Friesema, E.C., Ganguly, S., Abdalla, A., Manning Fox, J.E., Halestrap, A.P., Visser, T.J., 2003. Identification of monocarboxylate transporter 8 as a specific thyroid hormone transporter. J. Biol. Chem. 278, 40128–40135. https://doi.org/10.1074/jbc.M300909200.

Friesema, E.C., Grueters, A., Biebermann, H., Krude, H., von Moers, A., Reeser, M., Barrett, T.G., Mancilla, E.E., Svensson, J., Kester, M.H., Kuiper, G.G., Balkassmi, S., Uitterlinden, A.G., Koehrle, J., Rodien, P., Halestrap, A.P., Visser, T.J., 2004. Association between mutations in a thyroid hormone transporter and severe X-linked psychomotor retardation. Lancet 364, 1435–1437. https://doi.org/10.1016/S0140-6736(04)17226-7.

Friesema, E.C., Jansen, J., Milici, C., Visser, T.J., 2005. Thyroid hormone transporters. Vitam. Horm. 70, 137–167. https://doi.org/10.1016/S0083-6729(05)70005-4.

Hagenbuch, B., 2007. Cellular entry of thyroid hormones by organic anion transporting polypeptides. Best Pract. Res. Clin. Endocrinol. Metab. 21, 209–221. https://doi.org/10.1016/j.beem.2007.03.004.

Hsieh, M.T., Wang, L.M., Changou, C.A., Chin, Y.T., Yang, Y.S.H., Lai, H.Y., Lee, S.Y., Yang, Y.N., Whang-Peng, J., Liu, L.F., Lin, H.Y., Mousa, S.A., Davis, P.J., 2017. Crosstalk between integrin αvβ3 and ERα contributes to thyroid hormone-induced proliferation of ovarian cancer cells. Oncotarget 8, 24237–24249. https://doi.org/10.18632/oncotarget.10757.

Ihunnah, C.A., Wada, T., Philips, B.J., Ravuri, S.K., Gibbs, R.B., Kirisci, L., Rubin, J.P., Marra, K.G., Xie, W., 2014. Estrogen sulfotransferase/SULT1E1 promotes human adipogenesis. Mol. Cell. Biol. 34, 1682–1694. https://doi.org/10.1128/MCB.01147-13.

Kirat, D., Sallam, K.I., Kato, S., 2013. Expression and cellular localization of monocarboxylate transporters (MCT2, MCT7, and MCT8) along the cattle gastrointestinal tract. Cell Tissue Res. 352, 585–598. https://doi.org/10.1007/s00441-013-1570-5.

Kobayashi, N., Orisaka, M., Cao, M., Kotsuji, F., Leader, A., Sakuragi, N., Tsang, B.K., 2009. Growth differentiation factor-9 mediates follicle-stimulating hormone-thyroid hormone interaction in the regulation of rat preantral follicular development. Endocrinology 150, 5566–5574. https://doi.org/10.1210/en.2009-0262.

Krassas, G., Karras, S.N., Pontikides, N., 2015. Thyroid diseases during pregnancy: a number of important issues. Hormones 14, 59–69. https://doi.org/10.1007/BF03401381.

Lafrenière, R.G., Carrel, L., Willard, H.F., 1994. A novel transmembrane transporter encoded by the XPCT gene in Xq13.2. Hum. Mol. Genet. 3, 1133–1139. https://doi.org/10.1093/hmg/3.7.1133.

Liu, J., Tian, Y., Ding, Y., Heng, D., Xu, K., Liu, W., Zhang, C., 2017. Role of CYP51 in the regulation of T3 and FSH-induced steroidogenesis in female mice. Endocrinology 158, 3974–3987. https://doi.org/10.1210/en.2017-00249.

Macchiarelli, G., Palmerini, M.G., Nottola, S.A., Cecconi, S., Tanemura, K., Sato, E., 2013. Restoration of corpus luteum angiogenesis in immature hypothyroid rdw rats after thyroxine treatment: morphologic and molecular evidence. Theriogenology 79, 116–126. https://doi.org/10.1016/j.theriogenology.2012.09.016.

Maruo, T., Hayashi, M., Matsuo, H., Yamamoto, T., Okada, H., Mochizuki, M., 1987. The role of thyroid hormone as a biological amplifier of the actions of follicle-stimulating hormone in the functional differentiation of cultured porcine granulosa cells. Endocrinology 121, 1233–1241. https://doi.org/10.1210/endo-121-4-1233.

Mayerl, S., Müller, J., Bauer, R., Richert, S., Kassmann, C.M., Darras, V.M., Buder, K., Boelen, A., Visser, T.J., Heuer, H., 2014. Transporters MCT8 and OATP1C1 maintain murine brain thyroid hormone homeostasis. J. Clin. Invest. 124, 1987–1999. https://doi.org/10.1172/JCI70324.

Meng, L., Rijntjes, E., Swarts, H.J., Keijer, J., Teerds, K.J., 2017. Prolonged hypothyroidism severely reduces ovarian follicular reserve in adult rats. J. Ovarian Res. 10, 19. https://doi.org/10.1186/s13048-017-0314-7.

Müller, J., Heuer, H., 2014. Expression pattern of thyroid hormone transporters in the postnatal mouse brain. Front. Endocrinol. (Lausanne) 5, 92. https://doi.org/10.3389/fendo.2014.00092.

Muzzio, A.M., Noyes, P.D., Stapleton, H.M., Lema, S.C., 2014. Tissue distribution and thyroid hormone effects on mRNA abundance for membrane transporters Mct8, Mct10, and organic anion-transporting polypeptides (Oatps) in a teleost fish. Comp. Biochem. Physiol. A Mol. Integr. Physiol. 167, 77–89. https://doi.org/10.1016/j.cbpa.2013.09.019.

Navas, P.B., Redondo, A.L., Cuello-Carrión, F.D., Roig, L.M., Valdez, S.R., Jahn, G.A., Hapon, M.B., 2014. Luteal expression of thyroid hormone receptors during gestation and postpartum in the rat. Thyroid. 24, 1040–1050. https://doi.org/10.1089/thy.2013.0332.

Nishimura, M., Naito, S., 2008. Tissue-specific mRNA expression profiles of human solute carrier transporter superfamilies. Drug Metab. Pharmacokinet. 23, 22–44.

Obregon, M.J., 2014. Adipose tissues and thyroid hormones. Front. Physiol. 5, 479. https://doi.org/10.3389/fphys.2014.00479.

Panveloski-Costa, A.C., Serrano-Nascimento, C., Bargi-Souza, P., Poyares, L.L., Viana, G.S., Nunes, M.T., 2018. Beneficial effects of thyroid hormone on adipose inflammation and insulin sensitivity of obese Wistar rats. Physiol. Rep. 6, e13550. https://doi.org/10.14814/phy2.13550.

Pizzagalli, F., Hagenbuch, B., Stieger, B., Klenk, U., Folkers, G., Meier, P.J., 2002. Identification of a novel human organic anion transporting polypeptide as a high affinity thyroxine transporter. Mol. Endocrinol. 16, 2283–2296. https://doi.org/10.1210/me.2001-0309.

Rodríguez-Castelán, J., Anaya-Hernández, A., Méndez-Tepepa, M., Martínez-Gómez, M., Castelán, F., Cuevas-Romero, E., 2017a. Distribution of thyroid hormone and thyrotropin receptors in reproductive tissues of adult female rabbits. Endocr. Res. 42, 59–70. https://doi.org/10.1080/07435800.2016.1182185.

Rodríguez-Castelán, J., Méndez-Tepepa, M., Carrillo-Portillo, Y., Anaya-Hernández, A., Rodríguez-Antolín, J., Zambrano, E., Castelán, F., Cuevas-Romero, E., 2017b. Hypothyroidism reduces the size of ovarian follicles and promotes hypertrophy of periovarian fat with infiltration of macrophages in adult rabbits. Biomed Res. Int. 2017, 3795950. https://doi.org/10.1155/2017/3795950.

Schwartz, C.E., May, M.M., Carpenter, N.J., Rogers, R.C., Martin, J., Bialer, M.G., Ward, J., Sanabria, J., Marsa, S., Lewis, J.A., Echeverri, R., Lubs, H.A., Voeller, K., Simensen, R.J., Stevenson, R.E., 2005. Allan-Herndon-Dudley syndrome and the monocarboxylate transporter 8 (MCT8) gene. Am. J. Hum. Genet. 77, 41–53. https://doi.org/10.1086/431313.

Shinderman-Maman, E., Cohen, K., Weingarten, C., Nabriski, D., Twito, O., Baraf, L., Hercbergs, A., Davis, P.J., Werner, H., Ellis, M., Ashur-Fabian, O., 2016. The thyroid hormone-αvβ3 integrin axis in ovarian cancer: regulation of gene transcription and MAPK-dependent proliferation. Oncogene 35, 1977–1987. https://doi.org/10.1038/onc.2015.262.

Silva, J.F., Ocarino, N.M., Vieira, A.L., Nascimento, E.F., Serakides, R., 2013. Effects of hypo- and hyperthyroidism on proliferation, angiogenesis, apoptosis and expression of COX-2 in the corpus luteum of female rats. Reprod. Domest. Anim. 48, 691–698. https://doi.org/10.1111/rda.12149.

Sugiyama, D., Kusuhara, H., Taniguchi, H., Ishikawa, S., Nozaki, Y., Aburatani, H., Sugiyama, Y., 2003. Functional characterization of rat brain-specific organic anion transporter (Oatp14) at the blood-brain barrier: high affinity transporter for thyroxine. J. Biol. Chem. 278, 43489–43495. https://doi.org/10.1074/jbc.M306933200.

Sun, Y.N., Liu, Y.J., Zhang, L., Ye, Y., Lin, L.X., Li, Y.M., Yan, Y.Q., Chen, Z.P., 2014. Expression of organic anion transporting polypeptide 1c1 and monocarboxylate transporter 8 in the rat placental barrier and the compensatory response to thyroid dysfunction. PLoS One 9, e96047. https://doi.org/10.1371/journal.pone.0096047.

Thongrod, S., Wanichanon, C., Sobhon, P., 2019. Distribution of neuropeptide F in the ventral nerve cord and its possible role on testicular development and germ cell proliferation in the giant freshwater prawn, Macrobrachium rosenbergii. Cell Tissue Res. 376, 471–484. https://doi.org/10.1007/s00441-019-02999-8.

Trajkovic, M., Visser, T.J., Mittag, J., Horn, S., Lukas, J., Darras, V.M., Raivich, G., Bauer, K., Heuer, H., 2007. Abnormal thyroid hormone metabolism in mice lacking the monocarboxylate transporter 8. J. Clin. Invest. 117, 627–635. https://doi.org/10.1172/JCI28253.

Van Der Deure, W.M., Appelhof, B.C., Peeters, R.P., Wiersinga, W.M., Wekking, E.M., Huyser, J., Schene, A.H., Tijssen, J.G.P., Hoogendijk, W.J.G., Visser, T.J., Fliers, E., 2008. Polymorphisms in the brain-specific thyroid hormone transporter OATP1C1 are associated with fatigue and depression in hypothyroid patients. Clin. Endocrinol. (Oxf). 69, 804–811. https://doi.org/10.1111/j.1365-2265.2008.03267.x.

Vissenberg, R., Manders, V.D., Mastenbroek, S., Fliers, E., Afink, G.B., Ris-Stalpers, C., Goddijn, M., Bisschop, P.H., 2015. Pathophysiological aspects of thyroid hormone disorders/thyroid peroxidase autoantibodies and reproduction. Hum. Reprod. Update 21, 378–387. https://doi.org/10.1093/humupd/dmv004.

Visser, W.E., Friesema, E.C.H., Visser, T.J., 2011. Minireview: thyroid hormone transporters: the knowns and the unknowns. Mol. Endocrinol. 25, 1–14. https://doi.org/10.1210/me.2010-0095.

Visser, W.E., Wong, W.S., van Mullem, A.A.A., Friesema, E.C.H., Geyer, J., Visser, T.J., 2010. Study of the transport of thyroid hormone by transporters of the SLC10 family. Mol. Cell. Endocrinol. 315, 138–145. https://doi.org/10.1016/j.mce.2009.08.003.

Wakim, A.N., Paljug, W.R., Jasnosz, K.M., Alhakim, N., Brown, A.B., Burholt, D.R., 1994. Thyroid hormone receptor messenger ribonucleic acid in human granulosa and ovarian stromal cells. Fertil. Steril. 62, 531–534. https://doi.org/10.1016/S0015-0282(16)56941-6.

Yoshimura, T., 2013. Thyroid hormone and seasonal regulation of reproduction. Front. Neuroendocrinol. 34, 157–166. https://doi.org/10.1016/j.yfrne.2013.04.002.

Zhang, C., Guo, L., Zhu, B., Feng, Y., Yu, S., An, N., Wang, X., 2013. Effects of 3, 5, 3′-triiodothyronine (T3) and follicle stimulating hormone on apoptosis and proliferation of rat ovarian granulosa cells. Chin. J. Physiol. 56, 298–305. https://doi.org/10.4077/CJP.2013.BAB186.

Zheng, K., Sulieman, F.J., Li, J., Wei, Q., Xu, M., Shi, F., 2015. Nitric oxide and thyroid hormone receptor alpha 1 contribute to ovarian follicular development in immature hyper- and hypo-thyroid rats. Reprod. Biol. 15, 27–33. https://doi.org/10.1016/j.repbio.2014.11.002.

Published online 18 April 2019

Nucleic Acids Research, 2019, Vol. 47, No. 12 ***6425–6438***
doi: 10.1093/nar/gkz285

A screening platform to monitor RNA processing and protein-RNA interactions in ribonuclease P uncovers a small molecule inhibitor

Ezequiel-Alejandro Madrigal-Carrillo[1,†], Carlos-Alejandro Díaz-Tufinio[1,2,†], Hugo-Aníbal Santamaría-Suárez[1], Marcelino Arciniega[1] and Alfredo Torres-Larios[1,*]

[1]Department of Biochemistry and Structural Biology, Instituto de Fisiología Celular, Universidad Nacional Autónoma de México, Mexico City, Mexico and [2]Tecnologico de Monterrey, Escuela de Ingeniería y Ciencias, Mexico City, Mexico

Received October 26, 2018; Revised April 08, 2019; Editorial Decision April 09, 2019; Accepted April 10, 2019

ABSTRACT

Ribonucleoprotein (RNP) complexes and RNA-processing enzymes are attractive targets for antibiotic development owing to their central roles in microbial physiology. For many of these complexes, comprehensive strategies to identify inhibitors are either lacking or suffer from substantial technical limitations. Here, we describe an activity-binding-structure platform for bacterial ribonuclease P (RNase P), an essential RNP ribozyme involved in 5′ tRNA processing. A novel, real-time fluorescence-based assay was used to monitor RNase P activity and rapidly identify inhibitors using a mini-helix and a pre-tRNA-like bipartite substrate. Using the mini-helix substrate, we screened a library comprising 2560 compounds. Initial hits were then validated using pre-tRNA and the pre-tRNA-like substrate, which ultimately verified four compounds as inhibitors. Biolayer interferometry-based binding assays and molecular dynamics simulations were then used to characterize the interactions between each validated inhibitor and the P protein, P RNA and pre-tRNA. X-ray crystallographic studies subsequently elucidated the structure of the P protein bound to the most promising hit, purpurin, and revealed how this inhibitor adversely affects tRNA 5′ leader binding. This integrated platform affords improved structure-function studies of RNA processing enzymes and facilitates the discovery of novel regulators or inhibitors.

INTRODUCTION

Regulatory RNAs, ribozymes, and RNA-protein complexes are appealing antibiotic targets due to their essential functions in microbial metabolism (1–3). This clinical importance is exemplified by the ribosome, which is currently the target of roughly 50% of known antibiotics (4). The focus of this work is Ribonuclease P (RNase P), the only ribozyme other than the ribosome that is present in all three domains of life (see (5–8) for some reviews). This essential ribonucleoprotein complex remains to be exploited as a target for much-needed novel antibacterial agents (9).

The composition of RNase P varies across the three domains of life (10) and therefore may afford high selectivity in drug targeting (11,12). While in archaea and eukaryotes, RNase P is comprised of one RNA subunit and four to ten proteins (13), in bacteria, this complex is formed by an RNA subunit (P RNA, 350–400 nucleotides, 110–125 kDa) and a single protein (P protein, ∼110 amino acids, 13 kDa) (14). In all species, the P RNA serves as the primary biocatalyst (15) for the cleavage of the 5′-leader sequence of pre-tRNAs during tRNA maturation (16). The P protein, on the other hand, binds the distal 5′-leader region of the pre-tRNA substrate, enhances the affinity of metal ions, and assists in product release (17–20). RNase P is dependent on divalent metal ions (Mg^{2+} is needed for proper folding and activity (21–23)) and *in vitro*, high concentrations of Mg^{2+} are sufficient to allow P RNA catalysis, even in the absence of the protein subunit (15,24,25).

There are several known inhibitors of RNase P (reviewed in (12,26,27)), with iriginol hexaacetate and methylene blue being the most recently discovered (26,28). However, to date, neither natural nor highly specific RNase P inhibitors have been identified. The dynamic and flexible nature of the RNase P complex may have hindered the evolution of specific binders (29) and moreover, the protein subunit has some features of intrinsically disordered proteins, which

*To whom correspondence should be addressed. Tel: +52 55 5622 5640; Fax: +52 55 5622 5630; Email: torres@ifc.unam.mx
†The authors wish it to be known that, in their opinion, the first two authors should be regarded as joint First Authors.

© The Author(s) 2019. Published by Oxford University Press on behalf of Nucleic Acids Research.
This is an Open Access article distributed under the terms of the Creative Commons Attribution License (http://creativecommons.org/licenses/by/4.0/), which permits unrestricted reuse, distribution, and reproduction in any medium, provided the original work is properly cited.

Downloaded from https://academic.oup.com/nar/article/47/12/6425/5475076 by UNIVERSIDAD NACIONAL AUTONOMA DE MEXICO user on 20 October 2020

INFORME DE LABORES 2019

could hamper the stable binding of ligands (30). There also may be an inherent limitation for small molecules to compete with the protein for binding to the P RNA, depending on the relative affinity of the P RNA:P protein pair.

Monitoring RNase P activity has traditionally relied on using radiolabeled RNA substrates (31). In this method, radiolabeled RNA is mixed with RNase P. The reaction is then monitored by denaturing polyacrylamide gel electrophoresis (Urea-PAGE) followed by auto-radiography (31). Very recently, alternatives to measure the kinetics of RNase P on pre-tRNA substrates have emerged. A recent paper developed a fluorescence polarization-based activity assay to monitor RNase P activity on a full-length substrate (26).

To expand the repertoire of inhibitors that may serve as clinical leads as antibiotics, a robust platform for assessing RNase P activity in high throughput is essential. Current activity protocols are either inhibited by 1% (v/v) DMSO or not amenable to high-throughput screening. Additionally, validation methods to verify efficacious RNase P inhibition are lacking. Recognizing these shortcomings, we aimed to create improved methods for discovering small molecule inhibitors of RNase P. To accomplish this goal, we focused on the following strategy: (i) developing a novel method to measure real-time RNase P activity in solution; (ii) obtaining real-time measurements of the binding of the RNase P holoenzyme, P RNA and P protein to their native substrate and inhibitors and (iii) obtaining structural information, *in silico* and through X-ray crystallography, on the binding of potential inhibitors to the P protein.

In this work, we present an RNase P activity assay that exploits a previously reported minimal model substrate (pMini3bpUG, herein referred to as Minihelix or Mh) (32,33). This substrate utilizes a FRET mechanism in which the RNase P substrate couples both a 3′ fluorophore and a 5′ non-fluorescent quencher. Cleavage and release of the quencher molecule by RNase P enables the detection of enzymatic activity by measuring fluorescence emission over time, which is amenable for monitoring steady-state kinetics and for high-throughput screening assays.

We then implemented this method to assess a compound library of 2560 small molecules and found four compounds that inhibit RNase P activity. These inhibitors were effective in the presence of both a canonical pre-tRNA substrate and a novel pre-tRNA-like substrate (herein referred to as 'bipartite pre-tRNA') that is composed of two RNA oligonucleotides and monitors the reaction in an analogous way to the Mh substrate. To avoid the sensitivity of RNase P processing to organic solvents using the bipartite pre-tRNA substrate, we dissolved the hits in PEG 200 rather than DMSO. This procedure allowed us to validate the inhibitory properties of these molecules under varied conditions.

Positive hits were then verified and characterized using biolayer interferometry (34), which allowed us to perform the following tasks: (i) define the affinity parameters of the RNase P holoenzyme, P RNA and P protein to the RNA substrates, (ii) discriminate between the interactions of a given compound with the holoenzyme, P RNA, P protein or the substrate and (iii) determine if a given compound hinders the binding of the holoenzyme to pre-tRNA or the P protein to the 5′-leader.

Once validated, we performed docking and molecular dynamics simulations with each hit and identified putative binding sites for two inhibitors on the P protein. Furthermore, purpurin, a competitive inhibitor which behaved as the most consistent hit across our assays, was shown to bind the P protein by X-ray crystallography, with its binding site corresponding to part of the 5′-leader binding site.

MATERIALS AND METHODS

Selection of bacterial RNase P

We chose to work with RNase P from the thermophilic bacterium *Thermotoga maritima* for several reasons. First, it represents the ancestral and most common 'type A' ribozyme, the same that is present in *Escherichia coli* (35). Second, the crystal structure of the RNase P holoenzyme from *T. maritima* in complex with tRNA (19) as well as the apo-structure of the RNA subunit (36) are known, thus facilitating structure-function studies. Third, the folding protocol of the RNase P holoenzyme from *T. maritima* (described below) leads to crystals that present a functional and homogeneous molecular complex (19). Fourth, although the RNase P from *T. maritima* has optimal activity at 50°C (37), the holoenzyme is active in a temperature range of 20–55°C.

RNase P production

The preparation of P RNA and pre-tRNA from *T. maritima* was carried out by *in vitro* transcription and purified by denaturing 6% urea-PAGE with standard protocols as described previously (19,38). The P protein was purified according to (39). The A260/A280 ratio was between 0.6 and 0.7 for each preparation of purified protein.

RNase P reconstitution

The reconstitution of the RNase P holoenzyme was performed as described in (40,19). This protocol produces a homogeneous and functional ribozyme that can be crystallized by mixing P RNA and P protein in a 1:1.1 molar ratio in 1× TH buffer (33 mM Tris–HCl, 66 mM HEPES, pH 7.4) and 400 mM ammonium acetate (AmOAc). The mixture was heated to 95°C for 2 min in a water bath, then chilled on ice for 2 min, after which $MgCl_2$ was added to a final concentration of 100 mM. Although RNase P from *T. maritima* is catalytically active at 10 mM $MgCl_2$ (19), we found that for our minihelix substrate, 100 mM $MgCl_2$ demonstrated more robust activity. This higher concentration was used in all experiments described herein. The holoenzyme was further incubated at 50°C for 10 min and 37°C for 40 min. The final concentration of holoenzyme was 333 nM (35.6 μg/ml of P RNA and 4.7 μg/ml of P protein).

Substrate minihelix (Mh)

The minihelix (Mh) substrate (Figure 1A) was adopted from a previously characterized RNase P substrate, pMini3bpUG (32,33) and coupled to either Black Hole Quencher 1 (BHQ1) or Black Hole Quencher 2 (BHQ2) at the 5′-end and Alexa Fluor 488 at the 3′-end. This probe was

Downloaded from https://academic.oup.com/nar/article/47/12/6425/5475076 by UNIVERSIDAD NACIONAL AUTONOMA DE MEXICO user on 20 October 2020

INFORME DE LABORES 2019

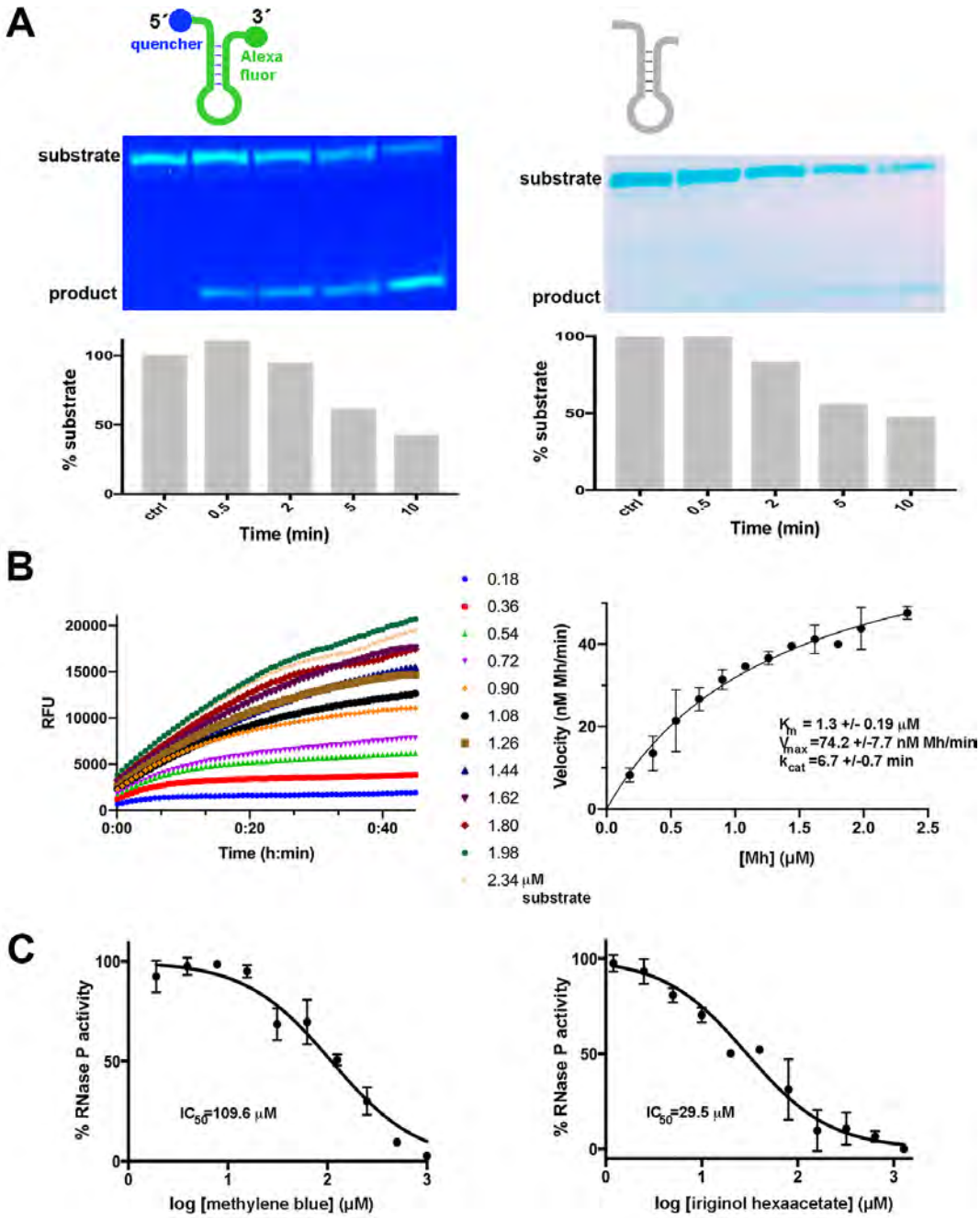

Figure 1. Validation of the fluorescent minihelix (Mh) substrate. (**A**) Cleavage by bacterial RNase P. Top. Schematic representation of the 24-nucleotide fluorescent (left) or non-fluorescent (right) minihelix (Mh) substrate with the predicted secondary structure according to Brannvall et al. (32). Middle left. RNase P holoenzyme from *Thermotoga maritima* cleaves the fluorescent Mh substrate, as visualized by 20% urea-PAGE under UV light. The fluorescence detected from both the substrate (upper band) and the product (lower band) is due to the unfolding of the Mh probe under the denaturing gel conditions. The time-dependent disappearance at 55°C of the 24 nt Mh fluorescent substrate (5 ng), with a simultaneous accumulation of the 15 nt product, confirms the catalytic cleavage of RNase P on the proposed minihelix. Middle right. FRET-pair addition does not affect the cleavage of RNase P on the fluorescent probe as visualized by UV after PAGE and ethidium bromide staining. Bottom. Similar time courses of substrate conversion are observed for the fluorescent (left) and non-fluorescent (right) Mh substrates. (**B**) Kinetic assays of RNase P with the fluorescent substrate show a typical Michaelis-Menten enzymatic behavior. Left. Representative plots of kinetic assays are shown. RNase P holoenzyme was incubated at 20°C at 11 nM, with increasing Mh concentrations as indicated. Right. Michaelis-Menten model fitting ($R^2 = 0.9368$). Initial velocities from three independent trials were plotted against substrate concentration; error bars indicate the standard error for each plot. (**C**) The reported RNase P inhibitors methylene blue and iriginol hexaacetate inhibit bacterial RNase P from *Thermotoga maritima*. Left. The inhibition of RNase P by methylene blue. Dose-response curve ($R^2 = 0.9543$) calculated from the normalized slope values from the linear portions of the kinetic assays in triplicate shown in Supplementary Figure S5. The reported K_i value using a conventional pre-tRNA substrate and the RNA subunit of different bacterial RNase P′s is between 14 and 28 μM (28). Right. Inhibition of RNase P by iriginol hexaacetate. Dose–response curve ($R^2 = 0.9556$) calculated from the normalized slope values from assays in triplicate. The reported IC_{50} value using a fluorescent pre-tRNA substrate is 0.8 μM for *Bacillus subtilis* RNase P (26).

Downloaded from https://academic.oup.com/nar/article/47/12/6425/5475076 by UNIVERSIDAD NACIONAL AUTONOMA DE MEXICO user on 20 October 2020

INFORME DE LABORES 2019

purchased either from Sigma-Aldrich or Integrated DNA Technologies (IDT). A requested scale of 0.05 mmol yielded between 6.3 and 20 nmol (57.5 to 181 μg, enough for 1300–4000 reactions depending on the experimental substrate concentration). Before use, the minihelix was diluted from a 100 μM stock (dissolved in water) to 3.6 μM in activity buffer H (33 mM Tris–HCl, 66 mM HEPES, pH 7.4, 400 mM AmOAc and 100 mM $MgCl_2$).

Substrate bipartite pre-tRNA

The bipartite pre-tRNA substrate derived from pre-$tRNA^{Phe}$ from *T. maritima* (Supplementary Figure S13) was designed for the ease of chemical synthesis and conceived from the fact that the anticodon loop is not required for RNase P recognition (Reiter *et al.*). As for the Mh substrate, fluorescent bipartite pre-tRNA was coupled to Black Hole Quencher 1 (BHQ1) at the 5′-end of the 5′ oligo, and to Alexa Fluor 488 at the 3′-end of the 3′ oligo (see Supplementary Table S1). The probes were purchased from Integrated DNA Technologies (IDT). A requested scale of 250 nmol yielded 27.4 nmol (0.36 mg) for the 5′ oligo and 3.8 nmol (50 μg) for the 3′ fluorescent oligo. Before use, the probes were diluted from a 100 μM stock (dissolved in water) and assembled by mixing and heating to 3.6 μM in activity buffer L (Tris–HCl pH 7.4 33 mM, HEPES 66 mM, 100 mM AmOAc and 10 mM $MgCl_2$).

Fluorescence-based activity assay

Reactions were performed in a total volume of 20 μl. Pipetting was done by hand using multichannel pipettes. First, an 18 μl reaction mixture containing 16.5 μl of activity buffer (H for Mh or L supplemented with 10% PEG 200 for bipartite pre-tRNA) and 270 nM (Mh) or 135 nM (bipartite pre-tRNA) (1.5 or 0.7 μl of the 3.6 μM stock) of the fluorescent substrate probe was pre-incubated on ice for at least 5 m in a black polystyrene 384-well microtiter microplate with a flat transparent bottom (Corning ref 3540). The holoenzyme was then added at a final concentration of 33 nM (2 μl of a 333 nM stock) in 1× TH buffer and mixed. Kinetic activity was monitored in a Synergy MX Multimode Detector (BioTek) at 37°C with rapid agitation. At least 20 readings were taken per well every 15 s. The probe was excited at 485 nm, and its emission was monitored at 535 nm with an integration time of 1 s. From the plots of relative fluorescent units (RFU) versus time, linear regression was used to determine the slopes in the linear portion of the curves, using at least 12 data points to obtain initial velocities. Non-linear fitting to obtain the Michaelis–Menten parameters was performed using GraphPad Prism® 6.01 software.

Gel-based activity assay

For gel-based activity assays, reactions were prepared as described in the previous section (fluorescence activity assay), incubated for 1–15 min at 37–50°C, then loaded onto a denaturing 7 M urea–20% acrylamide gel in the case of the Mh substrate or 19% acrylamide (40% acrylamide/bisacrylamide 38.5:1.5) for the bipartite pre-tRNA substrate. The activity conditions for the gel reported in Figure 3A, to monitor the cleavage of the holoenzyme and P RNA, were under 100 mM AmOAc and 10 mM $MgCl_2$. The gels (13 × 16 × 0.15 cm) were electrophoresed at 20 V/cm for 2–3 h. UV shadowing or ethidium bromide staining was used to visualize RNA cleavage. Detection of minihelix fluorescence was achieved without staining using a UV lamp with excitation at ∼254 nm.

Library screening

Screening was performed with the Spectrum Collection (MicroSource Discovery Systems, Inc), which comprises 2560 compounds, each dissolved in DMSO at 10 mM. For our initial screening, compounds from this collection were tested in cocktails; eight compounds were tested per well in 384-well format. The final concentration of each compound in the cocktail was 1.25 mM. For the activity assay, reactions were set up in a total volume of 20 μl (13.5 μl of activity buffer, 1.5 μl of fluorescent Mh at 3.6 μM, 3 μl of DMSO or cocktail). This set-up resulted in a final concentration of 187.5 μM for each compound. The control wells included for each experiment series were: (i) reaction with twice (3 μl) the fluorescent Mh amount to avoid a signal saturation for the rest of the wells, (ii) two reactions with 10% DMSO (no cocktail), (iii) Mh substrate only, with no ribozyme, (iv) reaction with 100 mM $CaCl_2$, which it is used as a negative control as it competes with $MgCl_2$ (EDTA was not used because metal ions are essential to maintaining the structure of P RNA (41)). The reaction was initiated by adding 2 μl of holoenzyme at 333 nM and monitored as described above. Each round of experiments contained twenty different cocktails corresponding to one row of a 384-well plate (Supplementary Figures S6 and S24). Cocktails that showed inhibition (those with a slope value lower than any of the positive controls in the same plate) were verified (Supplementary Figure S7) and deconvoluted (Supplementary Figure S8) to determine the individual fragment or fragments responsible for the inhibition. At this stage, each compound from the inhibitory cocktails was tested at a final concentration of 1 mM (2 μl of the 10 mM stock). We performed a gel-based assay for the nine selected compounds to qualitatively verify the results obtained by the fluorescence assay (Supplementary Figure S9). After deconvolution, each of the final four potential positive compounds was purchased individually from a different provider (Sigma-Aldrich) and tested inhibition using the *T. maritima* Mh, pre-tRNA and bipartite pre-tRNA substrates (Figure 2 and Supplementary Figures S10–S12 and S14).

Expression and purification of His-tagged P protein for binding assays

The gene encoding the P protein from *T. maritima* (gene synthesis performed by DNA 2.0 ATUM) was cloned into the expression vector TmP-pD454-GST as a Glutathione S-transferase (GST) fusion protein, with a TEV protease cleavage site and a His_6-tag at the N-terminus. This vector was transformed into *E. coli* BL21(DE3)pLysS cells. Cells were then used to inoculate 3 l of Luria-Bertani media and incubated with orbital shaking at 250 rpm and 37°C until

Downloaded from https://academic.oup.com/nar/article/47/12/6425/5475076 by UNIVERSIDAD NACIONAL AUTONOMA DE MEXICO user on 20 October 2020

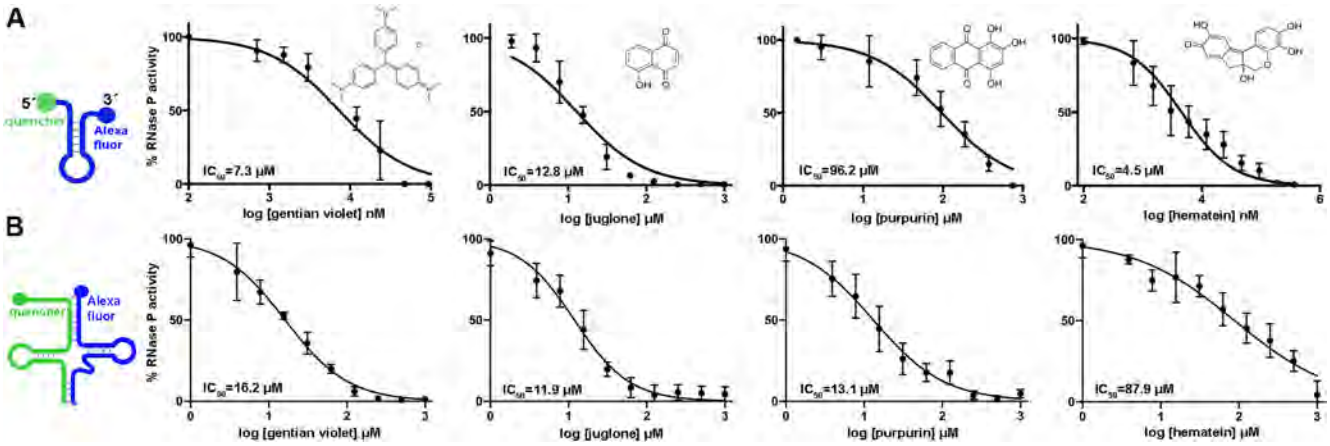

Figure 2. Four validated hits inhibit RNase P holoenzyme from *Thermotoga maritima* in the micromolar range using the substrates Mh and bipartite pre-tRNA. After the screening step (Supplementary Figures S6–S9), four compounds inhibit RNase P using substrates Mh (**A**) and bipartite pre-tRNA (**B**). See Supplementary Figure S13 for a description and validation of the bipartite pre-tRNA substrate. Experiments were performed using compounds from Sigma Aldrich in standard conditions and as described in Supplementary Figures S10 and S14. The four hits are gentian violet (tris(4-(dimethylamino)phenyl)methylium chloride), juglone (5-hydroxy-1, 4-naphthoquinone)., purpurin (1,2,4-trihydroxyanthraquinone) and hematein (3,4,6a,10-tetrahydroxy-6a,7-dihydroindeno[2,1-*c*]chromen-9(6H)-one. A brief description of some properties found of these compounds is given in the Supplementary Information.

the OD_{600} reached 0.6. Protein expression was then induced with IPTG at 1 mM for 6 h. The cell pellet was collected and sonicated in 40 ml of lysis buffer (20 mM sodium phosphate monobasic, pH 8.0, 500 mM NaCl, 20 mM imidazole, 10% glycerol, 1 mM TCEP). TEV protease (700 μg) was then added directly to the lysate and incubated for 16 h at 34°C. The lysate was centrifuged at 13 000*g* and solid urea was added to the supernatant to reach a final concentration of 5 M. The sample was then purified by Ni-NTA affinity chromatography column (HisTrap FF crude, GE Healthcare) equilibrated with binding buffer (20 mM sodium phosphate monobasic, 500 mM NaCl, 5 M urea, 30 mM imidazole, pH 8.0). A 30 min wash at 5 ml/min was performed after which the protein was eluted in 20 mM sodium phosphate monobasic, 500 mM NaCl, 5 M urea, 2 M imidazole, pH 8.0. The elution was then loaded onto a gel filtration column (HiPrep 26/10 desalting, GE Healthcare) equilibrated with desalting buffer (20 mM sodium phosphate monobasic, pH 8.0, 500 mM NaCl). The eluted protein was concentrated to 5 mg/ml and stored at 19°C until needed.

Biolayer interferometry assays (P RNA and holoenzyme)

Real-time binding assays of the holoenzyme, P RNA, P protein, the substrate minihelix and the 5′-leader to individual compounds were performed by biolayer interferometry using an Octet RED96 system (ForteBio). For the holoenzyme or P RNA, a 5′ biotinylated RNA oligonucleotide with the sequence 5′biotin-CAU**UCCAGACGAU** was immobilized on Super Streptavidin (SSA) biosensors. Then, a modified P RNA or holoenzyme was added. The P RNA modification consisted of a sequence with part of the P1 stem sequence complementary to the biotinylated oligonucleotide (AUCGUCUGGA) (Supplementary Figure S23A). P1 is far from the active site or other regions involved in specific interactions (Supplementary Figure S23B) (19). The activity of this construct was indistinguishable from the wild-type holoenzyme. Alternatively, the holoenzyme was immobilized through the His-tagged P protein from *T. maritima* at 0.05 mg/ml (3.4 μM) on Ni-NTA biosensors. Control biosensors were used to subtract non-specific binding of compounds to the biosensor surface. All assay steps (immobilization, wash, baseline, association, and dissociation) were performed in 20 mM HEPES pH 7.4, 100 mM ammonium acetate, 10 mM $MgCl_2$, 2.5% DMSO. The assays were performed on black bottom 96-well microplates (Greiner Bio-One 655209) in a total volume of 200 μl, at 30°C with orbital shaking at 1000 rpm. Experiments were controlled with the software Data Acquisition 8.2 (ForteBio, Inc.). Kinetic binding parameters were calculated using Data Analysis 8.2 (ForteBio, Inc.). After subtraction of reference biosensors, the binding curves were aligned to the X- and Y-axis and the association-dissociation inter-step curve in order to get a common baseline for the association and dissociation phases.

Biolayer interferometry assays (P protein)

Immobilization of the His-tagged P protein from *T. maritima* at 0.05 mg/ml (3.4 μM) was performed on Ni-NTA biosensors. For the initial binding tests to the P protein, a compound concentration of 1 mM was used. Periods for each step of the assay were as follows: immobilization (400 s), wash (100 s), baseline establishment (100s), association (250 s), dissociation (250 s). For each titration curve, six points were used corresponding to the 125, 62.5, 31.25, 15.6 and 7.8 μM compound concentrations. Control biosensors were used to subtract non-specific binding of compounds to the biosensor surface. All assay steps (immobilization, wash, baseline, association, and dissociation) were performed in 20 mM HEPES pH 7.4, 100 mM ammonium acetate, 10 mM $MgCl_2$, 5% DMSO. The assays were performed on black bottom 96-well microplates (Greiner Bio-One 655209) in a total volume of 200 μl, at 30°C with orbital shaking at 1000 rpm. Experiments were controlled with the software Data Acquisition 8.2 (Forte-

Downloaded from https://academic.oup.com/nar/article/47/12/6425/5475076 by UNIVERSIDAD NACIONAL AUTONOMA DE MEXICO user on 20 October 2020

INFORME DE LABORES 2019

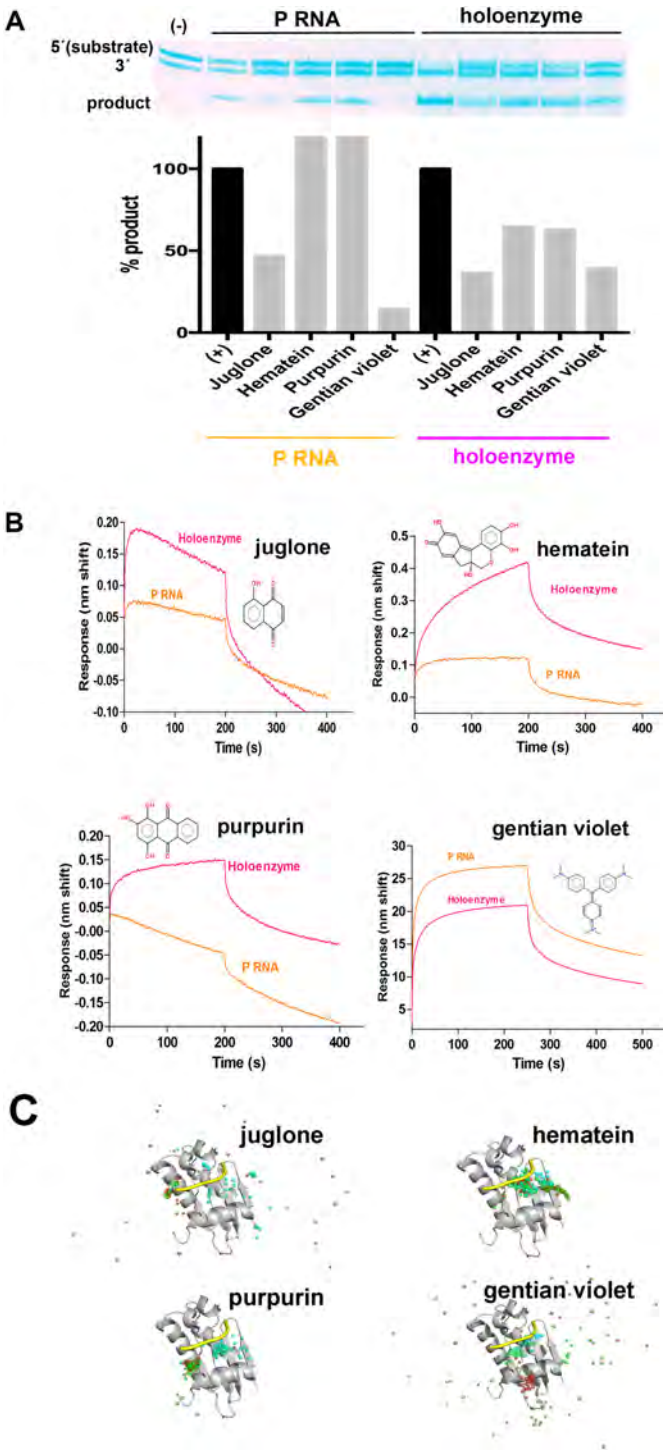

Figure 3. The inhibitors purpurin and hematein bind to the holoenzyme. (**A**) Top. 19% urea-PAGE demonstrates bipartite pre-tRNA substrate is processed with either P RNA or the RNase P holoenzyme from *T. maritima*. Bottom. Comparison of RNase P activity using P RNA (left) or the holoenzyme (right), indicates that purpurin and hematein do not inhibit the P RNA reaction, as derived by densitometry analysis of the lower band (product). (**B**) The relative affinities of the inhibitors for the P RNA or the holoenzyme differ. Binding sensorgrams obtained by biolayer interferometry (BLI). P RNA or RNase P holoenzyme was immobilized on super streptavidin (SSA) biosensors through a 5′-biotinylated RNA oligonucleotide complementary to a region on the P1 stem of P RNA (see Materials and Methods). Remarkably, purpurin does not bind to P RNA (orange). In contrast, gentian violet binds not only to P RNA but also to the Mh substrate (Supplementary Figure S16). (**C**) Molecular Dynamics (MD) simulations of RNase P protein in complex with the validated inhibitors. In each panel, semitransparent spheres represent the geometric center, over a 200 ns trajectory, of the corresponding tested compound. The 5′-leader (yellow) is shown for reference purposes only; it was not included in the simulation. Sphere color coding indicates the starting and final positions in blue and red, respectively. The starting complex conformation for gentian violet, juglone and hematein correspond to the best pose suggested by docking simulations. Purpurin's starting conformation corresponds to that observed in the crystal structure in complex with the P protein (PDB code: 6MAX. See Figure 5). Hematein and purpurin remain bound to the P protein throughout the dynamics protocol.

Bio, Inc.). Kinetic binding parameters were calculated using Data Analysis 8.2 (ForteBio, Inc.). After subtraction of reference biosensors, the binding curves were aligned to the X- and Y-axis and the association-dissociation inter-step curve in order to get a common baseline for the association and dissociation phases.

Biolayer interferometry assays (minihelix substrate)

3′-Biotinylated minihelix was purchased from Integrated DNA Technologies (IDT) (24-mer RNA sequence, 5′-GAUCUGAAUGCGGAAACGCGCCAC-3′-Biotin).
The biotinylated minihelix was immobilized on Super Streptavidin (SSA) biosensors at a concentration of 10 μM. An initial screening of compounds at 1 mM yielded a binding signal only for two compounds: gentian violet and methylene blue. For the titration experiments, 10 μM of 3′-biotinylated minihelix was immobilized for 300 s on Super Streptavidin (SSA) biosensors, followed by a wash step of 100 s and association and dissociation steps of 200 s in the presence of 6 different concentrations of compound ranging from 500 to 15.6 μM. SSA biosensors with no minihelix were used to measure non-specific binding of compounds. All other parameters (buffer, instrument control, analysis) are as described above.

Binding of the P protein to the 5′ RNA leader and binding hindrance

A 5′ RNA leader sequence with 10-bases 5′-GGAAAAAGAU-3′ was purchased from IDT and used at a concentration of 5 μM. This sequence is the same used to obtain the crystal structure of the RNase P holoenzyme (19). The His-tagged P protein was immobilized on Ni-NTA biosensors at 0.05 mg/ml (3.4 μM). The 5′ RNA leader does not bind to the Ni-NTA biosensor surface. The steps performed on the assay and their periods were: P protein immobilization (400 s), wash (100 s), baseline (100ms) (1000 rpm), compound association (800 s), compound dissociation (200 s) (500 rpm), baseline (100 s), 5′ leader association (200 s), 5′ leader dissociation (200 s) (1000 rpm). The assay was performed at 30°C. The compounds were used at 100 μM throughout. All assay steps were performed in 20 mM HEPES pH 7.4, 100 mM ammonium acetate, 10 mM $MgCl_2$, 5% DMSO.

Downloaded from https://academic.oup.com/nar/article/47/12/6425/5475076 by UNIVERSIDAD NACIONAL AUTONOMA DE MEXICO user on 20 October 2020

INFORME DE LABORES 2019

Molecular docking

In silico molecular docking of gentian violet, juglone, purpurin and hematein were performed on the RNase P protein from *Thermotoga maritima* (PDB code 1NZ0). The analysis was conducted using AutodockVina 1.2 (42). Protein and small molecule compounds' structures were prepared by employing scripts from AutoDockTools (43). Two search boxes, with sizes 30 Å × 30 Å × 30 Å, were explored, aiming to cover the tRNA 5′-leader binding region (PDB code 3Q1R). These two boxes were centered at (x = 51.45, y = –23.71, z = –3.4) and (x = 49.01, y = –18.63, z = –8.04). When indicated, side chain flexibility was considered for F17, K51, K53 and K90. Search parameters were set to their default values. The best-suggested pose from the two searches for each ligand was selected as a starting position to perform Molecular Dynamics simulations.

Molecular dynamics simulation

Molecular dynamics simulations were performed on the best binding modes (according to the docking score), for gentian violet, juglone and hematein. Purpurin's starting conformation corresponded to that observed in the crystal structure (PDB code: 6MAX). All systems were simulated with GROMACS 5.0.3 (44) using the AMBER99SB-ILDN all-atom force field (45) in an explicit water solvent scheme with periodic boundary conditions. The topology and force field parameters files for the gentian violet and purpurin compounds were generated with ACYPE (46). The protein protonation was performed with Molprobity (47). The water molecule model used was based on the transferable intermolecular potential with three sites (48). The solvent also included sodium chloride (NaCl) at 0.15 mM plus a small surplus of ions for electric charge neutralization. The long-range electrostatic interactions were computed using fast Particle-Mesh Ewald (PME) (49), using a grid spacing of 1.2 Å. The van der Waals and short-range electrostatic interactions were computed using a cutoff of 1.1 Å for both parameters. The neighbor list was updated every 20 steps using the Verlet cut-off scheme. All bonds were constrained using LINCS (50), enabling a simulation time step of 0.002 ps. The following startup protocol was applied to all modeled systems: Firstly, two following minimization processes with (i) 1000 steps under the steepest descendant algorithm and (ii) 500 steps using the conjugate gradient algorithm. Subsequently, the following two simulations were carried out to equilibrate the system at 300 K: (i) 500 ps in the canonical ensemble at 300 K using a V-rescale thermostat (τ = 0.1 ps) (51) and (ii) 500 ps in the isobaric-isothermal ensemble using Berendsen (52) pressure coupling at 1 bar (τ = 2.0 ps). During these processes, a restraint constant of 1000 kJ mol^{-1} nm^{-2} was applied to all heavy protein atoms and all main chain heavy atoms for the temperature and pressure equilibrations, respectively. An additional 500 ps were simulated within the isobaric–isothermal ensemble without restraints. Finally, 100 ns of molecular dynamics simulation was performed in the isobaric–isothermal ensemble using the Parrinello–Rahman barostat with no restraints (53). For all systems, the protocol was repeated three times starting from the minimized structures with a new assignment of velocities.

Protein crystallization, fragment screening, and structure determination

P protein from *T. maritima* in 50 mM Tris–HCl pH 7.5, 0.2 mM EDTA was crystallized at 3 mg/mL in 12% PEG-1000, 100 mm sodium acetate, pH 4.8, and 200 mM potassium sulfate by vapor diffusion in a sitting drop configuration in 96-well crystallization plates (Swissci™), where 1 μl of P protein plus 1 μl of mother liquor were mixed thoroughly. Crystals appeared in 3 days at 19°C with approximate dimensions of 300 × 200 × 90 μm. Due to the frequent appearance of salt crystals of similar morphology, the presence of protein crystals was checked under a CrystaLight™ 100 UV Source (Molecular Dimensions). P protein crystals were severely damaged at concentrations of DMSO as low as 5%. Thus, purpurin was solubilized in 50% PEG-400, which proved useful in dissolving this compound entirely and maintaining the integrity of P protein crystals. From this stock, a cryoprotectant solution was prepared at a final concentration of 20 mM purpurin, which additionally contained 35% PEG-1000, 100 mM sodium acetate, pH 5.2, 20 mM potassium sulfate and 1 mM DTT. Crystals were soaked for 3 months using the solution with purpurin. Crystals were flash-frozen and stored in liquid nitrogen until needed. Diffraction data were collected at 100 K at a wavelength of 0.9785 Å at the Life Sciences Collaborative Access Team (LS-CAT) 21-ID-F and 21-ID-G beamlines at the Advanced Photon Source (Argonne National Laboratory, Argonne, IL, USA). Data were indexed and processed with XDS (54) and reduced with Aimless (55).

For fragment screening, the reference structure was solved by molecular replacement using Phaser (56), with a search model based on the structure of the P protein from *Thermotoga maritima* (PDB entry: 1NZ0). There is one monomer in the asymmetric unit, with a crystal solvent content of 40%. The presence of purpurin was initially confirmed by difference Fourier maps calculated using the structure of the wild-type enzyme.

The ligand was manually fit, and the restraints for refinement were generated using the eLBOW program of the PHENIX suite (57) using the SMILES string C1 = CC = C2C(= C1)C(= O)C3 = C(C2 = O)C(= C(C = C3O)O)O. Refinement was alternated with manual building/refinement in COOT (58), PHENIX and the PDB_REDO server (59).

The B-factor of the ligand is 42.5 versus 16.0, 25.4 and 21.1 Å^2 for the surrounding residues Val33 Gln28 and Arg89, respectively and the density of the ligand is evident in the 2mF_o – DF_c map at a contour level of 1.5σ. σA-weighted, 2F_o – F_c simulated annealing omit maps (Supplementary Figure S19) were used to validate the presence of the ligand further.

The model presents no Ramachandran outliers. Data collection and refinement statistics are summarized in Supplementary Table S2. Figures were prepared with Pymol (The PyMOL Molecular Graphics System, Version 1.7.4, Schrödinger, LLC). The atomic coordinates and structure factors of the RNase P protein from T. maritima in the complex with purpurin have been deposited in the Protein Data Bank (PDB) with the accession code 6MAX.

Downloaded from https://academic.oup.com/nar/article/47/12/6425/5475076 by UNIVERSIDAD NACIONAL AUTONOMA DE MEXICO user on 20 October 2020

INFORME DE LABORES 2019

RESULTS

A new fluorescent probe as an RNase P substrate

In this work, we designed a synthetic oligonucleotide substrate probe with a fluorophore and a non-fluorescent quencher (NFQ) at the two termini (Figure 1A, Supplementary Table S1) based on a FRET detection mechanism. If the substrate is cleaved, physical separation of the quencher from the fluorophore allows light emission that can be detected with a fluorometer (60–62). A short RNase P substrate candidate that fulfills the assay design requirements was the minihelix (Mh) pMini3pbUG (Figure 1A), whose cleavage kinetics were previously characterized (32,33) and confirmed in the present study. Substrate functionality was first tested in a polyacrylamide gel-based assay (Figure 1A) to ascertain uniform cleavage of the substrate by the RNase P holoenzyme and ensure that the appended fluorophore and quencher did not hinder catalysis. After testing the RNase P activity on the modified FRET substrate and confirming the specific cleavage (Figure 1A), we also tested the minihelix construct without the fluorescent label. The same RNase P processing pattern was observed in both cases (Figure 1A) thus supporting that the fluorophore and the quencher do not affect the ability of this substrate to be enzymatically processed by RNase P. Finally, the titration of the Mh fluorescent substrate using unlabeled pre-tRNA or Mh (Supplementary Figure S1) in solution activity assays (described below) led to a decrease in the relative fluorescence in time-course measurements.

The Mh substrate can be used in a novel, real-time in-solution RNase P fluorescence-based assay.

The in-solution activity assays were performed at 37°C in a total volume of 20 μl on a fluorescence microplate reader in 384-well plates (Figures 1B, C, 2 and Supplementary Figures S1–S10). Supplementary Figure S2A demonstrates the stability over time and the FRET quenching efficiency of the substrate (fluorescent substrate or holoenzyme with $CaCl_2$ added as a negative control). Using the Mh substrate, we did not observe RNase P activity (Supplementary Figure S2A) at 10 mM $MgCl_2$. The kinetic analysis further demonstrated that this is indeed a viable and useful assay for monitoring RNase P activity (Figure 1B, left and Supplementary Figure S2B). A Michaelis–Menten fit was performed, and the kinetic parameters were calculated (Figure 1B, right). The obtained K_M and k_{cat} values are 1.3 μM and 6.7 min^{-1}, respectively. The only previously reported values for this substrate are $K_D = 2.8$ μM and $k_{obs} = 0.86$ min^{-1} using the RNase P from *E. coli* (33).

The novel fluorescence assay using Mh Is reproducible, tolerant of DMSO, sensitive to known RNase P inhibitors and amenable for high-throughput screening

Before performing this assay in a large-scale setup, we first assessed its reproducibility in 10–12 reactions usually performed in a single run (Supplementary Figure S3). To evaluate the robustness of the assay, we used a *Z*'-factor scoring method (63) for both the end-point of the assay (Supplementary Figures S3A, C) and the initial velocities of the reaction (Supplementary Figure S3B, D) (*Z*'-factor = 0.73). The linear responses in all cases were 3–5 min long (Figure 1B and Supplementary Figures S3–S10). In subsequent experiments, we considered the kinetics information given by the linear parameter to calculate the IC_{50} values for the inhibitors described in Figures 3 and 4. Most notably, we found that DMSO does not decrease the activity of RNase P on the cleavage of the Mh substrate up to a concentration of 30% (v/v) (Supplementary Figure S4). For the assays involving inhibitors (Figure 2A and Supplementary Figures S5–S10), we used a concentration of 10% DMSO.

To benchmark our assay against known inhibitors, we tested the activity of two newly-described RNase P inhibitors, methylene blue (33) (Figure 1C, left and Supplementary Figures S5A, B) and iriginol hexaacetate (26) (Figure 1C, right and Supplementary Figures S5C, D). Notably, we detected inhibition for both compounds, and IC_{50} values are in reasonable agreement with the published data (109 μM versus 62 μM (reported) for methylene blue and 29.5 μM versus 0.8 μM (reported) for iriginol hexaacetate). As expected, we did not detect inhibition by neomycin B or kanamycin B, as it is known that high Mg^{2+} concentrations nullify their effects on RNase P (64). These results corroborate the validity of the assay as we were able to detect inhibition in the same range as previously reported inhibitors and exclude non-specific interactors. Our chosen RNase P system and the developed assay (regarding substrate, real-time monitoring, volume, buffer composition, [E]/[S] ratio and DMSO tolerance) are a reliable platform to search for new inhibitors in a high-throughput manner.

Library screening and hit validation identifies four potential inhibitors of RNase P

We performed a screen of the Spectrum Collection library (Discovery Systems, Inc.) comprising 2560 compounds (Supplementary Figure S6). A schematic view of the overall workflow and results is presented in Supplementary Figure S22. In our setup, the screening strategy involved initial testing of cocktails with eight compounds per assay/well. To select a positive hit, we considered the inhibition of the initial velocity of the reaction based on its *Z*-factor robustness (Supplementary Figures S3B and D). Several cocktails exhibited initial velocity changes that were significantly decreased (Supplementary Figure S6). In general, we further analyzed the compounds that demonstrated an initial velocity slope lower than the positive control or a negative slope (Supplementary Figure S6. Red bar corresponds to the positive control). We verified the selected cocktails by a second round of selection (Supplementary Figure S7) and finally deconvoluted to identify active compounds (Supplementary Figure S8). The potential hits were further verified at this stage by the correspondence between the fluorescence-based assay and the canonical gel-based inhibition test using lower concentrations of compounds (Supplementary Figure S9).

Using this strategy, after the initial screening (Supplementary Figure S6), 37 cocktails were selected and verified again for inhibition (Supplementary Figure S7). Of these, ten cocktails with evident inhibition were retained and then deconvoluted to deduce the 10 active compounds in each

Downloaded from https://academic.oup.com/nar/article/47/12/6425/5475076 by UNIVERSIDAD NACIONAL AUTONOMA DE MEXICO user on 20 October 2020

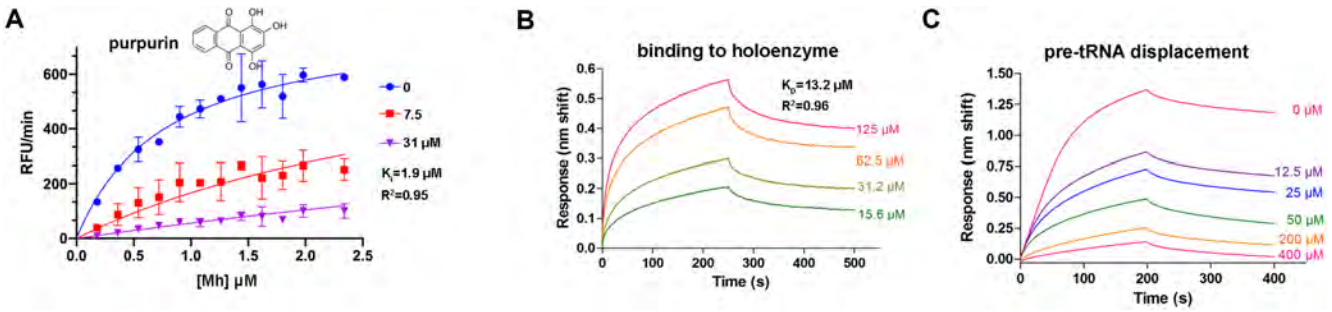

Figure 4. Characterization of the inhibition of *T. maritima* RNase P by purpurin. (**A**) Best global fit for inhibition of RNase P in the presence of varying concentrations of fluorescent Mh substrate. A competitive inhibition model best fit the data ($R^2 = 0.9549$) with $K_i = 1.9 \pm 0.5$ μM. Symbols represent the mean ± standard error as determined from three independent experiments at each concentration. See also Supplementary Figure S18. (**B**) The affinity of purpurin for the RNase P holoenzyme comparable to its K_i. Binding sensorgrams obtained by biolayer interferometry (BLI). RNase P holoenzyme at 400 nM was immobilized on Ni-NTA. (**C**) Purpurin displaces bound pre-tRNA in a dose-response behavior. Binding sensorgrams obtained by biolayer interferometry (BLI). RNase P holoenzyme was immobilized on Ni-NTA biosensors, incubated with purpurin at varying concentrations (0–400 μM), and then the association and dissociation pre-tRNA was monitored. Of the four inhibitors found in this study, only purpurin exhibited a dose–response behavior in this experiment. See also Supplementary Figure S17.

(Supplementary Figure S8). One compound, ethidium bromide, was discarded due to its known non-specific effects on nucleic acids. We thus proceeded with 9 compounds for confirmation of inhibition at a lower concentration (Supplementary Figure S9).

A gel-based inhibition assay was performed in parallel for the nine selected compounds to qualitatively verify the results obtained by the fluorescence-based assay of Supplementary Figure S9A for the nine selected compounds (Supplementary Figure S9B) (250 and 500 μM at this stage versus 1 mM for the deconvolution stage shown in Supplementary Figure S8). In this assay, the compound iodoquinol resulted in a false positive (the inhibition does not correlate in both assays, Supplementary Figures S9A and B). Pararoseaniline and emodin did not inhibit RNase P under the conditions tested in these assays (Supplementary Figure S9), nifursol is a weak inhibitor (Supplementary Figure S9), and alexidine hydrochloride seems to precipitate the holoenzyme (Supplementary Figure S9B and Supplementary Figure S8C). These results excluded five more compounds.

After this more restrictive analysis, four remaining compounds were pursued further: gentian violet (Tris(4-(dimethylamino)phenyl)methylium chloride), juglone (5-hydroxy-1, 4-naphthoquinone), purpurin (1,2,4-trihydroxyanthraquinone) and hematein (3,4,6a,10-tetrahydroxy-6a,7-dihydroindeno[2,1-*c*]chromen-9(6H)-one. We purchased these reagents from a different provider (Sigma Aldrich) and used these compounds to generate dose-response curves (Figure 2A and Supplementary Figure S10). The range of IC_{50} values was between 4.5 and 96.2 μM (Figure 2A).

Pre-tRNA and a pre-tRNA-like substrate allow validation of the four identified hits using gel and fluorescence-based assays

First, we qualitatively validated the results obtained using the fluorescent Mh substrate by gel-based assays using a canonical pre-tRNA substrate (Supplementary Figures S11 and S12). Next, to mimic a substrate similar to the natural pre-tRNA, we designed a new probe consisting of two individual oligonucleotides (39 and 38 nucleotides for the 5′ and 3′ components, respectively) (Figure 2B, right, Supplementary Figure S13 and Supplementary Table S1). This probe, named bipartite pre-tRNA, differs from a canonical pre-tRNA in the sense that it lacks the anticodon loop and it is composed of two oligonucleotides (Supplementary Figure S13A). Binding experiments of pre-tRNA and bipartite pre-tRNA substrates to the holoenzyme using biolayer interferometry show that their affinity is comparable (K_D values of 1.8 and 3.5 nM, Supplementary Figure S13B). For the binding experiments, we tested the agreement of the affinity values obtained by BLI with previous K_D determinations of the RNase P holoenzyme:pre-tRNA and the P RNA:P protein pairs (65,40). These K_D values are in excellent agreement with the published data (Supplementary Figure S15A, B). Finally, titration of fluorescent bipartite pre-tRNA, with a similar design to fluorescent Mh, in time-course fluorescence emission experiments using unlabeled substrates shows highly similar profiles (Supplementary Figure S13C). Thus, we used fluorescent bipartite pre-tRNA as an analog that is highly similar to pre-tRNA, and we obtained dose-response curves using this substrate in the presence of the four hits obtained using fluorescent Mh (Figure 2B and Supplementary Figure S14). As the sensitivity to DMSO for this assay using the bipartite pre-tRNA substrate was very high (no more than 2% DMSO was tolerated, similar to (26,17), we used 10% PEG 200 instead.

Overall, the fluorescent screening strategy—using both a model substrate, tolerant to high DMSO concentrations and a pre-tRNA-like substrate, useful to demonstrate the inhibition properties under low monovalent and Mg^{2+} conditions—demonstrates its utility to find new small molecule inhibitors directed against RNase P.

Purpurin and hematein bind to the RNase P holoenzyme

Gel-based assays performed using the bipartite pre-tRNA substrate (Figure 3A) under a single buffer condition where both P RNA and the holoenzyme display activity demon-

Downloaded from https://academic.oup.com/nar/article/47/12/6425/5475076 by UNIVERSIDAD NACIONAL AUTONOMA DE MEXICO user on 20 October 2020

INFORME DE LABORES 2019

strated that the hits purpurin and hematein inhibit the reaction catalyzed by the RNase P holoenzyme but not the P RNA alone (Figure 3A). The gel-assay using the bipartite pre-tRNA substrate allowed us to distinguish this behavior clearly. In agreement with this result, binding assays with immobilized P RNA or holoenzyme using a 5′ biotinylated RNA oligonucleotide (Figure 3B) show that purpurin does not bind to P RNA and hematein binds only slightly to P RNA (Figure 3B). In contrast with the behavior of these two hits, gentian violet inhibits the reaction *via* P RNA (Figure 3A) and also binds more strongly to it (Figure 3B). Moreover, unlike the other three hits, gentian violet binds to the biotinylated minihelix substrate in the micromolar range (Supplementary Figure S16). The hit juglone displayed a less clear behavior in these assays (Figure 3A, B).

Given that the main difference between P RNA and the holoenzyme is the presence of the P protein, we performed a preliminary interrogation of potential inhibitor interactions between the P protein and each of the four hits using docking and Molecular Dynamics (MD) (Figure 3C and Supplementary Figure S18). Small molecule docking studies of gentian violet, juglone and hematein were performed on the model obtained from crystallographic data of the RNase P protein from *T. maritima* (PDB codes 1NZ0, 3Q1R). Next, Molecular Dynamics (MD) simulations were performed on the four compounds with the best-scoring docking poses or the purpurin position as observed in complex with the P protein by X-ray crystallography (Figure 5C, PDB code: 6MAX). While the dynamics preserve the overall protein structure, the binding modes of the tested compounds were affected (Figure 3C and Supplementary Figure S20). While hematein and purpurin rearranged themselves into a new binding mode around the initial docking or crystallographic pose around the P protein (Figure 3C and Supplementary Figure S20), juglone and gentian violet did not adopt a stable arrangement (Figure 3C and Supplementary Figure S20).

Overall, the activity, binding, docking and MD experiments point to gentian violet as a non-specific inhibitor that binds to RNA, juglone as an inhibitor with an ambiguous mechanism and hematein and purpurin as inhibitors of *T. maritima* RNase P holoenzyme which may specifically target the P protein.

Purpurin inhibits RNase P holoenzyme through a competitive mechanism and shows a dose-response relationship on its binding to the holoenzyme and pre-tRNA displacement

We tested whether any of the four validated hits were capable of displacing the canonical substrate pre-tRNA from the holoenzyme in a binding assay. Purpurin displays a dose-response relationship and remarkably, none of the other three hits demonstrated this behavior (Figure 4C, Supplementary Figure S17). Together, all of the data collected for purpurin are in agreement with the activity and binding criteria to validate an RNase P inhibitor (Table 1). Further characterization shows that the K_i value of purpurin (Figure 4A, Supplementary Figure S18), obtained from an adjustment to a competitive inhibition model, is in general agreement with the K_D value obtained for RNase P holoenzyme-purpurin (Figure 4B, Table 1).

Purpurin has a binding site on the P protein in a region important for substrate binding

To further explore the possible binding of purpurin to the P protein, we tested the binding interference of an RNA oligonucleotide with the sequence of a 5′leader in the presence of this compound (Figure 5A). Remarkably, purpurin interferes with the binding of the leader to the P protein (Figure 5A). The three other hits were also tested in this manner (Supplementary Figure S19). Juglone and gentian violet do not impede the leader binding (Supplementary Figure S19). We discounted hematein because, although it displayed leader-binding hindrance (Supplementary Figure S19), unlike purpurin, it lacked a dose-response relationship on pre-tRNA displacement in the presence of the holoenzyme (see Figure 4C for purpurin). We next determined that purpurin binds to the P protein with micromolar affinity in a dose-response relationship (Figure 5B). Finally, the crystal structure of *T. maritima* P protein in complex with purpurin (Figure 5C, D Supplementary Figure S21 and Table S2) shows a binding region of the compound located in a hydrophobic patch formed by residues Val 33, Leu 35 and Ile 87. Additional hydrogen-bonding interactions are observed between purpurin and Gln 28 and Arg 89. Arg 89 is a conserved protein residue, essential for efficient *T. maritima* RNase P activity, that potentially contacts the pre-tRNA leader binding region (Figure 5D) (38). Taken together, the binding and X-ray crystallography results indicate the existence of a region in the P protein that is sensitive to the binding of inhibitory compounds of *T. maritima* RNase P and that this region is also crucial for substrate binding.

DISCUSSION

In this work, we developed and implemented novel methods to discover and validate inhibitory compounds against bacterial RNase P and gain insight into the structure and function of this ribozyme. Although FRET assays have been used for high-throughput screening of RNA-based targets (66,61,62), this is the first description of this type of method tailored for RNase P. The most noteworthy differences between the proposed method compared to the recent advances described by (26) are the DMSO tolerance (provided by the use of the Mh substrate), the salt tolerance (which reduces non-specific binding) and the development of a novel bipartite pre-tRNA substrate (which allows hit validation). In particular, the DMSO tolerance of the new assay allows for additional chemical space to be probed beyond what was previously explored. It should be noted however that, given the assay design, inhibitors that alter the fidelity of processing might appear as false negatives in the fluorescence-screening step. It should also be considered that there might be a quenching effect from cleaved 5′ leader that could lead to an underestimation of the catalytic activity. Despite these potential issues, the presented method offers a powerful way to discover new inhibitors under a variety of conditions and substrates.

Additionally, this work presents the first binding screening method amenable for high-throughput for RNase P. The method may be useful for enhanced characterization of known inhibitors (26) or to demonstrate specific binding to the holoenzyme, P RNA or P protein (67,68). Notably,

Downloaded from https://academic.oup.com/nar/article/47/12/6425/5475076 by UNIVERSIDAD NACIONAL AUTONOMA DE MEXICO user on 20 October 2020

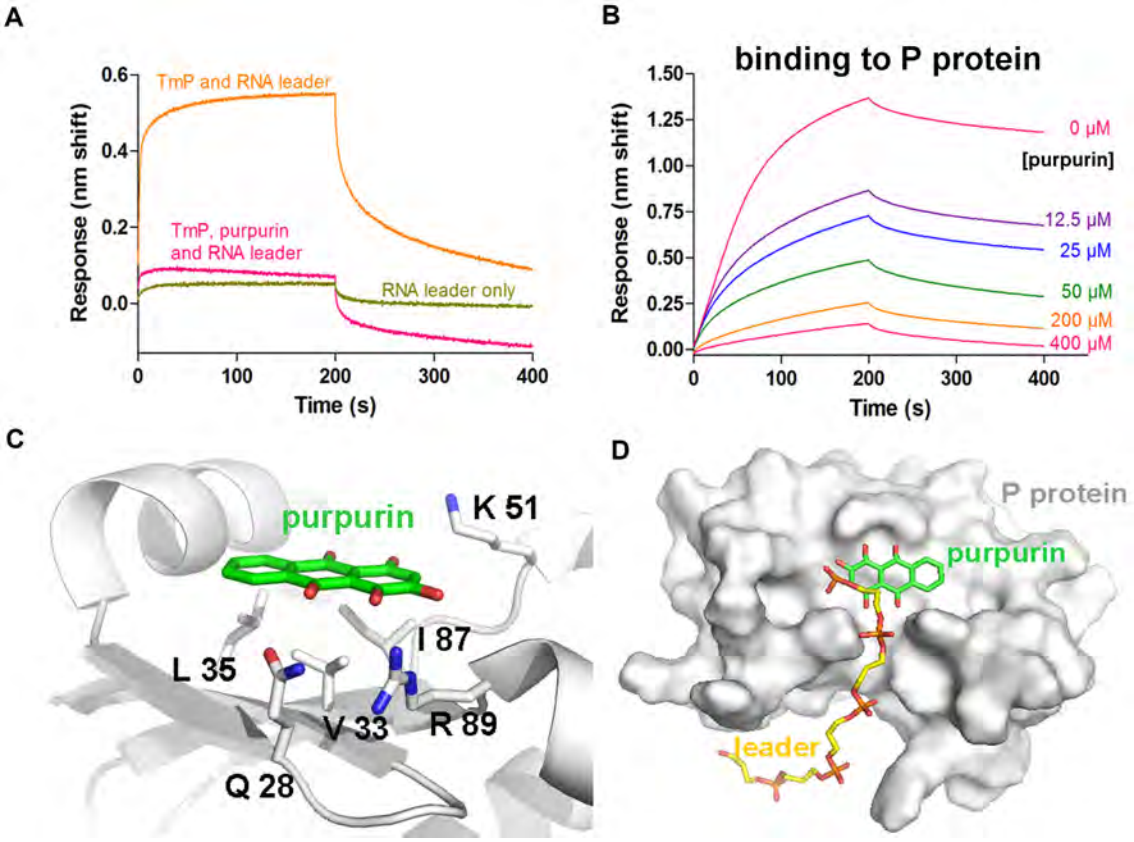

Figure 5. Purpurin binds the P protein. (**A**) Purpurin hinders the binding of the P protein to the 5′ RNA leader. Association and dissociation of the 5′ RNA leader to the P protein (TmP) is measured over time. P protein was immobilized on Ni-NTA biosensors while purpurin was assayed at 100 μM and the 5′ RNA leader at 5 μM. A 10-nt leader was used for these experiments. See Supplementary Figure S10 for the experimental design and testing of the other three inhibitors. (**B**) Purpurin binds to the P protein from *T. maritima* in a dose-response manner ($K_D = 6.8$ μM). Binding sensorgrams obtained by BLI. P protein was immobilized on Ni-NTA biosensors after which its association and dissociation from indicated compounds were monitored. Sensorgrams were fit to a 1:1 Langmuir binding model. (**C**) Location of purpurin (green) on the *T. maritima* P protein as determined by X-ray crystallography (PDB code: 6MAX; see Supplementary Figure S19 and Supplementary Table S2). (**D**) Location of the 5′ RNA leader (yellow) on the P protein in the context of the RNase P holoenzyme in complex with tRNA (19) (PDB code: 3Q1R). In both cases, residue Arg 89 (labeled in panel C) forms interactions with the different ligands.

Table 1. Summary of inhibition and affinity parameters for the four identified hits

Compound name	Mh IC_{50} (μM)	Bipartite pre-tRNA IC_{50} (μM)	Targets RNA	Dose–response displacement of pre-tRNA	K_i and K_d (holoenzyme) (μM)
Gentian violet	7.3 ± 1.6	16.2 ± 2.1	++ (substrate)	No	ND
Juglone	12.8 ± 1.9	11.9 ± 1.7	+	No	ND
Purpurin	96.2 ± 21.7	13.1 ± 2.3	-	Yes	1.9 ± 0.4, 13.2 ± 2.6
Hematein	4.5 ± 0.9	87.9 ± 19.7	-	No	ND

this method provided insights into the inhibitory mode of action via monitoring the pre-tRNA or the leader binding hindrance to the holoenzyme or the P protein. Overall, the results obtained point to the P protein as a promising target for the yet undiscovered inhibitors.

We also used molecular docking, molecular dynamics, and X-ray crystallography to elucidate the possible site of action for the validated hits. P protein is an ideal target for these techniques. Due to its small size (117 aa, 14 kDa), efficient MD protocols are executed successfully. The protein crystallizes in 3 days, the crystals diffract to high resolution (~1.5 Å), a structure of the holoenzyme is known, and the critical binding sites have been identified (19). Most importantly, the crystallization precipitant (PEG 1000) is fully compatible with the solvent used to solubilize fragments (PEG 400 50%). However, it has been challenging to obtain complexes of the P protein with different ligands, probably due to steric hindrance in the crystal packing. Nonetheless, we succeeded in obtaining the crystal structure of the P protein in complex with purpurin, which binds in a region important for the 5′-leader interaction with the protein (38). This region includes R89, a highly conserved residue that makes putative contacts with the phosphate backbone of N-5 of the pre-tRNA leader. The mutation of this residue has substantial effects on RNase P activity (38). These re-

Downloaded from https://academic.oup.com/nar/article/47/12/6425/5475076 by UNIVERSIDAD NACIONAL AUTONOMA DE MEXICO user on 20 October 2020

INFORME DE LABORES 2019

sults point to the P protein as an attractive component for targeted inhibition.

Table 1 shows a summary of the four validated hits and some parameters analyzed in this work. Most importantly, purpurin is the only compound that shows similar IC_{50} values using the fluorescent substrates Mh and bipartite pre-tRNA and presented a dose-response relationship on the pre-tRNA displacement assay. Moreover, the obtained K_D value to the holoenzyme and the K_i are in reasonable agreement. Holistically, this work demonstrates the necessity to consider several corroborating approaches before committing to an initial small-molecule inhibitor hit. While purpurin binds somewhat weakly, its relatively low molecular weight (256 Da), may allow its further optimization.

Three of the found hits—juglone, hematein, and purpurin—have characteristics of known non-specific inhibitors in drug screens, specifically catechol and quinone groups that are known to undergo addition reactions, complex with divalent metal ions, or act as redox cyclers (69–71). On the other hand, several lines of evidence point to purpurin as a potential inhibitor amenable to further optimization. This compound maintains inhibition even at remarkably high concentrations of $MgCl_2$ (100 mM) and ammonium acetate (400 mM), shows a dose–response relationship in binding the holoenzyme, binding P protein and displacing pre-tRNA, and it presents a specific binding site on the P protein, as revealed by the co-crystal structure.

Taken together, this work offers the following technological advances that may be more widely applied to the study of RNA-protein complexes: (i) establishment of biolayer interferometry as a real-time technique for measuring ligand interactions with all the components of RNase P (P RNA, P protein and substrate); (ii) demonstrating the utility of a novel, pre-tRNA-like substrate, which may be useful for the study of other tRNA-processing enzymes and (iii) highlighting the use of low molecular PEGs as substitutes for DMSO in the study of small ligands in complex with macromolecules. This work offers a multi-technique platform for inhibitor discovery and indicates, for the first time, that the P protein is a promising target for future antibiotics.

DATA AVAILABILITY

Atomic coordinates and structure factors for the reported crystal structure have been deposited in the Protein Data Bank under accession number 6MAX.

SUPPLEMENTARY DATA

Supplementary Data are available at NAR Online.

ACKNOWLEDGEMENTS

We thank Jonathan Ipsaro and Alfonso Mondragón for critical reading of the manuscript. Elizabeth Nallely Cabrera-González and María Teresa Lara Ortiz are thanked for their technical support. Adela Rodríguez-Romero is acknowledged for her support in the mass determination of purpurin. Gabriel del Río (G.D.R) is thanked for supporting us in the use of the Synergy MX (BioTek) equipment. Chi-Hao Luan from the High-Throughput Analysis Laboratory, Department of Molecular Biosciences, Northwestern University is greatly acknowledged for his support and guidance. E.A.M.C. is a recipient of a grant from CONACyT to perform graduate studies. Part of this work was performed to fulfill the requirements of a doctoral dissertation (E.A.M.C) in the Posgrado en Ciencias Bioquímicas, Universidad Nacional Autónoma de México.

Authors contributions: C.A.D.T., E.A.M.C., M.A.C. and A.T.L. conceived and designed the experiments; C.A.D.T., E.A.M.C., H.A.S.S., M.A.C. and A.T.L. performed the experiments; C.A.D.T., E.A.M.C., M.A.C. and A.T.L. analyzed the data; A.T.L. contributed reagents/materials/analysis tools; C.A.D.T., E.A.M.C., M.A.C. and A.T.L wrote the paper.

FUNDING

Fundación Marcos Moshinsky, México, Consejo Nacional de Ciencia y Tecnología (CONACyT) [CB-82308, CB-252316 to G.D.R. and CB-253323, PDCPN2014-47543 to A.T.L.]; Programa de Apoyo a Proyectos de Investigación e Innovación Tecnológica, Universidad Nacional Autónoma de México (PAPIIT-DGAPA) [IN202416 and IA202917, to A.T.L. and M.A.C.]; HP Cluster Platform 3000SL 'Miztli' [LANCAD-UNAM-DGTIC-320]; Use of the Advanced Photon Source, an Office of Science User Facility operated for the U.S. Department of Energy (DOE) Office of Science by Argonne National Laboratory, was supported by the U.S. DOE [DE-AC02-06CH11357]; use of the LS-CAT Sector 21 was supported by the Michigan Economic Development Corporation and the Michigan Technology Tri-Corridor [085P1000817]. Funding for open access charge: Instituto de Fisiología Celular, Universidad Nacional Autónoma de México.

Conflict of interest statement. None declared.

REFERENCES

1. Deigan,K.E. and Ferre-D'Amare,A.R. (2011) Riboswitches: discovery of drugs that target bacterial gene-regulatory RNAs. *Acc. Chem. Res.*, **44**, 1329–1338.
2. Dersch,P., Khan,M.A., Muhlen,S. and Gorke,B. (2017) Roles of regulatory RNAs for antibiotic resistance in bacteria and their potential value as novel drug targets. *Front. Microbiol.*, **8**, 803.
3. Matzov,D., Bashan,A. and Yonath,A. (2017) A bright future for antibiotics? *Annu. Rev. Biochem.*, **86**, 567–583.
4. McCoy,L.S., Xie,Y. and Tor,Y. (2011) Antibiotics that target protein synthesis. *Wiley Interdiscip. Rev. RNA*, **2**, 209–232.
5. Kazantsev,A.V. and Pace,N.R. (2006) Bacterial RNase P: a new view of an ancient enzyme. *Nat. Rev. Microbiol.*, **4**, 729–740.
6. McClain,W.H., Lai,L.B. and Gopalan,V. (2010) Trials, travails and triumphs: an account of RNA catalysis in RNase P. *J. Mol. Biol.*, **397**, 627–646.
7. Mondragon,A. (2013) Structural studies of RNase P. *Annu. Rev. Biophys.*, **42**, 537–557.
8. Klemm,B.P., Wu,N., Chen,Y., Liu,X., Kaitany,K.J., Howard,M.J. and Fierke,C.A. (2016) The diversity of ribonuclease P: protein and RNA catalysts with analogous biological functions. *Biomolecules*, **6**, E27
9. Brown,E.D. and Wright,G.D. (2016) Antibacterial drug discovery in the resistance era. *Nature*, **529**, 336–343.
10. Hernandez-Cid,A., Aguirre-Sampieri,S., Diaz-Vilchis,A. and Torres-Larios,A. (2012) Ribonucleases P/MRP and the expanding ribonucleoprotein world. *IUBMB Life*, **64**, 521–528.

Downloaded from https://academic.oup.com/nar/article/47/12/6425/5475076 by UNIVERSIDAD NACIONAL AUTONOMA DE MEXICO user on 20 October 2020

11. Willkomm,D.K., Gruegelsiepe,H., Goudinakis,O., Kretschmer-Kazemi Far,R., Bald,R., Erdmann,V.A. and Hartmann,R.K. (2003) Evaluation of bacterial RNase P RNA as a drug target. *Chembiochem*, **4**, 1041–1048.
12. Drainas,D. (2016) Antibiotics and RNase P. *Antibiotics (Basel)*, **5**, 15.
13. Esakova,O. and Krasilnikov,A.S. (2010) Of proteins and RNA: the RNase P/MRP family. *RNA*, **16**, 1725–1747.
14. Kole,R. and Altman,S. (1981) Properties of purified ribonuclease P from Escherichia coli. *Biochemistry*, **20**, 1902–1906.
15. Guerrier-Takada,C., Gardiner,K., Marsh,T., Pace,N. and Altman,S. (1983) The RNA moiety of ribonuclease P is the catalytic subunit of the enzyme. *Cell*, **35**, 849–857.
16. Altman,S. (2011) Ribonuclease P. *Philos. Trans. R Soc. Lond. B Biol. Sci.*, **366**, 2936–2941.
17. Kurz,J.C., Niranjanakumari,S. and Fierke,C.A. (1998) Protein component of Bacillus subtilis RNase P specifically enhances the affinity for precursor-tRNAAsp. *Biochemistry*, **37**, 2393–2400.
18. Kurz,J.C. and Fierke,C.A. (2002) The affinity of magnesium binding sites in the Bacillus subtilis RNase P x pre-tRNA complex is enhanced by the protein subunit. *Biochemistry*, **41**, 9545–9558.
19. Reiter,N.J., Osterman,A., Torres-Larios,A., Swinger,K.K., Pan,T. and Mondragon,A. (2010) Structure of a bacterial ribonuclease P holoenzyme in complex with tRNA. *Nature*, **468**, 784–789.
20. Niland,C.N., Anderson,D.R., Jankowsky,E. and Harris,M.E. (2017) The contribution of the C5 protein subunit of Escherichia coli ribonuclease P to specificity for precursor tRNA is modulated by proximal 5′ leader sequences. *RNA*, **23**, 1502–1511.
21. Smith,D. and Pace,N.R. (1993) Multiple magnesium ions in the ribonuclease P reaction mechanism. *Biochemistry*, **32**, 5273–5281.
22. Christian,E.L., Smith,K.M., Perera,N. and Harris,M.E. (2006) The P4 metal binding site in RNase P RNA affects active site metal affinity through substrate positioning. *RNA*, **12**, 1463–1467.
23. Hsieh,J., Koutmou,K.S., Rueda,D., Koutmos,M., Walter,N.G. and Fierke,C.A. (2010) A divalent cation stabilizes the active conformation of the B. subtilis RNase P x pre-tRNA complex: a role for an inner-sphere metal ion in RNase P. *J. Mol. Biol.*, **400**, 38–51.
24. Pannucci,J.A., Haas,E.S., Hall,T.A., Harris,J.K. and Brown,J.W. (1999) RNase P RNAs from some Archaea are catalytically active. *Proc. Natl. Acad. Sci. U.S.A.*, **96**, 7803–7808.
25. Kikovska,E., Svard,S.G. and Kirsebom,L.A. (2007) Eukaryotic RNase P RNA mediates cleavage in the absence of protein. *Proc. Natl. Acad. Sci. U.S.A.*, **104**, 2062–2067.
26. Liu,X., Chen,Y. and Fierke,C.A. (2014) A real-time fluorescence polarization activity assay to screen for inhibitors of bacterial ribonuclease P. *Nucleic Acids Res.*, **42**, e159.
27. Willkomm,D.K., Pfeffer,P., Reuter,K., Klebe,G. and Hartmann,R.K. (2010) In: Liu,F and Altman,S (eds). *Ribonuclease P*. Springer, Protein Reviews, pp. 235–256.
28. Wu,S., Mao,G. and Kirsebom,L.A. (2016) Inhibition of bacterial RNase P RNA by phenothiazine Derivatives. *Biomolecules*, **6**, E38
29. Kirsebom,L.A. (2007) RNase P RNA mediated cleavage: substrate recognition and catalysis. *Biochimie.*, **89**, 1183–1194.
30. Henkels,C.H., Kurz,J.C., Fierke,C.A. and Oas,T.G. (2001) Linked folding and anion binding of the Bacillus subtilis ribonuclease P protein. *Biochemistry*, **40**, 2777–2789.
31. Gossringer,M., Helmecke,D. and Hartmann,R.K. (2012) Characterization of RNase P RNA activity. *Methods Mol. Biol.*, **848**, 61–72.
32. Brannvall,M., Kikovska,E., Wu,S. and Kirsebom,L.A. (2007) Evidence for induced fit in bacterial RNase P RNA-mediated cleavage. *J. Mol. Biol.*, **372**, 1149–1164.
33. Wu,S., Chen,Y., Mao,G., Trobro,S., Kwiatkowski,M. and Kirsebom,L.A. (2014) Transition-state stabilization in Escherichia coli ribonuclease P RNA-mediated cleavage of model substrates. *Nucleic Acids Res.*, **42**, 631–642.
34. Abdiche,Y., Malashock,D., Pinkerton,A. and Pons,J. (2008) Determining kinetics and affinities of protein interactions using a parallel real-time label-free biosensor, the Octet. *Anal. Biochem.*, **377**, 209–217.
35. Masquida,B. and Westhof,E. (2011) RNase P: at last, the key finds its lock. *RNA*, **17**, 1615–1618.
36. Torres-Larios,A., Swinger,K.K., Krasilnikov,A.S., Pan,T. and Mondragon,A. (2005) Crystal structure of the RNA component of bacterial ribonuclease P. *Nature*, **437**, 584–587.
37. Paul,R., Lazarev,D. and Altman,S. (2001) Characterization of RNase P from Thermotoga maritima. *Nucleic Acids Res.*, **29**, 880–885.
38. Reiter,N.J., Osterman,A.K. and Mondragon,A. (2012) The bacterial ribonuclease P holoenzyme requires specific, conserved residues for efficient catalysis and substrate positioning. *Nucleic Acids Res.*, **40**, 10384–10393.
39. Krivenko,A.A., Kazantsev,A.V., Adamidi,C., Harrington,D.J. and Pace,N.R. (2002) Expression, purification, crystallization and preliminary diffraction analysis of RNase P protein from Thermotoga maritima. *Acta Crystallogr. D Biol. Crystallogr.*, **58**, 1234–1236.
40. Buck,A.H., Dalby,A.B., Poole,A.W., Kazantsev,A.V. and Pace,N.R. (2005) Protein activation of a ribozyme: the role of bacterial RNase P protein. *EMBO J.*, **24**, 3360–3368.
41. Chen,Y., Liu,X., Wu,N. and Fierke,C.A. (2017) Fluorescence-based real-time activity assays to identify RNase P inhibitors. *Methods Mol. Biol.*, **1520**, 201–225.
42. Trott,O. and Olson,A.J. (2010) AutoDock Vina: improving the speed and accuracy of docking with a new scoring function, efficient optimization, and multithreading. *J. Comput. Chem.*, **31**, 455–461.
43. Morris,G.M., Huey,R., Lindstrom,W., Sanner,M.F., Belew,R.K., Goodsell,D.S. and Olson,A.J. (2009) AutoDock4 and AutoDockTools4: automated docking with selective receptor flexibility. *J. Comput. Chem.*, **30**, 2785–2791.
44. Pronk,S., Pall,S., Schulz,R., Larsson,P., Bjelkmar,P., Apostolov,R., Shirts,M.R., Smith,J.C., Kasson,P.M., van der Spoel,D *et al.* (2013) GROMACS 4.5: a high-throughput and highly parallel open source molecular simulation toolkit. *Bioinformatics*, **29**, 845–854.
45. Lindorff-Larsen,K., Piana,S., Palmo,K., Maragakis,P., Klepeis,J.L., Dror,R.O. and Shaw,D.E. (2010) Improved side-chain torsion potentials for the Amber ff99SB protein force field. *Proteins*, **78**, 1950–1958.
46. Sousa da Silva,A.W. and Vranken,W.F. (2012) ACPYPE - AnteChamber PYthon Parser interfacE. *BMC Res. Notes*, **5**, 367.
47. Chen,V.B., Arendall,W.B. 3rd, Headd,J.J., Keedy,D.A., Immormino,R.M., Kapral,G.J., Murray,L.W., Richardson,J.S. and Richardson,D.C. (2010) MolProbity: all-atom structure validation for macromolecular crystallography. *Acta Crystallogr. D Biol. Crystallogr.*, **66**, 12–21.
48. Jorgensen,W., Chandrasekhar,J. and Madura,J. (1983) Comparison of simple potential functions for simulating liquid water. *J. Chem. Phys.*, **79**, 926–935.
49. Darden,T., York,D. and Pedersen,L. (1993) Particle mesh Ewald - an N.LOG(N) method for Ewald sums in large systems. *J.Chem.Phys.*, **98**, 10089.
50. Hess,B., Bekker,H., Berendsen,H.J.C. and Fraaije,J. (1997) LINCS: A linear constraint solver for molecular simulations. *Journal of Computational Chemistry*, **18**, 1463–1472.
51. Bussi,G., Donadio,D. and Parrinello,M. (2007) Canonical sampling through velocity rescaling. *J. Chem. Phys.*, **126**, 14101.
52. Berendsen,H.J.C., Postma,J.P.M., Vangunsteren,W.F., Dinola,A. and Haak,J.R. (1984) Molecular-dynamics with coupling to an external bath. *J. Chem. Phys.*, **81**, 3684–3690.
53. Parrinello,M. and Rahman,A. (1981) Polymorphic transitions in single-crystals—a new molecular dynamics method. *J. Appl. Phys.*, **52**, 7182–7190.
54. Kabsch,W. (2010) Xds. *Acta Crystallogr. D Biol. Crystallogr.*, **66**, 125–132.
55. Evans,P.R. (2011) An introduction to data reduction: space-group determination, scaling and intensity statistics. *Acta Crystallogr. D Biol. Crystallogr.*, **67**, 282–292.
56. McCoy,A.J., Grosse-Kunstleve,R.W., Adams,P.D., Winn,M.D., Storoni,L.C. and Read,R.J. (2007) Phaser crystallographic software. *J. Appl. Crystallogr.*, **40**, 658–674.
57. Adams,P.D., Afonine,P.V., Bunkoczi,G., Chen,V.B., Davis,I.W., Echols,N., Headd,J.J., Hung,L.W., Kapral,G.J., Grosse-Kunstleve,R.W *et al.* (2010) PHENIX: a comprehensive Python-based system for macromolecular structure solution. *Acta Crystallogr. D Biol. Crystallogr.*, **66**, 213–221.
58. Emsley,P. and Cowtan,K. (2004) Coot: model-building tools for molecular graphics. *Acta Crystallogr. D Biol. Crystallogr.*, **60**, 2126–2132.

Downloaded from https://academic.oup.com/nar/article/47/12/6425/5475076 by UNIVERSIDAD NACIONAL AUTONOMA DE MEXICO user on 20 October 2020

INFORME DE LABORES 2019

59. Joosten,R.P., Long,F., Murshudov,G.N. and Perrakis,A. (2014) The PDB_REDO server for macromolecular structure model optimization. *IUCrJ*, **1**, 213–220.
60. Thakur,C.S., Xu,Z., Wang,Z., Novince,Z. and Silverman,R.H. (2005) A convenient and sensitive fluorescence resonance energy transfer assay for RNase L and 2′,5′ oligoadenylates. *Methods Mol. Med.*, **116**, 103–113.
61. Wiseman,R.L., Zhang,Y., Lee,K.P., Harding,H.P., Haynes,C.M., Price,J., Sicheri,F. and Ron,D. (2010) Flavonol activation defines an unanticipated ligand-binding site in the kinase-RNase domain of IRE1. *Mol. Cell*, **38**, 291–304.
62. Di Grandi,M., Olson,M., Prashad,A.S., Bebernitz,G., Luckay,A., Mullen,S., Hu,Y., Krishnamurthy,G., Pitts,K. and O'Connell,J. (2010) Small molecule inhibitors of HIV RT Ribonuclease H. *Bioorg Med. Chem. Lett.*, **20**, 398–402.
63. Zhang,J.H., Chung,T.D. and Oldenburg,K.R. (1999) A simple statistical parameter for use in evaluation and validation of high throughput screening assays. *J. Biomol. Screen.*, **4**, 67–73.
64. Mikkelsen,N.E., Brannvall,M., Virtanen,A. and Kirsebom,L.A. (1999) Inhibition of RNase P RNA cleavage by aminoglycosides. *Proc. Natl. Acad. Sci. U.S.A.*, **96**, 6155–6160.
65. Talbot,S.J. and Altman,S. (1994) Gel retardation analysis of the interaction between C5 protein and M1 RNA in the formation of the ribonuclease P holoenzyme from Escherichia coli. *Biochemistry*, **33**, 1399–1405.
66. Klostermeier,D. and Millar,D.P. (2001) RNA conformation and folding studied with fluorescence resonance energy transfer. *Methods*, **23**, 240–254.
67. Olson,P.D., Kuechenmeister,L.J., Anderson,K.L., Daily,S., Beenken,K.E., Roux,C.M., Reniere,M.L., Lewis,T.L., Weiss,W.J., Pulse,M *et al.* (2011) Small molecule inhibitors of Staphylococcus aureus RnpA alter cellular mRNA turnover, exhibit antimicrobial activity, and attenuate pathogenesis. *PLoS Pathog.*, **7**, e1001287.
68. Lounsbury,N., Eidem,T., Colquhoun,J., Mateo,G., Abou-Gharbia,M., Dunman,P.M. and Wayne,E.C. (2018) Novel inhibitors of Staphylococcus aureus RnpA that synergize with muporicin. *Bioorg. Med. Chem. Lett.*, **28**, 1127–1131.
69. Baell,J. and Walters,M.A. (2014) Chemistry: Chemical con artists foil drug discovery. *Nature*, **513**, 481–483.
70. Dahlin,J.L., Nissink,J.W., Strasser,J.M., Francis,S., Higgins,L., Zhou,H., Zhang,Z. and Walters,M.A. (2015) PAINS in the assay: chemical mechanisms of assay interference and promiscuous enzymatic inhibition observed during a sulfhydryl-scavenging HTS. *J. Med. Chem.*, **58**, 2091–2113.
71. Dahlin,J.L. and Walters,M.A. (2016) How to triage PAINS-full research. *Assay Drug Dev. Technol.*, **14**, 168–174.

Downloaded from https://academic.oup.com/nar/article/47/12/6425/5475076 by UNIVERSIDAD NACIONAL AUTONOMA DE MEXICO user on 20 October 2020

SCIENTIFIC REPORTS

OPEN

Hippocampal neurogenesis regulates recovery of defensive responses by recruiting threat- and extinction-signalling brain networks

Received: 16 October 2018
Accepted: 18 January 2019
Published online: 27 February 2019

Alonso Martínez-Canabal[1], Grecia López-Oropeza[1], Abril Gaona-Gamboa[1], Paola Ballesteros-Zebadua[2], Olinca Galvan de la Cruz[2], Sergio Moreno-Jimenez[2] & Francisco Sotres-Bayon[1]

Safe exposure to a context that was previously associated with threat leads to extinction of defensive responses. Such contextual fear extinction involves the formation of a new memory that inhibits a previously acquired contextual fear memory. However, fear-related responses often return with the simple passage of time (spontaneous fear recovery). Given that contextual fear and extinction memories are hippocampus-dependent and hippocampal neurogenesis has been reported to modify preexisting memories, we hypothesized that neurogenesis-mediated modification of preexisting extinction memory would modify spontaneous fear recovery. To test this, rats underwent contextual fear conditioning followed by extinction. Subsequently, we exposed rats to an enriched environment or focal X-irradiation to enhance or ablate hippocampal neurogenesis, respectively. Over a month later, rats were tested to evaluate spontaneous fear recovery. We found that enhancing neurogenesis after, but not before, extinction prevented fear recovery. In contrast, neurogenesis ablation after, but not before, extinction promoted fear recovery. Using the neuronal activity marker c-Fos, we identified brain regions recruited in these opposing neurogenesis-mediated changes during fear recovery. Together, our findings indicate that neurogenesis manipulation after extinction learning modifies fear recovery by recruiting brain network activity that mediates the expression of preexisting contextual fear and extinction memories.

To survive in a dynamic environment, animals must be able to distinguish between a dangerous and a safe place. When a place is associated with an aversive consequence (e.g. a foot-shock) the brain forms a threat memory to that context (contextual fear memory), representing a dangerous place. After repeated re-exposure to the same context but without the aversive consequence (i.e. without foot-shock), the brain forms an extinction memory to that context, representing a safe place[1,2]. Later, exposure to the context evokes the extinction memory rather than fear memory, as indicated by low defensive responses to the threat. However, with the simple passage of time after extinction learning, expression of the fear memory returns, as indicated by high defensive responses to the threat[3–5]. This time-dependent phenomenon, known as spontaneous recovery of fear[6,7], is accentuated in patients with fear-related disorders[8]. Despite the importance of spontaneous fear recovery to study how animals distinguish between safe and dangerous contexts over time and how dysregulation of this phenomenon may relate to psychopathology, its underlying brain mechanisms are not clear.

Neural activity in the hippocampus is crucial for encoding contextual memories in rodents as in humans[1]. Recent reports show that the addition of new neurons (neurogenesis) to the adult dentate gyrus of the hippocampus can modify preexisting hippocampal-dependent memories[9–12]. Contextual memory that is hippocampus-dependent, and that is crucial for survival, involves encoding the association of a place with its

[1]Instituto de Fisiología Celular - Neurociencias, Universidad Nacional Autónoma de México, 04510, Ciudad de México, Mexico. [2]Instituto Nacional de Neurología y Neurocirugía – Radioneurocirugía, Ciudad de México, Mexico. Grecia López-Oropeza and Abril Gaona-Gamboa contributed equally. Correspondence and requests for materials should be addressed to F.S.-B. (email: sotres@ifc.unam.mx)

biological significance, as in fear and extinction memories[1,3,13]. It has been suggested that hippocampal neurogenesis modulates the expression of fear-related memories. Yet the accumulated evidence that supports this notion is conflicting. On one hand, evidence shows that facilitation of neurogenesis can increase fear context-specificity[14], decrease context-mediated fear-related responses[9,10] or have no effect[15]. On the other hand, there is evidence that blockade of neurogenesis can increase fear-related responses in infants[10], decrease fear-related responses in adults[16] or have no effect[17–19]. It is not clear whether the conflicting evidence in these different studies is due to neurogenesis manipulations being performed at different time points with respect to the formation of contextual fear and extinction memories. Thus, the time at which new neurons are added or not to the hippocampus circuitry may be crucial to understand its contribution to regulation of fear-related behaviours.

Spontaneous recovery of fear may be a particularly relevant phenomenon to study fear-related behaviours and contextual memory discrimination[2,5,20]. Testing memory retrieval during spontaneous recovery may allow to evaluate a time point when fear and extinction memories compete for the control of fear-related behaviours. Thereby this time point denotes a moment where the individual is required to distinguish between a dangerous and a safe place that may share some features[2,21]. Notably, this cognitive function (pattern separation), important for survival and mental health, has been associated with the addition of new neurons to the hippocampal circuits[22,23]. We hypothesized that a change in the hippocampal circuitry mediated by the addition or ablation of new-born neurons would modify the circuits that support fear expression during spontaneous recovery. Indeed, we found that increasing neurogenesis using environmental enrichment (EE) after, but not before or in absence of, fear extinction learning prevents spontaneous fear recovery. Consistently, we found that ablating hippocampal neurogenesis using focal X-irradiation[15] after, but not before or in the absence of, fear extinction learning promotes spontaneous fear recovery. Notably, using c-Fos expression as a neuronal activity marker, we identified that underlying brain activity involved in neurogenesis-mediated control of fear recovery levels involves opposing recruitment in the prefrontal-amygdala-habenula network.

Results

Environmental enrichment after extinction increases neurogenesis and prevents fear recovery. To test the hypothesis that adding more adult-born hippocampal neurons prevents fear recovery, we compared spontaneous fear recovery levels (freezing and bar presses per minute) before and after a month of either living in EE or in a standard home cage (non-EE). On day 1, rats were conditioned to fear a context (chamber) by pairing it with an aversive consequence (mild foot-shocks). The next day (day 2), rats extinguished their fear to the conditioned context by not receiving any aversive consequence. One day later (day 3), rats were tested for memory retrieval to the context. We used this first retrieval test to match groups (experimental and control) based on similar fear response levels. This matching allows for a fair comparison of fear response levels before and after living in an EE or non-EE. After matching, fear-related behaviours (freezing and presses per minute) were similar between groups during conditioning (day 1; freezing: $F_{(1,19)} = 1.80$, $p = 0.31$; bar-pressing: $F_{(1,19)} = 0.31$, $p = 0.58$), extinction (day 2; freezing: $F_{(1,19)} = 1.15$, $p = 0.29$; bar-pressing: $F_{(1,19)} = 1.24$, $p = 0.30$) and retrieval test (test 1 on day 3; freezing: $t_{(19)} = 0.52$, $p = 0.60$; bar-pressing: $t_{(19)} = 0.4$, $p = 0.96$). Over a month later rats were evaluated for a second retrieval test (day 38).

Rats either lived in an EE or in a non-EE for more than a month (35 days), the time that has been shown to be sufficient for adult-born new neurons to incorporate into hippocampal circuits[24]. On day 38, to evaluate spontaneous recovery of fear, rats were tested in the same context for a second retrieval test (test 2). We found, that rats that lived in an EE showed significantly lower levels of fear-related responses during test 2 as compared to rats that lived in a non-EE (freezing: EE: 23.72%; non-EE: 50.78%; $t_{(19)} = 2.33$, $p = 0.03$; bar-pressing: EE: 6.34 press/min; non-EE: 0.55 press/min; $t_{(19)} = 3.56$, $p = 0.002$), suggesting prevention of fear recovery (Fig. 1A). Moreover, rats that lived in an EE showed a robust increase in hippocampal neurogenesis, indicated by significantly higher numbers of doublecortin (DCX) positive cell density (+/mm^2), compared to rats that lived in a non-EE (Fig. 1B,C; EE: 475.47 DCX+/mm^2; non-EE: 212.70 DCX+/mm^2; $t_{(19)} = 3.56$, $p = 0.002$). Importantly, this effect was associated with specific local increase of hippocampal neurogenesis by EE as indicated by lack of effect on neurogenesis in the rostral migratory stream (EE: 0.53 ± 0.09 optical density units (OD), non-EE: 0.58 ± 0.03 OD; $t_{(14)} = 0.33$, $p = 0.74$). Further, we found that during test 2, fear response levels and levels of neurogenesis were related, as indicated by DCX+ neurons correlation with freezing ($R = -0.59$, $p = 0.0018$) and bar-pressing ($R = 0.52$, $p = 0.014$) (Fig. 1D). Together, these findings indicate that EE-mediated increase of hippocampal neurogenesis after extinction prevents fear recovery.

Hippocampal irradiation after extinction ablates neurogenesis and promotes fear recovery. Even though we showed that EE-mediated neurogenesis after extinction is sufficient to prevent fear recovery, it is possible that neurogenesis is not necessary to modulate fear recovery. To test this possibility, we ablated hippocampal neurogenesis by focal X-irradiation. To evaluate the effect of neurogenesis ablation on fear recovery, we compared spontaneous fear recovery levels (freezing and bar presses per minute) before and after three irradiation (IRR) or sham irradiation (non-IRR) sessions that occurred during a 35-day period to be comparable to the EE experiment above. Thus, on day 1, rats were conditioned to fear a context (chamber) by pairing it with an aversive consequence (mild foot-shocks). The next day (day 2), rats extinguished their fear to the conditioned context by not receiving any aversive consequence. One day later (day 3), rats were tested for memory retrieval to the context. We used this first test to match groups (experimental and control) based on similar fear response levels. This matching allows for a fair comparison of fear response levels before and after IRR or non-IRR. After matching, fear-related behaviour (freezing and presses per minute) was similar between groups during conditioning (day 1; freezing: $F_{(1,19)} = 0.47$, $p = 0.79$; bar-pressing: $F_{(1,19)} = 0.38$, $p = 0.95$), extinction (day 2; freezing: $F_{(1,19)} = 0.13$, $p = 0.73$; bar-pressing: $F_{(1,19)} = 0.20$, $p = 0.65$) and retrieval test (test 1 on day 3; freezing: $t_{(19)} = 0.28$, $p = 0.77$; bar-pressing: $t_{(19)} = 1.27$, $p = 0.21$). Then rats received either IRR or non-IRR.

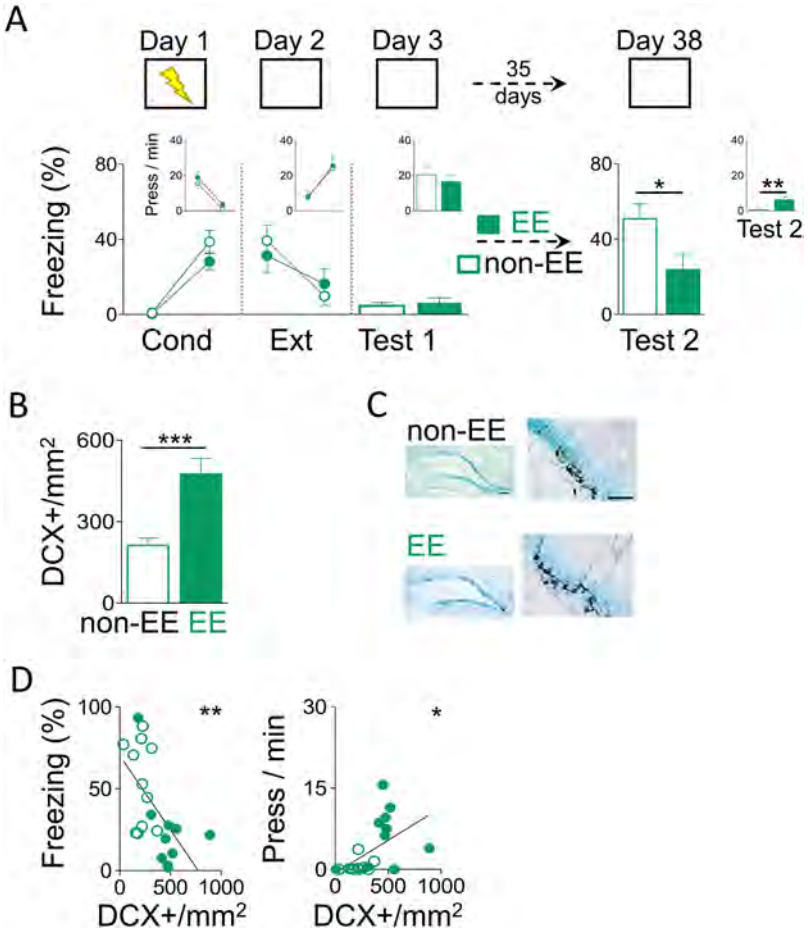

Figure 1. EE-mediated neurogenesis increase after extinction prevented spontaneous fear recovery. (**A**) Top, Rats were trained to associate a context with foot-shocks (day 1; conditioning). One day later, rats were trained to associate the same context with the absence of foot-shocks (day 2; extinction). The next day, rats were placed in the same context without foot-shocks (day 3; test 1). Then, rats were housed for over a month (35 days) either in an EE or a non-EE. Finally, rats were placed again in the same context alone to test for fear recovery (day 38; test 2). Bottom, EE after extinction training prevented spontaneous fear recovery, as indicated by low freezing and high bar presses per minute, when comparing EE with non-EE (EE: n = 10; non-EE: n = 11). Insets: bar-pressing behavior (press/min) across the different phases of the behavioral protocol. Data are shown for first block (early) and last block (late) of conditioning and extinction (5-minute blocks), and as a single block in test sessions (10-minute block). (**B**) Rats that lived in an EE for over a month showed more number of immature cells (DCX+) per area (mm^2) in the dentate gyrus of the hippocampus than rats that lived in a non-EE. (**C**) Representative immunohistochemically stained immature cells (DCX+; black) in the dentate gyrus of the hippocampus after EE or non-EE. Low magnification scale bar = 200 µm (left) and high magnification scale bar = 50 µm (right). (**D**) Negative correlation between number of DCX+/mm^2 and percent freezing response in Test 2 (R = −0.59; $p < 0.01$). Positive correlation between number of DCX+/mm^2 and presses per min in Test 2 (R = 0.52; $p < 0.05$). *$p < 0.05$, **$p < 0.01$, ***$p < 0.001$. Error bars indicate SEM. EE: enhanced environment; Cond: conditioning; Ext: extinction; DCX+: doublecortin positive cells.

On day 38, over a month after the first retrieval test, to evaluate spontaneous recovery of fear, rats were tested in the same context for a second retrieval test (test 2; Fig. 2A). We found that rats treated with IRR showed significantly higher levels of fear-related responses during test 2 as compared to rats treated with non-IRR (freezing: IRR: 62.64%; non-IRR: 30.34%; $t_{(19)} = 3.41$, $p = 0.003$**;** bar-pressing: IRR: 0.31 press/min; non-IRR: 9.39 press/min; $t_{(19)} = 3.41$, $p = 0.003$), suggesting promotion of fear recovery. Importantly, and consistent with previous reports[25], irradiated rats showed a robust decrease in hippocampal neurogenesis as compared to non-IRR rats, as indicated by significantly lower DCX+ neurons in the hippocampus of IRR-treated rats compared to non-IRR control rats (Fig. 2B,C; IRR: 350 DCX+/mm^2; non-IRR: 56.85 DCX+/mm^2; $t_{(19)} = 8.40$, $p < 0.0001$). Further, we found that this effect was due to specific local increase of hippocampal neurogenesis as indicated by lack of effect on neurogenesis in the rostral migratory stream (non-IRR: 0.64 ± 0.81 OD, IRR: 0.56 ± 0.06 OD; $t_{(14)} = 0.34$, $p = 0.74$). Further, we found that during test 2, fear response levels and levels of neurogenesis were related, as indicated by DCX+ neurons correlation with freezing (R = −0.58, $p = 0.03$) and bar-pressing (R = 0.47, $p = 0.03$)

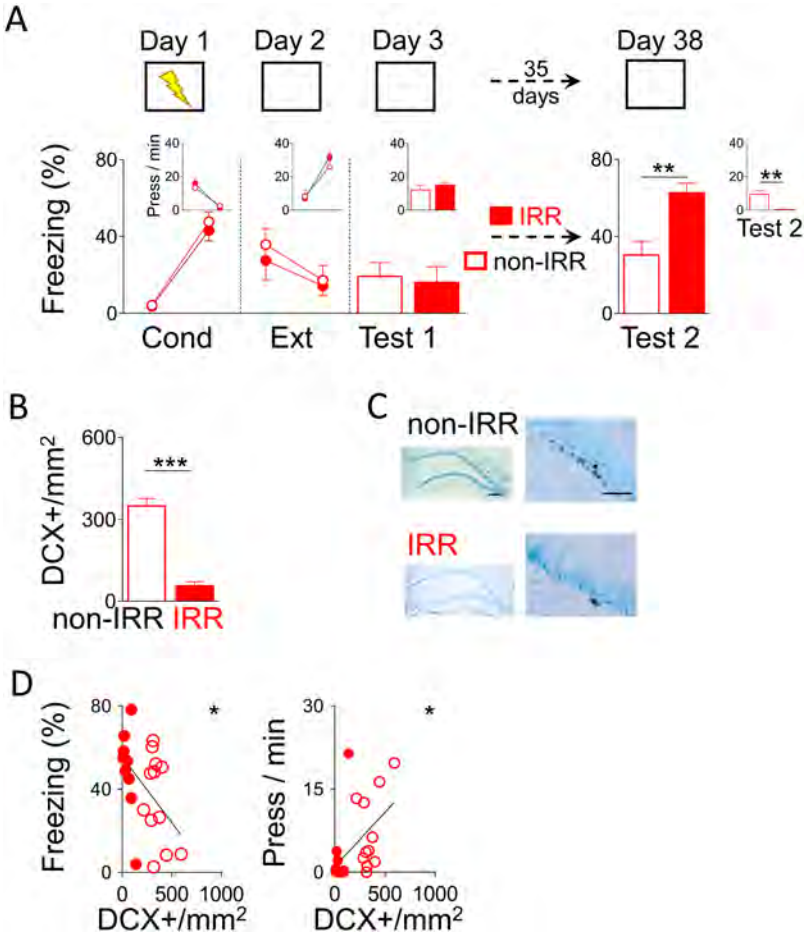

Figure 2. IRR-mediated neurogenesis ablation after extinction promoted spontaneous fear recovery. (**A**) Top, Rats were trained to associate a context with foot-shocks (day 1; conditioning). One day later, rats were trained to associate the same context with the absence of foot-shock (day 2; extinction). The next day, rats were placed in the same context without foot-shocks (day 3; test 1). Then, rats received three IRR or non-IRR sessions during a 35-day period. Finally, rats were placed again in the same context alone to test for fear recovery (day 38; test 2). Bottom, IRR after extinction training promoted spontaneous fear recovery, as indicated by high freezing and low bar presses per minute (inset), when comparing IRR with non-IRR (IRR: n = 9; non-IRR: n = 12). Insets: bar-pressing behavior (press/min) across the different phases of the behavioral protocol. Data are shown for first block (early) and last block (late) of conditioning and extinction (5-minute blocks), and as a single block in test sessions (10-minute block). (**B**) Rats subjected to IRR showed less number of immature cells (DCX+) per area (mm^2) in the dentate gyrus of the hippocampus than non-IRR. (**C**) Representative immunohistochemically stained immature cells (DCX+; black) in the dentate gyrus of the hippocampus after IRR or non-IRR. Low magnification scale bar = 200 µm and high magnification scale bar = 50 µm. (**D**) Negative correlation between DCX+/mm^2 and percent freezing response in Test 2 ($R = -0.58$; $p < 0.05$). Positive correlation between number of DCX+/mm^2 and presses per min in Test 2 ($R = 0.47$; $p < 0.05$). $^{**}p < 0.01$, $^{***}p < 0.001$. Error bars indicate SEM. IRR: irradiation; Cond: conditioning; Ext: extinction; DCX+: doublecortin positive cells.

(Fig. 2D). Together, these findings indicate that IRR-mediated ablation of hippocampal neurogenesis after extinction promotes fear recovery.

Neurogenesis-mediated fear recovery is associated with opposite changes in brain network activity. Our results of the manipulation of neurogenesis levels after extinction, using EE to increase it and IRR to ablate it, suggest that the amounts of adult-born neurons that are incorporated into the hippocampus is crucial to regulate spontaneous fear recovery. During fear recovery, both fear and extinction memories compete for the control of fear-related behaviour[21]. Interestingly, recent studies show that neurogenesis modifies pre-existing memories[10]. One way to evaluate whether neurogenesis manipulations modify preexisting memories is by assessing the recruitment of neuronal activity in structures involved in signalling threat and extinction memories[26]. To address this recruitment issue, rats from the previous experiments (EE vs. non-EE and IRR vs. non-IRR) were sacrificed and perfused 90 minutes after the second retrieval test (day 38). We used expression of the *c-fos* immediate early gene as a marker of recent neuronal activity (Fig. 3A). To directly compare c-Fos protein expression between candidate brain structures (hippocampus, amygdala, prefrontal cortex and dorsal

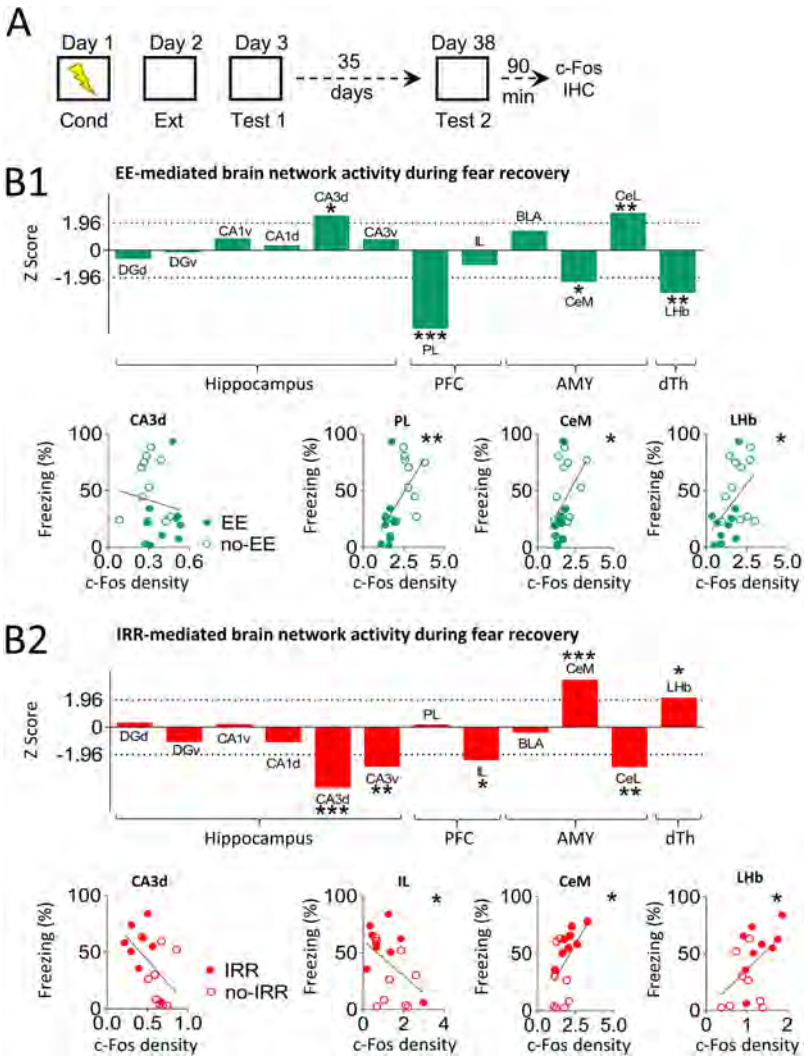

Figure 3. Opposing brain network recruitment during fear recovery mediated by neurogenesis manipulations. (**A**) Top, Rats were trained to associate a context with foot-shocks (day 1; conditioning). One day later, rats were trained to associate the same context with the absence of foot-shocks (day 2; extinction). The next day, rats were placed in the same context without foot-shocks (day 3; test 1). Then, separate groups of rats received different treatments to induce opposing neurogenesis effects (EE to enhance it or IRR to ablate it) during a 35-day period. After neurogenesis manipulations rats were placed again in the same context alone to test for fear recovery (day 38; test 2). Ninety minutes following this test, brains were removed and expression of activity-regulated gene *c-fos* was evaluated immunohistochemically. (**B**) Data represent normalized contrast of c-Fos immunoreactive cells in treated rats (EE and IRR) as compared to its control group (non-EE and non-IRR, respectively) (z-score). (**B1**) Top, Z-scores of c-Fos expression shows that EE, as compared to non-EE, increased recruitment (positive z-scores that exceeded 1.96; $p < 0.05$) of dorsal CA3 (CA3d) and centrolateral amygdala (CeL), while decreasing neuronal activity (negative z-scores that exceeded −1.96; $p < 0.05$) in prefrontal (PFC) prelimbic cortex (PL), centromedial amygdala (CeM) and lateral habenula (LHb). Bottom, Correlation analysis between percent freezing response during fear recovery (day 38) and c-Fos density (c-Fos positive cells per 100 µm^2) shows a positive correlation for PL ($R = 0.57$; $p < 0.01$), CeM ($R = 0.45$; $p < 0.05$) and LHb ($R = 0.48$; $p < 0.05$). (**B2**) Top, Z-scores of c-Fos expression shows that IRR, as compared to non-IRR, increased recruitment (positive z-scores that exceeded 1.96; $p < 0.05$) of centromedial amygdala (CeM) and lateral habenula (LHb), while decreasing neuronal activity (negative z-scores that exceeded −1.96; $p < 0.05$) in prefrontal (PFC) infralimbic cortex (IL), dorsal and ventral CA3 (CA3d and CA3v) as well as centrolateral amygdala (CeL). Bottom, Correlation analysis between percent freezing response during fear recovery (day 38) and c-Fos density (c-Fos positive cells per 100 µm^2) shows a positive correlation for LHb ($R = 0.48$; $p < 0.05$), CeM ($R = 0.49$; $p < 0.05$) and a negative correlation for CA3d ($R = -0.51$, $p < 0.05$) and IL ($R = -0.47$, $p < 0.05$). Both in z-score and correlation analysis: *$p < 0.05$, **$p < 0.01$, ***$p < 0.001$.

thalamus) and experiments (EE-mediated increase of neurogenesis and IRR-mediated ablation of neurogenesis), data were normalized using z-scores. On the one hand, we found that increased neurogenesis mediated by EE, (as compared with non-EE) was associated with c-Fos expression changes in specific brain sub-regions

related to threat and extinction signalling. This is indicated by the increase of c-Fos activity in the lateral region of the central amygdala (CeL) and dorsal cornu ammonis 3 (CA3d), as well as decreased c-Fos activity in the prelimbic region of the prefrontal cortex (PL), medial region of the central amygdala (CeM) and lateral region of the habenula (LHb) (Fig. 3B1; CeL: $z = 2.59$, $p = 0.01$; Ca3d: $z = 2.40$, $p = 0.016$; PL: $z = -5.52$, $p < 0.001$; CeM: $z = -2.16$, $p = 0.03$; LHb: $z = -2.94$, $p = 0.003$). This pattern of brain activity suggests that prevention of fear recovery behaviour, mediated by increased neurogenesis, recruits an amygdala subregion associated with decreased fear-related behaviour (CeL)[27,28], while at the same time engages inhibition of brain regions associated with increased fear-related behaviour (PL[29,30], CeM[27] and LHb[31]). Consistent with this interpretation, we found that brain activity pattern and freezing behaviour were inversely correlated (negative correlation) with CeL ($R = -0.44$, $p = 0.047$) and were directly correlated (positive correlation) with PL, CeM and LHb (PL: $R = 0.57$, $p = 0.006$; CeM: $R = 0.45$, $p = 0.042$; LHb: $R = 0.48$, $p = 0.03$) (Fig. 3B1).

On the other hand, we found that neurogenesis ablation mediated by IRR (as compared with non-IRR) was associated with c-Fos expression changes in brain regions related to fear and extinction memories, as indicated by increases of c-Fos activity in CeM and LHb, as well as decreased c-Fos activity CA3d, CA3v, IL and CeL (Fig. 3B2; CeM: $z = 3.29$, $p = 0.0009$; LHb: $z = 2.01$, $p = 0.044$; CA3d: $z = -4.21$, $p < 0.0001$, CA3v: $z = -2.72$, $p = 0.006$; IL: $z = -2.24$, $p = 0.024$; CeL: $z = -2.75$, $p = 0.006$). This pattern of brain activity suggests that promotion of fear recovery behaviour, mediated by ablated neurogenesis, recruits amygdala and dorsal thalamus subregions associated with increased fear-related behaviour (CeM[32] and LHb[33]), while at the same time engages inhibition of brain regions associated with decreased fear-related behaviour (IL[34], CeL[32] and CA3[35]). Consistent with this interpretation, we found that brain activity pattern and freezing behaviour were related, as indicated by direct correlation (positive correlation) of freezing behaviour and c-Fos expression in CeM and LHb (CeM: $R = 0.49$, $p = 0.041$; LHb: $R = 0.49$, $p = 0.041$), as well as inverse correlation (negative correlation) in IL, CA3 and CeL (IL: $R = -0.47$, $p = 0.045$; CA3d: $R = -0.51$, $p = 0.03$; CeL: $R = -0.29$, $p = 0.26$) (Fig. 3B2). Together, these findings indicate that neurogenesis manipulations to increase (using EE) and ablate (using IRR) neurogenesis after extinction modify, in opposing manner, the neuronal activity of brain subregions related to preexisting fear and extinction memories.

Neurogenesis after extinction is necessary for environmental enrichment-mediated prevention of fear recovery. We showed that EE-mediated neurogenesis increase after extinction prevents spontaneous fear recovery and IRR-mediated neurogenesis ablation after extinction promotes spontaneous fear recovery. However, despite hippocampal neurogenesis being one of the most notorious effects observed at molecular level due to EE[36], living in an EE could affect brain activity that is not limited to the hippocampus[37]. To exclude the possibility that the observed EE-mediated prevention of fear recovery is independent of hippocampal neurogenesis, we subjected rats with ablated hippocampal neurogenesis (using IRR) to an EE for over a month (35 days) after extinction and evaluated spontaneous fear recovery (day 38). As in our previous experiments in this study, rats were matched for similar levels of fear-related behaviour during the first retrieval test (day 3) (freezing: $t_{(14)} = -1.26$, $p = 0.23$; bar-pressing: $t_{(14)} = 0.76$, $p = 0.45$). This matching resulted in similar fear-related response levels between groups during conditioning (day 1; freezing: $F_{(1,14)} = 0.47$, $p = 0.49$; bar-pressing: $F_{(1,14)} = 0.02$, $p = 0.88$) and extinction (day 2; freezing: $F_{(1,14)} = 0.32$, $p = 0.58$; bar-pressing: $F_{(1,14)} = 2.271$, $p = 0.15$). We found that, rats treated with IRR followed by EE (IRR/EE) showed significantly higher levels of fear-related responses during test 2 as compared to rats treated with non-IRR followed by EE (non-IRR/EE) (Fig. 4A; freezing: IRR/EE: 51.66%; non-IRR/EE: 21.7%; $t_{(14)} = 2.79$, $p = 0.015$; bar-pressing: IRR/EE: 2.96 press/min; non-IRR-EE: 11.04 press/min; $t_{(14)} = 220$, $p = 0.045$), excluding the possibility that the observed EE-mediated effect on prevention of fear recovery is independent of hippocampal neurogenesis. Further, we confirmed that IRR decreases hippocampal neurogenesis as compared to non-IRR rats, as indicated by significantly lower DCX+ neurons in the hippocampus of IRR/EE-treated rats compared to non-IRR/EE control rats (Fig. 4B; IRR/EE: 126.34 DCX+/mm^2; non-IRR/EE: 389.62 DCX+/mm^2; $t_{(14)} = 5.66$, $p < 0.0001$); and that this neurogenesis ablation effect was specific to the hippocampus as indicated by lack of effect on neurogenesis in the rostral migratory stream (non-IRR: 0.58 ± 0.03 OD, IRR: 0.62 ± 0.02 OD; $t_{(10)} = 0.77$, $p = 0.45$). Consistently, we found that during test 2, freezing response and levels of neurogenesis are related, as indicated by DCX+ neurons correlation with freezing responses (freezing: $R = -0.57$, $p = 0.02$) (Fig. 4C). Together, these findings indicate that EE-mediated increase in neurogenesis after extinction, that in turn prevents spontaneous fear recovery, is dependent on hippocampal neurogenesis.

Neurogenesis manipulations before extinction do not affect fear recovery. In the present study, we have shown that neurogenesis manipulations after extinction learning, regulates the expression of spontaneous fear recovery: increased neurogenesis leads to low fear recovery and decreased neurogenesis leads to high fear recovery. However, it is possible that neurogenesis manipulations at other time points, besides after extinction, also have an impact on fear-related behaviour. To test this possibility, neurogenesis manipulations (EE-mediated increase or IRR-mediated ablation of neurogenesis) were performed before, rather than after extinction learning. Rats were matched for similar fear-related behaviour levels during conditioning (day 1; freezing: EE vs non-EE: $F_{(1,14)} = 0.02$, $p = 0.88$; IRR vs non-IRR: $F_{(1,11)} = 0.015$, $p = 0.9$; bar-pressing: EE vs non-EE: $F_{(1,14)} = 0,32$, $p = 0.84$; IRR vs non-IRR: $F_{(1,11)} = 1.25$, $p = 0.28$). The next day four different groups of rats were subjected to four different treatments: EE or non-EE and IRR or non-IRR. Over a month (35 days) after conditioning, rats extinguished fear to the context (day 36) and were tested for retrieval in two consecutive days (days 37 and 38). We found that neither increasing nor decreasing neurogenesis (using EE (Fig. 5A) or IRR (Fig. 5C), respectively) before extinction (after conditioning) affected fear expression, extinction learning or spontaneous fear recovery, as indicated by similar levels of fear-related behaviour during extinction between groups (freezing: EE vs non-EE: $F_{(1,14)} = 0.85$, $p = 0.37$; IRR vs non-IRR: $F_{(1,11)} = 0.84$, $p = 0.38$; bar-pressing: EE vs non-EE: $F_{(1,14)} = 0.42$,

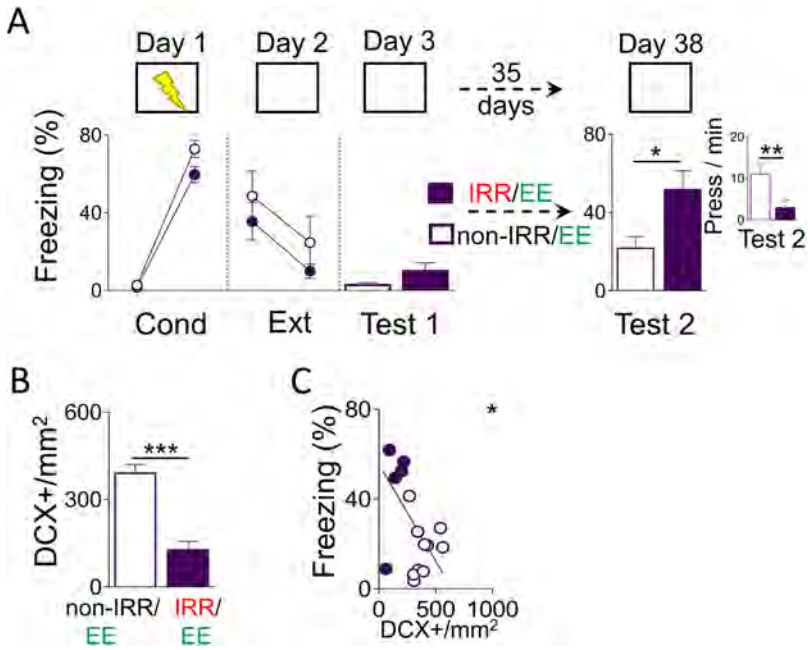

Figure 4. Irradiation arrest of EE-mediated neurogenesis increase after extinction restores spontaneous fear recovery. (**A**) Top, Rats were trained to associate a context with foot-shocks (day 1; conditioning). One day later, rats were trained to associate the same context with the absence of foot-shock (day 2; extinction). The next day, rats were placed in the same context without foot-shocks (day 3; test 1). Rats were housed for over a month (35 days) in an EE. At the beginning of EE rats received three IRR or non-IRR sessions. Finally, rats were placed again in the same context alone to test for fear recovery (day 38; test 2). Bottom, rats subjected to both IRR and EE (IRR/EE: n = 6) after extinction showed high spontaneous fear recovery, as indicated by high freezing and low bar pressing rate (inset) compared with rats subjected to both non-IRR and EE (non-IRR/EE: n = 12) after extinction. Data are shown for first block (early) and last block (late) of conditioning and extinction (5-minute blocks), and as a single block in test sessions (10-minute block). (**B**) Rats subjected to non-IRR/EE showed more number of DCX+ per area (mm^2) in the hippocampus than EE/IRR-treated rats. (**C**) Negative correlation between number of DCX+ per area (mm^2) and percent freezing response in Test 2 (R = −0.57; $p < 0.05$). *$p < 0.05$, **$p < 0.01$, ***$p < 0.001$. Error bars indicate SEM. EE: environmental enrichment; IRR: irradiation; Cond: conditioning; Ext: extinction; DCX+: doublecortin positive cells.

$p = 0.84$; IRR vs non-IRR: $F_{(1,11)} = 0.14$, $p = 0.71$) and two retrieval tests (test 1; freezing: EE vs non-EE: $t_{(14)} = 0.18$, $p = 0.88$; IRR vs non-IRR: $t_{(11)} = 0.11$, $p = 0.91$; bar-pressing: EE vs non-EE: $t_{(14)} = 0.28$, $p = 0.77$; IRR vs non-IRR: $t_{(11)} = 0.46$, $p = 0.65$; test 2: freezing: EE vs non-EE: $t_{(14)} = 1.353$, $p = 0.11$; IRR vs non-IRR: $t_{(14)} = 1.41$, $p = 0.18$; bar pressing: EE vs non-EE: $t_{(11)} = 0.88$, $p = 0.39$; bar-pressing: IRR vs non-IRR: $t_{(11)} = 1.57$, $p = 0.14$). Yet, as expected, we found significantly more DCX+ neurons in EE-treated rats as compared to non-EE rats (Fig. 5B; $t_{(14)} = 3.88$, $p = 0.043$) and significantly less DCX+ neurons in IRR-treated rats as compared to non-IRR rats (Fig. 5B; $t_{(11)} = -4.82$, $p = 0.02$), supporting the notion that EE increases neurogenesis and IRR ablates it, independently of when it occurs. Together these results indicate that for neurogenesis to influence spontaneous fear recovery it must occur after, but not before, extinction learning.

To assess whether the neurogenesis-mediated effect on fear expression we observed (low with EE and high with IRR) is dependent on the experience of extinction, rats were tested in a behavioural protocol that includes conditioning (day 1) and two different retrieval tests (day 2 and 38) separated by over a month (35 days), but without an extinction training session. After proper group matching during the first conditioning retrieval test (day 2; EE vs non-EE: $t_{(12)} = 1.08$, $p = 0.3$; IRR vs non-IRR: $t_{(10)} = 0.4$, $p = 0.69$), we found that neither EE nor IRR altered fear expression, as indicated by similar fear-related behaviours during the second retrieval test (day 38) (Fig. 5E,G; freezing: EE vs non-EE: $t_{(12)} = -1.55$, $p = 0.15$; IRR vs non-IRR: $t_{(10)} = 0.46$, $p = 0.64$; bar-pressing: EE vs non-EE: $t_{(12)} = 0.1.26$, $p = 0.23$; IRR vs non-IRR: $t_{(10)} = 0.14$, $p = 0.88$). Again, despite not having a behavioural effect, both manipulations used (EE and IRR) were effective at modifying neurogenesis levels (increase and ablate, respectively) (Fig. 5F,H; EE vs non-EE: $t_{(12)} = 4.54$, $p = 0.007$; IRR vs non-IRR: $t_{(10)} = 4.03$, $p = 0.0024$). These results indicate that neurogenesis-mediated effect on fear expression is dependent on extinction. Moreover, all together these findings highlight the importance of timing neurogenesis manipulations after extinction to influence the expression of spontaneous fear recovery.

Increased neurogenesis after extinction does not prevent cued fear recovery. Fear-related behaviour regulation can be triggered by context or specific environmental cues such as a tone. Contextual fear-related behaviour is dependent on the hippocampus, but cued fear-related behaviour is dependent on the amygdala[38]. Thus, to test whether neurogenesis-mediated prevention of spontaneous fear recovery is hippocampus dependent,

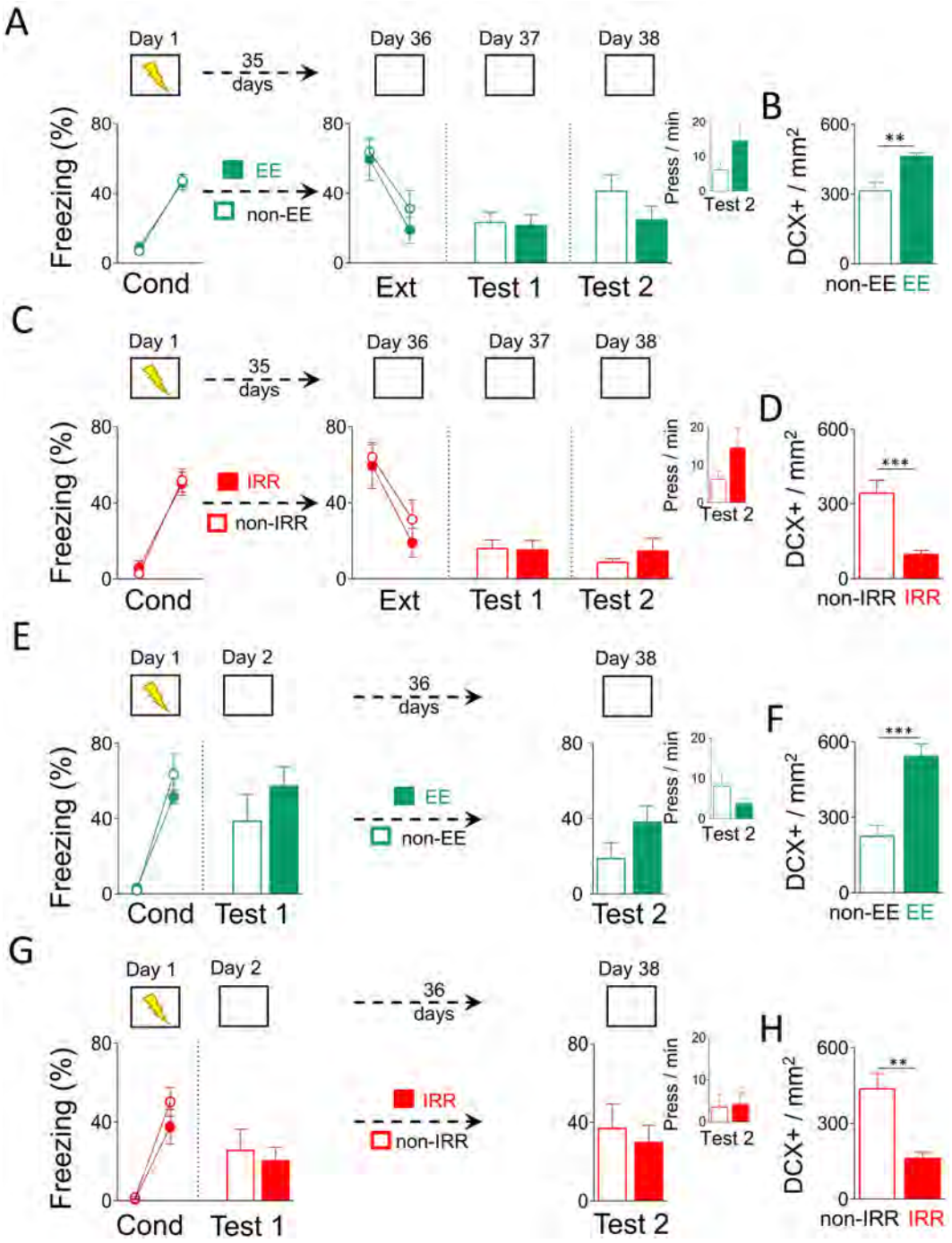

Figure 5. Neurogenesis increase by EE or decrease by IRR before or without extinction training does not alter fear-related behaviors. (**A**,**C**) Top, Rats that previously associated a context with foot-shocks (day 1; conditioning) were either housed in an EE or non-EE, or subjected to three IRR or non-IRR sessions, in a 35 day-period. On day 36, rats were exposed to the conditioning context without foots-shocks (extinction). The following two days, rats were exposed again to the same context alone (days 37 and 38; tests 1 and 2). Data are shown for first block (early) and last block (late) of conditioning and extinction (5-minute blocks), and as a single block in test sessions (10-minute block). (**A**) Bottom, EE before extinction training did not alter fear-related behaviors during extinction or test sessions, as compared to non-EE (EE: n = 8; non-EE: n = 8), as indicated by similar freezing responses and bar presses per minute (inset). (**B**) Rats that lived in an EE for over a month, before extinction training, showed more number of DCX+ per area (mm^2) in the hippocampus than non-EE. (**C**) Bottom, IRR before extinction training did not alter fear-related behaviors during extinction or test sessions, as compared to non-IRR (IRR: n = 7; non-IRR: n = 6), as indicated by similar freezing responses and bar presses per minute (inset). (**D**) Rats that were subjected to IRR, before extinction training, showed less number of DCX+/mm^2 in the hippocampus than non-IRR. (**E**,**G**) Rats that were trained to associate a context with foot-shocks (day 1; conditioning) were exposed to the conditioning context alone the next day (day 2; test 1). Then after over month (36 days) of either living in an EE or non-EE, or subjected to three IRR or

non-IRR sessions, rats were again exposed again to the conditioning context alone (day 38; test 2). (**E**) Bottom, EE after conditioning and a retrieval test (without extinction) did not alter fear-related behaviors during test sessions, as compared to non-EE (EE: n = 8; non-EE: n = 6), as indicated by similar freezing responses and bar presses per minute (inset). (**F**) Rats that lived in an EE for over a month, after conditioning and a retrieval test (without extinction), showed more number DCX+/mm^2 in the hippocampus than non-EE. (**G**) Bottom, IRR after conditioning and a retrieval test (without extinction) did not alter fear-related behaviors during test sessions, as compared to non-IRR (IRR: n = 6; non-IRR: n = 6), as indicated by similar freezing responses and bar presses per minute (inset). (**H**) Rats that were subjected to IRR, after conditioning and a retrieval test (without extinction), showed less number of DCX+/mm^2 in the hippocampus than non-IRR. Data are shown for early and late conditioning and extinction (5 min blocks) and for test sessions (10 min average). $^{**}p < 0.01$., $^{***}p < 0.001$. EE: environmental enrichment; IRR: irradiation; Cond: conditioning; Ext: extinction; DCX+: doublecortin positive cells.

we used a non-hippocampus dependent conditioning procedure (auditory fear conditioning). We compared spontaneous tone-elicited fear recovery before and after a month of either living in an enriched environment (EE) or a standard home cage (non-EE). On day 1, rats were conditioned to fear a sound (tone) by pairing it with an aversive consequence (mild foot-shocks). The next day (day 2), rats extinguished their fear to the conditioned tone by not receiving any aversive consequence. One day later (day 3), rats were tested for fear memory retrieval to the tone. After proper group matching during the first retrieval test (day 3; $t_{(13)} = 0.91$, $p = 0.92$), rats spent over a month in EE or non-EE until tested for a second retrieval test (day 38). We found that rats that lived in an EE showed similar tone-elicited fear-related behaviour levels during test 2 as compared to rats that lived in a non-EE (Fig. 6A; freezing: EE: 70.02%; non-EE: 55.36%; $t_{(13)} = 1.15$, $p = 0.26$; bar-pressing: EE: 1.031 press/min; non-EE: 3.43 press/min; $t_{(13)} = 0.99$, $p = 0.3$). Despite the consistent EE-induced increase of neurogenesis after extinction (Fig. 6B; $t_{(13)} = 3.13$, $p = 0.008$), our behavioural results indicate that neurogenesis-mediated prevention of spontaneous fear recovery is hippocampus dependent and amygdala independent.

Discussion

We investigated when adult hippocampal neurogenesis affects spontaneous fear recovery and its underlying brain network activity. We found that EE-mediated enhancement of neurogenesis prevented fear recovery. Consistently, we found that IRR-mediated ablation of neurogenesis promoted fear recovery. Interestingly, these opposing neurogenesis manipulations affected fear-related behaviours only if manipulations occurred after, but not before or in the absence of, extinction learning. These behavioural findings indicate that neurogenesis effect on fear-related behaviour during fear recovery is time- and extinction-dependent. Notably, assessment of neural activity revealed that recruitment of distinct prefrontal-amygdala-habenula networks correlates with opposing neurogenesis manipulations and fear-related response during fear recovery. These findings add to a growing body of evidence showing that neurogenesis regulates fear-related behaviour by altering activity in fear-signalling brain regions[9,10] and highlight the importance of timing neurogenesis manipulations after extinction learning.

New neurons are generated in the adult dentate gyrus of the hippocampus in mammals[39]; however, the functional impact of these adult-born neurons on hippocampus-dependent functions is still unclear. For instance, although the impact of neurogenesis on hippocampal-dependent contextual fear memories has been largely explored, current results are conflicting. Neurogenesis manipulations (using different methods to enhance or ablate it) can either increase[16], decrease[10] or have no effect[17] on fear-related responses. Here we show that identifying *when* neurogenesis is crucial and irreplaceable may be key to understand the role it plays in fear-related behaviour. We found that neurogenesis modulations alter the of expression fear-related behaviours only if neurogenesis manipulations occurred after, but not before, extinction training, suggesting a time-dependent effect. This post-training effect is consistent with the long-held notion that the hippocampus plays a key role in memory consolidation and its retrieval[13,40]. More interestingly, our behavioural findings are consistent with the recently emerged notion that neurogenesis is crucial to alter preexisting hippocampal-dependent memories[11,41]. It has been suggested that targeting neurogenesis after memory formation (post-training) is more disruptive because these memories are already committed to memory traces[42]. Further, recent studies have shown that neurogenesis manipulations after memory formation can alter the expression of the fear memory by either promoting memory consolidation[15] or forgetting[10]. But, we found that increasing neurogenesis after conditioning (before extinction) did not promote forgetting of fear memory. A possible explanation for the discrepancy with Akers *et al*., 2014 is twofold: stronger conditioning and saliency of bar-pressing across contexts in our study. The former explanation agrees with a recent report showing that spatial memory forgetting is prevented by long training[43]. The latter explanation agrees with another recent report showing spatial memory forgetting can be prevented by the addition of a salient retrieval reminder[44]. Although we cannot specify through which mechanism(s), our findings indicate that opposing neurogenesis manipulations timed after the formation of the extinction memory may alter the expression of fear-related contextual memories and thereby prevent or promote fear recovery.

Previous studies exploring the relationship between hippocampal neurogenesis and extinction of fear have shown conflicting data. One report found that neurogenesis ablation retards extinction learning[45], while another found the same manipulation had no effect[46]. Yet, the effect of manipulating neurogenesis after extinction learning had not been studied. By timing neurogenesis manipulation before or after extinction and evaluating spontaneous fear recovery, our findings reveal that neurogenesis manipulations after extinction learning, but not before, is crucial to modify fear levels during fear recovery. Notably, this effect on fear-related behaviours is not present in the absence of extinction training, suggesting it is an extinction-dependent effect. Given hippocampus' well-known role in consolidation[47], our results extend its role to neurogenesis-mediated consolidation of

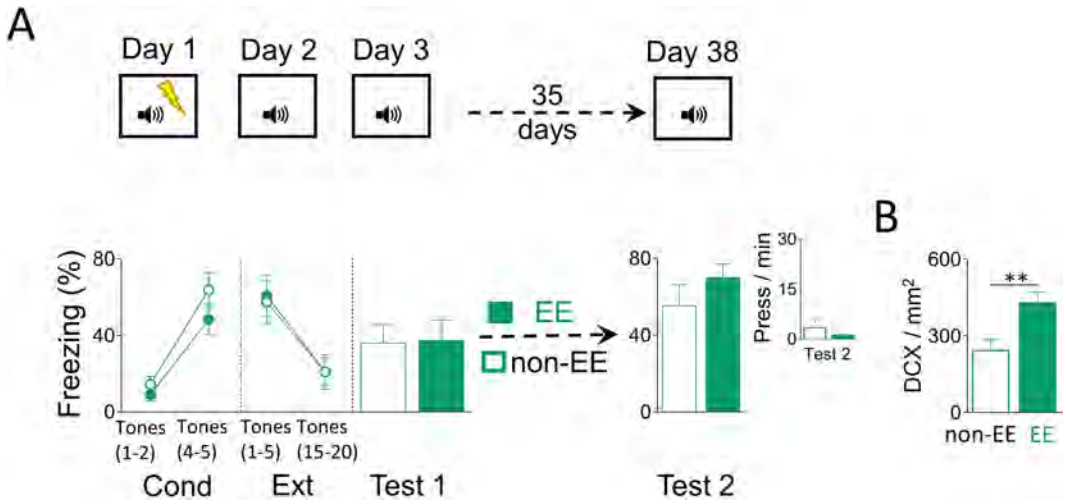

Figure 6. EE-mediated neurogenesis increase does not prevent tone-associated fear recovery. (**A**) Top, Rats were trained to associate a tone with foot-shock (five tone-shock pairings) (day 1; conditioning). One day later, rats were trained to associate the same tone (20 presentations) with the absence of foot-shock (day 2; extinction). The next day, rats were presented with the same tone without foot-shocks (day 3; test 1). Then, rats were housed for over a month (35 days) either in an EE or a non-EE. Finally, rats were presented with two tones alone in the same context to test for fear recovery (day 38; test 2). Data are shown for first block (early) and last block (late) of conditioning and extinction, and as a single block in test sessions (2-trial blocks). Bottom, EE after extinction training did not prevent tone-associated fear recovery, as indicated by similar freezing responses and bar presses per minute (inset), when comparing EE with non-EE (EE: n = 8; non-EE: n = 7). (**B**) Rats that lived in an EE for over a month showed more number of DCX+ per area (mm^2) in the dentate gyrus of the hippocampus than rats that lived in a non-EE. $^{**}p < 0.01$. Error bars indicate SEM. EE: enhanced environment; Cond: conditioning; Ext: extinction; DCX+ doublecortin positive cells.

extinction memory. Further, events that involve synaptic changes (including neurogenesis), mediated by hippocampal communication with the medial prefrontal cortex (mPFC) are necessary and recruited during consolidation of remote fear memory[15]. However, changes that mPFC undergoes (e.g. increased synaptic density) during remote memory consolidation[48,49] are reverted by extinction training, suggesting synaptic modifications in mPFC can be mediated by hippocampal neurogenesis during extinction. This is consistent with the presently observed PL decreased recruitment mediated by neurogenesis enhancement and IL decreased activity mediated by neurogenesis ablation during extinction consolidation.

It is also possible that the effect we observed is also due to modulation of other cognitive functions. It has been suggested that during fear recovery of extinguished fear, two memory traces (fear memory and extinction memory) compete for the control of fear-related behaviours[1,21]. Our results suggest that increasing neurogenesis may balance towards the expression of extinction memory and decreasing neurogenesis may balance towards the expression of fear memory. Given that in our study, both fear and extinction memories share the representation of the same context, it is possible that the observed neurogenesis-mediated effect on fear recovery also relies on a neurogenesis-dependent phenomenon known as pattern separation[50]. Neurogenesis may prevent fear recovery by facilitating the separation of similar contextual representations that may otherwise cause defensive responses based on ambiguous interpretations of the valence of the context (dangerous vs. safe environment)[51]. Further experiments are necessary to test this idea formally.

But what brain activity supports the observed neurogenesis-mediated time- and extinction-dependent effect on fear recovery? Consistent with previous results, we found that extinguished fear recovery involves recruitment of the canonical brain circuit involved in fear regulation (distinct regions of the hippocampus, medial prefrontal cortex and the amygdala[26,30,34]). Additionally, consistent with habenula´s role in signalling aversion[31], we found the habenula to be heavily correlated with fear recovery levels associated with opposing neurogenesis manipulations. Importantly, our findings suggest that modifications generated in the hippocampus mediated by adding new-born neurons modifies the activity of this circuitry. This is consistent with the idea that, through adulthood, new neurons are continuously generated and integrated into existing circuits in the hippocampus[52,53] modulating hippocampus-dependent information processing and associated circuitry[12]. Further, our brain activity findings are consistent with studies *in silico* that predict that neuronal plasticity mediated by adding new neurons alters brain activity associated to previously established memory traces[11,54]. Thus, together our results are consistent with the idea that hippocampal neurogenesis models (or remodels) connectivity of the brain network involved in fear-related behaviours linked to previous contextual experiences.

Fear-related disorders in humans are associated with high fear relapse rates[55], reduced hippocampal volume[56,57], hyperactivity in the dorsal anterior cingulate cortex[58] (a homolog of rodent PL[59]) and reduced activity in the ventromedial prefrontal cortex[60] (a homolog of rodent IL[61]). We found that high fear recovery mediated by neurogenesis ablation after extinction is associated with decreased hippocampal and IL activity, while low fear recovery mediated by increased neurogenesis is associated with conspicuously decreased PL activity.

Thus, targeting the promotion of neurogenesis (for example with regular aerobic exercise programs[62]) after extinction-based therapy may help restore activity of the fear regulation brain network and thereby prevent fear relapse in humans.

Methods

Subjects. A total of 107 male Wistar rats (180–220 g; Instituto de Fisiología Celular breeding colony) were housed in polyethylene cages and maintained on a standard 12 h light/dark schedule with *ad libitum* access to standard laboratory rat chow and water until bar-press training. All manipulations and behavioural procedures were performed during the light phase between 7:00 and 19:00 h. Animals were housed in groups of 2–3 per cage in a temperature-controlled environment (24 °C). All procedures were approved by the Institutional Animal Care and Use Committee of the Cellular Physiology Institute at the National Autonomous University of Mexico (FSB35–14 and FSB98-35), in compliance with the National Ministry of Health guidelines for the care of laboratory animals.

Behaviour. Food was restricted to 18 g/day of standard laboratory rat chow until rats reached 85% of their free-feeding weight. Rats were trained to press a lever for food (dustless precision pellets, 45 mg Bioserve, New Jersey) on a variable interval reinforcement schedule (VI 60 s). All rats received six bar-press training sessions until they reached a minimum of 12 presses per minute (each session lasted 30–35 min). Pressing maintains a constant level of activity against which freezing can be reliably measure. Bar-press training, fear conditioning, extinction and retrieval tests were performed in standard operant chambers (Coulbourn Instruments, Whitehall, PA) located inside sound-isolated cubicles (Med Associates, Burlington, VT). Bar-press training and fear conditioning protocols were performed in different conditions to control for potential context pre-exposure. Bar-press and fear conditioning contexts differed considerably. While fear conditioning context included a grid floor, white house light, clear plastic walls and constant background white noise, bar-press training context included a plastic floor, no house light, striped plastic walls and no background noise. The only element in common between operant and classical conditioning contexts was the lever-feeder. Between experiments, shock grids and floor trays were cleaned with soap and water, and the chamber walls were cleaned with wet paper towels.

Contextual fear conditioning, extinction and retrieval tests were performed in the same chambers. Rats were exposed to 5 min of habituation to the context immediately followed by conditioning consisting of five foot-shocks (2 s, 1 mA; inter shock interval was variable with an average of 2 min) during 15 min exposure to the context. Contextual extinction of fear consisted of 50 min exposure to the context in the absence of foot-shocks. Contextual memory retrieval test consisted of 10 min exposure to the context alone. Food pellets were available in the conditioning chambers on a VI 60 s schedule throughout all phases of the experiment. Freezing data were calculated as mean freezing per minute and expressed in graphs as average of 5 minutes in blocks (first block (early) and last block (late) of conditioning and extinction) or a 10-minute block (test sessions). Bar-pressing data were calculated as mean bar presses per minute and expressed in graphs as 5-minute blocks (first block (early) and last block (late) of conditioning and extinction) or a 10-minute block (test sessions).

Auditory fear conditioning, extinction and retrieval tests were performed in the same chambers. Auditory conditioning consisted on the presentation of five tones (30 s, 4 kHz, 75 dB) that co-terminated with foot-shocks (1 s, 0.8 mA). Auditory extinction of fear consisted on 20 tone-presentations in the absence of foot-shocks. Auditory fear memory retrieval test consisted on the presentation of 2 tones alone. In all sessions, the interval between tones was variable with an average of 2 min. Freezing and bar-pressing during the tone were used as a measure of cued fear. Food pellets were available in the conditioning chambers on a VI 60 s schedule throughout all phases of the experiment. Freezing data were calculated as mean freezing per minute during tone presentation (trial) and expressed in graphs as average of 2 trial in blocks (first block (early) and last block (late) of conditioning and extinction, and a single block in test sessions). Bar-pressing data were calculated as mean bar presses per minute during tone presentation (trial) and expressed in graphs as 2-trial blocks (first block (early) and last block (late) of conditioning and extinction, and a single block in test sessions).

Neurogenesis manipulations. Environmental enrichment: This procedure is used as an experimental tool to enhance adult hippocampal neurogenesis[37,62]. Rats were separated in two groups: those that lived in an enriched environment (EE) and those that lived in standard environment (non-EE). EE rats were housed in groups of 2–3 rats in standard large cages equipped with a running wheel for aerobic exercise (always available), an opaque plastic tunnel and chewing woods. Non-EE rats were also housed in groups of 2–3 rats in standard large cages but with no other material.

X–Irradiation: This procedure is used as an experimental tool to ablate adult hippocampal neurogenesis[16,25]. Rats were separated into two groups: those that were irradiated (IRR) and those that received sham-irradiation (non-IRR). All rats were anesthetized (ketamine 90 mg/kg and xylazine 10 mg/kg, i.p.). First, we obtained a cranial tomography to obtain the specific target coordinates to locally irradiate the hippocampus specifically. Then, rats were placed in a stereotaxic apparatus. The whole procedure was performed using a 6MV linear accelerator (Novalis, Brainlab-Varian). IRR rats received three arcs of circular irradiation per each side of the hippocampus; X-rays were confined to the hippocampus shape using a circular collimator (6 mm-Brainlab). Non-IRR rats were anesthetized in the same conditions and placed in the stereotaxic apparatus in the irradiation room, however, no X-irradiation was applied. For each rat, this process was repeated three times per session in three separate sessions distributed in 35 days. On each session, a dose of 5 Greys (Gy; Gy = J/kg) was applied, with a total dosage of 15 Gy for the three sessions. At the beginning and the end of each session vital signs were monitored. After each session, rats were put back in their home cages.

Immunohistochemistry. Ninety minutes after the final behavioural test, rats were overdosed with chloral hydrate (400 mg/Kg, Sigma) and transcardially perfused with cold saline solution (0.9%), and paraformaldehyde (PFA, 4%). Brains were collected and post-fixed in the same perfusate. One week later, brains were transferred into a 30% sucrose (Sigma) in PBS. Brains were mounted and cut (50 µm) using a cryostat (Leica, CM 1520) at −25 °C. Sections were collected into tissue culture plates with antifreeze (40% glycerol, 10% ethylene glycol in PBS). Then, brain sections were mounted into gelatinized slides. On the first immunohistochemistry day, the antigen retrieval protocol was performed. Slides were placed through an alcohol gradient. Then, slides were placed in citrate buffer solution (10 mM Citric Acid, 0.05 Tween 20, pH 6.0) and subsequently in a pressure cooker during 20 min. Next, tissue underwent endogenous peroxidases blocking (Hydrogen peroxide 3%, Sigma) for 10 min. Tissue was removed from slides and placed freely floating in a blocking solution (Bovine Serum Albumin, 1%, Santa Cruz Biotechnology, NGS 1%, Jackson Immunoresearch in TBS-T) during 1 hr. Tissues were then transferred to the primary antibody (1:2500, anti c-Fos, Ab-5, Polyclonal Rabbit, Millipore/Calbiochem or 1:5000, rabbit monoclonal anti-DCX, #4604 S, Cell Signaling Technology) for 48 h at 120 rpm. The second immunohistochemistry day, sections were washed six times with TBS-T for 10 min. Then, tissue was incubated in the secondary antibody (1:1000, anti-rabbit, Jackson Inmunoresearch) for 1 h at 120 rpm. Afterwards, six TBS-T washes were performed for 10 min and then incubated in ABC complex (1:250) (kit ABC-peroxidase, elite VECTASAN®, Vector) during 1 h. Next, six more TBS-T washes for 10 min were done. DAB-Ni (Sigma) solution was used as chromogen, forming a purple-black precipitate. Sections were mounted and counterstaining with methyl green (Sigma).

Cell counting and analysis. We quantified the number of c-Fos positive nuclei in the prelimbic (PL) and infralimbic cortex (IL), lateral habenula (LHb), basolateral (BLA) and central amygdala (CeA) as well as CA1, CA3 and dentate gyrus (DG) of the hippocampus. DCX positive cells (DCX+) were quantified in DG. The DCX+ cells were counted in all DG with a 40x objective (N.A 0.7) and images to measure the complete area were taken with 1X objective (N.A 0.04). Multiple images were captured for each brain region for c-Fos positive nuclei. All c-Fos images were taken with a microscope (Nikon Eclipse) with 10X objective (N.A 0.30) using the QCapturePro Program (7.05 v). For each region, the number of c-Fos positive nuclei were counted using the freely available image analysis software (ImageJ, 1.48 v, National Institutes of Health, US). Parameters we used to include c-Fos positive nuclei were: 52–250 µm area and 0.6–1 circularity. To directly compare c-Fos immunoreactivity in brain regions with different baselines, the expression of c-Fos was evaluated as a normalized contrast of c-Fos immunoreactive cells in treated rats (EE and IRR) relative to its control group (non-EE and non-IRR, respectively) (z-score; as in[63]). To obtain the density (numbers of cells per mm^2) of c-Fos positive nuclei and DCX+, we obtained the weighted mean of all the cells per area unit using ImageJ.

To control for DCX staining in the X-irradiation experiments, we quantified immunostained DCX+ cells in the rostral migratory stream (RMS). RMS can be found in the region that comprises the ependymal/olfactory ventricle (E/OV) at the level of the prefrontal cortext in the rat brain. Given the high concentration and entangled configuration of immature cells in RMS, it is not possible to reliably quantify immature cells one by one using the same methods described above for the hippocampus. Thus, we used optical density (OD) values to provide a quantitative and unbiased measurement of the density of immunostained doublecortin positive (DCX+) cells in RMS. OD values represent a standardized measurement of the intensity of dark deposit in an image. To obtain an effective contrast to quantify OD, DCX+ cells were immunostained in purple/black (stains the whole cell body, dendrites and axon) whereas DCX− cells appeared as a light green nuclear counterstaining. The dramatic contrast that resulted from this staining allowed to clearly differentiate between DCX+ and DCX− congregate cells, as evidenced by very distinct grey levels in images taken with a microscope equipped with a digital camera. Finally, we converted grey levels to quantifiable standard OD unit values using a software calibration tool (ImageJ).

Data collection and analysis. Behaviour was recorded with digital video cameras. Freezing was quantified from digitized video images using commercially available software (ANY-maze; Stoelting Co., IL, USA). The amount of time spent freezing per minute (contextual conditioning protocol) or per tone (auditory conditioning protocol) was expressed as a percentage of context exposure time or tone presentation, respectively. Bar-pressing was also used as conditioned fear-related response during context exposure or tone presentation. Groups were compared by using, when appropriate, unpaired Student's two-tailed *t* tests or repeated-measures analysis of variance (ANOVA; STATISTICA; StatSoft, Tulsa, OK).

References

1. Maren, S., Phan, K. L. & Liberzon, I. The contextual brain: implications for fear conditioning, extinction and psychopathology. *Nature reviews. Neuroscience* **14**, 417–428, https://doi.org/10.1038/nrn3492 (2013).
2. Bouton, M. E. Context, ambiguity, and unlearning: sources of relapse after behavioral extinction. *Biological psychiatry* **52**, 976–986 (2002).
3. Ji, J. & Maren, S. Hippocampal involvement in contextual modulation of fear extinction. *Hippocampus* **17**, 749–758, https://doi.org/10.1002/hipo.20331 (2007).
4. Sotres-Bayon, F., Cain, C. K. & LeDoux, J. E. Brain mechanisms of fear extinction: historical perspectives on the contribution of prefrontal cortex. *Biological psychiatry* **60**, 329–336, https://doi.org/10.1016/j.biopsych.2005.10.012 (2006).
5. Goode, T. D. & Maren, S. Animal models of fear relapse. *ILAR journal/National Research Council, Institute of Laboratory Animal Resources* **55**, 246–258, https://doi.org/10.1093/ilar/ilu008 (2014).
6. Rescorla, R. A. Spontaneous recovery. *Learn.Mem.* **11**, 501–509 (2004).
7. Quirk, G. J. Memory for extinction of conditioned fear is long-lasting and persists following spontaneous recovery. *Learn.Mem.* **9**, 402–407 (2002).
8. Vervliet, B., Craske, M. G. & Hermans, D. Fear extinction and relapse: state of the art. *Annual review of clinical psychology* **9**, 215–248, https://doi.org/10.1146/annurev-clinpsy-050212-185542 (2013).
9. Feng, R. *et al*. Deficient neurogenesis in forebrain-specific presenilin-1 knockout mice is associated with reduced clearance of hippocampal memory traces. *Neuron* **32**, 911–926 (2001).

10. Akers, K. G. *et al*. Hippocampal neurogenesis regulates forgetting during adulthood and infancy. *Science* **344**, 598–602, https://doi.org/10.1126/science.1248903 (2014).
11. Weisz, V. I. & Argibay, P. F. Neurogenesis interferes with the retrieval of remote memories: forgetting in neurocomputational terms. *Cognition* **125**, 13–25, https://doi.org/10.1016/j.cognition.2012.07.002 (2012).
12. Epp, J. R., Silva Mera, R., Kohler, S., Josselyn, S. A. & Frankland, P. W. Neurogenesis-mediated forgetting minimizes proactive interference. *Nature communications* **7**, 10838, https://doi.org/10.1038/ncomms10838 (2016).
13. Maren, S. & Holt, W. The hippocampus and contextual memory retrieval in Pavlovian conditioning. *Behav Brain Res* **110**, 97–108 (2000).
14. Sahay, A. *et al*. Increasing adult hippocampal neurogenesis is sufficient to improve pattern separation. *Nature* **472**, 466–470, https://doi.org/10.1038/nature09817 (2011).
15. Kitamura, T. *et al*. Adult neurogenesis modulates the hippocampus-dependent period of associative fear memory. *Cell* **139**, 814–827, https://doi.org/10.1016/j.cell.2009.10.020 (2009).
16. Winocur, G., Wojtowicz, J. M., Sekeres, M., Snyder, J. S. & Wang, S. Inhibition of neurogenesis interferes with hippocampus-dependent memory function. *Hippocampus* **16**, 296–304, https://doi.org/10.1002/hipo.20163 (2006).
17. Shors, T. J., Townsend, D. A., Zhao, M., Kozorovitskiy, Y. & Gould, E. Neurogenesis may relate to some but not all types of hippocampal-dependent learning. *Hippocampus* **12**, 578–584, https://doi.org/10.1002/hipo.10103 (2002).
18. Zhang, C. L., Zou, Y., He, W., Gage, F. H. & Evans, R. M. A role for adult TLX-positive neural stem cells in learning and behaviour. *Nature* **451**, 1004–1007, https://doi.org/10.1038/nature06562 (2008).
19. Jaholkowski, P. *et al*. New hippocampal neurons are not obligatory for memory formation; cyclin D2 knockout mice with no adult brain neurogenesis show learning. *Learning & memory* **16**, 439–451, https://doi.org/10.1101/lm.1459709 (2009).
20. Milad, M. R. & Quirk, G. J. Fear extinction as a model for translational neuroscience: ten years of progress. *Annu Rev Psychol* **63**, 129–151, https://doi.org/10.1146/annurev.psych.121208.131631 (2012).
21. Quirk, G. J. *Handbook of emotion regulation*. 27–46 (Guilford Press, 2007).
22. Clelland, C. D. *et al*. A functional role for adult hippocampal neurogenesis in spatial pattern separation. *Science* **325**, 210–213, https://doi.org/10.1126/science.1173215 (2009).
23. Aimone, J. B., Deng, W. & Gage, F. H. Resolving new memories: a critical look at the dentate gyrus, adult neurogenesis, and pattern separation. *Neuron* **70**, 589–596, https://doi.org/10.1016/j.neuron.2011.05.010 (2011).
24. Stone, S. S. *et al*. Functional convergence of developmentally and adult-generated granule cells in dentate gyrus circuits supporting hippocampus-dependent memory. *Hippocampus* **21**, 1348–1362, https://doi.org/10.1002/hipo.20845 (2011).
25. Wojtowicz, J. M. Irradiation as an experimental tool in studies of adult neurogenesis. *Hippocampus* **16**, 261–266, https://doi.org/10.1002/hipo.20158 (2006).
26. Sotres-Bayon, F. & Quirk, G. J. Prefrontal control of fear: more than just extinction. *Current opinion in neurobiology* **20**, 231–235, https://doi.org/10.1016/j.conb.2010.02.005 (2010).
27. Ciocchi, S. *et al*. Encoding of conditioned fear in central amygdala inhibitory circuits. *Nature* **468**, 277–282, https://doi.org/10.1038/nature09559 (2010).
28. Badrinarayan, A., Prater, K. E. & Orsini, C. A. The role of the central amygdala in selecting circuits and responses. *The Journal of neuroscience: the official journal of the Society for Neuroscience* **32**, 8431–8433, https://doi.org/10.1523/JNEUROSCI.1820-12.2012 (2012).
29. Burgos-Robles, A., Vidal-Gonzalez, I. & Quirk, G. J. Sustained conditioned responses in prelimbic prefrontal neurons are correlated with fear expression and extinction failure. *The Journal of neuroscience: the official journal of the Society for Neuroscience* **29**, 8474–8482, https://doi.org/10.1523/JNEUROSCI.0378-09.2009 (2009).
30. Sotres-Bayon, F., Sierra-Mercado, D., Pardilla-Delgado, E. & Quirk, G. J. Gating of fear in prelimbic cortex by hippocampal and amygdala inputs. *Neuron* **76**, 804–812, https://doi.org/10.1016/j.neuron.2012.09.028 (2012).
31. Zhang, J. *et al*. Presynaptic Excitation via GABAB Receptors in Habenula Cholinergic Neurons Regulates Fear Memory Expression. *Cell* **166**, 716–728, https://doi.org/10.1016/j.cell.2016.06.026 (2016).
32. Ehrlich, I. *et al*. Amygdala inhibitory circuits and the control of fear memory. *Neuron* **62**, 757–771, https://doi.org/10.1016/j.neuron.2009.05.026 (2009).
33. Goutagny, R. *et al*. Interactions between the lateral habenula and the hippocampus: implication for spatial memory processes. *Neuropsychopharmacology: official publication of the American College of Neuropsychopharmacology* **38**, 2418–2426, https://doi.org/10.1038/npp.2013.142 (2013).
34. Sierra-Mercado, D., Padilla-Coreano, N. & Quirk, G. J. Dissociable roles of prelimbic and infralimbic cortices, ventral hippocampus, and basolateral amygdala in the expression and extinction of conditioned fear. *Neuropsychopharmacology: official publication of the American College of Neuropsychopharmacology* **36**, 529–538, https://doi.org/10.1038/npp.2010.184 (2011).
35. Radwanska, K., Schenatto-Pereira, G., Ziolkowska, M., Lukasiewicz, K. & Giese, K. P. Mapping fear memory consolidation and extinction-specific expression of JunB. *Neurobiology of learning and memory* **125**, 106–112, https://doi.org/10.1016/j.nlm.2015.08.007 (2015).
36. Lee, M. C. *et al*. DNA microarray-based analysis of voluntary resistance wheel running reveals novel transcriptome leading robust hippocampal plasticity. *Physiological reports* **2**, https://doi.org/10.14814/phy2.12206 (2014).
37. Hirase, H. & Shinohara, Y. Transformation of cortical and hippocampal neural circuit by environmental enrichment. *Neuroscience* **280**, 282–298, https://doi.org/10.1016/j.neuroscience.2014.09.031 (2014).
38. Phillips, R. G. & LeDoux, J. E. Differential contribution of amygdala and hippocampus to cued and contextual fear conditioning. *Behavioral neuroscience* **106**, 274–285 (1992).
39. Ming, G. L. & Song, H. Adult neurogenesis in the mammalian central nervous system. *Annual review of neuroscience* **28**, 223–250, https://doi.org/10.1146/annurev.neuro.28.051804.101459 (2005).
40. Anagnostaras, S. G., Maren, S. & Fanselow, M. S. Temporally graded retrograde amnesia of contextual fear after hippocampal damage in rats: within-subjects examination. *The Journal of neuroscience: the official journal of the Society for Neuroscience* **19**, 1106–1114 (1999).
41. Frankland, P. W., Kohler, S. & Josselyn, S. A. Hippocampal neurogenesis and forgetting. *Trends in neurosciences* **36**, 497–503, https://doi.org/10.1016/j.tins.2013.05.002 (2013).
42. Ishikawa, R., Fukushima, H., Frankland, P. W. & Kida, S. Hippocampal neurogenesis enhancers promote forgetting of remote fear memory after hippocampal reactivation by retrieval. *eLife* **5**, https://doi.org/10.7554/eLife.17464 (2016).
43. Kodali, M. *et al*. Voluntary Running Exercise-Mediated Enhanced Neurogenesis Does Not Obliterate Retrograde Spatial Memory. *The Journal of neuroscience: the official journal of the Society for Neuroscience* **36**, 8112–8122, https://doi.org/10.1523/JNEUROSCI.0766-16.2016 (2016).
44. Guskjolen, A., Josselyn, S. A. & Frankland, P. W. Age-dependent changes in spatial memory retention and flexibility in mice. *Neurobiology of learning and memory* **143**, 59–66, https://doi.org/10.1016/j.nlm.2016.12.006 (2017).
45. Pan, Y. W., Chan, G. C., Kuo, C. T., Storm, D. R. & Xia, Z. Inhibition of adult neurogenesis by inducible and targeted deletion of ERK5 mitogen-activated protein kinase specifically in adult neurogenic regions impairs contextual fear extinction and remote fear memory. *The Journal of neuroscience: the official journal of the Society for Neuroscience* **32**, 6444–6455, https://doi.org/10.1523/JNEUROSCI.6076-11.2012 (2012).

46. Ko, H. G. *et al*. Effect of ablated hippocampal neurogenesis on the formation and extinction of contextual fear memory. *Molecular brain* **2**, 1, https://doi.org/10.1186/1756-6606-2-1 (2009).
47. Squire, L. R., Genzel, L., Wixted, J. T. & Morris, R. G. Memory consolidation. *Cold Spring Harbor perspectives in biology* **7**, a021766, https://doi.org/10.1101/cshperspect.a021766 (2015).
48. Vetere, G. *et al*. Extinction partially reverts structural changes associated with remote fear memory. *Learning & memory* **18**, 554–557, https://doi.org/10.1101/lm.2246711 (2011).
49. Restivo, L., Vetere, G., Bontempi, B. & Ammassari-Teule, M. The formation of recent and remote memory is associated with time-dependent formation of dendritic spines in the hippocampus and anterior cingulate cortex. *The Journal of neuroscience: the official journal of the Society for Neuroscience* **29**, 8206–8214, https://doi.org/10.1523/JNEUROSCI.0966-09.2009 (2009).
50. Aimone, J. B., Deng, W. & Gage, F. H. Adult neurogenesis: integrating theories and separating functions. *Trends in cognitive sciences* **14**, 325–337, https://doi.org/10.1016/j.tics.2010.04.003 (2010).
51. Nakashiba, T. *et al*. Young dentate granule cells mediate pattern separation, whereas old granule cells facilitate pattern completion. *Cell* **149**, 188–201, https://doi.org/10.1016/j.cell.2012.01.046 (2012).
52. Arruda-Carvalho, M., Sakaguchi, M., Akers, K. G., Josselyn, S. A. & Frankland, P. W. Posttraining ablation of adult-generated neurons degrades previously acquired memories. *The Journal of neuroscience: the official journal of the Society for Neuroscience* **31**, 15113–15127, https://doi.org/10.1523/JNEUROSCI.3432-11.2011 (2011).
53. Deng, W., Saxe, M. D., Gallina, I. S. & Gage, F. H. Adult-born hippocampal dentate granule cells undergoing maturation modulate learning and memory in the brain. *The Journal of neuroscience: the official journal of the Society for Neuroscience* **29**, 13532–13542, https://doi.org/10.1523/JNEUROSCI.3362-09.2009 (2009).
54. Meltzer, L. A., Yabaluri, R. & Deisseroth, K. A role for circuit homeostasis in adult neurogenesis. *Trends in neurosciences* **28**, 653–660 (2005).
55. Perez Benitez, C. I. *et al*. A 5-year longitudinal study of posttraumatic stress disorder in primary care patients. *Psychopathology* **45**, 286–293, https://doi.org/10.1159/000331595 (2012).
56. Gilbertson, M. W. *et al*. Smaller hippocampal volume predicts pathologic vulnerability to psychological trauma. *Nature neuroscience* **5**, 1242–1247, https://doi.org/10.1038/nn958 (2002).
57. O'Doherty, D. C., Chitty, K. M., Saddiqui, S., Bennett, M. R. & Lagopoulos, J. A systematic review and meta-analysis of magnetic resonance imaging measurement of structural volumes in posttraumatic stress disorder. *Psychiatry research* **232**, 1–33, https://doi.org/10.1016/j.pscychresns.2015.01.002 (2015).
58. Clancy, K., Ding, M., Bernat, E., Schmidt, N. B. & Li, W. Restless 'rest': intrinsic sensory hyperactivity and disinhibition in post-traumatic stress disorder. *Brain: a journal of neurology* **140**, 2041–2050, https://doi.org/10.1093/brain/awx116 (2017).
59. Preuss, T. M. Do rats have prefrontal cortex? The rose-woolsey-akert program reconsidered. *J Cogn Neurosci* **7**, 1–24, https://doi.org/10.1162/jocn.1995.7.1.1 (1995).
60. Phelps, E. A., Delgado, M. R., Nearing, K. I. & LeDoux, J. E. Extinction learning in humans: role of the amygdala and vmPFC. *Neuron* **43**, 897–905, https://doi.org/10.1016/j.neuron.2004.08.042 (2004).
61. Quirk, G. J. & Beer, J. S. Prefrontal involvement in the regulation of emotion: convergence of rat and human studies. *Current opinion in neurobiology* **16**, 723–727, https://doi.org/10.1016/j.conb.2006.07.004 (2006).
62. van Praag, H., Kempermann, G. & Gage, F. H. Running increases cell proliferation and neurogenesis in the adult mouse dentate gyrus. *Nature neuroscience* **2**, 266–270, https://doi.org/10.1038/6368 (1999).
63. Wheeler, A. L. *et al*. Identification of a Functional Connectome for Long-Term Fear Memory in Mice. *PLoS computational biology* **9**, e1002853, https://doi.org/10.1371/journal.pcbi.1002853 (2013).

Acknowledgements

We thank Dr. L. Ramírez-Lugo for technical assistance and Dr. C. Bravo-Rivera for comments on a previous version of the manuscript. This study was supported by grants from CONACyT (CB176639 and PN2463), DGAPA-UNAM (IA200715 and IN205417) and IBRO Return Home fellowship to FS-B. Also, DGAPA-UNAM (CJIC/CTIC/0030/2014) and CONACyT (49133) post-doctoral fellowships to AM-C and CONACyT (CB258296) grant to PB-Z.

Author Contributions

A.M.-C. and F.S.-B. designed research; A.M.-C., G.L.-O., A.G.-G., P.B.-Z., O.G.C. and S.M.-J. performed research; A.M.-C., G.L.-O., A.G.-G. and F.S.-B. analysed data; A.M.-C. and F.S.-B. wrote the paper.

Additional Information

Competing Interests: The authors declare no competing interests.

Publisher's note: Springer Nature remains neutral with regard to jurisdictional claims in published maps and institutional affiliations.

Open Access This article is licensed under a Creative Commons Attribution 4.0 International License, which permits use, sharing, adaptation, distribution and reproduction in any medium or format, as long as you give appropriate credit to the original author(s) and the source, provide a link to the Creative Commons license, and indicate if changes were made. The images or other third party material in this article are included in the article's Creative Commons license, unless indicated otherwise in a credit line to the material. If material is not included in the article's Creative Commons license and your intended use is not permitted by statutory regulation or exceeds the permitted use, you will need to obtain permission directly from the copyright holder. To view a copy of this license, visit http://creativecommons.org/licenses/by/4.0/.

© The Author(s) 2019

Martínez-Martínez *et al. AMB Expr* (2019) 9:155
https://doi.org/10.1186/s13568-019-0876-4

AMB Express

ORIGINAL ARTICLE

Open Access

Phasin PhaP1 is involved in polyhydroxybutyrate granules morphology and in controlling early biopolymer accumulation in *Azospirillum brasilense* Sp7

María de los Angeles Martínez-Martínez[1], Bertha González-Pedrajo[2], Georges Dreyfus[2], Lucía Soto-Urzúa[1] and Luis Javier Martínez-Morales[1*]

Abstract

Phasins are amphiphilic proteins involved in the regulation of the number and size of polyhydroxybutyrate (PHB) granules. The plant growth promoting bacterium *Azospirillum brasilense* Sp7 accumulates high quantities of bioplastic PHB as carbon and energy source. By analyzing the genome, we identified six genes that code for proteins with a Phasin_2 domain. To understand the role of *A. brasilense* Sp7 PhaP1 ($PhaP1_{Abs}$) on PHB synthesis, the *phaP1* gene (AMK58_RS17065) was deleted. The morphology of the PHB granules was analyzed by transmission electron microscopy (TEM) and the PHB produced was quantified under three different C:N ratios in cultures subjected to null or low-oxygen transfer. The results showed that $PhaP1_{Abs}$ is involved in PHB granules morphology and in controlling early biopolymer accumulation. Using RT-PCR it was found that phasin genes, except *phaP4*, are transcribed in accordance with the C:N ratio used for the growth of *A. brasilense*. *phaP1*, *phaP2* and *phaP3* genes were able to respond to the growth conditions tested. This study reports the first analysis of a phasin protein in *A. brasilense* Sp7.

Keywords: *Azospirillum brasilense* Sp7, Phasins, C:N ratio, Oxygen stress, PHB accumulation

Introduction

Since it was reported for the first time in 1926 (Lemoigne 1926), polyhydroxybutyrate (PHB) has been the best studied bacterial biopolymer. PHB exhibits similar characteristics with respect to petrochemical plastics in addition to its biodegradability and biocompatibility properties. These characteristics enable PHB convenient to reduce the use of petrochemical plastic derivatives (Madison and Huisman 1999; Anjum et al. 2016). Besides the significant advantages of PHB, it is currently not used in large quantities because of the high production costs (US$ 5.5/kg) (Brigham and Riedel 2018; Pavan et al. 2019), mainly caused by the expensive carbon sources and the ineffective recovery process. A solution for improve the large-scale production of PHB could be the use of economic carbon substrates for PHB production such as food wastes (Brigham and Riedel 2018). Nonetheless, usage of cheaper carbon source combined with optimized processes for PHA accumulation and extraction could reduce the cost of biopolymer production and this could allow to address the large-scale production challenge. Since the demand in the health industry, the making of renewable materials and the advances in technologies, will make the market increase at a rate of 6.3%, reaching 119.15 million dollars by 2025 (Global Polyhydroxyalkanoate (PHA) Market Analysis & Trends—Industry Forecast to 2025).

More than 300 microorganisms have been reported to be PHB-producers (Koller et al. 2010; Alarfaj et al. 2015). PHB-producing microorganisms synthesize PHB by three enzymatic reactions. β-ketothiolase (PhaA) condenses two acetyl-CoA into acetoacetyl-CoA, then

*Correspondence: luis.martinez@correo.buap.mx
[1] Centro de Investigaciones en Ciencias Microbiológicas, Instituto de Ciencias, Benemérita Universidad Autónoma de Puebla, Puebla, Mexico
Full list of author information is available at the end of the article

Springer Open

© The Author(s) 2019. This article is distributed under the terms of the Creative Commons Attribution 4.0 International License (http://creativecommons.org/licenses/by/4.0/), which permits unrestricted use, distribution, and reproduction in any medium, provided you give appropriate credit to the original author(s) and the source, provide a link to the Creative Commons license, and indicate if changes were made.

INFORME DE LABORES 2019

acetoacetyl-CoA is reduced to 3-hydroxybutyril-CoA by an acetoacetyl-CoA reductase (PhaB) and finally, 3-hydroxybutyril-CoA monomers are polymerized to PHB by a PHB synthase (PhaC) (Madison and Huisman 1999; Sagong et al. 2018).

Once synthesized, PHB is packaged into granules named carbonosomes which contain PHB covered by granule associated proteins (GAP's) (Steinbüchel et al. 1995; Jendrossek 2009; Pfeiffer and Jendrossek 2012). Four main GAP's have been reported: PHB synthases (PhaC), PHB depolymerases (PhaZ), regulators (PhaR or PhaM) and phasins (PhaP) (Steinbüchel et al. 1995; Tirapelle et al. 2013). Synthases and depolymerases are involved in PHB accumulation and utilization, respectively (Juengert et al. 2018; Mezzolla et al. 2018). Phasins are small amphiphilic proteins that coat and stabilize PHB in the cytoplasm (Sznajder et al. 2015) and therefore, phasins are involved in regulate the number and size of carbonosomes (Pfeiffer and Jendrossek 2012; Hauf et al. 2015). Regulator proteins (PhaR) control phasin synthesis (Maehara et al. 2002; Pötter et al. 2002; York et al. 2002) and possibly granule localization (PhaM) (Pfeiffer et al. 2011; Pfeiffer and Jendrossek 2014).

It has been demonstrated that phasins are the main GAP's (Steinbüchel et al. 1995: Sznajder et al. 2015). Studies on phasins have suggested possible interactions with PHB polymerases and PHB depolymerases depending on the PHB-producing microorganism (York et al. 2001; Fukui et al. 2001; Handrick et al. 2004a, b; Tian et al. 2005; Ushimaru et al. 2014). In *Aeromonas hydrophila* the PHB content increased twofold when the only PhaP was overexpressed (Ushimaru et al. 2014), also changes in the monomer composition of poly(3-hydroxybutyrate-*co*-3-hydroxyhexanoate) [P(HB-*co*-HHx)] copolyester were documented (Tian et al. 2005). It has also been shown that PHB is easily degraded in the presence of PhaP in *Rhodospirillum rubrum* (Handrick et al. 2004a, b; Kuchta et al. 2007).

PHB synthesis has been poorly studied in the α-proteobacterium *A. brasilense* Sp7. This bacterium accumulates up to 70% of its dry-cell weight (DCW) as PHB. The PHB accumulated energizes metabolic processes that favor bacterial survival under stressful environments (Tal and Okon 1985; Itzigsohn et al. 1995). PHB accumulation in *A. brasilense* Sp7 requires an excess in carbon and limited nitrogen sources (Tal and Okon 1985; Itzigsohn et al. 1995). Malic acid and ammonium chloride are the best carbon and nitrogen sources to improve PHB accumulation in *A. brasilense* Sp7 (Itzigsohn et al. 1995). Biochemical analyses of the PHB synthase and PHB depolymerase in *A. brasilense* have been carried out (Tal et al. 1990; Kadouri et al. 2002, 2003). However, there are no reports dealing with phasin proteins.

Our goal in this study was to analyze the function of the $PhaP1_{Abs}$ on the morphology of PHB granules and PHB accumulation using carbon:nitrogen (C:N) ratios of 30:1, 60:1 and 90:1, in cultures subjected to null or low-oxygen transfer. By means of bioinformatics analyses we found six genes that code for proteins containing a Phasin_2 domain (PF09361). In this work we deleted *phaP1* gene and the resulting mutant was characterized. The results showed that $PhaP1_{Abs}$ controls the morphology of the PHB granules and is involved in the control of early PHB synthesis in some of the growth conditions evaluated.

Materials and methods

Bacterial strains, plasmids and growth conditions

Bacteria used in this study are listed in Table 1. *Escherichia coli* strains were grown in Luria Bertani (LB) broth supplemented with the appropriate antibiotics at 37 °C and 150 rpm. LB composition per liter: yeast extract 5 g, casein peptone 10 g and NaCl 10 g. For *A. brasilense*, a minimal medium supplemented with malic acid and ammonium chloride as carbon and nitrogen sources, was used. Minimal medium composition per liter: Malic acid 4.355 g, NH_4Cl 0.2 g, K_2HPO_4 1.67 g, KH_2PO_4 0.87 g, $MgSO_4$ 0.29 g, NaCl 0.48 g, $CaCl_2$ 0.07 g, $FeCl_3{\cdot}6H_2O$ 0.01 g, $Na_2MoO_4{\cdot}2H_2O$ 0.025 g and 10 mL of trace element solution (containing $MnSO_4{\cdot}H_2O$ 250 mg, $ZnSO_4{\cdot}7H_2O$ 70 mg, $CoSO_4{\cdot}7H_2O$ 14 mg, $CuSO_4{\cdot}5H_2O$ 12.5 mg and H_3BO_3 3 mg per liter). *A. brasilense* Sp7 strains were cultured, with the appropriated antibiotics, at 32 °C and 110 rpm. All incubations were carried out in a 25 mm amplitude orbital shaker (INO-650M SEV®).

Bioinformatics analyses

Proteins containing a Phasin_2 domain (PF09361) in the *A. brasilense* Sp7 genome were searched on National Center for Biotechnology Information (NCBI) (Geer et al. 2009), Simple Modular Architecture Research Tool (SMART) (Letunic and Bork 2017) and PFAM databases (Finn et al. 2015). Secondary structures were predicted using the PSI-blast based secondary structure PREDiction (PSIPRED) software (Buchan et al. 2013) and Protein Homology/AnalogY Recognition Engine (Phyre2) server (Kelley et al. 2015). Three-dimensional structures of putative phasins were predicted by using the Iterative Threading ASSEmbly Refinement (I-TASSER) (Roy et al. 2010; Yang and Zhang 2015; Zhang et al. 2017) and SWISS-MODEL (Waterhouse et al. 2018) servers. The obtained three-dimensional structures were evaluated by Qualitative Model Energy ANalysis (QMEAN) (Benkert et al. 2011) and Ramachandran plots at SWISS-MODEL Structure Assessment server. Alignments were done using Clustal X software (Larkin et al. 2007). Identity and similarity percentages were calculated on the Sequence

INFORME DE LABORES 2019

Table 1 Strains and plasmids used in this study

Bacteria	Characteristics	Reference
Azospirillum brasilense Sp7	Wild type strain	Tarrand et al. (1978)
A. brasilense Δ*phaP1*	*A. brasilense* Sp7 deleted in *phaP1* gene.	This study
A. brasilense PhaP1^{+++}	*A. brasilense* Δ*phaP1* containing pMBA-12	This study
E. coli S17-1	*Smr*, *rec*A, *thi*, *pro*, *hsd*R-M+ RP4:2-*Tc:Mu:Km* Tn7, λ*pir*	Simon et al. (1983)
Plasmids	**Characteristics**	**References**
pCR2.1TOPO	Source of Km resistance cassette	Invitrogen
pGLO	Source of Ara promoter	BioRad
pMMB206	Expression vector	Morales et al. (1991)
pSUP202	Suicide vector	Roschanski and Strauch (2011)
pSUPAB	pSUP202 containing upstream and downstream *phaP1* flanking regions.	This study
pSUPAKB	pSUPAB containing Km resistance cassette of pCR2.1TOPO	This study
pMBA-2	Expression vector pMMB206 derivative containing Ara promoter	This study
pMBA-12	pMBA-2 with *phaP1*	This study

Manipulation Suite (Stothard 2000). For the phylogenetic analyses, 18 amino acid sequences of phasins from main PHB-producing microorganisms were aligned using Clustal X software (Larkin et al. 2007). The phylogenetic tree was inferred using the Neighbor-Joining method and the evolutionary distances were computed using the Poisson correction method at the Molecular Evolutionary Genetics Analysis software version 7.0 (MEGA 7.0) (Kumar et al. 2016). The number of replicates were 500. Amino acid sequences of *Ralstonia eutropha* phasins were used as outgroup for the tree.

DNA manipulation

DNA was obtained by the phenol:chloroform method as previously reported (Cheng and Jiang 2006). Briefly, bacterial cells were harvested by centrifugation (8000×*g* for 5 min), the supernatant was removed, and the pellet washed in Sodium chloride–Tris–EDTA (STE) buffer twice. Cells were recovered and resuspended in Tris–EDTA (TE) buffer. Tris-saturated phenol (pH 8) was added, and the samples were mixed by vortexing and centrifuged as above. Phenol traces and debris were cleaned by three chloroform washes and the aqueous phase containing nucleic acids was recovered. RNA was eliminated by adding RNase H (10 mg/mL) to the aqueous phase and incubating for 10 min at 37 °C followed by purification with phenol:chloroform (Invitrogen). Pure DNA was contained in the aqueous phase. Plasmid DNA was isolated by the miniprep technique (Sambrook et al. 1989). Cloning procedures such as PCR amplifications, digestions and ligations were performed according to the instructions provided by the manufacturer (ThermoScientific).

In frame deletion of the *phaP1* gene in *A. brasilense* Sp7

Upstream and downstream regions of the *phaP1* gene (AMK58_RS17065) were PCR amplified using the primers *phaP1*FA*Pst*I/*phaP1*RA*Xma*I (upstream) and *phaP1* FB*Xma*I/*phaP1*RB*Eco*RI (downstream) (Table 2). Primers were designed to contain *Pst*I/*Xma*I and *Xma*I/*Eco*RI restriction sites. PCR conditions consisted of an initial denaturalization step at 94 °C for 5 min, followed by 30

Table 2 Primers used in this study (restriction sites are underlined)

Primer	Sequence (5′ → 3′)
*pha*P1FA*Pst*I	gatactgcagcgccaacctgatcgagcata
*pha*P1RA*Xma*I	tatcccgggcttggccatggttctcaccc
*pha*P1FB*Xma*I	gatacccgggaagaagtaagcgtctctcccg
*pha*P1RB*Eco*RI	ctatgaattcaaggaactgctggtcatctc
*pha*P1-F*Mfe*I	ctagcaattgcatggccaagcagaccggtaa
*pha*P1-R*Sma*I	atacccgggttacttcttggcgatgcgggc
RT-16 s rRNA-F	ctgaacaaccagcgcatcga
RT-16 s rRNA-r	aagtcctcgcgcttcacg
RT-*pha*P1-F	gccgagatcgtccgttcct
RT-*pha*P1-R	gcgaccttgaccagttcgg
RT-*pha*P2-F	cccagtcctcgctggagaag
RT-*pha*P2-R	gtctcgaagctcgccttggc
RT-*pha*P3-F	agctcctgaagatctcctccga
RT-*pha*P3-R	cctcacgggtcagctcctcg
RT-*pha*P4-F	cctgtccgcacaagccca
RT-*pha*P4-R	ccattcgcgcatgatggac
RT-*pha*P5-F	gccaatccggagttcgtcc
RT-*pha*P5-R	ccctgcatcagggtcatcca
RT-*pha*P6-F	cgtcaaccagatgcagaccgtc
RT-*pha*P6-R	cggagcagccttcggagc

cycles of denaturing at 94 °C for 45 s, annealing at 58 °C for 45 s and extension at 72 °C for 1 min as suggested by the manufacturer (ThermoScientific). Finally, an additional extension of 5 min at 72 °C was carried out. Both PCR fragments were digested with the specified endonucleases and cloned into *Pst*I/*Eco*RI sites of the suicide vector pSUP202 generating the plasmid pSUPAB. Then, kanamycin resistance gene from pCR2.1TOPO vector was cloned into *Xma*I sites of pSUPAB. The resulting suicide vector, pSUPAKB, was mobilized into *A. brasilense* Sp7 using *E. coli* S17-1 as a donor strain as previously reported (Mishra et al. 2011). The *A. brasilense phaP1* deleted mutant strain (named *A. brasilense* Δ*phaP1*) was selected on minimal medium supplemented with kanamycin (50 μg/mL) and ampicillin (100 μg/mL).

Complementation of the *A. brasilense* Δ*phaP1* strain

The complementation of the *A. brasilense* Δ*phaP1* was done in two steps. First, the pMBA-2 vector was generated by cloning of the arabinose promoter and the *araC* gene from pGLO into *ApaI*/*EcoRI* sites of the expression vector pMMB206. Second, the *phaP1* gene was amplified by PCR using the primers *phaP1*-F*Mfe*I/*phaP1*-R*Sma*I and wild type total DNA as a template. The PCR product was digested and ligated into *Eco*RI/*Sma*I restriction sites of pMBA-2. The resulting pMBA-12 plasmid was mobilized into *A. brasilense* Δ*phaP1* using *E. coli* S17-1 as a donor strain. The complemented mutant (named *A. brasilense* PhaP1^{+++}) was selected on minimal medium supplemented with chloramphenicol (10 μg/mL), kanamycin (50 μg/mL) and ampicillin (100 μg/mL). Induction of the arabinose promoter for PhaP1$_{Abs}$ expression in pMBA-12 vector was carried out with 0.1% arabinose (Sigma-Aldrich).

Growth curves of *A. brasilense* strains

Flasks containing 50 mL of minimal medium supplemented with malic acid and ammonium chloride at C:N ratios of 30:1, 60:1 and 90:1 were inoculated with the *A. brasilense* strains to an optical density at 600 nm (OD600) of 0.01, then the cultures were grown at 32 °C at 110 rpm. The OD600 was determined every 3 h during 24 h.

PHB quantitation

Strains of *A. brasilense* were grown on minimal medium supplemented with malic acid and ammonium chloride at C:N ratios of 30:1, 60:1 and 90:1 in flasks subjected to null or low-oxygen transfer. To generate null-oxygen transfer condition, unbaffled Erlenmeyer flasks of 125 mL of capacity were filled with 25 mL of minimal medium and capped with a number 5 rubber stopper, which keep off from the atmospheric oxygen transfer throughout the assay. To generate low-oxygen transfer condition, unbaffled Erlenmeyer flasks of 125 mL of capacity were filled with 25 mL of minimal medium and capped with a 5 g cotton stopper, which keep off from the atmospheric oxygen transfer throughout the assay. The flasks containing the minimal medium were inoculated with an overnight culture to an OD600 of 0.01 and grown at 32 °C and 110 rpm. For each strain, four flasks with 25 mL of minimal medium were inoculated with the appropriated strain. One flask was uncovered at 24 h to determine PHB production, another flask was uncovered at 48 h and so on. This led us to maintain the oxygen conditions throughout the study. Samples of *A. brasilense* strains (10 mL) were taken at 24, 48, 72 and 96 h and harvested by centrifugation (6000×*g* for 5 min). Cells were washed with TE buffer twice, weighed and dried at 60 °C until weight was constant. PHB was extracted as reported elsewhere (Hahn et al. 1994) and quantified spectrophotometrically (Law and Slepecky 1961). Data were correlated with a commercial standard of PHB (Sigma-Aldrich). Determinations were carried out in triplicate. Results are shown as mean ± standard deviation of % PHB/DCW. Statistical analysis was performed in Statgraphics Centurion 18 software using One-way ANalysis Of VAriance (ANOVA) at 95% confidence level.

Transmission electron microscopy (TEM)

Samples of *A. brasilense* strains were grown at C:N ratios of 30:1, and 90:1, harvested (6000×*g* for 5 min) and washed with TE buffer twice. Cells were fixed in 2.5% (v/v) glutaraldehyde for 3 h, postfixed in 1% (w/v) OsO_4 for 2 h and rinsed 3 times in 50 mM of sodium cacodylate buffer (pH 7.2). Bacteria were dehydrated with a graded ethanol series and embedded in a low-viscosity epoxy resin that was subsequently dried at 60 °C for 24 h. Ultrathin sections were stained with uranyl acetate and examined on a Jeol JEM-1200 EX II transmission electron microscope.

RT-PCR analysis

RNA was extracted from cultures of *A. brasilense* strains (wild type, mutant and complemented) grown on minimal medium at C:N ratios of 30:1 and 90:1. The extraction was performed using the Trizol reagent method according to the instructions provided (Sigma-Aldrich). A mix consisting of: 1 μg of pure RNA, *phaP1* to *phaP6* gene-specific primers (RT-*pha*P1-R, RT-*pha*P2-R, RT-*pha*P3-R, RT-*pha*P4-R, RT-*pha*P5-R and RT-*pha*P6-R) (Table 2), dNTP mix, RNase inhibitor, RevertAid reverse transcriptase and the RevertAid reverse transcriptase buffer, was used to produce the cDNA according to the recommendations of the manufacturer (ThermoScientific). For the PCR amplification of each putative phasin gene (internal region of ~120 nucleotides), a mix

INFORME DE LABORES 2019

consisting of: cDNA (1 µL), dNTPs, gene specified pair of primers (RT-*pha*P1-F/RT-*pha*P1-R, RT-*pha*P2-F/RT-*pha*P2-R, RT-*pha*P3-F/RT-*pha*P3-R, RT-*pha*P4-F/RT-*pha*P4-R, RT-*pha*P5-F/RT-*pha*P5-R or RT-*pha*P6-F/RT-*pha*P6-R) (Table 2), Taq polymerase recombinant and Taq polymerase recombinant buffer, was utilized. PCR conditions consisted of an initial denaturalization step at 94 °C for 5 min, followed by 30 cycles of denaturing at 94 °C for 30 s, annealing at 58 °C for 30 s and extension at 72 °C for 1 min as suggested by the manufacturer (ThermoScientific). Finally, an additional extension of 5 min at 72 °C was carried out. 16S rRNA gene (AMK58_09830) was used as control. PCR products were analyzed by gel electrophoresis on 3% agarose gels and subsequent ethidium bromide staining. RT-PCR assays were repeated three times.

Results

A. brasilense Sp7 contains six putative *phaP* genes

In silico analyses of the *A. brasilense* Sp7 genome revealed six genes that code for proteins containing a Phasin_2 domain (PF09361). Two putative phasin genes are in plasmid 1: AMK58_RS17065 (Gene ID: 36110503) and AMK58_RS20955 (Gene ID: 36111302) and the other putative phasin genes are in the chromosome: AMK58_RS04265 (Gene ID: 36107916), AMK58_RS04270 (Gene ID: 36107917), AMK58_RS07520 (Gene ID: 36108566) and AMK58_RS13850 (Gene ID: 36109844) (Additional file 1). The putative phasin proteins were referred as $PhaP1_{Abs}$ to $PhaP6_{Abs}$ according to the e-value (Table 3) presented with respect to the Phasin_2 domain. The size of the PhaP proteins ranges from 15 to 29 kDa. Analysis of the predicted secondary structure showed that phasins $PhaP1_{Abs}$ to $PhaP5_{Abs}$ possess a high α-helix content (85 to 95%) in contrast to $PhaP6_{Abs}$ which shows a low percentage (14%) (Table 3).

The phasin amino acid sequences from other PHB-producing microorganisms [*R. eutropha* (PhaP1 to PhaP7 and PhaM), *Pseudomonas putida* (PhaI and PhaF), *Aeromonas hydrophila* (PhaP), *Herbaspirillum seropedicae* (PhaP1 and PhaP2) and *Azotobacter* FA8 (PhaP)] were used for protein alignment with the *A. brasilense* Sp7 phasins (Fig. 1a). The results obtained showed that some *A. brasilense* Sp7 phasins are moderately conserved among phasins previously reported, with identities ranging from 3 to 33.7% and similarities from 6 to 55.8% (Additional file 2). The low identity and similarity percentages between the analyzed phasins, occurs by the diversity of aligned amino acid sequences of phasins belonging to the α, β, and γ-proteobacteria classes and does not pretend to identify a phasin domain. Moreover, the entire amino acid phasin sequences from the above-mentioned microorganisms were used to make a Neighbor-Joining phylogenetic tree (Fig. 1b). The putative $PhaP2_{Abs}$, $PhaP3_{Abs}$, $PhaP4_{Abs}$ and $PhaP5_{Abs}$ were clustered together on the 500 bootstrap tree. $PhaP1_{Abs}$ maybe share a common

Table 3 Characteristics of *A. brasilense* Sp7 phasin proteins

Phasin protein	Location	E-value[a]	Length[b]	Phasin_2 domain location	α-helix		MW (KDa)
					Percentage	Position[c]	
$PhaP1_{Abs}$ (AMK58_RS17065)	ABSP7_p1: 722945–723373	$4.56e^{-15}$	142	29–125	85	P8–E20 V28–A79 E85–I139	15.23
$PhaP2_{Abs}$ (AMK58_RS04265)	Chr: 940913–941398	$3.59e^{-14}$	161	46–142	94	K4–L96 I101–K158	16.98
$PhaP3_{Abs}$ (AMK58_RS04270)	Chr: 941668–942204	$3.89e^{-12}$	178	67–162	92	T2–K8 F17–L116 L121–I176	18.57
$PhaP4_{Abs}$ (AMK58_RS07520)	Chr: 1633959–1634525	$4.61e^{-10}$	188	79–174	95	E4–M128 V133–R185	20.37
$PhaP5_{Abs}$ (AMK58_RS13850)	Chr: 2997626–2998141	$6.20e^{-03}$	171	61–155	87	P11–A49 I55–L109 P115–Q169	18.34
$PhaP6_{Abs}$ (AMK58_RS20955)	ABSP7_p1: 1595843–1596694	$3.42e^{-03}$	283	25–111	14	A3–F12 E31–A35 T38–A57 A80–R83	28.84

[a] The E-value was obtained from the alignment of each phasin protein with the Phasin_2 domain

[b] Amino acids

[c] Amino acids

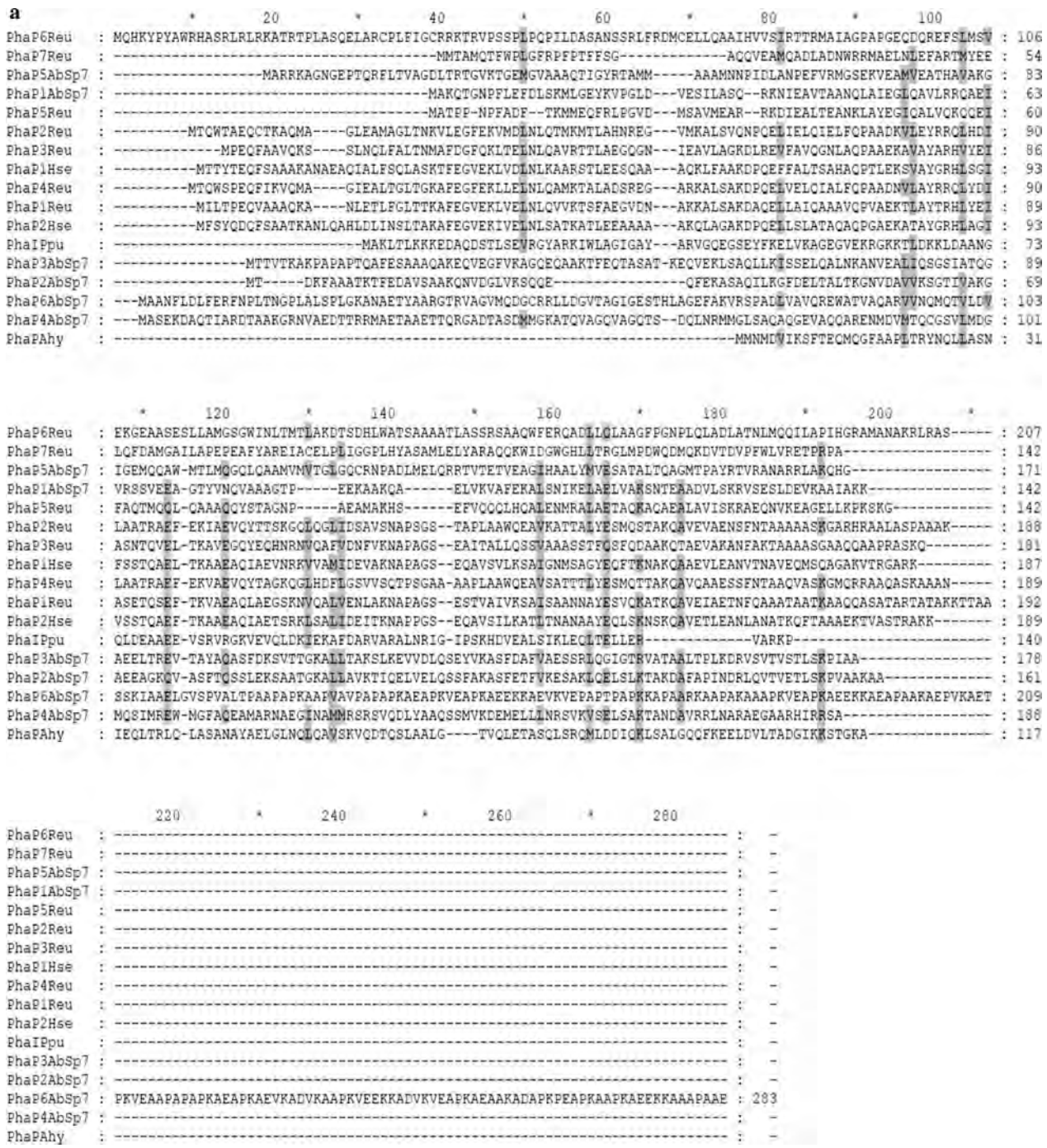

Fig. 1 Phylogeny of *A. brasilense* Sp7 phasin proteins. **a** The amino acids sequences of phasin proteins of PHB-producing microorganisms were aligned to *A. brasilense* Sp7 proteins containing a phasin domain (PF09361). The conserved residues are highlighted. **b** A phylogenetic tree based on amino acid sequences of phasins was inferred using the Neighbor-Joining method. The percentage of replicate trees in which the associated taxa clustered together in the bootstrap test (500 replicates) are shown next to the branches. The evolutionary distances were computed using the Poisson correction method and are in the units of the number of amino acid substitutions per site. The analysis involved 18 amino acid sequences. All the positions containing gaps and missing data were eliminated. PhaP1AbSp7 to PhaP6AbSp7 denotes the *A. brasilense* Sp7 PhaP1 to PhaP6. PhaP1Reu to PhaP7Reu indicates the phasins PhaP1 to PhaP7 of *R. eutropha*. PhaIPpu and PhaFPpu are the phasins PhaI and PhaF, respectively, of *P. putida*. PhaP1Hse and PhaP2Hse are the *H. seropedicae* PhaP1 and PhaP2. PhaPAhy denotes the *A. hydrophila* PhaP

INFORME DE LABORES 2019

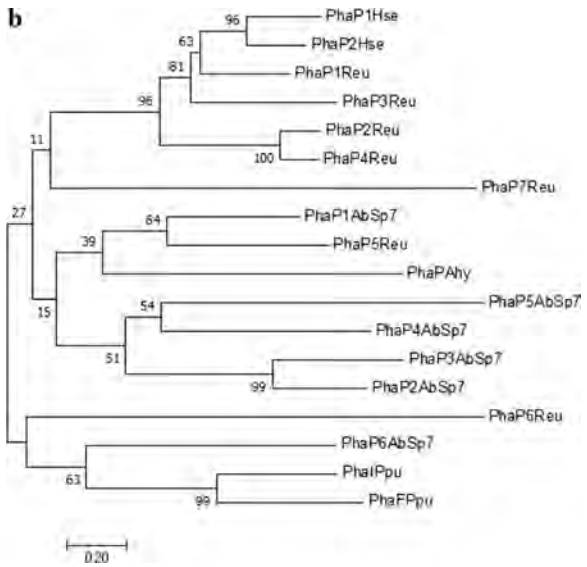

Fig. 1 (continued)

ancestor with this clade. The putative $PhaP6_{Abs}$ was clustered alone. A gene duplication event is suggested for $PhaP2_{Abs}$ and $PhaP3_{Abs}$. It is important to mention that was not possible enroot the phylogenetic tree due to the diversity of amino acid sequences of phasins used for tree construction.

Because of the non-existence of genetic, biochemical and structural information about phasin proteins of the most-well studied PHB-producing microorganisms, it was decided to analyze whether the putative *A. brasilense* Sp7 phasins share any structural homology with the crystal structure of $PhaP_{Ahy}$ (*Aeromonas hydrophila*) (PDB number 5IP0) (Zhao et al. 2016). The $PhaP_{Ahy}$ was used as template to predict the three-dimensional structures of the *A. brasilense* Sp7 phasins by the I-TASSER and SWISS-MODEL servers (Fig. 2 and Additional file 3). The results showed a good structural similarity for $PhaP1_{Abs}$ to $PhaP4_{Abs}$ models (QMEAN ranging from −1.03 to −3.60).

Due to the similarity between $PhaP1_{Abs}$ and $PhaP5_{Reu}$ (*R. eutropha* PhaP5) (55.8%) and based on the data that we obtained it was decided to focus on the analyses of the function of $PhaP1_{Abs}$ on PHB granule morphology and PHB accumulation.

PhaP1 does not affect growth of *A. brasilense*

Growth curves of *A. brasilense* strains were carried out using minimal medium containing malic acid and ammonium chloride at C:N ratios of 30:1, 60:1 and 90:1 (Fig. 3). At all evaluated C:N ratios, the exponential growth phase was reached at 15 h of culturing, whereas the stationary phase occurred at 21 h. As was expected, the strains of study grew better when a C:N ratio of 30:1 was used. By comparing the growth curves of the mutant (*A. brasilense* Δ*phaP1*) and complemented (*A. brasilense* $PhaP1^{+++}$) strains with respect to the wild type (*A. brasilense* Sp7) strain was shown that $PhaP1_{Abs}$ is not important for the growth of *A. brasilense*.

Deletion of *phaP1* gene affects the morphology of the PHB granules

Wild type, mutant and complemented strains were cultivated for 15 h in minimal medium at C:N ratios of 30:1 and 90:1. Ultra-thin sections of the strains were analyzed by TEM (Fig. 4). At a C:N ratio of 30:1, several PHB granules were observed in the wild type strain. These granules are distributed throughout the cytoplasm (Fig. 4a). On the contrary, the mutant strain produced few PHB granules that appear to be larger and are located either at the center or at the pole of the cell (Fig. 4b). By restoring the $PhaP1_{Abs}$ function in the complemented strain, the number and appearance of the PHB granules was restored (Fig. 4c). This suggests that at a C:N ratio of 30:1, $PhaP1_{Abs}$ is involved in the control of the number and size of the PHB granules. However, when the bacteria were grown at a C:N ratio of 90:1, no differences in the size or distribution of the PHB granules could be observed (Fig. 4d–f). These results could suggest the participation of other PhaP proteins that contribute in the maintenance of the architecture of the PHB granules at the evaluated conditions.

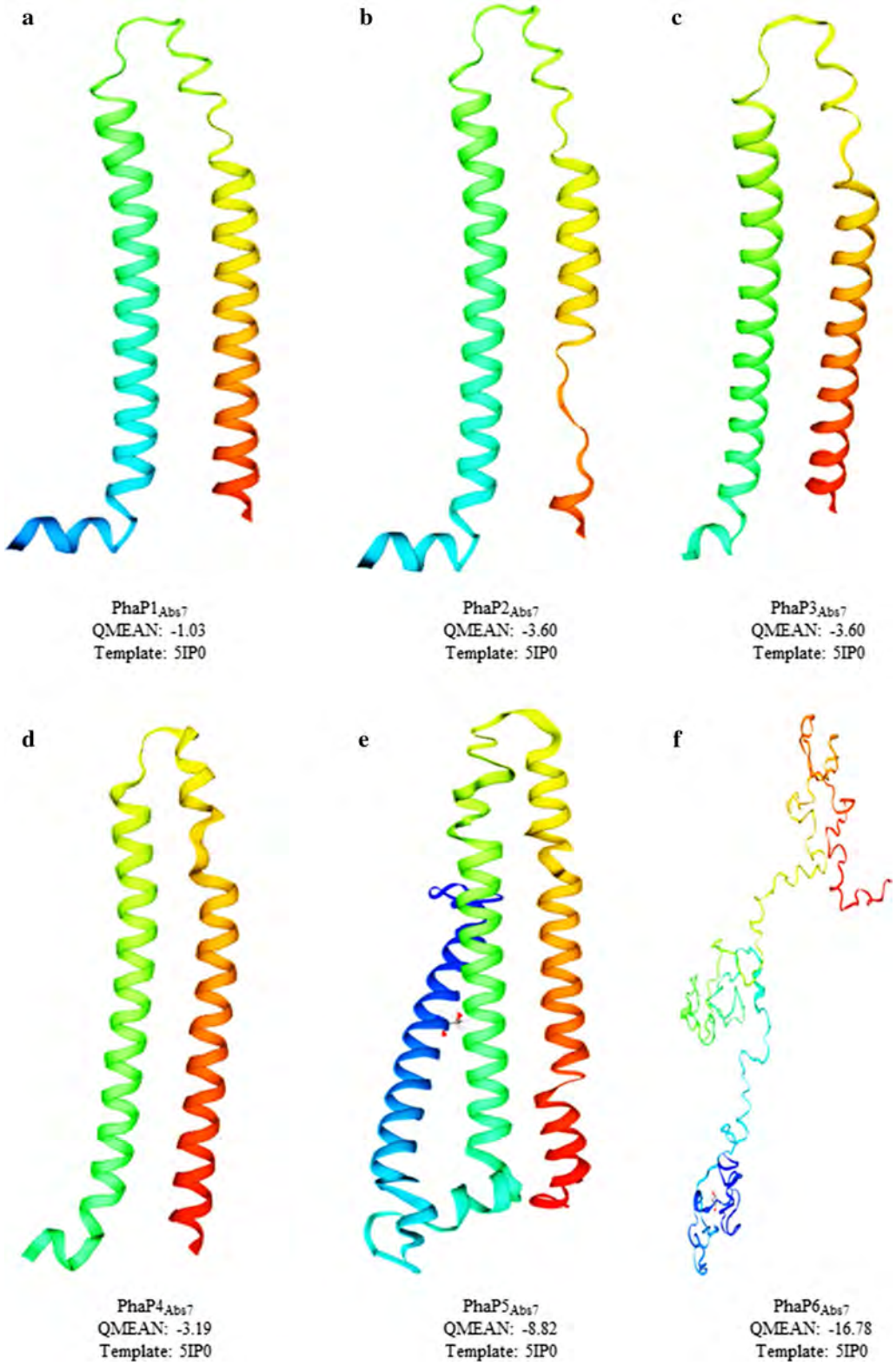

Fig. 2 Predicted three-dimensional structures of *A. brasilense* Sp7 phasins. Structures were predicted using the I-TASSER and SWISS-MODEL servers. The crystal structure of PhaP from *A. hydrophila* (PDB number 5IP0) was used as template. For each *A. brasilense* Sp7 phasin, the QMEAN value was calculated and the Ramachandran plots were obtained (see Additional file 3). **a** $PhaP1_{Abs}$, **b** $PhaP2_{Abs}$, **c** $PhaP3_{Abs}$, **d** $PhaP4_{Abs}$, **e** $PhaP5_{Abs}$ and **f** $PhaP6_{Abs}$

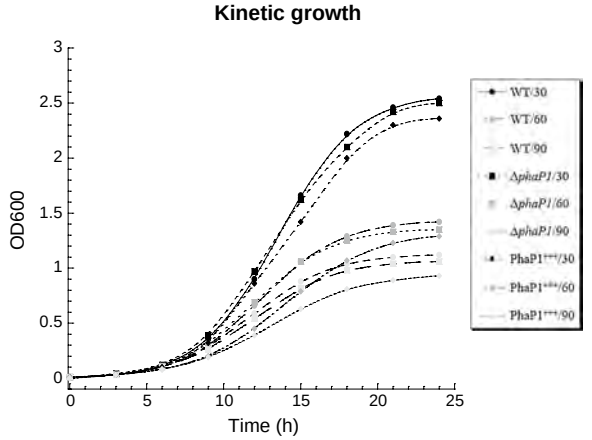

Fig. 3 Growth kinetic behavior of *A. brasilense* strains. *A. brasilense* strains were inoculated in flasks containing minimal medium supplemented with malic acid and ammonium chloride, at C:N ratios of 30:1, 60:1 and 90:1, to an OD600 of 0.01. Samples were taken every 3 h for 24 h and measured spectrophotometrically at an OD600. Growth of *A. brasilense* Sp7 (WT) (circles), *A. brasilense* Δ*phaP1* (Δ*phaP1*) (squares) and *A. brasilense* PhaP1^{+++} (PhaP1^{+++}) (diamonds). Dark spots indicate a C:N ratio of 30:1, gray spots for a C:N ratio of 60:1 and light gray spots denotes a C:N ratio of 90:1

The deletion of the *phaP1* gene affects early (24 h) PHB accumulation depending on the C:N ratio used

PHB accumulation was quantified to evaluate the possible involvement of PhaP1$_{Abs}$ on biopolymer metabolism. Malic acid and ammonium chloride were used at C:N ratios of 30:1, 60:1 and 90:1 in cultures subjected to low or null oxygen transfer (as described in materials and methods). General comparison of the growth conditions evaluated for PHB accumulation (C:N ratio with low or null-oxygen transfer) is observed that the oxygen transfer limits PHB accumulation by approximately 50% (Fig. 5).

Moreover, by analyzing the PHB accumulation at a C:N ratio of 30:1 in cultures with null-oxygen transfer (Fig. 5a) it can be observed that the PHB is accumulated at 24 h of growth and subsequently degraded in wild type and mutant strain. However, it is observed that the mutant strain accumulates 17% PHB/DCW with respect to 9.5% PHB/DCW that was accumulated by the wild type strain. In addition, the PHB produced by the mutant is easily degraded to similar levels as wild type strain. This suggests that PhaP1$_{Abs}$ somehow regulates the early stage of PHB accumulation. Moreover, the restoration of PhaP1$_{Abs}$ function in the complemented strain results in an increased PHB content to reach 17.5% PHB/DCW, it is about 90% more PHB with respect to the PHB accumulated by wild type strain. It should be noted that there was no signal observed for PHB degradation, since the PHB content decreased with time in the wild type and mutant strains but it was increased in the complemented strain. We also quantified the PHB accumulation in *A. brasilense* strains cultured at a C:N ratio of 30:1 but subjected to low-oxygen transfer (Fig. 5b). Both, wild type and mutant strains reported a similar behavior in PHB accumulation. In these strains, PHB content reach the maximum level at 24 h (~5% PHB/DCW) and it was subsequently decreased to minimum levels (~1% PHB/DCW) at the end of bacterial culturing time (96 h). Taken together data obtained is suggested that PhaP1$_{Abs}$ could be involved in the control of PHB synthesis or utilization at a C:N ratio of 30:1 in cultures subjected to null-oxygen transfer when early PHB synthesis occurs (24 h) (Fig. 5a). It should be noted that under low-oxygen transfer this does not occur (Fig. 5b).

To analyze whether the behavior observed is constant at other C:N ratios, it was decided to quantify PHB accumulation by increasing the C:N ratio to 60:1 and 90:1 under low or null-oxygen transfer (Fig. 5c–f). The data obtained at a C:N ratio of 60:1 in cultures with null-oxygen transfer showed a similar behavior by wild type, mutant and complemented strains from 72 to 96 h. However, at 24 h it appears that PHB synthesis in the mutant and complemented strains is delayed but at 48 h, they accumulated more PHB than the wild type strain (Fig. 5c). The observed phenotype may be due to the presence of another phasin protein that support PHB accumulation when a C:N ratio of 60:1 is combined with null-oxygen transfer. The above mentioned does not occur when PHB is measured in cultures subjected to low-oxygen transfer as can be observed in Fig. 5d.

Furthermore, when the PHB was quantified in cultures grown at a C:N ratio of 90:1 was observed that PHB is rapidly synthesized by the mutant strain when it is grown in cultures subjected to a null-oxygen transfer. At 24 h, the mutant strain accumulates approximately 50% PHB/DCW, whereas the wild type strain accumulates 35% PHB/DCW (Fig. 5e). It should be noted that the excess of PHB accumulated by the mutant strain is degraded after 48 h and remains constant up to 96 h of culture. Whereas, the PHB produced by the wild type strain increases over time. The complemented strain does not recover the wild type phenotype in PHB accumulation (Fig. 5e). Moreover, when cultures were grown at a C:N ratio of 90:1 and subjected to a low-oxygen transfer (Fig. 5f), it was found that, between 24 and 48 h of culture, the mutant strain increases the PHB content from 50 to 60% with respect to the wild type strain. PHB is accumulated rapidly by the mutant strain in contrast to a slow accumulation of PHB by the wild type.

INFORME DE LABORES 2019

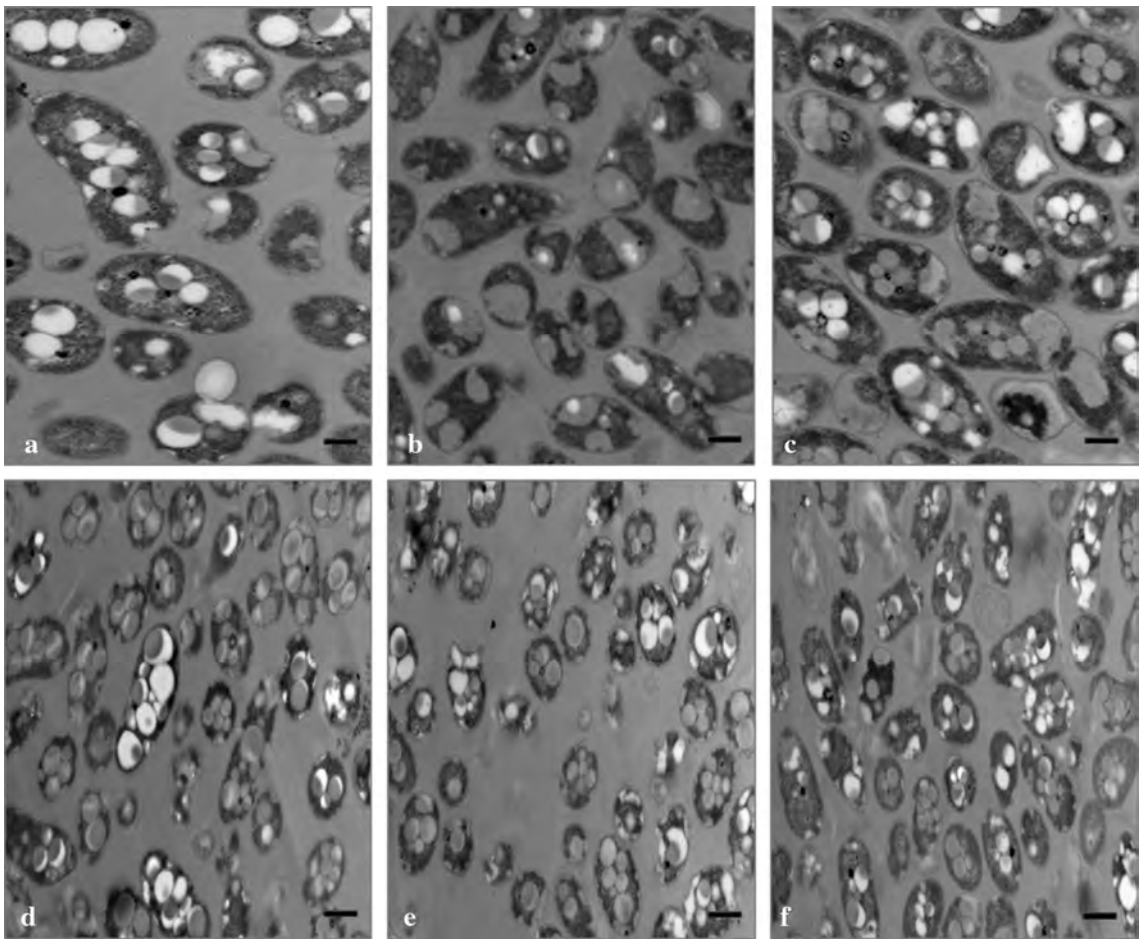

Fig. 4 Transmission electron microscopy of ultra-thin sections of *A. brasilense*. Strains were grown on minimal medium containing malic acid and ammonium chloride at C:N ratios of 30:1 (**a**–**c**) and 90:1 (**e**–**g**). Strains were incubated at 32 °C and 110 rpm for 24 h. PHB granules of wild type (*A. brasilense* Sp7) (**a** and **e**), mutant (*A. brasilense* Δ*phaP1*) (**b** and **f**) and complemented (*A. brasilense* PhaP1^{+++}) (**c** and **g**) strains are shown as intracellular granules. Label Scale bar = 1 µm

Differential transcription of putative phasin genes under three different C:N ratios

TEM images obtained from ultra-thin sections of *A. brasilense* strains grown at a C:N ratio of 90:1 showed no differences in the size and number of PHB granules by both, mutant and complemented strains, compared to the wild type strain (Fig. 4d–f). Additionally, the data obtained from the PHB quantification at C:N ratios of 60:1 and 90:1 showed an unclear phenotype. This suggests the possible involvement of other phasin proteins for the PHB accumulation and the maintenance of the structure of the PHB granules. To address this possibility, the transcripts of the *phaP* genes of wild type and mutant strains were evaluated by RT-PCR (Fig. 6). The results show that, *phaP1* and *phaP2* are the main genes transcribed in the wild type strain when cultures are grown at a C:N ratio of 30:1 (Fig. 6a). However, in the mutant, the *phaP2* transcript was the most prominent of all phasins and the *phaP3* transcript was partially increased (Fig. 6a). Nevertheless, it is still possible that the *phaP2* product could compensate for the lack of $PhaP1_{Abs}$ in the granule structure as well as the PHB content in the mutant strain. Transcripts of the *phaP4* and *phaP6* were not observed either in wild type and mutant strains and the transcript of *phaP5* was slightly detected at a C:N ratio of 30:1 (Fig. 6a). However, when *A. brasilense* was grown at a C:N ratio of 90:1 (Fig. 6b), *phaP3* transcript increased to levels similar to *phaP2* in the wild type strain. A similar behavior was observed for the mutant strain (Fig. 6b). It should be mentioned that the transcript of the *phaP4* gene was not observed in both, wild type and mutant strains, whereas the *phaP5* and *phaP6* transcripts were present at low levels (Fig. 6b). Our results suggest that the C:N ratio has important implications on phasin genes transcription in this bacterium.

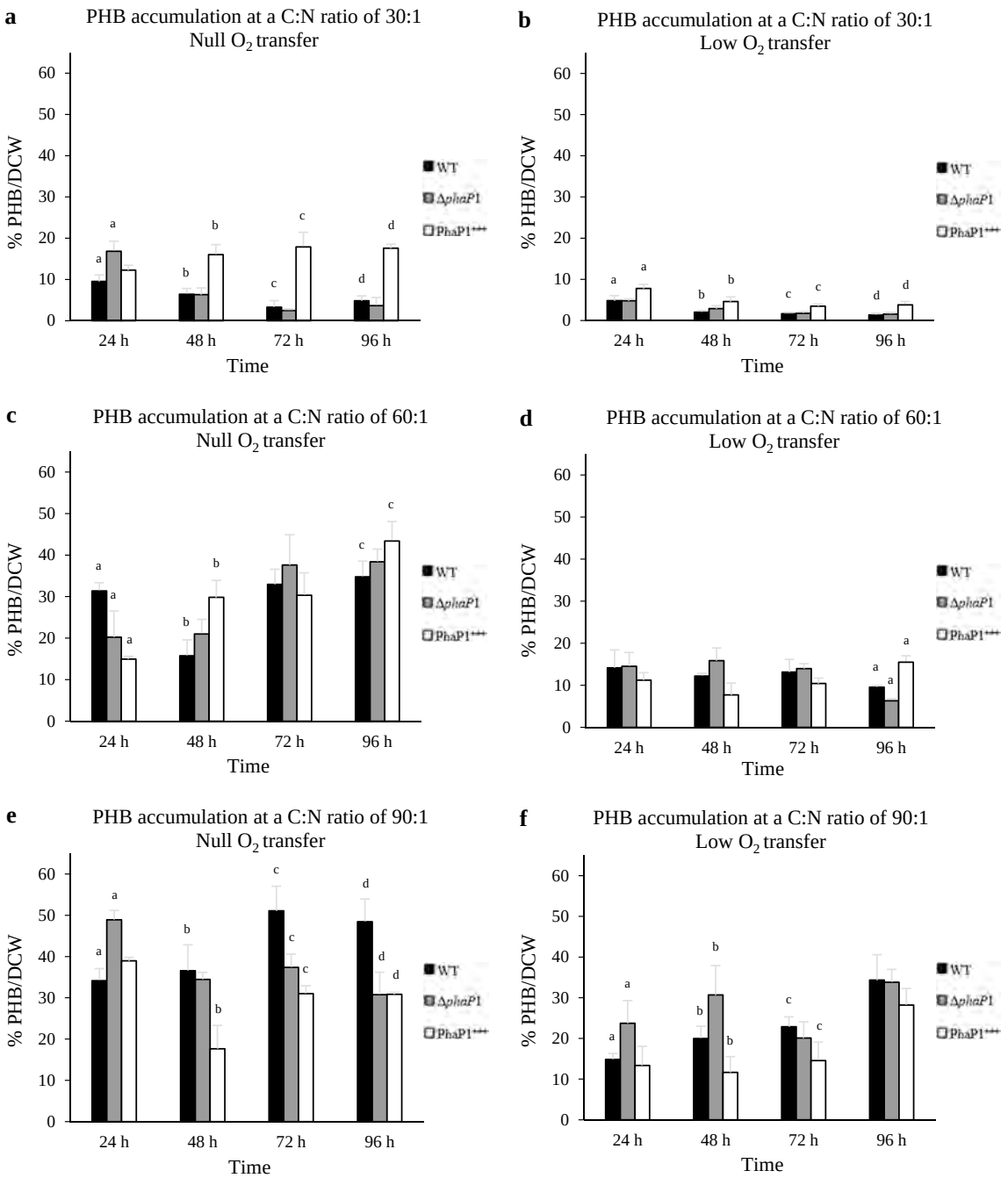

Fig. 5 PHB/DCW content in *A. brasilense* strains. For PHB quantitation, flasks containing minimal medium supplemented with malic acid and ammonium chloride at C:N ratios of 30:1 (**a** and **b**), 60:1 (**c** and **d**), and 90:1 (**e** and **f**) were inoculated with the *A. brasilense* strains in flasks subjected to null (**a**, **c** and **e**) or low (**b**, **d** and **f**) oxygen transfer. Samples of cultures of *A. brasilense* were taken every 24 h for 96 h. Cells were harvested and dried, then PHB was extracted and quantified. PHB produced by *A. brasilense* Sp7 (WT), *A. brasilense* Δ*phaP1* (Δ*phaP1*) and *A. brasilense* PhaP1+++ (PhaP1^{+++}) are shown. Data are presented as mean ± standard deviation of three independent experiments. Letters in each graphic denote significant differences ($p > 0.05$) according to a one-way ANOVA test

Discussion

The function of $PhaP1_{Abs}$ on PHB synthesis and PHB granule structure in *A. brasilense* was analyzed. Phasin proteins have been mainly implicated in PHB granule stabilization which occurs due to their amphiphilic properties (Pötter and Steinbüchel 2005) that avoid the

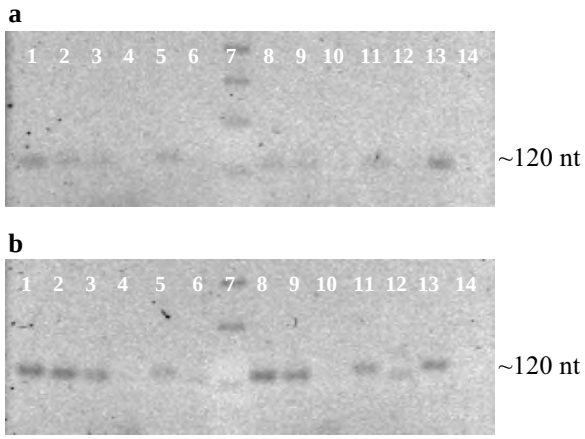

Fig. 6 Analysis of the transcription of *A. brasilense* Sp7 phasin genes. RT-PCR assays of the internal region of putative phasin genes were conducted using cDNA of wild type (*A. brasilense* Sp7) and mutant (*A. brasilense* Δ*phaP1*) strains. RNA was extracted from cultures grown on minimal medium containing malic acid and ammonium chloride at C:N ratios of 30:1 and 90:1. Transcripts were visualized on a 3% agarose gel electrophoresis. **a** Transcription analyses of putative phasin genes of wild type and mutant strains grown at a C:N ratio of 30:1. For wild type: *phaP1* (lane 1), *phaP2* (lane 2), *phaP3* (lane 3), *phaP4* (lane 4), *phaP5* (lane 5), *phaP6* (lane 6). GeneRuler 1 Kb DNA ladder ThermoScientific (lane 7). For mutant strain: *phaP2* (lane 8), *phaP3* (lane 9), *phaP4* (lane 10), *phaP5* (lane 11), *phaP6* (lane 12). 16S rRNA was used as positive control (lane 13). Negative control using cDNA of mutant strain with gene-specified primers for *phaP1* transcript was done (lane 14). **b** Transcription analyses of putative phasin genes in wild type and mutant strains grown at a C:N ratio of 90:1. For wild type strain: *phaP1* (lane 1), *phaP2* (lane 2), *phaP3* (lane 3), *phaP4* (lane 4), *phaP5* (lane 5), *phaP6* (lane 6). GeneRuler 1 Kb DNA ladder ThermoScientific (lane 7). For mutant strain: *phaP2* (lane 8), *phaP3* (lane 9), *phaP4* (lane 10), *phaP5* (lane 11), *phaP6* (lane 12). 16S rRNA was used as positive control (lane 13). Negative control using cDNA of mutant strain with gene-specified primers for *phaP1* transcript was done (lane 14)

coalescence of the PHB granules (Wieczorek et al. 1995; Pfeiffer et al. 2011). Every PHB-producing microorganism has at least one phasin, however there are reports of bacteria with several phasin proteins such as *R. eutropha* with seven PhaP proteins (Wieczorek et al. 1995; Pötter et al. 2004; Pfeiffer and Jendrossek 2011, 2012). Despite the existence of multiple homologues in some bacterial species and the fact that most of them can be bound to the PHB granule, only one or two are covering the PHB granules (Pötter et al. 2004; Yoshida et al. 2013). In this study, bioinformatic analyses of the *A. brasilense* Sp7 genome revealed six putative phasin genes, referred as *phaP1* to *phaP6*. The amino acid sequences of *A. brasilense* phasins are not highly conserved however similar results have been reported for phasins of *R. eutropha* (Pötter et al. 2004; Pfeiffer and Jendrossek 2012), *H. seropedicae* (Alves et al. 2016), *Bradyrhizobium japonicum* (Yoshida et al. 2013) and *Haloferax mediterranei* (Cai et al. 2012) among others. The predicted secondary structures of $PhaP1_{Abs}$ to $PhaP5_{Abs}$ reveals a high percentage of α-helix content as has been reported for this type of proteins (Mezzina and Pettinari 2016; Zhao et al. 2016).

The deletion of the main phasin that covers the PHB granules results in a single enlarged granule rather than five to ten granules that are observed in the wild type strains (Steinbüchel et al. 1995; Jurasek and Marchessault 2002; Cai et al. 2012). To analyze the role of the $PhaP1_{Abs}$ in the PHB granule morphology, the *phaP1* gene was deleted. TEM images of the carbonosomes from the mutant strain showed fewer PHB granules that were larger than those observed in the wild type strain. This strongly suggests that $PhaP1_{Abs}$ controls to a certain extent the number and size of the PHB granules.

Among other functions attributable to phasins are the regulation of synthesis and degradation of PHB (York et al. 2001; Handrick et al. 2004a, b; Cai et al. 2012) and the distribution of the PHB granules during cell division (Galán et al. 2011; Pfeiffer and Jendrossek 2011; Wahl et al. 2012; Bresan and Jendrossek 2017). To analyze the possible involvement of $PhaP1_{Abs}$ on PHB synthesis and degradation in *A. brasilense* Sp7, a *phaP1* mutant strain was constructed and PHB accumulation was determined. For that, minimal medium supplemented with malic acid and ammonium chloride at different C:N ratios in addition to either low or null-oxygen transfer conditions was used. The results showed that $PhaP1_{Abs}$ controls early PHB synthesis at a C:N ratio of 30:1 when the oxygen transfer is null. The overexpression of $PhaP1_{Abs}$ in the complemented strain resulted in the increase of PHB over time, suggesting a possible increment in the PHB synthesis or a decrement in the PHB utilization. However, when the accumulation of PHB in *A. brasilense* was quantified in cultures grown in minimal medium at C:N ratios of 60:1 and 90:1 and subjected to low or null-oxygen transfer, no clear effect caused by the lack or overexpression of $PhaP1_{Abs}$ was observed. This suggest a possible participation of other phasin proteins to maintain PHB accumulation.

By analyzing the behavior of phasins in *R. eutropha*, it was found that the *phaP1* mutant strain accumulates approximately 40% PHB/DCW less than the wild type strain (Pötter et al. 2005). However, the deletion of *phaP2*, *phaP3* or *phaP4* did not affect PHB accumulation (Pötter et al. 2005). In *H. seropedicae* SmR1, the deletion of *phaP1* reduced PHB accumulation by 50% PHB/DCW but the *pha*P2 deleted strain produced 30% PHB/DCW more than the wild type strain when grown on glucose as a carbon source, suggesting that $PhaP2_{Hse}$ (*Herbaspirillum seropedicae* PhaP2) compensates for the lack of $PhaP1_{Hse}$ (Alves et al. 2016). Similar results

have been obtained for *Methylobacterium extorquens* AM1 (Korotkova et al. 2002). The deletion of *phaP1* and *phaP2* in *H. seropedicae* and *phaP1* to *phaP4* in *R. eutropha* H16 abolished PHB accumulation (Pötter et al. 2005; Alves et al. 2016). These results, in addition to the changes observed in polymer accumulation allow to infer a possible interaction between phasin proteins and the PHB polymerase, which has been corroborated for *R. eutropha* (York et al. 2001), *Aeromonas caviae* (Fukui et al. 2001; Ushimaru et al. 2014) *A. hydrophila* (Tian et al. 2005), and, in this work, is suggested for *A. brasilense* Sp7, however the mechanism by which the interactions take place has not been elucidated.

Furthermore, a strong interaction between $PhaP5_{Reu}$ and the PHB depolymerase or the regulator protein (PhaR) has been proven (Pötter et al. 2005; Pfeiffer and Jendrossek 2011). Studies of $PhaP2_{Reu}$ and $PhaP4_{Reu}$ on PHB degradation conclude that both phasins, limit PHB degradation by interacting with the depolymerases PhaZ2, PhaZ3 and PhaZ7. Moreover, the expression of $PhaP1_{Reu}$ reduced the PHB content in *E. coli* when expressing the *phaCAB* operon of *R. eutropha* (Eggers and Steinbüchel 2014).

In conclusion, in this study we demonstrated that early PHB synthesis and the morphology of the PHB granules are influenced by $PhaP1_{Abs}$ when *A. brasilense* Sp7 is grown in a medium with a C:N ratio of 30:1. Nevertheless, when C:N ratios of 60:1 and 90:1 were used, PHB synthesis and the morphology of the PHB granules seem to be influenced by the coordinated action of several phasin proteins.

Supplementary information

Supplementary information accompanies this paper at https://doi.org/10.1186/s13568-019-0876-4.

Additional file 1. Putative phasin genes localization.

Additional file 2. Identity and similarity percentages between the entire amino acids sequences of phasins from PHB-producing microorganisms.

Additional file 3. Ramachandran plots of predicted three-dimensional structures of putative *A. brasilense* Sp7 phasins.

Abbreviations

PHB: polyhydroxybutyrate; [P(HB-*co*-HHx)]: poly(3-hydroxybutyrate-*co*-3-hydroxyhexanoate); GAP's: granule associated proteins; C:N: carbon:nitrogen ratio; LB: Luria–Bertani; h: hours; min: minutes; s: seconds; Kg: kilograms; g: grams; *g*: gravity; OD600: optical density at 600 nm; DCW: dry cell weight; TEM: transmission electron microscopy.

Acknowledgements

The Unidad de Imagenología of the Instituto de Fisiología Celular, UNAM.

Teresa Ballado, Javier de la Mora and Norma Espinosa for technical assistance.

Consejo Nacional de Ciencia y Tecnología (CONACyT) for the scholarship (474387) for MAMM.

Authors' contributions

LJMM and MAMM designed this study. MAMM performed the experiments. MAMM, LSU and LJMM interpreted the results. BGP and GD supported the project by critical evaluation of experimental results, TEM experiments and providing facilities required. MAMM, BGP, GD, LSU and LJMM participated substantially in writing the manuscript, critical evaluation and modifications. LJMM supervised the study. All authors read and approved the final manuscript for publication.

Funding

This work was supported in part by grants VIEP-BUAP; ID: 00249 to LJMM and ID: 00122 to LSU).

Availability of data and materials

Please contact to the authors for all request.

Ethics approval and consent to participate

Not applicable.

Consent for publication

Not applicable.

Competing interests

The authors declare that they have no competing interests.

Author details

[1] Centro de Investigaciones en Ciencias Microbiológicas, Instituto de Ciencias, Benemérita Universidad Autónoma de Puebla, Puebla, Mexico. [2] Departamento de Genética Molecular, Instituto de Fisiología Celular, Universidad Nacional Autónoma de México, Mexico City, Mexico.

Received: 21 May 2019 Accepted: 9 September 2019
Published online: 25 September 2019

References

Alarfaj AA, Arshad M, Sholkamy EN, Munusamy MA (2015) Extraction and characterization of polyhydroxybutyrates (PHB) from *Bacillus thuringiensis* KSADL127 isolated from Mangrove environments of Saudi Arabia. Braz Arch Biol Technol 58(5):781–788

Alves LPS, Teixeira CS, Tirapelle EF, Donatti L, Tadra-Sfeir MZ, Steffens MBR, De Souza EM, De Oliveira PF, Chubatsu LS, Müller-Santos M (2016) Backup expression of the PhaP2 phasin compensates for *pha*P1 deletion in *Herbaspirillum seropedicae*, maintaining fitness and PHB accumulation. Front Microbiol 7:739

Anjum A, Zuber M, Zia KM, Noreen A, Anjum MN, Tabasum S (2016) Microbial production of polyhydroxyalkanoates (PHAs) and its copolymers: a review of recent advancements. Int J Biol Macromol 89:161–174

Benkert P, Biasini M, Schwede T (2011) Toward the estimation of the absolute quality of individual protein structure models. Bioinformatics 27:343–350

Bresan S, Jendrossek D (2017) New insights into PhaM-PhaC-mediated localization of polyhydroxybutyrate granules in *Ralstonia eutropha* H16. Appl Environ Microbiol 83(12):e00505-17

Brigham CJ, Riedel SI (2018) The potential of polyhydroxyalkanoate production from food wastes. Appl Food Biotecnol. 6(1):7–18

Buchan DWA, Minneci F, Nugent TCO, Bryson K, Jones DT (2013) Scalable web services for the PSIPRED Protein Analysis Workbench. Nucleic Acids Res 41(W1):W340–W348

Cai S, Cai L, Liu H, Liu X, Han J, Zhou J, Xiang H (2012) Identification of the haloarchaeal type phasin (PhaP) that functions in polyhydroxyalkanoate accumulation and granule formation in *Haloferax mediterranei*. Appl Environ Microbiol. https://doi.org/10.1128/AEM.07114-11

Cheng HR, Jiang N (2006) Extremely rapid extraction of DNA from bacteria and yeasts. Biotechnol Lett 28(1):55–59

Eggers J, Steinbüchel A (2014) Impact of *Ralstonia eutropha*'s poly (3-Hydroxybutyrate) (PHB) depolymerases and phasins on PHB storage in recombinant *Escherichia coli*. Appl Environ Microbiol 80(24):7702–7709

Finn RD, Coggill P, Eberhardt RY, Eddy SR, Mistry J, Mitchell AL, Potter SC, Punta M, Qureshi M, Sangrador-Vegas A, Salazar GA, Tate J, Bateman A (2015) The Pfam protein families database: towards a more sustainable future. Nucleic Acids Res 44(D1):D279–D285

Fukui T, Kichise T, Iwata T, Doi Y (2001) Characterization of 13 kDa granule-associated protein in *Aeromonas caviae* and biosynthesis of Polyhydroxyalkanoates with altered molar composition by recombinant bacteria. Biomacromolecules 2(1):148–153

Galán B, Dinjaski N, Maestro B, De Eugenio LI, Escapa IF, Sanz JM, García JL, Prieto MA (2011) Nucleoid-associated PhaF phasin drives intracellular location and segregation of polyhydroxyalkanoate granules in Pseudomonas putida KT2442. Mol Microbiol 79(2):402–418

Geer LY, Marchler-Bauer A, Geer RC, Han L, He J, He S, Liu C, Shi W, Bryant SH (2009) The NCBI biosystems database. Nucleic Acids Res 38:D492–D496

Hahn SK, Chang YK, Kim BS, Chang HN (1994) Optimization of microbial poly (3-ß-hydroxybutyrate) recover using dispersions of sodium hypochlorite solution and chloroform. Biotechnol Bioengin 44(2):256–261

Handrick R, Reinhardt S, Schultheiss D, Reichart T, Schüler D, Jendrossek V, Jendrossek D (2004a) Unraveling the function of the *Rhodospirillum rubrum* activator of polyhydroxybutyrate (PHB) degradation: the activator is a PHB-granule-bound protein (phasin). J Bacteriol 186(8):2466–2475

Handrick R, Technow U, Reichart T, Reinhardt S, Sander T, Jendrossek D (2004b) The activator of the *Rhodospirillum rubrum* PHB depolymerase is a polypeptide that is extremely resistant to high temperature (121 C) and other physical or chemical stresses. FEMS Microbiol Lett 230(2):265–274

Hauf W, Watzer B, Roos N, Klotz A, Forchhammer K (2015) Photoautotrophic polyhydroxybutyrate granule formation is regulated by cyanobacterial phasin PhaP in *Synechocystis* sp. strain PCC 6803. Appl Environ Microbiol 81(13):4411–4422

Itzigsohn R, Yarden O, Okon Y (1995) Polyhydroxyalkanoate analysis in *Azospirillum brasilense*. Can J Microbiol 41(13):73–76

Jendrossek D (2009) Polyhydroxyalkanoate granules are complex subcellular organelles (carbonosomes). J Bacteriol 191(10):3195–3202

Juengert JR, Petterson C, Jendrossek D (2018) Poly (3-hydroxybutyrate) (PHB) polymerase PhaC1 and PHB depolymerase PhaZa1 of *Ralstonia eutropha* are phosphorylated in vivo. Appl Environ Microbiol 84(13):e00604-18

Jurasek L, Marchessault RH (2002) The role of phasins in the morphogenesis of poly (3-hydroxybutyrate) granules. Biomacromolecules 3(2):256–261

Kadouri D, Burdman S, Jurkevitch E, Okon Y (2002) Identification and isolation of genes involved in poly (β-hydroxybutyrate) biosynthesis in *Azospirillum brasilense* and characterization of a *phb*C mutant. Appl Environ Microbiol 68(6):2943–2949

Kadouri D, Jurkevitch E, Okon Y (2003) Poly β-hydroxybutyrate depolymerase (PhaZ) in *Azospirillum brasilense* and characterization of a *pha*Z mutant. Arch Microbiol 180(5):309–318

Kelley LA, Mezulis S, Yates CM, Wass MN, Sternberg MJ (2015) The Phyre2 web portal for protein modeling, prediction and analysis. Nat Protoc 10(6):845

Koller M, Salerno A, Dias M, Reiterer A, Braunegg G (2010) Modern biotechnological polymer synthesis: a review. Food Technol Biotechnol 48(3):255–269

Korotkova N, Chistoserdova L, Lidstrom ME (2002) Poly-β-hydroxybutyrate biosynthesis in the facultative methylotroph *Methylobacterium extorquens* AM1: identification and mutation of gap11, gap20, and phaR. J Bacteriol 184(22):6174–6181

Kuchta K, Chi L, Fuchs H, Pötter M, Steinbüchel A (2007) Studies on the influence of phasins on accumulation and degradation of PHB and nanostructure of PHB granules in *Ralstonia eutropha* H16. Biomacromol 8(2):657–662

Kumar S, Stecher G, Tamura K (2016) MEGA7: molecular evolutionary genetics analysis version 7.0 for bigger datasets. Mol Biol Evol 33(7):1870–1874

Larkin MA, Blackshields G, Brown NP, Chenna R, McGettigan PA, McWilliam H, Valentin F, Wallace IM, Wilm A, Lopez R, Thompson JD, Gibson TJ, Higgins DG (2007) Clustal W and Clustal X version 2.0. Bioinformatics 23:2947–2948

Law JH, Slepecky RA (1961) Assay of poly-β-hydroxybutyric acid. J Bacteriol 82(1):33–36

Lemoigne M (1926) Produits de dehydration et de polymerisation de l'acide ß-oxobutyrique. Bull Soc Chim Biol 8:770–773

Letunic I, Bork P (2017) 20 years of the SMART protein domain annotation resource. Nucleic Acids Res 46(D1):D493–D496

Madison LL, Huisman GW (1999) Metabolic engineering of poly (3-hydroxyalkanoates): from DNA to plastic. Microbiol Mol Biol Rev 63(1):21–53

Maehara A, Taguchi S, Nishiyama T, Yamane T, Doi Y (2002) A repressor protein, PhaR, regulates polyhydroxyalkanoate (PHA) synthesis via its direct interaction with PHA. J Bacteriol 184(14):3992–4002

Mezzina MP, Pettinari MJ (2016) Phasins, multifaceted polyhydroxyalkanoate granule-associated proteins. Appl Environ Microbiol 82(17):5060–5067

Mezzolla V, DÜrso O, Poltronieri P (2018) Role of PhaC type I and type II enzymes during PHA biosynthesis. Polymers 10(8):910

Mishra MN, Kumar S, Gupta N, Kaur S, Gupta A, Tripathi AK (2011) An extracytoplasmic function sigma factor cotranscribed with its cognate anti-sigma factor confers tolerance to NaCl, ethanol and methylene blue in *Azospirillum brasilense* Sp7. Microbiology 157(4):988–999

Morales VM, Bäckman A, Bagdasarian M (1991) A series of wide-host-range low-copy-number vectors that allow direct screening for recombinants. Gene 97(1):39–47

Pavan FA, Junqueira TL, Watanabe MD, Bonomi A, Quines LK, Schmidell W, de Aragao GM (2019) Economic analysis of polyhydroxybutyrate production by *Cupriavidus necator* using different routes for product recovery. Biochem Eng J 146:97–104

Pfeiffer D, Jendrossek D (2011) Interaction between poly (3-hydroxybutyrate) granule-associated proteins as revealed by two-hybrid analysis and identification of a new phasin in *Ralstonia eutropha* H16. Microbiology 157(10):2795–2807

Pfeiffer D, Jendrossek D (2012) Localization of PHB granule associated proteins during PHB granule formation and identification of two new phasins, PhaP6 and PhaP7, in *Ralstonia eutropha* H16. J Bacteriol. https://doi.org/10.1128/JB.00779-12

Pfeiffer D, Jendrossek D (2014) PhaM is the physiological activator of poly (3-hydroxybutyrate) (PHB) synthase (PhaC1) in *Ralstonia eutropha*. Appl Environ Microbiol 80(2):555–563

Pfeiffer D, Wahl A, Jendrossek D (2011) Identification of a multifunctional protein, PhaM, that determines number, surface to volume ratio, subcellular localization and distribution to daughter cells of poly (3-ß-hydroxybutyrate), PHB, granules in *Ralstonia eutropha* H16. Mol Microbiol 82(4):936–951

Pötter M, Steinbüchel A (2005) Poly (3-hydroxybutyrate) granule-associated proteins: impacts on poly (3-hydroxybutyrate) synthesis and degradation. Biomacromolecules 6(2):552–560

Pötter M, Madkour MH, Mayer F, Steinbüchel A (2002) Regulation of phasin expression and polyhydroxyalkanoate (PHA) granule formation in *Ralstonia eutropha* H16. Microbiology 148(8):2413–2426

Pötter M, Müller H, Reinecke F, Wieczorek R, Fricke F, Bowien B, Friedrich B, Steinbüchel A (2004) The complex structure of polyhydroxybutyrate (PHB) granules: four orthologous and paralogous phasins occur in *Ralstonia eutropha*. Microbiology 150(7):2301–2311

Pötter M, Müller H, Steinbüchel A (2005) Influence of homologous phasins (PhaP) on PHA accumulation and regulation of their expression by the transcriptional repressor PhaR in *Ralstonia eutropha* H16. Microbiology 151(3):825–833

Roschanski N, Strauch E (2011) Assessment of the mobilizable vector plasmids pSUP202 and pSUP404. 2 as genetic tools for the predatory bacterium *Bdellovibrio bacteriovorus*. Curr Microbiol 62(2):589–596

Roy A, Kucukural A, Zhang Y (2010) I-TASSER: a unified platform for automated protein structure and function prediction. Nat Protoc 5:725–738

Sagong HY, Son HF, Choi SY, Lee SY, Kim KJ (2018) Structural insights into polyhydroxyalkanoates biosynthesis. Trends Biochem Sci 43:790–805

Sambrook J, Fritsch EF, Maniatis T (1989) Molecular cloning: a laboratory manual. Cold spring harbor laboratory press, Cold Spring Harbor

Simon R, Priefer U, Pühler A (1983) A broad host range mobilization system for in vivo genetic engineering: transposon mutagenesis in gram negative bacteria. Nat Biotechnol 1(9):784

Steinbüchel A, Aerts K, Liebergesell M, Wieczorek R, Babel W, Föllner C, Hussien MM, Mayer F, Pieper-Fürst U, Pries A, Valentin HE (1995) Considerations on the structure and biochemistry of bacterial polyhydroxyalkanoic acid inclusions. Can J Microbiol 41(13):94–105

Stothard P (2000) The Sequence Manipulation Suite: javaScript programs for analyzing and formatting protein and DNA sequences. Biotechniques 28:1102–1104

Sznajder A, Pfeiffer D, Jendrossek D (2015) Comparative proteome analysis reveals four novel polyhydroxybutyrate (PHB) granule-associated proteins in *Ralstonia eutropha* H16. Appl Environ Microbiol 81(5):1847–1858

Tal S, Okon Y (1985) Production of the reserve material poly-β-hydroxybutyrate and its function in *Azospirillum brasilense* Cd. Can J Microbiol 31(7):608–613

Tal S, Smirnoff P, Okon Y (1990) The regulation of poly-β-hydroxybutyrate metabolism in *Azospirillum brasilense* during balanced growth and starvation. Microbiology 136(7):1191–1196

Tarrand JJ, Krieg NR, Döbereiner J (1978) A taxonomic study of the *Spirillum lipoferum* group, with descriptions of a new genus, *Azospirillum* gen. nov. and two species, *Azospirillum lipoferum* (Beijerinck) comb. nov. and *Azospirillum brasilense* sp. nov. Can J Microbiol 24(8):967–980

Tian SJ, Lai WJ, Zheng Z, Wang HX, Chen GQ (2005) Effect of over-expression of phasin gene from *Aeromonas hydrophila* on biosynthesis of copolyesters of 3-hydroxybutyrate and 3-hydroxyhexanoate. FEMS Microbiol Lett 244(1):19–25

Tirapelle EF, Müller-Santos M, Tadra-Sfeir MZ, Kadowaki MAS, Steffens MBR, Monteiro RA, Souza EM, Pedrosa FO, Chubatsu LS (2013) Identification of proteins associated with polyhydroxybutyrate granules from *Herbaspirillum seropedicae* SmR1-old partners, new players. PLoS ONE 8(9):e75066

Ushimaru K, Motoda Y, Numata K, Tsuge T (2014) Phasin proteins activate *Aeromonas caviae* polyhydroxyalkanoate (PHA) synthase but not *Ralstonia eutropha* PHA synthase. Appl Environ Microbiol 80(9):2867–2873

Wahl A, Schuth N, Pfeiffer D, Nussberger S, Jendrossek D (2012) PHB granules are attached to the nucleoid via PhaM in *Ralstonia eutropha*. BMC Microbiol 12(1):262

Waterhouse A, Bertoni M, Bienert S, Studer G, Tauriello G, Gumienny R, Heer FT, de Beer TAP, Rempfer C, Bordoli L, Lepore R, Schwede T (2018) SWISS-MODEL: homology modelling of protein structures and complexes. Nucleic Acids Res 46:W296–W303

Wieczorek R, Pries A, Steinbüchel A, Mayer F (1995) Analysis of a 24-kilodalton protein associated with the polyhydroxyalkanoic acid granules in *Alcaligenes eutrophus*. J Bacteriol 177(9):2425–2435

Yang J, Zhang Y (2015) I-TASSER server: new development for protein structure and function predictions. Nucleic Acids Res 43:W174–W181

York GM, Stubbe J, Sinskey AJ (2001) New insight into the role of the PhaP phasin of *Ralstonia eutropha* in promoting synthesis of polyhydroxybutyrate. J Bacteriol 183(7):2394–2397

York GM, Stubbe J, Sinskey AJ (2002) The *Ralstonia eutropha* PhaR protein couples synthesis of the PhaP phasin to the presence of polyhydroxybutyrate in cells and promotes polyhydroxybutyrate production. J Bacteriol 184(1):59–66

Yoshida KI, Takemoto Y, Sotsuka T, Tanaka K, Takenaka S (2013) PhaP phasins play a principal role in poly-β-hydroxybutyrate accumulation in free-living *Bradyrhizobium japonicum*. BMC Microbiol 13(1):290

Zhang C, Freddolino PL, Zhang Y (2017) COFACTOR: improved protein function prediction by combining structure, sequence and protein–protein interaction information. Nucleic Acids Res 45:W291–W299

Zhao H, Wei H, Liu X, Yao Z, Xu M, Wei D, Wang J, Wang X, Chen G (2016) Structural insights on PHA binding protein PhaP from *Aeromonas hydrophila*. Sci Rep 6:39424

Publisher's Note

Springer Nature remains neutral with regard to jurisdictional claims in published maps and institutional affiliations.

Submit your manuscript to a SpringerOpen journal and benefit from:

- ► Convenient online submission
- ► Rigorous peer review
- ► Open access: articles freely available online
- ► High visibility within the field
- ► Retaining the copyright to your article

Submit your next manuscript at ► springeropen.com

INFORME DE LABORES 2019

5746–5760 *Nucleic Acids Research, 2019, Vol. 47, No. 11* *Published online 10 April 2019*
doi: 10.1093/nar/gkz266

The mitoribosome-specific protein mS38 is preferentially required for synthesis of cytochrome *c* oxidase subunits

Jeffri-Noelle Mays[1], Yolanda Camacho-Villasana[2], Rodolfo Garcia-Villegas[2], Xochitl Perez-Martinez[2], Antoni Barrientos[1,3] and Flavia Fontanesi[1,*]

[1]Department of Biochemistry and Molecular Biology, University of Miami Miller School of Medicine, Miami, FL 33136, USA, [2]Departamento de Genetica Molecular, Instituto de Fisiologiía Celular, Universidad Nacional Autonoma de Mexico, Mexico City 04510, Mexico and [3]Department of Neurology, University of Miami Miller School of Medicine, Miami, FL 33136, USA

Received September 20, 2018; Revised March 26, 2019; Editorial Decision April 01, 2019; Accepted April 02, 2019

ABSTRACT

Message-specific translational regulation mechanisms shape the biogenesis of multimeric oxidative phosphorylation (OXPHOS) enzyme in mitochondria from the yeast *Saccharomyces cerevisiae*. These mechanisms, driven mainly by the action of mRNA-specific translational activators, help to coordinate synthesis of OXPHOS catalytic subunits by the mitoribosomes with both the import of their nucleus-encoded partners and their assembly to form the holocomplexes. However, little is known regarding the role that the mitoribosome itself may play in mRNA-specific translational regulation. Here, we show that the mitoribosome small subunit protein Cox24/mS38, known to be necessary for mitoribosome-specific intersubunit bridge formation and 15S rRNA H44 stabilization, is required for efficient mitoribogenesis. Consequently, mS38 is necessary to sustain the overall mitochondrial protein synthesis rate, despite an adaptive ∼2-fold increase in mitoribosome abundance in *mS38*-deleted cells. Additionally, the absence of mS38 preferentially disturbs translation initiation of *COX1*, *COX2,* and *COX3* mRNAs, without affecting the levels of mRNA-specific translational activators. We propose that mS38 confers the mitochondrial ribosome an intrinsic capacity of translational regulation, probably acquired during evolution from bacterial ribosomes to facilitate the translation of mitochondrial mRNAs, which lack typical anti-Shine-Dalgarno sequences.

INTRODUCTION

A major challenge in biology is to understand how protein expression is regulated to attend cellular needs. One of the orchestrating layers of regulation involves the translation machinery itself, where protein synthesis is tightly regulated to prevent wasting cellular resources (1). The mitochondrion, a eukaryotic organelle that possesses its own protein synthesis apparatus, has also evolved several mechanisms of translational control, some of which were identified and best studied in the yeast *Saccharomyces cerevisiae* (2). However, the possible role the mitochondrial ribosome plays in these mechanisms and whether it exerts an additional layer of intrinsic regulation remains largely unexplored.

The yeast mitochondrial genome (mtDNA) encodes eight proteins, two ribosomal RNAs (rRNAs) and a set of tRNAs. Seven hydrophobic proteins are components of the multimeric oxidative phosphorylation (OXPHOS) system enzymes, and the eighth is a soluble mitoribosomal protein of the small subunit (mtSSU). Regarding the OXPHOS system, one subunit (Cyt*b*) from the *bc1*-complex or complex III (CIII), three (Cox1, 2 and 3) from the cytochrome *c* oxidase (COX) or complex IV (CIV), and three (Atp6, 8 and 9) from the ATP synthase are encoded in the mtDNA. The remaining subunits of the OXPHOS system complexes, the mitoribosome proteins, and the factors required to assemble these macrostructures are all encoded by the nuclear genome, synthesized in cytoplasmic ribosomes and imported into mitochondria. Therefore, efficient protein synthesis and complex assembly within this organelle require careful coordination to synchronize mitochondrial and cytosolic translation programs (3).

Translation of mitochondrial mRNAs occurs in mitoribosomes, whose composition and structure are adapted to translate mitochondrial mRNAs that lack a typical anti-Shine-Dalgarno element, and to synthesize highly hydrophobic membrane proteins (4). The understanding of

*To whom correspondence should be addressed. Tel: +1 305 243 7215; Fax: +1 305 243 7404; Email: ffontanesi@med.miami.edu

© The Author(s) 2019. Published by Oxford University Press on behalf of Nucleic Acids Research.
This is an Open Access article distributed under the terms of the Creative Commons Attribution License (http://creativecommons.org/licenses/by/4.0/), which permits unrestricted reuse, distribution, and reproduction in any medium, provided the original work is properly cited.

Downloaded from https://academic.oup.com/nar/article/47/11/5746/5436776 by UNAM Instituto de Investigaciones Biomédicas user on 20 October 2020

these adaptations and their evolution from yeast to humans was recently illuminated by high-resolution cryo-EM reconstructions of the yeast, porcine and human mitoribosomes (5–8). These structures confirmed that some proteins present in bacterial ribosomes have been lost, proteins with homologs in bacteria have substantial extensions, and the mitoribosome has acquired many additional proteins. The assembly lines of the yeast (9) and human mitoribosomes (10) are also starting to emerge and provide insight into the essentiality of mitoribosome proteins for mitoribosome assembly and function.

The yeast mitoribosome small subunit (mtSSU) contains an almost complete set of proteins with homologs in bacteria, with the single exception of bS20 (8). It additionally contains 14 mitochondria-specific proteins, 7 of which have homologs in the mammalian mitoribosome (8). A protein in the latter group is Cox24, the yeast homolog of MRPS38, recently renamed as mS38 (8). Yeast Cox24 was reported to participate in *COX1* mRNA splicing and also translation, as *cox24*-deleted strains carrying intronless mtDNA have attenuated Cox1 synthesis (11). However, the mechanism/s by which Cox24 could influence or regulate *COX1* mRNA-specific translation remained unexplored. Now that Cox24 has been recognized as the mtSSU mS38 protein, the intrigue regarding how it can modulate mRNA-specific translation has only increased.

In the present study, we have used strains carrying intronless mtDNA to analyze the role of mS38 in mitoribosome assembly and function, and its requirement for mRNA-specific translation. We have demonstrated that mitoribosomes lacking mS38 are capable of synthesizing all proteins, although at a strongly attenuated overall mitochondrial translation rate. Importantly, we show that mS38 is preferentially required for translation initiation of not only *COX1* but also *COX2* and *COX3* mRNAs. The mechanism does not directly involve mRNA-specific translational activators, but it involves functional interactions of mS38 with the 5′UTRs of *COX1*, *COX2* and *COX3* mRNAs. Mitoribosome loading onto these mRNAs can occur in the absence of mS38, but their translation is inhibited. Our results suggest that mS38 was acquired by the mitoribosome before or concurrently with the remodeling of the mRNA channel to facilitate the translation of mitochondrial transcripts. The influence of mS38 on the flexibility of elements forming the mRNA channel and the interaction of mS38 with the *COX1–2-3* mRNAs would be required for the efficient translation of these mRNAs. In this way, our data support the concept of mitoribosome-mediated translational regulation.

MATERIALS AND METHODS

Yeast strains and media

All *S. cerevisiae* strains used are listed in supplemental Table S1. The composition of the standard culture medium used is defined in the Supplemental material.

Antibodies

Several attempts to obtain antibodies against an mS38 peptide were unsuccessful. However, a working antibody against purified recombinant mS38 was obtained using the services of GenScript. The antibody, however, produced multiple crossreacting bands in immunoblotting assays (Supplementary Figure S3A). Therefore, a GST-tagged version of mS38 was generated. A list of all antibodies used in this study is presented in supplemental Table S2.

Characterization of the mitochondrial respiratory chain and oxidative phosphorylation system

Endogenous cell respiration was assayed in whole cells in the presence of galactose using a Clark-type polarographic oxygen electrode from Hansatech Instruments (Norfolk, UK) at 30°C as described (12).

Mitochondria were prepared from the different strains as described (13) and used for spectrophotometric assays performed at 24°C to measure KCN-sensitive COX activity and antimycin A-sensitive NADH cytochrome *c* reductase, as described (12).

The abundance of OXPHOS complexes in mitochondrial extracts obtained in the presence of 1% lauryl-maltoside was analyzed by Blue Native polyacrylamide gel electrophoresis (BN-PAGE) using a linear 3–12% acrylamide gradient gel (14).

In vivo mitochondrial protein synthesis

Mitochondrial gene products were labeled with [^{35}S]-methionine (7 mCi/mmol, Perkin Elmer) in whole cells at room temperature in the presence of 0.2 mg/ml cycloheximide to inhibit cytoplasmic protein synthesis (12). In most experiments, we used 10 μCi [^{35}S]-methionine for a final methionine concentration of 17.2 nM. In some time-course experiments, we used a mixture of labeled (2.5 μCi; 4.3 nM) + cold methionine (12.9 nM). When indicated, mitochondrial translation was inhibited by addition of 0.08 mg/ml puromycin and 40 mM cold methionine and samples were chased for the indicated times. Equivalent amounts of total cellular proteins were separated by SDS-PAGE on a 17.5% polyacrylamide gel, transferred to a nitrocellulose membrane and exposed to X-ray film.

Sucrose gradients

The sedimentation properties in sucrose gradients of mS38, translational activators and mitoribosomal proteins from total mitochondrial extracts were analyzed essentially as previously described (13,15) and are further described in the supplemental experimental procedures.

Analysis of mitochondrial polysomes

Yeast cells were grown in medium supplemented with 4 mg/ml chloramphenicol (CAP) for 3 h and in fresh medium for 1 h before proceeding with mitochondrial isolation as described (16–18). Mitochondria were further purified using a step sucrose gradient as described (19). Mitochondrial extracts were prepared in the presence of 0.8% sodium deoxycholate (NaDOC), 10 mM Tris–HCl pH. 7.5, 100 mM NH_4Cl, 20 mM $MgCl_2$ and 200 U of RNaseOUT (Thermo Fisher) and loaded onto 10 ml 10–30% sucrose gradients.

Downloaded from https://academic.oup.com/nar/article/47/11/5746/5436776 by UNAM Instituto de Investigaciones Biomédicas user on 20 October 2020

INFORME DE LABORES 2019

The gradients were centrifuged in an SW41 Ti rotor (Beckman) at 32 700 rpm during 2.5 h at 4°C. Subsequently, the gradients were fractionated using a BR-188 Density Gradient Fractionation System (Brandel). Aliquots of each of 28 fractions were used for immunoblotting analysis of mitoribosomal markers. The rest was used for RNA extraction, to analyze the presence of the 15S and 21S rRNAs, and *COX1 and COB* mRNAs by cDNA synthesis followed by RT-PCR amplification.

RNA analysis

Methods for RNA isolation and quantitative real-time polymerase chain reaction (RT-PCR) are described in the supplemental experimental procedures.

Statistical analysis

All of the experiments were done at least in triplicate. The data are presented as the means ± S.D. of absolute values or percentages of control. The values for the several parameters studied, obtained for WT and Δ*mS38* mutant strains, were compared by Student's *t*-test. $P < 0.05$ was considered significant.

RESULTS AND DISCUSSION

mS38 is a mitoribosome SSU protein specifically required for the efficient synthesis of mtDNA encoded COX subunits

Yeast Cox24 was initially reported to act in *COX1* mRNA splicing and translation (11), and subsequently to be the mitoribosome-specific mtSSU protein mS38 (8). How a mtSSU structural subunit participates in mRNA-specific translation is intriguing. To ascertain the mechanism involved, we utilized for all our experiments a Δ*mS38* strain carrying intronless mtDNA (I^0), to avoid the described effects on *COX1* mRNA splicing, and started by assessing its ability to support mitochondrial mRNA translation and cellular respiration.

As previously reported (11), the Δm*S38* I^0 strain was found to grow poorly in respiratory YPEG media (Figure 1A). Furthermore, endogenous cell respiration was 45% of WT (Figure 1B). The respiratory defect can be partially attributed to a decrease in the activity of CIII since NADH-cytochrome *c* reductase activity (NCCR) was 70% of WT (Figure 1B). However, the major contributor to the respiratory defect appears to be COX, whose activity was severely decreased to 20% of WT (Figure 1B), in agreement with the markedly low levels of assembled CIV (Figure 1C) and COX subunits (Figure 1D), detected in Δ*mS38* I^0 mitochondria. The levels of several COX assembly factors were not affected by the *mS38* mutation (Figure 1D). This is particularly relevant for Mss51, a *COX1* mRNA translation activator and Cox1 chaperone (16,20) since the *mS38* gene on chromosome XII of *S. cerevisiae* genome is 'head to head' with *MSS51* and, as they share regulatory elements (21), the *mS38* deletion could have affected *MSS51* expression.

To confirm that the OXPHOS biogenesis defect in the Δ*mS38* strain stems from a defect in mtDNA gene expression, we performed *in vivo* mitochondrial translation experiments by following the rate of incorporation of [^{35}S]-methionine into the different translation products at increasing pulse times. Our results showed that Δ*mS38* cells could synthesize mitochondrial proteins albeit not efficiently (Figure 1E and Supplementary Figure S1). In the experiment presented in Figure 1E, the labeling reaction was supplemented with cold methionine to slow down and better estimate the rate of [^{35}S]-methionine incorporation into newly synthesized polypeptides. As previously reported, the Δ*mS38* mutation most specifically affected synthesis of Cox1 (11), but also of Cox2 and Cox3 (Figure 1E and Supplementary Figure S1). The incorporation of [^{35}S]-methionine into Cox1 in the mutant was ∼20% of WT, even at the later time points (Figure 1E and Supplementary Figure S1). For Cox2 and Cox3, labeling was ∼30–70% of WT after 1h of pulse-labeling (Figure 1E). For cytochrome *b* and Var1, although the rate of synthesis in the Δ*mS38* mutant was initially lower than in the WT, in the longer pulses these proteins reached WT labeling saturation (Figure 1E and Supplementary Figure S1).

The poor labeling of COX subunits in the Δ*mS38* mutant strain could be due to an effect of the *mS38* mutation on the rate of protein synthesis or turnover. However, the fact that incorporation of [^{35}S]-methionine into Cox1, Cox2 and Cox3 is undetectable after short pulses (Figure 1E, 2.5 min) and that the residual proteins synthesized after 1 h pulse are stable in chase experiments (Supplementary Figure S2A) argues against fast turnover. Likewise, the protein synthesis defect in Δ*mS38* cells is not due to a discrepancy in mRNA levels, as Δ*mS38* I^0 mitochondria had wild-type levels of *COX2* and *COB* mRNAs, and even enhanced levels of *COX1* mRNA (Figure 1F).

mS38 is required for translation initiation of *COX1*, *COX2* and *COX3* mRNAs

The general decrease in mitochondrial protein synthesis rate in the absence of mS38 could be attributed to a change in mtSSU structure near the decoding center and the mRNA exit channel, as well as to the absent intersubunit bridges that involve mS38 (see below). However, translation of a subset of mRNAs, *COX1*, *COX2* and at a lower extent *COX3*, is deeply affected. These mRNAs might undergo specific interactions with the mS38-containing mtSSU that are missing or attenuated in *ΔmS38* mitochondria.

To test the direct involvement of mS38 in the translation of *COX1*, *COX2* and *COX3* mRNAs, we used strains carrying a mitochondrion-encoded reporter gene (20) in either WT or Δ*mS38*. The strains are deleted for the nuclear *ARG8* gene, and the reporter is a recoded version of *ARG8,* termed *ARG8^m,* that encodes a matrix-localized biosynthetic enzyme, which allows us to look directly at mitochondrial translation by scoring the growth of yeast in the absence of arginine. In the strain YC162, the *COX1* coding sequence was completely replaced by *ARG8^m* (*cox1*Δ::*ARG8^m*). Similarly, *ARG8^m* gene replaced the *COX2* coding sequence in the strain RGV139 (*cox2*Δ::*ARG8^m*), the *COX3* coding sequence in the RGV140 strain (*cox3*Δ::*ARG8^m*), and as a control, the *COB* coding sequence in the RGV137 strain (*cob*Δ::*ARG8^m*) (Figure 2A). In these strains, *ARG8* mRNA translation is dependent on the 5′- and 3'- un-

Downloaded from https://academic.oup.com/nar/article/47/11/5746/5436776 by UNAM Instituto de Investigaciones Biomédicas user on 20 October 2020

INFORME DE LABORES 2019

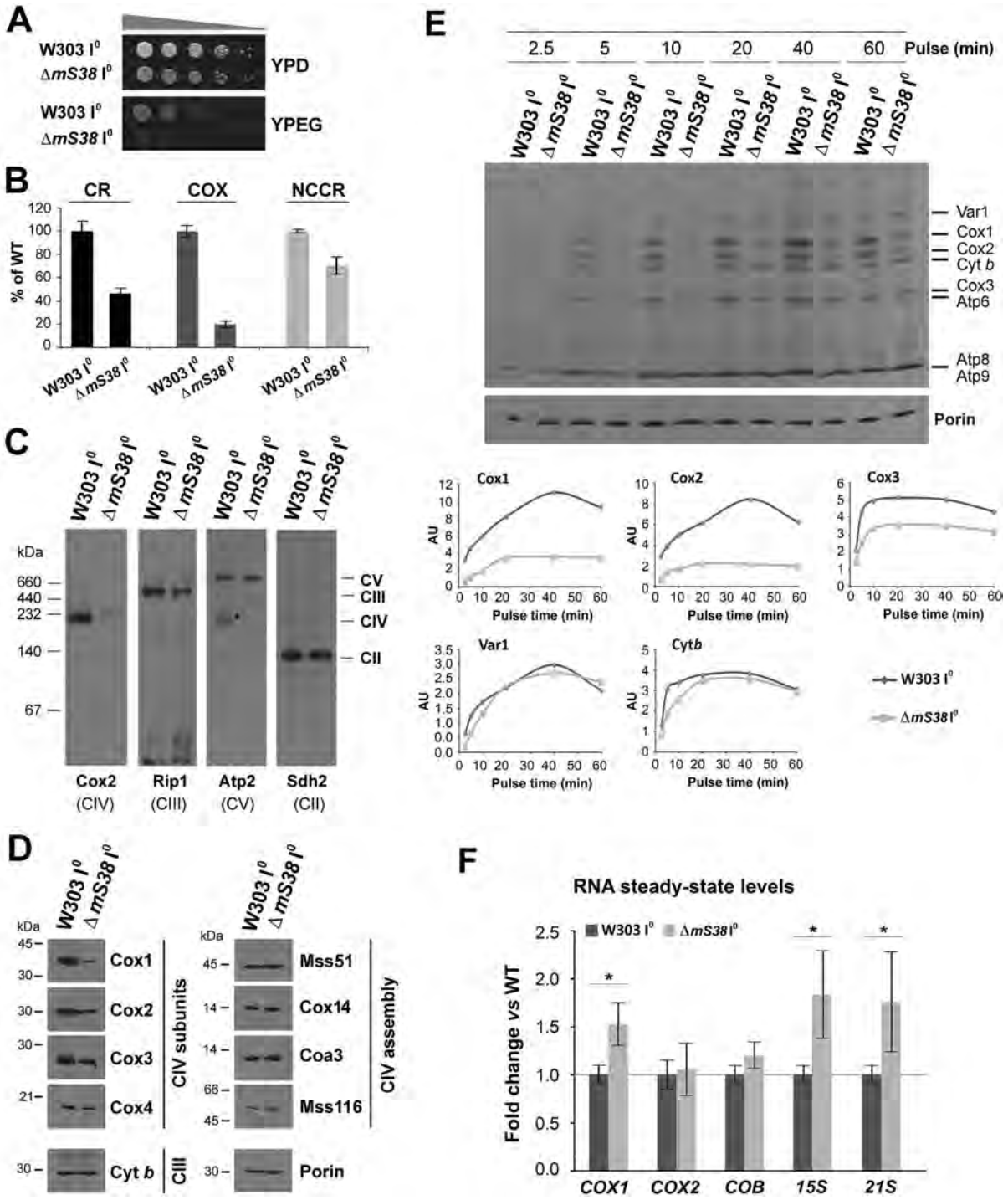

Figure 1. mS38 is specifically required for the efficient translation of *COX1*, *COX2,* and *COX3* mRNAs. See also Supplementary Figure S1. The intronless WT (W303 I^0) and Δ*mS38* mutant strains were characterized by: (**A**) Serial dilutions growth test in fermentable complete solid media containing glucose (YPD) and respiratory media containing ethanol and glycerol (YPEG). Pictures were taken after two days of growth at 30°C. (**B**) Measurement of OXPHOS parameters in the indicated cell strains. The graph shows the endogenous cell respiration rate (CR), and the enzymatic activities of CIV or cytochrome *c* oxidase (COX) and of NADH-cytochrome *c* reductase (NCCR), expressed as the percentage of WT. Bars represent the mean ± SD of three independent repetitions. (**C**) Steady-state levels of OXPHOS complexes extracted from isolated mitochondria with lauryl maltoside, analyzed by BN–PAGE and detected by immunoblotting with the indicated antibodies. (**D**) Immunoblot analyses of the steady-state levels of the indicated complex III (CIII) and complex IV (CIV) subunits and assembly factors. Porin was used as loading control. (**E**) Metabolic labeling with ^{35}S-methionine (2.5 μCi; 4.30 nM) + cold methionine (12.90 nM) of newly synthesized mitochondrial products in whole cells during increasing pulse times in the presence of cycloheximide to inhibit cytoplasmic protein synthesis. Immunoblotting for Porin was used as a loading control. Newly-synthesized polypeptides are identified on the right. In the lower panel, raw densitometry values for the indicated individual proteins were plotted to visualize their synthesis kinetics. (**F**) RT-qPCR analysis of mitochondrial RNA steady-state levels in WT (W303 I^0) and Δ*mS38* cells, expressed as fold change versus WT values. The bars represent the average ± SD of three independent repetitions. Student's *t*-test: $*P < 0.01$.

Downloaded from https://academic.oup.com/nar/article/47/11/5746/5436776 by UNAM Instituto de Investigaciones Biomédicas user on 20 October 2020

INFORME DE LABORES 2019

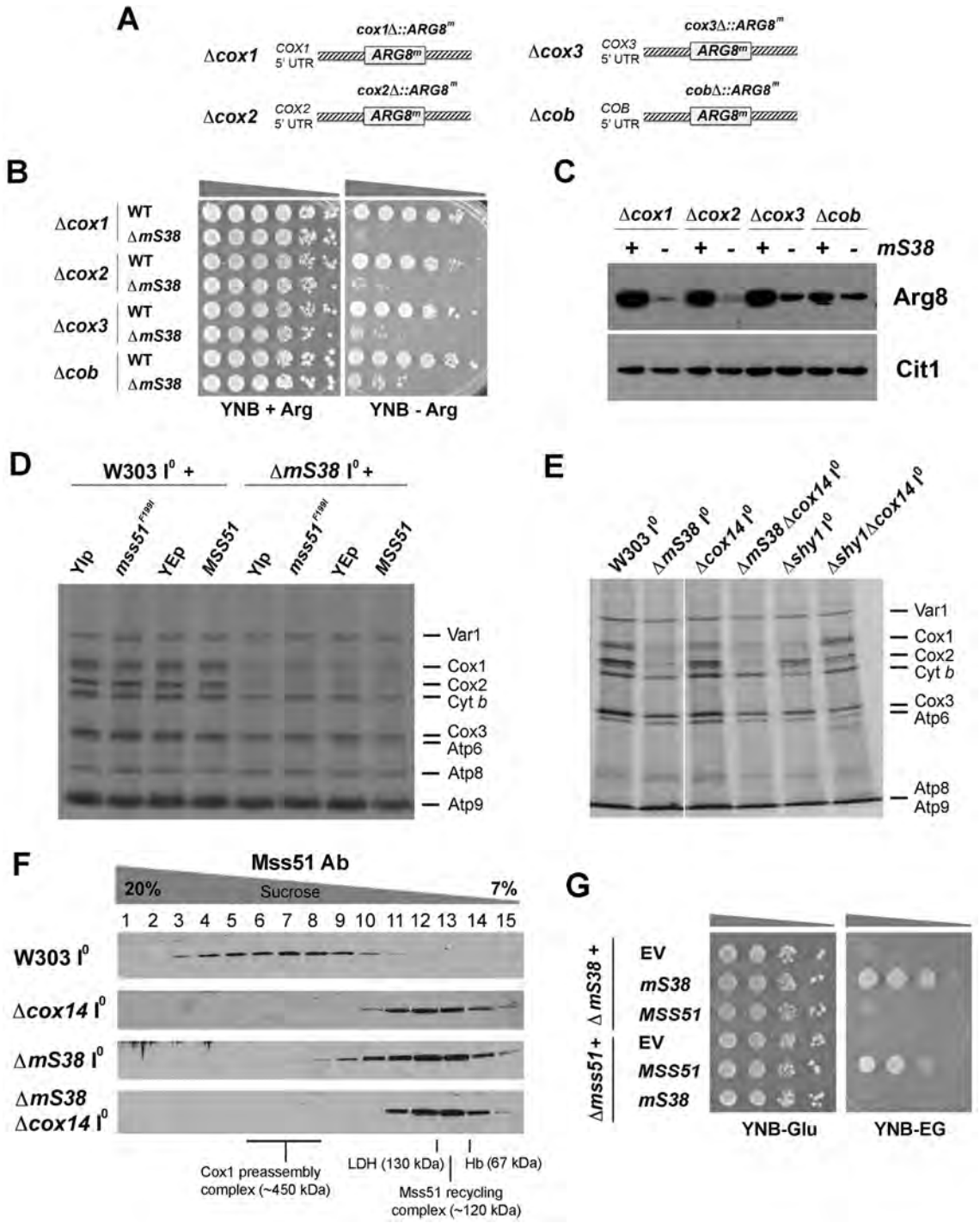

Figure 2. mS38 is required for translation initiation of mtDNA-encoded COX subunits. See also Supplementary Figure S2. (**A**) Scheme depicting the mitochondrial genotype of strains carrying mitochondrial *ARG8* (*ARG8^m*) as a reporter of mRNA translation. (**B**) Growth test using serial dilutions of the indicated strains in yeast nitrogen base minimum media (YNB) supplemented or not with arginine. Pictures were taken after 2 days of growth at 30°C. (**C**) Steady-state levels of mitochondrial Arg8 in the indicated strains, estimated by immunoblotting. Cit1 (mitochondrial citrate synthase) was used as loading control. (**D** and **E**) *In vivo* mitochondrial protein synthesis performed as in Figure 1E but using ^{35}S-labeled (10 μCi; 17.20 nM) and not cold methionine, and the indicated strains. In (**D**), the effect of extra copies of the wild-type *MSS51* or the heme-insensitive allele mss51^{F199I} was tested. YIp: empty integrative vector YIp211. YEp: empty episomal vector YEp351. In (**E**), the effect of a Δ*cox14* mutation was assessed. (**F**) Sucrose gradient sedimentation analyses of translational activator Mss51 on mitochondrial extracts prepared from the indicated strains carrying intronless mtDNA (I^0) in the presence of 0.8% digitonin. (**G**) Growth test using serial dilutions of the indicated strains in minimum media (YNB) supplemented with fermentable (D, dextrose) or non-fermentable (EG, ethanol-glycerol) carbon sources. Pictures were taken after 2 days of growth at 30°C.

Downloaded from https://academic.oup.com/nar/article/47/11/5746/5436776 by UNAM Instituto de Investigaciones Biomédicas user on 20 October 2020

INFORME DE LABORES 2019

translated regions (UTRs) of *COX1*, *COX2*, *COX3* and *COB* respectively (20). When carrying a WT allele of *mS38,* Arg8^{m} is synthesized in all strains and supports arginine-independent growth (Figure 2B). However, the Δ*mS38* mutation affected capacity of the strains to grow in the absence of exogenous arginine (Figure 2B) due to the general translation defect observed in the Δ*mS38* strain (Figure 1E). The deleterious effect was particularly prominent in the Δ*cox1* and Δ*cox2* strains, less prominent in the Δ*cox3* strain, and markedly less severe in the Δ*cob* control strain (Figure 2B). The growth results correlate well with the steady-state levels of Arg8^{m} detected in each of these strains (Figure 2C). These results indicated that whereas mitochondrial translation in mS38-less mitoribosomes is generally compromised, they are preferentially impaired in translation initiation of *COX1*, *COX2* and *COX3* RNAs.

The mS38-dependent Cox1 synthesis defect is not the result of Cox1 translational regulation

Synthesis of Cox1 is coupled to its assembly into COX by a translational negative feedback loop in which Mss51 plays an essential role (16,20). Mss51 acts on the *COX1* mRNA 5′-UTR to promote translation initiation and forms a complex with newly synthesized Cox1 that is stabilized by two specific chaperones, Cox14 and Coa3. Interactions with these chaperones trap Mss51 in a ∼450 kDa Cox1 pre-assembly complex until Cox1 is matured or interacts with its assembly partners (15,20,22–24). When this occurs, Mss51 is released from its interaction with the Cox1 polypeptide, forms a ∼120 kDa recycling complex with the Hsp70 chaperone (Ssc1) and becomes available to promote new rounds of *COX1* mRNA translation (15). To further test whether the decrease in Cox1 synthesis that we observed in the *mS38* mutant is due to a primary defect in translation and not the result of Cox1 synthesis downregulation, we followed two strategies to bypass feedback regulation of *COX1* mRNA translation. First, we previously reported that additional copies of wild-type *MSS51* or a single copy of the mutant allele *mss51*^{F199I} increases Cox1 synthesis in COX assembly mutants in which Cox1 synthesis is downregulated (12,16). As shown in Figure 2D, these strategies did not alleviate the Cox1 synthesis defect observed in the Δ*mS38* strain. Second, we introduced a Δ*cox14* mutation in the Δ*mS38* strain. In most COX assembly mutants, the absence of Cox14 destabilizes the complex of sequestered Mss51 with newly synthesized Cox1 and renders Mss51 available for translation, thus bypassing the regulatory feedback mechanism (16). As shown in Figure 2E, the absence of Cox14 suppressed the Cox1 synthesis downregulation in the control COX mutant strain Δ*shy1* but not in the Δ*mS38* strain. *SHY1* codes for the SURF1 homolog of yeast, a known conserved COX assembly factor (12). The additional Δ*cox14* mutation was not found deleterious for the residual Cox1 synthesis capacity retained by the Δ*mS38* strain (Figure 2E), as previously reported (11). Instead, using pulse-chase assays, we found that as in the Δ*cox14* strain, newly synthesized Cox1 is also very susceptible to degradation in the double mutant strain (Supplementary Figure S2A).

We subsequently followed the sedimentation pattern of Mss51 in sucrose gradients in Δ*cox14,* ΔmS38 and the double Δ*cox14*Δ*mS38 strain.* In WT mitochondria, most Mss51 sediments in the ∼450 kDa Cox1-preassembly complexes, whereas in Δ*cox14* mitochondria it sediments in the 120 kDa Mss51 recycling complex ((15) and Figure 2F). In the absence of mS38, only traces of Mss51 sediment in the ∼450 kDa complex, and the additional absence of Cox14 exerts an epistatic effect (Figure 2F). Furthermore, mS38 and Mss51 do not interact genetically, as overexpression of each protein does not compensate for the absence of the other in terms of protein synthesis (Figure 2D) and respiratory growth (Figure 2G).

We concluded that the Cox1 synthesis defect in the Δ*mS38* strain does not result from negative-feedback translation regulation, but from a *COX1* mRNA translation impairment affecting initiation according to the Arg8^{m} reporter experiments presented earlier, that can be extended to *COX2* and to a lesser extent also to *COX3* mRNAs.

Specific attenuation of the synthesis or assembly of mtDNA-encoded subunits has been reported in strains carrying point mutations in some mtLSU proteins, although the mechanisms involved differ from those underlying the Δ*mS38* phenotype. Temperature-sensitive point mutations in the mtLSU protein bL34 (such as the highly conserved R95 residue to W) result in specific alterations in the synthesis of Cox1 and Cox3, but normal Cox2 synthesis (25). The conserved bL34-R95 residue is in close contact with the 21S rRNA. bL34 also interacts with uL23 and uL24, two components of the polypeptide exit tunnel that was modified from bacteria to become adapted for the passage of hydrophobic polypeptides (5). It has been proposed that the bL34 mutations could slightly modify the exit tunnel cavity and then challenge or block the path for the most hydrophobic polypeptides such as Cox1 and Cox3 (25). Differently, strains expressing variants of mL38, a component of the mtLSU central protuberance, carrying point mutations in its phosphatidylethanolamine-binding protein (PEBP)-like domain (*mL38*^{Y275}) undergo normal synthesis of all proteins, even enhanced for Cox1, but have impaired COX assembly (26). The mL38-ts mutation might affect the functional integrity of Coa3, Cox14 and Mss51, three Cox1-binding proteins essential for Cox1 elongation, membrane insertion and stability (26,27).

The phenotype of Δ*mS38* is also reminiscent of that of Δ*mss116.* Mss116 is a DEAD-box helicase that plays distinct roles in *COX1* mRNA splicing, mtLSU biogenesis, and mitochondrial *COX* mRNA-specific translation, predominantly affecting Cox1 synthesis (28). The absence of Mss116 renders unstable the pentatricopeptide repeat protein Pet309, a *COX1* mRNA-specific translational activator, thus explaining the Cox1 synthesis defect. Cox14, Coa3, Mss51 and Mss116 were found stable in Δ*mS38* mitochondria (Figure 1D).

Therefore, mS38 is a mtSSU protein that could directly influence the selection of mitochondrial mRNAs for translation. A potential mechanism could involve mitoribosome heterogeneity, with mitoribosome pools containing or not mS38. However, this possibility is tempered by the fact that over-expression of mS38 in wild-type cells did not affect the synthesis rate of Cox1–3 or any other protein (Supplementary Figure S2B), as it would be expected for a mitoribosomal protein present in all mitoribosomes. Furthermore,

Downloaded from https://academic.oup.com/nar/article/47/11/5746/5436776 by UNAM Instituto de Investigaciones Biomédicas user on 20 October 2020

INFORME DE LABORES 2019

the cryo-EM structural reconstruction of the yeast mitoribosome did not display any heterogeneity involving mitoribosomal proteins (8).

Mitoribosomes are assembled and more abundant in mS38-depleted mitochondria

Recently, mS38 has been identified as a mtSSU subunit by cryo-EM analysis (8). However, the fact that the Δ*mS38* strain can perform mitochondrial translation, despite at a low rate, implies that mitoribosomes are assembled and somehow functional in the absence of mS38.

To further explore the role mS38 plays in mitoribosome biogenesis and function, we generated a polyclonal antibody against purified recombinant mS38 (Supplementary Figure S3A) that allowed us to determine that in wild-type mitochondria, all endogenous mS38 co-sediments with mtSSU markers (Figure 3A). Similarly, a near fully functional GST-tagged version of mS38 (Supplementary Figure S3B–D) co-sediments with the mtSSU and monosome fractions (Figure 3B) when using extracts prepared in the presence of Mg^{2+}. However, when mtSSU and mtLSU are separated by addition of EDTA, a portion of mS38-GST accumulates in a non-assembled pool (Figure 3C), suggesting that under these extraction conditions the large GST tag could destabilize the association of mS38 with the mtSSU. Association of mS38-GST with the mtSSU was further tested by treatment with high concentrations of RNase to disrupt ribosomal integrity. The RNAse treatment resulted in the accumulation of all mS38 in the smaller complex (Figure 3C), further confirming that mS38 is an integral component of the mtSSU.

To probe for a possible mitoribosome assembly defect, mitochondrial proteins were extracted from isolated WT mitochondria using 0.8% digitonin and 25 mM KCl and analyzed by sucrose gradient sedimentation. The sedimentation of the 74S monosome, the 54S mtLSU, and the 37S mtSSU were similar in the WT and Δ*mS38* strains in extracts prepared either in the presence of 0.5 mM $MgCl_2$ to preserve the intactness of the monosome or in the presence of 5 mM EDTA to promote subunit dissociation (Figure 3B and C). To obtain a comprehensive picture of potential differences in the composition of assembled mitoribosomal subunits, sucrose gradient fractions from Figure 3C, corresponding to the mtSSU were methanol/chloroform precipitated and analyzed by mass spectrometry (supplemental Table S3). Proteins mS38, mS47 and mS48 were not detected in any of the samples. The rest of the mtSSU proteins were detected in fractions from both WT and Δ*mS38* mitochondrial extracts, which indicates that the absence of mS38 does not prevent incorporation of the remaining proteins into the mtSSU.

To compare the accumulation of mitoribosome protein markers in WT and Δ*mS38* extracts, we ran in parallel, in a single gel, samples from the relevant sucrose gradient fractions (Figure 3D). We determined that the levels of mtSSU and mtLSU proteins were increased in the corresponding fractions and in the fractions where the monosome peaks. In agreement, the steady-state levels of mitoribosome proteins indicated that the concentrations of two mtSSU and five mtLSU proteins tested were enhanced in *ΔmS38* cells compared to the WT control (Figure 3E). Similarly, the steady-state levels of 15S and 21S rRNAs were also found ∼1.5–2-fold increased in Δ*mS38* mitochondria (Figure 1F). We concluded that the steady-state levels of mS38-less mitoribosomes are enhanced, probably to attempt compensating for their inefficient functional performance.

Mitoribosome loading onto *COX1* mRNA can occur in the absence of mS38

A failure of translational activators to bind their specific RNA is expected to prevent the proper mRNA loading onto the mitoribosome (29). To assess whether the absence of mS38 limits the mitoribosome-*COX1* mRNA association, we used highly purified mitochondria from WT and Δ*mS38* I^0 strains, both carrying a null allele of the unspecific mitochondrial nuclease *nuc1*, to avoid RNA degradation during sample processing, as reported (29). Yeast cells were grown in chloramphenicol (CAP) for 3 h and in fresh medium for 1 h prior to mitochondrial isolation (Figure 4A). The CAP treatment allows accumulation of cytoplasmically-synthesized proteins required for mitoribosome assembly and mitochondrial gene expression, which results in a robust increase in the proportion of mito-polysomes and of mitochondrial protein synthesis (16,17,28). Mitochondrial extracts were prepared in the presence of 0.8% NaDOC, 10 mM Tris pH 7.5, 100 mM NH_4Cl, 20 mM $MgCl_2$ and 200 U of RNaseOUT, and fractionated in sucrose gradients. Aliquots of each fraction were used for immunoblot analysis of mitoribosomal markers. The rest was used for RNA extraction and the presence of the 21S and 15S rRNAs, and the *COX1 and COB* mRNAs analyzed by cDNA synthesis followed by quantitative RT-PCR amplification (Figure 4A). Polysomes were detected in the two strains analyzed (Figure 4B). However, they were dramatically decreased in Δ*mS38* mitochondria compared to WT. In our experimental conditions, in both strains, all *COX1* and *COB* mRNAs were found cosedimenting with mitoribosomal particles and not in free pools (Figure 4B). In WT mitochondria, the proportion of *COX1* and *COB* mRNAs detected in the mtSSU was lower than in the monosome and polysome fractions (Figure 4B). On the contrary, in Δ*mS38* mitochondria, the proportion of *COB* and *COX1* mRNAs was higher in the mtSSU and monosome, and attenuated in the polysome fractions, indicating a general role of mS38 in translation. The proportion of *COX1* mRNA on Δ*mS38* polysome fractions was particularly attenuated (Figure 4B), which explains why only traces of newly synthesized Cox1 are detected in mitochondrial protein synthesis experiments (Figure 1E).

Using similar experiments, we previously reported that mitoribosome loading onto *COX1* mRNA could occur in the absence of Pet309 or Mss116 (28). However, the *COX1* mRNA was not detected in polysomes, thus supporting the requirement of Pet309 and Mss116 for *COX1* mRNA translation initiation (28). Similarly, the results presented here indicate the mS38 is not required for the loading of *COX1* mRNA on the mtSSU and the monosome, but rather for its translation.

The mRNA molecules in the cell often assume a secondary and a tertiary structure that might be tight for some

Downloaded from https://academic.oup.com/nar/article/47/11/5746/5436776 by UNAM Instituto de Investigaciones Biomédicas user on 20 October 2020

INFORME DE LABORES 2019

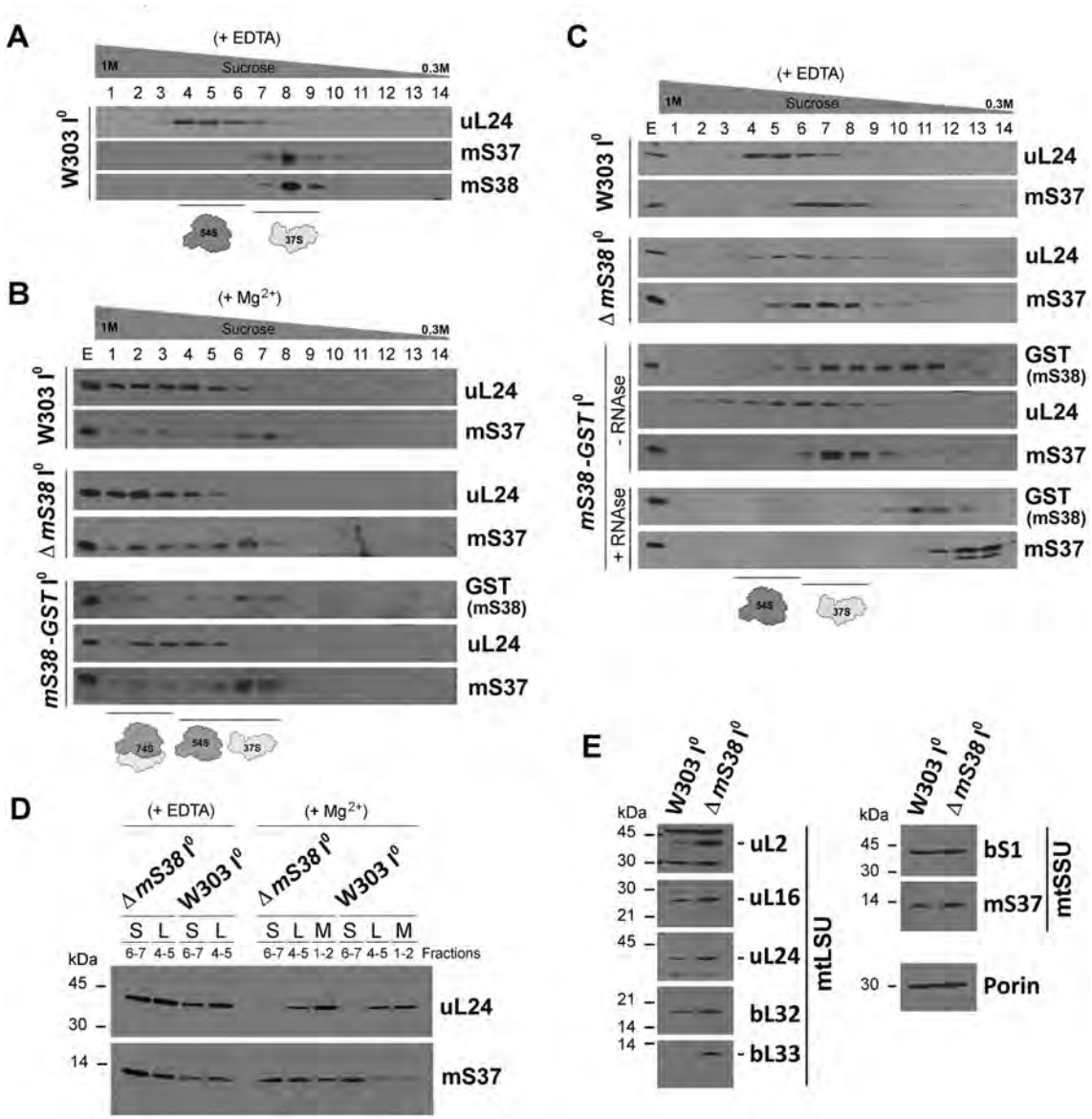

Figure 3. Mitoribosome particles are assembled and more abundant in mS38-depleted mitochondria. See also Supplementary Figure S3. (A–C) Sucrose gradient sedimentation analyses of mitoribosomal protein markers on mitochondrial extracts prepared from the indicated strains carrying intronless mtDNA (I^0) in the presence of 0.8% digitonin and the conditions stated including either EDTA (**A** and **C**) or Mg^{2+} (**B**). Extracts from a Δ*mS38* strain expressing mS38-GST from an integrative plasmid were prepared in the presence or absence of a high concentration of RNAse (600U) to disrupt mitoribosome integrity. (**D**) To compare the levels of mtSSU (S), mtLSU (L) or monosome (M) in the WT and Δ*mS38* strains, the indicated fractions from the sucrose gradients in panel (B), were pooled and equal volumes analyzed by SDS-PAGE and immunoblotting. (**E**) Steady-state levels of mitoribosomal proteins estimated by immunoblot analyses. Porin was used as a loading control.

genes, and loose for others. For translation to proceed, such structure must first allow ribosome binding and then needs to be threaded through the ribosome, thus providing an opportunity to regulate the translation efficiency of mRNAs (30,31). The 5′-UTRs of *S. cerevisiae* mitochondrial mRNAs are highly variable in length, from 54 nt for *COX2* to 954 nt for *COB*. Their structures have not been determined *in vivo*, where RNA-specific binding proteins are expected to modify them. However, models determined *in silico* by applying free energy rules using the *mfold* web server algorithms have shown that the secondary structures of all naked 5′-UTRs are complex (28). According to these structures, the *COX1* and *COB* 5′-UTRs contain convoluted stem–loops and *COX2* has the shorter and perhaps the simplest 5′-UTR. Although a single short stable hairpin can inhibit ribosome loading at the 5′-end of an mRNA (31), these models suggest that there is more than differences in 5′-UTR arrangements behind the disfavored *COX1–3* mRNAs translation observed in the absence of mS38.

Downloaded from https://academic.oup.com/nar/article/47/11/5746/5436776 by UNAM Instituto de Investigaciones Biomédicas user on 20 October 2020

INFORME DE LABORES 2019

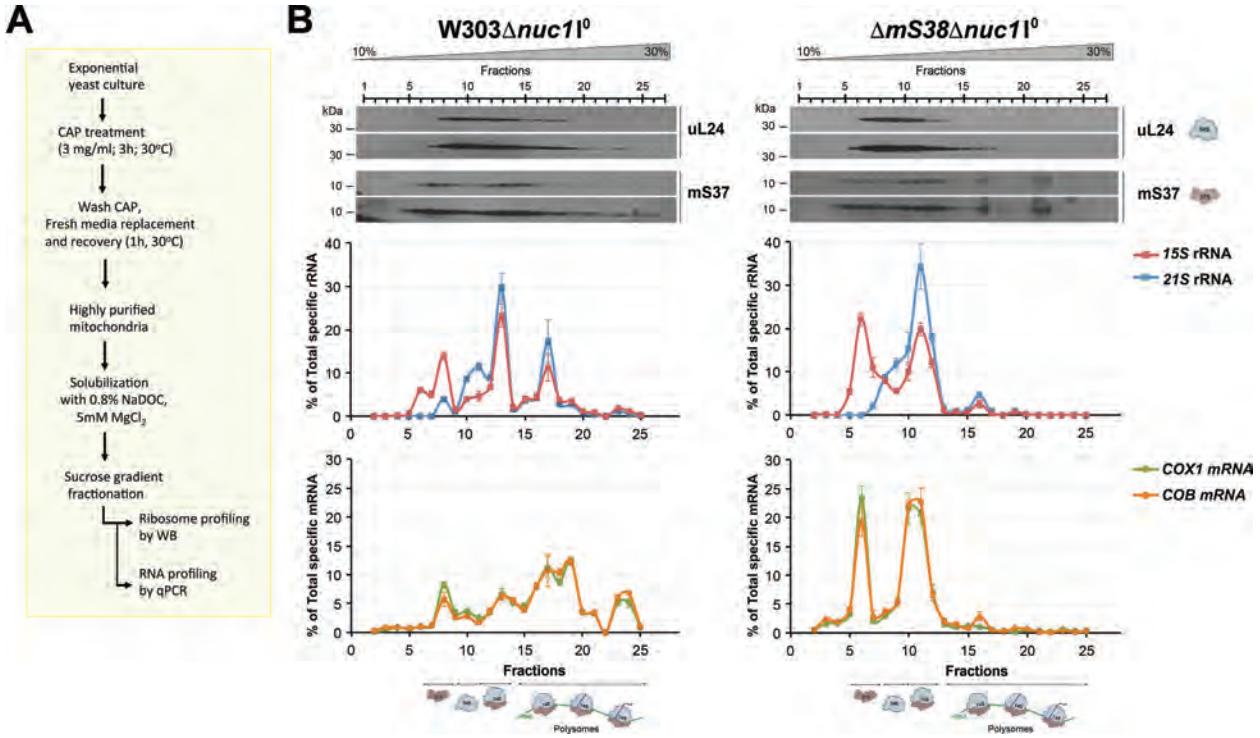

Figure 4. In the absence of mS38, *COX1* mRNA is loaded onto the mitoribosomes but is poorly detected in polysomes. (**A**) Scheme depicting the experimental protocol for mito-polysome profiling. (**B**) Sucrose gradient sedimentation analyses of mitoribosomal subunits, monosomes, and polysomes in extracts obtained from mitochondria isolated from the indicated strains. One representative image of three independent experiments is shown. The graphs in the lower panels represent the relative amount of the indicated rRNAs and mRNAs in the gradient fractions, estimated by RT-qPCR. The bars represent the average ± SD of three independent repetitions.

The preferential inability of mS38-less mitoribosomes to synthesize Cox1 is independent of the *COX1* mRNA-specific translational activators

Next, we investigated whether mS38 genetically or physically interacts with the *COX1* mRNA translational activators, Mss51, Mss116, Pet309, Mam33 and Pet54, which could facilitate the recruitment of the *COX1* mRNA to the mtSSU.

As mentioned above, the five proteins are required for intron splicing on the *COX1* transcript, a function that has also been proposed for mS38 (11), and have been shown to act on the *COX1* mRNA 5′-UTR to promote translation (16,20,28,32). Moreover, Pet54 is a multifunctional protein that acts primarily as a translational activator of *COX3* mRNA and plays a role in Cox1 synthesis possibly by rendering Mss51 competent as a *COX1* mRNA translational activator (33).

We started by testing whether overexpression of each translation activator suppresses the Δ*mS38* phenotype. Extra copies of *MSS51* (Figure 2D-G and Supplementary Figure S5C), *MSS116* (data not shown), *MAM33* (Supplementary Figure S5C) or *PET54* (Supplementary Figure S4F-G) failed to restore the respiratory growth or protein synthesis defects observed in the Δ*mS38* strain. Furthermore, the steady-state levels of endogenous Mss51 and Mss116 (Figure 1D) and functional tagged Pet54, Pet309 and Mam33 (Figure 5A, Supplementary Figure S4A and B and Supplementary Figure S5A and B), were not affected by the presence or absence of mS38. Additionally, no additive effect on the rate of Cox1 synthesis was observed in a double null mutant strain *Δpet54ΔmS38* compared to the single mutant *ΔmS38* (Supplementary Figure S4E).

Subsequently, we examined the association of the translational activators with mitoribosomes using sucrose gradient sedimentation analyses. A small fraction of Mss51 was found to co-sediment with the mtSSU in mitochondrial extracts prepared in the presence of EDTA from WT or from Δ*mS38* reconstituted with a GST-tagged version of mS38 (Figure 5B). The absence of mS38 abolished the co-sedimentation of Mss51 with 37S mitoribosomal particles (Figure 5B). This observation could suggest an mS38-mediated interaction of Mss51 with these particles. Alternatively, the Mss51-mitoribosome interaction is most probably mediated through newly synthesized Cox1 and then abolished in Δ*mS38* mitochondria in which Cox1 synthesis is strongly attenuated. To solidify this concept we performed similar experiments using strains carrying a Δ*cox11* mutation, since we have previously shown that the interaction of Mss51 with the mitoribosome is particularly prominent in strains deficient in Cox1 maturation or assembly, such as Δ*cox11,* in which Cox1 synthesis is stalled (15). Consistent with our hypothesis, that Mss51 could interact with the ribosome through newly synthesized Cox1, we observed that Mss51 co-sedimented with the 37S mitoribosome in Δ*cox11ΔmS38* mitochondrial extracts (Figure 5B). Also, a functional FLAG-tagged version of Pet54 (Supplementary Figure S4A and B) was found to co-sediment with 37S

Downloaded from https://academic.oup.com/nar/article/47/11/5746/5436776 by UNAM Instituto de Investigaciones Biomédicas user on 20 October 2020

INFORME DE LABORES 2019

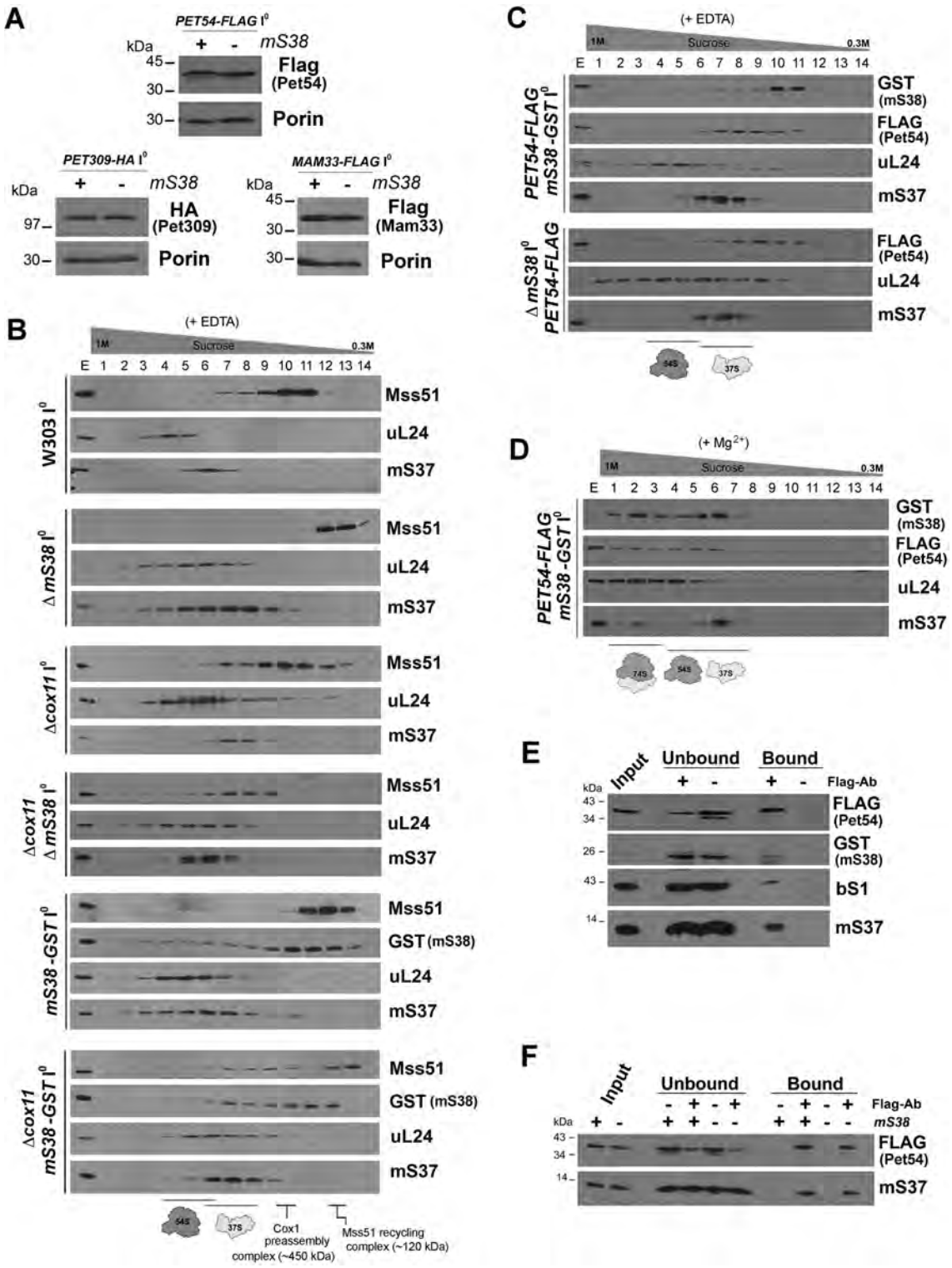

Figure 5. mS38-specific role in regulating *COX* mRNA translation does not directly involve translational activators. See also Supplementary Figure S4 and S5. (**A**) Steady-state levels in wild-type and Δ*ms38* of proteins that regulate *COX1* mRNA translation: Pet54, Pet309 and Mam33. Each strain was constructed by generating double mutants that were reconstituted with an integrated plasmid to express a functional tagged version of the protein being analyzed (Δ*ms38*Δ*pet54 +PET54-FLAG;* Δ*ms38*Δ*pet309 +PET309-HA, and* Δ*ms38*Δ*MAM33 +MAM33-FLAG).* Porin was used as a loading control. (**B–D**) Sucrose gradient sedimentation analyses of mitoribosomal protein markers and the translational activators Mss51 (B) or Pet54 (C-D) on mitochondrial extracts prepared from the indicated strains carrying intronless mtDNA (I^0) in the presence of 0.8% digitonin and either EDTA (B, C) or Mg^{2+} (D). (**E**) Co-immunoprecipitation of mS38-GST and Pet54-FLAG, using anti-FLAG-conjugated agarose beads. Protein A-conjugated beads were used as a negative control. (**F**) Co-immunoprecipitation of Pet54-Flag with a mtSSU marker in cells carrying WT or deletion alleles of *mS38* performed as in panel (E).

Downloaded from https://academic.oup.com/nar/article/47/11/5746/5436776 by UNAM Instituto de Investigaciones Biomédicas user on 20 October 2020

INFORME DE LABORES 2019

(Figure 5C and D) and 74S mitoribosomal particles (Figure 5D), although its sedimentation properties were not altered in the absence of mS38 (Figure 5C). Immunoprecipitation studies using a strain expressing *PET54-FLAG* (Figure 5E and F) further confirmed that the interaction of Pet54 with mitoribosomes is independent of mS38. Lastly, no sedimentation with the mitoribosomes was observed for a Flag-tagged functional version of Mam33 (data not shown).

As an additional relevant observation, we noted a different sedimentation pattern in sucrose gradients for Mss51 extracted from strains expressing wild-type mS38 or mS38-GST. The interaction of mS38-GST with the mitoribosome is labile, and a portion is removed from the mitoribosome particle in the presence of EDTA (Figures 3C and 5B), suggesting that the fusion protein may not be fully functional. In fact, although mS38-GST fully supports respiratory growth (Supplementary Figure S3B) and largely restores overall mitochondrial protein synthesis, the synthesis of Cox1 (and at a lesser extent also Cox2 and Cox3) is not fully restored (Supplementary Figure S3D and 7D). For this reason, a portion of Mss51 is trapped in the Mss51 recycling complex (Figure 5B). Importantly, the results obtained with the mS38-GST strain further support the predominant requirement of mS38 for the synthesis of COX subunits.

Overall, from the results presented in this section, we conclude that the preferential inability of mS38-less mitoribosomes to synthesize Cox1 is independent of the *COX1* mRNA-specific translational activators. The case reported here differs from other instances in which interplay between translational activators and mitoribosome subunits, has been reported. Such was the case of mutations in bS6 (former Mrp17) reported to compensate for a C-terminal truncation of Pet122, a *COX3* mRNA-specific translational activator (34).

The absence of mS38 modifies the decoding center in the mtSSU

In the mtSSU, mS38 interacts with the 15S rRNA helix 44 ((8) Figure 6A-B). This helix is an element present in all ribosomes that forms several inter-subunit bridges, which regulate the relative movement of the subunits, and is part of the decoding center. In bacteria, the lower part of the helix is rigid and anchored by bS20, whereas the middle part forms major intersubunit bridges, and the upper part is flexible being involved in tRNA translocation (35). These H44-involving bridges are also present in the yeast mitoribosome, which contains nine mitochondria-specific bridges, one of which involves mS38 (8). Specifically, mS38 aa residues 101–102, 105–106 and 109–110 connect with 21S rRNA helices H70 (nt 1832–1834), H71 (nt 1859–1860), H62 (nt 1643–1644) and H67 (nt 1739–1741 and 1874–1877), respectively. It has been proposed that the extensive intersubunit bridges may restrain the movement of the yeast mitoribosomal subunits (8). The lack of mS38 in yeast is then predicted to affect subunit association. Additionally, the upper part of H44 is largely more flexible in mitochondrial compared to bacterial ribosomes and its movement is mainly constrained by the presence of mS38. As a consequence, in mS38 absence, H44 is likely to be unrestricted, and decoding could be affected, due to loss of H44 base pairing.

To determine how the absence of mS38 affects H44 near the decoding center we exploited the fact that aminoglycoside antibiotics such as paromomycin bind to the 15S rRNA in the aminoacyl-tRNA site (A-site) to cause misreading of the genetic code and inhibit translocation. Studies in bacteria comparing the 30S subunit with and without paromomycin (36) confirmed an earlier model (37) in which bases 1492 and 1493 of the 16S rRNA are in a position to monitor the codon:anticodon fit via hydrogen bonding to the codon:anticodon duplex. Paromomycin alters the structure of the 16S rRNA to mimic conditions of a perfect codon:anticodon fit, so that incorrect aminoacyl-tRNAs may be selected. In yeast mitochondria, resistance to paromomycin (Par^R) arises from a single base change in the 15S rRNA H44 region ((39), Figure 6B). This mutation causes a base pair mismatch, which is likely to increase the flexibility of the decoding center. When the Δ*mS38* mutation was introduced into a Par^R mtDNA background strain, it did not affect respiratory growth of the resulting strain in regular media (Figure 6C) or its mitochondrial protein synthesis capacity (Figure 6D, E and Supplementary Figure S6) compared to the Par^S background. However, the double mutation conferred greater resistance to exogenous paromomycin than the Par^R mutation alone (Figure 6C). Notably, the lack of mS38 is associated with strong thermosensitivity. At 37°C, whereas WT mitochondrial translation was unaffected, the synthesis of Cox1, Cox2 and Cox3 was barely detected in Δ*mS38* Par^S or Par^R backgrounds (Figure 6E), and therefore resistance to exogenous paromomycin was eliminated (Figure 6C). An increase in temperature could also affect the decoding region structure, as reported for *Escherichia coli* ribosomes (38).

Together, these results indicate that the absence of mS38 modifies the decoding center in the mtSSU.

The mS38 N-terminus is sufficient to support SSU assembly and normal synthesis of all proteins other than COX subunits

Saccharomyces cerevisiae mS38 is a 111-aa protein that contains a predicted 15-aa N-terminal mitochondrial targeting sequence (MTS, shadowed in yellow in Figure 7A). The C-terminal aa 81–111 form an arginine-lysine-rich domain (shadowed in red in Figure 7A) conserved from yeast to human. As seen in the cryo-EM structure (8), from the C-terminus, this domain forms a helix that runs parallel to the 15S rRNA H44 at the subunit interface and contains the residues involved in intersubunit bridge formation ((8) and Figure 6B). mS38 then bends, probably restricting the movement of the upper part of H44 that forms the decoding center, and subsequently forces the mS38 N-terminus to protrude into the 15S rRNA (8). The structure of the N-terminal portion of the protein (aa 15–80), which is highly divergent (Figure 7A), was not resolved by cryo-EM. The most probable model of the structure of the full mature protein (aa 16–111), obtained using Quark (Supplementary Figure S8), is shown in Figure 7B. Quark is a computer algorithm for *ab initio* protein structure prediction and protein peptide folding, which aims to construct the correct protein 3D model from amino acid sequence only (39).

Downloaded from https://academic.oup.com/nar/article/47/11/5746/5436776 by UNAM Instituto de Investigaciones Biomédicas user on 20 October 2020

INFORME DE LABORES 2019

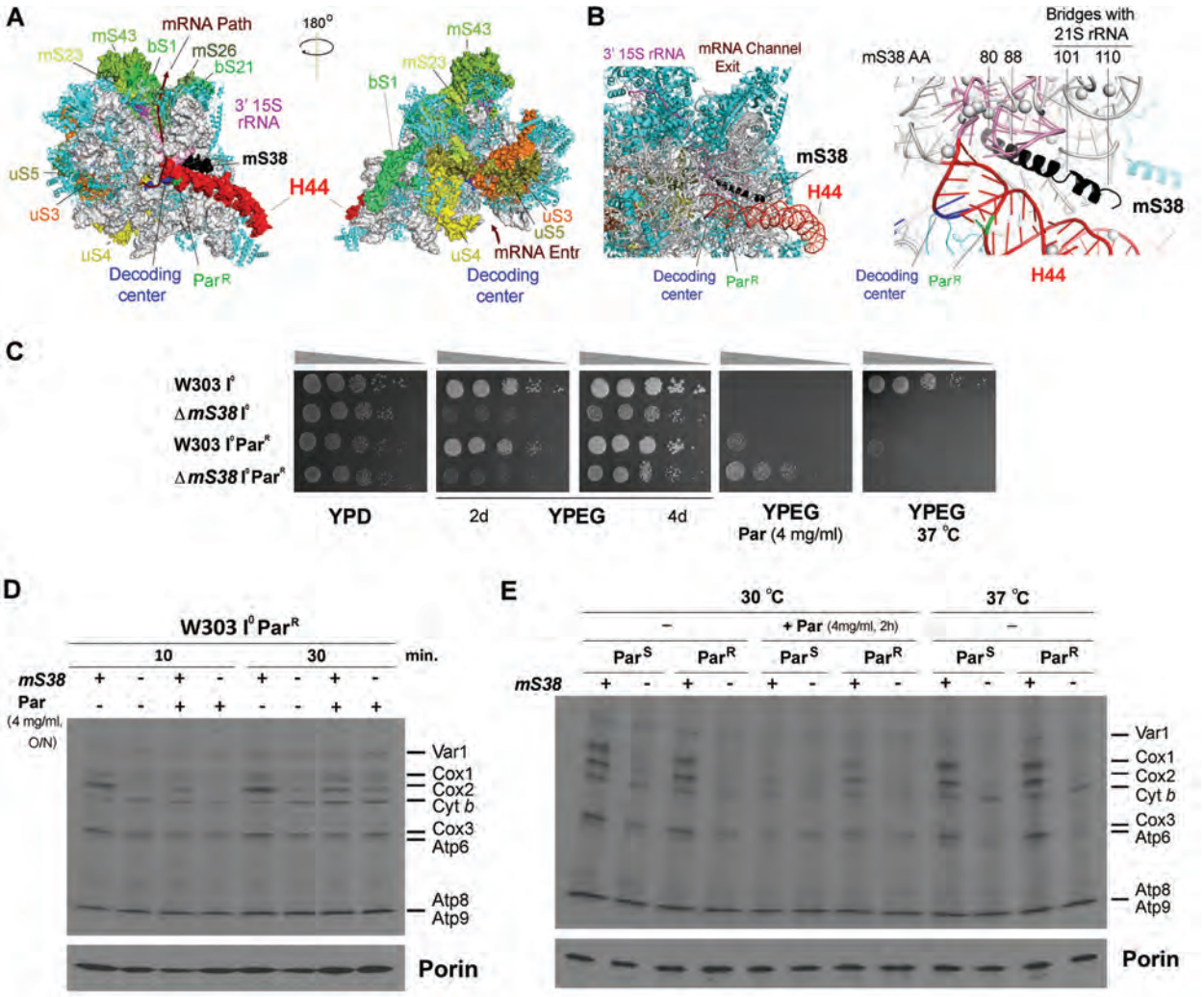

Figure 6. mS38 genetically interacts with mutations in the 15S rRNA helix 44. See also Supplementary Figure S6. (**A**) Localization of the mRNA path in the mtSSU, the proteins located at the entrance and exit channels, as well as mS38, the 15S rRNA helix 44 and the decoding center in the yeast mitoribosome structure (PDB 5MRC) (8). (**B**) Close-up of the mS38-h44 region in the mtSSU structure. The location of the paromomycin-resistance mutation (Par^R) and key amino acids in mS38 are indicated. (**C**) Serial dilutions growth test of the indicated strains in complete fermentable (YPD) or non-fermentable (YPEG) solid media. The effects of paromomycin supplementation and incubation at 37°C were also tested. Pictures were taken after two days of growth or the time indicated. (D, E) *In vivo* mitochondrial protein synthesis of the indicated strains performed as in Figure 2D. In (**D**), the intronless WT (W303 I^0) and Δ*mS38* strains with mtDNA carrying the paromomycin-resistant mutation (Par^R) were incubated or not overnight (ON) in the presence of 4 mg/ml of paromomycin (Par) and pulsed with ^{35}S-methionine for 10 or 30 min. In (**E**), the strains with mtDNA carrying paromomycin-sensitive or resistant 15S rRNA sequences were incubated at 30°C in the presence or absence of 4 mg/ml paromomycin for 2 hrs or 37°C and pulsed for 10 minutes with ^{35}S-methionine in the same conditions.

Once acquired by the mitoribosome, mS38 probably co-evolved with H44 and the downstream 3'-15S rRNA sequences that mark the mRNA exit path. As an example, the mS38 C-terminus is longer in human than in yeast (Figure 7A). Coevolution was tested by assessing heterologous complementation of the *S. cerevisiae* Δ*mS38* strain with *mS38* from human (also known as AURKAIP1) and several yeast and plant species (Supplementary Figure S7A-C). Human mS38 was unable to substitute for the *S. cerevisiae* protein even when the *S. cerevisiae* mS38 N-terminus was co-expressed (Supplementary Figure S7C). Among fungi, mS38 from *Kluyveromyces lactis* and *Yarrowia lipolytica* complemented the *S. cerevisiae* Δ*mS38* strain. Among plants, mS38 from *Arabidopsis thaliana* did it only partially, and that of *Oriza sativa* did not (Supplementary Figure S7A). These results highlight the structural diversity of mitoribosomes across evolution.

In an attempt to dissect the roles of the mS38 N- and C- termini, each half of the protein was expressed in the Δ*mS38* strain. Expression of either mS38 N-domain (aa 1–81) or mS38 C-domain (aa 1–15+81–111), both containing the 15-aa N-terminal mitochondrial targeting sequence, largely restored the respiratory growth defect of the Δ*mS38* strain (Figure 7C) by repairing its general mitochondrial protein synthesis deficiency (Figure 7D). However, translation of *COX1*, *COX2* and *COX3* mRNAs remained slightly inefficient in the $mS38^{1–81}$ strain and more attenuated, particularly *COX1* mRNA translation, in the

Downloaded from https://academic.oup.com/nar/article/47/11/5746/5436776 by UNAM Instituto de Investigaciones Biomédicas user on 20 October 2020

INFORME DE LABORES 2019

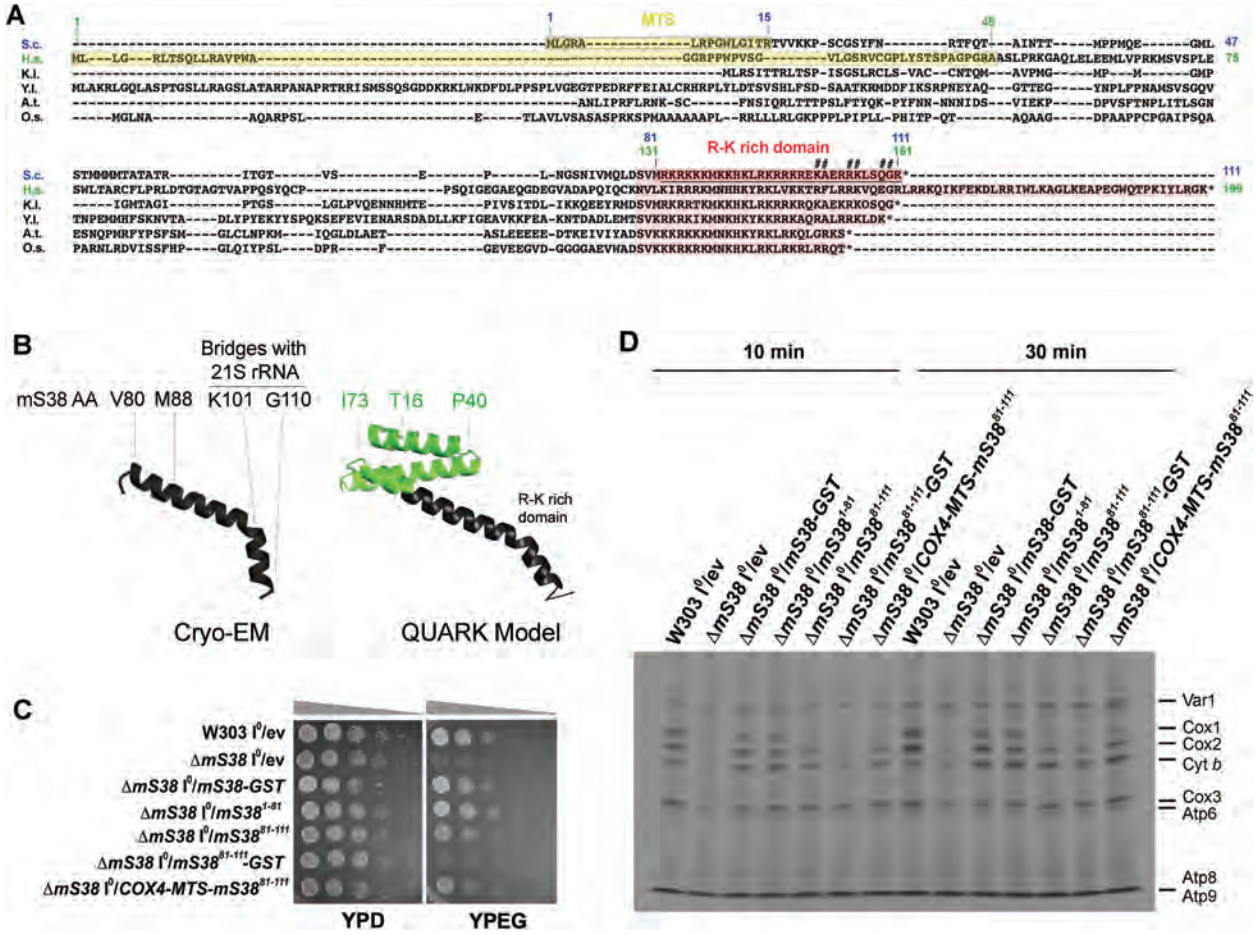

Figure 7. The N- and C-terminal portions of mS38 perform different roles in ribosome assembly and mRNA-specific translation. See also Supplementary Figures S7 and S8. (**A**) Alignment of mS38 sequences from *Saccharomyces cerevisiae (S.c.), Homo sapiens (H.s.),* other yeasts (*Kluyveromyces lactis*—K.l- and *Yarrowia lipolytica*—Y.l.) and plants (*Arabidopsis thaliana*—A.t., *Oriza sativa*—O.s.). The mitochondrial targeting sequence (MTS) in *S.c* and *H.s.* are marked in yellow. The arginine-lysine (R-G)-rich domain present in the C-terminus of all proteins is labeled in red. Numbers in blue indicate amino acids (aa) in the *S. cerevisiae* protein and numbers in green, amino acids in the human protein. The underlined region in *S. cerevisiae* mS38 is the region that was resolved in the cryo-EM structural reconstruction by (8). The # symbol indicates residues in *S. cerevisiae* mS38 involved in the formation of intersubunit bridge mB3 with elements of the 21S rRNA (8). Bridge mB3 is exclusive of mitochondrial ribosomes but conserved from yeast to mammals. (**B**) Structure of *S. cerevisiae* mS38 as obtained by cryo-EM including amino acids 80–111 (8) and a model of the whole mature protein (aa 16–111) obtained using Quark, a computer algorithm for *ab initio* protein structure prediction (39). Key amino acid residues are indicated. (**C**) Serial dilutions growth test of the indicated strains in complete media containing fermentable (YPD) or non-fermentable (YPEG) carbon sources. Pictures were taken after two days of growth at 30°C. (**D**) *In vivo* mitochondrial protein synthesis using the indicated strains and performed as in Figure 2D following ^{35}S-methionine pulses of the indicated increasing times.

mS38$^{81–111}$ strain (Figure 7D). Similar results were obtained using a strain in which mS38$^{81–111}$ contained the first 15 aa in mS38, predicted to form its mitochondrial targeting sequence (MTS), or when a COX4 MTS was used instead (Figure 7D). In the mS38$^{1–81}$ strain, the stability of newly synthesized polypeptides was as in the wild-type (Supplementary Figure S7D), which suggested that the potential presence of large amounts of aberrant proteins resulting from compromised translational fidelity unable to engage in OXPHOS complex assembly could be disregarded.

Together, the data presented in this section indicates that the N- and C-terminal portions of mS38 are each sufficient to functionally stabilize the mitoribosome and facilitate the translation of most mRNAs, including *COX2* and *COX3*. However, the N-terminal portion of mS38, which according to the structure would be expected to contact mtSSU elements that could influence the transit of mRNA throughout the channel, near the exit site, is particularly important for the translation of *COX1* mRNA.

CONCLUSION

A requisite property of all ribosomes is their ability to translate genetic information into polypeptides in an accurate and rapid manner. The SSU elements that ensure translation fidelity in bacteria are conserved in mitochondrial and eukaryotic ribosomes, although some adaptations have occurred. In the mitoribosome, these adaptations include the remodeling of the rRNA H44 and surrounding proteins. The mitochondrion-specific SSU protein mS38 was acquired to stabilize the upper part of H44 where the decoding center is located and to establish the critical mitoribosome-specific intersubunit bridge mB4 with the mt-LSU rRNA

Downloaded from https://academic.oup.com/nar/article/47/11/5746/5436776 by UNAM Instituto de Investigaciones Biomédicas user on 20 October 2020

INFORME DE LABORES 2019

H71. In this work, we report that *S. cerevisiae* mS38 plays an additional fundamental role in the selection of mRNAs that will be translated.

Our data show that although the absence of mS38 in *S. cerevisiae* attenuates mitochondrial protein synthesis globally, it particularly prevents efficient initiation of *COX1, COX2,* and *COX3* mRNA translation.

The analysis of eukaryotic and bacterial ribosomes across species might provide clues regarding mS38 function. Although mS38 is a mitoribosome-specific protein, it has been noticed by Desai and colleagues (8) that the location and structure of mS38 C-terminus resembles eL41, which is more strongly associated with the eukaryotic SSU 40S subunit than with the LSU 60S subunit and forms a eukaryotic-specific intersubunit bridge (eB14) that stabilizes the monosome (8). Therefore, eL41 and mS38 could be the products of convergent evolution. eL41 is not essential, but its absence reduces the binding efficiency of 60S subunits to translation pre-initiation complexes and also decreases peptidyltransferase activity while enhancing translocation efficiency (40). However, no effect of eL41 on selective mRNA translation has been so far reported.

In bacteria, resolution of the structure of the *Mycobacterium smegmatis* 70S ribosome has revealed the existence of a previously unknown protein, bS22, absent in the *E. coli* ribosome, which folds in a manner and occupies a location beneath the mRNA channel similar to mS38, thus indicating a common evolutionary origin (41). Like mitochondrial mS38, mycobacterial bS22 is rich in arginines and lysines, interacts with the rRNA H44 and probably contributes to its stabilization during translocation of tRNAs. Moreover, it has been proposed that contacts of bS22 with H45 might modify the mRNA channel near its exit site immediately upstream of the anti-Shine-Dalgarno sequence (41). Canonical translation initiation in bacteria requires mRNAs with a 5′-UTR and Shine Dalgarno sequence for ribosome assembly and start codon selection. However, the transcriptome of most bacteria contains 1–2% of leaderless mRNAs, and alternative translation mechanisms have been invoked (42). Remarkably, a quarter of the mycobacterial transcriptome is expressed as leaderless and lack both a 5′-UTR and Shine-Dalgarno sequence (43), raising the intriguing possibility that mycobacterial-specific ribosome proteins such as bS22 could facilitate leaderless translation initiation in mycobacteria (42).

Mammalian mitochondrial mRNAs are also leaderless and, although *S. cerevisiae* mitochondrial mRNAs have long 5′-UTR leaders, they lack Shine-Dalgarno sequences, and require transcript-specific translational activators to initiate translation (2). It is tempting to speculate that the acquisition of mS38 by mitochondrial ribosomes co-evolved with the loss of Shine-Dalgarno sequences in the mRNAs. However, it has been recently shown that in mammalian mitochondria, start codon selection could occur by mitoribosome-specific mRNA engagement and subsequent threading of the mRNA into the mRNA channel for start codon-anticodon interactions, which would be stabilized by a domain insertion that is present in the mammalian mitochondrial initiation factor 2 (44). Focusing on *S. cerevisiae*, although the 15S rRNA of yeast mitochondria lacks the Shine-Dalgarno sequence (45), it has been shown to have in its 3' end a 10-nucleotide sequence complementary to different extents with sequences in the 5′ leaders of the messages for *COX1* (10 nt), *COX2* (7 nt), *COX3* (7 nt) and *ATP6* (8 nt) (45). However, yeast mitoribosome structural studies have shown that the 3′ end of the 15S rRNA is not constrained to a position at the mRNA channel exit but extends into the mtSSU body where it is surrounded by mitoribosomal proteins (8). Different from bacteria, a wide V-shaped canyon flanked by mitoribosomal proteins forms at the mRNA channel exit, above which mRNA-specific translational activators may functionally interact (8). The presence of mRNA occupying this canyon during translation initiation would explain ribosome-profiling data, which have shown that the yeast mitoribosome protects longer mRNA stretches during active translation than cytosolic ribosomes (∼38 versus 28 nucleotides) (3). The absence of mS38 in the deletion strain might change the flexibility of the elements forming the mRNA exit channel. Such a modification could affect the transit of specific mRNAs (e.g. *COX1*, *COX2* and *COX3*), perhaps giving them a chance to interact with the 3′ end of the 15S rRNA unproductively or merely misfold, thus jamming the channel.

In conclusion, we propose that mS38 is a core component of the mitoribosomal SSU that may exert regulatory effects by interacting with specific mRNAs and by interfacing with structural elements in the mRNA exit channel to facilitate their correct translation initiation. This hypothesis is reminiscent of the 'ribosome filter' model according to which specific riboproteins would allow the ribosome to interface with specific subsets of mRNAs to regulate their translation (46).

SUPPLEMENTARY DATA

Supplementary Data are available at NAR Online.

ACKNOWLEDGEMENTS

We thank Dr Hyun-Jung Kim for critical reading of the manuscript. We thank Drs Sharon Ackerman, Mario Barros, Thomas D. Fox, Marin Ott, Rosemary Stuart, Alexander Tzagoloff and Dennis Winge for providing reagents.

FUNDING

AHA development grant [14SDG20040003 to F.F.]; NIH-R35 grant [GM118141 to A.B.]; MDA grant [MDA-381828 to A.B.]; PAPIIT-UNAM grant [IN209217 to X.P.M.]. Funding for open access charge: NIH-R35 grant [GM118141].
Conflict of interest statement. None declared.

REFERENCES

1. Hinnebusch,A.G., Ivanov,I.P. and Sonenberg,N. (2016) Translational control by 5′-untranslated regions of eukaryotic mRNAs. *Science*, **352**, 1413–1416.
2. Fontanesi,F. (2013) Mechanisms of mitochondrial translational regulation. *IUBMB Life*, **65**, 397–408.
3. Couvillion,M.T., Soto,I.C., Shipkovenska,G. and Churchman,L.S. (2016) Synchronized mitochondrial and cytosolic translation programs. *Nature*, **533**, 499–503.

Downloaded from https://academic.oup.com/nar/article/47/11/5746/5436776 by UNAM Instituto de Investigaciones Biomédicas user on 20 October 2020

INFORME DE LABORES 2019

4. De Silva,D., Tu,Y.T., Amunts,A., Fontanesi,F. and Barrientos,A. (2015) Mitochondrial ribosome assembly in health and disease. *Cell Cycle*, **14**, 2226–2250.
5. Amunts,A., Brown,A., Bai,X., Llácer,J.L., Hussain,T., Emsley,P., Long,F., Murshudov,G., Scheres,S.H.W. and Ramakrishnan,V. (2014) Structure of the yeast mitochondrial large ribosomal subunit. *Science*, **343**, 1485–1489.
6. Amunts,A., Brown,A., Toots,J., Scheres,S.H.W. and Ramakrishnan,V. (2015) The structure of the human mitochondrial ribosome. *Science*, **348**, 95–98.
7. Greber,B.J., Bieri,P., Leibundgut,M., Leitner,A., Aebersold,R., Boehringer,D. and Ban,N. (2015) Ribosome. The complete structure of the 55S mammalian mitochondrial ribosome. *Science*, **348**, 303–308.
8. Desai,N., Brown,A., Amunts,A. and Ramakrishnan,V. (2017) The structure of the yeast mitochondrial ribosome. *Science*, **355**, 528–531.
9. Zeng,R., Smith,E. and Barrientos,A. (2018) Yeast mitoribosome large subunit assembly proceeds by hierarchical incorporation of protein clusters and modules on the inner membrane. *Cell Metab.*, **27**, 645–656.
10. Bogenhagen,D.F., Ostermeyer-Fay,A.G., Haley,J.D. and Garcia-Diaz,M. (2018) Kinetics and mechanism of mammalian mitochondrial ribosome assembly. *Cell Rep.*, **22**, 1935–1944.
11. Barros,M.H., Myers,A.M., Van Driesche,S. and Tzagoloff,A. (2005) *COX24* codes for a mitochondrial protein required for processing of the *COX1* transcript. *J. Biol. Chem.*, **281**, 3743–3751.
12. Barrientos,A., Korr,D. and Tzagoloff,A. (2002) Shy1p is necessary for full expression of mitochondrial *COX1* in the yeast model of Leigh's syndrome. *EMBO J.*, **21**, 43–52.
13. De Silva,D., Fontanesi,F. and Barrientos,A. (2013) The DEAD-Box protein Mrh4 functions in the assembly of the mitochondrial large ribosomal subunit. *Cell Metab.*, **18**, 712–725.
14. Diaz,F., Barrientos,A. and Fontanesi,F. (2009) Evaluation of the mitochondrial respiratory chain and oxidative phosphorylation system using blue native gel electrophoresis. *Curr. Protoc. Hum. Genet.*, doi:10.1002/0471142905.hg1904s63.
15. Fontanesi,F., Soto,I.C., Horn,D. and Barrientos,A. (2010) Mss51 and Ssc1 facilitate translational regulation of cytochrome *c* oxidase biogenesis. *Mol. Cell. Biol.*, **30**, 245–259.
16. Barrientos,A., Zambrano,A. and Tzagoloff,A. (2004) Mss51p and Cox14p jointly regulate mitochondrial Cox1p expression in *Saccharomyces cerevisiae*. *EMBO J.*, **23**, 3472–3482.
17. Ibrahim,N.G. and Beattie,D.S. (1976) Regulation of mitochondrial protein synthesis at the polyribosomal level. *J. Biol. Chem.*, **251**, 108–115.
18. Herrmann,J.M., Stuart,R.A., Craig,E.A. and Neupert,W. (1994) Mitochondrial heat shock protein 70, a molecular chaperone for proteins encoded by mitochondrial DNA. *J. Cell Biol.*, **127**, 893–902.
19. Meisinger,C., Pfanner,N. and Truscott,K.N. (2006) Isolation of yeast mitochondria. *Methods Mol. Biol.*, **313**, 33–39.
20. Perez-Martinez,X., Broadley,S.A. and Fox,T.D. (2003) Mss51p promotes mitochondrial Cox1p synthesis and interacts with newly synthesized Cox1p. *EMBO J.*, **22**, 5951–5961.
21. Simon,M., Della Seta,F., Sor,F. and Faye,G. (1992) Analysis of the MSS51 region on chromosome XII of *Saccharomyces cerevisiae*. *Yeast*, **8**, 559–567.
22. Perez-Martinez,X., Butler,C.A., Shingu-Vazquez,M. and Fox,T.D. (2009) Dual functions of Mss51 couple synthesis of Cox1 to assembly of cytochrome *c* oxidase in *Saccharomyces cerevisiae* mitochondria. *Mol. Biol. Cell*, **20**, 4371–4380.
23. Pierrel,F., Bestwick,M.L., Cobine,P.A., Khalimonchuk,O., Cricco,J.A. and Winge,D.R. (2007) Coa1 links the Mss51 post-translational function to Cox1 cofactor insertion in cytochrome *c* oxidase assembly. *EMBO J.*, **26**, 4335–4346.
24. Soto,I.C. and Barrientos,A. (2016) Mitochondrial cytochrome *c* oxidase biogenesis Is regulated by the redox state of a heme-binding translational activator. *Antioxid. Redox Signal.*, **24**, 281–298.
25. Guedes-Monteiro,R.F., Ferreira-Junior,J.R., Bleicher,L., Nobrega,F.G., Barrientos,A. and Barros,M.H. (2017) Mitochondrial ribosome bL34 mutants present diminished translation of cytochrome *c* oxidase subunits. *Cell Biol. Int.*, **42**, 630–642.
26. Box,J.M., Kaur,J. and Stuart,R.A. (2017) MrpL35, a mitospecific component of mitoribosomes, plays a key role in cytochrome *c* oxidase assembly. *Mol. Biol. Cell.*, **28**, 3489–3499.
27. Richter-Dennerlein,R., Oeljeklaus,S., Lorenzi,I., Ronsor,C., Bareth,B., Schendzielorz,A.B., Wang,C., Warscheid,B., Rehling,P. and Dennerlein,S. (2016) Mitochondrial protein synthesis adapts to influx of nuclear-encoded protein. *Cell*, **167**, 471–483.
28. De Silva,D., Poliquin,S., Zeng,R., Zamudio-Ochoa,A., Marrero,N., Perez-Martinez,X., Fontanesi,F. and Barrientos,A. (2017) The DEAD-box helicase Mss116 plays distinct roles in mitochondrial ribogenesis and mRNA-specific translation. *Nucleic Acids Res.*, **45**, 6628–6643.
29. Kehrein,K., Schilling,R., Moller-Hergt,B.V., Wurm,C.A., Jakobs,S., Lamkemeyer,T., Langer,T. and Ott,M. (2015) Organization of mitochondrial gene expression in two distinct ribosome-containing assemblies. *Cell Rep.*, **10**, 843–853.
30. Schauder,B. and McCarthy,J.E. (1989) The role of bases upstream of the Shine-Dalgarno region and in the coding sequence in the control of gene expression in Escherichia coli: translation and stability of mRNAs in vivo. *Gene*, **78**, 59–72.
31. Wang,L. and Wessler,S.R. (2001) Role of mRNA secondary structure in translational repression of the maize transcriptional activator Lc(1,2). *Plant Physiol.*, **125**, 1380–1387.
32. Roloff,G.A. and Henry,M.F. (2015) Mam33 promotes cytochrome *c* oxidase subunit I translation in *Saccharomyces cerevisiae* mitochondria. *Mol. Biol. Cell*, **26**, 2885–2894.
33. Mayorga,J.P., Camacho-Villasana,Y., Shingu-Vazquez,M., Garcia-Villegas,R., Zamudio-Ochoa,A., Garcia-Guerrero,A.E., Hernandez,G. and Perez-Martinez,X. (2016) A novel function of Pet54 in regulation of Cox1 synthesis in *Saccharomyces cerevisiae* mitochondria. *J. Biol. Chem.*, **291**, 9343–9355.
34. Haffter,P. and Fox,T.D. (1992) Suppression of carboxy-terminal truncations of the yeast mitochondrial mRNA-specific translational activator *PET122* by mutations in two new genes, *MRP17* and *PET127*. *Mol. Gen. Genet.*, **235**, 64–73.
35. VanLoock,M.S., Agrawal,R.K., Gabashvili,I.S., Qi,L., Frank,J. and Harvey,S.C. (2000) Movement of the decoding region of the 16 S ribosomal RNA accompanies tRNA translocation. *J. Mol. Biol.*, **304**, 507–515.
36. Carter,A.P., Clemons,W.M., Brodersen,D.E., Morgan-Warren,R.J., Wimberly,B.T. and Ramakrishnan,V. (2000) Functional insights from the structure of the 30S ribosomal subunit and its interactions with antibiotics. *Nature*, **407**, 340–348.
37. Yoshizawa,S., Fourmy,D. and Puglisi,J.D. (1999) Recognition of the codon-anticodon helix by ribosomal RNA. *Science*, **285**, 1722–1725.
38. Noah,J.W. and Wollenzien,P. (1998) Dependence of the 16S rRNA decoding region structure on Mg^{2+}, subunit association, and temperature. *Biochemistry*, **37**, 15442–15448.
39. Xu,D. and Zhang,Y. (2012) Ab initio protein structure assembly using continuous structure fragments and optimized knowledge-based force field. *Proteins*, **80**, 1715–1735.
40. Dresios,J., Panopoulos,P., Suzuki,K. and Synetos,D. (2003) A dispensable yeast ribosomal protein optimizes peptidyltransferase activity and affects translocation. *J. Biol. Chem.*, **278**, 3314–3322.
41. Hentschel,J., Burnside,C., Mignot,I., Leibundgut,M., Boehringer,D. and Ban,N. (2017) The complete structure of the *Mycobacterium smegmatis* 70S ribosome. *Cell Rep.*, **20**, 149–160.
42. Sawyer,E.B., Grabowska,A.D. and Cortes,T. (2018) Translational regulation in mycobacteria and its implications for pathogenicity. *Nucleic Acids Res.*, **46**, 6950–6961.
43. Cortes,T., Schubert,O.T., Rose,G., Arnvig,K.B., Comas,I., Aebersold,R. and Young,D.B. (2013) Genome-wide mapping of transcriptional start sites defines an extensive leaderless transcriptome in *Mycobacterium tuberculosis*. *Cell Rep.*, **5**, 1121–1131.
44. Kummer,E., Leibundgut,M., Rackham,O., Lee,R.G., Boehringer,D., Filipovska,A. and Ban,N. (2018) Unique features of mammalian mitochondrial translation initiation revealed by cryo-EM. *Nature*, **560**, 263–267.
45. Li,M., Tzagoloff,A., Underbrink-Lyon,K. and Martin,N.C. (1982) Identification of the paromomycin-resistance mutation in the 15 S rRNA gene of yeast mitochondria. *J. Biol. Chem.*, **257**, 5921–5928.
46. Mauro,V.P. and Edelman,G.M. (2002) The ribosome filter hypothesis. *Proc. Natl. Acad. Sci. U.S.A.*, **99**, 12031–12036.

Downloaded from https://academic.oup.com/nar/article/47/11/5746/5436776 by UNAM Instituto de Investigaciones Biomédicas user on 20 October 2020

3028–3044 *Nucleic Acids Research, 2019, Vol. 47, No. 6* *Published online 30 January 2019*
doi: 10.1093/nar/gkz039

Plant organellar DNA polymerases repair double-stranded breaks by microhomology-mediated end-joining

Paola L. García-Medel[1], Noe Baruch-Torres[1], Antolín Peralta-Castro[1], Carlos H. Trasviña-Arenas[1], Alfredo Torres-Larios[2] and Luis G. Brieba[1,*]

[1]Laboratorio Nacional de Genómica para la Biodiversidad, Centro de Investigación y de Estudios Avanzados del IPN, Apartado Postal 629, Irapuato, Guanajuato, CP 36821, México and [2]Departamento de Bioquímica y Biología Estructural, Instituto de Fisiología Celular, Universidad Nacional Autónoma de México, Circuito Exterior s/n, Ciudad Universitaria, Apartado postal 70-243, Mexico City 04510, México

Received June 14, 2018; Revised December 23, 2018; Editorial Decision January 14, 2019; Accepted January 15, 2019

ABSTRACT

Double-stranded breaks (DSBs) in plant organelles are repaired via genomic rearrangements characterized by microhomologous repeats. These microhomologous signatures predict the existence of an unidentified enzymatic machinery capable of repairing of DSBs via microhomology-mediated end-joining (MMEJ) in plant organelles. Here, we show that organellar DNA polymerases from *Arabidopsis thaliana* (AtPolIA and AtPolIB) perform MMEJ using microhomologous sequences as short as six nucleotides. AtPolIs execute MMEJ by virtue of two specialized amino acid insertions located in their thumb subdomains. Single-stranded binding proteins (SSBs) unique to plants, AtWhirly2 and organellar single-stranded binding proteins (AtOSBs), hinder MMEJ, whereas canonical mitochondrial SSBs (AtmtSSB1 and AtmtSSB2) do not interfere with MMEJ. Our data predict that organellar DNA rearrangements by MMEJ are a consequence of a competition for the 3′-OH of a DSBs. If AtWhirlies or AtOSBs gain access to the single-stranded DNA (ssDNA) region of a DSB, the reaction will shift towards high-fidelity routes like homologous recombination. Conversely MMEJ would be favored if AtPolIs or AtmtSSBs interact with the DSB. AtPolIs are not phylogenetically related to metazoan mitochondrial DNA polymerases, and the ability of AtPolIs to execute MMEJ may explain the abundance of DNA rearrangements in plant organelles in comparison to animal mitochondria.

INTRODUCTION

Plant organellar genomes encode for macromolecular assemblies indispensable for oxidative phosphorylation and photosynthesis (1–3). Thus, faithful organellar replication and regulated transcription are necessary for cell survival. Contrary to the representation of a circular structure as the predominant form of mitochondrial DNA, plant mitochondrial genomes are heterogeneous linear molecules with a strong tendency to produce rearrangements (4–7). The notion that plastid DNA exists as a circular molecule is challenged by findings of linear molecules in maize seedlings and in *Medicago truncatula* (4,8,9). Although the mechanisms that mediate plant organellar DNA replication are unknown, DNA rearrangements in plant organelles are common and are attributed to the repair of double-strand breaks (DSBs) (6,10–14).

Repair of DSBs occurs by two main pathways: homologous recombination (HR) and non-homologous end joining (NHEJ) (Reviewed in (15)). HR is an error-free pathway in which identical DNA segments are used as templates. In contrast, NHEJ is an error-prone pathway. NHEJ is divided into two sub-pathways: Ku-dependent classical non-homologous end joining (c-NHEJ) and alternative end joining (alt-EJ). A subset of DNA breaks repaired by alt-EJ employs a mechanism that requires minimal base pairing of microhomologous sequences, dubbed microhomology-mediated end joining (MMEJ) (16–18).

MMEJ was discovered as a sub-pathway derived from the Archaeo-Prokaryotic (AP)-NHEJ. Within this sub-pathway bacterial DNAPs promote synapsis of DSBs using short microhomologous sequences, these annealed sequences assemble the 3′-OH primers and are extended by virtue of strand-displacement synthesis by specialized DNAPs

*To whom correspondence should be addressed. Tel: +52 462 166 3007; Email: luis.brieba@cinvestav.mx

© The Author(s) 2019. Published by Oxford University Press on behalf of Nucleic Acids Research.
This is an Open Access article distributed under the terms of the Creative Commons Attribution Non-Commercial License (http://creativecommons.org/licenses/by-nc/4.0/), which permits non-commercial re-use, distribution, and reproduction in any medium, provided the original work is properly cited. For commercial re-use, please contact journals.permissions@oup.com

Downloaded from https://academic.oup.com/nar/article/47/6/3028/5304310 by UNAM user on 20 October 2020

(19,20). Eukaryotic DNA polymerases θ (HsPolθ), β, λ and μ, also perform MMEJ using short microhomologous sequences. As in bacterial MMEJ, the proposed DSB repair mechanism involves annealing of microhomologous sequences in *trans* to create a template DNA synapse and nucleotide extension (21–24). Crystal structures of DNAPs during MMEJ illustrate that they promote the stabilization of microhomologous sequences via unique structural elements that mediate synapse formation (19,25,26).

The plant mitochondrial genome frequently recombines via homologous recombination of large size (>500 bp) or intermediate size repeats (50–500 bp). Break-Induced Replication (BIR) and Single-Strand Annealing (SSA) are postulated to drive illegitimate recombination events at intermediate size repeats (6,27,28). However, plant organellar genomes also undergo rearrangements attributed to illegitimate recombination at intermediate size repeats (>50 base pairs) (6,11,12,27,29–33). These rearrangements are associated with MMEJ, microhomology-mediated break-induced replication (MMBIR) and microhomology-mediated recombination (12,28–30). DSBs in Arabidopsis´ chloroplasts, generated by ciprofloxacin or by a homing endonuclease, are repaired using microhomologous sequences that rank between 4 and 18 nts (29,31,32). The nature of the sequences at the junctions of the DNA rearrangements indicates that DSBs are repaired by a route that involves annealing of microhomologous sequences. The length of these microhomologies resembles the length of microhomologous segments in metazoan DNA repaired by MMEJ (17) or MMBIR (34).

Flowering plants harbor two organellar family-A DNA polymerases, known as plant and protist DNA polymerases (POPs) that are not phylogenetically related to yeast or metazoan mitochondrial DNA polymerase γ and are the sole DNAPs in plant organelles (35–39). Both AtPolIs display lower nucleotide insertion fidelity that metazoan mitochondrial DNAPs, elongate RNA primers synthesized by the organellar DNA primase-helicase and harbor strand-displacement and 5′-deoxyribose phosphate lyase activities (29,40–43). From the DNAPs able to execute MMEJ, HsPolθ is the only one that belongs to the family-A of DNAPs. This enzyme harbors a polymerization domain linked to a helicase domain and seminal work demonstrated that both domains participate in MMEJ (44,45). Structure-function studies of HsPolθ indicate that a specific insertion in its polymerization domain is responsible for MMEJ (21) The ortholog of HsPolθ in plants (24), TEBICHI, is involved in T-DNA random integration by MMEJ (46,47). Although TEBICHI participates in nuclear MMEJ, a mechanism for MMEJ has not been identified in plant organelles.

AtPolIs and HsPolθ bypass DNA lesions via unique amino acid insertions in their polymerization domain (25,40). Because of this convergence, and the necessity of a unique amino acid insertion in HsPolθ to execute MMEJ (21,48), we wanted to determine whether AtPolIs could execute MMEJ. To our surprise, AtPolIs are able to efficiently mediate synapsis formation on microhomologies as short as 6-bp. We found that members of the single-stranded binding proteins unique to plants, Whirly-2 and Organellar Single-stranded DNA Binding proteins (OSBs), inhibit MMEJ by competing with the single-stranded overhang. In contrast, mtSSBs do not interfere with MMEJ formation. Our results indicate the MMEJ in plant organelles is mediated by the available concentration of single-stranded binding proteins and AtPolIs.

MATERIALS AND METHODS

Cloning of recombinant Single-Stranded DNA-Binding proteins

The coding regions corresponding to processed AtOSB2 (AT4G20010), AtOSB3 (AT5G44785), AtWhirly2 (AT1G71260), AtmtSBB1 (AT4G11060.1), AtmtSSB2 (AT3G18580.1) were PCR amplified from cDNA. The PCR products were digested and cloned into a modified pET19b or pET28b vectors. Positive clones were verified by DNA sequencing.

Expression and purification of recombinant proteins

In this study, we use recombinant AtPolIs that lack their first 257 amino acids. Those residues correspond to a dual targeting sequence (DTS) and a disordered region. Removal of those amino acids increases protein yield during heterologous purification without affecting exonucleolytic degradation or DNA polymerization (40) Thus, recombinantly expressed AtPolIs contain intact 3′-5′ exonuclease and polymerization domains, as metazoan DNAP γ and the Klenow fragment of bacterial DNAPs. The 3′-5′ exonuclease deficient variants of AtPolIs substitute two invariant carboxylates in exonuclease motif I of AtPolIA (D294 and D296) and AtPolIB (D287 and D289) to alanine. Exonuclease deficient AtPolIB (AtPolIB exo$^-$) was used as template to construct deletions in the unique insertions present in AtPolIs. The AtPolIB variant with a deletion in insertion 1 (AtPolIB-Δins1) eliminates residues 581 to 619, AtPolIB-Δins2 eliminates residues 648 to 712, and AtPolIB-Δins2 eliminates residues 845–869. All mutant polymerases are readily purified using three chromatographic steps (40) (Supplementary Figure S1).

AtmtSSB2 was purified following published protocols (49). Recombinant AtmtSSBs, AtOSB2, AtOSB3, and AtWhirly2 were expressed using an *Escherichia coli* BL21 PKJE7 strain. Cell cultures were grown until they reached an OD_{600} of 0.6 and were induced with 0.5 mM IPTG (isopropyl-1-thio-β-D-galactopyranoside) at 16°C during 18 h. Cells were recollected by centrifugation at 4°C and resuspended in 30 ml lysis buffer (25 mM HEPES pH 8, 600 mM NaCl, 10 mM imidazole, 10% glycerol and 1 mM PMSF). The lysate was supplemented with lysozyme 0.5 mg/ml and sonicated on ice. The clear lysate was filtrated and loaded onto a Ni-NTA column. The column was washed with lysis buffer containing 30 mM imidazole. Proteins were eluted using lysis buffer supplemented with 500 mM imidazole and dialyzed in buffer A (25 mM HEPES pH 8, 50 mM NaCl, 2 mM EDTA, 30% glycerol and 5 mM DTT). SSBs were loaded into a Hi-Trap heparin column, and further purified using a 0.1 M to 1 M NaCl gradient. Pure fractions were stored into a buffer B (25 mM HEPES pH 8.0, 100 mM NaCl, 2 mM EDTA, 50% glycerol and 5 mM DTT) at −20°C.

Downloaded from https://academic.oup.com/nar/article/47/6/3028/5304310 by UNAM user on 20 October 2020

INFORME DE LABORES 2019

Substrates

5′-End oligonucleotide labeling was performed with T4 polynucleotide kinase using [γ-^{32}P] ATP and purified with Nucleotide Removal Kit following manufacture's protocol. Oligonucleotides used for the MMEJ assay are described in Supplementary Table S1.

Microhomology-mediated end joining (MMEJ) assays

MMEJ assays were performed at 37°C using 20 nM 5′-end radiolabeled pssDNA, in a buffer containing 10 mM Tris–HCl pH 7.5, 50 mM NaCl, 1.5 mM DTT, 10% glycerol and 0.1 mg/ml BSA. The mix was incubated with 100 nM AtPolIs for 15 min and then supplemented with 500 μM of dNTPs and 10, 6 or 2 mM $MgCl_2$ for 30 min. The reactions were terminated using a stop buffer (95% formamide, 10 mM EDTA, 0.1% bromophenol blue and 0.1% xylene cyanol). The reactions were loaded on a 17% polyacrylamide denaturing gel and analyzed by phosphorimaging. In the MMEJ assay with singled-stranded DNA binding proteins, the same labeled pssDNA substrates were at 5 nM and AtSSBs were present at the concentrations described in the figure legends.

Electrophoretic-mobility shift assay (EMSA)

To investigate the binding of plant SSB to ssDNA we use a radioactively labeled poly-T of 70 nts oligonucleotide. Reactions were incubated in buffer containing 10 mM Tris–HCl pH 7.5, 50 mM NaCl, 1.5 mM DTT, 10% glycerol, 0.1 mg/ml BSA, 10 mM $MgCl_2$, using varying concentrations of SSBs. The reactions were run on 4% polyacrylamide nondenaturing gel at 4°C and visualized by phosphorimaging.

Fluorescence anisotropy binding assay

Dissociation constant (K_d) were measured using a fluorescein-labeled ssDNA of 45 nts ($ssDNA_{(45)}$) or a Cy3-labeled pssDNA-10 in 10 mM Tris–HCl pH 7.5, 50 mM NaCl, 0.05 mg/ml BSA,10% glycerol and 10 mM $MgCl_2$. Increased concentration of purified proteins (AtmtSSB1, AtOSB2 and AtWhy2) were individually evaluated. The reactions were incubated at 25°C in darkness during 20 min. Changes in anisotropy were quantified on an Infinite M1000 Microplate Reader (Tecan®) using excitation and emission wavelength (λ) of 470 and 525 nm, respectively. The data were analyzed using GraphPad Prism 6 according to the specific binding with Hill slope model following this equation: $Y = B_{max}*X^h/(K_d{}^h + X^h)$, where B_{max} indicates the maximum number of binding sites, K_d refers to ligand concentration that binds to half the receptor sites at equilibrium and h is the Hill slope.

Fluorescence resonance energy transfer (FRET) assay

For evaluation of DNA synapsis formation, oligonucleotides labeled with different fluorescence probes (Cy3 and Cy5) were annealed as described in the figure legends. Titration experiments were performed using equimolar concentration of labeled DNA (50 nM) with increasing concentrations of AtPolIs. Variations in fluorescence intensity upon incubation of AtPolIs were measured in an Infinite M1000 microplate reader using wavelengths (λ) of 530 nm for excitation and 675 nm for emission. Reactions were incubated in 10 mM Tris–HCl pH 7.5, 50 mM NaCl, 1.5 mM DTT, 10% glycerol, 0.1 mg/ml BSA and varying concentrations of AtPolIs. The reactions were incubated for 20 min in darkness at 25°C by triplicate. The data were normalized and analyzed in GraphPad Prism 6.

Gel filtration analysis

The elution profiles of plant SSBs in solution were evaluated using gel filtration. The proteins were injected into a Superdex 75 10/300 column equilibrated with 20 mM HEPES pH 8.0, 200 mM NaCl, 10% glycerol, 2 mM EDTA and 1 mM DTT. Elution peaks were analyzed using molecular weight markers.

Homology model

The homology model of AtPolIB was carried out using the homology modeling platform of the Swiss-Model Workspace (50) using as templates the Klenow fragments from the crystal structures of *Thermus aquaticus*, *Geobacillus stearothermophilus* and *Geobacillus kaustophilus*. From those homology models, we selected the one generated with the crystal structure of *G. kaustophilus* DNAP I in complex with dsDNA (PDB: 4DSE), because this model positions insertions 1 and 3 in an optimal position to interact with dsDNA.

SEC-MALS analysis

The SEC-MALS analysis was performed on a DAWN HELEOS multi-angle light scattering detector, with eighteen angles detectors and a 658.9 nm laser beam, (Wyatt Technology, Santa Barbara, CA, USA) and an Optilab T-rEX refractometer (Wyatt Technology) in-line with two coupled Superdex 200 Increase 10/300 GL size exclusion chromatography analytical columns. Experiments were performed using an isocratic pump (Agilent) with a flow of 0.5 ml/min at room temperature (25°C). Data collection was performed with ASTRA 6.1 software (Wyatt Technology). For the experiments, 300 μl at 1.3 mg/ml protein were loaded on the columns with running buffer of 25 mM HEPES pH 8, 10% glycerol, 300 mM NaCl and 2 mM EDTA. Calibration was performed with high-molecular weight markers from GE Healthcare (thyroglobulin, 669 000 Da; ferritin, 440 000 Da; aldolase, 158 000 Da; conalbumin, 75 000 Da; and ovoalbumin, 43 000 Da).

Strand-displacement assays

A 65mer DNA template (5′-CCT TGG CAC TAG CGC ACG ATG CCG CTA AGA ACC TCA GGG CCA GTT AGG TGG GCA GGT GGG CTG CG-3′) was annealed with a 5′-end radioactively labeled 24mer primer (5′-CGC AGC CCA CCT GCC CAC CTA ACT-3′) and a DNA blocking oligonucleotide (5′-GA GGT TCT TAG CGG CAT CGT GCG CTA GTG CCA AGG-3′) to create a gap of 6 nucleotides. Reactions were run at 37°C mixing 10 mM

Downloaded from https://academic.oup.com/nar/article/47/6/3028/5304310 by UNAM user on 20 October 2020

Tris–HCl pH 7.5, 50 mM NaCl, 0.2 mg ml^{-1} BSA, 1.5 mM DTT, 2 mM $MgCl_2$, 10% glycerol, 10 nM DNA substrate, 20 nM DNA polymerases and initiated adding 200 μM of dNTPs.

MicroScale Thermophoresis (MST)

MST analysis of the interactions between AtPolIB exo$^-$ and plant SSB's was carried out as follows. AtPolIB was purified with a 10× histidine tag at the N terminal and labeled using NanoTemper's Monolith His-Tag Labeling Kit RED-Tris-NTA at 100 nM. SSB's were purified and their His-tag was removed by addition of precision protease and gel filtration. SSBs were titrated against labeled AtPolIB in 16 serial dilutions from initial concentrations of 150, 200 and 250 μM for AtmtSSB1, AtOSB2 and AtWhy2, respectively. Reactions were incubated for 10 min at 25°C in PBS buffer + 0.05% Tween™ 20. The measurements were performed using a NanoTemper Monolith NT.115 pico instrument. Analyses were conducted at 10% LED power and 50% MST power on standard capillaries.

RESULTS

AtPolIs execute MMEJ on partially resected DSBs

Pioneering work by Herrin and Brisson´s laboratories revealed that DSBs in chloroplast are repaired using illegitimate recombination mechanisms attributed to MMEJ (12,29–31,33). The predicted melting points for several of those microhomologies is <37°C (51) (Figure 1A), suggesting that protein factors may be involved in stabilizing the annealing of microhomologous sequences that are repaired by MMEJ during DSBs. Plant organelles in *A. thaliana* harbor only two DNA polymerases, AtPolIA and AtPolB that have as a distinctive feature the presence of three insertions in their polymerization domain.

Given that HsPolθ performs TLS and MMEJ by a specific amino acid insertion and that unique amino acid insertions are responsible for TLS activity in AtPolIs, we hypothesize that AtPolIs may perform MMEJ via unique amino acid insertions (21,40). To investigate the putative MMEJ capabilities of AtPolIs, we used recombinant AtPolIA and AtPolIB harboring amino acid deletions of their first 257 amino acids. Those amino acids correspond to a predicted disordered protein region and their removal increases the yield of recombinant active protein (40). Thus, recombinant AtPolIs harbor both 3′-5′ exonuclease and polymerization domain activities (Figure 1B). The initial substrate used to test MMEJ, consisted of a partially resected DSB (pssDNA) with a 5′-CCCCGGGG-3′overhang sequence of 8 nts (pssDNA-8) with a predicted Tm for the microhomologous region of 22.5°C (Figure 1C). This substrate was formerly used to asses MMEJ formation by HsPolθ (21,48).

Synapse formation, followed by polymerization on the single-stranded portion of the template and strand-displacement would generate a MMEJ product of 56 nts (Figure 1C). MMEJ reactions were initially executed using 10 mM of $MgCl_2$ and 2 mM of $MnCl_2$, as those are optimal metal concentrations during primer extension on a canonical primer-template (data not shown) and high nucleotide concentrations (500 μM). Reaction products of 56 and 57 nts product were synthetized by exonuclease proficient AtPolIs, in the presence of Mg^{2+} (Figure 1D, lanes 2–5), whereas products of 56–58 nts were synthetized in reactions incubated with Mn^{2+} (Figure 1D, lanes 6–9). The presence of Mg^{2+} promotes the addition of an extra base, whereas incubation with Mn^{2+} promotes the addition of two extra bases, possibly due to terminal transferase activity. Thus, reactions incubated with pssDNA-8 generate MMEJ products in the presence of AtPolIs harboring an active exonuclease domain or exonuclease deficient DNAPs (Figure 1D). AtPolIs incubated with Mn^{2+} exhibit an increase in their 3′-5′ exonuclease activity. The exonuclease activity of AtPolIs is halted after digestion of 16 nts, at the boundary of the double-stranded DNA template (Figure 1D, lanes 2–9). Disruption of the exonuclease activity by site-directed mutagenesis in AtPolIs increases MMEJ activity, resulting in the appearance of a MMEJ product of 58 nts (Figure 1C, lanes 11–18).

In order to asses if AtPolIs could execute MMEJ at physiological nucleotide concentrations, we used a pssDNA-8 substrate that templates for 20 consecutive thymines or adenines, after the assembly of the MMEJ substrate. In this experiment, we used nucleotide concentrations that rank from 0.0037 to 245.76 μM (Figure 2A). At low micromolar dATP or dTTP concentrations (Figure 2A and B, lanes 2–5 and 12–15) a single MMEJ product of 56 nts is observed. At higher nucleotide concentrations, a band of 57 nts is shown in reactions incubated with dTTP and a band of 58 nts is observed in reactions incubated with dATP (Figure 2A and B, lanes 7–10 and 17–20). AtPolIB exhibits a nearly 20-fold higher K_M for dNTP during nucleotide incorporation on a canonical primer-template substrate with respect to AtPolIA (43). Thus, the observation that AtPolIA and AtPolIB exhibit similar MMEJ efficiency during all the assayed dNTP concentrations suggests that during MMEJ annealing the mechanism that dictates the affinity of the incoming nucleotide differs from the one during primer-template incorporation.

In order to determine the minimal microhomologous length in which AtPolls are able to execute MMEJ, we performed MMEJ reactions using substrates than contained microhomologies from 0 to 12 nts. We initially used similar reaction conditions to those previously reported for HsPolθ, but with the addition of 50 mM NaCl (21). Full nucleotide incorporations on these pssDNA substrates are designed to generate products from 54 to 98 nts, and only a pssDNA substrate containing a microhomology of 12 nts (pssDNA-12) exhibits a T_m higher than 37°C (Figure 2A).

The Klenow Fragment of *E. coli* DNA polymerase I (KF-DNAP I) control generates faint products of approximately 56 and 98 nts in reactions incubated with pssDNA-8 and pssDNA-12 and not with any other pssDNA substrates, indicating that transient alignment of the microhomologous sequence does not form a stable substrate for DNAPs (Figure 2B, lanes 18–21). This result contrasts with a previous report in which KF-DNAP I generates low molecular weight MMEJ products on a pssDNA containing a microhomology of 4nts (pssDNA-4) (21). Thus, exonuclease deficient KF-DNAP I is unable to efficiently use pssDNAs as substrates, including a pssDNA-12 substrate. In contrast, wild-type (AtPolIB exo$^+$) and exonuclease deficient

Downloaded from https://academic.oup.com/nar/article/47/6/3028/5304310 by UNAM user on 20 October 2020

INFORME DE LABORES 2019

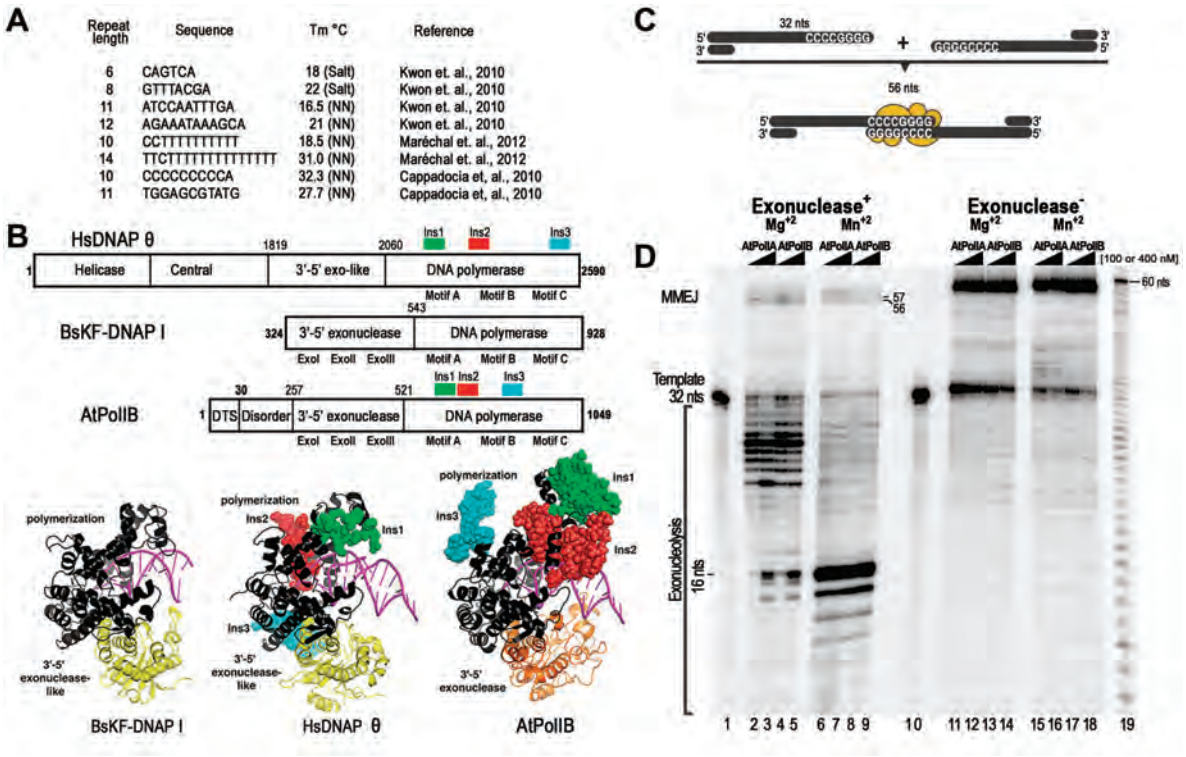

Figure 1. AtPolIs mediate MMEJ *in vitro*. (**A**) Representative microhomologous sequences present in chloroplast DNA from *A. thaliana* upon DSB repair (30–32). The calculated melting temperature (T_m) for single-stranded regions shorter than 8 nts were calculated using the salt-adjusted method (salt) and regions longer than 8 nts were calculated using the Nearest Neighbor (NN) method (51). (**B**) Structural comparison between a homology model of AtPolIs with the crystal structures of HsPolθ (25) (PDB: 4x0Q) and the Klenow fragment of *Bacillus* DNAP I (68) (PDB: 3BDP). The polymerization domains are colored in black, the active 3′-5′ exonuclease domain of AtPolIB in orange and the inactive 3′-5′ exonuclease domains of HsPolθ and *Bacillus* DNAP I in yellow. The unique amino acid insertions in HsPolθ and AtPolIB in comparison to bacterial DNAPs I are depicted in a ball-stick representation. In all DNAPs the dsDNA (magenta) is poised for nucleotide incorporation. (**C**) Proposed arrangement of a micromologous sequence of 8 nts showing DNA synapse formation and extension upon dNTPs incorporation by MMEJ. (**D**) Denaturing polyacrylamide gel showing MMEJ reactions catalyzed by wild-type and exonuclease deficient AtPolIs present at concentration of 100 or 400 nM. In the presence of Mg^{2+} or Mn^{2+}. AtPolIs extend the pss-DNA(8) substrate to MMEJ products of 56, 57 and 58 nts. The migration of the MMEJ products of 56, 57 and 58 nts and the pss-DNA(8) substrate are indicated.

AtPolIB (AtPolIB exo$^-$) efficiently use substrates with microhomologous sequences of 8 nts (pssDNA-8) to perform MMEJ (Figure 2B, lanes 1 to 16). A MMEJ product is not observed in reactions incubated with pssDNA-6, pssDNA-4, pssDNA-2, and pssDNA-0 substrates (Figure 2B, lanes 11, 12 and 13). The predicted Tms of the microhomologous regions in pssDNA-6 and pssDNA-8 are <37°C, suggesting that spontaneous template annealing is unfavorable and that MMEJ is mediated by AtPolIB. As the editing activity of AtPolIs hampers MMEJ, we subsequently utilized exonuclease deficient variants of AtPolIs to investigate their MMEJ properties.

AtPolIs exhibited limited terminal deoxynucleotidyl transferase activity

In the presence of high nucleotide concentrations, AtPolIs generate MMEJ products with additional non-templated nucleotides residues at the 3′ end (Figure 2A, lanes 6–10 and 16–20). Bacterial family-A DNAPs, like Taq DNA polymerase (Taq DNAP), present limited non-templated nucleotide or terminal transferase activity. In this reaction, one or two nucleotides, preferentially dATP, are added to a 3′-OH primer (52). In contrast, HsPolθ and terminal deoxynucleotidyl transferases exhibit a robust terminal transferase activity and are able to add several nucleotides the 3′-OH primer (48,53). To test the efficiency of the predicted terminal transferase activity by AtPolIs, we used three different substrates: a homopolymeric ssDNA poly-dT, a double-stranded blunt-ended DNA substrate, and a MMEJ substrate (Figure 3). AtPolIB exo$^-$ fails to incorporate any nucleotide having as a substrate a poly-dT oligonucleotide in the presence of individual nucleotides or in the presence of all nucleotides (Figure 3A). In contrast, AtPolIB exo$^-$ exhibits limited terminal transferase activity catalyzing the addition of one or two nucleotides on a double-stranded blunt-ended DNA substrate (Figure 3B). This activity is reminiscent of the limited terminal transferase exhibited by Taq DNAP. In the presence of Mg^{2+} as cofactor AtPolIB exo$^-$ efficiently incorporates two non-templated dAMP molecules (Figure 3B, lane 2), whereas all other nucleotides are incorporated only once (Figure 3B). AtPolIB exo$^-$ also shows limited terminate transferase activity when $MgCl_2$ is used as a cofactor (data not shown). In a MMEJ substrate, AtPolIB exo$^-$ synthesizes products that rank from 56 to 58 nts. This product corresponds to the annealing of the pssDNA-8 substrates plus the addition of two extra nucleotides. Using individual nucleotides, we

Downloaded from https://academic.oup.com/nar/article/47/6/3028/5304310 by UNAM user on 20 October 2020

INFORME DE LABORES 2019

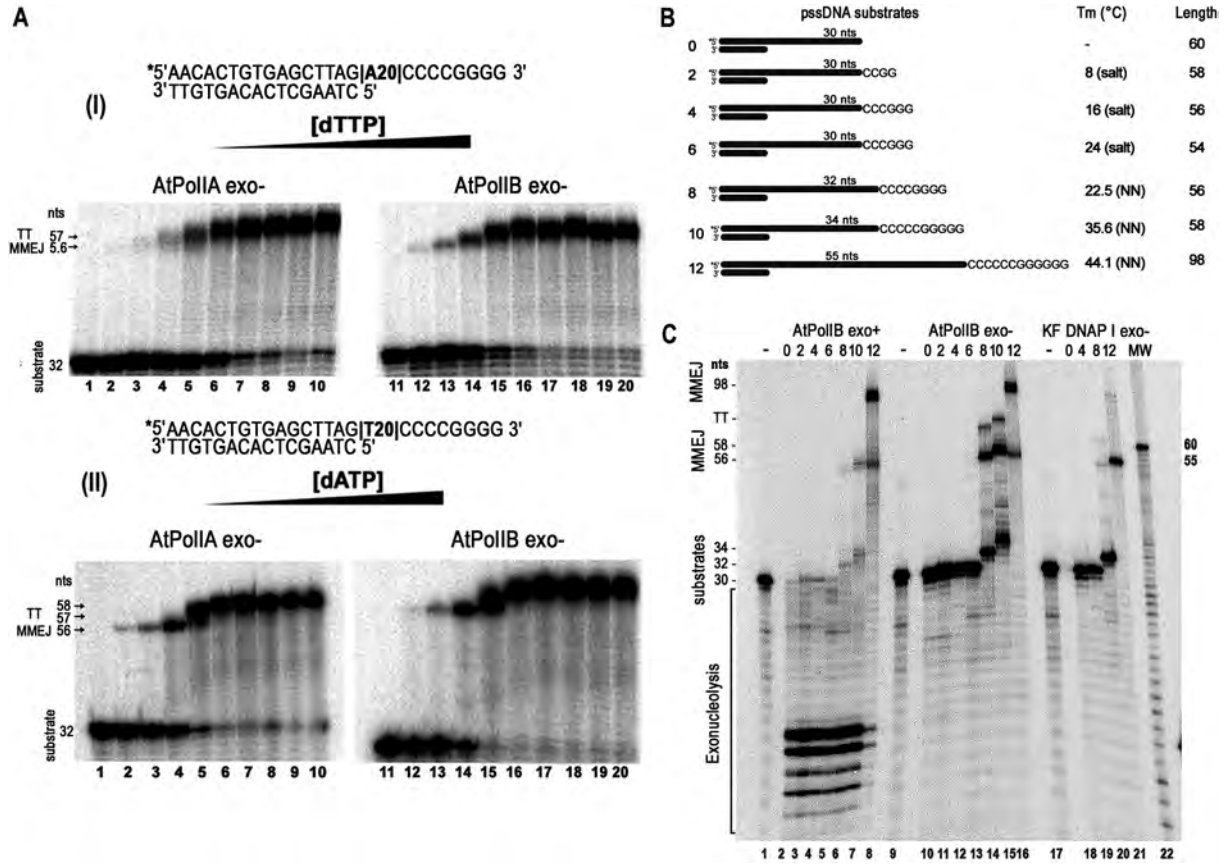

Figure 2. AtPolIs performs MMEJ using microhomology sequence longer than 8 nts at high $MgCl_2$ concentrations. (**A**) Exonuclease deficient AtPolIs execute MMEJ on a pss-DNA(8) substrate at physiological dNTP concentrations. Reactions incubated in the absence of dNTPs (lanes1 and 11) show the migration o the labeled substrate. MMEJ reactions were incubated using increasing dTTP (panel I) or dATP (panel II) from 0.0037 to 245.76 μM using four-fold increments (lanes 2–10 and 12–20). At low micromolar dNTP concentrations (lanes 2–5 and 12–15) a MMEJ product of 56 nts is observed. In contrast, a band of 57 nts is observed in reactions incubated with dTTP using high nucleotide concentrations and a band of 58 nts is observed in reactions incubated with high concentrations of dATP. (**B**) Schematic representation of the pssDNAs substrates used for MMEJ assays. Asterisks indicate the position of the 5′-radioactive label. The microhomology lengths (from 0 to 12 nts), the calculated Tm for DNA synapsis formation and the expected lengths of the MMEJ product are indicated at the right. (**C**) Denaturing sequencing gel showing MMEJ reactions by wild-type (lanes 2–8) and exonuclease deficient (lanes 10–16) AtPolIBs in comparison to reactions incubated with the exonuclease deficient Klenow Fragment of DNAP I (lanes 18–21). Al reactions contained 10 mM $MgCl_2$ as a cofactor. A control labeled substrate corresponding to pss-DNA(8) is present in lanes 1, 9 and 17. MMEJ products are observed in reactions incubated with AtPolIBs on substrates with microhomologies longer than eight nucleotides (lanes 6, 7, 8, 14, 15, 16). These products correspond to bands of 56, 58 and 98 nts respectively. In contrast, Klenow Fragment is unable to efficiently use MMEJ substrates and only low amounts of products are formed with pssDNAs of 8 and 12 nts (lanes 20 and 21). TT denotes products generated by a predicted terminal transferase activity.

observed an efficient nucleotide incorporation only when dCTP is present in the reaction (Figure 3C, lane 4). The pssDNA-8 substrate poises a template guanosine as the first template base after the annealing of the microhomologous CCCCGGGG sequence. The incorporation of two dCMPs on this substrate may be related to the low fidelity during nucleotide incorporation by AtPolIB (43) or to a transient misalignment of the 3′-OH (Figure 3C).

In order to discern if the observed MMEJ products could be due to a template-dependent extension in *cis* (snap-back replication), we used a single-stranded pssDNA-8 substrate in the presence of individual nucleotides. In this experiment, the single-stranded oligonucleotide is predicted to assemble a primer-template by the annealing of four cytidines and four guanosines in *cis* (Figure 3D). This snap-back assembly is predicted to position a template guanosine for dCMP incorporation. In the presence of dCTP both AtPolIs incorporate multiple dCMPs (Figure 3D, lanes 5 and 11) possible due to a misalignment of the primer-strand. The presence of products derived from the incorporation of multiple cytidines on a single-stranded template contrast with the incorporation of two dCMPs in a pssDNA-8 substrate predicted to form a synapse (Figure 3C, lane 5). In the sole presence of dGTP, AtPolIs efficiently incorporate a dGMP molecule, possibly due to an alignment of only three cytidines with three guanosines that generate that a cytidine poised for dGTP incorporation (Figure 3C, lanes 6 and 12).

AtPolIs use substrates with microhomologies longer than 6 nts

DSBs are repaired using microhomologous sequences as short as four nts in chloroplasts (30,32), suggesting that the machinery responsible of MMEJ should efficiently anneal pssDNA with short microhomologous regions. To investigate if AtPolIB exo$^-$ could perform MMEJ on these sub-

Downloaded from https://academic.oup.com/nar/article/47/6/3028/5304310 by UNAM user on 20 October 2020

INFORME DE LABORES 2019

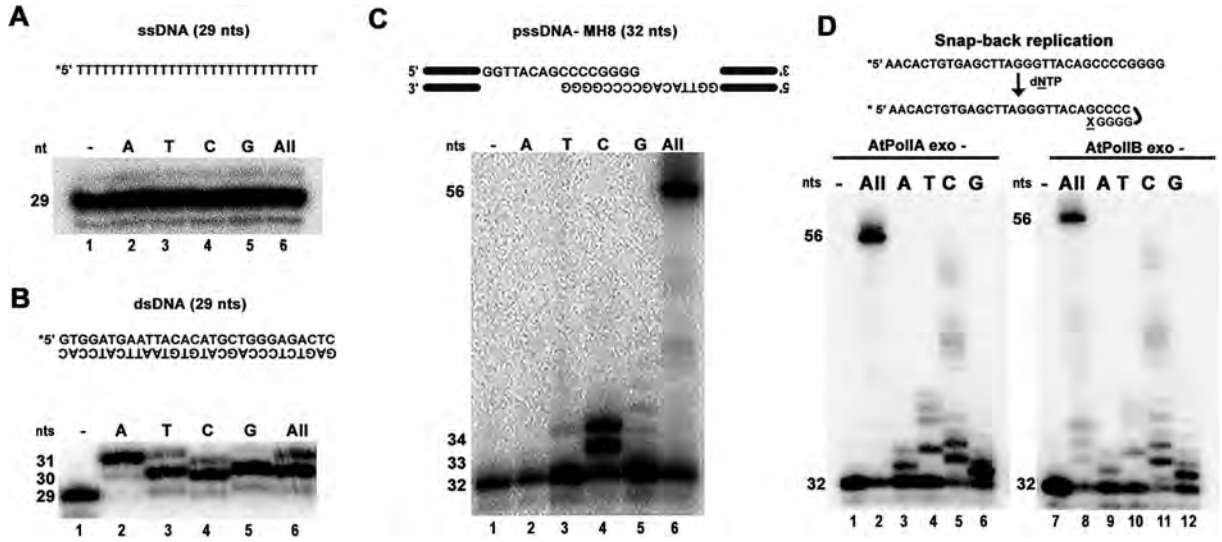

Figure 3. AtPolIB exhibits limited terminal transferase activity on double-stranded substrates. (**A**) Denaturing gel showing the lack of terminal transferase activity on a poly-dT ssDNA template incubated in the presence of individual nucleotides. (**B**) Denaturing acrylamide gel showing AtPolIB exo- nucleotide incorporation on a ds-DNA substrate in the presence of individual nucleotides. (**C**) AtPolIB performs MMEJ using DNA templates in *trans*. Denaturing gel showing MMEJ reactions incubated in the presence of individual nucleotides on pss-DNA(8) substrate. (**D**) AtPolIB performs limited snap-back replication. Denaturing gel showing reactions incubated in the presence of individual nucleotides on a MH-8 substrate with AtPolIA exo- (lanes 1–6) and AtPolIB exo – (lanes 7–12).

strates, we studied the effect of three different concentrations of $MgCl_2$ (10, 6 and 2 mM) on MMEJ. As previously shown, reactions incubated with 10 mM $MgCl_2$ produced a faint MMEJ-product on a pssDNA-6 substrate and efficiently uses a pssDNA-8 substrate (Figure 4A, lanes 22, 24). However, in reactions incubated with 2 and 6 mM $MgCl_2$, AtPolB exo$^-$ is able to use templates with microhomologous sequences of 6 nts (Figure 4A, lanes 6, 14).

We further investigated synapse formation by AtPolIs exo$^-$ using two substrates labeled with different fluorophores poised for fluorescence resonance energy transfer (FRET). Two pssDNA-8 substrates labeled with Cy3 or Cy5 dyes were incubated with AtPolIs in the absence of dNTPs. The efficiency of FRET increases in a proportional manner to the amount of AtPolIA exo$^-$ or AtPolIB exo$^-$ present in the reaction, indicating that AtPolIs drive DNA synapse formation of the fluorescent Cy3–Cy5 donor–acceptor pair (Figure 4B).

MMEJ by different DNAPs predict the formation of a synapse that is stabilized by two DNA polymerases in *trans* (19,21,25,26). To evaluate the possibility that AtPolIB assemblies in *trans* forming a dimer, we use size-exclusion chromatography (SEC)-coupled multiangle light scattering (MALS) on AtPolIBexo$^-$ incubated in the presence and absence of a DNA substrate (Figure 4C). These analyses found an average molecular weight for AtPolIB exo$^-$ of 180 kDa that corresponds to a molecular mass of two AtPolIB monomers (93 kDa). AtPolIB incubated with DNA increases its molecular mass to 235 kDa, a molecular mass that corresponds to two AtPolIB monomers interacting with two DNA molecules (27 kDa). Thus, the SEC-MALS analysis are consistent with synapse formation driven by a dimer assembly of AtPolIB and a pssDNA substrate.

MMEJ by AtPolIB is mediated by insertions 1 and 3

AtPolIs are family-A DNA polymerases that contain three unique insertions in their polymerization domain (35,37,40) (Figure 1B). In order to investigate if MMEJ would depend on these insertions, we used mutant polymerases harboring individual deletions. Deletion mutants eliminate 38, 64, and 24 amino acids corresponding to insertions 1, 2 and 3 respectively (Figure 5A). Insertions 1 and 2 are located at the thumb subdomain and structural modeling suggests that they are poised to interact with the primer-template, whereas insertion 3 is located at the fingers subdomain in a position that is predicted to be distant from DNA (40) (Figure 5A). Mutant polymerases harboring deletions in those insertions are active on a canonical primer-template, suggesting that these mutant polymerases do not have severe alterations in their structure (40). The ability of AtPolIB exo$^-$ deletion variants to execute synapse formation was assessed by FRET on a pssDNA-8 substrate in the absence of dNTPs (Figure 1B). As previously shown, AtPolIB exo$^-$ produces a concentration-dependent increase in fluorescence. However, AtPolIB exo$^-$ harboring deletions in insertions 1 and 3 (AtPolIB-Δins1 or AtPolIB-Δins3) failed to produce a concentration-dependent change in fluorescence (Figure 5B). In contrast, a mutant AtPolIB exo$^-$ harboring a deletion in insertion 2 (AtPolIB-Δins2) showed a FRET response that is dependent on protein concentration, albeit with less efficiency compared to an unmodified AtPolIB exo$^-$ (Figure 5B). Thus, the FRET experiments suggest that AtPolIB variants harboring deletions in insertions 1 and 3 are inefficient in MMEJ (Figure 5B). To corroborate this result, we performed MMEJ reactions on a pssDNA-8 substrate. As expected, a product band of 58 nts was observed in reactions incubated with AtPolIB exo$^-$ and AtPolIB-Δins2. In contrast, no product was synthesized in

Downloaded from https://academic.oup.com/nar/article/47/6/3028/5304310 by UNAM user on 20 October 2020

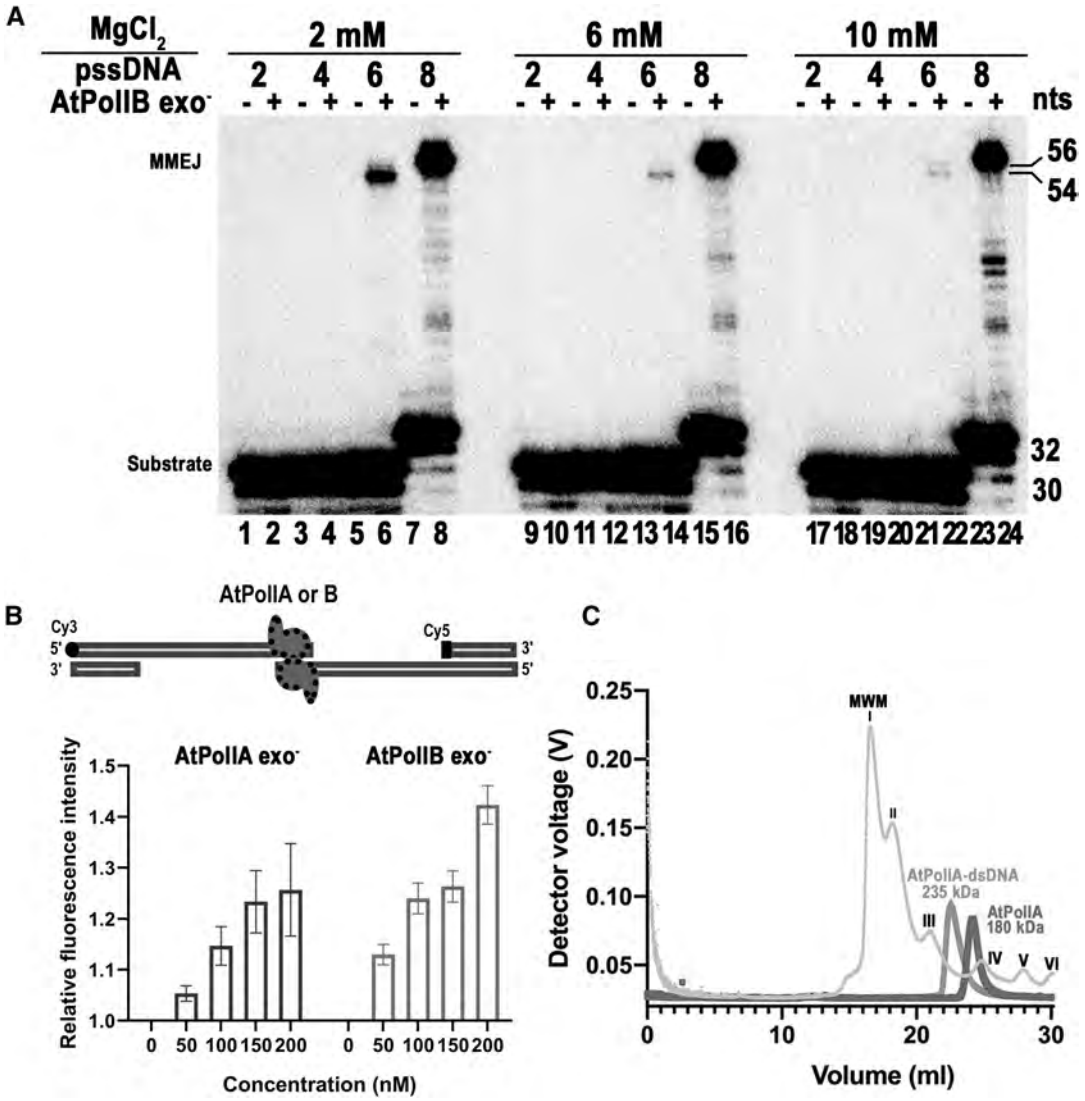

Figure 4. AtPolIs performs MMEJ in short homologous sequences at physiological MgCl2 concentrations and template synapse formation by AtPolIs. (**A**) MMEJ assays using three $MgCl_2$ concentrations (2, 6 and 10 mM) in psDNA templates with microhomologies ranking from 2 to 8 nts. MMEJ reactions were incubated in the absence of $MgCl_2$ (odd numbers) and with the indicated $MgCl_2$ concentration (even numbers). A defined MMEJ product band of 54 nts is observed in reactions incubated with 2 mM $MgCl_2$ on a pssDNA-6 substrate (lanes 6) whereas this product is hardly observed in reactions incubated with 6 and 10 mM $MgCl_2$ (lanes 14 and 22). Reactions incubated with pssDNA-2 and pssDNA-4 do not generate a MMEJ product at any metal concentration. (**B**) Changes in the intensity of fluorescence indicative of the formation of a Cy3–Cy5 intermediate upon incubation of AtPolIs. The relative fluorescence increases in relation to the amount of added of exonuclease deficient AtPolIA and AtPolIB. Experiments were performed in triplicate and the graph shows the mean and the standard deviation. (**C**) SEC-MALS analysis of the oligomerization state of AtPolIB exo- in the absence and presence of DNA substrate. The chromatogram shows the readings of the light scattering for the molecular mass standards and AtPolIB exo- incubated in the presence and absence of DNA. The molecular mass of the standards is indicated by roman numbers: I) blue dextran (2 000 000 Da), II) thyroglobulin (669 000 Da), III) ferritin (440 000 Da), IV) aldolase (158 000 Da), V) conalbumin (75 000 Da), and ovoalbumin (43 000 Da).

samples incubated with AtPolIB exo$^-$ mutants harboring a deletion in insertions 1 and 3 (Figure 5C). Therefore, only an AtPolIB exo$^-$ mutant harboring a deletion in insertions 2 is able to execute MMEJ, although their products are different from the wild-type AtPolIB.

To further corroborate the role of insertions 1 and 3 in MMEJ, we constructed a shortened version of deletion 1 (δ599–610) and point mutations to alanine of individual lysine and arginine residues in this loop. We also constructed a point mutant in residue K866 located in loop 3. An MMEJ reaction using those mutant polymerases, show that a shorted version of loop 1 decreases MMEJ formation by ∼90% and individual K590A and K593A mutations also decrease the amount of MMEJ product to 20 and 50% of the consumed substrate (Figure 5D, lanes 5, 6, 7). Interestingly an alanine mutant of residue K866 also decreases MMEJ formation by MMEJ by nearly 40% (Figure 5D, lane 13).

AtPolIB-Δins2 primarily generates a product of approximately 42 nts that correlates with the necessity to displace the 5′-end of the primer stand corresponding to the opposite template (Figures 5C and 3C). AtPolIs har-

Downloaded from https://academic.oup.com/nar/article/47/6/3028/5304310 by UNAM user on 20 October 2020

INFORME DE LABORES 2019

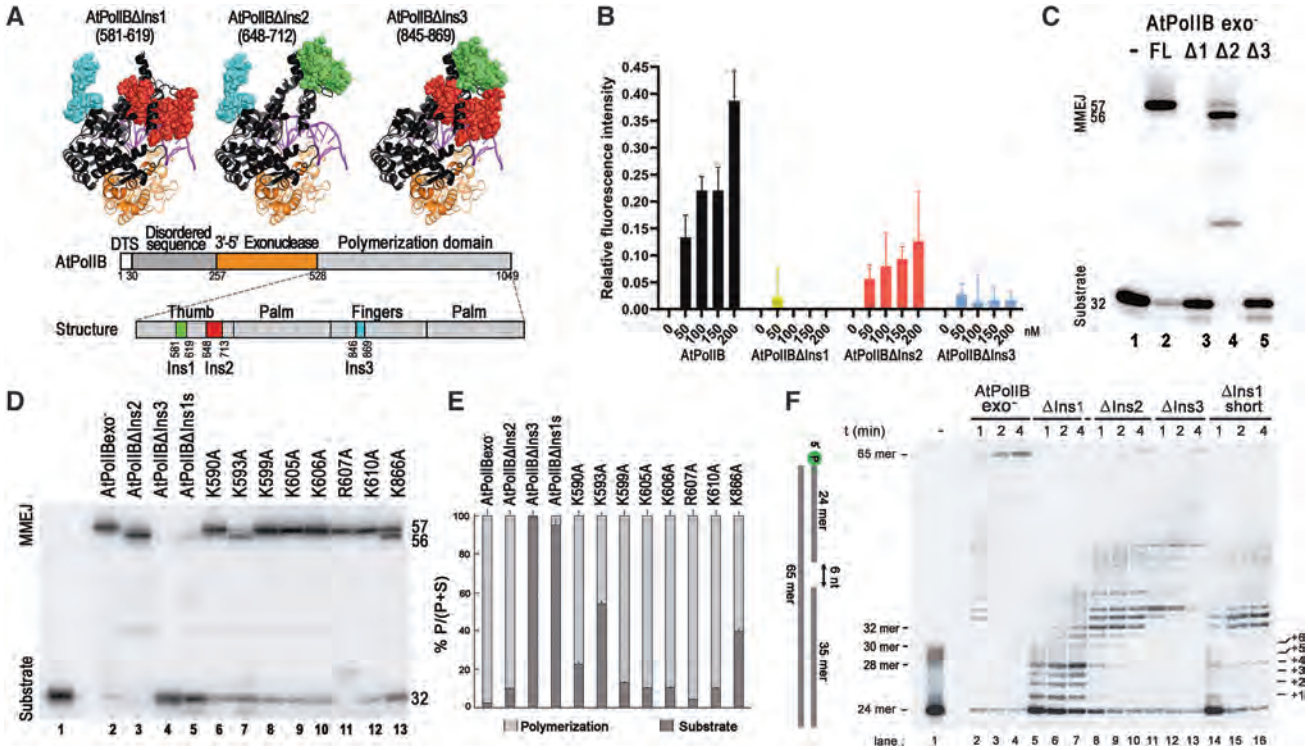

Figure 5. MMEJ by AtPolIs is mediated by unique amino acid insertions in their polymerization domain. (**A**) Homology model showing the predicted localization of the unique insertions in the polymerization domain of AtPolIB. Insertions 1 and 2 are located at the thumb subdomain (green and red colored, respectively), whereas insertion 3 (cyan colored) is located at the palm subdomain. A representative structure of mutant polymerases showing individual deletions is present. (**B**) FRET assay using exonuclease deficient AtPolIB and exonuclease deficient deletion mutants. AtPolIB and AtPolIB-Δins2 generate a concentration-dependent change in the relative fluorescence, whereas incubation with AtPolIB-ΔIns1 and AtPolIB-ΔIns3 do not have an effect on the relative fluorescence. Data show the mean of three independent experiments. (**C**) MMEJ reaction assays using AtPolIB deletion mutants on a pssDNA-8 substrate. A MMEJ product is observed upon incubation with full-length (FL) AtPolIB (lane2), in contrast AtPolIB-ΔIns1 and ΔIns3 mutants (Δ1 and Δ3) are severely deficient in MMEJ product formation (lanes 3 and 5), AtPolIB-ΔIns2 forms the expected MMEJ product reaction products of 56 and of lower molecular weight products (lane 4) that correlate with the observed strand-displacement deficiency of this mutant (lane 4). (**D** and **E**) MMEJ reactions by point and deletion mutants in loops 1 and 3. A short deletion of 11 amino acids (599–610) in loop 1 abolishes MMEJ formation (lane 5). Point mutants K590 and K593A in loop 1 decrease MMEJ formation by 20 and 50% respectively, whereas a point mutant. K886A (loop 3) decrease MMEJ formation by 35%. MMEJ formation is quantified as the percentage of MMEJ product (P) in relation to the total amount of product and substrate (P+S). The graphical representation shows the mean of three independent experiments. (**F**) Denaturing polyacrylamide gel showing a time course reaction (from 1 to 4 minutes) by AtPolIB exo- and deletion mutants on a gapped-substrate. The six-nucleotides gapped DNA substrates, the length of the primer (24-mer), the expected maximal extension (30-mer) before strand-displacement and the full-length strand-displacement (65-mer) are indicated in the left side of the figure.

bor strong strand-displacement capabilities (40,42), mutant AtPolIs harboring a deletion in loop 1 abolish strand-displacement on a 1-nt gap, whereas mutant AtPolIB-Δins2 and AtPolIB-Δins3 severely decrease this property (42). In order to investigate if the appearance of the band of 42 nts synthesized by AtPolIB-Δins2 is related to a decrease in strand-displacement, we compare the efficiencies for strand-displacement on a 6-nt gap for all deletion mutants. Nucleotide incorporation by AtPolIB-Δins2 and AtPolIB-Δins3 is halted two and four nucleotides after the 5′-end of the blocking DNA strand (32- and 34-mer products) (Figure 5F, lanes 8 and 11). The ability of AtPolIB-Δins2 to displace two nucleotides correlates with the observed MMEJ product of approximately 42 nts (32 nts from the primer, 8 nts for extension in *trans* and 2 nts due to strand-displacement) show on a pssDNA-8 substrate (Figure 5C). The presence of the 42 nts band by AtPolIB-Δins2 supports the ability of AtPolIs to assemble a synapse in *trans* as a product mediated by snap-back replication would not be affect by the decrease in strand-displacement.

AtPolIs execute MMEJ on mismatched substrates

Analysis of microhomologous sequences found in chloroplast DNA upon DSBs contain mismatches (30,32). This suggests that in plastids MMEJ is executed by a DNAP able to extend from mismatches or that the distortions generated by a mismatch in the DNA double helix would not hamper synapse formation and its extension. We thus, investigated whether AtPolIs would use pssDNA substrates containing mismatches. We assemble six substrates using six different nucleotides annealed to the MH-8 substrate (Figure 6A and Supplementary Table S1). The first set of substrates contain three consecutive mismatches, one and two nucleotides before the 3′-OH end of the microhomologous sequence (substrate I and II, respectively). The second set of substrates (III and IV) contained one and two mismatches at their 3′-

Downloaded from https://academic.oup.com/nar/article/47/6/3028/5304310 by UNAM user on 20 October 2020

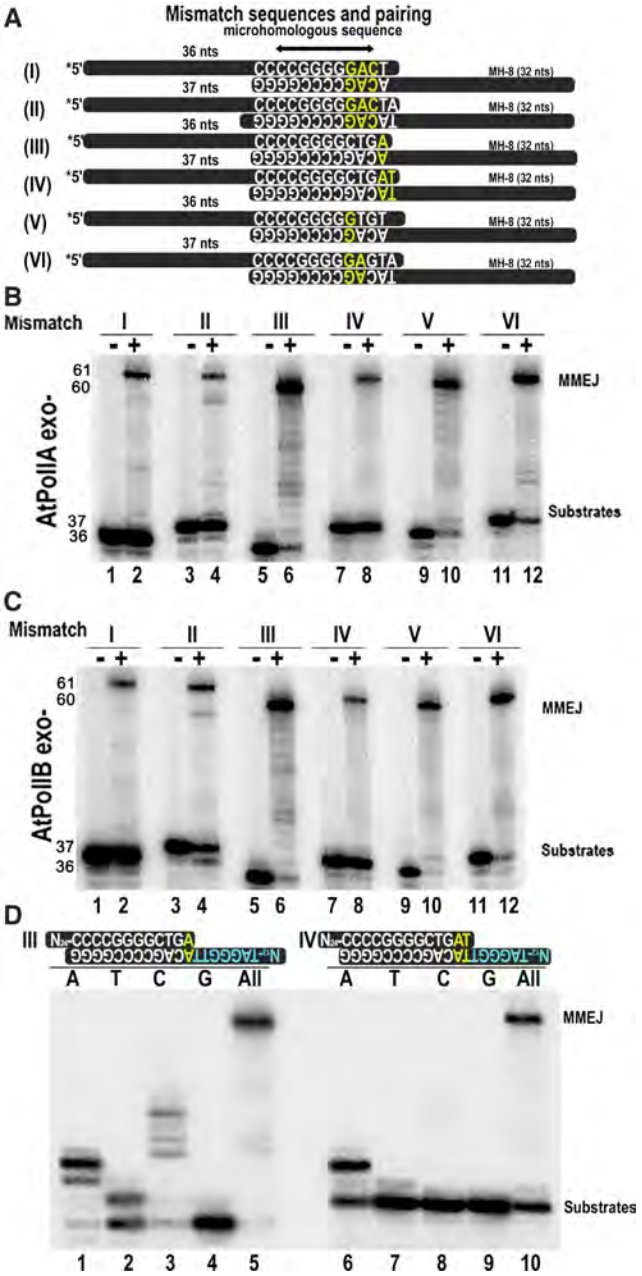

Figure 6. AtPolIA and AtPolIB execute MMEJ on mismatched substrates. (**A**) Oligonucleotide substrates containing mismatches annealed to promote MMEJ. The sequence of the microhomologous sequence of the single-stranded oligonucleotides is indicated. The mismatches are colored in red, whereas Watson-Crick pairs are colored in white. The arrangement includes mismatches located one and two nucleotides after the 3′-OH (I and II), located at the 3′-OH (III and IV), and located three and four nucleotides before the 3′-OH (V and VI). (B and C) MMEJ reactions executed by exonuclease deficient AtPolIA exo- (**B**) and AtPolIB exo$^-$ (**C**) on single-stranded substrates. The substrate without added polymerase is indicated by a negative sign (−), whereas reactions including DNA polymerase are indicated by a positive sign (+). The migration for substrates and MMEJ products are indicated. (**D**) Denaturing acrylamide gel showing the formation of MMEJ products by AtPolIB exo$^-$ on MMEJ with 3′-OH mismatches (substrates III and IV) annealed with the MH-8 oligonucleotide in the presence of individual nucleotides.

OH and the third set of substrates (V and VI) contained one and two mismatches three nucleotides before their 3′-OH (Figure 6A). To our surprise, all substrates, including a single mismatch (substrate III) and a double mismatch at the 3′-OH (substrate IV) were able to generate MMEJ products when incubated with AtPolIs exo$^-$ (Figure 6B and C). This result may relate to the fact that AtPolIs efficiently extend from a primer whose 3′-OH is confronted to an abasic site (40) and the ability of AtPolIs to extend mismatches in canonical primer-templates (43). Our data are congruent with the large repertoire of microhomologous sequences, because sequences that are not perfectly paired can be used as substrates by AtPolIs.

We decided to investigate the ability of AtPolIB exo$^-$ to incorporate individual nucleotides on substrates with one and two mismatches at their 3′-OH (substrates III and IV) (Figure 6D). On a substrate with a single nucleotide mismatch, AtPolIB exo$^-$ incorporates three dAMP nucleotides, in which two of them are expected to be template dependent and the third one due to misincorporation (Figure 6D, lane 1). AtPolIB exo$^-$ also misincoporates one adenine and several cytidines possibly due to misalignment (Figure 6D, lanes 2 and 3). On a substrate with two consecutive 3′-OH mismatches, AtPolIB exo$^-$ incorporates a dAMP molecule (Figure 6D, lane 6).

Plant specific DNA binding proteins AtmtSSBs, AtWhirlies and AtOSBs bind single-stranded DNA with different affinities

Organelles in *Arabidopsis* harbor three families of single-stranded DNA binding proteins (AtSSBs) and each family contains several members: A) The family of canonical mitochondrial DNA binding proteins (AtmtSSB) consisting of two members, B) Whirlies, which are composed of three members, and C) Organellar Single-stranded DNA Binding proteins (OSB), harboring four members (Figure 6A). AtmtSSBs contain an OB-domain follow by a C-terminal extension, AtOSBs, contain an N-terminal OB-like domain, followed by repeats (from one to four) of a PDF motif. This 50 amino acid motif is responsible for ssDNA binding. Whirlies assemble as tetramers and interact with ssDNA via the β-sheets of neighboring subunits (30,31,49,54–56) (Figure 7A).

Members of the OSB and Whirly families decrease the formation of illegitimate recombination products (31,54), whereas AtmtSSB1 promotes AtRecA strand-exchange activity (49). In order to investigate the possible role of AtSSBs in MMEJ, we directly measured their binding affinities for substrates containing ssDNAs of different lengths. In order to correctly measure their binding affinities, we first determined their oligomeric states. The elution profiles of purified AtmtSSB1, AtmtSSB2, AtOSB2, AtOSB3, and AtWhirly2 (Figure 7B, inset) on a gel filtration column revealed that all proteins assembled as tetramers in the absence of DNA (Figure 6B). In our binding studies, we used the molar concentration of the tetrameric SSBs and not the individual protomers. An EMSA on a labeled oligonucleotide of 70 nts illustrates the high binding

Downloaded from https://academic.oup.com/nar/article/47/6/3028/5304310 by UNAM user on 20 October 2020

INFORME DE LABORES 2019

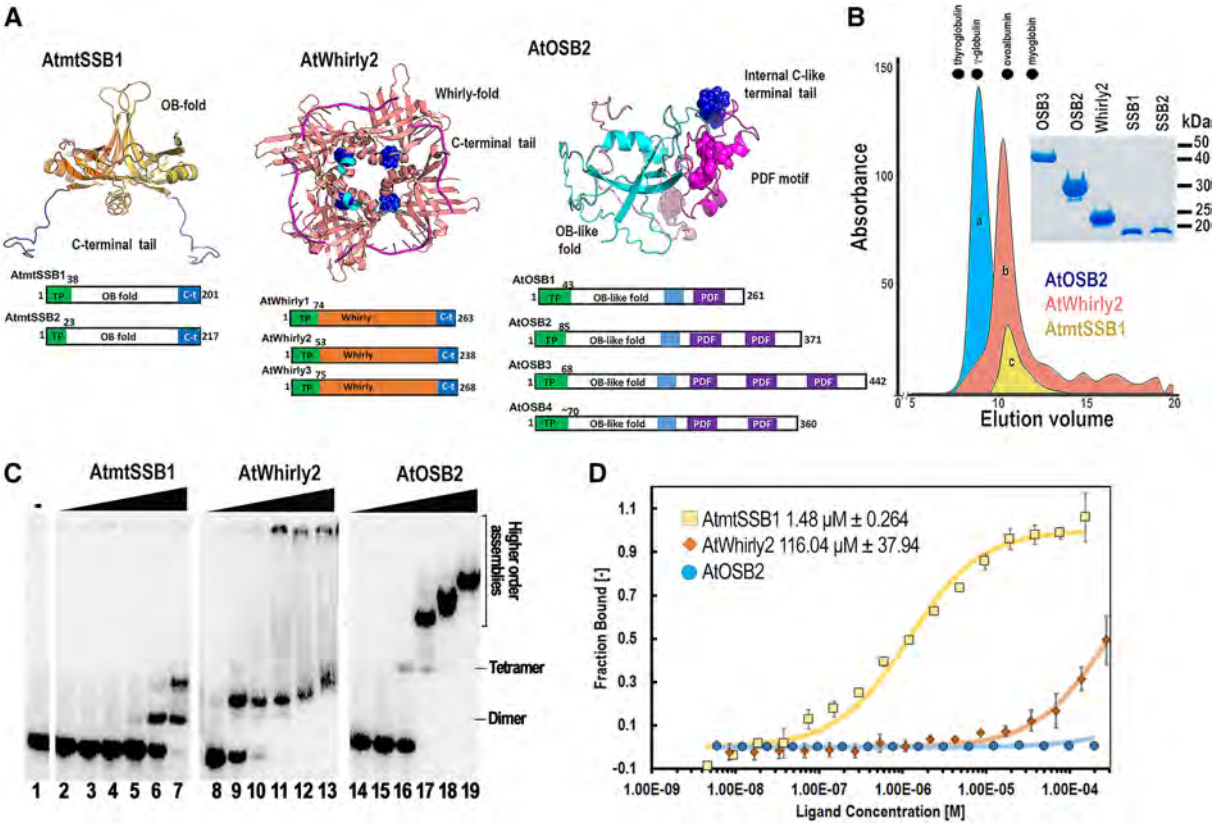

Figure 7. Arabidopsis harbors canonical and unique SSBs. (**A**) Structural organization of AtmtSSBs, AtWhirlies and AtOSBs. AtmtSSB1 and AtmtSSB2 are predicted to assemble as proteins with an oligonucleotide/oligosaccharide-binding (OB)-fold and a C-terminal disorder region, AtWhirlies (1–3) consists of a Whirly domain composed of two four-stranded β-sheets and two α–helices plus a disordered C-terminal extension (55,56), AtOSBs consist of an OB-like fold followed by one to three PDF motifs (54). The structural models of AtmtSSBs and AtOSBSs highlight the structural organization of the OB-fold domains and PDF motifs respectively. Structural modeling shows AtmtSSB1 and AtOSB1 as a dimer and monomer for clarity. The crystal structure of AtWhirly2 is shown in combination with the superimposed ssDNA co-crystallized in whirly2 from potato. The C-terminal amino acids of Whirlys are not present in their crystal structures and are proposed to be involved in protein-protein interactions. The AtWhirly2 structure illustrates the tetrameric organization and DNA binding of members this protein family. (**B**) Gel filtration profiles of purified AtmtSSB1, AtOSB2, and AtWhirly2 (inset) on a Superdex 75 column. Dots denote the elution profiles of molecular weight markers: thyroglobulin, γ globulin, ovoalbumin and myoglobin. The elution profiles of AtSSBs indicate their tetrameric assembly. (**C**) EMSA assay showing the binding of purified AtmtSSB1, AtOSB2, and AtWhirly2 to ssDNA. Reactions were incubated with increased concentration of the tetrameric SSBs (0, 1.15, 4.125, 14.87,53.5, 192.9, 694.2 nM) and 1 nM of a 5′-^{32}P-labeled 70-mer oligonucleotide. Binding reactions were resolved on an 8% non-denaturing polyacrylamide gel. (**D**) Langmuir isotherms showing the binding of AtmtSSB1 and AtWhirly2 to AtPolIB exo^{-} by MST.

affinity of AtWhirly2 for single-stranded DNA (Figure 7C, lanes 9–13). This binding is consistent with previous biochemical analyses of Whirly variants that bind ssDNA as tetramers with affinity constants of approximately 5 nM (30,55). In addition to binding as a tetramer, AtWhirly2 also forms high molecular weight complexes with ssDNA, as previously show by Cappadocia and coworkers (57). AtmtSSB1 forms two complexes that may correspond to dimeric and tetrameric assemblies in comparison to the tetrameric AtWhirly2 (Figure 7C, lanes 6 and 7). On the other hand, AtOSB2 initially binds ssDNA with a relative migration that corresponds to a tetrameric assembly, although high molecular assemblies are formed at higher protein concentrations (Figure 7C, lanes 14–19). An interesting point is the contrasting differences for ssDNA binding between plant SSBs. AtmtSSBs needs to be in a molar excess of 694-fold to shift all the 70-mer, whereas AtOSB2 and AtWhirly2 need to be in 53-fold excess (Figure 6C). Given these contrasting binding profiles, we measured the binding affinities for AtmtSSB1, AtOSB2 and AtWhirly2 on pssDNA-10 and ssDNA45-mer substrates using fluorescence anisotropy (Table 1). AtOSB2 and AtWhirly2 bind to a pssDNA-10 substrate with dissociation constants (K_d) of 8 and 22 nM respectively, whereas AtmtSSB1 was unable to bind to this substrate (Table 1). On the other hand, AtmtSSB1, AtOSB2, and AtWhirly2 bonded to a ssDNA 45-mer substrate with Kds of 62.8, 11.7 and 8.2 nM, respectively (Table 1). These values approximate the reported values for AtWhirly2 (30) and AtOSB2 (54). The EMSA and anisotropy experiments thus indicate that the binding affinity of AtmtSS1 for ssDNA substrates is weaker than the binding affinities of AtOSB2 and AtWhirly2.

AtmtSSB1, but not AtOSB2 and AtWhirly2, interact with AtPolIB with affinity constant similar to canonical replisomes

Several SSBs bind to their cognate DNA polymerases by virtue of their exposed C-terminal amino acids. In order

Downloaded from https://academic.oup.com/nar/article/47/6/3028/5304310 by UNAM user on 20 October 2020

INFORME DE LABORES 2019

Table 1. Dissociation constants of plant organellar SSBs in pssDNA and ssDNA templates

	pssDNA-10 Oligomeric State in solution	ssDNA-45 mer Oligomeric State in solution
Protein	K_d (nM)	K_d (nM)
AtmtSSB1	—	62.8 ± 3.6 (tetramer)
AtOSB2	8.6 ± 0.46 (tetramer)	11.7 ± 2.2 (tetramer)
AtWhirly2	22.1 ± 1.3 (tetramer)	8.2 ± 0.19 (tetramer)

*Dissociation constant were determined by three independent experiments.

to investigate if AtSSBs interact with the plant organellar DNA polymerases, we evaluated a potential interaction between AtSSBs and AtPolIB exo$^-$ by MST. We found that AtPolIB exo$^-$ interacts with AtmtSSB1 with an affinity constant of 1.48 μM. This affinity constant is similar to the 1.6 μM interaction between T7 DNA polymerase and T7 SSB in the absence of thioredoxin and the 1.6 μM interaction between DNAP III and SSB from *E. coli* (58,59). In contrast, AtWhirly2 at a concentration of 250 μM (6 mg/ml) is not able to saturate a binding isotherm, suggesting that the observed interaction is non-specific or that is larger than 250 μM. AtOSB2 shows no observable binding to AtPolIB exo$^-$ (Figure 7D).

AtWhirlies and AtOSBs decrease MMEJ on long ssDNA templates

Whirlies and OSBs are proposed to compete for a partially resected DSB and prevent MMEJ in organelles (31,54). In order to obtain biochemical evidence for this hypothesis, we performed MMEJ reactions using pssDNA with microhomologies of 8 nts, but with extra single-stranded DNA sequences that ranked from 0 to 65 nts. In these reactions, we used a 50-fold molar excess of tetrameric purified SSBs (AtmtSSB1, AtmtSSB2, AtOSB2, AtOSB3, and AtWhirly2) and 5-fold AtPolIB with respect to pssDNAs (Figure 8A and B). In reactions incubated using the microhomology of 8 nts without an extra single-stranded DNA segment, pssDNA-$8_{(0)}$, the presence of SSBs did not have an effect on MMEJ formation by AtPolIB (Figure 8A, lanes 1–7). The lack of MMEJ inhibition on a pssDNA-$8_{(0)}$ correlates with the absence of binding for SSBs to this substrate (30) a (Table 1) and also indicates that the presence of SSBs does not inhibit MMEJ by AtPolIB. When 4 nts were added to the microhomologous sequence of 8 nts (pssDNA-$8_{(4)}$), AtOSB2 and AtWhirly2 completely hampered MMEJ formation (Figure 8A, lanes 12 and 14). Inhibition by AtOSB2 and AtWhirly2 on a pssDNA-$8_{(4)}$ substrate, but not by AtmtSSB1 or AtmtSSB2, correlates with the binding of AtOSB2 and AtWhirly2 to a pssDNA-10 substrate (Table 1). The presence of AtOSB3, but not AtmtSSB1 and AtmtSSB2, in substrates with single-stranded DNA regions of 43 (pssDNA-$8_{(35)}$) and 73 (pssDNA-$8_{(65)}$) nucleotides decreased product formation in pssDNA-$8_{(35)}$ and pssDNA-$8_{(65)}$ substrates (Figure 8B). The lack of inhibition for AtmtSSB1 and AtmtSSB2 on longer partially single-stranded substrates was observed even with reactions incubated with 200-fold molar excess of those proteins with respect to the ppsDNA template (Supplementary Figure S2). The binding affinity of AtmtSSB1 for a 70-mer ssDNA substrate is approximately five times weaker than the binding affinity of AtOSB2 and AtWhirly2, so the lack of MMEJ product formation by AtPolIs in reactions incubated with AtmtSSBs is not explained by a lack of binding to single-stranded DNA.

MMEJ on long substrates is favored over exonucleolysis independently of the presence of mtSSBs

MMEJ reactions incubated with substrates containing longer single-stranded DNA regions of 43 and 73 nucleotides were more efficiently used than substrates with short regions (Figure 8A and B). Canonical SSBs recruit several enzymes to DNA replication forks via their acid C-terminal extension (60,61) and AtmtSSB1 interacts with AtPolIB with similar affinities to the interactions observed in other replisomes (Figure 8D). We therefore tested whether the presence of AtmtSSBs would promote MMEJ by wild-type AtPolIs in substrates with long single-stranded DNA regions. We used substrates with increased single-stranded DNA regions of 12, 43 and 73 nucleotides while maintaining a microhomology region of 8 nts (pssDNA-$8_{(4)}$, pssDNA-$8_{(35)}$ and pssDNA-$8_{(65)}$) in the presence of increased concentrations of AtmtSSB1 and AtmtSSB2 and exonuclease proficient AtPolIB (Figure 8C–E). In a pssDNA-$8_{(4)}$ substrate, AtPolIB executed MMEJ in the presence and absence of mtSSBs with similar efficiencies and most of the substrate was degraded to 15- or a 16-mer (Figure 8C). A comparison between the amount of MMEJ product synthesized by exonuclease deficient AtPolIB and the exonuclease active form of the enzyme on the pssDNA-$8_{(4)}$ substrate shows that AtPolIB exo- converts approximately 80% of the substrate to a MMEJ product, whereas wild-type AtPolIB converts <10% of the substrate to a MMEJ product in the absence of AtmtSSB1 (Figure 8C, lanes 2 and 3). In pssDNA-$8_{(35)}$ and pssDNA-$8_{(65)}$ substrates, the exonucleolytic degradation by wild-type AtPolIB substantially decreased independent of the presence or absence of AtmtSSBs (Figure 8D and E). MMEJ reactions incubated with a pssDNA-$8_{(35)}$ substrate exhibited almost no difference when incubated with exonuclease deficient or exonuclease proficient AtPolIB (Figure 8D, lanes 2 and 3) and the addition of AtmtSSBs had no effect on MMEJ (Figure 8D, lanes 4–11). Reactions incubated with wild-type AtPolIB generate a predominant MMEJ product of 110 nts and a minimal amount of exonucleolytic products that accumulate as 15 or 16-mers (Figure 8D, lanes 3–11). A similar decrease of the exonuclease degradation products by wild-type AtPolIB is also observed in reactions incubated

Downloaded from https://academic.oup.com/nar/article/47/6/3028/5304310 by UNAM user on 20 October 2020

INFORME DE LABORES 2019

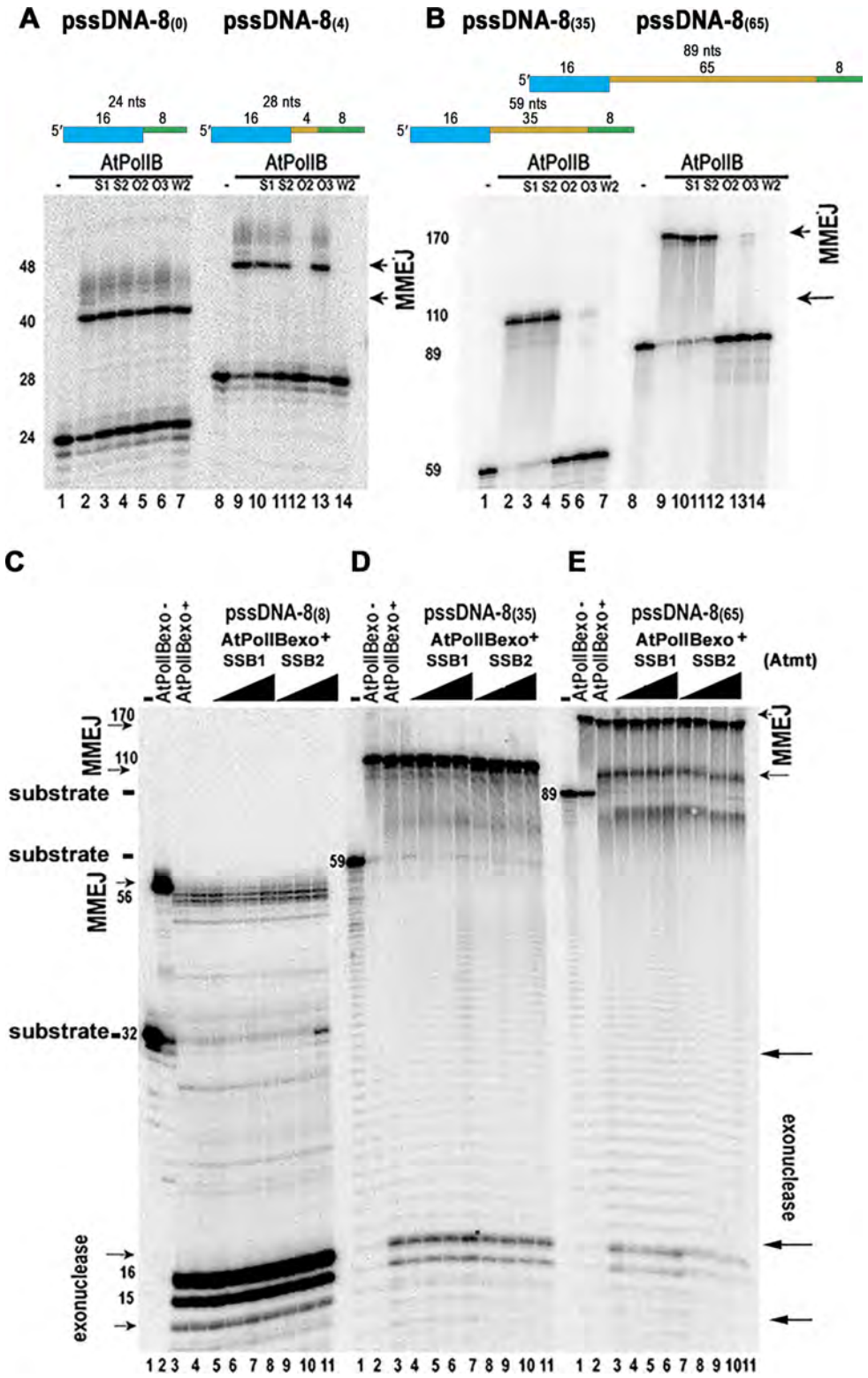

Figure 8. AtSSBs and single-stranded length of the DNA break regulate MMEJ. (**A**, **B**) Unique SSB from plant organelles hamper MMEJ on substrates with single-stranded regions longer than 8 nts. MMEJ formation by AtPolIs in the presence of plant SSBs (AtmtSSB1, S1; AtmtSSB2, S2; AtOSB2, O2; AtOSB3, O3; and AtWhirly2, W2) in MMEJ substrates with a constant microhomologous sequence of 8 nts, but varying single-stranded regions of 8 (panel A, lanes 1 to 7),12 (panel A, lanes 8–14) 43 (panel B, lanes 1–7) and 73 nts (panel B, lanes 8–14). The length of the MMEJ, single-stranded region and total oligonucleotide length of the substrates are indicated in the upper part of the panel. The length of the substrates and MMEJ products are indicated by arrows. (**C**–**E**) Wild-type AtPolIA and AtPolIB execute MMEJ with minimal exonucleolysis on substrates with single-stranded regions longer than 16 nts. (C) MMEJ reaction by AtPolIA (lanes 3–6) and AtPolIB (lanes 7–11) on a pssDNA with 8 bases of microhomologous sequence and 8 extra-bases of single-stranded DNA. The labeled substrate is indicated in lane 1 and the MMEJ product by and exonuclease deficient AtPolIB is shown in lane 2. (D and E) As in C, but with a substrate containing 35 nts or 65 nts of extra single-stranded DNA respectively.

Downloaded from https://academic.oup.com/nar/article/47/6/3028/5304310 by UNAM user on 20 October 2020

INFORME DE LABORES 2019

with a pssDNA-$8_{(65)}$ substrate in the presence and absence of AtmtSSBs (Figure 8E).

DISCUSSION

Here we demonstrate that organellar DNA polymerases from the plant model *A. thaliana*, AtPolIs, efficiently perform MMEJ on partially resected DSBs longer than 6 nts, proving an explanation for DSBs repair with MMEJ signatures in plant organelles (12,29,31,32). MMEJ requires the formation of a synapse between DNA strands to join otherwise unstably paired microhomologous sequences, while creating a 3′-OH necessary for nucleotide incorporation and extension. Short microhomologous sequences could transiently pair, however these intermediates are short-lived. AtPolIs in comparison to KF DNAP I is able to stabilize these intermediates and used them as substrates. AtPolIs harbor three unique amino acid insertions in their polymerization domain (35,37) and within these insertions, insertion 1 is indispensable for MMEJ. Thus, AtPolIs and HsPolθ converged in the use of insertions for MMEJ and lesion bypass (21,40).

Mismatches are an abundant feature in DSBs repaired by MMEJ in plant organelles. For example, the Brisson group showed that 91 out of 158 induced MMEJ rearrangements in plastid DNA contain mismatches (30). Thus, the machinery responsible to execute MMEJ in plant organelles must be able to extend from mismatches. The fact that AtPolIs can efficiently anneal and extend from microhomologus sequences harboring mismatches at their 3′-OH, supports the notion that these enzymes are biochemically equipped to execute MMEJ in plant organelles. In contrast to HsPolθ, AtPolIs contain an active exonuclease domain and its modulation should be essential for MMEJ *in vivo*. In substrates that contain a short single-stranded region, *i.e.* less than 12-nts, AtPolIs exonucleolytic degradation is preferred over MMEJ. An increase in the length of the single-stranded region, however, promotes MMEJ at levels in which exonuclease deficient and wild-type AtPolIs execute MMEJ with similar efficiencies. We speculate that the presence of extra nucleotides generates a binding platform for AtPolIs that promotes synapse formation (Figure 8D and E). The ability of exonuclease proficient AtPolIs to carry out MMEJ on substrates with long single-stranded regions with the same efficiency that exonuclease deficient AtPolIs reinforces the notion of the functional relevance of these enzymes to execute MMEJ *in organello*.

Arabidopsis plants harboring T-DNA insertion mutants in *why* and *osb1* genes accumulate DSBs that are repaired via MMEJ and an increase of ectopic recombination products (30,54). As MMEJ and ectopic homologous recombination are driven by annealing of short single-stranded DNA sequences, we analyzed the effect of AtmtSSBs, At Whirly2 and AtOSBs in MMEJ by AtPolIB. Whirlies and AtOSBs are proposed to counter MMEJ and ectopic homologus recombination by binding to 3′-OH resected ends (10,30,62). This binding is predicted to hamper the annealing of the microhomologous or short-homologous sequences. We demonstrated that the presence of AtWhirly2 and AtOSBs in templates containing single-stranded regions longer than 12 nts hampers MMEJ. AtOSB3 is unable to prevent MMEJ on a pssDNA with a single-stranded region of 12 nts, but efficiently hampers MMEJ on longer substrates (Figure 8A and B). This differential correlates with the presence of an extra PDF domain, suggesting that AtOSB3 needs a larger nucleotide length for binding (10).

AtmtSSB, AtWhirly2, and AtOSBs, bind single-stranded DNA and pssDNA substrates with different affinities (10,30,31,54) (Figure 8 and Table 1). Only AtWhirly2 and AtOSBs, however, completely block MMEJ by AtPolIs. The latter suggests that the concentration of AtmtSSBs needed to block MMEJ is much higher because of its weaker affinity for ssDNA, that AtmtSSBs easily dissociate from DNA, or that AtmtSSBs physically interact with AtPolls and displaces these proteins. The weak binding for ssDNA by mtSSB is observed for other proteins from the same family that have micromolar affinities for ssDNA binding (63). A weak binding of the plant organellar OB-fold maybe related to the modular structure of AtOSBs, in which their PDF domains are responsible for binding to single-stranded DNA and their associated OB-fold domain does not contribute to ssDNA binding (54).

MMEJ inhibition by AtOSBs and Whirlies is in agreement with previous models explaining the fate of genomic DNA upon DSBs in plant organelles (10,30,62,64). Plant organelles harbor a bacterial RecA orthologue that mediates homologous recombination and a Rad52-like single-stranded annealing protein, dubbed organellar DNA-binding protein 1 (ODB1). ODB1 has been proposed to direct SSBs displacement from single-strand DNA regions and promotes loading of RecA (10,65,66). In plant organelles, U-turn-like rearrangements are mediated by microhomologies. The absence of whirlies and AtRecA in Arabidopsis increases the amount of U-turn-like rearrangements (67). Zampini and coworkers postulate that RecA promotes accurate fork restart suggesting that in the absence of whirlies the single-stranded 3′-OH of a collapsed replication fork anneals to an opposite strand generating U-turn-like rearrangement (67). Based upon our biochemical results and previous genetic analysis (6,11,27,28,32,54,65,67), we propose a model in which AtOSBs and AtWhirlies limit MMEJ by blocking the access of a single-stranded 3′-OH to AtPolIs or AtmtSSBs. AtmtSSBs binding to the 3′-OH may result in recruiting AtPolIs or the HR machinery, and MMEJ would be favored only if AtPolIs reach the end of partially resected 3′-OH (Figure 9). If the proposed block of the single-stranded 3′-OH is limited by the absence of whirlies and HR is impaired by lack of AtRecA, other DNA repair routes like MMEJ would mediate DSB repair.

Both AtPolIA and AtPolB execute MMEJ, suggesting that *in vivo* MMEJ is executed by both polymerases. This contrasts with the role of AtPolIB in preventing MMEJ rearrangements in chloroplasts proposed by Parent and coworkers (29). A plausible explanation for the increase of MMEJ rearrangements in T-DNA insertion lines inactivating AtPolIB may lie in a differential in lesion bypass abilities between AtPolIA and AtPolIB. For instance, if AtPolA possesses less efficient lesion bypass than AtPolIB, organellar DNA replication under the sole presence of AtPolIA would have a greater tendency to collapse generating double-stranded breaks. Alternatively, it is possible that At-

Downloaded from https://academic.oup.com/nar/article/47/6/3028/5304310 by UNAM user on 20 October 2020

INFORME DE LABORES 2019

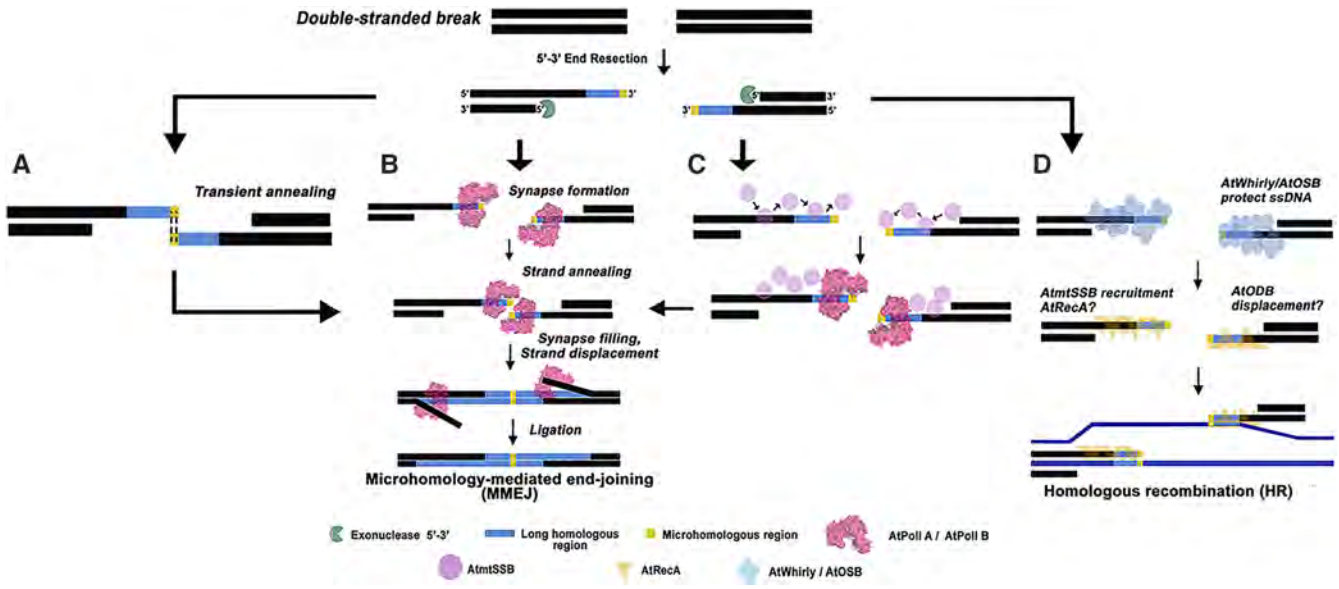

Figure 9. Proposed model for DSBs fate in plant organelles. Microhomology-mediated end-joining or Homologous Recombination is driven by the access of single-stranded binding proteins to a 3′-OH single-stranded end. Resected single-strand DNA regions with microhomologous (yellow) and long homologous (blue) sequences are produced upon DSBs. Plant SSBs and AtPolIs compete to bind the 3′-OH of a resected end. If single-stranded biding proteins AtOSBs or AtWhirlies bind to a resected end, they block the access to canonical AtmtSBB and AtPolIs. Binding of mtSSBs would promote MMEJ if sufficient AtPolIs is available to react with them. Conversely recruitment of RecA to a 3′-OH of a resected end would drive homologous recombination.

PolIB, but not AtPolIA, interacts with components of the HR machinery (29). Although the latter scenario is speculative, our data reveal that MMEJ in plant organelles is driven by a unique family of DNAPs. The presence of these polymerases, instead of metazoan DNAP γ, may account for the numerous MMEJ events in plant organelles. AtPolIs are functionally analogous to HsPolθ, in both lesion bypass and MMEJ. The functional similarities between AtPolIs and HsPolθ are and example of protein convergence in which nature has used amino acid insertions to decorate the active site of family-A DNA polymerases and execute novel DNA transactions.

SUPPLEMENTARY DATA

Supplementary Data are available at NAR Online.

ACKNOWLEDGEMENTS

We thank Corina Diaz-Quezada for technical support and Teri Markow for critical reading. P.L. G.-M. thanks CONACYT for her master's fellowship.

FUNDING

CONACYT-Ciencia Básica grant [253737 to L.G.B.]; CONACYT-Infrastructure [279896]. Funding for open access charge: CONACYT-PRODEP.
Conflict of interest statement. None declared.

REFERENCES

1. Gray,M.W. (2012) Mitochondrial evolution. *Cold Spring Harb. Perspect. Biol.*, **4**, a011403.
2. Raven,J.A. and Allen,J.F. (2003) Genomics and chloroplast evolution: what did cyanobacteria do for plants? *Genome Biol.*, **4**, 209.
3. Martin,W., Rujan,T., Richly,E., Hansen,A., Cornelsen,S., Lins,T., Leister,D., Stoebe,B., Hasegawa,M. and Penny,D. (2002) Evolutionary analysis of Arabidopsis, cyanobacterial, and chloroplast genomes reveals plastid phylogeny and thousands of cyanobacterial genes in the nucleus. *Proc. Natl. Acad. Sci. U.S.A.*, **99**, 12246–12251.
4. Oldenburg,D.J. and Bendich,A.J. (2004) Most chloroplast DNA of maize seedlings in linear molecules with defined ends and branched forms. *J. Mol. Biol.*, **335**, 953–970.
5. Backert,S. and Borner,T. (2000) Phage T4-like intermediates of DNA replication and recombination in the mitochondria of the higher plant Chenopodium album (L.). *Curr. Genet.*, **37**, 304–314.
6. Davila,J.I., Arrieta-Montiel,M.P., Wamboldt,Y., Cao,J., Hagmann,J., Shedge,V., Xu,Y.Z., Weigel,D. and Mackenzie,S.A. (2011) Double-strand break repair processes drive evolution of the mitochondrial genome in Arabidopsis. *BMC Biol.*, **9**, 64.
7. Sloan,D.B. (2013) One ring to rule them all? Genome sequencing provides new insights into the 'master circle' model of plant mitochondrial DNA structure. *New Phytol.*, **200**, 978–985.
8. Shaver,J.M., Oldenburg,D.J. and Bendich,A.J. (2008) The structure of chloroplast DNA molecules and the effects of light on the amount of chloroplast DNA during development in Medicago truncatula. *Plant Physiol.*, **146**, 1064–1074.
9. Bendich,A.J. (2004) Circular chloroplast chromosomes: the grand illusion. *Plant Cell*, **16**, 1661–1666.
10. Gualberto,J.M. and Newton,K.J. (2017) Plant mitochondrial Genomes: Dynamics and mechanisms of mutation. *Annu. Rev. Plant Biol.*, **68**, 225–252.
11. Tremblay-Belzile,S., Lepage,E., Zampini,E. and Brisson,N. (2015) Short-range inversions: rethinking organelle genome stability: template switching events during DNA replication destabilize organelle genomes. *Bioessays*, **37**, 1086–1094.
12. Marechal,A. and Brisson,N. (2010) Recombination and the maintenance of plant organelle genome stability. *New Phytol.*, **186**, 299–317.
13. Christensen,A.C. (2014) Genes and junk in plant mitochondria-repair mechanisms and selection. *Genome Biol. Evol.*, **6**, 1448–1453.
14. Christensen,A.C. (2013) Plant mitochondrial genome evolution can be explained by DNA repair mechanisms. *Genome Biol. Evol.*, **5**, 1079–1086.

Downloaded from https://academic.oup.com/nar/article/47/6/3028/5304310 by UNAM user on 20 October 2020

15. Lieber,M.R. (2010) The mechanism of double-strand DNA break repair by the nonhomologous DNA end-joining pathway. *Annu. Rev. Biochem.*, **79**, 181–211.
16. Chang,H.H.Y., Pannunzio,N.R., Adachi,N. and Lieber,M.R. (2017) Non-homologous DNA end joining and alternative pathways to double-strand break repair. *Nat. Rev. Mol. Cell Biol.*, **18**, 495–506.
17. Sfeir,A. and Symington,L.S. (2015) Microhomology-Mediated end Joining: A Back-up survival mechanism or dedicated pathway? *Trends Biochem. Sci.*, **40**, 701–714.
18. Chiruvella,K.K., Liang,Z. and Wilson,T.E. (2013) Repair of double-strand breaks by end joining. *Cold Spring Harb. Perspect. Biol.*, **5**, a012757.
19. Brissett,N.C., Pitcher,R.S., Juarez,R., Picher,A.J., Green,A.J., Dafforn,T.R., Fox,G.C., Blanco,L. and Doherty,A.J. (2007) Structure of a NHEJ polymerase-mediated DNA synaptic complex. *Science*, **318**, 456–459.
20. Pitcher,R.S., Brissett,N.C., Picher,A.J., Andrade,P., Juarez,R., Thompson,D., Fox,G.C., Blanco,L. and Doherty,A.J. (2007) Structure and function of a mycobacterial NHEJ DNA repair polymerase. *J. Mol. Biol.*, **366**, 391–405.
21. Kent,T., Chandramouly,G., McDevitt,S.M., Ozdemir,A.Y. and Pomerantz,R.T. (2015) Mechanism of microhomology-mediated end-joining promoted by human DNA polymerase theta. *Nat. Struct. Mol. Biol.*, **22**, 230–237.
22. Nick McElhinny,S.A., Havener,J.M., Garcia-Diaz,M., Juarez,R., Bebenek,K., Kee,B.L., Blanco,L., Kunkel,T.A. and Ramsden,D.A. (2005) A gradient of template dependence defines distinct biological roles for family X polymerases in nonhomologous end joining. *Mol. Cell*, **19**, 357–366.
23. Crespan,E., Czabany,T., Maga,G. and Hubscher,U. (2012) Microhomology-mediated DNA strand annealing and elongation by human DNA polymerases lambda and beta on normal and repetitive DNA sequences. *Nucleic Acids Res.*, **40**, 5577–5590.
24. McVey,M. and Lee,S.E. (2008) MMEJ repair of double-strand breaks (director's cut): deleted sequences and alternative endings. *Trends Genet.*, **24**, 529–538.
25. Zahn,K.E., Averill,A.M., Aller,P., Wood,R.D. and Doublie,S. (2015) Human DNA polymerase theta grasps the primer terminus to mediate DNA repair. *Nat. Struct. Mol. Biol.*, **22**, 304–311.
26. Brissett,N.C., Martin,M.J., Bartlett,E.J., Bianchi,J., Blanco,L. and Doherty,A.J. (2013) Molecular basis for DNA double-strand break annealing and primer extension by an NHEJ DNA polymerase. *Cell Rep.*, **5**, 1108–1120.
27. Arrieta-Montiel,M.P., Shedge,V., Davila,J., Christensen,A.C. and Mackenzie,S.A. (2009) Diversity of the Arabidopsis mitochondrial genome occurs via nuclear-controlled recombination activity. *Genetics*, **183**, 1261–1268.
28. Miller-Messmer,M., Kuhn,K., Bichara,M., Le Ret,M., Imbault,P. and Gualberto,J.M. (2012) RecA-dependent DNA repair results in increased heteroplasmy of the Arabidopsis mitochondrial genome. *Plant Physiol.*, **159**, 211–226.
29. Parent,J.S., Lepage,E. and Brisson,N. (2011) Divergent roles for the two PolI-like organelle DNA polymerases of Arabidopsis. *Plant Physiol.*, **156**, 254–262.
30. Cappadocia,L., Marechal,A., Parent,J.S., Lepage,E., Sygusch,J. and Brisson,N. (2010) Crystal structures of DNA-Whirly complexes and their role in Arabidopsis organelle genome repair. *Plant Cell*, **22**, 1849–1867.
31. Marechal,A., Parent,J.S., Veronneau-Lafortune,F., Joyeux,A., Lang,B.F. and Brisson,N. (2009) Whirly proteins maintain plastid genome stability in Arabidopsis. *Proc. Natl. Acad. Sci. U.S.A.*, **106**, 14693–14698.
32. Kwon,T., Huq,E. and Herrin,D.L. (2010) Microhomology-mediated and nonhomologous repair of a double-strand break in the chloroplast genome of Arabidopsis. *Proc. Natl. Acad. Sci. U.S.A.*, **107**, 13954–13959.
33. Odom,O.W., Baek,K.H., Dani,R.N. and Herrin,D.L. (2008) Chlamydomonas chloroplasts can use short dispersed repeats and multiple pathways to repair a double-strand break in the genome. *Plant J.*, **53**, 842–853.
34. Ottaviani,D., LeCain,M. and Sheer,D. (2014) The role of microhomology in genomic structural variation. *Trends Genet.*, **30**, 85–94.
35. Moriyama,T. and Sato,N. (2014) Enzymes involved in organellar DNA replication in photosynthetic eukaryotes. *Front. Plant Sci.*, **5**, 480.
36. Moriyama,T., Tajima,N., Sekine,K. and Sato,N. (2014) Localization and phylogenetic analysis of enzymes related to organellar genome replication in the unicellular rhodophyte Cyanidioschyzon merolae. *Genome Biol. Evol.*, **6**, 228–237.
37. Moriyama,T., Terasawa,K. and Sato,N. (2011) Conservation of POPs, the plant organellar DNA polymerases, in eukaryotes. *Protist*, **162**, 177–187.
38. Moriyama,T., Terasawa,K., Fujiwara,M. and Sato,N. (2008) Purification and characterization of organellar DNA polymerases in the red alga Cyanidioschyzon merolae. *FEBS J.*, **275**, 2899–2918.
39. Mori,Y., Kimura,S., Saotome,A., Kasai,N., Sakaguchi,N., Uchiyama,Y., Ishibashi,T., Yamamoto,T., Chiku,H. and Sakaguchi,K. (2005) Plastid DNA polymerases from higher plants, Arabidopsis thaliana. *Biochem. Biophys. Res. Commun.*, **334**, 43–50.
40. Baruch-Torres,N. and Brieba,L.G. (2017) Plant organellar DNA polymerases are replicative and translesion DNA synthesis polymerases. *Nucleic Acids Res.*, **45**, 10751–10763.
41. Peralta-Castro,A., Baruch-Torres,N. and Brieba,L.G. (2017) Plant organellar DNA primase-helicase synthesizes RNA primers for organellar DNA polymerases using a unique recognition sequence. *Nucleic Acids Res.*, **45**, 10764–10774.
42. Trasvina-Arenas,C.H., Baruch-Torres,N., Cordoba-Andrade,F.J., Ayala-Garcia,V.M., Garcia-Medel,P.L., Diaz-Quezada,C., Peralta-Castro,A., Ordaz-Ortiz,J.J. and Brieba,L.G. (2018) Identification of a unique insertion in plant organellar DNA polymerases responsible for 5′-dRP lyase and strand-displacement activities: Implications for Base Excision Repair. *DNA Repair (Amst.)*, **65**, 1–10.
43. Ayala-Garcia,V.M., Baruch-Torres,N., Garcia-Medel,P.L. and Brieba,L.G. (2018) Plant organellar DNA polymerases paralogs exhibit dissimilar nucleotide incorporation fidelity. *FEBS J.*, **285**, 4005–4018.
44. Chan,S.H., Yu,A.M. and McVey,M. (2010) Dual roles for DNA polymerase theta in alternative end-joining repair of double-strand breaks in Drosophila. *PLoS Genet.*, **6**, e1001005.
45. Beagan,K., Armstrong,R.L., Witsell,A., Roy,U., Renedo,N., Baker,A.E., Scharer,O.D. and McVey,M. (2017) Drosophila DNA polymerase theta utilizes both helicase-like and polymerase domains during microhomology-mediated end joining and interstrand crosslink repair. *PLoS Genet.*, **13**, e1006813.
46. van Kregten,M., de Pater,S., Romeijn,R., van Schendel,R., Hooykaas,P.J. and Tijsterman,M. (2016) T-DNA integration in plants results from polymerase-theta-mediated DNA repair. *Nat. Plants*, **2**, 16164.
47. Inagaki,S., Suzuki,T., Ohto,M.A., Urawa,H., Horiuchi,T., Nakamura,K. and Morikami,A. (2006) Arabidopsis TEBICHI, with helicase and DNA polymerase domains, is required for regulated cell division and differentiation in meristems. *Plant Cell*, **18**, 879–892.
48. Black,S.J., Kashkina,E., Kent,T. and Pomerantz,R.T. (2016) DNA polymerase theta: aunique multifunctional End-Joining machine. *Genes (Basel)*, **7**, 67.
49. Edmondson,A.C., Song,D., Alvarez,L.A., Wall,M.K., Almond,D., McClellan,D.A., Maxwell,A. and Nielsen,B.L. (2005) Characterization of a mitochondrially targeted single-stranded DNA-binding protein in Arabidopsis thaliana. *Mol. Genet. Genomics*, **273**, 115–122.
50. Biasini,M., Bienert,S., Waterhouse,A., Arnold,K., Studer,G., Schmidt,T., Kiefer,F., Gallo Cassarino,T., Bertoni,M., Bordoli,L. *et al.* (2014) SWISS-MODEL: modelling protein tertiary and quaternary structure using evolutionary information. *Nucleic Acids Res.*, **42**, W252–W258.
51. Kibbe,W.A. (2007) OligoCalc: an online oligonucleotide properties calculator. *Nucleic Acids Res.*, **35**, W43–W46.
52. Clark,J.M. (1988) Novel non-templated nucleotide addition reactions catalyzed by procaryotic and eucaryotic DNA polymerases. *Nucleic Acids Res.*, **16**, 9677–9686.
53. Kent,T., Mateos-Gomez,P.A., Sfeir,A. and Pomerantz,R.T. (2016) Polymerase theta is a robust terminal transferase that oscillates between three different mechanisms during end-joining. *Elife*, **5**, e13740.

Downloaded from https://academic.oup.com/nar/article/47/6/3028/5304310 by UNAM user on 20 October 2020

INFORME DE LABORES 2019

54. Zaegel,V., Guermann,B., Le Ret,M., Andres,C., Meyer,D., Erhardt,M., Canaday,J., Gualberto,J.M. and Imbault,P. (2006) The plant-specific ssDNA binding protein OSB1 is involved in the stoichiometric transmission of mitochondrial DNA in Arabidopsis. *Plant Cell*, **18**, 3548–3563.
55. Desveaux,D., Allard,J., Brisson,N. and Sygusch,J. (2002) A new family of plant transcription factors displays a novel ssDNA-binding surface. *Nat. Struct. Biol.*, **9**, 512–517.
56. Desveaux,D., Marechal,A. and Brisson,N. (2005) Whirly transcription factors: defense gene regulation and beyond. *Trends Plant Sci.*, **10**, 95–102.
57. Cappadocia,L., Parent,J.S., Zampini,E., Lepage,E., Sygusch,J. and Brisson,N. (2012) A conserved lysine residue of plant Whirly proteins is necessary for higher order protein assembly and protection against DNA damage. *Nucleic Acids Res.*, **40**, 258–269.
58. Hamdan,S.M., Marintcheva,B., Cook,T., Lee,S.J., Tabor,S. and Richardson,C.C. (2005) A unique loop in T7 DNA polymerase mediates the binding of helicase-primase, DNA binding protein, and processivity factor. *Proc. Natl. Acad. Sci. U.S.A.*, **102**, 5096–5101.
59. Glover,B.P. and McHenry,C.S. (1998) The chi psi subunits of DNA polymerase III holoenzyme bind to single-stranded DNA-binding protein (SSB) and facilitate replication of an SSB-coated template. *J. Biol. Chem.*, **273**, 23476–23484.
60. Kong,D. and Richardson,C.C. (1998) Role of the acidic carboxyl-terminal domain of the single-stranded DNA-binding protein of bacteriophage T7 in specific protein-protein interactions. *J. Biol. Chem.*, **273**, 6556–6564.
61. Antony,E., Weiland,E., Yuan,Q., Manhart,C.M., Nguyen,B., Kozlov,A.G., McHenry,C.S. and Lohman,T.M. (2013) Multiple C-terminal tails within a single E. coli SSB homotetramer coordinate DNA replication and repair. *J. Mol. Biol.*, **425**, 4802–4819.
62. Kühn,K. and Gualberto,J.M. (2012) In: Maréchal-Drouard,L (ed). *Advances in Botanical Research*. Elsevier, Vol. **63**, pp. 215–252.
63. He,Z.G., Rezende,L.F., Willcox,S., Griffith,J.D. and Richardson,C.C. (2003) The carboxyl-terminal domain of bacteriophage T7 single-stranded DNA-binding protein modulates DNA binding and interaction with T7 DNA polymerase. *J. Biol. Chem.*, **278**, 29538–29545.
64. Zampini,E., Truche,S., Lepage,E., Tremblay-Belzile,S. and Brisson,N. (2017) In: Li,XQ (ed). *Somatic Genome Variation in Animals, Plants, and Microorganisms*, John Wiley & Sons, Inc., pp. 119–163.
65. Janicka,S., Kuhn,K., Le Ret,M., Bonnard,G., Imbault,P., Augustyniak,H. and Gualberto,J.M. (2012) A RAD52-like single-stranded DNA binding protein affects mitochondrial DNA repair by recombination. *Plant J.*, **72**, 423–435.
66. Manchekar,M., Scissum-Gunn,K., Song,D., Khazi,F., McLean,S.L. and Nielsen,B.L. (2006) DNA recombination activity in soybean mitochondria. *J. Mol. Biol.*, **356**, 288–299.
67. Zampini,E., Lepage,E., Tremblay-Belzile,S., Truche,S. and Brisson,N. (2015) Organelle DNA rearrangement mapping reveals U-turn-like inversions as a major source of genomic instability in Arabidopsis and humans. *Genome Res.*, **25**, 645–654.
68. Kiefer,J.R., Mao,C., Braman,J.C. and Beese,L.S. (1998) Visualizing DNA replication in a catalytically active Bacillus DNA polymerase crystal. *Nature*, **391**, 304–307.

Downloaded from https://academic.oup.com/nar/article/47/6/3028/5304310 by UNAM user on 20 October 2020

Original Paper

Neuro
-endocrinology

Neuroendocrinology 2019;109:152–164
DOI: 10.1159/000499507

Received: February 19, 2019
Accepted after revision: March 9, 2019
Published online: May 15, 2019

Vasoinhibin Suppresses Nerve Growth Factor-Induced Differentiation and Survival of PC12 Pheochromocytoma Cells

Zesergio Melo[a] Ximena Castillo[a] Bibiana Moreno-Carranza[a] María G. Ledesma-Colunga[a] Edith Arnold[a, b] Fernando López-Casillas[c] Xarubet Ruíz-Herrera[a] Carmen Clapp[a] Gonzalo Martínez de la Escalera[a]

[a]Instituto de Neurobiología, Universidad Nacional Autónoma de México (UNAM), Campus UNAM-Juriquilla, Querétaro, Mexico; [b]Catedrática CONACYT, Instituto de Neurobiología, Universidad Nacional Autónoma de México (UNAM), Campus UNAM-Juriquilla, Querétaro, Mexico; [c]Instituto de Fisiología Celular, Universidad Nacional Autónoma de México (UNAM), Ciudad Universitaria, Mexico City, Mexico

Abstract

Background: Vasoinhibin, a protein derived from prolactin, regulates various vascular functions including endothelial cell survival. Of note, vasoinhibin is present in the central nervous system, where it triggers neuroendocrine and behavioral responses to stress. Moreover, vasoinhibin compromises nerve growth factor (NGF)-induced neurite outgrowth in primary sensory neurons of the peripheral nervous system. Nonetheless, information on the functions of vasoinhibin in developing neurons remains limited. The present study explored whether vasoinhibin affects the neurotrophic actions of NGF by measuring the cell differentiation and survival of PC12 pheochromocytoma cells. ***Methods:*** The effects of recombinant or lentiviral vector-transduced human vasoinhibin were tested on differentiating PC12 cells. Neurite outgrowth was quantified by measuring their length and density. The MTT assay was employed to assess cell viability, and ELISA was used to quantify DNA fragmentation as an index of apoptosis. Phosphorylated Akt and ERK1/2 were analyzed by Western blotting. ***Results:*** The addition of a human recombinant vasoinhibin, and the transduction of a lentiviral vector carrying a human vasoinhibin sequence, significantly reduced NGF-induced neurite outgrowth, cell survival, and phosphorylation of Akt and ERK1/2, and increased DNA fragmentation and caspase 3 activation in PC12 cells. ***Conclusions:*** Vasoinhibin downregulates NGF-induced differentiation and survival of PC12 cells, blocking tropomyosin receptor kinase A-triggered signaling pathways and increasing apoptosis. These results establish that vasoinhibin interaction with NGF and other neurotrophins may be critical in mediating pathways involved in neuronal survival and differentiation.
© 2019 S. Karger AG, Basel

Introduction

Vasoinhibin is an endocrine and autocrine/paracrine factor that downregulates blood vessel growth and function and upregulates inflammatory responses [for reviews see 1–3]. Vasoinhibin, previously referred to as "16-kDa PRL," is a posttranslational N-terminal cleavage

Z. Melo and X. Castillo contributed equally and thus share first authorship.

KARGER
© 2019 S. Karger AG, Basel

E-Mail karger@karger.com
www.karger.com/nen

Gonzalo Martínez de la Escalera, PhD
Instituto de Neurobiología, Universidad Nacional Autónoma de México (UNAM)
Campus UNAM-Juriquilla, Blvd. Juriquilla 3001
Querétaro 76230 (Mexico)
E-Mail gmel@unam.mx

Downloaded by:
Universidad Nacional Autónoma de México
132.248.16.208 - 10/20/2020 8:49:09 AM

product of prolactin (PRL), ranging in molecular mass between 11 and 18 kDa depending on the proteases involved in its generation, which include cathepsin D [4, 5], matrix metalloproteinases [6], and bone morphogenetic protein 1 [7]. Vasoinhibin antagonizes the angiogenesis, vasopermeability, and vasodilation induced by vascular endothelial growth factor and other vasoactive compounds [for reviews see 1–3] via a direct action on endothelial cells. Likewise, vasoinhibin stimulates inflammatory reactions in fibroblasts [8, 9].

Recent studies have revealed a diversity of roles for vasoinhibin beyond the vascular system. Nonetheless, information on the functions of vasoinhibin in the nervous system remains limited. Vasoinhibin operates in the central nervous system (CNS) and peripheral nervous system. Vasoinhibin was detected in the rat hypothalamus [10–12], specifically in the hypothalamic paraventricular and supraoptic nuclei, where it appears to function as a stimulator of vasopressin release [13] and as a functional inhibitor of vascular endothelial growth factor, whose expression is particularly high at these sites [10, 14]. Furthermore, the intracerebroventricular administration of vasoinhibin promotes behaviors associated with anxiety and depression [12], suggesting neuropeptide-like functions for vasoinhibin within the CNS. Recent studies on the peripheral nervous system have revealed direct actions of vasoinhibin on primary sensory neurons, including the inhibition of some neurotrophic actions of nerve growth factor (NGF), such as neurite outgrowth [15].

NGF is the prototypic member of the family of neurotrophins or neurotrophic factors [16] that control a variety of developmental and functional processes of the nervous system [for review see 17], including regulation of neuronal proliferation, survival, differentiation, and plasticity [18]. The signaling pathways involved in NGF-induced neuronal differentiation and survival have been extensively studied in PC12 pheochromocytoma cells [19, 20]. NGF exerts these effects through binding to two transmembrane receptors: the high-affinity tropomyosin receptor kinase A (TrkA) and the low-affinity p75. In the presence of NGF, TrkA and p75 form a cooperating receptor complex [21, 22]. TrkA receptor signaling involves initiating the phosphatidylinositol 3-kinase (PI3K)/Akt and the mitogen-activated protein kinase (MAPK)/extracellular signal-regulated kinase 1/2 (ERK1/2) pathways [18]. Activation of the PI3K/Akt axis is essential for NGF-specific protection of neuronal cells from apoptosis [23] and neuronal differentiation [24], while activation of the MAPK/ERK1/2 pathway appears to be critical for the NGF-induced neuronal differentiation of PC12 cells [25].

As mentioned earlier, vasoinhibin interferes with neurite outgrowth triggered by the binding of NGF to the TrkA/p75 receptor complex in dorsal root ganglion neurons [15]. Therefore, it is important to investigate the functional interaction of vasoinhibin with NGF, as well as their putative signaling cross-talk. If the hypothesis that vasoinhibin interferes with TrkA signaling is true, vasoinhibin would suppress NGF signaling and inhibit some of its neurotrophic actions. In this study, we present evidence that a recombinant human vasoinhibin, or the transduction of a human vasoinhibin with a lentiviral vector, markedly attenuated the differentiating effect of NGF in cultured PC12 cells, as revealed by the inhibition of neurite extension. Likewise, vasoinhibin blocked the prosurvival properties of NGF in serum-deprived PC12 cells. NGF treatment resulted in the rescue of cell survival in serum-deprived PC12 cells, suggesting that vasoinhibin might partially cross-talk with the signaling pathways triggered by NGF activation of TrkA receptors. Indeed, vasoinhibin blocked the NGF-induced phosphorylation/activation of Akt and ERK1/2. Also, vasoinhibin reversed the antiapoptotic effects of NGF in serum-deprived PC12 cells. These findings reveal the inhibitory effect of vasoinhibin in the downstream action of neurotrophin signaling and provide novel insights into the functional role of vasoinhibin in the nervous system.

Materials and Methods

Cell Culture

PC12 cells (American Type Culture Collection, Manassas, VA, USA) were cultured and maintained in RPMI-1640 medium supplemented with 10% heat-inactivated horse serum, 5% heat-inactivated fetal bovine serum, 2 mM glutamine, 100 U/mL penicillin, and 100 μg/mL streptomycin. Cells were routinely grown in 25 cm^2 tissue culture dishes (Corning, New York, NY, USA) at 37 °C in a humidified atmosphere containing 5% CO_2, and the medium was changed every 3 days [26]. The cell culture reagents and sera were purchased from Thermo Fisher Scientific, Waltham, MA, USA.

Cell Differentiation and Treatment

For NGF-induced differentiation into neuron-like cells, PC12 cells were cultured in serum-free RPMI-1640 medium supplemented with NGF-β (Sigma-Aldrich, St. Louis, MO, USA). In order to investigate the effects of vasoinhibin upon NGF-induced neurite outgrowth, i.e., increased cell viability and decreased apoptosis, some PC12 cell cultures were treated with a recombinant vasoinhibin containing the first 123 amino acids (aa) of the human PRL sequence and a tail of 7 histidines, generated as previously described [27]. In addition, NGF actions were also tested in PC12 cells transduced with a lentiviral vector expressing human vasoinhibin.

Downloaded by:
Universidad Nacional Autónoma de México
132.248.16.208 - 10/20/2020 8:49:09 AM

Generation of Vasoinhibin-Expressing PC12 Cells

Stable expression of vasoinhibin and green fluorescent protein (GFP) in PC12 cells was achieved by lentiviral transduction. To generate the lentiviral genome, the *GFP* gene from the self-inactivating pHR-SIN SEWe plasmid [28], kindly provided by PhD Brendel, Boston Children's Hospital, was substituted with a human 123-aa vasoinhibin sequence amplified by PCR from the full-length human PRL cDNA including the signal peptide from an existing construct [29]. Vasoinhibin- and GFP-expressing lentiviral vectors pseudotyped with vesicular stomatitis virus G glycoprotein were produced by transient cotransfection on HEK 293T cells, as described elsewhere [30]. Cell-free viral supernatants were concentrated and titrated by real-time PCR. To transduce the PC12 cells, 1×10^4 undifferentiated cells were seeded in 6-well plates in 1 mL of RPMI-1640 medium supplemented with 10% heat-inactivated horse serum, 5% heat-inactivated fetal bovine serum, 2 mM glutamine, 100 U/mL penicillin, and 100 µg/mL streptomycin, inoculated with 1×10^5 viral particles of the vasoinhibin- or GFP-expressing lentiviral vectors (MOI of 1), and cultured at 37 °C in a humidified atmosphere containing 5% CO_2 for 72 h.

Neurite Outgrowth Analysis

To measure neurite outgrowth, 1×10^4 wild-type PC12 cells and PC12 cells transduced with lentiviral vectors expressing either GFP or vasoinhibin were seeded in 12-well plates coated with poly-L-lysine and cultured in serum-free RPMI-1640 medium supplemented with 2 mM glutamine, 100 U/mL penicillin, and 100 µg/mL streptomycin. Cells were treated for either 1, 3, 5, or 7 days with NGF (50 ng/mL) with or without vasoinhibin (10 nM). Phase-contrast photographs were registered every day at the same time using an Olympus IX51 Inverted Microscope (Olympus, Tokyo, Japan) and a QImaging micropublisher 3.3 RTV camera (QImaging, Surrey, BC, Canada). Ten fields containing a total of at least 100 cells were randomly chosen for neurite growth assay. Cell processes longer than the cell body's diameter were counted as neurites. The length of the longest neurite was traced using ImageJ software (NIH, Bethesda, MD, USA) [31].

MTT Assay of Cell Viability

Cell viability was assessed by measuring the reduction of MTT (3-[4,5-dimethylthiazol-2-yl]-2,5-diphenyltetrazolium bromide) to produce a dark-blue formazan product. Wild-type PC12 cells and PC12 cells transduced with lentiviral vectors expressing either vasoinhibin or GFP were seeded in triplicate in flat-bottom 96-well plates (Corning) at a density of 1×10^4 cells/well. Cells were cultured in RPMI-1640 medium with or without serum and exposed to NGF (50 ng/mL), vasoinhibin (10 nM), or their combination for 7 days. MTT (Sigma-Aldrich) was added to each well to a final concentration of 500 µg/mL, and incubation continued for 4 h at 37 °C. The resulting formazan product was solubilized using a detergent reagent (0.4 N HCl and 10% SDS) in the dark for 2 h at room temperature, and absorbance was measured at 570 nm. The results are expressed as percent of absorbance relative to control cells cultured with serum. Each experiment was repeated 3 times.

TUNEL and Cleaved Caspase 3 Immunofluorescence Analysis of PC12 Cell Apoptosis

PC12 cells were cultured on 18-mm glass coverslips pretreated with poly-L-lysine, and exposed 24 h later to NGF (50 ng/mL), vasoinhibin (10 nM), or a combination of both, in the presence or absence of serum. After 7 days, the cells were fixed with 4% paraformaldehyde for 1 h at room temperature and washed twice with 1× PBS. Apoptosis was detected by the TUNEL method using the In Situ Cell Death Detection Kit (Roche Diagnostics, Risch-Rotkreuz, Switzerland). Blockage of nonspecific binding sites was achieved by incubation in 1× PBS, 0.05% Triton X-100, 1% bovine serum albumin, and 5% normal goat serum during 1 h. Immunostaining was carried out overnight at 4 °C in PBS containing 1% bovine serum albumin, 0.05% Triton X-100, and polyclonal anti-cleaved caspase 3 (1:200 dilution; Millipore, Burlington, MA, USA). The samples were then washed 3 times with PBS and incubated in a PBS solution containing an anti-rabbit IgG conjugated to Alexa 546 (1:500 dilution; Invitrogen, Eugene, OR, USA). The PC12 cells were mounted with VECTASHIELD mounting medium with DAPI (Vector Laboratories, Burlingame, CA, USA). The preparations were maintained at 4 °C until observation with a Zeiss LSM 510 Confocal Microscope (Zeiss, Feldbach, Switzerland).

DNA Fragmentation Analysis of PC12 Cell Damage

PC12 cell apoptosis was also assessed using a cell death detection ELISA (enzyme-linked immunosorbent assay kit; Roche Applied Science, Penzberg, Germany) to measure the fragmentation of DNA. Wild-type PC12 cells were seeded in triplicate in 48-well plates (Corning) at a density of 1×10^5 cells/well. The cells were cultured in RPMI-1640 medium with or without serum and exposed to NGF (50 ng/mL) alone or in combination with vasoinhibin (10, 100, or 1,000 nM). After 48 h, the cells were lysed and processed according to the manufacturer's instructions.

Western Blot Analysis

For analysis of protein phosphorylation, wild-type PC12 cells and PC12 cells transduced with lentiviral vectors expressing either vasoinhibin or GFP were incubated for 10 min in serum-free RPMI-1640 medium supplemented with 50 ng/mL NGF, and analyzed for phospho-Akt, Akt, phospho-ERK1/2, and ERK1/2. The cells were lysed at 4 °C in TNTE buffer (150 mM NaCl, 1 mM EDTA, and 0.5% Triton X-100, supplemented with protease inhibitors: 2 mM leupeptin, 1.5 mM pepstatin A, 1.4 mM E-64, 4 mM bestatin, 80 µM aprotinin, and 1 mM phenylmethylsulfonyl fluoride [Sigma-Aldrich] in 50 mM Tris buffer, pH 7.4). The proteins separated by SDS-PAGE 12% gel electrophoresis were then transferred onto a nitrocellulose membrane. The membranes were blocked with 5% nonfat skimmed milk in TBST buffer (20 mM Tris-HCl, pH 7.6, 137 mM NaCl, and 0.01% Tween 20) for 1 h at room temperature, followed by incubation with primary antibodies against phosphorylated ERK, phosphorylated Akt, ERK, or Akt. After extensive washing with TBST, the membrane was reprobed with 1:3,000 horseradish peroxidase-linked anti-rabbit or anti-mouse immunoglobulin in 5% nonfat skim milk-TBST for 40 min at room temperature. Immunoblots were visualized by enhanced chemiluminescence (SuperSignal West Femto Chemiluminescent Substrate; Thermo Fisher Scientific) according to the manufacturer's protocol. All experiments were repeated at least 3 times.

Statistical Analysis

All values are expressed as means ± SEM. Statistical significance was determined by one-way ANOVA, followed by Bonferroni's multiple-comparison post hoc test, with $p < 0.05$ considered statistically significant.

Downloaded by:
Universidad Nacional Autónoma de México
132.248.16.208 - 10/20/2020 8:49:09 AM

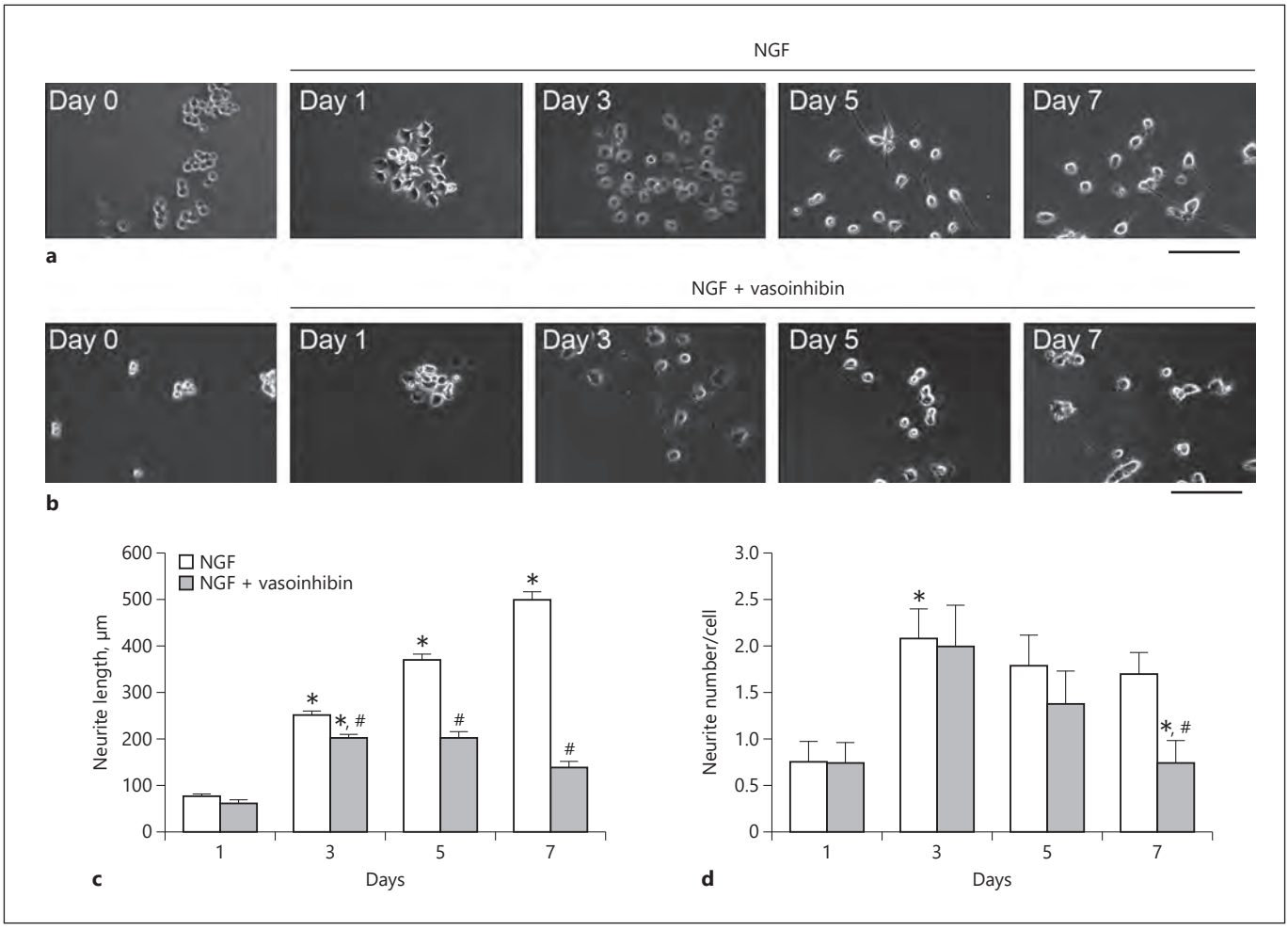

Fig. 1. Vasoinhibin inhibits nerve growth factor (NGF)-induced neurite outgrowth in differentiating PC12 cells. Serum-deprived PC12 cells were cultured in the presence of NGF (50 ng/mL) with or without human recombinant vasoinhibin (10 nM) for 1, 3, 5, or 7 days. **a** Changes in cell shape and neurite outgrowth induced by NGF. **b** Changes in cell shape and neurite outgrowth in PC12 cells exposed to NGF and vasoinhibin. **c** Quantification of neurite length extension. The length of the largest neurite from each cell was determined 1, 3, 5, and 7 days after stimulation with NGF alone or in combination with vasoinhibin. **d** Quantification of neurite density. The number of neurites longer than the cell body's diameter per cell was determined 1, 3, 5, and 7 days after stimulation with NGF alone or in combination with vasoinhibin. Values shown are means ± SEM of about 100 cells obtained from 3 independent experiments. * $p < 0.05$ versus previous time point; # $p < 0.05$ versus corresponding NGF alone. Scale bars, 100 µm.

Results

Vasoinhibin Inhibits NGF-Induced Neurite Outgrowth in Differentiating PC12 Cells

Neurite outgrowth represents a critical process in synapse formation during development. PC12 cells are known to differentiate into neuron-like cells in the presence of NGF [26]. We first confirmed the response to NGF in our sample PC12 cells. Treatment with 50 ng/mL NGF induced neurite outgrowth in most cells (Fig. 1a). We found that the cells were round to oval in shape without neurites in normal serum-containing medium. After treatment with 50 ng/mL NGF for 1 day, the serum-deprived PC12 cells began to develop neurites. By days 3, 5, and 7, almost all cells showed significant neurite outgrowth extension. The length of the longest neurites increased in a time-dependent manner between days 1 and 7 (Fig. 1c, white bars). The number of neurites per cell reached a plateau by day 3 (Fig. 1d, white bars).

We next investigated whether NGF-induced neurite outgrowth was affected by exogenous administration of

Downloaded by:
Universidad Nacional Autónoma de México
132.248.16.208 - 10/20/2020 8:49:09 AM

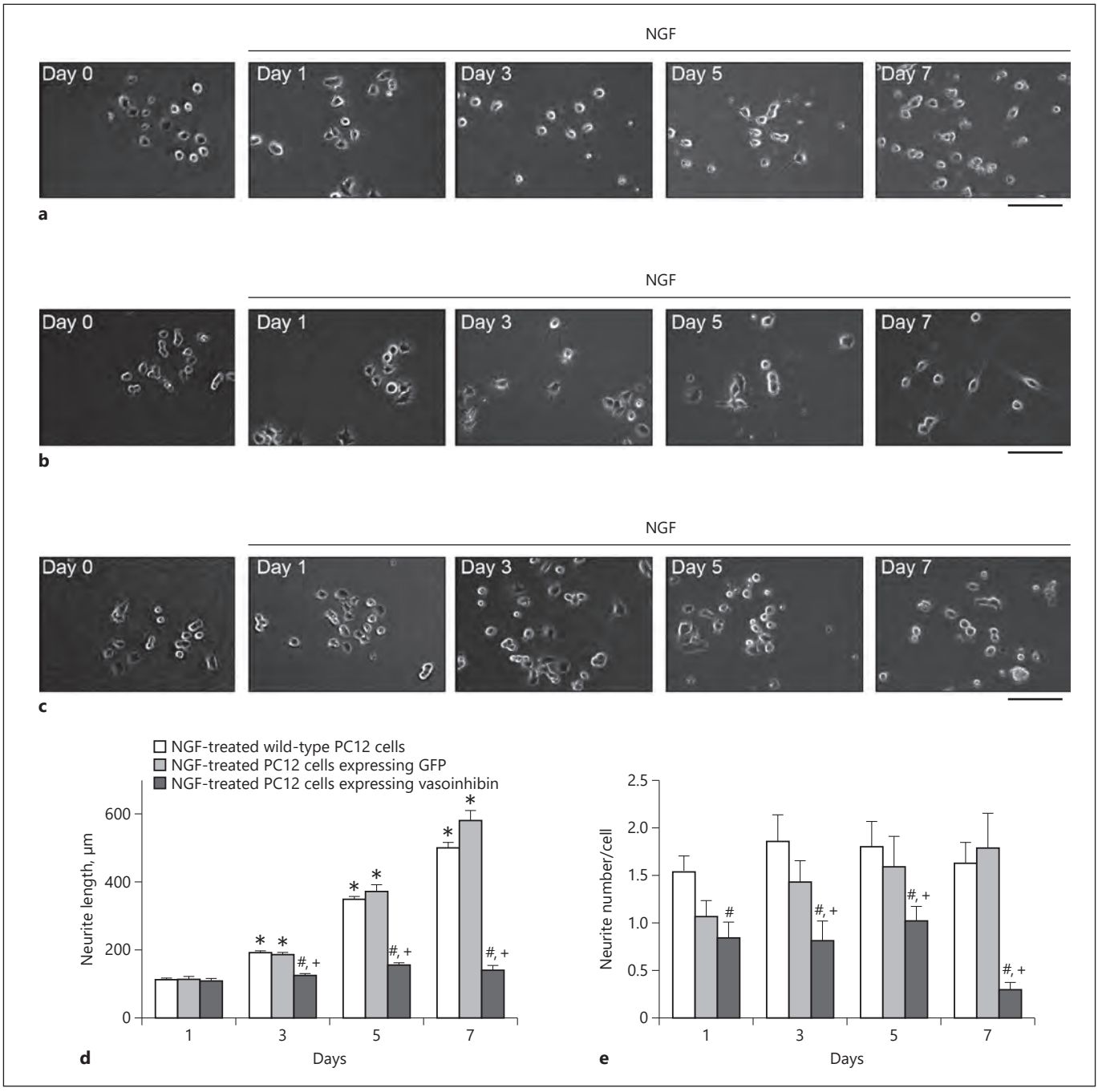

Fig. 2. Nerve growth factor (NGF)-induced neurite outgrowth is hampered in differentiating PC12 cells expressing vasoinhibin. Serum-deprived wild-type PC12 cells and PC12 cells transduced with lentiviral vectors expressing either green fluorescent protein (GFP) or vasoinhibin were cultured in the presence of NGF (50 ng/mL) for 1, 3, 5, and 7 days. **a** Changes in cell shape and neurite outgrowth induced by NGF in wild-type PC12 cells. **b** Changes in cell shape and neurite outgrowth induced by NGF in PC12 cells expressing GFP. **c** Changes in cell shape and neurite outgrowth induced by NGF in PC12 cells expressing human recombinant vasoinhibin. **d** Quantification of neurite length extension. The length of the largest neurite from each cell was determined 1, 3, 5, and 7 days after stimulation with NGF. **e** Quantification of neurite density. The number of neurites longer than the cell body's diameter per cell was determined 1, 3, 5, and 7 days after stimulation with NGF. Values shown are means ± SEM of about 100 cells obtained from 3 independent experiments. * $p < 0.05$ versus previous time point; # $p < 0.05$ versus corresponding wild-type PC12 cells; + $p < 0.05$ versus corresponding PC12 cells expressing GFP. Scale bars, 100 µm.

Neuroendocrinology 2019;109:152–164
DOI: 10.1159/000499507

Downloaded by:
Universidad Nacional Autónoma de México
132.248.16.208 - 10/20/2020 8:49:09 AM

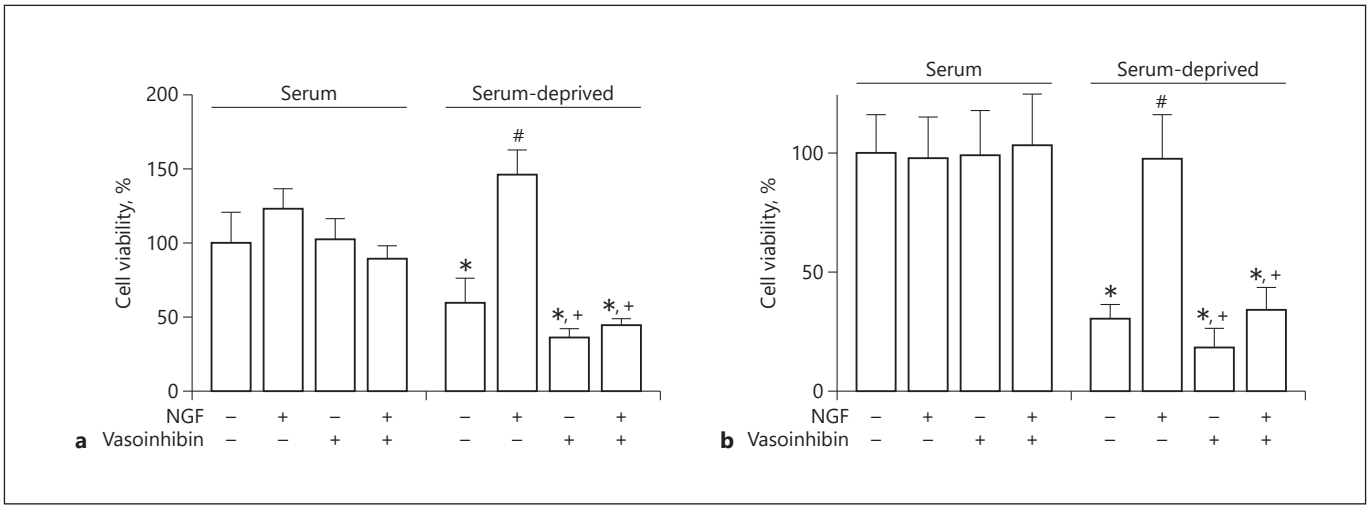

Fig. 3. Vasoinhibin decreased the prosurvival effect of nerve growth factor (NGF) in serum-deprived PC12 cells. Cell survival was analyzed by the MTT assay to quantify surviving PC12 cells. **a** Wild-type PC12 cells cultured with serum or exposed to serum starvation were challenged with NGF (50 ng/mL), vasoinhibin (10 nM), or both. **b** PC12 cells expressing green fluorescent protein (GFP) cultured with serum or exposed to serum starvation were challenged with NGF (50 ng/mL), vasoinhibin (10 nM), or both. Values shown are means ± SEM and expressed as percentage of the untreated cells cultured with serum. The experiments were repeated 3 times with similar results. * $p < 0.05$ versus corresponding serum condition; $^{\#}$ $p < 0.05$ versus untreated cells; $^{+}$ $p < 0.05$ versus NGF-treated cells.

vasoinhibin to differentiating PC12 cells. We treated serum-deprived PC12 cells with 50 ng/mL NGF and 10 nM human recombinant vasoinhibin. We found that the extent of neurite growth was significantly inhibited by the addition of vasoinhibin (Fig. 1b). The effect of vasoinhibin was mainly due to a significant reduction of the length of the neurites by days 3–7 (Fig. 1c, gray bars). The number of neurites per cell was not affected by vasoinhibin between days 1 and 5, but was significantly lower by day 7 (Fig. 1d, gray bars).

NGF-Induced Neurite Outgrowth Is Hampered in Differentiating PC12 Cells Expressing Vasoinhibin

To further investigate the effect of vasoinhibin on NGF-induced neurite outgrowth, we tested the effect of NGF on PC12 cells transduced with a lentiviral vector expressing human recombinant vasoinhibin. PC12 cells were transduced with a lentiviral vector containing a human vasoinhibin truncated at aa 123 of the human PRL sequence. In addition to wild-type PC12 cells, PC12 cells transduced with a lentiviral vector expressing GFP were used as controls. Again, treatment with 50 ng/mL NGF induced neurite outgrowth in most wild-type PC12 cells (Fig. 2a). The expression of GFP using a lentiviral vector did not alter NGF-induced neurite outgrowth (Fig. 2b). In both cell cultures, the length of the neurites increased in a time-dependent manner between days 1 and 7 (Fig. 2d, white bars).

In contrast, NGF was unable to induce neurite growth in PC12 cells transduced with a lentiviral vector expressing vasoinhibin (Fig. 2c). Both the length of the neurites and the number of neurites per cell were significantly inhibited in vasoinhibin-expressing PC12 cells (Fig. 2d, e). These results are consistent with a previous report showing that vasoinhibin inhibits neurite outgrowth of primary sensory neurons [15], and they demonstrate that our PC12 cell line responds to both types of vasoinhibin treatment.

Vasoinhibin Decreases the Prosurvival Effect of NGF in Serum-Deprived PC12 Cells

NGF is known to promote the survival of PC12 cells [26]. We first confirmed this effect investigating PC12 cell survival, as determined by the MTT assay. Serum starvation significantly decreased the cell viability of wild-type PC12 cells (Fig. 3a) and PC12 cells expressing GFP (Fig. 3b). NGF (50 ng/mL) rescued the viability of both wild-type PC12 cells (Fig. 3a) and PC12 cells expressing GFP (Fig. 3b) exposed to serum deprivation to the levels observed in cells cultured with serum. The addition of 10 nM vasoinhibin significantly suppressed the NGF-mediated neuroprotective effect on both wild-type PC12 cells

Downloaded by:
Universidad Nacional Autónoma de México
132.248.16.208 - 10/20/2020 8:49:09 AM

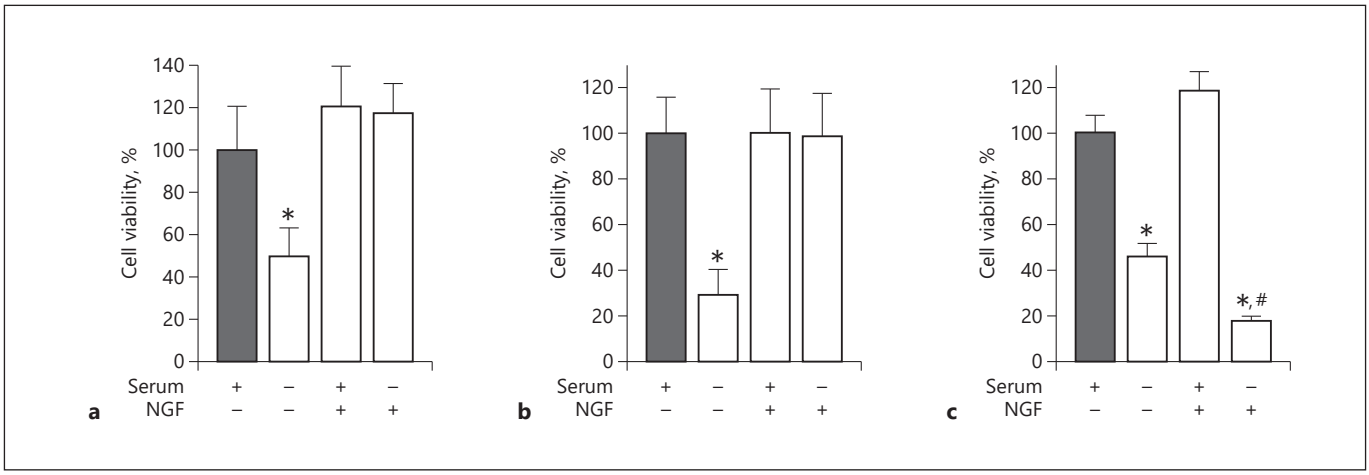

Fig. 4. The neuroprotective effect of nerve growth factor (NGF) on PC12 cells exposed to serum starvation is blocked by vasoinhibin. Cell survival was analyzed by the MTT assay to quantify surviving PC12 cells. **a** Wild-type PC12 cells, incubated with serum or exposed to serum starvation, were cultured with or without NGF (50 ng/mL). **b** PC12 cells expressing green fluorescent protein (GFP), incubated with serum or exposed to serum starvation, were cultured with or without NGF (50 ng/mL). **c** PC12 cells expressing human recombinant vasoinhibin, incubated with serum or exposed to serum starvation, were cultured with or without NGF (50 ng/mL). Values shown are means ± SEM and expressed as percentage of the untreated cells cultured with serum. The experiments were repeated 3 times with similar results. * $p < 0.05$ versus untreated cells cultured with serum; # $p < 0.05$ versus untreated cells cultured without serum.

(Fig. 3a) and PC12 cells expressing GFP (Fig. 3b). Vasoinhibin, by itself, had no effect on the cell viability of either cell type. Under serum condition, vasoinhibin was also unable to affect cell viability, either by itself or when tested with NGF.

We next quantified the protective effect of NGF in vasoinhibin-expressing PC12 cells, in comparison with wild-type and GFP-expressing PC12 cells (Fig. 4). In agreement with the effect shown by treatment with recombinant vasoinhibin, expression of vasoinhibin after lentiviral vector transduction prevented the neuroprotective effect of NGF (Fig. 4c) that was observed in wild-type PC12 cells (Fig. 4a) and in PC12 cells expressing GFP (Fig. 4b).

Vasoinhibin Reverts NGF Inhibition of Apoptosis, Caspase 3 Activation, and DNA Fragmentation in Serum-Deprived PC12 Cells

Apoptosis is the main process involved in serum deprivation-induced cell death in PC12 cells [32]. We first examined the effect of NGF on PC12 cell apoptosis by TUNEL assay, upon exposure of the cells to serum deprivation injury (Fig. 5a). Serum-deprived PC12 cells showed increased TUNEL staining, and this effect was prevented by NGF. Addition of vasoinhibin in combination with NGF completely abolished the protective effect of NGF. Cleaved caspase 3 followed the same pattern (Fig. 5b). Serum deprivation increased the number of cleaved caspase 3-positive cells, and again, this effect was prevented by NGF. Co-incubation of PC12 cells with NGF and vasoinhibin completely abolished the neuroprotective effect of NGF.

We next quantified DNA fragmentation as a third parameter of cellular apoptosis. Under conditions of serum deprivation, PC12 cells showed increased levels of DNA fragmentation as measured by ELISA (Fig. 6a). The effect of serum deprivation was prevented by incubating PC12 cells with 50 ng/mL NGF (Fig. 6a). On the other hand, 100 and 1,000 nM vasoinhibin significantly increased DNA fragmentation in PC12 cells cultured with serum (Fig. 6b). Likewise, increasing concentrations of vasoinhibin decreased the effect of NGF, as shown by the significant dose-dependent increase in DNA fragmentation in response to 100 and 1,000 nM vasoinhibin in serum-deprived PC12 cells cultured with 50 ng/mL NGF (Fig. 6c).

Vasoinhibin Prevents NGF-Induced Activation of PI3K and MAPK in Serum-Deprived PC12 Cells

PI3K and MAPK activation is necessary for NGF-induced neurite outgrowth and survival in PC12 cells [18, 33]. We examined the role of PI3K and MAPK activation

Downloaded by:
Universidad Nacional Autónoma de México
132.248.16.208 - 10/20/2020 8:49:09 AM

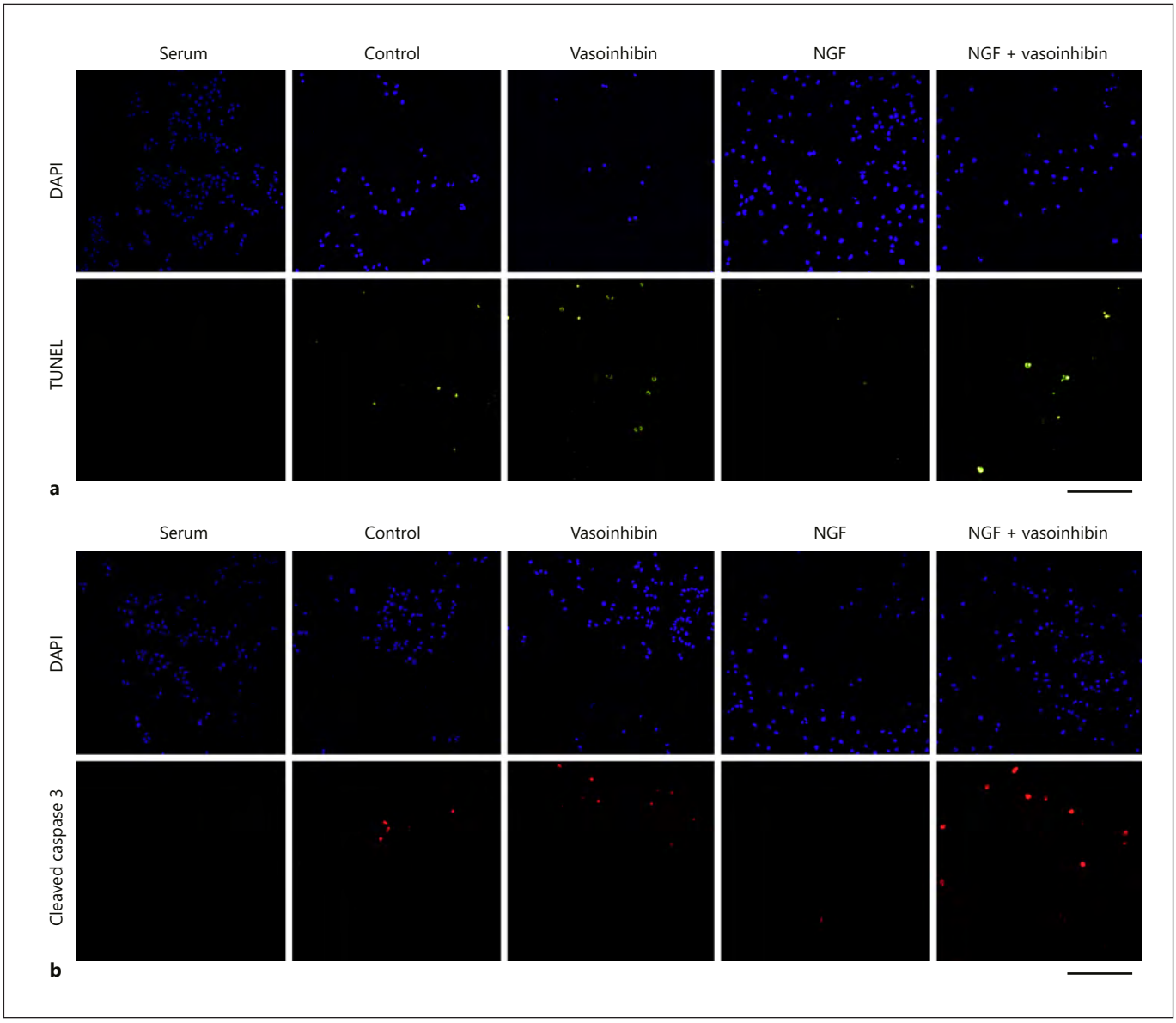

Fig. 5. Vasoinhibin prevented nerve growth factor (NGF) inhibition of apoptosis and caspase 3 activation in serum-deprived PC12 cells. Apoptosis was analyzed by TUNEL assay (**a**) and cleaved caspase 3 immunostaining (**b**) in PC12 cells. The effects of serum starvation for 24 h in the presence or absence of NGF (50 ng/mL), vasoinhibin (10 nM), or their combination are shown in representative photomicrographs of PC12 cells. **a** Green: TUNEL-positive cells. **b** Red: cleaved caspase 3 immunostaining using anti-cleaved caspase antibodies. Cells were co-stained with DAPI to demonstrate nuclear staining. Scale bars, 100 μm.

using Western blot analysis to test the ability of NGF to induce the phosphorylation of Akt and ERK1/2. The addition of NGF for 10 min enhanced Akt and ERK1/2 phosphorylation in protein extracts from wild-type and GFP-expressing PC12 cells (Fig. 7). The NGF-induced Akt and ERK1/2 phosphorylation was prevented in vasoinhibin-expressing PC12 cells.

Likewise, NGF-treated wild-type PC12 cells showed a long-term and time-dependent increase in Akt phosphorylation (Fig. 8a), which was prevented when the PC12 cells were co-treated with NGF and vasoinhibin (Fig. 8b). These results show that NGF is unable to activate the PI3K and MAPK pathways in PC12 cells in the presence of vasoinhibin.

Downloaded by:
Universidad Nacional Autónoma de México
132.248.16.208 - 10/20/2020 8:49:09 AM

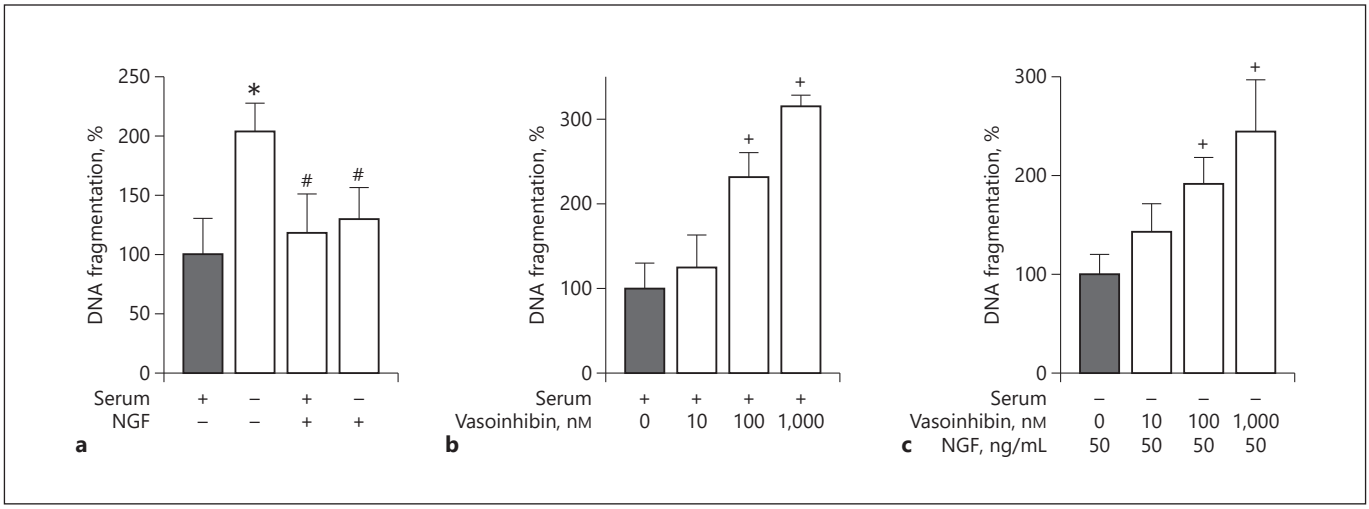

Fig. 6. Vasoinhibin prevented nerve growth factor (NGF) inhibition of DNA fragmentation in serum-deprived PC12 cells. DNA fragmentation was analyzed by ELISA in PC12 cells. The effects of serum starvation for 24 h in the presence or absence of NGF (50 ng/mL), vasoinhibin (10 nM), or their combination are shown in PC12 cells. **a** Effect of NGF on serum-deprived PC12 cells. **b** Dose-dependent effect of vasoinhibin on PC12 cells cultured with serum. **c** Dose-dependent effect of vasoinhibin on serum-deprived PC12 cells cultured with 50 ng/mL NGF. * $p < 0.05$ versus untreated PC12 cells cultured with serum; # $p < 0.05$ versus serum-deprived PC12 cells; + $p < 0.05$ versus vasoinhibin-untreated PC12 cells.

Discussion

In this study, we explored the effects of vasoinhibin, an N-terminal fragment of PRL [1], on TrkA tyrosine kinase receptor signaling in differentiating adrenal PC12 pheochromocytoma cells. We present evidence that treatment with a recombinant human vasoinhibin, either via its administration or expressed by its transduction via a lentiviral vector, markedly attenuated the differentiation, survival, and antiapoptotic effects of NGF in cultured PC12 cells. We also explored the effects of vasoinhibin on TrkA signaling and found a dramatic attenuation of NGF-triggered PI3K/Akt and MAPK/ERK activation, two signaling cascades eventually leading to neurite outgrowth and neuronal apoptosis and fostering cell survival. Our main findings are as follows: (1) vasoinhibin suppressed neurite outgrowth induced by NGF in serum-deprived PC12 cells; (2) vasoinhibin blocked the prosurvival properties of NGF; (3) vasoinhibin reversed the antiapoptotic effects of NGF; and (4) vasoinhibin suppressed TrkA signaling induced by NGF. This study provides the first demonstration that vasoinhibin is able to interfere with NGF actions beyond the promotion of neuronal differentiation, inhibiting the neuroprotective effects of NGF on apoptosis of PC12 cells. These findings reveal the contribution of vasoinhibin to the downstream functions of this neurotrophin, and they provide novel insights into the functional role of vasoinhibin in the nervous system.

In addition to the well-known actions on the vascular system [reviewed in 1, 3], emerging information shows that vasoinhibin can modulate the function of the CNS. Vasoinhibin is present in neurons of the hypothalamic supraoptic and the paraventricular nuclei and, in their projections, conforming the neurohypophysis [10, 11], where it stimulates vasopressin release [13]. Vasoinhibin also influences stress-related behavioral responses. Acute stress reduces the rate of cleavage of PRL to vasoinhibin in the hypothalamus, while the intracerebroventricular administration of vasoinhibin triggers behaviors associated with anxiety and depression [12]. Moreover, vasoinhibin interferes with neurite outgrowth induced by the binding of NGF to the TrkA/p75 receptor complex in newborn rat dorsal root ganglia in organ culture, and in primary sensory neurons in culture [15]. These results show that vasoinhibin acts directly on primary sensory neurons to downregulate NGF-induced developmental changes. Therefore, it was important to investigate the functional interaction of vasoinhibin with NGF, as well as their putative signaling cross-talk, since in this scenario, vasoinhibin may interfere with broad TrkA signaling. If

Downloaded by:
Universidad Nacional Autónoma de México
132.248.16.208 - 10/20/2020 8:49:09 AM

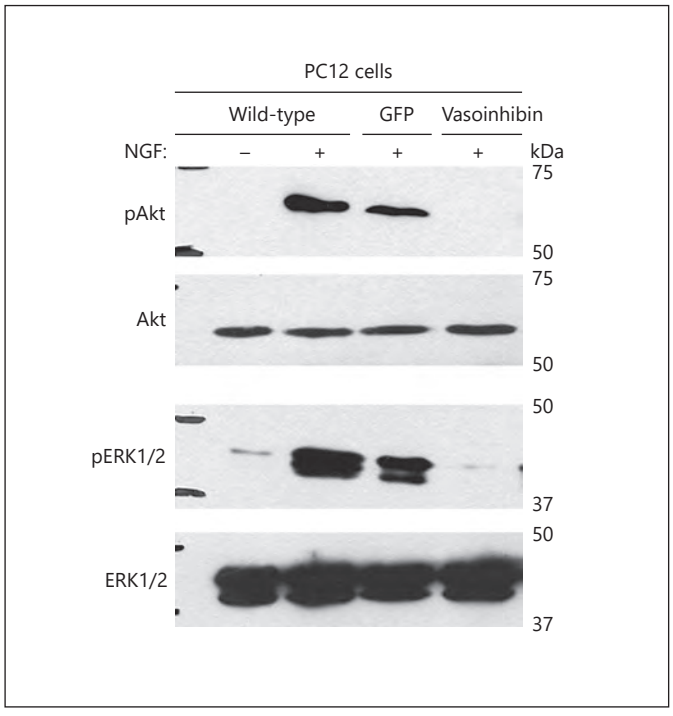

Fig. 7. Vasoinhibin prevented nerve growth factor (NGF)-induced activation of PI3K and MAPK in serum-deprived PC12 cells. NGF induced activation of Akt and ERK in PC12 cells and PC12 cells transduced with lentiviral vector to express green fluorescent protein (GFP) or vasoinhibin. Cells were serum starved and stimulated with NGF (50 ng/mL) for 10 min. Cell lysates were separated by SDS-PAGE and analyzed by immunoblotting. Activated PI3K and MAPK were specifically recognized with rabbit anti-phosphorylated Akt (pAkt) and anti-phosphorylated ERK1/2 (pERK1/2) antibodies. The blot was then reprobed with a rabbit antibody to total Akt or total ERK1/2. Total Akt and total ERK1/2 were used to verify equal protein loading in all lanes. Representative data from 3 independent experiments are shown.

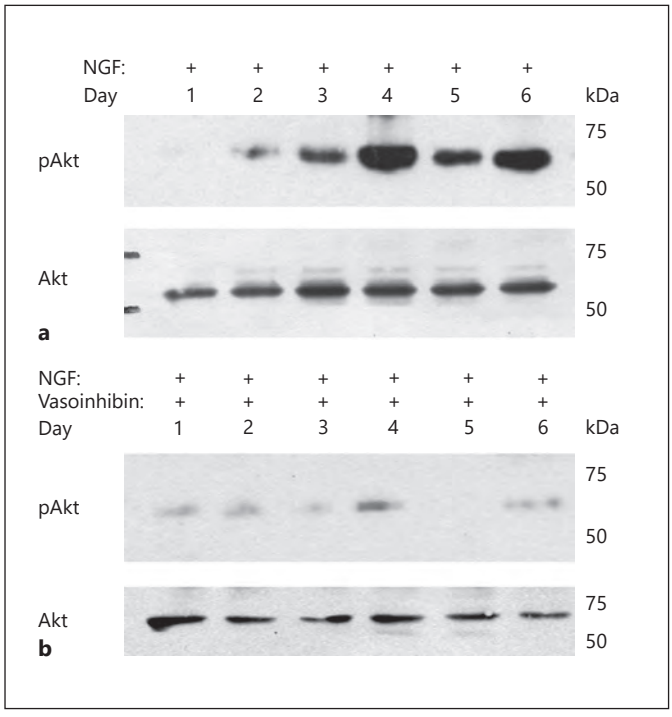

Fig. 8. Vasoinhibin prevented nerve growth factor (NGF)-induced activation of PI3K in serum-deprived PC12 cells. NGF induced activation of Akt in wild-type PC12 cells. **a** PC12 cells were serum starved and stimulated with NGF (50 ng/mL) for 1–6 days. **b** PC12 cells were serum starved and stimulated with NGF (50 ng/mL) and vasoinhibin (10 nM) for 1–6 days. Cell lysates were separated by SDS-PAGE and analyzed by immunoblotting. Activated PI3K was specifically recognized with a rabbit anti-phosphorylated Akt (pAkt) antibody. The blots were then reprobed with a rabbit antibody to total Akt. Total Akt was used to verify equal protein loading in all lanes. Representative data from 3 independent experiments are shown.

this hypothesis is true, vasoinhibin would suppress TrkA signaling and participate in the inhibition of neurotrophic actions induced by NGF. Due to the variable and complex in vivo environments, in the present study we used controlled, NGF-sensitive PC12 cells in vitro as our experimental model. PC12 is a cell line derived from the rat adrenal medulla, and it provides an exceptional experimental model system for the study of the neurotrophic actions of NGF [34]. When cultured in the presence of NGF, PC12 cells differentiate into morphological and functional sympathetic neuron-like cells [26].

The differentiation of PC12 cells in response to NGF is characterized by cell cycle arrest, neurite outgrowth, and the expression of neuron-specific differentiation markers [32, 35, 36]. In this report, we first confirmed that our PC12 cell line responded to NGF by showing that upon stimulation, TrkA signaling was activated and neurite outgrowths developed in these cells. Furthermore, incubation of serum-deprived PC12 cells with a recombinant human vasoinhibin resulted in severe inhibition of the enhanced neurite outgrowth promoted by NGF. Moreover, we succeeded in generating a stable pool of vasoinhibin-expressing PC12 cells via lentiviral vector-mediated cell transfer and found similar results regarding cell differentiation than in vasoinhibin-treated cells. Vasoinhibin expression completely prevented NGF-mediated neurite outgrowth. These results are in line with previous observations regarding vasoinhibin and primary sensory neurons [15], suggesting that vaso-

Downloaded by:
Universidad Nacional Autónoma de México
132.248.16.208 - 10/20/2020 8:49:09 AM

inhibin may have a potent inhibitory effect on the NGF promotion of neurite outgrowth in all neurons, a very important morphological change in synaptic formation during CNS development and post-injury axon path finding.

Vasoinhibin triggers antiproliferative and proapoptotic processes in different cell types. It promotes the apoptosis of mammary gland epithelial cells [37] and of anterior pituitary lactotropes [38]. Moreover, vasoinhibin inhibits the survival of endothelial cells and fibroblasts [for reviews see 2, 3] by activating proapoptotic proteins of the Bcl-2 family and the NF-κB-mediated activation of caspases [9, 39, 40]. These observations led us to hypothesize that vasoinhibin may also have antisurvival and proapoptotic effects on neurons in general, and on PC12 cells in particular. Consistent with this notion, we showed that vasoinhibin reduces the survival of PC12 cells, and that this effect occurs via activation of the caspase apoptosis signaling pathway. In this report, vasoinhibin prevented the protective action of NGF on the viability rate of serum-deprived PC12 cells. Interestingly, no change in PC12 cell survival was observed in PC12 cells cultured with serum, either in response to vasoinhibin alone or to co-treatment with NGF and vasoinhibin. Therefore, the sensitivity of PC12 cell viability to vasoinhibin was restricted to just NGF-stimulated response, and it did not occur regarding survival in response to other serum factors.

We showed a robust increase in apoptosis (as measured by TUNEL) and in caspase 3 activation in response to vasoinhibin in NGF-induced PC12 cells for 7 days. TUNEL staining and immunoreactive cleaved caspase 3, which is essential for stimulation of DNA fragmentation, were reduced by the action of NGF in comparison with serum-deprived PC12 cell cultures, and co-incubation with vasoinhibin blocked the antiapoptotic action of NGF. In agreement with these results, NGF blocked the increase in DNA fragmentation measured by ELISA in serum-deprived PC12 cells, and vasoinhibin stimulated DNA fragmentation in a dose-dependent manner in PC12 cells cultured for 7 days with or without NGF. Therefore, the sensitivity of PC12 cell DNA fragmentation to vasoinhibin is greater than the sensitivity of PC12 cell viability to vasoinhibin.

Our work provides information on the molecular mechanisms involved in the actions of vasoinhibin. It is well documented that neurotrophin-triggered signaling pathways in neurons are heavily redundant. ERK and Akt mediate many cellular processes including proliferation, differentiation, development, survival, and apoptosis [33, 36, 41, 42]. NGF-induced differentiation is accompanied by activation of the ERK1/2 cascade. In particular, there is compelling evidence that sustained ERK1/2 signaling is required for the neuronal differentiation of PC12 cells induced by NGF [41, 43]. On the other hand, neuronal survival and cessation of proliferation signals induced by TrkA are mediated by activation of PI3K and its main downstream mediator Akt [18, 44, 45]. In the present study, NGF treatment of PC12 cells and of PC12 cells transduced to express GFP led to a rapid increase in phosphorylated Akt and ERK1/2 levels within 10 min. NGF-induced phosphorylation of both Akt and ERK1/2 was severely blunted in PC12 cells transduced to express vasoinhibin, showing that the actions of vasoinhibin and NGF on PC12 cells share the downstream PI3K/Akt and MAPK/ERK axes. Furthermore, treatment with a recombinant vasoinhibin also blocked the long-term phosphorylation of Akt induced by NGF in PC12 cells. These findings indicate that vasoinhibin inhibits the NGF-induced activation of the PI3K/Akt and MAPK/ERK1/2 pathways, suggesting that the blockage of these signaling axes by vasoinhibin may be responsible, at least in part, for the inhibitory action of vasoinhibin on neuritogenesis and neuronal apoptosis.

PC12 cells are particularly well suited for elucidating the action of vasoinhibin on differentiating neurons in neuritogenesis, apoptosis, and the signal transduction pathways involved. Although our findings showing the action of vasoinhibin on PC12 cells are robust, they must be extended to central neurons, where vasoinhibin is known to trigger neuroendocrine and behavioral responses. The nature of the signaling cascades, the precise cross-talk modulating neurotrophin action, and, especially, the physiological context of such interactions need to be mapped and elucidated. Thus, much work is required to help establish whether the effects of vasoinhibin counteracting the differentiating and prosurvival actions of NGF can be generalized to neurons other than PC12 cells.

Perspectives and Significance

Our work demonstrates that vasoinhibin inhibits the neurotrophic effects of NGF that promote the survival and differentiation of PC12 pheochromocytoma cells. We suggest that vasoinhibin acts by blocking NGF-induced activation of TrkA signaling, leading to phosphorylation/activation of the MAPK/ERK and PI3K/Akt pathways. These findings expand the understanding of interactions between vasoinhibin and NGF and suggest that similar mechanisms operate on central neuronal populations, warranting further research.

Downloaded by:
Universidad Nacional Autónoma de México
132.248.16.208 - 10/20/2020 8:49:09 AM

Acknowledgements

We thank Fernando López-Barrera, Nydia Hernández-Rios, Valentín Mendoza, and Alejandra Castilla for their technical assistance, as well as Jessica González Norris for critically editing the manuscript.

Statement of Ethics

The authors have no ethical conflicts to disclose.

Disclosure Statement

The authors have no conflicts of interest to disclose.

Funding Sources

This research was supported by the National Council of Science and Technology of Mexico (CONACYT grants 251 and 251509 to G.M.d.l.E.).

Author Contributions

G.M.d.l.E., principal investigator, conceived and designed the research, supervised the study, and wrote the manuscript; Z.M. and X.C., planning and carrying out the study, analyzed the data and contributed to writing of the manuscript; B.M.-C. generated the lentiviral vectors and contributed to writing of the manuscript; M.G.L.-C. and X.R.-H. performed the experiments and contributed to the experimental design and analysis of the data; F.L.-C. generated the recombinant vasoinhibin; E.A. and C.C. critically supervised and revised the study and contributed to writing of the manuscript. All authors critically reviewed and/or revised the manuscript for important intellectual content and approved the manuscript.

References

1 Clapp C, González C, Macotela Y, Aranda J, Rivera JC, García C, et al. Vasoinhibins: a family of N-terminal prolactin fragments that inhibit angiogenesis and vascular function. Front Horm Res. 2006;35:64–73.
2 Clapp C, Thebault S, Jeziorski MC, Martínez de la Escalera G. Peptide hormone regulation of angiogenesis. Physiol Rev. 2009 Oct;89(4):1177–215.
3 Clapp C, Thebault S, Macotela Y, Moreno-Carranza B, Triebel J, Martínez de la Escalera G. Regulation of blood vessels by prolactin and vasoinhibins. Adv Exp Med Biol. 2015;846:83–95.
4 Baldocchi RA, Tan L, King DS, Nicoll CS. Mass spectrometric analysis of the fragments produced by cleavage and reduction of rat prolactin: evidence that the cleaving enzyme is cathepsin D. Endocrinology. 1993 Aug;133(2):935–8.
5 Piwnica D, Touraine P, Struman I, Tabruyn S, Bolbach G, Clapp C, et al. Cathepsin D processes human prolactin into multiple 16K-like N-terminal fragments: study of their antiangiogenic properties and physiological relevance. Mol Endocrinol. 2004 Oct;18(10):2522–42.
6 Macotela Y, Aguilar MB, Guzmán-Morales J, Rivera JC, Zermeño C, López-Barrera F, et al. Matrix metalloproteases from chondrocytes generate an antiangiogenic 16 kDa prolactin. J Cell Sci. 2006 May;119(Pt 9):1790–800.
7 Ge G, Fernández CA, Moses MA, Greenspan DS. Bone morphogenetic protein 1 processes prolactin to a 17-kDa antiangiogenic factor. Proc Natl Acad Sci USA. 2007 Jun;104(24):10010–5.
8 Corbacho AM, Nava G, Eiserich JP, Noris G, Macotela Y, Struman I, et al. Proteolytic cleavage confers nitric oxide synthase inducing activity upon prolactin. J Biol Chem. 2000 May;275(18):13183–6.
9 Macotela Y, Mendoza C, Corbacho AM, Cosío G, Eiserich JP, Zentella A, et al. 16K prolactin induces NF-kappaB activation in pulmonary fibroblasts. J Endocrinol. 2002 Dec;175(3):R13–8.
10 Clapp C, Torner L, Gutiérrez-Ospina G, Alcántara E, López-Gómez FJ, Nagano M, et al. The prolactin gene is expressed in the hypothalamic-neurohypophyseal system and the protein is processed into a 14-kDa fragment with activity like 16-kDa prolactin. Proc Natl Acad Sci USA. 1994 Oct;91(22):10384–8.
11 Torner L, Mejía S, López-Gómez FJ, Quintanar A, Martínez de la Escalera G, Clapp C. A 14-kilodalton prolactin-like fragment is secreted by the hypothalamo-neurohypophyseal system of the rat. Endocrinology. 1995 Dec;136(12):5454–60.
12 Zamorano M, Ledesma-Colunga MG, Adán N, Vera-Massieu C, Lemini M, Méndez I, et al. Prolactin-derived vasoinhibins increase anxiety- and depression-related behaviors. Psychoneuroendocrinology. 2014 Jun;44:123–32.
13 Mejía S, Torner LM, Jeziorski MC, González C, Morales MA, de la Escalera GM, et al. Prolactin and 16K prolactin stimulate release of vasopressin by a direct effect on hypothalamo-neurohypophyseal system. Endocrine. 2003 Feb-Mar;20(1-2):155–62.
14 Jakeman LB, Armanini M, Phillips HS, Ferrara N. Developmental expression of binding sites and messenger ribonucleic acid for vascular endothelial growth factor suggests a role for this protein in vasculogenesis and angiogenesis. Endocrinology. 1993 Aug;133(2):848–59.
15 Castillo X, Melo Z, Varela-Echevarría A, Tamáriz E, Aroña RM, Arnold E, et al. Vasoinhibins suppresses the neurotrophic effects of VEGF and NGF in newborn rat primary sensory neurons. Neuroendocrinology. 2018;106(3):221–33.
16 Cohen S. Purification of a nerve-growth promoting protein from the mouse salivary gland and its neuro-cytotoxic antiserum. Proc Natl Acad Sci USA. 1960 Mar;46(3):302–11.
17 Levi-Montalcini R. The nerve growth factor: thirty-five years later. EMBO J. 1987 May;6(5):1145–54.
18 Huang EJ, Reichardt LF. Neurotrophins: roles in neuronal development and function. Annu Rev Neurosci. 2001;24(1):677–736.
19 Segal RA, Greenberg ME. Intracellular signaling pathways activated by neurotrophic factors. Annu Rev Neurosci. 1996;19(1):463–89.
20 Kaplan DR, Miller FD. Neurotrophin signal transduction in the nervous system. Curr Opin Neurobiol. 2000 Jun;10(3):381–91.
21 Wehrman T, He X, Raab B, Dukipatti A, Blau H, Garcia KC. Structural and mechanistic insights into nerve growth factor interactions with the TrkA and p75 receptors. Neuron. 2007 Jan;53(1):25–38.

Downloaded by:
Universidad Nacional Autónoma de México
132.248.16.208 - 10/20/2020 8:49:09 AM

22 Ceni C, Kommaddi RP, Thomas R, Vereker E, Liu X, McPherson PS, et al. The p75NTR intracellular domain generated by neurotrophin-induced receptor cleavage potentiates Trk signaling. J Cell Sci. 2010 Jul;123(Pt 13):2299–307.

23 Vaillant AR, Mazzoni I, Tudan C, Boudreau M, Kaplan DR, Miller FD. Depolarization and neurotrophins converge on the phosphatidylinositol 3-kinase-Akt pathway to synergistically regulate neuronal survival. J Cell Biol. 1999 Sep;146(5):955–66.

24 Nusser N, Gosmanova E, Zheng Y, Tigyi G. Nerve growth factor signals through TrkA, phosphatidylinositol 3-kinase, and Rac1 to inactivate RhoA during the initiation of neuronal differentiation of PC12 cells. J Biol Chem. 2002 Sep;277(39):35840–6.

25 Schonhoff CM, Bulseco DA, Brancho DM, Parada LF, Ross AH. The Ras-ERK pathway is required for the induction of neuronal nitric oxide synthase in differentiating PC12 cells. J Neurochem. 2001 Aug;78(3):631–9.

26 Greene LA, Tischler AS. Establishment of a noradrenergic clonal line of rat adrenal pheochromocytoma cells which respond to nerve growth factor. Proc Natl Acad Sci USA. 1976 Jul;73(7):2424–8.

27 Galfione M, Luo W, Kim J, Hawke D, Kobayashi R, Clapp C, et al. Expression and purification of the angiogenesis inhibitor 16-kDa prolactin fragment from insect cells. Protein Expr Purif. 2003 Apr;28(2):252–8.

28 Moreno-Carranza B, Gentsch M, Stein S, Schambach A, Santilli G, Rudolf E, et al. Transgene optimization significantly improves SIN vector titers, gp91phox expression and reconstitution of superoxide production in X-CGD cells. Gene Ther. 2009 Jan;16(1):111–8.

29 Ramírez M, Wu Z, Moreno-Carranza B, Jeziorski MC, Arnold E, Díaz-Lezama N, et al. Vasoinhibin gene transfer by adenoassociated virus type 2 protects against VEGF- and diabetes-induced retinal vasopermeability. Invest Ophthalmol Vis Sci. 2011 Nov;52(12):8944–50.

30 Barde I, Salmon P, Trono D. Production and titration of lentiviral vectors. Curr Protoc Neurosci. 2010 Oct;Chapter 4:Unit 4.21.

31 Schneider CA, Rasband WS, Eliceiri KW. NIH Image to ImageJ: 25 years of image analysis. Nat Methods. 2012 Jul;9(7):671–5.

32 Hughes AL, Messineo-Jones D, Lad SP, Neet KE. Distinction between differentiation, cell cycle, and apoptosis signals in PC12 cells by the nerve growth factor mutant delta9/13, which is selective for the p75 neurotrophin receptor. J Neurosci Res. 2001 Jan;63(1):10–9.

33 Liu X, Wang X, Lu J. Tenuifoliside A promotes neurite outgrowth in PC12 cells via the PI3K/AKT and MEK/ERK/CREB signaling pathways. Mol Med Rep. 2015 Nov;12(5):7637–42.

34 Shafer TJ, Atchison WD. Transmitter, ion channel and receptor properties of pheochromocytoma (PC12) cells: a model for neurotoxicological studies. Neurotoxicology. 1991;12(3):473–92.

35 Fábián Z, Vecsernyés M, Pap M, Szeberényi J. The effects of a mutant p53 protein on the proliferation and differentiation of PC12 rat phaeochromocytoma cells. J Cell Biochem. 2006 Dec;99(5):1431–41.

36 Vaudry D, Stork PJ, Lazarovici P, Eiden LE. Signaling pathways for PC12 cell differentiation: making the right connections. Science. 2002 May;296(5573):1648–9.

37 Ishida M, Maehara M, Watanabe T, Yanagisawa Y, Takata Y, Nakajima R, et al. Vasoinhibins, N-terminal mouse prolactin fragments, participate in mammary gland involution. J Mol Endocrinol. 2014 Apr;52(3):279–87.

38 Ferraris J, Radl DB, Zárate S, Jaita G, Eijo G, Zaldivar V, et al. N-terminal prolactin-derived fragments, vasoinhibins, are pro-apoptoptic and antiproliferative in the anterior pituitary. PLoS One. 2011;6(7):e21806.

39 Martini JF, Piot C, Humeau LM, Struman I, Martial JA, Weiner RI. The antiangiogenic factor 16K PRL induces programmed cell death in endothelial cells by caspase activation. Mol Endocrinol. 2000 Oct;14(10):1536–49.

40 Tabruyn SP, Sorlet CM, Rentier-Delrue F, Bours V, Weiner RI, Martial JA, et al. The antiangiogenic factor 16K human prolactin induces caspase-dependent apoptosis by a mechanism that requires activation of nuclear factor-kappaB. Mol Endocrinol. 2003 Sep;17(9):1815–23.

41 Kao S, Jaiswal RK, Kolch W, Landreth GE. Identification of the mechanisms regulating the differential activation of the MAPK cascade by epidermal growth factor and nerve growth factor in PC12 cells. J Biol Chem. 2001 May;276(21):18169–77.

42 Markus A, Zhong J, Snider WD. Raf and Akt mediate distinct aspects of sensory axon growth. Neuron. 2002 Jul;35(1):65–76.

43 Marshall CJ. Specificity of receptor tyrosine kinase signaling: transient versus sustained extracellular signal-regulated kinase activation. Cell. 1995 Jan;80(2):179–85.

44 Dudek H, Datta SR, Franke TF, Birnbaum MJ, Yao R, Cooper GM, et al. Regulation of neuronal survival by the serine-threonine protein kinase Akt. Science. 1997 Jan;275(5300):661–5.

45 Zhou H, Summers SA, Birnbaum MJ, Pittman RN. Inhibition of Akt kinase by cell-permeable ceramide and its implications for ceramide-induced apoptosis. J Biol Chem. 1998 Jun;273(26):16568–75.

Downloaded by:
Universidad Nacional Autónoma de México
132.248.16.208 - 10/20/2020 8:49:09 AM

Journal of Bioenergetics and Biomembranes (2019) 51:103–119
https://doi.org/10.1007/s10863-019-09789-5

Mitochondrial uncoupling proteins UCP4 and UCP5 from the Pacific white shrimp *Litopenaeus vannamei*

Ofelia Mendez-Romero[1] · Salvador Uribe-Carvajal[2] · Natalia Chiquete-Felix[2] · Adriana Muhlia-Almazan[1]

Received: 26 October 2018 / Accepted: 10 February 2019 / Published online: 22 February 2019
© Springer Science+Business Media, LLC, part of Springer Nature 2019

Abstract

Mitochondrial uncoupling proteins (UCP) transport protons from the intermembrane space to the mitochondrial matrix uncoupling oxidative phosphorylation. In mammals, these proteins have been implicated in several cellular functions ranging from thermoregulation to antioxidant defense. In contrast, their invertebrate homologs have been much less studied despite the great diversity of species. In this study, two transcripts encoding mitochondrial uncoupling proteins were, for the first time, characterized in crustaceans. The white shrimp *Litopenaeus vannamei* transcript *LvUCP4* is expressed in all tested shrimp tissues/organs, and its cDNA includes a coding region of 954 bp long which encodes a deduced protein 318 residues long and a predicted molecular weight of 35.3 kDa. The coding region of *LvUCP5* transcript is 906 bp long, encodes a protein of 302 residues with a calculated molecular weight of 33.17 kDa. Both proteins share homology with insect UCPs, their predicted structures show the conserved motifs of the mitochondrial carrier proteins and were confirmed to be located in the mitochondria through a Western blot analysis. The genic expression of *LvUCP4* and *LvUCP5* was evaluated in shrimp at oxidative stress conditions and results were compared to some antioxidant enzymes to infer about their antioxidant role. *LvUCP4* and *LvUCP5* genes expression did not change during hypoxia/re-oxygenation, and no coordinated responses were detected with antioxidant enzymes at the transcriptional level. Results confirmed UCPs as the first uncoupling mechanism reported in this species, but their role in the oxidative stress response remains to be confirmed.

Keywords Hypoxia · Mitochondria · Re-oxygenation · Shrimp *Litopenaeus vannamei* · Uncoupling proteins

Introduction

Mitochondrial uncoupling proteins (UCPs) in the inner membrane mediate uncoupling of oxidative phosphorylation through a proton-transport mechanism that allows the return of protons to the mitochondrial matrix, dissipating the proton gradient and decreasing the organelle ability to produce ATP (Brand et al. 1994; Guerrero-Castillo et al. 2011). Although physiological uncoupling activity from mitochondria has been suggested to control the mitochondrial production of reactive oxygen species, no specific roles have been addressed to UCPs other than UCP1, which significantly contributes to the catabolic cascade of non-shivering thermogenesis in endotherms (Echtay 2007; Cannon et al. 2006). To date, the tissue-specific patterns of both, gene and protein tissue-specific expression patterns from UCPs, and their specific roles in mitochondrial function, are not fully understood even in the most commonly studied vertebrate model species such as rats or mice (Alan et al. 2009). This lack of information on the functionality of UCPs is far more conspicuous in ectotherm models including fish, invertebrates, and unicellular eukaryotes, where scarce information has been published (Bermejo-Nogales et al. 2010; Jarmuszkiewicz et al. 2010; Da-Ré et al. 2014).

To date, several functions have been suggested for mitochondrial proton leak including thermogenesis, control of body mass, regulation of metabolic energy, and control of reactive oxygen species (ROS) production. Although the physiological advantage of thermogenesis is evident for endotherms such as mammals, the contribution of proton leak reactions, and the basal proton conductance in isolated mitochondria of ectothermic organisms seems debatable.

✉ Adriana Muhlia-Almazan
amuhlia@ciad.mx

[1] Bioenergetics and Molecular Genetics Lab, Centro de Investigacion en Alimentacion y Desarrollo, A. C. Carretera a Ejido La Victoria Km 0.6, PO Box 1735, 83000 Hermosillo, Sonora, Mexico

[2] Department of Molecular Genetics, Instituto de Fisiologia Celular, Universidad Nacional Autonoma de Mexico, Ciudad Universitaria, PO Box 70-242, Mexico City, Mexico

INFORME DE LABORES 2019

Beside their leader role in ATP production, mitochondria are also the primary site producing non-enzymatic ROS such as the superoxide anion (O_2^-) (Guerrero-Castillo et al. 2011). As previously established, mitochondria may display as an initial response to avoid oxidative damage, the antioxidant defense system that includes active enzymes such as superoxide dismutase, catalase, peroxidase, low molecular weight antioxidants (ascorbate, glutathione, phenolics, tocopherols), and several electron carriers (ubiquinone, CoQ). In addition, mild and soft uncoupling mechanisms may produce a small decrease in the mitochondrial membrane potential, as the result of a natural antioxidant response to regulate O_2^- through the activation of uncoupling proteins (Echtay 2007; Mailloux and Harper 2011).

UCPs belong to a large family of mitochondrial anion carriers. UCPs catalyze proton leaking into the matrix, and dissipate the proton electrochemical gradient built up during electron transport through the mitochondrial respiratory chain. In mammals, five members of this group have been described including SLC25A7 (UCP1), SLC25A48 (UCP2), SLC25A9 (UCP3), SLC25A27 (UCP4), and SLC25A14 (UCP5) with a partially overlapping expression in various organs (Kim-Han et al. 2001; Krauss et al. 2005).

Even though there is no evidence for the existence of either UCP1, UCP2, and UCP3 in arthropods, it has been proposed that UCP4 and UCP5 homologs are present in these species (Sokolova and Sokolov 2005); however, the functional characterization and physiological relevance of UCP proteins in this group of animals is still poorly understood.

Earlier studies have been focused on the UCPs of the fruit fly *Drosophila melanogaster*, the cockroach *Gromphadorhina coquereliana*, the beetle *Zophobas atratus*, and the blood-sucking bug *Rhodnius prolixus* (Hanák and Ježek 2001; Fridell et al. 2004; Slocinska et al. 2011, 2012; Alves-Bezerra et al. 2014; Da-Ré et al. 2014). These studies have confirmed that UCP4 and UCP5 homologs, which are highly conserved among insects, may play a significant role in regulating both, the mitochondrial respiratory rate and ROS production. Since crustaceans and insects share a common ancestor, it may be inferred that crustacean UCPs may accomplish very similar functions to those described in insects.

This study aimed to identify and characterize for the first time in crustaceans, the cDNA sequence of two UCPs homologs, *LvUCP4* and *LvUCP5,* in the white shrimp *Litopenaeus vannamei*. Their phylogenetic relationships were established, and their expression profile at the transcriptional level in various shrimp tissues/organs was determined. Also, changes in the mRNA relative amounts of *LvUCP4* and *LvUCP5* were determined in shrimp under oxidative stress conditions as hypoxia and re-oxygenation, and the results were compared with the expression levels of four genes encoding shrimp antioxidant enzymes. Both UCPs were confirmed to be expressed in the isolated mitochondria of shrimp.

Materials and methods

Shrimp total RNA isolation and cDNA synthesis

Gills, pleopods, midgut gland, eye stalk, heart, nerve cord, gut and muscle were individually dissected from juvenile, healthy shrimp. Total RNA was isolated from 100 mg of each organ/tissues, used to amplify and sequence UCPs transcripts, and for determination of UCPs mRNA presence in shrimp tissues/organs. Total RNA was isolated by using TRIzol® reagent (Invitrogen, Carlsbad, CA) according to the manufacturer's instructions, and both, concentration and purity of RNA samples were determined spectrophotometrically at 260/280 nm (Nanodrop® ND-1000 v 3.5.2). Total RNA integrity was determined by electrophoresis in a 2% agarose gel as follows: 2.5 μg total RNA were added to 2.5 μL RNA-loading buffer (0.25% bromophenol blue, 0.25% xylene cyanol FF, and 30% glycerol), and heated at 65 °C for 10 min before it was loaded.

Genomic DNA contamination was eliminated from total RNA samples by using DNAse I (Roche, USA; 1 U/μg RNA) following the manufacturer's instructions. Afterwards, cDNA was synthesized from 5 μg of total RNA using the GoScript™ Reverse Transcription System kit (PROMEGA, USA). Briefly, total RNA was added to a mix containing oligo$(dT)_{15}$ (0.5 μg/reaction), incubated for 5 min at 70 °C, and cooled on ice for 1 min. Then 4 μL of GoScript™ 5X reaction buffer, 4 μL of 25 mM $MgCl_2$, 1 μL of 0.5 mM dNTP's mix, 1 μL recombinant RNasin® ribonuclease inhibitor and 1 μL of GoScript™ reverse transcriptase were added to the mixture, gently mixed and incubated at 25 °C for 5 min, 42 °C for 60 min. The reaction was completed by incubating at 70 °C for 15 min, and samples were immediately placed on ice.

Shrimp cDNA was used as a template in PCR reactions to sequence UCPs, to determine their expression in different shrimp tissues, and for the quantitative analysis by qRT-PCR of genes expression under oxidative stress conditions.

LvUCP4 and LvUCP5 cDNA sequences

Specific oligonucleotides were designed using previously reported sequences from other species, and some unidentified sequences (ESTs) found in the GenBank database (EX487810.1), in the Penaeus Genome Database (GO073506.1), and shrimp transcriptome (Ghaffari et al. 2014; comp38567_c1_seq1, comp41251_c0_seq4; Table 1).

The PCR amplification of cDNA encoding shrimp UCPs transcripts were carried out in a DNA Engine Thermocycler® Peltier Cycler (Bio-Rad, USA). The Taq PCR master mix kit (Qiagen, USA) was used, and each PCR reaction included: 12.5 μL of 2X Top Taq PCR master mix, 2.5 μL of 10X coral dye, 1 μL of each 20 μM forward and reverse oligonucleotides, cDNA as template (250 ng total RNA equivalents), and water to a total volume of 25 μL. Cycling conditions were:

INFORME DE LABORES 2019

Table 1 Specific oligonucleotides used for PCR amplification of shrimp *LvUCP4* and *LvUCP5*

Gene	Oligonucleotide name	Sequence (5'-3')	cDNA position (nts)
UCP4	UCP4Fw1	AGATGCAGATGGAGGGAC	446-463
	UCP4Fw2	CTCACCTTCTGGATCACCTAC	898-918
	UCP4Fw3	CAAAGCACTACGCAGATTCAG	35-55
	UCP4Fw4	GGACCGGTGTTGGAATTA	203-220
	UCP4Fw5	TGATCTGACCACCTACGACTC	603-623
	UCP4Rv1	GAGTCGTAGGTGGTCAGATCA	623-603
	UCP4Rv2	CTTCACGGGCCTGTATCAT	1417-1399
	UCP4Rv3	CTTCTTCGTCCCTCCATCT	470-452
	UCP4Rv4	GTAGGTGATCCAGAAGGTGAG	918-898
	UCP4Rv5	TAATTCCAACACCGGTCC	220-203
UCP5	UCP5Fw1	GTGTAATGGGACTGAGCG	-6-13
	UCP5Fw2	AGGTGTCAGGGCATTGTAT	192-210
	MITOCARFw1	ACACGCCTGATGAACCAAAG	682-701
	MITOCARFw2	GCAGTAAGTGGCAATGGT	721-738
	MITOCARFw3	CCGAAGGTCTATGTGGCATT	975-994
	MITOCARFw4	TGATGAAAGCAATGGACAAA	1169-1188
	MITOCARFw5	CCTACATGGCTGAGACTTGG	835-854
	UCP5Rv1	AGGTGTCAGGGCATTGTAT	210-192
	UCP5Rv2	AAAGAGCAGGGGTCATCGTA	534-515
	MITOCARRv1	CCAAGTCTCAGCCATGTAGG	854-835
	MITOCARRv2	TGCCACATAGACCTTCGG	992-975
	MITOCARRv3	TTTGTCCATTGCTTTCATCA	1188-1169
L8	L8LvFw3	ACTTCCGTGACCCTTATC	144-162
	L8LvRv3	GTCACCAGTCTTCTCCTC	313-296

94 °C for 1 min (1 cycle), 94 °C for 1 min, 55 °C for 1 min, 72 °C for 3 min, 94 °C for 1 min, 42 °C for 1 min, 72 °C for 3 min, 94 °C for 1 min, 55 °C for 1 min and 72 °C for 1 min (33 cycles), and a final extension step at 72 °C for 10 min. PCR products were analyzed in a 1% agarose gel stained with SYBR Safe DNA gel stain® (Invitrogen, USA).

To confirm the sequence of each transcript untranslated regions (UTRs), oligonucleotides SMART and CDS III/3 from the SMART cDNA library construction kit (Clontech, USA) were used according to the method of Jimenez-Gutierrez et al. (2013). PCR reactions were carried out in the following conditions: 95 °C for 3 min (1 cycle); 95 °C for 15 s, 68 °C for 6 min, and 95 °C for 15 s (25 cycles). The resulting PCR products were analyzed in 2% agarose gels, and stained with SYBR Safe DNA gel stain® (Invitrogen). PCR products were purified using the Nucleospin Extract II purification kit (Macherey-Nagel, Germany) according to the manufacturer's instructions, and sequenced at the Laboratory of Molecular and Systematic Evolution Facility at the University of Arizona (Tucson, AZ, USA). The nucleotides and deduced amino acid sequences of LvUCP4 and LvUCP5 were analyzed at Expasy (http://au.expasy.org/tools), and using Blast (N, X and P; Altschul et al. 1990), and Clustal Ω algorithms (Sievers et al. 2011).

Phylogenetic analysis of LvUCP4 and LvUCP5

Phylogenetic relationships of shrimp UCPs were determined including the complete protein sequences of LvUCP4 and LvUCP5. A total of 30 different vertebrate and invertebrate UCPs encoding sequences retrieved from the GenBank database were included in the analysis. A multiple alignment analysis was performed using the Clustal Ω algorithm (Sievers et al. 2011), and the phylogenetic tree was constructed using the Neighbor-Joining algorithm with partial deletion (Saitou and Nei 1987). Evolutionary distances were calculated using the matrix method based on JTT (Jones et al. 1992). The bootstrap method was used to assess the confidence analysis of clades based on 1000 replicates. Evolutionary analysis was conducted using the MEGA software version x (Kumar et al. 2018).

In silico structural model of LvUCP4 and LvUCP5

The predicted three-dimensional models of LvUCP4 and LvUCP5 were generated using homology modeling procedures and the coordinates of mouse UCP2 protein (PDB codes: 2lck.1; Berardi et al. 2011) as template, with 36 and 38% identities for LvUCP4 and LvUCP5, respectively. The

predicted model coordinates were built using the SWISS-MODEL server (Guex and Peitsch 1997; Schwede et al. 2003), and Phyre2 software (Kelley et al. 2015; http://swissmodel.expasy.org/ and http://www.sbg.bio.ic.ac.uk/~phyre2/). Visualization of theoretical models of LvUCP4 and LvUCP5 was performed in the PyMOL(™) molecular graphics system (V1.7.5.0), and CCP4MG (2.10.6) software (McNicholas et al. 2011).

LvUCP4 and LvUCP5 mRNA expression in shrimp tissues/organs

To determine whether shrimp UCPs transcripts were expressed in different shrimp tissues/organs including pleopods (Pl), midgut gland (MG), gills (G), muscle (M), eyes stalk (ES), heart (H), nerve cord (NC) and gut (I), the cDNAs from the previously isolated total RNAs were synthesized as described above, and used as template in the PCR amplification of each shrimp UCP. PCR reactions included 250 ng of total RNA equivalents, specific oligonucleotides (UCP4Fw3 and UCP4Rv5) for *LvUCP4*, (UCP5Fw2 and UCP5Rv2) *LvUCP5*, and (L8LvFw3 and L8LvRv3) for the ribosomal L8 protein as internal control (20 μM each, Table 1) in 25 μL volume reactions, PCR conditions were identical to those mentioned above. The PCR products were loaded into a 1% agarose gel, and image was documented in a Gel Doc EZ (Bio-Rad, USA), using the Image Lab TM software (Bio-Rad, USA).

LvUCP4 and LvUCP5 identification in shrimp isolated mitochondria by Western blot analysis

To confirm the LvUCPs location in shrimp mitochondria, these organelles were isolated and solubilized from shrimp pleopods following the method of Rodriguez-Armenta et al. (2018). The soluble protein of mitochondrial fractions was measured by Bradford method (1976), using γ-globulin as a standard. Samples (50 μg) were diluted in a 4 X buffer (0.5 M Tris, pH 6.8, 10% glycerol, 10% SDS, 0.05% beta-mercaptoethanol, and 0.01% bromophenol blue), boiled for 5 min and separated on 10% SDS-polyacrylamide gels (Laemmli 1970). Electrophoresis was run at 100 V for 10 min, 150 V for 10 min, and 200 V to the end.

Gels were electrotransferred into a PVDF membrane using transfer buffer (25 mM Tris, 192 mM glycine and 20% methanol, pH 7.0) (Towbin et al. 1979) and a Wet electroblotting system (BioRad, USA). Membranes were blocked with 5% Blotto nonfat dry milk in TBS-T (50 mM Tris, 104 mM NaCl, pH 7.6, 0.1% Tween 20) for 1 h, and incubated overnight at 4 °C with the primary monoclonal antibodies: UCP4 (A-5; sc-365,295) or BMCP1/KMCP1 (F-3; sc-376,172) (Santa Cruz Biotechnology, USA) diluted 1:1000 (*v*/v). Membranes were washed with TBS-T and incubated at 37 °C for 1 h with peroxidase-conjugated AffiniPure Goat Anti-Mouse IgG (H + L) secondary antibody (Jackson ImmunoResearch, USA) diluted in TBS-T 1:10,000 (v/v). Membranes were washed again and the bands were developed by chemiluminescence using an ECL kit (Amersham Biosciences, GE, Healthcare).

Hypoxia/ re-oxygenation assay

To evaluate and compare the genic expression of shrimp UCPs and antioxidant enzymes, shrimp samples from a hypoxia/re-oxygenation assay were obtained and analyzed. Briefly, 90 adults of *L. vannamei* (30 ± 1 g each) were maintained in laboratory conditions at CIBNOR in La Paz, BCS, Mexico. All shrimp were randomly distributed in 6 plastic tanks (1000 L capacity) with 300 L of seawater each. During acclimatization (8 days), experimental shrimp were maintained at 28 °C, 35 ppt salinity and a dissolved oxygen concentration in the water of 6 mg/L (normoxia). Shrimp from each tank ($n = 15$) were fed twice a day with pelletized food (35% protein), and 50% of total seawater was daily exchanged.

After acclimation, shrimp were fasted for 24 h prior to the experiment. Three tanks were kept at normoxia (6 mg/L) as controls, and hypoxia/re-oxygenation was induced in the remaining 3 tanks. To induce hypoxia in seawater, the air stones were removed from tanks and oxygen was replaced by bubbling nitrogen gas. The 3 tanks at hypoxia were covered with plastic sheets, and oxygen concentration was continuously monitored using a submersible digital oximeter (Ohaus, USA).

All along the assay, 3 organisms were sampled from each tank at different oxygen concentrations (6, 2, 1.5, 7 mg/L), and samples from shrimp at normoxia were taken at the same time than those at hypoxia/re-oxygenation. During hypoxia, the dissolved oxygen concentration of water decreased up to 2 mg/L, then it was maintained at this concentration for 6 h more, and shrimp were sampled; afterwards, oxygen decreased to 1.5 mg/L and after 6 h samples were taken. Finally, oxygen concentration was gradually increased by introducing air stones to reach a final oxygen dissolved concentration of 7 mg/L and after 6 h shrimp samples were taken.

A total of 400 μL of hemolymph were extracted from the base of the fifth pereiopod from each sampled shrimp using a 1 mL syringe containing two volumes of pre-cooled shrimp anticoagulant solution containing 450 mM NaCl,10 mM KCl, 10 mM Na_2-EDTA, 10 mM HEPES, pH 7.3 (Vargas-Albores et al. 1993). Each hemolymph sample was centrifuged at 700 *x g* for 10 min at 4 °C, plasma and hemocytes were separated and stored at −80 °C until use. Subsequently, shrimp were sacrificed and dissected. The dissected tissues/organs were immersed in liquid nitrogen and stored at −20 °C.

INFORME DE LABORES 2019

Lactate concentration measurement in shrimp plasma at hypoxia and re-oxygenation

Shrimp plasma L-lactate concentration was measured to confirm the hypoxia and re-oxygenation effect on experimental shrimp. Individually collected samples from the assay were used and the commercial kit LACTATE-PAP (RANDOX, UK), according to the manufacturer protocols using a Synergy micro plate reader (Bio-Tek Instruments). Briefly, each sample was tested in a final volume reaction of 200 μL, including 10 μL of plasma and 190 μL of reaction solution, absorbance was followed at 550 nm in triplicates. L-lactate concentration in plasma was determined in shrimp at normoxic, hypoxic and re-oxygenated conditions.

Determination of shrimp UCPs and antioxidant enzymes- relative genes expression by qRT-PCR

Specific TaqMan® probes for *LvUCP4, LvUCP5,* manganese superoxide dismutase *(MnSOD),* thioredoxin *(TRX),* glutation peroxidase *(GPX),* catalase *(CAT),* and the ribosomal protein L8 (as a reference gene) were used to amplify shrimp transcripts (Table 2). The relative quantification of genes expression in shrimp gills was done in triplicates using a Step One real-time PCR System (Applied Biosystems). Total volume reactions of 20 μL included 10 μL of 2x Brilliant II qRT-PCR OneStep master mix (Stratagene, USA), 1 μL of TaqMan® probe (20X), 0.8 μL of enzyme RT/RNase block enzyme mix, 150 ng of total RNA free of gDNA and water. Amplification conditions were 50 °C for 30 min, 95 °C for 15 min, followed by 45 cycles at 95 °C for 15 s and 60 °C for 1 min. Fluorescence was taken at 60 °C after each amplification cycle. Each transcript evaluation included a no-template control to confirm no contamination.

The PCR efficiency (E) of each evaluated transcript was determined by the formula $E = 10^{(-1/slope)}$ through a dynamic-range evaluation, and efficiency results were compared between transcripts to be equal. The $2^{-(\Delta\Delta CT)}$ method (Livak and Schmittgen 2001) was used to calculate mRNA changes in the expression of each transcript, relative to the reference gene L8 following the formula: $2^{-(\Delta\Delta Ct)} = 2^{-(mean\ CtGenX - mean\ CtL8)hypoxia) - (mean\ CtGenX - mean\ CtL8)normoxia)}$. Data were analyzed for normality and variances homogeneity. Statistical significance was evaluated by one way-ANOVA, the post hoc analysis was done using the Tukey test. Statistical significance was considered at $p < 0.05$. Analyses were performed using the NCSS 2007 software.

Results

LvUCP4 and LvUCP5 cDNA sequence

Two different nucleotide sequences were identified in the transcriptome of the white shrimp *L. vannamei* as putative uncoupling proteins UCP4 and UCP5 (Ghaffari et al. 2014). The cDNA sequence of *LvUCP4* consists of 1868 pb, the start codon ATG is found at position 1, and the stop codon is found at position 955 followed by a 3′-UTR of 911 pb that contains a polyadenylation signal TAAAT at position 1823, and a polyA tail at position 1840. The coding region of 954 bp encodes a deduced protein LvUCP4 of 318 amino acids, with a predicted molecular weight of 35.3 kDa, and an isoelectric point (pI) of 9.65 (Fig. 1).

The protein primary sequence shares identity with invertebrates such as the fruit fly *D. melanogaster* (44% isoform 4A, NP_573246.1; 53% isoform 4B, NP_608977.1; and 39% isoform 4C, NP_608976.1), the louse *Pediculus humanus corporis* (52%, XP_002429177.1), the pea aphid *Acyrthosiphon pisum* (55%, XP_001944640.1), the parasitic crustacean *Caligus rogercresseyi* (52%, ACO11693.1), the nematode *Caenorhabditis elegans* (43%, CCD68613.1), and various UCP4 vertebrate homologs such as the mouse *Mus musculus* (54%, NP_082987.1), domestic cow *Bos taurus* (54%, NP_001193123.1), and human *Homo sapiens* (54% isoform 1, NP_004268.3, and 50% isoform 2, NP_001190980.1).

The *LvUCP5* cDNA sequence consists of 2332 pb, the start codon is found at position 1, and the stop codon is found at

Table 2 Specific TaqMan® probes used in the real time qRT-PCR determination

Gene	Forward oligos (5–3′)	Reverse oligos (5–3′)	Probes (5′-3′)
LvUCP4	CACCTACGACTCAGTCAAGAGATAC	CTTGACAAAGCATGGGTCCAATATG	TATCGGGCAACCCC
LvUCP5	AGGGCATTGTATTTCGGTATTGCT	GGAGTAATAAATGCCAAACTTGATGGT	CCGTCAGGCAACATA
CAT	ACATGGTGCCGGGTATTGAG	AGAAAAGAGGCGACCTTGCA	TTCCCCTGACAAAATG
TRX	GTGGATGTGGATGAATGTGAAGAC	CAAGCTTCTGGCCATTCTTCATG	ATTGCCCAAGATAACC
GPX	TGCATCATTTGGACACCTGTCT	GCCGATGAGGAATTTCTCGAAGTT	CCGCTCTGACATTGC
MnSOD	AACATGGCTCCCGATGCT	CGTCAATGGCTTGTGCAACAG	CCTTGCGGCTCGCCAC
L8	ATTTGCAACCTTGAGGAGAAGACT	TGGGCAATGACCTGAGCATAATT	ATCCACGGGCAATACG

INFORME DE LABORES 2019

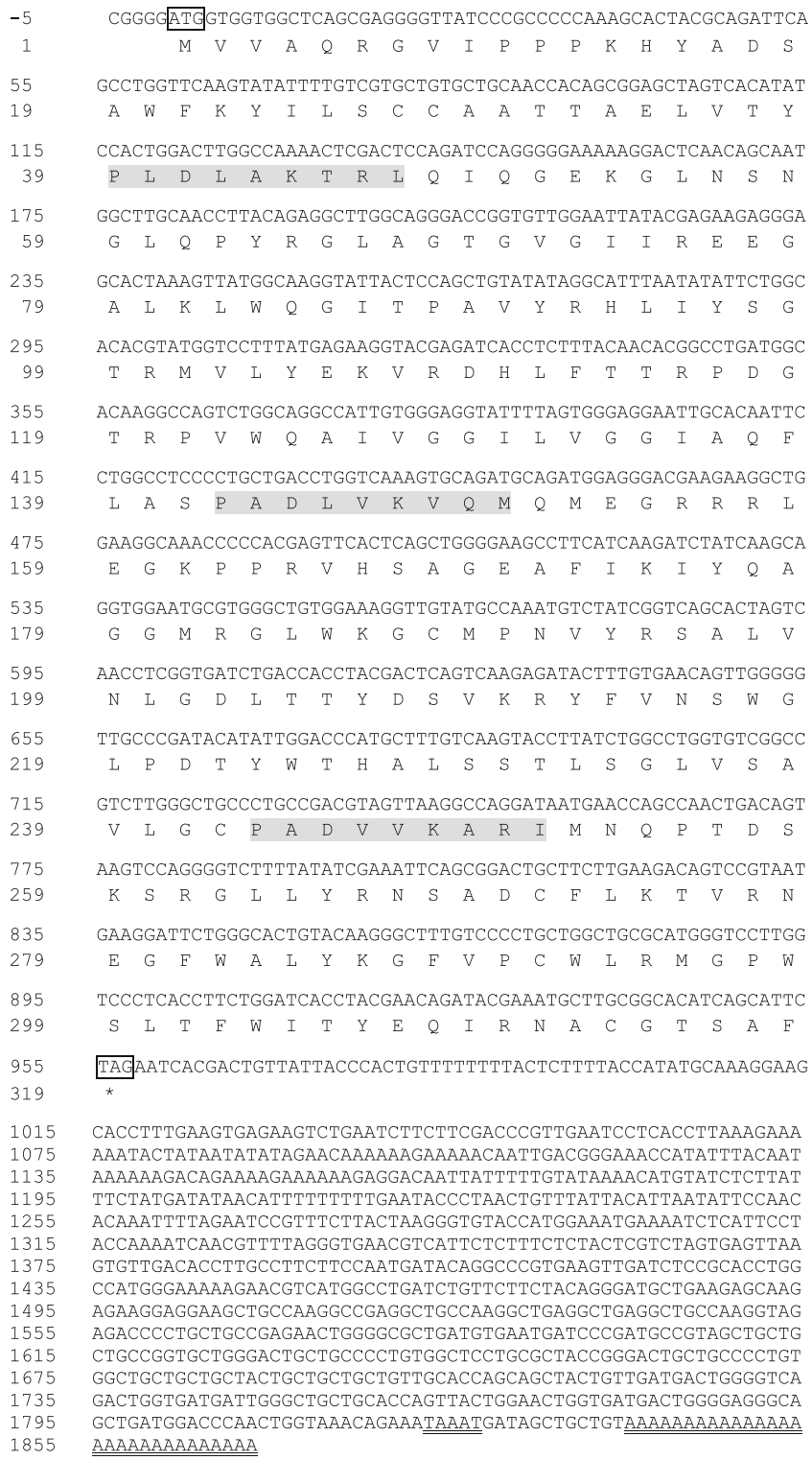

Fig. 1 UCP4 cDNA sequence and deduced amino acid from the white shrimp *L. vannamei*. The start and stop codons are framed. Double underlined nucleotides indicate the poly A signal and polyA tail. The mitochondrial carrier family signatures are shadowed in gray (Ježek 2002)

position 907 pb. The 3′-UTR is 1422 pb long and contains a polyadenylation signal TAAAT at position 2188, and a polyA tail at position 2303. This transcript encodes a deduced protein LvUCP5 of 303 residues with a predicted molecular weight of 33.17 kDa, and a pI of 9.58 (Fig. 2).

LvUCP5 amino acids sequence shows identity to other invertebrates as the fruit fly *D. melanogaster* (54% isoforms 5A NP_729738.1 and 5B NP_648501.1), the blood-sucking insect *R. prolixus* (57%, Alvares-Bezerra et al., 2014), the bee *Apis mellifera* (51%, XP_397152.2), the jewel wasp *Nasonia*

INFORME DE LABORES 2019

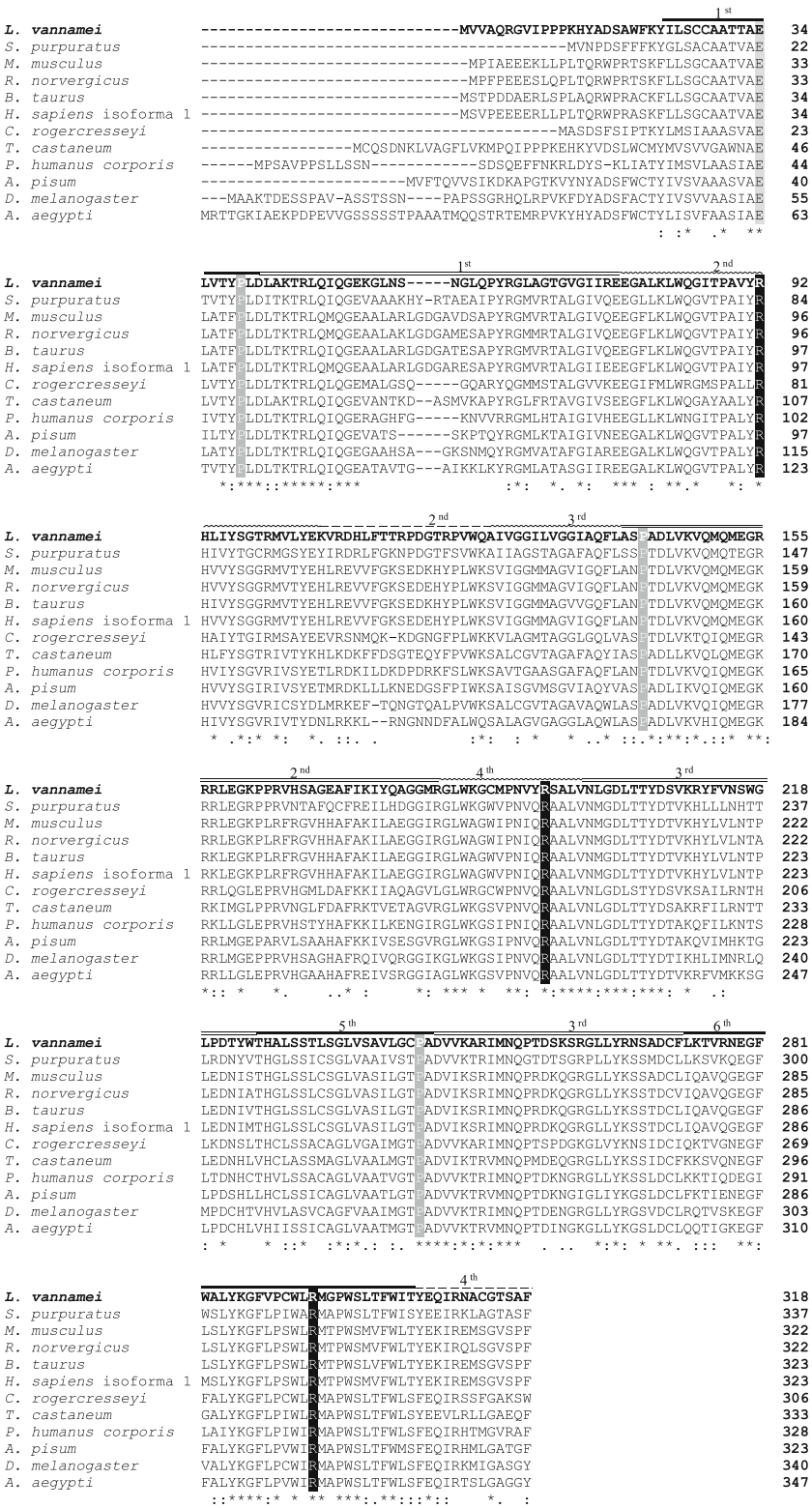

Fig. 2 UCP4 multiple protein alignment. Residues marked with (*) identical residues; (:) conservative substitutions; and (.) semiconservative substitutions. Underlined residues with (·– –·) are cytosolic segments, (▬)transmembrane segments, (═) matrix segments, and (〰) are the transmembrane helices (Ježek and Urbánková 2000). Proline residues are shadowed in light gray; negatively charged residues in gray, and residues involved in the binding site of purine nucleotides are shadowed in black

vitripennis (54%, XP_001606647.1), the bed bug *Cimex lectularius* (57%, XP_014251704.1), the mountain pine beetle *Dendroctonus ponderosae* (55%, AEE63135.1), the eastern oyster *Crassostrea virginica* (54%, ACQ57806.1), the Miyagi oyster *Crassostrea gigas* (54%, XP_011435266.1), and the UCP5 vertebrate homologs such as the cow *Bos taurus* (46%, NP _001039610.1), *Rattus norvegicus* (46%, NP_445953.1), and various human isoforms (45% isoforms 1 NP_001269124.1, and 2 NP_001269125.1; 40% isoform 3, NP_001269126.1, and 51% isoform 4, NP_001269127.1).

INFORME DE LABORES 2019

Both, LvUCP4 and LvUCP5 sequences, share a 27% identity between them, and include the signatures of the mitochondrial carrier family (Figs. 1 and 3). The repeated motifs in the cytosolic, transmembrane and matrix helices, were identified in both shrimp UCPs as shown in Figs. 2 and 4 (Ježek and Urbánková 2000). Both proteins show the conserved negatively charged residues Glu34 (UCP4) and Glu20 (UCP5) located in the transmembrane helix 1 (TMH1), which is involved in proton binding to UCPs (Echtay et al. 2000). Additionally, both proteins have three Pro residues in the odd-numbered helices (TMH1, −3 and − 5), and three Arg residues in the even-numbered helices (TMH2, −4 and − 6), all of them suggested as essential for purine nucleotides binding (Figs. 2 and 4).

```
-5      GTGTAATGGGACTGAGCGATTGGCGCCCTTTTGTATACGGGGGCGTGTCTGCCTGCATA
 1            M  G  L  S  D  W  R  P  F  V  Y  G  G  V  S  A  C  I

55      GCAGAGTTTGGGACGTTTCCCATCGACACCACCAAGACTCGGCTGCAGATCCAAGGAGCC
19       A  E  F  G  T  F  P  I  D  T  T  K  T  R  L  Q  I  Q  G  A

115     CGCAGCGATGGGGGCCAGATCGTTGCCAAGCGATACAAGGGCATGATCCATGCTCTTCTC
39       R  S  D  G  G  Q  I  V  A  K  R  Y  K  G  M  I  H  A  L  L

175     AAGATATCGAGTGAGGAAGGTGTCAGGGCATTGTATTTCGGTATTGCTCCAGCTGTCCTC
59       K  I  S  S  E  E  G  V  R  A  L  Y  F  G  I  A  P  A  V  L

235     CGTCAGGCAACATATGGAACCATCAAGTTTGGCATTTATTACTCCCTGAAACAGATGCTG
79       R  Q  A  T  Y  G  T  I  K  F  G  I  Y  Y  S  L  K  Q  M  L

295     ACAAAAAATCCCAATGAAGAGAGATTGGGCATCAACGTTTTTTGTGCAGTCACTGCAGGT
99       T  K  N  P  N  E  E  R  L  G  I  N  V  F  C  A  V  T  A  G

355     GTGGTGTCAAGTGCTATGGCCAACCCCACTGACGTCCTGAAAGTCAGGTTACAGAGTGGG
119      V  V  S  S  A  M  A  N  P  T  D  V  L  K  V  R  L  Q  S  G

415     CGTTCCGACTTCAAGGAGAAGTCTCTCCTTCAGGCATTTATTAGTATATATAACCAGGAG
139      R  S  D  F  K  E  K  S  L  L  Q  A  F  I  S  I  Y  N  Q  E

475     GGAATACAGGGCCTATGGAGAGGAGTTTGCCCAACGGCGCAAAGAGCAGGGGTCATCGTA
159      G  I  Q  G  L  W  R  G  V  C  P  T  A  Q  R  A  G  V  I  V

535     GGAGTAGAGCTGCCAATTTACGACATGTGCAAACACTATTTCATCAAGATGAACTTGCTG
179      G  V  E  L  P  I  Y  D  M  C  K  H  Y  F  I  K  M  N  L  L

595     CCAGATAATTCTACAAACCACTTCTTGTCGAGCTTCATATCTAGCCTGGGGGGTGCAGTT
199      P  D  N  S  T  N  H  F  L  S  S  F  I  S  S  L  G  G  A  V

655     GCATCAACGCCTCTGGATGTTGTGAGGACACGCCTGATGAACCAAAGAAAACTTAAAGCT
219      A  S  T  P  L  D  V  V  R  T  R  L  M  N  Q  R  K  L  K  A

715     CCAGCTGCAGTAAGTGGCAATGGTGCTGTTTGTACATCCCCAGTGTATGCTAGCACTGCA
239      P  A  A  V  S  G  N  G  A  V  C  T  S  P  V  Y  A  S  T  A

775     GACTGTTTCATACAGACTGTTAAGGCTGAGGGACCCTTGGCTCTCTATAAGGGCTTTATC
259      D  C  F  I  Q  T  V  K  A  E  G  P  L  A  L  Y  K  G  F  I

835     CCTACATGGCTGAGACTTGGCCCATGGAACATCATCTTCTTTGTCACCTTCGAGCAACTC
279      P  T  W  L  R  L  G  P  W  N  I  I  F  F  V  T  F  E  Q  L

895     AAGAAGTTTTATTAGGTTGTGTAGCAACTCCATTGGACCCATGTGAAGCTCAAGACATCT
299      K  K  F  Y  *

955     AATGAAGTTCCTGTTACCTTCCGAAGGTCTATGTGGCATTAAGAAGATCTAATGGGAAAC
1015    CTGGTAGCATTAAAGTGAAGTGCAGCTTATAATCTTGTTGTGATCTATGTCATAGATGGA
1075    GTTCATGGTTCAAAACCATTTCATGAACTAAAGAGCATTTCCTGGAATTTCATGTCTGAT
1135    GACTTGCATTTGTTCACCTACAGAGTTGTCCACTTGATGAAAGCAATGGACAAAAAAGGG
1195    GGGAAAAGTTTTGAAATTAAAAGGGAAGCTCTTTATTCTCATACTTTTTTTTAACATTTG
1255    AGACCTTAGCAGTGATTCTTCATAGCAAACACATTGCAAAGTCGTTTTGACAATCTGTAT
1315    GGAGAAACCTGTCTGTCAGATCTCATATTTCATAAATCAGATCCACATCACATCCATTTC
1375    TTTTGTTTTATAATCATATATGTCAGCCTCATTAATATAGGGTGCTCTTGTCAATTTCTC
1435    TCCTGTGGAGCAGGGGGACTCTTGTATAATATCAGAATGTCATGTTTGATATTAGTCATT
1495    CCAACTAGGAAGATCCTTCACCAGAATGAGATGTTGAAATGGTAATATATTTTATGGAGT
1555    TGTTTTTTTGTTTTTTTTTCTTCTTCTTAATGGAAGATGTAAATATCTCATTTTAGATCT
1615    ACTGTTCATAAGGTCTGTTTAAATTACTTCCTGGTTAAATGCAGTTGTGAAATGACTTGT
1675    GTGAAGACTGAAAGACTTTTCAGTGACCAAAGATTTGCTATTGATAAATGCAGCAGTGGA
1735    TCAACCAAGTTTTGACAGTGAGCATTGAATTACTAGGCATACAGCCATTTCACTTGCCTA
1795    GTCCTAGCACCAGTTTTTATTTTTGGTGAGATTGGCTTAAGTAGGATTATATGCTTTTAT
1855    GACCGTTGATGTTCTCTTCAAATTACAGTATTTAAGAAAGTATATTCAAGGAAACTATTG
1915    CTCACTTCCAAACTCAATCCTTGCTCTGTGTATATGATTACTTTTGACAAATGTATTGTG
1975    TAAATGTGAATTTATCTATTTTTGTAGAAAGTGAACGAGGTGAGATACAGATGAATGAAA
2035    CGCAGTGAAAAGATCAAAGAGTAATGGTGTGTGATAACATTAATTTATTTTGGTCTGGAT
2095    CTGAAGTAATTGCTTTTGTAAGTTTTTGTTATGTAGGTTGGAGAAATGGAATATTTGCCC
2155    TTTATCTACTCTTTCGGAAGTATTTATACATTGTAATACTCAAAAGCAATTGTAAATTAT
2215    CTTTTTTATGAATTGCAGTTTGTAAGAGTACATGGTGAGTGTTAGGATGTTCAGTAACTT
2275    ATTCTTCCAAATAAAAGTTATATCATACAAAAAAAAAAAAAAAAAAAAAAAAAAAAA
```

Fig. 3 UCP5 cDNA sequence and deduced amino acid UCP5 from white shrimp *L. vannamei*. The start and stop codons are framed. Double underlined nucleotides indicate the poly A signal and poly A tail; The mitochondrial carrier family signatures are shadowed in gray (Ježek 2002)

Phylogenetic relationships of UCPs of shrimp

A total of 53 protein sequences of UCP1, UCP2, UCP3, UCP4 and UCP5 from 31 different species from various taxa were included in the phylogenetic analysis, among these proteins 11 sequences of the dicarboxylate carrier protein SLC25A10 (DIC) were added since it is a member of the superfamily of mitochondrial solute carriers, and it has been proposed UCP4 and UCP5 are more closely related to oxoglutarate/malate and dicarboxylate carrier proteins (Palmieri 2013; Gaudry and Jastroch 2018). The resulting tree shows that both, UCP5 and UCP4, were grouped into different clades. Shrimp and insect UCP4 proteins were grouped into a single clade, which is separated from mammals, nematodes and the parasitic copepod *C. rogercresseyi* (Fig. 5).

The deduced protein LvUCP5 is grouped with the UCP5 proteins from insects, but vertebrate homologs including the various human isoforms were separated in a different clade (Fig. 5). Results confirm that the sequenced deduced proteins of *L. vannamei* are UCP4 and UCP5, sharing higher similarities with their vertebrates homologs UCP4 and UCP5, than to UCPs 1 to 3.

Predicted 3D structure of LvUCP4 and LvUCP5

Shrimp protein conformation resembles mouse UCP2. Both predictive models for LvUCP4 and LvUCP5 show secondary elements with a tripartite structure (Fig. 6a and 7a) and a central channel, this consists of three hydrophobic regions made up of two transmembrane α-helices each, extended through the MIM six times (transmembrane helices TMH 1–6). The two adjacent helices that form each repeated region are connected by an amphipathic helix (APH) matrix-oriented (Fig. 6b and 7b). The mitochondrial carrier family signature PxD/ExxK/RxK/R-(20–30 residues, where x is any residue) was observed in both shrimp UCPs (Ježek and Urbánková 2000). This motif is found in each repeated region, including slight modifications in one or both sequences signing some carriers (Krauss et al. 2005; Nury et al. 2006). The three repeated regions were located at positions 39–47, 142–150, and 243–251 in the LvUCP4 sequence, and at positions 25–33, 127–135, and 222–230 in the LvUCP5 sequence.

The N- (dark blue) and C-terminal (red) ends of these proteins are oriented toward the intermembrane space (Fig. 6 and 7a). The analysis of arginine conserved residues

INFORME DE LABORES 2019

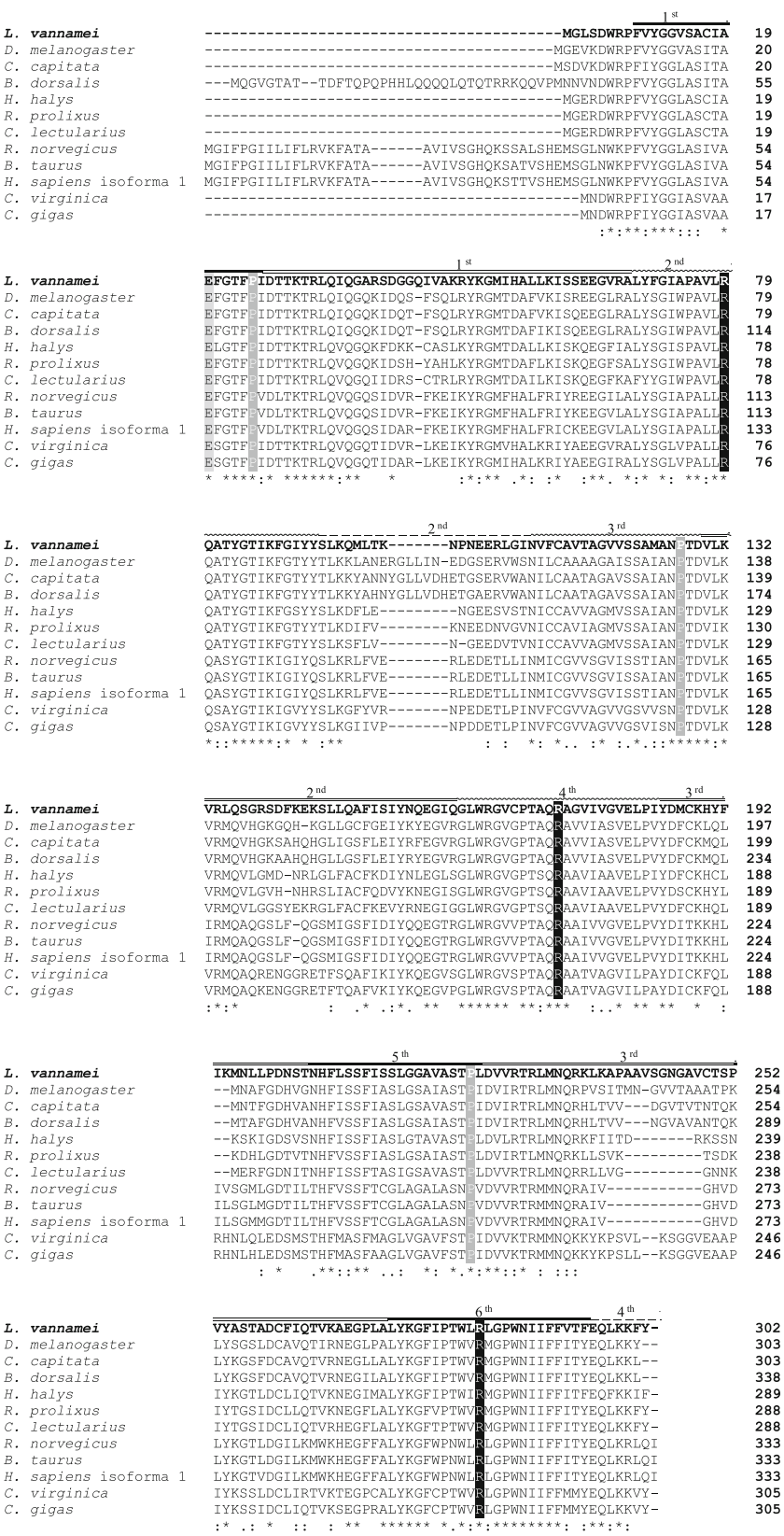

Fig. 4 UCP5 multiple protein alignment. Mitochondrial carrier family signatures (Ježek 2002) are shadowed in gray. Residues marked with (*) identical residues; (:) conservative substitutions; and (.) semiconservative substitutions. Underlined residues with (·– –·) are the cytosolic segments, (▬) transmembrane segments, (═) matrix segments, and (〰) are the transmembrane helices (Ježek and Urbánková 2000). Proline residues are shadowed in light gray; negatively charged residues in gray, and residues involved in the binding site of purine nucleotides are shadowed in black

in UCPs, which are known to be essential for purine nucleotide binding were located in the LvUCP4 model at positions R92 (TMH2), R194 (TMH4), and R294 (TMH6) (Fig. 6c), and in the LvUCP5 model at positions R79 (TMH2), R173 (TMH4), and R283 (THM6) (Fig. 7c). According to the arginine residues position in the predictive models of shrimp

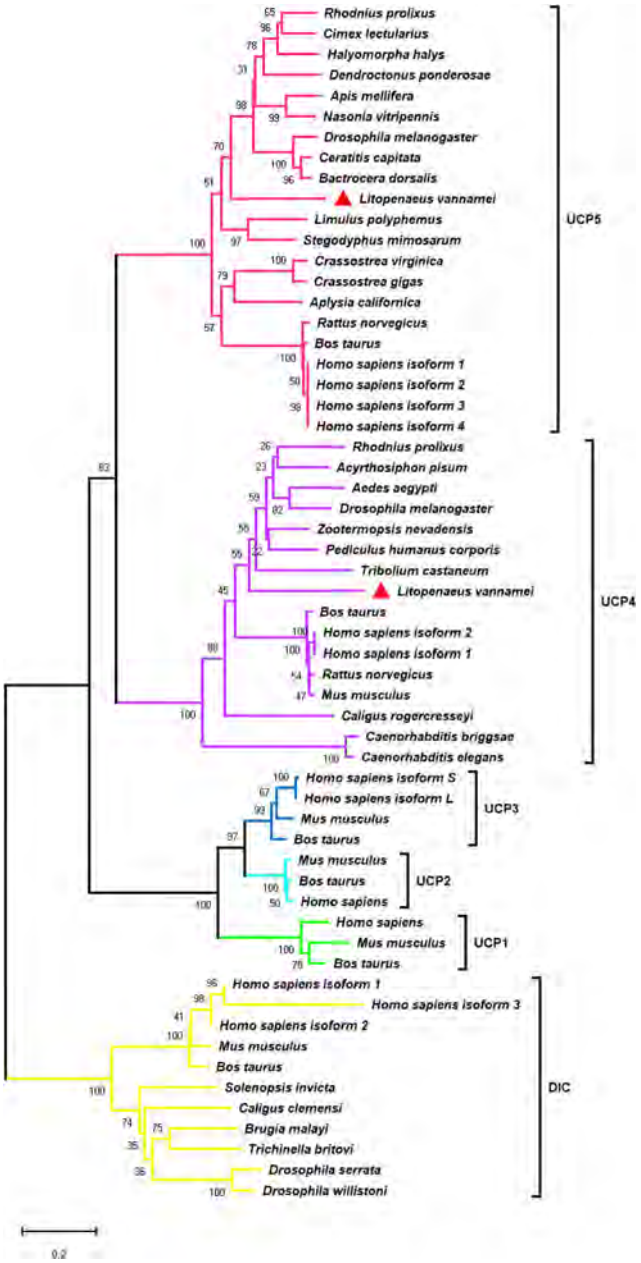

Fig. 5 Shrimp UCPs phylogenetic tree topology using neighbor-joining method with partial deletion from amino acid sequences. Numbers above/below the nodes indicate nonparametric bootstrap values (1000 replicates)

UCPs, the average distance between these three residues is >10 Å (Fig. 6c and 7c). Two additional residues, D202 in LvUCP4, and E181 in LvUCP5 were identified in the purine nucleotide binding sites (Fig. 6d and 7d).

LvUCP4 and LvUCP5 genes expression in shrimp tissues/organs

LvUCP4 was found to be ubiquitously expressed in all tested shrimp tissues and organs, being pleopods and gills, the sites where higher expression was detected. On the other hand, *LvUCP5* was observed to be only expressed in three of all tested organs including pleopods, gills, and muscle, being the gills the organ that expresses both transcripts and the one selected to determine *LvUCPs* genes expression (Fig. 8).

LvUCP4 and LvUCP5 identification in shrimp mitochondria

Western blot analysis confirmed that LvUCP4 and LvUCP5 are located in the isolated mitochondria of shrimp organs. Pleopods were used since higher amounts of mitochondria can be isolated from these appendages, and both transcripts were expressed in these organs. The isolated mitochondria protein fractions include both proteins, LvUCP4 and LvUCP5 in their monomeric and dimeric forms, with molecular masses of ~36 and 70 kDa, respectively (Fig. 9).

L-lactate concentration measurement in shrimp plasma at hypoxia and re-oxygenation

L-Lactate concentration in shrimp plasma significantly increased after 12 h at hypoxia (1.5 mg/L) ($p < 0.05$; Fig. 10). As hypoxia persisted, lactate levels increased becoming up to 11 times higher than at normoxia (6 mg/L); however, when the system was re-oxygenated to 7 mg/L, lactate concentration significantly diminished but it did not decrease to its initial concentration at normoxia.

Relative gene expression of UCPs and antioxidant enzymes from shrimp at hypoxia/re-oxygenation

The genic expression of *LvUCP*4 and *LvUCP5* and four antioxidant enzymes showed significant differences when shrimp were exposed to hypoxia and re-oxygenation. (Fig. 11a-f). No significant differences were detected in the *LvUCP4* and *LvUCP5* mRNA levels from shrimp at normoxia, hypoxia and re-oxygenation conditions ($p > 0.05$; Fig. 11a and b); however, the mean mRNA levels at hypoxia (2 mg/L) decreased 35% for *LvUCP4*, and 20% for *LvUCP5* when compared to normoxia, and these decreases continued at hypoxia (1.5 mg/L) and after re-oxygenation.

Among the mRNA changing levels of antioxidant enzymes, statistical differences were detected only for catalase (*CAT*) and glutathione peroxidase (*GPX*) transcripts ($p < 0.05$; Fig. 11d and e). However, some similarities were observed in the changing patterns of the four antioxidant enzymes along the assay. The *MnSOD*, *CAT* and *GPX* mRNA levels increased at hypoxia 2 mg/L and decreased at hypoxia 1.5 mg/L; however, no significant changes were detected in the transcripts levels at re-oxygenation, except *CAT*. These trends do not correspond to those for *LvUCP4* and *LvUCP5*, suggesting different regulation levels, different response times (whether ROS control is considered), or different functions in *L. vannamei*.

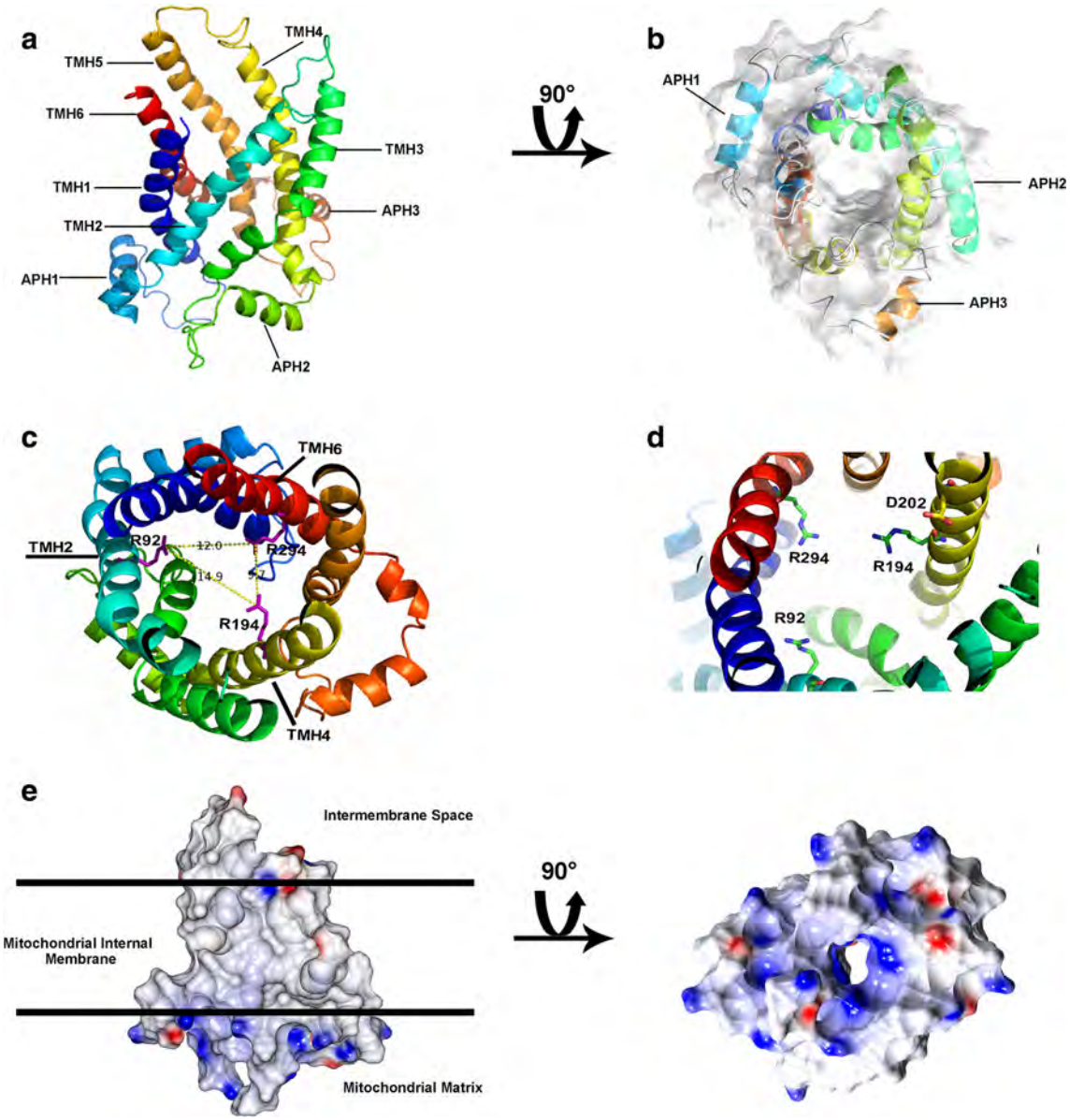

Fig. 6 Predictive structural model of *Lv*UCP4. **a** Secondary structure **b** View of the channel from the matrix with secondary structures and surface representation. **c** Conserved arginine residues. **d** View from the intermembrane space of conserved arginine residues. **e** Surface representation

Discussion

The mitochondrial ability to uncouple seems to be essential in cell physiology. Mitochondrial function is regulated by the transmembrane potential and proton gradient dissipation, which lead to control oxidative phosphorylation to synthesize ATP. Although different extrinsic and intrinsic uncoupling mechanisms have been described in eukaryotic cells (Guerrero-Castillo et al. 2011), to date no evidence exists that describes whether mitochondria from crustaceans exhibit physiological uncoupling. Previous studies have confirmed that isolated mitochondria from various shrimp species and artemia do not enter an uncoupled transition permeability state after a calcium overload (Menze et al. 2005; Holman and Hand 2009; Konrad et al. 2012; Rodriguez-Armenta et al., submitted). Additionally, no alternative oxidases or reductases were found as an uncoupling mechanism in the mitochondrial respiratory chain of the white shrimp L. vannamei (Rodriguez-Armenta et al. 2018).

Mitochondrial uncoupling proteins are widely distributed in nature, and this may suggest that regulating oxidative phosphorylation efficiency through physiological uncoupling mechanisms may be a general and helpful strategy (Miroux et al. 1993). Up to five different UCP isoforms, and some additional UCP-homologs have been described in birds, amphibians, fishes, insects, plants and unicellular organisms (Sokolova and Sokolov 2005); however, to our knowledge, no records for any crustacean UCP have been reported adequately described to date.

INFORME DE LABORES 2019

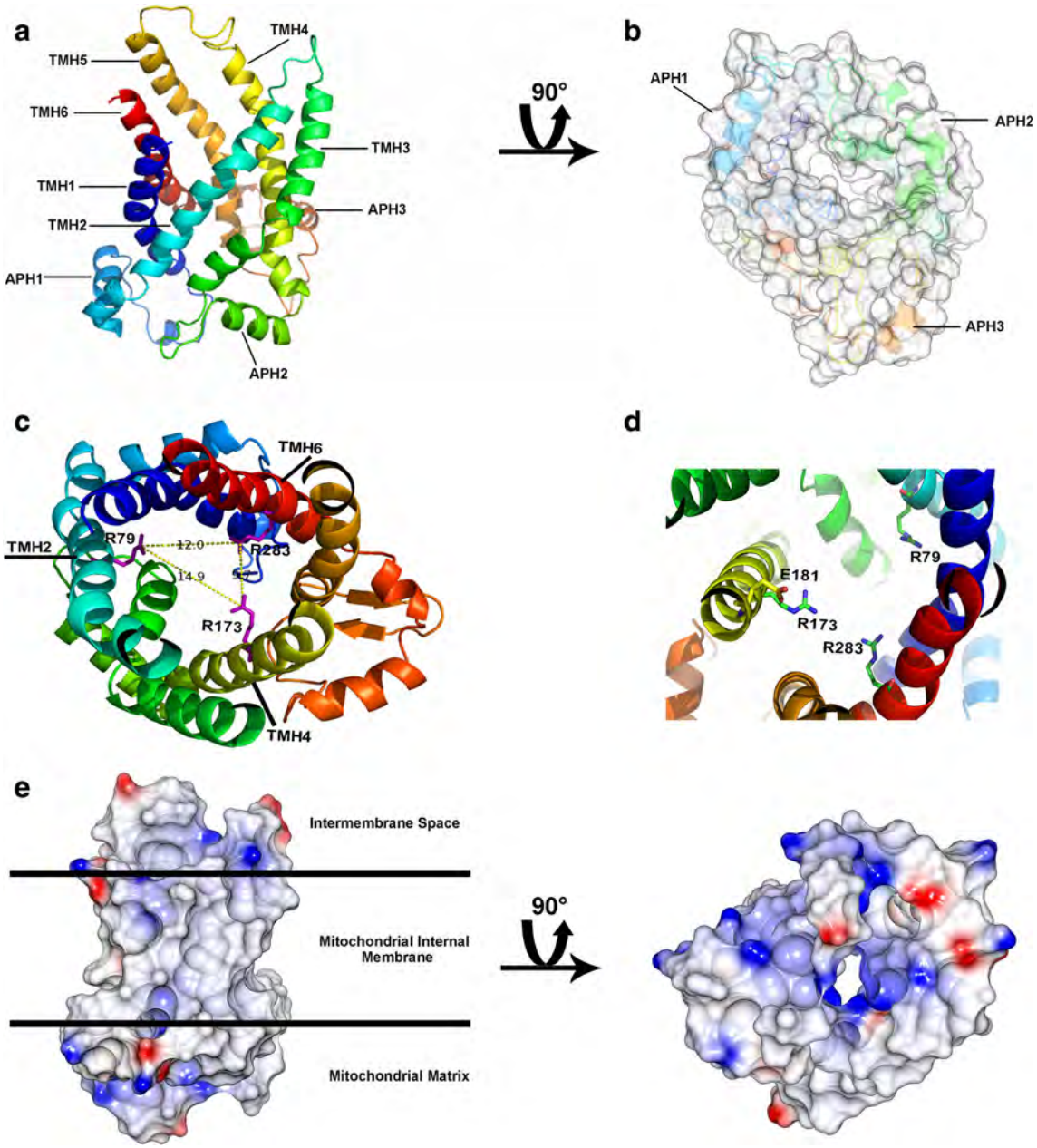

Fig. 7 Predictive structural model of *Lv*UCP5. **a** Secondary structure **b** View of the channel from the matrix with secondary structure and surface representation. **c** Conserved arginine residues. **d** View from the intermembrane space of conserved arginine residues. **e** Surface representation

In this study two transcripts, LvUCP4 and LvUCP5, were identified as uncoupling proteins in the white shrimp *L. vannamei*. This agrees with previous reports in other arthropod genomes /transcriptomes, that suggest that only UCP4 and UCP5 homologs are present in invertebrates (Sokolova and Sokolov 2005). Based on their phylogenetic

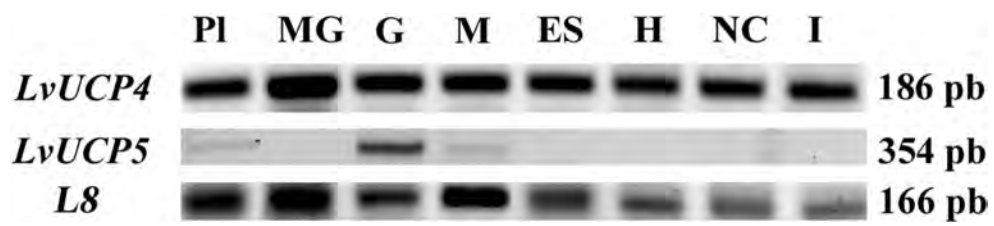

Fig. 8 *Lv*UCP4 and *Lv*UCP5 transcripts expressed on various tissues of the white shrimp *Litopenaeus vannamei*. (Pl) pleopods, (MG) midgut gland, (G) gills, (M) muscle, (ES) eye stalk, (H) heart, (NC) nerve cord and (I) gut

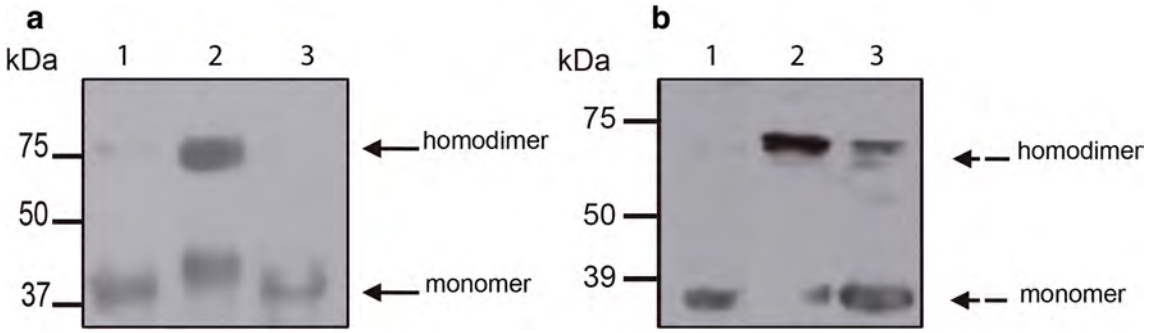

Fig. 9 Shrimp UCPs immunodetection in the isolated mitochondrial fractions. A) LvUCP4 detection of a homodimer (75 kDa) and monomer (37 kDa). B) LvUCP5 detection of a homodimer (72 kDa) and monomer (35 kDa). Isolated mitochondria were solubilized with RIPA buffer and PEG 400 1%. Lanes 1A and 1B mitochondria from shrimp pleopods; lanes 2A and 2B mitochondria from mouse liver; lanes 3A and 3B mitochondria from mouse brain

analysis, these two proteins are closely related to insect UCPs, and other invertebrate homologs, but they differ from the vertebrate proteins as the mammalian UCP1, UCP2 and UCP3 (Krauss et al. 2005). Their evolutionary origin seems to be clearly related to the ketoacid carriers subfamily as dicarboxylate carriers (DIC) since they share important amino acid similarities (Haferkamp and Schmitz-Esser 2012).

The *LvUCP4* transcript was found to be expressed in an ubiquitous manner, and *LvUCP5* was only expressed in specific organs mainly related to the high energy requirements of shrimp pleopods to swim, and to the respiratory activity of gills. Similar results with differentially expressed UCPs were obtained in the insect *R. prolixus*, whose *RpUCP4* mRNA was highly expressed in the anterior midgut and flight muscle (Alves-Bezerra et al. 2014), and in the gut of the fruit fly *D. melanogaster* larvae showing high gene expression of a UCP4 homolog (Da-Ré et al. 2014).

Structurally, LvUCPs share the main signatures of mitochondrial carriers and contain a high amount of basic and acid residues inserted in the transporter channel. Most arginine residues are located inside the channel, facilitating the purine nucleotide binding to a specific site to be inhibited. In this region, shrimp LvUCPs include the four conserved amino acids: three Arg residues and a Glu181 in LvUCP5, which in LvUCP4 is substituted by Asp202. The Glu residue acts as an interaction barrier between the three arginine residues and the acid groups of nucleotides as a result of the saline bonds formation. Once the glutamic acid is protonated, phosphate groups in nucleotides are able to interact with the three arginine residues, producing a tight complex (Luevano-Martinez and Uribe-Carvajal 2008).

The identity similarities of transcripts, and the structural characteristics of the predicted shrimp proteins described above suggests that these two deduced proteins are putatively UCP4 and UCP5, which may have the ability to transport protons through the MIM and to bind purine nucleotides being sensitive to their inhibitory effect (Echtay et al. 2000).

All previous results in addition to the confirmed presence of LvUCP4 and LvUCP5 in the isolated mitochondria of shrimp pleopods, allowed us to present this as the first report

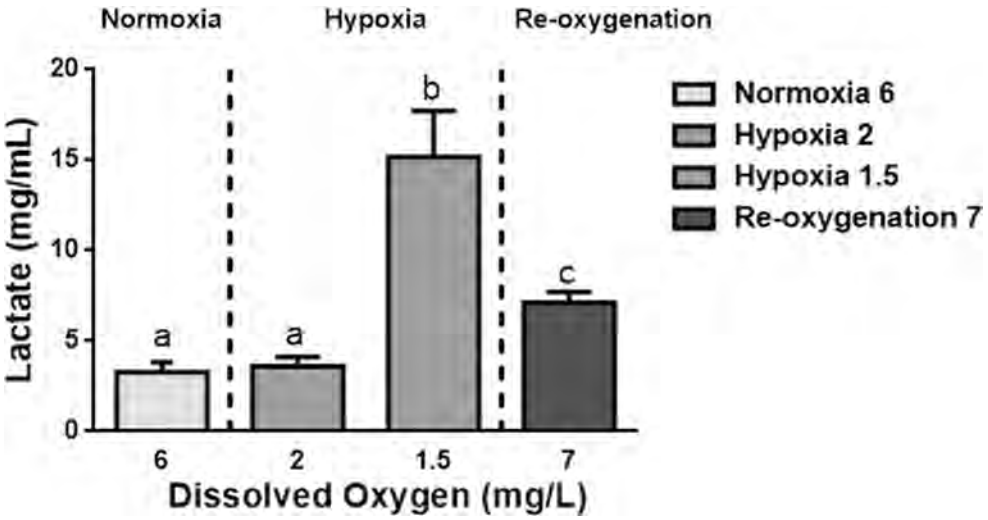

Fig. 10 Plasma L-lactate concentration in the white shrimp *L. vannamei* exposed to normoxia, hypoxia and re-oxygenation. Different letters show significant difference at $p < 0.05$. Bars represent means ± SEM

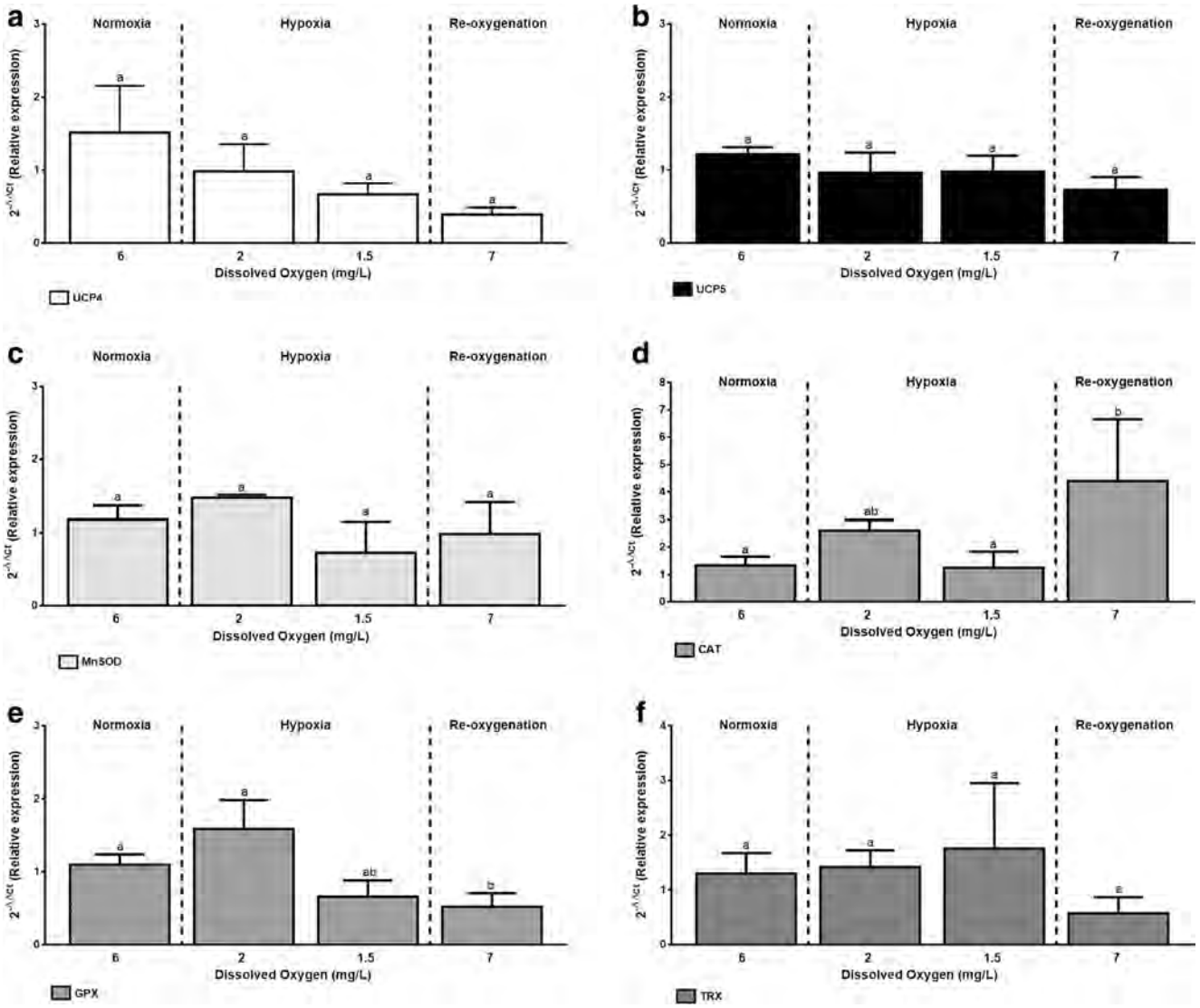

Fig. 11 Relative UCPs genes expression in the gills of shrimp at normoxia, hypoxia and re-oxygenation. **a** *UCP4,* **b** *UCP5,* **c** *MnSOD*, **d** *CAT*, **e** *GPX*, and **f** *TRX*. Data represent mean ± SEM. Different letters indicate statistical significant differences ($p < 0.05$)

that characterizes UCPs in crustaceans, to propose the proteins as the first uncoupling mechanism reported in shrimp mitochondria to dissipate protons gradient, and to hypothesize that this mechanism will also participate in controlling mitochondrial production of ROS, as it was observed in the mitochondria of *R. prolixus* (Alves-Bezerra et al. 2014), and *G. coquereliana* (Slocinska et al. 2011).

Hypoxia/re-oxygenation events represent an important physiological challenge for shrimp life, both in nature and culture systems. It has been suggested that the daily environmental changes in dissolved oxygen concentrations of seawater allow organisms to display highly specialized mechanisms to deal with ROS production when oxygen levels raise (Li et al. 2016).

Previously, it has been postulated that enzymes including catalase, glutathione peroxidase, peroxiredoxin, thioredoxin, and cytosolic manganese superoxide dismutase are part of an efficient initial antioxidant response that allows adapted marine invertebrates to survive after repetitive cycles of hypoxia/re-oxygenation by counteracting ROS production and, thus, preventing oxidative stress (Parrilla-Taylor and Zenteno-Savín 2011).

According to our results, hypoxia and re-oxygenation do not significantly affect any of the antioxidant enzymes as *MnSOD* and *TRX*, nor LvUCPs at the transcriptional level; however, *GPX* and *CAT* gene expression changed significantly according to the environmental oxygen concentration. In 2013, Trasviña-Arenas et al. reported the gene expression and activity of catalase in the gills of shrimp at hypoxia and re-oxygenation. The activity and transcript levels of the enzyme increased at both conditions being these results similar to those found in this study. TRX has also been reported as an

efficient electron donor to glutathione peroxidase, acting as a cofactor to thioredoxin peroxidases, known as peroxiredoxins, leading to the effective detoxification processes in humans. *TRX* gene expression is known to be regulated by the hypoxia-inducible transcription factor (HIF 1-α) in humans (Maulik and Das 2008). In the white shrimp *L. vannamei,* Aispuro-Hernandez et al. (2008) reported similar results to those observed in this study at hypoxia and re-oxygenation. Although no significant differences were observed in the *TRX-1* mRNA levels at hypoxia and re-oxygenation, they reported that the antioxidant capacity of recombinant TRX of *L. vannamei* exceeds that of glutathione, suggesting that a small amount of *TRX-1* may still be enough to maintain oxidative balance and protection from ROS-mediated cellular damage.

No comparable data were found about *MnSOD* and *GPX* genes expression at oxidative stress, but previous reports indicate that in *L. vannamei* hepatopancreas, gills and hemolymph, hypoxia promotes an increase in the activity of MnSOD and GPX, and re-oxygenation decreases both enzymes activity below those values observed at normoxia (Li et al. 2016). These two enzymes are known to play central roles in maintaining the balance of free radicals avoiding oxidative damage (Echtay 2007). At this point, our results indicate that changes in the antioxidant response to hypoxia and re-oxygenation are not all detected at the transcriptional level, but probably at post-translational level affecting enzymes activity.

In mammalians, reperfusion following ischemia results from an abnormal heart function, it induces a strong up-regulation of *UCP2* mRNA expression in rats kidney, which increased by 2.8-fold at day 1 after reperfusion and recovered to baseline at day 4 (Yoshida et al. 2002). This gene is involved in the modulation of superoxide anion radical and hydrogen peroxide generation in mitochondria, and is considered as an intracellular regulator of oxidative stress (Nègre-Salvayre et al. 1997).

In 2006, Mark et al. reported in the ectothermic fish *Zoarces viviparous* that *UCP2* expression is temperature dependent; authors found a general up-regulation during warm and cold adaptation, respectively. Up-regulation includes mRNA and protein expression levels, which showed the same trends in tissues of both high and low metabolic activities. They hypothesized that UCP holds an important position within mitochondrial energy metabolism of ectotherms, and especially during thermal stress may function as a regulatory protein, controlling the mitochondrial membrane potential to balance ROS formation and ATP production.

In contrast to rat and fish *UCP2*, in this study both shrimp *UCP4* and *UCP5* genes expression showed similar slight changes in response to hypoxia and re-oxygenation; differences were not statistically significant probably due to the endogenous individual variability, that promoted transcriptional levels remained unaffected, but also no changes may result from the shrimp mitochondrial oxyconformer response (Chimeo 2017), and to the hypoxia-tolerance this species display (Martinez-Cruz et al. 2017) as the consequence of repetitive exposure to cyclic variations in oxygen concentrations that these organisms face daily (Puente-Carreon 2009).

Finally, whether UCPs participate in controlling ROS production besides the efficient antioxidant system of shrimp cells (Zenteno-Savin et al. 2006) remains to be confirmed through additional evidence; their specific expression pattern suggest a primary role in the mitochondrial energy synthesis when animals respond to stress factors, however additional evidence on the functionality of shrimp UCPs including proteins expression, protein activation and inhibition responses, and RNAi experiments will help to better understand these proteins role in shrimp mitochondria.

Acknowledgements We thank Sandra Araujo Bernal for technical support and Consejo Nacional de Ciencia y Tecnologia (CONACYT, National Council for Research and Technology, Mexico) for grant 241670 to AMA and for a graduate scholarship to OAMR.

Publisher's note Springer Nature remains neutral with regard to jurisdictional claims in published maps and institutional affiliations.

References

Aispuro-Hernandez E, Garcia-Orozco KD, Muhlia-Almazan A, del-Toro-Sanchez L, Robles-Sanchez RM, Hernandez J, Sotelo-Mundo RR (2008) Shrimp thioredoxin is a potent antioxidant protein. Comp Biochem Phys C 148:94–99. https://doi.org/10.1016/j.cbpc.2008.03.013

Alan L, Smolkova K, Kronusova E, Santorova J, Jezek P (2009) Absolute levels of transcripts for mitochondrial uncoupling proteins UCP2, UCP3, UCP4 and UCP5 show different patterns in rat and mice tissues. J Bioenerg Biomembr 41:71–78. https://doi.org/10.1007/s10863-009-9201-2

Altschul SF, Gish W, Miller W, Myers EW, Lipman DJ (1990) Basic local alignment search tool. J Mol Biol 215:403–410. https://doi.org/10.1016/S0022-2836(05)80360-2

Alves-Bezerra M, Cosentino-Gomes D, Vieira LP, Rocco-Machado N, Gondim KC, Meyer-Fernandes JR (2014) Identification of uncoupling protein 4 from the blood-sucking insect *Rhodnius prolixus* and its possible role on protection against oxidative stress. Insect Biochem Molec 50:24–33. https://doi.org/10.1016/j.ibmb.2014.03.011

Berardi MJ, Shih WM, Harrison SC, Chou JJ (2011) Mitochondrial uncoupling protein 2 structure determined by NMR molecular fragment searching. Nature 476:109–113. https://doi.org/10.1038/nature10257

Bermejo-Nogales A, Calduch-Giner JA, Perez-Sanchez J (2010) Gene expression survey of mitochondrial uncoupling proteins (UXCP1/UCP3) in gilthead sea bream (*Sparus aurata* L). J Comp Physiol B 180:685–694. https://doi.org/10.1007/s00360-009-0441-6

Bradford MM (1976) A rapid and sensitive method for the quantitation of microgram quantities of protein utilizing the principle of protein-dye binding. Anal Biochem 72:248–254. https://doi.org/10.1016/0003-2697(76)90527-3

Brand MD, Chien LF, Ainscow EK, Rolfe DFS, Porter RK (1994) The causes and functions of mitochondrial proton leak. Biochim Biophys Acta 1187:132–139. https://doi.org/10.1016/0005-2728(94)90099-X

Cannon B, Shabalina IG, Kramarova TV, Petrovic N, Nedergaard J (2006) Uncoupling proteins: a role in protection against reactive oxygen species—or not? Biochim Biophys Acta 1757:449–458. https://doi.org/10.1016/j.bbabio.2006.05.016

Chimeo C (2017) El inhibidor endógeno IF1 del complejo mitochondrial ATPasa y su papel en el camarón blanco *Litopenaeus vannamei* durante la hipoxia-reoxigenación. PhD thesis. Centro de Investigación en Alimentacion y Desarrollo. Sonora Mexico, 95 pp

Da-Ré C, De Pittà C, Zordan MA, Teza G, Nestola F, Zeviani M, Bernardi P (2014) UCP4C mediates uncoupled respiration in larvae of *Drosophila melanogaster*. EMBO Rep 15:586–591. https://doi.org/10.1002/embr.201337972

Echtay KS (2007) Mitochondrial uncoupling proteins—what is their physiological role? Free Radic Biol Med 43:1351–1371. https://doi.org/10.1016/j.freeradbiomed.2007.08.011

Echtay KS, Winkler E, Bienengraeber M, Klingenberg M (2000) Site-directed mutagenesis identifies residues in uncoupling protein (UCP1) involved in three different functions. Biochemistry 39: 3311–3317. https://doi.org/10.1021/bi992448m

Fridell YW, Sánchez-Blanco A, Silvia B, Helfand S (2004) Functional characterization of a *Drosophila* mitochondrial uncoupling protein. J Bioenerg Biomembr 36:219–228. https://doi.org/10.1023/B:JOBB.0000031973.20153.c6

Gaudry MJ, Jastroch M (2018) Molecular evolution of uncoupling proteins and implications for brain function. Neurosci Lett 696:140–145. https://doi.org/10.1016/j.neulet.2018.12.027

Ghaffari N, Sanchez-Flores A, Doan R, Garcia-Orozco KD, Chen PL, Ochoa-Leyva A, Lopez-Zavala AA, Carrasco JS, Hong C, Brieba LG, Rudiño-Piñera E, Blood PD, Sawyer JE, Johnson CD, Dindot SV, Sotelo-Mundo RR, Criscitiello MF (2014) Novel transcriptome assembly and improved annotation of the whiteleg shrimp (*Litopenaeus vannamei*), a dominant crustacean in global seafood mariculture. Sci Rep 4:7081. https://doi.org/10.1038/srep07081

Guerrero-Castillo S, Araiza-Olivera D, Cabrera-Orefice A, Espinasa-Jaramillo J, Gutiérerz-Aguilar M, Luevano-Martínez LA, Zepeda-Bastida A, Uribe-Carvajal S (2011) Physiological uncoupling of mitochondrial oxidative phosphorylation. Studies in different yeast species. J Bioenerg Biomembr 43:323–331. https://doi.org/10.1007/s10863-011-9356-5

Guex N, Peitsch MC (1997) SWISS-MODEL and the Swiss-Pdb viewer: an environment for comparative protein modeling. Electrophoresis 18:2714–2723. https://doi.org/10.1002/elps.1150181505

Haferkamp I, Schmitz-Esser S (2012) The plant mitochondrial carrier family: functional and evolutionary aspects. Front Plant Sci 3:2. https://doi.org/10.3389/fpls.2012.00002

Hanák P, Ježek P (2001) Mitochondrial uncoupling proteins and phylogenesis – UCP4 as the ancestral uncoupling protein. FEBS Lett 495:137–141. https://doi.org/10.1016/S0014-5793(01)02338-9

Holman JD, Hand SC (2009) Metabolic depression is delayed and mitochondrial impairment averted during prolonged anoxia in the ghost shrimp, *Lepidophthalmus louisianensis* (Schmitt, 1935). J Exp Mar Biol Ecol 376:85–93. https://doi.org/10.1016/j.jembe.2009.06.008

Jarmuszkiewicz W, Woyda-Ploszczyca A, Antos-Krzeminska N, Sluse FE (2010) Mitochondrial uncoupling proteins in unicellular eukaryotes. Biochim Biophys Acta 1797:792–799. https://doi.org/10.1016/j.bbabio.2009.12.005

Ježek P (2002) Possible physiological roles of mitochondrial uncoupling proteins—UCPn. INT J BIOCHEM 34:1190–1206. https://doi.org/10.1016/S1357-2725(02)00061-4

Ježek P, Urbánková E (2000) Specific sequence motifs of mitochondrial uncoupling proteins. IUBMB Life 49:63–70. https://doi.org/10.1080/713803586

Jimenez-Gutierrez L, Hernandez-Lopez J, Islas-Osuna M, Muhlia-Almazan A (2013) Three nucleus-encoded subunits of mitochondrial cytochrome c oxidase of the whiteleg shrimp *Litopenaeus vannamei*: cDNA characterization, phylogeny and mRNA expression during hypoxia and reoxygenation. Comp Biochem Phys B 166:30–39. https://doi.org/10.1016/j.cbpb.2013.06.008

Jones DT, Taylor WR, Thornton JM (1992) The rapid generation of mutation data matrices from protein sequences. Comput Appl Biosci 8:275–282. https://doi.org/10.1093/bioinformatics/8.3.275

Kelley LA, Mezulis S, Yates CM, Wass MN, Sternberg MJE (2015) The Phyre2 web portal for protein modeling, prediction and analysis. Nat Protoc 10:845–858. https://doi.org/10.1038/nprot.2015.053

Kim-Han JS, Reichert SA, Quick KL, Dugan LL (2001) BMCP1: a mitochondrial uncoupling protein in neurons which regulates mitochondrial function and oxidant production. J Neurochem 79:658–668. https://doi.org/10.1046/j.1471-4159.2001.00604.x

Konrad C, Kiss G, Torocsik B, Adam-Vizi V, Chinopoulos C (2012) Absence of Ca^{2+}-induced mitochondrial permeability transition but presence of bongkrekate-sensitive nucleotide exchange in *C. crangon* and *P. serratus*. PLoS One 7:e39839. https://doi.org/10.1371/journal.pone.0039839

Krauss S, Zhang CY, Lowell BB (2005) The mitochondrial uncoupling-protein homologues. Nat Rev Mol Cell Biol 6:248–261. https://doi.org/10.1038/nrm1592

Kumar S, Stecher G, Li M, Knyaz C, Tamura K (2018) MEGA X: molecular evolutionary genetics analysis across computing platforms. Mol Biol Evol 35:1547–1549. https://doi.org/10.1093/molbev/msy096

Laemmli UK (1970) Cleavage of structural proteins during the assembly of the head of bacteriophage T4. Nature 227:680–685. https://doi.org/10.1038/227680a0

Li Y, Wei L, Cao J, Qiu L, Jiang X, Li P, Diao X (2016) Oxidative stress, DNA damage and antioxidant enzyme activities in the pacific white shrimp (*Litopenaeus vannamei*) when exposed to hypoxia and re-oxygenation. Chemosphere 144:234–240. https://doi.org/10.1016/j.chemosphere.2015.08.051

Livak KJ, Schmittgen TD (2001) Analysis of relative gene expression data using real-time quantitative PCR and the $2^{-\Delta\Delta CT}$ method. Methods 25:402–408. https://doi.org/10.1006/meth.2001.1262

Luevano-Martinez LA, Uribe-Carvajal S (2008) Advances in protein physical chemistry. In: Enrique Garcia-Hernandez and D. Alejandro Fernandez-Velasco (ed) Structure and mechanism of the mitochondrial uncoupling protein (UCP), 1st edn. Transworld research Network, pp 387–405

Mailloux RJ, Harper ME (2011) Uncoupling proteins and the control of mitochondrial reactive oxygen species production. Free Radic Biol Med 51:1106–1115. https://doi.org/10.1016/j.freeradbiomed.2011.06.022

Mark FC, Lucassen M, Pörtner HO (2006) Thermal sensitivity of uncoupling protein expression in polar and temperate fish. Comp Biochem Phys D 1:365–374. https://doi.org/10.1016/j.cbd.2006.08.004

Martinez-Cruz O, Chimeo C, Rodriguez-Armenta CM, Muhlia-Almazan A (2017) Crustaceans bioenergetics: mitochondrial adaprtive molecular responses to face environmentall challenges. J Shellfish Res 36: 771–786. https://doi.org/10.2983/035.036.0327

Maulik N, Das DK (2008) Emerging potential of thioredoxin and thioredoxin interacting proteins in various disease conditions. Biochim Biophys Acta 1780:1368–1382. https://doi.org/10.1016/j.bbagen.2007.12.008

McNicholas S, Potterton E, Wilson KS, Noble MEM (2011) Presenting your structures: the CCP4mg molecular-graphics software. Acta Crystallogr D 67:386–394. https://doi.org/10.1107/S0907444911007281

Menze MA, Hutchinson K, Laborde SM, Hand SC (2005) Mitochondrial permeability transition in the crustacean *Artemia franciscana*: absence of a calcium-regulated pore in the face of profound calcium

storage. Am J Physiol Regul Integr Comp Physiol 289:R68–R76. https://doi.org/10.1152/ajpregu.00844.2004

Miroux B, Frossard V, Raimbault S, Ricquier D, Bouillaud F (1993) The topology of the brown adipose tissue mitochondrial uncoupling protein determined with antibodies against its antigenic sites revealed by a library of fusion proteins. EMBO J 12:3739–3745. https://doi.org/10.1002/j.1460-2075.1993.tb06051.x

Nègre-Salvayre A, Hirtz C, Carrera G, Cazenave R, Troly M, Salvayre R, Casteilla L (1997) A role for uncoupling protein-2 as a regulator of mitochondrial hydrogen peroxide generation. The FASEB J 11:809–815. https://doi.org/10.1096/fasebj.11.10.9271366

Nury H, Dahout-Gonzalez C, Trezeguet V, Lauquin G, Brandolin G, Pebay-Peyroula E (2006) Relations between structure and function of the mitochondrial ADP/ATP carrier. Annu Rev Biochem 75:713–741. https://doi.org/10.1146/annurev.biochem.75.103004.142747

Palmieri F (2013) The mitochondrial transporter family SLC25: identification, properties and physiopathology. Mol Aspects Med 34(2–3):465–484. https://doi.org/10.1016/j.mam.2012.05.005

Parrilla-Taylor DP, Zenteno-Savín T (2011) Antioxidant enzyme activities in Pacific white shrimp (*Litopenaeus vannamei*) in response to environmental hypoxia and reoxygenation. Aquaculture 318:379–383. https://doi.org/10.1016/j.aquaculture.2011.05.015

Puente-Carreon E (2009) Respuesta fisiológica de juveniles de camarón blanco *Litopenaeus vannamei*, a condiciones oscilantes de oxígeno disuelto y temperatura. Centro Interdisciplinario de Ciencias Marinas, IPN. Tesis doctoral. La Paz Baja California

Rodriguez-Armenta C, Uribe-Carvajal S, Rosas-Lemus M, Chiquete-Felix N, Huerta-Ocampo JA, Muhlia-Almazan A (2018) Alternative mitochondrial respiratory chains from two crustaceans: *Artemia franciscana* nauplii and the white shrimp, *Litopenaeus vannamei*. J Bioenerg Biomembr 50:143–152. https://doi.org/10.1007/s10863-018-9753-0

Saitou N, Nei M (1987) The neighbor-joining method: a new method for reconstructing phylogenetic trees. Mol Biol Evol 4:406-425. https://doi.org/10.1093/oxfordjournals.molbev.a040454

Schwede T, Kopp J, Guex N, Peitsch MC (2003) SWISS-MODEL: an automated protein homology-modeling server. Nucleic Acids Res 31:3381–3385. https://doi.org/10.1093/nar/gkg520

Sievers F, Wilm A, Dineen D, Gibson TJ, Karplus K, Li W, Higgins DG (2011) Fast, scalable generation of high-quality protein multiple sequence alignments using Clustal omega. Mol Syst Biol 7:539. https://doi.org/10.1038/msb.2011.75

Slocinska M, Antos-Krzeminska N, Rosinski G, Jarmuszkiewicz W (2011) Identification and characterization of uncoupling protein 4 in fat body and muscle mitochondria from the cockroach *Gromphadorhina cocquereliana*. J Bioenerg Biomembr 43:717–727. https://doi.org/10.1007/s10863-011-9385-0

Slocinska M, Antos-Krzeminska N, Rosinski G, Jarmuszkiewicz W (2012) Functional characterization and regulation of UCP4 expression by adipokinetic hormone in larva and pupa fat body mitochondria from the beetle *Zophobas atratus*. BBA-Bioenergetics 1817:S116. https://doi.org/10.1016/j.bbabio.2012.06.312

Sokolova I, Sokolov E (2005) Evolution of mitochondrial uncoupling proteins: novel invertebrate UCP homologues suggest early evolutionary divergence of the UCP family. FEBS Lett 579:313–317. https://doi.org/10.1016/j.febslet.2004.11.103

Towbin H, Staehelin T, Gordon J (1979) Electrophoretic transfer of proteins from polyacrylamide gels to nitrocellulose sheets: procedure and some applications. P Natl Acad Sci USA 76:4350–4354. https://doi.org/10.1073/pnas.76.9.4350

Trasviña-Arenas CH, Garcia-Triana A, Peregrino-Uriarte AB, Yepiz-Plascencia G (2013) White shrimp *Litopenaeus vannamei* catalase: gene structure, expression and activity under hypoxia and reoxygenation. Comp Biochem Physiol B 164:44–52. https://doi.org/10.1016/j.cbpb.2012.10.004

Vargas-Albores F, Guzman MA, Ochoa JL (1993) An anticoagulant solution for haemolymph collection and prophenoloxidase studies of penaeid shrimp (*Penaeus californiensis*). Comp Biochem Phys A 106:299–303. https://doi.org/10.1016/0300-9629(93)90516-7

Yoshida T, Kurella M, Beato F, Min H, Ingelfinger JR, Stears RL, Swinford RD, Gullans SR, Tang S-S (2002) Monitoring changes in gene expression in renal ischemia-reperfusion in the rat. Kidney Int 61:1646–1654. https://doi.org/10.1046/j.1523-1755.2002.00341.x

Zenteno-Savin T, Saldierna R, Ahuejote-Sandoval M (2006) Superoxide radical production in response to environmental hypoxia in cultured shrimp. Comp Biochem Phys C 142:301–308. https://doi.org/10.1016/j.cbpc.2005.11.001

Fungal Biology 124 (2020) 253–262

Contents lists available at ScienceDirect

Fungal Biology

journal homepage: www.elsevier.com/locate/funbio

Yap1 homologs mediate more than the redox regulation of the antioxidant response in filamentous fungi

Ariann E. Mendoza-Martínez, Nallely Cano-Domínguez, Jesús Aguirre*

Departamento de Biología Celular y del Desarrollo, Instituto de Fisiología Celular, Universidad Nacional Autónoma de México, Apartado Postal 70-242, 04510 Ciudad de México, Mexico

ARTICLE INFO

Article history:
Received 30 January 2019
Received in revised form
2 April 2019
Accepted 3 April 2019
Available online 11 April 2019

Corresponding Editor: Drauzio E.N Rangel

Keywords:
ROS sensing
Fungal development
Reactive oxygen species
Secondary metabolism
Virulence

ABSTRACT

The regulation of gene expression in response to increased levels of reactive oxygen species (ROS) is a ubiquitous response in aerobic organisms. However, different organisms use different strategies to perceive and respond to high ROS levels. Yeast Yap1 is a paradigmatic example of a specific mechanism used by eukaryotic cells to link ROS sensing and gene regulation. The activation of this transcription factor by H_2O_2 is mediated by peroxiredoxins, which are widespread enzymes that use cysteine thiols to sense ROS, as well as to catalyze the reduction of peroxides to water. In filamentous fungi, Yap1 homologs and peroxiredoxins also are major regulators of the antioxidant response. However, Yap1 homologs are involved in a wider array of processes by regulating genes involved in nutrient assimilation, secondary metabolism, virulence and development. Such novel functions illustrate the divergent roles of ROS and other oxidizing compounds as important regulatory signaling molecules.
© 2019 The Authors. Published by Elsevier Ltd on behalf of British Mycological Society. This is an open access article under the CC BY-NC-ND license (http://creativecommons.org/licenses/by-nc-nd/4.0/).

1. Introduction

Aerobic respiration is one of the most important traits acquired during the evolution of life. In eukaryotes, respiration occurs in the mitochondria and it involves the use of oxygen as the final acceptor of the electrons that feed the electron transport chain, and the production of ATP. The incomplete reduction of O_2 to water generates the anion superoxide ($O_2^{\cdot -}$), which in turn generates hydrogen peroxide (H_2O_2), either spontaneously or by the activity of superoxide dismutase enzymes. Through different reactions, H_2O_2 can produce other reactive oxygen species (ROS) such as the hydroxyl radical ($^{\cdot}OH$). ROS can react with many different biomolecules, causing enzyme inactivation and degradation, lipid peroxidation and DNA damage. To avoid this, organisms evolved mechanisms to perceive and decompose ROS through coordinated cellular responses, collectively called the antioxidant response. Typical responses involve the up-regulation of ROS-decomposing enzymes such as superoxide dismutases (SOD), catalases (CAT), glutathione peroxidases (Gpx), glutathione S-transferases (GST) and peroxiredoxins (Prx), as well as enzymes involved in the production of reducing compounds such as NADPH and glutathione (Halliwell and Gutteridge, 2007).

For a long time, only the cell damaging aspects of ROS were considered as biologically relevant. Currently, increasing evidence from studies in many different biological systems supports our early view, in which ROS were proposed as signaling molecules important for cell differentiation (Aguirre et al., 2005; Hansberg and Aguirre, 1990), and several mechanisms for ROS perception, ROS signal transduction and ROS-induced gene regulation have been identified. Many of the regulatory roles of ROS are based on their ability to modify the activity of proteins sensitive to redox modifications. In turn, many of these modifications are mediated by the oxidation of cysteine residues, since its sulfhydryl group can be reversibly oxidized to form intra- or intermolecular disulfide bonds, affecting protein structure and function (D'Autreaux and Toledano, 2007; Holmstrom and Finkel, 2014).

2. Yap1, a paradigm in ROS signal transduction

Saccharomyces cerevisiae Yap1 is a transcription factor first identified as a member of the jun family, which includes AP-1 in mammalian cells (Harshman et al., 1988), which represents a paradigmatic example of the mechanisms that a cell utilizes to perceive and transduce ROS signals. YAP1 was also found as a gene

* Corresponding author.
E-mail address: jaguirre@ifc.unam.mx (J. Aguirre).

https://doi.org/10.1016/j.funbio.2019.04.001
1878-6146/© 2019 The Authors. Published by Elsevier Ltd on behalf of British Mycological Society. This is an open access article under the CC BY-NC-ND license (http://creativecommons.org/licenses/by-nc-nd/4.0/).

INFORME DE LABORES 2019

critical to survive the oxidative stress caused by H_2O_2, diamide (Kuge and Jones, 1994), cadmium and other heavy metals (Schnell and Entian, 1991). In addition, it was reported that Yap1 overexpression conferred pleiotropic drug resistance (Hertle et al., 1991).

There are excellent and recent reviews on Yap1 and its homologs in yeasts (Dantas Ada et al., 2015; Garcia-Santamarina et al., 2014). Here we describe a comparative analysis between Yap1 and its homologs in filamentous fungi. Yeast Yap1 contains five characteristic domains: a "b-ZIP" DNA binding domain, a N-terminal nuclear localization sequence (NLS), a C-terminal nuclear exportation sequence (NES), and two cysteine-rich (CRD) regions (Fernandes et al., 1997; Harshman et al., 1988). The first CRD (nCRD domain) contains Cys-303, Cys310 and Cys-315, while C-terminal CRD (cCRD domain) contains Cys-598, Cys-620 and Cys-629 (Fig. 1), and the oxidation of these cysteines is critical to regulate Yap1 nuclear localization (Delaunay et al., 2000; Kuge et al., 1997; Yan et al., 1998). When yeast cells are treated with H_2O_2, a Yap1 stepwise oxidation is initiated by the oxidation of the catalytic cysteine of the peroxiredoxin Gpx3, which then reacts with Yap1 Cys-598, forming a mixed Gpx3-Yap1 intermediate that immediately resolves in the formation of an intra-molecular bridge between Yap1 Cys-598 and Cys-303 (Delaunay et al., 2002). This generates a conformational change that hides the NES region and prevents its interaction with the Crm1 nuclear export factor, resulting in the accumulation of Yap1 in the nucleus (Delaunay et al., 2000; Kuge et al., 1997). The protein Ybp1 is necessary for this disulfide relay, very likely acting as a molecular scaffold protein and as a sulfenic acid chaperone (Bersweiler et al., 2017). Additionally, intermolecular disulfides Cys310−-Cys629 and Cys315−-Cys620 have been identified, all of which appear necessary for full Yap1 activation (Gulshan et al., 2005; Okazaki et al., 2007; Wood et al., 2003). Oxidized nuclear Yap1 is subject to phosphorylation, but the responsible kinase and the physiological consequences of this are yet unknown (Delaunay et al., 2000). However, the fact that *Candida albicans* Yap1 homolog Cap1 is also phosphorylated, suggests that this modification is physiologically important (Kos et al., 2016).

Yap1 cCRD cysteines can also be oxidized directly by synthetic as well as natural electrophilic compounds such as diamide, diethylmaleimide, menadione (Azevedo et al., 2003; Kuge et al., 1997; Wemmie et al., 1997), methylglyoxal (Maeta et al., 2004) and the garlic compound allicin (Gruhlke et al., 2017). This process is independent of Gpx3 and Ybp1 and also results in hiding of the NES motif and Yap1 nuclear accumulation. However, these two Yap1-activation mechanisms lead to the expression of different sets of genes and different adaptive responses. Indeed, Yap1 oxidation by H_2O_2 regulates the expression of around ~100 genes, including genes required for glutathione biosynthesis and redox balance proteins such as γ-glutamylcysteine synthetase GSH1, glutathione reductase GLR1 (Gasch et al., 2000) and thioredoxin gene TRX2 (Kuge and Jones, 1994). In contrast, Yap1 oxidation by electrophilic compounds results in the induction of genes related to xenobiotic detoxification, such as genes encoding major facilitator and ATP-binding cassette transporters (Alarco et al., 1997; Wemmie et al., 1994). Consistent with this, H_2O_2 and N-ethylmaleimide do not induce cross-protection against each other (Ouyang et al., 2011). The mechanism by which different oxidized forms of Yap1 regulate different sets of genes is not well understood. Part of the explanation involves Yap1 interaction with other transcriptional regulators such as Skn7, a response regulator also involved in the antioxidant response, and the mediator complex. About half of the genes regulated by Yap1 require its interaction with Skn7, while the other half is Skn7-independent (Lee et al., 1999; Mulford and Fassler, 2011). Mediator is a highly conserved multi-subunit protein complex involved in the transcriptional activation of many genes, including genes involved in multidrug resistance (Shahi et al., 2010; Uthe et al., 2017). The Yap1-mediated induction of the TRX2 gene depends on the mediator component Rox3 and a proper disulfide bonding between Yap1 n-CRD and c-CRD domains (Gulshan et al., 2005). Yap1 oxidized by either H_2O_2 or electrophilic compounds is subject to degradation (Gulshan et al., 2012) and can be reduced back by thioredoxin Trx2 and then translocated to the cytosol (Delaunay et al., 2000). In fact, deletion of *trx1* and *trx2* thioredoxin genes results in constitutive activation of Yap1 (Izawa et al., 1999).

Yap1 homologs Pap1 and Cap1 show very similar regulation in response to H_2O_2 in *Schizosaccharomyces pombe* (Toda et al., 1991; Toone et al., 1998) and *C. albicans* (Kos et al., 2016), respectively. However, in *S. pombe*, it is peroxiredoxin Tpx1 the enzyme which oxidizes Pap1, hiding the NES region and leading to Pap1 nuclear accumulation (Calvo et al., 2013), and the expression of ~50 genes (Chen et al., 2008) involved in the antioxidant response (catalases, peroxiredoxins, sulforedoxins), cellular detoxification and multiple drug resistance (Calvo et al., 2009). In *C. albicans*, peroxiredoxin Gpx3 and interacting protein Ybp1 are needed to relay H_2O_2 signaling to Cap1 (Patterson et al., 2013). Like Yap1, Pap1 regulates the expression of two subsets of genes. Notably, one subset requires Pap1 nuclear accumulation but not its oxidation, and includes genes related to multidrug resistance like *caf5*, which encodes an efflux pump to exclude drugs from the intracellular compartment. The second subset includes antioxidant genes such as catalase and thioredoxin reductase and depends on Pap1 nuclear localization as well as its oxidation and heterodimerization with Prr1, the Skn7 ortholog. Consistent with this, Pap1 binding to drug tolerance promoters is Prr1-independent, while Pap1 association with Prr1 enhances its affinity for antioxidant gene promoters (Calvo et al., 2012).

As indicated before, H_2O_2 signal is relayed to Yap1, Pap1 and Cap1 by specific peroxiredoxins (Prxs). Prxs constitute a large family of thiol-dependent peroxidases originally discovered as enzymes catalyzing the reduction of H_2O_2, alkyl hydroperoxides and peroxinitrite (Chae et al., 1994b; Jacobson et al., 1989; Peshenko and Shichi, 2001). All Prxs contain a conserved cysteine residue, designated as the peroxidatic cysteine (Cys_P), which is oxidized by peroxides (Choi et al., 1998; Ellis and Poole, 1997). Most, but not all Prxs contain an additional cysteine, designated as the resolving cysteine (Cys_R). Depending on their catalytic mechanism, Prxs are classified into three types: typical 2-Cys, atypical 2-Cys and 1-Cys Prxs. Each catalysis cycle can be divided into three steps. The first step, peroxidation, is where the sulfur atom of the Cys_P residue exerts a nucleophilic attack on the O—O bond of the peroxide substrate, releasing the corresponding molecule of alcohol or water, at the cost of Cys_P being oxidized to the cysteine sulfenic acid form. The second step, resolution, occurs when the Cys_R attacks the sulfenic acid, resulting in the formation of an inter- or intramolecular disulfide bond for typical and atypical 2-Cys Prxs, respectively, and the release of a water molecule. This step is omitted in 1-Cys Prxs, as they do not have a Cys_R residue and move directly to the third step, recycling, which occurs when the oxidized Prx is reduced by thiol-containing electron donors such as thioredoxin (Chae et al., 1994a). The regenerated Prx can then go through another catalytic cycle.

Clearly, the basic mechanisms by which Yap1 regulates gene expression in response to oxidative stress are well conserved in yeast fungi. However, as we will see below, is not clear yet to what extent these mechanisms are conserved in filamentous fungi, which are more complex organisms, containing about twice as many genes and showing more complex patterns of growth and cell differentiation.

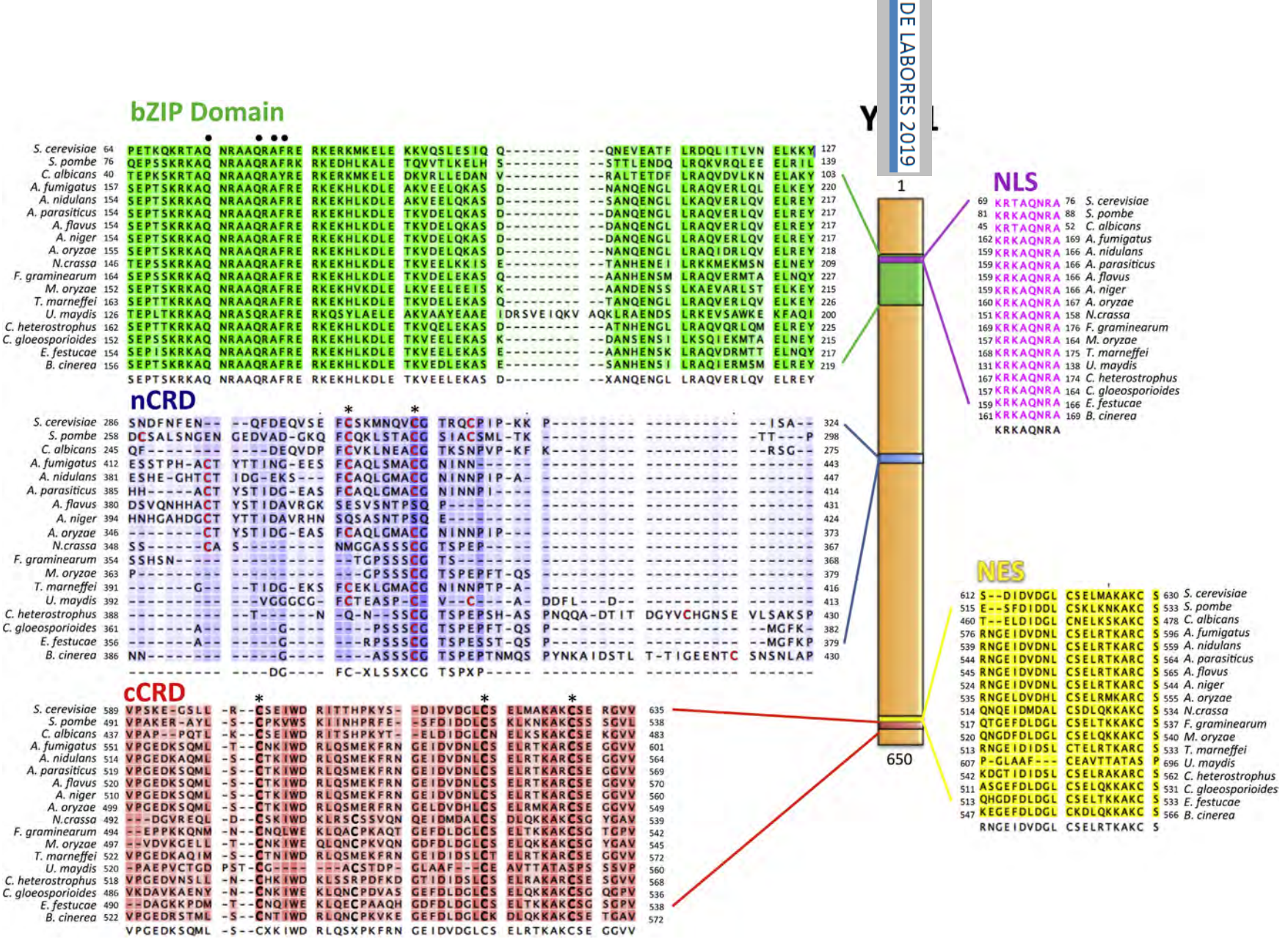

Fig. 1. Yap1 homologs from filamentous fungi contain the same domains described in yeast Yap1. The amino acid sequence of *Saccharomyces cerevisiae* Yap1 is aligned to homologous proteins from *Schizosaccharomyces pombe* (SPAC1783.07c), *Candida albicans* (C3_02220W), *Aspergillus fumigatus* (Afu6g09930), *Aspergillus nidulans* (AN7513), *Aspergillus parasiticus*, (P875_00065012), *Aspergillus flavus* (AFLA_129340), *Aspergillus niger* (An11g07980), *Aspergillus oryzae* (AO090001000627), *Neurospora crassa* (NCU03905), *Fusarium graminearum* (FGSG_08800T0), *Magnaporthe oryzae* (MGG_12814), *Talaromyces marneffei* (PMAA_063050), *Ustilago maydis* (um02191), *Cochliobolus heterostrophus* (estExt_Genewise1Plus.C_130082), *Colletotrichum gloeosporioides* (CGLO_14059), *Epichloe festucae* (KC121577) and *Botrytis cinerea* (FM957543). The b-ZIP binding domain is indicated in green and characteristic residues are indicated by black dots. The nuclear localization sequence (NLS) and nuclear exportation sequences (NESs) are indicated in pink and yellow, respectively. N-terminal cysteine rich domain (nCRD) is labeled in blue and conserved cysteines are indicated with asterisks. C-terminal cysteine rich domain (cCRD) is indicated in red and conserved cysteines are labeled with asterisks. The alignment was generated using software T-coffee (Notredame et al., 2000) and edited using CLC Sequence Viewer (https://www.qiagenbioinformatics.com/products/clc-genomics-workbench-direct-download/). (For interpretation of the references to color in this figure legend, the reader is referred to the Web version of this article.)

INFORME DE LABORES 2019

3. Yap1 homologs in filamentous fungi are also involved in the antioxidant response

Filamentous fungi contain Yap1 homologs, which contain the same domains described in Yap1 (Fig. 1). The b-ZIP domain covers a highly conserved region of about 64 amino acids with characteristic residues Q73, Q78, A80, F81 (Fernandes et al., 1997). NLS and NES regions with lengths of about 8 and 21 residues, respectively, are also conserved. However, there are clear differences in the total number of cysteines, as well as in their distribution within putative nCRD and cCRD domains (Fig. 1 and Table 2). The total number of cysteines in the Yap1 homologs studied up to now in filamentous fungi ranges from 4 in *Aspergillus niger* to 8 in *Ustilago maydis*. Within the nCRD, the number of cysteines varies from 1 in *Epichloe festucae* to 3 in several fungi, and from 3 to 4 in the cCRD domains (Fig. 1).

As indicated, the number and localization of cysteines is important because in Yap1 different cysteines are oxidized in response to different oxidizing agents (Kuge et al., 1997). However, it is not clear how these differences in cysteine number and distribution affect the function of Yap1 homologs in filamentous fungi. In fact, cysteine function has only been studied in *U. maydis* Yap1, where the simultaneous replacement of Cys399 and Cys407 by alanine resulted in sensitivity to H_2O_2, as in the null mutant, and a lack of nuclear localization (Molina and Kahmann, 2007).

Despite this limited information, most Yap1 null mutants reported in filamentous fungi are sensitive to some type of oxidant, such as H_2O_2, *t-butyl* hydroperoxide (*t*-BOOH) or menadione, indicating that the involvement of this transcription factor in the antioxidant response is highly conserved in fungi. However, there are interesting differences, likely related to differences in Yap1 structure and fungal life styles (Tables 1 and 2). *ΔyapA* mutants of endophytic fungus *E. festucae* show mycelial sensitivity to menadione (Md) and diamide, while only conidia are sensitive to H_2O_2 (Cartwright and Scott, 2013). In the animal pathogen *Aspergillus fumigatus*, *ΔAfyap1* mutants are susceptible to H_2O_2 and Md, but not to diamide (Lessing et al., 2007). In contrast, *Aspergillus parasiticus ΔApyapA* mutants show only slight growth defects in the presence of H_2O_2, Md and cumenehydroperoxide (CH), despite the fact that they showed reduced activity of antioxidant enzymes like SOD, GPX (glutathione peroxidase) and HPR (Hydrogen peroxide reducing enzymes) (Reverberi et al., 2008). Likewise, *Magnaporthe oryzae* mutants lacking MoAP1 show only mild sensitivity to H_2O_2 (Guo et al., 2011). In contrast, *Aspergillus nidulans* NapA is essential for resistance to H_2O_2 and Md in conidia, as well as in mycelia (Asano et al., 2007; Mendoza-Martinez et al., 2017). Although *ΔnapA* spores do not show a reduction in catalase CatA activity, mycelial CatB induction by H_2O_2 depends on both NapA and the Skn7 homolog SrrA (Mendoza-Martinez et al., 2017; Vargas-Perez et al., 2007). The differential sensitivity to H_2O_2 *vs.* electrophilic compounds could reflect the extent to which cysteines in these Yap1 homologs are available for either peroxiredoxin-mediated or direct oxidation. However, whether or not a peroxiredoxin is directly involved in Yap1 oxidation in filamentous fungi has not been answered yet. In *E. festucae*, double mutants lacking *S. cerevisiae* Gpx3 and *S. pombe Tpx1* homologs were still able to accumulate Yap1 in the nucleus in the presence of H_2O_2, ruling out these proteins as possible mediators of Yap1 oxidation (Cartwright and Scott, 2013). Likewise, in *A. nidulans* peroxiredoxins GpxA, TpxA and TpxB were not required for resistance to H_2O_2 or menadione, indicating that these proteins are not needed for NapA activation (Mendoza-Martinez et al., 2017). Similarly, the phenotypes of *A. fumigatus* mutants lacking PrxA, PrxB or PrxC are different from mutants lacking Yap1, arguing against the participation of these peroxiredoxins in Yap1 activation (Rocha et al., 2018). For a long time it was considered that fungi did not contain 2-Cys peroxiredoxins. However, PrxA has been characterized in *A. fumigatus* as Aspf3 (Hillmann et al., 2016) and in *A. nidulans* as PrxA (Xia et al., 2018), showing that it belongs to a family of atypical 2-Cys peroxiredoxins homologous to yeast peroxiredoxin Ahp1 (Lian et al., 2012). More recently, we (Mendoza-Martinez and Aguirre; unpublished) and others (Xia et al., 2018) have found that *A. nidulans* mutants lacking peroxiredoxin PrxA are highly sensitive to H_2O_2, opening the possibility that PrxA might regulate NapA in this fungus.

The Yap1 pathway is connected to other oxidative stress signaling pathways in yeast cells. For example, in *S. pombe*, Pap1 activation by Tpx1 occurs only at low H_2O_2 concentrations, while at high H_2O_2 concentrations Tpx1 is inactivated by over-oxidation of its catalytic cysteine. These conditions lead to the activation of the Sty1/Spc1 MAPK pathway, triggering a complementary antioxidant response (Vivancos et al., 2005). Therefore, differences in oxidative stress sensitivities observed in Yap1 mutants in filamentous fungi could also indicate different interactions among stress signaling pathways. Indeed, in addition to NapA (Mendoza-Martinez et al., 2017), Skn7 homolog SrrA (Vargas-Perez et al., 2007) and the Hog1/Sty1/Spc1 homologs SakA (Jaimes-Arroyo et al., 2015; Kawasaki et al., 2002; Lara-Rojas et al., 2011) and MpkC (Garrido-Bazan et al., 2018) are part of the antioxidant response in *A. nidulans*.

4. Nuclear localization of Yap1 homologs in filamentous fungi

The nuclear localization of Nap1 homologs has been studied fusing Yap1 to a reporter fluorescence protein and expressing it from its own promoter or from strong constitutive promoters, using H_2O_2 (or *t*-BOOH) as stressor agent. Although H_2O_2 concentrations and treatment times varied (Table 1), in all cases Yap1 nuclear accumulation was induced by the oxidant treatment. However, in contrast to the high basal expression of YAP1 observed in yeast cells, in most cases in which *yap1* was expressed from its native promoter, the initial fluorescence signal was low and increased only after the oxidant treatment. This is particularly notable in *A. nidulans*, where *napA* mycelial basal expression was low, as determined by qPCR and NapA::GFP fluorescence expression. In this fungus, the CCAAT-binding complex represses *napA* expression in the absence of oxidative stress. Interestingly, H_2O_2 can induce the formation of an intermolecular disulfide in CCAAT-binding complex subunit HapC, which results in the transcriptional activation of *napA* (Thon et al., 2010), creating a double redox switch in the antioxidant response in this fungus. Whether a similar regulation occurs in other filamentous fungi is not known. In addition to H_2O_2, other conditions have been reported to induce Yap1 nuclear accumulation in filamentous fungi. In the plant pathogen *Cochliobolus heterostrophus*, where *Chap1* initial expression is high in conidia and germ tubes, plant phenolic compounds like cinnamic acid trigger ChAP1 nuclear accumulation but this results in only a slight up regulation of specific antioxidant genes (Shalaby et al., 2012; Shanmugam et al., 2010). In *A. nidulans*, menadione, osmotic stress, glucose starvation stress and growth on ethanol as sole carbon source also induced NapA nuclear localization (Mendoza-Martinez et al., 2017). In *A. fumigatus* AfYap1 is accumulated in the nucleus under hypoxia, which correlates with an increased production of ROS and protein cysteine oxidation, under these conditions (Shekhova et al., 2019). One possible interpretation of these results is that all these different types of stress lead to oxidative stress (Hansberg and Aguirre, 1990).

INFORME DE LABORES 2019

Table 1
The function of Yap1 homologs in filamentous fungi.

Organism (reference)	Oxidant sensitivity	Nuclear localization	Genes regulated	Fungi–host interaction	Developmental phenotype	Other
Ustilago maydis (Molina and Kahmann, 2007)	*Δyap1* and *yap1*^{C399A,407A}::3XeGFP mutants sensitive to H_2O_2.	Native *yap1* locus replaced by yap1:3XeGFP fusion. Low accumulation in vacuoles without H_2O_2. Nuclear accumulation after 1 mM H_2O_2 (1 h) or during early biotrophic growth.	221 Yap1-dependent genes induced by 5 mM H_2O_2, including genes encoding ROS detoxifying enzymes and enzymes involved in NADPH and glutathione biosynthesis.	*Δyap1* mutants formed appressorium but were virtually non-virulent.	Brown pigment accumulation.	
Cochliobolus heterostrophus (Lev et al., 2005; Shalaby et al., 2012)	*Δchap1* mutants sensitive to H_2O_2 and menadione.	GFP-CHAP1 fusion under its own promoter. Strong cytoplasmic expression without stress in germ tubes and conidia. Nuclear localization induced by 50 mM H_2O_2, 1 mM menadione and plant phenolic signals.	Genes encoding to Thioredoxin reductase (ChTRR1), γ-glutamylcysteine synthetase (ChGSH1), glutathione reductase (ChGLR1), glutathione synthetase (ChGSH2) and thioredoxin (ChTRX1).	Virulence not affected in *Δchap1* mutants.	Similar to WT.	
Colletotrichum gloeosporioides (Li et al., 2017; Sun et al., 2016)	*ΔCgAP1* mutants sensitive to H_2O_2, menadione and *t*-BOOH.	*CgAP1::eGFP* fusion expressed from its own promoter. Low diffuse cytoplasmic fluorescence without stress. High expression and nuclear localization after 60 min with *t*-BOOH.	Genes encoding glutathione disulfide reductase, cytochrome P450 monooxygenase and glutathione peroxidase. 1505 CgAP1-dependent genes.	*ΔCgAP1* mutants show attenuated virulence on poplar leaves and are non-pathogenic on mango.	Similar to WT.	
Epichloe festucae (Cartwright and Scott, 2013)	*ΔyapA* spores sensitive to H_2O_2. Mycelia sensitive to menadione and diamide, but not to H_2O_2, *t*-BOOH or KO_2.	YapA-EGFP expressed from native promoter. Diffuse cytoplasmic fluorescence without stress. Nuclear localization after 30 min with 16 mM H_2O_2 and 30 min post-inoculation in plant.	Catalase gene *catA*.	Symbiotic interaction not affected in *ΔyapA* mutants.		
Fusarium graminearum (Montibus et al., 2013)	*ΔFgap1* mutants sensitive to H_2O_2, $CdCl_2$, sorbitol and NaCl.	Not determined.	Down-regulation of *cat1*, *cat2* and *cat3* catalase genes and two Cu/ZnSOD genes. Expression of genes *Tri4* and *Tri101* slightly up-regulated.	Virulence not affected in *ΔFgap1* mutants.	Similar to WT.	Mycotoxin genes and toxin production increased in *ΔFgap1* mutants.
Aspergillus fumigatus (Lessing et al., 2007; Qiao et al., 2008)	*ΔAfyap1* mutants sensitive to H_2O_2 and menadione but not to diamide and DETANO.	*fyap1-eGFP* gene expressed from heterologous promoter. Low and diffuse cytoplasmic fluorescence without stress. Nuclear localization after 60 min with 2 mM H_2O_2.	57 protein spots, decreased or increased in intensity in *ΔAfyap1* mutants treated with 2 mM H_2O_2, including catalases, peroxidases and peroxiredoxins.	Virulence not affected in *ΔAfyap1* mutants.	Slight growth reduction on malt agar.	Cat1 and Cat2 activity reduced in *ΔAfyap1* mutants.
Aspergillus parasiticus (Reverberi et al. 2007, 2008)	*ΔApyap1* mutants sensitive to H_2O_2, Cumene Hydroperoxide and menadione.	Not determined.	SOD, HRP and GPX activities reduced and early expression of *aflR* and *norA* genes, involved in alfatoxin biosynthesis, in a *ΔApyap1* mutant. Increased expression of transcription factor Skn7.		Increased and premature conidiogenesis.	Increased aflatoxin production.
Talaromyces marneffei (Dankai et al., 2016)	Mutant sensitive to H_2O_2, menadione and $NaNO_2$.	Not determined.	Not determined.	YapA necessary for virulence.	Slow growth and smaller colonies with more red pigment. Fewer aerial hyphae and conidia.	Swollen cells and no internal fission.
Magnaporthe oryzae (Guo et al., 2011)	*Moap1* mutant mycelia sensitive to H_2O_2.	MoAP1::eGFP expressed from *trpC* promoter. Low fluorescence signal throughout the cell without stress. Nuclear localization after 2 mM H_2O_2 (2 h).	1179 *Moap1*-dependent genes, including genes putatively involved in ROS detoxification.	MoAP1 is required for growth of invasive hyphae and for pathogenicity.	Decreased growth of aerial hypha and conidiation. Abnormal morphology of conidia.	High expression in conidia.

(*continued on next page*)

INFORME DE LABORES 2019

Table 1 (*continued*)

Organism (reference)	Oxidant sensitivity	Nuclear localization	Genes regulated	Fungi–host interaction	Developmental phenotype	Other
Botrytis cinerea (Temme and Tudzynski, 2009)	*Δbap1* mutants sensitive to H_2O_2 and menadione.	Not determined	99 H_2O_2-induced and Bap1-dependent genes.	Virulence not affected in *ΔApyap1* mutants.	Similar to WT.	
Aspergillus nidulans (Mendoza-Martinez et al., 2017)	Mutant mycelia and conidia sensitive to H_2O_2 and menadione.	*napA::gfp* fusion from its own promoter. Very low expression without stress. Increased expression and nuclear localization after 1–2 h with 2 mM H_2O_2, glucose starvation, ethanol as carbon source or osmotic stress.	214 NapA-dependent genes in isolated conidia.		Decreased asexual sporulation and highly derepressed sexual development.	*ΔnapA* mutants unable to grow on ethanol, sorbose and fructose as sole carbon sources.
Neurospora crassa (Takahashi et al., 2010; Tian et al., 2011)	Mutant *ΔNcAp-1* sensitive to H_2O_2 $CdCl_2$ and Menadione.	*Nap-1-sGFP* expressed from heterologous *ccg1* promoter. Strong cytoplasmic fluorescence without stress. Nuclear localization after 5 min with 50 μM menadione or 30 min with 30 mM H_2O_2 or 10 mM CdCl for 30 min.	16 *nap-1*-dependent genes induced by menadione (microarray). 45 genes *NcAp-1* dependent genes induced by 6 mM H_2O_2 (transcriptional profiling).		Growth and asexual reproduction similar to WT.	

Table 2
Protein size and total cysteine content in Yap1 homologs from filamentous fungi.

Organism	Protein name	Protein size (aa)	Total cysteines	Identity to Yap1 (%)
Ustilago maydis	Yap1	758	C396, C399, C405, C407, C526, C532, C536 and C546	40
Cochliobolus heterostrophus	CHAP1	589	C394, C418, C529, C553 and C562	51
Colletotrichum gloeospoiroides	CgAP1	566	C367, C497, C507, C521, C530 and C557	44
Epichloe festucae	YapA	580	C363, C410, C499, C509, C523 and C532	45
Fusarium graminearum	Fgap1	588	C365, C491, C503, C513, C527, C536 and C564	44
Aspergillus fumigatus	AfYap1	615	C419, C431, C438, C562, C586 and C595	52
Aspergillus parasiticus	ApyapA	583	C346, C388, C400, C407, C530, C554 and C563	44
Aspergillus nidulans	NapA	577	C388, C397, C404, C525, C549 and C558	41
Aspergillus flavus		584	C346, C388, C400, C407, C531, C555 and C564	41
Aspergillus oryzae		563	C346, C358, C365, C510, C534 and C543	41
Aspergillus niger		574	C402, C521, C545 and C554	34
Neurospora crassa	NcAp1	577	C350, C361, C500, C510, C524, C533, C561 and C565	39
Talaromyces marneffei	YapA	592	C400, C407, C533, C557 and C566.	42
Magnaporthe oryzae	MoAP1	576	C369, C506, C516, C530, C539 and C566	46
Botrytis cinerea	Bap1	601	C393 and C423, C533, C543, C557 and C566	44

5. Yap1 homologs in filamentous fungi and gene expression

Most studies showing that Yap1 regulates gene expression in response to oxidative stress in filamentous fungi have monitored the expression of specific antioxidant genes such as genes encoding catalases, peroxidases or genes involved in glutathione biosynthesis (Table 1). In more comprehensive studies, a proteomic study identified 29 proteins with decreased abundance in mutants lacking AfYap1 and treated with H_2O_2, including catalases, peroxidases, peroxiredoxins and chaperons (Lessing et al., 2007). Transcriptomic analysis in *Neurospora crassa* identified 16 NcAP-1-dependent genes induced by menadione (Takahashi et al., 2010) and 45 genes induced by H_2O_2 (Tian et al., 2011). Similar studies identified 99, 221, 214, 1179 and 1505 yap1-regulated genes induced by H_2O_2 in *Botrytis cinerea* (Temme and Tudzynski, 2009), *U. maydis* (Molina and Kahmann, 2007), *A. nidulans* (Mendoza-Martinez et al., 2017), *M. oryzae* (Guo et al., 2011) and *Colletotrichum gloeosporioides* (Li et al., 2017), respectively. By comparison, about 100 and 50 Yap1 and Pap1 regulated genes have been reported in *S. cerevisiae* (Gasch et al., 2000) and *S. pombe* (Chen et al., 2008), respectively. While most of these studies identified Yap1-dependent genes in response to oxidants, the transcriptomic study in *A. nidulans* analyzed NapA-dependent gene expression in isolated asexual spores, showing for the first time, a role for this transcription factor in developmental gene regulation. Notably, the set of genes that NapA regulates during conidiation is different from the set of genes normally induced by oxidants. Indeed, during conidiation NapA is required for full induction of 201 genes, which include genes encoding 12 putative transcription factors; 46 oxidoreductase enzymes; 32 membrane transporter proteins, putatively involved in sugar and amino acid transport, drug and metal detoxification; 29 predicted or confirmed hydrolases involved in ethanol and complex carbohydrate utilization, as well as 29 proteins with recognizable protein domains not included in the previous categories. Some of these enzymes would be involved in iron acquisition and the production of antibiotics and other secondary metabolites (Mendoza-Martinez et al., 2017). These results indicate that like in yeast cells, Yap1 homologs in filamentous fungi can regulate the expression of both antioxidant and drug detoxification genes. This might have clinical implications as in the opportunistic human pathogen *Aspergillus flavus* a Yap1 point mutation that would result in constitutive nuclear localization causes resistance to the antifungal voriconazole, mediated by the upregulation of the *atfR* gene, ecoding an ATP-binding cassette transporter (Ukai et al., 2018). In *Cryptococcus neoformans* CnYap1 is dispensable for virulence but required for resistance to the fungicide fluconazole (Paul et al., 2015) and for the fluconazole-mediated induction of the *AFR1* gene, encoding a major ABC-type pump critical for azole efflux (Chang et al., 2018).

INFORME DE LABORES 2019

6. Yap1 homologs regulate inter-kingdom communication in filamentous fungi

Major mechanisms of defense in plants and animals involve the production of ROS to prevent pathogen attack. Therefore, fungal pathogens need effective strategies for ROS detoxification, which could involve Yap1 homologs. In biotroph *U. maydis*, Yap1 is necessary for successful infection but not for the development of the infection structure called appressorium. H_2O_2 accumulation was detected at the plant infection point in *Δyap1* but not in WT strains, and the flavoenzyme inhibitor DPI prevented such H_2O_2 accumulation and restored *Δyap1* virulence, suggesting that Yap1 is essential to neutralize the ROS generated by the host NADPH oxidases (Molina and Kahmann, 2007). Similarly, in the hemibiotrophic pathogen *M. oryzae*, *Moap1* mutants are unable to infect the host plant but do form appressoria. In these mutants also the growth of invasive hyphae during infection was reduced and ROS accumulation was observed at the infection site (Guo et al., 2011), indicating that MoAp1 is necessary for ROS scavenging. Similar results were reported in hemibiotrophic *C. gloeosporioides*, where *ΔCgAP-1* mutants were unable to cause lesions on mango (Li et al., 2017) and showed decreased virulence on poplar leaves, despite not being affected in appresorium formation. Moreover, wild type CgAP1 was necessary to prevent ROS accumulation during early stages of biotrophic growth (Sun et al., 2016). Likewise, *Δ*Yap1 mutants of hemibiotrophic *Alternaria alternata* failed to incite necrotic lesions on wounded or unwounded Minneola leaves and the use of plant NADPH oxidase inhibitors partially restored virulence (Lin et al., 2009). However, Yap1 homologs are not essential for virulence or plant interactions in all pathogenic or symbiotic fungi studied. The biotrophic interaction of *E. festucae* with its host plant is not affected by the lack of Yap1, although Yap1 accumulates in nuclei during plant penetration (Cartwright and Scott, 2013). In *C. heterostrophus*, CHAP1 deletion does not affect virulence, despite that nuclear accumulation is induced from 2.5 to 30 h after infection (Lev et al., 2005). In necrotrophic *B. cinerea*, the deletion of *bap1* did not impact virulence (Temme and Tudzynski, 2009) and a *Fusarium graminearum Fgap1* deletion mutant was also not affected in pathogenicity (Montibus et al., 2013). These differences in Yap1 impact on fungal virulence may be related to the different type of associations established between plant and fungi, as Yap1 requirement for virulence appears to be more common in biotrophic and hemibiotrophic fungi. Biotrophic fungi establish a close association with the host through the development of specialized infection hyphae within living plant cells, from which nutrients are taken up (Mendgen and Hahn, 2002). Necrotrophic fungi secrete toxins and enzymes that kill host cells and then nutrients released from the dead tissue are taken up, while hemibiotrophic fungi combine both strategies (Horbach et al., 2011). An initial biotrophic phase, during which the host's immune system and cell death is actively suppressed, allows invasive hyphae to spread throughout the infected plant tissue. This is followed by a necrotrophic phase during which toxins are secreted by the pathogen to induce host cell death. For necrotrophs and hemibiotrophic fungi, ROS accumulation act as a virulence factor that induces cell death for successful infection (Mengiste, 2012). For most biotrophic fungi, the Yap1 pathway is probably sufficient and necessary to contend with ROS during the first stages of colonization, while necrotrophic fungi might use additional antioxidant pathways to counteract the oxidative stress produced by the host.

ROS also play critical roles in animal's immunity. Fungal human pathogens are usually opportunistic like *A. fumigatus*, which causes invasive pulmonary disease in immunocompromised patients. However, *Afyap1* mutants did not show attenuated virulence in a murine model (Lessing et al., 2007). In the dimorphic fungus *Talaromyces marneffei*, *ΔyapA* mutants showed decreased survival in human macrophages, suggesting that in this fungus YapA is important for virulence (Dankai et al., 2016).

7. Yap1 functions in secondary metabolism

Secondary metabolites are small non-essential molecules that work as chemical communication signals in complex ecosystems, defending the habitat from predators or inhibiting the growth of competitors. Fungal secondary metabolites like mycotoxins cause food contamination, affecting human health. In contrast, penicillin and others are used as medical treatment of infectious diseases, cancer, or as immunosuppressants (See (Keller, 2018) for a recent review).

In fungi, secondary metabolite production is generally related to developmental processes and in some cases development is regulated by secondary metabolites (Marquez-Fernandez et al., 2007; Soid-Raggi et al., 2016). In *A. nidulans*, *napA* overexpression results in increased tolerance to oxidative stress and decreased production of secondary metabolites, including sterigmatocystin, emericellin, asperthecin, shamixanthone, and epishamixanthone and a shift from sexual to asexual development (Yin et al., 2013). Consistent with this, *A. parasiticus ΔpyapA* mutants produce more hydroperoxides and aflatoxin during growth on maize seeds, compared to the wild type strain (Reverberi et al., 2007). These results suggest that NapA regulates secondary metabolism genes in a negative way. However, during development, NapA is necessary for the induction of several secondary metabolism genes in *A. nidulans*. During sexual development, NapA is needed for expression of a specific polyketide synthetase involved in the production of the cleistothecial melanin (Mendoza-Martinez et al., 2017), and during asexual development it is required for the conidial accumulation of mRNAs corresponding to two polyketide synthases genes and other genes involved in the biosynthesis of secondary metabolites such as sterigmatocystin, penicillin, monodictyphenone and prenyl xanthones, all with antimicrobial activity (Mendoza-Martinez et al., 2017). These results indicate that in filamentous fungi Yap1 homologs can repress as well as activate secondary metabolism genes, perhaps depending on the developmental stage. Further research is needed to determine the specific mechanisms.

8. ROS and Yap1 regulate development in filamentous fungi

Hansberg and Aguirre (1990) proposed that increased (localized) ROS levels, beyond certain threshold, induce cell differentiation. Such increase is a transient process as much as ROS induce the expression of ROS scavenging systems (Aguirre et al., 2005; Hansberg and Aguirre, 1990). In filamentous fungi, the nicotinamide adenine dinucleotide phosphate (NADPH) oxidases (NOX) connect ROS and cell differentiation processes. These enzymes transfer electrons from NADPH to produce superoxide, which can readily produce H_2O_2. NOX homologs are widely distributed in animals, plants and many multicellular microorganisms (Aguirre and Lambeth, 2010). The link between NOX activity and cell differentiation in fungi was first established in *A. nidulans*, where NoxA was shown to be necessary for fruiting body development (Lara-Ortiz et al., 2003). Similar results were obtained in *Podospora anserina* (Malagnac et al., 2004), *N. crassa* (Cano-Dominguez et al., 2008) and other fungi. In *B. cinerea*, NoxA and NoxB are necessary for the differentiation of sclerotia (Segmuller et al., 2008). Additional evidence indicating that ROS regulate fungal sexual development comes from experiments in *A. nidulans* showing a drastic increase in the production of fruiting bodies in mutants that either overexpress NoxA (Lara-Ortiz et al., 2003), lack catalases CatA, CatB

INFORME DE LABORES 2019

and CatC (Lara-Ortiz, 2004), or lack NapA (Mendoza-Martinez et al., 2017).

In different fashions, ROS and NapA have also been related to asexual development in filamentous fungi. In *A. alternata*, mutants lacking NoxB or its regulatory subunit NoxR show a drastic decrease in conidiation and YAP1 expression appears reduced in these mutants (Yang and Chung, 2012, 2013). In *T. marneffei*, *yapA* mutants produce conidiophores with fewer phialides and conidia, and conidia show decreased germination rates, while yeast cells fail to undergo binary fission (Dankai et al., 2016). In *M. oryzae* MoAP1 deletion led to a reduction of aerial hyphal growth, abnormal conidium morphology and reduced conidiation (Guo et al., 2011). In *A. nidulans*, NapA is also needed for full conidiation (Mendoza-Martinez et al., 2017), and the normal accumulation of 201 mRNAs in conidia. Lower conidiation in *ΔnapA* mutants might be related to their lower expression of *gmcA* gene, encoding a putative glucose-methanol-choline oxidoreductase required for early stages of conidiophore development (Etxebeste et al., 2012). In *A. fumigatus*, *gmcA* ortholog AFUA_3G01580 is induced by H_2O_2 in an AfYap1-dependent manner (Lessing et al., 2007), suggesting that *gmcA* regulation by NapA is conserved, at least in the *Aspergilli*.

9. Yap1 in nutrient assimilation

In *S. pombe* glucose limitation induces both, the activation of the stress activated MAPK Spc1/Sty1 pathway, and the nuclear accumulation of Pap1 (Madrid et al., 2004). *S. cerevisiae* Yap1 was also identified in a two-hybrid screen for proteins interacting with Sip2, a β subunit of the Snf1 protein kinase, which is important for adaptation to glucose. Yap1 also shows nuclear accumulation on glycerol as carbon source (Wiatrowski and Carlson, 2003) and *A. nidulans ΔnapA* mutants are unable to grow on ethanol or arabinose and show very reduced growth on fructose, as sole carbon sources. Consistent with their lack of growth on ethanol, *ΔnapA* mutant conidia show notably decreased levels of *alcR*, *alcA* and *aldA* mRNAs, and the corresponding proteins are essential for ethanol utilization (Mendoza-Martinez et al., 2017). Such connections between Yap1, oxidative stress and nutrient assimilation deserve a more detailed exploration in both, yeasts and filamentous fungi.

10. Concluding remarks

It is clear that Yap1 homologs in filamentous fungi regulate the antioxidant response, as well as virulence, secondary metabolism, development and nutrient assimilation. However, it is not clear if the same regulatory mechanisms operate under all these conditions. It is critical to determine which Yap1 nCRD and cCRD cysteines are critical for H_2O_2 *vs.* electrophilic compound oxidation and to determine if peroxiredoxins are involved in H_2O_2-mediated oxidation. As mentioned before, natural plant phenolic compounds like cinnamic acid can trigger ChAP1 nuclear accumulation but only a slight up regulation of specific antioxidant genes in *C. heterostrophus* (Shalaby et al., 2012; Shanmugam et al., 2010). This raises the possibility that phenolic compounds produced during fungal development (i.e conidiation, sexual development) could physiologically induce Yap1 direct oxidation, as opposed to H_2O_2-induced peroxiredoxin-dependent oxidation. Such possibility is supported by the fact that L-phenylalanine ammonia-lyase (PAL) activity, which catalyzes the deamination of phenylalanine to form *trans*-cinnamic acid and ammonia, and PAL-encoding genes have been detected not only in plants, but also in fungi, including *A. nidulans* (Hyun et al., 2011). Moreover, AfeA enzymes related to plant 4-coumarate ligases (4CL), have also been reported to regulate development in *A. nidulans* and be present in other fungi (Soid-Raggi et al., 2016). 4CL is the third enzyme in the phenylpropanoid biosynthesis pathway in plants and forms coenzyme esters from hydroxycinnamic acids such as coumaric, caffeic, or ferulic acids (Hahlbrock and Grisebach, 1970). Moreover, other Yap1 oxidizing physiological compounds like methylglyoxal could accumulate during development and induce the expression of drug detoxification genes. Finally, it is critical to determine if some Yap1 functions depend on its association with Skn7 homologs or other proteins, as it occurs in yeast cells, and to delimitate such functions.

Acknowledgments

Our work is supported by CONACYT grants Investigación en Fronteras de la Ciencia 2015-I-319, CONACYT-DFG 277869 and PAPIIT-UNAM IN200719 and IV200519. This article is part of the project granted for the International Symposium on Fungal Stress–ISFUS and the Brazilian agencies CAPES and FAPESP are acknowledged for their grants 88887.289326/2019-00 and 2018/20571-6, respectively.

References

Aguirre, J., Lambeth, J.D., 2010. Nox enzymes from fungus to fly to fish and what they tell us about Nox function in mammals. Free Radic. Biol. Med. 49, 1342–1353.
Aguirre, J., Rios-Momberg, M., Hewitt, D., Hansberg, W., 2005. Reactive oxygen species and development in microbial eukaryotes. Trends Microbiol. 13, 111–118.
Alarco, A.M., Balan, I., Talibi, D., Mainville, N., Raymond, M., 1997. AP1-mediated multidrug resistance in *Saccharomyces cerevisiae* requires FLR1 encoding a transporter of the major facilitator superfamily. J. Biol. Chem. 272, 19304–19313.
Asano, Y., Hagiwara, D., Yamashino, T., Mizuno, T., 2007. Characterization of the bZip-type transcription factor NapA with reference to oxidative stress response in *Aspergillus nidulans*. Biosci. Biotechnol. Biochem. 71, 1800–1803.
Azevedo, D., Tacnet, F., Delaunay, A., Rodrigues-Pousada, C., Toledano, M.B., 2003. Two redox centers within Yap1 for H_2O_2 and thiol-reactive chemicals signaling. Free Radic. Biol. Med. 35, 889–900.
Bersweiler, A., D'Autreaux, B., Mazon, H., Kriznik, A., Belli, G., Delaunay-Moisan, A., Toledano, M.B., Rahuel-Clermont, S., 2017. A scaffold protein that chaperones a cysteine-sulfenic acid in H_2O_2 signaling. Nat. Chem. Biol. 13, 909–915.
Calvo, I.A., Boronat, S., Domenech, A., Garcia-Santamarina, S., Ayte, J., Hidalgo, E., 2013. Dissection of a redox relay: H_2O_2-dependent activation of the transcription factor Pap1 through the peroxidatic Tpx1-thioredoxin cycle. Cell Rep. 5, 1413–1424.
Calvo, I.A., Gabrielli, N., Iglesias-Baena, I., Garcia-Santamarina, S., Hoe, K.L., Kim, D.U., Sanso, M., Zuin, A., Perez, P., Ayte, J., Hidalgo, E., 2009. Genome-wide screen of genes required for caffeine tolerance in fission yeast. PLoS One 4 e6619.
Calvo, I.A., Garcia, P., Ayte, J., Hidalgo, E., 2012. The transcription factors Pap1 and Prr1 collaborate to activate antioxidant, but not drug tolerance, genes in response to H_2O_2. Nucleic Acids Res. 40, 4816–4824.
Cano-Dominguez, N., Alvarez-Delfin, K., Hansberg, W., Aguirre, J., 2008. NADPH oxidases NOX-1 and NOX-2 require the regulatory subunit NOR-1 to control cell differentiation and growth in Neurospora crassa. Eukaryot. Cell 7, 1352–1361.
Cartwright, G.M., Scott, B., 2013. Redox regulation of an AP-1-like transcription factor, YapA, in the fungal symbiont *Epichloe festucae*. Eukaryot. Cell 12, 1335–1348.
Chae, H.Z., Chung, S.J., Rhee, S.G., 1994a. Thioredoxin-dependent peroxide reductase from yeast. J. Biol. Chem. 269, 27670–27678.
Chae, H.Z., Robison, K., Poole, L.B., Church, G., Storz, G., Rhee, S.G., 1994b. Cloning and sequencing of thiol-specific antioxidant from mammalian brain: alkyl hydroperoxide reductase and thiol-specific antioxidant define a large family of antioxidant enzymes. Proc. Natl. Acad. Sci. U. S. A. 91, 7017–7021.
Chang, M., Sionov, E., Khanal Lamichhane, A., Kwon-Chung, K.J., Chang, Y.C., 2018. Roles of three *Cryptococcus neoformans* and *Cryptococcus gattii* efflux pump-coding genes in response to drug treatment. Antimicrob. Agents Chemother. 62.
Chen, D., Wilkinson, C.R., Watt, S., Penkett, C.J., Toone, W.M., Jones, N., Bahler, J., 2008. Multiple pathways differentially regulate global oxidative stress responses in fission yeast. Mol. Biol. Cell 19, 308–317.
Choi, H.J., Kang, S.W., Yang, C.H., Rhee, S.G., Ryu, S.E., 1998. Crystal structure of a novel human peroxidase enzyme at 2.0 Å resolution. Nat. Struct. Biol. 5, 400–406.
D'Autreaux, B., Toledano, M.B., 2007. ROS as signalling molecules: mechanisms that generate specificity in ROS homeostasis. Nat. Rev. Mol. Cell Biol. 8, 813–824.
Dankai, W., Pongpom, M., Youngchim, S., Cooper Jr., C.R., Vanittanakom, N., 2016. The yapA encodes bZIP transcription factor involved in stress tolerance in pathogenic fungus *Talaromyces marneffei*. PLoS One 11 e0163778.

Dantas Ada, S., Day, A., Ikeh, M., Kos, I., Achan, B., Quinn, J., 2015. Oxidative stress responses in the human fungal pathogen, *Candida albicans*. Biomolecules 5, 142–165.

Delaunay, A., Isnard, A.D., Toledano, M.B., 2000. H_2O_2 sensing through oxidation of the Yap1 transcription factor. EMBO J. 19, 5157–5166.

Delaunay, A., Pflieger, D., Barrault, M.B., Vinh, J., Toledano, M.B., 2002. A thiol peroxidase is an H_2O_2 receptor and redox-transducer in gene activation. Cell 111, 471–481.

Ellis, H.R., Poole, L.B., 1997. Roles for the two cysteine residues of AhpC in catalysis of peroxide reduction by alkyl hydroperoxide reductase from *Salmonella typhimurium*. Biochemistry 36, 13349–13356.

Etxebeste, O., Herrero-Garcia, E., Cortese, M.S., Garzia, A., Oiartzabal-Arano, E., de los Rios, V., Ugalde, U., Espeso, E.A., 2012. GmcA is a putative glucose-methanol-choline oxidoreductase required for the induction of asexual development in *Aspergillus nidulans*. PLoS One 7 e40292.

Fernandes, L., Rodrigues-Pousada, C., Struhl, K., 1997. Yap, a novel family of eight bZIP proteins in *Saccharomyces cerevisiae* with distinct biological functions. Mol. Cell Biol. 17, 6982–6993.

Garcia-Santamarina, S., Boronat, S., Hidalgo, E., 2014. Reversible cysteine oxidation in hydrogen peroxide sensing and signal transduction. Biochemistry 53, 2560–2580.

Garrido-Bazan, V., Jaimes-Arroyo, R., Sanchez, O., Lara-Rojas, F., Aguirre, J., 2018. SakA and MpkC stress MAPKs show opposite and common functions during stress responses and development in Aspergillus nidulans. Front. Microbiol. 9, 2518.

Gasch, A.P., Spellman, P.T., Kao, C.M., Carmel-Harel, O., Eisen, M.B., Storz, G., Botstein, D., Brown, P.O., 2000. Genomic expression programs in the response of yeast cells to environmental changes. Mol. Biol. Cell 11, 4241–4257.

Gruhlke, M.C.H., Schlembach, I., Leontiev, R., Uebachs, A., Gollwitzer, P.U.G., Weiss, A., Delaunay, A., Toledano, M., Slusarenko, A.J., 2017. Yap1p, the central regulator of the S. cerevisiae oxidative stress response, is activated by allicin, a natural oxidant and defence substance of garlic. Free Radic. Biol. Med. 108, 793–802.

Gulshan, K., Rovinsky, S.A., Coleman, S.T., Moye-Rowley, W.S., 2005. Oxidant-specific folding of Yap1p regulates both transcriptional activation and nuclear localization. J. Biol. Chem. 280, 40524–40533.

Gulshan, K., Thommandru, B., Moye-Rowley, W.S., 2012. Proteolytic degradation of the Yap1 transcription factor is regulated by subcellular localization and the E3 ubiquitin ligase Not4. J. Biol. Chem. 287, 26796–26805.

Guo, M., Chen, Y., Du, Y., Dong, Y., Guo, W., Zhai, S., Zhang, H., Dong, S., Zhang, Z., Wang, Y., Wang, P., Zheng, X., 2011. The bZIP transcription factor MoAP1 mediates the oxidative stress response and is critical for pathogenicity of the rice blast fungus *Magnaporthe oryzae*. PLoS Pathog. 7 e1001302.

Hahlbrock, K., Grisebach, H., 1970. Formation of coenzyme a esters of cinnamic acids with an enzyme preparation from cell suspension cultures of parsley. FEBS Lett. 11, 62–64.

Halliwell, B., Gutteridge, J.M.C., 2007. Free Radicals in Biology and Medicine, fourth ed. Oxford University Press, Oxford, New York.

Hansberg, W., Aguirre, J., 1990. Hyperoxidant states cause microbial cell differentiation by cell isolation from dioxygen. J. Theor. Biol. 142, 201–221.

Harshman, K.D., Moye-Rowley, W.S., Parker, C.S., 1988. Transcriptional activation by the SV40 AP-1 recognition element in yeast is mediated by a factor similar to AP-1 that is distinct from GCN4. Cell 53, 321–330.

Hertle, K., Haase, E., Brendel, M., 1991. The SNQ3 gene of *Saccharomyces cerevisiae* confers hyper-resistance to several functionally unrelated chemicals. Curr. Genet. 19, 429–433.

Hillmann, F., Bagramyan, K., Strassburger, M., Heinekamp, T., Hong, T.B., Bzymek, K.P., Williams, J.C., Brakhage, A.A., Kalkum, M., 2016. The crystal structure of peroxiredoxin Asp f3 provides mechanistic insight into oxidative stress resistance and virulence of *Aspergillus fumigatus*. Sci. Rep. 6, 33396.

Holmstrom, K.M., Finkel, T., 2014. Cellular mechanisms and physiological consequences of redox-dependent signalling. Nat. Rev. Mol. Cell Biol. 15, 411–421.

Horbach, R., Navarro-Quesada, A.R., Knogge, W., Deising, H.B., 2011. When and how to kill a plant cell: infection strategies of plant pathogenic fungi. J. Plant Physiol. 168, 51–62.

Hyun, M.W., Yun, Y.H., Kim, J.Y., Kim, S.H., 2011. Fungal and plant phenylalanine ammonia-lyase. Mycobiology 39, 257–265.

Izawa, S., Maeda, K., Sugiyama, K., Mano, J., Inoue, Y., Kimura, A., 1999. Thioredoxin deficiency causes the constitutive activation of Yap1, an AP-1-like transcription factor in *Saccharomyces cerevisiae*. J. Biol. Chem. 274, 28459–28465.

Jacobson, F.S., Morgan, R.W., Christman, M.F., Ames, B.N., 1989. An alkyl hydroperoxide reductase from *Salmonella typhimurium* involved in the defense of DNA against oxidative damage. Purification and properties. J. Biol. Chem. 264, 1488–1496.

Jaimes-Arroyo, R., Lara-Rojas, F., Bayram, O., Valerius, O., Braus, G.H., Aguirre, J., 2015. The SrkA kinase is part of the SakA Mitogen-activated protein kinase interactome and regulates stress responses and development in *Aspergillus nidulans*. Eukaryot. Cell 14, 495–510.

Kawasaki, L., Sanchez, O., Shiozaki, K., Aguirre, J., 2002. SakA MAP kinase is involved in stress signal transduction, sexual development and spore viability in *Aspergillus nidulans*. Mol. Microbiol. 45, 1153–1163.

Keller, N.P., 2019 Mar. Fungal secondary metabolism: regulation, function and drug discovery. Nat. Rev. Microbiol. 17 (3), 167–180.

Kos, I., Patterson, M.J., Znaidi, S., Kaloriti, D., da Silva Dantas, A., Herrero-de-Dios, C.M., d'Enfert, C., Brown, A.J., Quinn, J., 2016. Mechanisms underlying the delayed activation of the Cap1 transcription factor in *Candida albicans* following combinatorial oxidative and cationic stress important for phagocytic potency. mBio 7 e00331.

Kuge, S., Jones, N., 1994. YAP1 dependent activation of TRX2 is essential for the response of *Saccharomyces cerevisiae* to oxidative stress by hydroperoxides. EMBO J. 13, 655–664.

Kuge, S., Jones, N., Nomoto, A., 1997. Regulation of yAP-1 nuclear localization in response to oxidative stress. EMBO J. 16, 1710–1720.

Lara-Ortiz, T., 2004. NoxA, una NADPH oxidasa homóloga a gp91phox, regula el desarrollo sexual en el hongo *Aspergillus nidulans*. Instituto de Fisiología Celular. Universidad Nacional Autónoma de México, p. 69.

Lara-Ortiz, T., Riveros-Rosas, H., Aguirre, J., 2003. Reactive oxygen species generated by microbial NADPH oxidase NoxA regulate sexual development in *Aspergillus nidulans*. Mol. Microbiol. 50, 1241–1255.

Lara-Rojas, F., Sanchez, O., Kawasaki, L., Aguirre, J., 2011. *Aspergillus nidulans* transcription factor AtfA interacts with the MAPK SakA to regulate general stress responses, development and spore functions. Mol. Microbiol. 80, 436–454.

Lee, J., Godon, C., Lagniel, G., Spector, D., Garin, J., Labarre, J., Toledano, M.B., 1999. Yap1 and Skn7 control two specialized oxidative stress response regulons in yeast. J. Biol. Chem. 274, 16040–16046.

Lessing, F., Kniemeyer, O., Wozniok, I., Loeffler, J., Kurzai, O., Haertl, A., Brakhage, A.A., 2007. The *Aspergillus fumigatus* transcriptional regulator AfYap1 represents the major regulator for defense against reactive oxygen intermediates but is dispensable for pathogenicity in an intranasal mouse infection model. Eukaryot. Cell 6, 2290–2302.

Lev, S., Hadar, R., Amedeo, P., Baker, S.E., Yoder, O.C., Horwitz, B.A., 2005. Activation of an AP1-like transcription factor of the maize pathogen *Cochliobolus heterostrophus* in response to oxidative stress and plant signals. Eukaryot. Cell 4, 443–454.

Li, X., Wu, Y., Liu, Z., Zhang, C., 2017. The function and transcriptome analysis of a bZIP transcription factor CgAP1 in *Colletotrichum gloeosporioides*. Microbiol. Res. 197, 39–48.

Lian, F.M., Yu, J., Ma, X.X., Yu, X.J., Chen, Y., Zhou, C.Z., 2012. Structural snapshots of yeast alkyl hydroperoxide reductase Ahp1 peroxiredoxin reveal a novel two-cysteine mechanism of electron transfer to eliminate reactive oxygen species. J. Biol. Chem. 287, 17077–17087.

Lin, C.H., Yang, S.L., Chung, K.R., 2009. The YAP1 homolog-mediated oxidative stress tolerance is crucial for pathogenicity of the necrotrophic fungus *Alternaria alternata* in citrus. Mol. Plant Microbe Interact. 22, 942–952.

Madrid, M., Soto, T., Franco, A., Paredes, V., Vicente, J., Hidalgo, E., Gacto, M., Cansado, J., 2004. A cooperative role for Atf1 and Pap1 in the detoxification of the oxidative stress induced by glucose deprivation in *Schizosaccharomyces pombe*. J. Biol. Chem. 279, 41594–41602.

Maeta, K., Izawa, S., Okazaki, S., Kuge, S., Inoue, Y., 2004. Activity of the Yap1 transcription factor in *Saccharomyces cerevisiae* is modulated by methylglyoxal, a metabolite derived from glycolysis. Mol. Cell Biol. 24, 8753–8764.

Malagnac, F., Lalucque, H., Lepere, G., Silar, P., 2004. Two NADPH oxidase isoforms are required for sexual reproduction and ascospore germination in the filamentous fungus *Podospora anserina*. Fungal Genet. Biol. 41, 982–997.

Marquez-Fernandez, O., Trigos, A., Ramos-Balderas, J.L., Viniegra-Gonzalez, G., Deising, H.B., Aguirre, J., 2007. Phosphopantetheinyl transferase CfwA/NpgA is required for *Aspergillus nidulans* secondary metabolism and asexual development. Eukaryot. Cell 6, 710–720.

Mendgen, K., Hahn, M., 2002. Plant infection and the establishment of fungal biotrophy. Trends Plant Sci. 7, 352–356.

Mendoza-Martinez, A.E., Lara-Rojas, F., Sanchez, O., Aguirre, J., 2017. NapA mediates a redox regulation of the antioxidant response, carbon utilization and development in *Aspergillus nidulans*. Front. Microbiol. 8, 516.

Mengiste, T., 2012. Plant immunity to necrotrophs. Annu. Rev. Phytopathol. 50, 267–294.

Molina, L., Kahmann, R., 2007. An *Ustilago maydis* gene involved in H_2O_2 detoxification is required for virulence. Plant Cell 19, 2293–2309.

Montibus, M., Ducos, C., Bonnin-Verdal, M.N., Bormann, J., Ponts, N., Richard-Forget, F., Barreau, C., 2013. The bZIP transcription factor Fgap1 mediates oxidative stress response and trichothecene biosynthesis but not virulence in *Fusarium graminearum*. PLoS One 8 e83377.

Mulford, K.E., Fassler, J.S., 2011. Association of the Skn7 and Yap1 transcription factors in the *Saccharomyces cerevisiae* oxidative stress response. Eukaryot. Cell 10, 761–769.

Notredame, C., Higgins, D.G., Heringa, J., 2000. T-Coffee: a novel method for fast and accurate multiple sequence alignment. J. Mol. Biol. 302, 205–217.

Okazaki, S., Tachibana, T., Naganuma, A., Mano, N., Kuge, S., 2007. Multistep disulfide bond formation in Yap1 is required for sensing and transduction of H_2O_2 stress signal. Mol. Cell 27, 675–688.

Ouyang, X., Tran, Q.T., Goodwin, S., Wible, R.S., Sutter, C.H., Sutter, T.R., 2011. Yap1 activation by H_2O_2 or thiol-reactive chemicals elicits distinct adaptive gene responses. Free Radic. Biol. Med. 50, 1–13.

Patterson, M.J., McKenzie, C.G., Smith, D.A., da Silva Dantas, A., Sherston, S., Veal, E.A., Morgan, B.A., MacCallum, D.M., Erwig, L.P., Quinn, J., 2013. Ybp1 and Gpx3 signaling in *Candida albicans* govern hydrogen peroxide-induced oxidation of the Cap1 transcription factor and macrophage escape. Antioxid. Redox. Signal. 19, 2244–2260.

Paul, S., Doering, T.L., Moye-Rowley, W.S., 2015. Cryptococcus neoformans Yap1 is required for normal fluconazole and oxidative stress resistance. Fungal Genet. Biol. 74, 1–9.

INFORME DE LABORES 2019

Peshenko, I.V., Shichi, H., 2001. Oxidation of active center cysteine of bovine 1-Cys peroxiredoxin to the cysteine sulfenic acid form by peroxide and peroxynitrite. Free Radic. Biol. Med. 31, 292–303.

Qiao, J., Kontoyiannis, D.P., Calderone, R., Li, D., Ma, Y., Wan, Z., Li, R., Liu, W., 2008. Afyap1, encoding a bZip transcriptional factor of *Aspergillus fumigatus*, contributes to oxidative stress response but is not essential to the virulence of this pathogen in mice immunosuppressed by cyclophosphamide and triamcinolone. Med Mycol 46, 773–782.

Reverberi, M., Zjalic, S., Punelli, F., Ricelli, A., Fabbri, A.A., Fanelli, C., 2007. Apyap1 affects aflatoxin biosynthesis during *Aspergillus parasiticus* growth in maize seeds. Food Addit. Contam. 24, 1070–1075.

Reverberi, M., Zjalic, S., Ricelli, A., Punelli, F., Camera, E., Fabbri, C., Picardo, M., Fanelli, C., Fabbri, A.A., 2008. Modulation of antioxidant defense in *Aspergillus parasiticus* is involved in aflatoxin biosynthesis: a role for the ApyapA gene. Eukaryot. Cell 7, 988–1000.

Rocha, M.C., de Godoy, K.F., Bannitz-Fernandes, R., Fabri, J., Barbosa, M.M.F., de Castro, P.A., Almeida, F., Goldman, G.H., da Cunha, A.F., Netto, L.E.S., de Oliveira, M.A., Malavazi, I., 2018. Analyses of the three 1-Cys peroxiredoxins from *Aspergillus fumigatus* reveal that cytosolic Prx1 is central to H_2O_2 metabolism and virulence. Sci. Rep. 8, 12314.

Schnell, N., Entian, K.D., 1991. Identification and characterization of a *Saccharomyces cerevisiae* gene (PAR1) conferring resistance to iron chelators. Eur. J. Biochem. 200, 487–493.

Segmuller, N., Kokkelink, L., Giesbert, S., Odinius, D., van Kan, J., Tudzynski, P., 2008. NADPH oxidases are involved in differentiation and pathogenicity in *Botrytis cinerea*. Mol. Plant Microbe Interact. 21, 808–819.

Shahi, P., Gulshan, K., Naar, A.M., Moye-Rowley, W.S., 2010. Differential roles of transcriptional mediator subunits in regulation of multidrug resistance gene expression in *Saccharomyces cerevisiae*. Mol. Biol. Cell 21, 2469–2482.

Shalaby, S., Horwitz, B.A., Larkov, O., 2012. Structure–activity relationships delineate how the maize pathogen *Cochliobolus heterostrophus* uses aromatic compounds as signals and metabolites. Mol. Plant Microbe Interact. 25, 931–940.

Shanmugam, V., Ronen, M., Shalaby, S., Larkov, O., Rachamim, Y., Hadar, R., Rose, M.S., Carmeli, S., Horwitz, B.A., Lev, S., 2010. The fungal pathogen *Cochliobolus heterostrophus* responds to maize phenolics: novel small molecule signals in a plant-fungal interaction. Cell Microbiol. 12, 1421–1434.

Shekhova, E., Ivanova, L., Kruger, T., Stroe, M.C., Macheleidt, J., Kniemeyer, O., Brakhage, A.A., 2019. Redox proteomic analysis reveals oxidative modifications of proteins by increased levels of intracellular reactive oxygen species during hypoxia adaptation of *Aspergillus fumigatus*. Proteomics e1800339.

Soid-Raggi, G., Sanchez, O., Ramos-Balderas, J.L., Aguirre, J., 2016. The adenylate-forming enzymes AfeA and TmpB are involved in *Aspergillus nidulans* self-communication during asexual development. Front. Microbiol. 7, 353.

Sun, Y., Wang, Y., Tian, C., 2016. bZIP transcription factor CgAP1 is essential for oxidative stress tolerance and full virulence of the poplar anthracnose fungus *Colletotrichum gloeosporioides*. Fungal Genet. Biol. 95, 58–66.

Takahashi, M., Yamashita, K., Shiozawa, A., Ichiishi, A., Fukumori, F., Fujimura, M., 2010. An AP-1-like transcription factor, NAP-1, regulates expression of the glutathione S-transferase and NADH:flavin oxidoreductase genes in *Neurospora crassa*. Biosci. Biotechnol. Biochem. 74, 746–752.

Temme, N., Tudzynski, P., 2009. Does *Botrytis cinerea* ignore H(2)O(2)-induced oxidative stress during infection? Characterization of botrytis activator protein 1. Mol. Plant Microbe Interact. 22, 987–998.

Thon, M., Al Abdallah, Q., Hortschansky, P., Scharf, D.H., Eisendle, M., Haas, H., Brakhage, A.A., 2010. The CCAAT-binding complex coordinates the oxidative stress response in eukaryotes. Nucleic Acids Res. 38, 1098–1113.

Tian, C., Li, J., Glass, N.L., 2011. Exploring the bZIP transcription factor regulatory network in *Neurospora crassa*. Microbiology 157, 747–759.

Toda, T., Shimanuki, M., Yanagida, M., 1991. Fission yeast genes that confer resistance to staurosporine encode an AP-1-like transcription factor and a protein kinase related to the mammalian ERK1/MAP2 and budding yeast FUS3 and KSS1 kinases. Genes Dev. 5, 60–73.

Toone, W.M., Kuge, S., Samuels, M., Morgan, B.A., Toda, T., Jones, N., 1998. Regulation of the fission yeast transcription factor Pap1 by oxidative stress: requirement for the nuclear export factor Crm1 (Exportin) and the stress-activated MAP kinase Sty1/Spc1. Genes Dev. 12, 1453–1463.

Ukai, Y., Kuroiwa, M., Kurihara, N., Naruse, H., Homma, T., Maki, H., Naito, A., 2018. Contributions of yap1 mutation and subsequent atrF upregulation to voriconazole resistance in *Aspergillus flavus*. Antimicrob. Agents Chemother. 62.

Uthe, H., Vanselow, J.T., Schlosser, A., 2017. Proteomic analysis of the mediator complex interactome in *Saccharomyces cerevisiae*. Sci. Rep. 7, 43584.

Vargas-Perez, I., Sanchez, O., Kawasaki, L., Georgellis, D., Aguirre, J., 2007. Response regulators SrrA and SskA are central components of a phosphorelay system involved in stress signal transduction and asexual sporulation in *Aspergillus nidulans*. Eukaryot. Cell 6, 1570–1583.

Vivancos, A.P., Castillo, E.A., Biteau, B., Nicot, C., Ayte, J., Toledano, M.B., Hidalgo, E., 2005. A cysteine-sulfinic acid in peroxiredoxin regulates H_2O_2-sensing by the antioxidant Pap1 pathway. Proc. Natl. Acad. Sci. U. S. A. 102, 8875–8880.

Wemmie, J.A., Steggerda, S.M., Moye-Rowley, W.S., 1997. The *Saccharomyces cerevisiae* AP-1 protein discriminates between oxidative stress elicited by the oxidants H_2O_2 and diamide. J. Biol. Chem. 272, 7908–7914.

Wemmie, J.A., Szczypka, M.S., Thiele, D.J., Moye-Rowley, W.S., 1994. Cadmium tolerance mediated by the yeast AP-1 protein requires the presence of an ATP-binding cassette transporter-encoding gene, YCF1. J. Biol. Chem. 269, 32592–32597.

Wiatrowski, H.A., Carlson, M., 2003. Yap1 accumulates in the nucleus in response to carbon stress in *Saccharomyces cerevisiae*. Eukaryot. Cell 2, 19–26.

Wood, M.J., Andrade, E.C., Storz, G., 2003. The redox domain of the Yap1p transcription factor contains two disulfide bonds. Biochemistry 42, 11982–11991.

Xia, Y., Yu, H., Zhou, Z., Takaya, N., Zhou, S., Wang, P., 2018. Peroxiredoxin system of *Aspergillus nidulans* resists inactivation by high concentration of hydrogen peroxide-mediated oxidative stress. J. Microbiol. Biotechnol. 28, 145–156.

Yan, C., Lee, L.H., Davis, L.I., 1998. Crm1p mediates regulated nuclear export of a yeast AP-1-like transcription factor. EMBO J. 17, 7416–7429.

Yang, S.L., Chung, K.R., 2012. The NADPH oxidase-mediated production of hydrogen peroxide (H(2)O(2)) and resistance to oxidative stress in the necrotrophic pathogen *Alternaria alternata* of citrus. Mol. Plant Pathol. 13, 900–914.

Yang, S.L., Chung, K.R., 2013. Similar and distinct roles of NADPH oxidase components in the tangerine pathotype of *Alternaria alternata*. Mol. Plant Pathol. 14, 543–556.

Yin, W.B., Reinke, A.W., Szilagyi, M., Emri, T., Chiang, Y.M., Keating, A.E., Pocsi, I., Wang, C.C., Keller, N.P., 2013. bZIP transcription factors affecting secondary metabolism, sexual development and stress responses in *Aspergillus nidulans*. Microbiology 159, 77–88.

INFORME DE LABORES 2019

Neuroscience Letters 712 (2019) 134506

Contents lists available at ScienceDirect

Neuroscience Letters

journal homepage: www.elsevier.com/locate/neulet

Research article

Glycine receptor is differentially expressed in the rat retina at early stages of streptozotocin-induced diabetes

Elizabeth Morales-Calixto[a,1], Miguel Ángel Velázquez-Flores[b,1], Gustavo Sánchez-Chávez[a,1], Ruth Ruiz Esparza-Garrido[c], Rocío Salceda[a,*]

[a] Departamento de Neurodesarrollo y Fisiología, Instituto de Fisiología Celular, Universidad Nacional Autónoma de México, Ciudad de México, Mexico
[b] Laboratorio de Genómica Funcional, Unidad de Investigación Médica en Genética Humana del Hospital de Pediatría "Silvestre Frenk Freund", Centro Médico Nacional Siglo XXI, Instituto Mexicano del Seguro Social (IMSS), Ciudad de México, Mexico
[c] Catedrática CONACyT, Laboratorio de Genómica Funcional, Unidad de Investigación Médica en Genética Humana del Hospital de Pediatría "Silvestre Frenk Freund", Centro Médico Nacional Siglo XXI, Instituto Mexicano del Seguro Social (IMSS), Ciudad de México, Mexico

ARTICLE INFO

Keywords:
Retina
Glycine
Glycine receptor
Streptozotocin
Diabetes

ABSTRACT

Diabetes mellitus is a metabolic disease that leads to several complications which include retinopathy. Neuronal abnormalities have been reported to appear before microvasculature alterations. We analyzed the expression levels of GlyR subunits in the retina at 7, 20, and 45 days after streptozotocin-induced diabetes to gain insight into the pathogenesis of diabetic retinopathy. We determined the mRNA and protein expression by qPCR and western blot, respectively. The mRNA and protein expression of the α1 subunit was not altered over the study period; however, they were slightly reduced in α2 yet statistically significant. While protein expression of α3 subunit was only reduced at 45 days diabetes. The mRNA and protein expression of the α4 subunit was remarkably decreased since day 7 of diabetes, remaining only ~20% on day 45 of diabetes. Surprisingly, the mRNA of the β subunit was highly increased, while its protein levels were not changed. The decrease in GlyR α subunits expression in the retina from diabetic animals suggest a perturbation in the inhibitory glycine signaling pathway, which might be related to the visual alterations observed in diabetes.

1. Introduction

Diabetic retinopathy is one of the most common complications of diabetes mellitus and it causes blindness in working-age adults [1]. Diabetic retinopathy usually refers to vascular abnormalities, but increasing evidence indicates the occurrence of neural alterations which precedes the microvascular pathology observed at later stages of the disease [2–4]. Abnormalities in oscillatory potentials and b waves of the electroretinogram, as well as in contrast sensitivity have been reported in diabetic patients and rodents [5–10]; in spite of this information, the underlying neural mechanisms involved are largely unknown.

Retina excitatory neurotransmission is modulated by glycine and GABA, the major inhibitory neurotransmitters in retina, localized in different types of amacrine cells, which carry out specific roles in the processing of visual signals [11]. Around 50% of the amacrine cells are glycinergic, which make synaptic contacts with bipolar, ganglion, and other amacrine cells [12,13].

The postsynaptic glycine receptors (GlyR) are pentameric ligand-gated chloride channel composed by α (1–4) and β subunits, assembled as homomeric (α subunits) or heteromeric (α-β subunits) receptors [14]. The β subunit is considered essential for clustering GlyR at synapses due to its direct interaction with the cytoplasmic clustering protein gephyrin [15]. All five subunits are expressed in the inner plexiform layer of the adult mammalian retina [16–18] and their characteristic distribution across the inner plexiform layer and neuronal subtype localization suggests they are involved with different neuronal circuits [13]. Therefore, the aim of the present study was to investigate whether changes on glycine receptor subunits expression occur in the retina at early diabetes induction in the rat.

* Corresponding author at: División de Neurociencias, Departamento de Neurodesarrollo y Fisiología, Instituto de Fisiología Celular, Universidad Nacional Autónoma de México, Apdo. Postal 70-253, CP 04510, Mexico.
E-mail address: rsalceda@ifc.unam.mx (R. Salceda).
[1] These authors contributed equally to this work.

https://doi.org/10.1016/j.neulet.2019.134506
Received 12 February 2019; Received in revised form 21 August 2019; Accepted 16 September 2019
Available online 18 September 2019
0304-3940/ © 2019 The Authors. Published by Elsevier B.V. This is an open access article under the CC BY-NC-ND license (http://creativecommons.org/licenses/BY-NC-ND/4.0/).

INFORME DE LABORES 2019

2. Methods

2.1. Animals

Female adult Long Evans rats (180–200 g) were used for the experiments. Diabetes was induced by a single intraperitoneal injection of streptozotocin (STZ) (90 mg/kg) [19]. No insulin was administered. Animals were considered diabetic if blood glucose levels were higher than 250 mg/dl. Rats were sacrificed after 7, 20, and 45 days after diabetes induction, along with non-treated animals (normal). Blood was collected and the eyes dissected. Eyes were equatorial sectioned and the retinas were shed away from the eye cups using fine pincers.

This study was carried out in strict accordance with the recommendations of the Mexican Institutes of Health Research (DOF. NOM-062-Z00-1999). The protocol was approved by our Institutional Laboratory Animal Care and Use Committee (CICUAL, in Spanish, Comité Institucional para el Cuidado y Uso de los Animales de Laboratorio del Instituto de Fisiología Celular de la Universidad Nacional Autónoma de México), Protocol Number RSS18-14; this was done in accordance with the Office of Laboratory Animal Welfare (OLAW), Assurance Number A5281-01.

All efforts were made to minimize animal suffering and to reduce the number of rats employed.

2.2. RNA extraction

Total retina RNA was extracted with TRIZOL and cDNA was synthesized with the RevertAid H Minus First Strand cDNA Synthesis Kit (Thermo Scientific) following the manufacturer instructions. RNA integrity and concentration was verified by spectrophotometry (NanoDrop1000, Thermo Scientific) and 2% agarose gels.

2.3. Quantitative real-time PCR

Absolute quantification of mRNA was performed according to the method described by Pffafl [20]. A standard curve was constructed from serial dilutions (51, 0.51, 0.0051, 0.000051, and 0.00000051 pg) of the purified 18S (18S ribosomal RNA) gene and it was run with each GlyR subunit: α1-α4 or β. PCR conditions were: holding stage (50 °C (2 min); 95 °C (2 min); forty cycles (95 °C, 15 s); TM (1 min); Melt curve (95 °C, 15 s); 60 °C (1 min); 72 °C (1 min). Primers were designed with the Primer 3 tool (Koressaar and Remm, 2007; Untergasser et al., 2012) and purchased from Oligo T4 (Guanajuato, Gto. Mexico). 18S (TM = 75.6 °C): Forward: Reverse: α1 (TM = 63.4 °C) Forward: 5´-ACTCTGCGATTCTACCTTTGG-3´, Reverse: 5´-ATATTCATTGTAGGCGAGACGG-3´. α2 (TM = 60.4 °C): Forward; 5´-CAGAGTTCAGGTTCCAGGG-3´, Reverse: 5´-TCCACAAACTTCTTCTTGATAG-3´. α3 (TM = 62.8 °C): Forward 5´-GTGAGACACTTTCGGACACTAC-3´, Reverse: 5´-GATGGGTCGAGGTCTAATGAATC-3´. β (TM = 65.1 °C): Forward: 5´-CTGTTCATATCAAGCACTTTGC-3´, Reverse: 5´- GGGATGACAGGCTTGGCAG-3´. The α4 subunit was amplified by using the Prime® qPCR Primers (Rn.PT.56a. 12226027; Exon location 7e8) from Integrated DNA Technologies (Coralville, IA, USA) Time Agarose gels (2%) were run to corroborate the specific amplification.

2.4. Western blotting

Retinas were homogenized in RIPA buffer (50 mM Tris-HCl pH 7.2, 150 mM NaCl, 2% triton X-100, 0.2% SDS) containing proteases and phosphatases inhibitors. Proteins were resolved through 10% SDS-PAGE and electro blotted to immobilon membranes. The membranes were blocked for 3 h in 5% no-fat milk, and incubated overnight at 4 °C with the primary antibodies prepared in Bovine serum albumin 5%: Rabbit anti- α1, 1:3000 (Synaptic Systems); rabbit anti- α2, 1:3000 (abcam); rabbit anti- α3, 1:1000 (abcam); rabbit anti- α4, 1:3000 (Biorbyt); rabbit anti- β, 1:2000 (abcam). After washing thoroughly, the membranes were incubated with the corresponding horseradish peroxidase-conjugated secondary antibodies (Amersham ECL Anti-Rabbit-HRP 1:45,000 for anti-α1; 1:30,000 for anti-α2, anti-α3, anti-α4 and 1:15,000 for anti-β).

The immunoreactive bands were visualized using a Chemiluminescent HRP Substrate (Immobilon Western Chemiluminescent HRP Substrate, Millipore Corp.) according to the manufacturer's instructions. Western blot densitometric analysis was normalized to the amount of actin, using a mouse monoclonal anti pan-actin 1:2000 (abcam) and Anti-Mouse-HRP 1:15,000 (Amersham). Densitometric images and data obtained with Alpha DigiDoc RT (Alpha Innotech, San Leandro, CA) were analyzed using Graph Pad Prism5 software (San Diego, CA, USA).

2.5. Statistical analysis

Data are expressed as the mean ± SEM. Statistical significance was determined by one way ANOVA analysis followed by Tukey´s test multiple comparison using Graph Pad Prisma 5. Statistical significance was assumed at $P \leq 0.05$.

3. Results

3.1. Metabolic state of streptozotocin-treated rats

The existence of diabetes in streptozotocin treated rats was inferred from hyperglycemia, impaired growth, polydipsia and polyuria (Table 1), (Sánchez-Chávez et al. 2008).

3.2. qPCR studies

mRNA GlyR subunits (α1- α4 and β) were evaluated by qPCR. Expression of all subunits was found in the normal rat retina, where the predominant subunits were α2 (5.7 ± 0.15 pg) and α1 (3.14 ± 0.85 pg), followed by α3 (1.33 ± 0.86 pg) and α4 (1.0 ± 0.07 pg); the β subunit showed high expression levels (5.0 ± 0.4 pg) [21]. The relative changes of each GlyR subunit mRNA in the diabetic stage are shown in Fig. 1. The α1 and α3 mRNA expression was not statistically significant over the diabetes study period (Fig. 1). Bizarrely, levels of α3 mRNA expression were founds significantly higher at 20-days of diabetes. On the contrary, the expression of the α2 mRNA expression showed a considerable reduction (30%) from 7 days after STZ administration (Fig. 1). Meanwhile, the α4 mRNA expression displayed a prominent and continuous decrease from day 7 of diabetes, showing values almost undetectable on day 45 of the STZ treatment. Regarding the β subunit mRNA expression values, these were remarkably increased (~2 folds) from early stages of diabetes (Fig. 1).

3.3. Western blotting studies

Western blot for normal rat retina revealed a band of 48–51 kDa for

Table 1
Characteristics of streptozotocin-diabetic rats.

Days	Body weight		Blood glucose	Water intake
	Control	STZ	mg/dl	% of increase
7	190 ± 10	173 ± 10	382 ± 18*	340 ± 25*
20	270 ± 22	180 ± 22*	480 ± 15*	300 ± 20*
45	370 ± 30	166 ± 20*	520 ± 29*	370 ± 15*

Values are the mean ± SEM of 7–12 animals per group. Glucose blood levels of normal (control) rats were 114 ± 4 mg/dl. Water intake in 12 h by normal rats was 33 ± 3 ml. *P < 0.01 compared to normal non streptozotocin treated rats.

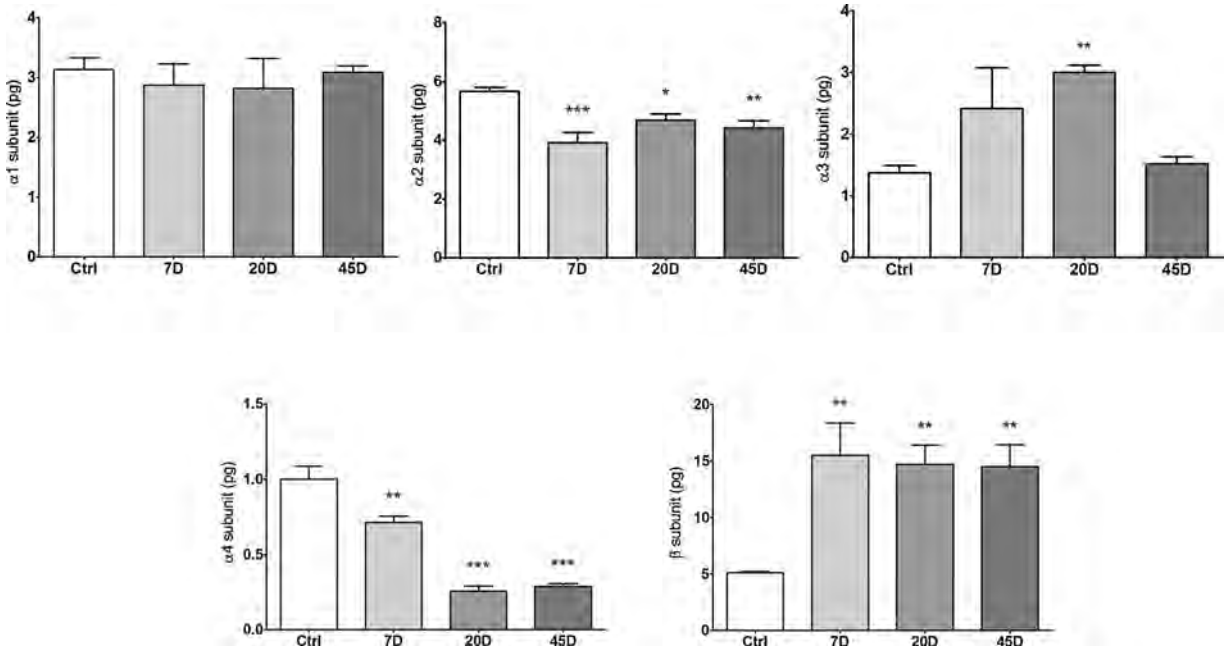

Fig. 1. Expression of GlyR subunits mRNAs in normal and diabetic rat retina. qRT-PCR analysis of GlyR α1 (A), α2 (B), α3 (C), α4 (D), and β (E) subunits in normal (N) and after 7, 20, and 45 days of diabetes induction. Data (± SEM) represent the results from six to nine different retinas carried out in duplicate. *P < 0.05, **P < 0.007, ***P < 0.0001 compared to normal non streptozotocin treated rats at the same ages.

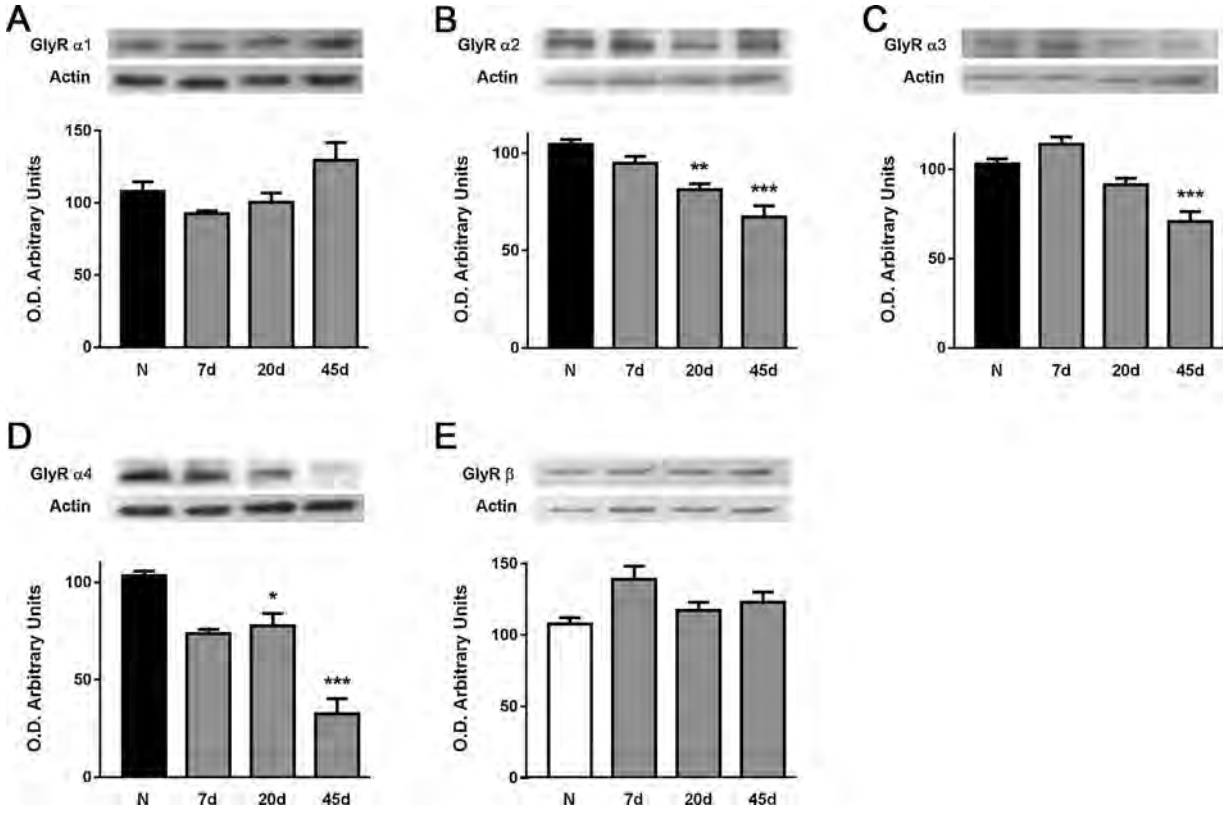

Fig. 2. Expression of GlyR subunits in rat retina at different periods of diabetes induction. Upper part, representative western blot analysis of GlyR subunits (48–49 kDa) and actin (43 kDa) in rat retina homogenates. Lower part, densitometric analysis of western blots of GlyR α1 (A), α2 (B), α3 (C), α4 (D), and β (E). The relative expression between the GlyR subunits normalized to actin was obtained considering as 100% the optical densities from the normal non-streptozotocin treated rats (N). Values are mean ± S.E.M. from three to five (7d), seven to eleven (20d, 45d) different retinas. *P < 0.0135, **P < 0.0014, ***P < 0.0001, compared to normal non-streptozotocin treated rats at the same ages.

INFORME DE LABORES 2019

all α subunits. The α1 and α2 subunits showed the higher expression, followed by the α3 and α4 (not shown), as previously reported [21].

Similar to that observed at mRNA level, the α1 GlyR subunit did not show expression changes under diabetic conditions (Fig. 2A), while the expression of the other α subunits was significantly reduced. The α2 subunit modestly decreased (20–30 %) at 20- and 45-days of diabetes (Fig. 2B), and the α3 subunit showed a considerable decrease (34%) at 45 days (Fig. 2C). Interestingly, the α4 subunit expression significantly decreased (25%) from day 7 of diabetes induction, remaining only 30% on day 45 of diabetes (Fig. 2D). Concerning the β subunit, western blot analysis revealed a 48.7 kDa protein band in both normal and diabetic rat retina. In the normal retina, the relative β subunit expression was around 5–6 folds higher than the α2 subunit (not shown). In the diabetic rat retina, the β subunit expression showed a small not significant increase over the period study (Fig. 2E).

4. Discussion

Diabetic retinopathy is clinically diagnosed by the onset of vascular disorders, suggesting that it is solely a microvascular disease [22,23]. However, early visual defects in diabetes appear to be a result of an impairment of the neural retina [2–4]. Abnormalities in the electroretinogram components have been reported in humans and rats with diabetes [5,8,9,24,25]. These alterations are accompanied by deficits in light and color sensitivity in patients at early diabetic retinopathy [6,7,10]. In addition, ganglion cell degeneration has been reported in diabetic patients as well as in animal models at long-term diabetes [2,26].

The glycinergic amacrine cells are known to generate inhibitory output into bipolar cells, ganglion cells and other amacrine cells. This signaling is essential in regulating the response properties of different classes of retinal ganglion cells [27–29]. Considerable evidence indicates that glycinergic inhibition modulates light responses of retinal neurons and is also involved in specificity, preferentially by crossover inhibition between the ON- and the OFF-channels. Glycine exerts its action through strychnine- sensitive ionotropic receptors, the GlyR, which open a chloride channel leading to hyperpolarization of the cell. GlyR are formed by α (1–4) subunits and a single β subunit, which are considered to form heteromeric receptors with stoichiometry of 2α/3β subunits [30]. The five subunits have been identified in the mammalian retina where they are expressed in the inner plexiform layer (IPL) [16,17,31]. Therefore, we aimed at analyzing whether diabetes influences retinal glycinergic neurotransmission to determine the expression of GlyR subunit isoforms.

We found that both mRNA and protein expression of α1 subunit, which is a main input to light transmitting ganglion cells [32], was not modified over the diabetes study. However, while the mRNA expression of the retina predominant α2 subunit [21] decreased over the diabetes study period, its protein dropped after 20–45 days of diabetes. It has been demonstrated that GlyRα2 is expressed by bipolar cell axon terminals and amacrine cells, and almost all ganglion cells [17]. Meanwhile, α3 mRNA expression was variable, but protein expression was reduced on the day 45 of the STZ treatment. The α3 subunit is distributed widely throughout the inner plexiform layer; in fact, all amacrine express α3β GlyR [13]. Although slight, the reduction in the expression of these subunits may be relevant, given that there is evidence that GlyRα2 and GlyRα3 inhibition enhance ganglion cells excitatory center responses, and GlyRα2 modulates crossover inhibition in both the ON and OFF pathways. In addition, GlyRα2 crossover and GlyRα3 serial inhibition are additive and independent in the ON retinal pathway.

Noteworthy, both the mRNA and protein expression of the α4 subunit were significantly reduced from very early diabetes stages. The GlyRα4 subunit is localized throughout the inner plexiform layer with highest density in cholinergic amacrine cells (starburst amacrine cells, SAC) [18], which play key roles in the direction selectivity [33,34]. Indeed, pharmacological studies showed that SAC lose direction selectivity in the absence of inhibition [35]. Interesting, decrease of cholinesterase activities were found in STZ-diabetic rats [36], and death of cholinergic cells in Ins2-Akita mice [37]. Remarkable, double labeling immunohistochemical experiments revealed that approximately 30% of the α4 containing synapses also express α2 subunit [18]. Therefore, our results suggest a decrease in α4- GlyR signaling in SAC and other amacrine and/or ganglion cells.

The β subunit is expressed throughout the IPL, which is expected, since β subunit is required for agonist binding [30], and all GlyR receptors appear to require the β subunit to target the membrane by means of its linking to gephyrin [15]. Biochemical evidence indicates that the β subunit does not assemble as pentameric homomers [38]; therefore, its higher mRNA expression must likely suggest changes in its synthesis and /or degradation, which has to be further studied.

5. Conclusion

We found a decrease in the expression of α4, α3, and α2 GlyR subunits in the rat retina at very early diabetes induction, suggesting alteration in retina glycinergic neurotransmission.

Statement of author contributions

R.S. designed the research.
E.M.C., M.A.V.F., G.S-CH., R.R.E-G performed the research.
E.M.C., M.A.V.F., G.S-CH., R.R.E-G, R.S. analyzed the data.
R.S. wrote the manuscript.
G.S-CH., M.A.V.F. made the figures.
All authors reviewed the paper.

Declaration of Competing Interest

The authors declare no conflict of interest.

Acknowledgments

This research was partially supported by the PAPIIT/UNAM, project IG200216 (RS), and FIS/IMSS/PROT/G17/1673 from Instituto Mexicano del Seguro Social (IMSS) (MAVF). The authors would like to thank the Animal Facilities and Molecular Biology Units, Instituto de Fisiología Celular, Universidad Nacional Autónoma de México. SINTAGMA TRANSLATIONS revised and corrected the English version.

References

[1] A.R. Shah, T.W. Gardner, Diabetic retinopathy: research to clinical practice, Clin. Diabetes Endocrinol. 3 (9) (2017) 1–7, https://doi.org/10.1186/s40842-017-0047-y.
[2] A.J. Barber, E. Lieth, S.A. Khin, D.A. Antonetti, A.G. Buchanan, T.W. Gardner, Neural apoptosis in the retina during experimental and human diabetes. Early onset and effect of insulin, J. Clin. Invest. 102 (4) (1998) 783–791, https://doi.org/10.1172/JCI2425.
[3] E. Lieth, A.J. Barber, B. Xu, C. Dice, M.J. Ratz, D. Tanase, J.M. Strother, Glial reactivity and impaired glutamate metabolism in short-term experimental diabetic retinopathy. Penn State Retina Research Group, Diabetes 47 (5) (1998) 815–820, https://doi.org/10.2337/diabetes.47.5.815.
[4] P.H. Peng, H.S. Lin, S. Lin, Nerve fibre layer thinning in patients with preclinical retinopathy, Can. J. Ophthalmol. 44 (4) (2009) 417–422, https://doi.org/10.3129/i09-112.
[5] M.A.J. Bearse, Y. Han, M.E. Schneck, A.J. Adams, Retinal function in normal and diabetic eyes mapped with the slow flash multifocal electroretinogram, Invest. Ophthalmol. Vis. Sci. 45 (1) (2004) 296–304, https://doi.org/10.1167/iovs.03-0424.
[6] A.A. Dosso, E.R. Bonvin, Y. Morel, A. Golay, J.P. Assal, P.M. Leuenberger, Risk factors associated with contrast sensitivity loss in diabetic patients, Graefes Arch. Clin. Exp. Ophthalmol. 234 (5) (1996) 300–305, https://doi.org/10.1007/BF00220704.
[7] M.S. Roy, R.D. Gunkel, M.J. Podgor, Color vision defects in early diabetic retinopathy, Arch. Ophthalmol. 104 (2) (1986) 225–228, https://doi.org/10.1001/archopht.1986.01050140079024.

[8] M. Segawa, Y. Hirata, S. Fujimori, K. Okada, The development of electroretinogram abnormalities and the possible role of polyol pathway activity in diabetic hyperglycemia and galactosemia, Metabolism 37 (5) (1988) 454–460, https://doi.org/10.1016/0026-0495(88)90046-7.

[9] K. Shinoda, R. Rejdak, F. Schuettauf, G. Blatsios, M. Volker, N. Tanimoto, et al., Early electroretinographic features of streptozotocin-induced diabetic retinopathy, Clin. Experiment. Ophthalmol. 35 (9) (2007) 847–854, https://doi.org/10.1111/j.1442-9071.2007.01607.x doi: CEO1607 [pii].

[10] S. Sokol, A. Moskowitz, B. Skarf, R. Evans, M. Molitch, B. Senior, Contrast sensitivity in diabetics with and without background retinopathy, Arch. Ophthalmol. 103 (1) (1985) 51–54, https://doi.org/10.1001/archopht.1985.01050010055018.

[11] R.G. Pourcho, Neurotransmitters in the retina, Curr. Eye Res. 15 (7) (1996) 797–803, https://doi.org/10.3109/02713689609003465.

[12] H. Wässle, Parallel processing in the mammalian retina, Nat. Rev. Neurosci. 5 (10) (2004) 747–757, https://doi.org/10.1038/nrn1497.

[13] H. Wässle, L. Heinze, E. Ivanova, S. Majumdar, J. Weiss, R.J. Harvey, S. Haverkamp, Glycinergic transmission in the Mammalian retina, Front. Mol. Neurosci. 2 (6) (2009) 1–12, https://doi.org/10.3389/neuro.02.006.2009.

[14] H. Betz, D. Langosch, N. Rundstrom, J. Bormann, A. Kuryatov, J. Kuhse, et al., Structure and biology of inhibitory glycine receptors, Ann. N. Y. Acad. Sci. 707 (1993) 109–115, https://doi.org/10.1111/j.1749-6632.1993.tb38046.x.

[15] M. Kneussel, H. Betz, Clustering of inhibitory neurotransmitter receptors at developing postsynaptic sites: the membrane activation model, Trends Neurosci. 23 (9) (2000) 429–435, https://doi.org/10.1016/S0166-2236(00)01627-1.

[16] U. Greferath, J.H. Brandstatter, H. Wassle, J. Kirsch, J. Kuhse, U. Grunert, Differential expression of glycine receptor subunits in the retina of the rat: a study using immunohistochemistry and in situ hybridization, Vis. Neurosci. 11 (4) (1994) 721–729 doi: S0952523800003023 [pii].

[17] S. Haverkamp, U. Muller, H.U. Zeilhofer, R.J. Harvey, H. Wassle, Diversity of glycine receptors in the mouse retina: localization of the alpha2 subunit, J. Comp. Neurol. 477 (4) (2004) 399–411, https://doi.org/10.1002/cne.20267.

[18] L. Heinze, R.J. Harvey, S. Haverkamp, H. Wassle, Diversity of glycine receptors in the mouse retina: localization of the alpha4 subunit, J. Comp. Neurol. 500 (4) (2007) 693–707, https://doi.org/10.1002/cne.21201.

[19] G. Sanchez-Chavez, J. Hernandez-Berrones, L.B. Luna-Ulloa, V. Coffe, R. Salceda, Effect of diabetes on glycogen metabolism in rat retina, Neurochem. Res. 33 (7) (2008) 1301–1308, https://doi.org/10.1007/s11064-007-9583-7.

[20] M.W. Pfaffl, A new mathematical model for relative quantification in real-time RT-PCR, Nucleic Acids Res. 29 (9) (2001) e45, https://doi.org/10.1093/nar/29.9.e45.

[21] G. Sánchez-Chávez, M. Velázquez-Flores, R. Ruiz Esparza-Garrido, R. Salceda, Glycine receptor subunits expression in the developing rat retina, Neurochem. Int. 108 (2017) 177–182, https://doi.org/10.1016/j.neuint.2017.03.013.

[22] R.N. Frank, Diabetic retinopathy, N. Engl. J. Med. 350 (1) (2004) 48–58, https://doi.org/10.1056/NEJMra021678.

[23] T.S. Kern, Interrelationships between the retinal neuroglia and vasculature in diabetes, Diabetes Metab. J. 38 (3) (2014) 163–170, https://doi.org/10.4093/dmj.2014.38.3.163.

[24] Q. Li, E. Zemel, B. Miller, I. Perlman, Early retinal damage in experimental diabetes: electroretinographical and morphological observations, Exp. Eye Res. 74 (5) (2002) 615–625, https://doi.org/10.1006/exer.2002.1170 S001448350291170X [pii].

[25] H. Sakai, Y. Tani, E. Shirasawa, Y. Shirao, K. Kawasaki, Development of electroretinographic alterations in streptozotocin-induced diabetes in rats, Ophthalmic Res. 27 (1) (1995) 57–63, https://doi.org/10.1159/000267571.

[26] M. Sasaki, Y. Ozawa, T. Kurihara, S. Kubota, K. Yuki, K. Noda, et al., Neurodegenerative influence of oxidative stress in the retina of a murine model of diabetes, Diabetologia 53 (5) (2010) 971–979, https://doi.org/10.1007/s00125-009-1655-6.

[27] U. Grünert, Distribution of GABA and glycine receptors on bipolar and ganglion cells in the mammalian retina, Microsc. Res. Technol. 50 (2) (2000) 130–140, https://doi.org/10.1002/1097-0029(20000715)50:2<130::AID-JEMT5>3.0.CO;2-I doi: 10.1002/1097-0029(20000715)50:2 < 130::AID-JEMT5 > 3.0.CO;2-I [pii].

[28] H. Wässle, P. Koulen, J.H. Brandstätter, E.L. Fletcher, C.M. Becker, Glycine and GABA receptors in the mammalian retina, Vision Res. 38 (10) (1998) 1411–1430, https://doi.org/10.1016/S0042-6989(97)00300-3.

[29] Z.J. Zhou, D.W. Marshak, G.L. Fain, Amino acid receptors of midget and parasol ganglion cells in primate retina, Proc. Natl. Acad. Sci. U. S. A. 91 (11) (1994) 4907–4911.

[30] J. Grudzinska, R. Schemm, S. Haeger, A. Nicke, G. Schmalzing, H. Betz, B. Laube, The beta subunit determines the ligand binding properties of synaptic glycine receptors, Neuron 45 (5) (2005) 727–739, https://doi.org/10.1016/j.neuron.2005.01.028 doi: S0896-6273(05)00060-7 [pii].

[31] S. Haverkamp, U. Muller, K. Harvey, R.J. Harvey, H. Betz, H. Wassle, Diversity of glycine receptors in the mouse retina: localization of the alpha3 subunit, J. Comp. Neurol. 465 (4) (2003) 524–539, https://doi.org/10.1002/cne.10852.

[32] S. Majumdar, L. Heinze, S. Haverkamp, E. Ivanova, H. Wässle, Glycine receptors of A-type ganglion cells of the mouse retina, Vis. Neurosci. 24 (4) (2007) 471–487, https://doi.org/10.1017/S0952523807070174.

[33] A.S. Mauss, A. Vlasits, A. Borst, M. Feller, Visual circuits for direction selectivity, Annu. Rev. Neurosci. 40 (2017) 211–230, https://doi.org/10.1146/annurev-neuro-072116-031335.

[34] W.R. Taylor, D.I. Vaney, Diverse synaptic mechanisms generate direction selectivity in the rabbit retina, J. Neurosci. 22 (17) (2002) 7712–7720.

[35] S. Lee, Z.J. Zhou, The synaptic mechanism of direction selectivity in distal processes of starburst amacrine cells, Neuron 51 (6) (2006) 787–799, https://doi.org/10.1016/j.neuron.2006.08.007.

[36] G. Sanchez-Chavez, R. Salceda, Effect of streptozotocin-induced diabetes on activities of cholinesterases in the rat retina, IUBMB Life 49 (4) (2000) 283–287, https://doi.org/10.1080/15216540050033140.

[37] M.J. Gastinger, R.S. Singh, A.J. Barber, Loss of cholinergic and dopaminergic amacrine cells in streptozotocin-diabetic rat and Ins2Akita-diabetic mouse retinas, Invest. Ophthalmol. Vis. Sci. 47 (7) (2006) 3143–3150, https://doi.org/10.1167/iovs.05-1376.

[38] N. Griffon, C. Büttner, A. Nicke, J. Kuhse, G. Schmalzing, H. Betz, Molecular determinants of glycine receptor subunit assembly, EMBO J. 18 (17) (1999) 4711–4721, https://doi.org/10.1093/emboj/18.17.4711.

frontiers in Pharmacology

REVIEW
published: 24 April 2019
doi: 10.3389/fphar.2019.00419

Molecular Interplay Between the Sigma-1 Receptor, Steroids, and Ion Channels

Sara L. Morales-Lázaro[1], Ricardo González-Ramírez[2] and Tamara Rosenbaum[1]*

[1] Departamento de Neurociencia Cognitiva, División de Neurociencias, Instituto de Fisiología Celular, Universidad Nacional Autónoma de México, Ciudad de México, Mexico, [2] Departamento de Biología Molecular e Histocompatibilidad, Hospital General Dr. Manuel Gea González, Secretaría de Salud, Ciudad de México, Mexico

Cell excitability is tightly regulated by the activity of ion channels that allow for the passage of ions across cell membranes. Ion channel activity is controlled by different mechanisms that change their gating properties, expression or abundance in the cell membrane. The latter can be achieved by forming complexes with a diversity of proteins like chaperones such as the Sigma-1 receptor (Sig-1R), which is one with unique features and exhibits a role as a ligand-operated chaperone. This molecule also displays high intracellular mobility according to its activation level since, depletion of internal Ca^{+2} stores or the presence of specific ligands, produce Sig-1R's mobilization from the endoplasmic reticulum toward the plasma membrane or nuclear envelope. The function of the Sig-1R as a chaperone is regulated by synthetic and endogenous ligands, with some of these compounds being a steroids and acting as key endogenous modifiers of the actions of the Sig-1R. There are cases in the literature that exemplify the close relationship between the actions of steroids on the Sig-1R and the resulting negative or positive effects on ion channel function/abundance. Such interactions have been shown to importantly influence the physiology of mammalian cells leading to changes in their excitability. The present review focuses on describing how the Sig-1R regulates the functional properties and the expression of some sodium, calcium, potassium, and TRP ion channels in the presence of steroids and the physiological consequences of these interplays at the cellular level are also discussed.

Keywords: Sig-1R, ion channels, steroids, NMDA – receptor, TRPV1, voltage-gated ion channel, progesterone

OPEN ACCESS

Edited by:
Tangui Maurice,
INSERM U1198 Mécanismes Moléculaires dans les Démences Neurodégénératives, France

Reviewed by:
Olivier Soriani,
Centre National de la Recherche Scientifique (CNRS), France
Carmela Parenti,
Università degli Studi di Catania, Italy

****Correspondence:***
Sara L. Morales-Lázaro
saraluzm@ifc.unam.mx

Specialty section:
This article was submitted to Experimental Pharmacology and Drug Discovery, a section of the journal Frontiers in Pharmacology

Received: *20 January 2019*
Accepted: *03 April 2019*
Published: *24 April 2019*

Citation:
Morales-Lázaro SL, González-Ramírez R and Rosenbaum T (2019) Molecular Interplay Between the Sigma-1 Receptor, Steroids, and Ion Channels. Front. Pharmacol. 10:419. doi: 10.3389/fphar.2019.00419

INTRODUCTION

The Sigma-1 receptor (Sig-1R) is a protein mainly localized to the endoplasmic reticulum (ER), where it functions as a ligand-operated chaperone (Hayashi and Su, 2003, 2007). The first studies related to Sig-1R incorrectly classified it as an opioid-type receptor (Martin et al., 1976; Su, 1982), although, Sig-1R displays high affinity for (+)-benzomorphans (such as (+)-SKF 10047) and not for the negative enantiomers of these compounds (Tam, 1983; Largent et al., 1987).

It was also hypothesized that its structure contained two transmembrane segments (Hayashi and Su, 2007; Aydar et al., 2016), however, the recent crystallographic structure for Sig-1R, shows only one transmembrane segment (Schmidt et al., 2016; **Figure 1**). The C-terminus of Sig-1R was also elucidated by crystallography, and it was proposed to be located facing toward the cell cytoplasm (Schmidt et al., 2016). Nonetheless, *in vivo* experiments later suggested that it is found facing the lumen of the ER (Mavylutov et al., 2018).

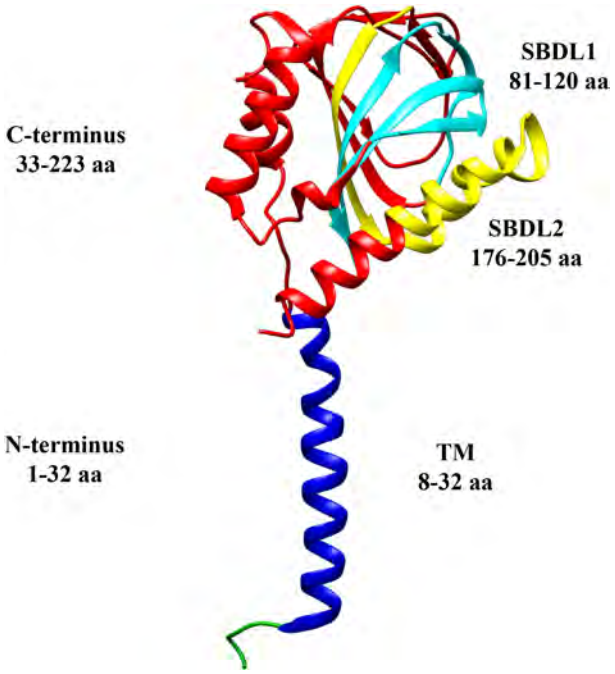

FIGURE 1 | Sigma-1 receptor topology. Structural domains of a monomer of the Sig-1R are shown in different colors: N-terminus (green and blue), transmembrane segment (TM, blue), C-terminus (red), and the two Steroid Binding Domain-Like (SBDL1, aqua, and SBDL2, yellow) which are located in the C-terminus. The amino acids (aa) comprising each domain are illustrated (PDB structure entry, 5HK).

The high affinity of Sig-1R for dextrorotatory isomers of specific opiate benzomorphans like (+) pentazocine (Tam and Cook, 1984; Prezzavento et al., 2017), was exploited to purify it from guinea pig liver and characterize it as a ∼25 kDa protein (Hanner et al., 1996). It was determined that its sequence shares no homology with any other mammalian protein, that it contains a typical ER-retention signal within the N-terminus and, initial hydrophobicity analysis, provided the first sign of the presence of a single transmembrane segment (Hanner et al., 1996). Also, it was defined that the C-terminus of this receptor (residues 33–223) contains the ligand binding-sites (Kruse, 2017), two steroid-like binding domains (SBDL1-2) (Pal et al., 2007) and the chaperone domain (**Figure 1**; Hayashi and Su, 2007; Ortega-Roldan et al., 2013). Another essential feature of Sig-1R is its intracellular mobility, although it is mostly localized to the mitochondria-associated membrane (MAM) of the ER (a domain with high cholesterol content; Hayashi and Su, 2007), it still exhibits movement toward the plasma membrane and nuclear envelope (Hayashi and Su, 2003). Under basal conditions, Sig-1R forms complexes with another ER resident protein, BiP (or Gpr78) and calcium depletion from the ER derives in the dissociation of these two proteins. Then, Sig-1R becomes available to perform its chaperone functions by contributing to the stability of targets proteins, such as the inositol triphosphate (IP3) receptor (IP3R) and others, as will be here discussed (Hayashi and Su, 2007).

An important property of the function of this receptor is its regulation by synthetic and endogenous ligands (Hayashi and Su, 2004; **Table 1**). According to the physiological responses that these ligands elicit, they can play a role as agonists by potentiating some physiological responses or by normalizing alterations produced during some pathological conditions. On the other hand, antagonists block these effects. For example, PRE084 is considered to be a Sig-1R agonist since it improves learning impairments induced by MK-801 (a non-competitive antagonist of NMDA receptors), while this effect is suppressed by a Sig-1R antagonist, haloperidol (Maurice et al., 1994). Another example of this is the psychomotor responsiveness induced by cocaine, which is Sig-1R-dependent, an effect that is prevented by the co- or pre-administration of Sig-1R antagonists (Kourrich et al., 2013).

It has been reported that some ligands allow for the dissociation of the Sig-1R/BiP complexes, facilitating the interaction of Sig-1R with other proteins (for example, ion channels), similar to what is described above for calcium (Hayashi and Su, 2007). Examples of ligands that promote the dissociation of Sig-1R from BiP are (+)-pentazocine, (+)-SKF 10047, PRE084, fluoxetine and cocaine (Hayashi and Su, 2007). In contrast, other Sig-1R ligands can preserve it in a silent state, either associated with BiP or by producing its oligomerization (Hayashi and Su, 2007; Mishra et al., 2015). Compounds representative of the latter are haloperidol, methamphetamine and NE-100 (Hayashi and Su, 2007; Mishra et al., 2015).

Interestingly, most of the endogenous ligands for Sig-1R are steroids (Su et al., 1988; Maurice et al., 1996). Among them are steroids synthesized in the nervous system (neurosteroids) that modulate the physiology of neuronal tissues (Corpechot et al., 1981). Neurosteroids such as pregnenolone-sulfate (PREG-S) and dehydroepiandrosterone sulfate (DHEA-S) have a role as Sig-1R agonists (Maurice et al., 1998; **Table 1**). Conversely, progesterone is an endogenous antagonist of this receptor, that displays the highest affinity for Sig-1R, as compared to the other steroid-type ligands (Su et al., 1988; Maurice et al., 1998; **Table 1**). On the other hand, testosterone, a steroid whose specific actions on Sig-1R are still unclear, only shows a partial affinity for the receptor (Su et al., 1988). In addition, cholesterol, the precursor of all steroids, can regulate Sig-1R through its binding to the C-terminus of Sig-1R (Palmer et al., 2007).

Altogether, the use of Sig-1R ligands has allowed establishing its role in neuroprotection, neurogenesis, pain, addiction, neurodegenerative and cardiovascular diseases (reviewed in Tsai et al., 2009). This review article will focus on our current understanding of how the interactions between Sig-1R and steroids regulate some ion channels such as voltage-gated potassium and sodium channels, NMDA receptors and TRP channels as well as on the resulting physiological effects of such interactions (**Figure 2**).

ION CHANNELS

An early event of evolution was the appearance of a plasma membrane that functioned as a barrier to separate and protect

INFORME DE LABORES 2019

TABLE 1 | Steroid Sig-1R ligands that regulate some ion channels.

Effect on Sig-1R	Name	Structure	Ion Channel Target
Agonist	Pregnenolone Sulfate K_i = 3.196 ± 0.823	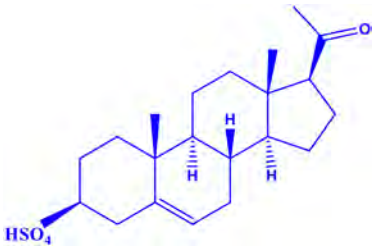	(–) L-type channels (+) NMDAr
	DHEA Sulfate K_i = 15.126 ± 7.69	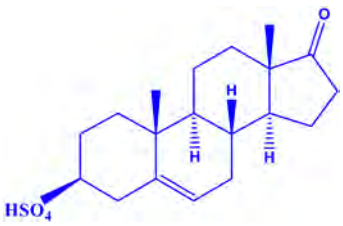	(–) Na_v channels (+) NMDAr
Antagonist	Progesterone K_i = 0.175 ± 0.55	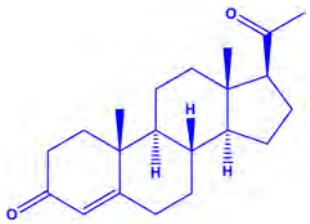	(–) TRPV1 channels (+) $Na_{v1.5}$ channels* (–) NMDAr** (–) hERG channels***

*K_i (μM) are indicated below the steroid name and represent the concentration of steroids necessary to inhibit in vitro binding of (+)-[3H]-SKF 10047 to brain homogenates (Su et al., 1988; Maurice et al., 1996). The column on the right indicates the ion channel that is the target of the steroid's actions through modulation of Sig-1R. (+) and (–) indicate the type of effect reported. *Progesterone prevents the inhibitory effects of DMT on Nav1.5 channels. **Progesterone disrupts the interaction between Sig-1R and NMDAr. ***This effect has not been directly demonstrated.*

the interior of cells from changes in the external conditions. This lipid barrier also allows for the separation of charges between the extracellular and intracellular regions, serving as a shelter for pore-forming proteins that allow for selective passage of ions from one side to the other which, in turn, results in the generation of a membrane potential (Hille, 2001). Some of these proteins, called voltage-gated ion channels (VGIC's; i.e., Na_v, K_v, and Ca_v), open their pores to ion conduction (sodium, potassium and calcium) in response to electrical changes, a phenomenon which is possible thanks to a voltage-sensitive domain that modulates the gating properties of these channels (Hille, 2001). Other channels are specifically activated by ligands (i.e., *N*-methyl-D-aspartate or NMDA receptors), which directly bind to certain regions of the channels modulating their gating (Hille, 2001). Also, there are polymodal ion channels, such as the Transient Receptor Potential or TRP channels, that are activated by several stimuli including those of thermal, chemical and osmotic natures (Li, 2017).

Different mechanisms can regulate the functions of ion channels that include specific pore blockers or modifiers of their gating properties (chemical compounds/toxins; Hille, 2001), post-translational modifications (phosphorylation, glycosylation) and interactions with other proteins, such as Sig-1R, among others.

Although several reports illustrate the regulation of ion channels by Sig-1R and its synthetic Sig-1R ligands, few studies have conclusively shown that endogenous Sig-1R ligands, such as steroids, modulate its interaction with some ion channels. Thus, examples of the latter will be discussed below.

STEROID-TYPE COMPOUNDS AS REGULATORS OF NA_V CHANNELS THROUGH SIG-1R

Voltage-gated sodium (Na_v) channels are molecular complexes primordial to cell depolarization in all excitable cells (Hille, 2001). They are constituted by α and β subunits (pore-forming and accessory subunits, respectively) and nine different Na_v channels have been identified ($Na_{v1.1-1.9}$) (Dhar Malhotra et al., 2001).

To date, it has been demonstrated that Sig-1R interacts with $Na_{v1.5}$ channels. These channels are expressed in the brain regulating neuronal excitation (Wu et al., 2002) and in cardiac tissue shaping the action potential in the heart (Veerman et al., 2015).

Balasuriya and collaborators demonstrated the association between Sig-1R and $Na_{v1.5}$ channels. They performed assays using HEK293 cells transiently expressing both, Sig-1R and $Na_{v1.5}$ channels, and determined, through atomic force microscopy (AFM) experiments, that Sig-1R directly interacts with $Na_{v1.5}$ tetramers with a 4-fold symmetry (Balasuriya et al., 2012).

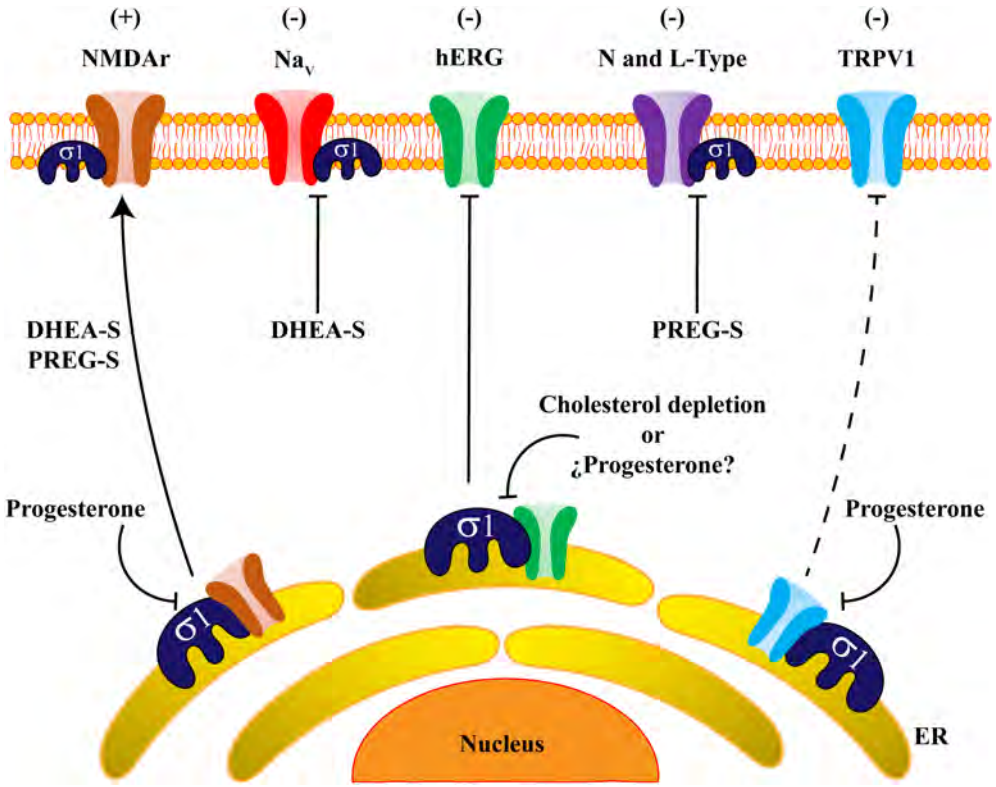

FIGURE 2 | Steroids regulate ion channels through Sigma-1 receptor actions. The scheme shows an overall view of ion channels regulated by the actions of steroids on Sig-1R. DHEA-S and PREG-S positively regulate (+) NMDAr trafficking and expression, whereas progesterone disrupts the association between NMDAr and Sig-1R and blocks the positive effects of the steroids on this channel's regulation. Otherwise, an adverse effect (–) is produced on Na^+ persistent currents by (DHEA-S). Indeed, hERG channels form protein complexes with Sig-1R, and this association is sensitive to cholesterol depletion. Also, L-type calcium channels are negatively regulated (–) by PREG-S in a strictly Sig-1R-dependent fashion. Finally, progesterone antagonizes Sig-1R which negatively regulates (–) the TRPV1 channel, producing protein instability of TRPV1 and reducing the amount of the channel in the plasma membrane. It is possible that progesterone has the same negative effects on hERG channel-expression.

This molecular association is disrupted by some of Sig-1R's synthetic ligands (haloperidol and pentazocine).

The physiological importance of the Sig-1R interaction with $Na_{v1.5}$ channels is exemplified in studies performed with some breast cancer cell lines, such as MDA-MB-231. This cell line constitutively expresses Sig-1R and $Na_{v1.5}$, where it has been shown that they form a protein complex (Aydar et al., 2016). The knockdown of Sig-1R expression reduces $Na_{v1.5}$ channels surface levels in this cancer breast cell line (Aydar et al., 2016), and the physiological consequence of this is a decrease in cell adhesion. This is a clear example of the importance of the Sig-1R/Nav1.5 protein complex in regulating the metastatic behavior of these cancer cells (Aydar et al., 2016).

Other studies have shown that the endogenous hallucinogen N,N-dimethyltryptamine (DMT) (Saavedra and Axelrod, 1972), is a ligand of Sig-1R (Fontanilla et al., 2009). DMT has been shown to reduce the activation of $Na_{v1.5}$ channels expressed in HEK293 cells and neonatal cardiac myocytes (Fontanilla et al., 2009). Effects of this Sig-1R agonist on Na^+ currents are strictly dependent upon Sig-1R expression since they are scarce in cells expressing low levels of Sig-1R, such as in the COS-7 cell line (Johannessen et al., 2009).

As for steroids and the roles of Sig-1R on the regulation of Na_v channels, it has been shown that DHEA-S negatively impacts on the function of persistent Na^+ currents. It is known that the increase of this type of currents leads to hyperexcitability of cells expressing these channels (Deng and Klyachko, 2016). The effects of DHEA-S on persistent Na^+ currents were evaluated in rat medial prefrontal cortex slices and were examined before and after DHEA-S perfusion (4.5 min) (Cheng et al., 2008). Whole-cell patch clamp recordings showed that DHEA-S reduces persistent Na^+ currents an action mimicked by carbetapentane citrate (a Sig-1R agonist) and blocked by Sig-1R antagonist (i.e., haloperidol) (Cheng et al., 2008). Although a change in the overall excitability of the tissue in question would have been expected in the presence of DHEA-S, this was not observed and the reasons for this remain unclear. Nonetheless, it has been suggested by the authors of this study that, such a lack of change in the tissue's excitability in the presence of DHEA-S, may be due to a positive effect of this compound on other molecular targets. This would lead to neutralization of the negative regulation of persistent Na^+ currents by DHEA-S and a neutral effect on neuronal excitability (Cheng et al., 2008).

Moreover, it has been suggested that the regulation of persistent Na^+ currents by DHEA-S, is probably relevant under pathological conditions such as brain ischemia. Under this scenario, negative regulation of persistent Na^+ currents by DHEA-S, through the actions of Sig-1R, would lead to a decrease in neuronal excitability, resulting in a neuroprotective effect. It has been proposed that DHEA-S may be a desirable candidate for therapeutic approaches directed toward relieving induced cerebral ischemia infarction (Yabuki et al., 2015).

In summary, there are only a few evidences showing the direct relationship between Sig-1R, steroids and Na_v channels. Nonetheless, available studies suggest that the negative role of synthetic Sig-1R ligands on Na^+ currents are similar to those promoted by steroidal Sig-1R agonists (i.e., DHEA-S) (**Figure 2**).

K_V CHANNELS ARE FUNCTIONAL TARGETS OF THE ACTIONS OF CHOLESTEROL ON SIG-1R

The generation of action potentials depends upon a fine-tuned coordination of different electrical phases, among which is repolarization. Through this process, the membrane potential is returned to negative voltage values to ensure that an excitable cell can respond to new stimuli. For repolarization to occur, the activation of voltage-gated K^+ channels (K_v) is essential (Hille, 2001; Kandel et al., 2012).

It has been shown that Sig-1R forms complexes with these ion channels regulating their function or abundance in the plasma membrane. Ligands of Sig-1R highly regulate the formation of some of these complexes. For instance, coimmunoprecipitation assays have demonstrated that Sig-1R is associated to $Kv_{1.4}$ in posterior pituitary nerve terminals from rat and also in Xenopus oocytes with heterologous expression of Sig-1R and $K_{v1.4}$ channels (Aydar et al., 2002). In the latter, whole-cell recordings showed that (+)-SKF 10047, downregulates $K_{v1.4}$ channel outward currents, indicating a negative role of Sig-1R on the function of these proteins (Aydar et al., 2002).

Conversely, cocaine triggers the dissociation of Sig-1R from BiP, leading to its interaction with $K_{v1.2}$ and facilitating channel translocation to the plasma membrane. As a result of this, $K_{v1.2}$ function is positively regulated, resulting in neuronal hypoactivity (Kourrich et al., 2013). These results highlight the physiological consequence of a cocaine-induced long-lasting association of these two proteins by which, an enduring experience-dependent plasticity phenomenon, occurs. This also pinpoints a mechanism that can shape neuronal and behavioral responses to cocaine, as suggested by Kourich and collaborators.

Despite the lack of direct experimental evidences showing the effects of steroids on the association of Sig-1R with K_v channels, some reports have demonstrated a possible interplay between them. For example, patch clamp experiments performed in the K562 leukemic cell line, which endogenously expresses Sig-1R and hERG channels (a K_v channel also expressed in cardiac tissues), showed that hERG currents are inhibited by igmesine and (+) pentazocine (both of which are Sig-1R ligands). In addition, silencing of Sig-1R using shRNA-based strategies, also demonstrated reduced hERG current-densities without affecting hERG-channel transcription, but rather by decreasing the amount of the mature form of the channel on the plasma membrane of the cells (Crottes et al., 2011).

It has also been reported that progesterone alters hERG-channel expression. By using HEK293 cells stably-expressing hERG channels and whole-cell voltage clamp recordings, it has been demonstrated that progesterone decreases hERG current-density. This effect was also observed in an hERG-channel endogenous expression system of rat neonatal cardiac myocytes (Wu et al., 2011). Confocal microscopy and western blot analysis of surface proteins showed that progesterone decreases the amount of the mature form of hERG-channel proteins in the plasma membrane and induces channel accumulation in the ER. Moreover, using filipin cell-staining techniques, it was shown that treatment with progesterone produces disruption of cholesterol homeostasis, impairing adequate hERG-channel folding and traffic to the Golgi compartment (Wu et al., 2011). Since progesterone is a Sig-1R antagonist, it could be hypothesized that these effects are produced through a disruption of the Sig-1R and hERG protein complexes. Alternatively, this could be the result of an alteration of cholesterol homeostasis, affecting the function or localization of Sig-1R. The consequences of both possibilities are an improper folding and traffic of hERG channels; thus, the overall effect of progesterone is negative regulation of channel expression in the plasma membrane (**Figure 2**).

Additionally, AFM imaging and homogenous time-resolved fluorescence experiments, have demonstrated that Sig-1R interacts with hERG channels with a 4-fold symmetry in the plasma membrane of HEK293 cells stably transfected with both proteins (Balasuriya et al., 2014). This is a similar scenario to the that reported for the formation of protein complexes between Sig-1R and $Na_{v1.5}$ channels (Balasuriya et al., 2012). Interestingly, this association is independent of Sig-1R's ligands but susceptible to cholesterol depletion (Balasuriya et al., 2014). Accordingly, it has been suggested that Sig-1R ligands can displace cholesterol from its binding site altering the distribution of the receptor in the cell and profoundly impacting on its association with other proteins (Palmer et al., 2007).

This experimental evidence suggests that Sig-1R supports a suitable assembly and folding of immature hERG channels in order to enable them to exit from the ER. Thus, it follows that progesterone and cholesterol affect Sig-1R actions and reduce hERG channel maturation.

Similar results have been obtained for SK3 channels, the small-conductance calcium-activated potassium channels, for which expression of these proteins is regulated by the cellular content of Sig-1R and cholesterol (Gueguinou et al., 2017). The molecular silencing of Sig-1R or the use of igmesine (a Sig-1R ligand) decreases the amount of SK3 channels localized to lipid-enriched nanodomains in breast cells. This, in turn, results in a reduction in the migration of these cancer cells (Gueguinou et al., 2017). Thus, these findings emphasize an interesting area of research in which, the regulation of Sig-1R activity, may be an alternative to control the metastatic potential of certain types of cancers where

the levels of Sig-1R are upregulated (i.e., colorectal or breast cancers) (Gueguinou et al., 2017).

REGULATION OF CA_V CHANNELS THROUGH SIG-1R'S ACTIVATION

Voltage-gated calcium channels (Ca_v) are the main transducers of membrane potential changes (Hille, 2001). Their activation produces the influx of Ca^{+2} ions to the cell, where they function as second messengers to activate different cell signaling pathways, leading to diverse physiological consequences. Ca_v channels are constituted by pore-forming subunits, α_1 (similar to Na_v channels) and by accessory subunits ($\alpha_2\delta$, β, and γ), which are necessary for a suitable function and expression of these channels. According to the types of Ca^{+2} currents that they generate, these proteins are classified as L-, N-, P/Q-, R-, and T-type calcium channels (reviewed in Catterall, 2000).

So far, there is interesting evidence about the interactions between Ca_v channels and Sig-1R. In this respect, the data show that Sig-1R activation by different synthetic agonists, negatively influences Ca_v channels functions, as shown in isolated intracardiac neurons of neonatal rats (Zhang and Cuevas, 2002). In this experimental model, Ca_v channel inactivation rates are increased, and the steady-state voltage-dependences of activation and inactivation are shifted to negative potentials.

The adverse effects of Sig-R ligands on Ca_v channel function have also been observed in cholinergic interneurons from the rat striatum. Here, agonists of Sig-1R such as (+)-SKF 10047 and PRE-084, inhibit N-type calcium currents and, as it would be expected, BD1047, a Sig-1R antagonist obliterates this phenomenon. FRET and coimmunoprecipitation experiments demonstrated that N-type channels and Sig-1R form protein-complexes when these proteins are expressed in HEK293 cells. The authors of this study proposed that Sig-1R agonists produce a conformational change in these protein complexes that negatively regulates N-type channels (Zhang et al., 2017).

Likewise, the negative roles of Sig-1R ligands on Ca_v channels have been observed in primary neuronal cultures from the hippocampus, where SA4503 (a Sig-1R agonist), inhibits N- and L-Type currents, producing an increase in axonal outgrowth (Li et al., 2017).

As for L-type ion channels, these have been shown to co-localize with Sig-1R in retinal ganglion cells (Mueller et al., 2013). Likewise, physical interactions between these proteins have also been demonstrated through coimmunoprecipitation assays in these cells (Tchedre et al., 2008).

Furthermore, an interplay between L-Type channels, Sig-1R and the neurosteroid, PREG-S, has been reported (Sabeti et al., 2007). This was evaluated using electrophysiological recordings from CA1 neurons of rat hippocampal slices perfused with PREG-S before and during the induction of long-term potentiation (LTP) of excitatory transmission. The data demonstrated that LTP increased in slices subjected to PREG-S perfusion. Suitably, nimodipine, an antagonist of L-type calcium channels, blocked PREG-S-induced LTP. Additionally, perfusion of PREG-S and BD1047, also blocked LTP in hippocampal slices, strongly supporting the role of PREG-S acting through Sig-1R in this process (Sabeti et al., 2007). Thus, in this neuronal context, regulation of the function of L-type channels confers synaptic plasticity (**Figure 2**).

REGULATION OF NMDA RECEPTORS BY NEUROSTEROID MOLECULES AND SIG-1R

The *N*-methyl-D-aspartate receptor (NMDAr) is a heterotetrameric ionotropic receptor formed by the assembly of two NR1 and two NR2 or NR3 subunits. NMDAr functions as a channel permeable to Ca^{+2}, its activation is produced by the binding of two different ligands (glutamate and glycine), profoundly impacting on neuronal plasticity, memory and learning processes (reviewed in Hansen et al., 2018).

Regulation of NMDAr by Sig-1R ligands has been extensively reported and, positive effects on their function, strongly correlate to Sig-1R's activation. A pioneering study by Monnet and collaborators demonstrated that a synthetic Sig-1R agonist potentiated neuronal activation induced by NMDAr in CA3 dorsal hippocampal neurons, an effect that was reverted by haloperidol (Monnet et al., 1990). Positive NMDAr regulation by Sig-1R's agonists leads to an improvement in learning and memory since it has been shown that PRE084, attenuates the impairment of learning in mice treated with an NMDAr antagonist (Maurice et al., 1994). A recent study showed that memory deficits produced in mice where brain ischemia was induced, were improved by the use of Sig-1R agonists while they were worsened by antagonism of the NR2 subunits (Xu et al., 2017).

Recently, a direct interaction between Sig-1R and the NR1 subunit of NMDAr has been revealed *in vitro* through the use of AFM imaging. Proximity-ligation assays also confirmed this interaction, supporting an *in vivo* association between these proteins (Balasuriya et al., 2013). This protein-complex is disrupted by some Sig-1R ligands such as BD1063, cannabidiol and progesterone, as demonstrated by pull-down assays (Rodriguez-Munoz et al., 2018). In addition, it has also been shown that the NR2 subunit of NMDAr is positively regulated by Sig-1R agonists, producing an upregulation in NR2-protein-expression and increasing traffic of NR2 to the plasma membrane (Pabba et al., 2014; **Figure 3A**). Finally, it has been shown that Sig-1R knockout mice display decreases in NMDAr-mediated currents and that these animals exhibit deficiencies in neurogenesis at the hippocampal dentate gyrus (Sha et al., 2013). These data suggest that Sig-1R activation positively influences NMDAr function during memory and learning processes.

Effects of steroid-type Sig-1R ligands on NMDAr functions have also been reported. For example, rats subjected to intraperitoneal injection of dizocilpine, (a competitive antagonist of NMDAr), exhibit spatial working and memory deficits. These effects are attenuated by DHEA-S and PREG-S or by a SA4503, all of which are Sig-1R agonists (**Figure 3B**). In contrast, progesterone or NE-100 (both of which constitute

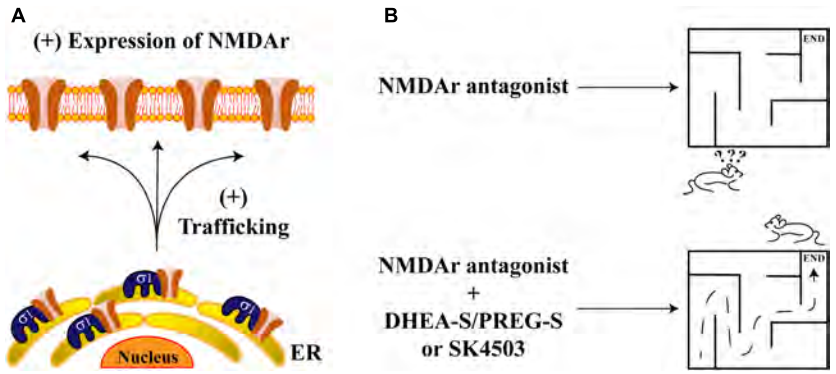

FIGURE 3 | Sigma-1 receptor and its endogenous ligands improve memory deficits. **(A)** The scheme represents the protein-complex between Sig-1R and NMDAr, which enhances the channel's trafficking to the plasma membrane. **(B)** NMDAr antagonism produces deficits in memory and spatial work (upper panel). Sig-1R's agonists such as DHEA-S, PREG-S, or SA4503, ameliorate memory impairments due to NMDAr antagonism (lower panel).

Sig-1R antagonists), block the ameliorative effects of DHEA-S and PREG-S on dizocilpine-induced memory deficits (Zou et al., 2000).

Similarly, some brain ischemia animal models display impairment of LTP at the hippocampal CA1 area, an effect that is prevented by DHEA-S. On the contrary, NE100 and progesterone revert the positive actions of DHEA-S in this model (Li et al., 2006). Finally, the protective effects of DHEA-S on spatial memory have also been reported and have demonstrated that they are dependent upon Sig-1R's actions (Li et al., 2009).

TRPV1: THE FIRST TRP CHANNEL SHOWN TO BE REGULATED BY SIG-1R

Transient Receptor Potential (TRP) ion channels allow for the influx of cations in a non-selective fashion. These proteins possess four subunits, giving rise to functional tetramers (reviewed in Ramsey et al., 2006). According to their structural features, these channels have been classified into seven subfamilies: TRPA (ankyrin), TRPC (canonical), TRPM (melastatin), TRPML (mucolipin), TRPN (no-mechanoreceptor potential C), TRPP (polycystic) and TRPV (vanilloid) (reviewed in Li, 2017). Several of the members of these subfamilies are implicated in the transduction of thermal, chemical and osmotic stimuli.

TRPV1 channels have been extensively studied for their roles in pain. They are mainly expressed by nociceptors (Aδ and C-Fibers) where they are essential for the transduction of noxious signals. These channels are activated by high temperatures ($\geq$ 42°C), irritant compounds (capsaicin, resiniferatoxin, allicin, etc.) (Caterina et al., 1997; Salazar et al., 2008) and by changes in extra- and intracellular pH (acid and basic, respectively) (Caterina et al., 1997; Jordt et al., 2000; Dhaka et al., 2009). Additionally, TRPV1's activation can also be achieved by some endogenous compounds released during inflammation or tissue injury, such as lysophosphatidic acid (LPA) (Nieto-Posadas et al., 2011), among other endogenous agonists (reviewed in Morales-Lazaro et al., 2013). Since TRPV1 exhibits a pivotal role in painful signal transduction, this channel has become a pharmacological target with several research groups around the world focusing on ways to regulate its function to relieve certain types of pain.

So far, several synthetic compounds and some of a natural origin (i.e., oleic acid) (Morales-Lazaro et al., 2016), have been described as negative regulators of TRPV1's activation. However, few studies have revealed alternative ways to regulate TRPV1's functions, including manipulating the abundance of this channel in the plasma membrane of nociceptors. Just recently, our group described that Sig-1R is a crucial molecular target that can regulate the amount of TRPV1 channels localized to the plasma membrane of cells, without affecting channel transcription (Ortiz-Renteria et al., 2018). This constituted the first report for a TRP channel as being regulated by Sig-1R, highlighting the role of a direct interaction between TRPV1 and Sig-1R in pain.

In this study, we found that a synthetic ligand of Sig-1R, BD1063, decreased TRPV1 protein levels in mice dorsal root ganglia (DRG) and HEK293 cells transiently expressing TRPV1. This effect was mimicked by the knockdown of Sig-1R expression in TRPV1-expressing HEK293 cells. Furthermore, progesterone also produced down-regulation of TRPV1 expression, as demonstrated by western blot assays. Worth noting is that the effects of progesterone on TRPV1 expression were found to be independent of its classical nuclear receptors (Ortiz-Renteria et al., 2018).

Also, whole-cell recordings showed that Sig-1R knockdown and the addition of BD1063 or progesterone to cell cultures, reduced the current-densities evoked by capsaicin, indicating that negative regulation of Sig-1R (either by reducing Sig-1R expression or using its antagonists), decreased the amount of TRPV1 localized to the plasma membrane. This negative effect on TRPV1 expression was prevented through the inhibition of proteasomal degradation, suggesting that Sig-1R is necessary for TRPV1 protein stability and confirms an independent effect of a transcriptional mechanism (Ortiz-Renteria et al., 2018).

Besides, we established a direct association between Sig-1R and the TRPV1 channel through coimmunoprecipitation and FRET experiments. We found that Sig-1R interacts with the transmembrane domain of TRPV1, similarly, to what had been previously reported for $K_{v1.3}$ ion channels (Kinoshita

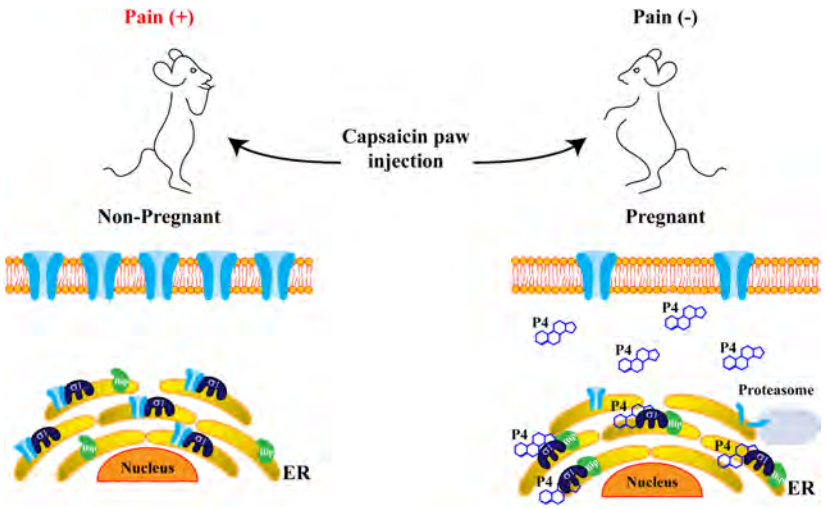

FIGURE 4 | Progesterone attenuates pain-related behavior through disruption of the Sig-1R/TRPV1 complex. Sig-1R and TRPV1 channels are physically associated in the endoplasmic reticulum (ER), improving TRPV1 stability and resulting in suitable TRPV1 expression in the plasma membrane, where the channel transduces painful signals. Consequently, non-pregnant mice display pain behaviors in response to capsaicin paw-injection (left). However, in pregnant mice (right), when progesterone levels considerably increase, the formation of the complex between Sig-1R and the Binding immunoglobulin protein (BiP), is promoted. This maintains Sig-1R in a sequestered state and blocks its association with the TRPV1 channel, improving protein instability and avoiding degradation through the proteasomal pathway. Thus, TRPV1 protein levels in the plasma membrane decrease, leading to an increased pain threshold in response to capsaicin in pregnant mice.

et al., 2012). Interestingly, this protein-complex was sensitive to Sig-1R ligands, since BD1063 and progesterone decreased the association between TRPV1 and Sig-1R. Furthermore, by confocal microscopy analysis, we observed that this protein-protein association is most prominent at the ER compartment and occurs less at the level of the plasma membrane. Together, all of these evidences pointed to a role of Sig-1R in conferring protein stability during the biogenesis of the channel, with Sig-1R preventing the misfolding of TRPV1 and avoiding its degradation by the proteasomal system (**Figure 4**).

Since, progesterone is the steroid with higher affinity for Sig-1R, its interactions with this receptor and the physiological consequences of such interplays have been a subject of focus in pregnancy, a physiological phase where progesterone levels are high (Bergeron et al., 1999). With this in mind, we explored if pain thresholds in response to capsaicin were different between non- and pregnant mice. The results indicated that, during pregnancy, pain-like behavior in response to the TRPV1 agonist was significantly decreased in mice, as compared to their non-pregnant counterparts (**Figure 4**). This led us to conclude that elevated levels of progesterone, such as those found during pregnancy, could confer protection against painful situations through the disruption of the protein complex between Sig-1R and TRPV1. This, in turn, would result in the downregulation of TRPV1's levels in the plasma membrane, ultimately decreasing the pain threshold associated with TRPV1's activation (**Figure 4**).

Several sources in the literature, together with our findings, have highlighted Sig-1R as a protein widely associated with nociception. For example, it has been reported that Sig-1R knockout mice, exhibit endurance to pain and mechanical allodynia induced by formalin and capsaicin, respectively (Cendan et al., 2005; Entrena et al., 2009).

Since Sig-1R is expressed in DRG neurons (Mavlyutov et al., 2016) and in specific regions of the spinal cord (Alonso et al., 2000), its actions are relevant at the pre and post-synaptic levels (reviewed in Romero et al., 2016). Thus, its roles in pain responses must involve more than one molecular target. For instance, several reports show that Sig-1R agonists induce and maintain central sensitization during painful states (Romero et al., 2012; Entrena et al., 2016; Choi et al., 2017). Some of Sig-1R's effects are through the upregulation or phosphorylation of the NR1 subunit of the NMDAr that lead to neuronal overexcitability (Roh et al., 2010). Conversely, antagonists of Sig-1R prevent or decrease pain in some neuropathic pain animal models since these compounds inhibit the upregulation of NR1 (Zhu et al., 2015). Besides it has been demonstrated that DHEA-S and PREG-S positively regulate the activity of P2X receptors resulting in the potentiation of the mechanical allodynia induced through these receptors (Kwon et al., 2016).

In conclusion, Sig-1R is essential for regulating peripheral and central sensitization by interacting with various molecular targets such as TRPV1 channels, P2X channels, NMDAr and it is possible that several other proteins involved in these processes, will be identified in the future.

Progesterone as a Prototypical Endogenous Ligand of Sig-1R

Up to this point, we have emphasized findings that link the actions of Sig-1R and steroids to the function of ion channels. It is important to stress that, the steroid concentrations used in most of the experiments here described, are well above the reported physiological range.

The low affinity of steroids to Sig-1R justifies the use of high concentrations of steroid ligands in different experimental systems. For example, a study by Su et al. (1988) showed that progesterone competes (Ki = 268 nM) with [H3](+)-SKF 10047 for the binding site in Sig-1R and exhibits higher affinity for this receptor. However, other steroids are required at much higher concentrations than those of progesterone to displace [H3](+)-SKF 10047 (Su et al., 1988). Nevertheless, this progesterone concentration is still too high to be normally circulating in blood but, in pregnancy, the circulating levels os this steroids can rise to 400 nM (Neill et al., 1969), reaching concentrations high enough to regulate Sig-1R.

In agreement with the results obtained by Su et al. (1988), Maurice et al. (1996) showed that progesterone displaces the binding of (+)-SKF 10047 to rat brain homogenates with a Ki of 175 nM. They showed that [H3](+)-SKF 10047 binding is significantly reduced in the hippocampus and the cortex from pregnant mice, as compared to non-pregnant female or male mice (Maurice et al., 1996).

These findings, together with ours where we showed that pregnant female mice display high pain-thresholds as compared to unpregnant mice (Ortiz-Renteria et al., 2018), suggesting that high circulating progesterone levels in pregnancy are enough to modify pain thresholds in mice.

Recently, a new high-affinity Sig-1R selective radiotracer ([^{18}F] FPS) has been developed. This compound has been used to perform PET studies in Rhesus monkeys showing high uptake of the radiotracer in brain regions where there are moderate densities of Sig-1R (Mach et al., 2005). Interestingly, animals pre-injected with progesterone displayed a significant reduction in the uptake of the radiotracer in the brain of the monkeys, confirming that progesterone displaces the radiotracer from Sig-1R's binding sites (Mach et al., 2005). In addition, this radiotracer was used to perform *in vitro* binding assays in rat forebrain homogenates showing that progesterone inhibits the binding of the radiotracer to Sig-1R. Notably, the Ki for progesterone is of 36 nM, a concentration of progesterone achieved during the luteal phase of the menstrual cycle (Neill et al., 1969). This finding further strengthens the notion that low progesterone levels also play a role in the activity of Sig-1R and that this steroid functions as an endogenous ligand of this receptor (Waterhouse et al., 2007).

CONCLUSION

Regulation of ion channel physiology has been a subject of intense research for several decades. The implications of such modifications of ion channel function are extremely diverse and important, and they are exemplified by the roles that these proteins play under normal physiological conditions but also in pathophysiological scenarios. Not only do these essential proteins regulate muscle contraction, neuronal excitability, and hormonal secretion but changes in their expression and function during pathological conditions lead to severe diseases such as epilepsy, diabetes, ataxia, pain, itch, etc. For many years, studies have focused on identifying molecular targets of synthetic and naturally-produced agents to regulate the activity of ion channels.

In addition to the identification of chemicals that specifically bind to members of different ion channel families to alter their biophysical properties, research groups have also focused on determining how protein-protein interactions regulate these. Among the proteins that can bind and change ion channel function and expression are chaperones and their roles and the consequences of their misfunctions are being studied in several diseases (Broadley and Hartl, 2009). The Sig-1R has been shown to play essential roles for the adequate function of several types of cells (Tsai et al., 2009), including those that are electrically excitable and hence express ion channels. Thus, from these studies and those discussed here, it is evident that a mechanism by which we may regulate ion channel physiology is through tools that allow us to manipulate the interactions between Sig-1R and these other proteins if this was to be possible without other severe consequences. But utmost important is that, by studying the interactions of Sig-1R with ion channels, we have gained valuable knowledge on how this receptor regulates ion channels. In turn, this has also helped us understand the physiological consequences of modifying the interplays between Sig-1R and ion channels for the function of the cells where these proteins are expressed.

AUTHOR CONTRIBUTIONS

All authors listed have made a substantial, direct and intellectual contribution to the work, and approved it for publication.

FUNDING

This work was supported by grants from Dirección General de Asuntos del Personal Académico (DGAPA)-Programa de Apoyo a Proyectos de Investigación e Innovación Tecnológica (PAPIIT) grant IN206819 and Estímulos a Investigaciones Médicas Miguel Alemán Valdés to SLM-L and Consejo Nacional de Ciencia y Tecnología (CONACyT) grant A1-S-8760, CONACyT Fronteras en la Ciencia No. 77 and DGAPA-PAPIIT grant IN200717 to TR.

REFERENCES

Alonso, G., Phan, V., Guillemain, I., Saunier, M., Legrand, A., Anoal, M., et al. (2000). Immunocytochemical localization of the sigma(1) receptor in the adult rat central nervous system. *Neuroscience* 97, 155–170.

Aydar, E., Palmer, C. P., Klyachko, V. A., and Jackson, M. B. (2002). The sigma receptor as a ligand-regulated auxiliary potassium channel subunit. *Neuron* 34, 399–410.

Aydar, E., Stratton, D., Fraser, S. P., Djamgoz, M. B., and Palmer, C. (2016). Sigma-1 receptors modulate neonatal Nav1.5 ion channels in breast cancer cell lines. *Eur. Biophys. J.* 45, 671–683.

Balasuriya, D., D'Sa, L., Talker, R., Dupuis, E., Maurin, F., Martin, P., et al. (2014). A direct interaction between the sigma-1 receptor and the hERG voltage-gated K^+ channel revealed by atomic force microscopy and homogeneous time-resolved fluorescence (HTRF$^{(R)}$). *J. Biol. Chem.* 289, 32353–32363. doi: 10.1074/jbc.M114.603506

Balasuriya, D., Stewart, A. P., Crottes, D., Borgese, F., Soriani, O., and Edwardson, J. M. (2012). The sigma-1 receptor binds to the Nav1.5 voltage-gated Na^+ channel with 4-fold symmetry. *J. Biol. Chem.* 287, 37021–37029. doi: 10.1074/jbc.M112.382077

Balasuriya, D., Stewart, A. P., and Edwardson, J. M. (2013). The sigma-1 receptor interacts directly with GluN1 but not GluN2A in the GluN1/GluN2A NMDA receptor. *J. Neurosci.* 33, 18219–18224. doi: 10.1523/JNEUROSCI.3360-13.2013

Bergeron, R., de Montigny, C., and Debonnel, G. (1999). Pregnancy reduces brain sigma receptor function. *Br. J. Pharmacol.* 127, 1769–1776. doi: 10.1038/sj.bjp.0702724

Broadley, S. A., and Hartl, F. U. (2009). The role of molecular chaperones in human misfolding diseases. *FEBS Lett.* 583, 2647–2653. doi: 10.1016/j.febslet.2009.04.029

Caterina, M. J., Schumacher, M. A., Tominaga, M., Rosen, T. A., Levine, J. D., and Julius, D. (1997). The capsaicin receptor: a heat-activated ion channel in the pain pathway. *Nature* 389, 816–824. doi: 10.1038/39807

Catterall, W. A. (2000). Structure and regulation of voltage-gated Ca^{2+} channels. *Annu. Rev. Cell Dev. Biol.* 16, 521–555. doi: 10.1146/annurev.cellbio.16.1.521

Cendan, C. M., Pujalte, J. M., Portillo-Salido, E., Montoliu, L., and Baeyens, J. M. (2005). Formalin-induced pain is reduced in sigma(1) receptor knockout mice. *Eur. J. Pharmacol.* 511, 73–74. doi: 10.1016/j.ejphar.2005.01.036

Cheng, Z. X., Lan, D. M., Wu, P. Y., Zhu, Y. H., Dong, Y., Ma, L., et al. (2008). Neurosteroid dehydroepiandrosterone sulphate inhibits persistent sodium currents in rat medial prefrontal cortex via activation of sigma-1 receptors. *Exp. Neurol.* 210, 128–136. doi: 10.1016/j.expneurol.2007.10.004

Choi, S. R., Moon, J. Y., Roh, D. H., Yoon, S. Y., Kwon, S. G., Choi, H. S., et al. (2017). Spinal D-serine increases PKC-dependent GluN1 phosphorylation contributing to the sigma-1 receptor-induced development of mechanical allodynia in a mouse model of neuropathic pain. *J. Pain* 18, 415–427. doi: 10.1016/j.jpain.2016.12.002

Corpechot, C., Robel, P., Axelson, M., Sjovall, J., and Baulieu, E. E. (1981). Characterization and measurement of dehydroepiandrosterone sulfate in rat brain. *Proc. Natl. Acad. Sci. U.S.A.* 78, 4704–4707.

Crottes, D., Martial, S., Rapetti-Mauss, R., Pisani, D. F., Loriol, C., Pellissier, B., et al. (2011). Sig1R protein regulates hERG channel expression through a post-translational mechanism in leukemic cells. *J. Biol. Chem.* 286, 27947–27958. doi: 10.1074/jbc.M111.226738

Deng, P. Y., and Klyachko, V. A. (2016). Increased persistent sodium current causes neuronal hyperexcitability in the entorhinal cortex of fmr1 knockout mice. *Cell Rep.* 16, 3157–3166. doi: 10.1016/j.celrep.2016.08.046

Dhaka, A., Uzzell, V., Dubin, A. E., Mathur, J., Petrus, M., Bandell, M., et al. (2009). TRPV1 is activated by both acidic and basic pH. *J. Neurosci.* 29, 153–158. doi: 10.1523/JNEUROSCI.4901-08.2009

Dhar Malhotra, J., Chen, C., Rivolta, I., Abriel, H., Malhotra, R., Mattei, L. N., et al. (2001). Characterization of sodium channel alpha- and beta-subunits in rat and mouse cardiac myocytes. *Circulation* 103, 1303–1310.

Entrena, J. M., Cobos, E. J., Nieto, F. R., Cendan, C. M., Gris, G., Del Pozo, E., et al. (2009). Sigma-1 receptors are essential for capsaicin-induced mechanical hypersensitivity: studies with selective sigma-1 ligands and sigma-1 knockout mice. *Pain* 143, 252–261. doi: 10.1016/j.pain.2009.03.011

Entrena, J. M., Sanchez-Fernandez, C., Nieto, F. R., Gonzalez-Cano, R., Yeste, S., Cobos, E. J., et al. (2016). Sigma-1 receptor agonism promotes mechanical allodynia after priming the nociceptive system with capsaicin. *Sci. Rep.* 6:37835. doi: 10.1038/srep37835

Fontanilla, D., Johannessen, M., Hajipour, A. R., Cozzi, N. V., Jackson, M. B., and Ruoho, A. E. (2009). The hallucinogen N,N-dimethyltryptamine (DMT) is an endogenous sigma-1 receptor regulator. *Science* 323, 934–937. doi: 10.1126/science.1166127

Gueguinou, M., Crottes, D., Chantome, A., Rapetti-Mauss, R., Potier-Cartereau, M., Clarysse, L., et al. (2017). The SigmaR1 chaperone drives breast and colorectal cancer cell migration by tuning SK3-dependent Ca^{2+} homeostasis. *Oncogene* 36, 3640–3647. doi: 10.1038/onc.2016.501

Hanner, M., Moebius, F. F., Flandorfer, A., Knaus, H. G., Striessnig, J., Kempner, E., et al. (1996). Purification, molecular cloning, and expression of the mammalian sigma1-binding site. *Proc. Natl. Acad. Sci. U.S.A.* 93, 8072–8077.

Hansen, K. B., Yi, F., Perszyk, R. E., Furukawa, H., Wollmuth, L. P., Gibb, A. J., et al. (2018). Structure, function, and allosteric modulation of NMDA receptors. *J. Gen. Physiol.* 150, 1081–1105. doi: 10.1085/jgp.201812032

Hayashi, T., and Su, T. P. (2003). Sigma-1 receptors (sigma(1) binding sites) form raft-like microdomains and target lipid droplets on the endoplasmic reticulum: roles in endoplasmic reticulum lipid compartmentalization and export. *J. Pharmacol. Exp. Ther.* 306, 718–725. doi: 10.1124/jpet.103.051284

Hayashi, T., and Su, T. P. (2004). Sigma-1 receptor ligands: potential in the treatment of neuropsychiatric disorders. *CNS Drugs* 18, 269–284.

Hayashi, T., and Su, T. P. (2007). Sigma-1 receptor chaperones at the ER-mitochondrion interface regulate Ca^{2+} signaling and cell survival. *Cell* 131, 596–610. doi: 10.1016/j.cell.2007.08.036

Hille, B. (2001). *Ionic Channels of Excitable Membranes*. Sunderland, MA: Sinauer.

Johannessen, M., Ramachandran, S., Riemer, L., Ramos-Serrano, A., Ruoho, A. E., and Jackson, M. B. (2009). Voltage-gated sodium channel modulation by sigma-receptors in cardiac myocytes and heterologous systems. *Am. J. Physiol. Cell Physiol.* 296, C1049–C1057. doi: 10.1152/ajpcell.00431.2008

Jordt, S. E., Tominaga, M., and Julius, D. (2000). Acid potentiation of the capsaicin receptor determined by a key extracellular site. *Proc. Natl. Acad. Sci. U.S.A.* 97, 8134–8139. doi: 10.1073/pnas.100129497

Kandel, E. R., Schwartz, J. H., Jessell, T. M., and Siegelbaum, S. A. (2012). *Principles of Neural Science*, 5th Edn. New York, NY: McGraw-Hill Education.

Kinoshita, M., Matsuoka, Y., Suzuki, T., Mirrielees, J., and Yang, J. (2012). Sigma-1 receptor alters the kinetics of Kv1.3 voltage gated potassium channels but not the sensitivity to receptor ligands. *Brain Res.* 1452, 1–9. doi: 10.1016/j.brainres.2012.02.070

Kourrich, S., Hayashi, T., Chuang, J. Y., Tsai, S. Y., Su, T. P., and Bonci, A. (2013). Dynamic interaction between sigma-1 receptor and Kv1.2 shapes neuronal and behavioral responses to cocaine. *Cell* 152, 236–247. doi: 10.1016/j.cell.2012.12.004

Kruse, A. (2017). Structural insights into sigma1 function. *Handb. Exp. Pharmacol.* 244, 13–25. doi: 10.1007/164_2016_95

Kwon, S. G., Yoon, S. Y., Roh, D. H., Choi, S. R., Choi, H. S., Moon, J. Y., et al. (2016). Peripheral neurosteroids enhance P2X receptor-induced mechanical allodynia via a sigma-1 receptor-mediated mechanism. *Brain Res. Bull.* 121, 227–232. doi: 10.1016/j.brainresbull.2016.02.012

Largent, B. L., Wikstrom, H., Gundlach, A. L., and Snyder, S. H. (1987). Structural determinants of sigma receptor affinity. *Mol. Pharmacol.* 32, 772–784.

Li, D., Zhang, S. Z., Yao, Y. H., Xiang, Y., Ma, X. Y., Wei, X. L., et al. (2017). Sigma-1 receptor agonist increases axon outgrowth of hippocampal neurons via voltage-gated calcium ions channels. *CNS Neurosci. Ther.* 23, 930–939. doi: 10.1111/cns.12768

Li, H. (2017). TRP channel classification. *Adv. Exp. Med. Biol.* 976, 1–8. doi: 10.1007/978-94-024-1088-4_1

Li, Z., Cui, S., Zhang, Z., Zhou, R., Ge, Y., Sokabe, M., et al. (2009). DHEA-neuroprotection and -neurotoxicity after transient cerebral ischemia in rats. *J. Cereb. Blood Flow Metab.* 29, 287–296. doi: 10.1038/jcbfm.2008.118

Li, Z., Zhou, R., Cui, S., Xie, G., Cai, W., Sokabe, M., et al. (2006). Dehydroepiandrosterone sulfate prevents ischemia-induced impairment of long-term potentiation in rat hippocampal CA1 by up-regulating tyrosine phosphorylation of NMDA receptor. *Neuropharmacology* 51, 958–966. doi: 10.1016/j.neuropharm.2006.06.007

Mach, R. H., Gage, H. D., Buchheimer, N., Huang, Y., Kuhner, R., Wu, L., et al. (2005). N-[18F]4'-fluorobenzylpiperidin-4yl-(2-fluorophenyl) acetamide ([18F]FBFPA): a potential fluorine-18 labeled PET radiotracer for imaging sigma-1 receptors in the CNS. *Synapse* 58, 267–274. doi: 10.1002/syn.20207

Martin, W. R., Eades, C. G., Thompson, J. A., Huppler, R. E., and Gilbert, P. E. (1976). The effects of morphine- and nalorphine- like drugs in the nondependent and morphine-dependent chronic spinal dog. *J. Pharmacol. Exp. Ther.* 197, 517–532.

Maurice, T., Roman, F. J., and Privat, A. (1996). Modulation by neurosteroids of the in vivo (+)-[3H]SKF-10,047 binding to sigma 1 receptors in the mouse forebrain. *J. Neurosci. Res.* 46, 734–743.

Maurice, T., Su, T. P., Parish, D. W., Nabeshima, T., and Privat, A. (1994). PRE-084, a sigma selective PCP derivative, attenuates MK-801-induced impairment of learning in mice. *Pharmacol. Biochem. Behav.* 49, 859–869.

Maurice, T., Su, T. P., and Privat, A. (1998). Sigma1 (sigma 1) receptor agonists and neurosteroids attenuate B25-35-amyloid peptide-induced amnesia in mice through a common mechanism. *Neuroscience* 83, 413–428.

Mavlyutov, T. A., Duellman, T., Kim, H. T., Epstein, M. L., Leese, C., Davletov, B. A., et al. (2016). Sigma-1 receptor expression in the dorsal root ganglion: Reexamination using a highly specific antibody. *Neuroscience* 331, 148–157. doi: 10.1016/j.neuroscience.2016.06.030

Mavylutov, T., Chen, X., Guo, L., and Yang, J. (2018). APEX2- tagging of Sigma 1-receptor indicates subcellular protein topology with cytosolic N-terminus and ER luminal C-terminus. *Protein Cell* 9, 733–737.

Mishra, A. K., Mavlyutov, T., Singh, D. R., Biener, G., Yang, J., Oliver, J. A., et al. (2015). The sigma-1 receptors are present in monomeric and oligomeric forms in living cells in the presence and absence of ligands. *Biochem. J.* 466, 263–271. doi: 10.1042/BJ20141321

Monnet, F. P., Debonnel, G., Junien, J. L., and De Montigny, C. (1990). N-methyl-D-aspartate-induced neuronal activation is selectively modulated by sigma receptors. *Eur. J. Pharmacol.* 179, 441–445.

Morales-Lazaro, S. L., Llorente, I., Sierra-Ramirez, F., Lopez-Romero, A. E., Ortiz-Renteria, M., Serrano-Flores, B., et al. (2016). Inhibition of TRPV1 channels by a naturally occurring omega-9 fatty acid reduces pain and itch. *Nat. Commun.* 7:13092. doi: 10.1038/ncomms13092

Morales-Lazaro, S. L., Simon, S. A., and Rosenbaum, T. (2013). The role of endogenous molecules in modulating pain through transient receptor potential vanilloid 1 (TRPV1). *J. Physiol.* 591, 3109–3121. doi: 10.1113/jphysiol.2013.251751

Mueller, B. H. II, Park, Y., Daudt, D. R. III, Ma, H. Y., Akopova, I., Stankowska, D. L., et al. (2013). Sigma-1 receptor stimulation attenuates calcium influx through activated L-type voltage gated calcium channels in purified retinal ganglion cells. *Exp. Eye Res.* 107, 21–31. doi: 10.1016/j.exer.2012.11.002

Neill, J. D., Johansson, E. D., and Knobil, E. (1969). Patterns of circulating progesterone concentrations during the fertile menstrual cycle and the remainder of gestation in the rhesus monkey. *Endocrinology* 84, 45–48.

Nieto-Posadas, A., Picazo-Juarez, G., Llorente, I., Jara-Oseguera, A., Morales-Lazaro, S., Escalante-Alcalde, D., et al. (2011). Lysophosphatidic acid directly activates TRPV1 through a C-terminal binding site. *Nat. Chem. Biol.* 8, 78–85. doi: 10.1038/nchembio.712

Ortega-Roldan, J. L., Ossa, F., and Schnell, J. R. (2013). Characterization of the human sigma-1 receptor chaperone domain structure and binding immunoglobulin protein (BiP) interactions. *J. Biol. Chem.* 288, 21448–21457. doi: 10.1074/jbc.M113.450379

Ortiz-Renteria, M., Juarez-Contreras, R., Gonzalez-Ramirez, R., Islas, L. D., Sierra-Ramirez, F., Llorente, I., et al. (2018). TRPV1 channels and the progesterone receptor Sig-1R interact to regulate pain. *Proc. Natl. Acad. Sci. U.S.A.* 115, E1657–E1666. doi: 10.1073/pnas.1715972115

Pabba, M., Wong, A. Y., Ahlskog, N., Hristova, E., Biscaro, D., Nassrallah, W., et al. (2014). NMDA receptors are upregulated and trafficked to the plasma membrane after sigma-1 receptor activation in the rat hippocampus. *J. Neurosci.* 34, 11325–11338. doi: 10.1523/JNEUROSCI.0458-14.2014

Pal, A., Hajipour, A. R., Fontanilla, D., Ramachandran, S., Chu, U. B., Mavlyutov, T., et al. (2007). Identification of regions of the sigma-1 receptor ligand binding site using a novel photoprobe. *Mol. Pharmacol.* 72, 921–933. doi: 10.1124/mol.107.038307

Palmer, C. P., Mahen, R., Schnell, E., Djamgoz, M. B., and Aydar, E. (2007). Sigma-1 receptors bind cholesterol and remodel lipid rafts in breast cancer cell lines. *Cancer Res.* 67, 11166–11175.

Prezzavento, O., Arena, E., Sanchez-Fernandez, C., Turnaturi, R., Parenti, C., Marrazzo, A., et al. (2017). (+)-and (−)-Phenazocine enantiomers: evaluation of their dual opioid agonist/sigma1 antagonist properties and antinociceptive effects. *Eur. J. Med. Chem.* 125, 603–610. doi: 10.1016/j.ejmech.2016.09.077

Ramsey, I. S., Delling, M., and Clapham, D. E. (2006). An introduction to TRP channels. *Annu. Rev. Physiol.* 68, 619–647. doi: 10.1146/annurev.physiol.68.040204.100431

Rodriguez-Munoz, M., Onetti, Y., Cortes-Montero, E., Garzon, J., and Sanchez-Blazquez, P. (2018). Cannabidiol enhances morphine antinociception, diminishes NMDA-mediated seizures and reduces stroke damage via the sigma 1 receptor. *Mol. Brain* 11:51.

Roh, D. H., Yoon, S. Y., Seo, H. S., Kang, S. Y., Moon, J. Y., Song, S., et al. (2010). Sigma-1 receptor-induced increase in murine spinal NR1 phosphorylation is mediated by the PKCalpha and epsilon, but not the PKCzeta, isoforms. *Neurosci. Lett.* 477, 95–99. doi: 10.1016/j.neulet.2010.04.041

Romero, L., Merlos, M., and Vela, J. M. (2016). Antinociception by sigma-1 receptor antagonists: central and peripheral effects. *Adv. Pharmacol.* 75, 179–215. doi: 10.1016/bs.apha.2015.11.003

Romero, L., Zamanillo, D., Nadal, X., Sanchez-Arroyos, R., Rivera-Arconada, I., Dordal, A., et al. (2012). Pharmacological properties of S1RA, a new sigma-1 receptor antagonist that inhibits neuropathic pain and activity-induced spinal sensitization. *Br. J. Pharmacol.* 166, 2289–2306. doi: 10.1111/j.1476-5381.2012.01942.x

Saavedra, J. M., and Axelrod, J. (1972). Psychotomimetic N-methylated tryptamines: formation in brain in vivo and in vitro. *Science* 175, 1365–1366.

Sabeti, J., Nelson, T. E., Purdy, R. H., and Gruol, D. L. (2007). Steroid pregnenolone sulfate enhances NMDA-receptor-independent long-term potentiation at hippocampal CA1 synapses: role for L-type calcium channels and sigma-receptors. *Hippocampus* 17, 349–369. doi: 10.1002/hipo.20273

Salazar, H., Llorente, I., Jara-Oseguera, A., Garcia-Villegas, R., Munari, M., Gordon, S. E., et al. (2008). A single N-terminal cysteine in TRPV1 determines activation by pungent compounds from onion and garlic. *Nat. Neurosci.* 11, 255–261. doi: 10.1038/nn2056

Schmidt, H. R., Zheng, S., Gurpinar, E., Koehl, A., Manglik, A., and Kruse, A. C. (2016). Crystal structure of the human sigma1 receptor. *Nature* 532, 527–530. doi: 10.1038/nature17391

Sha, S., Qu, W. J., Li, L., Lu, Z. H., Chen, L., Yu, W. F., et al. (2013). Sigma-1 receptor knockout impairs neurogenesis in dentate gyrus of adult hippocampus via down-regulation of NMDA receptors. *CNS Neurosci. Ther.* 19, 705–713. doi: 10.1111/cns.12129

Su, T. P. (1982). Evidence for sigma opioid receptor: binding of [3H]SKF-10047 to etorphine-inaccessible sites in guinea-pig brain. *J. Pharmacol. Exp. Ther.* 223, 284–290.

Su, T. P., London, E. D., and Jaffe, J. H. (1988). Steroid binding at sigma receptors suggests a link between endocrine, nervous, and immune systems. *Science* 240, 219–221.

Tam, S. W. (1983). Naloxone-inaccessible sigma receptor in rat central nervous system. *Proc. Natl. Acad. Sci. U.S.A.* 80, 6703–6707.

Tam, S. W., and Cook, L. (1984). Sigma opiates and certain antipsychotic drugs mutually inhibit (+)-[3H] SKF 10,047 and [3H]haloperidol binding in guinea pig brain membranes. *Proc. Natl. Acad. Sci. U.S.A.* 81, 5618–5621.

Tchedre, K. T., Huang, R. Q., Dibas, A., Krishnamoorthy, R. R., Dillon, G. H., and Yorio, T. (2008). Sigma-1 receptor regulation of voltage-gated calcium channels involves a direct interaction. *Invest. Ophthalmol. Vis. Sci.* 49, 4993–5002. doi: 10.1167/iovs.08-1867

Tsai, S. Y., Hayashi, T., Mori, T., and Su, T. P. (2009). Sigma-1 receptor chaperones and diseases. *Cent. Nerv. Syst. Agents Med. Chem.* 9, 184–189.

Veerman, C. C., Wilde, A. A., and Lodder, E. M. (2015). The cardiac sodium channel gene SCN5A and its gene product NaV1.5: role in physiology and pathophysiology. *Gene* 573, 177–187. doi: 10.1016/j.gene.2015.08.062

Waterhouse, R. N., Chang, R. C., Atuehene, N., and Collier, T. L. (2007). In vitro and in vivo binding of neuroactive steroids to the sigma-1 receptor as measured with the positron emission tomography radioligand [18F]FPS. *Synapse* 61, 540–546. doi: 10.1002/syn.20369

Wu, L., Nishiyama, K., Hollyfield, J. G., and Wang, Q. (2002). Localization of Nav1.5 sodium channel protein in the mouse brain. *Neuroreport* 13, 2547–2551. doi: 10.1097/01.wnr.0000052322.62862.a5

Wu, Z. Y., Yu, D. J., Soong, T. W., Dawe, G. S., and Bian, J. S. (2011). Progesterone impairs human ether-a-go-go-related gene (HERG) trafficking by disruption of intracellular cholesterol homeostasis. *J. Biol. Chem.* 286, 22186–22194. doi: 10.1074/jbc.M110.198853

Xu, Q., Ji, X. F., Chi, T. Y., Liu, P., Jin, G., Chen, L., et al. (2017). Sigma-1 receptor in brain ischemia/reperfusion: possible role in the NR2A-induced pathway to regulate brain-derived neurotrophic factor. *J. Neurol. Sci.* 376, 166–175. doi: 10.1016/j.jns.2017.03.027

Yabuki, Y., Shinoda, Y., Izumi, H., Ikuno, T., Shioda, N., and Fukunaga, K. (2015). Dehydroepiandrosterone administration improves memory deficits following transient brain ischemia through sigma-1 receptor stimulation. *Brain Res.* 1622, 102–113. doi: 10.1016/j.brainres.2015.05.006

Zhang, H., and Cuevas, J. (2002). Sigma receptors inhibit high-voltage-activated calcium channels in rat sympathetic and parasympathetic neurons. *J. Neurophysiol.* 87, 2867–2879. doi: 10.1152/jn.2002.87.6.2867

Zhang, K., Zhao, Z., Lan, L., Wei, X., Wang, L., Liu, X., et al. (2017). Sigma-1 receptor plays a negative modulation on N-type calcium channel. *Front. Pharmacol.* 8:302. doi: 10.3389/fphar.2017.00302

Zhu, S., Wang, C., Han, Y., Song, C., Hu, X., and Liu, Y. (2015). Sigma-1 receptor antagonist BD1047 reduces mechanical allodynia in a rat model of bone cancer pain through the inhibition of Spinal NR1 phosphorylation and microglia activation. *Mediators Inflamm.* 2015:265056. doi: 10.1155/2015/265056

Zou, L. B., Yamada, K., Sasa, M., Nakata, Y., and Nabeshima, T. (2000). Effects of sigma(1) receptor agonist SA4503 and neuroactive steroids on performance in a radial arm maze task in rats. *Neuropharmacology* 39, 1617–1627.

Conflict of Interest Statement: The authors declare that the research was conducted in the absence of any commercial or financial relationships that could be construed as a potential conflict of interest.

Copyright © 2019 Morales-Lázaro, González-Ramírez and Rosenbaum. This is an open-access article distributed under the terms of the Creative Commons Attribution License (CC BY). The use, distribution or reproduction in other forums is permitted, provided the original author(s) and the copyright owner(s) are credited and that the original publication in this journal is cited, in accordance with accepted academic practice. No use, distribution or reproduction is permitted which does not comply with these terms.

Cholesterol as a Key Molecule That Regulates TRPV1 Channel Function

Sara L. Morales-Lázaro and Tamara Rosenbaum

Abstract Cholesterol is the one of the major constituents of cell membranes providing these structures with a certain degree of rigidity. Proteins, such as ion channels, are molecules inserted in cell membranes and their activity is regulated by cholesterol and other molecules of a lipidic nature present in them. The molecular mechanisms underlying the regulation of ion channels by lipids and similar molecules have been an object of study for several years. A little over two decades ago, the first mammalian member of the Transient Receptor Potential (TRP) family of ion channels was cloned. This protein, the TRPV1 channel, was shown to integrate several types of noxious signals in sensory neurons and to participate in processes associated to the generation of pain. Thus, TRPV1 has become the target of intense research directed towards finding potential inhibitors of its activity in an effort to control pain. To date, several activators and positive modulators of the activity of TRPV1 have been described. However, very few naturally-occurring inhibitors are known. An endogenously-produced molecule that inhibits the activity of TRPV1 is cholesterol. This chapter focuses on describing the mechanisms by which the activity of TRPV1 can be regulated by this sterol.

Keywords TRPV1 · Cholesterol · Ion channel

1 Introduction

Evolution has allowed different organisms, from invertebrates to vertebrates, to develop the capacity to respond to a wide variety of harmful stimuli for the purpose of preserving their integrity [1]. Ion channels, which are specialized proteins present in the membranes of cells, are among the molecules that allow for the detection of

S. L. Morales-Lázaro (✉) · T. Rosenbaum (✉)
Departamento de Neurociencia Cognitiva, Instituto de Fisiología Celular, Universidad Nacional Autónoma de México, Coyoacan, México City, México
e-mail: saraluzm@ifc.unam.mx; trosenba@ifc.unam.mx

© Springer Nature Switzerland AG 2019

A. Rosenhouse-Dantsker, A. N. Bukiya (eds.), *Direct Mechanisms in Cholesterol Modulation of Protein Function*, Advances in Experimental Medicine and Biology 1135, https://doi.org/10.1007/978-3-030-14265-0_6

INFORME DE LABORES 2019

such noxious signals. Some of these ion channels can be activated, in a polymodal fashion, by thermal, chemical and mechanical signals. The activation of these multimeric proteins allows the fast passive diffusion of ions across cell membranes, converting different noxious messages into electrical signals [1].

The family of Transient Receptor Potential (TRP) non-selective cation channels are classified into seven subfamilies: TRPA (Ankyrin), TRPC (Canonical), TRPM (Melastatin), TRPML (Mucolipin), TRPP (Polycystic), TRPV (Vanilloid) and TRPN (no mechanoreceptor) [2]. Most of these channels have been described in mammals, however the TRPN channel has only been identified in insects, nematodes, zebrafish and amphibians [2].

TRP channels are structurally similar to voltage-gated ion channels [3], consisting of four subunits that are associated as homo or heterotretramers [4] (Fig. 1a). Each subunit is a protein that consists of six transmembrane domains (S1-6), with amino- and carboxyl-termini located intracellularly and an ionic conduction pore formed in the tetramer by the linker located between the S5 and S6 [4] (Fig. 1b). As in all other proteins, TRP channels exhibit a tight relationship between their structure and their function and contain amino acid residues that give rise to regions that constitute activation sites for the channels by diverse stimuli.

TRP channels of mammals are abundantly expressed in sensory neurons from dorsal root and trigeminal ganglia (DRG and TG, respectively), among other several types of cells, where they enable the detection of harmful signals [5]. Among these TRP channels, we find TRPA1, TRPM8, TRPM3 and some members of the vanilloid receptors (TRPV1-4) [5, 6]. All of these proteins are termed thermo-TRP channels because they can be activated by cold (TRPA1 and TRPM8) [7, 8] or by warm or hot temperatures (TRPM3, TRPV1-TRPV4) [6, 9–12]. These polymodal ion channels can also be activated by several chemical compounds found in plants. For example, TRPA1 is activated by isothiocyanates in garlic and mustard oil [13]; TRPM8 is acti-

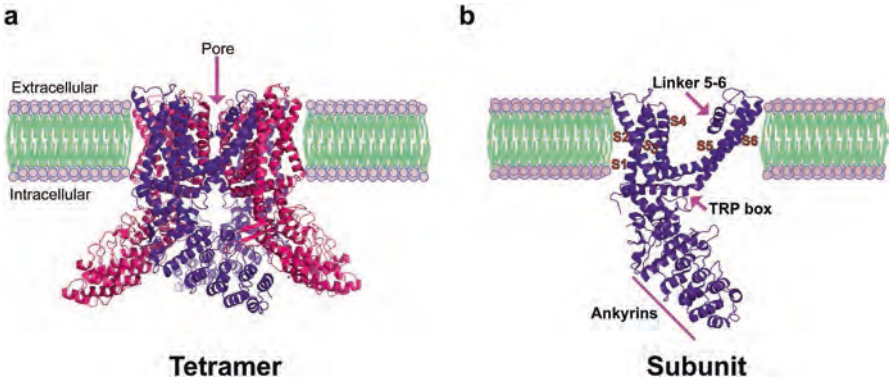

Fig. 1 TRPV1 ion channel topology. (**a**) Fourfold symmetry of TRP ion channel surrounded a pore the ion pore conduction (modified from PDB 3J5P). (**b**) The TRP subunit is composed of six transmembrane segments (S1–S6), an amino with a segment of six ankyrin repeats and carboxyl-end located intracellularly. The external pore the ion-conductivity pore is lined by linker between S5–6

INFORME DE LABORES 2019

vated by menthol [8] and TRPV1 is activated by capsaicin, the pungent compounds found in chili peppers of the *Capsicum* genus [10]. Additionally, some endogenous compounds (of a lipidic and/or peptidic nature) released during tissue injury or inflammation, are potent activators of these channels [14]. Thus, pathological states where there is an upregulation of these inflammatory mediators are accompanied by pain due to the activation of these ion channels located in the surface of sensory neurons.

To date, a large number of compounds that activate these channels has been identified and there is ongoing research focused on finding inhibitory molecules, which will be of therapeutic value if they can counteract the pain associated with the activation of these proteins [15]. TRPV1 has been the most studied member of the TRP-channel family due to its roles in acute and chronic pain, as will be discussed in detail in the next section.

2 TRPV1: More than a Capsaicin Receptor

The vanilloid subfamily contains the better studied member of the family of TRP ion channels, the capsaicin receptor (TRPV1). This receptor was first cloned in 1997 [10] and identified as a channel directly activated or modulated by several noxious inputs such as hot temperatures (≥42 °C), natural irritant compounds (i.e., capsaicin, allicin), toxins from plants or spider venoms (resiniferatoxin and double-Knot toxin, respectively), extracellular acid or intracellular alkaline pH and by endogenous lipid mediators such as anandamide, lysophosphatidic acid (LPA), diacylglycerol, phosphatidylinositol 4,5-biphosphate (PIP_2), and arachidonic acid or lipoxygenase products [10, 16].

Furthermore, the first high-resolution structure of TRP channels to be resolved was that of TRPV1 [17]. The resolved three-dimensional structure was obtained by using single particle electron cryomicroscopy (cryo-EM), corroborating that TRPV1 exhibits a fourfold symmetry that surrounds a central pore formed by the extracellular linker located between S5–S6 [17] (Fig. 1a). The S1–S4 voltage-sensing like domains are contiguous to S5-S6 and tetrameric organization is enabled by interactions between the intracellular domains: the amino and carboxy ends [17]. Interestingly, S1–S4 domains provide a long surface for the interaction of lipophilic ligands such as capsaicin, anandamide, resiniferatoxin or lipid mediators [17] and allicin binds to an ankyrin repeat domain in the N-terminus [18].

In this regard, our group has described that oleic acid, a lipophilic ligand, binds to the same pocket as capsaicin does; however, in contrast to capsaicin, the effect of this interaction is the inhibition of the activity of TRPV1, constituting one of the scarce antagonists described for this channel [19]. In this respect, it has also been reported that another lipophilic molecule, namely cholesterol, modulates TRPV1 function and such modulation has been proposed as a two-pronged mechanism: cholesterol indirectly regulates TRPV1 through changes in the properties of the membrane [20–23] or through a direct interaction with a region in the structure of TRPV1 [24, 25]. The following sections will describe the current knowledge on the effects of cholesterol on TRPV1 function.

INFORME DE LABORES 2019

3 Effects of Membrane Cholesterol Depletion on TRPV1 Function

Plasma membranes are composed of lipid molecules and proteins and the major lipid constituent in animal membranes is cholesterol, an amphipathic molecule formed by a rigid planar tetracyclic ring with an angular methyl group on a side, an aliphatic chain (isooctyl) attached to C7 and a β-hydroxyl group at the C3 position [26]. The latter is a functional group important for H-bond formation.

Cholesterol distribution in the plasma membrane is confined to microdomains called lipid rafts, which are cholesterol- and sphingolipid-enriched membrane domains characterized by their insolubility in Triton X-100 detergent, thus, they are also known as detergent-resistant membranes (DRMs) [27]. These membrane rafts form functional platforms for regulating signal pathways where some protein receptors are clustered [28]. Interestingly, some ligand-gated receptors, such as some ion channels, have been shown to be localized in these kinds of microdomains [29]. For example, the TRPV1 ion channel has been suggested to be localized in lipid rafts from DRG [21] or TG neurons, while transiently-transfected TRPV1 in cell lines like HEK293, has not been shown to be present in these specialized membrane domains [24].

Experimental evidences show that membrane depletion of cholesterol modifies the activation of TRPV1 by capsaicin and protons [21]. This was determined by performing whole-cell patch-clamp recordings in DRG neurons pretreated with methyl β-cyclodextrin (MβCD, which removes membrane-bound cholesterol). In these experiments, this pretreatment significantly decreased the amplitude of capsaicin- and proton-evoked currents as compared to untreated neurons [21]. Additionally, TRPV1 clusters localized to the surface of DRG neurons was drastically decreased when neurons were depleted of cholesterol [21]. Thus, the integrity of cholesterol in the plasma membranes of cells determines the appropriate localization and function of the TRPV1 channel.

Similarly, it was demonstrated that the effects of capsaicin and resiniferatoxin are abrogated in neurons from trigeminal ganglia depleted of cholesterol, since Ca^{2+} influx decreased in cells pretreated with MβCD [22]. Notably, this decrease was also observed when the neurons were treated with compounds that disrupt other lipid raft components such as sphingomyelin, indicating that lipid raft disruption affects Ca^{2+} influx related to the activation of TRPV1 [22].

In addition to these observations, recently it has been shown that rat TRPV1 channels transiently expressed in F11 (rat embryonic dorsal root ganglion) cells, co-localized with specific markers of lipid rafts such as flotillin [25], confirming the presence of TRPV1 in these specialized microdomains. Thus, lipid raft disruption could be a key way for the attenuation of TRPV1 activation and of the physiological effects linked to the function of this ion channel.

These experimental evidences show that TRPV1 localization to DMRs is dependent upon the presence of cholesterol in the membranes from DRG neurons, the native expression system. However, under experimental conditions where there is

INFORME DE LABORES 2019

transient expression of TRPV1 in epithelial cell lines, such as HEK293 cells, TRPV1 has not been found in these specialized microdomains [24]. These could be explained by the fact that different cells exhibit varying cholesterol contents. It is possible that neurons are a subtype of cells that contain higher cholesterol levels in their plasma membranes as compared to other types of cells and that cholesterol depletion leads to severe changes on the localization of particular proteins.

4 The TRPV1 Channel is Regulated by Cholesterol Via Specific Interactions

To date, numerous ion channels whose function can be modified by cholesterol have been identified. However, there are few channels have been shown to be regulated by this sterol through direct and specific interactions [30]. Among these channels are some potassium (K_{ir}, BK_{Ca}) channels [31–34], ligand-gated channels (GABA, nAChR, P2X) [35–37], and TRPV1 [24].

Specific interactions of cholesterol with ion channels are largely attributed to the presence of CRACs, which stands for Cholesterol Recognition/interaction Amino acid Consensus []. This short linear motif has the sequence (L/V)-X_{1-5}-(Y)-X_{1-5}-(K/R), where X represents any of one to five amino acids [38]. In addition, cholesterol can bind to an ion channel by interacting with an inverted CRAC motif named the CARC domain. This motif (K/R)-X_{1-5}-(Y/F)-X_{1-5}-(L/V) [39] is different from the CRAC sequence in its orientation and because the central amino acid can be either a tyrosine (Y) or a phenylalanine (F) [39]. Moreover, another cholesterol binding motif has been described as the Cholesterol Consensus Motif (CCM) that, unlike the other two motifs whose sequences are found in a continuous segment, the sequence of the CCM motif is bipartite, being located in two adjacent helices: the first sequence (W/Y)-(I/V/L)-(K/R) found on one helix and the amino acid (F/Y/R) on the other helix [30, 40].

Some of these cholesterol-binding motifs have only been described for two members of the vanilloid receptors: TRPV1 and TRPV4 [24, 25, 41]; however, a direct interaction of the lipid and a TRP channel, as well as the consequences on the activation of the protein, has only been demonstrated experimentally for TRPV1 [24].

Previous reports using whole-cell experiments in DRG neurons depleted of cholesterol yielded two possibilities to explain the reduction on capsaicin generated current densities: alteration of the activity of TRPV1 in the plasma membrane or modifications on channel trafficking to the membrane. In a study performed by our research group, we sought to examine the effects of cholesterol on TRPV1 channels using excised membranes from HEK293 cells expressing this channel. These experiments provided a tool to exclude the possible involvement of cholesterol on cell-trafficking mechanisms and to explore direct effects of the sterol on the ion channels. Depletion of cholesterol from these membrane patches with MβCD showed that TRPV1 activation by capsaicin was not affected by this treatment, as

assessed using inside-out patches with the patch clamp technique. However, the addition of cholesterol to inside-out membrane patches produced a significant reduction in rat TRPV1 activation by capsaicin, temperature and voltage. Since cholesterol enrichment did not modify parameters such as the Hill coefficient and the $K_{1/2}$ for activation by capsaicin, we concluded that binding of this agonist to TRPV1 was unmodified in the presence of cholesterol and not responsible for the effects of this lipid on channel function [24] .

To further detail the effects of cholesterol on rat TRPV1 function, we performed noise analysis experiments in inside-out patches from HEK293 cells expressing TRPV1 before and after cholesterol depletion in these excised patches. The results showed that the open probability (Po) of TRPV1 remained similar before and after cholesterol enrichment. However, the number of functional channels (*N*) decreased considerably [24]. These results were confirmed by excised patch single channel recordings, where cholesterol did not alter the magnitude of the single-channel currents nor the open probability of the channel. Nonetheless, after a few minutes of membrane enrichment with cholesterol we observed that the number of capsaicin-responsive channels decreased during our electrophysiological recordings [24].

In order to determine whether the reduction of the number of functional TRPV1 channels in cholesterol-enriched membranes was due to specific interactions of cholesterol with the channel, we searched sequences that resembled a possible CRAC motif and we found an inverted CRAC sequence (CARC motif) located in the S5 of TRPV1: $\underline{\mathbf{R}}_{579}F_{580}M_{581}\underline{\mathbf{F}}_{582}V_{583}Y_{584}\underline{\mathbf{L}}_{585}$ [24] (Fig. 2). We next evaluated the effects of cholesterol on rat TRPV1 mutant versions where the amino acids corresponding to the CARC motif were individually substituted by other residues. Our experiments showed that a charge reversal of the positive amino acid R576 to an aspartate (D), and the change of the aromatic F582 to a polar amino acid such as glutamine (Q), partially inhibited the effects of cholesterol on TRPV1 function [24]. Moreover, when L585 was changed to an isoleucine (I), the inhibitory effects of cholesterol on TRPV1 activity were completely abolished.

In order to demonstrate the stereospecificity of the interaction between cholesterol and TRPV1, we used a synthetic chiral cholesterol analogue, epicholesterol, which has the hydroxyl group in position 3α instead of position 3β. Membrane



Fig. 2 Alignment sequence between the CRAC and CARC domains from rat and human. Consensus sequence for the CARC motif found in rat TRPV1 channel, (NP_114188) alignment with the from human TRPV1 isoform 1 (iso1-hTRPV1) (NP_542435) and the genetic variant from human TRPV1, var-hTRPV1 (ABA06605.1). The alignment also shows that the CRAC motif is conserved between human and rat TRPV1 channels

INFORME DE LABORES 2019

patch incubation with epicholesterol did not modify capsaicin evoked currents, indicating that the effects of cholesterol on rat TRPV1 function are stereospecific [24].

The specificity of cholesterol interactions within the TRPV1 channel was simulated by molecular docking using the recently reported TRPV1 cryo-EM structure (Fig. 3). These molecular simulations suggest that TRPV1 interactions with cholesterol are mediated by CH-π stacking between the rings of cholesterol (α-face) and the aromatic ring of the tyrosine or phenylalanine residues located in the middle of the CARC domain in the channel; whereas leucine or valine make Van der Waals contacts with the aliphatic chains (methyl and isooctyl groups) located in the β-face of cholesterol (Fig. 3). Although the β-OH group of cholesterol on the CRAC motif is putatively capable of forming H-bonds with the phenol group of the tyrosine, this is impossible for the CARC motif (contained in the TRPV1 channel), since the aromatic ring of the phenylalanine lacks a hydroxyl group. However, it is possible that the hydroxyl group of cholesterol forms a H-bond with R585 at the inner leaflet, as has been recently described for other arginine residues located at the inner leaflet within the TRPV1 channel [25].

Finally, we also evaluated cholesterol effects on the human TRPV1 channel and found that the isoform 1 of human TRPV1 (iso1-hTRPV1, NP_542435) lacks the leucine in position 585 that is present in the rat TRPV1 sequence, Fig. 2. By further examining the literature on reported human TRPV1 sequences, we found a genetic variant (var-hTRPV1) with a single nucleotide polymorphism that contained a valine in this position (SNP: rs8065080) [42] (Fig. 2). This is an amino acid that actually forms part of the CARC motif, so we hypothesized that this variant would exhibit a similar behavior in response to cholesterol to the one we had observed in the rat TRPV1. Furthermore, isoform 1 human TRPV1 contains an isoleucine at position 585, a residue similar to the one we had introduced in the rat TRPV1 (L585I) and that

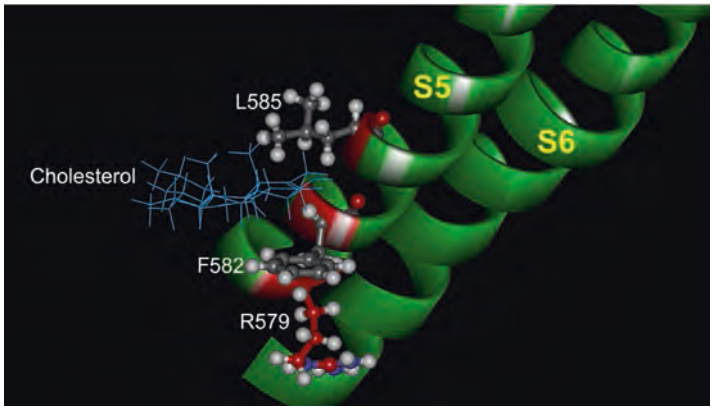

Fig. 3 Molecular docking simulation of cholesterol bound to TRPV1. Simulation using the cryo-EM structure of TRPV1 in the closed state (PDB 3J5P, chain a). Docking simulation shows the proximity between cholesterol and amino acids F582 and L585 located in the CARC motif of TRPV1

had produced channels resistant to inhibition by cholesterol. Indeed, it was not surprising to find that activation of the human TRPV1 isoform 1 was not inhibited by cholesterol. We also found that the substitution in this isoform 1 of I585 by a valine (as the one present in var-hTRPV1) rendered the channel partially susceptible to cholesterol [24]. Furthermore, when I585 from the iso1-hTRPV1 was mutated to leucine (emulating the amino acid contained in the rat TRPV1), this amino acid substitution conferred a marked susceptibility to cholesterol, producing iso1-hTRPV1-I585L channels that were inhibited in their activation by capsaicin when the membrane patches were enriched with this sterol [24].

The iso1-hTRPV1 does not contain a CARC domain at the same position where the rat TRPV1 CARC domain is located. So, it is possible that human or rat TRPV1 channels contain CRAC, CARC or CCM motifs in other sequence positions. Consistent with this idea, it was recently reported that human TRPV1 has two CRAC motifs (located in aa's 349-356 and 553-557), two CARC motifs (located in aa's 304-316 and 535-542) and one CCM motif (in aa's 433-447). Of these cholesterol-binding regions, the CRAC motif located in the S4 and linker S4-S5 region (553-557 aa) (Fig. 2) and the CCM motif, are the most conserved between TRPV1 channels from several species [25]. However, until now, there are only docking simulations showing the interaction of cholesterol with R557 located in the conserved CRAC motif and the functional significances of these motifs remain unresolved [25].

5 Cholesterol Depletion Modifies TRPV1 Permeability to Large-Cations

Plasma membranes properties can be modified according to their lipid composition (i.e. by cholesterol depletion or enrichment) [43]. Two important features of ion channels are their gating properties and their ion selectivity and both are highly dependent upon the membrane lipid content.

Ion selectivity has been considered as a fixed parameter for each channel, however, it has been described that some of them have dynamic pores, leading permeability to large cations, this process has been known as pore dilation [44–46]. Although, this concept has been reconsidered [47], there are experimental data demonstrating that some ion channels, such as TRPV1, can permeate large molecules under specific conditions.

In 2003 Meyers et al., provided the first evidence for the permeation of a large molecule, the nontoxic fluorescent cationic dye (FM1-43,) through the pore of TRPV1 [48]. Furthermore, Binshtok et al., demonstrated that when TRPV1 was activated by capsaicin, the permeation of a local cationic anesthetic QX-314 (a Na^+ ion channel blocker) is allowed, producing local pain inhibition without affecting other sensations [49]. Additionally, Chung et al., found that sustained TRPV1 exposure to capsaicin or protons induced a dilated pore allowing for the uptake of YO-PRO1 and FM1-43 into cells [45]. All these examples show how the TRPV1 can be modified, rendering the channel permeable to the passage of large cationic molecules.

INFORME DE LABORES 2019

Interestingly, these dynamic changes in the TRPV1 pore are susceptible to changes in the cholesterol content of membranes [20]. This was demonstrated in CHO cells (Chinese hamster ovary cells) with inducible human TRPV1 expression. The cholesterol content in these cells was depleted by ~54% through the treatment with MβCD:cholesterol (10:1) and whole cell patch clamp recordings were used to evaluate the effects of cholesterol depletion on the permeability to *N*-methyl-D-Glucamine (NMDG, a large monovalent cation) [20]. Sustained TRPV1 activation by capsaicin, under hypocalcemic conditions in cells depleted of cholesterol, decreased permeability to NMDG, indicating that cholesterol reduction in membrane affects the ion-permeability properties of the channel [20]. In addition, it has been shown that sustained TRPV1 activation by capsaicin in CHO cells, leads to YO-PRO1 uptake and cholesterol depletion decreases the uptake of this cationic large dye [20]. Similar effects were observed whether the channels are activated by protons under sustained and hypocalcemic conditions [20]. In contrast to these results, the permeability to these large cationic molecules in cells depleted of cholesterol were unaffected if TRPV1 was activated by temperature [20], indicating that the properties on TRPV1 ion-permeability also depend on the type of noxious stimulus that activates this channel.

6 Cholesterol Effects on TRPV1 Temperature Responses

We have discussed that cholesterol has strong influences on membrane fluidity [50] which affect the localization or function of transmembrane proteins as ion channels [43] but the amount of cholesterol in membranes also modifies the sensitivity of certain receptors to specific stimuli. For example, TRPV3 is also a thermosensitive channel [51] and it was reported that TRPV3 channels are sensitized to activation by lower temperatures (below 30 °C) in cholesterol-enriched cells [52].

Effects of cholesterol on TRPV1's temperature-sensitivity have been also evaluated [23]. Whole-cell recordings from TRPV1-expressing HEK293 cells with cholesterol enhancement showed that the temperature threshold for TRPV1 activation was significantly increased, since the half-activation temperature was 50 °C in comparison to 48 °C in untreated cells. Notably, the heat response of TRPV1 was unchanged in cholesterol-depleted cells. Therefore, the temperature threshold for TRPV1 activation is partially modified only when this sterol is increased in the membrane.

Thus, it is interesting to note that two structurally-related ion channels, TRPV3 and TRPV1, show distinct responses to cholesterol concentrations in the plasma membrane. Although it is not clear why these channels exhibit different responses to cholesterol, it is not uncommon that, even closely-related ion channels, respond differently to the same molecule. For example, the energetic transitions coupled to the opening or closing of the pore of a specific ion channel are not necessarily altered in the same way as what occurs in another ion channel. Moreover, in the particular cases of TRPV1 and TRPV3, the mechanism by which cholesterol

INFORME DE LABORES 2019

modulates thermal sensitivity of TRPV3 is unknown and could very well be through effects on membrane rigidity and not through a direct a mechanism as the one described for TRPV1.

7 Conclusion

Fifty years ago, it was unimaginable to consider cholesterol as a regulator of ion channels, since this sterol was only considered as a key component of the lipid bilayer where it maintains direct interaction with phospholipids. There is no doubt that cholesterol content modifies the properties of the membranes, having a strong influence in the regulation on ion channel function.

Furthermore, this sterol can regulate the function of these integral membrane proteins in a direct and specific fashion: through the interaction with specific amino acids within the sequence of these proteins.

This chapter has described the molecular mechanisms underlying the regulation of TRPV1 function by changes of cholesterol content in the cell plasma membrane or by direct interaction between the channel and the sterol.

Since cholesterol depletion modifies TRPV1 localization in the plasma membranes from sensory neurons affecting the calcium influx [21, 22], it has been concluded that TRPV1 is confined to specialized microdomains of the membrane: lipid rafts. The discrepancies observed in some cell lines where TRPV1 channels has not been identified in these detergent resistant domains [22, 24] could be attributed to differences in the amount of cholesterol between cell types. Moreover, cholesterol depletion from cells also modulates TRPV1 ion-permeability [20], indicating that the enlargement of the TRPV1 pore is strongly dependent upon cholesterol content. This differs from the idea that cholesterol only promotes stiffness of cellular membranes, since for the case of TRPV1, cholesterol has an important role on the elasticity of its pore. In addition, we have also discussed that cholesterol enrichment causes changes in TRPV1's threshold to heat [23]. Together, these experimental demonstrations, show that TRPV1 is highly susceptible to be regulated by changes on the amount of cholesterol in the membranes where it is expressed.

We have also detailed on how cholesterol directly inhibits TRPV1 activation by capsaicin, temperature and voltage through the specific interaction of cholesterol in a CARC motif located on the S4 from TRPV1 [24] and on the different TRPV1 susceptibilities to cholesterol of different species (rat and human isoform or variants) [36]. Data from our work group and further examination of the literature, has led us to conclude that cholesterol can inhibit human TRPV1 activation by interacting with other cholesterol binding domains recently described [25].

Now, cholesterol is considered as a molecule key in regulating TRPV1 function; however, the physiological consequences of this regulation have still to be explored.

Acknowledgments This work was supported by grants from Dirección General de Asuntos del Personal Académico (DGAPA)-Programa de Apoyo a Proyectos de Investigación e Innovación

INFORME DE LABORES 2019

Tecnológica (PAPIIT) IN206819 and by Estímulos a Investigaciones Médicas Miguel Alemán Valdés to S.LM.L. and Consejo Nacional de Ciencia y Tecnología (CONACyT) A1-S-8760, grant from Fronteras en la Ciencia No. 77 from CONACyT and DGAPA-PAPIIT IN200717 to T.R.

References

1. Smith ES, Lewin GR. Nociceptors: a phylogenetic view. J Comp Physiol A Neuroethol Sens Neural Behav Physiol. 2009;195:1089–106. https://doi.org/10.1007/s00359-009-0482-z.
2. Li H. TRP channel classification. Adv Exp Med Biol. 2017;976:1–8. https://doi.org/10.1007/978-94-024-1088-4_1.
3. Jiang Y, Lee A, Chen J, Ruta V, Cadene M, Chait BT, et al. X-ray structure of a voltage-dependent K+ channel. Nature. 2003;423:33–41. https://doi.org/10.1038/nature01580.
4. Ramsey IS, Delling M, Clapham DE. An introduction to TRP channels. Annu Rev Physiol. 2006;68:619–47. https://doi.org/10.1146/annurev.physiol.68.040204.100431.
5. Mickle AD, Shepherd AJ, Mohapatra DP. Nociceptive TRP channels: sensory detectors and transducers in multiple pain pathologies. Pharmaceuticals (Basel). 2016;9:E72. https://doi.org/10.3390/ph9040072.
6. Vandewauw I, De Clercq K, Mulier M, Held K, Pinto S, Van Ranst N, et al. A TRP channel trio mediates acute noxious heat sensing. Nature. 2018;555:662–6. https://doi.org/10.1038/nature26137.
7. Story GM, Peier AM, Reeve AJ, Eid SR, Mosbacher J, Hricik TR, et al. ANKTM1, a TRP-like channel expressed in nociceptive neurons, is activated by cold temperatures. Cell. 2003;112:819–29.
8. Bautista DM, Siemens J, Glazer JM, Tsuruda PR, Basbaum AI, Stucky CL, et al. The menthol receptor TRPM8 is the principal detector of environmental cold. Nature. 2007;448:204–8. https://doi.org/10.1038/nature05910.
9. Smith GD, Gunthorpe MJ, Kelsell RE, Hayes PD, Reilly P, Facer P, et al. TRPV3 is a temperature-sensitive vanilloid receptor-like protein. Nature. 2002;418:186–90. https://doi.org/10.1038/nature00894.
10. Caterina MJ, Schumacher MA, Tominaga M, Rosen TA, Levine JD, Julius D. The capsaicin receptor: a heat-activated ion channel in the pain pathway. Nature. 1997;389:816–24. https://doi.org/10.1038/39807.
11. Guler AD, Lee H, Iida T, Shimizu I, Tominaga M, Caterina M. Heat-evoked activation of the ion channel, TRPV4. J Neurosci. 2002;22:6408–14.
12. Caterina MJ, Rosen TA, Tominaga M, Brake AJ, Julius D. A capsaicin-receptor homologue with a high threshold for noxious heat. Nature. 1999;398:436–41. https://doi.org/10.1038/18906.
13. Jordt SE, Bautista DM, Chuang HH, McKemy DD, Zygmunt PM, Hogestatt ED, et al. Mustard oils and cannabinoids excite sensory nerve fibres through the TRP channel ANKTM1. Nature. 2004;427:260–5. https://doi.org/10.1038/nature02282.
14. Taberner FJ, Fernandez-Ballester G, Fernandez-Carvajal A, Ferrer-Montiel A. TRP channels interaction with lipids and its implications in disease. Biochim Biophys Acta. 2015;1848:1818–27. https://doi.org/10.1016/j.bbamem.2015.03.022.
15. Levine JD, Alessandri-Haber N. TRP channels: targets for the relief of pain. Biochim Biophys Acta. 2007;1772:989–1003. https://doi.org/10.1016/j.bbadis.2007.01.008.
16. Morales-Lazaro SL, Simon SA, Rosenbaum T. The role of endogenous molecules in modulating pain through transient receptor potential vanilloid 1 (TRPV1). J Physiol. 2013;591:3109–21. https://doi.org/10.1113/jphysiol.2013.251751.
17. Liao M, Cao E, Julius D, Cheng Y. Structure of the TRPV1 ion channel determined by electron cryo-microscopy. Nature. 2013;504:107–12. https://doi.org/10.1038/nature12822.

18. Salazar H, Llorente I, Jara-Oseguera A, Garcia-Villegas R, Munari M, Gordon SE, et al. A single N-terminal cysteine in TRPV1 determines activation by pungent compounds from onion and garlic. Nat Neurosci. 2008;11:255–61. https://doi.org/10.1038/nn2056.
19. Morales-Lazaro SL, Llorente I, Sierra-Ramirez F, Lopez-Romero AE, Ortiz-Renteria M, Serrano-Flores B, et al. Inhibition of TRPV1 channels by a naturally occurring omega-9 fatty acid reduces pain and itch. Nat Commun. 2016;7:13092. https://doi.org/10.1038/ncomms13092.
20. Jansson ET, Trkulja CL, Ahemaiti A, Millingen M, Jeffries GD, Jardemark K, et al. Effect of cholesterol depletion on the pore dilation of TRPV1. Mol Pain. 2013;9:1. https://doi.org/10.1186/1744-8069-9-1.
21. Liu M, Huang W, Wu D, Priestley JV. TRPV1, but not P2X, requires cholesterol for its function and membrane expression in rat nociceptors. Eur J Neurosci. 2006;24:1–6. https://doi.org/10.1111/j.1460-9568.2006.04889.x.
22. Szoke E, Borzsei R, Toth DM, Lengl O, Helyes Z, Sandor Z, et al. Effect of lipid raft disruption on TRPV1 receptor activation of trigeminal sensory neurons and transfected cell line. Eur J Pharmacol. 2010;628:67–74. https://doi.org/10.1016/j.ejphar.2009.11.052.
23. Liu B, Hui K, Qin F. Thermodynamics of heat activation of single capsaicin ion channels VR1. Biophys J. 2003;85:2988–3006. https://doi.org/10.1016/S0006-3495(03)74719-5.
24. Picazo-Juarez G, Romero-Suarez S, Nieto-Posadas A, Llorente I, Jara-Oseguera A, Briggs M, et al. Identification of a binding motif in the S5 helix that confers cholesterol sensitivity to the TRPV1 ion channel. J Biol Chem. 2011;286:24966–76. https://doi.org/10.1074/jbc.M111.237537.
25. Saha S, Ghosh A, Tiwari N, Kumar A, Kumar A, Goswami C. Preferential selection of Arginine at the lipid-water-interface of TRPV1 during vertebrate evolution correlates with its snorkeling behaviour and cholesterol interaction. Sci Rep. 2017;7:16,808. https://doi.org/10.1038/s41598-017-16780-w.
26. Song Y, Kenworthy AK, Sanders CR. Cholesterol as a co-solvent and a ligand for membrane proteins. Protein Sci. 2014;23:1–22. Epub 2013/10/25. https://doi.org/10.1002/pro.2385.
27. Rietveld A, Simons K. The differential miscibility of lipids as the basis for the formation of functional membrane rafts. Biochim Biophys Acta. 1998;1376:467–79.. Epub 1998/11/07
28. Lingwood D, Simons K. Lipid rafts as a membrane-organizing principle. Science. 2010;327:46–50. Epub 2010/01/02. https://doi.org/10.1126/science.1174621.
29. Dart C. Lipid microdomains and the regulation of ion channel function. J Physiol. 2010;588:3169–78. Epub 2010/06/04. https://doi.org/10.1113/jphysiol.2010.191585.
30. Levitan I, Singh DK, Rosenhouse-Dantsker A. Cholesterol binding to ion channels. Front Physiol. 2014;5:65. https://doi.org/10.3389/fphys.2014.00065.
31. Romanenko VG, Rothblat GH, Levitan I. Modulation of endothelial inward-rectifier K+ current by optical isomers of cholesterol. Biophys J. 2002;83:3211–22. https://doi.org/10.1016/S0006-3495(02)75323-X.
32. Singh DK, Rosenhouse-Dantsker A, Nichols CG, Enkvetchakul D, Levitan I. Direct regulation of prokaryotic Kir channel by cholesterol. J Biol Chem. 2009;284:30,727–36. https://doi.org/10.1074/jbc.M109.011221.
33. Rosenhouse-Dantsker A, Noskov S, Durdagi S, Logothetis DE, Levitan I. Identification of novel cholesterol-binding regions in Kir2 channels. J Biol Chem. 2013;288:31,154–64. https://doi.org/10.1074/jbc.M113.496117.
34. Bukiya AN, Belani JD, Rychnovsky S, Dopico AM. Specificity of cholesterol and analogs to modulate BK channels points to direct sterol-channel protein interactions. J Gen Physiol. 2011;137:93–110. https://doi.org/10.1085/jgp.201010519.
35. Addona GH, Sandermann H Jr, Kloczewiak MA, Miller KW. Low chemical specificity of the nicotinic acetylcholine receptor sterol activation site. Biochim Biophys Acta. 2003;1609:177–82.

INFORME DE LABORES 2019

36. Sooksawate T, Simmonds MA. Effects of membrane cholesterol on the sensitivity of the GABA(A) receptor to GABA in acutely dissociated rat hippocampal neurones. Neuropharmacology. 2001;40:178–84.
37. Robinson LE, Shridar M, Smith P, Murrell-Lagnado RD. Plasma membrane cholesterol as a regulator of human and rodent P2X7 receptor activation and sensitization. J Biol Chem. 2014;289:31983–94. https://doi.org/10.1074/jbc.M114.574699.
38. Li H, Papadopoulos V. Peripheral-type benzodiazepine receptor function in cholesterol transport. Identification of a putative cholesterol recognition/interaction amino acid sequence and consensus pattern. Endocrinology. 1998;139:4991–7. https://doi.org/10.1210/endo.139.12.6390.
39. Baier CJ, Fantini J, Barrantes FJ. Disclosure of cholesterol recognition motifs in transmembrane domains of the human nicotinic acetylcholine receptor. Sci Rep. 2011;1:69. https://doi.org/10.1038/srep00069.
40. Hanson MA, Cherezov V, Griffith MT, Roth CB, Jaakola VP, Chien EY, et al. A specific cholesterol binding site is established by the 2.8 A structure of the human beta2-adrenergic receptor. Structure. 2008;16:897–905. https://doi.org/10.1016/j.str.2008.05.001.
41. Kumari S, Kumar A, Sardar P, Yadav M, Majhi RK, Kumar A, et al. Influence of membrane cholesterol in the molecular evolution and functional regulation of TRPV4. Biochem Biophys Res Commun. 2015;456:312–9. https://doi.org/10.1016/j.bbrc.2014.11.077.
42. Cantero-Recasens G, Gonzalez JR, Fandos C, Duran-Tauleria E, Smit LA, Kauffmann F, et al. Loss of function of transient receptor potential vanilloid 1 (TRPV1) genetic variant is associated with lower risk of active childhood asthma. J Biol Chem. 2010;285:27532–5. https://doi.org/10.1074/jbc.C110.159491.
43. McIntosh TJ, Simon SA. Roles of bilayer material properties in function and distribution of membrane proteins. Annu Rev Biophys Biomol Struct. 2006;35:177–98. https://doi.org/10.1146/annurev.biophys.35.040405.102022.
44. Virginio C, MacKenzie A, Rassendren FA, North RA, Surprenant A. Pore dilation of neuronal P2X receptor channels. Nat Neurosci. 1999;2:315–21. https://doi.org/10.1038/7225.
45. Chung MK, Guler AD, Caterina MJ. TRPV1 shows dynamic ionic selectivity during agonist stimulation. Nat Neurosci. 2008;11:555–64. https://doi.org/10.1038/nn.2102.
46. Chen J, Kim D, Bianchi BR, Cavanaugh EJ, Faltynek CR, Kym PR, et al. Pore dilation occurs in TRPA1 but not in TRPM8 channels. Mol Pain. 2009;5:3. https://doi.org/10.1186/1744-8069-5-3.
47. Li M, Toombes GE, Silberberg SD, Swartz KJ. Physical basis of apparent pore dilation of ATP-activated P2X receptor channels. Nat Neurosci. 2015;18:1577–83. https://doi.org/10.1038/nn.4120.
48. Meyers JR, MacDonald RB, Duggan A, Lenzi D, Standaert DG, Corwin JT, et al. Lighting up the senses: FM1-43 loading of sensory cells through nonselective ion channels. J Neurosci. 2003;23:4054–65.
49. Binshtok AM, Bean BP, Woolf CJ. Inhibition of nociceptors by TRPV1-mediated entry of impermeant sodium channel blockers. Nature. 2007;449:607–10. https://doi.org/10.1038/nature06191.
50. de Meyer F, Smit B. Effect of cholesterol on the structure of a phospholipid bilayer. Proc Natl Acad Sci U S A. 2009;106:3654–8. https://doi.org/10.1073/pnas.0809959106.
51. Liu B, Qin F. Single-residue molecular switch for high-temperature dependence of vanilloid receptor TRPV3. Proc Natl Acad Sci U S A. 2017;114:1589–94. https://doi.org/10.1073/pnas.1615304114.
52. Klein AS, Tannert A, Schaefer M. Cholesterol sensitises the transient receptor potential channel TRPV3 to lower temperatures and activator concentrations. Cell Calcium. 2014;55:59–68. https://doi.org/10.1016/j.ceca.2013.12.001.

www.aging-us.com AGING 2019, Vol. 11, No. 16

Research Paper

Cortical neurons develop a senescence-like phenotype promoted by dysfunctional autophagy

Daniel Moreno-Blas[1], Elisa Gorostieta-Salas[1], Alexander Pommer-Alba[1], Gabriel Muciño-Hernández[1], Cristian Gerónimo-Olvera[2], Luis Angel Maciel-Barón[3], Mina Konigsberg[3], Lourdes Massieu[2], Susana Castro-Obregón[1]

[1]Departamento de Neurodesarrollo y Fisiología, División de Neurociencias, Instituto de Fisiología Celular, UNAM, Mexico City 04510, México
[2]Departamento de Neuropatología, División de Neurociencias, Instituto de Fisiología Celular, UNAM, Mexico City 04510, México
[3]Departamento de Ciencias de la Salud, Universidad Autónoma Metropolitana, Unidad Iztapalapa. Mexico City 09340, México

Correspondence to: Susana Castro-Obregón; **email:** scastro@ifc.unam.mx
Keywords: senescence, brain, neuron, autophagy, SASP (senescence-associated secretory phenotype)
Received: March 12, 2019 **Accepted:** August 9, 2019 **Published:** August 30, 2019

Copyright: Moreno-Blas et al. This is an open-access article distributed under the terms of the Creative Commons Attribution License (CC BY 3.0), which permits unrestricted use, distribution, and reproduction in any medium, provided the original author and source are credited.

ABSTRACT

Senescent cells accumulate in various tissues and organs with aging altering surrounding tissue due to an active secretome, and at least in mice their elimination extends healthy lifespan and ameliorates several chronic diseases. Whether all cell types senesce, including post-mitotic cells, has been poorly described mainly because cellular senescence was defined as a permanent cell cycle arrest. Nevertheless, neurons with features of senescence have been described in old rodent and human brains. In this study we characterized an *in vitro* model useful to study the molecular basis of senescence of primary rat cortical cells that recapitulates senescent features described in brain aging. We found that in long-term cultures, rat primary cortical neurons displayed features of cellular senescence before glial cells did, and developed a functional senescence-associated secretory phenotype able to induce paracrine premature senescence of mouse embryonic fibroblasts but proliferation of rat glial cells. Functional autophagy seems to prevent neuronal senescence, as we observed an autophagic flux reduction in senescent neurons both *in vitro* and *in vivo*, and autophagy impairment induced cortical cell senescence while autophagy stimulation inhibited it. Our findings suggest that aging-associated dysfunctional autophagy contributes to senescence transition also in neuronal cells.

INTRODUCTION

Aging is accompanied by a wide range of symptoms that reduce health span, such as cardiovascular dysfunction, osteoporosis, neurodegeneration and cancer, among other diseases. Amelioration of those symptoms has been achieved after pharmacological interventions using a novel class of drugs termed senolytics. These compounds clear senescent cells that accumulate late in life both in normal tissues and especially in those affected by age-related pathologies [1]. Nevertheless, senescent cells are harmful only when they persist, since transient senescent cells, which are eliminated by effector immune cells, contribute to wound healing, regeneration, immunity and even morphogenesis during development [2]. Therefore, it is fundamental to understand the molecular mechanisms of senescence establishment and maintenance.

Cellular senescence is a phenotype characterized by a durable cell cycle arrest (*i.e*. cells do not respond to mitogens) and a flattened and vacuolated morphology with stress granules collection. Even though there is no single marker of senescence, some of the most common features observed are: activation of the lysosomal enzyme senescence-associated β-galactosidase (SA-β-gal); persistent DNA damage response detected by γH2AX foci; expression of tumor suppressors $p21^{CIP1/WAF1}$ (encoded by *Cdkn1a)* and/or $p16^{INK4A}$ (encoded by *Cdkn2a)*; lipofuscin accumulation [3]; and nuclear deformation associated with nuclear envelop proteins degradation [4]. The most important activity of senescent cells is the secretion of a set of molecules, known as the senescence-associated secretory phenotype (SASP) that, depending on the physiological context, can be either beneficial or harmful. In early stages senescent cells secrete cytokines that promote the migration and infiltration of effector immune cells, as well as growth factors and proteases that facilitate tissue repair and remodeling. Yet, persisting signaling contributes to chronic inflammation, a hallmark of aging and a major contributor to age-related dysfunctions. SASP molecules also have an autocrine role, fostering the senescent phenotype, and a paracrine role inducing senescence in surrounding cells [5], inflammation and tumorigenesis [6, 7].

Autophagy is a catabolic process that degrades intracellular components, like proteins and damaged organelles, including mitochondria, through lysosomes. Similar to senescence, it is induced in response to stressful stimuli, therefore both senescence and autophagy are often observed simultaneously. The interplay between autophagy and senescence requires further investigation, since autophagy has been implicated in both promoting and inhibiting cellular senescence. While autophagy inhibition promotes senescence in normal proliferating cells [8], autophagy inhibition delays oncogene-induced senescence and the synthesis of SASP components [9]. A possible explanation for the opposing role of autophagy over senescence is that it could engulf alternative targets that regulate cellular senescence in opposite manners. For example, the stability of the transcription factor GATA4, a key activator of SASP genes, is regulated by autophagy. Upon senescence induction, GATA4 escapes autophagic degradation because its interaction with p62/SQSTM1 (an autophagy cargo receptor) decreases, leading to GATA4 accumulation [10]. On the other hand, during oncogene-induced senescence, autophagy fosters the SASP through a specialized compartment known as the TOR-autophagy spatial coupling compartment (TASCC), where mTOR localizes at the surface of autolysosomes, which are surrounded by endoplasmic reticulum; a flux of recycled amino acids and metabolites released from the autolysosomes are used by mTORC1 for supporting the synthesis of SASP factors, hence facilitating senescence [11]. Therefore, selective autophagy actively suppresses cellular senescence through the degradation of GATA4, whereas autophagic degradation of other proteins (perhaps long-lived proteins), facilitates the SASP [12].

The traditional view of senescence as a specific phenomenon where a proliferation-competent cell undergoes permanent growth arrest, has limited the study of senescence of post-mitotic cells. Accordingly, the limited studies on cellular senescence in the brain have mostly focused on glial cells [13]. Nonetheless, some senescent markers have been described in several studies of both physiological aging and neurodegenerative diseases [14]. For example, cortical and Purkinje neurons show several senescence features like SA-β-gal activity, lipofuscin accumulation, γH2AX and macroH2A foci, and IL6 expression, all in a $p21^{CIP1/WAF1}$-dependent manner [15]. Interestingly, human neurons might also senesce, since there is expression of *p16/Cdkn2a* in pyramidal neurons in the prefrontal cortex from human brains of people over 77 years old [10]. We are interested in understanding the molecular basis for neuronal senescence, because we hypothesize that when senescent neurons persist in the brain, they contribute to cognitive decline by impairing synaptic function, inducing paracrine senescence and chronic inflammation.

While cellular senescence of mitotic cells is induced mainly by stressful stimuli (most of them inducing DNA damage), telomere attrition during cell division, oncogene activation or developmental cues [2], the molecular mechanisms that induce post-mitotic cells senescence are less understood. Also, whether autophagy regulates senescence in any direction in post-mitotic cells is completely unknown. Several groups have observed that neuronal cells acquire some senescent features *in vitro*, providing a very helpful system to study the molecular basis of neuronal senescence. For example, primary cortical, hippocampal and cerebellar granule neurons become SA-β-gal-positive over time [16-20]. However, these studies were limited to the detection of SA-β-gal activity, which could be misleading [21]. Recent *in vitro* studies confirmed the presence of additional senescent features, including γH2AX foci in neurons from mouse neuro-glial co-cultures maintained up to 27 days *in vitro* (D*IV*) [22]. Taken together, these reports support the notion that cultured neurons *in vitro* are capable of undergoing cellular senescence with the same features that occur *in vivo*.

For senescent neurons to contribute to chronic inflammation and paracrine senescence, they must establish a senescent phenotype including the SASP. Paracrine senescence has been demonstrated to occur in mouse embryonic fibroblast exposed to conditioned media from senescent fibroblasts [5]. In this work we developed an *in vitro* model of neuronal senescence that recapitulates *in vivo* senescence markers, and secreted molecules able to induce paracrine glial proliferation as well as premature senescence in mouse embryonic fibroblasts, pointing towards a neuronal SASP. We found that senescent cortical cells secrete C-C motif chemokine 2, also known as monocyte chemotactic protein 1 (MCP-1), a known SASP factor able to induce paracrine senescence [23]. Interestingly, we found that rat primary cortical neurons displayed features of cellular senescence before glial cells did. As reported for proliferating cells, functional autophagy, perhaps selective, seems to prevent neuronal senescence, as we observed autophagic flux impairment. Accordingly, we observed more senescent cortical cells when autophagy was impaired and less when it was stimulated. Our findings suggest that a dysfunctional autophagy contributes to senescence transition also in post-mitotic cells.

RESULTS

Primary cortical neurons acquire several senescent features after long-term culture.

To establish an *in vitro* model to study the transition of neurons from a non-dividing terminal differentiation state into senescence *in vitro*, prenatal rat cortical cells were cultured for up to 40 days *in vitro* (D*IV*). Since several reports indicate the presence of senescent glial cells in old brains [13], we considered that glial cells could become senescent and then promote paracrine neuronal senescence; hence, we allowed the proliferation of glial cells during the culture of primary cortical cells. During the first days of culture (6 D*IV*), neurons (expressing βIII-TUBULIN) represented 96.8% (SD 2.2) of the cells with very few glial cells (expressing GFAP); due to proliferation of glial cells and some loss of neurons, by 26 D*IV* there were 51% (SD 6.9) neurons and 31% (SD 11.5) glial cells; and by 40 D*IV* 73% (SD 6.9) of the surviving cells were glial. The cells expressing βIII-TUBULIN did not expressed GFAP. On average, the total number of cells along the culture remained similar (Supplementary Figure 1S). Without any further stressful stimuli, cortical cells became SA-β-gal-positive over time and accumulated lipofuscin detected by autofluorescence and by Sudan Black B staining, a lipophilic dye [24] (Figures 1A-B). SBB staining seems to be more sensitive than SA-β-gal activity. An increment in both SA-β-gal-positive and lipofuscin accumulation was also confirmed in the cortex of old rat brains (Figures 1C-E).

Since different inducers of senescence in mitotic cells converge on the activation of the tumor suppressor $p21^{CIP1/WAF1}$, and indeed $p21^{CIP1/WAF1}$ has been suggested to mediate neuronal senescence in old brains [15], we reasoned that even though post-mitotic cells already express some CDK inhibitors to exit the cell cycle, they could still need to induce its expression for a pro-senescent activity from this protein. Therefore, we analyzed its expression on neurons or glial cells at different times of culture. As shown in Figure 2, in primary culture of cortical cells incubated 26 D*IV*, neurons but not yet glial cells expressed higher levels of $p21^{CIP1/WAF1}$. The number of glial cells with elevated expression of $p21^{CIP1/WAF1}$ increased until 40 D*IV*. This observation suggests that neurons acquire senescent features before glial cells. Interestingly, at 26 D*IV* $p21^{CIP1/WAF1}$ is slightly enriched at the nuclear periphery. This could be related to the recent finding that altered nuclear export is a common hallmark of aging [25]. We confirmed $p21^{CIP1/WAF1}$ expression is induced at transcriptional level in cortical cells at 26 D*IV* by qRT-PCR (Figure 2C).

Another hallmark of senescence is a persistent DNA damage response, commonly detected by the presence of γH2AX foci. As shown in Figure 3A, neuronal cells accumulated γH2AX foci at 26 D*IV*, accompanied by ruptures of DNA detected by Comet assay (Figure 3B). Even though we are not able to distinguish neurons from glial cells with this assay, it is conceivable that the nuclei with broken DNA come from neurons, since we observed that mainly neurons had γH2AX foci; these observations suggest that neurons accumulate DNA damage leading to a persistent DNA damage response. At both 26 and 40 D*IV*, only a small proportion of GFAP expressing cells had γH2AX foci. As expected, cortical neurons from old rat brains also contained more γH2AX foci (Figure 3C).

Finally, since during oncogene-induced senescence, replicative senescence and senescence induced by DNA damaging drugs occur nuclear morphology abnormalities associated with nuclear envelope proteins loss [26], and depletion of Lamin-B1 or Lamin-A/C is sufficient to induce senescent features [4], we wondered whether also senescent post-mitotic cells, such as neurons, would manifest nuclear morphology deformations. As shown in Figure 4, indeed both *in vitro* and *in vivo* senescent neurons had irregular nuclear morphology with folds of the nuclear envelope forming intra-nuclear Lamin-A/C structures that protrude into the nucleoplasm. Very few astrocytes showed abnormal distribution of Lamin-A/C at 26 D*IV*, strengthening the

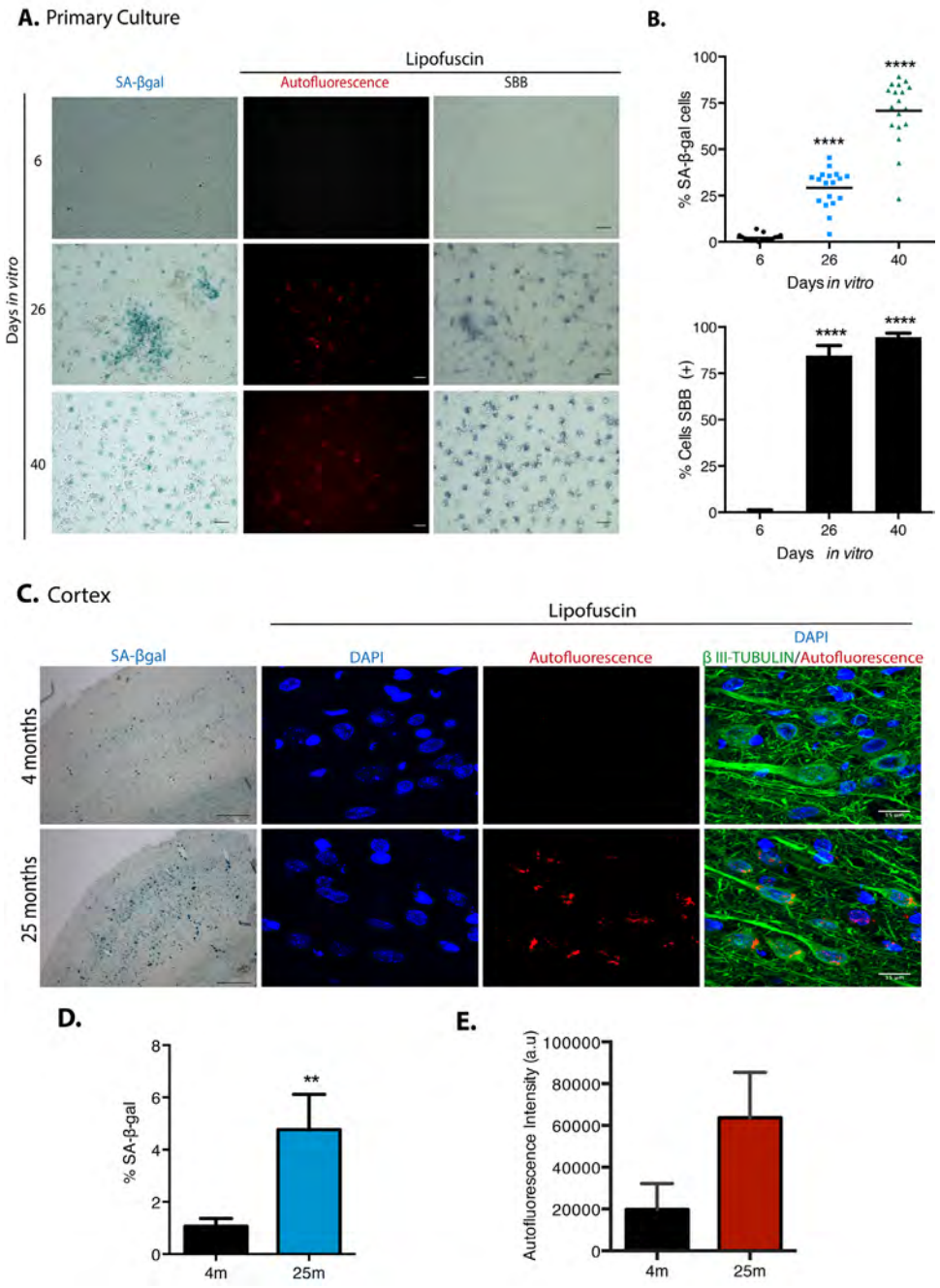

Figure 1. Cortical cells in long-term culture and in old rat brains had higher SA-β-gal activity and accumulated lipofuscin. (**A**) SA-β-gal activity or lipofuscin accumulation detected by autofluorescence or by Sudan Black B (SBB) staining were detected in primary rat cortical cells cultured for the indicated D*IV*. Notice that cortical cells have higher SA-β-gal activity and lipofuscin from 26 D*IV*. Images are representative of at least three independent experiments. Scales bar represent 100 μm. (**B**) Percentage of SA-β-gal or SBB positive cells in the cultures incubated at the indicated D*IV*. Quantification was made using NIS Elements software. The mean of three independent experiments, each done by quintupled replicas, is graphed. Bars in graphs represent SEM. Two-way RM ANOVA analysis, with Dunnett´s multiple comparison test. **** p< 0.0001 in comparison with 6 D*IV*. (**C**) Cortical neurons in old brains had higher SA-β-gal activity (scale bars represent 500 μm) and accumulated lipofuscin. Scale bar represents 15 μm. (**D**) The percentage of SA-β-gal positive area within each brain section is plot. The average of three brains per age is graphed; 15 sections from each brain were quantified. Bars in graphs represent SEM. Unpaired t Test, ** p< 0.01. (**E**) Quantification of autofluorescence intensity per section (arbitrary units). Bars in graphs represent SD. The average of three brains per age is graphed; 15 sections from each brain were quantified. Even though there was an evident increase in autofluorescence, no statistical significance was obtained.

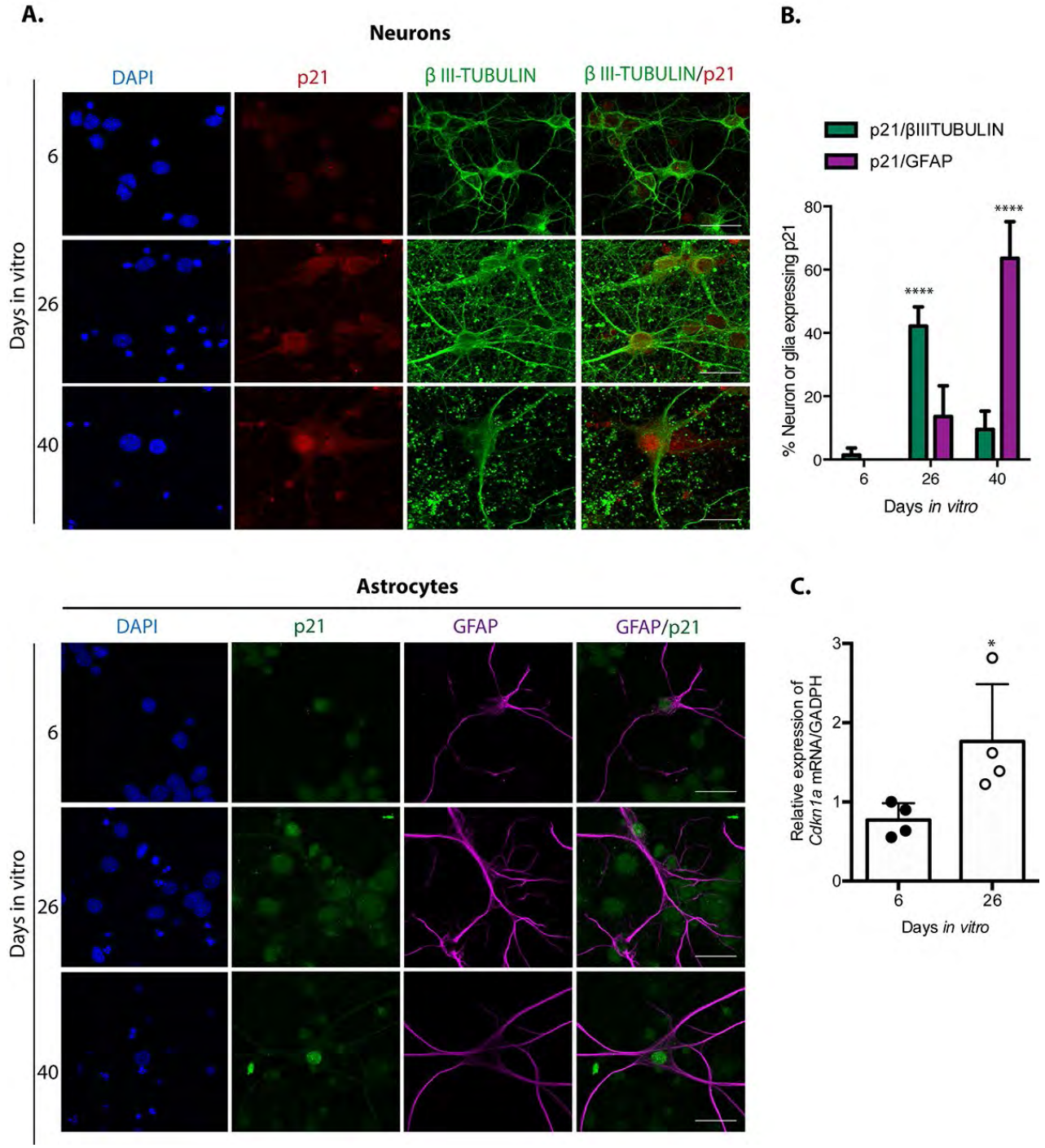

Figure 2. Neuronal cells in cortical long-term culture showed increased expression of p21$^{CIP1/WAF1}$. (**A**) Immunofluorescence to detect p21$^{CIP1/WAF1}$ (p21) in neurons (expressing βIII-TUBULIN) or astrocytes (expressing GFAP) in primary culture of cortical cells incubated during the indicated D*IV*. Notice that mostly neurons increased the abundance of p21$^{CIP1/WAF1}$ at 26 D*IV*, indicating that neurons acquired senescent features before glial cells. Scale bar represents 25 μm. Arrows indicate examples of cells with healthy nuclei counted (not all the healthy cells are indicated). (**B**) Percentage of neurons or glial cells expressing p21$^{CIP1/WAF1}$ over all cells. The mean of three independent experiments, each done by duplicate, is plotted. Bars represent standard deviation. Two-way RM ANOVA analysis, with Tukey´s multiple comparison test. **** p<0.0001. (**C**) qRT-PCR from total RNA purified from cortical primary cultures during the indicated days. The relative expression of *Cdkn1a* mRNA was normalized with *Gapdh* mRNA. Bars represent SD. * p=0.039 by unpaired t test two tailed. n=4.

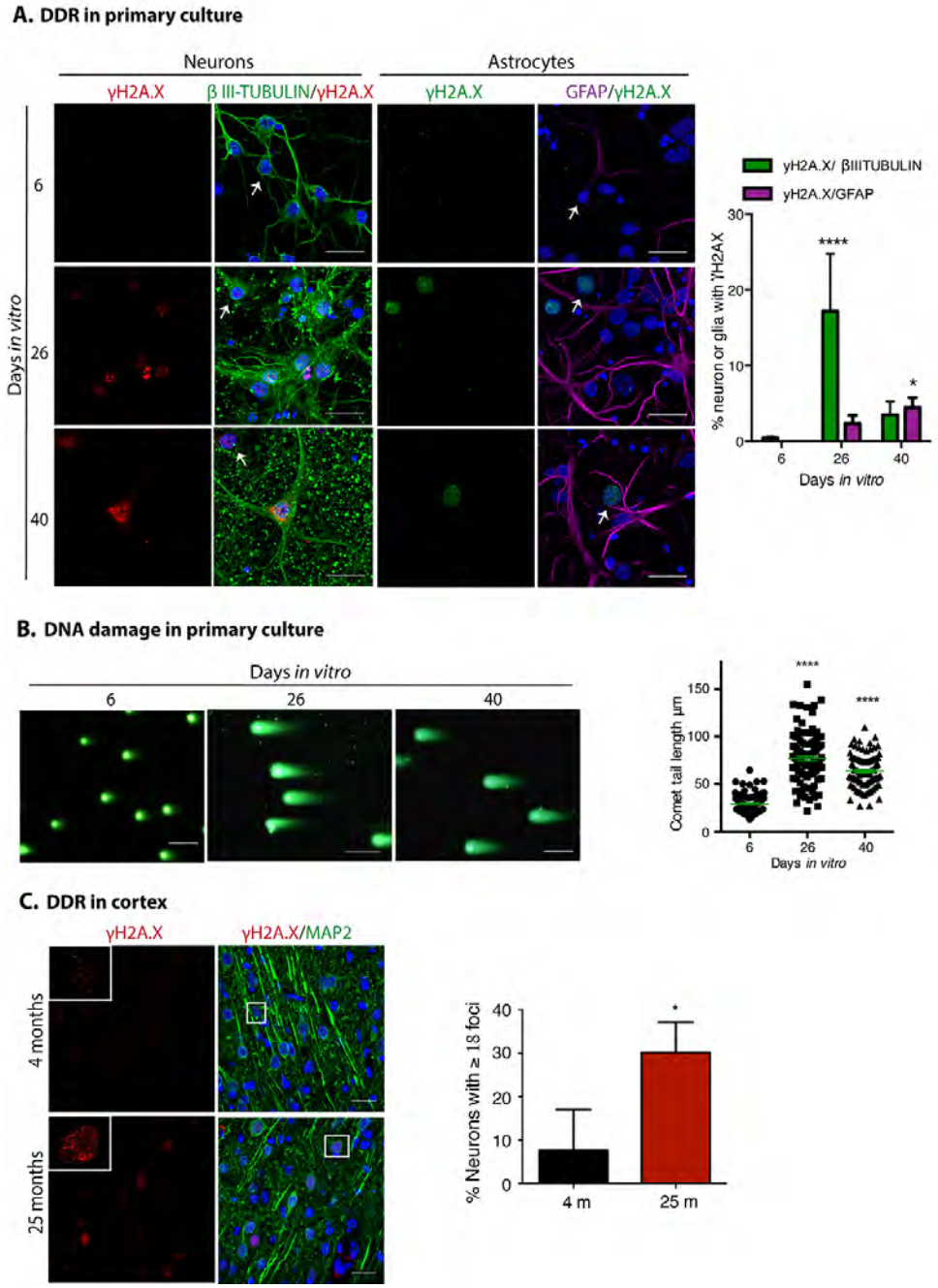

Figure 3. Neuronal cells in cortical long-term culture and in the cortex from old rat brains had a sustained DNA damage response (DDR). (**A**) Immunofluorescence to detect γH2AX foci in neurons (expressing βIII-TUBULIN) or astrocytes (expressing GFAP) in primary culture of cortical cells incubated during the indicated D*IV*. Notice that mostly neurons have γH2AX foci at 26 D*IV*. Scale bar represents 25 μm. Right, quantification of the percentage of neurons or glial cells with γH2AX foci over all cells. The mean of three independent experiments, each done by duplicate, is plotted. Bars represent SEM. Two-way RM ANOVA analysis, with Dunnett´s multiple comparison test. **** p< 0.0001 26 D*IV vs*. 6 D*IV*; * p<0.05 40 D*IV vs*. 6 D*IV*. Arrows indicate examples of cells with healthy nuclei counted (not all the healthy cells are indicated). (**B**) Comet assay to detect double strand breaks in genomic DNA from cells collected at the indicated days. Scale bars represent 100 μm. Right, the length of the tail of the comets, indicative of level of DNA damage, is plotted. 50 nuclei from each treatment, from two independent experiments, were analyzed by RM one-way ANOVA with Dennett's´ multiple comparison. **** p< 0.0001 between 26 D*IV* or 40 D*IV* in comparison with 6 D*IV*. (**C**) Immunofluorescence to detect γH2AX foci in cortical neurons (expressing MAP2) in rat brains from the indicated age. Nuclei were stained with DAPI. Scale bars represent 30 μm. Right, percentage of neurons with more than 18 foci per nucleus. More than 100 neurons were counted from 3 different brains of each age. Bars represent standard deviation. Unpaired t Test * p<0.01.

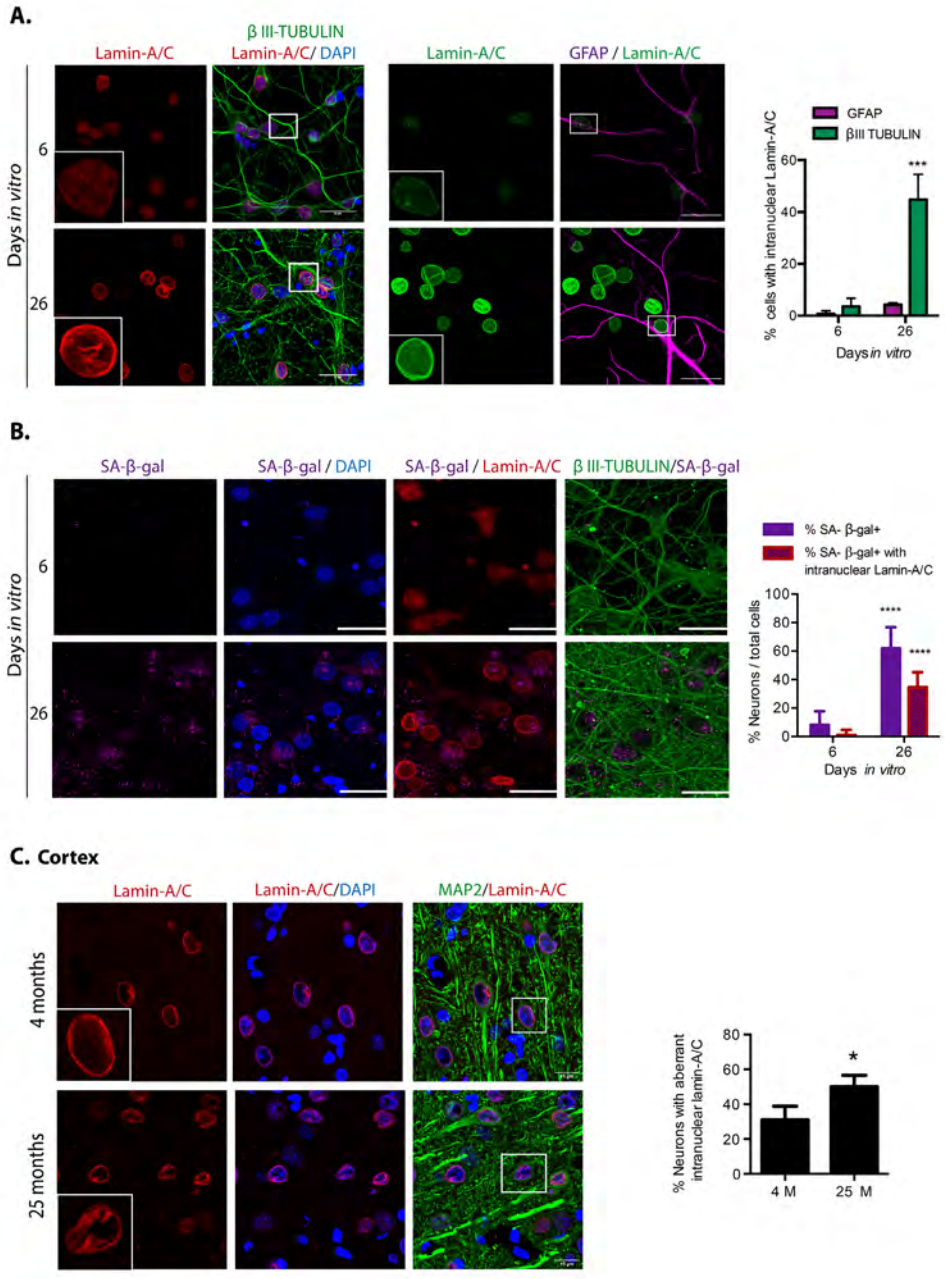

Figure 4. Cortical cells in long-term culture and in old rat brains had nuclear morphology abnormalities. (**A**) Immunofluorescence to detect Lamin-A/C in neurons (expressing βIII-TUBULIN) or astrocytes (expressing GFAP), in primary culture of cortical cells incubated during the indicated days *in vitro.* Squares indicate the magnified area shown in insets. Representative images of three independent experiments are shown. Scale bars represent 25 μm. Right, percentage of neurons or astrocytes with aberrant nuclear morphology over total cells. Bars represent SEM; two-way RM ANOVA analysis, *** p< 0.001 in comparison with 6 D*IV*. (**B**) Simultaneous detection of SA-β-gal activity (by confocal microscopy) and Lamina-A/C (by immunofluorescence) in neurons (expressing βIII-TUBULIN) in primary culture of cortical cells incubated during the indicated days *in vitro.* Representative images of three independent experiments are shown. Scale bars represent 25 μm. Right, percentage of neurons with visible SA-β-gal activity, and with both visible SA-β-gal activity and aberrant intranuclear Lamin-A/C over total cells. Five fields from three independent experiments were quantified. Bars represent SEM. Two-way RM ANOVA analysis, followed by Sidak´s multiple comparison test. **** p< 0.0001 in comparison with 6 D*IV*. C. Immunofluorescence to detect Lamin-A/C in cortical neurons in the internal pyramidal layer 5 from brain slices of the indicated age. Notice that also *in vivo,* neurons in old brains had nuclear deformations. Squares indicate the magnified area shown in insets. Scale bars represent 30 μm. Right, percentage of neurons in with aberrant nuclear morphology in cortical brain slices of the indicated age, as shown in (**C**). (n=3). Bars represent SD; unpaired t Test Student * p< 0.01.

notion that neurons become senescent before glial cells in this model. Since every senescent feature, alone, is not sufficient to confirm a senescent state, we simultaneously detected SA-β-gal activity and Lamin-A/C in neurons. As shown in Figure 4B, around half of the neurons with high SA-β-gal activity at 26 D*IV* also had an aberrant nuclear morphology, supporting the notion that neurons in long-term culture acquire senescent features. The observation that some neurons with high SA-β-gal show a normal nuclear morphology, is in agreement with previous observation that SA-β-gal activity alone is not a reliable marker of senescence [21]. We propose that nuclear deformations could be a more reliable marker for neuronal senescence. Since differentiated neurons express low levels of Lamin-B1 [27], we were unable to detect loss of Lamin-B1 in senescent neurons.

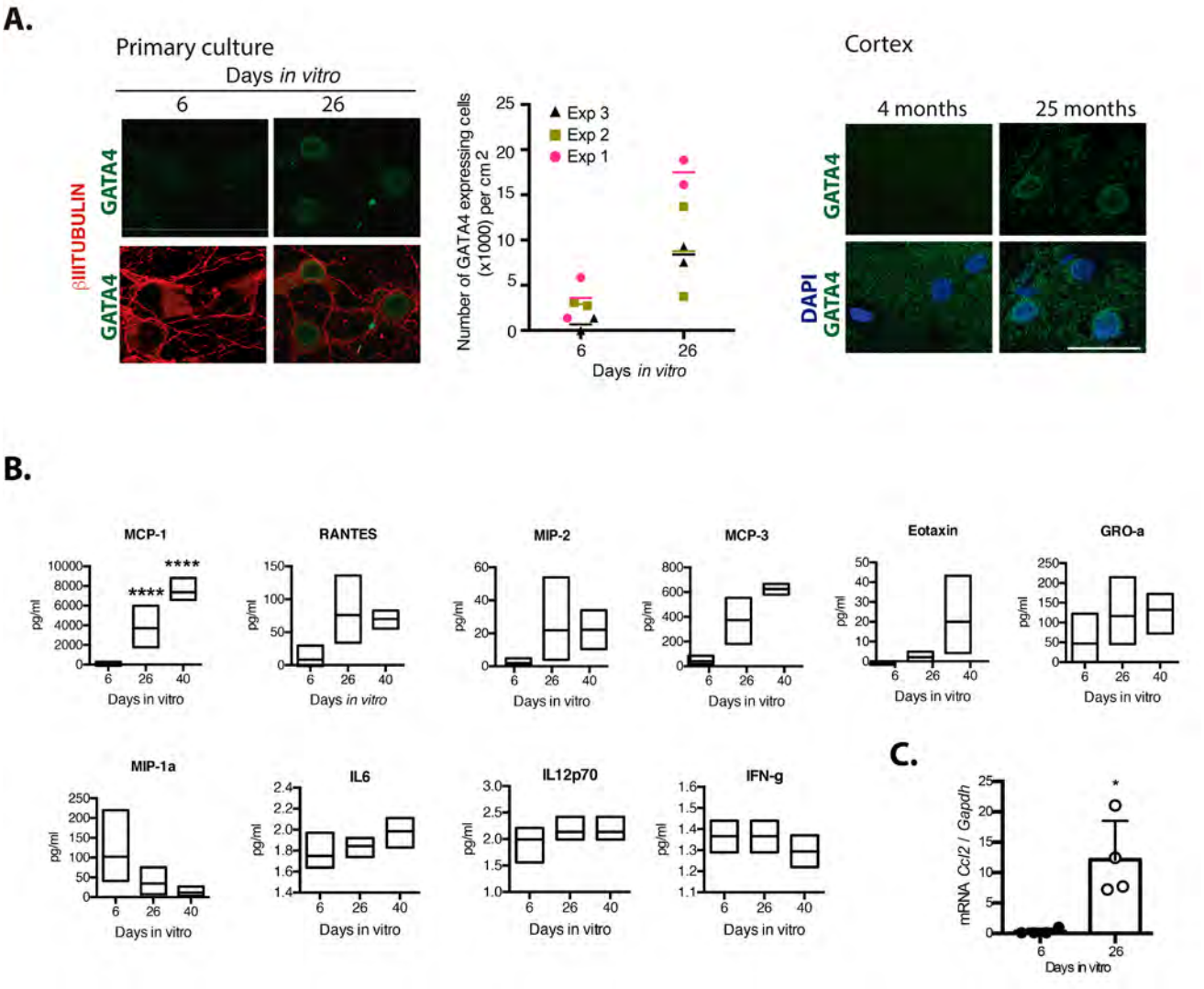

Figure 5. Senescent neurons increased the expression of GATA4 and cortical cells secreted MCP-1. (**A**) Immunofluorescence to detect GATA4 in neurons (expressing βIII-TUBULIN) in primary culture of cortical cells either incubated during the indicated days *in vitro* or in rat brains of the indicated age. Scale bars represent 25 μm. The number of cells with increased GATA4 abundance from three independent experiments, each performed in duplicate, is graphed. The mean of each experiment is represented by horizontal bars. (**B**) Quantification by multiplex immunoassay of the indicated cytokines, from conditioned media from cultures of the indicated days from three independent experiments. The maximum and minimum values are graphed. Bars indicate the mean of the three independent experiments. Data were analyzed by two-way ANOVA followed by Tukey´s multiple comparisons test analysis, only MCP-1 was significant. **** p<0.0001 relative to 6 D*IV*. (**C**) qRT-PCR from total RNA purified from cortical primary cultures during the indicated days. The relative expression of *Ccl2* mRNA was normalized with *Gapdh* mRNA. Bars represent SD. * p=0.0106 by unpaired t test two tailed. n=4.

Senescent cortical cells secrete molecules that induce premature paracrine senescence and glial proliferation, suggesting a neuronal SASP

We hypothesize that persistent senescent neurons, through the SASP, contribute to induce paracrine senescence and chronic inflammation in old brains. Therefore, we studied whether neurons would express GATA4, a transcription factor that promotes the expression of SASP factors [10]. As shown in Figure 5A, GATA4 accumulated in neuronal cells cultured for 26 D*IV*, as well in cortical neurons from old brains. To get an insight about the cytokines that senescent cortical cells could be secreting, we analyzed the presence of G-CSF, GM-CSF, IFNγ, IL-1α, IL-1β, IL-10, IL-12p70, IL-13, IL-17A, IL-2, IL-4, IL-5, IL-6, TNFα, EOTAXIN, GRO-α, IP-10, MCP-1, MCP-3, MIP-1α, MIP-2 and RANTES by a multiplex immunoassay. As shown in Figure 5B, MCP-1, RANTES, MIP-2, GRO-1, MCP-3 and EOTAXIN were more abundant in conditioned media from senescent cortical cultures, although only MCP-1 content showed a statistically significant difference at 26 and 40 D*IV* relative to 6 D*IV* cortical cultures; MIP-1a secretion was reduced in older cultures. To our surprise, IL6, a common SASP component, was barely detected and did not increase in conditioned media from senescent cells. Also, IL-12p70 and IFNγ secretion did not change along the time in culture and were secreted in a very small amount, at the threshold limit of detection. G-CSF, GM-CSF, IL-1α, IL-1β, IL-10, IL-13, IL-17A, IL-2, IL-4, IL-5, TNFα, GRO-α, IP-10 and MIP-1α were not detected at any time point. We further confirmed the induction of expression of *Ccl2* (gen coding for MCP-1) by qRT-PCR (Figre 5C).

Since MCP-1 has been shown to induce paracrine senescence [23], and GATA 4 is a mediator regulating MCP-1 expression during senescence induced by Lamin-A defects [28], we reasoned that senescent cortical cells could indeed acquire a functional SASP. To test this hypothesis, we analyzed whether conditioned media from senescent cortical cells could induce premature paracrine senescence (a schematic experimental design is shown in Figure 6A). To obtain conditioned media with accumulated secreted factors, the media was left for intervals of about a week in between fresh media changes over the cells, and it was collected at 6, 26 or 40 days of culture. Conditioned media was then added to young (1 D*IV*) prenatal cortical cells and after 6 D*IV* of treatment all the senescent markers described above were evaluated. Interestingly, conditioned media from cortical cells cultured for 26 D*IV* or 40 D*IV* induced abundant proliferation of glial cells (Figure 6B), suggesting that senescent cortical cells, potentially neurons, could indeed affect tissue organization. Nevertheless, we did not observe significant expression of senescent markers on young neurons (not shown). We reasoned that young neurons could be more resistant to paracrine senescence than mitotic cells; therefore, we tested whether the conditioned media from cortical cells cultured for 26 D*IV*, time at which most of the senescent cells are neurons, would induce paracrine senescence in mouse embryonic fibroblast (MEFs). Indeed, conditioned media from cortical cells cultured for 26 D*IV* induced key senescent features in MEFs, such as increased SA-β-gal activity; inhibition of proliferation (detected by Ki67 expression); DNA damage response identified by γH2AX foci; and increased expression of IL6, although this latter was not statistical different (Figure 6C). In summary, prenatal cortical cells exposed for 6 days to conditioned media from cortical cells cultured for 26 D*IV* or 40 D*IV* did not show senescent features, whereas MEFs did.

Taken together, our results confirm that neurons acquire senescent features potentially including the SASP, interestingly before glial cells. This observation suggests that senescent neurons could affect the function of surrounding cells, such as astrocytes. Intriguingly, young neurons were unresponsive to the SASP produced by senescent cortical cells, since they did not show senescent markers when exposed to the conditioned media from cortical cultures of 26 or 40 *DIV* (not shown).

Dysfunctional autophagy contributes to neuronal senescence

Abundant reports indicate that dysfunctional autophagy accompanies aging, and in the brain it causes neurodegeneration [29]. Accordingly, induction of autophagy ameliorates age-related cognition deficits [30]. Therefore, we evaluated whether dysfunctional autophagy would contribute to neuronal senescence establishment, with a similar mechanism as described for senescence transition of mitotic cells. First, we analyzed in senescent neurons whether autophagic flux is reduced, reflected by accumulation of autophagosomes and proteins associated to them like LC3 and p62/SQSTM1. As shown in Figure 7A, cortical cells at 26 D*IV*, a time point when neurons showed senescent features, had more autophagosomes detected with the specific dye CytoID® and by immunofluorescent detection of LC3. We confirmed the abundance of autophagosomes in senescent neurons by electron microscopy, labeling them with immunogold localization of LC3. As the autophagic receptor p62/SQSTM1 is degraded together with the cargo, it accumulates when the autophagic flux is interrupted. We analyzed the abundance of p62/SQSTM1 by

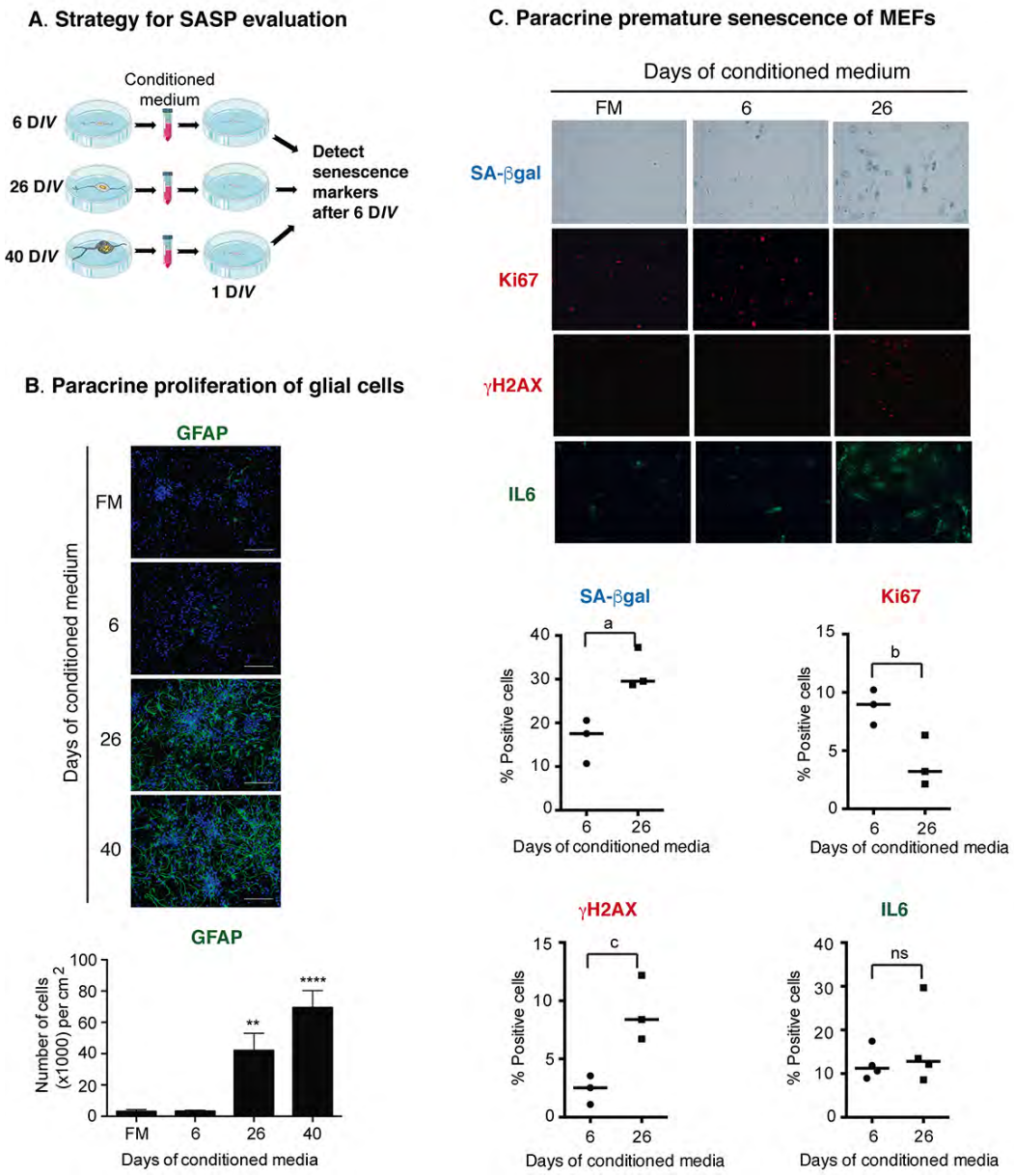

Figure 6. Senescent cortical cells develop a functional SASP. (**A**) Experimental design to evaluate the presence of secreted molecules with SASP activity from senescent cortical cells. Conditioned media was collected from cortical cells that had been incubated from 1-6 (6), 19-26 (26) or 32-40 (40) D*IV*. Either primary prenatal cortical cells or MEFs were cultured for 24 hr (1 D*IV)* before adding conditioned media; senescence markers were evaluated 6 days later. (**B**) Conditioned media from senescent cortical cells induced paracrine proliferation of glial cells in primary culture of prenatal cortical cells. Representative immunofluorescences to detect GFAP in cortical cells are shown. Cells were incubated with conditioned media collected from cortical cells that had been incubated during the indicated D*IV*. FM stands for fresh medium. Notice that conditioned media from 26 D*IV* and 40 D*IV* induced high proliferation of glial cells. Scale bars represent 500 μm. The bottom graph is a quantification of the number of GFAP expressing cells in three independent experiments, each done in duplicate. Data were analyzed by one-way ANOVA, with Dunnett´s multiple comparison test. ** p<0.01; ****p<0.0001 compared to FM. (**C**) Conditioned media from senescent cortical cells induced paracrine premature senescence in MEFs. MEFs were incubated with conditioned media collected from cortical cells that had been incubated during the indicated D*IV*. FM stands for fresh medium. Notice that senescent markers were higher in cells incubated with conditioned media from cortical cells cultured for 26 days. The bottom graphs are quantifications of the percentage of cells with blue or fluorescent signals. The signal (either blue or fluorescent) from cells incubated with 6 D*IV* conditioned media plus one standard deviation was deducted from the signal obtained from the cells treated with 26 D*IV* conditioned media. Three independent experiments, each performed in duplicate were quantified. Data were analyzed by unpaired T test. a, p=0.0175; b, p=.0.0327; c, p=0.0191.

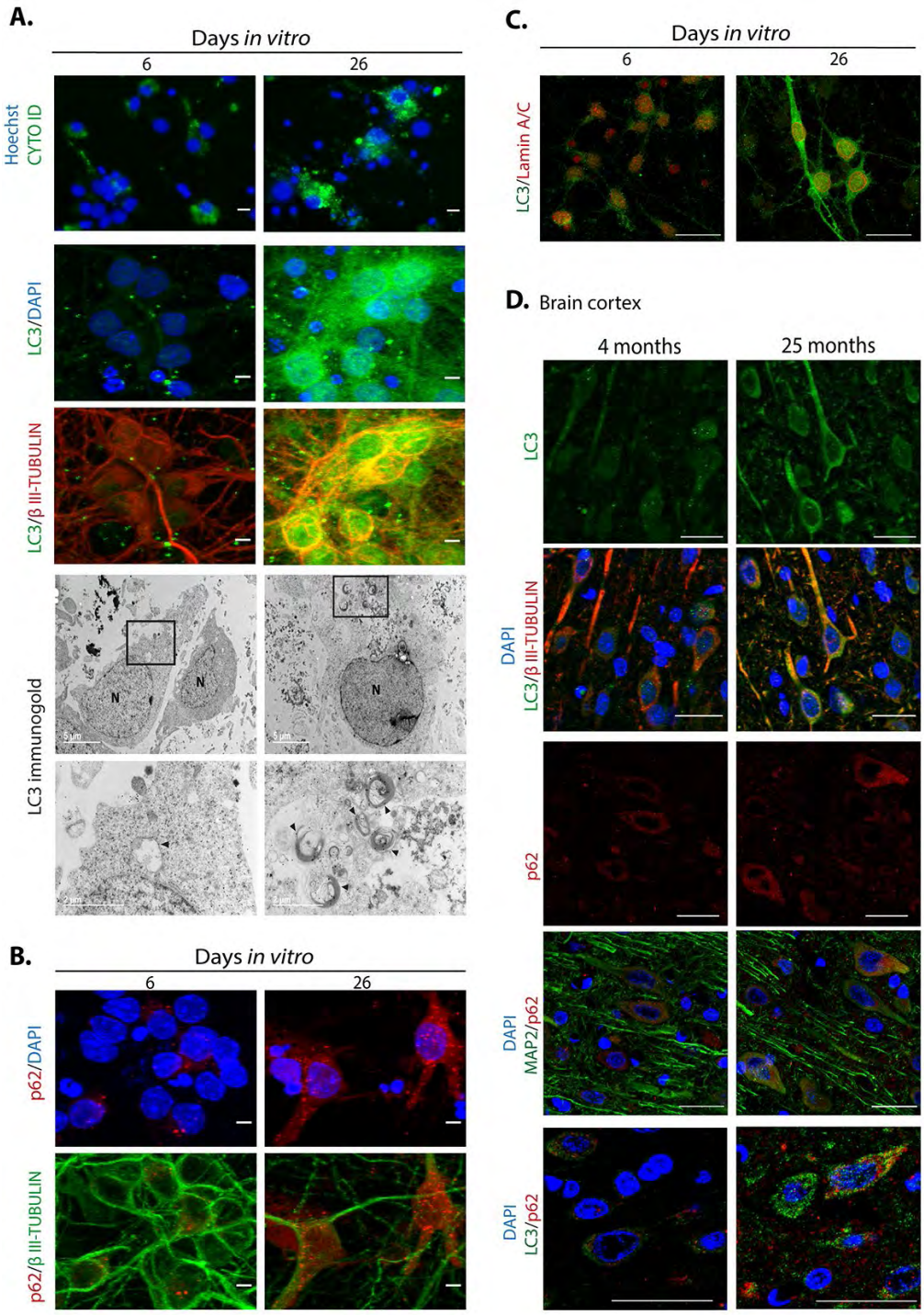

Figure 7. Autophagosomes accumulate during neuronal senescence. (**A**) Top row, autophagosomes were stained with CytoID® and nuclei with Hoechst in primary culture of cortical cells incubated during the indicated D*IV*; scale bars represent 15 μm. Middle rows, immunofluorescence to detect LC3 in neurons (expressing βIII-TUBULIN) of primary cortical cells cultivated during the indicated D*IV*. Scale bars represent 5 μm. Bottom rows, electron micrographs showing accumulation of autophagosomes in 26 D*IV* cortical cells, detected by immunogold localization of LC3 (arrow heads). Squares indicate the amplified area below. (**B**) Immunofluorescence to detect p62/SQSTM1 in cortical cells cultured during the indicated D*IV*. Nuclei were stained with DAPI. Notice that p62/SQSTM1 in neurons (expressing βIII-TUBULIN) accumulated at 26 D*IV*. Scale bars represent 5 μm. (**C**) Immunofluorescence to simultaneously detect LC3 and Lamin-A/C to observe intranuclear folds as a senescence marker, in cortical cells cultured during the indicated D*IV*. Scale bars represent 25 μm. (**D**) LC3 and p62/SQSTM1 also accumulate in cortical neurons (expressing βIII-TUBULIN or MAP2) form old rat brains. Scale bars represent 30 μm.

immunofluorescence (Figure 7B) and Western blot (Figure 8B), and we found that it was also accumulated in neurons at 26 D*IV*. To determine whether indeed senescent cells had more autophagosomes, we simultaneously detected LC3 and Lamin-A/C. As shown in Figure 7C, the same cells that had intranuclear folds of the nuclear envelop with Lamin-A/C at 26 D*IV* had LC3 accumulation (Figure 7C). Importantly, both LC3 and p62/SQSTM1 also accumulated in cortical neurons of old rat brains (Figure 7D). The accumulation of both autophagosomes and p62/SQSTM1 suggests dysfunctional lysosomes or impairment of the fusion of autophagosomes with lysosomes. We stained lysosomes with Lysotracker® and observed an accumulation of enlarged lysosomes in senescent cortical cells (Figure 8A), as it has been described in another model of neuronal senescence [21]. We confirmed altered lysosomal morphology by localizing the lysosomal protein LAMP1; we noticed that abundant p62/SQSTM1 puncta did not co-localize with LAMP1 at 26 D*IV* (Figure 8A), suggesting limited autolysosome maturation (*i.e.* reduced autophagosome-lysosome fusion), although further studies are needed to corroborate it.

p62/SQSTM1 accumulates when autophagy promotes the SASP through a compartmentalized structure coined TASCC (Tor-autophagy spatial coupling compartment),

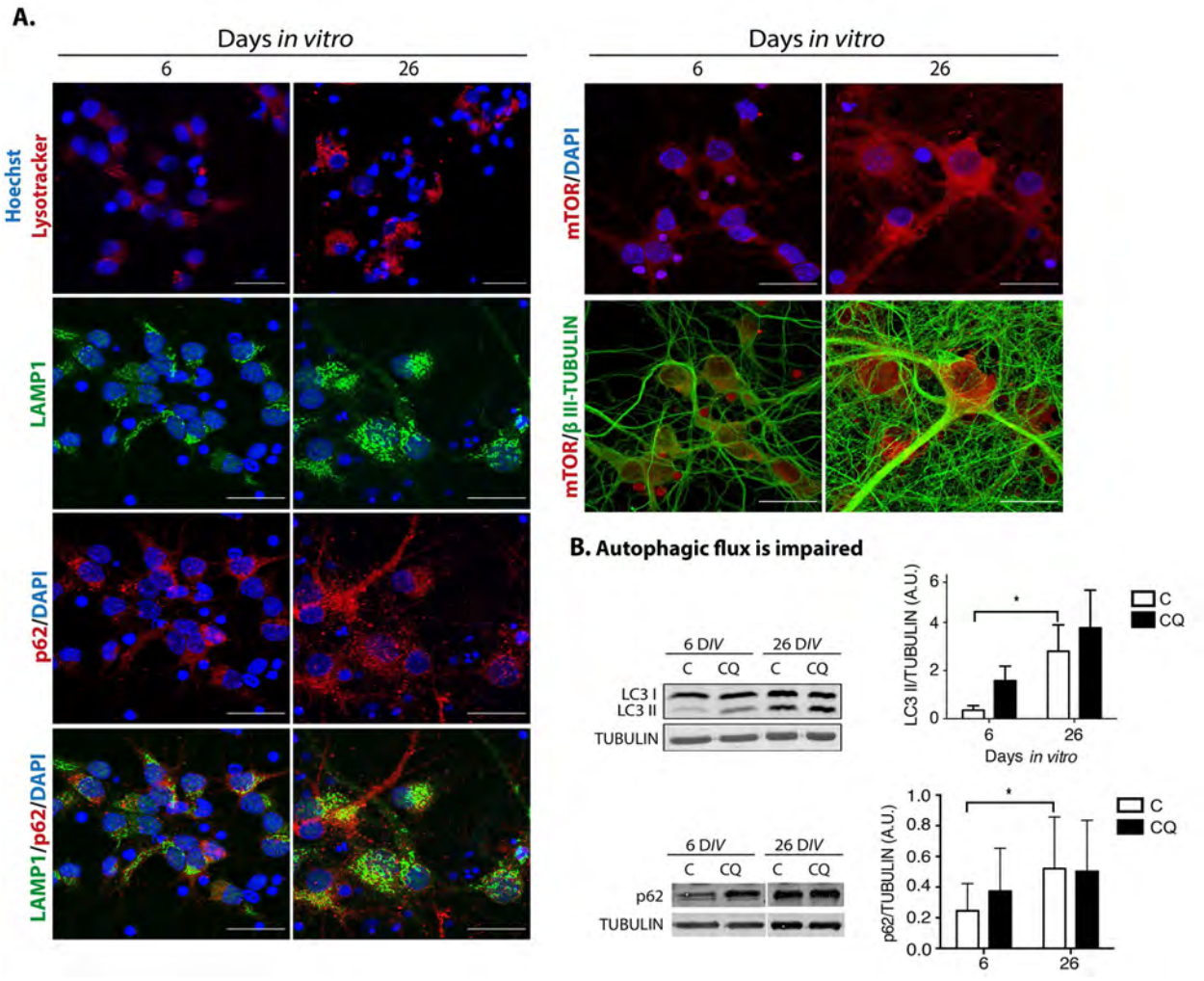

Figure 8. Dysfunctional autophagy contributes to neuronal senescence. (**A**) There was an accumulation of enlarged lysosomes and undigested p62/SQSTM1 in senescent neurons. Top row, lysosomes were detected with Lysotracker® and nuclei with Hoechst in primary culture of cortical cells incubated during the indicated D*IV*. Bottom rows, immunofluorescence to detect the indicated proteins in cortical cells cultured during 6 or 26 days. Nuclei were stained with DAPI. Notice that even though lysosomes and p62/SQSTM1 accumulated at 26 D*IV*, their intracellular distribution did not overlap. mTOR distribution did not change. Scale bars represent 25 μm. (**B**) The autophagic flux was impaired in senescent neurons. Western blot of total protein extracts from cortical cells cultured at 6 or 26 days, without (C) or with (CQ) 20 μM Chloroquine for 4 hr. Graphs represent the mean of densitometry analysis of four independent experiments. Bars represent SEM. Two-way RM ANOVA followed by Sidak´s multiple comparison test. *p<0.001.

which is where amino acids released by autolysosomes locally activate mTORC1, facilitating the synthesis of SASP proteins. The TASCC can be distinguished by the polarized co-localization of p62/SQSTM1, mTOR and LAMP2 [11]. Therefore, we analyzed whether during neuronal senescence these proteins were also distributed in a similar polarized intracellular localization (we observed LAMP1 instead of LAMP2). As can be seen in Figure 8A, neither the distribution of p62/SQSTM1 nor mTOR indicated a compartmentalized distribution. Even though lysosomes seemed to be mainly located on one side of the cells, it might reflect only the particular morphology of this type of cells, which have the cytoplasm mostly on one side of the cell. Therefore, we found no evidence of a TASCC during neuronal senescence, indicating that autophagy dysfunction, rather than function, accompanies neuronal senescence. To verify that the observed accumulation of autophagosomes was due to an impaired autophagic flux, instead of an enhanced activation of autophagy, cortical cells were incubated in the presence of Chloroquine, an agent that neutralizes lysosomes pH and impairs autophagosomes fusion with lysosomes. As shown in Figure 8B, the presence of Chloroquine did not increase the amount of LC3-II or p62/SQSTM1 accumulation at 26 D*IV*, indicating that the autophagic flux was already diminished in senescent neurons.

If a limited autophagic flux contributes to neuronal senescence, we would expect more senescent cells when autophagy is inhibited. Since basal autophagy is essential for survival, inhibition of autophagy by genetic means along the time of culture kills the neurons. Therefore, we inhibited autophagy only at distinct time windows (7 days long each) by adding Spautin-1, a molecule that indirectly induces BECN1 and PtdIns-3-kinase type 3/VPS34 (PI3KC3) degradation [31]. As shown in Figure 9B, we found that the number of cells with SA-β-gal activity increased when autophagy was inhibited during the second or third weeks of culture. When Spautin-1 was added at the fourth week of culture or later, it had no effect increasing the number of cells with SA-β-gal activity, suggesting that autophagy was already dysfunctional at this time. On the other hand, stimulating autophagy with trehalose, a disaccharide that mimics caloric restriction by preventing glucose uptake [32], reduced the number of cortical cells with SA-β-gal activity regardless of the time window of exposure, although a more noticeable protection was observed during the second and third weeks of culture. As a control to verify the function of Spautin-1 in neurons, we verified the reduction in the number of autophagosomes in cortical cells at 26 D*IV*, when we had previously observed abundant autophagosomes. We also tested that trehalose stimulates autophagy in neurons by detecting more autophagosomes in cortical cells at 6 D*IV*, which time we had observed neurons have a reduced amount of autophagosomes (Supplementary Figure 2S). To confirm that trehalose induction of autophagy indeed reduced the senescent phenotype and not just SA-β-gal activity, we repeated the experiment now immunodetecting Lamin-A/C to evaluate whether the intranuclear folds were reduced. As shown in Figure 9C, adding trehalose during one week windows statistical significantly reduced the degree of intranuclear Lamin-A/C folds. These results suggest that autophagy induction prevents senescence conversion and potentially reverts the senescent phenotype, although further experiments will be needed to address the latter.

DISCUSSION

Accumulating evidence shows the presence of senescent cells in brains from both physiologically aged subjects and with neurodegeneration [14]. In this work we have characterized an *in vitro* model useful to study the molecular basis for neuronal senescence transition and maintenance, as well as SASP components. We demonstrate that neurons, in spite of being post-mitotic cells, acquire multiple senescent features and notably they do so before glial cells. Every senescent marker we looked at in primary culture of senescent neurons was confirmed in old rat brains (25 months old), validating this *in vitro* neuronal senescence model. We demonstrated, to our knowledge for the first time, that senescent cortical cells develop a functional SASP, secreting components able to induced paracrine senescence in MEFs and glial proliferation. Since most of the senescent cells at 26 D*IV* are neurons, we suggest the existence of a neuronal SASP, although it is still possible that the few senescent astrocytes present in the culture secrete a very potent SASP. Nevertheless, a neuronal SASP is supported by other observations, such as the induction of expression of pro-inflammatory cytokines like TNF-α and CCL2 [33]. Interestingly, dopaminergic neurons with senescent phenotype due to lack of expression of SATB1, a DNA binding protein reduced in the vulnerable region of Parkinson´s Disease patients, express several SASP components, including MCP-1 [34], the cytokine we found significantly secreted by senescent cortical cells. MCP-1 is also secreted by senescent human mesenchymal stem cells and induces paracrine senescence; according to our findings, MCP-1 expression is mediated by GATA4 [28], a transcription factor we found increased in senescent cortical neurons. Further experiments are necessary to demonstrate that indeed MCP-1 secreted by senescent cortical neurons is the molecule responsible for the induction of paracrine senescence in MEFs. To our surprise, we did no detect secretions of IL6, as it is a very common SASP component and has

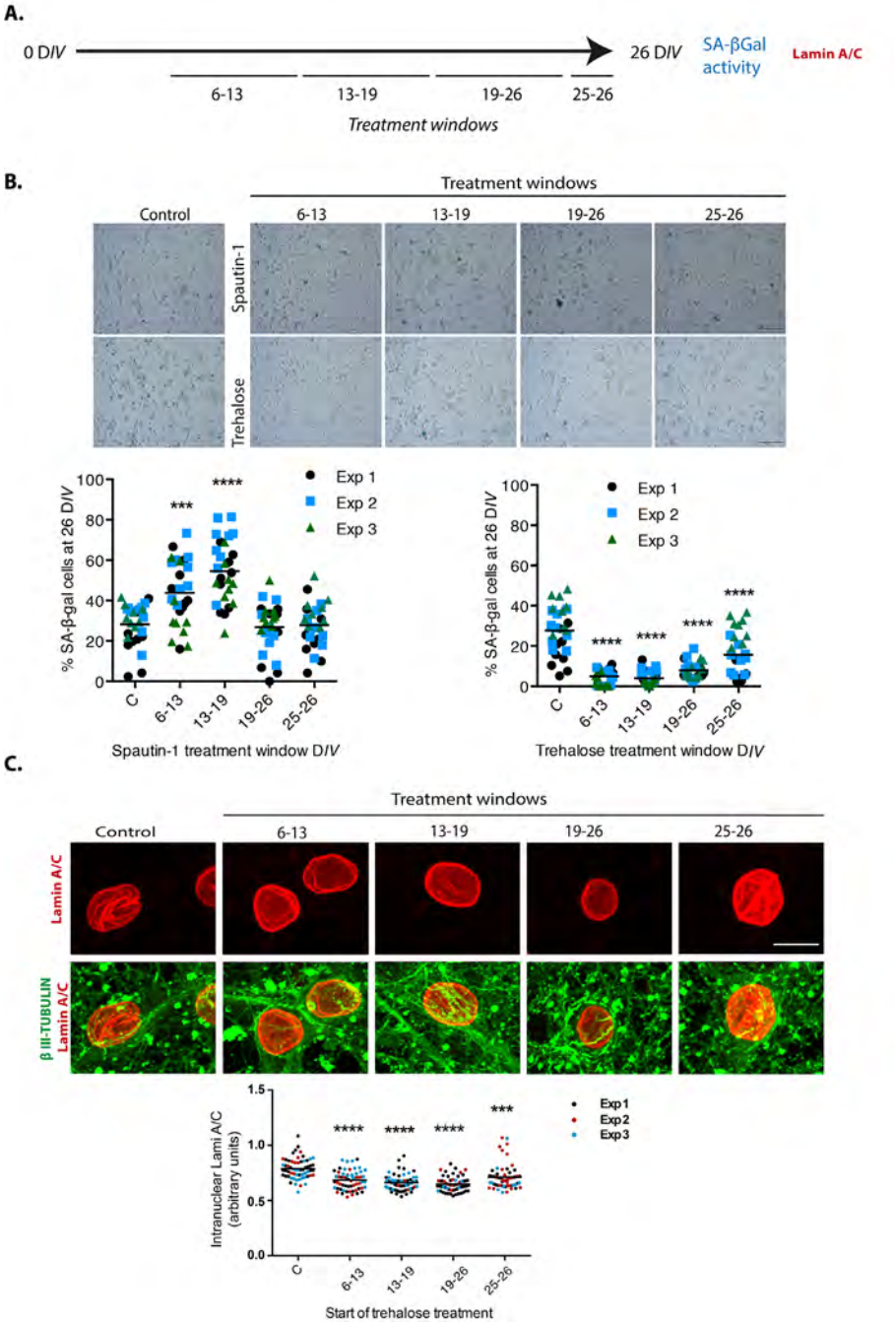

Figure 9. Autophagy modulation alters cortical cells senescence. (**A**) Experimental design. (**B**) Early inhibition of autophagy with Spautin1 increased the number of cells with SA-β-gal activity, while early induction of autophagy by adding trehalose reduced them. Spautin1 or trehalose were added during periods of several days, at the indicated time intervals in days of culture (D*IV*); after 26 D*IV* all cultures (including control with no treatment) were fixed to quantify the percentage of cells showing high SA-β-gal activity. Scale bars represent 500 μm. The bars in graphs represent the mean of each independent experiment, each done by triplicates. Three fields from each replica were scored (9 fields per experiment), each dot represent the percentage of SA-β-gal positive cells per field. Data were analyzed by two-way RM ANOVA, followed by Dunnett´s multiple comparison test. ***p<0.001 Spautin1 added during 6-13 D*IV* in comparison with control; **** p< 0.0001 Spautin1 added during 13-19 D*IV* in comparison with control, and Trehalose treatments in comparison with control. (**C**) Autophagy induction with trehalose reduced the abundance of intranuclear fold with Lamin-A/C. Trehalose were added during periods of several days, at the indicated time intervals in days of culture (D*IV*); after 26 D*IV* all cultures (including control with no treatment) were fixed to detect Lamin-A/C by immunofluorescence. Scale bar represents 5 μm. Representative images of three independent experiments are shown. At least 60 cells per treatment were quantified as described in Methods. Bars in the bottom graph represents mean. Data were analyzed by two-way RM ANOVA, followed by Dunnett´s multiple comparison test. ***p<0.001; **** p< 0.0001 with respect to control.

been found to be secreted in senescent neurons by others [22]. It is worth to note that the paracrine senescence signaling components seem to be conserved between rat and mouse, as the rat neuronal SASP was able to induce premature paracrine senescence in mouse fibroblasts (MEFs).

The finding that conditioned media from senescent cortical cells induced glial cell proliferation, suggests that persistent neuronal senescent cells could alter tissue organization. As opposed to replicative senescence, which is caused by critically short telomeres, premature senescence induced by oncogene activation initiates with hyper-proliferation, followed by a "transition phase" that signals to induce the senescent phenotype [35]. Further experiments are in progress to evaluate whether the increased proliferation of astrocytes we observed reflects a mitotic phase preceding senescence in response to the cortical SASP. Also, the finding that young neurons are resistant to undergo premature paracrine senescence in response to the SASP produced by senescent cortical cells deserves further investigation. It will be interesting to understand the molecular differences that render MEFs susceptible and prenatal cortical neurons resistant to paracrine senescence in response to the cortical SASP. Although we ought to mention that we observed in one out of six experiments an increase of young neurons with high SA-β–gal activity in response to conditioned media from senescent neurons, therefore, it is yet possible that senescent cortical cell secretes molecules able to induce neuronal paracrine senescence, but which are rather labile. We propose that persistent senescent cells in the brain would secrete molecules that induce chronic inflammation and propagate further paracrine senescence to nearby healthy cells within the brain, like astrocytes, microglia or endothelial cells, thereby spreading the senescent phenotype and thus contributing to brain aging and exacerbating neurodegeneration. In fact, chronic and low-grade inflammation (inflammaging) have been associated with neurodegeneration in aging [36, 37] and cellular senescence markers have been observed in brain tissues from Alzheimer's disease patients, such as $p16^{INK4A}$ expression, increased p38MAPK activity, and IL6 and TGFβ mRNA expression [38-41]. Actually, brain overexpression of IL6 in mice induces neurodegeneration [42]. Promising, two recent works demonstrate that eliminating senescent cells in the brain ameliorate Tau-dependent neuropathology in mice transgenic models. Bussian TJ, *et al.* did not find neurons with senescent features (looking for SA-β-gal activity and the mRNA expression of *p16*, *p19*, *p21*, *pai1* and *Il6* in an enriched population of cells expressing Cd56), and propose that senescent microglia and astrocytes induce Tau-containing neurofibrillary tangles (NFT) in neurons by an unknown mechanism [43]. Interestingly, Musi N *et al.* analyzed laser-captured microdissected cortical neurons from human brains with Alzheimer disease and compared their transcriptome signature with adjacent histopathologically normal neurons. NFT-containing neurons had a senescent gene expression profile. The same was observed in NFT-containing neurons in a Tau transgenic mouse line [44]. Therefore, it seems that all cell types in the brain are able to become senescent, but the timing of geroconversion could vary in different contexts. Since in both works senolytics ameliorated Tau-dependent neuropathology, to discover which cell type becomes senescent and how similar are senescent cells from different cell types, will be useful to design targeted therapies.

Considering that it has been widely documented that during aging autophagy becomes dysfunctional [45], that most of the interventions that improve health span and/or lifespan stimulate autophagy [46, 47], and our finding that Spautin-1 treatment increased the number of senescent cortical cells, we propose that dysfunctional autophagy during aging also contributes to cellular senescence in the brain, including neurons, which in turn contributes to synaptic dysfunction. It is fundamental, therefore, to understand the mechanisms of autophagy dysfunction with ageing in the brain. Perhaps the tubular morphology of lysosomes we observed in senescent cortical neurons interferes with lysosomes fusion with autophagosomes. Therefore, treatments that promote autolysosome maturation or prevent lysosomal dysfunction could solve or prevent the onset of neuronal senescence. Interestingly, our observation that trehalose reduced the number of senescent cortical cells suggests that the neuronal senescent phenotype is reversible. Supporting this notion, addition of resveratrol, an autophagy-inducer compound, also decreases senescent hallmarks of long-term neuroglial cocultures [22]. Further experiments are necessary to test the possible reversion of the neuronal senescent phenotype.

Having a molecular understanding of neuronal senescence, new targets for pharmacological intervention could be proposed, with potential impact to prevent or reduce both physiological brain aging and neurodegeneration.

MATERIALS AND METHODS

Animals

Wistar rats of the indicated age in each experiment were obtained from the animal house of the Institute of Cell Physiology at the National University of Mexico (UNAM) and were housed at 22 ^{0}C in 12h light/12h

dark cycle. All procedures were approved by the Internal Committee of Care and Use of Laboratory Animals of the Institute (IFC-SCO51-18). Rats had *ad libitum* access to water and food.

Cell Culture

Cortical primary cultures

Cortical primary cultures were prepared as described before [48], from Wistar rat embryos of 17 days of gestation. Cerebral cortices were isolated and dissociated by 1:1400 Trypsin-EDTA (15400054, INVITROGEN/GIBCO, Grand Island, NY, USA) digestion and trituration with a Pasteur pipette. Cells were suspended in Neurobasal medium (21103049, INVITROGEN/GIBCO, Grand Island, NY, USA) supplemented with 2% B27 (17504044, INVITROGEN/GIBCO, Grand Island, NY, USA), 200 mM GlutaMAX™ Supplement (35050061, GIBCO Life Technologies, Grand Island, NY, USA) and 0.02 mg/ml Gentamicin (15710064, INVITROGEN/GIBCO, Grand Island, NY, USA). Cells were plated at a density of 1.05 x 10^5/cm^2 in 12-well plates precoated with Poly-L-Lysine (P1524, SIGMA-ALDRICH St. Louis, MO, USA) (0.01 mg/ml). Cells were cultured up to 40 days *in vitro* (40 DIV) at 37ºC in a humidified, 5% CO_2 atmosphere. Half the medium was changed every 6 days.

Cell viability

Cell viability was estimated by staining with LIVE/DEAD viability/cytotoxicity kit (INVITROGEN/GIBCO, Grand Island, NY, USA). Alive cells were stained with Calcein, while dead cells were stained with Ethidium homodimer-1, following manufacturer´s instructions. For every experiment, only cells with healthy nuclear morphology (non apoptotic) were quantified.

MEFs culture

Mouse embryonic fibroblasts were isolated from CD1 mouse embryos at E13.5 following the standard protocol [49]. MEFs were seeded at a density of 2.6x10^3 cells/cm^2 with Dulbecco´s Modified Eagle Medium + GlutaMAX™, 10% FBS and Penicillin/Streptomycin 100 U/ml. Each experiment was performed with MEFs at cell passage 4 to avoid replicative senescence. For conditioned media experiments, one day after seeding, cells were cultured with 25% OptiMEM supplemented with GlutaMAX and 75% of conditioned media. Media and supplements were from GIBCO® Life Technologies™, Grand Island, NY, USA.

SA–β-galactosidase staining

The β-galactosidase activity was analyzed following the protocols described previously [50, 51]. Cells were fixed with 2% formaldehyde + 0.2% glutaraldehyde for 5 min, washed with PBS and stained with the staining solution containing: 20 mg/ml of X-gal (IB02260, IBI SCIENTIFIC, Peosta, IA, USA) in dimethylformamide, 0.2 M citric acid/sodium phosphate buffer pH=6, 100 mM potassium ferrocyanide, 5 M sodium chloride and 1 M magnesium chloride. Cells were incubated for 16 h at 37 °C. For colorimetric analysis, samples were observed in an inverted Nikon ECLIPSE Ti-U microscope, the number of positive cells was counted of at least 500 cells. For SA–β-galactosidase staining and immunofluorescence in the same samples, cells were stained for SA-β-gal as described above and then immunostained. Confocal detection of X-gal was performed as previously described [52].

Lipofuscin accumulation

Autofluorescence Detection

Lipofuscin auto-fluorescence was evidenced by excitation at 450-490 nm of unstained cortical cells using an inverted Nikon ECLIPSE Ti-U microscope.

Sudan Black B (SBB) staining

SBB staining was performed as described [24]. 0.7 g of SBB (199664, SIGMA-ALDRICH, St. Louis, MO, USA) were dissolved in 70% ethanol, covered with Parafilm® and thoroughly stirred overnight at room temperature. Afterwards the solution was filtered (paper filter Whatman™ 1001-110). Cells seeded on coverslips were fixed in 4% (wt/vol) formaldehyde/PBS for 30 min at room temperature and then washed three times at room temperature with PBS. Coverslips with fixed cells were incubated for 2 min in 70% ethanol. A drop of freshly prepared SBB was dropped on a clean slide. The coverslip with the cells was held facing down on the drop of SBB on the slide and was incubated for 10 seconds. The coverslip was carefully lifted and the SBB on the edges of the coverslip was wiped off manually from the back and along the edges of the coverslip with the help of an absorbent paper. The cells were then embedded into 50% ethanol for 1 min, transferred and washed with distilled water. The staining was observed under an inverted Nikon ECLIPSE Ti-U microscope and SBB staining was considered positive when cytoplasmic aggregates of blue-black granules were evident inside the cells. Three independent experiments, each done by quintupled replicas, were analyzed.

Immunofluorescence

Primary culture

Cells were fixed with 4% paraformaldehyde for 30 min, permeabilized with PBS / 0.5% Triton for 5 min, blocked with PBS/5% BSA and incubated at 4 °C with primary antibody overnight. AlexaFluor-conjugated

secondary antibodies were diluted in PBS/2%BSA (1:500, LIFE TECHNOLOGIES, Oregon, USA) and incubated for 1 h at room temperature. Nuclei were stained for 2 min with DAPI (1 μg/ml). Only cells with healthy nuclear morphology (non-apoptotic) were quantified.

Brain section

Wistar rat male brains 4 or 25 months old were isolated following IACUC guidelines. Rats were perfused transcardially with PBS, then with 4% paraformaldehyde. Brains were drop-fixed in 4% paraformaldehyde for 24h; for cryoprotection brains were immersed in PBS/30% sucrose for 24 h. Brain coronal sections (50 μm) from frontal cortex were mounted serially. The sections were permeabilized with PBS/ 0.3% Triton for 15 min, blocked with PBS/5% BSA for 1 hour at room temperature and incubated with primary antibody at 4 °C overnight in PBS/1% BSA. Next, sections were incubated with AlexaFluor-conjugated secondary antibodies (1:350, LIFE TECHNOLOGIES, Oregon, USA) in PBS / 2% BSA 1 h at room temperature; nuclei were stained with DAPI (1 μg/ml). To avoid lipofuscin autofluorescence slices were incubated with Sudan Black B.

The following primary antibodies were used: mouse anti class III β-TUBULIN (1:1000, ABCAM 14545, Cambridge, MA, USA), rabbit anti class III β-TUBULIN (1:1000, ABCAM 18207, Cambridge, MA, USA), rabbit anti- class III β-TUBULIN (1:500, BIOLEGEND, MRB435P-100, San Diego, CA, USA), rabbit anti-GFAP (1:1000, DAKO Z0334, Santa Clara, CA, USA), rat anti-GFAP (1:1000, INVITROGEN 13-0300, Camarillo, CA, USA), rabbit anti-p21 (1:25, ABCAM 7960 or 1:100 ABCAM 109199, Cambridge, MA, USA), mouse anti-γH2AX (1:500, ABCAM 26350, Cambridge, MA, USA), rabbit anti-LC3 (1:500, MBL PD014, Nagoya, Japan), mouse anti-p62 (1:300, ABCAM 56416, Cambridge, MA, USA), rabbit anti-LAMP1 (1:1000, SIGMA-ALDRICH L1418, St. Louis, MO, USA), rabbit anti-mTOR (1:200, CELL SIGNALING 2983, Beverly, MA, USA), rabbit anti-GATA4 (1:500, ABCAM 84593, Cambridge, MA, USA).

Images were acquired using a NIKON ECLIPSE Ti-U microscope or a confocal microscope Zeiss LSM 800. Images were processed using NIS Elements, Basic Research (NIKON INSTRUMENTS Inc ®, NY, USA) software, Version 3.13 or Fiji software.

Immunoelectron microscopy

Cortical cells were fixed with 3% glutaraldehyde. Following fixation, dehydration was performed in an ethanol gradient: 30-40-50-60-70-80-90-100 % ethanol at 4°C. Then, the cells were embedded in a LR White resin and polymerization was carried out at 50 °C. Ultrathin sections of 70-80 nm were cut from the polymer using an Ultracut-Recheirt-Jung and placed on nickel grids for immunogold assay.

The thin sections were washed twice for 2 min with deionized water and two times with PBS with 0.005 % Tween20. Sections were then incubated for 30 min with the blocking solution (50 mM glycine, 0.005 % Tween20, 0.01 % Triton X-100 and 0.1 % BSA in PBS) [53]. After blocking, sections were incubated with the primary antibody: rabbit anti-LC3 (1:500, MBL PD014, Nagoya, Japan). After rinsing three times in PBS with 0.005 % Tween20, the sections were incubated overnight at 4 °C with the secondary antibody: donkey anti-rabbit 25-nm gold conjugate (Electron Microscopy Science Aurion #25708). Samples were washed three times with PBS, 0.005 % Tween20 and post-fixed in 2 % glutaraldehyde in PBS for 10 min. The sections were then rinsed with distilled water twice for 5 min and contrasted with 2 % uranyl acetate, rinsed with water, dried and observed under a JEOL JEM 1200 EXII electron microscope.

Immunoblotting analysis

Cells grown in the presence or absence of 20 □M Chloroquine (C-6628 SIGMA-ALDRICH, St. Louis, MO, USA) for 4 hrs were lysed in an extraction buffer consisting of 25 mM Tris, 50 mM NaCl, 2% Igepal, 0.2% SDS and 2 mg/ml protease inhibitor 18 (Complete, Roche Molecular Diagnostics, pH 7.4). Thirty micrograms of total protein were separated by SDS-PAGE and electroblotted onto polyvinylidene fluoride (PVDF-FL) membranes (Millipore). Membranes were incubated overnight with the primary antibody at 4 °C, rabbit anti-LC3 (1:1000, MBL PD014, Nagoya, Japan), rabbit anti-p62 (1:500, CELL SIGNALING 5114S, Beverly, MA, USA), mouse anti-TUBULIN (1:10000, CELL SIGNALING 3873, Beverly, MA, USA). Following three washes with TTBS secondary antibody IRDye® 680RD goat anti-rabbit (925-68071, LI-COR) or IRDye® 800CW goat anti-mouse (925-32210, LI-COR) was applied at 1:10,000 dilution in TTBS. Membranes were scanned and analyzed using an Odyssey® IR scanner and Odyssey® Image Studio software 5.2.5.

Gene expression analysis

Total RNA was isolated using TRIzol™ reagent (Life Technologies), and cDNA was synthesized from 1 μg of RNA using the High Capacity cDNA Reverse Transcription Kit (Thermo Fisher Scientific #4368814).

The quantitative PCR (qPCR) reaction was performed with the SYBR Green mix (Kapa SYBR® Fast Universal #KK4602) in the Rotor-Gene Qthermocycler (Qiagene, Germantown, MD, USA). All reactions were performed in quadruplicate, and the expression was normalized using the glyceraldehyde-3-phosphate dehydrogenase (*Gapdh*) mRNA. The sequences of the primers used are as follows:

Cdkn1a F 5′-CCGAGAACGGTGGAACTTTGAC-3′;
Cdkn1a R 5′-GAACACGCTCCCAGACGTAGTTG-3′
Ccl2 (*Mcp-1*) F, 5′- ATGCAGTTAATGCCCCACTC;
Ccl2 (*Mcp-1*) R, 5′-TTCCTTATTGGGGTCAGCAC-3′
Gapdh F, 5′-CTCATGACCACAGTCCATGC-3′
Gapdh R, 5′-TTCAGCTCTGGGATGACCTT-3′.

Neutral Comet assay

Cells were resuspended in cold PBS at 10^3 cells/µL density. This suspension was mixed at a 1:5 ratio with 0.75% low-melting point agarose (BIO RAD Certified™ Low Melt Agarose #1613111, Hercules, California, USA) at 37°C. About 50 to 100 µL of the mix were placed on microscope slides pre-coated with 1% normal-melting point agarose (BIO RAD Certified™ PCR Agarose #1613103, Hercules, California, USA), spread with coverslips and incubated at 4° C for 2 min and 10 min more at room temperature. The coverslips were removed and slides were covered with pre-chilled lysis solution (0.03 M EDTA, 1% SDS) for 60 min at 4°C. After that, slides were washed and covered with unwinding/electrophoresis buffer (Tris 60 mM, Acetic acid 90 mM, EDTA 2.5 mM, pH 9.0) for 60 min. Electrophoresis was performed at 25 V for 20 min. Immediately, slides were rinsed and incubated for 10 min in neutralization buffer (Tris-HCl 500 mM, pH 7.5) 3 times. Finally, DNA was stained with SYBR green (SYBR™ green I Nucleic Acid Gel Stain, INVITROGEN™, Eugene, Oregon, USA) 1:10000 in PBS. For each sample 50 comet images were measured, using a Nikon ECLIPSE Ti-U fluorescence microscope. The length and area of the broken DNA were measured with NIS Elements Basic Research software (NIKON INSTRUMENTS Inc ®, NY, USA)-

SASP analysis of cortical cells

Conditioned medium was collected from neuronal cultures at 6, 26 and 40 days *in vitro* (DIV) and was frozen at -20 °C until use. Concentrations (pg/mL) of G-CSF, GM-CSF, IFN gamma, IL-1α, IL-1β, IL-10, IL-12p70, IL-13, IL-17A, IL-2, IL-4, IL-5, IL-6, TNF alpha, Eotaxin, Gro α, IP-10, MCP-1, MCP-3, MIP-1α, MIP-2 and RANTES in media conditioned by cortical cells were measured by ProcartaPlex® Multiplex Immunoassay (BIO RAD # 171K1002M). The conditioned medium was previously concentrated using centrifugal filter units Amicon Ultracel-3 kDa (Millipore # UFC800324) and a total of 50 µL of concentrated conditioned medium were examined following manufacturer's instructions. Data were obtained in a Luminex Instrument and the analytes concentration was measured calibrating with a standard curve for each cytokine provided by the manufacturer.

Cyto-ID autophagosomes detection and Lysotracker staining

The Cyto-ID (ENZO LIFE SCIENCES ENZ-51031-K200, Farmingdale, NY, USA) is an 488 nm-excitable green fluorescent reagent that specifically accumulates in autophagic vesicles. Cells were incubated in Cyto-ID (1 µl Cyto-ID/1ml cell culture medium) for 30 minutes at 37 °C, 5 % CO_2 and washed prior to analysis. Lysotracker dye (DND-99 LIFE TECHNOLOGIES, Oregon, USA) was incubated for 20 min at 37ºC. Cells were analyzed by Fluorescence Nikon ECLIPSE Ti-U microscope.

Cortical cells-derived conditioned medium collection and treatment

Conditioned medium was prepared by collecting half the medium from neuronal cultures at 6, 26 and 40 days *in vitro* (DIV) and freezing it at -20^{0}C until use. Conditioned media were diluted 3:1 with fresh medium and added to cells at 1 D*IV* in 12-well plates ($4x10^5$ cortical neurons cells/well; $1x10^4$ MEFs/well). For MEFs, to avoid adding unknown factors from serum, conditioned media were diluted with OptiMEM (GIBCO Life Technologies, Grand Island, NY, USA). Cells were incubated further for 6 days at 37°C and 5 % CO_2. At the end of incubation, the senescent markers were analyzed.

Quantification

The quantifications of cells with a particular phenotype were done using NIS Elements, Basic Research (NIKON INSTRUMENTS Inc ®, NY, USA) Version 3.13 software or Fiji software. The size of the samples analyzed is indicated in every figure legend. We counted at least 100 cells in each graph shown. To quantify data that corresponds to nuclear Lamin A/C invagination (Figure 4), we exploited the observation that internal Lamin A/C invaginations increase the signal intensity of intranuclear Lamin A/C that would otherwise be in the nuclear envelope as follows: Z-Stacked maximum intensity confocal images were utilized. Border ROIs were manually selected with the brush selection tool of FIJI, the brush size corresponded to the pixel number length closest to 500 nm, roughly

the nuclear envelope size (i.e. 101.41 μm x 101.41 μm 1024 pixels x 1024 pixels images required a brush of pixel size 5 and 1437 pixels x 1437 pixels images of the same metric size required a brush of pixel size 7). Border ROIs were selected manually including the most distal from the center of the nucleus signal of DAPI stained nuclei forming ring like ROIs. Central ROIs were selected to be exactly the internal part of the ring excluded from the border ROIs by using the clear outside function on the edit menu followed clicking on the internal part with the wand (tracing) tool of FIJI. The mean fluorescence intensity of these ROIs in Lamin A/C images was measured and the signal of the center was divided by the signal of the border so as to normalize for different Lamin A/C expression. Higher values correspond to more invagination.

Statistical Analysis.
All data were analyzed and graphed with Prism 6 (GraphPad Software Inc. La Jolla, CA, USA). Specific tests were performed according to each experimental design, and are indicated in each figure.

Abbreviations

BECN1: Beclin 1; CQ: Cloroquine; DAPI: 4′,6-Diamidine-2′-phenylindole dihydrochloride; DDR: DNA Damage Response; D*IV*: Days *in vitro;* FM: Fresh medium; GFAP: Glial fibrillary acidic protein; IL6: Interleukin-6; LAMP: Lysosomal-associated membrane protein; MEFs: Mouse embryonic fibroblasts; mH2A: Histone macroH2A; mTOR: mechanistic target of rapamycin; N2A: Neuro 2A; PI3KC3: Phosphatidylinositol 3-kinase class 3; p38MAPK: p38 mitogen-activated protein kinase; SA-β-gal: Senescence-Associated β-galactosidase; SAHF: Senescence-associated heterochromatin foci; SAMP8: senescence-accelerated mice prone; SASP: Senescence-associated secretory phenotype; SBB: Sudan Black B; Spautin-1: Specific and potent autophagy inhibitor 1; SQSTM1: Sequestosome 1; TASCC: TOR-autophagy spatial coupling compartment; TGFβ: Transforming growth factor-beta; Tre: Trehalose; 53BP1: p53-binding protein 1; MCP-1: monocyte chemotactic protein 1; official name C-C motif chemokine 2; GATA4: GATA binding protein 4.

AUTHOR CONTRIBUTIONS

DMB carried out most of the experiments and participated in project design. EGS characterized neuronal senescence in the cortex of old rat brains; APA studied the paracrine premature senescence on MEFs; LAM and MK analyzed SASP components; GMH analyzed the double strand DNA brakes in senescent neurons; CGO performed lysotracker staining and contributed to autophagy analysis; LM contributed to experimental design and data analysis. SCO conceived the study and wrote the manuscript. All authors edited and approved the final manuscript.

ACKNOWLEDGMENTS

We are thankful to Dr. Beatriz Aguilar for her technical assistance. We acknowledge the support given by M.Sc. Ana Maria Escalante and Francisco Pérez at the IT Unit and Claudia Rivero at the Animal Facility. We are thankful to Dr. Ruth Rincón for confocal analysis assistance, to M.Sc. Rodolfo Paredes for electron microscopy imaging and to Dr. Abraham Rosas for both confocal analysis and electron microscopy imaging, all at the Imagenology Unit. Data in this work are part of the doctoral dissertation in the “Programa de Doctorado en Ciencias Bioquímicas” at the Universidad Nacional Autónoma de México (UNAM) of DMB and GMH, of the doctoral dissertation of EGS in the “Programa de Doctorado en Ciencias Biomédicas” at UNAM, and of the master dissertation in the “Programa de Maestría en Ciencias Bioquímicas” at UNAM of APA. All are recipients of fellowships from CONACyT.

CONFLICTS OF INTEREST

The authors declare no conflict of interest.

FUNDING

This project was supported by a grant from the Secretaria de Educación, Ciencia, Tecnología e Innovación de la Ciudad de México SECITI/042/2018 (INGER-DI-CRECITES-008-2018) "Red Colaborativa de Investigación Traslacional para el Envejecimiento Saludable de la Ciudad de México (RECITES)"; by CONACyT FC-921 and CB2013-220515; and by UNAM-PAPIIT IN206015-IN206518 to SCO. DMB received CONACyT doctoral fellowship 588372; GMH received CONACyT doctoral fellowship 417724; EGS received CONACyT doctoral fellowship 586932 and APA received CONACyT master fellowship 485243.

REFERENCES

1. Soto-Gamez A, Demaria M. Therapeutic interventions for aging: the case of cellular senescence. Drug Discov Today. 2017; 22:786–95. https://doi.org/10.1016/j.drudis.2017.01.004 PMID:28111332

2. Muñoz-Espín D, Serrano M. Cellular senescence: from physiology to pathology. Nat Rev Mol Cell Biol. 2014; 15:482–96. https://doi.org/10.1038/nrm3823 PMID:24954210

3. Matjusaitis M, Chin G, Sarnoski EA, Stolzing A. Biomarkers to identify and isolate senescent cells. Ageing Res Rev. 2016; 29:1–12. https://doi.org/10.1016/j.arr.2016.05.003 PMID:27212009

4. Lenain C, Gusyatiner O, Douma S, van den Broek B, Peeper DS. Autophagy-mediated degradation of nuclear envelope proteins during oncogene-induced senescence. Carcinogenesis. 2015; 36:1263–74. https://doi.org/10.1093/carcin/bgv124 PMID:26354777

5. Acosta JC, Banito A, Wuestefeld T, Georgilis A, Janich P, Morton JP, Athineos D, Kang TW, Lasitschka F, Andrulis M, Pascual G, Morris KJ, Khan S, et al. A complex secretory program orchestrated by the inflammasome controls paracrine senescence. Nat Cell Biol. 2013; 15:978–90. https://doi.org/10.1038/ncb2784 PMID:23770676

6. Coppé JP, Desprez PY, Krtolica A, Campisi J. The senescence-associated secretory phenotype: the dark side of tumor suppression. Annu Rev Pathol. 2010; 5:99–118. https://doi.org/10.1146/annurev-pathol-121808-102144 PMID:20078217

7. Sieben CJ, Sturmlechner I, van de Sluis B, van Deursen JM. Two-Step Senescence-Focused Cancer Therapies. Trends Cell Biol. 2018; 28:723–37. https://doi.org/10.1016/j.tcb.2018.04.006 PMID:29776716

8. Kang HT, Lee KB, Kim SY, Choi HR, Park SC. Autophagy impairment induces premature senescence in primary human fibroblasts. PLoS One. 2011; 6:e23367. https://doi.org/10.1371/journal.pone.0023367 PMID:21858089

9. Young AR, Narita M, Ferreira M, Kirschner K, Sadaie M, Darot JF, Tavaré S, Arakawa S, Shimizu S, Watt FM, Narita M. Autophagy mediates the mitotic senescence transition. Genes Dev. 2009; 23:798–803. https://doi.org/10.1101/gad.519709 PMID:19279323

10. Kang C, Xu Q, Martin TD, Li MZ, Demaria M, Aron L, Lu T, Yankner BA, Campisi J, Elledge SJ. The DNA damage response induces inflammation and senescence by inhibiting autophagy of GATA4. Science. 2015; 349:aaa5612. https://doi.org/10.1126/science.aaa5612 PMID:26404840

11. Narita M, Young AR, Arakawa S, Samarajiwa SA, Nakashima T, Yoshida S, Hong S, Berry LS, Reichelt S, Ferreira M, Tavaré S, Inoki K, Shimizu S, Narita M. Spatial coupling of mTOR and autophagy augments secretory phenotypes. Science. 2011; 332:966–70. https://doi.org/10.1126/science.1205407 PMID:21512002

12. Kang C, Elledge SJ. How autophagy both activates and inhibits cellular senescence. Autophagy. 2016; 12:898–99. https://doi.org/10.1080/15548627.2015.1121361 PMID:27129029

13. Chinta SJ, Woods G, Rane A, Demaria M, Campisi J, Andersen JK. Cellular senescence and the aging brain. Exp Gerontol. 2015; 68:3–7. https://doi.org/10.1016/j.exger.2014.09.018 PMID:25281806

14. Walton CC, Andersen JK. Unknown fates of (brain) oxidation or UFO: close encounters with neuronal senescence. Free Radic Biol Med. 2019; 134:695–701. https://doi.org/10.1016/j.freeradbiomed.2019.01.012 PMID:30639615

15. Jurk D, Wang C, Miwa S, Maddick M, Korolchuk V, Tsolou A, Gonos ES, Thrasivoulou C, Saffrey MJ, Cameron K, von Zglinicki T. Postmitotic neurons develop a p21-dependent senescence-like phenotype driven by a DNA damage response. Aging Cell. 2012; 11:996–1004. https://doi.org/10.1111/j.1474-9726.2012.00870.x PMID:22882466

16. Chernova T, Nicotera P, Smith AG. Heme deficiency is associated with senescence and causes suppression of N-methyl-D-aspartate receptor subunits expression in primary cortical neurons. Mol Pharmacol. 2006; 69:697–705. https://doi.org/10.1124/mol.105.016675 PMID:16306232

17. Bhanu MU, Mandraju RK, Bhaskar C, Kondapi AK. Cultured cerebellar granule neurons as an in vitro aging model: topoisomerase IIβ as an additional biomarker in DNA repair and aging. Toxicol In Vitro. 2010; 24:1935–45. https://doi.org/10.1016/j.tiv.2010.08.003 PMID:20708677

18. Dong W, Cheng S, Huang F, Fan W, Chen Y, Shi H, He H. Mitochondrial dysfunction in long-term neuronal cultures mimics changes with aging. Med Sci Monit. 2011; 17:BR91–96. https://doi.org/10.12659/MSM.881706 PMID:21455101

19. Geng YQ, Guan JT, Xu XH, Fu YC. Senescence-associated beta-galactosidase activity expression in aging hippocampal neurons. Biochem Biophys Res Commun. 2010; 396:866–69. https://doi.org/10.1016/j.bbrc.2010.05.011 PMID:20457127

20. Xu T, Sun L, Shen X, Chen Y, Yin Y, Zhang J, Huang D, Li W, Li W. NADPH oxidase 2-mediated NLRP1 inflammasome activation involves in neuronal senescence in hippocampal neurons in vitro. Int Immunopharmacol. 2019; 69:60–70. https://doi.org/10.1016/j.intimp.2019.01.025 PMID:30677569

21. Piechota M, Sunderland P, Wysocka A, Nalberczak M, Sliwinska MA, Radwanska K, Sikora E. Is senescence-associated β-galactosidase a marker of neuronal senescence? Oncotarget. 2016; 7:81099–109. https://doi.org/10.18632/oncotarget.12752 PMID:27768595

22. Bigagli E, Luceri C, Scartabelli T, Dolara P, Casamenti F, Pellegrini-Giampietro DE, Giovannelli L. Long-term Neuroglial Cocultures as a Brain Aging Model: Hallmarks of Senescence, MicroRNA Expression Profiles, and Comparison With In Vivo Models. J Gerontol A Biol Sci Med Sci. 2016; 71:50–60. https://doi.org/10.1093/gerona/glu231 PMID:25568096

23. Jin HJ, Lee HJ, Heo J, Lim J, Kim M, Kim MK, Nam HY, Hong GH, Cho YS, Choi SJ, Kim IG, Shin DM, Kim SW. Senescence-Associated MCP-1 Secretion Is Dependent on a Decline in BMI1 in Human Mesenchymal Stromal Cells. Antioxid Redox Signal. 2016; 24:471–85. https://doi.org/10.1089/ars.2015.6359 PMID:26573462

24. Georgakopoulou EA, Tsimaratou K, Evangelou K, Fernandez-Marcos PJ, Zoumpourlis V, Trougakos IP, Kletsas D, Bartek J, Serrano M, Gorgoulis VG. Specific lipofuscin staining as a novel biomarker to detect replicative and stress-induced senescence. A method applicable in cryo-preserved and archival tissues. Aging (Albany NY). 2013; 5:37–50. https://doi.org/10.18632/aging.100527 PMID:23449538

25. García-Aguirre I, Alamillo-Iniesta A, Rodríguez-Pérez R, Vélez-Aguilera G, Amaro-Encarnación E, Jiménez-Gutiérrez E, Vásquez-Limeta A, Samuel Laredo-Cisneros M, Morales-Lázaro SL, Tiburcio-Félix R, Ortega A, Magaña JJ, Winder SJ, Cisneros B. Enhanced nuclear protein export in premature aging and rescue of the progeria phenotype by modulation of CRM1 activity. Aging Cell. 2019:e13002. [Epub ahead of print] https://doi.org/10.1111/acel.13002 PMID:31305018

26. Freund A, Laberge RM, Demaria M, Campisi J. Lamin B1 loss is a senescence-associated biomarker. Mol Biol Cell. 2012; 23:2066–75. https://doi.org/10.1091/mbc.e11-10-0884 PMID:22496421

27. Takamori Y, Tamura Y, Kataoka Y, Cui Y, Seo S, Kanazawa T, Kurokawa K, Yamada H. Differential expression of nuclear lamin, the major component of nuclear lamina, during neurogenesis in two germinal regions of adult rat brain. Eur J Neurosci. 2007; 25:1653–62. https://doi.org/10.1111/j.1460-9568.2007.05450.x PMID:17432957

28. Lee JY, Yu KR, Lee BC, Kang I, Kim JJ, Jung EJ, Kim HS, Seo Y, Choi SW, Kang KS. GATA4-dependent regulation of the secretory phenotype via MCP-1 underlies lamin A-mediated human mesenchymal stem cell aging. Exp Mol Med. 2018; 50:63. https://doi.org/10.1038/s12276-018-0092-3 PMID:29760459

29. Rubinsztein DC, Mariño G, Kroemer G. Autophagy and aging. Cell. 2011; 146:682–95. https://doi.org/10.1016/j.cell.2011.07.030 PMID:21884931

30. Yang F, Chu X, Yin M, Liu X, Yuan H, Niu Y, Fu L. mTOR and autophagy in normal brain aging and caloric restriction ameliorating age-related cognition deficits. Behav Brain Res. 2014; 264:82–90. https://doi.org/10.1016/j.bbr.2014.02.005 PMID:24525424

31. Liu J, Xia H, Kim M, Xu L, Li Y, Zhang L, Cai Y, Norberg HV, Zhang T, Furuya T, Jin M, Zhu Z, Wang H, et al. Beclin1 controls the levels of p53 by regulating the deubiquitination activity of USP10 and USP13. Cell. 2011; 147:223–34. https://doi.org/10.1016/j.cell.2011.08.037 PMID:21962518

32. Mayer AL, Higgins CB, Heitmeier MR, Kraft TE, Qian X, Crowley JR, Hyrc KL, Beatty WL, Yarasheski KE, Hruz PW, DeBosch BJ. SLC2A8 (GLUT8) is a mammalian trehalose transporter required for trehalose-induced autophagy. Sci Rep. 2016; 6:38586. https://doi.org/10.1038/srep38586 PMID:27922102

33. Song J, Lee B, Kang S, Oh Y, Kim E, Kim CH, Song HT, Lee JE. Agmatine Ameliorates High Glucose-Induced Neuronal Cell Senescence by Regulating the p21 and p53 Signaling. Exp Neurobiol. 2016; 25:24–32. https://doi.org/10.5607/en.2016.25.1.24 PMID:26924930

34. Riessland M, Kolisnyk B, Kim TW, Cheng J, Ni J, Pearson JA, Park EJ, Dam K, Acehan D, Ramos-Espiritu LS, Wang W, Zhang J, Shim J, et al. Loss of SATB1 Induces a p21 Dependent Cellular Senescence Phenotype in Dopaminergic Neurons. bioRxiv. 2018; 452243. 10.1101/452243

35. Narita M, Young AR, Narita M. Autophagy facilitates oncogene-induced senescence. Autophagy. 2009;

5:1046–47. https://doi.org/10.4161/auto.5.7.9444 PMID:19652542

36. Golde TE, Miller VM. Proteinopathy-induced neuronal senescence: a hypothesis for brain failure in Alzheimer's and other neurodegenerative diseases. Alzheimers Res Ther. 2009; 1:5. https://doi.org/10.1186/alzrt5 PMID:19822029

37. Franceschi C, Campisi J. Chronic inflammation (inflammaging) and its potential contribution to age-associated diseases. J Gerontol A Biol Sci Med Sci. 2014 (Suppl 1); 69:S4–9. https://doi.org/10.1093/gerona/glu057 PMID:24833586

38. McShea A, Harris PL, Webster KR, Wahl AF, Smith MA. Abnormal expression of the cell cycle regulators P16 and CDK4 in Alzheimer's disease. Am J Pathol. 1997; 150:1933–39. PMID:9176387

39. Lüth HJ, Holzer M, Gertz HJ, Arendt T. Aberrant expression of nNOS in pyramidal neurons in Alzheimer's disease is highly co-localized with p21ras and p16INK4a. Brain Res. 2000; 852:45–55. https://doi.org/10.1016/S0006-8993(99)02178-2 PMID:10661494

40. Luterman JD, Haroutunian V, Yemul S, Ho L, Purohit D, Aisen PS, Mohs R, Pasinetti GM. Cytokine gene expression as a function of the clinical progression of Alzheimer disease dementia. Arch Neurol. 2000; 57:1153–60. https://doi.org/10.1001/archneur.57.8.1153 PMID:10927795

41. Sun A, Liu M, Nguyen XV, Bing G. P38 MAP kinase is activated at early stages in Alzheimer's disease brain. Exp Neurol. 2003; 183:394–405. https://doi.org/10.1016/S0014-4886(03)00180-8 PMID:14552880

42. Campbell IL, Abraham CR, Masliah E, Kemper P, Inglis JD, Oldstone MB, Mucke L. Neurologic disease induced in transgenic mice by cerebral overexpression of interleukin 6. Proc Natl Acad Sci USA. 1993; 90:10061–65. https://doi.org/10.1073/pnas.90.21.10061 PMID:7694279

43. Bussian TJ, Aziz A, Meyer CF, Swenson BL, van Deursen JM, Baker DJ. Clearance of senescent glial cells prevents tau-dependent pathology and cognitive decline. Nature. 2018; 562:578–82. https://doi.org/10.1038/s41586-018-0543-y PMID:30232451

44. Musi N, Valentine JM, Sickora KR, Baeuerle E, Thompson CS, Shen Q, Orr ME. Tau protein aggregation is associated with cellular senescence in the brain. Aging Cell. 2018; 17:e12840. https://doi.org/10.1111/acel.12840 PMID:30126037

45. Martinez-Lopez N, Athonvarangkul D, Singh R. Autophagy and aging. Adv Exp Med Biol. 2015; 847:73–87. https://doi.org/10.1007/978-1-4939-2404-2_3 PMID:25916586

46. Gelino S, Hansen M. Autophagy - An Emerging Anti-Aging Mechanism. J Clin Exp Pathol. 2012 (Suppl 4); Suppl 4:006. PMID:23750326

47. Madeo F, Zimmermann A, Maiuri MC, Kroemer G. Essential role for autophagy in life span extension. J Clin Invest. 2015; 125:85–93. https://doi.org/10.1172/JCI73946 PMID:25654554

48. Gerónimo-Olvera C, Montiel T, Rincon-Heredia R, Castro-Obregón S, Massieu L. Autophagy fails to prevent glucose deprivation/glucose reintroduction-induced neuronal death due to calpain-mediated lysosomal dysfunction in cortical neurons. Cell Death Dis. 2017; 8:e2911. https://doi.org/10.1038/cddis.2017.299 PMID:28661473

49. Xu J. Preparation, culture, and immortalization of mouse embryonic fibroblasts. Curr Protoc Mol Biol. 2005; Chapter 28:Unit 28.1. https://doi.org/10.1002/0471142727.mb2801s70 PMID:18265366

50. Dimri GP, Lee X, Basile G, Acosta M, Scott G, Roskelley C, Medrano EE, Linskens M, Rubelj I, Pereira-Smith O. A biomarker that identifies senescent human cells in culture and in aging skin in vivo. Proc Natl Acad Sci USA. 1995; 92:9363–67. https://doi.org/10.1073/pnas.92.20.9363 PMID:7568133

51. Debacq-Chainiaux F, Erusalimsky JD, Campisi J, Toussaint O. Protocols to detect senescence-associated beta-galactosidase (SA-betagal) activity, a biomarker of senescent cells in culture and in vivo. Nat Protoc. 2009; 4:1798–806. https://doi.org/10.1038/nprot.2009.191 PMID:20010931

52. Levitsky KL, Toledo-Aral JJ, López-Barneo J, Villadiego J. Direct confocal acquisition of fluorescence from X-gal staining on thick tissue sections. Sci Rep. 2013; 3:2937. https://doi.org/10.1038/srep02937 PMID:24121824

53. Rosas-Arellano A, Villalobos-González JB, Palma-Tirado L, Beltrán FA, Cárabez-Trejo A, Missirlis F, Castro MA. A simple solution for antibody signal enhancement in immunofluorescence and triple immunogold assays. Histochem Cell Biol. 2016; 146:421–30. https://doi.org/10.1007/s00418-016-1447-2 PMID:27188756

SUPPLEMENTARY MATERIAL

Supplementary Figures

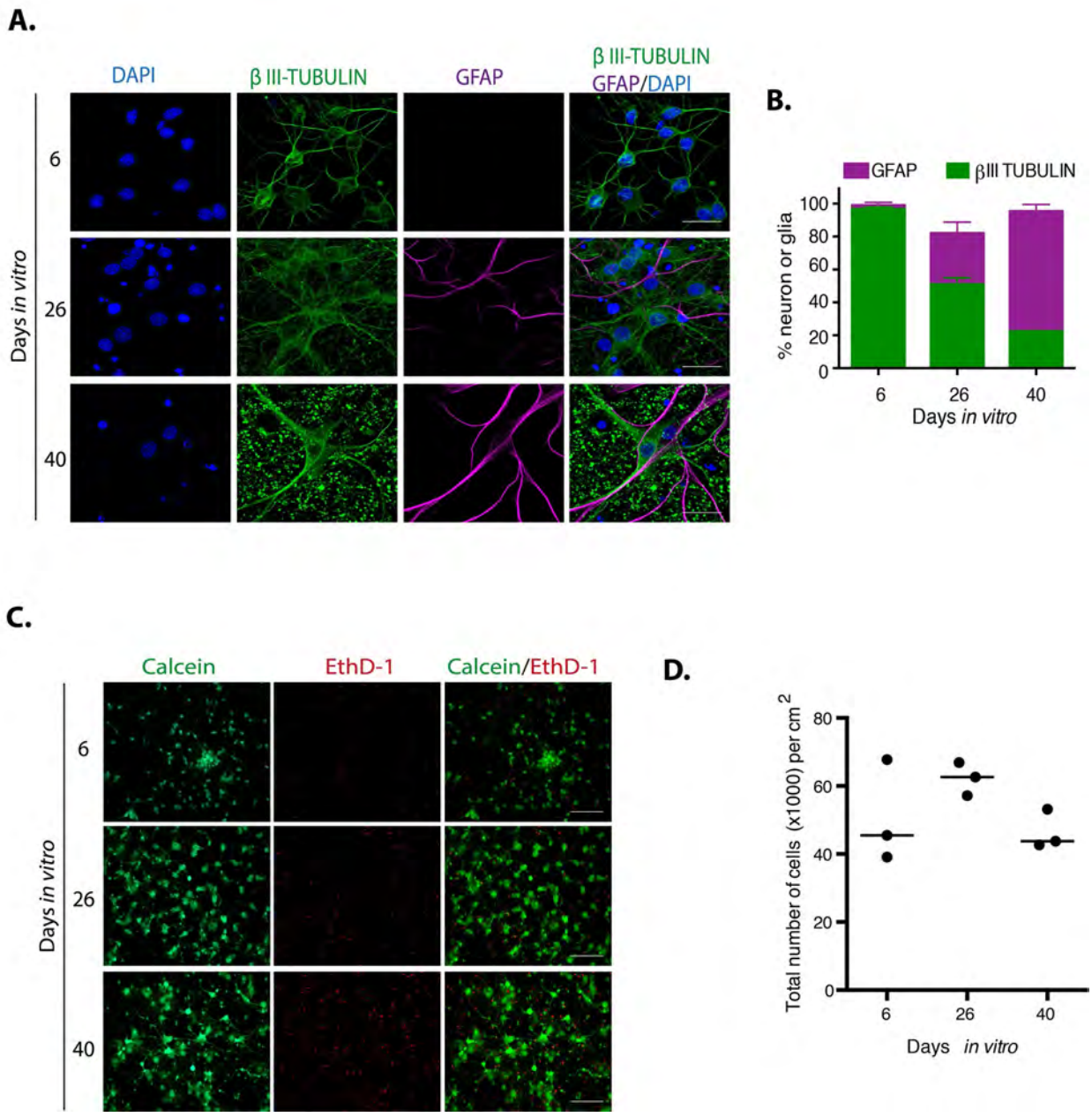

Supplementary Figure 1S. Rat prenatal cortex primary culture is viable up to 40 days *in vitro* (D*IV*). (**A**) Representative immunofluorescence used to quantify neurons (βIII-TUBULIN) and glial cells (GFAP) at 6, 26 or 40 D*IV* as indicated. Nuclei were stained with DAPI. Scale bars represent 25 µm. (**B**) The percentage of neurons or glial cells along the culture is graphed. It changes along the time of culture due to both neuronal death and glial proliferation. Bars represent SEM, n=3. (**C**) Cell viability was estimated by staining with LIVE/DEAD viability/cytotoxicity kit. Alive cells were stained with Calcein, while dead cells were stained with Ethidium homodimer-1 (EthD-1). Scale bars represent 500 µm. (**D**) The total number of cells per square cm remained similar along the culture. Each dot represents the average of three wells per experiment. Bars represent the average of three independent experiments. Although there was an increment in the average number of cells at 26 D*IV*, it was not statistically significant analyzed by two-way RM ANOVA, with Dunnett´s multiple comparison test.

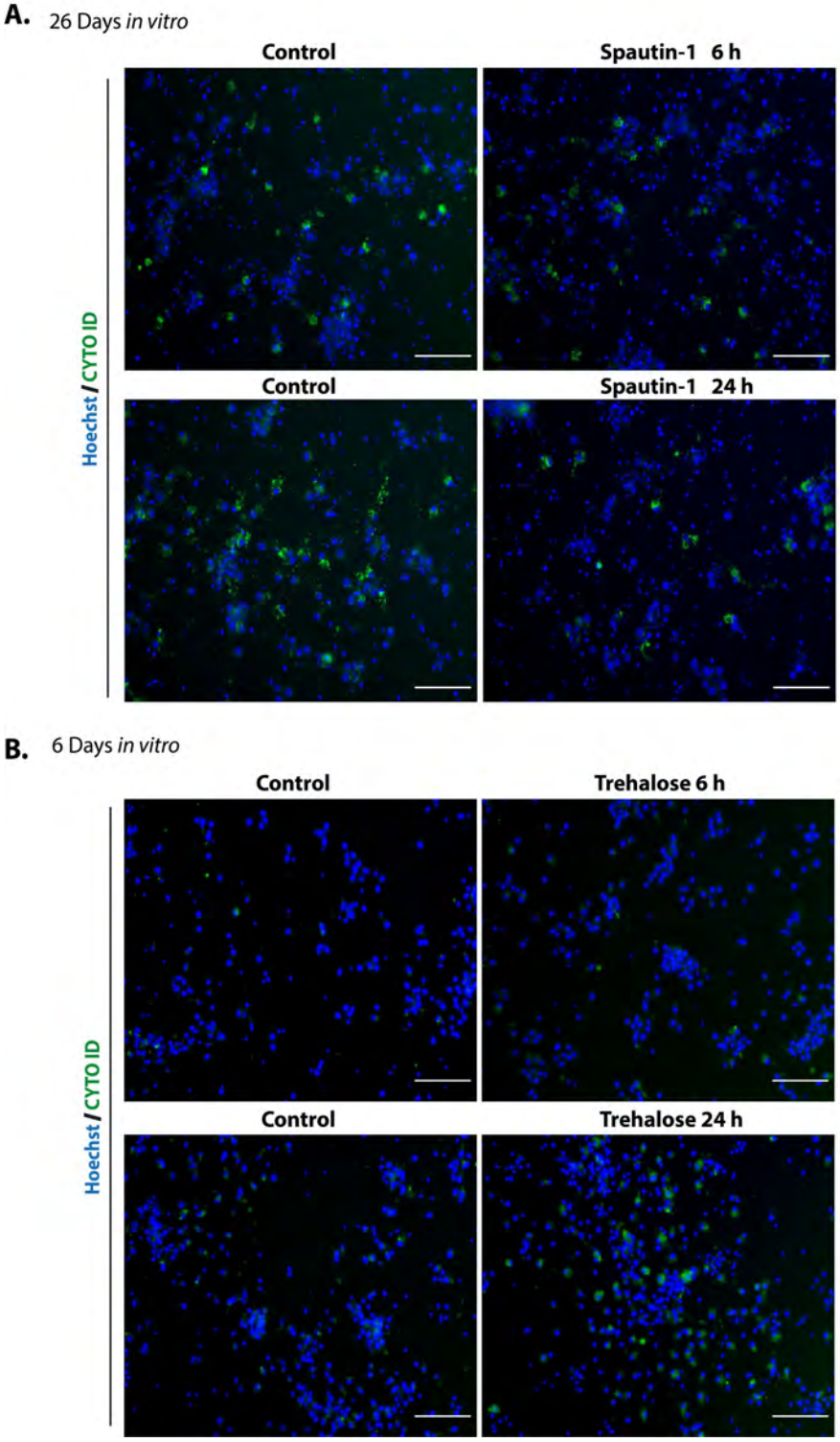

Supplementary Figure 2S. Spautin-1 inhibited autophagy and Trehalose induced autophagy on cortical primary cells. (**A**) Autophagosomes were stained with CytoID® to verify Spautin1 inhibition of autophagy on cortical cells cultured for 26 D*IV*, since at this time cells have abundant autophagosomes. Controls were treated with vehicle only. (**B**) Trehalose induction of autophagy was verified by adding it to cortical cells cultured for 6 D*IV*, since at this time cortical cells have only few autophagosomes. Controls were treated with vehicle only. Nuclei were stained with Hoechst. Scale bars represent 500 μm.

nature biotechnology

ARTICLES

https://doi.org/10.1038/s41587-019-0166-3

RNA proximity sequencing reveals the spatial organization of the transcriptome in the nucleus

Jörg Morf[1*], Steven W. Wingett[1,2], Irene Farabella[3,4], Jonathan Cairns[1,12], Mayra Furlan-Magaril[5], Luis F. Jiménez-García[6], Xin Liu[7], Frank F. Craig[7], Simon Walker[8], Anne Segonds-Pichon[2], Simon Andrews[2], Marc A. Marti-Renom[3,4,9,10] and Peter Fraser[1,11]

The global, three-dimensional organization of RNA molecules in the nucleus is difficult to determine using existing methods. Here we introduce Proximity RNA-seq, which identifies colocalization preferences for pairs or groups of nascent and fully transcribed RNAs in the nucleus. Proximity RNA-seq is based on massive-throughput RNA barcoding of subnuclear particles in water-in-oil emulsion droplets, followed by cDNA sequencing. Our results show RNAs of varying tissue-specificity of expression, speed of RNA polymerase elongation and extent of alternative splicing positioned at varying distances from nucleoli. The simultaneous detection of multiple RNAs in proximity to each other distinguishes RNA-dense from sparse compartments. Application of Proximity RNA-seq will facilitate study of the spatial organization of transcripts in the nucleus, including non-coding RNAs, and its functional relevance.

The spatial organization of nucleic acids in cell nuclei is critical for gene expression and ultimately cell physiology[1]. Different scales of the spatial organization of DNA and chromatin have been analysed; from promoter–enhancer interactions to megabase-sized topological association domains (TADs) and large-scale, higher-order folding of chromosomes into distinct compartments composed of transcriptionally active or inactive regions[2–4]. However, there is little understanding of where specific transcripts are synthesized, processed and/or sequestered in relation to nuclear landmarks. Large parts of transcriptomes have been spatially resolved in tissues[5] and single cells[6–8] with imaging techniques, but these methods do not infer colocalization or spatial associations between different RNA molecules. Pairwise probing of RNA–RNA interactions has thus far been limited to direct base-paired contacts[9] or to short-range distances between RNA ends allowing enzymatic ligations[10–13]. We therefore devised a widely applicable, massive-throughput method that determines spatial associations between pairs or groups of transcripts irrespective of the nature of their interaction to provide a functional readout of transcriptional genome activity in the nucleus.

Proximity RNA-seq uniquely barcodes RNAs in millions of subnuclear particles in parallel by a simple, rapid vortexing step combining fragmented nuclear particles with barcoded beads in a water-in-oil emulsion (Fig. 1a and Supplementary Fig. 1). Barcoded complementary DNAs are then sequenced to enable the reconstruction of proximities between chromatin-associated, nascent RNAs and non-coding RNAs in nuclei. We use Proximity RNA-seq to identify, characterize and map specific transcript families in relation to a major recognizable nuclear landmark, providing a cytological spatial map of RNAs in cells.

Results

Massive-throughput barcoding in emulsion. We first developed an on-bead PCR protocol in emulsion to uniquely barcode up to 1 billion beads individually for an experiment. We used conditions that favor the amplification of a single synthesized DNA template containing a 26-base-long random barcode on each bead in the emulsion[14,15] (Fig. 1b). The encapsulation of a single barcode with one bead can be approximated by diluting templates and beads sufficiently before emulsification. To estimate the fraction of singly barcoded beads, we first used two barcode templates of defined sequences (Supplementary Table 1) for PCR amplification on beads. Fluorescent probes were then hybridized to the amplified barcodes on beads before flow cytometry analysis and comparison with expected Poisson distributions (Fig. 1c,d). To optimize the yield of beads with individual random barcodes, we chose encapsulation conditions and template amounts according to a Poisson model that aimed at 50% barcoded beads, of which around 70% were covered with copies of a single barcode and 30% had copies of multiple barcodes. After PCR, barcode copies on beads were extended with 15 random bases to generate reverse transcription (RT) primers (Fig. 1b,e). Subnuclear particles from SH-SY5Y human neuroblastoma cells were obtained by minimal sonication to disrupt nuclei isolated from chemically crosslinked cells. After each sonication cycle, disruption of nuclei was examined by microscopy. We used ethylene glycol-bis(succinimidylsuccinate) (EGS), with a 16 Å spacer between reactive groups, in combination with formaldehyde for crosslinking, with the aim to increase the fraction of particles containing multiple RNA molecules. After sonication of nuclei, all the homogenate was encapsulated into droplets without prior centrifugation. In-droplet reverse transcription of

[1]Laboratory of Nuclear Dynamics, Babraham Institute, Cambridge, UK. [2]Bioinformatics, Babraham Institute, Cambridge, UK. [3]CNAG-CRG, Centre for Genomic Regulation, Barcelona Institute of Science and Technology, Barcelona, Spain. [4]CRG, Centre for Genomic Regulation, Barcelona, Spain. [5]Departamento de Genética Molecular, Instituto de Fisiología Celular, Universidad Nacional Autónoma de México, Mexico City, Mexico. [6]Department of Cell Biology, Faculty of Sciences, National Autonomous University of Mexico, Mexico City, Mexico. [7]Sphere Fluidics Limited, Babraham Research Campus, Cambridge, UK. [8]Imaging Facility, Babraham Institute, Cambridge, UK. [9]Universitat Pompeu Fabra, Barcelona, Spain. [10]Catalan Institution for Research and Advanced Studies, Barcelona, Spain. [11]Department of Biological Science, Florida State University, Tallahassee, FL, USA. [12]Present address: Quantitative Biology department, Discovery Sciences, IMED Biotech Unit, AstraZeneca, Cambridge, UK. *e-mail: jorg.morf@gmail.com

INFORME DE LABORES 2019

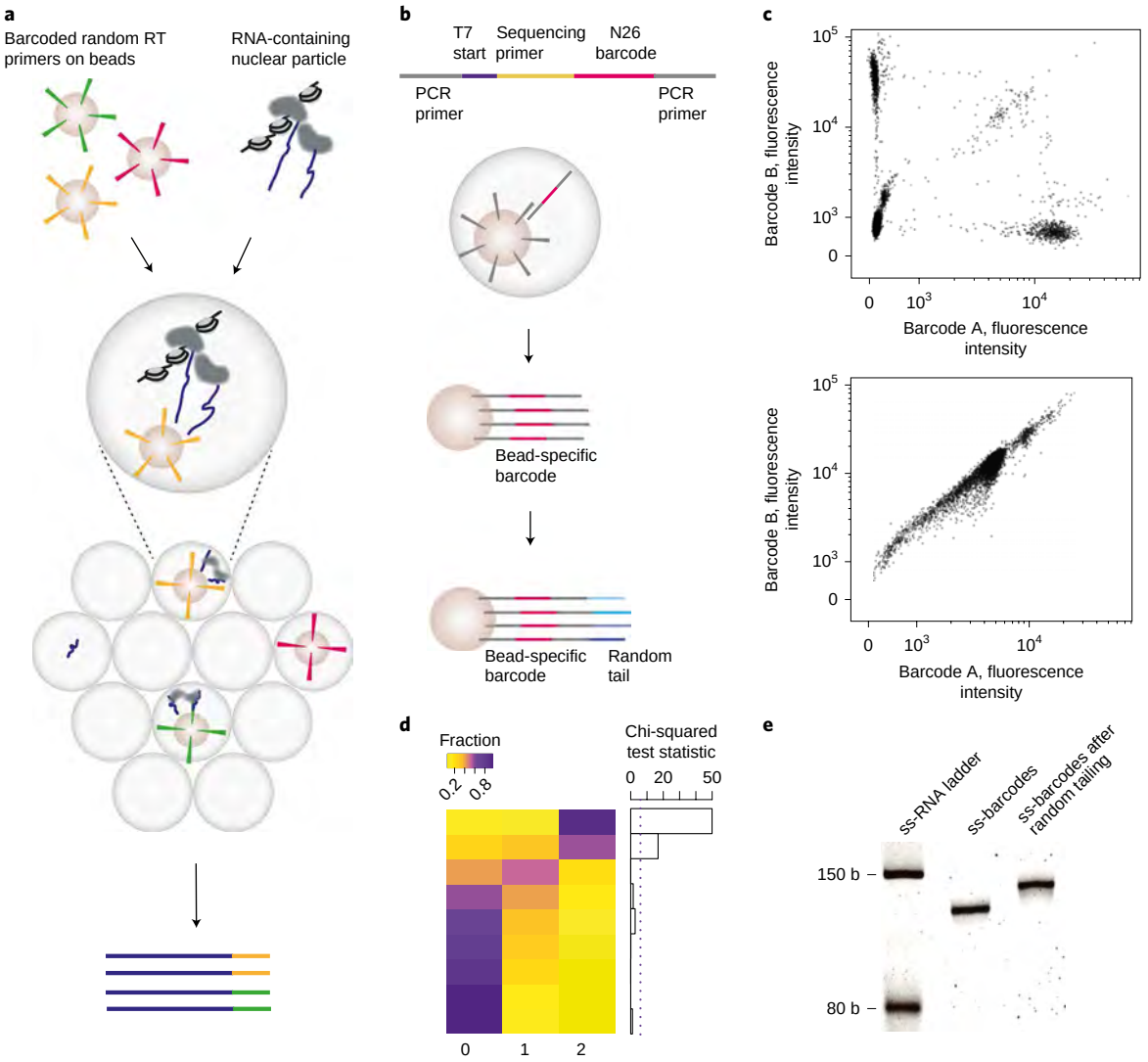

Fig. 1 | Proximity RNA-seq. a, Massive-throughput barcoding by RT of RNA-containing particles in water-in-oil droplets. **b**, Barcoding of magnetic beads with immobilized primers and diluted random DNA templates by emulsion PCR. Barcodes on beads were end-tailed with random nucleotides to subsequently serve as RT primers. **c**, To control barcoding and emulsion integrity, two barcodes of known sequence were amplified on beads in emulsion or solution prior to hybridization with complementary fluorescent probes and fluorescence-activated cell sorting (FACS) analysis to count empty, single and mixed barcoded beads. Top panel, PCR in emulsion; bottom panel, PCR in solution. Axes specify fluorescence signals of hybridized probes. **d**, Different two-barcode experiments, rows, were ordered according to increasing fractions of non-barcoded beads (yellow, low fraction; purple, high fraction). Fractions of beads containing no, one or both barcodes (columns) were compared with expected Poisson distributions (chi-squared test statistic, dashed line indicates $P = 0.05$). $n = 10{,}000$ beads per experiment were analysed. **e**, Acrylamide gel of single-stranded barcodes (ss-barcodes) before (lane 2) and after (lane 3) the addition of 15 random nucleotides. Single-stranded RNA ladder (ss-RNA ladder) was run in lane 1 ($n = 2$).

RNAs in crosslinked particles with barcoded beads followed by cDNA library amplification (Supplementary Fig. 1) resulted in a fragment length suitable for Illumina sequencing.

Proximity RNA-seq characterization and validation. Sequencing and mapping of RNAs in nuclear-enriched particles resulted in a fourfold increase in intron-to-exon read ratio compared with ribosomal RNA-depleted RNA-seq. In addition, the characteristic overrepresentation of reads at the 5′ ends in introns compared with the 3′ ends[16] demonstrated a clear enrichment for nascent transcripts (Fig. 2a,b). We trimmed three bases on either end of the barcode to account for offsets by a few bases of otherwise identical barcodes. The resulting barcode length of 20 random bases corresponds to a theoretical barcode complexity of 10^{12}, which exceeded an estimated 10^9 nascent RNA molecules in the input material. Multiple reads with the same barcode and mapping to the same transcript were dubbed a proxy read and counted as one transcript observation (Supplementary Fig. 2). Up to 25% of proxy reads were cobarcoded with proxy reads mapping to other transcripts identifying spatial RNA associations (Supplementary Fig. 3). Proximity RNA-seq benefits from sequencing into saturation to increase the number of RNAs identified on beads and cobarcoded proxy reads (Supplementary Fig. 4).

To validate spatial associations, we first analysed cobarcoding events of the abundant small RNA U3, which resides in the nucleolus together with hundreds of other small non-coding, nucleolar RNAs (snoRNAs)[17]. We found overwhelmingly significant cobarcoding of snoRNAs with U3 compared with the non-snoRNA transcriptome (Mann–Whitney U-test: $P = 4 \times 10^{-56}$; Cliff's delta effect size: 0.9; Fig. 2c). In contrast, control experiments using multi-barcoded

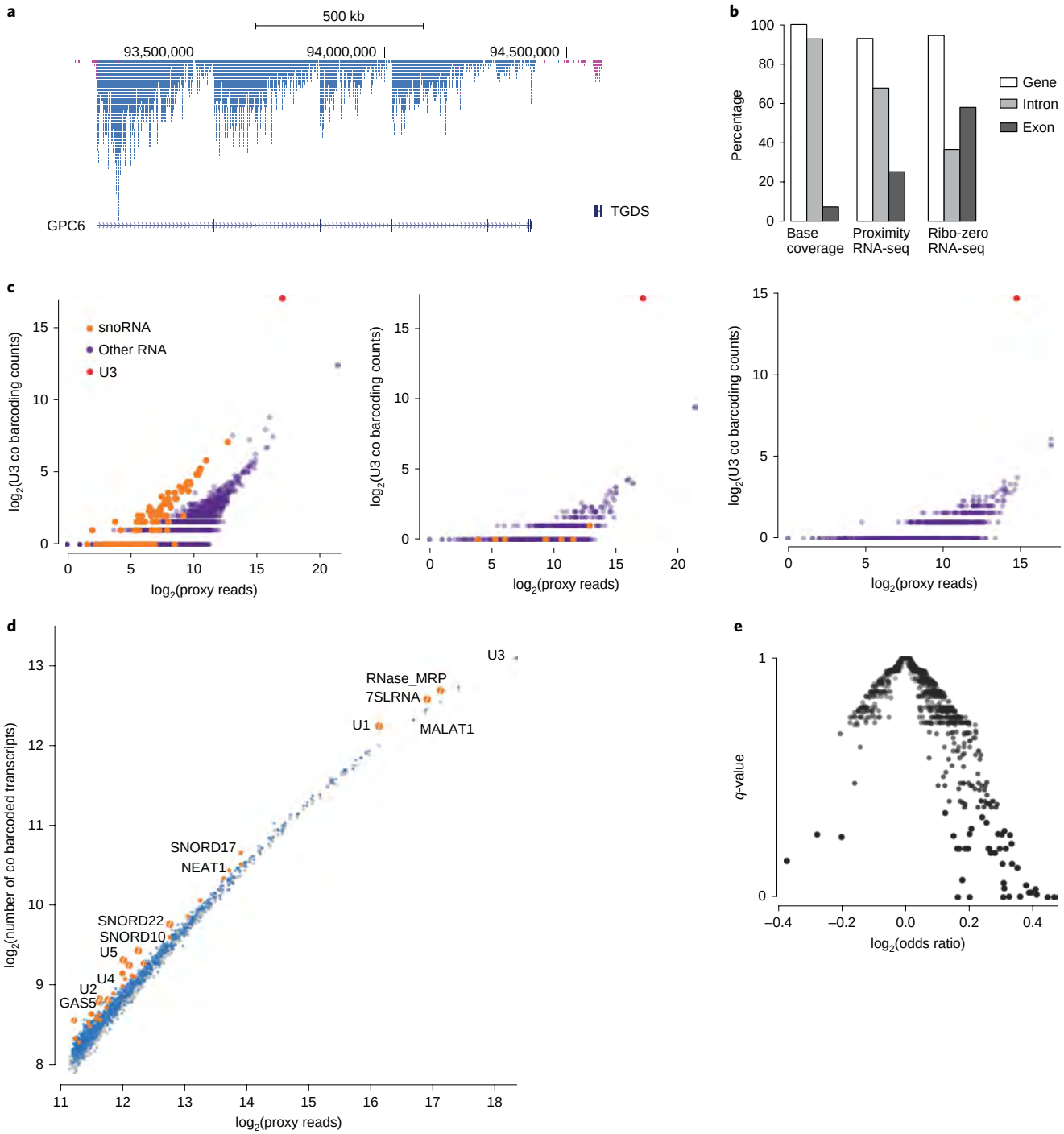

Fig. 2 | RNA cobarcoding and proximal transcriptomes. a, Proximity RNA-seq reads mapping to GPC6 (blue) and adjacent transcripts on the opposite strand (pink) illustrate both high intronic read densities and the saw-tooth read pattern along introns. **b**, Fractions in percentage of reads in transcript features. Proximity RNA-seq was compared with total RNA-seq after ribosomal depletion[39] and the base coverage of exons, introns and genes in the genome (set as 100), respectively. **c**, Counts of cobarcoding events involving U3 RNA plotted against the number of proxy reads of the other RNA. Left panel, crosslinked sample with uniquely barcoded beads; middle panel, control using crosslinked sample and randomly barcoded beads; right panel, control with purified RNA after crosslink reversal and uniquely barcoded beads. Of note, most snoRNAs are not plotted for control data, as no cobarcoding with U3 was detected. **d**, For the top 1,000 RNAs (combined data from $n = 3$ independent experiments), the number of cobarcoded transcripts was plotted against the number of proxy reads per RNA. Gray, randomized; blue, observed; orange, RNAs with high complexity of cobarcoded transcripts ($P < 0.01$); orange with white slash, $q < 0.05$ as derived in **e**. **e**, Transcripts with more complex composition of cobarcoded transcripts than expected at random were identified by Fisher's exact test, two-sided, and FDR adjustment (x axis, odds ratio with positive values indicating high complexity of cobarcoded transcripts).

beads produced by PCR amplification in a droplet-free solution showed essentially no cobarcoding between U3 and snoRNAs. Similarly, using crosslink-reversed and purified RNA and uniquely barcoded beads also showed no cobarcoding between U3 and snoRNAs. We next compared the crosslink-reversed control, the standard crosslinked condition used throughout the manuscript and a

INFORME DE LABORES 2019

prolonged crosslinked sample to assess the effects of sample preparation on particle encapsulation, RNA read counts and nuclear proximities. Global correlation in transcript abundance as measured by Proximity RNA-seq between standard crosslinked and crosslink-reversed samples (Spearman's rank correlation coefficient: 0.8) was found to be similarly high to that between replicates of crosslinked samples (Supplementary Fig. 3). Equal transcript abundances in both datasets suggested unbiased encapsulation of crosslinked RNA particles into droplets. As exemplified by U3 (Fig. 2c), the crosslink-reversed sample lacked information on RNA proximities, and global correlation in pairwise transcript cobarcoding between crosslinked and crosslink-reversed samples was poor (Spearman's rank correlation coefficient: 0.29). We then compared the sample with prolonged fixation with the standard sample preparation. The same number of sonication cycles was used for both samples to disrupt nuclei. We found that the fraction of ribosomal RNA reads increased from 43% in standard conditions to 87% with prolonged crosslinking. Of note, nuclei contribute less than the cytoplasm to a total of around 90% rRNA in whole cells[18,19]. Intronic reads decreased from 74% to 47% and exonic reads increased from 18% to 47% with prolonged crosslinking compared with standard conditions (Supplementary Fig. 5). We conclude that prolonged crosslinking copurified larger amounts of cytoplasmic RNA compared with standard crosslinking, which hampers the analysis of nuclear RNA organization. Nuclear particle preparation is therefore likely a trade-off between a high crosslinking efficiency, to increase cobarcoding of transcripts at the cost of cytoplasmic RNA contamination, and aiming for a cleaner preparation of nuclei with less crosslinking and less frequent cobarcoding of transcripts. Using our standard sample preparation in SH-SY5Y cells, high intron and modest rRNA contents suggested that the conditions were suitable to probe nuclear RNA proximities. Furthermore, correlations in pairwise transcript cobarcoding between different standard crosslinked replicates ranged between 0.71 and 0.83 (Spearman's rank correlation coefficient, Supplementary Fig. 3). These results demonstrate that our method reproducibly detects RNAs present in individual subnuclear particles. However, we cannot rule out the possibility that other conditions may be more suitable.

To calculate the significance of spatial associations between transcripts while taking their vastly different abundances into account, we randomized pairings of proxy reads and their barcodes 100,000 times to obtain simulated cobarcoding counts for pairs of transcripts (see Methods, Supplementary Fig. 3). Observed cobarcoded pairwise RNA proximities were compared with simulated counts to determine statistical significance (Supplementary Tables 2,3). These analyses verified known contacts between 18S and 28S rRNAs, MALAT1 and U1 (ref. [20]) and between spliceosomal RNAs, respectively ($q < 0.002$). To further test the analysis pipeline, we performed Proximity RNA-seq using a mixture of particles from different species. To a standard input of human particles equivalent to 50 ng RNA we added the same amount of fruit fly particles to obtain a conservative estimate of false positive RNA proximities. We first selected barcode groups with exactly two transcripts and found that 20% of all two-transcript barcode groups consisted of a fly and a human transcript (Supplementary Fig. 6). We then compared the whole dataset with randomizations and estimated the false positive rates of pairwise, inter-species RNA proximities. *P*-value cutoffs for pairwise RNA proximities at 0.01, 0.05 and 0.1 resulted in 0%, 2% and 6.4% false positive rates, respectively. This shows that Proximity RNA-seq and the analysis pipeline produce few false positives even in conditions with considerable species mixing in droplets.

Main RNA compartments and transcript positioning in nuclei. Next, we analysed the number of unique transcripts cobarcoded once or multiple times and irrespective of the significance of pairwise associations, with a given RNA molecule of the 1,000 highest expressed transcripts. We found that RNAs present at higher levels had higher cobarcoded transcript counts (Fig. 2d and Supplementary Table 4). Two factors likely underlie this trend. First, in cells, highly expressed RNAs have more opportunities to encounter other transcripts, and second, in droplets, abundant RNAs are more often cobarcoded with transcripts from distinct particles, according to the Poisson distribution of particles into droplets, thereby further increasing the number of unique cobarcoded transcripts. Notably, we identified RNAs cobarcoded with more unique transcripts than would be expected by their abundance. Such RNAs were often non-coding, rather than protein-coding, and included spliceosomal (U1, U2, U4 and U5), paraspeckle (NEAT1) and nucleolar (snoRNAs) transcripts (Fig. 2d,e). The more complex compositions of cobarcoded transcripts likely reflected transcriptome-wide functions in intron excision and exon splicing in the case of spliceosomal RNAs and supported the notion of some non-coding RNAs as spatial organizers or markers of larger RNA groups in nuclei.

In DNA contact assays, close distance on the linear genome largely increases contact strength between genomic regions. Significant but lower contact strength between regions further apart is indicative of higher-order chromatin folding. We therefore assumed that pairs of nascent RNAs, although not physically linked like DNA of the same chromosome, would show increased spatial association when the distance between their genes was small. Using randomization-derived *P* values for RNA pairs, we found higher levels of associations between transcripts encoded by genes located nearby in the linear genome than between transcripts from genes further apart or on different chromosomes (Supplementary Fig. 7). This shows that one factor that specifies spatial associations of a nascent transcript with other RNAs is linear genome proximity of the respective genes.

We then asked whether larger groups of nuclear-retained, non-coding and nascent coding transcripts preferentially associate with each other and thereby partition the nuclear transcriptome. Principal component analysis (PCA) on *P* values of pairwise associations between any RNA and the top 100 connected transcripts identified two main compartments for RNA in nuclei. Principal component 2 (PC2) separated snoRNAs as well as a set of protein-coding transcripts from the bulk of mostly protein-coding transcripts (Fig. 3a, Supplementary Table 5). We dubbed this transcript group, which is highly enriched for nucleolar transcripts, compartment I, based on the prevalent RNA polymerase I activity for rRNA synthesis within the nucleolus. Accordingly, compartment II was named after RNA polymerase II, which is predominant in the nucleoplasm (Fig. 3b). We then performed dual RNA fluorescence in situ hybridization (FISH) using U3 as a nucleolar marker and sets of 24 probes hybridizing to intronic sequences of 13 different RNAs (Fig. 3c,d). The results confirmed that nascent transcripts from compartment I are indeed preferentially synthesized in close proximity to the nucleolus, whereas nascent transcripts from compartment II are transcribed in the nucleoplasm at greater distances from the nucleolus. This validates the accuracy of Proximity RNA-seq to predict spatial distances between different transcripts and a major nuclear structure, the nucleolus, providing a 'magnetic north' reference point for genome function that is lacking in chromosome conformation capture (Hi-C) data. On average, median distances between the edge of the nearest nucleolus and transcripts of compartment I were $0.82 \pm 0.24\,\mu m$ (mean ± s.d.). Compartment II transcripts, on the other hand, were found at on average twofold increased distances from the nucleoli ($1.68 \pm 0.37\,\mu m$). Our findings suggest that the perinucleolar region, which has previously been associated with transcriptionally silent, compact chromatin[3,21], expresses a specific subgroup of RNAPII-transcribed genes.

We next analysed features of RNAs grouped into eight quantiles according to their relative nuclear position derived from PC2 values (Fig. 3b,e–g). Compartment I (quantiles 1–3) contained 370 (70%) and compartment II (quantiles 4–8) 784 protein-coding

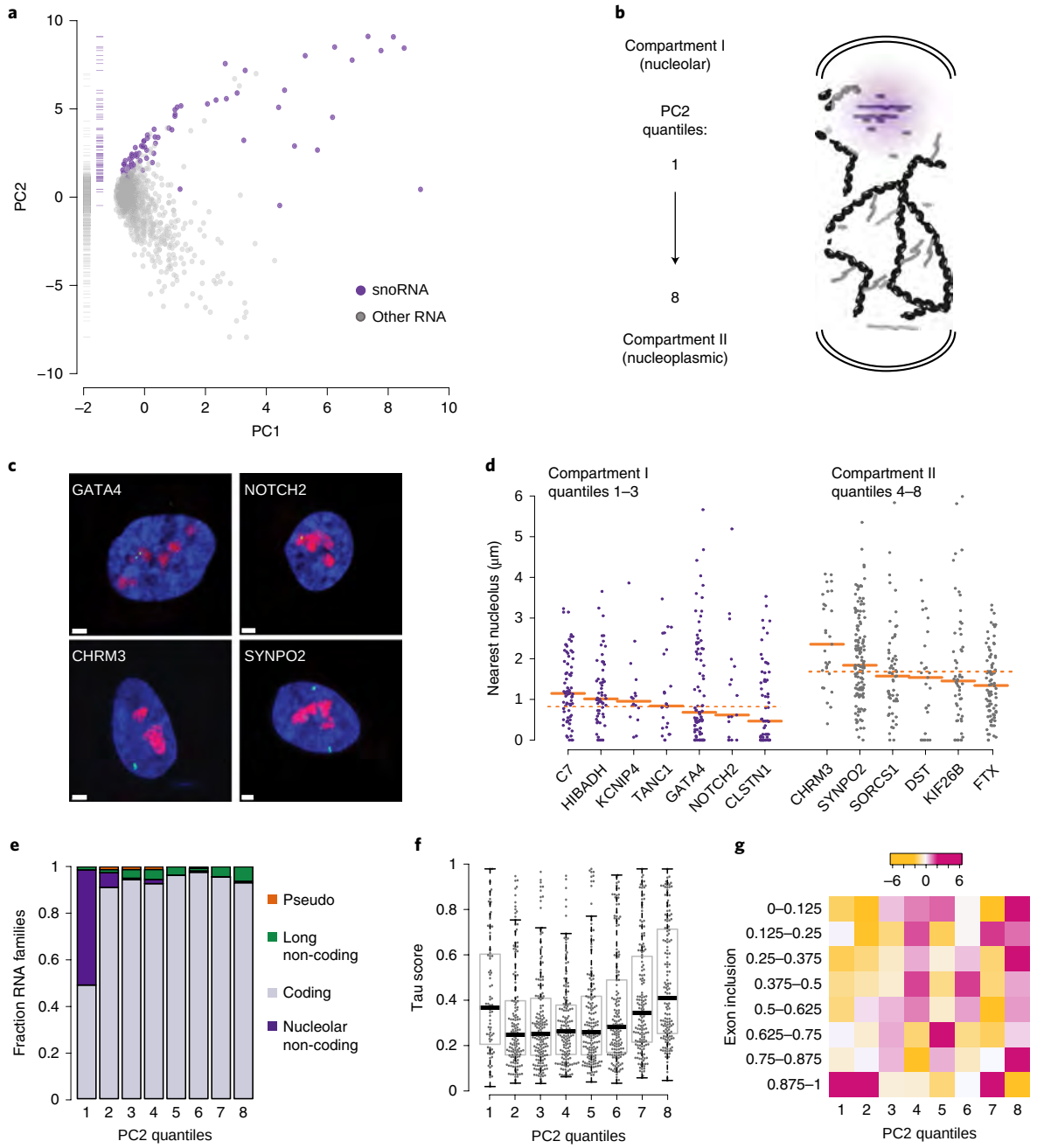

Fig. 3 | Bipartite nuclear transcriptome. a, PCA of transcripts ($n=1,388$) based on their pairwise proximity with the top 100 connected transcripts. **b**, Schematic of compartment I with transcripts in purple and compartment II with transcripts in gray. PC2 quantiles 1–8 are indicated. **c**, Examples of dual RNA-FISH. Red, U3; green, intronic probes against candidate RNA; blue, DAPI; scale bars, 2 µm. **d**, Spatial distances of intronic transcript spots to nearest nucleolus as measured by dual RNA-FISH. Compartment I transcripts are shown in purple, compartment II in gray (I versus II nested analysis of variance (ANOVA): $P=0.002$). C7 $n=72$ intronic spots, HIBADH 58, KCNIP4 16, TANC 24, GATA44 86, NOTCH2 17, DST 63, CHRM3 29, SNPO2 129, SORCS1 59, CLSTN1 27, KIF26B 55, FTX 88. Orange bar, median; dashed orange lines, mean of medians. **e**, Fractions of RNA families along PC2 axis (PC2 quantiles 1, 3, 6, 8: $n=174$, quantiles 2, 4, 5, 7: $n=173$). **f**, Tissue specificity (Tau scores, 0 for broadly expressed and 1 for tissue specific[22,23]) for each transcript in different proximity quantiles. The borders, bar and whiskers of the box plot represent the first (Q1) and third (Q3) quartiles, the median and the most extreme data points within 1.5× interquartile range from Q1 to Q3, respectively. **g**, Heatmap of Pearson residuals (yellow–magenta) from regression against PC2 quantiles (columns, PC2 quantiles 1–8: $n=1,214$, 2,017, 2,926, 3,070, 3,324, 3,884, 3,417, 3,225 exons) and bins of exon inclusion scores (rows).

transcripts (90%). We observed an accumulation of gene ontology terms, many specific to the neuronal cell type, in compartment II but few enriched terms in compartment I (Supplementary Fig. 8). Similarly, the number of transcripts with high tissue specificity[22,23] increased from compartment I to compartment II, with the exception of nucleolar quantile 1 (Fig. 3f). Consistently, genes encoding compartment II transcripts were closer in the linear genome to multi-enhancer domains crucial for cell identity (super-enhancers[24,25]) than genes whose transcripts were assigned to compartment I (Supplementary Fig. 8). Finally, alternative splicing of exons in protein-coding transcripts occurred less frequently in compartment I, as indicated by high exon inclusion[26]. In contrast, transcripts in

INFORME DE LABORES 2019

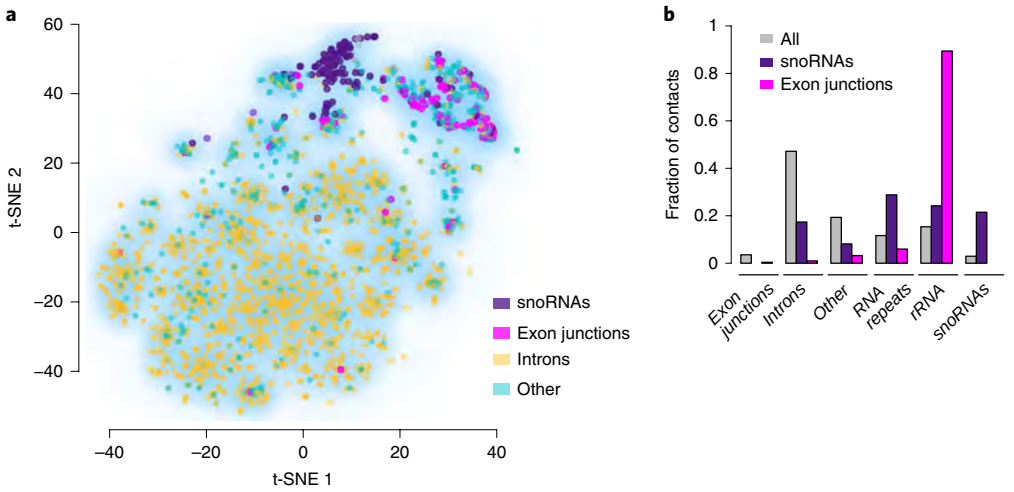

Fig. 4 | RNA proximities of nascent and processed transcripts. a, t-SNE visualization of intronic ($n=1,666$), exon junction ($n=105$) and other, ambiguous ($n=608$) RNA features based on their pairwise proximity with the top 100 connected features. Additionally, snoRNAs are colored in purple ($n=111$). **b**, Comparison of spatial RNA associations ($P\leq0.1$) between all features, snoRNAs and exon junctions with different classes of features (number of associations between features: all - exon junctions $n=1,022$, snoRNAs - exon junctions $n=0$, between pairs of exon junctions $n=4$, all - introns: $n=13,596$, snoRNAs - introns $n=147$, exon junctions - introns $n=10$, all - other $n=5,571$, snoRNAs - other $n=69$, exon junctions - other $n=33$, all - RNA repeats: $n=3,360$, snoRNAs - RNA repeats $n=244$, exon junctions - RNA repeats $n=61$, all - rRNA $n=4,426$, snoRNAs - rRNA $n=205$, exon junctions - rRNA $n=914$, all - snoRNAs $n=849$, between pairs of snoRNAs $n=182$, exon junctions - snoRNAs $n=0$).

compartment II exhibited variable and often lower exon inclusion (Fig. 3g). This suggests that the nuclear transcriptome is partitioned into broadly expressed, so-called housekeeping, transcripts in the vicinity of nucleoli in compartment I and tissue-specific RNAs and transcripts that are more frequently subject to alternative splicing in compartment II.

Precursor and processed RNA localization. To distinguish different spatial sites for precursor and processed RNA, we split reads for any transcript into three groups: overlapping introns for precursors, exon junctions for mature RNAs and a group of other, ambiguous stretches of transcripts. After comparison with random simulations (Supplementary Table 6), we visualized the high-dimensional spatial RNA association data by giving each RNA a position in a two-dimensional map using t-distributed Stochastic Neighbor Embedding (t-SNE[27]) (Fig. 4a). The clustering of snoRNAs apart from the bulk of precursor transcripts recapitulated the two compartments revealed by PCA and using gene-based transcript annotations. In addition, we found exon junctions clustered together, separated from nascent RNA and nucleolar transcript clusters. Strikingly, most pairwise RNA associations involving exon junctions were formed with ribosomal RNA (89%). Unlike snoRNAs, which contact each other and rRNA in nucleoli, exon junctions showed no association with snoRNAs (Fig. 4b). These results indicate that rRNA was captured at two distinct stages and locations: during synthesis and processing with snoRNAs in nucleoli, and as functional ribosomes, likely situated at the outer nuclear envelope and copurified from the cytoplasm by crosslinking to nuclei, in complex with spliced protein-coding RNAs as represented by exon junction reads.

Compartment- and transcript-specific local RNA density. Proximity RNA-seq enables the simultaneous detection of two or more proximal transcripts. We reasoned that frequent or rare simultaneous detection of multiple proximal transcripts is characteristic of a specific RNA and the nuclear region from which crosslinked particles originate and reflects high or low local RNA density, respectively. To derive local RNA density and/or connectivity for individual transcripts, we introduced a measure describing how often a transcript was detected singly or cobarcoded with one or multiple other RNA molecules. This so-called 'valency' of a given transcript was inferred from relative enrichments or depletions (z-score) in the number of reads mapping to the transcript in barcode groups encompassing one, two and three transcripts, respectively, compared with the nuclear transcriptome average (Fig. 5a, Supplementary Fig. 9, Supplementary Table 7). After assigning valency to individual transcripts, we analysed the distribution of valency in compartments I and II. We found that transcripts in compartment I overall exhibited high valency (that is, z-scores of valency $1<0$ and z-scores of valency 2 and $3>0$), indicating the increased RNA density in nucleoli[28]. Of note, spatial regions adjacent to nucleoli contained in PC2 quantiles 2 and 3 also exhibited high valency despite much reduced numbers of snoRNAs in such regions. In contrast, low-valency transcripts prevailed in compartment II (Fig. 5b). Further, we analysed valencies of whole proximal transcriptomes (association $P\leq0.1$) specific to the abundant non-coding RNAs 7SLRNA, 7SK and nuclear speckle-resident MALAT1, respectively (Fig. 5c). We first examined transcript assignments to PC2 quantiles and found 7SLRNA enriched in proximity to compartment I transcripts (quantiles 1–3). 7SK and MALAT1 colocalization with proximal transcripts peaked near the border of or within compartment II (quantiles 4–8), respectively (Fig. 5d). We then combined transcript-specific valencies for each proximal transcriptome. All three proximal transcriptomes showed decreased valency 1 and increased valency 2 and 3 compared with the entire transcriptome, indicative of locally increased RNA density (Fig. 5e) (tests for valency 1, compared with entire transcriptome, Kolmogorov–Smirnov, two-sided: 7SL $P=5\times10^{-5}$, 7SK $P=0.001$, MALAT1 $P=3\times10^{-5}$, Cliff's delta effect size: 7SL 0.25, 7SK 0.22, MALAT1 0.21). We next asked how the valency of proximal transcriptomes is affected through associations with high-valency nucleoli and snoRNAs. Removal of snoRNAs from the analysis reduced valencies 2 and 3 and increased valency 1 of 7SLRNA (Fig. 5e) (for valency 1 with and without snoRNAs, Kolmogorov–Smirnov, two-sided: $P=0.003$, Cliff's delta effect size: −0.23). Therefore, the proximal transcriptome of 7SLRNA increased RNA density through association with nucleolar transcripts. The valency of the 7SK transcriptome showed little change upon removal of snoRNAs (for valency 1 with and without

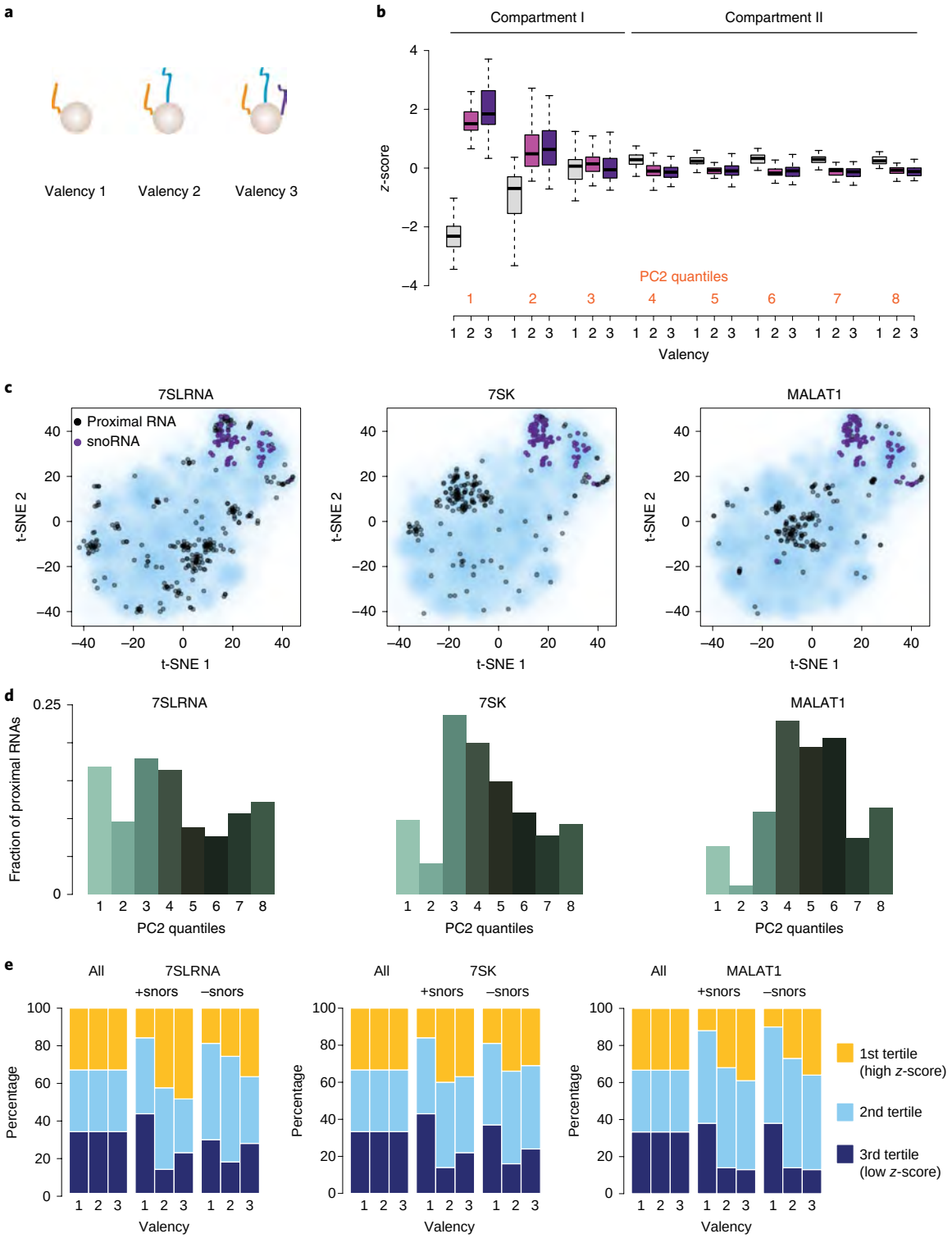

Fig. 5 | RNA valency. a, RNA valency was based on read counts of a given transcript in barcode groups with one, two or three transcripts. **b**, *z*-scores (*y* axis) of valencies (*x* axis: black numbers) along the PC2 axis (*x*: orange numbers, for PC2 quantiles 1 and 8 $n=58$, for quantiles 2–7 $n=57$ transcripts). The borders, bar and whiskers of the box plot represent the first (Q1) and third (Q3) quartiles, the median and the most extreme data points within 1.5× the interquartile range from Q1 to Q3, respectively. **c**, t-SNE visualization of transcripts (black) proximal ($P \leq 0.1$) to 7SLRNA ($n=415$), 7SK ($n=333$) and MALAT1 ($n=255$). SnoRNAs are indicated in purple. **d**, Fractions of transcripts proximal to 7SLRNA, 7SK and MALAT1, respectively, in different PC2 quantiles along the compartment I to II axis. **e**, Valency of proximal transcriptomes of 7SLRNA, 7SK, MALAT1 and of the whole transcriptome (all) before ($n=150$, 120, 103 and 2,486 transcripts, respectively) and after ($n=115$, 104, 95 and 2,411, respectively) removal of all snoRNAs from analysis (+snors, −snors). Tertiles were derived from whole-transcriptome distributions for valency 1, 2 and 3. Occurrences of transcripts proximal to 7SLRNA, 7SK and MALAT1 were counted in the tertiles and shown as percentages. For example, high valency is represented by a smaller first (yellow) and a larger third tertile (dark blue) for valency 1 and vice versa for valency 2 and 3 compared with whole-transcriptome tertiles.

INFORME DE LABORES 2019

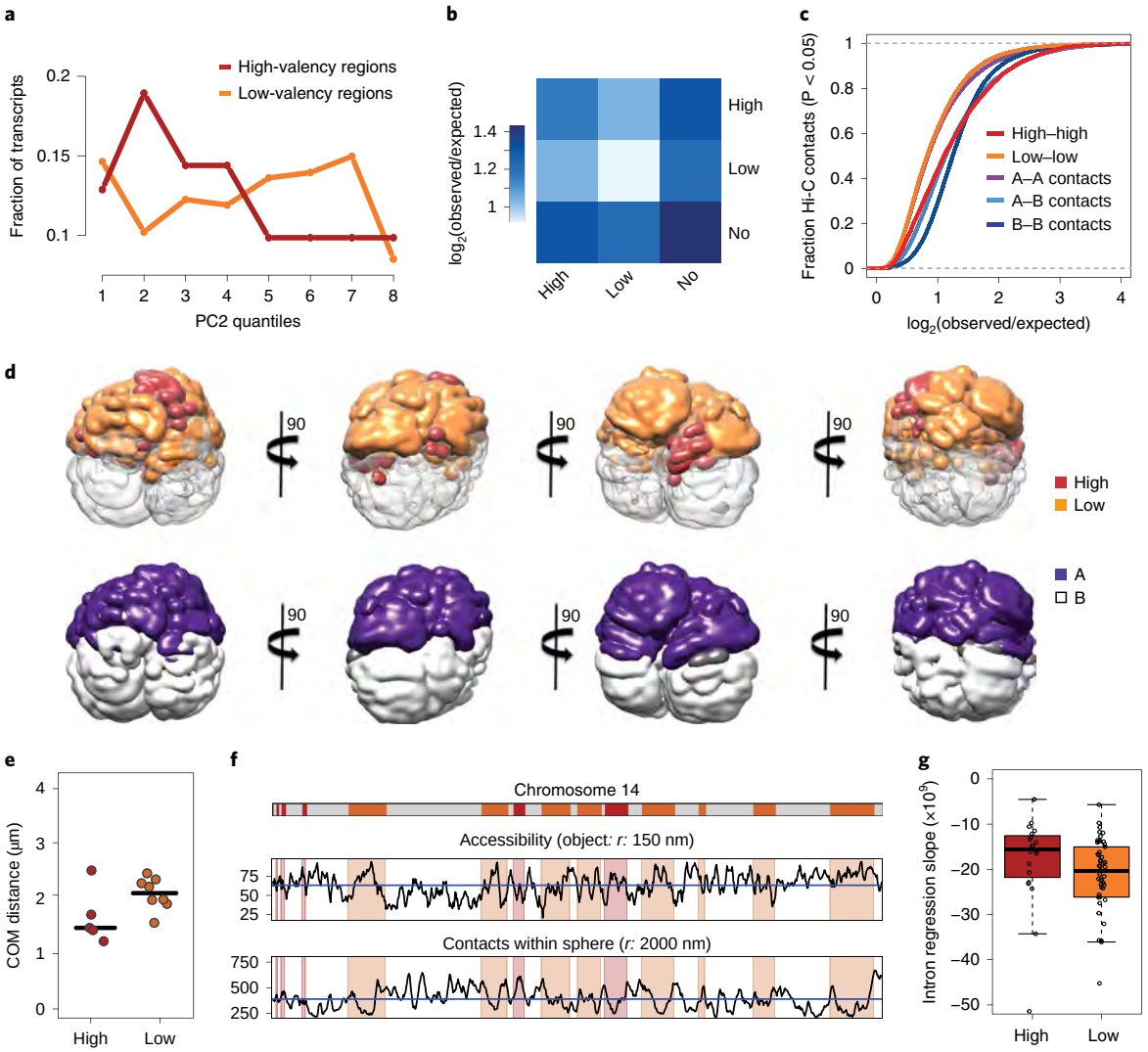

Fig. 6 | RNA valency and chromatin territories. a, Factions of transcripts with assigned valency in different PC 2 quantiles for high- and low-valency genomic regions. **b**, Mean Hi-C contact enrichments between high-, low- and no-valency regions. **c**, Cumulative distributions of Hi-C contact enrichments ($P \leq 0.05$) for high ($n = 5179$ contacts) and low ($n = 17{,}630$) valency segments in comparison with A–A ($n = 42{,}351$), A–B ($n = 22{,}217$) and B–B contacts ($n = 43{,}290$). Kolmogorov–Smirnov, two-sided, pairs of high-valency contacts versus pairs of low-valency contacts: $P = 0$, Cliff's delta effect size: 0.25. **d**, Density map of chromosome 14 ensemble model. **e**, Distances, median indicated as bar, between the center of mass (COM) of the B compartment and COM for high- ($n = 5$) and low-valency ($n = 8$) regions in chromosome 14, respectively (Mann–Whitney *U*-test, two-sided, $P = 0.1$). **f**, Local accessibility for a virtual object with radius of 150 nm and local contact density number within spherical volumes with radii 2,000 nm. High-valency regions in red, low-valency orange. **g**, Genome-wide intronic read density decays indicated faster transcription elongation in high- (red, $n = 20$) than low-valency (orange, $n = 50$) genomic regions (Kolmogorov–Smirnov, two-sided: $P = 0.03$, Cliff's delta effect size: 0.33). The borders, bar and whiskers of the box plot represent the first (Q1) and third (Q3) quartiles, the median and the most extreme data points within 1.5× the interquartile range from Q1 to Q3, respectively.

snoRNAs, Kolmogorov–Smirnov, two-sided: $P = 0.3$, Cliff's delta effect size: −0.13). Similarly to 7SK and in line with its architectural role in membrane-less nuclear bodies, autonomous from nucleoli, the proximal transcriptome of MALAT1 retained its valency state irrespective of snoRNAs (for valency 1 with and without snoRNAs, Kolmogorov–Smirnov, two-sided: $P = 0.9$, Cliff's delta effect size: −0.07). In conclusion, we found compartment I to be clearly distinguished from compartment II based on RNA density. Yet, the proximal transcriptome of MALAT1 was identified as a high-valency, RNA-dense body apart from compartment I, suggesting a heterogeneous RNA valency distribution throughout the relatively RNA-sparse compartment II.

RNA valency identifies dense, fast-transcribing chromatin. We next applied valency to differentiate transcriptionally active genomic subcompartments. Given that up to 80% of Proximity RNA-seq reads mapped to introns, we reasoned that Proximity RNA-seq-derived valency could be deployed to further classify transcript-encoding genome regions. We therefore performed Hi-C in SH-SY5Y cells and assigned average RNA valency scores to genomic regions. Hi-C studies have described open, transcriptionally active domains that preferentially contact other active domains in higher-order A compartments, while compact, poorly expressed domains preferentially contact each other in B compartments[2,29–31]. We found genomic A regions with high average RNA valency to be enriched in compartment I transcripts. Low-valency A regions more frequently encoded compartment II transcripts (Fig. 6a). As expected, genomic regions without assigned valency encompassed most B regions with low transcript expression (Supplementary Fig. 10) and showed very strong enrichment of chromatin contacts between

them by Hi-C (Fig. 6b). When comparing high- and low-valency genomic regions by Hi-C, we identified stronger DNA contact enrichments for pairs of high-valency compartment I regions, which resembled A to B contacts, whereas contact enrichments between low-valency regions were weaker, similar to A to A contacts (Fig. 6b,c, Kolmogorov–Smirnov, two-sided, pairs of high-valency contacts versus pairs of low-valency contacts: $P=0$, Cliff's delta effect size: 0.25). To gain further insights into distinct spatial distributions and local chromatin properties for different valency regions, we created three-dimensional (3D) models of a chromosome using Hi-C contact frequencies as spatial restraints[32]. In line with the contact enrichment profiles, high-valency domains in chromosome 14 were spatially closer to the B compartment than low-valency regions (Fig. 6d,e). Electron micrographs of nuclei likewise provided evidence for RNA-dense regions adjacent to compact chromatin (Supplementary Fig. 11)[33]. 3D model-derived estimates of local accessibility of a virtual object and of chromatin contact counts per volume suggested, furthermore, that high-valency regions were less accessible and more compact than low-valency regions (Fig. 6f, Supplementary Fig. 12). Finally, we observed increased transcription elongation rates in high-valency compared with low-valency regions (Fig. 6g, Supplementary Fig. 13) as estimated by regression of 5′ to 3′ read density within long introns measured by Proximity RNA-seq (Fig. 2a)[16,34]. This suggests that high- and low-valency territories are also distinguishable by local, apparent catalytic activities. In a reciprocal analysis in K562 haematopoietic cells we confirmed that fast-transcribing genomic regions, defined by BruDRB-seq[35], showed stronger Hi-C contact enrichments than slowly transcribed regions[36] (Supplementary Fig. 14).

Discussion

Much insight into RNA–RNA associations has so far been gained from methods using psoralen derivatives to specifically crosslink base-paired interactions. This approach has proved invaluable to map RNA secondary structure and to identify pairs of RNAs with complementary and hybridized sequence patches[9–13,37]. However, the larger 3D context of where RNA molecules are located and form contacts in cells has remained unaddressed. Proximity RNA-seq measures co-localization and positioning of RNAs in cellular 3D space at the resolution of individual transcripts, while psoralen methods identify base-paired regions within a transcript or a pair of transcripts. Dimensionality reduction of pairwise spatial RNA associations enabled us to accurately position transcripts to compartment I, encompassing the nucleolus and adjacent regions, and compartment II, the nucleoplasm and nuclear periphery, in strong agreement with 3D RNA-FISH. Previously, the detection and identification of the RNA-dense compartment I based on DNA proximity ligations has been hampered due to the low and repetitive DNA content in nucleoli. Furthermore, distances between genes distributed over the surface area of nucleoli are probably too large for ligation[3]. Measuring RNA proximities in subnuclear particles circumvents this limitation of DNA ligation assays to describe RNA-dense regions in nuclei. Ligation-free DNA proximity measurements mirror our finding of transcript compartments at the genome level[3].

Positioning of a gene to dense heterochromatin around nucleoli has been associated with gene repression[3,21]. However, the direct spatial mapping of transcriptional output here identified active RNA synthesis from specific genes at the periphery of nucleoli. Little is known about what defines the positioning of active genes and their nascent transcripts to either the nucleoplasm or nucleoli. Gene editing experiments, in which a compartment I gene, whose transcripts are close to nucleoli, replaces a gene encoding compartment II transcripts positioned further away from nucleoli, promise insights into whether DNA regions and/or the expressed transcript play roles in gene and RNA positioning.

Our in-emulsion barcoding and sequencing method enables not only the identification of pairwise spatial associations but also the simultaneous detection of more than two RNAs in proximity to each other. This allows transcripts to be characterized by valency, which can be interpreted as a local RNA density or connectivity. Transcripts can therefore be located and assigned to RNA-dense or sparse neighborhoods. For example, we mapped the proximal transcriptomes of 7SLRNA overlapping or at the border to high-valency compartment I, which explained the increased valency of the network. In contrast, the proximal transcriptome of MALAT1 in speckle bodies assigned to the often RNA-sparse compartment II showed increased valency independently of associations with nucleoli in compartment I.

The combined analysis of Hi-C chromatin contacts and RNA valency suggested that chromatin regions encoding compartment I transcripts with increased RNA valency exhibit stronger DNA contacts, reflecting proximity to the perinucleolar B compartment. These nucleic-acid-dense territories displayed faster transcription elongation compared with low-valency compartment II regions. We can only speculate that, besides genomic sequence and chromatin determinants, sequestering of certain protein factors might favor rapid transcription elongation in high-valency nuclear regions. Interestingly, transcription elongation factors have been shown to associate with chromatin in an RNA-dependent manner[38], which raises the possibility that transcripts themselves in crowded RNA-dense regions might accumulate elongation factors critical to speed up transcription and thereby sustain local high RNA valency.

The utility of Proximity RNA-seq will lie in its versatility to sequence different subcellular RNA-containing structures. Our understanding of the composition and functioning of RNA compartments beyond the nucleus, such as RNA-rich phase separations or aggregates in disease states, will benefit from the spatial RNA measurements introduced here. We envision that large-scale proximity measurements of RNA, a molecule with ubiquitous but non-random distribution throughout cells, will achieve a map of whole-cell spatial organization by means of sequencing.

Online content

Any methods, additional references, Nature Research reporting summaries, source data, statements of code and data availability and associated accession codes are available at https://doi.org/10.1038/s41587-019-0166-3.

Received: 12 July 2018; Accepted: 22 May 2019;
Published online: 1 July 2019

References

1. Zhao, R., Bodnar, M. S. & Spector, D. L. Nuclear neighborhoods and gene expression. *Curr. Opin. Genet. Dev.* **19**, 172–179 (2009).
2. Lieberman-Aiden, E. et al. Comprehensive mapping of long-range interactions reveals folding principles of the human genome. *Science* **326**, 289–293 (2009).
3. Quinodoz, S. A. et al. Higher-order inter-chromosomal hubs shape 3D genome organization in the nucleus. *Cell* **174**, 744–757 (2018).
4. Beagrie, R. A. et al. Complex multi-enhancer contacts captured by genome architecture mapping. *Nature* **543**, 519–524 (2017).
5. Stahl, P. L. et al. Visualization and analysis of gene expression in tissue sections by spatial transcriptomics. *Science* **353**, 78–82 (2016).
6. Lee, J. H. et al. Highly multiplexed subcellular RNA sequencing in situ. *Science* **343**, 1360–1363 (2014).
7. Chen, K. H., Boettiger, A. N., Moffitt, J. R., Wang, S. & Zhuang, X. RNA imaging. Spatially resolved, highly multiplexed RNA profiling in single cells. *Science* **348**, aaa6090 (2015).
8. Shah, S. et al. Dynamics and spatial genomics of the nascent transcriptome by Intron seqFISH. *Cell* **174**, 363–376.e16 (2018).
9. Weidmann, C. A., Mustoe, A. M. & Weeks, K. M. Direct duplex detection: an emerging tool in the RNA structure analysis toolbox. *Trends Biochem. Sci.* **41**, 734–736 (2016).
10. Nguyen, T. C. et al. Mapping RNA-RNA interactome and RNA structure in vivo by MARIO. *Nat. Commun.* **7**, 12023 (2016).

INFORME DE LABORES 2019

11. Kudla, G., Granneman, S., Hahn, D., Beggs, J. D. & Tollervey, D. Cross-linking, ligation, and sequencing of hybrids reveals RNA-RNA interactions in yeast. *Proc. Natl Acad. Sci. USA* **108**, 10010–10015 (2011).
12. Sugimoto, Y. et al. hiCLIP reveals the in vivo atlas of mRNA secondary structures recognized by Staufen 1. *Nature* **519**, 491–494 (2015).
13. Ramani, V., Qiu, R. & Shendure, J. High-throughput determination of RNA structure by proximity ligation. *Nat. Biotechnol.* **33**, 980–984 (2015).
14. Dressman, D., Yan, H., Traverso, G., Kinzler, K. W. & Vogelstein, B. Transforming single DNA molecules into fluorescent magnetic particles for detection and enumeration of genetic variations. *Proc. Natl Acad. Sci. USA* **100**, 8817–8822 (2003).
15. Shendure, J. et al. Accurate multiplex polony sequencing of an evolved bacterial genome. *Science* **309**, 1728–1732 (2005).
16. Ameur, A. et al. Total RNA sequencing reveals nascent transcription and widespread co-transcriptional splicing in the human brain. *Nat. Struct. Mol. Biol.* **18**, 1435–1440 (2011).
17. Scheer, U. & Hock, R. Structure and function of the nucleolus. *Curr. Opin. Cell Biol.* **11**, 385–390 (1999).
18. Neve, J. et al. Subcellular RNA profiling links splicing and nuclear DICER1 to alternative cleavage and polyadenylation. *Genome Res.* **26**, 24–35 (2016).
19. Gondran, P., Amiot, F., Weil, D. & Dautry, F. Accumulation of mature mRNA in the nuclear fraction of mammalian cells. *FEBS Lett.* **458**, 324–328 (1999).
20. Engreitz, J. M. et al. RNA-RNA interactions enable specific targeting of noncoding RNAs to nascent pre-mRNAs and chromatin sites. *Cell* **159**, 188–199 (2014).
21. Padeken, J. & Heun, P. Nucleolus and nuclear periphery: Velcro for heterochromatin. *Curr. Opin. Cell Biol.* **28**, 54–60 (2014).
22. Fagerberg, L. et al. Analysis of the human tissue-specific expression by genome-wide integration of transcriptomics and antibody-based proteomics. *Mol. Cell. Proteomics* **13**, 397–406 (2014).
23. Kryuchkova-Mostacci, N. & Robinson-Rechavi, M. A benchmark of gene expression tissue-specificity metrics. *Brief. Bioinform.* **18**, 205–214 (2017).
24. Whyte, W. A. et al. Master transcription factors and mediator establish super-enhancers at key cell identity genes. *Cell* **153**, 307–319 (2013).
25. van Groningen, T. et al. Neuroblastoma is composed of two super-enhancer-associated differentiation states. *Nat. Genet.* **49**, 1261–1266 (2017).
26. Busch, A. & Hertel, K. J. HEXEvent: a database of Human EXon splicing Events. *Nucleic Acids Res.* **41**, D118–124 (2013).
27. van der Maaten, L. Accelerating t-SNE using tree-based algorithms. *J. Mach. Learn. Res.* **15**, 3221–3245 (2015).
28. Edstrom, J. E., Grampp, W. & Schor, N. The intracellular distribution and heterogeneity of ribonucleic acid in starfish oocytes. *J. Biophys. Biochem. Cytol.* **11**, 549–557 (1961).
29. Dixon, J. R. et al. Topological domains in mammalian genomes identified by analysis of chromatin interactions. *Nature* **485**, 376–380 (2012).
30. Nora, E. P. et al. Spatial partitioning of the regulatory landscape of the X-inactivation centre. *Nature* **485**, 381–385 (2012).
31. Sexton, T. et al. Three-dimensional folding and functional organization principles of the Drosophila genome. *Cell* **148**, 458–472 (2012).
32. Serra, F. et al. Automatic analysis and 3D-modelling of Hi-C data using TADbit reveals structural features of the fly chromatin colors. *PLOS Comput. Biol.* **13**, e1005665 (2017).
33. Bernhard, W. A new staining procedure for electron microscopical cytology. *J. Ultrastruct. Res.* **27**, 250–265 (1969).
34. Jonkers, I., Kwak, H. & Lis, J. T. Genome-wide dynamics of Pol II elongation and its interplay with promoter proximal pausing, chromatin, and exons. *eLife* **3**, e02407 (2014).
35. Veloso, A. et al. Rate of elongation by RNA polymeraseII is associated with specific gene features and epigenetic modifications. *Genome Res.* **24**, 896–905 (2014).
36. Rao, S. S. et al. A 3D map of the human genome at kilobase resolution reveals principles of chromatin looping. *Cell* **159**, 1665–1680 (2014).
37. Ziv, O. et al. COMRADES determines in vivo RNA structures and interactions. *Nat. Methods* **15**, 785–788 (2018).
38. Battaglia, S. et al. RNA-dependent chromatin association of transcription elongation factors and Pol II CTD kinases. *eLife* **6**, e25637 (2017).
39. Rybak-Wolf, A. et al. Circular RNAs in the mammalian brain are highly abundant, conserved, and dynamically expressed. *Mol. Cell* **58**, 870–885 (2015).

Acknowledgements

J.M. was supported by a Swiss National Science Foundation early postdoc mobility fellowship, a Human Frontier Science Program long-term fellowship and the Babraham Science Policy Committee. The work of I.F. and M.A.M.-R. was partially supported by the European Research Council under the 7th Framework Program FP7/2007-2013 (ERC grant no. 609989) and the European Union's Horizon 2020 research and innovation program (grant no. 676556) to M.A.M.-R. M.A.M.-R. also acknowledges the support of the Spanish Ministry of Economy and Competitiveness (grant nos. BFU2013-47736-P and BFU2017-85926-P), Centro de Excelencia Severo Ochoa 2013-2017 (grant no. SEV-2012-0208) and the Agency for Management of University and Research Grants (AGAUR). M.F.-M. was supported by UNAM Technology Innovation and Research Support Program PAPIIT IA201817 and PAPIIT IN207319. We acknowledge Sphere Fluidics for their contribution of microfluidic knowhow and time and their free donation of surfactants. We thank Babraham sequencing, fluorescence-activated cell sorting and imaging facilities for technical support, and Peter Rugg-Gunn, Paulo Amaral and Lucas Edelman for helpful discussions.

Author contributions

J.M. designed the study, performed experiments, analysed data and wrote the manuscript with contributions from all authors. S.W.W. provided conceptual advice and analysed data. I.F., J.C., A.S.-P. and M.A.M.-R. analysed data. M.F.-M., L.F.J.-G. and S.W. performed experiments. X.L. and F.F.C. provided technical help. S.A. provided conceptual advice. P.F. designed and supervised the study and wrote the manuscript.

Competing interests

The authors declare no competing interests.

Additional information

Supplementary information is available for this paper at https://doi.org/10.1038/s41587-019-0166-3.

Reprints and permissions information is available at www.nature.com/reprints.

Correspondence and requests for materials should be addressed to J.M.

Publisher's note: Springer Nature remains neutral with regard to jurisdictional claims in published maps and institutional affiliations.

© The Author(s), under exclusive licence to Springer Nature America, Inc. 2019

Methods

Preparation of nuclear homogenates for Proximity RNA-seq. SH-SY5Y cells were cultured in high-glucose DMEM medium (Thermo Fisher Scientific) containing 10% fetal bovine serum (Hyclone) and Streptomycin, Penicillin (Thermo Fisher Scientific). At 70–80% confluency in 150 mm dishes, cells were crosslinked. Culture medium was replaced by 19.8 ml of pre-warmed 1× PBS and 0.2 ml of freshly prepared 10 mM EGS (Thermo Fisher Scientific) in dimethyl sulfoxide (DMSO) was added drop-wise for 1 mM final concentration. Cells were incubated for 10 min at 37 °C. Then, 1.4 ml of 16% formaldehyde (Agar Scientific) was added to dishes for a final concentration of 1%, and the incubation was extended for another 10 min at room temperature. The addition of 3.5 ml of 1 M glycine quenched crosslinking, and cells were scraped immediately and pelleted in a 50 ml Falcon tube at 210*g* for 5 min at 4 °C. Cell pellets were washed with 1× PBS supplemented with 125 mM glycine. A second wash with 1× PBS was carried out subsequently. Cell pellets were flash frozen in liquid nitrogen and stored at −80 °C until use.

Frozen cell pellets from single 150 mm dishes were thawed on ice in 1 ml of 20 mM Tris buffer pH 7.2, spun and resuspended in 1.5 ml of hypotonic Igepal C-630 lysis buffer (20 mM Tris, pH 7.2, 5 mM NaCl, 0.2% Igepal C-630, 2 mM EDTA, 1 mM EGTA) supplemented with 1× Complete, EDTA-free protease inhibitor cocktail (Roche Applied Science) and 0.5 units μl^{-1} SUPERase IN RNase inhibitor (Thermo Fisher Scientific). Cells were kept on ice for 30 min with occasional mixing. Nuclei were spun at 2,000 r.p.m. for 5 min in a benchtop centrifuge at room temperature, and the buffer exchanged with SDS washing buffer (20 mM Tris, pH 7.2, 5 mM NaCl, 0.3% SDS, 2 mM EDTA, 1 mM EGTA) supplemented with inhibitors as listed above. Samples were incubated for 10 min at room temperature in a thermoblock with constant mixing at 750 r.p.m. Triton X-100 was added for a final concentration of 1.7% and incubation prolonged for 10 min. Nuclei were then washed once in 10 mM Tris pH 7.2, 5 mM NaCl, 0.5 mM EDTA, 1% Triton X-100, supplemented with inhibitors as specified above, and once in the same buffer with only 0.05% Triton X-100. Nuclei were resuspended in 0.2 ml of wash buffer with 0.05% Triton X-100 and sonicated in 15 ml Falcon tubes using a bioruptor UCD-200 sonicator (Diagenode) with power set to medium for three to five cycles of 10 s on followed by 10 s off at 8 °C. After three cycles of sonication, the disruption of nuclei was inspected using Trypan blue staining and light microscopy. Sonicated nuclear homogenates were flash frozen in liquid nitrogen and stored at −80 °C until use.

Content and fragment length of RNA and DNA, respectively, were estimated after crosslink reversal and purification of nucleic acids using a spectrophotometer (NanoDrop) and agarose gel electrophoresis as follows. For DNA extraction, 20 µl of nuclear homogenate was supplemented with the following reagents to final concentrations of 50 mM Tris pH 8.0, 50 mM NaCl, 2 mM EDTA, 0.2% SDS and 5 µl of proteinase K (Roche Applied Science, 10 mg ml^{-1} stock concentration) for a total volume of 40 µl. DNA extraction mixes were first incubated for 4 h at room temperature followed by 2 h at 70 °C. Then, 2 µl of RNase A (Roche Applied Science, 10 mg ml^{-1} stock concentration) was added and samples were incubated for 1 h at 37 °C. DNA was purified by phenol/chloroform extraction and salt/isopropanol precipitation and resuspended in 10 µl of nuclease-free water (Ambion). To extract RNA, final concentrations of 100 mM sodium citrate pH 6.2, 2 mM EDTA, 0.2% SDS and 5 µl of proteinase K were added for a total volume of 40 µl. RNA extraction mixes were incubated for 4 h at room temperature followed by 1 h at 70 °C. 1 ml of Trizol LS (Thermo Fisher Scientific) was added and RNA isolated according to the manufacturer's manual and resuspended in 10 µl of water.

Barcoding of beads by emulsion PCR. For eight PCR reactions, 140 µl of MyOne streptavidin C1 magnetic beads (Thermo Fisher Scientific) was washed twice in polypropylene tubes (Treff) on a magnetic rack with high salt buffer (20 mM Tris pH 8.0, 1 M NaCl, 1 mM EDTA). After resuspension in 280 µl of high salt buffer, 48 µl of 100 µM dual-biotinylated primer R (Integrated DNA technologies) was added and beads were mixed briefly by vortexing. Binding was allowed for 20 min at room temperature with occasional vortexing. Beads were then washed twice in high salt buffer and once in TTLE buffer (10 mM Tris pH 8.0, 0.5 mM EDTA, 0.05% Triton X-100) with 0.04 µg ml^{-1} of molecular biology grade BSA (NEB). Beads were resuspended in 280 µl of TTLE buffer with 0.04 µg μl^{-1} BSA and stored for up to 2 d at 4 °C.

The aqueous phase for eight PCR reactions using AccuPrime HiFi Taq DNA polymerase and reagents (Thermo Fisher Scientific) was prepared on ice in DNA LoBind tubes (Eppendorf). To 943 µl of water were added 128 µl of 10× PCR buffer I, 32 µl of $MgSO_4$ (50 mM stock), 25 µl of dNTP mix (stock of 25 mM each dNTP, Thermo Fisher Scientific), 32 µl of Primer F (100 µM stock, Sigma) and 40 µl of 1 µM non-biotinylated primer R (Sigma). Then, 35 µl of beads carrying dual-biotinylated primer R were pipetted extensively and heated at 95 °C for 40 s before addition to the PCR mix on ice. After mixing by pipetting, 20 µl of AccuPrime HiFi Taq polymerase was added, and the mix was pipetted again. Next, 25 µl of 1 nM random barcode template was heated for 1 min at 95 °C before immediate addition to the PCR mix on ice. The mix was extensively pipetted on ice. The oil phase for one PCR reaction consisted of 480 µl of Pico-Surf 1–5% in Novec 7500 (Sphere Fluidics). To 480 µl of Pico-Surf in polypropylene tubes (Treff), 160 µl of the PCR mix was added. The water–oil phase-separated mixture was then emulsified by vortexing using a Vortex Genie 2 vortexer (Scientific Industries) on a horizontal tube holder at 4 °C for 20 min at maximum speed, and 50 µl aliquots of the emulsion were pipetted into each well of a 96-well hard-shell plate (Biorad). The PCR was carried out with a lid temperature of 100 °C. After 1 min at 94 °C, 35 cycles of 15 s at 94 °C, 30 s at 58 °C and 45 s at 68 °C were performed, followed by 5 min at 68 °C.

The 50 µl emulsion PCR reactions were pooled and spun at 2,000 r.p.m. for 1–2 min in a benchtop centrifuge or until non-emulsified oil phase appeared at the bottom. The lower oil phase was removed, three volumes of the initial aqueous phase of 5% Ficoll 400 was added, and the mixture was vortexed. Then, 350 µl of PFOH (1H,1H,2H,2H-Perfluorooctan-1-ol) was added, and after vortexing, the mixture was incubated at 37 °C for 5 min. To separate beads from the mixture, the tube was placed on a magnet and incubated at 37 °C for 5–10 min. The PFOH phase at the bottom and the aqueous upper phase, if transparent, were removed. Beads were resuspended in the remaining aqueous phase and TLE buffer (10 mM Tris pH 8.0, 0.5 mM EDTA) was added up to a total volume of around 300 µl. The PFOH extraction was repeated. Beads were then washed three to four times in TLE buffer and transferred into new tubes. Further washes as specified followed: three times in 1% SDS buffer (20 mM Tris pH 8.0, 5 mM NaCl, 1% SDS), once in TLE buffer supplemented with 1% Triton X-100, once in TTLE buffer with 0.04 µg μl^{-1} BSA. Beads from eight PCR reactions were pooled and resuspended in 50 µl of TTLE buffer with 0.04 µg μl^{-1} BSA.

Barcoding quality controls. Two-barcode quality control experiments (Fig. 1c,d) were carried out as described above except that random barcode pools were replaced with two barcode templates with defined sequences. To count barcoded beads of two-barcode experiments, fluorescently labeled probes base-pairing to barcode sequences were hybridized. Briefly, 2 µl of beads from a 50 µl batch of eight PCR reactions were mixed with 3 µl of 10× Accuprime PCR buffer I, 2 × 2 µl of the two barcode-specific probes or 1 × 2 µl of T7 probe (100 µM) and water up to 30 µl. Hybridization was carried out using the following temperature program: 2 min incubations at 94 °C and 80 °C, then from 75 °C to 61 °C a temperature decrease by 1° every 2 min, followed by 10 min at 60 °C and 2 min at 55 °C, 50 °C and 45 °C, respectively. Beads were washed once with 1% SDS buffer, once in high salt buffer, then resuspended in 1× Accuprime PCR buffer I, which was pre-warmed at 67 °C and incubated for 3 min at 67 °C. These washes were repeated two more times. After resuspension in TTLE buffer with 0.04 µg μl^{-1} BSA, beads were pipetted extensively before analysis by flow cytometry. We used a FACSAria III machine (BD Biosciences) with a 70 µm diameter nozzle and removed neutral density filter. For two-barcode experiments, fluorophores were detected with settings for PE 582/15 nm (Cy3) and APC 670/14 nm (Cy5).

To control the fraction of barcoded beads when using random template pools, we only used a Cy5-labeled DNA probe (T7 probe) hybridizing to a non-random region of the barcodes. We retained bead batches with 40–60% barcoding.

Random tailing of barcodes on beads. First, unused primers immobilized on beads were digested by an exonuclease I (NEB) treatment. One batch of beads from eight PCR reactions was resuspended in 65 µl of 10× Exo I buffer, 520 µl of water and 65 µl of exonuclease I and incubated at 37 °C for 90 min. Beads were then washed once in1% SDS buffer, once in TLE buffer with 1% Triton X-100 and once in TTLE buffer with 0.04 µg μl^{-1} BSA. To remove untemplated adenosine overhangs added by *Taq* polymerase, beads were incubated for 30 min at 20 °C in 10 µl of NEB Next End Repair Reaction Buffer, 5 µl of NEB Next End Repair Enzyme Mix (NEB) and 85 µl of water. Wash steps were repeated as outlined after exonuclease I treatment. Beads were then subjected to a T7 exonuclease treatment in 20 µl of NEB 4 buffer, 10 µl of T7 exonuclease (NEB) and 170 µl of water for 15 min at 25 °C to generate single-stranded barcodes immobilized via their dual-biotinylated 5′ ends, which are inert to exonuclease activity. The same wash steps as described above were repeated. To add random bases to barcode ends on beads, a primer with a 5′ random overhang was hybridized to the 3′ ends of barcodes and the overhang used as template to introduce 3′ random bases to barcodes. To do so, beads were resuspended in a Pfx polymerase mix (Thermo Fisher Scientific) consisting of 10 µl of 10× Platinum Pfx buffer, 84 µl of water, 3 µl of 10 mM nucleotides, 2 µl of 50 mM $MgSO_4$, 1 µl of Random tail primer (100 µM) and 1 µl of Pfx polymerase enzyme. The mix was incubated for 2 min at 94 °C, 5 min at 55 °C and 10 min at 68 °C. The wash steps as described above were repeated. The T7 exonuclease treatment to generate single-stranded barcodes was repeated as described above. Beads were resuspended in 50 µl of TTLE buffer with 0.04 µg μl^{-1} BSA and stored at −20 °C or 4 °C until use.

In-emulsion reverse transcription of RNA-containing particles and crosslink reversal. Two batches of beads, equivalent to 16 PCR reactions, were used to reverse-transcribe RNA-containing particles equivalent to 50 ng of purified RNA. The beads were resuspended in 30 µl of TTLE with 0.04 µg μl^{-1} BSA, and freshly prepared Actinomycin D (Sigma) in DMSO was added for a final concentration of 6 ng μl^{-1} to inhibit reverse transcriptase activity on DNA templates. Possible aggregates of beads were disrupted by extensive pipetting, followed by sonication using a bioruptor UCD-200 sonicator (Diagenode) with power set to medium for two cycles of 5 s on followed by 5 s off. The 160 µl of RT mixes (Thermo Fisher

INFORME DE LABORES 2019

Scientific) prepared in LoBind tubes (Eppendorf) contained 32 µl of 5× First-Strand Buffer, 8 µl of 10 mM dNTP Mix (each), 8 µl of 0.1 M dithiothreitol (DTT), 2 µl of RNase inhibitor, 0.32 µl of BSA for a final concentration of 0.04 µg µl^{-1} (NEB), 1.6 µl of $MgCl_2$ for a final concentration of 0.5 mM,16 µl of Superscript III, 2 µl of Actinomycin D, final concentration of 5 ng µl^{-1}, nuclear homogenate corresponding to 50 ng of RNA, and water. The beads were heated at 90 °C for 1 min before addition to the RT mix on ice. The emulsion was prepared with 550 µl of Pico-Surf on a vortexer as described above at 4 °C for 40 min at maximum speed, and 50 µl per well was added to a 96-well plate. A cycling temperature program was used to increase the probability of RNA priming. In a thermocycler with lid temperature at 55 °C, samples were incubated at 55 °C for 2 min, then placed on ice for 2 min, followed by 30 min at 22 °C. Then, the following cycle was repeated 60 times: 22 °C for 1 min, ramping to 50 °C with a rate of 0.5 °C s^{-1}, 50 °C for 1 min. Emulsions were broken as described earlier. Beads were resuspended in 200 µl of 20 mM Tris pH 8.0, 50 mM NaCl and incubated overnight at 65 °C. cDNA on beads was treated with 1 µl of RNase H (Thermo Fisher Scientific) and 0.5 µl of RNase A (Roche Applied Science, 10 mg ml^{-1} of stock concentration) in 5 µl of 10× RNaseH buffer l (Thermo Fisher Scientific) and 43.5 µl of water for 30 min at 37 °C. Beads were then washed once in 1% SDS buffer, once in TLE buffer with 1% Triton X-100 and once in TTLE buffer with 0.04 µg µl^{-1} BSA and resuspended in 1× TTLE buffer with 0.04 µg µl^{-1} BSA.

Proximity RNA-seq library preparation. The second Illumina sequence was introduced by PCR with a primer flanked by a poly-C stretch after G-tailing of the barcoded and immobilized cDNA. For G-tailing, beads were resuspended in 5 µl of 10× TdT buffer (NEB), 5 µl of cobalt chloride, 2.5 µl of 100 µM dGTP/ddGTP mix (95 µM dGTP (Thermo Fisher Scientific), 5 µM ddGTP (Sigma)), 5 µl of TdT enzyme (NEB, 2 units µl^{-1} final) and 32.5 µl of water and incubated for 20 min at 37 °C. Beads were washed once in 1% SDS buffer, once in TLE buffer with 1% Triton X-100, once in 10 mM Tris pH 8.0, 0.5 M NaCl, 0.5 mM EDTA, 0.05% Triton X-100 and twice in TTLE buffer with 0.04 µg µl^{-1} BSA.

Beads were resuspended in 5 µl of 10× Accuprime buffer I, 42.5 µl of water, 0.5 µl of RP1_long primer (50 µM stock), 0.5 µl of polyC12_cDNA adapter (50 µM stock) and 0.5 µl of Accuprime HiFi Taq pol (Thermo Fisher Scientific). After 1 min incubation at 94 °C, five cycles of 15 s at 94 °C, 45 s at 52 °C and 2 min 30 s at 68 °C were carried out. The beads were captured, the supernatant containing the barcoded cDNA library was transferred to a new tube and 150 µl of 20 mM Tris pH 8, 50 mM NaCl, 1 mM EDTA was added. Size selection of PCR products using AMPure XP beads (0.75× the sample volume, Beckman Coulter) was repeated twice.

To reduce non-specific amplification and PCR duplicates during library amplification with low input, an emulsion PCR was performed. The eluate from the preamplification was mixed with 20 µl of 10× Accuprime buffer I, 2 µl of RP1 long (50 µM), 2 µl of Index primer (50 µM), 1 µl of dNTPs (stock of 25 mM each dNTP, Thermo Fisher Scientific), 1 µl of $MgSO_4$ (50 mM stock), 4 µl of Accuprime HiFi Taq pol and water for a final volume of 200 µl. The mix was emulsified for 20 min with 600 µl of Pico-Surf as described above. The emulsion was transferred into wells of a 96-well plate and the following PCR program run: 94 °C for 1 min, 20–24 cycles of 15 s at 94 °C, 30 s at 52 °C and 2 min 30 s at 68 °C. After pooling the PCR reactions, the aqueous phase was recovered and DNA was size-selected in one round with 0.65× AMPure beads and a second round with 0.8× AMPure beads. The final libraries were eluted in 35 µl of TLE buffer. The concentration and fragment size distribution of libraries were determined by Bioanalyzer profiles (Agilent Technologies) and Kapa Illumina SYBR green qPCR (Kapa Biosystems) according to manufacturer's instructions.

Species-mixing control experiment. For the species-mixing experiment, 1182-4H *Drosophila melanogaster* cells were cultured in M3 medium (10% FCS) according to recommendations of the Drosophila Genomics Resource Center (DGRC). Nuclear particles were prepared as described above for human cells. Fly particles equivalent to 50 ng of purified RNA were added to the same amount of human particles before encapsulation into droplets together with barcoded beads for reverse transcription. All steps were carried out as described for libraries with human particles only.

Hi-C library generation. Hi-C libraries were generated for biological duplicates as described previously[40,41]. Briefly, after fixation in 2% formaldehyde for 10 min, nuclei from 2–10 million SH-SY5Y cells were digested with HindIII at 37 °C overnight, and DNA ends were labeled with biotin-14-dATP (Life Technologies) in a Klenow fill-in reaction and then re-ligated overnight. After treatment with proteinase K (Roche) and crosslink reversal at 65 °C for 16 h, DNA was purified and sheared to an average size of 400 base pairs (bp), following manufacturer's instructions (Covaris). The sheared DNA was end-repaired, A-tailed and size-selected using AMPure XP beads (Beckman Coulter) to isolate DNA ranging from 250 to 550 bp in size. Accessible biotin at fragment ends was removed, and internally biotinylated fragments were immobilized on MyOne Streptavidin C1 DynaBeads (Invitrogen). Paired-end adapters (Illumina) were ligated to fragment ends and Hi-C libraries were amplified by PCR.

Dual RNA-FISH. The smiFISH (single molecule inexpensive FISH) strategy adapted here has been developed by Tsanov et al[42]. The transcript-specific probes (usually 24) are unlabeled but contain a fixed sequence complementary to a fluorescently labeled detector probe (FLAP oligo, Supplementary Table 1). Transcript probe design was performed with Stellaris probe designer (www.biosearchtech.com) with the following settings: probe length 20 bases, human masking level 5, minimal spacing 2 bases. The first and/or second intron of transcripts was used for probe design. An equimolar mix of probes (100 µM) was prepared, and 2 µl of this mix and 200 pmol of the FLAP oligo were added to 50 mM Tris pH 8, 100 mM NaCl in a final volume of 20 µl. The mix was incubated at 85 °C for 1 min. To hybridize probes with FLAP oligo, the temperature was then gradually decreased at 1 °C intervals from 66 to 59 °C and the mix incubated for 1 min at each temperature. After a final incubation at 55 °C for 1 min, labeled probes were frozen. Cells were seeded on a coverglass to reach around 80% confluency the following day. Then, cells on coverglasses were washed in 1× PBS and crosslinked with 3.7% formaldehyde in 1× PBS for 10 min at room temperature followed by two 1× PBS washes. Cells were permeabilized in 1× PBS with 0.3% SDS for 10 min at room temperature followed by 1× PBS with 1% Triton X-100 for 5 min at room temperature. Subsequently, samples were washed in wash buffer (2× saline sodium citrate (Thermo Fisher Scientific), 10% deionized formamide (Ambion), 10 mM Ribonucleoside Vanadyl Complex (NEB)) for 2–5 min. Coverglasses with fixed cells were then incubated upside down on 200 µl of hybridization buffer (2× saline sodium citrate (Thermo Fisher Scientific), 10% dextran sulfate, 10% deionized formamide (Ambion), 10 mM Ribonucleoside Vanadyl Complex (NEB)) with U3 probes (100 ng) and candidate transcript probes (3 µl of mix) in a light-tight humidified chamber for 4 h at 37 °C. After in situ hybridization, samples were washed twice for 30 min in wash buffer at 37 °C. During the second wash step, 10 ng ml^{-1} of DAPI was added. Then, coverglasses with cells were washed twice in 1× PBS and mounted on microscope slides using Prolong Diamond Antifade Mountant (Thermo Fisher Scientific). Stacked images were taken with a confocal Zeiss 780 microscope (Zeiss) and 3D distances measured using the Imaris software (Bitplane).

Electron microscopy of nuclei after EDTA regressive staining. EDTA regressive staining was conducted as originally reported[33] with modifications as follows. Briefly, cell pellets were fixed in 2.5% glutaraldehyde and 4% paraformaldehyde. Samples were then dehydrated with increasing concentrations of ethanol (50%, 70%, 80%, 90%, 96%, for 10 min each and 100% ethanol three times for 10 min). Then, samples were treated three times with propylene oxide for 5 min each. Samples were embedded in epoxy resin and polymerized at 60 °C for 16 h. Thin sections of about 50 nm width were mounted on copper grids covered with formvar and treated with 3% uranyl acetate for 3 min, rinsed and then floated on 0.2 M EDTA for 18 min at room temperature. After rinsing, cells were contrasted with 0.2% lead citrate for 2 min. The grids were washed with bi-distilled water and air-dried. Imaging was done with a transmission electron microscope (Jeol JEM-1010, Peabody, MA) operating at 80 kV and a CCD (charge-coupled device) camera (CCD-300-RC, MT 1).

Filtering and mapping of barcode and cDNA reads generated by Proximity RNA-seq. Proximity RNA-seq libraries were sequenced on two to three sequencing lanes. We combined the FASTQ files, 150 bp single-end, derived from the same library into one FASTQ file.

Properly constructed sequence reads started at the 5′ end with a 26 bp random barcode, immediately followed by a fixed 20 bp sequence, which specified one of the primer sequences used to amplify barcodes on beads. The pipeline confirmed that this fixed sequence was present, allowing for a 2 bp mismatch. Reads lacking the fixed primer sequence were discarded.

Low-complexity polynucleotides, the same nucleotide 13 or more times in a 20 bp sequence, in barcodes were removed. We chose this threshold because the probability of a randomly generated 20 bp sequence containing the same nucleotide at least 13 times was less than 1 in 1,000 (it was assumed that each nucleotide occurred with equal frequency and that any combination of nucleotides was equiprobable). In addition, the software filtered out putative adapter artefacts by screening barcodes against adapter sequences used in the generation of the library.

To account for errors in barcodes introduced throughout the protocol, which could lead to an inflation of the barcode complexity of a library and reduce the number of identified spatial RNA associations, the pipeline allocated barcodes to groups of barcodes of very closely related sequences, most likely derived from the same barcode.

To create these groups, barcode sequences were extracted from all the sequenced reads. This dataset was then de-duplicated and concatenated into a single string, in which barcodes were separated from one to another by 24 unspecified bases (*N*). The produced file was in FASTA format and was subsequently converted to a Bowtie 2 FM-index (based on the Burrows–Wheeler transform). Each barcode was then mapped back to this index using Bowtie 2 in FASTA mode, reporting all alignments (-a)[43]. Barcodes either mapped uniquely to this index or mapped to multiple locations. In the latter scenario, the two locations to which the read mapped were considered members of the same barcode group. After mapping, all barcode groups sharing a common barcode were collapsed into a single barcode group comprising all the observed, slightly varying barcodes.

We noticed barcode sequences that were identical to one another but offset by a nucleotide. If artefactual, this would cause new barcodes to be generated and

potentially split otherwise cobarcoded groups of transcripts. For this reason, we trimmed barcodes by 3 bp at either end after extracting from the 150 bp sequenced read and before mapping to the virtual barcode genome, which consisted of the full 26 bp units.

Finally, to remove large, likely false positive transcript groups, we chose a conservative cutoff in which the pipeline modeled the variation in increasing barcode group size, that is, the number of cobarcoded transcripts, as a Poisson distribution. Barcode groups of a size so large that they would have been expected to occur with a probability of less than 0.001 were removed from the dataset.

For mapping cDNA sequences, the first 67 bp from the start of a read were removed (26 bp barcode, 20 bp barcode PCR primer, 15 bp random reverse transcription primer and six extra base pairs, which improved mapping efficiency); the next 50 bp were retained and mapped to the human genome using HISAT2 with default parameters[44] and known splice-sites (GRCh38.83).

Ribosomal RNA sequences in the reference human genome 38 were masked. The rRNA sequence was subsequently re-introduced into the genomic sequence as a separate chromosome (NCBI Reference Sequence: NR_046235.1).

Following mapping, exact read duplicates (reads sharing identical barcodes and mapping to the same position) were removed, but one representative copy was retained.

Custom transcriptome annotation. We used gene annotations from ENSEMBL Human Genome 38 (Ensembl 78: December 2014) as transcript units. We divided the reference annotation so that reads could be aligned unambiguously to a single feature. Since genes may overlap, we defined a hierarchy to establish how regions were classified (Supplementary Fig. 2). First, the pipeline used the ENSEMBL Human Genome 38 to retrieve gene coordinates and repeat masker to define RNA repeat regions in Human Genome 38 (http://www.repeatmasker.org). Opposing strands were treated separately with respect to overlapping genes, but regions of overlap between genes on the same strand were excluded. An exception to that rule was when genes were contained entirely within a surrounding gene. In such instances, the area of overlap was assigned to the inner gene. This was particularly important, since many genes, such as snoRNAs, are often located entirely within larger genes. Reads mapping to either strand of a RNA repeat region in the genome were assigned to single representations of 5S, HY1, HY3, HY4, HY5, U1, U2, U3, U4, U5, U6, U7, U8, U13, U14, U17, BC200, transfer RNA (all t-RNAs were collapsed into one feature), 7SLRNA and 7SK.

For gene features, only uniquely mapping reads were kept. The pipeline allowed multi-mapping as long as the best possible alignment corresponded to a predefined repeat region. Reads not mapping to any feature were discarded.

The pipeline grouped features into RNA particles or transcript groups based on the barcode read sequences. Multiple reads with the same barcode and mapping to the same transcript were counted as one observation, which we named a proxy read, due to the ambiguity of the multiple reads originating from a single RNA molecule or from several copies of the same transcript.

Monte Carlo simulation to identify preferential pairwise RNA contacts. We created a Monte Carlo simulation to identify preferential spatial associations or contacts between pairs of transcripts. The simulation took as input: (1) the number of transcript groups or RNA particles observed, which equals the number of unique barcodes in a dataset, (2) the barcode group size of each of those particles and (3) the frequency with which each transcript was observed in the dataset (number of proxy reads). The simulation first constructed frequency distributions for barcode group size and transcript abundance. Then, virtual RNA particles were created in silico by selecting a random value from the barcode group size distribution and then randomly selecting different transcripts from the transcript abundance distribution to fill up the barcode group. Again, the simulation allowed any combination of transcripts within a barcode group except combinations with multiple observations of the same transcript. On the occasion when a transcript was selected that was already present in the particle, the selection of the new transcript was rejected and instead added to a priority pool. Transcripts inside the priority pool were randomly picked for the generation of the following virtual RNA particle.

Following random particle generation, the cobarcoded pairwise RNA contacts were counted. In total, 100,000 simulations were performed, and the number of simulations in which a pairwise RNA contact occurred at least as many times as in the observed data was recorded. This gave a *P* value for the probability that an observed RNA–RNA contact in the real data could have occurred with that frequency by chance. One of the simulated randomized datasets was also passed to the Monte Carlo simulation to undergo 100,000 simulations. We intended that this would give us a measure of the variation between random datasets (but still retain comparable barcode group size and transcript abundance distributions to those of the observed datasets). There were now two groups of Monte Carlo simulations: the first the result of performing 100,000 simulations on the observed dataset (group 1) and the second the result of performing 100,000 simulations on one of the randomized datasets (group 2) of group 1.

Each *P* value assigned to an observed contact after comparison with group 1 was then added to a local distribution of 500 *P* values from the group 2 simulations. The local distributions were chosen to most closely match the RNA–RNA contact being examined in terms of the observed and simulated counts. Each distribution was modeled as a normal distribution to assign a probability of a given contact falling within that distribution. Consequently, for infrequent contacts the selected distributions generally exhibited high variability, whereas for frequent contacts the variability was lower, so the new *P* values calculated took this change in variability into account. These new, local-background-corrected *P* values obtained from the normal distribution, referred to simply as *P* values throughout the manuscript, were used when filtering spatial RNA associations and for principal component and t-SNE analyses. Furthermore, background-corrected *P* values were adjusted using Benjamini–Hochberg multiple testing correction.

Nascent versus processed transcriptome analysis. We categorized the Binary Alignment Map (BAM) format reads mapped by HISAT2 into one of three categories: 'Exon Junction', 'Nascent' or 'Other'. To achieve this, we defined regions in human genome assembly 38.78 as unambiguously intronic: that is, notated as an intron but never also notated as an exon in the case of overlapping isoforms or genes. After determining the genomic positions of these sequences, we identified BAM reads in which both ends overlapped an unambiguous intron sequence, and analysis of the Compact Idiosyncratic Gapped Alignment Report (CIGAR) string showed that the read was not split by HISAT2 during mapping. These were considered nascent reads. In contrast, we defined exon junction reads as those that that were split by HISAT2 during mapping and neither of the split read sequences overlapped with a predefined unambiguous intron region. All reads classified neither as exon junction nor as nascent were labeled as other.

Poisson distribution in bead barcoding. Bead barcoding, and in general the integrity of emulsions generated as described earlier, was controlled by applying a Poisson model to two-barcode PCR assay data (see section "Barcoding quality controls"). Specifically, flow cytometry analysis of barcoded beads was used to count the number of beads without barcodes, beads with both barcodes and beads with signal from only one of the two barcodes. However, beads for which we detected only one type of barcode could originate from PCR reactions with initially a single or multiple copies of one of the barcode templates. Similarly, beads with both barcode types could originate from more than two templates. We estimated the number of initial barcodes per droplet as follows. Let X and Y be the hidden number of initial barcode templates of each type on a bead. We assumed that $X \approx \text{Poisson}(\lambda_X)$ and $Y \approx \text{Poisson}(\lambda_Y)$, with X and Y independent. For each bead, we observe $I_X = I(X > 0)$ and $I_Y = I(Y > 0)$—that is, binary indicators of whether each Poisson variable is greater than zero. It can be shown that the maximum likelihood estimate of λ_X is $-\log(1 - \text{mean}(I_X))$, with a similar result for λ_Y. From this information, we estimated the number of beads with unique barcodes, which is $P(X+Y=1) = (\lambda_X + \lambda_Y)\exp(-\lambda_X - \lambda_Y)$ (since $X + Y \approx \text{Poisson}(\lambda_X + \lambda_Y)$). Similarly, the number of beads with multiple barcodes is $P(X+Y>1) = 1 - P(X<2) = 1 - (1 + \lambda_X + \lambda_Y)\exp(-(\lambda_X + \lambda_Y))$. Hence, we estimated the ratio of single-to-multiple barcodes as $P(X+Y=1)/P(X+Y>1)$. This assumption can be verified with the chi-squared test of independence—we used two degrees of freedom, since the total number of beads is not fixed and two parameters are estimated from the data.

Mapping statistics. We compared the percentage of reads mapping to genes, exons and introns (Ensembl 78: December 2014) from Proximity RNA-seq and ribosomal RNA-depleted total RNA library from SH-SY5Y cells[39] (SRX1007599) with the percentage of base coverage of the same features. Genes were set as 100.

U3 RNA proximities and experimental controls. The number of cobarcoding events was plotted against the number of proxy reads for each transcript. A Mann–Whitney *U*-test was performed on the log ratios ($\log_2$(cobarcoding counts) − $\log_2$(proxy reads)) for snoRNAs and non-snoRNAs.

Number of cobarcoded transcripts of top 1,000 RNAs. We restricted the analysis to the top 1,000 transcripts (based on the number of proxy reads in the observed dataset). For each of these transcripts, the number of unique, cobarcoded transcripts was counted irrespective of how many times a given pair of transcripts was observed together. The number of unique, cobarcoded transcripts was plotted against the number of proxy reads for the corresponding transcript of the top 1,000 list. Using the top 1,000 transcripts from the observed dataset, unique cobarcoded transcripts were retrieved from random simulations as well. Fisher's exact tests were performed for each transcript on 2 by 2 tables, which included the number of contacted, that is, cobarcoded, transcripts and the number of transcripts that were not cobarcoded of the top 1,000 transcriptome for the observed and the randomized data. The top 1,000 proximal transcriptome was defined as the union between observed and simulated datasets of all transcripts contacted at least once by any top 1,000 RNA. *P* values were false discovery rate (FDR)-adjusted to control for multiple testing.

RNA proximities and genomic distance. Monte Carlo simulation-derived $-\log_{10}$ *P* values, capped at 10, were plotted for RNA association pairs with more than three observations and after filtering out RNA repeats with multiple gene loci against genomic distance between the RNA-encoding genes.

INFORME DE LABORES 2019

Principal component analysis on pairwise RNA contacts. We performed PCA on a matrix of $-\log_{10} P$ values within each cell from pairwise spatial RNA associations. The top 100 connected transcripts were used as input variables (columns) and all transcripts as observations (rows). Including more transcripts as input variables resulted in failure of PCA due to violation of the normality assumption. Furthermore, we only used pairwise spatial RNA associations with more than three observations and a P value cutoff ≤ 0.1 as derived by the Monte Carlo simulations. We removed transcripts with only one reported pairing with another transcript and associations that involved mitochondrial ribosomal RNA. We restricted $-\log_{10} P$ values to a plateau at 5 and then subtracted the matrix mean from cells before performing PCA (R: princomp, using the correlation matrix). Transcripts were assigned to eight quantiles based on PC2.

Analysis of PC2 quantiles. Transcripts contained within the eight PC2 quantiles were assigned to RNA classifications retrieved from HGNC (HUGO gene nomenclature committee, http://www.genenames.org/).

We analysed enrichments of biological processes from gene ontology for transcripts in PC 2 quantiles using ToppCluster[45] (https://toppcluster.cchmc.org/). A P value cutoff ≤ 0.05 and Bonferroni correction were selected. Furthermore, limits of transcript number n (minimum and maximum number of transcripts allowed for an annotation) were set to $5 \leq n \leq 1{,}500$. Identified terms of biological processes were clustered for visualization in Supplementary Fig. 8 based on semantic grouping using the R package GOSemSim[46].

Tissue specificity of transcripts in PC2 quantiles based on Tau scores, where 0 means broadly expressed and 1 is specific, was retrieved from Kryuchkova-Mostacci and Robinson-Rechavi[23]. The expression data are based on RNA-seq measurements of 27 human tissues[22].

Exon inclusion scores, a measure for how often an exon is included in the mature transcript molecule, were used to estimate alternative splicing of transcripts in PC2 quantiles. For exons of known mRNA isoforms (excluding non-coding RNAs) as defined by the UCSC Genome Browser (GRCh37/hg19) scores were obtained from the HEXEvent database[26] (http://hexevent.mmg.uci.edu/). Furthermore, the exon inclusion scale from 0 to 1 was divided into eight equal interval groups. Thus, each exon had an assigned exon inclusion group and also a PC2 quantile. To identify overrepresented or underrepresented combinations of exon inclusion group and PC2 quantile, we used a Poisson generalized linear model (GLM). We counted the number of transcripts with each combination. This count was regressed against a linear combination of exon-inclusion-group-specific and PC2-quantile-specific parameters via a logarithmic link function. The Pearson residuals from this regression model were plotted in a heatmap.

t-SNE using introns, exon junctions and other features of transcripts or gene-based annotations. The same matrix as for PCA with $-\log_{10} P$ values within each cell from pairwise spatial RNA associations was used for t-SNE. The top 100 connected transcripts were used as input variables (columns) and all transcripts as observations (rows). Again, we only used pairwise spatial RNA associations with more than three observations and a P value cutoff ≤ 0.1 as derived by the Monte Carlo simulations. We removed transcripts with only one reported pairing with another transcript and associations that involved mitochondrial rRNA. We restricted $-\log_{10} P$ values to a plateau at 5 and then subtracted the matrix mean from cells before performing t-SNE (Rtsne package: seed 96, perplexity = 50, theta = 0.2). Similarly, for gene-based annotations the PCA matrix was used for t-SNE visualization (seed 96, perplexity = 46, theta = 0.1).

Assignment of valency to transcripts. Proxy reads for each transcript were counted in barcode groups of different size (named valencies). We then selected transcripts with the sum of valency 1, 2 and 3 (1: an observation of a single transcript, 2: two different transcripts detected with one barcode, 3: three different transcripts detected with one barcode) greater than 10 proxy reads. For each transcript, counts in valency 1, 2 and 3 were divided by the sum of all three valencies of that given transcript. Subsequently, the transcriptome-wide distributions of the three valencies were separately transformed into z-scores. Transcripts were then assigned to high- and low-valency classes, respectively. High-valency transcripts were defined based on z-scores of valency 1 <0 and a mean of valency 2 and 3 z-scores >0. Low-valency transcripts had z-scores of valency 1 >0 and a mean of valency 2 and 3 z-scores <0. Furthermore, only transcripts reproducibly assigned to high- and low-valency classes in Proximity RNA-seq triplicates were retained and used for further analysis. To analyse the valency of a group of transcripts proximal to a specific RNA, the mean valency z-scores were used.

Hi-C data processing. Sequencing data generated by Hi-C of two biological replicates were processed using HiCUP, which includes mapping to the reference genome, di-tag filtering and removal of artefacts[47].

Each chromosome contact matrix was normalized using TADbit[32]. Briefly, low-quality bins (those presenting low contacts numbers) were removed and ICE normalization[48]—also known as 'vanilla' normalization[36]—was performed using the default settings.

Identification of subnuclear genomic compartments. To segment the genome into A and B regions, the normalized Hi-C matrices at 100 kb resolution were transformed into correlation matrices using the Pearson product-moment correlation. The first component of a PCA (PC1) on each of these matrices was used as a quantitative measure of compartmentalization, and gene expression values (rpkm) from Proximity RNA-seq data were used to assign negative and positive PC1 categories to the correct compartments. If necessary, the sign of the PC1 (which is randomly assigned) was inverted so that positive PC1 values corresponded to A compartment regions and vice versa for the B compartment.

Integrative 3D chromosome modeling with TADbit. To assess the potential of the Hi-C data for modeling, we computed the MMP score (0.6) of the matrix and the predicted accuracy of the models, named distance Spearman correlation coefficient (0.5), using the MMP score as implemented in TADbit[32,49]. The MMP score is based on the matrix size, the contribution of significant eigenvectors in the matrix, and the skewness and kurtosis of the z-scores distribution of the matrix.

The normalized interaction matrix of chromosome 14 was used for modeling at a resolution of 100 kb. The short chromosome arm and the centromere were omitted due to the poor quality of the contact information. TADbit generates 3D models using a restraint-based modeling approach, where the experimental frequencies of interaction are transformed into a set of spatial restraints. The size of each particle in the models was defined by the relationship 0.01 nm bp^{-1} assuming the canonical 30 nm fibre[50]. Using a grid search approach, TADbit identified empirically the three optimal parameters to be used for modeling: (1) maximal distance between two non-interacting particles (maxdist set as 1,600 nm); (2) a lower-bound cutoff to define particles that do not interact frequently (lowfreq set as −1.6); and (3) an upper-bound cutoff to define particles that do interact frequently (upfreq set as 0.0). Once the three optimal parameters are defined, TADbit sets the type of restraints between each pair of particles considering an inverse relationship between the frequencies of interactions of the contact map and the corresponding spatial distances. Two consecutive particles were spatially restrained by a harmonic oscillator with an equilibrium distance that corresponds to the sum of their radii. Non-consecutive particles with contact frequencies above the upper-bound cutoff were restrained by a harmonic oscillator at an equilibrium distance, while those below the lower-bound cutoff were maintained further than an equilibrium distance by a lower-bound harmonic oscillator. To identify 3D models that best satisfy all the imposed restraints, the optimization procedure was then performed using a Monte Carlo simulated annealing sampling protocol as implemented in TADbit. A total of 5,000 models were generated and only the 1,000 that best satisfied the input restraints were used for further analysis. The contact map obtained from the final 1,000 models ensemble resulted in a Pearson correlation of 0.72 with the input Hi-C interaction matrix, which is indicative of good model accuracy[49].

Clustering was performed on the models ensemble to assess its structural similarity using a pairwise rigid-body superposition that minimizes the root mean squared deviation (r.m.s.d.) between the superimposed conformations, as implemented in TADbit.

Structural analysis of the 3D chromosome model. Using TADbit, a set of descriptive measures were calculated to analyse the structural properties of each particle in the ensemble model: (1) accessibility, measuring how accessible a particle is from an external object of radius of 150 nm; (2) density, measuring the local compactness of the chromatin fibre; (3) contact density, counting the number of particles within a given spatial distance (2× particle size) from a specified particle; and (4) walking angle, measuring the angle formed by a particle and its two immediate neighbor particles. Using these descriptive measurements, we calculate local proprieties of the ensemble model. We define local accessibility of a particle as the mean accessibility value of a given particle over all N models in the ensemble. Similarly, we define local contact density of a particle as the mean contact density of a given particle over all N models in the ensemble; this is used as a proxy for local packing density.

A density map is generated for each cluster in the ensemble using the *molmap* command in Chimera[51]. The density map is represented by intensities at points i (ρ_i) on a cubic grid with a grid space of resolution in kb divided a factor of 3. Each structure is defined by its beads coordinate in Cartesian space and a mass corresponding to 1 bead unit.

The density ρ_i is defined with a Gaussian function as:

$$\rho_i = \sum_N \frac{Z_N}{(\sigma\sqrt{2\pi})^3} e^{-\frac{(x-x_n)^2+(y-y_n)^2+(z-z_n)^2}{2\sigma^2}}$$

x, y and z are the Cartesian coordinates of particle N, Z_N is the mass and σ is set equal to the resolution in kb (100). Density maps for specific compartments or regions are generated accordingly.

The distances between the centers of mass (COMs) of different density map regions were calculated to analyse the relative positioning of high- and low-valency regions with respect to the B compartment. Analysis was performed with Chimera[51].

Hi-C contact enrichments between genomic valency segments. We computed contact enrichments between all PCA-derived Hi-C regions (A and B regions,

INFORME DE LABORES 2019

excluding chromosome X) using a statistical model based on a binomial test to estimate the significance of contacts as implemented in SeqMonk (https://www.bioinformatics.babraham.ac.uk/projects/seqmonk/). Contacts with P values ≤ 0.05 and at least five observations were reported. High- and low-valency transcripts (see method paragraph on valency) were scored as 1 and −1, respectively, and for every A, B genomic region the mean score of valency transcripts overlapping the region was calculated. We selected regions with at least three transcripts with assigned valency for further analysis. Low-valency regions were defined based on scores smaller than or equal to the median of all region valency scores; high-valency regions had bigger scores than the median. Regions that did not overlap with any valency transcript were classified as no-valency regions. Empirical cumulative distribution functions and means of $\log_2$ observed/expected contacts (contact enrichment) were plotted for groups of contact pairs as indicated (Fig. 6c).

Regression of intronic read density decay. We implemented a linear regression analysis to estimate the read decrease along introns into the SeqMonk suite (https://www.bioinformatics.babraham.ac.uk/projects/seqmonk/). Briefly, Proximity RNA-seq, pool of p2, p5, p8 and p7 libraries, was used as a 1D RNA-seq dataset after read de-duplication based on genomic position and ignoring RNA particle-specific barcodes. We only considered introns of at least 30 kb in length. Reads were binned into 500 bp windows for linear regression. Regressions were only reported if the slope was negative and the P value did not exceed 0.05. All slope values were reported multiplied by a factor of 1,000,000. For genomic intervals overlapped by multiple intron isoforms, the mean slope of all isoforms was used. Genomic regions with two or more valency transcripts and three or more introns with estimated elongation rates were included in the analysis.

Statistics. Proximity RNA-seq libraries were generated from multiple independent SH-SY5Y cell cultures. The frequency with which pairwise RNA cobarcoding occurred at least as many times in simulations as in observed data generated P values for RNA–RNA proximities. P values were then background-corrected based on local distributions of observed and simulated RNA–RNA proximity counts modeled as normal distributions.

In follow-up analyses exact sample sizes and statistical tests, all two-sided, are noted.

Reporting Summary. Further information on research design is available in the Nature Research Reporting Summary linked to this article.

Data availability

Proximity RNA-seq and Hi-C raw sequencing data are available on Gene Expression Omnibus accession: GSE129732.

Code availability

Code for Hi-C and Proximity RNA-seq analysis is available on github: https://github.com/3DGenomes/TADbit and https://github.com/StevenWingett/CloseCall, respectively.

References

40. Mifsud, B. et al. Mapping long-range promoter contacts in human cells with high-resolution capture Hi-C. *Nat. Genet.* **47**, 598–606 (2015).
41. Rubin, A. J. et al. Lineage-specific dynamic and pre-established enhancer-promoter contacts cooperate in terminal differentiation. *Nat. Genet.* **49**, 1522–1528 (2017).
42. Tsanov, N. et al. smiFISH and FISH-quant – a flexible single RNA detection approach with super-resolution capability. *Nucleic Acids Res.* **44**, e165 (2016).
43. Langmead, B. & Salzberg, S. L. Fast gapped-read alignment with Bowtie 2. *Nat. Methods* **9**, 357–359 (2012).
44. Kim, D., Langmead, B. & Salzberg, S. L. HISAT: a fast spliced aligner with low memory requirements. *Nat. Methods* **12**, 357–360 (2015).
45. Kaimal, V., Bardes, E. E., Tabar, S. C., Jegga, A. G. & Aronow, B. J. ToppCluster: a multiple gene list feature analyzer for comparative enrichment clustering and network-based dissection of biological systems. *Nucleic Acids Res.* **38**, W96–102 (2010).
46. Yu, G. et al. GOSemSim: an R package for measuring semantic similarity among GO terms and gene products. *Bioinformatics* **26**, 976–978 (2010).
47. Wingett, S. et al. HiCUP: pipeline for mapping and processing Hi-C data. *F1000Research* **4**, 1310 (2015).
48. Imakaev, M. et al. Iterative correction of Hi-C data reveals hallmarks of chromosome organization. *Nat. Methods* **9**, 999–1003 (2012).
49. Trussart, M. et al. Assessing the limits of restraint-based 3D modeling of genomes and genomic domains. *Nucleic Acids Res.* **43**, 3465–3477 (2015).
50. Gerchman, S. E. & Ramakrishnan, V. Chromatin higher-order structure studied by neutron scattering and scanning transmission electron microscopy. *Proc. Natl Acad. Sci. USA* **84**, 7802–7806 (1987).
51. Pettersen, E. F. et al. UCSF Chimera – a visualization system for exploratory research and analysis. *J. Comput. Chem.* **25**, 1605–1612 (2004).

nature research

Corresponding author(s): Jörg Morf

Reporting Summary

Nature Research wishes to improve the reproducibility of the work that we publish. This form provides structure for consistency and transparency in reporting. For further information on Nature Research policies, see Authors & Referees and the Editorial Policy Checklist.

Statistical parameters

When statistical analyses are reported, confirm that the following items are present in the relevant location (e.g. figure legend, table legend, main text, or Methods section).

n/a	Confirmed	
☐	☒	The exact sample size (*n*) for each experimental group/condition, given as a discrete number and unit of measurement
☐	☒	An indication of whether measurements were taken from distinct samples or whether the same sample was measured repeatedly
☐	☒	The statistical test(s) used AND whether they are one- or two-sided *Only common tests should be described solely by name; describe more complex techniques in the Methods section.*
☐	☒	A description of all covariates tested
☐	☒	A description of any assumptions or corrections, such as tests of normality and adjustment for multiple comparisons
☐	☒	A full description of the statistics including central tendency (e.g. means) or other basic estimates (e.g. regression coefficient) AND variation (e.g. standard deviation) or associated estimates of uncertainty (e.g. confidence intervals)
☐	☒	For null hypothesis testing, the test statistic (e.g. *F*, *t*, *r*) with confidence intervals, effect sizes, degrees of freedom and *P* value noted *Give P values as exact values whenever suitable.*
☒	☐	For Bayesian analysis, information on the choice of priors and Markov chain Monte Carlo settings
☒	☐	For hierarchical and complex designs, identification of the appropriate level for tests and full reporting of outcomes
☐	☒	Estimates of effect sizes (e.g. Cohen's *d*, Pearson's *r*), indicating how they were calculated
☐	☒	Clearly defined error bars *State explicitly what error bars represent (e.g. SD, SE, CI)*

Our web collection on statistics for biologists may be useful.

Software and code

Policy information about availability of computer code

Data collection	Read sequences were acquired using Illumina instrumentation and software. For dual RNA-FISH, probe design was performed with Stellaris probe designer (www.biosearchtech.com), 3D FISH distances were measured using the Imaris software (Bitplane).
Data analysis	All software and code used in this study has been described in published literature (Bowtie v2.2.6, HICUP v0.5.8, Bowtie v2.3.2, Hisat2 v2.1.0, SeqMonk v1.35.0, R v3.1.3, ToppCluster) or are custom made and available on github, https://github.com/3DGenomes/TADbit and https://github.com/StevenWingett/CloseCall.

For manuscripts utilizing custom algorithms or software that are central to the research but not yet described in published literature, software must be made available to editors/reviewers upon request. We strongly encourage code deposition in a community repository (e.g. GitHub). See the Nature Research guidelines for submitting code & software for further information.

Data

Policy information about availability of data

All manuscripts must include a data availability statement. This statement should provide the following information, where applicable:

- Accession codes, unique identifiers, or web links for publicly available datasets
- A list of figures that have associated raw data
- A description of any restrictions on data availability

Proximity RNA-seq and Hi-C sequencing data are available on Gene Expression Omnibus (GEO) accession: GSE129732.

Field-specific reporting

Please select the best fit for your research. If you are not sure, read the appropriate sections before making your selection.

☒ Life sciences ☐ Behavioural & social sciences ☐ Ecological, evolutionary & environmental sciences

For a reference copy of the document with all sections, see nature.com/authors/policies/ReportingSummary-flat.pdf

Life sciences study design

All studies must disclose on these points even when the disclosure is negative.

Sample size	Proximity RNA-seq with identical experimental parameters was performed using 3 biological replicates. Results were pooled for subsequent analysis. Hi-C experiments were performed in duplicates and reads pooled for further analysis.
Data exclusions	No data was excluded.
Replication	All attempts to replicate data were successful.
Randomization	No randomization was required for this study since no comparisons were made between samples/experimental groups.
Blinding	No blinding was required for this study since no comparisons were made between samples/experimental groups.

Reporting for specific materials, systems and methods

Materials & experimental systems

n/a	Involved in the study
☒	☐ Unique biological materials
☒	☐ Antibodies
☐	☒ Eukaryotic cell lines
☒	☐ Palaeontology
☒	☐ Animals and other organisms
☒	☐ Human research participants

Methods

n/a	Involved in the study
☒	☐ ChIP-seq
☒	☐ Flow cytometry
☒	☐ MRI-based neuroimaging

Eukaryotic cell lines

Policy information about cell lines

Cell line source(s)	SH-SY5Y human neuroblastoma cell line (Sigma)
Authentication	SH-SY5Y cells were identified based on RNA expression (Proximity RNA-seq expression) and gene ontology.
Mycoplasma contamination	Cell line was tested for mycoplasma contamination by vendor only.
Commonly misidentified lines (See ICLAC register)	No commonly misidentified cell line was used.

Arteriosclerosis, Thrombosis, and Vascular Biology

BASIC SCIENCES

Coronary Artery Disease Risk-Associated *Plpp3* Gene and Its Product Lipid Phosphate Phosphatase 3 Regulate Experimental Atherosclerosis

Paul A. Mueller, Liping Yang, Margo Ubele, Guogen Mao, Jason Brandon, Julia Vandra, Timothy C. Nichols, Diana Escalante-Alcalde, Andrew J. Morris, Susan S. Smyth

OBJECTIVE: Genome-wide association studies identified novel loci in *PLPP3* (phospholipid phosphatase 3) that associate with coronary artery disease risk independently of traditional risk factors. *PLPP3* encodes LPP3 (lipid phosphate phosphatase 3), a cell-surface enzyme that can regulate the availability of bioactive lysophopsholipids including lysophosphatidic acid (LPA). The protective allele of *PLPP3* increases LPP3 expression during cell exposure to oxidized lipids, however, the role of LPP3 in atherosclerosis remains unclear.

APPROACH AND RESULTS: In this study, we sought to validate LPP3 as a determinate of the development of atherosclerosis. In experimental models of atherosclerosis, LPP3 is upregulated and co-localizes with endothelial, smooth muscle cell, and CD68-positive cell markers. Global post-natal reductions in *Plpp3* expression in mice substantially increase atherosclerosis, plaque-associated LPA, and inflammation. Although LPP3 expression increases during ox-LDL (oxidized low-density lipoprotein)-induced phenotypic modulation of bone marrow-derived macrophages, myeloid *Plpp3* does not appear to regulate lesion formation. Rather, smooth muscle cell LPP3 expression is a critical regulator of atherosclerosis and LPA content in lesions. Moreover, mice with inherited deficiency in LPA receptor signaling are protected from experimental atherosclerosis.

CONCLUSIONS: Our results identify a novel lipid signaling pathway that regulates inflammation in the context of atherosclerosis and is not related to traditional risk factors. Pharmacological targeting of bioactive LPP3 substrates, including LPA, may offer an orthogonal approach to lipid-lowering drugs for mitigation of coronary artery disease risk.

VISUAL OVERVIEW: An online visual overview is available for this article.

Key Words: atherosclerosis ■ coronary artery disease ■ lipid phosphate phosphatase ■ lysophospholipids ■ lysophosphatidic acid

Downloaded from http://ahajournals.org by on October 20, 2020

Coronary artery disease (CAD) is a major component of cardiovascular disease and a leading cause of death worldwide. Due to the complexity of the disease, contributors to CAD risk can be divided into several factors, but more generally, they include both heritable and nonheritable risk factors. Genome-wide association studies identified heritable single nucleotide polymorphisms (SNPs) in *PLPP3* (phospholipid phosphatase 3), previously referred to as *PPAP2B*, as novel loci associated with risk of CAD and its complications independent of traditional risk factors.[1–3] LPP3 (lipid phosphate phosphatase 3), encoded by the gene *PLPP3*, is a cell surface enzyme that can regulate the availability and hence the signaling actions of bioactive lipids including lysophosphatidic acid (LPA). The risk-associated haplotype block is in the final intron of *PLPP3* and contains a CEBP-β (CCAAT enhancer binding protein-β) motif. The CAD risk allele disrupts transcriptional enhancer activity induced by CEBP-β binding.[4] CEBP-β binding increases transcription from the *PLPP3* promoter, and polymorphisms that disrupt this interaction are associated

Correspondence to: Susan S. Smyth, MD, PhD, Division of Cardiovascular, Medicine, The Gill Heart and Vascular Institute, 345 BBRSB, 741 S Limestone St, Lexington, KY 40536. Email susansmyth@uky.edu

This manuscript was sent to William Sessa, Senior Consulting Editor, for review by expert referees, editorial decision, and final disposition.

The online-only Data Supplement is available with this article at https://www.ahajournals.org/doi/suppl/10.1161/ATVBAHA.119.313056.

For Sources of Funding and Disclosures, see page 2271.

© 2019 American Heart Association, Inc.

Arterioscler Thromb Vasc Biol is available at www.ahajournals.org/journal/atvb

Nonstandard Abbreviations and Acronyms

BMDM	bone marrow-derived macrophages
CAD	coronary artery disease
CEBPβ	CCAAT enhancer binding protein beta
LPA	lysophosphatidic acid
LPAR4	LPA receptor 4
LPP3	lipid phosphate phosphatase 3
MYH11	myosin heavy chain 11
MβCD	methyl-β-cyclodextrin
ox-LDL	oxidized low-density lipoprotein
PLPP3	phospholipid phosphatase 3
SMC	smooth muscle cell
SNPs	single nucleotide polymorphisms
Tfam	transcriptional factor A mitochondrial

with lower *PLPP3* gene expression in monocytes exposed to ox-low-density lipoprotein (oxidized LDL).[4] In addition to identifying a local expression quantitative trait loci effect in monocytes, we have demonstrated that exposure of human monocytes to ox-LDL increases LPP3 expression and activity, and that the CAD risk allele in *PLPP3* is associated with lower LPP3 expression.[4,5] Others have reported similar findings in other vascular cells.[6]

We have previously demonstrated a protective role for LPP3 and its biological target LPA in vascular injury models in a tissue-specific manner.[7–9] In fact, the loss of LPP3 in vascular smooth muscle cells exacerbates local inflammation and proliferation after carotid artery ligation that leads to increased neointimal formation likely via heightened ERK (extracellular signal–regulated kinase) activity and Rho activation.[7] We also demonstrated vascular smooth muscle cells LPP3 expression increases after injury and vascular smooth muscle cells proliferation increases with exposure to LPA.[7] In addition, endothelial, but not hematopoietic, deletion of *Plpp3* increases vascular permeability in healthy mice and enhances sensitivity after inflammation-induced vascular leak.[8] Both pharmacological and genetic inhibition of LPA production attenuates the increased vascular leak observed in this model.[8] With respect to CAD, LPP3 expression in vascular endothelial cells is critical in maintaining an anti-inflammatory phenotype and vascular barrier integrity in regions of atheroprotective blood flow.[10] In addition, LPP3 expressed in the liver of mice limits atherosclerosis progression and modulates systemic LPA levels.[11] Finally, treating mice susceptible to atherosclerosis, either through diet or peritoneal injections, with unsaturated LPA species prone to oxidation accelerates lesion formation compared with mice fed saturated LPA species.[12,13] Cumulatively these data demonstrate LPP3 harbors a protective role against injury in the vasculature and that its regulation of bioavailable LPA may be a crucial mechanism.

Highlights

- LPP3 (lipid phosphatase 3) is augmented during atherosclerosis.
- *PLPP3* (phospholipid phosphatase 3 deficiency diminishes experimental atherosclerosis.
- Deficiency of smooth muscle cell LPP3 increases atherosclerosis.

Together these observations suggest a link between polymorphisms in *PLPP3* and CAD and, specifically, that upregulation of LPP3 after injury may protect against the development and complications of CAD in humans. To functionally validate these observations, we sought to determine whether LPP3 expressed globally, or in a tissue-specific manner, influences the development of experimental atherosclerosis. Herein, we present that the loss of *Plpp3* globally or in vascular smooth muscle cells alone accelerates the progression of experimental atherosclerosis possibly in part via LPA signaling through the LPA4 (LPA receptor 4).

METHODS

The data that support the findings of this study are available from the corresponding author on reasonable request.

Animals

All procedures conformed to the recommendations of Guide for the Care and Use of Laboratory Animals[14] and were approved by the Institutional Animal Care and Use Committee. The production, initial characterization, and backcrossing of mice have previously been described.[15] To generate mice susceptible to atherosclerosis, *Plpp3fl/fl* animals (fl/fl) with or without the MX1-Cre or smooth muscle cell (SMC-22) Cre (referred to as SM22-Δ) transgene were crossed to *Ldlr*$^{-/-}$ mice (The Jackson Laboratory; Bar Harbor, ME). Littermate pups with and without the MX1 Cre transgene were treated with polyinosinic-polycytidylic acid (Sigma) between post-natal days 3 o 5 to activate the MX1 promoter (referred to as MX1-Δ). To generate *Ldlr*$^{-/-}$ mice lacking *Plpp3* in myeloid cells, lethally irradiated animals (900 rads) were reconstituted with bone marrow from fl/fl mice without or with LysM-Cre transgene (referred to as LysM-Δ). To simulate LDL receptor deficiency, mice lacking *Lpar4*[16] were backcrossed to the C57BL/6J background and then bred to generate *Lpar4*$^{Y/+}$ and *Lpar4* $^{Y/-}$ mice, which were injected with PCSK9D377Y.AAV (1×10^{11} genomic copies/mouse; provided by University of Pennsylvania, Penn Vector Core) before feeding Western diet. Mice were housed in cages with HEPA-filtered air in rooms on 12-hour light cycles, and fed Western diet (Research Diets, New Brunswick, NJ, D12079B) ad libitum for 12–20 weeks. Both male and female mice were used for the MX1 and Sm22 models of *Plpp3* ablation, and their data combined as no sex-specific differences were observed (Data not shown). Due to a lack of differences in these models, only male mice were used for the LysM bone marrow transplant model of *Plpp3* ablation. Finally, because *Lpar4* is on the X-chromosome,

Downloaded from http://ahajournals.org by on October 20, 2020

both male and female mice were used and reported separately. For procedural anesthesia, 2% isoflurane was delivered using the Harvard Apparatus Anesthetic Vaporizer. For euthanasia, mice were anesthetized with 5% isoflurane followed by cervical dislocation. This study was designed in adherence to the guidelines for experimental atherosclerosis studies as recommended in the American Heart Association statement, which includes the use of our mouse models (including proper use of sample size and use of both sexes where appropriate), quantification of atherosclerosis, characterizing plasma lipids, statistical analyses, and presentation of data.[17]

Quantification of Atherosclerosis and Immunohistochemistry

Atherosclerosis was quantified along the proximal aorta by en face technique and also by measuring lesion size at the aortic root by oil-red-O staining of tissue sections. Aortas were cleaned of the adventitia and dissected from the aortic root to the iliac bifurcation. Aortas were cut open longitudinally, exposing the intimal surface, and atherosclerosis was quantified on the intimal surface of the aorta by an en face technique and reported as proportion of total area. Aortic roots were serially sectioned (10 µm) starting ≈3 mm from the base of the aortic root as described previously.[18] Sections were stained with filtered oil red-O (0.25% in 2-propanol), counterstained with hematoxylin, and oil red-O area was quantified in sections using ImageJ software[19] and reported as lesion area.

Immunohistochemistry

Primary antibodies were LPP3,[20] smooth muscle alpha-actin (2 µg/mL; Abcam AB5694), CD68 (10 µg/mL; Abcam AB53444), PECAM1 (platelet-endothelial cell adhesion molecule-1; 5 µg/mL; BD Biosciences 553370), and podocalyxin (2 µg/mL; R&D Systems AF1556). In situ hybridization and proximity, ligation assays were performed as previously described.[21] Imaging was performed using a Nikon A1R confocal microscope with a spectral detector (Nikon, Melville, NY). For lipid measurements, aortic roots were homogenized in 0.5 mL of 0.1 mol/L HCl and extracted and GC-MS/MS performed with internal standards as described previously.[22] Using this method, S1P was undetectable in the proximal aortic tissue.

Gene Expression Analysis of Proximal Aortas

Proximal aortas were homogenized and treated with the Qiagen RNeasy Fibrous Tissue Mini Kit (Qiagen, Germantown, MD, ID:74704), and RNA (1 µg) was used for the generation of a cDNA library using MultiScribe Reverse Transcriptase (Life Technologies, Waltham, MA, 4311235). cDNA was diluted 1:10 and used in a reaction with the TaqMan Fast Universal PCR Master Mix (2×; Life Technologies, Waltham, MA, 4364103) with VIC/FAM (fluorescent reporter dye VIC specific for allele "A"/6-carboxyfluorescein FAM specific for allele "B") primers from Life Technologies designed for specific gene targets.

Plasma Analysis

Whole blood was collected into CTAD tubes supplemented with EDTA, and plasma separated by centrifugation (12 000 rpm×4 minutes). Total plasma cholesterol was measured using the Wako Diagnostics Cholesterol E Assay (Wako Diagnostics, Richmond, VA, 999-02601), and plasma triglycerides were measured using the Wako Diagnostics L-type TG M Assay with the Multi-Calibrator Lipid Standard (Wako Diagnostics, Richmond, VA, 464-01601) according to the manufacturer's protocol. Plasma lipoproteins were separated by fast-performance liquid chromatography on to a Superose 6 column (Sigma-Aldrich, St Louis, MO) and were performed on individual mouse plasma samples (N=4/genotype). Cholesterol concentration in fractions was determined by enzymatic colorimetric assay (Wako Diagnostics, Richmond, VA).

Lysophosphatidic Acid Levels.

LPA was measured in plasma and tissue by LC-MS/MS as previously described by our group.[23]

Isolation and Culture of Bone Marrow-Derived Macrophages

To isolate bone marrow cells, femur and tibia were isolated and flushed with DMEM through a 25 gauge needle. Media-cell suspension was filtered through 70 µm nylon mesh and centrifuged at 1000×*g* for 5 minutes. Cells were plated at a concentration of 1 million cells per well in DMEM Glutamax containing 10% FBS, 1% PenStrep, and 10% L929 media. Media was changed every 2 to 3 days to generate bone marrow-derived macrophages (BMDM). To isolate SMC, aorta was separated from surrounding tissue starting from the arch to the renal arteries. The aorta was digested and SMC cultured as previously described.[9] Primary human coronary artery SMC (Clonetics, Lonza, Allendale, NJ) were treated with MβCD (methyl-β-cyclodextrin) cholesterol (20 µg/mL) or vehicle for 48 hours for the generation of SMC-derived foam cells. Twelve-well transwell (Sigma, St Louis MO) plates with 8.0 µm pore size were used for migration assays.

Statistical Analysis

All data are expressed as mean±SEM unless otherwise noted. Data were classified as parametric if it passed Shapiro-Wilk normality test and Brown-Forsythe equal variance tests or nonparametric if either test failed. Statistical analysis was performed using an unpaired, 2-tailed Student *t* test unless otherwise noted. *P* value <0.05 is regarded as significant. Two-way ANOVA and the Holm-Sidak post hoc test was used when multiple comparisons were made. Statistical analysis was performed using SigmaPlot 14.0 (Systat Inc, San Jose, CA). In cases where small sample sizes were used a power analysis was performed to determine the sample size required to detect differences of 30%. The data that support the findings of this study are available from the corresponding author on reasonable request.

RESULTS

LPP3 is Dynamically Upregulated During Atherosclerosis

The association of *PLPP3* alleles with human CAD risk and their correlation with gene and LPP3 protein expression in vascular cells suggests that regulation of

Downloaded from http://ahajournals.org by on October 20, 2020

LPP3 levels could influence the development of atherosclerotic vascular disease. LPP3 expression is readily detected in human atheromas.[4] To enable a detailed histological comparison of LPP3 expression in healthy and atherosclerotic coronary arteries, we took advantage of experimental pig models in which we could compare normal coronary arteries and well-characterized coronary atherosclerosis resembling lesions in humans from normocholesterolemic or heterozygous familial hypercholesterolemic pigs, respectively.[24] Healthy porcine coronary arteries displayed relatively low levels of LPP3 expression (Figure IA in the online-only Data Supplement, left). Coronary arteries from hypercholesterolemic animals fed a high-fat diet exhibited more prominent LPP3 immunostaining that co-localized with SMC makers and that was present in other cells within the vessel wall (Figure IA in the online-only Data Supplement, right). Next, we profiled LPP3 expression in 2 different murine models of atherosclerosis and observed prominent LPP3 expression in aortic root from both *Apoe*$^{-/-}$ mice (Figure IB in the online-only Data Supplement) and in *Ldlr*$^{-/-}$ mice fed a Western diet in comparison to wild-type controls (Figure IC and ID in the online-only Data Supplement). In the atherosclerotic aortic root lesions, LPP3 expression co-localized with the endothelial markers PECAM1 (Figure IC and ID in the online-only Data Supplement) and podocalyxin (Figure IE in the online-only Data Supplement), with CD68 (Figure IF in the online-only Data Supplement), and with SMC marker SM α-actin staining (Figure IG in the online-only Data Supplement). Upregulation of LPP3 protein, which is variably glycosylated as previously reported,[25] was detected by immunoblot analysis and was restricted to the atherosclerotic-prone proximal region of the aorta but not the descending thoracic aorta (Figure IH in the online-only Data Supplement). Together, these findings confirm that LPP3 is dynamically upregulated during atherosclerosis.

Post-Natal Reduction in Plpp3 Promotes Atherosclerosis

Having established that LPP3 levels are increased in several vascular cell types in atherosclerotic arteries, we investigated the consequences of global reduction of LPP3 expression in experimental models of murine atherosclerosis. Disruption of *Plpp3* in mice results in embryonic lethality due to defects in patterning and failure of the development of the extra-embryonic vasculature.[26,27] Therefore, we used a post-natal targeting strategy to broadly reduce *Plpp3* expression. Mice carrying a previously described floxed *Plpp3* allele and Cre recombinase under the control of the *Mx1* promoter were generated on the *Ldlr*$^{-/-}$ background.[8] Control (fl/fl) and Mx1-Cre expressing neonates were treated with pI-pC, to activate *Mx1* directed recombination (MX1-Δ). Sustained reduction in LPP3 expression was confirmed by analysis of bone marrow cells from adult mice (Figure IIA in the online-only Data Supplement) with some attenuation of overall protein expression in proximal aorta (Figure IIB in the online-only Data Supplement). After consuming Western diet for 12 weeks both fl/fl and MX1-Δ mice displayed hypercholesterolemia (Figure IIC in the online-only Data Supplement) without differences in plasma lipoprotein-associated cholesterol profiles (Figure IID and IIE in the online-only Data Supplement) or plasma triglyceride levels (Figure IIF in the online-only Data Supplement). We observed no differences in complete blood counts between fl/fl and MX1-Δ mice after 12 weeks on Western diet (Figure IIIA in the online-only Data Supplement). En face examination of proximal aortas revealed a 30% higher atherosclerotic burden in the MX1-Δ mice (Figure 1A; P=0.009). Similarly, oil red-O staining of the aortic sinus revealed a similar increase in lesion area in MX1-Δ mice (Figure 1B; P=0.028). Reduced LPP3 was accompanied by a nearly 2-fold increase in CD68-positive lesion area (P<0.001; Figure 1C) and an accompanying increase in inflammatory markers ICAM (intercellular adhesion molecule; Figure 1D) and CD68 mRNA levels (P<0.05; Figure 1E) in proximal aorta of the MX1-Δ mice. Global reduction of LPP3 increased plasma LPA, with increases in both saturated and unsaturated LPA species (Figure 1F). The global loss of LPP3 also led to an ≈2-fold increase in total LPA content in the proximal aorta (Figure 1G). Together, these findings support a role for LPP3 in attenuating inflammatory responses and atherosclerotic plaque development. However, the broad activity of the MX1 promoter does not provide information about cell types contributing the observed protective effect of LPP3 against experimental atherosclerosis. Thus, we employed cell-type specific approaches to attenuate LPP3 expression.

Myeloid LPP3 May Not be a Major Regulator of Atherosclerosis

We previously reported that levels of LPP3 in human monocyte/macrophages was extremely low and substantially increased in response to atherogenic ox-LDL in a manner that is governed by CAD risk alleles.[4] However, the functional consequences of LPP3 expression in macrophages is presently unknown. We, therefore, investigated whether monocyte/macrophage expression of LPP3 regulates the extent of atherosclerosis in mice. As observed with peripheral blood monocytes from humans, *Plpp3* expression in BMDM from control (fl/fl) mice is low and increased significantly after exposure to ox-LDL but not LDL (P<0.001; Figure 2A). BMDM isolated from mice with *Lys*M-Cre driven deletion of *Plpp3* (LysM-Δ) lacked LPP3 upregulation during ox-LDL stimulated foam cell formation. To determine if LPP3 regulates ox-LDL stimulated gene expression, responses of fl/fl control and LysM-Δ cells treated

Downloaded from http://ahajournals.org by on October 20, 2020

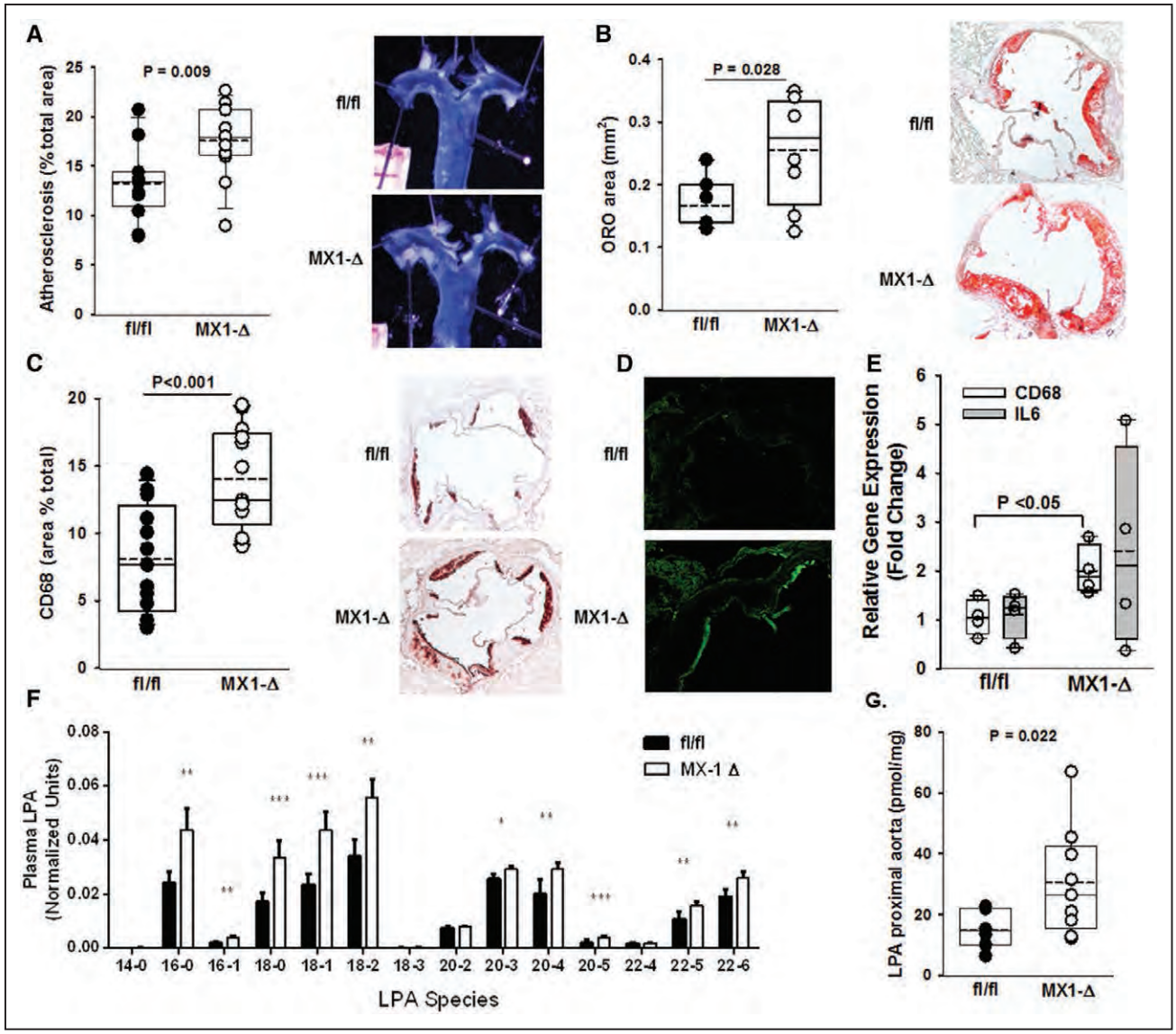

Figure 1. Global reduction in post-natal *Plpp3* expression accelerates atherosclerosis.
A, **Left**: En face analysis of atherosclerosis lesion area (% of arch area) in proximal aortas (n=12–14/group). **Right**: Representative proximal aortas from fl/fl and MX1-Δ mice on the *Ldlr*$^{-/-}$ background after 12 wk on Western diet. **B**, Oil red-O (ORO) staining of aortic sinus lesions reported as % area of aortic sinus (n=5–7/group). **C**, **Left**: Immunohistological quantification of CD68 from sections of aortic roots from fl/fl and MX1-Δ mice on the *Ldlr*$^{-/-}$ background after 12 wk on Western diet (n=12–14/group). **Right**: Representative images of CD68 staining in the aortic sinus. **D**, Immunofluorescence staining of ICAM-1 (intercellular adhesion molecule-1) in proximal aortic roots from fl/fl (**top**) and MX1-Δ (**bottom**) mice on the *Ldlr*$^{-/-}$ background after 12 wk on Western diet. **E**, *Cd68 and Il-6* (interleukin 6) gene expression (fold change; mean±SEM) determined by qRT-PCR from proximal aortas of fl/fl and MX1-Δ mice on the *Ldlr*$^{-/-}$ background after 12 wk on Western diet (n=4-5/group). **F**, Plasma lysophosphatidic acid (LPA) species quantification from fl/fl (black bars) and MX1-Δ (white bars) mice on the *Ldlr*$^{-/-}$ background after 12 wk on Western diet (n=15/group). **P*<0.05, ***P*<0.01, and ****P*<0.001. **G**, Total LPA content (pmol/mg tissue) in proximal aortas from fl/fl and MX1-Δ mice on the *Ldlr*$^{-/-}$ background 12 wk after Western diet (n=7–9/group).

without or with ox-LDL were compared. No difference in *Cebpb* expression occurred under any condition. *Fos*, *Tfam* (transcriptional factor A mitochondrial), and *Cd36* expression were substantially upregulated in LysM-Δ as compared with fl/fl BMDM at baseline, and *Cd36* was further amplified by environmental exposure to ox-LDL (Figure 2B). Having established dynamic regulation of LPP3 in murine BMDM and effects of LPP3 deficiency on ox-LDL stimulated gene expression in these cells, the role of myeloid LPP3 in experimental atherosclerosis was investigated by performing bone marrow transplant using fl/fl and LysM-Δ bone marrow cells into lethally irradiated *Ldlr*$^{-/-}$ mice that were subsequently fed a Western diet. After 12 weeks on Western diet, animals displayed characteristic hyperlipidemia with no differences in total plasma cholesterol or plasma LPA between the groups (Figure 2C and 2D). Development of atherosclerosis was also similar, without significant differences in the extent of atherosclerotic area by en face (Figure 2E) or by aortic root analysis (Figure 2F). These results indicate that

Downloaded from http://ahajournals.org by on October 20, 2020

INFORME DE LABORES 2019

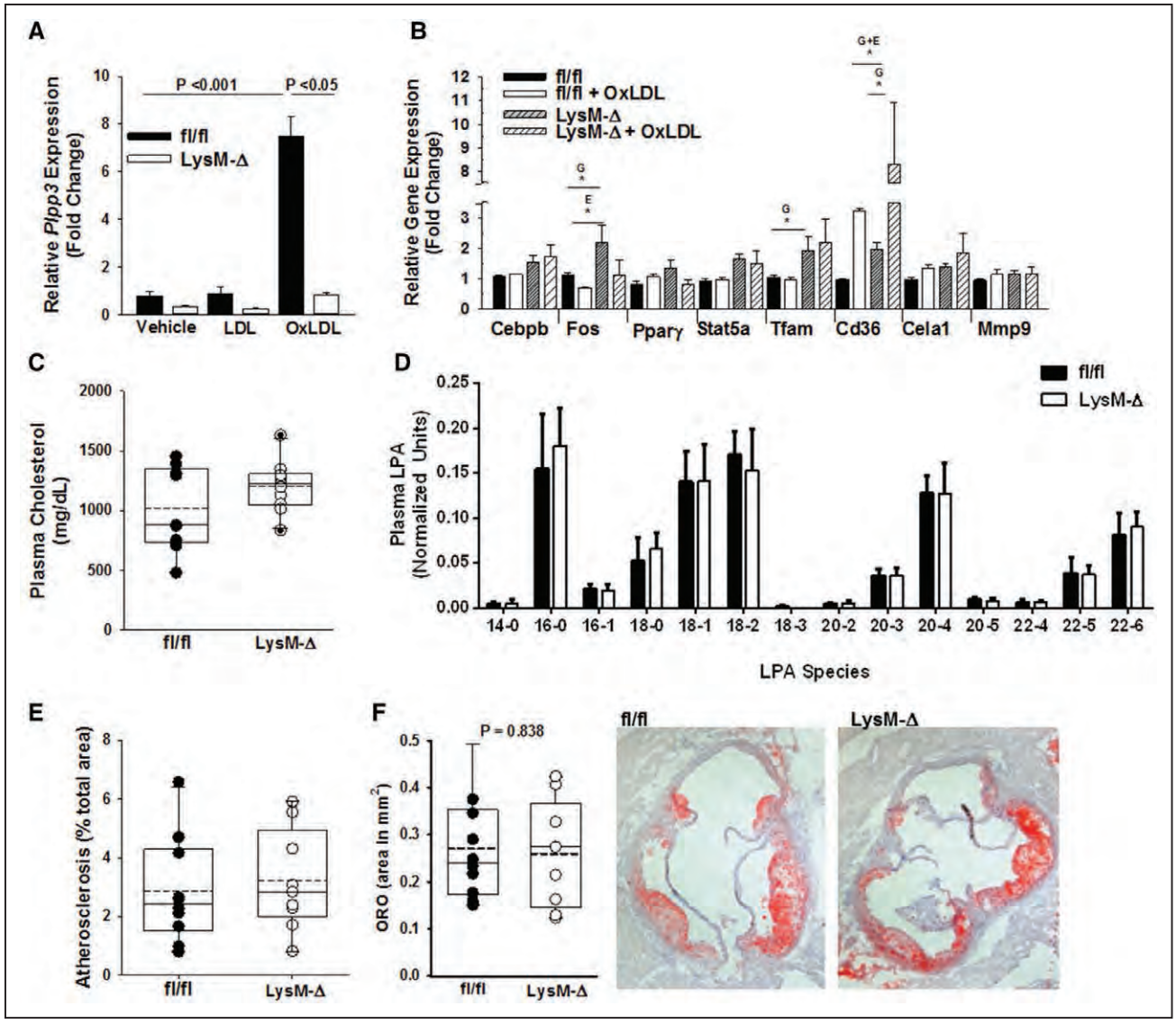

Figure 2. Myeloid deficiency of *Plpp3* does not alter atherosclerosis.
A, *Plpp3* gene expression (fold change; mean±SEM) in bone marrow-derived macrophages (BMDMs) from fl/fl and LysM-Δ mice (n=3–5 per group) treated with human LDL (low-density lipoprotein; 50 μg/mL), human ox-LDL (oxidized-LDL; 50 μg/mL) or vehicle for 18 h. Two-way ANOVA with Holm-Sidak pairwise multiple comparisons test was used to determine differences between treatment groups and genotype. **B**, Gene expression was profiled in BMDMs from fl/fl or LysM-Δ mice (n=3–5/group) exposed to vehicle or human ox-LDL. Two-way ANOVA with Holm-Sidak pairwise multiple comparisons test was used to analyze effects of genotype (*G*) and ox-LDL as an environmental stimulus for foam cell formation (*E*). **C**, Plasma cholesterol (mg/dL) in chimeric *Ldlr*$^{-/-}$ mice injected with bone marrow cells harvested from fl/fl (closed circles) or LysM-Δ (open circles) mice fed western diet for 12 wk beginning 4 wk after irradiation and reconstitution (n=10/group). **D**, Plasma lysophosphatidic acid (LPA) species quantification from fl/fl (black bars) and LysM-Δ (white bars) mice on the *Ldlr*$^{-/-}$ background after 12 wk on Western diet (n=10/group). **E**, En face analysis of atherosclerosis (% of arch area) in Wester diet fed, chimeric *Ldlr*$^{-/-}$ mice with fl/fl (closed circles) or LysM-Δ (open circles) bone marrow cells (n=10/group). **F**, Oil red-O staining of aortic sinus lesions reported as % area of aortic sinus (n=10/group). *P<0.05.

although *Plpp3* expression is dynamically regulated as macrophages assume a foam cell-like phenotype in vitro, myeloid LPP3 expression may not be a primary influencer of the development of experimental atherosclerosis.

Loss of SMC LPP3 Increases Atherosclerosis

In both murine and porcine vessels, LPP3 was prominently upregulated in cells expressing SM α-actin in atherosclerotic lesions. Our previous work established a role for LPP3 in regulating SMC responses to the bioactive lysolipid LPA, in particular, LPP3 attenuates LPA-promoted migration and RhoA and ERK activation in isolated SMC, likely due to LPP3-mediated degradation of LPA.[7] The absence of SMC LPP3 in mice promotes the development of intimal hyperplasia in normolipidemic mice, suggesting that the enzyme normally attenuates events associated with SMC migration and proliferation

Downloaded from http://ahajournals.org by on October 20, 2020

after injury.[7] Based on this evidence implicating LPP3 in SMC function, we examined the impact of loss of SMC-derived LPP3 (SM22-Δ) on the development of atherosclerosis in *Ldlr*$^{-/-}$ mice fed a Western diet. Measurement of LPP3 expression in primary cultures of SMC from fl/fl and SM22-Δ *Ldlr*$^{-/-}$ aortas confirmed efficiency of the knock-down strategy (Figure 3A). After 12 weeks on Western diet, no differences in plasma cholesterol levels were observed in fl/fl and SM22-Δ mice (Figure 3B). Unlike our MX1 mediated model of reduced *Plpp3*, no change in plasma LPA levels were detected between SM22-Δ and fl/fl mice (Figure 3C). However, SMC-specific deletion of LPP3 resulted in an approximate doubling of the extent of atherosclerosis in SM22-Δ mice as compared with the fl/fl control mice measured by en face (P=0.0002; Figure 3D) and confirmed in measurements of lesion areas in the aortic sinus by oil red-O staining (P=0.012; Figure 3E). SM22-Δ mice also displayed a significant increase in CD68 lesion area compared with fl/fl controls (P=0.006; Figure 3F). We observed a 3-fold higher expression of the inflammatory marker *Il-6* (interleukin 6) in SM22-Δ proximal aorta (P<0.05; Figure 3G). In keeping with the loss of local lipid degrading activity, aortic LPA content increased ≈2-fold in the SM22-Δ tissue (P=0.011; Figure 3H).

The results of tissue-specific targeting implicate SMC-derived, but not myeloid-derived, LPP3 as an intrinsic negative regulator of the development of atherosclerosis. Our earlier work suggests that the polymorphisms in humans associated with CAD risk influence upregulation of LPP3 in foam cells derived from monocytes. In particular, the protective allele results in higher LPP3 expression in macrophage foam cells. Cultured SMCs can assume a foam cell-like phenotype on loading with cholesterol, and intimal SMCs contribute to a substantial proportion of the foam cell population in advanced murine atherosclerosis.[28–30] Based on our findings in myeloid-derived foam cells, we sought to determine whether LPP3 expression was dynamically regulated during phenotypic modulation of SMC after cholesterol uptake. Exposure of human aortic SMCs to cholesterol reduced the SMC marker *ACTA2* and increased *CD68* consistent with downregulation of SMC markers and the assumption of an inflammatory phenotype (P<0.05; Figure 4A). Additionally, SMCs exposed to cholesterol displayed a 2-fold increased expression of *PLPP3* and more than a 10-fold increase in *LPAR4* (LPA receptor 4; P<0.05; Figure 4A). Cholesterol loading also significantly reduced cell migration in response to either serum or LPA (Figure 4B). SMC isolated from fl/fl and SM22-Δ mice respond to cholesterol loading by upregulating *Plpp3*, *Cd68*, and *Lpar4* similarly to human aortic SMCs (P<0.05; Figure 4C). LPP3 deficiency attenuated upregulation of *Cd68* and *Lpar4* (Figure 4D and 4E). These findings suggest that LPP3 may influence the phenotype of SMC-derived foam cells. To determine if LPP3 expression regulated the ability of intimal SMC to assume properties of foam cells within atherosclerotic plaque, in situ hybridization and proximity ligation assays were employed to visualize in tissue sections the H3K4dime marker of the MYH11 (myosin heavy chain 11) locus that is restricted to the SMC lineage.[21] Approximately 40% of the CD68^{+} staining cells within atherosclerotic lesions of control mice displayed the H3K4dime mark, which persists in phenotypically modulated SMC (Figure 4F). No difference was observed in sections from SM22-Δ mice (Figure 4F). These results indicate that the absence of LPP3 does not fundamentally alter the phenotype transition of SMC to foam cells, as assessed by CD68 staining. Instead, LPP3 may regulate functional response of the cells to bioactive lipids, such as LPA.

LPAR4 in Involved in the Development of Atherosclerosis

Based on the findings observed in SMC, we next focused on the role LPAR4 in the development of atherosclerosis. Control or *Lpar4*-deficient mice were injected with PCSK9D377Y.AAV to lower LDLR expression and phenotypically mimic the *Ldlr*$^{-/-}$ background, and then placed on Western diet to elicit hypercholesterolemia.[31] *Lpar4* is carried on the X-chromosome in mice, so analysis of both sexes was performed. After 16 weeks on Western diet, total plasma cholesterol was similar regardless of genotype (Figure 5A), although overall lower levels were detected in female mice injected with PCSK9 (proprotein convertase subtilisin/kexin type 9) virus. Despite similar levels of hyperlipidemia after PCSK9D377Y. AAV injection, both *Lpar4*$^{-/-}$ male (P=0.019) and female (P=0.011) mice were significantly protected from the development of atherosclerosis as measured by en face analysis (Figure 5B). Oil red-O staining of aortic sinus lesions revealed female *Lpar4*$^{-/-}$ mice were significantly protected from atherosclerosis compared with wild-type mice (P=0.008), and while male *Lpar4*$^{-/-}$ mice appeared to be protected from lesion formation the difference did not reach statistical significance (P=0.05; Figure 5C). The area of CD68 staining was statistically lower in aortic sinus lesions of male (P=0.046), but not female (P=0.11), *Lpar4*$^{-/-}$ mice compared with wild-type controls (Figure 5D) with a corresponding increase in the area of SMC α-actin staining (P=0.038; Figure 5E).

DISCUSSION

Heritable variant loci in *PLPP3* that associate with lower LPP3 expression are strong predictors of CAD risk.[1] We previously reported both a local and distant expression quantitative trait loci effect in monocyte/macrophages and found that higher expression of LPP3 was a characteristic of ox-LDL-induced foam cells from individuals with the protective allele.[4] In this report, we describe

Downloaded from http://ahajournals.org by on October 20, 2020

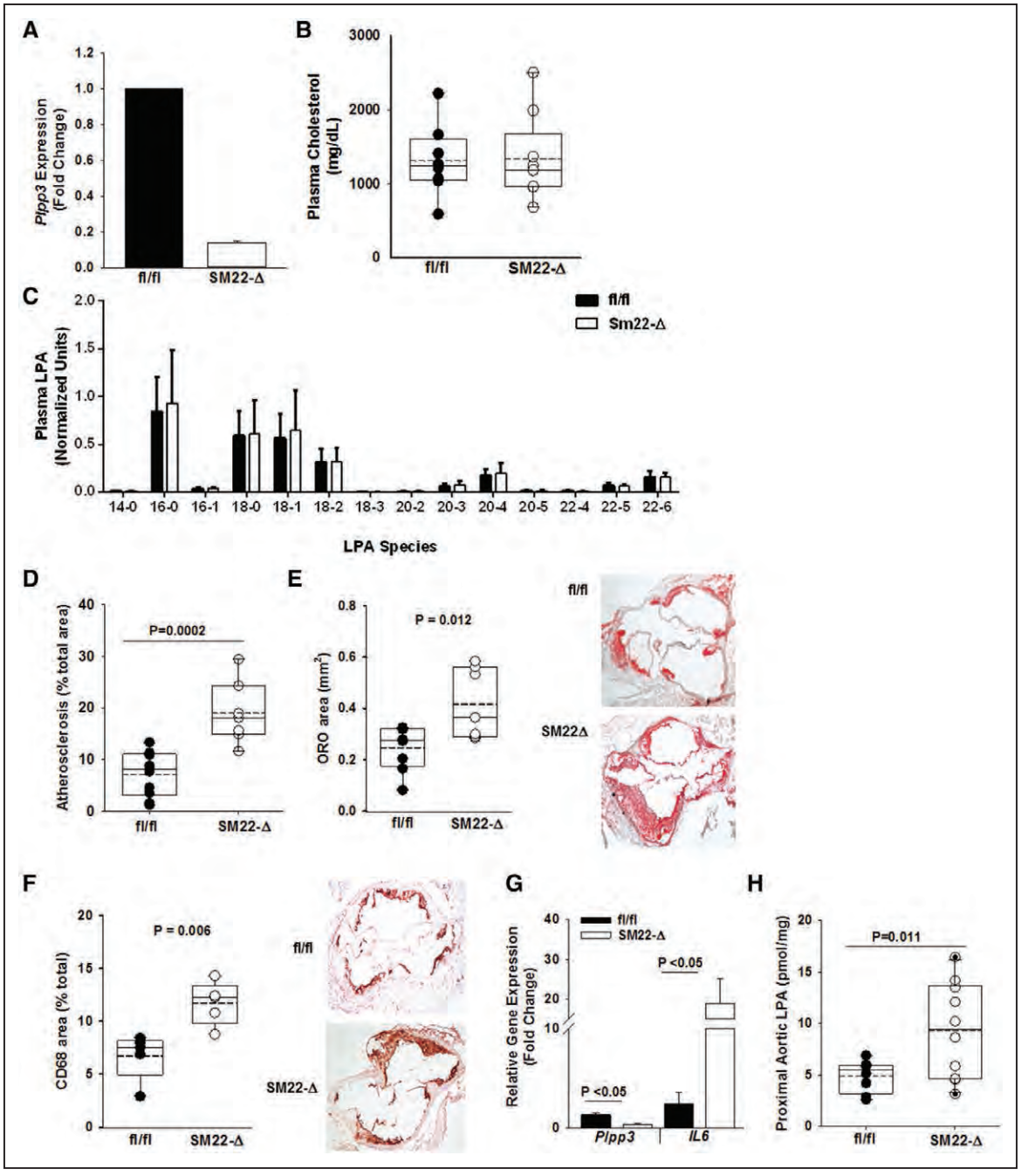

Figure 3. Smooth muscle cell (SMC) deficiency of *Plpp3* accelerates atherosclerosis.
A, *Plpp3* expression (fold change; mean±SEM) from SMC isolated from fl/fl (dark) and SM22-Δ (open) mice on the *Ldlr*$^{-/-}$ background (n=3/group). **B**, At 6 to 8 wk of age, fl/fl (dark circles) and SM22-Δ (open circles) mice on the *Ldlr*$^{-/-}$ background were placed on Western diet for 12 wk and total plasma cholesterol (mg/dL) measured (n=7/group). **C**, Plasma lysophosphatidic acid (LPA) species quantification from fl/fl (black bars) and Sm22-Δ (white bars) mice on the *Ldlr*$^{-/-}$ background after 12 wk on Western diet (n=9–11/group). **D**, En face analysis of atherosclerosis (% of arch area; n=7–9/group). **E**, Oil red-O (ORO) staining of aortic sinus lesions reported as % area of aortic sinus (n=5–6/group). **F**, **Left**: Immunohistological quantification of CD68 from sections of aortic roots from fl/fl and MX1-Δ mice on the *Ldlr*$^{-/-}$ background after 12 wk on Western diet (n=5–6/group). **Right**: Representative images of CD68 staining in the aortic sinus. **G**, Plpp3 (phospholipid phosphatase 3) and *Il-6* (interleukin 6) expression (fold change; mean±SEM) in proximal aortas from fl/fl and SM22-Δ (n=5/group). **H**, Total LPA content (pmol/mg) in proximal aortas of fl/fl and SM22-Δ (n=7–9/group).

dynamic upregulation of LPP3 during the development of atherosclerosis in porcine and murine models of atherosclerosis. Herein, we report that LPP3 serves as an intrinsic negative regulator of plaque formation in experimental models of murine atherosclerosis and its loss either globally or in SMCs coincide with increased plaque macrophage cellularity, increased inflammatory cytokine expression and elevated LPA levels in

Downloaded from http://ahajournals.org by on October 20, 2020

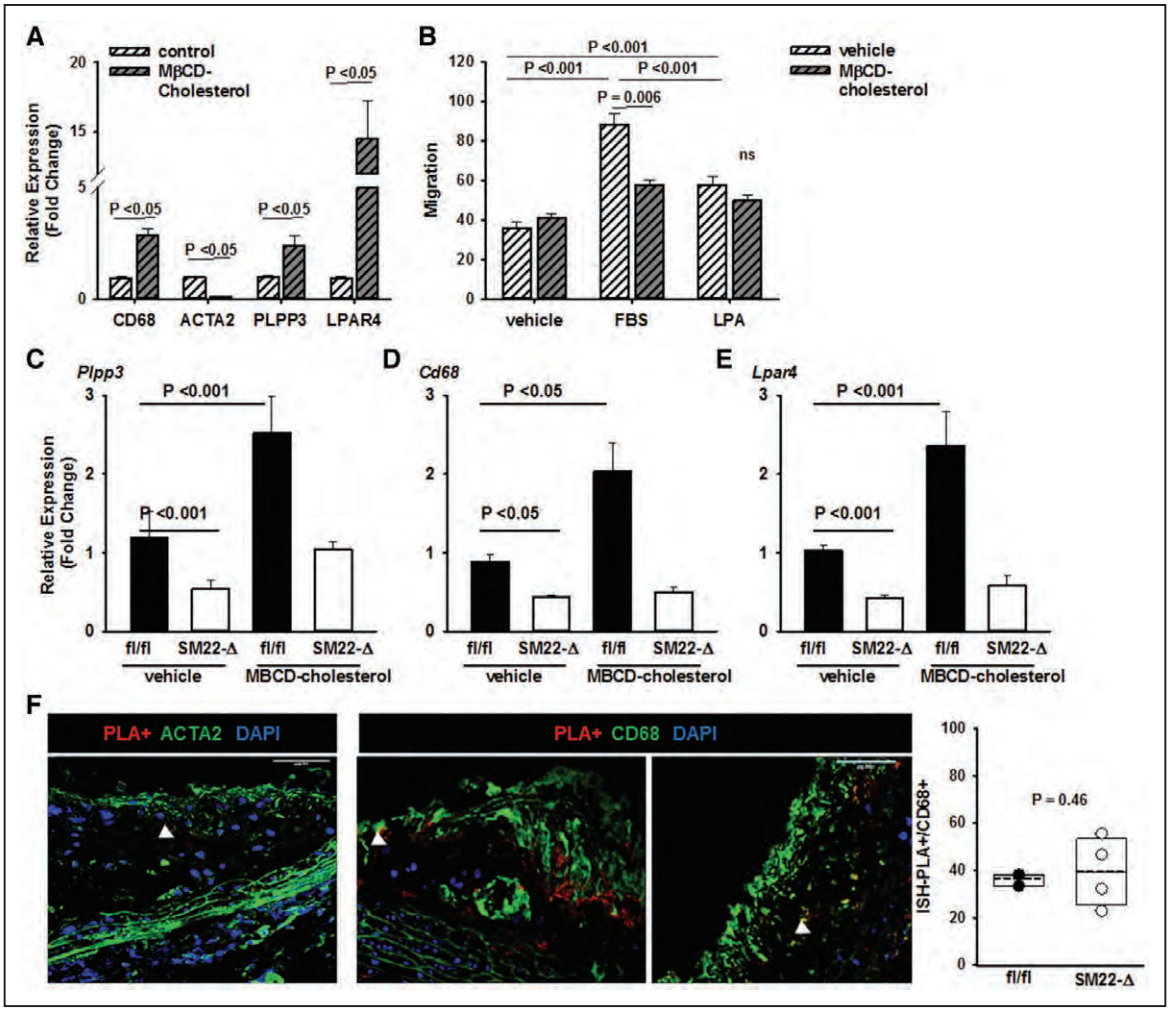

Figure 4. *PLPP3* expression is dynamically regulated during smooth muscle cell (SMC) phenotypic modulation.
A, Expression of the indicated genes in primary human coronary artery SMC treated with vehicle control or methyl-β-cyclodextrin (MβCD) complexed cholesterol (20 μg/mL) for 48 h to induce modulation towards a foam cell-like phenotype. Relative gene expression (fold change; mean±SEM) was determined. **B**, Cell migration to vehicle (DMEM with 0.01% FBS), FBS (DMEM with 10% FBS), or LPA (DMEM with 10 μmol/L 18:1 LPA) for 24 h (**right**; mean numbers of migrated cells±SEM). Two-way ANOVA was used to determine differences between treatment groups and chemotaxis agent. Relative gene expression (fold change; mean±SEM) of (**C**) *Plpp3*, (**D**) *Cd68*, and (**E**) *Lpar4* in primary SMCs from fl/fl and SM22-Δ on the *Ldlr*$^{-/-}$ background treated with vehicle or MβCD-cholesterol (20 μg/mL) for 48 h. Two-way ANOVA was used to determine differences between treatment groups and genotypes. **F**, H3K4me2 marker of the MYH11 (myosin heavy chain 11) promoter (red) visualized by in situ hybridization and proximity ligation assays in aortic root sections stained with ACTA (actin, alpha, skeletal muscle 1; green) and DAPI (blue). Cells positive for the H3K4me2 marker as a percentage of total CD68+cells (cells/field quantified) in aortic root sections from fl/fl and SM22-Δ animals on the *Ldlr*$^{-/-}$ background fed Western diet for 12 wk (n=2–4/group).

atheromas. Importantly, *Lpar4* expression is modulated by cholesterol loading in both human and murine SMCs and *Lpar4*$^{-/-}$ mice prone to atherosclerosis are protected against plaque formation suggesting that elevated LPA signaling may directly modulate CAD in mice. These findings provide functional validation and support a causal relationship of observations linking *PLPP3* alleles with LPP3 expression and risk of CAD.

Global reductions in LPP3 expression using the *Mx1-Cre* system substantially increase atherosclerosis and are accompanied by elevations in plaque-associated LPA and inflammation. Interestingly, although LPP3 expression increases during ox-LDL-induced phenotypic modulation of BMDM, myeloid *Plpp3* does not appear to regulate the development of atherosclerosis. Instead, SMC expression of LPP3 is a major determinant of the extent of both atherosclerosis and LPA content in lesions. Importantly, the pro-atherosclerotic effects of targeting LPP3 with either *Mx1-Cre* or *Sm22-Cre* are independent of changes in circulating lipoprotein or plasma triglyceride levels.

We previously reported that SMC LPP3 is a negative regulator of neointimal formation in the absence of hyperlipidemia, in part due to an ability to attenuate inflammatory cell accumulation and SMC migration.[22] In SMCs, LPP3 regulates LPA-induced ERK activity, Rho activation, and migration, and lentiviral expression of human or mouse LPP3 (but not catalytically inactive variants)

Downloaded from http://ahajournals.org by on October 20, 2020

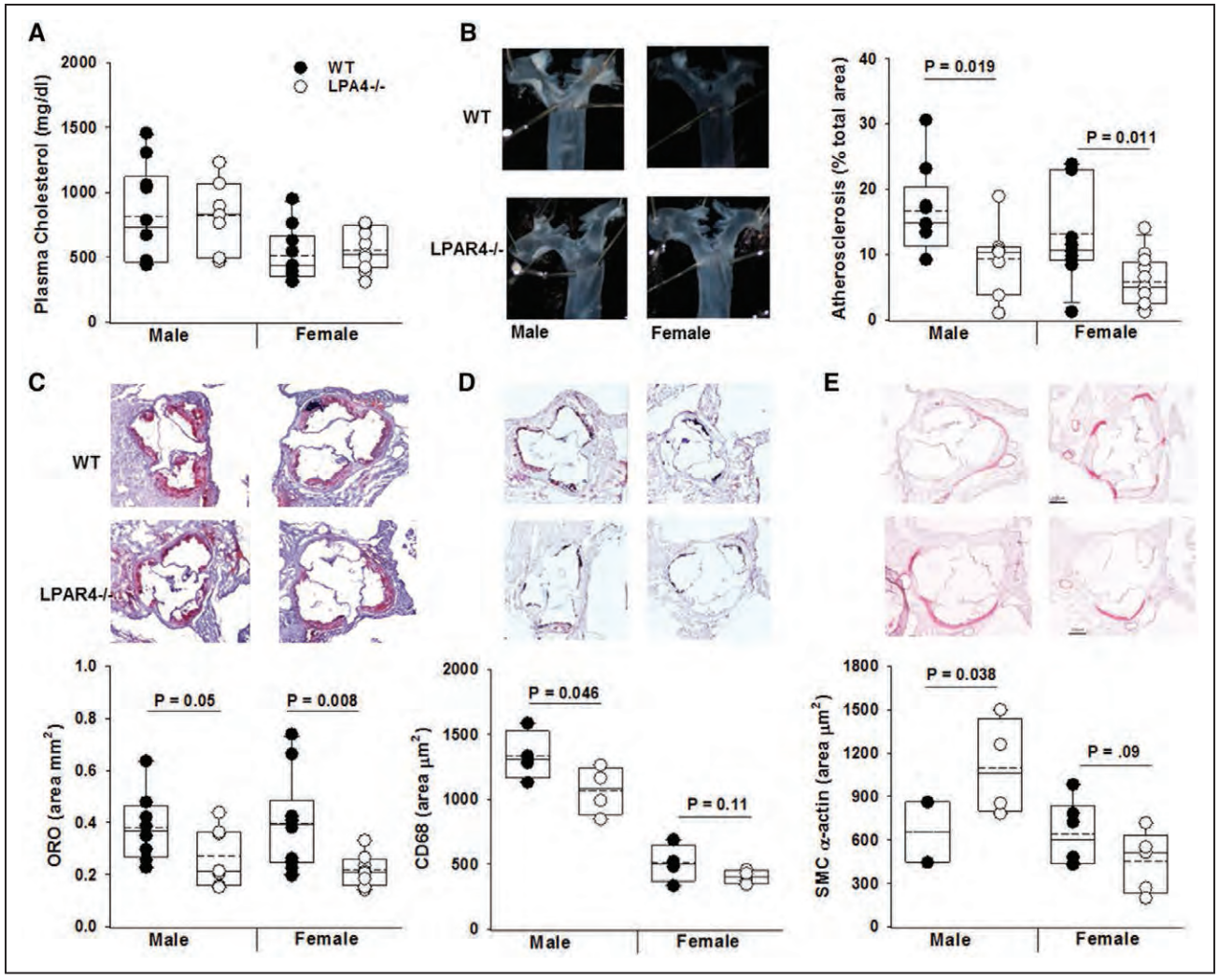

Figure 5. LPAR4 (LPA receptor 4) regulates experimental atherosclerosis.
A, Six to 8-week-old wild-type (WT; closed circle) control or *Lpar4*$^{-/-}$ (open circles) mice were infected with PCSK9 (proprotein convertase subtilisin/kexin type 9) adeno-associated virus. One week later, they were placed on Western diet for 16- weeks and total plasma cholesterol (mg/dL; n=7–9/group). **B**, **Left**: Representative images of proximal aorta. **Right**: En face analysis of atherosclerosis (% of arch area) in male and female WT (closed circle) and *Lpar4*$^{-/-}$ (open circles) mice infected with PCSK9 adeno-associated virus and Western diet-fed for 16-weeks (n=7–9/group). **C**, Oil red-O (ORO) staining and lesion area (% total aorta in root section; n=7–9/group). **D**, CD68 immunostaining (n=4/group) and (**E**) Smooth muscle cell (SM) α-actin staining from aortic root sections of male mice (n=2–5/group).

attenuates these effects.[22] These results imply that LPP3 may function within the vasculature to regulate responses to bioactive lipids, such as LPA. Herein, we expand these findings to demonstrate that LPP3 expression is upregulated in both human and murine primary SMCs as they assume a foam cell like phenotype characterized by upregulation of *CD68* and downregulation of SMC marker *ACTA2* in response to cholesterol uptake. In this context, upregulation of LPP3 is associated with decreased FBS-stimulated SMC migration. We also demonstrate that LPP3 regulates LPA levels in atherosclerotic vessels, in that tissue LPA levels are higher from mice with reduced LPP3. Thus, the effect of LPP3 on inflammation may be a consequence of broad effects on extracellular bioactive lipid levels and hence signaling responses of multiple cell types during the development of atherosclerosis.

While LPA is not the only substrate of LPP3, in support of a role for LPA-mediated pro-atherosclerotic effects, we demonstrate that global deletion of *Lpar4* in hyperlipidemic mice significantly reduced the development of atherosclerosis in the absence of an effect on plasma cholesterol. As to be expected with decreased atheroma size, we observed significantly less macrophage content in male *Lpar4*$^{-/-}$ mice; however, this effect was not observed in female mice. Additionally, we characterized SMC cell content in these knockout mice and observed a significant increase in SMC area in male *Lpar4*$^{-/-}$ lesions that also was not present in females. These data suggest that loss of *Lpar4*$^{-/-}$ may affect SMC proliferation and migration during atherosclerosis progression differently in males than females. Regardless of LPAR4's role in SMC modulation during atherosclerosis, the overall

Downloaded from http://ahajournals.org by on October 20, 2020

result was protection from atherosclerotic lesion formation. LPA signaling can promote CD14 and SR-A1 expression in these cells which may influence the mechanisms linking ox-LDL uptake and foam cell formation. Indeed, previous studies have reported an atherogenic role for LPA signaling via inducing endothelial expression of the monocyte adhesion molecule CXCL1.[12] Zhou et al[12] report that treatment of mice with unsaturated but not saturated LPA species increases atherogenesis and macrophage accumulation in aortic sinus lesions that can be attenuated via treatment with an inhibitor to LPA receptors 1 and 3. These data are supported by another report wherein intestinally derived unsaturated LPA species increased atherosclerotic lesion size in mice relative to normal rodent diet and saturated LPA fed mice.[13] It is important to note that our MX1 model of Plpp3 reduction did increase circulating LPA content; however, there were no species-specific modulation of LPA by global loss of LPP3. Additionally, the loss of SMC-derived LPP3 accelerated atherosclerosis progression independently of changes in circulating LPA. Our findings reported here propose a novel LPA signaling pathway through LPAR4 that modulates atherosclerosis progression.

While our work focuses attention on SMC LPP3 and LPAR4 as regulators of atherosclerosis, expression of LPP3 in other cell-types may also attenuate development of atherosclerotic lesions. We also observed increases in endothelial LPP3 in atherosclerotic lesions. We and others have demonstrated that LPP3 controls endothelial barrier function[8,31] perhaps by spatial restriction of LPA receptor signaling.[32] LPP3 also modulates mechanotransduction in endothelial cells in an anti-inflammatory manner[10,33]; thus, endothelial LPP3 expression may also protect against atherosclerosis progression. A recent report implicates hepatocyte LPP3 as a regulator of plasma LPA levels and experimental atherosclerosis.[11] These findings are intriguing because they suggest that LPP3 expression in the liver could have a systemic effect, likely by regulating levels of key bioactive lipids that stimulate atherosclerosis. However, in the models reported here, inactivation of mouse *Plpp3* was not associated with significant differences in plasma lipid or lipoprotein profiles or, as observed in the SM22-model, circulating levels of LPA.

It is important to note that *Sm22* expression has been observed in cells other than SMC, such as in monocytes and neutrophils in mice.[34] Therefore, it is possible that the results observed are not the result of the lack of LPP3 in SMC. However, loss of *Plpp3* in myeloid derived cells achieved with the LysM promoter had no impact on atherogenesis, suggesting that the primary effect of SM22-mediated knockdown of *Plpp3* is unlikely to be mediated by loss of expression in granulocytes. Importantly, due to the fact that SM22-mediated *Plpp3* deletion is constitutive, we cannot rule out that loss of SMC-derived LPP3 during development did not impact susceptibility of these mice to the development of atherosclerosis. Finally, it is worth mentioning that we did not directly test whether activation of the MX1-Cre recombinase alone modulated atherogenesis. While this cannot be excluded as a possibility, our model using MX1-Cre mediated deletion of *Plpp3* demonstrates increased plasma and atherosclerotic plaque LPA, the former of which has been previously reported as a mechanism driving atherogenesis.[11,13]

Allelic variation of *loci* within the final intron of *PLPP3* associates with inter individual differences in CAD risk. Functional genomic studies identify this as a dynamically regulated locus containing regulatory elements for C/EBP and AP1 family transcription factors. While these *loci* could act in *trans* to modulate expression of distal genes, our finding that *Plpp3* deficiency exacerbates experimental atherosclerosis is consistent with the concept that *cis* actions of these *loci* on activity of the *PLPP3* promoter account for or contribute to the CAD risk effect. Taken together, our results identify and validate the *PLPP3* gene as an associated biological pathway that regulates CAD risk but is not obviously related to traditional risk factors, in particular those involving elevations in circulating cholesterol and triglycerides. While strategies to elevate *PLPP3* expression to protect against atherosclerosis may not be feasible, our findings suggest that pharmacological targeting of LPA synthesis and signaling might offer an orthogonal approach to lipid-lowering drugs for mitigation of CAD risk.

ARTICLE INFORMATION

Received November 29, 2018; accepted August 30, 2019.

Affiliations

From the Division of Cardiovascular Medicine, The Gill Heart & Vascular Institute, University of Kentucky, Lexington (P.A.M., L.Y., M.U., G.M., J.B., J.V., A.J.M., S.S.S.); Department of Pathology and Laboratory Medicine, University of North Carolina at Chapel Hill (T.C.N.); División de Neurociencias, Instituto de Fisiología, Celular Universidad Nacional Autónoma de México, Ciudad de México, CDMX (D.E.-A.); and Department of Veterans Affairs Medical Center, Lexington, KY (A.J.M., S.S.S.).

Acknowledgments

P.A. Mueller designed and conducted experiments, performed analysis, and drafted article. L. Yang designed and conducted experiments, performed analysis, and critically reviewed article. G. Mao designed and conducted experiments, performed analysis, and critically reviewed article. M. Ubele designed and conducted experiments, performed analysis. J. Brandon designed and conducted experiments, performed analysis, and critically reviewed article. J. Vandra designed and conducted experiments, performed analysis, and critically reviewed article. T.C. Nichols provided essential reagents, critically reviewed article. D. Escalante-Alcalde provided essential reagents, critically reviewed article. A.J. Morris designed and analyzed experiments, drafted and reviewed article. S.S. Smyth designed and analyzed experiments, drafted, and reviewed article.

Sources of Funding

This project was supported by a grant from the Heart Lung and Blood Institute (R01HL120507), the National Center for Research Resources (P20RR021954), and by an IDeA award from the National Institute of General Medical Sciences (P20GM103527) of the National Institutes of Health. This material is the result of work supported in part with resources and the use of facilities at the Lexington VA Medical Center. This work was supported in part by VA merit Award No. BX002769 (Autotaxin) and BX001984 (SSS) from the United States Department of Veterans Affairs Biomedical Laboratory Research and Development

Downloaded from http://ahajournals.org by on October 20, 2020

Program. PM was supported in part by a grant from the Heart Lung and Blood Institute (T32HL072743) and National Center for Advancing Translational Sciences (TL1TR000115).

Disclosures

None.

REFERENCES

1. Schunkert H, König IR, Kathiresan S, Reilly MP, Assimes TL, Holm H, Preuss M, Stewart AF, Barbalic M, Gieger C, et al; Cardiogenics; CARDIoGRAM Consortium. Large-scale association analysis identifies 13 new susceptibility loci for coronary artery disease. *Nat Genet*. 2011;43:333–338. doi: 10.1038/ng.784
2. Sun YX, Gao CY, Lu Y, Fu X, Jia JG, Zhao YJ, Li LD, Dui HZ, Zhang XY, Li ZY, et al. Association between PPAP2B gene polymorphisms and coronary heart disease susceptibility in Chinese han males and females. *Oncotarget*. 2017;8:13166–13173. doi: 10.18632/oncotarget.14486
3. Wirtwein M, Melander O, Sjögren M, Hoffmann M, Narkiewicz K, Gruchala M, Sobiczewski W. Relationship between selected DNA polymorphisms and coronary artery disease complications. *Int J Cardiol*. 2017;228:814–820. doi: 10.1016/j.ijcard.2016.11.060
4. Reschen ME, Gaulton KJ, Lin D, Soilleux EJ, Morris AJ, Smyth SS, O'Callaghan CA. Lipid-induced epigenomic changes in human macrophages identify a coronary artery disease-associated variant that regulates PPAP2B expression through altered C/EBP-beta binding. *PLoS Genet*. 2015;11:e1005061. doi: 10.1371/journal.pgen.1005061
5. Smyth SS, Mueller P, Yang F, Brandon JA, Morris AJ. Arguing the case for the autotaxin-lysophosphatidic acid-lipid phosphate phosphatase 3-signaling nexus in the development and complications of atherosclerosis. *Arterioscler Thromb Vasc Biol*. 2014;34:479–486. doi: 10.1161/ATVBAHA.113.302737
6. Erbilgin A, Civelek M, Romanoski CE, Pan C, Hagopian R, Berliner JA, Lusis AJ. Identification of CAD candidate genes in GWAS loci and their expression in vascular cells. *J Lipid Res*. 2013;54:1894–1905. doi: 10.1194/jlr.M037085
7. Panchatcharam M, Miriyala S, Salous A, Wheeler J, Dong A, Mueller P, Sunkara M, Escalante-Alcalde D, Morris AJ, Smyth SS. Lipid phosphate phosphatase 3 negatively regulates smooth muscle cell phenotypic modulation to limit intimal hyperplasia. *Arterioscler Thromb Vasc Biol*. 2013;33:52–59. doi: 10.1161/ATVBAHA.112.300527
8. Panchatcharam M, Salous AK, Brandon J, Miriyala S, Wheeler J, Patil P, Sunkara M, Morris AJ, Escalante-Alcalde D, Smyth SS. Mice with targeted inactivation of ppap2b in endothelial and hematopoietic cells display enhanced vascular inflammation and permeability. *Arterioscler Thromb Vasc Biol*. 2014;34:837–845. doi: 10.1161/ATVBAHA.113.302335
9. Panchatcharam M, Miriyala S, Yang F, Rojas M, End C, Vallant C, Dong A, Lynch K, Chun J, Morris AJ, et al. Lysophosphatidic acid receptors 1 and 2 play roles in regulation of vascular injury responses but not blood pressure. *Circ Res*. 2008;103:662–670. doi: 10.1161/CIRCRESAHA.108.180778
10. Wu C, Huang RT, Kuo CH, Kumar S, Kim CW, Lin YC, Chen YJ, Birukova A, Birukov KG, Dulin NO, et al. Mechanosensitive PPAP2B regulates endothelial responses to atherorelevant hemodynamic forces. *Circ Res*. 2015;117:e41–e53. doi: 10.1161/CIRCRESAHA.117.306457
11. Busnelli M, Manzini S, Hilvo M, Parolini C, Ganzetti GS, Dellera F, Ekroos K, Janis M, Escalante-Alcalde D, Sirtori CR, et al. Liver-specific deletion of the Plpp3 gene alters plasma lipid composition and worsens atherosclerosis in apoE(-/-) mice. *Sci Rep*. 2017;7:44503. doi:10.1038/srep44503
12. Zhou Z, Subramanian P, Sevilmis G, Globke B, Soehnlein O, Karshovska E, Megens R, Heyll K, Chun J, Saulnier-Blache Jean S, et al. Lipoprotein-derived lysophosphatidic acid promotes atherosclerosis by releasing CXCL1 from the endothelium. *Cell Metabolism*. 2011;13:592–600. doi:https://doi.org/10.1016/j.cmet.2011.02.016
13. Navab M, Chattopadhyay A, Hough G, Meriwether D, Fogelman SI, Wagner AC, Grijalva V, Su F, Anantharamaiah GM, Hwang LH, et al. Source and role of intestinally derived lysophosphatidic acid in dyslipidemia and atherosclerosis. *J Lipid Res*. 2015;56:871–887. doi: 10.1194/jlr.M056614
14. National Research Council of the National Academes. *Guide for the Care and Use of Laboratory Animals*. 8th ed. Washington, DC: The National Academies Press; 2011.
15. Escalante-Alcalde D, Sánchez-Sánchez R, Stewart CL. Generation of a conditional Ppap2b/Lpp3 null allele. *Genesis*. 2007;45:465–469. doi: 10.1002/dvg.20314
16. Lee Z, Cheng CT, Zhang H, Subler MA, Wu J, Mukherjee A, Windle JJ, Chen CK, Fang X. Role of LPA4/p2y9/GPR23 in negative regulation of cell motility. *Mol Biol Cell*. 2008;19:5435–5445. doi: 10.1091/mbc.e08-03-0316
17. Daugherty A, Tall AR, Daemen M, Falk E, Fisher EA, Garcia-Cardena G, Lusis AJ, Owens AP III, Rosenfeld ME, Virmani R. Recommendation on design, execution, and reporting of animal atherosclerosis studies: a scientific statement from the American Heart Association. *Arterioscler Thromb Vasc Biol*. 2017;37:e131–e157. doi:10.1161/atv.0000000000000062
18. Daugherty A, Rateri DL. Development of experimental designs for atherosclerosis studies in mice. *Methods*. 2005;36:129–138. doi: 10.1016/j.ymeth.2004.11.008
19. Schneider CA, Rasband WS, Eliceiri KW. NIH Image to ImageJ: 25 years of image analysis. *Nat Methods*. 2012;9:671–675. doi: 10.1038/nmeth.2089
20. Sciorra VA, Morris AJ. Sequential actions of phospholipase D and phosphatidic acid phosphohydrolase 2b generate diglyceride in mammalian cells. *Mol Biol Cell*. 1999;10:3863–3876. doi: 10.1091/mbc.10.11.3863
21. Bjørklund MM, Hollensen AK, Hagensen MK, Dagnaes-Hansen F, Christoffersen C, Mikkelsen JG, Bentzon JF. Induction of atherosclerosis in mice and hamsters without germline genetic engineering. *Circ Res*. 2014;114:1684–1689. doi: 10.1161/CIRCRESAHA.114.302937
22. Vengrenyuk Y, Nishi H, Long X, Ouimet M, Savji N, Martinez FO, Cassella CP, Moore KJ, Ramsey SA, Miano JM, et al. Cholesterol loading reprograms the microRNA-143/145-myocardin axis to convert aortic smooth muscle cells to a dysfunctional macrophage-like phenotype. *Arterioscler Thromb Vasc Biol*. 2015;35:535–546. doi:10.1161/atvbaha.114.304029
23. Kraemer MP, Halder S, Smyth SS, Morris AJ. Measurement of lysophosphatidic acid and sphingosine-1-phosphate by liquid chromatography-coupled electrospray ionization tandem mass spectrometry. *Methods Mol Biol*. 2018;1697:31–42. doi: 10.1007/7651_2017_55
24. Nichols TC, Merricks EP, Bellinger DA, Raymer RA, Yu J, Lam D, Koch GG, Busby WH Jr, Clemmons DR. Oxidized LDL and fructosamine associated with severity of coronary artery atherosclerosis in insulin resistant pigs fed a high fat/high naCl diet. *PLoS One*. 2015;10:e0132302. doi: 10.1371/journal.pone.0132302
25. Smyth SS, Sciorra VA, Sigal YJ, Pamuklar Z, Wang Z, Xu Y, Prestwich GD, Morris AJ. Lipid phosphate phosphatases regulate lysophosphatidic acid production and signaling in platelets: studies using chemical inhibitors of lipid phosphate phosphatase activity. *J Biol Chem*. 2003;278:43214–43223. doi: 10.1074/jbc.M306709200M306709200
26. Tomsig JL, Snyder AH, Berdyshev EV, Skobeleva A, Mataya C, Natarajan V, Brindley DN, Lynch KR. Lipid phosphate phosphohydrolase type 1 (LPP1) degrades extracellular lysophosphatidic acid in vivo. *Biochem J*. 2009;419:611–618. doi: 10.1042/BJ20081888
27. Escalante-Alcalde D, Hernandez L, Le Stunff H, Maeda R, Lee HS, Jr-Gang-Cheng, Sciorra VA, Daar I, Spiegel S, Morris AJ, et al. The lipid phosphatase LPP3 regulates extra-embryonic vasculogenesis and axis patterning. *Development*. 2003;130:4623–4637. doi: 10.1242/dev.00635
28. Bennett MR, Sinha S, Owens GK. Vascular smooth muscle cells in atherosclerosis. *Circ Res*. 2016;118:692–702. doi:10.1161/circresaha.115.306361.
29. Gomez D, Shankman LS, Nguyen AT, Owens GK. Detection of histone modifications at specific gene loci in single cells in histological sections. *Nat Methods*. 2013;10:171–177. doi:10.1038/nmeth.2332.
30. Wang Y, Dubland JA, Allahverdian S, Asonye E, Sahin B, Erh Jaw J, Sin DD, Seidman MA, Leeper NJ, Francis GA. smooth muscle cells contribute the majority of foam cells in ApoE (Apolipoprotein E)-deficient mouse atherosclerosis. *Arterioscler Thromb Vasc Biol*. 2019;39:876–887. doi:10.1161/atvbaha.119.312434
31. Chatterjee I, Baruah J, Lurie EE, Wary KK. Endothelial lipid phosphate phosphatase-3 deficiency that disrupts the endothelial barrier function is a modifier of cardiovascular development. *Cardiovasc Res*. 2016;111:105–118. doi: 10.1093/cvr/cvw090
32. Yukiura H, Hama K, Nakanaga K, Tanaka M, Asaoka Y, Okudaira S, Arima N, Inoue A, Hashimoto T, Arai H, et al. Autotaxin regulates vascular development via multiple lysophosphatidic acid (LPA) receptors in zebrafish. *J Biol Chem*. 2011;286:43972–43983. doi: 10.1074/jbc.M111.301093
33. Touat-Hamici Z, Weidmann H, Blum Y, Proust C, Durand H, Iannacci F, Codoni V, Gaignard P, Thérond P, Civelek M, et al. Role of lipid phosphate phosphatase 3 in human aortic endothelial cell function. *Cardiovasc Res*. 2016;112:702–713. doi: 10.1093/cvr/cvw217
34. Shen Z, Li C, Frieler RA, Gerasimova AS, Lee SJ, Wu J, Wang MM, Lumeng CN, Brosius FC III, Duan SZ, et al. Smooth muscle protein 22 alpha-Cre is expressed in myeloid cells in mice. *Biochem Biophys Res Commun*. 2012;422:639–642. doi: 10.1016/j.bbrc.2012.05.041

Downloaded from http://ahajournals.org by on October 20, 2020

molecules

MDPI

Article

Heterologous Machine Learning for the Identification of Antimicrobial Activity in Human-Targeted Drugs

Rodrigo A. Nava Lara [1], Longendri Aguilera-Mendoza [2], Carlos A. Brizuela [2], Antonio Peña [3] and Gabriel Del Rio [1,*]

1 Department of biochemistry and structural biology, Instituto de Fisiología Celular, UNAM, Mexico City 04510, Mexico; rnava@email.ifc.unam.mx
2 Computer Science Department, CICESE Research Center, Ensenada, Baja California 22860, Mexico; longendri@gmail.com (L.A.-M.); cbrizuel@cicese.mx (C.A.B.)
3 Department of genetics, Instituto de Fisiología Celular, UNAM, Mexico City 04510, Mexico; apd@ifc.unam.mx
* Correspondence: gdelrio@ifc.unam.mx; Tel.: +52-55-5622-5663

Academic Editor: Julio Caballero
Received: 1 February 2019; Accepted: 14 March 2019; Published: 31 March 2019



Abstract: The emergence of microbes resistant to common antibiotics represent a current treat to human health. It has been recently recognized that non-antibiotic labeled drugs may promote antibiotic-resistance mechanisms in the human microbiome by presenting a secondary antibiotic activity; hence, the development of computer-assisted procedures to identify antibiotic activity in human-targeted compounds may assist in preventing the emergence of resistant microbes. In this regard, it is worth noting that while most antibiotics used to treat human infectious diseases are non-peptidic compounds, most known antimicrobials nowadays are peptides, therefore all computer-based models aimed to predict antimicrobials either use small datasets of non-peptidic compounds rendering predictions with poor reliability or they predict antimicrobial peptides that are not currently used in humans. Here we report a machine-learning-based approach trained to identify gut antimicrobial compounds; a unique aspect of our model is the use of heterologous training sets, in which peptide and non-peptide antimicrobial compounds were used to increase the size of the training data set. Our results show that combining peptide and non-peptide antimicrobial compounds rendered the best classification of gut antimicrobial compounds. Furthermore, this classification model was tested on the latest human-approved drugs expecting to identify antibiotics with broad-spectrum activity and our results show that the model rendered predictions consistent with current knowledge about broad-spectrum antibiotics. Therefore, heterologous machine learning rendered an efficient computational approach to classify antimicrobial compounds.

Keywords: machine-learning; antimicrobial peptide; non-peptidic antimicrobial compound; antimicrobial activity

1. Introduction

Drug-resistant microbes are one of the most important challenges for modern medicine [1] considering the increased rate in morbidity and mortality associated with antibiotic-resistant pathogens [2]. It is now commonly accepted that misuse of antibiotics is a major factor that promotes microbial resistance to these agents [3]; such is the case of broad-spectrum antibiotics that tend to promote resistance and are now prescribed in very restricted situations [4]. Furthermore, it has been noted that many non-antibiotic human-targeted drugs alter the gut microbiome in patients taking such drugs [5,6]. This alteration has been shown to be the consequence of a non-reported colateral antimicrobial activity, suggesting that microbe resistance to an antibiotic may emerge as

INFORME DE LABORES 2019

a consequence of using those human-targeted drugs [7]. Furthermore, some antibiotics may have not been tested against the gut microbiome and may as well promote the emergence of resistant microbes. Since the experimental validation of antimicrobial activity for the gut microbiome requires tests on hundreds/thousands of cultivable and non-cultivable microorganisms and the number of new human-targeted drugs may include dozens of compounds, it is relevant to develop efficient computational strategies for the identification of secondary antimicrobial activity of human-targeted drugs. In the present work we present a computational strategy aimed to improve the identification of compounds with antimicrobial activity using machine-learning-based approaches.

Previous computational approaches to identify antibiotics using Quantitative Structure-Activity Relationships (QSAR) [8,9] and machine-learning-based [10,11] procedures have been reported. In these computational approaches, non-peptidic chemical compounds (from now on referred to as NPCC) are represented by chemical descriptors (e.g., *LogP*, molecular weight, polarizability) and each compound is labeled as antibiotic or non-antibiotic; then a clustering algorithm separates antibiotics from non-antibiotics. An important limitation of these previous studies is that the number of chemical compounds used to train the models is limited (less than one thousand NPCC have been described with antimicrobial activity) and the reliability of these models requires further improvement. Alternatively, antimicrobial peptides now accumulate in more than 10,000 in different databases [12–14], and several computational models have been reported to effectively classify antimicrobial from non-antimicrobial peptides [15–17]. Although peptides represent an important new focus to develop pharmaceuticals, most human-targeted drugs are NPCC; therefore computational models to identify antimicrobial activity in these compounds should focus on NPCC. The need to use common molecular descriptors between polypeptides and NPCC has been previously noted for protein-ligand recognition and protein folding, as a fundamental aspect to deal with induced-fit or conformer selection mechanisms for molecular recognition [18]; the aim of this work though, is not to find common descriptors to peptides and NPCC since there are already packages that solve this problem (see below). Here we propose that combining peptides and NPCC increases the training set size and this should improve the reliability of the computational models. The present work tests this proposal and validates the idea that heterelogous (NPCC and peptides) training sets render the best classifying models. We then show how this improved model may assist in the identification of broad-spectrum antibiotics on FDA-approved NPCC.

2. Results

2.1. Training and Testing Gut Antimicrobial Classifiers

Building data sets to combine peptides and NPCC required the use of molecular descriptors common to both types of compounds; in our case, we used 1444 descriptors calculated by PadelDescriptor (see Methods). Then, to identify the best machine-learning model to classify gut antimicrobials, three groups of training sets were used (see Table 1). The first group included only peptides (TrOnlyPeptides), the second group comprises 4 sets and included only NPCC (TrNPCC1-4) and the third group combined these two previous sets (TrHeterologous1-4) resulting in a total of 9 training sets (see Table 1); this rendered a total of 45 training sets. These 45 sets were further processed to substitute any null or "Infinity" values using three different approaches, and a reduction of dimensions was performed via principal-component analysis (PCA, see Methods). This procedure rendered a total of 50 Training Sets; all these sets are included in Supplemental Tables S1(A–E)–S9(A–E).

Nine testing sets were built using the NPCC recently reported by Maier et al. [7] with and without gut antimicrobial activity (see Table 2). The same processing of these testing sets was performed as in the case of the training sets (see above), rendering again a total of 50 data sets (see Supplemental Tables S10(A–E)–S18(A–E)). Please note that in both training and testing sets all peptides included were tested against only one gut microbe assayed against the NPCC used in these sets and that although there are

INFORME DE LABORES 2019

many more peptides than NPCC in our training and testing sets, this imbalance is not relevant to find the border between antimicrobials and non-antimicrobials compounds.

Table 1. Training data sets.

Training Set	Entries	Description
TrOnlyPeptides	11,546	8000 antimicrobial peptides, 3546 peptides with no known antimicrobial activity
TrNPCC1	431	164 antimicrobial non-peptides, 267 non-peptides with no known antimicrobial activity
TrNPCC2	430	164 antimicrobial non-peptides, 266 non-peptides with no known antimicrobial activity
TrNPCC3	430	164 antimicrobial non-peptides, 266 non-peptides with no known antimicrobial activity
TrNPCC4	431	164 antimicrobial non-peptides, 267 non-peptides with no known antimicrobial activity
TrHeterologous1	6204	4164 antimicrobial compounds (4000 peptides and 164 non-peptidic compounds), 2040 no antimicrobial compounds (1773 peptides and 267 non-peptidic compounds)
TrHeterologous2	6203	4164 antimicrobial compounds (4000 peptides and 164 non-peptidic compounds), 2039 no antimicrobial compounds (1773 peptides and 266 non-peptidic compounds)
TrHeterologous3	6203	4164 antimicrobial compounds (4000 peptides and 164 non-peptidic compounds), 2039 no antimicrobial compounds (1773 peptides and 266 non-peptidic compounds)
TrHeterologous4	6204	4164 antimicrobial compounds (4000 peptides and 164 non-peptidic compounds), 2040 no antimicrobial compounds (1773 peptides and 267 non-peptidic compounds)

The original NPCC from Maier et al. [7], here referred to as OnlyNonPeptides, was used to build TrNPCC1 by taking only the odd listed compounds, TrNPCC2 by taking even listed compounds, TrNPCC3 and TrNPCC4, included the first and second half of the data set respectively. The OnlyPeptides data set was divided to generate TrHeterologous1, TrHeterologous2, TrHeterologous3 and TrHeterologous4 by taking the odds listed peptides, even listed peptides, first and second half, respectively. Then, these TrHeterologous1-4 data sets with peptides were combined with the TrNPCC1-4 to complete these sets.

Table 2. Testing data sets.

Testing Set	Entries	Description
TeOnlyPeptides	861	328 antimicrobial and 533 non-antimicrobial non-peptides
TeNPCC1	430	164 antimicrobial non-peptides, 266 non-peptides with no known antimicrobial activity. Same as TrNPCC2.
TeNPCC2	431	164 antimicrobial non-peptides, 267 non-peptides with no known antimicrobial activity. Same as TrNPCC1.
TeNPCC3	431	164 antimicrobial non-peptides, 267 non-peptides with no known antimicrobial activity. Same as TrNPCC4.
TeNPCC4	430	164 antimicrobial non-peptides, 266 non-peptides with no known antimicrobial activity. Same as TrNPCC3.
TeHeterologous1	430	Same as TeNPCC1.
TeHeterologous2	431	Same as TeNPCC2.
TeHeterologous3	431	Same as TeNPCC3.
TeHeterologous4	430	Same as TeNPCC4.

The original NPCC from Maier et al. [7], here referred to as OnlyNonPeptides, was used to build all Testing Sets. TeOnlyPeptides was built taking all the 861 listed compounds. TeNPCC1 and TeHeterologous1 were built by taking only the even listed compounds. TeNPCC2 and TeHeterologous2 included only the odd listed compounds. TeNPCC3 and TeHeterologous3 included the second half of OnlyNonPeptides, TeNPCC4 and TeHeterologous4 included the first half of the data set. Testing sets were built so they were the complement of the compounds listed for their Training sets, so, for example, if a training set was built using the even listed compounds (e.g., TrNPCC1), its Testing set would be built with the odd listed compounds (e.g., TeNPCC1). Heterologous Testing Sets were the same as OnlyNonPeptides Testing sets, due to the fact that the interest compounds are of non-peptidic nature.

INFORME DE LABORES 2019

Five different statistical parameters (adjusted estimated error rate on the training set (AEER); correctly classified instances in the training set after splitting 33% for testing (%Split); 10-fold cross-validation (%10FCV); correctly classified instances on the testing set (%CC); area under the receiver operator characteristic curve on the testing set (AUROC)) that evaluated the performance on either the training or testing sets (see Methods) were used to identify the best classifier.

As shown in Figure 1, the best models included heterologous compounds (peptides and NPCC): circles in Figure 1 represent heterologous training sets and accumulate on the upper part of Figure 1, that is, those models with highest statistical parameters evaluating the model performance (the actual data in this figure for these models are included in Supplemental Table S19). Treating the training set rendering the best model with the K-nearest neighbor or mean-imputation approaches did not improve the performance of the best model (see Supplemental Tables S6G, S6I, S6J and its corresponding test set in Table S15G; supplemental Tables S6K, S6L and their corresponding test sets in Supplemental Tables S15I and S15J).

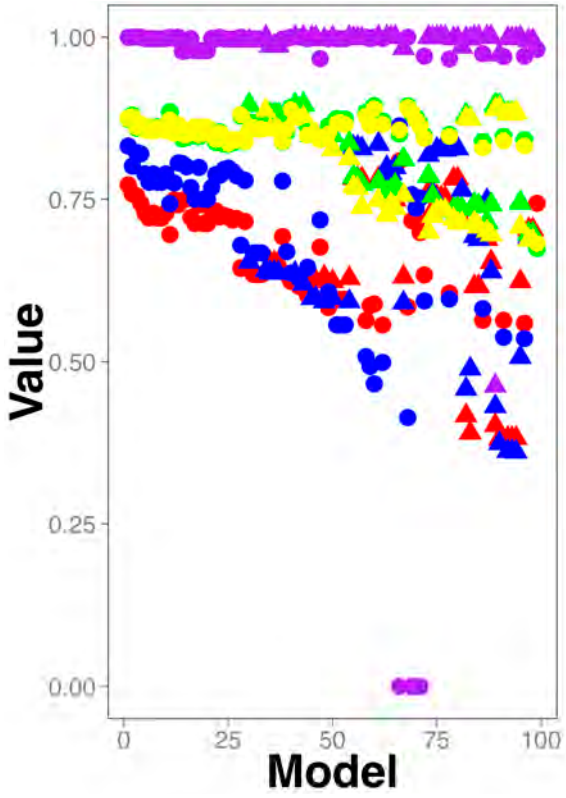

Figure 1. Classifiers performance. Five statistical parameters (yellow circle: Correctly classified instances in the test set after 67% of split validation of the training set; green circle: 10-fold cross-validation on training set; red circle: Correctly classified instances on the testing set; blue circle: AUROC on the testing set; purple circle: adjusted estimated error rate on the training set where the minimum error was represented by number 1.0) are sorted from highest to lowest values. Hence, the best parameter values are located on the left-upper part of the figure. The models using heterologous data are represented as circles; triangles are used otherwise. The actual data of this plot can be found in Supplementary Table S19.

Yet, none of these models surpassed the others in all 5 parameters. To aid in the visualization of this aspect of our results, Figure 1 displays the values in descending order from left to right; therefore, the models on the left side of the plot have better scores than those on the right. For instance, models using heterologous (represented by circles) testing sets (the red and blue circles, corresponding with the statistical parameters correctly classified instances and *AUROC*, respectively) laying on the left side of Figure 1, have better performance than those models using heterologous testing sets on the right

side of the plot, yet, those on the right side including either heterologous or non-heterologous training sets (green and yellow circles or triangles) have better scores than those models using heterologous or non-heterologous training sets on the left side of the plot. The models in the middle of the plot have on the other hand, intermediate performances. Please note that the statistical parameter adjusted estimated error rate is the value that AutoWeka optimizes, hence for all the reported models is close to 1.0 and consequently does not contribute to differentiate the performance of the models. This statistical parameter is shown in Figure 1 to note that all models have similar error rates, yet different statistical parameters, hence, the best model obtained from AutoWeka cannot be selected simply by considering the error rate value reported.

Thus, to aid in the identification of the best models, we used a previous score developed by our group that takes into account multiple statistical parameters, the Combined Score or simply *CScore* [19]:

$$CScore_i = \frac{1}{5}\sum_{n=1}^{5}\left[\sqrt{\frac{MaxS_n - S_{i,n}}{MaxS_n - MinS_n}}\right] \quad (1)$$

where $MaxS_n$ and $MinS_n$ represent the maximum and minimum scores for a given statistical parameter n over all models; $S_{i,n}$ is the score observed for a given statistical parameter n and model i; n represents the index of the statistical parameter to evaluate (in our case were 5 parameters: AEER, %Split, %10FCV, %CC and AUROC). Thus, formula 1 calculates *CScore* for each model i.

CScore averages the difference of each statistical parameter to its best value (e.g., true-positive rate best value is 1, so the difference between the observed true positive rate and 1 is included in the *CScore*), therefore the lower the *CScore* value the better the classifying model. Figure 2 (and Supplementary Table S20) shows that the five best models are those using heterologous training sets (the ones below the 0.3 line in Figure 2). Furthermore, we noticed that the top 5 best models overlapped on average in more than 70% of their classifications hence, these were mainly redundant (see Figure 3).

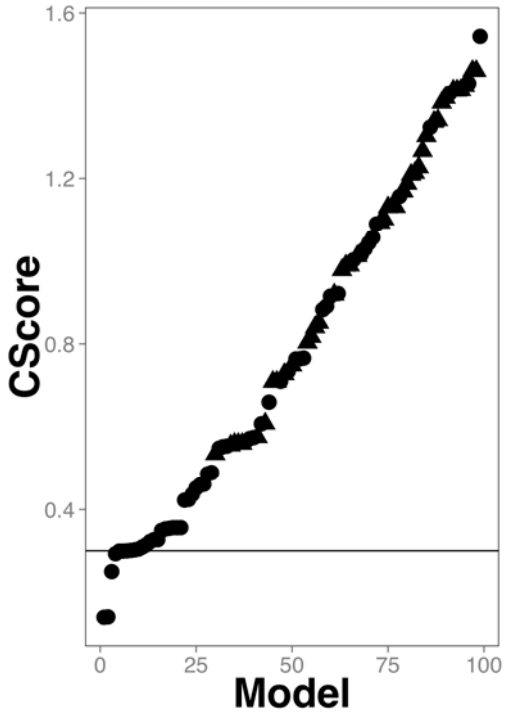

Figure 2. Classifiers combined scores. A circle represents each model; the best model has the lowest *CScore*. The line represents the *CScore* = 0.3, that separates the top 5 models from the rest. The models using heterologous data are represented as circles; triangles are used otherwise. The actual data of this plot can be found in Supplementary Table S20.

INFORME DE LABORES 2019

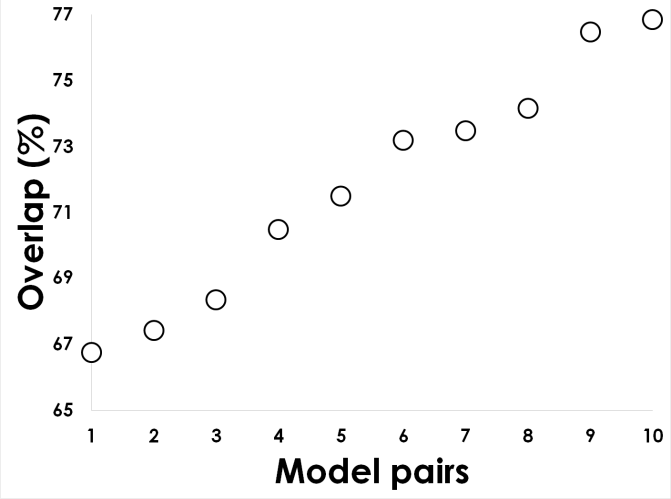

Figure 3. Classifiers overlap. The predictions of antimicrobial compounds of the top 5 models were compared to quantify their overlap. The image shows the 10 pairs of models generated from these 5 top models. The comparison was performed on the discovery set (see Methods) because not every model had the same testing set.

Therefore, we selected the best model based on the lowest *CScore*; such model was built using the RandomCommittee algorithm (see Supplemental Table S21 for the algorithm parameters) on the TrHeterologous1 set (see Table 1) that included 86 molecular PCA-reduced descriptors and achieved the following performance: AEER: 0.99955; %Split: 87.4; %10FCV: 87.3; %CC: 77.2; AUROC: 0.83 (model named TrHeterologous1-Reduced-With-99M-CRC20_CRF in Supplemental Table S21; the corresponding data set for this model is reported in Supplemental Table S6E).

2.2. Identifying Broad-Spectrum Antibiotics among FDA-Approved Compounds

We used the best model to predict NPCC with expected gut antimicrobial activity among FDA-approved drugs. The motivation to perform this prediction is not for testing purposes, as in the case of the training and testing sets used before. Hence, the set of compounds used in this prediction stage is referred to as the discovery set, because we aimed to discover potential compounds with gut antimicrobial activity. We used 756 FDA-approved compounds included in the ZINC database (see Methods) that were not part of the training or testing sets; these compounds included 111 antimicrobials and 645 compounds without any known antimicrobial activity; we also added 73 NPCC that included 22 antifungal compounds and 51 without any reported antifungal activity (see Supplementary Table S22). We have previously reported that these 22 antifungals work through a mechanism (alter calcium intake [20]) different from antibacterial compounds (e.g., penicillin derivates, sulphonamides, etc), thus we expected our model to predict few of these compounds as antibacterials. FDA-approved compounds on the other hand are expected not to have, or to have minor, gut antimicrobial activity otherwise their secondary gastrointestinal effects would be significant. We would expect that FDA-approved drugs would be less likely predicted to act against non-athogenic gut microbes than antifungals. To evaluate the reliability of our predictions using the discovery set, we considered that antibiotic compounds against the non-pathogenic gut flora among the FDA-approved drugs should be considered broad-spectrum antibiotics; please note that our classifier was not trained to predict this class of antibiotics, yet the combination of the predictions of our classifier on the FDA-approved drugs would render this information. The definition of broad-spectrum antibiotics is somehow arbitrary, for instance, it is considered that antibiotics that act on G(+) and G(−) are broad-spectrum antibiotics for some authors, while those acting against pathogenic and non-pathogenic microorganisms are classified as broad-spectrum antibiotics by others [21,22]. The list of broad-spectrum antibiotics was obtained from five recent works (see Methods), including 19

INFORME DE LABORES 2019

broad-spectrum and 3 narrow-spectrum antibiotics (see Supplementary Table S22). We were able to identify 72 true positives (FDA-approved antibiotics against pathogenic microbes predicted to act against non-pathogenic gut microbes) in the discovery set that we predicted should be considered as broad-spectrum antibiotics (see Table 3).

Table 3. Confusion matrix for the discovery set.

	Predicted Gut Antimicrobial	Predicted No Antimicrobial
Pathogenic antimicrobial	72	61
No antimicrobial	140	556

The actual data for this table can be found in Supplementary Table S22.

From these 72 antimicrobials, only 16 had been annotated as broad-spectrum antibiotics and 3 as narrow-spectrum antibiotics (see Supplemental Table S22). Hence, we propose that these 3 annotated narrow-spectrum antibiotics should be considered more likely as broad-spectrum antibiotics (see Table 4).

Table 4. True pathogenic antimicrobials predicted by the best classifier on the discovery set.

Compound Name	Annotation
Amoxicillin	Narrow spectrum
Phenoxymethylpenicillin	Narrow spectrum
Cephalexin	Narrow spectrum

On the other hand, among the 61 false negatives, 3 compounds were annotated as broad-spectrum antibiotics (see Supplemental Table S22). This annotation is consistent with our predictions, since these antibiotics directed towards pathogenic microorganisms are unlikely to affect the non-pathogenic gut microbes. Furthermore, 17 out of the 22 antifungal compounds were predicted as antimicrobials.

Thus, in total we were able to correctly identify 16 out of the 19 known broad-spectrum antibiotics and we suggest that 3 of the annotated narrow-spectrum antibiotics should be re-evaluated; hence, the reliability to identify broad-spectrum antibiotics was 84.2%. Furthermore, our results suggest that 56 (61 true negatives less 5 antifungals) (50.4%) out of 111 antibiotics approved by the FDA included in our discovery set are unlikely to affect gut microbes. In comparison, 5 (22.7%) out of 22 antifungals were predicted not to act against the gut microbes (see Supplemental Table S21). Thus, it is twice as much less likely that FDA-approved antibiotics would be toxic against gut microbes than antifungals.

3. Discussion

The identification of antimicrobial compounds assisted by machine-learning techniques has multiple advantages, such as reduction of the invested time to develop novel pharmaceuticals or to flag molecules that could have secondary antimicrobial activity [17]. An important aspect of these techniques is how to improve the reliability of these predictions. One way to achieve this is to increase the number of examples in the training and testing sets. In this work we propose that it is possible to use chemical compounds of different nature (peptides and NPCC) that are commonly modeled separately as antimicrobials to improve the reliability of the predictions. Here we show that indeed, the training sets that rendered the best classifiers of antimicrobial compounds were heterologous, those including NPCC and peptides (see Figures 1 and 2). We can compare our best classifier with previous works in terms of the learnability of our classes, that is, how well gut antimicrobial compounds are differentiated from non-antimicrobial gut compounds. In that sense, the numeric performance achieved by the best classifier on the testing set (AUC = 0.83) is comparable with the performance achieved with one of the best antimicrobial peptide classifiers (AUC = 0.85) recently reported [23], indicating that the learnability of heterologous training sets is as good as those of only peptides.

INFORME DE LABORES 2019

Another important aspect of our work is the molecular descriptors obtained to best classify gut antimicrobial compounds that included both peptides and NPCC. Although our goal was not to identify common descriptors for NPCC and peptides (these are already calculated by available packages, see Methods), we did look for those descriptors that are relevant to learn the difference between antimicrobials from non-antimicrobials. Our results indicate that the solution to this problem requires the transformation of 86 computed molecular descriptors, suggesting that other molecular descriptors, most likely associated to these 86 descriptors, may improve the current best-model performance.

In terms of improving the performance reported in this work, it is worth mentioning that we used peptides that were not tested by Maier et al. [7] yet, these peptides had reported antibiotic activity against at least one microorganism (*Escherichia coli*) found in the gut and tested by Maier and collaborators. On the other hand, the NPCC included in our work had antibiotic activity against at least one of the 40 gut microorganisms tested by Maier and collaborators. Hence, one alternative approach to improve the performance of classifiers aimed at identifying gut microorganisms would be to include antibiotics that target more common gut microorganisms; that would require further experimental data that is not currently available at present.

To the best of our knowledge, no previous machine-learning efforts to assist in the identification of broad-spectrum antibiotics have been reported; here the definition of broad-spectrum antibiotics was restricted to those acting against both pathogenic and non-pathogenic microorganisms. Hence, using a classifier trained to identify gut non-pathogenic antimicrobial compounds to predict this activity in FDA-approved antibiotics targeted against pathogenic microorganisms represents a way to identify broad-spectrum antibiotics. Our results suggest that half of the FDA-approved antibiotics are likely to have antimicrobial activity against the gut microorganisms indicating that these require further testing or investigation. For instance, two annotated narrow-spectrum antibiotics, amoxicillin and cephalexin, that were predicted to alter gut microbes are known to affect the gastrointestinal flora [24]. On the other hand, the broad-spectrum antibiotic ceftaroline fosamil recently approved by the FDA to treat bacterial pneumonia and skin infections, which was not predicted to affect the gut flora, was reported to have minor gastrointestinal effects during clinical trials [25].

How significant is our finding that almost half of the FDA-approved antibiotics are predicted to have a broad-spectrum activity? To address this question, we included in the discovery set a group of antifungal compounds. All microorganisms used to train our models were bacteria, hence we expected that these antifungals that act through a mechanism different from those reported for bacteria would be unlikely predicted to act against bacteria; lets refer to this negative prediction as *expectation-antifungal*. On the other hand, most FDA-approved antibiotics should unlikely present antibiotic activity against gut microbes, otherwise these would frequently have secondary gastrointestinal effects on patients; lets refer to this negative prediction as *expectation-FDA*. Then, to address the significance of our findings about broad-spectrum antibiotics requires evaluating *expectation-antifungal* and *expectation-FDA*; if FDA-approved drugs are less likely to act on gut microbes than antifungals then *expectation-FDA* < *expectation-antifungal*. Indeed, we observed that FDA-approved antibiotics are twice as much less likely to act against gut microbes than antifungals. Thus, our results indicate that even when FDA-approved antibiotics are safer (do not act against non-pathogenic resident gut bacteria) than our control group (antifungals), we identified some of these compounds that need to be re-assessed as potential promoters of resistance among microbes for their potential broad-spectrum activity.

In summary, we report a computational approach to use heterologous antimicrobial compounds (peptides and non-peptides) to improve the discriminatory power of machine-learning approaches. We show that training a classifier to identify antibiotics against the gut flora using heterologous training sets correctly anticipate adverse gastrointestinal reactions in patients receiving these antibiotics.

4. Materials and Methods

4.1. Materials

Peptides included in the training sets were obtained from the non-redundant data set of 20 public databases (see Table 5). Testing sets were derived from the work reported by Maier and collaborators (see Supplemental Tables S10–S18). Finally, a discovery set containing 750 FDA-approved drugs for treating human infectious diseases and 76 antifungal drugs was built from the ZINC database [26]. Molecular descriptors were computed with PadelDescriptor [27]. For every training and test set, we performed five different approaches to process the molecular descriptors for each peptide and/or NPCC. These included: no processing; eliminate every null value; substitute every "Infinity" value for 0 or 99,999,999; reduction of the dimensionality applying a principal component analysis implemented in WEKA package (see below). Since the substitution of Infinity values for 0 or 99,999,999 is not a conventional strategy, we performed an imputation of the Infinity and null values using the K nearest neighbor or mean imputation approaches, but only on the best model data set for comparison. That is, from the 9 training sets we generated a total of 45 training sets following the different approaches described before; the same applies to the 9 testing sets. For the discovery set only the transformation applied to the best classifier was performed.

Table 5. Antimicrobial peptide databases used in the present study.

Database	Focused on	Reference
BACTIBASE	Bacteriocins	[28]
Bagel	Bacteriocins	[29]
CAMP	General and Patented AMPs	[14]
DADP	Anuran AMPs	[30]
DAMPD	General AMPs *	[31]
DBAASP	General AMPs	[13]
Defensins	Defensins	[32]
HIPdb	Anti-HIV peptides	[33]
LAMP	General and Patented AMPs	[34]
MilkAMP	AMPs of dairy origin	[35]
PhytAMP	Plant AMPs	[36]
PenBase	Penaeidin AMPs	[37]
Peptaibol	Peptaibols	[38]
RAPD	Recombinant AMPs	[39]
AMPer	Eukaryotic AMPs	[40]
UniprotKb	General AMPs	[41]
YADAMP	General AMPs	[42]
AMSDb	Eukaryotic AMPs	[43]
APD	General AMPs	[44]
AVPdb	Antiviral peptides	[45]

* AMPs stands for Antimicrobial Peptides.

4.2. Method

To identify the best model to classify gut antimicrobial compounds, we followed a systematic method previously reported by our group [46]. Briefly, given the training sets, 52 different machine-learning algorithms implemented in WEKA [47] and their parameters were systematically

INFORME DE LABORES 2019

analyzed to identify the algorithm, parameters and molecular descriptors that renders the lowest possible error in classification; this systematic analysis was performed by the Bayesian optimization algorithm implemented in AutoWEKA [48]. We ran AutoWEKA against any training set for 10, 90, 720, 2880 and 4320 minutes to identify when the optimization has reached a plateau in the classification error. Afterwards, a 10-fold cross validation and 67% split tests were performed in WEKA. Finally, these classifiers were evaluated against their corresponding testing sets. Two statistical parameters were chosen to evaluate the performance of the classifiers during the testing, including: Area under the ROC curve and correctly classified instances on the testing set. Therefore, a total of 5 statistical parameters were used to define the best classifiers, three for the training phase (adjusted estimated error rate on the training set; correctly classified instances in the training set after splitting 33% for testing; 10-fold cross-validation) and two for the testing phase (AUROC and correctly classified instances).

To identify the intersection set between the top 5 classifiers, we compared the predictions of these classifiers rendering 10 possible pairs of predictions on the discovery set; we used this set because not every classifier had the same testing set. The best model was identified using a combined score (see formula 1): the model with the lowest combined score was chosen. The model then was used to predict gut antimicrobial compounds in the discovery set using WEKA command line (see Supplemental File S1). To annotate as broad-spectrum or narrow-spectrum antibiotics, we used five different previous works that classified antibiotic action [22,49–52].

Supplementary Materials: The following are available online at http://bis.ifc.unam.mx:8080/ironbios/heteroml/, File S1: Script to execute the best model to predict antimicrobials on FDA-approved drugs, Table S1A–E: Training sets in ARF format for TrOnlyPeptides, Table S2A–E: Training sets in ARFF format for TrNPCC1, Table S3A–E: Training sets in ARFF format for TrNPCC2, Table S4A–E: Training sets in ARFF format for TrNPCC3, Table S5A–E: Training sets in ARFF format for TrNPCC4, Table S6A–L: Training sets in ARFF format for TrHeterologous1, Table S7A–E: Training sets in ARFF format for TrHeterologous2, Table S8A–E: Training sets in ARFF format for TrHeterologous3, Table S9A–E: Training sets in ARFF format for TrHeterologous4, Table S10A–E: Testing sets in ARF format for TeOnlyPeptides, Table S11A–E: Testing sets in ARF format for TeNPCC1, Table S12A–E: Testing sets in ARF format for TeNPCC2, Table S13A–E: Testing sets in ARF format for TeNPCC3, Table S14A–E: Testing sets in ARF format for TeNPCC4, Table S15A–J: Testing sets in ARF format for TeHetrelogous1, Table S16A–E: Testing sets in ARF format for TeHetrelogous2, Table S17A–E: Testing sets in ARF format for TeHetrelogous3, Table S18A–E: Testing sets in ARF format for TeHetrelogous4, Table S19: Parameter values for all models tested, Table S20: CScore values for all model tested, Table S21: Best models algorithms and corresponding parameters and Table S22: Discovery set.

Author Contributions: Conceptualization, G.D.R.; methodology, G.D.R., C.A.B. and R.A.N.L.; software, G.D.R. and R.A.N.L.; validation, R.A.N.L. and G.D.R.; formal analysis, R.A.N.L.; investigation, G.D.R. and R.A.N.L.; resources, G.D.R., C.A.B. and A.P.; data curation, R.A.N.L. and L.A.-M.; writing—original draft preparation, G.D.R.; writing—review and editing, C.A.B., A.P., L.A.-M. and R.A.N.L.; visualization, G.D.R. and R.A.N.L.; supervision, G.D.R. and C.A.B.; project administration, G.D.R.; funding acquisition, G.D.R.

Funding: This research was funded by the following agencies: CONACyT (gran numbers FOIN-219 and CB-252316), Programa de Apoyo a Proyectos de Investigación y Tecnológicos of the UNAM (grant numbers IG100416 and IN208014) and the Instituto de fisiología celular at UNAM. RN is enrolled as a graduate student of the Programa de maestría en ciencias bioquímicas at UNAM and received support from CONACyT with the fellowship number 631360.

Acknowledgments: To María Teresa Lara Ortiz for her technical assistance.

Conflicts of Interest: The authors declare no conflict of interest. The funders had no role in the design of the study; in the collection, analyses, or interpretation of data; in the writing of the manuscript, or in the decision to publish the results.

References

1. Akova, M. Epidemiology of antimicrobial resistance in bloodstream infections. *Virulence* **2016**, *7*, 252–266. [CrossRef]
2. Aslam, B.; Wang, W.; Arshad, M.I.; Khurshid, M.; Muzammil, S.; Nisar, M.A.; Alvi, R.F.; Aslam, M.A.; Qamar, M.U.; Salamat, M.K.F.; et al. Antibiotic resistance: A rundown of a global crisis. *Infect. Drug Resist.* **2018**, *11*, 1645–1658. [CrossRef]

INFORME DE LABORES 2019

3. Roger, P.-M.; Montera, E.; Lesselingue, D.; Troadec, N.; Charlot, P.; Simand, A.; Rancezot, A.; Pantaloni, O.; Guichard, T.; Dautezac, V.; et al. Risk factors for unnecessary antibiotic therapy: A major role for clinical management. *Clin Infect Dis.* **2018**. [CrossRef] [PubMed]
4. Jackson, M.A.; Goodrich, J.K.; Maxan, M.-E.; Freedberg, D.E.; Abrams, J.A.; Poole, A.C.; Sutter, J.L.; Welter, D.; Ley, R.E.; Bell, J.T.; et al. Proton pump inhibitors alter the composition of the gut microbiota. *Gut* **2016**, *65*, 749–756. [CrossRef] [PubMed]
5. Rogers, M.A.M.; Aronoff, D.M. The influence of non-steroidal anti-inflammatory drugs on the gut microbiome. *Clin. Microbiol. Infect.* **2016**, *22*, 178.e1–178.e9. [CrossRef]
6. Flowers, S.A.; Evans, S.J.; Ward, K.M.; McInnis, M.G.; Ellingrod, V.L. Interaction between Atypical Antipsychotics and the Gut Microbiome in a Bipolar Disease Cohort. *Pharmacother. J. Hum. Pharmacol. Drug Ther.* **2017**, *37*, 261–267. [CrossRef] [PubMed]
7. Maier, L.; Pruteanu, M.; Kuhn, M.; Zeller, G.; Telzerow, A.; Anderson, E.E.; Brochado, A.R.; Fernandez, K.C.; Dose, H.; Mori, H.; et al. Extensive impact of non-antibiotic drugs on human gut bacteria. *Nature* **2018**, *555*, 623–628. [CrossRef] [PubMed]
8. González-Díaz, H.; Prado-Prado, F.J.; Santana, L.; Uriarte, E. Unify QSAR approach to antimicrobials. Part 1: Predicting antifungal activity against different species. *Bioorg. Med. Chem.* **2006**, *14*, 5973–5980. [CrossRef]
9. Rath, E.C.; Gill, H.; Bai, Y. Identification of potential antimicrobials against Salmonella typhimurium and Listeria monocytogenes using Quantitative Structure-Activity Relation modeling. *PLoS ONE* **2017**, *12*, e0189580. [CrossRef]
10. Murcia-Soler, M.; Pérez-Giménez, F.; García-March, F.J.; Salabert-Salvador, M.T.; Díaz-Villanueva, W.; Castro-Bleda, M.J.; Villanueva-Pareja, A. Artificial Neural Networks and Linear Discriminant Analysis: A Valuable Combination in the Selection of New Antibacterial Compounds. *J. Chem. Inf. Comput. Sci.* **2004**, *44*, 1031–1041. [CrossRef]
11. Nguyen, M.; Long, S.W.; McDermott, P.F.; Olsen, R.J.; Olson, R.; Stevens, R.L.; Tyson, G.H.; Zhao, S.; Davis, J.J. Using machine learning to predict antimicrobial minimum inhibitory concentrations and associated genomic features for nontyphoidal *Salmonella*. *J. Clin. Microbiol.* **2018**. Available online: http://www.ncbi.nlm.nih.gov/pubmed/30333126 (accessed on 19 January 2019). [CrossRef] [PubMed]
12. Wang, Z.; Wang, G. APD: The Antimicrobial Peptide Database. *Nucleic Acids Res.* **2004**, *32*, D590–D592. [CrossRef] [PubMed]
13. Pirtskhalava, M.; Gabrielian, A.; Cruz, P.; Griggs, H.L.; Squires, R.B.; Hurt, D.E.; Grigolava, M.; Chubinidze, M.; Gogoladze, G.; Vishnepolsky, B.; et al. DBAASP v.2: An enhanced database of structure and antimicrobial/cytotoxic activity of natural and synthetic peptides. *Nucleic Acids Res.* **2016**, *44*, D1104–D1112. [CrossRef] [PubMed]
14. Waghu, F.H.; Barai, R.S.; Gurung, P.; Idicula-Thomas, S. CAMP R3: A database on sequences, structures and signatures of antimicrobial peptides: Table 1. *Nucleic Acids Res.* **2016**, *44*, D1094–D1097. [CrossRef] [PubMed]
15. Del Rio, G.; Castro-Obregon, S.; Rao, R.; Ellerby, H.M.; Bredesen, D.E. APAP, a sequence-pattern recognition approach identifies substance P as a potential apoptotic peptide. *FEBS Lett.* **2001**, *494*, 213–219. [CrossRef]
16. Toropova, M.A.; Veselinović, A.M.; Veselinović, J.B.; Stojanović, D.B.; Toropov, A.A. QSAR modeling of the antimicrobial activity of peptides as a mathematical function of a sequence of amino acids. *Comput. Biol. Chem.* **2015**, *59*, 126–130. [CrossRef]
17. Durrant, J.D.; Amaro, R.E. Machine-Learning Techniques Applied to Antibacterial Drug Discovery. *Chem. Biol. Drug Des.* **2015**, *85*, 14–21. [CrossRef]
18. Battisti, A.; Zamuner, S.; Sarti, E.; Laio, A. Toward a unified scoring function for native state discrimination and drug-binding pocket recognition. *Phys. Chem. Chem. Phys.* **2018**, *20*, 17148–17155. [CrossRef]
19. Del Rio, G.; Koschützki, D.; Coello, G. How to identify essential genes from molecular networks? *BMC Syst. Biol.* **2009**, *3*, 102. [CrossRef] [PubMed]
20. Calahorra, M.; Sánchez, N.S.; Peña, A. Influence of phenothiazines, phenazines and phenoxazine on cation transport in Candida albicans. *J. Appl. Microbiol.* **2018**, *125*, 1728–1738. [CrossRef] [PubMed]
21. Acar, J. Broad- and narrow-spectrum antibiotics: An unhelpful categorization. *Clin. Microbiol. Infect.* **1997**, *3*, 395–396. [CrossRef]
22. Sarpong, E.M.; Miller, G.E. Narrow- and Broad-Spectrum Antibiotic Use among U.S. Children. *Health Serv. Res.* **2015**, *50*, 830–846. [CrossRef] [PubMed]

INFORME DE LABORES 2019

23. Beltran, J.A.; Aguilera-Mendoza, L.; Brizuela, C.A. Optimal selection of molecular descriptors for antimicrobial peptides classification: An evolutionary feature weighting approach. *BMC Genomics* **2018**, *19*, 672. [CrossRef]
24. NIH DailyMed. 26/November 2018. Available online: https://dailymed.nlm.nih.gov/dailymed/index.cfm (accessed on 19 January 2019).
25. File, T.M.; Wilcox, M.H.; Stein, G.E. Summary of Ceftaroline Fosamil Clinical Trial Studies and Clinical Safety. *Clin. Infect. Dis.* **2012**, *55*, S173–S180. [CrossRef] [PubMed]
26. Sterling, T.; Irwin, J.J. ZINC 15—Ligand Discovery for Everyone. *J. Chem. Inf. Model.* **2015**, *55*, 2324–2337. [CrossRef]
27. Yap, C.W. PaDEL-descriptor: An open source software to calculate molecular descriptors and fingerprints. *J. Comput. Chem.* **2011**, *32*, 1466–1474. [CrossRef]
28. Hammami, R.; Zouhir, A.; Le Lay, C.; Ben Hamida, J.; Fliss, I. BACTIBASE second release: A database and tool platform for bacteriocin characterization. *BMC Microbiol.* **2010**, *10*, 22. [CrossRef]
29. De Jong, A.; van Heel, A.J.; Kok, J.; Kuipers, O.P. BAGEL2: Mining for bacteriocins in genomic data. *Nucleic Acids Res.* **2010**, *38*, W647–W651. [CrossRef]
30. Novković, M.; Simunić, J.; Bojović, V.; Tossi, A.; Juretić, D. DADP: The database of anuran defense peptides. *Bioinformatics* **2012**, *28*, 1406–1407. [CrossRef] [PubMed]
31. Seshadri Sundararajan, V.; Gabere, M.N.; Pretorius, A.; Adam, S.; Christoffels, A.; Lehväslaiho, M.; Archer, J.A.C.; Bajic, V.B. DAMPD: A manually curated antimicrobial peptide database. *Nucleic Acids Res.* **2012**, *40*, D1108–D1112. [CrossRef]
32. Seebah, S.; Suresh, A.; Zhuo, S.; Choong, Y.H.; Chua, H.; Chuon, D.; Beuerman, R.; Verma, C. Defensins knowledgebase: A manually curated database and information source focused on the defensins family of antimicrobial peptides. *Nucleic Acids Res.* **2007**, *35*, D265–D268. [CrossRef]
33. Qureshi, A.; Thakur, N.; Kumar, M. HIPdb: A Database of Experimentally Validated HIV Inhibiting Peptides. *PLoS ONE* **2013**, *8*, e54908. [CrossRef] [PubMed]
34. Zhao, X.; Wu, H.; Lu, H.; Li, G.; Huang, Q. LAMP: A Database Linking Antimicrobial Peptides. *PLoS ONE* **2013**, *8*, e66557. [CrossRef] [PubMed]
35. Théolier, J.; Fliss, I.; Jean, J.; Hammami, R. MilkAMP: A comprehensive database of antimicrobial peptides of dairy origin. *Dairy Sci. Technol.* **2014**, *94*, 181–193. [CrossRef]
36. Hammami, R.; Ben Hamida, J.; Vergoten, G.; Fliss, I. PhytAMP: A database dedicated to antimicrobial plant peptides. *Nucleic Acids Res.* **2009**, *37*, D963–D968. [CrossRef] [PubMed]
37. Gueguen, Y.; Garnier, J.; Robert, L.; Lefranc, M.; Mougenot, I.; Lorgeril, J.; Janech, M.; Gross, P.S.; Warr, G.W.; Cuthbertson, B.; et al. PenBase, the shrimp antimicrobial peptide penaeidin database: Sequence-based classification and recommended nomenclature. *Dev. Comp. Immunol.* **2006**, *30*, 283–288. [CrossRef]
38. Whitmore, L.; Wallace, B.A. The Peptaibol Database: A database for sequences and structures of naturally occurring peptaibols. *Nucleic Acids Res.* **2004**, *32*, D593–D594. [CrossRef]
39. Li, Y.; Chen, Z. RAPD: A database of recombinantly-produced antimicrobial peptides. *FEMS Microbiol. Lett.* **2008**, *289*, 126–129. [CrossRef]
40. Fjell, C.D.; Hancock, R.E.W.; Cherkasov, A. AMPer: A database and an automated discovery tool for antimicrobial peptides. *Bioinformatics* **2007**, *23*, 1148–1155. Available online: http://www.ncbi.nlm.nih.gov/pubmed/17341497 (accessed on 23 January 2019). [CrossRef]
41. UniProt Consortium T. UniProt: the universal protein knowledgebase. *Nucleic Acids Res.* **2018**, *46*, 2699.
42. Piotto, S.P.; Sessa, L.; Concilio, S.; Iannelli, P. YADAMP: Yet another database of antimicrobial peptides. *Int. J. Antimicrob. Agents* **2012**, *39*, 346–351. [CrossRef] [PubMed]
43. Tossi, A.; Sandri, L. Molecular diversity in gene-encoded, cationic antimicrobial polypeptides. *Curr. Pharm. Des.* **2002**, *8*, 743–761. [CrossRef] [PubMed]
44. Wang, G.; Li, X.; Wang, Z. APD3: The antimicrobial peptide database as a tool for research and education. *Nucleic Acids Res.* **2016**, *44*, D1087–D1093. [CrossRef]
45. Qureshi, A.; Thakur, N.; Tandon, H.; Kumar, M. AVPdb: A database of experimentally validated antiviral peptides targeting medically important viruses. *Nucleic Acids Res.* **2014**, *42*, D1147–D1153. [CrossRef] [PubMed]

46. Corral-Corral, R.; Beltrán, J.; Brizuela, C.; Del Rio, G. Systematic Identification of Machine-Learning Models Aimed to Classify Critical Residues for Protein Function from Protein Structure. *Molecules* **2017**, *22*, 1673. [CrossRef]
47. Witten, I.H.; Ian, H.; Frank, E.; Hall, M.A.; Mark, A. *Data Mining: Practical Machine Learning Tools and Techniques*; Morgan Kaufmann: Burlington, MA, USA, 2011; 629p.
48. Kotthoff, L.; Thornton, C.; Hoos, H.H.; Hutter, F.; Leyton-Brown, K. Auto-WEKA 2.0: Automatic model selection and hyperparameter optimization in WEKA. *J. Mach. Learn. Res.* **2017**, *18*, 1–5.
49. Newland, J.G.; Stach, L.M.; De Lurgio, S.A.; Hedican, E.; Yu, D.; Prasad, P.A.; Jackson, M.A.; Myers, A.L.; Zaoutis, T.E. Impact of a Prospective-Audit-With-Feedback Antimicrobial Stewardship Program at a Children's Hospital. *J. Pediatric Infect. Dis. Soc.* **2012**, *1*, 179–186. [CrossRef]
50. Newman, R.E.; Hedican, E.B.; Herigon, J.C.; Williams, D.D.; Williams, A.R.; Jason, G. Newland. Impact of a Guideline on Management of Children Hospitalized With Community-Acquired Pneumonia. *Pediatrics* **2012**, *129*, e597–e604. [CrossRef]
51. Di Pentima, M.C.; Chan, S. Impact of Antimicrobial Stewardship Program on Vancomycin Use in a Pediatric Teaching Hospital. *Pediatr. Infect. Dis. J.* **2010**, *29*, 707–711. [CrossRef]
52. Kreitmeyr, K.; von Both, U.; Pecar, A.; Borde, J.P.; Mikolajczyk, R.; Huebner, J. Pediatric antibiotic stewardship: Successful interventions to reduce broad-spectrum antibiotic use on general pediatric wards. *Infection* **2017**, *45*, 493–504. [CrossRef] [PubMed]

Sample Availability: All data used in this study are available as supplemental data.



© 2019 by the authors. Licensee MDPI, Basel, Switzerland. This article is an open access article distributed under the terms and conditions of the Creative Commons Attribution (CC BY) license (http://creativecommons.org/licenses/by/4.0/).

frontiers in Physiology

INFORME DE LABORES 2019

ORIGINAL RESEARCH
published: 31 May 2019
doi: 10.3389/fphys.2019.00473

Thermodynamic Efficiency of Somatic Exocytosis of Serotonin

Paula Noguez[1], *J. Miguel Rubí*[2] *and Francisco F. De-Miguel*[3]*

[1] *Instituto de Fisiología Celular-Neurociencias, Universidad Nacional Autónoma de México, Mexico City, Mexico,* [2] *Facultat de Física, Universitat de Barcelona, Barcelona, Spain,* [3] *Centro de Ciencias de la Complejidad, Universidad Nacional Autónoma de México, Mexico City, Mexico*

Through somatic exocytosis neurons liberate immense amounts of transmitter molecules that modulate the functioning of the nervous system. A stream of action potentials triggers an ATP-dependent transport of transmitter-containing vesicles to the plasma membrane, that ends with a large-scale exocytosis. It is commonly assumed that biological processes use metabolic energy with a high thermodynamic efficiency, meaning that most energy generates work with minor dissipation. However, the intricate ultrastructure underlying the pathway for the vesicle flow necessary for somatic exocytosis challenges this possibility. To study this problem here we first applied thermodynamic theory to quantify the efficiency of somatic exocytosis of the vital transmitter serotonin. Then we correlated the efficiency to the ultrastructure of the transport pathway of the vesicles. Exocytosis was evoked in cultured Retzius neurons of the leech by trains of 10 impulses delivered at 20 Hz. The kinetics of exocytosis was quantified from the gradual fluorescence increase of FM1-43 dye as it became incorporated into vesicles that underwent their exo-endocytosis cycle. By fitting a model of the vesicle transport carried by motor forces to the kinetics of exocytosis, we calculated the thermodynamic efficiency of the ATP expenses per vesicle, as the power of the transport divided by total energy ideally produced by the hydrolysis of ATP during the process. The efficiency was remarkably low (0.1–6.4%) and the values formed a W-shape distribution with the transport distances of the vesicles. Electron micrographs and fluorescent staining of the actin cortex indicated that the slopes of the W chart could be explained by the interaction of vesicles with the actin cortex and the calcium-releasing endoplasmic reticulum. We showed that the application of thermodynamic theory permitted to predict aspects of the intracellular structure. Our results suggest that the distribution of subcellular structures that are essential for somatic exocytosis abates the thermodynamic efficiency of the transport by hampering vesicle mobilization. It is remarkable that the modulation of the nervous system occurs at the expenses of an efficient use of metabolic energy.

Keywords: somatic exocytosis, extrasynaptic, serotonin, thermodynamic efficiency, vesicle transport, kinesin, myosin, leech

OPEN ACCESS

Edited by:
Christoph Fahlke,
Julich Research Centre, Germany

Reviewed by:
Ulrich Zachariae,
University of Dundee, United Kingdom
Delany Torres-Salazar,
National Institutes of Health (NIH), United States

***Correspondence:**
Francisco F. De-Miguel
ffernand@ifc.unam.mx

Specialty section:
This article was submitted to Membrane Physiology and Membrane Biophysics, a section of the journal Frontiers in Physiology

Received: *08 November 2018*
Accepted: *04 April 2019*
Published: *31 May 2019*

Citation:
Noguez P, Rubí JM and De-Miguel FF (2019) Thermodynamic Efficiency of Somatic Exocytosis of Serotonin. Front. Physiol. 10:473. doi: 10.3389/fphys.2019.00473

INTRODUCTION

Extrasynaptic exocytosis, namely the release of transmitters and peptides from the neuronal soma, dendrites, and axons, is a source of modulators of the activity of the nervous system (De-Miguel and Fuxe, 2012; De-Miguel and Nicholls, 2015). Most low molecular weight transmitters and different peptides are released extrasynaptically by exocytosis (for review see Trueta and De-Miguel, 2012).

Molecules released in this manner diversify the responses of neural circuits to a given stimulus by integrating the activity of neurons, glia and capillaries (Fuxe et al., 2007; Rozanski et al., 2012; Hirasawa et al., 2015; Newman, 2015).

The mechanism for extrasynaptic exocytosis is substantially different from that for release at synapses and similar to the mechanism for exocytosis from endocrine cells. Somatic exocytosis involves a multi-regulated sequence of serial and parallel reactions that couple excitation with exocytosis (Ludwig and Stern, 2015; Del-Bel and De-Miguel, 2018). Vesicles -usually large and electrodense (see Trueta and De-Miguel, 2012) filled with signaling molecules, rest far from the plasma membrane. Bursts of electrical activity evoke a transmembrane calcium entry that triggers calcium release from the endoplasmic reticulum (review see Trueta and De-Miguel, 2012; Del-Bel and De-Miguel, 2018). The calcium wave induces an increase of cytosolic ATP that triggers the vesicle transport by the activation of molecular motors (Nicholls et al., 2003; Llorente-Folch et al., 2013; Rueda et al., 2014; Del-Pozo and De-Miguel, in preparation). Exocytosis starts as vesicles arrive at the plasma membrane (De-Miguel and Trueta, 2005). Calculations of the ATP expenses per vesicle fusing (ATP_{ves}) made by applying thermodynamic theory to the kinetics of somatic exocytosis of serotonin, unveiled that the amount of ATP_{ves} has a W-shape dependence on the transport distance of the vesicles (De-Miguel et al., 2012). This relationship may reflect the cytoarchitecture of the transport pathway, since electron micrographs contain endoplasmic reticulum and mitochondria -which are engines for somatic exocytosis- often invading the transport pathway of the vesicles (Trueta et al., 2004, 2012; De-Miguel et al., 2012). In addition, the actin cortex at rest prevents the vesicle transport, but after the onset of electrical activity turns into a component of the transport system by binding to myosin motors (Wang and Hatton, 2006; Tobin and Ludwig, 2007). Such observations raised the possibility that somatic exocytosis operates under low thermodynamic efficiency, opposing to the common assumption that biological processes make a high efficiency use of their metabolic energy. Theoretically, when friction forces hamper the work, a fraction of the energy dissipates in the form of heat, reducing the thermodynamic efficiency of the process. For this reason, measurements of the amount of energy provide only a partial story; it is also necessary to estimate how efficiently the energy is used. This focal problem was studied here by making use of the advantages of the well-known somatic exocytosis of serotonin by the Retzius neuron of the leech.

The large (~70 μm) soma of a Retzius neuron stores serotonin in astronomic numbers of 100 nm diameter electrodense vesicles (Coggeshall, 1972). At rest or following electrical stimulation with trains of 10 action potentials at 1 Hz (a frequency similar to the spontaneous firing of serotonergic neurons), vesicles remain

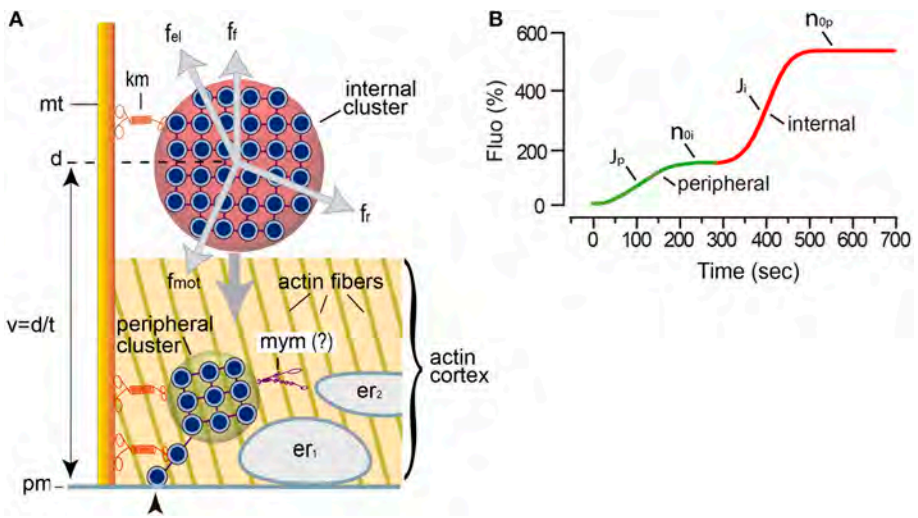

FIGURE 1 | Mechanism for somatic exocytosis in the Retzius neuron. **(A)** Schematic representation of the vesicle transport system. The scheme incorporates findings from this study. Vesicle clusters rest at variable distances from the plasma membrane. More than one cluster can be attached to the same microtubule (mt) bundle by kinesin motors (km). Internal clusters (red) lay across the actin cortex. The transport of vesicle clusters depends on four forces: the motor forces (f_{mot}), elastic forces (f_{el}), friction forces (f_f), and random forces (f_r). At rest, these forces are in equilibrium. The motor forces are microtubule- and kinesin-dependent (De-Miguel et al., 2012). Electrical stimulation produces a cascade of calcium-dependent events that activate the motor forces. Vesicle clusters are transported to the plasma membrane along a distance (d), at a velocity ($v = d/t$). Peripheral clusters (green) rest immersed in the actin cortex at the time of stimulation, flanked by two layers of endoplasmic reticulum (er_1, er_2). Inside the actin cortex, myosin motors (mym) add to kinesin motors to transport the vesicle clusters to the plasma membrane (pm). The reduced number of vesicles as clusters approach the plasma membrane seems to obey a continuous vesicle detachment and transport to the plasma membrane (Leon-Pinzon et al., 2014). Fusion of these vesicles (arrowhead) produces the constitutive release of serotonin that permits the large-scale exocytosis when whole clusters arrive at the plasma membrane in response to electrical stimulation. **(B)** Biophysical parameters measured from the FM1-43 kinetics upon electrical stimulation of exocytosis. The green segment is the contribution of a peripheral cluster; the red segment is the contribution of an internal cluster. The latency to the onset of release contains information on the distance and velocity ($t = d/v$) of the vesicle transport. The J value is the flux of vesicles (vesicles fused per second). The n_o values are the number of vesicles that fused per vesicle cluster.

clustered at variable distances from the plasma membrane and exocytosis does not occur (**Figure 1**; De-Miguel et al., 2012). By contrast, the same number of action potentials evoked at a high 20 Hz frequency triggers the massive transport of vesicle clusters to the plasma membrane and the large-scale exocytosis. Within the following hundreds of seconds, tens of thousands of vesicles distributed in ∼90 clusters will discharge their content from different parts of the soma (Trueta et al., 2003; De-Miguel et al., 2012). The large-scale exocytosis is sustained for long periods in absence of further transmembrane calcium entry, by the serotonin that has been released (Leon-Pinzon et al., 2014). Activation of serotonin autoreceptors evoke an intracellular IP3-dependent release of calcium from the endoplasmic reticulum adjacent to the plasma membrane. This localized calcium elevation maintains exocytosis until the fusion of the last vesicles in the clusters (Leon-Pinzon et al., 2014). It is common that a second and larger cluster of vesicles arrives at the same release site producing a second bulk of exocytosis (De-Miguel et al., 2012; Leon-Pinzon et al., 2014). **Figure 1** recapitulates the elementary aspects of this mechanism.

In this study we applied a thermodynamic theoretical approach to calculate the efficiency of somatic exocytosis of serotonin. As the reporter of exocytosis we used the fluorescence increase of FM1-43 dye, which stains the inside of vesicles that undergo their exocytosis/endocytosis cycle (Betz et al., 1992; De-Miguel et al., 2012). A mathematical approach applied to the kinetics of exocytosis permitted to calculate the transport distance, velocity and power of the whole process of somatic exocytosis from individual release sites. By incorporating new experimental data to the model fittings, we improved our previous estimates of the ATP expenses per vesicle fused (ATP_{ves}). The thermodynamic efficiency of the ATP_{ves} expenses was calculated from the work in the presence of friction forces, divided by the ideal energy generated by the ATP cleavage. The thermodynamic efficiency along the traveling distance of the vesicles was correlated with the ultrastructure of the transport pathway, analyzed from electron micrographs, and fluorescent staining of the actin cortex.

MATERIALS AND METHODS

Ethics Statement

Animal research was approved by the Animal Committee of the Instituto de Fisiología Celular, Universidad Nacional Autónoma de México.

Isolation and Culture of Neurons

Experiments were made using Retzius neurons of the medicinal leech *Hirudo sp*. For experiments with FM1-43, neurons were individually isolated by suction through a glass pipette after an enzyme treatment (Dietzel et al., 1986) and plated in glass-bottom culture dishes coated with concanavalin-A (Sigma, St. Louis, MO). The culture medium was L-15 (Sigma) supplemented with 6 mg/mL glucose, 0.1 mg/mL gentamycin and 2% fetal bovine serum (Gibco, Gaithersburg, MD). Experiments were made at 18°C after 1–3 days in culture.

Stimulation and Detection of Exocytosis

Exocytosis was quantified from the fluorescence increases produced by the incorporation of FM1-43 (2 μM; Molecular Probes) by the vesicles that undergo fusion and endocytosis (Betz and Bewick, 1993). Vesicle fusion permits the dye to enter the vesicles and stain their internal membrane. Endocytosis keeps the dye inside the vesicle. Therefore, each vesicle fusion contributes with a step to the fluorescence in the release site. We have previously shown that the large-scale exocytosis from vesicles arriving in a cluster lasts for hundreds of seconds, depending on the number of vesicles in the distance and the velocity of the transport. Upon endocytosis, the stained vesicles accumulate near the plasma membrane without being recycled to the releasable pool. Instead, they get packed forming multivesicular bodies that are later transported to the perikaryon (Trueta et al., 2012). Therefore, the gradual increase of fluorescence reflects accurately the kinetics of exocytosis; the plateau is reached once all the electrodense vesicles in the cluster have fused and the intensity of fluorescence indicates the number of vesicles that fused (De-Miguel et al., 2012). If any stained vesicle fuses again the amount of fluorescence does not increase because the vesicle is already stained.

Stimulation of exocytosis consisted of trains of 10 action potentials produced by intracellular injection of 10 ms current pulses at 20 Hz delivered every 2 min. The amplitude of the current pulses was adjusted in every neuron between 5 and 8 nA, to guarantee that each pulse in the train produced one action potential. The intracellular voltage was recorded using a Getting pre-amplifier operating in bridge balance mode. In eight other neurons the actin cortex was uncoupled by incubation with 1 μM cytochalasin D (Sigma-Aldrich) for 30 min at 18°C before stimulation.

Individual neurons were focused on their equator with a Nikon Eclipse TE 200 inverted microscope using a Nikon 100x oil immersion objective (NA 1.40). FM1-43 was excited at 488 nm and its fluorescent emission was measured at 543 nm. Images were taken every 2 s with a cooled CCD camera (IMAGO, Till Vision, Germany) at a 640 × 480-pixel resolution. Processing was made offline by using TILLvisION software.

The fluorescence measurements were made by linear interpolation, after non-specific fluorescence in each sequential image was subtracted from the intensity of the membrane. The area of release was estimated from the length of membrane in which fluorescence increased, by assuming that it was circular (De-Miguel et al., 2012). This number served as a reference for the model estimates of the number of vesicles (see Equation 1).

Exclusion Criteria

Neurons commonly moved after electrical stimulation. Therefore, the focus of each spot in the time series analysis had to be confirmed from a z axis scanning of the neurons at the end of the experiment. Only fluorescent spots that remained in focus during the whole experiment or that could be aligned digitally were included in the analysis. Clusters extending for more than 1 μm of membrane length were excluded to avoid out-of-focus fluorescent emissions due to large numbers of vesicles (De-Miguel et al., 2012). For these reasons, we eliminated

from our analysis a vast number of observations. However, the data from nine different neurons in which subsequent uncorrelated clusters of vesicles arrived at the same spot were a fair representation of the population.

Quantitative Analysis of Exocytosis

The model was developed based on the kinetic properties of the FM1-43 fluorescence increases during exocytosis (**Figure 2**). A full account of the theoretical development of the model is presented in De-Miguel et al. (2012). In brief, the fluorescence kinetics $F_{(t)}$ is proportional to the flux J_{ves} of vesicles arriving at the plasma membrane. The process of exocytosis is orders of magnitude faster than the speed of the vesicle transport. Therefore, the flux reflects the transport and can be defined as the number of vesicles fusing per second at an area A of the plasma membrane, according to:

$$F(t) = F_0 + Ab \int_0^t J_{ves}(d, t')dt' \quad (1)$$

In Equation (1), F_0 is the basal fluorescence produced by the interaction of the fluorescent dye with the extracellular layer of the plasma membrane; b is a proportionality factor relating the amount of fluorescence contributed by each vesicle. This proportionality stems from the fact that the internal membrane surface of the population of electrodense vesicles can be considered constant. The parameter "t" is the time, while "d" is the transport distance from the center of mass of the resting cluster to the plasma membrane. The distance was estimated by the model and was correlated with distances measured from electron micrographs of neurons stimulated with 1 Hz trains of impulses (De-Miguel et al., 2012). The plateau of the fluorescence increase indicates the total the number of vesicles (n_0) that fused (**Figure 1B**). The parameters used in the model are in **Table 1**. The contribution of the distance, velocity and number of vesicles to the kinetics of fluorescence are presented schematically in **Figure 1**.

As shown also in **Figure 1**, the flux of vesicles, J_{ves}, depends on four forces. The first two are a frictional force due to the resistance opposed by the medium to the vesicle motion and a random force produced by thermal agitation. These two forces produce the Brownian motion of the vesicles at the experimental temperature. The third force is elastic and confines the individual vesicles in a cluster. These forces are considered harmonic because the vesicle displacements they produce are small. This assumption simplifies the model. The fourth force is used by the motors to carry the vesicle clusters plus mitochondria at an average velocity "v_{ves}" (Svoboda and Block, 1994; Schnitzer and Block, 1997). The Force of the motor and the elastic forces acting together on the vesicles can be defined as:

$$F = f_{el} + f_{mot} = \omega^2(d - vt) \quad (2)$$

Where ω is the characteristic frequency at which the elastic forces confine the vesicles, as described by:

$$\omega = \sqrt{\frac{k}{m}} \quad (3)$$

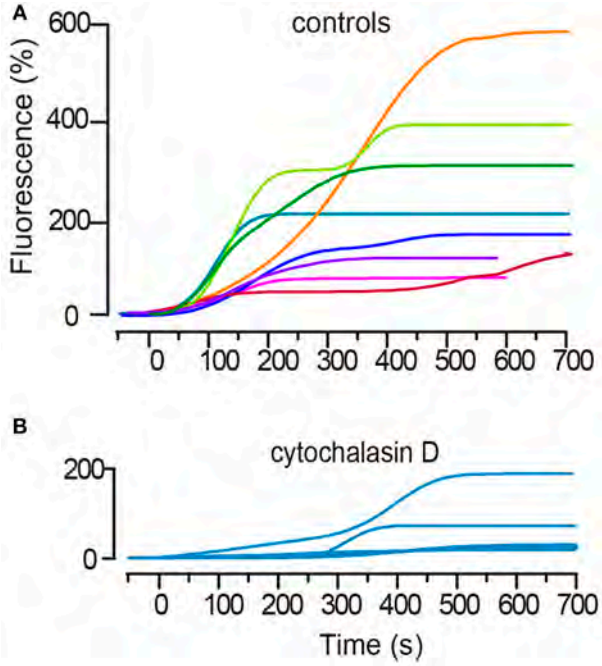

FIGURE 2 | Kinetics of the large-scale exocytosis as measured from the fluorescence increases of FM1-43. **(A)** Superimposition of the FM fluorescence (Fluo) kinetics of eight representative spots from an equal number of neurons. Stimulation occurred at $t = 0$. A subsequent stimulation train was delivered every 2 min. Fluorescence is plotted as the percentage increase over the baseline. Subsequent sigmoidal increases appear in most kinetics, with each reflecting exocytosis from a subsequent vesicle cluster. **(B)** Treatment of neurons with cytochalasin D that uncouples the actin cortex delayed and reduced the fluorescence increases in response to stimulation and abolished the second sigmoidal fluorescence increase. The plot superimposes six kinetics from an equal number of neurons. Note the difference in the fluorescence scale bars between **(A,B)**.

We consider that the vesicle motion toward the cell membrane is unidimensional and can be described in terms of the distance coordinate. Therefore, J_{ves} depends on the friction and motor forces plus the contribution of diffusion, where $J_{ves} = \rho v_{ves}$ and $v_{ves} = \beta^{-1}F$. Then J_{ves} can also be expressed as:

$$J_{ves} = -D\frac{\partial \rho}{\partial x} + \beta^{-1}\rho F \quad (4)$$

where the term $-D\frac{\partial \rho}{\partial x}$ accounts for diffusion, with D the being the diffusion coefficient, and the second term is the product of the friction ($\beta^{-1}\rho$) and the motor (F) forces, due to the effect of the driving force (De-Miguel et al., 2012).

These forces are modeled by a linear function of the position, which corresponds to a harmonic force. Harmonic forces yield in general an oscillatory motion in which the velocity of the particle decreases until it vanishes at a certain point, and then increases in the opposite direction. In this case the harmonic force acts only during forward motion. Therefore, that sole force can model the main movement of the vesicles to the plasma membrane.

TABLE 1 | Definition of the parameters used in the model.

Symbol	Definition	Dimensions
A	Area of a release site measured from the diameter of the fluorescence increase	L^2
ATP_{ves}	Number of ATP molecules hydrolyzed per vesicle fused.	–
β	Dimensionless constant referring to the fluorescence increase per vesicle fused	–
d	Transport distance of vesicle clusters measured from the center of mass of the cluster to the plasma membrane	L
ΔG	Gibb's free energy	ML^2T^{-2}
ΔG_{ATP}	Gibb's free energy of ATP hydrolysis	ML^2T^{-2}
F_0	Baseline value of the fluorescence intensity	a.u.
$F(t)$	Fluorescence as a function of time	a.u.
F	Force exerted by the motors	MLT^{-2}
f_f	Friction forces per mass unit	LT^{-2}
$f_{r(t)}$	Random forces due to thermal agitation per mass unit	LT^{-2}
f_{el}	Elastic forces per mass unit	LT^{-2}
f_{mot}	Molecular motor force per mass unit	LT^{-2}
Fv	Power of the large-scale exocytosis	ML^2T^{-3}
J_{ves}	Current density of vesicles	$L^{-2}T^{-1}$
κ	Elastic constant of the cytoskeleton	MT^{-2}
m	Mass	M
η	Thermodynamic efficiency	–
n_o	Number of vesicles per cluster	–
r	Rate constant of ATP hydrolysis	T^{-1}
v	Average velocity of vesicle cluster transport	LT^{-1}
ω	Characteristic frequency of the elastic force	T^{-1}
W	Work of the large-scale exocytosis	ML^2T^{-2}

Improved Estimates of ATP Consumption

The work that moves the vesicle cluster-mitochondria complex along a certain distance equals the change in free energy:

$$W_{tot} = k(d^2 - dvt) = \Delta G_{process} \tag{5}$$

In our previous calculations, the elastic (k) constant value of the molecular motors was a free parameter in the model. For such reason there were variations in its predicted value from one release site to another (De-Miguel et al., 2012). In this study, we fed the model with a unique $k = 0.027$ pN/nm value measured experimentally by Bruno et al. (2011).

Equation (6) expresses the total amount of energy provided by the cleavage of ATP that is necessary under ideal conditions, to transport a vesicle cluster for a certain distance without dissipation. Due to the heterogeneity of the vesicle cluster sizes, the energy is expressed as the number of ATP molecules hydrolyzed per vesicle fused (ATP_{ves}) by dividing the numerator by the number of vesicles in the cluster n_0:

$$ATP_{ves} = \frac{\Delta G_{process}}{n_0 \Delta G_{ATP}} \tag{6}$$

TABLE 2 | Ranges of parameter values contributing to the vesicle transport.

Cluster	Peripheral	Internal
η_0	98–490	52–930
d (μm)	0.6–2.1	1.9–6.2
v (nm/s)	15.0–95.0	11.5–60.0
J_{ves} (ves/sec)	0.2–4.0	0.9–10.33
Elastic force (N × 10^{-11})	1.2–4.2 (0.6–4.1)	3.8–12.0 (2.2–24.2)
Motor force (N × 10^{-10})	1.2–6.0 (0.6–4.4)	1.8–4.7 (1.4–3.5)
ATP_{ves}	10.9–49.4 (3.4–73.0)	13.6–260 (0.4–25.1)
Efficiency (%)	0.2–6.4	0.1–1.9

Data in red are the estimates calculated in this study; data in parenthesis are from our previous study (De-Miguel et al., 2012).

The ΔG_{ATP} value was 5.4×10^{-20} Joules (Alberty and Goldberg, 1992), and n_0 is the number of vesicles that fused (see Equation 1). **Table 2** compares the data obtained for the elastic and motor forces, and for the ATP_{ves} expenses reported here and in our previous study (De-Miguel et al., 2012). **Table 2** shows that the ATP_{ves} values presented here remained within similar orders of magnitude than those previously reported.

Thermodynamic Efficiency

Since energy dissipation due to the presence of frictional forces is expected to occur in a non-ideal transport by living neurons, we used the classical definition of efficiency as the ratio between the ideal and the lost work and applied as in De Groot and Mazur (1969), later applied to analyze the efficiency of the calcium ATP_{ase} by Lervik et al. (2012).

$$\eta = \frac{W_{ideal} - W_{lost}}{W_{ideal}} \tag{7}$$

The W_{ideal} is the given by:

$$W_{ideal} = -r\Delta_r G \tag{8}$$

Where r is the force-related rate of ATP cleaved by the molecular motors. The kinetics of force generation of molecular motors are consistent with a two-step reaction (Higuchi et al., 1997). The binding of ATP has a rate constant that depends on the concentration and therefore its units are $\mu M^{-1} \cdot s^{-1}$; a second rate constant r accounts for the force generation used here, and has s^{-1} units (Higuchi et al., 1997). The r value related to the force generation is the one that matters for our estimates, since according to De Groot and Mazur (1969, Equation 10 of Chapter X), it relates the reaction rate to the production of entropy. This definition is adequate to calculate the efficiency since the entropy production related to thermal dissipation. As in our previous equation, $\Delta_r G$ is the Gibbs free energy of the ATP cleavage.

The work lost (W_{lost}) can be obtained from the Gouy-Stodola theorem in Equation (7) (see Kjelstrup et al., 2010):

$$W_{lost} = T\sigma \tag{9}$$

where T is the constant temperature of the surroundings of the system and σ is the production of entropy that accounts for the thermal dissipation. In our case, the energy is dissipated during the transport of vesicles and in the process of the ATP hydrolysis at a rate given by:

$$T\sigma = -r\Delta G - J_{ves}\Delta\mu_{ves} \tag{10}$$

This expression was derived according to energy conservation along the transport path; $\Delta\mu_{ves}$ in a previous paper was an electroneutral exchange of ions by the calcium ATP_{ase} (22), and here it relates to the force F of the motors. We also considered a negligible thermal driving force (Lervik et al., 2012). This expression was also used by Caplan and Essig (1999), who considered the isothermal case and the linear regime of proper pathways.

The efficiency η of vesicle exocytosis can be given in terms of measurable quantities as:

$$\eta = \frac{-r\Delta G - T\sigma}{-r\Delta G} = \frac{J_{ves}\Delta\mu_{ves}}{-r\Delta G} \tag{11}$$

The numerator of this fraction involves the flux of particles J_{ves} and the chemical potential difference $\Delta\mu_{ves}$ between the initial and the final position of the vesicles, which corresponds to a force. Since in the experiments we follow the trajectories of the vesicles, the numerator that corresponds to the work applied to the vesicles to move with a velocity v_{ves} is given by the product $F_{ves}v_{ves}$. The efficiency is then:

$$\eta = \frac{F_{ves}v_{ves}}{r|\Delta G|} \tag{12}$$

where F_{ves} is the sum of elastic and motor forces given in Equation (2).

The efficiency per vesicle was calculated by dividing by the number of vesicles (n_0) in the cluster.

$$\eta = \frac{F_{ves}v_{ves}}{n_0 r|\Delta G_{ATP}|} \tag{13}$$

The rate constant r of the force generated by the ATP hydrolysis for kinesin motors is <100–300 s^{-1} (Higuchi et al., 1997; Cross, 2004). A similar range of values has been measured for myosin motors (Johnson and Taylor, 1978; De La Cruz et al., 1999). Therefore, the 100 s^{-1} value used here may account for either motor type acting separately and with non-additive effects.

Curve Fitting and Statistical Analysis

The kinetics of exocytosis of 19 release sites obtained from six neurons were fitted to the mathematical model, as in De-Miguel et al. (2012; see **Figure 5**). The traveling distance and number of vesicles were limited by the ranges of values determined previously from electron microscopy (De-Miguel et al., 2012). In this way we reduced the possible combinations of values estimated by the model and reduced the error in the fittings. The data were fitted manually by using our own routines made in MATLAB software (MathWorks, Massachusetts, USA). This procedure was preferred over minimum square methods because sigmoidal functions with two crossovers became smoothed in abrupt parts of curves that had strong contributions by the motor activity. A previous account on the quality of the fittings and the effects of varying the values of the free parameters has been presented in De-Miguel et al. (2012).

The data sets relating the ATP_{ves} expenses and the efficiency vs. distance presented in **Figure 6** were fitted to empirical polynomial functions to underscore the W-shape of the charts. The order of the polynomials was adjusted to obtain the best R^2 correlation values. The polynomial functions in our previous study had better fittings; data of peripheral clusters were fitted by a third-order polynomial function with $R^2 = 0.92$. Likewise, the fitting quality of the internal cluster data was $R^2 = 0.83$. The reason for the lower quality of the fittings presented here is the absence of data in the distance ranges of the minimum peaks (see **Figure 6A**). However, the polynomial fittings had no other intention than to give numeric support to the clear W-shaped trend of the data. In any case, due to the calculation improvements already described, we consider that the data sets in this study are more precise.

Staining of the Actin Cortex

The actin cortex was measured from fluorescent stainings made by use of phalloidin coupled to a fluorescent probe. Neurons were fixed right after stimulation with CytoSkelFix (Cytoskeleton) for 4 min at −20°C and permeabilized for 30 min with phosphate-buffer saline (PBS) solution containing 0.3% Triton X-100. SFB (10%) was added as a blocker for 2 days, during which the preparations were maintained at 4°C. Actin was stained by incubation for 30 min at 37°C with phalloidin coupled to Alexa-fluor 488 (0.16 μM, Invitrogen). Controls incubated in parallel without phalloidin were devoid of any staining.

Observations of fluorescence made using an Olympus Fluoview FV1000 upright confocal scanning microscope equipped with a 60X oil immersion objective (1.45 NA). Images were stored digitally using Fluoview 3.1 software (Olympus). The thickness of the actin cortex was measured from digital images using ImageJ software (NIH, USA).

Electron Microscopy

Neurons in isolated ganglia were fixed right after stimulation with 10 trains of 10 impulses at 1 or 20 Hz, delivered at 10 s intervals. The procedure to obtain thin (70–100 nm) sections for electron micrographs of Retzius cells were as in Kuffler et al. (1987). Sections were photographed in a JEOL 1010 electron microscope (JEOL USA Inc.).

RESULTS

Kinetics of Somatic Exocytosis

Electrical stimulation of Retzius neurons with 20 Hz trains produced FM1-43 fluorescence spots at the neuronal surface (Trueta et al., 2003). In this experimental situation each release site develops a fluorescent spot upon the subsequent fusion of electrodense vesicles. A first sigmoidal fluorescence increase (**Figure 2A**) reflects the fusion of vesicles forming a cluster that

rested at distances <2.0 μm from the plasma membrane (De-Miguel et al., 2012). Such clusters are named "peripheral" and data are presented as green symbols (**Figure 2B**). A second sigmoidal increase in the same spot is due to fusion of vesicles in clusters that traveled from more internal sites (see De-Miguel et al., 2012). These clusters are called "internal," and data are represented with red symbols (**Figure 2B**).

The model fittings predicted that 52–930 vesicles per cluster became fused in the 19 clusters analyzed from 10 neurons. There was no correlation between the number of vesicles, the distance, or the velocity of pairs of clusters arriving subsequently at the same release site ($R^2 \leq 0.4$ for all cases). For example, in a release site the peripheral cluster contained 95 vesicles that traveled along 0.6 μm at 70 nm/s, whereas the internal cluster contained 262 vesicles that traveled along 4.1 μm at 12 nm/s; in other release site the peripheral cluster also had 95 vesicles that traveled along 0.6 μm at 59 nm/s, but the internal cluster contained 675 vesicles that traveled along 2.7 μm at 18 nm/s. In a third release site the peripheral cluster was larger than the internal, however both traveled at the same 30 nm/s velocity. Data of the pairs of clusters can be seen in **Figure 10**.

It was previously shown that uncoupling microtubules by addition of colchicine to the neurons abolishes somatic exocytosis, most likely by uncoupling the actin-mediated transport (De-Miguel et al., 2012). In addition, the actin cortex in neurons and secretory cells imposes a barrier for the transport at rest, but electrical activity in the presence of myosin turns the actin cortex to an active transporter (Vitale et al., 1995; Lang et al., 2000; Oheim and Stühmer, 2000; Giner et al., 2005; Tobin and Ludwig, 2007; Gutiérrez and Gil, 2011; Torregrosa-Hetland et al., 2011). For its potential friction-generating qualities, we uncoupled the actin cortex to test its contribution to the ATP expenses and efficiency of the transport. Pre-incubation of six neurons with cytochalasin D in the bathing solution produced that in all but one case ($n = 8$ clusters from 6 neurons), the latency to the onset of exocytosis was increased from 50–80 s to ∼300 s. In addition, the amplitude of the plateau fluorescence was reduced to values corresponding to 40–107 vesicles fused (**Figure 2B**). It can also be seen that in all but one case the fluorescence increase lacked the second sigmoidal. This experiment shows that the actin cortex has a sophisticated contribution to somatic exocytosis.

The Rate of Vesicle Fusion Reflects the Transport Conditions

The calculations of the efficiency depended on the correct measure of the flux of vesicles (J_{ves}; see Equations 1 and 4 in the Methods section), indirectly representing the rate of exocytosis. For this reason, it was necessary to demonstrate that the area of membrane did not limit exocytosis. This possibility was confirmed by correlating J_{ves} with the number of vesicles that fused. The J_{ves} values ranged from 0.2 to 5.2 vesicles per second in the 19 clusters studied and had a linear relationship ($R^2 = 0.85$) with the area of release (**Figure 3A**). For internal clusters the relation was sublinear with a 0.76 exponent ($R^2 = 0.88$). The deviation from linearity occurred when the number of vesicles per cluster was above 600. Such large clusters may have encountered major constrains in their traveling path, as will be confirmed below. However, the large clusters can extend over wide areas of membrane, as seen in electron micrographs (Trueta et al., 2004). Therefore, we consider that the J_{ves} values reflect accurately the transport velocity of the vesicle clusters. In support to this, **Figure 3B** shows that the efficiency of the ATP expenses was uncorrelated with the J_{ves} values.

ATP-Dependence of the Thermodynamic Efficiency

The efficiency of the ATP_{ves} expenses of peripheral clusters spanned within more than one logarithmic unit from values as low as 0.2% for the smallest 11 ATP_{ves} value. From there, the efficiency increased to its largest 6.4% value when the ATP_{ves} cost was 49 molecules (**Figure 4**). The intermediate data were described by a supralinear relationship. The 1.9 potency slope ($R^2 = 0.7$) is consistent with the possible incorporation of a second type of motor, presumably myosin coupled to the actin cortex. This addition could increase the efficiency of ATP_{ves} expenses by incorporating the characteristic longer steps per ATP molecule of myosin motors (Kohler and Rohrbach, 2015). The internal vesicle clusters were distributed within an efficiency range from 0.1 to 1.9% and a large range of ATP_{ves} cost of 14 to

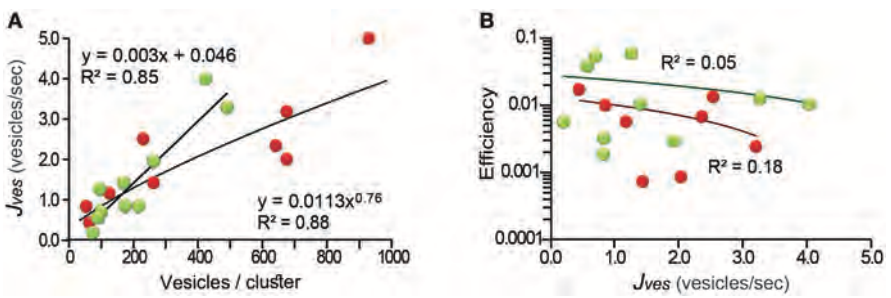

FIGURE 3 | The thermodynamic efficiency of the ATP per vesicle fused was independent from the rate of vesicle fusion (J_{ves}). **(A)** The J_{ves} values related linearly to the number of vesicles in peripheral clusters (green), and with a 0.76 exponent to the number of vesicles of internal clusters (red; for explanation see text). **(B)** The efficiency did not correlate with the rate of fusion of internal or external clusters (black lines), respectively. The equations giving the best fit to the data and the significance levels are presented.

260. The plot approximated a linear relationship ($R^2 = 0.6$) with a 0.9 exponent. This result is more consistent with the action of a single type of motor (kinesin) mediating the transport (Kohler and Rohrbach, 2015).

Uncoupling the actin cortex with cytochalasin D reduced the range of ATP_{ves} expenses to 1.3–19, and the efficiency to the lowest 0.06–0.4% range in the study (**Figure 4**). The small amount of exocytosis in this experimental situation suggests that only vesicles inside the cortex at the time of stimulation could fuse. This is in agreement with the 0.37–2.7 μm transport distances estimated for these clusters. The potency function that fitted these data, had again a slope of two ($R^2 = 0.90$). These data in addition with the short transport distances points to the possibility that short filaments of actin bound to myosin and contributed to move the proximal clusters that fused. Our conclusion from these sections is that the efficiency values are proportional to the ATP_{ves} expenses and may indicate additive effects on the vesicle transport.

Velocity as a Reporter of the Thermodynamic Efficiency

Figure 5 shows that the thermodynamic efficiency displayed a power law relationship with the transport velocity of the vesicles. This trend incorporated the whole population of data, although peripheral clusters traveled with a wider 15–95 nm/s range of velocities. The velocities above 60 nm/s were unreachable for internal clusters. As expected from Equation (12), the peripheral vesicles transported at higher velocities also displayed the largest -although yet low- thermodynamic efficiencies between 4.2 and 6.4%. This finding is not surprising from a different perspective: the peripheral clusters were small and had less mass to oppose to frictive obstacles. At velocities below 60 nm/s there was an extensive overlapping of both cluster populations in the chart, with the efficiencies of the internal clusters being ≤1.9%. Application of the actin depolymerizing agent cytochalasin D produced a reduction in the transport velocity to 1.5–17.0 nm/s that correlated with the lower 0.006–0.04% range of efficiency. This result seems more related to the lack of one motor system than to an increase in the frictive forces. Data from the internal and external clusters could be fitted independently to potency functions with equal 1.56 exponents and R^2 values of 0.69 and 0.41, respectively. However, the pooled data set, including those data collected in the presence of cytochalasin D were best described by a single function with a 1.63 slope ($R^2 = 0.86$). This property anticipates that the distribution of velocities expresses effects from other variables such as the size of the vesicle cluster and the cytoarchitecture of the pathway. To complement this scheme, we have also shown that the ATP_{ves} cost also increases with the velocity (De-Miguel et al., 2012).

Distance-Dependence of the ATP Expenses

The distance-dependence of the ATP_{ves} expenses reproduced the previously described W-shape (De-Miguel et al., 2012), with

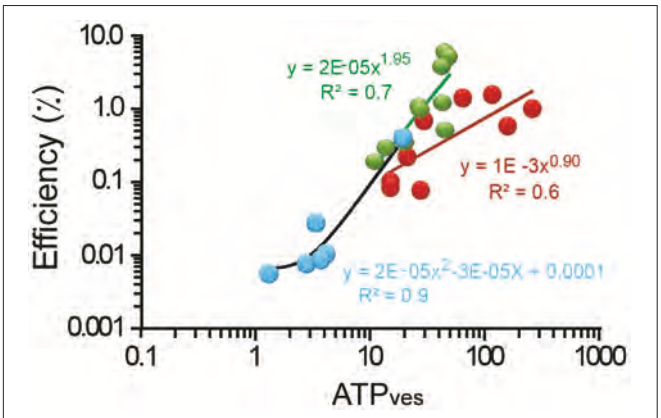

FIGURE 4 | Efficiency as a function of the ATP_{ves} expenses. Logarithmic plot of the efficiency as a function of the ATP_{ves}. The thermodynamic efficiency of exocytosis from peripheral clusters had a quadratic relationship with ATP_{ves} expenses (green line); internal clusters (red) the relationship had a 0.9 exponent (dark red line). Uncoupling the actin cortex with cytochalasin D (blue dots) reduced the range of the relationship by two logarithmic units. Data was fitted by a quadratic potency function (black line). The equations and their significance values are presented.

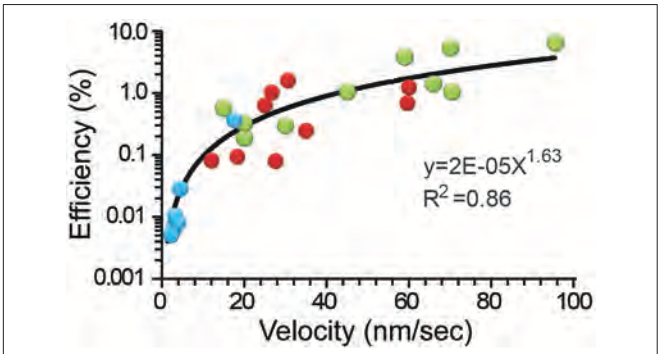

FIGURE 5 | The efficiency depended on the transport velocity. Data from internal (red), peripheral (green) clusters, and after addition of cytochalasin D (blue) were pooled together and fitted to a potency function (black line). The equation and significance level are presented.

certain differences in the ranges of ATP_{ves} values, that are presented in **Table 2**. The transport of external clusters along the shortest 0.6 μm resting distances had a high 52 ATP_{ves} cost. As the transport distance increased to 1.3 μm, the ATP_{ves} cost became gradually reduced to reach minimum of 13 ATP_{ves}. As the distance continued to increase, the trend of the energy cost reversed to reach 44 ATP_{ves} when the distance was 2.1 μm. This was the distance at which the high-energy barrier of the W curve appeared. This was also the site of convergence for external and internal clusters. The first internal cluster rested at 1.9 μm and release from its vesicles occurred at a high 118 ATP_{ves} cost (**Figure 6A**). From there, the ATP_{ves} expenses had a second decrease to reach the second minimum, which in this case was 14 ATP_{ves} in the segment between 2.3 and 4.3 μm. The last increase complemented the W shape by reaching the largest 260 ATP_{ves} value at 6.15 μm (**Figure 6A**). The polynomial

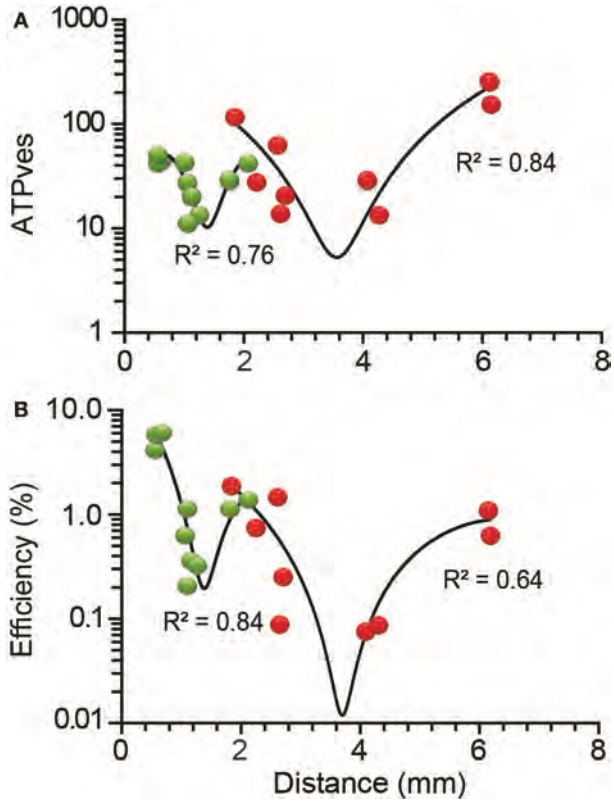

FIGURE 6 | Distance-dependence of the ATP_{ves} expenses and thermodynamic efficiency of exocytosis. **(A)** The ATP_{ves}-dependence on the distance had a W-shape. The short distance range of the plot contains information from peripheral (green) clusters, while distances above 1.9 μm contain information from internal (red) clusters. A maximum intermediate peak forming a high energy barrier appeared by 1.9 μm, with convergence of peripheral and internal clusters. **(B)** The distance-dependence of the thermodynamic efficiency of somatic exocytosis also was W-shaped, with each vesicle population separated by the intermediate maximum. The clusters that rested at the shortest distances had the largest efficiency values. The R^2 values are the significance of the polynomial functions fitted to the data (black lines).

fittings in the plots had the unique intention to underscore the W-shape distribution of the data without any use for the model calculations.

Distance-Dependence of the Thermodynamic Efficiency

As expected from the proportionality of the efficiency and the ATP_{ves} values in **Figure 4**, the thermodynamic efficiency also displayed a W-shape dependence on the transport distance (**Figure 6B**). The distance ranges of the efficiency plots were the same as for the ATP expenses. However, the efficiency of peripheral clusters covered a larger range of values than that of internal clusters. The first polynomial distribution in **Figure 6B** included the data from peripheral clusters ($R^2 = 0.84$). The low distance extreme had the higher 6.4% efficiency. At deeper distances the values first decreased to a 1.9% minimum and then increased to reach the intermediate 1.4% peak right where peripheral and internal clusters intersected. The second part of the chart had a sole contribution from internal clusters. This section could be approached by a polynomial function ($R^2 = 0.64$). The 0.08% second minimum efficiency occurred between 2.65 and 4.30 μm, although as discussed above, data with even lower values may be missing. At 6.15 μm the efficiency reached its internal maximum value of 1.1%. Our hypothesis to explain the W-distribution of the ATP_{ves} expenses and efficiency was that each component of the plot reflects a mechanical or ultrastructural interference on the vesicle pathway. An increase in the friction can be produced by a larger number of vesicles being transported or by obstacles in the pathway. It is worth to remark that the slopes of the W chart do not refer to the behavior of the vesicles within the range of distances covering that slope but indicate the amount of ATP expenses and efficiency over their whole trip to the membrane. Following this idea, those vesicles traveling the longest distances would have to overcome the obstacles that produce each of the four slopes of the chart. These possibilities were explored in the following parts of the study.

Ultrastructural Correlates of the Thermodynamic Efficiency

For its susceptibility to be affected by friction forces, the number of vesicles in the clusters was our first candidate to explain the components of the W chart. The plot in **Figure 6B** showed that the vesicle clusters near the plasma membrane had the largest efficiencies. **Figure 7** shows that those same clusters were small, as explained in **Figure 1**. Intuitively, the transport of small cargos occurs with higher efficiency owing to the smaller counteracting friction forces. However, the ATP_{ves} cost of the transport of these clusters was among the highest (**Figure 6A**). Moreover, the relationship between the size of the clusters and the efficiency did not follow the W shape. The number of vesicles per cluster increased as the clusters rested more internally, to reach 930 vesicles at 4.5 μm from the plasma membrane. Then the last cluster carried only 62 vesicles with a 1.1% efficiency. This small cluster was most likely being assembled near a Golgi apparatus (see Trueta et al., 2012). This result points to elements other than the vesicle numbers affecting the efficiency. Based on this reasoning we carried out a search for ultrastructural elements affecting the thermodynamic efficiency.

Ultrastructure of the Actin Cortex

The dual role of the actin cortex on the vesicle transport already described suggested its influence on the thermodynamic efficiency of the transport. The actin cortex of neurons stimulated with 1 Hz trains of impulses was stained with phalloidin coupled to Alexa fluorescent dye. The fluorescent label in equatorial images of the soma consisted of a thick 1.93 ± 0.74 μm (S.D.) array of radial bundles (**Figure 8**), as quantified from 46 counts of different parts of the cortex of five neurons. This thickness was similar to the distance at which we found the high energy barrier and high efficiency intermediate peak of the W distributions shown in **Figure 6**. Such value gives a possible explanation to the third slope of the W distributions in **Figure 6**. As internal clusters

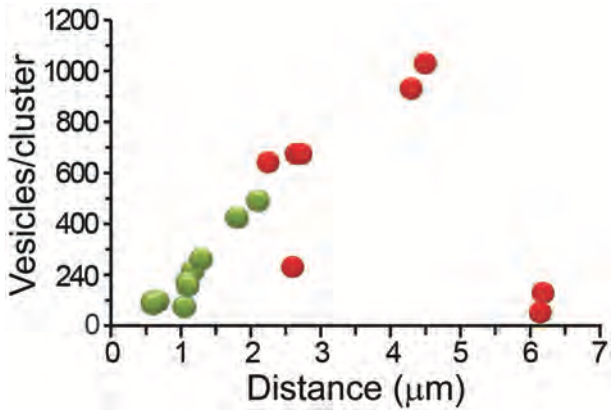

FIGURE 7 | Distance-dependence of the number of vesicles that fused per cluster. The number of vesicles in the clusters increased with the distance from the plasma membrane. The most internal clusters were small. Peripheral clusters are represented in green and internal in red.

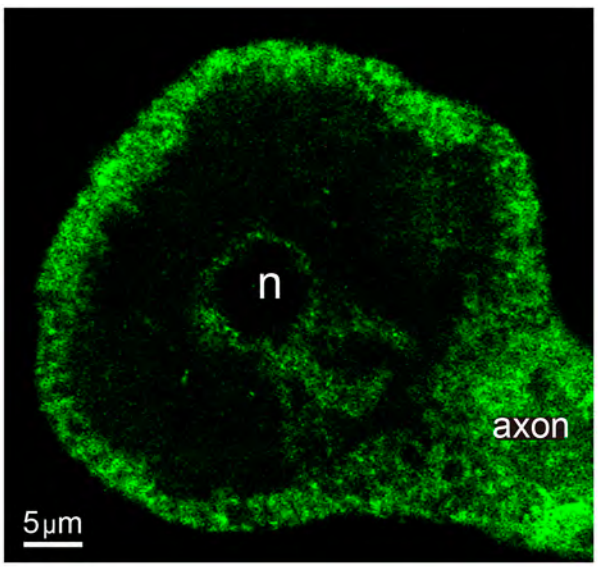

FIGURE 8 | Actin cortex of Retzius neurons. Confocal equatorial image of the soma of a Retzius neuron showing the fluorescence of Alexa dye coupled to phalloidin. The perinuclear region and primary axon also display a profuse staining. n indicates the position of the nucleus.

rested closer to the high energy barrier increasing amounts of vesicles were inside the actin cortex, where the myosin carried by the clusters assembles the actin-myosin transport with the actin filaments (Noguez et al., in preparation). As larger fraction of the clusters added the myosin-actin dymers to the kinesin-tubulin transport, the cost and efficiency of the transport would increase. However, this is a partial explanation. A fuller account comes from the origins of the two short distance slopes of the W charts, which are explained in the following paragraphs.

Distribution of Endoplasmic Reticulum

The search for alternative ultrastructural candidates to explain the ATP_{ves} expenses and thermodynamic efficiency of the first half of the W distributions took us to the endoplasmic reticulum. Electron micrographs showing release sites of neurons were obtained by fixing neurons right after 1 Hz stimulation ($n = 5$) to maintain the resting ultrastructure of the transport pathway (Trueta et al., 2004). The images in **Figure 9** contain structures immersed in the actin cortex, although the conventional fixation technique that we used to prepare the sections does not allow to resolve its structure. **Figure 9A** contains a cluster of electrodense vesicles resting distantly from the plasma membrane. Subsequent vesicles are bound by small fine filaments. The vesicle cluster was bound indirectly to the plasma membrane via a thick bundle of microtubules, according to the diameter of the individual fibers. Single vesicles appeared along the microtubules, presumably on their way to the plasma membrane (Leon-Pinzon et al., 2014; **Figure 1**). As explained in **Figure 1**, this vesicle migration explains the reduction of the number of vesicles as the peripheral clusters rest closer to the plasma membrane. An alignment of endoplasmic reticulum bags bordered the intracellular side of the plasma membrane; deeper and smaller bags of endoplasmic reticulum were scattered between the vesicles and the plasma membrane. One may wonder that vesicles being transported to the plasma membrane will find these bags on their way forming a bottleneck.

Electron micrographs obtained from neurons fixed after 20 Hz stimulation confirmed this idea. The image in **Figure 9B** shows vesicles from a large cluster reaching the plasma membrane by passing between endoplasmic reticulum. These obstacles bottlenecked the flux of vesicles and can be considered as sources of friction forces that reduce the thermodynamic efficiency of somatic exocytosis.

Countings of the distance between the plasma membrane and the center of mass of endoplasmic reticulum bags are presented in **Figure 9C**. The green and red lines fit the data distribution to two Gaussians, one with a mean $0.36 \pm 0.11\,\mu m$ (SD) distance from the plasma membrane, corresponding to the more external layer of endoplasmic reticulum. The red line fits the distribution of the scattered internal bags of endoplasmic reticulum, rendering a mean $0.93 \pm 0.12\,\mu m$ distance. This distribution supports that the endoplasmic reticulum is a source of friction forces that reduce the thermodynamic efficiency. Smaller vesicle clusters facing the plasma membrane seem to rest between the external layer of endoplasmic reticulum in absence of further obstacles to reach the plasma membrane.

Multiple Variables Affect the Thermodynamic Efficiency

The multivariable schemes in **Figure 10** integrate the data on the possible variables that determine the thermodynamic efficiency of somatic exocytosis. Each element of the transport pathway has been scaled based on the experimental evidence. The diameter of the circles representing each cluster was calculated from its number of vesicles. Peripheral clusters are organized in an

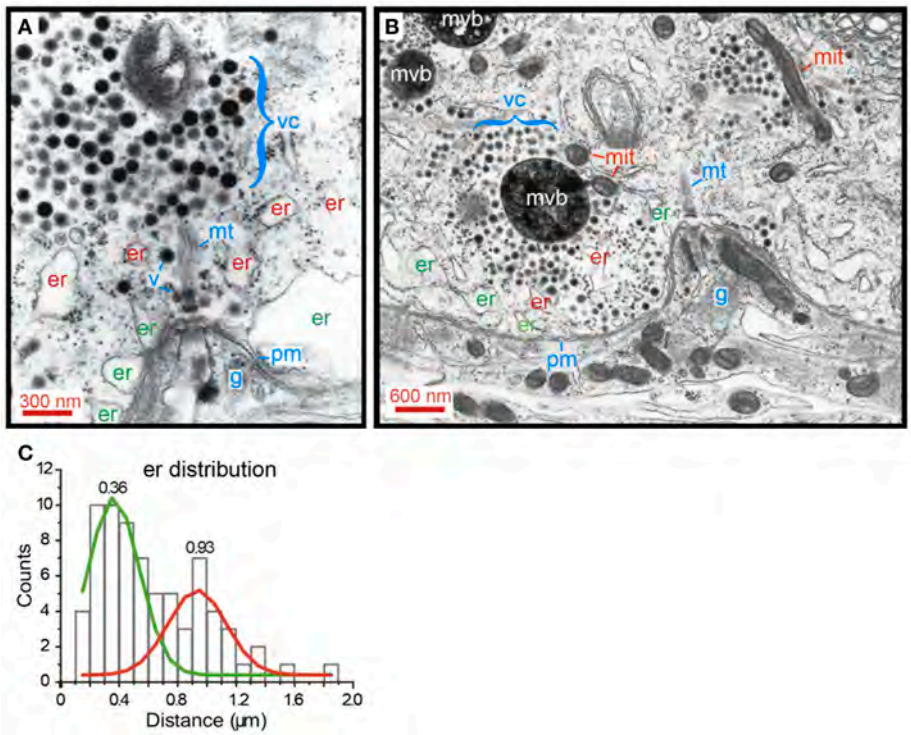

FIGURE 9 | Distribution of smooth endoplasmic reticulum in the soma shell. **(A)** Electron micrograph of a neuron that had been stimulated at 1 Hz. Vesicles remain at their resting states. A somatic vesicle cluster (vc) is bound to the membrane (pm) via a bundle of cytoskeletal fibers, most likely microtubules (mt). Peripheral endoplasmic bags (er) rest closely apposed to the plasma membrane. More internally, another layer of endoplasmic reticulum (er) contains smaller bags. Individual vesicles (v) can be seen in an apparent migration to the membrane, along the microtubule bundles (see also **Figure 1**). Glial cell processes (g) in an invagination of the Retzius neuron, right at the anchor site of microtubules to the plasma membrane. **(B)** Electron micrograph of a release site in a neuron that had been stimulated with 20 Hz trains. Vesicles in a large cluster are apposed to the membrane. Transport occurs through a bottleneck of endoplasmic reticulum. Mitochondria (mit) are common satellites of the clusters that travel with them. Multi-vesicular bodies (mvb) result from the incorporation of vesicles after exo/endocytosis (Trueta et al., 2012). Note that exocytosis occurs onto the glia. **(C)** Distribution of endoplasmic reticulum in the soma shell. The distances have the plasma membrane as reference. Peripheral (er) and internal (er) pools of endoplasmic reticulum were distinguished by Gaussian fittings to the histograms. The mean values for each distribution are indicated.

ascending order of efficiency. The distance from the plasma membrane to the center of mass of the clusters was determined by the model fittings. Pairs of clusters releasing in the same spot are associated by a black line representing the microtubule bundles. The efficiency of the ATP expenses per vesicle is indicated in the center of each cluster; the velocity of the transport is indicated on the right of each cluster. The actin cortex and endoplasmic reticulum are represented according to the morphometric analysis descried above. At first glance there is a good correlation between the size, the resting distance and the efficiency of peripheral clusters. The thermodynamic efficiency of the exocytosis process from vesicles in these peripheral clusters was inversely proportional to their resting distance. Similar correlations are unclear for the internal clusters in this representation, because although they were associated to a peripheral cluster, their biophysical properties were not correlated. The correlations between different variables of the clusters and the ultrastructure of the transport pathway are simplified in **Figure 10B**. The vesicle clusters were grouped from I to IV based on the distance, efficiency, size, velocity, and ultrastructural interactions. Both regions in which the ATP hydrolysis and efficiency had increasing slopes also had higher transport velocities. On the contrary, the regions in which the energy and efficiency had decreasing trends had slower velocity ranges. This result, which can be predicted from the formula of the thermodynamic efficiency in Equation (12), acquires a morphological correlate in **Figure 10**. **Table 3** summarizes the data according to the groups of vesicle clusters. For the small peripheral clusters in Group 1, the additive action of two motors and the clusters resting already between endoplasmic reticulum in the more peripheral layer may favor higher velocities and efficiencies at the expenses of the high ATP_{ves} cost. Group II has two friction barriers represented by the two layers of endoplasmic reticulum. As vesicles enter the barriers the thermodynamic efficiency decreases. This can be attributed to the friction exerted by the endoplasmic reticulum on the vesicle clusters. In group III, the large clusters are at least in part, immersed in the actin cortex. The assembly of two motors may increase the ATP expenses and efficiency. However, the effect of the endoplasmic reticulum barriers is

INFORME DE LABORES 2019

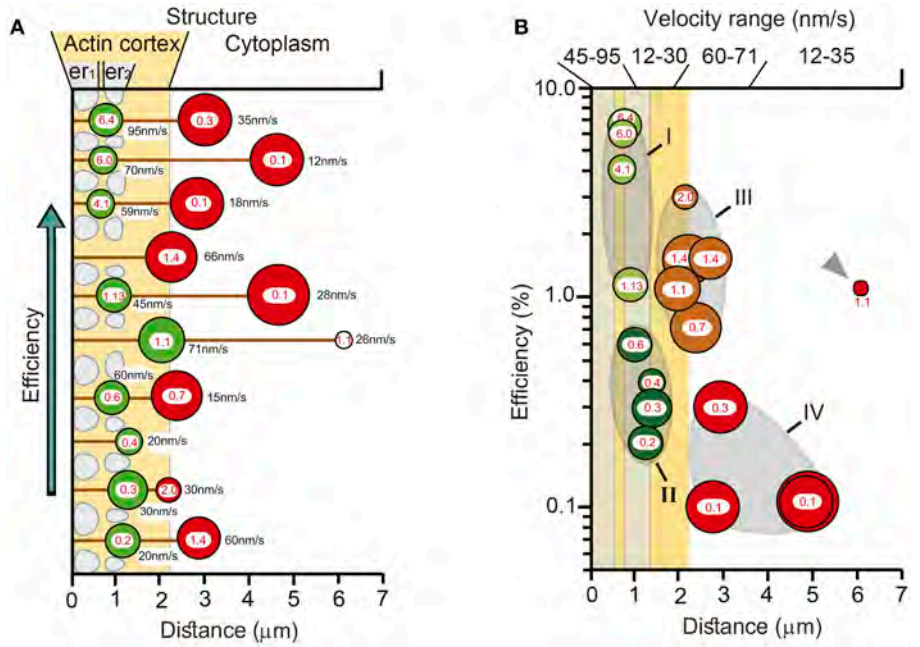

FIGURE 10 | Structural and biophysical correlations of the thermodynamic efficiency of the ATP_{ves} hydrolysis. **(A)** Pairs formed by peripheral (green circles) and internal (red circles) vesicle clusters that discharged in the same site are represented attached to microtubules (black lines). The distances were calculated by the model fittings from the mass center of the cluster to the plasma membrane. The diameter of the clusters corresponds to the number of vesicles in the cluster. For each cluster, the red numbers inside indicate the efficiency (%), and the black numbers on the right the transport velocity (nm/sec). The peripheral clusters are presented from bottom to top according to their increasingly efficiency values. Their paired internal clusters had independent efficiency values, velocities, sizes and traveling distances. The actin cortex is represented in pale orange. Both layers of endoplasmic reticulum, one immediately inside the plasma membrane (er_1) and the other ~1 μm inside (er_2) are represented as pale sacs. The number of vesicles decreased as the clusters approached the plasma membrane. The efficiency of the peripheral clusters decreased as the distance increased. The number of vesicles, the efficiency, the transport distance and velocity of their corresponding internal clusters were uncorrelated with those of their peripheral pairs. **(B)** Vesicle clusters were groped according to their efficiency, size, distance, and velocity. The thermodynamic efficiency of somatic exocytosis also correlated with the thickness of the actin cortex (pale orange) and both subsequent layers of endoplasmic reticulum (gray bars). Group I contains the smallest and more peripheral clusters, which also had the highest thermodynamic efficiency values. These clusters rested at the entrance of the submembrane barrier of endoplasmic reticulum (gray bar adjacent to the plasma membrane). Group II contained clusters embedded within the second layer of endoplasmic reticulum, (more internal gray bar). The transport velocities and efficiencies of these clusters were smaller than those of Group I. Group III (brown) rested in the limits of the actin cortex. These clusters were large, moved with high velocity and their efficiencies were above 1%. Group IV (red) contained large internal clusters that rested inside the actin cortex. Their velocities were smaller than those in Group III. The smaller cluster was the deeper (gray arrowhead). This cluster did not correlate with the rest of group IV for its size and for having a relatively large 1.1 efficiency, in spite of its low 26 nm/s velocity. Its size and position suggest that it was in the assembly process at the time of the stimulation series.

diminished. This can be explained if the flow of the peripheral clusters that precede the larger internal clusters has already diminished the friction forces by displacing the endoplasmic reticulum to the side, thus widening the spaces though which the internal clusters will flow. If so, the pairing of clusters in the same microtubule pathway would favor the transport of the internal larger vesicle clusters. The ATP expenses and thermodynamic efficiency of vesicles in Group IV may stem from their longer traveling distance, part of which is solely covered by the force of kinesin motors. In addition, entering the actin cortex may impose friction forces due to the accommodation of the vesicles within the entanglement of the actin fibers, before the coupling of the myosin motors. Another group that can be predicted contains the small clusters that are assembled and transported from the parikaryon (see Trueta et al., 2012). However, more evidence is required to strengthen this argument.

DISCUSSION

The application of thermodynamic theory to the study of somatic exocytosis predicts how the cytoarchitecture of the vesicle trafficking pathway influences the cost and thermodynamic efficiency of serotonin release. In spite of the common belief that biological systems operate with high efficiency levels, somatic exocytosis is far from an ideal system. Isolated myosin motors moving on actin fibers have efficiencies of 45% (Kjelstrup et al., 2013). Therefore, the low efficiency reported here shows the additive effects of the low efficiency of the motors and the frictive effects imposed by the ultrastructure of the transport pathway. Surprisingly, the thermodynamic efficiency of the simple calcium ATPase immersed in the plasma membrane, depends on the lipid composition of the membrane, with low efficiency values ≤12% (Lervik et al., 2012). Therefore, the values estimated here seem reasonable by considering the number of variables affecting the vesicle transport.

TABLE 3 | Variables contributing to the energy cost and efficiency of somatic exocytosis.

Cluster group	I	II	III	IV
Distance to membrane (μm)	0.6–1.1	1.0–2.3	1.8–2.6	2.7–6.1
Efficiency (0%)	1.0–6.4	0.2–0.6	0.7–2.0	1.1
ATP_{ves}	27–45	11–43	28–260	13–30
Velocity nm/s	45–95	12–30	60–71	35–12
Size of cluster	Small	Intermediate	Large	Larger
Vesicles per cluster	95–169	174–260	229–641 (65)	262–930 (52)
Intracellular structures	Actin cortex, Endoplasmic reticulum 1	Actin cortex, Endoplasmic reticulum 1+2	Actin cortex interface Endoplasmic reticulum 1+2	Cytoplasm Actin cortex interface Endoplasmic reticulum 1+2
Transport system	Kinesin Myosin	Kinesin Myosin	Kinesin Some Myosin	Kinesin Later Myosin

The red numbers correspond to the decreasing slopes of the W distributions of ATP_{ves} expenses and efficiency; the blue numbers correspond to the increasing slopes of the W distribution. Other colors underscore different structures; the tones indicate gradations. The number of vesicles in parenthesis are out of range. The value in Group IV corresponds to the most internal cluster, most likely under formation at the time of the stimulation of exocytosis. Endoplasmic reticulum 1 and 2 correspond to the external and internal layers in ***Figures 9****,* ***10****, respectively.*

It is pertinent to discuss a potential source of error in our measurements. The reports of the rate constant values of the ATP cleavage that fuels the actin and myosin motors have considerable variations depending on the subtype of motor and the experimental conditions of the measurements. Since these variations span over similar ranges 100–300 s^{-1}, we could choose one single value to represent both rate constants for our calculations. The choice for the low 100 s^{-1} value seemed the most accurate for our purposes, because the 18°C temperature at which our experiments were carried out—leeches are cold blooded animals—decreases the rate constants of chemical processes. We have no way to justify that this choice reflects the real values with which the vesicle transport operates in Retzius neurons since their motor subtypes are only superficially known. Antibodies against myosin type IV succeeded to bind myosin in other set of experiments and the contribution of each motor to somatic exocytosis has been blocked pharmacologically (Noguez et al., in preparation), but we still lack estimates of their rate constants. If the rate constant values were higher, the estimate of the efficiency would decrease linearly in proportion to the increase in the rate constant values, as predicted from Equation (12). For example, a 20% increase in the rate constant value from 100 to 125 s^{-1} would reduce the efficiency from 6.0 to 4.8%; likewise, a 200% increase in the rate constant value to 300 s^{-1} -which is near the largest estimate available (Johnson and Taylor, 1978; Apell et al., 1996; Higuchi et al., 1997; De La Cruz et al., 1999; Cross, 2004; De la Cruz and Ostap, 2009)- would reduce the efficiency to 0.2%. In any case, the values would move downwards linearly but not logarithmically. The additional possibility that each motor operates with a different rate constant value cannot be resolved with the tools of our study. The measures of the average velocity of the transport normalize these possible variations without sensitivity to separate them.

A duality has emerged between the structure/function relationship of the release sites and the thermodynamic efficiency of somatic exocytosis. Each slope of the W distribution of the efficiency vs. distance plot is influenced by the interaction of vesicles with a particular building block of the exocytosis process. The same structures that regulate the exocytosis machinery hamper the thermodynamic efficiency of the transport. For example, the endoplasmic reticulum is the fundamental source for intracellular calcium that first activates the vesicle transport in response to high frequency stimulation (Trueta et al., 2004), and later maintains the large-scale exocytosis in response to the activation of serotonin autoreceptors (Leon-Pinzon et al., 2014). In a previous study (Trueta et al., 2004) we have shown that very large vesicle clusters become apposed to the plasma membrane in response to electrical stimulation. This observation implies that they occupy positions that at rest contained endoplasmic reticulum. The endoplasmic reticulum may then be moved aside during transport of the peripheral vesicle cluster. As a positive consequence, the internal cluster that follows the same trajectory may find a cleared pathway to the plasma membrane, with a concomitant saving of energy and reduced heat dissipation.

The actin cortex adds another duality to neurons and excitable endocrine cells by preventing the entry of the vesicle clusters at rest and by propelling vesicles in response to electrical stimulation (Vitale et al., 1995; Lang et al., 2000; Oheim and Stühmer, 2000; Giner et al., 2005; Tobin and Ludwig, 2007; Gutiérrez and Gil, 2011; Torregrosa-Hetland et al., 2011). The third player is mitochondria, the fuel generator that in response to calcium produces ATP that activates the motors. Mitochondria travel along with the vesicle clusters, as suspected because both organelles appear together in electron micrographs after 1 or 20 Hz stimulation. The cargo imposed by the mitochondria may be as large as, or even larger than that imposed by the cluster of vesicles. Therefore, it is most likely that the mobilization of the energy generators along with the vesicle clusters increases the friction forces at the expenses of the thermodynamic efficiency.

A final question from our study concerns its general significance. Somatic exocytosis is part of a wider communication complex system that involves not only the soma, but every part

of the neuron. A remarkably similar mechanism for somato-dendritic exocytosis has been demonstrated in thalamic neurons releasing the peptides vasopressin and oxytocin (Ludwig and Stern, 2015). Moreover, the mobilization of serotonin-containing exocytosis structures in the isolated soma of Raphe neurons from mammals follow similar steps (Sarkar et al., 2012). The soma and dendrites of thalamic neurons releasing peptides contain an actin cortex whose activation promotes the vesicle transport and exocytosis (Tobin and Ludwig, 2007). The ATP expenses and efficiency of exocytosis have not been explored in those or in other types of neurons, but the highly conserved mechanism of somatic and in general extrasynaptic exocytosis (Trueta et al., 2012) suggest that the effects presented here may be of general interest. The dendrites and small axon varicosities, for example release of serotonin through a mechanism similar to that in the soma, although the transport distances of the vesicles are downscaled. The ATP expenses and the thermodynamic efficiency of the vesicle transport for their exocytosis may be scaled accordingly. Such smaller traveling distances may require less ATP and may operate with higher thermodynamic efficiencies.

The mechanism for somatic exocytosis seems to be highly conserved also for most signaling molecules in the central and peripheral nervous system (For review see Trueta and De-Miguel, 2012; Del-Bel and De-Miguel, 2018). Secretory cells follow similar mechanistic rules by transporting vesicles across an actin cortex in response to stimulation (Vitale et al., 1995; Lang et al., 2000; Oheim and Stühmer, 2000; Giner et al., 2005; Gutiérrez and Gil, 2011; Torregrosa-Hetland et al., 2011). These arguments suggest that our results represent general mechanisms in biology.

AUTHOR CONTRIBUTIONS

PN and FD-M designed and carried out the experiments, conducted the analysis and prepared the figures. MR designed the mathematical approach. FD-M wrote the manuscript.

FUNDING

Our work was funded by a Dirección General de Asuntos del Personal Académico (DGAPA) grant IN210317 from the Universidad Nacional Autónoma de México (UNAM) and grant 130031 from the Consejo Nacional de Ciencia y Tecnología (CONACyT) to FD-M. MR was supported by MINECO of the Spanish Government under grant Fis 2015-67837-P. PN is a doctoral student from Programa de Doctorado en Ciencias Biomédicas, Universidad Nacional Autónoma de México (UNAM) and received fellowship 193987 from CONACYT.

ACKNOWLEDGMENTS

We wish to express our gratitude to Mr. Bruno Mendez Ambrosio his excellent technical assistance during this study, and to Mrs. Sara Flores González for her invaluable assistance in the animal and laboratory care. We also express our gratitude to Mr. Francisco Perez for his continuous support in the computer unit and to Mr. Rodlfo Paredes and Dr. Fernando García Hernandez for their invaluable help in the preparation el the electron micrographs and fluorescence microscopy. The animal care facility at our Institute was fundamental for the good conditions of our animal colony. Professor J. G. Nicholls, Dr. Sharlen Moore, and Mrs. Sorel Achouna made critical readings of our manuscript.

REFERENCES

Alberty, R. A., and Goldberg, R. N. (1992). Standard thermodynamic formation properties for the adenosine 5'-triphosphate series. *Biochemistry* 3, 10610–10615. doi: 10.1021/bi00158a025

Apell, H. J., Roudna, M., Corrie, J. E., and Trentham, D. R. (1996). Kinetics of the phosphorylation of Na, K-ATPase by inorganic phosphate detected by a fluorescence method. *Biochemistry* 35, 10922–10930.

Betz, W. J., and Bewick, G. S. (1993). Optical monitoring of transmitter release and synaptic vesicle recycling at the frog neuromuscular junction. *J. Physiol.* 460, 287–309.

Betz, W. J., Bewick, G. S., and Ridge, R. M. (1992). Intracellular movements of fluorescently labeled synaptic vesicles in frog motor nerve terminals during nerve stimulation. *Neuron* 9, 805–813. doi: 10.1016/0896-6273(92)90235-6

Bruno, L., Salierno, M., Wetzler, D. E., Despósito, M. A., and Levi, V. (2011). Mechanical properties of organelles driven by microtubule-dependent molecular motors in living cells. *PLoS ONE* 6:e18332. doi: 10.1371/journal.pone.0018332

Caplan, S. R., and Essig, A. (1999). *Bioenergetics and Linear Nonequilibrium Thermodynamics: The Steady State*. Cambridge, MA: Harvard University Press.

Coggeshall, R. E. (1972). Autoradiographic and chemical localization of 5-hydroxytryptamine in identified neurons in the leech. *Anat. Rec.* 172, 489–498. doi: 10.1002/ar.1091720303

Cross, R. A. (2004). The kinetic mechanism of kinesin. *Trends Biochem Sci.* 29, 301–309. doi: 10.1016/j.tibs.2004.04.010

De Groot, S. R., and Mazur, P. (1969). "Chapter 7," in *Non-equilibrium Thermodynamics* (New York, NY: Dover Publications Inc.), p. 510.

De la Cruz, E. M., and Ostap, E. M. (2009). Kinetic and equilibrium analysis of the myosin ATPase. *Methods Enzymol.* 455, 157–192. doi: 10.1016/S0076-6879(08)04206-7

De La Cruz, E. M., Wells, A. L., Rosenfeld, S. S., Ostap, E. M., and Sweeney, H. L. (1999). The kinetic mechanism of myosin V. *Proc. Natl. Acad. Sci. U.S.A.* 96, 13726–13731. doi: 10.1073/pnas.96.24.13726

Del-Bel, E., and De-Miguel, F. F. (2018). Extrasynaptic neurotransmission mediated by exocytosis and diffusive release of transmitter substances. *Front. Synaptic Neurosci.* 10:13. doi: 10.3389/fnsyn.2018.00013

De-Miguel, F. F., and Fuxe, K. (2012). Extrasynaptic neurotransmission as a way of modulating neuronal functions. *Front. Physiol.* 3:16. doi: 10.3389/fphys.2012.00016

De-Miguel, F. F., and Nicholls, J. G. (2015). Release of chemical transmitters from cell bodies and dendrites of nerve cells. *Phil. Trans. R. Soc. B* 370:20140181. doi: 10.1098/rstb.2014.0181

De-Miguel, F. F., Santamaría-Holek, I., Noguez, P., Bustos, C., Hernández-Lemus, E., and Rubí, J. M. (2012). Biophysics of active vesicle transport, an intermediate step that couples excitation and exocytosis of serotonin in the neuronal soma. *PLoS ONE* 7:e45454. doi: 10.1371/annotation/b72afb21-407c-46e9-9870-7c59ab9e582c

De-Miguel, F. F., and Trueta, C. (2005). Synaptic and extrasynaptic exocytosis of serotonin. *Cell Mol. Neurobiol.* 2, 297–312. doi: 10.1007/s10571-005-3061-z

Dietzel, I. D., Drapeau, P., and Nicholls, J. G. (1986). Voltage dependence of 5-hydroxytryptamine release at a synapse between identified leech neurones in culture. *J. Physiol.* 372, 191–205.

Fuxe, K., Dahlström, A., Höistad, M., Marcellino, D., Jansson, A., Rivera, A., et al. (2007). From the Golgi-Cajal mapping to the transmitter based characterization of the neuronal networks leading to two modes of brain communication: wiring and volume transmission. *Brain Res. Rev.* 55, 17–54. doi: 10.1016/j.brainresrev.2007.02.009

Giner, D., Neco, P., Francés Medel, M., López, I., Viniegra, S., and Gutiérrez, L. M. (2005). Real-time dynamics of the F-actin cytoskeleton during secretion from chromaffin cells. *J. Cell Sci.* 118, 2871–2880. doi: 10.1242/jcs.02419

Gutiérrez, L. M., and Gil, A. (2011). Modeling F-actin cortex influence on the secretory properties of neuroendocrine cells. *Commun. Integr. Biol.* 4, 413–415. doi: 10.4161/cib.15251

Higuchi, H., Muto, E., Inoue, Y., and Yanagida, T. (1997). Kinetics of force generation by single kinesin molecules activated by laser photolysis of caged ATP. *Proc. Natl. Acad. Sci. U.S.A.* 94, 4395–4400. doi: 10.1073/pnas.94.9.4395

Hirasawa, H., Contini, M., and Raviola, E. (2015). Extrasynaptic release of GABA and dopamine by retinal dopaminergic neurons. *Phil. Trans. R. Soc. Lond. B Biol. Sci.* 370:20140186. doi: 10.1098/rstb.2014.0186

Johnson, K. A., and Taylor, E. W. (1978). Intermediate states of subfragment 1 and actosubfragment 1 ATPase: reevaluation of the mechanism. *Biochemistry*. 17, 3432–3442. doi: 10.1021/bi00610a002

Kjelstrup, S., Bedeaux, D., Johannessen, E., and Gross, J. (2010). *Non-Equilibrium Thermodynamics for Engineers*. Singapore: World Scientific.

Kjelstrup, S., Rubi, J. M., Pagonabarraga, I., and Bedeaux, D. (2013). Mesoscopic non-equilibrium thermodynamic analysis of molecular motors. *Phys. Chem. Chem. Phys.* 28, 19405–19414. doi: 10.1039/c3cp52339j

Kohler, F., and Rohrbach, A. (2015). Synchronization of elastically coupled processive molecular motors and regulation of cargo transport. *Phys. Rev. E Stat. Nonlin. Soft. Matter. Phys.* 91:012701. doi: 10.1103/PhysRevE.91.012701

Kuffler, D. P., Nicholls, J., and Drapeau, P. (1987). Transmitter localization and vesicle turnover at a serotoninergic synapse between identified leech neurons in culture. *J. Comp. Neurol.* 256, 516–526. doi: 10.1002/cne.902560404

Lang, T., Wacker, I., Wunderlich, I., Rohrbach, A., Giese, G., Soldati, T., et al. (2000). Role of actin cortex in the subplasmalemmal transport of secretory granules in PC-12 cells. *Biophys. J.* 78, 2863–2877. doi: 10.1016/S0006-3495(00)76828-7

Leon-Pinzon, C., Cercós, M. G., Noguez, P., Trueta, C., and De-Miguel, F. F. (2014). Exocytosis of serotonin from the neuronal soma is sustained by a serotonin and calcium-dependent feedback loop. *Front. Cell Neurosci.* 8:169. doi: 10.3389/fncel.2014.00169

Lervik, A., Bresme, F., Kjelstrup, S., and Rubí, J. M. (2012). On the thermodynamic efficiency of Ca^{2}?-ATPase molecular machines. *Biophys. J.* 19, 1218–1226. doi: 10.1016/j.bpj.2012.07.057

Llorente-Folch, I., Rueda, C. B., Amigo, I., del Arco, A., Saheki, T., Pardo, B., et al. (2013). Calcium-regulation of mitochondrial respiration maintains ATP homeostasis and requires ARALAR/AGC1-malate aspartate shuttle in intact cortical neurons. *J. Neurosci.* 33, 13957–13971. doi: 10.1523/JNEUROSCI.0929-13.2013

Ludwig, M., and Stern, J. (2015). Multiple signalling modalities mediated by dendritic exocytosis of oxytocin and vasopressin. *Philos. Trans. R. Soc. Lond. B Biol. Sci.* 370:20140182. doi: 10.1098/rstb.2014.0182

Newman, E. A. (2015). Glial cell regulation of neuronal activity and blood flow in the retina by release of gliotransmitters. *Philos. Trans. R. Soc. Lond. B Biol. Sci.* 370:20140195. doi: 10.1098/rstb.2014.0195

Nicholls, D. G., Vesce, S., Kirk, L., and Chalmers, S. (2003). Interactions between mitochondrial bioenergetics and cytoplasmic calcium in cultured cerebellar granule cells. *Cell Calcium* 34, 407–424. doi: 10.1016/S0143-4160(03)00144-1

Oheim, M., and Stühmer, W. (2000). Tracking chromaffin granules on their way through the actin cortex. *Eur. Biophys. J.* 29, 67–89. doi: 10.1007/s002490050253

Rozanski, G. M., Kim, H., Li, Q., Wong, F. K., and Stanley, E. F. (2012). Slow chemical transmission between dorsal root ganglion neuron somata. *Eur. J. Neurosci.* 36, 3314–3321. doi: 10.1111/j.1460-9568.2012.08233.x

Rueda, C. B., Llorente-Folch, I., Amigo, I., Contreras, L., González-Sánchez, P., Martínez-Valero, P., et al. (2014). Ca(2+) regulation of mitochondrial function in neurons. *Biochim. Biophys. Acta* 1837, 1617–1624. doi: 10.1016/j.bbabio.2014.04.010

Sarkar, B., Das, A. K., Arumugam, S., Kaushalya, S. K., Bandyopadhyay, A., Balaji, J., et al. (2012). The dynamics of somatic exocytosis in monoaminergic neurons. *Front. Physiol.* 3:414. doi: 10.3389/fphys.2012.00414

Schnitzer, M. J., and Block, S. M. (1997). Kinesin hydrolyses one ATP per 8-nm step. *Nature* 388, 386–390. doi: 10.1038/41111

Svoboda, K., and Block, S. M. (1994). Force and velocity measured for single kinesin molecules. *Cell* 77, 773–784. doi: 10.1016/0092-8674(94)90060-4

Tobin, V. A., and Ludwig, M. (2007). The role of the actin cytoskeleton in oxytocin and vasopressin release from rat supraoptic nucleus neurons. *J. Physiol.* 582, 1337–1348. doi: 10.1113/jphysiol.2007.132639

Torregrosa-Hetland, C. J., Villanueva, J., Giner, D., Lopez-Font, I., Nadal, A., Quesada, I., et al. (2011). The F-actin cortical network is a major factor influencing the organization of the secretory machinery in chromaffin cells. *J. Cell Sci.* 2011 124, 727–734. doi: 10.1242/jcs.078600

Trueta, C., and De-Miguel, F. F. (2012). Extrasynaptic exocytosis and its mechanisms: a source of molecules mediating volume transmission in the nervous system. *Front. Physiol.* 3:319. doi: 10.3389/fphys.2012.00319

Trueta, C., Kuffler, D. P., and De-Miguel, F. F. (2012). Cycling of dense core vesicles involved in somatic exocytosis of serotonin by leech neurons. *Front. Physiol.* 3:175. doi: 10.3389/fphys.2012.00175

Trueta, C., Méndez, B., and De-Miguel, F. F. (2003). Somatic exocytosis of serotonin mediated by L-type calcium channels in cultured leech neurons. *J. Physiol.* 547, 405–416. doi: 10.1113/jphysiol.2002.030684

Trueta, C., Sánchez-Armas, S., Morales, M. A., and De-Miguel, F. F. (2004). Calcium-induced calcium release contributes to somatic exocytosis of serotonin in leech retzius neurons. *J. Physiol.* 547, 309–316. doi: 10.1002/neu.20055

Vitale, M. L., Seward, E. P., and Trifaró, J. M. (1995). Chromaffin cell cortical actin network dynamics control the size of the release-ready vesicle pool and the initial rate of exocytosis. *Neuron* 14, 353–363. doi: 10.1016/0896-6273(95)90291-0

Wang, Y. F., and Hatton, G. I. (2006). Mechanisms underlying oxytocin-induced excitation of supraoptic neurons: prostaglandin mediation of actin polymerization. *J. Neurophysiol.* 3933–3947. doi: 10.1152/jn.01267.2005

Conflict of Interest Statement: The authors declare that the research was conducted in the absence of any commercial or financial relationships that could be construed as a potential conflict of interest.

Copyright © 2019 Noguez, Rubí and De-Miguel. This is an open-access article distributed under the terms of the Creative Commons Attribution License (CC BY). The use, distribution or reproduction in other forums is permitted, provided the original author(s) and the copyright owner(s) are credited and that the original publication in this journal is cited, in accordance with accepted academic practice. No use, distribution or reproduction is permitted which does not comply with these terms.

Olivas-Aguirre et al. *Cell Death and Disease* (2019)10:779
https://doi.org/10.1038/s41419-019-2024-0

Cell Death & Disease

ARTICLE Open Access

Cannabidiol directly targets mitochondria and disturbs calcium homeostasis in acute lymphoblastic leukemia

Miguel Olivas-Aguirre[1], Liliana Torres-López[1], Juan Salvador Valle-Reyes[1], Arturo Hernández-Cruz[2], Igor Pottosin[1] and Oxana Dobrovinskaya[1]

Abstract

Anticancer properties of non-psychoactive cannabinoid cannabidiol (CBD) have been demonstrated on tumors of different histogenesis. Different molecular targets for CBD were proposed, including cannabinoid receptors and some plasma membrane ion channels. Here we have shown that cell lines derived from acute lymphoblastic leukemia of T lineage (T-ALL), but not resting healthy T cells, are highly sensitive to CBD treatment. CBD effect does not depend on cannabinoid receptors or plasma membrane Ca^{2+}-permeable channels. Instead, CBD directly targets mitochondria and alters their capacity to handle Ca^{2+}. At lethal concentrations, CBD causes mitochondrial Ca^{2+} overload, stable mitochondrial transition pore formation and cell death. Our results suggest that CBD is an attractive candidate to be included into chemotherapeutic protocols for T-ALL treatment.

Introduction

Acute lymphoblastic leukemia (ALL) of T lineage (T-ALL) represents a highly aggressive cancer, resistant to chemotherapy and with increased risk of relapse, which occurs in 15% of childhood and 25% of adult ALL cases. In T-ALL, a long-term remission fails in ~20% of children and 40% of adult patients. The prognosis for these groups remains poor, with a 5-year survival rate of <25%[1–5]. Thus, novel therapeutic strategies for the T-ALL treatment are needed.

Cannabinoids are a group of more than 60 structurally related terpenophenolic compounds. Most of them exert their effects through cannabinoid CB1 and CB2 receptors, which belong to the family of G protein-coupled receptors. Lymphocytes mainly express CB2, whereas CB1 are highly expressed in the central nervous system (CNS). Cannabinoids have been used for decades in the field of palliative care. Recently two phytocannabinoids, Δ^9-tetrahydrocannabinol (THC) and cannabidiol (CBD), were found to possess antitumorigenic properties[6,7]. Contrary to THC, a well-known strong CB1 agonist with psychotropic effect, CBD has a low binding affinity for CB1/2 receptors and is considered as a "non-intoxicating drug"[8]. Molecular targets for CBD are uncertain. Among putative candidates, some members of the TRP channels´ family, orphan cannabinoid receptor GPR55, 5HT and PPARγ receptors have been proposed[6,9].

In the present study we addressed the immediate targets for CBD in leukemic cell lines, derived from T-ALL patients in relapse.

Results

CBD suppresses viability and impairs migration of leukemic T cells

Cytotoxic effect of CBD was first evaluated in leukemic cell lines of different lineages, including T-ALL, B lineage-

Correspondence: Igor Pottosin (pottosin@ucol.mx) or Oxana Dobrovinskaya (oxana@ucol.mx)
[1]Laboratory of Immunobiology and Ionic Transport Regulation, University Center for Biomedical Research, University of Colima, Av. 25 de Julio 965, Col. 28030 Colima, Mexico
[2]Department of Cognitive Neuroscience and National Laboratory of Channelopathies (LaNCa), Institute of Cellular Physiology, National Autonomous University of Mexico, Mexico-City, Mexico
Edited by M. Diederich

© The Author(s) 2019
Open Access This article is licensed under a Creative Commons Attribution 4.0 International License, which permits use, sharing, adaptation, distribution and reproduction in any medium or format, as long as you give appropriate credit to the original author(s) and the source, provide a link to the Creative Commons license, and indicate if changes were made. The images or other third party material in this article are included in the article's Creative Commons license, unless indicated otherwise in a credit line to the material. If material is not included in the article's Creative Commons license and your intended use is not permitted by statutory regulation or exceeds the permitted use, you will need to obtain permission directly from the copyright holder. To view a copy of this license, visit http://creativecommons.org/licenses/by/4.0/.

derived ALL (B-ALL), and chronic myelogenous leukemia (CML) by means of metabolic assay. T-ALL were the most CBD-sensitive among tested cell lines (Fig. 1a). However, there is an uncertainty in the interpretation of this result, which may be explained by mitochondrial metabolism inhibition, decreased proliferation rate, increased level of cell death, or combination of these effects. Then survival and proliferation of CBD- treated Jurkat cells were evaluated in long-lasting (72 h) cultures by counting live and dead cells CBD at 30–100 μM induced cell death, while at 10 μM the cells remained alive, but did not proliferate. Noteworthy, at low (1 μM) concentration, CBD stimulated the cell proliferation (Fig. 1b, left). Stimulation was also obtained in experiments with a sequential (1 μM every 24 h) CBD administration (Fig. 1b, right). Strikingly, dose dependence was very similar in both cases, irrespective to supposed CBD accumulation during sequential application. Apparently, cell fate was defined already by the first CBD administration.

In additional experiments, cervical and breast cancer cell lines were included for a comparison, because CBD effect on these types of cancer was reported earlier. Again, among 10 cell lines tested, cytotoxic effect of CBD was the most pronounced in T-ALL (Fig. 1c).

We also tested CBD toxicity in non-tumoral cells. Murine bone marrow-derived cell line OP9 displayed high resistance to CBD (Fig. 1d). Strikingly, in contrast to activated human $CD4^+$ T cells, resting $CD4^+$ T cells were relatively insensitive to CBD. Noteworthy, resting $CD4^+$ T cells pretreated with CBD (30 μM, 24 h) were able to respond to activating stimuli. At 72 h of activation their proliferative response was statistically indistinguishable from that of untreated $CD4^+$ cells (Fig. 1e).

The infiltration of lymph nodes and CNS by leukemic cells and formation of a mediastinal mass are tightly related to disease relapse and unfavorable prognosis in T-ALL[10]. Thus, the effect of CBD on the T-ALL cells migration was addressed. Since CXCL12/CXCR4 axis plays a significant role in the dissemination of leukemic cells[11,12], CXCL12 was used as a chemoattractant. Migration of T-ALL cells was shown to be significantly suppressed by 2 h preincubation with 30 μM CBD (Fig. 1f).

CBD (30–100 μM) triggered apoptosis in a part of the cell population (Annexin V - single positive cells). At the same time, loss of plasma membrane integrity was observed in a large cell population as early as at 4 h of treatment (Annexin V/ propidium iodide (PI) – double positive cells), indicating necrosis (Fig. 1g–i).

Transmission electron microscopy (TEM) imaging revealed multiple dramatic changes in cell morphology already after 2 h of CBD (30 μM) exposure (Fig. 2). Two of the most characteristic features were extensive cytoplasmic vacuolation and numerous swollen mitochondria, devoid of cristae. Golgi complex and endoplasmic reticulum (ER) were disassembled, which seems to be related to cytoplasmic vacuolation. Plasma membrane blebbing and apoptotic bodies (ApoBDs) formation were detected. The observed morphological changes pointed out to a complex mechanism, with both apoptotic and necrotic symptoms. In addition, double membrane vacuoles, containing degrading material (autophagosomes), were much more numerous in CBD-treated cells as compared to control.

Sublethal CBD concentrations activate autophagy in leukemic cells

Autophagy is a catabolic cellular process, representing an important strategy to ensure cell homeostasis by the elimination of defunct organelles in both physiological and pathological conditions[13]. Basal levels of autophagy serve a housekeeping function, whereas stress stimulates autophagy. CBD was shown to cause cell death by inducing a crosstalk between apoptosis and autophagy in breast cancer[14]. To reveal the ability of CBD to induce autophagy in T-ALL, LC3-I to LC3-II conversion and LC3-II turnover were monitored by immunoblotting. In the course of autophagy, microtubule-associated protein LC3-I first conjugates with phosphatidylethanolamine, forming LC3-II, followed by the LC3-II translocation to autophagosomes. An increased LC3-II level is considered as an indicator of the autophagy, but LC3-II is degraded by lysosomal proteases after autophagosome-lysosome fusion. Chloroquine (CQ) is known to prevent autophagosome-lysosome fusion and to inhibit the LC3-II degradation, thus LC3-II is accumulated in the presence of CQ[15,16]. Western blot analysis of LC3 variants demonstrated that sublethal CBD concentration (10 μM) effectively induced autophagy in Jurkat cells (Fig. 3a, b), since LC3-II level was higher in cells treated with both CBD (10 μM) and CQ (20 μM) when compared to either 20 μM CQ (basal autophagy) or 10 μM CBD treatment alone. Note that accumulation of LC3-II was diminished by its degradation during the autophagic flux in the samples without CQ.

Proceeding of the autophagic flux at the single-cell level was monitored using mCherry-GFP-LC3 expressing Jurkat cells. The mCherry-GFP-LC3 experimental strategy is based on the fact that GFP is quenched at acidic pH, found in the autophagolysosome, while mCherry is not. Accordingly, enhancement of the mCherry/GFP ratio sensitive to CQ indicates the autophagolysosome formation[17]. Figure 3c shows representative images from the experiment, in which Jurkat GFP-mCherry-LC3 cells were incubated with CBD (10 and 30 μM) and CQ, alone or in combination. High mCherry/GFP ratio, efficiently equalized by CQ, was observed in samples, treated with 10 μM CBD (Fig. 3d, e), evidencing a throughput of the autophagic pathway. In samples treated with 30 μM CBD this

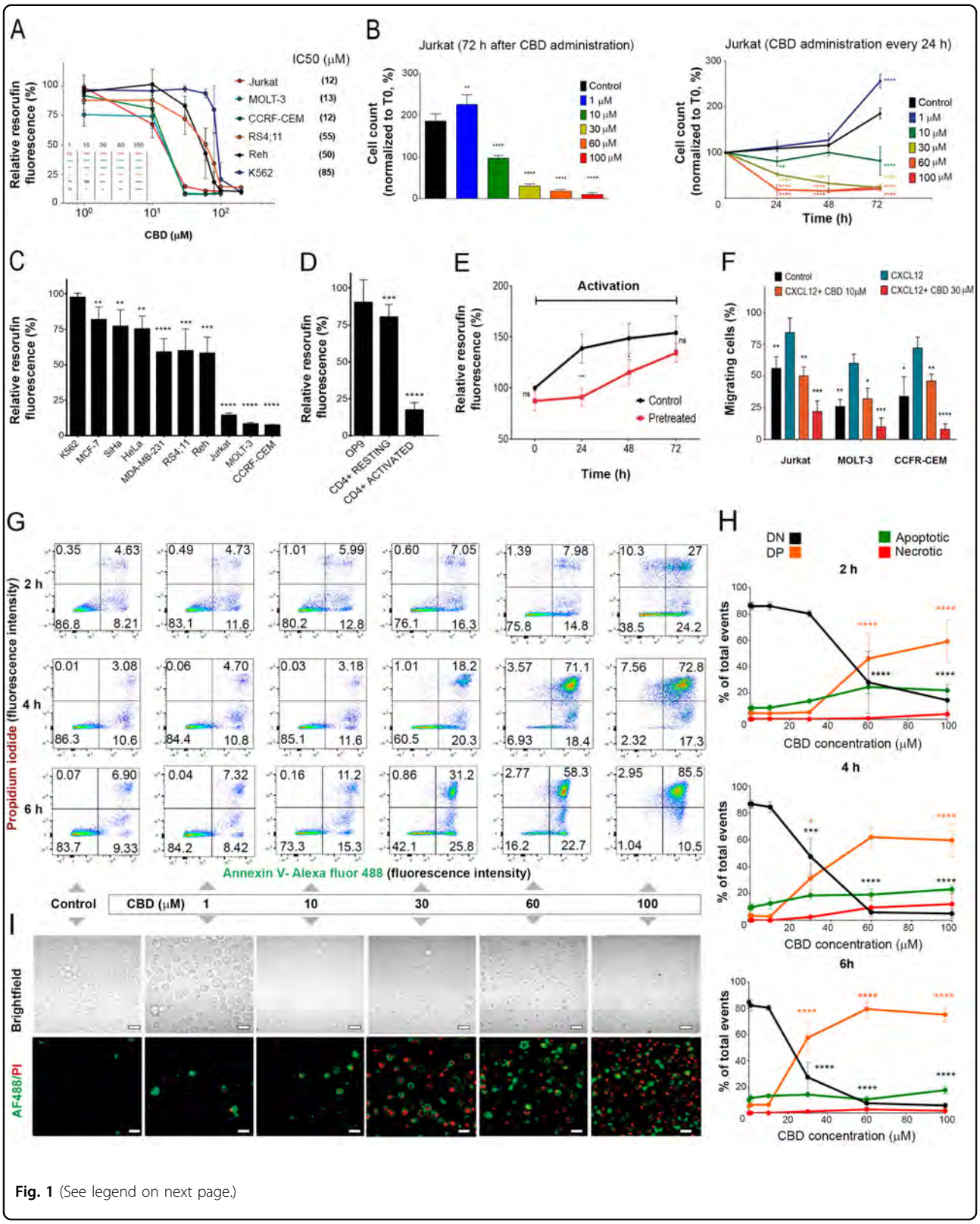

Fig. 1 (See legend on next page.)

(see figure on previous page)
Fig. 1 CBD effect on viability in different cancer cell lines. a Cell viability, evaluated by resazurin-based metabolic assay, as a function of CBD concentration in human leukemic cell lines of different lineages at 24 h of treatment. Cell lines derived from T-ALL (Jurkat, MOLT-3, and CEM), B-ALL (RS4;11 and Reh) and CML (K562) were tested. Data (resorufin fluorescence intensity, arbitrary units) were normalized to the vehicle-treated control and shown as mean ± SD ($n = 8$; *$p < 0.05$; **$p < 0.01$; ***$p < 0.001$; ****$p < 0.0001$; ns, not significant; one-way ANOVA). **b** Live cell count (trypan blue exclusion test) in long-lasting Jurkat cells cultures exposed to different CBD concentrations (0–100 μM). Left: cell count at 72 h after single CBD administration; right: fresh CBD was added, 50% of medium volume was changed and cells were counted every 24 h. Data are normalized to the initial point (0 h) and shown as mean ± SD ($n = 3$; **$p < 0.01$; ***$p < 0.001$; ****$p < 0.0001$, one-way ANOVA test). **c** Cell viability was evaluated by resazurin-based metabolic assay at 24 h of treatment with CBD (30 μM) in human tumor cell lines of different histogenesis, including CML (K562), B-ALL (Reh and RS4;11), T-ALL (CEM, MOLT-3, and Jurkat), cervical cancer (SiHa and HeLa), and breast cancer (MCF7-7 and MDA-MB-231). Data (resorufin fluorescence intensity) were normalized to vehicle-treated control and reported as mean ± SD ($n = 8$ of four independent experiments; (*$p < 0.05$; **$p < 0.01$; ***$p < 0.001$; ****$p < 0.0001$, Student's *t*-test). **d** Cell viability was evaluated by resazurin-based metabolic assay at 24 h of treatment with CBD (30 μM) in non-cancerous cells. Human $CD4^+$ cells were activated with anti-CD3/CD28 antibodies as described in Materials and Methods section. Data (resorufin fluorescence intensity) are normalized to the vehicle-treated control and reported as mean ± SD ($n = 8$ in at least three independent experiments; *$p < 0.05$; **$p < 0.01$; ***$p < 0.001$; ****$p < 0.0001$; Student's *t*-test). **e** After preincubation with CBD (30 μM, 24 h), non-cancerous $CD4^+$ cells were activated by anti-CD3/antiCD28 antibodies. Cell viability was evaluated by resazurin-based metabolic assay every 24 h. Data (resorufin fluorescence intensity) were normalized to 0 h time point and shown as mean ± SD ($n = 8$ in at least three independent experiments). Statistical comparison between control and pretreated samples was undertaken at each time point (*$p < 0.05$; **$p < 0.01$; ***$p < 0.001$; ****$p < 0.0001$, Student's *t*-test). **f** Migration capacity of Jurkat cells pretreated with CBD (10 or 30 μM, 2 h) was evaluated by chemotactic migration assay, using a Transwell system. Cells were allowed to migrate for 4 h, CXCL12 was used as a chemoattractant. The percentage of migrated cells was determined by cells count in the lower chamber. Data are mean ± SD ($n = 4$). Statistical comparison was made with respect to positive control (CXCL12) (*$p < 0.05$; **$p < 0.01$; ***$p < 0.001$; ****$p < 0.0001$, one-way ANOVA test). **g**–**i** Cell death was evaluation by flow cytometry (**g**, **h**) and fluorescent microscopy (**I**) in Jurkat cells treated with different concentrations of CBD using Annexin V-AF488/PI double staining. Representative dot plots (2, 4, and 6 h) and images (12 h) are shown in **g** and **i**, correspondingly. Scale bar: 20 μm. In every dot plot lower left quadrant represents Annexin V^-PI^- (DN) live cells, in the lower right quadrant are Annexin V^+PI^- (early apoptotic) cells, Annexin V^-PI^+ (primary necrotic) cells are in the upper left quadrant, whereas the double-stained population Annexin V^+PI^+ (DP) in the upper right quadrant represents dead cells, which may include necrotic and late apoptotic ones. Statistical analysis of flow cytometry data is given in **h** ($n = 3$; *$p < 0.05$; **$p < 0.01$; ***$p < 0.001$; ****$p < 0.0001$, one-way ANOVA test)

ratio was low (Fig. 3d, e). However, the number of autophagosomes was increased at early times after CBD administration (30 μM), as it was revealed by an enhanced level of both GFP^+ and $mCherry^+$ puncta (Fig. 3f, g). These data may be explained by a truncation of basal, and, possibly, also CBD-induced autophagy at late phases in damaged cells.

CBD causes mitochondrial damage and induces cytochrome C release

Dissipation of the mitochondrial transmembrane potential (ΔΨm) is a hallmark of the mitochondrial permeability transition (MPT) - driven necrosis as well as of intrinsic apoptosis. It involves an irreversible mitochondrial outer membrane permeabilization and a release of various pro-apoptotic factors, including cytochrome C (Cyt-C), to the cytosol. In the cytosol, Cyt-C contributes to the apoptosome formation, with a consequent activation of the initiator caspase 9, which cleaves and activates executioner caspases[18].

We monitored ΔΨm in Jurkat cells double-stained with green fluorescent dye MtGreen, which covalently binds to mitochondrial matrix proteins, and tetramethylrhodamine ethyl ester (TMRE), a cationic fluorescent dye that is readily sequestered by energized mitochondria (Fig. 4a). When exposed to CBD (30 μM), the intensity of TMRE fluorescence, in contrast to that of MtGreen, was gradually decreased within the first 10 min of treatment, indicating a rapid ΔΨm loss (Fig. 4a, Supplementary Movie 1). The loss of TMRE fluorescence was dose-dependent (Fig. 4b). To monitor Cyt-C release from mitochondria in a response to CBD treatment, Jurkat cells were transfected with EYFP-Cyt-C. In untreated cells, Cyt-C localization was restricted to mitochondria, as confirmed by punctate distribution of EYFP-Cyt-C staining and its colocalization with TMRE (Fig. 4c, d). After treatment with CBD (30 μM), EYFP-Cyt-C distribution in the cytoplasm of treated cells became more diffuse (Fig. 4e), indicating Cyt-C release from mitochondria, observed as early as within the first 20 min of treatment (Fig. 4f). Concomitantly, cell volume was significantly reduced, as it was previously reported for CBD-treated Jurkat cells by others[19]. Jurkat cells, exposed to CBD, exhibited an enhanced activity of caspases 9 and 3, confirming the triggering of intrinsic apoptotic pathway (Fig. 4g).

Collapse of the ΔΨm is frequently associated with the induction of the mitochondrial permeability transition pore (mPTP), a wide channel formed through inner and outer mitochondrial membranes. The formation of mPTP is potently blocked by cyclosporine A (CsA)[20]. Two distinct mechanisms, leading to the Cyt-C release from mitochondria were suggested: one is related to the mPTP and inhibited by CsA and another is Bax-dependent but CsA-insensitive[21,22]. In our experiments both CBD-induced phenomena, Cyt-C release from mitochondria and cell shrinkage were inhibited by CsA (Fig. 4h). mPTP opening is associated with the oxidative stress[20]. CBD-induced reactive oxygen species (ROS) overproduction

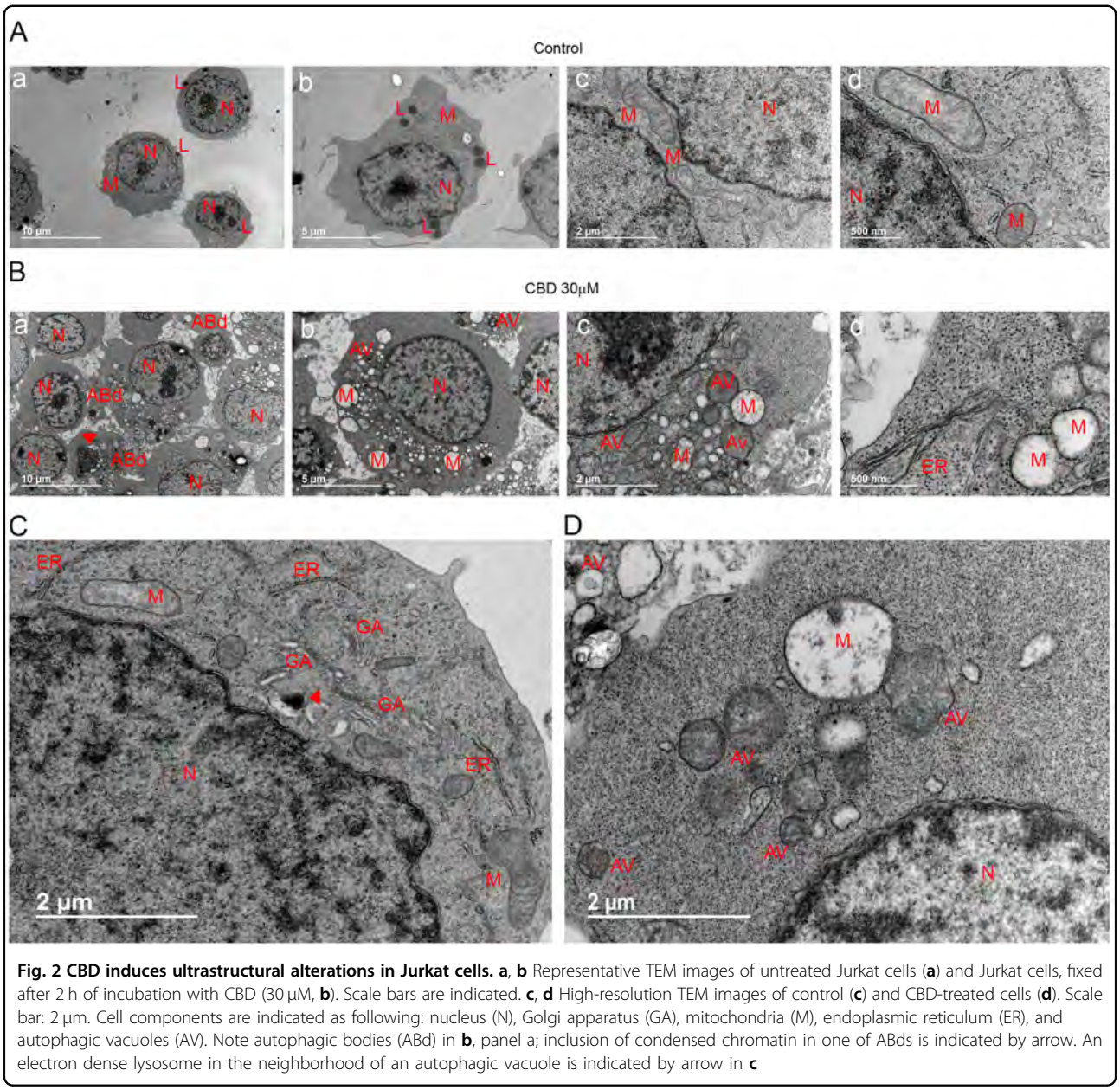

Fig. 2 CBD induces ultrastructural alterations in Jurkat cells. a, **b** Representative TEM images of untreated Jurkat cells (**a**) and Jurkat cells, fixed after 2 h of incubation with CBD (30 μM, **b**). Scale bars are indicated. **c**, **d** High-resolution TEM images of control (**c**) and CBD-treated cells (**d**). Scale bar: 2 μm. Cell components are indicated as following: nucleus (N), Golgi apparatus (GA), mitochondria (M), endoplasmic reticulum (ER), and autophagic vacuoles (AV). Note autophagic bodies (ABd) in **b**, panel a; inclusion of condensed chromatin in one of ABds is indicated by arrow. An electron dense lysosome in the neighborhood of an autophagic vacuole is indicated by arrow in **c**

was previously reported in different cell models[14,23]. As shown in the Fig. 4i, CBD within few minutes provoked a dose-dependent increase in ROS generation.

CBD-induced mitochondrial Ca^{2+} overload is responsible for the formation of mPTP

CBD-mediated elevation of the cytosolic free Ca^{2+} ($[Ca^{2+}]_i$) has been observed in several cancer and non-cancerous cells[24,25]. Calcium signal signature defines the cell fate, survival, or death scenarios[26]. Elevated intramitochondrial Ca^{2+} ($[Ca^{2+}]_m$) is a prerequisite for the mPTP formation[20]. It is generally assumed that $[Ca^{2+}]_m$ increase is triggered by an increase of $[Ca^{2+}]_i$. In many cases, Ca^{2+} source can be ER, whose membranes come to a very close proximity with the outer mitochondrial membrane (OMM)[27].

CBD promoted a dose-dependent elevation of $[Ca^{2+}]_i$ from the resting level of 100 nM up to 300 nM, both in T-ALL cells (Fig. 5a–d) and in healthy lymphocytes (Fig. 5e, f). Pharmacological analysis revealed that neither CB1/2 nor GPR55 receptors were involved in the CBD-induced $[Ca^{2+}]_i$ rise. Importantly, CBD-induced $[Ca^{2+}]_i$ rise was neither dependent on Ca^{2+} permeable channels in plasma membrane nor on extracellular Ca^{2+} (Fig. 5g–j). Thus, the source of CBD-induced $[Ca^{2+}]_i$ rise were intracellular Ca^{2+} stores. Blockage of plasma membrane

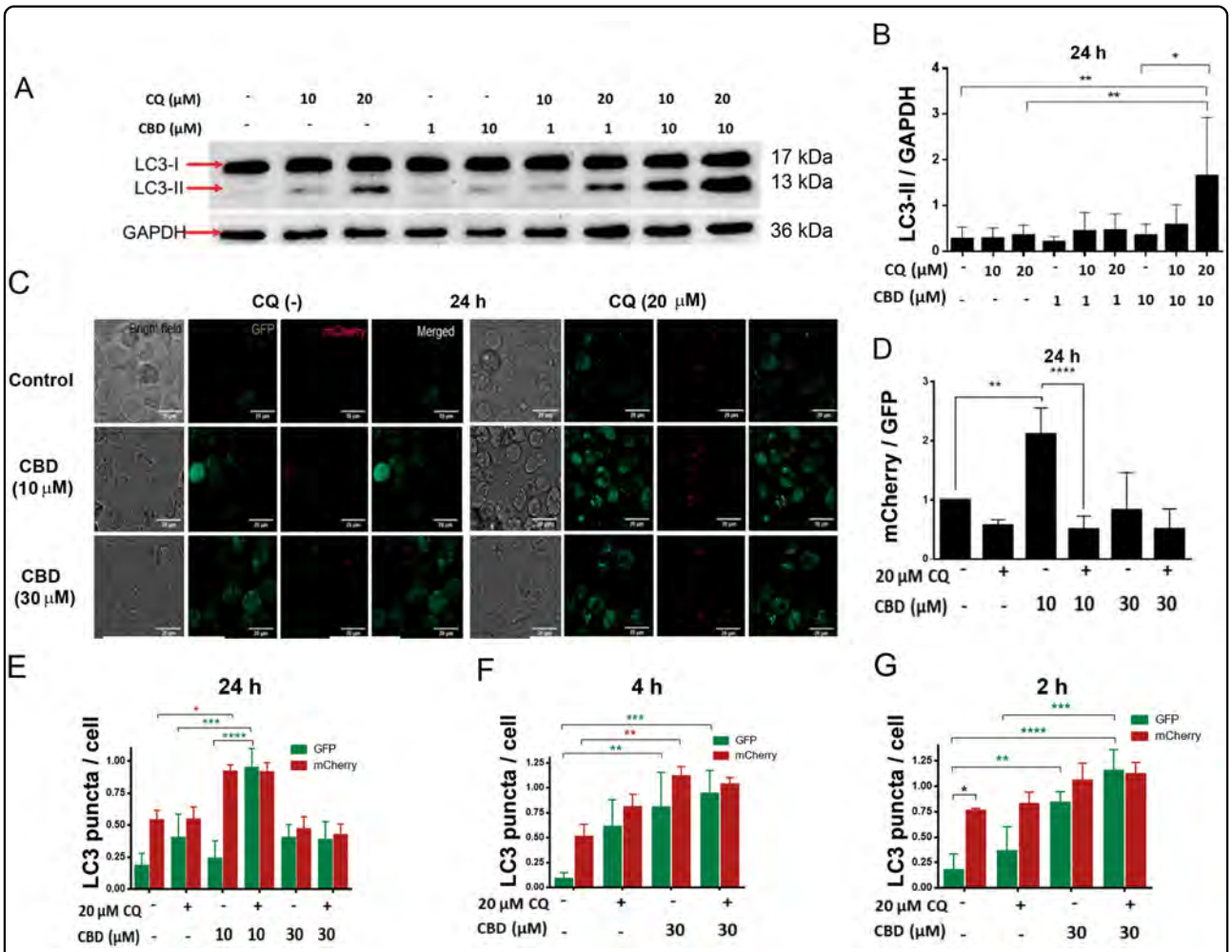

Fig. 3 CBD induces autophagy in Jurkat cells. a Representative Western blot of LC3-I/II protein expression in vehicle- or CBD- treated Jurkat cells (24 h). CQ was used to prevent the fusion of autophagosomes with lysosomes, where LC3-II is otherwise degraded. The concentrations of CQ and CBD are indicated. GAPDH was used as a loading control. Note that in absence of CQ the accumulation of LC3-II was observed neither in control (basal autophagy) nor in CBD-treated samples. In the presence of CQ LC3-II is accumulated and corresponding bands are more intense. **b** LC3-II/GAPDH density ratio in samples, obtained from Jurkat cells, grown in different conditions (as in example shown in **a**). Data are mean ± SD ($n \geq 4$; *$p < 0.05$; **$p < 0.01$). Control and different treatments were compared, using one-way ANOVA with Tukey's multiple comparisons tests. **c** Confocal microscopy images of mCherry-GFP Jurkat cells, incubated over 24 h at different conditions as indicated. CQ was used to prevent the fusion of autophagosomes with lysosomes during the autophagy flux. Note that the inhibition of autophagolysosomes formation by CQ results in prevention of GFP quenching in the acidic environment within a lysosome. **d** mCherry/GFP puncta ratio was calculated from confocal images of Jurkat cells as shown in **c**, incubated at different conditions. Quantification of the average number of mCherry and GFP puncta was performed using ImageJ "Particle analysis" tool. For each condition, 3 fields (10–20 cells/ field) were analyzed. Data from three independent experiments were averaged and are shown as mean ± SD. One-way ANOVA with Tukey's post-hoc tests were employed to compare statistical significance between groups (**$p < 0.01$; ****$p < 0.0001$). **e**–**g** LC3 puncta counts, where GFP and mCherry puncta were counted and analyzed separately in Jurkat cells in control samples or in samples treated with different combinations of CBD and CQ, and incubated during 24 h (**e**), 4 h (**f**) or 2 h (**g**). Quantification of the average number of mCherry and GFP puncta was performed using ImageJ "Particle analysis" tool. For each condition, 3 fields (10–20 cells/field) were analyzed. Data from four independent experiments were averaged and are shown as mean ± SD. Significance is depicted in green, when comparing GFP puncta between groups and in red for mCherry puncta comparison. Significance in black represents differences between GFP/mCherry puncta ($n \geq 4$, *$p < 0.05$; **$p < 0.01$; ***$p < 0.001$; ****$p < 0.0001$; two-way ANOVA with Tukey's post-hoc tests)

Ca^{2+} permeable channels by Gd^{3+} and ruthenium red (RR) did not protect leukemic cells against CBD (Fig. 5i, j).

To monitor $[Ca^{2+}]_m$, Jurkat cells were transfected with a Ca^{2+}-sensitive, mitochondrial targeted indicator CEPIA3mt (Kd = 11 μM)[28]. Specific mitochondrial targeting of CEPIA3mt was confirmed by its colocalization with TMRE (Fig. 6a). Concurrent measurement of $[Ca^{2+}]_i$ were conducted with cells loaded with a conventional cytosolic ratiometric dye Fura-2. CBD-induced $[Ca^{2+}]_i$ increase was preceded by $[Ca^{2+}]_m$ transient (Fig. 6b). Peak value for

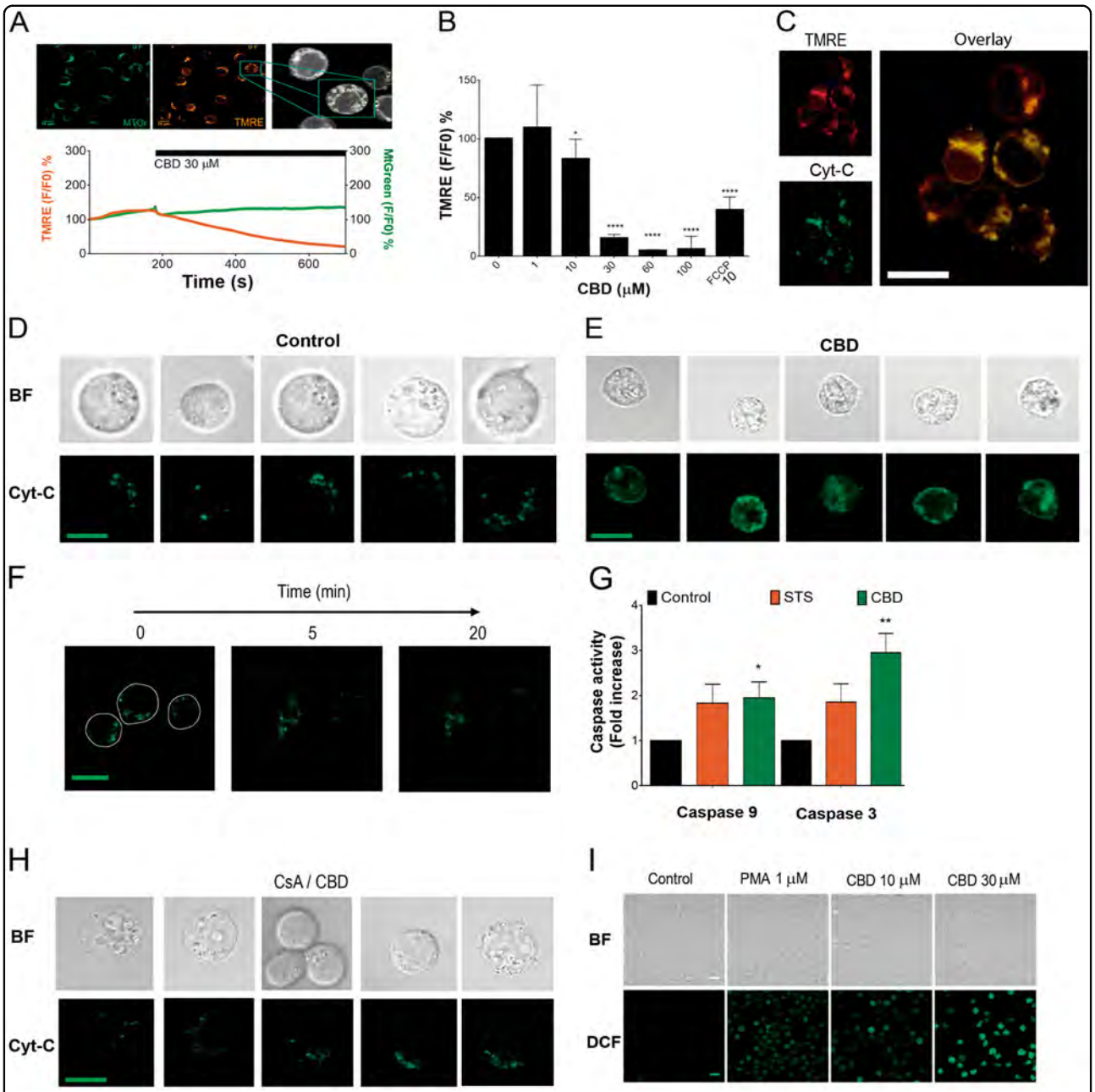

Fig. 4 CBD impairs mitochondrial function, induces Cyt-C liberation and ROS production. a Monitoring of Δψm loss in CBD-treated leukemic cells. Jurkat cells were double-stained with MtGreen and TMRE, mitochondria (ROI) were selected (upper panel) and intensity of fluorescence was monitored by confocal microscopy after CBD (30 μM) administration (lower panel, $n = 36$; see also Supplementary movie 1). **b** Intensity of TMRE fluorescence as an indicator of Δψm in Jurkat cells, treated with different concentrations of CBD (0–100 μM) during 10 min. FCCP (10 μM) was used as a positive control. Data are mean ± SD ($n = 8$ in three independent experiments). Statistical comparison with control was performed by means of one-way ANOVA test (*$p < 0.05$; ****$p < 0.0001$). **c** EYFP-Cyt-C is localized in mitochondria of Jurkat cells after 12 h of transfection. EYFP-Cyt-C and TMRE fluorescence are colocalized (200 nM TMRE, 200 ng EYFP-Cyt-C, pseudocolor). Images were acquired by confocal microscopy at 12 h after transfection, scale bar: 10 μm. **d** Representative images of five Jurkat cells, transfected with EYFP-Cyt-C (as in **c**). Dense green fluorescent puncta (pseudocolor) reflect Cyt-C localization in intact mitochondria. Scale bar: 10 μm. **e** Representative images of five Jurkat cells, transfected with EYFP-Cyt-C (as in **c**) and treated with CBD (30 μM, 1 h). Cyt-C was released from mitochondria as evidenced by a diffuse EYFP-CytC distribution. Scale bar: 10 μm. **f** EYFP-Cyt-C distribution in Jurkat cells, expressing EYFP-Cyt-C, at 0, 5, and 20 min with CBD (30 μM). Scale bar: 10 μm. **g** Caspase-9 and caspase-3 activity in vehicle- and CBD- treated (30 μM, 12 h) Jurkat cells. Staurosporine (STS, 5 μM) was used as a positive control. After incubation, cells were lysed, and caspase activity was determined by colorimetric assay (BioVision). Fold increase in activity compared to control was plotted as mean ± SE (four independent experiments). One-way ANOVA test was performed to compare CBD-treated to control group (*$p < 0.05$; **$p < 0.01$). **h** Pretreatment with mPTP inhibitor CsA (10 μM) prevents Cyt-C release, induced by CBD (30 μM; 1 h). Compare these images with Fig. 4d, e (vehicle- and CBD-treated cells) and note the protective effect of CsA. Scale bar: 10 μm. **i** ROS production as evaluated by fluorescent microscopy in DCF-loaded (2 μM) Jurkat cells. CBD effect on ROS production was monitored after 1 h of incubation. PMA (1 μM) was used as a positive control

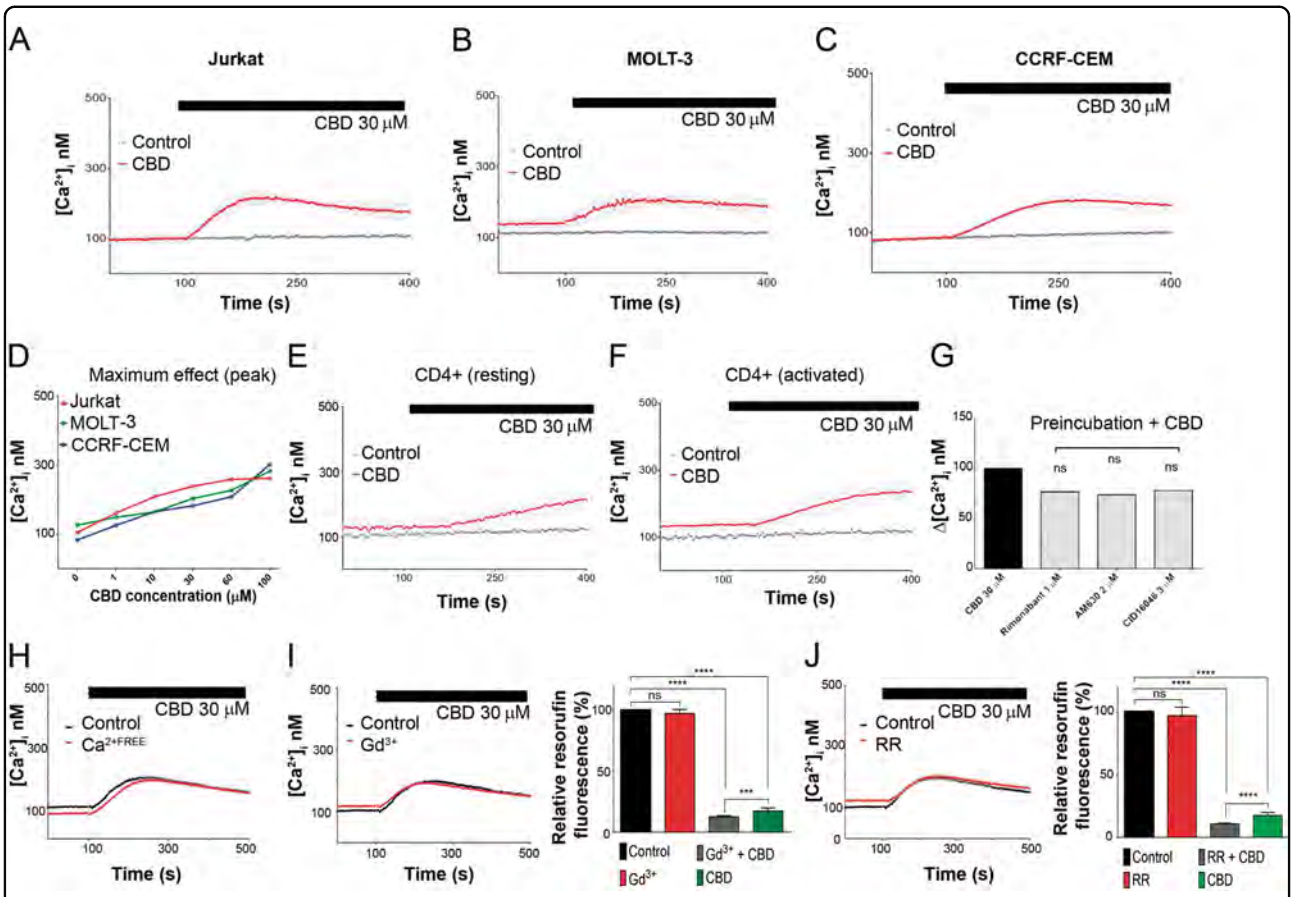

Fig. 5 CBD induces cytosolic Ca^{2+} rise in human T-ALL cell lines and non-cancerous T cells. a–c $[Ca^{2+}]_i$ monitoring in leukemic cells, treated with CBD. Traces represent the mean ± SD of at least six samples from independent experiments. **d** Dose dependence of peak $[Ca^{2+}]_i$ values in T-ALL cell lines, exposed to CBD. Data are mean ± SD for at least six samples from independent experiments. **e**, **f** $[Ca^{2+}]_i$ monitoring in non-cancerous T cells in resting (**e**) and activated (**f**) states. Traces represent the mean ± SD of at least six samples from independent experiments. **g** Pharmacological analysis of $[Ca^{2+}]_i$ rise in response to CBD. Before CBD treatment, cells were preincubated over 20 min with either CB1 antagonist, rimonabant (1 μM), CB2 inverse agonist, AM630 (2 μM), or GPR55 antagonist, CID16020046 (3 μM); values Δ $[Ca^{2+}]_i$ were obtained by subtracting the $[Ca^{2+}]_i$ baseline level from $[Ca^{2+}]_i$ maximum increase. Data are mean ± SD of at least 6 samples from independent experiments. **h** $[Ca^{2+}]_i$ monitoring in Jurkat cells, suspended in Ca^{2+}-free HBSS. Traces represent the mean ± SD of at least six samples from independent experiments. **i**, **j** Effect of Gd^{3+} and RR, non-selective blockers of plasma membrane Ca^{2+}- permeable channels, on $[Ca^{2+}]_i$ (**i** and **j**, left) and cell viability evaluated by resazurin-based metabolic assay (**i** and **j**, right). Gd^{3+} (1 μM) or RR (1 μM) were added to Jurkat cells 20 min before the $[Ca^{2+}]_i$ measurement. **i**, **j** left: traces represent the mean ± SD of at least six samples from independent experiments. **i**, **j** right: data (resorufin fluorescence intensity) were normalized to vehicle-treated control and reported as mean ± SD ($n = 8$ of four independent experiments (****$p < 0.0001$, Student's *t*-test)

$[Ca^{2+}]_m$ signal was ~5 μM, basing on the titration curve for CEPIA3mt[28]. Notably, CBD-induced $[Ca^{2+}]_m$ transient occurred at time when $[Ca^{2+}]_i$ remained at the resting level. Thus, causal relation between CBD-induced $[Ca^{2+}]_m$ and $[Ca^{2+}]_i$ increases was further addressed. Jurkat cells highly express functional H1 histamine receptors and histamine treatment was proved to induce the inositol 1,4,5-trisphosphate receptor (IP_3R)-dependent Ca^{2+} release from the ER for this cell model[29]. Artificial depletion of the ER Ca^{2+} by histamine or thapsigargin and block of the ER Ca^{2+} release via IP_3R channels by 2-aminoethoxydiphenyl borate (2-APB) abolished the CBD-induced $[Ca^{2+}]_i$ increase. Thus, ER was the source of the CBD-induced $[Ca^{2+}]_i$ rise (Fig. 6c, d, f). CBD-induced $[Ca^{2+}]_m$ rise was potentiated by ER Ca^{2+} release (and concomitant cytosolic Ca^{2+} rise) and reduced upon the conditions, when ER Ca^{2+} release was blocked (Fig. 6c–e). Thus, ER Ca^{2+} release partly fuels the CBD-induced $[Ca^{2+}]_m$ rise. However, note that $[Ca^{2+}]_m$ rise was switched first upon CBD administration, not by Ca^{2+} release from the ER per se. Mitochondria act as a sink for Ca^{2+}, artificially released from the ER prior to CBD application as evidenced by an abrupt decrease of $[Ca^{2+}]_i$ in a response to CBD (Fig. 6c, f).

Ca^{2+} uptake from the cytosol to mitochondria is mediated by voltage-dependent anion channel (VDAC) in the OMM and the mitochondrial Ca^{2+} uniporter (MCU)

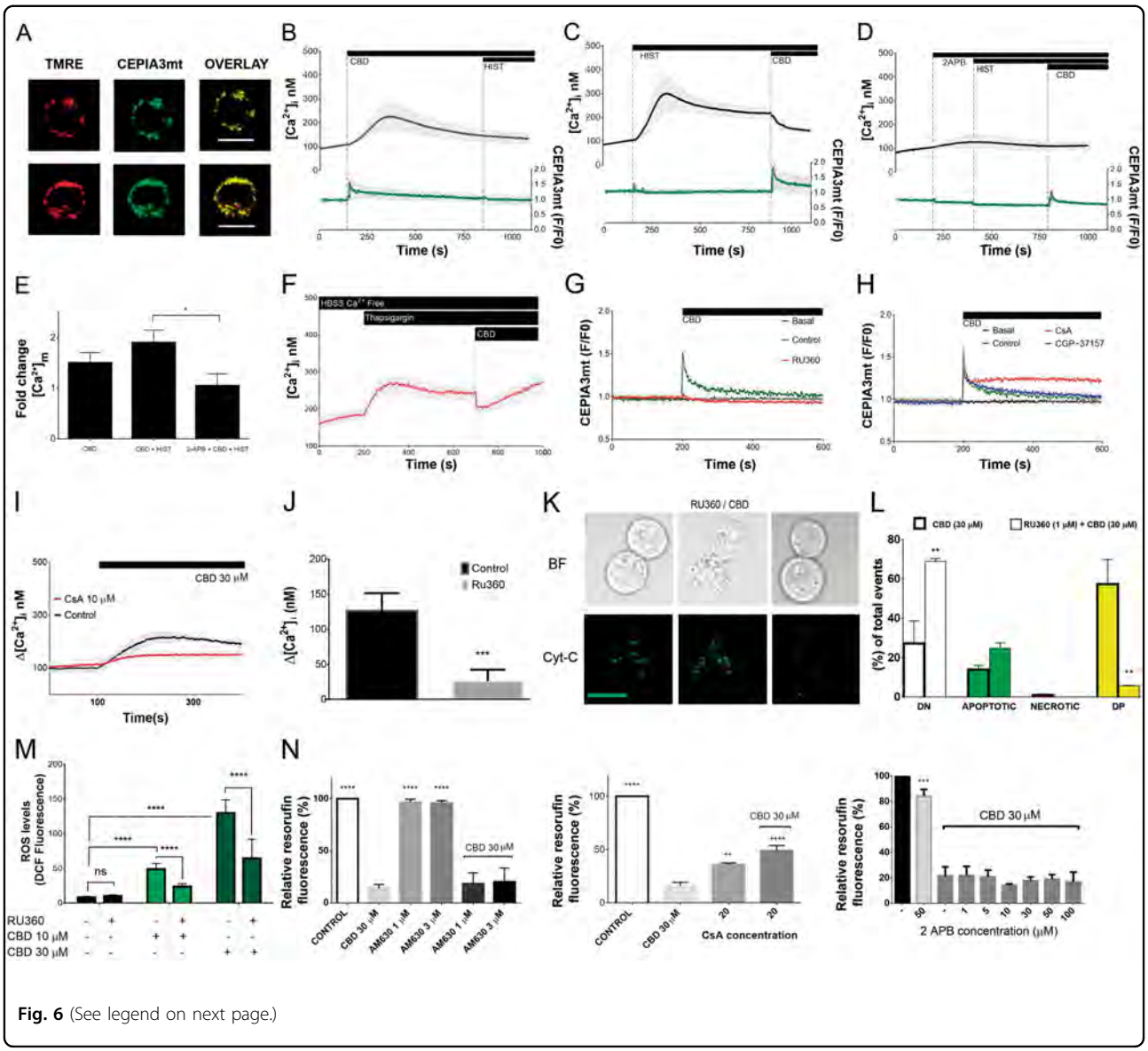

Fig. 6 (See legend on next page.)

in the inner mitochondrial membrane (IMM). In our experiments, CBD-induced $[Ca^{2+}]_m$ rise was completely suppressed by a permeable MCU blocker Ru360 (Fig. 6g), but not significantly affected by CGP-37157, the inhibitor of the inner membrane Na^+/Ca^{2+} exchanger, NCX (Fig. 6h). Specific inhibitor of mPTP, CsA, stabilized $[Ca^{2+}]_m$ at a high level (Fig. 6h). Of special note, the inhibition of mitochondrial Ca^{2+} overload and of mPTP by Ru360 and CsA, respectively, precluded the cytosolic Ca^{2+} rise (Fig. 6i–j). Thus, the ER Ca^{2+} release is causally dependent on the mitochondrial response. Collectively, our $[Ca^{2+}]_m$ data imply that CBD-induced Ca^{2+} uptake into the mitochondrial matrix via MCU caused a rapid $[Ca^{2+}]_m$ overload, which induced the mPTP opening and a subsequent $[Ca^{2+}]_m$ release. Thus, mitochondria appear to be a primary target for CBD and mPTP opening is required for the induction of Ca^{2+} release from the ER. MCU inhibitor Ru360 prevented CBD-induced ROS formation, Cyt-C release and cell death as revealed by Annexin V/PI assay (Fig. 6k–m). The last result is very essential, because it links mitochondrial Ca^{2+} overload to cell death. Remarkably, CsA, albeit per se possessing immunosuppressing activity, partially improved cell viability of CBD-treated cells, while CB2 inverse agonist AM630 and 2-APB were inefficient (Fig. 6n).

CBD interacts directly with mitochondria to promote the organelle dysfunction

To verify the conclusion that mitochondria are direct targets for CBD action, mitochondria were freshly isolated

(see figure on previous page)
Fig. 6 CBD directly induces mitochondrial Ca^{2+} overload and mPTP opening. a CEPIA3mt fluorescence is colocalized with mitochondrial marker TMRE in Jurkat cells. Scale bar: 10 µm. **b**–**d** Concurrent monitoring of $[Ca^{2+}]_i$ and $[Ca^{2+}]_m$ in Jurkat cells. $[Ca^{2+}]_i$ and $[Ca^{2+}]_m$ changes were evaluated with Fura-2 (2 µM) and CEPIA3mt, respectively. Note that cells were loaded either with Fura-2 or with CEPIA3mt; individual time courses for Fura-2 and CEPIA3mt, were synchronized with respect to the timepoint of CBD addition and averaged $[Ca^{2+}]_i$ and $[Ca^{2+}]_m$ responses were plotted at the upper and lower panels, respectively. CBD (30 µM), histamine (10 µM) and membrane-permeable IP_3R blocker 2 APB (50 µM µM) were added as indicated. Traces are mean ± SD of at least six samples from independent experiments. **e** Peak values for $[Ca^{2+}]_m$ changes, induced by CBD, from the experiments shown in **b**–**d**, with a variable level of $[Ca^{2+}]_i$ due to manipulations with Ca^{2+} release from the ER. Bars represent mean ± SD of at least six samples from independent experiments. One-way ANOVA test (*$p < 0.05$). **f** $[Ca^{2+}]_i$ monitoring in Jurkat cells, loaded with Fura-2 (2 µM). ER Ca^{2+} was depleted by thapsigargin (1 µM). Experiments were performed in Ca^{2+}-free medium (HBSS). Addition of CBD causes an abrupt decrease of $[Ca^{2+}]_i$ (*cf* with **c**). Traces are mean ± SD of at least three samples from independent experiments. **g**, **h** $[Ca^{2+}]_m$ monitoring in Jurkat cells, transfected with CEPIA3mt. CBD (30 µM) was added as indicated. When indicated, cells were preincubated over 20 min with either MCU blocker RU360 (1 µM), mPTP inhibitor CsA (10 µM), or inhibitor of mitochondrial Na^+/Ca^{2+} exchanger NCLX CGP37157 (1 µM). Traces are mean ± SD of at least six samples from independent experiments. **i** $[Ca^{2+}]_i$ monitoring in Jurkat cells, loaded with Fura-2 (2 µM). CBD (30 µM) was added as indicated. Cells were preincubated during 20 min with vehicle or CsA (10 µM), specific inhibitor of the mPTP. Values Δ $[Ca^{2+}]_i$ were obtained by subtracting the $[Ca^{2+}]_i$ baseline level from the peak $[Ca^{2+}]_i$. Traces are ±SD of at least six samples from independent experiments. **j** Cytosolic Ca^{2+} response to CBD (30 µM) in Jurkat cells was abolished by a preincubation with the MCU blocker Ru360 (1 µM) over 20 min. Values Δ $[Ca^{2+}]_i$ were obtained by subtracting the $[Ca^{2+}]_i$ baseline level from peak $[Ca^{2+}]_i$. Data are mean ± SD of a minimum of six independent experiments (**$p < 0.01$; ***$p < 0.001$; Student's *t*-test). **k** Representative images of Jurkat cells, transfected with EYFP-Cyt-C, pretreated with RU360 (1 µM, 20 min), and subsequently treated with CBD (30 µM, 1 h). Discrete green fluorescent puncta (pseudocolor) represent Cyt-C localization in intact mitochondria whereas Cyt-C release from mitochondria is evidenced by a more diffuse EYFP-Cyt-C distribution. Compare these images with Fig. 4d, **e** (vehicle- and CBD-treated cells) and note the protective effect of RU360. Scale bar: 10 µm. **l** MCU blocker RU360 effectively prevents CBD-induced cell death in Jurkat cells. Cell death was evaluated by flow cytometry, using Annexin V-AF488/PI double staining. Cells were preincubated with vehicle or RU360 (1 µM, 2 min), and then treated with CBD (30 µM, 6 h). Data of three independent experiments are present (**$p < 0.01$, one-way ANOVA test). **m** ROS levels were evaluated by DCF fluorescence intensity. Cells were either only treated with CBD (10 or 30 µM, 1 h, light and dark green bars, respectively) or additionally pretreated with RU360 (1 µM, 20 min). In all, 50 cells from at least three independent experiments were analyzed for each condition. Data are mean of ±SD. Statistic comparisons between control and CBD-treated samples, or between RU360-pretreated and non-pretreated samples were performed. ****$p < 0.0001$, one-way ANOVA. **n** Effects of the CB2 inverse agonist, AM630 ($n = 8$), mPTP inhibitor CsA ($n = 6$) and membrane-permeable IP_3R blocker 2APB ($n = 6$) on the viability of Jurkat cells, treated with CBD. Cell viability was evaluated by resazurin-based metabolic assay (24 h). Data are mean ± SD. Statistical comparison was made in relation to CBD-treated samples; *$p < 0.05$; **$p < 0.01$; ***$p < 0.001$; ****$p < 0.0001$, one-way ANOVA

from Jurkat cells. Mitochondria were stained with MtGreen and fluorescent Ca^{2+} indicator Rhod-2, and evaluated by flow cytometry. High percentage of double-stained particles evidenced high purity of mitochondria population (Fig. 7a). Upon exposure to 30 µM CBD isolated mitochondria exhibited $[Ca^{2+}]_m$ increase at external free Ca^{2+} of 100 nM, equal to the resting cytosolic Ca^{2+} level (Fig. 7b). The response of high affinity Ca^{2+} indicator Rhod-2 (Kd ~ 0.6 µM) was saturated, implying that free $[Ca^{2+}]_m$ level was above 1 µM for a long time. Incubation of isolated mitochondria with CBD over 10 min produced a strong dose-dependent decrease of ΔΨm (Fig. 7c), similar to that in whole cells (Fig. 4b).

CBD binding to VDAC: in silico evidences

In some cell models CBD can induce cell death via direct interaction with VDAC, promoting its closure to a conformational substate[30]. This substate possesses a reduced capacity to transport metabolites and increased Ca^{2+} permeability[31]. We performed in silico analysis of VDAC- CBD interactions. VDAC surface and N-terminus were tested for CBD binding. Among the main VDAC cavities, β9–12 and N-terminus regions exhibited the most suitable sites for the CBD binding, basing on respective free energy changes (docking score, see Supplementary Table 1). 3D analysis of the CBD-VDAC interaction revealed that more likely CBD interacts with 3 residues, Thr9, Asp12, and Leu13 at the N-terminus and neighboring pore residues Val146, Gln157, Gly175, Gln182, and His184 (Fig. 7d). Further analysis revealed that CBD binding is stabilized mainly by steric interactions and hydrogen bonds (Fig. 7e). Of putative CBD-interacting residues, Thr9, Asp 12, and Hist184 have a highest contribution to the overall binding energy (Supplementary Fig. 1, Supplementary Table 1).

Discussion

A crucial role of mitochondria in cell metabolism and bioenergetics, as well as in signaling pathways, regulation of transcriptional activity, proliferation, migration, and cell death is tightly related to their involvement into the intracellular Ca^{2+} dynamics[32]. In the present study, by means of concurrent monitoring of $[Ca^{2+}]_m$ and $[Ca^{2+}]_i$ in a response to the CBD treatment, we have provided the experimental evidences that mitochondria are primary CBD target in T-ALL. In the first place, acute transient $[Ca^{2+}]_m$ rise, preceding the $[Ca^{2+}]_i$ increase, was observed in a response to CBD (Fig. 6b). Furthermore, $[Ca^{2+}]_m$ increase together with a dissipation of ΔΨm was observed also in isolated mitochondria, treated with CBD (Fig. 7b, c). Ca^{2+} accumulation in mitochondrial matrix requires the crossing of both OMM and IMM. VDAC channel,

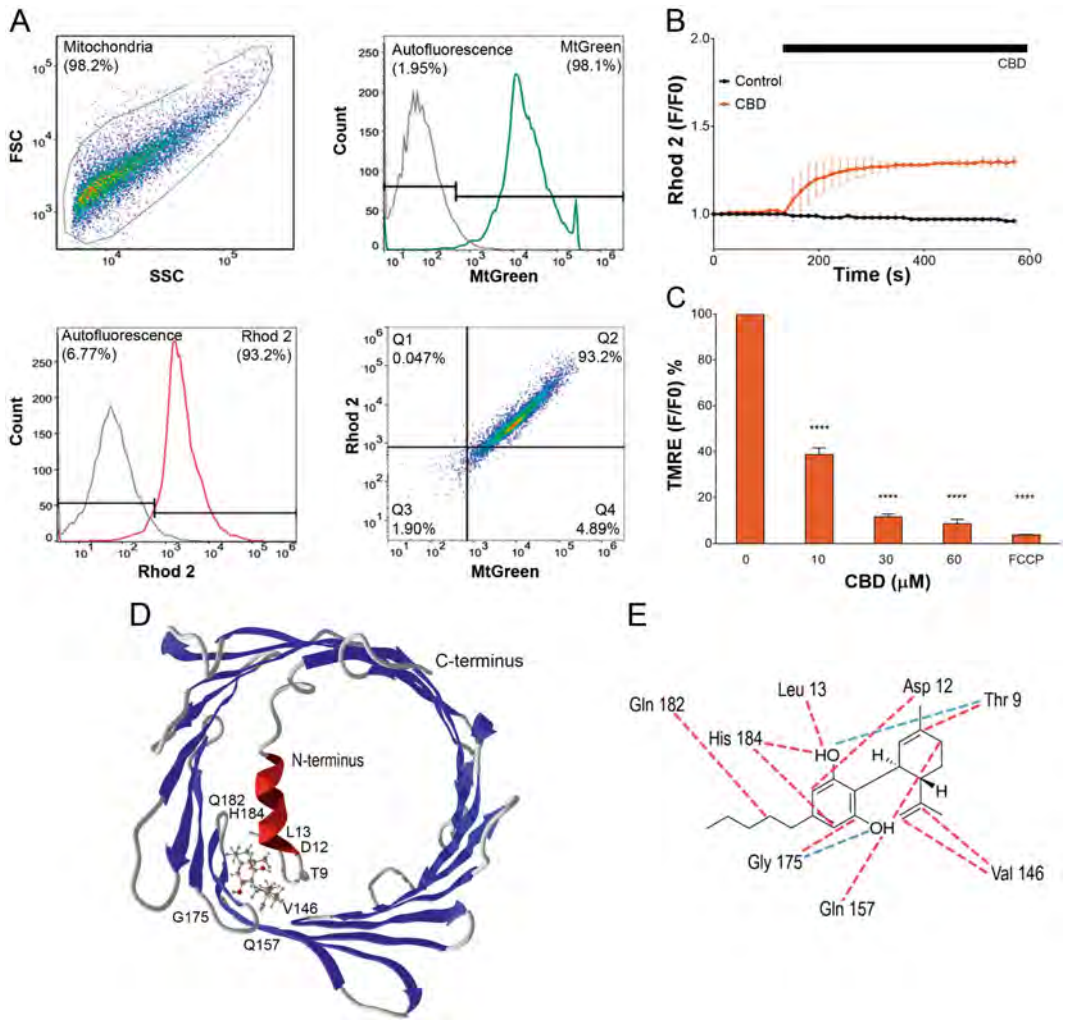

Fig. 7 CBD directly interacts with mitochondria. a Isolation of mitochondria from Jurkat cells was corroborated by flow cytometry analysis. Representative experiment is shown. The purity of mitochondria population was determined as a percentage of double positive particles after staining (20 min) with MtGreen (200 nM) and Rhod-2 (2 μM). First, the mitochondria population was visualized in FSC/SSC dot blot (upper left panel). Non-stained mitochondria were used to determine the autofluorescence interval (gray histograms and corresponding intervals in upper right and lower left panels). Accordingly, positive intervals for MtGreen (green histogram and corresponding interval in upper right panel) and Rhod-2 (red histogram and corresponding interval in lower left panel) were determined. More than 90% of freshly isolated mitochondria were double-positive (lower right panel). Freshly isolated mitochondria were assayed immediately. **b** $[Ca^{2+}]_m$ uptake by freshly isolated mitochondria in a response to vehicle or CBD (30 μM) treatments. Traces are mean ± SD for three independent experiments. **c** CBD effect on membrane potential (Δψm) in isolated mitochondria. Freshly isolated mitochondria were stained with TMRE (400 nM) and exposed to different CBD concentrations for 10 min. FCCP was used as a positive control. Data are mean ± SD of at least three independent experiments (****$p < 0.0001$, one-way ANOVA test). **d** In silico analysis predicts that CBD interacts with VDAC1 at N-terminus and β9–11 residues. **e** Residues, interacting with CBD are depicted; hydrogen bonding interactions are colored in red, whereas steric interactions are depicted in blue

ubiquitously expressed in OMM, is normally responsible for the OMM permeability to Ca^{2+}[33]. Under physiological conditions, VDAC permeability to Ca^{2+} at levels, required for an optimal function of TCA enzymes, is regulated by VDAC interaction with IP_3R in ER and chaperone 75 kDa glucose-regulated protein GRP75[34]. Our in silico analysis which demonstrated that CBD may interact directly with VDAC (Fig. 7) is in agreement with findings by others that CBD colocalizes with VDAC-rich mitochondrial membranes fraction from BV-2 microglia cell line and that purified VDAC, incorporated into lipid bilayers, is switched from fully open to major subconductance state by CBD[30]. Such "closed" channel state is known to be highly permeable for Ca^{2+}, due to the exposure of anionic groups within the channel pore[31].

Based on the available data, the following working model can be proposed (Fig. 8). Due to its direct interaction with CBD, VDAC1 is "fixed" in the Ca^{2+}-permeable state. This

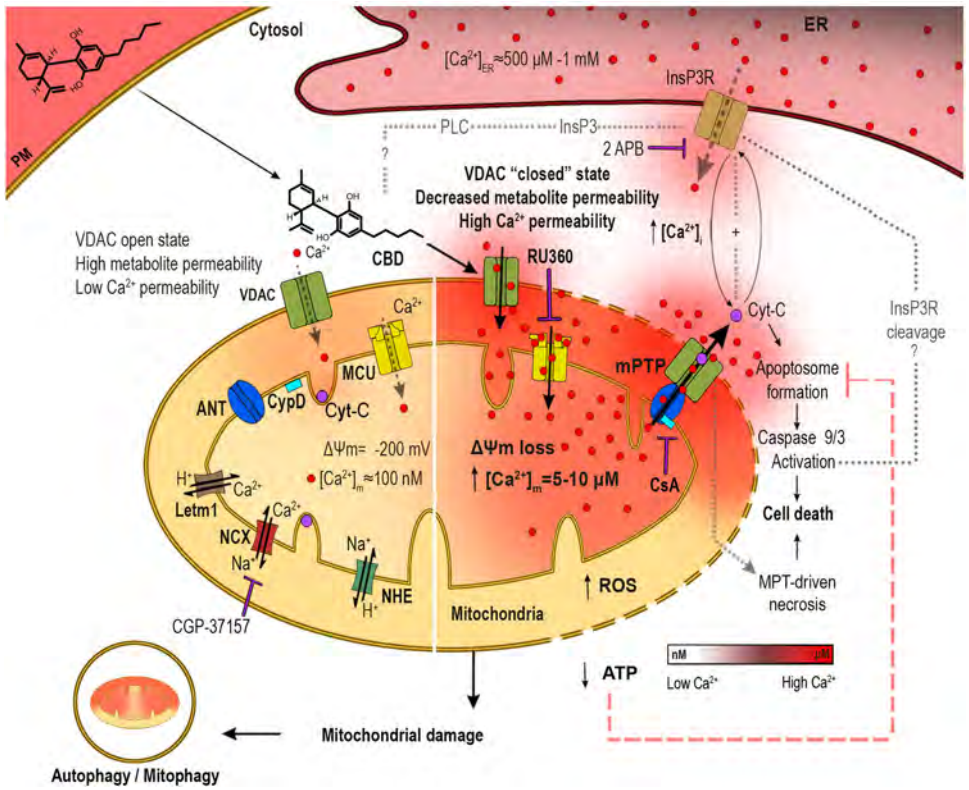

Fig. 8 Proposed mechanism for the CBD effect on T-ALL cells. Highly lipophilic CBD readily permeates plasma membrane and enters the cytosol, approaching mitochondria. Direct CBD interaction with VDAC favors the channel closed substate with increased Ca^{2+} permeability. It favors mitochondrial Ca^{2+} uptake through VDAC and MCU, leading to the mitochondrial Ca^{2+} overload that promotes the mPTP formation, Δψm loss, mitochondrial swelling, and cristae disruption. mPTP opening promotes the Cyt-C release from mitochondria. In cytoplasm, Cyt-C may orchestrate the apoptosome formation, caspases´ activation, and triggers the intrinsic apoptosis. mPTP rapidly triggers Ca^{2+} release from the ER, which tends to promote the mitochondrial Ca^{2+} overload in a feedforward manner. The CBD-induced dysfunction of mitochondria is accompanied by severe oxidative stress and rapid loss of ATP production, resulting in the MPT-driven necrosis. Autophagy occurs in T-ALL cells treated with sublethal CBD concentrations

causes Ca^{2+} entry into the intermembrane space. Ca^{2+} needs to concentrate to micromolar level there, to unlock and activate the MCU[35]. This is commonly believed to be induced by a substantial increase of extramitochondrial Ca^{2+}. Our data suggest that mitochondrial Ca^{2+} overload occurred already at resting 0.1 μM cytosolic Ca^{2+} (Figs. 6b, d and 7b). The driving force for Ca^{2+} accumulation within the intermembrane space could be a negative Donnan potential of −20 to −40 mV across the OMM[36]. This allows the concentration of Ca^{2+} in the intermembrane space up to 20-fold as compared to the cytosolic Ca^{2+} concentration, providing that the outer membrane is permeable for Ca^{2+}. The magnitude of the Donnan potential across the OMM depends on the accumulation of impermeable large anions within the intermembrane space. Such accumulation, e.g. of ATP, may be provoked by the same conformational shift within VDAC1, which not only increases its Ca^{2+} permeability, but also makes it adenine nucleotide-impermeable[36]. Activation of MCU along with a large negative potential across the IMM drives Ca^{2+} entry into the mitochondrial matrix, leading to a rapid $[Ca^{2+}]_m$ overload (Fig. 6). The latter triggers a stable mPTP formation, which causes depolarization of the IMM, mitochondrial dysfunction, severe oxidative stress, and Ca^{2+} and Cyt-C release into the cytosol.

Noteworthy, multiple leukemic phenotypes express higher levels of VDAC in a comparison to healthy cells and VDAC expression is increased upon chemotherapy. Moreover, the degree of overexpression is positively correlated with the cell death induction by anticancer agents[37–39].

We have observed different outcome of the CBD treatment depending on its concentration. At high CBD concentration, various scenarios of regulated cell death may be triggered in LLA-T (Fig. 8). In the present study, we reported apoptotic features such as Cyt-C release from mitochondria to cytosol, activation of caspases 9/3 and externalization of phosphatidylserine. On the other hand, appearance of the huge Annexin V^+PI^+ population in the early phases of CBD treatment evidenced MPT-driven

necrosis. One can hypothesize that development of MPT-driven apoptosis may be blocked due to energy penalty, a decreased ATP level caused by a cessation of oxidative phosphorylation by defunct mitochondria[40]. At sublethal (10 μM CBD) concentration, autophagy was induced and apparently efficiently prevented cell death (Fig. 1b, c, g, h; Fig. 3a–d). Low CBD concentrations even stimulated cell proliferation (Fig. 1b). This phenomenon may be explained in the frame of the same basic model, providing they promoted only limited $[Ca^{2+}]_m$ increase. Such moderate $[Ca^{2+}]_m$ accelerates metabolism due to Ca^{2+}-dependence of TCA cycle enzymes[41].

In conclusion, CBD directly targets mitochondria in T-ALL and changes their capacity to handle Ca^{2+}, which in turn affects multiple cellular functions, including ROS production and Ca^{2+} signaling, metabolic switch and the induction of autophagy and cell death. The latter is directly proved for our experimental model as the inhibitor of mitochondrial Ca^{2+} uptake Ru360 protected T-ALL cells from the CBD-induced cell death. Considering the pivotal role of mitochondria in oncogenic re-programming, CBD may be plausible candidate to be included into chemotherapeutic protocols. Importantly, resting T cells, representing major T lymphocyte population, were resistant to CBD and retained their ability to antigen activation. Healthy activated T cells were CBD-sensitive, but this population is small in T-ALL patients with a weakened immunologic system. However, contrasting effects of low and high CBD concentrations and possible differences in its tissue distribution and bioavailability requires further studies on animal models, with a focus on safety issues.

Materials/subjects and methods

Cell lines and culture conditions

Leukemic cell lines Jurkat (ATCC®TIB™, Clone E6-1, male, 14 years), MOLT-3 (ATCC®CRL-1552™, male, 19 years), CCFR-CEM (ATCC®CCL-119™, T-ALL, female, 4 years), K562 (ATCC®CCL-243™, female, 53 years), Reh (ATCC®CRL-8286™, female) and RS4;11 (ATCC®CRL-1873™, female, 32 years) purchased from ATCC® (Manassas, VA, USA) were grown in suspension in Advanced RPMI 1640 medium, supplemented with 5% (v/v) of heat-inactivated fetal bovine serum (FBS), 100 U/mL of penicillin, 100 μg/mL streptomycin and 1% of GlutaMAX™ (all from Invitrogene, Carlsbad, CA, USA). Tandem-labeled mCherry-GFP-LC3 Jurkat cells (gift from Dr. A. Thorburn, Colorado, USA) were maintained in complete growth medium (as for wild type Jurkat cells), additionally supplemented with 400 μg/mL of hygromycin B (Sigma, H3274) for selection. Suspension cells were maintained in the logarithmic growth phase by daily medium refreshment. Adherent cell lines MDA-MB-231 (ATCC®HTB-26™, female, 51 years), MCF7 (ATCC®HTB-22™, female, 69 years), SiHa (ATCC®HTB-35™, female, 55 years) and HeLa (ATCC®CCL-2™, female, 31 years) were maintained in DMEM medium supplemented with 10% (v/v) of heat-inactivated FBS, 100 U/mL of penicillin, 100 μg/mL streptomycin and 1% of GlutaMAX™. Adherent cells were passaged when they were in the logarithmic growth phase. All cells were cultured in a humidified incubator in 5% CO_2/95% air atmosphere at 37 °C.

Human samples

Blood samples (10 mL) from non-cancerous, apparently healthy volunteers (6 males and 6 females, younger than 35 years) were collected by capacitated personal under aseptic conditions. A written informed consent was obtained from all persons, prior to sample collection, according to the Declaration of Helsinki. Sample acquisition protocol was evaluated and approved by the Bioethics and Biosecurity Committee of the Biomedical Research Centre and the Faculty of Medicine of the University of Colima, in agreement with the federal laws (Artículo 100, Ley General de Salud).

Cannabidiol

CBD solution in methanol (10 mg/mL, equivalent to 32 mM) was purchased from Cayman Chemical (90081) and stored at −20 °C. Working solutions in complete growth medium were prepared daily. Methanol (154903, Merck) was used in vehicle-treated controls. Reference methanol concentration for a vehicle control was 0.3% v/v, which corresponds to that applied with the highest tested CBD concentration (100 μM).

Purification and activation of $CD4^+$ lymphocytes

Heparinized freshly isolated blood samples were diluted 1:1 with cold PBS. Peripheral blood mononuclear cells (PBMC) were separated by centrifugation in Ficoll (17-144002, Ficoll-Paque 1.073, GE Healthcare) gradient (1:1.5 blood/Ficoll ratio, 1000 × *g*, 30 min, RT). PBMC were collected from the interphase and carefully washed in PBS. Finally, cells were resuspended in a fresh RPMI 1640 medium, supplemented with 10% of FBS and incubated overnight for cell recovery. Next day, PBMC were subjected to negative selection (to avoid activation) with human $CD4^+$ T cell isolation kit (130-096-533, Miltenyi Biotec Miltenyi Biotec), following manufacturers' specifications. Briefly, PBMC were collected, washed (400 × *g*, 5 min) and the pellet was resuspended in cold MACS buffer. Live cells were counted (trypan blue exclusion test) and incubated with $CD4^+$ T cell biotin-antibody cocktail (1 μL/1 × 10^6 cells) against CD8a, CD11b, CD11c, CD19, CD45R (B220), CD49b (DX5), CD105, Anti-MHC Class II, Ter-119, and TCRγ/δ, for 20 min at 4 °C with agitation, followed by incubation with microbeads, conjugated to monoclonal anti- biotin antibodies (2 μL/1 × 10^6 cells)

over 20 min at 4 °C. Next, 1 mL of MACS buffer was added, cells were centrifuged (400 × *g*, 5 min), supernatant was discarded to remove the excess of antibodies and cells were resuspended in 1 mL of cold MACS buffer. $CD4^+$ T cell population was separated using a MACS separator. LS column was placed in the MAC separator, rinsed with 3 mL of MACS buffer and cell suspension was added. Enriched $CD4^+$ T (negative) cells were collected and column was washed three times with MACS buffer for a complete $CD4^+$ harvesting. Enriched $CD4^+$ T cell population was centrifuged (400 × *g*, 5 min), resuspended in complete Advanced RPMI 1640 medium and incubated at 37 °C in a humidified atmosphere (5% CO_2, 95% air) prior to the experiments. The population purity was more than 95% as verified by flow cytometry (FACSCanto II, BD Biosciences), using antiCD4 antibodies (BioLegend 357404).

For polyclonal activation, resting $CD4^+$ lymphocytes were pretreated in 96-well plates with antiCD3 monoclonal antibodies (5 µg/mL) (BD, 555336) for 2 h at 37 °C. Medium excess was removed and cells were further incubated with antiCD28 monoclonal antibodies (2 µg/mL) (BD, 555725) for 4 days. Ligation of CD3/CD28 provides an antigen-independent activation stimulus by cross-linking T cell receptor (TCR), resulting in transit from quiescent to proliferation state.

Resazurin-based metabolic assay

To estimate cell drug toxicity, resazurin-based metabolic assay was used. Bioreduction of resazurin reagent (Tox 8, Sigma-Aldrich) by viable cells reduces the amount of its oxidized form and concomitantly increases the amount of its fluorescent intermediate resorufin. The amount of dye conversion in solution was measured fluorometrically, using a fluorescence plate reader GloMax Discover (PROMEGA). Cells (10^6/mL) were seeded into 96-well plates in 180 µL of complete RPMI medium per well. Cells were incubated 24 h without or with CBD (1–100 µM). For assay, 20 µL aliquots of resazurin reagent were added to each well to a final volume of 200 µL and cells were further incubated for 4 h (37 °C). Samples' fluorescence was measured by excitation at 520 nm and emission was collected at 580–640 nm. RPMI fluorescence was subtracted for each condition. Samples were run in triplicate, in at least three independent experiments. Data obtained from resorufin fluorescence were averaged, normalized to their controls and expressed as cell viability.

Sequential CBD administration

Jurkat cells (2.5×10^5/mL per well) were seeded into a 48-well plate in complete Advanced RPMI medium. Cells were exposed to CBD (1–100 µM, dissolved in 500 µL of RPMI) and incubated for 24 h. After incubation, cell culture was gently resuspended, and 10 µL of suspension was taken for cell counting, using a hemocytometer and trypan blue exclusion test, to determine the number of viable cells. A second dose of CBD was administered, and cells were incubated for the next 24 h. The procedure was repeated one more time, so that total assay was completed in 72 h. Initial cell number was taken as 100%, and daily cell count was normalized to this point. Three cell counts ($n = 3$) from three independent experiments were averaged and expressed as percentage of viability.

$CD4^+$ T cell recovery test

Non-cancerous $CD4^+$ T-cells from healthy donors were cultured (1×10^6 cells/mL) in complete Advanced RPMI 1640 medium. Cells were preincubated with CBD (30 µM) or vehicle over 24 h. After CBD treatment, cells were washed and resuspended in a CBD-free medium and used for activation with antiCD3 and antiCD28 antibodies, as described earlier. Cell viability was determined by resazurin-based metabolic assay (Tox8, Sigma-Aldrich) as previously described, using a fluorescence plate reader (GloMax Discover, PROMEGA). Samples were excited at 520 nm and emission was collected at 580–640 nm. RPMI fluorescence was subtracted for each condition and data was generated in triplicate, in at least three independent experiments. Data obtained from resorufin fluorescence were averaged, normalized to their control values and expressed as cell viability.

Migration assay

Leukemic cells were seeded in 12-well plates (3422, Transwell system, Corning Inc.) and preincubated for 1 h with CBD. Pretreated cells (2×10^5) were placed in 400 µL of serum-free medium in the upper chamber of Transwell inserts (8 µM pore size). Recombinant human CXCL12 (Sigma-Aldrich) was used as a chemoattractant (100 ng/mL) in the lower chamber, filled with complete RPMI (10% FBS) medium. Cells were allowed to migrate over 4 hours. After incubation, insert was removed and cells from the lower chamber were counted, using hemocytometer. Migration was expressed as a percentage of migrated cells in relation to the total cell number.

Cell death analysis

For this assay, Alexa Fluor® 488 Annexin V/Dead Cell Apoptosis Kit (V13241, Thermo Fisher Scientific) was used, following manufacturer specifications. Kit provides a nucleophilic marker (propidium iodide, PI, Ex/Em max = 535/617 nm) as an indicator of plasma membrane damage and Annexin V-Alexa Fluor 488 (Ex/Em max = 488/510 nm), binding to externalized phosphatidylserine (a hallmark of apoptosis). Jurkat cells (10^6/mL) were seeded in a 24 well plate and incubated with or without CBD (0–100 µM) for determined period (2, 4, 6, or 12 h).

After the incubation period, cells were centrifuged (400 × *g*) and washed with cold PBS. Then cells (1×10^6) were resuspended in 100 µL of 1X Annexin V-binding buffer and 5 µL of Annexin V conjugate with 1 µL of PI working solution (200 µg/mL) were added. The mixture was incubated for 20 min at room temperature (protected from light), 200 µL of Annexin V - binding buffer was added and cells were analyzed either by confocal microscopy (LSM 700, Carl Zeiss) or by flow cytometry (FACSCanto II, BD Biosciences).

For confocal microscopy, cells were placed into home-made coverslips-bottomed chambers (poly-L-lysine-coated coverslips were fixed at the bottom of chamber using Dow corning® high vacuum grease). 40×/63x oil-immersion objectives were used. For excitation, 488 nm laser was used for both Alexa Fluor 488 and PI. Raw data were further processed, and images were generated using Zen software (Zeiss).

For flow cytometry analysis, color compensation (Alexa Fluor 488 vs PI) was performed previously to data acquisition. 488 nm laser was used for excitation. PI fluorescence was measured using 556LP mirror and 585/42 filter, Alexa Fluor 488 fluorescence was measured using 502LP mirror and 530/30 filter. Debris and doublets were gated out, and 10,000 events of single cells per sample were collected. Autofluorescence control was used to determine the positive fluorescence threshold. Annexin V^-PI^- populations were classified as healthy, Annexin V^+PI^- as early apoptotic, Annexin V^-PI^+ as primary necrotic, and Annexin V^+PI^+ as necrotic/late apoptotic. Data analysis was performed with FlowJo 10.2 software.

Determination of mitochondrial membrane potential

Jurkat cells (10^6/mL) were double-labeled with MitoTracker™ Green (100 nM, Ex/Em max = 490/518 nm; M7514, Thermo Fisher Scientific) and TMRE (200 nM, Ex/Em max = 555/582 nm; T669, Thermo Fisher Scientific), both from Thermo Fisher Scientific, by incubating over 30 min. After incubation period, cells were centrifuged (400 × *g*, 10 min) and washed with Hanks Balanced Salt Solution (HBSS; NaCl 143 mM, KCl 6 mM, $MgSO_4$ 5 mM, $CaCl_2$ 1 mM, HEPES 20 mM, BSA 0.1%, glucose 5 mM, pH 7.4, ≈300 mOsm) to remove excessive dye. For imaging, cells were placed in home-made coverslips-bottomed chambers and analyzed by confocal microscopy (LSM 700, Carl Zeiss) in a time series mode. Images were acquired every second and raw data were further processed by ImageJ program, where regions of interest (ROI) were defined, based on MitoTracker Green distribution. The fluorescence of each ROI for both dyes (TMRE/MtGr) was then averaged and expressed as a temporal ratio between the fluorescence of each frame and the initial fluorescence (F/F0). To evaluate drugs' effect, CBD (0–100 µM) or FCCP (10 µM; C2920, Merck) were administered, and cells were incubated for 10 min, centrifuged (400 × *g*, 10 min), resuspended in HBSS, and transferred to a 96-well plate. TMRE retention was assessed by measurement of fluorescence intensity, using a GloMax Discover plate reader, by exciting the sample at 549 nm and collecting the emission signal at 575 nm. Data from independent experiments were averaged and the effect of CBD/FCCP was expressed as percentage of TMRE signal in comparison to control.

EYFP-Cyt c transfection

DH5α competent bacteria (18258012, Thermo Fisher Scientific) were transformed by heat shock and EYFP-Cyt-C construct[42] was added and incubated for 14 h at 37 °C in LB agar (22700025, Thermo Fisher Scientific), supplemented with 100 µg/µL of ampicillin (11593027, Thermo Fisher Scientific). Colonies were selected and transferred to supplemented media for further incubation during 14 h for bacterial growth. Plasmid DNA was purified by NucleoBond XtraMidi (740410.10, Macherey-Nagel) kit, and DNA purity and concentration were evaluated spectrophotometrically by absorption at 260/280 nm. For transfection, 10^5 Jurkat cells were starved in Optimem reduced media for 12 h, then exposed to complexes composed by lipofectamine 3000 (L3000015, Thermo Fisher Scientific) and plasmidic DNA (500 ng) and centrifuged (400 × *g*) for 30 min to promote interaction. Transfected cells were incubated at 37 °C, with 5% CO_2 overnight, whereas FBS (10%) was added at the next day. Protein expression was monitored, and experiments were performed 12 h after transfection. Images were acquired using a confocal microscope (LSM 700, Carl Zeiss) equipped with ×40/×63 oil-immersion objectives.

Cyt-C release microscopic assay

Jurkat cells transfected with EYFP-Cyt-C (Ex/Em max = 514/526 nm) were labeled with TMRE (200 nM, 30 min) to confirm mitochondrial EYFP-Cyt-C localization. EYFP-Cyt-C expression and distribution were evaluated in Jurkat cells 12 h after transfection by confocal microscopy. The effect of CBD (30 µM) was monitored in transfected cells incubated for indicated period with the drug. To evaluate the effects of CsA and Ru360, cells were preincubated with one of these drugs for 10 min, followed by treatment with CBD. For data acquisition, cells were placed in home-made coverslips-bottomed chambers. The images were acquired using a confocal microscope (LSM 700, Carl Zeiss), equipped with ×40/×63 oil-immersion objectives.

ROS production

To evaluate ROS production, 2′,7′-Dichlorofluorescin diacetate (DCFDA, D6883, Merck) was used following manufacturer's recommendations. Jurkat cells (10^6/mL)

were loaded with permeable DCFDA (2 μM) for 30 min in HBSS. After this, cells were washed to remove extracellular dye. Cells were resuspended in RPMI1640 medium and allowed to recover and to hydrolyze the AM groups, producing the insoluble form. Culture media was removed, and cells were resuspended in HBSS and treated either with PMA (1 μM, P8139, Merck) as a positive control or with CBD (10 and 30 μM). For data acquisition, cells were placed in home-made coverslips-bottomed chambers. Images were acquired by confocal microscopy (LSM 700, Carl Zeiss), equipped with ×40/×63 oil-immersion objectives and analyzed by ZEN imaging software.

Caspase 3/9 assay

Caspase 3/9 colorimetric assays (K106/119, BioVision) were used following manufacturer's recommendations. Jurkat cells were grown in the presence of vehicle, staurosporine (positive control) or CBD during 12 h. After this period, 10^6 cells from each sample were washed, resuspended in lysis buffer and incubated over 10 min on ice. Then samples were centrifuged (10,000 × *g*, 15 min) and supernatants (cytosolic fraction) were transferred into new tubes. For caspase activity assays, 100 μg of protein (as estimated by BCA protein quantification kit, Merck) from every sample were mixed with 50 μL of reaction buffer (containing 10 mM DTT) and 5 μL (4 mM) of the caspases´ substrates (DEVD-*p*NA for caspase 3, LEHD-*p*NA for caspase 9). Mixtures were incubated for 2 h at 37 °C and placed into a 96-well plate. Absorbance was measured at 405 nm, using a GloMax Discover plate reader. Data from three independent experiments were averaged and normalized in relation to non-treated cells, yielding fold increase in caspase activity.

Transmission electron microscopy

Jurkat cells were treated with CBD (30 μM) for 2 h. Next, control or treated cells were centrifuged (400 × *g*), supernatants were discarded and the pellets were fixed with 2.5% glutaraldehyde and post-fixed in 1% OsO_4 and 0.8% $K_4Fe(CN)_6 \cdot 3H_2O$, and 5 mM Ca^{2+}. Post-fixed cells were dehydrated in acetone and embedded in Epon. Ultrathin sections were stained with uranyl acetate and lead citrate and examined under a JEOL JEM 12 000 EII transmission electron microscope at the Unidad de Imagenología, Instituto de Fisiología Celular (IFC), UNAM, Mexico City.

CEPIA3mt transfection

DH5α competent bacteria (18258012, Thermo Fisher Scientific) were transformed by heat shock and CEPIA3mt/pCMV construct (58219, Addgene) was added[27]. Samples were incubated for 14 h at 37 °C in LB agar (22700025, Thermo Fisher Scientific), supplemented with 100 μg/μl of ampicillin (11593027, Gibco). Colonies were selected and transferred to supplemented media for further incubation during 14 h for bacterial growth. Plasmid DNA was purified by NucleoBond XtraMidi (740410.10, Macherey-Nagel) kit and purity and DNA concentration were determined by spectrophotometry (absorption at 260/280 nm). For the transfection, 10^5 Jurkat cells were starved in Optimem reduced media over 12 h, collected, exposed to complexes of lipofectamine 3000 (L3000015, Thermo Fisher Scientific) and plasmidic DNA (1 μg), and centrifuged (400 × *g*) for 30 min to promote interaction. Cells were incubated at 37 °C with 5% CO_2 overnight, whereas FBS (10%) was added at the next day. Protein expression was monitored, and experiments were performed 24 h after transfection. For confocal imaging, cells were placed in home-made coverslips-bottomed chambers. Images were acquired using a confocal microscope (LSM 700, Carl Zeiss) equipped with ×40/×63 oil-immersion objectives.

Determination of the intracellular free Ca^{2+} concentration

For free $[Ca^{2+}]_i$ measurements, cells were loaded with ratiometric Ca^{2+} indicator Fura-2 (F1201, Thermo Fisher Scientific). Cells were twice washed with PBS and resuspended in a loading solution (HBSS, 0.01% pluronic acid, 2 μM Fura-2/AM), incubated for 30 min at room temperature protected from light, washed, and resuspended in HBSS. Changes in fluorescence were recorded with a F7000 spectrophotometer (Hitachi High-Technologies). Measurements were realized in quartz cuvettes, containing 1.5×10^6 cells/mL. Loaded cells were excited alternately at 340/380 nm and the fluorescence emission was collected every 2 s at 510 nm. Fluorescence was recorded by means of the FL-solutions software. Maximum and minimum free $[Ca^{2+}]$ levels were determined at the end of each experiment by adding 0.3% Triton X-100 and consequent addition of EGTA to a final concentration of 35 mM, respectively. Free $[Ca^{2+}]_i$ was calculated by using the following equation:

$$\left[Ca^{2+}\right]_i = K_d(R - R_{MIN})/(R_{MAX} - R)$$

where R stays for the ratio of fluorescence intensity upon excitation at 340 to that at 380 nm and R_{MIN} and R_{MAX} correspond to maximal and minimal values of this ratio, determined as described above[43].

In some experiments Ca^{2+}-free HBSS was used (NaCl 143 mM, KCl 6 mM, $MgSO_4$ 5 mM, HEPES 20 mM, BSA 0.1%, glucose 5 mM, EGTA 1 mM, pH 7.4, ≈300 mOsm).

Mitochondrial Ca^{2+} measurements

CEPIA3mt (Ex/Em max = 488/510 nm) expression and its mitochondrial localization were confirmed in transfected Jurkat cells, loaded with TMRE, by confocal microscopy (LSM700, Carl Zeiss). For $[Ca^{2+}]_m$

measurements, 10^5 cells (24 h after transfection) were placed in a quartz cuvette and fluorescence was evaluated by spectrofluorometry, using a F7000 HITACHI spectrofluorometer (FL solution software). Samples were excited at 488 nm and fluorescence was measured at 510 nm. $[Ca^{2+}]_m$ was evaluated as fluorescence intensity in relation to the initial fluorescence intensity (F/F0).

Mitochondria isolation

Mitochondria were isolated as reported earlier[39], with some modifications. Jurkat cells were harvested and centrifuged (400 × *g*) at 4 °C for 10 min, washed twice with PBS (pH 7.4) and resuspended in 10x of volume of isolation buffer (IB, HEPES-KOH 20 mM, PMSF 1 mM, sucrose 250 mM, mercaptoethanol 1 mM, EGTA 1 mM, EDTA 1 mM, $MgCl_2$ 1.5 mM, KCl 10 mM). Cells were incubated on ice for 10 min and homogenized with a Dounce homogenizer. Homogenate was then centrifuged at 650 × *g* for 10 min at 4 °C, pellet, containing nuclei, was discarded and the supernatant was collected for a further 12500 × *g* centrifugation for 30 min at 4 °C. Pellet containing the heavy membrane fractions (HMF) was collected and the supernatant was discarded. HMF were washed with IB and resuspended in isotonic sucrose buffer (sucrose 250 mM, EDTA 1 mM, Tris-HCl pH 7.4 10 mM). Homogenate was placed in a discontinuous sucrose gradient (sucrose 1/1.5 M, EDTA 1 mM, Tris-HCl pH 7.4 10 mM) and centrifuged for 25 min at 60,000 × *g*, 4 °C. Mitochondria were collected from the interphase, washed and resuspended in the experimental buffer (KCl 125 mM, KH_2PO_4 1 mM, Tris-HCl 10 mM, glutamate 5 mM, malate 2.5 mM, EGTA 1 mM, $CaCl_2$ 0.7 mM). Isolated mitochondria were suspended in the lysis buffer (Nonidet P-40 0.5% w/v, Tris-HCL 50 mM, NaCl 150 mM, EDTA 1 mM, and PMSM 1 mM) for 1 h and centrifuged at 15000 × *g* for 5 min. The supernatant was collected, and isolation yield was estimated by the protein content (BCA quantification assay). Finally, mitochondrial samples, containing 50 µg of protein, were used in the experiments. To evaluate the purity and integrity of isolated mitochondria, a small fraction was stained with MtGreen (200 nM, Ex/Em max = 490/510 nm; M7514, Thermo Fisher Scientific) as mitochondrial marker, followed by staining with Rhod (2 µM, Ex/Em max = 552/581 nm; R1244, Thermo Fisher Scientific) or TMRE (200 nM, Ex/Em max = 549/575 nm; T669, Thermo Fisher Scientific). Samples were acquired by flow cytometry (FACSCantoII, BD Biosciences) and data were analyzed by FlowJo software.

Ca^{2+} measurement in isolated mitochondria

Freshly isolated mitochondrial samples (50 µg of protein per sample) were incubated with Rhod2 (2 µM) over 30 min, washed by centrifugation (12500 × *g*, 5 min) and resuspended in experimental buffer (KCl 125 mM, KH_2PO_4 1 mM, TrisHCl 10 mM, glutamate 5 mM, malate 2.5 mM, EGTA 1 mM, $CaCl_2$ 0.7 mM). Samples were placed in a quartz cuvette, and fluorescence was evaluated by F7000 spectrophotometer (Hitachi High-Technologies), using excitation at 552 nm and collecting the fluorescence at 581 nm. Data was recorded using the FL-Solution software (Hitachi). $[Ca^{2+}]_m$ change was evaluated by taking fluorescence for each acquisition in relation to the initial fluorescence value, F/F0.

Membrane potential measurements on isolated mitochondria

Isolated mitochondria (50 µg of protein/sample) were stained with TMRE (200 nM; 30 min), treated with CBD (0–60 µM) or FCCP (10 µM) for 10 min, washed, resuspended in experimental buffer (KCl 125 mM, KH_2PO_4 1 mM, TrisHCl 10 mM, glutamate 5 mM, malate 2.5 mM, EGTA 1 mM, $CaCl_2$ 0.7 mM) and placed in a 96-well plate. Fluorescence was assayed using a GloMax Discover plate reader, by exciting the sample at 549 nm and collecting the emission at 575 nm. Data from independent experiments were averaged and the effect of CBD or FCCP on membrane potential value is defined as % of TMRE fluorescence with respect to control.

Detection of autophagic flux by LC3 immunoblotting

During autophagy, the amount of LC3-I decreases and that of LC3-II increases. But at the late phase after autophagolysosome formation LC3-II disappears being degraded by lysosomal proteases. If cells are treated with lysosomal protease inhibitors or with drugs inhibiting autophagosome-lysosome fusion, LC3-II degradation is prevented. Thus, LC3-II amount at a certain time point does *per se* serve a measure of the total autophagic flux. This flux should be more accurately evaluated by comparison of the amount of LC3-II between samples in the presence and absence of lysosomal protease inhibitors or compounds preventing autophagosome-lysosome fusion[15,44]. CQ was shown to prevent autophagosome-lysosome fusion[16] and was used therefore in the present work.

For Western blot analysis, cells after corresponding treatments (CQ, CBD, or CQ and CBD combination) were harvested and lysed with RIPA buffer (Tris-HCl 25 mM, pH 7.6, NaCl 150 mM, EDTA 5 mM, NP-40 1%, sodium deoxycholate 1%, SDS 0.1%), supplemented with protease inhibitors (11697498001, Complete, Roche). For protein quantification, BCA Protein Assay Kit (Sigma) was used. For each sample, 15 µg/line of protein were loaded on a 15% SDS-PAGE gel. After electrophoresis (100 V, ~2 h), proteins were transferred onto PVDF membranes. Membranes were blocked for 1 hour with 5% BSA in TBS Tween-20 buffer (TBS-T) and incubated overnight at 4 °C with anti-human LC3 rabbit antibodies

(Novus-Biologicals, NB100-2220, dilution 1:3000) and mouse monoclonal anti-human GAPDH antibodies (SCBT, sc-47724, dilution 1:1000) as a loading control. As secondary
antibodies, HRP-conjugated goat anti-rabbit IgG (Novus-Biologicals, NBP2-30348H, dilution 1:3000) and HRP-conjugated anti-mouse IgGκ (SCBT, sc-516102, dilution 1:1000) were used for LC3 and GAPDH, respectively. Membranes were incubated with secondary antibodies over 1 h at room temperature, followed by incubation with the ECL detection reagent (Bio-Rad, 170-5061). Protein bands were visualized with Bio-Rad Universal Hood II system and analyzed with Image Lab 5.0 software.

Autophagic flux measurement with mCherry-GFP-LC3

To measure autophagic flux at the single cell level, Jurkat cells, stably expressing tandem mCherry-GFP-LC3, were used[45]. Cells were cultured in the presence of CBD, CQ or their combination for 2, 4, and 24 h. After these periods, cells were collected by centrifugation ($100 \times g$), suspended in PBS and placed in a in home-made coverslips-bottomed chambers for microscopy imaging. Double positive mCherry + /GFP + puncta represented autophagosomes, whereas fusion with the lysosome (autophagolysosomes) caused quenching of the pH-sensitive GFP, resulting in appearance of mCherry + GFP- puncta. CQ prevents GFP quenching by inhibiting autophagosome-lysosome fusion[16]. Samples were analyzed by confocal microscopy (LSM700, Carl Zeiss). Alternatively, custom-made confocal microscope (Solamere Technology Group, Salt Lake City, USA) based on a Yakogawa spindisk confocal scan head (CSUX1M1, Yokogawa Electronic Co., Tokio, Japan), equipped with solid state Coherent Obis lasers (405, 488, 561 and 640 nm) was used. Autophagy flux was evaluated by counting red (mCherry+) and green (GFP+) puncta (0.5–3 μm^2) in the cells. Data analysis was performed using "Particle analysis" tool of ImageJ software, as reported by others[46–48]. Three fields for each condition (10–20 cells/ field) in at least three independent experiments were analyzed. Data are presented as mean of LC3 puncta/ cell or as mean of mCherry/GFP ratio.

Protein-ligand docking

To explore binding sites for CBD within human VDAC1 channel, molecular docking analysis was performed, using Molegro virtual docker 6.0 software. Chemical structure of CBD was obtained from Pubchem (NIH, 644019), whereas hVDAC1 channel structure was downloaded from the protein data bank (PDB, 2JK4). For the beginning, three main cavities for hVDAC1 were defined and explored as possible CBD-interacting sites. MolDock Optimizer was selected as a search algorithm, 20 runs (number of times that the docking is repeated for each ligand) was chosen, and 1000 ligand binding conformations were established. From them, the best 5, based on their docking score (MolDock Score), were selected for each cavity. For all 15 selected binding conformations the contribution of each participating residue in the CBD binding was evaluated (Ligand map > Ligand Energy Inspector). Finally, basing on Total energy/MolDock Score, the best binding conformation was revealed and plotted by creating backbone visualization in the workspace.

Acknowledgements

This study was funded by CONACyT grants 220793 to I.P., FC2015/1-140 to O.D., and PAPIIT IG200119 (DGAPA-UNAM) to A.H.C.; doctoral fellowships (M.O. A., L.T.L. and J.SV.R). We thank Dr. Boehning and Dr. Methner for providing EYFP-Cyt C and CEPIA3mt plasmids, Dr. Thorburn for gifting mCherry-GFP-LC3 expressing Jurkat cells, Dr. Rincón-Heredia and Dr. Díaz for sample preparation and data acquisition by TEM, and Dr. Gómez and Mr. Reyes for their assistance in the docking simulations. Technical assistance of L. Liñan-Rico and M. Flores (University of Colima), Dr. Picones, Dr. Loza, O. Lara, and L. Durán (National Laboratory of Channelopathies) is appreciated.

Conflict of interest

The authors declare that they have no conflict of interest.

Publisher's note

Springer Nature remains neutral with regard to jurisdictional claims in published maps and institutional affiliations.

Supplementary Information accompanies this paper at (https://doi.org/10.1038/s41419-019-2024-0).

Received: 21 May 2019 Revised: 22 August 2019 Accepted: 24 September 2019
Published online: 14 October 2019

References

1. Nguyen, K. et al. Factors influencing survival after relapse from acute lymphoblastic leukemia: a Children's Oncology Group Study. *Leukemia* **22**, 2142–2150 (2008).
2. Bassan, R. & Hoelzer, D. Modern therapy of acute lymphoblastic leukemia. *J. Clin. Oncol.* **29**, 532–543 (2011).
3. Pui, C. H. & Evans, W. E. A 50-year journey to cure childhood acute lymphoblastic leukemia. *Semin. Hematol.* **50**, 185–196 (2013).
4. Raetz, E. A. & Teachey, D. T. T-cell acute lymphoblastic leukemia. *Hematol. Am. Soc. Hematol. Educ. Program.* **2016**, 580–588 (2016).
5. Pui, C. H., Yang, J. J., Bhakta, N. & Galindo, C. Global efforts toward the cure of childhood acute lymphoblastic leukaemia. *Lancet Child Adolesc. Health* **2**, 440–454 (2018).
6. Solinas, M, Cinquina, V. & Parolaro, D. *Cannabidiol and Cancer — An Overview of the Preclinical Data, Molecular Considerations and Evolving Surgical Management Issues in the Treatment of Patients with a Brain Tumor*. Ch. 8. (IntechOpen, London, 2015).
7. Ladin, D. A., Soliman, E., Griffin, L. & Van Dross, R. Preclinical and clinical assessment of cannabinoids as anti-cancer agents. *Front. Pharmacol.* **7**, 361 (2016).
8. Russo, E. B. Cannabidiol claims and misconceptions. *Trends Pharmacol. Sci.* **38**, 198–201 (2017).
9. Massi, P., Solinas, M., Cinquina, V. & Parolaro, D. Cannabidiol as potential anticancer drug. *Br. J. Clin. Pharmacol.* **75**, 303–312 (2013).
10. Yadav, B. D. et al. Heterogeneity in mechanism of emergent resistant in pediatric T-cell acute lymphoblastic leukemia. *Oncotarget* **7**, 58728–58742 (2016).
11. Pitt, L. A. et al. CXCL12-producing vascular endothelial niches control acute T cell leukemia maintenance. *Cancer Cell* **27**, 755–768 (2015).
12. Passaro, D. et al. CXCR4 is required for leukemia-initiating cell activity in T cell acute lymphoblastic leukemia. *Cancer Cell* **27**, 769–779 (2015).

INFORME DE LABORES 2019

13. Galluzzi, L., Pietrocola, F., Levine, B. & Kroemer, G. Metabolic control of autophagy. *Cell* **159**, 1263–1376 (2014).
14. Shrivastava, A., Kuzontkoski, P. M., Groopman, J. E. & Prasad, A. Cannabidiol induces programmed cell death in breast cancer cells by coordinating the cross-talk between apoptosis and autophagy. *Mol. Cancer Ther.* **10**, 1161–1172 (2011).
15. Mizushima, N. & Yoshimori, T. How to interpret LC3 immunoblotting. *Autophagy* **3**, 542–545 (2007).
16. Mauthe, M. et al. Chloroquine inhibits autophagic flux by decreasing autophagosome-lysosome fusion. *Autophagy* **14**, 1435–1455 (2018).
17. Pankiv, S. et al. p62/SQSTM1 binds directly to Atg8/LC3 to facilitate degradation of ubiquitinated protein aggregates by autophagy. *J. Biol. Chem.* **282**, 24131–24145 (2007).
18. Galluzzi, L. et al. Molecular mechanisms of cell death: recommendations of the Nomenclature Committee on Cell Death 2018. *Cell Death Differ.* **25**, 486–541 (2018).
19. Kalenderoglou, N., Macpherson, T. & Wright, K. L. Cannabidiol reduces leukemic cell size - but is it important?. *Front. Pharmacol.* **8**, 144 (2017).
20. Giorgio, V., Guo, L., Bassot, C., Petronilli, V. & Bernardi, P. Calcium and regulation of the mitochondrial permeability transition. *Cell Calcium* **70**, 56–63 (2018).
21. Eskes, R. et al. Bax-induced cytochrome C release from mitochondria is independent of the permeability transition pore but highly dependent on Mg^{2+} ions. *J. Cell Biol.* **143**, 217–224 (1998).
22. Brustovetsky, N., Brustovetsky, T., Jemmerson, R. & Dubinsky, J. M. Calcium-induced cytochrome c release from CNS mitochondria is associated with the permeability transition and rupture of the outer membrane. *J. Neurochem.* **80**, 207–218 (2002).
23. McKallip, R. J. et al. Cannabidiol-induced apoptosis in human leukemia cells: a novel role of cannabidiol in the regulation of p22phox and Nox4 expression. *Mol. Pharmacol.* **70**, 897–908 (2006).
24. Ligresti, A. et al. Antitumor activity of plant cannabinoids with emphasis on the effect of cannabidiol on human breast carcinoma. *J. Pharmacol. Exp. Ther.* **318**, 1375–1387 (2006).
25. Ryan, D., Drysdale, A. J., Lafourcade, C., Pertwee, R. G. & Platt, B. Cannabidiol targets mitochondria to regulate intracellular Ca^{2+} levels. *J. Neurosci.* **29**, 2053–2063 (2009).
26. Orrenius, S., Gogvadze, V. & Zhivotovsky, B. Calcium and mitochondria in the regulation of cell death. *Biochem. Biophys. Res. Commun.* **460**, 72–81 (2015).
27. Giacomello, M. & Pellegrini, L. The coming of age of the mitochondria-ER contact: a matter of thickness. *Cell Death Differ.* **23**, 1417–1427 (2016).
28. Suzuki, J. et al. Imaging intraorganellar Ca^{2+} at subcellular resolution using CEPIA. *Nat. Commun.* **5**, 4153 (2014).
29. Kitamura, Y., Arima, T., Kitayama, Y. & Nomura, Y. Regulation of $[Ca^{2+}]i$ rise activated by doxepin-sensitive H1-histamine receptors in Jurkat cells, cloned human T lymphocytes. *Gen. Pharmacol.* **27**, 285–291 (1996).
30. Rimmerman, N. et al. Direct modulation of the outer mitochondrial membrane channel, voltage-dependent anion channel 1 (VDAC1) by cannabidiol: a novel mechanism for cannabinoid-induced cell death. *Cell Death Dis.* **4**, e949 (2013).
31. Tan, W. & Colombini, M. VDAC closure increases calcium ion flux. *Biochim. Biophys. Acta* **1768**, 2510–2505 (2007).
32. Rizzuto, R., De Stefani, D., Raffaello, A. & Mammucari, C. Mitochondria as sensors and regulators of calcium signaling. *Nat. Rev. Mol. Cell Biol.* **13**, 566–578 (2012).
33. Szabo, I. & Zoratti, M. Mitochondrial channels: ion fluxes and more. *Physiol. Rev.* **94**, 519–608 (2014).
34. Szabadkai, G. et al. Chaperone-mediated coupling of endoplasmic reticulum and mitochondrial Ca^{2+} channels. *J. Cell Biol.* **175**, 901–911 (2006).
35. De Stefani, D., Patron, M. & Rizzuto, R. Structure and function of the mitochondrial calcium uniporter complex. *Biochim. Biophys. Acta* **1853**, 2006–2011 (2015).
36. Colombini, M. Mitochondrial outer membrane channels. *Chem. Rev.* **112**, 6373–6387 (2012).
37. Rezaul, K., Wu, L., Mayva, V., Hwang, S. & Han, D. A systematic characterization of mitochondrial proteome from human T leukemia cells. *Mol. Cell Proteom.* **4**, 169–181 (2005).
38. Jiang, N. et al. Identification of prognosis protein biomarkers in childhood acute lymphoblastic leukemia (ALL). *J. Proteom.* **74**, 843–857 (2011).
39. Prezma, T. et al. VDAC1-based peptides: novel pro-apoptotic agents and potential therapeutics or B-cell chronic lymphocytic leukemia. *Cell Death Dis.* **4**, e809 (2013).
40. Bonora, M. & Pinton, P. The mitocondrial permeability transition pore and cancer: molecular mechanisms involved in cell death. *Front. Oncol.* **4**, 302 (2014).
41. Denton, R. Regulation of mitochondrial dehydrogenases by calcium ions. *Biochim. Biophys. Acta* **1787**, 1309–1316 (2009).
42. Boehning, D. et al. Cytochrome c binds to inositol (1,4,5) trisphosphate receptors, amplifying calcium-dependent apoptosis. *Nat. Cell Biol.* **5**, 1051–1061 (2003).
43. Grynkiewicz, G., Poenie, M. & Tsien, R. Y. A new generation of Ca^{2+} indicators with greatly improved fluorescence properties. *J. Biol. Chem.* **260**, 3440–3450 (1985).
44. Klionsky, D. J. et al. Guidelines for the use and interpretation of assays for monitoring autophagy. *Autophagy* **12**, 443 (2016).
45. Gump, J. M. & Thorburn, A. Sorting cells for basal and induced autophagic flux by quantitative ratiometric flow cytometry. *Autophagy* **10**, 1327–1334 (2014).
46. Zhou, C. et al. Monitoring autophagic flux by an improved tandem fluorescent-tagged LC3 (mTagRFP-mWasabi-LC3) reveals that high-dose rapamycin impairs autophagic flux in cancer cells. *Autophagy* **8**, 1215–1226 (2012).
47. Castillo, K., Valenzuela, V., Oñate, M. & Hetz, C. A molecular reporter for monitoring autophagic flux in nervous system in vivo. *Methods Enzymol.* **588**, 109–131 (2017).
48. Runwal, G. et al. LC3-positive structures are prominent in autophagy-deficient cells. *Sci. Rep.* **9**, 10147 (2019).

INFORME DE LABORES 2019

Behavioural Brain Research 376 (2019) 112193

Contents lists available at ScienceDirect

Behavioural Brain Research

journal homepage: www.elsevier.com/locate/bbr

Artificial taste avoidance memory induced by coactivation of NMDA and β-adrenergic receptors in the amygdala

Daniel Osorio-Gómez[a], Federico Bermúdez-Rattoni[a], Kioko Guzmán-Ramos[b,*]

[a] División de Neurociencias, Instituto de Fisiología Celular, Universidad Nacional Autónoma de México, Circuito Exterior, Ciudad Universitaria, 04510, Mexico City, Mexico

[b] Departamento de Ciencias de la Salud, División de Ciencias Biológicas y de la Salud Universidad Autónoma Metropolitana, Unidad Lerma Av. de las Garzas No. 10, Col. El Panteón, Lerma de Villada, Estado de México, C.P. 52005, Mexico

ARTICLE INFO

Keywords:
Amygdala
Insular cortex
Taste aversion
Glutamate
Memory induction

ABSTRACT

The association between a taste and gastric malaise allows animals to avoid the ingestion of potentially toxic food. This association has been termed conditioned taste aversion (CTA) and relies on the activity of key brain structures such as the amygdala and the insular cortex.

The establishment of this gustatory-avoidance memory is related to glutamatergic and noradrenergic activity within the amygdala during two crucial events: gastric malaise (unconditioned stimulus, US) and the post-acquisition spontaneous activity related to the association of both stimuli. To understand the functional implications of these neurochemical changes on avoidance memory formation, we assessed the effects of pharmacological stimulation of β-adrenergic and glutamatergic NMDA receptors through the administration of a mixture of L-homocysteic acid and isoproterenol into the amygdala after saccharin exposure on specific times to emulate the US and post-acquisition local signals that would be occurring naturally under CTA training. Our results show that activation of NMDA and β-adrenergic receptors generated a long-term avoidance response to saccharin, like a naturally induced rejection with LiCl. Moreover, the behavioral outcome was accompanied by changes in glutamate, norepinephrine and dopamine levels within the insular cortex, analogous to those displayed during memory retrieval of taste aversion memory. Therefore, we suggest that taste avoidance memory can be induced artificially through the emulation of specific amygdalar neurochemical signals, promoting changes in the amygdala-insular cortex circuit enabling memory establishment.

1. Introduction

Classical conditioning has been used as a model to study how neurotransmitters are involved in the acquisition and storage of information [1,2]. The neurochemical basis of memory formation emerged through pharmacological manipulations of receptors' activity before or after the learning phase. However, there is scarce information on how specific neurotransmitters participate in the encoding of both the conditioned stimulus (CS) and the unconditioned stimulus (US), triggering the mechanisms associated with the establishment of memory [3–7].

Taste aversion memory has been widely used as an associative learning paradigm in the search of the neurobiological mechanisms involved in memory processes. Animals' survival depends on their capacity to adapt to the environment by efficiently store the consequences of the ingestion of a specific food; specially the ones that might be toxic, this way, the animal will be able to display an avoidance response to evade aversive outcomes. In order to associate and store these memory traces, appropriate neurochemical representations on key brain structures have been described. Exposure to a novel taste produces increments of dopamine and norepinephrine in both the amygdala and the insular cortex (IC) [3–6]. Conversely, a malaise-inducing agent such as LiCl generates an elevation of glutamate [3,5,8] and norepinephrine [3] within the amygdala, suggesting that these neurotransmitters are related to the signaling of the aversive outcome. Furthermore, taste aversion memory can be enhanced by intra-amygdalar administration of glutamate when a weak US is given (low concentration of LiCl) [9,5]. Blockade of either noradrenergic [10] or glutamatergic [11] receptors within the amygdala before the induction of gastric malaise impairs aversive taste memory establishment. Altogether, this evidence suggests

Abbreviations: CS, conditioned stimulus; CTA, conditioned taste aversion; IC, insular cortex; ISO, isoproterenol; LHa, L-homocysteic acid; MIX, mixture of isoproterenol and homocysteic acid; SS, saline solution; US, unconditioned stimulus

* Corresponding author.
E-mail address: k.guzman@correo.ler.uam.mx (K. Guzmán-Ramos).

https://doi.org/10.1016/j.bbr.2019.112193
Received 22 May 2019; Received in revised form 7 August 2019; Accepted 28 August 2019
Available online 29 August 2019
0166-4328/ © 2019 Elsevier B.V. All rights reserved.

INFORME DE LABORES 2019

that glutamatergic and noradrenergic activity within the amygdala could be related to the encoding of the necessary signals to generate an aversive taste memory trace.

Memory consolidation involves post-acquisition processes whereby newly acquired information is maintained and established into long-term memory [12,13]. As part of these consolidation mechanisms, data suggest that electrical or neurochemical patterns of activity occur during post-acquisition wakefulness and during sleep in the absence of sensory information [3,4,14–17]. In this regard, it has been reported an increase in norepinephrine levels within the amygdala that remained elevated 2 h after inhibitory avoidance training [18]. Particularly, we demonstrated an increase of the extracellular levels of glutamate and norepinephrine within the amygdala [3], and dopamine and glutamate within the IC [4] about 45 min after taste and gastric malaise pairing. These changes of neurotransmitters levels are related to taste aversion consolidation, since amygdalar blockade of N-methyl-D-aspartate (NMDA) and β-adrenergic receptors during the timeframe of reactivation disrupts long-term memory consolidation [3]. Moreover, reversible inactivation of the amygdala at the time of reactivation impedes the release of glutamate and dopamine within the IC and impairs stabilization of conditioned taste aversion (CTA) [4]. These results strongly suggest that the amygdala modulates post-acquisition events within the IC required for CTA memory consolidation [19–21].

The aim of this study was to evaluate the effects of local amygdalar stimulation of noradrenergic β-receptors and glutamatergic NMDA receptors, in pursuance of emulating the neurochemical signals related to the US and to the post-acquisition spontaneous activity; that has been described within this structure during CTA formation and long-term stabilization. Thereby, we administrated a mixture of a NMDA receptor agonist (L-homocysteic acid) and a β-adrenergic receptor agonist (isoproterenol) into the amygdala to mimic the neurochemical signals triggered at different times. In addition, we monitored the neurochemical levels within the IC during memory retrieval as a result of the artificially induced taste avoidance and compared it with a naturally-induced taste aversion retrieval as previously reported [21].

2. Material and methods

2.1. Animals

Two-months old male Wistar rats, weighing 260–280 g at the time of surgery, were used in this study. Animals were obtained from the Instituto de Fisiología Celular animals production facility. Rats were housed individually and maintained on a 12 h light/12 h dark cycle with water and food ad libitum except when noted on the behavioral procedures. All procedures were completed during the light period and were approved by the Animal Care and Ethics Committee of the Instituto de Fisiología Celular (FBR 30-14) in accordance with the National Institutes of Health guidelines.

2.2. Intra-amygdalar drugs administration and taste avoidance assessment

Rats were implanted bilaterally with 12 mm long stainless-steel guide cannulae (23 gauges) directed to the central and basolateral amygdalar nuclei using standard stereotaxic procedures (AP-2.8 mm, L ± 4.8 mm, DV-6.5 mm relative to Bregma, [22]. After six days of surgery recovery, animals were deprived of water for 24 h; rats were allowed to drink 15 mL of tap water from two graded bottles for 15 min between 10:00 and 11:00 in their home cage to obtain a baseline water consumption over 6 days. Additional water access was allowed for 15 min in the afternoon (around 5 pm) to ensure proper hydration of the animals. To diminish handling-associated stress, daily handling was performed during 3 min every day prior to the infusion protocol. All drugs were dissolved in saline solution (0.9% wt/vol). We administered isoproterenol (2 μg/μL, Sigma Aldrich), L-homocysteic acid (18.315 μg/μL, Sigma Aldrich, [23]) or a mixture of isoproterenol and L-homocysteic acid (2 μg/μL; 18.315 μg/μL final concentrations respectively). There is evidence of central and basolateral nuclei participation in taste aversion formation, especially during LiCl administration [3,5,24,25]. Therefore, a total volume of 1 μL was injected per hemisphere in the amygdala (0.5 μL/min); the injector was left for another minute to allow diffusion into the tissue. Drug administration was made through 30-gauge dental needles that protruded 1 mm from the tip of the guide cannulae. Injection needles were connected via polyethylene tubing to two 10-mL Hamilton syringes, driven by an automated micro infusion pump (Carnegie Medicine).

On the acquisition day, rats were divided in 7 groups counterbalanced according to their mean baseline consumption of tap water. Two graded bottles were presented, one with 15 mL of a 0.1% (wt/vol) saccharin solution (Sigma Aldrich) and the other with 15 mL of tap water. Rats were allowed to drink for 15 min. After a 15 min delay, rats received an intra-amygdalar injection and 30 min later rats were infused again according to the administration protocol. Experimental groups were separated as follows (final number of animals on each group is shown): saline solution - saline solution (SS-SS, n = 6); isoproterenol - isoproterenol (ISO - ISO, n = 6); L-homocysteic acid - L-homocysteic acid (LHa-LHa, n = 6); saline solution-mix of isoproterenol and L-homocysteic acid (SS-MIX, n = 6); mix of isoproterenol and L-homocysteic acid-saline solution (MIX-SS, n = 6) and mix of isoproterenol and L-homocysteic acid-mix of isoproterenol and L-homocysteic acid (MIX-MIX, n = 7). We compared the behavioral response of an artificially induced taste avoidance to a naturally induced rejection through gastric malaise caused by LiCl; hence a positive control group received an i.p. injection of LiCl (0.15 M, 7.5 mL/kg) (LiCl 0.15 M, n = 5) 15 min after saccharin acquisition consumption during acquisition. Seventy-two hours after training, all animals could drink from two graded bottles, one with saccharin solution (0.1% (wt/vol) and the other with tap water for 15 min; the consumption measurements of each bottle were obtained. Data is presented as Preference index (Preference index = Saccharin mL / Saccharin mL + tap water mL).

2.3. Collection of cortical neurotransmitters related to an artificially-induced taste avoidance

Unilateral microdialysis cannula (22-gauge, shaft length 14 mm. CMA Microdialysis) aiming the insular cortex (AP + 1.2 mm; L + 5.5 mm; DV -4.5 mm, [22]) and bilateral steel cannulas (12 mm length and 23 gauge) aiming the amygdala (AP -2.8 mm, L ± 4.8 mm, DV −6.5, [22]) were implanted using standard stereotaxic protocols. Six days after surgery, animals were deprived of water for 24 h and placed in the microdialysis chamber during 3 h for six days to let them habituate to the context and constant manipulation. Rats were allowed to drink 30 mL of tap water from a graded bottle for 15 min to obtain a water baseline consumption intake. Microinfused drugs were dissolved in saline solution (0.9% wt/vol) and a total volume of 1 μL was injected per hemisphere in the amygdala (0.5 μL/min) as described above. On the acquisition day, rats were divided into 3 groups counterbalanced according to their mean baseline tap water consumption and were exposed for 15 min to a graded bottle with 30 mL of a 0.1% (wt/vol) saccharin solution. After a 15 min delay, rats received a first intra-amygdalar injection and 30 min later rats were infused again according to the administration protocol. Experimental groups were separated as follows: one group received saline solution-saline solution (SS-SS, n = 8); a second group received a mix of isoproterenol and L-homocysteic acid-mix of isoproterenol and L-homocysteic acid (MIX-MIX, n = 8) and a third group (positive control) that received a LiCl i.p. injection (0.15 M, 7.5 mL/kg) (LiCl 0.15 M, n = 6) 15 min after saccharin consumption.

Seventy-two hours after training, a dialysis probe with a 3 mm membrane (CMA 12 MD Probe, CMA Microdialysis) was connected to the microinfusion pump system (CMA Microdialysis), which infused

artificial cerebrospinal fluid (NaCl 125 mM, KCl 5 mM, $NaH_2PO_4H_2O$ 1.25 mM, $MgSO_4$ •$7H_2O$ 1.5 mM, $NaHCO_3$ 26 mM, $CaCl_2$ 2.5 mM, glucose 10 mM) at a rate of 1 μL/min. After insertion of the probe, 1 h of fluid stabilization was allowed; samples were collected every 4 min in vials containing 1 μL of an antioxidant mixture (0.25 mM ascorbic acid, Na_2EDTA 0.27 mM, 0.1 M acetic acid) and immediately frozen at −80 °C. Three fractions were collected as baseline samples, afterward, a 0.1% (wt/vol) saccharin solution was presented for 15 min. We obtained five more fractions after CS exposure onset. The saccharin consumption was measured during retrieval and it was reported as percentage of consumption of saccharin during the acquisition intake (acquisition consumption percentage = saccharin solution intake during retrieval × 100/saccharin intake during acquisition). During microdialysis experiments, animals were trained and evaluated with one bottle of saccharin to avoid changes in neurotransmitter levels associated with water preference.

2.4. Analysis of glutamate, norepinephrine and dopamine in microdialysis samples

Neurotransmitters levels were determined by capillary electrophoresis. Briefly, microdialysis samples were derivatized with 6 μL of 16.58 mM 3-(2-furoyl) quinoline-2-carboxaldehyde (Molecular Probes, Eugene, OR, USA) in the presence of 2 μL of KCN 25 mM in 10 mM borate buffer (pH 9.2) and 1 μL of internal standard (0.075 mM O-methyl-L-threonine). The mixture was allowed to react in the dark at 65 °C for 15 min. Separation and analysis were conducted in a capillary electrophoresis system (Beckman-Coulter PACE/MDQ, Glycoprotein System, Beckman Coulter, Brea, CA, USA) with laser-induced fluorescence detection; light at 488 nm from an argon ion laser was used to excite the 3-(2-furoyl) quinoline-2-carboxaldehyde-labeled analytes. A micellar electrokinetic chromatography buffer system was used to separate the dialyzed compounds. The borate buffer included 35 mM borates, sodium dodecylsulphate 25 mM, 13% (vol/vol) methanol HPLC grade, final pH 9.6. The samples were injected hydro-dynamically at 0.5 psi for 5 s in a 75 μm i.d. capillary (Beckman Coulter); then the separation was performed at 25 kV. After each sample, the capillary was flushed with 0.1 M NaOH, water and running buffer. The glutamate, norepinephrine and dopamine peaks were identified by matching the migration pattern with those in a spiked sample and corrected by relating the area under the curve of the unknown sample with the area under the curve of the internal standard. Data were analyzed using Karat System Gold (Beckman Coulter). Results are expressed as percentage of basal concentration (percentage of basal concentration = analyte concentration × 100/mean of the three first samples).

2.5. Histology

Cannulae placement was verified at the end of behavioral procedures, animals were sacrificed with an overdose of sodium pentobarbital and transcardially perfused with a physiological saline solution. Brains were removed and stored in paraformaldehyde (4% solution in phosphate buffered saline) for 24 h. After a sucrose gradient treatment, coronal sections of 40 μm were cut and stained with cresyl violet. Samples were then examined under a light microscope to corroborate the correct placement of cannulas; those tips that were not located in the aimed area were removed from the statistical analysis (Fig. 3).

2.6. Statistical analysis

For all experiments, animals were assigned to each treatment group after balancing their average consumption of tap water. Preference consumption indexes were calculated as follows: mL saccharin consumption/mL saccharin + mL tap water consumption. A preference consumption index equal to 0.5 reflects a random choice for saccharin. Preference consumption indexes were analyzed using One-sample Student's *t*-tests compared to a hypothetical value of 0.5 (chance level) to determine taste preference. Additionally, we used a One-way ANOVA with Dunnet's post hoc test to compare preference consumption indexes of the different groups in comparison to the control group and effect size was calculated with Cohen's d. In order to assure that treatments did not cause adipsia or a general reduction in consumption, we compared total fluid intake (mL saccharin + mL tap water) among groups with One-way ANOVA (Fig. 2).

Changes in the extracellular levels of neurotransmitters within the insular cortex were analyzed using Repeated measures ANOVA with Bonferroni post hoc test. For the behavioral response during microdialysis protocol, one-way ANOVA with Dunnet's post hoc test was used to compare avoidance response during test in contrast with the control group. The accepted level of significance was p-value ≤ 0.05. Data are presented as mean ± SEM. Statistical analysis was performed using StatView version 4.57 and graphs were obtained with GraphPad Prism version 6.00, GraphPad software.

3. Results

3.1. Emulation of amygdalar representation of the US and reactivation signals by pharmacological activation of NMDA and β-receptors elicits taste avoidance

From the histological analysis the following rats with cannulae misplacement were removed from results and statistical analysis: ISO-ISO n = 1; MIX-SS n = 2; MIX-MIX n = 1. Fig. 1A represents the behavioral protocol previously described in the methodology. The two-bottle protocol was used because is considered more sensitive since the animals have access to saccharin and water at the same time, enhancing the detection of the avoidance. The animals got accustomed to having two-bottles available for drinking during the baseline monitoring and they alternate between bottles throughout the experiment (Table 1). Table 2 shows the mean consumption of liquid during acquisition and test; no difference on total volume consumption (water + saccharin) was observed among groups during long-term memory test ($F_{6,35}$) = 1.376, p = 0.253). Table 3 shows the raw consumption of the different groups during the long-term memory test; statistical analysis showed significant differences in the saccharin preference among groups ($F_{6,35}$) = 6.629, $p < 0.001$), post hoc analysis revealed that both naturally (LiCl 0.15 M) and artificially induced (MIX-MIX) taste avoidance are reflected as a significantly lower saccharin preference when compared to the SS-SS group ($p < 0.001$, d = 4.721 and p = 0.003, d = 3.461, respectively). The ISO-ISO, LHa-LHa, MIX-SS and SS-MIX groups exhibited a similar saccharin preference compared to SS-SS groups and did not have significant differences (SS-SS vs ISO-ISO p = 0.970, d = 0.367; SS-SS vs Lha-Lha p = 0.269, d = 0.901; SS-SS vs MIX-SS p = 0.995, d = 0.245; SS-SS vs SS-MIX p = 0.854, d = 0.879). Moreover, no differences were observed in saccharin preference between LiCl 0.15 M and MIX-MIX groups (p = 0.807 d = 1.4). The groups LiCl 0.15 M (p = 0.004) and MIX-MIX (p = 0.017) showed preference indexes below chance, indicating a clear avoidance of saccharin, whereas the SS-SS (p = 0.003) and SS-MIX (p = 0.018) groups showed a preference index above chance, demonstrating a predilection for saccharin, hence no avoidance. Therefore, only double intra-amygdalar infusions of a mixture of isoproterenol and L-homocysteic acid, which resemble the US encoding and reactivation signaling, induced a long-term avoidance memory, which is like a naturally developed response after taste and malaise pairing (Fig. 1B).

3.2. Artificially and naturally induced taste avoidance elicit similar neurochemical representations within the insular cortex

During microdialysis experiments (protocol representation in Fig. 2A), regarding extracellular levels of glutamate, repeated measures

INFORME DE LABORES 2019

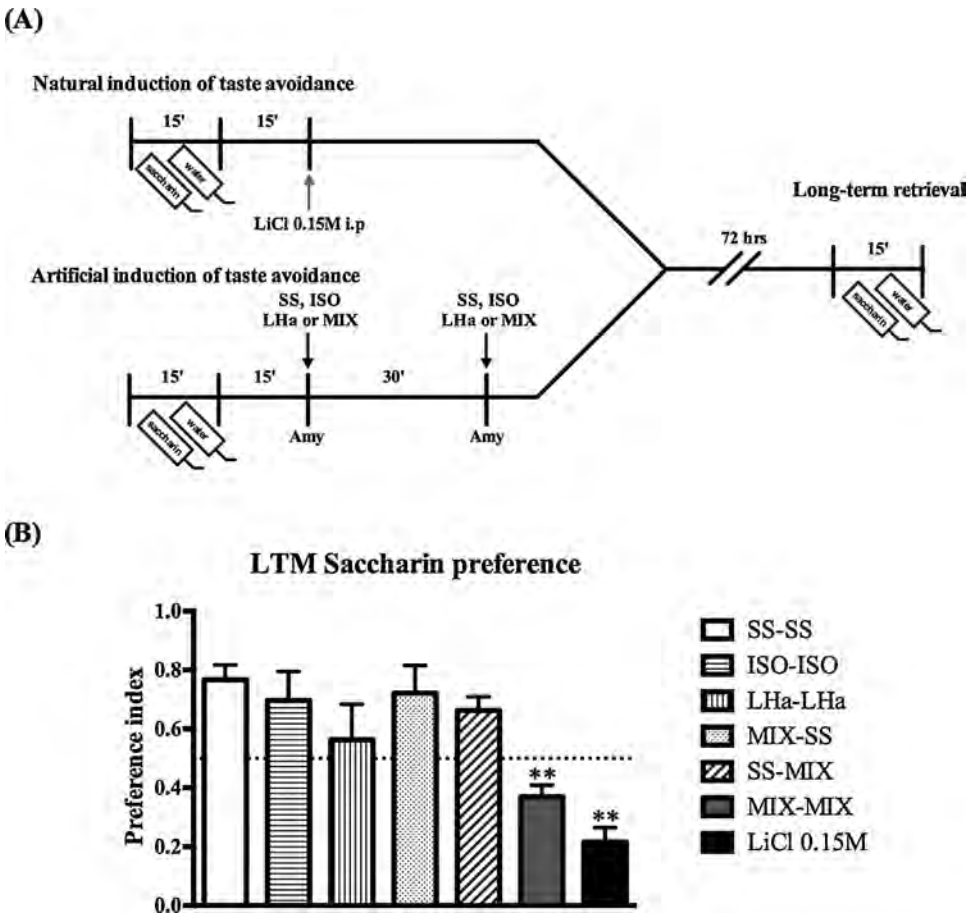

Fig. 1. Effect of pharmacological manipulation in the amygdala over saccharin preference during taste avoidance retrieval. (A) Schematic representation of the behavioral and micro-infusion protocols used. (B) Long-term memory (LTM) for saccharin preference, MIX-MIX and LiCl 0.15 M groups showed reduced preference for saccharin during taste avoidance retrieval, whereas SS-SS, ISO-ISO, LHa-LHa, MIX-SS, and SS-MIX did not. Dark arrows represent micro-infusions into the amygdala (Amy); gray arrow represent LiCl i.p. administration. The graphic is expressed as means of saccharin preference index ± SEM. Dotted line represents consumption on chance level (0.5); ** $p < 0.01$ versus SS-SS group. LHa: L-homocysteic acid; ISO: isoproterenol; MIX: L-homocysteic acid + isoproterenol; SS: saline solution; LTM: Long-term memory.

ANOVA analysis revealed significant differences among fractions ($F_{8,190}$) = 2.232, p = 0.030) and an interaction effect ($F_{16,190}$) = 1.777, p = 0.044) with no groups differences ($F_{2,190}$) = 1.058, p = 0.349). Bonferroni's post hoc test showed that artificially induced avoidance (MIX-MIX) and LiCl 0.15 M groups were different in comparison to SS-SS group at fraction 6 (p = 0.006 and p = 0.028, respectively), i.e., when animals were exposed to the conditioned stimulus during retrieval. Our data demonstrated that a naturally or artificially induced taste avoidance caused a significant augmentation in the extracellular levels of glutamate within the IC during memory retrieval (Fig. 2B).

For norepinephrine release, statistical analysis showed significant differences among fractions ($F_{8,167}$) = 2.117, p = 0.041) with an interaction effect ($F_{16,167}$) = 1.770, p = 0.043), without group effect ($F_{2,167}$) = 0.477, p = 0.621). Bonferroni's post hoc analysis revealed that MIX-MIX ($p < 0.001$) and LiCl 0.15 M ($p < 0.001$) groups were different in comparison to SS-SS group at fraction 6 (saccharin exposure). Therefore, memory retrieval produces an elevation of norepinephrine levels in the IC during both artificial and natural-induced avoidance (Fig. 2C).

Regarding the dopamine release (Fig. 2D), two-way ANOVA revealed differences in dopamine levels among fractions ($F_{8,185}$) = 3.345, p = 0.015) with no group effect ($F_{2,185}$) = 0.414, p = 0.668) and no interaction effect ($F_{16,185}$) = 1.187, p = 0.288). Post-hoc analysis showed that MIX-MIX ($p < 0.001$) and LiCl 0.15 M (p = 0.01) groups were different in comparison to SS-SS group at fraction 6 when the animals were exposed to the conditioned stimulus. We observed a clear increase in dopamine extracellular levels within the IC when animals were exposed to the saccharin after artificial or natural induced avoidance.

In the behavioral assessment of these animals we observed significant differences in saccharin consumption during taste avoidance retrieval among groups ($F_{2,18}$) = 6.017, p = 0.039), post hoc analysis showed that saccharin consumption in LiCl 0.15 M (p = 0.021, d = 1.89) and MIX-MIX (p = 0.044, d = 1.046) groups were different from SS-SS group, whereas no difference was observed between LiCl 0.15 M and MIX-MIX groups (p = 0.588, d = 0.290) (Fig. 2E).

4. Discussion

During the last decades, memory research has focused on how cellular and molecular mechanisms are involved in the codification and consolidation of memory. In CTA memory establishment, the amygdalar glutamatergic activity has been related to visceral signaling of the US [3,5,8,11,25]; whereas noradrenergic transmission is probably implicated with a stress response due to the administration of the malaise-inducing agent [3]. Specifically, β-adrenergic and NMDA receptors within the amygdala play an essential role in the US processing [5,9–11]. However, it has been reported that microinfusions of glutamate into the amygdala did not generate taste aversion or avoidance, unless it was paired with a subthreshold dose of LiCl [10,5]. Our experiments confirm that concomitant activation of β-adrenergic and NMDA receptors at 15 min post-intake is not enough to induce an avoidance response during retrieval, and subsequent reactivation of these receptors appears to prompt the long-term memory.

Long-term memory stabilization involves post-acquisition reactivation patterns of activity [17] that can be reflected as extracellular changes in neurotransmitters after the CS-US pairing [3,4]. Coactivation of NMDA and β-adrenergic receptors during the post-acquisition reactivation timeframe has demonstrated to be necessary for taste aversion memory consolidation within the amygdala [3]. The present results further support the idea that glutamatergic and noradrenergic activities during the post-acquisition period are part of the

Table 1
Mean consumption ± standard error of the two bottles presented throughout the experiments.

mL of liquid intake												
Day 1		Day 2		Day 3		Day 4		Acquisition		Test		
Bottle 1	Bottle 2	Bottle 1	Bottle 2	Bottle 1	Bottle 2	Bottle 1	Bottle 2	Saccharin	Water	Saccharin	Water
6.11 ± 0.84	9.66 ± 0.66	7.28 ± 0.81	9.29 ± 0.61	8.53 ± 0.65	9.16 ± 0.59	11.07 ± 0.74	8.57 ± 0.47				

mL of liquid intake												
Day 5		Day 6		Acquisition		Test						
Bottle 1	Bottle 2	Bottle 1	Bottle 2	Saccharin	Water	Saccharin	Water					
8.01 ± 0.82	10.79 ± 0.88	11.55 ± 0.87	8.012 ± 0.82	9.14 ± 0.74	8.41 ± 0.68	10.51 ± 0.68	8.04 ± 0.75					

Table 2
Total fluid intake during acquisition and test stages. (Mean ± standard error).

Group	Consumption during acquisition (mL)	Consumption during test (mL)
SS-SS	17.50 ± 2.48	17.50 ± 2.50
ISO-ISO	18.17 ± 1.37	18.00 ± 1.52
LHa-LHa	16.83 ± 1.22	17.33 ± 1.45
MIX-SS	17.17 ± 1.24	16.33 ± 1.60
SS-MIX	19.00 ± 1.15	22.17 ± 1.55
MIX-MIX	16.14 ± 1.68	21.29 ± 1.01
LiCl 0.15 M	18.33 ± 1.99	16.83 ± 0.94
SS-SS	17.50 ± 2.48	17.50 ± 2.50
ISO-ISO	18.17 ± 1.37	18.00 ± 1.52
LHa-LHa	16.83 ± 1.22	17.33 ± 1.45
MIX-SS	17.17 ± 1.24	16.33 ± 1.60
SS-MIX	19.00 ± 1.15	22.17 ± 1.55
MIX-MIX	16.14 ± 1.68	21.29 ± 1.01
LiCl 0.15 M	18.33 ± 1.99	16.83 ± 0.94
SS-SS	17.50 ± 2.48	17.50 ± 2.50
ISO-ISO	18.17 ± 1.37	18.00 ± 1.52
LHa-LHa	16.83 ± 1.22	17.33 ± 1.45
MIX-SS	17.17 ± 1.24	16.33 ± 1.60
SS-MIX	19.00 ± 1.15	22.17 ± 1.55
MIX-MIX	16.14 ± 1.68	21.29 ± 1.01
LiCl 0.15 M	18.33 ± 1.99	16.83 ± 0.94

Table 3
Mean consumption ± standard error and preference index values during test.

Group	Saccharin consumption (mL) during test	Water consumption (mL) during test	Preference index
SS-SS	12.83 ± 1.24	4.66 ± 1.38	0.76 ± 0.05
ISO-ISO	12.17 ± 1.53	5.83 ± 2.023	0.69 ± 0.09
Lha-Lha	9.83 ± 2.12	7.5 ± 2.094	0.56 ± 0.12
MIX-SS	11.67 ± 1.68	4.66 ± 1.94	0.72 ± 0.09
SS-MIX	14.33 ± 0.42	7.83 ± 1.64	0.66 ± 0.04
MIX-MIX	8.00 ± 1.17	13.29 ± 0.68	0.36 ± 0.04 **
LiCl	5.16 ± 1.60	11.67 ± 1.46	0.29 ± 0.09**

** $p < 0.01$ vs SS-SS. Preference index = Sac mL/(Sac mL + H_2O mL).

neurobiological mechanisms involved in the consolidation of taste aversive memory. According to our observations, it is indispensable to generate both the US signaling and the post-acquisition signaling in the amygdala to induce a reliable taste avoidance response reflecting or representing the establishment of a taste memory trace. Therefore, it is possible that US signaling through the activation of NMDA and β-adrenergic receptors initiates molecular pathways involved in synaptic modifications, whereas post-learning reactivation activity patterns underlies long-term memory persistence.

Although the period between administrations was calculated according to the US and post-acquisition events reported previously, it is possible that kinetics of drug's action may be altered by the co-administration of isoproterenol and LHa. It has been reported that isoproterenol promotes LHa release from astrocytes, as it is an endogenous excitatory aminoacid [26]. Therefore, it is possible that β-adrenergic activation leads to a higher concentration of LHa within the amygdala altering the kinetics of NMDA activation.

The activation of β-adrenergic and NMDA receptors leads to a synergistic effect for the establishment of taste avoidance memory. It has been demonstrated that synaptic plasticity is facilitated by β-adrenergic activation, probably as a result of the enhancement of P/Q type calcium currents in amygdalar neurons, generating an increase in intracellular calcium levels [27]. In addition, isoproterenol enhances synaptic transmission through an increase in presynaptic Ca^{2+} influx in the amygdala [28], producing a higher response mediated by AMPA [27] and NMDA currents [29]. Activation of β-adrenergic receptors

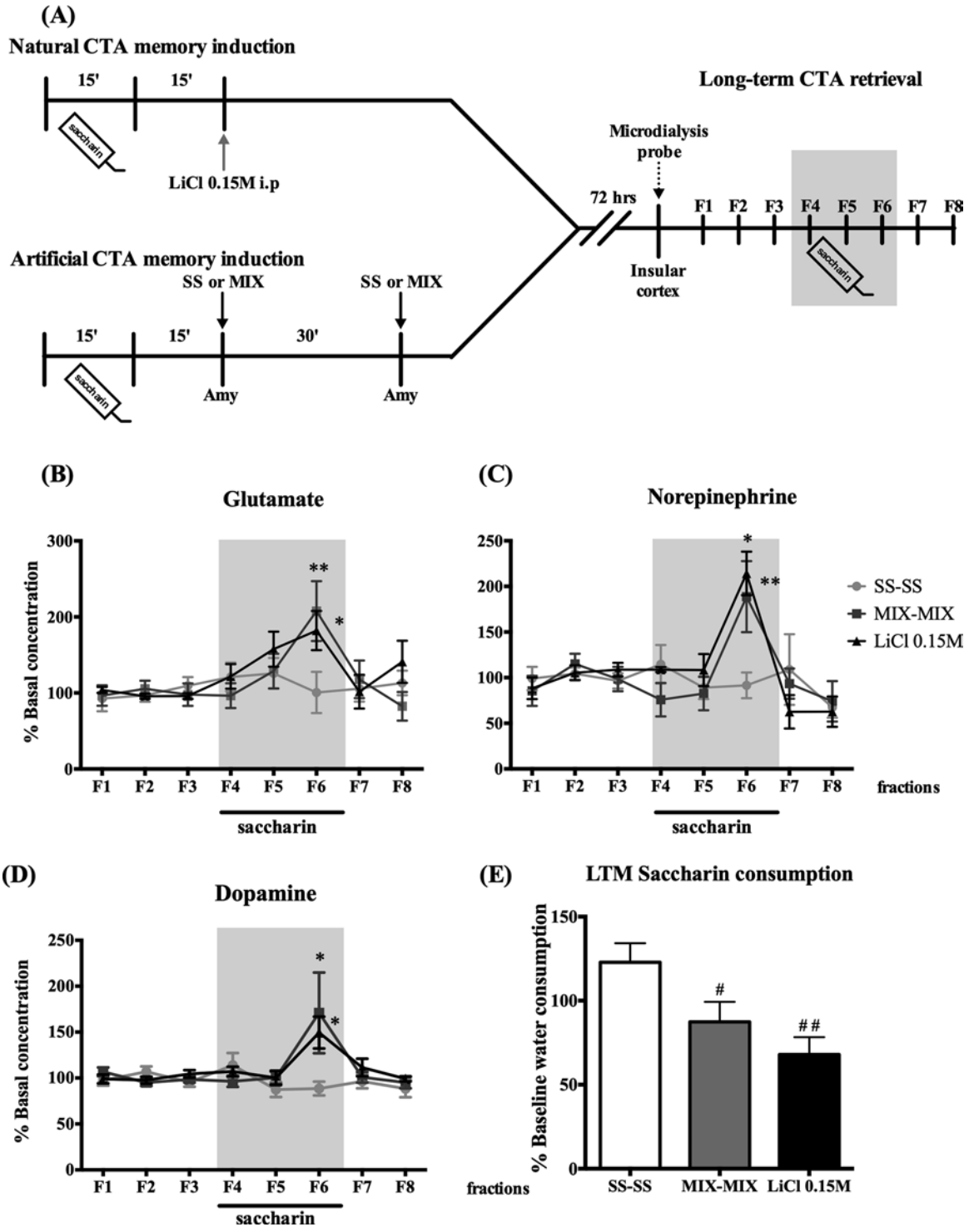

Fig. 2. Taste avoidance responses and extracellular levels of glutamate, norepinephrine, and dopamine in the insular cortex during taste avoidance retrieval. (A) Schematic representation of the microdialysis protocol used. Changes in (B) glutamate, (C) norepinephrine, and (D) dopamine levels in SS-SS, LiCl 0.15 M and MIX-MIX groups during retrieval of either naturally or artificially induced avoidance. Exposure to saccharin elicits an augmentation in glutamate, norepinephrine, and dopamine in the LiCl 0.15 M and MIX-MIX groups during taste avoidance retrieval. (E) Saccharin consumption during microdialysis procedure as percentage of the first saccharin exposure. MIX-MIX and LiCl 0.15 M groups display a taste avoidance response during memory retrieval. Dark arrows represent micro-infusions into the amygdala (Amy); gray arrow represents LiCl i.p. administration; and dotted arrow represent the insertion of the microdialysis probe in the insular cortex. Graphics are expressed as means of percentage of basal concentration ± SEM. (∗) $p < 0.05$ and (∗∗) $p < 0.01$ versus SS-SS group. Behavioral response graph is expressed as the mean of percentage of saccharin intake during acquisition phase ± SEM. (#) $p < 0.05$ versus SS-SS group. MIX: L-homocysteic acid + isoproterenol; SS: saline solution. LTM: Long-term memory.

promotes the stimulation of adenylate cyclase that triggers cAMP formation and subsequent activation of cyclic-AMP-dependent kinase (PKA) and mitogen-activated protein kinase (MAPK) [30]. The activated PKA phosphorylates many synaptic and intracellular targets including cAMP response element binding pathway (CREB) [31,32]. The β-adrenergic activation causes the strengthening of intracellular

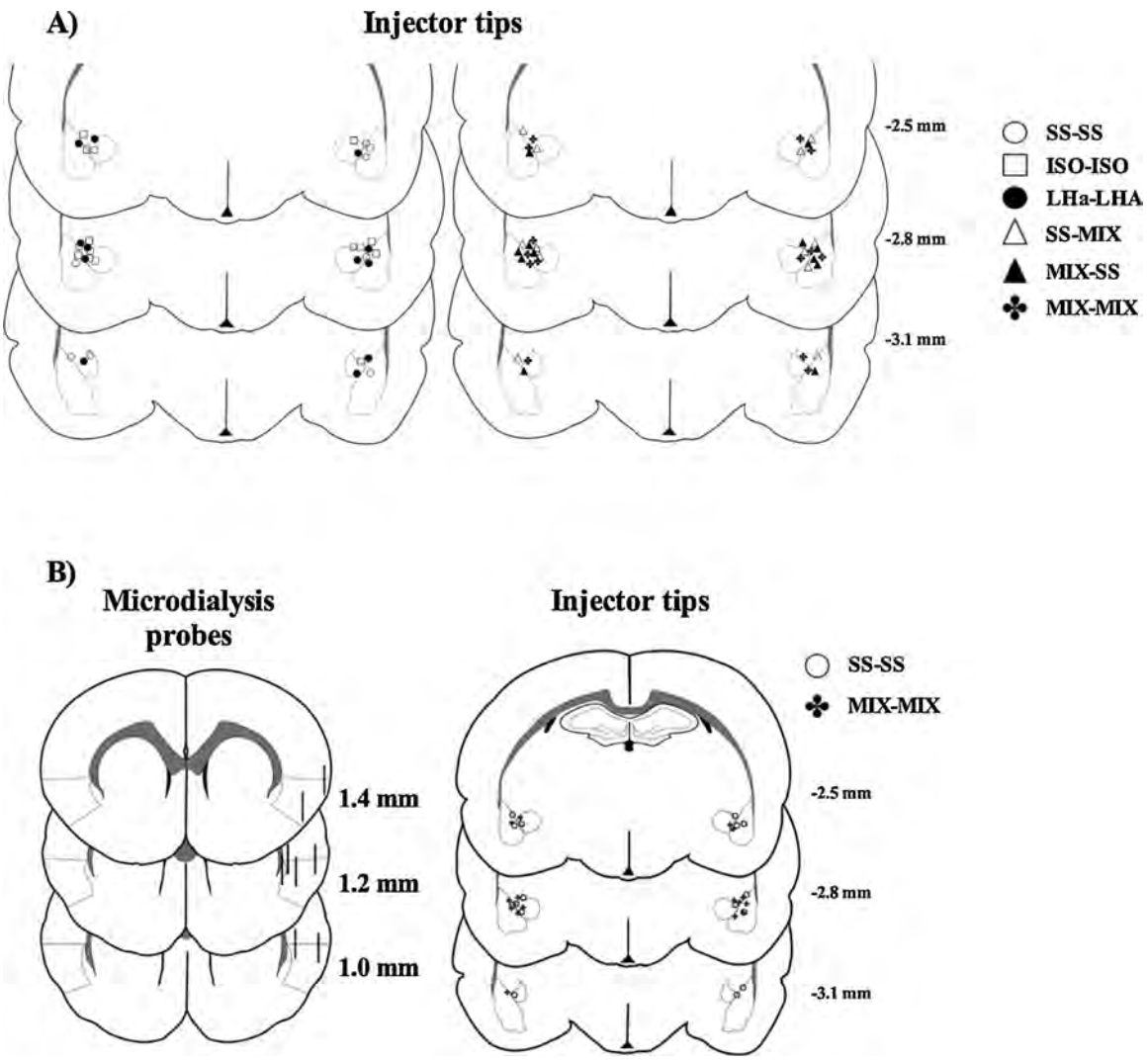

Fig. 3. Summary of injector tips and microdialysis probes. (A) Representation of the tips of the injectors aiming the amygdala in the pharmacological activation experiment. (B) Representation of the tips of the injectors aiming the amygdala and the microdialysis probes within the insular cortex.

processes, resulting in a greater response to a given input, in this case the activation of glutamatergic receptors. PKA also facilitates AMPA receptors trafficking [33] and phosphorylation of NMDA receptors by PKA enhances Ca^{2+} conductivity [34,35]. The increased intracellular flow of Ca^{2+} promotes the activation of adenylate cyclase through calcium / calmodulin kinase by improving cAMP production [36] and the subsequent intracellular events described before. Therefore, the synergistic activation of adenylate cyclase, as a consequence of the activation of β-adrenergic receptors and NMDA, improves the activity of MAPK, CREB and transcription factors; that determine in a coordinated way the transcription and translation of genes. All these processes culminate in the increase in protein synthesis required for neuronal remodeling within the neural networks necessary to acquire and consolidate taste avoidance memories [37].

In this regard, it has been proposed that a single molecular event triggered during acquisition may not be sufficient to maintain long-term memory; and the persistence of memory requires rounds of consolidation-like processes during different time windows [38–41]. Therefore, we suggest that emulation of US amygdalar events is necessary to initiate the molecular pathways involved in modifications of the amygdala-insular network and the coactivation of NMDA and β-adrenergic receptors during the post-learning period facilitates the taste avoidance memory consolidation through protein synthesis-dependent mechanisms.

Although unspecific modifications between the amygdala and different brain structures could be induced by our pharmacological manipulations, we focused on the response in the IC considering that taste aversion memory involves the functional integrity of this structure [42–46]; it is also possible that the communication of the amygdala-insular cortex had been modified affecting the trace of the taste in a way that an avoidance response is displayed in a second encounter.

The amygdala has afferents to the IC [47,48] and receives feedback information from the insula [49]. The functional connectivity between the amygdala and the IC has been demonstrated by the tetanic stimulation of the amygdala that generates a long-term potentiation in the IC, promoting an improved retention of CTA [19,50]. Although the amygdala-IC pathway appears to be predominantly glutamatergic [9,43,50], it can also be modulated by dopaminergic activity from the ventral area tegmental [51], and norepinephrine from the locus coeruleus [52]. During the time frame following the acquisition of CTA, levels of dopamine and glutamate involved in the maintenance of long-term memory also increase within the IC. Interestingly, when the amygdala is transiently inactivated, there is an impairment of the reactivation signaling within the IC and CTA memory consolidation [4]. All these results suggest that the interaction of the amygdala-IC plays an important role in the formation and stabilization of taste memories where an aversive outcome is avoided.

Recently, it has been demonstrated that during the taste aversion

INFORME DE LABORES 2019

retrieval, the presentation of a CS stored as aversive induces an elevation of glutamate, dopamine and norepinephrine levels within the IC [21]. As shown, the artificial induction of taste avoidance promoted a similar increase in glutamate during memory retrieval. Glutamatergic neurotransmission seems to be relevant for the retrieval and maintenance of CTA since the infusions of α-amino-3-hidroxi-5-metilo-4-isoxazolpropionic (AMPA) receptor antagonists in the IC hinders taste aversion retrieval [21,53]. Moreover, the presentation of an aversive or stressful stimulus causes an increase in norepinephrine levels in the forebrain [54], including the IC [55]. Similarly, injections of the malaise-inducing agent (the US) induce an increase in norepinephrine levels within the IC [4]. Thus, exposure to an aversively-conditioned taste stimulus generates an elevation of norepinephrine within the IC as reported previously [56]. In relation to dopamine release, a novel or salient stimulus cause activation of dopaminergic neurons [57,58]. Hence, consumption of an aversively conditioned taste stimulus promotes an increase in dopamine levels within the IC. This elevation of dopamine probably reflects the response to the salient stimulus generated by the relevance of the aversive taste. Therefore, the consumption of a taste stimulus associated with aversive signals, artificially stimulated or naturally associated with gastric malaise, produces an elevation of the extracellular levels of glutamate, norepinephrine and dopamine inside the IC. Our results demonstrate that the pharmacological activation of NMDA and β-adrenergic receptors in the amygdala could induce behavioral and neurochemical responses like a naturally-induced taste avoidance memory.

Even though other neurotransmitter systems are involved in CTA formation, such as acetylcholine [59,60], cortical extracellular changes of this neurotransmitter have been related mostly to the novelty of the stimulus [6] and apparently is not required during CTA retrieval [59,61]. Other monoamines, such as serotonin participate in the CTA formation within the IC or the amygdala, but have been less studied during the retrieval phase in the amygdala [62] or the insular cortex [63].

5. Conclusion

The confirmation of the functional role of the neurochemical signals that have been described during and after the acquisition of an aversive taste memory allow us to better understand the mechanisms that underly memory formation. We suggest that the induction of an artificial taste aversion memory, through pharmacological activation of NMDA and β-adrenergic receptors within the amygdala, promotes changes in the amygdala-insular cortex circuit enabling aversive memory establishment. It is important to note that during memory retrieval, behavioral and neurotransmitters patterns response within the IC are indistinguishable from an artificially induced or true avoidance memory.

Author contributions

Conceptualization and writing DOG, FBR, KGR; data curation and methodology DOG and KRG; funding acquisition FBR and KGR.

The authors declare no competing financial interests to disclose.

Funding and disclosures

This work was supported by CONACyT (CB-250870), DGAPA PAPIIT-UNAM (IN212919), FOSSIS-CONACyT (273308) and SEP-PROMEP (UAM-PTC-585) grants.

Acknowledgments

Authors thank Dr. Luis Rodríguez-Durán for his technical assistance. Special thanks to Auraly Axell Luyen Díaz and Luz del Carmen Medellín Cruz for their excellent assistance during the experiments.

References

[1] E.R. Kandel, T. Abrams, L. Bernier, T.J. Carew, R.D. Hawkins, J.H. Schwartz, Classical conditioning and sensitization share aspects of the same molecular cascade in Aplysia, Cold Spring Harb. Symp. Quant. Biol. 48 (1983) 821–830, https://doi.org/10.1101/SQB.1983.048.01.085.

[2] J. Lisman, K. Cooper, M. Sehgal, A.J. Silva, Memory formation depends on both synapse-specific modifications of synaptic strength and cell-specific increases in excitability, Nat. Neurosci. 21 (2018) 309–314, https://doi.org/10.1038/s41593-018-0076-6.

[3] K. Guzmán-Ramos, D. Osorio-Gómez, P. Moreno-Castilla, F. Bermúdez-Rattoni, Post-acquisition release of glutamate and norepinephrine in the amygdala is involved in taste-aversion memory consolidation, Learn. Mem. 19 (2012) 231–238, https://doi.org/10.1101/lm.024703.111.

[4] K. Guzmán-Ramos, D. Osorio-Gómez, P. Moreno-Castilla, F. Bermúdez-Rattoni, Off-line concomitant release of dopamine and glutamate involvement in taste memory consolidation, J. Neurochem. 114 (2010) 226–236, https://doi.org/10.1111/j.1471-4159.2010.06758.x.

[5] M.I. Miranda, G. Ferreira, L. Ramirez-Lugo, F. Bermudez-Rattoni, Glutamatergic activity in the amygdala signals visceral input during taste memory formation, Proc. Natl. Acad. Sci. U. S. A. 99 (2002) 11417–11422, https://doi.org/10.1073/pnas.182200499.

[6] M.I. Miranda, L. Ramírez-Lugo, F. Bermúdez-Rattoni, Cortical cholinergic activity is related to the novelty of the stimulus, Brain Res. 882 (2000) 230–235.

[7] G.L. Quirarte, R. Galvez, B. Roozendaal, J.L. McGaugh, Norepinephrine release in the amygdala in response to footshock and opioid peptidergic drugs, Brain Res. 808 (1998) 134–140.

[8] S. Tucci, P. Rada, L. Hernandez, Role of glutamate in the amygdala and lateral hypothalamus in conditioned taste aversion, Brain Res. 813 (1998) 44–49.

[9] G. Ferreira, M.I. Miranda, V. De la Cruz, C.J. Rodríguez-Ortiz, F. Bermúdez-Rattoni, Basolateral amygdala glutamatergic activation enhances taste aversion through NMDA receptor activation in the insular cortex, Eur. J. Neurosci. 22 (2005) 2596–2604, https://doi.org/10.1111/j.1460-9568.2005.04440.x.

[10] M.I. Miranda, R.T. LaLumiere, T.V. Buen, F. Bermudez-Rattoni, J.L. McGaugh, Blockade of noradrenergic receptors in the basolateral amygdala impairs taste memory, Eur. J. Neurosci. 18 (2003) 2605–2610.

[11] Y. Yasoshima, T. Morimoto, T. Yamamoto, Different disruptive effects on the acquisition and expression of conditioned taste aversion by blockades of amygdalar ionotropic and metabotropic glutamatergic receptor subtypes in rats, Brain Res. 869 (2000) 15–24.

[12] J.L. McGaugh, Memory–a century of consolidation, Science 287 (2000) 248–251.

[13] J.L. McGaugh, Time-dependent processes in memory storage, Science 153 (1966) 1351–1358.

[14] S. Deyama, T. Katayama, N. Kondoh, T. Nakagawa, S. Kaneko, T. Yamaguchi, M. Yoshioka, M. Minami, Role of enhanced noradrenergic transmission within the ventral bed nucleus of the stria terminalis in visceral pain-induced aversion in rats, Behav. Brain Res. 197 (2009) 279–283, https://doi.org/10.1016/j.bbr.2008.08.024.

[15] G.B. Feld, J. Born, Sculpting memory during sleep: concurrent consolidation and forgetting, Curr. Opin. Neurobiol. 44 (2017) 20–27, https://doi.org/10.1016/j.conb.2017.02.012.

[16] D.J. Foster, M.A. Wilson, Reverse replay of behavioural sequences in hippocampal place cells during the awake state, Nature 440 (2006) 680–683, https://doi.org/10.1038/nature04587.

[17] K.L. Hoffman, B.L. McNaughton, Coordinated reactivation of distributed memory traces in primate neocortex, Science 297 (2002) 2070–2073, https://doi.org/10.1126/science.1073538.

[18] C.K. McIntyre, T. Hatfield, J.L. McGaugh, Amygdala norepinephrine levels after training predict inhibitory avoidance retention performance in rats, Eur. J. Neurosci. 16 (2002) 1223–1226.

[19] M.L. Escobar, V. Chao, F. Bermúdez-Rattoni, In vivo long-term potentiation in the insular cortex: NMDA receptor dependence, Brain Res. 779 (1998) 314–319.

[20] S.E. Grossman, A. Fontanini, J.S. Wieskopf, D.B. Katz, Learning-related plasticity of temporal coding in simultaneously recorded amygdala-cortical ensembles, J. Neurosci. 28 (2008) 2864–2873, https://doi.org/10.1523/JNEUROSCI.4063-07.2008.

[21] D. Osorio-Gómez, K. Guzmán-Ramos, F. Bermúdez-Rattoni, Memory trace reactivation and behavioral response during retrieval are differentially modulated by amygdalar glutamate receptors activity: interaction between amygdala and insular cortex, Learn. Mem. 24 (2017) 14–23, https://doi.org/10.1101/lm.042895.116.

[22] G. Paxinos, C. Watson, The Rat Brain in Stereotaxic Coordinates, 4th ed., Academic Press, San Diego, CA, 1998.

[23] J.P. Johansen, H.L. Fields, Glutamatergic activation of anterior cingulate cortex produces an aversive teaching signal, Nat. Neurosci. 7 (2004) 398–403, https://doi.org/10.1038/nn1207.

[24] J. St. Andre, K. Albanos, S. Reilly, C-fos expression in the rat brain following lithium chloride induced-illness, Brain Res. 1135 (2007) 122–128, https://doi.org/10.1016/j.brainres.2006.12.010.

[25] T. Yamamoto, N. Sako, N. Sakai, A. Iwafune, Gustatory and visceral inputs to the amygdala of the rat: conditioned taste aversion and induction of c-fos-like immunoreactivity, Neurosci. Lett. 226 (1997) 127–130, https://doi.org/10.1016/S0304-3940(97)00265-6.

[26] K.Q. Do, B. Benz, O. Sorg, L. Pellerin, P.J. Magistretti, Beta-Adrenergic stimulation promotes homocysteic acid release from astrocyte cultures: evidence for a role of astrocytes in the modulation of synaptic transmission, J. Neurochem. 68 (1997)

2386–2394, https://doi.org/10.1046/j.1471-4159.1997.68062386.x.
[27] L. Liebmann, H. Karst, M. Joëls, Effects of corticosterone and the beta-agonist isoproterenol on glutamate receptor-mediated synaptic currents in the rat basolateral amygdala, Eur. J. Neurosci. 30 (2009) 800–807, https://doi.org/10.1111/j.1460-9568.2009.06882.x.
[28] C.C. Huang, K.S. Hsu, P.W. Gean, Isoproterenol potentiates synaptic transmission primarily by enhancing presynaptic calcium influx via P- and/or Q-type calcium channels in the rat amygdala, J. Neurosci. 16 (1996) 1026–1033.
[29] C.C. Huang, C.H. Lin, P.W. Gean, Potentiation of N-methyl-D-aspartate currents by isoproterenol in the acutely dissociated rat amygdalar neurons, Neurosci. Lett. 253 (1998) 9–12, https://doi.org/10.1016/s0304-3940(98)00571-0.
[30] C.B. Sindreu, Z.S. Scheiner, D.R. Storm, Ca2+ -stimulated adenylyl cyclases regulate ERK-dependent activation of MSK1 during fear conditioning, Neuron 53 (2007) 79–89, https://doi.org/10.1016/j.neuron.2006.11.024.
[31] B. Ferry, B. Roozendaal, J.L. McGaugh, Basolateral amygdala noradrenergic influences on memory storage are mediated by an interaction between beta- and alpha1-adrenoceptors, J. Neurosci. 19 (1999) 5119–5123.
[32] K.C. Liang, J.L. McGaugh, H.Y. Yao, Involvement of amygdala pathways in the influence of post-training intra-amygdala norepinephrine and peripheral epinephrine on memory storage, Brain Res. 508 (1990) 225–233.
[33] E.M. Snyder, M. Colledge, R.A. Crozier, W.S. Chen, J.D. Scott, M.F. Bear, Role for A kinase-anchoring proteins (AKAPS) in glutamate receptor trafficking and long term synaptic depression, J. Biol. Chem. 280 (2005) 16962–16968, https://doi.org/10.1074/jbc.M409693200.
[34] V.A. Skeberdis, V. Chevaleyre, C.G. Lau, J.H. Goldberg, D.L. Pettit, S.O. Suadicani, Y. Lin, M.V.L. Bennett, R. Yuste, P.E. Castillo, R.S. Zukin, Protein kinase A regulates calcium permeability of NMDA receptors, Nat. Neurosci. 9 (2006) 501–510, https://doi.org/10.1038/nn1664.
[35] W.G. Tingley, M.D. Ehlers, K. Kameyama, C. Doherty, J.B. Ptak, C.T. Riley, R.L. Huganir, Characterization of protein kinase A and protein kinase C phosphorylation of the N-methyl-D-aspartate receptor NR1 subunit using phosphorylation site-specific antibodies, J. Biol. Chem. 272 (1997) 5157–5166.
[36] D.M. Chetkovich, J.D. Sweatt, NMDA receptor activation increases cyclic AMP in area CA1 of the hippocampus via calcium/calmodulin stimulation of adenylyl cyclase, J. Neurochem. 61 (1993) 1933–1942, https://doi.org/10.1111/j.1471-4159.1993.tb09836.x.
[37] A. Yiannakas, K. Rosenblum, The insula and taste learning, Front. Mol. Neurosci. 10 (2017) 335, https://doi.org/10.3389/fnmol.2017.00335.
[38] P. Bekinschtein, M. Cammarota, L.M. Igaz, L.R.M. Bevilaqua, I. Izquierdo, J.H. Medina, Persistence of long-term memory storage requires a late protein synthesis- and BDNF- dependent phase in the hippocampus, Neuron 53 (2007) 261–277, https://doi.org/10.1016/j.neuron.2006.11.025.
[39] L.M. Igaz, M.R.M. Vianna, J.H. Medina, I. Izquierdo, Two time periods of hippocampal mRNA synthesis are required for memory consolidation of fear-motivated learning, J. Neurosci. 22 (2002) 6781–6789, https://doi.org/10.1523/JNEUROSCI.22-15-06781.2002.
[40] A. Martínez-Moreno, L.F. Rodríguez-Durán, M.L. Escobar, Late protein synthesis-dependent phases in CTA long-term memory: BDNF requirement, Front. Behav. Neurosci. 5 (2011) 61, https://doi.org/10.3389/fnbeh.2011.00061.
[41] L.A. Rodríguez-Blanco, A. Rivera-Olvera, M.L. Escobar, Consolidation of an aversive taste memory requires two rounds of transcriptional and epigenetic regulation in the insular cortex, Behav. Brain Res. 356 (2019) 371–374, https://doi.org/10.1016/j.bbr.2018.09.009.
[42] S.K. Barot, Y. Kyono, E.W. Clark, I.L. Bernstein, Visualizing stimulus convergence in amygdala neurons during associative learning, Proc. Natl. Acad. Sci. U. S. A. 105 (2008) 20959–20963, https://doi.org/10.1073/pnas.0808996106.
[43] F. Bermudez-Rattoni, J.L. McGaugh, Insular cortex and amygdala lesions differentially affect acquisition on inhibitory avoidance and conditioned taste aversion, Brain Res. 549 (1991) 165–170.
[44] J.-Y. Lin, J. Arthurs, S. Reilly, Gustatory insular cortex, aversive taste memory and taste neophobia, Neurobiol. Learn. Mem. 119 (2015) 77–84, https://doi.org/10.1016/j.nlm.2015.01.005.
[45] L. Nerad, V. Ramírez-Amaya, C.E. Ormsby, F. Bermúdez-Rattoni, Differential effects of anterior and posterior insular cortex lesions on the acquisition of conditioned taste aversion and spatial learning, Neurobiol. Learn. Mem. 66 (1996) 44–50.
[46] L.A. Schier, G.D. Blonde, A.C. Spector, Bilateral lesions in a specific subregion of posterior insular cortex impair conditioned taste aversion expression in rats, J. Comp. Neurol. 524 (2016) 54–73, https://doi.org/10.1002/cne.23822.
[47] A. Pitkänen, Connectivity of the rat amygdaloid complex, The Amygdala: A Functional Analysis, Oxford University Press, Oxford, New York, 2000, pp. 31–115.
[48] P. Sah, E.S.L. Faber, M. Lopez De Armentia, J. Power, The amygdaloid complex: anatomy and physiology, Physiol. Rev. 83 (2003) 803–834, https://doi.org/10.1152/physrev.00002.2003.
[49] C.J. Shi, M.D. Cassell, Cortical, thalamic, and amygdaloid connections of the anterior and posterior insular cortices, J. Comp. Neurol. 399 (1998) 440–468.
[50] M.L. Escobar, F. Bermúdez-Rattoni, Long-term potentiation in the insular cortex enhances conditioned taste aversion retention, Brain Res. 852 (2000) 208–212.
[51] J. Kaufling, P. Veinante, S.A. Pawlowski, M.-J. Freund-Mercier, M. Barrot, Afferents to the GABAergic tail of the ventral tegmental area in the rat, J. Comp. Neurol. 513 (2009) 597–621, https://doi.org/10.1002/cne.21983.
[52] J.M. Cedarbaum, G.K. Aghajanian, Afferent projections to the rat locus coeruleus as determined by a retrograde tracing technique, J. Comp. Neurol. 178 (1978) 1–16, https://doi.org/10.1002/cne.901780102.
[53] D.E. Berman, S. Hazvi, V. Neduva, Y. Dudai, The role of identified neurotransmitter systems in the response of insular cortex to unfamiliar taste: activation of ERK1-2 and formation of a memory trace, J. Neurosci. 20 (2000) 7017–7023.
[54] D.A. Morilak, G. Barrera, D.J. Echevarria, A.S. Garcia, A. Hernandez, S. Ma, C.O. Petre, Role of brain norepinephrine in the behavioral response to stress, Prog. Neuropsychopharmacol. Biol. Psychiatry 29 (2005) 1214–1224, https://doi.org/10.1016/j.pnpbp.2005.08.007.
[55] D. Funk, J. Stewart, Role of catecholamines in the frontal cortex in the modulation of basal and stress-induced autonomic output in rats, Brain Res. 741 (1996) 220–229.
[56] D. Osorio-Gómez, K. Guzmán-Ramos, F. Bermúdez-Rattoni, Differential involvement of glutamatergic and catecholaminergic activity within the amygdala during taste aversion retrieval on memory expression and updating, Behav. Brain Res. 307 (2016) 120–125, https://doi.org/10.1016/j.bbr.2016.03.038.
[57] E.S. Bromberg-Martin, M. Matsumoto, O. Hikosaka, Dopamine in motivational control: rewarding, aversive, and alerting, Neuron 68 (2010) 815–834, https://doi.org/10.1016/j.neuron.2010.11.022.
[58] M.A. Ungless, Dopamine: the salient issue, Trends Neurosci. 27 (2004) 702–706, https://doi.org/10.1016/j.tins.2004.10.001.
[59] M.I. Miranda, F. Bermúdez-Rattoni, Reversible inactivation of the nucleus basalis magnocellularis induces disruption of cortical acetylcholine release and acquisition, but not retrieval, of aversive memories, Proc. Natl. Acad. Sci. U. S. A. 96 (1999) 6478–6482, https://doi.org/10.1073/pnas.96.11.6478.
[60] C. Naor, Y. Dudai, Transient impairment of cholinergic function in the rat insular cortex disrupts the encoding of taste in conditioned taste aversion, Behav. Brain Res. 79 (1996) 61–67.
[61] L. Ramírez-Lugo, M.I. Miranda, M.L. Escobar, E. Espinosa, F. Bermúdez-Rattoni, The role of cortical cholinergic pre- and post-synaptic receptors in taste memory formation, Neurobiol. Learn. Mem. 79 (2003) 184–193.
[62] F. Borsini, E.T. Rolls, Role of noradrenaline and serotonin in the basolateral region of the amygdala in food preferences and learned taste aversions in the rat, Physiol. Behav. 33 (1984) 37–43, https://doi.org/10.1016/0031-9384(84)90010-6.
[63] K.J. Tuerke, C.L. Limebeer, P.J. Fletcher, L.A. Parker, Double dissociation between regulation of conditioned disgust and taste avoidance by serotonin availability at the 5-HT(3) receptor in the posterior and anterior insular cortex, J. Neurosci. 32 (2012) 13709–13717, https://doi.org/10.1523/JNEUROSCI.2042-12.2012.

INFORME DE LABORES 2019

Neuropharmacology 146 (2019) 84–94

Contents lists available at ScienceDirect

Neuropharmacology

journal homepage: www.elsevier.com/locate/neuropharm

Early memory consolidation window enables drug induced state-dependent memory

Daniel Osorio-Gómez[a,*], Karina S. Saldivar-Mares[a], Aldo Perera-López[a], James L. McGaugh[b], Federico Bermúdez-Rattoni[a]

[a] División de Neurociencias, Instituto de Fisiología Celular, Universidad Nacional Autónoma de México, Circuito Exterior, Ciudad Universitaria, 04510, Mexico City, Mexico
[b] Department of Neurobiology and Behavior, Center for the Neurobiology of Learning and Memory, University of California, Irvine, CA, 92697, USA

HIGHLIGHTS

- Anisomycin induces state-dependent recognition memory.
- DRB, an elongation RNA inhibitor, induces state-dependent recognition memory.
- The duration of drug action is a boundary condition for the induction of state-dependent recognition memory.
- Drugs induce state-dependent memory only when infused at early consolidation window.

ARTICLE INFO

Keywords:
Anisomycin
DRB
Memory consolidation
Recognition memory

ABSTRACT

It is well established that newly acquired information is stabilized over time by processes underlying memory consolidation, these events can be impaired by many drug treatments administered shortly after learning. The consolidation hypothesis has been challenged by a memory integration hypothesis, which suggests that the processes underlying new memories are vulnerable to incorporation of the neurobiological alterations induced by amnesic drugs generating a state-dependent memory. The present experiments investigated the effects of amnesic drugs infused into the insular cortex of male Wistar rats on memory for object recognition training. The findings provide evidence that infusions of several amnesic agents including a protein synthesis inhibitor, an RNA synthesis inhibitor, or an NMDA receptor antagonist administered both after a specific period of time and before retrieval induce state-dependent recognition memory. Additionally, when amnesic drugs were infused outside the early consolidation window, there was amnesia, but the amnesia was not state-dependent. Data suggest that amnesic agents can induce state-dependent memory when administered during the early consolidation window and only if the duration of the drug effect is long enough to become integrated to the memory trace. In consequence, there are boundary conditions in order to induce state-dependent memory.

1. Introduction

Memory consolidation refers to the post-learning processes by which recently acquired information is stabilized and strengthened into long-term memory (Müller and Pilzecker, 1900; McGaugh, 1966, 2000). There is extensive evidence that memory consolidation can be either impaired or enhanced by post-learning administration of treatments that affect neuronal functioning. Many kinds of treatments, including electroconvulsive shock (Duncan, 1949) and protein synthesis inhibitors impair consolidation when administered shortly after learning but not when administered several hours after learning (Agranoff, 1967; Davis and Squire, 1984; Packard and Teather, 1997; Lechner et al., 1999; Roullet et al., 2001). Some evidence suggests that memory consolidation may consist of multiple stages, at least during two sensitive windows in which amnesic agents can induce amnesia, one early phase immediately after memory acquisition and a second period of time between 120 and 240 min later (Bourtchouladze et al., 1998; Roullet et al., 2001; Igaz et al., 2002). Such findings indicate that there are different post-learning time-windows when memories are labile and vulnerable to amnesic events.

* Corresponding author. Laboratory BL-201, División de Neurociencias, Instituto de Fisiología Celular, Universidad Nacional Autónoma de México, Circuito Exterior s/n, Ciudad Universitaria, Coyoacán, 04510, Mexico City, Mexico.
E-mail address: dosorio@ifc.unam.mx (D. Osorio-Gómez).

https://doi.org/10.1016/j.neuropharm.2018.11.033
Received 7 June 2018; Received in revised form 20 November 2018; Accepted 21 November 2018
Available online 25 November 2018
0028-3908/ © 2018 Elsevier Ltd. All rights reserved.

Early studies reported that administration of protein-synthesis inhibitors immediately after acquisition impairs long-term memory (Flexner et al., 1963; Agranoff et al., 1965). These findings, and those of many subsequent experiments using protein synthesis inhibitors, suggested that memory consolidation depends on *de novo* protein synthesis, in which newly synthesized proteins modify functional connectivity between neurons that were involved in learning (Dudai, 2004). Subsequent experiments investigated the effects of many different protein synthesis inhibitors, including anisomycin, acetoxycycloheximide, cycloheximide and puromycin. Each of these drugs blocks the translation of proteins by a different mechanism of action (see Davis and Squire, 1984; Rao and Grollman, 1967; Barbacid and Vazquez, 1975; Hazzalin et al., 1998; Alberini, 2008).

The findings of these and many other studies appear to provide compelling evidence that protein synthesis inhibitors impair memory by blocking memory consolidation. However, a recent study reported evidence that memory impairment induced by injections of cycloheximide after training was reversed by the re-administration of cycloheximide before retrieval. These findings suggest that under some conditions the amnesia induced by protein-synthesis inhibitors is due to a difference in the brain state induced by the protein synthesis inhibitor shortly after learning, i.e., during the consolidation process, and the brain state during subsequent testing. That is, the brain state occurring after learning, during consolidation, may be required for subsequent memory retrieval (Gisquet-Verrier and Riccio, 2012; Gisquet-Verrier et al., 2015).

Memory consolidation impairment has also been found in experiments using the RNA elongation inhibitor 5,6-dichloro-1-β-D-ribofuranosylbenzimidazole (DRB) (Sherry et al., 2010; Prado-Alcalá et al., 2017; Ozawa et al., 2017; Steinmetz et al., 2017). Also, NMDA receptor antagonists impair memory consolidation based on aversive (Ferreira et al., 2002; Guzmán-Ramos et al, 2010; Guzmán-Ramos et al., 2012), as well as non-aversive training experiences (Baker and Kim, 2002; Winters and Bussey, 2005). The possibility that memory consolidation impairments induced by treatments affecting RNA elongation and NMDA receptors might also be the consequence of state-dependent memory induction, as suggested by the memory integration hypothesis), has not, as yet been investigated (Gisquet-Verrier et al., 2015). To investigate this issue the present experiments examined the effects of several amnesic agents to determine whether integration hypothesis might account for their influences on memory.

The experiments investigated drug influences on the consolidation of object recognition memory (ORM) (Brown and Aggleton, 2001). ORM is assessed by a single brief training session and a testing session and does not use aversive or rewarded training. Rodents have a natural tendency to explore novel objects rather than previously encountered ones. Consolidation of ORM involves several brain areas including the insular cortex (Bermudez-Rattoni et al., 2005; Balderas et al., 2008). The insular cortex has been proposed as a dynamic center in the salience network (Menon, 2015) that is critical to process novel-familiar information in recognition memory (Bermudez-Rattoni et al., 2005; Balderas et al., 2008; Bermudez-Rattoni, 2014; Schmahmann et al., 2007). The aim of this study was to determine whether amnesic treatments other than protein synthesis inhibitors also induce state-dependent recognition memory when infused into the insular cortex and provide additional understanding of dissociation between memory consolidation impairments and state-dependent memory.

2. Material and methods

2.1. Animals

A total amount of 210 adult male Wistar rats weighing 260–280 g were used in this study. Animals were obtained from the Instituto de Fisiología Celular and were housed individually at 22 °C in a 12 h light/12 h dark cycle starting at 7 a.m. All procedures were performed during the light cycle and were approved by the animal care and ethics committee of the institute (IFC-FBR 30–14). Rats had *ad libitum* access to water and food.

2.2. Guide cannulae implantation

Rats were implanted bilaterally with 9 mm (23G) steel cannulae aiming at the insular cortex using standard stereotaxic procedures. The coordinates for the insular cortex were AP + 1.2 mm; L ± 5.5 mm; DV -3 mm from Bregma (Paxinos and Watson, 1998). Cannulae were fixed to the skull using two screws with dental acrylic cement. Stylets were inserted to prevent clogging. Animals were allowed to recover from surgery for six days before behavioral protocols.

2.3. Object recognition memory protocol

The apparatus and general protocol used have been reported previously (Balderas et al., 2008, 2012). Briefly, all procedures were conducted in the experimental room where animals were left for 1 h before and 1 h after each session. During three consecutive days, animals were introduced into the open-field arena without any objects for 10 min and afterwards, rats were handled for 3 min to avoid handling-stress effects at the infusion sessions. During the sample session, rats were placed in the arena facing to the wall opposite the objects and were allowed to freely explore two identical objects (O1 and O2) for 5 min. Memory recognition test session was conducted 24 h later. At memory test, rats were allowed to explore freely one copy of the previously presented object (Familiar object, FO) together with a new one (Novel object, NO) for 5 min. The objects to be discriminated were white glass bulbs (6 cm in diameter and 11 cm in length) and transparent glass jars (5.5 cm in diameter and 5 cm in height). All objects were fixed to the floor at the back corners of the arena (10 cm from walls) with Velcro to prevent them from being displaced by the rats. To avoid olfactory cues, objects were thoroughly cleaned with 70% ethanol and the sawdust was stirred after each trial. Object exploration was defined as directing the nose at a distance of less than 1 cm from the object or touching the object with the nose. Object exploration was not scored when animals sat on the object or when the rats used the object to move backwards with the rat's nose facing the ceiling (Balderas et al., 2008; Albasser et al., 2010).

2.4. General microinfusion procedure

During infusion session, stylets were removed, and injectors were inserted into cannulae aiming at the insular cortex extending 2 mm bellow the tip. Injection needles were connected via polyethylene tubing to 10 μL Hamilton syringes, driven by an automated micro-infusion pump (Carnegie Medicine, Stockholm, SE). A volume of 1 μL (0.5 μL/min) was injected per hemisphere in the insular cortex (Balderas et al., 2008; García de la Torre et al., 2009), the volume and site of infusion have been demonstrated to be restricted to the insular cortex (Adaikkan and Ronseblum, 2015; Merhav and RosenblumK, 2008; Levitan et al., 2016); the injectors were left for another minute to allow diffusion into the tissue. Stylets were inserted again to prevent clogging. Infusion times are described later.

2.5. Drugs

Protein synthesis inhibitor anisomycin (ANI 120 mg/mL, Sigma-Aldrich, Missouri, US) was dissolved in an equimolar HCl-Ringer solution (NaCl 118 mM, KCl 4.7 mM, $NaH_2PO_4H_2O$ 1.2 mM, $MgSO_47H_2O$ 1.2 mM, $NaHCO_3$ 19 mM, $CaCl_2$ 2.5 mM, glucose 3.3 mM; pH was adjusted to 7.4). Vehicle solution was Ringer solution with HCl and adjusted pH to 7.4 (VEH). The RNA elongation inhibitor 5,6-dichloro-1-β-D-ribofuranosylbenzimidazole (DRB 40 ng/μL, Sigma-Aldrich, Missouri, US) was dissolved in 1 M PBS and 8% of dimethyl sulfoxide (DMSO,

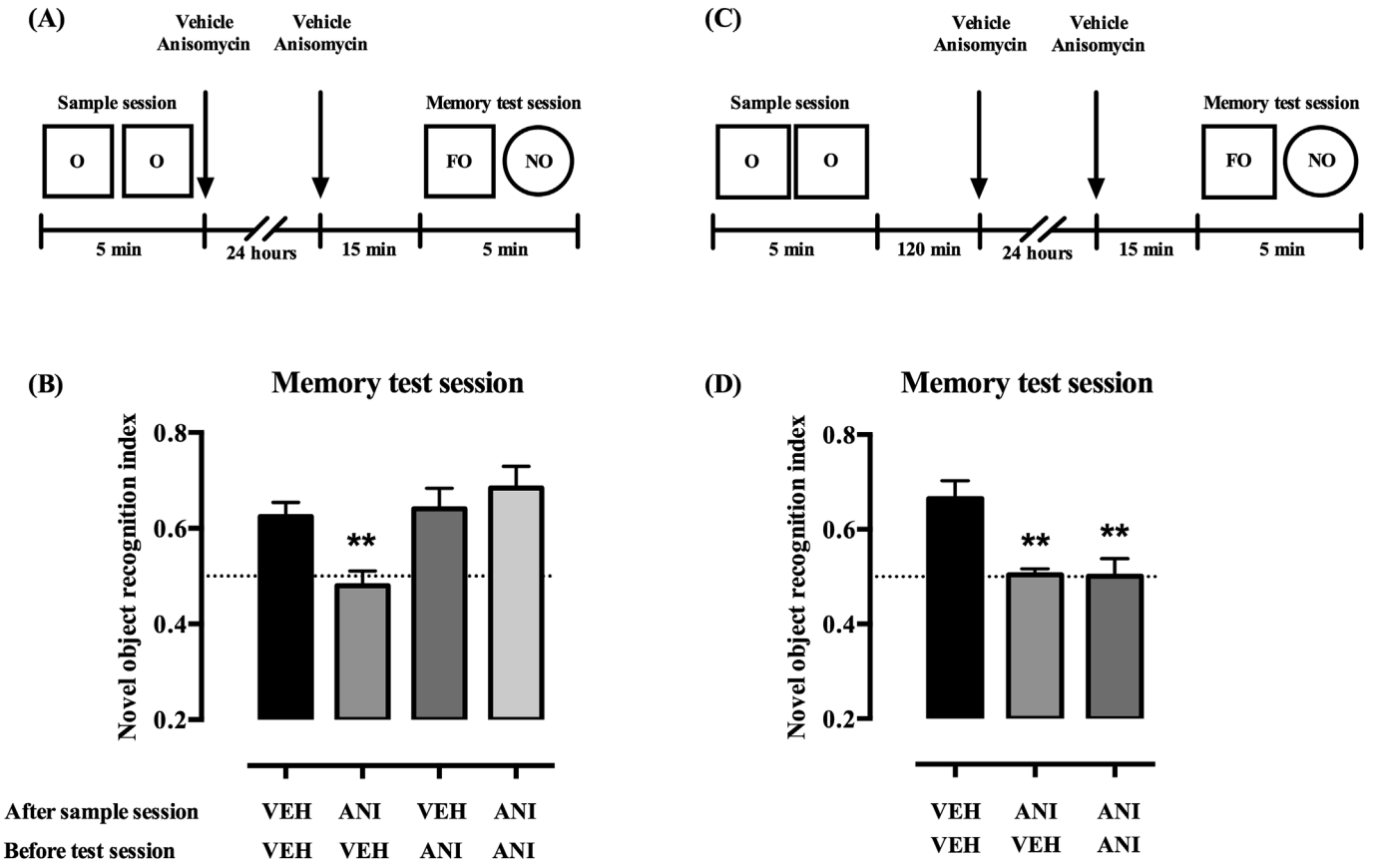

Fig. 1. Protein-synthesis inhibitor induces state-dependent memory when infused into the insular cortex during early consolidation window. (A) Schematic representation of the behavioral and intra-cortical infusion protocol used. (B) Novel object recognition index during memory recognition test session, VEH-VEH, VEH-ANI, and ANI-ANI groups showed preference for the novel object; whereas the group ANI-VEH did not. (C) Schematic representation of the behavioral and intra-cortical infusion protocol used in anisomycin administration at 120 min. (D) Novel object recognition index during memory recognition test session, the group VEH-VEH (120 min) showed preference for the novel object; whereas the groups ANI-VEH (120 min) and ANI-ANI (120 min) did not show preference for any object. Object (O), Familiar Object (FO) and Novel object (NO). Arrows represent micro-infusions into the insular cortex. Graphics are expressed as means of recognition index ± SEM. Dotted line represents exploration chance (0.5); **p < 0.01 versus VEH-VEH.

Sigma-Aldrich, Missouri, US). Vehicle solution was PBS 1 M with 8% DMSO (VEH). The NMDA receptor antagonist, DL-2-amino-5-phosphonovaleric acid (APV 10 mg/mL, Tocris Bioscience; Bristol, UK) was dissolved in saline solution (0.9% wt/vol). Saline solution was used as vehicle (VEH). We have administered the doses that have been shown to induce amnesia in various tasks and brain structures (Tronel and Sara, 2003; Guzmán-Ramos et al., 2010; Igaz et al., 2002; Prado-Alcalá et al., 2017; Balderas et al., 2008), since higher doses could cause nonspecific reactions masking state-dependent memory.

2.6. Drug injection protocol

In order to determine whether the infusion of anisomycin, DRB or APV induces state-dependent recognition memory, we used the following administration protocol. All drugs or vehicle were infused into the insular cortex immediately after ORM sample phase and 15 min before ORM retrieval. This yielded VEH-VEH, ANI-VEH, VEH-ANI, ANI-ANI, DRB-VEH, VEH-DRB, DRB-DRB, APV-VEH, VEH-APV and APV-APV groups (Please see, Fig. 1A, Fig. 2A, and Fig. 3A).

It has been suggested that amnesic drugs generate amnesia during the early stages of consolidation (Tronel and Sara, 2003). Thus, it is possible that induction of state-dependent memory occurs during the same sensitive window. To determine whether infusion of anisomycin or DRB outside the early consolidation window (120 min, Bourtchouladze et al., 1998; Igaz et al., 2002; Roullet et al., 2001) induces state-dependent recognition memory. We administrated vehicle, anisomycin or DRB into the insular cortex 120 min after ORM sample phase and 15 min before ORM retrieval. In order to reduce animal testing, we focused only on the groups VEH-VEH, ANI-VEH, ANI-ANI, DRB-VEH and DRB-DRB (see, Figs. 1C and 2C); since we have previously shown that administration of ANI before ORM retrieval did not affect memory expression (VEH-ANI), and DRB infusion before test (VEH-DRB) disrupts memory retrieval.

As anisomycin and DRB inhibit protein synthesis by different mechanisms, it is important to determine what anisomycin and DRB might have in common that underlies induction of state-dependent memory in comparison to APV. A possible explanation for this effect is the half-life of these drugs, as it has been reported that anisomycin (Wanisch and Wotjak, 2008) and DRB (Nguyen et al., 1994) induce sustained protein synthesis inhibition effect (hours), whereas the APV plasticity inhibition lasted ~60 min (Ji et al., 2005). Therefore, we investigated whether a prolonged exposure to APV, by a double administration into the insular cortex, could induce a state-dependent recognition memory. In brief, vehicle or APV were administrated after ORM sample phase, 60 min after ORM sample phase and 15 min before ORM retrieval. We aimed to evaluate VEH-VEH-VEH, VEH-APV-VEH, VEH-APV-APV, APV-APV-VEH and APV-APV-APV groups considering that administration of APV immediately after ORM sample phase induced recognition amnesia (APV-VEH), memory impairment could not be reversed by the administration of APV before retrieval (APV-APV) and APV infusion did not affect memory retrieval (VEH-APV); hence the APV-VEH-VEH, APV-VEH-APV and VEH-VEH-APV groups were omitted in the study due to the above-mentioned reasons (Please see Fig. 3C).

Considering that early consolidation phase is vulnerable to

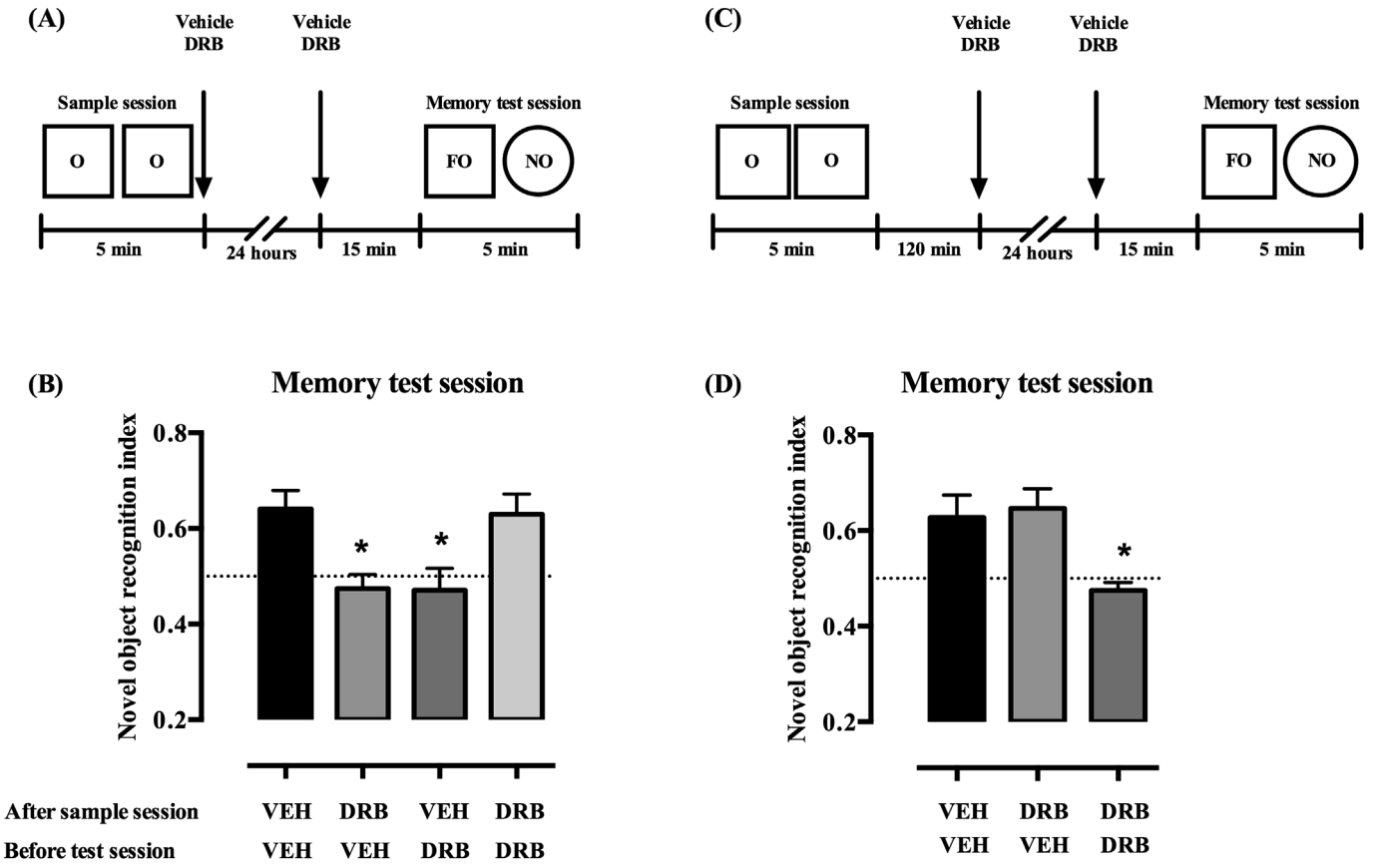

Fig. 2. RNA elongation inhibitor induces state-dependent memory when infused into the insular cortex during early consolidation window. (A) Schematic representation of the behavioral and intra-cortical infusion protocol used. (B) Novel object recognition index during memory recognition test session, the groups VEH-VEH and DRB-DRB showed preference for the novel object; whereas VEH-DRB and DRB-VEH groups did not. (C) Schematic representation of the behavioral and intra-cortical infusion protocol used in DRB administration at 120 min. (D) Novel object recognition index during memory recognition test session, VEH-VEH and DRB-VEH groups (120 min) showed preference for the novel object; whereas DRB-DRB (120 min) group did not. Object (O), Familiar Object (FO) and Novel object (NO). Arrows represent micro-infusions into the insular cortex. Graphics are expressed as means of recognition index ± SEM. Dotted line represents exploration chance (0.5); *p < 0.05 versus VEH-VEH.

induction of state-dependent recognition memory, we evaluated whether state-dependent recognition memory can occur when APV administrations are separated by a longer time window (120 min). We infused vehicle or APV into the insular cortex immediately after ORM sample phase, 120 min after ORM sample phase and 15 min before ORM retrieval. We determined the following groups: VEH-VEH′-VEH, VEH-APV′-VEH, VEH-APV′-APV, APV-VEH′-APV, APV-APV′-VEH and APV-APV′-APV (Please see Fig. 4A). VEH-VEH′-APV and APV-VEH′-VEH groups were excluded because we have observed that APV spared recognition memory retrieval (VEH-APV) and APV impaired memory recognition establishment (APV-VEH) (See, Fig. 3B).

2.7. Histology

At the end of the experiments, animals were injected i.p. with an overdose of sodium pentobarbital, and perfused intracardially with 0.9% saline solution. The brains were removed and stored at 4 °C in 4% paraformaldehyde in phosphate buffered saline. After treatment with sucrose gradient, 40 μm coronal sections were cut and stained with cresyl violet. Samples were examined by light microscopy to corroborate placement of the cannulae.

2.8. Experimental design and statistical analysis

For all experiments, objects and open-fields arenas were counterbalanced. Animals were randomly assigned to each treatment group. Timing and video analysis were conducted by an experimenter who was blind to the treatment condition. Recognition indexes for each object were calculated as follows: time of exploration of the object/total time of exploration during test. Also, we calculated the percentage of exploration time in comparison to vehicle group. Percentage of vehicle exploration time = (Total exploration time of experimental group/Total exploration time of vehicle group) * 100. We compared the novel object recognition indexes to a hypothetical value of 0.5 (chance level) using One-sample Student's *t*-test in order to determine preference for an object. Additionally, we used One-way ANOVA with Dunnett's *post hoc* test to compare the mean novel object exploration indexes versus the mean exploration index of control group. We compared the mean percentage of exploration time during ORM test amongst groups with One-way ANOVA with Dunnett's *post hoc* test. The accepted level of significance was p value ≤ 0.05. Data are presented as mean ± SEM. Effect size was determined by calculating Cohen's *d* statistic. Statistical analysis was performed using GraphPad Prism version 6.00, GraphPad software.

3. Results

3.1. Verification of cannula placements

Coronal sections (40 μm) were cut and stained with cresyl violet. The location sites of the cannulae for the micro-infusions were observed in the insular cortex region (Please see Fig. 5). Twelve animals with misplaced cannulae were not included in further analyses.

INFORME DE LABORES 2019

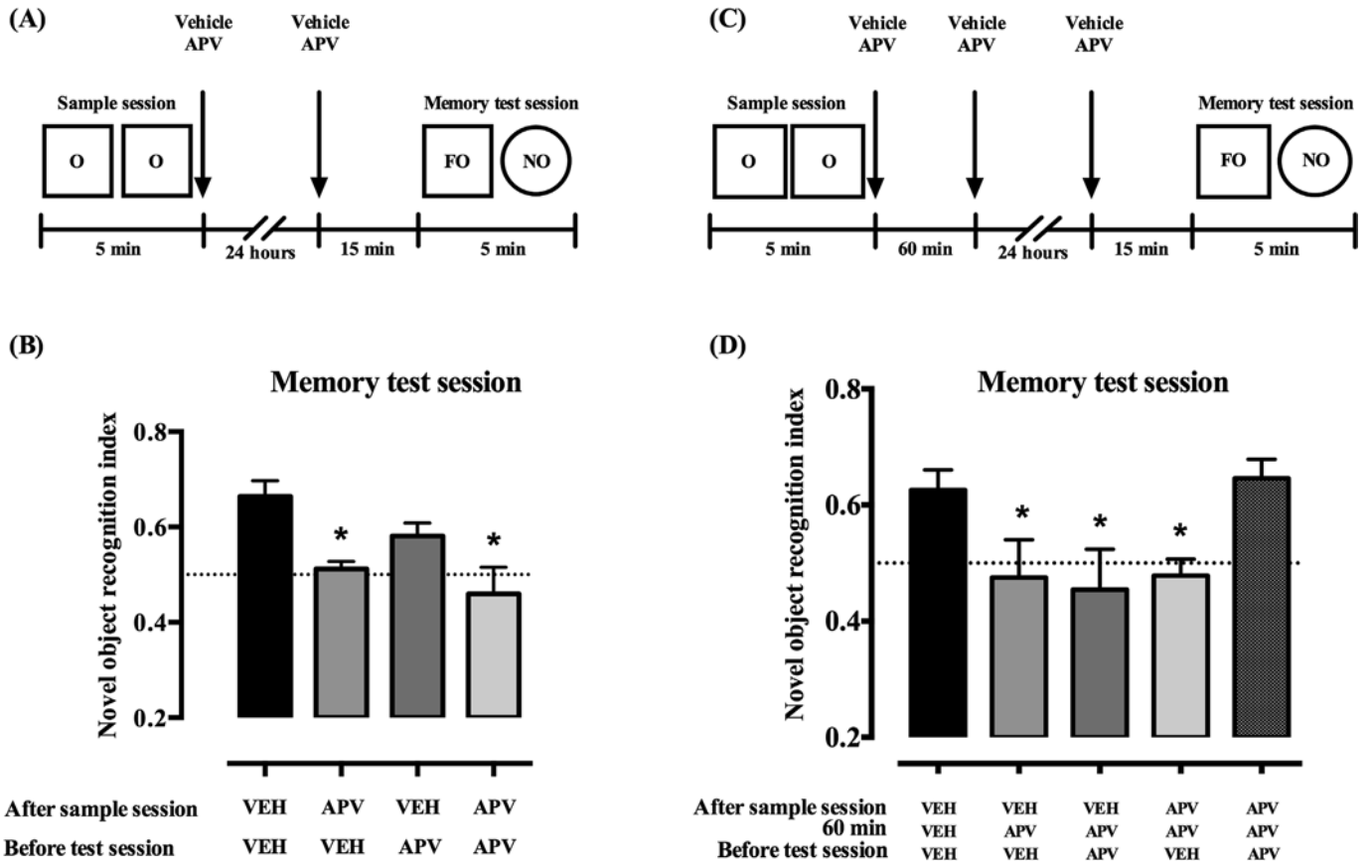

Fig. 3. Prolonged exposure to APV generates state dependent recognition memory. (A) Schematic representation of the behavioral and intra-cortical infusion protocol used. (B) Novel object recognition index during memory recognition test session, VEH-VEH and VEH-APV groups showed preference for the novel object; whereas APV-VEH, and APV-APV groups did not show preference for novel object. (C) Schematic representation of the behavioral and intra-cortical infusion protocol used in prolonged exposure to APV experiments. (D) Novel object recognition index during memory recognition test session, VEH-VEH-VEH and APV-APV-APV groups showed preference for the novel object; whereas VEH-APV-VEH, VEH-APV-APV and APV-APV-VEH groups did not show preference. Object (O), Familiar Object (FO) and Novel object (NO). Arrows represent micro-infusions within the insular cortex. Graphics are expressed as means of recognition index ± SEM. Dotted line represents exploration chance (0.5); *p < 0.05 versus VEH-VEH or VEH-VEH-VEH, respectively.

3.2. Induction of state-dependent memory with anisomycin

During object recognition memory retrieval, the groups VEH-VEH (n = 8; $t = 4.225$; $p = 0.003$; Mean = 0.625; SD = 0.083; $d = 1.494$; *t*-test), VEH-ANI (n = 8; $t = 3.278$; $p = 0.013$; Mean = 0.641; SD = 0.122; $d = 1.159$; *t*-test), and ANI-ANI (n = 8; $t = 4.040$; $p = 0.004$; Mean = 0.684; SD = 0.129; $d = 1.485$; *t*-test) explored the novel object above the chance; whereas the group ANI-VEH (n = 8; $t = 0.655$; $p = 0.5337$; Mean = 0.480; SD = 0.086; $d = -0.231$; *t*-test) did not (Fig. 1, (B) Memory test session). One-way ANOVA analysis showed significant differences in novel object recognition indexes among groups ($F_{(3,28)} = 5.481$, $p = 0.004$, overall effect size $d = 0.718$). Dunnett's multiple comparison test revealed differences in the ANI-VEH group ($p = 0.030$; $d = 0.479$) compared with the VEH-VEH group. The groups VEH-ANI ($p = 0.988$; $d = 0.053$ ANI-ANI ($p = 0.556$; $d = 0.196$ and VEH-VEH exhibited similar novel recognition indexes. ANOVA analysis showed that all groups spent a similar percentage of vehicle exploration time during test session ($F_{(3,28)} = 1.725$, $p = 0.199$) (Table 1). These data indicate that VEH-VEH, VEH-ANI and ANI-ANI groups recognized the novel object, whereas ANI-VEH group did not. These results show that anisomycin did not affect ORM retrieval, and ORM was consolidated in a state-dependent manner. Anisomycin induced recognition memory deficits and could be reversed by the re-administration of anisomycin before retrieval, exhibiting an anisomycin state-dependent memory.

3.3. Anisomycin impairs memory consolidation at 120 min after acquisition

Concerning anisomycin experiments outside early consolidation window (120 min), only the VEH-VEH (n = 7; $t = 4.392$; $p = 0.004$; Mean = 0.665; SD = 0.099; $d = 1.660$; *t*-test) explored the novel object above the chance; regardless of ANI-VEH (n = 7; $t = 0.272$; $p = 0.794$; Mean = 0.503; SD = 0.033; $d = 0.103$; *t*-test) and ANI-ANI (n = 7; $t = 0.020$; $p = 0.984$; Mean = 0.501; SD = 0.098; $d = 0.008$; *t*-test) groups (Fig. 1, (D) Memory recognition test session). Statistical analysis revealed significant differences in novel object recognition indexes among groups ($F_{(2,18)} = 9.002$, $p = 0.002$, ANOVA; overall effect size $d = 0.928$); Dunnett's multiple comparison test showed that VEH-VEH group was different in comparison to ANI-VEH ($p = 0.003$; $d = 0.797$) and ANI-ANI ($p = 0.003$; $d = 0.809$) groups. During memory recognition test session, all groups spent a similar percentage of vehicle exploration time ($F_{(2,18)} = 0.615$, $p = 0.552$, ANOVA; Table 1). These results show that during memory recognition test, VEH-VEH recognized the novel object, whereas ANI-VEH and ANI-ANI groups did not. Therefore, exposure to anisomycin 120 min after sample phase disrupted consolidation of recognition memory. However, memory deficits could not be reversed by the re-administration of anisomycin before memory retrieval. These results suggest that infusion of anisomycin into the insular cortex outside the early consolidation induced amnesia, but the amnesia was not state-dependent. Data obtained in this study evidence that anisomycin induces a state-dependent recognition memory only when administrated immediately after acquisition, and interrupts

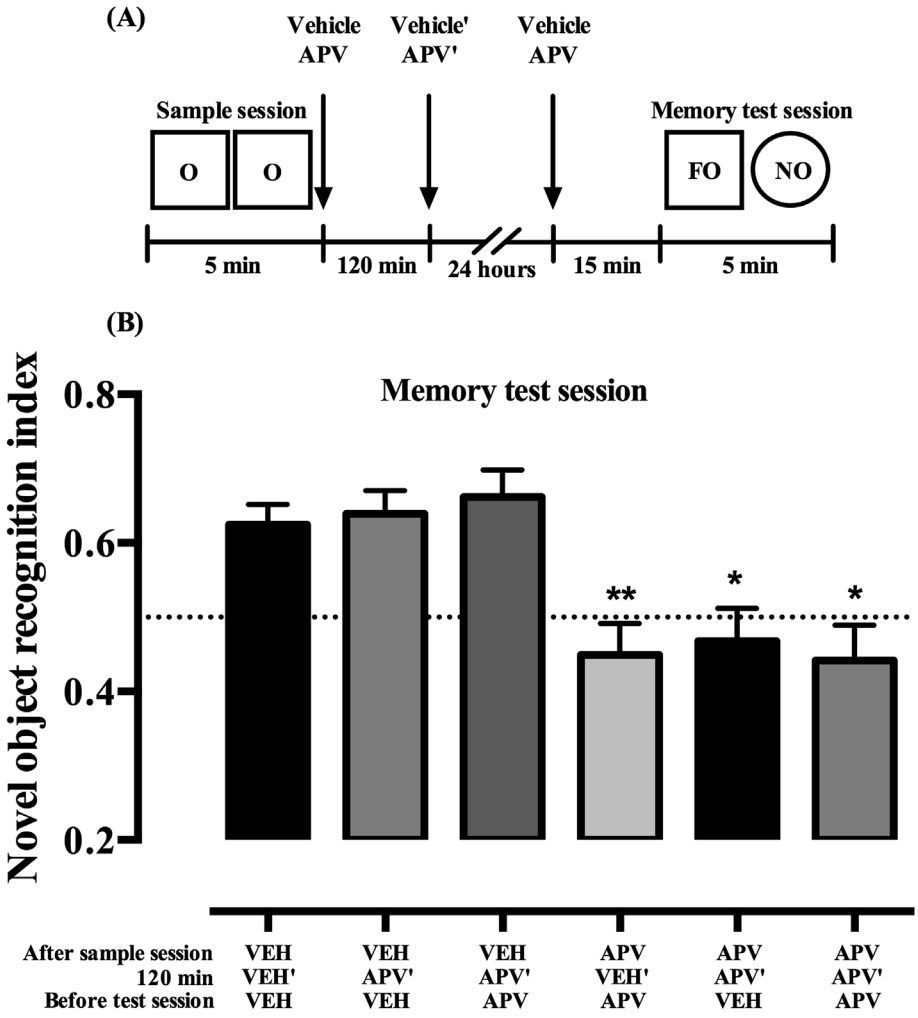

Fig. 4. Prolonged exposure to APV outside early consolidation window does not induce state-dependent recognition memory. (A) Schematic representation of the behavioral and intra-cortical infusion protocol used. (B) Novel object recognition index during memory recognition test session, VEH-VEH′-VEH, VEH-APV′-VEH and VEH-APV′-APV groups showed preference for the novel object; whereas APV-VEH′-APV, APV-APV′-VEH and APV-APV′-APV groups did not show preference. Object (O), Familiar Object (FO) and Novel object (NO). Arrows represent micro-infusions into the insular cortex. Graphics are expressed as means of recognition index ± SEM. Dotted line represents exploration chance (0.5); **p < 0.01 and * p < 0.05 versus VEH-VEH′-VEH, respectively.

recognition memory consolidation when infused at a later stage of consolidation.

3.4. Induction of state-dependent memory with DRB

Amongst DRB experiments, the groups VEH-VEH (n = 7; $t = 3.586$; $p = 0.031$; Mean = 0.641; SD = 0.104; $d = 1.355$; *t*-test) and DRB-DRB (n = 6; $t = 3.048$; $p = 0.028$; Mean = 0.629; SD = 0.104; $d = 1.245$; *t*-test) explored the novel object above the chance, whereas VEH-DRB (n = 7; $t = 0.647$; $p = 0.541$; Mean = 0.470; SD = 0.121; $d = -0.244$; *t*-test) and DRB-VEH (n = 7; $t = 0.865$; $p = 0.42$; Mean = 0.474; SD = 0.078; $d = -0.327$; *t*-test) groups did not. One-way ANOVA analysis showed that novel object recognition indexes were different among groups ($F_{(3,23)} = 4.378$, $p = 0.004$; overall size effect $d = 0.792$) (Fig. 2, (B) Memory test session); Dunnett's test revealed differences in VEH-DRB ($p = 0.013$; $d = 0.595$) and DRB-VEH ($p = 0.016$; $d = 0.580$) groups compared to VEH-VEH group. Animals in the VEH-VEH and DRB-DRB groups exhibited similar novel recognition indexes ($p = 0.995$; $d = 0.036$). During test session, percentage of vehicle exploration times were similar in all groups ($F_{(3,23)} = 0.388$, $p = 0.762$, ANOVA) (Table 2). These results indicate that VEH-VEH and DRB-DRB groups recognized the novel object during memory evaluation, whereas VEH-DRB and DRB-VEH groups did not differentiate the novel object from the familiar one. Our results show that DRB administration established a state-dependent recognition memory. ORM could be retrieved only when the same condition induced by DRB is present during consolidation and retrieval.

3.5. DRB does not induce state-dependent memory when infused 120 min after acquisition

Data obtained from intracortical administration of DRB outside early consolidation window (120 min) shows that VEH-VEH (n = 8; $t = 2.722$; $p = 0.029$; Mean = 0.627; SD = 0.133; $d = 0.962$; *t*-test) and DRB-VEH (n = 8; $t = 3.535$; $p = 0.009$; Mean = 0.646; SD = 0.117; $d = 1.249$; *t*-test) groups explored the novel object above the chance; DRB-DRB group did not show preference for the novel object (n = 7; $t = 1.494$; $p = 0.185$; Mean = 0.475; SD = 0.442; $d = -0.565$; *t*-test) (Fig. 2, (D) Memory recognition test session). Statistical analysis revealed significant differences in novel object recognition indexes among groups ($F_{(2,21)} = 3.972$, $p = 0.034$, ANOVA; overall size effect $d = 0.715$); Dunnett's test showed that VEH-VEH group was different in comparison to DRB-DRB ($p = 0.023$; $d = 0.587$), whereas VEH-VEH and DRB-VEH explored the novel object similarly ($p = 0.917$; $d = 0.074$). During memory recognition test session, all groups spent a similar percentage of vehicle exploration time ($F_{(2,21)} = 0.661$, $p = 0.526$, ANOVA; Table 2). In summary, VEH-VEH and DRB-VEH recognized the novel object, whereas DRB-DRB group did not. These results indicate that DRB infusion 120 min after sample phase did not impair consolidation of recognition memory and did not induce state-dependent recognition memory. Memory deficits observed in the DRB-DRB group are the consequence of DRB impairment on memory retrieval as described previously in Fig. 2 (B, VEH-DRB group). We observed that DRB infusion induces a state-dependent recognition memory only when administered immediately after memory acquisition.

INFORME DE LABORES 2019

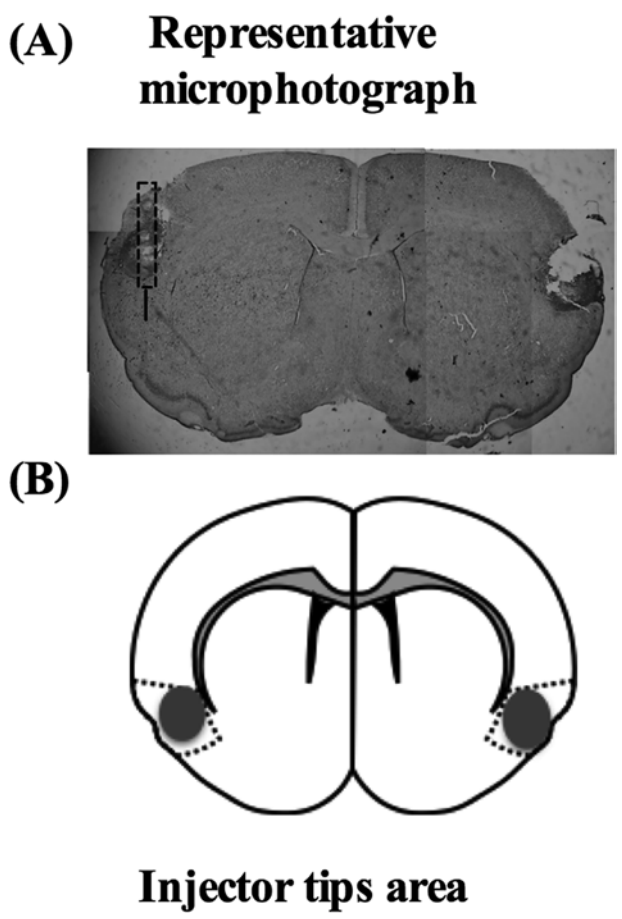

Fig. 5. Representation of the injector tips within the insular cortex. (A) Representative microphotographs of the insular cortex with injector tip. (B) Representation of injector tips location areas.

Taken together, administration of protein synthesis and RNA elongation inhibitors in the insular cortex induces a state-dependent-recognition memory only when infused immediately after acquisition, whereas pharmacological manipulation outside the early consolidation period does not induce state-dependent recognition memory.

3.6. APV impairs memory consolidation, but the amnesia is not state-dependent

Regarding APV experiments, statistical analysis showed that VEH-VEH (n = 7; $t = 3.154$; $p = 0.019$; Mean = 0.664; SD = 0.0818; $d = 2.002$; *t*-test) and VEH-APV groups (n = 6; $t = 2.936$; $p = 0.032$; Mean = 0.581; SD = 0.067; $d = 1.199$; *t*-test) explored the novel object above the chance; whereas APV-VEH (n = 7; $t = 0.722$; $p = 0.497$; Mean = 0.5117; SD = 0.043; $d = 0.274$; *t*-test) and APV-APV (n = 6; $t = 0.726$; $p = 0.500$; Mean = 0.459; SD = 0.135; $d = -0.296$; *t*-test) did not recognize the novel object above the chance (Fig. 3, (B) Memory recognition test session). One-way ANOVA analysis showed that there were significant differences in novel object recognition indexes among groups ($F_{(3,22)} = 4.132$, $p = 0.018$; overall size effect $d = 0.853$); Dunnett's post hoc analysis unveil differences in the APV-VEH ($p = 0.013$; $d = 0.619$) and APV-APV ($p = 0.011$; $d = 0.799$) groups compared to the VEH-VEH group; whereas VEH-VEH and VEH-APV ($p = 0.257$; $d = 0.326$) exhibited similar novel recognition indexes. All groups spent a similar percentage of vehicle exploration time during memory evaluation ($F_{(3,22)} = 0.427$, $p = 0.735$, ANOVA; Table 3). These results indicate that during memory recognition test, VEH-VEH and VEH-APV groups recognized the novel object, whereas APV-VEH and APV-APV groups did not. These results enlighten that APV did not hinder ORM retrieval but impaired recognition memory establishment. Memory deficits could not be rescued by the re-administration of APV before retrieval. Therefore, APV induced amnesia in a non-state dependent manner.

3.7. The increase of APV duration effects establishes a state-dependent memory

Statistical analysis show that VEH-VEH-VEH (n = 6; $t = 3.631$; $p = 0.015$; Mean = 0.626; SD = 0.085; $d = 1.482$; *t*-test) and APV-APV-APV (n = 7; $t = 4.473$; $p = 0.004$; Mean = 0.646; SD = 0.086; $d = 1.00$; *t*-test) groups explored the novel object above the chance, whereas VEH-APV-VEH (n = 7; $t = 0.382$; $p = 0.715$; Mean = 0.475; SD = 0.172; $d = -0.144$; *t*-test), VEH-APV-APV (n = 7; $t = 0.655$; $p = 0.536$; Mean = 0.454; SD = 0.184; $d = -0.248$; *t*-test) and APV-APV-VEH (n = 7; $t = 1.779$; $p = 0.135$; Mean = 0.478; SD = 0.747; $d = -0.290$; *t*-test) groups did not. One-way ANOVA analysis showed that exploration indexes for the novel object were different among groups ($F_{(5,37)} = 3.351$, $p = 0.026$; overall size effect $d = 0.768$) (Fig. 3, (D) Memory test session); Dunnett's multiple comparison analysis revealed novel object recognition index differences in the VEH-APV-VEH ($p = 0.042$; $d = 0.435$), VEH-APV-APV ($p = 0.025$; $d = 0.495$) and APV-APV-VEH ($p = 0.046$; $d = 0.425$) groups compared with VEH-VEH-VEH group; whereas VEH-VEH-VEH and APV-APV-APV groups exhibited similar novel recognition indexes ($p = 0.936$; $d = 0.059$). ANOVA analysis showed no differences in the percentage of vehicle exploration time among groups ($F_{(4,29)} = 0.825$, $p = 0.5219$) (Table 4). These results indicate that VEH-VEH-VEH and APV-APV-APV groups recognized the novel object during the memory test, while VEH-APV-VEH, VEH-APV-APV, and APV-APV-VEH did not. These data provide evidence that a single administration of APV at 60 min after acquisition impaired recognition memory, which was not state-dependent. However, an extended duration of APV effects by a double administration of APV, immediately and 60 min after acquisition, induced a state-dependent recognition memory. Our results suggest that the duration of drug effects is a boundary condition in state-dependency formation.

3.8. Prolonged APV duration effects can induce state-dependent memory only when administered during the early consolidation window

Statistical analysis in APV experiments outside early consolidation window (120 min) showed that VEH-VEH′-VEH (n = 7; $t = 4.526$; $p = 0.004$; Mean = 0.624; SD = 0.073; $d = 1.710$; *t*-test), VEH-APV′-VEH (n = 7; $t = 4.420$; $p = 0.004$; Mean = 0.639; SD = 0.083; $d = 1.671$; *t*-test), VEH-APV′-APV groups (n = 8; $t = 4.396$; $p = 0.003$; Mean = 0.662; SD = 0.104; $d = 1.554$; *t*-test) explored the novel object above the chance; in spite of APV-VEH′-APV (n = 7; $t = 1.194$; $p = 0.277$; Mean = 0.449; SD = 0.112; $d = -0.451$; *t*-test), APV-APV′-VEH (n = 7; $t = 0.046$; $p = 0.964$; Mean = 0.467; SD = 0.108; $d = -0.300$; *t*-test) and APV-APV′-APV (n = 7; $t = 0.329$; $p = 0.752$; Mean = 0.442; SD = 0.117; $d = -0.500$; *t*-test) groups (Fig. 4, (B) Memory recognition test session). Statistical analysis revealed significant differences in novel object recognition indexes among groups ($F_{(5,37)} = 5.056$, $p = 0.001$, ANOVA; overall size effect $d = 0.950$); Dunnett's test revealed that APV-VEH′-APV ($p = 0.010$; $d = 0.508$) APV-APV′-VEH ($p = 0.032$; $d = 0.437$) and APV-APV′-APV ($p = 0.011$; $d = 0.509$) groups were different in comparison to VEH-VEH′-VEH group. In addition, VEH-APV′-APV ($p = 0.923$; $d = 0.112$) and VEH-APV′-VEH ($p = 0.9985$; $d = 0.043$) exhibited similar novel object recognition indexes compared to VEH-VEH′-VEH. During memory recognition test session all groups spent a similar amount of percentage of vehicle exploration time ($F_{(5,37)} = 0.897$, $p = 0.491$, ANOVA; Table 5). Our results show that VEH-VEH′-VEH, VEH-APV′-VEH and VEH-APV′-APV groups recognized the novel object, whereas APV-VEH′-APV, APV-APV′-VEH and APV-APV′-APV groups did not. These findings indicate

that administration of APV 120 min after sample phase did not impair recognition memory and confirm that recognition memory was impaired by the infusion of APV immediately after acquisition and could not be rescued by the re-administration of APV before retrieval. Infusion of APV into the insular cortex at both times, 120 min after ORM acquisition and 15 min before retrieval, spared recognition memory. This effect seems to be as a result of lack of APV effect in memory recognition on late consolidation window and memory retrieval. However, memory impairment observed in APV-APV′-APV group was the result of the immediate infusion of APV after ORM acquisition, since a long temporal separation between administrations restrained drug-induced state integration in recognition memory.

Altogether, our results indicate that there are boundary conditions in order to establish a state-dependent recognition memory: a short half-life of the drug seems to be insufficient to be integrated to the memory trace; and the timing of pharmacological manipulation, since drug administration during the early but not late consolidation window induces state-dependent recognition memory.

4. Discussion

Previous studies have provided experimental evidence of state-dependent memories; memories may be more readily retrieved when a drug-induced brain state during recall is similar to the drug-induced brain state when learning occurred (Overton, 1991; Jovasevic et al., 2015). There is also some evidence suggesting that drugs that are administered shortly after learning may induce state-dependent learning. Such findings propose that, while new memories are active and being consolidated, they may integrate the drug effects into the memory and thus require a similar drug state for subsequent expression of memory (Thompson and Neely, 1970; Thompson and Grossman, 1972; Hinderliter et al., 1975; Mactutus and Riccio, 1978; Mactutus et al., 1980; Bradley and Galal, 1988; Millin and Newman, 2008; Briggs and Olson, 2013; Gisquet-Verrier and Riccio, 2012; Gisquet-Verrier et al., 2015).

In this study, we found that immediate post-training infusions of anisomycin into the insular cortex induces state-dependent recognition memory. This finding is similar to the effect previously observed with cycloheximide (Briggs and Olson, 2013; Gisquet-Verrier et al., 2015). We also found that administration of DRB, an RNA elongation inhibitor, also induced a state-dependent recognition memory. It is important to note that administration of anisomycin or DRB 120 min after ORM acquisition did not induce state-dependent recognition memory. Thus, our findings provide additional support for the idea that as suggested by the integration hypothesis, newly formed memories are susceptible to integrate drug-induced effects that can induce state-dependent memory.

Unlike the state-dependency generated by anisomycin or DRB, cortical administration of APV immediately after training induced amnesia that was not recovered by the infusion of APV before retrieval. Interestingly, the absence of state dependent memory with APV has been reported previously when infused into the amygdala (Maren et al., 1996). However, this lack of effect on state-dependent memory formation might be due to the short half-life of APV (Ji et al., 2005) compared to anisomycin (Wanisch and Wotjak, 2008) and DRB (Nguyen et al., 1994). In support of this possibility, we investigated whether state-dependent memory could be induced when we extended the duration of the APV effect by a double administration, immediately and 60 min after memory acquisition. Our results indicate that the effects of a prolonged duration of APV could be integrated into the processes mediating the newly-formed recognition memory. Importantly, a brief exposure to APV immediately or 60 min after ORM acquisition, impaired memory recognition and could not be reversed when APV was administered before memory retrieval. As the half-life of APV is short, amnesia is observed as a result of an incomplete incorporation of the brain state induced by APV. Our results suggest that induction of state-dependent memory with APV depends on the extended effect that comprises the early consolidation window between 0 and 120 min, since administration of APV during later consolidation window failed to induce state-dependent recognition memory.

Previous findings suggest that progressive stabilization of newly learned information occurs at least during two sensitive windows in which protein-synthesis inhibitors induce amnesia, one early phase immediately after training and a second phase between 2 and 4 h later (Bourtchouladze et al., 1998; Quevedo et al., 1999; Igaz et al., 2002). Here, we observed that infusion of anisomycin into the insular cortex immediately or 120 min after ORM training impaired recognition memory. Additionally, DRB administration into the insular cortex immediately after training impaired recognition memory, but not when administered 120 min after training. Memory deficits induced by anisomycin or DRB administration have been also found in many memory studies using different learning tasks (Balderas et al., 2008; Sherry et al., 2010; Prado-Alcalá et al., 2017; Ozawa et al., 2017; Steinmetz et al., 2017). Thus, memory consolidation may be sensitive to two-time periods (Igaz et al., 2002) in which differential effects of anisomycin or DRB are due to differences in time of infusion and concentration used (Agranoff, 1967; Igaz et al., 2002). In addition, infusion of APV into the insular cortex immediately or 60 min after the acquisition impairs recognition memory; APV administration 120 min after training is ineffective. Previously, we have reported that memory consolidation is affected by the administration of APV into the insular cortex up to 45 min after training (Guzmán-Ramos et al., 2010). However, administration of APV 120 min after training does not alter consolidation processes (Roullet et al., 2001; Tronel and Sara, 2003).

In general, our findings support the idea that induction of state-dependent memory and memory deficits could be differentially generated during two sensitive windows, an early consolidation stage affected by anisomycin, DRB and APV up to 60 min, and a late consolidation phase blocked only by anisomycin. A possible explanation for the differential effects observed between times of drug-administration, is that during early consolidation window, NMDA receptor activation constitutes the principal cellular mechanism for initiating memory processes. NMDA receptor activity has been associated with the regulation of protein synthesis; calcium entry through NMDA receptors modulates several signaling pathways including, among others, CREB and elongation factors (Hoeffer and Klann, 2006; Tran et al., 2007). Thus, increased phosphorylation of CREB factor promotes RNA synthesis, new RNA and pre-existing RNA are translated in proteins required for setting up permanent synaptic changes (Igaz et al., 2002; Tran et al., 2007; Stewart and Schuman, 2001). Modification in any of these molecular events during early consolidation window, disrupts memory establishment. Nevertheless, protein synthesis is critical in both early and late consolidation windows; during the early phase, the pre-existing RNA of the immediate genes is translated into proteins necessary for the synaptic modifications, while the window of late consolidation undergoes structural changes that require new proteins involved in the long-term synaptic remodeling (Igaz et al., 2002; Stewart and Schuman, 2001).

As mentioned, the IC belongs to a dynamic network for salience detection; the salience network has been principally associated with the IC and the nucleus accumbens, but also includes limbic areas such as the amygdala, ventral striatum, dorsomedial thalamus, hypothalamus, substantia nigra and the ventral tegmental area (Menon, 2015). Therefore, the possible key role of the IC of the salience network is recognizing familiar/novel stimuli. In this regard, it has been observed that the IC activity is increased with the strength on familiarity (Morin et al., 2011; Kafkas and Montaldi, 2014). Therefore, the IC can be seen as a dynamic center for detection and selection of salient stimuli (novel vs familiar) (Menon, 2015) and the IC-limbic pathway is critical for processing novel-familiar information (Schmahmann et al., 2007). In addition, there is evidence from animal and human studies suggesting that a network of temporal cortical regions, including the perirhinal,

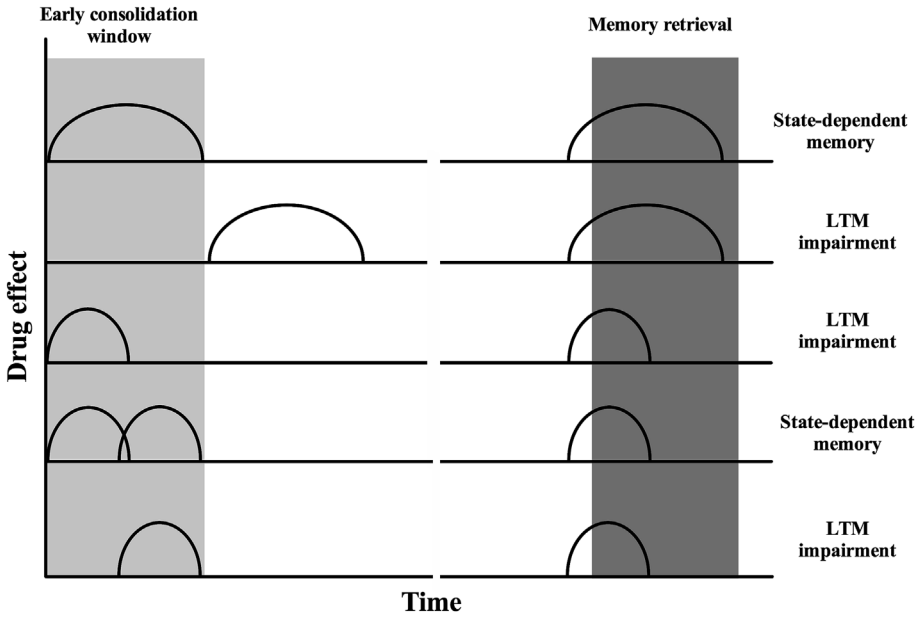

Fig. 6. Schema of the induction of state-dependent memory by amnesic drugs. There are boundary conditions in order to establish a state-dependent memory: a short half-life of the drug seems to be insufficient to be integrated to the memory trace; and the timing of pharmacological manipulation. It is only during early consolidation phase that newly acquired memories integrate information of the induced brain state generated by a long duration of drug effects.

parahippocampal, entorhinal and insular cortices and the hippocampus participates in recognition memory (Tang et al., 1997; Aggleton and Brown, 1999; Malkova and Mishkin, 2003; Reed et al., 2004; Bermúdez-Rattoni et al., 2005; Balderas et al., 2008; Bermúdez-Rattoni, 2014). Thus, a suggested key role of the IC is the detection of behaviorally relevant stimuli during recognition tasks (Menon, 2015). The induction of state-dependent recognition memory through pharmacological manipulations within the IC could be explained as a result of the incorporation of the drug-induced state into the familiar trace of the memory of the object necessary for the novel-familiar recognition.

Interestingly, our results provide evidence that induction of memory dependent on the state could be supported by several brain regions, since intracortical administration of a protein synthesis inhibitor generates state-dependent memories similar to those injected in the hippocampus or intracerebroventricular (Gisquet-Verrier et al., 2015 Jafari-Sabet et al., 2016). However, it remains to study the cellular and molecular mechanisms involved in the formation of state-dependent memory (Radulovic et al., 2017).

Despite the extensive evidence that amnesia induced by anisomycin, DRB or APV is explained by well-known molecular mechanisms, our data indicate that, under some special conditions, memory consolidation is not impaired by such treatments, but rather, is consolidated in a state-dependent manner. Induction of state dependent memory occurs during early consolidation window when memory establishment takes place; it is possible that infusion of drugs with long-lasting effects alters the molecular events of the insular cortex that are capable of inducing a brain state that becomes part of the novel-familiar memory trace in a state-dependent manner. However, amnesia is induced as a result of an incomplete incorporation of the brain state induced by drugs with short-lasting effect during early consolidation window, or by hindering memory long-term structural changes during late consolidation phase.

Differences in the time required for the consolidation and retrieval processes may explain why the integration of a prolonged exposure to drugs during consolidation is necessary, whereas a single injection is sufficient to induce a state that serves as a reference for retrieval. Memory consolidation events are required to make persistent modifications in functional connectivity that are accomplished within the first minutes to hours after memory acquisition (Dudai, 2004). However, memory retrieval processes are consummated very quickly, even in less than a second (Thorpe et al., 1996). Therefore, it is possible that the integration of the brain state induced by a drug requires a longer exposure to drugs compared to a short exposure that serves as a cue-signal during memory retrieval.

In agreement with previous studies (Rodríguez-Ortiz et al., 2012; Igaz et al., 2002; Ozawa et al., 2017; García-Delatorre et al., 2014, Osorio-Gómez et al., 2016; Liang et al., 1996; Izquierdo et al., 2002; Roullet et al., 2001; Winters and Bussey, 2005), we observed that anisomycin and APV do not disrupt memory retrieval. However, we found that administrations of DRB impaired ORM retrieval as reported previously (Igaz et al., 2002; Ozawa et al., 2017). Although memory retrieval impairments reported in literature are explained in terms of retrieval-related mechanisms, an alternative explanation is that memory expression is impaired because the brain-state during retrieval is different from the induced-state during memory formation. Nevertheless, our findings indicate that only DRB, but not anisomycin or APV, disrupted memory retrieval. However, all drugs used in this study serve as a state-dependent cue for recognition memory retrieval.

5. Conclusion

Summarizing, our data indicate that incorporation of the brain state induced by anisomycin and DRB in a state-dependent memory manner is due to their prolonged half-life. State-dependency could also be induced with APV when the duration of action was extended by double administration. The time of administration is crucial to state-dependent memory formation. Integration of drug-induced effects into memory occurs strictly at early consolidation window, whereas later consolidation window is vulnerable to consolidation disruption in a non-state dependent nature. Taken together, these results indicate that drugs' half-life and time of administration are boundary conditions creating state-dependent memory (see Fig. 6).

Declaration of interest

None.

Funding

This work was supported by CONACYT (250870) and DGAPA PAPIIT-UNAM (IN208616) grants.

Acknowledgments

We thank Dr. Luis Rodríguez-Durán for his technical assistance. We

also wish to acknowledge the excellent assistance of Julio César Abarca Magaña, Arturo Hernández-Matias and José Jaimes Cabrera during the experiments.

Appendix A. Supplementary data

Supplementary data to this article can be found online at https://doi.org/10.1016/j.neuropharm.2018.11.033.

References

Adaikkan, C., Ronseblum, K., 2015. A molecular mechanism underlying gustatory memory trace for an association in the insular cortex. Elife 4, e07582. https://doi.org/10.7554/eLife.07582.

Aggleton, J.P., Brown, M.W., 1999. Episodic memory, amnesia, and the hippocampal-anterior thalamic axis. Behav. Brain Sci. 22 (3), 425–444 discussion 444-89.

Agranoff, B.W., 1967. Memory and protein synthesis. Proc.Natl. Scientific American 216 (6), 115–122.

Agranoff, B.W., Davis, R.E., Brink, J.J., 1965. Memory fixation in the goldfish. Proc.Natl. Acad. Sci. 54, 788–793.

Albasser, M.M., Chapman, R.J., Amin, E., Iordanova, M.D., Vann, S.D., Aggleton, J.P., 2010. New behavioral protocols to extend our knowledge of rodent object recognition memory. Learn. Mem. 17 (8), 407–419. https://doi.org/10.1101/lm.1879610.

Alberini, C.M., 2008. The role of protein synthesis during the labile phases of memory: revisiting the skepticism. Neurobiol. Learn. Mem. 89 (3), 234–246.

Baker, K.B., Kim, J.J., 2002. Effects of stress and hippocampal NMDA receptor antagonism on recognition memory in rats. Learn. Mem. 9 (2), 58–65.

Balderas, I., Rodriguez-Ortiz, C.J., Salgado-Tonda, P., Chavez-Hurtado, J., McGaugh, J.L., Bermudez-Rattoni, F., 2008. The consolidation of object and context recognition memory involve different regions of the temporal lobe. Learn. Mem. 15 (9), 618–624. https://doi.org/10.1101/lm.1028008.

Balderas, I., Morin, J.P., Rodriguez-Ortiz, C.J., Bermudez-Rattoni, F., 2012. Muscarinic receptors activity in the perirhinal cortex and hippocampus has differential involvement in the formation of recognition memory. Neurobiol. Learn. Mem. 97 (4), 418–424. https://doi.org/10.1016/j.nlm.2012.03.006.

Barbacid, M., Vazquez, D., 1975. Ribosome changes during translation. J. Mol. Biol. 93 (4), 449–463.

Bermudez-Rattoni, F., 2014. The forgotten insular cortex. Neurobiol. Learn. Mem. 109, 207–216. https://doi.org/10.1016/j.nlm.2014.01.001.

Bermudez-Rattoni, F., Okuda, S., Roozendaal, B., McGaugh, J.L., 2005. Insular cortex is involved in consolidation of object recognition memory. Learn. Mem. 12 (5), 447–449.

Bourtchouladze, R., Abel, T., Berman, N., Gordon, R., Lapidus, K., Kandel, E.R., 1998. Different training procedures recruit either one or two critical periods for contextual memory consolidation, each of which requires protein synthesis and PKA. Learn. Mem. (4–5), 365–374.

Bradley, P.M., Galal, K.M., 1988. State-dependent recall can be induced by protein synthesis inhibition: behavioural and morphological observations. Brain Res. 468, 243–251.

Briggs, J.F., Olson, B.P., 2013. Reexposure to the amnestic agent alleviates cycloheximide-induced retrograde amnesia for reactivated and extinction memories. Learn. Mem. 20, 285–288.

Brown, M.W., Aggleton, J.P., 2001. Recognition Memory: what are the roles of the perirhinal cortex and the hippocampus? Nat. Rev. Neurosci. 2 (1), 51–56. https://doi.org/10.1038/35049064.

Davis, H.P., Squire, L.R., 1984. Protein synthesis and memory: a review. Psychol. Bull. 96 (3), 518–559.

Dudai, Y., 2004. The neurobiology of consolidations, or, how stable is the engram? Annu. Rev. Psychol. 55, 51–86.

Duncan, C.P., 1949. The retroactive effect of electroshock on learning. J. Comp. Physiol. Psychol. 42, 32–44.

Ferreira, G., Gutiérrez, R., De La Cruz, V., Bermúdez-Rattoni, F., 2002. Differential involvement of cortical muscarinic and NMDA receptors in short- and long-term taste aversion memory. Eur. J. Neurosci. 16 (6), 1139–1145.

Flexner, J.B., Flexner, L.B., Stellar, E., 1963. Memory in mice as affected by intracerebral puromycin. Science 141, 57–59.

García-Delatorre, P., Rodriguez-Ortiz, C.J., Arreguin-Martinez, J.L., Cruz-Castañeda, P., Bermúdez-Rattoni, F., 2009. Simultaneous but not independent anisomycin infusions in insular cortex and amygdala hinder stabilization of taste memory when updated. Learn. Mem. 16 (9), 514–519. https://doi.org/10.1101/lm.1356509.

García-Delatorre, P., Pérez-Sánchez, C., Guzmán-Ramos, K., Bermúdez-Rattoni, F., 2014. Role of glutamate receptors of central and basolateral amygdala nuclei on retrieval and reconsolidation of taste aversive memory. Neurobiol. Learn. Mem. 111, 35–40.

Gisquet-Verrier, P., Riccio, D.C., 2012. Memory reactivation effects independent of reconsolidation. Learn. Mem. 19 (9), 401–409. https://doi.org/10.1101/lm.026054.112.

Gisquet-Verrier, P., Lynch 3rd, J.F., Cutolo, P., Toledano, D., Ulmen, A., Jasnow, A.M., Riccio, D.C., 2015. Integration of new information with active memory accounts for retrograde Amnesia: a challenge to the consolidation/reconsolidation hypothesis? J. Neurosci. 35 (33), 11623–11633.

Guzmán-Ramos, K., Osorio-Gómez, D., Moreno-Castilla, P., Bermúdez-Rattoni, F., 2010. Off-line concomitant release of dopamine and glutamate involvement in taste memory consolidation. J. Neurochem. 114 (1), 226–236.

Guzmán-Ramos, K., Osorio-Gómez, D., Moreno-Castilla, P., Bermúdez-Rattoni, F., 2012. Post-acquisition release of glutamate and norepinephrine in the amygdala is involved in taste-aversion memory consolidation. Learn. Mem. 19 (6), 231–238.

Hazzalin, C.A., Le Panse, R., Cano, E., Mahadevan, L.C., 1998. Anisomycin selectively desensitizes signalling components involved in stress kinase activation and fos and jun induction. Mol. Cell Biol. 18 (4), 1844–1854.

Hinderliter, C.F., Webster, T., Riccio, D.C., 1975. Amnesia induced by hypo-thermia as a function of treatment-test interval and recooling in rats. Anim. Learn. Behav. 3, 257–263.

Hoeffer, C.A., Klann, E., 2006. NMDA receptor and translational control. In: In: Van Dongen, A.M. (Ed.), Biology of the NMDA Receptor CRC Press/Taylor & Francis, Boca Raton (FL.

Igaz, L.M., Vianna, M.R., Medina, J.H., Izquierdo, I., 2002. Two time periods of hippocampal mRNA synthesis are required for memory consolidation of fear-motivated learning. J. Neurosci. 22 (15), 6781–6789.

Izquierdo, I., Vianna, M.R., Izquierdo, L.A., Barros, D.M., Szapiro, G., Coitinho, A.S., Muller, L., Cammarota, M., Bevilaqua, L.R., Medina, J.H., 2002. Memory retrieval and its lasting consequences. Neurotox. Res. 4 (5–6), 573–593.

Jafari-Sabet, M., Jafari-Sabet, A.R., Dizaji Ghadim, A., 2016. Tramadol state-dependent memory: involvement of dorsal hippocampal muscarinic acetylcholine receptors. Behav Pharmacol. Aug 27 (5), 470–478. https://doi.org/10.1097/FBP.0000000000000239.

Ji, W., Suga, N., Gao, E., 2005. Effects of agonists and antagonists of NMDA and ACh receptors on plasticity of bat auditory system elicited by fear conditioning. J. Neurophysiol. 94 (2), 1199–1211.

Jovasevic, V., Corcoran, K.A., Leaderbrand, K., Yamawaki, N., Guedea, A.L., Chen, H.J., Shepherd, G.M., Radulovic, J., 2015. GABAergic mechanisms regulated by miR-33 encode state-dependent fear. Nat. Neurosci. 18 (9), 1265–1271.

Kafkas, A., Montaldi, D., 2014. Two separate, but interacting, neural systems for familiarity and novelty detection: a dual-route mechanism. Hippocampus 24 (5), 516–527. https://doi.org/10.1002/hipo.22241. 2014 May.

Lechner, H.A., Squire, L.R., Byrne, J.H., 1999. 100 years of consolidation–remembering Müller and Pilzecker. Learn. Mem. 6 (2), 77–87 1999.

Levitan, D., Gal-Ben-Ari, S., Heise, C., Rosenberg, T., Elkobi, A., Inberg, S., Sala, C., Rosenblum, K., 2016. The differential role of cortical protein synthesis in taste memory formation and persistence. NPJ Sci Learn 1, 16001.

Liang, K.C., Hu, S.J., Chang, S.C., 1996. Formation and retrieval of inhibitory avoidance memory: differential roles of glutamate receptors in the amygdala and medial prefrontal cortex. Chin. J. Physiol. 39 (3), 155–166.

Mactutus, C.F., Riccio, D.C., 1978. Hypothermia-induced retrograde amnesia: role of body temperature in memory retrieval. Physiol. Psychol. 6, 18–22.

Mactutus, C.F., Ferek, J.M., Riccio, D.C., 1980. Amnesia induced by hyperthermia: an unusually profound, yet reversible, memory loss. Behav. Neural. Biol. 30, 260–277.

Malkova, L., Mishkin, M., 2003. One-trial memory for object-place associations after separate lesions of hippocampus and posterior parahippocampal region in the monkey. J. Neurosci. 23 (5), 1956–1965.

Maren, S., Aharonov, G., Stote, D.L., Fanselow, M.S., 1996. N-methyl-D-aspartate receptors in the basolateral amygdala are requires for both acquisition and expression of conditional fear in rats. Behav. Neurosci. 110 (6), 1365–1374.

McGaugh, J.L., 1966. Time-dependent processes in memory stage. Science 153 (3742), 1351–1358.

McGaugh, J.L., 2000. Memory–a century of consolidation. Science 287 (5451), 248–251.

Menon, V., 2015. Salience network. In: Toga, Arthur W. (Ed.), Brain Mapping: an Encyclopedic Reference. vol. 2. Academic Press: Elsevier, pp. 597–611.

Merhav, M., Rosenblum, K., 2008. Facilitation of taste memory acquisition by experiencing previous novel taste is protein-synthesis dependent. Learn. Mem. 15 (7), 501–507. https://doi.org/10.1101/lm.986008.

Millin, P., Newman, E., 2008. A comparison of the effects of state and non-state reminder treatments on morphine state-dependency and cycloheximide-induced retrograde amnesia. J. Behav. Neurosci. Res. 6, 6–14.

Morin, J.P., Quiroz, C., Mendoza-Viveros, L., Ramirez-Amaya, V., Bermudez-Rattoni, F., 2011. Familiar taste induces higher dendritic levels of activity-regulated cytoskeleton-associated protein in the insular cortex than a novel one. Learn. Mem. 18 (10), 610–616. https://doi.org/10.1101/lm.2323411.

Müller, G.E., Pilzecker, A., 1900. Experimentelle Beiträge zur Lehre vom Gedächtnis. Z. Psychol. Ergänzungsband 1, 1–300.

Nguyen, P.V., Abel, T., Kandel, E.R., 1994. Requirement of critical a period of transcription for induction of a late phase of LTP. Science 265 (5175), 1104–1107.

Osorio-Gómez, D., Guzmán-Ramos, K., Bermúdez-Rattoni, F., 2016. Differential involvement of glutamatergic and catecholaminergic activity within the amygdala during taste aversion retrieval on memory expression and updating. Behav. Brain Res. 307, 120–125.

Overton, D.A., 1991. Historical context of state dependent learning and discriminative drug effects. Behav. Pharmacol. 2 (4 And 5), 253–264.

Ozawa, T., Yamada, K., Ichitani, Y., 2017. Differential requirements of hippocampal de novo protein and mRNA synthesis in two long-term spatial memory tests: spontaneus place recognition and delay-interposed radial maze performance in rats. PLoS One 12 (2), e0171629.

Packard, M.G., Teather, L.A., 1997. Posttraining injections of MK-801 produce a time-dependent impairment of memory in two water maze tasks. Neurobiol. Learn. Mem. 68 (1), 42–50.

Paxinos, G., Watson, C., 1998. The Rat Brain in Stereotaxic Coordinates, fourth ed. Academic Press, San Diego, CA.

Prado-Alcalá, R.A., Medina, A.C., Bello-Medina, P.C., Quirarte, G.L., 2017. Inhibition of transcription and translation in the striatum after memory reactivation: lack of

evidence of reconsolidation. Neurobiol. Learn. Mem. 142 (A), 21–29.
Quevedo, J., Vianna, M.R., Roesler, R., de-Paris, F., Izquierdo, I., Rose, S.P., 1999. Two time windows of anisomycin-induced amnesia for inhibitory avoidance training in rats: protection from amnesia by pretraining but not pre-exposure to the task apparatus. Learn. Mem. (6), 600–607.
Radulovic, J., Jovasevic, V., Meyer, M.A., 2017. Neurobiological mechanisms of state-dependent learning. Curr. Opin. Neurobiol. 45, 92–98. https://doi.org/10.1016/j.conb.2017.05.013.
Rao, S.S., Grollman, A.P., 1967. Cycloheximide resistance in yeast: a property of the 60s ribosomal subunit. Biochem. Biophys. Res. Commun. 29 (5), 696–704.
Reed, C.L., Shoham, S., Halgren, E., 2004. Neural substrates of tactile object recognition: an fMRI study. Hum. Brain Mapp. 21 (4), 236–246.
Rodríguez-Ortiz, C.J., Balderas, I., García-Delatorre, P., Bermúdez-Rattoni, F., 2012. Taste aversion memory reconsolidation is independent of its retrieval. Neurobiol. Learn. Mem. 98 (3), 215–219.
Roullet, P., Sargolini, F., Oliverio, A., Mele, A., 2001. NMDA and AMPA antagonist infusions into the ventral striatum impair different steps of spatial information processing in a nonassociative task in mice. J. Neurosci. 21 (6), 2143–2149.
Schmahmann, J.D., Pandya, D.N., Wang, R., Dai, G., D'Arceuil, H.E., de Crespigny, A.J., Wedeen, V.J., 2007. Association fibre pathways of the brain: parallel observations from diffusion spectrum imaging and autoradiography. Brain 130 (Pt 3), 630–653.
Sherry, J.M., Milsome, S.L., Crowe, S.F., 2010. The roles of RNA synthesis and protein translation during reconsolidation of passive-avoidance learning in the day-old chick. Pharmacol. Biochem. Behav. 94 (3), 438–446.
Steinmetz, A.B., Ng, K.H., Freeman, J.H., 2017. Memory consolidation within the central amygdala is not necessary for modulation of cerevellar learning. Learn. Mem. 24 (6), 225–230.
Stewart, O., Schuman, E.M., 2001. Protein synthesis at synaptic sites on dendrites. Annu. Rev. Neurosci. 24, 299–325.
Tang, Y., Mishkin, M., Aigner, T.G., 1997. Effects of muscarinic blockade in perirhinal cortex during visual recognition. Proc. Natl. Acad. Sci. U. S. A 94 (23), 12667–12669.
Thompson, C.I., Grossman, L.B., 1972. Loss and recovery of long-term memories after ECS in rats: evidence for state-dependent recall. J. Comp. Physiol. Psychol. 78 (2), 248–254.
Thompson, C.I., Neely, J.E., 1970. Dissociated learning in rats produced by electroconvulsive shock. Physiol. Behav. 5 (7), 783–786.
Thorpe, S., Fize, D., Marlot, C., 1996. Speed of processing in the human visual system. Nature 381 (6582), 520–522.
Tran, D.H., Gong, R., Tang, S.J., 2007. Differential roles of NR2A and NR2B subtypes in NMDA receptor-dependent protein synthesis in dendrites. Neuropharmacology 53 (2), 252–256.
Tronel, S., Sara, S.J., 2003. Blockade of NMDA receptors in prelimbic cortex induces an enduring amnesia for odor-reward associative learning. J. Neurosci. 23 (13), 5472–5476.
Wanisch, K., Wotjak, C.K., 2008. A Time course and efficiency of protein synthesis inhibition following intracerebral and systemic anisomycin treatment. Neurobiol. Learn. Mem. 90 (3), 485–494.
Winters, B.D., Bussey, T.J., 2005. Glutamate receptors in perirhinal cortex mediate encoding, retrieval, and consolidation of object recognition memory. J. Neurosci. 25 (17), 4243–4251.

Free Radical Biology and Medicine 135 (2019) 102–115

Contents lists available at ScienceDirect

Free Radical Biology and Medicine

journal homepage: www.elsevier.com/locate/freeradbiomed

Original article

Reduced lifespan of mice lacking catalase correlates with altered lipid metabolism without oxidative damage or premature aging

José Raúl Pérez-Estrada[a], David Hernández-García[a], Francisco Leyva-Castro[a], Javier Ramos-León[a], Osiris Cuevas-Benítez[a], Mauricio Díaz-Muñoz[b], Susana Castro-Obregón[a,1], Ramiro Ramírez-Solís[c], Celina García[a], Luis Covarrubias[a,*]

[a] Instituto de Biotecnología, Universidad Nacional Autónoma de México, Cuernavaca, Mor, Mexico
[b] Instituto de Neurobiología, Universidad Nacional Autónoma de México, Cuernavaca, Mor, Mexico
[c] University of Texas, Health Science Center, San Antonio, TX, USA

A B S T R A C T

The relationship between the mechanisms that underlie longevity and aging and the metabolic alterations due to feeding conditions has not been completely defined. In the present work, through the deletion of the gene encoding catalase, hydrogen peroxide (H_2O_2) was uncovered as a relevant regulator of longevity and of liver metabolism. Mice lacking catalase ($Cat^{-/-}$) fed ad libitum with a regular diet showed a shorter lifespan than wild type mice, which correlated with reduced body weight, blood glucose levels and liver fat accumulation, but not with increased oxidative damage or consistent premature aging. High fat diet (HFD) and fasting increased oxidative damage in the liver of wild type animals but, unexpectedly, this was not the case for that of $Cat^{-/-}$ mice. Interestingly, although HFD feeding similarly increased the body weight of $Cat^{-/-}$ and wild-type mice, hyperglycemia and liver steatosis did not develop in the former. Fat accumulation due to fasting, on the other hand, was diminished in mice lacking catalase, which correlated with increased risk of death and low ketone body blood levels. Alteration in expression of some metabolic genes in livers of catalase deficient mice was consistent with reduced lipogenesis. Specifically, *Pparγ2* expression up-regulation in response to a HFD and down-regulation upon fasting was lower and higher, respectively, in livers of $Cat^{-/-}$ than of wild type mice, and a marked decay was observed during $Cat^{-/-}$ mice aging. We propose that catalase regulates lipid metabolism in the liver by an evolutionary conserved mechanism that is determinant of lifespan without affecting general oxidative damage.

1. Introduction

Aging is the process of organism deterioration that progressively reduces the capacity to keep the general organism homeostasis, increasing the likelihood of death. In contrast, longevity is the length of life from birth to death. Aging is a complex process involving multiple factors going from genetic to environmental and acting at different stages of organism life, including gestation [1]. Since all factors causing aging also reduce lifespan, delaying aging may not extend longevity, but it would extend the healthy life (i.e., health-span; [1,2]).

The good correlation between cellular oxidative damage and aging has been on the basis of the prevalent but still controversial oxidative theory of aging [3]. A premise of this theory is that molecular oxidation causes the cellular damage that accompanies aging. Therefore, lifespan would be determined by the amount of reactive oxygen species (ROS) produced and the capacity to protect against oxidation (e.g., by antioxidants) or the toxic effect of oxidized macromolecules (e.g., by repair or removal; [4]). However, attempts to change the maximal lifespan by increasing or reducing oxidative stress in mice have not resulted in consistent correlations predicted by the oxidative theory, but it does influence the development of a pathology [5]. These observations suggest that under chronic stress, proper function of antioxidant mechanisms could contribute to health-span. Therefore, the role of oxidative stress on aging and health-span is worth of further investigation.

The fact that ROS are unavoidable molecules produced during the process of oxidative phosphorylation as well as of other metabolic reactions such as the β-oxidation of fatty acids implies that metabolic activity would be an intrinsic component of the aging process. Metabolic activity might be a limiting determinant of lifespan as suggested by the key role of the insulin/IGF1 signaling pathway in *Caenorhabditis elegans* (*C. elegans*) and the extension of lifespan promoted by caloric restriction in several species. However, the level at which the control of lifespan due to changes in metabolic activity relies on oxidative damage or ROS-mediated signaling is yet to be determined.

Several antioxidant systems contribute to keep the redox state

* Corresponding author. Av. Universidad 2001, Cuernavaca, Mor, 62210, Mexico.
E-mail address: covs@ibt.unam.mx (L. Covarrubias).
[1] Present address: Instituto de Fisiología Celular, Universidad Nacional Autónoma de México, Ciudad de México, México.

https://doi.org/10.1016/j.freeradbiomed.2019.02.016
Received 23 October 2018; Received in revised form 11 February 2019; Accepted 15 February 2019
Available online 25 February 2019
0891-5849/ © 2019 Elsevier Inc. All rights reserved.

INFORME DE LABORES 2019

required for normal cell functioning and the prevention of cell damage. For example, controlled balance of cofactors such as NAD^+/NADH and $NADP^+$/NADPH is necessary for a broad diversity of reactions, including the ones involved in metabolism and aging [6]. Antioxidant enzymes are expected to contribute to this regulation and, generally, to the control of ROS levels; however, their intracellular localization indicates more specific cellular functions, some directly related with metabolic activity [7]. For example, the mitochondrial localization of superoxide dismutase 2 controls the superoxide produced by the oxidative phosphorylation [8]. On the other hand, the membrane localization of glutathione peroxidase 4 suggests that it protects lipids from peroxidation [9]. In the cytosol, many antioxidant enzymes are present, but the glutathione peroxidase 1 (GPX1) appears to be relevant for proper insulin signaling [10]. Catalase is preferentially located in the peroxisome where likely regulates the levels of H_2O_2 produced as a by-product of, among other oxidation reactions, the very long chain fatty acid β-oxidation [11–13]. These functions appear to be irrelevant during mammalian embryogenesis, but the abnormal phenotypes observed in the absence of some of them suggest a function during adult life [14–17].

The liver can be considered a metabolic center where signals from the nervous system and peripheral organs (e.g., pancreas, adipose tissue) converge to maintain the homeostasis of many metabolites required for the well-functioning of cells and organs. In particular, lipid metabolism in hepatocytes is fundamental for the maintenance of systemic energy homeostasis, such that under fed condition insulin promotes lipogenesis and lipoprotein secretion, whereas under fasting, fatty acid oxidation increases eventually producing ketone bodies, an essential energetic resource when glucose is depleted. These processes are critically altered in obesity resulting in accumulation of fat in the liver, a condition that often correlates with the hyperglycemia and insulin resistance that typically characterize type 2 diabetes [18]. Hepatocytes are rich in peroxisomes where catalase is the main protein component, though has also been detected in the cytosol and mitochondria [11,19]. Therefore, it is expected that catalase perform a key antioxidant role in hepatocytes, especially during active fatty acid oxidation.

The catalase of mammals is a homotetrameric enzyme that contains a heme moiety in the active site of each subunit [11]. Mammals have a single gene encoding catalase or homologous enzymes. The catalytic reaction of catalase uses two H_2O_2 molecules, the only natural substrate known, to oxidize iron in the heme and release water and oxygen. Catalase activity is among the highest known to be able of degrading H_2O_2 in a wide range of concentrations [11]. In the present work, we found that mice lacking catalase have a shorter lifespan than wild type mice and reduced fat accumulation, without an evident increase in oxidative damage. Therefore, we explored the role of catalase in liver under conditions that promote degradation of fatty acids in the liver, a high fat diet and fasting. Our data support a relevant role of peroxisomal H_2O_2 in the regulation of lipid metabolism in the liver, a process that could significantly influence lifespan by an evolutionary conserved mechanism.

2. Material and methods

2.1. Cat null allele generation

The null mutation in the gene encoding catalase (*Cat*) was generated in embryonic stem (ES) cells (AB2.2 line) by standard gene targeting procedures. The 5'- (3.5 kb) and the 3'- (3.3 kb) arms specific for the *Cat* genomic region were inserted in the pPGKNeoloxPA vector containing the Neo^r gene under the control of the PGK promoter flanked by loxP sequences (Fig. S1A). Because of homologous recombination, a 6.2 kb region, containing exons 4–6 and a fragment of 7, was deleted (Figs. S1A and B). The chimeric mice, resulting after blastocyst ES cell injection, were backcrossed with mice of the C57BL/6NJ strain obtained from Jackson Laboratories for more than 10 generations giving rise to the heterozygous $Cat^{+/-}$ line used in the present work. Heterozygous $Cat^{+/-}$ mice were intercrossed to produce mice with $Cat^{+/+}$, $Cat^{+/-}$ and $Cat^{-/-}$ genotype and, in some cases, $Cat^{-/-}$ mice were also produced by incrosses. Mice were genotyped by PCR with specific primers for the wild-type (forward TTGTTACCGCTTTCCTAAACTCC; reverse: TGACTTCCTTGGTCAGATCAAATG) and mutant alleles (forward TGTC ATTCTATTCTGGGGGG; reverse: GGACGACACTTATGAAGCAATC).

2.2. Animal protocols

The mice were maintained in plastic cages within a pathogen-free animal facility with humidity-monitored rooms and a 12-h light/dark cycle. Male mice were used for all experiments and were euthanized by cervical dislocation and collected tissues and blood samples stored at −70 °C. Survival along aging was determined in cohorts consisting of 28, 30 and 31 male mice with the $Cat^{+/+}$, $Cat^{+/-}$ and $Cat^{-/-}$ genotypes, respectively, which were maintained in cages with 2–3 individuals, fed with regular chow ad libitum, had free access to water and received standard animal care. The exact birth and death date were recorded, and mice that developed acute skin ulcers, typical of C57BL/6NJ strain, were euthanized and not considered for the survival analysis; relevant to mention is that emergence of skin ulcers did not correlate with the *Cat* genotype (14/28 $Cat^{+/+}$, 11/30 $Cat^{+/-}$ and 14/31 $Cat^{-/-}$) but it did correlate with age (2/89 of 2–9 months, 19/79 of 10–17 months and 18/51 of 18–25 months). Ambulatory and fine activity of individual 12- or 24-month-old (mo) mice $Cat^{+/+}$ or $Cat^{-/-}$ was determined with the Photobeam Activity System (San Diego Instruments Inc, San Diego, CA, USA) and the data analyzed with the PAS Home Cage software (San Diego Instruments Inc, San Diego, CA, USA). Briefly, the activity chamber (11.75" (W) x 18.75" (L)) records the number of times the mouse crosses a photobeam grid oriented on an x and y axis; consecutive photobeam breaks occurring in adjacent photobeams were scored as an ambulatory movement while breaks occurring at same photobeam were scored as fine activity. Cumulative ambulatory and fine activity counts were recorded every 5 min for 24 h (7:00–7:00 daytime); the total activity was the sum of ambulatory and fine activity. Groups of at least 3 mice with the $Cat^{+/+}$ and $Cat^{-/-}$ genotype were collected for each diet or feeding condition. High fat diet (HFD; 60% calories from fat; D12492, Diets Research, New Brunswick, NJ, USA) feeding was initiated, either immediately after winning (i.e., at 21 days of age) and continued for 6 months, or at 3 months of age and continued for 2 or 12 weeks. HFD-control low fat diet for these experiments was the one recommended by the provider (10% calories from fat; D1245B, Diets Research, New Brunswick, NJ, USA). For starvation protocols, 3-mo male mice with a defined *Cat* genotype were collected, fed with a standard diet (1218SX, Envigo, Indianapolis, IN, USA) and food removed at 7:00 daytime and animals sacrificed 24 or 48 h later; in some cases, refeeding was allowed for 12 h starting at 7:00 daytime. Newborn mice with the genotype required for starvation experiments were produced by timed matings of homozygous mice with the desired genotype ($Cat^{+/+}$ *or* $Cat^{-/-}$); at 19 days post coitum a cesarean was performed on pregnant mice. Newly delivered mice were kept in a humidified chamber at 37 °C and continuously monitored to determine survival. Another group of pregnant mice gave birth naturally, and 12 h later pups were transferred to the humidified chamber to follow survival. For the capture of X-Ray images, mice were anesthetized with intranasal 1% isoflurane (Sofloran Vet, PiSA Agropecuaria, Guadalajada, JAL, México) and images captured in a 15 cm^2 view field, aperture f/stop of 2.8 and an acquisition time of 5 s with a 0.4 mm filter using the Multimodal Animal Rotation System (MARS) in the In-vivo Xtreme instrument (Bruker, Germany). The AKT activation by insulin was performed in 2-mo mice fed with the standard diet; mice were fasted for 12 h before ip injection of insulin (3 U/kg) or of a saline solution and euthanized 30 min later. All animal procedures described were approved by the Bioethical Committee of our Institute and

rigorously meet international standards.

2.3. Blood and serum analysis

Blood was collected from the tail or by cardiac puncture after sacrifice. To obtain serum, blood was incubated for 2 h at room temperature and centrifuged at 2000 g for 10 min; the supernatant recovered was stored at −70 °C until used. Levels of glucose and ketone bodies were determined with the Ascencia Countour glucometer (Bayer, Japan) or the FreeStyle ketone/glucometer (Abbot, Maidenhead, UK), respectively. Insulin was measured with the Ultra-Sensitive Mouse Insulin ELISA kit (Crystal Chem, Downers Grove, IL, USA). Triglycerides and cholesterol in serum were determined using the Triglycerides reagent (BioSystem, Costa Brava, Barcelona, Spain) or the Cholesterol reagent (BioSystem, Costa Brava, Barcelona, Spain) following the manufacturer's instruction. For the glucose tolerance test, glucose (2 mg/kg) was intraperitoneally (ip) injected after a 12 h starvation period and blood glucose concentration immediately measured (time "0") and then at 15, 30, 60 and 120 min after injection. For the insulin tolerance test, 4 h-starved mice were ip injected with a recombinant human insulin (Gibco, Invitrogene, CarlsBad, CA, USA) and blood glucose concentration immediately measured (time "0") and then at 15, 30, 60 and 120 min after injection.

2.4. Quantification of total hepatic cholesterol, triglycerides and glycogen

Lipids of liver were extracted by homogenization of 50 mg of tissue in 1 mL of PBS, followed by the addition of 4 ml of Folch reactive (chloroform/methanol 2:1). After vortexing, the suspension was centrifuged at 3000 g for 10 min, and the organic phase transferred to a glass vial for evaporation to dryness at 37 °C overnight. The precipitate was resuspended in 500 µl of 1% sodium deoxycholate solution, and triglycerides and cholesterol concentration determined using the Triglycerides reagent (BioSystem, Costa Brava, Barcelona, Spain) or the Cholesterol reagent (BioSystem, Costa Brava, Barcelona, Spain) following the manufacturer's instruction. For hepatic glycogen content, 40–100-mg of tissue were homogenized in 100 µl of 30% KOH at 100 °C for 30 min. The homogenates were cooled to room temperature and then 100 µl of 20% Na_2SO_4 followed by 1 ml ethanol were added. The mixture was left at −20 °C for 6 h and then centrifugated at 3000 g for 10 min; after removal of the supernatant, the pellet was resuspended in 500 µl of 0.2 M sodium acetate buffer pH 4.8 and incubated with 5 units of amyloglucosidase (Sigma-Adrich, Saint Louis, MO, USA) for 8 h at 55 °C. Finally, glucose concentration was measured using the Glucose reagent (BioSystem, Costa Brava, Barcelona, Spain); the data were expressed as nmol equivalents of glucose/g liver.

2.5. Determination of conjugated dienes and catalase activity

Livers were homogenized in PBS and total amount of protein recovered determined with the Bradford reagent (Bio-Rad, Hercules, CA, USA) for each resulting sample. Conjugated dienes were determined in lipids extracted as referred above and using previously described procedures [20]. The catalase activity was determined in whole liver homogenates by two methods: (a) in-gel activity, detected by the absence of the Prussian blue precipitate in non-denaturing gels embedded first with H_2O_2 and then with a potassium ferrocyanide/ferric chloride solution, or (b) by spectrophotometrically determining the decline in concentration of H_2O_2 substrate with time. Both methods were performed following the protocol described by Weydert and Cullen [21].

2.6. Histological analysis

Liver tissue samples were fixed with 4% paraformaldehyde overnight and embedded in paraffin wax or in Tissue-Tek (Sakura Finetek, Torrance, CA, USA) for microtome (RM2145, Leica, Nussloch, Germany) or freezing Cryostate sections (CM1850, Leica, Nussloch, Germany), respectively. Paraffin-embedded liver slices were stained with a hematoxylin-eosin cocktail (Sigma-Adrich, Saint Louis, MO, USA) following the manufacturer's instructions. Slices from frozen tissues were stained with red-oil and counterstained with hematoxylin (Sigma-Adrich, Saint Louis, MO, USA), or stained for β-galactosidase activity at pH 6 using the Beta-Galactosidase Tissue Stain Base Solution (Merk-Millipore, Darmstadt, Germany) and counterstained with eosin (Sigma-Adrich, Saint Louis, MO, USA) following the manufacturer's instructions. Similar procedure was followed for hematoxylin-eosin staining of adipose tissue slices but Bouin's fixing solution (Sigma-Adrich, Saint Louis, MO, USA) was used. Bright-field images were acquired using the Olympus BX51 microscope and a C-5050 camera (Olympus, Tokyo, Japan). β-gal-eosin images were quantified using the Image J software (version 2.0.0). Briefly, H&E color deconvolution was applied to each image and the layer corresponding to 'hematoxylin" was selected and converted to a 8-bit format before establishing a threshold. After that, the analysis of particles was performed to obtain the count of blue spots, the mean average of spot size and the total stained area; three images per liver were analyzed.

2.7. Immunoblotting

Liver tissue lysates (35 µg protein) prepared in RIPA lysis buffer (50 mM Tris pH7.5, 150 mM NaCl, 1% Triton X-100, 0.5% sodium deoxycholate, 0.1% SDS with protease and phosphatase inhibitors) were separated by electrophoresis on 10% SDS-PAGE gels and transferred to Immobilon-FL membranes (Merk-Millipore, Darmstadt, Germany). The blots were blocked with the Odyssey blocking buffer (LI-COR Biosciences, Lincoln, NE, USA) at room temperature for 1 h and then incubated overnight with the primary antibodies obtained from Cell Signaling (Cell Signaling Technology, Danvers, MA, USA): anti-AMPK (#2532, 1:2000 dilution), anti-pAMPK (#2535, 1:1000 dilution), anti-tubulin (#3873, 1:7000 dilution), anti-AKT (#9272, 1:1000 dilution), anti-pAKT (#2965, 1:1000 dilution), anti-SQSTM1/p62 (#23214, 1:1000 dilution) anti-LC3A/B (#4599, 1:100 dilution). After washing 3 times for 5 min each in a Tris-buffered saline-Tween 20 (0.1%, vol:vol) solution, the membranes were incubated with a goat anti-rabbit IgG or anti-mouse IgG secondary antibodies coupled to infrared fluorophores (emission at 689 or 778 nm; LI-COR Biosciences, Lincoin, NE, USA) at room temperature for 1 h. After washing, the protein bands were visualized in the Odyssey Classic Imaging System (LI-COR Biosciences, Lincoin, NE, USA). Twenty percent SDS-PAGE was used only for the detection of LC3 using liver lysates prepared with RIPA containing 1% SDS. Protein carbonylation was determined using the OxyBlot Oxidation Detection Kit (Merk-Millipore, Darmstadt, Germany). Briefly, carbonyls in proteins were derivatized into 2,4-dinitrophenyhydrazone (DNP-hydrazone) and then processed for western-blot; oxidized proteins were detected with an anti-DNP antibody and visualized in the Odyssey Classic Imaging System (LI-COR Biosciences, Lincoin, NE, USA). Protein bands were quantified by densitometry using the ImageJ software (version 2.0.0).

2.8. Gene expression analysis

Total liver RNA was obtained using the RiboEx total RNA isolation solution (GeneAll Biotecnology, Seoul, Korea) following the manufacturer's instructions. This RNA was used as template to synthesize cDNA with the HyperScrip reverse transcriptase (GeneAll Biotecnology, Seoul, Korea) using random hexamers as primers (Invitrogen, US). The quantitative PCR (qPCR) reaction was performed with the SYBR Green mix (KAPA Biosystems, Cape Town, South Africa) in the Rotor-Gene Q thermocycler (Qiagene, Germantown, MD, USA). The sequence of specific oligonucleotides were taken from either reports of others or designed by us using the PrimerBlast3 (see Table S1 for details). In some cases, equal amounts of cDNA from at least 3 individuals were

mixed before qPCR. The relative gene expression level was estimated by the ΔΔCT method, using *Rplp0* expression as an internal control and the indicated mouse group as experimental control.

2.9. Statistical analysis

All statistical analyses were done with the Prism software version 5.0b (La Jolla, CA, US) using the Long-Rank test for survival and the two-way variance analysis followed by the Bonferroni test for the other rest of experiments; minimal significance considered was 0.05 (*0.05, **0.01, ***0.001) with a "n" minimal value of 3. All graphs shown are the media ± standard deviation.

3. Results

3.1. Catalase gene (Cat) inactivation causes premature death without signs of increased oxidative damage or general advanced aging

The *Cat* gene is abundantly expressed in early mouse embryos (Figs. S1C and D) and in several adult organs and tissues like liver, kidney and spleen (Fig. S1E). To determine the function of catalase during embryogenesis and in adult life, we generated a null *Cat* allele by deleting a region (exons 4–6) encoding an essential catalase domain in embryonic stem cells (Figs. S1A and B). Mice homozygous for this null allele ($Cat^{-/-}$) did not show catalase activity (Fig. S1E) supporting that, at least in the tissues tested, there is no other homologous gene that encodes an enzyme with a similar activity. $Cat^{-/-}$ mice were viable, born with the expected mendelian ratio but, interestingly, showed a decreased lifespan in comparison with $Cat^{+/+}$ and $Cat^{+/-}$ mice (Fig. 1A). Twelve-months old (mo) or 24-mo mice lacking catalase did not show evident signs of more advanced aging than wild type such as higher density of gray hairs, alopecia or reduced motor activity (Fig. 1B and C). Accordingly, the increasing lipid peroxidation observed along the first 10 months of life in several organs was similar between wild type and mice lacking catalase (Fig. 1D) or even lower in livers of 24-mo $Cat^{-/-}$ mice (see below). However, X-ray images revealed kyphosis (hunchback) in $Cat^{-/-}$ mice since 12-months of age, a phenotype that was more pronounced in 24-mo mice (Fig. 1E). Despite this latter evident phenotype associated with advanced aging, no other data indicated premature aging as the cause of death. Relevant to mention is that, although initial increase in weight with age was similar, mutant 24-mo mice were slimmer than wild type mice (Fig. 1E and F), despite the fact that there were no signs of any sickness (e.g., piloerection, presence of tumors) and that, in general, animals were active near death (Fig. 1C). In addition, the characteristic hyperglycemia of old mice did not develop in mice lacking catalase (Fig. 1G), though insulin levels increased with age as in wild-type mice (Fig. 1H). Circulating levels of triglycerides, cholesterol and ketone bodies were as in wild-type mice (Fig. 1I–K).

Since a distinctive characteristic of liver is the presence of high catalase activity, this organ of $Cat^{-/-}$ mice would be expected to show detectable cellular and molecular alterations. Increased lipid oxidative damage occurred in the liver of wild type mice with aging but, unexpectedly, this was not found in the liver of $Cat^{-/-}$ mice, which showed even reduced lipid oxidative damage at the age of 24 months (Fig. 2A) and there was no difference in liver protein oxidation between $Cat^{-/-}$ and wild type mice at 12- and 24-months of age (Fig. 2B). No compensatory activity of peroxidases (Fig. S1E) or an antioxidant response were detected in the liver of mice lacking catalase (Fig. S1F). In contrast, staining for β-galactosidase at pH6, a commonly used indicator of cellular senescence within a tissue, emerged in livers of $Cat^{-/-}$ at earlier age and spots were in higher number and covered a larger area than in those of $Cat^{+/+}$ mice (Fig. 2C). However, the association of this difference with cellular senescence could not be established because, as expected, livers of wild type and of $Cat^{-/-}$ mice showed similarly increasing levels with age in *p16*, *p21* and *p53* expression (Fig. 2D). Interestingly, liver fat accumulation with aging, as revealed by red oil staining, in *Cat* deficient mice was lower than in wild type mice (Fig. 2E), and particularly coincided with triglycerides and cholesterol levels detected in livers of 24-mo mice (Fig. 2F and G). No difference in liver glycogen content was found between wild-type and $Cat^{-/-}$ mice at any age tested (Fig. 2H). Therefore, the liver of $Cat^{-/-}$ mice do not show consistent characteristic of premature aging.

3.2. The lack of catalase prevents from oxidative damage and fat accumulation in the liver in response to feeding with a HFD

Oxidative damage or premature aging was not obviously related with the reduction in lifespan of catalase deficient mice. Instead, the slim appearance of old mutant mice together with their relatively low levels of blood glucose and of accumulated liver fat suggested that metabolic alterations are behind premature death. In agreement with the participation of catalase in fat metabolism in the liver (Fig. 3A), wild type mice fed with a HFD markedly decreased catalase activity (Fig. 3B) with a corresponding increment in lipid peroxidation (Fig. 3C). Paradoxically, the liver of $Cat^{-/-}$ mice did not show the increment in lipid peroxidation in response to HFD, though increased levels were detected when these mice were fed with the HFD-control diet (Fig. 3C). The contrasting difference between this latter observation and the one shown above (Fig. 2A) could be due to the diet composition; particularly, the HFD-control has 2/3 of the amount of polyunsaturated fat in standard chow, and the caloric supply of fat and carbohydrates in HFD-control is lower and higher, respectively, than those in standard chow (see more details in Table S2). These data together indicate that the absence of catalase prevents from the rise in ROS levels in association with a HFD.

An evident sign of the effect on fat metabolism due to a long-term HFD feeding is the accumulation of fat in liver, pathology known as hepatic steatosis. In agreement with the absence of evident abnormalities due to the lack of catalase, $Cat^{-/-}$ and $Cat^{+/+}$ mice fed with a HFD-control diet did not show body weight or feeding behavior differences during adult life (Fig. 3D, Fig. S2A). In addition, the pattern of increase in body weight and feeding behavior under a HFD was also similar for mice with either genotype (Fig. 3D, Fig. S2A). However, mice lacking catalase showed attenuated hepatic steatosis (Fig. 3E) and decreased triglycerides and cholesterol content in liver in comparison with wild type mice after 3 months feeding with a HFD (Fig. 3F and G), though an alteration in liver weight associated with the lack of catalase was not evident (Fig. S2B). The absence of catalase did not seem to affect adipocyte size or level of macrophage infiltration in the white tissue of epididymus (Fig. S2C), common in obese mice. Brown subcutaneous interscapular or white epidydimal fat tissue weight did not change in association with the levels of catalase (Figs. S2D and E) and evident accumulation of white adipose tissue was noted in all mice fed with a HFD (Fig. S2F). Therefore, HFD, instead of increasing oxidative damage in livers of $Cat^{-/-}$ mice, causes changes in the lipid metabolic pathways that generate steatosis (see below).

3.3. Mice lacking catalase fed with HFD do not develop hyperglycemia and glucose intolerance

It is widely known that mice fed for a long term with a HFD causes obesity and, consequently, hyperglycemia, glucose intolerance and insulin resistance. Recent data have also shown that these alterations in glycemia are strongly associated with liver steatosis [22]. The glycemia determined at 12-weeks after feeding with a HFD showed that $Cat^{-/-}$ mice did not develop the typical hyperglycemia observed in wild type mice, and glucose levels remained in a similar range as mice fed with the HFD-control diet (Fig. 3H). In agreement with this observation, the increase in insulin, typical in response to HFD feeding, was not observed in $Cat^{-/-}$ mice (Fig. 3I) and levels were similar to those observed in mice fed with the standard diet (Fig. 1H). Accordingly, and in

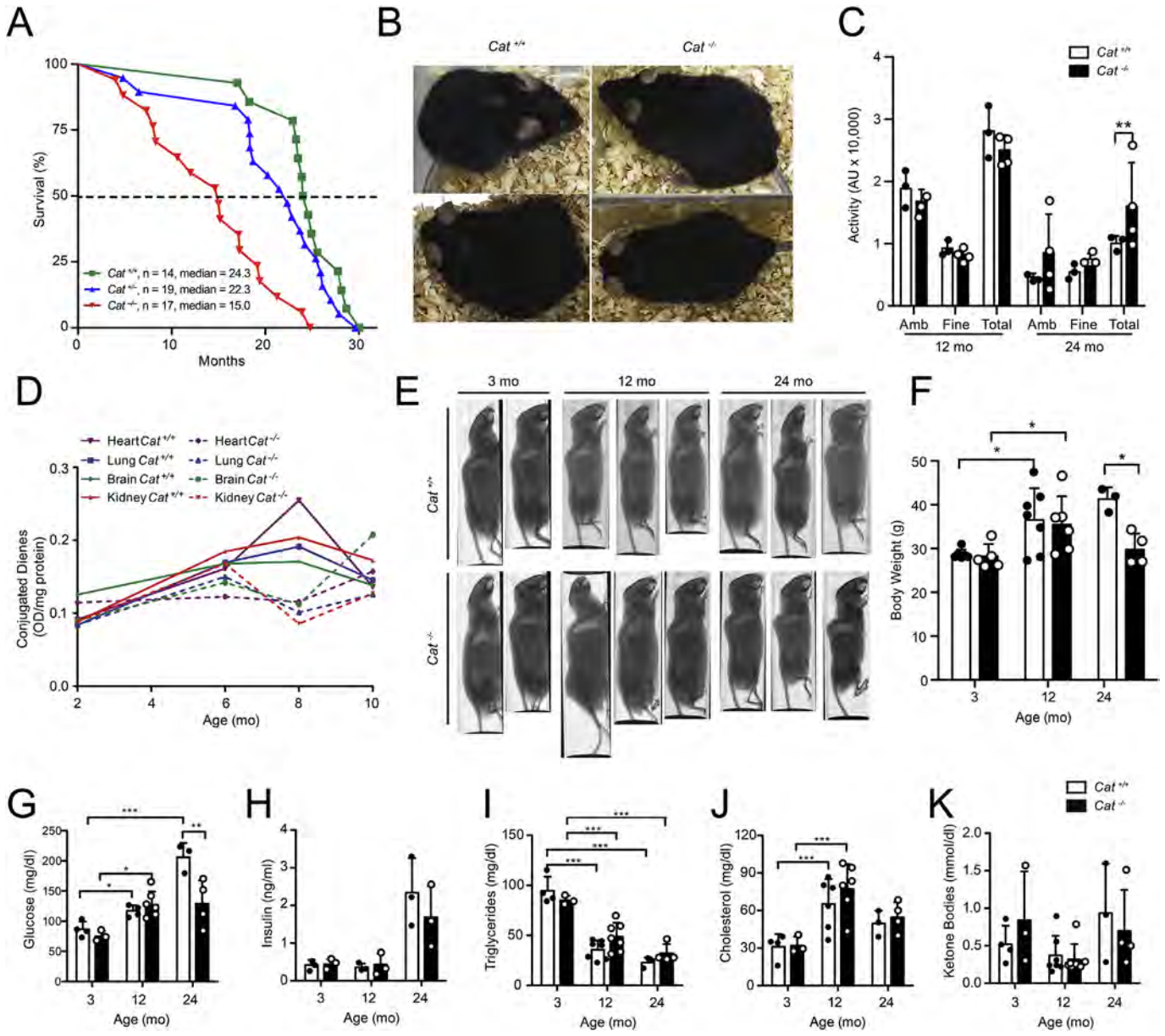

Fig. 1. Lifespan and aging parameters of mice with ($Cat^{+/+}$) or without ($Cat^{-/-}$) catalase. (A) Lifespan of $Cat^{+/+}$, $Cat^{+/-}$ and $Cat^{-/-}$ mice. Survival difference between $Cat^{+/+}$ and $Cat^{-/-}$ mice is statistically significant ($p < 0.0001$, Long-Rank test) and also between $Cat^{+/-}$ and $Cat^{-/-}$ mice ($p < 0.0012$) but not between $Cat^{+/+}$ and $Cat^{\pm}$ mice ($p < 0.1773$). (B) Representative photographs of 18-mo $Cat^{+/+}$ and $Cat^{-/-}$ mice. (C) Motor ambulatory (Amb), Fine (F) and Total (T), activity of 12- and 24-mo $Cat^{+/+}$ and $Cat^{-/-}$ mice. (D) Lipid oxidation, as estimated by the amount conjugated dienes, in whole extracts of heart, lung, brain and kidney of 2–10-mo mice. (E, F) X-ray images (E) and body weight (F) of 3-, 12- and 24-mo mice. (G–K) Glucose (G), insulin (H), triglycerides (I), cholesterol (J) and ketone bodies (K) levels in serum of 3-, 12- and 24-mo mice. Note that the lack of catalase in mice did not correlate with increased oxidative damage in several organs or consistent premature aging, but lower blood glucose levels and body weight were observed in mice lacking catalase. All values shown are the mean ± SD; n = 3–9. $*p < 0.05$, $**p < 0.01$ and $***p < 0.001$ (two-way variance analyses).

contrast with wild type animals, the $Cat^{-/-}$ mice fed with a HFD responded to an elevation in blood glucose concentration in a similar manner as wild type or mutant mice fed with the HFD-control diet (Fig. 3J). Interestingly, the response to high insulin dose of $Cat^{-/-}$ mice fed with a HFD-control diet was as of wild type mice, whereas when feeding was with a HFD, the initial response was similar among mice with any *Cat* genotype but recovery towards normal glucose levels was notoriously more rapid in animals lacking catalase (Fig. 3K). This phenomenon does not seem to be related to alterations in insulin signaling, since basal and insulin-stimulated levels of AKT phosphorylation were not modified by the absence of catalase (Fig. 3L,M; see also data below); nonetheless, increased gluconeogenesis could be responsible of the rapid recovery in glucose levels after the decline induced by insulin. These data are in agreement with the reduced accumulation of fat in the liver of $Cat^{-/-}$ mice that, consequently, prevents from losing the homeostatic control of glucose under a HFD.

3.4. The lack of catalase decreases the viability of mice under fasting conditions

Another condition that causes significant changes in lipid metabolism is fasting. Shortly after food deprivation, free fatty acids are brought from the adipose tissue to the liver causing the accumulation of fat in the form of lipid droplets [23]. The immediate source of glucose under food deprivation is glycogen but later fatty acids are directed to produce ketone bodies which are used as a major energetic source when

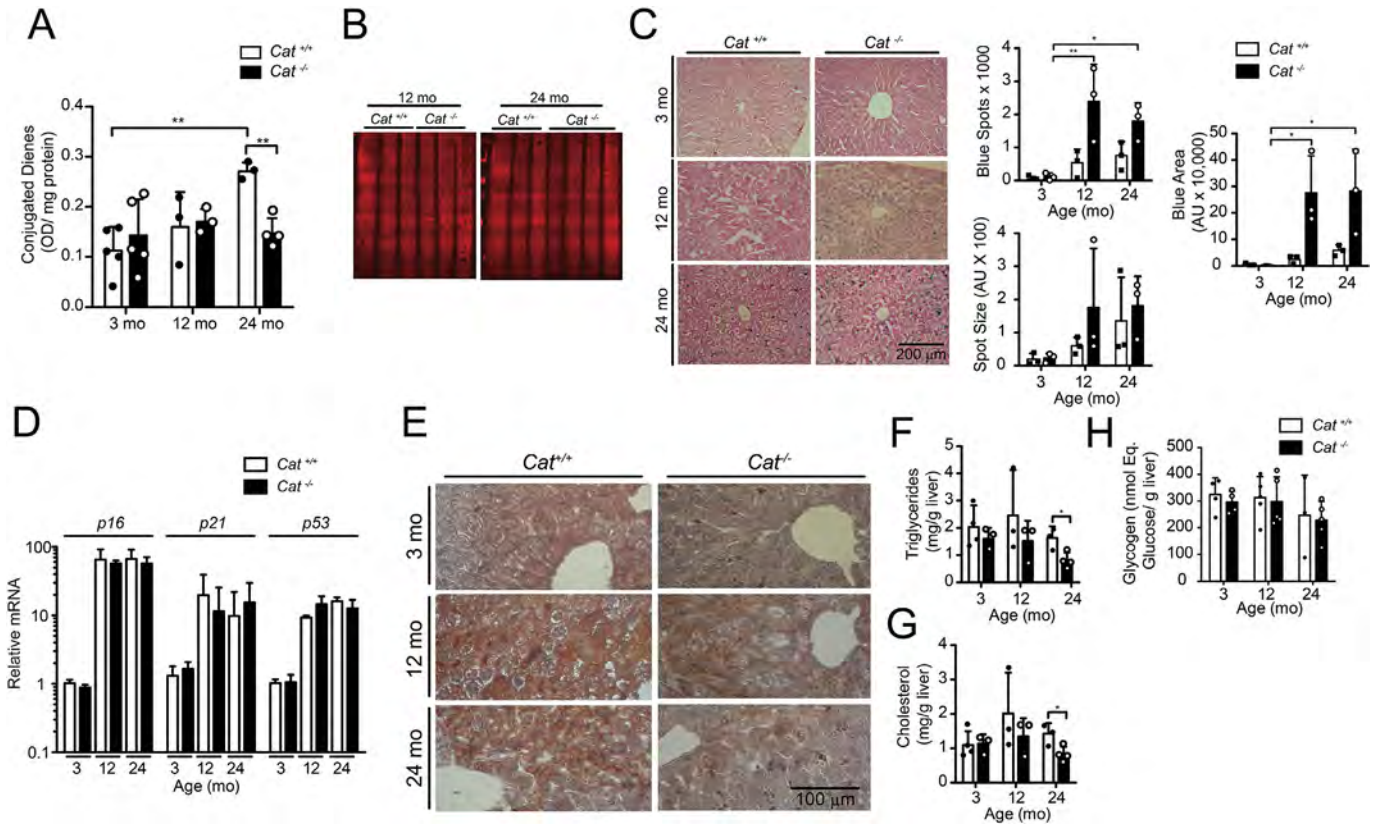

Fig. 2. Oxidative damage, cellular senescence and fat accumulation in livers of aging mice with ($Cat^{+/+}$) and without ($Cat^{-/-}$) catalase. Determinations were done in 3-, 12- and 24-mo mice. (A) Lipid oxidation in liver as determined by the amount of conjugated dienes. (B) Protein oxidation (immunoreactivity against DNP) in livers of 12- and 24-mo mice; no signal was detected before carbonyl derivatization into DNP-hydrazone. (C) Representative images of β-galactosidase stained liver sections. Level of staining was determined by counting the number of blue dots and estimating the area covered by them in representative sections of livers. (D) Expression of the senescence-related genes indicated determined by qRT-PCR. (E) Representative images of red-oil stained liver sections. (F, G, H) Triglycerides (E), cholesterol (F) and glycogen (H) content in liver. Note that the levels of oxidative damage correlated better with fat accumulation than with markers of cellular senescence. All values shown are the mean ± SD; n = 3–5. $*p < 0.05$, $**p < 0.01$ and $***p < 0.001$ (two-way variance analyses).

glucose supply is short [24].

In wild type mice, catalase activity and expression of its gene decreased during fasting, and their recovery was still incomplete 12 h after refeeding (Fig. 4A, Fig. S3A). In agreement with the decrease in catalase activity, the lipoperoxidation increased (Fig. 4B), suggesting that catalase normally participates in the metabolic changes associated with this condition. Weight loss throughout 48 h fasting and the corresponding weight gain after refeeding was not markedly altered in $Cat^{-/-}$ mice in comparison with wild type mice (Fig. 4C). Also, the lack of catalase did not cause significant differences in the early elevation and abrupt decline of blood glucose (Fig. S3B), and the expected increase in ketone bodies (Fig. 4D). Blood levels of cholesterol and triglycerides, and the liver glycogen content after 24 h and 48 h fasting in $Cat^{-/-}$ was as in wild type mice (Fig. S3 C-E). In contrast, the characteristic fat accumulation (Fig. 4E–G) and increased lipoperoxidation at 48 h (Fig. 4B) in the liver of wild type mice was reduced in $Cat^{-/-}$ mice. In agreement with a rise in protein recycling due to fasting, expression of autophagy/lysosome genes (*Atg5*, *Atg7*, *LC3B*, *p62*, *Lamp2*) and a gene associated with activation of ubiquitin-proteosome (*Atrogin-1*) increased in livers of $Cat^{-/-}$ and $Cat^{+/+}$ mice after 24 h of fasting (Fig. S3F). However, although the levels of p62 decreased similarly in livers of mice of both genotypes, the levels of LC3II, the autophagosome-associated form of LC3I that reflects autophagy activity [25], were moderately higher in livers of mice lacking catalase (Fig. S3G). Therefore, as in the HFD feeding condition, reduced fat accumulation accompanied by a lower oxidative damage was the major consequence of fasting in livers of mice lacking catalase.

The metabolic alterations described above were apparently no life-threatening for $Cat^{-/-}$ mice. However, it was common to find that some catalase deficient mice at 48 h of starvation, just before sacrifice, got still, a characteristic that correlated with an evident necrotic small bowel and was considered a sign of imminent death (Fig. 4H). Interestingly, these dying $Cat^{-/-}$ mice also showed an abrupt exhaust of ketone bodies (Fig. 4D, red dots). No wild type mice showed any of these characteristics at this time of fasting. Since it is well-known that the viability of starved newborn mice strongly depends on their capacity to use the energetic resources available (e.g., glycogen and ketone bodies; [26,27]), we tested the viability of newborn $Cat^{-/-}$ mice. Interestingly, the survival of $Cat^{-/-}$ newborn mice was reduced in comparison with wild type newborn mice under acute (Fig. 4I) or moderate starvation (Fig. 4J). Serum ketone bodies sharply decreased in $Cat^{-/-}$ mice after 6-h fasting, whereas reduction in $Cat^{+/+}$ mice was noted until 12-h fasting (Fig. 4K). Likewise, glucose levels decreased earlier in $Cat^{-/-}$ than in wild type (2-h vs. 6-h fasting; Fig. 4L), though this effect did not correlate with glycogen content (Fig. S3H). No major differences were detected in cholesterol and triglycerides liver content (Figs. S3I and J). Therefore, the depletion of substrates needed for production of ketone bodies might be behind the reduced viability, although the reduction in other energetic resources relevant under these conditions (e.g., amino acids; [28]) should also be considered.

3.5. Catalase deficiency reduces lipogenesis and maintains relatively high AMPK activity in the liver

The previous results suggest that the absence of catalase promote metabolic alterations that are detected when mice are subjected to

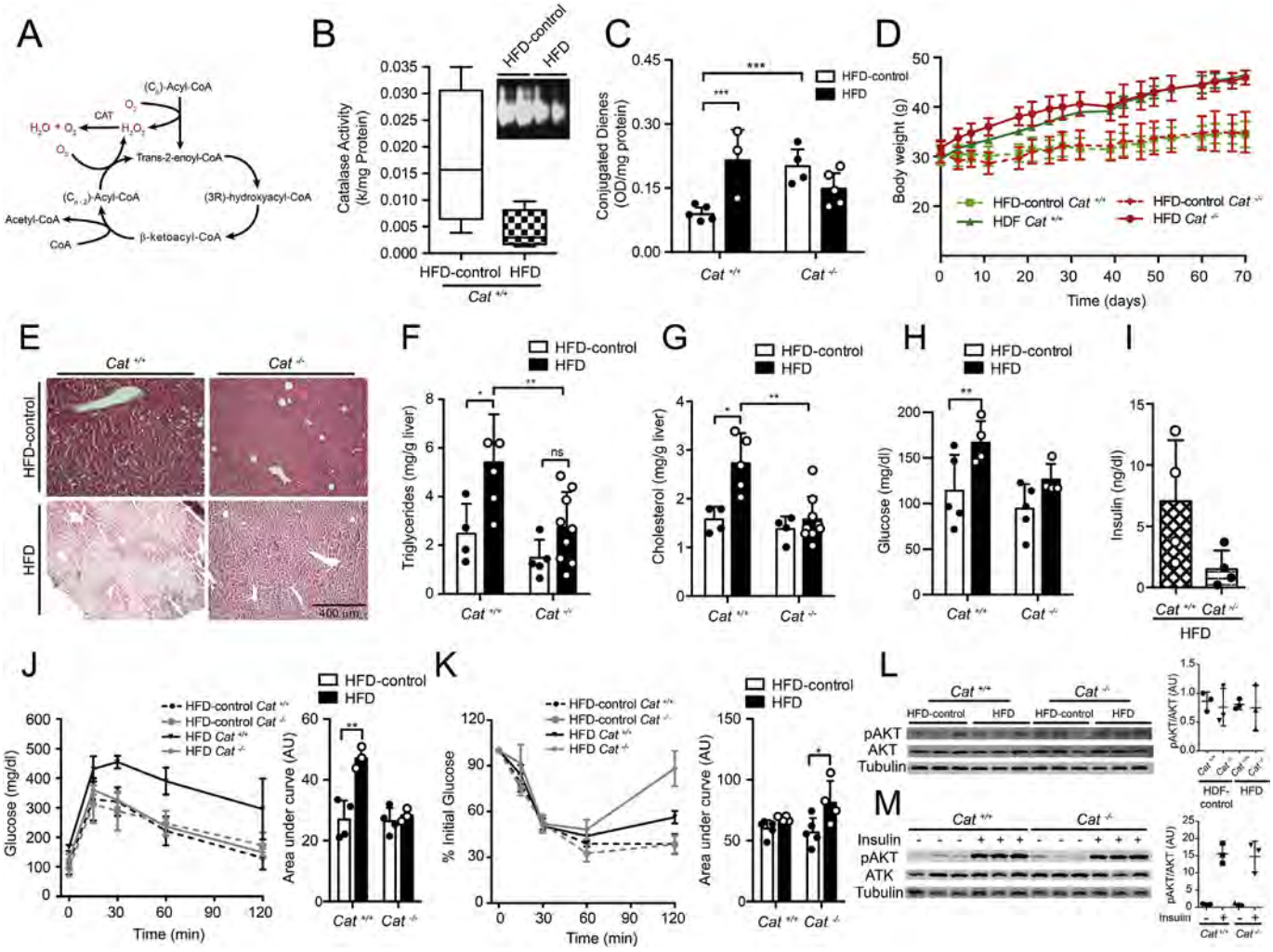

Fig. 3. Liver oxidative damage and metabolic parameters in mice with ($Cat^{+/+}$) and without ($Cat^{-/-}$) catalase under a high fat diet. Determinations were done in samples from mice fed with HFD-control diet or high fat diet (HFD) for 6 months. (A) Schematic representation of H_2O_2 production throughout every cycle of peroxisomal fatty acid β-oxidation. (B) Liver catalase activity. Inset shows catalase activity determined by a gel-based assay. (C) Liver oxidative damage, as estimated by the amount of conjugated dienes. (D) Body weight gain. (E) Representative images of hematoxilin-eosin stained liver sections. (F, G) Triglycerides (F) and cholesterol (G) content in liver. (H, I) Glucose (H) and insulin (I) serum levels. (J, K) Glucose levels during the glucose (J) and insulin (K) tolerance tests performed on mice after fed with the diets indicated. Areas under the curve are shown for statistical comparative analyses. (L, M) Liver pAKT and AKT, determined by western-blot, in mice fed with HFD-control and HFD (L) and after insulin infusion to mice fed with standard chow (M). Note that the liver oxidative damage and fat accumulation in response to HFD did not occur in mice lacking catalase, observations that correlated with the apparent increased insulin sensitivity. All values shown are the mean ± SD; n = 3–9. *$p < 0.05$, **$p < 0.01$ and ***$p < 0.001$ (two-way analysis variance).

feeding regimes that affect lipid metabolism. In order to get insights into the metabolic pathways altered in the liver by the lack of catalase, we estimated the expression levels of metabolic genes. In basal conditions (i.e., ad libitum ingestion of standard chow), gene expression showed downregulation of several selected genes (e.g., *Gck, Pparγ2, Spot14, Fasn*) in the liver of $Cat^{-/-}$ mice (Fig. S4A). When this comparison was done with liver samples from animals fed with food pellets of different composition (i.e., HFD-control diet; Tables S2–S4), some of the genes tested showed a contrasting expression pattern (*Gck*, *Pck1*, *G6pc*, *Fgf21*, *Cpt1a*) and downregulation of some lipogenic genes was not as evident in livers of mutant mice (e.g., *Spot14, Fasn*; Fig. S4B). This differential gene expression detected is possibly due to the nutrient composition of food pellets provided (Tables S2–S4) that, as described above, also affected the levels of lipid peroxidation.

Under feeding with a HFD for 3 months, mRNA levels of lipogenic genes (*Acc, Fasn*, *Elov6, Scd1* and *mGpat*), included the positive regulators *Pparγ2* and *Spot14*, were lower in livers of $Cat^{-/-}$ than of wild type mice (Fig. S4C). The expected expression up-regulation of *Fasn*, *Spot14* and *Pparγ2* was detected since 15 days after HFD feeding in the liver of wild type mice, whereas no or a mild effect was observed in the liver of mice lacking catalase (Fig. 5A); of note was the significant response of the *Pparγ2* gene in livers of wild type mice that, although upregulated in livers of $Cat^{-/-}$ mice, the increase in mRNA levels was much lower. Significant difference in the liver expression levels of gluconeogenic genes was not detected when comparing wild type mice with mice lacking catalase fed with a HFD (Fig. 5A). The downregulation of lipogenic gene expression in the liver of $Cat^{-/-}$ mice under a HFD is in agreement with the key role of lipogenesis in the generation of hepatic steatosis [22,29].

On the other hand, the mRNA levels of genes associated with catabolism such as *Gck* (encoding the first enzyme in the degradation of glucose), *Acox1* (encoding the first enzyme of the peroxisomal fatty acid β-oxidation pathway) and *Fgf21* (encoding a growth factor released in association with lipolysis) were higher in $Cat^{-/-}$ mice after 3 months of HFD feeding (Fig. S4C). Among these genes, only the expression of *Gck* responded to two-weeks HFD feeding (Fig. 5A), showing upregulation in livers of wild type mice as previously reported [30], but this effect was reduced in those of $Cat^{-/-}$ mice. These data together suggest

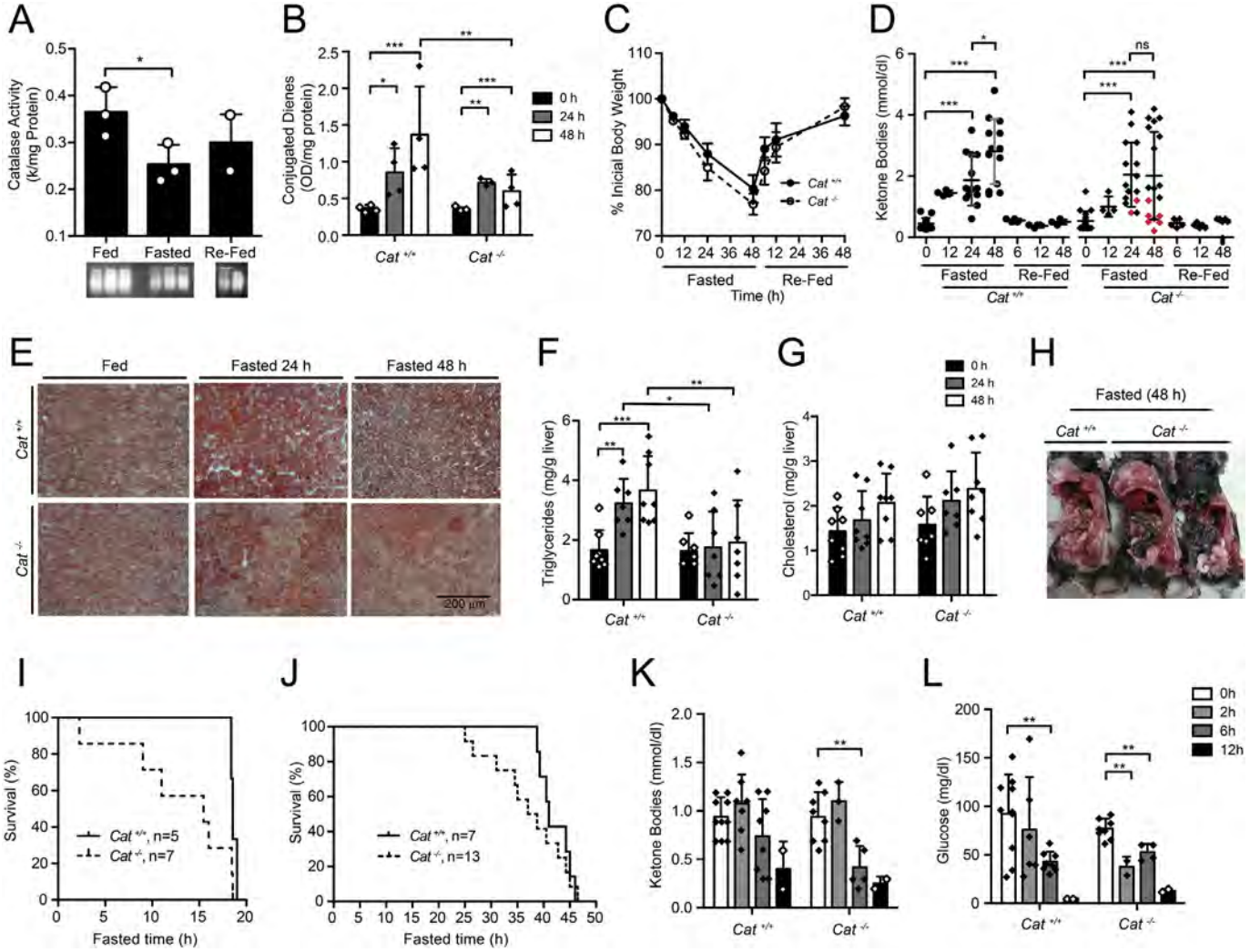

Fig. 4. Oxidative damage and fat accumulation in livers of mice with ($Cat^{+/+}$) and without ($Cat^{-/-}$) catalase after fasting. Adult mice were fasted for up to 48 h and measurements were done at the same daytime (9 AM). (A) Liver catalase activity after 24 h fasting and after refeeding for 12 h. The picture below shows catalase activity determined by a gel-based assay. (B) Liver oxidative damage, as estimated by the amount of conjugated dienes. (C) Percent of body weight loss across 48 h fasting/48 h refeeding. (D) Serum ketone body levels across 48 h fasting/48 h refeeding. Red dots are serum ketone body levels of mice that are about to die (i.e., still and did not respond to touch) at the time of fasting indicated. (E) Representative images of red-oil stained sections from livers of mice, fed or fasted, with the genotype indicated. (F, G) Triglycerides (F) and cholesterol (G) content in livers. (H) Aspect of bowel of mice after 48 h fasting. Note the necrotic aspect of the bowel of fasted mice lacking catalase. (I, J) Survival of fasted (I) or 6 h-fed (J) newborn mice. (K, L) Serum ketone body (K) and glucose (L) levels of newborn mice across fasting. Note that, apparently, reduced fat accumulation and ketone body production is the cause of reduced survival of mice lacking catalase. All values shown are the mean ± SD; n = 3–10. $*p < 0.05$, $**p < 0.01$ and $***p < 0.001$ (two-way analysis variance). (For interpretation of the references to color in this figure legend, the reader is referred to the Web version of this article.)

that the lack of catalase causes a reduction in lipogenesis leading the metabolic balance to favor catabolic activity.

Fasting is a short-term metabolic shift that could reveal the direct metabolic consequence of lacking catalase. The expression of *Pparγ2, Spot14*, *Fasn*, *Scd1* and *Gck* was similarly reduced upon fasting for 24 h, though the recovery to the level before fasting did not occur in all these genes at 12 h after refeeding. In contrast with the downregulation observed in the expression of lipogenic genes and *Gck*, the expression of gluconeogenic (*Pck1*) and catabolism-associated (*Ppara*, *Fgf21*, *Cpt1a*) genes was upregulated upon fasting and downregulated after refeeding (Fig. 5B and C). Despite the expression level of some genes in livers of $Cat^{-/-}$ were lower than those of wild type mice, generally the regulatory patterns described above were similar, although it was particularly interesting to note that *Pparγ2* downregulation upon fasting was more pronounced in samples of $Cat^{-/-}$ mice (7- vs. 16-fold reduction; Fig. 5B). In newborns, *Gck* in livers of $Cat^{-/-}$ mice was expressed at higher levels than in livers of $Cat^{+/+}$ mice, and a pronounced downregulation was detected in the former but not in the latter after fasting; the liver expression of other genes tested similarly changed in newborn mice of either genotype in response to fasting (Fig. 5D). The downregulation and upregulation response upon fasting of lipogenic and gluconeogenic genes, respectively, in livers of adult $Cat^{-/-}$ mice indicate that the main insulin/glucagon regulatory pathways that control metabolic gene expression are not markedly affected due to the lack of catalase and, thus, reduced lipogenesis and fat accumulation in mice lacking catalase is rather due to an affected central modulator of liver metabolism.

Activation of AMPK by phosphorylation reduces lipogenesis and increases general catabolism [31]. Under HFD-control diet for at least 2 weeks, the liver of mutant mice showed higher levels of activated AMPK than the liver of wild type mice (Fig. 6A), and no change in pAMPK levels could be detected when HFD was provided for as long as 3 months to either $Cat^{-/-}$ or $Cat^{+/+}$ mice (Fig. 6B). Feeding with the standard chow did not result in consistent higher levels of pAMPK in

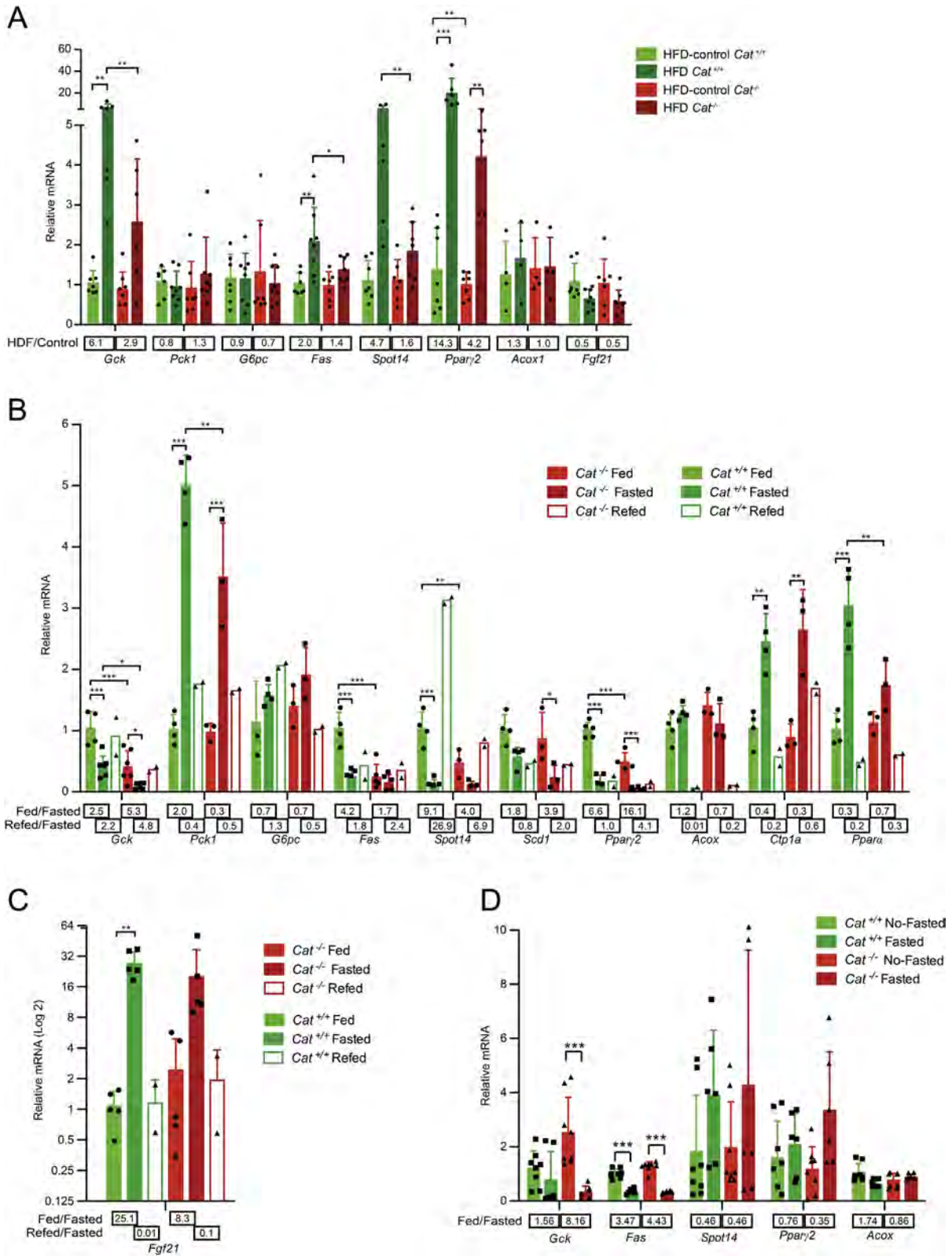

Fig. 5. Expression of metabolic genes in livers of mice with (*Cat*$^{+/+}$) and without (*Cat*$^{-/-}$) catalase fed with high fat diet or fasted. Expression levels in the liver of individual mouse either fed with a high fat diet (HFD) for 2 weeks or fasted for 24 h were determined for the genes indicated. (A) Gene expression in livers of mice fed with HFD-control diet or HFD. (B–C) Gene expression in livers of fed, fasted or refed mice. (D) Gene expression in livers of 12 h fasted newborn mice. Numbers within squares are the fold difference between bars above (estimated from the ratio of corresponding averages). Note the reduced up-regulation (upon HFD) or expression levels (before and after fasting) of *Gck* and lipogenic genes. All values shown are the mean ± SD; n = 3–5. *$p < 0.05$, **$p < 0.01$ and ***$p < 0.001$ (two-way analysis variance).

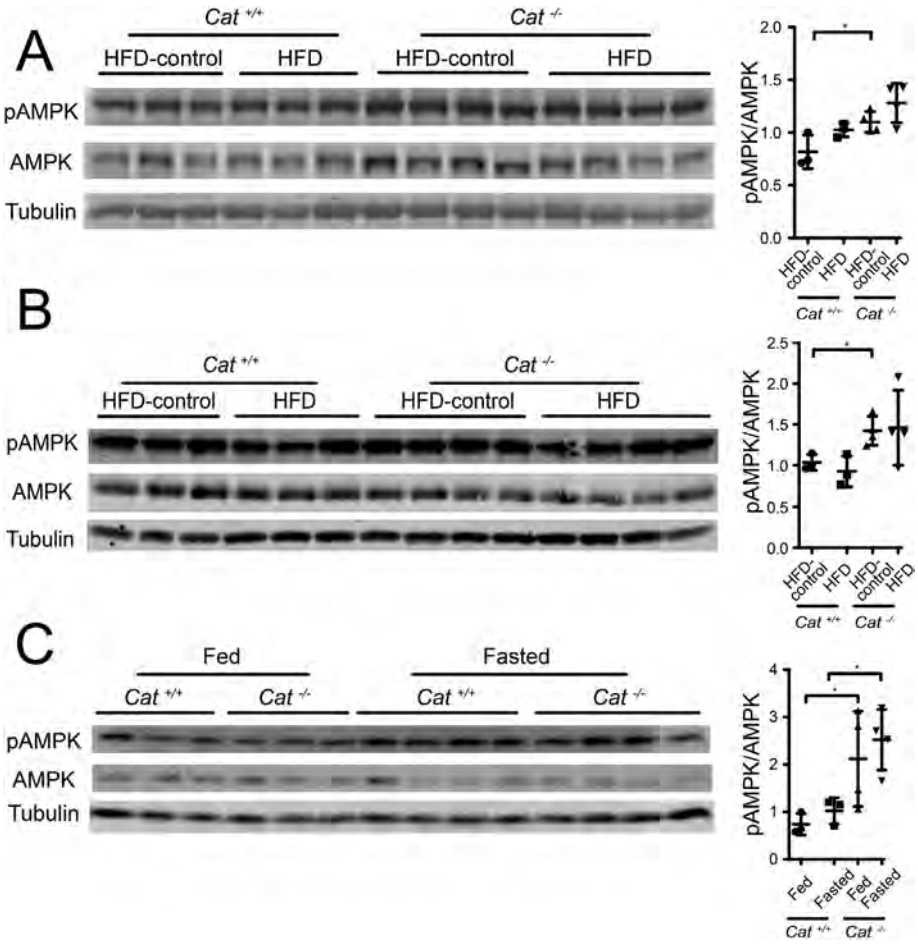

Fig. 6. Levels of activated AMPK in livers of mice with (*Cat*$^{+/+}$) and without (*Cat*$^{-/-}$) catalase fed with high fat diet or fasted. AMPK activation in liver was inferred from levels of phosphorylated AMPK (pAMPK) determined by western-blot. Quantification of the pAMPK/AMPK ratio is shown in graphs. (A, B) Activated AMPK in liver of mice fed with HFD-control diet and HFD for 2 weeks (A) or for 3 months (B). (C) Activated AMPK in liver of mice fed or fasted for 24 h. Note a higher level of activated AMPK in livers of mice lacking catalase. All values shown are the mean ± SD; n = 3–4. *$p < 0.05$ (two-way analysis variance).

livers of *Cat*$^{-/-}$ mice in comparison with those of *Cat*$^{+/+}$ mice but, as expected, the proportion of pAMPK increased in response to fasting (Fig. 6C). Therefore, at least in the presence of HFD, higher levels of activated AMPK in livers lacking catalase could contribute to lipogenesis downregulation.

3.6. Downregulation of the lipogenic master gene Pparγ2 and the lipolytic gene Fgf21 could contribute to the reduction in lifespan of mice lacking catalase

Short longevity of *Cat*$^{-/-}$ mice could be related to the metabolic alterations described above. Aged mice (12-mo or 24-mo) showed elevated expression levels of gluconeogenic genes in livers of both *Cat*$^{+/+}$ and *Cat*$^{-/-}$ mice in comparison with their corresponding young animals (3 mo; Fig. 7A), which might be expected due to the development of insulin resistance with aging [32]. *Fasn* expression increased with age (3-mo, 12-mo and 24-mo) in both wild type and mice lacking catalase and, although the difference in level of expression remained, was not significant in old animals. Higher levels of pAMPK were particularly notorious in 24-mo mutant mice (Fig. 7B). In previous experiments the pattern of *Fasn* expression positively correlated with that of *Spot14*, however, during aging, *Spot14* expression levels did not change in mice of either *Cat* genotype. Remarkably, while *Pparγ2* expression in liver did not markedly change along wild type mice aging, it was reduced with age in *Cat*$^{-/-}$ mice. Also, the liver of 24-mo mice lacking catalase showed significant lower levels of *Fgf21* expression than the liver of 24-mo wild type mice; low expression levels of *Fgf21* correlated with reduced expression of other catabolic genes such as *Cpt1* and *Acox* (Fig. 7A). In kidney, *Pparγ2* has shown to be a positive transcriptional regulator of *α-Klotho* [33], a gene involved in the control of longevity [34]. In the liver, *β-Klotho* is much more abundant than *α-Klotho* [35] and is the specific co-receptor of Fgf21 [36], therefore, we investigated whether its expression correlated with the one determined for *Pparγ2*. Despite the great difference in *α-* and *β-Klotho* expression level in liver (estimated of more than 100-fold), the expression levels of both *Klotho* genes increased in aged mice (i.e., 12- and 24-mo) regardless of the presence or absence of catalase (Fig. 7C). Autophagy was not notably affected by the absence of catalase along aging (Fig. 7D, Fig. S4D), though a consistent LC3 isoform of slightly higher molecular weight than LC3-II was exclusively present in livers of 12-mo and 24-mo *Cat*$^{-/-}$ mice (Fig. 7D). In summary, low fat accumulation, involving the participation of PPARγ2 activity, and diminished catabolic activity, involving the participation of FGF21 signaling, in the liver could be the cause of the limited lifespan of aged *Cat*$^{-/-}$ mice.

4. Discussion

Traditionally, ROS have been considered damaging molecules for the cell but, presently, a variety of studies indicate that ROS play a regulatory role in many cell processes [37,38]. The fact that the activity of many proteins depends on their oxidation state is in agreement with this regulatory role of ROS. Here we propose that H_2O_2, rather than

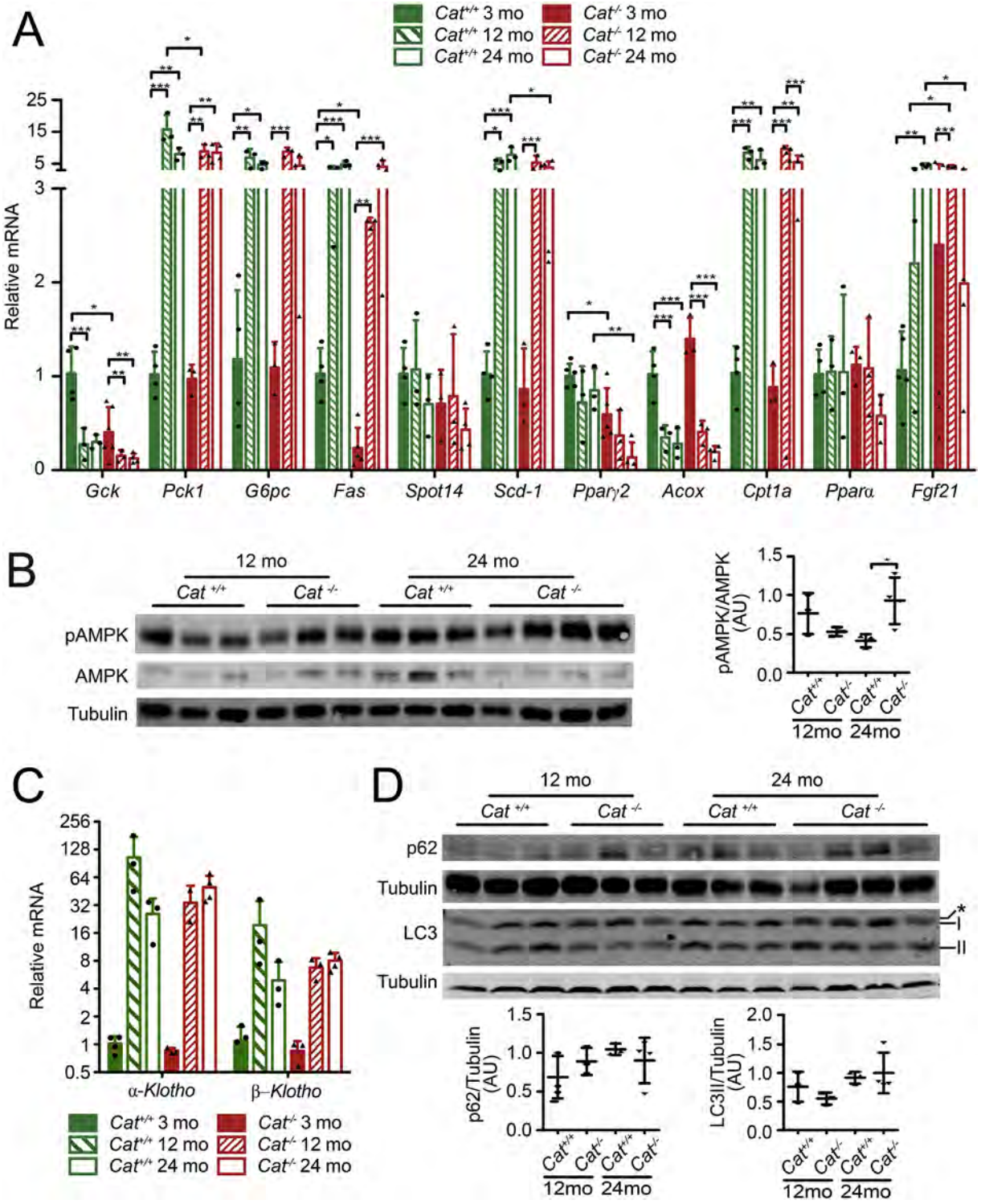

Fig. 7. Metabolic gene expression and levels of activated AMPK in livers of aging mice with (*Cat*$^{+/+}$) and without (*Cat*$^{-/-}$) catalase. Determinations were done in livers of 3-, 12- and 24-mo mice. (A) Expression of selected metabolic genes. (B) Levels of activated AMPK (pAMPK). Quantification of the pAMPK/AMPK ratio is shown in graphs. Note the marked up-regulation of gluconeogenic genes in 12- and 24-mo mice of either genotype and the contrasting pattern of *Pparγ2* expression across aging. Also, pAMPK was very abundant in livers of 24-mo mice lacking catalase. (C) Expression of *α-Klotho* and *β-Klotho* genes. (D) Levels of autophagy markers p62 and LC3; asterik in blot photograph points the extra band above LC3-I detected only in livers of mice lacking catalase. All values shown are the mean ± SD; n = 3–4. $p < 0.05$, $^{**}p < 0.01$ and $^{***}p < 0.001$ (two-way analysis variance).

causing a general macromolecular damage, alters metabolism with consequences in the mechanisms that determine longevity. Apparently, the metabolic pathways affected by the lack of catalase are influenced by feeding conditions and additional genetic factors [39,40].

4.1. Peroxisome and lipid metabolism

Due to the many oxidase reactions occurring in the peroxisome, this organelle produces a high amount of H_2O_2 [12,13]. Accordingly, peroxisomes are also rich in many antioxidants, among which catalase is

the most abundant. H_2O_2 could diffuse throughout the peroxisomal membrane passively and the derived ROS (i.e., hydroxyl radical) generally damage cellular macromolecules. However, it is apparent that intraperoxisomal-produced ROS restricts their influence to the redox state of peroxisomes and mitochondria, whereas, peroxisomes are rather resistant to oxidation by ROS produced from different cell compartment including mitochondria [41]. Therefore, the absence of general increased lipid oxidation due to the expected rise in H_2O_2 in mice lacking catalase could be due to the restricted oxidation of macromolecules in peroxisomes and mitochondria, whereas the diminished liver oxidative damage caused by a HFD or fasting could be a consequence of the metabolic alterations downstream resulting from specific protein oxidation or changes in the redox balance within these organelles (see below). Hormesis, possibly generated from the moderate increase in ROS in mice lacking catalase, could also contribute to explain the better handling of the rise in ROS under a HFD or fasting, however, up to date we have not detected evidence of a compensatory antioxidant response (Figs. S1E and F), in agreement with other reports [39,42].

The function of peroxisomes in fatty acid metabolism is presently well established [12]. Without disregarding other fundamental functions such as synthesis of ether-phospholipids, biliary acids and essential precursors of cholesterol, one major function of peroxisomes, as mitochondrial β-oxidation efficiency reduces, is a significant contribution to oxidation of long-chain fatty acids and the exclusive oxidation of very long-chain fatty acids [12,13]. Our results indicate that catalase has a relevant function in the regulation of fatty acid metabolism in the liver such that lack of catalase resulted in reduced lipid storage. Under a HFD, liver lipid storage is increased, at least in part, by increased lipogenesis [43]. Lipogenesis upregulation in this condition could derive from AMPK downregulation followed by the rise in SREBP-1c activity due to reduced AMPK-mediated phosphorylation and, consequently, upregulation of lipogenic genes [43]. Contribution of PPARγ2 is particularly relevant in this regard, functioning as a positive regulator of lipogenesis and also of fat storage, causing steatosis when upregulated [44]. In addition, the increase in *Gck* expression observed under a HFD, might provide the essential amount of NADPH to fuel lipogenesis [45]. The relatively higher levels than wild type of pAMPK and reduced upregulation of *Pparγ2* and *Gck* in livers of $Cat^{-/-}$ mice, which correlated with lower amount of *Fasn* and *Acc* mRNA are in accordance with reduced lipogenesis as the cause of limited steatosis after a HFD. Although there is not a clear mechanism by which alterations in the peroxisome could affect lipogenesis, products of peroxisomal lipolysis could represent either a significant amount of substrates for lipogenesis or PPARγ2 ligands [46]. Since liver steatosis upon feeding with a HFD can occur in the absence of peroxisomes and with decreased lipogenesis [47], indirect effects of lack of catalase on fatty acid transport and storage should also be considered (see below).

Fasting is another condition that promotes liver fat accumulation which, paradoxically, is associated with increased lipolysis and reduced lipogenesis [23]. A simple explanation to this phenomenon is the inability of liver to process all fatty acids released from the adipose tissue and imported into the liver under this condition; however, the actual mechanism is still a puzzle. Based on the regulation of gene expression, the reduced fat accumulation in the liver of mice lacking catalase upon fasting could hardly be due to the reduced expression levels of lipogenic genes before food deprivation, though it should not be discarded the possibility that a precondition (i.e., hormesis) is set in association to the reduced basal lipogenic activity under fed conditions. Increased lipolysis seems unlikely too, since not only minor differences were detected in levels of lipolytic gene expression, but also ketone bodies reached similar levels than wild type up to 48 h of fasting. Interestingly, NRF2, a transcription factor that controls an antioxidant response, prevents of excess fat accumulation in the liver upon fasting, apparently, by a mechanism that does not involve major alterations in lipogenesis or lipolysis [48,49]. It is tempting to speculate that increased β-oxidation due to fasting together with the lack of catalase elevates H_2O_2 to a level that does not cause significant oxidative damage and maintains NRF2 during fasting and, as a consequence, causes reduced fat accumulation. This mechanism could also contribute to reduced fat accumulation during a HFD, since lack of NRF2 promote hepatic steatosis. The regulation of *Pparγ* by NRF2 supports a role of this latter transcription factor in the liver metabolic phenotype of mice lacking catalase [50,51].

4.2. Lipid metabolism and aging

The effects of lack of catalase on liver fat accumulation point to lipid metabolism as the cause of shorter than wild type lifespan of $Cat^{-/-}$ mice. Accordingly, body weight and liver fat accumulation was reduced in aged $Cat^{-/-}$ mice. Although the cause of death of old animals has not been identified, this could be related to the mechanism that causes death of fasted mice. Survival of fasted mice is critically dependent on the existing energetic reserves at the time of food deprivation. In particular, after glycogen exhaustion in fasting conditions, fatty acid β-oxidation in the liver becomes essential for the production of ketone bodies, the systemic energetic source when glucose is scarce. Thus, survival of fasted newborn mice is compromised by the absence of ketolysis [26]. Newborn mice lacking catalase died upon fasting with a similar pattern as mice unable to use ketone bodies and, although the rapid use of ketone bodies limited the detection of their complete depletion before death, the decline in ketone bodies at 6 h of fasting were significant only in mice lacking catalase. In agreement with this view, adult $Cat^{-/-}$ mice that died under fasting correlated with an abrupt reduction in ketone bodies. Although we cannot discard that other reserves distinct from lipids also limit the survival of $Cat^{-/-}$ mice under fasting, our data suggest lipid shortage as a determinant of survival in conditions of food restriction or during aging. In agreement with this conclusion, the gene encoding PPARγ2, which promote lipid storage and its absence causes premature aging [52], was downregulated before fasting and in aged $Cat^{-/-}$ mice.

The participation of lipid metabolism in survival under food restriction and longevity has been previously determined. In *C. elegans*, DAF-16, a classical promotor of longevity in association with reduced insulin/IGF signaling, induces lipid synthesis [53]. However, the role of lipid metabolism in longevity is remarked by the increased lifespan of *C. elegans* lacking germ cells in which fat accumulation is an evident characteristic [54]. Interestingly, *SKN1*, a functionally-related *Nrf* homologous gene, is required for extended longevity in this condition, and although it protects against oxidative stress, also limits excess accumulation of fat [55]. Suggesting the participation of peroxisomal catalase in this phenomenon, *C. elegans* deficient in *ctl-3*, the gene encoding the peroxisomal catalase in this organism, exhibit, as in mice, shortened lifespan and reduced oxidative damage [56]. In addition, lack of peroxisomal catalase or H_2O_2 derived from fatty acid β-oxidation rescue *C. elegans* lacking AMPK from death under the hibernation-like dauer state by increasing, with minimal oxidative damage, accumulation of fat, an energetic reserve required for survival in this condition [57]. Therefore, the function of peroxisomal catalase in the regulation of lipid metabolism, maintenance of fat reserves, and longevity is conserved among distant organisms, though the mechanism may vary depending on environmental or genetic conditions.

4.3. Concluding remarks

The present work reveals a relevant role of catalase in the modulation of lipid metabolism. Physical interaction between lipid droplets and peroxisomes [12] suggests that peroxisomal activity and, thus, peroxisomal H_2O_2, are part of the regulatory mechanism. Since long fatty acids can be degraded in peroxisomes, this metabolic activity might explain why the penetrance of *Cat* deficiency in lipid metabolism was mainly revealed when mice ingested HFD or under extended

INFORME DE LABORES 2019

fasting. Genetic factors also appear to have a profound effect on the consequences associated with reduced catalase activity. For instance, an opposite phenotype to the one reported here (i.e., increased body weight and fat accumulation) has been observed in a mouse strain with in a slightly different genetic background (i.e., C57BL/6J vs. C57BL/6 N of the present study) [39,40]; the possible genetic modifier in this case is *Nnt*, a nuclear gene encoding the mitochondrial nicotinamide nucleotide transhydrogenase that is expected to affect the balance NAD^+/NADH and $NADP^+$/NADPH in mitochondria and has been related to body weight gain and obesity [58,59].

Catalase deficiency uncovers a mechanism by which ROS regulate lipid metabolism without oxidative damage, with implications in the mechanism that control longevity. Although alterations determined in the liver due to the lack of catalase are sufficient to provoke systemic metabolic alterations that can put at risk animal survival, direct cell autonomous damages in other tissue cannot be discarded. The ability of peroxisomal catalase to diminish cellular replicative senescence of human fibroblast [60] indicate that this enzyme can perform cell autonomous functions. However, the origin of the phenotype of animals lacking catalase cannot be conclusively attributed at this time to a cell autonomous function in hepatocytes, and non-cell autonomous functions involving, among others, adipose tissue should be considered.

The production and efficient use of reserves should be especially important for animals in the wild, since food is not equally available during the whole year. Thus animals, should have evolved mechanisms to survive under shortage of food, including those to store energetic resources and to efficiently use them [61]. Catalase can be an essential enzyme in these mechanisms that, through the control of peroxisomal H_2O_2, supports an optimal metabolic balance by regulating, at least, lipid metabolism. In this context, it is tempting to speculate that lifespan determination during evolution was critically influenced by the capacity of animals to survive under food restriction. The peroxisomal catalase could, then, be an evolutionary conserved component required for optimal use of metabolic reserves, before than protecting from the oxidative damage that characterizes aging.

Acknowledgements

We appreciate the support by members of our group throughout fruitful discussions. We thank to all service units in our institution, in particular, the animal facility (supervised by Graciela Cabeza, Sergio Trujillo and Elizabeth Mata) and the DNA synthesis unit, without their assistance this work would not be possible. We also appreciate the technical contribution of Olivia Vázquez-Martínez, Deisy Gasca-Martínez and Mayra L. López-Cervantes of the INB-UNAM, and of Concepción Valencia of the IBT-UNAM. We also thank all the support provided by Landsteiner Scientific, SA de CV. This work was supported by grants IN209813 and IN213416 from PAPIIT-UNAM. JRPE was recipients of a CONACYT fellowship for graduate studies.

Appendix A. Supplementary data

Supplementary data to this article can be found online at https://doi.org/10.1016/j.freeradbiomed.2019.02.016.

References

[1] C. López-Otín, M.A. Blasco, L. Partridge, M. Serrano, G. Kroemer, The hallmarks of aging, Cell 153 (2013), https://doi.org/10.1016/j.cell.2013.05.039.
[2] J. a. Mattison, G.S. Roth, T.M. Beasley, E.M. Tilmont, A.M. Handy, R.L. Herbert, D.L. Longo, D.B. Allison, J.E. Young, M. Bryant, D. Barnard, W.F. Ward, W. Qi, D.K. Ingram, R. de Cabo, Impact of caloric restriction on health and survival in rhesus monkeys from the NIA study, Nature 489 (2012) 318–321, https://doi.org/10.1038/nature11432.
[3] J. Viña, C. Borras, K.M. Abdelaziz, R. Garcia-Valles, M.C. Gomez-Cabrera, The free radical theory of aging revisited: the cell signaling disruption theory of aging, Antioxidants Redox Signal. 19 (2013) 779–787, https://doi.org/10.1089/ars.2012.5111.
[4] T. Finkel, N.J. Holbrook, Oxidants, oxidative stress and the biology of ageing, Nature 408 (2000) 239–247, https://doi.org/10.1038/35041687.
[5] V.I. Pérez, A. Bokov, H. Van Remmen, J. Mele, Q. Ran, Y. Ikeno, A. Richardson, Is the oxidative stress theory of aging dead? Biochim. Biophys. Acta 1790 (2010) 1005–1014, https://doi.org/10.1016/j.bbagen.2009.06.003.Is.
[6] S. Imai, J. Yoshino, The importance of NAMPT/NAD/SIRT1 in the systemic regulation of metabolism and ageing, Diabetes Obes. Metab. 15 (2013) 26–33, https://doi.org/10.1111/dom.12171.
[7] L. Moldovan, N.I. Moldovan, Oxygen free radicals and redox biology of organelles, Histochem. Cell Biol. 122 (2004) 395–412, https://doi.org/10.1007/s00418-004-0676-y.
[8] M.P. Murphy, How mitochondria produce reactive oxygen species, Biochem. J. 417 (2009) 1–13, https://doi.org/10.1042/BJ20081386.
[9] G. Cozza, M. Rossetto, V. Bosello-Travain, M. Maiorino, A. Roveri, S. Toppo, M. Zaccarin, L. Zennaro, F. Ursini, Glutathione peroxidase 4-catalyzed reduction of lipid hydroperoxides in membranes: the polar head of membrane phospholipids binds the enzyme and addresses the fatty acid hydroperoxide group toward the redox center, Free Radic. Biol. Med. 112 (2017) 1–11, https://doi.org/10.1016/j.freeradbiomed.2017.07.010.
[10] K. Loh, H. Deng, A. Fukushima, X. Cai, B. Boivin, S. Galic, C. Bruce, B.J. Shields, B. Skiba, L.M. Ooms, N. Stepto, B. Wu, C.A. Mitchell, N.K. Tonks, M.J. Watt, M.A. Febbraio, P.J. Crack, S. Andrikopoulos, T. Tiganis, Reactive oxygen species enhance insulin sensitivity, Cell Metabol. 10 (2009) 260–272, https://doi.org/10.1016/j.cmet.2009.08.009.
[11] H.N. Kirkman, G.F. Gaetani, Mammalian catalase: a venerable enzyme with new mysteries, Trends Biochem. Sci. 32 (2007) 44–50, https://doi.org/10.1016/j.tibs.2006.11.003.
[12] I.J. Lodhi, C.F. Semenkovich, Peroxisomes: a nexus for lipid metabolism and cellular signaling, Cell Metabol. 19 (2014) 380–392, https://doi.org/10.1016/j.cmet.2014.01.002.
[13] M. Schrader, J. Costello, L.F. Godinho, M. Islinger, Peroxisome-mitochondria interplay and disease, J. Inherit. Metab. Dis. 38 (2015) 681–702, https://doi.org/10.1007/s10545-015-9819-7.
[14] J.M. Flynn, S. Melovn, SOD2 in mitochondrial dysfunction and neurodegeneration, Free Radic. Biol. Med. 62 (2013) 4–12, https://doi.org/10.1016/j.freeradbiomed.2013.05.027.
[15] R.S. Esworthy, R. Aranda, M.G. Martín, J.H. Doroshow, S.W. Binder, F.F. Chu, Mice with combined disruption of Gpx1 and Gpx2 genes have colitis, Am. J. Physiol. Gastrointest. Liver Physiol. 281 (2001) G848–G855.
[16] C. a Neumann, D.S. Krause, C.V. Carman, S. Das, D.P. Dubey, J.L. Abraham, R.T. Bronson, Y. Fujiwara, S.H. Orkin, R. a Van Etten, Essential role for the peroxiredoxin Prdx1 in erythrocyte antioxidant defence and tumour suppression, Nature 424 (2003) 561–565, https://doi.org/10.1038/nature01819.
[17] M.L. Sentman, M. Granström, H. Jakobson, A. Reaume, S. Basu, S.L. Marklund, Phenotypes of mice lacking extracellular superoxide dismutase and copper- and zinc-containing superoxide dismutase, J. Biol. Chem. 281 (2006) 6904–6909, https://doi.org/10.1074/jbc.M510764200.
[18] J.T. Haas, J. Miao, D. Chanda, Y. Wang, E. Zhao, M.E. Haas, M. Hirschey, B. Vaitheesvaran, R.V. Farese, I.J. Kurland, M. Graham, R. Crooke, F. Foufelle, S.B. Biddinger, Hepatic insulin signaling is required for obesity-dependent expression of SREBP-1c mRNA but not for feeding-dependent expression, Cell Metabol. 15 (2012) 873–884, https://doi.org/10.1016/j.cmet.2012.05.002.
[19] R. Radi, J.F. Turrens, L.Y. Chang, K.M. Bush, J.D. Crapo, B.A. Freeman, Detection of catalase in rat heart mitochondria, J. Biol. Chem. 266 (1991) 22028–22034.
[20] D. Luna-Moreno, O. Vázquez-Martínez, A. Báez-Ruiz, J. Ramírez, M. Díaz-Muñoz, Food restricted schedules promote differential lipoperoxidative activity in rat hepatic subcellular fractions, Comp. Biochem. Physiol. – A Mol. Integr. Physiol. 146 (2007) 632–643, https://doi.org/10.1016/j.cbpa.2006.02.039.
[21] C.C.J. Weydert, J.J. Cullen, Measurement of superoxide dismutase, catalase and glutathione peroxidase in cultured cells and tissue, Nat. Protoc. 5 (2009) 51–66, https://doi.org/10.1038/nprot.2009.197.
[22] Y.A. Moon, G. Liang, X. Xie, M. Frank-Kamenetsky, K. Fitzgerald, V. Koteliansky, M.S. Brown, J.L. Goldstein, J.D. Horton, The Scap/SREBP pathway is essential for developing diabetic fatty liver and carbohydrate-induced hypertriglyceridemia in animals, Cell Metabol. 15 (2012) 240–246, https://doi.org/10.1016/j.cmet.2011.12.017.
[23] J. Lee, J. Choi, S. Scafidi, M.J. Wolfgang, Hepatic fatty acid oxidation restrains systemic catabolism during starvation, Cell Rep. 16 (2016) 201–212, https://doi.org/10.1016/j.celrep.2016.05.062.
[24] T. Fukao, G.D. Lopaschuk, G.A. Mitchell, Pathways and control of ketone body metabolism: on the fringe of lipid biochemistry, Prostagl. Leukot. Essent. Fat. Acids 70 (2004) 243–251, https://doi.org/10.1016/j.plefa.2003.11.001.
[25] N. Mizushima, T. Yoshimori, B. Levine, Methods in mammalian autophagy research, Cell 140 (2010) 313–326, https://doi.org/10.1016/j.cell.2010.01.028.
[26] D.A. Cotter, David G. Avignon, A.E. Wentz, M.L. Weber, P.A. Crawford, Obligate role for ketone body oxidation in neonatal metabolic homeostasis, J. Biol. Chem. 286 (2011) 6902–6910, https://doi.org/10.1074/jbc.M110.192369.
[27] K.J. Lei, H. Chen, C.J. Pan, J.M. Ward, B. Mosinger, E.J. Lee, H. Westphal, B.C. Mansfield, J.Y. Chou, Glucose-6-phosphatase dependent substrate transport in the glycogen storage disease type-1a mouse, Nat. Genet. (1996), https://doi.org/10.1038/ng0696-203.
[28] J. Ezaki, N. Matsumoto, M. Takeda-Ezaki, M. Komatsu, K. Takahashi, Y. Hiraoka, H. Taka, T. Fujimura, K. Takehana, M. Yoshida, J. Iwata, I. Tanida, N. Furuya, D.M. Zheng, N. Tada, K. Tanaka, E. Kominami, T. Ueno, Liver autophagy contributes to the maintenance of blood glucose and amino acid levels, Autophagy 7 (2011) 727–736, https://doi.org/10.4161/auto.7.7.15371.

[29] K. Matsusue, M. Haluzik, G. Lambert, S.H. Yim, O. Gavrilova, J.M. Ward, B. Brewer, M.L. Reitman, F.J. Gonzalez, Liver-specific disruption of PPARγ in leptin-deficient mice improves fatty liver but aggravates diabetic phenotypes, J. Clin. Invest. 111 (2003) 737–747, https://doi.org/10.1172/JCI200317223.

[30] S. Tsukita, T. Yamada, K. Uno, K. Takahashi, K. Kaneko, Y. Ishigaki, J. Imai, Y. Hasegawa, S. Sawada, H. Ishihara, Y. Oka, H. Katagiri, Hepatic glucokinase modulates obesity predisposition by regulating BAT thermogenesis via neural signals, Cell Metabol. 16 (2012) 825–832, https://doi.org/10.1016/j.cmet.2012.11.006.

[31] Y.C. Long, J.R. Zierath, AMP-activated protein kinase signaling in metabolic regulation, J. Clin. Invest. 116 (2006) 1776–1783, https://doi.org/10.1172/JCI29044.1776.

[32] R.I. Fink, O.G. Kolterman, J. Griffin, J.M. Olefsky, Mechanisms of insulin resistance in aging, J. Clin. Invest. 71 (1983) 1523–1535 http://www.ncbi.nlm.nih.gov/pubmed/6345584.

[33] H. Zhang, Y. Li, Y. Fan, J. Wu, B. Zhao, Y. Guan, S. Chien, N. Wang, Klotho is a target gene of PPAR-γ, Kidney Int. 74 (2008) 732–739, https://doi.org/10.1038/ki.2008.244.

[34] M. Kuro-o, Y. Nabeshima, Y. Matsumura, H. Aizawa, H. Kawaguchi, T. Suga, T. Utsugi, Y. Ohyama, M. Kurabayashi, T. Kaname, E. Kume, H. Iwasaki, A. Iida, T. Shiraki-Iida, S. Nishikawa, R. Nagai, Mutation of the mouse *klotho* gene leads to a syndrome resembling ageing, Nature 390 (1997) 45–51, https://doi.org/10.1038/36285.

[35] Y. Xu, Z. Sun, Molecular basis of klotho: from gene to function in aging, Endocr. Rev. 36 (2015) 174–193, https://doi.org/10.1210/er.2013-1079.

[36] S.Y. Shi, Y.W. Lu, J. Richardson, X. Min, J. Weiszmann, W.G. Richards, Z. Wang, Z. Zhang, J. Zhang, Y. Li, A systematic dissection of sequence elements determining β-Klotho and FGF interaction and signaling, Sci. Rep. 8 (2018) 1–15, https://doi.org/10.1038/s41598-018-29396-5.

[37] L. Covarrubias, D. Hernández-García, D. Schnabel, E. Salas-Vidal, S. Castro-Obregón, Function of reactive oxygen species during animal development: passive or active? Dev. Biol. 320 (2008) 1–11, https://doi.org/10.1016/j.ydbio.2008.04.041.

[38] R.B. Hamanaka, A. Glasauer, P. Hoover, S. Yang, H. Blatt, A.R. Mullen, S. Getsios, C.J. Gottardi, R.J. DeBerardinis, R.M. Lavker, N.S. Chandel, Mitochondrial reactive oxygen species promote epidermal differentiation and hair follicle development, Sci. Signal. 6 (2013), https://doi.org/10.1126/scisignal.2003638 ra8-ra8.

[39] L. Piao, J. Choi, G. Kwon, H. Ha, Endogenous catalase delays high-fat diet-induced liver injury in mice, Korean J. Physiol. Pharmacol. 21 (2017) 317–325, https://doi.org/10.4196/kjpp.2017.21.3.317.

[40] C. Heit, S. Marshall, S. Singh, X. Yu, G. Charkoftaki, H. Zhao, D.J. Orlicky, K.S. Fritz, D.C. Thompson, V. Vasiliou, Catalase deletion promotes prediabetic phenotype in mice, Free Radic. Biol. Med. 103 (2017) 48–56, https://doi.org/10.1016/j.freeradbiomed.2016.12.011.

[41] O. Ivashchenko, P.P. Van Veldhoven, C. Brees, Y.-S. Ho, S.R. Terlecky, M. Fransen, Intraperoxisomal redox balance in mammalian cells: oxidative stress and interorganellar cross-talk, Mol. Biol. Cell 22 (2011) 1440–1451, https://doi.org/10.1091/mbc.E10-11-0919.

[42] Y.S. Ho, Y. Xiong, W. Ma, A. Spector, D.S. Ho, Mice lacking catalase develop normally but show differential sensitivity to oxidant tissue injury, J. Biol. Chem. 279 (2004) 32804–32812, https://doi.org/10.1074/jbc.M404800200.

[43] Y. Li, S. Xu, M.M. Mihaylova, B. Zheng, X. Hou, B. Jiang, O. Park, Z. Luo, E. Lefai, J.Y.J. Shyy, B. Gao, M. Wierzbicki, T.J. Verbeuren, R.J. Shaw, R.A. Cohen, M. Zang, AMPK phosphorylates and inhibits SREBP activity to attenuate hepatic steatosis and atherosclerosis in diet-induced insulin-resistant mice, Cell Metabol. 13 (2011) 376–388, https://doi.org/10.1016/j.cmet.2011.03.009.

[44] M. Bedoucha, E. Atzpodien, U.A. Boelsterli, Diabetic KKAy mice exhibit increased hepatic PPARγ1 gene expression and develop hepatic steatosis upon chronic treatment with antidiabetic thiazolidinediones, J. Hepatol. 35 (2001) 17–23, https://doi.org/10.1016/S0168-8278(01)00066-6.

[45] E.S. Jin, M.H. Lee, R.E. Murphy, C.R. Malloy, Pentose phosphate pathway activity parallels lipogenesis but not antioxidant processes in rat liver, Am. J. Physiol. Metab. 314 (2018) E543–E551, https://doi.org/10.1152/ajpendo.00342.2017.

[46] I.J. Lodhi, L. Yin, A.P.L. Jensen-Urstad, K. Funai, T. Coleman, J.H. Baird, M.K. El Ramahi, B. Razani, H. Song, F. Fu-Hsu, J. Turk, C.F. Semenkovich, Inhibiting adipose tissue lipogenesis reprograms thermogenesis and PPARγ activation to decrease diet-induced obesity, Cell Metabol. 16 (2012) 189–201, https://doi.org/10.1016/j.cmet.2012.06.013.

[47] H. Weng, X. Ji, Y. Naito, K. Endo, X. Ma, R. Takahashi, C. Shen, G. Hirokawa, Y. Fukushima, N. Iwai, Pex11 deficiency impairs peroxisome elongation and division and contributes to nonalcoholic fatty liver in mice, AJP Endocrinol. Metab. 304 (2013) E187–E196, https://doi.org/10.1152/ajpendo.00425.2012.

[48] Y. Li, X. Chao, L. Yang, Q. Lu, T. Li, W.X. Ding, H.M. Ni, Impaired fasting-induced adaptive lipid droplet biogenesis in liver-specific Atg5-deficient mouse liver is mediated by persistent nuclear factor-like 2 activation, Am. J. Pathol. 188 (2018) 1833–1846, https://doi.org/10.1016/j.ajpath.2018.04.015.

[49] J. Paek, J.Y. Lo, S.D. Narasimhan, T.N. Nguyen, K. Glover-Cutter, S. Robida-Stubbs, T. Suzuki, M. Yamamoto, T.K. Blackwell, S.P. Curran, Mitochondrial SKN-1/Nrf mediates a conserved starvation response, Cell Metabol. 16 (2012) 526–537, https://doi.org/10.1016/j.cmet.2012.09.007.

[50] V.R. More, J. Xu, P.C. Shimpi, C. Belgrave, J.P. Luyendyk, M. Yamamoto, A.L. Slitt, Keap1 knockdown increases markers of metabolic syndrome after long-term high fat diet feeding, Free Radic. Biol. Med. 61 (2013) 85–94, https://doi.org/10.1016/j.freeradbiomed.2013.03.007.

[51] Y. Tanaka, L.M. Aleksunes, R.L. Yeager, M. a Gyamfi, N. Esterly, G.L. Guo, C.D. Klaassen, NF-E2-Related factor 2 inhibits lipid accumulation and oxidative stress in mice fed a high-fat diet, J. Pharmacol. Exp. Therapeut. 325 (2008) 655–664, https://doi.org/10.1124/jpet.107.135822.

[52] C. Argmann, R. Dobrin, S. Heikkinen, A. Auburtin, L. Pouilly, T.A. Cock, H. Koutnikova, J. Zhu, E.E. Schadt, J. Auwerx, Pparγ2 is a key driver of longevity in the mouse, PLoS Genet. 5 (2009), https://doi.org/10.1371/journal.pgen.1000752.

[53] M. McCormick, K. Chen, P. Ramaswamy, C. Kenyon, New genes that extend Caenorhabditis elegans' lifespan in response to reproductive signals, Aging Cell 11 (2012) 192–202, https://doi.org/10.1111/j.1474-9726.2011.00768.x.

[54] C. Longevity, M.C. Wang, E.J.O. Rourke, G. Ruvkun, Fat metabolism links germline stem, Science (80) 322 (2008) 957–960.

[55] M.J. Steinbaugh, S.D. Narasimhan, S. Robida-Stubbs, L.E. Moronetti Mazzeo, J.M. Dreyfuss, J.M. Hourihan, P. Raghavan, T.N. Operaña, R. Esmaillie, T.K. Blackwell, Lipid-mediated regulation of SKN-1/Nrf in response to germ cell absence, Elife 4 (2015) 1–30, https://doi.org/10.7554/eLife.07836.

[56] O.I. Petriv, R.A. Rachubinski, Lack of peroxisomal catalase causes a progeric phenotype in Caenorhabditis elegans, J. Biol. Chem. 279 (2004) 19996–20001, https://doi.org/10.1074/jbc.M400207200.

[57] M. Xie, R. Roy, Increased levels of hydrogen peroxide induce a HIF-1-dependent modification of lipid metabolism in AMPK compromised C. elegans dauer larvae, Cell Metabol. 16 (2012) 322–335, https://doi.org/10.1016/j.cmet.2012.07.016.

[58] A. Nicholson, P.C. Reifsnyder, R. Malcolm, C. a Lucas, R. Grant, W. Zhang, E.H. Leiter, B. Harbor, Diet induced obesity in two C57BL/6 substrains with intact or mutant Nicotinamide Nucleotide Transhydrogenase (Nnt) gene, Obesity 18 (2011) 1902–1905, https://doi.org/10.1038/oby.2009.477.Diet.

[59] J.A. Ronchi, T.R. Figueira, F.G. Ravagnani, H.C.F. Oliveira, A.E. Vercesi, R.F. Castilho, A spontaneous mutation in the nicotinamide nucleotide transhydrogenase gene of C57BL/6J mice results in mitochondrial redox abnormalities, Free Radic. Biol. Med. 63 (2013) 446–456, https://doi.org/10.1016/j.freeradbiomed.2013.05.049.

[60] J.E. Legakis, Peroxisome senescence in human fibroblasts, Mol. Biol. Cell 13 (2002) 4243–4255, https://doi.org/10.1091/mbc.E02-06-0322.

[61] J.A. Viscarra, R.M. Ortiz, Cellular mechanisms regulating fuel metabolism in mammals: role of adipose tissue and lipids during prolonged food deprivation, Metabolism 62 (2013) 889–897, https://doi.org/10.1016/j.metabol.2012.12.014.

INFORME DE LABORES 2019

RESEARCH ARTICLE

Characterization of FlgP, an Essential Protein for Flagellar Assembly in *Rhodobacter sphaeroides*

Caleb Pérez-González,[a] Clelia Domenzain,[b] Sebastian Poggio,[a] Diego González-Halphen,[b] Georges Dreyfus,[b] Laura Camarena[a]

[a]Instituto de Investigaciones Biomédicas, Universidad Nacional Autónoma de México, Mexico City, Mexico
[b]Instituto de Fisiología Celular, Universidad Nacional Autónoma de México, Mexico City, Mexico

ABSTRACT The flagellar lipoprotein FlgP has been identified in several species of bacteria, and its absence provokes different phenotypes. In this study, we show that in the alphaproteobacterium *Rhodobacter sphaeroides*, a Δ*flgP* mutant is unable to assemble the hook and the filament. In contrast, the membrane/supramembrane (MS) ring and the flagellar rod appear to be assembled. In the absence of FlgP a severe defect in the transition from rod to hook polymerization occurs. In agreement with this idea, we noticed a reduction in the amount of intracellular flagellin and the chemotactic protein CheY4, both encoded by genes dependent on σ^{28}. This suggests that in the absence of *flgP* the switch to export the anti-sigma factor, FlgM, does not occur. The presence of FlgP was detected by Western blot in samples of isolated wild-type filament basal bodies, indicating that FlgP is an integral part of the flagellar structure. In this regard, we show that FlgP interacts with FlgH and FlgT, indicating that FlgP should be localized closely to the L and H rings. We propose that FlgP could affect the architecture of the L ring, which has been recently identified to be responsible for the rod-hook transition.

IMPORTANCE Flagellar based motility confers a selective advantage on bacteria by allowing migration to favorable environments or in pathogenic species to reach the optimal niche for colonization. The flagellar structure has been well established in *Salmonella*. However, other accessory components have been identified in other species. Many of these have been implied in adapting the flagellar function to enable faster rotation, or higher torque. FlgP has been proposed to be the main component of the basal disk located underlying the outer membrane in *Campylobacter jejuni* and *Vibrio fischeri*. Its role is still unclear, and its absence impacts motility differently in different species. The study of these new components will bring a better understanding of the evolution of this complex organelle.

KEYWORDS bacterial flagellum, FlgH, FlgJ, FlgP, L ring, *Rhodobacter sphaeroides*, flagellar basal disk, outer membrane, rod-hook transition

The bacterial flagellum is a rotary nanomachine embedded in the cell envelope. The motor is powered by the electrochemical ion gradient formed across the cytoplasmic membrane. The rotating part has three well-defined structures: the basal body, which expands from the cytoplasm to the outer membrane; the hook that is the first extracellular structure; and the helical filament that thrusts the cell forward through rotation of the flagellar motor (1, 2). The rotor is surrounded by a stator formed by multiple transmembrane subunits of MotA/MotB, or PomA/PomB in bacteria with H^+- or Na^+-driven motors, respectively (3–7). These proteins form a channel that conveys ions across the membrane and couples ion flow to rotation (8–10). In *Escherichia coli* and *Salmonella enterica* serovar Typhimurium (from here on *Salmonella*), the basal body is formed by four rings and a rod that expands from the cytoplasm to the outer

Citation Pérez-González C, Domenzain C, Poggio S, González-Halphen D, Dreyfus G, Camarena L. 2019. Characterization of FlgP, an essential protein for flagellar assembly in *Rhodobacter sphaeroides*. J Bacteriol 201:e00752-18. https://doi.org/10.1128/JB.00752-18.

Editor Ann M. Stock, Rutgers University-Robert Wood Johnson Medical School

Copyright © 2019 American Society for Microbiology. All Rights Reserved.

Address correspondence to Georges Dreyfus, gdreyfus@ifc.unam.mx, or Laura Camarena, rosal@servidor.unam.mx.

Received 6 December 2018
Accepted 12 December 2018
Accepted manuscript posted online 17 December 2018
Published 31 January 2019

Downloaded from http://jb.asm.org/ on October 20, 2020 at UNAM INST DE INVEST BIOMEDICAS

membrane (OM), while the membrane/supramembrane (MS) ring is formed by 26 subunits of FliF that is located at the inner membrane (IM) (11, 12). At the cytoplasmic side the MS ring connects with the C-ring that is formed by FliG, FliM, and FliN; these proteins have been implicated in torque generation and morphogenesis (13–15). The periplasmic side of the MS ring couples with the flagellar rod through the adaptor protein FliE (16, 17). The rod formed by FlgB, FlgC, FlgF, and FlgG spans the cell wall and the OM crossing the P and L rings, which act as bushings for the rotating rod (18–21). FlgI and FlgH form the P and L rings, respectively (22). It has been recently proposed that L-ring formation contributes to dislodging the scaffolding protein FlgJ from the tip of the growing rod; this enables the transition from rod to the polymerization of the hook (23). The hook is the first extracellular structure, and it is formed by approximately 120 subunits of FlgE. The flagellar filament is formed by thousands of flagellin subunits and connects to the hook by means of the hook-associated proteins FlgK and FlgL (12, 24, 25).

Recently, electron cryotomography (ECT) of cells from different bacterial species allowed *in situ* visualization of the intact flagellum. These studies have revealed that the basal body has a central core structure that is conserved; however, around it a great diversity of additional components were observed (5, 7, 26, 27). The protein composition of these additional elements is still mostly unknown. In this regard, it has also been recognized that the presence of certain flagellar proteins is restricted to specific bacterial groups, and their characterization is incipient. This is the case for FlgT and FlgP, which are both absent in *E. coli* and *Salmonella*. FlgT is present in several species of *Vibrio* and *Aeromonas*, whereas FlgP has been reported to be present in species of *Vibrio* and in *Campylobacter jejuni* (28–32).

FlgT forms the H ring that covers the L and P rings and which is instrumental in supporting the high swimming velocities reported for several species of *Vibrio* (28). FlgP is a lipoprotein that was first identified and characterized in *Vibrio cholerae* and *C. jejuni* (29, 30, 32). In *V. cholerae* the absence of FlgP provokes a reduction in the number of flagellated cells, and morphologically the filaments were shorter than those observed in wild-type cells (29, 32). In contrast, a *flgP* mutant strain of *C. jejuni* was able to assemble a normal flagellum that showed a paralyzed phenotype (Mot$^-$) (30). Recently, flagella of a *flgP* mutant of *V. fischeri* and *C. jejuni* were observed by ECT, and the reconstructed images were compared to those of the wild-type cells. It was suggested that FlgP is a component of a structure named basal disk, which seems to be in contact with the OM (7). The basal disk is required to form other flagellar structures such as the medial and proximal rings in *C. jejuni* or to recruit the stator complexes in *V. fischeri* (7). These authors also observed that in the *flgP* mutant of *C. jejuni* the flagellum is formed, which agrees with previous reports; however, in contrast to what had been reported for *V. cholerae*, the *flgP* mutant of *V. fischeri* seldom forms a flagellum (7).

Rhodobacter sphaeroides is an alphaproteobacterium with two different flagellar systems (33). Transcription of the *fla1* set produces a single subpolar flagellum that is expressed constitutively under the growth conditions commonly used in the laboratory (33, 34). The products encoded by the *fla2* set produce several polar flagella (33, 35). However, the expression of the *fla2* genes is achieved only under very particular conditions. Fla2 flagella were detected in a mutant strain lacking the master activator of the *fla1* genes that acquired a gain of function mutation in the histidine kinase CckA (36). Phylogenetic analysis of these flagellar gene systems suggested that the *fla1* set was acquired by *R. sphaeroides* from an ancestral gammaproteobacterium, whereas the *fla2* set is vertically inherited (33).

The *fla1* system of *R. sphaeroides* includes the *flgT* and *flgP* genes. FlgT forms the periplasmic H-ring that covers the P and L rings, similar to the observed situation in *Vibrio* species; however, the phenotype of the *flgT* mutant strain differs from that of these bacteria, given that in *V. cholerae* and *V. alginolyticus* the absence of FlgT results in a reduction of the number of flagellated cells, but in *R. sphaeroides* the absence of FlgT yields a Mot$^-$ phenotype, where the flagellum is paralyzed (37–40).

Downloaded from http://jb.asm.org/ on October 20, 2020 at UNAM INST DE INVEST BIOMEDICAS

INFORME DE LABORES 2019

In this study, we characterized FlgP from *R. sphaeroides*. This protein is absolutely required for the assembly of the Fla1 flagellum, and its absence results in the lack of hook and filament. FlgP was detected in isolated wild-type filament basal body structures, and evidence is presented suggesting that FlgP interacts with FlgH and FlgT.

(This study was conducted by C. Pérez-González in partial fulfillment of the requirements for a Doctorado en Ciencias Biomédicas degree from the Universidad Nacional Autónoma de Mexico, Mexico City, Mexico.)

RESULTS

FlgP is required for swimming and filament assembly. In *R. sphaeroides* the gene *flgP* encodes a 177-amino-acid polypeptide. The N terminus shows a short sequence similar to the consensus sequence recognized by the signal peptidase II (SPaseII) that has a predicted cleavage site between Ala20 and Cys21, with Ala at position +2. The identity of the residue at the +2 position after the cleavage site indicates if the polypeptide will be retained at the IM or directed to the OM (41, 42). Therefore, the presence of Ala at this position, suggests that FlgP is localized in the OM (Fig. 1A). This protein shows a 25/27% identity with homologs in *V. cholerae* and *C. jejuni*. In *R. sphaeroides flgP* is the first gene of a putative operon formed by *flgP*, *flgT*, *flgA*, *flgM*, and RSWS8N_05380 *orf* (Fig. 1A). The first three genes show overlapping of the translation stop and start codons. *flgT* encodes the protein that forms the H ring, which is present is some bacterial species (28), FlgA is a chaperone that assists in the assembly of the L ring and, FlgM is the anti-σ^{28} factor required to transcribe the late flagellar genes. RSWS8N_05380 encodes a 123-amino-acid protein that has not been reported to be involved in either flagellar biogenesis or swimming.

To characterize the role of FlgP in the flagellar biogenesis of *R. sphaeroides*, a mutant strain in *flgP* (Δ*flgP*::*aadA*) was constructed. This mutant was unable to swim and introduction of the plasmid that expresses *flgP* (pRK_flgP) did not restore swimming; however, when the plasmid pRK_flgPT (that drives the expression of *flgP* and *flgT*) was introduced, swimming was recovered (Fig. 1B). These results suggest that the allele Δ*flgP*::*aadA* generates a polar effect on the expression of *flgT*. Nevertheless, the role of FlgP on swimming was clearly appreciated in the Δ*flgP*/pRK_flgT strain, since the expression of *flgT* did not restore swimming, suggesting the absence of *flgP* by itself is responsible of this defect. The presence in these strains of FlgP and FlgT was verified by Western blotting (Fig. 1C) and, as expected, FlgT is absent in the strain carrying the Δ*flgP*::*aadA* allele but is present in the nonmotile Δ*flgP*/pRK_flgT strain. Furthermore, FlgP was detected in the wild-type strain and also in the Δ*flgP* strain harboring pRK_flgP and pRK_flgPT (Fig. 1C). Given that in this bacterium the flagellar hierarchy is controlled by the master activator FleQ (43), the absence of FlgP in the Δ*fleQ* mutant strain indicates that *flgP* is expressed as a part of the flagellar regulon (Fig. 1C).

Overlapping of the translation stop and start codons *of flgP*, *flgT*, and *flgA* suggests that these genes form an operon. We noticed that the Δ*flgP*::*aadA* allele affects the expression of *flgT* but not the expression of *flgA*, since the Δ*flgP*::*aadA*/pRK_flgPT strain was fully motile (and the lack of FlgA would have produced a Fla$^-$ phenotype). From these observations, it could be hypothesized that the absence of FlgT in the Δ*flgP*::*aadA* mutant could be caused by translational coupling. This possibility would also explain why the insertion of the nonpolar gene *aadA* (44) could affect the expression of the downstream gene; alternatively, in the absence of FlgP, FlgT could be unstable. Unfortunately, several attempts to isolate a *flgP* mutant without a resistance marker were unsuccessful; therefore, we carried out experiments to characterize the Δ*flgP* (Δ*flgP*::*aadA*) mutant always in the presence of the plasmid pRK_flgT. In this strain the amount of FlgT detected by Western blotting is similar to the amount detected in WS8N (Fig. 1C), suggesting that FlgT should not be limiting for flagellum formation and functioning.

Filaments were easily detected in the microscope in the wild-type strain, but this structure was not observed in Δ*flgP* and Δ*flgP*/pRK_flgT strains, indicating that these

Downloaded from http://jb.asm.org/ on October 20, 2020 at UNAM INST DE INVEST BIOMEDICAS

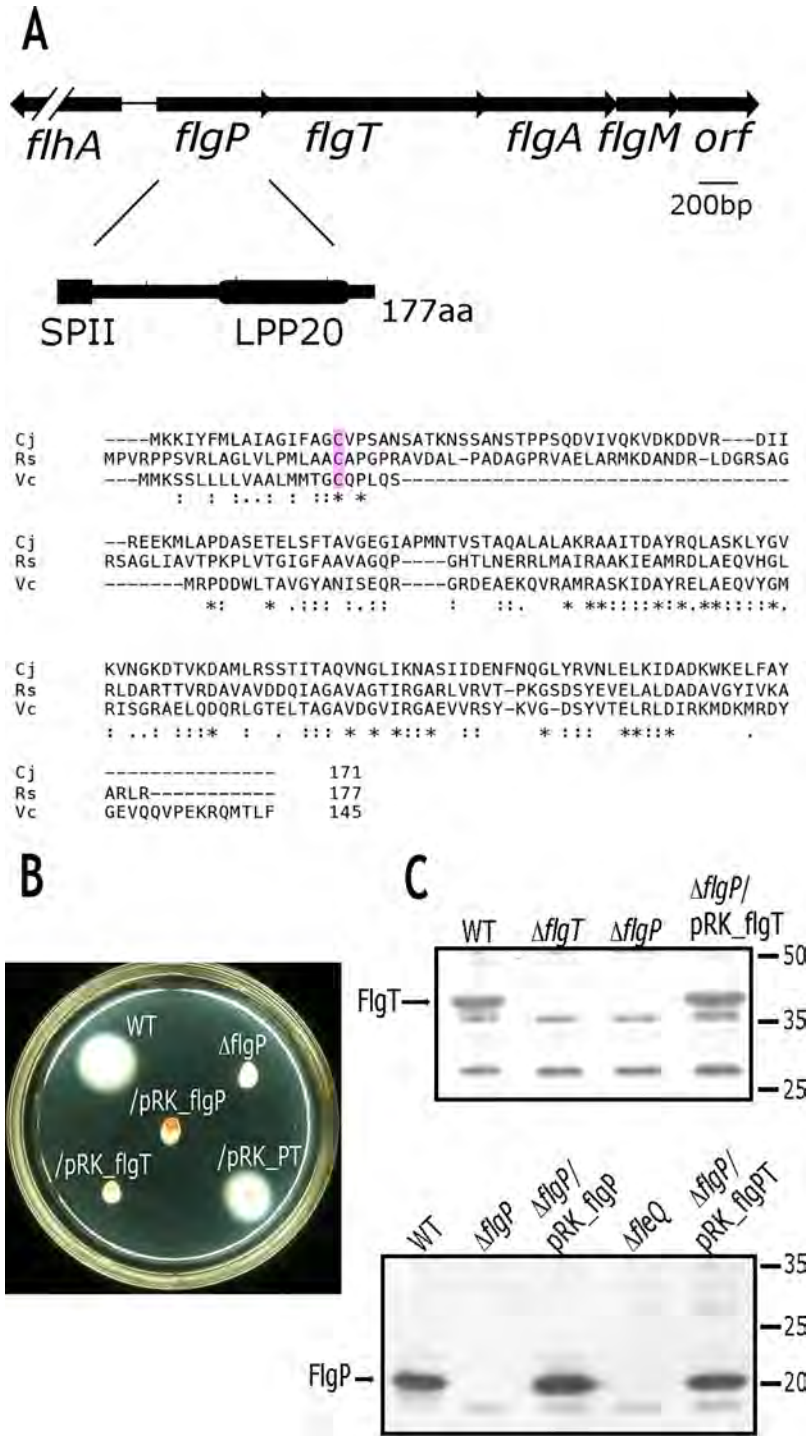

FIG 1 The role of FlgP on swimming in *R. sphaeroides*. (A) Genetic context of *flgP* and domain composition. SPII, signal protease II; LPP20, pfam PF02169. Amino acid sequence alignment of FlgP with homologs from *C. jejuni* and *V. cholerae*. The invariant cysteine in the lipobox is shown in pink. (B) Swimming of the Δ*flgP*::*aadA* mutant and complementation test. (C) Immunodetection of FlgT and FlgP in total cell extracts of the Δ*flgP*::*aadA* mutant and strains expressing FlgP, FlgT, and FlgPT from the promoter of pRK415. WT, wild-type strain WS8N.

two mutant strains are Fla$^-$ (Fig. 2). In contrast, the filament was visible in Δ*flgP*/pRK_flgP cells. Given that a strain lacking of *flgT* shows a Mot$^-$ phenotype (37), the presence of the flagellar filament in the Δ*flgT* mutant was expected (Fig. 2). From these results, we conclude that the absence of FlgP causes the loss of the flagellar filament.

Downloaded from http://jb.asm.org/ on October 20, 2020 at UNAM INST DE INVEST BIOMEDICAS

INFORME DE LABORES 2019

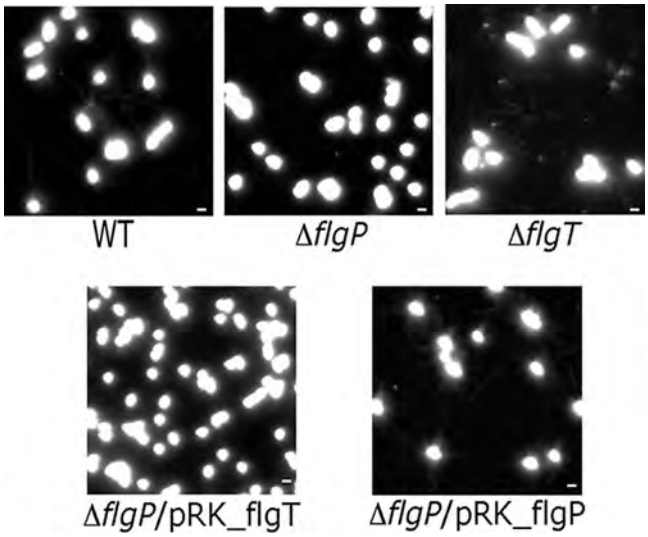

FIG 2 Flagellar filament detection. Cells were stained with DAPI and observed by fluorescence microscopy as indicated in Materials and Methods. WT, wild-type strain WS8N. Scale bars, 1 μm.

This phenotype is different from that reported for *C. jejuni* and *V. cholerae* (29, 30) but is similar to what was observed in *V. fischeri* (7).

Role of FlgP in the formation of other flagellar structures. Given that the flagellar filament is absent in the Δ*flgP*/pRK_flgT mutant cells, we proceeded to investigate whether the flagellar hook would be assembled in the absence of FlgP. For this, Δ*flgP*/pRK_flgT cells were labeled with an anti-FlgE antibody previously conjugated with Alexa Fluor 488 and then observed by fluorescence microscopy. The hook was readily observed as small fluorescent foci that are placed laterally on wild-type strain cells (Fig. 3A). In contrast, the Δ*flgP*/pRK_flgT mutant strain did not show fluorescent foci, indicating that the hook is not formed in the absence of FlgP (Fig. 3A).

A simple explanation for the lack of hook and filament in the Δ*flgP*/pRK_flgT strain could be that FlgE and FliC were not being synthesized. This possibility was tested by probing total cell extracts by Western blotting using anti-FliC and anti-FlgE antibodies (Fig. 3B). The intensity of the signal for FlgE was similar in the wild-type cells and Δ*flgP*/pRK_flgT mutant, indicating that the absence of the hook is not due to a lack of protein. However, the amount of FliC was severely reduced in the mutant strain (Δ*flgP*/pRK_flgT). This is the logical outcome of a lack of hook, since the anti-sigma factor FlgM cannot be exported from the cells, and transcription by σ^{28} of the late flagellar genes does not take place (43, 45–47). The expression of CheY4 was used to corroborate this notion, given that it is also σ^{28} dependent (48). As expected, a severe reduction in the amount of CheY4 was observed in the Δ*flgP*/pRK_flgT strain (Fig. 3B).

In Δ*flgP*/pRK_flgT cells, the hook was not detected but FlgE was observed in total cell extracts, raising the possibility that FlgE could be exported from the cell but not assembled. To test this idea, the supernatants of WS8N and Δ*flgP*/pRK_flgT cultures were probed by Western blotting for the presence of FlgE. No protein was detected in these samples, indicating that FlgE is not exported (data not shown). As a control, the cells of these cultures were vigorously vortexed to promote the mechanical shearing of the flagella. After centrifugation, the supernatants were tested by Western blotting. In these samples, FlgE was detected in the culture supernatant of WS8N but not in the Δ*flgP*/pRK_flgT strain (see Fig. S1 in the supplemental material), confirming the notion that, in the absence of FlgP, FlgE is not exported or assembled.

To determine whether the MS ring is formed in the absence of FlgP, we evaluated the localization of the GFP-FliF fusion protein as an indirect evidence of the presence of this structure. As shown in Fig. 4A, GFP-FliF was detected as a single focus in wild-type and Δ*flgP* cells, suggesting that the formation of the MS ring is not affected by the absence of FlgP.

Downloaded from http://jb.asm.org/ on October 20, 2020 at UNAM INST DE INVEST BIOMEDICAS

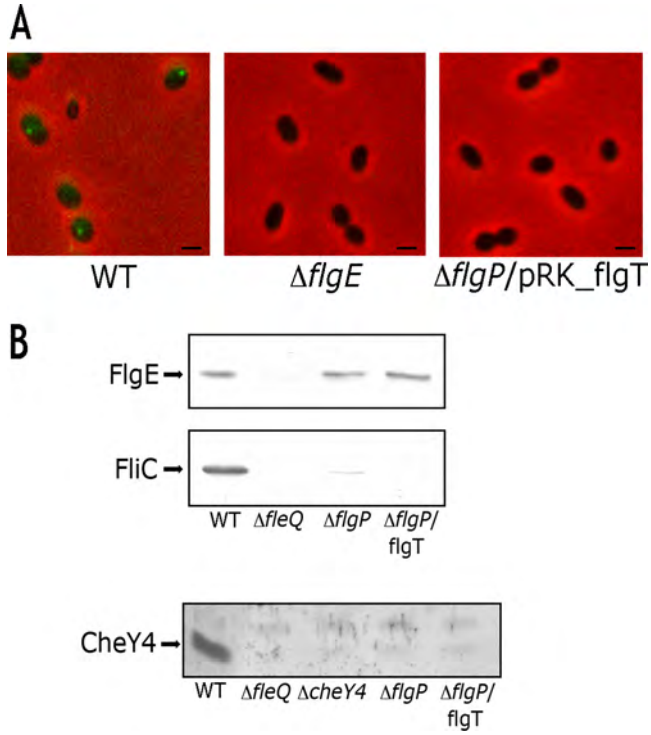

FIG 3 Immunofluorescent detection of the flagellar hook in complete cells. (A) Cells were incubated in the presence of anti-FlgE prestained with Alexa Fluor 488 and observed by fluorescence microscopy. WT, wild-type strain WS8N. Scale bars, 1 μm. (B) Western blots of total cell extracts of the indicated strains, using anti-FlgE, anti-FliC, and anti-CheY4 antibodies. WT, wild-type strain WS8N.

It has been shown that in *Salmonella* FlgE is degraded in strains where the rod genes have been deleted. This was caused by the high sensitivity of FlgE to periplasmic proteases (49). We tested by Western blot analysis whether FlgE could be detected in rod mutants, type III export apparatus mutants, and the Δ*flgP*/pRK_flgT mutant. Total cell extracts of these strains revealed the presence of FlgE in the wild-type strain, in the export apparatus mutants (*fliE*, *fliR*, and *fliO*), and also in the Δ*flgP* mutant (Δ*flgP*/pRK_flgT) and its absence in the rod mutants (Δ*flgB* and Δ*flgC*) (Fig. 4B). A reduction of

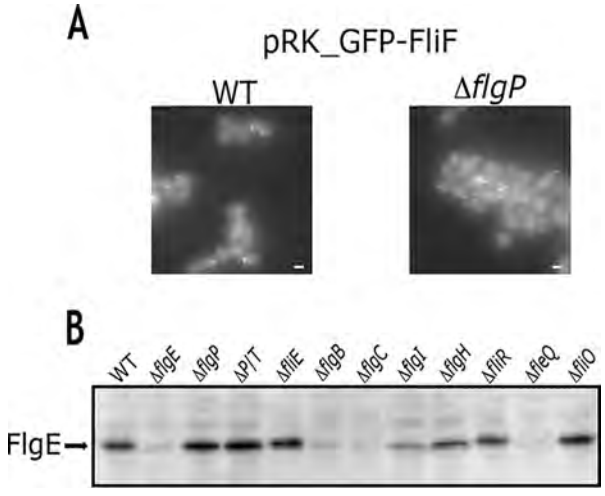

FIG 4 GFP-FliF detection by fluorescence microscopy. (A) Wild-type (WT), WS8N, and Δ*flgP*::*aadA*/pRK_flgT cells. Scale bars, 1 μm. (B) Immunodetection of FlgE by Western blotting in the indicated genetic background.

Downloaded from http://jb.asm.org/ on October 20, 2020 at UNAM INST DE INVEST BIOMEDICAS

INFORME DE LABORES 2019

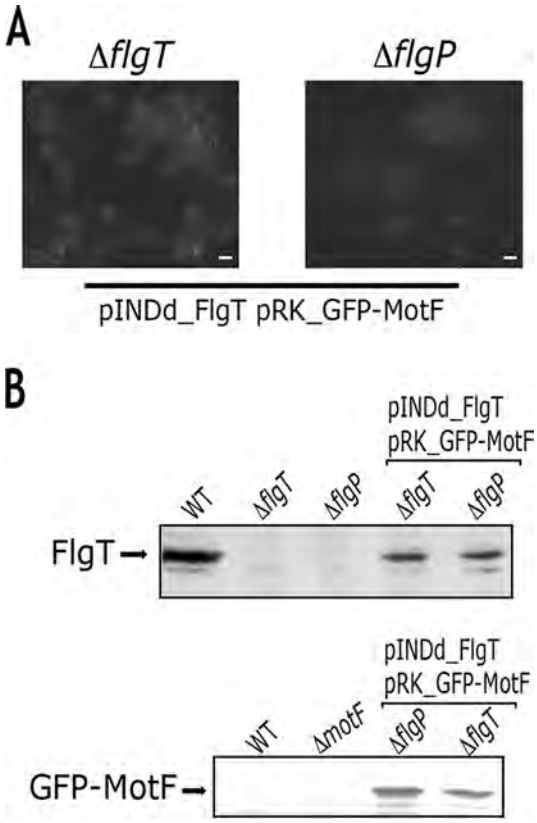

FIG 5 GFP-MotF detection by fluorescence microscopy. (A) Cells expressing FlgT from pINDd and GFP-MotF from pRK415. Scale bars, 1 μm. (B) Immunoblotting detection of FlgT and GFP-MotF in total cell extracts of the indicated strains. WT, wild-type strain WS8.

FlgE in the Δ*flgI* mutant was noted; this is in accordance with the results previously reported for *Salmonella* (49). The mutants lacking the flagellar master regulator, *fleQ*, and the hook gene *flgE* were included as negative controls. The presence of FlgE in Δ*flgP*/pRK_flgT cells (Fig. 4B) suggests that in the absence of FlgP the rod is completed since FlgE is not degraded by the periplasmic proteases, as has been previously reported (49).

FlgT is another flagellar protein localized in the periplasm, it is required to form the H ring that covers the P and L rings. In *R. sphaeroides* the absence of FlgT did not affect flagellar biogenesis (37). To determine whether FlgT is present in the flagellum in the absence of FlgP, we took advantage of the fact that the flagellar protein MotF (present exclusively in *R. sphaeroides*) requires the presence of FlgT to be localized (50). Therefore, we determined if green fluorescent protein (GFP)-MotF is localized in the absence of FlgP. We used strain SF3 (Δ*flgT*) carrying the plasmids pINDd_flgT and pRK_GFP-MotF as a positive control for this experiment. We observed the presence of fluorescent foci in these cells, suggesting that GFP-MotF is localized in the flagellar structure (Fig. 5A). However, no fluorescent foci were detected in Δ*flgP* cells carrying pINDd_flgT and pRK_GFP-MotF, suggesting that in the absence of FlgP the H ring could be destabilized or severely affected. The presence of FlgT and GFP-MotF in total cell extracts of these strains was detected by immunoblotting (Fig. 5B).

FlgP is an integral protein of the basal body and is stable in different genetic backgrounds. We isolated filament basal body structures of WS8N cells and used this preparation for electron microscopy (EM) and for immunodetection of FlgP. An example of the EM images obtained from intact flagellar structures, shows the H ring covering the L and P rings, as previously reported (37) (Fig. 6A). In this same sample, we were able to detect FlgP by immunoblotting, indicating that this protein is a part of this structure (Fig. 6B).

Downloaded from http://jb.asm.org/ on October 20, 2020 at UNAM INST DE INVEST BIOMEDICAS

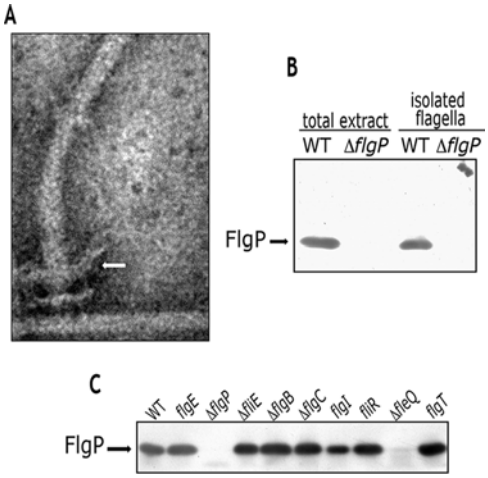

FIG 6 Presence of FlgP in isolated filament basal body preparations and stability of FlgP in the absence of other flagellar components. (A) Sample of an isolated flagellum from the wild-type strain. The arrow denotes the H ring. (B) Immunoblotting of total cell extracts using anti-FlgP antibodies (left lanes) and isolated flagella (right lanes). (C) Stability of FlgP in different genetic backgrounds. Western blots of total cell extracts were probed with anti-FlgP antibodies. WT, wild-type strain WS8N.

In *C. jejuni* FlgP was generally absent or present at low levels in whole-cell lysates of proximal rod (*flgB* and *flgC*) and type III export apparatus (*flip* and *flhA*) mutants (7), indicating that FlgP stability was dependent on other flagellar components. In contrast, we detected FlgP in rod (*flgB* and *flgC*) and type III export apparatus (*fliE* and *fliR*) mutants (Fig. 6C), demonstrating that in *R. sphaeroides* this protein is not particularly unstable.

FlgP interacts with FlgT and FlgH. Given that FlgP is part of the flagellar basal body structure, we evaluated possible interactions of FlgP with other periplasmic flagellar proteins, such as FlgH, FlgT, and MotF. The interactions of the periplasmic region of FlgP with the periplasmic regions of FlgH, FlgT, and MotF were tested using a yeast two hybrid assay. In this assay, we observed that FlgP interacts with FlgH and FlgT (Fig. 7). The possible interaction between FlgP with MotF could not be evaluated given the autoactivation of these proteins (Fig. 7). It should be noted that Gal4BD-FlgP by itself allows growth in the absence of histidine; therefore, only strong interactions that alleviate adenine auxotrophy were considered positives (Fig. 7). In this assay, the interaction of FlgP with FlgP does not occur, since a yeast strain expressing AD-FlgP and BD-FlgP recovered the prototrophy only for histidine (data not shown). Interestingly, FlgH showed a positive interaction with FlgT (Fig. 7).

The interaction of FlgP with FlgP was evaluated by blue native polyacrylamide gel electrophoresis (PAGE). Two different species of FlgP were detected: one with an apparent molecular mass around 36 kDa that may represent the monomeric form and another that was around 56 kDa (Fig. 8A), suggesting that under these conditions FlgP could form a dimer. In these experiments, we also detected the monomeric and dimeric forms of FlgT (54 and 113 kDa, respectively). When FlgP and FlgT were mixed together, a weak but conspicuous band of around 90 kDa appeared, which was interpreted to represent the oligomeric complex formed by the association of FlgP with FlgT. Since high-molecular-weight markers were used in this native electrophoresis, the apparent molecular masses of the complexes may be overestimated. Denaturing two-dimensional SDS-PAGE (lanes 2 to 4) show that the bands observed in the native gels belong exclusively to FlgP, to FlgT, or to the FlgP/FlgT mixture (Fig. 8B).

The interaction of FlgP with FlgT was also detected by pulldown using glutathione *S*-transferase (GST)–FlgP as a bait (Fig. 9A). In contrast, the interaction between FlgP and FlgH could not be detected using this assay, given that FlgH showed nonspecific interactions with GST (data not shown). Nonetheless, we were able to corroborate the

Downloaded from http://jb.asm.org/ on October 20, 2020 at UNAM INST DE INVEST BIOMEDICAS

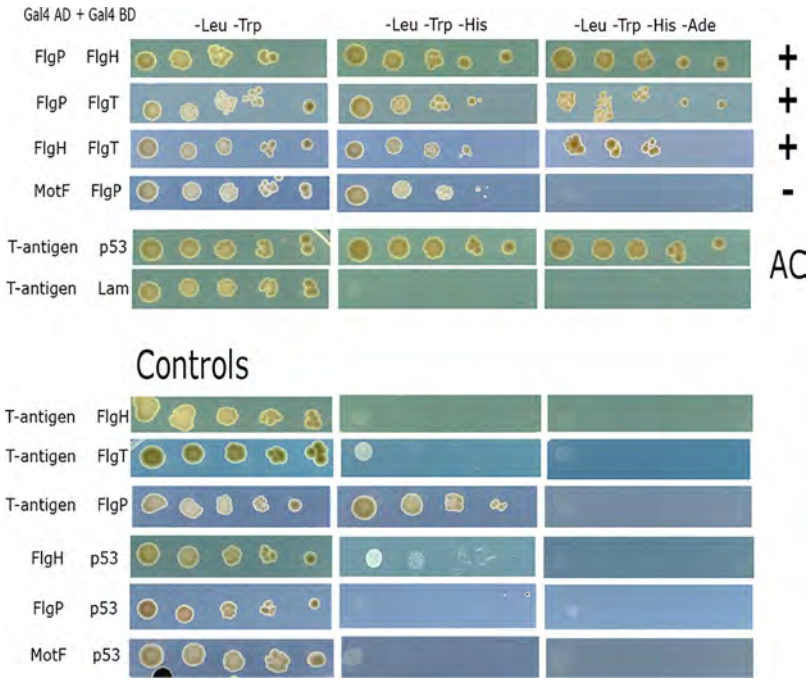

FIG 7 Double hybrid assay. Yeast were transformed with the plasmids indicated at the left. The pairs Gal4AD T-antigen with Gal4 p53, and Gal4AD T-antigen with Gal4 BD Lam served as positive and negative controls, respectively (labeled "AC" [assay controls]). Transformant cells were seeded on the medium indicated at the top. To rule out spurious activation of the reporter genes, yeast cells transformed with a control plasmid, either Gal4 AD T-antigen or Gal4 BD p53, and a flagellar gene in the BD or AD plasmid. The growth of these cells was tested and corresponds to the six combinations in the lower part of the figure (Controls).

interaction between FlgP and FlgH by far-Western analysis (Fig. 9B). For this experiment, GST-FlgP was incubated with the blotted proteins $His_{6\times}$-FlgH and $His_{6\times}$-GFP. The presence of complexes was tested using anti-FlgP antibodies (Fig. 9B). The blotted proteins were also incubated with GST, and the absence of unspecific complexes was confirmed using anti-GST (Sigma) antibodies (Fig. S2).

DISCUSSION

Several new ancillary proteins different from the well-characterized flagellar components of *E. coli* and *Salmonella* have been identified in various bacterial species. These new elements in some cases improve flagellar rotation by recruiting a larger number of stator complexes (7); in others, they contribute to remodel other bacterial structures such as the outer membrane (OM) (51). FlgP is absent in *E. coli* and *Salmonella* but is present in several species of *Vibrio* and many *Epsilonproteobacteria* (29, 30, 52). ECT images suggest that FlgP could form a basal disk located underneath the OM. It has also been suggested that the basal disk (FlgP) attaches to the motor via the P ring (FlgI) in *C. jejuni* and in *V. fischeri* through the H ring (FlgT) (7).

In *R. sphaeroides*, the absence of FlgP causes a Fla$^-$ phenotype that contrasts with the phenotypes observed in other species so far studied. In *C. jejuni*, a Δ*flgP* mutant forms flagella (30), whereas a reduction in the number of flagellated cells was observed for the Δ*flgP* mutant in *V. cholerae* (29). This suggests that in *R. sphaeroides* the role of this protein is not redundant; perhaps the absence of flagellar rings, such as the T ring (present in *Vibrio*) or the proximal and medial disks (found in *C. jejuni*), makes flagellar assembly impossible in the absence of FlgP.

A closer inspection of the Δ*flgP* strain of *R. sphaeroides* revealed that the flagellar hook is not assembled even though the presence of the hook protein FlgE was detected by Western blotting. In addition, the fact that flagellin (FliC) and the chemotactic protein CheY4 were not detected in total cell extracts of the Δ*flgP* mutant

Downloaded from http://jb.asm.org/ on October 20, 2020 at UNAM INST DE INVEST BIOMEDICAS

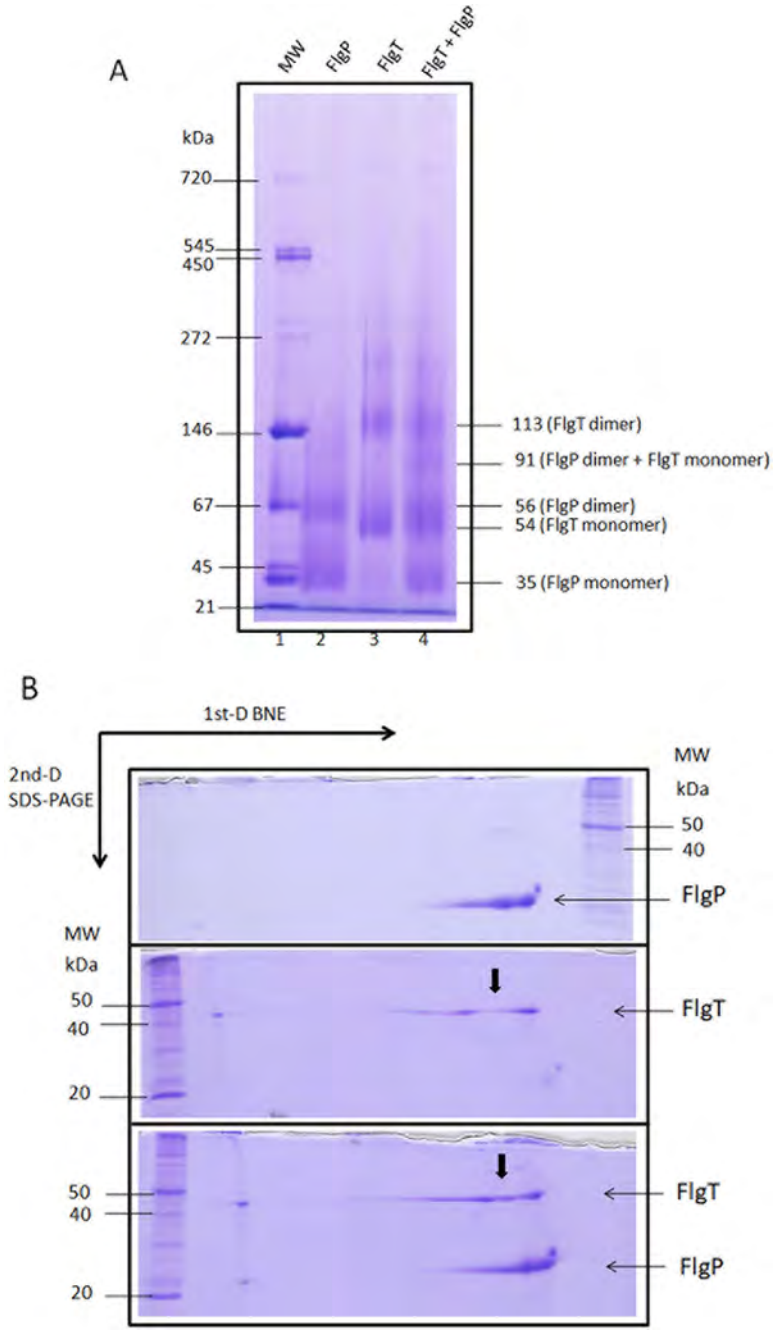

FIG 8 Blue native gel electrophoresis. (A) Portions (100 μg) of $His_{6\times}$-FlgPp (lane 2), FlgTp-$His_{6\times}$ (lane 3), or a mixture of both proteins (lane 4) were dialyzed overnight in PBS (pH 7.4), mixed with sample buffer, and loaded into a native 4 to 12% acrylamide gradient gel. Lane 1 was loaded with molecular weight protein markers. Gel casting and electrophoresis were performed as described previously (44). (B) Parallel lanes of each sample of interest from panel A were cut and subjected to denaturing two-dimensional SDS-PAGE (14%). The presence of FlgT in the complex formed with FlgP is indicated by an arrow.

indicates that the anti-sigma factor FlgM is not exported. This is consistent with the well-established idea that a structural defect in the hook basal body (HBB) impairs secretion of FlgM (45–47). Nevertheless, in the absence of FlgP, the flagellar rod is assembled, and FlgE was not detected in the culture supernatant. Therefore, the absence of FlgP could be altering the rod to filament transition. This idea is in accordance with the images observed by ECT for the *flgP* mutant of *V. fischeri*, where the rod and the P, L, H, and T rings are formed, but the presence of the hook is not evident (7).

Downloaded from http://jb.asm.org/ on October 20, 2020 at UNAM INST DE INVEST BIOMEDICAS

INFORME DE LABORES 2019

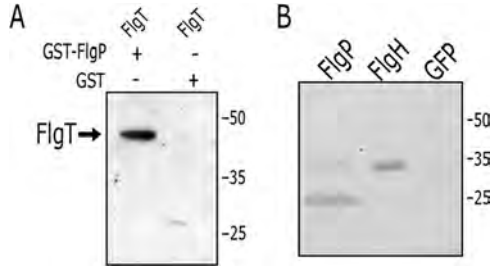

FIG 9 FlgP interaction with FlgT and FlgH. (A) Pulldown assay using glutathione-agarose beads containing either GST-FlgP or GST, followed by incubation with FlgT. After a washing step, the presence of FlgT retained by the tested proteins was revealed by Western blotting. (B) Interaction between FlgP and FlgH tested by far-Western analysis. Purified $His_{6\times}$-FlgP, $His_{6\times}$-FlgH, and $His_{6\times}$-GFP were subject to 12% SDS-PAGE and blotted on nitrocellulose. The membrane was incubated with GST-FlgP for 2 h. After a washing step, the presence of FlgP was detected using anti-FlgP antibodies.

As a result of the absence of FlgT (H ring) in *R. sphaeroides*, MotF is not localized in the flagellar motor (37). Furthermore, we have observed in the present study that in the absence of FlgP, MotF is not recruited to the flagellum, suggesting that the H ring is not formed or that the architecture of the H ring is modified. In agreement with the possible remodeling of these rings as they are being assembled, it was observed in *V. fischeri* that in the absence of FlgP, all the rings were formed (i.e., P, L, T, and H rings), but the stator complexes were not recruited, suggesting that FlgP could modify the architecture of the H and T rings (7).

It is conceivable that the flagellar structure of *R. sphaeroides* has a basal ring similar to that observed in *C. jejuni* and *V. fischeri*. In this regard, our results indicate that FlgP can interact with itself, suggesting that it could be a part of an oligomeric structure, such as the basal disk. Besides this interaction, FlgP also interacts with FlgT, indicating that the OM is in close contact with the H ring through FlgP. In spite of the strong interaction between FlgP and FlgT, recruitment of FlgP to the growing structure should not be dependent only on FlgT, given that the flagellum is formed in its absence (37) but not in the absence of FlgP. This indicates that even in the absence of FlgT, FlgP must be recruited to the growing flagellum. This recruitment could be achieved by a FlgP-FlgH interaction. This is in contrast to the observed situation in *V. fischeri*, where it was proposed that the H ring provides a platform for assembly of FlgP (7).

We observed that FlgP is stable in the different flagellar mutants tested. In contrast, in *C. jejuni*, FlgP was not detected in total cell extracts of proximal rod and type III export apparatus mutants (7). This difference could be explained by a different intrinsic stability of these proteins or by the presence of ancillary flagellar proteins, such as FlgQ and FlgO (52), that are absent in *R. sphaeroides*. FlgQ is required for FlgP stability in *C. jejuni* (30), whereas FlgO of *Vibrio* seems to be a part of the H ring and is located at the OM similar to FlgP (29).

To explain the Fla^- phenotype of the Δ*flgP* strain, we propose that the L ring could be remodeled by the basal disk. This event could be part of the check point that involves the removal of the rod scaffolding protein FlgJ to enable hook assembly. It is possible that in other species in which the flagellar hook can be assembled in the absence of FlgP, other proteins collaborate to form an L ring suitable for the removal of FlgJ or that FlgH could accomplish this task by itself, as occurs in *E. coli* and *Salmonella*. A model summarizing the findings reported in this is presented in Fig. 10.

MATERIALS AND METHODS

Strains, plasmids, growth conditions, and oligonucleotides. All strains and plasmids used in this study are listed in Table 1. *R. sphaeroides* was grown in Sistrom's minimal medium at 30°C (53). Cultures were grown heterotrophically in Erlenmeyer flasks with orbital shaking (200 rpm). *E. coli* was grown in Luria broth at 37°C (54). When needed, the following antibiotics were used at the indicated concentrations: 25 μg/ml kanamycin, 50 μg/ml spectinomycin, and 1 μg/ml tetracycline. For *E. coli*, the antibiotics used were 100 μg/ml ampicillin, 50 μg/ml kanamycin, 50 μg/ml spectinomycin, 30 μg/ml gentamicin, 25 μg/ml chloramphenicol, and 10 μg/ml tetracycline. The oligonucleotides used are also listed in Table 1.

Downloaded from http://jb.asm.org/ on October 20, 2020 at UNAM INST DE INVEST BIOMEDICAS

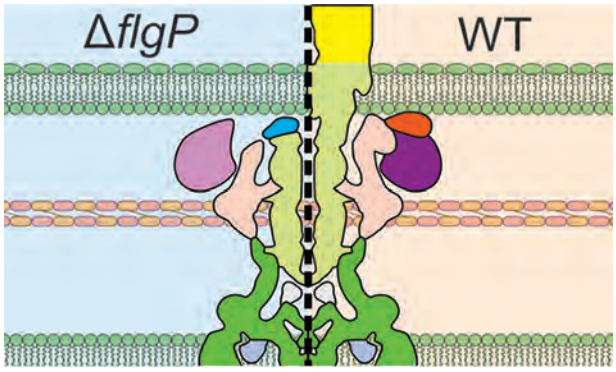

FIG 10 Model showing the possible role of FlgP during flagellar biogenesis in *R. sphaeroides*. The right side depicts the wild-type flagellum where FlgP (orange) interacts with FlgH (pink) and FlgT (violet). The hook (yellow) is formed. The left side shows that, in the absence of FlgP, the hook is not assembled. A possible perturbation in the formation of the L ring (formed by FlgH) prevents the progression of the flagellar biogenesis beyond the outer membrane. In the absence of FlgP, the possible presence of FlgJ (blue) at the tip of the growing flagellum is shown. In addition, FlgT is shown in light violet, indicating that it may also be absent.

Molecular biology techniques. Standard methods were used to isolate and analyze chromosomal or plasmid DNA (54). Restriction and other DNA-modifying enzymes were purchased either from New England BioLabs (NEB, Ipswich, MA), Roche (Basel, Switzerland), or Invitrogen (Carlsbad, CA). Plasmids used for sequencing were purified using an Illustra plasmidPrep minispin kit (GE Healthcare Life Sciences, Buckinghamshire, UK). DNA was amplified with the appropriate oligonucleotides using PrimeSTAR HS DNA polymerase (TaKaRa Bio, Inc., Mountain View, CA) according to the manufacturer's recommendations.

Isolation of mutant strains. The CP1 strain (Δ*flgP*::*aadA*) was obtained by cloning together two PCR products that amplified the upstream and downstream regions of *flgP* in pTZ19R. The 756-bp product from the upstream region of *flgP* was obtained using the oligonucleotides orf_11 and RvRSP0035B, whereas the downstream product of 1,293 bp was obtained with the oligonucleotides FwRSP0035B and orf_12. These PCR products were joined through a BglII site designed in the oligonucleotides and cloned in pTZ19R. A 1.4-kb PCR fragment carrying the *aadA* gene, which encodes the streptomycin/spectinomycin adenylyltransferase (Spc^r) (44), was cloned into pTZ_ΔflgPup-down previously digested with BglII. The resultant plasmid, pTZ_ΔflgP::aadA, was digested with XbaI, and the fragment carrying the allele Δ*flgP*::*aadA* was subcloned in plasmid pQJ200mp18. To obtain the CP2 strain (Δ*flgH*::*aadA*), a similar strategy to that used to obtain CP1 was followed; in this case, the 700-bp product from the upstream region of *flgH* was obtained using the oligonucleotides Fw_flgH and Rvi_flgH, whereas a downstream product of 1,008 bp was obtained with Fwi_flgH and Rv_flgH. These products were joined through a BamHI site designed in the oligonucleotides and cloned in pTZ19R_BamHI−. The fragment carrying the *aadA* gene was cloned in pTZ_flgHup-down previously digested with BamHI. The fragment carrying Δ*flgH*::*aadA* was subcloned in pJQ200mp18.

Plasmid constructions. pRK415_flgP plasmid carries a 1,086-bp fragment that includes the coding region of *flgP* (534 bp), 501 bp upstream and 51 bp downstream. pRK_flgPT carries a 2,300-bp fragment that includes the coding regions of *flgP* and *flgT* (1,083 bp), 501 bp upstream of *flgP* and 186 bp downstream of the stop codon of *flgT*. pINDd_flgT was obtained by cloning the 1,083-bp PCR product encoding the complete polypeptide of FlgT in pINDd.

Protein purification. The coding region of *flgP* lacking the segment corresponding to the signal peptide was amplified by PCR using the oligonucleotides 0035fwBAD and 0035RvBAD and cloned in pBAD-HisB. The resultant plasmid was introduced to the strain LMG194 strain. A culture of this strain was grown until midexponential phase and induced with 0.2% arabinose for 6 h at 28°C. The culture was harvested and resuspended in buffer containing 50 mM Tris, 5% glycerol, 50 mM NaCl, and 1 mg/ml lysozyme (pH 8). The cell suspension was sonicated on ice with three bursts of 10 s. Cell debris were removed by centrifugation. The supernatant was mixed with nickel-nitrilotriacetic acid (Ni-NTA)–agarose beads (1/250 of the original culture volume) and incubated by 1 h on ice, with occasional mixing. The beads were washed with 3 volumes of phosphate-buffered saline (PBS; pH 7.4). The protein was eluted in PBS containing 20% glycerol and 200 mM imidazole. The purity of the $His_{6\times}$-FlgPp (periplasmic region of FlgP) was evaluated by SDS-PAGE and Coomassie blue staining. The sample was dialyzed overnight using PBS (pH 7.4). To purify FlgH, the fragment encoding from Ala58 to the stop codon of *flgH* (FlgHp) was amplified by PCR using the oligonucleotides flgH-pGABfw and flgH-pBADB and cloned in pET28a. The purification protocol was similar to the procedure used to purify $His_{6\times}$-FlgPp, except that induction of the cell culture was carried out with 0.25 mM IPTG for 4 h at 28°C. FlgTp-His_{6X} and $His_{6\times}$-MotFp were purified using the procedures previously described (37, 50). The plasmid expressing glutathione *S*-transferase fused to the mature polypeptide of FlgP (GST-FlgPp) was constructed by cloning in pGEX-4T-2, the PCR product obtained with the oligonucleotides 0035FwpGEX and 0035RvpGEX that encompasses the coding region of *flgP*, excluding the segment that encodes the signal peptide

Downloaded from http://jb.asm.org/ on October 20, 2020 at UNAM INST DE INVEST BIOMEDICAS

INFORME DE LABORES 2019

TABLE 1 Strains and plasmids used in this study[a]

Strain, plasmid, or source oligonucleotide	Relevant characteristics or sequence	Reference or source
Strains		
E. coli		
LMG194	Δ*lacX74 galE thi rpsL* Δ*phoA* Δ*ara714 leu*::Tn*10*	Invitrogen
S17-1	*recA endA thi hsdR* RP4-2 Tc::Mu::Tn*7*	58
TOP10	Cloning strain	Invitrogen
Rosetta	Protein expression strain; Cm^r	Novagen
Yeast AH109	Yeast reporter strain for HIS3, ADE2, and *lacZ*	Clontech
R. sphaeroides		
CP1	Δ*flgP*::*aadA*	This study
CP2	Δ*flgH*::*aadA*	This study
LC1	*flgE*::*aadA*	44
RsgI-np	*flgI*::*aadA*	59
SF3	*flgT*::*aadA*	37
SP2	*fliR*::*uidA-aadA*	60
SP13	Δ*fleQ*::*aadA*	43
SP30	Δ*fliE*::*aadA*	Laboratory collection
SP31	Δ*flgC*::*aadA*	Laboratory collection
SP32	Δ*flgB*::*aadA*	Laboratory collection
SP33	Δ*fliO*::*aadA*	Laboratory collection
WS8N	Wild-type strain	61
Plasmids		
pBAD His-motFp	Vector expressing $His_{6\times}$-MotFp	50
pBAD_FlgPp	Vector expressing $His_{6\times}$-FlgPp	This study
pBAD/HisB	Expression vector of $His_{6\times}$-tagged proteins	Invitrogen
pBAD/Myc-HisA-flgT	Vector expressing FlgT-$His_{6\times}$	37
pET28_FlgHp	Vector expressing $His_{6\times}$-FlgHp	This study
pET28a	Expression vector $His_{6\times}$-tagged proteins	Novagen
pGAD_flgH	pGAD derivative expressing GAL4 AD-FlgHp	This study
pGAD_flgP	pGAD derivative expressing GAL4 AD-FlgPp	This study
pGAD_motFp	pGAD derivative expressing GAL4 AD-MotFp	37
pGADT7	GAL4 activation domain, LEU2	Clontech
pGBD_flgH	pGAD derivative expressing GAL4 BD-FlgHp	This study
pGBD_flgP	pGAD derivative expressing GAL4 BD-FlgPp	This study
pGBD_flgT	pGAD derivative expressing GAL4 BD-FlgTp	37
pGBKT7	GAL4 DNA binding domain, TRP1	Clontech
pGEX-4T-2	Expression vector for GST fusions	Amersham
pGEX-4T-2_flgP	Plasmid expressing the fusion GST-FlgPp	This study
pIND4	IPTG-inducible expression vector for *R. sphaeroides*	62
pINDd	pIND4 Δ*lacI*	This study
pINDd_flgT	pINDd expressing *flgT*	This study
pJQ_ flgH::aadA	pJQ carrying Δ*flgH*::*aadA*	This study
pJQ_ΔflgP::aadA	pJQ carrying Δ*flgP*::*aadA*	This study
pJQ200mp18	Mobilizable suicide vector for *R. sphaeroides*	63
pRK_flgH	pRK415 expressing *flgH*	This study
pRK_flgP	pRK415 expressing *flgP*	This study
pRK_flgPT	pRK415 expressing *flgPT*	This study
pRK_flgT	pRK415 expressing *flgT*	37
pRK_GFP-FliF	pRK expressing GFP-FliF	Laboratory collection
pRK_GFP-MotF	pRK415 expressing the GFP-MotF fusion	50
pRK415	Vector used for expression in *R. sphaeroides*	64
pTZ_ΔflgP::aadA	pTZ carrying Δ*flgP*::*aadA*	This study
pTZ_ΔflgPup-down	pTZ carrying flgPupdown	This study
pTZ19R	Cloning vector	Thermo Fisher Scientific
pTZ19R_Bam−	pTZ19R without BamHI site	Laboratory collection
pTZBam_flgH::aadA	pTZ carrying Δ*flgH*::*aadA*	This study
pTZBam_flgHup-down	pTZ carrying flgHupdown	This study
Oligonucleotides		
orf_11	GCTCTAGACCTTGCCCGCCGCATCGTGG	
RvRSP0035B	GCAGATCTGCCCGGCTGGCCCGCGACGG	
FwRSP0035B	GCAGATCTTATCGTCAAGGCGGCACGGCTG	
orf_12	GCTCTAGACGTTCAGCGCCTCCACATGG	
Fw_flgH	GCTCTAGAGGTGCTGATGCCCGACGG	
Rvi_flgH	GCGGATCCACGATGTCGCCCACCCGC	
Fwi_flgH	GCGGATCCGCTCGACGACGGGGTGCT	

(Continued on next page)

Downloaded from http://jb.asm.org/ on October 20, 2020 at UNAM INST DE INVEST BIOMEDICAS

TABLE 1 (Continued)

Strain, plasmid, or source oligonucleotide	Relevant characteristics or sequence	Reference or source
Rv_flgH	CGGAATTCGCGCACGCGGATCGAGGT	
0035fwBAD	GCAGATCTGCGCCGGGGCCGCGCGCGGTC	
0035RvBAD	GCGAATTCGAAGCCGTTTCACCGCAGCCG	
flgH-pGABfw	GCGAATTCTCGACCTATGTCGAGGACCGC	
flgH-pGABrv	GCGGATCCGAAGCGCTGCGAGAAGGAGAG	
0035fw pGA-pGB	GCCCATGGCGCCGGGGCCGCGCGCGGTC	
0035rvBAD	GCGAATTCGAAGCCGTTTCACCGCAGCCG	
flgH-pBADB	GCAAGCTTGAAGCGCTGCGAGAAGGAGAG	
0035FwpGEX	GCGAATTCCCGCGCCGGGGCCGCGCGCGGTC	
0035RvpGEX	GCGTCGACGAAGCCGTTTCACCGCAGCCG	

[a]Cm[r], chloramphenicol resistance.

sequence. The resultant plasmid was used to transform the *E. coli* strain Rosetta. The resultant cells were grown in Luria broth medium (30 ml) supplemented with chloramphenicol and ampicillin at 37°C to an optical density at 600 nm (OD_{600}) of 0.6. The culture was induced by the addition of IPTG (isopropyl-β-D-thiogalactopyranoside) to a final concentration of 0.25 mM, cultured for 4 h at 30°C, and collected by centrifugation. The cell pellet was resuspended in 1 ml of PBS containing 20% glycerol (pH 7.4) and 1 mg/ml lysozyme. The cell suspension was let stand on ice for 1 h before sonication with three bursts of 9 s. Cell debris was removed by centrifugation. The supernatant was mixed with 100 μl of glutathione-agarose beads and incubated for 1 h on ice, mixing by inversion every 10 min. The beads were washed with 3 volumes of PBS. GST-FlgPp protein was eluted in elution buffer (50 mM Tris HCl, 10 mM reduced glutathione [pH 8]). GST was purified according to a similar protocol.

Immunoblotting and antibody production. Samples were obtained from heterotrophically grown cultures at an OD_{600} of 0.6. At this point, the cells were harvested and lysed by boiling in a solution containing 2% SDS, 1% β-mercaptoethanol, and 50 mM Tris (pH 7.5). Western blotting was performed as previously described (55). Briefly, these samples were separated using 12% SDS-PAGE. After electrophoresis, proteins were transferred to nitrocellulose membranes. Membranes were blocked with 2% fat-free milk in TBST (20 mM Tris, 150 mM NaCl, containing 0.1% Tween 20 [pH 7.4]) for 12 h. After a wash in TBST, the membranes were incubated with the primary antibody in the same buffer, as indicated. Removal of excess primary antibody was carried out by washing the membrane three times in TBST. The secondary antibody (phosphatase alkaline-conjugated, anti-mouse IgG secondary antibody) diluted 1:30,000 was incubated with the membrane in TBST for 1 h. After being washed, the membranes were incubated with CDP-Star (Thermo Fisher Scientific, Waltham, MA) reagent for detection on X-ray films. Polyclonal antibodies were raised in female BALB/c mice against $His_{6\times}$-FlgPp and $His_{6\times}$-FlgHp according to previously reported protocols (55).

Microscopy. Slides were covered with an agarose pad containing Sistrom's culture medium. Images were taken with a Hamamatsu Orca-ER camera and a Nikon E600 microscope. The flagellum was stained DAPI (4′,6′-diamidino-2-phenylindole) according to a previous report (50). Immunofluorescent detection of FlgE was carried out by fixing cells from a heterotrophically grown culture, where cells were swimming (OD_{600}, ~0.6) with paraformaldehyde (3%); after 20 min at room temperature, the paraformaldehyde was removed by centrifugation. The cell pellet was resuspended in 1/10 of the original volume in PBS–1% bovine serum albumin (BSA). Anti-FlgE γ-globulins were stained with Alexa Fluor 488 (Invitrogen, Carlsbad, CA) according to the manufacturer's instructions.

Yeast two-hybrid assays. The assays were performed according to the directions of the manufacturer (Clontech). In summary, yeast cells of the strain AH109 were cotransformed with pGBKT7 and pGADT7 plasmids expressing the mature polypeptide of FlgP, or FlgH, fused to the activation (AD) or DNA binding (BD) domain of Gal4. The DNA fragment encoding the periplasmic regions of FlgP and FlgH was obtained by PCR using the oligonucleotides 0035fw pGA-pGB and 0035rvBAD or the oligonucleotides flgH-pGABfw and flgH-pBADB, respectively. The plasmid expressing pGBD-flgT was previously reported (37). pGBKT7 and pGADT7 plasmids restore prototrophy for leucine (LEU) and tryptophan (TRP), respectively. For interaction assays, the AH109 strain carrying the appropriated plasmids was grown overnight in synthetic defined (SD) minimal medium supplemented with histidine (HIS) and adenine (ADE), washed in SD medium without HIS and ADE, diluted at OD_{600} of 0.5, and serially diluted in the same medium. From these dilutions, 10-μl aliquots were seeded on plates containing SD supplemented with HIS and ADE (–LEU –TRP), ADE (–LEU –TRP –HIS), or HIS (–LEU –TRP –ADE).

Blue native PAGE. A total of 100 μg of $His_{6\times}$-FlgPp, FlgTp-$His_{6\times}$, or a mixture of both proteins was dialyzed overnight in PBS (pH 7.4), mixed with sample buffer, and loaded in a native 4 to 12% acrylamide gradient gel. Gel casting and electrophoresis were performed as described before (56). The lines of each sample were cut and subjected to denaturing two-dimensional SDS-PAGE (14%).

Pulldown interaction assay. Next, 5 μg of GST-FlgPp or GST bound to glutathione-agarose beads in PBS (pH 7.4) was mixed with FlgT-$His_{6\times}$ in a 1:1 molar ratio. The volume was adjusted to 250 μl with PBS containing 10% glycerol and 3% BSA. The mixture was incubated for 2 h at 4°C, with mixing by inversion every 10 min. The beads were collected by centrifugation for 1 min at 3,000 rpm. The supernatant was discarded, and the beads were washed three times with 1 ml of PBS. To elute the protein, the beads were resuspended in 100 μl of buffer containing 100 mM Tris (pH 8) and 10 mM reduced L-glutathione. After 10 min, the sample was centrifuged for 1 min at 5,000 rpm. An aliquot (10 μl) of the supernatant was analyzed by Western blotting with Penta-His antibodies (Qiagen).

Downloaded from http://jb.asm.org/ on October 20, 2020 at UNAM INST DE INVEST BIOMEDICAS

Far-Western assay. Far-Western blotting was performed according to a method reported previously (57). Briefly, 5 μg of $His_{6\times}$-FlgHp and $His_{6\times}$-GFP protein was mixed with an equal volume of 2× Laemmli sample buffer without β-mercaptoethanol, loaded onto 12% acrylamide (wt/vol), and electrophoresed at 100 V. Proteins were transferred electrophoretically to nitrocellulose membranes as described previously (55). Membranes were incubated in blocking buffer (5% nonfat dry milk in PBS [pH 7.4] and 0.05% Tween 20) for 1 h with shaking. Blocked membranes were incubated with 17 μg of purified GST-FlgPp or GST proteins in 10 ml of blocking buffer for 1 h with shaking. Membranes were washed three times for 5 min in PBS (pH 7.4) and 0.05% Tween 20, followed by incubation with anti-FlgP or anti-GFP antibodies diluted 1:5,000, for 1 h, and then washed again three times for 10 min in PBS–0.05% Tween 20, followed by incubation with anti-mouse AP antibody (Sigma, 1:30,000) for 45 min. Antibody binding was detected by incubation with CDP-Star reagent according to the manufacturer´s instructions and visualized by autoradiography.

SUPPLEMENTAL MATERIAL

Supplemental material for this article may be found at https://doi.org/10.1128/JB.00752-18.

SUPPLEMENTAL FILE 1, PDF file, 0.6 MB.

ACKNOWLEDGMENTS

We are indebted to Aurora Osorio, Javier de la Mora, Teresa Ballado, Jorge Omar García Rebollar, and Miriam Vázquez for technical assistance. We thank the Molecular Biology Unit at IFC-UNAM for sequencing facilities.

C.P.-G. was supported by a fellowship from CONACyT (2013 to 2018). This study was partially supported by DGAPA-UNAM (PAPIIT-IN204317) and CONACyT (CB2014-235996).

REFERENCES

1. Berg HC. 2003. The rotary motor of bacterial flagella. Annu Rev Biochem 72:19–54. https://doi.org/10.1146/annurev.biochem.72.121801.161737.
2. Terashima H, Kojima S, Homma M. 2008. Flagellar motility in bacteria structure and function of flagellar motor. Int Rev Cell Mol Biol 270:39–85. https://doi.org/10.1016/S1937-6448(08)01402-0.
3. Khan S, Dapice M, Reese TS. 1988. Effects of *mot* gene expression on the structure of the flagellar motor. J Mol Biol 202:575–584. https://doi.org/10.1016/0022-2836(88)90287-2.
4. Murphy GE, Leadbetter JR, Jensen GJ. 2006. *In situ* structure of the complete *Treponema primitia* flagellar motor. Nature 442:1062–1064. https://doi.org/10.1038/nature05015.
5. Chen S, Beeby M, Murphy GE, Leadbetter JR, Hendrixson DR, Briegel A, Li Z, Shi J, Tocheva EI, Muller A, Dobro MJ, Jensen GJ. 2011. Structural diversity of bacterial flagellar motors. EMBO J 30:2972–2981. https://doi.org/10.1038/emboj.2011.186.
6. Liu J, Lin T, Botkin DJ, McCrum E, Winkler H, Norris SJ. 2009. Intact flagellar motor of *Borrelia burgdorferi* revealed by cryo-electron tomography: evidence for stator ring curvature and rotor/C-ring assembly flexion. J Bacteriol 191:5026–5036. https://doi.org/10.1128/JB.00340-09.
7. Beeby M, Ribardo DA, Brennan CA, Ruby EG, Jensen GJ, Hendrixson DR. 2016. Diverse high-torque bacterial flagellar motors assemble wider stator rings using a conserved protein scaffold. Proc Natl Acad Sci U S A 113:E1917–E1926. https://doi.org/10.1073/pnas.1518952113.
8. Sowa Y, Berry RM. 2008. Bacterial flagellar motor. Q Rev Biophys 41:103–132. https://doi.org/10.1017/S0033583508004691.
9. Asai Y, Kojima S, Kato H, Nishioka N, Kawagishi I, Homma M. 1997. Putative channel components for the fast-rotating sodium-driven flagellar motor of a marine bacterium. J Bacteriol 179:5104–5110. https://doi.org/10.1128/jb.179.16.5104-5110.1997.
10. Blair DF, Berg HC. 1990. The MotA protein of *E. coli* is a proton-conducting component of the flagellar motor. Cell 60:439–449. https://doi.org/10.1016/0092-8674(90)90595-6.
11. Ueno T, Oosawa K, Aizawa S. 1992. M ring, S ring and proximal rod of the flagellar basal body of *Salmonella typhimurium* are composed of subunits of a single protein, FliF. J Mol Biol 227:672–677. https://doi.org/10.1016/0022-2836(92)90216-7.
12. Jones CJ, Macnab RM, Okino H, Aizawa S. 1990. Stoichiometric analysis of the flagellar hook-(basal-body) complex of *Salmonella typhimurium*. J Mol Biol 212:377–387. https://doi.org/10.1016/0022-2836(90)90132-6.
13. Irikura VM, Kihara M, Yamaguchi S, Sockett H, Macnab RM. 1993. Salmonella typhimurium *fliG* and *fliN* mutations causing defects in assembly, rotation, and switching of the flagellar motor. J Bacteriol 175:802–810. https://doi.org/10.1128/jb.175.3.802-810.1993.
14. Sockett H, Yamaguchi S, Kihara M, Irikura VM, Macnab RM. 1992. Molecular analysis of the flagellar switch protein FliM of *Salmonella typhimurium*. J Bacteriol 174:793–806. https://doi.org/10.1128/jb.174.3.793-806.1992.
15. Sircar R, Borbat PP, Lynch MJ, Bhatnagar J, Beyersdorf MS, Halkides CJ, Freed JH, Crane BR. 2015. Assembly states of FliM and FliG within the flagellar switch complex. J Mol Biol 427:867–886. https://doi.org/10.1016/j.jmb.2014.12.009.
16. Minamino T, Yamaguchi S, Macnab RM. 2000. Interaction between FliE and FlgB, a proximal rod component of the flagellar basal body of *Salmonella*. J Bacteriol 182:3029–3036. https://doi.org/10.1128/JB.182.11.3029-3036.2000.
17. Muller V, Jones CJ, Kawagishi I, Aizawa S, Macnab RM. 1992. Characterization of the *fliE* genes of *Escherichia coli* and *Salmonella typhimurium* and identification of the FliE protein as a component of the flagellar hook-basal body complex. J Bacteriol 174:2298–2304. https://doi.org/10.1128/jb.174.7.2298-2304.1992.
18. Kubori T, Shimamoto N, Yamaguchi S, Namba K, Aizawa S. 1992. Morphological pathway of flagellar assembly in *Salmonella typhimurium*. J Mol Biol 226:433–446. https://doi.org/10.1016/0022-2836(92)90958-M.
19. Homma M, Kutsukake K, Hasebe M, Iino T, Macnab RM. 1990. FlgB, FlgC, FlgF and FlgG. A family of structurally related proteins in the flagellar basal body of *Salmonella typhimurium*. J Mol Biol 211:465–477. https://doi.org/10.1016/0022-2836(90)90365-S.
20. DePamphilis ML, Adler J. 1971. Fine structure and isolation of the hook-basal body complex of flagella from *Escherichia coli* and *Bacillus subtilis*. J Bacteriol 105:384–395.
21. Jones CJ, Macnab RM. 1990. Flagellar assembly in *Salmonella typhimurium*: analysis with temperature-sensitive mutants. J Bacteriol 172:1327–1339. https://doi.org/10.1128/jb.172.3.1327-1339.1990.
22. Jones CJ, Homma M, Macnab RM. 1989. L-, P-, and M-ring proteins of the flagellar basal body of *Salmonella typhimurium*: gene sequences and deduced protein sequences. J Bacteriol 171:3890–3900. https://doi.org/10.1128/jb.171.7.3890-3900.1989.
23. Cohen EJ, Hughes KT. 2014. Rod-to-hook transition for extracellular flagellum assembly is catalyzed by the L-ring-dependent rod scaffold removal. J Bacteriol 196:2387–2395. https://doi.org/10.1128/JB.01580-14.

Downloaded from http://jb.asm.org/ on October 20, 2020 at UNAM INST DE INVEST BIOMEDICAS

24. Wagenknecht T, DeRosier DJ, Aizawa S, Macnab RM. 1982. Flagellar hook structures of *Caulobacter* and *Salmonella* and their relationship to filament structure. J Mol Biol 162:69–87. https://doi.org/10.1016/0022-2836(82)90162-0.
25. Matsunami H, Barker CS, Yoon YH, Wolf M, Samatey FA. 2016. Complete structure of the bacterial flagellar hook reveals extensive set of stabilizing interactions. Nat Commun 7:13425. https://doi.org/10.1038/ncomms13425.
26. Zhao X, Norris SJ, Liu J. 2014. Molecular architecture of the bacterial flagellar motor in cells. Biochemistry 53:4323–4333. https://doi.org/10.1021/bi500059y.
27. Terashima H, Kawamoto A, Morimoto YV, Imada K, Minamino T. 2017. Structural differences in the bacterial flagellar motor among bacterial species. Biophys Physicobiol 14:191–198. https://doi.org/10.2142/biophysico.14.0_191.
28. Minamino T, Imada K. 2015. The bacterial flagellar motor and its structural diversity. Trends Microbiol 23:267–274. https://doi.org/10.1016/j.tim.2014.12.011.
29. Martinez RM, Dharmasena MN, Kirn TJ, Taylor RK. 2009. Characterization of two outer membrane proteins, FlgO and FlgP, that influence *Vibrio cholerae* motility. J Bacteriol 191:5669–5679. https://doi.org/10.1128/JB.00632-09.
30. Sommerlad SM, Hendrixson DR. 2007. Analysis of the roles of FlgP and FlgQ in flagellar motility of *Campylobacter jejuni*. J Bacteriol 189:179–186. https://doi.org/10.1128/JB.01199-06.
31. Merino S, Tomas JM. 2016. The FlgT protein is involved in *Aeromonas hydrophila* polar flagella stability and not affects anchorage of lateral flagella. Front Microbiol 7:1150.
32. Morris DC, Peng F, Barker JR, Klose KE. 2008. Lipidation of an FlrC-dependent protein is required for enhanced intestinal colonization by *Vibrio cholerae*. J Bacteriol 190:231–239. https://doi.org/10.1128/JB.00924-07.
33. Poggio S, Abreu-Goodger C, Fabela S, Osorio A, Dreyfus G, Vinuesa P, Camarena L. 2007. A complete set of flagellar genes acquired by horizontal transfer coexists with the endogenous flagellar system in *Rhodobacter sphaeroides*. J Bacteriol 189:3208–3216. https://doi.org/10.1128/JB.01681-06.
34. Armitage JP, Macnab RM. 1987. Unidirectional, intermittent rotation of the flagellum of *Rhodobacter sphaeroides*. J Bacteriol 169:514–518. https://doi.org/10.1128/jb.169.2.514-518.1987.
35. de la Mora J, Uchida K, del Campo AM, Camarena L, Aizawa S, Dreyfus G. 2015. Structural Characterization of the Fla2 Flagellum of *Rhodobacter sphaeroides*. J Bacteriol 197:2859–2866. https://doi.org/10.1128/JB.00170-15.
36. Vega-Baray B, Domenzain C, Rivera A, Alfaro-López R, Gómez-César E, Poggio S, Dreyfus G, Camarena L. 2015. The flagellar set Fla2 in *Rhodobacter sphaeroides* is controlled by the CckA pathway and is repressed by organic acids and the expression of Fla1. J Bacteriol 197:833–847. https://doi.org/10.1128/JB.02429-14.
37. Fabela S, Domenzain C, De la Mora J, Osorio A, Ramirez-Cabrera V, Poggio S, Dreyfus G, Camarena L. 2013. A distant homologue of the FlgT protein interacts with MotB and FliL and is essential for flagellar rotation in *Rhodobacter sphaeroides*. J Bacteriol 195:5285–5296. https://doi.org/10.1128/JB.00760-13.
38. Cameron DE, Urbach JM, Mekalanos JJ. 2008. A defined transposon mutant library and its use in identifying motility genes in *Vibrio cholerae*. Proc Natl Acad Sci U S A 105:8736–8741. https://doi.org/10.1073/pnas.0803281105.
39. Martinez RM, Jude BA, Kirn TJ, Skorupski K, Taylor RK. 2010. Role of FlgT in anchoring the flagellum of *Vibrio cholerae*. J Bacteriol 192:2085–2092. https://doi.org/10.1128/JB.01562-09.
40. Terashima H, Koike M, Kojima S, Homma M. 2010. The flagellar basal body-associated protein FlgT is essential for a novel ring structure in the sodium-driven *Vibrio* motor. J Bacteriol 192:5609–5615. https://doi.org/10.1128/JB.00720-10.
41. Juncker AS, Willenbrock H, Von Heijne G, Brunak S, Nielsen H, Krogh A. 2003. Prediction of lipoprotein signal peptides in Gram-negative bacteria. Protein Sci 12:1652–1662. https://doi.org/10.1110/ps.0303703.
42. Seydel A, Gounon P, Pugsley AP. 1999. Testing the '+2 rule' for lipoprotein sorting in the *Escherichia coli* cell envelope with a new genetic selection. Mol Microbiol 34:810–821. https://doi.org/10.1046/j.1365-2958.1999.01647.x.
43. Poggio S, Osorio A, Dreyfus G, Camarena L. 2005. The flagellar hierarchy of *Rhodobacter sphaeroides* is controlled by the concerted action of two enhancer-binding proteins. Mol Microbiol 58:969–983. https://doi.org/10.1111/j.1365-2958.2005.04900.x.
44. Ballado T, Camarena L, Gonzalez-Pedrajo B, Silva-Herzog E, Dreyfus G. 2001. The hook gene (*flgE*) is expressed from the *flgBCDEF* operon in *Rhodobacter sphaeroides*: study of an *flgE* mutant. J Bacteriol 183:1680–1687. https://doi.org/10.1128/JB.183.5.1680-1687.2001.
45. Kutsukake K. 1994. Excretion of the anti-sigma factor through a flagellar substructure couples flagellar gene expression with flagellar assembly in *Salmonella typhimurium*. Mol Gen Genet 243:605–612.
46. Karlinsey JE, Tsui HC, Winkler ME, Hughes KT. 1998. Flk couples *flgM* translation to flagellar ring assembly in *Salmonella typhimurium*. J Bacteriol 180:5384–5397.
47. Hughes KT, Gillen KL, Semon MJ, Karlinsey JE. 1993. Sensing structural intermediates in bacterial flagellar assembly by export of a negative regulator. Science 262:1277–1280. https://doi.org/10.1126/science.8235660.
48. Hernandez-Valle J, Domenzain C, de la Mora J, Poggio S, Dreyfus G, Camarena L. 2017. The master regulators of the Fla1 and Fla2 flagella of *Rhodobacter sphaeroides* control the expression of their cognate CheY proteins. J Bacteriol 199:e00670-16. https://doi.org/10.1128/JB.00670-16.
49. Bonifield HR, Yamaguchi S, Hughes KT. 2000. The flagellar hook protein, FlgE, of *Salmonella enterica* serovar Typhimurium is posttranscriptionally regulated in response to the stage of flagellar assembly. J Bacteriol 182:4044–4050. https://doi.org/10.1128/JB.182.14.4044-4050.2000.
50. Ramirez-Cabrera V, Poggio S, Domenzain C, Osorio A, Dreyfus G, Camarena L. 2012. A novel component of the *Rhodobacter sphaeroides* Fla1 flagellum is essential for motor rotation. J Bacteriol 194:6174–6183. https://doi.org/10.1128/JB.00850-12.
51. Zhu S, Nishikino T, Hu B, Kojima S, Homma M, Liu J. 2017. Molecular architecture of the sheathed polar flagellum in *Vibrio alginolyticus*. Proc Natl Acad Sci U S A 114:10966–10971. https://doi.org/10.1073/pnas.1712489114.
52. Chaban B, Coleman I, Beeby M. 2018. Evolution of higher torque in *Campylobacter*-type bacterial flagellar motors. Sci Rep 8:97. https://doi.org/10.1038/s41598-017-18115-1.
53. Sistrom WR. 1962. The kinetics of the synthesis of photopigments in *Rhodopseudomonas sphaeroides*. J Gen Microbiol 28:607–616. https://doi.org/10.1099/00221287-28-4-607.
54. Ausubel FM, Brent R, Kingston RE, Moore DD, Seidman JG, Smith JA, Struhl K. 1987. Current protocols in molecular biology. John Wiley, New York, NY.
55. Harlow E, Lane D. 1988. Antibodies: a laboratory manual. Cold Spring Harbor Laboratory Press, Cold Spring Harbor, New York.
56. Schagger H, Cramer WA, von Jagow G. 1994. Analysis of molecular masses and oligomeric states of protein complexes by blue native electrophoresis and isolation of membrane protein complexes by two-dimensional native electrophoresis. Anal Biochem 217:220–230. https://doi.org/10.1006/abio.1994.1112.
57. Edmondson DG, Roth SY. 2001. Identification of protein interactions by far Western analysis. Curr Protoc Mol Biol Chapter20:Unit 20.26.
58. Simon R, Priefer U, Pühler A. 1983. A broad host range mobilization system for *in vivo* genetic engineering: transposon mutagenesis in Gram-negative bacteria. Bio/Technology 1:37–45.
59. Gonzalez-Pedrajo B, de la Mora J, Ballado T, Camarena L, Dreyfus G. 2002. Characterization of the *flgG* operon of *Rhodobacter sphaeroides* WS8 and its role in flagellum biosynthesis. Biochim Biophys Acta 1579:55–63. https://doi.org/10.1016/S0167-4781(02)00504-3.
60. Poggio S, Aguilar C, Osorio A, Gonzalez-Pedrajo B, Dreyfus G, Camarena L. 2000. σ54 promoters control expression of genes encoding the hook and basal body complex in *Rhodobacter sphaeroides*. J Bacteriol 182:5787–5792. https://doi.org/10.1128/JB.182.20.5787-5792.2000.
61. Foster, Jca SRE, Armitage JP. 1990. Molecular biology of the *Rhodobacter sphaeroides* flagellum. FEMS Symp 53:473–479.
62. Ind AC, Porter SL, Brown MT, Byles ED, de Beyer JA, Godfrey SA, Armitage JP. 2009. Inducible-expression plasmid for *Rhodobacter sphaeroides* and *Paracoccus denitrificans*. Appl Environ Microbiol 75:6613–6615. https://doi.org/10.1128/AEM.01587-09.
63. Quandt J, Hynes MF. 1993. Versatile suicide vectors which allow direct selection for gene replacement in Gram-negative bacteria. Gene 127:15–21.
64. Keen NT, Tamaki S, Kobayashi D, Trollinger D. 1988. Improved broad-host-range plasmids for DNA cloning in Gram-negative bacteria. Gene 70:191–197.

Downloaded from http://jb.asm.org/ on October 20, 2020 at UNAM INST DE INVEST BIOMEDICAS

INFORME DE LABORES 2019

LETTER

https://doi.org/10.1038/s41586-019-1641-1

Population imaging of neural activity in awake behaving mice

Kiryl D. Piatkevich[1,2,11], Seth Bensussen[3,11], Hua-an Tseng[3,11], Sanaya N. Shroff[3], Violeta Gisselle Lopez-Huerta[4], Demian Park[1,2], Erica E. Jung[1,5], Or A. Shemesh[1,2], Christoph Straub[6], Howard J. Gritton[3], Michael F. Romano[3], Emma Costa[1], Bernardo L. Sabatini[6], Zhanyan Fu[4], Edward S. Boyden[1,2,7,8,9,10]* & Xue Han[3]*

A longstanding goal in neuroscience has been to image membrane voltage across a population of individual neurons in an awake, behaving mammal. Here we describe a genetically encoded fluorescent voltage indicator, SomArchon, which exhibits millisecond response times and is compatible with optogenetic control, and which increases the sensitivity, signal-to-noise ratio, and number of neurons observable several-fold over previously published fully genetically encoded reagents[1–8]. Under conventional one-photon microscopy, SomArchon enables the routine population analysis of around 13 neurons at once, in multiple brain regions (cortex, hippocampus, and striatum) of head-fixed, awake, behaving mice. Using SomArchon, we detected both positive and negative responses of striatal neurons during movement, as previously reported by electrophysiology but not easily detected using modern calcium imaging techniques[9–11], highlighting the power of voltage imaging to reveal bidirectional modulation. We also examined how spikes relate to the subthreshold theta oscillations of individual hippocampal neurons, with SomArchon showing that the spikes of individual neurons are more phase-locked to their own subthreshold theta oscillations than to local field potential theta oscillations. Thus, SomArchon reports both spikes and subthreshold voltage dynamics in awake, behaving mice.

Near-infrared genetically encoded voltage indicators (GEVIs) derived from rhodopsins offer high temporal fidelity, and are compatible with optogenetics[1,12,13], whereas green fluorescent GEVIs derived from the voltage-sensing domains of phosphatases or opsins are often slower and brighter[2,3,14–17]. Translating these voltage sensors into the living mammalian brain has been challenging, because of poor membrane localization, low photostability, and low signal-to-noise ratio (SNR). So far, amongst fully genetically encoded reagents, only Ace2N and paQuasAr3-s have been used to optically report voltage dynamics in a living mouse brain, reporting the activities of up to four cells in one field of view (FOV) in awake mice[4,17]. Recently, we developed a robotic directed-evolution approach and created the improved GEVI Archon1[13]. To further improve SNR in the dense, living mammalian brain, we conducted a screen for peptides to localize Archon1 to the soma[18–21], so that neuropil contamination could be reduced (Extended Data Fig. 1; see Supplementary Table 1 for the sequences of the motifs). The molecule Archon1–KGC–EGFP–K_V2.1-motif–ER2, which we call SomArchon (Fig. 1a), exhibited the highest relative change in fluorescence ($\Delta F/F$) during 100-mV voltage steps (Fig. 1g) and was well-localized to the soma (Extended Data Fig. 1h–k).

SomArchon fluorescently reported action potentials in mouse brain slices after in utero electroporation (IUE) into the cortex and hippocampus, and after adeno-associated virus (AAV)-mediated expression in the cortex, striatum, and thalamus (Extended Data Fig. 2). SomArchon was localized primarily to the membrane within 30–45 μm of the cell body in the cortex, striatum, and hippocampus (Fig. 1b, Extended Data Fig. 1h–k). The sensitivity of SomArchon was about twofold greater (Fig. 1c, d) than our previously published values for Archon1[13], and it had comparable kinetics (Fig. 1e) and SNR (defined as the maximum fluorescence change observed during an action potential divided by the standard deviation of the baseline) (Fig. 1f). SomArchon linearly reported voltage (Fig. 1g), and did not alter membrane properties or resting potential in mouse brain slices, induce gliosis, or mediate light-induced phototoxicity (Extended Data Figs. 3, 4). It has previously been demonstrated that Archon1 exhibits essentially no crosstalk under blue light illumination as used commonly for optogenetic neural activation[13]. We used a bicistronic expression system (Fig. 1h) to co-express SomArchon and the high-performance channelrhodopsin CoChR[22] in the same cell, and demonstrated that brief blue light pulses could reliably evoke action potentials that were visible in SomArchon fluorescence (Fig. 1i, j).

We performed a side-by-side comparison of SomArchon with soma-localized versions of several next-generation voltage sensors—specifically QuasAr3-s[4], paQuasAr3-s[4], ASAP3[5], and Voltron$_{525}$[6]—in mouse cortical brain slices under identical expression conditions, focusing on layer 2/3 neurons (Supplementary Table 3). The spectrally similar sensors QuasAr3-s, paQuasAr3-s, and SomArchon were recorded under identical imaging conditions (1.5 W mm^{-2}) during CoChR-mediated action potentials. ASAP3 and Voltron were recorded with the filter sets described[5,6] under similar excitation intensities as used in the initial description of Voltron[6] (25–29 mW mm^{-2}), during action potentials evoked upon application of 4-aminopyridine. Under these conditions, SomArchon exhibited the highest $\Delta F/F$ and SNR per action potential (Extended Data Fig. 5); in addition, SomArchon exhibited values higher than those previously reported for Ace2N-mNeon[7], ASAP1[2], MacQ-mCitrine[3], and QuasAr2[8] (Supplementary Table 3). In addition, SomArchon showed higher photostability than soma-localized versions of ASAP3 and Voltron$_{525}$ under comparable imaging conditions in cultured neurons (Extended Data Fig. 5e).

We virally expressed SomArchon in vivo in the mouse motor cortex, visual cortex, striatum, and hippocampus, and imaged neural activity while mice were awake with their heads fixed under a conventional one-photon microscope (Fig. 2a) using a scientific complementary metal-oxide semiconductor (sCMOS) camera and laser excitation light at 637 nm, at a power of around 1.6 W mm^{-2} (75 mW; 20× objective lens), 4 W mm^{-2} (75 mW; 40× objective lens), or 1.6 W mm^{-2} (95 mW; 16× objective lens). Cells expressing SomArchon could be resolved at depths of about 50–150 μm below the imaging surface (Fig. 2b). We could detect individual spikes in single cells in all four brain regions (Fig. 2c, e, g, i, Supplementary Video 1). The SNR per action potential ranged from about 7 to about 16 across the brain regions examined (Fig. 2d, f, h, j). To our knowledge, no other paper has reported SNR

[1]Media Lab, MIT, Cambridge, MA, USA. [2]MIT McGovern Institute for Brain Research, MIT, Cambridge, MA, USA. [3]Department of Biomedical Engineering, Boston University, Boston, MA, USA. [4]Stanley Center for Psychiatric Research, Broad Institute of MIT and Harvard, Cambridge, MA, USA. [5]Department of Mechanical and Industrial Engineering, University of Illinois, Chicago, IL, USA. [6]Howard Hughes Medical Institute, Department of Neurobiology, Harvard Medical School, Boston, MA, USA. [7]Department of Biological Engineering, MIT, Cambridge, MA, USA. [8]MIT Center for Neurobiological Engineering, MIT, Cambridge, MA, USA. [9]Department of Brain and Cognitive Sciences, MIT, Cambridge, MA, USA. [10]Koch Institute, MIT, Cambridge, MA, USA. [11]These authors contributed equally: Kiryl D. Piatkevich, Seth Bensussen, Hua-an Tseng. *e-mail: esb@media.mit.edu; xuehan@bu.edu

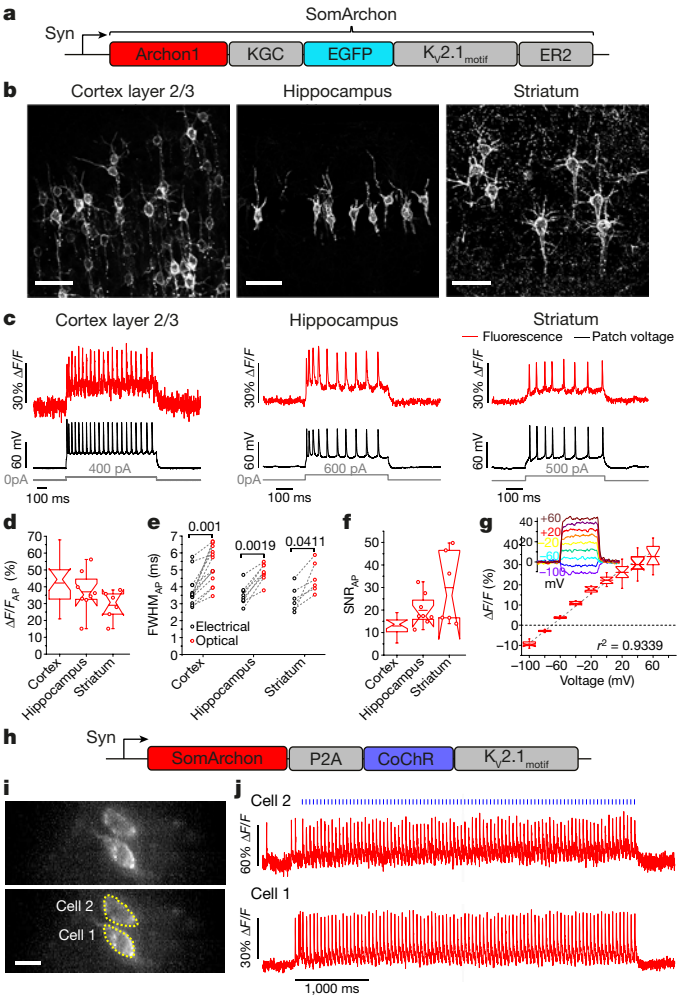

Fig. 1 | SomArchon enables high-fidelity voltage imaging in brain slices. a, Diagram of the SomArchon construct. **b**, Confocal images of SomArchon-expressing neurons in cortex layer 2/3 (left), hippocampus (middle), and striatum (right). Excitation wavelength (λ_{ex}) = 488 nm laser, emission wavelength (λ_{em}) = 525/50 nm (representative images selected from 8, 10 and 6 slices, respectively, from 2 mice each). Scale bars, 50 μm. **c**, Single-trial SomArchon fluorescence (red), and concurrent membrane voltage recorded via whole-cell patch-clamp (black), during action potentials evoked by current injection (grey); λ_{ex} = 637 nm laser at 0.8, 1.5, and 1.5 W mm^{-2} for cortex, hippocampus, and striatum, respectively. **d**, $\Delta F/F$ per action potential across recordings exemplified in **c** (representative traces selected from n = 18, 8, and 6 neurons from 5, 2, and 2 mice, respectively). Box plots: 25th and 75th percentiles with notch, median; whiskers, 1.5× interquartile range from the 25th and 75th percentiles; middle horizontal line, mean; individual data points, open circles when $n < 9$). **e**, Electrical and optical action potential waveform full-width-at-half-maximum ($FWHM_{AP}$; dashed lines connect the same neurons) across recordings exemplified in **c** (P values above brackets are from two-sided Wilcoxon rank-sum test; Supplementary Table 2). **f**, SNR per action potential across recordings exemplified in **c**. **g**, Population fluorescence of SomArchon in response to voltage steps in voltage-clamp mode, normalized to the fluorescence at −70 mV (inset, optical recordings for a representative neuron) recorded in cortex (n = 12 neurons from 2 mice). **h**, Diagram of SomArchon–P2A–CoChR–$K_V2.1_{motif}$. **i**, Fluorescence image of neurons in hippocampal slice expressing SomArchon–P2A–CoChR–$K_V2.1_{motif}$ (top) with two cells identified (bottom); λ_{ex} = 637 nm, exposure time 1.3 ms (selected from n = 3 slices from 2 mice). Scale bar, 25 μm. **j**, Representative single-trial optical voltage traces from cells shown in **i** with blue light stimulation (2 ms pulse at 20 Hz). Acquisition rate, 777 Hz.

values per action potential in living mouse brain, so we cannot directly compare our molecule to others in this regard. We were able to resolve short segments of proximal dendrites next to the soma, and detected voltage fluctuation patterns that sometimes differed from those in the soma (Extended Data Fig. 6c–f). In addition, simultaneous optical control and voltage imaging was feasible using the strategy shown in Fig. 1h, in awake behaving mice (Fig. 2k–m).

Electrophysiological studies have shown that many striatal neurons increase their responses during movement[9,23], while others decrease their responses[9,10]. Although electrophysiological recordings largely discard spatial information regarding the relative locations of the neurons being observed, recent calcium imaging studies have revealed that spatially clustered striatal neurons are activated by similar aspects of movement[11]. These calcium imaging studies focused on the increases in activity during movement; decreases in activity are harder to observe with calcium imaging. We performed voltage imaging while mice ran on a spherical treadmill (Fig. 3a), identified cell bodies and spikes from cells in the striatum (Fig. 3b–d), and aligned spiking activity to movement (Fig. 3d). Some neurons exhibited firing patterns known to occur in striatal fast spiking interneurons[24] or cholinergic interneurons[25] (Extended Data Fig. 7a–d). We found that 4 of the 14 neurons imaged were positively modulated by movement speed, and that 2 were negatively modulated by movement speed (Fig. 3e, f, Extended Data Fig. 7e, f; see Supplementary Table 2 for statistics). Furthermore, adjacent neurons did not respond to movement speed in identical ways. For example, in two recordings of three neurons each, one of the three neurons was positively modulated by movement speed whereas the other two were not (Fig. 3f, Extended Data Fig. 7a, c (cells 1, 2, 3 and cells 6, 7, 8), Supplementary Table 2). Thus, SomArchon can readily detect decreases in striatal neuron spiking during movement, and can help to disambiguate activity changes amongst spatially clustered striatal neurons.

We performed wide-field voltage imaging with SomArchon in hippocampal CA1 neurons in awake, head-fixed mice, while simultaneously recording local field potentials (LFPs). In vivo patch-clamp recordings have shown that the spikes of a CA1 neuron are more strongly phase-locked to its own intracellular theta frequency (4–10 Hz) oscillations than to the theta oscillations of the across-neuron averaged LFP[26,27]. We found that 6 of the 16 neurons had spikes phase-locked to both intracellular and LFP theta oscillations (Fig. 4a), and that 9 were phase-locked only to intracellular theta oscillations and not to LFP theta oscillations (Fig. 4b). As a population, neurons exhibited stronger phase-locking to intracellular theta oscillations than to LFP theta oscillations (Fig. 4c, d). SomArchon thus supports the analysis of subthreshold intracellular oscillations, although interpretation of these measurements must take into account background fluorescence, which—in densely labelled tissue—may result in crosstalk that affects correlations.

We evaluated the photostability of SomArchon in vivo, and found a slight decrease in fluorescence intensity in both the striatum and the hippocampus over time. However, the SNR remained largely stable in both brain regions (Extended Data Fig. 8). In the hippocampus, firing rates remained constant over time, and we were able to continuously image for up to 80 s with minimal changes in SNR (Extended Data Fig. 8i–m, Supplementary Video 1). This lack of toxicity is consistent with our results from cultured neurons (Extended Data Fig. 3).

Owing to the high performance and soma-targeted nature of SomArchon, we were able to routinely image multiple neurons at once in both cortical and subcortical brain regions (Figs. 2k, l, 3b, c, Extended Data Fig. 6a, b). In the hippocampus, using a 20× objective lens, we were able to record from 14 neurons at once, 8 of which were spiking (Fig. 4e, f). In addition, using a 16× objective lens, we routinely recorded from around 13 cells at once (n = 13.1 ± 3.5 (mean ± s.d.) neurons per FOV from 13 recording sessions in 2 awake mice). Of the 170 manually identified neurons, 107 (63%) spiked during the recording periods (duration: 13.5–27 s) (Extended Data Fig. 6g–j, Supplementary Table 4). The ability to record from multiple neurons simultaneously enabled us to examine the correlation and coherence of subthreshold activities between pairs of neurons, although background fluorescence crosstalk between nearby neurons will need to

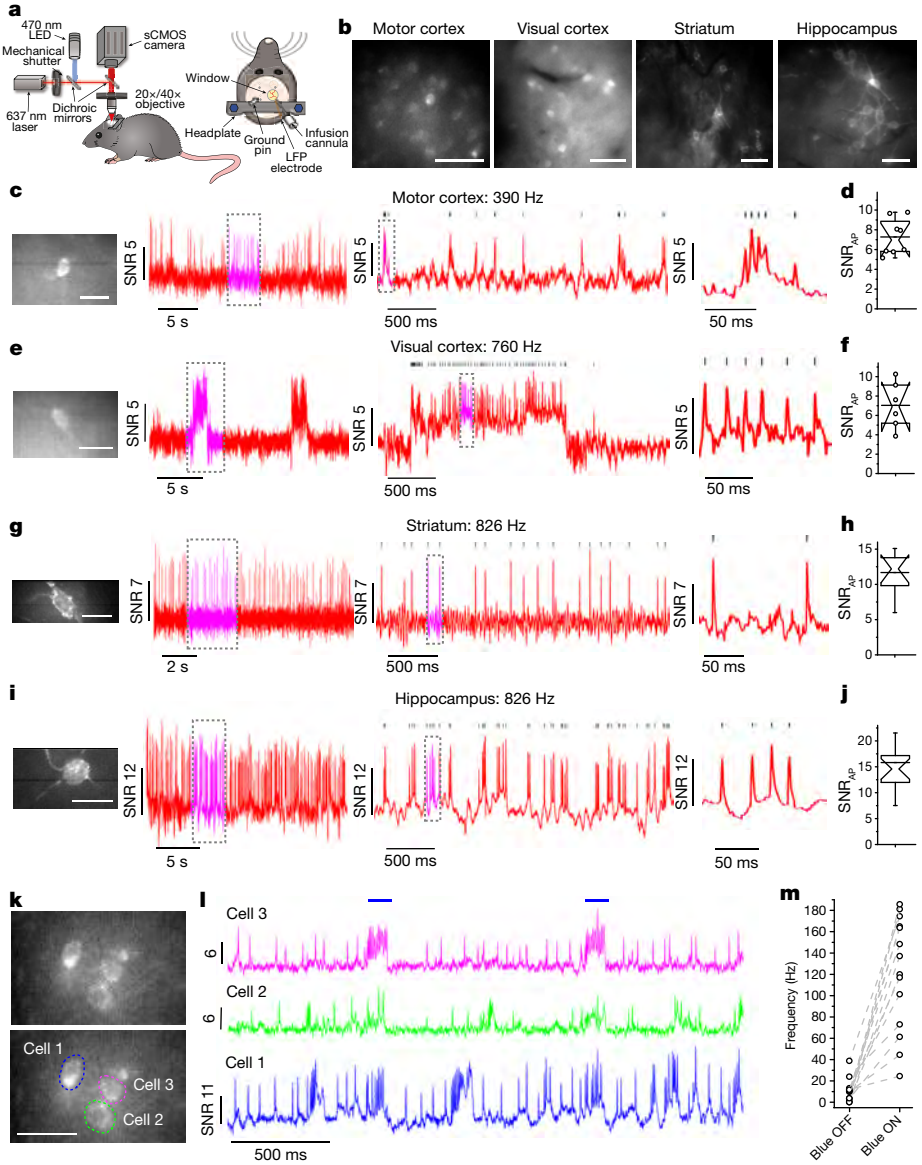

Fig. 2 | SomArchon enables single-cell voltage imaging in multiple brain regions of awake mice, using a simple wide-field imaging setup. **a**, Experimental setup. Left, awake mice had their heads fixed under a wide-field microscope; right, surgical window implant coupled with an infusion cannula and an LFP recording electrode. **b**, Representative SomArchon-expressing neurons visualized via EGFP fluorescence in motor cortex, visual cortex, striatum, and hippocampus (λ_{ex} = 470/25 nm LED, λ_{em} = 525/50 nm). Scale bars, 50 μm. **c**, **e**, **g**, **i**, Voltage imaging in motor cortex (**c**), visual cortex (**e**), striatum (**g**), and hippocampus (**i**). Left, SomArchon fluorescence image of the cell in vivo; right, optical voltage trace acquired from the cell (dashed boxes indicate time intervals shown at successively expanded time scales; vertical bars indicate peaks of action potentials identified by a custom spike-sorting algorithm). λ_{ex} = 637 nm laser at 1.6 W mm^{-2} for visual cortex and motor cortex, 4 W mm^{-2} for striatum and hippocampus, λ_{em} = 664 long-pass. Scale bars, 25 μm. **d**, **f**, **h**, **j**, Quantification of SNR per action potential for motor cortex (**d**), visual cortex (**f**), striatum (**h**), and hippocampus (**j**). Box plots as in Fig. 1. In **b**–**j**, representative images and traces were selected from, and statistics performed on, n = 8, 6, 10, and 17 cells from 3, 2, 3, and 4 mice for the motor cortex, visual cortex, striatum, and hippocampus, respectively. **k**, Fluorescence image of selected FOV showing hippocampal neurons expressing SomArchon–P2A–CoChR–$K_V2.1_{motif}$ (top) with neurons identified (bottom); λ_{ex} = 637 nm, exposure time 1.2 ms. Scale bar, 20 μm. **l**, Representative single-trial optical voltage traces from cells shown in **k** with blue light stimulation (100 ms pulse). Image acquisition rate, 826 Hz. **m**, Firing rate changes during blue light off versus blue light on conditions in individual neurons. In **k**–**m**, representative image selected from, and statistics performed on, n = 14 cells from 2 mice.

be considered when interpreting pairwise correlation and coherence measurements (Extended Data Figs. 9e–h, 10, Supplementary Discussion).

Compared to existing fully genetically encoded voltage indicators, SomArchon achieves a severalfold improvement in the number of cells that can be imaged simultaneously, while using inexpensive one-photon microscopy. The previously published record for fully genetically encoded voltage imaging was four spiking cells recorded simultaneously in an awake behaving mouse, but this required a specialized imaging setup that combined two-photon structural imaging to support patterned single-photon excitation illumination targeting individual cell bodies, as well as the blue-light-gated molecule paQuasAr3, which is incompatible with commonly used pulsed blue light optogenetic modulation[4]. ASAP3 has been used to image three dendrites at once, with 2-photon microscopy, but this approach can be used to record only single cells at the fast rates typical for voltage imaging[5]. The hybrid GEVI sensor Voltron enables imaging of 46 neurons[6], but requires the addition of chemicals delivered to the living brain that complicate in vivo mammalian use, is not compatible with optogenetics, and exhibits a lower dynamic range than SomArchon (Extended Data Fig. 5). Voltron, ASAP3, and Ace2N-mNeon all exhibit crosstalk with rhodopsins, hampering their use with optogenetic actuators. Voltage

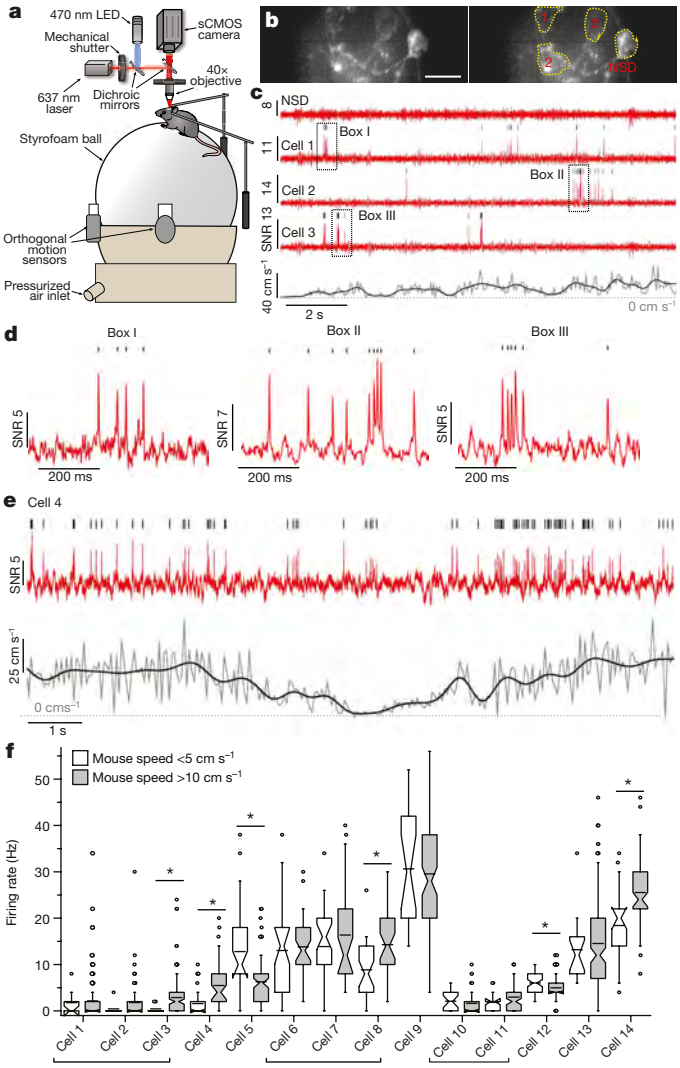

Fig. 3 | Voltage imaging of striatal neurons during locomotion. a, Schematic of the experimental setup, similar to that in Fig. 2a, but with mice positioned on a spherical treadmill. Imaging was performed with a 40× objective lens. **b**, Left, SomArchon fluorescence image of striatal cells; right, identified regions of interest (ROIs) corresponding to somas. $\lambda_{ex} = 637$ nm, exposure time 1.2 ms (representative image selected from $n = 9$ FOV from 2 mice). Scale bar, 20 μm. NSD, no spikes detected. **c**, Optical voltage traces acquired from cells in **b** and corresponding mouse movement speed (black, low-pass-filtered at 1.5 Hz; grey, raw data; representative traces selected from $n = 2$ FOV from one mouse). Image acquisition rate, 826 Hz. **d**, Magnified views of the three periods indicated by black boxes in **c**. **e**, Optical voltage trace (red) for a neuron modulated by movement speed and corresponding movement speed (black and grey; representative trace selected from $n = 14$ neurons from 2 mice). **f**, Firing rates of individual striatal neurons, during periods with low (open box plots) versus high (grey box plots) movement speed ($n = 14$ neurons from 2 mice, brackets indicate neurons from the same FOV). $^*P < 0.05$, two-sided Wilcoxon rank-sum test. Box plots as in Fig. 1.

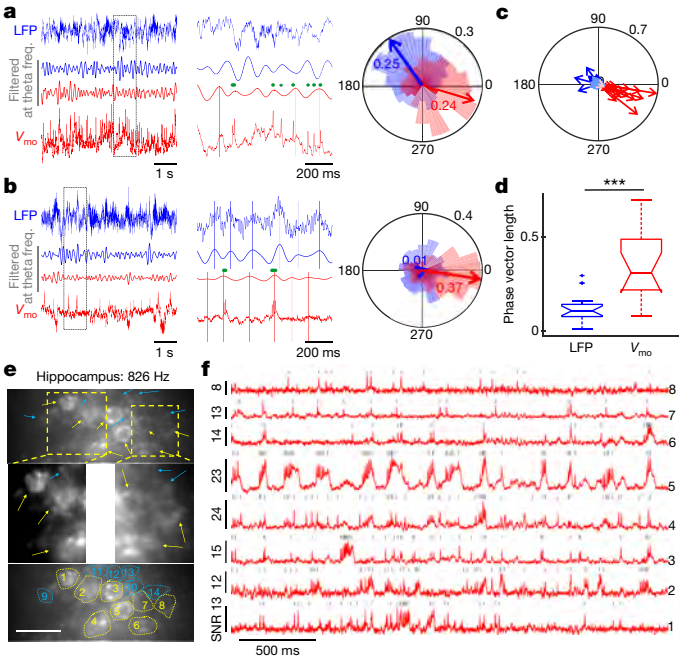

Fig. 4 | Population voltage imaging of spikes and subthreshold voltage activities in CA1 neurons. a, Neuron with spikes phase-locked to theta oscillations of LFPs (blue) and optically recorded membrane voltage (V_{mo}, red). Left, raw LFPs (top) and V_{mo} (bottom), and theta frequency-filtered traces (middle). Middle, magnified view of the boxed period on the left. Theta oscillation peaks are indicated by blue and red vertical lines, and spikes by green dots. Right, probability distribution of the timing of spikes relative to the phases of the LFP (blue) and V_{mo} (red) oscillations at theta frequency. Arrows indicate the average phase vector (with vector length indicated). Outer circle number indicates probability. Example selected from $n = 16$ neurons in 7 FOVs from 4 mice. **b**, As in **a**, but for an example neuron phase-locked to V_{mo} theta oscillations, but not to LFP theta oscillations. **c**, Population spike–phase vectors relative to theta oscillations of LFP (blue and light blue) and V_{mo} (red and pink). Each vector represents the average vector from one neuron (blue and red, $P < 0.05$; light blue and pink, not significant; χ^2 test, spike–phase distribution of each neuron against uniform distribution; $n = 198$–1,077 spikes per neuron; 16 neurons in 7 FOVs from 4 mice). **d**, Population spike–phase relationship. $^{***}P = 5.0 \times 10^{-5}$, two-tailed paired Student's t-test, $n = 16$ neurons in 7 FOVs from 4 mice. Box plots: 25th and 75th percentiles with notch, median; whiskers, all data points not considered outliers; plus, outliers. **e**, SomArchon fluorescence images of CA1 neurons (top) with ROIs overlaid (bottom; $n = 14$ FOV from 3 mice). Middle, zoomed-in views of the yellow boxes from the top. Yellow arrows, example spiking cells with optical voltage traces shown in **f**; blue arrows, neurons not active during the period shown. $\lambda_{ex} = 637$ nm laser at 1.5 W mm^{-2}. Scale bar, 20 μm.

imaging with SomArchon or QuasAr3 is limited mainly by the high power and illumination spot of the 637-nm excitation laser; however, our data suggest that high-powered 637-nm excitation does not induce more phototoxicity than is seen with common, lower-powered 470-nm excitation (Extended Data Fig. 3). In conclusion, SomArchon is fully genetically encoded, is compatible with conventional easily accessible one-photon wide-field fluorescence microscopes, is fully compatible with blue-light-driven optogenetics, and enables routine imaging of around 13 neurons in a single FOV. We anticipate that the practicality of SomArchon will enable its rapid deployment into a variety of contexts in neuroscience. As camera performance improves in years to come, and as further evolution of GEVIs continues, we anticipate that it might be possible to image tens to hundreds of neurons using simple one-photon optics in the near future.

Online content

Any methods, additional references, Nature Research reporting summaries, source data, extended data, supplementary information, acknowledgements, peer review information; details of author contributions and competing interests; and statements of data and code availability are available at https://doi.org/10.1038/s41586-019-1641-1.

Received: 23 August 2018; Accepted: 28 August 2019;
Published online 9 October 2019.

1. Hochbaum, D. R. et al. All-optical electrophysiology in mammalian neurons using engineered microbial rhodopsins. *Nat. Methods* **11**, 825–833 (2014).
2. St-Pierre, F. et al. High-fidelity optical reporting of neuronal electrical activity with an ultrafast fluorescent voltage sensor. *Nat. Neurosci.* **17**, 884–889 (2014).

3. Gong, Y., Wagner, M. J., Zhong Li, J. & Schnitzer, M. J. Imaging neural spiking in brain tissue using FRET-opsin protein voltage sensors. *Nat. Commun.* **5**, 3674 (2014).
4. Adam, Y. et al. Voltage imaging and optogenetics reveal behaviour-dependent changes in hippocampal dynamics. *Nature* **569**, 413–417 (2019).
5. Chavarha, M. et al. Fast two-photon volumetric imaging of an improved voltage indicator reveals electrical activity in deeply located neurons in the awake brain. Preprint at https://www.biorxiv.org/content/10.1101/445064v2 (2018).
6. Abdelfattah, A. S. et al. Bright and photostable chemigenetic indicators for extended *in vivo* voltage imaging. *Science* **365**, 699–704 (2019).
7. Gong, Y. et al. High-speed recording of neural spikes in awake mice and flies with a fluorescent voltage sensor. *Science* **350**, 1361–1366 (2015).
8. Lou, S. et al. Genetically targeted all-optical electrophysiology with a transgenic Cre-dependent optopatch mouse. *J. Neurosci.* **36**, 11059–11073 (2016).
9. Jin, X., Tecuapetla, F. & Costa, R. M. Basal ganglia subcircuits distinctively encode the parsing and concatenation of action sequences. *Nat. Neurosci.* **17**, 423–430 (2014).
10. Shi, L. H., Luo, F., Woodward, D. J. & Chang, J. Y. Neural responses in multiple basal ganglia regions during spontaneous and treadmill locomotion tasks in rats. *Exp. Brain Res.* **157**, 303–314 (2004).
11. Gritton, H. J. et al. Unique contributions of parvalbumin and cholinergic interneurons in organizing striatal networks during movement. *Nat. Neurosci.* **22**, 586–597 (2019).
12. Flytzanis, N. C. et al. Archaerhodopsin variants with enhanced voltage-sensitive fluorescence in mammalian and *Caenorhabditis elegans* neurons. *Nat. Commun.* **5**, 4894 (2014).
13. Piatkevich, K. D. et al. A robotic multidimensional directed evolution approach applied to fluorescent voltage reporters. *Nat. Chem. Biol.* **14**, 352–360 (2018).
14. Jin, L. et al. Single action potentials and subthreshold electrical events imaged in neurons with a fluorescent protein voltage probe. *Neuron* **75**, 779–785 (2012).
15. Chamberland, S. et al. Fast two-photon imaging of subcellular voltage dynamics in neuronal tissue with genetically encoded indicators. *eLife* **6**, e25690 (2017).
16. Zou, P. et al. Bright and fast multicoloured voltage reporters via electrochromic FRET. *Nat. Commun.* **5**, 4625 (2014).
17. Gong, Y. et al. High-speed recording of neural spikes in awake mice and flies with a fluorescent voltage sensor. *Science* **350**, 1361–1366 (2015).
18. Shemesh, O. A. et al. Temporally precise single-cell-resolution optogenetics. *Nat. Neurosci.* **20**, 1796–1806 (2017).
19. Baker, C. A., Elyada, Y. M., Parra, A. & Bolton, M. M. L. Cellular resolution circuit mapping with temporal-focused excitation of soma-targeted channelrhodopsin. *eLife* **5**, e14193 (2016).
20. Daigle, T. L. et al. A suite of transgenic driver and reporter mouse lines with enhanced brain-cell-type targeting and functionality. *Cell* **174**, 465–480.e22 (2018).
21. Wu, C., Ivanova, E., Zhang, Y. & Pan, Z. H. rAAV-mediated subcellular targeting of optogenetic tools in retinal ganglion cells *in vivo*. *PLoS ONE* **8**, e66332 (2013).
22. Klapoetke, N. C. et al. Independent optical excitation of distinct neural populations. *Nat. Methods* **11**, 338–346 (2014).
23. Kravitz, A. V. & Kreitzer, A. C. Striatal mechanisms underlying movement, reinforcement, and punishment. *Physiology (Bethesda)* **27**, 167–177 (2012).
24. Koós, T. & Tepper, J. M. Inhibitory control of neostriatal projection neurons by GABAergic interneurons. *Nat. Neurosci.* **2**, 467–472 (1999).
25. Zhou, F. M., Wilson, C. J. & Dani, J. A. Cholinergic interneuron characteristics and nicotinic properties in the striatum. *J. Neurobiol.* **53**, 590–605 (2002).
26. Bittner, K. C. et al. Conjunctive input processing drives feature selectivity in hippocampal CA1 neurons. *Nat. Neurosci.* **18**, 1133–1142 (2015).
27. Harvey, C. D., Collman, F., Dombeck, D. A. & Tank, D. W. Intracellular dynamics of hippocampal place cells during virtual navigation. *Nature* **461**, 941–946 (2009).

Publisher's note Springer Nature remains neutral with regard to jurisdictional claims in published maps and institutional affiliations.

© The Author(s), under exclusive licence to Springer Nature Limited 2019

METHODS

Molecular cloning. To screen candidates for the soma-localized Archon1 voltage sensor in primary hippocampal neurons, we synthesized DNAs coding for candidate localization motifs de novo with mammalian codon optimization and subcloned them with the genes for Archon1 (GenBank ID MG250280.1) and EGFP into the pAAV-CAG vector to obtain the final constructs (Supplementary Table 1; gene synthesis and subcloning performed by Epoch Life Science). For in vivo expression in the mouse brain via IUE, the genes encoding Archon1–KGC–EGFP–$K_V2.1_{motif}$–ER2, QuasAr3–PP–Citrine–$K_V2.1_{motif}$–ER2 (QuasAr3-s), paQuasAr3–PP–Citrine–$K_V2.1_{motif}$–ER2 (paQuasAr3-s) and CoChR–mTagBFP2–$K_V2.2_{motif}$–ER2 were subcloned into the pCAG-WPRE vector. The genes encoding QuasAr3–PP–Citrine–$K_V2.1$–ER2 and paQuasAr3–PP–Citrine–$K_V2.1$–ER2 were synthesized de novo (GenScript Biotech) based on the reported sequences[28]. The gene for CoChR–mTagBFP2–$K_V2.2_{motif}$–ER2 was assembled by Epoch Life Science using pAAV-Syn–CoChR–GFP (Addgene plasmid no. 59070) and pBAD–mTagBFP2 (Addgene plasmid no. 34632) as the source of the genes for CoChR and mTagBFP2, respectively; the $K_V2.2$ motifs were synthesized de novo with mammalian codon optimization (Epoch Life Science). The pAAV-Syn-Archon1-KGC-EGFP-$K_V2.1_{motif}$-P2A-CoChR-$K_V2.1_{motif}$ plasmid was also cloned by Epoch Life Science. We used the Kv2.1 motif fused to CoChR for the following reason: in our original paper on soma-targeted CoChR[18], we used the KA2 sequence, which worked best with CoChR–GFP, but in this paper we used fluorophore-free CoChR, which did not express well with KA2, and rather worked better with $K_V2.1$; we also sometimes used the corresponding sequence from $K_V2.2$ as described in the text. Plasmid amplification was performed using Stellar (Clontech Laboratories) or NEB10-beta (New England BioLabs) chemically competent *Escherichia coli* cells. Small-scale isolation of plasmid DNA was performed with Mini-Prep kits (Qiagen); large-scale DNA plasmid purification was done with GenElute HP Endotoxin-Free Plasmid Maxiprep Kits (Sigma-Aldrich). The genes for ASAP3-Kv and Voltron-ST were synthesized de novo by GenScript, based on the reported sequences[5,6], and cloned into the pCAG-WPRE vector.

Neuronal culture and transfection. All mouse procedures were performed in accordance with the National Institute of Health Guide for Laboratory Animals and approved by the Massachusetts Institute of Technology Institutional Animal Care and Use and Biosafety Committees. For preparation of dissociated hippocampal mouse neuron cultures, we used postnatal day 0 or 1 Swiss Webster mice without regard to sex (Taconic Biosciences) as previously described[13]. In brief, dissected hippocampal tissue was digested with 50 units of papain (Worthington Biochemical) for 6–8 min at 37 °C, and the digestion was stopped by incubation with ovomucoid trypsin inhibitor (Worthington Biochemical) for 4 min at 37 °C. The tissue was then gently dissociated with Pasteur pipettes, and dissociated neurons were plated at a density of 20,000–30,000 per glass coverslip coated with Matrigel (BD Biosciences). Neurons were seeded in 100 µl plating medium containing MEM (Life Technologies), glucose (33 mM, Sigma), transferrin (0.01%, Sigma), HEPES (10mM, Sigma), Glutagro (2 mM, Corning), insulin (0.13%, Millipore), B27 supplement (2%, Gibco), and heat-inactivated FBS (7.5%, Corning). After cell adhesion, additional plating medium was added. AraC (0.002 mM, Sigma) was added when glia density was 50–70% of confluence. Neurons were grown at 37 °C and 5% CO_2 in a humidified atmosphere.

For in vitro screening of candidate soma-localized Archon1 sensors, primary hippocampal neuron cultures were transfected with 500 ng plasmid DNA per well using a commercial calcium phosphate transfection kit (Life Technologies) after 4 days in vitro (DIV), as previously described[13]. After 30–60 min of incubation of cultured neurons with DNA-calcium phosphate precipitate at 37 °C, neurons were washed twice with acidic MEM buffer (pH 6.7–6.8) to remove residual calcium phosphate particles and returned to the original plating medium. All measurements on cultured neurons were taken between DIV 14 and DIV 18 (about 9–14 d post transfection) to allow sodium channel maturation (and thus spiking). No cultured neuron recordings were supplemented with all-*trans*-retinal.

Electrophysiology and fluorescence microscopy in cultured primary hippocampal neurons. Whole-cell patch-clamp recordings of cultured neurons for Supplementary Table 1 were acquired via an Axopatch 700B amplifier (Molecular Devices) and Digidata 1440 digitizer (Molecular Devices). Neurons were patched between DIV 14 and DIV 18 and were bathed in Tyrode's solution (125 mM NaCl, 2 mM KCl, 3 mM $CaCl_2$, 1 mM $MgCl_2$, 10 mM HEPES, 30 mM glucose, pH 7.3 (NaOH adjusted)) at 32 °C during measurements. Synaptic blockers (2,3-dihydroxy-6-nitro-7-sulfamoyl-benzo[f]quinoxaline (NBQX), 10 µM; D(−)-2-amino-5-phosphonovaleric acid, 25 µM; gabazine, 20 µM; Tocris) were added to the extracellular solution for single-cell electrophysiology. Borosilicate glass pipettes with an outer diameter of 1 mm and a wall thickness of 0.2 mm were pulled to produce electrodes with resistance of 3–10 MΩ and were filled with an internal solution containing 135 mM potassium gluconate, 8 mM NaCl, 10 mM HEPES, 4 mM Mg-ATP, 0.4 mM Na-GTP, 0.6 mM $MgCl_2$, 0.1 mM $CaCl_2$, pH 7.25 (KOH adjusted) at 295 mOsm. Measurements from primary neuron cultures were performed on the electrophysiology setup described above. Patch-clamp data were acquired only if the resting potential was below −45 mV and access resistance was <25 MΩ. Access resistance was compensated at 30–70%. Fluorescence imaging was performed on an inverted fluorescence microscope (Nikon Ti), equipped with a red laser (637 nm, 100 mW, Coherent, OBIS 637LX, Pigtailed) expanded by a beam expander (Thorlabs) and focused onto the back focal plane of a 40× NA 1.15 objective lens (Nikon).

Two-photon imaging of SomArchon-expressing neurons was performed using an Olympus FVMPE-RS equipped with two lasers for fluorescence excitation. An InSight X3 laser (Spectra-Physics) tuned to 1,150 nm at 50% transmissivity was used to excite SomArchon, and a MaiTai HP Ti:Sapphire laser (Spectra-Physics) tuned to 920 nm at 15% transmissivity was used to excite EGFP. The laser beams were focused using a 25× 1.05 NA water-immersion objective lens (Olympus). SomArchon emission was separated using a 590-nm dichroic mirror and imaged with 660–750 nm and 495–540 nm filters for near-infrared and green fluorescence, respectively, and signals were collected onto separate photomultiplier tubes. Imaging was performed at 2.0 µs per pixel sampling speed with one-way galvano scanning.

Phototoxicity and photobleaching measurements in cultured neurons. For phototoxicity and photostability measurements, primary mouse neuron cultures, prepared as described above, were imaged using an inverted Eclipse Ti-E microscope (Nikon) equipped with an sCMOS camera (OrcaFlash4.2, Hamamatsu), LED light source (Spectra, Lumencor), a 637-nm laser (637 LX, OBIS) focused on the back focal plane of a 40× NA 1.15 water immersion objective lens (Nikon), and a Polygon400 Multi-wavelength Patterned Illuminator (Mightex) with a 470-nm LED (ThorLabs). To express SomArchon, neurons were infected with AAV2-CaMKII-SomArchon or AAV2-Syn-SomArchon-P2A-CoChR-$K_V2.1_{motif}$ at DIV 5. To express ASAP3-Kv and Voltron-ST, neurons were transfected with the pCAG-ASAP3-Kv-WPRE and pCAG-Voltron-ST-WPRE plasmids, respectively, using the calcium phosphate method described above. For imaging of Voltron-expressing neurons, the cells were incubated with JF525 at final concentration 1.25 µM for 60 min at 37 °C (application of higher concentrations of JF525 resulted in marked internalization of the dye within 40 min of incubation at 37 °C, thus preventing functional imaging owing to the high background fluorescence). After incubation, the cells were washed 3 times with fresh plating medium for 3 h to removed unbound dye. The reactive oxygen species (ROS) measurements were performed using CellRox Orange dye (Invitrogen) according to the manufacturer's protocol. In brief, neurons were incubated with the CellROX Orange reagent at a final concentration of 5 µM for 30 min at 37 °C in darkness, and then washed once with fresh plating medium before imaging. Immediately before imaging, cells were supplemented with the NucGreen Dead 488 reagent for detection of plasma membrane integrity, which we used to indicate cell death. Cells that showed a more than ten times increase in green fluorescence in the nucleus over background fluorescence levels were considered dead. Neurons were imaged between DIV 14 and DIV 18 in the plating medium at 22 °C. CellROX Orange fluorescence was acquired using 510/25 nm excitation at 0.8 mW/mm^2 and 545/40 nm emission. NucGreen fluorescence was acquired using 475/36 nm excitation at 3.5 mW/mm^2 and 527/50 nm emission.

IUE, AAV injection, and acute brain slice preparation. For IUE, embryonic day (E)15.5 timed-pregnant female Swiss Webster (Taconic Biosciences) mice were deeply anaesthetized with 2% isoflurane. Uterine horns were exposed and periodically rinsed with warm sterile PBS. Plasmid DNA (1–2 µg total at a final concentration of about 2–3 µg/µl diluted in sterile PBS) was injected into the lateral ventricle of one cerebral hemisphere of an embryo. Five voltage pulses (50 V, 50 ms duration, 1 Hz) were delivered using 5-mm round plate electrodes (ECM 830 electroporator, Harvard Apparatus), with the anode or cathode placed on top of the skull to target the cortex or hippocampus, respectively. Electroporated embryos were placed back into the dam, and allowed to mature to delivery. Brain slices were prepared from electroporated mice without regard to sex at postnatal day (P)12–P22.

The electroporated mice were anaesthetized by isoflurane inhalation and decapitated, and cerebral hemispheres were quickly removed and placed in cold choline-based cutting solution consisting of (in mM): 110 choline chloride, 25 $NaHCO_3$, 2.5 KCl, 7 $MgCl_2$, 0.5 $CaCl_2$, 1.25 NaH_2PO_4, 25 glucose, 11.6 ascorbic acid, and 3.1 pyruvic acid (339–341 mOsm/kg; pH 7.75 adjusted with NaOH) for 2 min, then blocked and transferred into a slicing chamber containing ice-cold choline-based cutting solution. For mice electroporated with Voltron-ST, 50 µl JF525 dye (Janelia Farm; 12.5 nM JF525 in 10µl DMSO mixed with 10 µl Pluronic F-127 (20% w/v in DMSO; Invitrogen) and 30 µl sterile PBS) was injected into the retro-orbital sinus one day before slicing. Coronal slices (300 µm thick) were cut with a Compresstome VF-300 slicing machine, then transferred to a holding chamber with artificial cerebrospinal fluid (ACSF) containing (in mM) 125 NaCl, 2.5 KCl, 25 $NaHCO_3$, 2 $CaCl_2$, 1 $MgCl_2$, 1.25 NaH_2PO_4 and 11 glucose (300–310 mOsm/kg; pH 7.35 adjusted with NaOH), and allowed to recover for 10 min at 34 °C, followed by another 30 min at room temperature. Slices were subsequently maintained at room

temperature (22 °C) until use. Both cutting solution and ACSF were constantly bubbled with 95% O_2 and 5% CO_2.

For AAV injection, 21-day-old C57 BL/6J mice were anaesthetized with isoflurane and placed in a small animal stereotaxic apparatus (David Kopf Instruments). Animals were injected with 200 nl rAAV8-Syn-Archon1-KGC-EGFP-Kv2.1motif-ER2 using a Nanoject (Drummond Scientific) via glass pipettes with 20–30-μm diameter tips into the striatum: anteroposterior (AP) 1.2 mm, mediolateral (ML) 2.1 mm, dorsoventral (DV) 3.2 mm relative to bregma. Brain slices were then prepared from these AAV-injected mice at P30–35. Mice were deeply anaesthetized with isoflurane and perfused transcardially using cold saline containing (in mM): 194 sucrose, 30 NaCl, 4.5 KCl, 1.2 NaH_2PO_4, 0.2 $CaCl_2$, 2 $MgCl_2$, 26 $NaHCO_3$, and 10 D-(+)-glucose saturated with 95% O_2 and 5% CO_2, pH 7.4 adjusted with NaOH, 320–340 mOsm/l. Coronal slices (250–300 μm thick) were cut using a slicer (VT1200 S, Leica Microsystems) and then incubated for 10–15 min in a holding chamber (BSK4, Scientific System Design) at 32 °C with regular ACSF containing (in mM): 136 NaCl, 3.5 KCl, 1 $MgCl_2$, 2.5 $CaCl_2$, 26 $NaHCO_3$ and 11 glucose saturated with 95% O_2 and 5% CO_2, followed by at least 1 h recovery at room temperature (21–25 °C) before recording.

Concurrent electrophysiology and fluorescence imaging in acute brain slices. For the recordings shown in Fig. 1 and Extended Data Fig. 3a–c, individual slices were transferred to a recording chamber mounted on an upright microscope (Olympus BX51WI, see below) and continuously superfused (2–3 ml/min) with carbogenated ACSF at room temperature. Whole-cell patch-clamp recordings were performed with borosilicate glass pipettes (KG33, King Precision Glass) heat-polished to obtain direct current resistances of ~4–6 MΩ. For cortex recordings, pipettes were filled with an internal solution containing in mM: 120 K-gluconate, 2 $MgCl_2$, 10 HEPES, 0.5 EGTA, 0.2 Na_2ATP, and 0.2 Na_3GTP. For hippocampus and striatum recordings, pipettes were filled with an internal solution containing in mM: 131 K-gluconate, 17.5 KCl, 9 NaCl, 1 $MgCl_2$, 10 HEPES, 1.1 EGTA, 2 Na_2ATP, and 0.2 Na_3GTP. Voltage clamp recordings were made with a microelectrode amplifier (Multiclamp 700B, Molecular Devices). Cell membrane potential was held at −60 mV, unless specified otherwise. Signals were low-pass-filtered at 2 kHz and sampled at 10–20 kHz with a Digidata 1440A (Molecular Devices), and data were stored on a computer for subsequent offline analysis. Cells in which the series resistance (R_s, typically 8–12 MΩ) changed by >20% were excluded from subsequent data analysis. In addition, cells with R_s more than 25 MΩ at any time during the recordings were discarded. In some cases, conventional characterization of neurons was made in both voltage and current clamp configurations. Positive neurons were identified for recordings on the basis of EGFP expression visualized with a microscope equipped with a standard GFP filter (BX-51WI, Olympus). Optical voltage recordings were taken through a 40× water immersion objective (Olympus LUMFL N 40x/0.8W). Fluorescence was excited using a fibre-coupled 637-nm red laser (140 mW, Coherent Obis 637-140 LX), and the emission was filtered through a 664-nm long-pass filter. Images were collected on an EMCCD camera (Andor iXON Ultra 888) or sCMOS camera (Andor Zyla4.2 Plus Andor) in a reduced pixel window to enable acquisition at about 1 kHz. Each trial was about 30 s in duration. Of the 18 cortical neurons reported in Fig. 1, 4 neurons were not analysed for Fig. 1e because the electrophysiology files were inadvertently not saved, owing to a problem with the manual save process.

For optical recordings shown in Fig. 1i, j and Extended Data Figs. 1a–g, 2, 5, acute brain slices were transferred to a recording chamber mounted on an inverted Eclipse Ti-E (Nikon) equipped with a CMOS camera (Zyla5.5, Andor), LEDs (Spectra, Lumencor), a 637-nm laser (637 LX, OBIS) focused on the back focal plane of a 40× NA 1.15 objective (Nikon), and a Polygon400 Multiwavelength Patterned Illuminator (Mightex) with 470-nm LED (ThorLabs), and continuously superfused (2–3 ml/min) with carbogenated ACSF at room temperature. Positive cells were imaged under 0.8 or 1.5 W/mm^2 (55 mW) excitation light power at 637 nm from the laser. 4-Aminopyridine at a final concentration of 1 mM was added to induce neuronal activity for experiments shown in Extended Data Figs. 2c, d, g, h, 5. For Fig. 1i, j and Extended Data Fig. 5, cells were illuminated with 2-ms blue light pulses at light power in the range from 0.1 to 1.0 mW/mm^2.

Mouse surgery. All in vivo mouse procedures were performed in accordance with the National Institute of Health Guide for Laboratory Animals and approved by the Boston University Institutional Animal Care and Use and Biosafety Committees.

Virus injection surgery. All AAVs were produced by the University of North Carolina Chapel Hill Vector Core. Adult female C57BL/6 mice (Charles River Laboratories) or Chat-cre mice (Chat-cre;129S6-Chattm2(cre)Lowl/J, the Jackson Laboratory), 8–12 weeks old at the time of surgery, were used for all experiments. AAV-Syn-SomArchon (5.9×10^{-12} genome copies (GC)/ml) or AAV-syn-SomArchon-P2A-CoChR-Kv2.1 (2.19×10^{-13} GC/ml) was injected into the motor cortex (AP: +1.5 mm, ML: ±1.5 mm, DV: −0.3 mm relative to bregma, 0.5 μl virus), visual cortex (AP: −3.6 mm, ML: ±2.5 mm, DV: −0.3 mm, 0.5 μl virus), hippocampus (AP: −2.0 mm, ML: +1.4 mm, DV: −1.6 mm, 1 μl virus) or striatum (AP: +0.8 mm, ML: −1.8 mm, DV: −2.1 mm, 1 μl virus). Viral injection occurred at 50–100 nl/min (10 min total) using a 10-μl syringe (NANOFIL, World Precision Instruments) fitted with a 33-gauge needle (World Precision Instruments, NF33BL) and controlled by a microinfusion pump (World Precision Instruments, UltraMicroPump3–4). The syringe was left in place for an additional 10 min after injection to facilitate viral spread. About one week after the viral injection, mice underwent a second surgery to implant the cranial window for in vivo imaging.

Cortex imaging window implantation. The imaging window consisted of a stainless steel cannula (OD: 3.17 mm, ID: 2.36 mm, height: 1 mm, AmazonSupply, B004TUE45E) fitted with a circular coverslip (no. 0, OD: 3 mm, Deckgläser Cover Glasses, Warner Instruments, 64-0726 (CS-3R-0)) adhered using a UV curable glue (Norland Products, Norland Optical Adhesive 60, P/N 6001). A craniotomy of about 3 mm in diameter was created, with the dura left intact, over the motor cortex (centred at AP: +1.5 mm, ML: ±1.75 mm) or visual cortex (AP: −3.6 mm, ML: ±2.15 mm). The imaging window was positioned over the cortex so that it was flush with the surface of the dura. Kwik-sil adhesive (World Precision Instruments, KWIK-SIL) was applied around the edges of the imaging window to hold the imaging window in place and to prevent any dental cement from touching the brain. Three small screws (J.I. Morris, F000CE094) were screwed into the skull to further anchor the imaging window to the skull. Dental cement was then gently applied to affix the imaging window to the exposed skull, and to mount an aluminium headbar posterior to the imaging window. Supplementary Fig. 1a, b provides the window placement.

Hippocampus and striatum imaging window implantation. Hippocampal and striatal window surgeries were performed in a similar way to those previously described[11,29]. For each imaging window, a virus/drug infusion cannula (26G, PlasticsOne, C135GS-4/SPC) was attached to a stainless steel imaging cannula (OD: 3.17 mm, ID: 2.36 mm, height: 1 or 2 mm, AmazonSupply, B004TUE45E). The bottom of the infusion cannula was flush with the base of the stainless steel cannula, and a circular coverslip (no. 0, OD: 3mm, Deckgläser Cover Glasses, Warner Instruments, 64-0726 (CS-3R-0)) was adhered using a UV curable glue (Norland Products, Norland Optical Adhesive 60, P/N 6001). An additional insulated stainless steel wire (diameter: 130 μm, PlasticsOne, 005SW-30S, 7N003736501F) was glued to the viral/drug infusion cannula with super glue (Henkel, Loctite 414 and Loctite 713) and protruded from the bottom of the infusion cannula and imaging window by about 200 μm for LFP recordings.

A craniotomy about 3 mm in diameter was made over the hippocampus CA1 region (AP: −2.0 mm, ML: +2.0 mm) or the striatum (AP: +0.8 mm, ML: −1.8 mm). A small notch was made on the posterior edge of the craniotomy to accommodate the infusion cannula and LFP recording electrode. The overlying cortex was gently aspirated using the corpus callosum as a landmark. The corpus callosum was then carefully thinned to expose the hippocampus CA1 region or the dorsal striatum. The imaging window was positioned in the craniotomy, and Kwik-sil adhesive (World Precision Instruments, KWIK-SIL) was applied around the edges of the imaging window to hold it in place and to prevent any dental cement from touching the brain. Three small screws (J.I. Morris, F000CE094) were screwed into the skull to further anchor the imaging window to the skull, and a small ground pin was inserted into the posterior part of the brain near the lambda suture as a ground reference for LFP recordings. Dental cement was then gently applied to affix the imaging window to the exposed skull, and to mount an aluminium headbar posterior to the imaging window. Supplementary Fig. 1c, d provides the window placement.

In mice that did not receive a virus injection before window implantation, 1 μl of AAV-syn-SomArchon (5.9×10^{12} GC/ml) or 1 μl of AAV-syn-SomArchon-P2A-CoChR-Kv2.1 (2.19×10^{13} GC/ml), or 1 μl of AAV-CAG-FLEX-SomArchon (6.3×10^{12} GC/ml) was injected through the virus/drug infusion cannula at 100 nl/min through an internal infusion cannula (33G, PlasticsOne, C315IS-4/SPC) connected to a microinfusion pump (World Precision Instruments, UltraMicroPump3–4), one week after the window implantation surgery. The internal infusion cannula was left in place for 10 min after injection to facilitate viral spread. Mice were awake and their heads were fixed throughout the injection period.

All mice were treated with buprenex for 48 h after surgery and single-housed to prevent any damage to the headbar or window implant.

In vivo imaging in the live mouse brain. All optical recordings were acquired on a conventional one-photon fluorescence microscope equipped with an ORCA Flash 4.0 V3 Digital CMOS camera (Hamamatsu Photonics K.K., C13440-20CU) or Hamamatsu ORCA Fusion Digital CMOS camera (Hamamatsu Photonics K.K., C14440-20UP), 10× NA0.25 LMPlanFI air objective (Olympus), 40× NA0.8 LUMPlanFI/IR water immersion objective (Olympus), 20× NA1.0 XLUMPlanFL N water immersion objective (Olympus), 16× NA0.8 CFI LWD Plan Fluorite water immersion objective (Nikon), 470-nm LED (ThorLabs, M470L3), 140-mW 637-nm red laser (Coherent Obis 637-140X), a green filter set with a 470/25-nm bandpass excitation filter, a 495-nm dichroic, and a 525/50-nm bandpass emission filter, and a near infrared filter set with a 635-nm laser dichroic filter, and a 664-nm

long-pass emission filter. The near-infrared laser illuminated a circular area of about 60–80 μm, about 80–140 μm, and about 100–200 μm in diameter in brain tissue, with FOV height (limited by camera acquisition rate) 40–60 μm, 80–100 μm, and 100–120 μm under 40×, 20×, and 16× objective lenses, respectively. A mechanical shutter (Newport, model 76995) was positioned in the laser path to control the timing of illumination over the imaging window. Optical recordings were acquired at 390–900 Hz with HCImage Live (Hamamatsu Photonics K.K.) or NIS Elements (Nikon) software. HC Image Live data were stored as DCAM image files (DCIMG), and further analysed offline in Fiji/ImageJ and MATLAB (Mathworks). NIS Elements data were stored as .nd2 files and further analysed offline using the NIS Elements software.

The GFP signal of SomArchon was acquired in the green channel ($\lambda_{ex} = 470$ nm) at 1,024 × 1,024 pixels with 2 × 2 binning to show cell structure and distribution. Optical voltage recordings were imaged in the near infrared channel ($\lambda_{ex} = 637$ nm) with 2 × 2 or 4 × 4 binning. OmniPlex system (PLEXON) was used to synchronize data acquisition from different systems. In all experiments, the OmniPlex system recorded the start of image acquisition from the sCMOS camera, the acquisition time of each frame, and other experiment-dependent signals described below.

Optical imaging of spontaneous neural activity. All in vivo optical imaging of spontaneous neural activity was performed when mice were awake with their heads fixed in a custom holder that allowed attachment of the headplate at the anterior end. Animals were covered with an elastic wrap to prevent upward movement. Spontaneous neural activity recordings lasted continuously for up to 30,000 frames (about 36 s).

Eye puff. During some in vivo hippocampal imaging recordings, an eye puff was applied to evoke high-frequency local field potential responses in the hippocampus (Extended Data Fig. 9a–d). The mice had their heads fixed in a custom holder that allowed attachment of the headplate at the anterior end, and they were covered with an elastic wrap to prevent upward movement. Each experimental session consisted of 20–30 trials, with each trial lasting for 5,000 frames (about 6 s). Three seconds after the start of image acquisition, the sCMOS camera sent a TTL pulse to a function generator (Agilent Technologies, model 33210A), which triggered a 100-ms-long air puff. The air puff was 5–10 psi, and administered via a 0.5-mm cannula placed 2–3 cm away from the eye of the mouse. The puff TTL pulses were also recorded with the OmniPlex system (PLEXON). Eye movement was monitored using a USB webcam (Logitech, Carl Zeiss Tessar 2.0/3.7 2MP Autofocus).

Optopatch blue light stimulation. All in vivo optopatch (that is, optogenetics plus voltage imaging) experiments were performed when mice were awake with their heads fixed in a custom holder that allowed attachment of the headplate at the anterior end. Mice were covered with an elastic wrap to prevent upward movement. A 470-nm LED (ThorLabs, M470L3) was coupled to a Polygon400 Multiwavelength Patterned Illuminator (Mightex), and the blue light was focused through the objective lens to illuminate the centre of the FOV. At the onset of imaging, the sCMOS camera sent a TTL pulse to trigger Axon CNS (Molecular Devices, Digidata 1440A) which controlled the 470-nm LED (ThorLabs). Each trial lasted 1.1 s and consisted of a single 100-ms-long blue light pulse, 500 ms after trial onset. Each recording session consisted of 10 trials with increasing blue light power from 0.1 to 1 mW/mm^2, with a step of about 0.1 mW/mm^2 per trial. The OmniPlex system (PLEXON) recorded the timing of TTL pulses used to trigger the Axon CNS.

Head-fixed voluntary movement experiments. All voluntary movement experiments were performed while awake, head-fixed mice were freely navigating a spherical treadmill. The spherical treadmill was constructed as described[30]. In brief, a 3D spherical Styrofoam ball was supported by air, and motion was tracked using two computer mouse sensors positioned roughly ±45° from the centre along the equator of the ball. All motion-sensor displacement data were acquired at 100 Hz on a separate computer and synthesized using a custom Python script. Motion sensor displacement data were then sent to the image acquisition computer to be accumulated using a modified ViRMEn MATLAB script. The timing of each motion sensor displacement data point was also recorded using the OmniPlex system (PLEXON) to synchronize movement data with optical voltage recordings.

To determine the mouse movement speed, ball movement was first calibrated. The ball was pinned on the two sides and rotated vertically to calibrate sensor displacement.

All mice were habituated on the spherical treadmill for at least 3 days, at least 20 min per day, before image acquisition. During optical imaging, mice were imaged while freely navigating the spherical treadmill. Each FOV was recorded for at least 36 s in total. In some fields of view, we performed multiple trials, and each trial was at least 12 s in duration with an inter-trial interval of at least 30 s in duration.

Local field potential recording. Local field potentials were recorded using an OmniPlex system (PLEXON) at a 1 kHz sampling rate. To synchronize optical recordings with LFP recordings, the camera sent out a TTL pulse to the OmniPlex system at the onset of imaging and after each acquired frame.

Motion correction. In Figs. 2i, 3, 4, motion correction was performed with a custom Python script. For FOV, if multiple video imaging files were collected for the same FOV, we started with the first imaging file to ensure speedy data processing (a single video file contains a series of images). We first generated the reference image by averaging across all images within the file. We then performed a series of image processing procedures to enhance the contrast of the reference image and every image in the file to facilitate motion correction. We first removed 10% of the pixels along all edges of an image to remove any camera induced artefact. We then applied a high-pass filter (Python scipy package, ndimage.gaussian_filter, sigma = 50) to remove low-frequency components within the images. To enhance the boundaries of high intensity areas, we identified the boundaries as the difference between two low-pass-filtered images (sigma = 2 and 1). We then enhanced the boundary by adding 100 times the boundary back to the low-pass-filtered image (sigma = 2). We then limited the intensity range of the processed images within one standard deviation above and below the average intensity of the image, by setting the pixels with intensity higher than mean + s.d. as mean + s.d., and the pixels with intensity lower than mean − s.d. as zero. Finally, to counter any potential bleaching over time, we normalized the intensity of each image by shifting the mean intensity to zero and divided intensity values by the s.d. of all pixel intensities in that image. After image processing, we calculated the displacement of each image, by identifying the maximum cross-correlation coefficient between each image and the reference image, and then corrected motion by shifting the displacement in the original, unenhanced image sequence. If the same FOV was imaged over an extended period of time, during which multiple files were acquired, we motion-corrected subsequent files by aligning them to the first file, so that the same ROIs from the same FOV could be applied across the entire imaging session. Specifically, we first refined the reference frame by generating the mean intensity projection image from the motion-corrected first imaging file. The refined reference image was then used to motion-correct all files of the same FOV, including the first file, using the procedure described above. The motion-corrected, original, unenhanced image sequences were then used for subsequent manual ROI segmentation and further analysis.

ROI identification. We imported the image files (motion-corrected as above, if necessary) into Fiji/ImageJ or NIS Elements and manually segmented ROIs by examining the time-series images to identify areas with clear neuron outlines and/or intensity dynamics over time. The optically recorded voltage traces for each ROI were generated from the motion-corrected image sequences using the multiple measurement function and were then used for analyses.

The wide dynamic range (16 bit) of the raw images meant that to select dim as well as bright cells, we had to create maximum projection and standard deviation images of the entire raw video, and stretched their look-up tables to enhance visibility. For Fig. 4 and Extended Data Fig. 9e–h, cells were densely packed, so we identified and tracked ROIs semi-manually across image sequences without performing motion correction. We first visually inspected all image sequences and identified those with minimal motion and with an SNR greater than about 2 for further analysis. We then performed an iterative ROI-selection procedure to identify ROIs that best fit each cell. Specifically, we started by manually selecting ROIs from the maximum projection image of the entire image sequence. The image sequence was then visually inspected to identify frames with cells that exhibited shifts of more than three pixels from the defined ROI. We then used these frames to separate the image sequence into multiple time intervals, and obtained a new set of maximum projection images to identify new ROIs within these time intervals for these cells. This procedure was repeated iteratively until the ROI represented the cell across all image frames in their corresponding time intervals without the cell moving out of the ROI. Thus, with this procedure, we created multiple ROIs representing the same cell across different frames. For each cell, we extracted traces for every ROI during its corresponding time interval, and stitched the baseline-normalized traces for the same cell(s) in time. The fluorescence traces of each cell were then detrended for further analysis. Supplementary Fig. 2 provides an example of raw and processed traces for two cells in the same FOV.

Hippocampal spike detection. Spikes were associated with a rapid increase in intensity, followed by a rapid decrease. By contrast, occasional motion artefacts were usually associated with a decrease in intensity as a neuron moved out of the ROI. To facilitate spike detection, we first removed motion artefacts. For each time point of the fluorescence intensity trace for each ROI, we calculated the change in intensity from that of the prior time point (I_{change}). We then defined noise as the time points at which instantaneous I_{change} was 3 s.d. below the mean value of I_{change} across the entire trace. We excluded any time points at which the I_{change} of the previous time point was more than 1 s.d. above the average I_{change}, because this might have indicated a spike. These noise time points and their following three time points (as we found that motion artefacts are typically >4 ms) were then considered motion artefacts, and removed from further analysis. We then recalculated the standard deviation of I_{change}, excluding the data points related to the motion artefact. The peaks of spikes were then identified as time points that

met the following two criteria: (1) the intensity change of the time point combined with that of its preceding time point was more than 3 s.d. above the average I_{change}, and (2) the intensity change over the next two time points was less than 2 s.d. below the average I_{change}.

Hippocampal spike–phase calculation. Hippocampal spike–phase analysis was performed on 16 neurons from 7 FOVs in 4 mice. For each FOV, we analysed data collected over 10 trials (about 60 s in total) during which animals experienced an eye puff in each trial, as described above. To calculate the phase of spikes at theta frequency (4–10 Hz), we first band-pass-filtered both the optical voltage trace and the simultaneously recorded LFP at theta frequency (eegfilt, EEGLAB toolbox). The peaks of theta oscillation power were then identified using the findspike function in MATLAB. For each spike, we obtained the phase of the spike by calculating the timing of each spike relative to the period of that oscillation cycle in degrees. We averaged the phases of all spikes from the same neuron as the average phase of a given neuron.

Analysis for pairwise coherence between hippocampal neurons and LFPs. The coherence analysis was performed on nine FOVs that contained multiple neurons from four mice. Each FOV contained imaging data over a period of 6–36 s. For each FOV, we first re-sampled the LFP at the acquisition rate of the optical imaging. We then divided the optical voltage traces and LFPs into segments of 1,000 data points. We then calculated the averaged coherence, at theta frequency (4–10 Hz), with the functions in the Chronux toolbox (optical voltage trace to optical voltage trace or LFP: coherencyc, and spike to spike: coherencypt) with tapers = [10 19], fpass = [4 10] and trialave = 1. To compare V_{mo}–V_{mo} coherence with V_{mo}–LFP coherence across nine FOVs, we averaged the coherence of neurons in the same FOV to obtain the mean coherence of that FOV, and then performed statistical tests across FOVs using the mean coherences of the individual FOVs. To understand the relationships between pairs of coherence, we used the MATLAB function fitlm to perform a linear regression between coherent pairs and obtain the P and r^2 values.

To estimate background fluorescence crosstalk, we calculated pairwise coherence and correlation between background doughnut areas surrounding a neuron. To select background doughnut areas, we excluded the edges (5%) of each FOV, because the edge may be missing for a particular image frame when image frames were shifted during motion correction. The background doughnut of a neuron was determined as the area 3–10 μm from the neuron boundary, excluding any pixels within 10 μm of the boundary of another neuron. One neuron was excluded from this analysis owing to dense labelling where we could not identify its doughnut area. Fluorescence traces of the background doughnut area were then processed as for neurons, and their pairwise coherence and Pearson correlations were calculated.

Spike detection for striatum, motor cortex, and visual cortex. After motion correction, we first identified large fluorescence increases using a threshold of 4 s.d. above the baseline. The baseline was manually selected as a period of >500 ms without spiking or drifting due to z-plane shifting or photobleaching. From these large fluorescence increases, we selected those with rise times and decay times shorter than 4 ms as spikes.

Firing rate comparison of striatal neurons during high- and low-speed movement. Movement data of mice were first interpolated to the voltage imaging frame rate with MATLAB function interp1, and then smoothed using a 1.5-Hz low-pass Butterworth filter to remove any motion sensor artefacts. We calculated the average movement speed at 0.5-s intervals and defined low-speed periods as intervals during which the average speed was ≤5 cm/s and high-speed periods as intervals during which the average speed was ≥10 cm/s. The firing rates during these high- and low-speed motion periods were compared, and a two-sided Wilcoxon rank-sum test was used to identify significant differences between these periods.

SNR calculation for in vivo photostability evaluation over imaging duration in striatum and hippocampus. We defined noise as the standard deviation of the fluorescence intensity across the entire trial period. For each neuron, we first calculated the SNR for each action potential by dividing the intensity change observed during an action potential by the noise, and then calculated the average SNRs across all spikes detected in a trial as the corresponding SNR for the trial. For the striatum dataset, only neurons imaged over at least five consecutive trials were analysed. For the hippocampus dataset, all neurons were analysed.

Detrending. All optically recorded SomArchon traces reported in the manuscript (except those shown in Fig. 4a–d) were corrected for photobleaching or focus shift by subtracting baseline fluorescence traces that were low-pass-filtered and fit to a double or single exponential function.

Histology. Mice were transcardially perfused with PBS followed by 4% paraformaldehyde. The brain was gently extracted from the skull and post-fixed in 4% paraformaldehyde for 1–4 h at room temperature or overnight at +4 °C. Fixed brains were transferred to a 30% sucrose–PBS solution and rotated for 24–48 h at 4 °C for cryoprotection. Cryoprotected brains were frozen in OCT in a dry ice bath and sliced (coronally) to 50-μm thickness using a cryostat. Glial and microglial antibody staining were performed with anti-GFAP[29] (1:250, Clone N206/A8, Neuromab) and anti-IBA1[31] (1:500, 019-19741, Wako Chemicals) primary antibodies, respectively, followed by Alexa Fluor 568 (1:1,000, goat anti-mouse IgG (H+L) cross-adsorbed secondary antibody, A11004, InVitrogen) and 633 secondary antibodies (1:1,000, goat anti-rabbit IgG (H+L) cross-adsorbed secondary antibody, A21070, InVitrogen). All antibodies were used according to protocols that have been validated by their suppliers. Slice imaging was performed using an inverted Nikon Eclipse Ti microscope equipped with a spinning disk sCSUW1 confocal scanner unit (Yokogawa), 488-, 561-, and 642-nm solid state lasers, 525/25-nm, 579/34-nm, and 664LP emission filters, a 20× NA0.75 air objective lens (Nikon), and a 4.2 PLUS Zyla camera (Andor), controlled by NIS-Elements AR software. Acquired images were contrast-enhanced to improve visualization.

Brain temperature measurements. Under general anaesthesia, a craniotomy about 3 mm in diameter was made to expose the brain surface, with a small notch on the posterior edge to accommodate the insertion of a temperature probe (Physitemp, IT-1E) coupled to a Thermocouple DAQ (DATAQ Instruments, Model DI-245). An imaging window, identical to those used in all imaging experiments, was positioned on the craniotomy. Kwik-sil adhesive was applied around the edges of the imaging window to hold it in place, but not around the craniotomy notch, to allow insertion of the temperature probe. Dental cement was then gently applied to affix the imaging window to the skull and to mount an aluminium headbar. Once mice had recovered from anaesthesia, they had their heads fixed while awake and the temperature probe was inserted under the imaging window above the brain surface, through the craniotomy notch. The 637-nm laser was directed through the 40× objective under identical conditions to those used while imaging (75–95 mW laser power), and brain temperature was recorded. We noted a temperature increase of 1.88 ± 0.80 °C (mean ± s.d., n = 3 mice) over the 12-s illumination period commonly used in our experiments. These changes are similar to, or smaller than, changes commonly seen with two-photon imaging, optogenetics, and the making of craniotomies for neural imaging[32–36].

Sample size. No statistical methods were used to estimate sample size for mouse studies throughout. We did not perform a power analysis, as our goal was to create a new technology, as recommended by the NIH: "In experiments based on the success or failure of a desired goal, the number of animals required is difficult to estimate..."[37]. As noted in the aforementioned paper, "The number of animals required is usually estimated by experience instead of by any formal statistical calculation, although the procedures will be terminated [when the goal is achieved]." These numbers reflect our past experience in developing neurotechnologies.

Data exclusions. Voltage imaging datasets with significant motion or in which no spikes were detected were excluded from analysis. Significant motion was defined as a shift of more than 20 μm in any direction. In Extended Data Fig. 1i–k, data points that corresponded to overlapping neurites were excluded. Data exclusion criteria were not pre-established.

Replication. All attempts at replication were successful.

Randomization and blinding. There were no treatment conditions to compare in this study. All recording sessions were randomly performed with different voltage sensors or in different brain regions. On recording days, cultured cells or brain slices expressing specific sensors were known. On in vivo recording days, mouse conditions were known. Voltage trace extraction and subsequent analysis were performed with the investigators unaware of specific mouse conditions. For analysis of movement modulation of striatal neuron spiking, a computer algorithm was used to identify periods with different movement parameters. For analysis of spike–phase relationships, or subthreshold membrane voltage relationships, a computer algorithm was used across all conditions. For histology, sections were selected and images were taken from slides by a researcher not aware of the conditions or antibody used. Cells were also counted and quantified from these sections by a researcher blinded to the experimental conditions or antibody used.

Reporting summary. Further information on research design is available in the Nature Research Reporting Summary linked to this paper.

Code availability

Computer code used to generate results for this study is available at https://github.com/HanLabBU/somarchon-imaging.

Data availability

The data that support the findings of this study are available from the corresponding author upon reasonable request; raw data essential to the work are available online as Source Data files. Sequences of the reported proteins are available at GenBank at the following accession codes: SomArchon MN091368; SomArchon-P2A-CoChR-$K_V2.1_{motif}$, MN091369.

28. Adam, Y. et al. Voltage imaging and optogenetics reveal behaviour-dependent changes in hippocampal dynamics. *Nature* **569**, 413–417 (2019).
29. Hansen, K. R. et al. Mild blast injury produces acute changes in basal intracellular calcium levels and activity patterns in mouse hippocampal neurons. *J. Neurotrauma* **35**, 1523–1536 (2018).

30. Dombeck, D. A., Khabbaz, A. N., Collman, F., Adelman, T. L. & Tank, D. W. Imaging large-scale neural activity with cellular resolution in awake, mobile mice. *Neuron* **56**, 43–57 (2007).
31. Fields, I. E. et al. Noninvasive deep brain stimulation via temporally interfering electric fields. *Cell* **169**, 1029–1041.e16 (2017).
32. Kalmbach, A. S. & Waters, J. Brain surface temperature under a craniotomy. *J. Neurophysiol.* **108**, 3138–3146 (2012).
33. Podgorski, K. & Ranganathan, G. Brain heating induced by near-infrared lasers during multiphoton microscopy. *J. Neurophysiol.* **116**, 1012–1023 (2016).
34. Arias-Gil, G., Ohl, F. W., Takagaki, K. & Lippert, M. T. Measurement, modeling, and prediction of temperature rise due to optogenetic brain stimulation. *Neurophotonics* **3**, 045007 (2016).
35. Stujenske, J. M., Spellman, T. & Gordon, J. A. Modeling the spatiotemporal dynamics of light and heat propagation for in vivo optogenetics. *Cell Rep.* **12**, 525–534 (2015).
36. Christie, I. N. et al. fMRI response to blue light delivery in the naïve brain: implications for combined optogenetic fMRI studies. *Neuroimage* **66**, 634–641 (2013).
37. Dell, R. B., Holleran, S. & Ramakrishnan, R. Sample size determination. *ILAR J.* **43**, 207–213 (2002).

Acknowledgements We thank T. Ta for help with histology; M. Murdock for help with mouse work; N. Pak, A. Badon and J. Mertz for help with assembling the in vivo imaging setup; and Y. Bando for helping with the Supplementary Video. E.S.B. acknowledges funding from Edward and Kay Poitras, NIH Director's Pioneer Award 1DP1NS087724, NIH 1R01GM104948, NIH 1R01EB024261, NIH 1R01DA045549, NIH 1R01MH114031, Charles Hieken, NIH 1R01NS102727, John Doerr, NSF Grant 1734870, the HHMI-Simons Faculty Scholars Program, Human Frontier Science Program RGP0015/2016, NIH 1R43MH109332, US Army Research Laboratory and the US Army Research Office under contract/grant number W911NF1510548, NIH 2R01DA029639, and NSF CBET 1344219. X.H. acknowledges funding from the NIH Director's Office (1DP2NS082126), NINDS (1R01NS109794-01, 1R01NS087950-01), NSF CBET-1848029, the Grainger Foundation, the Pew Foundation, and Boston University Biomedical Engineering Department. S.B. and S.N.S. acknowledge funding from the NIH/NIGMS T32 Quantitative Biology and Physiology Fellowship (GM008764) through the Boston University Biomedical Engineering Department. The funders had no role in study design, data collection and analysis, decision to publish, or preparation of the manuscript.

Author contributions K.D.P. and E.S.B. initiated the project. K.D.P., S.B., H.T., S.N.S., X.H., and E.S.B. designed all in vivo experiments and interpreted the data. K.D.P. developed SomArchon and together with E.E.J., O.A.S., and E.C. characterized all constructs in cultured cells. K.D.P., V.G.L.-H., D.P., C.S., Z.F., and B.L.S. performed characterization of SomArchon in acute brain slices. S.B., S.N.S. and H.J.G. performed all mouse surgeries for in vivo experiments. M.F.R. assisted on imaging setups. K.D.P, S.B., H.T., and S.N.S performed all in vivo imaging experiments and analysed all in vivo imaging data. K.D.P., S.B., H.T., S.N.S, X.H. and E.S.B. wrote the paper with contributions from all of the authors. E.S.B. and X.H. oversaw all aspects of the project.

Competing interests The authors declare no competing financial interests.

Additional information

Supplementary information is available for this paper at https://doi.org/10.1038/s41586-019-1641-1.

Correspondence and requests for materials should be addressed to E.S.B. or X.H.

Peer review information *Nature* thanks Kenneth Harris, Lin Tian, Christian Wilms and the other, anonymous, reviewer(s) for their contribution to the peer review of this work.

Reprints and permissions information is available at http://www.nature.com/reprints.

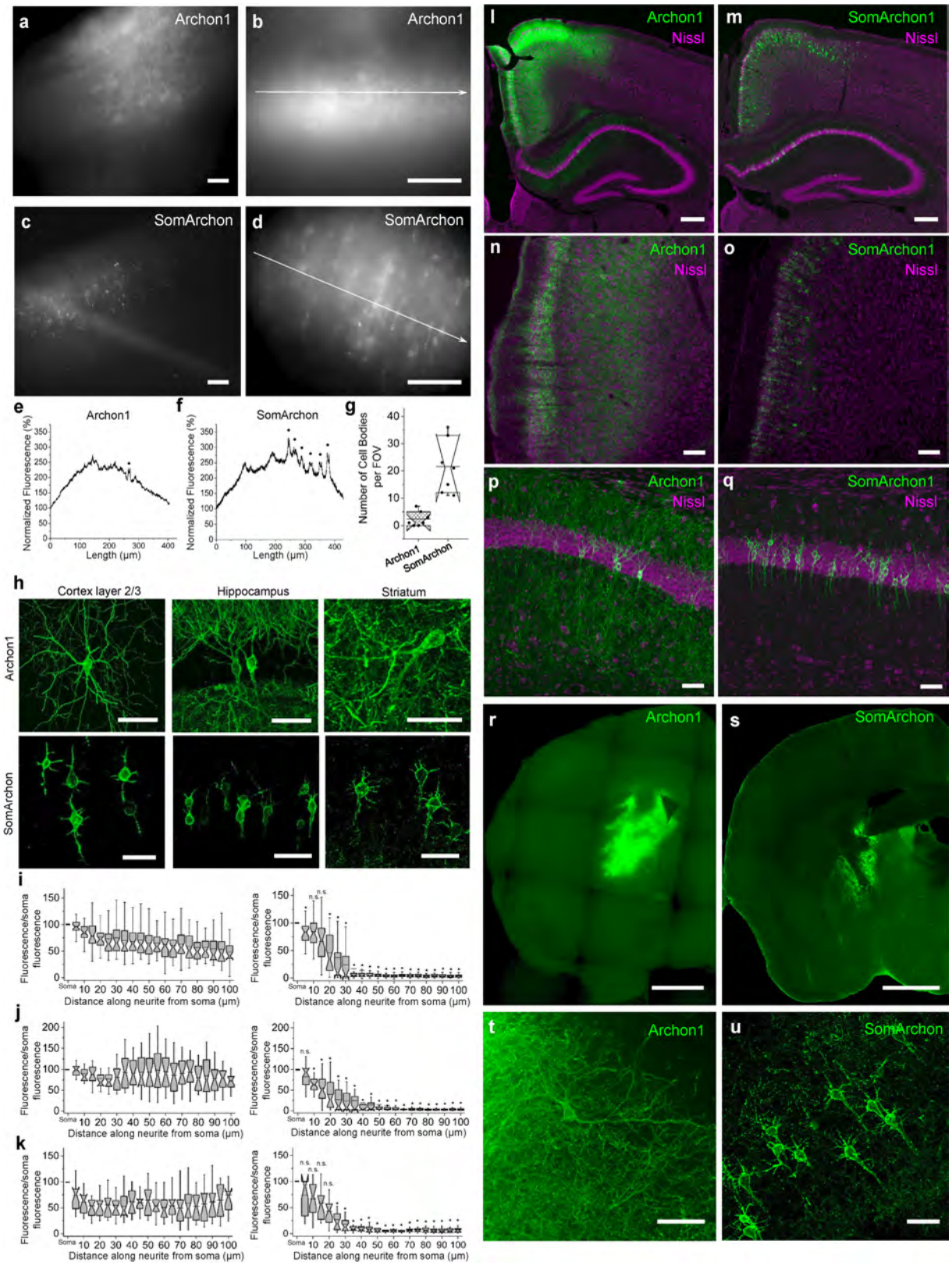

Extended Data Fig. 1 | See next page for caption.

Extended Data Fig. 1 | Expression of Archon1 and SomArchon in mouse brain. a–d, Representative images of mouse brain slices expressing Archon1 (**a**, **b**) and SomArchon (**c**, **d**) (CAG promoter, via IUE) imaged with a wide-field microscope with 10× (**a**, **c**) and 40× (**b**, **d**) objective lenses (from $n = 7$ slices from 2 mice each). **e**, **f**, Normalized EGFP fluorescence along white arrows shown in **b**, **d**, respectively. Black dots correspond to resolvable cells. **g**, Number of resolvable cells per FOV for brain slices expressing Archon1 or SomArchon (2.4 ± 2.5 and 22 ± 9 neurons per FOV ($350 \times 415\ \mu m^2$) for Archon1 and SomArchon, respectively). Mean ± s.d.; $n = 7$ slices from 2 mice each; box plots as in Fig. 1. Further confocal analysis with larger FOVs of $500 \times 500 \times 50\ \mu m^3$ revealed that SomArchon can resolve around 15 times more neurons in the cortex than Archon1 ($n = 4$, 8, 9, 11, 11, 18, and 20 neurons from 7 slices for Archon1, versus $n = 180$, 187, and 137 neurons from 3 slices for SomArchon). **h**, Representative confocal images of neurons in cortex layer 2/3 (left), hippocampus (middle), and striatum (right) expressing Archon1 (top) and SomArchon (bottom). **i–k**, EGFP fluorescence along a neurite, normalized to soma, for neurons expressing Archon1 (left) or SomArchon (right) in cortex layer 2/3 (**i**, $n = 39$ and 37 neurites from 10 cells from 2 mice each), hippocampus (**j**, $n = 20$ and 34 neurites from 9 and 17 cells from 2 mice each), and striatum (**k**, $n = 17$ and 20 neurites from 7 cells from 2 mice each). Box plots as in Fig. 1. $^*P < 0.002$ compared to Archon1 at corresponding position away from the soma; n.s., not significant. Two-sample Kolmogorov–Smirnov test, see Supplementary Table 2. **l–u**, Representative confocal fluorescence images of brain slices expressing Archon (left) or SomArchon (right) via IUE (**l–q**) or AAV injection (**r–u**) in cortex layer 2/3 (**n**, **o**; $n = 8$ slices from 2 mice), hippocampus (**p**, **q**; $n = 8$ slices from 2 mice), and striatum (**t**, **u**; $n = 6$ slices from 2 mice). Green, EGFP; magenta, Nissl staining. Scale bars, 100 μm (**a–d**), 50 μm (**h**, **n–q**, **t**, **u**), 250 μm (**l**, **m**, **r**, **s**).

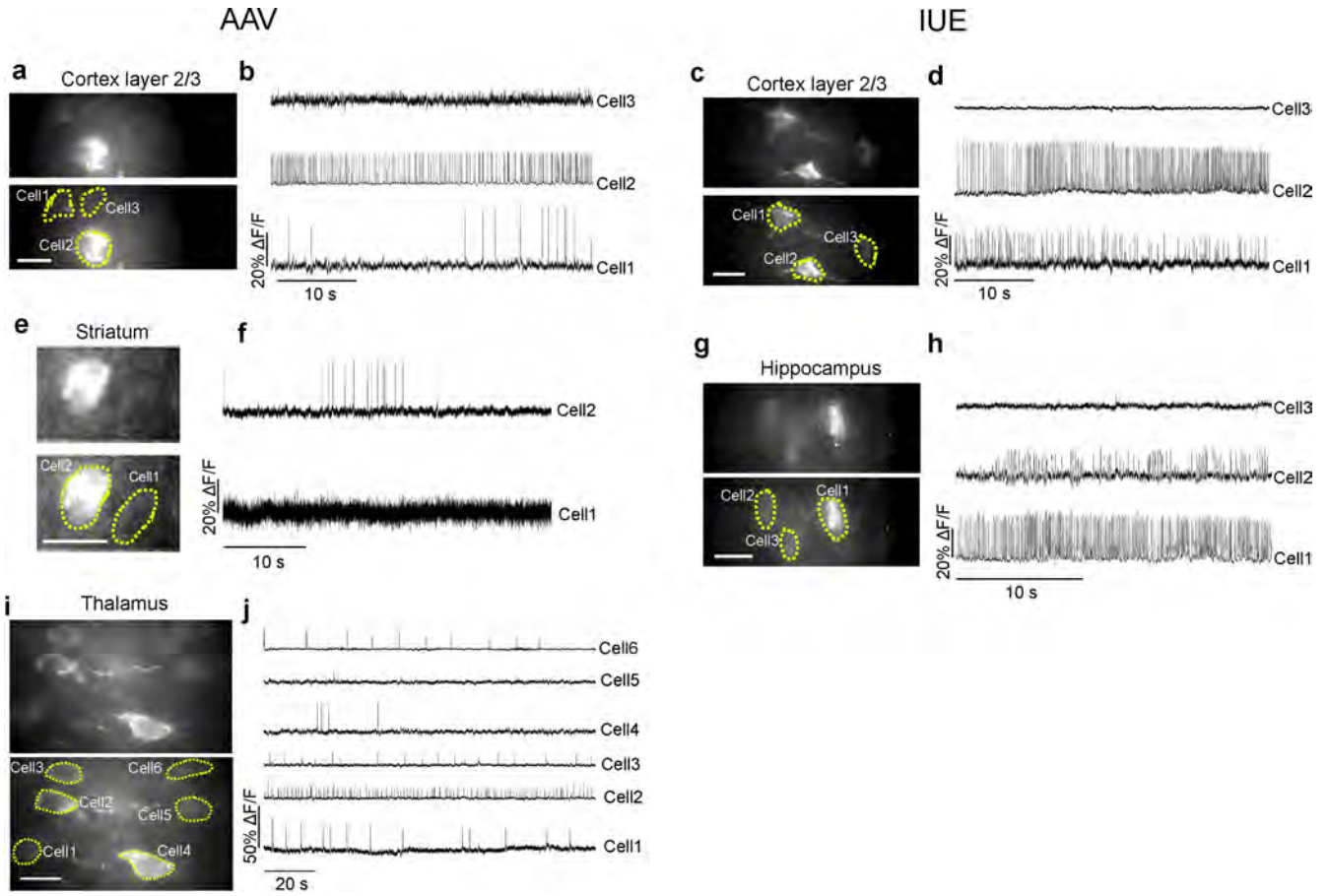

Extended Data Fig. 2 | Voltage imaging using SomArchon in mouse brain slices. a–**d**, Representative fluorescence wide-field images of cortex layer 2/3 neurons expressing SomArchon via AAV transduction (**a**) or IUE (**c**) with selected ROIs (bottom), and corresponding fluorescence traces (**b**, **d**; $n = 6$ and 13 slices from 2 and 4 mice for AAV transduction and IUE, respectively). Acquisition rate, 632 Hz (**b**) or 440 Hz (**d**). **e**, **f**, Representative fluorescence wide-field images of striatal neurons expressing SomArchon via AAV transduction (top) with selected ROIs (bottom) (**e**), and corresponding fluorescence traces (**f**; $n = 8$ slices from 2 mice). Acquisition rate, 733 Hz. **g**, **h**, Representative fluorescence wide-field images of hippocampal neurons expressing SomArchon via IUE (top) with selected ROIs (bottom) (**g**), and corresponding fluorescence traces (**h**; $n = 8$ slices from 2 mice). Acquisition rate, 333 Hz. **i**, **j**, Fluorescence wide-field images of thalamus neurons expressing SomArchon (top) via AAV transduction with selected ROIs (bottom) (**i**), and corresponding fluorescence traces (**j**; $n = 5$ slices from 2 mice). Acquisition rate, 333 Hz. Scale bars, 25 μm.

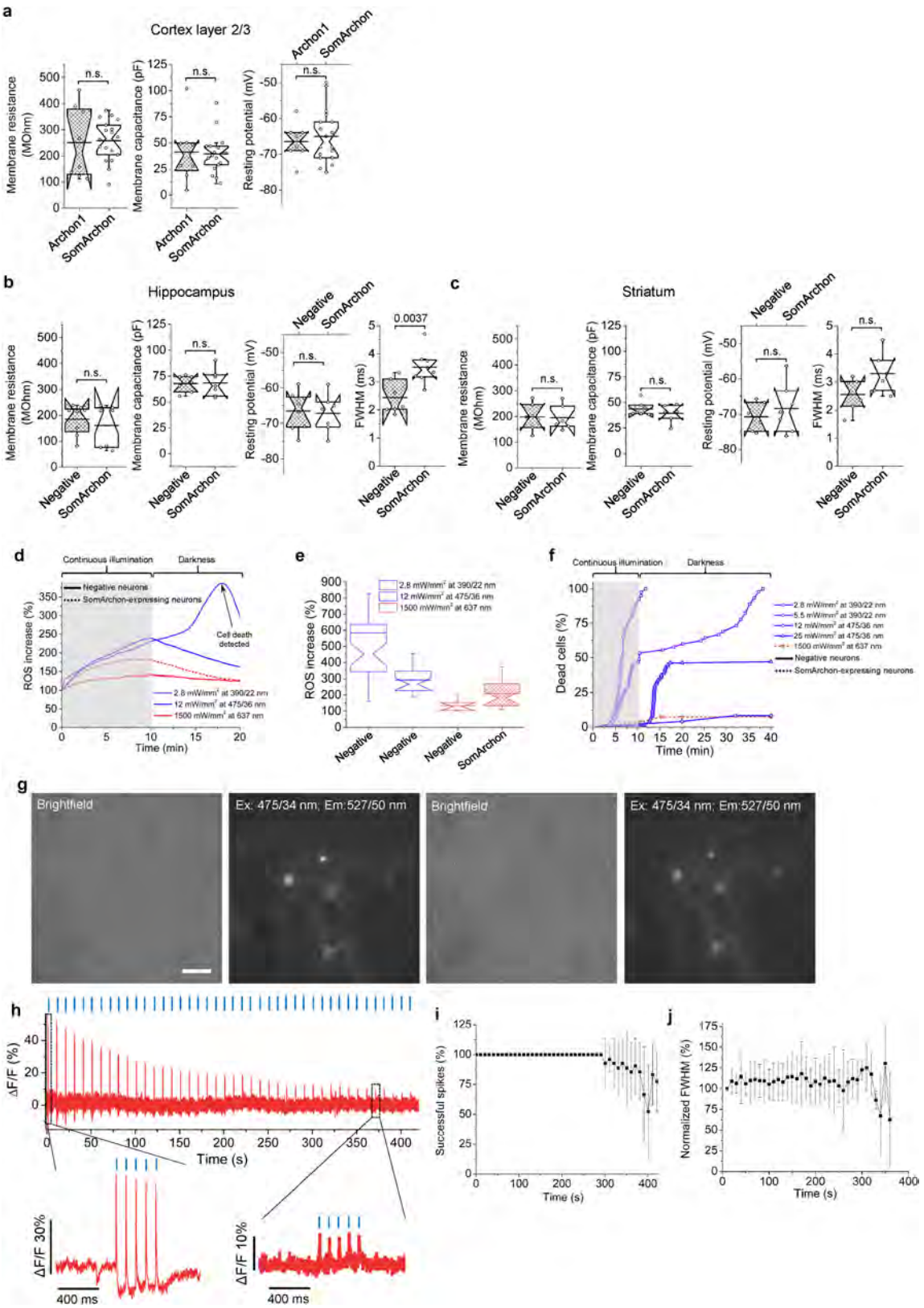

Extended Data Fig. 3 | See next page for caption.

Extended Data Fig. 3 | Expression of SomArchon and voltage imaging do not alter membrane properties or cause phototoxicity. a, Membrane properties of neurons expressing Archon (hashed boxes) or SomArchon (open boxes) in cortex layer 2/3 brain slices ($P = 0.8026$, 0.8895, and 0.8236 for resistance, capacitance, and resting potential, respectively; two-sided Wilcoxon rank-sum test comparing Archon1 versus SomArchon; $n = 8$ and 18 cells from 1 and 2 mice for Archon1 and SomArchon, respectively). **b**, Similar to **a** but in hippocampus ($P = 0.6294$, 0.9720, 0.8880, and 0.0037 for resistance, capacitance, resting potential, and FWHM, respectively; two-sided Wilcoxon rank-sum test comparing negative versus SomArchon; $n = 8$ and 7 cells from 2 mice each for negative and SomArchon for resistance and resting potential; $n = 7$ and 7 cells from 2 mice each for negative and SomArchon for capacitance; $n = 7$ and 8 cells from from 2 mice each for negative and SomArchon for FWHM). **c**, Similar to **a** but in striatum ($P = 0.7380$, 0.8357, 0.7751, and 0.0931 for resistance, capacitance, resting potential and FWHM, respectively; two-sided Wilcoxon rank-sum test comparing negative and SomArchon; $n = 7$ and 6 cells from 2 mice each for negative and SomArchon for resistance and capacitance; $n = 6$ and 7 cells from 2 mice each for negative and SomArchon for resting potential; $n = 6$ and 6 cells from 2 mice each for negative and SomArchon for FWHM). **d**, Changes in relative ROS concentration (normalized to that before illumination) over time in negative (solid line) and SomArchon-expressing (dashed line) cultured mouse neurons under various illumination protocols. **e**, Maximal increase in ROS concentration during continuous illumination for conditions performed in **d** ($n = 45$, 24, and 8 negative neurons from 2, 2, and 1 cultures for 390/22 nm, 475/36 nm, and 637 nm illumination, respectively; $n = 24$ SomArchon-expressing neurons for 637 nm illumination from 1 culture). **f**, Cell death for negative (solid line) and SomArchon-expressing (dashed line) cultured neurons at DIV 14–18 under various illumination protocols ($n = 45$, 35, 91, 40, and 27 neurons from 2, 1, 2, 1, and 1 cultures, respectively, for 390/22 nm at 2.8 mW mm^{-2}, 390/22 nm at 5.5 mW mm^{-2}, 475/36 nm at 12 mW mm^{-2}, 475/36 nm at 25 mW mm^{-2}, and 637 nm at 1,500 mW mm^{-2} illumination). **g**, Bright-field and fluorescence images of representative neurons expressing SomArchon before and after 10 min of continuous 637-nm laser illumination at 1,500 mW mm^{-2}, followed by 10 min in darkness (93% of imaged cells did not exhibit noticeable changes in morphology; $n = 27$ cells from 1 culture; non-illuminated cells did not show any changes in morphology; $n = 10$ cells from 1 cultures). Scale bar, 50 μm. **h**, Representative SomArchon fluorescence trace from neuron co-expressing SomArchon and CoChR-$K_v2.1_{motif}$. **i**, Normalized spike rates (to initial value) elicited by blue light illumination dropped after 300 s of continuous recording, owing to decrease in spike amplitude as a result of photobleaching ($n = 10$ neurons from 1 culture; plotted as mean ± s.d.). **j**, Normalized (to initial value) FWHM of spikes elicited by continuous light exposure as in **h**. Box plots as in Fig. 1.

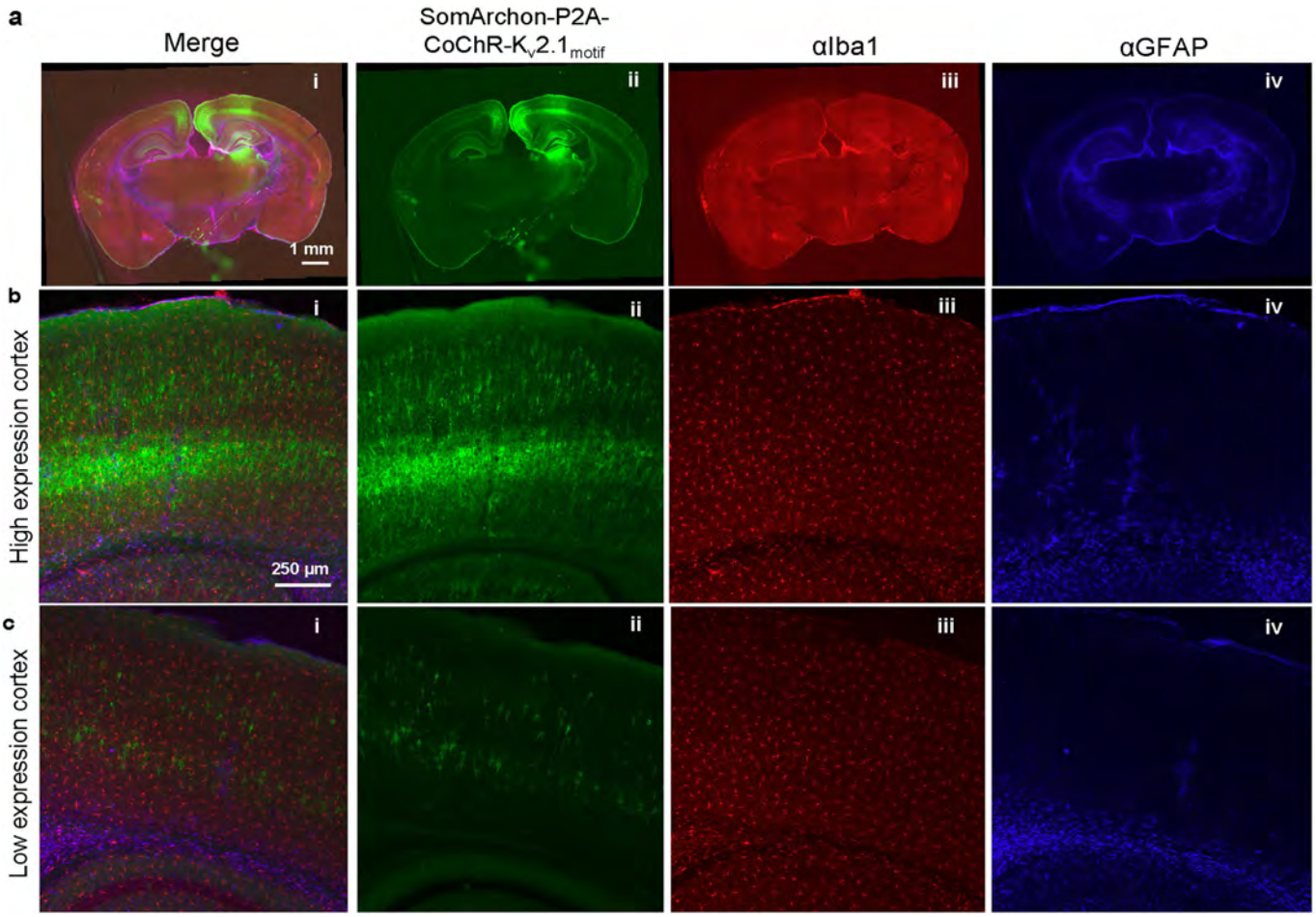

Extended Data Fig. 4 | SomArchon expression in vivo does not cause gliosis. SomArchon was expressed in the mouse brain by AAV2.9-Syn-SomArchon-P2A-CoChR-K$_V$2.1$_{motif}$ injection into the cortex in P0 Swiss Webster mice. Brain tissues were analysed 63 days after viral injection. Merged fluorescence images from 50-μm-thick coronal sections (i) were visualized via EGFP fluorescence of SomArchon (ii), anti-IBA1 immunofluorescence (iii), and anti-GFAP immunofluorescence (iv; $n = 4$ slices from 2 mice). **a**, Expression throughout the coronal section. **b**, Zoomed-in view of the virally injected area (high-expression cortex). **c**, Zoomed-in view of the non-injected contralateral hemisphere (low-expression cortex). The commonly used glial and microglial markers GFAP and IBA1 appeared similarly in both hemispheres, suggesting that expression of SomArchon did not cause gliosis. Scale bars, 1 mm (**a**), 250 μm (**b**, **c**).

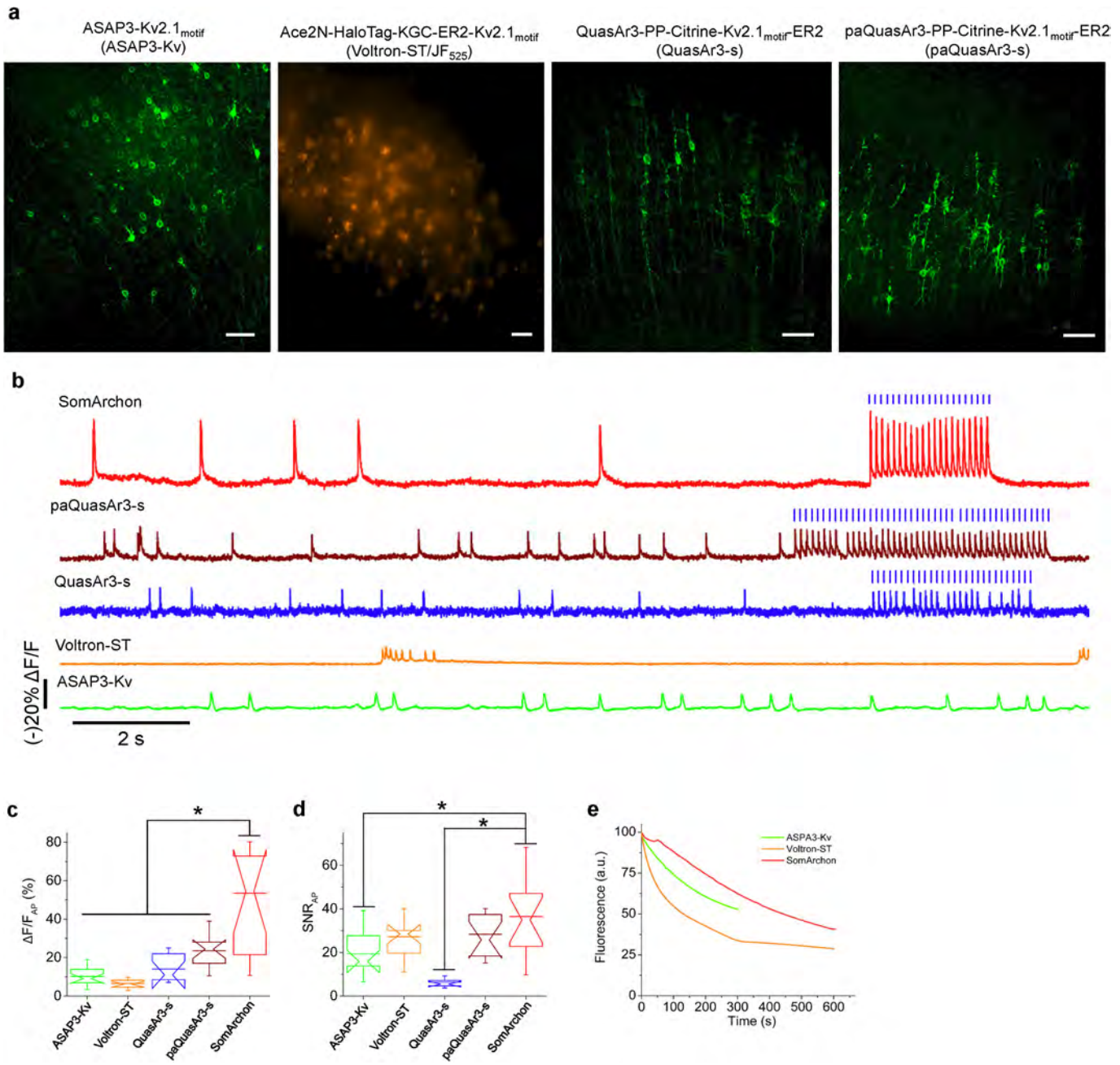

Extended Data Fig. 5 | Side-by-side comparison of next-generation voltage indicators in mouse brain slices. a, Representative fluorescence images of mouse cortex layer 2/3 neurons expressing ASAP3-$K_V2.1_{motif}$ (ASAP3-Kv), Ace2N-HaloTag-KGC-ER2-$K_V2.1_{motif}$ (Voltron-ST/JF_{525}), QuasAr3-PP-mCitrine-$K_V2.1_{motif}$-ER2 (QuasAr3-s), and paQuasAr3-PP-mCitrine-$K_V2.1_{motif}$-ER2 (paQuasAr3-s). ASAP3-Kv, QuasAr3-s and paQuasAr3-s were visualized via cpGFP, mCitrine, and mCitrine fluorescence, respectively, using laser excitation at 488 nm and emission at 525/50 nm under a confocal microscope. Voltron-ST/JF_{525} was visualized via JF525 fluorescence using LED excitation at 510/25 nm and emission at 545/40 nm under a wide-field microscope. Scale bar, 50 μm. **b**, Single-trial optical recordings of ASAP3-Kv (green) and Voltron-ST/JF_{525} (orange) fluorescence responses during neuronal activity evoked with 4-aminopyridine, and QuasAr3-s (blue), paQuasAr3-s (brown), and SomArchon (red) fluorescence responses during neuronal activity evoked with CoChR-mTagBFP2-$K_V2.2_{motif}$. Acquisition rate, about 500 Hz. Blue light pulses (470/20 nm, 2 ms per pulse, 10 Hz; vertical blue bars) were used to activate CoChR to evoke spiking. **c**, **d**, Quantification of $\Delta F/F$ (**c**) and SNR (**d**) per action potential across all recordings ($n = 18$, 14, 9, 13, and 14 neurons from 1, 2, 2, 2, and 2 mice for ASAP3-Kv, Voltron-ST/JF_{525}, QuasAr3-s, paQuasAr3-s, and SomArchon, respectively). Box plots as in Fig. 1. *$P < 0.01$, Wilcoxon rank-sum test; see Supplementary Table 2 for statistics. **e**, Photobleaching curves of ASAP3-Kv, Voltron-ST/JF_{525}, and SomArchon under continuous illumination ($n = 11$, 8, and 17 neurons from 1 culture, respectively).

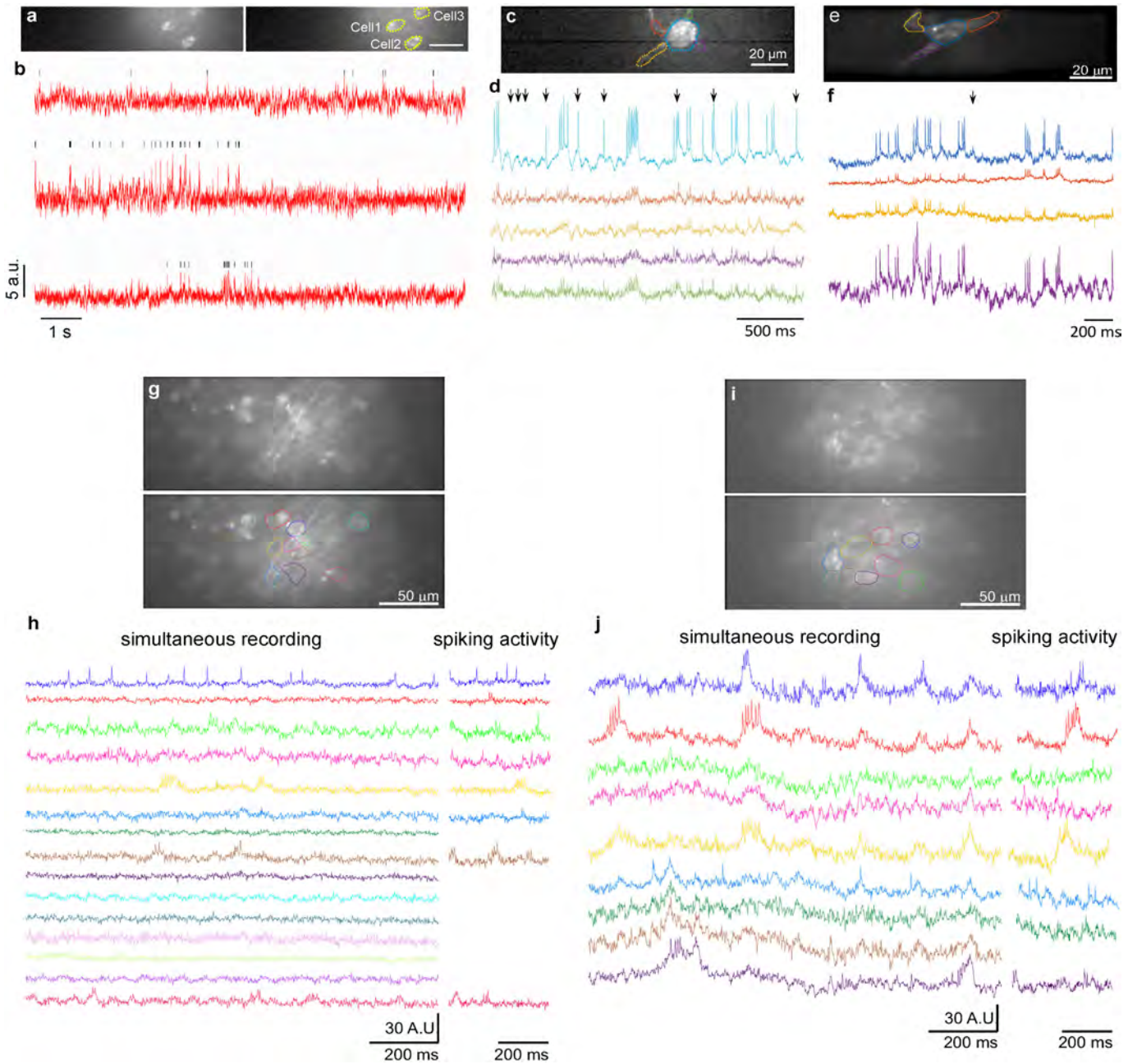

Extended Data Fig. 6 | SomArchon enables both local dendritic and population imaging of neurons in multiple brain regions in vivo. **a**, Fluorescence images of selected FOV in motor cortex (left) with selected ROIs corresponding to somas of 3 neurons (right) ($n = 1$ FOV from 1 mouse). Scale bar, 50 µm. **b**, Representative fluorescence traces from **a** with detected spikes (black ticks). **c**, Fluorescence image of a hippocampal neuron expressing SomArchon with ROIs selected at the soma and on 4 proximal dendrites ($n = 1$ neuron from 1 mouse). Scale bar, 20 µm. **d**, Optical voltage traces from the selected ROIs shown in **c**. **e**, Fluorescence image of a striatal neuron expressing SomArchon with ROIs selected at the soma and on 3 proximal dendrites ($n = 1$ neuron from 1 mouse). Scale bar, 20 µm. **f**, Optical voltage traces from the selected ROIs shown in **e**. Black arrows in **d**, **f** highlight instances in which dendritic voltages differed visibly from those on the soma. **g**–**k**, In vivo population voltage imaging in the hippocampus CA1 region ($n = 14$ FOVs from 3 mice). **g**, **i**, Average intensity projection image for each video (top), with identified ROIs (bottom). **h**, **j**, Optical voltage traces for each neuron shown in **g**, **i**, respectively, with colours matching corresponding ROI colours. Panels show 1.2 s of simultaneously recorded voltage for all neurons (left), and a period with prominent spikes (right). Image acquisition rate for all recordings, 826 Hz.

a

	Firing Rate (Hz)	Area (um²)	ISI (mean+/- SD)
Cell 1	2	187.59	403.8+/-881.5
Cell 2	1.6686	144.073	530.2+/-953.4
Cell 3	2.7771	172.803	300.4+/-542.4
Cell 4	2.9167	175.338	273.3+/-509.6
Cell 5	7.933	175.76	124.4+/-198.3
Cell 6	13.2778	89.993	71.3+/-88.6
Cell 7	15.1389	69.29	64.8+/-87.6
Cell 8	11.7222	86.612	83.7+/-98.9
Cell 9	29.95	131.82	33.2+/-39.8
Cell 10	2.0167	117.455	462.6+/-586.2
Cell 11	2.7667	149.143	351.2+/-470.7
Cell 12	5.4271	361.66	182.4+/-133.1
Cell 13	14.3626	181.253	69.1+/-96.8
Cell 14	23.1753	191.393	43.0+/-44.0

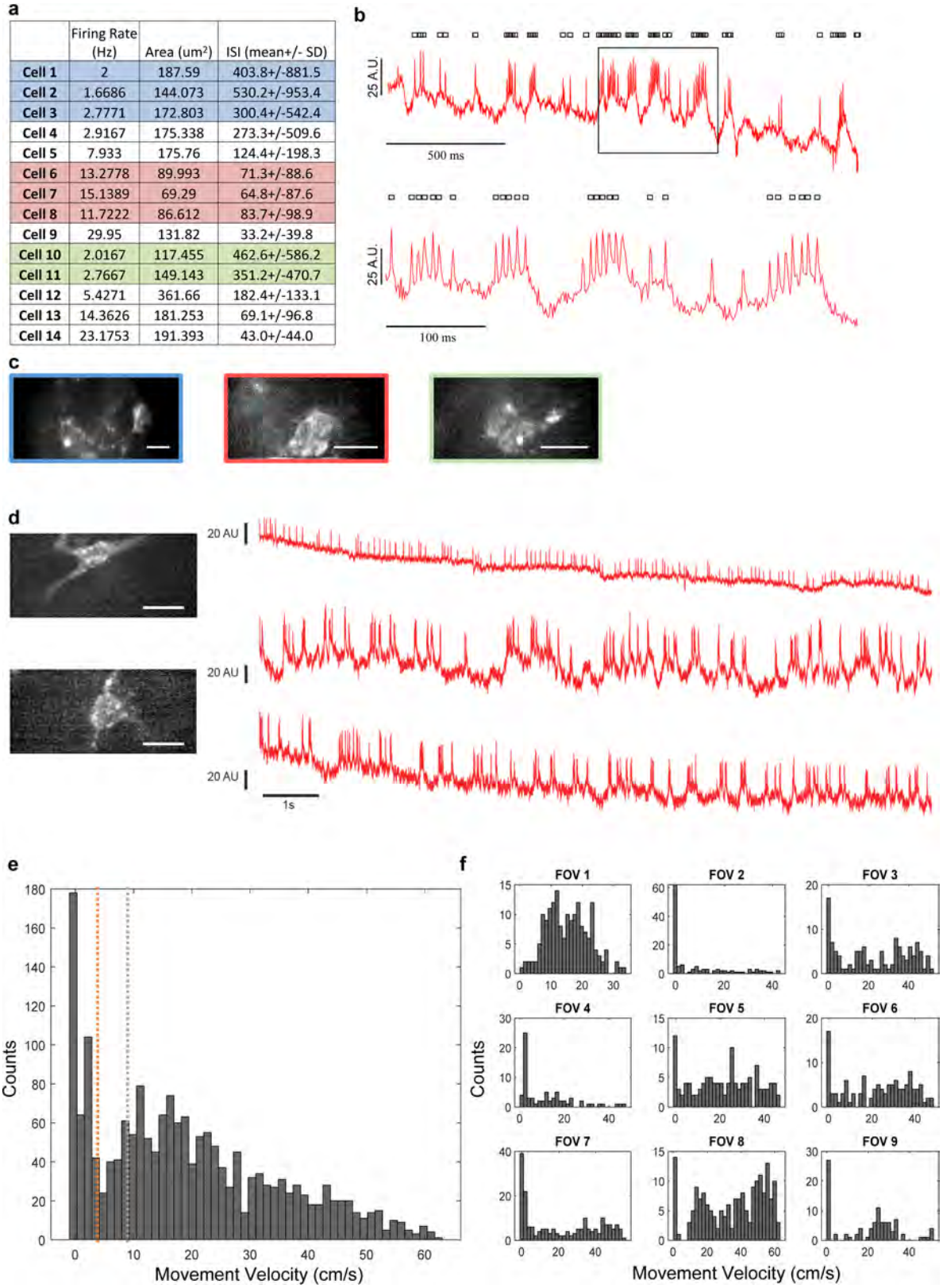

Extended Data Fig. 7 | See next page for caption.

Extended Data Fig. 7 | Properties of striatal neurons and movement thresholds. a, Average firing rate, size, and interspike interval (ISI) for 14 neurons recorded in 9 FOV in 2 mice. Cells simultaneously recorded in the same FOV are colour-coded (blue, red and green). Cells in rows with a white background were recorded individually. **b**, Selected trace from cell 9 exhibiting spike bursting (top), and a zoomed-in view of the boxed region (bottom). A.U., arbitrary unit. Identified spikes are indicated by the marks on top of the trace. **c**, Single frame images for FOVs with multiple neurons, colour-coded as in **a**. Scale bars, 20 μm. **d**, Representative optical traces from two Cre-dependent SomArchon-expressing striatal cholinergic interneurons in a ChAT-Cre mouse (left; scale bar, 20 μm), recorded in 3 sessions, while mouse was awake with head fixed and navigating a spherical treadmill ($n = 2$ neurons from 1 mouse). Top trace corresponds to top neuron on left; two bottom traces correspond to bottom neuron. Image acquisition rate, 826 Hz. **e**, Histogram of instantaneous movement speeds for all FOVs shown in Fig. 3 (nine FOVs in two mice). Instantaneous movement speed was calculated as average speed during each 0.5-s time interval. Red line, threshold for low movement speed identification; green line, threshold for high movement speed identification. **f**, Histogram of instantaneous movement speed for individual FOVs analysed.

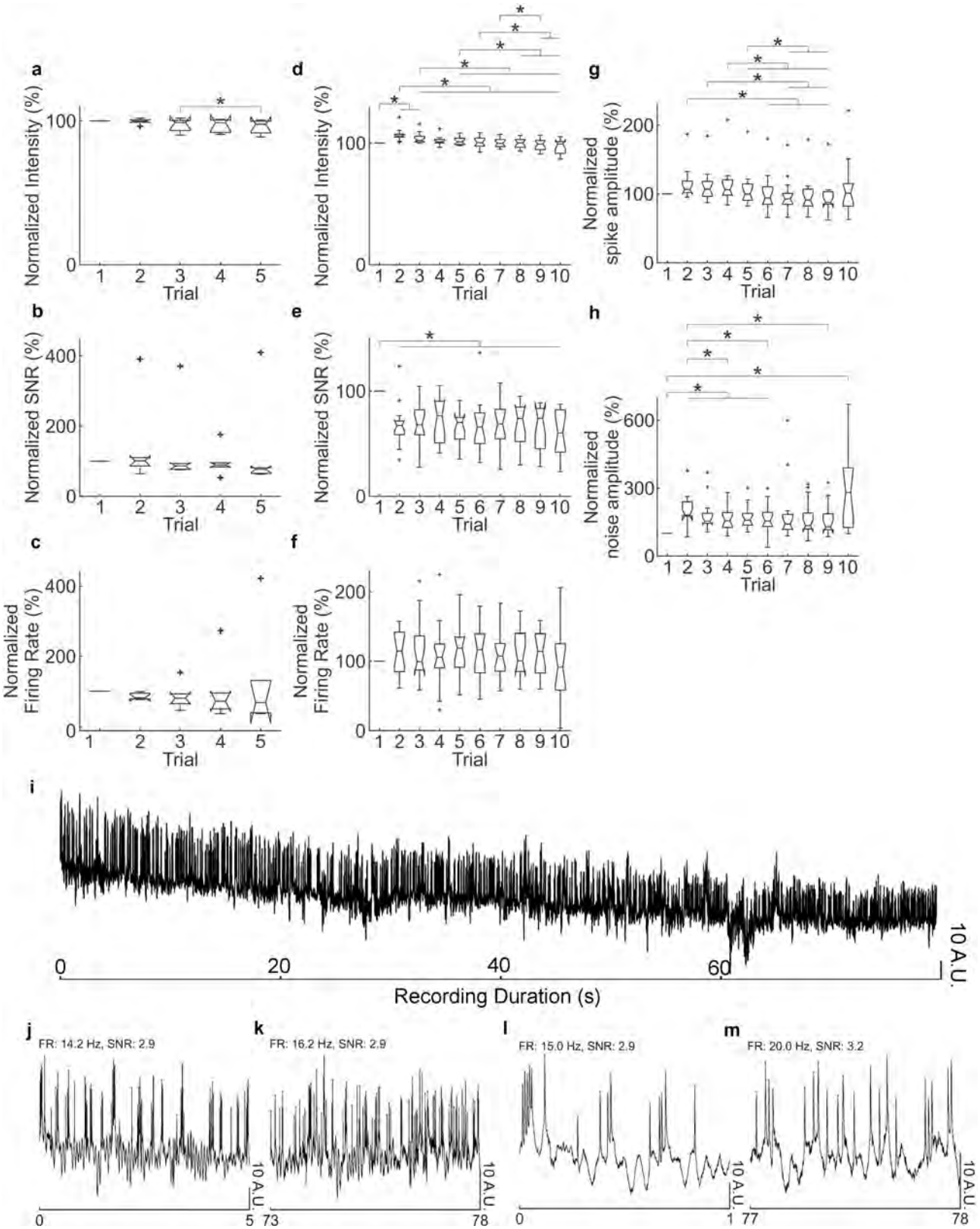

Extended Data Fig. 8 | See next page for caption.

Extended Data Fig. 8 | In vivo SomArchon performance over time in the striatum and hippocampus of awake mice. a–h, Average fluorescence intensity, SNR per spike, and firing rates of neurons in the striatum and hippocampus of awake mice, over multiple trials. **a–c**, In each striatal recording session, we performed 5 trials, each 12-s long, with inter-trial intervals of 30–60 s. Average fluorescence intensity (**a**) decreased slightly; spike SNR (**b**) and firing rates (**c**) remained constant throughout the recording session (repeated-measures analysis of variance (ANOVA), $n = 6$ neurons in 5 FOVs from 1 mouse). **d–h**, In each hippocampal recording session, we performed 10 trials, each 6-s long, with inter-trial intervals of 20–30 s. Average fluorescence intensity (**d**) showed a slight but significant decrease across trials. SNR (**e**) decreased between the first and second trials but not afterwards, and firing rate (**f**) remained constant. Spike amplitude (**g**) fluctuated randomly over trials, and there was a significant increase in baseline noise (**h**) between the first and second trials (repeated-measures ANOVA; $^*P < 0.05$, post-hoc test: Tukey's HSD test, $n = 16$ neurons in 7 FOVs from 4 mice, Supplementary Table 2). Measurements were normalized to the first trial for each neuron. Box plots as in Fig. 4. **i–m**, A representative continuous optical trace of a hippocampal neuron over 80 s in an awake, head-fixed mouse (**i**), with zoomed-in views (**j–m**) at the beginning and end of the recording highlighting comparable firing rates and SNRs ($n = 16$ neurons in 7 FOVs from 4 mice).

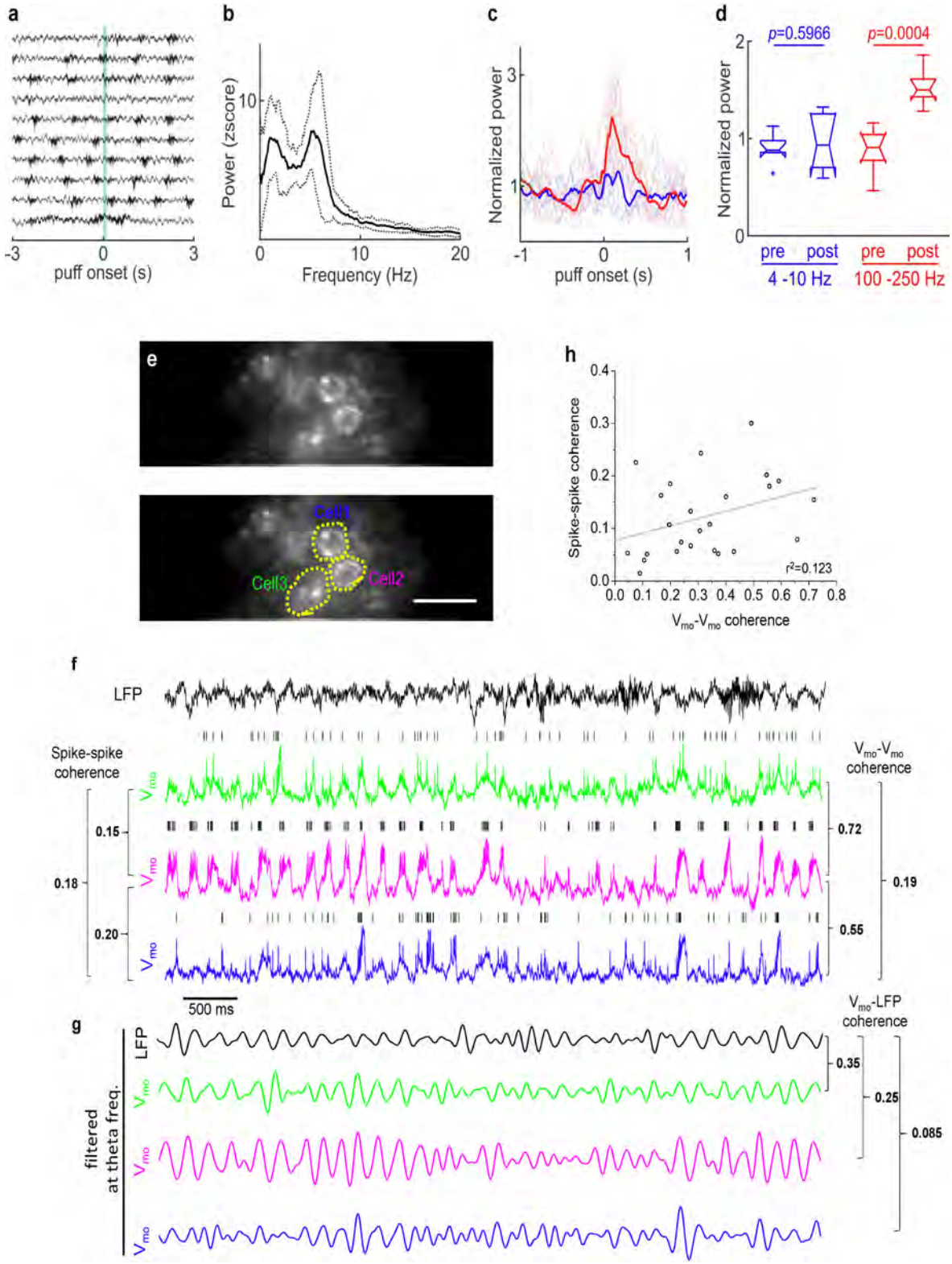

Extended Data Fig. 9 | Analysis of LFP and subthreshold membrane voltage oscillation in the hippocampus. a, Example hippocampal LFP recordings from a session with ten trials, aligned to the onset of an air puff (green shading) directed to one eye in awake, head-fixed mice. **b**, LFP power spectrum shows strong theta oscillations. Mean ± s.d., $n = 10$ trials in 1 session. **c**, Oscillation power at high frequencies (100–250 Hz, red) and at theta frequencies (blue), aligned to puff onset. Each thin line represents an individual recording session, and the thick lines denote means ($n = 7$ sessions in 4 mice). **d**, Eye puff evoked a significant increase in LFP power at high frequency, but not at theta frequency (theta frequency $P = 0.5966$; high frequency $P = 0.0004$; two-tailed paired Student's t-test, $n = 7$ sessions in 4 mice). Box plots as in Fig. 4. **e**, Fluorescence image of a representative FOV (top) with selected ROIs (bottom). **f**, Membrane voltage recorded optically (V_{mo}) from neurons identified in **e**, and simultaneously recorded LFPs. Black vertical ticks above V_{mo}s denote spikes. Spike–spike coherence values between neurons are shown on the left and V_{mo}–V_{mo} theta coherence values are shown on the right. **g**, Theta-frequency-filtered LFPs and V_{mo}s for the four traces shown in **f**. V_{mo}–LFP coherence values are shown on the right. **h**, Scatter plot of V_{mo}–V_{mo} theta frequency coherence and spike–spike coherence from all neuron pairs, fitted with a linear regression ($n = 25$ pairs, $P = 0.08$, t-statistic, $r^2 = 0.12$).

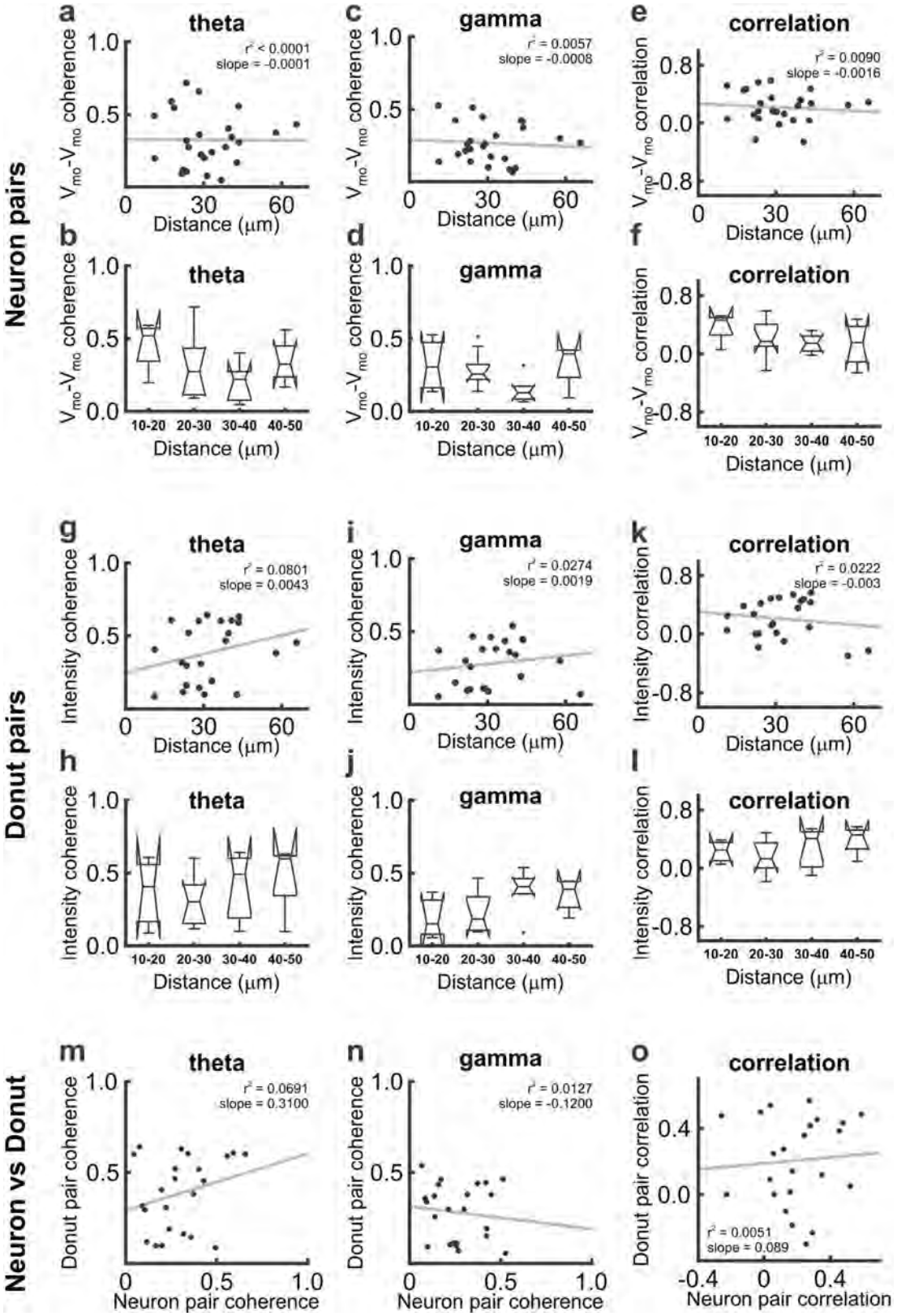

Extended Data Fig. 10 | See next page for caption.

Extended Data Fig. 10 | Pairwise coherence and correlation measures over spatial distance. To investigate the potential of background fluorescence signals under wide-field imaging to produce shared crosstalk signals on neuron pairs, we examined the relationship of various coherence and correlation measures between neurons and background fluorescence over spatial distance. **a**, **b**, Pairwise coherence at theta frequencies between neurons. V_{mo}–V_{mo} coherence did not decrease significantly with spatial distance. (**a**, $n = 25$ pairs analysed with spatial distance of 11–66 μm, centre to centre; **b**, $n = 23$ pairs within 50 μm of each other; $F = 1.44$, $P = 0.26$, one-way ANOVA). **c**, **d**, Pairwise V_{mo}–V_{mo} coherence at gamma frequencies (30–50 Hz) was not dependent on spatial distance (**c**, $n = 25$ pairs; **d**, $n = 23$ pairs within 50 μm of each other; $F = 2.10$, $P = 0.13$, one-way ANOVA). **e**, **f**, Pairwise correlation between neurons did not decrease significantly with spatial distance (**e**, $n = 25$ pairs; **f**, $n = 23$ pairs within 50 μm of each other; $F = 1.00$, $P = 0.42$, one-way ANOVA). **g**–**l**, Same analysis as in **a**–**f** performed in background doughnut ROIs surrounding each neuron (Methods). Similar to results from neuron pairs, we found that theta frequency coherence between background doughnut ROIs was not dependent on spatial distance (**g**, $n = 23$ pairs; **h**, $n = 21$ pairs; $F = 0.65$, $P = 0.59$, one-way ANOVA), nor was gamma frequency coherence (**i**, $n = 23$ pairs; **j**, $n = 21$ pairs; $F = 1.93$, $P = 0.16$, one-way ANOVA), or the correlation coefficient (**k**, $n = 23$ pairs; **l**, $n = 21$ pairs; $F = 1.02$, $P = 0.41$, one-way ANOVA). **m**–**o**, The coherence between neurons and their corresponding doughnuts was not correlated at theta frequency (**m**), at gamma frequency (**n**), or for the Pearson correlation coefficients (**o**). Box plots are as in Fig. 4.

nature research

Corresponding author(s): Xue Han, Edward S. Boyden

Last updated by author(s): Apr 25, 2019

Reporting Summary

Nature Research wishes to improve the reproducibility of the work that we publish. This form provides structure for consistency and transparency in reporting. For further information on Nature Research policies, see Authors & Referees and the Editorial Policy Checklist.

Statistics

For all statistical analyses, confirm that the following items are present in the figure legend, table legend, main text, or Methods section.

n/a	Confirmed
☐	☒ The exact sample size (*n*) for each experimental group/condition, given as a discrete number and unit of measurement
☐	☒ A statement on whether measurements were taken from distinct samples or whether the same sample was measured repeatedly
☐	☒ The statistical test(s) used AND whether they are one- or two-sided *Only common tests should be described solely by name; describe more complex techniques in the Methods section.*
☒	☐ A description of all covariates tested
☐	☒ A description of any assumptions or corrections, such as tests of normality and adjustment for multiple comparisons
☐	☒ A full description of the statistical parameters including central tendency (e.g. means) or other basic estimates (e.g. regression coefficient) AND variation (e.g. standard deviation) or associated estimates of uncertainty (e.g. confidence intervals)
☐	☒ For null hypothesis testing, the test statistic (e.g. *F*, *t*, *r*) with confidence intervals, effect sizes, degrees of freedom and *P* value noted *Give P values as exact values whenever suitable.*
☒	☐ For Bayesian analysis, information on the choice of priors and Markov chain Monte Carlo settings
☒	☐ For hierarchical and complex designs, identification of the appropriate level for tests and full reporting of outcomes
☒	☐ Estimates of effect sizes (e.g. Cohen's *d*, Pearson's *r*), indicating how they were calculated

Our web collection on statistics for biologists contains articles on many of the points above.

Software and code

Policy information about availability of computer code

Data collection	Data were recorded using NIS-Elements Advance Research software v4.60.00, HC Image 4.5, OmniPlex system 1.6.0, and MATLAB 2014b.
Data analysis	Data were analyzed offline using NIS-Elements Advance Research software v4.60.00, OriginPro 8 (OriginLab), C, Excel 2016 (Microsoft), ImageJ(Fiji) 1.52i, Python 3.6.8. and 3.7.1, BoxPlotR, and MATLAB 2017a, 2018a, 2018b.

For manuscripts utilizing custom algorithms or software that are central to the research but not yet described in published literature, software must be made available to editors/reviewers. We strongly encourage code deposition in a community repository (e.g. GitHub). See the Nature Research guidelines for submitting code & software for further information.

Data

Policy information about availability of data

All manuscripts must include a data availability statement. This statement should provide the following information, where applicable:

- Accession codes, unique identifiers, or web links for publicly available datasets
- A list of figures that have associated raw data
- A description of any restrictions on data availability

Code availability. Computer codes used to generate results for this study are available at https://github.com/HanLabBU/somarchon-imaging.
Data availability. The data that support the findings of this study are available from the corresponding author upon reasonable request; raw data essential to the work is avalible online at nature.com. Sequences of the reported proteins are available at Genbank at the following accession codes: SomArchon MN091368; SomArchon-P2A-CoChR-KV2.1motif, MN091369.

Field-specific reporting

Please select the one below that is the best fit for your research. If you are not sure, read the appropriate sections before making your selection.

☒ Life sciences ☐ Behavioural & social sciences ☐ Ecological, evolutionary & environmental sciences

For a reference copy of the document with all sections, see nature.com/documents/nr-reporting-summary-flat.pdf

Life sciences study design

All studies must disclose on these points even when the disclosure is negative.

Sample size	No statistical methods were used to estimate sample size for animal studies throughout. We did not perform a power analysis, since our goal was to create a new technology; in the reference (Dell, R. B., Holleran, S. & Ramakrishnan, R. Sample size determination. ILAR. J. 43, 207–213 (2002)), as recommended by the NIH, "In experiments based on the success or failure of a desired goal, the number of animals required is difficult to estimate..." As noted in the aforementioned paper, "The number of animals required is usually estimated by experience instead of by any formal statistical calculation, although the procedures will be terminated [when the goal is achieved]." These numbers reflect our past experience in developing neurotechnologies.
Data exclusions	Voltage imaging datasets with significant motion or where no spikes were detected were excluded from analysis. Significant motion was defined as a shift for more than 20 µm in any direction. In Extended Data Figure 1i,j,k data points that corresponded to overlapping neurites were excluded. Data exclusion criteria were not pre-established.
Replication	All attempts at replication were successful. The detailed experimental protocols are provided to facilitate replication by others.
Randomization	There were no treatment conditions to compare in this study. All recording sessions were randomly performed with different voltage sensors or in different brain regions. On recording days, cultured cells or brain slices expressing specific sensors were known. On in vivo recording days, mouse conditions were known. Voltage trace extraction and subsequent analysis were performed with the investigators unaware of specific mouse conditions. For analysis of movement modulation of striatal neuron spiking, a computer algorithm was used to identify periods with different movement parameters. For analysis of spike-phase relationships, or subthreshold membrane voltage relationships, a computer algorithm was used across all conditions. For histology,- sections were selected and images were taken from slides by a researcher not aware of the conditions or antibody used. Cells were also counted and quantified from these sections by a researcher blinded to the experimental conditions or antibody used.
Blinding	

Reporting for specific materials, systems and methods

We require information from authors about some types of materials, experimental systems and methods used in many studies. Here, indicate whether each material, system or method listed is relevant to your study. If you are not sure if a list item applies to your research, read the appropriate section before selecting a response.

Materials & experimental systems

n/a	Involved in the study
☐	☒ Antibodies
☒	☐ Eukaryotic cell lines
☒	☐ Palaeontology
☐	☒ Animals and other organisms
☒	☐ Human research participants
☒	☐ Clinical data

Methods

n/a	Involved in the study
☒	☐ ChIP-seq
☒	☐ Flow cytometry
☒	☐ MRI-based neuroimaging

Antibodies

Antibodies used	Primary antibodies anti-GFAP (1:250, Clone N206/A8, Neuromab) and anti-IBa1 (1:500, 019-19741, Wako Chemicals) and secondary antibodies Alexa Fluor 568 (1:1000, Goat anti-Mouse IgG (H+L) Cross-Adsorbed Secondary Antibody, A11004, InVitrogen) 633 secondary antibodies (1:1000, Goat anti-Rabbit IgG (H+L) Cross-Adsorbed Secondary Antibody, A21070, InVitrogen)were used in the study.
Validation	For anti-GFAP please see: http://neuromab.ucdavis.edu/datasheet/N206A_8.pdf For anti IBa1, please see: http://www.e-reagent.com/uh/Shs.do?now=1550070200673 Validation methods are references in Methods.

Animals and other organisms

Policy information about studies involving animals; ARRIVE guidelines recommended for reporting animal research

Laboratory animals	Species, strain, sex, and age are reported for each experiment in the Methods
Wild animals	The study did not involve wild animals

Field-collected samples	This study did not involve samples collected in the field.
Ethics oversight	Boston University Institutional Animal Care and Use and Biosafety Committee, Massachusetts Institute of Technology Institutional Animal Care and Use and Biosafety Committee

Note that full information on the approval of the study protocol must also be provided in the manuscript.

frontiers in Neuroscience

METHODS
published: 21 February 2019
doi: 10.3389/fnins.2019.00128

Reimplantable Microdrive for Long-Term Chronic Extracellular Recordings in Freely Moving Rats

Leopoldo Emmanuel Polo-Castillo[1,2], Miguel Villavicencio[3], Leticia Ramírez-Lugo[4], Elizabeth Illescas-Huerta[4], Mario Gil Moreno[3], Leopoldo Ruiz-Huerta[1,2], Ranier Gutierrez[3], Francisco Sotres-Bayon[4]* and Alberto Caballero-Ruiz[1,2]**

[1] Instituto de Ciencias Aplicadas y Tecnología, Universidad Nacional Autónoma de México, Mexico City, Mexico, [2] National Laboratory for Additive and Digital Manufacturing, Mexico City, Mexico, [3] Laboratory of Neurobiology of Appetite, Department of Pharmacology, Centro de Investigación y de Estudios Avanzados, Mexico City, Mexico, [4] Instituto de Fisiología Celular - Neurociencias, Universidad Nacional Autónoma de México, Mexico City, Mexico

OPEN ACCESS

Edited by:
Ulrich G. Hofmann, Freiburg University Medical Center, Germany

Reviewed by:
Robert W. Komorowski, Massachusetts Institute of Technology, United States
Ronen Segev, Ben-Gurion University of the Negev, Israel

***Correspondence:**
Ranier Gutierrez
ranier@cinvestav.mx
Francisco Sotres-Bayon
sotres@ifc.unam.mx
Alberto Caballero-Ruiz
alberto.caballero@icat.unam.mx

Specialty section:
This article was submitted to Neural Technology, a section of the journal Frontiers in Neuroscience

Received: *23 October 2018*
Accepted: *05 February 2019*
Published: *21 February 2019*

Citation:
Polo-Castillo LE, Villavicencio M, Ramírez-Lugo L, Illescas-Huerta E, Moreno MG, Ruiz-Huerta L, Gutierrez R, Sotres-Bayon F and Caballero-Ruiz A (2019) Reimplantable Microdrive for Long-Term Chronic Extracellular Recordings in Freely Moving Rats. Front. Neurosci. 13:128. doi: 10.3389/fnins.2019.00128

Extracellular recordings of electrical activity in freely moving rats are fundamental to understand brain function in health and disease. Such recordings require a small-size, lightweight device that includes movable electrodes (microdrive) to record either a new set of neurons every day or the same set of neurons over time. Ideally, microdrives should be easy to implant, allowing precise and smooth displacement of electrodes. The main caveat of most commercially available microdrives is their relatively short half-life span, in average ranging from weeks to a month. For most experiments, recording days–weeks is sufficient, but when the experiment depends on training animals for several months, it is crucial to develop new approaches. Here, we present a low-cost, reusable, and reimplantable device design as a solution to extend chronic recordings to long-term. This device is composed of a baseplate that is permanently fixed to the rodent's skull, as well as a reusable and replaceable microdrive that can be attached and detached from the baseplate, allowing its implantation and reimplantation. Reimplanting this microdrive is particularly convenient when no clear neuronal signal is present, or when the signal gradually decays across days. Our microdrive incorporates a mechanism for moving a 16 tungsten-wire bundle within a small (∼15 mm^3) lightweight device (∼4 g). We present details of the design, manufacturing, and assembly processes. As a proof of concept, we show that recordings of the nucleus accumbens core (NAcc) in a freely behaving rat are stable over a month. Additionally, during a lever-press task, we found, as expected, that NAc single-unit activity was associated with rewarded lever presses. Furthermore, we also show that NAc shell (NAcSh) responses evoked by freely licking for sucrose, consistent with our previously published results, were conserved from a first implant to a second microdrive reimplant in the same rat, notably showing reimplantation is possible without overtly affecting the functional responses of the area of interest. In sum, here we present a novel microdrive design (low-cost, small size, and light weight) that can be used for long-term chronic recordings and reimplanted in freely behaving rats.

Keywords: microdrive, extracellular chronic recording, reimplantable microdrive, electrophysiology, additive manufacturing

INTRODUCTION

Electrophysiological recording of brain activity is a valuable technique to understand the neural correlates of behavior in health and disease (Esmaeili and Grace, 2013). Recordings of electrical neural activity in rodents provide useful insights into how the brain represents information about the internal and external world (Nicolelis et al., 1995; Buzsáki, 2004; Hasegawa et al., 2015), uncovering the neuronal correlates from sensory and perceptual processing to decision making (Feierstein et al., 2006; Fonseca et al., 2018). In general, the methods in electrophysiology can be divided into intracellular and extracellular recordings. Unlike the former, the latter is widely used in freely moving animals, which allows stable recordings for several minutes or even hours (Ribeiro et al., 2004; Jovalekic et al., 2017). However, the loss of signal becomes a fundamental problem, especially, in studies involving either extensive behavioral training (spanning from weeks to months) or in animal models characterizing the development of chronic human diseases (Vlamings et al., 2012; Ellens and Leventhal, 2013; Sesia et al., 2013; Saddoris et al., 2016). To circumvent this issue, it is needed a reimplantable microdrive to record, the same animal, over an extended period.

Although it is not fully understood why electrical signals degrade along time, it has been speculated that the loss of signal could be caused by tiny vibrations produced by the animal's movement or by biological reasons such as tissue reaction surrounding the electrode, resulting in neuronal migration, neuronal death, or glial encapsulation of the recording tips (Muthuswamy et al., 2005, 2011; Branchaud et al., 2006). Also, researchers face the problem of oversampling the same neuropil over days, which reduces the biological replicates within a dataset. In this regard, previous microdrives were developed to move the wires and to record from a new set of neurons every day (Gutierrez et al., 2010) or record from the same neurons for a few days (Sotres-Bayon et al., 2012). In any case, most commonly movable electrodes are permanently implanted and cemented to the skull which precludes reimplantation in the same subject and thus increased the number of experimental animals needed (Fitts, 2011).

Multiple designs have been used for building microdrives. Manually movable microdrives have been used in the past decades with limited success. Morrow (1980) reported a manual mechanism which is based on four parts with a mounting sleeve, a carrier tube and an electrode drive screw that moves the electrode. Later, O'Keefe and Recce (1993) reported the use of a microdrive with a mechanism that avoids the rotation of the cannula or electrodes. Gothard et al. (1996) developed a conic and bulky microdrive able to move 14 tetrodes independently. Looking for a low-cost, low-weight, and easy-fabrication device, the "Scribe microdrive" was presented by Bilkey and Muir (1999). It is composed of the parts of a pen, a guide cannula and a screw, whose motion is transmitted using a contact point between the screw and the pen nib, allowing only forward displacement. Lansink et al. (2007) reported the development of a multi-electrode microdrive for chronic recording in two brain areas simultaneously, based on a microdrive presented by Gothard et al. (1996). This system allows reusing some parts of the microdrive. More recently, Chang et al. (2013) developed a home-made microdrive consisting of two joined brass guides. This microdrive uses four tetrodes displaced by a screw, and an electronic interface board (EIB-18, Neuralynx) for proper connections, which resulted in stable single-unit recordings for several weeks. Also, the same manuscript shows the steps for assembling a commercially available microdrive (Versa Drive 4, Neuralynx) based on a Mill-Max commercial connector and containing four drive screws (Chang et al., 2013).

The main disadvantage of manually driven microdrives is the limited precision to move electrodes and the stress to which the animal is subjected when lowering them. To solve this problem, several automatic movable microdrives have been developed. Fee and Leonardo (2001) introduced a microdrive consisting of a brushless dc micromotor. In 2007, a microdrive based on a hydraulic system was presented. This device can move 22 wires independently along 4 mm in intervals of 50 μm (Sato et al., 2007). Yamamoto and Wilson (2008) reported a motorized system with 21 drivers, each composed of five parts: a dc brushless servomotor with planetary gearbox, a threaded rod, a slotted PEEK tube, a shuttle lock, and a shuttle. A microdrive for mice containing a piezo-motor (TULA 35, Piezoelectric Technology Co., Ltd.) with 1 μm accuracy was presented by Yang et al. (2011). This motorized microdrive comprises 13 components. Another lightweight microdrive that uses a dc micromotor with threaded output was developed in 2012 by Otchy and Ölveczky, which consists of seven major components. In 2014, Caballero-Ruiz et al. (2014) proposed a high-precision displacement system based on a piezo motor (SQL-RV-1.8, New Scale Technologies Inc.) and a Hall-effect sensor (Allegro A1324 MicroSystems, Inc.) comprising six assembly parts and three more for the closed-loop positioning system. In 2017, Jovalekic et al. (2017) developed another micropositioning system consisting of a piezo motor (SQL-RV-1.8, New Scale Technologies Inc.) and a Hall-effect sensor (NSE-5310, New Scale Technologies, Inc.). These electrodes could be replaced, increasing the yield of neurons recorded. However, to further increase the number of neurons recorded, there is a need for a reimplantable microdrive for chronic recordings in freely behaving animals. This is particularly relevant in experiments in which much time and effort are devoted to training animals in tasks where reusing and reimplanting microdrives would increase the gathering of neural data.

Among the many microdrives developed so far, the power screw mechanism is the most commonly used for electrode positioning, whether it is a manual or automated mechanism. Most of the automated ones, in addition to the screw, use geared brushless dc micromotors, reaching resolutions about 1 μm. As suggested by Sato et al. (2007), and in spite of the high resolutions achieved by this kind of mechanisms, the backlash present in the gears and leadscrews introduces a significant amount of imprecision which could cause lateral deviations along the vertical displacement (as it can be seen in the work carried out by Chang et al., 2013) and, even more, the micro motion between the electrode and

the surrounding tissue, due to the natural movements (i.e., heartbeat and respiration) of the animal, could results in loss of signal (Muthuswamy et al., 2011). To address this problem, Sato et al. (2007) put forward a hydraulic system in which electrode positioning can be estimated accurately with a pre-pressurized system. Although the hydraulic microdrive can precisely displace the electrodes, it is too heavy and bulky. From another standpoint, electrode motion can be performed using piezoelectric motors. Unlike electromagnetic devices, the piezoelectric ones are electromagnetic noise-free, and their efficiency is insensitive to size (Heywang et al., 2008). Besides considering low weight, low cost, small dimensions, and high precision as important requirements for the development of microdrives, it is also important to consider the half-life of electrodes. Long-term experiments require a reliable microdrive to record neural signals over a long period able to overcome biotic and abiotic factors that could affect impedance (Sankar et al., 2014).

In this work, we present the development of a reusable and reimplantable microdrive that increases the success of electrophysiological studies in freely moving rats. Such a microdrive is based on a smooth displacement mechanism and a reimplantable system. It also accomplishes the low weight, low cost, small dimension, and high precision requirements mentioned above. The proposed mechanism prevents lateral motion along the electrode stroke, which results in stable recordings. The motion can be manually or automated performed, depending on the preference of the user. Moreover, a baseplate is fixed to the skull without using dental acrylic, and the microdrive is attached to the baseplate. Thus, it can be easily replaced. The efficiency of the microdrive was demonstrated using electrophysiological experiments in freely behaving rats. First, we characterized the stability of our microdrive. We found stable responses in a single neuron recorded in the nucleus accumbens core (NAcc) while a rat pressed a lever to obtain food. Then, in a separate rat, the spontaneous activity of two neurons was successfully recorded for over a month (40 days). Having demonstrated the stability of the microdrive, we evaluated if our microdrive could be reimplanted, in the same rat, without overtly damaging the functional activity of the brain region of interest. To this end, single-unit recordings from the NAc shell (NAcSh) were performed while rats licked for sucrose. In the same animals, we found that the signal quality between the first electrode implant and the second one was not statistically different, indicating that the proposed reimplantable microdrive can potentially extend the half-life of the electrophysiological experiments. Also, it revealed that reimplantation did not impair the normal function of the recorded brain region since our data replicated a well-known function of the NAcSh. That is, the majority of NAcSh neurons were either Lick-Inactive whereas the minority were Lick-Active during consummatory behavior, in the same proportion than previous observations (Krause et al., 2010; Tellez et al., 2012; Villavicencio et al., 2018). In sum, we demonstrated that the proposed reimplantable microdrive could be a reliable solution to extend chronic extracellular neuronal recording in freely behaving rats.

MATERIALS AND METHODS

In this section, the design, fabrication, assembly, and implementation of a reimplantable microdrive to smoothly displace electrode bundles for extracellular recordings is presented. Such a microdrive is based under the following requirements: small-size less than 15 mm × 15 mm × 15 mm; weight less than 5 g; mechanical stability; able to move a bundle of 16 microelectrodes; able to be actuated manually or by motor (for manual actuating, using a resolution between 50 and 100 μm; while for motorized actuating, employing a resolution less than 10 μm); able to be reimplanted and easy to be installed and reused.

Microdrive Design

Figure 1 depicts the exploded view of the proposed microdrive, which has eight overall components: a micropositioning mechanism, composed of an electrode shuttle system (1) able to move the electrodes by means of either a nut-screw linear motion system (2a), for manual configuration, or a piezoelectric motor (SQL-RV-1.8; NewScale Tech.) (2b), for motorized configuration; in order to obtain precise displacements, a closed-loop position control system is used based on a Hall-effect sensor (Allegro A1324 MicroSystems, Inc.) (3). Inside the housing (4), the mechanism, the actuator and the gold-plated electronic interface board (EIB; 5) are located. Also, the design has two covers, one that is designated to protect the EIB (6) and the other one to protect the electrodes (7). Finally, the entire assembly lies on top of the baseplate (8), which is the only piece permanently fixed on the skull of the rat.

In order to fulfill the requirements for high resolution and mechanical stability, the linear motion is generated by either a nut-screw system [**Figure 1(2a)**], for the manual configuration, or by a piezoelectric actuator [**Figure 1(2b)**], for the motorized configuration, which is coupled to an electrode shuttle system (see **Figure 2**). The electrode shuttle system is composed of an element acting as a piston [**Figure 2 (2a)**] through a bushing (2b) in order to constrain the displacement. A compression spring (2c) introduces a pre-load between the piston and the nut-screw system or the piezoelectric actuator, warranting cero backlash. In this way, the mechanism exhibits high stiffness, load capacity and resistance to shock and vibration. The piston works as a shuttle, in which a stainless-steel guide cannula (2e) with a polyimide tube (2d) concentrically arranged is fixed. To prevent short circuits between the microelectrodes and the cannula, the polyamide tube is used, and the cannula guide improves the shuttle system alignment. For the motorized configuration, a magnet (2f), sensed by the Hall effect sensor, is employed.

The housing element (**Figure 3**) and the two covers shape the casing. Inside the first one, the micropositioning mechanism is located, as it can be seen in the lateral view (dashed line, red square). In the housing element, two internal conduits [**Figure 3 (4a)**] permit guiding the electrodes to the EIB, protecting them from damages caused by the natural movements of the animal. In this way, the electrodes can be led from the top to the bottom of the structure in order to be finally cut and connected to the EIB. The clamping element (4g) permits a stable attachment between the connector and the headstage using an

INFORME DE LABORES 2019

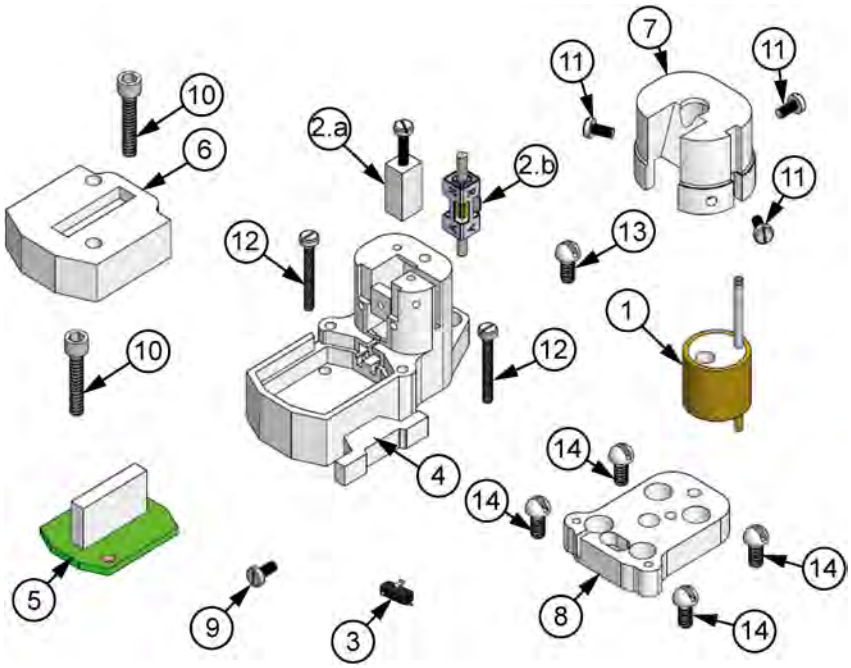

FIGURE 1 | Exploded view of the microdrive proposed. **(1)** Electrode shuttle system, **(2a)** nut-screw linear motion system, **(2b)** piezoelectric motor, **(3)** Hall-effect sensor, **(4)** housing element, **(5)** EIB-18, **(6)** EIB-18 cover, **(7)** electrode cover, **(8)** baseplate, **(9)** fixing screw of the motor or nut, **(10)** EIB cover-housing fixing screw (×2), **(11)** electrode cover-housing fixing screws (×3), **(12)** posterior housing-baseplate fixing screws (×2), **(13)** anterior housing-baseplate fixing screw, **(14)** baseplate-skull fixing screws (×4).

elastic rubber band. The EIB cover is fastened to the housing element using two screws through the holes (4f). Using three screws, the electrode cover is fixed to the housing, completing in this way the protection of the electrodes from the movements of the animal.

The baseplate (see **Figure 4**) is the element that facilitates the mounting on the skull of the rat. Such a baseplate can be easily designed for a desired position. It allows the device to be replaced in case of loss of signal, increasing the experiment time without the necessity of a second surgery. Through the fastening holes [**Figure 4 (8a)**], four screws have the function of fixing the baseplate to the skull. A groove (8b) allows joining the ground wire to the proper pin of the EIB. The alignment between the slotted guide groove (8c) and the guide wedge [**Figure 3(4b)**] makes it easier to assemble the housing element on the baseplate; also, three screws permit fixing both elements by means of an anterior fastening hole (8d) and two posterior fastening holes (8e). Also, the baseplate includes a hole (8f) through which the piston travels in a vertical path together with the bundle of electrodes in the recording site hole (8g). A microdrive design that includes such baseplate provides the opportunity to easily replace the device if there is an error during surgery.

Microdrive Fabrication and Assembly

To develop the microdrive presented, manufacturing processes criteria such as the shape of the components, type of the required materials as well as resolution and cost were considered. For the micropositioning mechanism, high resolution is a critical requirement, hence CNC manufacturing was used; through the milling process, the bushing and the piston were manufactured: the bushing was made of brass, with overall dimensions of 6 mm in internal diameter, 7 mm in external diameter, 6 mm in height and a weight of 0.29 g; while the piston was made of acrylic and has overall sizes of 2 mm in the inner diameter, 6 mm in the outer diameter, 6 mm in height and a weight of 0.069 g. The baseplate (weight: 0.52 g), the housing element (weight: 1.42 g), the covers (electrode cover weight: 0.42 g and EIB cover weight: 0.35094 g), and the nut (weight: 0.045 g) were manufactured using an additive manufacturing process (material jetting) because of the complexity of their shapes; the equipment employed was a Connex 3 by Stratasys, and the material used was VeroClear resin (RGD810). This technology has the advantage of reducing manufacturing costs when the production batch increases. The other components are commercial. The compression spring used (by Industrial Springs Corp.) is made of stainless steel and has a mean diameter of 2 mm, a free length of 5 mm and a weight of 0.01 g. The polyimide tube (Polyimide 0.0135 ID by Neuralynx) has a length of 18 mm and weighs only 0.002 g, while the guide cannula (20G by Lanceta HG) has a length of 13.5 mm and weighs 0.37 g. The magnet (R063-063 by Amazing Magnets LLC) weights 0.023 g and has overall sizes of 1.59 mm diameter and 1.59 mm length. The Hall-effect sensor (A1324LLHLT-T by Allegro MicroSystems) has overall sizes of 2 × 3 × 1 mm and weighs 0.015 g. In order to avoid rust problems, stainless steel screws were used which, according to

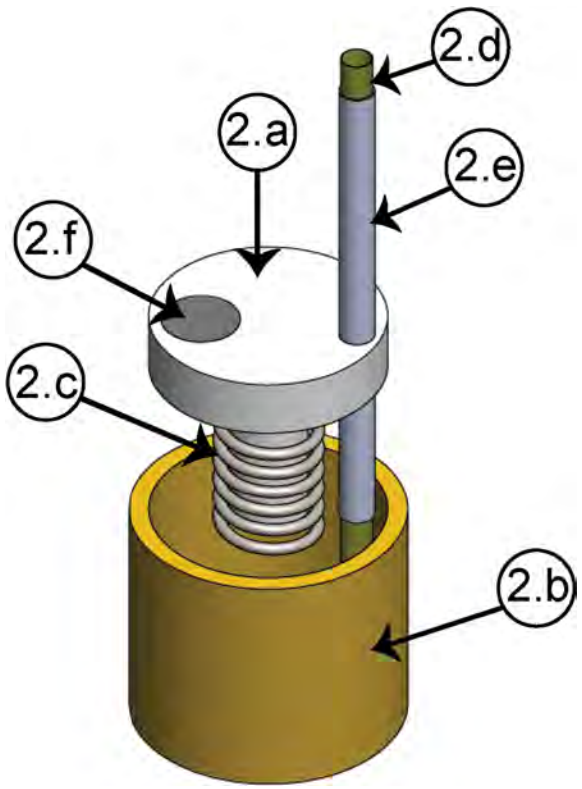

FIGURE 2 | Electrode shuttle system. **(2a)** Piston, **(2b)** bushing, **(2c)** compression spring, **(2d)** polyimide tube, **(2e)** cannula guide, **(2f)** magnet.

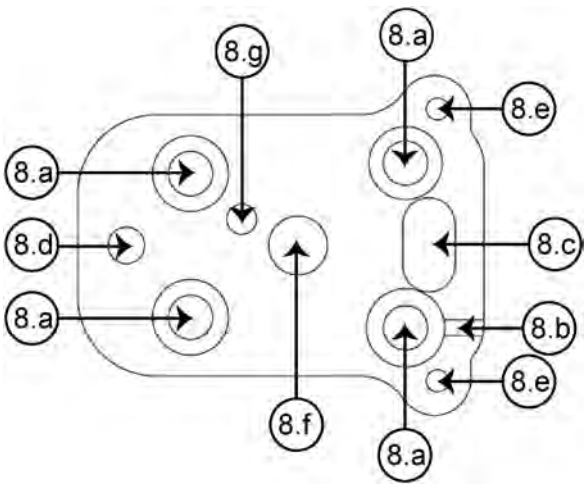

FIGURE 4 | Superior view of the baseplate. **(8a)** Baseplate-skull fastening hole (×4), **(8b)** groove for the ground wire, **(8c)** slotted guide groove, **(8d)** anterior fastening hole, **(8e)** posterior fastening hole (×2), **(8f)** piston blind hole, **(8g)** recording site (for the right NAcSh).

their application on the microdrive design, can be classified into three types: power screw, housing fixing screws and skull fixing screws. The first one (#21475 by MetricScrews) is M1-0.25 × 10 mm and weighs 0.045 g. The second one is composed of three different screws: four pieces of M1-0.25 × 3 mm (#20694 by MetricScrews) with a weight of 0.07760 g, two pieces of M1-0.25 × 8 mm (#21474 by MetricScrews) screws with a weight of 0.068 g and one 0–80 × 1/8 (by Plastics One Inc.) screw with a weight of 0.058 g. Finally, the skull fixing screws consist of four 0–80 × 1/8" screws with a weight of 0.23332 g. For the automated microdrive, a piezoelectric SQL-RV-1.8 actuator by New Scale Technologies is used, such an actuator has overall sizes of 2.8 × 2.8 × 6 mm and a weight of 0.16 g.

The complete assembly can be divided into three stages: the first one is related with the assembly of the micro positioning system; the second one involves the insertion and connection of the electrodes, and the last one is concerned with the placement of the protection covers with the appropriate fixing screws. The complete process can be seen in **Figure 5**. As a first step, the electrode shuttle system is assembled by fixing the polyimide tube and cannula (**Figure 5A**) to the piston

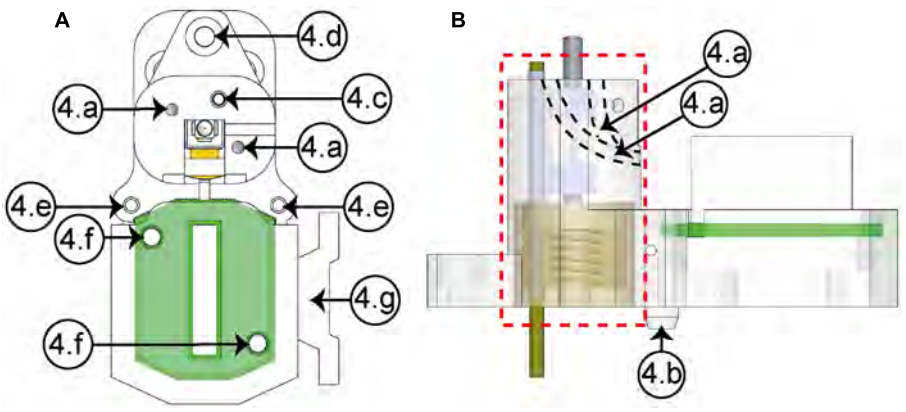

FIGURE 3 | Housing element (**A**, upper view; **B**, lateral view). **(4a)** Conduits (×2), **(4b)** guide wedge, **(4c)** cannula hole, **(4d)** anterior fastening hole, **(4e)** posterior fastening holes (×2), **(4f)** EIB's fastening holes (×2), **(4g)** headstage clamping element.

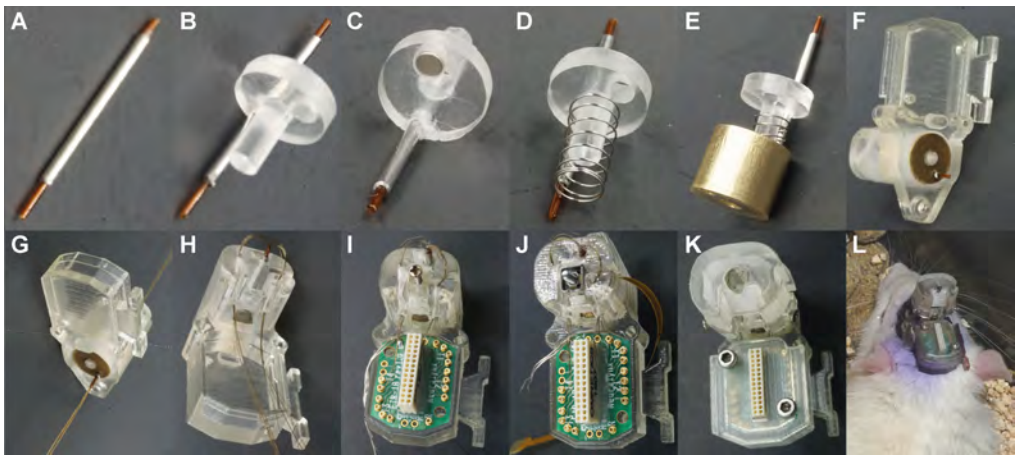

FIGURE 5 | Reimplantable microdrive assembly. **(A)** Polyimide tube in the guide cannula. **(B)** Guide cannula fixed to the piston. **(C)** A magnet placed in the piston. **(D)** Compression spring placed concentrically to the piston rod. **(E)** Piston placed concentrically and aligned to the bushing. **(F)** Electrode shuttle system assembled with the housing element. **(G)** Electrodes introduced through the polyimide tube. **(H)** Electrodes introduced through the conduits. **(I)** Nut-screw and EIB placed in the housing element. **(J)** Piezoelectric actuator placed in the housing element for the automated configuration. **(K)** Final assembly with the two covers and the housing fixing screws. **(L)** Illustrative picture of a rat implanted with a reimplantable microdrive.

(**Figure 5B**), the polyimide tube projects 2 mm from the lower face of the baseplate. Then, the magnet is placed in the piston hole (**Figure 5C**) and the compression spring is placed concentrically to the piston rod (**Figure 5D**); after that, all these parts are put concentrically in the bushing (**Figure 5E**), which in turn is placed in the housing element (**Figure 5F**). After this, the nut-screw or the piezoelectric actuator can be placed and fixed with a screw. This stage takes about 10 min. The second stage consists in introducing the electrodes through the polyimide tube (**Figure 5G**) and the conduits (**Figure 5H**). After this, the electrodes are cut 7.5 mm from the lower face of the baseplate for the NAcSh, and 6 mm for the NAcc in order to reach the region of interest (see **Supplementary Figure S1**); next, the EIB is placed in the housing element; and finally, the electrodes are connected to the EIB by means of gold-plated pins (**Figure 5I**). **Figure 5J** shows the assembly with the piezoelectric actuator. It is important to handle the electrodes carefully, making sure they do not bend. This task takes around 30 min. The last stage consists in protecting the EIB and the exposed part of the electrodes by fixing the covers with the housing element (**Figure 5K**). At the end of this stage, the final assembly time is less than 70 min. Including the weight of the baseplate, the total weight of the reimplantable microdrive is about 4.08 g when the nut-screw is used, and 4.15 g if the piezoelectric motor is implemented. In both configurations, its overall dimensions are 27.73 × 15.95 × 21.50 mm. Finally, before the implantation, the electrodes can be gold plated and then the device is ready. **Supplementary Table S2** depicts the cost of all components to build one microdrive. In the case of the automated microdrive, the total cost of the parts is 280.2 USD. Considering that the actuator and the EIB are reusable, the total cost of each microdrive is approximately 53 USD (and it could be cheaper by producing a larger batch). All STL files are provided in the **Supplementary Data Sheet S1**.

Gold Plating of Electrodes

The impedance of the electrodes was controlled by electroplating the tip of the wires. Electroplating prevents impedance damping and improves the signal-to-noise ratio (Ferguson et al., 2009). Before implantation (and reimplantation), the 16 tungsten wires with 35 μm in diameter were electro-plated with a gold plating solution and the recommended Neuralynx stepped protocol (**Supplementary Table S1**) using a nanoZ^{TM} multi-electrode impedance tester (Plexon, Dallas, TX, United States). Impedances were reduced to 70 kΩ.

Microdrive in Freely Behaving Rats

The proposed microdrive was tested in freely behaving animals. Testing involved two separate experiments in different laboratories. In both laboratories, the activity in the nucleus accumbens (NAc) of the ventral striatum was recorded, a brain region involved with reward processing and appetitive behaviors (Castro et al., 2015). Experiments differ in the use of microdrive connectors: the first one uses the Mill-Max connector, while the second one uses an Omnetics connector. They also differ in the rat strain (Wistar and Sprague-Dawley rats) and task used to assess the microdrive: one experiment involves an instrumental task pressing-lever to obtain food while the other one involves a licking task to obtain a liquid solution.

Subjects

Two male Wistar rats (280–300 g; Instituto de Fisiología Celular's breeding colony) were housed in polyethylene cages. Rats were maintained on a 12 h light/dark cycle and fed standard laboratory rat chow in a restricted manner (18 g/day) until they reached 85% of their free-feeding weight. Rats had free access to water throughout the experiment. All manipulations and behavioral procedures were performed during the light phase. Animals were housed individually in a temperature-controlled environment

(24°C) for at least 4 days before surgery. Animals were handled daily to diminish stress responses.

Five male Sprague-Dawley rats (300–350 g; CINVESTAV bioterium). Rats were housed in polyethylene cages and maintained on a 12 h light/dark cycle (lights on 0700; and lights off 1900). These rats were under a water restriction of 23 h per day, with 1 h of access to tap water in their home-cages following each recording session (see below). Such water restriction protocol is necessary for rats to maintain high levels of motivation for operant conditioning tasks (Hughes et al., 1994), without affecting the health of the rats (Rowland, 2007). Chow food diet (LabDiet, 5008) was available *ad libitum* in their home cages. All manipulations and behavioral procedures were performed during the light phase. Animals were housed individually in a temperature-controlled environment (21–24°C) for at least 4 days before surgery.

All procedures were approved by the Institutional Animal Care and Use Committee of the UNAM and CINVESTAV, in compliance with the National Ministry of Health guidelines for the care of laboratory animals.

Surgery

Figure 6 depicts the microdrive implantation procedure. Following behavioral training, Wistar rats were anesthetized using isoflurane, and Sprague-Dawley rats with an intraperitoneal injection of ketamine (90 mg/kg)/xylazine (8 mg/kg).

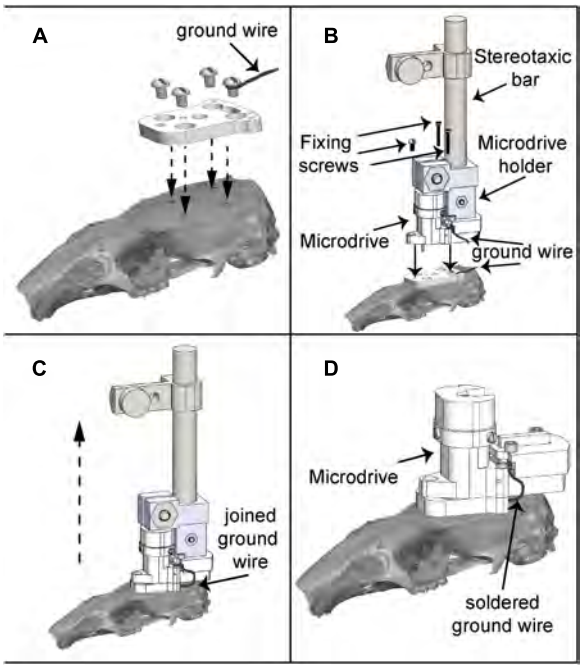

FIGURE 6 | Microdrive implantation procedure. **(A)** The baseplate is located on the cranium of the rat according to the recording site and fixed using four screws. **(B)** The microdrive holder allows a smooth and precise mounting of the microdrive, which is fixed to the baseplate using three screws. **(C)** After the ground wire fixation, the microdrive is released from the holder and ready to use. **(D)** Microdrive firmly attached on the baseplate.

The microdrive contained a 16-channel electrode bundle. For the five Sprague-Dawley rats the electrode bundle was implanted targeting the nucleus accumbens shell (NAcSh; +1.4 mm AP, −1 mm ML, and −7.5 mm DV, from bregma; Tellez et al., 2012), whereas Wistar rats aimed the NAcc (2.0 mm AP, +1.4 mm ML, and −6.0 mm DV, from bregma). Rats were positioned in a stereotaxic apparatus to perform a ∼2 × 2 mm craniotomy above the implantation site. Later, four additional Ø1.5 mm holes were made in the skull. The positions of these holes matched the holes in the baseplate where the microdrive was mounted. Then, the baseplate was fixed to the skull by screwing it through the holes. A drop of glue (cyanoacrylate, Krazy Kola Loka) was added to strengthen the fixation to the scalp. Finally, the reimplantable microdrive, positioned above the baseplate was lowered using a holder to introduce the electrode array in the brain. Once the microdrive was settled in, it was screwed to the baseplate. Following surgery, a triple antibiotic ointment was applied to the wound and enrofloxacin (45 mg/kg) was administered for three additional days. Rats were allowed to recover for 7–14 days before initiating recordings.

Behavior

Wistar rats were trained in standard operant chambers (Coulbourn Instruments, Allentown, PA, United States) located inside sound-attenuating boxes (MED Associates, Burlington, VT, United States) to press a bar to obtain food pellets (Bioserve, Inc., Frenchtown, NJ, United States) on a continuous reinforcement schedule. Recordings were performed in freely behaving rats or during lever pressing sessions.

Sprague-Dawley animals were recorded at the same time of the day between 2:00 and 3:00 p.m. Specifically, three rats were recorded while performing a brief-access test as described in Villavicencio et al. (2018). Briefly, taste stimuli consisted of reagent-grade sucrose (Sigma-Aldrich, Mexico) dissolved in deionized water. For the brief-access taste test, four semi-logarithmically spaced sucrose concentrations were used: 3, 5.8, 10.7, and 20 wt./vol. % (0.087, 0.168, 0.31, 0.58 M, respectively). For the brief-access test, in each trial, rats licked the spout to receive one randomly selected sweet concentration during a 5-s reward period. Moreover, the other two Sprague-Dawley rats performed an *ad libitum* freely licking sucrose test, in which only a sucrose solution of 10 wt./vol. % was available at all times (Tellez et al., 2012). Sweet tastants were prepared daily and used at room temperature. The behavioral box contained a V-shaped licking port where the spout was located (Med Associates, St. Albans, VT, United States). The licks given to the spout were recorded with a photobeam diode (Med Associates), and each lick delivered a 10-μL drop directly onto the rats' tongue as described in Gutierrez et al. (2010).

Data Analysis

Custom-made Matlab (The MathWorks Inc., Natick, MA, United States) codes were used to analyze behavioral and single unit activity. To identify neurons whose activity was modulated while the rats licked for sucrose in both licking tasks (**Figure 9D**), the rhythmic licking behavior was first segmented into bouts. A lick bout was considered to be a train of contiguous licks

with inter-lick intervals <500 ms (Spector et al., 1998; Tellez et al., 2012). Then, the neuronal firing rate was calculated during a baseline period encompassing −1 to −0.5 s before the onset of every lick bout and the firing rate during the lick bouts. Finally, to determine whether each neuron was modulated by licking or not, the firing rate in the baseline was compared with that in the licking period (lick bout) with a one-way ANOVA ($\alpha = 0.05$). All neurons with a significant difference were classified as modulated by licking and the difference between the firing rate during the two periods was used to classify the direction of the modulation into Lick-Active (increases in firing rate) or Lick-Inactive (decreases). The proportion of Lick-Active and Lick-Inactive neurons found during the first and second implant was compared against that previously reported in Tellez et al. (2012), using the chi-squared test ($\alpha = 0.05$; **Figure 9E**).

Furthermore, to compare the performance between two consecutive implants in the same animal, we performed the following statistical analyses. We counted the number of neurons recorded in each session using either a First or Second implant and compared among them with a Kruskal–Wallis test ($\alpha = 0.05$; **Figure 9B**). Also, we counted the number of days each microdrive recorded unitary activity and compared between First and Second implants with a Kruskal–Wallis test ($\alpha = 0.05$; **Figure 9C**). To control for the lower number of repetitions (implants), we modeled the number of recording days for either the First and Second implants by resampling. To achieve this, we bootstrap the data 10,000 times with replacement. Then, we calculated the confidence intervals (CI's) centered at the 95% from the resulting distributions and looked if CI's from the First and Second implants overlapped, to determine significant differences.

Multi-Channel Unit Recording

For the Wistar rats, individual neurons were recorded extracellularly using the present microdrive (with a Mill-Max connector), in freely behaving rats or while they pressed for food. Extracellular waveform signals exceeding a voltage threshold were amplified (gain × 100), digitized at 40 kHz using an OmniPlex Neural Data Acquisition system (Plexon, Dallas, TX, United States), and stored on a disk for further off-line analysis. Waveforms were recorded during 10 min periods of spontaneous activity. Single units were isolated using principal component analysis and template matching (Offline Sorter; Plexon, Dallas, TX, United States). We applied semi-automated (automated followed by manual correction) processing techniques to sort spikes from single units in clusters. Automated processing involved using a valley-seeking scan algorithm (Offline Sorter; Plexon, Dallas, TX, United States), one channel at a time, and then evaluated using sort quality metrics. For manual verification of automated clustering techniques, a cluster was considered to be generated from a single neuron if the cluster was distinct from clusters for other units in the principal component space. Also, the cluster had to exhibit a clear refractory period (>1 ms). Only stable clusters of single units during recording were considered for analysis. Timestamps of neural spiking and flags for the occurrence of bar-pressing were imported to NeuroExplorer (NEX Technologies, Littleton, MA, United States) for analysis. Long-term single-unit stability isolation was evaluated using Wavetracker (Plexon, Dallas, TX, United States) in which principal component space-cylinders were calculated from a 10 min segment of data spontaneously recorded session. Straight and overlapped cylinders or tubes suggest that the same single unit was recorded over different sessions (as in Herry et al., 2008).

For the Sprague-Dawley rats, extracellular single-unit activity from the NAcSh was recorded using a Multichannel Acquisition Processor (Plexon, Dallas, TX, United States). Specifically, voltage signals were sampled at 40 kHz and digitalized at 12-bit resolution. Single unit timestamps were extracted from the raw signal by using an online band-pass filter with a low cutoff of 154 Hz and high cutoff of 8.8 KHz. Only single neurons with action potentials having greater than 3:1 signal to noise ratio were analyzed. The action potentials were isolated online using voltage-time threshold windows and a three principal component contour template algorithm. Furthermore, for all recordings, off-line spike sorting (Plexon offline sorter) was performed, and only single units with stable waveforms across the entire session were included in the analysis (Gutierrez et al., 2010). As electrodes tips were positioned in the dorsal region of the NAcSh, we sampled neuronal responses across the dorsoventral axis by lowering down the electrodes every day. To this end, the lead screw driving the micro positioning system was turned one rotation before each experiment, pushing down the electrode bundle ∼250 μm. As the total displacement length of the reimplantable microdrive is 2.5 mm, after 10 days of recording (thus, traveling all the way down) the microdrive was replaced. For that purpose, rats were anesthetized and positioned in the stereotaxic frame. Once there, the microdrive was unscrewed and removed, leaving the baseplate fixed to the skull of the rat. A new microdrive was immediately reimplanted in the NAcSh using the same brain coordinates and screwed to the baseplate. During the following 3 days, rats had access to water in their home cages. Note that the reimplantable microdrives were lowered each day to test their capability to record single-unit activity all the way down and to replace the microdrives rapidly. However, of course, the experimenter can decide to lower and replace the microdrives, when considered necessary, depending on the intended duration of the experiment and the quality of the extracellular recordings.

Microdrive Placement and Electrode Location

To identify the location and integrity of the microdrive implant, a computed tomography (CT) was performed of the head of the rat using a Nikon CT, model XT H 225. **Figure 9B** is a representative X-ray image of the rat's head with the microdrive implant in place. Upon completion of all experiments, rats were transcardially perfused with 0.9% saline solution followed by an overdose of pentobarbital (150 mg/kg, i.p.). Brains were extracted and fixed in a 30% sucrose/10% formalin solution (Sigma-Aldrich, St. Louis, MO, United States). Electrode placements were verified by cutting coronal sections 40–50 μm thick using a cryostat (Leica, CM1520), subsequently mounted on slides and stained for Nissl bodies with cresyl violet. Only rats with electrode locations within the borders of the target structure were included in the statistical analysis.

RESULTS

Microdrive Assessment

To evaluate the implantation and reimplantation procedures of the microdrive, the time required for each procedure was measured. For the first case, the procedure consists in the surgery for attaching the baseplate by means of four screws, one of these with a silver ground wire soldered (**Figure 6A**); to place the microdrive at its final position, a customized microdrive holder was attached to the stereotaxic incisor bar; once the microdrive was on the baseplate, it was fixed by means of three fastener screws (**Figure 6B**); after this, the microdrive holder was released (**Figure 6C**); finally, the silver ground wire had to be soldered to the microdrive ground wire (**Figure 6D**).

For microdrive reimplantation, the procedure consists in releasing three fastener screws to remove the old microdrive (using the microdrive holder), cutting the ground wire in half (leaving at least 2 cm of ground wire from the ground screw attached to the skull to ground the EIB pin), cleaning the baseplate top and, after that, the procedure followed for implantation must be repeated (see **Figure 6**). We found that the average temperature on the ground screw after five soldering iterations (3 s per iteration) was 23.2°C (see **Supplementary Figure S3**). Even if soldering lasted as much as 10 s, we found that heating only reached 32°C, suggesting that heating due to re-soldering does not damage the underlying brain tissue.

The total weight of the reimplantable microdrive, including the weight of the baseplate, is about 4.08 g when the nut-screw is used, and 4.15 g if the piezoelectric motor is implemented. In both configurations, its overall dimensions are 27.73 × 15.95 × 21.50 mm. The microdrive offers a travel range of 2.5 mm, which is a reasonable distance to cover most brain regions in a rat. To assess the movable mechanism proposed in the microdrive, two different characterizations were performed. The first one was related with assessing the smoothness of the displacements for demonstrating the reliability of the micropositioning system to record neural activity to a certain depth without lateral motions of the tip of the wire. The second one was focused on assessing the position capabilities of the microdrive. For both evaluations, an optical comparator NIKON Profile Projector V-16D with an ×20 magnification was employed, which is a precise instrument suitable for measuring different shapes of workpieces with a resolution of 0.1 μm. Both evaluations were performed in manual and open-loop motorized configurations. Once the microdrive was fixed on the profile projector stage, for the manual system, the screw was rotated 22 times in half-turn increments to generate forward and backward displacements with a theoretical value of 125 μm in each event. Three experiments were performed, and the experimental displacements were plotted versus the theoretical position (see **Figure 7A**). The mean displacements for the three experiments were 123, 122.1, and 122.5 μm, respectively. While the mechanism was displaced forward and backward, it was noticed that the electrodes have minimal, if any, lateral motion, which warranties a smooth displacement. The same procedure was performed using the automated microdrive with open-loop control. To generate the control signals, the NSD-2101 piezo motor driver by Austria Microsystems was employed. The actuator works by voltage pulses. To evaluate the displacement of the automated microdrive in an open-loop control, three experiments were performed. Each experiment was composed of 64 steps, and each step was programmed with 10 pulses, duration of 1 ms, and intervals of 1 ms. For this case, **Figure 7B** shows the experimental displacement as a function of the motor steps for the three experiments, thereby obtaining an average displacements of 35.145, 33.193, and 30.919 μm, respectively. As was observed in the first experiment, lateral deviations were not present.

Long-Term Stable Neuronal Recordings in Freely Moving Rats

To assess the stability of the microdrive *in vivo*, we recorded NAcc neurons (**Figure 8**) in Wistar rats that were either in their home cage or during a behavioral task. Superimposed waveforms from two different units recorded simultaneously in the same electrode show them separated from noise. Offline sorting of two units using the voltage-time threshold, principal component time-space surface, interspike interval histogram,

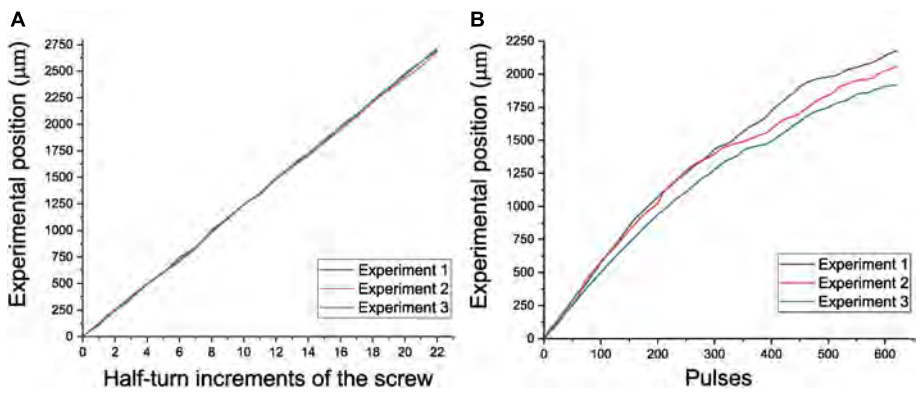

FIGURE 7 | Performance of the electrode positioning system. **(A)** Experimental position versus half-turn increments of the screw. **(B)** Experimental position versus motor steps in open loop.

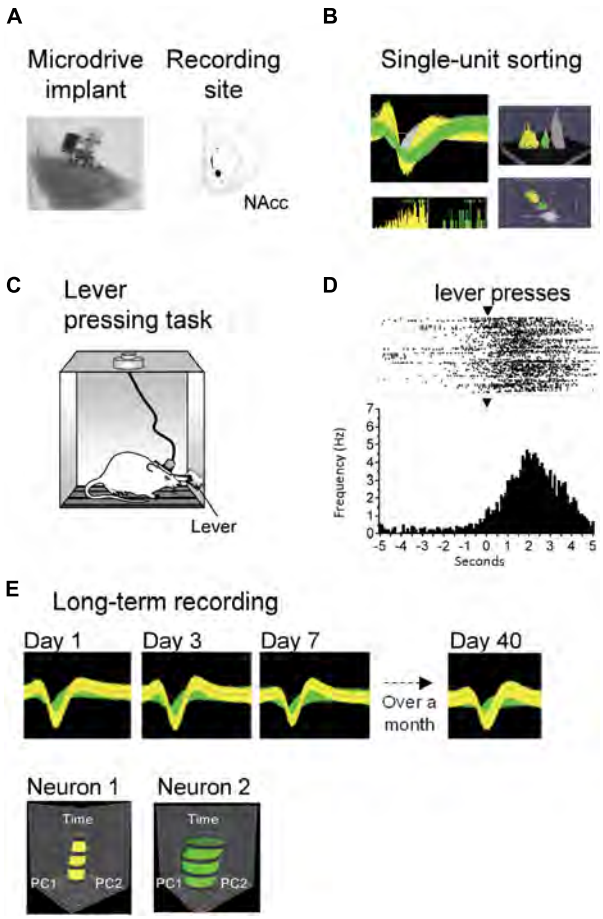

FIGURE 8 | Long-term stable recordings of NAcc neurons in freely behaving rats. **(A)** Left: X-ray of the head of the rat showing location of the microdrive implant. Right: Histological reconstruction of the location of electrode tips in NAc of the ventral striatum. **(B)** Left top: Superimposed waveforms from two different units (green and yellow) recorded simultaneously in the same electrode and separated from noise (gray). Grid: 400 μV, 800 μs. Left bottom: Interspike interval histogram of the two units. Right: Offline sorting of two units using voltage-time threshold, principal component time-space surface (top) and 3D (bottom). **(C)** Freely behaving rats pressed a lever to obtain a food pellet, in a fixed ratio 1 reinforcement schedule. **(D)** Raster plot (top) and peri-event time histogram (bottom) for a neuron exhibiting an increase in firing rate after lever pressing (time = 0 s; the waveform of this neuron is shown in yellow in panel **B**). In the raster, a black tick indicates one action potential; the bin size was 100 ms. Arrowheads (▼) indicate the time of lever pressing (time = 0 s). **(E)** We tested the stability of recordings during spontaneous activity sessions in another freely behaving Wistar rat. Top: Waveforms of two separate neurons (yellow and green) recorded from the same single electrode for over a month (40 days). For visualization purposes, only waveforms in days 1, 3, 7, and 40 are shown. Bottom: Verification of long-term stable single-unit recordings using principal component space cylinders. A straight cylinder indicates that the same single unit was recorded in different sessions across time (days).

and 3D were used to verify they were separate units (**Figure 8B**). To validate the microdrive and evaluate its recording stability, freely behaving rats were trained in a lever-pressing task (**Figure 8C**). Spontaneous neural activity was recorded while rats were pressing a bar to obtain a food pellet. The response of one individual neuron is shown in the raster plot in **Figure 8D**. This neuron responded vigorously when pressing the lever to obtain food. This result is consistent with previous reports showing lever press response-related activity in NAcc (e.g., Morrison and Nicola, 2014). This neuron was recorded for three consecutive days (data not shown). These results indicate that the microdrive can be used for short-term (less than a week) recordings in rats performing a simple behavioral lever-press task. Further, in a different rat and to evaluate if the microdrive can be used for long-term recordings (over a month), we recorded spontaneous NAcc neuronal activity of two single neurons for 40 days. The response of these two individual neurons with a stable waveform for over 40 days is shown in **Figure 8E**. Quantitative verification of long-term stable single-unit recordings was performed using principal component space cylinders. A straight principal component space cylinder indicates that the same single unit was recorded in different sessions (days) across time. Taken together these results indicate that the microdrive is stable for short-term and, most importantly for long-term recordings in freely behaving rats. Yet, because of the limited dataset (one recording channel with two clearly isolatable units tracked for over a month), we acknowledge that implanting more rats with this microdrive would be necessary to evaluate quantitatively further the degree of long-term recording stability.

Neuronal Recordings for the First and Second Microdrive Implant

Having characterized the stability of the microdrive, we then assessed if it was feasible to re-implant it without overtly affecting the functional activity of the targeted brain region. To do this, we performed extracellular single-unit recordings in five Sprague-Dawley rats performing a sucrose licking task. In total, the activity of 262 single neurons was recorded and analyzed to test the efficacy of our reimplantable microdrive. **Figure 9** shows a representative example of two neurons recorded by the same tungsten wire. Note that the clusters of waveforms were stable and well separated in the principal component-time space, as well as in a voltage-time window (Inset) during the 1-h experiment, demonstrating once more that our microdrive can perform stable recordings in freely moving rats (in **Supplementary Figure S2** can be found the raw data of online sorting of a single recording day).

Next, we characterized the quality of the recordings in two consecutive implants, performed in the same animal. The frequency to record single neurons between the First and Second implant was not statistically different (Kruskal–Wallis, $\chi^2_{(1,9)} = 0.55$, $p = 0.45$; **Figure 9B**; 4.7 and 3.2 neurons per session, respectively). Moreover, in average the activity recorded from the Second implant lasted roughly the same number of days than the First implant (**Figure 9C**; Kruskal–Wallis, $\chi^2_{(1,9)} = 2.18$, $p = 0.14$; $n = 10$ implants), suggesting that the process of degradation of the electrode's signal was similar between both implants. To further validate this point, we resample with replacement the number of recorded days with signal. The averages of resampled data were 8.05 (CI = 1–7) and 5.33 (CI = 5–11) days with signal for the First and Second

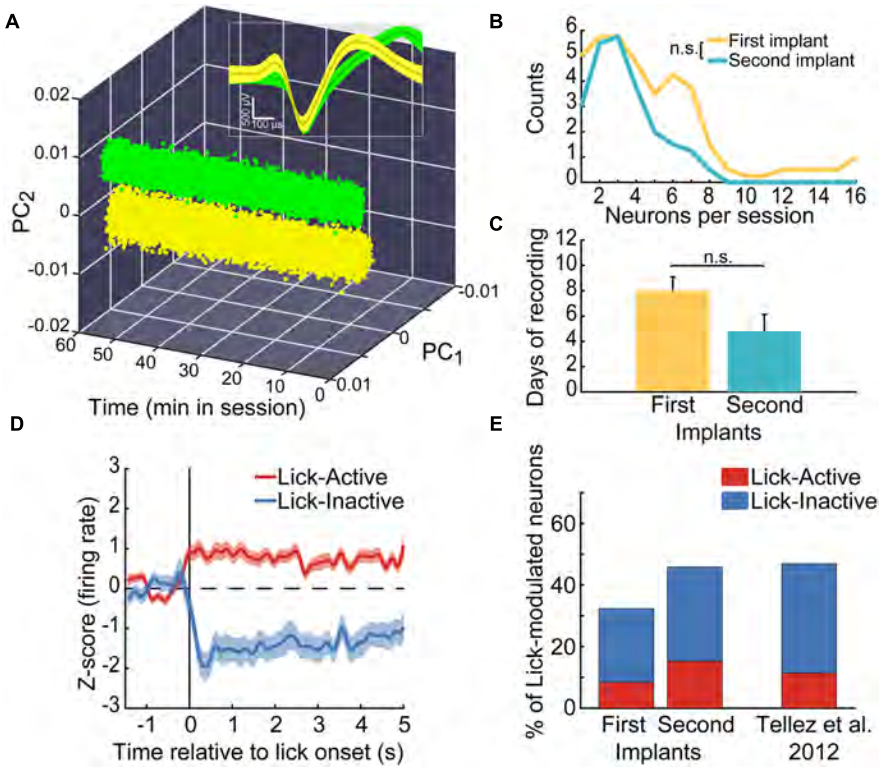

FIGURE 9 | In the same animals, we recorded a similar proportion of lick-modulated NAcSh neurons in the first and second microdrive implant. **(A)** Action potentials (dots) of two single-neurons recorded in the same channel (yellow and green, respectively) within a 1 h freely licking behavioral session. Values are plotted in a three-dimensional space built with the first two principal components (PCs) of the voltage signals vs. time. Inset: Depicts the time-voltage window showing the mean ± SEM of action potential waveforms. These neurons were recorded from the "first" implant. **(B)** Histogram depicting the number of single neurons recorded in the first and second implant across sessions. **(C)** Number of daily sessions where single-unit activity was recorded in the first and second implant. **(D)** The population activity (normalized to z-score) of neurons that were either Lick-Active (red) or Lick-Inactive (blue) around the initiation of licking (vertical line at time = 0 s). The baseline level of neuronal activity (z-score = 0) is indicated by a horizontal dashed line and was taken from –1.5 to –0.5 s relative to the lick onset. **(E)** Histograms of the percentage of Lick-Active and Lick-Inactive neurons found in the NAcSh using the first and the second implant of the microdrive and the proportion of the lick modulated neurons reported in a study published elsewhere (Tellez et al., 2012). The proportions of neurons were not statistically different relative to data from Tellez et al. (2012) (chi-square test; Lick-Active neurons of the first and second implants vs. Tellez, $\chi^2 = 0.004$, and $\chi^2 = 0.005$, respectively; Lick-Inactive of the first and second implants vs. Tellez, $\chi^2 = 0.017$ and $\chi^2 = 0.003$, respectively; all p's > 0.05).

implants, respectively. Since confidence intervals did overlap, then it indicates no statistical difference, at a 95% confidence, exists between the First and Second re-implant. Nevertheless, we do acknowledge that in our second implant, we could not record more than eight simultaneous neurons in a single session (**Figure 9B**), further studies should confirm this trend. These data suggest that good-quality recordings can be obtained from a second implant in the same rat. Also, these results demonstrate that recordings in freely moving animals can be extended for at least one more implant (perhaps more), but this remains to be tested.

To further characterize if there is any reliable advantage in the yield of neurons recorded with our microdrive, we compared the yield obtained with our reimplantable microdrive against a permanently implanted movable electrode from our previously published study (Tellez et al., 2012) (see **Table 1**). In average, in the First implant, we recorded 36.8 neurons per animal, whereas with a permanently implanted electrode 38.3 (Mann–Whitney Rank p = n.s.), producing a yield of 4.7 vs. 5.7 neurons/session, respectively (p = n.s.). Thus, our microdrive results in a similar yield than other tungsten electrodes, at least, in the First implant. As noted above, the advantage of our drive mainly resides on the ability to be reimplanted (and to be reused). As can be appreciated in **Table 1**, we recorded, from the same rats, in average 16.2 new neurons in the Second implant (see **Table 1**; Second implant). Nevertheless, we acknowledge that not in all subjects the Second implant recorded more neurons than the First implant (see for example rat R02). Nonetheless, it is important to note that we also found cases (such as in subject R01) where the Second implant improved the yield of neurons, demonstrating the advantage of using our microdrive.

After demonstrating the recording capabilities of our microdrive, we evaluated whether the two consecutive implants lead to recording the same type of functional ensembles in the NAcSh. A considerable amount of evidence has consistently shown the existence of a small proportion of Lick-Active and a larger population of Lick-Inactive neurons in the NAcSh (Roitman et al., 2005; Krause et al., 2010; Tellez et al.,

INFORME DE LABORES 2019

TABLE 1 | Comparison of the yield of neurons obtained in First and Second implant, and against Tellez's database with a permanently implanted electrode.

	First implant			Second implant		
Name rat	**Sessions**	**Neurons**	**Neu/Sess**	**Sessions**	**Neurons**	**Neu/Sess**
R01	6	6	1	6	22	3.6
R02	9	33	3.6	1	3	3
R03	11	71	6.4	7	25	3.5
R04	9	25	2.7	7	17	2.4
R05	5	49	9.8	4	14	3.5
Average	8	36.8	4.7	5	16.2	3.2

	Permanent implantation		
Name rat	**Sessions**	**Neurons**	**Neu/Sess**
Cooper	5	26	5.2
Floyd	8	59	7.3
Orec	3	10	3.3
Rhino	9	45	5
Silverio	14	147	10.5
Zero	5	15	9.4
Stan	1	4	4
Cua	1	1	1
Average	5.7	38.3	5.7

2012; Villavicencio et al., 2018), suggesting that these neuronal populations reflect the functional organization of the NAcSh. Thus, to address this issue, we first identified NAcSh neurons that were modulated during consummatory licking behavior. **Figure 9D** shows the populational activity of all NAcSh neurons that either increased their activity during licking (see red line) or suppressed it (blue line). Thus, the proportions of Lick-Active and Lick-Inactive neurons using our reimplantable microdrive was compared against the proportions reported in our previously published study (Tellez et al., 2012) (**Figure 9E**). For this analysis, the licking-modulated neurons from both, the brief-access taste test and the free-licking task, were pooled. No statistical differences were found in the percentage of active or inactive licking-modulated populations for the first or second implant in comparison with the data reported by Tellez et al. (2012) (chi-square test; all p's > 0.05, $n = 87$ Lick modulated neurons from our microdrive vs. $n = 124$ from Tellez et al., 2012). This result suggests that the reimplanted microdrive can record the same functional ensembles as other standard electrodes without affecting the functional activity of the NAcSh. Altogether, the data obtained indicate that the microdrive is suitable for *in vivo* recordings involving simultaneous behavioral testing and, more importantly, that it can extend recordings for an extra period, without affecting neither their quality nor the functionality of the brain region targeted.

DISCUSSION

A novel microdrive design is presented here. This microdrive met the low cost, small size, and lightweight criteria, which are ideal features for experiments involving freely moving rodents. The assembly and implantation, as well as the re-implantations, resulted easy and quick. Also, the design presented here incorporates a mechanism based on two concentric cylinders that produce smooth displacements in both the manual and automated versions. Most important, it was demonstrated that the micropositioning system could reliably advance the electrode bundle in the space without lateral motions artifacts. One of the innovative aspects of the device is that is it potentially reusable. We have indeed been reusing parts from our microdrive by cleaning, re-plating and sterilizing the device (or by simply replacing the tungsten wires). This suggests that our microdrive allows for users to potentially re-use microdrives across animals, greatly decreasing cost and time of experiments. As a proof of concept, single unit recordings using the microdrives were tested in rats performing behavioral tasks or during spontaneous activity. We found a high-quality neuronal signal that was comparable between a first standard implant and a re-implant in the same subjects. Also, it was demonstrated that such a signal could last over a month. Thus, the microdrive design proposed here is an original and useful device to facilitate the collection of neuronal activity datasets, especially for experiments where time, training, and resources employed are critical.

Micropositioning System

The microdrive presented incorporates a mechanism based on two concentric cylinders that produce smooth displacements; the mechanism is coupled to the lead screw by pressure, avoiding any backlash and system misaligning, which are the main drawbacks in mechanisms based on leadscrew and cannula guides (e.g., Fee and Leonardo, 2001; Venkateswaran et al., 2005; Otchy and Ölveczky, 2012; Jovalekic et al., 2017), in which the electrodes can be subject to mechanical drift and in consequence the loss of signal. The microdrive proposed exhibited good stability over several recording days. Another advantage of the microdrive presented is the possibility to choose between a manual or automated actuation. The use of the piezoelectric motor SQL-RV-1.8 allows replacing it with a nut and a screw with the same geometrical characteristics decreasing the microdrive's cost. The mechanical characterization demonstrated that there were not lateral displacements along the displacement stroke. Related to the displacement characterization, for the manual configuration, a resolution of about 125 μm per half turn was obtained; but if the user requires a lower displacement, he/she only needs to decrease the rotation of the screw; for example, a quarter of a turn represents a displacement of about 60 μm. For the automatic configuration (open-loop control), it was observed that there was no similarity in the three experiments. Such a behavior is related to the actuator and the mechanism employed: ultrasonic PZT actuators usually do not have a constant behavior because their principle work is based on friction; on the other hand, the spring employed in the mechanism produces a non-constant preload force to the motor, which changes depending on the position in the microdrive stroke. Despite this drawback, using close control loop can improve the precision of the displacement, as demonstrated in Caballero-Ruiz et al. (2014), where a resolution of 1.3 μm with an average error of 2.2 μm was obtained with

the prototype of the presented mechanism, making it a high-performance system.

Manufacturing

The use of additive manufacturing technologies helps us to generate a microdrive housing with internal conduits to protect the microelectrodes form possible damages caused by the natural behavior of the animal; this is an important issue in extracellular recording experiments with rodents. Also, we incorporated a baseplate and a holder that permits the easy installation of the microdrive and the possibility of reimplanting a new one in case of loss of signal. This represents an advantage when trained animals are used for the experiment. The microdrive presented can displace a bundle of 16 microelectrodes, which makes it impossible to determine the specific location of each of them, individually. It is necessary to work on a proposal that allows moving a microelectrode array with a specific distance between the electrodes to avoid the possible crosstalk phenomena and to know the specific location of each electrode. The recording experiments were performed in the NAc of the ventral striatum, but the design can be easily modified to target other brain regions. The additive manufactured baseplate allows for a flexible recording location, located between AP ± 3.5 mm and ML ± 2.5 mm; with some minimal modifications in the 3D model, it is possible to achieve more distant regions; however, not for all brain regions, for example, this design cannot offer recordings in very lateral areas such as in the posterior insular cortex (ICp); therefore, designing a universal baseplate that can be used on any region of the brain can be considered. The final weight and dimensions of the proposed microdrive are appropriate for extracellular recording in rats. For smaller rodent species, such as mice, it will be necessary to miniaturize its components and redesign the baseplate and the microdrive. Another caveat of our microdrive is that all electrodes are moved in a bundle rather than an independent placement of each electrode individually. Nevertheless, this limitation allows us to reduced device weight and, for a future version, it could save space to introduce a second driver to record two simultaneous brain regions.

Gold Plating of Electrodes

Sixteen tungsten wires with 35 μm in diameter were gold-plated in order to reduce the impedance to 70 kΩ. However, the user can flexibly choose electrodes with other diameters and materials. It has been demonstrated that tungsten is a good choice of material for chronic implants since it is a stable and inert metal (Freire et al., 2011), and it has been successfully used in single unit recordings (Gutierrez et al., 2010). This diameter is stiff enough to maintain stability and rigidity at lengths <7 mm. We note that larger diameters >50 μm are not optimal for isolating single unit activity. Furthermore, in Patrick et al. (2011), it was demonstrated gold-plated in tungsten electrodes. Additionally, Prasad et al. (2014) reported that with tungsten electrodes, the best yield is for the impedance range 40–150 kΩ. Further studies should analyze different materials and diameters in order to characterize the best option of electrodes and impedance range.

Datasets Collection

The main advantage of using the microdrive is, of course, reducing the number of experimental subjects, which is a fundamental ethical issue as expressed by Institutional Animal Care and Use Committees (Fitts, 2011). We believe that our microdrive will be especially valuable for preparations for which extensive behavioral training is needed (Erlich et al., 2011; Jaramillo and Zador, 2014; Liu et al., 2014; Fonseca et al., 2018); or in animal models for chronic diseases that take months to develop, such as diet-induced obesity (Benedikz et al., 2009; Avena, 2012). We expect our reimplantable microdrive to become a critical implementation for extracellular recordings that facilitate the collection of larger neuronal activity databases over long periods.

In sum, here we presented the design of a novel microdrive that resulted in stable recordings over days to a month, and more important, when necessary it could be reimplanted, in the same animal, with the intent to extend the half-life of extracellular recordings. Altogether, the structural and functional features of the present microdrive make it ideal to further study the neuronal correlates of behaviors, in health and disease, from perception to decision making that requires stable recordings across several weeks and give the opportunity to reuse it and reimplant it if there is an error during surgery.

DATA AVAILABILITY

The datasets generated for this study are available on request to the corresponding author.

AUTHOR CONTRIBUTIONS

LR-H, FS-B, RG, and AC-R designed the research. LP-C, LR-L, MV, MM, and EI-H performed the research. AC-R, LR-H, RG, and FS-B analyzed the data. LR-H, MV, FS-B, RG, LP-C, and AC-R wrote the manuscript.

FUNDING

This work was supported by grants CONACyT LN280867 and DGAPA PE-106417 (given to LR-H); CONACyT CB176639 and APN 2463, DGAPA IN205417, and the International Brain Research Organization, Return Home fellowship (given to FS-B). The project was also supported by Productos Medix (3247), Fundación Miguel Aleman, and CONACyT: grants FOINS 63 and APN 464 (given to RG).

ACKNOWLEDGMENTS

The authors would like to thank Fabiola Hernandez-Olvera for her invaluable assistance with animal care; Gerardo Ruiz Botello for the assistance during the positioning characterization process; and Nora E. Reyes-Rocafuerte for proofreading.

SUPPLEMENTARY MATERIAL

The Supplementary Material for this article can be found online at: https://www.frontiersin.org/articles/10.3389/fnins.2019.00128/full#supplementary-material

FIGURE S1 | Distance from baseplate to end of electrode bundle (7 mm). **(A)** Length of electrodes without the baseplate. **(B)** Same as in **(A)** but with the baseplate in place.

FIGURE S2 | Single-unit activity recorded from the reimplantable microdrive. Screenshot of the acquisition system's user interface software showing single-unit activity recorded during an ongoing experiment (online sorting). At the right, it is seen different time-voltage windows corresponding to different channels from where single-unit activity was recorded. Yellow and green traces distinguish different neuronal signals recorded in a single channel. At left side of the screenshot, it is shown an expansion of the channel "4" seen at the left (see window framed by a magenta rectangle).

FIGURE S3 | Soldering process and temperature measurement. **(A)** Temperature measured with an infrared thermometer before soldering. **(B)** The ground wires have been joined. **(C)** The ground wires have been soldered and an average temperature of 23.2°C has been obtained.

TABLE S1 | NanoZ stepped protocol used to perform the electroplating in the electrodes. This protocol was applied to each channel. The interval is the time between bi-phasic pulses within a run. Runs are the maximum number of attempts per step to reach a target impedance. n/a, not applicable.

TABLE S2 | Costs for microdrive parts. For the automated microdrive, the total cost of the parts is 280,2 USD, while for the manual configuration is 155,2 USD. Both estimations were made considering the cost of the electronic interface board (101.65 USD), which is reusable. Without the cost of the electronic interface board, the total cost of each microdrive is 53,55 USD.

DATA SHEET S1 | STL files and G code for manufacturing the parts of the microdrive.

REFERENCES

Avena, N. M. (2012). *Animal Models of Eating Disorders*. Totowa, NJ: Humana Press.

Benedikz, E., Kloskowska, E., and Winblad, B. (2009). The rat as an animal model of Alzheimer's disease. *J. Cell. Mol. Med.* 13, 1034–1042. doi: 10.1111/j.1582-4934.2009.00781.x

Bilkey, D. K., and Muir, G. M. (1999). A low cost, high precision subminiature microdrive for extracellular unit recording in behaving animals. *J. Neurosci. Methods* 92, 87–90. doi: 10.1016/S0165-0270(99)00102-8

Branchaud, E. A., Burdick, J. W., and Andersen, R. A. (2006). "An algorithm for autonomous isolation of neurons in extracellular recordings," in *Proceedings of the First IEEE/RAS-EMBS International Conference on Biomedical Robotics and Biomechatronics, BioRob 2006*, Pisa. doi: 10.1109/BIOROB.2006.1639212

Buzsáki, G. (2004). Large-scale recording of neuronal ensembles. *Nat. Neurosci.* 7, 446–451. doi: 10.1038/nn1233

Caballero-Ruiz, A., Garcia-Beltran, L. I., Ruiz-Huerta, L., and Heredia-Lopez, F. (2014). "Micropositioning system for the study of neural activity in free-behaving rats," in *Proceedings of the 2014 International Conference on Mechatronics, Electronics and Automotive Engineering*, (Washington, DC: IEEE). doi: 10.1109/ICMEAE.2014.30

Castro, D. C., Cole, S. L., and Berridge, K. C. (2015). Lateral hypothalamus, nucleus accumbens, and ventral pallidum roles in eating and hunger: interactions between homeostatic and reward circuitry. *Front. Syst. Neurosci.* 9:90. doi: 10.3389/fnsys.2015.00090

Chang, E. H., Frattini, S. A., Robbiati, S., and Huerta, P. T. (2013). Construction of microdrive arrays for chronic neural recordings in awake behaving mice. *J. Vis. Exp.* 77:e50470. doi: 10.3791/50470

Ellens, D. J., and Leventhal, D. K. (2013). Review: electrophysiology of basal ganglia and cortex in models of Parkinson disease. *J. Parkinsons Dis.* 3, 241–254. doi: 10.3233/JPD-130204

Erlich, J. C., Bialek, M., and Brody, C. D. (2011). A cortical substrate for memory-guided orienting in the rat. *Neuron* 72, 330–343. doi: 10.1016/j.neuron.2011.07.010

Esmaeili, B., and Grace, A. A. (2013). Afferent drive of medial prefrontal cortex by hippocampus and amygdala is altered in MAM-treated rats: evidence for interneuron dysfunction. *Neuropsychopharmacology* 38, 1871–1880. doi: 10.1038/npp.2013.64

Fee, M. S., and Leonardo, A. (2001). Miniature motorized microdrive and commutator system for chronic neural recording in small animals. *J. Neurosci. Methods* 112, 83–94. doi: 10.1016/S0165-0270(01)00426-5

Ferguson, J. E., Boldt, C., and Redish, A. D. (2009). Creating low-impedance tetrodes by electroplating with additives. *Sens. Actuators A Phys.* 156, 388–393. doi: 10.1016/j.sna.2009.10.001

Feierstein, C. E., Quirk, M. C., Uchida, N., Sosulski, D. L., and Mainen, Z. F. (2006). Representation of spatial goals in rat orbitofrontal cortex. *Neuron* 51, 495–507. doi: 10.1016/j.neuron.2006.06.032

Fitts, D. A. (2011). Ethics and animal numbers: informal analyses, uncertain sample sizes, inefficient replications, and type I errors. *J. Am. Assoc. Lab. Anim. Sci.* 50, 445–453.

Fonseca, E., de Lafuente, V., Simon, S. A., and Gutierrez, R. (2018). Sucrose intensity coding and decision-making in rat gustatory cortices. *Elife* 7:e41152. doi: 10.7554/eLife.41152

Freire, M. A. M., Morya, E., Faber, J., Santos, J. R., Guimaraes, J. S., Lemos, N. A. M., et al. (2011). Comprehensive analysis of tissue preservation and recording quality from chronic multielectrode implants. *PLoS One* 6:e27554. doi: 10.1371/journal.pone.0027554

Gothard, K. M., Skaggs, W. E., Moore, K. M., and McNaughton, B. L. (1996). Binding of hippocampal CA1 neural activity to multiple reference frames in a landmark-based navigation task. *J. Neurosci.* 16, 823–835. doi: 10.1523/JNEUROSCI.16-02-00823.1996

Gutierrez, R., Simon, S. A., and Nicolelis, M. A. L. (2010). Licking-induced synchrony in the taste-reward circuit improves cue discrimination during learning. *J. Neurosci.* 30, 287–303. doi: 10.1523/JNEUROSCI.0855-09.2010

Hasegawa, T., Fujimoto, H., Tashiro, K., Nonomura, M., Tsuchiya, A., and Watanabe, D. (2015). A wireless neural recording system with a precision motorized microdrive for freely behaving animals. *Sci. Rep.* 5:7853. doi: 10.1038/srep07853

Herry, C., Ciocchi, S., Senn, V., Demmou, L., Müller, C., and Lüthi, A. (2008). switching on and off fear by distinct neuronal circuits. *Nature* 31, 600–606. doi: 10.1038/nature07166

Heywang, W., Lubitz, K., and Wersing, W. (2008). *Piezoelectricity: Evolution and Future of a Technology*. Berlin: Springer Science & Business Media.

Hughes, J. E., Amyx, H., Howard, J. L., Nanry, K. P., and Pollard, G. T. (1994). Health effects of water restriction to motivate lever-pressing in rats. *Lab. Anim. Sci.* 44, 135–140.

Jaramillo, S., and Zador, A. M. (2014). Mice and rats achieve similar levels of performance in an adaptive decision-making task. *Front. Syst. Neurosci.* 8:173. doi: 10.3389/fnsys.2014.00173

Jovalekic, A., Cavé-Lopez, S., Canopoli, A., Ondracek, J. M., Nager, A., Vyssotski, A. L., et al. (2017). A lightweight feedback-controlled microdrive for chronic neural recordings. *J. Neural Eng.* 14:026006. doi: 10.1088/1741-2552/aa5848

Krause, M., German, P. W., Taha, S. A., and Fields, H. L. (2010). A pause in nucleus accumbens neuron firing is required to initiate and maintain feeding. *J. Neurosci.* 30, 4746–4756. doi: 10.1523/JNEUROSCI.0197-10.2010

Lansink, C. S., Bakker, M., Buster, W., Lankelma, J., van der Blom, R., Westdorp, R., et al. (2007). A split microdrive for simultaneous multi-electrode recordings from two brain areas in awake small animals. *J. Neurosci. Methods* 162, 129–138. doi: 10.1016/j.jneumeth.2006.12.016

Liu, D., Gu, X., Zhu, J., Zhang, X., Han, Z., Yan, W., et al. (2014). Medial prefrontal activity during delay period contributes to learning of a working memory task. *Science* 346, 458–463. doi: 10.1126/science.1256573

Morrison, S. E., and Nicola, S. M. (2014). Neurons in the nucleus accumbens promote selection bias for nearer objects. *J. Neurosci.* 34, 14147–14162. doi: 10.1523/JNEUROSCI.2197-14.2014

Morrow, T. J. (1980). Improved technique for recording single unit activity in awake animals. *Brain Res. Bull.* 5, 91–93. doi: 10.1016/0361-9230(80)90289-0

Muthuswamy, J., Anand, S., and Sridharan, A. (2011). Adaptive movable neural interfaces for monitoring single neurons in the brain. *Front. Neurosci.* 5:94. doi: 10.3389/fnins.2011.00094

Muthuswamy, J., Okandan, M., Jain, T., and Gilletti, A. (2005). Electrostatic microactuators for precise positioning of neural microelectrodes. *IEEE Trans. Biomed. Eng.* 52, 1748–1755. doi: 10.1109/TBME.2005.855712

Nicolelis, M. A., Baccala, L. A., Lin, R. C., and Chapin, J. K. (1995). Sensorimotor encoding by synchronous neural ensemble activity at multiple levels of the somatosensory system. *Science* 268, 1353–1358. doi: 10.1126/science.7761855

O'Keefe, J., and Recce, M. L. (1993). Phase relationship between hippocampal place units and the EEG theta rhythm. *Hippocampus* 3, 317–330. doi: 10.1002/hipo.450030307

Otchy, T. M., and Ölveczky, B. P. (2012). Design and assembly of an ultra-light motorized microdrive for chronic neural recordings in small animals. *J. Vis. Exp.* 69:4314. doi: 10.3791/4314

Patrick, E., Orazem, M. E., Sanchez, J. C., and Nishida, T. (2011). Corrosion of tungsten microelectrodes used in neural recording applications. *J. Neurosci. Methods* 198, 158–171. doi: 10.1016/j.jneumeth.2011.03.012

Prasad, A., Xue, Q.-S., Dieme, R., Sankar, V., Mayrand, R. C., Nishida, T., et al. (2014). Abiotic-biotic characterization of Pt/Ir microelectrode arrays in chronic implants. *Front. Neuroeng.* 7:2. doi: 10.3389/fneng.2014.00002

Ribeiro, S., Gervasoni, D., Soares, E. S., Zhou, Y., Lin, S.-C., Pantoja, J., et al. (2004). Long-lasting novelty-induced neuronal reverberation during slow-wave sleep in multiple forebrain areas. *PLoS Biol.* 2:E24. doi: 10.1371/journal.pbio.0020024

Roitman, M. F., Wheeler, R. A., and Carelli, R. M. (2005). Nucleus accumbens neurons are innately tuned for rewarding and aversive taste stimuli, encode their predictors, and are linked to motor output. *Neuron* 45, 587–597. doi: 10.1016/j.neuron.2004.12.055

Rowland, N. E. (2007). Food or fluid restriction in common laboratory animals: balancing welfare considerations with scientific inquiry. *Comp. Med.* 57, 149–160.

Saddoris, M. P., Wang, X., Sugam, J. A., and Carelli, R. M. (2016). Cocaine self-administration experience induces pathological phasic accumbens dopamine signals and abnormal incentive behaviors in drug-abstinent rats. *J. Neurosci.* 36, 235–250. doi: 10.1523/JNEUROSCI.3468-15.2016

Sankar, V., Patrick, E., Dieme, R., Sanchez, J. C., Prasad, A., and Nishida, T. (2014). Electrode impedance analysis of chronic tungsten microwire neural implants: understanding abiotic vs. biotic contributions. *Front. Neuroeng.* 7:13. doi: 10.3389/fneng.2014.00013

Sato, T., Suzuki, T., and Mabuchi, K. (2007). A new multi-electrode array design for chronic neural recording, with independent and automatic hydraulic positioning. *J. Neurosci. Methods* 160, 45–51. doi: 10.1016/j.jneumeth.2006.08.009

Sesia, T., Bizup, B., and Grace, A. A. (2013). Evaluation of animal models of obsessive-compulsive disorder: correlation with phasic dopamine neuron activity. *Int. J. Neuropsychopharmacol.* 16, 1295–1307. doi: 10.1017/S14611457120015 4X

Sotres-Bayon, F., Sierra-Mercado, D., Pardilla-Delgado, E., and Quirk, G. J. (2012). Gating of fear in prelimbic cortex by hippocampal and amygdala inputs. *Neuron* 76, 804–812. doi: 10.1016/j.neuron.2012.09.028

Spector, A. C., Klumpp, P. A., and Kaplan, J. M. (1998). Analytical issues in the evaluation of food deprivation and sucrose concentration effects on the microstructure of licking behavior in the rat. *Behav. Neurosci.* 112, 678–694. doi: 10.1037/0735-7044.112.3.678

Tellez, L. A., Perez, I. O., Simon, S. A., and Gutierrez, R. (2012). Transitions between sleep and feeding states in rat ventral striatum neurons. *J. Neurophysiol.* 108, 1739–1751. doi: 10.1152/jn.00394.2012

Venkateswaran, R., Boldt, C., Parthasarathy, J., Ziaie, B., Erdman, A. G., and Redish, A. D. (2005). A motorized microdrive for recording of neural ensembles in awake behaving rats. *J. Biomech. Eng.* 127, 1035–1040. doi: 10.1115/1.2049332

Villavicencio, M., Moreno, M. G., Simon, S. A., and Gutierrez, R. (2018). Encoding of sucrose's palatability in the nucleus accumbens shell and its modulation by exteroceptive auditory cues. *Front. Neurosci.* 12:265. doi: 10.3389/fnins.2018.00265

Vlamings, R., Benazzouz, A., Chetrit, J., Janssen, M. L. F., Kozan, R., Visser-Vandewalle, V., et al. (2012). Metabolic and electrophysiological changes in the basal ganglia of transgenic Huntington's disease rats. *Neurobiol. Dis.* 48, 488–494. doi: 10.1016/j.nbd.2012.07.006

Yamamoto, J., and Wilson, M. A. (2008). Large-scale chronically implantable precision motorized microdrive array for freely behaving animals. *J. Neurophysiol.* 100, 2430–2440. doi: 10.1152/jn.90687.2008

Yang, S., Cho, J., Lee, S., Park, K., Kim, J., Huh, Y., et al. (2011). Feedback controlled piezo-motor microdrive for accurate electrode positioning in chronic single unit recording in behaving mice. *J. Neurosci. Methods* 195, 117–127. doi: 10.1016/j.jneumeth.2010.09.006

Conflict of Interest Statement: The authors declare that the research was conducted in the absence of any commercial or financial relationships that could be construed as a potential conflict of interest.

Copyright © 2019 Polo-Castillo, Villavicencio, Ramírez-Lugo, Illescas-Huerta, Moreno, Ruiz-Huerta, Gutierrez, Sotres-Bayon and Caballero-Ruiz. This is an open-access article distributed under the terms of the Creative Commons Attribution License (CC BY). The use, distribution or reproduction in other forums is permitted, provided the original author(s) and the copyright owner(s) are credited and that the original publication in this journal is cited, in accordance with accepted academic practice. No use, distribution or reproduction is permitted which does not comply with these terms.

INFORME DE LABORES 2019

Neuroscience Letters 701 (2019) 58–64

Contents lists available at ScienceDirect

Neuroscience Letters

journal homepage: www.elsevier.com/locate/neulet

Research article

Prolactin prevents mitochondrial dysfunction induced by glutamate excitotoxicity in hippocampal neurons

N.A. Rivero-Segura[a,b], Ma. I. Coronado-Mares[a], R. Rincón-Heredia[c], I. Pérez-Torres[d], T. Montiel[b], N. Pavón[e], E.A. Cabrera-Reyes[a], L. Massieu[b], M. Cerbón[a,*]

[a] Unidad de Investigación en Reproducción Humana, Instituto Nacional de Perinatología-Facultad de Química, Universidad Nacional Autónoma de México, Ciudad de México, Mexico
[b] División de Neurociencias, Instituto de Fisiología Celular, Universidad Nacional Autónoma de México, Ciudad de México, Mexico
[c] Unidad de Imagenología, Instituto de Fisiología Celular, Universidad Nacional Autónoma de México, México
[d] Departamento de Patología, Instituto Nacional de Cardiología Ignacio Chávez, Ciudad de México, Mexico
[e] Departamento de Farmacología, Instituto Nacional de Cardiología Ignacio Chávez, Ciudad de México, Mexico

ARTICLE INFO

Keywords:
Prolactin
Neuroprotection
Excitotoxicity
Mitochondria
Antioxidant
Hippocampal neurons

ABSTRACT

Prolactin (PRL) is a pleiotropic hormone secreted by several cells and tissues in the body, such as mammary glands, T-lymphocytes, hypothalamus, among others. This hormone possess neuroprotective properties against glutamate-excitotoxicity through the activation of NF-kB, suggesting it could exert an antioxidant action. However, the role of PRL on the antioxidant defense during glutamate-induced excitotoxicity is not clear to date. Therefore, in the present study, we have evaluated the effect of PRL on SOD activity and protein content of both of its isoforms (Mn^{2+}-SOD and Cu^{2+}/Zn^{2+}-SOD), as well as, its action on mitochondrial activity in primary culture of hippocampal neurons of rats. Additionally, we have evaluated the possible antioxidant effect of PRL through the determination of lipid peroxidation products (LPO), measured as malondialdehyde (MDA). Results show that PRL enhances the activity and the protein content of Mn^{2+}-SOD and Cu^{2+}/Zn^{2+}-SOD in neurons exposed to glutamate-induced excitotoxicity. Moreover, our results demonstrate that PRL prevents mitochondrial dysfunction induced by glutamate and significantly decreases the levels of LPO products. To our knowledge, this is the first time that a potential antioxidant effect of PRL has been described in hippocampal neurons exposed to glutamate excitotoxicity, opening questions of its potentiality for therapeutics.

1. Introduction

Glutamate (Glu) is the primary excitatory neurotransmitter in the brain [1]; under physiological conditions, astrocytes maintain Glu concentration in the extra-synaptic space in a low concentration (≈1 μM) preventing excitotoxicity [2]. However, in some neurodegenerative disorders astrocyte function is compromised leading to Glu-induced excitotoxicity [3]. One of the main characteristics of this condition is the overstimulation of the glutamate receptors which leads to the intracellular calcium ($[Ca^{2+}]i$) overload and concomitantly the mitochondrial dysfunction. High intracellular concentrations of Ca^{2+} induce the opening of the mitochondrial permeability transition pore, which impairs the energy balance and enhances reactive oxygen species production (ROS). As a result, the release of pro-apoptotic factors to the cytoplasm, such as cytochrome c is favored, leading to apoptosis.

Moreover, oxidative stress recognized as the dominant player in the pathology of several neurological disorders, such as Parkinson's, Alzheimer's, stroke and ischemia; and has been extensively described as the major contributor to neuronal death, since ROS damage organelles and macromolecules, such as proteins, nucleic acids and lipids [4]. Mainly, lipid peroxidation resulting from the attack by free radicals on fatty acids in membranes promotes an increase in lipid peroxidation

Abbreviations: ΔΨm, mitochondrial transmembrane potential; $[Ca^{2+}]i$, intracellular calcium concentration DIV days *in vitro*; FCCP, carbonyl cyanide-*p*-trifluoromethoxy phenylhydrazone; GH, growth hormone; Glu, glutamate; LPO, lipid peroxidation; MAPK, mitogen-activated protein kinase; MDA, malondialdehyde; PI3K, phosphoinositide-3-kinase; PRL, prolactin; rhGH, human recombinant growth hormone; SOD, super oxide dismutase; STAT-3, signal inducer and activator of transcription 3; TBARS, thiobarbituric acid reactive substances; TRMP2, transient receptor potential cation channel subfamily M member 2; TUNEL, terminal deoxynucleotidyl transferase (TdT) dUTP nick-end labeling

* Corresponding author at: Unidad de Investigación en Reproducción Humana, Instituto Nacional de Perinatología-Facultad de Química, Universidad Nacional Autónoma de México, Calle Montes Urales 800, Lomas - Virreyes, Lomas de Chapultepec IV Secc, 11000 Ciudad de México, CDMX, Mexico.
E-mail address: mcerbon85@yahoo.com.mx (M. Cerbón).

https://doi.org/10.1016/j.neulet.2019.02.027
Received 27 November 2018; Received in revised form 12 February 2019; Accepted 18 February 2019
Available online 18 February 2019
0304-3940/ © 2019 Published by Elsevier B.V.

products (LPO), such as malondialdehyde (MDA) [5]. LPO products interfered with the mitochondrial electron transport chain leading to the loss of the mitochondrial membrane potential (ΔΨm) and enhanced ROS as superoxide anion and hydrogen peroxide [6]. Although, neurons possess robust antioxidant defences, such as peroxiredoxin V, Cu^{2+}/Zn^{2+}-SOD (SOD1), Mn^{2+}-SOD (SOD2), glutathione peroxidase and catalase (in low amount), during neurodegeneration: the function of antioxidant defences is compromised [7].

On the other hand, prolactin (PRL) a peptidic hormone biosynthesised by the pituitary and by other extrapituitary tissues [8,9], has been described to exert more than 300 biological functions, including neuroprotection against Glu and kainic acid-induced excitotoxicity both *in vivo* and *in vitro* models [10–14]. Recently, our group reported, that PRL neuroprotection against Glu-induced excitotoxicity is mediated by $[Ca^{2+}]$i modulation and by NF-κB activation [11]. NF-κB plays several roles in cognition, inflammation, cell survival and cell death. Particularly in cell survival, NF-κB promotes the transcription of anti-apoptotic genes, such as *bcl-2* and inhibitor of apoptosis proteins (IAPs), in several models of excitotoxicity. Additionally, NF-κB activation induces the expression of both SOD isoforms in neurons [15]. However, few studies have investigated the antioxidant actions of PRL.

In this context, Melendez-García et al. suggested that PRL promotes cell survival in retinal pigment epithelium cells *via* anti-apoptotic and antioxidant actions, the latter associated to the inhibition of the oxidant-induced sirtuin 2-dependent activation of TRPM2 channels [16]. Nevertheless, in hippocampal neurons, the antioxidant action of PRL against excitotoxicity is not clear to date. Here, we evaluate whether PRL prevents apoptotic cell death *via* the stimulation of SOD antioxidant defence. Our results demonstrate that PRL treatment prevents apoptosis and mitochondrial dysfunction in primary cultures of hippocampal neurons through the increase in the protein content of both isoforms of SOD (SOD1 and SOD2) and the SOD activity, even during glutamate exposure. Interestingly, this results correlates with a decrease in LPO produced during Glu-induced excitotoxicity.

2. Materials and methods

2.1. Cell culture

Primary cultures of hippocampal neurons were obtained from Wistar rat embryos from 17 to 18 days of gestation as described by [11]. Briefly, neurons were suspended in Neurobasal medium supplemented with B-27 minus antioxidants (1%, Gibco, NY, USA), gentamicin (20 μg/mL, Gibco, NY, USA) and L-glutamine (0.5 mM, Sigma-Aldrich, Missouri, USA). For protein isolation, TBARS determination and SOD activity assay, neurons were cultured at a density of 3×10^5 cell/cm^2 in 35 mm cell culture plates (Costar, NY, USA), previously precoated with Poly-L-lysine (5 μg/10 mL, Sigma-Aldrich, Missouri, USA). For TUNEL and mitochondrial activity assays, cells were cultured in 12-well plate (Costar, NY, USA) on rounded coverslips (18 mm diameter) at a density of 185×10^3 cells/cm^2. Neurons were cultured in standard culture conditions (37 °C in a humidified 5% CO_2/ 95% O_2 air atmosphere) for ten days. At the 4 DIV, neurons were treated with cytosine arabinoside (0.8 μM, Sigma-Aldrich, Costar, NY, USA).

2.2. Cell treatment

At 8 DIV, all neurons received a partial replacement of Neurobasal medium and some cultures were treated with PRL (10 ng/mL solubilised in sterile saline solution during 72 h, Sigma-Aldrich, Missouri, USA) or with sterile saline solution alone. At 10 DIV, pre-treated neurons with PRL were exposed to Glu (100 μM) for 24 h while other culture wells were exposed to Glu alone to induce excitotoxicity as described by [11,12]. All experiments were carried out at the 11 DIV.

2.3. TUNEL assay

After treatments (11 DIV), primary cultures platted in rounded coverslips were washed with PBS and fixed with PFA (4% during 10 min) at RT. TUNEL assay (*in situ* cell death detection kit TMR Red, ROCHE, Basel, Switzerland) was performed according to the supplier´s instructions to. We counterstained nuclei with Hoechst (0.005%) and consider TUNEL-positive neurons those with condensed or fragmented nuclei, as reported by Mandelkow et al. [17]. Samples were observed under an epifluorescence microscope (Nikon H550S) using a UV-2A DM400 filter for Hoechst and Rhodamine filter for TUNEL. Images from five different fields, containing about 20–30 cells in three independent experiments, were analysed by ImageJ. Data are expressed as percent of TUNEL-positive neurons relative to the total number of nuclei labelled with Hoechst, as reported by García de la Cadena et al. [18].

2.4. Mitochondrial activity determination

Mitochondrial activity was measured with the JC-1 fluorescent marker. JC-1 is a mitochondrial transmembrane potential (ΔΨm) sensor, which emits fluorescence at 590 nm (red) when mitochondrion are polarised (active), and at 530 nm (green) when mitochondrion are depolarised (dysfunctional). Neurons cultured on coverslips and exposed to the different treatments were incubated with JC-1 (100 nM during 30 min covered from light at standard culture conditions, Thermo-Fisher Scientific, Massachusetts, USA). As a positive control of mitochondrial dysfunction, 1 μM of carbonyl cyanide-p-trifluoromethoxy phenylhydrazone (FCCP, Sigma-Aldrich, Missouri, USA) was incubated for 5 min. Afterwards, coverslips were transferred to a chamber with Lockey´s buffer at 37 °C and observed under a confocal microscope (Leica TCS-SP5) using the argon laser, at Unidad de Imagenología del Instituto de Fisiología Celular, UNAM. Images were analysed according to Lijima et al. [19], calculating the 530/590 nm ratio in the soma region.

2.5. Western blotting

Protein isolation, quantification, and Western blot assays were performed as described in [11]. Briefly, neurons cultured in 35 mm plates were washed with cold PBS and lysed with RIPA buffer supplemented with 5 mM of a protease inhibitor cocktail (mini-Complete, ROCHE, Basel, Switzerland). Protein quantification was determined with the DC protein assay kit (Bio-Rad, CA, USA), following the manufacturer's protocol and 40 μg of protein from each condition were loaded onto 12.5% SDS-PAGE and subsequently transferred to PVDF membranes (Millipore, Massachusetts, USA). Membranes were incubated with anti-SOD1 (1:100, cat. sc-11407), anti-SOD2 (1:200, sc-30080) or β-actin (1:10000, cat. sc-1615) overnight at 4 °C. Hybridised membranes were incubated with the corresponding secondary antibodies conjugated with horseradish peroxidase: anti-rabbit (1:7000, cat. 2301) or anti-goat (1:10000, cat. 2033) (Santa Cruz Biotechnology, CA, USA). The signal from each antibody was detected by chemiluminescence using the Immobilon Western Chemiluminescent HRP substrate (Millipore, Massachusetts, USA) with a blot-scanner (LI − COR, NE, USA). Densitometry analysis was performed with Image Studio 3.1. SOD1 and SOD2 content were normalised against β-actin.

2.6. SOD activity assay

SOD activity was quantified with the SOD determination kit Assay (Sigma-Aldrich, Missouri, USA) following the supplier´s instructions, based on the McCord and Fridovich´s principle. Neurons cultivated in 35 mm plates were washed with cold PBS and homogenised in lysis buffer. After centrifugation (14,000 *g* X 10 min at 4 °C), the supernatant from each condition was used for measuring SOD activity. Data represent the percentage of SOD activity.

2.7. Lipid peroxidation products determination

Lipid peroxidation (LPO) products were measured by the thiobarbituric acid reactive substances (TBARS) as described by [20]. Neurons were washed with cold PBS and subsequently homogenised in lysis buffer containing: Tris − HCl (25 mM, pH 7.5), SDS (1%), EDTA (1 mM, pH 8), mini-complete protease inhibitor and PMSF (5 mM, Sigma-Aldrich, Missouri, USA). Homogenates were centrifuged at 10,000 *g* X 10 min at 4 °C and protein content were determined by Lowry´s method. 100 µg of protein from each sample was mixed with BHT (4%, Sigma-Aldrich, Missouri, USA) and PBS at 100 °C during 30 min. Afterwards, each sample was incubated with thiobarbituric acid (0.8 M, Sigma-Aldrich, Missouri, USA) during 1 h at 100 °C. Samples were transferred to an ice bath, in order to stop the reaction, and then they were rapidly mixed with KCl (5%) and n-butanol. Finally, samples were centrifuged (400 *g* X 5 min at RT) and the aqueous phase as isolated to a measure absorbance at 532 nm.

2.8. Statistics

All data were analysed by GraphPad Prism® software by one-way ANOVA followed by a Bonferroni´s *post hoc* test. Values are expressed as the mean ± S.E.M. of 3–5 independent experiments. Significant differences were considered when $p < 0.05$ or $p < 0.01$.

3. Results

3.1. Prolactin prevents glu-induced excitotoxicity in hippocampal neurons

It has been reported that PRL induces neuroprotection against Glu-induced excitotoxicity in primary cultures of hippocampal neurons [11–14]. As a control for following experiments, we performed TUNEL assay in primary cultures of hippocampal neurons. Results depicted in Fig. 1S (supplementary material), show that PRL treatment does not alter the percentage of TUNEL positive neurons with condensed nuclei, in comparison with the control (Ctrl) group. However, in the PRL/Glu group, PRL reduces 50% of the TUNEL positive cells as compared with those exposed only Glu (Fig. 1S A and B, panel g–i and j–l), meaning that PRL induces neuroprotection against Glu-induces excitotoxicity as reported previously.

3.2. Prolactin-induced neuroprotection is associated with the preservation of the mitochondrial activity

Glu-induced excitotoxicity alters the intracellular calcium homeostasis leading to mitochondrial damage affecting the electron transport chain and the OxPhos [21,22]. Once we reproduce the neuroprotective effect of PRL against Glu-induced excitotoxicity, we aim to evaluate whether PRL treatment prevents the mitochondrial dysfunction during excitotoxicity. Since the ratio between 530 nm and 590 nm is more than 1 after Glu exposure (Fig. 1B), data suggest that Glu treatment collapses the mitochondrial potential in a similar proportion as showed in the neurons stimulated with FCCP (Fig. 1 A; panel k and n), as expected. On the other hand, neurons pretreated to PRL and then insulted with Glu, showed a ratio similar to the vehicle-treated neurons, indicating that PRL preserves the mitochondrial function during excitotoxicity. Additionally, we evaluated if PRL induces *per se* alterations in mitochondrial function and interestingly, our data showed a significant increase in the red fluorescence, which results in a significant decrease in the 530/ 590 nm ratio (Fig. 1 A; panel e, and Fig. 1. B), suggesting that PRL sustains mitochondrial membrane potential.

3.3. Prolactin enhances total SOD activity and both isoforms of protein content

As mention above, PRL induces NF-κB p65 activation in hippocampal neurons, and several studies report that this activation induces the expression of several proteins involved in neuroprotection, survival and the antioxidant defense. In this context, we evaluated whether PRL affects the protein content and the total activity of both isoforms of SOD in primary cultures of hippocampal neurons. Our results showed that PRL treatment during 72 h increases the protein content of both, SOD-1 and SOD-2 significantly, in contrast with the vehicle. Interestingly, this effect is also observed in the PRL/Glu group in comparison with the neurons that were only treated with Glu, which show a significant decrease in both isoforms, as expected (Fig. 2 A and B). Additionally, we evaluate whether PRL modifies the total SOD activity since the protein content evaluated by Western blot does not reveal their activity. As seen in Fig. 2C, PRL treatment doubles the total SOD activity, from 20% to 40%, as compared with the control and maintain this effect even in the neurons from the PRL/Glu condition (30%). While neurons treated only with Glu decreases to 10%, the total SOD activity compares with the PRL/Glu group.

3.4. Total SOD activity and protein content increase correlate with a low concentration of LPO products

LPO products increase significantly during Glu-induced excitotoxicity as result from mitochondrial dysfunction [23–25]. Since we observed that PRL maintains the mitochondrial membrane potential and increases the activity and the protein content of SOD, we quantified the LPO products concentration in hippocampal neurons treated with PRL or Glu alone or as a mixture (PRL/Glu), in order to determine indirectly the effect of PRL on lipid oxidation induced by ROS during excitotoxicity. As depicted in Fig. 3, LPO products concentration increase significantly in neurons treated only with Glu alone (100 µM). However, PRL pretreatment prevented this effect in PRL/Glu group, as the LPO products concentration decrease to 2µM/ µg of protein. Regarding the PRL-treated group, the LPO products concentration remained close to control values (Fig. 3).

4. Discussión

Excitotoxicity is implicated in neuronal death during ischemia, stroke and neurodegenerative disorders, among other neuropathological conditions [26]. This process caused by a rise in the extracellular Glu concentration is characterized by the impairment of mitochondrial activity and a significant increase in ROS production, mainly. Besides, excitotoxicity is accompanied by the decline in the antioxidant defences, such as catalase, glutathione peroxidase and SOD, among others [7,27]. Previously, we reported that PRL-induced neuroprotection against excitotoxicity is mediated by NF-κB activation [11]. Hence, in the present study, we have evaluated whether PRL mediates neuroprotection *via* the induction of the antioxidant enzymes SOD1 and SOD2.

First, we evaluated whether PRL prevents the cell death induced by Glu, in order to confirm the neuroprotective effect displayed by PRL previously reported by our group [11,12]. Our results demonstrate that PRL significantly decreases the percentage of TUNEL-positive neurons, which correspond mainly to apoptotic cells. Interestingly, other groups have also described that human PRL (hPRL) increases cell survival and decreases the number of apoptotic cells in human retinal pigment epithelial cells (ARPE-19) exposed to H_2O_2 [16].

Once we confirm that PRL decrease the percentage of TUNEL-positive cell, we demonstrated for the first time that PRL-induced neuroprotection is associated with the enhanced activity and a significant increase in the content of both SOD isoforms. These data are following those in rat luteinized granulosa cells exposed to PRL treatment (1 ng/mL for four days), in which both, the protein content and the mRNA of SOD1 and SOD2 increases significantly [28]. Moreover, in another study in pancreatic β-islets exposed to PRL (1 µg/mL for 24 h), it has been reported that PRL increases 8-times SOD1 mRNA, probably

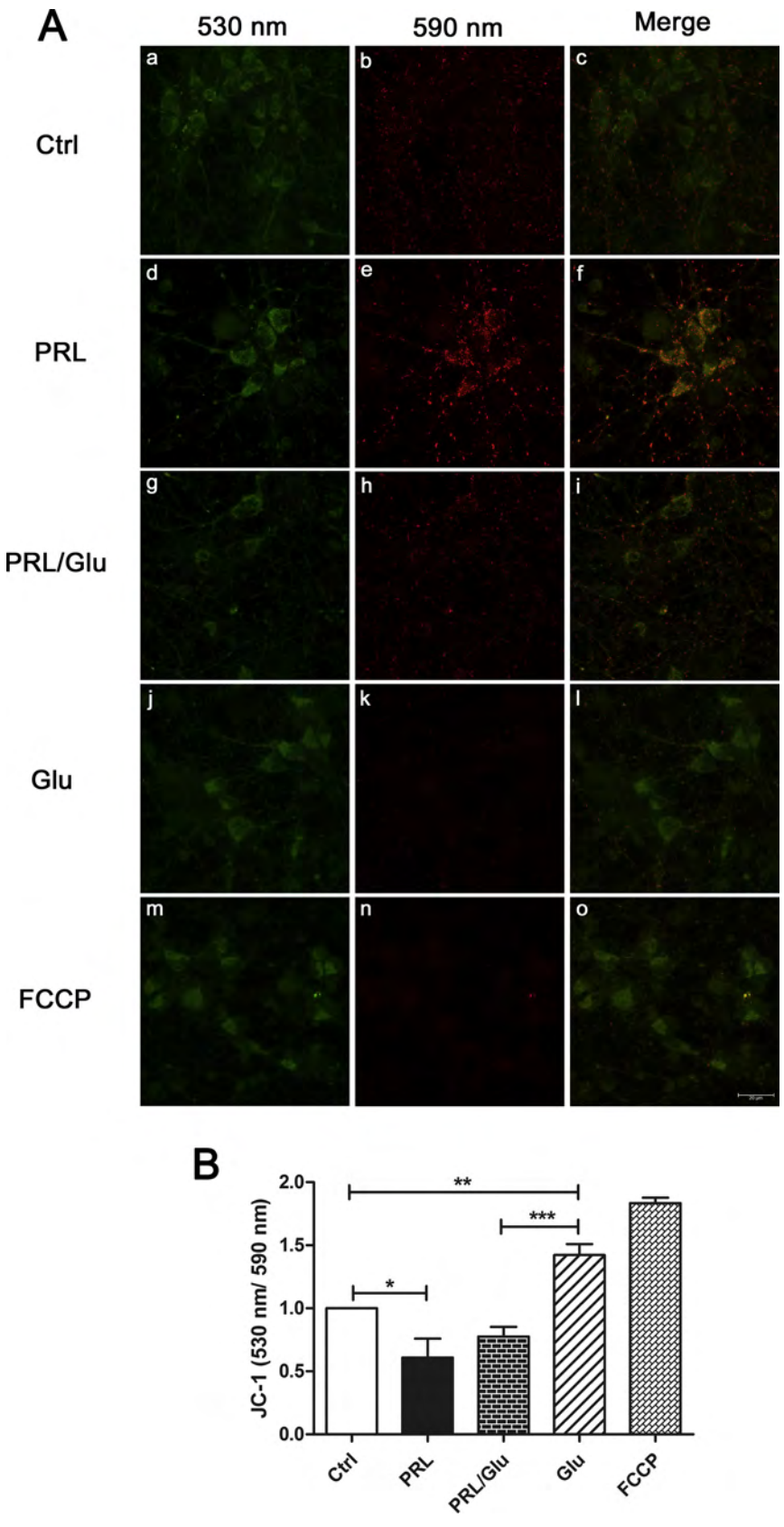

Fig. 1. Prolactin-induced neuroprotection is associated to the preservation of the mitochondrial activity. (**A**) Representative images from the hippocampal neurons stained with the JC-1 dye, treated with Control (saline solution); PRL (10 ng/mL); PRL/Glu (10 ng/mL and 100 μM, respectively), Glu (100 μM) and FCCP (1 μM for 5 min). (**B**) JC-1 ratio between both wavelengths (530 nm/590 nm), depolarized neurons show increased green fluorescence while neurons with active mitochondria increases the red fluorescence resulting in a decreased JC-1 ratio. Bars represent the mean ± SD of the JC-1 ratio from four independent experiments. Data were analyzed by one-way ANOVA followed by a Bonferroni´s post hoc test ** $p < 0.01$ PRL/Glu *vs.* Glu and Ctrl *vs.* Glu. Scale bar: 20 μm.

through the MAPK and STAT-3 activation [29]. However, contrary to these observations, another study showed that PRL induce antioxidant effects in retinal epithelium cells by SOD-independent mechanisms [16], suggesting that further experiments are required to investigate the effects of PRL on other antioxidant defense systems in hippocampal neurons.

Our results also demonstrate that PRL enhances total SOD activity, while Glu significantly decrease it, as compared with control values.

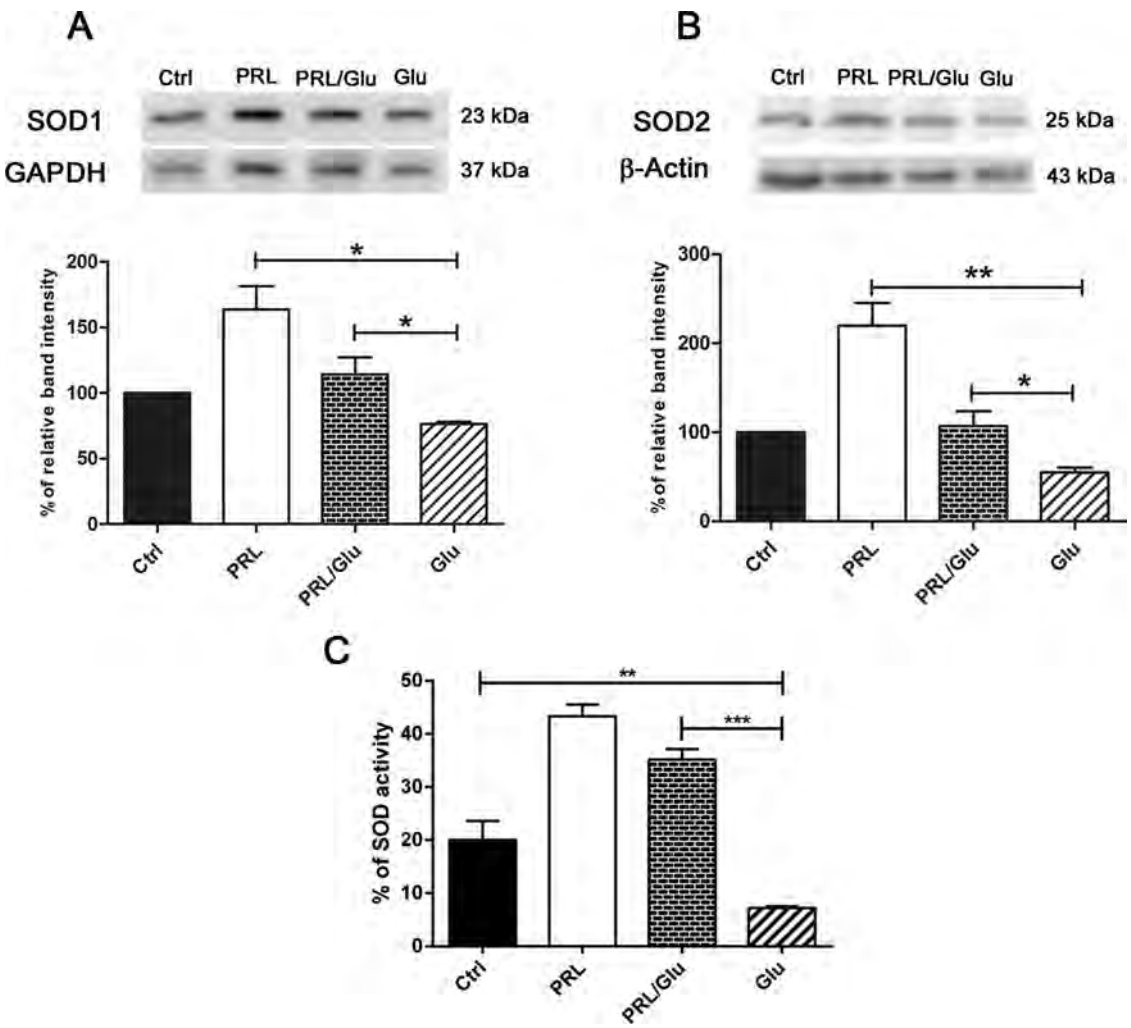

Fig. 2. Prolactin enhances SOD activity and protein content. (**A-B**) Representative western blots from both SOD isoforms. Densitometry analyses represent the relative ratio SOD1 or SOD2 normalized against GADPH or β-Actin, respectively. (**C**) Percentage of SOD activity in hippocampal neurons treated with PRL (10 ng/mL), PRL/Glu (10 ng/mL and 100 μM, respectively) and Glu alone. Bars represent the mean ± SD of five independent experiments. Data were analyzed by one-way ANOVA followed by a Bonferroni´s post hoc test *p < 0.05 PRL vs Glu; ** p < 0.01 PRL *vs.* Glu and Ctrl *vs.* Glu, *** p < 0.001 PRL/Glu *vs.* Glu.

These are in accordance with the literature. For instance, Bolzán et al. demonstrated that PRL positively regulates the SOD activity in liver and thymus in 29-month-old Sprague-Dawley female rats in a dose-dependent manner [30]; and Sun et al. reported that Glu-induced excitotoxicity impairs SOD activity in human neuroblastoma SH-SY5Y cells 24 h after Glu treatment [31]. Interestingly, our results demonstrate for the first time that enhanced PRL-induced SOD activity also occurs during Glu exposure, suggesting the increase in this antioxidant system even during the excitotoxic insult. This correlates with the increased protein content of SOD1 and SOD2, suggesting that PRL can augment both the constitutively expressed SOD1 [32] and the PI3K/Akt pathway-dependent SOD2 [15,33]. We hypothesize that PI3K/Akt pathway might induces SOD 2 expression, since PRL is able to activate this pathway through PRL receptor (PRLR) and hippocampal neurons express the long and short isoforms [12]. In fact, the PI3K/Akt pathway activation induced by PRL is under study in our group. The significant increase of both activity and protein content of SOD-1 and SOD-2 is probably *via* NF-kB activation; however, to address this effect to this transcriptional factor we are currently performing experiments with selective inhibitors of this pathway such as SN-50, PDTC.

Other interesting findings from this study is the effect of PRL on LPO products and the ΔΨm. We report for the first time that PRL prevents the increase in LPO and mitochondrial depolarisation induced by GLU, suggesting the preservation of mitochondrial function. PRL effects in the hippocampus have been poor studied only a few studies have focused on its antioxidant effects and none on the direct effect of PRL on lipid peroxidation, or mitochondrial function. However, a large number of studies are available regarding the antioxidant effect of growth hormone (GH), a protein hormone that belongs to the same protein family protein as PRL that exhibits antioxidant effects in several models. For instance, the human growth hormone (rhGH) prevents mitochondrial dysfunction and excitotoxicity, through the down-regulation of the mRNA of the NMDA receptor subunits GluN1, GluN2a and GluN2b [34]. Based on this finding we suggest that PRL could also modulate the expression and activity of the NMDA receptor complex, leading to a decrease in the intracellular Ca^{2+} overload and the concomitant preservation of the mitochondrial function. Actually, our group is on the effect of PRL on the expression, function and Glu binding affinity to AMPA, NMDA and KA ionotropic Glu receptors.

The mechanism underlying the decrease in LPO concentration by PRL is still not precise. In contrast, the effect of GH in the LPO products has been widely explored. It is known that patients with severe GH deficiency exhibit a high LPO serum concentration [35]. Likewise, GH decreases LPO products levels in the liver, heart, kidney and spleen of ovariectomized aged female rats, through the restoration of reduced glutathione and the increase in the reduced/ oxidised glutathione ratio [36]. This observation suggests that PRL induce a similar effect in the present conditions. Further LPO determinations in our *in vivo* model of

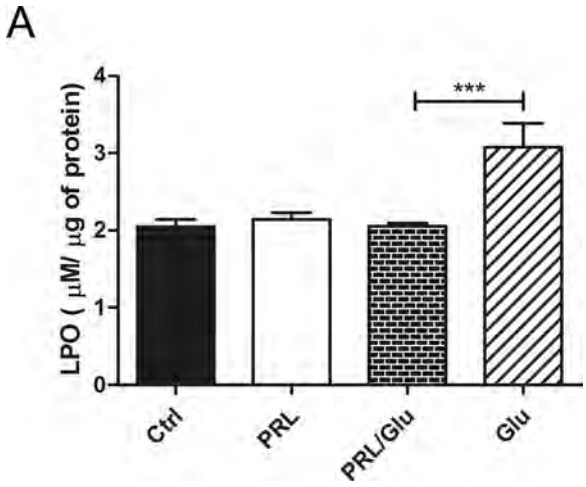

Fig. 3. SOD protein content and activity correlates with a decrease in the LPO products concentration induced by Glu. Bars represent the LPO products concentration correct per μg of protein from the hippocampal neurons exposed to PRL (10 ng/mL); PRL/Glu (10 ng/mL and 100 μM, respectively) or with Glu alone (100 μM). Each bar represent the mean ± SD of four independent experiments. Data were analyzed by one-way ANOVA followed by a Bonferroni´s post hoc test *** $p < 0.001$ *vs.* Glu.

neuroprotection induced by the exogenous administration of PRL, are required.

Finally, the present study provides evidence for the first time of the antioxidant effect of PRL during Glu-induced excitotoxicity in hippocampal neurons, suggesting novel properties for this hormone in the brain, which have been neglected for a long time, and offers new knowledge supporting the potentiality of PRL for the treatment of multiple targets affected by excitotoxicity.

Conflict of interest

The authors declare no competing financial interests

Acknowledgements

This study receive grants from DGAPA-PAPIIT-UNAM (to Dr. Lourdes Massieu, IN205416, and to Dr. Marco Cerbón, IN216817) and PAIP-Facultad de Química-UNAM (to Dr. Marco Cerbón, 5000-9108). Dr. Nadia Rivero receives a postdoctoral fellowship by DGAPA-UNAM.

Appendix A. Supplementary data

Supplementary material related to this article can be found, in the online version, at doi:https://doi.org/10.1016/j.neulet.2019.02.027.

References

[1] J.T. Brosnan, M.E. Brosnan, Glutamate: a truly functional amino acid, Amino Acids 45 (2013) 413–418.
[2] F. Schubert, J. Gallinat, F. Seifert, H. Rinneberg, Glutamate concentrations in human brain using single voxel proton magnetic resonance spectroscopy at 3 Tesla, Neuroimage 21 (2004) 1762–1771.
[3] A.J.B. Markowitz, M.G. White, D.L. Kolson, K.L. Jordan-Sciutto, Cellular interplay between neurons and glia: toward a comprehensive mechanism for excitotoxic neuronal loss in neurodegeneration, Cellscience 4 (2007) 111–146.
[4] X.-X. Dong, Y. Wang, Z.-H. Qin, Molecular mechanisms of excitotoxicity and their relevance to pathogenesis of neurodegenerative diseases, Acta Pharmacol. Sin. 30 (2009) 379–387.
[5] P. Kumar, H. Kalonia, A. Kumar, Role of LOX/COX pathways in 3-nitropropionic acid-induced Huntington's Disease-like symptoms in rats: protective effect of licofelone, Br. J. Pharmacol. 164 (2011) 644–654.
[6] P.R. Angelova, A.Y. Abramov, Role of mitochondrial ROS in the brain: from physiology to neurodegeneration, FEBS Lett. 592 (2018) 692–702.
[7] A. Mehta, M. Prabhakar, P. Kumar, R. Deshmukh, P.L. Sharma, Excitotoxicity: bridge to various triggers in neurodegenerative disorders, Eur. J. Pharmacol. 698 (2013) 6–18.
[8] E.A. Cabrera-Reyes, O. Limón-Morales, N.A. Rivero-Segura, I. Camacho-Arroyo, M. Cerbón, Prolactin function and putative expression in the brain, Endocrine 57 (2017) 199–213.
[9] M.E. Freeman, B. Kanyicska, A. Lerant, G. Nagy, Prolactin: Structure, Function, and regulation of secretion, Physiol. Rev. 80 (2000) 1523–1631.
[10] A.M. Corbacho, G. Martínez De La Escalera, C. Clapp, Roles of prolactin and related members of the prolactin/growth hormone/placental lactogen family in angiogenesis, J. Endocrinol. 173 (2002) 219–238.
[11] N.A. Rivero-Segura, E. Flores-Soto, S. García de la Cadena, I. Coronado-Mares, J.C. Gomez-Verjan, D.G. Ferreira, E.A. Cabrera-Reyes, L.V. Lopes, L. Massieu, M. Cerbón, Prolactin-induced neuroprotection against glutamate excitotoxicity is mediated by the reduction of [Ca2+]i overload and NF-κB activation, PLoS One 12 (2017) e0176910.
[12] E. Vergara-Castañeda, D.R. Grattan, H. Pasantes-Morales, M. Pérez-Domínguez, E.A. Cabrera-Reyes, T. Morales, M. Cerbón, Prolactin mediates neuroprotection against excitotoxicity in primary cell cultures of hippocampal neurons via its receptor, Brain Res. 1636 (2016) 193–199.
[13] A. Vanoye-Carlo, T. Morales, E. Ramos, A. Mendoza-Rodríguez, M. Cerbón, Neuroprotective effects of lactation against kainic acid treatment in the dorsal hippocampus of the rat, Horm. Behav. 53 (2008) 112–123.
[14] D. Tejadilla, M. Cerbón, T. Morales, Prolactin reduces the damaging effects of excitotoxicity in the dorsal hippocampus of the female rat independently of ovarian hormones, Neuroscience 169 (2010) 1178–1185.
[15] L. Miao, D.K. St Clair, Regulation of superoxide dismutase genes: implications in disease, Free Radic. Biol. Med. 47 (2009) 344–356.
[16] R. Meléndez García, D. Arredondo Zamarripa, E. Arnold, X. Ruiz-Herrera, R. Noguez Imm, G. Baeza Cruz, N. Adán, N. Binart, J. Riesgo-Escovar, V. Goffin, B. Ordaz, F. Peña-Ortega, A. Martínez-Torres, C. Clapp, S. Thebault, Prolactin protects retinal pigment epithelium by inhibiting sirtuin 2-dependent cell death, EBioMedicine 7 (2016) 35–49.
[17] R. Mandelkow, D. Gümbel, H. Ahrend, A. Kaul, U. Zimmermann, M. Burchardt, M.B. Stope, Detection and quantification of nuclear morphology changes in apoptotic cells by fluorescence microscopy and subsequent analysis of visualized fluorescent signals, Anticancer Res. 37 (2017) 2239–2244.
[18] S.G. de la Cadena, K. Hernández-Fonseca, I. Camacho-Arroyo, L. Massieu, Glucose deprivation induces reticulum stress by the PERK pathway and caspase-7- and calpain-mediated caspase-12 activation, Apoptosis 19 (2014) 414–427.
[19] T. Iijima, T. Mishima, M. Tohyama, K. Akagawa, Y. Iwao, Mitochondrial membrane potential and intracellular ATP content after transient experimental ischemia in the cultured hippocampal neuron, Neurochem. Int. 43 (2003) 263–269.
[20] I. Pérez-Torres, M. El Hafidi, O. Infante, G. Baños, Effects of sex hormone levels on aortic vascular reactivity and variables associated with the metabolic syndrome in sucrose-fed female rats, Can. J. Physiol. Pharmacol. 86 (2008) 25–35.
[21] M.R. Duchen, Mitochondria, calcium-dependent neuronal death and neurodegenerative disease, Pflugers Arch. 464 (2012) 111–121.
[22] C.B. Rueda, I. Llorente-Folch, J. Traba, I. Amigo, P. Gonzalez-Sanchez, L. Contreras, I. Juaristi, P. Martinez-Valero, B. Pardo, A. Del Arco, J. Satrustegui, Glutamate excitotoxicity and Ca2+-regulation of respiration: role of the Ca2+ activated mitochondrial transporters (CaMCs), Biochim. Biophys. Acta 1857 (2016) 1158–1166.
[23] T. Cassano, L. Pace, G. Bedse, A.M. Lavecchia, F. De Marco, S. Gaetani, G. Serviddio, Glutamate and Mitochondria: Two Prominent Players in the Oxidative Stress-Induced Neurodegeneration, Curr. Alzheimer Res. 13 (2016) 185–197.
[24] M.W. Fariss, Role of Mitochondria in toxic oxidative stress, Mol. Interv. 5 (2005) 94–111.
[25] H.K. Kim, C. Isaacs-Trepanier, N. Elmi, S.I. Rapoport, A.C. Andreazza, Mitochondrial dysfunction and lipid peroxidation in rat frontal cortex by chronic NMDA administration can be partially prevented by lithium treatment, J. Psychiatr. Res. 76 (2016) 59–65.
[26] H. Prentice, J.P. Modi, J.-Y. Wu, Mechanisms of Neuronal Protection against Excitotoxicity, Endoplasmic Reticulum Stress, and Mitochondrial Dysfunction in Stroke and Neurodegenerative Diseases, Oxid. Med. Cell. Longev. 2015 (2015) 964518.
[27] J.A. Dykens, Free radicals and mitochondria dysfunction in excitotoxicity and neurodegenerative disease, Cell Death and Diseases of the Nervous System, (1999), pp. 45–68.
[28] N. Sugino, M. Hirosawa-Takamori, L. Zhong, C.M. Telleria, K. Shiota, G. Gibori, Hormonal regulation of copper-zinc superoxide dismutase and manganese superoxide dismutase messenger ribonucleic acid in the rat corpus luteum: induction by prolactin and placental lactogens, Biol. Reprod. 59 (1998) 599–605.
[29] S. Bordin, M.E.C. Amaral, G.F. Anhê, V. Delghingaro-Augusto, D.A. Cunha, J.E. Nicoletti-Carvalho, A.C. Boschero, Prolactin-modulated gene expression profiles in pancreatic islets from adult female rats, Mol. Cell. Endocrinol. 220 (2004) 41–50.
[30] A.D. Bolzán, O.A. Brown, R.G. Goya, M.S. Bianchi, Hormonal modulation of antioxidant enzyme activities in young and old rats, Exp. Gerontol. 30 (1995) 169–175.
[31] Z.-W. Sun, L. Zhang, S.-J. Zhu, W.-C. Chen, B. Mei, Excitotoxicity effects of glutamate on human neuroblastoma SH-SY5Y cells via oxidative damage, Neurosci. Bull. 26 (2010) 8–16.
[32] E. Minc, P. de Coppet, P. Masson, L. Thiery, S. Dutertre, M. Amor-Guéret, C. Jaulin, The human copper-zinc superoxide dismutase gene (SOD1) proximal promoter is regulated by Sp1, Egr-1, and WT1 via non-canonical binding sites, J. Biol. Chem. 274 (1999) 503–509.
[33] A.I. Rojo, M. Salinas, D. Martín, R. Perona, A. Cuadrado, Regulation of Cu/Zn-superoxide dismutase expression via the phosphatidylinositol 3 kinase/Akt pathway

and nuclear factor-kappaB, J. Neurosci. 24 (2004) 7324–7334.
[34] E. Nylander, A. Grönbladh, S. Zelleroth, S. Diwakarla, F. Nyberg, M. Hallberg, Growth hormone is protective against acute methadone-induced toxicity by modulating the NMDA receptor complex, Neuroscience 339 (2016) 538–547.
[35] A. Kokoszko, M. Karbownik, A. Lewiński, Increased lipid peroxidation in growth hormone-deficient adult patients, Neuro Endocrinol. Lett. 27 (2006) 225–230.
[36] I. Baeza, J. Fdez-Tresguerres, C. Ariznavarreta, M. De la Fuente, Effects of growth hormone, melatonin, oestrogens and phytoestrogens on the oxidized glutathione (GSSG)/reduced glutathione (GSH) ratio and lipid peroxidation in aged ovariectomized rats, Biogerontology 11 (2010) 687–701.

Send Orders for Reprints to reprints@benthamscience.ae

304 *Current Protein and Peptide Science,* **2019,** *20,* **304-315**

REVIEW ARTICLE

Medical and Veterinary Importance of the Moonlighting Functions of Triosephosphate Isomerase

Mónica Rodríguez-Bolaños* and Ruy Perez-Montfort*

Departamento de Bioquímica y Biología Estructural, Instituto de Fisiología Celular, Universidad Nacional Autónoma de México, Av. Universidad 3000, Coyoacán, 04510 México DF, México

ARTICLE HISTORY

Received: December 20, 2017
Revised: October 16, 2018
Accepted: October 18, 2018

DOI:
10.2174/1389203719666181026170751

Abstract: Triosephosphate isomerase is the fifth enzyme in glycolysis and its canonical function is the reversible isomerization of glyceraldehyde-3-phosphate and dihydroxyacetone phosphate. Within the last decade multiple other functions, that may not necessarily always involve catalysis, have been described. These include variations in the degree of its expression in many types of cancer and participation in the regulation of the cell cycle. Triosephosphate isomerase may function as an auto-antigen and in the evasion of the immune response, as a factor of virulence of some organisms, and also as an important allergen, mainly in a variety of seafoods. It is an important factor to consider in the cryopreservation of semen and seems to play a major role in some aspects of the development of Alzheimer's disease. It also seems to be responsible for neurodegenerative alterations in a few cases of human triosephosphate isomerase deficiency. Thus, triosephosphate isomerase is an excellent example of a moonlighting protein.

Keywords: Triosephosphate isomerase, moonlighting, cancer, antibody, virulence factor, allergen, cryopreservation, Alzheimer's disease, neurodegeneration.

1. INTRODUCTION

Glycolysis is a catabolic pathway involving ten steps, in which one glucose molecule is converted to two pyruvate molecules, consuming two ATPs, but gaining four molecules of ATP for each transformed glucose [1]. Triosephosphate isomerase (TIM) catalyzes the fifth step of glycolysis, reversibly isomerizing glyceraldehyde-3-phosphate (GAP) and dihydroxyacetone phosphate (DHAP). Even though TIM is not a regulatory enzyme, it is in charge of providing metabolites that connect with other metabolic pathways including (i) the pentose phosphate pathway, in which complex sugars can be formed from GAP [2]; (ii) the de novo synthesis of NAD+ via the synthesis of quinolinic acid (QA): here aspartate is oxidized to iminoaspartate, which condenses with a molecule of DHAP to form QA; QA is then phosphorylated to be converted into nicotinic acid mononucleotide, one of the precursors of NAD+ [3]; (iii) gluconeogenesis, in which GAP or DHAP may be formed starting from pyruvate or oxaloacetate [4] and (iv) biosynthesis of triacylglycerols in adipose tissue, where DHAP is used for the synthesis of triacylglycerols [5].

*Address correspondence to these authors at the Departamento de Bioquímica y Biología Estructural, Instituto de Fisiología Celular, Universidad Nacional Autónoma de México, Circuito Exterior S/N, Delegación Coyoacán, 04510 México D.F., Mexico;
Tel: + 52 55 5622 5657; Fax: + 52 55 5622 5630;
E-mails: mbolanos@email.ifc.unam.mx (MR-B), ruy@ifc.unam.mx (RP-M)

TIM is present in all organisms [6, 7] and, in most known cases, has approximately 250 amino acids per monomer chain (molecular mass ~ 27,000 Da), even though the length of the protein, and the molecular mass, can vary considerably in different species. The first crystallized structure of TIM revealed it had a $(\beta/\alpha)_8$-barrel topology [8], currently known as the TIM barrel. This is the most frequent structural motif in soluble proteins. Close to 10 % of the enzymes with known structure are TIM barrels [9, 10]. TIM does not require any ion or cofactor to perform its catalytic function [11, 12]. TIM is only active as a dimer, but both monomers have all catalytic residues. From an evolutionary and kinetic point of view, TIM is considered a perfect catalyst, since only the velocity of diffusion of the substrate to the active site is the limiting step for catalysis. Both, the function and the catalytic mechanism of TIM have been conserved in all species throughout evolution [1, 10, 11]. TIM is a well-studied glycolytic enzyme that has been thoroughly characterized from an enzymatic point of view.

After years of research on many enzymes, new functions, which are not related to their catalytic function, have been discovered [13]. Some examples can be found in glycolytic enzymes, which besides their main function, also regulate the activity of other proteins. For example, aldolase helps in the assembly and function of the vacuolar-type ATPase, hexokinase regulates the function of the apoptotic proteins Bax, Bak, and Bad, glyceraldehyde-3-phosphate dehydrogenase regulates the transcription of the gene of histone H2B during the progress of the cellular cycle, and glucose-6-

1389-2037/19 $58.00+.00 **© 2019 Bentham Science Publishers**

INFORME DE LABORES 2019

phosphate isomerase participates in inducing cellular motility through secretion and binding to the tumor autocrine motility factor receptor gp 78 [6].

This review focuses on new non-catalytic functions of TIM in multiple biochemical systems, most of them medical and one of them of veterinary importance. It has been reported that, depending on its location and oligomeric state, TIM can have different functions. For example, TIM expression levels are associated and seem to be important markers of different types of cancers [14]. TIM is also involved in the cellular cycle via its interaction with cyclin 2 dependent kinase (Cdk2) [15-17]. In other cases, TIM secreted to the surrounding medium may function as a virulence factor [18]. TIM may also function as an allergen that easily elicits immune responses [19]. Modification of TIM allows adequate signaling for the maturation of highly specialized cells like spermatozoa [20]. It has also been proposed that TIM must be assembled correctly for an optimal function of neurons. And finally, TIM also seems to play an important role in Alzheimer's disease [7] and in neurodegeneration problems in some cases of the rare human TIM deficiency disease [21, 22].

2. TIM AND CANCER

2.1. Variation in the Degree of TIM Expression

The incidence of cancer seems to be increasing in recent years and is becoming more prevalent in its numerous varieties (https://www.cancer.gov/about-cancer/understanding/statistics). Many tools for early detection and diagnosis of different types of cancers lack sensitivity and often positive confirmation of its presence occurs only in the advanced stages of the disease [23]. The dysfunction of tumor suppressors and oncogenes produce modifications in several intracellular signaling pathways, which reprogram the metabolism of tumor cells to favor their survival and growth. Glycolysis is a central degradation pathway in eukaryotes, but in the majority of cases, cells acquire their ATP stores from oxidative phosphorylation. In several cancers, metabolic alterations trigger the transformation of healthy cells into diseased cells. One of these alterations, called the Warburg effect, is when the cancer cell uses glycolysis as its main pathway to produce ATP. Depending on the cell type, the mRNA expression of TIM increases 5 to 20-fold when the cells start proliferating [24, 25]. The deregulation of the levels of expression for TIM is one of the characteristics of cancer [14]. The level of expression of this enzyme in different cells and its clinical implications are not defined and, in some cases, result in beneficial effects and in other cases they become deleterious [25-27].

The expression of TIM is associated with the suppression of the development of the tumor and metastasis in some types of cancers like hepatocarcinoma and carcinoma of the stomach [24, 25]. In liver cancer, the effect of suppression of the tumors has been described both *in vitro* and *in vivo* in YY-88103, Hep3B, and Huh7 cells and in tumors extracted from patients with hepatocarcinoma. Even though the mechanism of how TIM affects the progression of the disease is not well understood, it has been shown that the overexpression of TIM, in this type of cancer, inhibits cellular growth arresting the cells in phases G1/S of the cell cycle [25]. Some of the genes that participate in the modulation of phases G1/S are P53, P16, P27, cyclin D1, and Rb. The alteration of their levels increases cell growth and the risk of tumor formation [28]. Additionally, high levels of TIM, modify the expression patterns of regulatory proteins like P53, P16, P27, cyclin, Rb, and β-catenin. The increase in the expression of P53 and P27 produces a decrease in the expression of cyclin D1, which leads to a cellular arrest and stops propagation, while β-catenin, an enzyme closely related to metastasis, reduces its expression [25].

TIM expression is deregulated in all cases of gastric cancer [27]. Overexpression of TIM in gastric carcinoma cells with phenotype SGC7901/VCR, which are multi-resistant to the drugs used to treat the illness, helps reduce this multiresistance. Similarly, a reduction of the expression of TIM favors resistance to those drugs [24]. This indicates that overexpression of TIM helps in the treatment of gastric cancer.

Another TIM that has a suppressor effect on the growth of cells is the TIM from a species of mollusk called *Arca inflata*. It has a toxic effect on adenocarcinoma cells with A549 and SPC-A-1 phenotypes and also on HEP G2 liver carcinoma cells [29].

In different ways, expression of TIM in different types of gastric cancers is related to an increase in invasion, metastasis and the proliferation of tumor cells [26]. In gastric carcinoma cell lines with the BGC-823 phenotype, overexpression of TIM promotes cellular proliferation, migration, and invasion, but does not generate any changes in the cell cycle. However, when TIM expression is suppressed in cells with phenotype MGC-803, proliferation decreases and an apoptosis signal is turned on, producing an arrest of the cell cycle in phase G2/M [14, 23, 27]. Thus, the intracellular concentration of TIM in these cells is of great importance for their disease-producing behavior.

Additionally, the levels of expression of TIM are also altered in other types of cancers such as cancer of the urinary tract [14], carcinoma of the ovaries [30], lung adenocarcinoma [14], cancer of the colon with a high metastatic potential [23], gastric carcinoma [26], thyroid cancer [31], breast cancer [32, 33], squamous cell carcinoma of the esophagus [34], pancreatic cancer [31], kidney cancer [35, 36], esophageal carcinoma [26] and squamous lung cell carcinoma [14, 23, 25]. In all cases, TIM is related to the metastatic and invasive behavior of the diseases.

2.2. TIM Expression Levels as Markers for the Prognosis of Different Cancers

The differential expression of TIM in cancerous cells and in normal cells has an important diagnostic value and relates to the prognosis of the patient. The possibilities of survival can be predicted depending on the type of cancer, the size of the tumor, the presence of metastasis, the degree of histologic differentiation of the cells and the overexpression of TIM [26, 37].

In gastric cancers, survival is diminished in patients with high levels of TIM expression and who have tumors larger than 5 cm, in comparison with those who have tumors of the same size but low expression levels of TIM [26]. In cases of

INFORME DE LABORES 2019

papillary and follicular cancer of the thyroid, a differential expression of this enzyme has been found [31]. It has been observed that this expression, together with that of other proteins such as A2, cofilin1, PCNA, and HSP27, allows differentiation between both types of cancer, helping in its timely and appropriate treatment [31]. In breast cancer cells expression of TIM is also elevated in comparison to healthy cells, making it a good biomarker for the disease [33].

Metastasis is a common complication of cancer, which typically worsens the prognosis of the patients. The detection of the places where the cancer has spread is of utmost importance for the treatment of the disease. In the case of some gynecological cancers, there are some deregulated proteins that function as biomarkers. For example, in endometrial and ovarian cancer, TIM is expressed more intensely in the secondary tumors than in the primary tumor [38]. Numerous proteins have been described that can serve as biomarkers in different types of cancer, but, interestingly, TIM seems to be deregulated very frequently in a great number of varieties of this illness and, in many cases, can be a useful marker.

2.3. Anti-TIM Antibodies

The immune response is one of the primary and fundamental lines of defense against pathogenic agents. During the first stages of tumor formation, many proteins or peptides are expressed on the surface of cancerous cells. These molecules may initiate an immune response in the patient against the tumor [39]. Humoral responses against cancer have been demonstrated with the identification of many different surface and intracellular antigens in different types of tumors. However, the concentration of antigens tends to be very low, particularly during the initial stages of the ailments [23]. Early detection and diagnosis are of vital importance in many malignancies. The detection of autoantibodies is one of the widely used approaches for the detection of these illnesses today [32].

TIM is distributed in all the cytoplasm of cells and it is overexpressed to high levels in tissues with high glycolytic activity, like cancer cells. One of the theories about why TIM may have immunogenic activity is that during the development of the tumor it produces aberrant or mutated proteins that can elicit an immune response [34]. Anti-endogenous TIM antibodies have been reported in squamous cell carcinoma of the lung [23], gastrointestinal carcinoma [26], esophageal carcinoma [34], breast cancer [32, 33], hepatoma [34] and carcinoma of the kidney [35], among others.

As mentioned before, one of the theories about the generation of autoimmune responses is the production of aberrant proteins, but the mechanism of the autoantibody response against intracellular proteins remains unknown. In some cases, the response is generated because variant proteins are expressed as results of the activation of alternative promoters after the cancerous transformation of the cells [33] or different isoforms of the protein are expressed [36, 39]. Moreover, it has been proposed that most tumor antigens are not products of damaged genes. Instead, tumor antigens are overexpressed proteins during cellular differentiation [23, 39] that change their expression level depending on the status of the tumor and direct the progression of the disease [36].

In squamous cell carcinoma of the lung, TIM is secreted to the extracellular medium assisting the recognition of the disease by the immune system. Pieper and coworkers [40] suggest that a mutation of threonine 28 for an isoleucine, produces a new epitope which increases the immune response. These autoantibodies also exist in other diseases such as hepatitis, but these antibodies are more reactive in patients with hepatic cancer than in those with hepatitis [34].

The humoral immune response against TIM is apparently dependent on certain post-transcriptional modifications such as protein glycosylation. Antibodies can recognize glycosylated TIM but not TIM without modifications [34, 39]. The high specificity with which the antibodies recognize glycosylated TIM, could yield clues to the metabolic changes that occur in the course of the disease.

In addition to cancer, anti-TIM antibodies have been detected in a variety of diseases. These include systemic lupus erythematosus, particularly its neurologic manifestation known as neuropsychiatric lupus erythematosus [41-43], in osteoarthritis, where they are associated with chronic inflammation [44] and in patients with hepatitis type A and mononucleosis, in which the antibodies cause hemolysis, the reactivation of the Epstein-Barr virus [45] and multiple sclerosis [46].

In general, each tissue or organ in the body has a different molecular composition, depending on its location and function. The mechanism of production of auto-antibodies against many of their extracellular and intracellular proteins is still not fully understood.

3. TIM AS A VIRULENCE FACTOR

Virulence factors are molecules with which a microorganism invades and colonizes other organisms and provokes sickness. Virulence factors can be proteins, carbohydrates or lipids which are usually located on the surface of the pathogen [47]. There are reports on a great number of virulence factors, and notably in some parasites and protozoans, some enzymes that are normally intracellular have been found in the extracellular matrix. Some of them are glycolytic enzymes among which are glyceraldehyde-3-phosphate dehydrogenase (GAPDH), enolase and TIM. It has been demonstrated that the function of these enzymes in the extracellular matrix is not catalytic [18, 48]. The mechanism of secretion to the exterior of the cell of these enzymes is unknown [47]. No signal sequence or anchoring motif that may help bind TIM, GAPDH or elongation factor thermo unstable (EF-Tu) to the surface of the cells has been identified [18]. Together with other proteins, TIM has been identified on the surface of Gram-positive bacteria [49]. Usually, proteins that anchor on the surface of cells with their C-terminal domain, maintain their N-terminal domain as a recognition peptide [47].

The cell surface has two types of adhesins: one type are proteins that are covalently associated with the membrane, the other type are proteins that are bound to the cellular surface using ionic interactions. In the case of *Lactobacillus plantarum*, it was shown that TIM, GAPDH, and EF-Tu were bound to the membrane with these ionic interactions [50].

INFORME DE LABORES 2019

TIM has also been reported as an external adhesion molecule in organisms like *Trichomonas vaginalis* [51], *Lactobacillus plantarum* [50] and *Paracoccidiodes brasiliensis* [48]. In these organisms, TIM interacts with the epithelial cells and with the proteins of the extracellular matrix like laminin and fibronectin. TIM from *Staphylococcus aureus* mimic lectin activity and permits binding with sugars on the surface of *Cryptococcus neoformans*. The association of *S. aureus* TIM with the glyco-capsule of *C. neoformans* triggers apoptosis, and thus elimination of this pathogen [48, 52]. Furthermore, TIM from *S. aureus* together with enolase regulates fibrinolysis and fibrinogenesis, potentiating its capacity to invade tissue [47, 53].

In some parasites, one way to evade the immune response of the host is the continuous interchange of epitopes on the surface of their cells [54]. In some parasites like *Brugia malayi*, *Schistosoma mansoni* and *Haemonchus contortus*, variations in the quantities of TIM excreted to the medium, depending on the phase of their vital cycle, have been described [55]. It has also been reported that a certain concentration of TIM secreted to the medium is necessary for the maturation *of Brugia malayi*, indicating that TIM plays a role in the evasion/modulation of the host's immune response [56].

Drastic changes in the expression levels of TIM, related to viral replication, have also been reported in viral infections [57]. After viral infection, the machinery of the cell is sequestered by the virus to favor its replication or evade the immune response. The Warburg effect has been observed during infection of the cells of *Exopalaemon carinicauda* by the white spot syndrome virus (WSSV). This includes an increase of activity of glycolysis and a redirecting of the infected cells to different replication states. The levels of TIM are particularly altered, indicating that TIM has a major role in WSSV infection [57, 58].

4. TIM AS AN ALLERGEN

Food allergies are caused by an induced abnormal immune response to certain foods. The eight great groups of foodstuffs that are capable of generating this type of response are peanuts, nuts, soy, wheat, fish, oysters, milk and eggs. Allergies have increased all over the world in the last years, due to the increased consumption of certain foods [59, 60].

Typically, all allergens are proteins and, in some cases, these proteins exist in all organisms. Allergens usually have a low molecular mass (of approximately 10-70 kDa), a high solubility, a high thermic stability, and acid isoelectric points [60, 61]. The most common allergens in the groups of foodstuffs mentioned above have been known for decades, but there are still many that have not been identified and studied. There are databases that enlist details about certain molecular, biochemical and clinical properties of some of these proteins. An example is the list of allergens of the Allergen Nomenclature Sub-Committee of the World Health Organization and the International Union of Immunological Societies (www.allergen.org).

Among numerous families of proteins present in food, it has been found that most allergens belong to a small group of proteins with restricted biochemical role [62]. Surprisingly, the TIM-barrel is the most frequent motif among the allergens [63].

TIM has been described as a new allergen, mainly in marine organisms and in certain invertebrates. Some of these species are: *Octopus fangsiao* [60], *Blattella germanica* [19], *Penaeus monodon* [64], *Procambarus clarkii* [65], *Citrullus lanatus* [59], *Forcipomyia taiwana* [66], latex (rubber) [67], *Litchi chinensis* [61], *Crangon crangon* [68], *Solea solea* [69] and *Sarcoptes scabiei* [70].

Pan-allergens are proteins that are present in all organisms and have the capacity of cross-reacting [64, 71]. Cross-reactions are immune responses against similar antigenic epitopes, which come from different sources. They generally occur with proteins that have at least 35% homology in their sequences [65]. For example, human TIM cross-reacts with TIMs from other species such as crustaceans, insects, dust mites and mollusks [64]. TIM from *B. germanica* (cockroach) has 60.7% sequence homology with wheat TIM and 19 other TIMs [19]. Thus, patients that are allergic against TIM from *B. germanica* can also react when exposed to other TIMs. Cross-reaction also occurs between TIM and other proteins. For example, TIM from *P. clarkii* has crossed-reactivity with Filamin C (FLN c), which is a protein that binds actin in this same organism [65]. It has also been proposed that hypersensitivity against watermelon (*C. lanatus*) TIM is due to cross-reactivity with the pollen of other plants. In the case of lychee TIM, cross-reaction has been seen with latex (rubber) TIM [67]. TIM from *S. scabiei* var. *canis* shows cross-reactivity with sera from rabbits that have been infected with other parasites. TIM from *S. scabiei* also shows great homology with 25 allergens of dust mites [70].

The mechanism by which TIM generates immune reactivity is not yet fully understood. Rosenberg and coworkers [72], proposed that the formation of homo and hetero-oligomeric aggregates between TIM itself or with other proteins considerably favors the humoral immune response against those proteins. An analysis of the structures of several crystallized allergens showed that 80% of them are dimers [64]. Since the oligomeric state can be important in the induction of the immune response, the treatment of the food before it is ingested is a factor that influences the generation of allergic responses. Generally, food receives treatment with heat (cooking) and is then subjected to changes in pH and enzymatic digestion when it is eaten. Most of the time there is either an increase or decrease in the hyper-reactivity caused by the proteins, in particular by TIM [60]. However, protein in its native conformation is not always the causative agent of allergic reaction [73]. In some cases, as is the case with the TIM from *O. fangsiao*, there is no decrease in the response when it is treated with heat. In contrast, TIM from *P. monodon* loses its immunogenicity under the same conditions [60].

There are two types of antigen epitopes: linear and conformational [73]. It is thought that epitopes of TIM from *O. fangsiao* are of the linear type because their conformations are not affected by hydrolysis and denaturation, but epitopes of TIM from *P. monodon* are conformational.

INFORME DE LABORES 2019

Much is unknown about the epitopes that initiate an anti-TIM allergy. Nevertheless, in the case of crustaceans and arthropods, such as the dust mite and *S. scabiei*, use of an antibody against anti-TIM IgE has been proposed as a good marker for allergy prediction [64, 70].

Due to their immense nutritional contribution to world food consumption, marine products can frequently produce allergies and hypersensitivity problems. Several common proteins that can elicit an immune response have been identified in these foods, which include tropomyosin, arginine kinase, the light chain of myosin, the sarcoplasmic calcium-binding protein, troponin C, hemocyanin and TIM [60, 73].

5. TIM AS A BIOMARKER OF CRYOPRESERVED SEMEN

Spermatozoa are highly differentiated cells which lack endoplasmic reticulum, Golgi apparatus, peroxisomes, lysosomes, and ribosomes and therefore lack transcription and translation. Expression of proteins necessary for fecundation is completed before they are ejected to the environment [74]. Cryopreservation of semen is a technique that permits the conservation and dissemination of gametes of different species. Frequently, the procedure causes structural and functional damage to spermatozoa. The increase in reactive oxygen species (ROS), osmotic stress, mechanical damage and the formation of crystals, are the main causes of the decrease in the quality of sperm during cryopreservation. Changes in any of these variables affect the mobility and potential fertility of the sperm [75]. TIM is located in the membranes of the acrosomes of the spermatozoa and it plays an important role in the capacitation reaction and the binding of sperm to the pellucid zone of the oocyte [76]. Additionally, high levels of TIM have been found in asthenozoospermia (a diminishment in the motility of sperm) in boars. In bulls, high levels of TIM are associated with a lower quantity of sperm and low fertility levels [20, 77].

Analysis of the patterns of overexpression of spermatic proteins under various conditions revealed that cryopreservation produces changes in levels of expression of 41 enzymes [74]. These proteins belong to three groups: enzymes for the organization of the flagellum, detoxification proteins, and metabolic energy proteins. Among these enzymes, TIM modifies its quantity to an important degree. In studies of the quality of sperm for cryopreservation, two populations of cells have been identified with different levels of TIM expression. Those with low quantities of TIM before freezing had a better viability after thawing and those with high TIM levels had a low survival rate [20, 77].

It is thought that after thawing the high amounts of TIM predispose the cell to an "early capacitation"; that involves all the cellular modifications that allow the sperm to bind to the oocyte [20, 78, 79]. If capacitation occurs before the right time, the motility of the spermatozoa is affected.

During freezing and thawing of sperm cells, the lipids in their membranes are rearranged. These changes increase the fluidity of the membranes, causing alterations in intracellular calcium permeability, accelerating capacitation and diminishing the viability of the spermatozoa [75, 80, 81].

Additionally, it has been observed that cryopreservation induces important changes in phosphorylation and the redox state via carbonylation of the proteins of sperm. One of the proteins most affected by this reaction is TIM. Carbonylation of proteins is the direct result of the oxidative stress caused by cryopreservation [75].

Changes in the oxidation state of the proteins cause physio-pathological conditions due to the modification of their structure and function. For example, carbonylation of TIM and other enzymes promotes early capacitation of sperm [75].

Protein carbonylation can be a crucial component of redox signaling in certain mammalian tissues. It may be a part of the mechanism for cryo-capacitation, a method commonly used for mammalian sperm [75].

In vivo, infertility is frequently associated with low sperm count (azoospermia), but it has also been found that the production of anti-TIM antibodies hinders capacitation of sperm and their binding to the pellucid zone [76].

6. THE ROLE OF TIM IN ALZHEIMER'S DISEASE

The reactive species of oxygen and nitrogen (ROS and NOS) are normally produced in small amounts in mammalian cells, where they act as physiological messengers. Changes in the cellular environment, exposure to toxins or changes in metabolism change the balance of the concentration of these species. All cells in an organism are vulnerable to the damage caused by an unbalance of ROS. In particular, neurons have increased sensitivity because of their high energy demand and low concentration of antioxidants in these cells [82-84].

One of the hallmarks of Alzheimer's disease is the presence of plaques and neurofibrillary tangles due to the accumulation of the amyloid peptide (Aβ) and paired helical filaments of Tau protein [85, 86]. The main function of Tau protein is to stabilize microtubules, which are necessary for axonal transport. TIM interacts with Tau protein under normal and also under pathological conditions. Under normal conditions, when there is little oxidative stress, Tau protein protects TIM, preventing modifications that may affect TIM's activity [85]. It is known that Aβ is capable of reducing the Cu^{2+} and Fe^{3+} ions, with the concurrent production of H_2O_2, which creates a cascade of ROS. The superoxide anion (O_2^-) reacts with nitric oxide (NO) to produce the peroxynitrite anion (ONOO-), which nitrates the tyrosines of proteins. This process is known as nitrotyrosination. This reaction, which involves the addition of a nitro (NO_2) group to a tyrosine, is irreversible and yields 3-nitrotyrosine as a product [87, 88]. In Alzheimer's disease, 45 proteins have been found that undergo this modification [84].

One of the proteins that are most affected by nitrotyrosination is TIM. TIM is the only glycolytic protein whose malfunction is associated with a loss of memory and with cerebral dysfunction and neurodegeneration [6, 7, 89]. When tyrosines of TIM are nitrated, its catalytic efficiency is decreased 15 times with respect to the wild-type enzyme [90]. Human TIM has 4 tyrosines, but the derivatization of Y164 and Y208 have a greater impact on the structure of the enzyme [90].

INFORME DE LABORES 2019

Enzymatic catalysis of TIM is usually accomplished in a special medium that enables isomerization. This setting is provided by the catalytic loop which remains open when there is no substrate and closed when catalysis is ongoing [91, 92]. Nitration of Y164 and Y208 prevents the loop from closing. Y164 interacts with T168 forming a hydrogen bond that reduces the mobility of the loop. Besides, the hydroxyl group of Y209 (of yeast TIM) is of highest importance for the stabilization of the loop in closed position. When this Y209 has nitrated the catalytic loop remains open, favoring the entrance of water to the active site and, with it, the formation of methylglyoxal (MEG) [88, 90, 93].

MEG is capable of glycosylating other amino acids in proteins and nucleic acids. Arginine is its most frequent target, producing argpyrimidine glycation of Aβ [84, 87, 88, 90, 94, 95], that accelerates the deposit of the amyloid peptide and considerably increases its toxicity [90].

The modifications brought by oxidative stress, as well as those created by the accumulation of MEG, produce compounds that are capable of modifying the permeability of the mitochondrial membrane [86]. For example, 4-hydroxy-2-trans-nonenal, a product of the peroxidation of the lipids of the membrane, interacts with some amino acids such as cysteine, lysine, and histidine which generate conformational changes in membrane proteins. The damage to the structure of the membrane can be so severe that its permeability may induce cellular death. Additionally, MEG accumulation diminishes the mitochondrial membrane potential and as a result, the amount of pro-apoptotic proteins Bax and caspase -3 are increased [88, 96, 97].

Other studies indicate that nitrotyrosinated TIM has a greater tendency to aggregate. In an alignment of the sequence of amyloid peptide and TIM, a fragment of TIM showed 20% homology with the amyloid peptide [98]. Accumulation of nitrotyrosinated TIM aggregates that cannot be degraded by the proteasome act as seeds for the fibrogenesis of other proteins.

TIM has an important functional and structural role in Alzheimer's disease. It has been shown that the modification of the structure of the dimer is enough to induce neurodegeneration [7]. Likewise, modification of its function provokes the formation of toxic structures such as neurofibrillary plaques and tangles. Another common feature of Alzheimer's disease is a low level of ATP in the cells, which also correlates with the low activity of TIM [87, 99]. Figure **1** depicts a summary of the pathological processes in which TIM plays a role in Alzheimer's disease.

7. HUMAN DEFICIENCY OF TRIOSEPHOSPHATE ISOMERASE

Human TIM deficiency is a rare autosomal recessive disease that was first described in 1965. It belongs to a class of diseases called glycolytic enzymopathies which show symptoms such as chronic hemolytic anemia, cardiomyopathy, high susceptibility to infection, neurologic dysfunction and premature death [7, 89, 100].

Thirteen mutations of the gene that codifies for TIM (in chromosome 12p13) have been described for this disease, and all of them result in a diminished enzyme activity that results in the excessive accumulation of DHAP. However, the most common mutation is in the codon for the amino acid in position 104, where a glutamic acid is substituted for an aspartic acid, producing the mutant enzyme TIM E104D. This mutation occurs in 80% of the cases. Other less frequent mutations are the substitution of cysteine 41 for tyrosine (TIM C41Y) and isoleucine 170 for valine (TIM I170V) [7, 101, 102]. Both mutations affect the dimerization of TIM and the binding of the substrate. There are other mutations that have been identified like the change of phenylalanine for leucine in position 240, glycine for arginine in position 122 or valine for methionine in positions 154 and 231 [22, 100, 101, 103, 104].

There are mainly two types of symptoms caused by this illness: the first is clearly due to the reduced catalytic function of the enzyme, which causes severe metabolic disorders and which are not in the scope of this review. The second type of symptoms, which are absent in very few patients, are associated with neurodegeneration.

7.1. Possible Causes of Neurodegeneration in Human TIM Deficiency

TIM deficiency is different from other glycolytic enzymopathies because none of these are associated with neurologic dysfunction. Although the precise causes for neurodegeneration in TIM deficiency are not known, there are some observations that could potentially explain it. When the catalytic activity of TIM is diminished there is an accumulation of DHAP in all cells [101]. For example, in patients with mutation TIM E145Stop /TIM F240L, the concentration of DHAP inside the erythrocytes is 60 times higher than normal. Even though the accumulation of high concentrations of DHAP is not toxic, the molecule tends to transform non-enzymatically to MEG, which is toxic and capable of modifying proteins and nucleic acids (see section 5 "The role of TIM in Alzheimer's disease" and Fig. **1**). Under conditions of high oxidative and nitrative stress, glyoxalases cannot cope with the accumulation of MEG [21] and the glycated proteins, together with the oxidative stress and the damaged DNA, contribute to the neuronal symptoms [22, 101].

DHAP is also a precursor of acyl-DHAP, which is an intermediary in the synthesis of alkyl glycerol ethers and plasmalogens. DHAP can also be converted to non-ether derived glycerolipids, which produces an abnormal metabolism of lipids [105]. It has been reported that plasmalogen levels in the membranes of erythrocytes and lymphocytes can influence several processes related to protection mechanisms from oxidative stress [101, 106]. Coincidentally, the plasmalogen levels in erythrocytes from patients with TIM deficiencies due to TIME104D and TIM F240L/E145stop are diminished [101]. DHAP also inhibits competitively the activity of myoinositol 3 phosphate synthase, an enzyme that involved in the de novo synthesis of inositol. A deficiency in the concentration of inositol has been described in several pathological conditions like bipolar disorder, Down's syndrome and peripheral diabetic neuropathy, which suggests that the deficit in TIM activity can contribute to neurodegeneration [101].

Other studies that could explain the development of neurodegeneration are those made by Roland *et al*., [6, 7, 89],

INFORME DE LABORES 2019

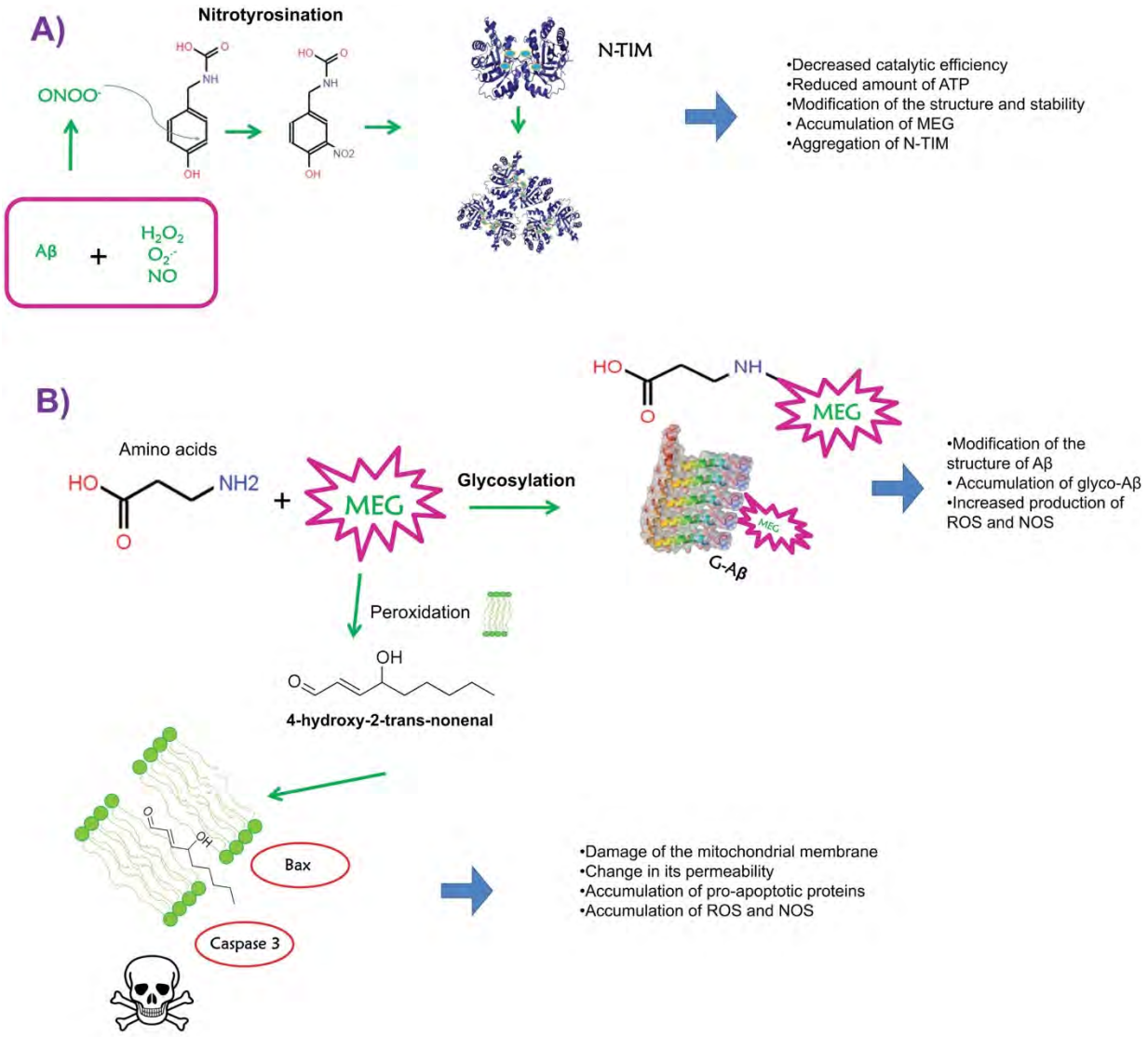

Fig. (1). Role of TIM in Alzheimer's disease. A) The accumulation of the amyloid peptide (Aβ), together with the oxidative/nitrative stress produce peroxynitrite which modifies tyrosines in proteins. During the progress of the disease, TIM is nitrotyrosinated (N-TIM), decreasing its catalytic activity, lowering ATP levels in the cells and favoring the formation of methylglyoxal (MEG), a highly toxic molecule. **B**) The accumulation of MEG generates further oxidative/nitrative stress in the cell. The contact of MEG with membranes produces 4-hydroxy-2-trans-nonenal, which damages the membrane and changes the membrane potential of the mitochondria generating apoptosis [96]. MEG can also glycosylate proteins like Aβ (G-Aβ). Accumulation of G-Aβ further favors production of reactive oxygen species and reactive nitrogen species, and N-TIM aggregates can function as seeds to form new fibrillar structures.

Ralser *et al.* [100] and Rodríguez-Almazán *et al.* [107]. These studies indicate that TIM deficiency is produced by changes in the conformation of the protein, more than because of the metabolic defects caused by the loss of activity. Specifically, problems in dimerization and/or the assembly of the enzyme are the main cause of the disease. One proposal is that TIM participates in the dynamics of the vesicles in the synapse as the main source of the ATP (through glycolysis) that feeds the process and, when this pathway is inhibited, the traffic of the vesicles stops. Another proposal suggests that TIM participates in the mobilization of vesicles as an activator of other molecules that facilitate vesicular traffic [7, 108, 109]. Recently it has been found that TIM binds to cofilin, which is a regulatory protein of actin, and that, the formation of a TIM-cofilin complex seems to regulate vesicle traffic [7, 110]. Thus, an anomaly in the structure of either protein could influence the formation of this complex, affecting neuronal communication [7].

It has also been reported that TIM can associate with the N-terminus of the transmembrane protein Band 3 from erythrocytes and that this association diminishes its catalytic activity [101, 111]. The N-terminus of protein Band 3 has great sequence similarity with the C-terminus of tubulin, which is the end with which tubulin is bound to the microtubules. It has therefore been suggested that TIM can also bind to the microtubules, which are the main component of neuronal axons, and thus provoke an energetic destabilization [87, 101].

INFORME DE LABORES 2019

8. DISCUSSION

There is a great discrepancy in the great size of the human genome and the number of synthesized proteins [13]. This difference implies the utilization of the limited amount of synthesized proteins to fulfill multiple functions. The case of TIM, as mentioned previously, is an enzyme present in all organisms, so that its reuse or moonlighting functions is a common occurrence.

TIM has several roles that are different from its traditional main function. But, relatively little is known of the properties and mechanisms that allow it to perform the varied functions described here. TIM seems to have a role in cell cycle signaling. It interacts with proteins like Cdk2, whose activity is essential in meiosis and the adequate control of cellular proliferation, repair, and death [15-17]. Its maximal activity is between phases S and G2, even though it is active in phases G1-S. It has been reported that Cdk2 is able to phosphorylate TIM, reducing its glycolytic activity and causing a disturbance in other pathways, which generate cellular arrest [96].

Cellular proliferation is strictly controlled and TIM, together with other enzymes seems to form a part of the controls. In certain types of gastric cancer, the levels of TIM are unbalanced, initiating the loss of control in cellular proliferation. This makes TIM a good biomarker for this type of ailment [24, 25].

The reason why a difference of expression levels of TIM between one type of cancer and another can vary the prognosis of the patients suffering these diseases is unknown. Yet, one of the aspects that have not been examined is that there may be several isoforms of this protein or that this enzyme may be subjected to different types of post-transcriptional modifications. In some cases, these modifications bring beneficial effects like in the maturation of sperm, where the active form of TIM is the one that is carbonylated [75]. Furthermore, there are other modifications that result in pathological processes like Alzheimer's disease [87, 88] and the formation of anti-TIM autoantibodies [34, 39]. For example, three isoforms of TIM are overexpressed in some types of pulmonary cancer, and, the clinical outcome of the disease varies depending on the isoform that is expressed. Interestingly these isoforms vary only in the type of modifications they show, with phosphorylation being the most common [112].

One of the factors that control post-transcriptional modifications in these proteins is the redox balance of the cell. Cdk2 is also related to the nitric oxide signaling pathway so that any failure in this pathway can cause important modifications in TIM and other proteins [96].

Whenever TIM suffers changes due to oxidative stress, it reduces its activity and changes its conformation favoring the production of MEG and the propagation of the oxidative damage in the cell.

As mentioned earlier, TIM expression has an impact on the prognosis of various cancer patients. The repercussions are different, depending on the type of tumor that develops. This may also be due to a high genetic variation between tumors and the way in which their metabolism varies, thus affecting the differential response in TIM expression and the prognosis of the patient. Renal tumors have the greatest genetic variation and 3 types of mutations may be found among them. Clear cell renal carcinoma cells have a specific deletion in chromosome 3P, while papillary renal cell carcinoma cells have trisomies and chromosome Y losses and chromophobe renal cell carcinoma cells have losses in chromosomes 1, 2, 6 and 10 [35].

A novel therapeutic strategy in cancer treatment is the inhibition of glycolysis. The disruption of this pathway, using Cdk2 to inactivate TIM, could produce the death of malignant cells [96].

It is interesting to note that in several diseases like cancer and Alzheimer's disease, overexpression of TIM also coincides with the overexpression of other proteins such as cofilin. This is a protein that binds actin and regulates the length of the microfilaments; it also acts in the reorganization of the microtubules for vesicle traffic. It is now known that cofilin associates with TIM so that they can be translocated by the plasmatic membrane and bind to the Na/K ATPase [110]. As described previously, the mechanisms by which TIM is transported outside the cell, or induces the formation of antibodies, or functions as a virulence factor, are unknown. Perhaps, its ability to associate with proteins related with cellular traffic (cofilin, Band 3 and microtubules) could give a clue.

The presence of TIM autoantibodies in cancer represents a type of "fingerprint" or "signature" of the immune system responding to the progression of the disease. Antibodies can sometimes be detected years or months before the main symptoms of the disease are apparent, giving signs of the dynamics of the carcinogenic process [34]. In neuropsychiatric lupus, anti-TIM antibodies appear in great quantities and they show a high specificity of 94.7%, making them a good marker for this disease [42].

It is thought that antibodies arise due to the exposure of misfolded proteins, however, misfolding is not necessary for immunogenicity. The reason could be the form in which protein is associated with itself or with other proteins [72].

Surprisingly, even though TIM is so immunogenic in certain pathologies, this enzyme also contributes to the evasion of the immune response. Certain parasites and bacteria use it as a protecting shield just for that purpose. In immune tolerance, the immune system recognizes a non-self or self-antigen, but no response is elicited. Tolerance depends on the situation in which the recognition of the antigen takes place [113].

CONCLUSION

TIM belongs to the group of moonlighting proteins, which carry multiple functions. Even though TIM is not a regulating enzyme, it seems to have an important metabolic role in the development of several cancers. The correct assembly of the protein is necessary for normal neuronal function, with structural modifications leading to neurodegeneration. Depending on the cellular environment TIM can be a potent allergen or induce immune tolerance.

New protein moonlighting functions are being discovered and may have evolved as a means of communication and

INFORME DE LABORES 2019

cooperation between different pathways necessary for fundamental functions in the complex world of different types of cells, within an organism [13].

Finally, further research is required considering TIM and its multiple functions, trying to elucidate the mechanisms by which it accomplishes all these different tasks, either to apply them biotechnologically or to prevent and treat a select group of diseases.

LIST OF ABBREVIATIONS

Abbreviations are defined when first used in the text.

CONSENT FOR PUBLICATION

Not applicable.

CONFLICT OF INTEREST

The authors declare no conflict of interest, financial or otherwise.

ACKNOWLEDGEMENTS

This work was supported by grant no. 254694 from the Consejo Nacional de Ciencia y Tecnologia (to R.P.-M.). MR-B was the recipient of a fellowship from CONACyT (no. 262118).

REFERENCES

[1] Katebi, A.R.; Jernigan, R.L. The critical role of the loops of triosephosphate isomerase for its oligomerization, dynamics, and functionality. *Protein Sci.*, **2014**, *23*, 213-228.

[2] Bar-Even, A.; Flamholz, A.; Noor, E.; Milo, R. Rethinking glycolysis: On the biochemical logic of metabolic pathways. *Nat. Chem. Biol.*, **2012**, *8*, 509-517.

[3] Osterman, A. Biogenesis and homeostasis of nicotinamide adenine dinucleotide cofactor. *EcoSal Plus* **2009**, *3*, doi: 10.1128/ecosalplus.3.6.3.10.

[4] Richard, J.P. Restoring a metabolic pathway. *ACS Chem. Biol.*, **2008**, *3*, 605-607.

[5] Lincet, H.; Icard, P. How do glycolytic enzymes favour cancer cell proliferation by nonmetabolic functions? *Oncogene*, **2015**, *34*, 3751-3759.

[6] Roland, B.P.; Stuchul, K.A.; Larsen, S.B.; Amrich, C.G.; VanDemark, A.P.; Celotto, A.M.; Palladino, M.J. Evidence of a triosephosphate isomerase non-catalytic function crucial to behavior and longevity. *J. Cell Sci.*, **2013**, *126*, 3151-3158.

[7] Roland, B.P.; Zeccola, A.M.; Larsen, S.B.; Amrich, C.G.; Talsma, A.D.; Stuchul, K.A.; Heroux, A.; Levitan, E.S. VanDemark A.P. Palladino M.J. Structural and genetic studies demonstrate neurologic dysfunction in triosephosphate isomerase deficiency is associated with impaired synaptic vesicle dynamics. *PLoS Genet.*, **2016**, *12*, e1005941.

[8] Banner, D.W; Bloomer, A.C.; Petsko, G.A; Phillips, D.C; Pogson, C.I.; Wilson, I.A.; Corran, P.H.; Furth, A.J.; Milman, J.D.; Offord, R.E.; Priddle, J.D.; Waley, S.G. Structure of chicken muscle triose phosphate isomerase determined crystallographically at 2.5 Å resolution: Using amino acid sequence data. *Nature*, **1975**, *255*, 609-614.

[9] Lesk, A.M.; Brändén, C.I; Chothia, C. Structural principles of α/β barrel proteins: the packing of the interior of the sheet. *Proteins*, **1989**, *5*, 139-148.

[10] Wierenga, R.K. The TIM-barrel fold: A versatile framework for efficient enzymes. *FEBS Lett.*, **2001**, *492*, 193-198.

[11] Alber, T.; Banner, D.W.; Bloomer, A.C.; Petsko, G.A.; Phillips, D.; Rivers, P.S.; Wilson, I.A. On the three-dimensional structure and catalytic mechanism of triose phosphate isomerase. *Philos. Trans. R. Soc. Lond. B Biol. Sci.*, **1981**, *293*, 159-171.

[12] Wierenga, R.K.; Kapetaniou, E.G.; Venkatesan, R. Triosephosphate isomerase: A highly evolved biocatalyst. *Cell. Mol. Life Sci.*, **2010**, *67*, 3961-3982.

[13] Jeffery, C.J. Moonlighting proteins: old proteins learning new tricks. *Trends Genet.*, **2003**, *19*, 415-417.

[14] Dang, Y.; Wang, Z.; Guo, Y.; Yang, J.; Xing, Z.; Mu, L.; Zhang, X.; Ding, Z. Overexpression of triosephosphate isomerase inhibits proliferation of chicken embryonal fibroblast cells. *Asian Pac. J. Cancer Prev.*, **2011**, *12*, 3479-3482.

[15] Beranova-Giorgianni, S.; Zhao, Y.; Desiderio, D.M; Giorgianni, F. Phosphoproteomic analysis of the human pituitary. *Pituitary*, **2006**, *9*, 109-120.

[16] Dephoure, N.; Zhou, C.; Villén, J.; Beausoleil, S.A.; Bakalarski, C.E.; Elledge, S.J.; Gygi, S.P. A quantitative atlas of mitotic phosphorylation. *Proc. Natl. Acad. Sci. USA*, **2008**, *105*, 10762-10767.

[17] Imami, K.; Sugiyama, N.; Kyono, Y.; Tomita, M.; Ishihama, Y. Automated phosphoproteome analysis for cultured cancer cells by two-dimensional nanoLC-MS using a calcined titania / C18 biphasic column. *Anal. Sci.*, **2008**, *24*, 161-166.

[18] Pancholi, V.; Chhatwal, G.S. Housekeeping enzymes as virulence factors for pathogens. *Int. J. Med. Microbiol.*, **2003**, *293*, 391-401.

[19] Chuang, J.G.; Su, S.N.; Chiang, B.L.; Lee, H.J.; Chow, L.P. Proteome mining for novel IgE-binding proteins from the German cockroach (*Blattella germanica*) and allergen profiling of patients. *Proteomics*, **2010**, *10*, 3854-3867.

[20] Vilagran, I.; Castillo, J.; Bonet, S.; Sancho, S.; Yeste, M.; Estanyol, J.M.; Oliva, R. Acrosin-binding protein (ACRBP) and triosephosphate isomerase (TPI) are good markers to predict boar sperm freezing capacity. *Theriogenology*, **2013**, *80*, 443-450.

[21] Ahmed, N.; Battah, S.; Karachalias, N.; Babaei-Jadidi, R.; Horányi, M.; Baróti, K.; Hollan, S.; Thornalley, P.J. Increased formation of methylglyoxal and protein glycation, oxidation and nitrosation in triosephosphate isomerase deficiency. *Biochim. Biophys. Acta*, **2003**, *1639*, 121-132.

[22] Schneider, A.S. Triosephosphate isomerase deficiency: Historical perspectives and molecular aspects. *Baillieres Best Pract. Res. Clin. Haematol.*, **2000**, *13*, 119-140.

[23] Yang, F.; Xiao, Z.Q.; Zhang, X.Z.; Li, C.; Zhang, P.F.; Li, M.; Chen, Y.; Zhu, G.Q.; Sun, Y.; Liu, Y.F.; Chen, Z.C. Identification of tumor antigens in human lung squamous carcinoma by serological proteome analysis. *J. Proteome Res.*, **2007**, *6*, 751-758.

[24] Wang, X.; Lu, Y.; Yang, J.; Shi, Y.; Lan, M.; Liu, Z.; Zhai, H.; Fan, D. Identification of triosephosphate isomerase as an anti-drug resistance agent in human gastric cancer cells using functional proteomic analysis. *J. Cancer Res. Clin. Oncol.*, **2008**, *134*, 995-1003.

[25] Jiang, H.; Ma, N.; Shang, Y.; Zhou, W.; Chen, T.; Guan, D.; Li, J.; Wang, J.; Zhang, E.; Feng, Y.; Yin, F.; Yuan, Y.; Fang, Y.; Qiu, L.; Xie, D.; Wei, D. Triosephosphate isomerase 1 suppresses growth, migration and invasion of hepatocellular carcinoma cells. *Biochem. Biophys. Res. Commun.*, **2017**, *482*, 1048-1053.

[26] Chen, T.; Huang, Z.; Tian, Y.; Lin, B.; He, R.; Wang, H.; Ouyang, P.; Chen, H.; Wu, L. Clinical significance and prognostic value of triosephosphate isomerase expression in gastric cancer. *Medicine (Baltimore)*, **2017**, *96*, e6865.

[27] Chen, T; Huang, Z.; Tian, Y.; Wang, H.; Ouyang, P.; Chen, H.; Wu, L.; Lin, B.; He, R. Role of triosephosphate isomerase and downstream functional genes on gastric cancer. *Oncol. Rep.*, **2017**, *38*, 1822-1832.

[28] Ford, H.L.; Pardee, A.B. Cancer and the cell cycle. *J. Cell. Biochem.*, **1999**, (*Suppl. 32-33)*, 166-172.

[29] Zhu, J.; Xu, J.; Wang, Y.; Li, C.; Chen, Z.; Song, L.; Gao, J.; Yu, R. Purification and structural characterization of a novel-tumor protein from *Arca inflata*. *Int. J. Biol. Macromol.*, **2017**, *105*, 103-110.

[30] Toyama, A.; Suzuki, A.; Shimada, T.; Aoki, C.; Aoki, Y.; Umino, Y.; Nakamura, Y.; Aoki, D.; Sato, T.A. Proteomic characterization of ovarian cancers identifying annexin-A4, phosphoserine aminotransferase, cellular retinoic acid-binding protein 2, and serpin B5 as histology-specific biomarkers. *Cancer Sci.*, **2012**, *103*, 747-755.

[31] Parichartanakul, N.M.; Saharat, K.; Chokchaichamnankit, D.; Punyarit, P.; Srisomsap, C.; Svasti, J. Unveiling a novel biomarker panel for diagnosis and classification of well-differentiated thyroid carcinomas. *Oncol. Rep.*, **2016**, *35*, 2286-2296.

[32] Desmetz, C.; Bibeau, F.; Boissière, F.; Bellet, V.; Rouanet, P.; Maudelonde, T.; Mangé, A.; Solassol, J. Proteomics-based identification of HSP60 as a tumor-associated antigen in early stage breast

INFORME DE LABORES 2019

cancer and ductal carcinoma *in situ*. *J. Proteome Res*., **2008**, *7*, 3830-3837.

[33] Zamani-Ahmadmahmudi, M.; Nassiri, S.M.; Rahbarghazi, R. Serological proteome analysis of dogs with breast cancer unveils common serum biomarkers with human counterparts. *Electrophoresis*, **2014**, *35*, 901-910.

[34] Gao, H.; Zheng, Z.; Mao, Y.; Wang, W.; Qiao, Y.; Zhou, L.; Liu, F.; He, H.; Zhao, X. Identification of tumor antigens that elicit a humoral immune response in the sera of chinese esophageal squamous cell carcinoma patients by modified serological proteome analysis. *Cancer Lett.*, **2014**, *344*, 54-61.

[35] Valera, V.A.; Li-Ning, T.E.; Walter, B.A.; Roberts, D.D.; Linehan, W.M.; Merino, M.J. Protein expression profiling in the spectrum of renal cell carcinomas. *J. Cancer*, **2010**, *1*, 184-196.

[36] Unwin, R.D.; Craven, R.A.; Harnden, P.; Hanrahan, S.; Totty, N.; Knowles, M.; Eardley, I.; Selby, P.J.; Banks, R.E. Proteomic changes in renal cancer and co-ordinate demonstration of both the glycolytic and mitochondrial aspects of the Warburg effect. *Proteomics*, **2003**, *3*, 1620-1632.

[37] Wang, J.W.; Peng, S.Y.; Li, J.T.; Wang, Y.; Zhang, Z.P.; Cheng, Y.; Cheng, D.Q.; Weng, W.H.; Wu, X.S.; Fei, X.Z.; Quan, Z.W.; Li, Z.Y.; Li, S.G.; Liu, Y.B. Identification of metastasis-associated proteins involved in gallbladder carcinoma metastasis by proteomic analysis and functional exploration of chloride intracellular channel 1. *Cancer Lett.*, **2009**, *281*, 71-81.

[38] Yoshida, A.; Okamoto, N.; Tozawa-Ono, A.; Koizumi, H.; Kiguchi, K.; Ishizuka, B.; Kumai, T.; Suzuki, N. Proteomic analysis of differential protein expression by brain metastases of gynecological malignancies. *Hum. Cell*, **2013**, *26*, 56-66.

[39] Hong Y, Huang J. Autoantibodies against tumor-associated antigens for detection of hepatocellular carcinoma. *World J. Hepatol*., **2015**, *7*, 1581-1585.

[40] Pieper, R.; Christian, R.E.; Gonzales, M.I.; Nishimura, M.I.; Gupta, G.; Settlage, R.E.; Shabanowitz, J.; Rosenberg, S.A.; Hunt, D.F.; Topalian, S.L. Biochemical identification of a mutated human melanoma antigen recognized by CD4(+) T cells. *J. Exp. Med*., **1999**, *189*, 757-766.

[41] Sato, S.; Yashiro, M.; Asano, T.; Kobayashi, H.; Watanabe, H.; Migita, K. Association of anti-triosephosphate isomerase antibodies with aseptic meningitis in patients with neuropsychiatric systemic lupus erythematosus. *Clin. Rheumatol.*, **2017**, *36*, 1655-1659.

[42] Watanabe, H.; Seino, T.; Sato, Y. Antibodies to triosephosphate isomerase in patients with neuropsychiatric lupus. *Biochem. Biophys. Res. Commun*., **2004**, *321*, 949-953.

[43] Sasajima, T.; Watanabe, H.; Sato, S.; Sato, Y.; Ohira, H. Anti-triosephosphate isomerase antibodies in cerebrospinal fluid are associated with neuropsychiatric lupus. *J. Neuroimmunol.*, **2006**, *181*, 150-156.

[44] Xiang, Y.; Sekine, T.; Nakamura, H.; Imajoh-Ohmi, S.; Fukuda, H.; Nishioka, K.; Kato, T. Proteomic surveillance of autoimmunity in osteoarthritis: identification of triosephosphate isomerase as an autoantigen in patients with osteoarthritis. *Arthritis Rheum.*, **2004**, *50*, 1511-1521.

[45] Ritter, S.; Schröder, S.; Uy, A.; Ritter, K. Haemolysis in hepatitis A virus infections coinciding with the occurrence of autoantibodies against triosephosphate isomerase and the reactivation of latent persistent Epstein-Barr virus infection. *J. Med. Virol.*, **1996**, *50*, 272-275.

[46] Kolln, J.; Ren, H.M.; Da, R.R.; Zhang, Y.; Spillner, E.; Olek, M.; Hermanowicz, N.; Hilgenberg, L.G.; Smith, M.A.; van den Noort, S.; Qin, Y. Triosephosphate isomerase- and glyceraldehyde-3-phosphate dehydrogenase-reactive autoantibodies in the cerebrospinal fluid of patients with multiple sclerosis. *J. Immunol.*, **2006**, *177*, 5652-5658.

[47] Furuya, H.; Ikeda, R. Interaction of triosephosphate isomerase from *Staphylococcus aureus* with plasminogen. *Microbiol. Immunol.*, **2011**, *55*, 855-862.

[48] Furuya, H.; Ikeda, R. Interaction of triosephosphate isomerase from the cell surface of *Staphylococcus aureus* and alpha-(1->3)-mannooligosaccharides derived from glucuronoxylomannan of *Cryptococcus neoformans*. *Microbiology*, **2009**, *155*, 2707-2713.

[49] Ramiah, K.; van Reenen, C.A.; Dicks, L.M.T. Surface-bound proteins of *Lactobacillus plantarum* 423 that contribute to adhesion of Caco-2 cells and their role in competitive exclusion and displacement of *Clostridium sporogenes* and *Enterococcus faecalis*. *Res. Microbiol.*, **2008**, *159*, 470-475.

[50] Kinoshita, H.; Ohuchi, S.; Arakawa, K.; Watanabe, M.; Kitazawa, H.; Saito, T. Isolation of lactic acid bacteria bound to the porcine intestinal mucosa and an analysis of their moonlighting adhesins. *Biosci. Microbiota Food Health*, **2016**, *35*, 185-196.

[51] Miranda-Ozuna, J.F.; Hernández-García, M.S.; Brieba, L.G.; Benítez-Cardoza, C.G.; Ortega-López, J.; González-Robles, A.; Arroyo, R. The glycolytic enzyme triosephosphate isomerase of *Trichomonas vaginalis* is a surface-associated protein induced by glucose that functions as a laminin- and fibronectin-binding protein. *Infect. Immun.*, **2016**, *84*, 2878-2894.

[52] Yamaguchi, M.; Ikeda, R.; Nishimura, M.; Kawamoto, S. Localization by scanning immunoelectron microscopy of triosephosphate isomerase, the molecules responsible for contact-mediated killing of *Cryptococcus*, on the surface of *Staphylococcus*. *Microbiol. Immunol.*, **2010**, *54*, 368-370.

[53] Ikeda, R.; Ichikawa, T. Interaction of surface molecules on *Cryptococcus neoformans* with plasminogen. *FEMS Yeast Res.*, **2014**, *14*, 445-450.

[54] Ditgen, D.; Anandarajah, E.M.; Meissner, K.A.; Brattig, N.; Wrenger, C.; Liebau, E. Harnessing the helminth secretome for therapeutic immunomodulators. *Biomed. Res. Int.*, **2014**, *2014*, 964350.

[55] Bennuru, S.; Semnani, R.; Meng, Z.; Ribeiro, J.M.C.; Veenstra, T.D.; Nutman, T.B. *Brugia malayi* excreted/secreted proteins at the host/parasite interface: stage- and gender-specific proteomic profiling. *PLoS Negl. Trop. Dis*., **2009**, *3*, e410.

[56] Hewitson, J.P.; Rückerl, D.; Harcus, Y.; Murray, J.; Webb, L.M.; Babayan, S.A.; Allen, J.E.; Kurniawan, A.; Maizels, R.M. The secreted triose phosphate isomerase of *Brugia malayi* is required to sustain microfilaria production *in vivo*. *PLoS Pathog.*, **2014**, *10*, e1003930.

[57] Liu, F.; Li, S.; Liu, G.; Li, F. Triosephosphate isomerase (TPI) facilitates the replication of WSSV in *Exopalaemon carinicauda*. *Dev. Comp. Immunol.*, **2017**, *71*, 28-36.

[58] Vester, D.; Rapp, E.; Kluge, S.; Genzel, Y.; Reichl, U. Virus-host cell interactions in vaccine production cell lines infected with different human influenza A virus variants: A proteomic approach. *J. Proteomics*, **2010**, *73*, 1656-1669.

[59] Pastor, C.; Cuesta-Herranz, J.; Cases, B.; Pérez-Gordo, M.; Figueredo, E.; de las Heras, M.; Vivanco, F. Identification of major allergens in watermelon. *Int. Arch. Allergy Immunol.*, **2009**, *149*, 291-298.

[60] Yang, Y.; Chen, Z.W.; Hurlburt, B.K.; Li, G.L.; Zhang, Y.X.; Fei, D.X.; Shen, H.W.; Cao, M.J.; Liu, G.M. Identification of triosephosphate isomerase as a novel allergen in *Octopus fangsiao*. *Mol. Immunol.*, **2017**, *85*, 35-46.

[61] Hoppe, S.; Steinhart, H.; Paschke, A. Identification of a 28 kDa Lychee allergen as a triose-phosphate isomerase. *Food Agric. Immunol.*, **2006**, *17*, 9-19.

[62] Radauer, C.; Bublin, M.; Wagner, S.; Mari, A.; Breiteneder, H. Allergens are distributed into few protein families and possess a restricted number of biochemical functions. *J. Allergy Clin. Immunol.*, **2008**, *121*, 847-852.

[63] Hoffmann-Sommergruber, K.; Bruckmüller, M. Watermelon contains 92 % water but it also contains allergens! *Int. Arch. Allergy Immunol.*, **2009**, *149*, 289-290.

[64] Kamath, S.D.; Rahman, A.M.; Voskamp, A.; Komoda, T.; Rolland, J.M.; O'Hehir, R.E.; Lopata, A.L. Effect of heat processing on antibody reactivity to allergen variants and fragments of black tiger prawn: A comprehensive allergenomic approach. *Mol. Nutr. Food Res.*, **2014**, *58*, 1144-1155.

[65] Yang, Y.; Zhang, Y.X.; Liu, M.; Maleki, S.J.; Zhang, M.L.; Liu, Q.M.; Cao, M.J.; Su, W.J.; Liu, G.M. Triosephosphate isomerase and Filamin C share common epitopes as novel allergens of *Procambarus clarkii*. *J. Agric. Food Chem.*, **2017**, *65*, 950-963.

[66] Chen, Y.H.; Lee, M.F.; Lan, J.L.; Chen, C.S.; Wang, H.L.; Hwang, G.Y.; Wu, C.H. Hypersensitivity to *Forcipomyia taiwana* (biting midge): Clinical analysis and identification of major For t 1 , For t 2 and For t 3 allergens. *Allergy*, **2005**, *60*, 1518-1523.

[67] Posch, A.; Chen, Z.; Wheeler, C.; Dunn, M.J.; Raulf-Heimsoth, M.; Baur, X. Characterization and identification of latex allergens by two-dimensional electrophoresis and protein microsequencing. *J. Allergy Clin. Immunol*., **1997**, *99*, 385-395.

[68] Bauermeister, K.; Wangorsch, A.; Garoffo, L.P.; Reuter, A.; Conti, A.; Taylor, S.L.; Lidholm, J.; Dewitt, A.M.; Enrique, E.; Vieths, S.; Holzhauser, T.; Ballmer-Weber, B.; Reese, G. Generation of a

INFORME DE LABORES 2019

comprehensive panel of crustacean allergens from the north sea shrimp *Crangon crangon*. *Mol. Immunol.*, **2011**, *48*, 1983-1992.

[69] Pérez-Gordo, M.; Pastor Vargas, C.; Cases, B.; De Las Heras M.; Sanz A.; Vivanco, F.; Cuesta-Herranz, J. New allergen involved in a case of allergy to *Solea solea*, common sole. *Ann. Allergy Asthma Immunol.*, **2010**, *104*, 352-353.

[70] He, R.; Zhang, H.; Shen, N.; Guo, C.; Ren, Y.; Xie, Y.; Gu, X.; Lai, W.; Peng, X.; Yang, G. Molecular characterization and allergenicity potential of triosephosphate isomerase from *Sarcoptes scabiei*. *Vet. Parasitol*., **2018**, *257*, 40-47.

[71] Hauser, M.; Roulias, A.; Ferreira, F.; Egger, M. Panallergens and their impact on the allergic patient. *Allergy Asthma Clin. Immunol.*, **2010**, *6*, 1.

[72] Rosenberg, A.S. Effects of protein aggregates: an immunologic perspective. *AAPS J.*, **2006**, *8*, E501-E507.

[73] Mao, H.Y.; Cao, M.J.; Maleki, S.J.; Cai, Q.F.; Su, W.J.; Yang, Y.; Liu, G.M. Structural characterization and IgE epitope analysis of arginine kinase from *Scylla* paramamosain. *Mol. Immunol.*, **2013**, *56*, 463-470.

[74] Cheng, C.Y.; Chen, P.R.; Chen, C.J.; Wang, S.H.; Chen, C.F.; Lee, Y.P.; Huang, S.Y. Differential protein expression in chicken spermatozoa before and after freezing-thawing treatment. *Anim. Reprod. Sci.*, **2015**, *152*, 99-107.

[75] Mostek, A.; Dietrich, M.A.; Słowińska, M.; Ciereszko, A. Cryopreservation of bull semen is associated with carbonylation of sperm proteins. *Theriogenology*, **2017**, *92*, 95-102.

[76] Zangbar, M.S.; Keshtgar, S.; Zolghadri, J.; Gharesi-Fard, B. Antisperm protein targets in azoospermia men. *J. Hum. Reprod. Sci.*, **2016**, *9*, 47-52.

[77] Vilagran, I.; Castillo-Martín, M.; Prieto-Martínez, N.; Bonet, S.; Yeste, M. Triosephosphate isomerase (TPI) and epididymal secretory glutathione peroxidase (GPX5) are markers for boar sperm quality. *Anim. Reprod. Sci*., **2016**, *165*, 22-30.

[78] Bailey, J.L.; Tardif, S.; Dubé, C.; Beaulieu, M.; Reyes-Moreno, C.; Lefièvre, L.; Leclerc, P. Use of phosphoproteomics to study tyrosine kinase activity in capacitating boar sperm. kinase activity and capacitation. *Theriogenology*, **2005**, *63*, 599-614.

[79] Bone, W.; Jones, A.R.; Morin, C.; Nieschlag, E.; Cooper, T.G. Susceptibility of glycolytic enzyme activity and motility of spermatozoa from rat, mouse, and human to inhibition by proven and putative chlorinated antifertility compounds *in vitro*. *J. Androl.*, **2001**, *22*, 464-470.

[80] Cormier, N.; Bailey, J.L. A differential mechanism is involved during heparin- and cryopreservation-induced capacitation of bovine spermatozoa. *Biol. Reprod.*, **2003**, *69*, 177-185.

[81] Pons-Rejraji, H.; Bailey, J.L.; Leclerc, P. Cryopreservation affects bovine sperm intracellular parameters associated with capacitation and acrosome exocytosis. *Reprod. Fertil. Dev.*, **2009**, *21*, 525-537.

[82] Nakamura, T.; Cho, D.H.; Lipton, S.A. Redox regulation of protein misfolding, mitochondrial dysfunction, synaptic damage, and cell death in neurodegenerative diseases. *Exp. Neurol.*, **2012**, *238*, 12-21.

[83] Nakamura, T.; Tu, S.; Akhtar, M.W.; Sunico, C.R.; Okamoto, S.; Lipton, S.A. Aberrant protein S-nitrosylation in neurodegenerative diseases. *Neuron*, **2013**, *78*, 596-614.

[84] Zahid, S.; Khan, R.; Oellerich, M.; Ahmed, N.; Asif, A.R. Differential S-nitrosylation of proteins in Alzheimer's disease. *Neuroscience*, **2014**, *256*, 126-136.

[85] Park, S.A.; Park, H.W.; Kim, N.H.; Kim, Y.H.; Kwak, M.J.; Shin, J.S.; Kim, C.W. Effects of Tau on the activity of triose phosphate isomerase (TPI) in brain cells. *Neurochem. Int.*, **2010**, *56*, 886-892.

[86] Hu, H.; Tan, C.C.; Tan, L.; Yu, J.T. A mitocentric view of Alzheimer's disease. *Mol. Neurobiol.*, **2017**, *54*, 6046-6060.

[87] Coma, M.; Guix, F.X.; Uribesalgo, I.; Espuña, G.; Solé, M.; Andreu, D.; Muñoz, F.J. Lack of oestrogen protection in amyloid-mediated endothelial damage due to protein nitrotyrosination. *Brain*, **2005**, *128*, 1613-1621.

[88] Tajes, M.; Eraso-Pichot, A.; Rubio-Moscardó, F.; Guivernau, B.; Bosch-Morató, M.; Valls-Comamala, V.; Muñoz, F.J. Methylglyoxal reduces mitochondrial potential and activates Bax and caspase-3 in neurons: Implications for Alzheimer's disease. *Neurosci. Lett.*, **2014**, *580*, 78-82.

[89] Roland, B.P.; Amrich, C.G.; Kammerer, C.J.; Stuchul, K.A.; Larsen, S.B.; Rode, S.; Aslam, A.A.; Heroux, A.; Wetzel, R.; VanDemark, A.P.; Palladino, M.J. Triosephosphate isomerase I170V alters catalytic site, enhances stability and induces pathology in a Drosophila model of TPI deficiency. *Biochim. Biophys. Acta*, **2015**, *1852*, 61-69.

[90] Guix, F.X.; Ill-Raga, G.; Bravo, R.; Nakaya, T.; de Fabritiis, G.; Coma, M.; Miscione, G.P.; Villà-Freixa, J.; Suzuki, T.; Fernández-Busquets, X.; Valverde, M.A.; de Strooper, B.; Muñoz, F.J. Amyloid-dependent triosephosphate isomerase nitrotyrosination induces glycation and tau fibrillation. *Brain*, **2009**, *132*, 1335-1345.

[91] Knowles J.R. Enzyme catalysis: Not different, just better. *Nature*, **1991**, *350*, 121-124.

[92] Rozovsky, S.; McDermott, A.E. The time scale of the catalytic loop motion in triosephosphate isomerase. *J. Mol. Biol.*, **2001**, *310*, 259-270.

[93] Gao, W.; Zhao, J.; Li, H.; Gao, Z. Triosephosphate isomerase tyrosine nitration induced by heme – $NaNO_2$ – H_2O_2 or peroxynitrite : effects of different natural phenolic compounds. *J. Biochem. Mol. Toxicol.*, **2017**, *31*, doi: 10.1002/jbt.21893.

[94] Ill-Raga, G.; Ramos-Fernández, E.; Guix, F.X.; Tajes, M.; Bosch-Morató, M.; Palomer, E.; Godoy, J.; Belmar, S.; Cerpa, W.; Simpkins, J.W.; Inestrosa, N.C.; Muñoz, F.J. Amyloid-β peptide fibrils induce nitro-oxidative stress in neuronal cells. *J. Alzheimers Dis.*, **2010**, *22*, 641-652.

[95] Kim, C.; Lim, Y.; Yoo, B.C.; Won N.H.; Kim, S.; Kim, G. Regulation of post-translational protein arginine methylation during HeLa cell cycle. *Biochim. Biophys. Acta*, **2010**, *1800*, 977-985.

[96] Lee, W.H.; Choi, J.S.; Byun, M.R.; Koo, K.T.; Shin, S.; Lee, S.K.; Surh Y.J. Functional inactivation of triosephosphate isomerase through phosphorylation during etoposide-induced apoptosis in HeLa cells: Potential role of Cdk2. *Toxicology*, **2010**, *278*, 224-228.

[97] Sultana, R.; Butterfield, D.A. Identification of the oxidative stress proteome in the brain. *Free Radic. Biol. Med.*, **2011**, *50*, 487-494.

[98] Contreras, C.F.; Canales, M.A.; Alvarez, A.; Ferrari, G.V.; Inestrosa, N.C. Molecular modeling of the amyloid- beta -peptide using the homology to a fragment of triosephosphate isomerase that forms amyloid *in vitro*. *Protein Eng.*, **1999**, *12*, 959-966.

[99] Butterfield, D.A. Proteomics: A new approach to investigate oxidative stress in Alzheimer's disease brain. *Brain Res.*, **2004**, *1000*, 1-7.

[100] Ralser, M.; Heeren, G.; Breitenbach, M.; Lehrach, H.; Krobitsch, S. Triose phosphate isomerase deficiency is caused by altered dimerization--not catalytic inactivity--of the mutant enzymes. *PLos One*, **2006**, *1*, e30.

[101] Orosz, F.; Oláh, J.; Ovádi, J. Triosephosphate isomerase deficiency: Facts and doubts. *IUBMB Life*, **2006**, *58*, 703-715.

[102] Orosz, F.; Oláh, J.; Ovádi, J. Reappraisal of the triosephosphate isomerase deficiency. *Eur. J. Haematol.*, **2011**, *86*, 265-267.

[103] Serdaroglu, G.; Aydinok, Y.; Yilmaz, S.; Manco, L.; Özer, E. Triosephosphate isomerase deficiency: A patient with Val231Met mutation. *Pediatr. Neurol.*, **2011**, *44*, 139-142.

[104] Cabrera, N.; Torres-Larios, A.; García-Torres, I.; Enríquez-Flores, S.; Perez-Montfort, R. Differential effects on enzyme stability and kinetic parameters of mutants related to human triosephosphate isomerase deficiency. *Biochim. Biophys. Acta*, **2018**, *1862*, 1401-1409.

[105] Hollán, S.; Magócsi, M.; Fodor, E.; Horányi, M.; Harsányi, V.; Farkas, T. Search for the pathogenesis of the differing phenotype in two compound heterozygote Hungarian brothers with the same genotypic triosephosphate isomerase deficiency. *Proc. Natl. Acad. Sci. USA*, **1997**, *94*, 10362-10366.

[106] Hollán, S.; Dey, I.; Szollár, L.; Horányi, M. Magócsi, M.; Harsányi, V.; Farkas, T. Erythrocyte lipids in triose-phosphate isomerase deficiency. *Proc. Natl. Acad. Sci. USA*, **1995**, *92*, 268-271.

[107] Rodríguez-Almazán, C.; Arreola, R.; Rodríguez-Larrea, D.; Aguirre-López, B.; de Gómez-Puyou, M.T.; Pérez-Montfort, R.; Costas, M.; Gómez-Puyou, A.; Torres-Larios, A. Structural basis of human triosephosphate isomerase deficiency: mutation E104D is related to alterations of a conserved water network at the dimer interface. *J. Biol. Chem*., **2008**, *283*, 23254-23263.

[108] Görlich, A.; Wolf, M.; Zimmermann, A.M.; Gurniak, C.B.; Al Banchaabouchi, M.; Sassoè-Pognetto, M.; Witke, W.; Friauf, E.; Rust, M.B. N- cofilin can compensate for the loss of ADF in excitatory synapses. *PLoS One*, **2011**, *6*, e26789.

[109] Wolf, M.; Zimmermann, A.M.; Görlich, A.; Gurniak, C.B.; Sassoè-Pognetto, M.; Friauf, E.; Witke, W.; Rust, M.B. ADF/Cofilin con-

INFORME DE LABORES 2019

trols synaptic actin dynamics and regulates synaptic vesicle mobilization and exocytosis. *Cereb. Cortex,* **2015**, *25*, 2863-2875.

[110] Jung, J.; Yoon, T.; Choi, E.C.; Lee, K.; Interaction of cofilin with triose-phosphate isomerase contributes glycolytic fuel for Na,K-ATPase via Rho-mediated signaling pathway. *J. Biol. Chem.*, **2002**, *277*, 48931-48937.

[111] Knull, H.R.; Walsh, J.L. Association of glycolytic enzymes with the cytoskeleton. *Curr. Top. Cell. Regul.*, **1992**, *33*, 15-30.

[112] Chen, G.; Gharib, T.G.; Huang, C.C.; Thomas, D.G.; Shedden, K.A.; Taylor, J.M.; Kardia, S.L.; Misek, D.E.; Giordano, T.J.; Iannettoni, M.D.; Orringer, M.B.; Hanash, S.M.; Beer, D.G. Proteomic analysis of lung adenocarcinoma: Identification of a highly expressed set of proteins in tumors. *Clin. Cancer Res.*, **2002**, *8*, 2298-2305.

[113] Wawrzyniak, M.; O'Mahony, L.; Akdis, M. Role of regulatory cells in oral tolerance. *Allergy Asthma Immunol. Res.*, **2017**, *9*, 107-115.

DISCLAIMER: The above article has been published in Epub (ahead of print) on the basis of the materials provided by the author. The Editorial Department reserves the right to make minor modifications for further improvement of the manuscript.

PMID: 30370845

Journal of Neurochemistry

INFORME DE LABORES 2019

JOURNAL OF NEUROCHEMISTRY | 2020 | 153 | 10–32

doi: 10.1111/jnc.14900

REVIEW

Construction and reconstruction of brain circuits: normal and pathological axon guidance

Sergi Roig-Puiggros[1,*], Robin J. Vigouroux[1,*], Danielle Beckman[2], Nadia I. Bocai[3,4], Brian Chiou[5], Joshua Davimes[6], Gimena Gomez[7], Sara Grassi[8], Ashfaqul Hoque[9], Thomas K. Karikari[10,11,12], Frederico Kiffer[13,14,15], Mary Lopez[16], Giulia Lunghi[17], Pedzisai Mazengenya[18], Sonja Meier[19], Mauricio Olguín-Albuerne[20], Mauricio M. Oliveira[21], Juan Paraíso-Luna[22,23], Jonu Pradhan[24], Andressa Radiske[25], Ana Belén Ramos-Hryb[26,27], Mayara C. Ribeiro[28], Roberta Schellino[29], Maria Clara Selles[30], Shripriya Singh[31], Paschalis Theotokis[32] and Alain Chédotal[1]

[1]*Sorbonne Université, INSERM, CNRS, Institut de la Vision, Paris, France*

[2]*California National Primate Research Center, UC Davis, Davis, California, USA*

[3]*Laboratory of Amyloidosis and Neurodegeneration, Fundación Instituto Leloir, Buenos Aires, Argentina*

[4]*Instituto de Investigaciones Bioquímicas de Buenos Aires, Consejo Nacional de Investigaciones Científicas y Técnicas (CONICET), Buenos Aires, Argentina*

[5]*Department of Pediatrics, University of California - San Francisco, San Francisco, California, USA*

[6]*Faculty of Health Sciences School of Anatomical Sciences, University of the Witwatersrand, Parktown Johannesburg, South Africa*

[7]*Laboratorio de Parkinson Experimental, Instituto de Investigaciones Farmacológicas (ININFA-CONICET-UBA), Ciudad Autónoma de Buenos Aires, Argentina*

[8]*Department of Medical Biotechnology and Translational Medicine, University of Milan, Milan, Italy*

[9]*Metabolic Signalling Laboratory, St Vincent's Institute of Medical Research, Fitzroy, Victoria, Australia*

[10]*Department of Psychiatry and Neurochemistry, Institute of Neuroscience and Physiology, The Sahlgrenska Academy at the University of Gothenburg, Gothenburg, Sweden*

[11]*School of Life Sciences, University of Warwick, Coventry, UK*

[12]*Midlands Integrative Biosciences Training Partnership, University of Warwick, Coventry, UK*

[13]*Division of Radiation Health, College of Pharmacy, University of Arkansas for Medical Sciences, Little Rock, Arkansas, USA*

[14]*Department of Pharmaceutical Sciences, College of Pharmacy, University of Arkansas for Medical Sciences, Little Rock, Arkansas, USA*

[15]*Department of Anesthesiology and Critical Care Medicine, Children's Hospital of Philadelphia, Philadelphia, Pennsylvania, USA*

[16]*Institute for Stroke and Dementia Research, LMU Munich, Munich, Germany*

[17]*Department of Medical Biotechnology and Translational Medicin, University of Milano, Segrate, Italy*

Received August 16, 2019; revised manuscript received October 14, 2019; accepted October 17, 2019.

Address correspondence and reprint requests to Alain Chédotal, Sorbonne Université, INSERM, CNRS, Institut de la Vision, 17 rue Moreau, F-75012 Paris, France. E-mail: alain.chedotal@inserm.fr

*Equal contribution.

Abbreviations: CC, corpus callosum; Dcc, deleted in colorectal cancer; Sema3C, semaphorin3C; Nrp1, neuropilin 1; RGCs, retinal ganglion cells; OC, optic chiasm; Zic2, Zic family member 2.

© 2019 International Society for Neurochemistry,

REVIEW

[18]*School of Anatomical Sciences, Faculty of Health Sciences, University of the Witwatersrand, Johannesburg, South Africa*
[19]*Queensland Brain Institute, The University of Queensland, St Lucia, Queensland, Australia*
[20]*División de Neurociencias, Instituto de Fisiología Celular, Universidad Nacional Autónoma de México, Ciudad de México, México*
[21]*Institute of Biophysics Carlos Chagas Filho, Federal University of Rio de Janeiro, Rio de Janeiro, Brazil*
[22]*Ramón* y Cajal Institute of Health Research (IRYCIS), Department of Biochemistry and Molecular Biology and University Research Institute in Neurochemistry (IUIN), Complutense University, Madrid, Spain
[23]*Network Center for Biomedical Research in Neurodegenerative Diseases (CIBERNED), Madrid, Spain*
[24]*Faculty of Medicine, School of Biomedical Sciences, The University of Queensland, Brisbane, Queensland, Australia*
[25]*Memory Research Laboratory, Brain Institute, Federal University of Rio Grande do Norte, Natal, Brazil*
[26]*Instituto de Biología* y Medicina Experimental (IBYME)-CONICET, Buenos Aires, Argentina
[27]*Grupo de Neurociencia de Sistemas, Instituto de Fisiología* y Biofísica (IFIBIO) Bernardo Houssay, Universidad de Buenos Aires, CONICET, Buenos Aires, Argentina
[28]*Department of Biology, Program in Neuroscience, Syracuse University, Syracuse, New York, USA*
[29]*Neuroscience Department "Rita Levi-Montalcini" and Neuroscience Institute Cavalieri Ottolenghi, University of Torino, Torino, Italy*
[30]*Institute of Medical Biochemistry Leopoldo de Meis, Federal University of Rio de Janeiro, Rio de Janeiro, Brazil*
[31]*System Toxicology and Health Risk Assessment Group, CSIR*-Indian Institute of Toxicology Research, Lucknow, India
[32]*Department of Neurology, Laboratory of Experimental Neurology and Neuroimmunology, AHEPA University Hospital, Thessaloniki, Macedonia, Greece*

Abstract
Perception of our environment entirely depends on the close interaction between the central and peripheral nervous system. In order to communicate each other, both systems must develop in parallel and in coordination. During development, axonal projections from the CNS as well as the PNS must extend over large distances to reach their appropriate target cells. To do so, they read and follow a series of axon guidance molecules. Interestingly, while these molecules play critical roles in guiding developing axons, they have also been shown to be critical in other major neurodevelopmental processes, such as the migration of cortical progenitors. Currently, a major hurdle for brain repair after injury or neurodegeneration is the absence of axonal regeneration in the mammalian CNS. By contrasts, PNS axons can regenerate. Many hypotheses have been put forward to explain this paradox but recent studies suggest that hacking neurodevelopmental mechanisms may be the key to promote CNS regeneration. Here we provide a seminar report written by trainees attending the second Flagship school held in Alpbach, Austria in September 2018 organized by the International Society for Neurochemistry (ISN) together with the *Journal of Neurochemistry* (JCN). This advanced school has brought together leaders in the fields of neurodevelopment and regeneration in order to discuss major keystones and future challenges in these respective fields.
Keywords: JNC-ISN Flagship School, review, cell therapy, spinal cord, axon guidance, regeneration.
J. Neurochem. (2020) **153**, 10–32.

The first anatomical reference of the brain dates back to the ancient Egyptian mummifications. However, the tremendous complexity of this organ was revealed by the work of the world-renowned neuroscientist Santiago Ramón y Cajal. Nevertheless, his anatomical descriptions could not fully explain the cellular and molecular events at the origin of behavioral, motor or sensitive responses. Today, it is clear that the CNS is the processing center for these events. Moreover fine sensory perception and intricate motor control are orchestrated by a discrete and permanent communication

between the CNS and the PNS. In the last century, neuroscientists have investigated the mechanisms involved in the development and plasticity of this structure. To address these fundamental questions, researchers made use of simple and accessible animal models. *Drosophila melanogaster* was one of the first organisms used because of several technical advantages: amenability to genetic manipulation, short lifespan and large number of offsprings. Studies emanating from this model system paved the path toward our understanding of major neurodevelopmental mechanisms involved in vertebrate behavior, neuronal migration and differentiation among many others (Bellen *et al.* 2010). *Danio rerio* (zebrafish), quickly emerged as an attractive more complex animal model. Like the *Drosophila melanogaster*, the zebrafish model also possessed a short lifespan and a large number of offsprings. However, it provided the advantage of studying neurodevelopmental mechanisms in vertebrates (d'Amora and Giordani 2018). While findings in these two models have led to major findings in the field of neuroscience, there are still significant gaps in our understanding of human development. Over the last 50 years, *Mus musculus* and *Rattus norvegicus* are classic models in neuroscience research because of their closer phylogenetic proximity to humans (Ellenbroek and Youn 2016).

In parallel to these findings, a large number of pathologies related to the CNS have emerged over the last century. This is mainly related to the aging population, encountering previously unknown neuro-degenerative diseases. The rising prevalence of these neurodegenerative diseases has urged the need for novel and more effective therapies (Gitler *et al.* 2017). Quickly, the idea emerged that developmental processes could be reinitiated to induce regeneration and brain repair. In an effort to target these fundamental questions, the Journal of Neurochemistry organized in September 2018 a workshop in Alpbach, Austria, gathering some of the most prominent researchers in the field of developmental neurobiology and regeneration in order to discuss the most significant findings and current challenges in these fields. Trainees attending this workshop have drafted a seminar report of this workshop listing the major advances and putting forward major questions in the field.

The developing nervous system

Metazoans all possess an axis of symmetry. In contrast to *radiata* (radial symmetry), *Bilateria* possess a two-fold symmetry. Thus, *bilateria* have a front and rear as well as left and right sides. To connect its two lateral halves, the CNS of *bilateria* possesses commissural neurons. These neurons, which are born embryonically, project their axons contralaterally to connect the left and right side of the organism. Together, these commissural networks not only allow for integration and coordination of left-right neuronal activities, but are essential for the correct processing and interpretation of various sensory information, the coordination of motor responses and other brain functions (Stoeckli 2018; Gaudet and Fonken 2018; Ducuing *et al.* 2019). Many commissural tracts exist in the CNS (Chédotal 2014). Here, we will discuss the three major systems: the corpus callosum, the ventral commissure of the spinal cord, and the optic chiasm.

Forebrain

The forebrain possesses two main cortical projection neurons: cortico-cortical, that form the corpus callossum, and cortico-fugal, further subdivided into corticothalamic and coroticospinal tracts (Leyva-Díaz and López-Bendito 2013).

The corpus callosum (CC) is the largest brain commissure and develops alongside neocortex expansion. Interestingly, this structure is unique to eutherian mammals and relays information between left and right hemispheres via the midline (Gazzaniga 2000; Suárez *et al.* 2014). Corpus Callosum dysgenesis affects ~ 1 : 4000 live births that result in either partial or complete absence (agenesis) of the CC (Edwards *et al.* 2014). Initially the two hemispheres are separated, at the midline, by the interhemispheric fissure (Rakic and Yakovlev 1968). This region is lined by specialized astroglial and neuronal cells that are required for proper CC tract formation (Silver *et al.* 1982; Niquille *et al.* 2009; Gobius *et al.* 2016; Gobius *et al.* 2017). In addition to providing a permissive substrate for callosal growth cones to grow across the midline, midline cells also secrete guidance cues. Pre-crossing CC axons are sensitive to Slit2, expressed by these astroglia, which acts as a repulsive cue to constrain callosal axons expressing the Roundabout (Robo) receptors 1/2 (Unni *et al.* 2012). In contrast, netrin-1, expressed by the cingulate cortex, counteracts the Slit2 repulsive signal by attracting callosal axons expressing the transmembrane receptor deleted in colorectal cancer (Dcc) (Fothergill *et al.* 2014). Indeed, loss of Dcc or netrin-1 leads to CC agenesis (Serafini *et al.* 1996; Fothergill *et al.* 2014). In addition to netrin-1, semaphorin (Sema3C) is secreted at the midline and attracts callosal axons expressing the receptor neuropilin 1 (Nrp1, Fig. 1a) (Niquille *et al.* 2009). Once CC axons have reached and crossed the midline, this attractive signal is switched off (Mire *et al.* 2018). This coincides with an up-regulation of the transmembrane protein ephrin-B1 in post-crossing CC axons. Interestingly, ephrin-B1 possesses a unique Asparagine residue (N-139), not shared by other ephrins, which once glycosylated can allow ephrin-B1 interaction with Nrp1 and silence Sema3C/Nrp1 attraction (Mire *et al.* 2018) (Fig. 1b). These findings identify a novel mechanism involving interaction between Sema3c/Nrp1 and Ephrinb1 during midline crossing in the corpus callosum (Fig. 1).

Optic chiasm

Another critical component of the CNS is visual perception. The functional unit of the eye is the retina (Fig. 2a), which is

INFORME DE LABORES 2019

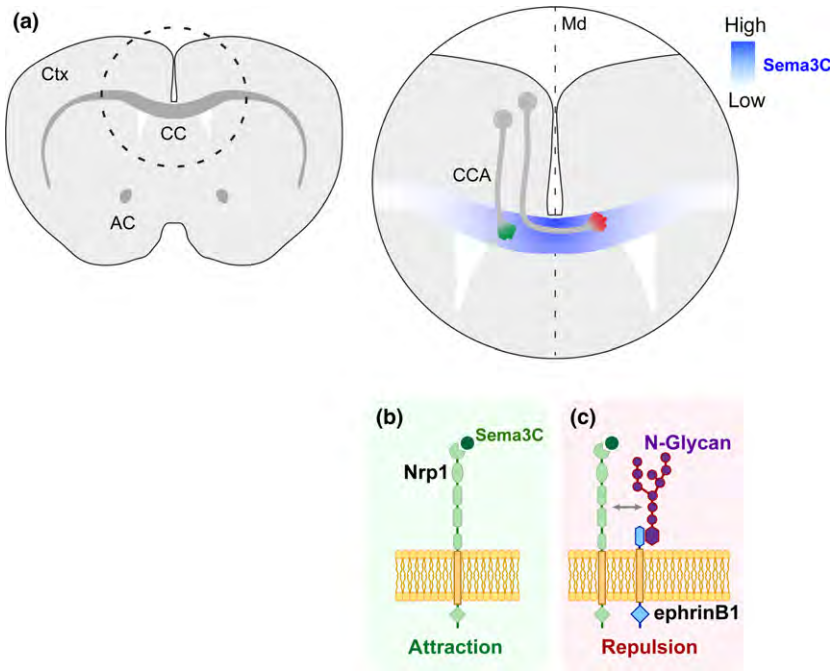

Fig. 1 Sema3C controls midline crossing in the developing *corpus callosum*. (a) The role of semaphorin in midline crossing in the *corpus callosum* has been recently elucidated. Sema3C is expressed in a gradient across the callosal midline. It binds the Nrp1 receptor on callosal axon growth cones (b) acting as an attractive cue. (c) The Sema3C/Nrp1 complex is silenced by the presence of trans-membrane protein ephrinB1. This requires an N-Glycan post-traductional modification of ephrinB1. Ctx, cortex; CC, *corpus callosum*; AC, anterior commissure; CCA, *corpus callosum* axon.

a highly organized structure. Photoreceptor cells are photosensitive cells that transform photons of light into an electrical impulse that is transmitted to bipolar cells and subsequently to Retinal ganglion cells (RGCs). RGCs relay this electrical signal to the brain along their axons that form the optic nerve. Importantly, whilst other retinal cell types can modulate the electrical signal mediated by photoreceptor cells, such as amacrine and horizontal cells, RGCs are the only output neuron from the retina and connecting it to the brain. During visual system development, retinal ganglion cells (RGCs) extend axons toward a specialized structure at the midline, named the optic chiasm (OC). At this point, RGCs will either project to the same hemisphere (ipsi-lateral) or cross the midline to project to the opposite hemisphere (contra-lateral). Therefore, two types of RGCs, ipsilateral RGCs (iRGCs) and contralateral RGCs (cRGCs) can be defined by the laterality of their projections (Williams *et al.* 2004).

This process is critical for depth perception, stereopsis. Indeed, since both eyes will obtain a "picture" of our environment, by combining these pictures we will generate a three-dimensional (3D) representation of the picture. Interestingly, the amount of overlap between each eye is directly proportional to the amount of ipsi-lateral projections. For instance, species with laterally positioned eyes, such as mice, possess only 3–5% of ipsi-laterally projecting RGCs. However, humans and primates, with more frontally positioned eyes, possess approximately 50% of ipsi-laterally projecting RGCs (Guillery *et al.* 1995; Jeffery and Erskine 2005; Herrera *et al.* 2019). Mouse iRGCs and cRGCs are characterized by specific transcriptional patterns and, in part, spatial localization, with iRGCs residing in the ventro-temporal retina, and cRGCs being dispersed across the retina (Herrera *et al.* 2003; Pak *et al.* 2004; Williams *et al.* 2006; García-Frigola *et al.* 2008; Kuwajima *et al.* 2017) (Fig. 2b and c).

In order to control the crossing of RGC axons at the OC, two processes take place: repulsion of axons with an ipsi-lateral fate, and the crossing of contralateral axons across the midline (Fig. 2d). EphB1/ephrin-B2 signaling pathway is a key component of ipsi-lateral axon repulsion. Expression of the EphB1 tyrosine kinase receptor is restricted to axons of iRGCs, while its ligand, the repulsive axon guidance molecule ephrin-B2, is expressed at the OC (Williams *et al.* 2003). When the axons reach the proximity of the OC, a chemo-repulsive gradient of ephrin-B2 leads to growth cone collapse and pausing of axonal outgrowth, eventually causing changes of trajectory and driving the axon toward ipsi-lateral visual nuclei (Petros *et al.* 2010). It was further shown that RGC axon laterality is transcriptionally regulated. The transcription factor Zic family member 2 (Zic2) was identified as a key regulator of iRGCs identity (Herrera *et al.* 2003; Wang *et al.* 2016). Furthermore, Zic2 is sufficient to induce the expression of EphB1 receptor in iRGCs (Lee *et al.* 2008; García-Frigola *et al.* 2008) (Fig. 2c). In addition, the transcription factor Forkhead box D1 was shown to be critical in maintaining iRGCs fate by promoting the expression of Zic2 (Herrera 2004). In addition to the EphB1/ephrin-B2 repulsion pathway, another pathway also controls ipsilateral RGC repulsion: Shh is expressed by contralateral RGCs and transported axonally and anterogradely to the optic chiasm (Peng *et al.* 2018). At the optic chiasm, ipsilateral

INFORME DE LABORES 2019

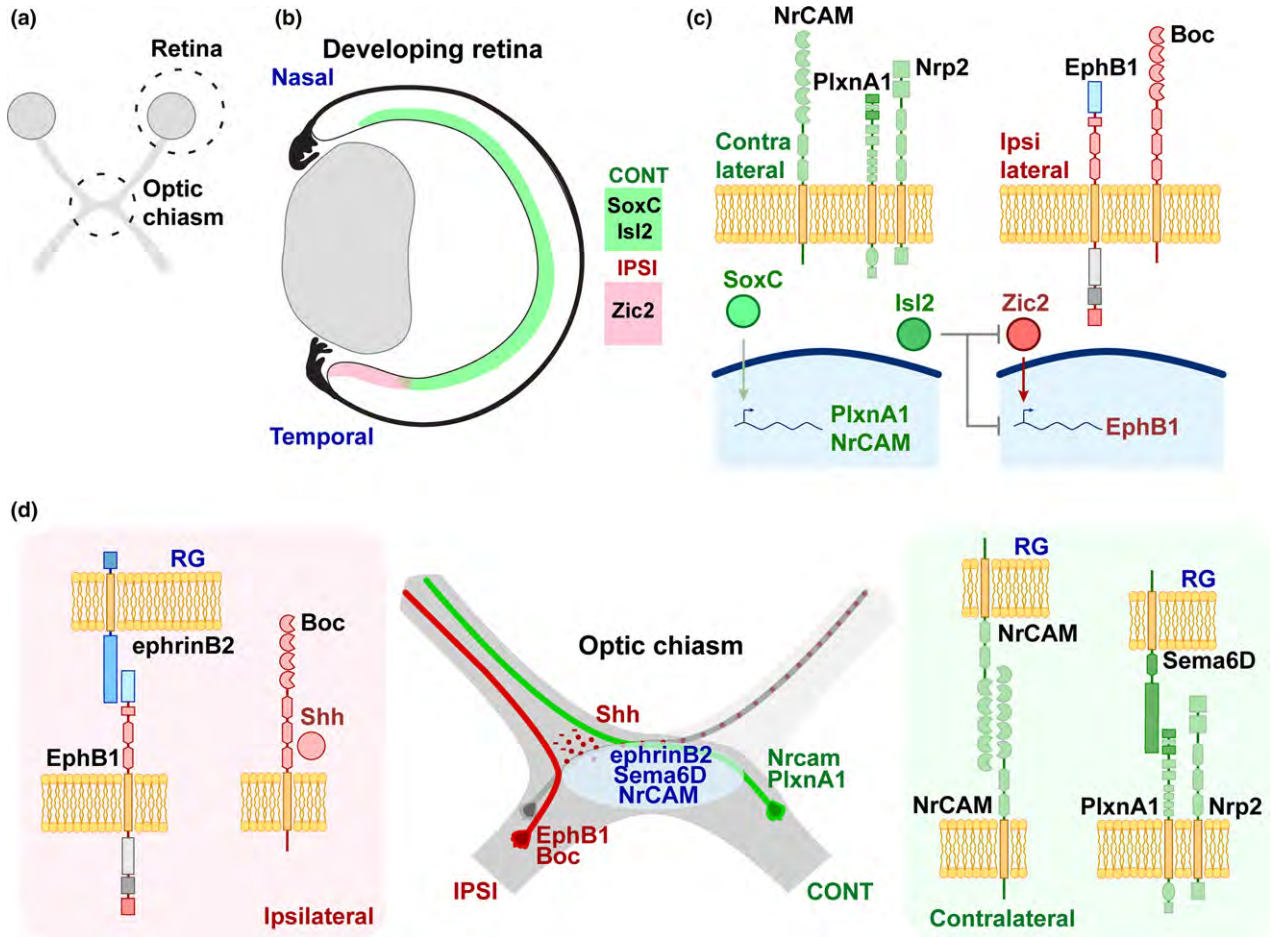

Fig. 2 Retinal ganglion cells development and their pathfinding at the optic chiasm. (a) In the developing visual system, retinal ganglion cells (RGCs) project from the retina to the brain nuclei. During this process, some RGC axons cross the midline at the optic chiasm. (b) RGCs projecting towards the contra or ipsilateral side are already specified in the retina by two sets of transcription factors: *SoxC* and *Islet2* in contralateral RGCs and *Zic2* in ipsilateral RGCs. The Sonic hedgehog (Shh) receptor Boc, is also expressed by ipsilateral RGCs. (c) These two different combinations allow the expression of guidance effectors, regulating the pathfinding choices at the optic chiasm. Moreover *Islet2* is also blocking the expression of *Zic2* and *Boc* expression in contralateral RGCs. (d) The optic chiasm is the intermediate target where contralateral RGCs (green) project towards the contralateral side of the CNS whereas ipsilateral RGCs (red) follow the visual tract on their original side. Shh, transported by the contra-lateral RGCs (gray), is released at the optic chiasm. Ipsi-lateral RGCs expressing the transmembrane receptors Boc as well as EphB1 are repelled by Shh and ephrinB2 at the optic chiasm. An attraction of contralateral RGCs to the midline is mediated by the cell adhesion molecule NrCAM and transmembrane semaphorin Sema6D, through their interaction with NrCAM and the complex PlexinA1-Neuropilin2. RG, radial glia.

RGCs, which express the Shh receptor Boc, are repelled by Shh and therefore do not cross the optic chiasm, remaining ipsilateral (Fabre *et al.* 2010; Peng *et al.* 2018) (Fig. 2d).

In contrast, cRGC axons express the L1 cell adhesion molecule, the neuronal cell adhesion molecule (NrCAM), and the semaphorin receptor Plexin-A1. Together, these molecules provide a permissive substrate for cRGCs to invade and cross the OC (Williams *et al.* 2006; Kuwajima *et al.* 2012). Transcriptionally, the Sox C family of transcription factors (Sox4, Sox11, Sox12) was identified as key regulators for cRGC fate by regulating NrCAM and PlexinA1 expression (Kuwajima *et al.* 2017) (Fig. 2c and d). In addition, the transcription factor Islet2 is expressed by ~ 30% of cRGCs, mainly expressed by late-born cRGCs (Pak *et al.* 2004; Kuwajima *et al.* 2017). Furthermore, the leucine-rich repeat receptor Islr2 has been shown to be expressed on cRGCs and its deletion leads to aberrant ipsi-lateral projections in *Danio Rerio* (Panza *et al.* 2015).

Interestingly, binocular vision is impaired in patients with albinism (an absence of melanin production of the retinal pigmented epithelium). This led researchers to study the role of pigmentation on iRGCs. It was found that albino mice have less iRGCs, but a normal number of cRGCs (Rebsam *et al.* 2012). This appears to be linked to the timing of RGC

INFORME DE LABORES 2019

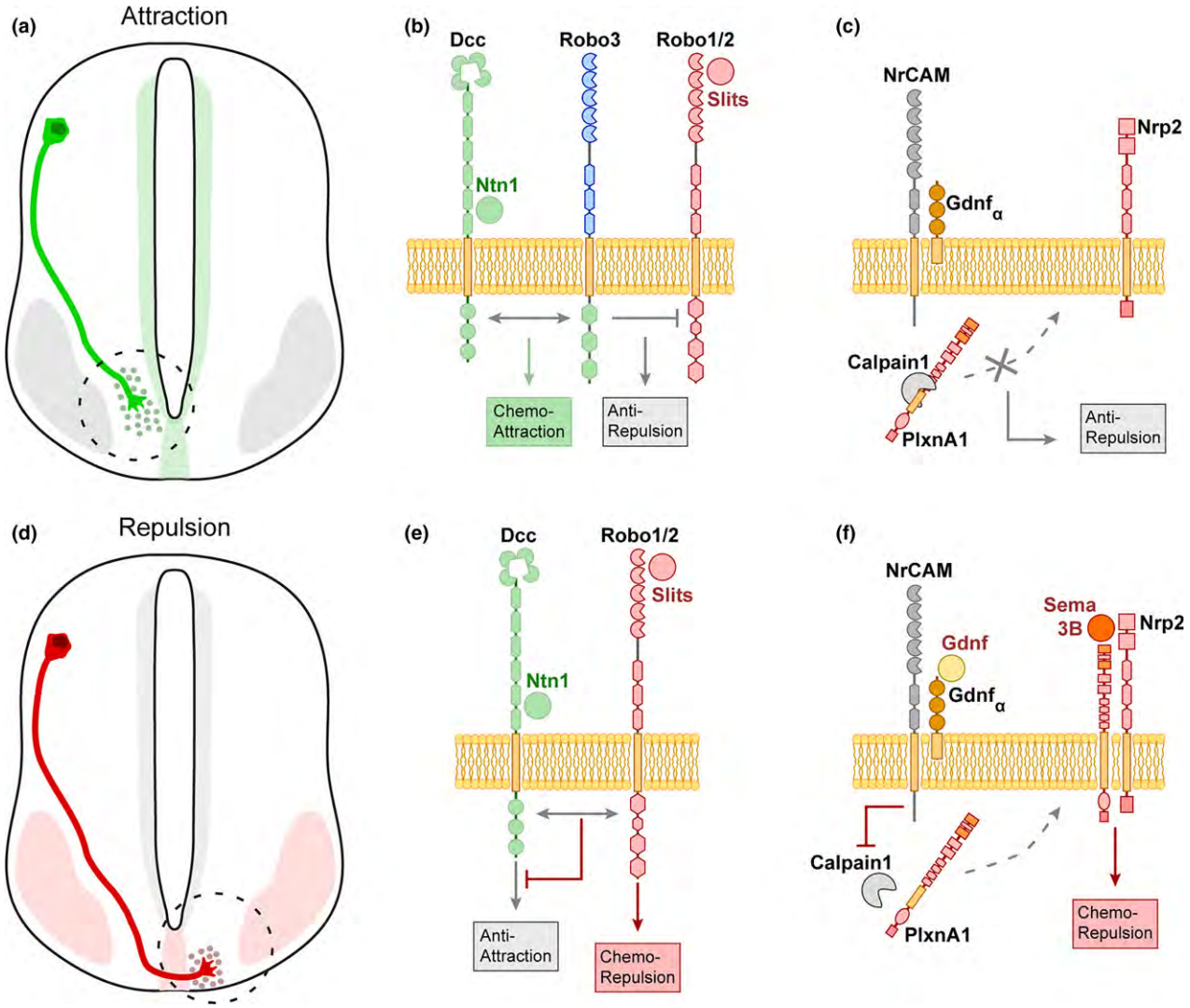

Fig. 3 Spinal cord commissural axons development: pre and post-crossing guidance mechanisms. (a) Commissural axons arise from the dorsal portion of the spinal cord. To cross the midline, they first have to be guided to the floor plate. This first process involves several guidance receptors that trigger the axon outgrowth toward the ventral midline. (b) Pre-crossing axons express the Roundabout 3 (Robo3) receptor. Robo3 interacts with deleted in colorectal cancer (Dcc) receptor and both promote axon extension to the floor plate in response to Netrin-1. Netrin-1 was first thought to act as long-range cue but recent studies suggest that it acts as short-range cue. Robo3 might also prevent Slit repulsion by interacting with the Robo1/2 receptors. (c) Moreover in pre-crossing commissural axons, the presence of calpain induces a cleavage of the PlexinA1 receptor, inactivating this repulsive signalling pathway. (d) After midline crossing, commissural axons switch from midline attraction to repulsion. They become sensitive to repulsive cues secreted by floor plate cells which prevent midline re-crossing. Axon then start to extend rostrally toward their final targets. (e) At the floor plate, Robo3 is down-regulated, and Robo1/2 interaction with Slits blocks the Dcc-Netrin-1 attractive signalling. (f) In addition, the expression of Gdnf by floor plate cells inhibits calpain activity on crossing fibres, allowing PlexinA1 to reach the membrane where it interacts with Neuropilin2, where this receptor complex triggers midline repulsion upon binding Sema3B.

differentiation: albino animals have a shorter time window during which iRGCs are born which is compensated by an increased number of cRGCs (Bhansali *et al.* 2014). Furthermore, the functional comparison of gene expression in albino and pigmented retinas, showed that the Wnt-pathway, which controls iRGC differentiation and cell proliferation, is dysregulated in albino animals (Iwai-Takekoshi *et al.* 2018). Rescue of ipsi-lateral deficit via blockage of Nr-CAM may improve visual capability in albino animals, thereby providing a paradigm for functionally investigating the consequences of natural ipsi-lateral depletion (Williams *et al.* 2006).

Interestingly, the existence of another population of RGCs has been described to project between the two retinas (retino-

retinal projection) in various vertebrate species (Müller and Holländer 1988; Tóth and Strznicky 1989; Nadal-Nicolás *et al.* 2015). More recently, it was described that this population resides in the ventro-nasal retina and is transient (E16.5 to postnatal day 4) (Murcia-Belmonte *et al.* 2019). These late-born RGCs were shown to express Unc5c, a netrin-1 receptor. Upon reaching the optic chiasm, Unc5c-positive RGCs are repelled by netrin-1 and project into the contralateral optic nerve. Indeed, Unc5c is both sufficient and necessary for retino-retinal projections (Murcia-Belmonte *et al.* 2019). However, the precise connection and function of this projection remains to be characterized. Moreover the implication of this projection in co-ordinating spontaneous activity remains to be studied.

Spinal cord

In the developing spinal cord, midline crossing takes place ventrally through a structure named the floor plate (FP). The FP is a crucial patterning center composed of specialized cells that contribute to the specification of the neuronal lineages of the neural tube and adjacent territories.

Moreover the FP is a source of both growth-promoting and growth-repulsive cues for commissural axons, such as netrin-1 and Slits (Chédotal 2019). In vertebrates, spinal commissural axons navigate first ventrally toward the floor plate (Fig. 3a), cross the midline and then turn rostrally or caudally (Fig. 3d). According to the current model, the sensitivity to midline repellents is silenced in pre-crossing commissural growth cones as they navigate toward the FP. However, during FP crossing, commissural growth cones gain responsiveness to FP repulsive cues. The post-crossing commissural neurons are thus expelled from the midline, and also prevented from re-crossing the FP. At later stages, they follow rostro-caudal gradients of guidance cues, turning rostrally or caudally in the ventral or lateral funiculi (Gaudet and Fonken 2018; Ducuing *et al.* 2019; Chédotal 2019).

Commissural axon guidance before midline crossing

The earliest born spinal commissural neurons will extend their axons toward the pial surface of the spinal cord and ventrally toward the FP (Fig. 3a). For many years it was thought that a long-range gradient of the secreted protein netrin-1 is generated by the FP and attracts commissural neurons ventrally upon binding the receptor Dcc (Hiramoto *et al.* 2000; Finci *et al.* 2015). However, recent studies have challenged this model and rather support a local and haptotactic function of netrin-1. Indeed, netrin-1 is not only expressed by FP cells but also by the neural progenitors of the ventricular zone of the spinal cord and brainstem. In support to this model, specific deletion of netrin-1 at the FP, does not perturb commissural axon crossing in the hindbrain (Dominici *et al.* 2017; Yamauchi *et al.* 2017). Interestingly, in the spinal cord, midline crossing appears slightly delayed (Moreno-Bravo *et al.* 2019) and some axons are misguided before crossing (Varadarajan *et al.* 2017; Moreno-Bravo *et al.* 2019; Wu *et al.* 2019). These results suggest that floor plate-derived netrin-1 is dispensable for commissural axon crossing, but also highlight a different mechanism of action of netrin-1 between the hindbrain and the spinal cord. Importantly, ablating netrin-1 expression in ventricular zone progenitors severely perturbs midline crossing in the brainstem (Dominici *et al.* 2017; Yamauchi *et al.* 2017) but only mildly in the spinal cord (Moreno-Bravo *et al.* 2019). However, the simultaneous deletion of ventricular and FP derived netrin-1 prevents midline crossing (Moreno-Bravo *et al.* 2019). Therefore, in the spinal cord, both sources of netrin-1 cooperate to guide commissural neuron at the midline. Other secreted proteins such as VEGF (Ruiz de Almodovar *et al.* 2011) and Shh (Charron *et al.* 2003; Bovolenta and Sanchez-Arrones 2012; Sloan *et al.* 2015; Wu *et al.* 2019) are expressed at the floor plate and act redundantly with netrin-1 to attract axons as they get close to the FP.

Robo3, a member of the Roundabout (Robo) family, plays a key role in midline guidance. This receptor is expressed transiently by commissural axons in mouse spinal cord, midbrain and hindbrain and then is rapidly down-regulated after the axons have crossed the FP (Belle *et al.* 2014; Zelina *et al.* 2014). It is expressed in human pontine neurons (Jen *et al.* 2004) and in hindbrain and spinal cord commissural axons of birds (Philipp *et al.* 2012; Escalante *et al.* 2013; Friocourt and Chédotal 2017) and other vertebrate species (Friocourt *et al.* 2019). The absence of Robo3 leads to a complete loss of several commissures in mice and in humans (Jen *et al.* 2004; Marillat *et al.* 2004; Sabatier *et al.* 2004; Renier *et al.* 2010; Michalski *et al.* 2013). The mechanism through which Robo3 controls commissure development is not completely understood. However, it was proposed that Robo3 expression in pre-crossing commissural neurons repress Slit/Robo repulsion (Fig. 3b), thus allowing commissural axons to reach, enter, and cross the ventral midline in response to netrin-1 attraction (Sabatier *et al.* 2004; Jaworski *et al.* 2010; Chédotal 2011). This mechanism has been validated in the spinal cord and lateral reticular nucleus. Interestingly, the inferior olivary nucleus does not seem to follow the same mechanism (Di Meglio *et al.* 2008). However, it was initially proposed that Robo3 may facilitate attraction of commissural neurons to the floor plate, independently of Slit/Robo signaling (Sabatier *et al.* 2004; Di Meglio *et al.* 2008; Jaworski *et al.* 2010). More recent studies support this notion. Indeed, whilst non-mammalian Robo3 retained its ability to bind Slits, the mammalian orthologue of Robo3 has lost key residues in the Slit/Robo binding domain (Zelina *et al.* 2014). Instead, it possesses the ability to bind to netrin-1, by creating a receptor complex between Dcc and Robo3 via Src kinases, on a conserved tyrosine residue and contributes to the attractive actions of netrin-1 (Zelina *et al.* 2014). Therefore, Robo3 might

promote attraction to the ventral midline rather than counteract repulsion.

To date, several transcription factors have been associated with the most dorsal commissural population, dI1, which arises from the *Atoh1*$^{+}$ domain (Chédotal 2014). These interneurons are divided in two different subtypes depending on the location of their targets: ipsilateral (dI1i) or contralateral (dI1c) (Wilson *et al.* 2008). Interestingly, their projection pattern relies on the balance between the expression of two transcription factors *Lhx2* and *Lhx9* (Lim homeobox) and their upstream activation by the transcription factor *Barhl2* (Ding *et al.* 2012). Lhx2 is able to directly bind to the regulatory region of *Robo3* and modulate its expression in a dose-dependent manner. Moreover in *Lhx2/9* knockouts, most of dI1 interneurons fail to cross the midline and project ipsilaterally (Wilson *et al.* 2008; Marcos-Mondejar *et al.* 2012).

Furthermore, the transcription factor Zic2 triggers an ipsilateral transcriptional program but also inactivates a contralateral one (Escalante *et al.* 2013). Indeed, down-regulation of *Zic2* by *in utero* electroporation of siRNA induces an abnormal up-regulation of Robo3 and a contralateral projection of dorsal horn neurons. A *Zic2* gain of function has the reverse effect, reducing *Robo3* expression and an increase of ipsilateral projections. In addition to modulating Robo3 expression, Zic2 is necessary and sufficient to induce EphA4 expression and commissural neuron repulsion in response to midline ephrinB's.

Commissural axon guidance after midline crossing

Upon FP crossing, commissural axons become sensitive to a myriad of repulsive guidance molecules expressed at the FP. However, prior to midline crossing, commissural axons do not express the receptors (at the surface) required to sense this repulsive environment. One such example is the repulsive receptor, PlexinA1, which is down-regulated at the surface of commissural neurons prior to midline crossing (Fig. 3c). PlexinA1 down-regulation at the growth cone involves the protease, Calpain-1 (Nawabi *et al.* 2010; Charoy *et al.* 2012). However upon FP entry, commissural neurons become exposed to the NrCAM that inhibits calpain-1 activity (Fig. 3f). As a result, PlexinA1 can accumulate at the growth cone which becomes sensitive to the repulsive cue Sema3B (expressed at the FP) (Nawabi *et al.* 2010; Charoy *et al.* 2012). In addition to PlexinA1, the semaphorin receptor Neuropilin 2 (Nrp2) is also expressed at the growth cone following FP entry. Indeed, Sema3B and Nrp2 double mutants display FP stalling as well as post-crossing misrouting (Nawabi *et al.* 2010; Parra and Zou 2010).

Slits are other repulsive cues expressed at the FP (Brose *et al.* 1999). As with PlexinA1 and Nrp2, commissural axon growth cones start expressing the Robo 1 and Robo2 receptors only after midline crossing, and become sensitive to Slit repulsion (Fig. 3e). Indeed, deletion of Robo receptors results in commissural axons stalling at the FP (Long *et al.* 2004; Garbe and Bashaw 2007; Blockus and Chédotal 2016). However, Silts can also function independently of Robo receptors. In vertebrates, Slits can be cleaved into two separate fragments (Brose *et al.* 1999; Wang *et al.* 1999). The shorter fragment (Slit-C) is able to bind to PlexinA1 in commissural neurons to induce growth cone collapse (Delloye-Bourgeois *et al.* 2015).

Once commissural axons have exited the FP, they are then guided by other cues to continue either rostrally or caudally. Little is known about the cues guiding postcrossing axons along the midline. However, Wnt signaling has been shown to be critical in this process (Onishi *et al.* 2014). An expression gradient of several Wnt family proteins controls the rostral turning of post-crossing commissural axons through an attractive mechanism involving the Frizzled3 (Fzd3) receptor (Lyuksyutova *et al.* 2003; Yoshikawa *et al.* 2003). The disruption of the Wnt gradient, results in a randomization of the growth of post-crossing commissural axons, which randomly turn toward the anterior or posterior part (Yoshikawa *et al.* 2003; Zou 2004). Recently, a mechanism orchestrating Wnt activation has been proposed. During FP crossing, commissural neurons expressing Smoothened (Smo) are exposed to the morphogen sonic hedgehog (Shh). This interaction leads to the reduction in mRNA translation of Shisa2, a well-known Wnt signaling inhibitor. Shisa2 inhibits the Wnt receptor Frizzled (Fzd3) trafficking to the cell surface by interfering with its glycosylation, inactivating Wnt signaling (Onishi and Zou 2017). Moreover it has been shown that components of the planar cell polarity signaling pathway mediate Wnt attraction and the anterior turning of commissural axons (Lyuksyutova *et al.* 2003; Zou 2012; Onishi *et al.* 2014). In addition to the planar cell polarity pathway, the canonical Wnt signaling pathway is critical in mediating post-crossing commissural neuron turning. Indeed, down-regulation of both Lrp5 and Lrp6 (Low density lipoprotein receptor-related protein, co-receptors for Frizzled), which are required in the β-catenin-mediated canonical Wnt pathway, lead to major defects in post-crossing commissural neurons (Avilés *et al.* 2016).

Shh also guides post-crossing commissural axons (Bourikas *et al.* 2005; Yam *et al.* 2012). After crossing, commissural axons become repelled by Shh and project anteriorly along a posterior-high Shh and anterior-high Wnt4 gradients. However, instead of mediating its action through Patched or smoothened, Shh acts through the Hedgehog interacting protein. Further experiments showed that this switch in Shh responsiveness depended on the levels of 14-3-3 proteins, which are low in pre-crossing and high in post-crossing commissural neurons, and modulate Protein Kinase A activity (Yam *et al.* 2012).

Peripheral nervous system development

The bilaterian nervous system is subdivided in two main components: the central and the peripheral nervous systems

(CNS and PNS). Permanent cross-talk between the CNS and PNS is critical for integration of sensory inputs. In the 4th century BC, *Alcmaeon of Croton* (Goddard *et al.* 1996) (Zolog 1994) proposed the first theory about channels ("poroi" in ancient greek) that would connect the senses and the brain, this last one being the center of human perception. Later, it became clear that all sensory perception being mechanical, auditory, gustatory, and olfactory were relayed to the CNS through the "nerves" (Mazengenya and Bhikha 2017). Indeed, the precise interplay between these two networks develop in parallel during embryonic development (Ben-Arie *et al.* 2000). Additionally, it has been demonstrated that both axon guidance and neuronal activity can strongly modulate connections between the PNS and the CNS (Bonanomi and Pfaff 2010; Wang and Bergles 2015). Nevertheless, the PNS is itself formed by different components, each specialized in the transmission of a specific signal to the CNS. These signals are transmitted by mechanosensory, chemical or thermal receptors projecting to the mammalian spinal cord via nociceptive afferents.

Drosophila bristles are sensory organs that are tightly distributed and contain one single mechanosensory neuron that specifically projects to the CNS. These axons can be guided by cell adhesion molecules, such as Neuroglian or Flamingo (Martin *et al.* 2008; Steinel and Whitington 2009), but also by other guidance molecules, such as Plexins or semaphorins (Wu *et al.* 2011). Down syndrome cell adhesion molecule (DSCAM) is a transmembrane receptor of the immunoglobulin-superfamily (Chen *et al.* 2006). DSCAM has since been described to regulate cell targeting, axon branch specification, and dendrite patterning (Schmucker *et al.* 2000; Wang *et al.* 2002a; Dascenco *et al.* 2015). The repulsive molecule, Slit, has been shown to bind and signal through DSCAM1 independently of Robo receptors (Chen *et al.* 2006). Indeed, local binding to Slit drives spatial specificity of axon collateral formation. Furthermore, Chen *et al.* (2006) report that many DSCAM isoforms exist and particular DSCAM isoform mosaicism in a specific growth cone appears to dictate local guidance decisions, such as the formation of axon collateral projections.

The inner ear is essential for the transmission of sounds and their integration by the CNS. This complex sensory organ is composed of bipolar spiral ganglion neurons (SGN) that connect the ipsilateral cochlear nucleus and the mechanosensory inner and outer hair cells located in the organ of Corti (Nayagam *et al.* 2011). SGNs project to both the inner (IHC) and the outer hair cells (OHC). During the course of development, both type I and II project to the OHC but type I SGNs appear to refine in later stages and only project to the IHC (Huang *et al.* 2012; Safieddine *et al.* 2012; Druckenbrod and Goodrich 2015). The use of molecular markers to target single spiral ganglia has revealed key morphological differences between type I and type II SGNs as well as their specific projection patterns to the IHC or outer hair cells OHC (Druckenbrod and Goodrich 2015; Coate *et al.* 2015). Indeed, type I and II SGNs were shown to be molecularly different. Type I SGNs express the semaphorin receptor Nrp2 and its co-receptor PlexinA3 (Coate *et al.* 2015). Upon binding Sema3F, secreted by the OHC, type I SGNs are repulsed and restrict their projections to the IHC (Coate *et al.* 2015). More recently, the use of single sequencing has allowed a more in depth characterization of SGNs. In this study, Shrestha *et al.* (2018) identified that type I SGNs can be further classified into three different subtypes. These data suggest a growing complexity of the auditory system formation and integration of external signals.

These examples underline the complexity of PNS development. With the aim of understanding the surrounding environment, each of these systems seems to have its own guidance mechanisms, which through a tight and orchestrated regulation, establish an essential pathway between sensory neurons and superior brain areas. Novel genetic and technical approaches also highlight the cellular heterogeneity in these systems, most of them considered quite homogeneous until recently. The understanding of the molecular differences between cell types in a determined structure is a key element in establishing therapeutic approaches such as stem cell therapy. Moreover these molecular differences can also help to understand the possible effects of different known guidance mechanisms. Lastly, several groups have tried to understand the role of spontaneous activity in these structures. Neural activity has been observed to happen randomly in most structures, since early development (Shrestha *et al.* 2018). This neuronal activity could be essential to pattern and reinforce synapses, as was shown in the visual system (Ackman and Crair 2014).

Non-traditional roles of axon guidance molecules

Axon guidance molecules have been extensively studied during axonal development but have also been shown to be critical in many diverse biological processes such as angiogenesis and cell migration (Castets and Mehlen 2010; Aberle 2019). Undeniably, cortical development is dependent on cellular migration. A fundamental question for the past decades has been the emergence of the neocortex, a specific feature of the mammalian brain (Finlay and Darlington 1995; Northcutt 2006). Cortical development begins with the division of radial glial progenitor cells (RGPCs), which gives rise to all cortical neurons and glia. RGPCs are aligned at the cortical ventricular zone and undergo mitosis to either self-renew (symmetric division = indirect neurogenesis), or differentiate into cortical neurons (asymmetric division = direct neurogenesis). However, in mammals RGPCs can also divide symmetrically to give rise to an intermediate progenitor cell (IPCs) (Haubensak *et al.* 2004; Noctor *et al.* 2004; Miyata *et al.* 2004). IPCs can either self renew or differentiate into cortical neurons.

Thus, IPCs have been proposed to serve as the main determinant for cortex expansion in mammals (Malatesta *et al.* 2000; Noctor *et al.* 2001; Smart 2002; Noctor *et al.* 2004; Kriegstein *et al.* 2006; Hansen *et al.* 2010). Recently, Cárdenas *et al.* (2018) have identified a novel role for Robo 1/2 in regulating radial glia cortical migration. By comparing the mouse olfactory bulb (OB) (reminiscent of the reptilian paleocortex) to the cortex (Cx), Cárdenas *et al.* (2018) observed that the OB solely developed by direct neurogenesis whereas the Cx was developed mostly by indirect neurogenesis. Interestingly, Robo1/2 were expressed in a gradient, with a high-low expression in the OB compared to the Cx. Furthermore, it was shown that Robo1/2 can regulate the notch canonical signaling pathway via Delta-like 1 as well as the ligands *jagged* 1 (*Jag1*) and *Jag2*. The mechanism put forward is that high Robo1/2 expression in the OB reduces Delta-like 1 expression and increases *Jag1* and *Jag2* expression, resulting in asymmetric division and direct neurogenesis. Indeed, gain of function experiments showed that high Robo1/2 expression is sufficient to induce direct neurogenesis in the mouse Cx (Cárdenas *et al.* 2018). Interestingly, amniotes deprived of a neocortex, such as birds and reptiles, show high Robo1/2 expression in the cortex (Cárdenas *et al.* 2018). Thus, the authors propose silencing of Robo1/2 as an evolutionary switch giving rise to indirect neurogenesis in mammals.

The Fibronectin Leucine Rich-repeat Transmembrane (FLRTs) proteins have also been identified as axon guidance molecules. For instance, thalamocortical axons expressing Dcc are not sensitive to the netrin-1 gradient present in the thalamus because of Robo1 silencing (Leyva-Díaz *et al.* 2014). However, FLRT3 can sequester Robo1 to allow for Dcc expression at the surface of thalamocortical neurons, thereby activating netrin-1 responsiveness (Leyva-Díaz *et al.* 2014). More recently, FLRTs have also been implicated with cortical progenitor migration (del Toro *et al.* 2017). In mammals the cortex initially forms as a laminar sheet. Whilst some mammals (mice and rats) will retain this smooth cortical development (lissencephaly, Fig. 4a), other mammals (primates and ferrets) develop cortical folds (gyrencephaly, Fig. 4b). FLRT1/3 have recently been shown to be critical players in this process (del Toro *et al.* 2017). Interestingly, genetic ablation in mice of FLRT1/3 promotes cortical folding (del Toro *et al.* 2017). Whilst the proliferation rate of radial glia cells was unchanged, their migratory patterns were significantly perturbed. Indeed, loss of FLRT1/3 increased neuronal clustering and radial migration rate. This creates columns of migrating progenitors, inducing an asymmetric proliferation across the surface of the cortex and as a result creating sulci. Of note, FLRT1/3 expression is reduced in gyrencephalic species, suggesting that the abundance of FLRT1/3 during evolution promoted cortical smoothing (lissencephaly).

Whilst typical axon guidance proteins such as Slits and ephrins have been largely discussed, a growing body of literature has shown that some lipids could be atypical guidance molecules. Phospholipids are considered the major components of cell membranes and they have the ability to form amphipathic lipid bilayers. Their role in axon guidance was first proposed by some in vitro experiments in which Lysophosphatidic acid, an intermediate substance of lipid synthesis, was shown to be able to induce growth cone collapse, neurite retraction and cell rounding in neuroblastoma-derived neuronal cell cultures (Jalink *et al.* 1993). Later on, further evidence highlighted their role on primary cultured chick embryo neurons and on isolated retinal growth cones (Saito 1997; Campbell and Holt 2001). Additional *in vivo* evidence of the axon guidance role of lysophospholypids were obtained in the *Xenopus* visual system. In absence of sphingosine 1-phosphate, retinal projections were misguided and invaded abnormal areas (Strochlic *et al.* 2007). Recently, a novel role for phospholipids on axon guidance was brought to light: Phosphatidyl-B-D-Glucoside (PtdGlc) is localized in radial glia and nascent astrocytes *in vivo* (Nagatsuka *et al.* 2006; Kinoshita *et al.* 2009). PtdGlc can be hydrolysed in *lyso*PtdGlc and released into the extracellular environment (Guy *et al.* 2015). In the embryonic chick and mouse spinal cord, TrkA and TrkC dorsal root ganglion axons enter the CNS through the dorsal root entry zone. Only TrkC axons get into the primordial dorsal funiculus where *Lyso*PtdGlc is found (Guy *et al.* 2015), suggesting a possible repulsive role for nociceptive afferences (TrkA). TrkA enriched dorsal root ganglia (DRG) explants showed chemorepulsion *in vitro* in presence of a *lyso*PtdGlc gradient. Furthermore, blocking antibodies for *lyso*PtdGlc used *in ovo*, showed a misprojection of TrkA axons in the primordial dorsal funiculus. Finally, a receptor screening proposed GPR55 as putative receptor for this extracellular cue. GPR55 *knockout* mice phenocopy the DRG axon misprojections induced by *lyso*PtdGlc blocking antibodies, confirming the role of this receptor-sensing glia released *lyso*PtdGlc in this system (Guy *et al.* 2015).

Axonal regeneration

In the early 20th century, pioneering studies from Ramón y Cajal showed that the mammalian CNS is unable to regenerate following a lesion (Ramón y Cajal 1914). Neuroscientists have since delved on the idea that understanding CNS development could be the key to hi-jack regenerative mechanisms following CNS injury. Interestingly, similar lesion experiments carried out on dorsal root ganglia axons (which belong to the PNS) resulted in robust regeneration of their peripheral branch and functional recovery following the lesion, whereas their central branch projecting into the CNS did not regenerate. Therefore, something either intrinsic or extrinsic to CNS neurons is responsible for their lack of regeneration (Fig. 5a). This fundamental question has sparked years of intensive research

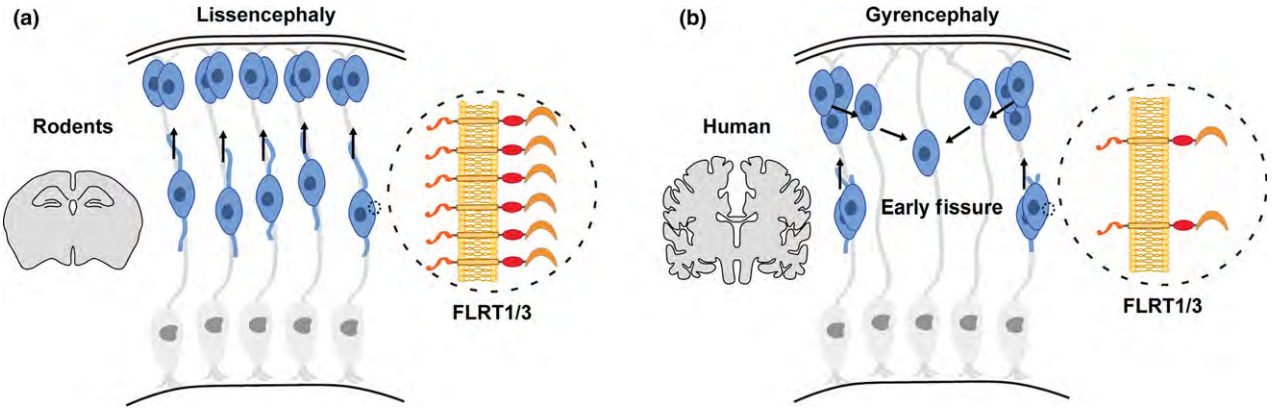

Fig. 4 Cortical folding relies on Fibronectin Leucine Rich-repeat Transmembranes (FLRTs) expression. Cortical folding appears to be dependent on the presence of the cell adhesion proteins FLRT1 and FLRT3 during cortical expansion, where (a) higher expression in migrating cortical progenitors is associated with parallel migration, resulting in a lissencephalic cortex. Conversely, (b) lower FLRT1 and 3 expression favors lower migration rates, and promotes lateral adhesion resulting in a gyrencephalic cortex.

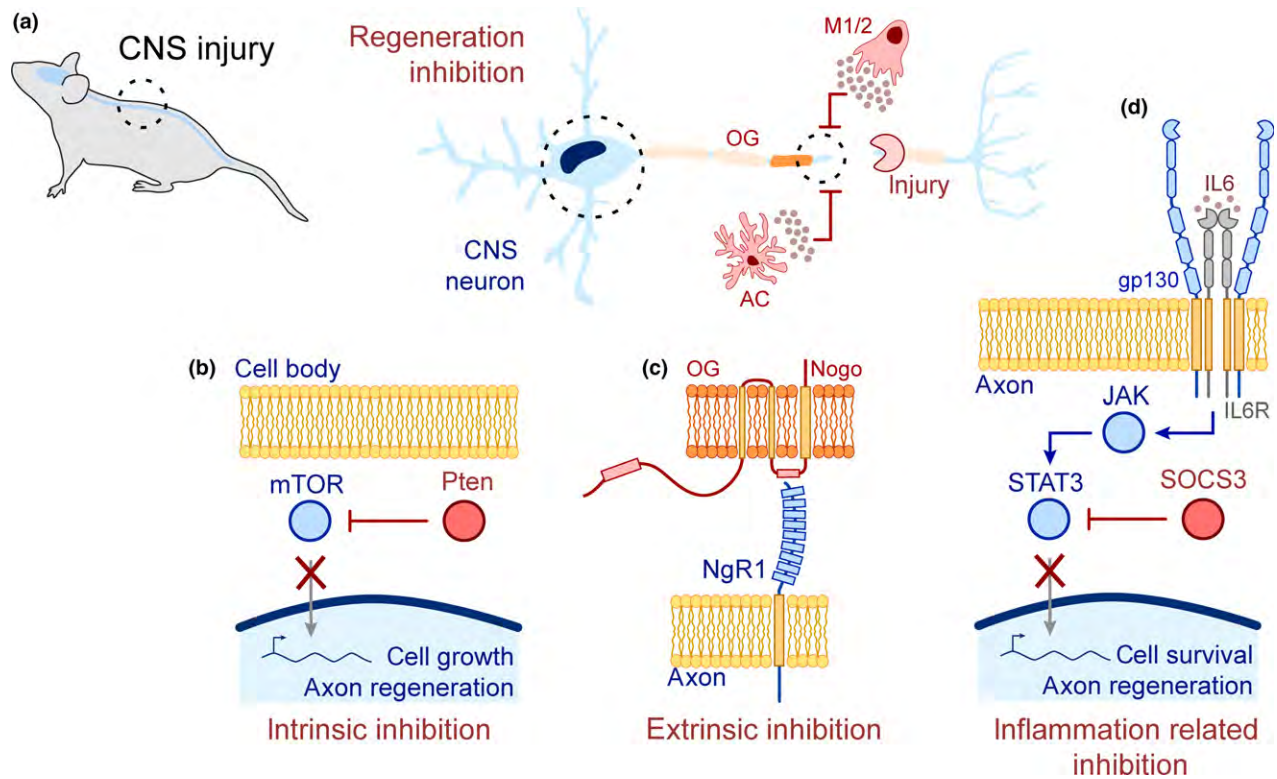

Fig. 5 Molecular mechanisms for CNS regeneration. (a) After CNS injury, extrinsic and intrinsic mechanisms impair axonal regeneration. These events occur both in the cell soma and the injure site and they are the main targets of strategies aiming at promoting regeneration. Most of the extrinsic inhibition comes from the recruitment of astrocytes and macrophages to the injury area and the "activation" of local oligodendrocytes. (b) In injured neurons, Pten blocks the mammalian target of rapamycin (mTOR) pathway that induces axon regeneration. The complete or conditional depletion of Pten in RGCs or corticospinal tract neurons, promotes the regeneration of their axons after injury. (c) Moreover oligodendrocytes at the lesion site, start to express inhibitory signalling molecules such as Nogo and myelin associated glycoproteins that will block axonal regeneration. The simultaneous depletion of Pten and Nogo, significantly promotes axonal regeneration. (d) Finally, The expression of cytokines by macrophages also promote axon outgrowth. Suppressor of cytokine signaling 3 (SOCS3) expression in lesioned axons blocks signal transducer and activator of transcription 3 (STAT3), a downstream effector of this cascade. Together with Pten, the depletion of SOCS3 also increases the regeneration rate of RGC axons.

to understand the molecular mechanisms activated after axotomy and to develop strategies for inducing axonal regeneration. Here, we will discuss some of the current approaches and challenges in regeneration of CNS and PNS axons.

Central nervous system regeneration

Visual system regeneration

Optic nerve (ON) transection or crush, have become a predominant models for studying CNS regeneration. The ON only contains axons which originate from RGC neurons in the retina. Directly following ON lesions, multiple inhibitory pathways are triggered. The activator protein 1 and the transcription factor subunit c-Jun (Fos-binding protein p39) both act in synergy to trigger cell death in RGCs following an experimental axotomy (Hüll and Bähr 1994). In addition, interplay between c-Jun and the activating transcription factor 2 dictates cell fate following ON crush. When both are up-regulated, they promote cell survival. However, reduction in activating transcription factor 2 expression induces apoptosis (Martin-Villalba *et al.* 1998). The activation of c-Jun is driven by calcium influx, since specific inhibition of calcium channels leads to reduction of c-Jun activity in ON crush models. Remarkably, the inhibition of calcium channels not only reduces acute axon neurodegeneration, but also improves axonal regeneration (Ribas *et al.* 2017). The RhoA/ROCK/LIMK pathway, which can be activated by a variety of cytokines and inflammatory mediators, is another critical inhibitory mechanism that mediates repulsive signals in the injured CNS. The knockdown of either Rho associated coiled-coil containing protein kinase 2 (ROCK2) or its downstream substrate LIM domain kinase 1 promotes neuronal regeneration following ON crush. However, only ROCK2 knockdown was found to be neuroprotective in RGCs following ON axotomy (Koch *et al.* 2014). ROCK2 down-regulation leads to reduced calpain and caspase3 activity and a concurrent increase in protein kinase B (Akt) activity (Koch *et al.* 2014). Pharmacological inhibition of RhoA/ROCK pathway through Y-27632 or Fasudil administration promotes neuronal regeneration in a dose-dependent manner, probably because of enhanced MAPK and Akt phosphorylation (Lingor *et al.* 2007; Lingor *et al.* 2008). Pharmacological modulation of this pathway, thus, could represent a therapeutic approach for CNS cell restoration.

Another inhibitory pathway exists in the surrounding environment of the lesion (Fig. 5b-d). The myelin inhibitory proteins: Nogo, myelin-associated glycoprotein (MAG), and oligodendrocyte-myelin glycoprotein suppress axonal growth in the optic nerve by acting through Nogo receptors where they act in an orchestrated manner with other co-receptors, such as p75 neurotrophin receptor and epidermal growth factor receptor (Domeniconi *et al.* 2002; Wang *et al.* 2002b; Wang *et al.* 2002c; Koprivica 2005). Notably, deletion of its downstream signaling pathway, through protein kinase C appears to restore axonal growth by blocking Rho activation (Sivasankaran *et al.* 2004). Furthermore, the over-expression of dominant negative Nogo receptors in RGCs promoted axonal regeneration (Fischer 2004).

Alternatively to extrinsic factors inhibiting axon regeneration, many groups have shown that the intrinsic mechanisms prevent CNS axon regeneration (He and Jin 2016). One critical pathway, put forward by the group of Zhigang He, was the phosphoinositide 3-kinase/mammalian target of rapamycin (mTOR) signaling pathway. Following ON crush, a dramatic decrease in phosphoinositide 3-kinase/mTOR activity is observed (Park *et al.* 2008). Indeed, following ON crush, mTOR activity is suppressed by the phosphatase and tensin homolog (PTEN) (Fig. 5b). Genetically deleting PTEN in RGCs, using an adeno-associated virus, induces robust and long-distance axon regeneration following ON crush (Park *et al.* 2008). Interestingly, PTEN deletion following ON crush only stimulates the regeneration of a subset of RGCs (Park *et al.* 2008). A large number of RGC types exists with distinct physiology and projection patterns (Sanes and Masland 2015; Martersteck *et al.* 2017). Therefore, it is not surprising that distinct RGCs types respond heterogeneously to injury. Further studies have shown that a specific subtype of RGCs, the α-RGCs, are able to survive following ON crush and express insulin-like growth factor receptor (IGF1) as well as osteopontin (OPN) (Duan *et al.* 2015). Reprogramming of RGCs after injury is accompanied by changes in mRNA expression profiles. The transcription factors that are expressed after injury appear to determine whether a specific sub-type of RGC will regrow. The Kruppel-like factors 4 and 9 (KLF4 and KLF9), for example, play a major role suppressing axon development (Qin *et al.* 2013; Apara *et al.* 2017). KLF4 interacts with Tyr705-phosphorylated signal transducer and activator of transcription 3 (STAT3) suppressing its activity and function as an intrinsic barrier for regeneration of damaged adult RGC axons (Qin *et al.* 2013). KLF9 functions as another intrinsic inhibitor for axon regeneration as shRNA mediated knockdown of KLF9 promote RGC survival and axon regeneration following optic nerve injury *in vivo* (Apara *et al.* 2017). This KLF9-mediated inhibition is via interaction of the upstream kinase c-Jun N-terminal kinase 3 (JNK3) (Apara *et al.* 2017). Recent findings indicate that micro RNAs 135a and 135b (miRNA135s) could regulate KLF4 expression during axon development. Intravitreal administration of miRNA135 induced axon regeneration following ON injury, in part by suppressing KLF4 expression in RGCs (van Battum *et al.* 2018). SOX11, on the other hand, plays a dual role. When overexpressed, it can stimulate axon growth of non-α-RGCs while it induces cell death of α-RGCs following ON crush (Norsworthy *et al.* 2017). In addition to intrinsic growth metabolism, neuroinflammation has been shown to be critical

for RGCs axonal regeneration (Smith *et al.* 2009). The simple intraocular injection of Zymosan (protein-carbohydrate complexes derived from yeast cell wall), which enhances macrophage infiltration in the injured ON, greatly stimulates the expression of GAP-43 in RGC axons, resulting in accelerated axonal regeneration (Leon *et al.* 2000).

During the past decades, major effort has been made toward the development of combinatorial therapeutic approaches, targeting two or more neuronal pathways. Over stimulating cell growth programs by deleting PTEN and suppressor of cytokine signaling 3 (SOCS3) promotes a well-sustained axon regeneration (Fig. 5d), by brake-releasing two independent pathways that converge into axon growth-related gene expression (Sun *et al.* 2011). In an alternative approach, the use of the pro-inflammatory Zymosan, in combination to PTEN inhibition and cAMP analogue administration promotes axonal regeneration, and allows the recovery of long distance axonal degeneration (Kurimoto *et al.* 2010). The critical step following regeneration and functional synapses formation is the restoration of the conductance and visual function following injury. Treatment with the voltage-gated potassium channel blocker 4-aminopyridine (4-AP) or its methyl derivative 4-AP-3-Me restores conduction and visual acuity following PTEN/SOCS3 co-deletion. Similar phenomena were observed when mice were treated with 4-AP following OPN overexpression in the presence of IGF1 and ciliary neurotrophic factor. This highlights the importance of combination therapy for axon regeneration and improving visual conduction (Bei *et al.* 2016).

Spinal cord regeneration

Another attractive model for studying CNS regeneration is that of spinal cord injury (SCI). In addition to its scientific interest, SCI has a dramatic clinical impact, with the world health organization approximating between 250 000 to 500 000 people suffer from SCI each year (Courtine and Sofroniew 2019). The Cortico spinal neurons (CSNs) located in the mammalian neocortex are the major output from the brain to the spinal cord (making up to 90% of projections), which mediate both motor and sensory functions (Wang *et al.* 2017). Indeed, corticospinal tract (CST) lesions, such as a bilateral pyramidotomy, lead to the complete loss of voluntary movement. Following a spinal cord lesion, extrinsic mechanisms such as growth inhibitors or glial scars, inhibit axonal regeneration (Gaudet and Fonken 2018). Several inhibitory signaling molecules have since been identified such as Nogo or myelin-associated glycoproteins (Caroni and Schwab 1988; McKeon *et al.* 1991; Afshari *et al.* 2009; Lang *et al.* 2015). Indeed silencing these inhibitory cues in mouse or rat models of spinal cord injury has shown some success (Schmandke *et al.* 2014). Another approach, led by Zhigang He's group, questioned whether the inability of CNS neurons to regenerate involved intrinsic factors. They identified that mTOR (mammalian target of rapamycin) activity and *de novo* protein synthesis are suppressed after CNS lesions (Park *et al.* 2008). Reactivation of the mTOR pathway by silencing of PTEN (phosphatase and tensin homolog) and TSC1 (tuberous sclerosis complex 1), leads to extensive CST axon regeneration (Park *et al.* 2008). Together, these findings proved that both intrinsic and extrinsic mechanisms were responsible for inhibiting CST axon regeneration after spinal cord injury. Accordingly, the combined genetic deletion of Nogo receptors and PTEN, led to a major increase in the regeneration and sprouting of lesioned CSNs (Geoffroy *et al.* 2015). However, there was little to no functional amelioration in lesioned animals.

The lack of functional rescue observed in double mutants of Nogo and PTEN led to the idea that a better understanding of the locomotor system was required. Indeed, very little was known about the localization, development, and function of the CSNs responsible for voluntary movement. Using retrograde viral tracing strategies, it was found that CSNs were localized in both the motor and somatosensory cortex. Two major nuclei were identified, the rostral forelimb area (RFA) and the caudal forelimb area (CFA) (Wang *et al.* 2017). To better understand the precise function of RFA and CFA CSNs in voluntary task, a food pellet retrieval task was used to tease apart which CSNs were responsible for specific motor movements. Using AAV:Cre-driven GCamp6 expression in CSNs, it was shown that RFA CSNs fired prior to grasping the food-pellet, whereas CFA CSNs fired prior to reaching as well as post-grasping the food pellet (Wang *et al.* 2017). These data provide evidence supporting a parallel organization of motor tasks responsible for specific behavior organized in a topographic manner.

While much work has focused on spinal cord lesions, the majority of patients suffer from partial lesions. However, partial spinal cord injuries still result in complete loss of motor function below the site of injury. This hints toward the idea that unlesioned axons are unable to properly function despite being spared from injury. By carrying out a staggered hemisection of the thoracic spinal cord on opposing sides, Chen *et al.* (2018) took advantage of a partial spinal cord injury model to carry out a small compound screening approach. They identified that an agonist of the potassium/chloride transporter (KCC2) resulted in increased weight bearing strength in mice following lesion (Chen *et al.* 2018). Because of the complexity of spinal circuits, they questioned whether KCC2 activity was required by multiple or distinct neuronal subsets (excitatory, inhibitory, motor). Interestingly, only overexpression of KCC2 in inhibitory neurons (Vgat:Cre) resulted in an improved weight-bearing strength in injured mice. Moreover inhibitory neurons below the staggered lesion were dispensable for this rescue, since overexpressing KCC2 only in inhibitory neurons between the lesions was sufficient to rescue the weight bearing strength. Overall, this identifies a crucial role for inhibitory interneurons in a closed-circuit to be critical in associating the

excitation to inhibition ratio required to regulate functional recovery following a lesion (Chen *et al.* 2018).

The translation of these findings to the treatment of spinal cord injury, won't be simple as the genetic manipulation of tumor suppressor genes may not be suitable for the clinic. Attractive treatment alternatives could consist of applying growth factors (which occur endogenously in the CNS). However, adult CNS neurons lose their sensitivity to growth factors such as brain-derived neurotrophic factor (Liu *et al.* 2017). Moreover adult CSNs treated with OPN can be sensitized to the IGF1 by reactivating the mTOR pathway (Liu *et al.* 2017).

Furthermore, the identification that spared axons following partial spinal cord injury could be re-synchronized to induce functional recovery opens many questions, one of which, is the importance of inhibitory synapses conserved amongst other species. Indeed, the complexity in human spinal cord circuitry may pose a major challenge toward this clinical implication.

For instance, how does our current understanding on excitatory/inhibitory ratios in the rodent spinal cord translate to the human spinal cord? This is a daunting question since inhibitory feedback loops in human spinal cord may be more complex and thus more challenging to re-stimulate. Furthermore, more research should focus on understanding the coordinated action between neurons and glial cells. Synaptic activity, axonal and dendritic growth and regeneration are fine-tuned by glial cells (Liu *et al.* 2017). There are a few studies investigating how glial scar-induced disruption may be overcome by improving the communication between neurons and glial cells. Of note, exosomes released by glial cells in the PNS have shown to promote robust axonal regeneration and survival (Lopez-Leal and Court 2016). A similar result was obtained from mesenchymal stem cells releasing exosomes following spinal cord injury (Li *et al.* 2018; Liu *et al.* 2019).

Peripheral nerve regeneration

Insults such as physical trauma, chemotherapy or metabolic disorders can lead to peripheral nerve damage (Scholz *et al.* 2009). As previously mentioned, PNS axons have retained considerable capacity to regenerate following injury and to form functional connections with their original targets (Bremer *et al.* 2017). This seems in part because of a cell-intrinsic growth-promoting response of PNS neurons and to a favorable environment for axonal regeneration (Bremer *et al.* 2017). However, many aspects of this process, including how regenerating axons navigate across the lesion site and select their original trajectory at branch choice points, are not well understood *in vivo*. Whilst many animal models have been used to study PNS regeneration, the zebrafish has been heavily studied because of its transparency (allowing for *in vivo* live imaging) as well as the ability for genetic manipulation. Adult and larval fish both have well-defined PNS circuits and stereotyped behaviors, facilitating cell biology studies underlying PNS axon regrowth and synapse re-establishment (He and Jin 2016; Rasmussen and Sagasti 2017).

In vertebrates, spinal motor nerve degeneration after transection occurs through morphological hallmarks characteristic of Wallerian degeneration (Fig. 6a), a stereotyped form of degeneration (Waller 1851). Live imaging on zebrafish showed that following nerve transection, degradation of the distal axon happens within 120–240 min (Rosenberg *et al.* 2012). Moreover it highlighted that individual axons within the transected nerves initiate fragmentation at different times independent of myelination and thickness of the axons. Once initiated, fragmentation occurs along the entire length of the axon within minutes. Recruitment of macrophages to the injury site starts between 60–120 min before nerve fragmentation, and with the onset of axonal fragmentation, macrophages enter the nerve and begin to phagocytose nerve debris. Experimental elimination of Schwann cells through genetic ablation does not change the recruitment and behavior of macrophages to the injury site suggesting that this process is independent on Schwann cells (Dutton *et al.* 2001; Rosenberg *et al.* 2012).

In zebrafish, 80% of regenerating axons retain the ability to select their original branch-specific trajectory in both ventral and dorsal nerve branches following complete nerve transection (Isaacman-Beck *et al.* 2015). After complete nerve transection, usually a single axon emerges from the proximal nerve stump to pioneer a regenerative path across the injury site. At later stages, multiple emerging axons join the pioneering axon and extend with about twice the speed of the pioneering axon across the injury gap. The synaptic low-density lipoprotein receptor-related protein 4 is critical for the regrowth of follower axons across the injury gap and toward their original targets (Gribble *et al.* 2018) (Fig. 6c). Live-cell imaging shows that Schwann cells provide directionality to axons, by crossing the injury site and navigating to their original trajectory. An interaction between Schwann cells and motor axons is triggered following motor nerve transection leading to highly coordinated changes in axonal and Schwann cell morphology during both degeneration and regeneration (Fig. 6b). For instance, once axons start to fragment, Schwann cell membranes, localized distal to the lesion site, undergo dramatic morphological changes returning to a more immature state (Rosenberg *et al.* 2014). Lrp4 promotes the morphological changes associated with Schwann cells re-differentiation after injury-induced de-differentiation. *In vivo* evidence suggests that low-density lipoprotein receptor-related protein 4 promotes peripheral nerve regeneration through a non-canonical, Agrin/MuSK independent signalling pathway that is critical for neuromuscular synapse development in mammals and zebrafish (Gribble *et al.* 2018). The importance of this process in promoting vertebrate nerve regeneration is also confirmed by

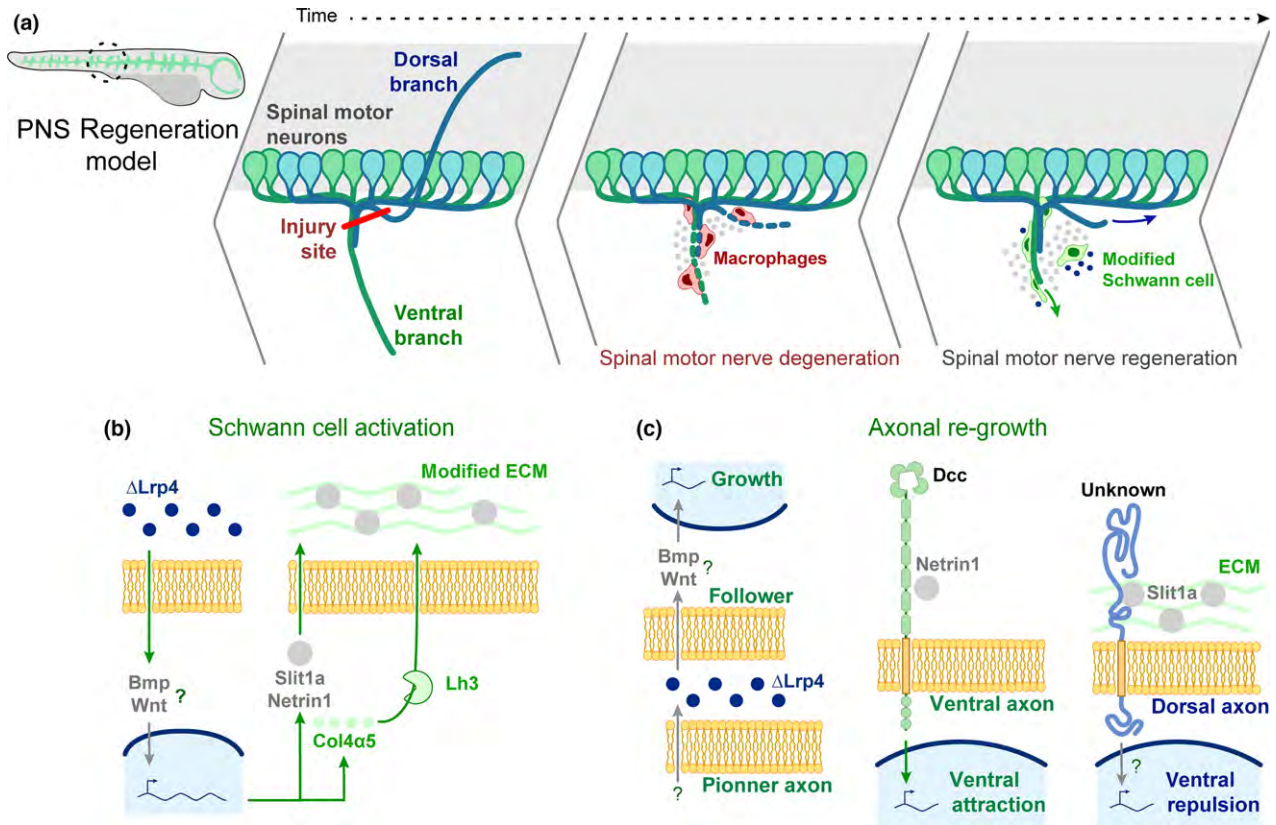

Fig. 6 PNS axon regeneration in zebrafish spinal motor nerves. (a) Zebrafish has extensively been used as PNS regeneration model. Its transparency allows live-imaging of axons and genetic manipulations remain simpler than in mammals. In this model, a transection of both, dorso-ventral spinal cord motor branches is performed. First, a Wallerian degeneration of the sectioned nerves occurs, dependent on macrophages activity. Then, spontaneous regeneration occurs, promoted by intrinsic and extrinsic signals. (b) After injury, 80% of the lesioned axons retain the ability to regenerate. This relies on Schwann cell activation that will ensure the proper pathfinding of the regenerating axons through different mechanisms. This activation occurs by exposure to ΔLrp4 and triggers the expression of axon guidance molecules (Netrin-1 and Slit1a) and the remodelling of the extracellular matrix (ECM). (c) There is evidence that nerve regrowth relies on the extension of a single pioneer axon that will be used as migration scaffold by follower axons. This process seems dependent on ΔLrp4 but no receptors have been identified yet. Axon guidance of dorsal or ventral projections differs. Netrin-1 and Dcc promotes the growth of ventral axons while Slit1a prevent dorsal axon from growing dorsally, through a yet unknown receptor.

the impairment of peripheral nerve regeneration by Topoisomerase I inhibitor, identified through a fin removal assay performed by Bremer and colleagues, which hypothesizes that Topoisomerase I promotes peripheral nerve regeneration by regulating gene transcription specifically in de-differentiated Schwann cells (Bremer *et al.* 2017).

In zebrafish mutants lacking Schwann cells, 50–80% of transected nerves show a failure in regenerating axons along their original trajectory through the ventral myotome compared with 20% in wild-type (Rosenberg *et al.* 2014). Netrin1 and its receptor DCC have been implicated in promoting the extent of axon regeneration (Fig. 6c): *in vivo Netrin1b* mRNA is expressed in Schwann cells before and after motor nerve transection, and *dcc* mRNA is detectable in motor neurons during initial axonal regrowth. In $dcc^{zm130198}$ mutants, characterized by a 90% reduction of *dcc* mRNA, 40% of regenerating motor axons extended not only along their original path but also along ectopic lateral trajectories. This suggests that DCC is required to guide regenerating ventral motor axons across the injury gap toward their original trajectory *in vivo* (Rosenberg *et al.* 2014).

Early after transection (7–11 h post transection), dorsal axons sprout growth cones that explore the environment with multi-directional extensions and retractions. In the following 2–4 h, only the growth cones extending along the correct dorsal path are stabilized and quickly extend, supporting the existence of extrinsic cues that drive the growth cones through the branch point (Isaacman-Beck *et al.* 2015). Among these cues, the collagen-modifying glycosyltransferase lysyl hydroxylase 3 (*lh3*), expressed by Schwann cells, has a crucial role in promoting target selectivity of regenerating dorsal, but not ventral nerve axons (Fig. 6b). For this

process, equally fundamental is Collagen4a5 (col4a5), the *lh3* substrate, which is over expressed in a small group of Schwann cells located ventral and ventrolaterally to the transection gap. Col4a5 destabilizes mistargeted axons, directing regenerating axons toward their original targets. Following the nerve transection there is an up-regulation of the canonical axon guidance repellent *slit1a* in cells expressing col4a5. Hypothetically, in response to injury, Schwann cells ventral to the transection site, secrete col4a5, which binds and accumulates Slit, thereby forming a repulsive barrier to direct dorsal axons onto their original dorsal path (Isaacman-Beck *et al.* 2015) (Fig. 6c).

Real-time imaging on live zebrafish has allowed deciphering some of the intrinsic and extrinsic mechanisms responsible for peripheral nerve regeneration, but the molecular mechanisms and the specific cellular interactions which are vital for axon regeneration are not completely understood. Furthermore, the identification of other regeneration-promoting molecules could allow the development of new neuronal repair strategies. Based on that premise a fin removal assay was developed that enabled to perform the first whole organism small molecule screen to identify pathways that promote vertebrate nerve regeneration (Bremer *et al.* 2017). The approach utilized the regeneration of the ring-like nerve of zebrafish larvae pectoral fin after removal as readout of axonal regrowth. 480 bioactive compounds with known biological targets were screened to identify molecular pathways promoting nerve regrowth. After excluding 134 compounds which affected larvae health, the remaining compounds were combined in 69 distinct pools and added each of these pool to larvae immediately following fin amputation to evaluate the re-formation of regenerating axons of a ring-like nerve network at the fin base that normally occurs in 24 hours. In larvae exposed to 15 pools regenerating axons failed to form the characteristic ring-like network. Next, each of the compounds was tested within a given pool individually. This failed to identify a singly effective compound in 20% of pools which reduced nerve regrowth in the first pass of the screen. Despite the fin removal assay is a powerful screening method to study nerve regeneration, the high false positive rate indicates the importance of a second method to confirm the results (Fig. 7).

Other strategies for CNS/PNS repair

Many strategies have shown incredible potential for regeneration of the CNS following an injury, but a major concern remains the significant death of neurons (Ling *et al.* 2015; Mckee and Daneshvar 2015). Moreover complex diseases such as stroke, amyloid-β plaque accumulation and inflammatory-mediated neurodegeneration lead to broad defects such as defective communication, glial scar formation and ultimately neuronal loss, which make it challenging to repair (Chauhan 2014; Albrecht *et al.* 2015). In such cases, the development of cell therapy has shown some promising results (Gates *et al.* 2000). Stem cell manipulation is a powerful tool to understand neurodevelopment and its integration into developing tissue can recapitulate neurogenesis. In vivo strategies based on stem cell replacement such as human and mice-derived embryonic stem cells (ESCs) for brain repair in models of neurological diseases, have made significant progress in pre-clinical trials (Barker *et al.* 2015; Péron *et al.* 2017). It is known that the lack of endogenous repair in the brain leads to a condition of life-long disease and disability after a neuronal damage. Thus, understanding how well the transplanted neurons are able to mature and integrate into damaged circuits is a challenging task (Fig. 7a).

Because of the complexity of the organization of the cerebral cortex in terms of highly specific topography and connectivity (Guillemot *et al.* 2006; Tiberi *et al.* 2012), the replacement of lost neurons is a daunting challenge. A notable initial attempt at regenerative cortical cell therapy showed that transplanting embryonic cortical tissue from transgenic mice to lesioned cortex in an adult brain could regenerate neurons and establish neuronal projections and synaptic connections (Wernig 2004; Gaillard *et al.* 2007). These findings have been corroborated by data from other studies which have shown that not only ESCs have intrinsic mechanisms of corticogenesis (Gaspard *et al.* 2008) but induced pluripotent stem cell-derived neurons also can regenerate functional cortical neurons (Falkner *et al.* 2016; Espuny-Camacho *et al.* 2018).

There are certain prerequisites for the ESCs to successfully integrate the malfunctioning adult cortex (Fig. 7b). Re-establishment of neuronal connectivity and function requires identity match between the damaged brain area and the transplanted material (Michelsen *et al.* 2015). Human embryonic stem cell-derived visual cortical neurons, once grafted into the lesioned adult murine cortex, are able to mature and integrate into the corresponding cortical layers, acquiring a visual-like identity and rewiring the circuit with appropriate inputs and outputs (Espuny-Camacho *et al.* 2018). Interestingly, Human embryonic stem-derived cells transplanted into motor cortical areas showed a reduced maturation and a lower capacity to send long-range projections, suggesting that the areal identity match represents an important factor for successful cortical transplantation.

Another key factor accompanying identify match (Fig. 7c), is the adaptation to the extrinsic *in vivo* environment to establish polarity, such as microenvironment generated by blood vessels (Javaherian and Kriegstein 2009) or composition of extracellular matrix (Fietz *et al.* 2012). Context-wise, junctional complexes block the incorporation of grafted cells at the apical surface (Espuny-Camacho *et al.* 2013). For this reason, a new grafting method called TETCaD (transplantation to epithelial tissue with calcium depletion) has been developed, using moderate concentrations of EGTA (ethylene glycol tetra-acetic acid) to chelate calcium,

INFORME DE LABORES 2019

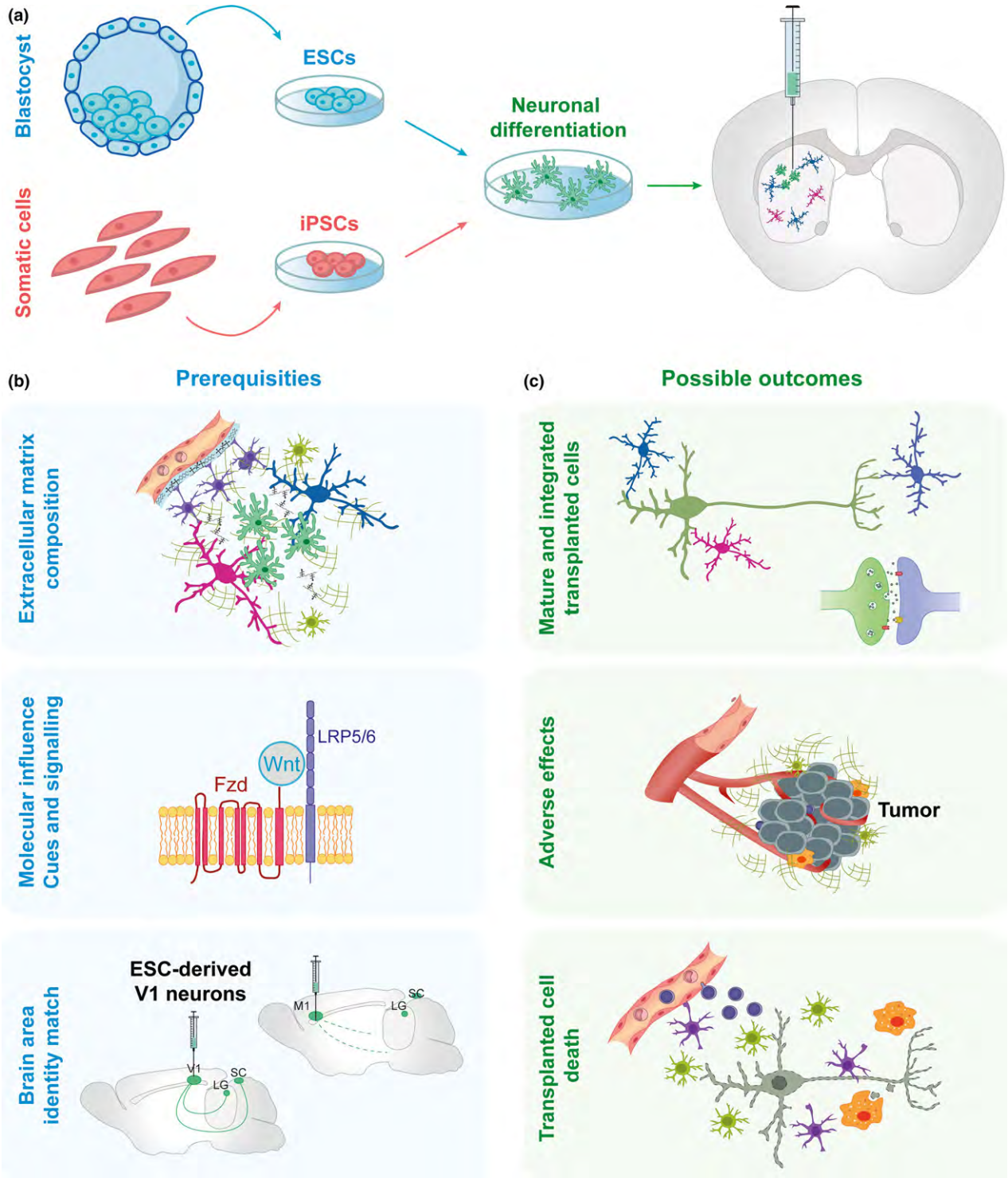

Fig. 7 Cell therapy. (a) Strategies based on stem cell replacement such as human- and mouse-derived embryonic stem cells (ESCs) and induced pluripotent stem cell (iPSC)-derived neurons. Grafting iPSC-derived neurons in brain circuits requires (b) adaptation to the extrinsic in vivo microenvironment or composition of extracellular matrix, lesion site-specific cues and signalling pathways, and identity match between the damaged brain area and the transplanted material. (c) Transplanted neurons could mature and integrate into damaged circuits; however, potential adverse effects as tumors or neuron death should be addressed before these strategies are transferred to the clinic.

increasing efficiency of transplantation and dissociating adherents junctions in the epithelial tissue (Nagashima *et al.* 2014). Lastly in the molecular level, lesion site-specific cues and signalling pathways such as the WNT signalling and NOTCH2NL genes have been implicated in human corticogenesis (Raitano *et al.* 2015; Fiddes *et al.* 2018; Suzuki *et al.* 2018). *In vitro* and *in vivo* use of induced pluripotent stem cells in animal models simulating human diseases such as stroke (Tornero *et al.* 2013), Alzheimer's disease (AD) (Espuny-Camacho *et al.* 2017) and multiple sclerosis (Theotokis *et al.* 2015), highlight the hallmarks of synaptic activity, connectivity and cortical neuronal maturation (Suzuki and Vanderhaeghen 2015). Specifically for AD, the significant expression of non- coding RNA sequences in grafted human neurons further opens up an entirely new avenue for investigating the involvement of non-coding RNAs in AD-induced neurodegeneration.

Altogether, establishing the molecular mechanisms regulating fate acquisition and plasticity after cell transplantation is of great importance in the light of preclinical studies. Determining which cues are involved in fate maintenance, area specificity and functional integration in the adult brain will be pivotal for successful outcomes in stem cell-based therapies. These signaling events may also play major roles in neurodegeneration so targeting pathways such as the Wnt pathway, may result in the establishment of novel therapeutic approaches. Nonetheless, potential adverse effects and host-transplant compatibility should be addressed before these approaches can be considered for clinical applications.

Acknowledgements and conflict of interest disclosure

This Review was invited following the 2nd JNC-ISN Flagship School held in 2018 in Alpbach, Austria. Alain Chédotal was the Scientific Head of that Flagship School. The co-authors are students participating in the Flagship School.

References

Aberle H. (2019) Axon guidance and collective cell migration by substrate-derived attractants. *Front. Mol. Neurosci.* **12**, 148.

Ackman J. B. and Crair M. C. (2014) Role of emergent neural activity in visual map development. *Curr. Opin. Neurobiol.* **24**, 166–175.

Afshari F. T., Kappagantula S. and Fawcett J. W. (2009) Extrinsic and intrinsic factors controlling axonal regeneration after spinal cord injury. *Expert Rev. Mol. Med.* **11**, e37.

Albrecht J. S., Liu X., Smith G. S., Baumgarten M., Rattinger G. B., Gambert S. R., Langenberg P. and Zuckerman I. H. (2015) Stroke incidence following traumatic brain injury in older adults. *J. Head Trauma Rehabil.* **30**, E62–E67.

Apara A., Galvao J., Wang Y. *et al*. (2017) KLF9 and JNK3 interact to suppress axon regeneration in the adult CNS. *J. Neurosci.* **37**, 9632–9644.

Avilés E. C., Stoeckli E. T., Avil E. C. and Stoeckli E. T. (2016) Canonical wnt signaling is required for commissural axon guidance. *Dev. Neurobiol.* **76**, 190–208.

Barker R. A., Drouin-Ouellet J. and Parmar M. (2015) Cell-based therapies for Parkinson disease—past insights and future potential. *Nat. Rev. Neurol.* **11**, 492–503.

van Battum E. Y., Verhagen M. G., Vangoor V. R. *et al*. (2018) An image-based miRNA screen identifies miRNA-135s as regulators of CNS axon growth and regeneration by targeting Krüppel-like factor 4. *J. Neurosci.* **38**, 613–630.

Bei F., Lee H. H. C., Liu X. *et al*. (2016) Restoration of visual function by enhancing conduction in regenerated axons. *Cell* **164**, 219–232.

Belle M., Godefroy D., Dominici C., Heitz-Marchaland C., Zelina P., Hellal F., Bradke F. and Chédotal A. (2014) A simple method for 3D analysis of immunolabeled axonal tracts in a transparent nervous system. *Cell Rep.* **9**, 1191–1201.

Bellen H. J., Tong C. and Tsuda H. (2010) 100 years of Drosophila research and its impact on vertebrate neuroscience: a history lesson for the future. *Nat. Rev. Neurosci.* **11**, 514–522.

Ben-Arie N., Hassan B. A., Bermingham N. A., Malicki D. M., Armstrong D., Matzuk M., Bellen H. J. and Zoghbi H. Y. (2000) Functional conservation of atonal and Math1 in the CNS and PNS. *Development* **127**, 1039–48.

Bhansali P., Rayport I., Rebsam A. and Mason C. (2014) Delayed neurogenesis leads to altered specification of ventrotemporal retinal ganglion cells in albino mice. *Neural Dev.* **9**, 11.

Blockus H. and Chédotal A. (2016) Slit-Robo signaling. *Development* **143**, 3037–3044.

Bonanomi D. and Pfaff S. L. (2010) Motor axon pathfinding. *Cold Spring Harb. Perspect. Biol.* **2**, a001735.

Bourikas D., Pekarik V., Baeriswyl T., Grunditz Å., Sadhu R., Nardó M. and Stoeckli E. T. (2005) Sonic hedgehod guides commissural axons along the longitudinal axis of the spinal cord. *Nat. Neurosci.* **8**, 297–304.

Bovolenta P. and Sanchez-Arrones L. (2012) Shh goes multidirectional in axon guidance. *Cell Res.* **22**, 611–613.

Bremer J., Skinner J. and Granato M. (2017) A small molecule screen identifies in vivo modulators of peripheral nerve regeneration in zebrafish. *PLoS ONE*.

Brose K., Bland K. S., Wang K. H., Arnott D., Henzel W., Goodman C. S., Tessier-Lavigne M. and Kidd T. (1999) Slit proteins bind robo receptors and have an evolutionarily conserved role in repulsive axon guidance. *Cell* **96**, 795–806.

Campbell D. S. and Holt C. E. (2001) Chemotropic responses of retinal growth cones mediated by rapid local protein synthesis and degradation. *Neuron* **32**, 1013–1026.

Cárdenas A., Villalba A., Juan Romero C. *et al*. (2018) Evolution of cortical neurogenesis in amniotes controlled by robo signaling levels. *Cell* **174**, 590–606.e21.

Caroni P. and Schwab M. E. (1988) Antibody against myelin associated inhibitor of neurite growth neutralizes nonpermissive substrate properties of CNS white matter. *Neuron* **1**, 85–96.

Castets M. and Mehlen P. (2010) Netrin-1 role in angiogenesis: to be or not to be a pro-angiogenic factor? *Cell Cycle* **9**, 1466–71.

Charoy C., Nawabi H., Reynaud F., Derrington E., Bozon M., Wright K., Falk J., Helmbacher F., Kindbeiter K. and Castellani V. (2012) gdnf Activates midline repulsion by Semaphorin3b via NCAM during commissural axon guidance. *Neuron* **75**, 1051–1066.

Charron F., Stein E., Jeong J., McMahon A. P. and Tessier-Lavigne M. (2003) The morphogen sonic hedgehog is an axonal chemoattractant that collaborates with netrin-1 in midline axon guidance. *Cell* **113**, 11–23.

Chauhan N. B. (2014) Chronic neurodegenerative consequences of traumatic brain injury. *Restor. Neurol. Neurosci.* **32**, 337–65.

Chédotal A. (2011) Further tales of the midline. *Curr. Opin. Neurobiol.* **21**, 68–75.

Chédotal A. (2014) Development and plasticity of commissural circuits: from locomotion to brain repair. *Trends Neurosci.* **37**, 551–562.
Chédotal A. (2019) Roles of axon guidance molecules in neuronal wiring in the developing spinal cord. *Nat. Rev. Neurosci.* **20**, 380–396.
Chen B. E., Kondo M., Garnier A., Watson F. L., Püettmann-Holgado R., Lamar D. R. and Schmucker D. (2006) The molecular diversity of dscam is functionally required for neuronal wiring specificity in Drosophila. *Cell* **125**, 607–620.
Chen B., Li Y., Yu B. *et al*. (2018) Reactivation of dormant relay pathways in injured spinal cord by KCC2 manipulations. *Cell*.
Coate T. M., Spita N. A., Zhang K. D., Isgrig K. T. and Kelley M. W. (2015) Neuropilin-2/Semaphorin-3F-mediated repulsion promotes inner hair cell innervation by spiral ganglion neurons. *Elife* **4**, e07830.
Courtine G. and Sofroniew M. V. (2019) Spinal cord repair: advances in biology and technology. *Nat. Med.* **25**, 898–908.
d'Amora M. and Giordani S. (2018) The utility of Zebrafish as a model for screening developmental neurotoxicity. *Front. Neurosci.* **12**, 976.
Dascenco D., Erfurth M.-L., Izadifar A. *et al*. (2015) Slit and receptor tyrosine phosphatase 69D confer spatial specificity to axon branching via Dscam1. *Cell* **162**, 1140–1154.
Delloye-Bourgeois C., Jacquier A., Charoy C. *et al*. (2015) PlexinA1 is a new Slit receptor and mediates axon guidance function of Slit C-terminal fragments. *Nat. Neurosci.* **18**, 36–45.
Di Meglio T., Nguyen-Ba-Charvet K. T., Tessier-Lavigne M., Sotelo C., Di Meglio T. and Chédotal A. (2008) Molecular mechanisms controlling midline crossing by precerebellar neurons. *J. Neurosci.* **28**, 6285–94.
Ding Q., Joshi P., Xie Z., Xiang M. and Gan L. (2012) BARHL2 transcription factor regulates the ipsilateral/contralateral subtype divergence in postmitotic dl1 neurons of the developing spinal cord. *Proc. Natl Acad. Sci. USA* **109**, 1566–1571.
Domeniconi M., Cao Z., Spencer T. *et al*. (2002) Myelin-associated glycoprotein interacts with the Nogo66 receptor to inhibit neurite outgrowth. *Neuron* **35**, 283–290.
Dominici C., Moreno-Bravo J. A., Puiggros S. R., Rappeneau Q., Rama N., Vieugue P., Bernet A., Mehlen P. and Chédotal A. (2017) Floor-plate-derived netrin-1 is dispensable for commissural axon guidance. *Nature* **545**, 350–354.
Druckenbrod N. R., and Goodrich L.V. (2015) Sequential retraction segregates SGN processes during target selection in the cochlea. *J. Neurosci.* **35**, 16221–16235.
Duan X., Qiao M., Bei F., Kim I. J., He Z. and Sanes J. R. (2015) Subtype-specific regeneration of retinal ganglion cells following axotomy: effects of osteopontin and mtor signaling. *Neuron* **85**, 1244–1256.
Ducuing H., Gardette T., Pignata A., Tauszig-Delamasure S. and Castellani V. (2019) Commissural axon navigation in the spinal cord: a repertoire of repulsive forces is in command. *Semin. Cell Dev. Biol.* **85**, 3–12.
Dutton K. A., Pauliny A., Lopes S. S., Elworthy S., Carney T. J., Rauch J., Geisler R., Haffter P. and Kelsh R. N. (2001) Zebrafish colourless encodes sox10 and specifies non-ectomesenchymal neural crest fates. *Development* **128**, 4113–25.
Edwards T. J., Sherr E. H., Barkovich A. J. and Richards Linda J. (2014) Clinical, genetic and imaging findings identify new causes for corpus callosum development syndromes. *Brain* **137**, 1579–613.
Ellenbroek B. and Youn J. (2016) Rodent models in neuroscience research: is it a rat race? *Dis. Model. Mech.* **9**, 1079–1087.
Escalante A., Murillo B., Morenilla-Palao C., Klar A. and Herrera E. (2013) Zic2-dependent axon midline avoidance controls the formation of major ipsilateral tracts in the CNS. *Neuron* **80**, 1392–1406.
Espuny-Camacho I., Michelsen K. A., Gall D. *et al*. (2013) Pyramidal neurons derived from human pluripotent stem cells integrate efficiently into mouse brain circuits in vivo. *Neuron* **77**, 440–456.
Espuny-Camacho I., Arranz A. M., Fiers M. *et al*. (2017) Hallmarks of Alzheimer's disease in stem-cell-derived human neurons transplanted into mouse brain. *Neuron* **93**, 1066–1081.e8.
Espuny-Camacho I., Michelsen K. A., Linaro D., Bilheu A., Acosta-Verdugo S., Herpoel A., Giugliano M., Gaillard A. and Vanderhaeghen P. (2018) Human pluripotent stem-cell-derived cortical neurons integrate functionally into the lesioned adult murine visual cortex in an area-specific way. *Cell Rep.* **23**, 2732–2743.
Fabre P. J., Shimogori T. and Charron F. (2010) Segregation of ipsilateral retinal ganglion cell axons at the optic chiasm requires the Shh receptor Boc. *J. Neurosci.* **30**, 266–75.
Falkner S., Grade S., Dimou L., Conzelmann K.-K., Bonhoeffer T., Götz M. and Hübener M. (2016) Transplanted embryonic neurons integrate into adult neocortical circuits. *Nature* **539**, 248–253.
Fiddes I. T., Lodewijk G. A., Mooring M., Salama S. R., Jacobs F. M. J. and Haussler D. (2018) Human-specific NOTCH2NL genes affect notch signaling and cortical neurogenesis. *Cell* **173**.
Fietz S. A., Lachmann R., Brandl H. *et al*. (2012) Transcriptomes of germinal zones of human and mouse fetal neocortex suggest a role of extracellular matrix in progenitor self-renewal. *Proc. Natl Acad. Sci. USA* **109**, 11836–11841.
Finci L., Zhang Y., Meijers R. and Wang J.-H. (2015) Signaling mechanism of the netrin-1 receptor DCC in axon guidance. *Prog. Biophys. Mol. Biol.* **118**, 153–160.
Finlay B. and Darlington R. (1995) Linked regularities in the development and evolution of mammalian brains. *Science* **268**, 1578–1584.
Fischer D. (2004) Counteracting the Nogo receptor enhances optic nerve regeneration if retinal ganglion cells are in an active growth state. *State. J. Neurosci.* **24**, 1646–1651.
Fothergill T., Donahoo A.-L. S., Douglass A., Zalucki O., Yuan J., Shu T., Goodhill G. J. and Richards L. J. (2014) Netrin-DCC signaling regulates corpus callosum formation through attraction of pioneering axons and by modulating Slit2-mediated repulsion. *Cereb. Cortex* **24**, 1138–1151.
Friocourt F. and Chédotal A. (2017) The Robo3 receptor, a key player in the development, evolution, and function of commissural systems. *Dev. Neurobiol.* **77**, 876–890.
Friocourt F., Kozulin P., Belle M., Suárez R., Di-Poï N., Richards L. J., Giacobini P. and Chédotal A. (2019) Shared and differential features of Robo3 expression pattern in amniotes. *J. Comp. Neurol.* **527**, 2009–2029.
Gaillard A., Prestoz L., Dumartin B., Cantereau A., Morel F., Roger M. and Jaber M. (2007) Reestablishment of damaged adult motor pathways by grafted embryonic cortical neurons. *Nat. Neurosci.* **10**, 1294–1299.
Garbe D. S. and Bashaw G. J. (2007) Independent functions of Slit-Robo repulsion and Netrin-Frazzled attraction regulate axon crossing at the midline in Drosophila. *J. Neurosci.* **27**, 3584–92.
García-Frigola C., Carreres M. I., Vegar C., Mason C. A. and Herrera E. (2008) Zic2 promotes axonal divergence at the optic chiasm midline by EphB1-dependent and -independent mechanisms. *Development* **135**, 1833–1841.
Gaspard N., Bouschet T., Hourez R. *et al*. (2008) An intrinsic mechanism of corticogenesis from embryonic stem cells. *Nature* **455**, 351–357.
Gates M. A., Fricker-Gates R. A. and Macklis J. D. (2000) Reconstruction of cortical circuitry. *Prog. Brain Res.* **127**, 115–156.
Gaudet A. D. and Fonken L. K. (2018) Glial cells shape pathology and repair after spinal cord injury. *Neurotherapeutics* **15**, 554–577.

Gazzaniga M. S. (2000) Cerebral specialization and interhemispheric communication: does the corpus callosum enable the human condition? *Brain* **123**, 1293–1326.

Geoffroy C. G., Lorenzana A. O., Kwan J. P. *et al*. (2015) Effects of PTEN and Nogo codeletion on corticospinal axon sprouting and regeneration in mice. *J. Neurosci.* **35**, 6413–6428.

Gitler A. D., Dhillon P. and Shorter J. (2017) Neurodegenerative disease: models, mechanisms, and a new hope. *Dis. Model. Mech.* **10**, 499–502.

Gobius I., Morcom L., Suárez R. *et al*. (2016) Astroglial-mediated remodeling of the interhemispheric midline is required for the formation of the corpus callosum. *Cell Rep.* **17**, 735–747.

Gobius I., Suárez R., Morcom L., Paolino A., Edwards T. J., Kozulin P. and Richards L. J. (2017) Astroglial-mediated remodeling of the interhemispheric midline during telencephalic development is exclusive to eutherian mammals. *Neural Dev.* **12**, 9.

Goddard J. M., Rossel M., Manley N. R. and Capecchi M. R. (1996) Mice with targeted disruption of Hoxb-1 fail to form the motor nucleus of the VIIth nerve. *Development* **122**, 3217–28.

Gribble K. D., Walker L. J., Saint-Amant L., Kuwada J. Y. and Granato M. (2018) The synaptic receptor Lrp4 promotes peripheral nerve regeneration. *Nat. Commun.* **9**, 2389.

Guillemot F., Molnár Z., Tarabykin V. and Stoykova A. (2006) Molecular mechanisms of cortical differentiation. *Eur. J. Neurosci.* **23**, 857–868.

Guillery R. W., Mason C. A. and Taylor J. S. H. (1995) Developmental determinants at the mammalian optic chiasm. *J. Neurosci.* **15**, 4727–4737.

Guy A. T., Nagatsuka Y., Ooashi N. *et al*. (2015) Glycerophospholipid regulation of modality-specific sensory axon guidance in the spinal cord. *Science* **349**, 974–977.

Hansen D. V., Lui J. H., Parker P. R. L. and Kriegstein A. R. (2010) Neurogenic radial glia in the outer subventricular zone of human neocortex. *Nature* **464**, 554–561.

Haubensak W., Attardo A., Denk W. and Huttner W. B. (2004) Neurons arise in the basal neuroepithelium of the early mammalian telencephalon: a major site of neurogenesis. *Proc. Natl Acad. Sci. USA* **101**, 3196–201.

He Z. and Jin Y. (2016) Intrinsic control of axon regeneration. *Neuron* **90**, 437–451.

Herrera E. (2004) Foxd1 is required for proper formation of the optic chiasm. *Development* **131**, 5727–5739.

Herrera E., Brown L., Aruga J., Rachel R. A., Dolen G., Mikoshiba K., Brown S. and Mason C. A. (2003) Zic2 patterns binocular vision by specifying the uncrossed retinal projection. *Cell* **114**, 545–557.

Herrera E., Erskine L. and Morenilla-Palao C. (2019) Guidance of retinal axons in mammals. *Semin. Cell Dev. Biol.* **85**, 48–59.

Hiramoto M., Hiromi Y., Giniger E. and Hotta Y. (2000) The Drosophila netrin receptor frazzled guides axons by controlling netrin distribution. *Nature* **406**, 886–889.

Huang L. C., Barclay M., Lee K., Peter S., Housley G. D., Thorne P. R. and Montgomery J. M. (2012) Synaptic profiles during neurite extension, refinement and retraction in the developing cochlea. *Neural Dev.* **7**, 38.

Hüll M. and Bähr M. (1994) Differential regulation of c-JUN expression in rat retinal ganglion cells after proximal and distal optic nerve transection. *Neurosci. Lett.* **178**, 39–42.

Isaacman-Beck J., Schneider V., Franzini-Armstrong C. and Granato M. (2015) The lh3 glycosyltransferase directs target-selective peripheral nerve regeneration. *Neuron* **88**, 691–703.

Iwai-Takekoshi L., Balasubramanian R., Sitko A., Khan R., Weinreb S., Robinson K. and Mason C. (2018) Activation of Wnt signaling reduces ipsilaterally projecting retinal ganglion cells in pigmented retina. *Development* **145**, dev163212.

Jalink K., Eichholtz T., Postma F. R., van Corven E. J. and Moolenaar W. H. (1993) Lysophosphatidic acid induces neuronal shape changes via a novel, receptor-mediated signaling pathway: similarity to thrombin action. *Cell Growth Differ* **4**, 247–255.

Javaherian A. and Kriegstein A. (2009) A stem cell niche for intermediate progenitor cells of the embryonic cortex. *Cereb. Cortex* **19**, i70–i77.

Jaworski A., Long H. and Tessier-Lavigne M. (2010) Collaborative and specialized functions of Robo1 and Robo2 in spinal commissural axon guidance. *J. Neurosci.* **30**, 9445–9453.

Jeffery G. and Erskine L. (2005) Variations in the architecture and development of the vertebrate optic chiasm. *Prog. Retin. Eye Res.* **24**, 721–753.

Jen J. C., Chan W.-M. M., Bosley T. M., *et al*. (2004) Mutations in a human ROBO gene disrupt hindbrain axon pathway crossing and morphogenesis. *Science* **304**, 1509–1513.

Kinoshita M. O., Furuya S., Ito S. *et al*. (2009) Lipid rafts enriched in phosphatidylglucoside direct astroglial differentiation by regulating tyrosine kinase activity of epidermal growth factor receptors. *Biochem. J.* **419**, 565–575.

Koch J. C., Tönges L., Barski E., Michel U., Bähr M. and Lingor P. (2014) ROCK2 is a major regulator of axonal degeneration, neuronal death and axonal regeneration in the CNS. *Cell Death Dis.* **5**, e1225–e1225.

Koprivica V. (2005) EGFR activation mediates inhibition of axon regeneration by myelin and chondroitin sulfate proteoglycans. *Science* **310**, 106–110.

Kriegstein A., Noctor S. and Martínez-Cerdeño V. (2006) Patterns of neural stem and progenitor cell division may underlie evolutionary cortical expansion. *Nat. Rev. Neurosci.* **7**, 883–890.

Kurimoto T., Yin Y., Omura K., Gilbert H.-Y., Kim D., Cen L.-P., Moko L., Kugler S. and Benowitz L. I. (2010) Long-distance axon regeneration in the mature optic nerve: contributions of oncomodulin, cAMP, and pten gene deletion. *J. Neurosci.* **30**, 15654–15663.

Kuwajima T., Yoshida Y., Takegahara N., Petros T. J., Kumanogoh A., Jessell T. M., Sakurai T. and Mason C. (2012) Optic chiasm presentation of Semaphorin6D in the context of plexin-A1 and Nr-CAM promotes retinal axon midline crossing. *Neuron* **74**, 676–690.

Kuwajima T., Soares C. A., Sitko A. A., Lefebvre V. and Mason C. (2017) SoxC transcription factors promote contralateral retinal ganglion cell differentiation and axon guidance in the mouse visual system. *Neuron* **93**, 1110–1125.e5.

Lang B. T., Cregg J. M., DePaul M. A. *et al*. (2015) Modulation of the proteoglycan receptor PTPσ promotes recovery after spinal cord injury. *Nature* **518**, 404–408.

Lee R., Petros T. J. and Mason C. A. (2008) Zic2 Regulates retinal ganglion cell axon avoidance of ephrinB2 through inducing expression of the guidance receptor EphB1. *J. Neurosci.* **28**, 5910–5919.

Leon S., Yin Y., Nguyen J., Irwin N. and Benowitz L. I. (2000) Lens injury stimulates axon regeneration in the mature rat optic nerve. *J. Neurosci.* **20**, 4615–26.

Leyva-Díaz E. and López-Bendito G. (2013) In and out from the cortex: development of major forebrain connections. *Neuroscience* **254**, 26–44.

Leyva-Díaz E., del Toro D., Menal M. J., Cambray S., Susín R., Tessier-Lavigne M., Klein R., Egea J. and López-Bendito G. (2014) FLRT3 is a Robo1-interacting protein that determines Netrin-1 attraction in developing axons. *Curr. Biol.* **24**, 494–508.

Li D., Zhang P., Yao X., Li H., Shen H., Li X., Wu J. and Lu X. (2018) Exosomes derived from miR-133b-modified mesenchymal stem cells promote recovery after spinal cord injury. *Front. Neurosci.* **12**, 845.

INFORME DE LABORES 2019

Ling H., Hardy J. and Zetterberg H. (2015) Neurological consequences of traumatic brain injuries in sports. *Mol. Cell. Neurosci.* **66**, 114–122.

Lingor P., Teusch N., Schwarz K., Mueller R., Mack H., Bähr M. and Mueller B. K. (2007) Inhibition of Rho kinase (ROCK) increases neurite outgrowth on chondroitin sulphate proteoglycan in vitro and axonal regeneration in the adult optic nerve in vivo. *J. Neurochem.* **103**, 181–9.

Lingor P., Tönges L., Pieper N., Bermel C., Barski E., Planchamp V. and Bähr M. (2008) ROCK inhibition and CNTF interact on intrinsic signalling pathways and differentially regulate survival and regeneration in retinal ganglion cells. *Brain* **131**, 250–263.

Liu Y., Wang X., Li W. *et al*. (2017) A sensitized IGF1 treatment restores corticospinal axon-dependent functions. *Neuron* **95**, 817–833.e4.

Liu W., Wang Y., Gong F. *et al*. (2019) Exosomes derived from bone mesenchymal stem cells repair traumatic spinal cord injury by suppressing the activation of A1 neurotoxic reactive astrocytes. *J. Neurotrauma* **36**, 469–484.

Long H., Sabatier C., Ma L., Plump A., Yuan W., Ornitz D. M., Tamada A., Murakami F., Goodman C. S. and Tessier-Lavigne M. (2004) Conserved roles for Slit and Robo proteins in midline commissural axon guidance. *Neuron* **42**, 213–223.

Lopez-Leal R. and Court F. A. (2016) Schwann cell exosomes mediate neuron–glia communication and enhance axonal regeneration. *Cell. Mol. Neurobiol.* **36**, 429–436.

Lyuksyutova A. I., Lu C.-C., Milanesio N., King L. A., Guo N., Wang Y., Nathans J., Tessier-Lavigne M. and Zou Y. (2003) Anterior-posterior guidance of commissural axons by Wnt-frizzled signaling. *Science* **302**, 1984–8.

Malatesta P., Hartfuss E. and Götz M. (2000) Isolation of radial glial cells by fluorescent-activated cell sorting reveals a neuronal lineage. *Development* **127**, 5253–63.

Marcos-Mondejar P., Peregrin S., Li J. Y., Carlsson L., Tole S. and Lopez-Bendito G. (2012) The Lhx2 transcription factor controls thalamocortical axonal guidance by specific regulation of Robo1 and Robo2 receptors. *J. Neurosci.* **32**, 4372–4385.

Marillat V., Sabatier C., Failli V., Matsunaga E., Sotelo C., Tessier-Lavigne M. and Chédotal A. (2004) The slit receptor Rig-1/Robo3 controls midline crossing by hindbrain precerebellar neurons and axons. *Neuron* **43**, 69–79.

Martersteck E. M., Hirokawa K. E., Evarts M. *et al*. (2017) Diverse central projection patterns of retinal ganglion cells. *Cell Rep.* **18**, 2058–2072.

Martin V., Mrkusich E., Steinel M. C., Rice J., Merritt D. J. and Whitington P. M. (2008) The L1-type cell adhesion molecule Neuroglian is necessary for maintenance of sensory axon advance in the Drosophila embryo. *Neural Dev.* **3**, 10.

Martin-Villalba A., Winter C., Brecht S., Buschmann T., Zimmermann M. and Herdegen T. (1998) Rapid and long-lasting suppression of the ATF-2 transcription factor is a common response to neuronal injury. *Mol. Brain Res.* **62**, 158–166.

Mazengenya P. and Bhikha R. (2017) The structure and function of the central nervous system and sense organs in the canon of medicine by avicenna. *Arch. Iran. Med.* **20**, 67–70.

Mckee A. C. and Daneshvar D. H. (2015) The neuropathology of traumatic brain injury. *Handb. Clin. Neurol.* 45–66.

McKeon R. J., Schreiber R. C., Rudge J. S. and Silver J. (1991) Reduction of neurite outgrowth in a model of glial scarring following CNS injury is correlated with the expression of inhibitory molecules on reactive astrocytes. *J. Neurosci.* **11**, 3398–411.

Michalski N., Babai N., Renier N., Perkel D. J., Chédotal A. and Schneggenburger R. (2013) Robo3-driven axon midline crossing conditions functional maturation of a large commissural synapse. *Neuron* **78**, 855–68.

Michelsen K. A., Acosta-Verdugo S., Benoit-Marand M., Espuny-Camacho I., Gaspard N., Saha B., Gaillard A. and Vanderhaeghen P. (2015) Area-specific reestablishment of damaged circuits in the adult cerebral cortex by cortical neurons derived from mouse embryonic stem cells. *Neuron* **85**, 982–997.

Mire E., Hocine M., Bazellières E., Jungas T., Davy A., Chauvet S. and Mann F. (2018) Developmental upregulation of Ephrin-B1 silences Sema3C/Neuropilin-1 signaling during post-crossing navigation of corpus callosum axons. *Curr. Biol.* **28**, 1768–1782.e4.

Miyata T., Kawaguchi A., Saito K., Kawano M., Muto T. and Ogawa M. (2004) Asymmetric production of surface-dividing and non-surface-dividing cortical progenitor cells. *Development* **131**, 3133–45.

Moreno-Bravo J. A., Roig Puiggros S., Mehlen P. and Chédotal A. (2019) Synergistic activity of floor-plate- and ventricular-zone-derived netrin-1 in spinal cord commissural axon guidance. *Neuron* **101**, 625–634.e3.

Müller M. and Holländer H. (1988) A small population of retinal ganglion cells projecting to the retina of the other eye - an experimental study in the rat and the rabbit. *Exp. Brain Res.* **71**, 611–617.

Murcia-Belmonte V., Coca Y., Vegar C. *et al*. (2019) A retino-retinal projection guided by Unc5c emerged in species with retinal waves. *Curr. Biol.* **29**, 1149–1160.e4.

Nadal-Nicolás F. M., Valiente-Soriano F. J., Salinas-Navarro M., Jiménez-López M., Vidal-Sanz M. and Agudo-Barriuso M. (2015) Retino-retinal projection in juvenile and young adult rats and mice. *Exp. Eye Res.* **134**, 47–52.

Nagashima F., Suzuki I. K., Shitamukai A., Sakaguchi H., Iwashita M., Kobayashi T., Tone S., Toida K., Vanderhaeghen P. and Kosodo Y. (2014) Novel and robust transplantation reveals the acquisition of polarized processes by cortical cells derived from mouse and human pluripotent stem cells. *Stem Cells Dev.* **23**, 2129–2142.

Nagatsuka Y., Horibata Y., Yamazaki Y., Kinoshita M., Shinoda Y., Hashikawa T., Koshino H., Nakamura T. and Hirabayashi Y. (2006) Phosphatidylglucoside exists as a single molecular species with saturated fatty acyl chains in developing astroglial membranes. *Biochemistry* **45**, 8742–8750.

Nawabi H., Briancon-Marjollet A., Clark C. *et al*. (2010) A midline switch of receptor processing regulates commissural axon guidance in vertebrates. *Genes Dev.* **24**, 396–410.

Nayagam B. A., Muniak M. A. and Ryugo D. K. (2011) The spiral ganglion: connecting the peripheral and central auditory systems. *Hear. Res.* **278**, 2–20.

Niquille M., Garel S., Mann F. *et al*. (2009) Transient neuronal populations are required to guide callosal axons: a role for semaphorin 3C. *PLoS Biol.* **7**, e1000230.

Noctor S. C., Flint A. C., Weissman T. A., Dammerman R. S. and Kriegstein A. R. (2001) Neurons derived from radial glial cells establish radial units in neocortex. *Nature* **409**, 714–720.

Noctor S. C., Martínez-Cerdeño V., Ivic L. and Kriegstein A. R. (2004) Cortical neurons arise in symmetric and asymmetric division zones and migrate through specific phases. *Nat. Neurosci.* **7**, 136–44.

Norsworthy M. W., Bei F., Kawaguchi R. *et al*. (2017) Sox11 expression promotes regeneration of some retinal ganglion cell types but kills others. *Neuron* **94**, 1112–1120.e4.

Northcutt R. G. (2006) Understanding vertebrate brain evolution. *Integr. Comp. Biol.* **42**, 743–756.

Onishi K. and Zou Y. (2017) Sonic hedgehog switches on Wnt/planar cell polarity signaling in commissural axon growth cones by reducing levels of Shisa2. *Elife* **6**, 1–20.

Onishi K., Hollis E. and Zou Y. (2014) Axon guidance and injury-lessons from Wnts and Wnt signaling. *Curr. Opin. Neurobiol.* **27**, 232–40.

Pak W., Hindges R., Lim Y.-S., Pfaff S. L. and O'Leary D. D. M. (2004) Magnitude of binocular vision controlled by Islet-2 repression of a

genetic program that specifies laterality of retinal axon pathfinding. *Cell* **119**, 567–578.

Panza P., Sitko A. A., Maischein H.-M., Koch I., Flötenmeyer M., Wright G. J., Mandai K., Mason C. A. and Söllner C. (2015) The LRR receptor Islr2 is required for retinal axon routing at the vertebrate optic chiasm. *Neural Dev.* **10**, 23.

Park K. K., Liu K., Hu Y., *et al*. (2008) Promoting axon regeneration in the adult CNS by modulation of the PTEN/mTOR pathway. *Science* **322**, 963–966.

Parra L. M. and Zou Y. (2010) Sonic hedgehog induces response of commissural axons to Semaphorin repulsion during midline crossing. *Nat. Neurosci.* **13**, 29–35.

Peng J., Fabre P. J., Dolique T. and Swikert S. M. (2018) Sonic hedgehog is a remotely produced cue that controls axon guidance trans-axonally at a midline choice point. *Neuron* **97**, 326–340.

Péron S., Droguerre M., Debarbieux F., Ballout N., Benoit-Marand M., Francheteau M., Brot S., Rougon G., Jaber M. and Gaillard A. (2017) A delay between motor cortex lesions and neuronal transplantation enhances graft integration and improves repair and recovery. *J. Neurosci.* **37**, 1820–1834.

Petros T. J., Bryson J. B. and Mason C. (2010) Ephrin-B2 elicits differential growth cone collapse and axon retraction in retinal ganglion cells from distinct retinal regions. *Dev. Neurobiol.* **70**, 781–794.

Philipp M., Niederkofler V., Debrunner M., Alther T., Kunz B. and Stoeckli E. T. (2012) RabGDI controls axonal midline crossing by regulating Robo1 surface expression. *Neural Dev.* **7**, 36.

Qin S., Zou Y. and Zhang C.-L. (2013) Cross-talk between KLF4 and STAT3 regulates axon regeneration. *Nat. Commun.* **4**, 2633.

Raitano S., Ordovàs L., Muynck L. *et al*. (2015) Restoration of progranulin expression rescues cortical neuron generation in an induced pluripotent stem cell model of frontotemporal dementia. *Stem Cell Rep.* **4**, 16–24.

Rakic P. and Yakovlev P. I. (1968) Development of the corpus callosum and cavum septi in man. *J. Comp. Neurol.* **132**, 45–72.

Ramón y Cajal S. (1914) *Estudios sobre la degeneración y regeneración del sistema nerviosa*, Vol. **2**. Hijos de Nicolás Moza, Madrid.

Rasmussen J. P. and Sagasti A. (2017) *Learning to Swim, Again: Axon Regeneration in Fish*. Academic Press, Cambridge, MA.

Rebsam A., Bhansali P. and Mason C. A. (2012) Eye-specific projections of retinogeniculate axons are altered in albino mice. *J. Neurosci.* **32**, 4821–4826.

Renier N., Schonewille M., Giraudet F., Badura A., Tessier-Lavigne M., Avan P., Zeeuw C. I. and De Chédotal A. (2010) Genetic dissection of the function of hindbrain axonal commissures. *PLoS Biol.* **8**, e1000325.

Ribas V. T., Koch J. C., Michel U., Bähr M. and Lingor P. (2017) Attenuation of axonal degeneration by calcium channel inhibitors improves retinal ganglion cell survival and regeneration after optic nerve crush. *Mol. Neurobiol.* **54**, 72–86.

Rosenberg A. F., Wolman M. A., Franzini-Armstrong C. and Granato M. (2012) In vivo nerve-macrophage interactions following peripheral nerve injury. *J. Neurosci.* **32**, 3898–3909.

Rosenberg A. F., Isaacman-Beck J., Franzini-Armstrong C. and Granato M. (2014) Schwann cells and deleted in colorectal carcinoma direct regenerating motor axons towards their original path. *J. Neurosci.* **34**, 14668–81.

Ruiz de Almodovar C., Fabre P. J., Knevels E. *et al*. (2011) VEGF mediates commissural axon chemoattraction through its receptor Flk1. *Neuron* **70**, 966–978.

Sabatier C., Plump A. S., Le Ma, Brose K., Tamada A., Murakami F., Lee E. Y.-H. and Tessier-Lavigne M. (2004) The divergent robo family protein Rig-1/Robo3 is a negative regulator of slit responsiveness required for midline crossing by commissural axons. *Cell* **117**, 157–169.

Safieddine S., El-Amraoui A. and Petit C. (2012) The auditory hair cell ribbon synapse: from assembly to function. *Annu. Rev. Neurosci.* **35**, 509–528.

Saito S. (1997) Effects of lysophosphatidic acid on primary cultured chick neurons. *Neurosci. Lett.* **229**, 73–76.

Sanes J. R. and Masland R. H. (2015) The types of retinal ganglion cells: current status and implications for neuronal classification. *Annu. Rev. Neurosci.* **38**, 221–246.

Schmandke A., Schmandke A. and Schwab M. E. (2014) Nogo-A: multiple roles in CNS development, maintenance, and disease. *Neuroscientist* **20**, 372–386.

Schmucker D., Clemens J. C., Shu H., Worby C. A., Xiao J., Muda M., Dixon J. E. and Zipursky S. L. (2000) Drosophila Dscam is an axon guidance receptor exhibiting extraordinary molecular diversity. *Cell* **101**, 671–84.

Scholz T., Krichevsky A., Sumarto A., Jaffurs D., Wirth G., Paydar K. and Evans G. (2009) Peripheral nerve injuries: an international survey of current treatments and future perspectives. *J. Reconstr. Microsurg.* **25**, 339–344.

Serafini T., Colamarino S. A., Leonardo E. D., Wang H., Beddington R., Skarnes W. C. and Tessier-Lavigne M. (1996) Netrin-1 is required for commissural axon guidance in the developing vertebrate nervous system. *Cell* **87**, 1001–14.

Shrestha B. R., Chia C., Wu L., Kujawa S. G., Liberman M. C. and Goodrich L. V. (2018) Sensory neuron diversity in the inner ear is shaped by activity. *Cell* **174**, 1229–1246.e17.

Silver J., Lorenz S. E., Wahlsten D. and Coughlin J. (1982) Axonal guidance during development of the great cerebral commissures: descriptive and experimental studies, in vivo, on the role of preformed glial pathways. *J. Comp. Neurol.* **210**, 10–29.

Sivasankaran R., Pei J., Wang K. C., Zhang Y. P., Shields C. B., Xu X.-M. and He Z. (2004) PKC mediates inhibitory effects of myelin and chondroitin sulfate proteoglycans on axonal regeneration. *Nat. Neurosci.* **7**, 261–268.

Sloan T. F. W. W., Qasaimeh M. A., Juncker D., Yam P. T. and Charron F. (2015) Integration of shallow gradients of Shh and netrin-1 guides commissural axons. *PLOS Biol.* **13**, e1002119.

Smart I. H. M. (2002) Unique morphological features of the proliferative zones and postmitotic compartments of the neural epithelium giving rise to striate and extrastriate cortex in the monkey. *Cereb. Cortex* **12**, 37–53.

Smith P. D., Sun F., Park K. K., Cai B., Wang C., Kuwako K., Martinez-Carrasco I., Connolly L. and He Z. (2009) SOCS3 deletion promotes optic nerve regeneration in vivo. *Neuron* **64**, 617–623.

Steinel M. C. and Whitington P. M. (2009) The atypical cadherin Flamingo is required for sensory axon advance beyond intermediate target cells. *Dev. Biol.* **327**, 447–457.

Stoeckli E. T. (2018) Understanding axon guidance: are we nearly there yet? *Development* **145**, dev151415.

Strochlic L., Dwivedy A., van Horck F. P. G., Falk J.and Holt C. E. (2007) A role for S1P signalling in axon guidance in the Xenopus visual system. *Development* **135**, 333–342.

Suárez R., Gobius I. and Richards L. J. (2014) Evolution and development of interhemispheric connections in the vertebrate forebrain. *Front. Hum. Neurosci.* **8**, 497.

Sun F., Park K. K., Belin S. *et al*. (2011) Sustained axon regeneration induced by co-deletion of PTEN and SOCS3. *Nature* **480**, 372–375.

Suzuki I. K. and Vanderhaeghen P. (2015) Is this a brain which I see before me? Modeling human neural development with pluripotent stem cells. *Development* **142**, 3138–3150.

Suzuki I. K., Gacquer D., Heurck R. *et al*. (2018) Human-specific NOTCH2NL genes expand cortical neurogenesis through Delta/Notch regulation. *Cell* **173**, 1370–1384.e16.

INFORME DE LABORES 2019

Theotokis P., Kleopa K. A., Touloumi O. *et al*. (2015) Connexin43 and connexin47 alterations after neural precursor cells transplantation in experimental autoimmune encephalomyelitis. *Glia* **63**, 1772–1783.

Tiberi L., Vanderhaeghen P. and van den Ameele J. (2012) Cortical neurogenesis and morphogens: diversity of cues, sources and functions. *Curr. Opin. Cell Biol.* **24**, 269–276.

Tornero D., Wattananit S., Grønning Madsen M. *et al*. (2013) Human induced pluripotent stem cell-derived cortical neurons integrate in stroke-injured cortex and improve functional recovery. *Brain* **136**, 3561–3577.

del Toro D., Ruff T., Cederfjäll E., Villalba A., Seyit-Bremer G., Borrell V. and Klein R. (2017) Regulation of cerebral cortex folding by controlling neuronal migration via FLRT adhesion molecules. *Cell* **169**, 621–635.e16.

Tóth P. and Strznicky C. (1989) Retino-retinal projections in three anuran species. *Neurosci. Lett.* **104**, 43–47.

Unni D. K., Piper M., Moldrich R. X., Gobius I., Liu S., Fothergill T., Donahoo A.-L. S., Baisden J. M., Cooper H. M. and Richards L. J. (2012) Multiple Slits regulate the development of midline glial populations and the corpus callosum. *Dev. Biol.* **365**, 36–49.

Varadarajan S. G., Kong J. H., Phan K. D., Kao T.-J., Panaitof S. C., Cardin J., Eltzschig H., Kania A., Novitch B. G. and Butler S. J. (2017) Netrin1 produced by neural progenitors, not floor plate cells, is required for axon guidance in the spinal cord. *Neuron* **94**, 790–799.e3.

Waller A. (1851) Experiments on the section of the glosso-pharyngeal and hypoglossal nerves of the frog, and observations of the alterations produced thereby in the structure of their primitive fibres. *Edinburgh Med. Surg. J.* **76**, 369–376.

Wang H. C. and Bergles D. E. (2015) Spontaneous activity in the developing auditory system. *Cell Tissue Res.* **361**, 65–75.

Wang K. H., Brose K., Arnott D., Kidd T., Goodman C. S., Henzel W. and Tessier-Lavigne M. (1999) Biochemical purification of a mammalian Slit protein as a positive regulator of sensory axon elongation and branching. *Cell* **96**, 771–784.

Wang J., Zugates C. T., Liang I. H., Lee C.-H. J. and Lee T. (2002a) Drosophila Dscam is required for divergent segregation of sister branches and suppresses ectopic bifurcation of axons. *Neuron* **33**, 559–71.

Wang K. C., Kim J. A., Sivasankaran R., Segal R. and He Z. (2002b) p75 interacts with the Nogo receptor as a co-receptor for Nogo, MAG and OMgp. *Nature* **420**, 74–78.

Wang K. C., Koprivica V., Kim J. A., Sivasankaran R., Guo Y., Neve R. L. and He Z. (2002c) Oligodendrocyte-myelin glycoprotein is a Nogo receptor ligand that inhibits neurite outgrowth. *Nature* **417**, 941–944.

Wang Q., Marcucci F., Cerullo I. and Mason C. (2016) Ipsilateral and contralateral retinal ganglion cells express distinct genes during decussation at the optic chiasm. *eNeuro* **3**, ENEURO.0169-16.2016.

Wang X., Liu Y., Li X. *et al*. (2017) Deconstruction of corticospinal circuits for goal-directed motor skills. *Cell* **171**, 440–455.e14.

Wernig M. (2004) Functional integration of embryonic stem cell-derived neurons in vivo. *J. Neurosci.* **24**, 5258–5268.

Williams S. E., Mann F., Erskine L., Sakurai T., Wei S., Rossi D. J., Gale N. W., Holt C. E., Mason C. A. and Henkemeyer M. (2003) Ephrin-B2 and EphB1 mediate retinal axon divergence at the optic chiasm. *Neuron* **39**, 919–35.

Williams S. E., Mason C. A. and Herrera E. (2004) The optic chiasm as a midline choice point. *Curr. Opin. Neurobiol.* **14**, 51–60.

Williams S. E., Grumet M., Colman D. R., Henkemeyer M., Mason C. A. and Sakurai T. (2006) A role for Nr-CAM in the patterning of binocular visual pathways. *Neuron* **50**, 535–547.

Wilson S. I., Shafer B., Lee K. J. and Dodd J. (2008) A molecular program for contralateral trajectory: Rig-1 control by LIM homeodomain transcription factors. *Neuron* **59**, 413–424.

Wu Z., Sweeney L. B., Ayoob J. C., Chak K., Andreone B. J., Ohyama T., Kerr R., Luo L., Zlatic M. and Kolodkin A. L. (2011) A Combinatorial semaphorin code instructs the initial steps of sensory circuit assembly in the Drosophila CNS. *Neuron* **70**, 281–298.

Wu Z., Makihara S., Yam P. T. *et al*. (2019) Long-range guidance of spinal commissural axons by Netrin1 and sonic hedgehog from midline floor plate cells. *Neuron* **101**, 635–647.e4.

Yam P. T., Kent C. B., Morin S., Farmer W. T., Alchini R., Lepelletier L., Colman D. R., Tessier-Lavigne M., Fournier A. E. and Charron F. (2012) 14-3-3 Proteins regulate a cell-intrinsic switch from sonic hedgehog-mediated commissural axon attraction to repulsion after midline crossing. *Neuron* **76**, 735–749.

Yamauchi K., Yamazaki M., Abe M., Sakimura K., Lickert H., Kawasaki T., Murakami F. and Hirata T. (2017) Netrin-1 derived from the ventricular zone, but not the floor plate, directs hindbrain commissural axons to the ventral midline. *Sci. Rep.* **7**, 11992.

Yoshikawa S., McKinnon R. D., Kokel M. and Thomas J. B. (2003) Wnt-mediated axon guidance via the Drosophila derailed receptor. *Nature* **422**, 583–588.

Zelina P., Blockus H., Zagar Y. *et al*. (2014) Signaling switch of the axon guidance receptor Robo3 during vertebrate evolution. *Neuron* **84**, 1258–1272.

Zolog A. (1994) Somatic motor nerve and function as conceived by Alcmaeon of Croton. *J. Hist. Neurosci.* **3**, 261–262.

Zou Y. (2004) Wnt signaling in axon guidance. *Trends Neurosci.* **27**, 528–532.

Zou Y. (2012) Does planar cell polarity signaling steer growth cones? *Curr. Top. Dev. Biol.* **101**, 141–160.

Neuron
Previews

CellPress

Low Dimensionality, High Robustness in Neural Population Dynamics

Román Rossi-Pool[1,*] and Ranulfo Romo[1,2,*]
[1]Instituto de Fisiología Celular–Neurociencias, Universidad Nacional Autónoma de México, 04510 Mexico City, Mexico
[2]El Colegio Nacional, 06020 Mexico City, Mexico
*Correspondence: romanr@ifc.unam.mx (R.R.-P.), rromo@ifc.unam.mx (R.R.)
https://doi.org/10.1016/j.neuron.2019.06.021

Neuronal populations respond within a small number of relevant dimensions. New research by Trautmann et al. (2019) shows that spike sorting is not necessary to extract the important features of this low-dimensional population signal. Combined responses of multiple neurons (multiunit activity) only generate small changes in the extracted signals.

Neural population dynamics do condense to a few meaningful signals. Several thousands of single-neuron responses give rise to a small number of significant population dynamics ("*E pluribus pauca*"). Low dimensionality of neural data appears to be a general biological feature, observed in several experiments and animal models (Gao and Ganguli, 2015; Kobak et al., 2016; Rossi-Pool et al., 2017). Further, the dimension-reduced representation of the neural data across time constitutes a surface with smooth curvature (manifold). In recent years, different dimensionality reduction methods have been employed to infer the relevant latent population signals. Neural responses at a macroscopic level have helped neuroscientists to infer computational principles hidden in the heterogeneous activity of single neurons (Ames et al., 2014; Churchland et al., 2012; Kaufman et al., 2014; Rossi-Pool et al., 2019). This means that structures and invariant features of the data emerge by zooming out from single-neuron responses. However, what are the biological implications of the low dimensionality and smooth curvature of the population dynamics?

In general, population analyses employ a weighted sum of single-unit activity to compute the meaningful population signals from data. Therefore, to obtain each component of the population dynamics, different weights (importance) are given to each individual neuron of the network. Multiunit activity, recorded with a simple voltage threshold at each single channel, randomly combined activity from several neurons (Figure 1A). Notably, single neurons with analogous or different coding dynamics (high tuning correlation) are mixed spatially (see Figure S2 in Trautmann et al., 2019). Then, each multiunit response constitutes a random selection of single units that could be compelling for the same or different population components. Considering that the neural response is low dimensional, is it possible to obtain population dynamics employing multiunit instead of single-unit activity?

In this issue of *Neuron*, Trautmann et al. (2019) address this question, offering important new evidence of the robustness of population dynamics. The authors found that spike sorting is not necessary to accurately determine which population signals are most meaningful. To endorse this claim, they replicate results from three previous studies, originally spike sorted (Ames et al., 2014; Churchland et al., 2012; Kaufman et al., 2014) but now directly using the unsorted multiunit activity. Notably, they were able to extract population signals, employing threshold-crossing multiunit activity, with only minor differences with respect to the signals found in the previous studies. When dimensionality reduction methods are applied to random linear combinations of single-unit responses, they yield analogous neural trajectories. Equivalent hidden population responses emerged from both approaches (Figure 1A). Not only do these results have great implications for facilitating future population studies, they also provide new evidence of the robustness and stability of population signals. Moreover, multiunit responses include hash activity that cannot be sorted into isolated neurons. This unsortable activity could carry relevant signals that increase the statistical power of the population analysis.

In addition to the previously recorded neurons, the authors collected new neural data using silicon Neuropixels probes during a motor reaching task. Employing this new high-density recording technique (~20 μm site spacing), Trautmann et al. (2019) were able to sort hundreds of single neurons per trial. Again, the same population dynamics were obtained with the well-isolated single neurons. Importantly, their results suggest that more independent observations of the neural population are fundamental to compute the important aspect of the network. Contrary to that, redundancy given by high-density electrodes will not improve accuracy to infer the underlying neural signals. However, the authors used this new recording technique to provide significant additional evidence that nearby neurons do not share similar tuning properties. The results show that there are no spatially organized clusters of neurons with similar selectivity. This finding opens new questions that could be tackled with these high-density recordings. Is noise correlation higher between nearby neurons? Is there any relationship between distance, tuning, and noise correlation? These important questions could help to understand the underlying architecture of neural microcircuits.

As the authors assert across the manuscript, these results are restrained to population analysis. Crucial to this point, there are still many important questions to be addressed with single units. To evaluate individual cells' properties, like tuning to

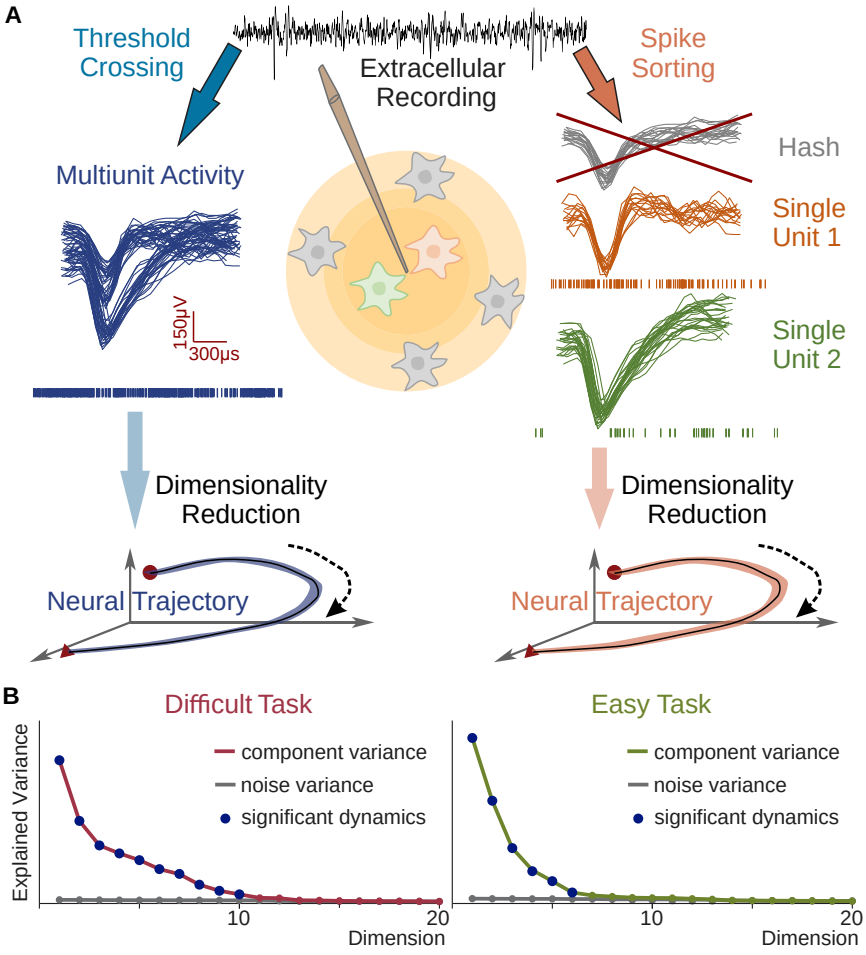

Figure 1. Single-Unit Versus Multiunit Activity in Low-Dimensional Neural Trajectories
(A) Single-unit activity obtained with spike sorting or multiunit activity obtained from threshold crossing gives rise to similar neural dynamics. Note that in the single-neuron approach, hash activity is discarded. (B) Easy and difficult tasks exhibit low dimensionality. Few significant dynamics explain most of the variance. A more difficult task displays more significant dynamics (above noise) than an easier task.

a stimulus parameter, spike sorting is still imperative. Studies based on single units are extremely important to understand the basic operations employed by neuronal circuits. Some of the most profound understandings of the neural mechanisms of working memory and decision making were obtained from studies of single-neuron activity across brain areas (Hernández et al., 2010). Furthermore, to our knowledge, there are no population-level studies analyzing neural features across areas.

To give a deeper interpretation of their results, the authors apply the theory of random projections (Ganguli and Sompolinsky, 2012). This theory is pertinent when a low-dimensional neural response is enclosed in a high-dimensional space. In this case, each single-neuron activity represents one axis of the high-dimension space. While the number of significant dimensions in a neural state is around ten, the number of recorded neurons could be on the order of thousands (Gao and Ganguli, 2015). Under these circumstances, recording small numbers of random linear combinations of single-neuron activity (multiunit activity) is enough to extract the meaningful population responses (Figure 1). Applying this theory, Trautmann et al. (2019) show that higher-dimensional neural data require a larger number of multiunit channels to properly estimate the population dynamics. Importantly, recent results suggest that dimensionality is associated with the complexity of the task (Rossi-Pool et al., 2017, 2019). When a task is too easy, the number of relevant dimensions decreases (Figure 1B). Note that to consider a neural dimension as significant, its explained variance should be higher than the noise variance associated with this component. Markedly, several tasks have shown that many significant dimensions and most of the network variance is captured by pure temporal latent signals (Kobak et al., 2016). These timing signals could be understood as a necessary substrate on which parameter coding responses can develop (Rossi-Pool et al., 2019).

Another important problem to be answered in future research is the relevance of the population-level responses. Do population responses reveal fundamental processes of brain circuits or do they only represent suitable pictures of their dynamics? Are the population responses, calculated with dimensional reduction approaches, still meaningful when the task is much more complex? Is it possible to establish an electrophysiological relationship between population signals and the oscillatory activity computed with local field potentials, which is considered to measure the level of synchronization of neural activity? These and other important questions are still open for future studies.

The work of Trautmann et al. (2019) leads the way to some other important, unresolved questions. Which are the biological reasons to have population neural responses with low dimensionality and high robustness? One possible hypothesis is that neurons from a downstream area could obtain the relevant neural information from upstream areas combining randomly single-unit activity. This population feature could help to facilitate communication across brain areas. Another complementary hypothesis is that low dimensionality gives stability and redundancy to the network. Once a complex task is learned, the neuronal population response could be prone to tolerate perturbation in its dynamic. However, under this stability, how do the networks learn a completely new task or variations of a previously acquired task? Is the dimensionality of the population higher when the subject is being trained

in a new task? New experiments, computational analyses, and theoretical biology developments are necessary to clear up these propositions.

To conclude, Trautmann et al. (2019) present a meticulous study showing how dimensionality reduction methods can be employed with multiunit instead of single-unit activity, and by doing so, they provide new evidence to the actual debate about the functional roles of dimensionality, robustness, stability, and redundancy of neural network dynamics.

REFERENCES

Ames, K.C., Ryu, S.I., and Shenoy, K.V. (2014). Neural dynamics of reaching following incorrect or absent motor preparation. Neuron *81*, 438–451.

Churchland, M.M., Cunningham, J.P., Kaufman, M.T., Foster, J.D., Nuyujukian, P., Ryu, S.I., and Shenoy, K.V. (2012). Neural population dynamics during reaching. Nature *487*, 51–56.

Ganguli, S., and Sompolinsky, H. (2012). Compressed sensing, sparsity, and dimensionality in neuronal information processing and data analysis. Annu. Rev. Neurosci. *35*, 485–508.

Gao, P., and Ganguli, S. (2015). On simplicity and complexity in the brave new world of large-scale neuroscience. Curr. Opin. Neurobiol. *32*, 148–155.

Hernández, A., Nácher, V., Luna, R., Zainos, A., Lemus, L., Alvarez, M., Vázquez, Y., Camarillo, L., and Romo, R. (2010). Decoding a perceptual decision process across cortex. Neuron *66*, 300–314.

Kaufman, M.T., Churchland, M.M., Ryu, S.I., and Shenoy, K.V. (2014). Cortical activity in the null space: permitting preparation without movement. Nat. Neurosci. *17*, 440–448.

Kobak, D., Brendel, W., Constantinidis, C., Feierstein, C.E., Kepecs, A., Mainen, Z.F., Qi, X.-L., Romo, R., Uchida, N., and Machens, C.K. (2016). Demixed principal component analysis of neural population data. eLife *5*, e10989.

Rossi-Pool, R., Zainos, A., Alvarez, M., Zizumbo, J., Vergara, J., and Romo, R. (2017). Decoding a Decision Process in the Neuronal Population of Dorsal Premotor Cortex. Neuron *96*, 1432–1446.e7.

Rossi-Pool, R., Zizumbo, J., Alvarez, M., Vergara, J., Zainos, A., and Romo, R. (2019). Temporal signals underlying a cognitive process in the dorsal premotor cortex. Proc. Natl. Acad. Sci. USA *116*, 7523–7532.

Trautmann, E.M., Stavisky, S.D., Lahiri, S., Ames, K.C., Kaufman, M.T., O'Shea, D.J., Vyas, S., Sun, X., Ryu, S.I., Ganguli, S., and Shenoy, K.V. (2019). Accurate Estimation of Neural Population Dynamics without Spike Sorting. Neuron *103*, this issue, 292–308.

How to Break a Fever: A Feedback Circuit for Body Temperature Control

Bo Duan[1,*] and X.Z. Shawn Xu[2,3,*]
[1]Department of Molecular, Cellular and Developmental Biology, University of Michigan, Ann Arbor, MI 48109, USA
[2]Life Sciences Institute, University of Michigan, Ann Arbor, MI 48109, USA
[3]Department of Molecular and Integrative Physiology, University of Michigan, Ann Arbor, MI 48109, USA
*Correspondence: bduan@umich.edu (B.D.), shawnxu@umich.edu (X.Z.S.X.)
https://doi.org/10.1016/j.neuron.2019.06.023

Body temperature control is a critical brain function. In this issue of *Neuron*, Wang et al. identify a negative feedback circuit in mouse preoptic area of the hypothalamus that regulates body temperature to counter fever.

Body temperature regulation is a fundamental homeostatic function in mammals. The maintenance of a constant body core temperature (T_c) at approximately 37°C is controlled by a central nervous network in an orchestrated manner. The thermoregulation system also plays a key role in host defense against pathogens through elevation of T_c, a response called fever. How is this accomplished? As a concept, the thermoregulation system consists of three components: sensory afferents, the central integration center, and command outputs (Morrison and Nakamura, 2019). The thermoregulatory center in the brain receives information through sensory afferents from thermoreceptors in the skin to detect ambient temperature and from thermoreceptors in viscera, muscle, spinal cord, and brain to detect body temperature. The thermal information is integrated in the thermoregulatory center, and then the center provides commands to thermoeffectors to control heat production or heat loss (Morrison and Nakamura, 2019). Work in the past decade has greatly advanced our understanding of the role of the temperature-sensitive TRP (transient receptor potential) family of cation channels in cutaneous thermosensation, particularly heat sensation (Dhaka et al., 2006). However, the molecular and cellular mechanisms underlying body temperature regulation in the brain remain largely unknown.

In mammals, the preoptic area (POA), located in the rostral pole of the hypothalamus, is thought to function as the thermoregulatory center in which a variety of thermal information, including ambient and body temperature, is integrated for the maintenance of temperature homeostasis (Morrison and Nakamura, 2019) (Figure 1). In their classic work in 1938, Magoun and colleagues precisely defined the thermosensitive area in the POA (Magoun et al., 1938). Later, single-unit studies in 1960s to 1980s showed that about 30% of POA neurons are warm-sensitive, 10%

Check for updates

Temporal signals underlying a cognitive process in the dorsal premotor cortex

Román Rossi-Pool[a,1], Jerónimo Zizumbo[a], Manuel Alvarez[a], José Vergara[a], Antonio Zainos[a], and Ranulfo Romo[a,b,1]

[a]Instituto de Fisiología Celular–Neurociencias, Universidad Nacional Autónoma de México, 04510 Mexico City, Mexico; and [b]El Colegio Nacional, 06020 Mexico City, Mexico

Contributed by Ranulfo Romo, February 19, 2019 (sent for review December 5, 2018; reviewed by Miguel Maravall and Adrián Ponce-Alvarez)

During discrimination between two sequential vibrotactile stimulus patterns, the primate dorsal premotor cortex (DPC) neurons exhibit a complex repertoire of coding dynamics associated with the working memory, comparison, and decision components of this task. In addition, these neurons and neurons with no coding responses show complex strong fluctuations in their firing rate associated with the temporal sequence of task events. Here, to make sense of this temporal complexity, we extracted the temporal signals that were latent in the population. We found a strong link between the individual and population response, suggesting a common neural substrate. Notably, in contrast to coding dynamics, these time-dependent responses were unaffected during error trials. However, in a nondemanding task in which monkeys did not require discrimination for reward, these time-dependent signals were largely reduced and changed. These results suggest that temporal dynamics in DPC reflect the underlying cognitive processes of this task.

behaving monkeys | dorsal premotor cortex | temporal signals | context-dependent signals | ramping activity

Our ability to anticipate the occurrence of future events is crucial when performing many cognitively demanding behaviors. For example, the benefits of anticipating the arrival of sensory inputs can be decisive in our perceptual behavior (1–3). In this way, neural circuits engaged in cognitive processes of this type would profit from employing temporal signals. Thus, the timing information contained in those signals may then constitute a mechanism to anticipate future task events. In fact, during experiments it is common to find neurons that display noteworthy temporal dependencies in their firing rate (4–9). In particular, a large proportion of the individual neurons from the frontal lobe cortices exhibit intricate time-dependent responses that mesh in myriad ways with stimulus identity and decision outcomes during behavioral tasks (4, 10–12). However, individual neurons must be reflecting a more widespread response across the network; temporal signals that represent anticipation of task events and stimulus identity must be coded at the population level. Recently, these neuronal population signals from the frontal lobe cortex were studied employing methods that reduced the dimensionality of network dynamics (11, 13). These methodological approaches facilitated the recognition of latent population responses during cognitive tasks (14–17). Notably, large differences between the population variance related to purely temporal signals and task parameter coding were observed (11, 13). Markedly, even if the tasks examined were completely different and employed two types of animal models, the temporal signals always captured more than 65% of the total variance. These results indicate that temporal signals occupy a central role during the execution of any behavioral task.

Here, to further investigate the temporal responses in single units and neuronal population, we employed the network activity recorded in dorsal premotor cortex (DPC) during a temporal pattern discrimination task (TPDT) (18, 19). Monkeys were trained to report whether the temporal patterns of two vibrotactile stimuli (P1 and P2) of equal mean frequency were the same or different (Fig. 1*A* and *SI Appendix*) by pressing one of two push-buttons (pbs). In two prior works, we studied the coding capacity of DPC single neurons (18) and population responses (19). In the first work, we showed that DPC neurons coded the stimulus patterns as broader categories and signaled them during the working memory, comparison, and decision periods of the TPDT. Furthermore, neurons exhibited mixed selectivity (20) and an extreme heterogeneity in their coding dynamics (21, 22). In our second work, we showed that this heterogeneous population activity can be condensed into two major coding components: one that persistently represented in working memory both the first stimulus identity and the postponed informed choice, and another that transiently coded the initial sensory information and the result of the comparison between the two stimuli. These dynamics, hidden in the neuronal coding heterogeneity, emerged in the DPC population response.

An important hypothesis is that the temporal signals should adjust to different cognitive contexts. Here, we tested this conjecture employing single-unit and population methodological approaches. First, focusing on the cognitively demanding TPDT, we compared the variance related to coding against time-dependent variance, using both single DPC neurons and population average. In the two cases, the results were analogous: the proportion of variance related with timing is much higher than that associated with task parameter coding. This means that temporal dynamics is responsible for the

Significance

When trained monkeys discriminate between two sequential vibrotactile stimulus patterns, neurons in the dorsal premotor cortex (DPC) code current and remembered inputs and the commands expressing the decision report. Additionally, responses of these neurons and neurons with no coding responses also reflect the timing of the task sequence. What is the cognitive relevance of these time-dependent signals? We show that time-dependent signals reflected the temporal sequence of the task during both hits and error trials but diminished or disappeared during a nondemanding cognitive task that did not require discrimination for reward. Also, strong links were detected between neuronal population and individual neurons' time-dependent signals. These time-dependent responses may function as the substrate network dynamics on which task coding components emerge.

Author contributions: R.R.-P. and R.R. designed research; M.A., A.Z., and R.R. performed research; R.R.-P., J.Z., and J.V. analyzed data; R.R.-P. and R.R. supervised all stages of the study; and R.R.-P. and R.R. wrote the paper.

Reviewers: M.M., University of Sussex; and A.P.-A., University Pompeu Fabra.

The authors declare no conflict of interest.

Published under the PNAS license.

Data deposition: Neuronal data related to this paper is available at https://drive.google.com/open?id=1zpqqOZm2bl0IGWSWLki29W0me6x7B6Ow.

[1]To whom correspondence may be addressed. Email: romanr@ifc.unam.mx or rromo@ifc.unam.mx.

This article contains supporting information online at www.pnas.org/lookup/suppl/doi:10.1073/pnas.1820474116/-/DCSupplemental.

Published online March 27, 2019.

Downloaded at Instituto de Biotecnología/UNAM on October 20, 2020

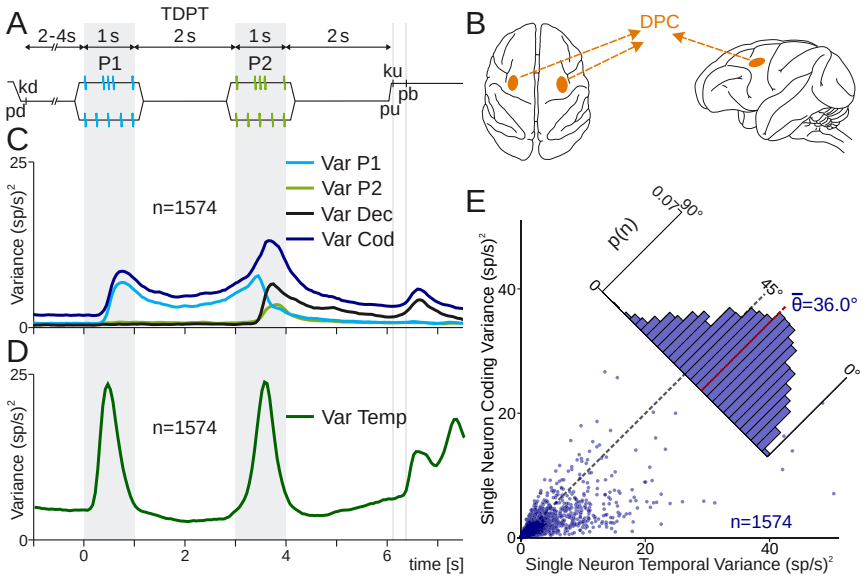

Fig. 1. Temporal pattern discrimination task (TPDT), single DPC neuron, and population variances. (*A*) Trial sequence of events. The mechanical probe is lowered (pd), indenting the glabrous skin of one fingertip of the right restrained hand; the monkey places its free hand on an immovable key (kd). After a variable prestimulus period (uniformly distributed from 2 to 4 s), the probe vibrates, generating one of two possible stimulus patterns [P1, either grouped (G) or extended (E); 1 s duration; mean frequency of 5 Hz]; after a first delay (2-s length, from 1 to 3 s) between P1 and P2, the second stimulus is delivered, again either of the two possible patterns (P2, either G or E; 1-s duration; mean frequency of 5 Hz); after a second fixed delay (2-s length, from 4 to 6 s) between P2 and pu, the monkey releases the key (ku) and presses the push-button (pb) to indicate whether P1 and P2 were the same or different (P2 ≠ P1). (*B*) Top (*Left*) and lateral (*Right*) views of the brain. Dark orange spots mark the location of the dorsal premotor cortex (DPC). Single DPC neurons were recorded from both hemispheres, while trained monkeys performed the TPDT. (*C*) Population instantaneous coding variance (Var_{COD}, blue, *SI Appendix*, Eq. **S1**), P1 variance (Var_{P1}, cyan trace), P2 variance (Var_{P2}, light green trace), and decision variance (Var_{DEC}, black trace). (*D*) Population instantaneous temporal variance (Var_{Temp}, green trace). (*E*) Single-neuron temporal variance (*x* axis, *SI Appendix*) is plotted against single-neuron coding variance (*y* axis, *SI Appendix*). Each dot corresponds to one neuron (n = 1,574). Diagonal line (45°) indicates equality between both measures. *Inset* histogram show angular distributions for the population (<θ> = 36.0°). In general, $SNVar^{i}_{Temp}$ is higher than $SNVar^{i}_{Cod}$.

large proportion of DPC firing rate fluctuations during the TPDT. In addition, we identified several DPC neurons with pure temporal responses. These responses also proved to be heterogeneous. Furthermore, we focused on the pure temporal signals that emerged from the DPC population. Most of the population variance was captured by these pure temporal components. These signals were engaged during relevant periods of the task: they reflected stimulus arrival and button presses, and had ramping activity during delays.

To further address our hypothesis, we investigated the role of these temporal signals in two different cognitive contexts. First, when the monkeys performed the TPDT and after during a nondemanding variation of the task [light control task (LCT)]. During this control task, no parameter encoding was found in single neurons and population dynamics. Notable, the time-dependent signals observed in the TPDT reduced their intensity or completely vanished during this nondemanding task. Additionally, the temporal variance was diminished in single-unit responses and in their population average. Several temporal neurons reflected this decline in their temporal responses. These results show that pure temporal responses were bound to the cognitive processes of the TPDT. Second, we focused on the relevance of the temporal responses during error trials. Noteworthy, temporal variance remained unaffected in both single neurons and population average during the animals' hit and error responses. These findings support the idea that the temporal-dependent signals code the temporal sequence of this task. Collectively, our results indicate that time-dependent signals observed in both levels, single units and population dynamics, could be interpreted as a necessary substrate on which the coding responses can develop to reach a decision during the TPDT.

Results

Previously, we identified and classified single neurons associated with relevant task parameter coding during the TPDT (ref. 18 and *SI Appendix*, Fig. S1 *A–L*). DPC neurons (Fig. 1*B*) exhibited a high heterogeneity among their responses during the TPDT. Additionally, several single units coded more than one task parameter throughout the task. This is illustrated in *SI Appendix*, Fig. S1, where we display 12 DPC neurons that coded different task parameters (P1, decision and class identity). Most of these neurons showed mixed selectivity in their coding responses (18, 20). We then condensed these heterogeneous single-unit responses into two major population signals that built an elegant and compact solution for the task, consistent with the monkeys' psychophysical performance (19).

Here, to measure the response's variability associated with task parameters coding, we calculated the population instantaneous coding variance during the TPDT (Var_{COD}, *SI Appendix*; Fig. 1*C*, blue trace). This metric quantified the firing rate fluctuations among classes and neurons at each time point. Clearly, time bins in which more neurons code task parameters usually give rise to higher instantaneous coding variance. Additionally, we calculated the population variance associated with each task parameter: P1 (Var_{P1}, *SI Appendix*; Fig. 1*C*, cyan trace), P2 (Var_{P2}, *SI Appendix*; Fig. 1*C*, light green trace), and decision period (Var_{Dec}, *SI Appendix*; Fig. 1*C*, black trace). In a previous work (18), we quantified the coding dynamic as the percentage of cells that coded each task parameter. Notably, those coding dynamics closely resembled the specific task parameter variances observed here. This means that there was a close relationship between the number of neurons coding a task parameter and the population coding variance associated with it. Notice that before the arrival of P1 (prestimulus period), there is no task parameter to be coded. Thus, one could expect that the population variance associated with each task parameter should be zero. Nevertheless, all of the traces shown in Fig. 1*C* exhibit a positive value before P1. This nonzero instantaneous variance observed during the prestimulus period could be interpreted as an estimate of the basal variances associated with residual fluctuations. When each type of variance is higher than its basal value, these larger fluctuations must be associated with task parameter coding.

Population and Single-Unit Temporal Variance During the TPDT. We wondered how much population variance could be associated with temporal dynamics during the TPDT. To quantify this, we calculated the population instantaneous temporal variance with respect to its mean response (Var_{Temp}, *SI Appendix*; Fig. 1*D*). At each time bin, Var_{Temp} quantifies the quadratic square sum among the neuron's responses of the difference between their mean firing rates for each time bin [$r^{i}(t)$] and mean firing rates across the whole task

Downloaded at instituto de Biotecnologia/UNAM on October 20, 2020

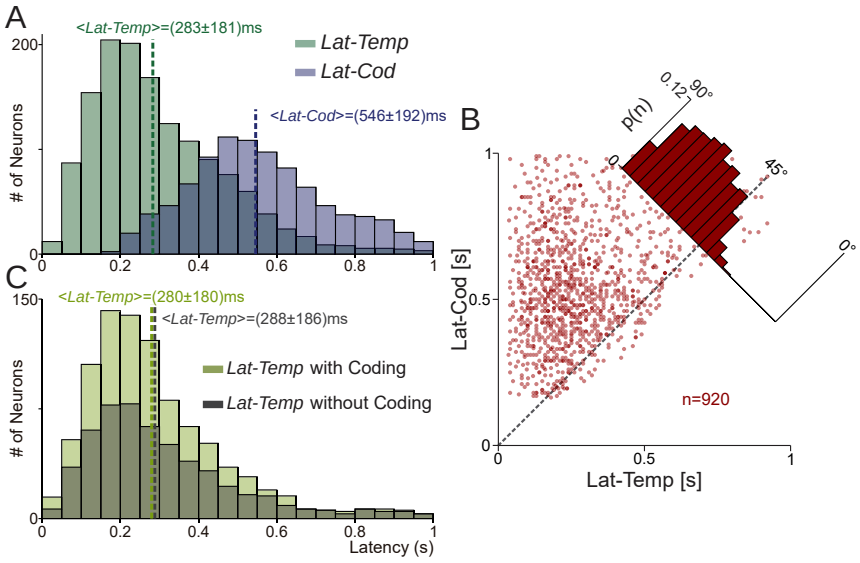

Fig. 2. Temporal and coding latency variances. (*A*) Latency distribution for neurons with temporal (green; n = 1,436) or coding (blue; n = 946) variance statistically different from their basal values during P1. In general, pure temporal signal ($<Lat_{Temp}>$ = 283 ± 181 ms) appeared before coding signals ($<Lat_{Cod}>$ = 546 ± 192 ms). (*B*) Neurons with significant latencies of temporal and coding variances (n = 920). Lat_{Temp} (x axis) is plotted against Lat_{Cod} (y axis). Each dot corresponds to one neuron. Single-neuron latencies were higher for coding than for temporal variances. (*C*) Latency distributions of temporal variance for neurons with significant Lat_{Temp} and Lat_{Cod} (n = 920; light green) and for neurons with only significant Lat_{Temp} (n = 516; dark green). Latency distributions are statistically the same in both groups ($<Lat_{Temp}>$ = 280 ± 180 ms vs. $<Lat_{Temp}>$ = 288 ± 186 ms). Response temporal latencies were very much alike for neurons with significant temporal and coding responses and for neurons with only significant temporal signals.

(^{i}, from −1 to 7.5 s). Whenever the mean population activity departs from its mean value, the temporal variance will increase. Remarkably, the instantaneous temporal population variance was much higher than the coding variance at any time bin (Fig. 1*C* vs. Fig. 1*D*). The same effect was observed using the temporal population fluctuation $Fluc_{Temp}$ computed with respect to the mean basal firing rate (*SI Appendix*, Fig. S2*A* and Eq. **S6**). Hence, most of the population variance in firing rate over the extent of a trial corresponded to variability across the sequential events of the task rather than across classes. Even though $Fluc_{Temp}$ was highest at stimulus arrival, it exhibited large values during both working memory (from 1 to 3 s) and postponed decision (from 4 to 6 s) delay periods. Additionally, Var_{Temp} and $Fluc_{Temp}$ displayed high values after pb presses.

To further study temporal variance, we focused on single-neuron responses. For each unit, we compared the variance associated with parameter coding ($SNVar^i_{COD}$) with the temporal variance ($SNVar^i_{Temp}$) during the whole task period (from −1 to 7.5 s). On one hand, $SNVar^i_{COD}$ measures the variance of the firing rate among classes from each individual cell (*SI Appendix*, Eq. **S7**). On the other hand, $SNVar^i_{Temp}$ computes the average temporal variance for each neuron across the whole task (*SI Appendix*, Eq. **S8**). Note, in these single-neuron metrics (Fig. 1*E*), we averaged across time bins for each unit, whereas in Fig. 1*D* we averaged across neurons for each time bin. Each point in Fig. 1*E* represents one neuron response, and the position in the plot was defined by $SNVar^i_{Temp}$ (x axis) and $SNVar^i_{COD}$ (y axis). In concordance with the results observed in Fig. 1*D*, individual neurons displayed higher values of $SNVar^i_{Temp}$ than $SNVar^i_{COD}$. Hence, the mean value of the angular distributions was $<\theta>$ = 36.0° (Fig. 1*E*, red dotted line), which means that most of the neurons were closer to the temporal than the coding axis. Analogous results were found computing the single-neuron temporal fluctuation ($SNFluc^i_{Temp}$, *SI Appendix*, Eq. **S9**) with respect to their mean basal firing rate (from −1 to 0 s, *SI Appendix*, Fig. S2*B*). Looking at the distribution shown in Fig. 1*E* and *SI Appendix*, Fig. S2*B*, we can see that there were no neurons with coding variance only. Thus, it is unlikely to find cells with significant task parameter coding and where the firing rate curves cancel out when averaged over trials of different classes.

Temporal Versus Coding Latencies. We wondered whether the pure temporal responses increased earlier than the task parameter coding variances. For each neuron, we quantified the time bin at which the temporal and the coding variance increased significantly with respect to its basal value during P1 (from 0 to 1 s). These time bins defined two different latencies: Lat_{Temp} and Lat_{Cod}. Fig. 2*A* shows the latency distributions for Lat_{Temp} and Lat_{Cod}. During P1, more neurons displayed a significant increase in the temporal variance (n = 1,436; 91.2%) than in the coding response variance (n = 946; 60.1%). Importantly, the temporal signals emerged before than the coding signals (Fig. 2*A*, $<Lat_{Temp}>$ = 283 ± 181 ms vs. $<Lat_{Cod}>$ = 546 ± 192 ms). Thus, pure temporal responses could act as a precursor for task parameter coding. Previously, similar response and coding latencies were found using a completely different approach (18). In addition, most of the neurons with significant Lat_{Cod} exhibit significant Lat_{Temp} (n = 920). For each of these neurons, we plotted Lat_{Temp} (Fig. 2*B*, x axis) against Lat_{Cod} (y axis). In general, the single-neuron temporal responses appeared before the coding signals. This was further documented by dividing the temporal latency (n = 1,436) during P1 into two groups: one with significant coding latency (n = 920) and another without coding (n = 516). Notably, we show that Lat_{Temp} distributions were statistically the same for these two groups of neurons (Fig. 2*C*). This means that the temporal signals from single neurons emerged independently of whether the neurons significantly encoded task parameters.

Temporal Responses of Single DPC Neurons. We employed $SNVar^i_{Temp}$ and $SNFluc^i_{Temp}$ to identify neurons with strong temporal signals. Fig. 3 and *SI Appendix*, Fig. S3 illustrate typical temporal activity of single DPC neurons. Clearly, all of these neurons' responses are not essentially related with task parameter coding. Most of these neurons do not code any task parameters during the task. These neurons exhibit response dynamics that vary over time, but not in a manner that encodes task variables. Furthermore, DPC neurons exhibited a large repertoire of neuronal responses associated with pure temporal dynamics. Some of these neurons were involved in stimulus arrival with positive (Fig. 3*F* and *SI Appendix*, Fig. S3 *B*, *D*, and *F*–*H*), negative (Fig. 3*E* and *SI Appendix*, Fig. S3 *C* and *I*), or mixed (Fig. 3*C* and *SI Appendix*, Fig. S3*A*) responses. Another group of neurons was associated with ramping activity during the delay periods (Fig. 3 *A*, *B*, and *D* and *SI Appendix*, Fig. S3 *A*, *F*, *G*, and *I*). Finally, another overlapping group of neurons was related to temporal responses after pb (Fig. 3 *A*, *D*, and *F* and *SI Appendix*, Fig. S3 *A*, *C*–*E*, and *G*–*I*). Interestingly, there were neurons that only respond during pb,

Downloaded at instituto de Biotecnologia/UNAM on October 20, 2020

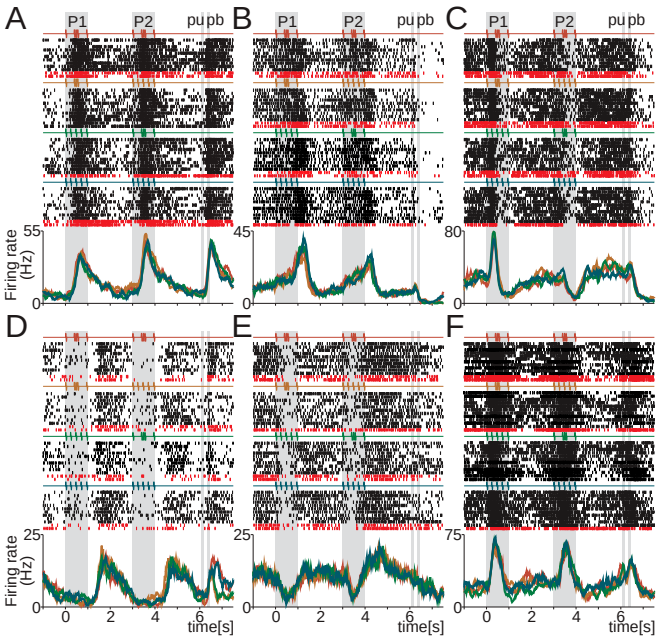

Fig. 3. Single DPC neurons with notable temporal activity during the TPDT. (*A–F*) Raster plots of six temporal exemplary neurons sorted according to the four possible classes. Each row of ticks is one trial, and each tick is an action potential. Trials were randomly delivered and were sorted by class afterward (only 10 out of 20 trials per class are shown). Correct and incorrect trials are indicated by black and dark red ticks, respectively. Traces below the raster plots are average per-class firing rates [peristimulus time histograms (PSTHs)] for each temporal neuron. Each color refers to one of the four possible classes: G-G (red); G-E (orange); E-G (green); and E-E (blue). Neurons exhibit pure temporal dynamics without coding any task parameter.

independently of the decision outcome (*SI Appendix*, Fig. S3*E*). Therefore, even for temporal signals, the complexity and diversity of responses was broad. To handle this temporal heterogeneity, we applied dimensional reduction methods of the population activity to reveal temporal latent signals.

Population Principal Components Exhibit Temporal Signals. Such dimensional reduction was done using a condensed population-level representation of the data, based on the state space of neural responses. The state of the DPC population was represented by a point in a n-dimensional (n = 1,574) space of firing rate responses. Each dimension, at each time point, corresponded to the firing rate of one neuron. The dynamics of the network was described by combining 1,574 firing rates mostly recorded separately (15, 19, 23–25). As neurons' activity evolves over time, the point moves through the space, forming a trajectory that represents the response of the population.

We first employed principal-component analysis (PCA) to identify a lower dimensional subspace underlying the DPC network dynamics (26). The covariance matrix used for PCA was quantified from the whole task (*SI Appendix*, Eq. **S10**). Even if PCA could be used to reduce the dimensionality of the dynamics, the new subspace was deficient in highlighting temporal signals or task parameter dynamics (*SI Appendix*, Fig. S4). Overall, PCA gave a much more complex picture of the population dynamics, dominated by strong temporal signals mixed with parameter coding responses. The first five PCs were ordered by the amount of explained total variance (ETV) (*SI Appendix*, Eq. **S15**). For each PC, we displayed the population activity projections sorted by classes. In general, PCs exhibited strong temporal signals that dominate the population dynamics. Notice that the fifth PC displayed a ramping temporal activity during the first (from 1 to 3 s) and second (from 4 to 6 s) delay periods (*SI Appendix*, Fig. S4). Even though PCA was a fully unsupervised approach, it was possible to recognize almost pure temporal responses such as the fifth PC.

Population Temporal Dynamics. Then, to focus on the task timing signals from the population activity, we applied demixed PCA (dPCA) (13). Employing dPCA, we were able to extract a low-dimensional subspace more sensitive to the pure temporal responses. Contrary to other approaches, dPCA split the population variability associated with different task parameters employing marginalized matrices. Here, we center our analysis on decomposing the population temporal responses. In a previous study (19), we studied the population components associated with coding task parameters. Fig. 4*A* displayed the first five temporal dPCs that captured most of the variance during the task. To calculate the temporal dPCs, we applied a temporal marginalization of the population activity. Then, we averaged the responses of all of the trials without considering class identity. The temporal dPCs were optimized to maximize (*SI Appendix*, Eq. **S13**) the ETV (*SI Appendix*). Due to this optimization, the population activity of the four classes overlapped when they were projected onto this axis (Fig. 4*A*). We selected class E-G (c3, green trace) to be on top of the other four traces.

The first temporal dPC displayed an intense response during P1 and P2 periods (Fig. 4*A*). This component captured 23.9% ETV and represented the most relevant demixed signal. We remark that there was no component with higher variance associated with task parameter coding. This means that the sensory stimulation gave rise to strong temporal dynamics that underlay the coding of the stimulus pattern. Notably, second temporal dPC (Fig. 4*A*) exhibited a strong temporal response immediately after the pb press. This signal contrasted highly with the first dPC: It was less involved in stimulus presentation and more engaged with a population dynamic after the animals reported their decisions. Although this component was related with the last period of the trial, it explained 13.5% of the total variance. This signal was presumably linked with the strong decision signal that emerged after pb (ref. 18 and Fig. 1*C*). By construction, this second temporal dPC was orthogonal to the first dPC. This means that the sensory temporal signal (first dPC) was independent of the signal after pb presses (second dPC). The third temporal dPC projections showed a mixed dynamic with sensory and persistent responses (Fig. 4*A*, 9.5% ETV). It exhibited a stepped change during P1 followed by persistence during the first delay; after that, it showed another stepped response during P2, again followed by persistence during the second delay between P2 and pu. Remarkably, the neural projections onto the fourth temporal dPC presented a temporal pacemaker during both delays (Fig. 4*A*). This component, which explained 8.25% ETV, begins in each stimulus period with a negative value and reaches peak values during P1, P2, and pb. We notice the resemblance between this component and the fifth PC shown in *SI Appendix*, Fig. S4. We hypothesize that this pacemaker component could act as an internal time estimator that allows the network to predict the arrival of relevant events during this cognitively demanding task. Last, the fifth temporal dPC showed a ramping temporal activity during the first delay, and with markedly smaller one during the second delay (5.84% ETV).

Task Dimensionality and Temporal Signals. Subsequently, we studied the dimensionality of the population across the TPDT. We wonder: How many dimensions or components were necessary to explain the network dynamics? Moreover, how many of these relevant dimensions were pure temporal signals? To estimate quantitatively the dimensionality, we used both dPCA and PCA. We constructed a noise population covariance matrix that only included single-trial variability (X_{noise}; *SI Appendix*, Eq. **S16**). Using this noise

Downloaded at Instituto de Biotecnologia/UNAM on October 20, 2020

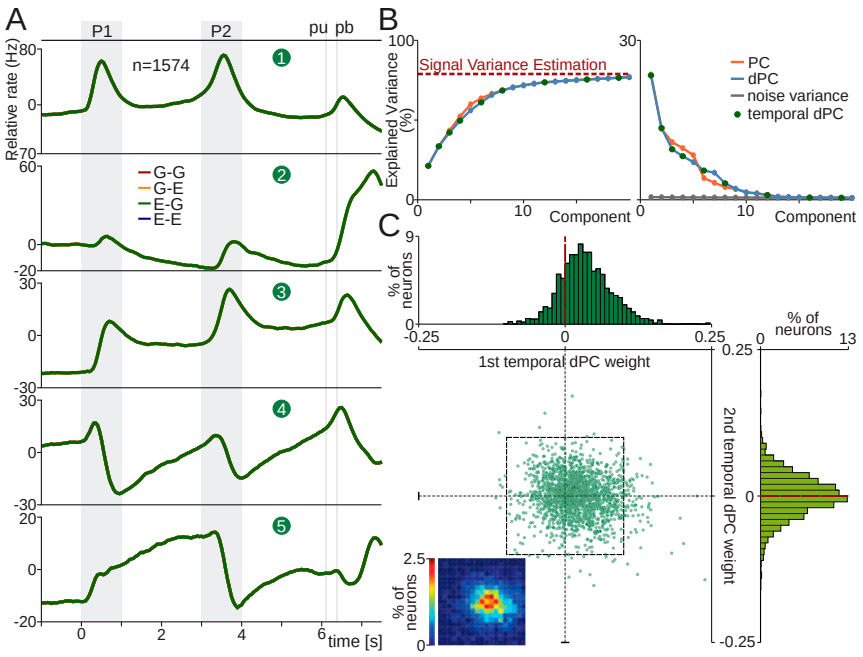

Fig. 4. DPC population temporal signals during the TPDT. (*A*) dPCA was applied to the temporal marginalized covariance matrix obtained from the TPDT. Population activity, sorted by classes, was projected onto the temporal dPCs. Temporal dPCs were ordered according to their explained total variance (ETV). First five temporal dPCs: first ETV, 23.9%; second ETV, 13.5%; third ETV, 9.5%; fourth ETV, 8.25%; fifth ETV, 5.84%. (*B*) Cumulative sum of explained signal-plus-noise variance (*Left*, ESNV). The dashed red line shows an estimate of the fraction of task-related variance. ESNV per component (*Right*). The red traces correspond to PCs; the blue traces are for dPCs. The gray trace represents the percentage of noise variance explained by the dPCs. The green points indicate which dPCs are temporal. (*C*) Central graph: For each neuron, we use its first and second temporal-dPC weights to plot its location on the plane. Heat-map *Inset* (*Bottom Left*) shows the joint weight distribution (20 × 20 grid, 0.01 bin side length, corresponds to black dashed square; color scale goes from 0 to 2.5%). First temporal-dPC weight distribution tends to positive values: $\mu = 0.028$; $\sigma = 0.035$ (*Top*). Second temporal-dPC weights are equally distributed for positive and negative values: $\mu = 0.0001$; $\sigma = 0.029$ (*Right*).

covariance matrix, we estimated the fraction of the "signal-plus-noise" variance that was related to noise. The percentage of variance that was related with signal and not with noise ($1 - Var_{Noise}$) determined the red dashed line in Fig. 4*B*. In Fig. 4*B*, *Left*, we compared the cumulative explained variance for PCs and dPCs. Using both techniques, we obtained analogous results: Few components are necessary to reach the signal variance estimation. In addition, the dimensionality of the population responses estimated with dPCA was equivalent to the one calculated with PCA. Consistently, in Fig. 4*B*, *Right*, we showed that there were only few dPCs that captured higher explained signal-plus-noise variance (ESNV) than noise variance (*SI Appendix*). This means that the inherent population fluctuations (noise) projected onto the dPCs captured significantly less variance, but only compared with the first few components. Keep in mind that there were 1,574 possible dimensions. However, few components are enough to explain the relevant dimensions of the network. We calculated that around 12 dPCs are at least 50% above inherent noise variance. This number estimates the dimensionality of the population responses during the TPDT. In a previous study, this approach was applied to estimate the dimensionality of the dynamic in a frequency discrimination task (11).

Most notably, 7 out of 12 relevant dimensions are pure temporal signals (green dots in Fig. 4*B*). Then, a large proportion of the dimensions of the network are only related to time. Even more, the first four dimensions, which captured 55.15% ETV (48.1% of ESNV), are temporal signals. These results are strong evidence that temporal signals are a relevant part of the network response and that they might act as a substrate for coding dynamics.

A Common Anatomical Substrate for Temporal Signals. We speculated on whether there were separate categories of neurons involved in different temporal components. To explore this possibility, we plotted for each neuron their first and second temporal-dPC weights (Fig. 4*C*). We did not identify evidence for separate clusters of neurons. Even if we showed individual neurons with responses that resembled each of these two components (*SI Appendix*, Fig. S3 *G* and *F* for first dPC, and *SI Appendix*, Fig. S3*E* for second dPC), this was not the general trend. Analogous results were observed when we plotted the weights of other temporal dPCs. Thus, although these temporal signals can be read out independently, they were built from the same anatomical substrate. Analogous results were found in previous studies for other types of components and tasks (11, 13, 19, 27).

Additionally, we calculated the distribution of the weights given by this dPCs for each of the 1,574 neurons. Note that the weight distribution for the first temporal dPC (Fig. 4*C*, *Top*) exhibited a bias to positive values ($\mu = 0.028$; $\sigma = 0.035$). This means that the sensory temporal signals were in general positive (excitatory). Although it was possible to identify negative (inhibitory) temporal sensory neurons (Fig. 3*E* and *SI Appendix*, Fig. S3 *C* and *I*), they were not as abundant as the positive sensory neurons (Fig. 3*F* and *SI Appendix*, Fig. S3 *B*, *D*, and *F*–*H*). However, the weights given by the second temporal dPCs (Fig. 4*C*, *Right*) were equally distributed for both positive and negative values. These results agree with previous studies that found that coding components behave like zero-centered Gaussians distributions (11, 13, 19). Similar distributions were found for higher-order temporal dPCs. Thus, except for the first dPC, the other components exhibited zero-centered weight distributions. Furthermore, the unimodal weight distributions also suggested that there was not a clear division between single neurons that might have participated in temporal signals from those neurons that did not.

Population and Single-Unit Temporal Variances During the LCT. To further quantify whether the DPC temporal signals depended on the animal's task performance, many of the neurons ($n = 462$) were also tested in a control variant of the TPDT. In each trial, the monkeys received identical stimuli as in the TPDT, but the correct answer was indicated by a continual visual cue (Fig. 5*A*). We refer to this task as LCT.

As before, we calculated the population instantaneous coding variance during the LCT (Var_{COD}, *SI Appendix*; Fig. 5*B*). Analogously, we calculated the population variance associated with each task parameter: P1 (Var_{P1}; Fig. 5*B*), P2 (Var_{P2}), and decision (Var_{Dec}). Under the LCT, the population coding variance was no longer related to the identity of the stimulus pattern or the decision report (Fig. 5*B*). Accordingly, the population coding variance stayed constant and equal to its basal value during the whole task. These results agree with the coding dynamics of individual

Downloaded at instituto de Biotecnologia/UNAM on October 20, 2020

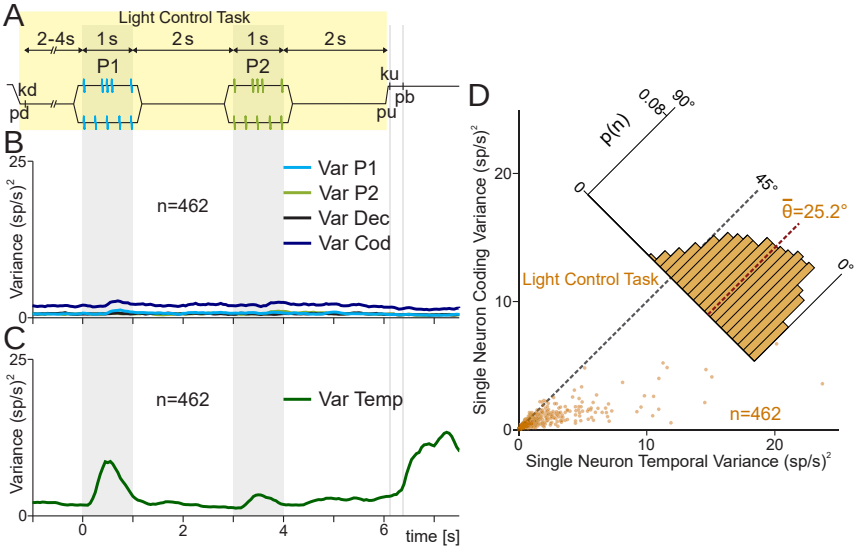

Fig. 5. Single DPC neuron and population variances during the LTC. (*A*) During LCT, events proceeded exactly as in Fig. 1*A*, except that when the probe touched the skin, the correct pb was illuminated. The light was turned off after pu, triggering the pb press. Thus, stimuli and movements were identical to the TPDT, but were cued by visual stimuli. Performance in the LCT was 100% across classes. (*B*) LCT population instantaneous variances: Var_{COD} (blue, *SI Appendix*); Var_{P1} (cyan trace), Var_{P2} (light green trace), and Var_{DEC} (black trace). Note the marked differences with Fig. 1. (*C*) LCT population instantaneous temporal variance (Var_{Temp}, green trace). (*D*) Single-neuron temporal variance during LCT (*x* axis, *SI Appendix*) is compared against single-neuron coding variance during LCT (*y* axis). Each dot corresponds to one neuron ($n = 462$). *Inset* histogram show angular distributions for the population ($\langle\theta\rangle = 25.2°$). During the LCT, $SNVar^i_{Temp}$ is much higher than $SNVar^i_{Cod}$.

neurons observed before (18). Even though stimuli and final movements were the same as in the TPDT, no coding variance modulation was observed. Thus, the population coding variance increased above its basal state only when the task demanded it.

Again, we wonder how much population variance could be associated with temporal dynamics. We remark that although coding variance was not modulated, the firing rate of the neurons evolved during the LCT. To further show this, we quantified the population instantaneous temporal variance (Var_{Temp}, *SI Appendix*, Fig. 5*C*) during the LCT. In contrast to coding variances, Var_{Temp} evolved during the LCT. Thus, fluctuations in firing rate are only involved in timing of the task events. However, the values Var_{Temp} are not as high as during the TPDT (compare Fig. 5*C* with Fig. 1*D*). Thus, we could speculate that part of the temporal signals were still present during LCT, but other temporal dynamics diminished or disappeared. In addition, we compared the variance associated with coding ($SNVar^i_{COD}$) and temporal ($SNVar^i_{Temp}$) for each neuron during the LCT. Each dot in Fig. 5*D* represents one neuron during LCT ($SNVar^i_{Temp}$, *x* axis; $SNVar^i_{COD}$, *y* axis). In concordance, neurons displayed much higher temporal than coding responses. Coding variance remained at small values for all 462 neurons and the angular distribution was biased to small angles ($\langle\theta\rangle = 25.2°$; Fig. 5*D*).

Temporal Responses of Single Neurons in the TPDT vs. the LCT. Do the responses of single neurons undergo their own decrease in temporal variability during LCT? To quantify this, we chose neurons with high temporal variance during the TPDT that were also tested in the LCT. In Fig. 6 and *SI Appendix*, Fig. S5, we show typical DPC temporal activity under both task conditions. In concordance with the differences in Var_{Temp} between Figs. 1*D* and 5*C*, most of the temporal responses declined or vanished during LCT. Notably, even the sensory temporal signal during the stimulus arrival are diminished noticeably during the LCT (Fig. 6 and *SI Appendix*, Fig. S5 *A–C*). All ramping activity observed during the TPDT ceased (Fig. 6 *A* and *C* and *SI Appendix*, Fig. S5 *A–E*). Some of the temporal signals after pb presses remained during both task

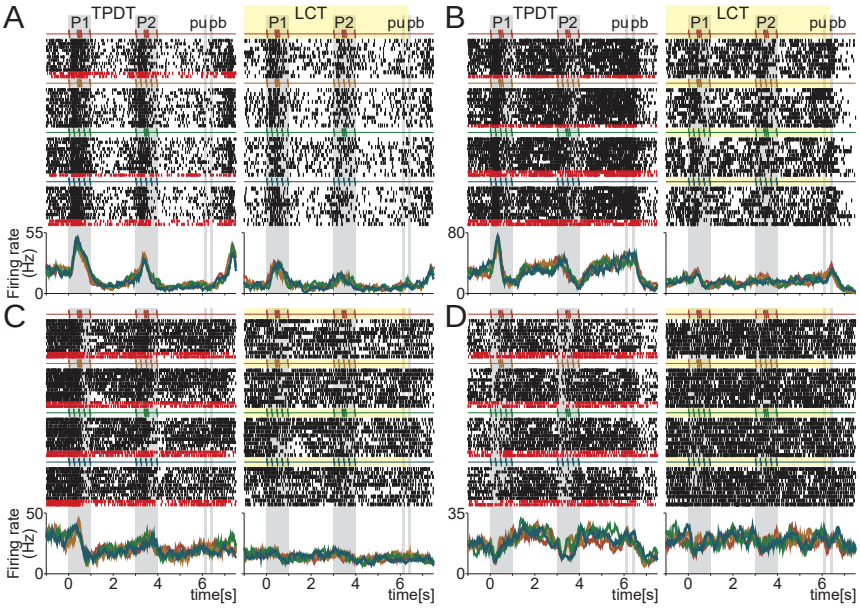

Fig. 6. Single DPC neurons with notable temporal activity compared between TPDT and LCT. (*A–D*) Raster plots of four temporal exemplary neurons tested in both conditions: TPDT (*Left*) and LCT (*Right*). Responses are sorted according to the four possible combinations of G and E stimulus patterns delivered during P1 and P2. Correct and incorrect (only in TPDT) trials are indicated by black and dark red ticks, respectively. Traces below the raster plots are average per-class firing rates (PSTHs) for each neuron and condition. Each color refers to one of the four possible stimulus combinations of G and E; the resulting four classes are c1 (G-G, red), c2 (G-E, orange), c3 (E-G, green), and c4 (E-E, blue). Note that these neurons are different from those shown in other figures.

Downloaded at instituto de Biotecnologia/UNAM on October 20, 2020

conditions (*SI Appendix*, Fig. S5 *D–F*). In summary, during the LCT, the temporal signals of individual neurons diminished or ceased, while the coding responses disappeared (18).

Population PCs During the LCT. To investigate whether population temporal signals depended on the cognitive context, we implemented the same population analysis to a subgroup of neurons (n = 462) recorded during TPDT and LCT. First, we applied PCA to the population response under each condition (*SI Appendix*, Fig. S6). We displayed the first five PCs during the TPDT for this subpopulation. We remark that although the number of neurons decreased from 1,574 to 462 (29.3%), the dynamics remained approximately the same (compare *SI Appendix*, Fig. S4 with *SI Appendix*, Fig. S6*A*). This suggests that network dynamics was robust and stable under changes in the number of neurons.

Next, we computed the PCs for the same group of neurons under the LCT (*SI Appendix*, Fig. S6*B*). Although the PCs did not show task-related coding, they exhibited prominent temporal responses. Moreover, all of the components appeared to be associated with the stimulus arrivals or the pb presses. Notably, the PCs' dynamics during delay periods are much weaker than in TPDT. Furthermore, the ramping temporal activity was no longer present under LCT.

Single-Neuron Temporal Variance Compared Between the TPDT and LCT. Based on the results shown in the previous three sections, we speculated that single neurons may diminish their temporal variance under a nondemanding cognitive task (LCT). To test this hypothesis, we compared $SNVar^{i}_{Temp}$ under both task variants. Each point in Fig. 7*A* was determined by the two values: the TPDT $SNVar^{i}_{Temp}$ (x axis) and the LCT $SNVar^{i}_{Temp}$ (y axis). In concordance, cells presented much higher temporal variance under the demanding task (TPDT) than the nondemanding task (LTC). Additionally, the distribution (Fig. 7*A*) was biased to small angles (<θ> = 27.5°). Similar results were found comparing $SNFluc^{i}_{Temp}$ for each task condition (*SI Appendix*, Fig. S7*A*). This is further evidence that several temporal signals were recruited only when the task was demanding enough.

Task Dimensionality and Temporal Signals During the LCT. We applied dPCA to obtain the temporal components optimized for the LCT population. Then, we estimated the dimensionality of the responses during LCT. In Fig. 7*B*, *Top*, we displayed the cumulative sum of total variance captured by the dPCs. We computed the fraction of the total population variance associated with the signal variance (red dashed line). Consistently, few components were enough to reach the estimated signal variance. Additionally, the first six components are pure temporal dPCs. In Fig. 7*B*, *Bottom*, we estimated ESNV from each LCT component and its fraction associated with noise (gray trace). Notably, only six temporal components were significantly above the noise variance estimate. This means that the dimensionality of the network dynamic diminished from 12 dPCs during the TPDT to 6 dPCs during the LCT. Similar results were found using the same neurons (n = 462) to calculate the dimensionality of the network under both task conditions (*SI Appendix*, Fig. S6 *C* and *D*). This dimensionality reduction was due to two factors: the lack of coding dynamics and the decline of temporal signals during LCT.

In Fig. 7*C*, we show the temporal dPCs optimized for the LCT activity. Comparing the temporal dPC from TPDT and LCT, the persistent activity and the ramping responses of Figs. 4*A* and 7*D* were no longer present in Fig. 7*C*. This means that temporal signals are not equivalent in LCT and TPDT, except for those related to stimuli or pb presses. Nevertheless, the intensity of the

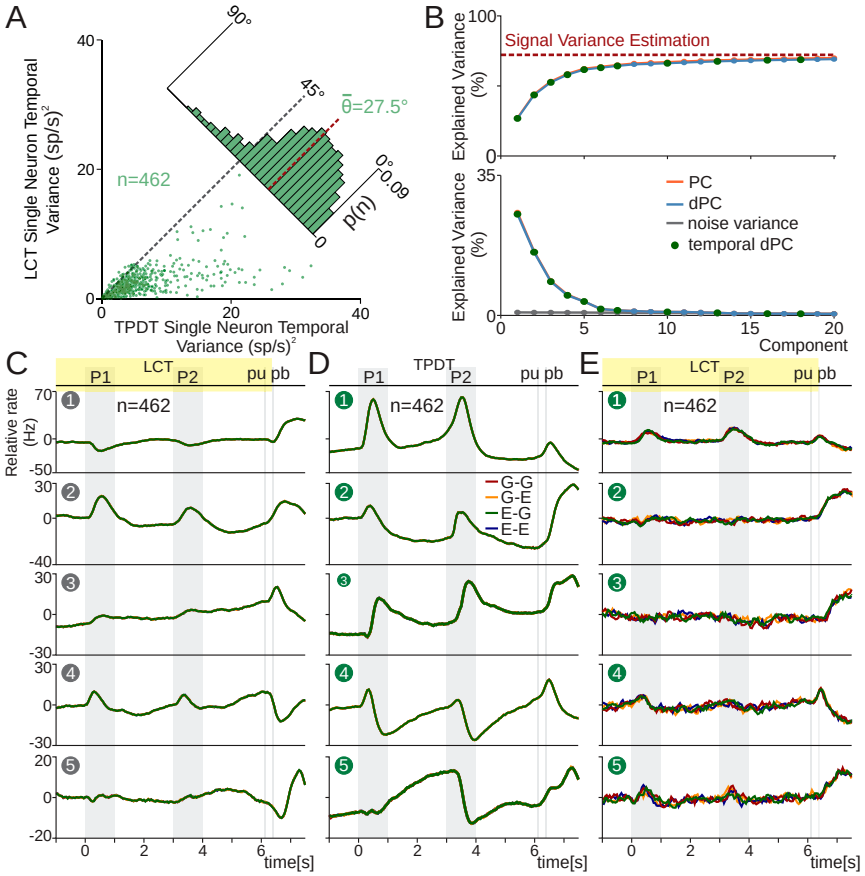

Fig. 7. DPC population temporal signals during the LCT. In this figure, we restricted our analysis to the neurons that were recorded during both TPDT and LCT (n = 462). (*A*) $SNVar^{i}_{Temp}$ in TPDT (x axis, *SI Appendix*) is compared with $SNVar^{i}_{Temp}$ in LCT (y axis). Each dot corresponds to one neuron tested in both conditions (n = 462). *Inset* histogram show angular distributions for the population (<θ> = 27.5°). $SNVar^{i}_{Temp}$ is much higher in TPDT than LCT. (*B*) Cumulative sum of the explained signal-plus-noise variance (ESNV) of the PCs and dPCs during LCT (*Top*). The dashed red line shows an estimate of the fraction of task-related variance. (*Bottom*) ESNV of PCs (red) or dPCs (blue). The gray trace represents the percentage of noise variance explained by each dPCs. The green points indicate the temporal dPC. (*C–E*) Population activity, sorted by class identity, was projected onto each dPC. Components were ordered by their explained total variance (ETV). The same y scale was used among projections to facilitate comparison. (*C*) First five temporal dPCs optimized for the LCT. First ETV, 30.5%; second ETV, 19.5%; third ETV, 10.6%; fourth ETV, 6.4%; fifth ETV, 4.3%. (*D*) dPCA was applied to the temporal marginalized covariance matrix obtained from the whole TPDT (n = 462). These signals are similar to those in Fig. 4*A*. First ETV, 25.1%; second ETV, 14.8%; third ETV, 10.3%; fourth ETV, 9.1%; fifth ETV, 6.4%. (*E*) LCT activity was projected into exactly the same axes than in *D*. Since dPCs were optimized for TPDT population activity, projections of LCT activity showed more fluctuations.

Downloaded at Instituto de Biotecnología/UNAM on October 20, 2020

sensory component clearly diminished during the LCT. The most plausible explanation is that as task parameter coding was not necessary during LCT, the temporal responses that supported this coding ceased or disappeared. Note that the first temporal dPC explained 30.5% of the total variance and was mainly associated with the signal after pb presses. Furthermore, the second dPC was involved with stimulus arrival and pb signal (19.5% ETV). Moreover, the absence of coding during LCT, except for the timing of the task events, entailed similar results when we used dPC or PC projections (compare Fig. 7*C* vs. *SI Appendix*, Fig. S6*B*).

Context-Dependent Temporal Signals. To examine the differences between TPDT and LCT temporal signals, we benefited from the 462 neurons recorded in both task conditions. We calculated the temporal dPCs, now restricted to only those neurons during TPDT. The results were presented in Fig. 7*D*. Again, as with PCA, the temporal dPCs of this subgroup of neurons (n = 462) matched those of the full population (Fig. 4*A*). Then, the number of neurons was reduced from 1,574 to 462, and the temporal components remained unaltered. On the other hand, when we used the TPDT temporal dPCs to project the LCT population activity, we observed a pronounced disappearance of most of the temporal signals (Fig. 7*E*). Thus, the same temporal axes were used to project the TPDT (Fig. 7*D*) and LCT (Fig. 7*E*) population activities. This analysis allowed us to compare between task conditions, the temporal signals that remained or disappeared within the components. Consistent with our previous result, the persistent and ramping responses calculated during the TPDT (Fig. 7*D*) were no longer present in LCT projections (Fig. 7*E*). However, the temporal responses observed after pb during TPDT, remained unaltered across all LCT projections. This is evidence that pb temporal signals are unconnected to those during the delays. All of these results agree with what was observed across the exemplary neurons (Fig. 6 and *SI Appendix*, Fig. S5). Collectively, our population findings suggest a close relationship between the temporal dynamics and task execution. These results are strong evidence that some temporal signals were only recruited when parameter coding was needed to solve the TPDT.

Population and Single-Neuron Temporal Variances During Hit and Error Trials. We wanted to determine to what degree the pure temporal signals in the DPC population predicted the monkeys' performance. We investigated whether the evoked temporal variance was somehow different between correct (hit) vs. incorrect (error) trials during the TPDT. For this, we computed (Var_{Temp}) during hit and error trials (Fig. 8*A*). We restricted this analysis to a subgroup of neurons with at least three error trials in each of the four classes (n = 547). Note that during LCT there were no error trials to analyze; the performance was consistently 100%; this reflects that this guided task was not cognitively demanding, which was part of the intended design.

Notably, Fig. 8*A* shows that Var_{Temp} evolved together during hit and error trials (the same conclusion was obtained employing $Fluc_{Temp}$; *SI Appendix*, Fig. S7*B*). In other words, at each time point, the quadratic distance between the population mean and the basal firing rate during hit and error trials was approximately the same. This means that it is impossible to use Var_{Temp} or $Fluc_{Temp}$ to predict the animals' choice. This result gave us a first suggestion that temporal responses were the same for error and correct choices. We then evaluated the error effect in temporal variance of single neurons. This was made by measuring the $SNVar^{i}_{Temp}$ for each cell during hit and error trials. Similar as we have done previously, on Fig. 8*B* we compared on the same plot the $SNVar^{i}_{Temp}$ associated with hit (x axis) and error (y axis) trials for each single neuron (n = 547). We found that $SNVar^{i}_{Temp}$ evoked by the two types of trials were statistically identical (Fig. 8*B*; $\langle\theta\rangle = 46.9 \pm 10.1°$). The same effect was observed when $SNFluc^{i}_{Temp}$ is compared in hit vs. error trials (*SI Appendix*, Fig. S7*C*). This means that it would also be impossible to differentiate between hit and error trials, based on the temporal variance of single DPC neurons.

Population Temporal Signals During Hit and Error Trials. Finally, we investigated the relationship between the population temporal signals and monkeys' behavior. For this purpose, we studied the differences between hit and error trials on the temporal dPCs. We constructed single-trial activity matrices by pseudorandomly selecting trials from all neurons. Then, we plotted the average and SD of repeated projections (1,000) of single-trial activity onto the temporal axis used in Fig. 4*A*. For error trials, we randomly chose one error trial per iteration for each neuron in each class. Since all neurons (n = 1,574) had at least one error trial per class, we employed the full population for this analysis. The average (solid lines) and SD (shading) of single-hit trial projections are shown in Fig. 8*C*. Note the similarity between the traces in Figs. 4*A* and 8*C*. In addition, the single-trial projection onto each temporal dPC produced small values of SD throughout the task.

Even if it is possible to think that an error in the temporal signal could contribute to an error report, this is not in agreement with our

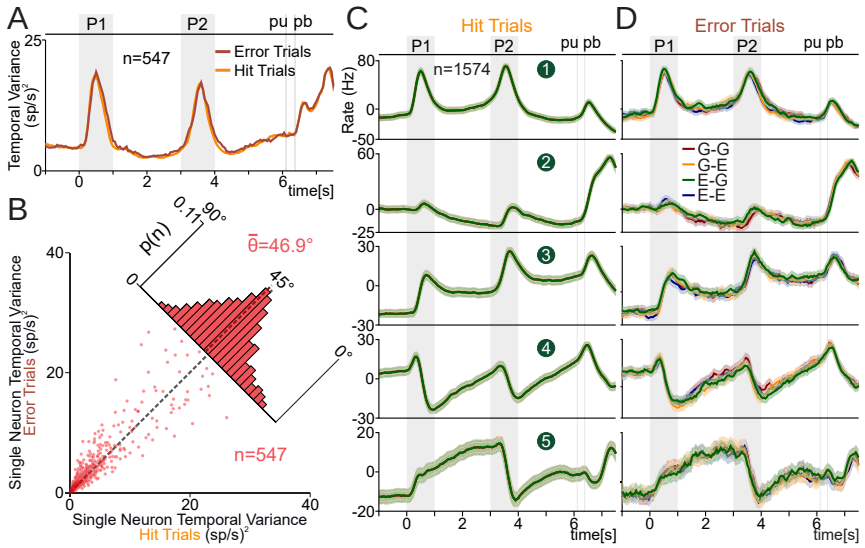

Fig. 8. DPC temporal signals during hit vs. error trials. (*A* and *B*) We restricted our analysis to the neurons (n = 547) with at least three error trials for each class. (*A*) Var_{Temp} (*SI Appendix*) for hit (red) and error (orange) trials. (*B*) $SNVar^{i}_{Temp}$ during hit trials (x axis) is compared against $SNVar^{i}_{Temp}$ during error trials (y axis). Each dot corresponds to one neuron (n = 547). *Inset* histogram show angular distributions ($\langle\theta\rangle = 46.9°$). $SNVar^{i}_{Temp}$ are statistically the same in hit and error trials. (*C*) Temporal dPCs, calculated with hit trials, were used to repeatedly project the population activity of single hit trials. First five temporal dPCs were ordered according to their ETV. Traces show the average (solid line) and SD (shading) for 1,000 hit trial projections. (*D*) The same temporal dPCs as for *C* (calculated with hit trails) were used to project the population activity in single-error trials. The solid lines and shadings were constructed in the same manner, but with error trial population activities.

Downloaded at Instituto de Biotecnología/UNAM on October 20, 2020

results. Clearly, there was a high correspondence between the temporal signals in error (Fig. 8*D*) and hit (Fig. 8*C*) trials. In general, our findings suggest that errors were not associated with the temporal signals. This finding is complemented by previous studies that have shown strong evidence that error trials were associated with task parameter miscoding (18, 28). We remark the notable differences between the temporal signals found in error trials (Fig. 8*D*) with the LCT temporal components (Fig. 7*C*). On one hand, a nondemanding task led to a decline in temporal responses (Fig. 7*C*). On the other hand, during error trials, the temporal signals remained unchanged (Fig. 8*D*).

Discussion

Previously, we showed that DPC codes the relevant task parameters of the TPDT. Here, we found that although a large percentage of DPC neurons were involved in coding dynamics, the variance related to coding task parameters was small in comparison with the size of temporal variance over time. We observed this by using both single-unit and population-averaged approaches. In both cases, the time-dependent responses showed higher variance than task parameter coding.

Contrary to the neuronal responses recorded in the active task (TPDT), during the control task (LCT), DPC neurons did not code task parameters. Furthermore, the only task-related responses that remained during LCT were some pure temporal fluctuations, but their variance were reduced in comparison with the TPDT. Again, this observation was corroborated using both single-unit and population-averaged approaches. Nevertheless, focusing on the error trials, the total amount of temporal variance was similar to hit trials. Then, fluctuations in firing rate related to time were not affected during the animals' errors. Thus, it is not possible to predict an error employing neither single neurons nor population temporal variance.

To extend our analyses to the neuronal population level, we employed dimensionality reduction methods (15, 23–25, 29). We found that the population dynamics were robust and stable despite the high variability in the single neuron's responses. Consistently, a recent study has shown that population responses are unaffected using multiunit threshold crossing activity instead of sorted individual neurons (30). Although PCA served to reduce the dimensionality of the data, most of the components did not reveal a useful representation of the data (13, 14). Consequently, we used dPCA to focalize on the temporal signals of the network responses (13). Thus, we split the whole DPC responses into a more tractable problem. Notable, although temporal dPCs are not linked to task parameter coding, their high explained variance suggested that they constituted a crucial element of task execution. Importantly, these temporal population signals were unaffected during error trials. However, previous studies have shown that coding signals noticeably changed during animals' errors (18, 19, 28). Combining both results, we hypothesize that errors emerge as task parameter miscoding, but not due to the pure temporal signals. This is further supported by the fact that LCT temporal population signals significantly decreased their intensities or disappeared. These results agree with the decreased in variance measured in single units during the LCT. Thus, a big proportion of the temporal signals appeared only when the animals performed the TPDT. The population signals that remained during LCT were only associated with the stimulus arrival and pb responses. To further understand the role of temporal signals during nondemanding tasks, future studies could employ passive tasks (31–34). Under this condition, stimuli remain the same, but animals are not required to push a button to receive reward. Since there was no decision report and no overt attention is necessary in this context, temporal signals in DPC could cease entirely. In support of this conjecture, other studies have shown that coding dynamics vanish completely in frontal cortices during the passive condition (31, 34).

Several studies have shown that neural activity was often sensitive to the temporal task sequence. In particular, a significant proportion of frontal lobe cortex neurons respond to the amount of time elapsed during the delay period between two events. Cells with these types of responses are generally called ramping neurons (4, 10). Note that it was not necessary for the subject to estimate the duration of the delay period to provide an appropriate answer. If they appear, as they do, it should be because they offer some advantage or alternatively, due to some constraint upon the network dynamics. Here, we showed that these ramping responses are commonly found in DPC neurons during both delays (from 1 to 3 s and from 4 to 6 s). Furthermore, we observed that peacemaker-shaped signals prominently emerged from the population response during the TPDT. Notably, they disappeared during the nondemanding task. This suggests that ramping signals were only generated during the active task. Since the network did not code task parameter during the LCT, it did not need to infer the arrival of the task events. Based on those results, we speculate that as the pacemaker component was no longer necessary, it vanished. Future studies could examine the relevance of this ramping activity during task designs in which each trial consists of delay periods of different durations (6, 35–37). Under duration uncertainty, peacemaker signals could adapt, or become useless to predict the stimulus arrival.

We would like to emphasize that a large proportion of the TPDT network dimensions were only associated with time events. In addition, there was a large disparity between the variance captured by population temporal signals vs. the variance associated with task parameters coding. Furthermore, most of the significant TPDT components were only associated with the temporal sequences of task events: 7 out of 12 relevant dimensions were pure temporal signals. However, during the LCT the dimensionality was even smaller than in the TPDT, and all significant components were associated with the temporal signals. These results are in concordance with a recent theoretical work (38) that showed that network's dimensionality increases from a simple task to a more complex one. Altogether, this is further evidence that time-dependent signals emerging in relation to different stages in the task constitute an essential element of the network dynamics during cognitive tasks.

A functional distinction between task coding components and time-dependent variations in firing rates has been proposed previously (11, 39). These studies suggested that functional separation appears at the population level, but not at the single neuron's responses. Our results indicate that temporal readouts arose from diffuse combinations of the single neuron's responses. The distributions of the weights given to each neuron indicate that they share a common anatomical substrate: the distributions were unimodal and Gaussian-like. Despite this, it was still possible to identify single neurons with temporal dynamics that resembled the population dynamics. This means that although these temporal signals emerge at the population level, there are usually stereotypical neuron responses that mimic these temporal responses. However, we were not able to separate them into different categories or give them labels; neuronal response exists in a continuum. This agrees with the notion that the functional separation does not emerge at the single-neuron level (13, 27).

Another important question regarding time-dependent signals is how they are generated. One possibility is that they are generated by a mechanism independent of the task parameter coding dynamics; a sort of master clock that could allow timing across a variety of contexts (40). However, we are inclined to think that our results point in the direction of a different mechanism that has been already proposed: Neuronal populations can inherently produce temporal signals relevant to the task being performed (41). Many networks models have been put forth to address this issue: Recurrent networks could supply a robust and flexible dynamics to encode the passage of time (42–44).

In previous studies, it was suggested that pure time-dependent signals could adapt much faster than task coding components (5, 10, 11). In other words, temporal signals during delays could readapt in blocks of trials with different durations. This mechanism

Downloaded at Instituto de Biotecnología/UNAM on October 20, 2020

could increase the flexibility for coding dynamics to solve the same task under different durations (45–47). Although in our experiment we could not test this hypothesis, it is an important question to address in future experiments.

To conclude, we propose that the temporal signals in DPC (or in any other brain areas) could be interpreted as a substrate necessary to supply a framework on which the task parameter coding dynamics can be computed during sequential events required to reach a decision report. Whether these signals are gradually constructed, beginning in sensory areas or whether they arise abruptly in the frontal lobe cortex remain open questions. This yields at least two possibilities: there exist specific brain areas that construct temporal signals such as the ones extracted here, which are broadcast to other regions, or, rather, the capacity to estimate time through these signals is embedded in the circuits across the brain. Further work is needed to answer these possibilities.

Materials and Methods

Monkeys were trained to report whether the temporal structure of two vibrotactile stimuli of equal frequency was the same or different (*SI Appendix*). Neuronal recordings were obtained in DPC while the monkeys performed the TPDT. Methods for single-unit and population analysis are provided in *SI Appendix*. Animals were handled in accordance with standards of the National Institutes of Health and Society for Neuroscience. All protocols were approved by the Institutional Animal Care and Use Committee of the Instituto de Fisiología Celular, Universidad Nacional Autónoma de México.

ACKNOWLEDGMENTS. We thank the technical assistance of Hector Diaz, Rafael Pulido, Ana Escalante, Francisco Pérez, and Sergio Méndez. This work was supported in part by Dirección de Asuntos del Personal Académico de la Universidad Nacional Autónoma de México (PAPIIT-IN210819 and PAPIIT- IN202716), Consejo Nacional de Ciencia y Tecnología (CONACYT) (CONACYT-240892) (to R.R.). J.V. and J.Z. are doctoral students from Programa de Doctorado en Ciencias Biomédicas, Universidad Nacional Autónoma de México, and received Fellowship 255865 from CONACYT.

1. Mauk MD, Buonomano DV (2004) The neural basis of temporal processing. *Annu Rev Neurosci* 27:307–340.
2. Finnerty GT, Shadlen MN, Jazayeri M, Nobre AC, Buonomano DV (2015) Time in cortical circuits. *J Neurosci* 35:13912–13916.
3. Merchant H, Harrington DL, Meck WH (2013) Neural basis of the perception and estimation of time. *Annu Rev Neurosci* 36:313–336.
4. Romo R, Brody CD, Hernández A, Lemus L (1999) Neuronal correlates of parametric working memory in the prefrontal cortex. *Nature* 399:470–473.
5. Mita A, Mushiake H, Shima K, Matsuzaka Y, Tanji J (2009) Interval time coding by neurons in the presupplementary and supplementary motor areas. *Nat Neurosci* 12: 502–507.
6. Janssen P, Shadlen MN (2005) A representation of the hazard rate of elapsed time in macaque area LIP. *Nat Neurosci* 8:234–241.
7. MacDonald CJ, Lepage KQ, Eden UT, Eichenbaum H (2011) Hippocampal "time cells" bridge the gap in memory for discontiguous events. *Neuron* 71:737–749.
8. Itskov V, Curto C, Pastalkova E, Buzsáki G (2011) Cell assembly sequences arising from spike threshold adaptation keep track of time in the hippocampus. *J Neurosci* 31: 2828–2834.
9. Kunimatsu J, Suzuki TW, Ohmae S, Tanaka M (2018) Different contributions of preparatory activity in the basal ganglia and cerebellum for self-timing. *eLife* 7:e35676.
10. Brody CD, Hernández A, Zainos A, Romo R (2003) Timing and neural encoding of somatosensory parametric working memory in macaque prefrontal cortex. *Cereb Cortex* 13:1196–1207.
11. Machens CK, Romo R, Brody CD (2010) Functional, but not anatomical, separation of "what" and "when" in prefrontal cortex. *J Neurosci* 30:350–360.
12. Merchant H, Zarco W, Pérez O, Prado L, Bartolo R (2011) Measuring time with different neural chronometers during a synchronization-continuation task. *Proc Natl Acad Sci USA* 108:19784–19789.
13. Kobak D, et al. (2016) Demixed principal component analysis of neural population data. *eLife* 5:e10989.
14. Mante V, Sussillo D, Shenoy KV, Newsome WT (2013) Context-dependent computation by recurrent dynamics in prefrontal cortex. *Nature* 503:78–84.
15. Carnevale F, de Lafuente V, Romo R, Barak O, Parga N (2015) Dynamic control of response criterion in premotor cortex during perceptual detection under temporal uncertainty. *Neuron* 86:1067–1077.
16. Elsayed GF, Cunningham JP (2017) Structure in neural population recordings: An expected byproduct of simpler phenomena? *Nat Neurosci* 20:1310–1318.
17. Cunningham JP, Yu BM (2014) Dimensionality reduction for large-scale neural recordings. *Nat Neurosci* 17:1500–1509.
18. Rossi-Pool R, et al. (2016) Emergence of an abstract categorical code enabling the discrimination of temporally structured tactile stimuli. *Proc Natl Acad Sci USA* 113: E7966–E7975.
19. Rossi-Pool R, et al. (2017) Decoding a decision process in the neuronal population of dorsal premotor complex. *Neuron* 96:1432–1446.e7.
20. Rigotti M, et al. (2013) The importance of mixed selectivity in complex cognitive tasks. *Nature* 497:585–590.
21. Pagan M, Rust NC (2014) Quantifying the signals contained in heterogeneous neural responses and determining their relationships with task performance. *J Neurophysiol* 112:1584–1598.
22. Churchland MM, Shenoy KV (2007) Temporal complexity and heterogeneity of single-neuron activity in premotor and motor cortex. *J Neurophysiol* 97:4235–4257.
23. Barak O, Tsodyks M, Romo R (2010) Neuronal population coding of parametric working memory. *J Neurosci* 30:9424–9430.
24. Kamiński J, et al. (2017) Persistently active neurons in human medial frontal and medial temporal lobe support working memory. *Nat Neurosci* 20:590–601.
25. Murray JD, et al. (2017) Stable population coding for working memory coexists with heterogeneous neural dynamics in prefrontal cortex. *Proc Natl Acad Sci USA* 114: 394–399.
26. Diamantaras KI, Kung SY (1996) *Principal Component Neural Networks: Theory and Applications* (Wiley, New York).
27. Raposo D, Kaufman MT, Churchland AK (2014) A category-free neural population supports evolving demands during decision-making. *Nat Neurosci* 17:1784–1792.
28. Vergara J, Rivera N, Rossi-Pool R, Romo R (2016) A neural parametric code for storing information of more than one sensory modality in working memory. *Neuron* 89: 54–62.
29. Chaisangmongkon W, Swaminathan SK, Freedman DJ, Wang XJ (2017) Computing by robust transience: How the fronto-parietal network performs sequential, category-based decisions. *Neuron* 93:1504–1517.e4.
30. Trautmann EM, et al. (2017) Accurate estimation of neural population dynamics without spike sorting. bioRxiv:10.1101/229252. Preprint, posted December 5, 2017.
31. Hernández A, et al. (2010) Decoding a perceptual decision process across cortex. *Neuron* 66:300–314.
32. Salinas E, Hernandez A, Zainos A, Romo R (2000) Periodicity and firing rate as candidate neural codes for the frequency of vibrotactile stimuli. *J Neurosci* 20:5503–5515.
33. Vázquez Y, Zainos A, Alvarez M, Salinas E, Romo R (2012) Neural coding and perceptual detection in the primate somatosensory thalamus. *Proc Natl Acad Sci USA* 109:15006–15011.
34. Romo R, Merchant H, Zainos A, Hernández A (1997) Categorical perception of somesthetic stimuli: Psychophysical measurements correlated with neuronal events in primate medial premotor cortex. *Cereb Cortex* 7:317–326.
35. de Lafuente V, Romo R (2006) Neural correlate of subjective sensory experience gradually builds up across cortical areas. *Proc Natl Acad Sci USA* 103:14266–14271.
36. Genovesio A, Tsujimoto S, Wise SP (2009) Feature- and order-based timing representations in the frontal cortex. *Neuron* 63:254–266.
37. Leon MI, Shadlen MN (2003) Representation of time by neurons in the posterior parietal cortex of the macaque. *Neuron* 38:317–327.
38. Gao P, et al. (2017) A theory of multineuronal dimensionality, dynamics and measurement. bioRxiv:10.1101/214262. Preprint, posted November 5, 2017.
39. Singh R, Eliasmith C (2006) Higher-dimensional neurons explain the tuning and dynamics of working memory cells. *J Neurosci* 26:3667–3678.
40. Ivry RB, Schlerf JE (2008) Dedicated and intrinsic models of time perception. *Trends Cogn Sci* 12:273–280.
41. Muller T, Nobre AC (2014) Perceiving the passage of time: Neural possibilities. *Ann N Y Acad Sci* 1326:60–71.
42. Laje R, Buonomano DV (2013) Robust timing and motor patterns by taming chaos in recurrent neural networks. *Nat Neurosci* 16:925–933.
43. Karmarkar UR, Buonomano DV (2007) Timing in the absence of clocks: Encoding time in neural network states. *Neuron* 53:427–438.
44. Cueva C, et al. (2018) Delay activity dynamics: Task dependent time encoding and low dimensional trajectories. bioRxiv:10.1101/504936. Preprint, posted December 29, 2018.
45. Wang J, Narain D, Hosseini EA, Jazayeri M (2018) Flexible timing by temporal scaling of cortical responses. *Nat Neurosci* 21:102–110.
46. Remington ED, Egger SW, Narain D, Wang J, Jazayeri M (2018) A dynamical systems perspective on flexible motor timing. *Trends Cogn Sci* 22:938–952.
47. Remington ED, Narain D, Hosseini EA, Jazayeri M (2018) Flexible sensorimotor computations through rapid reconfiguration of cortical dynamics. *Neuron* 98: 1005–1019.e5.

Downloaded at Instituto de Biotecnología/UNAM on October 20, 2020

MBoC | ARTICLE

Key within-membrane residues and precursor dosage impact the allotopic expression of yeast subunit II of cytochrome *c* oxidase

Diana Rubalcava-Gracia[a], Juan García-Rincón[a], Ruy Pérez-Montfort[a], Patrice Paul Hamel[b,c], and Diego González-Halphen[a,*]

[a]Instituto de Fisiología Celular, Universidad Nacional Autónoma de México, Ciudad de México 04510, Mexico; [b]Department of Molecular Genetics and [c]Department of Biological Chemistry and Pharmacology, The Ohio State University, Columbus, OH 43210

ABSTRACT **Experimentally relocating mitochondrial genes to the nucleus for functional expression (allotopic expression) is a challenging process. The high hydrophobicity of mitochondria-encoded proteins seems to be one of the main factors preventing this allotopic expression. We focused on subunit II of cytochrome *c* oxidase (Cox2) to study which modifications may enable or improve its allotopic expression in yeast. Cox2 can be imported from the cytosol into mitochondria in the presence of the W56R substitution, which decreases the protein hydrophobicity and allows partial respiratory rescue of a *cox2*-null strain. We show that the inclusion of a positive charge is more favorable than substitutions that only decrease the hydrophobicity. We also searched for other determinants enabling allotopic expression in yeast by examining the *COX2* gene in organisms where it was transferred to the nucleus during evolution. We found that naturally occurring variations at within-membrane residues in the legume *Glycine max* Cox2 could enable yeast *COX2* allotopic expression. We also evidence that directing high doses of allotopically synthesized Cox2 to mitochondria seems to be counterproductive because the subunit aggregates at the mitochondrial surface. Our findings are relevant to the design of allotopic expression strategies and contribute to the understanding of gene retention in organellar genomes.**

Monitoring Editor
Thomas D. Fox
Cornell University

Received: Dec 11, 2018
Revised: Jun 28, 2019
Accepted: Jul 11, 2019

INTRODUCTION

Most mitochondrial proteins are encoded in the nuclear genome, translated by cytosolic ribosomes, and directed to mitochondria. However, migration of mitochondrial genes to the nucleus occurs widely in nature (Adams and Palmer, 2003; Burger *et al.*, 2003; Timmis *et al.*, 2004). These relocalized nucleotide sequences acquire more complex regulation and tend to exhibit lower mutation rates (Martin and Herrmann, 1998). Mitochondrial genomes mainly encode subunits of oxidative phosphorylation (OXPHOS) complexes. In general, these proteins are embedded in membranes and are highly hydrophobic, a feature that is considered to be one of the main driving forces for the retention of a genome in mitochondria (Johnston and Williams, 2016).

Experimentally relocating mitochondrial genes to the nucleus holds promise for the development of treatments of mitochondrial diseases (De Grey, 2000; DiMauro *et al.*, 2006; Kyriakouli *et al.*, 2008). A mutation in the mitochondrial genome, yielding a defective protein, could be overcome in principle by the import of a nucleus-encoded functional version of the protein. Multiple efforts have been undertaken to express mitochondria-encoded genes allotopically using yeast or mammalian model systems, but conflicting and inconsistent results call for careful interpretation of results and warrant further experimental testing (Oca-Cossio *et al.*, 2003; Perales-Clemente *et al.*, 2011).

The *COX2* gene, encoding subunit 2 (Cox2) of cytochrome *c* oxidase (C*c*O), provides an example of natural migration of a mitochondrial gene to the nucleus. This gene is generally mitochondria-encoded, but in a few organisms it is found in the nuclear

This article was published online ahead of print in MBoC in Press (http://www.molbiolcell.org/cgi/doi/10.1091/mbc.E18-12-0788) on July 18, 2019.

*Address correspondence to: Diego González-Halphen (dhalphen@ifc.unam.mx).

Abbreviations used: C*c*O, cytochrome *c* oxidase; Cox2, subunit 2 of cytochrome *c* oxidase; MTS, mitochondrial targeting sequence; TIM, translocase of the inner membrane; TMS, transmembrane segment; TOM, translocase of the outer membrane.

© 2019 Rubalcava-Gracia *et al.* This article is distributed by The American Society for Cell Biology under license from the author(s). Two months after publication it is available to the public under an Attribution–Noncommercial–Share Alike 3.0 Unported Creative Commons License (http://creativecommons.org/licenses/by-nc-sa/3.0).

"ASCB®," "The American Society for Cell Biology®," and "Molecular Biology of the Cell®" are registered trademarks of The American Society for Cell Biology.

genome (Adams *et al.*, 1999; Pérez-Martínez *et al.*, 2001; Szafranski, 2017). For example, *COX2* was transferred to the nucleus in some members of the legume lineage, resulting in mitochondrial and nuclear versions of *COX2*. The representative species of this lineage encode Cox2 in the nuclear DNA, in the mitochondrial DNA, or in both genomes, depending on which copy was activated and/or inactivated (Adams *et al.*, 1999; Daley *et al.*, 2002a,b). Also, the *COX2* gene has been relocalized experimentally to the yeast nucleus (Supekova *et al.*, 2010), and subsequent studies have provided supporting genetic and biochemical evidence for successful allotopic expression (Cruz-Torres *et al.*, 2012; Elliott *et al.*, 2012; Rubalcava-Gracia *et al.*, 2018). The substitution of a tryptophan for an arginine in position 56 ($Cox2^{W56R}$), within the first transmembrane segment (TMS) of allotopically produced Cox2, decreases its hydrophobicity and allows the partial respiratory rescue of a *cox2*-null yeast strain, with an estimated ~60% recovery of CcO levels as compared with the wild-type strain (Cruz-Torres *et al.*, 2012). This partial complementation can be attributed solely to diminished import, since a mitochondrial *COX2* gene producing the W56R variant cannot be distinguished from wild-type (Rubalcava-Gracia *et al.*, 2018). The decrease in hydrophobicity of the first TMS in Cox2 also occurred during the natural relocation of the *COX2* gene to the nucleus in legumes (Daley *et al.*, 2002b). Other necessary modifications for successful allotopic expression include recoding the mitochondrial gene to the nuclear genetic code and fusing a sequence encoding a mitochondrial targeting sequence (MTS) to the open reading frame. Given that the W56R substitution was found in a random mutagenesis screen of 20,000 alleles (Supekova *et al.*, 2010), it is likely that this is the only permissible change that enables import from the cytosol to the mitochondria and at the same time maintains CcO functionality. This underscores the power of such an approach to uncover mutations allowing the allotopic production of other mitochondria-encoded proteins.

Here, we further explored the W56 position in Cox2 by testing whether other residues with similar properties to arginine could confer allotopic expression. We also tested whether naturally occurring changes in the legume *Glycine max* Cox2 enable yeast Cox2 to be imported from the cytosol into mitochondria and assembled into a functional CcO. Finally, we evidenced that dosage of the cytosol-synthesized Cox2 precursor is critical for the outcome of allotopic expression.

RESULTS

Other substitutions at residue 56 enable the allotopic expression of *COX2*

First, we tested whether other changes at position 56, besides the tryptophan-to-arginine substitution (Supekova *et al.*, 2010) (W56R), can restore the respiratory growth of a *cox2*-null strain expressing an allotopic version of *COX2*. We substituted W56 for two residues sharing at least one physicochemical property with arginine: lysine (W56K), which also has a positive charge, and glutamine (W56Q), which has the closest hydrophobicity score to arginine (Calado-Botelho *et al.*, 2011). Upon introduction of the allotopic constructs encoding $Cox2^{W56K}$ or $Cox2^{W56Q}$ into a *cox2*-null strain, we observed a restoration of respiratory growth. Respiratory growth of the strain with the W56K substitution was comparable to that of the strain carrying the W56R substitution, while the recovery of respiratory competence by $Cox2^{W56Q}$ was significantly less (Figure 1A). Hence, the growth behavior of yeast carrying these constructs was $Cox2^{W56R} = Cox2^{W56K} > Cox2^{W56Q}$. As a negative control, we included a strain expressing an allotopic wild-type *COX2* gene (producing the $Cox2^{WT}$ subunit). As expected, neither this construct producing $Cox2^{WT}$, nor the empty plasmid, was able to restore respiratory growth in the *cox2*-null strain (Figure 1A).

Previous work evidenced that most of the allotopically synthesized $Cox2^{W56R}$ protein accumulates as an unprocessed precursor (i.e., still carrying its MTS) detected in the mitochondrial fraction (Supekova *et al.*, 2010; Cruz-Torres *et al.*, 2012; Rubalcava-Gracia *et al.*, 2018). We thus performed cellular fractionations to test the cytosolic versus mitochondrial distribution of $Cox2^{WT}$, $Cox2^{W56K}$, and $Cox2^{W56Q}$. Most of the Cox2 precursors were found associated with mitochondria (Figure 1B), indicating that, similarly to $Cox2^{W56R}$, the limiting step occurs before their processing into mature forms in the mitochondrial matrix. Our results show that other residues at position 56 allow allotopic expression of *COX2* and that the inclusion of a positive charge in the first TMS (W56K) is favorable over a substitution that only diminishes hydrophobicity (W56Q).

Mutations that allow the nuclear expression of *COX2* in legumes also confer allotopic expression in yeast

Next, we sought to identify other changes in Cox2 that might enable its allotopic expression in the yeast system. We reasoned that in organisms that naturally encode *COX2* in the nucleus, the protein

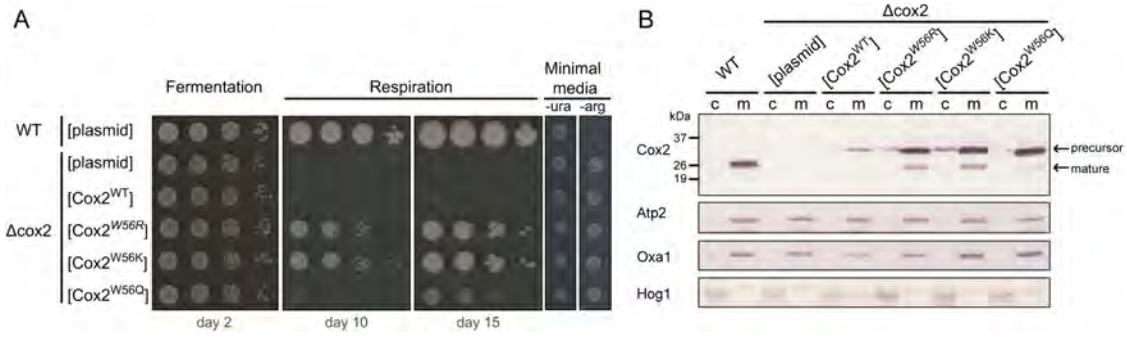

FIGURE 1: Substituting residues of properties similar to those of arginine in position 56 of allotopic Cox2 restores cellular respiration to a *cox2*-null strain. (A) Tenfold serial dilutions of yeast liquid cultures from strains transformed with the indicated constructs or with an empty vector (plasmid) were plated on fermentable (glucose), respiratory (ethanol + glycerol), and minimal, selective media (-ura or -arg, for verifying the presence of the transforming plasmid or the mitochondrial genome, respectively). (B) Immunoblots decorated with an anti-Cox2 antibody of cytosolic (c; 100-µg) and mitochondrial (m; 50-µg) fractions of the indicated yeast strains. The Cox2 precursor and mature forms of Cox2 are indicated. Antibodies anti-Atp2 and anti-Oxa1 were used to immunodetect the corresponding mitochondrial markers and anti-Hog1 was used for the cytosolic marker. Squared brackets indicate Cox2 variants expressed from plasmids. All the Cox2 variants contain an MTS from Oxa1.

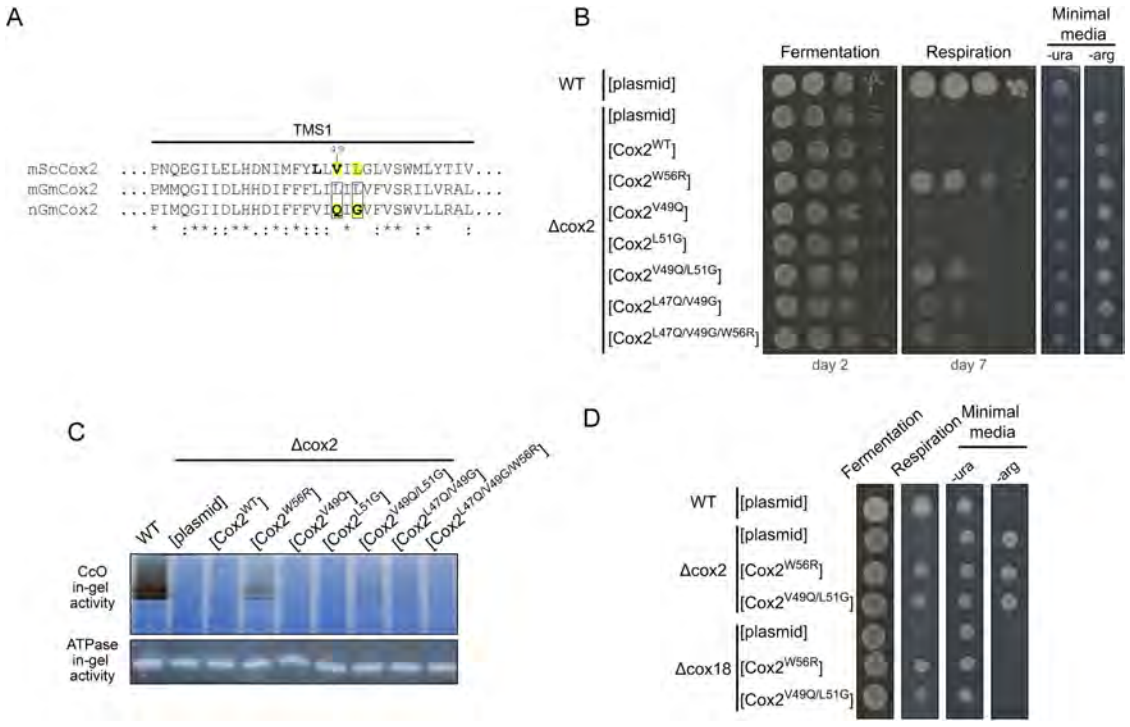

FIGURE 2: Mutations that allow the nuclear expression of *COX2* in legumes also confer allotopic expression in yeast. (A) Sequence alignments of the first transmembrane segment (TMS1) from the yeast Cox2 (mScCox2) and the mitochondrial and nuclear Cox2 versions of *Glycine max*, mGmCox2 and nGmCox2, respectively. An asterisk (*) indicates positions that have a single, fully conserved residue. A colon (:) indicates conservation between groups of strongly similar properties (scoring >0.5 in the Gonnet PAM 250 matrix). A period (.) indicates conservation between groups of weakly similar properties (scoring ≤0.5 in the Gonnet PAM 250 matrix). Key residues that are critical for import of the legume Cox2 from the cytosol are boxed (see text). Two yeast Cox2 constructs were designed based on this alignment: $Cox2^{V49Q/L51G}$ and $Cox2^{L47Q/V49G}$. (B) Tenfold serial dilutions of yeast cultures from the indicated strains were spotted on fermentable (glucose), respiratory (ethanol + glycerol), and minimal, selective media (-ura or -arg). (C) In-gel activity staining of complex IV and of complex V as a loading control. Isolated mitochondria (250 µg) from the indicated strains were solubilized with lauryl maltoside and resolved by BN-PAGE. (D) Strains (WT, Δ*cox2*, and Δ*cox18*) were plated on fermentable (glucose), respiratory (lactate), and minimal, selective media (-ura or -arg). Squared brackets indicate Cox2 variants expressed from plasmids. All the Cox2 variants contain an MTS from Oxa1.

sequence must carry determinants for import into the mitochondria and subsequent assembly into a functional holoenzyme. For example, the legume *Glycine max* expresses the *COX2* gene from both nuclear and mitochondrial genomes (Adams *et al.*, 1999). Previous research showed that a two-residue substitution within the first TMS of Cox2 is necessary and sufficient for the mitochondrial version of Cox2 to be imported into isolated mitochondria. Accordingly, the nucleus-encoded Cox2 protein could no longer be imported into the organelle when the residues (Q and G) at these two positions were modified to the ones (L and L) present in the mitochondria-encoded Cox2 (Daley *et al.*, 2002b; Figure 2A). The conclusion from this study is that this two-residue substitution was determinant in facilitating the import of Cox2 from the cytosol to the mitochondria.

To test whether this two-residue substitution could confer allotopic expression in the yeast system, we sought to reproduce the legume *COX2* mutations in the *COX2* sequence from yeast. We generated an alignment of the two legume Cox2 subunits with the one from yeast and identified that the key residues conferring import of the legume Cox2 correspond to a valine and a leucine at positions 49 and 51 in the yeast sequence (Figure 2A). We therefore engineered the mutations corresponding to the single and double substitutions V49Q and L51G in yeast *COX2*. We observed that only the $Cox2^{V49Q/L51G}$ variant was able to restore respiratory growth in a *cox2*-null strain, while the $Cox2^{V49Q}$ and $Cox2^{L51G}$ variants could not (Figure 2B), demonstrating that both changes are required for successful allotopic expression of *COX2*. However, the respiratory growth of the $Cox2^{V49Q/L51G}$ strain was less than that of the $Cox2^{W56R}$ strain. To test whether the overall decrease in hydrophobicity within the first TMS of Cox2 is sufficient for restoring respiratory growth, we substituted other aliphatic residues at other positions, resulting in the construct $Cox2^{L47Q/V49G}$. To explore any additive effect, a triple *COX2* mutant corresponding to W56R combined with a double substitution (L47Q/V49G/W56R) was also generated. All these constructs could restore the respiratory growth of a *cox2*-null strain, although to a lesser extent than the construct producing $Cox2^{V49Q/L51G}$. We also could not observe any additive effect in the strain producing the $Cox2^{V49Q/L51G/W56R}$ variant. Using *in-gel* activity staining, we verified that CcO activity correlated with the observation that the $Cox2^{W56R}$ variant exhibits increased respiratory growth compared with that in the variants containing two-residue substitutions (Figure 2C). In contrast, another OXPHOS complex, ATPase, exhibited comparable activity for all strains.

Next, we questioned whether $Cox2^{V49Q/L51G}$ follows the same biogenesis pathway as that of allotopically produced $Cox2^{W56R}$. In contrast to orthodox Cox2, synthesized in mitochondria, allotopically

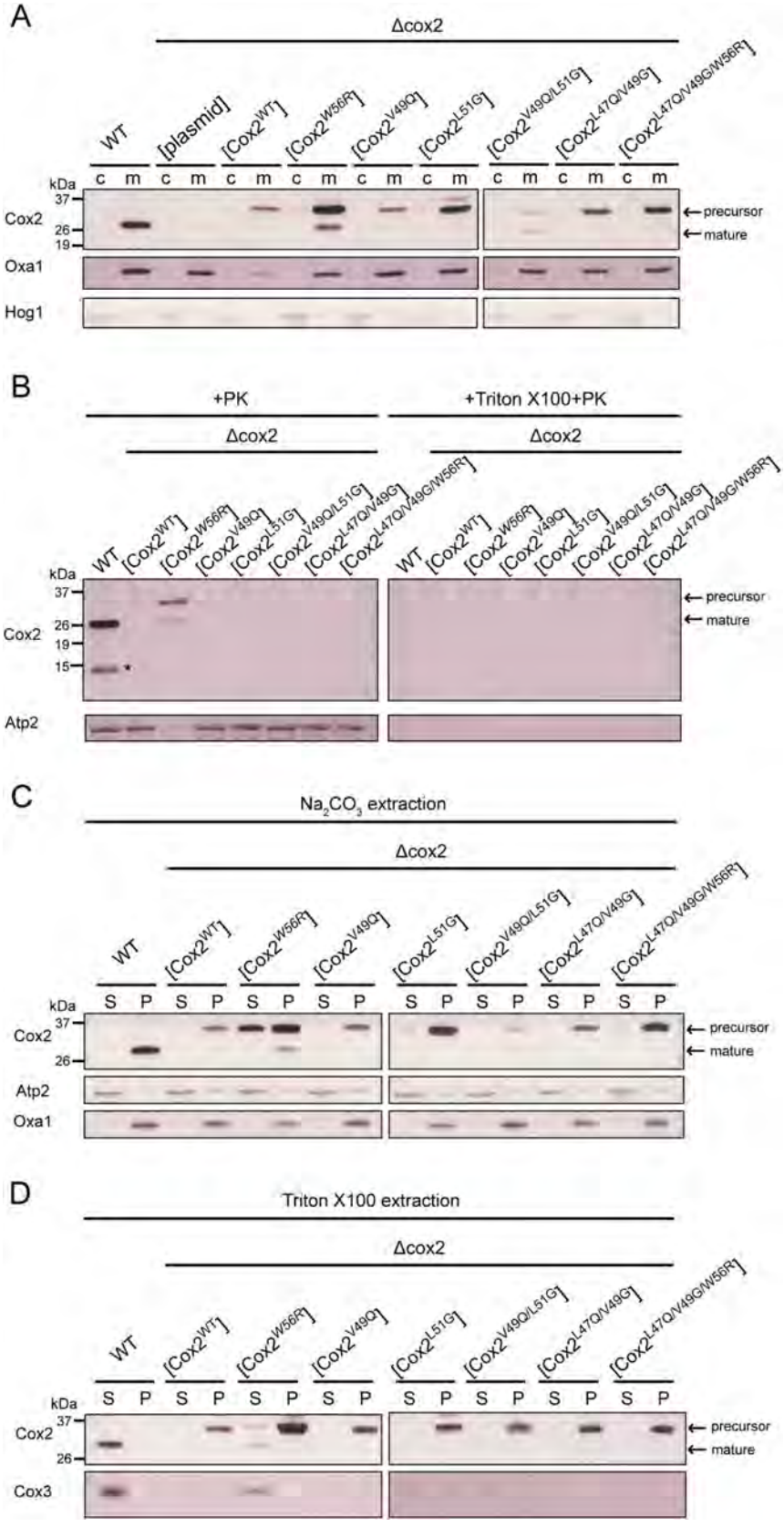

FIGURE 3: The allotopically synthesized proteins face the limiting step by aggregating at the mitochondrial periphery. (A) Immunoblots decorated with anti-Cox2 of cytosolic (c; 100-μg) and mitochondrial (m; 50-μg) fractions. Arrows indicate the precursor and mature forms of Cox2. The mitochondrial markers Oxa1 and the cytosolic marker Hog1 were decorated with their corresponding antibodies. (B) Isolated mitochondria (50 μg) were treated with proteinase K (PK) to degrade proteins external to the outer membrane. Parallel samples were preincubated with Triton X-100 to dissolve the membranes and to make all mitochondrial proteins accessible to protease degradation. The asterisk indicates partial degradation of Cox2, possibly due to imperfect mitochondrial preparation. (C) Carbonate extraction separating the membrane extrinsic proteins in the supernatant (S) from the integral membrane proteins in the pellet (P) from yeast expressing the indicated constructs. Atp2 was used as a soluble protein marker and Oxa1 as an integral membrane protein marker. (D) Triton X-100 extraction separating the detergent-solubilized proteins in the supernatant (S) from the (detergent-resistant) aggregated proteins in the pellet (P) from yeast expressing the indicated constructs. Cox3 was used as a solubilized membrane protein marker. Squared brackets indicate Cox2 variants expressed from plasmids. All the Cox2 variants contain an MTS from Oxa1.

synthesized $Cox2^{W56R}$ does not require the Cox18 translocase for the correct insertion of its second TMS into the inner membrane (Elliott *et al.*, 2012), and it was postulated to be released laterally into this membrane directly from the TIM23 complex (Rubalcava-Gracia *et al.*, 2018). We observed that, similarly to the $Cox2^{W56R}$ strain, the $Cox2^{V49Q/L51G}$ variant is able to restore respiration when expressed in a *cox18*-null (Figure 2D), indicating that the Cox18 translocase is completely dispensable. This suggests that the second TMS of $Cox2^{V49Q/L51G}$ is released laterally into the inner mitochondrial membrane by the TIM23 translocator.

We observed that while the mature forms of Cox2 were protected from degradation upon incubation of mitochondria-enriched fractions with proteinase K (PK), a result indicative of mitochondrial localization, the Cox2 precursors were mostly degraded by the protease (Figure 3, A and B). These results may be interpreted in two ways: either the precursors are associated with the external face of the outer mitochondrial membrane or they are retained while in transit through the TOM and TIM23 complexes with their C-termini still exposed to the cytosol (note that our anti-Cox2 antibody recognizes the C-terminus of Cox2). To distinguish between these two possibilities, we performed carbonate and Triton X-100 extractions of the mitochondrial fractions. We found that the precursors are mostly resistant to both carbonate (Figure 3C) and detergent treatments (Figure 3D). As expected, mature Cox2 proteins resist carbonate extraction but are solubilized into the supernatant upon Triton extraction (Figure 3, C and D). These observations suggest that most Cox2 precursors aggregate at the external mitochondrial surface, thus preventing their import.

Taken together, our data show that substitutions at a position different from that of W56

enable the successful allotopic expression of *COX* and that a major limiting step for importing allotopic Cox2 into mitochondria is its aggregation.

Lowering the dose of allotopic *COX2* expression enhances Cox2 import and assembly in CcO

While the use of a multicopy plasmid for allotopic expression of *COX2* to ensure successful complementation seemed justified a priori (Supekova *et al.*, 2010), we wondered whether reducing the allotopic expression of *COX2* would decrease the rescue of the respiratory defect proportionally. For this purpose, we opted to test allotopic expression under a condition where the same *COX2* construct carried in the multicopy plasmid was used as a single copy. To achieve this, we integrated the *COX2*-expressing construct (under the same phosphoglycerate kinase promoter and terminator present in the multicopy plasmid) in the nuclear genome. Surprisingly, we observed a notable increase in respiratory growth in the strains expressing the nuclear-integrated constructs producing $Cox2^{W56R}$ and $Cox2^{V49Q/L51G}$ in comparison with the strains producing the same Cox2 variants from a multicopy plasmid (Figure 4A). Growth of the yeast containing the single-copy $COX2^{W56R}$ construct was even comparable to that of a wild-type strain, and the strain containing the single-copy $COX2^{V49Q/L51G}$ exhibited more robust respiratory growth than the one with the high-copy $COX2^{W56R}$. The strain producing $Cox2^{WT}$ did not display any growth in respiratory medium, even at low doses. Immunodetection of Cox2 in mitochondria-enriched fractions of these strains showed that, at low dosage, $Cox2^{W56R}$ and $Cox2^{V49Q/L51G}$ only accumulated in their mature forms at levels similar to those of the WT strain (Figure 4B). As previously observed, at high dosage, $Cox2^{W56R}$ and $Cox2^{V49Q/L51G}$ were mainly observed as precursors, with only a fraction converted to the

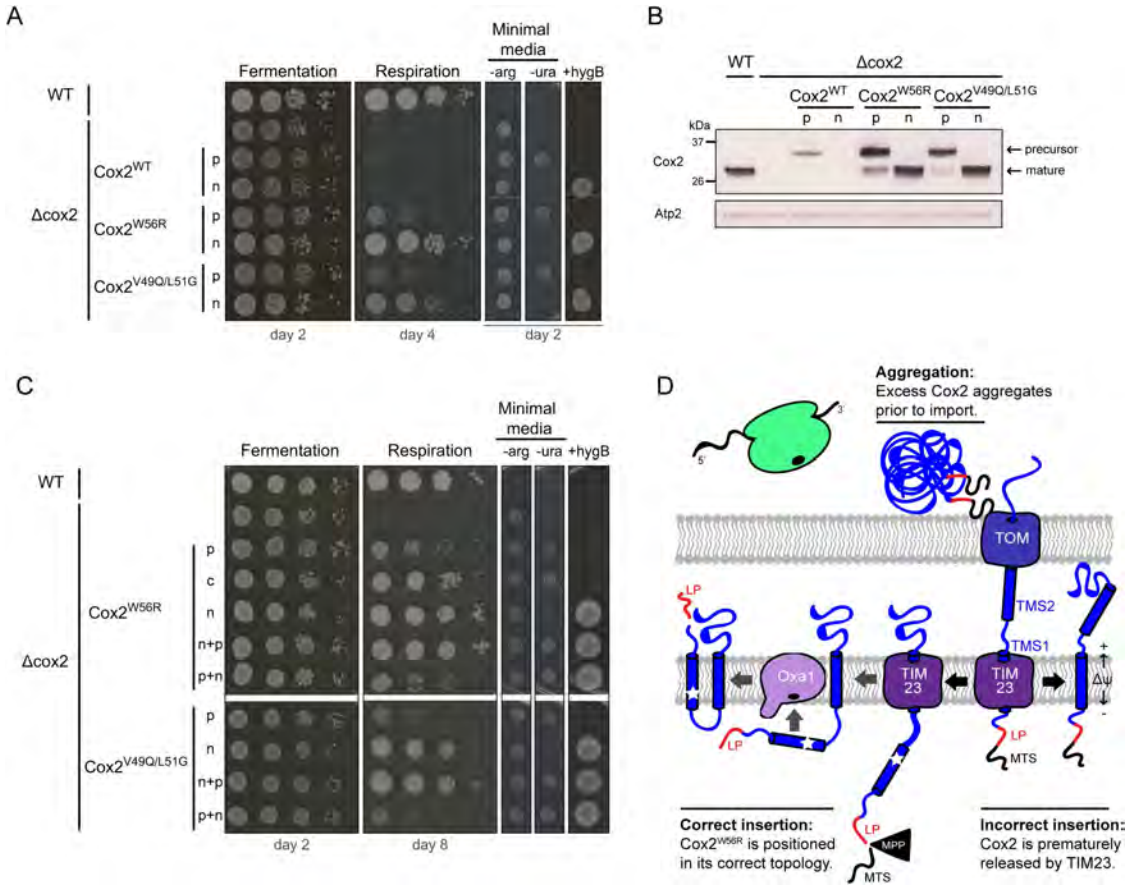

FIGURE 4: Lowering the expression of allotopic *COX2* in a *cox2*-null strain improves rescue of the respiratory growth. (A) Tenfold serial dilutions of yeast cultures from the indicated strains were plated on fermentable (glucose), respiratory (ethanol + glycerol), and minimal, selective media (-arg or -ura) and in the presence of hygromycin B (+hygB). The letter p represents expression from a multicopy plasmid, and the letter n represents expression from a single copy inserted in the nuclear genome. (B) Cox2 steady-state levels in isolated mitochondria (50 µg) from the indicated strains. Arrows indicate the precursor and mature forms of Cox2. The letters p and n indicate expression levels as in A. (C) Tenfold serial dilutions of yeast cultures from the indicated strains were plated on fermentable (glucose); respiratory (ethanol + glycerol), and minimal, selective media (-arg or -ura) and in the presence of hygromycin B (+hygB). The letter c represents expression from a centromeric plasmid. The order of the letters indicates the order in which *COX2*-expressing constructs were introduced into yeast cells. All the Cox2 variants contain an MTS from Oxa1. (D) Biogenesis model of allotopically synthesized Cox2. On the left, insertion of Cox2 results in its correct topology. On the right, the high hydrophobicity of the first TMS leads the cytosol-synthesized Cox2 to aggregate at the mitochondrial periphery or to be prematurely released by TIM23 into an incorrect topology. TOM: translocase of the outer membrane, TIM: translocase of the inner membrane, MPP: mitochondrial processing peptidase, LP: leader peptide, MTS: mitochondrial targeting sequence, TMS: transmembrane segment.

mature form. In line with the absence of respiratory growth of the strains carrying the *COX2*^{WT} construct, the Cox2^{WT} protein was observed only as a precursor and, at low dosage, its steady-state level was probably extremely low, as we could not detect it under our experimental conditions (Figure 4B). We observed the same behavior, that is, enhanced respiratory growth, lower accumulation of precursors, and higher levels of mature forms of Cox2, when the same constructs were expressed in few copies from a centromeric plasmid (Figure 4C and unpublished data). To test the importance of high versus low doses of Cox2 for the rescue of respiratory growth, we increased the dosage by producing the high-copy Cox2 variants (p) in a strain already encoding a single-copy Cox2 in the nuclear genome (n). We observed that this strain (n+p) grew in respiratory medium to levels similar to those of the strain expressing Cox2 encoded only in the nucleus (Figure 4C) and verified the presence of the precursors by immunoblotting (unpublished data). Unexpectedly, these increased levels of expression did not show the same growth defect of the high-copy Cox2 strain. However, when we inverted the order of production of allotopic Cox2 variants in the cells by integrating Cox2 into the nuclear genome in a strain already encoding a high-copy Cox2 (p+n), we observed that this strain showed the same level of respiratory growth as the strain expressing a high-copy Cox2 from a plasmid (Figure 4C).

The aforementioned results suggest that, although overexpression of allotopic *COX2* constructs is able to restore respiration to *cox2*-null strains, directing high doses of these proteins to mitochondria at the same time is counterproductive. Because the limiting step resides in the import of allotopic Cox2, low-dose expression seems to have a better outcome in terms of aggregation propensity and recovery of the respiratory growth.

DISCUSSION

The experimental relocation of mitochondrial genes to the nucleus has paved the way for the development of therapies intended to treat syndromes caused by mutations in the mitochondrial genome (González-Halphen *et al.*, 2004; Taylor and Turnbull, 2005; Kyriakouli *et al.*, 2008; Calvo and Mootha, 2010; Gorman *et al.*, 2016). Ongoing research has unveiled several constraining factors that limit allotopic expression (Claros *et al.*, 1995; Oca-Cossio *et al.*, 2003; Figueroa-Martínez *et al.*, 2011; Björkholm *et al.*, 2017). Because most proteins encoded in the mitogenome are integral to the membrane, the high hydrophobicity and the number of TMSs in these proteins seem to be major limiting factors for their import when synthesized in the cytosol (Claros *et al.*, 1995; Johnston and Williams, 2016). In this work we also found that aggregation propensity, which is directly correlated with high hydrophobicity (Chiti *et al.*, 2003; Dobson, 2004), contributes to the efficiency of importability before assembly of allotopic Cox2 into cytochrome *c* oxidase. Average hydrophobicities for the first TMSs of the different Cox2 variants used in this work are shown in Table 1.

First, we turned our attention to the Cox2 subunit to examine the importance of the residues enabling its allotopic production. Previous work demonstrated that substituting a tryptophan for an arginine decreases the hydrophobicity of the first TMS of Cox2 by adding a positive charge (Supekova *et al.*, 2010). In this study, substitution of a lysine or glutamine in the same position also allowed recovery of the respiratory growth, but residues containing a positive charge (arginine and lysine) yield better rescue than a residue decreasing the hydrophobicity (glutamine). It is possible that Cox2^{W56Q} is poorly inserted into the mitochondrial inner membrane, because the key determinant for importability is the presence of a positive charge (R^+ or K^+) and not reduction of the hydrophobicity

Cox2 variant	TMS1	H
Cox2^{WT}	IMFYLLVILGLVSWMLYTIVMTYS	0.349
Cox2^{W56K}	IMFYLLVILGLVSKMLYTIVMTYS	0.367
Cox2^{L51G}	IMFYLLVIGGLVSWMLYTIVMTYS	0.375
Cox2^{W56Q}	IMFYLLVILGLVSQMLYTIVMTYS	0.395
Cox2^{W56R}	IMFYLLVILGLVSRMLYTIVMTYS	0.427
Cox2^{V49Q}	IMFYLLQILGLVSWMLYTIVMTYS	0.435
Cox2$^{V49Q/L51G}$	IMFYLLQIGGLVSWMLYTIVMTYS	0.461
Cox2$^{L47Q/V49G}$	IMFYQLGILGLVSWMLYTIVMTYS	0.461
Cox2$^{L47Q/V49G/W56}$	IMFYQLGILGLVSRMLYTIVMTYS	0.540

Average hydrophobicity for the first transmembrane segment of each Cox2 variant used in this work. The "biological scale" was experimentally obtained and provides a hydrophobicity value for each residue present in the TMS of a model yeast mitochondrial protein (Calado-Botelho *et al.*, 2011). Cox2 variants are ordered by decreasing hydrophobicity (increasing hydrophilicity). Residue substitutions are underlined.

TABLE 1: Average hydrophobicity of the Cox2 variants.

(Q) at this position (von Heijne, 1992; Andersson and von Heijne, 1994) (see Table 1). This view is supported by the fact that while a similar number of Cox2 variant precursors accumulate in the mitochondria, the mature form of Cox2^{W56Q} is significantly less abundant than those of Cox2^{W56R} and Cox2^{W56K} (Figure 1B). This indicates that Cox2^{W56Q} is probably limited in its insertion in the inner membrane because it is more prone to aggregation. That mature Cox2^{W56K} and Cox2 ^{W56R} accumulate at the same level reinforces the view that a positive charge at this position is the key determinant of Cox2 importation into mitochondria when it originates from the cytosol.

Here, we designed allotopic Cox2 variants in yeast based on naturally evolving alterations in legumes. Notably, we observed that the double substitution reported as key for nuclear expression of Cox2 in *Glycine max* also allowed the allotopically expressed yeast *COX2* to restore respiration to a *cox2*-null mutant. Similarly to what was observed in in vitro import assays in legumes (Daley *et al.*, 2002b), each single-substitution V49Q or L51G was insufficient to restore respiration. In line with the cytosol-synthesized Cox2 biogenesis model (Daley *et al.*, 2002a; Jiménez-Suárez *et al.*, 2012; Rubalcava-Gracia *et al.*, 2018), the first TMS (TMS1) of Cox2 is transferred to the matrix through the TIM23 translocase, while the second TMS is laterally released into the inner membrane by TIM23 (Figure 4D). As a final step, TMS1 is inserted from the matrix in the inner membrane by Oxa1, positioning Cox2 in its correct topology (Figure 4D). We assume that in the presence of either substitution (V49Q or L51G), the proteins aggregate at the mitochondrial periphery before import because they are too hydrophobic (Figure 4D and Table 1). Accordingly, only the double substitution, which diminishes the overall hydrophobicity of the TMS1 of Cox2, allows its correct insertion into the inner membrane.

It should be mentioned that the legume Cox2 substitutions (V49Q/L51G) are less efficient in conferring respiratory growth than the W56R that was identified through random mutagenesis (Supekova *et al.*, 2010). Indeed, the W56R substitution meets Goldilocks conditions: besides maintaining CcO activity intact (Rubalcava-Gracia *et al.*, 2018), it balances the need to diminish the hydrophobicity of Cox2 TMS1, but at the same time, it maintains the ability of TMS1 to be recognized as a transmembrane domain by the inner membrane translocator Oxa1. Notably, in the mitochondrial Cox2 sequence from *Glycine max*, the residue corresponding

to position 56 contains an arginine, indicating that a positive charge in the first TMS of Cox2 is permissible, at least in some organisms. Production of low levels of $Cox2^{V49Q/L51G}$ results in the accumulation of mature Cox2 at a level similar to that of $Cox2^{W56R}$, suggesting that insertion in the inner membrane occurs to the same extent for both Cox2 variants (Figure 4B). However, the fact that the rescue with $Cox2^{V49Q/L51G}$ is significantly less efficient indicates that the V49Q/L51G modifications impact the biogenesis of Cox2 or the activity of the yeast enzyme. Furthermore, we observed that the combination of W56R substitution with the V49Q and L51G changes did not further improve respiratory growth, and resulted in lower C*c*O activity, as observed in Figure 2C. We assume that, despite the fact that these mutations enable respiratory growth, they may also affect C*c*O activity. Another possibility is that the hydrophobicity of the first TMS of the $Cox2^{L47Q/V49G/W56R}$ subunit is lowered to such an extent (Table 1) that it is not promptly recognized as a transmembrane domain and is therefore only partially routed for insertion into the inner membrane by the Oxa1 translocator.

Our experiments indicate that allotopically expressed proteins face a limiting step by aggregating before their import into mitochondria. When we lowered the *COX2* expression levels by integrating the *COX2* gene into the nuclear genome, we observed a notable increase in the rescue of the *cox2*-null strain, which correlated with lower levels of precursor and corresponding enhanced levels of mature Cox2. It is conceivable that excess cytosol-synthesized Cox2 aggregates at the mitochondrial surface, limiting the import of allotopic Cox2 (Figure 4D). These aggregates do not affect the import of other mitochondria-targeted proteins, as the precursors of Oxa1 and Atp2 were not observed to accumulate in our mitochondrial preparations (Figures 1B, 3A, and 4B). We noted that aggregation can also be avoided if large doses of Cox2 are produced in a strain already synthesizing small doses of allotopic Cox2. We explain this observation by the importing competence of *cox2*-null mitochondria. If large doses of the precursors of Cox2 are directly produced in a *cox2*-null mutant, most precursors aggregate and only a fraction assemble into C*c*O, resulting in difficulties in restoring respiration and in building up the electrochemical gradient required for further protein import. At small doses, aggregation of Cox2 is prevented and its assembly into C*c*O is enhanced, giving rise to an optimal transmembrane gradient that facilitates further import of cytosolic proteins. These results suggest that expression levels of the allotopic gene (from a centromeric plasmid or a high-copy plasmid) define the levels of importability versus aggregation of Cox2. It is also conceivable that cytosolic chaperones and other aggregation-response proteins might play a role in preventing the aggregation of Cox2 precursors.

Aggregation propensity is directly related to hydrophobicity and has been an underinvestigated factor in the study of allotopic expression. Highly hydrophobic proteins imported from the cytosol must avoid aggregating at the mitochondrial periphery to cross both mitochondrial membranes. All reports of allotopic expression in either yeast or cell cultures use high-level expression plasmids to ensure a high accumulation of the desired protein products inside the mitochondria (Guy *et al.*, 2002; Manfredi *et al.*, 2002; Ojaimi *et al.*, 2002; Bokori-Brown and Holt, 2006; Bonnet *et al.*, 2008; Figueroa-Martínez *et al.*, 2011; Cwerman-Thibault *et al.*, 2015; Boominathan *et al.*, 2016). Here, we found that a high level of the allotopically expressed Cox2 protein may be detrimental to the mitochondrial import system.

In summary, we provide a proof of principle that mimicking the modifications found in an organism that naturally transferred its mitochondrial gene to the nucleus can result in successful allotopic expression. This strategy includes expressing a gene with adequate mutations in a low copy number to ensure that moderate protein quantities are produced for mitochondrial import. Our results underscore that dosage, a previously unexplored important parameter, may be critical for allotopic expression in mammals, especially in human cell lines. The relevance of our finding is high, since allotopic expression still represents a promising strategy for developing treatments for patients with mitochondrial diseases. Our data also stress the relevance of studying organisms that naturally and atypically encode hydrophobic mitochondrial OXPHOS proteins in the nuclear genome.

MATERIALS AND METHODS

Strains, gene constructs, and culture conditions

The *Saccharomyces cerevisiae* strains used in this study were derived from the D273-10B parental strain. We used NB40-36A as the wild-type strain *(MATα, arg8::hisG, leu2-3, 112, lys2, ura3-52,* [rho+]), EHW154 as the Δ*cox2* strain (*MATa, arg8::hisG, his3-ΔHindIII, leu2-3, 112, lys2, ura3-52,* [rho+] *cox2-208::ARG8m*), and CAB116 as the Δ*cox18* strain (*MATa*, *arg8::hisG, his3-ΔHindIII, leu2-3,112, lys2, ura3-53, cox18Δ::KanMX4* [rho+]). Cells were grown on YPD as fermentable medium (1% yeast extract, 2% bactopeptone, and 2% dextrose) or YPEG as nonfermentable medium (1% yeast extract, 2% bactopeptone, 3% ethanol, and 3% vol/vol glycerol). Minimal medium was SD or SGal (0.17% yeast nitrogen base [without amino acids and $(NH_4)_2SO_4$], 0.5% $(NH_4)_2SO_4$, 2% glucose or galactose supplemented with specific amino acids and nucleotides). All strains were grown at 30°C in liquid (with shaking) or solid medium (containing 1.75% agar). We calculated duplication times by measuring the absorbance of cultures with an initial $O.D._{600}$ of 0.01 every 2 h in a Bioscreen C spectrophotometer (Growth Curves, USA). Dilution series were performed by diluting 10-fold a culture of 0.5 $O.D._{600}$ and plating 3 µl on Petri dishes with the indicated medium.

The yeast allotopic $COX2^{W56R}$ gene was recoded for expression from the nucleus and a sequence encoding the MTS of Oxa1 was added at the 5′ end, as previously described (Supekova *et al.*, 2010). The construct was chemically synthesized (GeneScript, Piscataway, NJ) and cloned at the *Not*I site in the pFL61 vector, which contains a phosphoglycerate kinase (*PGK*) promoter and terminator (Minet *et al.*, 1992).

Additional *COX2* mutations (WT, W56K, W56Q, V49Q, L51G, V49Q/L51G, L47Q/V49G, L47Q/V49G/W56R) were constructed using the pFL61 plasmid containing the $COX2^{W56R}$ insert via site-directed mutagenesis, according to the manufacturer's instructions (QuikChange II site-directed mutagenesis kit, Agilent Technologies). The presence of the site-directed mutations was confirmed by DNA sequencing. For the expression of the constructs from centromeric plasmids, the fragments containing the *COX2* constructs flanked by the *PGK* promoter and terminator were cloned from pFL61 into pRS306H upon digestion with *Hin*dIII and *Sma*I restriction enzymes. Nuclear localization was achieved by integration transformation at the *URA3* nuclear locus using the pRS306H plasmid and hygromycin B resistance as a selection (Taxis and Knop, 2006).

Yeast cells were transformed in the presence of lithium acetate and salmon sperm DNA as described (Gietz and Schiestl, 2007). At least 12 transformed individual colonies were grown in Petri dishes containing fresh SD medium and then were replica-plated into YPEG to ensure that the selected colonies had respiratory growth similar to the rest of the transformants.

Isolation of yeast mitochondria

Mitochondria were isolated from 100–200 ml of liquid SGal cultures as previously reported (Herrmann *et al.*, 1994). Briefly, cells were harvested at logarithmic growth phase ($O.D._{600}$ 0.8–1.0), washed with H_2O at 4500 rpm in a Beckman Coulter JA-25.5 rotor (2500 × *g*) for 5 min, resuspended in TD buffer (100 mM Tris, 10 mM dithiothreitol), and centrifuged at 4500 rpm (2500 × *g*) for 5 min. The cells were resuspended in 10 ml of zymoliase buffer (1.2 mM sorbitol, 20 mM KH_2PO_4 [pH 7.4], 3–5 mg zymoliase/g of wet weight), incubated for 1 h in a shaker at 30°C, and centrifuged at 4500 rpm (2500 × *g*) for 5 min at 4°C. The pellet was resuspended in 1 ml of Dounce buffer (0.6 M sorbitol, 10 mM Tris [pH 7.4], 1 mM EDTA, 0.2% bovine serum albumin, 1 mM phenylmethylsulfonyl fluoride [PMSF]) using a homogenizer and pestle (30 strokes). Samples were transferred to 1.5-ml tubes and centrifuged at 4500 rpm in a microcentrifuge (2000 × *g*) for 5 min at 4°C. The supernatants were transferred to new tubes and centrifuged at 12,000 rpm (13,500 × *g*) for 10 min at 4°C. The supernatant (cytosolic fraction) was collected in new tubes and the pellet (mitochondrial fraction) was resuspended in 100 µl of SH buffer (0.6 M sorbitol, 20 mM HEPES, pH 7.4). Protein concentration was determined by a modified Lowry method (Markwell *et al.*, 1978). Mitochondria and cytosolic fractions were frozen and stored at –70°C until use.

Proteinase K protection assays

For protease treatment of mitochondria, 50 µg of mitochondria was gently resuspended in 100 µl of SH buffer and incubated at 20°C for 30 min in the presence of 100 µg/ml Proteinase K; parallel reactions were made in the presence of 1% Triton X-100. PMSF was added to all suspensions (at 4 mM final concentration), which were then incubated on ice for 10 min and centrifuged at 14,000 rpm (18,400 × *g*) for 10 min. Most of the supernatant in each tube was discarded; the pellet was resuspended with 4 µl of 6× loading buffer (375 mM Tris-HCl [pH 6.8], 6% SDS, 48% glycerol, 9% β-mercaptoethanol) + 4 mM PMSF and incubated for 1 min in boiling water before being loaded onto 12% SDS-tricine-PAGE gels.

Sodium carbonate and Triton X-100 extractions

Integral membrane proteins were separated from peripheral or soluble proteins by carbonate extraction. Aggregated proteins were separated from membrane proteins by Triton X-100 extraction. Briefly, 50 µg of mitochondria was incubated with 100 µl of cold 0.1 M Na_2CO_3 (pH 11.0) or with 9.4 µl of 1% Triton X-100 (2 mg Triton X-100/mg protein) for 30 min on ice. The samples were centrifuged at 90,000 × *g* in a TLA 55 rotor for 30 min at 4°C. Supernatants and pellets were incubated with 500 µl of 12.5% TCA for 15 min on ice, followed by centrifugation for 15 min at 14,000 rpm (18,400 × *g*) at 4°C. Samples were washed by adding 500 µl of cold 100% acetone, centrifuged for 10 min at 14,000 rpm (18,400 × *g*) at 4°C, and dried for ~10 min at room temperature. The dried pellets were resuspended in 15 µl of 1× loading buffer and incubated for 1 min in boiling water before loading onto 12% SDS-tricine-PAGE gels.

Gel electrophoresis and in-gel enzymatic activities

Denaturing gel electrophoresis was carried out via SDS-tricine-polyacrylamide gels with 12% acrylamide (Schagger, 1994a). Sample preparation and blue native polyacrylamide gel electrophoresis (BN-PAGE) were carried out as described (Schagger, 1994b). Briefly, mitochondria were washed twice in 250 mM sorbitol, 50 mM Bis-Tris (pH 7.0), and centrifuged at 12,000 rpm (13,500 × *g*) for 10 min at 4°C. The pellet was resuspended in sample buffer (750 mM aminocaproic acid, 50 mM Bis-Tris, pH 7.0) and solubilized with 2 g of lauryl maltoside per g of protein for 30 min with gentle stirring and centrifuged at 13,200 rpm (16,400 × *g*) at 4°C for 12 min. The supernatants were loaded on 5–15% polyacrylamide gradient gels. The stacking gel contained 4% (wt/vol) polyacrylamide. In-gel activities were carried out following established procedures for C*c*O activity (Wittig *et al.*, 2007; Wittig and Schägger, 2007) and ATPase activity (Zerbetto *et al.*, 1997; Wittig and Schägger, 2005). Gels were stained with Coomassie solution (50% ethanol, 10% acetic acid, 0.1% Coomassie Brilliant Blue G) or otherwise transferred and then subjected to immunodetection.

Immunodetection

From SDS-tricine-PAGE, proteins were electrotransferred onto a nitrocellulose Trans-Blot membrane (Bio-Rad) for immunodetection. Membranes were washed, blocked, and independently incubated for 4 h with the following antibodies: anti-Cox2 antibody at a 1:9000 dilution (Invitrogen; Molecular Probes), anti-Oxa1 antibody at a 1:1000 dilution, anti-Hog1 antibody at a 1:2000 dilution (Santa Cruz Biotechnology), and anti-Atp2 antibody at a 1:50,000 dilution. Alkaline phosphatase-conjugated IgGs (1:15,000 for 2 h) were used as secondary antibodies. Insoluble black–purple precipitates were formed upon addition of nitro-blue tetrazolium chloride and 5-bromo-4-chloro-3′-indolyl phosphate *p*-toluidine salt. Images of the immunodecorated polypeptide bands were captured in an HP Scanjet G4050. For immunodetection on previously probed membranes using a different primary antibody, membranes were stripped by incubation for 45 min at 50°C in the presence of 2% SDS, 62.5 mM Tris-HCl, pH 6.8, and 100 mM β-mercaptoethanol.

In silico protein sequence analysis

A TMS1 of 24 residues was considered for the yeast Cox2. The hydrophobicity calculations were performed using the "biological" hydrophobicity scale (Calado-Botelho *et al.*, 2011).

ACKNOWLEDGMENTS

We are grateful to Miriam Vázquez-Acevedo and Nallely Cabrera (Universidad Nacional Autónoma de México [UNAM]) for their expert technical assistance in making some of the constructs used in the present study. We thank Thomas D. Fox (Cornell University) for the gift of most of the strains used in this project, Soledad Funes (UNAM) for the kind gift of the Hog1 antibody and the Δ*cox18* strain, and Johannes M. Herrmann (Technische Universität Kaiserslautern) for the kind gift of the Oxa1 antibody. We also acknowledge Soledad Funes and Juan Miranda Ríos for insightful comments throughout this project. This work was partially supported by Grants 239219 and 279125 from the Consejo Nacional de Ciencia y Tecnología (CONACyT, Mexico) and IN 208917 from the Dirección General de Asuntos del Personal Académico (DGAPA-UNAM, Mexico) to D.G.-H. CONACyT also supported the graduate studies of D.R.-G. with a fellowship. The two summer research stays of P.P.H. in Mexico (2015 and 2016) and the posdoctoral fellowship of J.G.-R. were supported by DGAPA-UNAM. This article partially fulfills the requirements of D.R.-G. for a PhD from the Biomedical Sciences PhD program (Programa de Doctorado en Ciencias Biomédicas, Universidad Nacional Autónoma de México).

REFERENCES

Adams K, Palmer JD (2003). Evolution of mitochondrial gene content: gene loss and transfer to the nucleus. Mol Phylogenet Evol 29, 380–395.

Adams KL, Song K, Roessler PG, Nugent JM, Doyle JL, Doyle JJ, Palmer JD (1999). Intracellular gene transfer in action: dual transcription and multiple silencings of nuclear and mitochondrial cox2 genes in legumes. Proc Natl Acad Sci USA 96, 13863–13868.

Andersson H, von Heijne G (1994). Membrane protein topology: effects of delta mu H+ on the translocation of charged residues explain the "positive inside" rule. EMBO J 13, 2267–2272.
Björkholm P, Ernst AM, Hagström E, Andersson SGE (2017). Why mitochondria need a genome revisited. FEBS Lett 591, 65–75.
Bokori-Brown M, Holt IJ (2006). Expression of algal nuclear ATP synthase subunit 6 in human cells results in protein targeting to mitochondria but no assembly into ATP synthase. Rejuvenation Res 9, 455–469.
Bonnet C, Augustin S, Ellouze S, Bénit P, Bouaita A, Rustin P, Sahel J-A, Corral-Debrinski M (2008). The optimized allotopic expression of ND1 or ND4 genes restores respiratory chain complex I activity in fibroblasts harboring mutations in these genes. Biochim Biophys Acta 1783, 1707–1717.
Boominathan A, Vanhoozer S, Basisty N, Powers K, Crampton AL, Wang X, Friedricks N, Schilling B, Brand MD, O'Connor MS (2016). Stable nuclear expression of ATP8 and ATP6 genes rescues a mtDNA complex V null mutant. Nucleic Acids Res 44, 9342–9357.
Burger G, Gray MW, Lang BF (2003). Mitochondrial genomes: anything goes. Trends Genet 19, 709–716.
Calado-Botelho S, Osterberg M, Reichert AS, Yamano K, Björkholm P, Endo T, von Heijne G, Kim H (2011). TIM23-mediated insertion of transmembrane α-helices into the mitochondrial inner membrane. EMBO J 30, 1003–1011.
Calvo SE, Mootha VK (2010). The mitochondrial proteome and human disease. Annu Rev Genomics Hum Genet 11, 25–44.
Chiti F, Stefani M, Taddei N, Ramponi G, Dobson CM (2003). Rationalization of the effects of mutations on peptide and protein aggregation rates. Nature 424, 805–808.
Claros MG, Perea J, Shu Y, Samatey FA, Popot JL, Jacq C (1995). Limitations to in vivo import of hydrophobic proteins into yeast mitochondria. The case of a cytoplasmically synthesized apocytochrome b. Eur J Biochem 771, 762–771.
Cruz-Torres V, Vázquez-Acevedo M, García-Villegas R, Pérez-Martínez X, Mendoza-Hernández G, González-Halphen D (2012). The cytosol-synthesized subunit II (Cox2) precursor with the point mutation W56R is correctly processed in yeast mitochondria to rescue cytochrome oxidase. Biochim Biophys Acta 1817, 2128–2139.
Cwerman-Thibault H, Augustin S, Lechauve C, Ayache J, Ellouze S, Sahel J-A, Corral-Debrinski M (2015). Nuclear expression of mitochondrial ND4 leads to the protein assembling in complex I and prevents optic atrophy and visual loss. Mol Ther—Methods Clin Dev 2, 15003.
Daley DO, Adams KL, Clifton R, Qualmann S, Millar AH, Palmer JD, Pratje E, Whelan J (2002a). Gene transfer from mitochondrion to nucleus: novel mechanisms for gene activation from Cox2. Plant J 30, 11–21.
Daley DO, Clifton R, Whelan J (2002b). Intracellular gene transfer: reduced hydrophobicity facilitates gene transfer for subunit 2 of cytochrome c oxidase. Proc Natl Acad Sci USA 99, 10510–10515.
De Grey ADNJ (2000). Mitochondrial gene therapy: an arena for the biomedical use of inteins. Trends Biotechnol 18, 394–399.
DiMauro S, Hirano M, Schon EA (2006). Approaches to the treatment of mitochondrial diseases. Muscle Nerve 34, 265–283.
Dobson CM (2004). Principles of protein folding, misfolding and aggregation. Semin Cell Dev Biol 15, 3–16.
Elliott LE, Saracco SA, Fox TD (2012). Multiple roles of the Cox20 chaperone in assembly of *Saccharomyces cerevisiae* cytochrome c oxidase. Genetics 190, 559–567.
Figueroa-Martínez F, Vázquez-Acevedo M, Cortés-Hernández P, García-Trejo JJ, Davidson E, King MP, González-Halphen D (2011). What limits the allotopic expression of nucleus-encoded mitochondrial genes? the case of the chimeric Cox3 and Atp6 genes. Mitochondrion 11, 147–154.
Gietz RD, Schiestl RH (2007). Quick and easy yeast transformation using the LiAc/SS carrier DNA/PEG method. Nat Protoc 2, 35–37.
González-Halphen D, Funes S, Pérez-Martínez X, Reyes-Prieto A, Claros MG, Davidson E, King MP (2004). Genetic correction of mitochondrial diseases. Ann NY Acad Sci 1019, 232–239.
Gorman GS, Chinnery PF, DiMauro S, Hirano M, Koga Y, McFarland R, Suomalainen A, Thorburn DR, Zeviani M, Turnbull DM (2016). Mitochondrial diseases. Nat Rev Dis Prim 2, 1–23.
Guy J, Qi X, Pallotti F, Schon EA, Manfredi G, Carelli V, Martinuzzi A, Hauswirth WW, Lewin AS (2002). Rescue of a mitochondrial deficiency causing Leber hereditary optic neuropathy. Ann Neurol 52, 534–542.
Herrmann JM, Fölsch H, Neupert W, Stuart RA (1994). Isolation of yeast mitochondria and study of mitochondrial protein translation. In: Cell Biology: A Laboratory Handbook, Vol. 1, ed. JE Celis, San Diego: Academic Press, 538–544.
Jiménez-Suárez A, Vázquez-Acevedo M, Rojas-Hernández A, Funes S, Uribe-Carvajal S, González-Halphen D (2012). In *Polytomella* sp. mitochondria, biogenesis of the heterodimeric COX2 subunit of cytochrome c oxidase requires two different import pathways. Biochim Biophys Acta 1817, 819–827.
Johnston IG, Williams BP (2016). Evolutionary inference across eukaryotes identifies specific pressures favoring mitochondrial gene retention. Cell Syst 2, 101–111.
Kyriakouli DS, Boesch P, Taylor RW, Lightowlers RN (2008). Progress and prospects: gene therapy for mitochondrial DNA disease. Gene Ther 15, 1017–1023.
Manfredi G, Fu J, Ojaimi J, Sadlock JE, Kwong JQ, Guy J, Schon EA (2002). Rescue of a deficiency in ATP synthesis by transfer of MTATP6, a mitochondrial DNA-encoded gene, to the nucleus. Nat Genet 30, 394–399.
Markwell MAK, Haas SM, Bieber LL, Tolbert NE (1978). A modification of the Lowry procedure to simplify protein determination in membrane and lipoprotein samples. Anal Biochem 87, 206–210.
Martin W, Herrmann RG (1998). Update on gene transfer from organelles to the nucleus. Gene transfer from organelles to the nucleus: how much, what happens, and why? Plant Physiol 118, 9–17.
Minet M, Dufour M, Lacroute F (1992). Complementation of *Saccharomyces cerevisiae* auxotrophic mutants by *Arabidopsis thaliana* cDNAs. Plant J 2, 417–422.
Oca-Cossio J, Kenyon L, Hao H, Moraes CT (2003). Limitations of allotopic expression of mitochondrial genes in mammalian cells. Genetics 165, 707–720.
Ojaimi J, Pan J, Santra S, Snell WJ, Schon EA (2002). An algal nucleus-encoded subunit of mitochondrial ATP synthase rescues a defect in the analogous human mitochondrial-encoded subunit. Mol Biol Cell 13, 3836–3844.
Perales-Clemente E, Fernández-Silva P, Acín-Pérez R, Pérez-Martos A, Enríquez JA (2011). Allotopic expression of mitochondrial-encoded genes in mammals: achieved goal, undemonstrated mechanism or impossible task? Nucleic Acids Res 39, 225–234.
Pérez-Martínez X, Antaramian A, Vazquez-Acevedo M, Funes S, Tolkunova E, d'Alayer J, Claros MG, Davidson E, King MP, González-Halphen D (2001). Subunit II of cytochrome c oxidase in chlamydomonad algae is a heterodimer encoded by two independent nuclear genes. J Biol Chem 276, 11302–11309.
Rubalcava-Gracia D, Vázquez-Acevedo M, Funes S, Pérez-Martínez X, González-Halphen D (2018). Mitochondrial versus nuclear gene expression and membrane protein assembly: the case of subunit 2 of yeast cytochrome c oxidase. Mol Biol Cell 29, 820–833.
Schagger H (1994a). Denaturing electrophoretic techniques. In: A Practical Guide to Membrane Protein Purification, ed. G von Jagow and H Schagger, San Diego: Academic Press, 55–79.
Schagger H (1994b). Native gel electrophoresis. In: A Practical Guide to Membrane Protein Purification, ed. G von Jagow and H Schagger, San Diego: Academic Press, 81–104.
Supekova L, Supek F, Greer JE, Schultz PG (2010). A single mutation in the first transmembrane domain of yeast COX2 enables its allotopic expression. Proc Natl Acad Sci USA 107, 5047–5052.
Szafranski P (2017). Evolutionarily recent, insertional fission of mitochondrial cox2 into complementary genes in bilaterian metazoa. BMC Genomics 18, 269.
Taxis C, Knop M (2006). System of centromeric, episomal, and integrative vectors based on drug resistance markers for saccharomyces cerevisiae. Biotechniques 40, 73–78.
Taylor RW, Turnbull DM (2005). Mitochondrial DNA mutations in human disease. Nat Rev Genet 6, 389–402.
Timmis JN, Ayliffe MA, Huang CY, Martin W (2004). Endosymbiotic gene transfer: organelle genomes forge eukaryotic chromosomes. Nat Rev Genet 5, 123–135.
von Heijne G (1992). Membrane protein structure prediction. Hydrophobicity analysis and the positive-inside rule. J Mol Biol 225, 487–494.
Wittig I, Karas M, Schägger H (2007). High resolution clear native electrophoresis for in-gel functional assays and fluorescence studies of membrane protein complexes. Mol Cell Proteomics 6, 1215–1225.
Wittig I, Schägger H (2005). Advantages and limitations of clear-native PAGE. Proteomics 5, 4338–4346.
Wittig I, Schägger H (2007). Electrophoretic methods to isolate protein complexes from mitochondria. Methods Cell Biol 80, 723–741.
Zerbetto E, Vergani L, Dabbeni-Sala F (1997). Quantification of muscle mitochondrial oxidative phosphorylation enzymes via histochemical staining of blue native polyacrylamide gels. Electrophoresis 18, 2059–2064.

INFORME DE LABORES 2019

Received: 20 April 2018 | Revised: 26 July 2018 | Accepted: 13 August 2018

DOI: 10.1111/tbed.12998

Check for updates

ORIGINAL ARTICLE

WILEY Transboundary and Emerging Diseases

Identification and genomic characterization of influenza viruses with different origin in Mexican pigs

Manuel Saavedra-Montañez[1] | Luis Vaca[2] | Humberto Ramírez-Mendoza[1] | Carmen Gaitán-Peredo[3] | Rebeca Bautista-Martínez[3] | René Segura-Velázquez[4] | Jacquelynne Cervantes-Torres[5] | José Ivan Sánchez-Betancourt[3]

[1]Departamento de Microbiología e Inmunología, Facultad de Medicina Veterinaria y Zootecnia (FMVZ), Universidad Nacional Autónoma de México (UNAM), México City, CP,México

[2]Instituto de Fisiología Celular UNAM, México City, CP,México

[3]Departamento de Medicina y Zootecnia de Cerdos, FMVZ-UNAM, México City, CP, México

[4]Unidad de Investigación FMVZ-UNAM, México City, CP,México

[5]Instituto de Investigaciones Biomédicas, UNAM, México City, CP, México

Correspondence
José Ivan Sánchez Betancourt, Departamento de Medicina y Zootecnia de Cerdos FMVZ-UNAM, México City, CP 04510, México.
Email: aisb_7@yahoo.com.mx

Funding information
CONACYT, Grant/Award Number: 254244, 393094; PAPIIT, Grant/Award Number: IN223514

Abstract

Swine influenza is a worldwide disease, which causes damage to the respiratory system of pigs. The H1N1 and H3N2 subtypes circulate mainly in the swine population of Mexico. There is evidence that new subtypes of influenza virus have evolved genetically and have been rearranged with human viruses and from other species; therefore, the aim of our study was to identify and characterize the genetic changes that have been generated in the different subtypes of the swine influenza virus in Mexican pigs. By sequencing and analyzing phylogenetically the eight segments that form the virus genome, the following subtypes were identified: H1N1, H3N2, H1N2 and H5N2; of which, a H1N1 subtype had a high genetic relationship with the human influenza virus. In addition, a H1N2 subtype related to the porcine H1N2 virus reported in the United States was identified, as well as, two other viruses of avian origin from the H5N2 subtype. Particularly for the H5N2 subtype, this is the first time that its presence has been reported in Mexican pigs. The analysis of these sequences demonstrates that in the swine population of Mexico, circulate viruses that have suffered punctual-specific mutations and rearrangements of their proteins with different subtypes, which have successfully adapted to the Mexican swine population.

KEYWORDS
complete sequences, H5N2, phylogenetic analysis, swine influenza virus Mexico

1 | INTRODUCTION

Swine influenza is a worldwide disease that causes damage to the respiratory system of pigs (Bouvier & Palese, 2008). Influenza viruses belong to the Orthomixoviridae family and have a genome composed of eight segments of ssRNA (–), where each one encodes for one or two proteins (Flint & Racaniello, 2001; King, Adams, Carstens, & Lefkowitz, 2012). The evolution of these viruses occurs through antigenic drift (Drift), characterized by the selection of new strains that contain amino acid changes in hemagglutinin (HA) and neuraminidase (NA) proteins; these changes are responsible for seasonal influenza infections (Carrat & Flahault, 2007; Treanor, 2004). In addition, these viruses can also have genetic rearrangements (Shift) associated with the emergence of pandemic viruses; these occur when a host cell is infected by more than one different virus subtype and the viral genomic segments are rearranged, generating a new combination (Boni, 2008; Webster, Laver, Air, & Schild, 1982; Zambon, 1999). Some accumulated and continuous mutations in the HA protein of the influenza virus have generated new antigenic strains that cause annual epidemics (Liao, Lee, Ko, & Hsiung, 2008). Pigs can naturally or experimentally be infected with viruses of avian or human origin because in the epithelial cells of the trachea, they express avian and

human type receptors (Ito et al., 1998; Scholtissek, Bürger, Bachmann, & Hannoun, 1983), which is why they are considered as mixing containers (Castrucci et al., 1993; Christoph Scholtissek, 1995). Currently, three subtypes of influenza viruses circulate mainly in pigs around the world: H1N1, H3N2 and H1N2 (Chambers, Hinshaw, Kawaoka, Easterday, & Webster, 1991). In the Mexican swine population, it has been reported the circulation of the H1N1 and H3N2 subtypes (Avalos, Sanchez, & Trujillo, 2011; López-Robles, Montalvo-Corral, Caire-Juvera, Ayora-Talavera, & Hernández, 2012); however, there are several studies showing the circulation of new subtypes of influenza virus, which have evolved genetically and have been rearranged with human viruses and from other species (Aguirre et al., 2014; Escalera-Zamudio et al., 2012; Nelson, Culhane et al., 2015; Nelson, Schaefer, Gava, Cantão, & Ciacci-zanella, 2015). On the other hand, there is evidence of the transmission of influenza viruses between different species (bird, pig, equine and human), as well as, rearrangements with different subtypes (H9N2, H4N6, H2N3, H3N8, H3N1, H5N2) in distinct parts of the world (Karasin, Brown, Carman, & Olsen, 2000; Lee et al., 2009; Ma et al., 2007; Peiris et al., 2001; Shin et al., 2006; Tu et al., 2009). These events highlight the requirement for a greater epidemiological surveillance, emphasizing the interest of isolating and characterizing the influenza viruses that circulate currently in the Mexican swine population.

2 | MATERIALS AND METHODS

2.1 | Samples

The research was carried out using 486 pig lung tissue samples from different production units located in twelve states of Mexico (Jalisco, State of Mexico, Guanajuato, Sonora, Michoacan, Puebla, Morelos, Yucatan, Queretaro, Hidalgo, Veracruz and Nuevo Leon) (Figure 1). The criterion for obtaining the samples was to use pigs that presented suggestive signology to infection with influenza virus.

The samples were remitted and processed in the Biosafety Laboratory Level 3 of the Medicine and Zootechnics Swine Department (DMZC) from the Veterinary Medicine and Zootechnics Faculty (FMVZ), National Autonomous University of Mexico (UNAM).

2.2 | RNA extraction

A total of 0.5 gr from each lung tissue was powdered in liquid nitrogen and homogenized in extraction buffer in order to obtain the RNA. RNA extraction was performed with the column technique using the QIAamp Viral RNA mini kit (QIAGEN, Germany) commercial kit, following the manufacturer's specifications. The purified nucleic acid was resuspended in 60 µl of elution buffer and stored at -70°C.

2.3 | qRT-PCR for the M gene

In order to confirm the presence of influenza virus A in the lung samples, a Real Time Reverse Transcription and Polymerase Chain Reaction (qRT-PCR) assay was performed using the FIND-IT INFLUENZA® (Biotecmol, México) commercial kit, directed to the identification of the matrix gene (M) and under the following conditions: 42°C for 30 min for reverse transcription, 95°C for 10 min for initial denaturation, 40 cycles at 95°C for 15 s for denaturation, 60°C for 45 s for annealing and 72°C for 5 min for extension.

2.4 | Sequencing of the Influenzavirus genome

The positive lung samples to the presence of influenza viruses were subjected to RT-PCR for the amplification of the eight gene segments of the virus, using the PathAmp™ FluA Reagents kit (Life Technologies, Carlsbad, CA) and a GeneAmp 9700 end point thermocycler (Applied Biosystems, CA). The RT-PCR products were visualized by electrophoresis in a 0.8% agarose gel.

Once the amplifications were obtained, the eight viral segments were sequenced using an Ion Torrent Genome Machine (PGM) System, following the manufacturer's specifications. Briefly, 100 ng of DNA input was used to prepare a library using the Ion Xpress™ Plus Fragment Library Kit (Life Technologies) by physical fragmentation of genome segments with the Bioruptor® Sonication System, in order to generate fragments of approximately 200 base pairs (bp). DNA fragments were linked to Ion-compatible adapters and amplified using the Ion PGM™Hi-Q™ OT2 Kit (Life Technologies) on an Ion OneTouch™ 2 System. The sequencing reaction was carried out using an Ion 314 Chip v2 and the Ion PGM™ Hi-Q™ Sequencing kit (Life Technologies). The obtained readings were subjected to quality filtering using the FastQC plug-in, and all of them were aligned with a Q-score ≥ 20 and assembled with the AssemblerSPAdes v 5.4.0 program. The average genomic coverage depth of the Ion Torrent PGM was up to 300-fold.

2.5 | Phylogenetic analysis

The obtained sequences were compared with those reported in the GenBank, selecting those with an identity percentage higher than 95%, using BLAST (Basic Local Alignment Search Tool) from the NCBI (National Center for Biotechnology) ("Nucleotide BLAST 2017: Search nucleotide databases using a nucleotide query"). The phylogenetic analysis was performed independently for each genomic segment with the MEGA 7.0.26 software the evolutionary history was inferred using the Maximum Likelihood method based on the General Time Reversible (GTR) model and discrete Gamma distribution with invariant sites was used (Kumar, Stecher, & Tamura, 2016; Nei & Kumar, 2000). The trees were edited with the FIGTREE v1.4.3 program ("FigTree 2017: Molecular evolution, Phylogenetics and Epidemiology").

2.6 | Viral isolation

For viral isolation, sterile 200 µl of lung suspension were inoculated into the allantoic cavity of ALPES1® embryos of 9–11 days, free of specific pathogens (SPF) and incubated at 37°C. The allantoic fluid

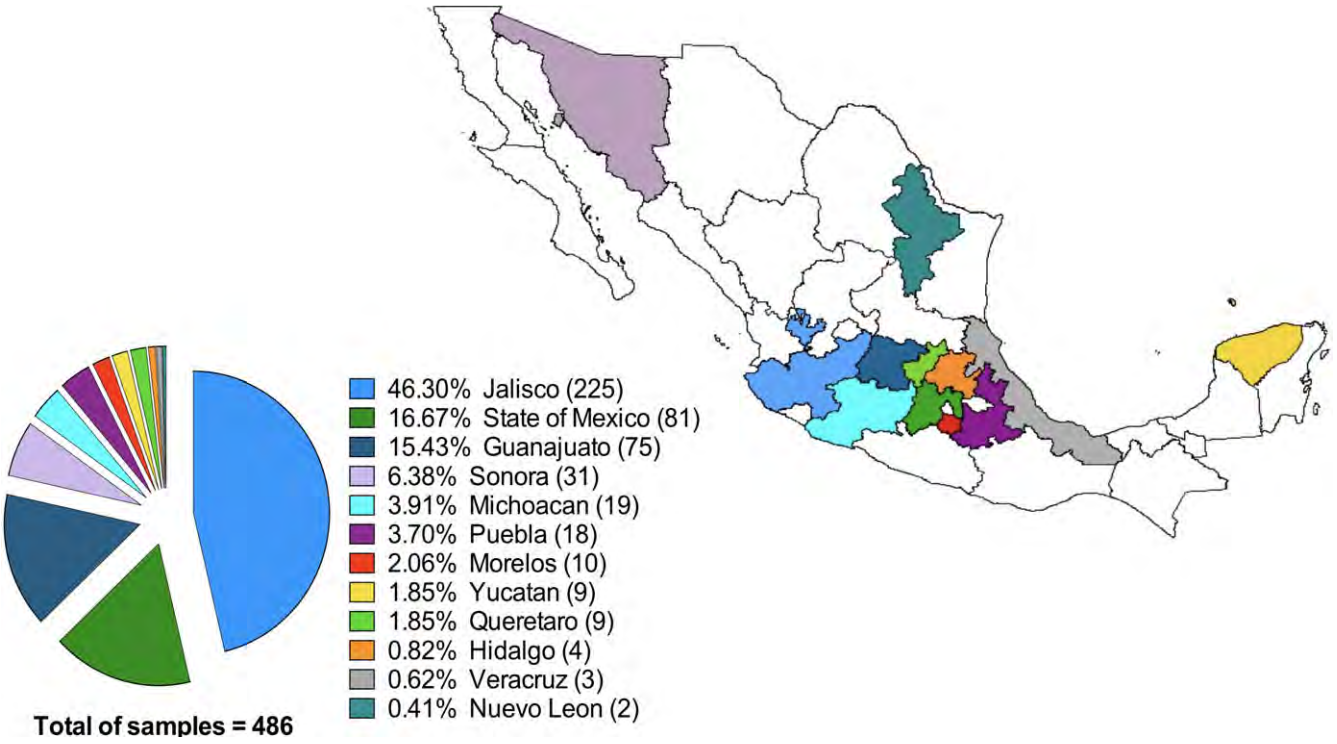

FIGURE 1 Percentage and number of samples per state. Different colors in the map represent the sampled states; whereas the graph shows the percentage and number of samples obtained for each state [Colour figure can be viewed at wileyonlinelibrary.com]

was collected at 24, 48 and 72 hr after inoculation and centrifuged at 423 *g* for 5 min (World Organisation for Animal Health, 2015). The viruses were titrated by hemagglutination (Ramírez, Carreón, & Mercado, 1996).

3 | RESULTS

Of 486 pig pulmonary samples, 10 (0.48%) were positive for influenza virus and 476 (99.52%) negative to the presence of this virus. From the positive samples, the complete genome of 8 influenza viruses was sequenced; three samples corresponded to the H1N1 subtype from the states of Guanajuato (2) and Jalisco (1), and two corresponded to the H3N2 subtype from the states of Jalisco and Hidalgo. An isolated H1N2 sequence was also obtained in the state of Guanajuato, while two H5N2 sequences came from Guanajuato and the State of Mexico (Table 1).

3.1 | Phylogenetic analysis of HA and NA genes

Regarding the evolutionary structure of the inferred topologies of the HA gene, the analysis of the sequences indicated that the HA protein of the GtoDMZC01(H1N2) virus was found in a clade with porcine and human H1N2 influenza viruses, reported in the United States in the period 2005-2010; whereas the HA of the GtoDMZC02(H5N2) and EdoMexDMZC03(H5N2) viruses, were found in a clade of avian influenza H5N2 viruses isolated in Mexico during 1994 and 1995. The HA of the GtoDMZC04(H1N1) virus was found in a clade of H1N1 human influenza viruses, isolated in the United States in 2013 and with one from Mexico isolated in 2014. On the other hand, there is homology between the HAs of JalDMZC05(H1N1) and GtoDMZC09(H1N1) viruses, which were found in a clade of porcine H1N1 influenza viruses isolated in Mexico in the period 2012-2014. The HA of the HgoDMZC11(H3N2) virus was found in a clade of Mexican H3N2 swine influenza viruses isolated in 2012 and 2013. The HA of the JalDMZC12(H3N2) virus was found in a clade with porcine influenza viruses from Canada and the United States, isolated during 2005 and 2006 (Figure 2).

Regarding the evolutionary structure of the inferred topologies from the NA gene, the analysis of the sequences indicated that the NA proteins of the GtoDMZC01(H1N2) and HgoDMZC11(H3N2) viruses were found in a clade with the Mexican H3N2 swine influenza viruses isolated in 2012 and 2013; while the NA of the GtoDMZC02(H5N2) and EdoMexDMZC03(H5N2) viruses were found in a clade of avian influenza H5N2 viruses isolated in Mexico during 1994 and 1995, and with the influenza viruses isolated in the United States in 1994 and 1995. The NA of the GtoDMZC04(H1N1) virus was found in a clade with H1N1 human influenza viruses isolated in the United States during 2013 and 2014. The analysis of the sequences indicated that the NA protein of the JalDMZC05(H1N1) and GtoDMZC09(H1N1) viruses were found in a clade of porcine H1N1 influenza viruses isolated in Mexico in the period of 2012–2014. The NA of the JalDMZC12(H3N2) virus was found in a clade with porcine influenza viruses from Canada and the United States, isolated during 2005 and 2006 (Figure 3).

TABLE 1 Number of positives and negatives according to the origin and subtype of the obtained sequences in our study

	State	(−)*	(+)*	Sequences obtained	Identification in trees**
Slaughterhouse					
	Jalisco	207	1	A/swine/Mexico/JalDMZC12/2015(H3N2)[a] JalDMZC12(H3N2)[b] MH006723-MH006730[c]	JalDMZC12H3N2_swine_MEX_2015.
	State of Mexico	78	0	-	
	Guanajuato	60	1	A/swine/Mexico/GtoDMZC09/2015(H1N1)[a] GtoDMZC09(H1N1)[b] MH006699-MH006706[c]	GtoDMZC09H1N1_swine_MEX_2015.
	Michoacan	3	1	-	
	Hidalgo	2	1	A/swine/Mexico/HgoDMZC11/2015(H3N2)[a] HgoDMZC11(H3N2)[b] MH006715-MH006722[c]	HgoDMZC11H3N2_swine_MEX_2015.
	Puebla	3	0	-	
Farm					
	Sonora	30	1	-	
	Jalisco	16	1	A/swine/Mexico/JalDMZC05/2015(H1N1)[a] JalDMZC05(H1N1)[b] MH013200-MH013207[c]	JalDMZC05H1N1_swine_MEX_2015.
	Michoacan	15	0	-	
	Puebla	15	0	-	
	Guanajuato	11	3	A/swine/Mexico/GtoDMZC04/2015(H1N1)[a] GtoDMZC04(H1N1)[b] MH013192-MH013199[c] A/swine/Mexico/GtoDMZC01/2014(H1N2)[a] GtoDMZC01(H1N2)[b] KT225468-KT225475[c] A/swine/Mexico/GtoDMZC02/2014(H5N2)[a] GtoDMZC02(H5N2)[b] KU141369-KU141376[c]	GtoDMZC04H1N1_swine_MEX_2015. GtoDMZC01H1N2_swine_MEX_2014. GtoDMZC02H5N2_swine_MEX_2014.
	Morelos	10	0	-	
	Queretaro	9	0	-	
	Yucatan	9	0	-	
	Veracruz	3	0	-	
	State of Mexico	2	1	A/swine/Mexico/EdoMexDMZC03/2015(H5N2)[a] EdoMexDMZC03(H5N2)[b] MH013208-MH013215[c]	EMXDMZC03H5N2_swine_MEX_2015.
	Nuevo Leon	2	0	-	
	Hidalgo	1	0	-	
Total		**476**	**10**	**8**	

[a]International classification for each virus. [b]Abbreviations used for each virus. [c]Genbank accession numbers for each virus. [d]by the qRT-PCR assay. [e]Identification used in the construction of inferred phylogenetic trees.

Regarding the origin identification of the eight genetic segments of the influenza viruses isolated in Mexico, it is clear that the eight segments that form the GtoDMZC01(H1N2) virus have a porcine origin; the genes of the PB1, PA, NP and NS proteins correspond to the H1N1 subtype, the NA to the H3N2 subtype and the proteins PB2, HA and M to the H1N2 subtype. In the case of the GtoDMZC02(H5N2) and EdoMexDMZC03(H5N2) viruses, their eight segments have an avian origin and correspond to the H5N2 subtype. On the other hand, the eight segments of the GtoDMZC04(H1N1) virus have a human origin and correspond to the H1N1 subtype; whereas, the eight segments of the JalDMZC05 (H1N1) virus have a porcine origin and also correspond to the H1N1 subtype. The eight segments of the GtoDMZC09(H1N1) virus have a porcine origin and the PB2, PB1, PA, HA, NP, NA and M proteins correspond to the H1N1 subtype; however, NS belongs to the H3N2 subtype. The eight segments of the HgoDMZC11

INFORME DE LABORES 2019

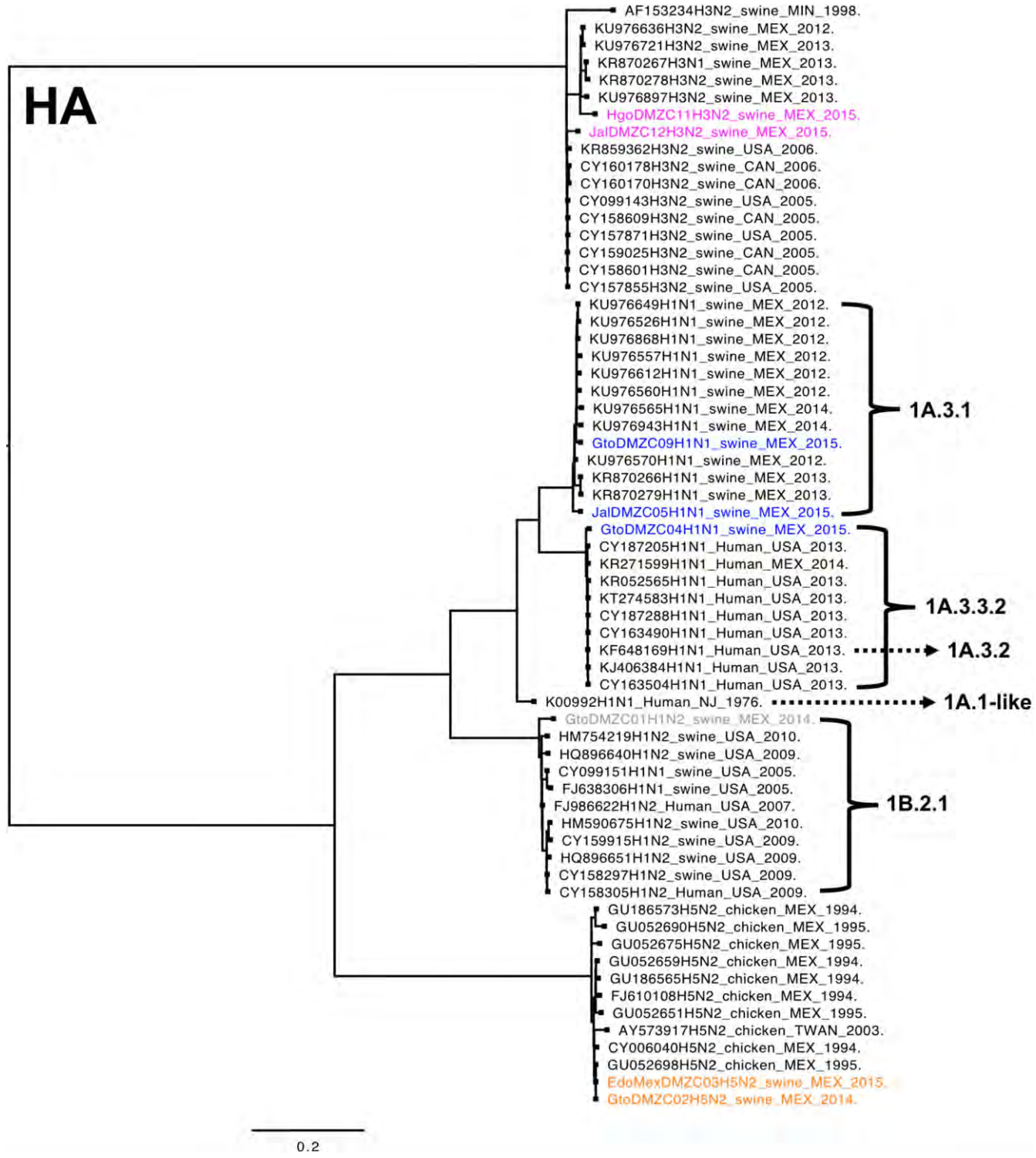

FIGURE 2 The tree is drawn to scale, with branch lengths corresponding to the number of substitutions per site. Mexican isolates are observed in color depending on the subtype: H1N1 (blue), H3N2 (pink), H1N2 (gray), H5N2 (orange). The brackets and arrows indicate the classification of Anderson et al., 2016 [Colour figure can be viewed at wileyonlinelibrary.com]

(H3N2) virus have a porcine origin; the PB1, NP, M and NS proteins correspond to the H1N1 subtype and the PB2, PA, HA and NA proteins to the H3N2 subtype. Finally, the eight segments of the JalDMZC12(H3N2) virus have a porcine origin and correspond to the H3N2 subtype (Table 2).

4 | DISCUSSION

In our study, the central region of Mexico is where the largest number of sequences was obtained; therefore, it could be the region where the largest number of rearrangements occur with viruses of

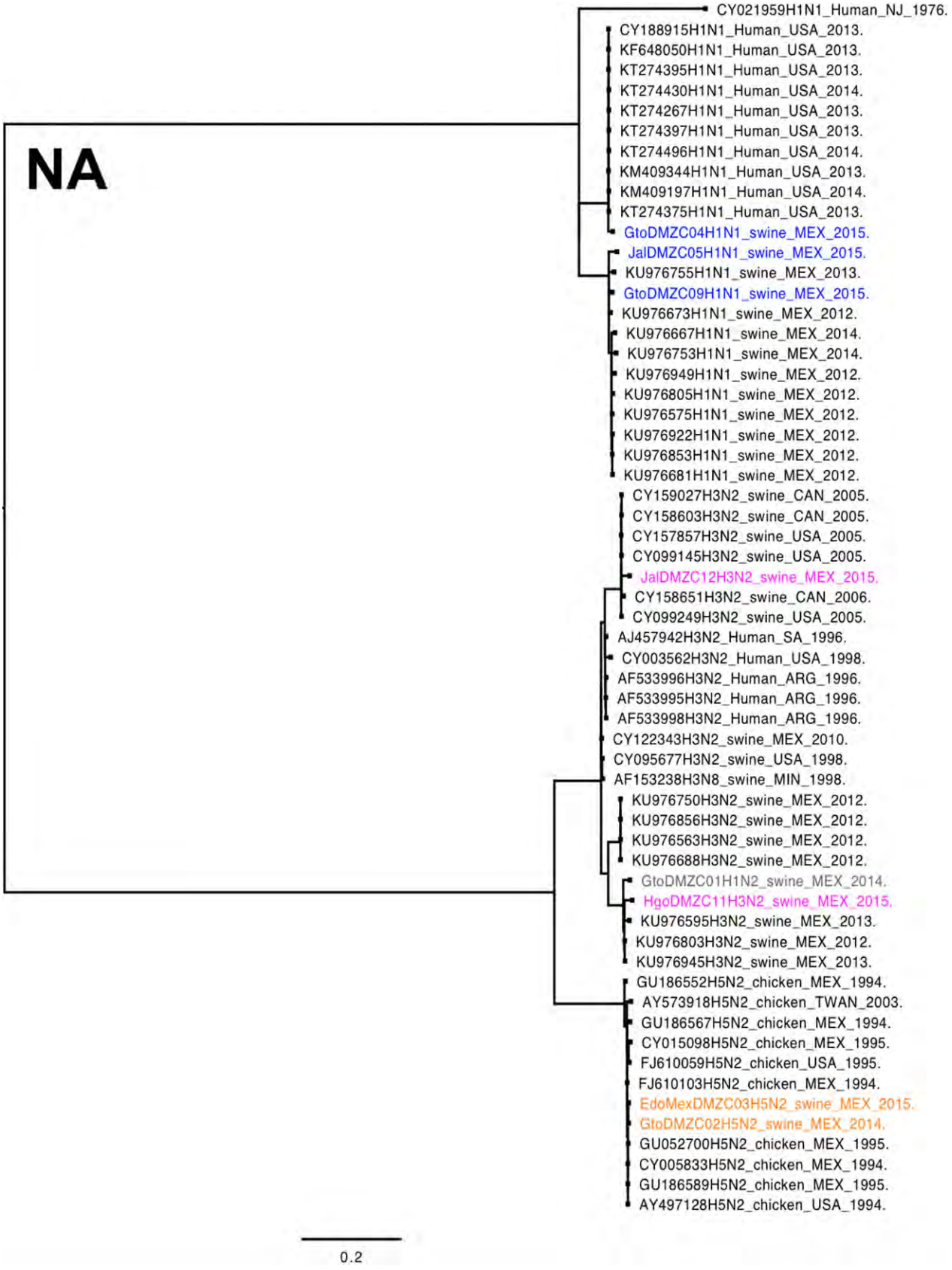

FIGURE 3 The tree is drawn to scale, with branch lengths corresponding to the number of substitutions per site. Mexican isolates are observed in color depending on the subtype: H1N1 (blue), H3N2 (pink), H1N2 (gray), H5N2 (orange) [Colour figure can be viewed at wileyonlinelibrary.com]

TABLE 2 Origin of the genetic segments of swine influenza viruses identified in Mexico [Colour table can be viewed at wileyonlinelibrary.com]

SEGMENT	1	2	3	4	5	6	7	8
PROTEIN	PB2	PB1	PA	HA	NP	NA	M	NS
A/swine/Mexico/GtoDMZC01/2014(H1N2)	S	S	S	S	S	S	S	S
A/swine/Mexico/GtoDMZC02/2014(H5N2)	C	C	C	C	C	C	C	C
A/swine/Mexico/EdoMexDMZC03/2015(H5N2)	C	C	C	C	C	C	C	C
A/swine/Mexico/GtoDMZC04/2015(H1N1)	H	H	H	H	H	H	H	H
A/swine/Mexico/JalDMZC05/2015(H1N1)	S	S	S	S	S	S	S	S
A/swine/Mexico/GtoDMZC09/2015(H1N1)	S	S	S	S	S	S	S	S
A/swine/Mexico/HgoDMZC11/2015(H3N2)	S	S	S	S	S	S	S	S
A/swine/Mexico/JalDMZC12/2015(H3N2)	S	S	S	S	S	S	S	S

Notes. The Mexican isolates are located in the left side column and the segments of each protein are represented by a color chart depending on the subtype to which they belong: H1N1 (blue), H3N2 (pink), H1N2 (gray) and H5N2 (orange).
The letters that are inside the coloring boxes indicate the species to which they correspond: swine (S), chicken (C) and human (H).

different subtypes, due to production conditions where different species interact in the same habitat (INEGI, 2007).

In our analysis, we identified that in the GtoDMZC01(H1N2), GtoDMZC09(H1N1) and HgoDMZC11(H3N2) viruses, there are rearrangements between different subtypes. On the other hand, the inter-species barrier crossing was appreciated in the following viruses: GtoDMZC02(H5N2) and EdoMexDMZC03(H5N2), which were transferred intact from chicken to pig; and in GtoDMZC04 (H1N1) which was transferred intact from human to pig. Only two viruses were found without change JalDMZC05(H1N1) and JalDMZC12(H3N2). Several phylogenetic analyzes suggest that the transmission between species has occurred from birds to pigs (Karasin et al., 2000; Lee et al., 2009; Peiris et al., 2001), horses to pigs (Tu et al., 2009), and from humans to pigs (Nelson, Gramer, Vincent, & Holmes, 2012; Nelson et al., 2014).

There are several studies that have reported the transmission of influenza viruses between humans and pigs, suggesting that these viruses have circulated without being detected (Cappuccio et al., 2011; Nelson, Culhane et al., 2015; Nelson, Schaefer et al., 2015). In our study, we identified one subtype of viruses of human origin in Mexican pigs and although there are surveillance data regarding influenza viruses in the human population of this country ("Dirección General de Epidemiología, 2017", "FluNet, 2017"). Although, it has been reported that the H1N1 and H3N2 subtypes are officially circulating in the Mexican swine population, until 2012, a seroprevalence of 80.26% was reported for the first time in Mexico for the H1N2 subtype (Lara-Puente, 2012); whereas in other study, the serological evidence for the H1N2 subtype was shown since 2010 (Gaitán-Peredo, 2016). In addition, a virus was isolated in the central region of Mexico, where the genetic characterization and phylogenetic analysis determined that it corresponded to an H1N2 influenza virus, and that the segments came from humans and pigs, besides reporting a 26.74% seroprevalence towards the same subtype (Sánchez-Betancourt, Cervantes-Torres, Saavedra-Montañez, & Segura-Velázquez, 2017). In our study, an H1N2 influenza virus was phylogenetically analyzed, showing that all of its segments have a porcine origin; however, it is rearranged with the H1N1 and H3N2 subtypes.

In 2008, two H5N2 viruses were reported in Korea and were isolated from pigs. The sequencing and phylogenetic analysis of the proteins determined that the Sw/Korea/C12/08 isolate corresponds to a fully avian virus from wild birds (Lee et al., 2009), similar to the H5N2 viruses reported in our study, where all their proteins correspond to an avian virus. However, in our analysis, the H5N2 subtypes were located in a clade of influenza viruses that originated from production birds (chicken) that were isolated and characterized in Mexico during 1994 and 1995. This coincided with several low-pathogenicity outbreaks of influenza viruses in 1994, which mutated into a high pathogenicity H5N2 strain during 1995 ("Servicio Nacional de Sanidad, Inocuidad y Calidad Agroalimentaria, 2017").

In Mexico there is an evident scenario for the transmission of chicken virus to pigs, due to the existence of mixed production systems, where two different species (chicken and pigs) share physical spaces (INEGI, 2007). However, the participation of dogs in the dissemination and the interspecies transmission of influenza viruses should not be ruled out (Giese et al., 2008; Song et al., 2013). In China during 2009, an H5N2 influenza virus was isolated from a dog that showed respiratory signs (Guang-jian, Zong-shuai, Yan-li, Shi-jin, & Zhi-jing, 2012). Later on, the transmission of this virus from dog to dog was confirmed (Song et al., 2013). Afterwards, infective manifestations of this H5N2 virus were observed in cats and chickens (Hai-xia et al., 2014).

Our results show that in Mexico, there are viruses with gene rearrangements and viruses that have crossed the inter-species barrier; for this reason, it is important to continue characterizing the A-type influenza viruses circulating in animal populations, in order to identify the new variants, particularly those closely associated with humans to avoid potential zoonotic threats.

Based on the phylogenetic analysis, we conclude that within the Mexican swine population, there are circulating viruses that have undergone punctual mutations and protein rearrangements with different subtypes. On the other hand, we also determined that some segments of human influenza viruses have been rearranged with swine influenza viruses, and these have been detected in Mexican pigs (see figures S1–S6).

ACKNOWLEDGEMENTS

This study was partially funded by the project: CONACYT 254244 and PAPIIT IN223514. "Determination of the infectious capacity of swine viruses in human cells". J. M. Saavedra-Montañez is a fellow of the National Council of Science and Technology (CONACyT, ID 393094). The authors also thank the Production and Animal Health Sciences Postgraduate, UNAM.

CONFLICT OF INTEREST

The authors declare no financial or commercial conflict interest.

ORCID

René Segura-Velázquez http://orcid.org/0000-0001-8392-4919
Jacquelynne Cervantes-Torres http://orcid.org/0000-0002-2610-2860
José Ivan Sánchez-Betancourt http://orcid.org/0000-0001-8201-9669

REFERENCES

Aguirre, V. M. C., del García, M. C. M., Ortega, M. E. T., Elvira, S. E. M., Haspra, P. I., Paz, L. F. P., … Sánchez-Betancourt, J. I. (2014). Cambios genéticos en los genes internos del virus de influenza porcina aislado en México. *Veterinaria México OA*, *1*, 1–22.

Anderson, T. K., Macken, C. A., Lewis, N. S., Scheuermann, R. H., Van Reeth, K., Brown, I. H., … Vincent, A. L. (2016). A phylogeny-based global nomenclature system and automated annotation tool for H1 hemagglutinin genes from swine influenza A viruses. *mSphere*, *1*(6): e00275–16. https://doi.org/10.1128/mSphere.00275-16

Avalos, G. P., Sanchez, B. J., & Trujillo, O. M. (2011). *Influenza Porcina en México*, 1ra edn. España: Editorial Academica Española.

Boni, M. F. (2008). Vaccination and antigenic drift in influenza. *Vaccine*, *26*, C8–C14. https://doi.org/10.1016/j.vaccine.2008.04.011

Bouvier, N. M., & Palese, P. (2008). The biology of influenza viruses. *Vaccine*, *26*, D49–D53. https://doi.org/10.1016/j.vaccine.2008.07.039

Cappuccio, J. A., Pena, L., Diba, M., Rimondi, A., Pin, P., Insarralde, L., … Insarralde, A. (2011). Outbreak of swine influenza in Argentina reveals a non-contemporary human H3N2 virus highly transmissible among pigs. *Journal of General Virology*, *92*, 2871–2878. https://doi.org/10.1099/vir.0.036590-0

Carrat, F., & Flahault, A. (2007). Influenza vaccine: The challenge of antigenic drift. *Vaccine*, *25*, 6852–6862. https://doi.org/10.1016/j.vaccine.2007.07.027

Castrucci, M. R., Donatelli, I., Sidoli, L., Barigazzi, G., Kawaoka, Y., & Webster, R. G. (1993). Genetic reassortment between avian and human influenza A viruses in Italian pigs. *Virology*, *193*, 503–506. https://doi.org/10.1006/viro.1993.1155

Chambers, T. M., Hinshaw, V. S., Kawaoka, Y., Easterday, B. C., & Webster, R. G. (1991). Influenza viral infection of swine in the United States 1988-1989. *Archives of Virology*, *116*, 61–265. https://doi.org/10.1007/BF01319247

Dirección General de Epidemiología. (2017). Retrieved from https://www.gob.mx/salud/acciones-y-programas/direccion-general-de-epidemiologia-informes-semanales-para-la-vigilancia-epidemiologica

Escalera-Zamudio, M., Cobián-Güemes, G., de los Dolores Soto-del Río, M., Isa, P., Sánchez-Betancourt, I., Parissi-Crivelli, A., … Arias, C. F. (2012). Characterization of an influenza A virus in Mexican swine that is related to the A/H1N1/2009 pandemic clade. *Virology*, *433*, 176–182. https://doi.org/10.1016/j.virol.2012.08.003

FigTree: (2017). Molecular evolution, phylogenetics and epidemiology. Retrieved from http://tree.bio.ed.ac.uk/software/figtree/

Flint, J., & Racaniello, V. (2001). Principles of virology. In D. M. Knipe & P. M. Howley (Eds), *Fields Virology*. Philadelphia, PA: Lippincot Williams and Wilkins.

FluNet. (2017). Retrieved from http://www.who.int/influenza/gisrs_laboratory/flunet/en/

Gaitán-Peredo, C. A. (2016). Análisis serológico retrospectivo del virus de influenza porcina subtipo H1N2 en los últimos seis años (2010-2015) en la República Mexicana. Universidad Nacioinal Autónoma de México.

Giese, M., Harder, T. C., Teifke, J. P., Klopfleisch, R., Breithaupt, A., Mettenleiter, T. C., & Vahlenkamp, T. W. (2008). Experimental infection and natural contact exposure of dogs with avian influenza virus (H5N1). *Emerging Infectious Diseases*, *14*, 308–310. https://doi.org/10.3201/eid1402.070864

Guang-jian, Z., Zong-shuai, L., Yan-li, Z., Shi-jin, J., & Zhi-jing, X. (2012). Genetic characterization of a novel influenza A virus H5N2 isolated from a dog in China. *Veterinary Microbiology*, *155*, 409–416. https://doi.org/10.1016/j.vetmic.2011.08.017

Hai-xia, F., Yuan-yuan, L., Qian-qian, S., Zong-shuai, L., Feng-xia, Z., Yan-li, Z., … Zhi-jing, X. (2014). Interspecies transmission of canine influenza virus H5N2 to cats and chickens by close contact with experimentally infected dogs. *Veterinary Microbiology*, *170*, 414–417. https://doi.org/10.1016/j.vetmic.2014.02.040

INEGI. (2007). Censo Agrícola, Ganadero y Forestal 2007. Retrieved from http://www.inegi.org.mx/est/contenidos/proyectos/agro/ca2007/resultados_agricola/

Ito, T., Couceiro, J. N., Kelm, S., Baum, L. G., Krauss, S., Castrucci, M. R., … Kawaoka, Y. (1998). Molecular basis for the generation in pigs of influenza A viruses with pandemic potential. *Journal of Virology*, *72*, 7367–7373.

Karasin, A. I., Brown, I. H., Carman, S., & Olsen, C. W. (2000). Isolation and Characterization of H4N6 Avian Influenza Viruses from Pigs with Pneumonia in Canada. *Journal of Virology*, *74*, 9322–9327. https://doi.org/10.1128/JVI.74.19.9322-9327.2000

King, A. M. Q., Adams, M. J., Carstens, E. B., & Lefkowitz, E. J. (2012). Virus Taxonomy Classification and Nomenclature of Viruses Ninth Report of the International Committee on Taxonomy of Viruses.

Kumar, S., Stecher, G., & Tamura, K. (2016). MEGA7: Molecular Evolutionary Genetics Analysis version 7.0 for bigger datasets. *Molecular Biology and Evolution*, *33*, 1870–1874. https://doi.org/10.1093/molbev/msw054

Lara-Puente, J. (2012). *Detección de Anticuerpos por IH contra los subtipos H1N1, H3N2 y H1N2 de influenza porcina (2006–2012) en México* (pp. 207). Guadalajara, Mexico: Memorias AMVEC.

Lee, J. H., Pascua, P. N. Q., Song, M., Baek, Y. H., Kim, C., Choi, H., … Choi, Y. K. (2009). Isolation and Genetic Characterization of H5N2 Influenza Viruses from Pigs in Korea. *Journal of Virology*, *83*, 4205–4215. https://doi.org/10.1128/JVI.02403-08

Liao, Y. C., Lee, M. S., Ko, C. Y., & Hsiung, C. A. (2008). Bioinformatics models for predicting antigenic variants of influenza A/H3N2 virus. *Bioinformatics*, *24*, 505–512. https://doi.org/10.1093/bioinformatics/btm638

López-Robles, G., Montalvo-Corral, M., Caire-Juvera, G., Ayora-Talavera, G., & Hernández, J. (2012). Seroprevalence and Risk Factors for Swine Influenza Zoonotic Transmission in Swine Workers from Northwestern Mexico. *Transboundary and Emerging Diseases*, *59*, 183–188. https://doi.org/10.1111/j.1865-1682.2011.01250.x

Ma, W., Vincent, A. L., Gramer, M. R., Brockwell, C. B., Lager, K. M., Janke, B. H., … Richt, A. (2007). Identification of H2N3 influenza A

viruses from swine in the United States. *Proceedings of the National Academic of Sciences of the United States of America*, *104*, 20949–20954. https://doi.org/10.1073/pnas.0710286104

Nei, M., & Kumar, S. (2000). *Molecular Evolution and Phylogenetics*. New York: Oxford University Press.

Nelson, M., Culhane, M. R., Rovira, A., Torremorell, M., Guerrero, P., & Norambuena, J. (2015). Novel human-like influenza A Viruses circulate in swine in Mexico and Chile. *PLoS Currents*, *7*, 1–20. https://doi.org/10.1371/currents.outbreaks.c8b3207c9bad98474eca3013fa933ca6

Nelson, M. I., Gramer, M. R., Vincent, A. L., & Holmes, E. C. (2012). Global transmission of influenza viruses from humans to swine. *Journal of General Virology*, *93*, 2195–2203. https://doi.org/10.1099/vir.0.044974-0

Nelson, M. I., Schaefer, R., Gava, D., Cantão, M. E., & Ciacci-zanella, J. R. (2015). Influenza A Viruses of Human Origin in Swine, Brazil. *Emerging Infectious Diseases*, *21*, 1339–1347. https://doi.org/10.3201/eid2108.141891

Nelson, M. I., Wentworth, D. E., Culhane, M. R., Vincent, A. L., Viboud, C., LaPointe, M. P., … Detmer,, S. E. (2014). Introductions and Evolution of Human-Origin Seasonal Influenza A Viruses in Multinational Swine Populations. *Journal of Virology*, *88*, 10110–10119. https://doi.org/10.1128/JVI.01080-14

Nucleotide BLAST: Search nucleotide databases using a nucleotide query. (2017). Retrieved from https://blast.ncbi.nlm.nih.gov/Blast.cgi?PAGE_TYPE=BlastSearch. January 8, 2017.

Peiris, J. S., Guan, Y., Markwell, D., Ghose, P., Webster, R. G., & Shortridge, K. F. (2001). Cocirculation of avian H9N2 and contemporary "human" H3N2 influenza A viruses in pigs in southeastern China: Potential for genetic reassortment? *Journal of Virology*, *75*, 9679–9686. https://doi.org/10.1128/JVI.75.20.9679-9686.2001

Ramírez, M. H., Carreón, N. R., & Mercado, G. C. (1996). Hemoaglutinación e inhibición de la hemoaglutinación del paramixovirus porcino a través de la modificación de algunas variables que participan en la prueba. *Veterinaria México OA*, *27*, 257–259.

Sánchez-Betancourt, J. I., Cervantes-Torres, J. B., Saavedra-Montañez, M., & Segura-Velázquez, R. A. (2017). Complete genome sequence of a novel influenza A H1N2 virus circulating in swine from Central Bajio region, Mexico. *Transboundary and Emerging Diseases*, *64*, 2083–2092. https://doi.org/10.1111/tbed.12620

Scholtissek, C. (1995). Molecular evolution of influenza viruses. *Virus Genes*, *11*, 209–215. https://doi.org/10.1007/BF01728660

Scholtissek, C., Bürger, H., Bachmann, P. A., & Hannoun, C. (1983). *Genetic relatedness of hemagglutinins of the H1 subtype of influenza a viruses isolated from swine and birds*. *Virology*, *129*, 521–523. https://doi.org/10.1016/0042-6822(83)90194-0

Servicio Nacional de Sanidad, Inocuidad y Calidad Agroalimentaria. (2017). Retrieved from https://www.gob.mx/senasica/acciones-y-programas/campana-nacional-para-la-prevencion-control-y-erradicacion-de-la-influenza-aviar-notificable

Shin, J.-Y., Song, M.-S., Lee, E. H., Lee, Y.-M., Kim, S.-Y., Kim, H. K., & Choi, Y.-K. (2006). Isolation and characterization of novel H3N1 swine influenza viruses from pigs with respiratory diseases in Korea. *Journal of Clinical Microbiology*, *44*, 3923–3927. https://doi.org/10.1128/JCM.00904-06

Song, Q. Q., Zhang, F. X., Liu, J. J., Ling, Z. S., Zhu, Y. L., Jiang, S. J., & Xie, Z. J. (2013). Dog to dog transmission of a novel influenza virus (H5N2) isolated from a canine. *Veterinary Microbiology*, *161*, 331–333. https://doi.org/10.1016/j.vetmic.2012.07.040

Treanor, J. (2004). Influenza Vaccine — Outmaneuvering Antigenic Shift and Drift. *New England Journal of Medicine*, *350*, 218–220. https://doi.org/10.1056/NEJMp038238

Tu, J., Zhou, H., Jiang, T., Li, C., Zhang, A., Guo, X., … Jin, M. (2009). Isolation and molecular characterization of equine H3N8 influenza viruses from pigs in China. *Archives of Virology*, *154*, 887–890. https://doi.org/10.1007/s00705-009-0381-1

Webster, R. G., Laver, W. G., Air, G. M., & Schild, G. C. (1982). Molecular mechanisms of variation in influenza viruses. *Nature*, *296*, 115–121. https://doi.org/10.1038/296115a0

World Organisation for Animal Health. (2015). Influenza A virus of swine. Manual of Diagnostic Tests and Vaccines for Terrestrial Animals. Retrieved from http://www.oie.int/en/international-standard-setting/terrestrial-manual/access-online/

Zambon, M. C. (1999). Epidemiology and pathogenesis of influenza. *Journal of Antimicrobial Chemotherapy*, *44*, 3–9. https://doi.org/10.1093/jac/44.suppl_2.3

SUPPORTING INFORMATION

Additional supporting information may be found online in the Supporting Information section at the end of the article.

How to cite this article: Saavedra-Montañez M, Vaca L, Ramírez-Mendoza H, et al. Identification and genomic characterization of influenza viruses with different origin in Mexican pigs. *Transbound Emerg Dis*. 2019;66:186–194. https://doi.org/10.1111/tbed.12998

Article

Molecular Cell

RNA Interactions Are Essential for CTCF-Mediated Genome Organization

Graphical Abstract

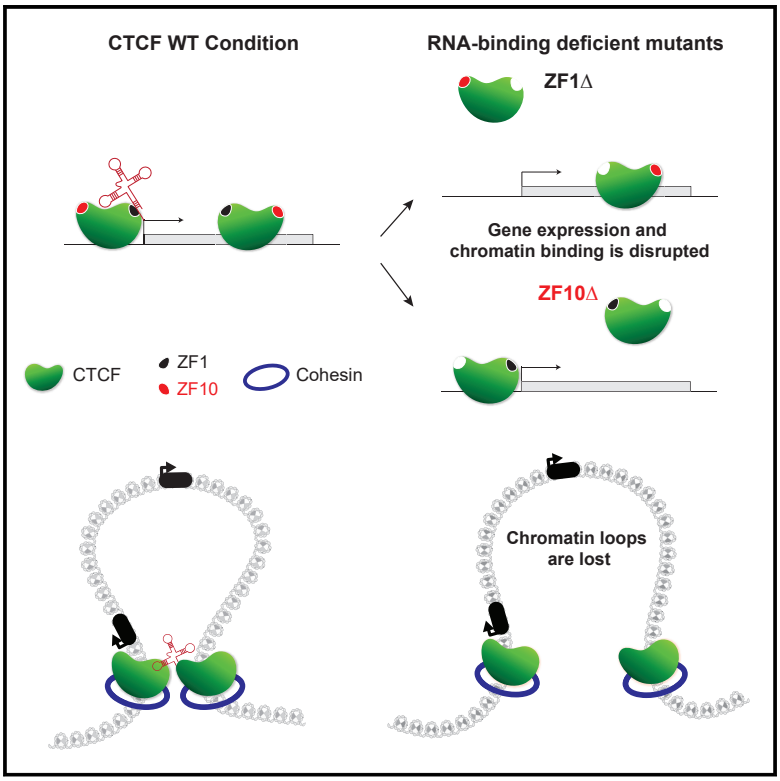

Authors

Ricardo Saldaña-Meyer, Javier Rodriguez-Hernaez, Thelma Escobar, ..., Mayra Furlan-Magaril, Jane Skok, Danny Reinberg

Correspondence

ricardo.saldana-meyer@nyulangone.org (R.S.-M.), danny.reinberg@nyulangone.org (D.R.)

In Brief

RNA binding promotes CTCF-dependent chromatin loops. Saldaña-Meyer et al. show that mutation of the RNA-binding regions in CTCF (ZF1 and ZF10) disrupts gene expression, chromatin binding, and the formation of chromatin loops.

Highlights

- Transcriptional inhibition disrupts CTCF binding to chromatin
- RNA-binding regions (RBRs) in CTCF are found within ZF1 and ZF10
- Gene expression and chromatin binding are disrupted by RBR mutants
- Chromatin loops are markedly decreased in ZF1Δ and ZF10Δ mutant rescues

Saldaña-Meyer et al., 2019, Molecular Cell *76*, 412–422
November 7, 2019 © 2019 Elsevier Inc.
https://doi.org/10.1016/j.molcel.2019.08.015

CellPress

Molecular Cell
Article

RNA Interactions Are Essential for CTCF-Mediated Genome Organization

Ricardo Saldaña-Meyer,[1,2,*] Javier Rodriguez-Hernaez,[3] Thelma Escobar,[1,2] Mayilaadumveettil Nishana,[3] Karina Jácome-López,[5] Elphege P. Nora,[6,7] Benoit G. Bruneau,[6,7,8,9] Aristotelis Tsirigos,[3,4] Mayra Furlan-Magaril,[5] Jane Skok,[3] and Danny Reinberg[1,2,10,*]

[1]Department of Biochemistry and Molecular Pharmacology, NYULSoM, New York, NY, USA
[2]Howard Hughes Medical Institute, NYU Langone Health, New York, NY, USA
[3]Department of Pathology, NYULSoM, New York, NY, USA
[4]Applied Bioinformatics Laboratories, NYU School of Medicine, New York, NY 10016, USA
[5]Departamento de Genética Molecular, Instituto de Fisiología Celular, Universidad Nacional Autónoma de México, Mexico City, Mexico
[6]Gladstone Institutes, San Francisco, CA 94158, USA
[7]Roddenberry Center for Stem Cell Biology and Medicine at Gladstone, San Francisco, CA 94158, USA
[8]Department of Pediatrics, University of California, San Francisco, San Francisco, CA 94143, USA
[9]Cardiovascular Research Institute, University of California, San Francisco, San Francisco, CA 94158, USA
[10]Lead Contact
*Correspondence: ricardo.saldana-meyer@nyulangone.org (R.S.-M.), danny.reinberg@nyulangone.org (D.R.)
https://doi.org/10.1016/j.molcel.2019.08.015

SUMMARY

The function of the CCCTC-binding factor (CTCF) in the organization of the genome has become an important area of investigation, but the mechanisms by which CTCF dynamically contributes to genome organization are not clear. We previously discovered that CTCF binds to large numbers of endogenous RNAs, promoting its self-association. In this regard, we now report two independent features that disrupt CTCF association with chromatin: inhibition of transcription and disruption of CTCF-RNA interactions through mutations of 2 of its 11 zinc fingers that are not required for CTCF binding to its cognate DNA site: zinc finger 1 (ZF1) or zinc finger 10 (ZF10). These mutations alter gene expression profiles as CTCF mutants lose their ability to form chromatin loops and thus the ability to insulate chromatin domains and to mediate CTCF long-range genomic interactions. Our results point to the importance of CTCF-mediated RNA interactions as a structural component of genome organization.

INTRODUCTION

Spatial and temporal control of gene expression is crucial for the development of multicellular organisms. Improper gene expression leads to developmental abnormalities and diseases such as cancer. In addition to the "linear" genetic information, the three-dimensional (3D) spatial organization of the eukaryotic genome within the nucleus contributes to genome function (Bonev and Cavalli, 2016; Merkenschlager and Nora, 2016).

The 3D genome is hierarchically organized: from nuclear compartments, to large insulated chromatin domains, to short-range *cis*-interactions. These chromatin domains are designated throughout the literature as topological associated domains (TADs), topologically constrained domains, physical domains, insulated neighborhoods, contact domains, or loop domains depending on their characteristics, size, and the algorithms used to identify them (Lieberman-Aiden et al., 2009; Dixon et al., 2012; Dowen et al., 2014; Nora et al., 2017; Rao et al., 2017). To avoid confusion, we simply call them chromatin-interacting domains. These domains are formed and delimited primarily by the interaction of CTCF with the cohesin complex, and proteins such as YY1, the Mediator complex, and others yet to be discovered. CTCF and the cohesin complex are pivotal to 3D structure formation (Rowley and Corces, 2018). The depletion of either factor has drastic effects on chromatin structure, with chromatin-interacting domains essentially disappearing (Nora et al., 2017; Rao et al., 2017). The most widely accepted explanation of how chromatin organizes 3D structure is through the loop extrusion model (Fudenberg et al., 2017). This model proposes that cohesin rings create loops by actively extruding DNA until the cohesin complex contacts two CTCF-binding sites in convergent orientation to serve as anchors. This simplifies the underlying mechanism of chromatin organization, but many questions remain unanswered as to how these domains are regulated temporally and in a cell type-specific manner and the repertoire of factors that participate in this process.

Although most chromatin domain boundaries are enriched by CTCF and cohesin, the majority of CTCF-bound sites are found elsewhere in the genome (Merkenschlager and Nora, 2016). Furthermore, CTCF and cohesin binding sites are significantly conserved among cell types, yet many of them, as well as many chromatin-interacting domains, display cell type-specific patterns and changes during differentiation as a result of stage-specific transcription factors (Narendra et al., 2016; Pękowska et al., 2018; Stadhouders et al., 2018).

Together with CTCF, YY1, cohesin, and Mediator complexes are also implicated in defining chromatin architecture at

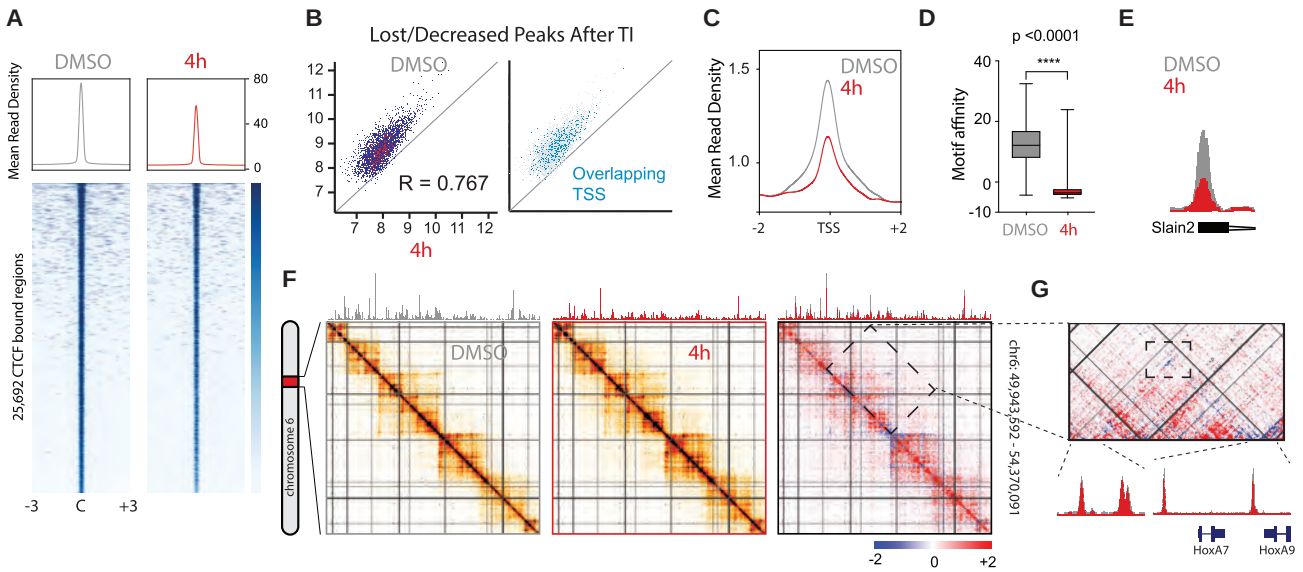

Figure 1. Transcriptional Inhibition Disrupts CTCF Binding Predominantly in TSS

Transcription was inhibited in mESCs for 4 h with co-incubation of DRB and triptolide. Cells incubated with DMSO served as control.

(A) Shows CTCF ChIP-seq heatmaps centered and rank-ordered on CTCF-binding sites. Corresponding average density profiles are plotted at the top of the heatmaps to illustrate differences between DMSO and 4 h of TI.

(B) A subset of peaks exhibit dramatically reduced CTCF enrichment after 4 h of TI. Overlapping peaks for TSS are highlighted in blue.

(C) Average density profiles for the same ChIP-seq as (A) but centered on TSS.

(D) Boxplot showing the motif affinity scores for CTCF-binding sites lost after transcriptional inhibition versus a random set of CTCF-binding sites in the control (Mann-Whitney test, $p < 0.0001$).

(E) Representative example of a CTCF peak with decreased binding to the TSS of the Slain2 gene. ChIP-seq tracks for DMSO (gray) and 4 h of TI (red) are overlapped for comparison.

(F) 5C heatmap depicting the interaction frequency between restriction fragments across a 4 Mb region surrounding the *HoxA* cluster (data were binned in 15 kb windows; step size 5 kb; the median is shown). Comparative 5C heatmap shows increased (red) and decreased (blue) interactions after TI. Overlapped ChIP-seq tracks above illustrate decreased binding of CTCF. Darker colors represent increasing interaction frequency.

(G) Zoom into a chromatin domain delimited by CTCF sites (top). Overlapped ChIP-seq tracks for DMSO (gray) and 4 h of TI (red) illustrate no change in CTCF binding for the loop enclosed in a rectangle (bottom).

different topological ranges and all of these proteins bind RNA (Lai et al., 2013; Li et al., 2013; Phillips-Cremins et al., 2013; Saldaña-Meyer et al., 2014; Sigova et al., 2015). A growing number of examples demonstrate that RNA can recruit and either stabilize or destabilize protein binding to chromatin, as in the case of the PRC2 complex or YY1, respectively (Beltran et al., 2016; Kaneko et al., 2014a, 2014b; Sigova et al., 2015; Xiao et al., 2019). Furthermore, both CTCF and YY1 can form dimers and oligomers in an RNA-dependent manner, which may account for the regulation of far *cis*-interactions on chromatin (Saldaña-Meyer et al., 2014; Weintraub et al., 2017).

Here, we sought to identify the functional relevance of CTCF-RNA interactions using two strategies: (1) inhibiting transcription and (2) rescuing the loss of wild-type endogenous CTCF through the expression of RNA binding-deficient mutants. We concentrated on three distinct levels of regulation: (1) gene expression using single-cell RNA sequencing (RNA-seq) and bulk RNA-seq; (2) chromatin binding via ChIP-seq; and (3) chromatin structure via 5C and Hi-C. We demonstrate that decreased RNA binding to CTCF disturbs its stability on chromatin with direct and likely indirect effects on gene expression and 3D chromatin organization.

RESULTS

Transcriptional Inhibition Disrupts CTCF Binding to Chromatin

To unbiasedly test if RNA binding is integral to CTCF activity genome-wide, we first performed chromatin immunoprecipitation followed by deep sequencing (ChIP-seq) after transcriptional inhibition (TI) by treating mouse embryonic stem cells (mESCs) with both DRB and triptolide. This treatment, which inhibits initiation and elongation of transcription and promotes degradation of RNAP II (Bensaude, 2011), had no impact on CTCF protein levels (Figure S1A). Nonetheless, we detected an overall modest decrease in CTCF association with chromatin genome-wide (Figure 1A). Similar results were observed after depleting RNA by incubation with RNase A (Figure S1B). Because CTCF is widely present throughout the genome within both intragenic and intergenic regions (Bonev and Cavalli, 2016), we next focused on the specific genomic distribution between individual CTCF-binding sites in the control versus those sites whose binding was significantly decreased after TI and RNase A treatment (Table S1). We found that CTCF-binding sites within transcription start sites (TSSs) and promoters were the

most significantly affected (Figures 1B, 1C, S1B, and S1C). To quantify the affinity of those affected sites, we used DeepBind, a deep-learning algorithm that has been trained on numerous ChIP-seq datasets and can be used to score the affinity of any given sequence for the CTCF motif. Remarkably, sites perturbed by TI were those with motifs with significantly lower affinity compared with a random sample of stable CTCF-bound regions ($p < 0.0001$, Mann-Whitney test; Figure 1D).

Regarding chromatin structure, 5C experiments targeting a 4 Mb region showed that throughout this region (chr6: 49,943592–54,370,091), CTCF binding was decreased together with a general increase in chromatin interactions (Figures 1F and S1D). Remarkably, the chromatin loop whose right anchor resides at the *HoxA* cluster boundary was disrupted (Figures 1G and S1E), without the loss of CTCF binding in the boundary, as illustrated by the overlapping ChIP-seq tracks (Figure 1G, bottom). These results favor the hypothesis that the role of CTCF in 3D chromatin structure is subject to at least two levels of regulation: (1) direct binding to chromatin and (2) regulation of CTCF-CTCF interactions in complex with RNA molecules to form chromatin loops at sites surrounding the *HoxA* cluster and probably others throughout the genome.

High-Resolution Mapping of RNA-Binding Regions (RBRs) in CTCF

The observations above are suggestive but cannot distinguish between a direct disruption of CTCF-RNA interactions or the various possible indirect effects of inhibiting transcription. To directly test the former case, we first defined putative RNA binding-deficient mutants. We focused on two regions detected by RBR-ID (He et al., 2016): one overlapping part of zinc finger 1 (ZF1) (aa 264–275; KTFQCELCSYTCPR) and another within ZF10 (aa 536–544; QLLDMHFKR), the latter having been identified previously through biochemical mapping of CTCF (Saldaña-Meyer et al., 2014) (Figure 2A; Table S2). Henceforward, the deletion of these 14 and 9 amino acids from ZF1 and ZF10, respectively, will be denoted as ZF1Δ and ZF10Δ.

Given that homozygous deletion of CTCF is embryonically lethal (Kemp et al., 2014; Moore et al., 2012), we induced the rapid degradation of endogenously tagged CTCF-GFP using the auxin-inducible degron (AID) system as previously described (Nora et al., 2017) and rescued the cells with either wild-type (WT) or RNA binding-deficient CTCF mutants; degradation of CTCF without rescue was lethal after 2–4 days (Nora et al., 2017). To bypass this issue, we transduced cells with lentivirus containing a vector encoding an internal ribosomal entry site (IRES) that allows a WT or mutant version of CTCF and the red fluorescent protein mCherry to be simultaneously expressed from a single mRNA transcript. We then sorted the successfully infected cells (mCherry positive and GFP negative; Figure 2B) to obtain a pooled population of steady-state rescues after degradation of the endogenous CTCF protein via AID (Figures 2B and S2A).

Although both ZF1Δ and ZF10Δ mutants rescued the lethality of endogenous CTCF depletion and had comparable levels of expression (Figures 2C and S2B), the cells exhibited a significantly slower proliferation rate relative to the WT rescue but presented no drastic changes in their cell cycle (Figures S2C–S2E). These results suggested that an important biological role of CTCF involves ZF1 and ZF10. Our previous report on CTCF-RNA interactions shows that an internal deletion (aa 574–614) within the RBR-ZF10 (aa 520–727) displays significant defects in self-association but no defects in binding to the cohesin complex (Saldaña-Meyer et al., 2014). ZF1Δ also retained its ability to interact with the cohesin complex, with apparently the same efficiency as that of ZF10Δ and WT CTCF (Figure 2C). We then performed the rescues in the absence of auxin and probed for the capacity of endogenous CTCF to co-precipitate the rescue proteins using an antibody against GFP (endogenous CTCF was readily distinguishable from the rescues given the molecular weight differences). Both mutants displayed defects in interaction with endogenous CTCF, reflecting a defect in self-association (~60%) compared with the WT rescue (Figure 2D).

To directly test the RNA-binding capacity of these mutants, we used photoactivatable ribonucleoside-enhanced cross-linking and immunoprecipitation (PAR-CLIP). The WT rescue showed robust binding to RNA molecules, whereas both ZF1Δ and ZF10Δ mutants displayed drastic reductions in binding, as evidenced by a significantly decreased signal in radiolabeled RNA compared with the WT rescue (Figure 2E). Notably, naturally occurring mutations in endometrial and breast cancer within ZF1 (H284N) and ZF10 (C528S) target the histidine or cysteine residues that are essential for zinc binding in C_2H_2 type ZFs (Kemp et al., 2014) (Figure 2F). Surprisingly, point mutations within ZF1 (H284N) or ZF10 (C528S) had no detectable defect on RNA binding (Figures 2E and 2F). These results suggest that CTCF binding to RNA is not just a consequence of simple RNA affinity to its ZFs but instead requires a structural conformation or binding of other components that are disrupted independently by deletion of the respective RBRs in ZF1 and ZF10.

Deletion of RBRs in CTCF Disturbs Gene Expression

To test if the presence of RNA binding-defective mutants had any effect on gene expression, we subjected the rescue cell lines to single-cell RNA-seq (scRNA-seq). Principal-component analysis (PCA) showed similarities between the different rescues but also underscored the clear distinction between each population of cells (Figure 3A; Table S3). Further analysis on the differential expression represented as heatmaps showed that downregulated genes are similar in both mutant rescues, but distinct clusters of genes are upregulated for ZF1Δ and ZF10Δ (Figures 3B and S3A).

scRNA-seq allows us to monitor the variability and consistency of the phenotypes we observe at the single-cell level, but it is not regularly used to test differential expression, because of the lower sequencing depth per cell (Rizzetto et al., 2017). Given these limitations, we also performed regular bulk RNA-seq and compared the two approaches. The differentially expressed genes (DEGs) for ZF1Δ and ZF10Δ rescue cell lines showed good overlap (687 genes, false discovery rate [FDR] < 0.05) even at different thresholds of significance (215 genes, FDR < 0.001) between bulk and scRNA-seq (232 genes) (Figure 3C). Comparing all DEGs from both RNA binding-deficient mutants with all DEGs from cells depleted of CTCF for 24 and 48 h provided similar overlaps (824 genes, FDR < 0.05) (Figure 3C; Table S4). Remarkably, all these different DEGs

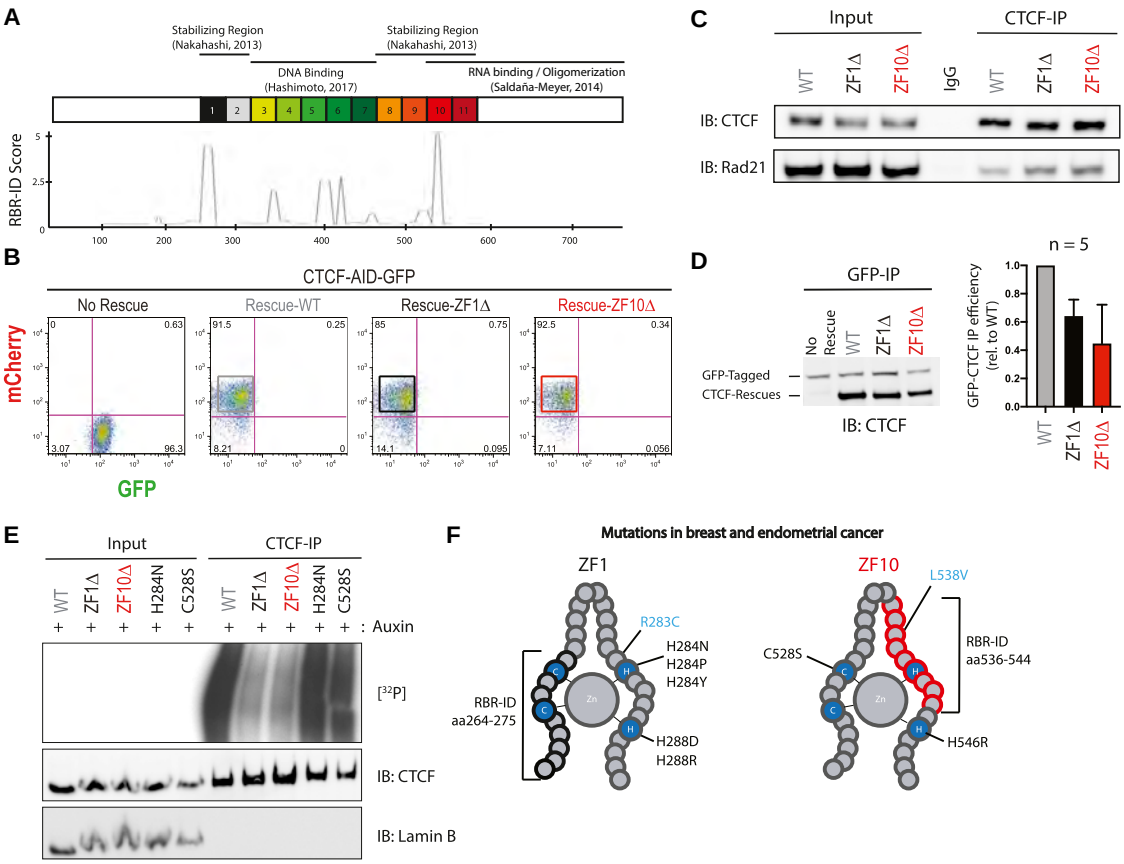

Figure 2. Deletions in ZF1 and ZF10 Independently Abolish CTCF Binding to RNA

(A) Schematic representation of known domains of WT CTCF with its 11 zinc fingers being numbered (top); smoothed residue-level RBR-ID score (He et al., 2016), plotted along the primary sequence (bottom).

(B) FACS analysis highlighting percentage of GFP+ or mCherry+ CTCF-AID-GFP mESCs with or without rescue of CTCF: WT, ZF1Δ, or ZF10Δ.

(C) Immunoprecipitation of all rescue cell lines indicated and immunoblots for CTCF and Rad21.

(D) Representative image of GFP-CTCF incubated with each rescue, immunoprecipitated with a GFP antibody and blotted against CTCF (left); bar graph quantification of each rescue protein relative to the GFP-CTCF (n = 5) (right).

(E) PAR-CLIP of stably expressed WT and mutant CTCF in mESCs. Autoradiography for ^{32}P-labeled RNA (top) and control western blot (middle and bottom).

(F) Schematic representation of ZF1 and ZF10 of CTCF; mutations found in breast and endometrial cancer that alter zinc binding are shown in black; mutations that do not alter zinc binding are in blue, and RBR-ID deletions are in brackets.

displayed a distinctive similarity with promoters and/or gene bodies containing CTCF-binding sites, a feature that is significantly lower for randomly picked genes (Figure 3D). Furthermore, using DeepBind to examine the motif affinity of CTCF sites at TSSs and intragenic regions of DEGs, we observed a significantly lower score compared with control sites (Mann-Whitney test, $p < 0.001$; Figure 3E). Considering the binding profile of CTCF on the TSSs of DEG, we can distinguish at least two groups: one that has CTCF binding enriched at or near TSSs and one without it in the WT situation (Figure S3B). It was previously shown that after 24 h of CTCF depletion, downregulated genes are enriched for CTCF-binding sites at TSSs (Nora et al., 2017), yet our results suggest no distinction between down- and upregulated genes.

These data indicate that although both ZF1Δ and ZF10Δ have similar deficiencies in RNA binding (and self-association), yet retain efficient interaction with the cohesin complex (Figure 2), they appear to engender distinct gene expression profiles that partially but do not completely overlap with each other and with acute depletion of CTCF.

Deletion of RBRs in CTCF Disturbs Its Chromatin Binding

Next, we focused on the genome-wide binding of the mutant rescues. Findings from ChIP-seq experiments reflect those presented above for TI and RNase A digestion (Figures 1 and S1). To identify specific differences between rescues, we used the R package DiffBind, which incorporates statistical analyses developed for RNA-seq (DESeq2) that have been modified to analyze ChIP-seq data. We observed that most binding sites were unchanged between conditions (Figure S4A; Table S5). Importantly, we found 2,528 differentially bound sites in ZF1Δ and 2,823 in ZF10Δ, of which only 174 were shared (FDR = 0.05, log2 fold change > 1) (Figures 4A, S4A, and S4B).

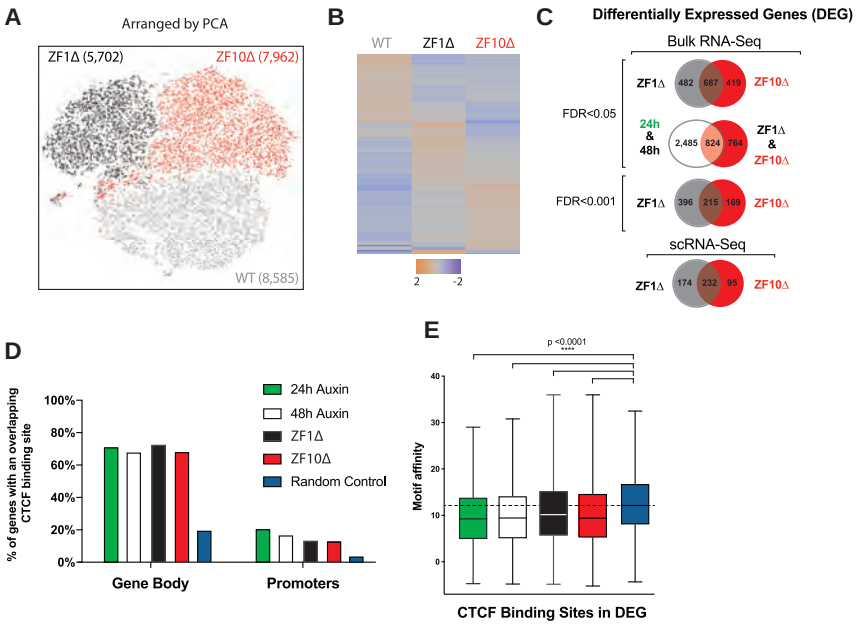

Figure 3. Gene Expression Defects Are Partially Preserved between RBR Deletions

(A) Principal-component analysis (PCA)-based representation of single-cell RNA-seq data for rescue cell lines from WT (gray), ZF1Δ (black), and ZF10Δ (red). Each dot represents a single cell, and dots are arranged on the basis of PCA. The final number of cells sequenced per condition is noted in parentheses.

(B) Heatmaps depicting differentially expressed genes from scRNA-seq.

(C) Venn diagrams showing the overlap between differentially expressed genes for the different conditions and levels of significance.

(D) Bar graph illustrating the percentage of genes that have at least one CTCF-binding site for CTCF in the promoter region or gene body.

(E) Boxplot showing the motif affinity scores for CTCF-binding sites within DEG represented in (B) compared with a random sample of genes (Mann-Whitney test, $p < 0.0001$).

Furthermore, this differential binding seems to be mediated by a change in enrichment from an adenine to a guanine in the eighth position of the CTCF consensus sequence in ZF1Δ, but not for ZF10Δ (Figure 4B). This base is part of a triplet that ZF6 binds, suggesting that the binding site change is not a direct effect of the mutation (Hashimoto et al., 2017). Notably, we found that the CTCF-binding sites lost in the ZF1Δ rescue were located primarily at promoters, whereas ZF10Δ mutations were located mainly in intronic and intergenic regions. However, both binding sites correlated with a lower motif affinity compared with control sites (Mann-Whitney test, $p < 0.0001$; Figures 4C, 4D, and S4C).

By integrating ChIP-seq and RNA-seq results, we can appreciate that the decrease in promoter binding can directly correlate with the change in gene expression, especially for ZF1Δ, which exhibited a more drastic decrease in CTCF binding. In some instances, ZF10Δ also resulted in reduced binding to promoters, as in the case of the *Cdkn2a* gene (Figures 4E, 4F, and S3B). Taken together, these results suggest that although many similarities exist between ZF1Δ and ZF10Δ, the preference for specific sequences in the genome can partially account for their different phenotypes. This and the other differences observed are likely a result of the deletions disrupting RNA-dependent interactions with other proteins.

Deletion of RBRs in CTCF Disturbs 3D Chromatin Structure

To study 3D chromatin conformation, we performed Hi-C and generated approximately 6 billion Hi-C contacts from each rescue cell line (~2.0 billion per condition) (Figures S5A and S5B). First, we focused on chromatin loops that are evident in Hi-C maps by the appearance of a higher frequency spot at the corner of a chromatin-interacting domain (a region that interacts more frequently than expected), indicative of a CTCF-CTCF-mediated chromatin loop.

To quantify the differences between mutants, we used the aggregate peak analysis (APA) method (Durand et al., 2016), which superimposes the signals from all loops (peak pixels), giving a combined signal for each condition. The genome-wide APA signal was strong for the WT rescue (2.38), while it was decreased for both ZF1Δ (1.18) and ZF10Δ (1.93) (Figures 5A and 5B). These decreases directly correlated with a lower number of annotated loops for the mutants (Figure 5C). For the WT rescue cells, we annotated 9,578 loops. Strikingly, loops mostly disappeared in the ZF1Δ rescue, whose binding sites are specifically lost at promoters, with a loss of ~70% of loops (Figure 5C) that was obviously evident by visual examination. For ZF10Δ, for which the affected binding sites are located primarily within intergenic regions, we annotated 7,668 loops, and although most loops were intact as determined by visual examination, the pixel intensity was reduced compared with WT loops (Figures 5A–5C). By integrating ChIP-seq and Hi-C maps, we observed at least two general types of loops exhibiting either (1) the loss of CTCF binding on at least one anchor (Figures 5D and S5C) or (2) loop disruption without the loss of CTCF binding at either anchor (Figures 5E and S5D).

Using Arrowhead to annotate chromatin-interacting domains, we observed a modest reduction in the two mutants, with ZF1Δ being the most affected, having fewer but larger domains; similar results were obtained using Hicratio. We annotated 6,501 and 3,311 chromatin-interacting domains for WT, 5,310 and 3,054 for ZF1Δ, and 5,749 and 3,118 for ZF10Δ using Arrowhead and Hicratio, respectively (Figure S5F; Table S6). Chromatin-interacting domains were also called using Crane insulation scores (Crane et al., 2015) at 40 kb bin resolution with an insulating window of 103 or 500 kb, both of which identified similar numbers of chromatin domains (Figure S5F).

Next, we tested if there were any changes in the interaction frequency within conserved chromatin-interacting domains. We classified these domains in terms of decreased, increased,

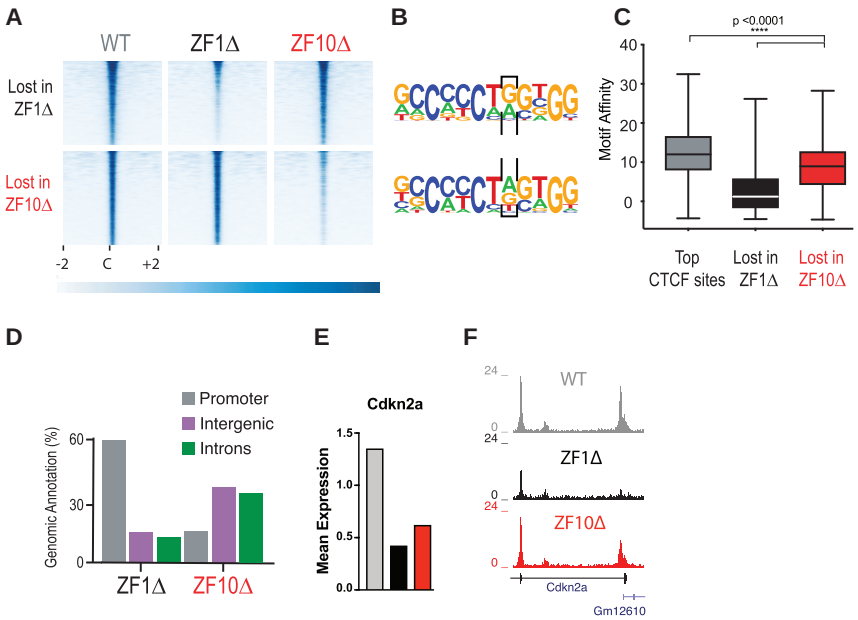

Figure 4. Deletion of RBRs in CTCF Disturb Its Chromatin Binding

(A) CTCF ChIP-seq for WT (gray), ZF1Δ (black), and ZF10Δ (red) rescue cell lines. Heatmaps were generated by centering and rank-ordering on CTCF-binding sites. Those lost for ZF1Δ (top) or ZF10Δ (bottom) are shown.

(B) *De novo* motif discovery was called for binding sites in (A), and a black box encloses the eighth position in which A to G was specifically preferred by ZF1Δ.

(C) Boxplot showing the motif affinity scores for CTCF-binding sites in (A) compared with unchanged sites (Mann-Whitney test, $p < 0.0001$).

(D) Bar graph representing the top three genomic regions for CTCF sites in (A).

(E and F) Mean expression levels for differentially expressed gene *Cdkn2a* (E) and corresponding ChIP-seq tracks (F) under each condition.

or stable activity (FDR < 0.1). Regardless of the algorithm used to call chromatin-interacting domains, we observed that compared with the WT rescue, both mutants had a predominantly increased interaction frequency in domains with altered activity (Figure 6A; Figure S5E), a trend that reflected the 5C results from TI and RNase A conditions (Figures 1F, 1G, S1D, and S1E).

Importantly, about 60% of ZF1Δ sites with decreased binding were located in gene promoters. An obvious assumption would be that CTCF is functioning as a transcription factor in these cases. Nonetheless, ZF1Δ presented the most striking phenotype of chromatin loop disruption. Thus, we analyzed the frequency at which TSSs are found within chromatin loop anchors. By overlapping all TSSs with the 9,578 annotated loops for the WT rescue, we found that 14% of loop anchors overlapped with a TSS, and of those, the majority were delimited by CTCF binding on each side of a chromatin-interacting domain called by Arrowhead (Figure S5G), a significantly higher enrichment than the 3% overlap seen in the random control. These results suggested that CTCF can function as both a transcription factor and an insulator at the same time. Indeed, such is the case for some DEGs for ZF1Δ or ZF10Δ that are contained within a chromatin-interacting domain that is disrupted along with loss of CTCF in their promoter region, which also serves as an anchor for a chromatin loop (Figure 6C).

Next, we attempted to correlate gene expression with the increased activity within chromatin-interacting domains. To do this, we assigned a DEG (FDR < 0.05, log2 fold change > 1) to a common chromatin-interacting domain when its promoter overlapped with the domain. We assessed statistical significance for downregulated or upregulated DEG for each mutant. Only the downregulated genes for ZF1Δ showed a significant correlation with increased interactions within a chromatin-interacting domain (Figure 6B).

Finally, we focused on genomic compartmentalization using PCA and hierarchical clustering, which reveals spatial segregation into A "active" and B "inactive" chromatin compartments. Neither RNA binding-deficient mutant rescue showed changes in the plaid pattern, as defined by the eigenvectors of the Hi-C correlation map, or in compartment domains, compared with the WT control (Figure S6). This finding is consistent with previous observations revealing that genomic compartmentalization relies on mechanisms independent of CTCF and cohesin (Nora et al., 2017; Rao et al., 2017).

The results above indicate that the formation of chromatin loops requires CTCF to properly interact with RNA, and mutations in its RBRs disturb their formation with direct and indirect effects on gene expression and chromatin organization (Figure 6D).

DISCUSSION

We previously demonstrated the ability of CTCF to bind large numbers of RNAs (Saldaña-Meyer et al., 2014), findings that were subsequently corroborated by others (Kung et al., 2015). In this study, we were able to dissect a fundamental and general role for RNA binding to CTCF. Importantly, we describe a clear co-dependency of CTCF-RNA interaction and chromatin binding that affects both 3D chromatin structure and transcription.

Some examples exist of individual RNAs that have important and specific functions, and we expect that more will surface in the future, especially for different cell types or during specific stages of development and differentiation. Regardless, we favor the view that most RNA molecules, not only non-coding (nc) RNAs, have a structural and stabilizing role inside the nucleus, as well as the potential to mediate or increase protein-protein interactions without showing any obvious sequence specificity.

The concept of RNA as a structural component of the nucleus originated in 1989, when the Sheldon Penman group reported that the nuclear matrix fibers collapse and aggregate after treatment with RNase A or actinomycin D in detergent-extracted cells. They proposed that RNA is a structural component of the nuclear matrix, which in turn might organize the higher order

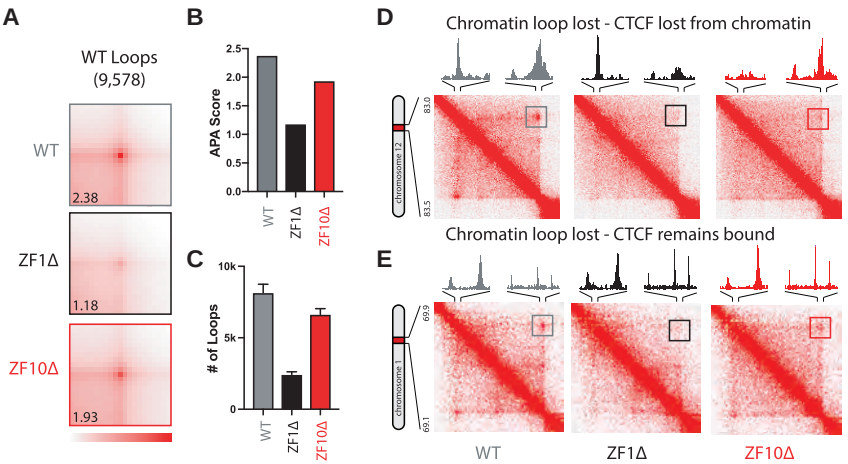

Figure 5. RBR Mutants Disturb Chromatin Loops

(A) Aggregate peak analysis (APA) was used to measure the aggregate strength of chromatin loops annotated by HICCUPS on the WT rescue. Loop strength is indicated by the extent of focal enrichment at the center of the plot. APA scores are shown on the bottom left.

(B) Bar graph representing APA scores between rescue conditions.

(C) Bar graph representing the number of chromatin loops annotated by HICCUPS for each individual condition.

(D) Representative contact matrix (at 5 kb resolution) shows that the chromatin loop in the WT rescue (left) disappears in the ZF1Δ (middle) or loses strength in ZF10Δ (right), while CTCF binding is lost at one of the anchors.

(E) Same as (D), but in this example CTCF remains bound under all conditions.

structure of chromatin (Nickerson et al., 1989). More recently, Hall et al. (2014) showed that RNAs transcribed from repetitive LINE1 elements stably associate with interphase chromosomes and are stable under TI. Furthermore, the loss of these nuclear RNAs from euchromatin disrupts proper chromatin condensation, underscoring the putative structural role for transposons including LINEs and other repetitive sequences that together constitute more than half of the human genome (de Koning et al., 2011; Hall et al., 2014).

CTCF is highly conserved across species (Heger et al., 2012; Vietri Rudan et al., 2015), and the presence of its 11 ZFs suggests that it can bind DNA in multiple ways (Filippova et al., 1996; Nakahashi et al., 2013). The 20 bp DNA core motif (Holohan et al., 2007; Kim et al., 2007; Schmidt et al., 2010; Xie et al., 2007) was suggested to be engaged by ZFs 4–7 *in vivo* (Nakahashi et al., 2013). This motif is present in most of the known CTCF-binding sites identified by ChIP-seq, and the nonspecific engagement of ZFs other than 4–7 with the flanking DNA sequence was proposed to stabilize CTCF binding (Nakahashi et al., 2013). Recently, the crystal structure of overlapping stretches of CTCF's ZFs bound to the core motif was resolved, showing that ZFs 3–7 engage the major groove of the core DNA motif. Importantly, it also revealed the lack of a specific function in DNA recognition and binding for ZF1, ZF10, and ZF11 (Hashimoto et al., 2017). Furthermore, mutating the histidine of ZF1 was previously shown to modestly affect the binding of CTCF to chromatin (Nakahashi et al., 2013). Our results show that a comparable point mutation did not affect RNA binding, but a deletion within ZF1 had a significant decrease in both RNA and chromatin binding (Figures 2, 3, and 4). Last, point mutations in ZF1 or ZF10 that do and do not affect the binding of ZFs to DNA are found in cancer (Figure 2F) (Kemp et al., 2014). In the context of this study, together these data suggest that the main property of ZF1 and ZF10 is binding to RNA rather than DNA.

Thus far, CTCF binding to DNA seems unaffected by other factors, as the knockdown of most of its binding partners is ineffectual. One exception is the general transcription factor II-I (TFII-I), which seems to stabilize CTCF binding at promoter regions (Peña-Hernández et al., 2015). In the context of our observations under TI (Figure 1), the knockdown of TFII-I most likely affects the transcription of its target genes, and hence the decrease in CTCF binding might be an indirect effect of disrupting transcription. Here, we showed that the CTCF-binding sites affected are those whose sequence diverged from the core DNA-binding motif (Figures 1D, 3E, and 4C), suggesting that this difference can have important roles in regulatory mechanisms, with RNA binding at its core.

CTCF was originally described as a TF, and there are several examples showing that CTCF binding to gene promoters is necessary for proper transcription of tumor suppressor genes, such as BRCA1, RB, TP53, and p16INK4a (Butcher and Rodenhiser, 2007; De La Rosa-Velázquez et al., 2007; Soto-Reyes and Recillas-Targa, 2010; Witcher and Emerson, 2009). Yet because CTCF was described as having a role as an architectural protein, little attention has been afforded to its role as a TF. Most arguments against CTCF being important for gene expression rest on the relatively small number (~200–400) of genes that are affected upon its knockdown or even its acute depletion using an AID (Nora et al., 2017; Zuin et al., 2014). In this context, our ZF1Δ and ZF10Δ rescue cell lines also exhibited a modest number of DEGs, although this varied depending on the threshold applied: ~1,000 genes (FDR < 0.05) to ~400 genes (FDR < 0.001).

Additionally, when analyzing the relative occupancy of CTCF as measured by ChIP-seq, promoter regions have significantly less occupancy compared with its overall binding sites (Figures 1A–1C) (Weintraub et al., 2017). CTCF-binding sites with low occupancy that diverge from the core DNA motif were associated with regulated binding during mESC differentiation (Plaschaert et al., 2014). In our study, we noticed that CTCF-binding sites within DEGs share these same characteristics, and chromatin binding is destabilized in both ZF1Δ and ZF10Δ rescue cell lines compared with WT (Figures 4D and 4E).

It is our view that CTCF has a significant role in regulating gene expression on the basis of the following observations: (1) Hemizygous mice for CTCF succumb to cancer in 80% of animals tested, highlighting that chronically lower levels of CTCF have

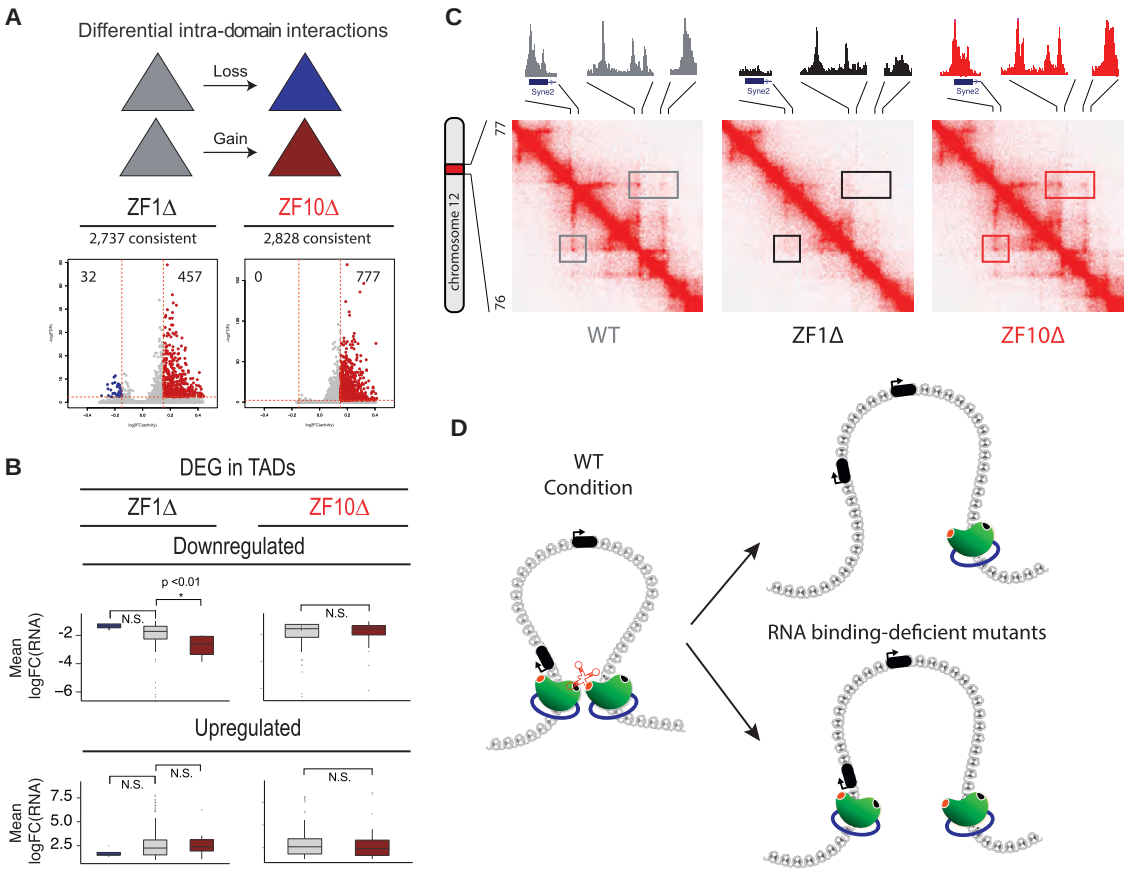

Figure 6. RBR Mutants Disturb Chromatin Loops

(A) Intra-domain interaction changes in WT versus ZF1Δ and WT versus ZF10Δ for common domains. CTCF mutant rescues are associated with gain (red) and loss (blue) of intra-domain interactions.

(B) Boxplots representing the correlation between DEG and chromatin domains whose interactions are increased. Only downregulated genes for ZF1Δ are significantly correlated with increased intra-domain interactions, while all others are not significantly correlated.

(C) Representative contact matrix (at 5 kb resolution) show that the chromatin loop anchor on the left overlaps with the promoter of the *Syne2* gene. In the WT rescue (left), the loop disappears in the ZF1Δ (middle) and is stable in ZF10Δ (right), while CTCF binding is lost only at the promoter and anchor for ZF1Δ. Syne2 is upregulated only under the ZF1Δ condition.

(D) Graphical representation of a chromatin loop formed by two CTCF proteins (green) and cohesin rings (blue), stabilized by an RNA in the WT condition (left diagram). Two outcomes are observed for the RNA binding-deficient mutants (ZF1Δ and ZF10Δ): (1) the loop is lost and a CTCF protein loses its binding to chromatin (top, right diagram), or (2) both CTCF proteins remain bound to chromatin yet the chromatin loop is still lost (bottom, right diagram).

clear dramatic effects on the biology of the cell and seem to be a hallmark of carcinogenesis (Kemp et al., 2014). (2) DEGs have significantly more CTCF-binding sites in their promoters and gene bodies (Figure 4B). (3) CTCF orientation at promoters is in the same direction as transcription and these form loops with internal CTCF-binding sites close to exons. These loops are prevalent and significant for alternative splicing (Ruiz-Velasco et al., 2017). We also found that a significant number of TSSs overlap with anchor sites delimiting chromatin-interacting domains, suggesting that CTCF can function as both a TF and an insulator at the same time (Figure S5G). (4) Differences between cell-type specificity of CTCF binding fit with the transcription trapping hypothesis: RNA contributes to the maintenance and recognition of its binding site for certain TFs such that "transcription of regulatory elements produce a positive-feedback loop that contributes to the stability of gene expression programs" (Sigova et al., 2015). All these features together underscore the relevance of CTCF as a TF and the interplay between transcription and chromatin organization.

In this study, we provide new insight into the relevance of CTCF-RNA interactions. We demonstrate that chromatin looping requires not only CTCF binding to chromatin but also to RNA. The reduced looping capability observed in RNA binding-deficient mutants causes an overall increase in interactions, highlighting the need for RNA molecules to stabilize the appropriate connections. Specifically, both ZF1Δ and ZF10Δ show an increase in interactions within chromatin-interacting domains (Figure 6A). These results suggest that altered *cis*-interactions and chromatin loops that are formed throughout the genome alter cell proliferation (Figure S2B). Furthermore, gene expression alterations are enriched at boundary regions (Figure S6E), possibly through new or disrupted promoter-enhancer contacts

or aberrant inter-domain interactions, suggesting that these are important regulatory regions.

We previously hypothesized that RNA molecules would stabilize CTCF-CTCF loops *in vivo* after describing that CTCF self-association was RNA dependent *in vitro* (Saldaña-Meyer et al., 2014). In our previous study, we termed the RBR (aa 520–727) as the region of CTCF from ZF10 to the end of the C terminus and a deletion within that RBR (aa 574–614) was found to be necessary for CTCF self-association and affected RNA binding *in vitro* (Saldaña-Meyer et al., 2014). Unexpectedly and in contrast to *in vitro* results, PAR-CLIP on full-length CTCF with the internal deletion resulted in only a modest reduction in RNA binding, compelling us to pursue further mapping of RBRs that are now presented in this study. In parallel to this study, Hansen et al. (2019) (in this issue of *Molecular Cell*) showed that the internal deletion in the RBR had significant defects on self-association and clustering but the RNA-binding defect is more modest than the ZF1Δ and ZF10Δ mutants. Regardless, half of the chromatin loops were disrupted in this mutant (Hansen et al., 2019). Together, these two studies suggest that there are several regions within CTCF than can associate with RNA and likely with other factors, which together contribute to the stability of CTCF binding to chromatin and to the formation of chromatin loops.

Many questions remain to be explored if transcription is considered to be a main factor contributing to the regulation of chromatin-interacting domains in a temporal and cell type-specific manner. Perhaps other RNA-binding proteins can account for specific structural roles. Many chromatin-interacting domains are gene poor, or the genes they contain are largely silenced. In these cases, the contribution of nascent RNA as a structural component appears untenable. Yet it is possible that abundant long-lived transcripts such as those from repetitive regions (Hall et al., 2014) could have a general function in chromatin organization of these repressed regions. On the basis of the large number of RNA interactors that are pulled down with CTCF (Kung et al., 2015; Saldaña-Meyer et al., 2014), we envision that these interactions might be highly redundant. Of note, experiments performed to date have examined interactions between bulk RNA and CTCF and, importantly, have yet to be designed to detect potential specificity of the interacting RNA in the context of distinct CTCF DNA-binding sites. Determining exactly how CTCF interacts in complex with DNA and RNA as well as with its protein partners will be an exciting new research avenue. Advances in technical approaches will be needed to improve our understanding of these highly complex regulatory mechanisms.

STAR★METHODS

Detailed methods are provided in the online version of this paper and include the following:

- KEY RESOURCES TABLE
- LEAD CONTACT AND MATERIALS AVAILABILITY
- EXPERIMENTAL MODEL AND SUBJECT DETAILS
  - Mouse ESC culture
- METHOD DETAILS
  - Transcriptional inhibition
  - RNase A treatment
  - Rescue cell line generation
  - Cell isolation and flow cytometry
  - PAR-CLIP
  - ChIP-seq
  - Bulk RNA-seq
  - Single-cell RNA-seq library preparation
  - Hi-C library preparation
  - Definition of regulatory regions
- QUANTIFICATION AND STATISTICAL ANALYSIS
  - Bulk RNA-seq Analysis
  - Single-cell RNA-seq Analysis
  - ChIP-seq Analysis
  - *De Novo* Motif Discovery
  - Motif Analysis
  - Hi-C data processing and quality control
  - Quality Control
  - Downstream Analysis
- DATA AND CODE AVAILABILITY

SUPPLEMENTAL INFORMATION

Supplemental Information can be found online at https://doi.org/10.1016/j.molcel.2019.08.015.

ACKNOWLEDGMENTS

We thank Dr. L. Vales for comments on the manuscript; Dr. Roberto Bonasio for sharing unpublished results for RBR-ID; Drs. Esteban Mazzoni and Pedro Lee for continuing discussions; Drs. Robert Tjian and Anders Hansen for early access to their manuscript; Dr. Angelica Menchaca at RNA Life Sciences Consulting for help with figure curation; the New York University Langone Medical Center (NYULMC) Genome Technology Center; the NYULMC Cytometry and Cell Sorting Core for help with fluorescence-activated cell sorting (FACS); Programa de Apoyo a Proyectos de Investigación e Innovación Tecnológica (PAPIIT; IA201817 and IN207319) for financial support to M.F.-M; and Laboratorio Nacional de Ciencias de la Sostenibilidad (LANCIS, UNAM) and Ing. Rodrigo García Herrera for access and technical support with the computer cluster. The NYULMC Genome Technology Center and the NYUMC Cytometry and Cell Sorting Core are partially supported by the Cancer Center Support Grant P30CA016087 at the Laura and Isaac Perlmutter Cancer Center. This work used computing resources at the High-Performance Computing Facility of the Center for Health Informatics and Bioinformatics at the NYULMC. K.J.-L. was supported by (CVU 631104) and R.S.-M. (CVU 224211) received a postdoctoral award from CONACYT. This work was supported by grants from the NIH (R01NS100897 and R01CA199652 to D.R. and 1R35GM122515 and 1R01-CA222131 to J.S.) and the Howard Hughes Medical Institute (to D.R.).

AUTHOR CONTRIBUTIONS

R.S.-M. and D.R. conceived the project, designed the experiments, and wrote the paper with input from all authors. R.S.-M. performed all experiments and bioinformatic data analysis. T.E. performed the cell-cycle analyses. E.P.N. generated the CTCF degron cell lines in the lab of B.G.B. J.R.-H. and M.N. analyzed Hi-C data in the laboratory of J.S. with supervision from A.T. K.J.-L. analyzed Hi-C data in the laboratory of M.F.-M.

DECLARATION OF INTERESTS

D.R. is a co-founder of Constellation Pharmaceuticals and Fulcrum Therapeutics. R.S.-M. is a co-founder of RNA Life Sciences Consulting. All other authors declare no competing interests.

Received: January 29, 2019
Revised: July 15, 2019
Accepted: August 16, 2019
Published: September 12, 2019

REFERENCES

Alipanahi, B., Delong, A., Weirauch, M.T., and Frey, B.J. (2015). Predicting the sequence specificities of DNA- and RNA-binding proteins by deep learning. Nat. Biotechnol. *33*, 831–838.

Beltran, M., Yates, C.M., Skalska, L., Dawson, M., Reis, F.P., Viiri, K., Fisher, C.L., Sibley, C.R., Foster, B.M., Bartke, T., et al. (2016). The interaction of PRC2 with RNA or chromatin is mutually antagonistic. Genome Res. *26*, 896–907.

Bensaude, O. (2011). Inhibiting eukaryotic transcription: which compound to choose? How to evaluate its activity? Transcription *2*, 103–108.

Bonev, B., and Cavalli, G. (2016). Organization and function of the 3D genome. Nat. Rev. Genet. *17*, 661–678.

Butcher, D.T., and Rodenhiser, D.I. (2007). Epigenetic inactivation of BRCA1 is associated with aberrant expression of CTCF and DNA methyltransferase (DNMT3B) in some sporadic breast tumours. Eur. J. Cancer *43*, 210–219.

Crane, E., Bian, Q., McCord, R.P., Lajoie, B.R., Wheeler, B.S., Ralston, E.J., Uzawa, S., Dekker, J., and Meyer, B.J. (2015). Condensin-driven remodelling of X chromosome topology during dosage compensation. Nature *523*, 240–244.

de Koning, A.P.J., Gu, W., Castoe, T.A., Batzer, M.A., and Pollock, D.D. (2011). Repetitive elements may comprise over two-thirds of the human genome. PLoS Genet. *7*, e1002384.

De La Rosa-Velázquez, I.A., Rincón-Arano, H., Benítez-Bribiesca, L., and Recillas-Targa, F. (2007). Epigenetic regulation of the human retinoblastoma tumor suppressor gene promoter by CTCF. Cancer Res. *67*, 2577–2585.

Dixon, J.R., Selvaraj, S., Yue, F., Kim, A., Li, Y., Shen, Y., Hu, M., Liu, J.S., and Ren, B. (2012). Topological domains in mammalian genomes identified by analysis of chromatin interactions. Nature *485*, 376–380.

Dowen, J.M., Fan, Z.P., Hnisz, D., Ren, G., Abraham, B.J., Zhang, L.N., Weintraub, A.S., Schujiers, J., Lee, T.I., Zhao, K., and Young, R.A. (2014). Control of cell identity genes occurs in insulated neighborhoods in mammalian chromosomes. Cell *159*, 374–387.

Durand, N.C., Shamim, M.S., Machol, I., Rao, S.S.P., Huntley, M.H., Lander, E.S., and Aiden, E.L. (2016). Juicer provides a one-click system for analyzing loop-resolution Hi-C experiments. Cell Syst. *3*, 95–98.

Filippova, G.N., Fagerlie, S., Klenova, E.M., Myers, C., Dehner, Y., Goodwin, G., Neiman, P.E., Collins, S.J., and Lobanenkov, V.V. (1996). An exceptionally conserved transcriptional repressor, CTCF, employs different combinations of zinc fingers to bind diverged promoter sequences of avian and mammalian c-myc oncogenes. Mol. Cell. Biol. *16*, 2802–2813.

Fudenberg, G., Abdennur, N., Imakaev, M., Goloborodko, A., and Mirny, L.A. (2017). Emerging evidence of chromosome folding by loop extrusion. Cold Spring Harb. Symp. Quant. Biol. *82*, 45–55.

Gao, Z., Zhang, J., Bonasio, R., Strino, F., Sawai, A., Parisi, F., Kluger, Y., and Reinberg, D. (2012). PCGF homologs, CBX proteins, and RYBP define functionally distinct PRC1 family complexes. Mol. Cell *45*, 344–356.

Hall, L.L., Carone, D.M., Gomez, A.V., Kolpa, H.J., Byron, M., Mehta, N., Fackelmayer, F.O., and Lawrence, J.B. (2014). Stable C0T-1 repeat RNA is abundant and is associated with euchromatic interphase chromosomes. Cell *156*, 907–919.

Hansen, A.S., Hsieh, T.-H.S., Cattoglio, C., Pustova, I., Saldaña-Meyer, R., Reinberg, D., Darzacq, X., and Tjian, R. (2019). Distinct classes of chromatin loops revealed by deletion of an RNA-binding Region in CTCF. Mol. Cell *76*. Published online September 12, 2019. https://doi.org/10.1016/j.molcel.2019.07.039.

Hashimoto, H., Wang, D., Horton, J.R., Zhang, X., Corces, V.G., and Cheng, X. (2017). Structural basis for the versatile and methylation-dependent binding of CTCF to DNA. Mol. Cell *66*, 711–720.e3.

He, C., Sidoli, S., Warneford-Thomson, R., Tatomer, D.C., Wilusz, J.E., Garcia, B.A., and Bonasio, R. (2016). High-resolution mapping of RNA-binding regions in the nuclear proteome of embryonic stem cells. Mol. Cell *64*, 416–430.

Heger, P., Marin, B., Bartkuhn, M., Schierenberg, E., and Wiehe, T. (2012). The chromatin insulator CTCF and the emergence of metazoan diversity. Proc. Natl. Acad. Sci. U S A *109*, 17507–17512.

Heinz, S., Benner, C., Spann, N., Bertolino, E., Lin, Y.C., Laslo, P., Cheng, J.X., Murre, C., Singh, H., and Glass, C.K. (2010). Simple combinations of lineage-determining transcription factors prime cis-regulatory elements required for macrophage and B cell identities. Mol. Cell *38*, 576–589.

Holohan, E.E., Kwong, C., Adryan, B., Bartkuhn, M., Herold, M., Renkawitz, R., Russell, S., and White, R. (2007). CTCF genomic binding sites in Drosophila and the organisation of the bithorax complex. PLoS Genet. *3*, e112–e112.

Imakaev, M., Fudenberg, G., McCord, R.P., Naumova, N., Goloborodko, A., Lajoie, B.R., Dekker, J., and Mirny, L.A. (2012). Iterative correction of Hi-C data reveals hallmarks of chromosome organization. Nat. Methods *9*, 999–1003.

Kaneko, S., Bonasio, R., Saldaña-Meyer, R., Yoshida, T., Son, J., Nishino, K., Umezawa, A., and Reinberg, D. (2014a). Interactions between JARID2 and noncoding RNAs regulate PRC2 recruitment to chromatin. Mol. Cell *53*, 290–300.

Kaneko, S., Son, J., Bonasio, R., Shen, S.S., and Reinberg, D. (2014b). Nascent RNA interaction keeps PRC2 activity poised and in check. Genes Dev. *28*, 1983–1988.

Kemp, C.J., Moore, J.M., Moser, R., Bernard, B., Teater, M., Smith, L.E., Rabaia, N.A., Gurley, K.E., Guinney, J., Busch, S.E., et al. (2014). CTCF haploinsufficiency destabilizes DNA methylation and predisposes to cancer. Cell Rep. *7*, 1020–1029.

Kim, T.H., Abdullaev, Z.K., Smith, A.D., Ching, K.A., Loukinov, D.I., Green, R.D., Zhang, M.Q., Lobanenkov, V.V., and Ren, B. (2007). Analysis of the vertebrate insulator protein CTCF-binding sites in the human genome. Cell *128*, 1231–1245.

Kung, J.T., Kesner, B., An, J.Y., Ahn, J.Y., Cifuentes-Rojas, C., Colognori, D., Jeon, Y., Szanto, A., del Rosario, B.C., Pinter, S.F., et al. (2015). Locus-specific targeting to the X chromosome revealed by the RNA interactome of CTCF. Mol. Cell *57*, 361–375.

Lai, F., Orom, U.A., Cesaroni, M., Beringer, M., Taatjes, D.J., Blobel, G.A., and Shiekhattar, R. (2013). Activating RNAs associate with Mediator to enhance chromatin architecture and transcription. Nature *494*, 497–501.

Langmead, B., and Salzberg, S.L. (2012). Fast gapped-read alignment with Bowtie 2. Nat. Methods *9*, 357–359.

Lazaris, C., Kelly, S., Ntziachristos, P., Aifantis, I., and Tsirigos, A. (2017). HiC-bench: comprehensive and reproducible Hi-C data analysis designed for parameter exploration and benchmarking. BMC Genomics *18*, 22.

Li, H., Handsaker, B., Wysoker, A., Fennell, T., Ruan, J., Homer, N., Marth, G., Abecasis, G., and Durbin, R.; 1000 Genome Project Data Processing Subgroup (2009). The Sequence Alignment/Map format and SAMtools. Bioinformatics *25*, 2078–2079.

Li, W., Notani, D., Ma, Q., Tanasa, B., Nunez, E., Chen, A.Y., Merkurjev, D., Zhang, J., Ohgi, K., Song, X., et al. (2013). Functional roles of enhancer RNAs for oestrogen-dependent transcriptional activation. Nature *498*, 516–520.

Lieberman-Aiden, E., van Berkum, N.L., Williams, L., Imakaev, M., Ragoczy, T., Telling, A., Amit, I., Lajoie, B.R., Sabo, P.J., Dorschner, M.O., et al. (2009). Comprehensive mapping of long-range interactions reveals folding principles of the human genome. Science *326*, 289–293.

Merkenschlager, M., and Nora, E.P. (2016). CTCF and cohesin in genome folding and transcriptional gene regulation. Annu. Rev. Genomics Hum. Genet. *17*, 17–43.

Moore, J.M., Rabaia, N.A., Smith, L.E., Fagerlie, S., Gurley, K., Loukinov, D., Disteche, C.M., Collins, S.J., Kemp, C.J., Lobanenkov, V.V., and Filippova, G.N. (2012). Loss of maternal CTCF is associated with peri-implantation lethality of Ctcf null embryos. PLoS ONE *7*, e34915.

Nakahashi, H., Kieffer Kwon, K.R., Resch, W., Vian, L., Dose, M., Stavreva, D., Hakim, O., Pruett, N., Nelson, S., Yamane, A., et al. (2013). A genome-wide map of CTCF multivalency redefines the CTCF code. Cell Rep. *3*, 1678–1689.

Narendra, V., Bulajić, M., Dekker, J., Mazzoni, E.O., and Reinberg, D. (2016). CTCF-mediated topological boundaries during development foster appropriate gene regulation. Genes Dev. *30*, 2657–2662.

Nickerson, J.A., Krochmalnic, G., Wan, K.M., and Penman, S. (1989). Chromatin architecture and nuclear RNA. Proc. Natl. Acad. Sci. U S A *86*, 177–181.

Nora, E.P., Goloborodko, A., Valton, A.-L., Gibcus, J.H., Uebersohn, A., Abdennur, N., Dekker, J., Mirny, L.A., and Bruneau, B.G. (2017). Targeted degradation of CTCF decouples local insulation of chromosome domains from genomic compartmentalization. Cell *169*, 930–944.e22.

Pękowska, A., Klaus, B., Xiang, W., Severino, J., Daigle, N., Klein, F.A., Oleś, M., Casellas, R., Ellenberg, J., Steinmetz, L.M., et al. (2018). Gain of CTCF-anchored chromatin loops marks the exit from naive pluripotency. Cell Syst. *7*, 482–495.e10.

Peña-Hernández, R., Marques, M., Hilmi, K., Zhao, T., Saad, A., Alaoui-Jamali, M.A., del Rincon, S.V., Ashworth, T., Roy, A.L., Emerson, B.M., and Witcher, M. (2015). Genome-wide targeting of the epigenetic regulatory protein CTCF to gene promoters by the transcription factor TFII-I. Proc. Natl. Acad. Sci. U S A *112*, E677–E686.

Phillips-Cremins, J.E., Sauria, M.E.G., Sanyal, A., Gerasimova, T.I., Lajoie, B.R., Bell, J.S.K., Ong, C.-T., Hookway, T.A., Guo, C., Sun, Y., et al. (2013). Architectural protein subclasses shape 3D organization of genomes during lineage commitment. Cell *153*, 1281–1295.

Plasschaert, R.N., Vigneau, S., Tempera, I., Gupta, R., Maksimoska, J., Everett, L., Davuluri, R., Mamorstein, R., Lieberman, P.M., Schultz, D., et al. (2014). CTCF binding site sequence differences are associated with unique regulatory and functional trends during embryonic stem cell differentiation. Nucleic Acids Res. *42*, 774–789.

Ramírez, F., Ryan, D.P., Grüning, B., Bhardwaj, V., Kilpert, F., Richter, A.S., Heyne, S., Dündar, F., and Manke, T. (2016). deepTools2: a next generation web server for deep-sequencing data analysis. Nucleic Acids Res. *44* (W1), W160–W165.

Rao, S.S.P., Huang, S.-C., Glenn St Hilaire, B., Engreitz, J.M., Perez, E.M., Kieffer-Kwon, K.-R., Sanborn, A.L., Johnstone, S.E., Bascom, G.D., Bochkov, I.D., et al. (2017). Cohesin loss eliminates all loop domains. Cell *171*, 305–320.e24.

Rizzetto, S., Eltahla, A.A., Lin, P., Bull, R., Lloyd, A.R., Ho, J.W.K., Venturi, V., and Luciani, F. (2017). Impact of sequencing depth and read length on single cell RNA sequencing data of T cells. Sci. Rep. *7*, 12781.

Robinson, J.T., Thorvaldsdóttir, H., Winckler, W., Guttman, M., Lander, E.S., Getz, G., and Mesirov, J.P. (2011). Integrative genomics viewer. Nat. Biotechnol. *29*, 24–26.

Rowley, M.J., and Corces, V.G. (2018). Organizational principles of 3D genome architecture. Nat. Rev. Genet. *19*, 789–800.

Ruiz-Velasco, M., Kumar, M., Lai, M.C., Bhat, P., Solis-Pinson, A.B., Reyes, A., Kleinsorg, S., Noh, K.-M., Gibson, T.J., and Zaugg, J.B. (2017). CTCF-mediated chromatin loops between promoter and gene body regulate alternative splicing across individuals. Cell Syst. *5*, 628–637.e6.

Saldaña-Meyer, R., González-Buendía, E., Guerrero, G., Narendra, V., Bonasio, R., Recillas-Targa, F., and Reinberg, D. (2014). CTCF regulates the human p53 gene through direct interaction with its natural antisense transcript, Wrap53. Genes Dev. *28*, 723–734.

Schmidt, D., Schwalie, P.C., Ross-Innes, C.S., Hurtado, A., Brown, G.D., Carroll, J.S., Flicek, P., and Odom, D.T. (2010). A CTCF-independent role for cohesin in tissue-specific transcription. Genome Res. *20*, 578–588.

Servant, N., Varoquaux, N., Lajoie, B.R., Viara, E., Chen, C.J., Vert, J.-P., Heard, E., Dekker, J., and Barillot, E. (2015). HiC-Pro: an optimized and flexible pipeline for Hi-C data processing. Genome Biol. *16*, 259.

Sigova, A.A., Abraham, B.J., Ji, X., Molinie, B., Hannett, N.M., Guo, Y.E., Jangi, M., Giallourakis, C.C., Sharp, P.A., and Young, R.A. (2015). Transcription factor trapping by RNA in gene regulatory elements. Science *350*, 978–981.

Soto-Reyes, E., and Recillas-Targa, F. (2010). Epigenetic regulation of the human p53 gene promoter by the CTCF transcription factor in transformed cell lines. Oncogene *29*, 2217–2227.

Stadhouders, R., Vidal, E., Serra, F., Di Stefano, B., Le Dily, F., Quilez, J., Gómez, A., Collombet, S., Berenguer, C., Cuartero, Y., et al. (2018). Transcription factors orchestrate dynamic interplay between genome topology and gene regulation during cell reprogramming. Nat. Genet. *50*, 238–249.

Stark, R., and Brown, G. (2011). DiffBind: differential binding analysis of ChIP-Seq peak data. R Package version 2.2.7 http://bioconductor.org/packages/DiffBind/.

Thorvaldsdóttir, H., Robinson, J.T., and Mesirov, J.P. (2013). Integrative Genomics Viewer (IGV): high-performance genomics data visualization and exploration. Brief. Bioinform. *14*, 178–192.

Trapnell, C., Roberts, A., Goff, L., Pertea, G., Kim, D., Kelley, D.R., Pimentel, H., Salzberg, S.L., Rinn, J.L., and Pachter, L. (2012). Differential gene and transcript expression analysis of RNA-seq experiments with TopHat and Cufflinks. Nat. Protoc. *7*, 562–578.

Tsirigos, A., Haiminen, N., Bilal, E., and Utro, F. (2012). GenomicTools: a computational platform for developing high-throughput analytics in genomics. Bioinformatics *28*, 282–283.

Vietri Rudan, M., Barrington, C., Henderson, S., Ernst, C., Odom, D.T., Tanay, A., and Hadjur, S. (2015). Comparative Hi-C reveals that CTCF underlies evolution of chromosomal domain architecture. Cell Rep. *10*, 1297–1309.

Weintraub, A.S., Li, C.H., Zamudio, A.V., Sigova, A.A., Hannett, N.M., Day, D.S., Abraham, B.J., Cohen, M.A., Nabet, B., Buckley, D.L., et al. (2017). YY1 is a structural regulator of enhancer-promoter loops. Cell *171*, 1573–1588.e28.

Whyte, W.A., Orlando, D.A., Hnisz, D., Abraham, B.J., Lin, C.Y., Kagey, M.H., Rahl, P.B., Lee, T.I., and Young, R.A. (2013). Master transcription factors and mediator establish super-enhancers at key cell identity genes. Cell *153*, 307–319.

Witcher, M., and Emerson, B.M. (2009). Epigenetic silencing of the p16(INK4a) tumor suppressor is associated with loss of CTCF binding and a chromatin boundary. Mol. Cell *34*, 271–284.

Xiao, R., Chen, J.-Y., Liang, Z., Luo, D., Chen, G., Lu, Z.J., Chen, Y., Zhou, B., Li, H., Du, X., et al. (2019). Pervasive chromatin-RNA binding protein interactions enable RNA-based regulation of transcription. Cell *178*, 107–121.e18.

Xie, X., Mikkelsen, T.S., Gnirke, A., Lindblad-Toh, K., Kellis, M., and Lander, E.S. (2007). Systematic discovery of regulatory motifs in conserved regions of the human genome, including thousands of CTCF insulator sites. Proc. Natl. Acad. Sci. U S A *104*, 7145–7150.

Yu, G., Wang, L.-G., and He, Q.-Y. (2015). ChIPseeker: an R/Bioconductor package for ChIP peak annotation, comparison and visualization. Bioinformatics *31*, 2382–2383.

Zhang, Y., Liu, T., Meyer, C.A., Eeckhoute, J., Johnson, D.S., Bernstein, B.E., Nusbaum, C., Myers, R.M., Brown, M., Li, W., and Liu, X.S. (2008). Model-based analysis of ChIP-Seq (MACS). Genome Biol. *9*, R137–R139.

Zuin, J., Dixon, J.R., van der Reijden, M.I.J.A., Ye, Z., Kolovos, P., Brouwer, R.W.W., van de Corput, M.P.C., van de Werken, H.J.G., Knoch, T.A., van IJcken, W.F.J., et al. (2014). Cohesin and CTCF differentially affect chromatin architecture and gene expression in human cells. Proc. Natl. Acad. Sci. USA *111*, 996–1001.

STAR★METHODS

KEY RESOURCES TABLE

REAGENT or RESOURCE	SOURCE	IDENTIFIER
Antibodies		
Anti-CTCF (IP, ChIP)	Abcam Cat# ab70303	RRID:AB_1209546
Anti-CTCF (WB)	Millipore # 07-729	RRID:AB_441965
Anti-Lamin B	Abcam Cat# ab16048	RRID:AB_10107828
Anti-Gapdh	Abcam Cat# ab8245	RRID:AB_2107448
Anti-YY1	Santa Cruz # sc-7341 X	RRID:AB_2257497
Chemicals, Peptides, and Recombinant Proteins		
Triptolide	Sigma-Aldrich Cat# T3652	N/A
DRB	Sigma-Aldrich Cat# D1916	N/A
Indole-3-acetic acid sodium salt (auxin analog)	Sigma-Aldrich Cat# I5148-2G	N/A
CHIR99021	Stemgent	N/A
PD0325901	Stemgent	N/A
Critical Commercial Assays		
TruSeq Stranded mRNA Kit	illumina	N/A
Kapa Library Prep Kit	Roche	N/A
Arima Hi-C Kit	Arima	N/A
Deposited Data		
Hi-C, 5C, RNA-Seq, scRNA-Seq and ChIP-Seq data	This paper	GSE125595
Unprocessed gel images for Figures 2, S1 and S2	This paper	https://doi.org/10.17632/xbrf8x7k22.1
Experimental Models: Cell Lines		
mESC e14 CTCF-GFP-Tir1-TIGER	Nora et al., 2017	N/A
mESC e14 CTCF-GFP-Tir1-TIGER-WT-Rescue	This paper	N/A
mESC e14 CTCF-GFP-Tir1-TIGER-ZF1Δ-Rescue	This paper	N/A
mESC e14 CTCF-GFP-Tir1-TIGER-ZF10Δ-Rescue	This paper	N/A
mESC e14 CTCF-GFP-Tir1-TIGER-ZF1-H284N-Rescue	This paper	N/A
mESC e14 CTCF-GFP-Tir1-TIGER-ZF10- H528S-Rescue	This paper	N/A
Recombinant DNA		
pLVX-EF1a-IRES-mCherry Vector (pLVX)	Clontech	Cat# 631987
Oligonucleotides		
See Table S2	This paper	N/A
Software and Algorithms		
RStudio	RStudio	RRID:SCR_000432
Samtools	Li et al., 2009	RRID:SCR_002105
Integrative Genomics Viewer	Robinson et al., 2011; Thorvaldsdóttir et al., 2013	RRID:SCR_011793
Bowtie2	Langmead and Salzberg, 2012	RRID:SCR_005476
deepTools	Ramírez et al., 2016	RRID:SCR_016366
MACS	Zhang et al., 2008; https://github.com/taoliu/MACS/	RRID:SCR_013291
HiC-Pro	Servant et al., 2015	https://github.com/nservant/HiC-Pro
DESeq2	https://www.bioconductor.org	RRID:SCR_015687
HiC-Bench	Lazaris et al., 2017	https://github.com/NYU-BFX/hic-bench

(*Continued on next page*)

Continued

REAGENT or RESOURCE	SOURCE	IDENTIFIER
Juicer 1.5	Durand et al., 2016; https://github.com/aidenlab/juicer/wiki	RRID:SCR_017226
tophat 2.1.1	Trapnell et al., 2012; https://github.com/cole-trapnell-lab/cufflinks	RRID:SCR_013035
Homer 4.10	Heinz et al., 2010; http://homer.ucsd.edu/homer/	RRID:SCR_010881
DiffBind	Stark and Brown, 2011; http://bioconductor.org/packages/DiffBind/	RRID:SCR_012918
ChIPseeker	Yu et al., 2015	http://bioconductor.org/packages/ChIPseeker/
DeepBind	Alipanahi et al., 2015	http://tools.genes.toronto.edu/deepbind/

LEAD CONTACT AND MATERIALS AVAILABILITY

Further information and requests for resources and reagents should be directed to and will be fulfilled by the Lead Contact, Danny Reinberg (Danny.Reinberg@nyulangone.org).

EXPERIMENTAL MODEL AND SUBJECT DETAILS

Mouse ESC culture

E14Tga2 (ATCC, CRL-1821) mESCs were grown in standard medium supplemented with LIF, 1 uM MEK1/2 inhibitor (PD0325901, Stemgent) and 3 uM GSK3 inhibitor (CHIR99021, Stemgent); rescue cell lines were also grown with 500mM of indole-3-acetic acid (IAA, chemical analog of auxin) in the medium as in Nora et al. (2017).

METHOD DETAILS

Transcriptional inhibition

mESCs were incubated with a combination of transcriptional inhibitors (Triptolide 1 μM and DRB 100μM) for 1 or 4 hours. After treatment cells were immediately harvested for immunoblot, ChIP and 5C experiments.

RNase A treatment

The treatment was performed as in Beltran et al. (2016). Briefly, mESCs nuclei were permeabilized with 0.05% Tween-20 in PBS for 10 min at 4C, washed once and resuspended in PBS and finally incubated with RNase A (1 mg/ml) or a mock reaction for 30 minutes. After treatment cells were immediately harvested for ChIP and 5C experiments.

Rescue cell line generation

HEK293T to cells were grown to ~90% confluency, split 1:4 and grown for one day. Cell were then transfected with pLVX-EF1a-IRES-mCherry encoding CTCF WT, ZF1Δ, ZF10Δ, H284N or C528S along with their respective packaging vectors. After 4 hours of transfection the medium was changed to complete DMEM and finally to ESC culture medium after 32-40hr of transfection. Then, the viral supernatant was harvested, filtered through 0.45um syringe filter and added polybrene to 8μg/μl. Added the mix to cells and spin infect (500 g X 60min). Change medium the next day. Sorted for mCherry positive cells after ~2 days of infection for each condition.

Cell isolation and flow cytometry

Single-cell suspensions were prepared passing through 40-μm cell strainers (BD Biosciences) and sorted for mCherry+ mESCs using SY3200 cell sorter. For cell cycle analysis, Click-It Edu AlexaFluor 488 Flow Cytometry Assay (Invitrogen) was used following manufacturing protocol and counterstaining with Propidium Iodide. Stained cells were assayed with BD LSRII flow cytometer and all results were analyzed using FlowJo software.

PAR-CLIP

PAR-CLIP was performed as in Saldaña-Meyer et al. (2014) with some modifications. Briefly, cells were grown under standard conditions and pulsed with 400 mM 4-SU (Sigma) for 2 h. After washing the plates with PBS, cells were cross- linked with 400 mJ/cm2 UVA (312 nm) using a Stratalinker UV cross-linker (Stratagene). Whole nuclear lysates (WNLs) were obtained by fractionation and nuclei were then incubated for 10 min at 37°C in an appropriate volume of CLIP buffer (20 mM HEPES at pH 7.4, 5 mM EDTA,

150 mM NaCl, 2% EMPIGEN) supplemented with protease inhibitors, 20 U/mL Turbo DNase (Life technologies), and 200 U/mL murine RNase inhibitor (New England Biolabs). After clearing the lysate by centrifugation, immunoprecipitations were carried out using 200 μg of WNLs, CTCF antibody, in the same CLIP buffer for 4h at 4°C and then added protein G-coupled Dynabeads (Life Technologies) for an additional hour. Contaminating DNA was removed by treating the beads with Turbo DNase (2 U in 20 mL). Cross-linked RNA was labeled by successive incubation with 5 U of Antarctic phosphatase (New England Biolabs) and 5 U of T4 PNK (New England Biolabs) in the presence of 10 mCi [^{32}P] ATP (PerkinElmer). Labeled material was resolved on 8% Bis-Tris gels, transferred to nitrocellulose membranes, and visualized by autoradiography. The same membrane was then blocked with TBS-T and 5% milk and blotted for CTCF and Lamin-B.

ChIP-seq

ChIP-seq experiments were performed as described previously (Gao et al., 2012). Briefly, cells were fixed with 1% Formaldehyde. Nuclei were isolated using buffers in the following order: LB1 (50 mM HEPES, pH 7.5 at 4C, 140 mM NaCl, 1 mM EDTA, 10% Glycerol, 0.5% NP40, 0.25% Triton X; 10 min at 4C), LB2 (10 mM Tris, pH 8 at 4C, 200 mM NaCl, 1 mM EDTA, 0.5 mM EGTA; 10 min at RT), and LB3 (10 mM Tris, pH 7.5 at 4C, 1 mM EDTA, 0.5 mM EGTA, and 0.5% N-Lauroylsarcosine sodium salt). Chromatin was fragmented to an average size of 250 bp using a Diagenode Bioruptor. Chromatin immunoprecipitation was performed with CTCF or K27ac antibodies. ChIP-seq libraries were prepared using the Kapa Library Prep Kit.

Bulk RNA-seq

Total RNA from ESCs was isolated with TRIzol (Life Technologies). Stranded libraries were then prepared with 2 μg of total RNA as starting material using TruSeq Stranded mRNA kits following the manufacturer's instructions.

Single-cell RNA-seq library preparation

Single-cell RNA-seq libraries were prepared using the Chromium Controller (10X Genomics). Briefly, single cells in 0.04% BSA in PBS were separated into droplets and then reverse transcription and library construction was performed according to the 10X Chromium Single Cell 30 Reagent Kit User Guide and sequenced on an Illumina Novaseq 6000.

Single-cell RNaseq analysis was performed for three 10X libraries (WT, ZF1Δ and ZF10Δ rescues) and sequenced on a paired-end 26/98 Illumina NovaSeq 6000 S2 run. Per-read per-sample FASTQ files were generated using the bcl2fastq Conversion software (v2.20) to convert BCL base call files outputted by the sequencing instrument into the FASTQ format. The 10X Genomics analysis software, Cell Ranger (v2.1.0), specifically the "cellranger count" pipeline, was used to align reads from the generated FASTQ files to the mouse reference genome mm10, generate gene-barcode expression matrices, and perform clustering and differential gene expression analysis. The outputs of the three conditions (WT, ZF1Δ and ZF10Δ) from the "cellranger count" pipeline were aggregated using the "cellranger aggr" pipeline of Cell Ranger, normalizing the combined output to the same sequencing depth and recomputing the gene-barcode matrices and expression analysis accordingly for the aggregated data.

Hi-C library preparation

Hi-C libraries were constructed using the Arima kit following the manufacturer's instructions. Briefly, cells were crosslinked with 2% formaldehyde to obtain 1-5 μg of DNA per Arima-HiC reaction. Importantly, the crosslinked cell pellet for each Arima-HiC reaction should not occupy more than 20 μL of volume in the sample tube and be devoid of any residual liquid. The Arima kit uses an enzyme cocktail that cuts at the following motifs, where '^' is the cut site on the + strand: ^GATC, G^ANTC (N can be either of the 4 genomic bases). Because a digested end produced by one enzyme can be ligated to a digested end produced by the other enzyme, there are 4 possible ligation junction signatures in the chimeric reads: GATC-GATC, GANT-GATC, GANT-ANTC, GATC-ANTC. All enzymatic reactions were made in PCR tubes and incubation was performed using a thermocycler. Libraries were prepared using the Kapa Library Prep Kit with a modified protocol provided by Arima.

Definition of regulatory regions

Enhancers

For Figures S1C and S3B. Typical-enhancer coordinates were downloaded from Whyte et al. (2013)

5C Library Preparation

5C was performed as in Narendra et al. (2016). Briefly, 5C primers were annealed at 48°C for 16hrs atop the 3C libraries from each sample. 1fmol of each primer was used in the annealing reaction with 1 μg of 3C template and 1 μg of salmon sperm DNA. 16 separate annealing reactions were performed per sample, along with control reactions with individual components removed. Forward and reverse primers that annealed to adjacent regions of the 3C template were ligated with 10U of Taq ligase for 60' at 48°C. Successfully ligated forward-reverse primer pairs were then amplified in 6 separate PCR reactions per annealing reaction, using primers specific to the T7 and T3 overhangs. PCR reactions from the equivalent initial sample were then pooled, purified, and run on a gel to ensure the control reactions did not show an amplification product. Libraries were then generated from the purified PCR product to allow for deep sequencing.

QUANTIFICATION AND STATISTICAL ANALYSIS

Bulk RNA-seq Analysis

Raw sequencing files were aligned against the mouse reference genome (GRCm38/mm10) using tophat 2.1.1 and differentially expressed genes were called using DESeq2 with adjusted p values 0.05 and 0.001.

Single-cell RNA-seq Analysis

Sequencing data was demultiplexed using the 10X Genomics Cell Ranger software (version 2.0.0) and aligned to the mm10 transcriptome. Unique molecular identifiers were collapsed into a gene-barcode matrix representing the counts of molecules per cell as determined and filtered by Cell Ranger using default parameters. Normalized expression values were generated using Cell Ranger using the default parameters.

ChIP-seq Analysis

Raw sequencing files were aligned against the mouse reference genome (GRCm38/mm10) using Bowtie2 (version 2.3.4.1) (parameters: -N 1 -k 1 -q -x). Ambiguous reads were filtered to use uniquely mapped reads in the downstream analysis. PCR duplicates were removed using Picard-tools (version 1.88). MACS version 2.0.10 was used to call narrow peaks (parameters: -g 1.87e9–qvalue 0.01). To create heatmaps we used deepTools (version 2.4.1) (Ramírez et al., 2016). We first ran bamCoverage (–binSize 50–extendReads 200 -of bigwig) and normalized read numbers to RPKM or to the spike-in *Drosophila* DNA (–scaleFactor sf), obtaining read coverage per 50-bp bins across the whole genome (bigWig files). We then used the bigWig files to compute read numbers centered on CTCF peaks called by MACS, on TSSs or enhancers (computeMatrix reference-point–sortRegions descend–sortUsing mean–averageTypeBins mean). Finally, heatmaps were created with plotHeatmap (–colorMap = 'Blues'–sortRegions = no).

We used the DiffBind package to identify CTCF sites with significant increase or decrease in binding affinity (Parameters: summits = 250, FDR < 0.01, log2FoldChange > 1).

De Novo Motif Discovery

De novo motif discovery was carried out using the Homer pipeline (Heinz et al., 2010) using coordinates for peaks lost in ZF1Δ and ZF10Δ conditions (findMotifsGenome.pl -size 200).

Motif Analysis

To quantify the affinity of each CTCF motif instance identified from our ChIP-seq data we used DeepBind (Alipanahi et al., 2015), a deep learning algorithm that has been trained on large amounts of ChIP-seq data and can be used to score the affinity of any given sequence for the CTCF motif. 500 bp DNA sequences were used to score their motif affinity with DeepBind v0.11, using motif D00328.018 (CTCF).

Hi-C data processing and quality control

Processing

HiC-Bench (Lazaris et al., 2017) was used to align and filter the Hi-C data, identify chromatin-interacting domains, and generate Hi-C heatmaps. To generate Hi-C filtered contact matrices, the Hi-C reads were aligned against the mouse reference genome (GRCm38/mm10) by bowtie2 (Langmead and Salzberg, 2012) (version 2.3.1). Mapped read pairs were filtered by the GenomicTools (Tsirigos et al., 2012) tools-hic filter command integrated in HiC-bench for known artifacts of the Hi-C protocol. The filtered reads include multi-mapped reads ('multihit'), read-pairs with only one mappable read ('single sided'), duplicated read-pairs ('ds.duplicate'), low mapping quality reads (MAPQ < 20), read-pairs resulting from self-ligated fragments, and short-range interactions resulting from read-pairs aligning within 25kb ('ds.filtered'). For the downstream analyses, all the accepted intra-chromosomal read-pairs ('ds.accepted intra') were used.

The Hi-C filtered contact matrices were corrected using the ICE ''correction'' algorithm (Imakaev et al., 2012) built into HiC-bench. Chromatin-interacting domains were annotated in all conditions using Arrowhead at 10kb resolutions using default parameters (Durand et al., 2016). We also assessed chromatin loops with aggregate peak analysis (APA). We analyzed the data at 10kb resolution (-r 10000 -x 42 -k KR). HiC heatmaps for regions of interest were generated in juicer.

Chromatin domains and boundaries were called using Crane (Crane et al., 2015) at 40 kb bin resolution with an insulating window of 103 kb and 500kb. We also called domains using the Hicratio algorithm (Lazaris et al., 2017) at 40kb resolution.

Quality Control

Quality assessment analysis shows that the total numbers of reads per biological replicate for each condition ranged from ~600 million reads to ~1.1 billion. The percentage of reads aligned was always over 98% in all samples. The proportion of accepted reads ('ds-accepted-intra' and 'ds-accepted-inter') was ~40%, which in all cases was sufficient to annotate chromatin loops with HICCUPS.

Downstream Analysis

The data was aligned against the mm10 reference genome. All contact matrices used for further analysis were KR-normalized. Chromatin loops were annotated for all conditions using HiCCUPS (Durand et al., 2016). Loops were called at 5kb and 10kb resolutions and merged using default parameters.

Compartments

Compartment analysis was carried out using the Homer pipeline (Heinz et al., 2010) (v4.6). Homer performs a principal component analysis of the normalized interaction matrices and uses the PCA1 component to predict regions of active (A compartments) and inactive chromatin (B compartments). Homer works under the assumption that gene-rich regions with active chromatin marks have similar PC1 values, while gene deserts show differing PC1 values. HiC filtered matrices were given as input to Homer together with H2K27ac peaks for compartment prediction. H2K27ac was used by Homer as prior information of active regions.

To determine if significantly altered compartments were present in the mutants, we used Homer's getHiCcorrDiff.pl pipeline to correlate the interaction profile of each locus in the mutants to the interaction profile of that same locus in the wild-type condition. As a result, no significant altered compartment region was identified. We generated density plots to compare the cis-eigenvector 1 values of the mutants and the wild-type by using 50kb genomic bins. Pearson correlation coefficients were also calculated ('Cor' function in R).

Intra-domain interactions

We used the 'domains-diff' pipeline present in HiC-Bench to assess statistically significant intra-domain interactions.

First, the domains-diff pipeline identifies overlapped or positionally consistent domain (common chromatin-interacting domains). This approach establishes a minimum domain length parameter (default: 10 bins) and extends either side of the domain by 3 bins (+/−120 kb in 40kb resolution). chromatin-interacting domains across two samples are considered positionally consistent if their boundaries are as close as 3 bins. The boundaries of the common chromatin-interacting domains are then set to those which yield the largest domain. The set of common domains between any two samples s_1 and s_2 is denoted as T. In the next step, a paired two-sided t test is performed on each single interaction bin within each common domain between the two samples. It calculates the difference between the average scores of all interaction intensities within such domains. A multiple testing correction by calculating the false-discovery rate per common domain (using the R function p.adjust with method = "fdr") is also calculated.

$$Chromatin-interacting\ domain(t) = \left(\frac{\sum i \in I_t\ ^{S}2i}{\#I_t}\right) - \left(\frac{\sum i \in I_t\ ^{S}1i}{\#I_t}\right)$$

for each $t \in T$, and I_t being all intra-domain interactions for domains t.

We classified the common domains in terms of increased, decreased or stable intra-domain interactions by using FDR < 0.1 and absolute domain interactions change > 0.15. A minimum common domains length of 240 kb was considered in the intra-domain interactions differential analysis (6 bins).

Gene expression analysis in Common domains

To assess the correlation of RNA expression with the intra-domain activity status of the common domains in the ZF1 and ZF10 mutants, we assigned a differentially expressed gene (FDR < 0.05) to a common domain when its promoter overlapped with a common domain (overlap > 1 bp). Then, the mean fold change of the RNA expression inside each common domain was computed for upregulated and downregulated DEGs, separately, and compared between the common domain groups (increased-activity, decreased-activity, stable-activity). Statistical significance was assessed by performing a wilcoxon test (unpaired) and boxplots were generated in R.

Annotation of the differential CTCF sites

We used the ChIPSeeker library to annotate the differential CTCF sites obtained in the DiffBind analysis. Annotation packages: 'TxDb.Mmusculus.UCSC.mm10.knownGene' and 'org.Mm.eg.db' (Bioconductor).

To annotate the CTCF differential sites in domains or boundaries we used the domains and boundaries obtained using Crane (w = 500kb). A CTCF site was assigned to a boundary if the complete CTCF peak was found within the boundary coordinates.

DATA AND CODE AVAILABILITY

Data can be found at GEO with accession GEO: GSE125595. Original gel images were uploaded to Mendeley Data: https://doi.org/10.17632/xbrf8x7k22.1

Sanchez-Sandoval and Gomora
Cancer Cell Int (2019) 19:35
https://doi.org/10.1186/s12935-019-0757-6

Cancer Cell International

PRIMARY RESEARCH

Open Access

Contribution of voltage-gated sodium channel β-subunits to cervical cancer cells metastatic behavior

Ana Laura Sanchez-Sandoval and Juan Carlos Gomora*

Abstract

Background: Voltage-gated sodium (Na_V) channels are heteromeric proteins consisting of a single pore forming α-subunit associated with one or two auxiliary β-subunits. These channels are classically known for being responsible of action potential generation and propagation in excitable cells; but lately they have been reported as widely expressed and regulated in several human cancer types. We have previously demonstrated the overexpression of $Na_V1.6$ channel in cervical cancer (CeCa) biopsies and primary cultures, and its contribution to cell migration and invasiveness. Here, we investigated the expression of Na_V channels β-subunits ($Na_V\beta$s) in the CeCa cell lines HeLa, SiHa and CaSki, and determined their contribution to cell proliferation, migration and invasiveness.

Methods: We assessed the expression of $Na_V\beta$s in CeCa cell lines by performing RT-PCR and western blotting experiments. We also evaluated CeCa cell lines proliferation, migration, and invasion by in vitro assays, both in basal conditions and after inducing changes in $Na_V\beta$s levels by transfecting specific cDNAs or siRNAs. The potential role of $Na_V\beta$s in modulating the expression of Na_V α-subunits in the plasma membrane of CeCa cells was examined by the patch-clamp whole-cell technique. Furthermore, we investigated the role of $Na_V\beta1$ on cell cycle in SiHa cells by flow cytometry.

Results: We found that the four $Na_V\beta$s are expressed in the three CeCa cell lines, even in the absence of functional Na_V α-subunit expression in the plasma membrane. Functional in vitro assays showed differential roles for $Na_V\beta1$ and $Na_V\beta4$, the latter as a cell invasiveness repressor and the former as a migration abolisher in CeCa cells. In silico analysis of $Na_V\beta4$ expression in cervical tissues corroborated the downregulation of this protein expression in CeCa vs normal cervix, supporting the evidence of $Na_V\beta4$'s role as a cell invasiveness repressor.

Conclusions: Our results contribute to the recent conception about $Na_V\beta$s as multifunctional proteins involved in cell processes like ion channel regulation, cell adhesion and motility, and even in metastatic cell behaviors. These non-canonical functions of $Na_V\beta$s are independent of the presence of functional Na_V α-subunits in the plasma membrane and might represent a new therapeutic target for the treatment of cervical cancer.

Keywords: Voltage-gated sodium channel β-subunits, Cervical cancer, Proliferation, Migration, Invasion, Cell-adhesion molecule

*Correspondence: jgomora@ifc.unam.mx
Departamento de Neuropatología Molecular, División de Neurociencias, Instituto de Fisiología Celular, Universidad Nacional Autónoma de México, 04510 Mexico City, Mexico

© The Author(s) 2019. This article is distributed under the terms of the Creative Commons Attribution 4.0 International License (http://creativecommons.org/licenses/by/4.0/), which permits unrestricted use, distribution, and reproduction in any medium, provided you give appropriate credit to the original author(s) and the source, provide a link to the Creative Commons license, and indicate if changes were made. The Creative Commons Public Domain Dedication waiver (http://creativecommons.org/publicdomain/zero/1.0/) applies to the data made available in this article, unless otherwise stated.

Background

Cervical cancer (CeCa) is the fourth most common cancer in women worldwide, with more than 500,000 new cases each year and an estimated 260,000 deaths, of which approximately 87% occur in developing countries [1]. Despite the implementation of vaccination against Human Papillomavirus infection, it will take decades before the impact on the cervical cancer incidence became clear, giving the natural history of this disease [2]. Therefore, it is necessary to better understand the biology of this type of cancer in order to improve the early detection and treatment.

Voltage-gated sodium (Na_V) channels are heteromeric transmembrane proteins that consist of a single pore forming α-subunit associated with one or more auxiliary β-subunits (Na_Vβs) [3]. These channels are known to be responsible for action potential generation and propagation in excitable cells, but they are also widely expressed and upregulated in a variety of human cancer types, including breast, prostate, colon, ovarian, lung, gastric, melanoma, astrocytoma and uterine cervix, where the Na_V α-subunit activity has been associated mainly, but not exclusively, with cell motility and invasiveness [4–14]. So far, four Na_Vβs (Na_Vβ1–Na_Vβ4) have been described. These are multifunctional type I transmembrane proteins that modulate Na_V α-subunit gating, localization and transit to the plasma membrane. Additionally, they possess a V-type immunoglobulin repeat in the extracellular domain similar to the family of neural cell adhesion molecules (CAMs), thus, their role as CAMs in a trans-homophilic and trans-heterophilic way, and with other molecules, in presence or absence of the α-subunits has been described in numerous reports and in different expression systems [15–22].

The role of Na_Vβs in cancer has also been studied, although not as widely as for the α-subunits. In prostate cancer (PCa), it has been found that the overexpression of Na_Vβs is associated with the increasing metastatic potential of PCa cell lines [23], and when overexpressing Na_Vβ2 in LnCaP cells, the cells acquired a fibroblastic-like morphology, became more invasive and had enhanced migration in vitro; in contrast, these cells had a reduced tumor volume in vivo [24, 25]. On the other hand, the overexpression of Na_Vβ3 in Saos-2 (osteosarcoma) and T98G (glioblastoma) cells, seems to activate an apoptotic pathway mediated by the tumor suppressor protein p53 [26]. However, most of the studies have been done in breast cancer, where it has been demonstrated that Na_Vβ1 is overexpressed in the low metastatic MCF-7 cell line vs highly metastatic MDA-MB-231 cells [27]. Overexpressing Na_Vβ1 in these last cells produced a drastic reduction on in vitro transwell migration and an increase in cellular adhesiveness. In contrast, MDA-MB-231 cells stably transfected with Na_Vβ1 produced larger tumors in an in vivo model compared with those generated by wild type MDA-MB-231 cells. In addition, overexpression of Na_Vβ1 induced a reduction in caspase activity in these cells [28]. More recently, the potential role of Na_Vβ4 as a metastasis-suppressor gene has been described in breast cancer cells, associated with the small GTPase RhoA activity and therefore with the cytoskeleton remodeling during migration and invasiveness [29].

We have previously demonstrated the overexpression of Na_V α-subunits in cervical cancer biopsies vs non-cancerous cervix, and furthermore, we reported the functional expression of these proteins in primary cultures derived from human cervical cancer biopsies and their contribution to the cell migration and invasiveness. Specifically, Na_V1.6 showed to be the most overexpressed α-subunit and the one responsible of the augmented invasive potential as the specific blockade of this channel was able to diminish the invasive potential with the same effectiveness as the blockade of all the Na_V α-subunits by TTX [14, 30]. In the present work, we investigated the electrophysiological activity of Na_V channels and the expression of Na_Vβs in three cervical cancer cell lines (HeLa, SiHa and CaSki) as well as their contribution to three metastatic cell behaviors: in vitro proliferation, transwell migration and invasiveness.

Methods

Cell lines and cell culture

Cervical cancer cell lines SiHa, CaSki (both HPV-16 positive) and HeLa (HPV-18 positive) were grown in DMEM supplemented with 10% fetal bovine serum (FBS), 100 U/ml penicillin, and 100 µg/ml streptomycin at 37 °C in a humidified 5% CO_2 incubator. All cell culture reagents were purchased from Gibco-Thermo Fisher Scientific (Waltham, MA). The three cell lines were authenticated by short tandem repeat profiling prior to the experiments (data not shown).

Overexpression and downregulation of Na_Vβs expression

Plasmids containing each of the Na_Vβs from rat were kindly donated by Dr. L. Isom (University of Michigan). Overexpression of each Na_Vβ in CeCa cells was achieved by transient transfections using the JetPEI transfection reagent (PolyPlus Transfection; Illkirch, France), according to the manufacturer's instructions. On the other hand, downregulation of Na_Vβs expression was performed using two or three different predesigned siRNAs (Sigma-Aldrich; St. Louis, MO) for each Na_Vβ (100 nM each); in all cases, we chose the one with the best efficiency. Optimal siRNA transfection conditions were stablished previously by using 50 nM of siGLO Green Transfection Indicator (Sigma-Aldrich), a fluorescent

Table 1 RT-PCR primers information

mRNA	*GenBank* access	Primer pair sequence (5′ → 3′)	PCR Product (bp)	Annealing Temp (°C)
$Na_V\beta1$	NM_001037	F: AGAAGGGCACTGAGGAGTTT R: GCAGCGATCTTCTTGTAGCA	379	60
$Na_V\beta2$	NM_004588	F: GCCCACCCGACTAACATCTC R: ATGCGGAACTGGAGGAACA	285	62
$Na_V\beta3$	NM_018400	F: CTGGCTTCTCTCGTGCTTAT R: TCAAACTCCCGGGACACATT	353	60
$Na_V\beta4$	NM_174934	F: CACGCCACCATCTTCCTCCAA R: TGCAGCTGCTCAGCCCGAAG	284	65
β-actin	NM_001101	F: GCTCGTCGTCGACAACGGCTC R: CAAACATGATCTGGGTCATCTTCTC	353	60

F forward primer, *R* reverse primer

siRNA for determining transfection efficiency. Efficiency of both experimental strategies to manipulate the expression levels of each $Na_V\beta$ was evaluated by RT-PCR and western blot (see Additional file 1).

Electrophysiology

Detailed methods for whole-cell patch-clamp recordings and protocols have been previously described [14, 30]. Sodium currents of native or transiently transfected CeCa cells were recorded at room temperature (20–23 °C) using an Axopatch 200B amplifier, a Digidata 1320A/D converter, and the pCLAMP 10.0 software (Molecular Devices; Sunnyvale, CA). As a positive control for sodium currents, we used transiently transfected CeCa cells with the $Na_V1.6$ channel.

Standard PCR (RT-PCR)

The $Na_V\beta$s mRNA expression levels of CeCa cell lines were assessed by RT-PCR with specific primers for each β-subunit and β-actin as control (Table 1) as described before [30]. Briefly, total RNA of each cell line was isolated with Trizol reagent (Invitrogen; Carlsbad, CA) and RT-PCR reactions were performed in a final volume of 25 µl using the Super-Script One-step RT-PCR kit (Invitrogen) with 250 ng of total RNA, 0.5 µl of enzyme mix, 0.2–0.5 µM of each primer, and 12.5 µl of 2X buffer containing 0.4 mM of each dNTP and 2.4 mM $MgSO_4$.

Real-time PCR (qPCR)

Total RNA was extracted using the RNeasy Mini Kit (Qiagen; Hilden, Germany), then reverse-transcribed with the High Capacity cDNA Reverse Transcription kit (Applied Biosystems; Foster City, CA) according to the manufacturer's instructions using 2 µg of total RNA in a final volume of 20 µl. Real-time PCR was carried out in a Rotor-Gene Q (Qiagen) using Custom TaqMan Gene Expression Assays (Applied Biosystems) as described before [14]. Briefly, 100 ng of cDNA, 0.4 µl of the TaqMan assay (Table 2) and 5 µl of TaqMan Universal PCR Master Mix (Applied Biosystems) were mixed in a final reaction volume of 10 µl for each qPCR reaction. At least three independent experiments were done, and each assay was performed in triplicate. The results were analyzed by the $2^{-\Delta\Delta Ct}$ method [31] using HPRT1 expression as the normalizing gene control and results are shown as relative expression values of $Na_V\beta1$ in HeLa cells.

Table 2 qPCR primers information

mRNA	*GenBank* access	Primer pair sequence (5′ → 3′)	PCR product (bp)
$Na_V\beta1$	NM_001037	F: GGAGGATGAGCGCTTCGA R: CAGATCCTGCAGGTCTTTGGT P: CCCCGGCTGCCATT	70
$Na_V\beta2$	NM_004588	F: TGCAGCCGGAGGATGAG R: GAGGACCTGCAGATGGATCTTG P: CCCCTGACCGCCACCG	92
$Na_V\beta3$	NM_018400	F: CGCCAGCCCCAGAAGAT R: CACAGGGAAGCAGACACTGA P: TTTCCCCTGGCTTCTC	90
$Na_V\beta4$	NM_174934	F: AAGAAGTGGACAACACAG TGACA R: TGAGTTTCTTGATCAGCAGGA TGAG P: ACCCCGCCCACGACAG	93

F forward primer, *R* reverse primer, *P* TaqMan probe

Western blot

Total protein from native or transiently transfected CeCa cells was extracted 24, 48, 72 and 96 h post-transfection (with cDNA or siRNAs, for overexpression or inhibition of the $Na_V\beta$ expression respectively) using RIPA buffer (25 mM Tris–HCl, pH 7.4; 150 mM NaCl; 1% IGEPAL; 1% Sodium deoxycholate, and 1% SDS) supplemented with complete EDTA-free protease inhibitors (Roche, Switzerland), and quantified by Bradford assay. Equal amounts of protein (100 µg) were subjected to

SDS-PAGE, transferred onto a polyvinylidene difluoride membrane (Millipore, Billerica MA) and probed overnight with the following primary antibodies: rabbit anti-$Na_V\beta1$ (1:3000; LifeSpan BioSciences Inc.; Seattle, WA); rabbit anti-$Na_V\beta2$ (1:1000; LifeSpan BioSciences Inc.); rabbit anti-$Na_V\beta3$ (1:5000; Abcam; Cambridge, UK), rabbit anti-$Na_V\beta4$ (1:3000; Novus Biologicals; Littleton, CO) and a homemade mouse anti-β-actin antibody (1:1000) used as a loading control. Blots were subsequently probed with an anti-rabbit or an anti-mouse (as the case may be) secondary antibody conjugated with horseradish peroxidase (1:10,000; Santa Cruz Biotechnology; Dallas, TX) for 1 h at room temperature and visualized using the SuperSignal West Pico chemiluminescent substrate (Thermo Fisher Scientific). Signal intensity of immunoblots was calculated with ImageJ software.

Proliferation assays

Cell proliferation was determined using the colorimetric 3-[4,5-dimethylthiazol-2-yl]-2,5-diphenyltetrazolium bromide (MTT) assay. Briefly, cells were plated in 48-well microplates at an initial density of 2×10^3 cells per well. To measure cell proliferation at 24, 48, 72 and 96 h after seeding, 10 µl of MTT solution (5 mg/ml) were added in each well after replacing the culture medium with 200 µl of fresh culture medium. The cells were incubated at 37 °C, and 3 h later, cell culture and MTT solution were removed and 150 µl of dimethyl sulfoxide was added into the plate to dissolve formazan crystals. The absorbance at a wavelength of 562 nm was recorded using an Eppendorf AG 22331 Biophotometer (Eppendorf; Hamburg, Germany). For analyzing the role of $Na_V\beta$s on proliferation, after overnight incubation, cells were transfected with the respective cDNA to overexpress or the specific siRNA to downregulate each β-subunit expression, and finally, MTT assay was performed 24, 48, 72 and 96 h after transfection.

Cell cycle analysis by flow cytometry

The role of $Na_V\beta1$ on cell cycle in SiHa cells was assessed by flow cytometry after staining the cells with propidium iodide (PI; Molecular Probes, Life Technologies; Grand Island, NY). Briefly, 2×10^5 cells were seeded onto 12-well plates, incubated in normal conditions for 24 h, synchronized by serum-reduced conditions (0.2% FBS) for 48 h and then transfected with the specific cDNA or siRNA. After incubating for 48 h, cells were collected and fixed with ice-cold 70% ethanol, stored for at least 24 h at −20 °C, treated with RNase and stained with PI for 1 h at 37 °C. For each condition, 2×10^4 cells (singlets) were analyzed in an Accuri C6 cytometer (BD Biosciences; San Jose, CA), and the percentages of cells in each cell cycle phase were analyzed with FlowJo software (Tree Star; Ashland, OR) using the Dean-Jett-Fox algorithm by three independent tests for each condition. Appropriate gating was used to select the single cell population and used on all samples.

In vitro migration and invasion assays

Migration and invasion assays were done using culture inserts with 8-µm pore size membranes covered or not with Matrigel (Corning Inc., Corning, NY) for invasion and migration respectively. The upper compartment was seeded with 5×10^4 for migration and 1×10^5 cells for invasion in DMEM supplemented with 5% FBS, and the lower compartment was filled with DMEM supplemented with 15% FBS as a chemoattractant. The number of cells migrating or invading (according to the circumstances) over 48 h at 37 °C was evaluated using the MTT assay described before. Results were compiled as the mean of at least three repeats, each time done by duplicate, and compared with control conditions.

In silico immunohistochemistry (IHC) staining analysis

Expression of $Na_V\beta4$ in CeCa and normal cervical tissues was examined using the Human Protein Atlas (http://www.proteinatlas.org/) [32, 33], a Swedish-based online tool for human protein expression analysis. Representative CeCa and normal tissues cores were chosen for illustrative purposes.

Statistical analysis

All quantitative results are given as the mean ± S.D. Differences in means were tested with an unpaired two-tailed Student's *t* test.

Results

Cervical cancer cell lines do not express plasma-membrane voltage-gated sodium currents

Our previous results showed the functional expression of Na_V channels in CeCa primary cultures and specifically demonstrated the relevance of the $Na_V1.6$ channel in the invasiveness of cervical cancer [14, 30]. Thus, in order to further investigate the role of Na_V channels in the biology of CeCa, we intended to use CeCa cell lines for such experiments. However, we found that SiHa, CaSki and HeLa cell lines do not express functional Na_V channels at the plasma-membrane as determined by whole-cell patch-clamp experiments. ($n = 30$ cells total; see Additional file 2), even though we have previously shown that they do express the $Na_V1.6$ mRNA and at least one isoform of the $Na_V1.6$ protein [34].

Endogenous expression of $Na_V\beta$s in cervical cancer cell lines

In previous studies, we described the role of Na_V α-subunits in the invasive potential of CeCa primary cultures. In this work, we wanted to analyze the possible role of $Na_V\beta$s in different CeCa cellular processes. To that end, endogenous expression of $Na_V\beta$s was first evaluated by RT-PCR using specific primers for each subunit. In most of cases, the mRNA was abundant as evidenced by the generation of the expected amplicon for each β-subunit (Fig. 1a), suggesting the very likely presence of these proteins. Along with the expected bands, additional PCR amplicons were observed when analyzing the expression of $Na_V\beta2$ and $Na_V\beta4$ by RT-PCR (Fig. 1a). The ≈150 bp DNA fragment observed in the $Na_V\beta4$ line matches with a splice variant that has been already reported [23], that would produce a highly truncated protein (if translated) with an unknown functionality. The larger non-specific bands in $Na_V\beta2$ and $Na_V\beta4$ RT-PCR do not correspond to any reported variants of such isoforms, and we cannot

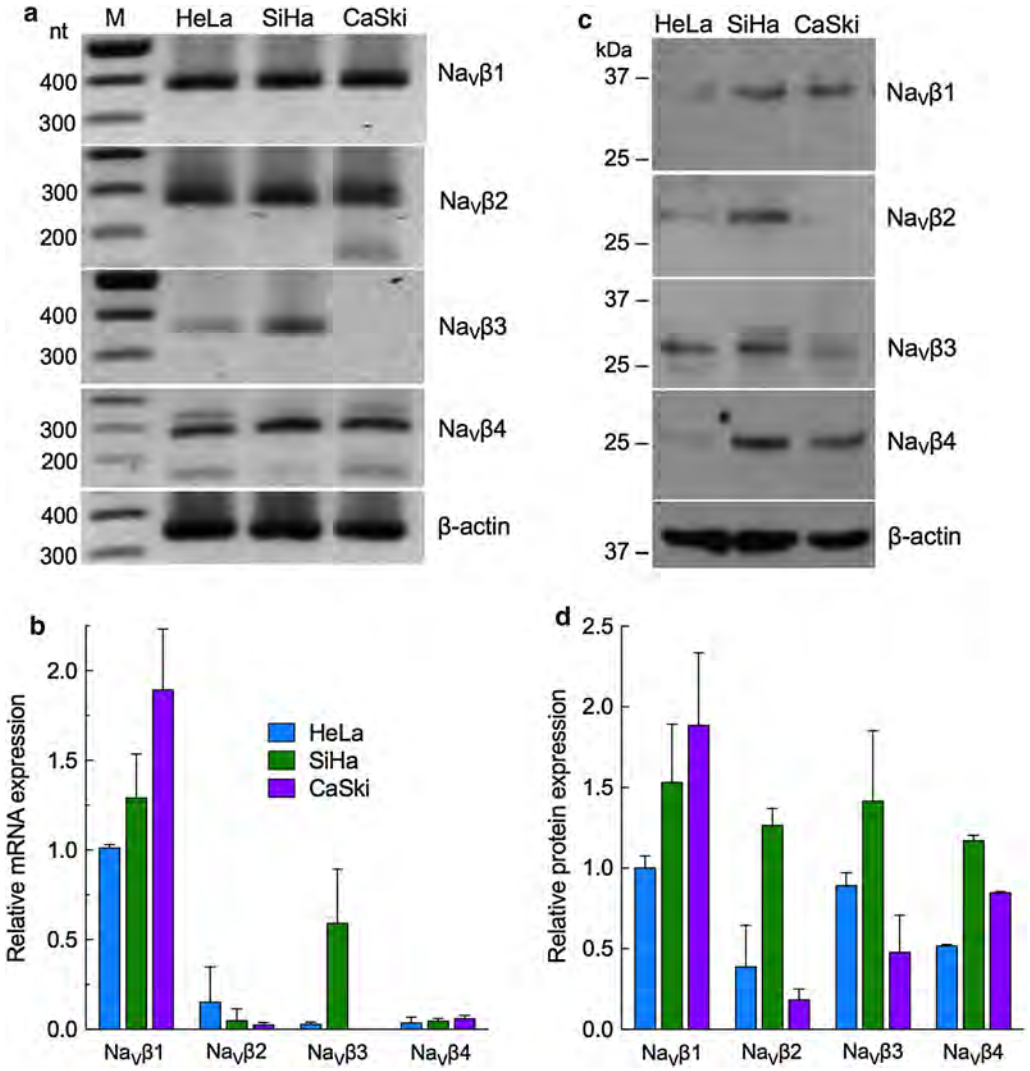

Fig. 1 Expression of $Na_V\beta$s in cervical cancer cell lines. **a** Total RNA isolated from CeCa cell lines was analyzed by conventional RT-PCR using specific primers for the indicated $Na_V\beta$ and β-actin as a loading control. Expected fragment sizes for each gene are shown on the right of each panel. M: molecular marker. **b** Quantitative differences in $Na_V\beta$s mRNA expression of CeCa cells analyzed by qPCR, normalized with HPRT1 mRNA levels and relative to $Na_V\beta1$ in HeLa. Each bar denotes mean ± S.D. of three independent experiments. **c** Western blot with 100 µg of total protein per lane from each of the cell lines indicated. Specific antibodies against each $Na_V\beta$ were used and β-actin antibody as a control for loading. **d** Quantified data for $Na_V\beta$s protein expression normalized with β-actin expression for each cell line, and relative to $Na_V\beta1$ expression in HeLa. Each bar denotes mean ± S.D. of three independent experiments

rule out the possibility of a non-specific amplification with these primers. A more detailed study is required to analyze the $Na_V\beta$s isoforms expressed in the CeCa cells and their potential function and/or contribution to the cancerous phenotype. Nevertheless, to carry out a more quantitative analysis of the $Na_V\beta$s expression levels in the different CeCa cell lines we performed qPCR experiments. Results exhibited substantial differences in $Na_V\beta$s mRNA expression, but in all cases, $Na_V\beta1$ showed to be highly expressed, whereas $Na_V\beta3$ displayed the lowest expression levels, except in SiHa cells (Fig. 1b). In addition, evaluation of protein expression by western blot for each $Na_V\beta$ indicates that the four $Na_V\beta$s are expressed in the three CeCa cell lines (Fig. 1c). Interestingly, SiHa was the only cell line that express very similar levels of all four $Na_V\beta$s (Fig. 1d). Also, SiHa and CaSki cells expressed significantly higher levels of $Na_V\beta1$ and $Na_V\beta4$ than HeLa cells. While $Na_V\beta3$ levels were similar among the CeCa cell lines, and $Na_V\beta2$ was the lees expressed except in SiHa cells (Fig. 1d). The western blot results suggest the absence of additional variants of $Na_V\beta$s isoforms, as we only observed the protein of the expected size.

Proliferation, migration and invasion of CeCa cell lines under basal conditions

In order to evaluate the metastatic potential of each CeCa cell line, we analyzed three key metastatic behaviors: proliferation, migration and invasiveness in vitro. HeLa cells demonstrated to be the most aggressive cell line as these cells proliferated, migrated and invaded the most, followed by SiHa cells, and CaSki cells (Fig. 2).

Increasing or decreasing the expression of $Na_V\beta$s is not enough to promote the functional activity of α-subunits in the plasma membrane

First, to evaluate the siRNA transfection efficacy, we used the siGLO Green Transfection Indicator, a fluorescent dye attached to a scramble siRNA, and analyzed the cells 24 h later by epifluorescent microscopy. The results indicated that almost 100% of the cells were transfected with the siRNAs, as can be appreciated in Additional file 3. Thus, we followed the same conditions to transfect the specific siRNAs against each of the $Na_V\beta$s.

It is well known that some of the $Na_V\beta$s are implicated in the correct trafficking of the Na_V α-subunits to the plasma membrane, as has been shown with the heterologous in vitro expression of $Na_V\beta1$ and $Na_V\beta2$ in Xenopus oocytes [15, 35], and in vivo with $Na_V\beta2$ knocked-out mice [36]. These evidences made us wonder if the sole overexpression or even the down regulation of the expression of $Na_V\beta$s was enough to promote the functional expression of the pore-forming sodium channels in the plasma membrane and therefore the appearance of voltage-gated sodium currents. To address this question, HeLa and SiHa cells were analyzed by the whole-cell patch-clamp technique 24, 48, 72 and 96 h after transfection to increase or decrease the expression of each of the $Na_V\beta$s. More than 130 cells were successfully investigated with this technique, but we did not find any voltage-gated sodium currents, suggesting that the regulation of the expression of $Na_V\beta$s is not enough to promote the functional activity of Na_V α-subunits in the plasma membrane (see Additional file 2).

Role of $Na_V\beta$s on proliferation

Next, we investigated whether the expression of $Na_V\beta$s had an effect on cell proliferation. This was evaluated in CeCa cell lines 24, 48, 72 and 96 h post-transfection with the cDNA or with the specific siRNA for each $Na_V\beta$ subunit to increase or to reduce the expression respectively. Only $Na_V\beta1$ had an effect on proliferation of SiHa cells: the overexpression of $Na_V\beta1$ increased cell proliferation, whereas its downregulation decreased cell duplication (Fig. 3a; center panels). This is similar to what was found

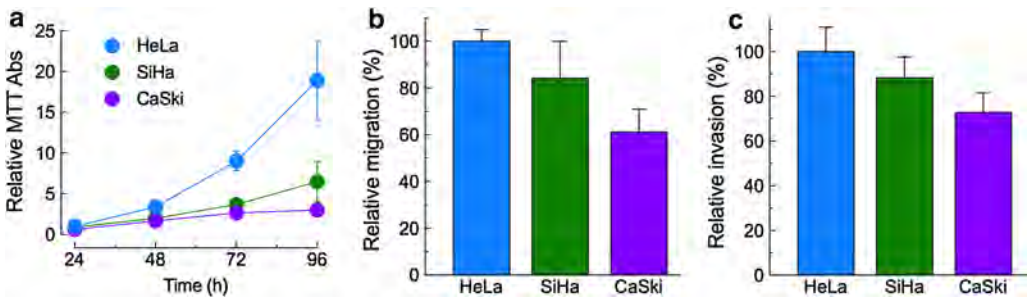

Fig. 2 Proliferation, migration and invasion of CeCa cells. **a** Proliferation was evaluated by MTT assays 24, 48, 72 and 96 h after seeding the cells (2×10^3 per well). Means ± S.D. of three independent experiments, each one done by triplicate. Migration (**b**) and invasion (**c**) of CeCa cells were assessed by Boyden transwell assays for 48 h. Results expressed as percentages of values obtained for HeLa cells. Means ± S.D. of three independent experiments, each done by duplicate. HeLa cells showed to be the most aggressive, as they proliferated, migrated and invaded the most

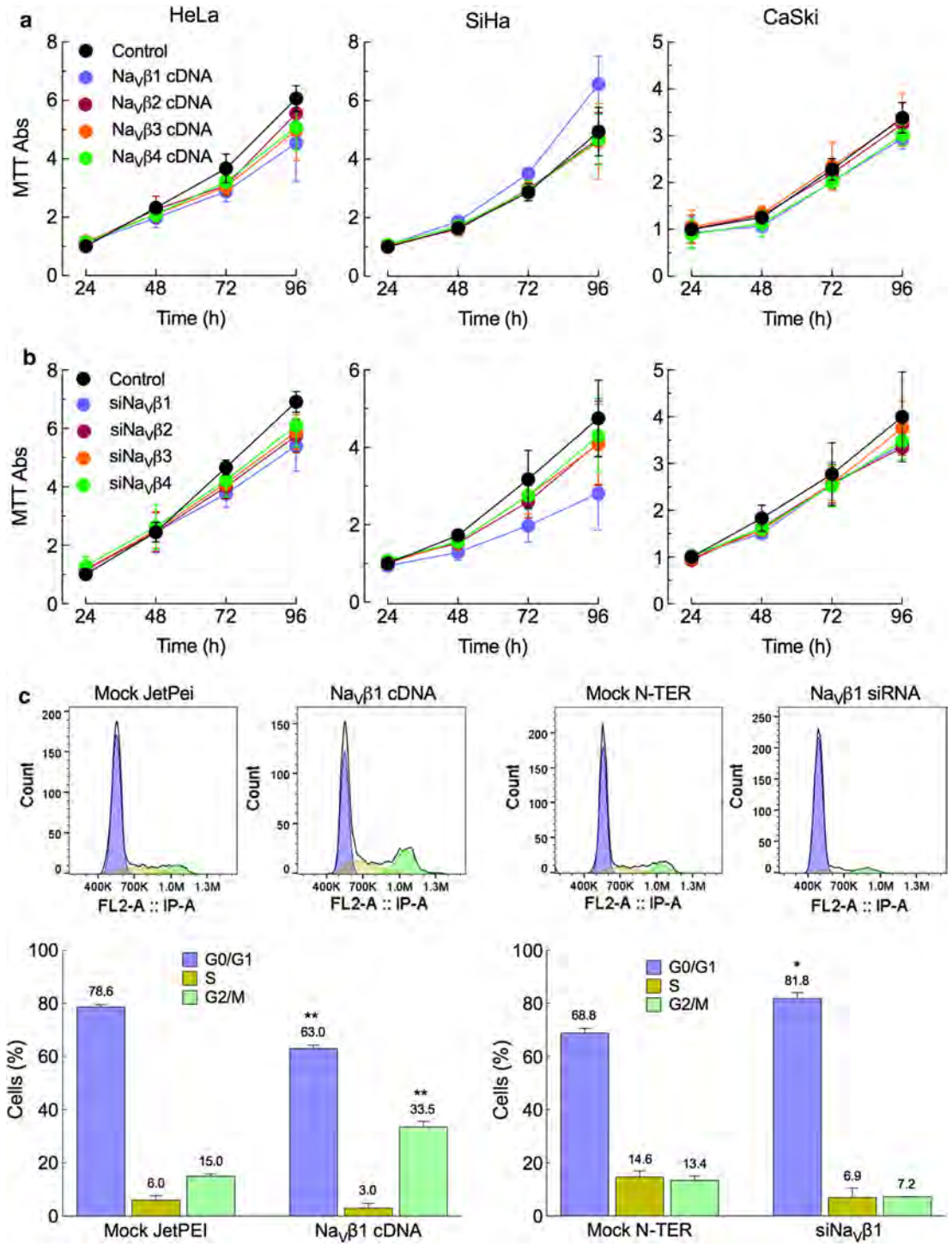

Fig. 3 Effect of $Na_V\beta$s on proliferation and cell-cycle of CeCa cells. Proliferation was evaluated by MTT assays 24, 48, 72 and 96 h post-transfection with plasmids (**a**) or with specific siRNAs (**b**) for the β-subunits. The results show the participation of $Na_V\beta1$ on proliferation of SiHa cells, as it increases when the protein is overexpressed and decreases when it is downregulated. The other three $Na_V\beta$s showed no effect on proliferation of SiHa cells, and none of the β-subunits were involved in proliferation of HeLa and CaSki cells. **c** Cell cycle analysis by flow cytometry in SiHa cells performed 48 h after transfection of synchronized cells with $Na_V\beta1$ cDNA or with the specific siRNA against this subunit. Cells were fixed with ice-cold 70% ethanol, stored for at least 24 h at − 20 °C, treated with RNase and stained with PI for 1 h at 37 °C. For each condition, 2×10^4 cells (singlets) were analyzed. Representative histograms of the control mock conditions and the transfected cells (upper panels) of three independent experiments summarized in the bar graphs (bottom panels) as means ± S.D. of the relative percentage of cells in each cell cycle phase. Significance: $^*P < 0.05$, $^{**}P < 0.01$

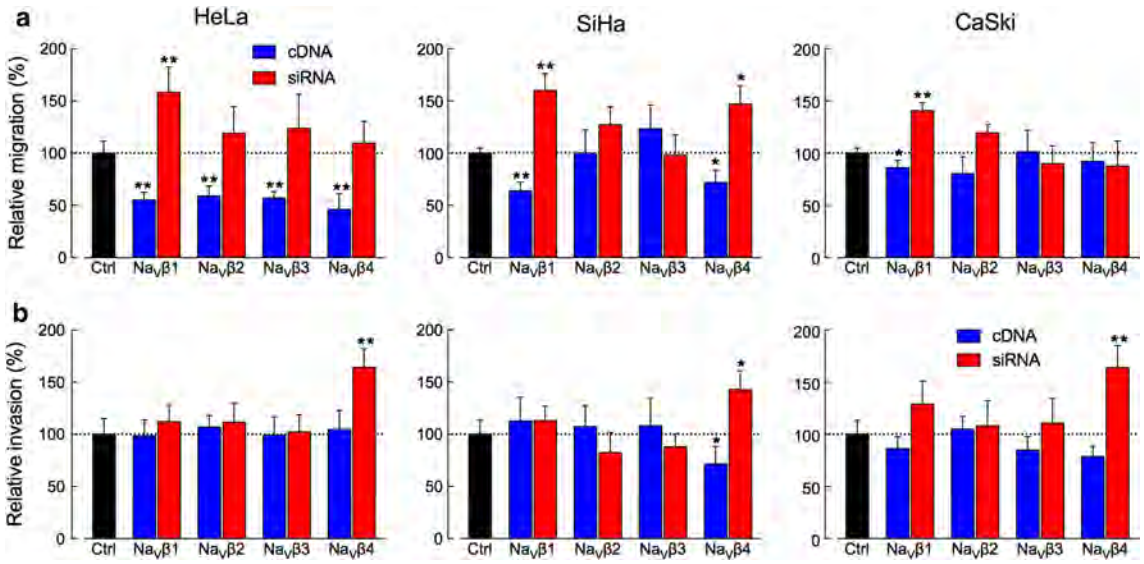

Fig. 4 Effect of $Na_V\beta$s on migration and invasiveness of CeCa cells. Migration (**a**) and invasion (**b**) experiments were performed with HeLa, SiHa and CaSki cells in Boyden transwell chambers for 48 h. Bars indicate mean ± S.D. of at least three independent experiments, each performed in duplicate and presented as a percentage of control conditions. Overexpression of $Na_V\beta$s in HeLa cells induced a reduction in approximately 50% in cellular migration, while the downregulation of $Na_V\beta1$ by siRNAs increased it in 58%. $Na_V\beta1$ is also involved in SiHa and CaSki migration. On the other hand, downregulation of $Na_V\beta4$ with siRNAs increased cellular invasiveness in the three cell lines. Significance: $^*P < 0.05$, $^{**}P < 0.01$

with the breast cancer cell line MDA-MB-231, where the overexpression of $Na_V\beta1$ in these cells led to the development of larger tumors in mice [28]. To corroborate this observation, we decided to perform a cell cycle assay by flow cytometry. First, for standardization purposes, SiHa cells were arrested at the G0/G1 phase by incubation in serum-reduced conditions for 24 and 48 h. To estimate the proportion of cells in different phases of the cell cycle, cells were stained with PI and analyzed by flow cytometry. Results show a consistent arrest of cells when treated for 48 h, as the proportion of the cells in G0/G1 phase increased significantly whereas the percentage of cells in G2/M phase was smaller compared to control (normal medium) conditions (see Additional file 4). Once synchronized cells were transfected with either cDNA or siRNA for $Na_V\beta1$ subunit under the experimental conditions indicated above. Results show a significant increase in the proportion of cells in G2/M phase when overexpressing $Na_V\beta1$ vs the control condition (JetPEI mock control), as well as a significant decrease in the proportion of cells in G0/G1 phase. In the same sense, the downregulation of the expression of $Na_V\beta1$ generated a significantly larger proportion of cells in G0/G1 phase, with no significant changes in the proportion of cells in G2/M phase compared with the N-TER mock control (Fig. 3b). These results suggest a positive role of $Na_V\beta1$ in the proliferation of SiHa cells, but not in HeLa or CaSki cells.

Role of $Na_V\beta$s on migration and invasion

The role of $Na_V\beta$s on in vitro migration and invasion of CeCa cell lines was evaluated 48 h post-transfection with the cDNA or with the siRNA for each β-subunit to overexpress or to downregulate the expression of $Na_V\beta$s respectively. Migration results show that overexpression of $Na_V\beta$s in HeLa cells induces a significant reduction in migration capability (around 50% in all cases), regardless of the type of $Na_V\beta$, accompanied by a tendency to increase the invasive capability when the $Na_V\beta$s are downregulated, being the effect of the treatment with siRNAs against $Na_V\beta1$ the most substantial (a 58% increment). In SiHa cells, a similar result was found with $Na_V\beta1$ and $Na_V\beta4$; a significant reduction on the migration capability (36% and 28% respectively) when they are overexpressed, and an increment (60% and 47% respectively) when they are downregulated, while the manipulation of the expression of $Na_V\beta2$ and $Na_V\beta3$ did not alter the migration of these cells. Finally, in CaSki cells, only $Na_V\beta1$ showed to have a role on cellular migration: the overexpression of this subunit decreased the migration by 14%, whereas the transfection with siRNAs increased it by 41% (Fig. 4a). It is worth of notice that only the effect of $Na_V\beta1$ (negative regulation) in migration remains constant and statistically significant in the three cell lines, suggesting a potential role of $Na_V\beta1$ in CeCa migration capability.

With regards to the in vitro invasion, results show that the downregulation of $Na_V\beta4$ increased the invasiveness of the three cell lines: 64% in HeLa, 43% in SiHa and 63% in CaSki cells. Accordingly, the overexpression of this protein induced a reduction on the invasiveness of SiHa and CaSki cells by 28% and 21% respectively, suggesting a potential role of $Na_V\beta4$ as an invasion suppressor. The rest of the $Na_V\beta$s did not significantly modified the invasion capacity of the CeCa cells (Fig. 4b).

Given all these results, we decided to corroborate whereas the diminished expression of $Na_V\beta4$ was associated with the presence of CeCa vs normal cervix tissues. For that purpose, we analyzed in silico the expression $Na_V\beta4$ in CeCa biopsies and normal cervical tissues from the Human Protein Atlas. Although the database only has a small number of IHC normal cervix and CeCa biopsies stained for $Na_V\beta4$ ($n=3$ for normal cervix, and $n=12$ for cervical cancer), the relationship between the expression of the protein and the presence or absence of cervical cancer is evident: the staining results indicate that three out of three normal cervix tissues have moderate $Na_V\beta4$ expression, while in the CeCa biopsies no signal of $Na_V\beta4$ was detected in twelve out of twelve cases (see Additional file 5). Taken together, these results strongly suggest that $Na_V\beta4$ expression is downregulated in CeCa, leading to an increase in the invasive capacity of the cells, and thus, the metastatic potential.

Discussion

For many years, $Na_V\beta$s were considered only as "auxiliary" Na_V subunits commissioned of regulating the α-subunit kinetics and cellular localization. Nowadays plenty of evidence shows the multifunctionality of these proteins, participating in a wide variety of cellular processes like cell adhesion, cytoskeleton remodeling, filopodia and invadopodia formation, transcriptional regulation, cell cycle regulation and even apoptosis [21, 29].

For the present work, we chose three different CeCa cell lines in order to cover a wide range of CeCa cases, and to analyze the potential role of $Na_V\beta$s in the malignant behavior of this disease. SiHa and CaSki cells are HPV-16 positive (the most frequently detected viral type in CeCa, found in approximately 57% of cases) whereas HeLa cells arise from a HPV-18 positive tumor (the second most frequent virus; 16% of cases) [37]. Furthermore, HeLa and SiHa cells derived from a primary tumor, while CaSki cells were taken from a metastatic tumor. In addition, the patients' ethnicity and the cellular origins of the three cell lines are different [38–40].

Here we demonstrated the presence (expression) of $Na_V\beta$s in the three different CeCa cell lines (Fig. 1), even in the absence of functional Na_V α-subunit expression in the plasma membrane (evidenced by whole-cell patch-clamp recordings, see Additional file 2), suggesting that their role in cancer cell biology is independent of the pore-forming Na_V α-subunit.

When we evaluated the aggressiveness of each cell line, by analyzing the basal proliferation, migration and invasiveness in vitro, HeLa cells demonstrated to be the most aggressive cell line, as these cells proliferated, migrated and invaded the most, followed by SiHa cells. CaSki cells were the less proliferative, and they migrated and invaded the less (Fig. 2). As far as we are concerned, this is the first report about the differences in the metastatic behavior among these CeCa cell lines.

We have previously reported the role of $Na_V1.6$ (the most overexpressed Na_V α-subunit in CeCa biopsies) in the invasiveness potential of CeCa primary cultures [14]. In agreement with our recent findings [34], in the present work we did not find voltage-gated sodium currents in any of the CeCa cell lines studied with the patch-clamp technique. This could be due to at least two possibilities: either the sodium channels are being correctly synthetized but are not reaching the plasma membrane for some unknown reason; or these cells are expressing a non-functional splicing variant. In this regard, it has been reported that $Na_V\beta$s participate in the appropriate traffic and localization of the Na_V α-subunits in the plasma membrane [15, 35, 36]. Moreover, it has been shown that $Na_V\beta2$ can be cleaved by secretases, generating small intracellular peptides capable of reaching the cell nucleus and promoting the transcriptional upregulation of genes including SCN1A, which encodes for $Na_V1.1$ [41, 42]. Hence, we thought that maybe by modifying the expression of these proteins we could promote the functional localization of conducting Na_V channels in the plasma membrane, however our results suggest this is not the case, as the manipulation of the expression of the $Na_V\beta$s in HeLa and SiHa cells was not enough to promote the appearance of voltage-dependent sodium currents (see Additional file 2). Yet, there are many other molecules such as hormones and growth factors that could be involved in the correct trafficking of the channel. In fact, we have examined the possibility that Na_Vs functional expression in CeCa cell lines could be regulated by β-estradiol or EGF, but we did not find sodium currents under any of the experimental conditions tested (data not shown). Another likely explanation could be related to the oxygen conditions in which the cell lines are cultured. It has been reported that hypoxia can change both the expression and activity of Na_Vs. Tumor cells usually experience severe hypoxia, which has been correlated with a more robust expression and activity of Na_Vs [43, 44]. On the contrary, CeCa cell lines have been cultured

in normoxic tissue culture conditions, which might have modified the Na_Vs expression and/or trafficking.

It is also possible that CeCa cell lines are expressing a non-conducting channel with a different and unknown function and/or localization in the cell. It remains to be investigated whether Na_V α-subunits are expressed in intracellular compartments, as well as their possible role in invasion. The existence of functional intracellular sodium channels has been demonstrated in macrophages where the activity of this sodium channel contributes to cellular invasion through a mechanism involving sodium ions release from cationic intracellular stores, followed by a subsequent mitochondrial calcium release mediated by the Na^+/Ca^{2+} exchanger, which in turn facilitates cytoskeletal remodeling and invadopodia formation [12]. In fact, recent data from our group suggests the presence of intracellular $Na_V1.6$ channels in CeCa cell lines [34]. However, more experiments are needed to fully elucidate this discrepancy between Na_Vs functional expression in CeCa primary cultures vs cell lines.

Regarding to the effect of Na_Vβs on cell proliferation, we found that only Na_Vβ1 had an effect on this process and only in SiHa cells: the overexpression of Na_Vβ1 increased cell proliferation, whereas the downregulation of the expression of this protein decreased it (Fig. 3a). This is in agreement with observations reported by Nelson et al. [28] demonstrating that Na_Vβ1 enhances breast tumor growth and metastasis in vivo, by increasing cell proliferation and reducing apoptosis. The fact that we only observed this effect in one out of three CeCa cell lines shows that it is a particularity of the cell line (SiHa) rather than a general role of Na_Vβ1 on proliferation in cervical cancer.

On the other hand, it has been suggested that Na_Vβ3 mediates a p53-dependent apoptotic pathway [26]. In breast cancer cells, for example, this subunit is totally absent, although it is normally expressed in non-cancerous breast cells (Sanchez-Sandoval et al., unpublished data). However, the overexpression or down regulation of this subunit did not alter the proliferation rate of the CeCa cell lines analyzed here, suggesting a lack of the pro-apoptotic activity of Na_Vβ3 in these cells. This might be related to the p53 protein status in CeCa cell lines. It has been reported that the association between the E6 protein (one of the two main HPV oncogenes) with p53 leads to the specific ubiquitination and degradation of p53 protein [45], therefore inactivating any pro-apoptotic effect due to the Na_Vβ3 expression in basal conditions. This is one of the several ways the HPV genome secures the growing of the tumor. However, the intermediate steps that Na_Vβ3 must undergo to promote apoptosis is still unknown, as well as why Na_Vβ3 had no pro-apoptotic effect in CeCa cells when overexpressed. A possible explanation could be the existence of a positive (and necessary) feedback regulation between p53 (or one of its multiple target genes) and Na_Vβ3, leading to a lack of pro-apoptotic activity of Na_Vβ3 in the absence of functional p53.

On the contrary, our migration experiments show a clear participation (negative regulation) of Na_Vβ1 on the ability of CeCa cells to perform transwell migration across of an 8 μm-pore membrane. When we induced the overexpression of this subunit, the migration rate decreased in the three CeCa cell lines, being HeLa cells the most affected (almost 50% inhibition in cell migration). Correspondingly, the inhibition of Na_Vβ1 expression by siRNAs led to significant increments in cell migration of HeLa, SiHa and CaSki cells (Fig. 4a). Thus, Na_Vβ1 could be acting as a cell adhesion molecule, promoting the cell–cell adhesion and therefore making it difficult to move across the membrane. It is also worth of notice that, among the three cell lines, HeLa have the lowest Na_Vβ1 expression compared to the other two CeCa cell lines (Fig. 1), and they also have the greatest migration capacity. In the same sense, CaSki cells are the ones with the bigger expression of Na_Vβ1, and the lowest migration behavior (Fig. 2b).

A study made on breast cancer cell lines revealed that the overexpression of Na_Vβ1 in highly metastatic MDA-MB-231 cells increased cell–cell adhesion and decreased in vitro migration, consistent with the proposed role of Na_Vβ1 as a cell adhesion molecule [27]. However, the *trans*-homophilic interactions through Na_Vβ1 can also mediate the process outgrowth in vivo, as in neurons, generating an elongated morphology and therefore potentiating metastasis, as has been reported for the same breast cancer cells but using mouse models instead of transwell experiments [28]. Something similar could be happening with CeCa cell lines. Thus, the persistent contribution of Na_Vβ1 in the three CeCa cell lines migration is indicative of its role as a negative regulator of the in vitro migration, regardless the HPV type present in the CeCa cell line. Although it remains to be investigated whether this behavior also occurs in vivo.

With respect to the contribution of Na_Vβs in invasiveness, our results show that downregulation of Na_Vβ4 expression resulted in a significant increase in the in vitro invasiveness of the three cell lines studied here (Fig. 4b), suggesting the role of this subunit as a metastasis suppressor protein. These observations agree with the in silico analysis of Na_Vβ4 expression performed with the Human Protein Atlas data: normal cervix biopsies show moderated Na_Vβ4 expression, while in CeCa biopsies it seems to be absent (see Additional file 5). Taken together, these results strongly suggest that Na_Vβ4 expression is downregulated in CeCa, which in turn increases the

invasive capacity of the cells. In accordance with this interpretation, out of the three CeCa cell lines studied in the present work, the HeLa cell line showed the lowest expression of $Na_V\beta4$ and the highest index of cell invasion.

In breast cancer cell lines, it has been found that increasing $Na_V\beta1$ expression promotes the overexpression of $Na_V1.5$, the main Na_V α-subunit involved in the invasiveness of this type of cancer [27]. However, according to our results, this is not the case for CeCa cell lines, as the overexpression of $Na_V\beta1$ or $Na_V\beta4$ did not promote the expression of conducting $Na_V1.6$ channels in the plasma membrane, the principal Na_V α-subunit involved in the invasive potential of these cells. Thus, we conclude that the pathways used by these proteins to induce cell migration and invasion, are independent of the activity of $Na_V1.6$ or other Na_V α-subunits in the plasma membrane of CeCa cell lines.

Other groups have also reported the downregulation of $Na_V\beta4$ expression in cancer vs normal tissue. This is the case of prostate cancer [23], papillary thyroid cancer [46], and breast cancer [29]. The latter study, performed by the group of Dr. Sebastien Roger at the University of Tours, reported solid evidence about the possible mechanistic pathway through which $Na_V\beta4$ prevents metastasis in cancer cells. They showed an increased activity of the small GTPase RhoA (crucial for cytoskeleton remodeling during migration and invasion) when $Na_V\beta4$ was silenced in breast cancer MDA-MB-231 cells. This effect was independent of $Na_V1.5$ channel activity, the main Na_V α-subunit implicated in BCa invasiveness. A similar mechanism might be taking place in CeCa cells: a downregulation of the $Na_V\beta4$ subunit that leads to an increased activity of RhoA and therefore, a more robust invasive potential, which is independent of the $Na_V1.6$ expression in the plasma membrane. However, we speculate that additional cellular mechanisms might be involved in this phenomenon, as the effects of $Na_V\beta4$ in cellular migration were not significant in our study, meaning that the sole change on cellular motility cannot explain the dramatic increase on cellular invasiveness when $Na_V\beta4$ is downregulated. A more recent study showed that $Na_V\beta4$ is downregulated in papillary thyroid cancer (PTC) compared with normal thyroid tissues. More interestingly, the authors also found that preserved $Na_V\beta4$ expression might independently predict favorable recurrence-free survival in classical PTC [46]. Altogether, these data reinforce the notion of using $Na_V\beta4$ as a biomarker for cancer metastasis and a potential new therapeutic target for the treatment of cervical cancer.

Conclusions

In conclusion, our results show that even though cervical cancer cell lines do not generate Na_V currents, they do express $Na_V\beta$ subunits, which could play a role in proliferation ($Na_V\beta1$ only in SiHa cells), migration ($Na_V\beta1$ in the three cell lines), and invasion ($Na_V\beta4$ in the three cell lines studied). The results support the recent knowledge about $Na_V\beta$s as multifunctional proteins involved in cell processes like ion channel regulation, cell adhesion and motility, and even in metastatic cell behaviors. Finally, the evidence presented here contributed to propose $Na_V\beta1$ and $Na_V\beta4$ as prognostic markers for cervical cancer tumor progression.

Additional files

Additional file 1. Evaluation of $Na_V\beta$s expression after transfecting HeLa cells with siRNAs or cDNAs. Real-time PCR and western blot data of $Na_V\beta$s expression in HeLa cells after transfection with corresponding cDNAs or siRNAs.

Additional file 2. Analysis of the expression of voltage-gated sodium currents in CeCa cells. Whole-cell patch-clamp experiments performed in CeCa cells to investigate the presence of functional Na_V α-subunits in the plasma membrane.

Additional file 3. Efficiency of siRNA transfection in CeCa cells. Micrographs of CeCa cells showing the efficiency of siRNA transfection using a fluorescent transfection indicator.

Additional file 4. Synchronization of SiHa cells. Flow cytometry results for synchronization of SiHa cells.

Additional file 5. Analysis of $Na_V\beta4$ expression in CeCa biopsies and normal cervical tissue. Representative immunohistochemical images of cervical cancer biopsies and normal cervix tissues showing the absence of $Na_V\beta4$ in CeCa biopsies and the moderate expression of the protein in normal cervix.

Abbreviations

BCa: breast cancer; CAMs: cell adhesion molecules; CeCa: cervical cancer; DMEM: Dulbecco's Modified Eagle's Medium; FBS: fetal bovine serum; Na_V: voltage-gated sodium channels; $Na_V\beta$s: voltage-gated sodium channels β-subunits; $Na_V1.6$: voltage-gated sodium channel coded by the *SCN8A* α-subunit; PI: propidium iodide; PTC: papillary thyroid cancer; qPCR: real-time polymerase chain reaction; RT-PCR: reverse transcription polymerase chain reaction.

Authors' contributions

ALSS conducted all the experiments, analyzed the results, and wrote the original version of the manuscript. JCG conceived the idea for the project, analyzed results and wrote the manuscript with ALSS. Both authors read and approved the final manuscript.

Acknowledgements

We are very grateful with Dr. Lori L. Isom for the donation of the four $Na_V\beta$s vectors; and Dr. Laura Ongay, from Unidad de Biología Molecular at Instituto de Fisiología Celular, UNAM, for expert technical support.

Competing interests

The authors declare that they have no competing interests.

Availability of data and materials
All data generated or analyzed during this study are included in this published article [and its additional information files].

Consent for publication
Not applicable.

Ethics approval and consent to participate
Not applicable.

Funding
This work was supported by grants from CONACYT-México (167790-B) and PAPIIT-DGAPA-UNAM (IN206917) to JCG. Ana Laura Sanchez-Sandoval is a doctoral student from Programa de Doctorado en Ciencias Bioquímicas, Universidad Nacional Autónoma de México (UNAM) and received fellowship from CONACYT. The funding bodies had no role in the design of the study and collection, analysis, and interpretation of data and in writing the manuscript.

Publisher's Note

Springer Nature remains neutral with regard to jurisdictional claims in published maps and institutional affiliations.

Received: 17 October 2018 Accepted: 12 February 2019
Published online: 15 February 2019

References

1. Torre LA, Bray F, Siegel RL, Ferlay J, Lortet-Tieulent J, Jemal A. Global cancer statistics, 2012. CA Cancer J Clin. 2015;65(2):87–108.
2. Rana MM, Huhtala H, Apter D, Eriksson T, Luostarinen T, Natunen K, et al. Understanding long-term protection of human papillomavirus vaccination against cervical carcinoma: cancer registry-based follow-up. Int J Cancer J Int du Cancer. 2013;132(12):2833–8.
3. Catterall WA. Voltage-gated sodium channels at 60: structure, function and pathophysiology. J Physiol. 2012;590(Pt 11):2577–89.
4. Fraser SP, Diss JK, Chioni AM, Mycielska ME, Pan H, Yamaci RF, et al. Voltage-gated sodium channel expression and potentiation of human breast cancer metastasis. Clin Cancer Res. 2005;11(15):5381–9.
5. Brisson L, Gillet L, Calaghan S, Besson P, Le Guennec JY, Roger S, et al. Na(V)1.5 enhances breast cancer cell invasiveness by increasing NHE1-dependent H(+) efflux in caveolae. Oncogene. 2011;30(17):2070–6.
6. Laniado ME, Lalani EN, Fraser SP, Grimes JA, Bhangal G, Djamgoz MB, et al. Expression and functional analysis of voltage-activated Na+ channels in human prostate cancer cell lines and their contribution to invasion in vitro. Am J Pathol. 1997;150(4):1213–21.
7. Diss JK, Archer SN, Hirano J, Fraser SP, Djamgoz MB. Expression profiles of voltage-gated Na(+) channel alpha-subunit genes in rat and human prostate cancer cell lines. Prostate. 2001;48(3):165–78.
8. House CD, Vaske CJ, Schwartz AM, Obias V, Frank B, Luu T, et al. Voltage-gated Na+ channel SCN5A is a key regulator of a gene transcriptional network that controls colon cancer invasion. Cancer Res. 2010;70(17):6957–67.
9. Gao R, Shen Y, Cai J, Lei M, Wang Z. Expression of voltage-gated sodium channel alpha subunit in human ovarian cancer. Oncol Rep. 2010;23(5):1293–9.
10. Roger S, Rollin J, Barascu A, Besson P, Raynal PI, Iochmann S, et al. Voltage-gated sodium channels potentiate the invasive capacities of human non-small-cell lung cancer cell lines. Int J Biochemis Cell Biol. 2007;39(4):774–86.
11. Xia J, Huang N, Huang H, Sun L, Dong S, Su J, et al. Voltage-gated sodium channel Nav 1.7 promotes gastric cancer progression through MACC1-mediated upregulation of NHE1. Int J Cancer. 2016;139(11):2553–69.
12. Carrithers MD, Chatterjee G, Carrithers LM, Offoha R, Iheagwara U, Rahner C, et al. Regulation of podosome formation in macrophages by a splice variant of the sodium channel SCN8A. J Biol Chem. 2009;284(12):8114–26.
13. Xing D, Wang J, Ou S, Wang Y, Qiu B, Ding D, et al. Expression of neonatal Nav1.5 in human brain astrocytoma and its effect on proliferation, invasion and apoptosis of astrocytoma cells. Oncol Rep. 2014;31(6):2692–700.
14. Hernandez-Plata E, Ortiz CS, Marquina-Castillo B, Medina-Martinez I, Alfaro A, Berumen J, et al. Overexpression of NaV 1.6 channels is associated with the invasion capacity of human cervical cancer. Int J Cancer J Int du Cancer. 2012;130(9):2013–23.
15. Isom LL, Ragsdale DS, De Jongh KS, Westenbroek RE, Reber BF, Scheuer T, et al. Structure and function of the beta 2 subunit of brain sodium channels, a transmembrane glycoprotein with a CAM motif. Cell. 1995;83(3):433–42.
16. Malhotra JD, Kazen-Gillespie K, Hortsch M, Isom LL. Sodium channel beta subunits mediate homophilic cell adhesion and recruit ankyrin to points of cell-cell contact. J Biol Chem. 2000;275(15):11383–8.
17. Ratcliffe CF, Westenbroek RE, Curtis R, Catterall WA. Sodium channel beta1 and beta3 subunits associate with neurofascin through their extracellular immunoglobulin-like domain. J Cell Biol. 2001;154(2):427–34.
18. Malhotra JD, Koopmann MC, Kazen-Gillespie KA, Fettman N, Hortsch M, Isom LL. Structural requirements for interaction of sodium channel beta 1 subunits with ankyrin. J Biol Chem. 2002;277(29):26681–8.
19. Yu FH, Westenbroek RE, Silos-Santiago I, McCormick KA, Lawson D, Ge P, et al. Sodium channel beta4, a new disulfide-linked auxiliary subunit with similarity to beta2. J Neurosci. 2003;23(20):7577–85.
20. McEwen DP, Isom LL. Heterophilic interactions of sodium channel beta1 subunits with axonal and glial cell adhesion molecules. J Biol Chem. 2004;279(50):52744–52.
21. Brackenbury WJ, Isom LL. Na channel beta subunits: overachievers of the ion channel family. Front Pharmacol. 2011;2:53.
22. Yereddi NR, Cusdin FS, Namadurai S, Packman LC, Monie TP, Slavny P, et al. The immunoglobulin domain of the sodium channel beta3 subunit contains a surface-localized disulfide bond that is required for homophilic binding. FASEB J. 2013;27(2):568–80.
23. Diss JK, Fraser SP, Walker MM, Patel A, Latchman DS, Djamgoz MB. Beta-subunits of voltage-gated sodium channels in human prostate cancer: quantitative in vitro and in vivo analyses of mRNA expression. Prostate Cancer Prostatic Dis. 2008;11(4):325–33.
24. Jansson KH, Lynch JE, Lepori-Bui N, Czymmek KJ, Duncan RL, Sikes RA. Overexpression of the VSSC-associated CAM, beta-2, enhances LNCaP cell metastasis associated behavior. Prostate. 2012;72(10):1080–92.
25. Jansson KH, Castillo DG, Morris JW, Boggs ME, Czymmek KJ, Adams EL, et al. Identification of beta-2 as a key cell adhesion molecule in PCa cell neurotropic behavior: a novel ex vivo and biophysical approach. PLoS ONE. 2014;9(6):e98408.
26. Adachi K, Toyota M, Sasaki Y, Yamashita T, Ishida S, Ohe-Toyota M, et al. Identification of SCN3B as a novel p53-inducible proapoptotic gene. Oncogene. 2004;23(47):7791–8.
27. Chioni AM, Brackenbury WJ, Calhoun JD, Isom LL, Djamgoz MB. A novel adhesion molecule in human breast cancer cells: voltage-gated Na + channel beta1 subunit. Int J Biochemis Cell Biol. 2009;41(5):1216–27.
28. Nelson M, Millican-Slater R, Forrest LC, Brackenbury WJ. The sodium channel beta1 subunit mediates outgrowth of neurite-like processes on breast cancer cells and promotes tumour growth and metastasis. Int J Cancer J Int du Cancer. 2014;135(10):2338–51.
29. Bon E, Driffort V, Gradek F, Martinez-Caceres C, Anchelin M, Pelegrin P, et al. SCN4B acts as a metastasis-suppressor gene preventing hyperactivation of cell migration in breast cancer. Nat Commun. 2016;7:13648.
30. Diaz D, Delgadillo DM, Hernandez-Gallegos E, Ramirez-Dominguez ME, Hinojosa LM, Ortiz CS, et al. Functional expression of voltage-gated sodium channels in primary cultures of human cervical cancer. J Cell Physiol. 2007;210(2):469–78.
31. Livak KJ, Schmittgen TD. Analysis of relative gene expression data using real-time quantitative PCR and the 2(-Delta Delta C(T)) Method. Methods. 2001;25(4):402–8.
32. Uhlen M, Fagerberg L, Hallstrom BM, Lindskog C, Oksvold P, Mardinoglu A, et al. Proteomics. Tissue-based map of the human proteome. Science. 2015;347(6220):1260419.
33. Uhlen M, Oksvold P, Fagerberg L, Lundberg E, Jonasson K, Forsberg M, et al. Towards a knowledge-based human protein atlas. Nat Biotechnol. 2010;28(12):1248–50.
34. Lopez-Charcas O, Espinosa AM, Alfaro A, Herrera-Carrillo Z, Ramirez-Cordero BE, Cortes-Reynosa P, et al. The invasiveness of human cervical cancer associated to the function of NaV1.6 channels is mediated by MMP-2 activity. Sci Rep. 2018;8(1):12995.

INFORME DE LABORES 2019

35. Isom LL, De Jongh KS, Patton DE, Reber BF, Offord J, Charbonneau H, et al. Primary structure and functional expression of the beta 1 subunit of the rat brain sodium channel. Science. 1992;256(5058):839–42.
36. Chen C, Bharucha V, Chen Y, Westenbroek RE, Brown A, Malhotra JD, et al. Reduced sodium channel density, altered voltage dependence of inactivation, and increased susceptibility to seizures in mice lacking sodium channel beta 2-subunits. Proc Natl Acad Sci USA. 2002;99(26):17072–7.
37. Crosbie EJ, Einstein MH, Franceschi S, Kitchener HC. Human papillomavirus and cervical cancer. Lancet. 2013;382(9895):889–99.
38. Gey GO, Coffman WD, Kubicek MT. Tissue culture studies of the proliferative capacity of cervical carcinoma and normal epithelium. Can Res. 1952;12(4):264–5.
39. Friedl F, Kimura I, Osato T, Ito Y. Studies on a new human cell line (SiHa) derived from carcinoma of uterus. I. Its establishment and morphology. Proc Soc Exp Biol Med. 1970;135(2):543–5.
40. Pattillo RA, Hussa RO, Story MT, Ruckert AC, Shalaby MR, Mattingly RF. Tumor antigen and human chorionic gonadotropin in CaSki cells: a new epidermoid cervical cancer cell line. Science. 1977;196(4297):1456–8.
41. Kim DY, Carey BW, Wang HB, Ingano LAM, Binshtok AM, Wertz MH, et al. BACE1 regulates voltage-gated sodium channels and neuronal activity. Nat Cell Biol. 2007;9(7):755–64.
42. Kim DY, Ingano LAM, Carey BW, Pettingell WH, Kovacs DM. Presenilin/gamma-secretase-mediated cleavage of the voltage-gated sodium channel beta 2-subunit regulates cell adhesion and migration. J Biol Chem. 2005;280(24):23251–61.
43. Ju YK, Saint DA, Gage PW. Hypoxia increases persistent sodium current in rat ventricular myocytes. J Physiol-London. 1996;497(2):337–47.
44. Fearon IM, Brown ST. Acute and chronic hypoxic regulation of recombinant hNa(v)1.5 alpha subunits. Biochem Bioph Res Co. 2004;324(4):1289–95.
45. Scheffner M, Huibregtse JM, Vierstra RD, Howley PM. The HPV-16 E6 and E6-AP complex functions as a ubiquitin-protein ligase in the ubiquitination of p53. Cell. 1993;75(3):495–505.
46. Gong Y, Yang J, Wu W, Liu F, Su A, Li Z, et al. Preserved SCN4B expression is an independent indicator of favorable recurrence-free survival in classical papillary thyroid cancer. PLoS ONE. 2018;13(5):e0197007.

Ready to submit your research? Choose BMC and benefit from:

- fast, convenient online submission
- thorough peer review by experienced researchers in your field
- rapid publication on acceptance
- support for research data, including large and complex data types
- gold Open Access which fosters wider collaboration and increased citations
- maximum visibility for your research: over 100M website views per year

At BMC, research is always in progress.

Learn more biomedcentral.com/submissions



Article

J. Mex. Chem. Soc. **2019**, *63*(1)
©2018, Sociedad Química de México
ISSN-e 2594-0317

Co-localization of the Receptor for Advanced Glycation End Products (RAGE) with S100 Calcium-Binding Protein B (S100B) in Human Umbilical Vein Endothelial

I. N. Serratos[1,*], A. López-Macay[2], P. Castellanos[3], J. G. Córdoba-Herrera[1], R. Pérez-Montfort[4], N. Cabrera[4], F. Arechavaleta-Velasco[5], P. Domínguez-López[5], A. Santamaría[6,*]

[1]Departamento de Química, Universidad Autónoma Metropolitana-Iztapalapa, México.
[2]Laboratorio de Enfermedades Neuromusculares, División de Neurociencias, Instituto Nacional de Rehabilitación, SSA. México.
[3]Departamento de Ingeniería Eléctrica, Universidad Autónoma Metropolitana-Iztapalapa, México.
[4]Departamento de Bioquímica y Biología Estructural, Instituto de Fisiología Celular, Universidad Nacional Autónoma de México. México.
[5]Unidad de Investigación Médica en Medicina Reproductiva, Hospital Gineco-Obstetricia, IMSS, México.
[6]Laboratorio de Aminoácidos Excitadores, Instituto Nacional de Neurología y Neurocirugía, SSA. México.

***Corresponding authors:** Iris N. Serratos and Abel Santamaria. Departamento de Química, Universidad Autónoma Metropolitana-Iztapalapa. Avenida San Rafael Atlixco 186, Leyes de Reforma 1ra Sección, 09310 Iztapalapa, CDMX. Tel.: (+5255) 5804-4667 (x14). E-mail address: absada@yahoo.com

Received May 21st, 2018; Accepted February 16th, 2019.

DOI: http://dx.doi.org/10.29356/jmcs.v63i1.574

Abstract. The receptor for advanced glycation end products (RAGE) has been involved in the actions of inflammatory proteins such as S100 calcium binding protein B (S100B), among several others. Despite there being many studies available proposing several different modes of interaction between the receptor and the protein, it is necessary to reconcile these binding hypotheses. We evaluated the co-localization of RAGE and S100B in human umbilical vein endothelial cells (HUVEC's) exposed to acute pro-inflammatory lipopolysaccharide (LPS). Co-localization of the receptor and the protein in umbilical cells exposed to pro-inflammatory stimuli was analyzed using an immunofluorescent assay. RAGE was present in umbilical cells, and its co-localization with S100B was stimulated in the presence of LPS. Our findings suggest an interaction between these proteins, possibly producing early inflammatory responses in umbilical cells. The understanding of the molecular mechanisms of this recognition is relevant to characterize the nature of the signaling associated with this receptor in inflammatory processes.
Keywords: Inflammation; Lipopolysaccharide; Molecular recognition; Co-localization; Umbilical endothelial cells.

Resumen. El receptor para productos finales de glucosilación avanzada (RAGE) ha sido involucrado en las acciones de proteínas inflamatorias tales como la proteína S100B unida a calcio (S100B), entre muchas otras. A pesar de los múltiples estudios disponibles que proponen diferentes modos de interacción entre el receptor y la proteína, es necesario reconciliar estas hipótesis. Se evaluó la co-localización de este receptor con la proteína S100B en células endoteliales de la vena del cordón umbilical humano (HUVEC's) expuestas de manera aguda al agente pro-inflamatorio lipopolisacárido (LPS). La co-localización del receptor y la proteína en células umbilicales expuestas al estímulo pro-inflamatorio se analizó mediante un ensayo de inmunofluorescencia. RAGE se presentó en células umbilicales, y su co-localización con S100B fue estimulada por LPS. Estos hallazgos sugieren el reconocimiento entre estas proteínas, posiblemente produciendo respuestas inflamatorias tempranas en células umbilicales. La comprensión de los mecanismos moleculares de este reconocimiento es relevante para caracterizar la naturaleza de la señalización asociada a este receptor en procesos inflamatorios.
Palabras clave: Inflamación; Lipopolisacárido; Reconocimiento molecular; Co-localización; Células endoteliales umbilicales.

Article *J. Mex. Chem. Soc.* **2019**, *63*(1)
©2018, Sociedad Química de México
ISSN-e 2594-0317

Introduction

The receptor for advanced glycation end products (RAGE) binds multiple ligands, including advanced glycation end products (AGEs) [1,2], the high mobility group box-1 protein (HMGB1) [3-5], several members of the S100 calcium-binding protein family, notably S100B [6-9], and the amyloid β peptide [10,11], among several others, which are expressed in inflammatory disorders [6,12-14]. Several studies exploring this concept have been carried out in *in vitro* conditions with human cells from the immune system, as well as in murine models. These findings include the activation of the membrane surface RAGE receptor upon binding the DNA-HMGB1 complex, HMGB1 or S100B [15]. These interactions induce the expression of pro-inflammatory molecules such as interleukin 8 (IL8), RAGE, HMGB1, and the S100 protein genes [16,17]. In different disease models, such as lupus, diabetes, viral infections and cancer, changes in the levels of soluble RAGE (sRAGE) and membrane RAGE have been observed, suggesting a major role for this protein in the amplification of inflammatory responses [18]. Leukocytes have been the most frequently used cell preparation to study cell receptor-ligand interactions at the membrane level [19]. However, more recently, other cell types have been studied in inflammatory microenvironments, including epithelial and endothelial cells, fibroblasts, and other cells that can respond to various inflammatory stimuli or cell damage. The endothelial cells of veins and arteries can be in direct contact with these pro-inflammatory ligands through RAGE and other receptors, such as Toll-like or cytokine receptors, to activate the MAPK pathways. In turn, these kinases can regulate transcription factors linked to inflammation. The nuclear factor kappa B (NFκB) requires kinase activation to amplify the response to injury or infection. This knowledge is derived from observations of *in vitro* models that primarily use specific inhibitors or antibodies that block the binding of membrane receptors to their ligands on the cell surface, thus emphasizing the importance of these interactions for cell responses. For instance, in 2003, Treutiger *et al.* [20] demonstrated that the use of anti-RAGE antibodies reduced the adhesion of neutrophils to human umbilical vein endothelial cells (HUVEC's) via NFκB signaling in inflammatory conditions elicited by lipopolysaccharide (LPS) or tumor necrosis factor-alpha (TNF-α). Similar results were obtained when HUVEC's were pre-activated using AGE-albumin induction and exposed to proteins of the S100 family as RAGE ligands [6]. Affinity studies of the S100 family as RAGE ligands have also been reported using surface plasmon resonance (SPR) analysis, and a stoichiometry of 2:1 (S100:RAGE) was determined [7,8,21,22]. These studies also demonstrated that these interactions induce pro-inflammatory responses in cells (including HUVEC's and macrophages); however, the binding of RAGE to its ligands remains unverified at the cytochemical level. Therefore, in this study, we characterized the early co-localization of endogenous RAGE with endogenous S100B in HUVEC's challenged with the pro-inflammatory stimulus LPS. In order to confirm the co-localization of these proteins and their interactions. Since, it is known that the activation of RAGE induced by S100B constitutes an important pro-inflammatory pathway during the progression of acute and chronic inflammatory diseases [7,23,24], our study provides insights into the co-localization of these proteins in unstimulated and LPS-stimulated HUVEC's. Our results represent a basis for ongoing studies involving the entire RAGE-S100B complex and for novel approaches to interfere with inflammatory responses.

Experimental

Materials and Methods

Reagents

Primary antibodies against RAGE (Ab3611 for immunofluorescence assays against the V and C2 domains) and secondary antibodies were purchased from Abcam (Cambridge, MA, USA). The antibody recognizing S-100B (AB11178) was also purchased from Abcam.

Cell cultures and experimental treatments

Endothelial cells from the veins of human umbilical cords (HUVEC's) were obtained from eutocic births and caesarean sections, according to the procedure described by Jaffe [25]. Samples were obtained at the Hospital of Obstetrics and Gynecology "Dr. Luis Ayala Castelazo", IMSS, Mexico City, following a clinical protocol previously approved by the Ethics Committee of the Hospital. Cords were processed within the first 3 h after being obtained, washed and cleaned with sterile saline solution. Once collected, the veins were cut into 5 cm pieces in order to use samples of the same length. The veins were placed in containers with phosphate buffered saline (PBS) supplemented with antibiotic-antimycotic (penicillin/streptomycin 1.5%; GIBCO, Life Technologies, USA plus

Article *J. Mex. Chem. Soc.* **2019**, *63*(1)
©2018, Sociedad Química de México
ISSN-e 2594-0317

Amphotericin B, Biowest S.A.S., USA). The vascular endothelium was disaggregated enzymatically by adding 10 ml of 0.02 % collagenase (type 4, Worthington Biochemical Corporation) dissolved in PBS. Endothelial cells were dissociated and collected in fetal bovine serum (FBS, Invitrogen, Mexico). The cells obtained after enzymatic digestion were centrifuged at 800 × *g* for 5 min in a Labofuge 400 Heraeus Instruments centrifuge (Thermo Scientific, Waltham, Massachusetts, USA) using a rotor model 8179. The pellets were resuspended in M199 medium (GIBCO, Rockville, Maryland, USA) supplemented with 1 % glutamine (GIBCO), 0.1 mg/ml of endothelial growth factor (Biomedical Technologies Inc., Alfa Aesar, Ward Hill, Massachusetts, USA), 0.1 mg/ml of heparin (Sigma-Aldrich Co., St. Louis, Missouri, USA) and 10 % FBS. Streptomycin and penicillin were added in a 1 % dilution (GIBCO). All cells were maintained by incubation at 37° C with controlled relative humidity and 5 % CO_2. For experimental purposes, cells were dissociated from the culture dish with a trypsin/versene solution (GIBCO) for 2 min and reseeded in 48 or 6 wheel-plates at densities ranging from 30,000 to 50,000 cells per wheel for the 48 wheel-plates, or 250,000 for the 6 wheel-plates, in M-199 medium supplemented as previously mentioned. All experiments were performed 24 h later.

The assay for inflammatory activation is based on previous studies under *in vitro* and *ex vivo* conditions in HUVEC's and human umbilical veins stimulated with TNF-α [26]. In these cases, it is known that concentrations of 1-10 ng/ml during 2-6 hours of exposure induce the expression of adhesion molecules and pro-inflammatory cytokines that promote leukocyte adhesion in response to TNF-α. The concentration of LPS that we used in this study is the most commonly used in studies of leukocyte activation involving 2-12 h periods of exposure [27]. Endothelial cell activation was determined after induction with LPS (10 ng/ml). TNF-α (5 ng/ml) was employed in additional experiments as a positive control of inflammation; this concentration was determined from a concentration curve in a leukocyte/endothelial cell adhesion assay, ranging from 0.5 to 10 ng/ml. Endothelial cells were washed twice in PBS and placed in new culture medium with 10 ng/ml of TNF-α or LPS for 3 hours at 37 °C, 5% of CO_2 and 95% air. Immediately thereafter, all samples were washed and fixed for immunofluorescence assays. The observation and capture of images was performed with a LSM-50 Confocal Scanning Microscope (Carl Zeiss, Germany).

Immunofluorescence assay

RAGE and S100B were detected in HUVEC's exposed to inflammatory stimuli. The observation and analysis were performed using immunofluorescence staining with specific antibodies (Abcam Co., Cambridge, Massachusetts, USA). For the *in vitro* assays, HUVEC's were washed three times with PBS at pH 7.2, fixed in 4% paraformaldehyde (PFA) for 15 minutes, and washed three times with PBS. These preparations were incubated in 0.6 M glycine for 20 minutes, to remove the autofluorescence of aldehydes and washed three times with PBA (PBS albumin, 0.5%). Samples were then blocked for 20 minutes with PBA 1% to eliminate nonspecific reactions of the antibodies, and subsequently washed three times with PBA 0.5%. Immunoreactions were carried out diluting the mouse primary antibody specific for S100B 1:100 (SH-B1, ab11178, Biotech, Cambridge, UK), or the polyclonal rabbit antibody for RAGE (ab3611, Biotech) in PBA 1%, and cells or tissue slices were incubated for 1 hour at 4 °C. They were subsequently washed three times with PBA 1 %. The secondary antibodies (Alexa 647 for S100B and Alexa-488 for RAGE, Life Technologies) were diluted 1:400 and incubated with the samples for 1 h; afterwards, the preparations were washed with PBA 1%. Nuclei were stained blue with DAPI (Vectashield, Vector Laboratories, Inc., Burlingame, California, USA) and visualized using a fluorescent microscope (Floid Cell Imaging Station, Life Technologies).

Image processing

In order to estimate the co-localization of RAGE and S100B in cells, the merge area from the fluorescent labeling was analyzed by Otsu's method for segmentation of the region of interest [28]. A value of 50 is used as a threshold for the red and green color image components. Contours are found applying a Laplacian operator of 3 x 3 pixels to the binary image after segmentation. The area is represented by the number of pixels different to the background in the binary image. The average of the intensity is computed in the region of interest. Z-stack processing was also employed for depth improvement of images containing HUVEC's. This method is commonly used to improve the analysis of three-dimensional images, hence allowing more detailed recognition of cellular structures and better localization of proteins.

Article

J. Mex. Chem. Soc. **2019**, *63*(1)
©2018, Sociedad Química de México
ISSN-e 2594-0317

Statistical analysis

All experiments were carried out in duplicate. Mean ± standard error medium (S.E.M.) were determined for all parameters. Statistical significance among groups was determined by Student's t-test or one-way analysis of variance followed by Bonferroni's *post-hoc* analysis. Values of $P<0.05$ were considered as statistically significant.

Results

LPS induced an early and enhanced co-expression of RAGE and S100B in HUVEC's after 3 h of exposure

Fig. 1 shows the co-localization of RAGE and S100B in HUVEC's exposed for 3 h to pro-inflammatory stimuli induced by LPS or TNF-α (as a positive control). Cells were labeled for immunofluorescence in blue (DAPI nuclei), green (RAGE) and red (S100B). The first line corresponds to the sequence of untreated (control) cells, where moderate co-localization areas of both proteins can be observed in the merge (Fig. 1A). In addition, in these cells, the segmentation method revealed the specific points of co-localization evidenced by a labeling area (16230 pixels per field). Quantification of these co-localization areas was achieved also with the segmentation method (Fig. 1 A-B). The second sequence of images (second line) depicts the effect of LPS on RAGE and S100B co-localization; this treatment produced an increased number of labeled cells for both proteins when co-localized in the merge, as compared to untreated cells. Concomitantly, the RAGE and S100B co-localization areas (segmentation) in LPS-treated cells were enhanced when compared with control cells (186 % above the control). In the third line, the sequence of images shows that the exposure of cells to TNF-α produced a prominent RAGE and S100B co-localization (in the merge), as well as an increased labeling area (334 % above the control).

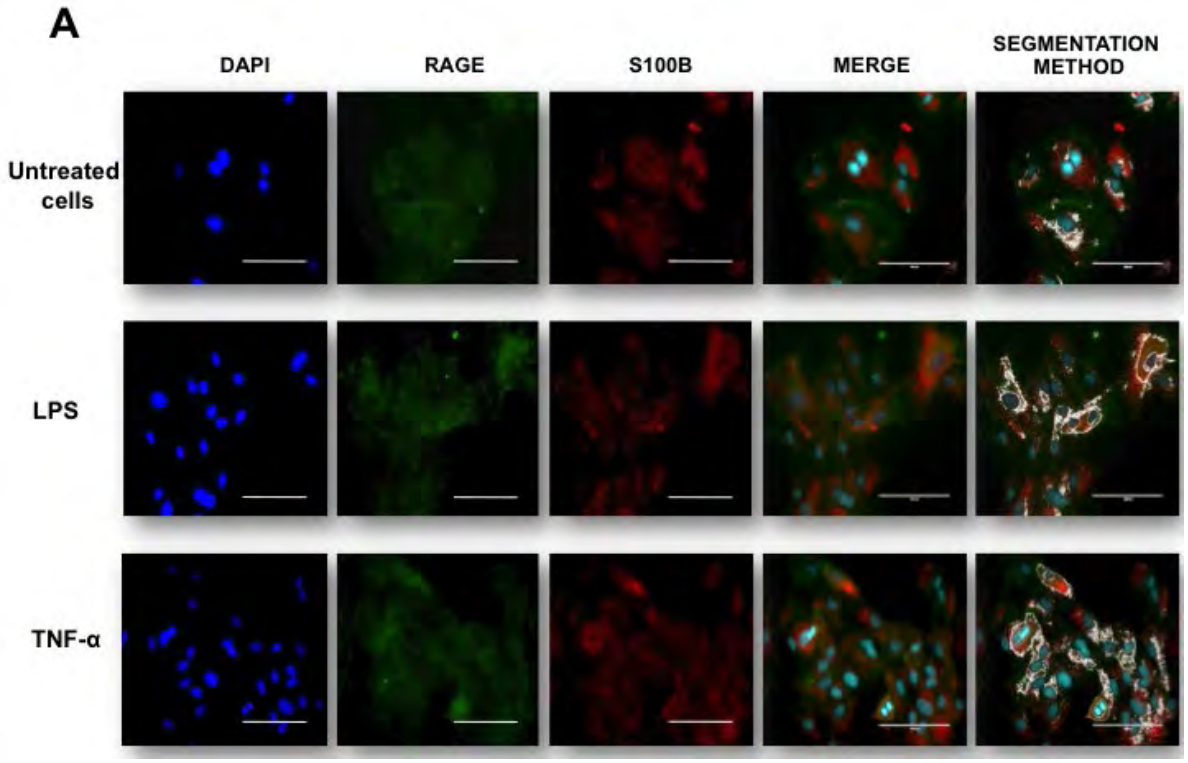

J. Mex. Chem. Soc. **2019**, *63*(1)
©2018, Sociedad Química de México
ISSN-e 2594-0317

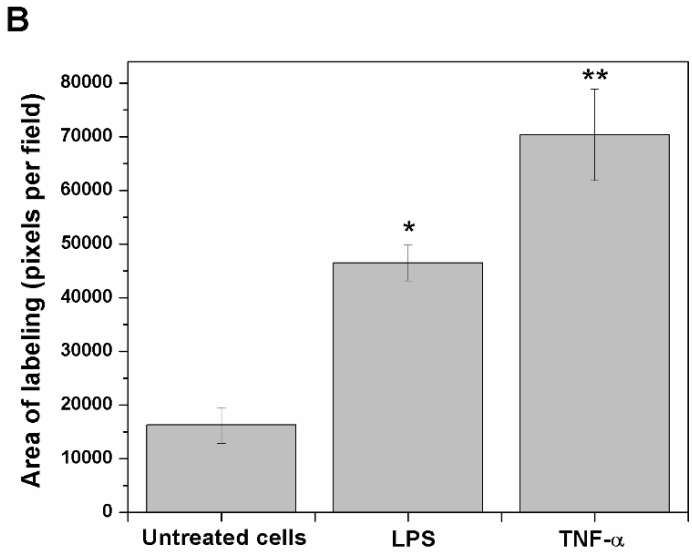

Fig. 1. RAGE and S100B co-localization in human umbilical vein endothelial cells (HUVEC's) obtained from umbilical cord. Cells were challenged with acute inflammatory stimuli (TNF-α [5 ng/ml] or LPS [10 ng/ml]). RAGE and S100B were detected early by immunofluorescence after exposure to pro-inflammatory agents for 3 h. In **A**, the localization of RAGE (green column) and S100B (red column) are shown. Nuclei were stained in blue (DAPI). In the fourth and fifth columns, the images show the co-localization (merge) and image analysis (segmentation algorithm) of both proteins, respectively. The horizontal bars indicate a length of 100 µm in all panels. In **B**, the graphic representation of the merge area (as percent) in untreated (Control) and TNF-α- or LPS-treated cells is shown. Bars represent quantification of two images per treatment. One-way ANOVA followed by Bonferroni's test; *p<0.05, **p<0.01, different from untreated cells.

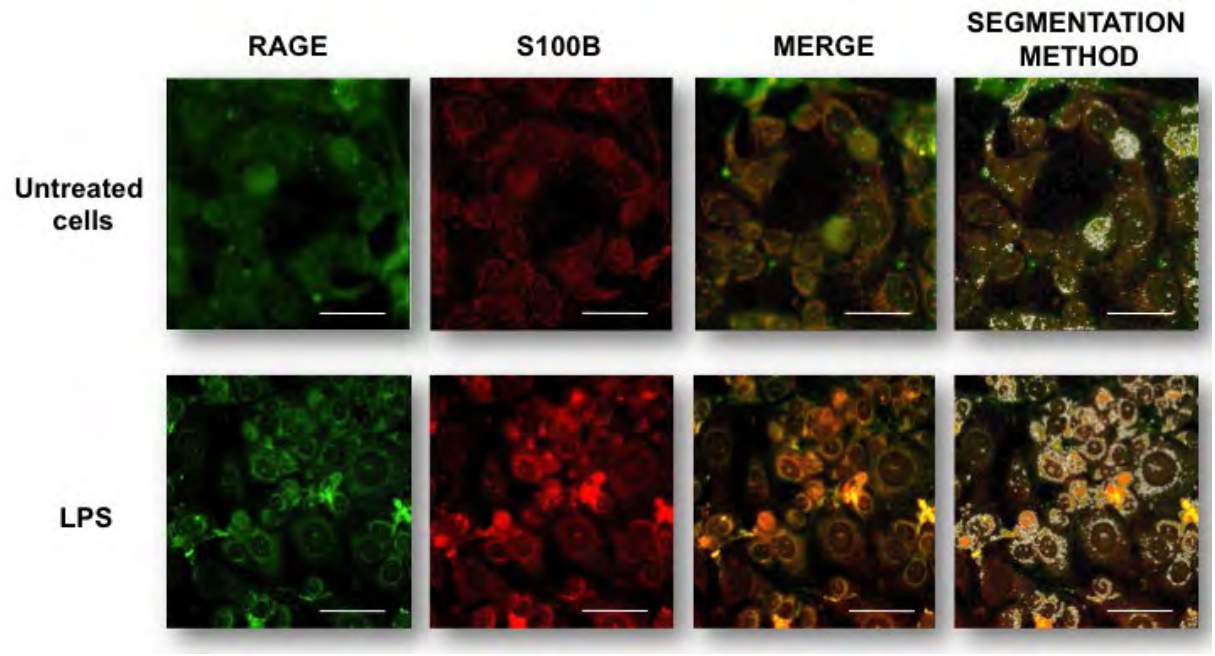

Article

J. Mex. Chem. Soc. **2019**, *63*(1)
©2018, Sociedad Química de México
ISSN-e 2594-0317

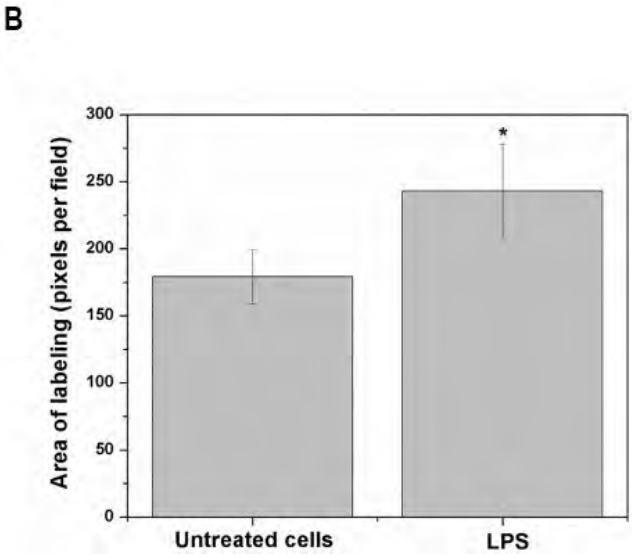

Fig. 2. Detailed images (20 μm bar scale) showing untreated cells (upper line) and LPS-treated HUVEC's (lower line). In **A**, Images correspond to three-dimensional reconstructions using the Z-stack to display the expression of RAGE (first column in green), S100B (second column in red) and the merge (third column). RAGE was constructed with 18 photos, whereas S100B was built up with 12 photos. The fourth column depicts the segmentation in the co-localization images. In **B**, the graphic representation of the merge area (as percent) in untreated (Control) and LPS-treated cells is shown. Bars represent quantification of two images per treatment. Student's t-test; *$p<0.05$, different from untreated cells.

Discussion

Endothelial dysfunction and inflammatory cell adhesion have been regarded as early and important factors in various pathologies. In fact, inflammation is a major event for both, the healing and the damaging processes. In turn, LPS is a pro-inflammatory molecule involved in the pathogenesis of inflammatory disorders. While chronic inflammation is more commonly associated with pathological stages, the characterization of acute inflammation is of major relevance since this event establishes the borders between healing and injury. How cells and tissues respond to acute inflammation is the clue to anticipate whether they will survive or initiate deadly cascades, leading further to tissue damage. Therefore, in this study we considered the early effects (3 h exposure) of LPS on HUVEC's in order to complement previous reports describing its actions on cell viability at different times (1 and 24 h) [29]. Further support for an early role of LPS and TNF-α as inflammatory promoters for HUVEC's can be found in related reports [30,31]. The response of endothelial cells *in vitro* was sensed after LPS stimulation upon the assumption that this pro-inflammatory molecule binds to Toll-like membrane receptors and RAGE, thereby inducing changes in their phenotype at short times [32].

Here, we demonstrated an early co-localization of RAGE and S100B proteins in HUVEC's subjected to inflammatory stimuli, thus suggesting that this interaction might eventually be responsible for inflammatory events through signaling cascades involving factors like NFκB [33]. In this regard, several studies have suggested that RAGE activation during inflammatory processes involving the S100B protein, is taking place [34]. Indeed, the elicited inflammatory cascades induced by RAGE probably perpetuate the organ dysfunction in inflammatory processes [6]. The interaction of these two proteins for triggering acute and/or chronic inflammation and its biological role has already been characterized [7,35,36]; yet, a still unresolved issue is the minimal size of the S100B-RAGE complex that can promote signaling, bringing together the cytoplasmic tails of the RAGE dimers.

Despite it being currently assumed that different ligands can bind to RAGE, directly or through other molecules (i.e., forming bridges with AGEs) [37], all possible interactions between these molecules or their effects on cells, have not been explored yet. RAGE activation by S100B is a major pro-inflammatory pathway occurring in acute and chronic inflammatory diseases [23,38]. Some members of the S100 protein family, such as S100B, are known to form active tetramers, hexamers or larger oligomers [7,39].

Article *J. Mex. Chem. Soc.* **2019**, *63*(1)
©2018, Sociedad Química de México
ISSN-e 2594-0317

The co-localized areas for RAGE and S100B could suggest either an increase in the expression of these proteins, or their mere re-location with additional interactions. It is therefore fair to mention that our results are focused exclusively on S100B from endothelial cells, where this protein can act as a chemokine that is subsequently released to the surrounding environment. Based on these conditions, the characterization of the interactions between RAGE and S100B and their effects are of major relevance, since they can serve for the design of more specific *in vivo* models of disorders involving inflammatory components.

Finally, the occurrence of the RAGE-S100B interaction in HUVEC's establishes the basis for the understanding of the inflammatory events taking place during the gestational and/or birth processes under normal or pathological conditions, though such interaction has also been described in other biological preparations, including different tumor cells, neurons, astrocytes, microglia, etc. This is relevant as RAGE has been shown to interact with several other ligands, including diverse members of the S100 protein family, thus participating in disorders like cancer, cardiovascular disease, CNS disorders, etc. [40,41]. Therefore, the many biological implications that the RAGE-S100B interaction represent for the compromise of physiological homeostasis deserves deeper and more detailed investigation in different biological scenarios

Acknolwedgements

The authors wish to thank the National Science and Technology Council of Mexico (CONACYT) for project No. 168692 and SEP-PRODEP. We also acknowledge the support of the Committee for Aid and Education in Neurochemistry (CAEN) in category 1B: Research Supplies for Use in the Applicant's Home Laboratory. We are particularly grateful to M.Sc. Ana María Soto-Estrada, I.Q. Tania Tapia-Esquivel and I.Q. Brenda Segura-Bailón for their fine and timely professional technical assistance.

References

1. Mueller, G.A.; Maleki, S.J.; Johnson, K.; Hurlburt, B.K.; Cheng, H.; Ruan, S.; Nesbit, J.B.; Pomés, A.; Edwards, L.L.; Schorzman, A.; Deterding, L.J.; Park, H.; Tomer, K.B.; London, R.E.; Williams, J.G. *Allergy*. **2013**, 68, 1546-1554.
2. Matsumoto, S.; Yoshida, T.; Murata, H.; Harada, S.; Fujita, N.; Nakamura, S.; Yamamoto, Y.; Watanabe, T.; Yonekura, H.; Yamamoto, H.; Ohkubo, T.; Kobayashi. Y. *Biochem*. **2008**, 47, 12299-12311.
3. Chen, R.C.; Yi, P.P.; Zhou, R.R.; Xiao M.F.; Huang, Z.B.; Tang, D.L.; Huang, Y.; Fan, X.G. *Mol Cell Biochem*. **2014**, 390, 271-280.
4. Tian, J.; Avalos, A.M.; Mao, S.Y.; Chen, B.; Senthil, K.; Wu, H.; Parroche, P.; Drabic, S.; Golenbock, D.; Sirois, C.; Hua, J.; An, L.L.; Audoly, L.; La Rosa, G.; Bierhaus, A.; Naworth, P.; Marshak-Rothstein, A.; Crow, M.K.; Fitzgerald, K.A.; Latz, E.; Kiener, P.A.; Coyle, A.J. *Nat Immunol*. **2007**, 85, 487-496.
5. Kang, R.; Tang, D.; Schapiro, N.E.; Loux, T.; Livesey, K.M.; Billiar, T.R.; Wang, H.; Van Houten, B.; Lotze, M.T.; Zeh, H.J. *Oncogene*. **2014**, 335, 567-577.
6. Ehlermann, P.; Eggers, K.; Bierhaus, A.; Most, P.; Weichenhan, D.; Greten, J.; Nawroth, P.P.; Katus, H.A.; Remppis, A. *Cardiovasc Diabetol.* **2006**, 5, 6.
7. *Ostendorp, T.; Leclerc, E.; Galichet,* A.; Koch, M.; Demling, N.; Weigle, B.; Heizmann, C.W.; Kroneck, P.M.; Fritz, G. *EMBO J. **2007**, 26, 3868-3878.*
8. Koch, M.; Chitayat, S.; Dattilo, B.M.; Schiefner, A.; Diez, J.; Chazin, W.J.; Fritz, G. *Structure*. **2010**, 18, 1342-1352.
9. Leclerc, E.; Sturchler, E.; Vetter, S.W. *Cardiovasc Psychiatry Neurol.* **2010**, 2010, 539581.
10. Gospodarska, E.; Kupniewska-Kozak, A.; Goch, G.; Dadlez, M. *Biochim Biophys Acta.* **2011**, 1814, 592-609.
11. Chaney, M.O.; Stine, W.B.; Kokjohn, T.A.; Kuo, Y.M.; Esh, C.; Rahman, A.; Luehrs, D.C.; Schmidt, A.M.; Stern, D.; Yan S.D.; Roher, A.E. *Biochim Biophys Acta*. **2005**, 1741, 199-205.
12. Sparvero, L.J.; Asafu-Adjei, D.; Kang, R.; Tang, D.; Amin, N.; Im, J.; Rutledge, R.; Lin, B.; Amoscato, A.A.; Zeh, H.J.; Lotze, M.T. *J Transl Med.* **2009**, 7, 17.
13. Yan, S.F.; Yan, S.D.; Ramasamy, R.; Schmidt, A.M. *Ann Med*. **2009**, 41, 408-422.

J. Mex. Chem. Soc. **2019**, *63*(1)
©2018, Sociedad Química de México
ISSN-e 2594-0317

14. Ramasamy, R.; Vannucci, S.J.; Yan, S.S.D.; Herold, K.; Yan, S.F.; Schmidt, A.M. *Glycobiology.* **2005**,15, 16R-28R.
15. Bianchi, M.E.; Manfredi, A.A. *Immunol Rev.* **2007**, 220, 35-46.
16. Marenholz, I.; Heizmann, C.W.; Fritz, G. *Biochem Biophys Res Commun*. **2004**, 322, 1111-1122.
17. Donato, R.; Cannon, B.R.; Sorci, G.; Riuzzi, F.; Hsu, K.; Weber, D.J.; Geczy, C.L. *Curr Mol Med.* **2013**, 13, 24-57.
18. Chuah, Y.K.; Basir, R.; Talib, H.; Tie, T.H.; Nordin, N. *Int J Inflam.* **2013**, 2013, 403460.
19. Prasad, K.; Dhar, I.; Caspar-Bell, G. *Int J Angiol*. **2015**, 24, 75-80.
20. Treutiger, C.J.; Mullins, G.E.; Johansson, A.S.; Rouhiainen, A.; Rauvala, H.M.; Erlandsson-Harris, H.; Andersson, U.; Yang, H.; Tracey, K.J.; Andersson, J.; Palmblad, J.E. *J Intern Med*. **2003**, 254, 375-385.
21. Leclerc, E. *Methods Mol Biol*. **2013**, 963, 201-213.
22. Park, H.; Adsit, F.G.; Boyington, J.C. *J Biol Chem*. **2010**, 285, 40762-40770.
23. Hofmann, M.A.; Drury, S.; Fu, C.; Qu, W., Taguchi, A.; Lu, Y.; Avila, C.; Kambham, N.; Bierhaus, A.; Nawroth, P.; Neurath, M.F.; Slattery, T.; Beach, D.; McClary, J.; Nagashima, M.; Morser, J.; Stern, D.; Schmidt. A.M. *Cell*. **1999**, 97, 889-901.
24. Yan, S.S.; Wu, Z.Y.; Zhang, H.P.; Furtado, G.; Chen, X.; Yan, S.F.; Schmidt, A.M.; Brown, C.; Stern, A.; LaFaille, J.; Chess, L.; Stern, D.M.; Jiang, H. *Nat Med*. **2003**, 9, 287-293.
25. Jaffe, E.A.; Nachman, R.L.; Becker, C.G.; Minick, C.R. *J Clin Invest*. **1973**, 52, 2745-56.
26. López-Macay, A.; Ruiz-Medina, E.J.; Ventura-Gallegos, J.L.; Arechavaleta-Velasco, F.; Gómez-Quiroz, L.E.; Königsberg-Fainstein, M.; Zentella-Dehesa, A. *Gac Med Mex*. **2015**, 151, 206-2015.
27. Monk, J.M.; Liddle, D.M.; Brown, M.J.; Zarepoor, L.; De Boer, A. A.; Ma, D.W.; Power, K.A.; Robinson, L.E. *Mol Nutr Food Res*. **2016**, 60, 621-630.
28. González, R.C. Woods RE. Digital Image Processing, third ed., Upper Saddle River, N.J: Prentice Hall, 2007.
29. Mbanya, D.N.; Kesteven, P.J.; Saunders, P.W. *Cent Afr J Med.* **2001**, 47, 177-181.
30. Ren, D.C.; Du, G.H.; Zhang, J.T. *Yao Xue Xue Bao*. **2003**, 38, 405-408.
31. Rodríguez-González, R.; Baluja, A.; Veiras Del Río, S.; Rodríguez, A.; Rodríguez, J.; Taboada, M.; Brea, D.; Álvarez, J. *J Transl Med.* **2013**, 11, 87.
32. Zhou, X.Y.; Zhang, W.J.; Huang, Q.B.; Guo, X. H. *Nan Fang Yi Ke Da Xue Xue Bao*. **2015**, 35, 6-11.
33. Cuevas, E.; Lantz, S.; Newport, G.; Divine, B.; Wu, Q.; Paule, M.G.; Tobón-Velasco, J.C.; Ali, S.F.; Santamaria, A. *Neurosci Lett*. **2010**, 474, 74-78.
34. Piazza, O.; Leggiero, E.; De Benedictis, G.; Pastore, L.; Salvatore, F.; Tufano, R.; De Robertis, E. *Int J Immunopathol Pharmacol*. **2013**, 26, 383-391.
35. Xu, D.; Young, J.H.; Krahn, J.M.; Song, D.; Corbett, K.D.; Chazin, W.J.; Pedersen, L.C.; Esko, J.D. *ACS Chem Biol*. **2013**, 8, 1611-1620.
36. Reddy, M.A.; Li, S.L.; Sahar, S.; Kim, Y.S.; Xu, Z.G.; Lanting, L.; Natarajan, R. *J Biol Chem*. **2006**, 281, 13685-13693.
37. Cárdenas-León, M.; Díaz-Díaz, E.; Argüelles-Medina, R.; Sánchez-Canales, P.; Díaz-Sánchez, V.; Larrea, F. *Rev Invest Clin*. **2009**, 61, 505-520.
38. Yan, S.F.; Ramasamy, R.; Naka, Y.; Schmidt, A.M. *Circ Res.* **2003**, 93, 1159-1169.
39. Leclerc, E.; Fritz, G.; Vetter, S.W.; Heizmann, C.W. *Biochim Biophys Acta*. **2009**, 1793, 993-1007.
40. Leclerc, E.; Heizmann CW. *Front Biosci (Schol Ed)*. **2011**, 3, 1232-1262.
41. Sorci, G; Bianchi, R.; Riuzzi, F.; Tubaro, C.; Arcuri, C.; Giambanco, I.; Donato, R. C*ardiovasc Psychiatry Neurol.* **2010**, 2010, 656481.

Check for updates

Rhes, a striatal-enriched protein, promotes mitophagy via Nix

Manish Sharma[a,1], Uri Nimrod Ramírez Jarquín[a,1], Oscar Rivera[a], Melissa Kazantzis[b], Mehdi Eshraghi[a], Neelam Shahani[a], Vishakha Sharma[a], Ricardo Tapia[c], and Srinivasa Subramaniam[a,2]

[a]Department of Neuroscience, The Scripps Research Institute, Jupiter, FL 33458; [b]Metabolic Core, The Scripps Research Institute, Jupiter, FL 33458; and [c]División de Neurociencias, Instituto de Fisiología Celular, Universidad Nacional Autónoma de México, Ciudad de México 04510, México

Edited by Solomon H. Snyder, Johns Hopkins University School of Medicine, Baltimore, MD, and approved October 6, 2019 (received for review July 25, 2019)

Elimination of dysfunctional mitochondria via mitophagy is essential for cell survival and neuronal functions. But, how impaired mitophagy participates in tissue-specific vulnerability in the brain remains unclear. Here, we find that striatal-enriched protein, Rhes, is a critical regulator of mitophagy and striatal vulnerability in brain. In vivo interactome and density fractionation reveal that Rhes coimmunoprecipitates and cosediments with mitochondrial and lysosomal proteins. Live-cell imaging of cultured striatal neuronal cell line shows Rhes surrounds globular mitochondria, recruits lysosomes, and ultimately degrades mitochondria. In the presence of 3-nitropropionic acid (3-NP), an inhibitor of succinate dehydrogenase, Rhes disrupts mitochondrial membrane potential ($\Delta\Psi_m$) and promotes excessive mitophagy and cell death. Ultrastructural analysis reveals that systemic injection of 3-NP in mice promotes globular mitochondria, accumulation of mitophagosomes, and striatal lesion only in the wild-type (WT), but not in the Rhes knockout (KO), striatum, suggesting that Rhes is critical for mitophagy and neuronal death in vivo. Mechanistically, Rhes requires Nix (BNIP3L), a known receptor of mitophagy, to disrupt $\Delta\Psi_m$ and promote mitophagy and cell death. Rhes interacts with Nix via SUMO E3-ligase domain, and Nix depletion totally abrogates Rhes-mediated mitophagy and cell death in the cultured striatal neuronal cell line. Finally, we find that Rhes, which travels from cell to cell via tunneling nanotube (TNT)-like cellular protrusions, interacts with dysfunctional mitochondria in the neighboring cell in a Nix-dependent manner. Collectively, Rhes is a major regulator of mitophagy via Nix, which may determine striatal vulnerability in the brain.

striatal neuronal vulnerability | tunneling nanotubes | mitophagy ligand | SUMO-E3 ligase | mitophagosomes

Understanding mitophagy mechanisms and its dysregulation leading to pathological abnormalities in human diseases is a major challenge in modern biology. Reduced mitochondrial functions are linked to aging and many neurodegenerative disorders. Parkinson disease (PD) is the best example linked to mitochondrial dysfunction, because the most vulnerable neurons of PD, the substantia nigra pars compacta, show mitochondrial abnormalities. Familial PD genes, such as PTEN-induced kinase-1 (Pink1), parkin, and leucine-rich repeat kinase 2, are implicated in mitochondrial dysfunction (1–3). Decline in mitochondrial enzyme activity is reported more in Alzheimer disease and amyotrophic lateral sclerosis patients compared to control subjects (4). Impaired mitochondrial function is observed in Huntington disease (HD) as patients continue to drop weight, even though they have a high caloric intake (5). Oligomers of amyloid, mutant superoxide dismutase 1, and mutant huntingtin can affect mitochondrial membrane potentials and impair mitochondria trafficking and function (6–12). Despite these important studies, how mitochondrial dysfunction leads to selective neuronal vulnerability remains unknown. For example, although the familial PINK1 and parkin mutants are ubiquitously expressed (13), the mechanisms by which they elicit lesion in the substantia nigra remains largely unclear. Similarly, how mitochondrial toxins induce tissue-specific lesion in the brain is also unclear. It is well known that 3-nitropropionic acid (3-NP) promotes lesion in the striatum but not in the cortex or cerebellar neurons, resulting in HD-like motor deficits (14, 15). MPTP (1-methyl-4-phenyl-1,2,3,6-tetrahydropyridine) or rotenone promotes substantia nigra pars compacta neurodegeneration, sparing the cortex or striatum, resulting in PD-like symptoms (16–18). The major difference between these toxins that promote brain region-specific lesion are that 3-NP blocks complex II, succinate dehydrogenase (SDH) (19), whereas rotenone and MPTP block complex I (NADH [nicotinamide adenine dinucleotide, reduced] dehydrogenase) (20, 21). Thus, what determines the substantia nigra neuron to MPTP-induced lesion and striatal neuron to 3-NP–induced lesion remains unclear. The differences in their brain penetrability may not account for the tissue-specific lesion, as these toxins block mitochondrial function throughout the brain and peripheral tissue. Therefore, although mitochondrial dysfunction is ubiquitous, it is insufficient to elicit selective neuronal death, suggesting that there are additional mechanisms that may play a role in the brain (22, 23).

Rhes belongs to a small GTPase (guanosine triphosphate hydrolase) family of proteins highly enriched in the brain's striatum, which controls psychiatric, cognitive, and motor functions. Rhes is induced by thyroid hormones and can inhibit the cAMP/PKA (cyclic adenosine monophosphate/protein kinase A) pathway, dopaminergic signaling, and N-type Ca^{2+} channels (Cav 2.2) (24–27).

Significance

Damaged mitochondria are eliminated by lysosomes, a process called mitophagy. However, the brain tissue specific roles and mechanisms of mitophagy remain unknown. We report that Rhes, a protein highly enriched in the striatum, eliminates damaged mitochondria via mitophagy, a function that may regulate the optimum number and function of mitochondria in the striatum. However, when mitochondria are irreversibly damaged, as in the presence of 3-NP (an inhibitor of complex II, SDH), Rhes exacerbates mitophagy in association with Nix, a mitophagy receptor and promotes cell death. Intriguingly, Rhes can travel via membranous protrusions from a healthy cell to the neighboring cell and interacts with the damaged mitochondria via Nix. Collectively, Rhes acts as "mitochondrial surveillant," and excessive mitophagy may account for striatal vulnerability in brain.

Author contributions: M.S. and S.S. designed research; M.S., U.N.R.J., O.R., M.K., M.E., N.S., and V.S. performed research; R.T. contributed new reagents/analytic tools; M.S., U.N.R.J., M.K., and N.S. analyzed data; and S.S. wrote the paper.

The authors declare no competing interest.

This article is a PNAS Direct Submission.

This open access article is distributed under Creative Commons Attribution-NonCommercial-NoDerivatives License 4.0 (CC BY-NC-ND).

[1]M.S. and U.N.R.J. contributed equally to this work.

[2]To whom correspondence may be addressed. Email: SSubrama@scripps.edu.

This article contains supporting information online at www.pnas.org/lookup/suppl/doi:10.1073/pnas.1912868116/-/DCSupplemental.

First published November 1, 2019.

Downloaded at Instituto de Biotecnología/UNAM on October 20, 2020

Over the years, we have found several roles for Rhes in the striatum. Rhes can regulate the mammalian target of rapamycin complex 1 (mTORC1), SUMOylation, and HD toxicity in cell and mouse models (28–32). Independent studies show a link for Rhes in striatal toxicity in various models of HD (33–38). Rhes knockout (KO) mice are also resistant to 3-NP–induced striatal lesion (39). Yet the mechanisms by which Rhes promotes neuronal vulnerability in the brain remains unclear.

Here we report that Rhes is a critical regulator of mitophagy in the striatum. Using ultrastructure, biochemical, and cell and molecular biology tools, we demonstrate that Rhes up-regulates mitophagy via Nix receptor, leading to striatal cell death. Our study reveals mitophagy mechanisms by which Rhes might promote striatal vulnerability in the brain.

Results

Rhes Associates with Mitochondria and Lysosomes In Vivo and In Vitro. We took an unbiased approach by comparing our previously identified in vivo striatal interactome of Rhes (40) with a publicly available database of mitochondrial (www.mrc-mbu.cam.ac.uk/impi) and lysosomal proteins (41). We found 64 (3.5%) and 20 (1.8%) out of 307 high-confidence striatal interactors of Rhes with potential association to mitochondria (for example, Vdac1, Rhot1) and lysosomes (Atp6v0d1, Nid1), respectively (Fig. 1 *A* and *B*). Next, using sucrose gradient density, we separated organelles from the striatal brain tissue homogenate from wild-type (WT) and Rhes KO and found that endogenous Rhes cosedimented in mitochondrial (as detected by SDH subunit A [SDHA]) and lysosomal (Microtubule associated protein light chain 3 [LC3] and lysosome associated membrane protein 1) fractions in WT striatum, and, as expected, no Rhes signal was detected in KO (Fig. 1*C*). In order to further understand the Rhes's mitochondrial role, we employed striatal neuronal cell lines (also known as ST*Hdh*$^{Q7/Q7}$) isolated from the striatum of knock-in mice, which contain a targeted insertion of a chimeric mouse with human Htt exon 1 with 7 polyglutamine repeats (control) (42). These cells do not express endogenous Rhes (30, 43), so we think this is a suitable model for studying the function of exogenously added Rhes, as it is the only source of Rhes, and it would not compete with endogenous function of Rhes. Similar to endogenous Rhes in the striatum, the cultured striatal neuronal cell line expressing GFP-Rhes, not GFP alone (control), also cosedimented in the mitochondrial and lysosomal fractions (*SI Appendix*, Fig. S1*A*). Next, we carried live-cell time-lapse fluorescence confocal microscopy to determine Rhes interaction and function with mitochondria and lysosomes. We found that 1) Rhes interacted preferentially with globular mitochondria in primary striatal neurons processes (Fig. 1 *D*, *Insets d1*, *d2*, and 3D rendered images,

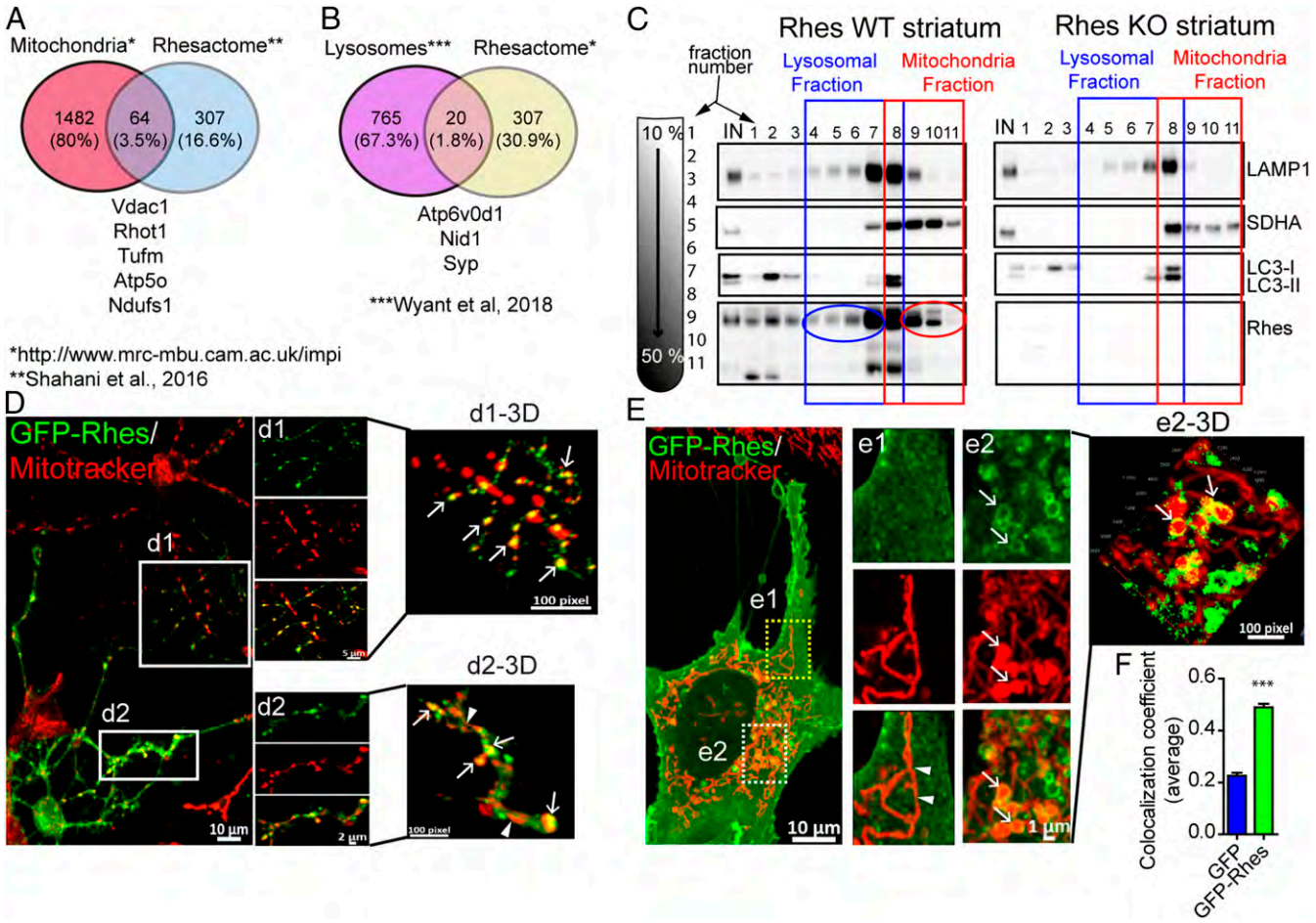

Fig. 1. Rhes associates with mitochondria and lysosome in vitro and in vivo. (*A* and *B*) Venn diagram showing mitochondrial and lysosomal proteins found in Rhes interactome in vivo, "Rhesactome," compared with available database of mitochondrial and lysosomal proteins (40, 41). (*C*) Sucrose density gradient and Western blotting of striatal tissue from WT or Rhes KO mice indicating lysosomal (blue) and mitochondrial (red) proteins across different fractions. (*D* and *E*) Representative confocal images (their respective *Insets* or 3D rendered images) of (*D*) primary striatal neuron and (*E*) striatal neuronal cells transfected with GFP-Rhes and costained with mitotracker orange (red). Arrow and arrowhead depict globular and elongated mitochondria, respectively, in neuronal processes. (*F*) Bar graph depicting average Pearson's coefficient of colocalization (n = 35 to 40 striatal neuronal cells per group, Student's t test; ***$P < 0.001$; data are mean ± SEM).

Downloaded at Instituto de Biotecnología/UNAM on October 20, 2020

d1-3D, *d2-3D*, arrows) and striatal neuronal cell line cytoplasm (Fig. 1 *E*, *Insets e1*, *e2*, and *e2-3D*) but not with the elongated mitochondria (Fig. 1 *D* and *E*, arrowheads); 2) Rhes formed a circular structure around the globular mitochondria (Fig. 1 *E*, *e2-3D*, arrow), and strongly colocalizes with it (Fig. 1*F*); 3) Rhes colocalizes with lysosomes in primary striatal neuronal processes (*SI Appendix*, Fig. S1 *B*, *Insets b1* and *b1-3D*, arrow) as well as striatal neuronal cell lines (*SI Appendix*, Fig. S1 *C*, *Inset c1-3D*, arrow and Fig. S1*D*); and 4) triple staining reveals Rhes localizes with both mitochondria and lysosomes in striatal neuronal cell (*SI Appendix*, Fig. S1 *E*, *Insets e1* and *e1-3D*). GFP alone did not show colocalization with mitotracker or lysosome in striatal neuronal cells or primary neurons (*SI Appendix*, Fig. S2). Next, we performed live-cell imaging of striatal neuronal cells transfected with GFP-Rhes (green) and costained with mitotracker (red) and lysotracker (blue) (Movie S1 with *Insets*). We found that GFP-Rhes was enriched with globular mitochondria, which becomes positive for lysosome in a time-dependent fashion (Movie S1, arrows). Intriguingly, enhanced GFP-Rhes signal intensity was associated with loss of mitotracker intensity, suggestive of mitochondrial degradation (Movie S1, arrow in GFP-Rhes). Collectively, these data indicated that Rhes associates with mitochondrial as well as lysosomal components in the intact striatum, primary neurons, and the striatal neuronal cell line, where we found stronger association with globular mitochondria.

Rhes Affects Basal Mitophagy but Not Mitochondrial Functions. Lysosomal localization of Rhes-positive globular mitochondria (Movie S1 and *SI Appendix*, Fig. S1*E*) leads us to investigate the role of Rhes in mitochondrial degradation or mitophagy. Using cycloheximide (CHX) chase experiments, we tested whether Rhes affects basal mitophagy. As expected, CHX treatment resulted in the degradation of SDHA (inner mitochondrial protein), VDAC1 (outer mitochondrial protein), and cytochrome C (intermembrane mitochondrial protein), whose levels were further diminished by GFP-Rhes compared to GFP-alone overexpression (Fig. 2*A*). Note that levels of mTOR or Bip were not altered by CHX between the groups in these cells, and down-regulation of LC3-II was similar between GFP-expressing and GFP-Rhes–expressing cells (Fig. 2*B*). To further confirm the role of Rhes in regulation of basal mitophagy, we assessed the mitochondrial mass by CHX chase experiment in striatal neuronal cells infected with validated adenovirus empty (Ad-null) or adenovirus-Rhes (Ad-Rhes) (32), using mitotracker green, a molecular probe that binds to mitochondria regardless of its membrane potential (44). We found that Rhes-positive cells stained with mitotracker green showed less fluorescent intensity in CHX treatment compared to control, indicating rapid mitochondrial degradation, suggesting Rhes regulates basal mitophagy (*SI Appendix*, Fig. S3 *A* and *B*). Next, we wondered, whether Rhes can affect overall mitochondrial functions. To test this, we used seahorse assay, which measures the mitochondrial respiratory functions. We infected striatal neuronal cell lines with Ad-null or Ad-Rhes. As shown in *SI Appendix*, Fig. S3 *C* and *D*, Rhes expression did not affect the mitochondrial functions basally or in the absence or the presence of oligomycin (an inhibitor of ATP [adenosine triphosphate] synthase), Carbonyl cyanide-4-(trifluoromethoxy)phenylhydrazone (FCCP, uncouples oxidative phosphorylation), or rotenone (complex I inhibitor). Similarly, Rhes expression did not affect FCCP-induced mitophagy (*SI Appendix*, Fig. S3 *E* and *F*). Thus, Rhes enhances basal mitophagy in CHX conditions, but may not affect the overall mitochondrial functions basally or in the presence of certain pharmacological modulators of mitochondria.

Rhes Diminishes Mitochondrial Functions and Up-Regulates Mitophagy in the Presence of 3-NP. To further assess the role of Rhes in mitochondrial functions, we investigated the effect of Rhes in the presence of 3-NP in seahorse assay. The rationale for testing 3-NP is 2-fold: 1) 3-NP is known to promote lesion selectively in the striatum, and 2) previously, we found that Rhes KO mice are totally prevented from 3-NP–induced striatal lesion compared to WT control (39). In sea horse assay, as in *SI Appendix*, Fig. S3*C*, Rhes alone did not affect mitochondrial function in vehicle conditions. But, in the presence of 3-NP, which diminished both the basal and maximal mitochondrial respiration, Rhes further potentiated

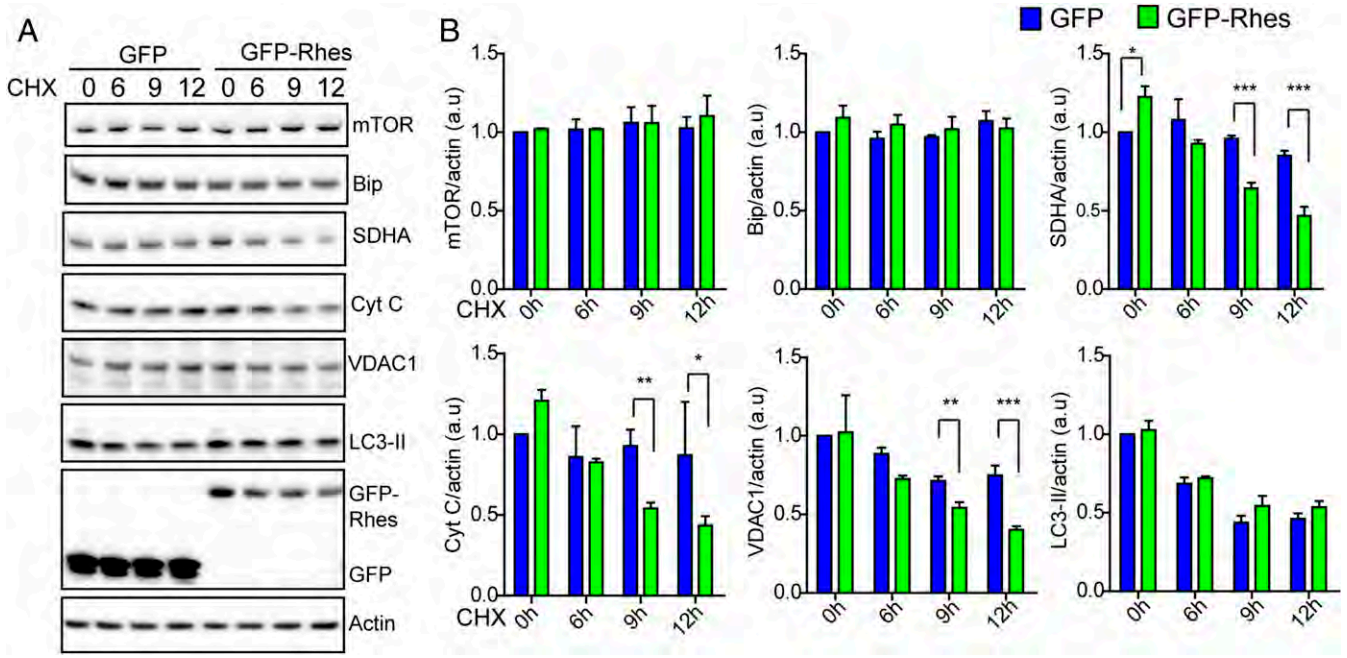

Fig. 2. Rhes regulates basal mitophagy. (*A*) Western blots from GFP-transfected or GFP-Rhes–transfected striatal neuronal cells treated with vehicle or cycloheximide (CHX, 100 μM) at indicated time point. Blots were probed with indicated antibodies. (*B*) Bar graph shows quantification of band intensities of indicated proteins in *A*. Protein levels were normalized to actin ($n = 3$, Student's t test; $^{*}P < 0.05$, $^{**}P < 0.01$, $^{***}P < 0.001$; data are mean ± SEM).

Downloaded at instituto de Biotecnologia/UNAM on October 20, 2020

the effect (*SI Appendix*, Fig. S4). This indicated that Rhes selectively worsens the 3-NP–induced mitochondrial dysfunctions, but not oligomycin, FCCP, or rotenone.

To investigate the mechanisms, we assessed the effect of Rhes on mitophagy in striatal neuronal cell line or primary striatal neurons using biochemical and confocal imaging approaches. We used cycloheximide chase experiment to assess the mitophagy, and Rhes markedly enhances mitophagy. As shown in Fig. 3 *A* and *B*, in GFP alone, there was a gradual loss of SDHA, in both vehicle and 3-NP conditions at 6, 9, and 12 h after CHX treatment. In the presence of GFP-Rhes, mTOR and Bip protein levels are not affected, but loss of SDHA is more rapid in vehicle and almost all (>90%) of SDHA was eliminated in 3-NP, which is also accompanied by enhanced LC3-II production (Fig. 3 *A* and *B*). Next, we transiently expressed GFP, GFP-Rhes WT, and GFP-Rhes C263S (mutant defective in membrane binding) in striatal neuronal cells by staining them with mitotracker and exposing them to vehicle or 3-NP (*SI Appendix*, Fig. S5). As expected, in vehicle-treated neuronal cells, we found that GFP-Rhes WT interacted with mitochondria (*SI Appendix*, Fig. S5, *Inset a4-2.5D*, arrow) and that mitotracker staining was observed throughout the GFP-Rhes WT–transfected (yellow arrowhead) and untransfected (blue arrowhead) neuronal cells (*SI Appendix*, Fig. S5, *Inset a3*). Contrary to this observation, in 3-NP–treated neuronal cells, the dispersed mitotracker staining was completely disrupted in the GFP-Rhes–transfected cells (*SI Appendix*, Fig.S5, *Inset a9*, yellow arrowhead) but not in untransfected neuronal cells (*SI Appendix*, Fig. S5, *Inset a9*, blue arrowhead). Also, in the presence of 3-NP, numerous globular mitochondria that were positive for Rhes were observed in GFP-Rhes–transfected cells (*SI Appendix*, Fig. S5, *Inset a10-2.5D*, arrow). Consistent with our previous work (28, 30, 45), we found that mutation of Rhes C263, which is a farnesylation consensus site, leads to its mislocalization into the nucleus (*SI Appendix*, Fig. S5, *Insets a5* and *a11*). Note that, in GFP-alone– or GFP-Rhes

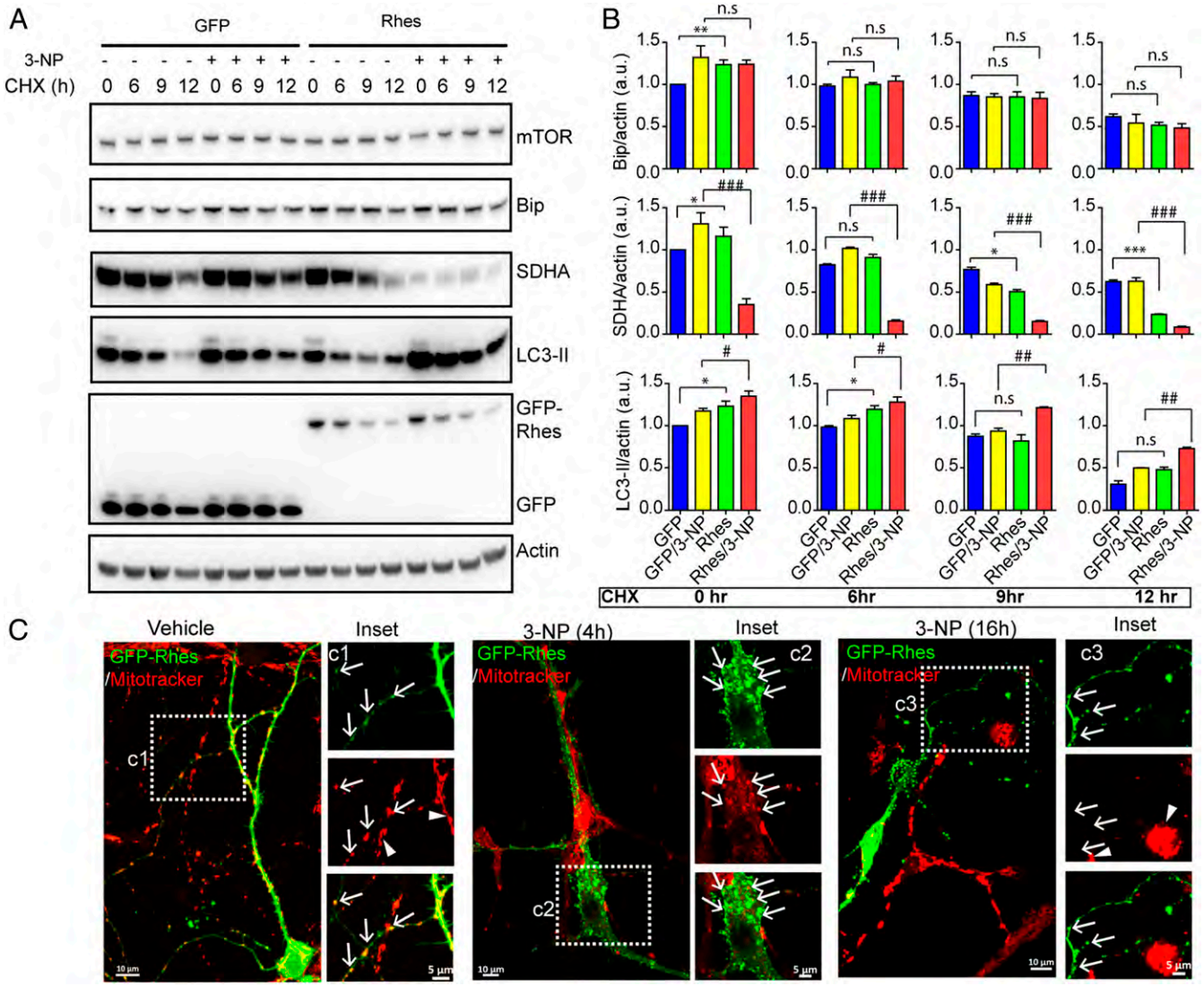

Fig. 3. Rhes promotes mitophagy in the presence of SDH inhibitor 3-NP. (*A*) Western blots of striatal neuronal cells transfected with GFP or GFP-Rhes, treated with vehicle or 3-NP (10 mM for 1 h) or with CHX (100 μM). (*B*) Bar graph shows the quantification of indicated proteins in *A* (*$P < 0.05$, **$P < 0.01$, ***$P < 0.001$, between GFP/vehicle and GFP-Rhes/Vehicle; $^{\#}P < 0.05$, $^{\#\#}P < 0.01$, $^{\#\#\#}P < 0.001$ between GFP/3-NP and GFP-Rhes/3-NP; 1-way ANOVA test followed by Tukey post hoc test; $n = 3$; data are mean ± SEM; n.s, not significant). (*C*) Representative confocal image and corresponding *Insets* of GFP-Rhes–transfected primary striatal neuron treated with vehicle or 3-NP (10 mM) at indicated time points. Cells were stained with mitotracker orange (red). Arrow indicates GFP-Rhes–positive neuronal processes colocalized with mitochondria in vehicle, and 4-h 3-NP–treated neuron but not in 16-h 3-NP–treated neuron. Arrowheads indicate that the mitotracker intensity is not affected in untransfected neighboring cell in the same field in either vehicle or 3-NP treatment.

Downloaded at instituto de Biotecnologia/UNAM on October 20, 2020

C263S-transfected cells, the mitotracker signal appears undisrupted, and no obvious association of GFP or GFP-Rhes C263S with mitochondria was observed in either vehicle (*SI Appendix*, Fig. S5, *Insets a2-2.5D* and *a6-2.5D*, arrowhead) or 3-NP–treated cells (*SI Appendix*, Fig. S5, *Insets a8-2.5D* and *a12-2.5D*, arrowhead). We further analyzed the mitotracker intensity by flow cytometry in striatal neuronal cells, infected with either Ad-null or Ad-Rhes, treated with vehicle or 3-NP. We found that mitotracker intensity was reduced by 30% in Ad-Rhes–infected cells compared to Ad-null infection after 3-NP treatment (*SI Appendix*, Fig. S6), indicating Rhes robustly diminishes mitochondrial intensity upon 3-NP treatment. Analogous to striatal cell lines, in primary striatal neurons, we also found that GFP-Rhes interacted with mitochondria (Fig. 3 *C*, *Inset c1*, arrow) and that mitotracker staining was observed throughout the GFP-Rhes WT-transfected and untransfected primary neuronal processes (Fig. 3 *C*, *Inset c1*, arrowhead). However, in 3-NP–treated primary neurons at 4 h, the mitotracker staining was reduced and globular mitochondria were surrounded by GFP-Rhes (Fig. 3 *C*, *Inset c2*, arrows). At a later time point of 3-NP treatment (16 h), mitotracker staining was almost completely abolished in the GFP-Rhes–transfected cells (Fig. 3 *C*, *Inset c3*, arrow) but not in untransfected neuronal cells (Fig. 3 *C*, *Inset c3*, arrowhead), indicating that Rhes diminishes mitochondrial functions in a time-dependent manner in the presence of 3-NP. Note that GFP-alone (control)–transfected primary neuron does not show reduction in mitotracker staining after 3-NP treatment (*SI Appendix*, Fig. S7). Together, these data indicate that Rhes exacerbates mitochondrial dysfunction and promotes mitophagy in the presence of SDHA inhibitor 3-NP.

Rhes Promotes Mitophagy Flux in the Presence of 3-NP. Next, we biochemically estimated whether Rhes alters the mitophagy flux in striatal neuronal cell lines in gradient fractionation (*SI Appendix*, Fig. S8*A*) and in total lysate (*SI Appendix*, Fig. S8 *B–E*). In Ad-null condition (control), as expected, we found an accumulation of SDHA in the mitochondrial fraction in the vehicle-treated groups (*SI Appendix*, Fig. S8*A*). Addition of 3-NP resulted in a robust accumulation of SDHA in the lysosomal fractions (compare green circles). Blocking autophagy with chloroquine (CQ), however, resulted in a diminished accumulation of SDHA and enhanced LC3-II levels in control, indicating that 3-NP might induce new mitochondrial production, in control condition. In Ad-Rhes, however, higher levels of SDHA were found in vehicle-treated conditions. Treatment of 3-NP in Ad-Rhes condition resulted in a reduction of SDHA levels in the lysosomal fractions (compare red circles). Cotreatment with CQ showed increased SDHA levels in lysosomal fraction, which is also accompanied by a rapid up-regulation of LC3 conversion (*SI Appendix*, Fig. S8*A*).

Apart from mitophagy, we also checked mitobiogenesis by investigating expression level of genes such as *Nrf1, Nrf2, Pgc1α*, and *Tfam* involved in the mitochondrial biogenesis in GFP-containing and GFP-Rhes–containing cells treated with 3-NP alone or in combination with CQ. We found that 3-NP treatment up-regulated the expression of mitobiogenesis regulatory genes, but the combination of 3-NP and CQ diminished their expression in both control and Rhes-containing cells (*SI Appendix*, Fig. S9). This indicates that the lysosomal activity is necessary for biogenesis in 3-NP–treated cells. Mitochondrial degradation and biosynthesis are tightly regulated processes (46). Thus, the reduced SDHA levels in 3-NP + Rhes are presumably due to higher degradation of mitochondria compared to biogenesis. This notion is consistent with enhanced abundance of SDHA in GFP-Rhes + 3-NP + CQ, compared to GFP + 3-NP + CQ (*SI Appendix*, Fig. S8*A*). Together, biochemical fractionation data suggest that Rhes up-regulates mitophagy flux in 3-NP condition.

In total lysate, in both vehicle-treated GFP-expressing and GFP-Rhes–expressing cells, we found there was no major difference in SDHA levels (*SI Appendix*, Fig. S8 *B* and *C*). Upon 3-NP treatment, however, there were increased SDHA levels in GFP-expressing cells, but, in GFP-Rhes–expressing cells, the SDHA levels were diminished, which is also accompanied by a rapid up-regulation of autophagy, as measured by increased LC3 conversion (*SI Appendix*, Fig. S8 *B* and *C*). Addition of CQ has further increased the SDHA and LC3-II levels in 3-NP condition (*SI Appendix*, Fig. S8 *D* and *E*). Together, these data indicate that Rhes increases autophagosome and lysosome accumulation around mitochondria and mediates mitophagy flux in the presence of 3-NP. Similarly, in immunocytochemistry, SDHA staining is also diminished in GFP-Rhes–transfected striatal neuronal cells, treated with 3-NP compared to vehicle treatment (*SI Appendix*, Fig. S10). Next, we investigated whether Rhes recruits lysosomes to globular mitochondria using lysotracker and GFP-LC3, by confocal microscopy. As predicted, we observed colocalization of lysotracker with GFP-Rhes–positive globular mitochondria (stained with mitotracker) in vehicle-treated cells, and this colocalization was further enhanced in the presence of 3-NP (*SI Appendix*, Fig. S11 *A* and *B*, arrow). The 3-NP–treated, GFP-alone–transfected cells also showed increase in colocalization between mitochondria and lysosomes, but only GFP-Rhes–positive cells show disrupted mitotracker staining (*SI Appendix*, Fig. S11, arrow). Similarly, there was an enhanced number of GFP-LC3 puncta (*SI Appendix*, Fig. S12 *A* and *B*, arrow) and increased colocalization between GFP-LC3 and mCherry TOMM20, a mitochondrial marker, in 3-NP–treated Myc-Rhes–expressing cells (*SI Appendix*, Fig. S12*C*). Thus, Rhes associates with mitochondria and lysosomes and activates mitophagy, upon 3-NP treatment.

Rhes Promotes the Formation of Mitophagosomes In Vivo. Since Rhes interacted with globular mitochondria and lysosomes (Fig. 1 and *SI Appendix*, Fig. S1) and modulates basal mitophagy which is further up-regulated in 3-NP (Figs. 2 and 3), we posited that Rhes may activate mitophagy in vivo. To test this thoroughly in vivo, we carried out behavioral, pathological, and ultrastructural analysis (using transmission electron microscopy) of the striatum in WT and Rhes KO mice after systemic injection of 3-NP (see experimental scheme, Fig. 4*A*). Consistent with our earlier report (39), 3-NP administration to WT mice promoted motor abnormalities that were diminished in Rhes KO mice (Fig. 4 *B–E*). The 3-NP also induced striatal-specific lesion in WT striatum, which was completely prevented in the Rhes KO striatum (Fig. 4*F*, arrowhead) (39). Microscopic analysis of the 3-NP–induced striatal-specific lesions found pyknotic nuclei and a diminished neuronal staining in WT mice, while KO striatum displayed healthy nuclei and normal neural staining (Fig. 4*F*, *Insets f1* and *f2*, compare WT and KO) (39). Thus, 3-NP promotes lesions selectively in the striatum of the WT mice but not in the Rhes KO striatum, a highly reproducible phenotype (39). To address why Rhes KO are resistant to 3-NP–induced lesion, we hypothesized that ultrastructural analysis might provide a clue. We carried out time-lapse ultrastructural analysis using serial corticostriatal section electron microscopy of the second and third days after systemic administration of 3-NP. On the second day (d2), we found no gross changes in the overall cell morphology or mitochondria ultrastructure between WT and KO, which were similar to control (Fig. 4 *G*, *Insets*). On the third day (d3), in WT, we found neuronal shrinkage and abnormal, swollen mitochondria with broken inner membrane and matrix in the striatum (Fig. 4 *G*, *Insets*, arrowhead). And, those abnormal striatal neuronal changes were completely absent in the Rhes KO (Fig. 4*G*). Mitochondrial circularity index (length/breadth) and area analysis showed that the frequency of circular mitochondria is high in Rhes WT compared to Rhes KO neuron after 3-NP treatment (Fig. 4*H*). Cortex from either genotype showed no lesion (*SI Appendix*, Fig. S13, arrowhead) or mitochondrial abnormalities (*SI Appendix*, Fig. S13,

Downloaded at Instituto de Biotecnología/UNAM on October 20, 2020

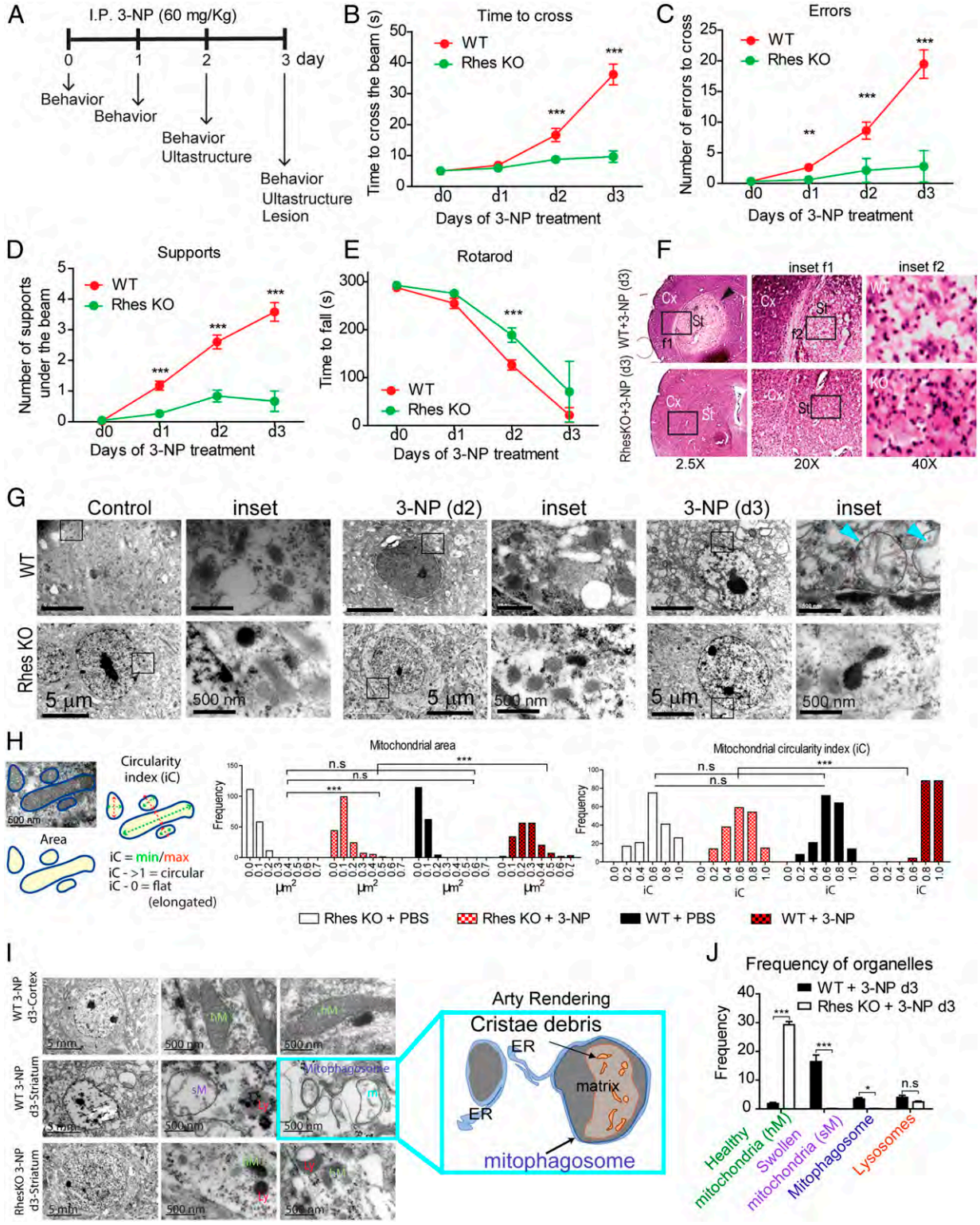

Fig. 4. Rhes promotes mitophagy in vivo. (*A*) Experimental design for 3-NP treatment in mice (I.P.: intraperitoneal injection). (*B–D*) Beam walk analysis during 3-NP treatment for WT (red circles) and Rhes-KO (green circles) groups. (*E*) Changes in the latency to fall for the rotarod test during 3-NP treatment. $^{**}P < 0.01$, $^{***}P < 0.001$; 2-way ANOVA followed by Bonferroni's post hoc test. (*F*) Representative hematoxylin/eosin-stained sections for WT and Rhes KO mice after 3 d of 3-NP treatment; Cx, cortex; St, striatum. *Insets f1* and *f2* show the magnified region from the selected area (arrowhead shows the 3-NP striatal lesion). (*G*) Representative electron micrographs from striatum of WT and Rhes KO mice at day 2 (d2) and day 3 (d3) of 3-NP treatment; *Insets* are high magnification (blue arrowheads show mitochondria with broken inner membrane). (*H*) Ultrastructural changes analysis using frequency histograms of the mitochondrial area and circularity index (iC) for the WT and Rhes KO groups treated with vehicle (PBS) or 3-NP. One-way ANOVA (Bartlett's test), Bonferroni's post hoc test. $^{***}P < 0.001$; n.s, not significant. (*I*) Representative electron micrographs from striatum and cortex of indicated groups after 3 d of 3-NP treatment. Arty Rendering shows the swollen mitochondria in mitophagosome. (*J*) Quantification of the healthy and swollen mitochondria, lysosomes, and mitophagosomes frequency in the striatum of WT and Rhes KO mice at day 3 of 3-NP treatment. $^{*}P < 0.05$, $^{***}P < 0.001$, n.s: not significant, determined by 2-way ANOVA, Bonferroni's post hoc test.

Downloaded at Instituto de Biotecnologia/UNAM on October 20, 2020

Insets a1 and *b1*), indicating that 3-NP–induced lesion (arrow) and mitochondrial abnormalities (*SI Appendix*, Fig. S13, *Inset b2*) are selective to the striatum, and require Rhes. Further examination of ultrastructure revealed numerous mitophagosomes, where the mitochondria with cristae debris were engulfed within the double-layer membranes resembling autophagosomes (Fig. 4*I*, and arty rendering), and there was a diminished frequency of the number of healthy looking mitochondria, but enhanced swollen mitochondria and mitophagosomes in Rhes WT striatum, compared to Rhes KO (Fig. 4*J*). Thus, Rhes deletion prevents the formation of neuronal shrinkage, mitochondrial swelling, and induction of mitophagosomes by 3-NP treatment. All together, these data indicated that Rhes physiologically regulates 3-NP–induced mitochondrial dysfunction and promotes the formation of globular mitochondria and mitophagosomes, which coincides with worsening motor phenotype in vivo.

Rhes Diminishes Mitochondrial Potential ($\Delta\Psi_m$) and Promotes Cell Death in the Presence of 3-NP. To understand the mechanisms, and because Rhes can interact with VDAC1 (Fig. 1*A*), which is a component of membrane permeability pore, we rationalized that Rhes may affect mitochondrial potential ($\Delta\Psi_m$). To investigate this, we tested whether Rhes alters $\Delta\Psi_m$ using tetramethyl rhodamine (TMRM), a widely used cell-permeable fluorescent dye that binds mitochondria with intact $\Delta\Psi_m$. We infected striatal neuronal cell lines with Ad-null or Ad-Rhes for ~32 h and added TMRM. We quantified TMRM signal intensity using FACS (fluorescence-activated cell sorting) in vehicle or 3-NP treatment at 15 min, 30 min, and 2 h (Fig. 5*A*). Notably, TMRM (red) signals were not altered in vehicle condition in both Ad-null– and Ad-Rhes–expressing cells. But, in the presence of 3-NP, the TMRM signal intensity is rapidly diminished only in Ad-Rhes–expressing cells but not Ad-null in a time-dependent manner, indicating a rapid loss of $\Delta\Psi_m$ by Rhes (Fig. 5*A*). This effect is specific to Rhes WT, as GFP-Rhes C263S mutant failed to alter TMRM signal, which is like GFP control (Fig. 5 *B* and *C*). Next, as Rhes is required for 3-NP induced striatal lesion in vivo (ref. 39 and Fig. 4), we investigated whether Rhes modulates striatal cell death in vitro, using propidium iodide (PI) staining, a fluorescent dye that enters cells only when they are compromised (47), and FAC sorting. As shown in Fig. 5*D*, we found that Ad-null control expressing cells did not show changes in PI+ cells in either vehicle or 3-NP condition (~5 to 7%). Similarly, Ad-Rhes–expressing cells in vehicle did not show changes in PI+ cells (~5%). However, in Ad-Rhes and 3-NP condition, there was a robust increase in PI+ cells (~25%; Fig. 5*E*). To further establish that cell death effect is specific to Rhes WT, we FAC-sorted GFP alone, GFP-Rhes WT, and GFP-Rhes C263S cells and added vehicle or 3-NP (see scheme in *SI Appendix*, Fig. S14*A*). As shown in *SI Appendix*, Fig. S14 *B* and *C*, Rhes WT showed ~27% cell death as measured by PI staining in the presence of 3-NP, whereas GFP or GFP-Rhes C263S showed ~5 to 10% cell death. Collectively, these

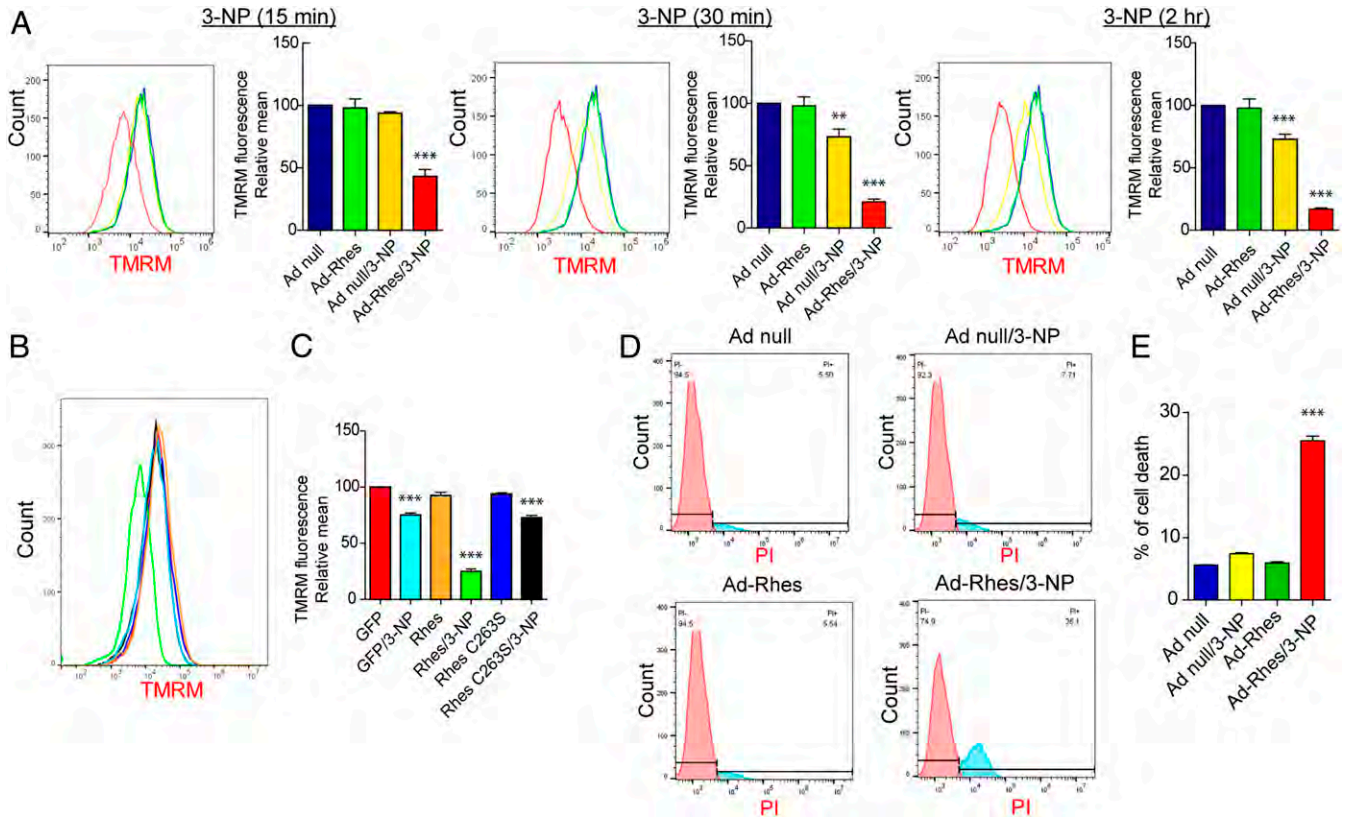

Fig. 5. Rhes diminishes mitochondrial membrane potential ($\Delta\Psi_m$) and promotes cell death in the presence of 3-NP. (*A*) Representative flow cytometry plot of striatal neuronal cells infected with Ad-null or Ad-Rhes in the presence of vehicle or 3-NP (10 mM, for 15 min, 30 min, or 2 h). Cells were stained for TMRM ($\Delta\Psi_m$ indicator) and analyzed in flow cytometry. Bar graph shows the relative TMRM mean intensity. $^{**}P < 0.01$, $^{***}P < 0.001$ vs. Ad-null and vehicle ($n = 3$ per group; data are mean ± SEM; 1-way ANOVA followed by Tukey post hoc test). (*B*) Flow cytometry plot of striatal neuronal cells transfected with GFP or GFP-Rhes or GFP-Rhes C263S treated with vehicle or 3-NP (10 mM and for 2 h) and stained for TMRM. (*C*) Bar graph shows the relative TMRM mean intensity for *B*. $^{***}P < 0.001$ vs. GFP/Vehicle sample ($n = 3$ per group; data are mean ± SEM; 1-way ANOVA followed by Tukey post hoc test). (*D*) Flow cytometry plot of striatal neuronal cells infected with Ad-null or Ad-Rhes treated with vehicle or 3-NP (10 mM for 8 h), stained with PI. (*E*) Bar graph shows the percent of cell death in indicated groups. $^{***}P < 0.001$ vs. Ad-null/Vehicle ($n = 3$ per group; data are mean ± SEM; 1-way ANOVA followed by Tukey post hoc test).

Downloaded at instituto de Biotecnologia/UNAM on October 20, 2020

data indicate Rhes diminishes $\Delta\Psi_m$ and promotes cell death in the presence of 3-NP.

Rhes Promotes Mitophagy, Disrupts $\Delta\Psi_m$, and Promotes Cell Death via Nix. To investigate the mechanisms by which Rhes may activate mitophagy, we considered whether Rhes interacts with well-known mitophagy modulators, such as Parkin, PINK1, DRP1 (Dynamin related protein 1), or Nix (48). In an affinity purification experiment, GST-Rhes did not interact with Parkin but readily interacted with mTOR (Fig. 6*A*), as shown in our previous report (28). We did not observe interaction of Rhes with either DRP1 or Pink1 (*SI Appendix*, Fig. S15 *A* and *B*). However, GST-Rhes readily interacted with Nix, a known mitophagy receptor (49) (Fig. 6 *B* and *C*). Rhes interaction with overexpressed Nix (Fig. 6*B*) or endogenous Nix (Fig. 6*C*), increases with 3-NP treatment; however, Rhes interaction with mTOR remains unaltered (Fig. 6*C*). GST-Rhes is also affinity-purified with LC3 without or with 3-NP and showed a consistent and enhanced interaction with Nix in the presence of 3-NP (Fig. 6*D*). Next, we found that the C-terminal SUMO E3 ligase domain (171 to 266 aa), but not the N-terminal GTPase (1 to 181 aa), or the fragment (147 to 216 aa) interacted strongly with Nix (Fig. 6*E*). Additionally, we found that membrane-binding defective mutant Rhes C263S, but not GTP-binding mutant (Rhes S33N), fails to interact with Nix (*SI Appendix*, Fig. S15*C*). Interaction of Rhes with mTOR, on the other hand, seems to be more toward the N-terminal side of Rhes (Fig. 6*E*). Thus, Rhes associates strongly with Nix in the presence of 3-NP, and the binding requires intact membrane binding domain.

Because Rhes interacted strongly with Nix, we hypothesized that Rhes may promote mitophagy via Nix. To test this hypothesis, we depleted endogenous Nix in the striatal cells using CRISPR/Cas9 tools. While GFP-Rhes promoted a significant loss of SDHA and increased LC3-II productions in CRISPR/Cas9 control cells, it completely failed to do so in CRISPR/Cas9 Nix-depleted cells (Fig. 6 *F* and *G*), which resulted in ~90% depletion of Nix (*SI Appendix*, Fig. S19*A*). This finding indicated that Nix is essential for Rhes-induced mitophagy. Furthermore, when we reconstituted Nix in Nix-depleted cells, Rhes was able to restore mitophagy and increase LC-3 conversion (*SI Appendix*, Fig. S16 *A* and *B*), suggesting that Nix is critical for Rhes-mediated mitophagy. Consistent with this, in confocal data, we found that, in CRISPR/Cas9 control cells, upon 3-NP treatment, Rhes promoted rapid loss of mitotracker intensity, and formation of numerous globular mitochondria colocalized with GFP-Rhes (Fig. 6*H*, arrow). However, in Nix-depleted GFP-Rhes expressing cells, most of the mitotracker

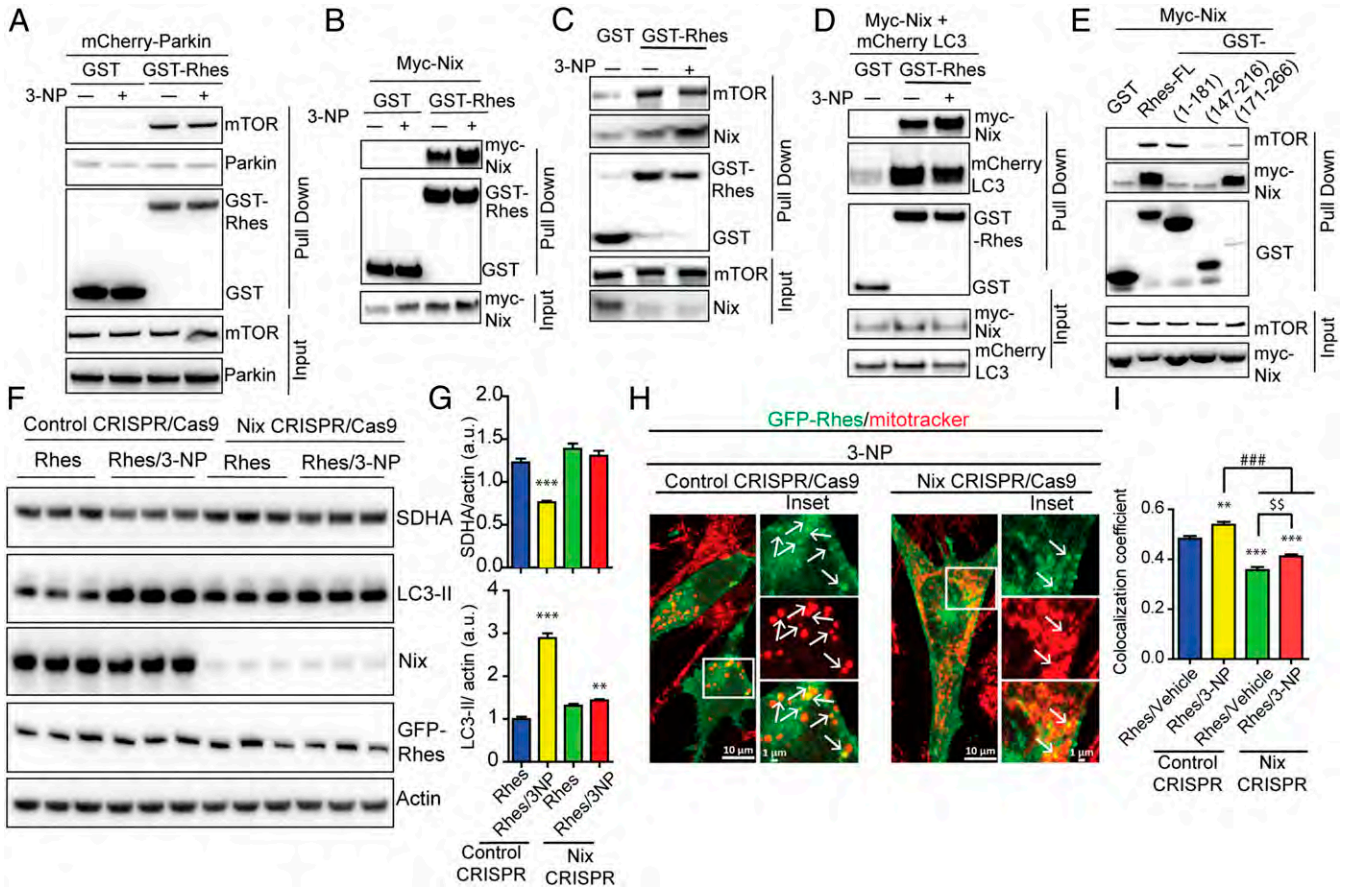

Fig. 6. Rhes interacts with Nix and promotes mitophagy. (*A–E*) Representative Western blot of indicated proteins after glutathione affinity purification of HEK 293 cells transfected with GST or GST-Rhes (full length [FL] or fragments), mCherry-Parkin, myc-Nix, or mCherry-LC3 plasmids that are exposed to vehicle or 3-NP (10 mM, 2 h) wherever indicated. Input is 5% of total lysate. (*F*) Representative Western blot of control or CRISPR/Cas9-mediated Nix-depleted striatal neuronal cells that were transfected with GFP or GFP-Rhes and treated with vehicle or 3-NP (10 mM, 2 h). (*G*) Bar graph shows the quantification for normalized SDHA and LC3-II proteins. $^{**}P < 0.01$, $^{***}P < 0.001$ vs. Rhes control CRISPR/vehicle ($n = 4$, data are mean ± SEM; 1-way ANOVA followed by Tukey post hoc test). (*H*) Representative confocal images and their *Insets* of control CRISPR/Cas9 or Nix CRISPR/Cas9 striatal neuronal cells transfected with GFP-Rhes and costained for mitotracker (red) that were treated with 3-NP (10 mM for 2 h). Arrows represents the globular mitochondria, positive for GFP-Rhes. (*I*) Bar graph shows the average of Pearson's coefficient of colocalization between GFP-Rhes and mitochondria in indicated groups ($n = 33$ to 37 cells per group; $^{**}P < 0.01$, $^{***}P < 0.001$ vs. Rhes/vehicle control CRISPR; $^{\#\#\#}P < 0.001$, $^{\$\$}P < 0.01$ between indicated groups; data are mean ± SEM; 1-way ANOVA followed by Tukey post hoc test).

Downloaded at Instituto de Biotecnología/UNAM on October 20, 2020

signal intensity remained unaltered by 3-NP treatment and colocalization between GFP-Rhes and mitotracker was significantly reduced (Fig. 6 *H*, arrows and *I*). In vehicle treatment, Rhes was unable to interact with globular mitochondria in Nix-depleted cells compared to control cells (*SI Appendix*, Fig. S16*C*, arrowhead). Together, these data suggest that Rhes interacts with globular mitochondria and promotes mitophagy via Nix.

Next, as Rhes decreases $\Delta\Psi_m$ in the presence of 3-NP, we wondered whether this process requires Nix. As shown in Fig. 7 *A* and *B*, while Rhes diminishes TMRM signals in control cells, this effect is not observed in Nix-depleted cells. Similarly, the observed Rhes-induced cell death in the presence of 3-NP in control cells was also markedly diminished in Nix-depleted cells (Fig. 7 *C* and *D*). Moreover, reconstitution of Nix significantly elevated Rhes-mediated cell death in 3-NP–treated cells (Fig. 7*D*). Nix is localized to endoplasmic reticulum (ER) as well as mitochondria (50). Using ER-targeted Nix, where transmembrane (TM) domain of Nix was replaced by CytoB, and mitochondria-targeted Nix, where TM domain was replaced with monoamine oxidase located in the outer mitochondrial membrane (50), we found Rhes affinity with both ER- and mitochondrial-targeted Nix (*SI Appendix*, Fig. S17 *A* and *B*). However, in a reconstitution FACS/TMRM experiment, we found that replenishing only the mitochondria-targeted Nix, but not ER-targeted Nix, restores the loss of TMRM signal by Rhes (*SI Appendix*, Fig. S17 *C* and *D*). Collectively, these data indicate that Rhes interacts with both ER- and mitochondrial-targeted Nix and disrupts $\Delta\Psi_m$ mostly via the latter.

Rhes Travels from Cell to Cell and Interacts with the Globular Mitochondria in the Neighboring Cells via Nix. We recently reported that Rhes induces the biogenesis of tunneling nanotube (TNT)-like cellular protrusion, "Rhes tunnel," through which Rhes travels from cell to cell (45). It is unknown whether intercellular signaling can regulate mitochondrial turnover. So, we considered whether Rhes can interact with damaged mitochondria in the neighboring cells. We designed an experiment in which we cocultured FACS-sorted GFP-Rhes–expressing cells (donor cells) with the acceptor cells that were exposed to 3-NP or vehicle (acceptor cells), followed by confocal imaging with mitotracker (see scheme in Fig. 8*A*). As expected, we found GFP-Rhes–positive TNT-like protrusions (closed arrow) and numerous GFP-Rhes (open arrow) in the neighboring cell in both vehicle-treated and 3-NP–treated cells (Fig. 8*B* and *SI Appendix*, Fig. S18). Interestingly, we found numerous GFP-Rhes puncta that were colocalized with globular mitochondria in cells that are exposed to 3-NP (yellow arrowhead) in control acceptor cell. But, when GFP-Rhes donor cells are cocultured with Nix-depleted acceptor cells, we do observe TNT-like protrusions (closed arrow) and numerous puncta (open arrow), but we failed to observe GFP puncta (white arrowhead) localization with globular mitochondria in the Nix-depleted acceptor cell treated

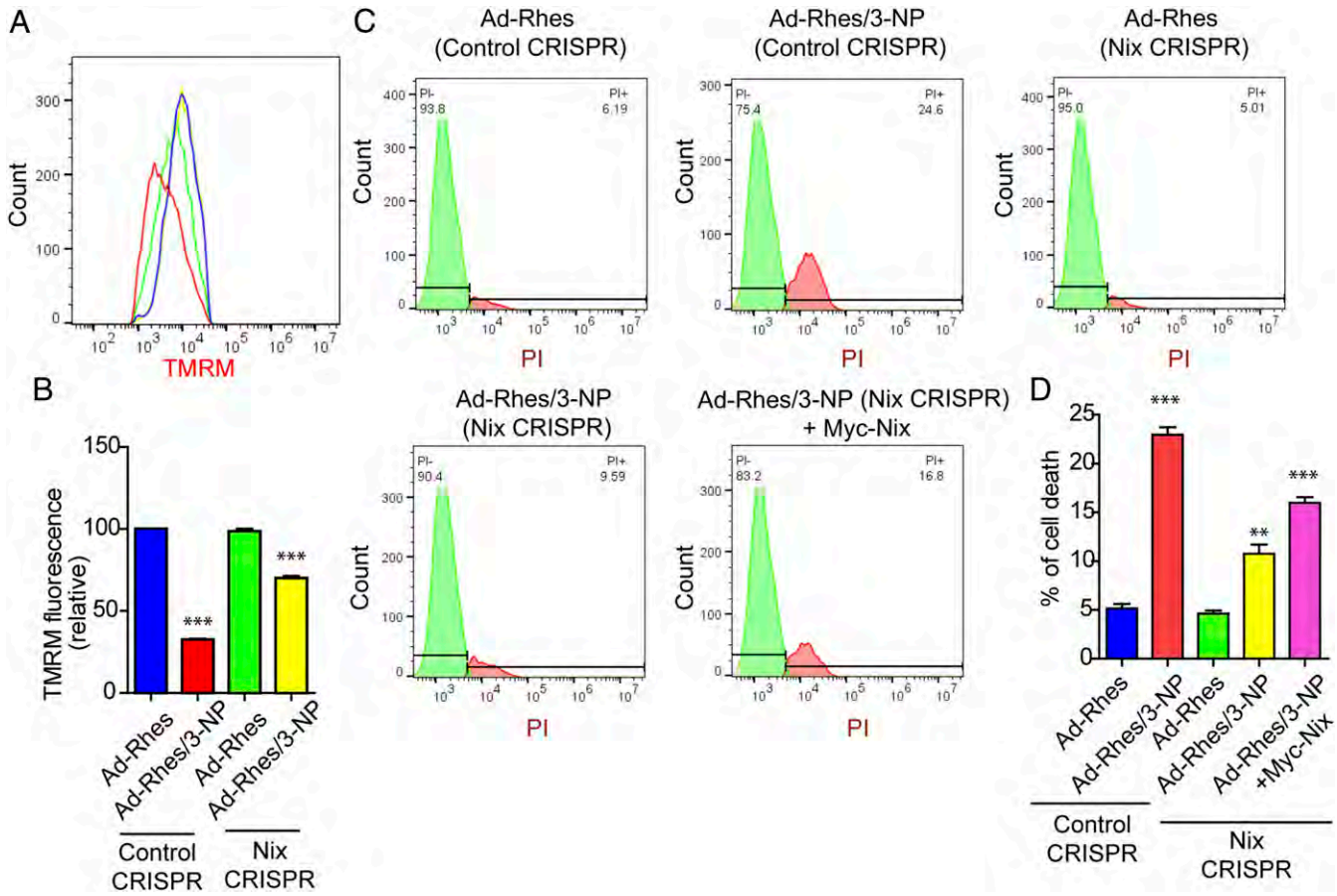

Fig. 7. Rhes promotes cell death and disrupts mitochondrial potential ($\Delta\Psi_m$) via Nix. (*A*) Flow cytometry plots of control CRISPR/Cas9 and or Nix CRISPR/Cas9 striatal neuronal cells, infected with either Ad-null or Ad-Rhes viral particles. (*B*) Bar graph shows the relative TMRM fluorescence intensity for *A*. ***$P < 0.001$ ($n = 3$ per group; data are mean ± SEM; 1-way ANOVA followed by Tukey post hoc test). (*C*) Flow cytometry plot of control CRISPR/Cas9 and or Nix CRISPR/Cas9 striatal neuronal cells infected with Ad-null or Ad-Rhes treated with vehicle or 3-NP (10 mM for 8 h) that are stained with PI. Nix CRISPR/Cas9 striatal neuronal cells reconstituted with Nix by transfecting myc-Nix cDNA. (*D*) Bar graph shows the percent of cell death in indicated groups (**$P < 0.01$, ***$P < 0.001$; $n = 3$ per group; data are mean ± SEM; 1-way ANOVA followed by Tukey post hoc test).

Downloaded at instituto de Biotecnologia/UNAM on October 20, 2020

with 3-NP (Fig. 8*B*). Pearson's colocalization coefficient further confirmed a marked reduction in Rhes localization with mitochondria in Nix-depleted cells (Fig. 8*C*). This indicates that Rhes can travel from cell to cell and interact with damaged mitochondria via Nix. Thus, these data raise a possibility that Rhes can act as an intercellular mitochondrial surveillance factor.

Discussion

To date, the brain tissue-specific regulator(s) of mitophagy or its role in neuronal vulnerability remains poorly understood. By using neuronal and mouse model combined with electron and live-cell confocal microscopy, we have systematically investigated the role of Rhes in mitophagy. We found striatal-enriched protein Rhes promotes mitophagy via Nix, a known mitophagy receptor (49). Despite abundant and comparable expression of Nix in the striatum of both WT and Rhes KO mice (*SI Appendix*, Fig. S19*B*), the removal of damaged mitochondria via mitophagy requires Rhes demonstrating its "mitophagy ligand-like" capabilities in vivo. In addition, this study demonstrate the role of Rhes in intercellular surveillance of mitochondria through the cellular protrusion that we recently discovered (45) and lays a foundation for understanding the unprecedented complexity by which Rhes may signal mitophagy within and outside the striatum.

Half-lives of mitochondria in rat whole brain were estimated to be ~24 d (51). Striatum is considered to be one of the metabolically active regions of the brain (52); the exact half-life of mitochondria remains unknown. Although Rhes appears to regulate basal mitophagy, the functional relevance of this has yet to be determined. Rhes KO mice are hyperactive to dopaminergic drugs, but whether the lack of mitophagy may contribute to such hyperactive phenotype remains largely unknown. It has long been known that 3-NP elicits striatal-specific lesion (53, 54), and mechanisms such as oxidative stress and excitotoxicity were implicated (55, 56). Oxidative stress or excitotoxicity can also occur in the cortex; however, 3-NP

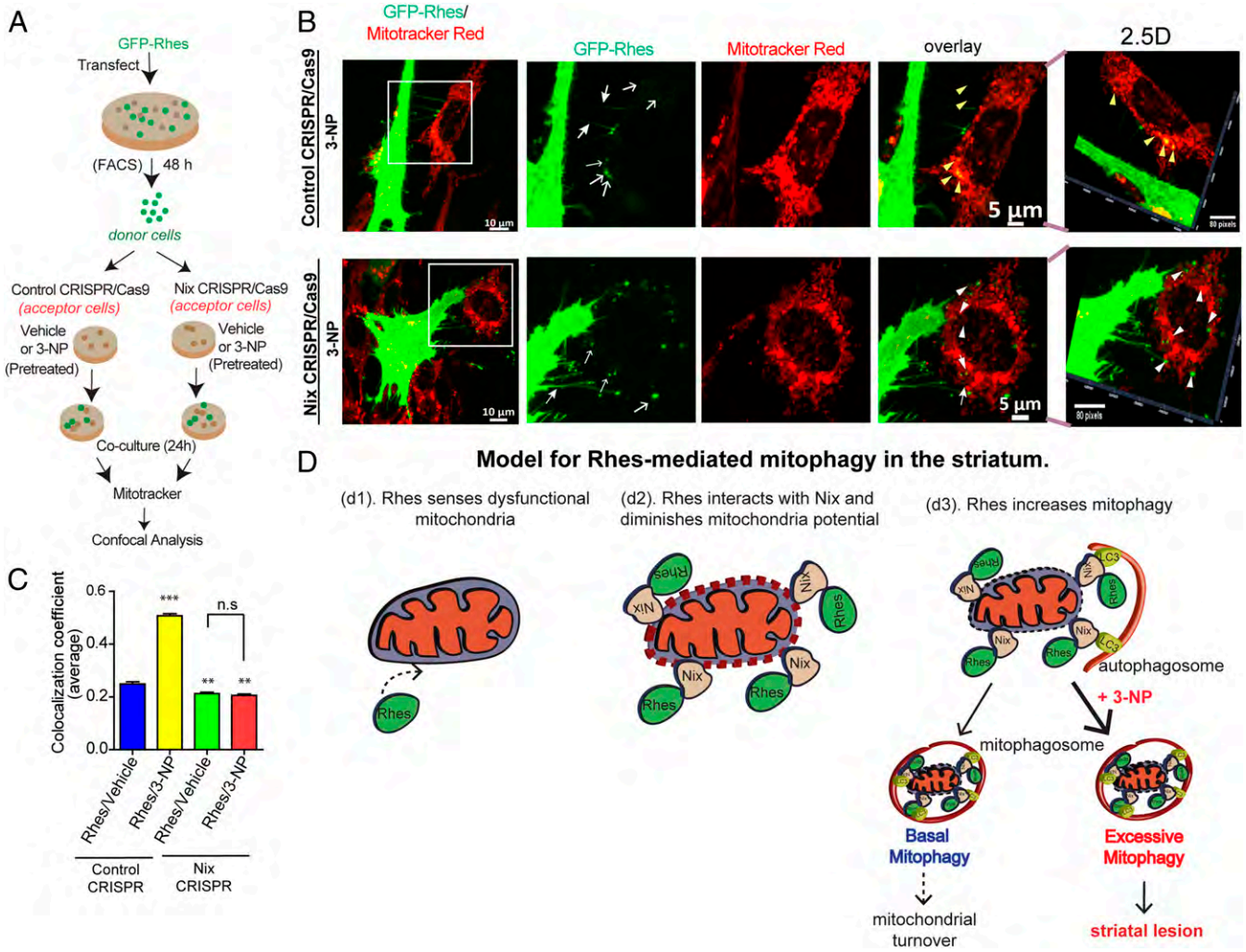

Fig. 8. Rhes travels Intercellularly and interacts with damaged mitochondria via Nix. (*A*) Experimental design for *B*. (*B*) Representative confocal image of GFP-Rhes (FAC-sorted) striatal neuronal cells (donor cells) cocultured with vehicle-treated or 3-NP–treated control or Nix-depleted (Nix CRISPR) cells (acceptor cells). *Insets* show the magnified region from selected area. Corresponding *Insets* were processed for 2.5-dimensional rendering. Closed arrow indicates Rhes-induced TNT-like protrusions. Open arrow represents GFP-Rhes puncta in acceptor cell. Yellow and white arrowheads indicate presence or lack, respectively, of colocalization of GFP-Rhes with mitotracker. (*C*) Bar graph shows average of Pearson's coefficient of colocalization between GFP puncta and mitotracker in neighboring acceptor cells where Rhes is transported from donor cell; $n = 72$ to 90 GFP-Rhes puncta per group were counted from 13 to 18 cells per group. $^{**}P < 0.01$, $^{***}P < 0.001$; 1-way ANOVA followed by Tukey post hoc test; n.s, not significant. (*D*) Model for Rhes-mediated mitophagy in the striatum. Rhes senses dysfunctional mitochondria (d1). Rhes interacts with Nix and diminishes membrane potential (d2). Rhes-Nix interaction recruits autophagosomes via LC3 and formation of mitophagosomes to promote mitochondrial degradation (d3). Basal mitophagy may lead to mitochondrial turnover; however, excessive mitophagy in the presence of mitochondrial toxin, 3-NP, may promote striatal lesion.

Downloaded at Instituto de Biotecnologia/UNAM on October 20, 2020

does not elicit lesion in the cortex (*SI Appendix*, Fig. S13). Therefore, the molecular details that contribute to 3-NP–induced striatal lesion has remained enigmatic. Now this study provides a clear molecular route for striatal lesion by 3-NP. Our data indicate that Rhes's role is to protect neurons by removing damaged mitochondria via mitophagy. However, upon exposure to mitochondrial toxin such as 3-NP, which irreversibly damages the mitochondria, the Rhes-mediated mitophagy processes are exacerbated that lead to depletion of the mitochondria and neuronal death (Fig. 8*D*). Because Rhes selectively mediates 3-NP–induced toxicity, it raises the question of whether Rhes contains special mechanisms to sense SDHA dysfunction in the brain.

Based on the data presented in this report, our current model predicts that Rhes may sense the dysfunctional mitochondria and binds to Nix to disrupt the $\Delta\Psi_m$ and initiate mitophagy. Rhes and Nix together may alter the membrane permeability pore, leading to the diminishment of $\Delta\Psi_m$. Nix alone cannot disrupt $\Delta\Psi_m$, because there was no difference in TMRM signal intensity between Nix WT and Nix KO cells with or without 3-NP (Fig. 7). Moreover, as mentioned above, Nix alone cannot elicit mitophagy in vivo because the levels of Nix between WT and Rhes KO striatum were similar (*SI Appendix*, Fig. S19*B*), and yet Rhes KO shows diminished mitophagy compared to WT (Fig. 4). Mechanistically, as loss of $\Delta\Psi_m$ is a major initial step in the mitophagy up-regulation, we hypothesize that altering the $\Delta\Psi_m$ by Rhes is the likely step to initiate mitophagy. Rhes's effect on mitophagy appears to be specific to 3-NP but not FCCP (Fig. 2 and *SI Appendix*, Fig. S3 *E* and *F*). How is this specificity accomplished? One possibility would be that Rhes, via yet unknown mechanisms, may particularly react to dysfunctional complex II of mitochondria. Analogous to this, some factors in the substantia nigra may sense MPTP- or rotenone- induced mitochondrial dysfunction related to complex I. Such tissue-specific regulator may set the stage for eliciting tissue-specific vulnerability through mitophagy. But the identity of such regulators in the substantia nigra remains unknown.

An earlier study showed that mitochondria from the axonal protrusions could be degraded in astrocytes via mitophagy, supporting the existence of intercellular mitophagy mechanisms in the brain (57). The implication that Rhes can travel from cell to cell and interacts with damaged mitochondria thus raises the intriguing possibility that Rhes may act like "mitochondrial surveillant" in the striatum. We imagine that Rhes "scans" for damaged mitochondria in the surrounding cells and travels there via TNT-like membranous tubes to eliminates them. Conceptually, such a process in brain sounds like "science fiction." Considering the complexity of brain, the surveillance ability of Rhes to monitor defective mitochondria may be needed for an effective coordination of billions of densely packed neurons in the brain. Collectively, this study reveals Rhes as a mediator of mitophagy and its impact on the regulation of striatal vulnerability. Development of therapeutic approaches that modulates mitophagy in the striatum may offer benefits for dysfunction related to the striatal region of the brain.

Materials and Methods

Cell Culture and Chemicals. Mouse normal striatal neuronal cells (ST*Hdh*$^{Q7/Q7}$) (42) were cultured in growth medium containing Dulbecco's modified Eagle's medium (Thermo Fisher Scientific) with 10% fetal bovine serum, 1% penicillin–streptomycin, as described in our previous work (30, 40, 58).

Generation of Nix KO Cell Line. Nix KO cell line was generated using Nix CRISPR/Cas9 plasmids from Santa Cruz Biotechnologies. First, we transfected the striatal neuronal cells with Nix CRISPR/Cas9 plasmid (SC-419357) or CRISPR/Cas9 control plasmid (SC-418922) in a 10-cm dish. After 48 h, we sorted the cells based on GFP fluorescence and recultured them. We passaged them 2 to 3 times and prepared lysate to confirm the Nix protein depletion by Western blotting using Nix antibody.

Mice. For in vivo experiments, we used Rhes KO mice, and we used C57BL/6J mice as a control group. Rhes KO mice were obtained from A. Usiello (25) and were backcrossed with C57BL/6J mice at least 8 generations; homozygous Rhes KO were used for all of the experiments. WT mice (C57BL/6) were obtained from Jackson Laboratory and maintained in our animal facility according to Institutional Animal Care and Use Committee at The Scripps Research Institute. The 3-NP injections were based on previous studies (14, 39). Briefly, 3-NP was dissolved in sterile phosphate-buffered saline (PBS; 0.1 M, 10 mg/mL), and pH was adjusted to pH 7.4 using sodium hydroxide. Mice received intraperitoneal injections twice a day (60 mg/kg doses), with 2 h between injections for 3 consecutive days. In this study, we used female and male mice; all of them were between 16 wk and 20 wk of age.

ACKNOWLEDGMENTS. We thank Dr. Long Yan of Max Plank Institute of Neuroscience, Jupiter, FL, for imaging help; and Alta Johnson and Bivian Torres of Flow Cytometry Core, Scripps Research, Jupiter, FL, for help in cell sorting and data analysis. We thank Melissa Benilous for administrative support, and Sumitha Rajendra Rao and Stephen Zorc for technical assistance. We thank Rodolfo Paredes for electron microscopic technical assistance. This part of the work was supported by Dirección General de Asuntos del Personal Académico, Universidad Nacional Autónoma de México (Project IN206719). This research was partially supported by a training grant in Alzheimer's Drug Discovery from the Lottie French Lewis Fund of the Community Foundation for Palm Beach and Martin Counties. This research was supported by funding from NIH/National Institute of Neurological Disorders and Stroke grant R01-NS087019-01A1, NIH/National Institute of Neurological Disorders and Stroke grant R01-NS094577-01A1, and grants from Cure Huntington Disease Initiative (CHDI) Foundation.

1. S. K. Barodia, R. B. Creed, M. S. Goldberg, Parkin and PINK1 functions in oxidative stress and neurodegeneration. *Brain Res. Bull.* **133**, 51–59 (2017).
2. X. Wang *et al.*, LRRK2 regulates mitochondrial dynamics and function through direct interaction with DLP1. *Hum. Mol. Genet.* **21**, 1931–1944 (2012).
3. C. Vives-Bauza *et al.*, PINK1-dependent recruitment of Parkin to mitochondria in mitophagy. *Proc. Natl. Acad. Sci. U.S.A.* **107**, 378–383 (2010).
4. L. Zhang *et al.*, Altered brain energetics induces mitochondrial fission arrest in Alzheimer's disease. *Sci. Rep.* **6**, 18725 (2016).
5. B. G. Jenkins, W. J. Koroshetz, M. F. Beal, B. R. Rosen, Evidence for impairment of energy metabolism in vivo in Huntington's disease using localized 1H NMR spectroscopy. *Neurology* **43**, 2689–2695 (1993).
6. A. V. Panov *et al.*, Early mitochondrial calcium defects in Huntington's disease are a direct effect of polyglutamines. *Nat. Neurosci.* **5**, 731–736 (2002).
7. S. E. Browne *et al.*, Oxidative damage and metabolic dysfunction in Huntington's disease: Selective vulnerability of the basal ganglia. *Ann. Neurol.* **41**, 646–653 (1997).
8. L. Zhang *et al.*, Differential effect of amyloid beta peptides on mitochondrial axonal trafficking depends on their state of aggregation and binding to the plasma membrane. *Neurobiol. Dis.* **114**, 1–16 (2018).
9. S. D. Yan *et al.*, An intracellular protein that binds amyloid-beta peptide and mediates neurotoxicity in Alzheimer's disease. *Nature* **389**, 689–695 (1997).
10. M. Mattiazzi *et al.*, Mutated human SOD1 causes dysfunction of oxidative phosphorylation in mitochondria of transgenic mice. *J. Biol. Chem.* **277**, 29626–29633 (2002).
11. J. M. Oliveira, Nature and cause of mitochondrial dysfunction in Huntington's disease: Focusing on huntingtin and the striatum. *J. Neurochem.* **114**, 1–12 (2010).
12. P. Shi, J. Gal, D. M. Kwinter, X. Liu, H. Zhu, Mitochondrial dysfunction in amyotrophic lateral sclerosis. *Biochim. Biophys. Acta* **1802**, 45–51 (2010).
13. D. Truban, X. Hou, T. R. Caulfield, F. C. Fiesel, W. Springer, PINK1, parkin, and mitochondrial quality control: What can we learn about Parkinson's disease pathobiology? *J. Parkinsons Dis.* **7**, 13–29 (2017).
14. E. Brouillet, C. Jacquard, N. Bizat, D. Blum, 3-Nitropropionic acid: A mitochondrial toxin to uncover physiopathological mechanisms underlying striatal degeneration in Huntington's disease. *J. Neurochem.* **95**, 1521–1540 (2005).
15. E. Brouillet *et al.*, Chronic mitochondrial energy impairment produces selective striatal degeneration and abnormal choreiform movements in primates. *Proc. Natl. Acad. Sci. U.S.A.* **92**, 7105–7109 (1995).
16. W. D. Parker Jr, S. J. Boyson, J. K. Parks, Abnormalities of the electron transport chain in idiopathic Parkinson's disease. *Ann. Neurol.* **26**, 719–723 (1989).
17. J. R. Cannon *et al.*, A highly reproducible rotenone model of Parkinson's disease. *Neurobiol. Dis.* **34**, 279–290 (2009).
18. J. W. Langston, P. Ballard, J. W. Tetrud, I. Irwin, Chronic Parkinsonism in humans due to a product of meperidine-analog synthesis. *Science* **219**, 979–980 (1983).
19. L. S. Huang *et al.*, 3-nitropropionic acid is a suicide inhibitor of mitochondrial respiration that, upon oxidation by complex II, forms a covalent adduct with a catalytic base arginine in the active site of the enzyme. *J. Biol. Chem.* **281**, 5965–5972 (2006).
20. R. R. Ramsay *et al.*, Interaction of 1-methyl-4-phenylpyridinium ion (MPP+) and its analogs with the rotenone/piericidin binding site of NADH dehydrogenase. *J. Neurochem.* **56**, 1184–1190 (1991).

Downloaded at Instituto de Biotecnología/UNAM on October 20, 2020

21. W. J. Nicklas, I. Vyas, R. E. Heikkila, Inhibition of NADH-linked oxidation in brain mitochondria by 1-methyl-4-phenyl-pyridine, a metabolite of the neurotoxin, 1-methyl-4-phenyl-1,2,5,6-tetrahydropyridine. *Life Sci.* **36**, 2503–2508 (1985).
22. R. Banerjee, A. A. Starkov, M. F. Beal, B. Thomas, Mitochondrial dysfunction in the limelight of Parkinson's disease pathogenesis. *Biochim. Biophys. Acta* **1792**, 651–663 (2009).
23. B. Thomas, K. P. Mohanakumar, Melatonin protects against oxidative stress caused by 1-methyl-4-phenyl-1,2,3,6-tetrahydropyridine in the mouse nigrostriatum. *J. Pineal Res.* **36**, 25–32 (2004).
24. P. Vargiu *et al*., The small GTP-binding protein, Rhes, regulates signal transduction from G protein-coupled receptors. *Oncogene* **23**, 559–568 (2004).
25. F. Errico *et al*., The GTP-binding protein Rhes modulates dopamine signalling in striatal medium spiny neurons. *Mol. Cell. Neurosci.* **37**, 335–345 (2008).
26. V. Ghiglieri *et al*., Rhes influences striatal cAMP/PKA-dependent signaling and synaptic plasticity in a gender-sensitive fashion. *Sci. Rep.* **5**, 10933 (2015).
27. L. M. Harrison, Y. He, Rhes and AGS1/Dexras1 affect signaling by dopamine D1 receptors through adenylyl cyclase. *J. Neurosci. Res.* **89**, 874–882 (2011).
28. S. Subramaniam *et al*., Rhes, a striatal-enriched small G protein, mediates mTOR signaling and L-DOPA-induced dyskinesia. *Nat. Neurosci.* **15**, 191–193 (2011).
29. S. Subramaniam *et al*., Rhes, a physiologic regulator of sumoylation, enhances cross-sumoylation between the basic sumoylation enzymes E1 and Ubc9. *J. Biol. Chem.* **285**, 20428–20432 (2010).
30. S. Subramaniam, K. M. Sixt, R. Barrow, S. H. Snyder, Rhes, a striatal specific protein, mediates mutant-huntingtin cytotoxicity. *Science* **324**, 1327–1330 (2009).
31. S. Subramaniam, S. H. Snyder, Huntington's disease is a disorder of the corpus striatum: Focus on Rhes (Ras homologue enriched in the striatum). *Neuropharmacology* **60**, 1187–1192 (2011).
32. S. Swarnkar *et al*., Ectopic expression of the striatal-enriched GTPase Rhes elicits cerebellar degeneration and an ataxia phenotype in Huntington's disease. *Neurobiol. Dis.* **82**, 66–77 (2015).
33. S. Okamoto *et al*., Balance between synaptic versus extrasynaptic NMDA receptor activity influences inclusions and neurotoxicity of mutant huntingtin. *Nat. Med.* **15**, 1407–1413 (2009).
34. T. Seredenina, O. Gokce, R. Luthi-Carter, Decreased striatal RGS2 expression is neuroprotective in Huntington's disease (HD) and exemplifies a compensatory aspect of HD-induced gene regulation. *PLoS One* **6**, e22231 (2011).
35. B. A. Baiamonte, F. A. Lee, S. T. Brewer, D. Spano, G. J. LaHoste, Attenuation of Rhes activity significantly delays the appearance of behavioral symptoms in a mouse model of Huntington's disease. *PLoS One* **8**, e53606 (2013).
36. J. I. Sbodio, B. D. Paul, C. E. Machamer, S. H. Snyder, Golgi protein ACBD3 mediates neurotoxicity associated with Huntington's disease. *Cell Rep.* **4**, 890–897 (2013).
37. B. Lu, J. Palacino, A novel human embryonic stem cell-derived Huntington's disease neuronal model exhibits mutant huntingtin (mHTT) aggregates and soluble mHTT-dependent neurodegeneration. *FASEB J.* **27**, 1820–1829 (2013).
38. M. Argenti, "The role of mitochondrial dysfunction in Huntington's disease pathogenesis and its relation with striatal rhes protein," PhD thesis, Università degli Studi di Padova, Padova, Italy (2014).
39. R. G. Mealer, S. Subramaniam, S. H. Snyder, Rhes deletion is neuroprotective in the 3-nitropropionic acid model of Huntington's disease. *J. Neurosci.* **33**, 4206–4210 (2013).
40. N. Shahani *et al*., RasGRP1 promotes amphetamine-induced motor behavior through a Rhes interaction network ("Rhesactome") in the striatum. *Sci. Signal.* **9**, ra111 (2016).
41. G. A. Wyant *et al*., NUFIP1 is a ribosome receptor for starvation-induced ribophagy. *Science* **360**, 751–758 (2018).
42. F. Trettel *et al*., Dominant phenotypes produced by the HD mutation in STHdh(Q111) striatal cells. *Hum. Mol. Genet.* **9**, 2799–2809 (2000).
43. M. Eshraghi *et al*., Global ribosome profiling reveals that mutant huntingtin stalls ribosomes and represses protein synthesis independent of fragile X mental retardation protein. bioRxiv:10.1101.629667 (7 May 2019).
44. E. Doherty, A. Perl, Measurement of mitochondrial mass by flow cytometry during oxidative stress. *React. Oxyg. Species (Apex)* **4**, 275–283 (2017).
45. M. Sharma, S. Subramaniam, Rhes travels from cell to cell and transports Huntington disease protein via TNT-like protrusion. *J. Cell Biol.* **218**, 1972–1993 (2019).
46. C. Ploumi, I. Daskalaki, N. Tavernarakis, Mitochondrial biogenesis and clearance: A balancing act. *FEBS J.* **284**, 183–195 (2017).
47. S. Subramaniam *et al*., ERK activation promotes neuronal degeneration predominantly through plasma membrane damage and independently of caspase-3. *J. Cell Biol.* **165**, 357–369 (2004).
48. S. M. Jin, R. J. Youle, PINK1- and Parkin-mediated mitophagy at a glance. *J. Cell Sci.* **125**, 795–799 (2012).
49. I. Novak *et al*., Nix is a selective autophagy receptor for mitochondrial clearance. *EMBO Rep.* **11**, 45–51 (2010).
50. W. Mughal *et al*., Myocardin regulates mitochondrial calcium homeostasis and prevents permeability transition. *Cell Death Differ.* **25**, 1732–1748 (2018).
51. R. A. Menzies, P. H. Gold, The turnover of mitochondria in a variety of tissues of young adult and aged rats. *J. Biol. Chem.* **246**, 2425–2429 (1971).
52. L. L. Brown *et al*., Differential metabolic activity in the striosome and matrix compartments of the rat striatum during natural behaviors. *J. Neurosci.* **22**, 305–314 (2002).
53. M. F. Beal *et al*., Neurochemical and histologic characterization of striatal excitotoxic lesions produced by the mitochondrial toxin 3-nitropropionic acid. *J. Neurosci.* **13**, 4181–4192 (1993).
54. G. Cirillo, M. Cirillo, F. Panetsos, A. Virtuoso, M. Papa, Selective vulnerability of basal ganglia: Insights into the mechanisms of bilateral striatal necrosis. *J. Neuropathol. Exp. Neurol.* **78**, 123–129 (2019).
55. R. L. Albin, J. T. Greenamyre, Alternative excitotoxic hypotheses. *Neurology* **42**, 733–738 (1992).
56. M. F. Beal, Energetics in the pathogenesis of neurodegenerative diseases. *Trends Neurosci.* **23**, 298–304 (2000).
57. C. H. Davis *et al*., Transcellular degradation of axonal mitochondria. *Proc. Natl. Acad. Sci. U.S.A.* **111**, 9633–9638 (2014).
58. W. M. Pryor *et al*., Huntingtin promotes mTORC1 signaling in the pathogenesis of Huntington's disease. *Sci. Signal.* **7**, ra103 (2014).

Downloaded at Instituto de Biotecnología/UNAM on October 20, 2020

MICROBIOLOGY

RESEARCH ARTICLE

Soto-Aceves *et al.*, *Microbiology* 2019;165:425–432

DOI 10.1099/mic.0.000778

Inactivation of the quorum-sensing transcriptional regulators LasR or RhlR does not suppress the expression of virulence factors and the virulence of *Pseudomonas aeruginosa* PAO1

Martín P. Soto-Aceves,[1] Miguel Cocotl-Yañez,[2] Enrique Merino,[3] Israel Castillo-Juárez,[4] Humberto Cortés-López,[4] Bertha González-Pedrajo,[5] Miguel Díaz-Guerrero,[5] Luis Servín-González[1] and Gloria Soberón-Chávez[1,*]

Abstract

Pseudomonas aeruginosa is an environmental bacterium but is also an opportunistic pathogen. The aim of this work is to evaluate the contribution of *P. aeruginosa* LasR and RhlR transcriptional regulators of the quorum-sensing response (QSR) to the production of virulence factors, and to its virulence in a mouse abscess model. The QSR is a complex regulatory network that modulates the expression of several virulence factors, including elastase, pyocyanin and rhamnolipids. LasR, when complexed with the auto-inducer 3-oxo-dodecanoyl lactone (3O-C12-HSL), produced by LasI, is at the top of the QSR regulatory cascade since it activates transcription of some genes encoding virulence factors (such as the gene coding for elastase, *lasB*) and also transcription of both *rhlR* and *rhlI,* encoding the synthase of the auto-inducer butanoyl-homoserine lactone (C4-HSL). In turn RhlR, coupled with C4-HSL, activates the transcription of genes encoding for the enzymes involved in pyocyanin and rhamnolipid production. Several efforts have been made to obtain inhibitors of LasR activity that would suppress the QSR. However, these attempts have used chemical compounds that might not be specific for LasR inactivation. In this work we show that individual inactivation of either *lasR* or *rhlR* did not block the QSR, nor did it impair *P. aeruginosa* virulence, and that even a *lasR rhlR* double mutant still presented residual virulence, even lacking the production of virulence factors. These results show that the inhibition of either *lasR* or *rhlR* is not a straightforward approach to blocking *P. aeruginosa* virulence, due to the great complexity of the QSR.

INTRODUCTION

Pseudomonas aeruginosa is an environmental bacterium, but is also an important opportunistic pathogen that represents a health problem due to its high incidence of infection among hospitalized patients, its high intrinsic antibiotic resistance and the susceptibility of cystic fibrosis patients to severe lung infections caused by this bacterium [1, 2]. The pathogenesis of *P. aeruginosa* is dependent on the fine-tuned, coordinated expression and secretion of multiple factors, most of which are regulated at the transcriptional level by the quorum-sensing response (QSR) [3, 4].

The QSR is mediated by the bacterial production of auto-inducers (AIs), which are mainly acyl-homoserine lactones acting as signal molecules by interaction with transcriptional regulators. The *P. aeruginosa* QSR is dependent on two transcriptional regulators of the LuxR family, LasR and RhlR, which are arranged in a hierarchical regulatory cascade: LasR forms a complex with 3-oxo-dodecanoyl-homoserine lactone (3O-C12-HSL) produced by the LasI enzyme, and activates the transcription of several genes encoding virulence factors, such as *lasB*, that codes for elastase, and also of *rhlR*, *lasI* and *rhlI*. In turn, *rhlR* encodes the second quorum-sensing transcriptional regulator, while the product of *rhlI* is the enzyme that produces butanoyl-homoserine lactone (C4-HSL), which is among the AIs that interact with RhlR [5, 6]. RhlR, coupled with AIs, promotes the expression of genes responsible for the production of several

Received 10 November 2018; Accepted 15 January 2019; Published 1 February 2019

Author affiliations: [1]Departamento de Biología Molecular y Biotecnología, Instituto de Investigaciones Biomédicas, Universidad Nacional Autónoma de México Apdo, Postal 70228, Ciudad Universitaria, 04510, CDMX, México; [2]Departamento de Microbiología y Parasitología, Facultad de Medicina, Universidad Nacional Autónoma de México, CDMX, México; [3]Departamento de Microbiología Molecular, Instituto de Biotecnología, Universidad Nacional Autónoma de México, Cuernavaca Mor, México; [4]Colegio de Postgraduados, Campus Montecillo, Texcoco, México; [5]Departamento de Genética Molecular, Instituto de Fisiología Celular, Universidad Nacional Autónoma de México, Ciudad Universitaria, 04510, CDMX, México.

***Correspondence:** Gloria Soberón-Chávez, gloria@biomedicas.unam.mx

Keywords: quorum-sensing response; *Pseudomonas aeruginosa*; virulence.

Abbreviations: 3O-C12-HSL, 3-oxo-dodecanoyl-homoserine lactone; AIs, auto-inducers; C4-HSL, butanoyl-homoserine lactone; HHQ, 4-hydroxy-2-heptylquinoline; PQS, 2-heptyl-3, 4-dihydroxyquinoline; PYO, pyocianin; QSR, quorum-sensing response; RL, rhamnolipids; SN, supernatant; T3SS, type III secretion system.

Supplementary file is available with the online version of this article.

000778 © 2019 The Authors

virulence factors, including rhamnolipids (RL) and pyocyanin (PYO). In addition, the *P. aeruginosa* QSR also involves the regulon that is dependent on the auto-inducer 2-heptyl-3,4-dihydroxyquinoline (PQS) and its precursor 4-hydroxy-2-heptylquinoline (HHQ), which interact with the transcriptional regulator PqsR that is a member of the LysR-family [3, 4]. LasR/3O-C12-HSL activates the transcription of *pqsR* [3, 4]. The virulence traits that are dependent on PqsR/PQS regulation are mainly produced by the enhancement of RhlR-dependent QSR, giving rise to a complex network of positive and negative interactions that exist between the LasR- and RhlR-dependent regulons [3, 4]. PqsE, which forms part of the PqsR/PQS regulon, produces a hitherto unidentified AI that interacts with RhlR and permits transcription activation of certain genes [6].

The current model of *P. aeruginosa* QSR was established almost exclusively by studying the type strains PAO1 (the strain used in this work) and PA14. However, it has been shown that there is a high phenotypic variability in the expression of the QSR among environmental and clinical *P. aeruginosa* isolates [7, 8], and that there is a high incidence of virulent isolates that have mutations in genes involved in the QSR, especially strains lacking a functional *las* system that are still able to produce virulence factors, which suggests a somewhat loosely based hierarchy [9–12].

The central role of the *P. aeruginosa* QSR in the establishment of pathogenic interactions by this bacterium has driven numerous research efforts to isolate compounds that might inhibit this complex genetic network. Most of the research has focused on blocking LasR transcriptional activity [13–16], because this protein has been hierarchically located in the highest part of the *P. aeruginosa* QSR [3, 4]. However, other targets, such as the transcriptional regulator RhlR [17], elastase activity [18], acyl-homoserine lactone synthesis [19] and the activity of the transcriptional regulator PqsR [20], have also been explored. Nevertheless, the specificity of the use of chemical compounds to block the activity of QSR proteins is questionable. That is why we decided to use mutants in the genes *lasR* and *rhlR*, or both genes and an antisense RNA, to specifically block *lasR* translation.

In the development of a strategy to block *P. aeruginosa* virulence through inhibition of the QSR, it is important to consider not only the variability of this genetic network among isolates, as mentioned previously, but also the undesired effects that might be encountered, such as promoting the selection of derivatives with increased virulence, as previously reported [12, 21]. In addition, it has been queried whether it is feasible to reduce *P. aeruginosa* virulence by interfering with the QSR, since there are many mechanisms that could cause resistance to this inhibition [22] or interfere with other regulons such as that encoding the type III secretion systems (T3SS), relevant for the virulence of this pathogen [23]. The importance of this secretion system can be seen with regard to the fact that the PA14 type strain has been shown to present increased virulence due to deregulated expression of T3SS caused by a mutation in the gene *ladS* [24].

The aim of this work is to evaluate the effect of specifically eliminating the expression of either *lasR, rhlR* or both genes (using deletion mutants) in the production of elastase, PYO, RL and virulence, using a murine cutaneous abscess model [25]. Our results show that elimination of eithet *lasR* or *rhlR* had a partial effect on the production of virulence-associated traits, while the double mutant completely lacked the expression of these factors but was still able to produce lesions in the murine model, albeit at a reduced level. We also evaluated an antisense RNA to interfere with the translation of *lasR*, but achieved only a low level of inhibition that did not affect the production of virulence factors.

We measured the secretion of effectors via T3SS in the Δ*lasR*–Δ*rhlR* double mutant compared to the PAO1 wild-type strain, and found that the ExoS and ExoT effectors in this double mutant are expressed and secreted at the same level as in the PAO1 wild-type strain. We thus conclude that the ability of this mutant to infect mice is due, at least in part, to the secretion of toxins by this secretion system. These results are compatible with the idea that virulence is multifactorial, and thus the contribution of single virulence factor, or even the QSR, to the establishment of an infection is variable [26].

METHODS

A more detailed description of the methods used in this work is included in the supplementary information section.

Microbiological methods

The strains and plasmids used in this work are shown in Table S1 (available in the online version of this article). In all experiments performed we used strain MPAO1, provided by the University of Washington (Table S1), referred to as PAO1. In order to rule out potential effects on virulence of an undetected mutation in *vfr*, we checked that the particular strain PAO1 that was used to select the described deletion mutants used in this work had no mutations in this gene (data not shown). The strains were routinely cultured in LB broth. To analyse phenotypic traits, cultures were inoculated at an optical density at 600 nm of 0.05 and were incubated for 16 (except for quinolones that were determined at 9 h), with continuous shaking (225 r.p.m.) at 37 °C.

Determination of the production of virulence factors and quinolones PQS and HHQ

PYO was extracted and its concentration was measured as reported previously [27]. Elastase activity was determined using the Elastin Congo Red protocol [28], with certain modifications. RL thin-layer chromatography was performed as reported previously [29]. Western blot for LasR detection was performed as reported previously [7]. Biofilm formation was measured in 96-well microtitre plates as previously described [30].

INFORME DE LABORES 2019

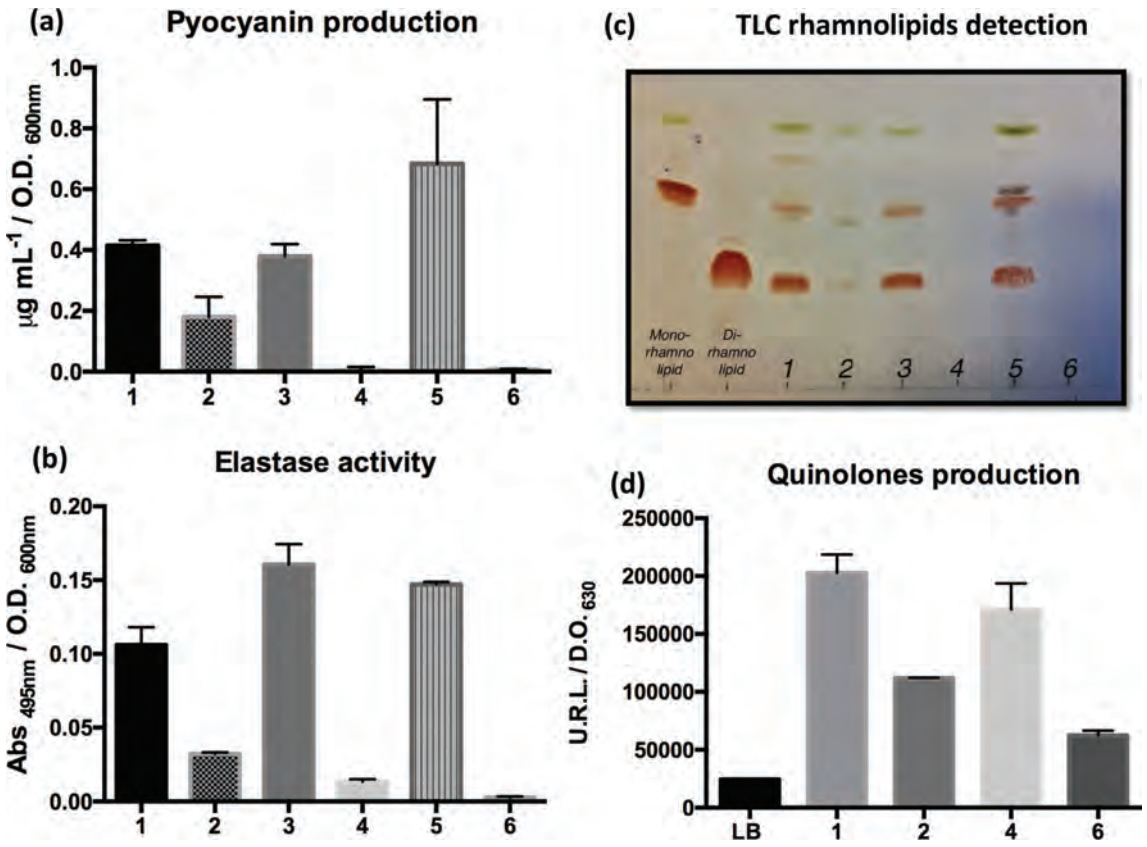

Fig. 1. Virulence factors and quinolone AIs production in *P. aeruginosa* PAO1 derivatives. Production of PYO (a), elastase (b), RL (detected on TLC plates) (c) and quinolones PQS and HHQ (d) in the PAO1 strain and its derived mutants in LB broth. Strains: 1) PAO1, 2) Δ*lasR*, 3) Δ*lasR*+pMT1(*lasR*), 4) Δ*rhlR*, 5) Δ*rhlR*+pGMYC(*rhlR*), 6) Δ*lasR*–Δ*rhlR*. The empty complementation vector (pUCP20) was also tested, showing no effect on any strain (data not shown). Results shown are the means of three biological replicates, and error bars denote standard deviation.

Bioluminescence to measure PQS and HHQ concentration was determined as previously reported [31].

DNA manipulation and construction of mutants

Oligonucleotides used in this work are listed in Table S2. DNA was purified and manipulated using standard techniques [32]. All plasmids were routinely maintained in *Escherichia coli* DH5α and were introduced by electroporation into *P. aeruginosa* as described previously [33]. The Δ*lasR* mutant was generated by construction and insertion of the pXLRt plasmid into the PAO1 strain following the protocol reported by Choi *et al.* [34]. The Δ*lasR*–Δ*rhlR* double mutant was also obtained with the same plasmid and technique but using the Δ*rhlR* mutant as recipient strain.

His-tagged ExoS protein purification and antibody production

The *exoS* gene was PCR amplified from PAO1 genomic DNA using primers exoS forward and exoS reverse, and cloned into the pET19b vector to generate plasmid pNEexoS. Animals used to produce antibodies were handled and cared for in accordance with the official Mexican guidelines, and with the approval of the local Animal Use and Care Committee (CICUAL) of the Instituto de Fisiología Celular, UNAM for protocol BGP70-15.

Type III protein secretion assay

The type III protein secretion assay was performed as reported previously [35]. Proteins were separated by 15 % SDS-PAGE, transferred onto a nitrocellulose membrane and probed for the presence of ExoS and ExoT by immunoblotting. ExoS antibodies recognize epitopes present on the ExoT protein.

Construction of the plasmid coding for the *lasR* antisense RNA, *lasR* translational fusion and *lasB* transcriptional fusion

Plasmid pLRL was constructed by cloning the annealed complementary primers 7582 and 7583 into the *Eco*RI and *Xho*I sites of pME6032 [36]. This sequence contains a region complementary to the *lasR* Shine Dalgarno (SD) sequence, since it has been reported that in most cases the strength of gene silencing coincides with RNAs having

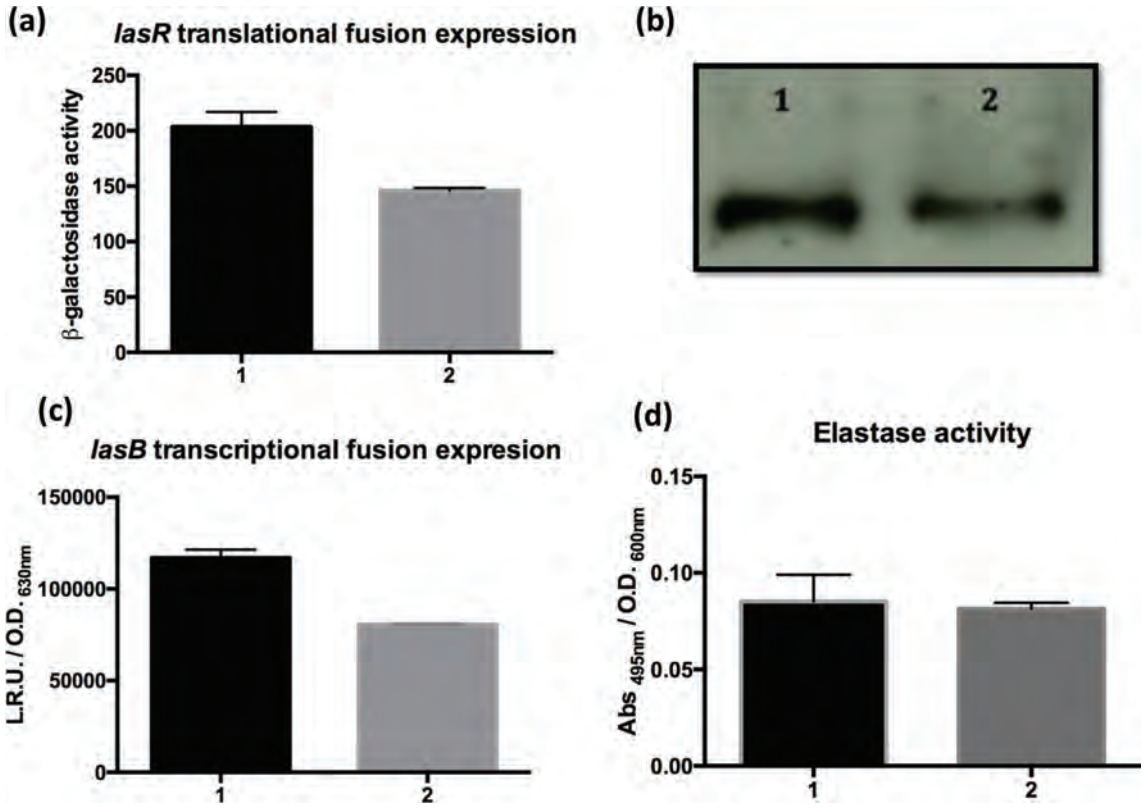

Fig. 2. Effect of the LRL antisense RNA on LasR expression and activity. (a) Effect of LRL on *lasR'-lacZ* translational fusion. (b) Western blot of LasR. (c) Effect of LRL on LasR transcriptional activity as measured by the expression of a *lasB-lux* transcriptional fusion. (d) Elastase activity in PAO1 with and without the expression of LRL. Strains: 1) PAO1 with pME6032 (empty vector), 2) PAO1 carrying pLRL (both strains also contain pSLR plasmid containing the *lasR'-lacZ* translational fusion). Results shown are the means of three biological replicates, and error bars denote the standard deviation.

sequences complementary to the SD sequence [37], and an intrinsic transcriptional terminator sequence.

Plasmids pSLR and pMLBX that encodes for a *lasR* translation and *lasB* transcriptional fusions, respectively, were constructed as described in the Supplementary Materials section.

Measurement of reporter fusion activity

Expression of LRL antisense RNA from pLRL was performed by the addition of 0.5 mM IPTG to cultures. β-galactosidase activity of the *lasR'-lacZ* fusion was measured using standard protocols [38]. Activity of the *lasB-lux* transcriptional fusion was measured using clear-bottomed 96-well black plates. Plates were incubated 18 h at 37 °C in Synergy HT (Biotek), and luminescence measurements were recorded automatically by the equipment every 0.5 h.

Determination of *P. aeruginosa* virulence by its ability to induce abscess in mice

Four- to eight-week-old CD-1 male mice were obtained from the General Vivarium of the Facultad de Estudios Superiores Iztacala, Universidad Nacional Autónoma de México. The indications given in NOM-062-ZOO-1999 for the handling and use of laboratory animals, as well as regulations for the use and care of animals destined for research, were followed at all times. All animals were housed under standard conditions and were provided with food and water *ad libitum*. The mouse abscess model was derived as previously described [25, 39].

RESULTS AND DISCUSSION

Production of virulence traits by *lasR* and *rhlR* single mutants and a Δ*lasR*–Δ*rhlR* double mutant

We measured the production, in LB broth, of elastase, PYO, RL and quinolone AIs PQS and HHQ in the wild-type PAO1 strain and its derived Δ*lasR and* Δ*rhlR* mutants and Δ*lasR*–Δ*rhlR* double mutant (Fig. 1). We found that the three virulence factors are strictly regulated by the QSR, since their production was completely impaired in the double Δ*lasR*–Δ*rhlR* mutant. In addition, the production of PQS and HHQ was also impaired. However, *lasR* deletion did not completely impair production of the virulence factors and quinolones, which would be expected if the QSR had a strict regulatory hierarchy with LasR at the top of the

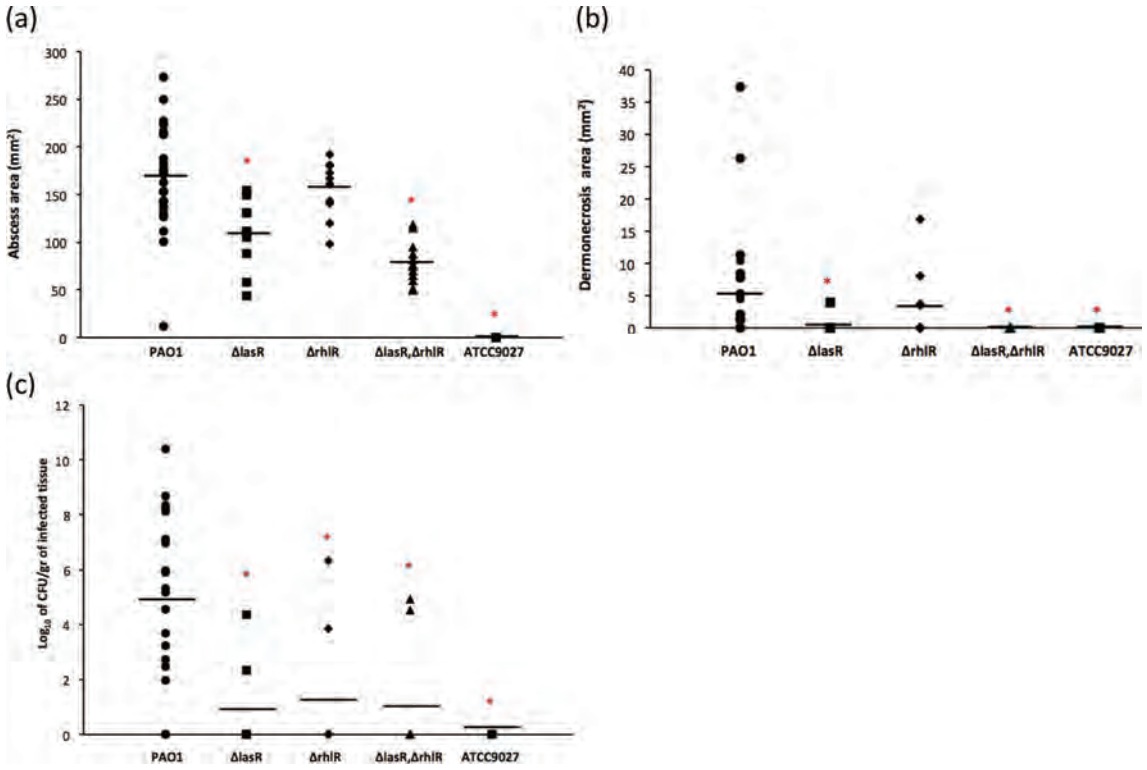

Fig. 3. Evaluation of virulence of *P. aeruginosa* strains by their formation of abscesses in mice. Points represent data for each abscess obtained after 4 days of inoculation with *P. aeruginosa* strains. Horizontal bars represent the mean of the results obtained (all animals in each experiment were inoculated with ~10^6 c.f.u. in a volume of 60 µl). Data were averaged for a minimum of two independent experiments with at least three animals per experiment. The number of animals inoculated with each strain was as follows: PAO1=22, Δ*lasR*=10, Δ*rhlR*=10, Δ*lasR*-Δ*rhlR*=10. For the avirulent ATCC 9027 used as negative control we performed one experiment with four animals. Red asterisks denote a significant difference from the wild-type (P<0.05). The results were analysed by the two-tailed Mann–Whitney test. (a) area of abscess; (b) extent dermonecrosis resulting from infection; (c) logarithm of bacterial c.f.u. g^{-1} recovered from damaged tissue. A file containing the complete dataset for all mice studied is provided, with the average and standard deviation for all experiments performed with each strain.

cascade as has been proposed [3, 4]. Moreover, the production of the three virulence factors was affected more in the Δ*rhlR* mutant that in the Δ*lasR* mutant; production of both PYO and RL was completely abrogated in the Δ*rhlR* mutant, revealing that RhlR coupled with its cognate AIs directly activates the transcription of the genes involved in RL and PYO production.

Even though the Δ*lasR* mutant had a more pronounced effect on quinolone production than the Δ*rhlR* mutant (which is in accordance with the participation of LasR/3O-C12-HSL in the expression of *pqsR*), it is clear that only the double Δ*lasR*–Δ*rhlR* mutant completely reduced the production of these AIs.

Taken together, these results show that there is considerable expression of the regulons Rhl and PQS that is independent of LasR/3O-C12-HSL, and that inhibition of the transcriptional activity of LasR is not sufficient to block the expression of *P. aeruginosa* QSR.

Selection of an antisense *lasR* RNA and its effect on LasR expression, *lasB* transcription and elastase production

In order to mimic the effect of a compound that would selectively inactivate LasR, we designed an antisense RNA that is complementary to the *lasR* messenger RNA comprising the SD sequence LRL. The expression of LRL in strain PAO1 caused reduced expression of a translational fusion of *lacZ* to the *lasR* gene, as evidenced by the lower levels of β-galactosidase (Fig. 2a), and also reduced the concentration of LasR (Fig. 2b). Furthermore, transcription of the *lasB* gene, which encodes for the elastase enzyme and is transcriptionally activated by LasR, was also decreased (Fig. 2c). However this reduction was not sufficient to diminish elastase activity (Fig. 2d). The limited effect of LRL on LasR expression, and the null effect of this reduction on the expression of LasR-dependent expression of elastase, show that LRL cannot be used to evaluate the effect of selective blocking of the LasR

INFORME DE LABORES 2019

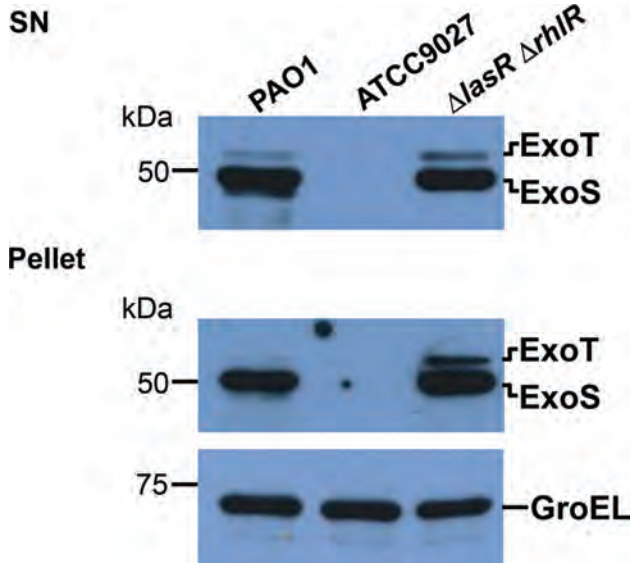

Fig. 4. Secretion of ExoT and ExoS by T3SS in PAO1 and its derived Δ*lasR*-Δ*rhlR* double mutant. The effectors ExoT and ExoS were detected by Western blot assay in whole cells (Pellet) and culture supernatant (SN) of the wild-type PAO1 strain and its derived Δ*lasR*–Δ*rhlR* double mutant. *P. aeruginosa* ATCC 9027, lacking T3SS, was used as negative control. Results are shown for one representative experiment repeated five times.

transcriptional regulator on the expression of virulence factors and the pathogenicity of *P. aeruginosa*.

The low efficiency of antisense RNAs on gene silencing in *P. aeruginosa* has been reported [40]. Even though in the present study the designed LRL RNA targeted the SD sequence as described for *E. coli* [37], this approach was insufficient to obtain good results. As native antisense RNAs rarely have a perfect base-pair match with the mRNA [41], these results reinforce the complexity of RNAs-mediated gene silencing in bacteria.

Effect of *lasR* and/or *rhlR* inactivation on *P. aeruginosa* virulence using a murine model of abscess formation

We evaluated the effect of the inactivation of LasR and RhlR transcriptional regulators using a murine model of abscess formation (Figs 3 and S1). Our results show that the QSR has a central role in *P. aeruginosa* pathogenicity, as previously reported using mutants in the *rhlI* and *lasI* single and double mutants in a burnt mouse model [42].

In the abscess model used in this work, the single Δ*lasR* mutant – and especially the Δ*lasR*–Δ*rhlR* double mutant – were attenuated but retained a high level of pathogenicity as judged by the size of the abscesses produced, the area of dermonecrosis and the number of bacteria recovered from damaged tissue (Fig. 3). These results differ from previously reported data using a burnt mouse model, which showed that the Δ*lasI*–Δ*rhlI* double mutant presented a more severely reduced virulence, even being avirulent [42]. This variation in results is probably due to the different pathogenicity models used, since the abscess model was designed to cause a local infection resembling a chronic, non-fatal situation [25] while the burnt model mimic an acute infection.

It was reported that, in the abscess model, the level of expression of genes involved in the production of phenazines such as PYO is reduced [25]. This finding might reflect the fact that the RhlR-dependent regulon is not induced, and this effect could explain why in our experiments the Δ*rhlR* mutant showed a significant reduction in neither abscess size nor the area of dermonecrosis compared to the wild-type strain (Fig. 3). However, it is clear that the RhlR-dependent regulon played an important part in the infection process in the abscess model considering that the Δ*lasR*–Δ*rhlR* double mutant showed reduced virulence compared to the Δ*lasR* mutant, and that the number of colony-forming units recovered from the abscesses caused by the Δ*rhlR* mutant was significantly less than that obtained from infections caused by the PAO1 wild-type strain (Fig. 3).

Because the ability to form biofilms has been implicated in *P. aeruginosa* infections [43], we wished to determine whether the deletion mutants in the QSR regulators would show a defect in biofilm-forming ability that correlated with their virulence. We found that the Δ*lasR* mutant and the Δ*lasR*–Δ*rhlR* double mutant showed decreased ability to form biofilm, while the Δ*rhlR* mutant produced more biofilm than the PAO1 strain (Fig. S2). It is highly likely that the increment in biofilm formation shown by the Δ*rhlR* mutant is due to increased production of exopolysaccharides involved in biofilm matrix formation in the absence of RL synthesis [44].

Secretion of type III effectors in PAO1 and its derived Δ*lasR*–Δ*rhlR* double mutant

In order to determine whether the remaining virulence of the PAO1 Δ*lasR*–Δ*rhlR* double mutant was due to secretion of the effectors ExoS and ExoT by T3SS, we compared the production and secretion of these toxins between strain PAO1 and its derived Δ*lasR*–Δ*rhlR* double mutant. It was apparent that the secretion of ExoT and ExoS is fully functional in the Δ*lasR*–Δ*rhlR* double mutant, and that this occurs at a level similar to that in the wild-type PAO1 strain (Fig. 4). These results suggest that the secretion of effectors by T3SS may cause the remaining virulence in the Δ*lasR*–Δ*rhlR* double mutant that is completely impaired in the QSR, since the effectors secreted by this system have been implicated in virulence levels using the same abscess model used in the present study [39].

Concluding remarks

Here we show that current opinion on the QSR hierarchy, with LasR at the top of the regulatory cascade as reported in the PAO1 type strain, should be revised since expression of RhlR-dependent virulence factors was not completely abrogated in a PAO1 Δ*lasR* mutant (Fig. 1). Moreover, we show

INFORME DE LABORES 2019

that *P. aeruginosa* PAO1 is able to induce abscess formation when lacking either one or both of the LasR and RhlR transcriptional regulators, albeit at a reduced level (Fig. 3). The remaining virulence of the Δ*lasR*-Δ*rhlR* double mutant may be due to the secretion of the effectors ExoT and ExoS by T3SS (Fig. 4).

Understanding of the molecular mechanism of *P. aeruginosa* pathogenicity is of considerable scientific and clinical importance. It is especially important to evaluate the role played by the QSR in this process, since significant efforts have been made to isolate compounds that inhibit this intricate regulatory network to reduce *P. aeruginosa* virulence. In this respect, it was recently reported that expression of genes involved in the QSR is at at a low level in human infections, thus questioning the importance of this regulon in *P. aeruginosa* pathogenicity and of the therapeutic impact of its inhibition [45].

The results presented here show that the development of a therapeutic approach towards the treatment of *P. aeruginosa* infections, based on the use of compounds that interfere with the production of virulence factors dependent on the QSR, and in particular those that are focused on LasR inactivation, should be taken with caution because (1) the hierarchy of this regulon is not very strict and (2) *P. aeruginosa* pathogenicity is multifactorial and several virulence factors participate, not all dependent on the QSR [26]. In addition the phenotypic variation in different *P. aeruginosa* isolates with respect to the production of virulence factors regulated by the QSR is considerable [7–10], and therefore the strategy developed by blocking this regulatory network using a type strain, such as PAO1 strain used in this work, might not be efficient with strains encountered in a clinical setting.

Funding information
This work was supported in part by grant No.IN201819 from Programa de Apoyo a Proyectos de Investigación e Innovación Tecnológica (Dirección General de Asuntos del Personal Académico–UNAM) and grant No.252269 from Consejo Nacional de Ciencia y Tecnología (CONACYT).

Acknowledgements
MPSA is a doctoral student of Programa de Maestría y Doctorado en Ciencias Bioquímicas, Universidad Nacional Autónoma de México (UNAM). MPSA (CVU-741217) received a fellowship from CONACYT. We acknowledge Abigail González-Valdez and Norma Espinosa Sánchez for technical assistance. We thank Stephan Heeb and Miguel Cámara (both Nottingham University) for providing plasmids mini-CTX-lux and pME6032; and Esteban Martínez (Centro Nacional de Biotecnología-España) and Cinthia Núñez (Instituto de Biotecnología-UNAM) for plasmids pUJ9 and pSEVA421.

Authors and contributors
Tuthors' contribution according to the CRediT taxonomy from CASRAI is as follows: MPSA, MCY, EM, LSG, BGP, ICJ and GSC participated in conceptualization, validation and supervision. MPSA, MCY, EM, LSG, BGP, ICJ, MDG and HCL participated in methodology, writing (review and editing) and visualization and investigation. ICJ was responsible for formal analysis. GSC was responsible for writing (original draft preparation), project administration and funding.

Conflicts of interest
The authors declare that there are no conflicts of interest.

References

1. Driscoll JA, Brody SL, Kollef MH. The epidemiology, pathogenesis and treatment of *Pseudomonas aeruginosa* infections. *Drugs* 2007; 67:351–368.
2. Gellatly SL, Hancock RE. *Pseudomonas aeruginosa*: new insights into pathogenesis and host defenses. *Pathog Dis* 2013;67:159–173.
3. Williams P, Cámara M. Quorum sensing and environmental adaptation in *Pseudomonas aeruginosa*: a tale of regulatory networks and multifunctional signal molecules. *Curr Opin Microbiol* 2009;12: 182–191.
4. Lee J, Zhang L. The hierarchy quorum sensing network in *Pseudomonas aeruginosa*. *Protein Cell* 2015;6:26–41.
5. Mukherjee S, Moustafa D, Smith CD, Goldberg JB, Bassler BL *et al.* The RhlR quorum-sensing receptor controls *Pseudomonas aeruginosa* pathogenesis and biofilm development independently of its canonical homoserine lactone autoinducer. *PLoS Pathog* 2017;13:e1006504.
6. Mukherjee S, Moustafa DA, Stergioula V, Smith CD, Goldberg JB *et al.* The PqsE and RhlR proteins are an autoinducer synthase-receptor pair that control virulence and biofilm development in *Pseudomonas aeruginosa*. *Proc Natl Acad Sci USA* 2018;115: E9411–E9418.
7. Grosso-Becerra MV, Santos-Medellín C, González-Valdez A, Méndez JL, Delgado G *et al.* *Pseudomonas aeruginosa* clinical and environmental isolates constitute a single population with high phenotypic diversity. *BMC Genomics* 2014;15:318.
8. García-Contreras R, Peréz-Eretza B, Jasso-Chávez R, Lira-Silva E, Roldán-Sánchez JA *et al.* High variability in quorum quenching and growth inhibition by furanone C-30 in *Pseudomonas aeruginosa* clinical isolates from cystic fibrosis patients. *Pathog Dis* 2015;73:ftv040.
9. Feltner JB, Wolter DJ, Pope CE, Groleau MC, Smalley NE *et al.* LasR variant cystic fibrosis isolates reveal an adaptable quorum-sensing hierarchy in *Pseudomonas aeruginosa*. *MBio* 2016;7: e01513–01516.
10. Morales E, González-Valdez A, Servín-González L, Soberón-Chávez G. *Pseudomonas aeruginosa* quorum-sensing response in the absence of functional LasR and LasI proteins: the case of strain 148, a virulent dolphin isolate. *FEMS Microbiol Lett* 2017; 364.
11. Schaber JA, Carty NL, McDonald NA, Graham ED, Cheluvappa R *et al.* Analysis of quorum sensing-deficient clinical isolates of *Pseudomonas aeruginosa*. *J Med Microbiol* 2004;53:841–853.
12. Köhler T, Ouertatani-Sakouhi H, Cosson P, van Delden C. QsrO a novel regulator of quorum-sensing and virulence in *Pseudomonas aeruginosa*. *PLoS One* 2014;9:e87814.
13. Amara N, Mashiach R, Amar D, Krief P, Spieser SA *et al.* Covalent inhibition of bacterial quorum sensing. *J Am Chem Soc* 2009;131: 10610–10619.
14. Jakobsen TH, Bjarnsholt T, Jensen PØ, Givskov M, Høiby N. Targeting quorum sensing in *Pseudomonas aeruginosa* biofilms: current and emerging inhibitors. *Future Microbiol* 2013;8:901–921.
15. O'Brien KT, Noto JG, Nichols-O'Neill L, Perez LJ. Potent Irreversible Inhibitors of LasR Quorum Sensing in *Pseudomonas aeruginosa*. *ACS Med Chem Lett* 2015;6:162–167.
16. O'Loughlin CT, Miller LC, Siryaporn A, Drescher K, Semmelhack MF *et al.* A quorum-sensing inhibitor blocks *Pseudomonas aeruginosa* virulence and biofilm formation. *Proc Natl Acad Sci USA* 2013;110:17981–17986.
17. Eibergen NR, Moore JD, Mattmann ME, Blackwell HE. Potent and Selective Modulation of the RhlR Quorum Sensing Receptor by Using Non-native Ligands: An Emerging Target for Virulence Control in *Pseudomonas aeruginosa*. *Chembiochem* 2015;16:2348–2356.
18. Gi M, Jeong J, Lee K, Lee KM, Toyofuku M *et al.* A drug-repositioning screening identifies pentetic acid as a potential therapeutic agent for suppressing the elastase-mediated virulence of

INFORME DE LABORES 2019

Pseudomonas aeruginosa. *Antimicrob Agents Chemother* 2014;58:7205–7214.

19. **Chang CY, Krishnan T, Wang H, Chen Y, Yin WF *et al.*** Non-antibiotic quorum sensing inhibitors acting against N-acyl homoserine lactone synthase as druggable target. *Sci Rep* 2014;4:7245.
20. **Allegretta G, Weidel E, Empting M, Hartmann RW.** Catechol-based substrates of chalcone synthase as a scaffold for novel inhibitors of PqsD. *Eur J Med Chem* 2015;90:351–359.
21. **Köhler T, Perron GG, Buckling A, van Delden C.** Quorum Sensing inhibition selects for virulence and cooperation in *Pseudomonas aeruginosa* . *PLoS Pathog* 2010;6:e1000883.
22. **García-Contreras R.** Is Quorum Sensing Interference a Viable Alternative to Treat *Pseudomonas aeruginosa* Infections? *Front Microbiol* 2016;7:1454.
23. **Dacheux D, Attree I, Schneider C, Toussaint B.** Cell death of human polymorphonuclear neutrophils induced by *a Pseudomonas aeruginosa* cystic fibrosis isolate requires a functional type III secretion system. *Infect Immun* 1999;67:6164–6167.
24. **Mikkelsen H, McMullan R, Filloux A.** The *Pseudomonas aeruginosa* reference strain PA14 displays increased virulence due to a mutation in *ladS*. *PLoS One* 2011;6:e29113.
25. **Pletzer D, Mansour SC, Wuerth K, Rahanjam N, Hancock RE.** New mouse model for chronic infections by Gram-negative bacteria enabling the study of anti-infective efficacy and host-microbe interactions. *MBio* 2017;8:e00140–17.
26. **Granato ET, Harrison F, Kümmerli R, Ross-Gillespie A.** Do bacterial "virulence factors" always increase virulence? A meta-analysis of pyoverdine production in *Pseudomonas aeruginosa* as a test case. *Front Microbiol* 2016;7:7.
27. **Essar DW, Eberly L, Hadero A, Crawford IP.** Identification and characterization of genes for a second anthranilate synthase in *Pseudomonas aeruginosa*: interchangeability of the two anthranilate synthases and evolutionary implications. *J Bacteriol* 1990;172:884–900.
28. **Beatson SA, Whitchurch CB, Sargent JL, Levesque RC, Mattick JS.** Differential regulation of twitching motility and elastase production by Vfr in *Pseudomonas aeruginosa*. *J Bacteriol* 2002;184:3605–3613.
29. **Matsuyama T, Sogawa M, Yano I.** Direct colony thin-layer chromatography and rapid characterization of *Serratia marcescens* mutants defective in production of wetting agents. *Appl Environ Microbiol* 1987;53:1186–1188.
30. **Coffey BM, Anderson GG.** Biofilm formation in the 96-well microtitre plate. In: Filloux A and Ramos J-L (editors). *Pseudomonas Methods and Protocols. Methods in Molecular Biology 1149*. New York, NY: Springer Protocols, Humana Press,; 2014. pp. 631–641.
31. **Diggle SP, Fletcher MP, Cámara M, Williams P.** Detection of 2-alkyl-4-quinolone using biosensors. In: Rumbaugh Kendra P (editor). *Quorum Sensing: Methods and Protocols*, vol. 692: Methods in Molecular Biology; 2011.
32. **Sambrook J, Fritsch EF, Maniatis T.** *Molecular Cloning: A Laboratory Manual*, 2nd ed. Cold Spring Harbor, NY: (Cold Spring Harbor Lab Press); 1989.
33. **Cadoret F, Soscia C, Voulhoux R.** Gene transfer: transformation/electroporation. In: Filloux A and Ramos J-L (editors). *Pseudomonas Methods and Protocols. Methods in Molecular Biology 1149*. New York, NY: Springer Protocols, Humana Press; 2014. pp. 271–279.
34. **Choi KH, Schweizer HP.** An improved method for rapid generation of unmarked *Pseudomonas aeruginosa* deletion mutants. *BMC Microbiol* 2005;5:30.
35. **Toska J, Sun Y, Carbonell DA, Foster AN, Jacobs MR *et al.*** Diversity of virulence phenotypes among type III secretion negative *Pseudomonas aeruginosa* clinical isolates. *PLoS One* 2014;9:e86829.
36. **Heeb S, Blumer C, Haas D.** Regulatory RNA as mediator in GacA/RsmA-dependent global control of exoproduct formation in *Pseudomonas fluorescens* CHA0. *J Bacteriol* 2002;184:1046–1056.
37. **Sharma V, Yamamura A, Yokobayashi Y.** Engineering artificial small RNAs for conditional gene silencing in *Escherichia coli*. *ACS Synth Biol* 2012;1:6–13.
38. **Miller JH.** *Experiments in Molecular Genetics*, Vol. 433. Cold Spring Harb NY: Cold Spring Harb Lab Press; 1972. pp. 352–355.
39. **Berube BJ, Murphy KR, Torhan MC, Bowlin NO, Williams JD *et al.*** Impact of type III secretion effectors and of phenoxyacetamide inhibitors of type III secretion on abscess formation in a mouse model of *Pseudomonas aeruginosa* infection. *Antimicrob Agents Chemother* 2017;61:e01202–01217.
40. **Gong FY, Zhang DY, Zhang JG, Wang LL, Zhan WL *et al.*** siRNA-mediated gene silencing of MexB from the MexA-MexB-OprM efflux pump in *Pseudomonas aeruginosa*. *BMB Rep* 2014;47:203–208.
41. **Gottesman S.** Micros for microbes: non-coding regulatory RNAs in bacteria. *Trends Genet* 2005;21:399–404.
42. **Rumbaugh KP, Griswold JA, Iglewski BH, Hamood AN.** Contribution of quorum sensing to the virulence of *Pseudomonas aeruginosa* in burn wound infections. *Infect Immun* 1999;67:5854–5862.
43. **Castillo-Juarez I, López-Jácome LE, Soberón-Chávez G, Tomás M, Lee J *et al.*** Exploiting Quorum Sensing inhibition for the control of *Pseudomonas* aeruginosa and *Acinetobacter baumanni* biofilms. *Curr Top Med Chem* 2017;17:1915–1927.
44. **Wang S, Yu S, Zhang Z, Wei Q, Yan L *et al.*** Coordination of swarming motility, biosurfactant synthesis, and biofilm matrix exopolysaccharide production in *Pseudomonas aeruginosa*. *Appl Environ Microbiol* 2014;80:6724–6732.
45. **Cornforth DM, Dees JL, Ibberson CB, Huse HK, Mathiesen IH *et al.*** *Pseudomonas aeruginosa* transcriptome during human infection. *Proc Natl Acad Sci USA* 2018;115:E5125–E5134.

Edited by: S. P. Diggle and M. Whiteley

Five reasons to publish your next article with a Microbiology Society journal

1. The Microbiology Society is a not-for-profit organization.
2. We offer fast and rigorous peer review – average time to first decision is 4–6 weeks.
3. Our journals have a global readership with subscriptions held in research institutions around the world.
4. 80% of our authors rate our submission process as 'excellent' or 'very good'.
5. Your article will be published on an interactive journal platform with advanced metrics.

Find out more and submit your article at microbiologyresearch.org.

Descubrimiento de la proteína reguladora de apoptosis 2 como determinante en la muerte de células tumorales

*Juana Virginia Tapia-Vieyra y Jaime Mas-Oliva**
Universidad Nacional Autónoma de México, Instituto de Fisiología Celular, Ciudad de México, México

Resumen

El cáncer es una enfermedad multifactorial que constituye un problema de salud pública mundial. Las etapas avanzadas del cáncer de próstata están asociadas con el desarrollo de tumores independientes de andrógeno y un fenotipo resistente a la apoptosis que progresa a metástasis. Al estudiar células de cáncer de próstata de nódulo linfoide (LNCaP) independientes de andrógeno inducidas a la apoptosis por eliminación de suero, identificamos la activación de un canal catiónico no selectivo de 23pS de conductancia que promueve corrientes entrantes de Ca^{2+} así como las etapas finales de la apoptosis. El cDNAarp2 fue aislado e identificado del mismo tipo celular y el ARN mensajero fue expresado en ovocitos de Xenopus laevis, asociándolo con la activación de las corrientes entrantes de Ca^{2+} y la inducción a la apoptosis. El ADN complementario que codifica para la proteína reguladora de apoptosis 2 (ARP2) fue sobreexpresado en células LNCaP y células de ovario de hámster chino, induciendo apoptosis. Nuestra evidencia sugiere que la sobreexpresión y tránsito de la proteína ARP2 a la membrana celular permite una corriente de entrada de Ca^{2+} aumentada, iniciadora del proceso de apoptosis en células de tipo epitelial cuyo fenotipo muestra resistencia a la muerte celular programada.

PALABRAS CLAVE: *Apoptosis. Proteína ARP2. Carcinoma epitelial. Cáncer de próstata.*

Abstract

Cancer is a multifactorial disease that constitutes a serious public health problem worldwide. Prostate cancer advanced stages are associated with the development of androgen-independent tumors and an apoptosis-resistant phenotype that progresses to metastasis. By studying androgen-independent lymphoid nodule carcinoma of the prostate (LNCaP) cells induced to apoptosis by serum elimination, we identified the activation of a non-selective cationic channel of 23pS conductance that promotes incoming Ca^{2+} currents, as well as apoptosis final stages. arp2cDNA was isolated and identified to be of the same cell type, and mRNA was expressed in Xenopus laevis oocytes, which was found to be associated with the activation of incoming Ca^{2+} currents and induction to apoptosis. cDNA, which encodes the ARP2 protein, was overexpressed in LNCaP cells and Chinese hamster ovary cells, which induced apoptosis. Our evidence suggests that protein ARP2 overexpression and transit to the cell membrane allows an increased Ca^{2+} incoming current that initiates the apoptosis process in epithelial-type cells whose phenotype shows resistance to programmed cell death.

KEY WORDS: *Apoptosis. ARP2 protein. Epithelial carcinoma. Prostate cancer.*

Correspondencia:
*Jaime Mas-Oliva
E-mail: jmas@ifc.unam.mx

Fecha de recepción: 25-03-2019
Fecha de aceptación: 27-03-2019
DOI: 10.24875/GMM.19005186

Gac Med Mex. 2019;155:546-553
Disponible en PubMed
www.gacetamedicademexico.com

Introducción

El cáncer es una enfermedad multifactorial y la segunda causa de muerte de la población general en el mundo. Su causalidad está relacionada con los hábitos de vida, predisposición genética y estados psicológico y anímico de los individuos.[1] La prevalencia del cáncer ha aumentado en los últimos años, por lo que es un problema de salud que demanda un nivel muy alto de atención.[2,3] En el hombre, los porcentajes más altos de incidencia de cáncer ocurren en próstata, pulmón, bronquios, colon, recto y vejiga urinaria; en las mujeres, en mama, pulmón, bronquios, colon, recto, útero y tiroides. Lo anterior es un indicador de que los tipos de cáncer más comunes en hombres y mujeres, respectivamente, son de próstata y mama.[4] En los niños, la incidencia más alta en cáncer se observa en médula ósea, cerebro y nódulos linfoides.[5,6]

El cáncer epitelial es uno de los tipos más agresivos. Particularmente en el cáncer de próstata, el tratamiento dependerá de la etapa en que se identifique la enfermedad, sin embargo, es muy común que esta progrese y desarrolle un fenotipo de resistencia a la apoptosis y, por lo tanto, de independencia de la hormona, por lo que las células continúan la proliferación hasta alcanzar la metástasis, de ahí que resulte indispensable el desarrollo de nuevas estrategias terapéuticas que impidan que la enfermedad alcance etapas avanzadas.

Durante el proceso de apoptosis de numerosos tipos de células, el incremento sostenido de Ca^{2+} citoplásmico ha sido definido como determinante en el inicio de la muerte celular programada.[7] Considerando este fundamento, desde hace años hemos trabajado en el estudio de los mecanismos de control de la homeostasis del calcio citoplásmico y el impacto del nivel alterado de Ca^{2+} en diversos tipos celulares y neoplásicos.

Hemos podido demostrar que un nivel aumentado de calcio citoplásmico da como resultado el inicio de la muerte celular programada en líneas celulares epiteliales de cáncer de próstata y de ovario de hámster chino. En este sentido, nuestro grupo de investigación descubrió un canal catiónico no selectivo permeable a Ca^{2+} de 23pS de conductancia, expresado en condiciones de apoptosis inducida mediante eliminación del suero del medio de cultivo en células de cáncer de próstata de nódulo linfoide (LNCaP, *lymph node carcinoma of the prostate*) independientes de andrógeno.[8] Asimismo, se logró aislar el ADN complementario (ADNc) de células LNCaP que codifica para la proteína reguladora de apoptosis 2 (la cual denominamos ARP2), la cual al ser sobreexpresada induce a la apoptosis en ovocitos de *Xenopus laevis* y células LNCaP independientes de andrógeno, de donde originalmente fue aislada ARP2.[9] Se demostró que la sobreexpresión de ARP2 induce la apoptosis de células de ovario de hámster chino. Estos hallazgos demuestran que los niveles aumentados de Ca^{2+} son una condición indispensable para dar inicio a la apoptosis en diversas líneas celulares de tipo epitelial, por lo que esa proteína pudiera constituir en un futuro una excelente herramienta en el tratamiento de la enfermedad, al evitar la progresión hacia las etapas avanzadas que culminan con un proceso metastásico.

Cáncer de próstata

El cáncer de próstata es la segunda causa de muerte por cáncer en Estados Unidos y la quinta en el mundo.[10-12] La prevalencia de esta enfermedad se incrementa conforme la edad avanza. El cáncer de próstata es encontrado durante la autopsia en más de la mitad de hombres de Estados Unidos mayores de 50 años, aunque esta enfermedad haya sido la causa de muerte solo en 3 %. Es una enfermedad asintomática hasta la aparición de lesiones metastásicas que generalmente son descubiertas en tejido óseo. Las terapias iniciales para dar tratamiento incluyen cirugía, radiación, uso de inhibidores de la 5-alfa reductasa que promueve la formación de andrógenos más potentes a partir de testosterona.[13] Los métodos iniciales de tratamiento a menudo causan disfunción sexual, urinaria e intestinal.[14]

Desde el punto de vista molecular, esta enfermedad se manifiesta en etapas tempranas y tardías. En las primeras, la proliferación de las células prostáticas es lenta y dependiente de los andrógenos, por lo que durante el tratamiento con agentes quimioterapéuticos las células alcanzan a reparar el daño y continúan proliferándose. Con el tiempo, las células se independizan de las hormonas androgénicas para proliferar, por lo que culminan en el desarrollo de metástasis que lleva al paciente a la muerte.[15]

Apoptosis y enfermedad

La muerte celular programada o apoptosis es un evento celular intrínseco de relevante importancia en procesos como la homeostasis celular, el desarrollo

embrionario y el inicio y mantenimiento de varias enfermedades como el cáncer y la aterosclerosis.[16,17] Este mecanismo se desarrolla mediante dos vías; la del receptor de muerte celular y la vía mitocondrial.[18] A su vez, el proceso apoptótico se desarrolla en varias etapas: la primera se relaciona con los estímulos que disparan la muerte celular programada, la segunda involucra los procesos de transducción de las señales, en la tercera participan enzimas efectoras que se ocupan del desensamble celular, como las caspasas activas y, finalmente, en la cuarta ocurre la condensación de la cromatina, la degradación del ADN y la formación de los cuerpos apoptóticos.[18,19]

Existen diversas vías apoptóticas como la extrínseca o de receptor de muerte, cuya caspasa iniciadora es la caspasa 8, y la intrínseca o mitocondrial, que tiene como proteína intermediaria al citocromo C y a la caspasa 9 como iniciadora. Ambas pueden converger en el conjunto de caspasas efectoras, principalmente las caspasas 3 y 7, que se activan a través del autoprocesamiento o activación en cascada, por lo que las mismas caspasas se autoactivan y activan entre ellas.[20,21] Existe otra vía alternativa denominada de la perforina-granzima,[22,23] que corresponde a un complejo de serina proteasas importante en la apoptosis inducida mediante células T citotóxicas, activando vías independientes de caspasas.

Ca^{2+} como segundo mensajero determinante en el proceso de apoptosis

Las variaciones en la concentración del Ca^{2+} intracelular promueven el comienzo de eventos celulares como la regulación del metabolismo, la mitosis, la secreción de neurotransmisores y de hormonas, así como la contracción de miofilamentos, por lo que se considera un segundo mensajero determinante para las funciones celulares.[24,25] Los niveles de Ca^{2+} también están involucrados en los mecanismos regulatorios de la muerte celular programada apoptótica.[26,27] Un nivel de Ca^{2+} superior al basal se considera altamente tóxico, ya que genera la activación de proteasas y fosfolipasas que participan en el desensamble celular.[28] El incremento de Ca^{2+} puede ocurrir en etapas tempranas y tardías de la apoptosis, mediante la salida de Ca^{2+} del retículo endoplásmico y la entrada de Ca^{2+} al citoplasma a través de canales activados por liberación de Ca^{2+}.[7,29] Es necesario tener en cuenta que parte del Ca^{2+} intracelular se mueve al retículo endoplásmico a través de la bomba de calcio del retículo endoplásmico y el Ca^{2+} es liberado de estos almacenes por receptores inositol 1,4,5 trifosfato o receptores de rianodina. Adicionalmente, en diversos organelos intracelulares (como el aparato de Golgi, núcleo y mitocondria) existen sistemas especializados para el transporte de Ca^{2+}.[30]

El calcio entra a la célula a través de proteínas transmembranales llamadas canales de calcio.[31] El calcio pasa a través de los canales mediante mecanismos distintos dependiendo del tipo de canal o voltaje o bien a través de receptores; estas vías no requieren energía, a diferencia de las bombas de calcio que envían calcio citoplásmico al exterior de la célula a expensas de la utilización de adenosín trifosfato.

En colaboración con el doctor Agustín Guerrero del CINVESTAV, en el laboratorio del Instituto de Fisiología Celular, Universidad Nacional Autónoma de México, para la obtención de registros electrofisiológicos se combinó técnica de fijación de membranas (*patch clamp*) y mediciones simultáneas de Ca^{2+} en célula única, con el propósito de estudiar la activación de canales permeables a Ca^{2+} mediante el uso de dos diferentes inductores: un ionóforo (ionomicina) y la eliminación del suero.[8] La última priva a las células de componentes nutricionales esenciales como proteínas, factores de crecimiento y vitaminas, induciendo a las células a la muerte.[32,33]

Los resultados demostraron la activación de un canal catiónico no selectivo y permeable a Ca^{2+} de 23pS de conductancia. Los niveles aumentados de Ca^{2+} indujeron a las células a la apoptosis, lo cual demostró que la activación de este canal promueve el desarrollo de la muerte programada de las células LN-CaP, lo que constituyen un importante hallazgo para la inducción de la muerte programada en este tipo celular (Figura 1).

Continuando con esta línea de investigación, en nuestro grupo se aisló, identificó y caracterizó cDNA*arp2*, que codifica para ARP2 de células LNCaP independientes de andrógeno, inducidas a la apoptosis mediante la eliminación del suero.[9] La secuencia de esta proteína muestra homología con el factor de empalme o *splicing* Prp8 (un componente del spliceosoma)[34] y funciones proapoptóticas en distintos tipos celulares (Figura 2). El mecanismo de corte y empalme de tipo alternativo es definido como una propiedad que prevalece en los organismos superiores para producir proteínas múltiples de un gen simple.[35,36] La actividad de unión a ubiquitina de la proteína Prp8 sugiere que algunos factores de corte y empalme para el pre-mARN pueden ser ubiquitinados para tener una interacción con Prp8.[37]

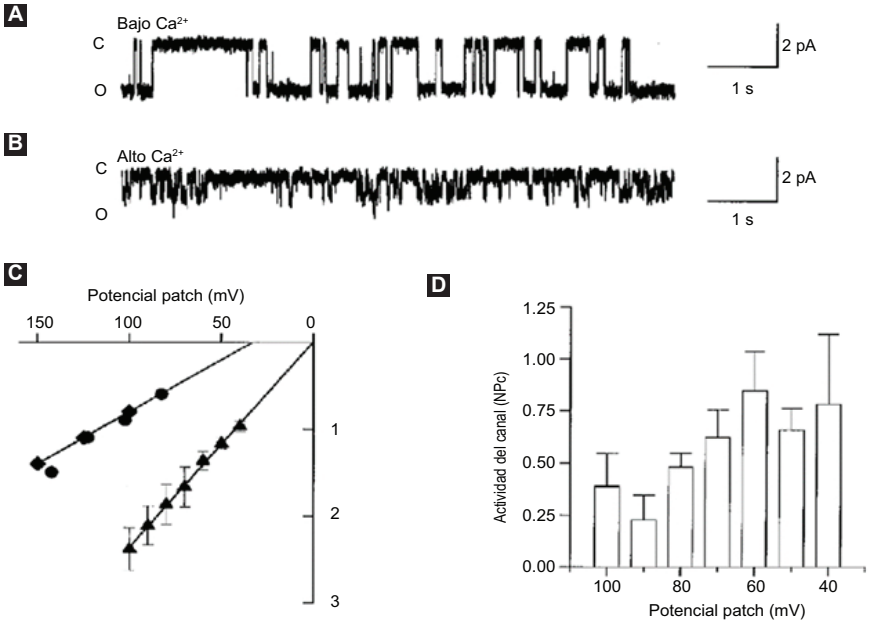

Figura 1. *Caracterización de canales iónicos asociados con el segundo aumento en Ca^{2+}.* **A:** *Registros de corriente de canal simple en la configuración de célula adherida con un potencial patch de −100 mV y solución de Na^{+}-Ca^{2+};* **B:** *Registros de canal simple con 110 mM de $CaCl_2$ en la solución de la pipeta y un potencial patch de −100 mV. En el lado izquierdo del registro se indican los niveles cerrado (C) y abierto (O);* **C:** *Curvas de corriente-voltaje obtenidas en solución $Na^{+}Ca^{2+}$ (▲), 110 mM de $CaCl_2$ (♦) o 110 mM de calcio glutamato (•) como transportadores de carga;* **D:** *En los potenciales de membrana indicados (n = 4) se muestra media ± desviación estándar de la actividad de estado basal del canal de 23pS. Tomada de referencia 8.*

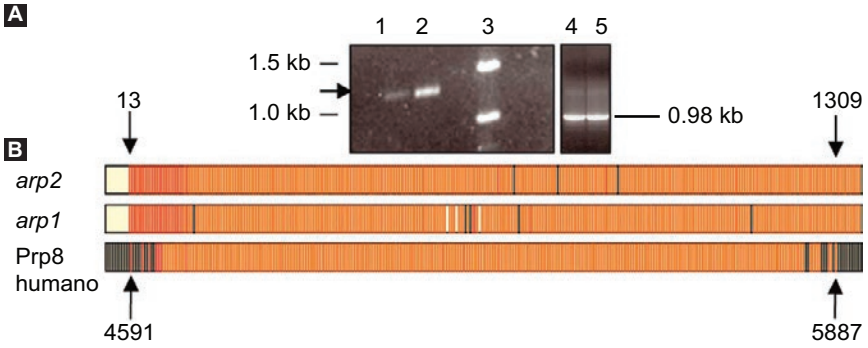

Figura 2. *Clonación de arp1 y arp2.* **A:** *Agarosa a 1 % (w/v), productos de la reacción en cadena de la polimerasa de las clonas arp2. Carril 1, producto de las células creciendo en la presencia de suero (control). Carril 2, producto de las células cultivadas en la ausencia de suero. Carril 3, marcadores de peso molecular (GIBCO BRL, ADN 1 kb). Carriles 4 y 5, controles GAPDH;* **B:** *Alineamiento múltiple de ADNc arp1 y arp2 con el ADNc Prp8 humano. Los nucleótidos 4591-5887 corresponden a la región de Prp8 humano que sobrelapa con secuencias de los ADNc arp1 y arp2. Las líneas negras indican los nucleótidos que no muestran homología entre los ADNc. Los espacios amarillos entre las líneas rojas corresponden a espacios vacíos de nucleótidos entre los ADNc. Las flechas negras señalan los nucleótidos 13 y 1309 de arp1 y arp2 y los nucleótidos 4591 y 5887 de Prp8. Tomada de referencia 9.*

Ovocitos de la rana *Xenopus laevis* inyectados con el mARN de *arp2* presentaron formación de ampollas a partir de las 12 horas de la inyección; se observó que estos cambios morfológicos aumentan cuando los ovocitos son tratados con tapsigargina (Figura 3A y 3B, respectivamente). También fue posible observar que los ovocitos sufrieron disminución en el potencial de membrana en reposo: de un valor control de −46.8 ± 6.6 mV pasaron a −5.9 ± 3.4 mV (5-8 ovocitos, dos ranas) (Figura 4). La incubación de las células con tapsigargina aceleró y aumentó los cambios morfológicos, siendo evidente la pérdida de la definición de los polos animal y vegetal, que se observó a las 36 horas de la inyección con el mARN *arp2* y ocho horas después de la incubación con tapsigargina (Figura 3B).

Los cambios morfológicos y la depolarización membranal observados en nuestro estudio han sido descritos en ovocitos de *Xenopus laevis* cuando son inyectados con citocromo C para disparar el

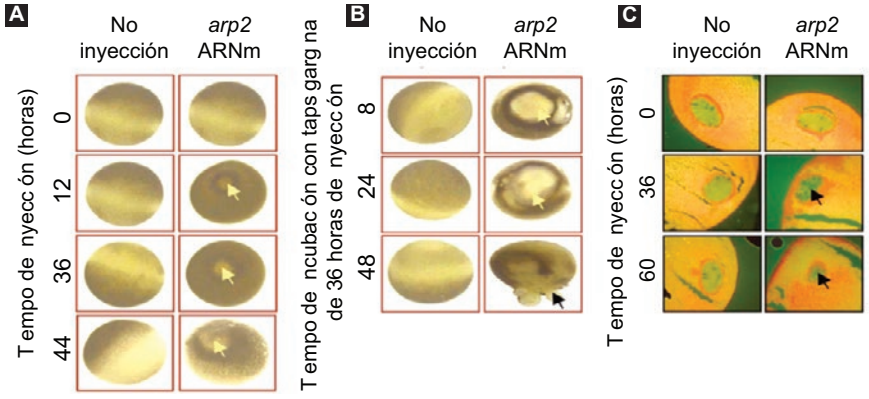

Figura 3. *Cambios morfológicos de ovocitos de Xenopus laevis relacionados con apoptosis después de la inyección del ARNm arp2;* **A:** *Inducción de apoptosis en ovocitos de Xenopus laevis por microinyección de ARNm arp2. Las columnas verticales corresponden a ovocitos que no recibieron inyección y ovocitos inyectados con ARNm arp2. Las líneas horizontales muestran los tiempos de inyección (0, 12, 36, 44 horas). Las flechas amarillas muestran las ampollas formadas;* **B:** *Progresión de la muerte celular en ovocitos de Xenopus laevis inyectados con el ARNm arp2 y la incubación con 5 µM de tapsigargina. Las columnas verticales muestran ovocitos control que no recibieron inyección y ovocitos inyectados con ARNm. Las líneas horizontales muestran los tiempos de incubación con tapsigargina de 36 horas de inyección y 8, 24, y 48 horas de incubación con tapsigargina;* **C:** *Cambios morfológicos en el núcleo de ovocitos de Xenopus laevis observados después de la inyección de ARNm arp2. Las columnas verticales muestran secciones histológicas de ovocitos no inyectados y ovocitos inyectados con ARNm arp2. Las líneas horizontales muestran tiempo de incubación después de la inyección de ARNm (0, 36, 60 horas) Las flechas negras muestran la condensación de la cromatina. Tomada de referencia 9.*

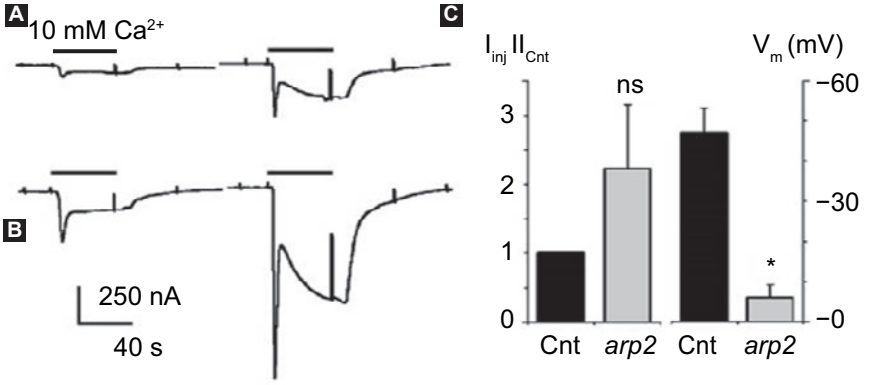

Figura 4. *Expresión funcional del ARNm arp2 en ovocitos de Xenopus laevis. Corrientes iónicas generadas por dos pulsos consecutivos de 10 mM Ca^{2+} en solución Ringer-Mg^{2+} después de la incubación de los ovocitos en ausencia de Ca^{2+} y en presencia de 5 µM de tapsigargina;* **A:** *Corrientes entrantes generadas en un ovocito control no inyectado;* **B:** *Corriente en un ovocito inyectado con ARNm arp2. Histograma que muestra la media ± desviación estándar de la corriente generada en ovocitos control (n = 3) y ovocitos inyectados con el ARNm arp2 (n = 6). También se muestran los cambios en el potencial de reposo (Vm) observados entre los diferentes grupos de ovocitos (ocho control y seis inyectados). Todos los ovocitos de esta figura fueron del mismo donador; resultados similares fueron obtenidos de una segunda rana. Cnt = control, ns = no significativo, *p ≤ 0.05. Tomada de referencia 9.*

mecanismo apoptótico,[38] al igual que en ovocitos inyectados con la molécula proapoptótica Bcl-xs.[9,39] La tapsigargina, un fármaco que descarga los almacenes intracelulares de Ca^{2+} por la inhibición específica de la Ca^{2+}-ATPasa del retículo endoplásmico, provoca que se activen canales independientes de voltaje de la membrana citoplasmática (TRP, *transient receptor potential*).[40]

De esta forma hemos reunido evidencia suficiente de que ARP2 es promotora de la apoptosis en las células LNCaP independientes de andrógeno y en células epiteliales de ovario de hámster chino,[41] favoreciendo incrementos mantenidos de Ca^{2+} al interactuar directamente con canales de membrana permeables a Ca^{2+} o presentando una función de canal de membrana. Por otro lado, considerando la homología de la secuencia del ADNc que codifica para ARP2 con el factor de corte y empalme Prp8, hasta el momento se desconoce si esta proteína pudiera tener adicionalmente alguna participación en el ensamble o funcionamiento del spliceosoma o estar relacionada con los mecanismos de regulación de corte y empalme alternativo de los ARNm que codifican para las proteínas de la maquinaria apoptótica. Existe

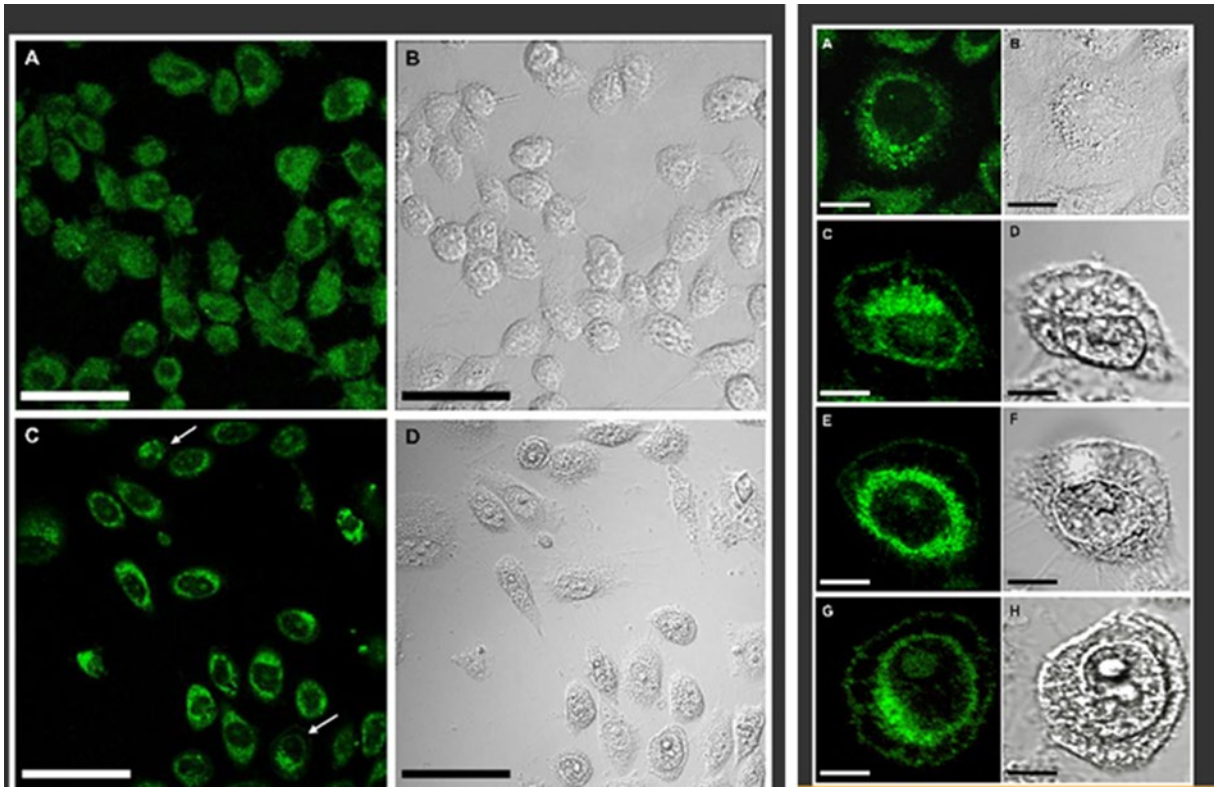

Figura 5. *Microscopia confocal de la proteína de fusión ARP2 expresada en células de ovario de hámster chino (CHO). Células CHO transfectadas con egfp ADNc fueron observadas 24 horas postransfección.* **A:** *Microscopia diferencial de contraste de interferencia;* **B:** *Células CHO transfectadas con arp2-egfp ADNc también fueron observadas 24 horas postransfección;* **C:** *Microscopia diferencial de contraste de interferencia;* **D:** *Escala de la barra 50 µm. Flechas blancas indican que ARP2 se localiza en la región perinuclear. Lado derecho: las células CHO transfectadas con ADNc arp2-egfp examinadas a las 16, 24, 48 y 72 horas postransfección (***A, C, E y G***, respectivamente); lo anterior pero con microscopia diferencial de contraste de interferencia (***B, D, F y H,** *respectivamente). Escala de la barra 10 µm. Tomada de referencia 41.*

un estudio en el que se observó que la proteína Prp8 se une a uno de los dominios del receptor a andrógeno de células de cáncer de próstata y, en consecuencia, pudiera estar interviniendo en la funcionalidad de este durante el desarrollo de la enfermedad.[42] Asimismo, se reportó que algunos factores de corte y empalme que conforman el spliceosoma están vinculados con el desarrollo de cáncer de mama, como el factor SNW1.[43]

Continuando con el proyecto, el ADNc que codifica para ARP2 fue clonado en un plásmido de expresión y transfectado a células LNCaP independientes de andrógeno y células de ovario de hámster chino. La sobreexpresión de ARP2 indujo a las células a desarrollar apoptosis, con impacto importante sobre la viabilidad celular y la activación de las caspasas efectoras 3 y 7, resultados comparados con los de células en inanición y tratadas con ionomicina.[41] En este estudio fue posible evidenciar mediante microscopia confocal que ARP2 inicialmente está localizado en la región perinuclear de las células y migra a lo largo del tiempo a la membrana plasmática[41] (Figuras 6). Tomando en cuenta nuestros resultados, consideramos que ARP2 se inserta en la membrana plasmática, con una función semejante a la de un canal de membrana, de esta forma constituye un blanco valioso para modular el flujo y la concentración de Ca^{2+} en el citoplasma de células de cáncer epitelial que muestran un fenotipo resistente a la apoptosis[41] (Figura 6).

Perspectivas

El mecanismo de apoptosis en fenotipos celulares malignos resistentes ha sido tema de amplio estudio en los últimos años. Debido al fuerte impacto del desarrollo del cáncer, es urgente la implementación de estrategias moleculares exitosas que apoyen los tratamientos contra esta enfermedad. Nuestro grupo ha demostrado que la sobreexpresión de la proteína ARP2 induce la muerte celular programada de diferentes tipos celulares: células de cáncer de próstata de nódulo linfoide independientes de andrógeno, de donde originalmente fue aislada, células de ovario de hámster chino, células de riñón embrionario humano

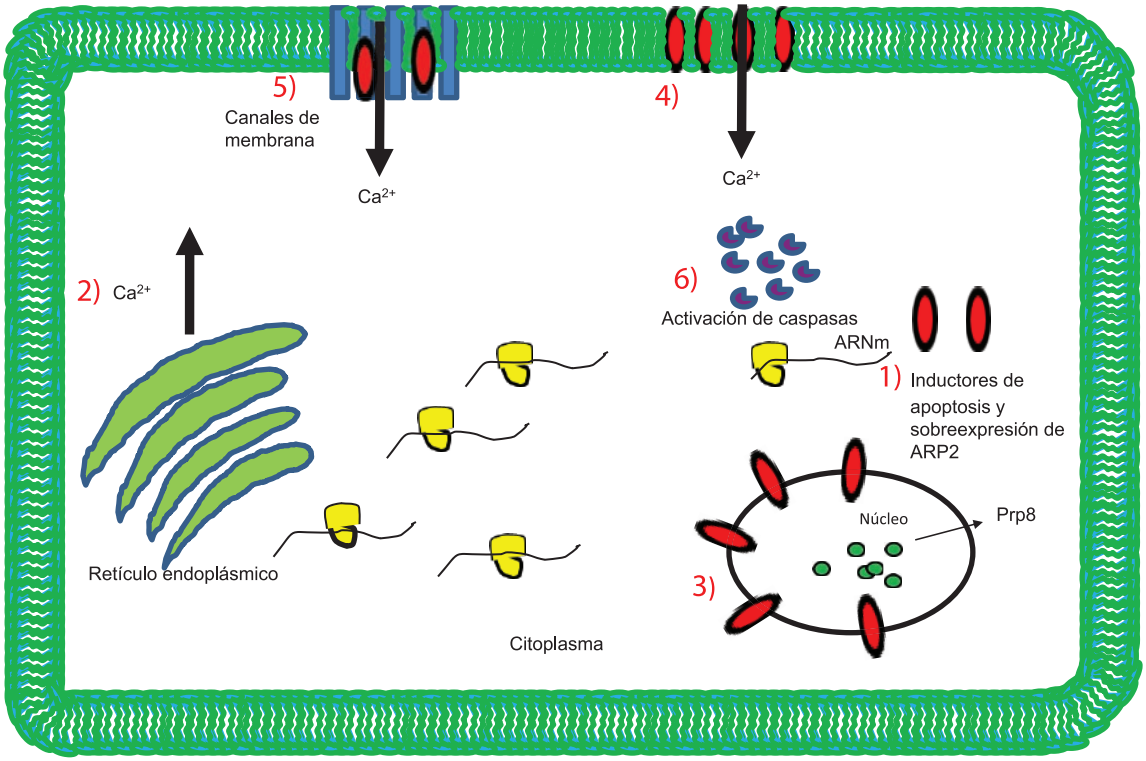

Figura 6. *Modelo de acción de ARP2.* **1:** *Inductores de apoptosis y sobreexpresión de ARP2;* **2:** *La sobreexpresion de ARP2 promueve incremento de Ca^{2+} proveniente de retículo endoplásmico y membrana citoplasmática;* **3:** *ARP2 localizada en membrana perinuclear en interacción con el complejo del spliceosoma, lo que promueve influjos de Ca^{2+};* **4:** *ARP2 insertándose en la membrana citoplasmática, con lo que forma posibles canales de membrana o regula la activación de canales permeables a Ca^{2+}* **(5)***; estos influjos de Ca^{2+} favorecen la actividad del complejo del spliceosoma y el desarrollo del mecanismo de apoptosis* **(6)**.

y células endoteliales de arteria coronaria (datos no mostrados).

Dadas las evidencias experimentales reunidas, consideramos que ARP2 pudiera estar contribuyendo durante su sobreexpresión al incremento de los niveles intracelulares de Ca^{2+} como una molécula mensajera o como una proteína insertada en la membrana que favorece la entrada de Ca^{2+}. Además de encontrarse en la región membranal, también observamos su localización perinuclear y debido a la homología con el factor Prp8 cabe la posibilidad de que esté participando en los mecanismos de corte y empalme alternativo de moléculas proapoptóticas.[44-46] En este sentido y tomando en cuenta de que la transcripción a través de mecanismos de corte y empalme alternativos son procesos moleculares altamente regulados por el nivel intracelular de Ca^{2+}, entre otros,[47,48] es factible pensar que ARP2 pudiera tener una doble función: en el control del flujo plasmático de Ca^{2+} y en mecanismos moleculares de corte y empalme alternativo.

Con fundamento en la evidencia de que genes de muerte celular están desregulados en el cáncer, fenómeno asociado con el control de sus patrones de corte y empalme alternativo, es justificado pensar que el proceso de apoptosis se manifiesta como una respuesta positiva a la quimioterapia.[49] Si tomamos en cuenta que la eficacia de los fármacos contra el cáncer puede también depender de la activación de la apoptosis o de una forma de inducción aguda de senescencia celular, consideramos que la sobreexpresión de la proteína ARP2 potencialmente podría ser empleada como una nueva herramienta en el tratamiento del cáncer de tipo epitelial.

Bibliografía

1. Vineis P, Wild CP. Global cancer patterns: causes and prevention. Lancet. 2014;383:549-557.
2. Siegel R, Naishadham D, Jemal A. Cancer statistics, 2013. CA Cancer J Clin. 2013;63:11-30.
3. Hossein-Hassanpour S, Dehghani M. Review of cancer from perspective of molecular. J Cancer Res Pract. 2017;4:127-129.
4. Siegel RL, Miller KD, Jemal A. Cancer statistics, 2016. CA Cancer J Clin. 2016;66:7-30.
5. Schottenfeld D, Fraumeni JF. Cancer epidemiology and prevention. Inglaterra: Oxford Scholarship Online; 2006.
6. Yoo KY, Shin HR. Cancer epidemiology and prevention. Korean J Epidemiol. 2003;25:1-15.
7. Pinton P, Giorgi C, Siviero R, Zecchini E, Rizzuto R. Calcium and apoptosis: ER-mitochondria Ca2+ transfer in the control of apoptosis. Oncogene. 2008;27:6407-6418.
8. Gutiérrez AA, Arias JM, García L, Mas-Oliva J, Guerrero-Hernández A. Activation of a Ca2+ permeable cation channel by two different inducers of apoptosis in a human prostatic cancer cell line. J Physiol. 1999;15:95-107.

9. Tapia-Vieyra JV, Arellano RO, Mas-Oliva J. ARP2 a novel protein involved in apoptosis of LNCaPcells shares a high degree homology with splicing factor Prp8. Mol Cel Biochem. 2005;269:189-201.
10. Ferlay J, Soerjomataram I, Dikshit R, Eser S, Mathers C, Rebelo M, et al. Cancer incidence and mortality worldwide: sources, methods and major patterns in GLOBOCAN 2012. Int J Cancer. 2015;136:E359-E386.
11. Dall'Era MA, Albertsen PC, Bangma C, Carroll PR, Carter HB, Cooperberg MR, et al. 2012. Active surveillance for prostate cancer: a systematic review of the literature. Eur Urol. 2012;62:976-983.
12. Siegel RL, Miller KD, Jemal A. Cancer statistics, 2015. CA Cancer J Clin. 2015;65:5-29.
13. Thompson IM, Goodman PJ, Tangen CM, Lucia MS, Miller GJ, Ford LG, et al. The influence of finasteride on the development of prostate cancer. N Engl J Med. 2003;349:215-224.
14. Talcott JA. In the clinic. Prostate cancer. Ann Intern Med. 2015;163:ITC1-ITC12.
15. Quinn DI, Sandler HM, Horvath LG, Goldkorn A, Eastham JA. The evolution of chemotherapy for the treatment of prostate cancer. Ann Oncol. 2017;28:2658-2669.
16. Kerr JF, Wyllie AH, Currie AR. Apoptosis: a basic biological phenomenon with wide-ranging implications in tissue kinetics. Br J Cancer. 1972;26:239-257.
17. Tapia-Vieyra JV, Delgado-Coello B, Mas-Oliva J. Atherosclerosis and cancer; a resemblance with far-reaching implications. Arch Med Res. 2017;48:12-26.
18. Chen M, Wang J. Initiator caspases in apoptosis signaling pathways. Apoptosis. 2002;7:313-319.
19. Cooper KF. Till death do us part: the marriage of autophagy and apoptosis. Oxidative Med Cell Longevity. 2018;1:1-13.
20. Fulda S, Debatin KM. Extrinsic versus intrinsic apoptosis pathways in anticancer chemotherapy. Oncogene. 2006;25:4798-4811.
21. Hassan M, Watari H, AbuAlmaaty A, Ohba Y, Sakuragi N. Apoptosis and molecular targeting therapy in cancer. Biomed Res Int. 2014;2014:150845.
22. Elmore S. Apoptosis: a review of programmed cell death. Toxicol Pathol. 2007;35:495-516.
23. Adams JM. Ways of dying: multiple pathways to apoptosis. Genes Dev. 2003;17:2481-2495.
24. Mason RP. Calcium channel blockers, apoptosis and cancer: is there a biologic relationship? J Am Coll Cardiol. 1999;34:1857-1866.
25. Clapham DE. Calcium signaling. Cell. 2007;131:1047-1058.
26. Rizzuto R, Pinton P, Ferrari D, Chami M, Szabadkai G, Magalhães PJ, et al. Calcium and apoptosis: facts and hypotheses. Oncogene. 2003;22:8619-8627.
27. Giorgi C, Romagnoli A, Pinton P, Rizzuto R. Ca2+ signaling, mitochondria and cell death. Curr Mol Med. 2008;8:119-130.
28. Fariss MW, Pascoe GA, Reed DJ. Vitamin E reversal of the effect of extracellular calcium on chemically induced toxicity in hepatocytes. Science. 1985;227:751-754.
29. Pinton P, Rizzuto R. Bcl-2 and Ca2+ homeostasis in the endoplasmic reticulum. Cell Death Differ. 2006;13:1409-1418.
30. Görlach A, Bertram K, Hudecova S, Krizanova O. Calcium and ROS: a mutual interplay. Redox Biol. 2015;6:260-271.
31. Tapia-Vieyra JV, Mas-Oliva J. Apoptosis and cell death channels in prostate cancer. Arch Med Res. 2001;32:175-185.
32. Schamberger CJ, Gerner C, Cerni C. Caspase-9 plays a marginal role in serum starvation-induced apoptosis. Exp Cell Res. 2005;302:115-128.
33. Braun F, Bertin-Ciftci J, Gallouet AS, Millour J, Juin P. Serum-nutrient starvation induces cell death mediated by Bax and Puma that is counteracted by p21 and unmasked by Bcl-xL inhibition. PlosOne. 2011;6:e23577.
34. Kelemen O, Convertini P, Zhang Z, Wen Y, Shen M, Falaleeva M, et al. Function of alternative splicing. Gene. 2017;514:1-30.
35. Black DL. Mechanisms of alternative pre-messenger RNA splicing. Annu Rev Biochem. 2003;72:291-336.
36. Blencowe BJ. Alternative splicing: new insights from global analyses. Cell. 2006;126:37-47.
37. Bellare P, Kutach AK, Rines AK, Guthrie C, Sontheimer EJ. Ubiquitin binding by a variant Jab1/MPN domain in the essential pre-mRNA splicing factor Prp8p. RNA. 2006;12:292-302.
38. Bhuyan AK, Varshney A, Mathew MK. Resting membrane potential as a marker of apoptosis: studies of xenopus oocytes microinjected with cytochrome c. Cell Death Differ. 2001;8 63-69.
39. Braun T, Dar S, Vorobiov D, Lindenboim L, Dascal N, Stein R. 2003. Expression of Bcl-x(S) in xenopus oocytes induces BH3-dependent and caspase-dependent cytochrome c release and apoptosis. Mol Cancer Res. 2003;1:186-194.
40. Boulay G, Zhu X, Peyton M, Jiang M, Hurst R, Enrico S, et al. Cloning and expression of a novel mammalian homolog of Drosophila transient receptor potential (Trp) involved in calcium entry secondary to activation of receptors coupled by the G_q class of G protein. J Biol Chem. 1997;272:29672-29680.
41. Mas-Oliva J, Navarro-Vidal E, Tapia-Vieyra JV. ARP2, a novel pro-apoptotic protein expressed in epithelial prostate cancer LNCaP cells and epithelial ovary CHO transformed cells. PLoS One. 2014;9 e86089.
42. Wang D, Nguyen MM, Masoodi KZ, Singh P, Jing Y, O'Malley K, et al. Splicing factor Prp8 interacts with NES(AR) and regulates androgen receptor in prostate cancer cells. Mol Endocrinol. 2015;29:1731-1742.
43. Sato N, Maeda M, Sugiyama M, Ito S, Hyodo T, Masuda A, et al. 2015. Inhibition of SNW1 association with spliceosomal proteins promotes apoptosis in breast cancer cells. Cancer Med. 2015;4:268-277.
44. Maniatis T, Tasic B. Alternative pre-mRNA splicing and proteome expansion in metazoans. Nature. 2002;418:236-243.
45. Schwerk C, Schulze-Osthoff K. Regulation of apoptosis by alternative pre-mRNA splicing. Mol Cell. 2005;19:1-13.
46. Moore MJ, Wang Q, Kennedy CJ, Silver PA. An alternative splicing network links cell-cycle control to apoptosis. Cell. 2010;142:625-636.
47. Krebs J. The influence of calcium signaling on the regulation of alternatives splicing. Biochim Biophys Acta. 2009;1793:979-984.
48. Tarn WY. Cellular signals modulate alternative splicing. J Biomed Sci. 2007;14:517-522.
49. Bracco L, Kearsey J. The relevance of alternative RNA splicing to pharmacogenomics. Trends Biotechnol. 2003;21:346-353.

INFORME DE LABORES 2019

Localization of chloride co-transporters in striatal neurons

Dagoberto Tapia, Paola Suárez, Mario A. Arias-García, Brisa Garcia-Vilchis, Miguel Serrano-Reyes, José Bargas and Elvira Galarraga

The ionic driving force for the chloride-permeable $GABA_A$ receptor is subject to spatial control and distribution of chloride transporters. NKCC1 and KCC2 are mostly expressed in neurons in a specific manner. In the striatum, the localization of these transporters in identified neurons is unknown. In this study, the expression of these transporters was found to be different between projection neurons and interneurons. NKCC1 immunoreactivity was observed in the soma of adult BAC-D1-eGFP+ and D2-eGFP+ striatal projection neurons (SPNs). KCC2 was not expressed in either projection neuron and immunoreactivity to this transporter was observed only in the neuropile. However, NKCC1 and KCC2 co-transporters were not localized in intracellular biocytin-injected dendrites of SPNs of the direct or indirect pathways (D1-SPNs and D2-SPNs). Experiments with PV^+ Cre transgenic mice transfected with Cre-dependent adeno-associated viruses containing tdTomato in the striatum showed a cell-type-specific distribution of KCC2 chloride transporter co-expression associated with PV^+ interneurons. Thus, depolarizing actions of GABA responses in adult projection neurons can be explained by the expression and somatic localization of the NKCC1 transporters. A somato/dendritic distribution of KCC2 expression was observed only in striatal interneurons and corresponds to the hyperpolarizing action of GABA recorded in these cells. This correlates the different roles for GABA actions in striatal neuronal excitability with the expression of specific chloride transporters. *NeuroReport* **30:457–462** **Copyright © 2019 Wolters Kluwer Health, Inc. All rights reserved.**

NeuroReport 2019, **30**:457–462

Keywords: D1-SPN, D2-SPN, $GABA_A$, KCC2, NKCC1, PV interneuron

Neuroscience Division, Cell Physiology Institute, Autonomous National University of Mexico, Mexico City, Mexico

Correspondence to Elvira Galarraga, PhD, División de Neurociencias, Instituto de Fisiología Celular, Universidad Nacional Autónoma de México, Mexico City 04510, Mexico
Tel: +52 55 5622 5621; fax: +52 55 5622 5607; e-mail: egalarra@ifc.unam.mx

Received 22 February 2019 **accepted** 7 March 2019

Downloaded from http://journals.lww.com/neuroreport by BhDMf5ePHKav1zEoum1tQfN4a+kJLhEZgbsIHo4XMi0hCywCX1AWnYQp/IlQrHD3Z0I3TR16A9fyKVvB4BX9hRpJzV1hKjWBSZ8eB4WJvAb4f5K6t58w== on 10/20/2020

Introduction

One parameter that can establish differences in the actions of GABAergic synapses is the ionic driving force for the chloride-permeable $GABA_A$ receptor.

The concentration of intracellular chloride ions in mammalian neurons is mainly controlled by two transporters.

NKCC1 accumulates chloride ions inside the cell using the sodium concentration gradient; KCC2 exports chloride outside the cell using the potassium concentration gradient [1,2]. Co-transporters are expressed in a cell-type-specific manner in the brain [3]. In the striatum, NKCC1 and KCC2 co-transporters are present [4], but their expression in specific striatal neurons is unknown. Reversal inhibitory potential is above the resting potential in all striatal projection neurons (SPNs) recorded by numerous studies using different techniques, including intracellular recordings and gramicidin patches [5–10]. GABAergic postsynaptic potentials have reversal potentials around −65 mV. Therefore, a depolarizing inhibition is present in all adult SPNs synaptic responses, considering chloride reversal potential. However, it is also well established that the expression of different chloride co-transporters can be distributed in separate compartments of the somato/dendritic membrane of a neuron, determining the polarity of the response to GABA [2,11–13]. In the present work, we studied the expression pattern among the SPNs and PV^+ interneurons of the co-transporters NKCC1 and KCC2, the subcellular anatomical distribution, and their role in regulating the different GABAergic responses in SPNs and PV^+ interneurons.

Materials and methods

All experiments were conducted in accordance with the international guidelines for the ethical use of experimental animals established in the NIH and detailed protocols were submitted and approved by the Institutional Committee for Laboratory Animals Care of the Instituto de Fisiología Celular, UNAM (NOM-062-Z00-1999; laboratory procedures EGP-41-14). Rodents were housed in a temperature-controlled, pathogen-free room, on a 12 : 12 light : dark cycle, and allowed food and water *ad libitum* to minimize the number of animals required to achieve statistical significance and the avoidance of animal suffering. Tg (Drd1-EGFP, $n=6$) X60Gsat/Mmmh (BAC-D1, GENSAT#: 000297-MU; Nathaniel Heintz, The Rockefeller University, New York City, New York, USA), Tg (Drd2-EGFP, $n=7$) S118Gsat/Mmnc (BAC-D2, 000230-UNC; Nathaniel Heintz, The Rockefeller University), C57BL/6 NCRL ($n=12$), and 12P2-*Pvalb*$^{tm1(cre)Arbr}$/J (PV-Cre, stock# 008069; Silvia Arber, Friedrich Miescher Institute, Basel, Switzerland and Jackson Labs, Bar Harbor, Maine, USA), PV-Cre mice ($n=5$), were used.

0959-4965 Copyright © 2019 Wolters Kluwer Health, Inc. All rights reserved.

DOI: 10.1097/WNR.0000000000001234

Copyright © 2019 Wolters Kluwer Health, Inc. Unauthorized reproduction of this article is prohibited.

INFORME DE LABORES 2019

Slice preparation

Animals (45 postnatal day) were anesthetized, decapitated, and their brains were removed and submerged in an iced saline solution containing (in mM): 120 NaCl, 3 KCl, 25 $NaHCO_3$, 2 $CaCl_2$, 1 $MgCl_2$, and 11 glucose (33–35°C, 300 mOsm/l with glucose, pH 7.4, after bubbling with 95% O_2 + 5% CO_2). Briefly, and as described previously in detail, 350 µm thick parasagittal slices were cut [14] on a vibratome and left to equilibrate for at least 1 h at room temperature in the same saline. Thereafter, slices were transferred to a recording chamber and superfused continuously with the same saline at 33–35°C.

Identification of recorded neurons

Intracellular recordings were performed from spiny neurons of the dorsal neostriatum using sharp electrodes filled with potassium acetate 3 M and 1% biocytin (DC resistance 80–120 MΩ). SPNs were identified by their intrinsic electrophysiological properties during corticostriatal synaptic responses as described previously [9,14, 15]. In all cases, neurons were injected with biocytin-CY3 to determine the somato/dendritic morphology ($n = 13$).

Immunohistochemistry

Neurons obtained from BAC-D1 or BAC-D2-eGFP mice were identified as belonging to direct or indirect pathways. Thereafter, fixed slices were infiltrated with 30% sucrose and cut on a vibratome into 40-µm thick sections and incubated for 30 min with 1% bovine albumin to block nonspecific binding sites and for 36 h with a rabbit polyclonal antibody against NKCC1 1 : 1000 (59791; Abcam, Cambridge, UK) or KCC2 1 : 1000 (07–432; Millipore, Burlington, Massachusetts, USA), dissolved in PBS containing 0.25% Triton-X. The slices were then rinsed thrice with PBS and incubated with a goat versus rabbit secondary antibody 1 : 100 for 1 h. This antibody was conjugated with CY3 (Jackson immunoResearch, West Grove, Pennsylvania, USA). The specificity of antibodies was verified by negative experiments.

In the case of intracellular dendritic-injected biocytin, streptavidin conjugated with Cy3 1 : 200 was used and FITC for NKCC1 and KCC2 antibodies. Identification of PV-Cre^+ interneurons labeled with tdTomato and FITC for KCC2 antibody was used. Samples were mounted with vectashield (Vector Laboratories, Burlingame, California, USA) and observed in a confocal microscope Olympus FV-1000 [15].

Results

Projection neurons express the NKCC1 transporter on the soma

To investigate the expression pattern of the NKCC1 chloride transporter in the SPNs identified, we analyzed striatal confocal images from D2-eGFP BAC mice (Fig. 1a, in green) with the anti-NKCC1 antibody labeling (Fig. 1b, in red). Both D2-eGFP-positive neurons (arrow) as well as D2-eGFP-negative neurons 'putative D1-SPNs' (arrow head) co-express the red fluorescence labeling of the NKCC1 transporter (Fig. 1c, yellow and red).

The KCC2 co-transporter expression pattern was not found in either the soma of D2-eGFP-positive (arrow) or D2-eGFP-negative neurons (arrow head, Fig. 1d–f). The same results were found in D1-eGFP mice brain slices (Fig. 1g–l; also see Fig. 2a and c and Fig. 3a–c). Images from striatal D1-eGFP neurons (Fig. 1g, in green) labeled with NKCC1 antibody (Fig. 1h, in red). Again, both D1-eGFP-positive neurons (arrow) as well as D1-eGFP-negative neurons (arrow head) co-expressed the red fluorescence labeling of the NKCC1 transporter (Fig. 1i, yellow and red). The KCC2 co-transporter expression pattern was not found in either the soma of D1-eGFP-positive (arrow), D1-eGFP-negative neurons (Fig. 1j–l, arrow head), or green dendrites of D1-eGFP-positive cells (Fig. 1l).

However, the KCC2 was highly expressed in striatal neuropile (big arrows Fig. 1e and k), although it was not present in the somato/dendritic membrane of the SPNs (Fig. 2f). The somatic expression of the NKCC1 chloride co-transporter contributes toward understanding the known depolarizing synaptic effects of GABA in SPNs [9,10,14,15].

NKCC1 and KCC2 are not expressed in dendrites of SPNs

The electrophysiological reversal potential for GABA-induced currents has been reported to vary between different cellular compartments in some neurons [3,11–13]. Therefore, we explored the possibility of NKCC1 and KCC2 expressions in intracellular labeled dendrites of D1-SPNs and D2-SPNs identified by their different corticostriatal synaptic responses [9,10]. Neurons injected with biocytin-CY3 were examined for double labeling along the dendrites; at least four dendrites from the soma to the tip in each cell (52 dendrites of 13 cells; seven dSPNs and six iSPNs, half of them subsequently labeled for KCC2 or NKCC1) were quantified. From this quantification, we concluded that dendrites of SPNs do not express the NKCC1 or the KCC2 co-transporters.

Figure 2a and b shows photomicrographs of intracellular injected projection neurons with biocytin streptavidin-conjugated Cy3. The NKCC1 antibody was only observed within the soma of neuron in Fig. 2c (arrow), not in dendrites of the biocytin-injected neuron (Fig. 2e, arrow). Note the labeled somata of other NKCC1-positive cells (Fig. 2e, arrow head). Figure 2b shows the somato/dendritic morphology of another SPN injected intracellularly with biocytin; in this case, no KCC2 expression was observed in the soma (Fig. 2d, arrow). Some positive KCC2 neuronal perikarya can be observed in the field (Fig. 2d, arrow heads). The KCC2 antibody was not expressed in the dendrites of this SPN (Fig. 2f, red arrow), but some positive dendritic processes were observed in the field (Fig. 2f, green arrow head).

These data show that intracellular labeled dendrites with biocytin (dendrites in red) in SPNs do not express the NKCC1 or the KCC2 (Fig. 2e and f) co-transporters. NKCC1

Copyright © 2019 Wolters Kluwer Health, Inc. Unauthorized reproduction of this article is prohibited.

INFORME DE LABORES 2019

Fig. 1

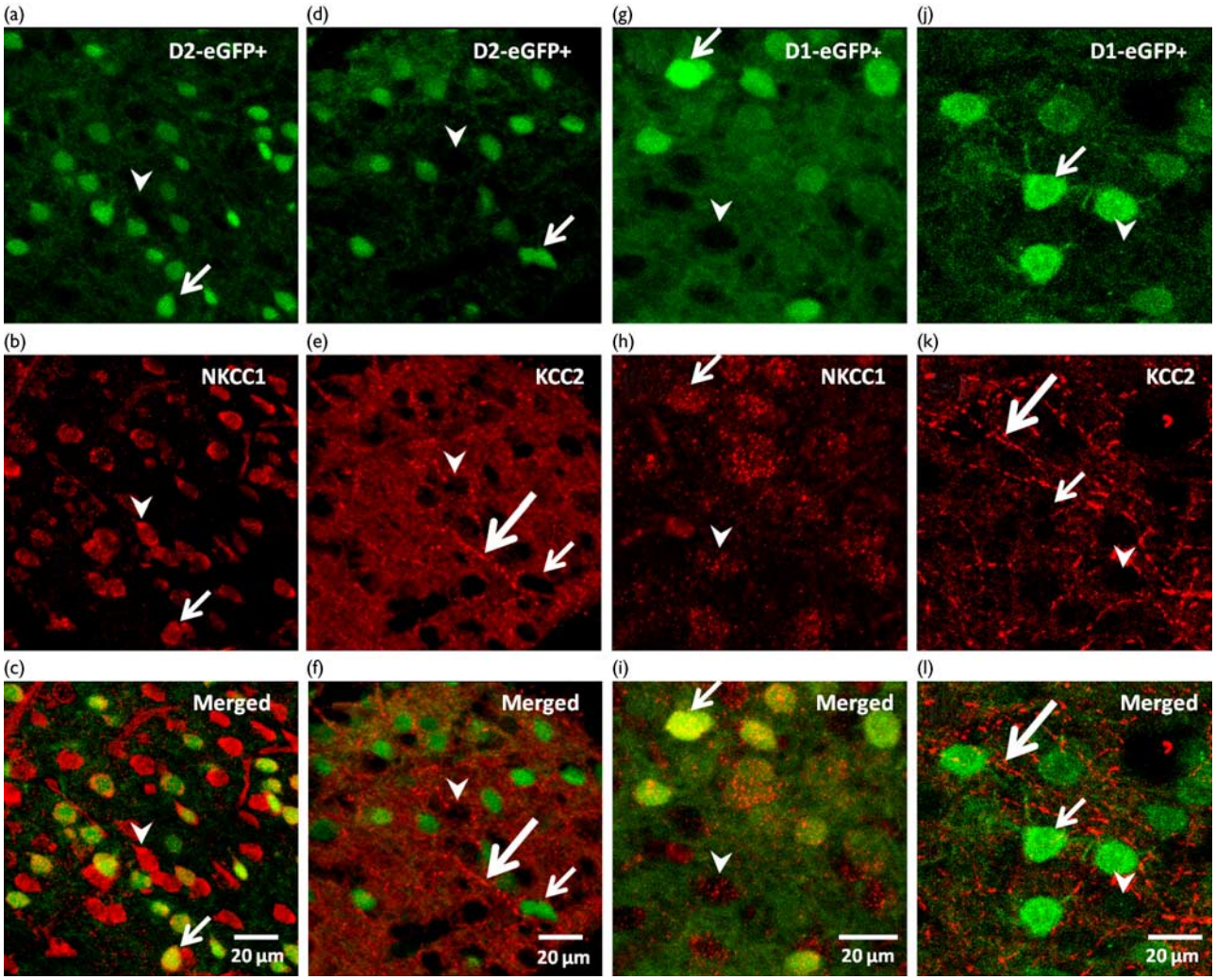

Striatal projection neurons (SPNs) only express the NKCC1 transporter in the soma. Confocal images of the striatum double stained for D2-eGFP-positive neurons (a, in green), and the anti-NKCC1 antibody (b, c, in red) and for D2-eGFP and KCC2 antibody (d–f). Some neurons seen in the merged images (c, in yellow) co-express the green fluorescence and the NKCC1 transporter (arrows). D2-eGFP-negative neurons also co-express the NKCC1 antibody immunoreactivity (a–c, arrow heads). Note that KCC2 is highly expressed in the neuropile of the striatum (e, big arrow), but the antibody is not expressed in either D2-eGFP-positive (arrows) or D2-eGFP-negative (f, arrow heads) SPNs. D1-eGFP-positive neurons (g, in green), and the anti-NKCC1 antibody (h and I, in red) and for D1-eGFP and KCC2 antibody (j–l). Some neurons seen in the merged images (c, in yellow) co-express the green fluorescence and the NKCC1 transporter (arrows).

was only observed on the soma of SPNs and not in the neuropile, as in the case of KCC2 (arrows in Fig. 2e and f).

The KCC2 chloride transporter is expressed in PV$^+$ interneurons

Figure 3a shows D1-eGFP-positive SPNs (in green). In Fig. 3b, KCC2 immunoreactivity (in red), confirms that D1-eGFP-positive neurons are not immunoreactive (Fig. 3a–c, small arrows). KCC2 immunoreactivity was observed on the somatic periphery of negative D1-eGFP cells (Fig. 3a–c, big arrows) and the thin dendritic profiles in Fig. 3b and c (arrow heads). To identify the KCC2-positive striatal cell population, we utilized PV-Cre transgenic mice transfected with tdTomato. Several PV$^+$ neurons were identified in the striatum (Fig. 3d, in red) and were positively immunoreactive to the KCC2 antibody (Fig. 3e, in green). Double labeling is shown on the right (Fig. 3f, neurons in yellow). As in other brain areas, these experiments show that KCC2 immunoreactivity was distributed in the somatodendritic axis of PV$^+$ interneurons, helping to understand GABAergic inhibition onto PV$^+$ interneurons [16,17].

Discussion

Most striatal neurons are GABAergic. D1-SPNs and D2-SPNs receive inhibitory inputs from axon collaterals of each other, from neurons belonging to the same pathway [16–19], and

Copyright © 2019 Wolters Kluwer Health, Inc. Unauthorized reproduction of this article is prohibited.

INFORME DE LABORES 2019

Fig. 2

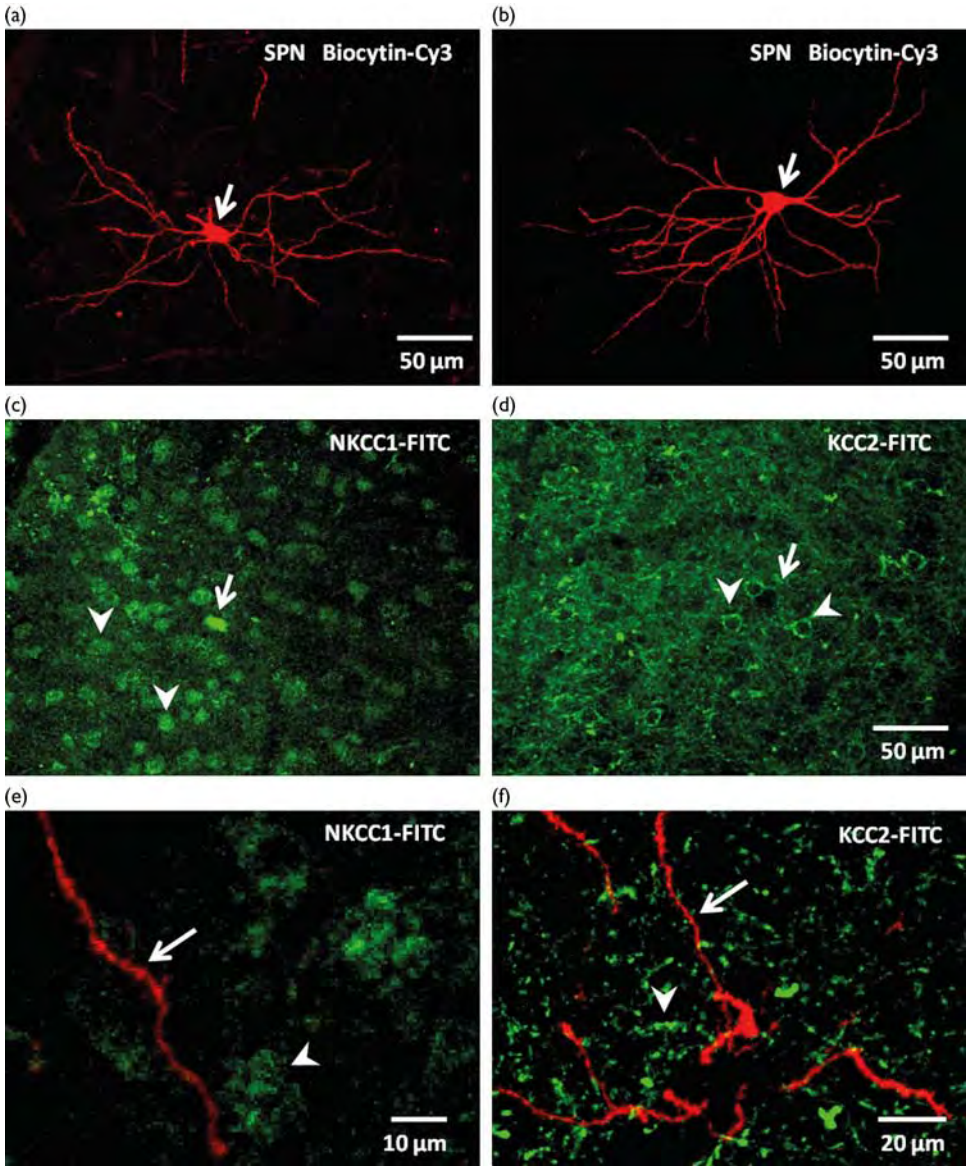

Cellular compartmentalization of co-transporters NKCC1 and KCC2 in the somato/dendritic membrane of striatal projection neurons (SPNs). In (a) and (b) intracellularly recorded SPNs filled with biocytin are in red. The neuron in (a) was positive to the NKCC1 antibody (c, arrow), while the neuron in (b) was negative to the KCC2 antibody (d, arrow). Some positive neurons are shown (arrow heads). Intracellular labeled dendrites of SPNs (e, f, in red) were not associated with the antibodies, instead they were associated with the perikarya of SPNs (e, arrow head) and the neuroplie (f, arrow head).

from several types of GABAergic interneurons including tonic inhibition because of extra synaptic gabaergic receptors [7–9,19]. Feedback and feedforward inhibition have been studied previously in striatal neurons [17,19]. All these inputs contribute toward the synaptic integrated output of SPNs. GABAergic inputs contact the peri-somatic region and distal dendrites interacting with glutamatergic cortical and thalamic inputs [20] and with intrinsic dendritic channels that determine synaptic integration and dynamics [10,14,15]. GABA is generally inhibitory in the adult brain, but it can also mediate depolarizing synaptic responses in immature animals [2,21]. In addition, depolarizing actions of GABA with respect to resting potential have been reported in adult neurons [5–7,22,23] and are important in the adult brain not only to regulate neuronal excitability but also for synaptic integration [9]. However, depolarizing GABA signals may maintain their inhibitory influence because of shunting inhibition [9,23,24]. It has been known for a long time that GABA is depolarizing in adult SPNs [5–9]. Here, we show that somatic depolarizing actions of GABA in adult projection neurons can in part be explained by the expression and somatic localization of the NKCC1 transporters in these cells. However, depolarizing GABA

Copyright © 2019 Wolters Kluwer Health, Inc. Unauthorized reproduction of this article is prohibited.

INFORME DE LABORES 2019

Fig. 3

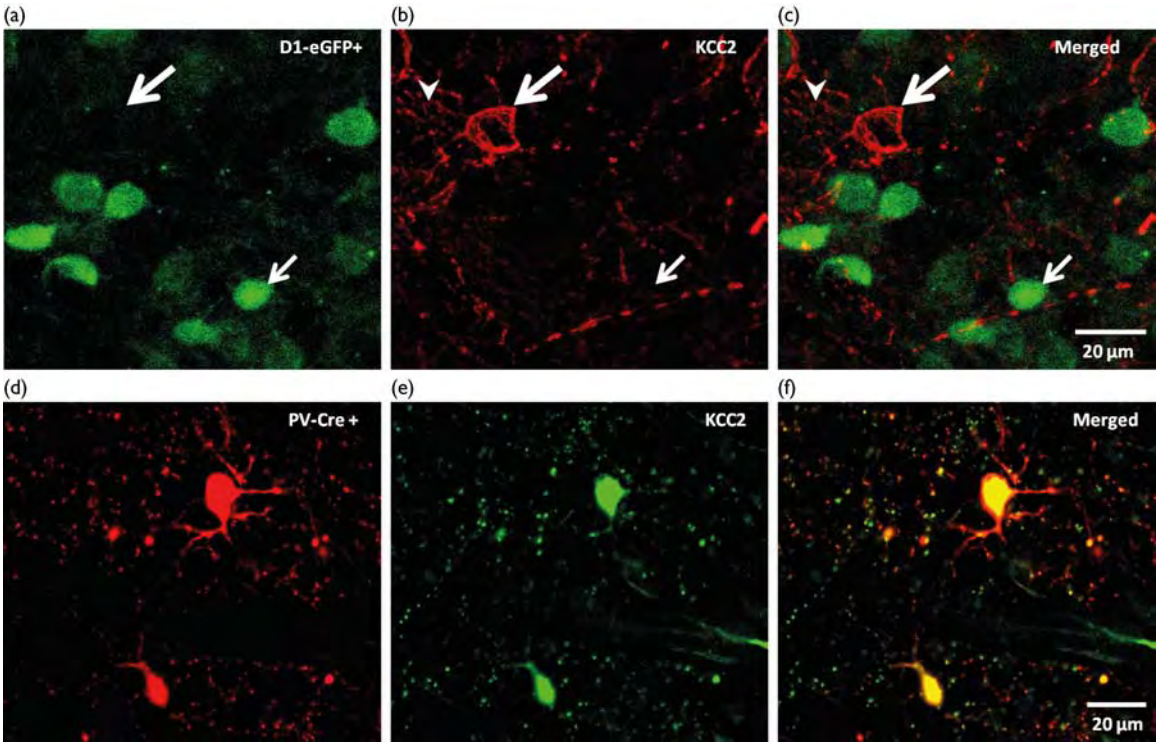

Cell-type-specific distribution of KCC2 chloride transporter. Expression of the KCC2 transporter was associated with PV^+ striatal interneurons. (a) Positive striatal projection neurons (SPNs) from a BAC-D1-eGFP mouse in green (small arrow). (b) KCC2 immunoreactivity is observed in some sparse somatic and dendritic processes (big arrow and arrow head). In (c), a and b are merged, showing that the KCC2 chloride transporter is not expressed in D1-eGFP-positive neurons (small arrow). In (d) PV-Cre^+ interneurons interpunct. In (e) KCC2 immunoreactivity was distributed along the somato/dendritic axis of PV-Cre^+ interneurons. In (f), d and e are merged.

signals may maintain their inhibitory influence because of shunting inhibition at threshold potentials, for example, restraining firing at the beginning of a synaptic response, but supporting a prolonged plateau depolarization at later times in D1-SPNs. The inhibitory GABA response can also be revealed by bicuculline application in D2-SPNs in which a larger dendritic calcium contribution is observed [6,8–10,15]. To conclude, depolarizing GABA actions in the striatum are correlated here with specific chloride transporters expression described in this work.

Conclusion

In the presented work, the expression of chloride co-transporters was described in a cell-type-specific manner in SPNs and PV^+ interneurons. The results show for the first time that KCC2 is found in PV^+ striatal interneurons, whereas NKCC1 is expressed within the somatic region of both SPNs classes. The presence of the KCC2 transporter in other striatal interneurons cannot be discarded and remains to be studied. The possible presence of other transporter proteins is not discarded. GABA actions are important to understand the functional integration of microcircuits.

Acknowledgements

The authors thank, Antonio Laville, Gabriela X. Ayala, and Ariadna Aparicio for technical support and advice, Dr Claudia Rivera for animal care, and Merlin J. Fair for manuscript review.This work was supported by grants from Consejo Nacional de Ciencia y Tecnología, México (CONACyT 251144 to E.G.) and Dirección General de Asuntos del Personal Académico, Universidad Nacional Autónoma de México (DGAPA-UNAM IN201517 to E.G. and IN 201417 to J.B.).

Conflicts of interest

There are no conflicts of interest.

References

1 Plotkin MD, Kaplan MR, Peterson LN, Gullans SR, Hebert SC, Delpire E. Expression of the Na^+–K^+–$2Cl^-$ cotransporter BSC2 in the nervous system. *Am J Physiol* 1997; **272**:173–183.

2 Chamma I, Chevy Q, Poncer JC, Lévi S. Role of the neuronal K–Cl co-transporter KCC2 in inhibitory and excitatory neurotransmission. *Frontiers Cel Neurosci* 2012; **6**:5.

3 Belenky MA, Sollars PJ, Mount DB, Alper SL, Yarom Y, Pickard DGE. Cell-type specific distribution of chloride transporters in the rat suprachiasmatic nucleus. *Neuroscience* 2010; **165**:1519–1537.

4 Kanaka C, Ohno K, Okabe A, Kuriyama T, Itoh T, Fukuda A, *et al.* The differential expression patterns of messenger RNAS encoding K–Cl

Copyright © 2019 Wolters Kluwer Health, Inc. Unauthorized reproduction of this article is prohibited.

cotransporters (KCC1,2) and Na–K–2Cl cotransporter (NKCC1) in the rat nervous system. *Neuroscience* 2001; **104**:933–946.
5 Misgeld U, Wagner A, Ohno T. Depolarizing IPSPs and depolarization by GABA of rat neostriatum cells in vitro. *Exp Brain Res* 1982; **45**:108–114.
6 Jiang Z, North R. Membrane properties and synaptic responses of rat striatal neurons in vitro. *J Physiol* 1991; **443**:533–553.
7 Kita H. Glutamatergic and GABAergic postsynaptic responses of striatal spiny neurons to intrastriatal and cortical stimulation recorded in slice preparations. *Neuroscience* 1996; **70**:925–940.
8 Bracci E, Panzeri S. Excitatory GABAergic effects in striatal projection neurons. *J Neurophysiol* 2006; **95**:1285–1290.
9 Flores-Barrera E, Vizcarra-Chacón BJ, Tapia D, Bargas J, Galarraga E. Different corticostriatal integration in spiny projection neurons from direct and indirect pathways. *Front Syst Neurosci* 2010; **4**:15.
10 Garcia-Vilchis B, Suárez P, Serrano-Reyes M, Arias-García M, Tapia D, Duhne M, *et al*. Differences in synaptic integration between direct and indirect striatal projection neurons: role of Ca_V3 channels. *Synapse* 2019; **73**:e22079.
11 Gavrikov KE, Nilson JE, Dmitriev AV, Zucker CL, Mangel SC. Dendritic compartmentalization of chloride cotransporters underlies directional responses of starburst amacrine cells in retina. *Proc Natl Acad Sci USA* 2006; **103**:18793–18798.
12 Wright R, Raimondo JV, Akerman CJ. Spatial and temporal dynamics in the ionic driving force for $GABA_A$ receptors. *Neural Plasticity* 2011; **2011**:728395.
13 Báldi R, Varga C, Tamás G. Differential distribution of KCC2 along the axo-somatodendritic axis of hippocampal principal cells. *Eur J Neurosci* 2010; **32**:1319–1325.
14 Vizcarra-Chacón BJ, Arias-García MA, Pérez-Ramírez MB, Flores-Barrera E, Tapia D, Drucker-Colin R, *et al*. Contribution of different classes of glutamate receptors in the corticostriatal polysynaptic responses from striatal direct and indirect projection neurons. *BMC Neurosci* 2013; **14**:60.
15 Arias-García MA, Tapia D, Flores-Barrera E, Pérez-Ortega JE, Bargas J, Galarraga E. Duration differences of corticostriatal responses in striatal projection neurons depend on calcium activated potassium currents. *Front Syst Neurosci* 2013; **7**:63.
16 Deleuze C, Pazienti A, Bacci A. Autaptic self-inhibition of cortical GABAergic neurons: synaptic narcissism or useful introspection? *Curr Opin Neurobiol* 2014; **26**:64–71.
17 Russo G, Nieus TR, Maggi S, Taverna S. Dynamics of action potential firing in electrically connected striatal fast-spiking interneurons. *Front Cell Neurosci* 2013; **7**:209.
18 Taverna S, Van Dongen YC, Groenewegen HJ, Pennartz CM. Direct physiological evidence for synaptic connectivity between medium-sized spiny neurons in rat nucleus accumbens in situ. *J Neurophysiol* 2004; **91**:1111–1121.
19 Gustafson N, Gireesh-Dharmaraj E, Czubayko U, Blackwell KT, Plenz DA. Comparative voltage and current clamp analysis of feedback and feedforward synaptic transmission in the striatal microcircuit in vitro. *J Neurophysiol* 2005; **95**:737–752.
20 Arias-García MA, Tapia D, Laville JA, Calderón VM, Ramiro-Cortés Y, Bargas J, *et al*. Functional comparison of corticostriatal and thalamostriatal postsynaptic responses in striatal neurons of the mouse. *Brain Struct Funct* 2018; **223**:1229–1253.
21 Ben-Ari Y. Excitatory actions of GABA during development: the nature of the nurture. *Nat Rev Neurosci* 2002; **3**:728–739.
22 Haam J, Popescu IR, Morton LA, Halmos KC, Teruyama R, Ueta Y, *et al*. GABA is excitatory in adult vasopressinergic neuroendocrine cells. *J Neurosci* 2012; **32**:572–582.
23 Randle JC, Renaud LP. Actions of gamma-aminobutyric acid on rat supraoptic nucleus neurosecretory neurones in vitro. *J Physiol* 1987; **387**:629–647.
24 Bartos M, Vida I, Jonas P. Synaptic mechanisms of synchronized gamma oscillations in inhibitory interneuron networks. *Nat Rev Neurosci* 2007; **8**:45–56.

Copyright © 2019 Wolters Kluwer Health, Inc. Unauthorized reproduction of this article is prohibited.

Check for updates

Feed-forward information and zero-lag synchronization in the sensory thalamocortical circuit are modulated during stimulus perception

Adrià Tauste Campo[a,b,1], Yuriria Vázquez[c,d], Manuel Álvarez[c], Antonio Zainos[c], Román Rossi-Pool[c], Gustavo Deco[b,e], and Ranulfo Romo[c,f,1]

[a]Barcelonaβeta Brain Research Center (BBRC), Pasqual Maragall Foundation, 08005 Barcelona, Spain; [b]Center for Brain and Cognition, Department of Information and Communication Technologies, Universitat Pompeu Fabra, 08003 Barcelona, Spain; [c]Instituto de Fisiología Celular–Neurociencias, Universidad Nacional Autónoma de México, 04510 Mexico City, Mexico; [d]Laboratory of Neural Systems, The Rockefeller University, New York, NY 10065; [e]Institució Catalana de Recerca i Estudis Avançats, 08010 Barcelona, Spain; and [f]El Colegio Nacional, 06020 Mexico City, Mexico

Contributed by Ranulfo Romo, February 20, 2019 (sent for review November 8, 2018; reviewed by Sonja Grün and Stefano Panzeri)

The direction of functional information flow in the sensory thalamocortical circuit may play a role in stimulus perception, but, surprisingly, this process is poorly understood. We addressed this problem by evaluating a directional information measure between simultaneously recorded neurons from somatosensory thalamus (ventral posterolateral nucleus, VPL) and somatosensory cortex (S1) sharing the same cutaneous receptive field while monkeys judged the presence or absence of a tactile stimulus. During stimulus presence, feed-forward information (VPL → S1) increased as a function of the stimulus amplitude, while pure feed-back information (S1 → VPL) was unaffected. In parallel, zero-lag interaction emerged with increasing stimulus amplitude, reflecting externally driven thalamocortical synchronization during stimulus processing. Furthermore, VPL → S1 information decreased during error trials. Also, VPL → S1 and zero-lag interaction decreased when monkeys were not required to report the stimulus presence. These findings provide evidence that both the direction of information flow and the instant synchronization in the sensory thalamocortical circuit play a role in stimulus perception.

behaving monkeys | somatosensory thalamocortical circuit | tactile detection task | simultaneous single-unit recordings | directed information-theoretic measure

A major challenge in systems neuroscience involves understanding how perceptual experiences arise from coordinated neural activity, and how functional information flows among the interacting neurons (1–5). The sensory thalamus is an essential node within the perceptual circuit, relaying stimulus information from the periphery to cortex (6). Given the connectivity between the thalamus and cortex, feed-back corticothalamic inputs could modulate feed-forward thalamocortical stimulus information transmission during perception (7–10). Thus, the thalamus could act as a processing unit in continuous interaction with the cortex (6, 11, 12). Evidence supporting this view comes from previous studies in anesthetized (13–15) and awake animals (10, 16). However, it is unclear how feed-forward and feed-back information flows coexist within the thalamocortical circuit and whether they correlate with the subject's perception.

To address these questions, we recorded the simultaneous activity of single neurons in the ventral posterolateral nucleus (VPL) of the somatosensory thalamus and in primary somatosensory cortex (S1) sharing the same cutaneous receptive field while monkeys performed a vibrotactile detection task. The animals were trained to report the presence or absence of a tactile stimulus of variable amplitude. In this task, previous work showed that VPL and S1 neurons encode mostly the physical features of the stimulus (17, 18). These findings raise several questions. First, how is sensory information communicated between the VPL and S1 at the level of single neurons? Second, what is the balance between the information flowing in a feed-forward direction (VPL → S1) and in a feed-back (S1 → VPL) direction? Third, does the information flow between VPL and S1 correlate with the subject's perception?

In the current work, we addressed the above questions by detecting time-varying directional couplings between the recorded VPL and S1 neuron pairs across many trials as a measure of the functional thalamocortical information flow needed to perform a vibrotactile detection task. During the stimulus presence, feed-forward (VPL → S1) information largely prevailed over feed-back (S1 → VPL) information. Interestingly, zero-lag interactions emerged with the stimulus amplitude above detection threshold, suggesting the existence of cortical common inputs facilitating the transmission of stimulus information. Critically, at the stimulus onset, feed-forward information correlated with the subject's perception. During a variant of the detection task (passive condition, in which no response was required from the animal), feed-forward information was reduced during the expected stimulation windows of stimulus-present and stimulus-absent trials, while zero-lag interaction was mainly reduced in the first half of the stimulus. Taken together, our results characterize the functional information flow between VPL–S1 neuron pairs during tactile perception. They reveal that besides relaying stimulus information

Significance

The direction of information flow between brain circuits may be key in cognitive functions. We addressed this problem by evaluating a directional correlation measure between simultaneously recorded neurons from somatosensory thalamus (ventral posterolateral nucleus, VPL) and somatosensory cortex (S1) sharing the same cutaneous receptive field while monkeys judged presence or absence of tactile stimuli. During stimulus presence, feed-forward (VPL → S1) information increased as a function of stimulus amplitude, while feed-back (S1 → VPL) information was unaffected. Simultaneously, zero-lag interaction emerged with increasing stimulus amplitude, contributing to thalamocortical synchronization. Furthermore, VPL → S1 information decreased during error trials. Also, both VPL → S1 and zero-lag interactions decreased when monkeys were not required to report stimulus presence. Thus, directional and coordinated information in the thalamocortical circuit is associated with stimulus perception.

Author contributions: A.T.C. and R.R. designed research; Y.V., M.Á., A.Z., and R.R. performed research; A.T.C. and R.R. contributed new reagents/analytic tools; A.T.C., R.R.-P., and G.D. analyzed data; and A.T.C., Y.V., R.R.-P., G.D., and R.R. wrote the paper.

Reviewers: S.G., Research Center Juelich; and S.P., Italian Institute of Technology.

The authors declare no conflict of interest.

Published under the PNAS license.

[1]To whom correspondence may be addressed. Email: adria.tauste@gmail.com or rromo@ifc.unam.mx.

This article contains supporting information online at www.pnas.org/lookup/suppl/doi:10.1073/pnas.1819095116/-/DCSupplemental.

Published online March 25, 2019.

Downloaded at Instituto de Biotecnología/UNAM on October 20, 2020

feed-forward information conveys task-context information, whereas zero-lag interactions might reflect the cortically driven coordinated activity of VPL and S1 that is required for information transmission during task performance.

Results

Two monkeys *(Macaca mulatta)* were trained to perform a tactile detection task (2, 3). In each trial, the animal had to report whether the tip of a mechanical stimulator vibrated or not (Fig. 1*A*). Stimuli were sinusoidal, had a fixed frequency of 20 Hz, and were delivered to the glabrous skin of one fingertip; crucially, they varied in amplitude across trials. Stimulus-present trials were interleaved with an equal number of stimulus-absent trials in which no mechanical vibrations were delivered (Fig. 1*A*). The presence or absence of the stimulus (0.5 s) was preceded by a variable prestimulus period (1.5 to 3 s), followed by a fixed poststimulus delay period of 3 s before the monkey reported its decision by pressing one of two push buttons (Fig. 1*A*). In stimulus-absent trials, we will refer to the possible window of stimulation (PWS) as the temporal windows when the monkeys may expect the stimulus (19). Stimulus detection thresholds were calculated from the behavioral responses (Fig. 1*B*, *Left*). Importantly, depending on the monkeys' responses, trials could be classified into four types: hits and misses in the stimulus-present trials and correct rejections and false alarms in the stimulus-absent condition (Fig. 1*B*, *Right*). Once the animals performed the task at near detection threshold (8 μm), we recorded the simultaneous activity of spike trains from individual neurons from VPL and S1 (areas 3b or 1; Fig. 1*C*) while monkeys performed the task. Here, it is important to highlight that the recorded neuron pairs (n = 84) from the VPL and S1 shared exactly the same cutaneous receptive fields (Fig. 1*D*). Fig. 1*E* qualitatively shows that the neurons of VPL and S1 modulate their firing rate during the stimulus-present condition (Fig. 1*E*, *Left*), but not during the stimulus-absent condition (Fig. 1*E*, *Right*). Thus, it appears an optimal experimental condition for assessing the functional time-varying information flow between neuron pairs from VPL and S1 during the detection task.

Assessing Directional Information Flow Between VPL and S1. It is well-established that the VPL relays information from the skin mechanoreceptors up to S1 (Fig. 1 *C* and *D*). This knowledge allows us to test the following hypothesis in the detection task: After the stimulus onset, the flow of functional information becomes crucially larger in the VPL → S1 direction than in the S1 → VPL direction. However, given the stronger anatomical connectivity from S1 to VPL than from VPL to S1 (12), the second hypothesis is that the flow of functional information is higher from S1 → VPL than from VPL → S1. Importantly, we also hypothesize that the information flow between VPL and S1 could be affected by task conditions (Fig. 1*B*). We addressed all these hypotheses by using a nonparametric method that measures directional information flows between the simultaneously recorded spike trains of pairs of VPL–S1 neurons in single trials and within slicing time windows of 0.25 ms using a directed information-theoretic measure (5, 20, 21) (*SI Appendix*). The method is illustrated in Fig. 2*A*. To measure single-neuron interactions on a fine temporal scale along each task trial, we estimated delayed versions of the directed information-theoretic measure (*SI Appendix*, Eq. **S1**) in both directions (VPL → S1 and S1 → VPL) for every pair of simultaneous VPL–S1 spike trains at the short time delays [0, 2, 4, . . ., 20 ms] (Fig. 2*A*, *Left*). To infer the significance of each estimation, we defined a maximizing-delay statistic (*SI Appendix*, Eq. **S2**) and built the corresponding null distribution using circular shifts of the target spike-train sequences (Y^T), which preserved the firing rate and the short-range (0 to 50 ms) autocorrelation of both spike trains while destroying their temporal alignment (Fig. 2*A*, *Middle*). For

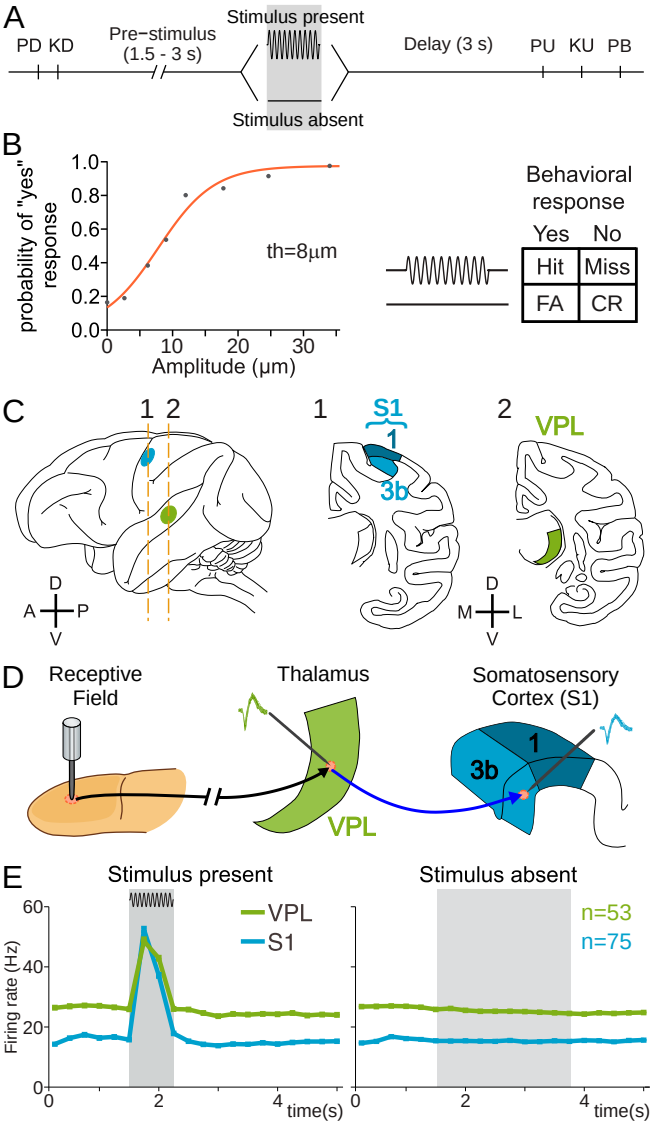

Fig. 1. Detection task, psychophysical performance, recording sites, and neuronal responses during the task. (*A*) Vibrotactile detection task. Trials began when the stimulator probe indented the skin of one fingertip of the monkey's restrained right hand (probe down, PD); the monkey reacted by placing its left, free hand on an immovable key (key down, KD). After a variable prestimulus period (1.5 to 3 s), a vibratory stimulus of variable amplitude (1 to 34 μm, 20 Hz, 0.5-s duration) was presented on one half of the trials; no stimulus was presented on the other half of the trials. Following the stimulus presentation period or a period where no stimulus was delivered, the monkey waited for 3 s until the probe was lifted off from the skin (PU, probe up), then the animal removed its free hand from the key (KU, key up) and pressed one of two push buttons (PBs) to report whether the stimulus was present or absent. Lateral and medial buttons were used for reporting stimulus presence and stimulus absence, respectively. Stimulus-present and stimulus-absent trials were randomly interleaved within a run. (*B*) The button pressed indicated whether the monkey felt the stimulus (henceforth referred as yes and no responses, respectively). (*B*, *Left*) Mean psychometric function depicting the probability of the monkey's reporting yes as a function of the stimulus amplitude (th = 8 μm, detection threshold). (*B*, *Right*) Behavioral responses depending on the stimulus presence (Hit or Miss) or stimulus absence (CR, correct rejection; FA, false alarm). (*C*) Recording sites in the ventral posterior lateral (VPL) nucleus (green) of the thalamus and in areas 1 and 3b of the primary somatosensory cortex (S1, cyan). (*D*) Scheme depicting how the neural activity from single neurons in the VPL and S1 (3b or area 1) sharing the same cutaneous receptive field was simultaneously recorded during the detection task. (*E*) Mean firing rate for the simultaneously recorded VPL (n = 53) and S1 (n = 75) neurons during the stimulus-present and stimulus-absent trials.

Downloaded at Instituto de Biotecnología/UNAM on October 20, 2020

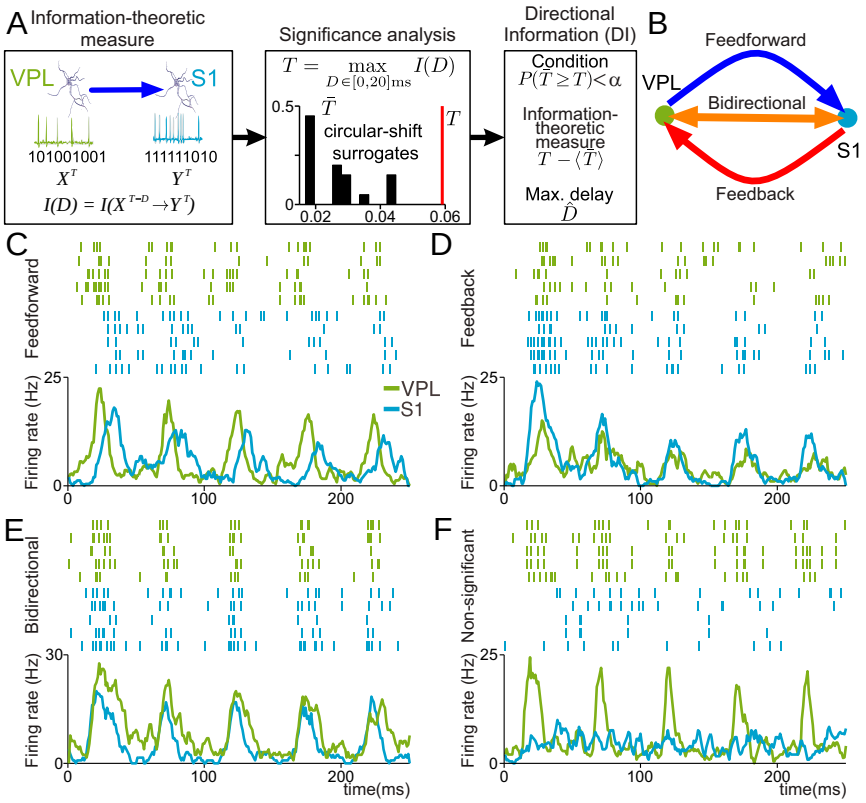

Fig. 2. Assessing DI between pairs of VPL and S1 neurons during the detection task. (*A*) Sequential scheme representing the method to infer DI at single-trial level. (*Left*) Information-theoretic measure is estimated between single-trial spike trains of the simultaneously recorded neurons in VPL and S1 for delays (0, 2, . . ., 20) ms. (*Middle*) Significance is locally determined via nonparametric testing ($\alpha = 0.05$) of a maximizing-delay statistic. (*Right*) Every significant statistic ($P < \alpha$) is associated with an unbiased information-theoretic measure value ($T - \langle T \rangle$) and a maximizing delay ($\hat{D}$). (*B*) Graphical representation for feed-forward (VPL → S1, in blue), feed-back (S1 → VPL, in red), and bidirectional (S1 ↔ VPL, in orange) information between VPL and S1 neurons. (*C–F*) Raster plots and spike density functions depicting the neural activity occurring during the first 250 ms of stimulation (34 μm) for examples of VPL (green) and S1 (cyan) neuron pairs involved in feed-forward (*C*), feed-back (*D*), and bidirectional (*E*) information and nonsignificant (*F*) statistic values.

each directional spike-train pair, (X^T, Y^T), the method assessed the significance of the statistic together with an unbiased estimation of the statistic value and the maximizing delay (Fig. 2*A*, *Right*). Directional spike-train pairs associated with significant estimators ($\alpha = 0.05$) will be referred to as directional information (DI) trials (*SI Appendix*) and will be represented for different experimental conditions as a percentage over the corresponding pairs and trials. Finally, statistical comparisons between percentages were assessed with nonparametric methods (21) and validated via Cohen's *H* (22) effect size (*H*) for proportion differences (*SI Appendix*).

A first characterization of the VPL–S1 simultaneous activity was done by measuring the percentage of DI (*SI Appendix*, Fig. S1*A*) as well as the mean DI value (*SI Appendix*, Fig. S1*B*) for VPL → S1 and S1 → VPL directions during the time course of the detection task for spike trains above a firing rate threshold (35 Hz). Both quantities were calculated separately for the stimulus-present (*SI Appendix*, Fig. S1*B*, *Left*) and stimulus-absent (*SI Appendix*, Fig. S1*B*, *Right*) trials. For the analysis of stimulus-present trials here and in the subsequent figures, we removed the variable-time prestimulus period in every trial and aligned all trials to the stimulus onset time. The analysis showed that for the stimulus-present trials the amount of VPL → S1 DI (trials = 3,216 in neuron pairs = 84, $P < 0.01$, $H > 0.5$, cyan line; *SI Appendix*, Fig. S1*A*, *Left*) was significantly larger than the amount of S1 → VPL DI during the first half (250 ms) of the stimulus period and weaker but still significant during the second half ($H < 0.5$). However, the strongest effect at stimulus onset was not mimicked by the mean DI value ($P < 0.01$, $D < 0.3$; *SI Appendix*, Fig. S1*B*, *Left*). In contrast, for stimulus-absent trials, the greatest differences were manifested by the amount of DI (trials = 4,371 in neuron pairs = 84, $P < 0.01$, $H > 0.3$; *SI Appendix*, Fig. S1*A*, *Right*) during the PWS (1.5 to 3.5 s) with no counterpart evidence from the mean DI value (*SI Appendix*, Fig. S1*B*, *Right*). Despite its moderate statistical effect ($H < 0.5$), *SI Appendix*, Fig. S1 shows a positive gap between VPL → S1 and S1 → VPL directions already during the prestimulus period, which could reflect an underlying directionality imbalance facilitating subsequent sensory information transmission. In conclusion, we restricted our analysis to the percentage of DI (rather than the mean DI value) due to its greater sensitivity to detect directionality differences during the stimulus and possible stimulation windows.

As a first approach, we considered exclusively two directionality cases: VPL → S1 and S1 → VPL (*SI Appendix*, Fig. S1). However, when studying DI flow for two simultaneous spike *T*-length trains X^T and Y^T at a given time interval (e.g., 250 ms) one may instead consider three disjoint cases: The spike trains are coupled in only one direction ($X^T \rightarrow Y^T$), in only the opposite direction ($Y^T \rightarrow X^T$) or simultaneously coupled in both directions ($X^T \leftrightarrow Y^T$). In principle, these three cases correspond to neurons in each pair taking three different roles—driver, target, or both—which may be associated with distinct functional mechanisms (24). According to this notion, we classified DI estimates by pairing the location and role of each neuron per trial. In short, we defined as feed-forward information (VPL → S1) those DI estimates involving pairs where the neuron of VPL was only driver and the neuron of S1 was only target. Similarly, we

Downloaded at instituto de Biotecnologia/UNAM on October 20, 2020

defined as feed-back information (S1 → VPL) where the neuron of S1 was only driver and the VPL neuron was only target. Finally, pairs where the neuron in VPL and the neuron in S1 were simultaneously drivers and targets (at possible different delays) of that interaction were labeled as bidirectional information. Fig. 2*B* shows a schematic representation for the three types of DI and Fig. 2 *C*–*E* shows four example pairs of neurons (five repetitive trials; green for VPL raster plots and cyan for S1 raster plots) responding during the first 250 ms after stimulus onset holding feed-forward (Fig. 2*C*), feed-back (Fig. 2*D*), and bidirectional (Fig. 2*E*) information, together with neuron pairs with nonsignificant statistic values (Fig. 2*F*). Since the significance analysis leading to DI is always single-trial, the choice of five trials in Fig. 2*D* is only for illustrative purposes here.

Stimulus Presence Modulates Feed-Forward and Bidirectional Information. Having set the above definitions, we first examined for each type of DI the average DI delay as a putative intrinsic property of each directionality case (*SI Appendix*, Fig. S2). Bidirectional information occurred at shorter delays than unidirectional information for both stimulus-present (trials = 3,217 in neuron pairs = 84, $D = 0.35$, time-average Cohen's d; *SI Appendix*, Fig. S2*A*, *Left*) and stimulus-absent trials (trials = 4,731 in neuron pairs = 84, $D = 0.37$, time-average Cohen's d; *SI Appendix*, Fig. S2*A*, *Right*). The delay histograms (*SI Appendix*, Fig. S2*B*, *Top*) outside the stimulus period or the PWS revealed that these differences were, in general, due to higher percentage of zero-delay couplings (around 33%) in bidirectional information compared with unidirectional information (around 15%). Further, we examined the DI delay distribution during the stimulus period (*SI Appendix*, Fig. S2*B*). We found that the arrival of the stimulus increased the relative amount of bidirectional information at zero delay (from 33 to 49%). However, the relative amount of feed-forward (from 9 to 19%) and feed-back information (from 9 to 15%) was enhanced at 8 ms.

Second, we investigated two main questions regarding feed-forward, feed-back, and bidirectional information: (*i*) What was the contribution of each DI type to a greater amount of VPL → S1 DI observed during the stimulus presence? and (*ii*) What was the contribution of each neuron pair to this effect? Fig. 3*A* depicts the percentages of DI according to their types (feed-forward, feed-back, and bidirectional) for stimulus-present (Fig. 3*A*, *Left*) and stimulus-absent trials (Fig. 3*A*, *Right*) during the time course of the task. The proposed decomposition highlighted the contribution of each type into the directionality differences illustrated in *SI Appendix*, Fig. S1. The increment in the VPL → S1 DI, especially after the stimulus onset, was mainly contributed by feed-forward information (trials = 3,216 in neuron pairs = 84, $P < 0.05$, $H = 0.23$; blue trace in Fig. 3*A*, *Left*) and lesser by the bidirectional information (trials = 3,216, neuron pairs = 84, $P < 0.05$, $H = 0.1$; orange trace in Fig. 3*A*, *Left*). In contrast, the increase in the S1 → VPL direction (*SI Appendix*, Fig. S1) could only be explained by an increase in bidirectional information. Indeed, genuine feed-back information was not significantly modulated during the stimulus presence ($P > 0.05$; red trace in Fig. 3*A*, *Left*). However, for stimulus-absent trials, no DI type showed a significant modulation (trials = 4,271 in neuron pairs = 84, $P > 0.05$; Fig. 3*A*, *Right*).

We then investigated the contribution of each neuron pair to the increment in feed-forward and bidirectional information during the first half of the stimulus period in the stimulus-present trials. To do so, we repeated the analysis of Fig. 3*A* for every VPL–S1 pair and obtained a stimulus-driven effect size per pair. Fig. 3*B* illustrates these results by sorting the neuron pairs independently for each DI type in a descending effect size order. Consistent with our previous findings, there were more neuron pairs exhibiting large stimulus effects in feed-forward and bidirectional information than in feed-back information. Besides that, ~40% (33/84) and 20% (18/84) of the neuron pairs increased the number

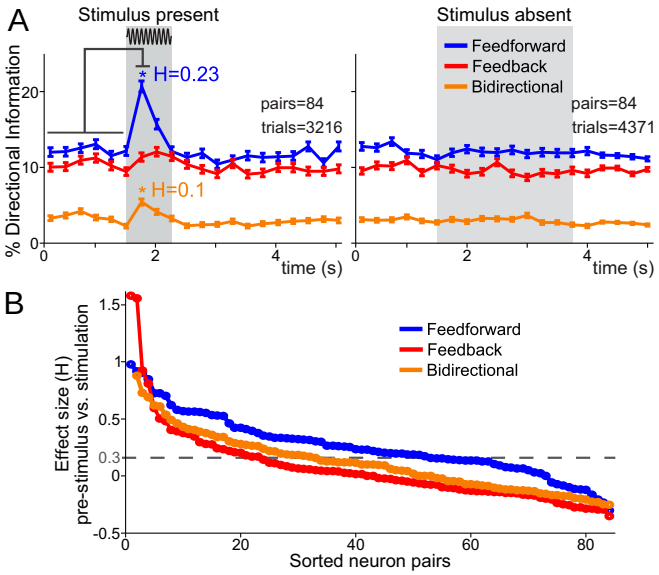

Fig. 3. VPL–S1 feed-forward, feed-back, and bidirectional information during the detection task. We analyzed hit and correct rejection trials across all recorded VPL–S1 neuron pairs. (*A*) Percentage of feed-forward, feed-back, and bidirectional information during the time course of the task during the stimulus-present (*Left*, trials = 3,216 hits; neuron pairs = 84) and stimulus-absent trials (*Right*, trials = 4,371 correct rejections; neuron pairs = 84). Error bars denote the SEM. In all figures, gray boxes depict the stimulus period for the stimulus-present trials and the PWS for the stimulus-absent trials. Asterisks denote significant differences ($P < 0.05$) between the prestimulus (first six task intervals, 1.5 s) and the first half (0 to 0.25 s) of the stimulus period (nonparametric test, $\alpha = 0.05$). H denotes the effect size (Cohen's H) of significant differences. Here and in the next time-varying figures, we removed the variable-time prestimulus period in every stimulus-present trial and aligned all trials to the stimulus onset. In stimulus-absent trials, we aligned the trials to the probe down event (PD). (*B*) Effect size of the difference between the percentage of each DI type during the prestimulus period and during the first stimulus interval as a function of the neuron pairs. Each curve is represented by ordering the neuron pairs in descending order according to the magnitude of the effect size for each particular DI type. The black horizontal dashed line represents the effect size threshold ($H \geq 0.3$).

of feed-forward and bidirectional information, respectively, with moderate and large effect sizes ($H > 0.3$; Fig. 3*B*).

Next, we asked how often a VPL–S1 neuron pair could simultaneously handle both DI modulations during the stimulus period. To address this question, we correlated the stimulus effect sizes associated with each DI type across all of the recorded VPL–S1 neuron pairs. The correlation value between the effect sizes was rather low ($\rho = -0.11$, $P > 0.5$, Spearman's rho), suggesting that feed-forward and bidirectional information might be modulated by a different thalamocortical mechanism. We also analyzed how neuron pairs were differently modulated during stimulus-absent trials (*SI Appendix*, Fig. S3). To this end, we compared the percentage of feed-forward, feed-back, and bidirectional information per neuron pair during the first interval of the stimulus window and during the first interval of the PWS. Each point in *SI Appendix*, Fig. S3 represents a VPL–S1 neuron pair and the histograms of all points' angles with respect to the stimulus-present axis (x axis: stimulus present; y axis: stimulus absent) are shown as insets. Therefore, angular values smaller than 45° indicated a stronger amount of DI during the stimulus period. Thus, mean angular values indicated that the stimulus-present effect ($\theta < 45°$) was more prominently manifested in feed-forward ($\theta = 30.5°$; *SI Appendix*, Fig. S3) and bidirectional information ($\theta = 25.2°$; *SI Appendix*, Fig. S3) than in feed-back information ($\theta = 41.1°$; *SI Appendix*, Fig. S3). In sum, we provided

Downloaded at Instituto de Biotecnologia/UNAM on October 20, 2020

consistent evidence from independent analyses that tactile stimuli mainly modulated feed-forward and bidirectional information in the VPL–S1 neuron pairs.

Correlation Between the Firing Rate and the Type of Directional Information. The statistical method used in this study infers DI measurements by preserving the firing rate of both sequences in the null distribution, thus avoiding to a large extent the bias introduced by fluctuations of the neuronal spikes (25, 26). To empirically corroborate this fact, we examined the influence of the firing rate into the observed VPL–S1 DI. In previous related work (17, 18) we showed that the average firing rate was larger in VPL than in S1 neurons (Fig. 1*E*). Therefore, the reported increase of feed-forward information (compared with feed-back information) occurred while the VPL and S1 neurons exhibited similar firing rates. This initially suggested a low dependence between the firing rate and the existence of DI. We then tested this hypothesis by correlating the firing rate driver and target neurons with the existence of incoming/outgoing DI (*SI Appendix*). The obtained Spearman correlation coefficients were significant but rather low for both driver (intervals = 206,360 in neuron pairs = 84, $\rho = 0.11$, $P < 0.05$; *SI Appendix*, Fig. S4*A*) and target neurons (intervals = 206,360 in neuron pairs = 84, $\rho = 0.07$, $P < 0.05$; *SI Appendix*, Fig. S4*A*). Moreover, these results were stable during stimulus-absent trials (intervals = 206,280 in neuron pairs = 84, $\rho = 0.1$ for driver spike trains, $\rho = 0.07$ for target spike trains, $P < 0.05$; *SI Appendix*, Fig. S4*B*). This shows that the increase in the number of DI estimates during the stimulus period could not be explained merely by an increase in the mean firing rate of either the VPL or S1 neurons.

The results shown above suggested that the firing rate might be poorly correlated with the distinct DI types. To specifically address this question, we first computed the time-varying correlation (Spearman's rho) between the firing rate in VPL and S1 neurons (*SI Appendix*, Fig. S4 *C* and *D*) associated with feed-forward, feed-back, and bidirectional information for stimulus-present (trials = 3,216 in neuron pairs = 84; *SI Appendix*, Fig. S4 *C* and *D*, *Left*) and stimulus-absent (trials = 4,371 in neuron pairs = 84; *SI Appendix*, Fig. S4 *C* and *D*, *Right*). The results show that the correlation values obtained during the entire time course of the task were upper-bounded by 0.1 for VPL neurons and by 0.2 for S1 neurons. For S1 neurons specifically, the correlation values decreased during the stimulus period. This implies that, for a substantial number of S1 neurons, the reported increase in firing rate (Fig. 1*E*) during the stimulus presence was not accompanied by an increase of incoming/outgoing DI with VPL. Besides, during the stimulus presence, the correlation values were larger for bidirectional information (rather than unidirectional) in VPL and S1 neurons, suggesting that neurons holding bidirectional information were particularly prone to have large firing rates. To further study this question, we examined the firing rate of VPL and S1 neurons associated with feed-forward, feed-back, and bidirectional information (Fig. 4 and *SI Appendix*). Our analysis revealed that the firing rate of VPL and S1 neurons was not significantly different ($n = 53$ and $n = 75$, respectively, Wilcoxon rank-sum test, $P > 0.05$; Fig. 4) between feed-forward and feed-back information across all task intervals, including those from the stimulus period. In contrast, neurons holding bidirectional information showed a significant increase in their firing rate with respect to the unidirectional case during the first interval of the stimulus period ($P < 0.05$; Fig. 4), in agreement with the reported larger correlation observed in the bidirectional type (*SI Appendix*, Fig. S4 *C* and *D*). These increases were manifested at suprathreshold stimulus amplitudes for VPL neurons ($n = 53$, $P < 0.001$; Fig. 4) during the entire stimulus period but for S1 neurons ($n = 75$, $P < 0.05$; Fig. 4) only during the first interval of the stimulus period. Interestingly, for stimulus-absent trials, bidirectional neurons showed enhanced firing

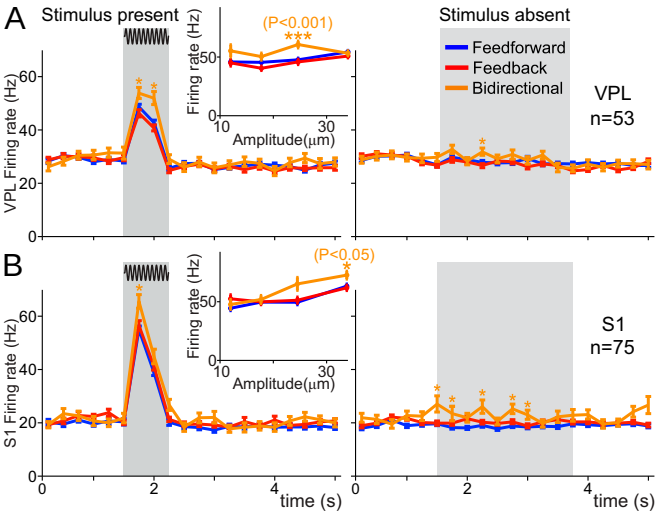

Fig. 4. Mean firing rate of VPL and S1 neurons during the detection task for feed-forward, feed-back, and bidirectional information. We analyzed hit and correct rejection trials across all recorded neurons in VPL and S1. For all panels, gray boxes depict the stimulus period for the stimulus-present trials (*Left*) and the PWS for the stimulus-absent trials (*Right*). Blue, red, and orange traces depict the mean firing rate for neurons holding feed-forward, feed-back, and bidirectional information, respectively, during the time course of the detection task (neuron pairs = 84). Error bars denote the SEM. (*A*) Mean firing rate for VPL neurons ($n = 53$; *Left*, trials = 1,995 hits; *Right*, trials = 2,764 correct rejections). Insets depict the mean firing rate as a function of the stimulus amplitude during the stimulus period. Asterisks denote significant differences (*$P < 0.05$, ***$P < 0.001$, Wilcoxon rank-sum test) among the firing rate of neurons holding distinct DI. (*B*) Similar to *A*, but for S1 neurons ($n = 75$; *Left*, trials = 2,853 hits; *Right*, trials = 3,854 correct rejections).

rates during PWS intervals compared with unidirectional neurons. In sum, these results show that firing rates were not able to discriminate between unidirectional information (feed-forward vs. feed-back) but could be significantly higher for bidirectional information during specific task intervals regardless of the stimulus presence.

Finally, we simulated a stochastic model to evaluate the performance of the DI estimation method as a function of the neuronal firing rate and assess any potential bias in the reported empirical correlations with the firing rate (*SI Appendix*, Fig. S5; details provided in the legend). The results of the model for parameter values that approximated the average firing rate of neurons and the percentage of DI measured in the real data validated that the spurious correlations introduced by the DI estimation method were very low for both unidirectional and bidirectional models (Spearman's rho < 0.08). In the meantime, the DI estimation method was shown to attain large sensitivity values (>90%) even for low firing rates (~35 Hz).

The Amount of VPL–S1 Directional Information Is Modulated by the Stimulus Amplitude. We showed above that both feed-forward and bidirectional VPL–S1 information was enhanced by the stimulus presence, while feed-back information was minimally affected (Fig. 3). Furthermore, each DI type could be modulated by different neuronal populations. This prompted us to hypothesize that feed-forward and bidirectional information could be differently related to the stimulus amplitude. To further investigate this question, we divided the stimulus-present trials into three groups based on the stimulus amplitude. We grouped the 9-μm trials within the near-threshold (Fig. 5*A*, *Top Right*) group and defined the suprathreshold (Fig. 5*A*, *Top Left*) and subthreshold (Fig. 5*A*, *Bottom Left*) groups as those stimulus-present trials above and below 9 μm, respectively. We choose 9 μm as the cutoff amplitude since it is the closer amplitude to the monkey's

Downloaded at Instituto de Biotecnologia/UNAM on October 20, 2020

mean detection threshold (8 μm; Fig. 1*B*). We also considered stimulus-absent trials for comparison (Fig. 5*A*, Bottom Right). First, we quantified the amount of DI within each group (Fig. 5*A*). Notably, we found that the stimulus effect observed for all amplitudes (Fig. 3*B*) was mainly due to the suprathreshold group (>9 μm). At these amplitudes, feed-forward and bidirectional information showed a significant incremental effect (trials = 2,237 in neuron pairs = 84, $P < 0.01$, $H = 0.26$ and $H = 0.14$; Fig. 5*A*, *Top Left*), while feed-back information was not significantly altered ($P > 0.05$). In contrast, for the near-threshold group, the feed-forward increment was preserved (trials = 443 in neuron pairs = 84, $P < 0.01$, $H = 0.2$; Fig. 5*A*, *Top Right*), while bidirectional information dropped dramatically ($P > 0.05$). Finally, the subthreshold amplitudes only showed a weaker significant increase in the amount of feed-forward information (trials = 536 in neuron pairs = 84, $P < 0.01$, $H = 0.13$; Fig. 5*A*, *Bottom Left*). Thus, the results illustrated in Fig. 5*A* demonstrated that the amount of DI was amplitude-dependent. To examine this dependency, we focused on the first 250 ms of the stimulus-present period and plotted the percentage of DI types as a function of the stimulus amplitude (Fig. 5*B*). In addition, we computed single-trial (r) and average-trial (R) Spearman's rho correlations between the amount of DI and amplitude values (*SI Appendix*). During the first 250 ms the amount of each DI type was correlated with the stimulus amplitude values as measured by single-trial types ($P < 0.05$; Fig. 5*B*). However, when considering average-trial correlations, the significance analysis provided different outcomes across DI types. Indeed, Fig. 5*B* shows that feed-forward (trials = 7,587, $r = 0.12$ in neuron pairs = 84, $R = 0.96$, $P < 0.01$; Fig. 5*B*, *Left*) and bidirectional (trials = 7,587, $r = 0.07$ in neuron pairs = 84, $R = 0.87$, $P < 0.05$; Fig. 5*B*, *Right*) information exhibited a significant monotonic modulation, while feed-back information remained approximately constant over the amplitude values (trials = 7,587, $r = 0.03$ in neuron pairs = 84, R = 0.26, $P > 0.05$; Fig. 5*B*, *Middle*). These effects are further illustrated in *SI Appendix*, Fig. S6 by representing feed-back and bidirectional against feed-forward information, which suggested that the bidirectional trend was mainly driven by suprathreshold amplitudes. These results complemented the analysis of Fig. 5*A*, revealing that the amount of feed-forward and bidirectional information was monotonically associated with the stimulus amplitude. Overall, feed-forward and bidirectional information was enhanced by the stimulus presence and they could convey information about the stimulus amplitude.

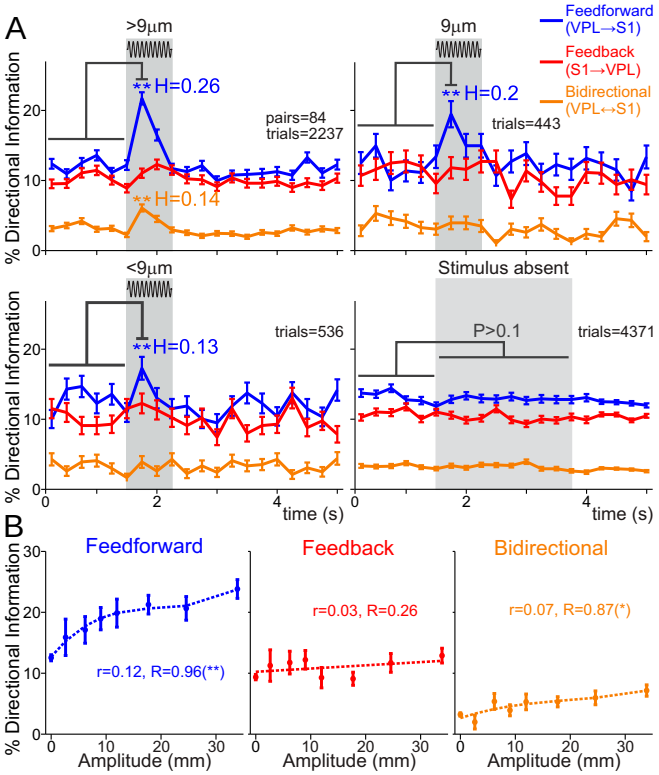

Fig. 5. VPL–S1 feed-forward and bidirectional information is modulated by the stimulus amplitude. We analyzed hit and correct rejection trials across all VPL–S1 neuron pairs. Hit trials were subdivided into three categories (suprathreshold, near threshold, and subthreshold). (*A*) Time course of the percentage of feed-forward (VPL → S1, blue), feed-back (S1 → VPL, red), and bidirectional (S1 ↔ VPL, orange) information between VPL and S1 neurons during stimulus-present and stimulus-absent trials. From left to right and from top to bottom: percentage of DI for suprathreshold (>9 μm, neuron pairs = 84; trials = 2,237 hits; *Top Left*), near threshold (9 μm, neuron pairs = 84; trials = 443 hits; *Top Right*), subthreshold (<9 μm, neuron pairs = 84; trials = 536 hits; *Bottom Left*) stimulus amplitudes, and stimulus-absent trials (neuron pairs = 84; trials = 4,371 correct rejections; *Bottom Right*). Asterisks denote significance levels (**$P < 0.01$; nonparametric test) between the prestimulus (first six task intervals, 1.5 s) and the first half (0 to 0.25 s) of the stimulus period. *H* denotes the effect size (Cohen's *H*) of significant percentage differences. Error bars denote the SEM. (*B*) Mean percentage of feed-forward, feed-back, and bidirectional information as a function of the stimulus amplitude during the first half of the stimulus period (*Left*, 250 ms). The value r is the correlation between the stimulus amplitude and the existence of DI in each type across all trials (no amplitude averages) with Spearman correlation (trials = 7,587). The value R is the analogous correlation considering amplitude-average values (number of stimulus amplitudes = 8). Asterisks depict significance (*$P < 0.05$, **$P < 0.01$, Spearman correlation). Error bars denote the SEM.

Influence of Task Context in Thalamocortical Directional Information. We showed above that for most recorded VPL–S1 neuron pairs there was more feed-forward than feed-back information during the first half (250 ms) of the stimulus-present trials. This differentiated amount of DI was related exclusively to sensory information processing, but whether it was also influenced by the task's context remained unknown. To investigate this question, we applied our directionality analysis to a control task in which the monkey was passively stimulated by the same set of tactile stimuli but no perceptual report was required. Using task-balanced datasets (*SI Appendix*), we repeated some of the previous analyses for stimulus-present trials (neuron pairs = 36, trials = 1,307 hits) and stimulus-absent trials (neuron pairs = 36, trials = 1,364 control rejects) in both task conditions, exploring potential differences in the percentage of DI when the monkey was passively stimulated (Fig. 6). Based on the previous analysis of amplitude modulation (Fig. 5), we restricted our analysis during stimulus-present trials to near-threshold and suprathreshold amplitudes for feed-forward information (neuron pairs = 36, trials = 1,105 hits) and suprathreshold amplitudes for feed-back and bidirectional information (neuron pairs = 36, trials = 932 hits).

We first revisited the firing rate of single neurons in VPL and S1 (17, 18) and found that the average (over neurons) firing rate of each area was not substantially altered during the time course of the passive stimulation task (Fig. 6*A*). Consistent with this quantification, we thereafter analyzed the percentage of DI during the passive condition over all neuron pairs that had been recorded in both task conditions. For these paired samples, we outlined task intervals where the difference was significant and the effect size was larger than 0.3. In general, our analysis revealed task-specific variations at the level of DI, which occurred around the stimulus period for stimulus-present trials (Fig. 6 *B–D*, *Left*). Compared with the vibrotactile task, the arrival of the (suprathreshold) stimulus in passive trials produced a lesser increase of bidirectional information (neuron pairs = 36; Fig. 6*D*, *Left*) during the second half of the stimulus window and a specific increase of feed-back information during the first 250 ms

Downloaded at Instituto de Biotecnología/UNAM on October 20, 2020

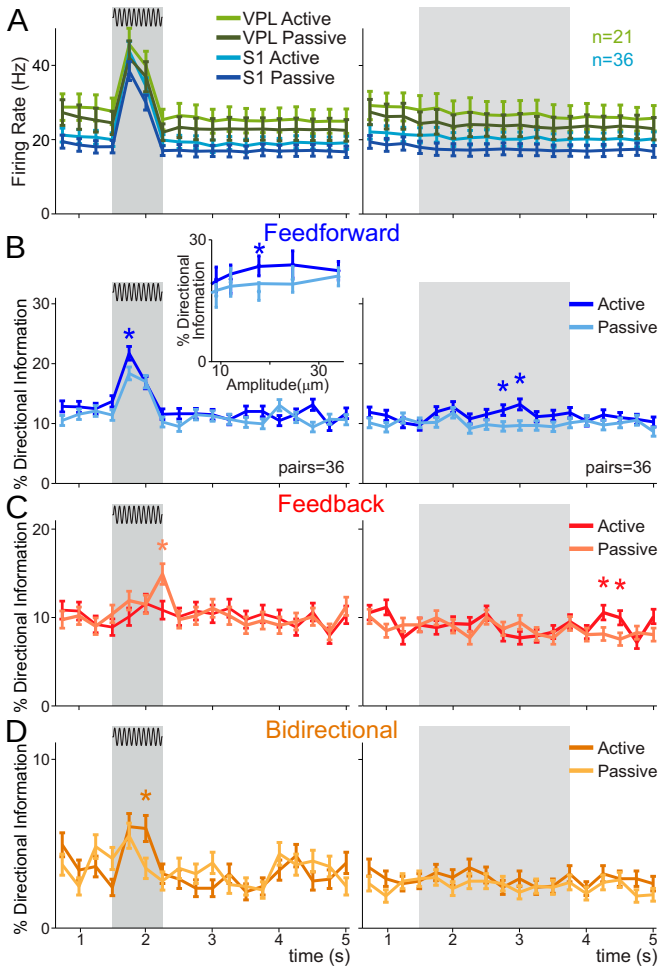

Fig. 6. VPL–S1 DI during passive stimulation. For the comparison between the vibrotactile detection task and the passive stimulation task, we analyzed supra- and near-threshold hit trials for feed-forward information and suprathreshold hit trials for feed-back and bidirectional information in addition to correct rejection trials. The left panels depict stimulus-present trials, whereas the right side depict stimulus-absent trials. Dark and light colors depict DI data belonging to the active and passive conditions, respectively. (*A*) Time course of the mean firing rates for VPL (n = 21) and S1 (n = 36) neurons. The same neuron pairs (pairs = 36) were simultaneously recorded during the detection task and passive stimulation. (*B*) Time course of the percentage of feed-forward information (pairs = 36; trials = 1,105 hits; trials = 1,364 correct rejections). (*Inset*) The percentage of feed-forward information as a function of stimulus amplitude. (*C*) Percentage of feed-back information for the active and passive conditions across time (pairs = 36; trials = 932 hits; trials = 1,364 correct rejections). (*D*) Percentage of bidirectional information across time (pairs = 36; trials = 932 hits; trials = 1,364 correct rejections). Asterisks denote significance levels (*P < 0.05, nonparametric balanced test) associated with effect sizes (Cohen's H) larger than 0.3.

of the poststimulation window (neuron pairs = 36; Fig. 6*C*, *Left*). Notably, feed-forward information was significantly higher in the active than the passive condition, both during the stimulus period (Fig. 6*B*, *Left*) and PWS (Fig. 6*B*, *Right*). Thus, our findings show that DI across VPL–S1 neuron pairs was sensitive to the task context. In particular, passive stimulation mitigated the amount of bidirectional information during stimulus delivery while enhancing feed-back information with a certain delay.

Influence of the Task on Zero-Lag Interactions. A priori, we defined DI types by matching the location of driver or target neurons to either VPL, S1, or both. However, the characterization of each DI type presented in *SI Appendix*, Fig. S2 unraveled features that could give rise to new characterizations. More specifically, the large percentage of bidirectional information occurring at zero delay (≥33%; *SI Appendix*, Fig. S2*B*) suggested that the zero-delay case could partially explain the trends reported for the bidirectional type. To study this question in detail, we decomposed bidirectional information into two subtypes: zero lag, for which both DI statistics (one per direction) were significant at zero delay, and non-zero lag, for which both statistics were simultaneously significant at non-zero delays (*SI Appendix*). We repeated most of the previous analyses on these two subtypes (Fig. 7). To begin with, we represented the time-varying percentage of each DI subtype during the time course of the task (Fig. 7*A*). Crucially, Fig. 7*A* shows that only zero-lag bidirectional information was significantly increased during the first 250 ms of the stimulus period ($P < 0.05$, $H > 0.14$; Fig. 7*A*, *Left*) and hence the reported overall bidirectional increase ($H = 0.1$; Fig. 7*A*, *Left*) was due to the zero-delay subtype. We then related zero-lag and non-zero lag bidirectional information with the firing rate of neurons in VPL and S1 ($n = 53$ and $n = 75$, respectively; Fig. 7 *B* and *C*). The results highlight that the firing rate of neurons holding zero-lag bidirectional information was frequently larger than those with non-zero lag (Wilcoxon rank-sum test, $P < 0.05$). Nonetheless, *SI Appendix*, Fig. S7 *A* and *B* validated that this enhancement of the firing rate did not simply follow from a larger correlation between the firing rate and zero-lag bidirectional information compared with other DI types (Spearman's rho < 0.2). Another reported feature of bidirectional information was its monotonic association with the stimulus amplitude (Fig. 5 and *SI Appendix*, Fig. S7*C*, *Left*). Hence, in light of the new decomposition, we investigated the contribution of the zero-lag sub-type to this trend. Performing the same analysis of Fig. 5*B*, we found that the modulation of bidirectional information by the stimulus amplitude was mostly explained by zero-lag bidirectional information (trials = 7,587, r = 0.06 in neuron pairs = 84, $R = 0.81$, $P < 0.05$; *SI Appendix*, Fig. S7*B*). Finally, we investigated the influence of the task context into zero-lag bidirectional information (Fig. 7*D*). In line with our previous analysis (Fig. 6*D*), we considered suprathreshold amplitudes (neuron pairs = 36, trials = 932 hits) and compared the amount of zero-lag bidirectional information across the same neurons pairs in both tasks. Critically, as compared to the original task ($P < 0.05$), zero-lag bidirectional information was not altered by the stimulus presence during passive stimulation. In contrast, this context effect was not observed in non-zero-lag bidirectional information. Taken together, we concluded that the distinctive features of bidirectional information reported so far were essentially occurring at zero delay. For the sake of interpretability, zero-lag bidirectional information will be referred to hereafter in short as zero-lag interaction.

Feed-Forward Information Correlates with the Animal's Task Performance. An important question is whether the DI across VPL–S1 neuron pairs is modulated by the animal's task performance. To further examine this question, we first analyzed the differences between hit and miss trials during the stimulus-present condition (Fig. 8*A*, *Left*) and between correct rejections and false-alarm trials during stimulus-absent trials (Fig. 8*A*, *Right*) across single neuron firing rates (Fig. 8*A*) and DI types (Fig. 8 *B*–*D*). In stimulus-present trials, we controlled for the effect of stimulus amplitudes by analyzing the difference between hits and misses at the near-threshold amplitude value (9 μm), where the number of samples was the most balanced between hit (trials = 443 hits in neuron pairs = 79) and miss responses (trials = 389 misses in neuron pairs = 79). In both experimental conditions, we controlled for a possible sample bias and experimental sessions effect, by using group-based permutation tests at the level of neuron pairs (*SI Appendix*). We then outlined task

Downloaded at Instituto de Biotecnología/UNAM on October 20, 2020

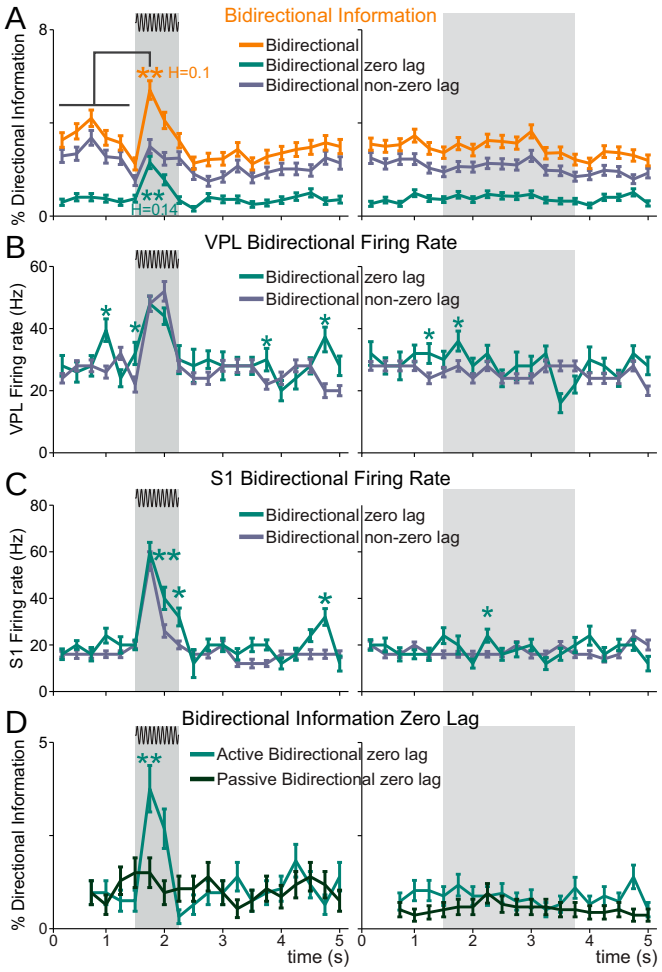

Fig. 7. Bidirectional information across zero-lag and non-zero-lag trials. We analyzed suprathreshold hit and correct rejection (CR) trials across neuron pairs. Error bars denote the SEM. (*A*) Percentage of overall bidirectional information (pairs = 84), zero-lag, and non-zero-lag bidirectional information across the task during stimulus-present (*Left*, trials = 3,216 hits) and stimulus-absent trials (*Right*, trials = 4,371 CR). Asterisks denote significant differences (**$P < 0.01$, nonparametric test) between the prestimulus (first six task intervals, 1.5 s) and the first half (0 to 0.25 s) of the stimulus period. H denotes the effect size (Cohen's *H*) of significant differences. (*B*) Mean firing rate for VPL neurons ($n = 53$; *Left*, trials = 1,995 hits; *Right*, trials = 2,764 CR). Asterisks denote significant differences (*$P < 0.05$; **$P < 0.01$; Wilcoxon rank-sum test) among the firing rate of neurons holding zero-lag and non-zero-lag bidirectional information. (*C*) Similar to *B*, but for S1 neurons ($n = 75$; *Left*, trials = 2,853 hits; *Right*, trials = 3,854 CR). (*D*) Percentage of zero-lag and non-zero-lag bidirectional information during suprathreshold and stimulus-absent trials (n pairs = 36; trials = 932 hits; trials = 1,364 CR) across the detection task and passive stimulation. Asterisks denote significance levels (**$P < 0.01$; nonparametric balanced test) associated with effect sizes (Cohen's *H*) larger than 0.3.

intervals where the difference was significant and the effect size was larger than 0.2. Our analysis primarily revealed that the amount of feed-forward information during the first half of the stimulus period in stimulus-present trials was significantly larger ($P < 0.05$, $H > 0.2$) in hit trials (Fig. 8*A*, *Left*). In contrast, our data did not unravel strong significant differences between correct rejections and false alarms during stimulus-absent trials (trials = 4,188 correct rejections and false alarm trials = 933 in neuron pairs = 82; Fig. 8*A*, *Right*). Overall, our results indicate that the amount of feed-forward information during the first half of the stimulus window was correlated with the monkey's behavior and could potentially predict the monkey's performance in stimulus-present trials (Fig. 8*B*, *Left*).

Discussion

Here, we sought to determine the functional roles of thalamocortical information flows in perception at a fine temporal scale. This was done by estimating a directional information measure (referred to as DI) between simultaneously recorded VPL–S1 neuron pairs sharing the same cutaneous receptive field while monkeys performed a vibrotactile detection task. Notably, the estimated DI could not be merely explained by increases in the firing rates of neurons within VPL or S1 during the stimulus period. We found that the stimulus presence elicited a significant increment on the amount of feed-forward information (VPL → S1) and zero-lag interaction. In

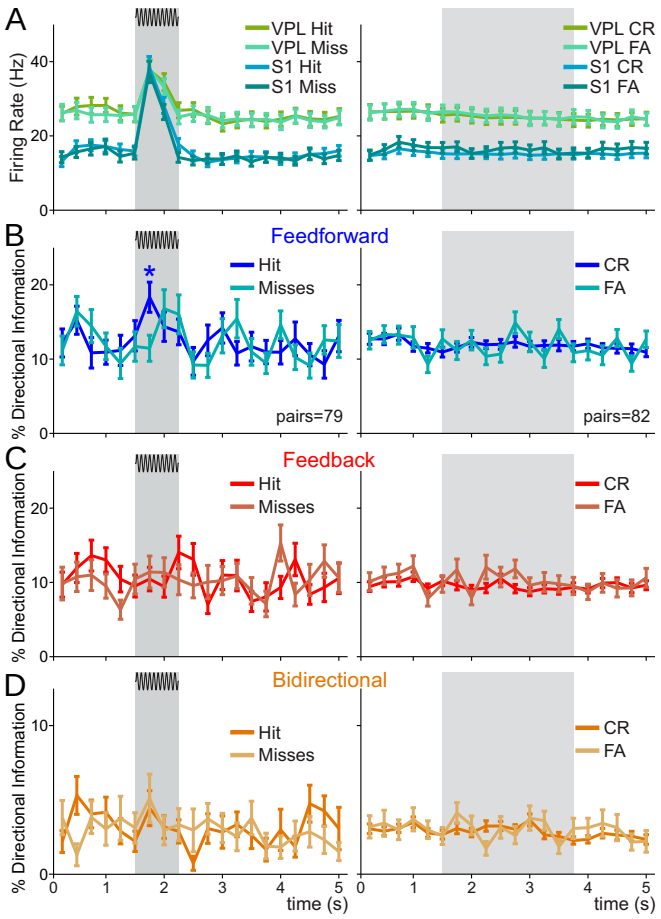

Fig. 8. VPL–S1 DI during correct and error trials. We analyzed hit and miss trials for near-threshold (9 μm) amplitudes as well as correct rejection trials and false alarms across all VPL–S1 neuron pairs. (*A*) Time course of the mean firing rate VPL ($n = 48$) and S1 ($n = 70$) neurons during stimulus-present trials and for VPL ($n = 51$) and S1 ($n = 73$) neurons during stimulus-absent trials. Neuronal responses were separated according to the monkey's behavioral output. (*Left*) Hits and misses for the stimulus-present trials. (*Right*) Correct rejections and false alarms for stimulus-absent trials. Neurons and pairs were selected to have more than two trials at near-threshold amplitude for each condition. (*B*) Time course for the percentage of feed-forward information. (*C*) Time course for the percentage of feed-back information. (*D*) Time course for the percentage of bidirectional information. (*B–D*, *Left*) Hits (dark colors) and misses (light colors) for the stimulus-present trials (neuron pairs = 79; trials = 443 hits; trials = 389 misses). (*B–D*, *Right*) Correct rejections (dark colors) and false alarms (light colors) for the stimulus-absent trials (neuron pairs = 82; trials = 4,188 correct rejections; trials = 933 false alarms). Asterisk denotes significance level (*$P < 0.05$; nonparametric test) associated with effect sizes (Cohen's *H*) larger than 0.2.

Downloaded at Instituto de Biotecnología/UNAM on October 20, 2020

contrast, pure feed-back (S1 → VPL) information remained practically unaltered during the stimulus presence. Remarkably, increments in feed-forward and zero-lag interaction were differently modulated as a function of the stimulus amplitude. Specifically, we found a monotonic relationship between both feed-forward and zero-lag interaction and the stimulus amplitude. However, zero-lag interaction only emerged significantly with suprathreshold sensory inputs during task performance. Additionally, we identified that thalamic and cortical neurons involved in bidirectional information exhibited higher firing rates during stimulus presence. Interestingly, the amount of feed-forward information was correlated with the monkeys' performance when they judged the presence at near-threshold stimuli. Also, during a passive stimulation task, when the monkeys were not required to report their percepts, both feed-forward and, more prominently, zero-lag interaction were reduced during the stimulus presence. This suggests that feed-forward information and zero-lag interaction are modulated by the task context. We discuss these findings below.

In the current study, we extended previous spectral and neural population studies on thalamocortical directionality (10, 27–29) to the temporal domain, at the level of single-neuron activity. To achieve this, we analyzed the DI between VPL and S1 neuronal spike trains with a nonlinear measure (5, 20, 21). Indeed, we decomposed single-neuron DI into three types, feed-forward, feed-back, and bidirectional, and explored their temporal evolution from the prestimulus up to the poststimulus intervals of the detection task. In particular, the lack of pure feed-back modulation (i.e., not concurrent to feed-forward information) during the stimulus period suggests that the spike-field coherence increment in the S1 → VPL direction shown in ref. 29 could be associated with increments in zero-lag interaction. Our data analysis approach involved the use of nonparametric significance tests (30) and the choice of the percentage of significant DI estimates as a relevant connectivity metric (5). Both choices were critical to detect nonlinear spike-train temporal correlations in a way that was shown to be weakly dependent on the firing rate in real and simulated data. As a result, we were able to analyze neuronal data in a dimension that was quasi-orthogonal to the firing rates (17, 18), while still showing rich stimulus modulations. It is important to mention the differences between the DI measure used here and the widespread measure of noise correlation (31, 32). Noise correlation averages across trials under the same stimulus condition, correlating fluctuations in firing rate of two neurons. In contrast, DI quantifies, in a single trial and for any given time, the information that the recent past and present spike train of a given neuron has about the present spike train of the other, simultaneously recorded, neuron.

Notably, feed-forward VPL–S1 information was modulated during the stimulus period. Further, the modulation was stronger 250 ms immediately after the stimulus onset. These findings are congruent with the adaptation of feed-forward information over the stimulus period. Indeed, previous studies have shown that thalamic and cortical neurons become adapted to tactile stimuli after several pulses (17, 18, 33). Moreover, it has been reported that this adaptation changes the neural code of cortical neurons and thalamic synchrony from a detection to a discrimination modality (34). As stated above, our directionality measure is poorly correlated with differences in firing rate of VPL and S1 neurons. Therefore, our results are congruent with the adaptive coding paradigm (34), by showing that feed-forward and zero-lag interactions exhibit the strongest modulation during the first part of the stimulus presence. In sum, we hypothesize that feed-forward adaptation reflects an internal mechanism that prioritizes the information contained within the first pulses of the sinusoidal stimulus to further transmit this information to the cortex and, therefore, for stimulus detection during this task.

According to the standard classification of thalamic sensory nuclei (6), VPL is considered a first-order relay nucleus that mainly transmits afferent information to S1 in the presence of cortical feedback (9, 35, 36). Our results support this view by showing that feed-forward information alone was primarily boosted during the first 250 ms immediately after the stimulus onset. The increment in feed-forward information was concentrated at a delay of 8 ms, which is consistent with previous literature (37). Moreover, these increments were reduced during incorrect trials and, to a lesser extent, during the passive control condition. In particular, the relationship between feed-forward information and the monkey's performance during stimulus-present trials is of special novelty. In previous related studies, this correlation did not arise either in spiking activity (18) or in the oscillatory activity (29). This result suggests that perceptual detection might be related to the amount of stimulus information flowing from VPL to S1. In contrast, pure feed-back information did not display substantial task modulations. We hypothesize that pure feed-back information might be relevant for perceptual detection but is generally less frequent than feed-forward information. However, cortical areas and higher-order thalamic nuclei (reviewed in ref. 38) might show more prominent feed-back corticothalamic information, perhaps related not only to facilitating the gating of the stimulus but also to some other cognitive aspects not detected in this task (however, see the discussion below).

Our study revealed that feed-back information could take place concurrently with feed-forward information, suggesting the emergence of a thalamocortical loop, denominated here in sum as bidirectional information. In particular, our analysis identified that bidirectional information showed bimodality between those cases where DI simultaneously occurred at zero delay (zero-lag interaction) and those cases at non-zero delay. Crucially, only zero-lag interaction was modulated by the stimulus presence, involved neurons exhibiting higher firing rates than in the unidirectional case, and was significantly diminished in the passive stimulation task. Hence, zero-lag interaction conveyed both stimulus and contextual information, thus indicating that its mechanism might be different from the non-zero subtype. Unlike the feed-forward type, we suggest that zero-lag interaction may not reflect direct routing of information (39). Instead, it could be established by common inputs from mediating cortical neurons. In particular, it will be interesting in future studies to simultaneously record the activity of higher-order areas like prefrontal cortex to examine how common cortical inputs driving zero-lag interactions (40) are associated with the expectancy caused by different prestimulus period times, a variable that was out of the scope of this study. In light of the existing models of corticothalamic circuitry (ref. 7 and Fig. 1), we hypothesize that the inferred feed-forward thalamocortical information could be related to layer 4 (15) as well as deep cortical layers 5/6 in S1 (41). In fact, future experiments involving multicontact electrodes and inactivation are needed to shed light on the contribution of the distinct cortical layers to the information flow within the thalamocortical circuit. However, we consider that the task-context modulation of zero-lag interaction requires the engagement of downstream cortical areas in this loop. Specifically, in concordance with computational models supporting zero-lag brain interarea synchronization (42–44), we propose that zero-lag interaction could be originated by a top-down modulation of cortical areas, establishing a similarly delayed reciprocal loop with both S1 and the thalamus (9, 45).

Recently, a study in monkeys performing a visual detection task was also able to relate the propagation of neural activity along the visual pathway with the monkey's detection accuracy (46). The authors showed that information about unreported stimuli may be lost at any stage of the pathway (V1–V4–prefrontal cortex) with an overall excursion that depended on the stimulus strength. Despite the methodological differences with the study presented here [the authors recorded cortical areas along the visual

Downloaded at Instituto de Biotecnologia/UNAM on October 20, 2020

pathway, analyzed multiunit activity (MUA) instead of single-unit activity, indirectly measured activity propagation via local MUA, and used microstimulation, among others], their results suggest that stimulus perception of near-threshold stimuli may depend on the feed-forward information flow across the early stages of the sensory pathway. More specifically, they explain their results with a model involving thalamocortical and corticocortical propagation, but no corticothalamic projections. While our main findings may fit in this model (see also ref. 3), the task modulation of zero-lag interaction between VPL and S1 suggests the additional existence of indirect corticothalamic pathways toward VPL in the somatosensory model.

In brief, the present study employed a fine-temporal methodology supporting that the increment of VPL → S1 neuronal DI (as opposed to S1 → VPL) at around 8 ms during the stimulus period reflects the effective transmission of tactile information from thalamus to cortex. Moreover, it suggests that the amount of feed-forward information occurring during the first 250 ms of stimulation correlates with the monkey's stimulus perception and with the behavioral task performance. Meanwhile, zero-lag interaction, which was reduced when monkeys were not required to report stimulus presence, may reflect the top-down modulation of the corticothalamic circuitry needed for stimulus perception. Our results, therefore, contribute to understanding the DI functional flow between the VPL and S1 during the detection of a tactile stimulus. Finally, the minimalistic approach used here, that is, the simultaneous recording of VPL–S1 neuron pairs sharing the same receptive field, together with the estimation of DI flow, could be used not only to investigate the functional role of the thalamocortical DI during perception but also across other brain areas in this and other behavioral tasks.

Materials and Methods

Monkeys were trained to report whether or not they felt the stimulus (*SI Appendix*). Neuronal recordings were obtained in VPL and S1 while the monkeys performed the detection task. Directional information was calculated between neuron pairs simultaneously recorded in VPL and S1 (*SI Appendix*). Animals were handled in accordance with standards of the National Institutes of Health and Society for Neuroscience. All protocols were approved by the Institutional Animal Care and Use Committee of the Instituto de Fisiología Celular, Universidad Nacional Autónoma de México.

ACKNOWLEDGMENTS. This work was supported by Dirección General de Asuntos del Personal Académico de la Universidad Nacional Autónoma de México Grants PAPIIT- IN202716 and PAPIIT-IN210819, Consejo Nacional de Ciencia y Tecnología Grant 240892 (to R.R.), Spanish Research Project PSI2016-75688-P [Agencia Estatal de Investigación/Fondo Europeo de Desarrollo Regional (AEI/FEDER), European Union] (to G.D.), by the European Union's Horizon 2020 Research and Innovation Programme under Grants 720270 [Human Brain Project Specific Grant Agreement 1 (HBP SGA1)] and 785907 (HBP SGA2) (to G.D.), and by the Catalan Agència de Gestió d'Ajuts Universitaris i de Recerca (AGAUR) Programme 2017 Suport als Grups de Recerca (SGR) 1545 (to G.D.). Y.V. was supported by a Pew Latin American Fellowship and a Charles H. Revson Biomedical Science Fellowship.

1. Salinas E, Hernández A, Zainos A, Romo R (2000) Periodicity and firing rate as candidate neural codes for the frequency of vibrotactile stimuli. *J Neurosci* 20:5503–5515.
2. de Lafuente V, Romo R (2005) Neuronal correlates of subjective sensory experience. *Nat Neurosci* 8:1698–1703.
3. de Lafuente V, Romo R (2006) Neural correlate of subjective sensory experience gradually builds up across cortical areas. *Proc Natl Acad Sci USA* 103:14266–14271.
4. Hernández A, et al. (2010) Decoding a perceptual decision process across cortex. *Neuron* 66:300–314.
5. Tauste Campo A, et al. (2015) Task-driven intra- and interarea communications in primate cerebral cortex. *Proc Natl Acad Sci USA* 112:4761–4766.
6. Sherman SM (2016) Thalamus plays a central role in ongoing cortical functioning. *Nat Neurosci* 19:533–541.
7. Alitto HJ, Usrey WM (2003) Corticothalamic feedback and sensory processing. *Curr Opin Neurobiol* 13:440–445.
8. Briggs F, Usrey WM (2007) A fast, reciprocal pathway between the lateral geniculate nucleus and visual cortex in the macaque monkey. *J Neurosci* 27:5431–5436.
9. Crandall SR, Cruikshank SJ, Connors BW (2015) A corticothalamic switch: Controlling the thalamus with dynamic synapses. *Neuron* 86:768–782.
10. Wang JY, et al. (2007) Corticofugal influences on thalamic neurons during nociceptive transmission in awake rats. *Synapse* 61:335–342.
11. Jones EG (2002) Thalamic circuitry and thalamocortical synchrony. *Philos Trans R Soc Lond B Biol Sci* 357:1659–1673.
12. Sherman SM, Guillery RW (2006) *Exploring the Thalamus and Its Role in Cortical Function* (MIT Press, Cambridge, MA).
13. Alonso JM, Usrey WM, Reid RC (1996) Precisely correlated firing in cells of the lateral geniculate nucleus. *Nature* 383:815–819.
14. Ahissar E, Sosnik R, Haidarliu S (2000) Transformation from temporal to rate coding in a somatosensory thalamocortical pathway. *Nature* 406:302–306.
15. Bruno RM, Sakmann B (2006) Cortex is driven by weak but synchronously active thalamocortical synapses. *Science* 312:1622–1627.
16. Bruno RM (2011) Synchrony in sensation. *Curr Opin Neurobiol* 21:701–708.
17. Vázquez Y, Zainos A, Alvarez M, Salinas E, Romo R (2012) Neural coding and perceptual detection in the primate somatosensory thalamus. *Proc Natl Acad Sci USA* 109:15006–15011.
18. Vázquez Y, Salinas E, Romo R (2013) Transformation of the neural code for tactile detection from thalamus to cortex. *Proc Natl Acad Sci USA* 110:E2635–E2644.
19. Carnevale F, de Lafuente V, Romo R, Barak O, Parga N (2015) Dynamic control of response criterion in premotor cortex during perceptual detection under temporal uncertainty. *Neuron* 86:1067–1077.
20. Massey J (1990) Causality, feedback and directed information. *Proceedings of International Symposium on Information Theory and its Applications* (Institute of Electronics, Information and Communication Engineers, Tokyo), pp 27–30.
21. Jiao J, Permuter HH, Zhao L, Kim YH, Weissman T (2013) Universal estimation of directed information. *IEEE Trans Inf Theory* 59:6220–6242.
22. Winkler AM, Ridgway GR, Webster MA, Smith SM, Nichols TE (2014) Permutation inference for the general linear model. *Neuroimage* 92:381–397.
23. Cohen J (1988) Statistical power analysis for the behavioral sciences. *Stat Power Anal Behav Sci* 2:567.
24. Deschênes M, Veinante P, Zhang ZW (1998) The organization of corticothalamic projections: Reciprocity versus parity. *Brain Res Brain Res Rev* 28:286–308.
25. Pipa G, Wheeler DW, Singer W, Nikolić D (2008) NeuroXidence: Reliable and efficient analysis of an excess or deficiency of joint-spike events. *J Comput Neurosci* 25:64–88.
26. Louis S, Gerstein GL, Grün S, Diesmann M (2010) Surrogate spike train generation through dithering in operational time. *Front Comput Neurosci* 4:127.
27. Fitzgerald TH, Valentin A, Selway R, Richardson MP (2013) Cross-frequency coupling within and between the human thalamus and neocortex. *Front Hum Neurosci* 7:84.
28. Bastos AM, Briggs F, Alitto HJ, Mangun GR, Usrey WM (2014) Simultaneous recordings from the primary visual cortex and lateral geniculate nucleus reveal rhythmic interactions and a cortical source for γ-band oscillations. *J Neurosci* 34:7639–7644.
29. Haegens S, et al. (2014) Thalamocortical rhythms during a vibrotactile detection task. *Proc Natl Acad Sci USA* 111:E1797–E1805.
30. Gilson M, Tauste Campo A, Chen X, Thiele A, Deco G (2017) Nonparametric test for connectivity detection in multivariate autoregressive networks and application to multiunit activity data. *Netw Neurosci* 1:357–380.
31. Ecker AS, et al. (2014) State dependence of noise correlations in macaque primary visual cortex. *Neuron* 82:235–248.
32. Kohn A, Coen-Cagli R, Kanitscheider I, Pouget A (2016) Correlations and neuronal population information. *Annu Rev Neurosci* 39:237–256.
33. Khatri V, Hartings JA, Simons DJ (2004) Adaptation in thalamic barreloid and cortical barrel neurons to periodic whisker deflections varying in frequency and velocity. *J Neurophysiol* 92:3244–3254.
34. Wang Q, Webber RM, Stanley GB (2010) Thalamic synchrony and the adaptive gating of information flow to cortex. *Nat Neurosci* 13:1534–1541.
35. Blomquist P, et al. (2009) Estimation of thalamocortical and intracortical network models from joint thalamic single-electrode and cortical laminar-electrode recordings in the rat barrel system. *PLoS Comput Biol* 5:e1000328.
36. Ahissar E, Oram T (2015) Thalamic relay or cortico-thalamic processing? Old question, new answers. *Cereb Cortex* 25:845–848.
37. Briggs F, Usrey WM (2008) Emerging views of corticothalamic function. *Curr Opin Neurobiol* 18:403–407.
38. Halassa MM, Kastner S (2017) Thalamic functions in distributed cognitive control. *Nat Neurosci* 20:1669–1679.
39. Besserve M, Lowe SC, Logothetis NK, Schölkopf B, Panzeri S (2015) Shifts of gamma phase across primary visual cortical sites reflect dynamic stimulus-modulated information transfer. *PLoS Biol* 13:e1002257.
40. Riehle A, Grün S, Diesmann M, Aertsen A (1997) Spike synchronization and rate modulation differentially involved in motor cortical function. *Science* 278:1950–1953.
41. Constantinople CM, Bruno RM (2013) Deep cortical layers are activated directly by thalamus. *Science* 340:1591–1594.
42. Fischer I, et al. (2006) Zero-lag long-range synchronization via dynamical relaying. *Phys Rev Lett* 97:123902.
43. Vicente R, Gollo LL, Mirasso CR, Fischer I, Pipa G (2008) Dynamical relaying can yield zero time lag neuronal synchrony despite long conduction delays. *Proc Natl Acad Sci USA* 105:17157–17162.
44. Gollo LL, Mirasso C, Sporns O, Breakspear M (2014) Mechanisms of zero-lag synchronization in cortical motifs. *PLoS Comput Biol* 10:e1003548.
45. Collins DP, Anastasiades PG, Marlin JJ, Carter AG (2018) Reciprocal circuits linking prefrontal cortex with ventral and dorsal thalamic nuclei. *Neuron* 98:366–379.e4.
46. van Vugt B, et al. (2018) The threshold for conscious report: Signal loss and response bias in visual and frontal cortex. *Science* 360:537–542.

Downloaded at Instituto de Biotecnología/UNAM on October 20, 2020

INFORME DE LABORES 2019

Cellular Signalling 54 (2019) 91–101

Contents lists available at ScienceDirect

Cellular Signalling

journal homepage: www.elsevier.com/locate/cellsig

Interplay between interferon-stimulated gene 15/ISGylation and interferon gamma signaling in breast cancer cells

Angeles C. Tecalco-Cruz[a,*], Carlo César Cortés-González[b], Eduardo Cruz-Ramos[a], Josué O. Ramírez Jarquín[c], Aline Kay Romero-Mandujano[b], Marcela Sosa-Garrocho[c]

[a] Instituto de Investigaciones Biomédicas, Universidad Nacional Autónoma de México, Mexico City 04510, Mexico
[b] Unidad de Investigación Biomédica en Cáncer, Instituto Nacional de Cancerología-Instituto de Investigaciones Biomédicas, Tlalpan, C.P. 14080 Mexico City, Mexico
[c] Instituto de Fisiología Celular, Universidad Nacional Autónoma de México, Mexico City 04510, Mexico

ARTICLE INFO

Keywords:
ISG15
ISGylation
Breast cancer
Interferon gamma
Cytoskeleton

ABSTRACT

Interferon-stimulated gene 15 (ISG15) is a ubiquitin-like protein that conjugates to its target proteins to modify them through ISGylation, but the relevance of *ISG15* expression and its effects have been not completely defined. Herein, we examined the interplay between ISG15/ISGylation and the interferon-gamma (IFN-γ) signaling pathway in mammary tumors and compared it with that in normal mammary tissues. Our results indicated that mammary tumors had higher levels of *ISG15* mRNA and ISG15 protein than the adjacent normal mammary tissue. Furthermore, the expression of IFN-γ signaling components was altered in breast cancer. Interestingly, IFN-γ treatment induced morphological changes in MCF-7 and MDA-MB-231 breast cancer cell lines due to cytoskeletal reorganization. This cellular process seems to be related to the increase in ISGylation of cytoplasmic IQ Motif Containing GTPase Activating Protein 1 (IQGAP1). Interactome analysis also indicated that IFN-γ signaling and the ISGylation system are associated with several proteins implicated in cytoskeletal remodeling, including IQGAP1. Thus, ISG15 may present a potential biomarker for breast cancer, and IFN-γ signaling and protein ISGylation may participate in the regulation of the cytoskeleton in breast cancer cells.

1. Introduction

IFN-γ is a unique member of the type II interferon family, and possesses important immunomodulatory and antiviral properties but has ambiguous functions in several cancers. The canonical signaling of IFN-γ requires a specific heterotetrameric receptor complex formed by IFNGR1 and IFNGR2 subunits and the JAK-STAT1 system. In response to the binding of IFN-γ to its receptor complex, activated JAKs1/2 (associated with the receptor complex in the intracellular region) mediates STAT1 phosphorylation. Activated STAT1 homodimers bind to the gamma interferon activated site (GAS) localized in the regulatory sequences of IFN-γ target genes to modulate gene expression [1,2]. Genes induced by IFN-γ include *IRF-1/2* [3–5], *RIG-1* [6–9], *SOCS1/3* [10] *SMAD7* [11], and genes implicated in antigen presentation by major histocompatibility complex (MHC) class I and II [12,13] *IRF-1* mediates IFN-γ-induced expression of late genes, while *IRF-2* represses the transcription of these genes [5]; *RIG-1* has antiviral, immunomodulatory, and suppressor tumor activities and regulates the expression of some genes [6–9]. *SOCS1/3* inhibits IFNs-signaling, and *SMAD7* is a negative regulator of TGFβ signaling [10,11]. Interestingly, in breast cancer, it has been suggested that IFN-γ induces apoptosis and cell cycle arrest, and also that there is autocrine signaling by IFN-γ in these cells [14,15]. Additionally, a gene signature regulated by IFNs may be associated with sensitivity and/or resistance to chemotherapy and endocrine therapy observed in breast cancer cells [16,17].

There is a high rate of heterogeneity observed in breast cancers. Approximately 70% of the cases are estrogen receptor-α positive (ERα+), and the residual cases are ERα-. In both cases, mechanisms that modulate ERα activity and expression appear to be deregulated [18–20]. Previously, we demonstrated that IFN-γ increases ISG15 (Interferon-stimulated gene 15) protein levels in ERα + and ERα- breast cancer cells in addition to type I interferons (IFN-α and IFN-β) that had been previously considered to be the exclusive inducers of ISG15 in other cell types [21–24].

ISG15 is a 15 kDa ubiquitin-like protein that conjugates to its target proteins in a covalent manner through an enzymatic process similar to ubiquitination [25–28]. This process is known as ISGylation and the enzymes involved are the E1-activating (UBE1L), E2-conjugating (UBCH8) [29], and E3 ligase enzymes (HERC5, EFP, and HHARI) [30–33], as well as the de-ISGylase enzyme USP18 that removes

* Corresponding author.
E-mail address: atecalco@iibiomedicas.unam.mx (A.C. Tecalco-Cruz).

https://doi.org/10.1016/j.cellsig.2018.11.021
Received 11 August 2018; Received in revised form 25 November 2018; Accepted 26 November 2018
Available online 27 November 2018
0898-6568/ © 2018 Elsevier Inc. All rights reserved.

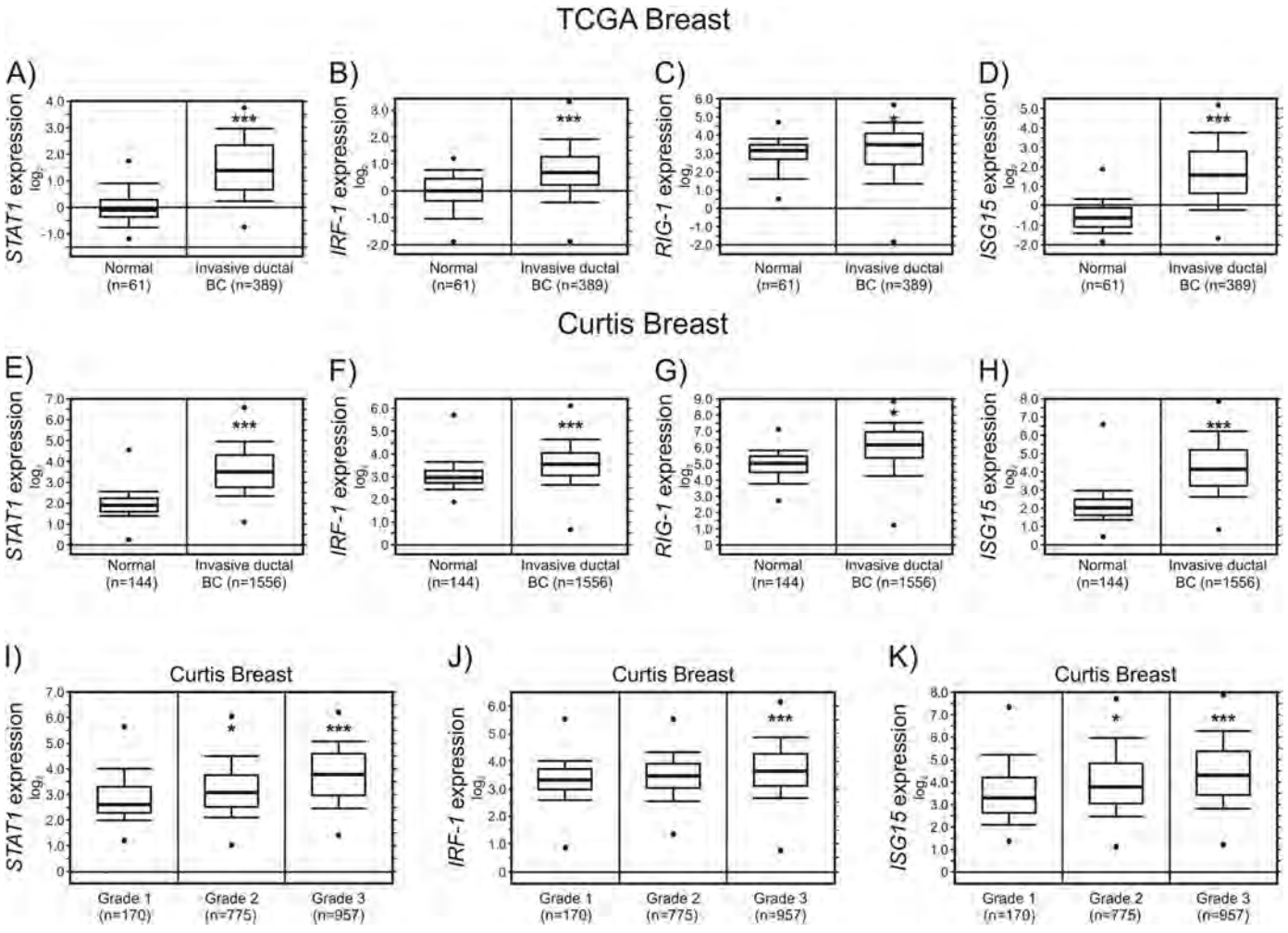

Fig. 1. Increased expression of *STAT1*, *RIG-1*, and *ISG15* in mammary tumors. A-D) TCGA (The Cancer Genome Atlas) and *E*-H) Curtis datasets from Oncomine were analyzed to evaluate *STAT1, IRF-1, RIG1*, and *ISG15* expression in human mammary tumors compared to those in normal tissue. I—K) Curtis dataset was analyzed to determine the *STAT1, IRF-1,* and *ISG15* expression in mammary tumors of grade 1, 2, and 3. Results are considered significant when $p < .05$ (*), $p < .01$ (**) and $p < .001$ (***).

ISGylation of proteins [34]. Additionally, ISG15 can also be detected as free ISG15 when it is not covalently bound to a target protein [35–37]. The function of ISGylated proteins is unclear, as this modification can interfere with and also collaborate with the ubiquitination pathway [38–42].

In breast cancer, it has been shown *in vivo* experiments using athymic mice models demonstrate that depletion of ISG15 enhances tumor development. In contrast, downregulation of ISG15 has been shown to decrease proliferation and migration in breast cancer cell lines *in vitro* [38,43,44]. Although ISGylation functions are yet to be elucidated, since only a limited number of proteins modified by ISG15 are known, it is evident that expression of ISG15 affects the malignancy of breast cancer cells, and many proteins may be modulated by ISGylation under this condition.

In order to explore the significance of ISG15 expression in patients diagnosed with breast cancer, we analyzed the levels of ISG15 and the expression of IFN-γ signaling components in normal and mammary tumor tissues. We probed the effect of IFN-γ on viability, morphology, and protein ISGylation in breast cancer cells. Our data indicate that ISG15 can act as a potential biomarker for breast cancer. Our findings also suggest important implications for IFN-γ induced protein ISGylation in the biology of breast cancer cells.

2. Materials and methods

2.1. Reagents and cell lines

Recombinant human IFN-γ (285-IF-00) was obtained from R&D systems, culture media were obtained from Invitrogen, and reagents were obtained from Sigma, AMRESCO-VWR, and Bio-Rad. The MDA-MB-231 (ERα-, triple negative breast cancer cells), and MCF-7 (ERα + breast cancer cells) cell lines were maintained in Dulbecco's modified Eagle's medium supplemented with 5% fetal bovine serum and penicillin/streptomycin.

2.2. Subcellular fractionation and total extracts

Nuclear and cytoplasmic fractions were obtained by subcellular fractionation as described previously [23,45]. Using homogenization buffer (250 mM sucrose, 3 mM imidazole protease, and phosphatase inhibitors), the cells were homogenized and then passed 15 times through a 22-gauge needle. The homogenized cells were then centrifuged at 700 × *g* for 10 min to separate the supernatant (cytoplasmic fraction) from the pellet (nuclear fraction). Both fractions were lysed with RIPA buffer (50 mM Tris-HCl pH 7.4, 150 mM NaCl, 1 mM EDTA, 0.5% deoxycholic acid, 1% NP-40, and 0.1% SDS) containing protease and phosphatase inhibitors. For total extracts, the cells were directly

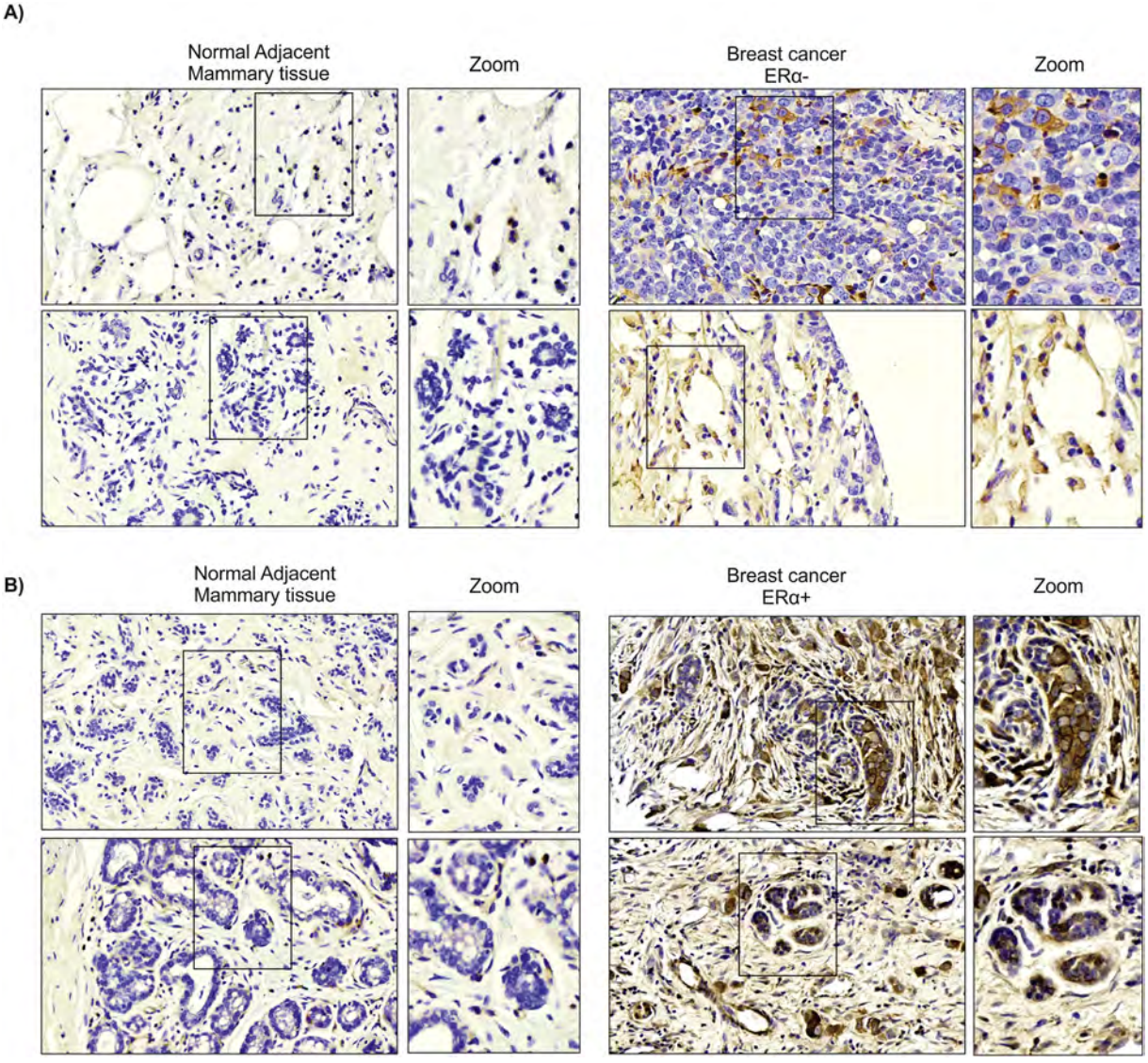

Fig. 2. ISG15 is detected at higher levels in mammary tumors than in adjacent normal mammary tissue.
A, B) Immunohistochemical (IHC) analysis of ISG15 protein expression in invasive ERα + and ERα- breast carcinomas. ISG15 protein expression is predominant in ERα + and ERα- breast cancer tissue in comparison with that in normal adjacent mammary tissue. 20× magnification of representative images. ISG15 protein is mainly detected in the cytoplasm of ERα + and ERα- mammary tumors from patients (A and B, zoom).

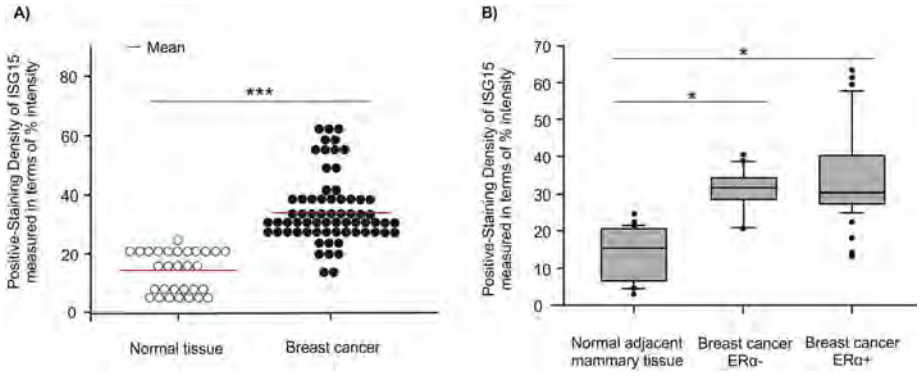

Fig. 3. Statistical analysis of immunohistochemical data from mammary tumors and adjacent normal mammary tissue. Immunohistochemical (IHC) analysis of ISG15 protein in invasive ERα + and ERα- breast carcinomas. A) Analysis of ISG15 protein signal in mammary tumors compared to signal in adjacent normal tissue. The Mann-Whitney rank sum test was performed, and the red line indicates the mean. B) Analysis of ISG15 protein signaling in ERα + and ERα- mammary tumors and in adjacent normal tissues. Kruskal-Wallis one way analysis of variance on ranks was performed to analyze the IHC data. Results are considered significant when $p < .001$ (***) and $p < .05$ (*). (For interpretation of the references to colour in this figure legend, the reader is referred to the web version of this article.)

lysed with RIPA buffer. Lysis was performed at 4 °C for 1 h, and protein extracts were quantified using the Bradford method for WB and immunoprecipitation assays.

2.3. Cell viability assays

For the determination of cellular viability, calcein-AM (green) and propidium iodide or PI (red) assays were performed. Viable cells

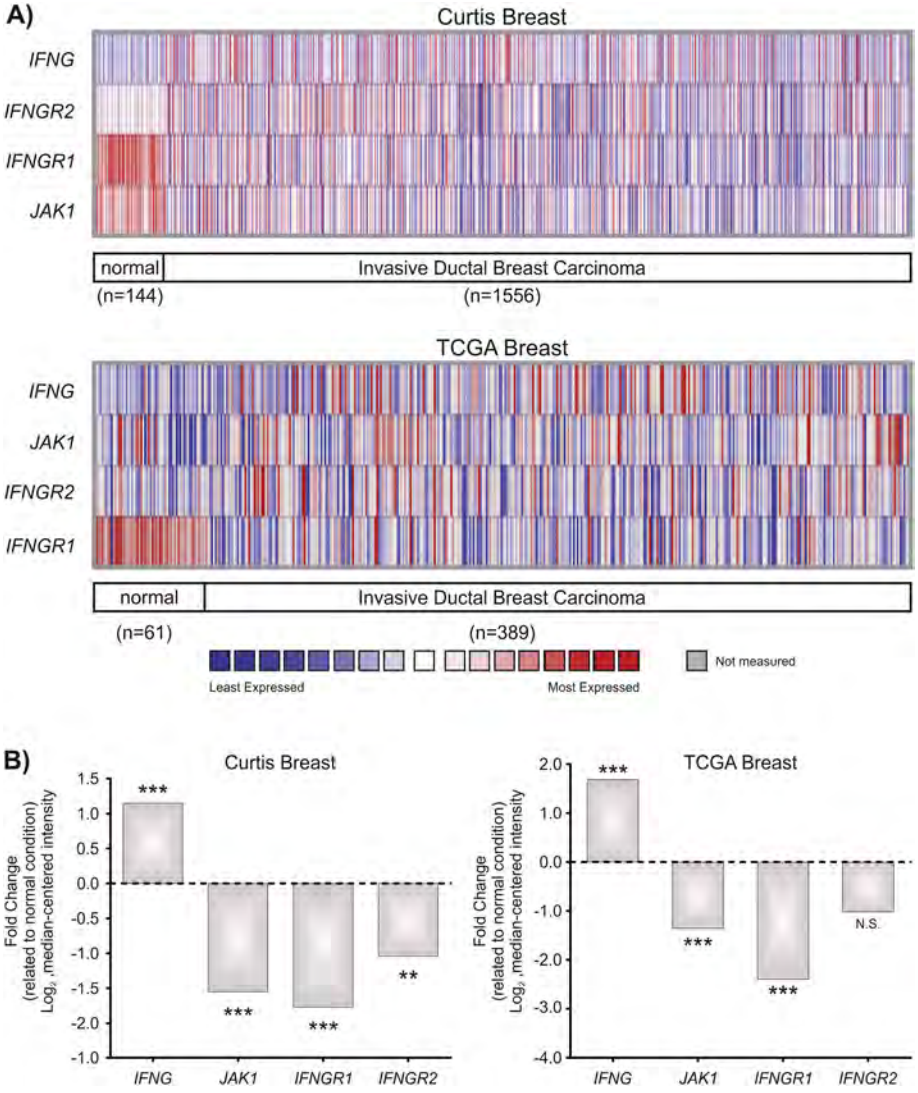

Fig. 4. Expression of IFN-γ signaling components in breast cancer. Heat maps for gene expression of IFN-γ signaling components. A) Curtis and TCGA (The Cancer Genome Atlas) datasets from Oncomine were analyzed to evaluate *IFNG, IFNGR2, IFNGR1* and *JAK1* expression in human mammary tumors and normal tissue. B) Analysis of *IFNG, JAK1*, *IFNGR1* and *IFNGR2* expression in mammary tumors compared to those in normal mammary tissue. Results are expressed as significant when $p < .01$ (**), and $p < .001$ (***). Non-significant differences are indicated by N.S.

possess an active metabolism, allowing intracellular esterases to convert non-fluorescent calcein-AM to green fluorescent calcein. In non-viable cells, a red fluorescence signal is generated when PI binds to DNA indicating that the nuclear membrane is disrupted. Cells treated with or without IFN-γ were incubated with calcein-AM (1 μM) and PI (5 mM) at 37 °C for 30 min, and the cells were then analyzed by fluorescence microscopy.

2.4. Co-immunoprecipitation assays and western blotting

Cytoplasmic and nuclear extracts or total extracts were used for immunoprecipitation assays as described previously [24]. Immunoprecipitation was performed using a specific anti-ISG15 (Santa Cruz Biotechnology) antibody. The immunoprecipitated complexes were separated by SDS-PAGE followed by immunoblotting with specific primary anti-IQGAP1 antibody (H-109, Santa Cruz Biotechnology). As input, cytoplasmic and nuclear extracts (25–100 μg of protein lysates) were used and separated by SDS-PAGE and then immunoblotted with anti-ISG15 (1:1000) (F-9, sc-166,755), anti-α-tubulin (1:3000) (B7, sc-5286) obtained from Santa-Cruz Biotechnology, and anti-lamin B1(1:2000) obtained from Cell Signaling (D4Q4Z). A secondary anti-rabbit IgG antibody was used (1:10000) against anti-lamin B1 (sc-2004; Santa Cruz Biotechnology), and peroxidase Affinipure goat anti-mouse antibody (1:10000) was used for anti-tubulin and anti-ISG15 (115–035-003, Jackson). Protein detection was performed using SuperSignal West Pico chemiluminescent substrates (Thermo Scientific) or Immobilon Western (Millipore) reagents. The experiments were performed in triplicate, and representative images are shown.

2.5. Immunofluorescence assay

The cells were fixed in 4% paraformaldehyde for 10 min, permeabilized with 0.1% Triton X-100 for 10 min, and blocked with 1% albumin for 1 h. Cells were incubated overnight with anti-ISG15 (F-9, sc-166,755; 1:100), and then the cells were washed and incubated with Alexa Fluor 647 anti-mouse IgG secondary antibody (ab150107, Abcam; 1:750) for 1 h in the dark. The slides were prepared with ProLong Diamond Antifade Mountant containing DAPI (Invitrogen). For phalloidin assays, after blocking, the cells were incubated for 1 h with phalloidin (1:40) and mounted with DAPI solution. An Olympus IX2 confocal laser-scanning microscope was used to visualize the cells, and ImageJ software was used for imaging, processing, and analyzing the

INFORME DE LABORES 2019

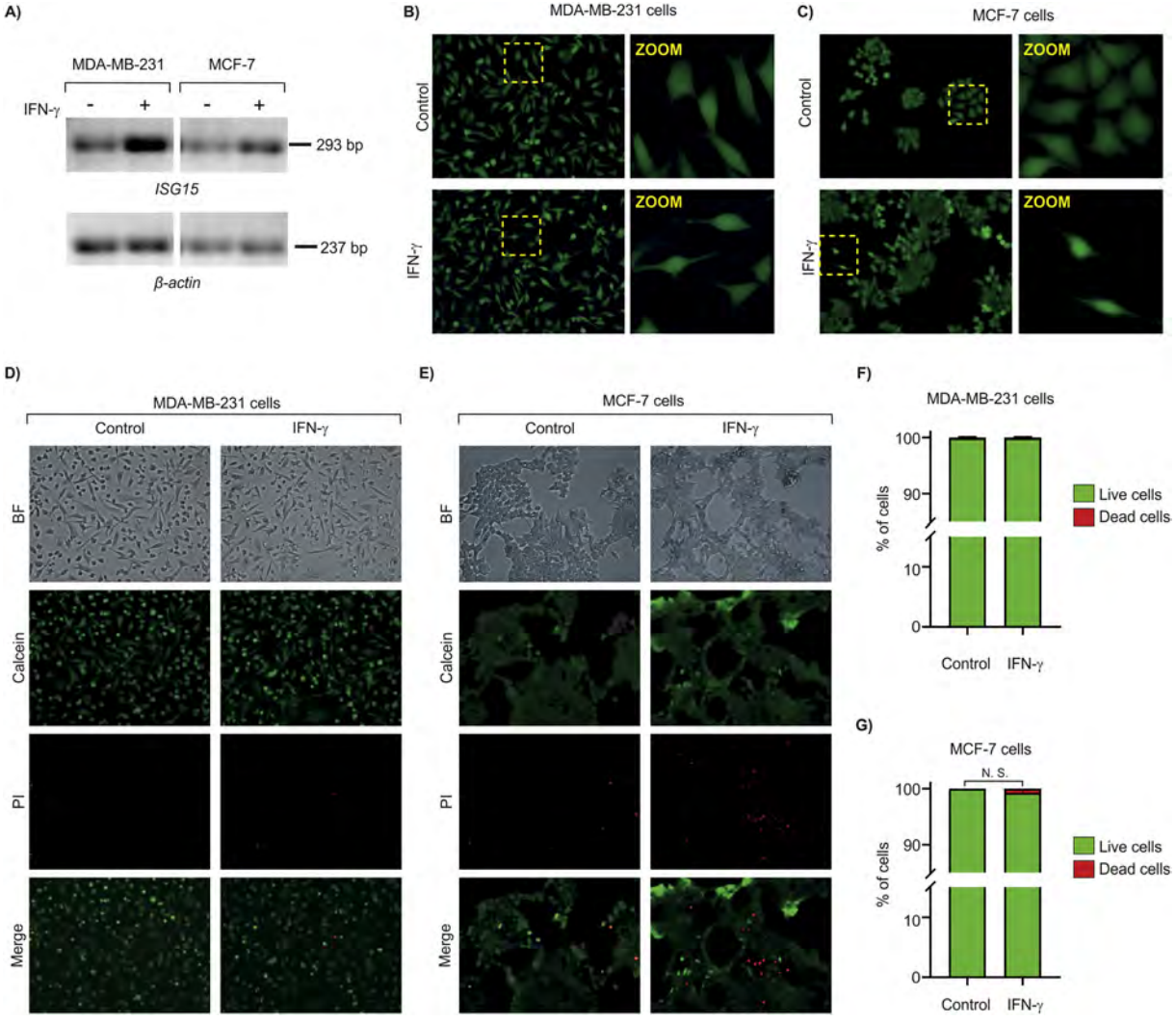

Fig. 5. IFN-γ affects the morphology of breast cancer cells. A) Total RNA was isolated from MDA-MB-231 and MCF-7 cells with or without IFN-γ (100 ng/ml) treatment and subjected to RT-PCR analysis. Specific primers for *ISG15* and *β-actin* were used. PCR products of 237 bp for *β-actin* and 293 bp for *ISG15* are shown. B, C) Calcein staining for MDA-MB-231 and MCF-7 cells with or without IFN-γ treatment for 24 h. D, E) Cellular viability assays using calcein/propidium iodide or PI on MDA-MB-231 and MCF-7 cells with or without IFN-γ treatment. Cells stained green represent viable cells and those stained red represent dead cells. F, G) Quantification of cell viability is shown. Non-significant differences are indicated by N.S. (For interpretation of the references to colour in this figure legend, the reader is referred to the web version of this article.)

results.

2.6. Gene expression analysis

The cancer microarray database Oncomine (www.oncomine.org) was used to analyze gene expression in patient-derived mammary tumors and normal mammary tissue. The datasets used were The Cancer Genome Atlas (TCGA) and Curtis.

2.7. In silico analysis

The analysis of protein–protein interactions was carried out using STRING 10.5 version software (https://string-db.org/cgi/network.pl) [46].

2.8. Human breast cancer tissue microarray

Breast cancer and normal tissue arrays, along with corresponding control tissues derived from the same patient (16 cases/48 cores), were purchased from Biomax (BRC481, U.S. Biomax human breast cancer tissue microarray). This microarray was composed of formalin-fixed, paraffin-embedded tissue.

2.9. Immunohistochemical assay

The microarrays were examined by immunohistochemical (IHC) analysis using a monoclonal antibody specific for ISG15 (F-9, sc-166,755 from Santa-Cruz Biotechnology). Samples were initially deparaffinized in xylene followed by rehydration in graded alcohol. Endogenous peroxide activity was quenched using 3% hydrogen peroxide (5 min) and samples were blocked using horse serum solution. Samples were then incubated with anti-mouse IgG (peroxidase). Results were visualized after incubation using DAB solution. Slides were dehydrated and cleared in xylene baths, and then mounted. A counterstain with Hematoxylin was also performed. Positive and negative controls (negative control: lacking the ISG15 antibody) were used.

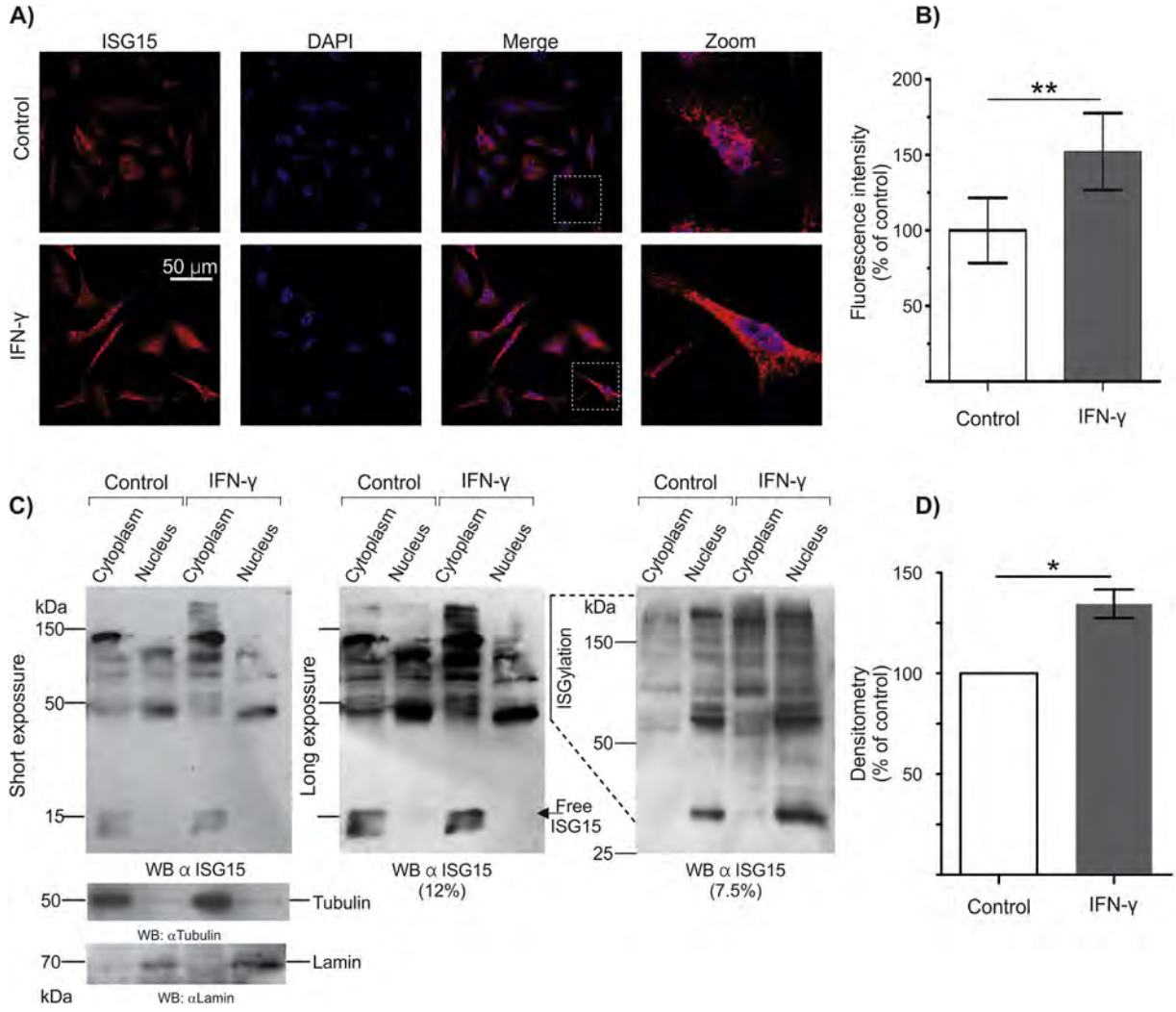

Fig. 6. IFN-γ increases cytoplasmic ISGylation marks in MDA-MB-231 cells. A) Subcellular localization of ISG15 in MDA-MB-231 cells with or without IFN-γ (100 ng/ml) treatment were evaluated by immunofluorescence. Changes in morphology are visible in the zoomed image. B) Quantification of ISG15 fluorescence intensity in MDA-MB-231 cells with or without IFN-γ treatment. C) Cytoplasmic and nuclear extracts taken from MDA-MB-231 cells with or without IFN-γ (100 ng/ml) treatment were used for WB analysis of ISG15 (gels 12%, short and long exposure). Cytoplasmic and nuclear fractions were also separated in 7.5% acrylamide gels for WB against ISG15. Lamin and tubulin were used as controls for the cytoplasmic and nuclear fractions, respectively. D) Densitometry analysis of the cytoplasmatic levels of protein ISGylation. Results are considered significant when $p < .05$ (*), and $p < .01$ (**).

2.10. Immunohistochemical analysis

2.10.1. Image acquisition

IHC photomicrographs were captured using an AxioScan.Z1 microscope (Zeiss, Germany) equipped with an AxioCam MRc5 camera (Zeiss, Germany). Light and camera settings were operated by ZEN2.3 software (blue edition, Carl Zeiss microscopy GmbH, 2011). Images were captured under 20× and 40× objective lenses.

2.10.2. Digital Image Analysis

IHC photomicrographs were used for developing a semi-automated analysis protocol called IHC profiler [47]. Quantitative analysis was performed using photomicrographs of 4 randomly selected fields taken from each representative tumor tissue on the microarray.

2.11. RT-PCR assay

ISG15 and *β-actin* mRNA levels were detected by RT-PCR. TRIzol (Invitrogen) was used to isolate total RNA from MCF-7 and MDA-MB-231 cells treated with or without IFN-γ (100 ng/ml) for 24 h. Total RNA (2 μg) was used for cDNA synthesis, and random hexamers and Moloney murine leukemia virus RT (Invitrogen) were used to promote the reaction. PCR was performed using a *Taq* PCR Master Mix kit (Qiagen) and primers specific for *ISG15* (Sense 5′-3′: GGT GGA CAA ATG CGA CGA AC and antisense 5′-3′: ATG CTG GTG GAG GCC CTT AG) and *β-actin* (Sense 5′-3′: GGG TCA GAA GGA TTC CTA TG and antisense 5′-3′: GGT CTC AAA CAT GAT CTG GG). PCR products were analyzed by agarose gel electrophoresis.

2.12. Statistical analysis

The data presented in our figures are representative of 3 or more independent experiments. Densitometry for WB, quantification of cell viability assays and fluorescence intensity percentages were performed using Fiji-ImageJ. Data were shown as percentages. Unpaired student's *t*-tests were performed using *GraphPad Prism* 5 software (GraphPad). Results were considered significant when $p < .05$ (*), $p < .01$ (**), and $p < .001$ (***). Non-significant differences were by N.S. Mann-Whitney rank sum test, and Kruskal-Wallis One Way Analysis of Variance on Ranks were performed to analyze IHC data.

INFORME DE LABORES 2019

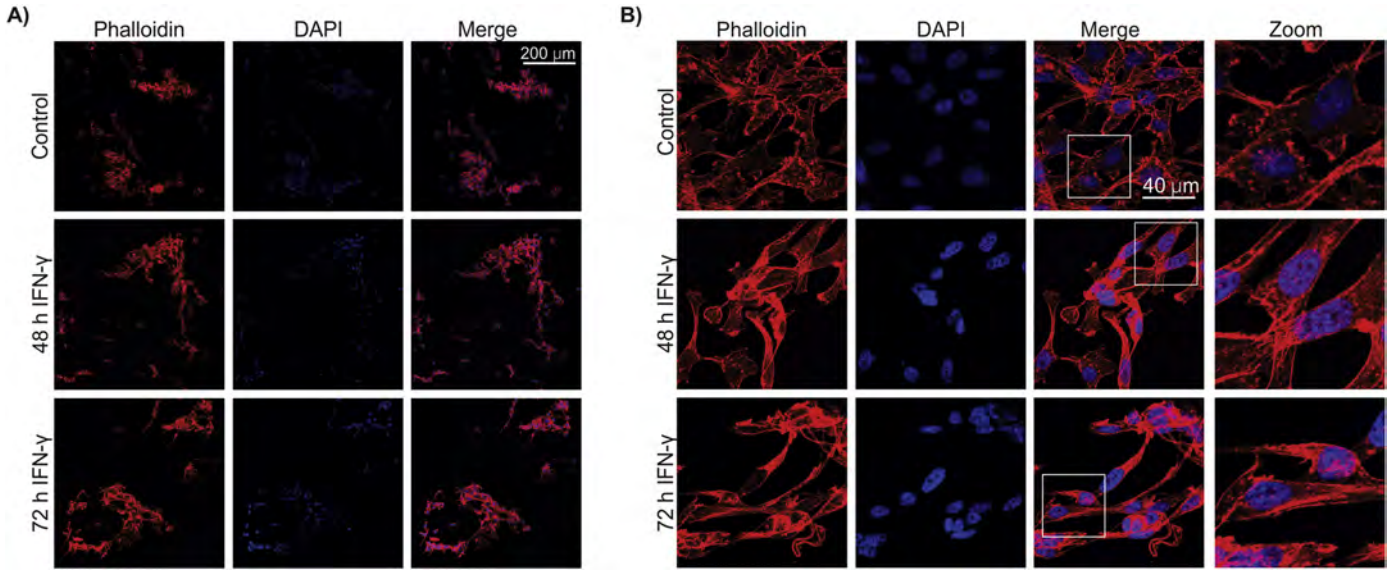

Fig. 7. IFN-γ modulates cytoskeletal remodeling of breast cancer cells. A, B) Phalloidin staining for MDA-MB-231 cells with or without IFN-γ (100 ng/ml) treatment for 48 and 72 h.

3. Results

3.1. Expression of STAT1, IRF-1, RIG-1, and ISG15 is increased in breast cancer

Approximately 80% of breast cancers develop in the mammary ducts and are invasive [48]. In order to explore the expression of factors activated by IFN-γ signaling (*STAT1, IRF-1,* and *RIG-1*) and *ISG15*, we evaluated their mRNA levels in tumors of patients diagnosed with invasive ductal breast cancer and compared them with their corresponding levels in normal mammary tissue using TCGA (450 patients) and Curtis (1700 patients) datasets. Our analysis of both datasets showed that the expression of all four genes (*STAT1, IRF-1, RIG-1*, and *ISG15*) were significantly increased in breast cancer (Fig. 1A-1H). Additionally, using the Curtis dataset (1902 patients), we found that the mRNA levels of *STAT1, IRF-1* and *ISG15* increased in a tumor-grade dependent manner. Expression levels were lower in grade 1 tumor tissues (well differentiated, tumor tissues appear similar to normal mammary tissues) and increased in grade 2 tumors (moderately differentiated) that grow and spread slowly. The mRNA levels of *STAT1, IRF-1*, and *ISG15* were highest in grade 3 tumors, which were poorly differentiated with a rapid growth and spread (Fig. 1I-1K). These results indicated that the expression of *STAT1*, *IRF-1*, *RIG-1*, and *ISG15* were increased in mammary tumors, and in particular, *STAT1, IRF-1*, and *ISG15* expression seemed to be critical in the progression of breast cancer.

Interestingly, other IFN-γ target genes were also upregulated in mammary tumors when compared to normal mammary tissue. These included *SOCS1* and *SMAD7*, whereas other IFN-γ regulated genes such as *SOCS3* and *IRF-2* were downregulated in breast cancer when compared to healthy breast tissue (Supplementary fig. 1). Furthermore, genes associated with antigen presentation by MHC class I and II were generally upregulated in breast cancer (Supplementary fig. 2). These results indicate that the IFN-γ-driven transcriptome may be deregulated in breast cancer.

3.2. ISG15 protein levels are enhanced in mammary tumor samples compared to normal adjacent tissue

Because *ISG15* is one the upregulated genes in breast cancer, we first decided to analyze the protein levels of ISG15 in tumors of patients with breast cancer. We evaluated a breast cancer microarray that contained 16 cases of invasive breast cancer in duplicates with adjacent uninvolved tissue from the same patients, and we detected ISG15 protein by immunohistochemistry (IHC). A strong signal was detected for ISG15 protein in different cases of ERα- and ERα + mammary tumors compared to signals detected in normal mammary tissue (Fig. 2A and B). The ISG15 signal was mostly detected in the cytoplasm in all cases. However, in some cells, ISG15 was also detected in the nucleus (Fig. 2A and B, zoom). Our statistical analysis demonstrated that ISG15 protein expression was significantly higher in breast cancer samples than in the normal mammary tissue (Fig. 3A). We performed the same analysis by classifying the tumors as ERα- and ERα + , and our results indicated that these tumors also have higher levels of ISG15 protein than the adjacent normal mammary tissue and was independent of ERα status (Fig. 3B). These results indicate that the ISG15 modifier protein is upregulated in breast cancers, and this upregulation may lead to the ISGylation of target proteins to modulate their activities.

3.3. Expression of the IFN-γ signaling pathway elements IFNGRs, JAK2, and IFNG is also altered in breast cancer

Expression of *STAT1* and *ISG15* is positively associated with tumor grade, and ISG15 protein levels are increased in breast cancer cells. Since STAT1 and ISG15 are linked to IFN-γ signaling, we analyzed the expression of the elements of this pathway including *IFNGR1*, *IFNGR2*, and *JAK1*, as well as the expression of the gene that encodes for IFN-γ cytokine (*IFNG*) in mammary tumors. These analyses were performed using Curtis and TCGA datasets derived from Oncomine. The analysis of these two datasets indicated that the IFN-γ signaling pathway is deregulated in mammary tumors, as the mRNA levels of *JAK1*, *IFNGR2*, and *IFNGR1* were decreased in these tumors in comparison to those found in normal tissue, and the expression of *IFNG* was increased (Fig. 4A, B). Taken together, these results suggest that IFN-γ production and secretion may be enhanced in mammary tumors, and the activation of the IFN-γ pathway and some of its effectors may be altered in comparison with normal mammary tissue.

3.4. IFN-γ affects the morphology of breast cancer cells

Previously, we demonstrated that the protein levels of free ISG15 and protein ISGylation are increased in response to IFN-γ treatment in MCF-7 and MDA-MB-231 breast cancer cells [24]. To examine if *ISG15* is an IFN-γ-induced gene in these breast cancer cells, we performed an

INFORME DE LABORES 2019

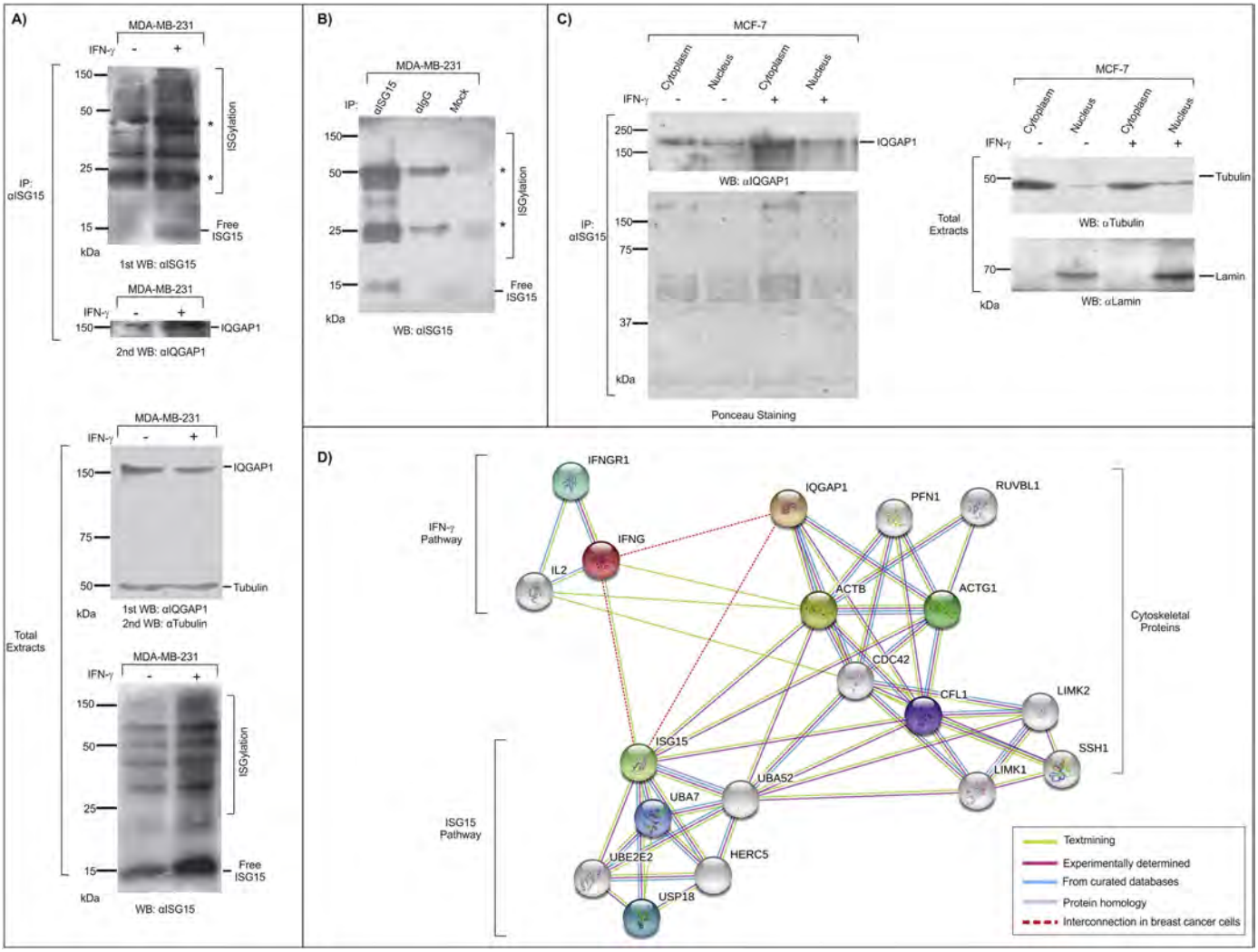

Fig. 8. Association between ISG15 and IQGAP1 is increased by IFN-γ treatment of breast cancer cells. A) Endogenous ISG15 immunoprecipitation (IP) followed by WB for ISG15, and then for IQGAP1, using total extracts from MDA-MB-231 cells with or without IFN-γ (100 ng/ml) treatment. IQGAP1 and ISG15 levels were also evaluated by WB, and tubulin was used as a loading control. B) Mock and IgG were used as controls to evaluate the specificity of ISG15 IP (*IgG). C) Cytoplasmic and nuclear extracts derived from MCF-7 cells with or without IFN-γ (100 ng/ml) treatment were immunoprecipitated using the ISG15 antibody and analyzed by WB for IQGAP1. Lamin and tubulin were used as loading controls for nuclear and cytoplasmic fractions, respectively. Ponceau staining was used on IP membrane. E) Interactome analysis using STRING software for IFN-γ signaling, ISGylation, and cytoskeletal remodeling associated proteins. The association between ISG15, IQGAP1, and IFN-γ is shown as a dashed red line. Known interactions from curated databases, text mining, experimental findings, and protein homology are indicated in blue, green, purple, and dark blue lines, respectively. (For interpretation of the references to colour in this figure legend, the reader is referred to the web version of this article.)

RT-PCR assay using RNA obtained from cells treated or untreated with IFN-γ for 24 h. Our results indicated that *ISG15* mRNA levels are up-regulated by IFN-γ (Fig. 5A), suggesting that these cell lines may provide a useful system to study the effects of IFN-γ/ISG15 signaling. Since IFN-γ signaling pathway seems to be deregulated in breast cancer cells, we decided to examine the effect of IFN-γ treatment on the morphology and viability of MCF-7 and MDA-MB-231 human breast cancer cells. Initially, the cells were treated with IFN-γ for 24 h, followed by calcein staining, and as a result we detected morphological changes in MCF-7 and MDA-MB-231 cells, since some of the cells were more elongated in comparison with cells without IFN-γ treatment (Fig. 5B, C, zoom). We then evaluated the viability of these cells after IFN-γ treatment for 48 h using cell viability assays (Calcein-AM/propidium iodide (PI)). Calcein emits a green fluorescence when it is released from Calcein-AM by esterases enzymatic activity of viable cells. PI emits a red fluorescence when it passes the membranes of dead cells to intercalate with nuclear DNA. As a result, Calcein-AM stains viable cells green and PI stains dead cells red. Our results indicated that MDA-MB-293 cells with or without IFN-γ treatment were viable, as the majority stained green for calcein (Fig. 5D and F). Similarly, the viability of MCF-7 cells treated with IFN-γ was not decreased by IFN-γ stimulation (Fig. 5E and G). Our statistical analysis, determined that the percentage of dead cells was not significantly different between the IFN-γ treated and untreated cells (Fig. 5F and G). Thus, our assays revealed that MCF-7 and MDA-MB-231 breast cancer cells undergo morphological changes in response to IFN-γ, and IFN-γ treatment does not appreciably affect the viability of these cells.

3.5. IFN-γ increases the marks of ISGylation in the cytoplasm of MDA-MB-231 breast cancer cells

We have evidenced changes in the morphology of breast cancer cells when they were treated with IFN-γ. For this reason, we performed an immunofluorescence assay to evaluate the subcellular distribution of ISG15 in response to IFN-γ treatment and its possible relation with the changes in morphology of MDA-MB-231 cells in this condition. As a

INFORME DE LABORES 2019

result, ISG15 signal was detected in the cytoplasm and nucleus of breast cancer cells without IFN-γ treatment. After IFN-γ treatment we also detected changes in the morphology of some of these cells (cell shape more elongated) in comparison with untreated cells (Fig. 6A, zoom). We also observed that IFN-γ treatment had no effect on ISG15 subcellular distribution in these cells, but a stronger signal for ISG15 was detected (Fig. 6A). Our analysis demonstrated that fluorescence intensity for ISG15 was significantly higher in MDA-MB-231 cells treated with IFN-γ compared with that detected in untreated cells (Fig. 6B).

Additionally, we performed a western blot (WB) to specifically detect the distribution of ISGylation marks between the cytoplasmic and nuclear compartments in MDA-MB-231 cells treated with or without IFN-γ (Fig. 6C short/long exposure, 12% and 7.5% gels). We detected statistically significant increase in ISGylation marks within the cytoplasm in response to IFN-γ (Fig. 6D). Hence, IFN-γ induces changes in the morphology of breast cancer cells and also increases ISG15 levels, while exerting no effects on subcellular distribution of this protein. ISGylation marks were mainly detected in the cytoplasm, suggesting that this interferon promotes the conjugation of ISG15 to several cytoplasmic proteins to modify them and modulate their functions.

3.6. *IFN-γ induces changes in the actin cytoskeleton and ISGylation of some cytoplasmic proteins could be implicated*

To further explore if IFN-γ could modulate the actin cytoskeleton of breast cancer cells, we performed phalloidin staining of actin filaments (also known as F-actin) in IFN-γ treated and untreated MDA-MB-231 cells. We observed changes in the actin cytoskeleton that were promoted by IFN-γ treatment. F-actin was concentrated in various subcellular areas but was reorganized into stress fibers following 48 h and 72 h of IFN-γ treatment (Fig. 7A and B). A similar effect was observed in MCF-7 cells expressing the ISGylation system (Supplementary Fig. 3). Given these observations, modifications in the morphology of breast cancer cells are clearly linked to cytoskeletal remodeling in response to IFN-γ treatment.

The changes in the cytoskeleton of breast cancer cells promoted by IFN-γ treatment could be linked to ISGylation of cytoplasmic proteins, but few ISGylation-target proteins have been identified to date. IQGAP1 is a protein that participates in the regulation of cytoskeletal dynamics, and interestingly, is one of the few proteins that appears to be ISGylated [49–51]. Based on this, we evaluated the effect of IFN-γ treatment on ISGylation of IQGAP1. Using total extracts obtained from MDA-MB-231 cells that were untreated or treated with IFN-γ, we performed an immunoprecipitation assay to enrich the modifier protein ISG15. A first WB against ISG15 was performed to probe the efficiency of immunoprecipitation, displaying a pattern of ISG15-conjugated proteins that increased in response to IFN-γ treatment (Fig. 8A, 1st WB:αISG15). Then, a second WB against IQGAP1 showed that IFN-γ also increased association between ISG15 and IQGAP1 (Fig. 8A, 2nd WB:αIQGAP1). Furthermore, the detection of tubulin from total extracts was used as a loading control, and it was observed that the IQGAP1 levels were not affected by IFN-γ. In contrast, ISGylation levels increased when the cells were treated with IFN-γ (Fig. 8A, bottom). Additionally, the use of IgG and mock controls were used to evaluate the specificity of ISG15 immunoprecipitation (Fig. 8B). IFN-γ treatment also increased this association between ISG15 and IQGAP1 in the cytoplasm of MCF-7 breast cancer cells (Fig. 8C). This ISG15 immunoprecipitation was probed using Ponceau staining. Therefore, proteins such as IQGAP1 that are involved in cytoskeletal remodeling may associate with ISG15 *via* ISGylation, and be modulated by IFN-γ in breast cancer cells.

To investigate the relationship between the IFN-γ signaling pathway, ISG15, and the ISGylation system in the context of the modulation of cytoskeletal reorganization, we performed an interactome analysis using STRING software. Our analysis showed a connection between these pathways, where the actin proteins (ACTB, ACTG1) are key players along with other proteins that regulate the cytoskeleton. Importantly, we observed a novel association between IFN-γ, ISGylation, and IQGAP1 in the cytoskeletal dynamics of breast cancer cells (Fig. 8D).

4. Discussion

Our study revealed increased expression of *STAT1, IRF-1, RIG-1* (factors that mediate IFN-γ signaling), and *ISG15* genes in breast cancer cells compared to their expression in normal mammary tissues, suggesting a possible interplay between IFN-γ and ISG15-regulated molecular pathways. We also observed increase in the expression of *STAT1, IRF-1*, and *ISG15* in grade 3 mammary tumors in comparison to grade 1 tumors, demonstrating the relevance of the expression of these genes in the progression of breast cancer.

Additionally, the observation that the levels of the modifier ISG15 are elevated in mammary tumors in comparison with those in normal adjacent tissue suggests that protein ISGylation may be a highly active modification in breast cancer cells. Under this condition, the function of several proteins may be affected by ISGylation, and some of them may be linked to proliferation and metastasis. As ISG15 expression and protein levels are increased in breast cancer, this may provide a potential biomarker for this cancer type. It must be noted that ISG15 upregulation has also been reported in other cancer types [52–56], but the mechanism of action is unclear.

Breast cancer cells exhibit a characteristic profile of free ISG15 and ISGylation that is upregulated by IFN-γ [23,24] and not exclusively by IFN-α/β as in some cell types. Given this, IFN-γ signaling may also play a critical role in breast cancer by mediating the modification of proteins by ISGylation and the gene expression characteristic of these cells. For example, it has also been reported that patient-derived mammary tumor xenografts in athymic mice can secrete IFN-γ, and a gene signature regulated by interferons may be associated with the grade of sensitivity to chemotherapy. Additionally, IFN-γ autocrine signaling has been associated with sensitivity to fulvestrant treatment [14–17].

Accordingly, IFN-γ may be a key component of the mammary tumor microenvironment and may function to generate autocrine and paracrine signals to induce protein ISGylation. Here, our results suggest that the *IFNG* gene that encodes for IFN-γ is increased in mammary tumors relative to control tissue, and as a consequence the production and secretion of IFN-γ may be increased in these tumors. Our analysis also indicated, however, that expression of IFN-γ signaling elements such as receptors and JAK1 is decreased in breast cancer. It is unclear if the deregulation of these IFN-γ signaling components is a compensatory mechanism to regulate this signaling, but this deregulation may have serious implications in for intercellular communication within the tumor microenvironment. Additionally, the deregulation of IFN-γ signaling in breast cancer may affect the expression of IFN-γ target genes, including those that allow for recognition of tumor cells by the antitumor immunity system (Supplementary fig. 2), and may also affect the pattern of proteins regulated by ISGylation.

Although there are alterations in the expression IFN-γ signaling elements in mammary tumors from patients, MCF-7 and MDA-MB-231 breast cancer cell lines are responsive to this molecule. Cellular outcomes, however, may be different due to crosstalk with other signaling pathways such as ERα and other nuclear receptor pathways that possess altered regulatory mechanisms that affect signaling in certain cancer types [57]. MCF-7 cells are ERα+, and the viability of these cells is not altered in a statistically significant manner when treated with IFN-γ. Additionally, MDA-MB-231 cells are ERα- and their viability is also unaffected by IFN-γ stimulation. Interestingly, in both cell types, IFN-γ treatment induced changes in cellular morphology, and our results suggest that these changes are linked to cytoskeletal reorganization. A deregulation of the IFN-γ signaling pathways may be associated with breast cancer progression.

The changes in the morphology of breast cancer cells induced by IFN-γ can, in part, be mediated *via* ISGylation of cytoplasmic proteins,

INFORME DE LABORES 2019

as IFN-γ increases ISGylation mark mainly in the cytoplasm. Here, we analyzed IQGAP1, a protein that is associated with cytoskeletal remodeling that has also been identified as an ISGylation target. Our findings suggest that the interaction between ISG15 and IQGAP1 is increased by IFN-γ treatment.

An important challenge is to identify other ISG15-interacting proteins that modulate the cytoskeletal organization and determine the specific function of this modification. To date, protein ISGylation has been determined principally as monoISGylation, regulating the protein stability either by inhibiting or promoting the ubiquitination pathway. Also, functions unrelated to protein stability have been proposed, in which ISGylation appears to modulate protein–protein interactions. For example, filamin B is another protein associated with actin that connects actin filaments to the cell membrane. When filamin B is not ISGylated, it acts as a scaffold for RAC1, MEKK1, and MKK4 proteins allowing IFN-α/β induced JNK signaling for the induction of apoptosis. When filamin B becomes ISGylated, however, its interactions with RAC1, MEKK1, and MKK4 proteins are lost, resulting in the inhibition of JNK signaling. Therefore, filamin B ISGylation blocks IFN-α/β induced JNK signaling [58]. In our study, we observed that IQGAP1 levels were not altered by IFN-γ stimulus (Fig. 8 A (bottom) and Supplementary fig. 4), and it is likely that ISGylation modulates the interaction of IQGAP1 with other proteins. Additionally, our interactome study indicated a close relationship between IFN-γ signaling, the ISGylation system, and proteins, such as IQGAP1, present in the cytoskeleton that may participate in cytoskeletal organization. Many of these proteins may be regulated by IFN-γ-induced ISGylation and/or modulated at the transcriptional level by IFN-γ. Thus, our findings may provide insight between these pathways in breast cancer cells. More studies may help to demonstrate functional and mechanistic implications of these pathways in the growth and progression of mammary tumors, as well as, their potential for the diagnosis, prognosis, and treatment of breast cancer.

5. Conclusion

In conclusion, our results indicate that the expression of elements involved in IFN-γ signaling pathway, IFN-γ target genes, and protein ISGylation are deregulated in mammary tumors. IFN-γ in breast cancer cells increases *ISG15* expression and subsequent protein ISGylation, and induces changes in cellular morphology associated with the cytoskeleton. ISG15 can be a potential biomarker for breast cancer, and the target of ISGylation, as IQGAP1, may present important implications in this context.

Funding

This work was supported by the DGAPA-UNAM (grant numbers PAPIIT-IA200916 to A.C.T.-C.).

Declaration of interest

The authors report no conflicts of interest in this work.

Author contributions

A.C.T.-C. designed research, performed some WB, conducted cellular viability assays, performed the *in silico* analysis, and wrote the manuscript. C.C. performed the IHC assays and analyzed data. E.C.-R. performed the IF and Co-IP experiments and prepared some figs. J.O.R.-J. prepared some figures and improved the manuscript. A.R.-M. assisted in the IHC assays. M.S-G performed the RT-PCR assay.

Acknowledgements

We thank Dr. Miguel Tapia Rodríguez (Instituto de Investigaciones Biomédicas, Unidad de Microscopia, UNAM) for his technical support in analyzing the immunofluorescence. We thank Claudia Rivera Cerecedo for her comments on the manuscript.

Appendix A. Supplementary data

Supplementary data to this article can be found online at https://doi.org/10.1016/j.cellsig.2018.11.021.

References

[1] M. Mojic, K. Takeda, Y. Hayakawa, The Dark Side of IFN-gamma: its Role in Promoting Cancer Immunoevasion, Int. J. Mol. Sci. 19 (1) (2017).
[2] M.R. Zaidi, G. Merlino, The two faces of interferon-gamma in cancer, Clinical Cancer Research 17 (19) (2011) 6118–6124.
[3] E.J. Kim, J.M. Lee, S.E. Namkoong, S.J. Um, J.S. Park, Interferon regulatory factor-1 mediates interferon-gamma-induced apoptosis in ovarian carcinoma cells, J. Cell. Biochem. 85 (2) (2002) 369–380.
[4] A. Rettino, N.M. Clarke, Genome-wide Identification of IRF1 Binding Sites Reveals Extensive Occupancy at Cell Death Associated Genes, J Carcinog Mutagen S6 (2013) 009, https://doi.org/10.4172/2157-2518.S6-009.
[5] Y. Wang, D. Liu, P. Chen, H.P. Koeffler, X. Tong, D. Xie, Negative feedback regulation of IFN-gamma pathway by IFN regulatory factor 2 in esophageal cancers, Cancer Res. 68 (4) (2008) 1136–1143.
[6] X.F. Cui, T. Imaizumi, H. Yoshida, E.C. Borden, K. Satoh, Retinoic acid-inducible gene-I is induced by interferon-gamma and regulates the expression of interferon-gamma stimulated gene 15 in MCF-7 cells, Biochemistry and cell biology, Biochimie et biologie cellulaire 82 (3) (2004) 401–405.
[7] T. Imaizumi, M. Hatakeyama, K. Yamashita, H. Yoshida, A. Ishikawa, K. Taima, K. Satoh, F. Mori, K. Wakabayashi, Interferon-gamma induces retinoic acid-inducible gene-I in endothelial cells, Endothelium : journal of endothelial cell research 11 (3–4) (2004) 169–173.
[8] T. Imaizumi, N. Yagihashi, M. Hatakeyama, K. Yamashita, A. Ishikawa, K. Taima, H. Yoshida, I. Inoue, T. Fujita, S. Yagihashi, K. Satoh, Expression of retinoic acid-inducible gene-I in vascular smooth muscle cells stimulated with interferon-gamma, Life Sci. 75 (10) (2004) 1171–1180.
[9] E. Yuzawa, T. Imaizumi, T. Matsumiya, H. Yoshida, R. Fukuhara, H. Kimura, A. Fukui, K. Tanji, F. Mori, K. Wakabayashi, S. Fujii, H. Mizunuma, K. Satoh, Retinoic acid-inducible gene-I is induced by interferon-gamma and regulates CXCL11 expression in HeLa cells, Life Sci. 82 (11 – 12) (2008) 670–675.
[10] G.B. Lesinski, J.M. Zimmerer, M. Kreiner, J. Trefry, M.A. Bill, G.S. Young, B. Becknell, W.E. Carson 3rd, Modulation of SOCS protein expression influences the interferon responsiveness of human melanoma cells, BMC Cancer 10 (2010) 142.
[11] H. Weng, P.R. Mertens, A.M. Gressner, S. Dooley, IFN-gamma abrogates profibrogenic TGF-beta signaling in liver by targeting expression of inhibitory and receptor Smads, J. Hepatol. 46 (2) (2007) 295–303.
[12] S.K. Browne, J.R. Roesser, S.Z. Zhu, G.D. Ginder, Differential IFN-gamma stimulation of HLA-A gene expression through CRM-1-dependent nuclear RNA export, J. Immunol. 177 (12) (2006) 8612–8619.
[13] A.A. Mostafa, D. Codner, K. Hirasawa, Y. Komatsu, M.N. Young, V. Steimle, S. Drover, Activation of ERalpha signaling differentially modulates IFN-gamma induced HLA-class II expression in breast cancer cells, PLoS One 9 (1) (2014) e87377.
[14] J.L. Gooch, R.E. Herrera, D. Yee, The role of p21 in interferon gamma-mediated growth inhibition of human breast cancer cells, Cell growth & differentiation : the molecular biology journal of the American Association for, Cancer Res. 11 (6) (2000) 335–342.
[15] X.L. Niu, Y. Wang, Z. Yao, H. Duan, Z. Li, W. Liu, H. Zhang, W.M. Deng, Autocrine interferon-gamma may affect malignant behavior and sensitivity to tamoxifen of MCF-7 via estrogen receptor beta subtype, Oncol. Rep. 34 (6) (2015) 3120–3130.
[16] M.E. Legrier, I. Bieche, J. Gaston, A. Beurdeley, V. Yvonnet, O. Deas, A. Thuleau, S. Chateau-Joubert, J.L. Servely, S. Vacher, M. Lassalle, S. Depil, G.C. Tucker, J.J. Fontaine, M.F. Poupon, S. Roman-Roman, J.G. Judde, D. Decaudin, S. Cairo, E. Marangoni, Activation of IFN/STAT1 signalling predicts response to chemotherapy in oestrogen receptor-negative breast cancer, Br. J. Cancer 114 (2) (2016) 177–187.
[17] Y. Ning, R.B. Riggins, J.E. Mulla, H. Chung, A. Zwart, R. Clarke, IFNgamma restores breast cancer sensitivity to fulvestrant by regulating STAT1, IFN regulatory factor 1, NF-kappaB, BCL2 family members, and signaling to caspase-dependent apoptosis, Mol. Cancer Ther. 9 (5) (2010) 1274–1285.
[18] A.A. Jitariu, A.M. Cimpean, D. Ribatti, M. Raica, Triple negative breast cancer: the kiss of death, Oncotarget 8 (28) (2017) 46652–46662.
[19] A.C. Tecalco-Cruz, I.A. Perez-Alvarado, J.O. Ramirez-Jarquin, L. Rocha-Zavaleta, Nucleo-cytoplasmic transport of estrogen receptor alpha in breast cancer cells, Cell. Signal. 34 (2017) 121–132.
[20] A.C. Tecalco-Cruz, J.O. Ramirez-Jarquin, Mechanisms that increase Stability of Estrogen Receptor Alpha in Breast Cancer, Clinical breast cancer 17 (1) (2017) 1–10.
[21] O.A. Malakhova, M. Yan, M.P. Malakhov, Y. Yuan, K.J. Ritchie, K.I. Kim, L.F. Peterson, K. Shuai, D.E. Zhang, Protein ISGylation modulates the JAK-STAT signaling pathway, Genes Dev. 17 (4) (2003) 455–460.
[22] M. Recht, E.C. Borden, E. Knight Jr., A human 15-kDa IFN-induced protein induces

the secretion of IFN-gamma, J. Immunol. 147 (8) (1991) 2617–2623.
[23] A.C. Tecalco Cruz, K. Mejia-Barreto, Cell type-dependent regulation of free ISG15 levels and ISGylation, Journal of cell communication and signaling 11 (2) (2017) 127–135.
[24] A.C. Tecalco-Cruz, E. Cruz-Ramos, Protein ISGylation and free ISG15 levels are increased by interferon gamma in breast cancer cells, Biochem. Biophys. Res. Commun. 499 (4) (2018) 973–978.
[25] E. Knight Jr., D. Fahey, B. Cordova, M. Hillman, R. Kutny, N. Reich, D. Blomstrom, A 15-kDa interferon-induced protein is derived by COOH-terminal processing of a 17-kDa precursor, J. Biol. Chem. 263 (10) (1988) 4520–4522.
[26] K.R. Loeb, A.L. Haas, The interferon-inducible 15-kDa ubiquitin homolog conjugates to intracellular proteins, J. Biol. Chem. 267 (11) (1992) 7806–7813.
[27] J.L. Potter, J. Narasimhan, L. Mende-Mueller, A.L. Haas, Precursor processing of pro-ISG15/UCRP, an interferon-beta-induced ubiquitin-like protein, J. Biol. Chem. 274 (35) (1999) 25061–25068.
[28] N. Reich, B. Evans, D. Levy, D. Fahey, E. Knight Jr., J.E. Darnell Jr., Interferon-induced transcription of a gene encoding a 15-kDa protein depends on an upstream enhancer element, Proc. Natl. Acad. Sci. U. S. A. 84 (18) (1987) 6394–6398.
[29] C. Zhao, S.L. Beaudenon, M.L. Kelley, M.B. Waddell, W. Yuan, B.A. Schulman, J.M. Huibregtse, R.M. Krug, The UbcH8 ubiquitin E2 enzyme is also the E2 enzyme for ISG15, an IFN-alpha/beta-induced ubiquitin-like protein, Proc. Natl. Acad. Sci. of the United States of America 101 (20) (2004) 7578–7582.
[30] A. Dastur, S. Beaudenon, M. Kelley, R.M. Krug, J.M. Huibregtse, Herc5, an interferon-induced HECT E3 enzyme, is required for conjugation of ISG15 in human cells, The J. Biol. Chem. 281 (7) (2006) 4334–4338.
[31] F. Okumura, W. Zou, D.E. Zhang, ISG15 modification of the eIF4E cognate 4EHP enhances cap structure-binding activity of 4EHP, Genes Dev. 21 (3) (2007) 255–260.
[32] J.J. Wong, Y.F. Pung, N.S. Sze, K.C. Chin, HERC5 is an IFN-induced HECT-type E3 protein ligase that mediates type I IFN-induced ISGylation of protein targets, Proc. Natl. Acad. Sci. U. S. A. 103 (28) (2006) 10735–10740.
[33] W. Zou, D.E. Zhang, The interferon-inducible ubiquitin-protein isopeptide ligase (E3) EFP also functions as an ISG15 E3 ligase, The J. Biol. Chem. 281 (7) (2006) 3989–3994.
[34] A. Basters, P.P. Geurink, F. El Oualid, L. Ketscher, M.S. Casutt, E. Krause, H. Ovaa, K.P. Knobeloch, G. Fritz, Molecular characterization of ubiquitin-specific protease 18 reveals substrate specificity for interferon-stimulated gene 15, FEBS J. 281 (7) (2014) 1918–1928.
[35] J. D'Cunha, E. Knight Jr., A.L. Haas, R.L. Truitt, E.C. Borden, Immunoregulatory properties of ISG15, an interferon-induced cytokine, Proc. Natl. Acad. Sci. U. S. A. 93 (1) (1996) 211–215.
[36] J. D'Cunha, S. Ramanujam, R.J. Wagner, P.L. Witt, E. Knight Jr., E.C. Borden, In vitro and in vivo secretion of human ISG15, an IFN-induced immunomodulatory cytokine, J. Immunol. 157 (9) (1996) 4100–4108.
[37] E. Knight Jr., B. Cordova, IFN-induced 15-kDa protein is released from human lymphocytes and monocytes, J. Immunol. 146 (7) (1991) 2280–2284.
[38] J. Burks, R.E. Reed, S.D. Desai, ISGylation governs the oncogenic function of Ki-Ras in breast cancer, Oncogene 33 (6) (2014) 794–803.
[39] S.D. Desai, A.L. Haas, L.M. Wood, Y.C. Tsai, S. Pestka, E.H. Rubin, A. Saleem, E.K.A. Nur, L.F. Liu, Elevated expression of ISG15 in tumor cells interferes with the ubiquitin/26S proteasome pathway, Cancer Res. 66 (2) (2006) 921–928.
[40] J.B. Fan, K. Arimoto, K. Motamedchaboki, M. Yan, D.A. Wolf, D.E. Zhang, Identification and characterization of a novel ISG15-ubiquitin mixed chain and its role in regulating protein homeostasis, Sci. Rep. 5 (2015) 12704.
[41] Y.F. Huang, D.V. Bulavin, Oncogene-mediated regulation of p53 ISGylation and functions, Oncotarget 5 (14) (2014) 5808–5818.
[42] M. Liu, X.L. Li, B.A. Hassel, Proteasomes modulate conjugation to the ubiquitin-like protein, ISG15, The Journal of biological chemistry 278 (3) (2003) 1594–1602.
[43] J. Burks, R.E. Reed, S.D. Desai, Free ISG15 triggers an antitumor immune response against breast cancer: a new perspective, Oncotarget 6 (9) (2015) 7221–7231.
[44] S.D. Desai, R.E. Reed, J. Burks, L.M. Wood, A.K. Pullikuth, A.L. Haas, L.F. Liu, J.W. Breslin, S. Meiners, S. Sankar, ISG15 disrupts cytoskeletal architecture and promotes motility in human breast cancer cells, Exp. Biol. Med. 237 (1) (2012) 38–49.
[45] T. Grewal, J. Heeren, D. Mewawala, T. Schnitgerhans, D. Wendt, G. Salomon, C. Enrich, U. Beisiegel, S. Jackle, Annexin VI stimulates endocytosis and is involved in the trafficking of low density lipoprotein to the prelysosomal compartment, J. Biol. Chem. 275 (43) (2000) 33806–33813.
[46] D. Szklarczyk, J.H. Morris, H. Cook, M. Kuhn, S. Wyder, M. Simonovic, A. Santos, N.T. Doncheva, A. Roth, P. Bork, L.J. Jensen, C. von Mering, The STRING database in 2017: quality-controlled protein-protein association networks, made broadly accessible, Nucleic Acids Res. 45 (D1) (2017) D362–D368.
[47] F. Varghese, A.B. Bukhari, R. Malhotra, A. De, IHC Profiler: an open source plugin for the quantitative evaluation and automated scoring of immunohistochemistry images of human tissue samples, PLoS One 9 (5) (2014) e96801.
[48] D.P. Arps, P. Healy, L. Zhao, C.G. Kleer, J.C. Pang, Invasive ductal carcinoma with lobular features: a comparison study to invasive ductal and invasive lobular carcinomas of the breast, Breast Cancer Res. Treat. 138 (3) (2013) 719–726.
[49] B. Cerikan, E. Schiebel, DOCK6 inactivation highlights ISGylation as RHO-GTPase balancer, Cell Cycle 16 (4) (2017) 304–305.
[50] B. Cerikan, R. Shaheen, G.P. Colo, C. Glasser, S. Hata, K.P. Knobeloch, F.S. Alkuraya, R. Fassler, E. Schiebel, Cell-Intrinsic Adaptation Arising from Chronic Ablation of a Key Rho GTPase Regulator, Dev. Cell 39 (1) (2016) 28–43.
[51] L.A. Durfee, N. Lyon, K. Seo, J.M. Huibregtse, The ISG15 conjugation system broadly targets newly synthesized proteins: implications for the antiviral function of ISG15, Mol. Cell 38 (5) (2010) 722–732.
[52] R.H. Chen, Y. Du, P. Han, H.B. Wang, F.Y. Liang, G.K. Feng, A.J. Zhou, M.Y. Cai, Q. Zhong, M.S. Zeng, X.M. Huang, ISG15 predicts poor prognosis and promotes cancer stem cell phenotype in nasopharyngeal carcinoma, Oncotarget 7 (13) (2016) 16910–16922.
[53] H. Mao, M. Wang, B. Cao, H. Zhou, Z. Zhang, X. Mao, Interferon-stimulated gene 15 induces cancer cell death by suppressing the NF-kappaB signaling pathway, Oncotarget 25 (7(43)) (2016) 70143–70151.
[54] E. Padovan, L. Terracciano, U. Certa, B. Jacobs, A. Reschner, M. Bolli, G.C. Spagnoli, E.C. Borden, M. Heberer, Interferon stimulated gene 15 constitutively produced by melanoma cells induces e-cadherin expression on human dendritic cells, Cancer Res. 62 (12) (2002) 3453–3458.
[55] H. Satake, K. Tamura, M. Furihata, T. Anchi, H. Sakoda, C. Kawada, T. Iiyama, S. Ashida, T. Shuin, The ubiquitin-like molecule interferon-stimulated gene 15 is overexpressed in human prostate cancer, Oncol. Rep. 23 (1) (2010) 11–16.
[56] X.X. Wan, H.C. Chen, M.A. Khan, A.H. Xu, F.L. Yang, Y.Y. Zhang, D.Z. Zhang, ISG15 inhibits IFN-alpha-resistant liver cancer cell growth, Biomed. Res. Int. 2013 (2013) 570909.
[57] A.C. Tecalco-Cruz, Molecular pathways involved in the transport of nuclear receptors from the nucleus to cytoplasm, J. Steroid Biochem. Mol. Biol. 178 (2018) 36–44.
[58] Y.J. Jeon, J.S. Choi, J.Y. Lee, K.R. Yu, S.M. Kim, S.H. Ka, K.H. Oh, K.I. Kim, D.E. Zhang, O.S. Bang, C.H. Chung, ISG15 modification of filamin B negatively regulates the type I interferon-induced JNK signalling pathway, EMBO Rep. 10 (4) (2009) 374–380.

Send Orders for R INFORME DE LABORES 2019 et

Current Drug Targets, 2019, *20*, 690-704

REVIEW ARTICLE

Estrogen Receptor Alpha and its Ubiquitination in Breast Cancer Cells

Angeles C. Tecalco-Cruz[1,*], Josué O. Ramírez-Jarquín[2] and Eduardo Cruz-Ramos[1]

[1]*Instituto de Investigaciones Biomédicas. Universidad Nacional Autónoma de México. Mexico City, 04510 Mexico;* [2]*Instituto de Fisiología Celular. Universidad Nacional Autónoma de México. Mexico City, 04510 Mexico*

ARTICLE HISTORY

Received: September 18, 2018
Revised: October 09, 2018
Accepted: October 09, 2018

DOI:
10.2174/1389450119666181015114041

Abstract: More than 70% of all breast cancer cases are estrogen receptor alpha-positive (ERα). ERα is a member of the nuclear receptor family, and its activity is implicated in the gene transcription linked to the proliferation of breast cancer cells, as well as in extranuclear signaling pathways related to the development of resistance to endocrine therapy. Protein-protein interactions and posttranslational modifications of ERα underlie critical mechanisms that modulate its activity. In this review, the relationship between ERα and ubiquitin protein (Ub), was investigated in the context of breast cancer cells. Interestingly, Ub can bind covalently or non-covalently to ERα resulting in either a *proteolytic* or *non-proteolytic* fate for this receptor. Thereby, Ub-dependent molecular pathways that modulate ERα signaling may play a central role in breast cancer progression, and consequently, present critical targets for treatment of this disease.

Keywords: Estrogen receptor alpha, breast cancer, monoubiquitination, polyubiquitination, non-covalent ubiquitin binding, endocrine therapy.

1. INTRODUCTION

Over 70% of all breast cancer cases are diagnosed as estrogen receptor-positive (ERα+) [1-5]. ERα is a nuclear receptor having nuclear and extranuclear activities related to gene transcription and signal transduction pathways, respectively. These activities of ERα are possible because of its structural organization into several domains, including the ligand-binding domain (LBD), the DNA-binding domain (DBD), and a hinge region that separates the LBD and the DBD. LBD recognizes estrogenic hormones, mainly 17-beta-estradiol (E2), while DBD binds to specific palindromic sequences in enhancer and promoter regions of its target genes [6-8]. Activation function domain-1 (AF-1), localized in the N-terminus, and activation function domain-2 (AF-2), localized in the C-terminus, recruit several proteins, including transcriptional coregulators. Functions of AF-1 and AF-2 domains are tissue-specific, where AF-1 functions in an E2 hormone-independent manner, and AF-2 in an E2 hormone-dependent manner [9-13].

ERα is a central element in the signal transduction pathways of breast cancer cells, both inside and outside the nucleus (Fig. **1**). Outside the nucleus, ERα is present in the cell membrane due to palmitoylation or association with other transmembrane proteins [14, 15]. ERα is also localized in the cytoplasm, where it interacts with several protein mediators of signaling pathways, such as MNAR, MTA1, MEMO, and RB, related to endocrine resistance in breast cancer [16-20]. Despite these important extranuclear functions, this receptor is well known by its function as a transcription factor, as well as a coregulator of other transcription factors, such as Sp1, AP1, and NF-kappa B [21, 22]. Importantly, ERα activity is promoted in response to the E2 hormone. However, growth factors, such as EGF and IGF, also promote ERα activity in an E2 hormone-independent manner by inducing its phosphorylation [23, 24].

In order to regulate transcription of its target genes in response to E2 hormone in breast cancer cells, ERα is recruited on enhancer and promoter sequences facilitated by pioneer factors, such as FOXA1 and GATA3 [25, 26]. Over 300 coregulators (coactivators and corepressors) have been identified as modulators of ERα activity that are frequently deregulated in breast cancers. For example, in breast cancer, coactivators are commonly upregulated while corepressors are downregulated. Coactivator complexes open chromatin to facilitate transcription and corepressor complexes compact chromatin to inhibit gene expression [27-31]. Although coregulators are central for modulating ERα activity, other mechanisms such as protein-protein interactions and post-translational modifications which regulate the stability and subcellular localization of this receptor, also act as crucial regulatory factors of ERα function [32-34].

Due to the importance of ERα and its signaling pathways in breast cancer cells, detection of ERα is an indicator for the administration of *endocrine therapy,* which includes the use of aromatase inhibitors, selective estrogen receptor degraders or downregulators (SERDs) and selective estrogen receptor modulators (SERMs). Aromatase inhibitors such as anastrozole and letrozole are used to reduce E2 levels by inhibiting

*Address correspondence to this author at the Instituto de Investigaciones Biomédicas. Universidad Nacional Autónoma de México. Mexico City, 04510 Mexico; Tel: +52 155 54197390; E-mail: 12anget@gmail.com

 ©2019 Bentham Science Publishers

Current Drug Targets

INFORME DE LABORES 2019

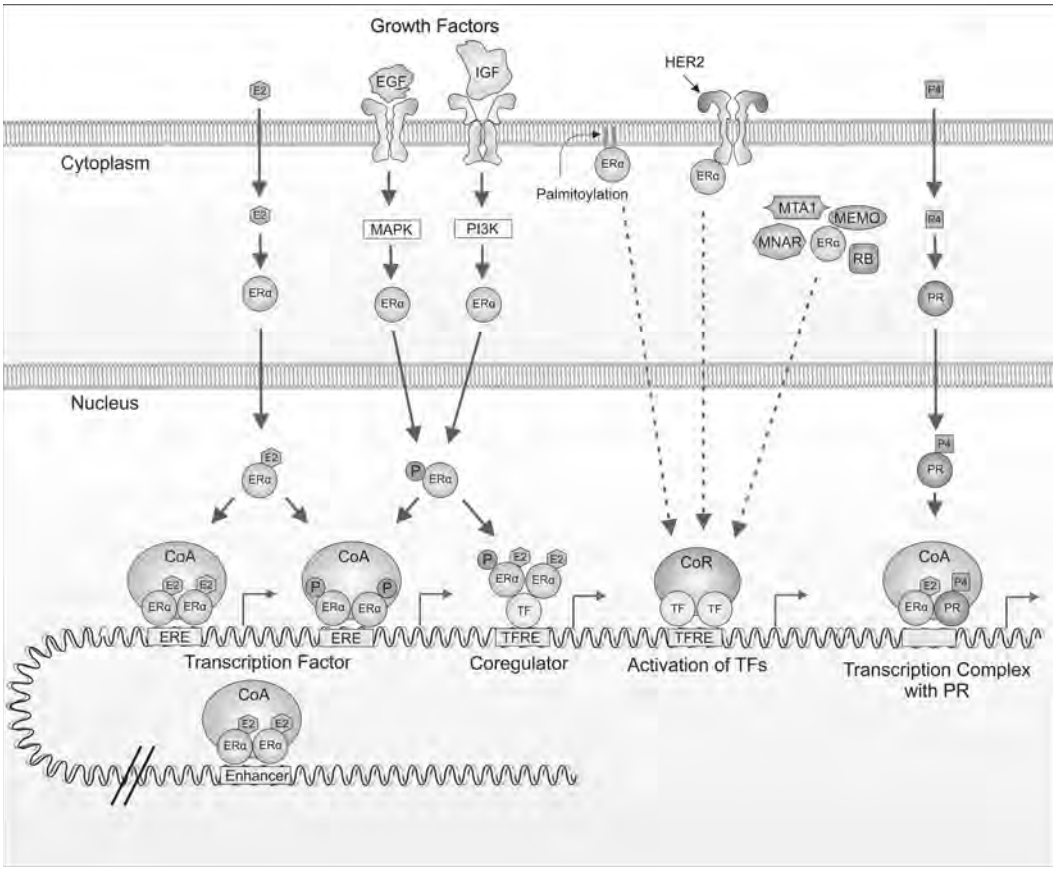

Fig. (1). Pathways of ERα in breast cancer cells. ERα is activated by E2 binding in the cytoplasm and/or nucleus. ERα recognizes AGGTCAnnnTGACCT sequence (estrogen response elements: EREs) in target enhancers and promoters. Coactivators (CoA) promote ERα-dependent gene expression. E2 induces ERα phosphorylation. Growth factors (EGF and IGF) also induce E2-independent ERα phosphorylation. This modification regulates ERα activity as a transcription factor or coregulator for some transcription factors (TFs). ERα is also out of the nucleus, membrane-localized by palmitoylation, with transmembrane receptors such as HER2, and/or associated with proteins such as MEMO, MTA1, MNAR and RB in the cytoplasm. In this manner, ERα is associated with kinase-dependent signaling that may activate other TFs and coregulator (CoR) complexes. Additionally, progesterone receptor (PR) may interact with ERα and re-direct its binding to chromatin regions to modulate gene expression.

the conversion of testosterone into E2 hormone [35-37]. Moreover, SERDs such as fulvestrant, and SERMs such as tamoxifen, are antiestrogens, which compete with E2 hormone for binding to ERα to decrease its abundance and/or activity, respectively. In summation, E2, SERDs and SERMs are ligands that bind to LBD of ERα, inducing a conformational change in the receptor depending on the ligand type. As a result, E2 induces ERα-dependent transcription, fulvestrant promotes the degradation of ERα, and tamoxifen binds to ERα and inhibits the induction of E2 hormone-target genes by recruiting several transcriptional corepressors [37-39]. Some breast cancer patients do not respond to endocrine therapy, presenting a *de novo resistance*, whereas many others develop resistance to these therapies later, presenting an *acquired resistance.* Mechanisms underlying both cases have not been completely defined yet [36, 40].

In this review, we focus on the modulation of ERα actions by Ub-associated pathways, and its potential implications in endocrine resistance to SERMs and SERDs in breast cancers.

1.1. Literature Search

The PubMed database was searched, using terms associated with ERα in relation to Ub, degradation and stability, with particular reference to human breast cancer including the treatment of this disease and implications for endocrine resistance. Articles included several original research such as studies on human breast cancer cell lines, *in vivo* studies on xenotransplantation to athymic mice from patients and analysis of tumor samples from patients. These articles contained data related to gene expression profiles, molecular mechanisms, and functional effects resulting from the interconnection of Ub-ERα pathways. The data were evaluated using several approaches, including clinical, molecular, and novel techniques such as NGS, ddPCR and CRISPR-Cas. Moreover, some critical general reviews were also perused.

2. BASICS OF THE UBIQUITIN PROTEIN AND UBIQUITINATION

Ubiquitin (Ub), a highly conserved protein in organisms ranging from yeast to humans, is composed of 76 amino acids (8-kDa). Ub contains a conjugation motif in its C-terminus, through which it is covalently attached to target proteins. The conjugation motif facilitates the formation of an isopeptide bond between Ub and specific lysine residues of its target protein, mediated by a sequential system of three enzymes: E1-ubiquitin-activating enzyme, E2-ubiquitin-

INFORME DE LABORES 2019

conjugating enzyme and E3-ubiquitin ligase enzyme. The substrate specificity for ubiquitination is determined by the E3 ligases because they attach the Ub to a lysine residue of the target protein [41-43]. In general, there are three main types of E3 ligases: Really Interesting New Gene E3 (*RING* E3) ligases, which contain a RING domain or U-box domain; Homologous to the E6AP Carboxyl Terminus (*HECT* E3) ligases, which are divided into 3 subfamilies (RCC1-like domains, tryptophan-tryptophan domains and ones lacking these domains), and RING-between RING-RING (*RBR* E3) ligases that contain an *in-between-RING domain* (IBR) which separates two predicted *RING domains* (RING1 and RING2). Ub is transferred from the E2-ubiquitin-conjugating enzyme to the substrate protein directly (in one step) by RING E3 ligases, whereas HECT and RBR ligases first transfer Ub from the E2-ubiquitin-conjugating enzyme to themselves and then to the substrate (in two steps). There are more than 600 members of the E3 ligase family, and RING E3 ligases are the most abundant [41, 44-46].

Ub chains are formed by the sequential attachment of Ubs to one another. Ub lysine residues 6, 11, 27, 29, 33, 48, and 63 can be used for polyubiquitin chain extension. Hence, there are homotypic chains *via* the link through one lysine of Ub, and also *via* several lysines of Ub. Moreover, several branched Ub structures can also be generated by other amino acid residues such as cysteine, serine, and threonine, but these have been scarcely studied. On the other hand, more than 100 deubiquitinases (DUBs) which break the isopeptide bond and reverse Ub binding of ubiquitinated proteins have been described in humans so far [47-50].

Covalent attachment of Ub to proteins can occur as monoubiquitination, multiubiquitination (monoubiquitination of several residues), or polyubiquitination, where each of these modifications results in a different cellular outcome. Monoubiquitination is associated with DNA repair, gene expression regulation, endocytosis, and protein stability, whereas polyubiquitination is mostly considered as a signal initiating selection of proteins for degradation by the 26S proteasome, and this coupling is known as the ubiquitin-proteasome system (UPS). Nevertheless, certain non-proteolytic functions have also been suggested for specific polyubiquitination cases [51-55].

3. MONOUBIQUITINATION AND UBIQUITIN-BINDING DOMAINS OF ERα IN BREAST CANCER CELLS

ERα is modified by both mono-and polyubiquitination but there are dissimilarities between these two modifications (Fig. **2**). For example, ERα polyubiquitination is induced by E2, whereas ERα monoubiquitination is negatively regulated by E2 in breast cancer cells [56]. In addition, while polyubiquitination is strongly related with E2-induced degradation of ERα by the UPS, ERα monoubiquitination does not induce its degradation by this system. Instead, monoubiquitination of this receptor modulates its stability, its interactions and DNA-binding activity as a transcriptional regulator [57-59].

Previous studies have indicated that ERα was monoubiquitinated *in vitro* in a BRCA1/BARD1 activity-dependent manner. Endogenous ERα monoubiquitination was observed in breast cancer cells, along with a decrease in monoubiquitinated ERα levels in response to E2 treatment. However, E2-dependent cellular proliferation seems to be promoted by ERα monoubiquitination. In these reports, ERα K302 and K303 residues were proposed as monoubiquitination sites of this receptor [57, 59, 60].

Monoubiquitination confers stability to ERα by inhibiting its polyubiquitination and degradation *via* the proteasome in breast cancer cells. E3-ubiquitin ligase RING finger proteins, such as RNF8 and RNF31 have been identified as modifiers of ERα *via* monoubiquitination. In particular**,** RNF8 associates with ERα to modulate its functions in two interconnected ways: 1) RNF8 induces monoubiquitination of ERα to stabilize it, and 2) RNF8 is a coactivator for ERα, increasing the expression of its target genes, such as pS2 and c-Myc. RNF8 downregulation decreases proliferation of breast cancer cells, whereas its upregulation is common in breast cancer, correlating with ERα levels [61]. Similarly, RNF31 associates with ERα and catalyzes its monoubiquitination to block the polyubiquitination, increasing ERα protein levels and its transcriptional activity. However, RNF31 is not a coactivator of ERα and is not recruited to ERα-dependent DNA regulatory regions [62].

SHARPIN also acts as an E3-ubiquitin ligase that stabilizes ERα by inducing its monoubiquitination to inhibit its polyubiquitination [63]. Thus, monoubiquitination and polyubiquitination compete to modify to ERα in order to modulate its stability and degradation, respectively. The deregulation of these modifications may be a key factor in regulating ERα functions in breast cancer, where ERα monoubiquitination seems to occur predominantly to confer more stability to the receptor and enhance E2 signaling in breast cancer cells.

It has been demonstrated that several proteins with ubiquitin-binding surfaces or domains (UBDs) may bind noncovalently with mono/polyubiquitinated proteins and Ub chains to stimulate signaling pathways, leading to several outcomes [53, 55, 64, 65]. These UBDs apparently lack shared, well-defined features, but it has been proposed that they possess regular secondary structures, such as α-helixes and/or Zn2+-fingers. Proteins modified *via* monoubiquitination also appear to contain one or more UBDs [66-68].

Importantly, UBDs have been reported to be present within the LBD of ERα (Fig. **2**). An interaction between ERα UBDs with ubiquitinated proteins or with recombinant Ub chains was demonstrated *in vitro* studies. Moreover, L429 and A430 residues of ERα were proposed as the key sites in UBDs of this receptor, as mutating these residues affected E2-dependent transcriptional functions of ERα. In addition, it was observed that when L429 and A430 residues in UBDs were mutated, the monoubiquitination of ERα receptor was blocked [69, 70]. These data indicate that these UBDs may have a functional significance for ERα monoubiquitination and for assembly of multiprotein complexes with ERα. Thus, the interactions of ERα *via* its UBDs seem to be critical in the progression of mammary tumors.

4. ERα POLYUBIQUITINATION IN BREAST CANCER CELLS

Certain E3-ubiquitin ligases such as CHIP, E6AP, BRCA1, BARD1, SKP2, and MDM2 are associated with

INFORME DE LABORES 2019

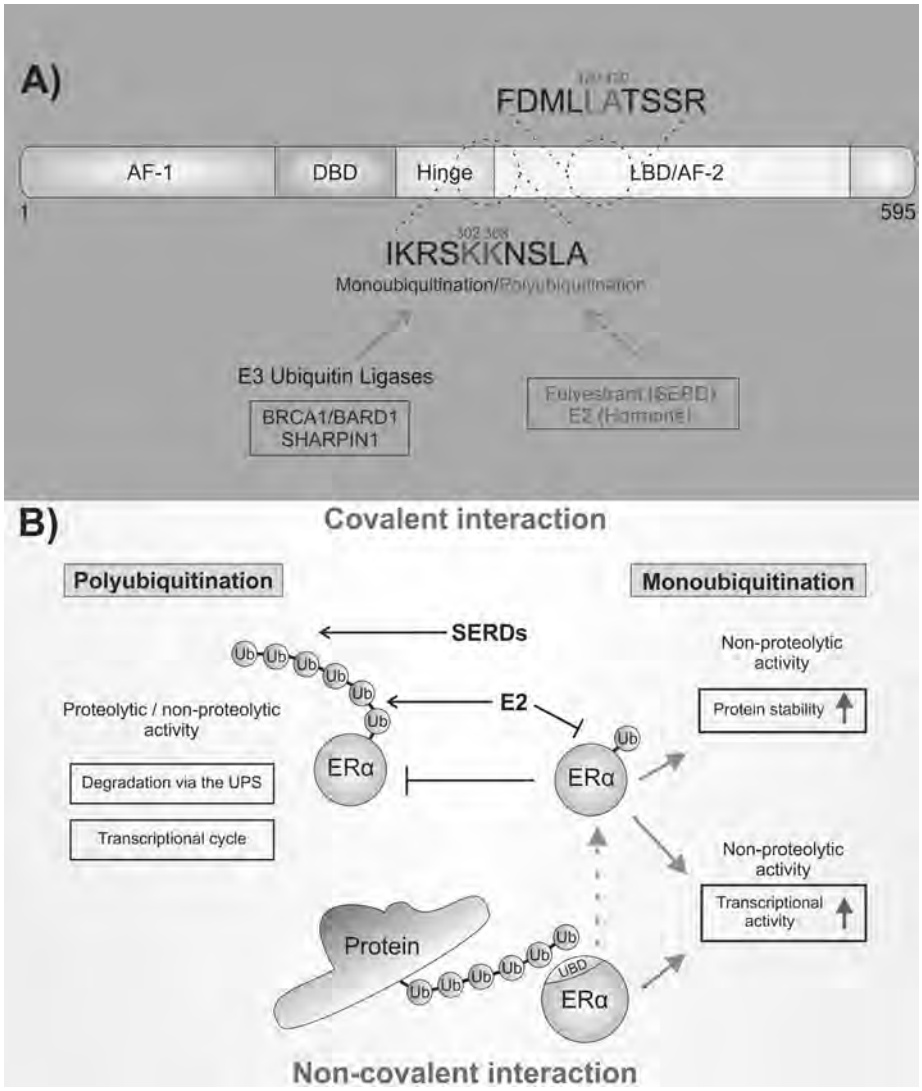

Fig. (2). ERα is modulated by ubiquitin-dependent pathways. A) Residues of ERα for interaction with ubiquitin protein. BRCA1/BARD1 and SHARPIN induces ERα monoubiquitination. E2 hormone and fulvestrant promote ERα polyubiquitination and degradation. ERα contains ubiquitin-binding domains (UBDs) to interact with ubiquitinated proteins. The residues are indicated. **B) Types of interactions between ERα and ubiquitin protein (Ub)**. Covalent (monoubiquitination and polyubiquitination) and non-covalent *via* UBDs. These interactions lead to proteolytic or non-proteolytic pathways for this receptor. ERα monoubiquitination appears to compete with its polyubiquitination in breast cancer cells. SERDs and E2 stimulate ERα polyubiquitination followed by degradation *via* the UPS. E2 decreases ERα monoubiquitination, but some E2-induced actions may require monoubiquitinated ERα.

ERα ubiquitination. Although it is known that polyubiquitination of ERα is followed by its degradation by 26S proteasome, not all ubiquitinated lysine residues of ERα have been identified, and direct interaction between ERα and all E3-ubiquitin ligases has not yet been demonstrated [57, 71-75]. Despite limited mechanistic details, ERα polyubiquitination is a regulatory factor, which controls its abundance or levels, as well as its functions.

In the absence of E2 hormone, the half-life of ERα protein oscillates between 3-5 h depending on cell type, whereas when the cells were exposed to E2, its half-life decreased to 1 h after treatment [76, 77]. Initially, the UPS system was suggested to be crucial to maintain the balance of ERα protein levels and E2 signaling [78]. However, studies performed by Leonard *et al.*, suggested that the interaction between ERα and its coactivators may be important for E2-induced downregulation of this receptor. This study highlighted the strong relationship between the process of degradation and transcriptional activity of ERα [79] (Fig. **2**).

Later, Reid G *et al.* proposed that, in the absence of ligand, ERα may bind to estrogen response elements (ERE) and recruit E3-ubiquitin ligases, promoting polyubiquitination and degradation of ERα, in order to restart the cycle with new receptors. In the presence of E2, ERα binds to ERE and recruits coactivators and E3-ubiquitin ligases. These coactivators facilitate the expression of ERα target genes, while E3-ubiquitin ligases mediate polyubiquitination and degradation of this receptor. Consequently, the cycle frequency, without or with ligand bound ERα, is estimated to be 20 and 45 min, respectively. This study elucidated that when ERα degradation is inhibited, Pol II is not recruited to EREs [80]. Moreover, intranuclear dynamics of unliganded and liganded

INFORME DE LABORES 2019

ERα is nullified when cells are treated with transcription or proteasome inhibitors [81]. A dynamic turnover of ERα protein is associated with its binding to DNA regulatory sequences for an active, cooperative, functional, and cyclical expression of its target genes [80, 82]. Thus, there is a complex relationship between ERα polyubiquitination and proteasomal degradation with the cycling of its transcriptional activity.

Several coactivators of ERα may also function as E3-ubiquitin ligases such as E6AP, RNF8, and SKP2, which may account for the link between polyubiquitination and the transcriptional cycle of ERα [48, 61, 75, 83]. One interesting E3 ligase/coactivator for ERα is SKP2, which functions as an E3-ubiquitin ligase for ERα degradation with a short E2 stimulation time. By contrast, with a longer stimulation time, SKP2 acts as a coactivator of ERα to induce transcription of late E2 target genes linked to cell cycle progression [83]. Similar to SKP2, several E3 ligases/coactivators of ERα may dynamically participate in the processes of degradation and transcription in an E2 hormone stimulation time-dependent manner.

In addition, the phosphorylation of ERα by certain kinases such as ERK7 [84], CDK11 [85], p38 [71], PKC [32], cyclin E-CDK2 [83], and Src [75] is required for its polyubiquitination and degradation [32]. ERα residues S118, S294, S341, and Y537 are phosphorylated in response to E2 stimulation, inducing ERα polyubiquitination [71, 83, 86]. A fine case in point is the phosphorylation of ERα at Y537 by Src following E2 treatment, which induces ERα polyubiquitination by E6AP (an E3-ubiquitin ligase/coactivator) [75]. Interestingly, mutations in this ERα residue, which affect its phosphorylation and degradation, have been detected in the mammary tumors of breast cancer patients resistant to endocrine therapy. Such coupling of phosphorylation and polyubiquitination of ERα may be central to recruiting E3-ubiquitin ligases with dual roles as coactivators to modulate ERα.

5. INHIBITION OF ERα POLYUBIQUITINATION IN BREAST CANCER CELLS

The complex relationship between ERα polyubiquitination with its degradation and transcriptional function may be affected in mammary tumors. Several studies indicate that many proteins directly or indirectly inhibit ERα polyubiquitination in breast cancer cells (Table **1**).

5.1. ERα Polyubiquitination Inhibitor Proteins (EPIPs) in Breast Cancer Cells

MUC1, PIN1, GSK3, LMTK3, cABL, RB, RNF31, RNF8, SMURF1 and SHARPIN proteins interact with ERα to protect it from polyubiquitination and degradation [87]. These ERα-interacting proteins act as ERα polyubiquitination inhibitor proteins (EPIPs). However, the mechanisms underlying the inhibition of ERα polyubiquitination by EPIPs are known to differ (Fig. **3** and Table **1**).

ERα polyubiquitination inhibition appears to be critical for ERα+ breast cancer cells. Polyubiquitinated ERα levels are increased when any EPIP is downregulated, and under this condition, ERα is degraded *via* the UPS, decreasing its abundance. In consequence, an inhibition of survival, proliferation, and migration of breast cancer cells is promoted. However, knockdown cells for each EPIP that are treated with MG132 (proteasome inhibitor) result in a partial restoration of ERα levels and its pro-tumor effects (Fig. **3**). Furthermore, EPIPs seem to be expressed mainly in breast cancer tissue compared to normal mammary tissue. For instance, RNF31 levels in mammary tumors were higher compared to those in adjacent normal mammary tissue [62]. Furthermore, a direct correlation between ERα protein levels and RNF8 or SHARPIN was observed in biopsies of patients with breast cancer [61, 63]. Interestingly, RB is decreased or lost in ERα– breast cancer [17].

5.2. Other Mechanisms Underlying Inhibition of ERα Polyubiquitination in Breast Cancer Cells

Other ERα polyubiquitination inhibitors include phosphatidylethanolamine-binding protein 4 (PEBP4), REG gamma (REG) protein and posttranslational modification processes such as acetylation and palmitoylation of ERα. PEBP4 interacts with Src kinase to block its interaction with ERα, leading to decreased phosphorylation of this receptor which inhibits its subsequent polyubiquitination and degradation [88, 89]. Moreover, REG expression, which correlates to high ERα levels, is increased in breast cancer and results in a poor clinical prognosis. REG-knockdown cells exhibited low ERα levels, probably due to its polyubiquitination and degradation, which recovered when treated with MG132 proteasome inhibitor [88].

Additionally, it has been reported that p300 protein may acetylate ERα at K266, K268, K299, K302, and K303 residues; and acetylation of ERα at K266 and K268 residues has been shown to increase its DNA-binding and transcriptional activities [90-93]. In addition to acetylation, methylation at K302 residue by SET7 has also been associated with ERα stability [94]. On the other hand, human ERα is also modified by palmitoylation at C447 by DHHC7 and DHHC21 palmitoyl acyltransferases to promote its association with the cell membrane [95]. Importantly, each of these modifications can also inhibit polyubiquitination and degradation of ERα in breast cancer cells (Table **1**).

Thus, several mechanisms protect ERα from polyubiquitination (Fig. **3**). Inhibition of ERα polyubiquitination leads to a decrease in the degradation of this receptor, and consequently, to an altered transcriptional activity, which seems to enhance the gene expression profile linked to breast cancer cell proliferation and resistance to endocrine therapy.

5.3. Effects Associated with ERα Polyubiquitination Inhibition in Breast Cancer Cells

When ERα levels are increased due to inhibition of its polyubiquitination and degradation, other changes may occur. For instance, high ERα protein levels may affect the induction of proteolysis and efficiency of ERα degradation [77, 96, 97]. Consequently, when ERα concentration is high, its transactivation function is activated by non-classical mechanisms, in which E2, growth factors or phosphorylation at S104, S106, and S118 are not involved. Therefore, the transcriptional activity of ERα as a result of its high levels is called *concentration-inducible ERα function*, which includes

INFORME DE LABORES 2019

Table 1. Molecular mechanisms associated with ERα stability in breast cancer cells.

	Mechanisms Associated to ERα Stability		References
EPIPs	MUC1	MUC1 interacts with ERα on the DNA and recruits SRC1/GRIP1 coactivators, preventing the degradation of ERα and stimulating the expression of target genes.	[149]
	PIN1	PIN1 interacts with phosphorylated ERα at the S118 residue to block association of the receptor with E6AP, thus inhibiting its degradation. In addition, PIN1 mediates ERα isomerization increasing its binding to DNA and transcriptional activity.	[86]
	LMTK3	LMTK3 interacts with and phosphorylates ERα to avoid its degradation, stabilizing it. Moreover, LMTK3 increases FOXO3-induced ERα expression by decreasing the enzymatic activity of PKC and AKT.	[105]
	GSK3	GSK3 interacts with and phosphorylates ERα (at S102, S104, and S106) to stabilize it in E2 absence. In E2 stimulated cells, GSK3 phosphorylates ERα S118, enhancing its transcriptional activity.	[150]
	cABL	cABL interacts with and phosphorylates ERα at Y52 and Y219 stabilizing it by inhibiting its polyubiquitination and degradation *via* the UPS.	[108]
	RB	RB forms a complex with ERα and HSP90 chaperone proteins, thus avoiding polyubiquitination of the receptor, enhancing its stability.	[17]
	RNF8	RNF8 monoubiquitinates ERα and functions as a coactivator modulating its activity	[61]
	RNF31	RNF31 and SHARPIN postranslationally modify ERα *via* its monoubiquitination	[62]
	SHARPIN		[63]
	SMURF1	SMURF1 also blocks ERα polyubiquitination and increases its stability, however, the molecular mechanism is not yet known.	[151]
Other ERα polyubiquitination inhibitors	Other modifications for ERα stability	Palmitoylation at C447 residue by DHHC7/DHHC21 Acetylations probably at K302/303 by p300 Methylation at K302 residue by SET7.	[95] [92] [94]
	PEBP4	PEBP4 interrupts the interaction between ERα and Src because PEBP4 competes with ERα for the Src protein, increasing ERα stability and its transcriptional activity.	[89]
	REG	ERα protein levels are decreased in REG-knockdown cells. Treatment with MG132 recovers ERα protein levels in these cells. Correlation between high levels of REG with high levels of ERα in breast tumors and poor clinical prognosis.	[88]

an unusual ERα recruitment to EREs, and thereby alters gene expression, such as changes in the magnitude of gene induction or expansion of new E2 target genes. Moreover, p160 coactivators are not required for gene transcription induced by high concentrations of ERα [98, 99].

INFORME DE LABORES 2019

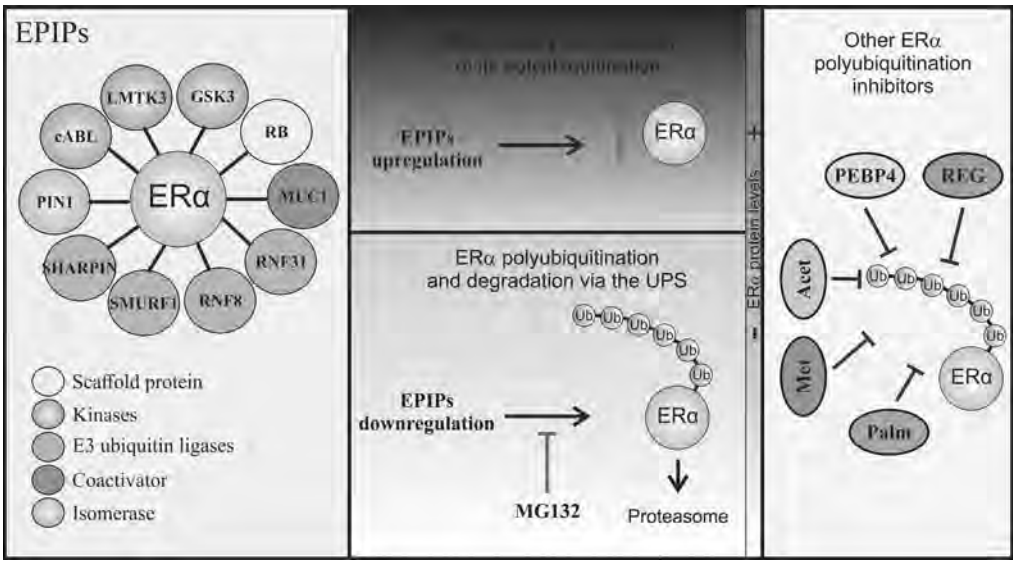

Fig. (3). ERα polyubiquitination inhibitor proteins in breast cancer cells. ERα polyubiquitination inhibitor proteins (EPIPs)**.** EPIPs interact with ERα in breast cancer cells. The upregulation of EPIPs increases ERα stability by inhibiting its polyubiquitination. In knockdown cells for each EPIP (by specific RNA interference), ERα protein levels are decreased by degradation *via* the UPS (Ubiquitin proteasome system). However, treatment with MG132 (proteasome inhibitor) restores ERα protein levels in knockdown cells. ERα modifications such as acetylation (Acet), methylation (Met) and palmitoylation (Palm), and PEBP4 and REG protein have also been associated with ERα stability in breast cancer cells.

6. ERα UBIQUITINATION PATHWAY IN ENDOCRINE RESISTANCE

Because ERα is the target for endocrine therapies using SERMs and SERDs, loss or reduction of ERα in breast cancer cells is the first critical factor in resistance to endocrine therapy. A study indicated that CUEDC2 protein promotes ERα polyubiquitination and degradation *via* the proteasome. Interestingly, CUEDC2 levels were inversely correlated with ERα levels in tumors of breast cancer patients. Moreover, high expression levels of CUEDC2 resulted in resistance to tamoxifen [100, 101]. In addition, the dysfunction or loss of RB in breast cancer has been also linked with resistance to tamoxifen. Likewise, RB tumor suppressor is reported to be lost in ERα– mammary tumors [102, 103]. In RB knockdown breast cancer cell lines, polyubiquitination and degradation of ERα are increased, compared to that in breast cancer cell line controls, but ERα downregulation in these cells is rescued by MG132 treatment [17].

Controversially, cellular processes that protect ERα from polyubiquitination and degradation have also been associated with endocrine resistance. For example, MUC1 forms a transcription complex with ERα inhibiting its polyubiquitination and thereby inducing the expression of genes linked to endocrine resistance, such as *Rab31* [104]. Moreover, ERα phosphorylation by LMTK3 inhibits its polyubiquitination. It has been reported that downregulation of LMTK3 restores the response to tamoxifen [105-107]. Similarly, the upregulation of other EPIPs such as cABL, PIN1, RNF8, and SHARPIN has been associated with the progression of breast cancer and endocrine resistance [61, 63, 108, 109]. In addition, inhibition of ERα polyubiquitination *via* several mechanisms may also facilitate resistance to SERDs used in breast cancer treatments.

7. SELECTIVE ESTROGEN RECEPTOR DEGRADERS (SERDS) IN BREAST CANCER

It is important to note that resistance to tamoxifen is a common phenomenon in the treatment of breast cancer. For this reason, the use of SERDs appears to be a potential therapy alternative for this cancer. ERα polyubiquitination is an essential step for its downregulation *via* the UPS, and this forms the basis for the mode of action of endocrine therapies with SERDs such as fulvestrant. When breast cancer cells are treated for 1 h with fulvestrant, ERα protein levels decrease due to its polyubiquitination and degradation *via* the UPS [35, 38, 39, 90, 110, 111].

Novel drugs based on SERDs other than fulvestrant have been discovered and are being studied to control ERα abundance in breast cancer cells. These include AZD9496 [112], bazedoxifene [113], RAD1901 [114], GDC-0810 [115], ZB716 [116] and LSZ102 [117]. However, fulvestrant is the only clinically approved SERD, with a known tumor growth reduction effect. Fulvestrant has been approved for first-line endocrine therapy, as well as for breast cancers for which tamoxifen or aromatase inhibitor treatment failed [118].

Residues targeted for polyubiquitination induced by fulvestrant and E2 appear to be K302 and K303 of ERα [90]. These same residues are involved in ERα SHARPIN-induced monoubiquitination, which inhibits polyubiquitination and degradation of ERα [63]. Apparently, these sites could be also monoubiquitinated by the BRCA1/BARD1 complex. In addition, these residues are also linked with the stability of the receptor under basal conditions in breast cancer [56, 57, 59, 60, 90]. In this context, ERα monoubiquitination by E3 ligases such as RNF31, RNF8, and SHARPIN may compete with the polyubiquitination of this receptor [34].

INFORME DE LABORES 2019

Remarkably, breast cancer cells may become insensitive to treatment with SERDs, if ERα is protected from polyubiquitination and degradation. Thereby, proteins and modifications that inhibit ERα polyubiquitination may play a crucial role in resistance to SERD, where ERα seems to be stabilized by losing its capacity to be degraded by the UPS (Fig. **3**).

In addition, elements of the Hippo pathway, large tumor suppressor kinases 1 and 2 (LATS1 and 2) promote ERα ubiquitination. LATS downregulation inhibits polyubiquitination and degradation of ERα, increasing the protein levels of this receptor and the expression of its target genes, thereby decreasing sensitivity to fulvestrant and its anti-tumor effects in breast cancer cells. Patients with breast cancer lacking ERα have higher levels of LATS1/2 and shorter relapse-free survival. Thus, LATS and its molecular relationship with ERα and the Hippo signaling pathway may be affected in breast cancer, leading to alterations in sensitivity to fulvestrant treatment [119].

8. *ESR1* MUTATIONS AND SERDs IN BREAST CANCER

8.1. Generalities Related to *ESR1* Mutations in Breast Cancer

ESR1 mutations, Y537S, Y537N, Y537C, D538G, and E380Q, have been discovered *via* large-scale next-generation sequencing (NGS) in mammary tumors from patients. Generally, these mutations are detected in metastatic breast cancer than in early stage breast cancer, facilitating their detection in circulating tumor DNA using droplet digital PCR [120, 121]. Interestingly, *ESR1* mutations have been identified mainly in the LBD of ERα generating conformational changes and E2-independent activity. Moreover, these mutations are associated with an acquired resistance to endocrine therapy [122].

Some of these mutations have been experimentally generated in breast cancer cell lines using CRISPR/Cas genome editing techniques, whereas their activities have been evaluated *via* NGS technologies such as whole-genome sequencing (WGS), ChIP-sequencing (ChIP-seq), whole-exome sequencing (WES) and RNA sequencing (RNA-Seq). These breast cancer cell lines with *ESR1* mutations also display E2-independent ERα activity and resistance to endocrine therapy. Surprisingly, a specific gene profile is altered by each of these *ESR1* mutations with a limited number of target genes in common, suggesting the molecular complexity of the endocrine resistance [123]. Moreover, a cistrome study of these mutants showed that cis-acting targets on genomes of breast cancer cells are different for each *ESR1* mutation, and may be linked to several genes involved in metastasis and endocrine resistance, compared to the E2-bound wild-type ERα protein [124].

ERα mutations detected in breast cancer (including Y537S/N/C, D538G, E380Q or S463P) are associated with resistance to aromatase inhibitors and SERMs, but appeared to have no effect on the response to SERDs (fulvestrant and AZD9496), with the exception of *ESR1* mutations in Y537 residue [121, 123, 125]. Moreover, in breast cancer cell lines with acquired endocrine resistance due to long-term E2 deprivation, *ESR1* mutations Y537C and Y537S were detected after acquiring resistance. These *ESR1* mutants display an alteration in genome binding, target gene transcription, and interactions with other proteins [126].

8.2. *ESR1* Mutations Involved in ERα Ubiquitination in Breast Cancer

As mentioned above, *ESR1* mutations in Y537 residue are commonly detected in mammary tumors of patients. This residue is associated with ERα polyubiquitination. In response to E2, ERα is phosphorylated at its Y537 residue by Src kinase, and then polyubiquitinated by E6AP E3 ubiquitin ligase and degraded *via* the UPS. Because E6AP is an E3-ubiquitin ligase and coactivator for ERα, the interaction with E6AP can also promote ERα binding to chromatin and ERα-mediated gene expression. Accordingly, a laboratory-generated mutant of this residue prevented ERα degradation, thereby affecting its activity and ability to respond to endocrine therapies [75, 127]. Therefore, mutations of the Y537 residue are involved in ERα stability and play an important role in SERD resistance.

In addition, K303 residue has been suggested as the target of polyubiquitination/monoubiquitination and acetylation [57, 59, 90, 92, 94]. Mutations in this residue have been detected in premalignant breast lesions and may be important in breast cancer progression [128, 129].

9. DISCUSSION

Approximately 70% of human breast cancers are ERα+. This nuclear receptor regulates the transcription of certain pro-tumor genes and mediates extranuclear signaling in breast cancer cells. High ERα levels have been detected in ERα+ mammary tumors [130-132], and ERα-dependent gene signatures are differentially expressed in breast cancer cells and mammary tumors of patients with varying clinical outcomes [133-135]. Additionally, nucleocytoplasmic transport seems to be differentially modulated in ERα– and ERα+ breast cancer cells [136]. Thus, ERα expression has important implications for breast cancer biology. More importantly, ERα is the target for endocrine therapies using SERDs and SERMs, but some ERα+ breast cancers are non-responsive or develop resistance to these treatments. Therefore, ERα and its modulatory mechanisms are central to the progression of this cancer. In this context, Ub-dependent pathways have emerged as important regulators of ERα levels and functions in breast cancer.

Ubiquitination system elements (E1, E2, E3 enzymes and DUBs) seem to be altered in mammary tumors compared to normal mammary tissue [137-142]. Furthermore, ERα regulation by Ub is complex since Ub is able to interact either covalently (mono or polyubiquitination) or non-covalently with ERα.

Monoubiquitination increases ERα stability and transcriptional activity. In contrast, ERα polyubiquitination signals ERα degradation *via* the UPS but also acts as a marker, which in combination with proteasome activity, is associated with the transcriptional cycle of ERα. E2 hormone positively regulates polyubiquitination of ERα, but negatively modulates its monoubiquitination, suggesting that a balance between these processes control ERα activity.

INFORME DE LABORES 2019

9.1. Molecular Mechanisms for ERα Ubiquitination

E2 hormone signaling induces several phosphorylations in ERα, one of which is catalyzed by Src kinase at the Y537 residue, which is a prerequisite for recruiting the E6AP E3 ligase/coactivator that mediates polyubiquitination and degradation of ERα in breast cancer cells (Fig. **4**). This is important because metastatic mammary tumors presenting endocrine resistance display mutations in this residue. Moreover, phosphorylation of Y537 can be interrupted by PIN1 that interacts with ERα to block its interaction with E6AP, thereby protecting it from degradation. Also, PEBP4 interacts with Src kinase to inhibit its association with ERα and its subsequent phosphorylation-dependent degradation [75, 86, 89]. Furthermore, the interaction between ERα and EPIPs, alterations in the interactome for its degradation, and its posttranslational modifications such as acetylation, palmitoylation and methylation can increase ERα stability affecting its levels and functions in breast cancer cells (Table **1**, Fig. **3**).

Monoubiquitination is a posttranslational modification that confers ERα stability by inhibiting its polyubiquitination [87]. Interestingly, as the sites for monoubiquitination and polyubiquitination appear to be the same, competition between these modifications may exist. E3 ligases that participate in these processes are different. Ligases, BRCA1, RNF31, and SHARPIN, have been associated with ERα monoubiquitination, whereas RNF8 which acts as a coactivator also induces monoubiquitination of ERα [59, 61-63]. Instead, polyubiquitination of ERα is mediated by different enzymes with dual roles, as E3 ligases and transcriptional coactivators, such as E6AP [75]. Lysine residues responsible for mono/polyubiquitination may also be implicated in acetylation and methylation of ERα which may affect its stability [90, 92-94]. Additionally, ERα has UBDs that interact with ubiquitinated proteins, which apparently are also required for transcriptional activity of the receptor and its monoubiquitination.

Thus, molecular mechanisms that modulate ERα by Ub-mediated pathways are multifaceted and regulate not only the degradation (polyubiquitination), and stability (monoubiquitination) of ERα, but also the transcriptional cycle and ERα-driven gene transcription. Therefore, many posttranslational modifications and interactions appear to be involved in Ub-dependent ERα modulation. Notably, ERα UBDs may also enable interactions with other ubiquitinated modulators of ERα, which remain to be identified.

Mechanisms that underlie ERα stability may also induce serious changes in nuclear and extranuclear activities as well as in ERα crosstalk, thus affecting the response to SERMs. Furthermore, SERDs are drugs that mediate the downregulation of ERα *via* polyubiquitination and degradation by the proteasome. Then, mechanisms that stabilize ERα in breast cancer may be critical in the development of resistance to SERDs.

9.2. ERα Ubiquitination in Endocrine Resistance

Conflicting data exist concerning the effects of inducing or inhibiting polyubiquitination and degradation of ERα, on endocrine resistance in breast cancer. Based on these data, it may be concluded that both induction and inhibition may influence endocrine resistance, but in a different manner. In ERα– breast cancer, polyubiquitination and degradation of ERα may be a factor in the negativity of this receptor [143]. In fact, proteins that promote ERα degradation by the UPS (as CUEDC2 and LATS1/2) are increased in ERα– mammary tumors. Hence, high levels of CUEDC2 and LATS1/2 are correlated with low ERα levels, whereas proteins that protect it from degradation, like RB, seem to be downregulated in ERα– breast cancer [101, 119]. Thus, polyubiquitination of ERα is important in ERα– mammary tumors. The absence of ERα precludes the use of endocrine therapy, these cells being resistant to such therapies.

The exact opposite of the above process may occur in ERα+ breast cancer, where ERα expression is considered as an indicator for the initiation of endocrine therapy. However, these breast cancer cells can present *de novo* or acquired resistance to endocrine therapy even in the presence of ERα, *via* mechanisms that are not completely understood. Based on some data, it is hypothesized that ERα stability may promote endocrine resistance in ERα+ breast cancer. When ERα stability is enhanced, its turnover is affected and levels of ERα+ are sustained. Sustained levels of ERα may stimulate persistent extranuclear and nuclear signaling associated with endocrine resistance and alter crosstalk between pathways, generating new signaling routes that promote the progression of this cancer.

9.3. Future Challenges

Endocrine resistance develops mainly against aromatase inhibitors and tamoxifen than against fulvestrant, indicating its potential as a drug central to breast cancer treatment. Currently, the ERα degrader, fulvestrant, is the first-in-class SERD member used in breast cancer patients. However, this drug has certain setbacks such as poor biodisponibility and the need for intramuscular administration. Therefore, development of new SERDs that can be administered *via* the oral route, with enhanced biodisponibility is being mulled. Currently, several newer SERDs are in the clinical investigation phase and may be nearing release pending approval [37, 40]. In this context, a better understanding of mechanisms that promote as well as inhibit polyubiquitination and degradation of ERα may be important for preventing resistance to SERDs. Hence, mechanisms underlying ERα stability may be targeted in the development of new therapeutic strategies as well as indicators of endocrine therapy selection.

Additionally, ERα LBD mutations linked to endocrine therapy resistance have been identified in metastatic breast cancer patients [121]. Interestingly, the use of Selective Estrogen Receptor Covalent Antagonists (SERCAs), which inactivate both wild-type and mutated ERα has been suggested, but these drugs may require further screening [144]. The need to develop novel drugs, such as E2 antagonists, as well as drugs that target domains other than ERα LBDs, has been recognized. Proteolysis targeting chimeric molecules known as PROTACs that target ERα proteolysis, are being designed [145]. PROTACs show promise as part of a therapeutic strategy involving downregulation of ERα *via* the UPS. Moreover, PROTACs may be useful in regulating proteins that modulate ERα stability. Therefore, modulation of

INFORME DE LABORES 2019

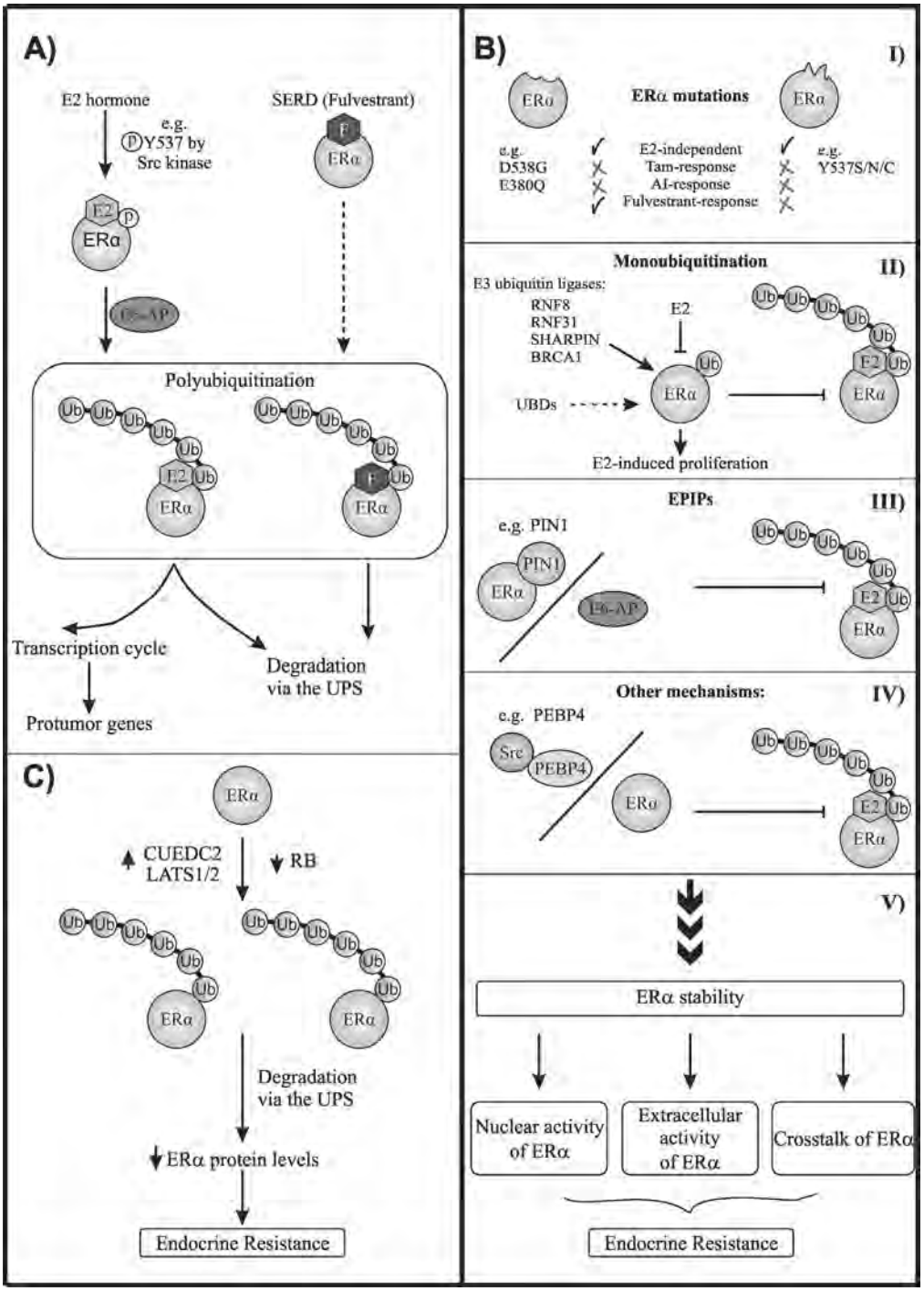

Fig. (4). Molecular pathways in the regulation of ERα by Ub in breast cancer cells. A) E2 activates ERα *via* binding to LBD to induce the expression of pro-tumor genes. E2 also induces phosphorylation in ERα *e.g.* in the Y537 residue by Src kinase. This modification allows the recruitment of E6AP E3 ligase/coactivator to induce its polyubiquitination (polyUb). The polyUb of ERα is required for its transcriptional cycle and its degradation *via* the UPS. SERDs as fulvestrant also induce the polyUb and degradation of ERα but without its transcription activation. **B**) I) In ERα+ advanced breast cancer with endocrine resistance, mutations in ERα were found to be associated with E2-independent activity and insensitivity to endocrine therapy, some of which occur at Y537 residue, also affecting the response to SERDs. II) Moreover, in ERα+ breast cancer cells, monoubiquitination by some E3 ligases inhibit polyUb and degradation of ERα to stabilize it. III) The interaction with EPIPs also confers ERα stability, *e.g.*, PIN1 interacts with ERα to inhibit its interaction with E6AP. IV) Other modifications and proteins can also stabilize ERα, *e.g.* PEBP4 interacts with Src kinase blocking its interaction with ERα avoiding its polyUb and degradation. V) ERα stability can lead to its sustained signaling, and the expression related to endocrine resistance and alterations in its crosstalk with other pathways. **C**) A decrease in ERα stability may be a factor in the negativity of ERα in breast cancer cells. Proteins that promote (CUEDC2 and LATS1/2) the polyUb and degradation are upregulated in ERα– breast cancer cells, whereas proteins (*e.g.* RB) that protect it from degradation seem to be downregulated. As a result, ERα is degraded *via* the UPS, contributing to the reduction of ERα levels. Tam= tamoxifen, AI= aromatase inhibitors.

INFORME DE LABORES 2019

ERα *via* Ub related pathways appear to be key to the development of novel therapeutic strategies for breast cancer control.

Finally, some Ub-like proteins are deregulated in breast cancer. ISG15 is upregulated in mammary tumors in comparison with normal tissue [146, 147]. Similarly, SUMO which modifies ERα is upregulated in breast cancer cells [148]. This indicates that ERα functions may be regulated by other Ub-like proteins. An understanding of these mechanisms may also enable the detection of novel molecular targets for this disease.

CONCLUSION

Ub is a small protein with enormous implications in the regulation of ERα in breast cancer cells. A better understanding of the relationship between ERα and Ub may reveal mechanisms underlying the modulation of ERα signaling by Ub-dependent processes in breast cancer cells, which, in turn, may be useful in determining novel strategies for treatment of this cancer.

LIST OF ABBREVIATIONS

AF = Activation Function
AP1 = Activator Protein 1
BARD1 = BRCA1-associated RING domain protein 1
BRCA1 = Breast Cancer Type 1 susceptibility protein
cABL = Abelson tyrosine-protein kinase
CDK11p58 = Cyclin-dependent kinase 11B
CDK2 = Cyclin-dependent kinase 2
CHIP = Carboxyl terminus of HSC70-interacting protein
CUED2 = CUE domain-containing protein 2
DBD = DNA Binding Domain
ddPCR = droplet digital PCR
DUB = Deubiquitinase
E2 = 17-Beta Estradiol
E6AP = E6-associated protein
EGF = Epidermal Growth Factor
EPIIPs = ER polyubiquitination inhibitor proteins
EREs = Estrogen Response Elements
ERK7 = Extracellular signal-regulated kinase 7
ERα = Estrogen Receptor Alpha
ESR1 = Estrogen Receptor 1
FOXA1 = Forkhead box protein A1
GSK3 = Glycogen Synthase Kinase 3
HECT = Homologous to the E6AP Carboxyl Terminus
HSP90 = Heat Shock Protein 90
IGF = Insulin-like Growth Factor
LATS1 = Large Tumor Suppressor kinase 1
LATS2 = Large Tumor Suppressor kinase 2
LBD = Ligand Binding Domain
LMTK3 = Lemur Tyrosine Kinase 3
MDM2 = Murine Double Minute 2
MEMO = Mediator of ERBB2-driven cell Motility
MNAR = Modulator of Non-genomic Actions of the Estrogen Receptor
MTA1 = Metastasis-Associated Protein 1
MUC1 = Mucin 1
NF-kappaB = Nuclear Factor kappa-light-chain-enhancer of activated B cells
NGS = Next Generation Sequencing
p38MAPK = p38 Mitogen-activated protein kinase
PEBP4 = Phosphatidyl ethanolamine-binding protein 4
PIN1 = Peptidyl-propyl cis-trans isomerase NIMA-interacting 1
PKC = Protein Kinase C
RB = Retinoblastoma
REG = REGgamma
RING = Really Interesting New Gene
RNF31 = RING finger protein 31
RNF8 = RING finger protein 8
SERD = Selective Estrogen Receptor Degraders
SERM = Selective Estrogen Receptor Modulator
SHARPIN1 = Shack-associated RH domain-interacting protein
SKP2 = S-phase kinase-associated protein 2
SMURF1 = SMAD ubiquitination regulatory factor
Ub = Ubiquitin
UBD = Ubiquitin-binding Domain
UPS = Ubiquitin-Proteasome System

CONSENT FOR PUBLICATION

Not applicable.

CONFLICT OF INTEREST

The authors declare no conflict of interest, financial or otherwise.

ACKNOWLEDGEMENTS

A.C.T.-C. designed the research, discussed and integrated the information for all sections, and wrote the manuscript. J.O.R.-J helped in the discussion and integration of information, modified the figures, and improved the manuscript. E.C.-R. helped in the integration of some papers and figures, and prepared the abbreviations list. This work was supported by the DGAPA-UNAM (grants number PAPIIT–IA200916).

REFERENCES

[1] Chen T, Zhang N, Moran MS, *et al.* Borderline er-positive primary breast cancer gains no significant survival benefit from endocrine therapy: A systematic review and meta-analysis. Clinical Breast Cancer 2018; 18: 1-8.
[2] Collins LC, Botero ML, Schnitt SJ. Bimodal frequency distribution of estrogen receptor immunohistochemical staining results in breast cancer: an analysis of 825 cases. Am J Clin Pathol 2005; 123: 16-20.
[3] Curigliano G, Burstein HJ, E PW, *et al.* De-escalating and escalating treatments for early-stage breast cancer: the St. Gallen International Expert Consensus Conference on the Primary Therapy of Early Breast Cancer 2017. Ann Oncol 2017; 28: 1700-12.
[4] Hammond ME, Hayes DF, Dowsett M, *et al.* American society of clinical oncology/college of american pathologists guideline recommendations for immunohistochemical testing of estrogen and progesterone receptors in breast cancer. J Clin Oncol 2010; 28: 2784-95.
[5] Yi M, Huo L, Koenig KB, *et al.* Which threshold for ER positivity? a retrospective study based on 9639 patients. Ann Oncol 2014; 25: 1004-11.
[6] Kumar R, Zakharov MN, Khan SH, *et al.* The dynamic structure of the estrogen receptor. J Amino Acids 2011; 2011: 812540.
[7] Mader S, Chambon P, White JH. Defining a minimal estrogen receptor DNA binding domain. Nucleic Acids Res 1993; 21: 1125-

INFORME DE LABORES 2019

32.

[8] Nardulli AM, Greene GL, Shapiro DJ. Human estrogen receptor bound to an estrogen response element bends DNA. Mol Endocrinol 1993; 7: 331-40.

[9] Billon-Gales A, Krust A, Fontaine C, *et al.* Activation function 2 (AF2) of estrogen receptor-alpha is required for the atheroprotective action of estradiol but not to accelerate endothelial healing. Proc Natl Acad Sci USA 2011; 108: 13311-6.

[10] Metivier R, Penot G, Flouriot G, Pakdel F. Synergism between ERalpha transactivation function 1 (AF-1) and AF-2 mediated by steroid receptor coactivator protein-1: requirement for the AF-1 alpha-helical core and for a direct interaction between the N- and C-terminal domains. Mol Endocrinol 2001; 15: 1953-70.

[11] Smirnova NF, Fontaine C, Buscato M, *et al*. The Activation function-1 of estrogen receptor alpha prevents arterial neointima development through a direct effect on smooth muscle cells. Circ Res 2015; 117: 770-8.

[12] Vrtacnik P, Ostanek B, Mencej-Bedrac S, Marc J. The many faces of estrogen signaling. Biochem Med (Zagreb) 2014; 24: 329-42.

[13] Zwart W, de Leeuw R, Rondaij M, *et al*. The hinge region of the human estrogen receptor determines functional synergy between AF-1 and AF-2 in the quantitative response to estradiol and tamoxifen. Journal of cell science 2010; 123: 1253-61.

[14] Acconcia F, Ascenzi P, Fabozzi G, *et al*. S-palmitoylation modulates human estrogen receptor-alpha functions. Biochem Biophys Res Commun 2004; 316: 878-83.

[15] Pedram A, Razandi M, Deschenes RJ, Levin ER. DHHC-7 and -21 are palmitoylacyltransferases for sex steroid receptors. Molecular biology of the cell 2012; 23: 188-99.

[16] Acconcia F, Kumar R. Signaling regulation of genomic and nongenomic functions of estrogen receptors. Cancer Lett 2006; 238: 1-14.

[17] Caligiuri I, Toffoli G, Giordano A, Rizzolio F. pRb controls estrogen receptor alpha protein stability and activity. Oncotarget 2013; 4: 875-83.

[18] Frei A, MacDonald G, Lund I, *et al.* Memo interacts with c-Src to control Estrogen Receptor alpha sub-cellular localization. Oncotarget 2016; 7: 56170-82.

[19] Kumar R, Wang RA, Mazumdar A, *et al*. A naturally occurring MTA1 variant sequesters oestrogen receptor-alpha in the cytoplasm. Nature 2002; 418: 654-7.

[20] Vadlamudi RK, Balasenthil S, Sahin AA, *et al*. Novel estrogen receptor coactivator PELP1/MNAR gene and ERbeta expression in salivary duct adenocarcinoma: potential therapeutic targets. Hum Pathol 2005; 36: 670-5.

[21] Bjornstrom L, Sjoberg M. Estrogen receptor-dependent activation of AP-1 *via* non-genomic signalling. Nuclear Receptor 2004; 2: 3.

[22] Frasor J, Weaver A, Pradhan M, *et al*. Positive cross-talk between estrogen receptor and NF-kappaB in breast cancer. Cancer Res 2009; 69: 8918-25.

[23] Kato S. Estrogen receptor-mediated cross-talk with growth factor signaling pathways. Breast Cancer 2001; 8: 3-9.

[24] Lee AV, Cui X, Oesterreich S. Cross-talk among estrogen receptor, epidermal growth factor, and insulin-like growth factor signaling in breast cancer. Clin Cancer Res 2001; 7: 4429s-35s; discussion 11s-12s.

[25] Carroll JS, Liu XS, Brodsky AS, *et al*. Chromosome-wide mapping of estrogen receptor binding reveals long-range regulation requiring the forkhead protein FoxA1. Cell 2005; 122: 33-43.

[26] Theodorou V, Stark R, Menon S, Carroll JS. GATA3 acts upstream of FOXA1 in mediating ESR1 binding by shaping enhancer accessibility. Genome Res 2013; 23: 12-22.

[27] Fleming FJ, Hill AD, McDermott EW, *et al*. Differential recruitment of coregulator proteins steroid receptor coactivator-1 and silencing mediator for retinoid and thyroid receptors to the estrogen receptor-estrogen response element by beta-estradiol and 4-hydroxytamoxifen in human breast cancer. J Clin Endocrinol Metab 2004; 89: 375-83.

[28] Hah N, Kraus WL. Hormone-regulated transcriptomes: lessons learned from estrogen signaling pathways in breast cancer cells. Mol Cell Endocrinol 2014; 382: 652-64.

[29] Hah N, Murakami S, Nagari A, *et al*. Enhancer transcripts mark active estrogen receptor binding sites. Genome Res 2013; 23: 1210-23.

[30] Hervouet E, Cartron PF, Jouvenot M, Delage-Mourroux R. Epigenetic regulation of estrogen signaling in breast cancer. Epigenetics 2013; 8: 237-45.

[31] Manavathi B, Samanthapudi VS, Gajulapalli VN. Estrogen receptor coregulators and pioneer factors: the orchestrators of mammary gland cell fate and development. Front Cell Dev Biol 2014; 2: 34.

[32] Marsaud V, Gougelet A, Maillard S, Renoir JM. Various phosphorylation pathways, depending on agonist and antagonist binding to endogenous estrogen receptor alpha (ERalpha), differentially affect ERalpha extractability, proteasome-mediated stability, and transcriptional activity in human breast cancer cells. Mol Endocrinol 2003; 17: 2013-27.

[33] Tecalco-Cruz AC, Perez-Alvarado IA, Ramirez-Jarquin JO, Rocha-Zavaleta L. Nucleo-cytoplasmic transport of estrogen receptor alpha in breast cancer cells. Cell Signal 2017; 34: 121-32.

[34] Tecalco-Cruz AC, Ramirez-Jarquin JO. Mechanisms that Increase Stability of Estrogen Receptor Alpha in Breast Cancer. Clinical breast cancer 2017; 17: 1-10.

[35] Howell SJ, Johnston SR, Howell A. The use of selective estrogen receptor modulators and selective estrogen receptor down-regulators in breast cancer. Best practice & research Clinical endocrinology & metabolism 2004; 18: 47-66.

[36] Osborne CK, Schiff R. Mechanisms of endocrine resistance in breast cancer. Annu Rev Med 2011; 62: 233-47.

[37] Patel HK, Bihani T. Selective estrogen receptor modulators (SERMs) and selective estrogen receptor degraders (SERDs) in cancer treatment. Pharmacology & therapeutics 2018; 186: 1-24.

[38] Osborne CK, Wakeling A, Nicholson RI. Fulvestrant: an oestrogen receptor antagonist with a novel mechanism of action. Br J Cancer 2004; 90 Suppl 1: S2-6.

[39] Wardell SE, Marks JR, McDonnell DP. The turnover of estrogen receptor alpha by the selective estrogen receptor degrader (SERD) fulvestrant is a saturable process that is not required for antagonist efficacy. Biochem Pharmacol 2011; 82: 122-30.

[40] AlFakeeh A, Brezden-Masley C. Overcoming endocrine resistance in hormone receptor-positive breast cancer. Current oncology 2018; 25: S18-S27.

[41] Bernassola F, Karin M, Ciechanover A, Melino G. The HECT family of E3 ubiquitin ligases: multiple players in cancer development. Cancer Cell 2008; 14: 10-21.

[42] Deshaies RJ, Joazeiro CA. RING domain E3 ubiquitin ligases. Annual review of biochemistry 2009; 78: 399-434.

[43] Metzger MB, Pruneda JN, Klevit RE, Weissman AM. RING-type E3 ligases: master manipulators of E2 ubiquitin-conjugating enzymes and ubiquitination. Biochim Biophys Acta 2014; 1843: 47-60.

[44] Morreale FE, Walden H. Types of Ubiquitin Ligases. Cell 2016; 165: 248- e1.

[45] Scheffner M, Kumar S. Mammalian HECT ubiquitin-protein ligases: biological and pathophysiological aspects. Biochim Biophys Acta 2014; 1843: 61-74.

[46] Zheng N, Shabek N. Ubiquitin Ligases: Structure, Function, and Regulation. Ann Rev Biochem 2017; 86: 129-57.

[47] D'Arcy P, Wang X, Linder S. Deubiquitinase inhibition as a cancer therapeutic strategy. Pharmacol Ther 2015; 147: 32-54.

[48] Helzer KT, Hooper C, Miyamoto S, Alarid ET. Ubiquitylation of nuclear receptors: new linkages and therapeutic implications. J Mol Endocrinol 2015; 54: R151-R67.

[49] Mevissen TET, Komander D. Mechanisms of Deubiquitinase Specificity and Regulation. Annual review of biochemistry 2017; 86: 159-92.

[50] Sadowski M, Suryadinata R, Tan AR, *et al*. Protein monoubiquitination and polyubiquitination generate structural diversity to control distinct biological processes. IUBMB life 2012; 64: 136-42.

[51] Bonacci T, Audebert S, Camoin L, *et al*. Regulation of nub1 activity through non-proteolytic mdm2-mediated ubiquitination. PLoS One 2017; 12: e0169988.

[52] Fei C, Li Z, Li C, *et al*. Smurf1-mediated Lys29-linked nonproteolytic polyubiquitination of axin negatively regulates Wnt/beta-catenin signaling. Mol Cell Biol 2013; 33: 4095-105.

[53] Hurley JH, Lee S, Prag G. Ubiquitin-binding domains. Biochem J 2006; 399: 361-72.

[54] Kuslansky Y, Sominsky S, Jackman A, *et al*. Ubiquitin ligase E6AP mediates nonproteolytic polyubiquitylation of beta-catenin independent of the E6 oncoprotein. J Gen Virol 2016; 97: 3313-30.

[55] Scott D, Oldham NJ, Strachan J, *et al*. Ubiquitin-binding domains: mechanisms of ubiquitin recognition and use as tools to investigate ubiquitin-modified proteomes. Proteomics 2015; 15: 844-61.

INFORME DE LABORES 2019

[56] La Rosa P, Marino M, Acconcia F. 17beta-estradiol regulates estrogen receptor alpha monoubiquitination. IUBMB life 2011; 63: 49-53.

[57] Eakin CM, Maccoss MJ, Finney GL, Klevit RE. Estrogen receptor alpha is a putative substrate for the BRCA1 ubiquitin ligase. Proc Natl Acad Sci USA 2007; 104: 5794-9.

[58] La Rosa P, Acconcia F. Signaling functions of ubiquitin in the 17beta-estradiol (E2):estrogen receptor (ER) alpha network. J Steroid Biochem Mol Biol 2011; 127: 223-30.

[59] Ma Y, Fan S, Hu C, *et al*. BRCA1 regulates acetylation and ubiquitination of estrogen receptor-alpha. Mol Endocrinol 2010; 24: 76-90.

[60] La Rosa P, Pesiri V, Marino M, Acconcia F. 17beta-Estradiol-induced cell proliferation requires estrogen receptor (ER) alpha monoubiquitination. Cell Signal 2011; 23: 1128-35.

[61] Wang S, Luo H, Wang C, *et al*. RNF8 identified as a co-activator of estrogen receptor alpha promotes cell growth in breast cancer. Biochim Biophys Acta 2017; 1863: 1615-28.

[62] Zhu J, Zhao C, Kharman-Biz A, *et al*. The atypical ubiquitin ligase RNF31 stabilizes estrogen receptor alpha and modulates estrogen-stimulated breast cancer cell proliferation. Oncogene 2014; 33: 4340-51.

[63] Zhuang T, Yu S, Zhang L, *et al.* SHARPIN stabilizes estrogen receptor alpha and promotes breast cancer cell proliferation. Oncotarget 2017; 8: 77137-51.

[64] Di Fiore PP, Polo S, Hofmann K. When ubiquitin meets ubiquitin receptors: a signalling connection. Nature reviews Molecular Cell Biol 2003; 4: 491-7.

[65] Wang X, Terpstra EJ. Ubiquitin receptors and protein quality control. J Mole Cell Cardiol 2013; 55: 73-84.

[66] Dikic I, Wakatsuki S, Walters KJ. Ubiquitin-binding domains - from structures to functions. Nature Rev Mol Cell Biol 2009; 10: 659-71.

[67] Husnjak K, Dikic I. Ubiquitin-binding proteins: decoders of ubiquitin-mediated cellular functions. Ann Rev Biochem 2012; 81: 291-322.

[68] Woelk T, Sigismund S, Penengo L, Polo S. The ubiquitination code: a signalling problem. Cell Div 2007; 2: 11.

[69] Pesiri V, Di Muzio E, Polticelli F, Acconcia F. Selective binding of estrogen receptor alpha to ubiquitin chains. IUBMB life 2016; 68: 569-77.

[70] Pesiri V, La Rosa P, Stano P, Acconcia F. Identification of an estrogen receptor alpha non covalent ubiquitin-binding surface: role in 17beta-estradiol-induced transcriptional activity. J Cell Sci 2013; 126: 2577-82.

[71] Bhatt S, Xiao Z, Meng Z, Katzenellenbogen BS. Phosphorylation by p38 mitogen-activated protein kinase promotes estrogen receptor alpha turnover and functional activity *via* the SCF(Skp2) proteasomal complex. Mol Cell Biol 2012; 32: 1928-43.

[72] Fan M, Park A, Nephew KP. CHIP (carboxyl terminus of Hsc70-interacting protein) promotes basal and geldanamycin-induced degradation of estrogen receptor-alpha. Mol Endocrinol 2005; 19: 2901-14.

[73] Hashizume R, Fukuda M, Maeda I, *et al*. The RING heterodimer BRCA1-BARD1 is a ubiquitin ligase inactivated by a breast cancer-derived mutation. J Biol Chem 2001; 276: 14537-40.

[74] Saji S, Okumura N, Eguchi H, *et al*. MDM2 enhances the function of estrogen receptor alpha in human breast cancer cells. Biochem Biophys Res Commun 2001; 281: 259-65.

[75] Sun J, Zhou W, Kaliappan K, *et al*. ERalpha phosphorylation at Y537 by Src triggers E6-AP-ERalpha binding, ERalpha ubiquitylation, promoter occupancy, and target gene expression. Mol Endocrinol 2012; 26: 1567-77.

[76] Alarid ET. Lives and times of nuclear receptors. Mol Endocrinol 2006; 20: 1972-81.

[77] Alarid ET, Bakopoulos N, Solodin N. Proteasome-mediated proteolysis of estrogen receptor: a novel component in autologous down-regulation. Mol Endocrinol 1999; 13: 1522-34.

[78] Nawaz Z, Lonard DM, Dennis AP, *et al*. Proteasome-dependent degradation of the human estrogen receptor. Proc Natl Acad Sci USA 1999; 96: 1858-62.

[79] Lonard DM, Nawaz Z, Smith CL, O'Malley BW. The 26S proteasome is required for estrogen receptor-alpha and coactivator turnover and for efficient estrogen receptor-alpha transactivation. Mol Cell 2000; 5: 939-48.

[80] Reid G, Hubner MR, Metivier R, *et al*. Cyclic, proteasome-mediated turnover of unliganded and liganded ERalpha on responsive promoters is an integral feature of estrogen signaling. Mol Cell 2003; 11: 695-707.

[81] Stenoien DL, Patel K, Mancini MG, *et al.* FRAP reveals that mobility of oestrogen receptor-alpha is ligand- and proteasome-dependent. Nature cell biology 2001; 3: 15-23.

[82] Metivier R, Reid G, Gannon F. Transcription in four dimensions: nuclear receptor-directed initiation of gene expression. EMBO Reports 2006; 7: 161-7.

[83] Zhou W, Srinivasan S, Nawaz Z, Slingerland JM. ERalpha, SKP2 and E2F-1 form a feed forward loop driving late ERalpha targets and G1 cell cycle progression. Oncogene 2014; 33: 2341-53.

[84] Henrich LM, Smith JA, Kitt D, *et al*. Extracellular signal-regulated kinase 7, a regulator of hormone-dependent estrogen receptor destruction. Mol Cell Biol 2003; 23: 5979-88.

[85] Wang Y, Zong H, Chi Y, *et al*. Repression of estrogen receptor alpha by CDK11p58 through promoting its ubiquitin-proteasome degradation. J Biochem 2009; 145: 331-43.

[86] Rajbhandari P, Schalper KA, Solodin NM, *et al*. Pin1 modulates ERalpha levels in breast cancer through inhibition of phosphorylation-dependent ubiquitination and degradation. Oncogene 2014; 33: 1438-47.

[87] Tecalco-Cruz AC, Ramirez-Jarquin JO. Polyubiquitination inhibition of estrogen receptor alpha and its implications in breast cancer. World J Clin Oncol 2018; 9: 60-70.

[88] Chai F, Liang Y, Bi J, *et al*. REGgamma regulates ERalpha degradation *via* ubiquitin-proteasome pathway in breast cancer. Biochem Biophys Res Commun 2015; 456: 534-40.

[89] Liu H, Qiu J, Li N, *et al*. Human phosphatidylethanolamine-binding protein 4 promotes transactivation of estrogen receptor alpha (ERalpha) in human cancer cells by inhibiting proteasome-dependent ERalpha degradation *via* association with Src. J Biol Chem 2010; 285: 21934-42.

[90] Berry NB, Fan M, Nephew KP. Estrogen receptor-alpha hinge-region lysines 302 and 303 regulate receptor degradation by the proteasome. Mol Endocrinol 2008; 22: 1535-51.

[91] Kim MY, Woo EM, Chong YT, *et al.* Acetylation of estrogen receptor alpha by p300 at lysines 266 and 268 enhances the deoxyribonucleic acid binding and transactivation activities of the receptor. Mol Endocrinol 2006; 20: 1479-93.

[92] Kim SH, Kang HJ, Na H, Lee MO. Trichostatin A enhances acetylation as well as protein stability of ERalpha through induction of p300 protein. Breast Cancer Res 2010; 12: R22.

[93] Wang C, Fu M, Angeletti RH, *et al*. Direct acetylation of the estrogen receptor alpha hinge region by p300 regulates transactivation and hormone sensitivity. J Biol Chem 2001; 276: 18375-83.

[94] Subramanian K, Jia D, Kapoor-Vazirani P, *et al*. Regulation of estrogen receptor alpha by the SET7 lysine methyltransferase. Mol Cell 2008; 30: 336-47.

[95] La Rosa P, Pesiri V, Leclercq G, *et al*. Palmitoylation regulates 17beta-estradiol-induced estrogen receptor-alpha degradation and transcriptional activity. Mol Endocrinol 2012; 26: 762-74.

[96] Preisler-Mashek MT, Solodin N, Stark BL, *et al*. Ligand-specific regulation of proteasome-mediated proteolysis of estrogen receptor-alpha. Am J Physiol Endocrinol Metab 2002; 282: E891-8.

[97] Valley CC, Solodin NM, Powers GL, *et al*. Temporal variation in estrogen receptor-alpha protein turnover in the presence of estrogen. J Mol Endocrinol 2008; 40: 23-34.

[98] Fowler AM, Solodin N, Preisler-Mashek MT, *et al*. Increases in estrogen receptor-alpha concentration in breast cancer cells promote serine 118/104/106-independent AF-1 transactivation and growth in the absence of estrogen. FASEB 2004; 18: 81-93.

[99] Fowler AM, Solodin NM, Valley CC, Alarid ET. Altered target gene regulation controlled by estrogen receptor-alpha concentration. Mol Endocrinol 2006; 20: 291-301.

[100] Musgrove EA. Estrogen receptor degradation: a CUE for endocrine resistance? Breast Cancer Res 2011; 13: 312.

[101] Pan X, Zhou T, Tai YH, *et al.* Elevated expression of CUEDC2 protein confers endocrine resistance in breast cancer. Nat Med 2011; 17: 708-14.

[102] Lehn S, Ferno M, Jirstrom K, *et al.* A non-functional retinoblastoma tumor suppressor (RB) pathway in premenopausal breast cancer is associated with resistance to tamoxifen. Cell Cycle 2011; 10: 956-62.

[103] Trere D, Brighenti E, Donati G, *et al*. High prevalence of retinoblastoma protein loss in triple-negative breast cancers and its as-

INFORME DE LABORES 2019

sociation with a good prognosis in patients treated with adjuvant chemotherapy. Ann Oncol 2009; 20: 1818-23.

[104] Jin C, Rajabi H, Pitroda S, *et al*. Cooperative interaction between the MUC1-C oncoprotein and the Rab31 GTPase in estrogen receptor-positive breast cancer cells. PLoS One 2012; 7: e39432.

[105] Giamas G, Filipovic A, Jacob J, *et al.* Kinome screening for regulators of the estrogen receptor identifies LMTK3 as a new therapeutic target in breast cancer. Nat Med 2011; 17: 715-9.

[106] Stebbing J, Filipovic A, Ellis IO, *et al.* LMTK3 expression in breast cancer: association with tumor phenotype and clinical outcome. Breast Cancer Res Treat 2012; 132: 537-44.

[107] Stebbing J, Filipovic A, Lit LC, *et al.* LMTK3 is implicated in endocrine resistance *via* multiple signaling pathways. Oncogene 2013; 32: 3371-80.

[108] He X, Zheng Z, Song T, *et al*. c-Abl regulates estrogen receptor alpha transcription activity through its stabilization by phosphorylation. Oncogene 2010; 29: 2238-51.

[109] Kim JA, Kim MR, Kim O, *et al*. Amurensin G inhibits angiogenesis and tumor growth of tamoxifen-resistant breast cancer *via* Pin1 inhibition. Food Chem Toxicol 2012; 50: 3625-34.

[110] Long X, Nephew KP. Fulvestrant (ICI 182,780)-dependent interacting proteins mediate immobilization and degradation of estrogen receptor-alpha. J Biol Chem 2006; 281: 9607-15.

[111] Yeh WL, Shioda K, Coser KR, *et al*. Fulvestrant-induced cell death and proteasomal degradation of estrogen receptor alpha protein in MCF-7 cells require the CSK c-Src tyrosine kinase. PLoS One 2013; 8: e60889.

[112] De Savi C, Bradbury RH, Rabow AA, *et al*. Abstract 3650: Discovery of the clinical candidate AZD9496: a potent and orally bioavailable selective estrogen receptor downregulator and antagonist. Cancer Res 2015; 75: 3650.

[113] Wardell SE, Nelson ER, Chao CA, McDonnell DP. Bazedoxifene exhibits antiestrogenic activity in animal models of tamoxifen-resistant breast cancer: implications for treatment of advanced disease. Clin Cancer Res 2013; 19: 2420-31.

[114] Garner F, Shomali M, Paquin D, *et al*. RAD1901: a novel, orally bioavailable selective estrogen receptor degrader that demonstrates antitumor activity in breast cancer xenograft models. Anticancer Drugs 2015; 26: 948-56.

[115] Lai A, Kahraman M, Govek S, *et al*. Identification of gdc-0810 (arn-810), an orally bioavailable selective estrogen receptor degrader (serd) that demonstrates robust activity in tamoxifen-resistant breast cancer xenografts. J Med Chem 2015; 58: 4888-904.

[116] Guo S, Zhang C, Bratton M, *et al*. ZB716, a steroidal selective estrogen receptor degrader (SERD), is orally efficacious in blocking tumor growth in mouse xenograft models. Oncotarget 2018; 9: 6924-37.

[117] Tria GS, Abrams T, Baird J, *et al*. Discovery of LSZ102, a Potent, orally bioavailable selective estrogen receptor degrader (serd) for the treatment of estrogen receptor positive breast cancer. J Med Chem 2018; 61: 2837-64.

[118] Deeks ED. Fulvestrant: a review in advanced breast cancer not previously treated with endocrine therapy. Drugs 2018; 78: 131-7.

[119] Britschgi A, Duss S, Kim S, *et al.* The Hippo kinases LATS1 and 2 control human breast cell fate *via* crosstalk with ERalpha. Nature 2017; 541: 541-5.

[120] Angus L, Beije N, Jager A, *et al*. ESR1 mutations: Moving towards guiding treatment decision-making in metastatic breast cancer patients. Cancer Treatment Rev 2017; 52: 33-40.

[121] Toy W, Weir H, Razavi P, *et al*. Activating ESR1 mutations differentially affect the efficacy of er antagonists. Cancer Discov 2017; 7: 277-87.

[122] Reinert T, Goncalves R, Bines J. Implications of ESR1 mutations in hormone receptor-positive breast cancer. Curr Treatment Options Oncol 2018; 19: 24.

[123] Bahreini A, Li Z, Wang P, *et al.* Mutation site and context dependent effects of ESR1 mutation in genome-edited breast cancer cell models. Breast Cancer Res 2017; 19: 60.

[124] Jeselsohn R, Bergholz JS, Pun M, *et al*. Allele-specific chromatin recruitment and therapeutic vulnerabilities of ESR1 activating mutations. Cancer Cell 2018; 33: 173-86 e5.

[125] Harrod A, Fulton J, Nguyen VTM, *et al*. Genomic modelling of the ESR1 Y537S mutation for evaluating function and new therapeutic approaches for metastatic breast cancer. Oncogene 2017; 36: 2286-96.

[126] Martin LA, Ribas R, Simigdala N, *et al*. Discovery of naturally occurring ESR1 mutations in breast cancer cell lines modelling endocrine resistance. Nat Commun 2017; 8: 1865.

[127] Chu I, Arnaout A, Loiseau S, *et al*. Src promotes estrogen-dependent estrogen receptor alpha proteolysis in human breast cancer. J Clin Invest 2007; 117: 2205-15.

[128] Fuqua SA, Wiltschke C, Zhang QX, *et al*. A hypersensitive estrogen receptor-alpha mutation in premalignant breast lesions. Cancer Res 2000; 60: 4026-9.

[129] Herynk MH, Parra I, Cui Y, *et al*. Association between the estrogen receptor alpha A908G mutation and outcomes in invasive breast cancer. Clin Cancer Res 2007; 13: 3235-43.

[130] Holst F, Singer CF. ESR1-amplification-associated estrogen receptor alpha activity in breast cancer. Trends Endocrinol Metab 2016; 27: 751-2.

[131] Laenkholm AV, Knoop A, Ejlertsen B, *et al*. ESR1 gene status correlates with estrogen receptor protein levels measured by ligand binding assay and immunohistochemistry. Mol Oncol 2012; 6: 428-36.

[132] Nielsen KV, Ejlertsen B, Muller S, *et al*. Amplification of ESR1 may predict resistance to adjuvant tamoxifen in postmenopausal patients with hormone receptor positive breast cancer. Breast Cancer Res Treat 2011; 127: 345-55.

[133] Glidewell-Kenney C, Weiss J, Lee EJ, *et al.* ERE-independent ERalpha target genes differentially expressed in human breast tumors. Mol Cell Endocrinol 2005; 245: 53-9.

[134] Lin CY, Strom A, Vega VB, *et al*. Discovery of estrogen receptor alpha target genes and response elements in breast tumor cells. Genome Biol 2004; 5: R66.

[135] Ross-Innes CS, Stark R, Teschendorff AE, *et al*. Differential oestrogen receptor binding is associated with clinical outcome in breast cancer. Nature 2012; 481: 389-93.

[136] Cruz-Ramos E, Sandoval-Hernandez A, Tecalco-Cruz AC. Differential expression and molecular interactions of chromosome region maintenance 1 and calreticulin exportins in breast cancer cells. J Steroid Biochem Mol Biol 2019; 185: 7-16.

[137] Chen C, Zhou Z, Ross JS, *et al*. The amplified WWP1 gene is a potential molecular target in breast cancer. Int J Cancer 2007; 121: 80-7.

[138] Chen C, Zhou Z, Sheehan CE, *et al*. Overexpression of WWP1 is associated with the estrogen receptor and insulin-like growth factor receptor 1 in breast carcinoma. Int J Cancer 2009; 124: 2829-36.

[139] Karunarathna U, Kongsema M, Zona S, *et al*. OTUB1 inhibits the ubiquitination and degradation of FOXM1 in breast cancer and epirubicin resistance. Oncogene 2016; 35: 1433-44.

[140] Liu X, Sun L, Gursel DB, *et al*. The non-canonical ubiquitin activating enzyme UBA6 suppresses epithelial-mesenchymal transition of mammary epithelial cells. Oncotarget 2017; 8: 87480-93.

[141] Stanisic V, Malovannaya A, Qin J *et al*.. OTU Domain-containing ubiquitin aldehyde-binding protein 1 (OTUB1) deubiquitinates estrogen receptor (ER) alpha and affects ERalpha transcriptional activity. J Biol Chem 2009; 284: 16135-45.

[142] Tedesco D, Zhang J, Trinh L, *et al*. The ubiquitin-conjugating enzyme E2-EPF is overexpressed in primary breast cancer and modulates sensitivity to topoisomerase II inhibition. Neoplasia 2007; 9: 601-13.

[143] Gajulapalli VNR, Malisetty VL, Chitta SK, Manavathi B. Oestrogen receptor negativity in breast cancer: a cause or consequence? Biosci Reports 2016; 36.

[144] Puyang X, Furman C, Zheng GZ, *et al*. Discovery of selective estrogen receptor covalent antagonists for the treatment of eralpha(wt) and eralpha(mut) breast cancer. Cancer Discov 2018; 8: 1176-93.

[145] Jiang Y, Deng Q, Zhao H, *et al*. Development of stabilized peptide-based protacs against estrogen receptor alpha. ACS Chem Biol 2018; 13: 628-35.

[146] Tecalco Cruz AC, Mejia-Barreto K. Cell type-dependent regulation of free ISG15 levels and ISGylation. J Cell Commun Signaling 2017; 11: 127-35.

[147] Tecalco-Cruz AC, Cruz-Ramos E. Protein ISGylation and free ISG15 levels are increased by interferon gamma in breast cancer cells. Biochem Biophys Res Commun 2018; 499: 973-8.

[148] Wu F, Mo YY. Ubiquitin-like protein modifications in prostate and breast cancer. Frontiers in bioscience: J Virtual Lib 2007; 12: 700-11.

[149] Wei X, Xu H, Kufe D. MUC1 oncoprotein stabilizes and activates

INFORME DE LABORES 2019

estrogen receptor alpha. Mol Cell 2006; 21: 295-305.
[150] Grisouard J, Medunjanin S, Hermani A, *et al*. Glycogen synthase kinase-3 protects estrogen receptor alpha from proteasomal degradation and is required for full transcriptional activity of the receptor. Mol Endocrinol 2007; 21: 2427-39.
[151] Yang H, Yu N, Xu J, *et al*. SMURF1 facilitates estrogen receptor a signaling in breast cancer cells. J Exp Clin Cancer Res 2018; 37: 24.

PMID: 30324876

Met-Flow: A Strategy for Single-Cell Metabolic Analysis

Free Webinar
Oct 21, 2020
1pm SGT



John Connolly, PhD
Baylor University

REGISTER HERE

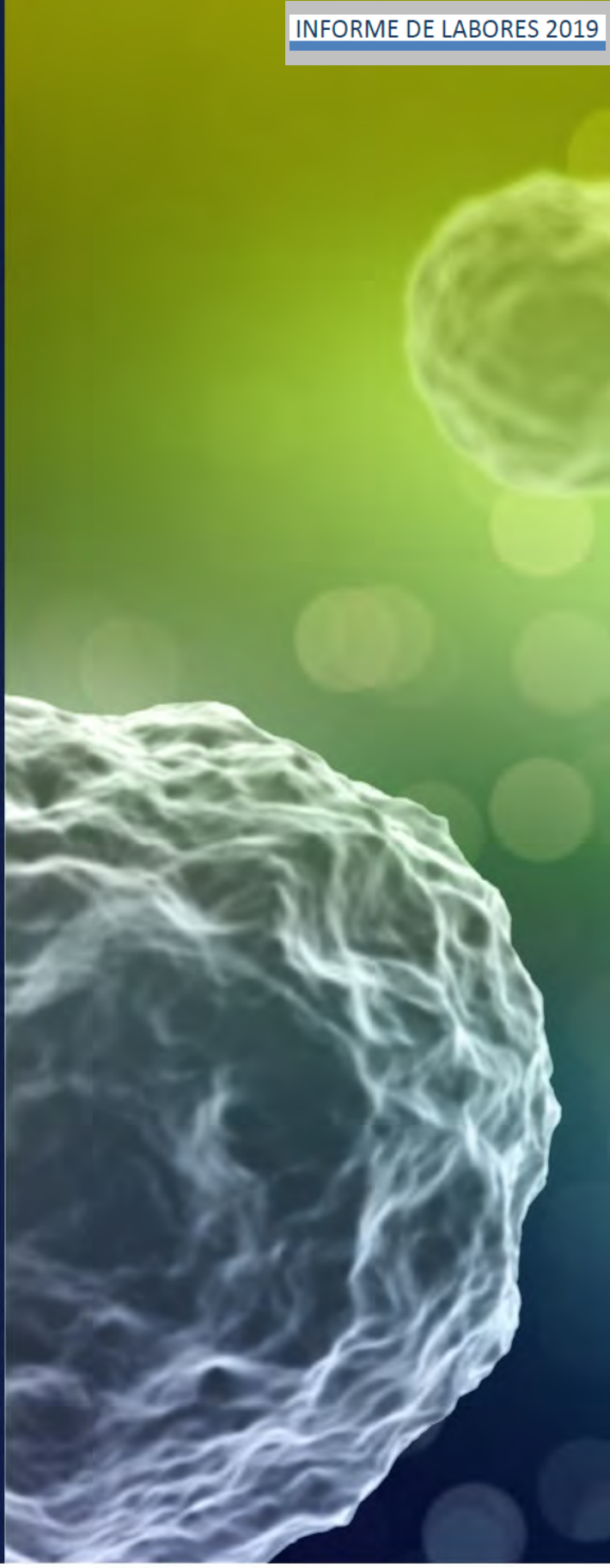

Sponsored by: BD

Provided by: CURRENT PROTOCOLS A Wiley Brand | WILEY

JLB JOURNAL OF LEUKOCYTE BIOLOGY

Check for updates

DOI: 10.1002/JLB.2VMA0818-328R

ARTICLE

Tamoxifen induces toxicity, causes autophagy, and partially reverses dexamethasone resistance in Jurkat T cells

Liliana Torres-López[1,2] | Paola Maycotte[3] | Andrómeda Liñán-Rico[4] | Liliana Liñán-Rico[1] | Luis Donis-Maturano[5] | Iván Delgado-Enciso[6] | Carmen Meza-Robles[6] | Clemente Vásquez-Jiménez[1] | Arturo Hernández-Cruz[7,8] | Oxana Dobrovinskaya[1]

[1]University Center for Biomedical Research, University of Colima, Colima, Mexico

[2]Faculty for Chemical Sciences, University of Colima, Colima, Mexico

[3]CONACYT-Biomedical Research Center of the East, Mexican Social Security Institute, Puebla, Mexico

[4]CONACYT-University Center for Biomedical Research, University of Colima, Colima, Mexico

[5]Ensenada Biomedical Innovation Department, Center for Scientific Research and Higher Education, Ensenada, Baja California, Mexico

[6]Medical School, University of Colima and Cancerology Institute of Colima State, Health Services, Colima, Mexico

[7]National Laboratory of Channelopathies (LaNCa), National Autonomous University of Mexico, Mexico City, Mexico

[8]Department of Cognitive Neuroscience-Institute of Cellular Physiology, National Autonomous University of Mexico, Mexico City, Mexico

Correspondence
Oxana Dobrovinskaya, University Center for Biomedical Research, University of Colima, 25 de Julio Av. Colima, Col. 28030, Mexico.
Email: oxana@ucol.mx

Abstract

Estrogens demonstrate biological activity in numerous organ systems, including the immune system, and exert their effects through estrogen receptors (ER) of two types: intracellular ERα and ERβ that activate transcriptional factors and membrane G protein-coupled ER GPER. The latter is capable to mediate fast activation of cytosolic signaling pathways, influencing transcriptional events in response to estrogens. Tamoxifen (TAM), widely used in chemotherapy of ERα-positive breast cancer, is considered as an ERα antagonist and GPER agonist. TAM was shown to possess "off-target" cytotoxicity, not related to ER in various tumor types. The present work was designed to study biological effects of TAM on the glucocorticoid (GC)-resistant cell line Jurkat, derived from acute lymphoblastic leukemia of T lineage (T-ALL). We have shown that T-ALL cell lines, in contrast to healthy T cells, express only GPER, but not ERα or ERβ. TAM compromised mitochondrial function and reduced the viability and proliferation of Jurkat cells. Additionally, TAM induced autophagy in a GPER-dependent manner. Gene expression profiling revealed the up-regulation of autophagy-related gene *ATG5*. Interestingly, TAM sensitized Jurkat cells to dexamethasone (DEX) treatment, which may be related to its capacity to cause autophagy. We suggest that TAM-based adjuvant therapy may represent a novel strategy in T-ALL patients handling.

KEYWORDS

tamoxifen, Jurkat cells, estrogen receptors, GPER, autophagy, apoptosis, cell cycle, proliferation, glucocorticoid resistance

1 | INTRODUCTION

Estrogens are known to have an important biological function in both female and male physiology and pathology in various organ and systems, including the immune system.[1–3] Their effects are mediated through binding ER to two types of ER: first, intracellular or intranuclear ERα and ERβ that activate transcription[4]; and second, membrane G protein-coupled ER, GPER or GPR30, that were identified later.[5] The latter mediate rapid triggering of signaling pathways by estrogens and antiestrogens, through MAPK activation, and early gene expression. Although ERα and ERβ are known to be expressed in immune cells and some lymphomas,[6] the information available on GPER expression in lymphoid cells is limited. Recently, it was reported that GPER contribute to the proliferation and survival of mantle cell lymphoma cells.[7] It has also been proposed that GPER regulates CXCR4 signaling in pre-B cell ALL.[8] Remarkably, GPER mediates the proliferative

Abbreviations: ALL, Acute lymphoblastic leukemia; ANOVA, Analysis of variance; B-ALL, Lymphoblastic leukemia cells of B lineage; BCLAF1, Bcl-2 associated factor 1; CFSE, Carboxy-fluorescein succinimidyl ester; CQ, Chloroquine; DEX, Dexamethasone; ER, Estrogen receptors(s); FBS, Fetal bovine serum; FCCP, Carbonyl cyanide 4-(trifluoromethoxy)phenylhydrazone; GC, Glucocorticoid(s); GPER, G protein-coupled estrogen receptor(s); GR, Glucocorticoid receptor(s); HSC, Hematopoietic stem cell; LC3I, Microtubule-associated protein light chain3-I; MDC, Monodansylcadaverine; MFI, Median fluorescence intensity; MNC, Mononuclear cells; PI, Propidium Iodide; Rhod-123, Rhodamine-123; T-ALL, Acute lymphoblastic leukemia of T lineage; TAM, Tamoxifen; TCR, T cell receptor; $\Delta\Psi m$, Mitochondrial membrane potential.

Received: 30 August 2018 | Revised: 30 November 2018 | Accepted: 5 December 2018

 ©2019 Society for Leukocyte Biology

effect of estrogen in numerous cancer types.[9,10] Accordingly, GPER agonist G-1 was shown to inhibit tumor growth in triple-negative breast cancer cells,[11] adrenocortical carcinoma,[12] lung cancer,[13] and ovarian cancer.[14]

TAM is considered as an ERα antagonist and GPER agonist,[15,16] which has been the first-line targeted therapy for the management of ERα positive breast cancers for almost 60 years.[17] However, several recent reports have pointed out some novel, "off-target" or non-ER-related anticancer effects of TAM, independent of nuclear ER.[18,19] Among these are target proteins involved in the regulation of proliferation, cell cycle progression, autophagy, and chemoresistance. In this regard, TAM-induced apoptosis of breast cancer MCF-7 cells via GPER/PI3K/MAPK pathway has also been reported.[20]

At doses significantly higher than those used for breast cancer treatment, but still in the therapeutic range, TAM caused an inhibitory effect on PKC, which is overexpressed in different malignancies, particularly in gliomas, glioblastoma, and anaplastic astrocytomas, resulting in cell toxicity.[21–25] Using TAM as a coadjuvant therapy, a significant improvement in the outcome of pancreatic cancer patients was archived.[26–28] Besides, there is evidence that TAM is a potent inducer of autophagy, and that its cytotoxic effect is related to the induction of autophagy previous to cell death.[29] On the other hand, autophagy may also have a protective effect in tumor cells and induce chemoresistance in cancer.[30] Then, the activation or inhibition of autophagy in every type of cancer should be studied in detail, to find the best strategy for targeting this process for cancer treatment. TAM-based coadjuvant therapy may represent an attractive approach in anticancer treatment, and TAM-mediated activation of autophagy may have an important relevance in this process. In this regard, we would like to mention the study published by Laane and colleagues[31] who demonstrated that GC, the first choice drugs used for the treatment of lymphoid malignancies, induced autophagy upstream of apoptosis in acute lymphoblastic leukemia cells of B lineage (B-ALL). The crucial role of autophagy in DEX-induced cell death was confirmed by the fact that autophagy inhibition precluded apoptosis in these cells. Because GC are administered to leukemic patients during all phases of therapy, GC resistance represents an essential challenge to improve the outcome of these patients.[32] At the same time, the referenced work represents the only study relating GC resistance with the autophagic process. Since there is no previously published evidence on the biological effects of TAM-induced autophagy in T-ALL, the present work was designed to study the antileukemic effect of TAM, its capability to induce autophagy and reverse GC-resistance in the Jurkat cell line derived from a T-ALL sample in relapse.

2 | MATERIALS AND METHODS

2.1 | Cell lines and culture conditions

Cell lines established from peripheral blood of a T-ALL patient in relapse were purchased from ATCC: Jurkat, clone E6-1, from a 14-year-old male (ATCC TIB); MOLT-3 from a 19-year-old male (ATCC CRL-1552); CCRF-CEM, from a 4-year-old girl (ATCC CCL-119). The cells were cultured in suspension in Advanced RPMI 1640 Medium supplemented with 5% (v/v) heat-inactivated fetal bovine serum (FBS), 2 mM GlutaMAX, 10 mM HEPES, and 100 U/ml penicillin, 100 μg/ml streptomycin (all from Gibco, Thermo Fisher Scientific). In some experiments, to count the number of autophagosomes and autolysosomes, tandem-labeled mCherry-GFP-LC3 Jurkat cells (gift from Dr. A. Thorburn, Colorado, USA) were used. These cells were maintained in complete growth medium (as for wild type Jurkat cells) additionally supplemented with 400 μg/ml of hygromycin B (Sigma, H3274) for selection. Cell lines were cultured in a humidified incubator in 5% CO_2 atmosphere at 37 °C. Cells were maintained in the logarithmic growth phase by daily medium refreshment.

2.2 | Chemicals

TAM (Sigma, T5648), G-36 (Cayman Chemical, 14397), and Chloroquine (CQ) (Sigma, C6628) were used. Stock solutions of TAM (in ethanol), G-36 (in DMSO), and CQ (in PBS) were prepared at 20 mM and stored at −20°C. DEX was acquired as solution for intravenous injections at 4 mg/ml (Chinoin Pharmaceutical Products, Aguascalientes, Mexico) and stored at 4 °C. All working solutions were prepared from stock solutions in growth medium immediately before experiments. Ethanol and DMSO used as vehicles in concentrations up to 1% did not demonstrate any effect in the protocols used in this study.

2.3 | Purification and activation of CD4$^+$ lymphocytes

Mature CD4$^+$ lymphocytes were obtained from peripheral blood of healthy donors. Peripheral blood was taken by trained personnel under aseptic condition with sterile material for each donor. The protocol was approved by Bioethics and Biosecurity Committee of the Biomedical Research Centre according to Federal (Artículo 100, Ley General de Salud), State, and local laws. Informed consent was obtained from each participant. Blood samples were diluted 1 : 1 with PBS. The mononuclear cells (MNC) were separated by Ficoll gradient (Ficoll-Paque PLUS, GE Healthcare). MNC were subjected to negative selection (to avoid activation) with CD4$^+$ T cell isolation kit, following Miltenyi Biotec specifications. The CD4$^+$ T cells were cultured in complete RPMI 1640 medium, in 24-well plates (no more than 1.5×10^6 cells per ml), for 24 h. For polyclonal activation, resting lymphocytes were pretreated in 96-well plates with anti-CD3 monoclonal antibodies (5 μg/ml) (BD, 555336) for 2 h at 37 °C; medium excess was removed and 1×10^5 cells were incubated with (2 μg/ml) anti-CD28 monoclonal antibodies (BD, 555725) for 4 days. Ligation of CD3/CD28 provides a powerful antigen-independent stimulus by cross-linking T cell receptor (TCR) resulting in transit from quiescent to proliferation state.

2.4 | Cell viability

Jurkat cells or activated CD4$^+$ lymphocytes (1×10^5 per well) were seeded in 96-well plates, treated with corresponding concentrations of TAM alone, or with vehicle, and incubated during 24–96 h. Every 24 h, cell count was performed using a hemocytometer and trypan blue dye.

Additionally, cell viability was determined using metabolic resazurin-based in vitro Toxicology Assay Kit (Sigma-Aldrich, TOX-8) according to manufacturer's recommendations. Kit mix, 10% (v/v) of the final volume, was added to each well and incubated during 4–6 h at 37°C. Resazurin (non-fluorescent) to resorufin (fluorescent) conversion was measured fluorometrically (Ex/Em = 560/590 nm) using GloMax Discover Multimode Microplate reader (Cat. GM3000, Promega). Three or more replicates were prepared for each concentration in all experiments to decrease variability.

2.5 | CFSE cell proliferation assay

CFSE cell proliferation assay was carried out as described earlier[33] with some modifications. Cells were washed, resuspended in PBS at a concentration of 1×10^6/ml and stained with carboxy-fluorescein succinimidyl ester (CFSE, ThermoFisher, C34554) to a final concentration of 0.5 μM or 1 μM for Jurkat cells and $CD4^+$ lymphocytes, respectively. Cells were incubated for 30 min at room temperature, with agitation every 5 min. Labeled Jurkat cells were washed with PBS, seeded in fresh culture medium into 24-well plates (5×10^5 cells/well) in the presence of increasing TAM concentrations, harvested every 24 h, and CFSE fluorescence intensity was measured by flow cytometry (FACSCanto II, BD Biosciences). $CD4^+$ lymphocytes were activated as described previously and TAM was added after 24 h. Lymphocytes were harvested after 72 h of culture for cytometric analysis. Data analysis was performed using FlowJo 10.2 Software.

2.6 | Western blot analysis

For LC3 immunoblotting, cells treated with CQ alone or in combination with TAM were harvested and lysed with RIPA buffer supplemented with protease inhibitors (Complete, Roche, 11697498001). Protein was quantitated using BCA Protein Assay Kit (Sigma, BCA1); 10 μg (for LC3-II) of protein were loaded in a 15% SDS-PAGE, transferred onto PVDF membrane, blocked for 1 h with 5% BSA in TBS Tween-20 buffer (TBS-T) and incubated overnight at 4 °C with anti-human LC3 rabbit antibody (Novus-Biologicals, NB100-2220, dilution 1:3000). For estrogen receptor evaluation, 20 μg of protein were loaded in a 10% SDS-PAGE; primary antibodies were: anti-human ERα (Novus-Biologicals, NBP2-84827, dilution 1:500), anti-human ERβ (Novus-Biologicals, NBP2-16379, dilution 1:1000) and GPER (Novus-Biologicals, NBP1-31239, dilution 1:1000), all produced in rabbit. Rabbit anti-human GAPDH antibodies (abcam, ab9485, dilution 1:2000) were used as a loading control. HRP-conjugated goat anti-rabbit IgG (Novus-Biologicals, NBP2-30348H, 1:3000) was used as secondary antibody and incubated 1 h at room temperature. The membranes were incubated with ECL detection reagent (Bio-Rad, 170–5061), protein bands were visualized with a Bio-Rad Universal Hood II system and analyzed with Image Lab 5.0 software.

2.7 | Mitochondrial membrane potential measurement

To evaluate changes in mitochondrial membrane potential ($\Delta\Psi$m), the fluorescent dye rhodamine-123 (Rhod-123) (Sigma, R8004) was used, which stains mitochondria directly proportional to $\Delta\Psi$m. After treatment with TAM, or carbonyl cyanide 4-(trifluoromethoxy) phenylhydrazone (FCCP) (Sigma, C2920) as a positive control of mitochondrial membrane depolarization, Jurkat cells were harvested, counted (trypan blue exclusion test), washed with PBS and stained with Rhod-123 (100 μl Rhod-123 2 μM for each 2.5×10^5 cells) for 30 min at room temperature. Changes in $\Delta\Psi$m before cell death were observed through flow cytometry (FACSCanto II, BD Biosciences) by selecting live population (PI exclusion) and Rhod-123 fluorescence measurement (Ex/Em = 507/530). Data analysis was performed with FlowJo 10.2 Software.

2.8 | DNA content/cell cycle progression

Samples of untreated or TAM-treated cells were counted (trypan blue exclusion test), harvested, washed with cold PBS and fixed with ice-cold 70% ethanol overnight. Next day, after two washes with PBS, cells were treated for 15 min with 0.1% Triton X-100 in PBS for permeabilization. Finally, 500 μl of PBS working solution containing 0.15 μM of Propidium Iodide (Invitrogen, PNN1011), 10 μg/ml RNase (Sigma, R4875), and 0.1% BSA (Research Organics, 1336A) were added to every sample of 1×10^6 cells. Due to more condensed DNA, PI penetration and staining is less efficient in G2 than G1 cells. Then, to insure PI DNA staining saturation, the samples were incubated in working solution at least 24 h at 4 °C, giving good delineation of G1 versus G2 peaks (G2/G1 ratio usually more than 1.95). For data acquisition, FACSCanto II cytometer (BD Biosciences) was used, equipped by 488 laser, 556 LP mirror, and 585/42 filter, to detect PI (Ex/Em max = 538/617 nm) fluorescence intensity. Cell cycle phase distribution was evaluated after appropriate gating of cell population in FSC versus SSC plot to exclude debris, following by gating in PI-FL (area) versus PI-FL (weight) plot to exclude doublets. Events (50,000) were analyzed in each sample. Data analysis was performed using ModFit 5.0 Software in Trial Version.

2.9 | Immunofluorescence assays for cell death and autophagy

After TAM treatment, cells were stained with cell death kit (Invitrogen, V13245) for 15 min, according to manufacturer's instructions with some modifications. It is well known that externalization of phosphatidylserine on the outer leaflet of the plasma membrane is a feature of apoptotic cells. Annexin V specifically binds to phosphatidylserine, and apoptotic cells are positively stained with Annexin V-Alexa Fluor 488 conjugate (Ex/Em max = 495/519), whereas PI (Ex/Em max = 538/617nm) binds to nucleic acids, permeating only into the necrotic/late apoptotic cells with disintegrated plasma membrane. The double positive fraction then represented late apoptosis and necrosis. For the assay, 3 μl of Annexin V-Alexa Fluor 488 and 0.2 μl PI were added for each 1×10^6 cells. For autophagolysosome accumulation monitoring, cells were incubated with monodansylcadaverine at 60 μM (MDC, Ex/Em max = 335/518 nm; Sigma, 30432). Fluorescence was measured either by flow cytometry (FACSCanto II, BD Biosciences) or confocal microscopy (ZEISS LSM 700) with a ×40 objective. For excitation, 405 nm laser was used for MDC, and 488 nm laser for Alexa

INFORME DE LABORES 2019

TABLE 1 Summary of nucleotide sequences

Gene	Forward primer	Reverse primer
BCLAF1	5′-AGAAAAGAAATGGGTCGCTCC-3′	5′-CGAGACCTAGAACTGTATCGC-3′
CFLAR	5′-AGAGGTAAGCTGTCTGTCGG-3′	5′-CAGCACTCTATAGTCCGAAACAAGG-3′
CARD8	5′-TCACGGAAACTGTTGGTTGAC-3′	5′-GCTCCCTGTATACCGTATCATTTG-3′
TRADD	5′-GGTCAGCCTGTAGTGAATCGG-3′	5′-CATTTGAGACCCACAGAGCG-3′
DIDO1	5′-TTGGACCCAGAGGTTTCGTC-3′	5′-TCCATACCTGCTCCAACACTG-3′
ATG5	5′-GCTTGGAGTAGGTTTGGCTTTG-3′	5′-AACCACACATCTCGAAGCAC-3′
COX7A2L	5′-CAAGTTTAGTGGCTTCACGC-3′	5′-GCTTTAATCCCTGCGGGC-3′
IL4	5′-TCCGATTCCTGAAACGGCTC-3′	5′-TGGTTGGCTTCCTTCACAGG-3′
CYP1B1	5′-CTCCTCCTCTTCACCAGGTATC-3′	5′-TCACCCATACAAGGCAGACG-3′
ESR1	5′-TATGTGTCCAGCCACCAACC-3′	5′-TCGGTCTTTTCGTATCCCACC-3′
ESR2	5′-GAGTCCGATGAATGTGCTTG-3′	5′-GGGCAAGTATAATGGCTTCAG-3′
GPER1	5′-TCTAAACTGCGGTCAGATGTGGC-3′	5′-TGTGAGGAGTGCAAGGTGACCAG-3′

Fluor 488 and PI. In cytometry, data were collected using 510/50 nm, 530/30 nm; 585/42 nm filters. Annexin V-Alexa Fluor 488 and PI negative populations were classified as viable, Annexin V-Alexa Fluor 488 positive, PI negative as apoptotic, Annexin V-Alexa Fluor 488 negative, PI positive as necrotic, and Annexin V-Alexa Fluor 488 and PI positive as late apoptotic or necrotic. Data analysis was performed with FlowJo 10.2 and ZEN 2.3 software.

2.10 | Autophagic flux measurement with mCherry-GFP-LC3

We used stably expressing tandem mCherry-GFP-LC3 Jurkat cells to measure autophagic flux. Upon autophagy induction, microtubule-associated protein light chain 3-I (LC3I) is conjugated to phosphatidylethanolamine (LC3II) and localized to the autophagosomes. However, LC3II is also degraded inside the lysosomes or de-conjugated by Atg4, decreasing its intracellular content. One approach to measure autophagic flux is the use of a tandem/tagged LC3 construct. Thus, LC3II positive autophagosomes would be double mCherry and GFP positive. On the other hand, since GFP signal is more sensitive to the acidic conditions in the lysosomal lumen, after autophagosome fusion with the lysosome, acidic lysosomal pH quenches the pH-sensitive GFP fluorescence and autophagolysosomes would be mCherry+GFP−. Thus, a ratio of mCherry+/GFP+ cells is an indication of autophagosome formation and degradation within the lysosome or autophagic flux as previously described.[34]

After TAM and/or G-36 treatment, LC3 accumulation was observed with ×40 objective using confocal microscopy. Images were acquired using Carl Zeiss LSM 700 system coupled to an inverted Observer Z1 microscope equipped with 488 and 555 nm lasers, or custom made confocal microscope (Solamere Technology Group, Salt Lake city, USA) based on a Yakogawa spindisk confocal scan head (CSUX1M1, Yokogawa Electronic Co., Tokyo, Japan), equipped with solid state Coherent Obis lasers (405, 488, 561, and 640 nm). Autophagy evaluation was assessed by counting red (mCherry+) and green (GFP+) dots in the cell. Cells were treated with TAM ± autophagy blocker CQ which neutralizes lysosomal pH and avoids GFP quenching produced by lysosomal acidic pH. Based on the GFP+ or mCherry+ average dots observed in control conditions, a cell was considered as GFP+ when it had more than two green dots and mCherry+ with six or more red dots. Data analysis was performed with ZEN 2.3 software. Three fields by sample were considered and the mean of mCherry/GFP relation of three independent experiments was graphed.[35]

2.11 | Changes in genetic transcription patterns

Jurkat cells were treated with 7.5 μM TAM for 24 h. In controls, the corresponding concentration of vehicle (ethanol) was used. TRizol reagent (ThermoFisher, 15596018) was used for RNA isolation according manufacturer's instructions. RNA concentration was measured with QuantiFluor RNA System (Promega, E3310), RNA purity and integrity were observed through gel electrophoresis.

Total RNA extracted from 1.5×10^6 cells was used to generate microarray expression data at the microarray facility in the Cell Physiology Institute (UNAM, Mexico). House double channel platform was used and microarrays were printed with a human 50-mer oligo library set "A" from MWG BiotechOligo Sets. The microarray contains approximately 10,000 specific gene oligonucleotide probes representing the best-annotated human genes. Chips were opposite stained with Alexa 555 and Alexa 647 as experimental and SWAP repetitions. The analysis was carried out using Genarise software and the lists of up- and down-regulated genes were obtained (Z-Score cuts 1.5). The data of microarrays were deposited in a public functional genomics data repository Gene Expression Omnibus (GEO) with a reference number GSE122852. Ten genes of interest were selected to confirm their expression level using qRT-PCR.

To quantify the expression of genes of interest in Jurkat cells, or to verify the expression of various estrogen receptors in different cell lines, the qRT-PCR was performed as follows: 500 ng of total RNA was reverse transcribed using QIAGEN Quantitec Reverse Transcription Kit (cat no. 205313), following the manufacturer's instructions, in a final volume of 20 μl; cDNA was diluted 1 : 3 in nuclease-free water. Samples were processed in triplicates. The primers nucleotide sequences are summarized in Table 1.

Quantitative PCR was performed using Maxima SYBR Green qPCR Master Mix (2X) and PikoReal Real-Time PCR System (Thermo

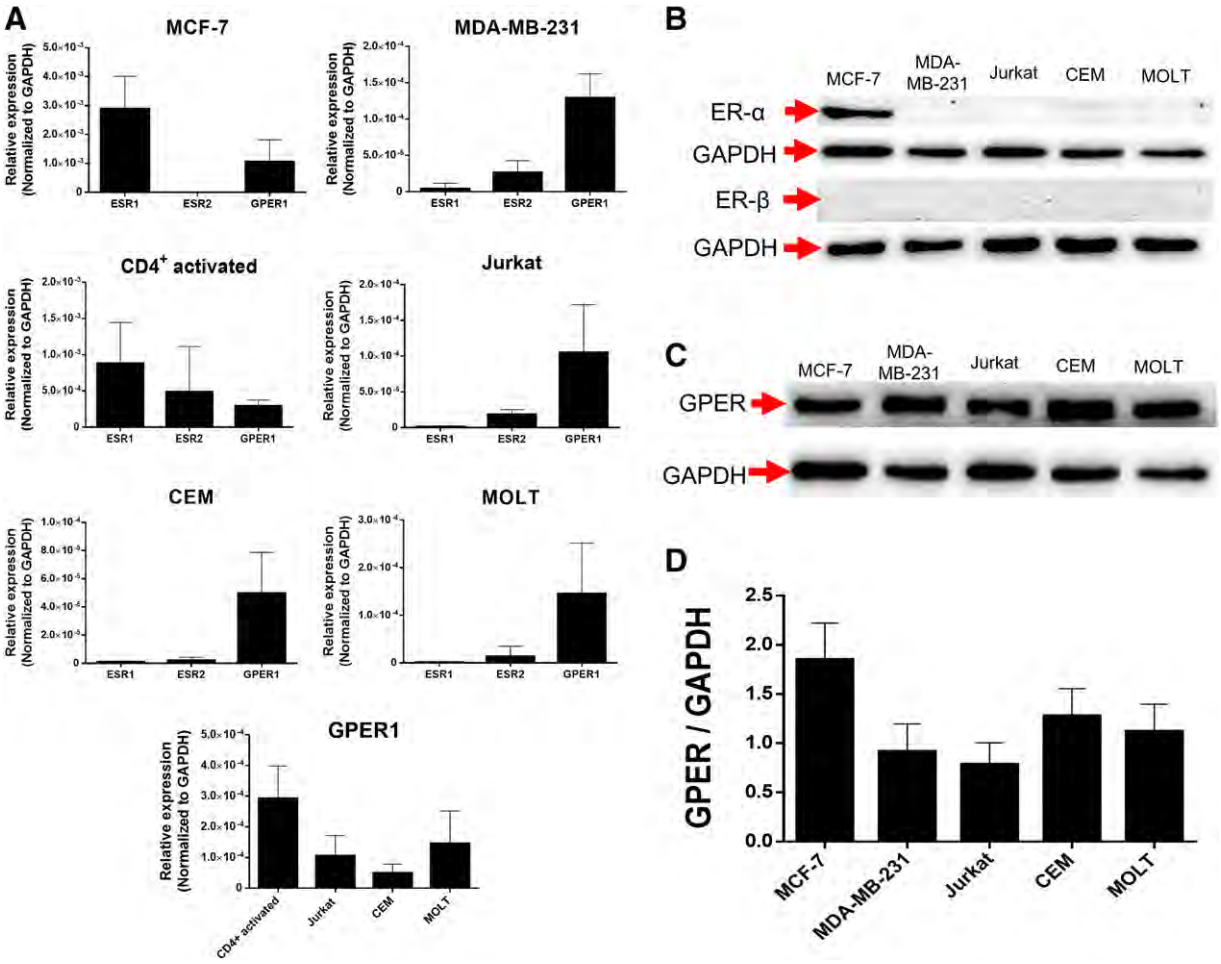

FIGURE 1 **RNA and protein expression of estrogen receptors in leukemic cell lines.** MCF-7, MDA-MB-231, and nonleukemic CD4+ T lymphocytes were used as reference. (**A**) mRNA expression of all ER: *ESR1* (ERα), *ESR2* (ERβ), and *GPER1* (GPER/GPR30). Expression was normalized to GAPDH as housekeeping gene ($2^{\wedge(-\Delta CT)}$). Data are mean ± SEM; $N \geq 4$. (**B**) Representative Western blot of ERα (~69 kDa) and ERβ (~55 kDa) in different cell lines. (**C**) Representative Western blot of GPER protein (~80 kDa) expression. (**D**) Relative protein band density values were calculated as the ratio of GPER to that of GAPDH in different cell lines. Data are mean ± SEM; $N \geq 5$

Scientific). The reaction was performed as follows: 10 min at 95 °C, and 38 cycles (denaturing at 95 °C for 15 s, annealing at 60 °C for 30 s, and extension at 72 °C for 30 s). Data collection was made after annealing step. The melt curve protocol was performed from 60 to 95 °C. Each gene was normalized to *GAPDH* and the relative gene expression levels were normalized to Jurkat cells with vehicle, using the comparative $2^{\wedge(-\Delta\Delta Ct)}$ method. The expression level of ER genes relative to *GAPDH* in different cell lines and healthy lymphocytes was evaluated by $2^{\wedge(-\Delta Ct)}$ method.

2.12 | Data analysis and statistics

All experiments were performed at least three times in independent form. Data were analyzed using GraphPad Prism 6.0 software and were expressed as mean values ± standard error. A comparison of individual treatments was performed, statistical significance was calculated and compared between control (without treatment) and treated samples using the analysis of variance (ANOVA) with Dunnett post hoc testing; also, comparison between every mean with every other mean was performed and statistical significance was calculated using ANOVA with Tukey post hoc testing. Comparisons in levels of gene expression between two groups of data (treated vs. untreated Jurkat cells) was made with unpaired *t*-test. Significance was defined as $P < 0.05$.

3 | RESULTS/DISCUSSION

3.1 | T-ALL cell lines express G protein-coupled estrogen receptor

First of all, our goal was to determine the pattern of estrogen receptors (ER) expression in T-ALL cell lines (Jurkat, CEM, and MOLT), both at mRNA as well as at protein level. MCF-7 and MDA-MB-231 breast cancer cell lines, and activated $CD4^+$ T cells isolated from peripheral blood of nonleukemic volunteers were used for reference. As shown in Fig. 1A, of the tree receptors analyzed, *ESR1* (ERα) displayed the highest expression level in MCF-7 (*ESR1* > *GPER1* > *ESR2*), whereas in nonleukemic $CD4^+$ T cells its expression level was the lowest (*GPER1* > *ESR2* > *ESR1*). *ESR1* (ERα) mRNA was not detected in any leukemic T cell line. *ESR2* (ERβ) mRNA was detected in MDA-MB-231 and activated healthy T cells, but in leukemic T cells, it showed a

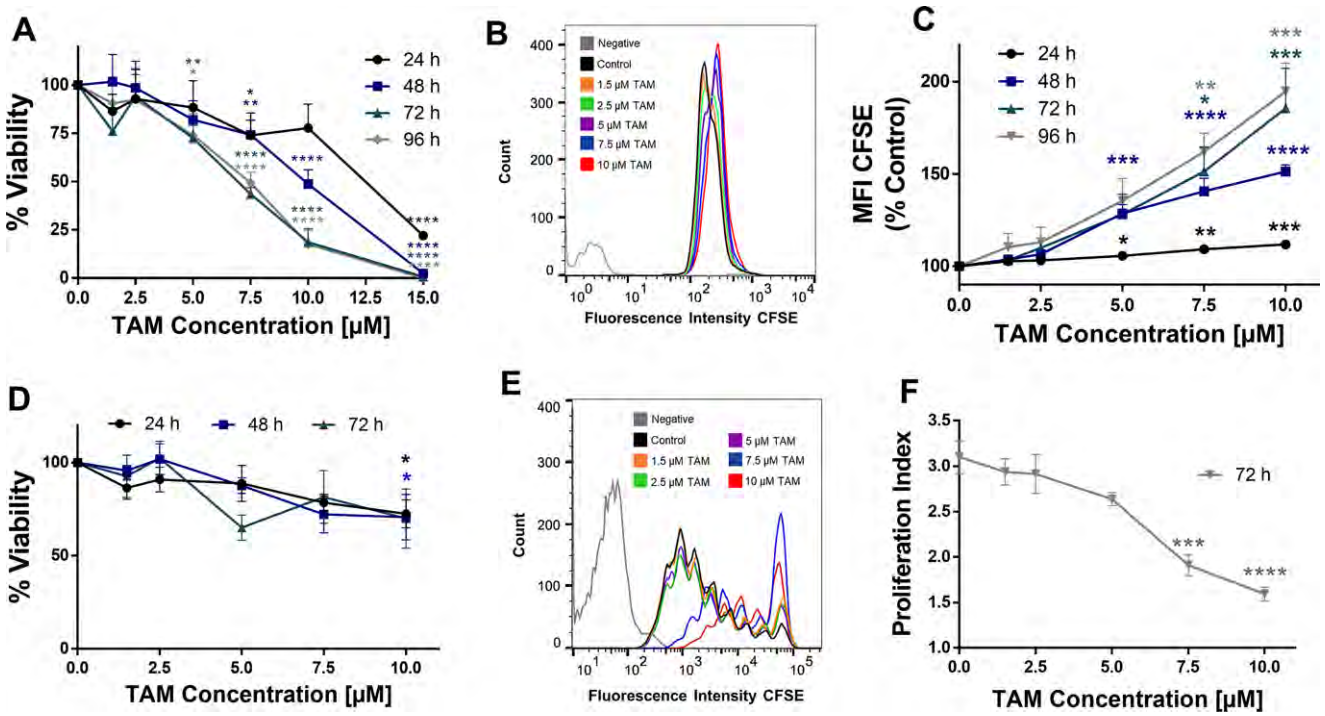

FIGURE 2 **TAM demonstrates cytotoxic and antiproliferative effects in leukemic cells.** Jurkat cells (**A–C**) and CD4$^+$ nonleukemic T lymphocytes (**D–F**) were incubated in presence of growing TAM concentrations during indicated time periods. (**A** and **D**). Cell viability evaluated by cell count (trypan blue exclusion test) after indicated time periods. Data are mean ± SEM; $N \geq 3$; $^*P < 0.05$, $^{**}P < 0.01$, $^{***}P < 0.001$, $^{****}P < 0.0001$. For each time point, comparison between control (without treatment) and treated samples was made by one-way ANOVA with Dunnett post hoc testing. (**B**) A representative histogram of changes in CFSE fluorescence intensity of Jurkat cells in presence of increasing concentrations of TAM after 48 h of treatment, where the shift of the mean fluorescence peak (MFI) to the left reflects Jurkat cell proliferation. (**C**) MFI of CFSE normalized to control (without treatment) as a function of TAM concentration. Cell proliferation decreased as TAM concentration increased. Data are mean ± SEM; $N = 3$; $^*P < 0.05$, $^{**}P < 0.01$, $^{***}P < 0.001$, $^{****}P < 0.0001$. For each time point, comparison between control and treated samples was made by one-way ANOVA with Dunnett post hoc testing. (**E**) Representative histograms of CFSE fluorescence intensity measured in CD4$^+$ activated (24 h) lymphocytes treated with different TAM concentrations for 72 h. (**F**) Proliferation index calculated for each TAM concentration with FlowJo Software (proliferation tool). Data are mean ± SEM; $N = 3$; $^{***}P < 0.001$, $^{****}P < 0.0001$. For each TAM concentration, comparison between control and treated samples was made by one-way ANOVA with Dunnett post hoc testing

very low expression level. Neither ERα nor ERβ proteins were detected in T-ALL cells (Fig. 1B), being in line with an earlier report where it was described that Jurkat cells do not express nuclear ER.[36] In contrast, *GPER1* mRNA expression was detected in all leukemic cell lines (Fig. 1A), which was also confirmed at protein level showing a high expression similar to GAPDH (Fig. 1C and D). To our knowledge, the present study is the first one to detect high expression levels of GPER at both mRNA and protein level in cell lines derived from T-ALL samples. Remarkably, the pattern of ER expression in T-ALL cell lines is quite different when compared to activated T cells. Whether this pattern is related to T cell maturation or T leukemogenesis, should be revealed in the future studies.

3.2 | TAM reduced viability and proliferation of ER-negative Jurkat cells

Cytotoxic "off-target" effect of TAM has been demonstrated in different types of cells that do not express nuclear ERα or ERβ.[18,19] To reveal whether TAM is toxic for leukemic cells, we performed viability assays in Jurkat cells, where healthy CD4$^+$ T cells were tested for reference. Effect of TAM on cell viability was evaluated by cell count using cell-impermeable dye trypan blue. As shown in Fig. 2A, significant cytotoxic effect was observed in Jurkat cells at TAM concentrations 5 μM and higher.

To evaluate the antiproliferative effect of TAM, fluorescence intensity of cells loaded with nontoxic concentrations of cell permeable cell tracker (CFSE) was measured using flow cytometry. In this assay, every division resulted in dye distribution between daughter cells and decrease of fluorescence intensity. Accordingly, median fluorescence intensity (MFI) evaluated in cell population is shifted to a lower fluorescence intensity as the cells divide. Starting at the concentration of 5 μM, TAM inhibited cell proliferation, as evidenced by decreased MFI shift in relation to the control population (Fig. 2B and C).

Remarkably, TAM was less toxic for activated CD4$^+$ T cells than for Jurkat cells (Fig. 2D), but reduced their proliferation, as clearly seen by the decrease in proliferation index at concentrations higher than 5 μM (Fig. 2E and F).

3.3 | TAM-induced cell cycle arrest in G1 phase

To further reveal whether TAM-induced toxicity is related to an arrest in the cell cycle progression, flow cytometric cell cycle profiling was performed every 24 h of incubation, during 48 h. DNA content, corresponding to G1, S, and G2 phases in living cells was evaluated

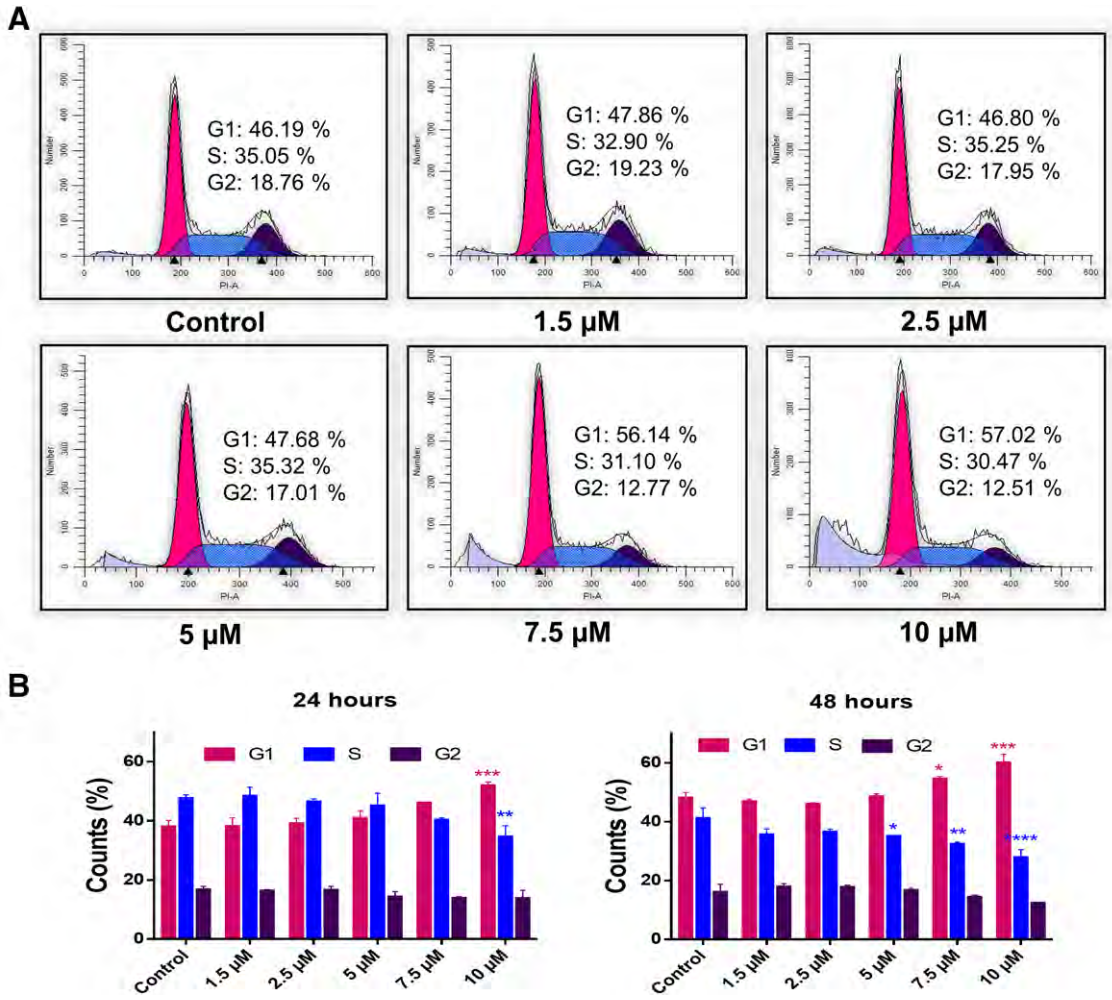

FIGURE 3 **TAM-induced arrest in G1 phase of cell cycle.** Jurkat cells were incubated in presence of growing TAM concentrations (1.5–10 μM) during 48 h. Cell cycle phase profiling was performed every 24 h by flow cytometry. (**A**) As an example of typical experiment, ModFit histograms of cell samples at 48 h of incubation with different TAM concentration are shown. G0/G1 peak is pink, G2/M peak is purple, S phase between G0/G1 and G2/M is blue, and subG1 damaged population is light-purple. (**B**) Cell count of cell subpopulations corresponding to G1, S, and G2 cell cycle phases were graphed at different times of TAM treatment. Data are mean ± SEM; $N = 3$; $^{*}P < 0.05$, $^{**}P < 0.01$, $^{***}P < 0.001$, $^{****}P < 0.0001$. For each cell cycle phase, comparison between control (without treatment) and different TAM concentrations was made by two-way ANOVA with Dunnett post hoc testing

using PI staining. Sub-G1 population, corresponding to dead cells with degraded DNA, was excluded from this analysis. In the Fig. 3A, representative cell cycle histograms of Jurkat cells after 48 h of treatment with different TAM concentrations are shown. After 24–48 h of treatment, statistical analysis revealed that TAM in the 5–10 μM range caused cell cycle arrest in G1 phase (Fig. 3B).

3.4 | TAM treatment caused mitochondrial dysfunction

Mitochondria are multifunctional organelles that link bioenergetics, biosynthesis and many signaling pathways in cancer.[37] Anabolic metabolism of rapidly proliferating T-ALL cells is highly dependent on both aerobic glycolysis and oxidative phosphorylation, and mitochondria are indispensable for fulfillment, fine regulation, and plasticity of these processes.[38] Therefore, mitochondria have been proposed as targets for cancer chemotherapy.[39] Mitochondria were suggested recently as the "gateway" for TAM-induced injury in liver. It was shown that TAM can bind directly to mitochondrial proteins. In particular, it was shown that TAM disrupted mitochondrial functions by mechanism related to alteration of inner mitochondrial membrane fluidity, which in turn affected lipid environment and function of membrane integral proteins, with suppression of 1–5 membrane complexes and impairment of oxidative phosphorylation.[40]

We evaluated whether mitochondria were involved in TAM-induced toxicity in leukemic cells. Reduced $\Delta\Psi$m is a classic indicator of mitochondrial damage, and thus we evaluated this parameter in TAM-treated Jurkat cells using mitochondria specific fluorescent probe Rhod-123 and flow cytometry. The assay was performed after 4 and 8 h of treatment, independently for populations of live and dead cells since cell death is closely linked to loss of $\Delta\Psi$m. Cell-impermeable fluorescent dye PI was used to detect dead cells that have lost plasma membrane integrity (Fig. 4A), and MFI of Rhod-123 was determined separately in dead PI-positive and live PI-negative

INFORME DE LABORES 2019

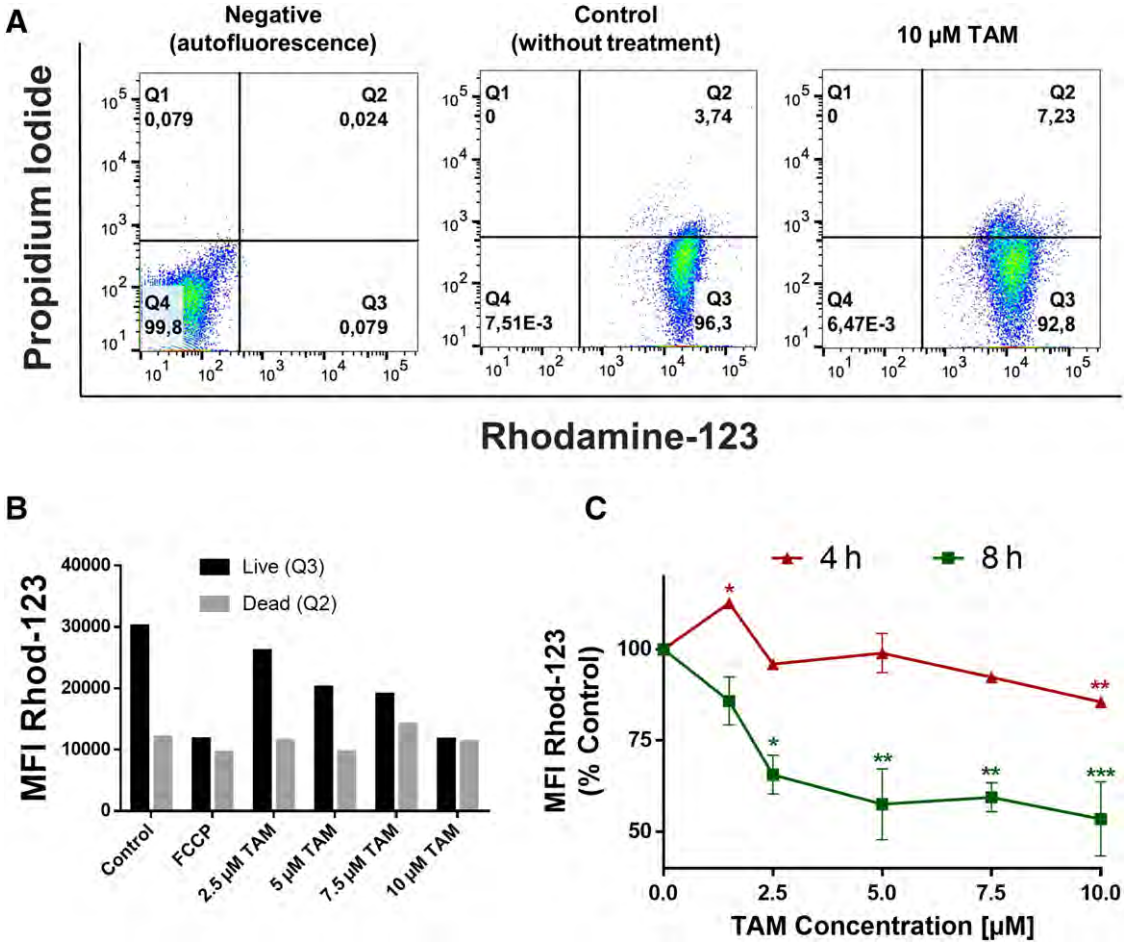

FIGURE 4 **Jurkat cells lost mitochondrial membrane potential after treatment with TAM.** (**A**) Representative dot plots obtained by flow cytometry analysis of Jurkat cells treated with TAM (48 h) and costained with Rhod-123 and PI. (**B**) For each treatment, MFI of Rhod-123 was graphed separately for live PI-negative population (Q3, black bars) and dead PI-positive population (Q2, in gray bars). Data of representative experiment corresponding to 48 h of incubation are present. (**C**) Only populations of PI-negative live cells (Q3) were analyzed: MFI of Rhod-123 was normalized to control (without treatment) and graphed as function of TAM concentration at 4 and 8 h of treatment. Statistical significance is expressed with respect to control. Data are mean ± SEM; $N \geq 3$. For each time, comparison between control and treated samples was made by one-way ANOVA with Dunnett post hoc testing

populations (Fig. 4B). A potent mitochondrial oxidative phosphorylation uncoupler FCCP (20 μM) was used as positive control. It was demonstrated that $\Delta\Psi$m was gradually decreased in live TAM-treated cells (Fig. 4C), indicating that TAM cytotoxicity in leukemic Jurkat cells is linked to mitochondrial damage.

Intrinsic apoptosis pathway is well known to be tightly related to mitochondrial damage.[41] Damaged mitochondria are subjected to degradation by mitophagic/autophagic process as an evolutionally designed mechanism to control mitochondrial number and health.[42] Therefore we decided to monitor apoptosis and autophagy in TAM-treated Jurkat cells.

3.5 | High TAM concentrations induced apoptotic cell death in Jurkat cells

Taking into the account that in our experiments, TAM compromised mitochondria and that mitochondria is an important regulator of the intrinsic apoptotic pathway, apoptotic and necrotic cell death caused by TAM (2.5–15 μM) were monitored at 8, 24, 48 h by confocal microscopy and flow cytometry (Fig. 5). Only high TAM concentrations caused apoptosis evaluated by externalization of phosphatidylserine, in a small part of the cell population. In relation to this result, it should be mentioned here that, in addition to the intrinsic apoptotic pathway, there are some other types of programmed cell death, related to mitochondria. In particular, mitochondrial permeability transition-driven cell death may be initiated by some perturbation of intracellular microenvironment such as oxidative stress and cytosolic Ca^{2+} overload, resulting in rapid $\Delta\Psi$m dissipation. The mechanism of this form of cell death is under intense research and debates.[41] In this regard, TAM was demonstrated to interact directly with mitochondrial membrane proteins,[40] as well as with nonclassical TAM targets including PKC, mTOR, cannabinoid receptors, and multidrug resistance proteins.[18,19] One can suggest also that the same drug may produce multitarget effects, with a complex cross-talk between underlying mechanisms.

3.6 | TAM treatment-induced autophagy in Jurkat cells

Autophagy is a catabolic cellular process highly conserved in evolution and characterized by lysosomal self-digestion of cytoplasmic

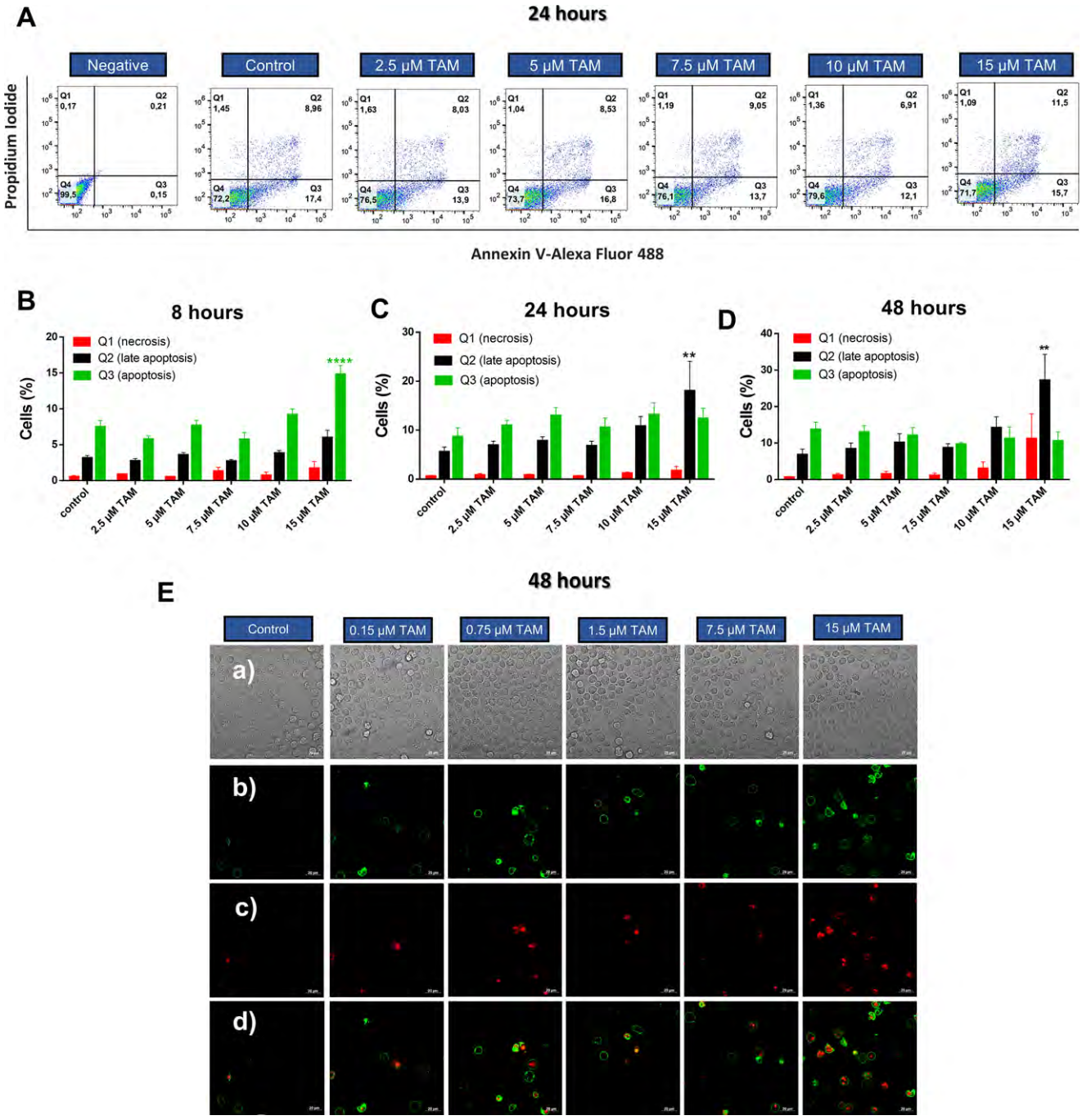

FIGURE 5 **High TAM concentrations produced apoptosis.** (**A**) Representative dot plots obtained by flow cytometry analysis of Jurkat cells treated with different TAM concentrations during 24 h. Q1: necrotic PI-positive population; Q2: late apoptosis/necrosis (double positive) population; Q3: apoptotic Annexin V/AlexaFluor488-positive population; Q4: viable double negative cells. (**B–D**) Bar charts show percentage of viable, necrotic, and apoptotic cells after treatment with TAM for 8 h (**B**); 24 h (**C**) and 48 h (**D**). Data are mean ± SEM; $N \geq 4$; $^{**}P < 0.01$, $^{****}P < 0.0001$. For each time and for each population (Q1–Q4), comparison between control (without treatment) and different TAM concentrations was made by two-way ANOVA with Dunnett post hoc testing. (**E**) Microscopic visualization of apoptosis and necrosis caused by TAM, after 48 h of incubation with indicated TAM concentrations: a) bright field, b) Annexin V-Alexa Fluor 488 (phosphatidylserine externalization), c) PI (plasma membrane integrity), and d) merge Alexa Fluor 488 and PI. Confocal microscopy (×40). Scale bar: 20 μm

material. This process has a multifunctional role in cell physiology. Basal autophagy is responsible for normal turnover of macromolecules and organelles, and during nutrient starvation cells resort to autophagy as a survival strategy. Autophagy is also in charge of removing damaged organelles and unfolded proteins from the cell. In cancer, autophagy has been shown to be involved in the chemoresistance of some types of tumors.[43–48] On the other hand, it has also been suggested that an excessive activation of this self-degradation process may also lead to nonapoptotic autophagic programmed cell death.[41,49] So, some studies suggest that the autophagic process could be a potential chemotherapeutic target for apoptosis-resistant malignancies.[50] In particular, many compounds have been proposed to

induce autophagic cell death instead of cell survival in hematologic malignancies.[51] So, understanding of the precise role of autophagy and its contribution either to cell survival or cell death will facilitate the future design of optimized protocols for treatments for T-ALL and other types of cancers.

TAM is known as a potent inducer of autophagy in different cell types, with different outcomes. In breast cancer, autophagy induced by TAM was considered as cause of chemoresistance, although the underlying mechanisms have not been completely clarified yet.[52,53] In contrast, TAM was shown to induce cytotoxic autophagy in glioblastoma.[54] Remarkably, cell death induced by DEX in B-ALL was shown to be mediated through induction of autophagy upstream of apoptosis.[31] Thus, we tested whether TAM is able to induce autophagy in the GC-resistant T-ALL cell line Jurkat.

In our initial experiments, we used the fluorescent acidophilic compound MDC to evaluate if TAM is able to cause formation and accumulation of autophagolysosomes in Jurkat cells.[55] Confocal microscopy and flow cytometry revealed accumulation of autophagolysosomes as the TAM concentration increased, after 48 h of treatment (Fig. 6A and B). An increased number of autophagolysosomes could result either from an enhanced formation of autophagosomes (increased autophagic flux) or, in contrast, a decreased degradation of autophagolysosomes (decreased autophagic flux). To address this issue, in the next experiments, we used more specific LC3-I-based strategies.

Cytosolic microtubule-associated protein LC3-I translocates to the autophagosomes after conjugation with phosphatidylethanolamine (LC3-II formation) during autophagy. It is known that LC3-II is essential for phagophore elongation and autophagosomes formation. This two forms can be easily distinguished in an SDS-PAGE due to the fact that LC3-II migrates faster than LC3-I. However, LC3-II itself is known to be degraded by autophagy after autophagosome–lysosome fusion, and therefore it is recommended to evaluate LC3-II levels both in the presence and in the absence of lysosomal protease inhibitors.[56] In our experiments, CQ was used to avoid LC3-II degradation. Western blot analysis of LC3 demonstrated that 5 μM TAM-induced autophagic flux in Jurkat cells since LC3II levels were higher in 5 μM TAM + 20 μM CQ when compared to either 20 μM CQ or 5 μM TAM treatment alone (Fig. 6C and D). We also used a more precise method to measure autophagic flux induction by the use of tandem mCherry-GFP-LC3 expressing Jurkat cells.[57] GFP is known to be sensitive to an acidic pH like the one found in the autophagolysosomes (structures produced by autophagosome fusion with the lysosomes). On the other hand, mCherry is stable in this acidic environment. Then, colocalization of GFP and mCherry indicates LC3 positive nonacidic compartments (autophagosomes), whereas mCherry+GFP- puncta correspond to autophagosomes which have fused with acidic endosomes or lysosomes (amphisomes or autophagolysosomes). Figure 6E shows a representative experiment in which Jurkat GFP-mCherry-LC3 cells were incubated with different TAM concentrations. Yellow puncta (GFP+mCherry+) correspond to autophagosomes, while red spots (GFP-mCherry+) correspond to autophagolysosomes, mCherry/GFP ratio was used as a measurement of autophagic flux (autophagosome degradation/formation) and was calculated at 24 and 48 h of treatment (Fig. 6F). High mCherry/GFP ratio effectively blocked by 10 and 20 μM CQ was observed at 5 μM TAM indicating effective TAM concentration to induce autophagy.

Finally, we tested whether TAM-induced autophagy functioned as a cell survival or a cell death mechanism in leukemic cells and if its blocking would produce a change in cell viability. For this purpose, cells were incubated 24 and 48 h with TAM alone, or in combination with CQ. Cell death was evaluated by staining with Annexin V-Alexa Fluor 488 and PI (Fig. 6G–H), where a decrease in cell viability was observed with the combined treatment with CQ.

3.7 | The specific GPER receptor antagonist G-36 efficiently prevented TAM-induced autophagy but not cytotoxicity

Several reports argued that membrane ER GPR30/GPER are able to mediate some estrogenic nongenomic actions.[58–60] Since Jurkat cells express GPER receptors (Fig. 1), we decided to examine whether the observed TAM-induced effects were triggered through GPER activation. G-36 was reported as a highly selective antagonist of GPER.[61] In our experiments, a 30 min pre-incubation of Jurkat cells with G-36 almost completely prevented TAM-induced autophagy (Fig. 7A).

To test if TAM-induced cytotoxicity is also related to GPER, concentration–response curves for different conditions were constructed, namely for TAM alone and TAM after a pre-incubation with different nontoxic doses of G-36 (Fig. 7B and C). If cytotoxicity is associated with GPER, under conditions of pre-incubation with the GPER antagonist, the curve would be expected to shift to the right, which was not actually observed. Instead, G-36 potentiated the cytotoxic effect of TAM, because cell viability in samples pre-treated with G-36 decreased, in a manner dependent on the G-36 concentration. It would be interesting to understand the mechanism of this phenomenon, but this task was beyond the scope of the present study. Of note, TAM is a highly lipophilic small molecule, which is able to modulate structure and mechanical properties of the cell membrane.[62] One may speculate that TAM cytotoxicity in Jurkat cells is related to "off-target" mechanisms, including PKC inhibition or direct effects on mitochondria, as it was demonstrated for some types of cells.[18,19] Our present findings also pinpointed the mitochondria as an important TAM target (Section 3.4). A synergistic effect of G-36 may be related to its capacity to prevent autophagy, which will to be addressed in future studies.

3.8 | Gene expression profiling revealed up-regulation of autophagy- and apoptosis-related genes in Jurkat cells treated with TAM

Next, we were interested in knowing if TAM induces any change in gene expression, in particular in those genes related to cell survival, before the mechanism of cell death was triggered. First, RNA microarray analysis was performed using RNA isolated from Jurkat cells treated with 7.5 μM TAM during 24 h. Several genes of interest related to autophagy and apoptosis were selected based on microarray analysis results, and relative level of their expression was confirmed by RT-qPCR (Fig. 8).

It was revealed, that the autophagy-related *ATG5* gene which is an indispensable component involved in the control of autophagic vesicle

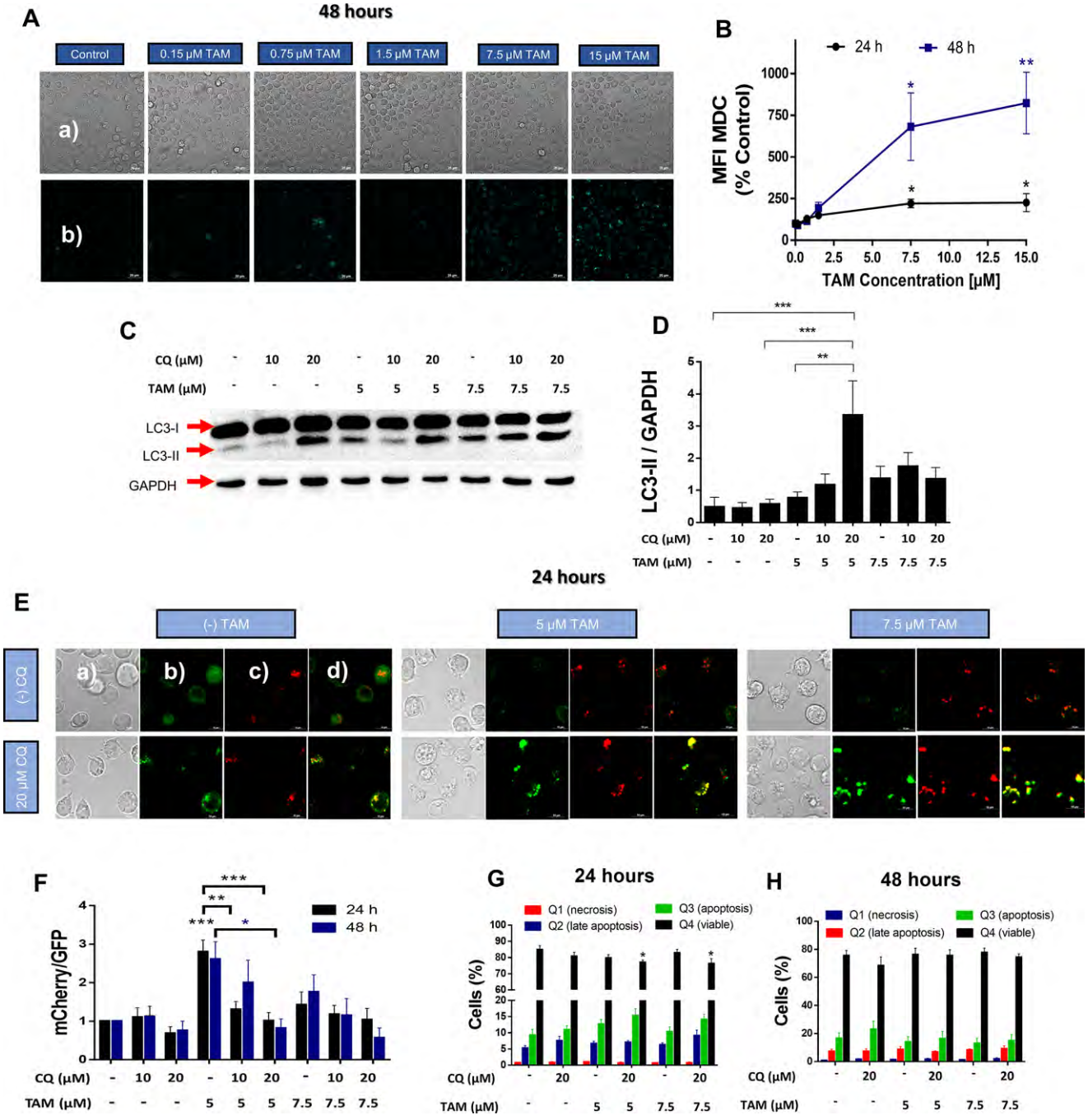

FIGURE 6 **Autophagy is induced by TAM in Jurkat cells.** (**A**) Autophagolysosomas accumulation caused by TAM, after 48 h of incubation revealed by MDC using confocal microscopy (×40). a) Bright field, b) MDC (autophagic lysosomes). Scale bar: 20 μm. (**B**) MFI of MDC measured by flow cytometry in Jurkat cells after treatment with TAM at indicated times. Data are mean ± SEM; $N = 3$; $^{*}P < 0.05$, $^{**}P < 0.01$. For each time point, comparison between control and treated samples was made by one-way ANOVA with Dunnett's multiple comparisons test. (**C**) Representative Western blot of LC3-I/II protein expression after treatment with TAM and/or CQ. (**D**) LC3-II/GAPDH-related density, mean ± SEM; $N \geq 5$; $^{**}P < 0.01$, $^{***}P < 0.001$, compared control (without treatment) with other treatment combinations (TAM+CQ) with one-way ANOVA with Tukey's multiple comparisons test. (**E**) Representative images of TAM-treated mCherry-GFP Jurkat cells obtained with confocal microscopy: a) bright field, b) GFP excitation, c) mCherry excitation, d) merge GFP-mCherry. (**F**) mCherry/GFP ratio was calculated individually in at least in three visual fields for each sample. Data are mean ± SEM; $N \geq 3$; $^{*}P < 0.05$, $^{**}P < 0.01$, $^{***}P < 0.001$. Comparison to control (without treatment) of each treatment combination (TAM+CQ) was made by one-way ANOVA with Tukey's multiple comparisons test. (**G and H**) Bar charts showing percentage of viable, necrotic and apoptotic cells after treatment with TAM and/or CQ for 24 h (**G**) and 48 h (**H**). Data are mean ± SEM; $N \geq 5$; $^{*}P < 0.05$. For each time and for each population (Q1–Q4), comparison between control (without treatment) and other treatment combinations (TAM+CQ) was made by two-way ANOVA with Tukey post hoc testing

INFORME DE LABORES 2019

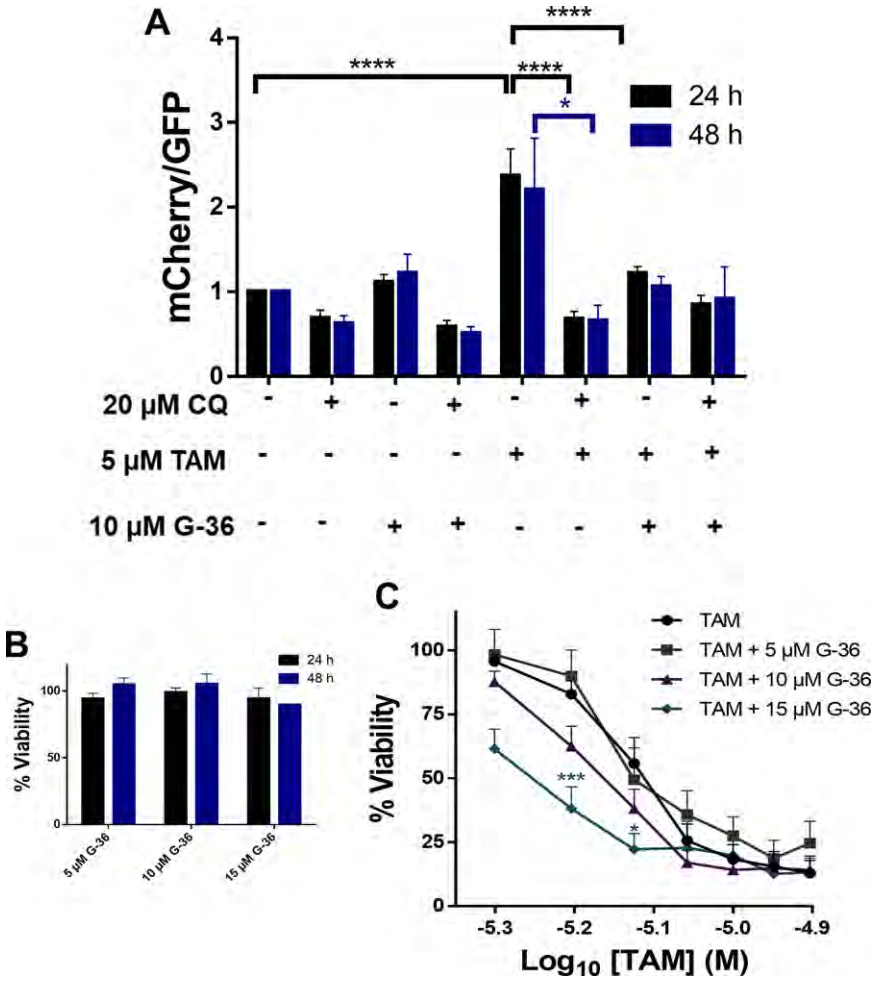

FIGURE 7 G-36 efficiently prevented TAM-induced autophagy but not cytotoxicity. (**A**) mCherry/GFP ratio was calculated individually in at least in three visual fields for each sample. Data are mean ± SEM; $N \geq 3$; $^{*}P < 0.05$, $^{**}P < 0.01$, $^{***}P < 0.001$. Comparison to control (without treatment) of each treatment combination (TAM+CQ+G-36) was made by one-way ANOVA with Tukey's multiple comparisons test. (**B**) Effect of G-36 on cell viability, evaluation was made by metabolic assay. (**C**) Concentration–response curves obtained after 24 h of treatment with TAM alone or with pre-treatment with different concentrations of selective GPER antagonist G-36. Evaluation was realized by resazurin-based metabolic assay, in absence of FBS. Statistical significance is expressed with respect to TAM group (black line). Data are mean ± SEM; $N \geq 4$; $^{*}P < 0.05$, $^{***}P < 0.001$. Comparison between TAM alone and TAM+G-36 was made by two-way ANOVA with Dunnett post hoc testing

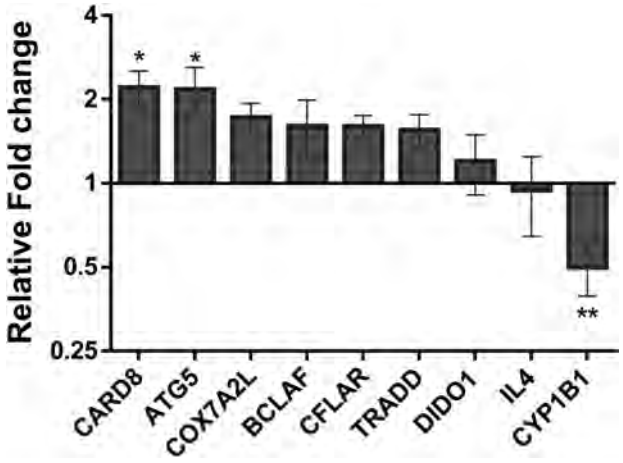

FIGURE 8 TAM-induced differential gene expression. RT-qPCR validation of a subset of genes selected after RNA microarray analysis. RNA was isolated after 24 h of cultivation of Jurkat cells treated with 7.5 μM TAM. Data were graphed (log-scale) as $2^{\wedge(-\Delta\Delta Ct)}$; *GAPDH* was used as an internal control to normalize the target RNA. Data are mean ± SEM; $N \geq 6$; $^{*}P < 0.05$, $^{**}P < 0.01$; unpaired *t*-test was used for comparison with mRNA of Jurkat cells treated with vehicle

formation and expansion in mammals is up-regulated. Remarkably, *Atg5* and LC3 conjugation are required for the canonical autophagy pathway.[63] Also, several apoptosis-related genes, involved in the extrinsic apoptotic pathway, including *CFLAR*, *CARD8*, and *TRADD* genes, were also overexpressed. Although the mechanisms linking autophagy and apoptosis are not fully defined yet, there are some evidences of their interactions. In particular, TAM in the range of 1–5 μM was demonstrated to stimulate Fas/CD95-dependent apoptosis in vitro in human cholangiocarcinoma cells,[64] and caspase-10 was shown to control autophagic cell death in multiple myeloma.[65]

Bcl-2 associated factor 1 (*BCLAF1*) was also up-regulated. *BCLAF1* has been shown to be related to thymocyte development and essential for T cell homeostasis. *BCLAF1* is able to interact with Bcl-2 family members. Although its overexpression was suggested to contribute to apoptosis, this hypothesis still remains a topic of debate.[66] On the other hand, *BCLAF1* has been associated with autophagic cell death in myeloma cells.[65] In addition, we observed a slight increase in *COX7AR*, a stress-inducible COX subunit.[67] On the other hand, we found down-regulation in *CYP1B1* gene, which is related to estrogenic metabolism.[68] Importantly, CYP1B1 protein is found to be overexpressed in various cancer tissues; it has been suggested as a tumor biomarker and a target for anticancer therapy.[68]

3.9 | TAM sensitized GC-resistant cells Jurkat to DEX treatment

GCs play central role in all protocols for ALL treatment representing the most effective agents.[69,70] These hormones are able to induce apoptosis in lymphoid cells acting through GC receptor (GR), a member

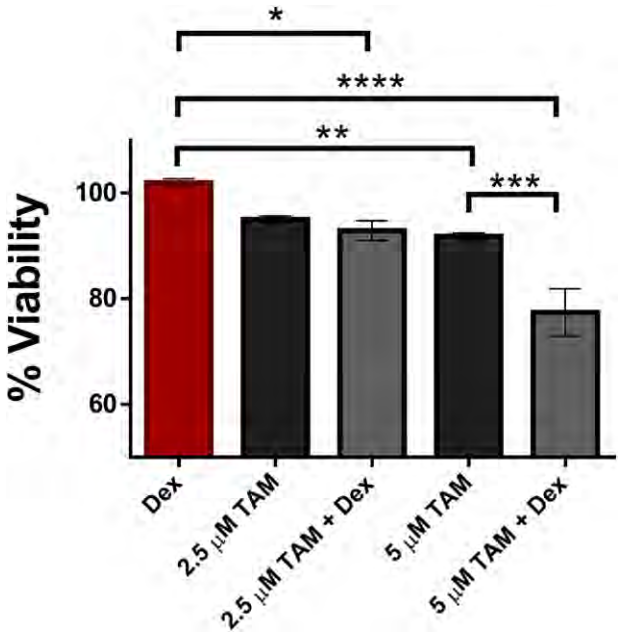

FIGURE 9 **TAM sensitized Jurkat cells to dexamethasone.** Evaluation was realized by resazurin-based metabolic assay. Data are mean ± SEM; $N \geq 3$; $^{*}P < 0.05$, $^{**}P < 0.01$, $^{***}P < 0.001$, $^{****}P < 0.0001$. Data were normalized to control (without treatment, considered as 100% viability). Comparison between DEX (0.021 μM) with other treatment combinations (TAM alone or TAM+DEX) was made by one-way ANOVA with Tukey post hoc testing

of the nuclear receptor family.[70] Although a significant number of LLA patients respond well to GC treatment during the initial phases, some patients show primary resistance; prolonged treatment sometimes leads to secondary resistance as well.[71] Generally, patient response to GC treatment has been proven to be a reliable prognostic indicator.[72] Although the underlying mechanism has not been completely understood yet, it was proposed that the resistance was due to alterations in GR expression. On the other hand, it was recently demonstrated, that in specimens derived directly from leukemia patients, GR alterations are rarely found.[73] Jurkat cell line used in the present study is GC-resistant, but expresses GR.[74] Taking into account the published data that GC-triggered cell death is related to autophagy process in early phases,[31] we decided to perform the experiments combining effective autophagy trigger TAM with GC DEX to treat GC-resistant Jurkat cell line. The results of these experiments are shown in the Fig. 9. Jurkat cells were exposed to a DEX concentration that corresponds to those reached in human plasma during chemotherapeutic treatment (0.021 μM). Since Jurkat is a GC-resistant cell line, no effect in cell viability was observed at this concentration. The viability of leukemic cells treated with DEX combined with 2.5 μM TAM, was slightly decreased. In contrast, when DEX was applied together with a TAM concentration effective in autophagy induction (5 μM), this combination caused a significant reduction of cellular vitality, when compared with DEX or TAM treatment alone ($P < 0.001$). Together with studies reported by Laane and collegues,[31] our data provide evidence about a possible relation between GC resistance and the autophagic pathway. We hope that our findings prompt further studies aimed at a better understanding of the mechanisms connecting autophagy and GC resistance of ALL.

4 | CONCLUDING REMARKS

Altogether, we have provided here the first evidence that: (1) lymphoblastic cell lines Jurkat, MOLT3, and CEM, derived from clinical T-ALL samples in relapse expressed high levels of GPER/GPR30 both at mRNA and protein level; (2) in contrast, studied cell lines derived from T-ALL samples did not express neither *ESR1* (ERα) nor *ESR2* (ERβ); (3) we were able to demonstrate dramatic differences in the expression pattern of ER and GPER between healthy activated T CD4^{+} cells and leukemic cells: activated T cells did express *ESR1* (ERα), *ESR2* (ERβ), and *GPER1*(GPER/GPR30); (4) TAM-reduced viability and proliferation of Jurkat cells in GPER-independent manner and induced cell cycle arrest in G1 phase; (5) TAM caused mitochondrial dysfunction in T-ALL Jurkat cell lines; (6) TAM treatment up-regulated autophagy-related gene *ATG5* and down-regulated cancer biomarker *CYP1B1* in Jurkat cells; (7) TAM treatment-induced autophagy in Jurkat cells in a GPER-dependent manner, which may partially sensitize these GC-resistant cells to DEX treatment.

Our findings are in agreement with recently published reports regarding antileukemic properties of TAM in myeloproliferative neoplasms, carried out using murine models.[75,76] Namely, it was shown that TAM, through apoptotic effects on malignant progenitors, inhibited the growth of JAK2^{V617F}-induced myeloproliferative neoplasms and sensitized MLL-AF9-induced myeloid leukemias to chemotherapy. Importantly, the effect of TAM in normal hematopoiesis was also studied. A potential effect of TAM on hematopoietic stem cells (HSC) and normal hematopoiesis is certainly an important issue, because a negative regulation of lymphopoiesis by estrogens is well known.[77] Numerous studies carried out on rodent and human models demonstrated that estrogen is involved in the regulation of proliferation and lineage commitment of pluripotent stem cells, and also in the modulation of the HSC niche in the bone marrow.[78] Adult bone marrow CD34^{+} cells were shown to express both ERα and ERβ,[79] though data regarding GPER expression is not available yet. As for specific TAM properties, it exerted antiestrogenic effects on breast cancer cells, but acted as an ERα agonist in the HSC. Remarkably, TAM treatment-induced contrasting effects in different types of HSC: it caused apoptosis in short-term HSC and multipotent progenitors, and simultaneously activated proliferation in quiescent long-term HSC.[75] As a result, although rapid reduction of bone marrow cellularity after TAM treatment was observed, long-term hematological parameters were almost unchanged, and TAM was considered to have a minor impact on a steady-state normal hematopoiesis.[75] Accordingly, antileukemic properties against myeloid leukemias[75] and T-ALL (this work), without negative effect on normal hematopoiesis,[75] and a long history of its clinical use, makes TAM a good candidate for future clinical trials with leukemic patients. Among the relevant issues for the immediate future research are: a) profiling of GPER expression and GPER-related effects in human HSC, hematopoietic precursors and mature leukocytes; and b) identification of the precise mechanisms of TAM-induced effects in leukemic cells, with a special focus on the link between autophagy and GC resistance in ALL.

We hope that further studies will reveal the underlying mechanisms of biologic effects of TAM in T-ALL, resulting in potential use of novel

TAM-based adjuvant therapy for this kind of disorders and representing a big challenge in patients' handling.

AUTHORSHIP

O.D. conceived and designed the study. L.T-L. conceived, designed, and performed most of experiments, analyzed the data, prepared the figures. P.M. conceived and designed autophagy experiments. A.L-R. contributed in primers' design and PCR data analysis. L.L-R. participated in acquisition and analysis of flow cytometry data. L.D-M. participated in experiments on mitochondria and cell proliferation analysis. C.M-R. performed the experiments on synergetic effect of DEX and TAM. I.D-E. contributed to the microarray and molecular biology data analysis, and designed the experiments on synergetic effect of DEX and TAM. O.D. and L.T-L. wrote the manuscript. O.D. and A.H-C. contributed to the experiments and received grants. L.T-L., P.M., A.L-R., L.L-R., L.D-M., I.D-I., C.M-R., C.V-J., A.H-C., and O.D. contributed to data analysis and result discussion, and reviewed the final draft of the manuscript.

ACKNOWLEDGMENTS

We thank Dr. Georgina Valencia-Cruz for expert technical assistance, MC Juan Salvador Valle-Reyes for purification and activation of $CD4^+$ lymphocytes, and for his contribution into statistical analysis, and Mr. Scott Hayes for his assistance in editing this manuscript. This study was funded by CONACyT: grant FC 2015-1/114 to OD, and Laboratorio Nacional de Canalopatías 279820 and (DGAPA-UNAM) PAPIIT-IN211616, IG200119 to AH-C. Doctoral fellowship and short academic stay fellowship to LTL.

DISCLOSURES

The authors declare no conflict of interest.

ORCID

Oxana Dobrovinskaya https://orcid.org/0000-0003-1526-6517

REFERENCES

1. Gustafsson JA. What pharmacologists can learn from recent advances in estrogen signaling. *Trends Pharmacol Sci*. 2003;24:479–485.
2. Ahmed SA, Karpuzoglu E, Khan D. Effect of sex steroids on innate and adaptive immunity. In: Klein SL, Roberts CW, eds. *Sex Hormones and Immunity to Infection*. Berlin, Heidelberg: Springer; 2010:19–51.
3. Khan D, Cowan C, Ahmed SA. Estrogen and signaling in the cells of immune system. *Adv Neuroimm Biol*. 2012;3:73–93.
4. Heldring N, Pike A, Andersson S, et al. Estrogen receptors: how do they signal and what are their targets. *Physiol Rev*. 2007;87:905–931.
5. Filardo EJ, Quinn JA, Bland KI, Frackelton Jr AR. Estrogen-induced activation of Erk-1 and Erk-2 requires the G protein-coupled receptor homolog, GPR30, and occurs via trans-activation of the epidermal growth factor receptor through release of HB-EGF. *Mol Endocrinol*. 2000;14:1649–1660.
6. Yakimchuk K, Jondal M, Okret S. Estrogen receptor α and β in the normal immune system and in lymphoid malignancies. *Mol Cell Endocrinol*. 2013;375:121–129.
7. Rudelius M, Rauert-Wunderlich H, Hartmann E, et al. The G protein-coupled estrogen receptor 1 (GPER-1) contributes to the proliferation and survival of mantle cell lymphoma cells. *Haematologica*. 2015;100:e458–e461.
8. Catusse J, Wollner S, Leick M, Schröttner P, Schraufstätter I, Burger M. Attenuation of CXCR4 responses by CCL18 in acute lymphocytic leukemia B cells. *J Cell Physiol*. 2010;225:792–800.
9. Albanito L, Madeo A, Lappano R, et al. G protein-coupled receptor 30 (GPR30) mediates gene expression changes and growth response to 17beta-estradiol and selective GPR30 ligand G-1 in ovarian cancer cells. *Cancer Res*. 2007;67:1859–1866.
10. Vivacqua A, Bonofiglio D, Recchia AG, et al. The G protein-coupled receptor GPR30 mediates the proliferative effects induced by 17β-estradiol and hydroxytamoxifen in endometrial cancer cells. *Mol Endocrinol*. 2006;20:631–646.
11. Weißenborn C, Ignatov T, Ochel H-J, et al. GPER functions as a tumor suppressor in triple-negative breast cancer cells. *J Cancer Res Clin Oncol*. 2014;140:713–723.
12. Chimento A, Sirianni R, Casaburi I, et al. GPER agonist G-1 decreases adrenocortical carcinoma (ACC) cell growth in vitro and in vivo. *Oncotarget*. 2015;6:19190–19203.
13. Kurt AH, Çelik A, Kelleci BM. Oxidative/antioxidative enzyme-mediated antiproliferative and proapoptotic effects of the GPER1 agonist G-1 on lung cancer cells. *Oncol Lett*. 2015;10:3177–3182.
14. Lv X, Wang C. G-1: new potential therapeutic option for ovarian cancer. *Cancer Cell Microenviron*. 2014;1:e27-1–e27-3.
15. Jordan VC. Tamoxifen: catalyst for the change to targeted therapy. *Eur J Cancer*. 2008;44:30–38.
16. Filardo EJ, Quinn JA, Frackelton Jr AR, Bland KI. Estrogen action via the G protein-coupled receptor, GPR30: stimulation of adenylyl cyclase and cAMP-mediated attenuation of the epidermal growth factor receptor-to-MAPK signaling axis. *Mol Endocrinol*. 2002;16:70–84.
17. Obiorah I, Jordan VC. Progress in endocrine approaches to the treatment and prevention of breast cancer. *Maturitas*. 2011;70:315–321.
18. Bogush T, Dudko E, Bogush E, Polotsky B, Tjulandin S, Davydov M. Tamoxifen non-estrogen receptor mediated molecular targets. *Oncol Rev*. 2012;6:e15-122–e15-129.
19. Bogush TA, Polezhaev BB, Mamichev IA, et al. Tamoxifen never ceases to amaze: new findings on non-estrogen receptor molecular targets and mediated effects. *Cancer Invest*. 2018;36:211–220.
20. Rouhimoghadam M, Safarian S, Carroll JS, Sheibani N, Bidkhori G. Tamoxifen-induced apoptosis of MCF-7 cells via GPR30/PI3K/MAPKs interactions: verification by ODE modeling and RNA sequencing. *Front Physiol*. 2018;9:907-1–907-14.
21. Couldwell WT, Hinton DR, Surnock AA, et al. Treatment of recurrent malignant gliomas with chronic oral high-dose tamoxifen. *Clin Cancer Res*. 1996;2:619–622.
22. Chamberlain MC, Kormanik PA. Salvage chemotherapy with tamoxifen for recurrent anaplastic astrocytomas. *Arch Neurol*. 1999;56:703–708.
23. Tang P, Roldan G, Brasher PM, et al. A phase II study of carboplatin and chronic high-dose tamoxifen in patients with recurrent malignant glioma. *J Neurooncol*. 2006;78:311–316.
24. Di Cristofori A, Carrabba G, Lanfranchi G, Menghetti C, Rampini P, Caroli M. Continuous tamoxifen and dose-dense temozolomide in recurrent glioblastoma. *Anticancer Res*. 2013;33:3383–3390.
25. Odia Y, Kreisl TN, Aregawi D, Innis EK, Fine HA. A phase II trial of tamoxifen and bortezomib in patients with recurrent malignant gliomas. *J Neurooncol*. 2015;125:191–195.

26. Xie X, Wu M-Y, Shou L-M, et al. Tamoxifen enhances the anticancer effect of cantharidin and norcantharidin in pancreatic cancer cell lines through inhibition of the protein kinase C signaling pathway. *Oncol Lett*. 2015;9:837–844.
27. Keating J, Johnson P, Cochrane A, et al. A prospective randomised controlled trial of tamoxifen and cyproterone acetate in pancreatic carcinoma. *Br J Cancer*. 1989;60:789–792.
28. Theve NO, Pousette A, Carlström K. Adenocarcinoma of the pancreas – a hormone sensitive tumor? A preliminary report on Nolvadex treatment. *Clin Oncol*. 1983;9:193–197.
29. Kohli L, Kaza N, Coric T, Byer SJ, et al. 4-Hydroxytamoxifen induces autophagic death through K-ras degradation. *Cancer Res*. 2013;73: 4395–4405.
30. Maycotte P, Thorburn A. Autophagy and cancer therapy. *Cancer Biol Ther*. 2011;11:127–137.
31. Laane E, Tamm KP, Buentke E, et al. Cell death induced by dexamethasone in lymphoid leukemia is mediated through initiation of autophagy. *Cell Death Differ*. 2009;16:1018–1029.
32. Serafin V, Capuzzo G, Milani G, et al. Glucocorticoid resistance is reverted by LCK inhibition in pediatric T-cell acute lymphoblastic leukemia. *Blood*. 2017;130:2750–2761.
33. Quah BJC, Warren HS, Parish CR. Monitoring lymphocyte proliferation in vitro and in vivo with the intracellular fluorescent dye carboxyfluorescein diacetate succinimidyl ester. *Nat Protoc*. 2007;2: 2049–2056.
34. Gump JM, Thorburn A. Sorting cells for basal and induced autophagic flux by quantitative ratiometric flow cytometry. *Autophagy*. 2014;10: 1327–1334.
35. Mizushima N, Yoshimori T, Levine B. Methods in mammalian autophagy research. *Cell*. 2010;140:313–326.
36. Nagahara Y, Shiina I, Nakata K, Sasaki A, Miyamoto T, Ikekita M. Induction of mitochondria-involved apoptosis in estrogen receptor-negative cells by a novel tamoxifen derivative, ridaifen-B. *Cancer Sci*. 2008;99:608–614.
37. Vyas S, Zaganjor E, Haigis MC. Mitochondria and cancer. *Cell*. 2016; 166:555–566.
38. Kishton RJ, Barnes CE, Nichols AG, et al. AMPK is essential to balance glycolysis and mitochondrial metabolism to control T-ALL cell stress and survival. *Cell Metab*. 2016;23:649–662.
39. Maximchik PV, Kulikov AV, Zhivotovsky BD, Gogvadze VG. Cellular energetics as a target for tumor cell elimination. *Biochemistry (Mosc)*. 2016;81:65–79.
40. Ribeiro MP, Santos AE, Custódio JBA. Mitochondria: the gateway for tamoxifen-induced liver injury. *Toxicology*. 2014;323:10–18.
41. Galluzzi L, Vitale I, Aaronson SA, et al. Molecular mechanisms of cell death: recommendations of the Nomenclature Committee on Cell Death 2018. *Cell Death Differ*. 2018;25:486–541.
42. Rambold AS, Lippincott-Schwartz J. Mechanisms of mitochondria and autophagy crosstalk. *Cell Cycle*. 2011;10:4032–4038.
43. Barnard RA, Wittenburg LA, Amaravadi RK, Gustafson DL, Thorburn A, Thamm DH. Phase I clinical trial and pharmacodynamic evaluation of combination hydroxychloroquine and doxorubicin treatment in pet dogs treated for spontaneously occurring lymphoma. *Autophagy*. 2014;10:1415–1425.
44. Mahalingam D, Mita M, Sarantopoulos J, et al. Combined autophagy and HDAC inhibition. *Autophagy*. 2014;10:1403–1414.
45. Rangwala R, Chang YC, Hu J, et al. Combined MTOR and autophagy inhibition. Phase I trial of hydroxychloroquine and temsirolimus in patients with advanced solid tumors and melanoma. *Autophagy*. 2014; 10:1391–1402.
46. Rangwala R, Leone R, Chang YC, et al. Phase I trial of hydroxychloroquine with dose-intense temozolomide in patients with advanced solid tumors and melanoma. *Autophagy*. 2014;10:1369–1379.
47. Rosenfeld MR, Ye X, Supko JG, et al. A phase I/II trial of hydroxychloroquine in conjunction with radiation therapy and concurrent and adjuvant temozolomide in patients with newly diagnosed glioblastoma multiforme. *Autophagy*. 2014;10:1359–1368.
48. Vogl DT, Stadtmauer EA, Tan KS, et al. Combined autophagy and proteasome inhibition: a phase 1 trial of hydroxychloroquine and bortezomib in patients with relapsed/refractory myeloma. *Autophagy*. 2014;10:1380–1390.
49. Galluzzi L, Vitale I, Abrams JM, et al. Molecular definitions of cell death subroutines: recommendations of the Nomenclature Committee on Cell Death 2012. *Cell Death Differ*. 2012;19:107–120.
50. Shimizu S, Konishi A, Nishida Y, et al. Involvement of JNK in the regulation of autophagic cell death. *Oncogene*. 2010;29:2070–2082
51. Banerji V, Gibs BS. Targeting metabolism and autophagy in the context of haematologic malignancies. *Int J Cell Biol*. 2012;2012:1–9.
52. Thomas S, Thurn KT, Biçaku E, Marchion DC, Münster PN. Addition of a histone deacetylase inhibitor redirects tamoxifen-treated breast cancer cells into apoptosis, which is opposed by the induction of autophagy. *Breast Cancer Res Treat*. 2011;130:437–447.
53. Cook KL, Wärri A, Soto-Pantoja DR, et al. Hydroxychloroquine inhibits autophagy to potentiate antiestrogen responsiveness in ER+ breast cancer. *Clin Cancer Res*. 2014;20:3222–3232.
54. Graham CD, Kaza N, Klocke BJ, et al. Tamoxifen induces cytotoxic autophagy in glioblastoma. *J Neuropathol Exp Neurol*. 2016;75: 946–954.
55. Biederbick A, Kern HF, Elsässer HP. Monodansylcadaverine (MDC) is a specific in vivo marker for autophagic vacuoles. *Eur J Cell Biol*. 1995;66:3–14.
56. Mizushima N, Yoshimori T. How to interpret LC3 immunoblotting. *Autophagy*. 2007;3:542–545.
57. Pankiv S, Clausen TH, Lamark T, et al. p62/SQSTM1 binds directly to Atg8/LC3 to facilitate degradation of ubiquitinated protein aggregates by autophagy. *J Biol Chem*. 2007;282:24131–24145.
58. Ariazi EA, Brailoiu E, Yerrum S, et al. The G protein-coupled receptor GPR30 inhibits proliferation of estrogen receptor-positive breast cancer cells. *Cancer Res*. 2010;70:1184–1194.
59. Meyer MR, Field AS, Kanagy NL, Barton M, Prossnitz ER. GPER regulates endothelin-dependent vascular tone and intracellular calcium. *Life Sci*. 2012;91:623–627.
60. Luo H, Yang G, Yu T, et al. GPER-mediated proliferation and estradiol production in breast cancer-associated fibroblasts. *Endocr Relat Cancer*. 2014;21:355–369.
61. Dennis MK, Field AS, Burai R, et al. Identification of a GPER/GPR30 antagonist with improved estrogen receptor counterselectivity. *J Steroid Biochem Mol Biol*. 2011;127:358–366.
62. Khadka NK, Cheng X, Ho CS, Katsaras J, Pan J. Interactions of the anticancer drug tamoxifen with lipid membranes. *Biophys J*. 2015;108: 2492–2501.
63. Mizushima N, Levine B. Autophagy in mammalian development and differentiation. *Nat Cell Biol*. 2010;12:823–830.
64. Pan G, Vickers SM, Pickens A, et al. Apoptosis and tumorigenesis in human cholangiocarcinoma cells. Involvement of Fas/APO-1 (CD95) and calmodulin. *Am J Pathol*. 1999;155:193–203.
65. Lamy L, Ngo VN, Emre NCT, et al. Control of autophagic cell death by caspase-10 in multiple myeloma. *Cancer Cell*. 2013;23:435–449.
66. Sarras H, Alizadeh Azami S, McPherson JP. In search of a function for BCLAF1. *Sci World J*. 2010;10:1450–1461.

INFORME DE LABORES 2019

67. Zhang K, Wang G, Zhang X, et al. COX7AR is a stress-inducible mitochondrial COX subunit that promotes breast cancer malignancy. *Sci Rep*. 2016;6:31742-1–31742-12.
68. Murray GI. The role of cytochrome P450 in tumour development and progression and it potential to therapy. *J Pathol*. 2000;192:419–426.
69. Pui CH, Relling MV, Downing JR. Acute lymphoblastic leukemia. *N Engl J Med*. 2004;350:1535–1548.
70. Greenstein S, Ghias K, Krett NL, Rosen ST. Mechanisms of glucocorticoid mediated apoptosis in hematological malignancies. *Clin Cancer Res*. 2002;8:1681–1694.
71. Kaspers GJ, Pieters R, Klumper E, De Waal FC, Veerman AJ. Glucocorticoid resistance in childhood leukemia. *Leuk Lymphoma*. 1994;13:187–201.
72. Roderick J, Gallagher KM, Tang KM, et al. Identifying mechanisms of glucocorticoid resistance in relapsed pediatric T-ALL. *Blood*. 2016;128:2769.
73. Bachmann PS, Gorman R, Mackenzie KL, Lutze-Mann L, Lock RB. Dexamethasone resistance in B-cell precursor childhood acute lymphoblastic leukemia occurs downstream of ligand-induced nuclear translocation of the glucocorticoid receptor. *Blood*. 2005;105:2519–2526.
74. Bachmann PS, Gorman R, Papa RA, et al. Divergent mechanisms of glucocorticoid resistance in experimental models of pediatric acute lymphoblastic leukemia. *Cancer Res*. 2007;67:4482–4490.
75. Sánchez-Aguilera A, Arranz L, Martín-Pérez D, et al. Estrogen signaling selectively induces apoptosis of hematopoietic progenitors and myeloid neoplasms without harming steady-state hematopoiesis. *Cell Stem Cell*. 2014;15:791–804.
76. Sánchez-Aguilera A, Méndez-Ferrer S. Regulation of hematopoietic progenitors by estrogens as a basis for new antileukemic strategies. *Mol Cell Oncol*. 2016;3:e1009728-1–e1009728-3.
77. Kincade PW, Medina KL, Smithson G. Sex hormones as negative regulators of lymphopoiesis. *Immunol Rev*. 1994;137:119–134.
78. Heo HR, Chen L, An B, Kim KS, Ji J, Hong SH. Hormonal regulation of hematopoietic stem cells and their niche: a focus on estrogen. *Int J Stem Cells*. 2015;8:18–23.
79. Igarashi H, Kouro T, Yokota T, Comp PC, Kincade PW. Age and stage dependency of estrogen receptor expression by lymphocyte precursors. *Proc Natl Acad Sci U S A*. 2001;98:15131–15136.

How to cite this article: Torres-López L, Maycotte P, Liñán-Rico A, et al. Tamoxifen induces toxicity, causes autophagy, and partially reverses dexamethasone resistance in Jurkat T cells. *J Leukoc Biol*. 2019;105:983–998. https://doi.org/10.1002/JLB.2VMA0818-328R

frontiers in Microbiology

REVIEW
published: 07 June 2019
doi: 10.3389/fmicb.2019.01100

Relationship Between Quorum Sensing and Secretion Systems

Rocio Trastoy Pena[1†], Lucia Blasco[1†], Antón Ambroa[1], Bertha González-Pedrajo[2], Laura Fernández-García[1], Maria López[1], Ines Bleriot[1], German Bou[1], Rodolfo García-Contreras[3†], Thomas Keith Wood[4] and Maria Tomás[1*†]*

[1] Deapartamento de Microbiología y Parasitología, Complejo Hospitalario Universitario A Coruña (CHUAC), Instituto de Investigación Biomédica (INIBIC), Universidad de A Coruña (UDC), A Coruña, Spain, [2] Departamento de Genética Molecular, Instituto de Fisiología Celular, Universidad Nacional Autónoma de México, Mexico City, Mexico, [3] Departamento de Microbiología y Parasitología, Facultad de Medicina, Universidad Nacional Autónoma de México, Mexico City, Mexico, [4] Department of Chemical Engineering, Pennsylvania State University, University Park, PA, United States

OPEN ACCESS

Edited by:
Tom Defoirdt, Ghent University, Belgium

Reviewed by:
Romé Voulhoux, UMR7255 Laboratoire d'Ingénierie des Systèmes Macromoléculaires (LISM), France
Jin Zhou, Tsinghua University, China

***Correspondence:**
Rodolfo García-Contreras
rgarc@bq.unam.mx
Maria Tomás
MA.del.Mar.Tomas.Carmona@sergas.es

† These authors have contributed equally to this work

Specialty section:
This article was submitted to Microbial Physiology and Metabolism, a section of the journal Frontiers in Microbiology

Received: *20 February 2019*
Accepted: *30 April 2019*
Published: *07 June 2019*

Citation:
Pena RT, Blasco L, Ambroa A, González-Pedrajo B, Fernández-García L, López M, Bleriot I, Bou G, García-Contreras R, Wood TK and Tomás M (2019) Relationship Between Quorum Sensing and Secretion Systems. Front. Microbiol. 10:1100. doi: 10.3389/fmicb.2019.01100

Quorum sensing (QS) is a communication mechanism between bacteria that allows specific processes to be controlled, such as biofilm formation, virulence factor expression, production of secondary metabolites and stress adaptation mechanisms such as bacterial competition systems including secretion systems (SS). These SS have an important role in bacterial communication. SS are ubiquitous; they are present in both Gram-negative and Gram-positive bacteria and in *Mycobacterium* sp. To date, 8 types of SS have been described (T1SS, T2SS, T3SS, T4SS, T5SS, T6SS, T7SS, and T9SS). They have global functions such as the transport of proteases, lipases, adhesins, heme-binding proteins, and amidases, and specific functions such as the synthesis of proteins in host cells, adaptation to the environment, the secretion of effectors to establish an infectious niche, transfer, absorption and release of DNA, translocation of effector proteins or DNA and autotransporter secretion. All of these functions can contribute to virulence and pathogenesis. In this review, we describe the known types of SS and discuss the ones that have been shown to be regulated by QS. Due to the large amount of information about this topic in some pathogens, we focus mainly on *Pseudomonas aeruginosa* and *Vibrio* spp.

Keywords: quorum, secretion, virulence, motility, competence

INTRODUCTION

Microorganisms coexist in competitive environments with other species, and they must develop different survival strategies to compete for space, nutrients and ecological niches. Bacteria have developed several molecular mechanisms that enable them to survive under stress conditions in different environments. The general stress response (RpoS) (Battesti et al., 2011), tolerance to reactive oxygen species (ROS) (Zhao and Drlica, 2014; Van den Bergh et al., 2017), energy metabolism (cytochrome *bd* complex) (Korshunov and Imlay, 2010) and Tau metabolism (Javaux et al., 2007), drug efflux pumps (Blanco et al., 2016), SOS response (Baharoglu and Mazel, 2014), (p)ppGpp signaling under starvation conditions (Hauryliuk et al., 2015), toxin-antitoxin (TA) systems (Wood et al., 2013) and quorum sensing (QS), which we will discuss in detail in this review, are the main molecular mechanisms of tolerance and bacterial persistence (Harms et al., 2016; Trastoy et al., 2018).

Quorum sensing acts by monitoring cell density through chemical signals that allow communication between bacteria in order to regulate the expression of genes involved in virulence, competition, pathogenicity and resistance (Nealson et al., 1970; Hawver et al., 2016; Paul et al., 2018). In general, QS systems are species-dependent and contribute to processes such as cell maintenance, biofilm formation and horizontal gene transfer. QS also plays a role in other events involving the synchronization of the whole population such as antibiotic production (Abisado et al., 2018), natural competence (Shanker and Federle, 2017), sporulation (Rai et al., 2015) and the expression of secretion systems (SS). In this review, we will focus on the relationship between QS networks and SS in two important bacterial pathogens *Pseudomonas aeruginosa* and *Vibrio* spp.

QS NETWORK

To explain the structure and functioning of the QS network, we will focus on Gram-negative bacteria, in which the signaling pathways are better described. In general terms, QS systems are composed of synthase proteins that produce QS signals, QS signals, and response regulators that bind QS signals and reprogram gene expression (Ng and Bassler, 2009). *N*-acyl homoserine lactones (AHLs) are the most common QS signals in Gram-negative bacteria (Geske et al., 2008). Other QS signals include autoinducer-2 (AI-2) in *Vibrio harveyi* (Surette et al., 1999), PQS (*Pseudomonas* quinolone signal) (Pesci et al., 1999), DSF (diffusible signaling factor) in *Xanthomonas campestris* (Barber et al., 1997), indole in *Escherichia coli* (Lee and Lee, 2010), and PAME (hydroxyl-palmitic acid methyl ester) in *Ralstonia solanacearum* (Flavier et al., 1997). The LuxI/LuxR QS system of *Vibrio fischeri* is the prototypical model system for Gram-negative bacteria (Engebrecht et al., 1983; Engebrecht and Silverman, 1984). Homologs of *luxI* (which encode synthase proteins) and *luxR* (which encode response regulators) are present in many bacteria (Case et al., 2008). AHL signals are produced inside the cell and most of them are transported freely to the local environment. When the concentration of AHL reaches a certain level outside of the cell, the molecule re-enters the cell (or binds surface receptors) and binds/activates the LuxR-type receptor to alter gene expression. AHL signals with small structural differences are involved in the process of gene regulation (Fuqua et al., 1994; Whiteley et al., 2017; Paul et al., 2018).

Pseudomonas aeruginosa possesses three well-known QS systems: LasI/LasR, RhlI/RhlR, and PQS (*Pseudomonas* quinolone signal)/PqsR (MvfR). The Las system consists of LasI, a synthase protein which produces the AHL *N*-(3-oxododecanoyl)-L-homoserine lactone (3O-C12-HSL), and LasR, the transcriptional regulator (Seed et al., 1995; Stintzi et al., 1998; Kariminik et al., 2017). Likewise, the RhlI/RhlR system produces the N-hexanoyl-L-homoserine lactone (C4-HSL) signal and the RhlR transcriptional regulator. Finally, the PQS system comprises 2-heptyl-3-hydroxy-4(1H)-quinolone (PQS signal) and the PqsR (MvfR) receptor (Xiao et al., 2006; Jimenez et al., 2012). In 2016, James and collaborators, analyzed the role of a new binding receptor for PQS signals, i.e., MexG, an inner membrane protein of the *mexGHI-opmD* operon and a component of a resistance-nodulation-cell division (RND) efflux pump (Hodgkinson et al., 2016).

Quorum quenching (QQ) enzymes have also been shown to be important in the functioning of QS systems (Zhang and Dong, 2004; Dong et al., 2007; Bzdrenga et al., 2017). Our research group has recently described a new QQ enzyme (AidA) which participates in the QS network in *Acinetobacter baumannii* clinical strains (Lopez et al., 2017b, 2018).

SECRETION SYSTEMS

Bacterial pathogens secrete proteins through their cell membranes in a fundamental process that enables them to attack other microorganisms, evade the host immune system, produce tissue damage and invade the host cells. Secreted proteins can act as virulence factors that generate toxic products to the host cells and may also facilitate adhesion to these cells. Translocation of proteins across the phospholipid membranes is carried out by several types of SS (Green and Mecsas, 2016). SS play a significant role in bacterial communication. To date, 8 types of SS (T1SS, T2SS, T3SS, T4SS, T5SS, T6SS, T7SS, and T9SS) have been made defined on their structure, composition and activity (**Figure 1**). These differences can be attributed to the differences between Gram-negative and Gram-positive bacteria (Desvaux et al., 2009; Sato et al., 2010; Costa et al., 2015). The characteristics of each type of SS are described in detail below.

T1SS

The type I secretion system is widely distributed in Gram-negative bacteria such as *P. aeruginosa*, *Salmonella enterica*, *Neisseria meningitidis,* and *E. coli* (Thomas et al., 2014).

The type I secretion system (T1SS), which has three structural elements (ABC transporter protein, a membrane fusion protein and an outer membrane factor), can transfer substrates across both bacterial membranes in Gram negative bacteria in a one-step process (Green and Mecsas, 2016). T1SS uses proteins as substrates, e.g., proteases and lipases of different sizes and with different functions; these proteins have a C-terminal uncleaved secretion signal which is recognized by the ABC transporter protein to form the translocation complex (Delepelaire, 2004; Kanonenberg et al., 2013).

There are two systems described so far that regulate the expression and secretion of substrates of T1SS, the Has system of *S. marcescens* and *P. aeruginosa,* and the hemolysins of *Vibrio cholerae*, *N. meningitidis* and in particular of uropathogenic *E. coli* (Thomas et al., 2014).

T2SS

The type II secretion system (T2SS), which is conserved in most Gram negative bacteria, is responsible for secreting folded proteins from the periplasm. These proteins are first transported through the IM by the general secretory (Sec) or twin-arginine translocation (Tat) pathways, and then secreted from the periplasm into the extracellular medium by the T2SS (Nivaskumar and Francetic, 2014; Green and Mecsas, 2016).

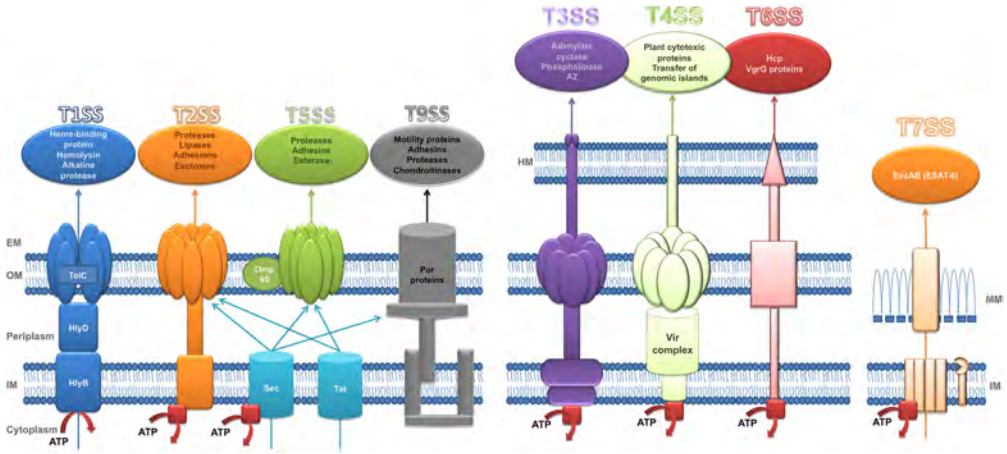

FIGURE 1 | Structure of secretion systems. Schematic representation of secretory systems: type I (T1SS), type II (T2SS), type V (T5SS), type IX (T9SS), type III (T3SS), type IV (T4SS), type VI (T6SS), and type VII (T7SS). The type I pathway is exemplified by hemolysin A (HlyA) secretion in *E. coli* where TolC, HlyD, and HlyB are the three components which constitute the channel to transport HlyA to extracellular space. Sec (general secretion route) and Tat (twin-arginine translocation pathway) transfer the substrates of T2SS and T5SS across the inner membrane. Sec also participates in the transport of T9SS substrates across de inner membrane. T9SS is also called Por Secretion System (PoSS). T4SS is represented by VirB/D system of *Agrobacterium tumefaciens*. The T7SS is based on a system in Mycobacteria. Red squares represent the ATPases. HM, host membrane; EM, extracellular medium; OM, outer membrane; IM, inner membrane; MM, mycomembrane. Substrates secreted by each secretory system are included in a circle in the top of the figure. Adapted from Tseng et al. (2009).

The Sec pathway consists of three structural parts: a protein targeting component, a motor protein and a membrane integrated conducting channel called SecYEG translocase. This mechanism transports unfolded proteins with a hydrophobic sequence at the N-terminus. Moreover, the secreted protein either remains in the periplasm or is transported to the extracellular space. The proteins may contain a SecB-specific signal sequence for transport to the periplasm or the extracellular milieu; however, if it has the signal recognition particle (SRP) signal it can follow the SRP pathway and remain in the inner membrane (Green and Mecsas, 2016; Tsirigotaki et al., 2017).

By contrast, the Tat secretion pathway consists of 2–3 subunits, TatA and TatB, which form a unique multifunctional protein in Gram-positive bacteria, and TatC. This mechanism translocates folded proteins with a twin-arginine motif. In Gram-positive bacteria, most proteins are transported out of the cell, while in Gram-negative bacteria the protein can remain in the periplasm or it can be translocated to the extracellular space by the T2SS (Patel et al., 2014; Green and Mecsas, 2016).

The T2SS, a complex structure composed of 15 proteins, named general secretion pathway proteins (Gsp) in *E. coli* (Korotkov et al., 2012), Eps in *V. cholera* (Abendroth et al., 2009; Sloup et al., 2017) and Xcp in *P. aeruginosa* (Filloux et al., 1998; Robert et al., 2005), has a wide range of substrates with diverse functions, although all share one feature, an N-terminal signal which enables them pass to the periplasm via the Sec or Tat secretion mechanisms (Nivaskumar and Francetic, 2014; Green and Mecsas, 2016).

The main function of the T2SS is to acquire nutrients (Nivaskumar and Francetic, 2014). It is responsible for secreting numerous exoproteins, most of which are hydrolytic enzymes and other proteins such as toxins, adhesins and cytochromes that have various roles in respiration, biofilm formation and motility (Nivaskumar and Francetic, 2014). The T2SS has been described in various environmental strains and also human pathogens such as *V. cholera* (Overbye et al., 1993), *P. aeruginosa, Aeromonas* sp. and enterotoxigenic *Escherichia coli* (ETEC) (Nivaskumar and Francetic, 2014).

T3SS

The type III secretion system (T3SS) or injectisome, is a double-membrane-embedded apparatus found in multiple pathogenic Gram-negative bacteria such as *Salmonella* spp., *Yersinia* spp., enteropathogenic and enterohemorrhagic *E. coli*, *Shigella* spp. and *Pseudomonas* spp. (Cornelis, 2006; Gaytan et al., 2016; Deng et al., 2017). This complex nanomachine promotes the transfer of virulence proteins called effectors from the bacterial cytoplasm into the eukaryotic cell in a single step (Galan and Waksman, 2018).

The T3SS is composed of approximately 25 proteins assembled in three main structures: the basal body, a set of rings spanning the two membranes of the bacterium; a hollow needle-shaped component through which the semi-unfolded effectors are transported (these first two structures are collectively called "needle complex"); and the translocon, made up of a hydrophilic protein that serves as a scaffold for forming a translocation pore, constituted by two hydrophobic proteins, which is inserted into the host cell membrane and through which effectors are directly translocated. A unique set of effectors is delivered by each pathogen, which subverts specific host-cell signaling pathways to allow bacterial colonization (Izore et al., 2011; Notti and Stebbins, 2016; Deng et al., 2017).

The export apparatus associated with the basal body is formed by five poly topic inner membrane proteins that are essential

for substrate secretion. This protein complex, together with a cytoplasmic sorting platform and the ATPase complex are responsible for substrate recruitment and classification, and for energizing the secretion process enabling chaperone-effector dissociation and protein unfolding for initial entry into the T3SS central channel that serves as the secretion pathway. These components are highly conserved between different T3SS systems and with the flagella, which is evolutionarily related to the injectisome (Abby and Rocha, 2012; Galan and Waksman, 2018; Lara-Tejero and Galan, 2019).

Several effectors of T3SS have been described such as ExoS, ExoT, ExoU, and ExoY in *P. aeruginosa*; Tir and EspE in *E. coli* and YopE, YopH, YopM, YopJ/P, YopO/YpkA, and YopT in *Yersinia* sp. (Cornelis and Van Gijsegem, 2000).

T4SS

The type IV secretion system family is found in Gram-negative and Gram-positive bacteria as well as in *Archaea*. T4SS is the most cosmopolitan secretion system and differs from other SS as it is able to transfer DNA in addition to proteins (Cascales and Christie, 2003). More specifically, T4SS is capable of performing contact-dependent secretion of effector molecules into eukaryotic cells, conjugative transfer of mobile DNA elements and also exchange of DNA without any contact with the outside of the cell (Green and Mecsas, 2016; Grohmann et al., 2018). T4SS can be divided on the basis of its functionality into two subfamilies: conjugation systems and effector translocators. Conjugation systems are responsible for the transfer of antibiotic resistance genes and virulence determinants among bacteria. The effector translocators introduce virulence factors into the host cell (Christie, 2016). However, in Gram-negative bacteria T4SS has been divided into two different subfamilies: IVA and IVB. The *E. coli* conjugation apparatuses and VirB/D system of *Agrobacterium tumefaciens* are the models used to study the structure of type IVA of T4SS (Grohmann et al., 2018). The VirB/D apparatus consists of 12 proteins which form a complex envelope-spanning structure that facilitate the translocation function. Two of these proteins, VirB2 and VirB5, make up the pilus, while another three proteins act as ATPases, and VirB1 is a lytic transglycosylase (Costa et al., 2015; Green and Mecsas, 2016). The *Legionella pneumophila* Dot/Icm (Defective for organelle trafficking/Intracellular multiplication) system is the model used to study the IVB subfamily of T4SS (Nagai and Kubori, 2011; Grohmann et al., 2018).

T5SS

The type V secretion system is unique because its substrates transport themselves across the outer membrane. The substrates use the Sec translocase to pass through the inner membrane to the periplasm space. Various different types of T5SS have been identified: autotransporters (T5aSS), two-partner passenger-translocators (T5bSS), trimeric autotransporters (T5cSS), hybrid autotransporters (T5dSS) and inverted autotransporters (T5eSS) (Henderson et al., 2004; Leo et al., 2012; Rojas-Lopez et al., 2017). In general, the T5SS transports proteins across the asymmetric outer membrane (OM) that contains lipopolysaccharides, through their own C-terminal translocation domain that inserts into the OM as a β-barrel to complete the secretion of the N-terminal passenger domain via the barrel pore. Several periplasmic chaperones also participate in transport through the OM, specifically the β-barrel assembly machinery (BAM complex) and the translocation and assembly module (TAM complex) facilitate protein secretion (Rojas-Lopez et al., 2017).

A T5SS has been described in human pathogens such as *Bordetella pertussis* and *Haemophilus influenzae*, which have two-partner SS and uropathogenic *E. coli*, which has chaperone-usher systems (Costa et al., 2015; Green and Mecsas, 2016).

YadA of *Yersinia enterocolitica* and SadA of *Salmonella* are T5SS type c (Leo et al., 2012). Intimin of *E. coli* and invasin of enteropathogenic *Yersinia* spp. are type Ve SS (Leo et al., 2012).

A self-transporter (T5aSS) (Wilhelm et al., 2007) and three T5bSS: LepA /LepB system (Kida et al., 2008), the CupB system (Ruer et al., 2008) and PdtA/PdtB system (Faure et al., 2014), have been reported in *P. aeruginosa*. In *B. cenocepacia,* four T5SS (Holden et al., 2009) have been found, two with pertactin domains and two with haemagglutinin autotransporters; this last type is also present in *S. maltophilia* (Ryan et al., 2009).

T6SS

The type VI secretion system is widely represented in Gram-negative bacteria (Coulthurst, 2013; Gallique et al., 2017b). T6SS is an integrated secretion device within the membrane and it transfers substrates, which are toxic effectors to eukaryotic (Pukatzki et al., 2007) and prokaryotic cells (Russell et al., 2014). It plays a crucial role in the pathogenesis and competition among bacteria (Ho et al., 2014; Zoued et al., 2014; Costa et al., 2015; Gallique et al., 2017a). The origin of T6SS is related to bacteriophages (Leiman et al., 2009). T6SS is a huge apparatus and consists of 13 core components organized into a *trans*-membrane complex, a baseplate-like structure at the cytoplasmic face of the inner membrane, and a sheathed inner tube, which is the effector delivery module that is ejected to the target cell. The tube-sheath complex is assembled from the baseplate in the cytoplasm and the hollow tube is built from hexamers of the hemolysin co-regulated protein (Hcp). The sheath contracts and pushes the tube with the associated effectors into targeted cells, using a puncturing mechanism similar to the one used by the contractile tails of phages (Russell et al., 2011, 2014; Cianfanelli et al., 2016; Green and Mecsas, 2016; Galan and Waksman, 2018).

T7SS

Type VII secretory system has been described in some Gram-positive bacteria such as *Staphylococcus aureus* and in species of *Mycobacterium* and *Corynebacterium*. This SS was reported for the first time in 2003 in *Mycobacterium tuberculosis* and it was called ESX-1 (Stanley et al., 2003), which is an important virulence factor in *M. tuberculosis*. To date, five T7SS have been identified in *Mycobacterium* sp. but the transport mechanisms across the mycobacterial membrane are almost unknown (Costa et al., 2015; Ates et al., 2016; Green and Mecsas, 2016).

Most of the substrates of T7SS belong to EscAB clan which includes six protein families: Esx, PE, PPE, LXG, DUF2563,

and DUF2580. ESAT-6 is a *M. tuberculosis* protein which belongs to Esx family and which is secreted with EsxB (CFP-10) (Ates et al., 2016).

T9SS

The type IX secretion system (T9SS) or Por secretion system (PorSS) is the most recently discovered system (Lasica et al., 2017). Its function is to transport molecules across the outer membrane. Its substrates must include a Sec signal, which allows transfer of proteins through the inner membrane with the aid of the Sec system. The T9SS system has been described in almost all members of the phylum *Bacteroidetes,* but it has mainly been studied in oral pathogens such as *Porphyromonas gingivalis* and *Tannerella forsythia.* In *P. gigivalis*, the T9SS system consists of 16 proteins with structural and functional activity, and another two proteins involved in the regulation of the transport process (Sato et al., 2010; Lasica et al., 2017).

REGULATION OF SECRETION SYSTEMS BY QUORUM SENSING NETWORKS (TABLE 1)

Pseudomonas aeruginosa

T1SS

Transcriptional studies in *P. aeruginosa* suggest that in this bacterium T1SS is positively regulated by QS, since the expression of its effector, the alkaline protease AprA, depends on QS. In addition, the genes of the AprA inhibitor *aprI* and the structural genes *aprDEF* also appear to be positively regulated by QS (Hentzer et al., 2003; Schuster et al., 2003; Wagner et al., 2003).

T2SS

Three T2SS systems, the Xcp, Hxc and Txc systems, have been described in *P. aeruginosa*. The first of these, Xcp, secretes the QS regulated virulence factors elastase A and B (LasA and LasB) as well as the exotoxin A (ExoA) and it is itself positively regulated by QS (**Figure 2**). Accordingly, recently it was demonstrated by ChIPseq analysis that MvfR (the receptor of the PQS autoinducer) is able to directly bind *xcpQ-xcpP-xcpR* regions and this is related to their induction in the presence of MvfR (Maura et al., 2016).

The second T2SS, Hxc, is regulated by the availability of phosphate and secretes LapA a low-molecular weight alkaline phosphatase (Wagner et al., 2003; Michel et al., 2007). Two genes, *xphA* and *xqhA*, which encode the PaQa subunit of the Xcp functional hybrid system, have been described. These genes, which are located outside the *xcp* locus, are regulated by environmental conditions but not by QS, in contrast to what occurs with the rest of the Xcp system (Michel et al., 2007, 2011). In contrast to the first two systems, the third system Txc has just recently been described and so far only identified in a region of genome plasticity of the strain PA7; it is regulated by a two component system (TtsSR) and secretes the chitin binding protein CpbE (Cadoret et al., 2014).

T3SS

Current evidence suggest that as in *Vibrio* spp., QS in *P. aeruginosa* negatively regulates the expression of T3SS, specifically the RhlI/RhlR system, as transcription of the T3SS genes and secretion of ExoS increase significantly in a *rhlI* mutant and return to basal levels on the addition of exogenous C4-HSL (Bleves et al., 2005; Kong et al., 2009; **Figure 2**). In agreement, the expression of *exoS* is also negatively regulated by QS, specifically by the RhlI/RhlR system, as well as by the stationary phase sigma factor RpoS (Hogardt et al., 2004).

The fact that the T3SS genes do not appear to be repressed by QS in some global transcriptomic studies with mutants may be explained by the presence of high calcium concentrations in the media, or by the lack of resolution of DNA microarrays (Hentzer et al., 2003; Schuster et al., 2003). More striking is the fact that some QS inhibitors like 6-gingerol and coumarin inhibit rather than increase the expression of T3SS (Zhang et al., 2018). Nevertheless, these studies were done in the presence of high calcium, and QS-independent inhibition of T3SS has not been ruled out. Moreover, a recent study in the PA01 strain, using a *lasR rhlR* double mutant, demonstrated that it remains virulent in a murine abscess model, despite that it does not produce QS-dependent virulence factors and that the secretion of ExoT and ExoS is fully functional in this mutant. Hence the authors hypothesized that T3SS is the cause of the remaining virulence (Soto-Aceves et al., 2019).

The *P. aeruginosa* QS network and its T3SS are also related by the fact that VqsM, an AraC-family transcription factor, binds to both the promoter region of *lasI* and the promoter of *exsA*, which encodes a master regulator of the T3SS, regulating both mechanisms (Liang et al., 2014; **Figure 2**).

T6SS

The T6SS is involved in iron transport, and a connection has been observed between T6SS and QS through the TseF protein, which is a substrate of T6SS and interacts with PQS (Lin et al., 2017; **Figure 2**).

In *P. aeruginosa,* three loci which encode T6SS have been found to be regulated by QS proteins (LasR and MvfR) (Lesic et al., 2009). Expression of the second loci, H2-T6SS, is regulated by the Las and Rhl QS systems in PAO1 strains (Sana et al., 2012; **Figure 2**) and by the direct binding of MvfR in PA14 (Maura et al., 2016).

Vibrio sp.

T2SS

The formation of biofilms has multifactorial regulation in *V. cholerae* as in other pathogens. The QS network controls directly biofilm production which is related to type II secretion system in *V. cholerae* (Teschler et al., 2015). Several proteins such as RbmA, RbmC and Bap1, which are involved in the formation of biofilms, are transported by T2SS. In addition, mutant strains with inactivated T2SS have reduced biofilm formation (Johnson et al., 2014; Teschler et al., 2015).

TABLE 1 | Pathogens and QS elements related to secretion systems.

Type secretion system	SS element	QS regulation	QS element	Microorganisms	References
T1SS	Lip	+	*Swr*	*Serratia liquefaciens*	Riedel et al., 2001
T2SS	Xcp	+	*lasR/lasI rhLR/rhlI*	*Pseudomonas aeruginosa*	Wagner et al., 2003; Michel et al., 2007
			DSF-type	*Xanthomonas* species	Qian et al., 2013
T3SS	LEE operon	+	*luxS*	*Escherichia coli*	Sperandio et al., 1999
		−		*Vibrio parahaemolyticus Vibrio harveyi*	Henke and Bassler, 2004
	ExsA		*lasI*	*Pseudomonas aeruginosa*	Liang et al., 2014
	Yop-Ysc	+	Hfq	*Yersinia pseudotuberculosis Yersinia pestis*	Schiano et al., 2014
T4SS	VirB/D	+	VjbR (LuxR-type QS)	*Brucella abortus*	Arocena et al., 2010; Li et al., 2017
		+	*luxI*	Roseobacter group	Patzelt et al., 2013, 2016
T6SS				*Vibrio alginolyticus*	Yang et al., 2018
	Hcp		HapR and LuxO	*Vibrio cholerae*	Ishikawa et al., 2009; Zheng et al., 2010; Kitaoka et al., 2011; Leung et al., 2011
				Burkholderia thailandensis	Majerczyk et al., 2016
			AHL	*Pseudomonas fluorescens*	Gallique et al., 2017b
	TseF		PQS	*Pseudomonas* spp.	Lin et al., 2017
			LasR and MvfR	*Pseudomonas aeruginosa*	Lesic et al., 2009
	VipA,Hcp-1, VipB		AbaR/AbaI	*Acinetobacter baumannii*	Lopez et al., 2017b

T3SS

In *V. parahaemolyticus* and *V. harveyi* (unlike in *E. coli*), both the HAI-1 and AI-2 QS systems inhibit the expression of T3SS genes (Henke and Bassler, 2004). QS also represses T3SS during *V. harveyi* infections of gnotobiotic brine shrimp (Ruwandeepika et al., 2015). Waters et al. (2010) have described the regulatory pathway by which QS controls T3SS. At low cell density when LuxR is repressed, which entails the derepression of two promoters of the *exsBA* operon and the *exsA* operon, ExsA activates the expression of genes that encode the structural proteins of the type III secretion system. However, when the cell density is high, LuxR directly represses transcription of the PB promoter, preventing the production of ExsA and consequently decreasing the expression of structural genes of T3SS (Waters et al., 2010; Ball et al., 2017). OpaR inhibits the T3SS1 in *V. parahaemolyticus* which is the most important factor in its cytotoxicity (Gode-Potratz and McCarter, 2011).

T6SS

Several researchers have demonstrated the regulation of T6SS by QS networks in *Vibrio* spp. We present the main findings in this field here. In *V. alginolyticus*, activation of T6SS and the QS network has been found to be coordinated by the serine/threonine kinase PpkA cascade (Yang et al., 2018). PpkA2 is autophosphorylation and it transfers the phosphate group to VstR. Phosphorylated VstR promotes the expression of both of the T6SS in *V. alginolyticus* through the inhibition of LuxO activity, which acts to impede the expression of LuxR, a promoter of the T6SS. LuxR inhibits the expression of the first T6SS (T6SS1) or promotes the expression of the second T6SS (T6SS2) (Yang et al., 2018).

At low cell population density, LuxO is phosphorylated, which activates the expression of specific small regulatory RNAs (sRNAs) in conjunction with alternative sigma factor σ^{54} (Sheng et al., 2012). sRNAs inhibit the expression of LuxR with the help of RNA chaperone Hfq (Liu et al., 2011). However, at high cell population density, LuxO is dephosphorylated turning off the transcription of the sRNAs and allowing the translation of LuxR (Waters and Bassler, 2005; Milton, 2006). Sheng et al. (2012) also demonstrated that the expression of the *hcp* T6SS gene is growth phase-dependent and the QS regulators controls the haemolysin co-regulated protein, which is one of the main proteins of the T6SS functioning as an effector of the system and/or an effector binding protein (**Figure 2**). The phosphatase PppA also acts on the QS (modulating the transcription of LuxR) and the expression and secretion of *hcp1* and *hcp2* (Sheng et al., 2013). It is important to highlight that PppA permits the cross-talk between the two T6SS in *V. alginolyticus* (Sheng et al., 2013).

Rpo N (σ^{54}) collaborates with QS in the regulation of T6SS genes. It is involved in the regulation of the expression of *hcp* and *vgrG3* operons that encode T6SS secreted molecules, but does not control the genes that encode the structural and sheath components of T6SS (Ishikawa et al., 2009; Dong and Mekalanos, 2012).

There are a few more studies in *V. cholerae* related to this topic than other species. Two QS autoinducers, CAI-I (cholerae autoinducer) and AI-2 (autoinducer-2), co-operate to control the gene expression depending on the cell density

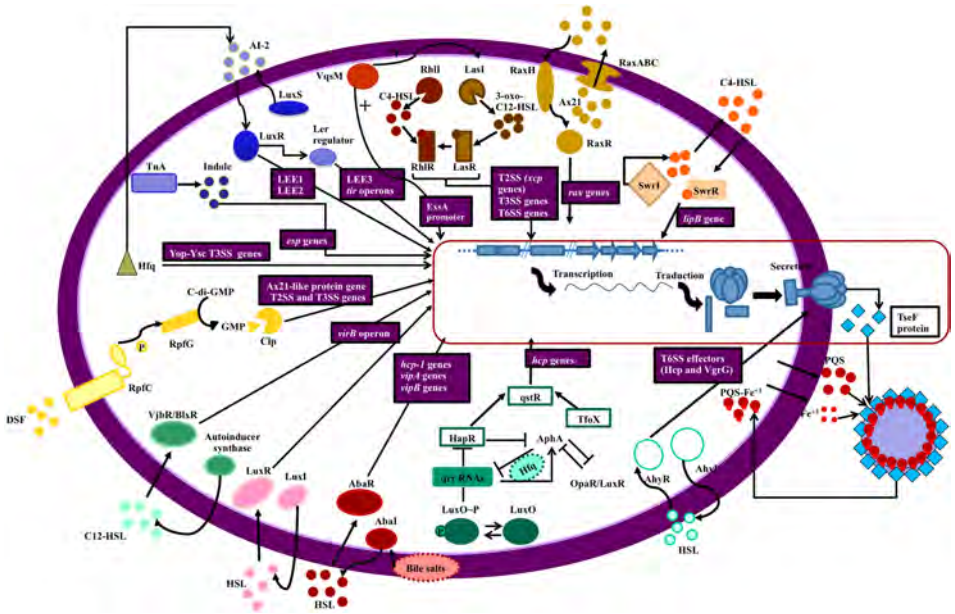

FIGURE 2 | Secretion systems and QS network elements. The figure shows the relationship between QS networks and expression of secretion systems (blue squares). The genes regulated by QS are in purple boxes. Each QS network is represented by a different color. Starting at the top right of the figure: The swr QS system of *S. liquefaciens* controls the *lipB* genes of the T1SS (orange); Ax21 (QS effector) and QS system Rax regulate RaxABC TOSS (T1SS) in gram negative bacteria (ochre); QS (RhlIR and LasIR) regulates expression of T2SS, T3SS, and T6SS in *P. aeruginosa* (brown); VqsM (an AraC family transcription factor) interacts with the LasIR and ExsA promoters (a master regulator of T3SS) in *P. aeruginosa* (dark orange); T2SS is regulated by LuxS/LuxI/AI-2 QS in *E. coli* and indole production by TnA (tryptophanase) regulates *esp* genes expression (T2SS) in this bacterium (blue); in *Yersinia* sp. the Hfq chaperone is connected with QS (AI-2) and regulates the Yop-Ysc type III secretion system (T3SS) (green); in *Xanthomonas* sp. T2SS and T3SS are regulated by DSF (diffusible signal factor) which is a quorum sensing signal (yellow); T4SS (*virB* operon) is regulated by VjbR (LuxR like protein) and LuxI in *Brucella* (turquoise) and *Roseobacter* (pink), respectively; a connection between *Acinetobacter baumanii* QS (AbaI/AbaR, controlled by bile salts) and T6SS has been established (maroon); in *Vibrio* sp. there is a complex network which relates QS (LuxO/HapR/TfoX) with T6SS (aquamarine); AhyRI (a QS network) in *Aeromonas* sp. and *P. atrosepticum* is involved in Hcp and VgrG secretion (sky blue) and finally, iron is transported across the cell membrane accompanied by PQS, a quorum sensing signal in *P. aeruginosa*, and this process depend on Tse a substrate of T6SS, which binds to OMVs (outer membrane vesicles) containing PQS- Fe^{3+}.

(Ng and Bassler, 2009). Two enzymes are necessary for the biosynthesis of these autoinducers: CqsA and LuxS, respectively (Schauder et al., 2001; Miller et al., 2002; Chen et al., 2002; Higgins et al., 2007). These signal molecules are detected by two sensor kinases, LuxQ (sensor of CAI-I) and CqsS (sensor of AI-2). Both pathways merge on LuxU, a phosphotranfer protein. At low cell density (LCD), the two sensor kinases phosphorylate LuxU due to the absence of their respective autoinducers. There are two histidine kinases which also contribute to the phosphorylation of LuxU: VpsS and CqsR (Jung et al., 2015). Then, LuxU transfers the phosphorylate group to a DNA-binding response regulator protein called LuxO. Phosphorylated LuxO activates the expression of sRNA molecules (known as qrr1-4) when the cell density is low thanks to the interaction with the alternative sigma factor σ^{54} (Freeman et al., 2000; Lenz et al., 2004). In conjunction with the RNA-binding protein Hfq, LuxO represses the expression of HapR (Lenz et al., 2004), a TetR-family global transcriptional regulator which acts on QstR (Tsou et al., 2009; Shao and Bassler, 2014; Watve et al., 2015; **Figure 2**). HapR is accumulated when the cell density is high (Lenz et al., 2004) because LuxO is not phosphorylated and transcription of the sRNAs is blocked. QstR is a master regulator of the T6SS belonging to the LuxR-type family of regulators (Jaskólska et al., 2018). QstR binds to the promoter region of the T6SS cluster inducing the expression of the genes. The regulation of the T6SS by cAMP-CRP pathway is not clear, but it is possible that it influences T6SS genes through regulation of QS and chitin-induced competency (Liang et al., 2007; Blokesch, 2012). It is known that CRP positively regulates T6SS (Ishikawa et al., 2009). Apart from the activation of QstR via QS, it is also regulated by chitin and arabinose (Lo Scrudato and Blokesch, 2012, 2013).

The expression of the three T6SS gene clusters in *V. cholerae* requires TfoX, CytR, HapR, and QstR for the highest level of expression (Watve et al., 2015). CytR and TfoX are required for the expression of the T6SS genes but their regulatory effects are only mediated by QstR (**Figure 2**).

Other Pathogens

T1SS

The *swr* QS system, which controls swarming motility, regulates the Lip secretion system, a T1SS responsible for the secretion of lipases, metalloproteases and S-layer proteins in *Serratia liquefaciens* MG1 (Riedel et al., 2001). The *swr* QS system consists of SwrI, which synthesizes C4-HSL, and SwrR, which regulates gene transcription after binding the diffusible signal C4-HSL.

QS-mediated regulation of *lipB*, which encodes the LipB exporter, was demonstrated in *swrI* mutants with *luxAB* insertions, in which the level of secreted proteins was lower (Riedel et al., 2001; **Figure 2**). Other relationships between T1SS and QS have also been observed. The rice pathogen recognition XA21 receptor recognizes a sulphated peptide (axY^S22) derived from the Ax21 protein (activator of XA21-mediated immunity) and confers resistance to *Xanthomonas oryzae* strains. Ax21 may have a key biological role because it is conserved in *Xanthomonas* spp., *Xylella fastidiosa,* and *Stenotrophomonas maltophilia*. Ax21 requires RaxABC TOSS (type I secretion system) for secretion and activity. The expression of *rax* genes which encode T1SS has been demonstrated to be QS-dependent due to the cell-density dependency (Han et al., 2011). These data indicate that Ax21 could have a role as a signaling molecule and a direct relationship between the QS network and T1SS is established (**Figure 2**; Lee et al., 2006).

T2SS

In *Xanthomonas* species, QS is mediated by the diffusible signal factor (DSF). A proteomic analysis conducted in 2013 revealed 33 proteins that are controlled by DSF. Their putative functions are associated with QS and include cellular processes, intermediary metabolism, oxidative adaption, macromolecule metabolism, cell-structure, protein catabolism, and hypothetical functions (Qian et al., 2013). In this study, it was observed that three genes encoding T2SS-dependent proteins and one gene which encodes Ax21 (activator of XA21-mediated immunity)-like protein are regulated by QS and are essential for virulence-associated functions, including extracellular protease, cell motility, antioxidative ability, extracellular polysaccharide biosynthesis (EPS), colonization, and biofilm (Qian et al., 2013; **Figure 2**).

T3SS

The relationship between QS and T3SS in *E. coli* was first demonstrated by Sperandio et al. (1999), who showed that expression of the locus of enterocyte effacement (LEE) operons that encode the T3SS is activated by QS in both enterohemorrhagic (EHEC) and enteropathogenic (EPEC) *E. coli* due to transcriptional control of the LEE operons by LuxS, which directly activates the LEE1 and LEE2 operons and indirectly activates (via the Ler regulator) the LEE3 and *tir* operons (**Figure 2**). These researchers proposed that activation of the T3SS by the AI-2 autoinducer synthesized by commensal *E. coli* resident in the large intestine could explain the high infectivity of *E. coli* O157: H7, which has an infectious dose of about 50 bacterial cells (Sperandio et al., 1999).

The major virulence factors of EHEC and EPEC are intimin (T5eSS), Tir (the receptor for intimin) and the three secreted proteins EspA, EspB and EspD. T3SS functions in the secretion of the Tir and Esp proteins. The LuxR-type response regulator SdiA negatively regulates the expression of EspD and intimin in the same bacterium, indicating multifactorial regulation of the T3SS by bacterial QS signals (Kanamaru et al., 2000).

Indole, which is produced by tryptophanase (TnA) in enteric bacteria and reaches high concentrations in the gut, is another signaling molecule that influences expression of T3SS in *E. coli* (Lee et al., 2007, 2008). Indole increases the production and secretion of the translocators EspA and EspB in EHEC O157:H7 (Hirakawa et al., 2009; **Figure 2**); hence, indole promotes the development of attaching and effacing (A/E) lesions in HeLa cells.

The involvement of the RNA chaperone protein Hfq, which also participates in QS, in T3SS expression was demonstrated in *Yersinia pseudotuberculosis* and *Yersinia pestis* (Schiano et al., 2014; **Figure 2**). Moreover, Schiano et al., 2014 have demonstrated the regulation of T3SS by QS through virulence regulators LcrF and YmoA in *Y. pseudotuberculosis* (Amy, 2018).

In *Aeromonas hydrophila*, an unique QS system, encoded in *ahyR/ahyI* loci, has been described (Vilches et al., 2009; Garde et al., 2010). Vilches et al. (2009) have used the *A. hydrophila* AH-3 strain to study the T3SS regulation. AH-3: ahyI and AH-3: ahyR mutants have reduced activity of the *aopN-aopB* promoter (promoter of T3SS components) compared to the wild-type strain (**Figure 2**). So they concluded that QS could be involved in the positive regulation of the production of the T3SS component in the AH-3 strain (Vilches et al., 2009).

T4SS

In *Brucella abortus,* there is a clear relationship between the QS network and T4SS. For the *virB* operon, which encodes the T4SS regulated by VjbR, a LuxR-type QS is responsible for the virulence characteristics of *B. abortus* (Li et al., 2017). The *virB* operon is responsible for establishing the replicative niche of the bacterium once it enters the host cell. The T4SS in *B. abortus,* as in other bacteria, translocates effector proteins into the host cell to avoid the immune defense mechanisms, making it one of the two main virulence factors for *Brucella.* Arocena et al. (2010) described the binding site of VjbR to the *virB* operon (Li et al., 2017). Otherwise, the conjugation process between two members of the *Roseobacter* group mediated by T4SS, encoded in RepABC-type plasmids, is controlled by the QS network. This was demonstrated by construction of *luxI* mutant and the addition of external long chain AHLs, which restored the phenotype (Patzelt et al., 2013, 2016; **Figure 2**).

T6SS

Quorum sensing has been reported to control expression of T6SS toxin-immunity systems in *Burkholderia thailandensis*. Moreover, a new role for T6SS in constraining the proliferation of QS mutants has been described in *B. thailandensis* (Majerczyk et al., 2016). Interestingly, it has been observed that T6SS effectors function as cell-to-cell signals in a *Pseudomonas fluorescens* MFE01 strain lacking the AHL QS pathway (Gallique et al., 2017b).

In *A. hydrophila*, Hcp and VgrG- two of the "core" proteins and also effectors of the T6SS- secretion have been suggested to be regulated by the AhyRI QS regulon (Khajanchi et al., 2009; **Figure 2**). Finally, our research group has described the association between T6SS machinery and the activation of the QS system by bile salts in *A. baumannii* clinical strains (Lopez et al., 2017a; **Figure 2**).

T7SS

As with other bacteria, *Mycobacterium* spp regulate biofilm formation by QS (Virmani et al., 2018). The second messenger c-di-cGMP, an intracellular signaling molecule, coordinates

biofilm production and QS signaling (Sharma et al., 2014). Both *M. tuberculosis* (Kulka et al., 2012) and diverse species of non-tuberculous mycobacteria (*M. smegmatis, M. marinum, M. fortuitum, M. chelonae, M. ulcerans, M. abscessus, M. avium,* and *M. bovis*) produce biofilm depending on certain environmental conditions such as the availability of nutrients or the pH of the medium (Hall-Stoodley et al., 1998; Bardouniotis et al., 2003; Ojha et al., 2005; Marsollier et al., 2007; Johansen et al., 2009; Rhoades et al., 2009).

In the recent work of Lai et al. (2018) it was demonstrated that *the espE, espF, espG,* and *espH* genes, located in the T7SS ESX-1 operon, are crucial for sliding motility and biofilm formation in *M. marinum*. Esp proteins, which regulate substrate transport, are involved also in virulence. This paper clearly demonstrates the role of *M. marinum* T7SS in the production of biofilm which, as already mentioned, is related to QS (Lai et al., 2018).

The T7SS of *S. aureus*, a virulence factors export machinery, plays a key role in the promotion of bacterial survival and long-term persistence of subpopulations of staphylococci. The expression of T7SS is regulated by the bacterial interaction with host tissues (Lopez et al., 2017c) mediated by the secondary sigma factor (σB) (Schulthess et al., 2012). Schulthess et al. (2012) reported that the repression of *esxA* by σB is due to the transcription of *sarA* induced by σB, which leads to a strong repression of *esxA*. The activation of the *esxA* transcript, on the other hand, is stimulated by *arlR*, the response regulator of the ArlRS two-component system, SpoVG, a σ-dependent element, and the Agr quorum detection system (Schulthess et al., 2012). Agr QS system is composed by AIP (self-activating peptide), the inducer ligand of AgrC which is the receptor of the agr signal. In the case of the QS Agr system, the effector of global gene regulation is an important regulatory RNA, RNAIII (Novick and Geisinger, 2008).

T9SS

Moreover, an important relationship between T9SS and biofilm formation has been observed in periodontopathogenic pathogens such as *Capnocytophaga ochracea*, *Porphyromonas* spp., *Fusobacterium* spp. and *Prevotella* spp. (Kita et al., 2016). In the study by Kita et al. (2016), the participation of T9SS in the formation of biofilm of *C. ochracea* is demonstrated. The formation of biofilm of *C. ochracea* is crucial for the development of dental plaque and the same happens with other periodontal pathogens, in which it has also been seen that genes related to T9SS are present. Therefore, the components of the T9SS could be potential targets to inhibit the formation of biofilm and thus avoid the formation of dental plaque (McBride and Zhu, 2013; Kita et al., 2016). However, in depth analysis of the relationship between T9SS and QS network in different pathogens is required.

DISCUSSION

To date, the T1SS, T2SS, T3SS, T4SS, T6SS, T7SS, and T9SS SS have been found to have important relationships with QS networks. The involvement of the T1SS system (Lip B which is part of the Lip exporter) in the QS network (*swr* quorum system) of *S. liquefaciens* MG1 has been investigated (Riedel et al., 2001). In *P. aeruginosa,* two QS systems (*lasR/lasI* and *rhLR/rhlI*) are linked to T2SS system by microarrays and proteomic studies (Chapon-Herve et al., 1997; Wagner et al., 2003; Michel et al., 2007), and DSF-type systems are also linked to T2SS in *Xanthomonas* species through proteome analysis (Qian et al., 2013). The QS signal AI-2 has been associated with a T3SS system in *E. coli* (Sperandio et al., 1999) and *Vibrio* spp. (Henke and Bassler, 2004). Moreover, this T3SS system has been related to QS proteins in another two pathogens, *P. aeruginosa* and *Yersinia* spp. (Liang et al., 2014; Schiano et al., 2014).

Several T4SS (*virB* operon) are controlled by VjbR protein which is a LuxR-type quorum-sensing regulator in *B. abortus* (Arocena et al., 2010; Li et al., 2017). Moreover, in the *Roseobacter* group, the conjugation of plasmids, which encode T4SS, is QS-controlled and the QS system may detect a broad range of long-chain AHLs at the cell surface (Patzelt et al., 2013, 2016).

There is a wealth of information relating the T6SS to QS in pathogens such as *Vibrio* spp. For example, Hcp and VasH from the T6SS system in *V. cholerae* are involved in QS (Ishikawa et al., 2009; Zheng et al., 2010; Kitaoka et al., 2011; Leung et al., 2011; Yang et al., 2018). For *Pseudomonas* spp,. there are numerous works where the different T6SS are regulated by QS networks (Lesic et al., 2009; Gallique et al., 2017b; Lin et al., 2017). In other pathogens as *Burkholderia thailandensis* (Majerczyk et al., 2016), and in *A. baumannii,* the relationship between QS and SS has begun to be studied (Lopez et al., 2017a).

In *M. marinum,* the relationship between biofilm formation, which is tightly connected with QS, and T7SS, has been demonstrated (Lai et al., 2018). Also in *S. aureus,* the Agr QS network has been related to T7SS (Schulthess et al., 2012). An important relationship between T9SS and biofilm formation has been observed in periodontopathogenic pathogens (Kita et al., 2016). Finally, although the involvement of T5SS secretion system in virulence, motility and competence is well-known, these systems and their association with QS must be studied in greater depth in order to clarify their roles.

Taking *P. aeruginosa* as a reference point, the positive effect of QS in the expression of T1SS and T2SS could be related to the fact that this organism secretes exoproducts that are public goods (proteases and lipases); hence, it is better to produce and secrete these compounds when a high cell density is reached, since these products are costly and the benefits associated to their production are higher at high cell densities. Similarly, the T6SS, which is involved in killing competitors by contact, will be more efficient at high cell densities since the probability of finding target bacteria is higher. In contrast, the T3SS appears to be negatively regulated by QS, and this may be related to its role in an acute infection and its "inhibition by QS" may be a way to facilitate the transition to a chronic infection state. In addition to its well established role in infections, T3SS has a broader ecological role suggested by its role in killing biofilm associated *Acanthamoeba castellanii* amoeba (Matz et al., 2008). Furthermore, it was recently demonstrated that T3SS is susceptible of cheating by mutants that do not produce it, allowing their establishment in infections (Czechowska et al., 2014); hence, the selective forces that act over T3SS are complex.

Therefore, research into the relationship between QS and SS must be further developed in order to better understand human infections.

AUTHOR CONTRIBUTIONS

RTP, LB, AA, BG-P, LF-G, ML, IB, and GB developed the redaction of the manuscript, figures and table. RG-C, TW, and MT designed the review, assigned writing tasks to co-authors, contributed to writing and proofread the final version.

FUNDING

This study was funded by grant PI16/01163 awarded to MT within the State Plan for R+D+I 2013–2016 (National Plan for Scientific Research, Technological Development and Innovation 2008–2011) and co-financed by the ISCIII-Deputy General Directorate for Evaluation and Promotion of Research – European Regional Development Fund "A way of making Europe" and Instituto de Salud Carlos III FEDER, Spanish Network for the Research in Infectious Diseases (REIPI, RD16/0016/0001 and RD16/0016/0006) and by the Study Group on Mechanisms of Action and Resistance to Antimicrobials, GEMARA (SEIMC, http://www.seimc.org/). MT was financially supported by the Miguel Servet Research Programme (SERGAS and ISCIII). RTP and LF-G were financially supported by, respectively, a post-speciality grant awarded by the Fundación Novoa Santos (CHUAC-SERGAS, Galicia) and predoctoral fellowship from the Xunta de Galicia (GAIN, Axencia de Innovación). RG-C research is supported by the grant PAPIIT-UNAM number IN214218. BG-P was supported by grants PAPIIT-UNAM IN209617 and CONACYT 284081.

REFERENCES

Abby, S. S., and Rocha, E. P. (2012). The non-flagellar type III secretion system evolved from the bacterial flagellum and diversified into host-cell adapted systems. *PLoS Genet.* 8:e1002983. doi: 10.1371/journal.pgen.1002983

Abendroth, J., Mitchell, D. D., Korotkov, K. V., Johnson, T. L., Kreger, A., Sandkvist, M., et al. (2009). The three-dimensional structure of the cytoplasmic domains of EpsF from the type 2 secretion system of *Vibrio cholerae*. *J. Struct. Biol.* 166, 303–315. doi: 10.1016/j.jsb.2009.03.009

Abisado, R. G., Benomar, S., Klaus, J. R., Dandekar, A. A., and Chandler, J. R. (2018). Bacterial quorum sensing and microbial community interactions. *mBio* 9:e02331-17. doi: 10.1128/mBio.02331-17

Amy, S. (2018). *Unraveling the Regulatory Relationship between Quorum Sensing and the Type III Secretion System in Yersinia pseudotuberculosis*. Ph.D. thesis, University of Nottingham, Nottingham.

Arocena, G. M., Sieira, R., Comerci, D. J., and Ugalde, R. A. (2010). Identification of the quorum-sensing target DNA sequence and N-Acyl homoserine lactone responsiveness of the *Brucella abortus* virB promoter. *J. Bacteriol.* 192, 3434–3440. doi: 10.1128/JB.00232-10

Ates, L. S., Houben, E. N., and Bitter, W. (2016). Type VII secretion: a highly versatile secretion system. *Microbiol. Spectr.* 4. doi: 10.1128/microbiolspec.VMBF-0011-2015

Baharoglu, Z., and Mazel, D. (2014). SOS, the formidable strategy of bacteria against aggressions. *FEMS Microbiol. Rev.* 38, 1126–1145. doi: 10.1111/1574-6976.12077

Ball, A. S., Chaparian, R. R., and van Kessel, J. C. (2017). Quorum sensing gene regulation by LuxR/HapR master regulators in vibrios. *J. Bacteriol.* 199:e00105-17. doi: 10.1128/JB.00105-17

Barber, C. E., Tang, J. L., Feng, J. X., Pan, M. Q., Wilson, T. J., Slater, H., et al. (1997). A novel regulatory system required for pathogenicity of *Xanthomonas campestris* is mediated by a small diffusible signal molecule. *Mol. Microbiol.* 24, 555–566. doi: 10.1046/j.1365-2958.1997.3721736.x

Bardouniotis, E., Ceri, H., and Olson, M. E. (2003). Biofilm formation and biocide susceptibility testing of *Mycobacterium fortuitum* and *Mycobacterium marinum*. *Curr. Microbiol.* 46, 28–32. doi: 10.1007/s00284-002-3796-4

Battesti, A., Majdalani, N., and Gottesman, S. (2011). The RpoS-mediated general stress response in *Escherichia coli*. *Annu. Rev. Microbiol.* 65, 189–213. doi: 10.1146/annurev-micro-090110-102946

Blanco, P., Hernando-Amado, S., Reales-Calderon, J. A., Corona, F., Lira, F., Alcalde-Rico, M., et al. (2016). Bacterial multidrug efflux pumps: much more than antibiotic resistance determinants. *Microorganisms* 4:E14. doi: 10.3390/microorganisms4010014

Bleves, S., Soscia, C., Nogueira-Orlandi, P., Lazdunski, A., and Filloux, A. (2005). Quorum sensing negatively controls type III secretion regulon expression in *Pseudomonas aeruginosa* PAO1. *J. Bacteriol.* 187, 3898–3902. doi: 10.1128/JB.187.11.3898-3902.2005

Blokesch, M. (2012). Chitin colonization, chitin degradation and chitin-induced natural competence of *Vibrio cholerae* are subject to catabolite repression. *Environ. Microbiol.* 14, 1898–1912. doi: 10.1111/j.1462-2920.2011.02689.x

Bzdrenga, J., Daudé, D., Rémy, B., Jacquet, P., Plener, L., Elias, M., et al. (2017). Biotechnological applications of quorum quenching enzymes. *Chem. Biol. Interact.* 267, 104–115. doi: 10.1016/j.cbi.2016.05.028

Cadoret, F., Ball, G., Douzi, B., and Voulhoux, R. (2014). Txc, a new type II secretion system of *Pseudomonas aeruginosa* strain PA7, is regulated by the TtsS/TtsR two-component system and directs specific secretion of the CbpE chitin-binding protein. *J. Bacteriol.* 196, 2376–2386. doi: 10.1128/JB.01563-14

Cascales, E., and Christie, P. J. (2003). The versatile bacterial type IV secretion systems. *Nat. Rev. Microbiol.* 1, 137–149. doi: 10.1038/nrmicro753

Case, R. J., Labbate, M., and Kjelleberg, S. (2008). AHL-driven quorum-sensing circuits: their frequency and function among the *Proteobacteria*. *ISME J.* 2, 345–349. doi: 10.1038/ismej.2008.13

Chapon-Herve, V., Akrim, M., Latifi, A., Williams, P., Lazdunski, A., and Bally, M. (1997). Regulation of the xcp secretion pathway by multiple quorum-sensing modulons in *Pseudomonas aeruginosa*. *Mol. Microbiol.* 24, 1169–1178. doi: 10.1046/j.1365-2958.1997.4271794.x

Chen, X., Schauder, S., Potier, N., Van Dorsselaer, A., Pelczer, I., Bassler, B. L., et al. (2002). Structural identification of a bacterial quorum-sensing signal containing boron. *Nature* 415, 545–549. doi: 10.1038/415545a

Christie, P. J. (2016). The mosaic type IV secretion systems. *Ecosal Plus* 7. doi: 10.1128/ecosalplus.ESP-0020-2015

Cianfanelli, F. R., Monlezun, L., and Coulthurst, S. J. (2016). Aim, load, fire: the type VI secretion system, a bacterial nanoweapon. *Trends Microbiol.* 24, 51–62. doi: 10.1016/j.tim.2015.10.005

Cornelis, G. R. (2006). The type III secretion injectisome. *Nat. Rev. Microbiol.* 4, 811–825. doi: 10.1038/nrmicro1526

Cornelis, G. R., and Van Gijsegem, F. (2000). Assembly and function of type III secretory systems. *Annu. Rev. Microbiol.* 54, 735–774. doi: 10.1146/annurev.micro.54.1.735

Costa, T. R., Felisberto-Rodrigues, C., Meir, A., Prevost, M. S., Redzej, A., Trokter, M., et al. (2015). Secretion systems in Gram-negative bacteria: structural and mechanistic insights. *Nat. Rev. Microbiol.* 13, 343–359. doi: 10.1038/nrmicro3456

Coulthurst, S. J. (2013). The Type VI secretion system - a widespread and versatile cell targeting system. *Res. Microbiol.* 164, 640–654. doi: 10.1016/j.resmic.2013.03.017

Czechowska, K., McKeithen-Mead, S., Al Moussawi, K., and Kazmierczak, B. I. (2014). Cheating by type 3 secretion system-negative *Pseudomonas aeruginosa*

during pulmonary infection. *Proc. Natl. Acad. Sci. U.S.A.* 111, 7801–7806. doi: 10.1073/pnas.1400782111

Delepelaire, P. (2004). Type I secretion in gram-negative bacteria. *Biochim. Biophys. Acta* 1694, 149–161. doi: 10.1016/j.bbamcr.2004.05.001

Deng, W., Marshall, N. C., Rowland, J. L., McCoy, J. M., Worrall, L. J., Santos, A. S., et al. (2017). Assembly, structure, function and regulation of type III secretion systems. *Nat. Rev. Microbiol.* 15, 323–337. doi: 10.1038/nrmicro.2017.20

Desvaux, M., Hebraud, M., Talon, R., and Henderson, I. R. (2009). Secretion and subcellular localizations of bacterial proteins: a semantic awareness issue. *Trends Microbiol.* 17, 139–145. doi: 10.1016/j.tim.2009.01.004

Dong, T. G., and Mekalanos, J. J. (2012). Characterization of the RpoN regulon reveals differential regulation of T6SS and new flagellar operons in *Vibrio cholerae* O37 strain V52. *Nucleic Acids Res.* 40, 7766–7775. doi: 10.1093/nar/gks567

Dong, Y. H., Wang, L. Y., and Zhang, L. H. (2007). Quorum-quenching microbial infections: mechanisms and implications. *Philos. Trans. R. Soc. Lond. B Biol. Sci.* 362, 1201–1211. doi: 10.1098/rstb.2007.2045

Engebrecht, J., Nealson, K., and Silverman, M. (1983). Bacterial bioluminescence: isolation and genetic analysis of functions from *Vibrio fischeri*. *Cell* 32, 773–781. doi: 10.1016/0092-8674(83)90063-6

Engebrecht, J., and Silverman, M. (1984). Identification of genes and gene products necessary for bacterial bioluminescence. *Proc. Natl. Acad. Sci. U.S.A.* 81, 4154–4158. doi: 10.1073/pnas.81.13.4154

Faure, L. M., Garvis, S., de Bentzmann, S., and Bigot, S. (2014). Characterization of a novel two-partner secretion system implicated in the virulence of *Pseudomonas aeruginosa*. *Microbiology* 160(Pt 9), 1940–1952. doi: 10.1099/mic.0.079616-0

Filloux, A., Michel, G., and Bally, M. (1998). GSP-dependent protein secretion in gram-negative bacteria: the Xcp system of *Pseudomonas aeruginosa*. *FEMS Microbiol. Rev.* 22, 177–198. doi: 10.1111/j.1574-6976.1998.tb00366.x

Flavier, A. B., Clough, S. J., Schell, M. A., and Denny, T. P. (1997). Identification of 3-hydroxypalmitic acid methyl ester as a novel autoregulator controlling virulence in *Ralstonia solanacearum*. *Mol. Microbiol.* 26, 251–259. doi: 10.1046/j.1365-2958.1997.5661945.x

Freeman, J. A., Lilley, B. N., and Bassler, B. L. (2000). A genetic analysis of the functions of LuxN: a two-component hybrid sensor kinase that regulates quorum sensing in *Vibrio harveyi*. *Mol. Microbil.* 35, 139–149. doi: 10.1046/j.1365-2958.2000.01684.x

Fuqua, W. C., Winans, S. C., and Greenberg, E. P. (1994). Quorum sensing in bacteria: the LuxR-LuxI family of cell density-responsive transcriptional regulators. *J. Bacteriol.* 176, 269–275. doi: 10.1128/jb.176.2.269-275.1994

Galan, J. E., and Waksman, G. (2018). Protein-injection machines in bacteria. *Cell* 172, 1306–1318. doi: 10.1016/j.cell.2018.01.034

Gallique, M., Bouteiller, M., and Merieau, A. (2017a). The type VI secretion system: a dynamic system for bacterial communication? *Front. Microbiol.* 8:1454. doi: 10.3389/fmicb.2017.01454

Gallique, M., Decoin, V., Barbey, C., Rosay, T., Feuilloley, M. G., Orange, N., et al. (2017b). Contribution of the *Pseudomonas fluorescens* MFE01 type VI secretion system to biofilm formation. *PLoS One* 12:e0170770. doi: 10.1371/journal.pone.0170770

Garde, C., Bjarnsholt, T., Givskov, M., Jakobsen, T. H., Hentzer, M., Claussen, A., et al. (2010). Quorum sensing regulation in *Aeromonas hydrophila*. *J. Mol. Biol.* 396, 849–857. doi: 10.1016/j.jmb.2010.01.002

Gaytan, M. O., Martinez-Santos, V. I., Soto, E., and Gonzalez-Pedrajo, B. (2016). Type three secretion system in attaching and effacing pathogens. *Front. Cell. Infect. Microbiol.* 6:129. doi: 10.3389/fcimb.2016.00129

Geske, G. D., O'Neill, J. C., and Blackwell, H. E. (2008). Expanding dialogues: from natural autoinducers to non-natural analogues that modulate quorum sensing in Gram-negative bacteria. *Chem. Soc. Rev.* 37, 1432–1447. doi: 10.1039/b703021p

Gode-Potratz, C. J., and McCarter, L. L. (2011). Quorum sensing and silencing in *Vibrio parahaemolyticus*. *J. Bacteriol.* 193, 4224–4237. doi: 10.1128/JB.00432-11

Green, E. R., and Mecsas, J. (2016). Bacterial secretion systems: an overview. *Microbiol. Spectr.* 4. doi: 10.1128/microbiolspec.VMBF-0012-2015

Grohmann, E., Christie, P. J., Waksman, G., and Backert, S. (2018). Type IV secretion in Gram-negative and Gram-positive bacteria. *Mol. Microbiol.* 107, 455–471. doi: 10.1111/mmi.13896

Hall-Stoodley, L., Keevil, C. W., and Lappin-Scott, H. M. (1998). *Mycobacterium fortuitum* and *Mycobacterium chelonae* biofilm formation under high and low nutrient conditions. *J. Appl. Microbiol.* 85(Suppl. 1), 60s–69s. doi: 10.1111/j.1365-2672.1998.tb05284.x

Han, S. W., Sriariyanun, M., Lee, S. W., Sharma, M., Bahar, O., Bower, Z., et al. (2011). Small protein-mediated quorum sensing in a Gram-negative bacterium. *PLoS One* 6:e29192. doi: 10.1371/journal.pone.0029192

Harms, A., Maisonneuve, E., and Gerdes, K. (2016). Mechanisms of bacterial persistence during stress and antibiotic exposure. *Science* 354:aaf4268. doi: 10.1126/science.aaf4268

Hauryliuk, V., Atkinson, G. C., Murakami, K. S., Tenson, T., and Gerdes, K. (2015). Recent functional insights into the role of (p)ppGpp in bacterial physiology. *Nat. Rev. Microbiol.* 13, 298–309. doi: 10.1038/nrmicro3448

Hawver, L. A., Jung, S. A., and Ng, W. L. (2016). Specificity and complexity in bacterial quorum-sensing systems. *FEMS Microbiol. Rev.* 40, 738–752. doi: 10.1093/femsre/fuw014

Henderson, I. R., Navarro-Garcia, F., Desvaux, M., Fernandez, R. C., and Ala'Aldeen, D. (2004). Type V protein secretion pathway: the autotransporter story. *Microbiol. Mol. Biol. Rev.* 68, 692–744. doi: 10.1128/MMBR.68.4.692-744.2004

Henke, J. M., and Bassler, B. L. (2004). Quorum sensing regulates type III secretion in *Vibrio harveyi* and *Vibrio parahaemolyticus*. *J. Bacteriol.* 186, 3794–3805. doi: 10.1128/JB.186.12.3794-3805.2004

Hentzer, M., Wu, H., Andersen, J. B., Riedel, K., Rasmussen, T. B., Bagge, N., et al. (2003). Attenuation of *Pseudomonas aeruginosa* virulence by quorum sensing inhibitors. *EMBO J.* 22, 3803–3815. doi: 10.1093/emboj/cdg366

Higgins, D. A., Pomianek, M. E., Kraml, C. M., Taylor, R. K., Semmelhack, M. F., and Bassler, B. L. (2007). The major *Vibrio cholerae* autoinducer and its role in virulence factor production. *Nature* 450, 883–886. doi: 10.1038/nature06284

Hirakawa, H., Kodama, T., Takumi-Kobayashi, A., Honda, T., and Yamaguchi, A. (2009). Secreted indole serves as a signal for expression of type III secretion system translocators in enterohaemorrhagic *Escherichia coli* O157:H7. *Microbiology* 155(Pt 2), 541–550. doi: 10.1099/mic.0.020420-0

Ho, B. T., Dong, T. G., and Mekalanos, J. J. (2014). A view to a kill: the bacterial type VI secretion system. *Cell Host Microbe* 15, 9–21. doi: 10.1016/j.chom.2013.11.008

Hodgkinson, J. T., Gross, J., Baker, Y. R., Spring, D. R., and Welch, M. (2016). A new *Pseudomonas* quinolone signal (PQS) binding partner: MexG. *Chem. Sci.* 7, 2553–2562. doi: 10.1039/c5sc04197j

Hogardt, M., Roeder, M., Schreff, A. M., Eberl, L., and Heesemann, J. (2004). Expression of *Pseudomonas aeruginosa exoS* is controlled by quorum sensing and RpoS. *Microbiology* 150(Pt 4), 843–851. doi: 10.1099/mic.0.26703-0

Holden, M. T., Seth-Smith, H. M., Crossman, L. C., Sebaihia, M., Bentley, S. D., Cerdeno-Tarraga, A. M., et al. (2009). The genome of *Burkholderia cenocepacia* J2315, an epidemic pathogen of cystic fibrosis patients. *J. Bacteriol.* 191, 261–277. doi: 10.1128/JB.01230-08

Ishikawa, T., Rompikuntal, P. K., Lindmark, B., Milton, D. L., and Wai, S. N. (2009). Quorum sensing regulation of the two *hcp* alleles in *Vibrio cholerae* O1 strains. *PLoS One* 4:e6734. doi: 10.1371/journal.pone.0006734

Izore, T., Job, V., and Dessen, A. (2011). Biogenesis, regulation, and targeting of the type III secretion system. *Structure* 19, 603–612. doi: 10.1016/j.str.2011.03.015

Jaskólska, M., Stutzmann, S., Stoudmann, C., and Blokesch, M. (2018). QstR-dependent regulation of natural competence and type VI secretion in *Vibrio cholerae*. *Nucleic Acids Res.* 46, 10619–10634. doi: 10.1093/nar/gky717

Javaux, C., Joris, B., and De Witte, P. (2007). Functional characteristics of TauA binding protein from TauABC *Escherichia coli* system. *Protein J.* 26, 231–238. doi: 10.1007/s10930-006-9064-x

Jimenez, P. N., Koch, G., Thompson, J. A., Xavier, K. B., Cool, R. H., and Quax, W. J. (2012). The multiple signaling systems regulating virulence in *Pseudomonas aeruginosa*. *Microbiol. Mol. Biol. Rev.* 76, 46–65. doi: 10.1128/MMBR.05007-11

Johansen, T. B., Agdestein, A., Olsen, I., Nilsen, S. F., Holstad, G., and Djonne, B. (2009). Biofilm formation by *Mycobacterium avium* isolates originating from humans, swine and birds. *BMC Microbiol.* 9:159. doi: 10.1186/1471-2180-9-159

Johnson, T. L., Fong, J. C., Rule, C., Rogers, A., Yildiz, F. H., and Sandkvist, M. (2014). The Type II secretion system delivers matrix proteins for biofilm formation by *Vibrio cholerae*. *J. Bacteriol.* 196, 4245–4252. doi: 10.1128/JB.01944-14

Jung, S. A., Chapman, C. A., and Ng, W. L. (2015). Quadruple quorum-sensing inputs control *Vibrio cholerae* virulence and maintain system robustness. *PLoS Pathog.* 11:e1004837. doi: 10.1371/journal.ppat.1004837

Kanamaru, K., Tatsuno, I., Tobe, T., and Sasakawa, C. (2000). SdiA, an *Escherichia coli* homologue of quorum-sensing regulators, controls the expression of virulence factors in enterohaemorrhagic *Escherichia coli* O157:H7. *Mol. Microbiol.* 38, 805–816. doi: 10.1046/j.1365-2958.2000.02171.x

Kanonenberg, K., Schwarz, C. K., and Schmitt, L. (2013). Type I secretion systems - a story of appendices. *Res. Microbiol.* 164, 596–604. doi: 10.1016/j.resmic.2013.03.011

Kariminik, A., Baseri-Salehi, M., and Kheirkhah, B. (2017). *Pseudomonas aeruginosa* quorum sensing modulates immune responses: an updated review article. *Immunol. Lett.* 190, 1–6. doi: 10.1016/j.imlet.2017.07.002

Khajanchi, B. K., Sha, J., Kozlova, E. V., Erova, T. E., Suarez, G., Sierra, J. C., et al. (2009). N-acylhomoserine lactones involved in quorum sensing control the type VI secretion system, biofilm formation, protease production, and in vivo virulence in a clinical isolate of *Aeromonas hydrophila*. *Microbiology* 155(Pt 11), 3518–3531. doi: 10.1099/mic.0.031575-0

Kida, Y., Higashimoto, Y., Inoue, H., Shimizu, T., and Kuwano, K. (2008). A novel secreted protease from *Pseudomonas aeruginosa* activates NF-kappaB through protease-activated receptors. *Cell Microbiol.* 10, 1491–1504. doi: 10.1111/j.1462-5822.2008.01142.x

Kita, D., Shibata, S., Kikuchi, Y., Kokubu, E., Nakayama, K., Saito, A., et al. (2016). Involvement of the type IX secretion system in *Capnocytophaga ochracea* gliding motility and biofilm formation. *Appl. Environ. Microbiol.* 82, 1756–1766. doi: 10.1128/AEM.03452-15

Kitaoka, M., Miyata, S. T., Brooks, T. M., Unterweger, D., and Pukatzki, S. (2011). VasH is a transcriptional regulator of the type VI secretion system functional in endemic and pandemic *Vibrio cholerae*. *J. Bacteriol.* 193, 6471–6482. doi: 10.1128/JB.05414-11

Kong, W., Liang, H., Shen, L., and Duan, K. (2009). [Regulation of type III secretion system by Rhl and PQS quorum sensing systems in *Pseudomonas aeruginosa*]. *Wei Sheng Wu Xue Bao* 49, 1158–1164.

Korotkov, K. V., Sandkvist, M., and Hol, W. G. (2012). The type II secretion system: biogenesis, molecular architecture and mechanism. *Nat. Rev. Microbiol.* 10, 336–351. doi: 10.1038/nrmicro2762

Korshunov, S., and Imlay, J. A. (2010). Two sources of endogenous hydrogen peroxide in *Escherichia coli*. *Mol. Microbiol.* 75, 1389–1401. doi: 10.1111/j.1365-2958.2010.07059.x

Kulka, K., Hatfull, G., and Ojha, A. K. (2012). Growth of *Mycobacterium tuberculosis* biofilms. *J. Vis. Exp.* 60:3820. doi: 10.3791/3820

Lai, L. Y., Lin, T. L., Chen, Y. Y., Hsieh, P. F., and Wang, J. T. (2018). Role of the *Mycobacterium marinum* ESX-1 secretion system in sliding motility and biofilm formation. *Front. Microbiol.* 9:1160. doi: 10.3389/fmicb.2018.01160

Lara-Tejero, M., and Galan, J. E. (2019). The injectisome, a complex nanomachine for protein injection into mammalian cells. *Ecosal Plus* 8. doi: 10.1128/ecosalplus.ESP-0039-2018

Lasica, A. M., Ksiazek, M., Madej, M., and Potempa, J. (2017). The type IX secretion system (T9SS): highlights and recent insights into its structure and function. *Front. Cell. Infect. Microbiol.* 7:215. doi: 10.3389/fcimb.2017.00215

Lee, J., Bansal, T., Jayaraman, A., Bentley, W. E., and Wood, T. K. (2007). Enterohemorrhagic *Escherichia coli* biofilms are inhibited by 7-hydroxyindole and stimulated by isatin. *Appl. Environ. Microbiol.* 73, 4100–4109. doi: 10.1128/AEM.00360-07

Lee, J., Zhang, X-S., Hegde, M., Bentley, W. E., Jayaraman, A., and Wood, T. K. (2008). Indole cell signaling occurs primarily at low temperatures in *Escherichia coli*. *ISME J.* 2, 1007–1023. doi: 10.1038/ismej.2008.54

Lee, J. H., and Lee, J. (2010). Indole as an intercellular signal in microbial communities. *FEMS Microbiol. Rev.* 34, 426–444. doi: 10.1111/j.1574-6976.2009.00204.x

Lee, S. W., Han, S. W., Bartley, L. E., and Ronald, P. C. (2006). From the academy: colloquium review. Unique characteristics of *Xanthomonas oryzae* pv. *oryzae* AvrXa21 and implications for plant innate immunity. *Proc. Natl. Acad. Sci. U.S.A.* 103, 18395–18400. doi: 10.1073/pnas.0605508103

Leiman, P. G., Basler, M., Ramagopal, U. A., Bonanno, J. B., Sauder, J. M., Pukatzki, S., et al. (2009). Type VI secretion apparatus and phage tail-associated protein complexes share a common evolutionary origin. *Proc. Natl. Acad. Sci. U.S.A.* 106, 4154–4159. doi: 10.1073/pnas.0813360106

Lenz, D. H., Mok, K. C., Lilley, B. N., Kulkarni, R. V., Wingreen, N. S., and Bassler, B. L. (2004). The small RNA chaperone Hfq and multiple small RNAs control quorum sensing in *Vibrio harveyi* and *Vibrio cholerae*. *Cell* 118, 69–82. doi: 10.1016/j.cell.2004.06.009

Leo, J. C., Grin, I., and Linke, D. (2012). Type V secretion: mechanism(s) of autotransport through the bacterial outer membrane. *Philos. Trans. R. Soc. Lond. B Biol. Sci.* 367, 1088–1101. doi: 10.1098/rstb.2011.0208

Lesic, B., Starkey, M., He, J., Hazan, R., and Rahme, L. G. (2009). Quorum sensing differentially regulates *Pseudomonas aeruginosa* type VI secretion locus I and homologous loci II and III, which are required for pathogenesis. *Microbiology* 155(Pt 9), 2845–2855. doi: 10.1099/mic.0.029082-0

Leung, K. Y., Siame, B. A., Snowball, H., and Mok, Y. K. (2011). Type VI secretion regulation: crosstalk and intracellular communication. *Curr. Opin. Microbiol.* 14, 9–15. doi: 10.1016/j.mib.2010.09.017

Li, P., Tian, M., Bao, Y., Hu, H., Liu, J., Yin, Y., et al. (2017). *Brucella* rough mutant induce macrophage death via activating IRE1alpha pathway of endoplasmic reticulum stress by enhanced T4SS secretion. *Front. Cell. Infect. Microbiol.* 7:422. doi: 10.3389/fcimb.2017.00422

Liang, H., Deng, X., Li, X., Ye, Y., and Wu, M. (2014). Molecular mechanisms of master regulator VqsM mediating quorum-sensing and antibiotic resistance in *Pseudomonas aeruginosa*. *Nucleic Acids Res.* 42, 10307–10320. doi: 10.1093/nar/gku586

Liang, W., Pascual-Montano, A., Silva, A. J., and Benitez, J. A. (2007). The cyclic AMP receptor protein modulates quorum sensing, motility and multiple genes that affect intestinal colonization in *Vibrio cholerae*. *Microbiology* 153(Pt 9), 2964–2975. doi: 10.1099/mic.0.2007/006668-0

Lin, J., Zhang, W., Cheng, J., Yang, X., Zhu, K., Wang, Y., et al. (2017). A *Pseudomonas* T6SS effector recruits PQS-containing outer membrane vesicles for iron acquisition. *Nat. Commun.* 8:14888. doi: 10.1038/ncomms14888

Liu, H., Wang, Q., Liu, Q., Cao, X., Shi, C., and Zhang, Y. (2011). Roles of Hfq in the stress adaptation and virulence in fish pathogen *Vibrio alginolyticus* and its potential application as a target for live attenuated vaccine. *Appl. Microbiol. Biotechnol.* 91, 353–364. doi: 10.1007/s00253-011-3286-3

Lo Scrudato, M., and Blokesch, M. (2012). The regulatory network of natural competence and transformation of *Vibrio cholerae*. *PLoS Genet.* 8:e1002778. doi: 10.1371/journal.pgen.1002778

Lo Scrudato, M., and Blokesch, M. (2013). A transcriptional regulator linking quorum sensing and chitin induction to render *Vibrio cholerae* naturally transformable. *Nucleic Acids Res.* 41, 3644–3658. doi: 10.1093/nar/gkt041

Lopez, M., Blasco, L., Gato, E., Perez, A., Fernandez-Garcia, L., Martinez-Martinez, L., et al. (2017a). Response to bile salts in clinical strains of *Acinetobacter baumannii* lacking the AdeABC efflux pump: virulence associated with quorum sensing. *Front. Cell. Infect. Microbiol.* 7:143. doi: 10.3389/fcimb.2017.00143

Lopez, M., Mayer, C., Fernandez-Garcia, L., Blasco, L., Muras, A., Ruiz, F. M., et al. (2017b). Quorum sensing network in clinical strains of *A. baumannii*: aidA is a new quorum quenching enzyme. *PLoS One* 12:e0174454. doi: 10.1371/journal.pone.0174454

Lopez, M. S., Tan, I. S., Yan, D., Kang, J., McCreary, M., Modrusan, Z., et al. (2017c). Host-derived fatty acids activate type VII secretion in *Staphylococcus aureus*. *Proc. Natl. Acad. Sci. U.S.A.* 114, 11223–11228. doi: 10.1073/pnas.1700627114

Lopez, M., Rueda, A., Florido, J. P., Blasco, L., Fernandez-Garcia, L., Trastoy, R., et al. (2018). Evolution of the Quorum network and the mobilome (plasmids and bacteriophages) in clinical strains of *Acinetobacter baumannii* during a decade. *Sci. Rep.* 8:2523. doi: 10.1038/s41598-018-20847-7

Majerczyk, C., Schneider, E., and Greenberg, E. P. (2016). Quorum sensing control of Type VI secretion factors restricts the proliferation of quorum-sensing mutants. *eLife* 5:e14712. doi: 10.7554/eLife.14712

Marsollier, L., Brodin, P., Jackson, M., Kordulakova, J., Tafelmeyer, P., Carbonnelle, E., et al. (2007). Impact of *Mycobacterium ulcerans* biofilm on transmissibility to ecological niches and Buruli ulcer pathogenesis. *PLoS Pathog.* 3:e62. doi: 10.1371/journal.ppat.0030062

Matz, C., Moreno, A. M., Alhede, M., Manefield, M., Hauser, A. R., Givskov, M., et al. (2008). *Pseudomonas aeruginosa* uses type III secretion system to kill biofilm-associated amoebae. *ISME J.* 2, 843–852. doi: 10.1038/ismej.2008.47

Maura, D., Hazan, R., Kitao, T., Ballok, A. E., and Rahme, L. G. (2016). Evidence for direct control of virulence and defense gene circuits by the *Pseudomonas*

aeruginosa quorum sensing regulator, MvfR. *Sci. Rep.* 6:34083. doi: 10.1038/srep34083

McBride, M. J., and Zhu, Y. (2013). Gliding motility and Por secretion system genes are widespread among members of the phylum bacteroidetes. *J. Bacteriol.* 195, 270–278. doi: 10.1128/JB.01962-12

Michel, G. P., Aguzzi, A., Ball, G., Soscia, C., Bleves, S., and Voulhoux, R. (2011). Role of fimV in type II secretion system-dependent protein secretion of *Pseudomonas aeruginosa* on solid medium. *Microbiology* 157(Pt 7), 1945–1954. doi: 10.1099/mic.0.045849-0

Michel, G. P., Durand, E., and Filloux, A. (2007). XphA/XqhA, a novel GspCD subunit for type II secretion in *Pseudomonas aeruginosa*. *J. Bacteriol.* 189, 3776–3783. doi: 10.1128/JB.00205-07

Miller, M. B., Skorupski, K., Lenz, D. H., Taylor, R. K., and Bassler, B. L. (2002). Parallel quorum sensing systems converge to regulate virulence in *Vibrio cholerae*. *Cell* 110, 303–314. doi: 10.1016/S0092-8674(02)00829-2

Milton, D. L. (2006). Quorum sensing in vibrios: complexity for diversification. *Int. J. Med. Microbiol.* 296, 61–71. doi: 10.1016/j.ijmm.2006.01.044

Nagai, H., and Kubori, T. (2011). Type IVB secretion systems of *Legionella* and other gram-negative bacteria. *Front. Microbiol.* 2:136. doi: 10.3389/fmicb.2011.00136

Nealson, K. H., Platt, T., and Hastings, J. W. (1970). Cellular control of the synthesis and activity of the bacterial luminescent system. *J. Bacteriol.* 104, 313–322.

Ng, W. L., and Bassler, B. L. (2009). Bacterial quorum-sensing network architectures. *Annu. Rev. Genet.* 43, 197–222. doi: 10.1146/annurev-genet-102108-134304

Nivaskumar, M., and Francetic, O. (2014). Type II secretion system: a magic beanstalk or a protein escalator. *Biochim. Biophys. Acta* 1843, 1568–1577. doi: 10.1016/j.bbamcr.2013.12.020

Notti, R. Q., and Stebbins, C. E. (2016). The structure and function of type III secretion systems. *Microbiol. Spectr.* 4. doi: 10.1128/microbiolspec.VMBF-0004-2015

Novick, R. P., and Geisinger, E. (2008). Quorum sensing in staphylococci. *Annu. Rev. Genet.* 42, 541–564. doi: 10.1146/annurev.genet.42.110807.091640

Ojha, A., Anand, M., Bhatt, A., Kremer, L., Jacobs, W. R. Jr., and Hatfull, G. F. (2005). GroEL1: a dedicated chaperone involved in mycolic acid biosynthesis during biofilm formation in mycobacteria. *Cell* 123, 861–873. doi: 10.1016/j.cell.2005.09.012

Overbye, L. J., Sandkvist, M., and Bagdasarian, M. (1993). Genes required for extracellular secretion of enterotoxin are clustered in *Vibrio cholerae*. *Gene* 132, 101–106. doi: 10.1016/0378-1119(93)90520-D

Patel, R., Smith, S. M., and Robinson, C. (2014). Protein transport by the bacterial Tat pathway. *Biochim. Biophys. Acta* 1843, 1620–1628. doi: 10.1016/j.bbamcr.2014.02.013

Patzelt, D., Michael, V., Pauker, O., Ebert, M., Tielen, P., Jahn, D., et al. (2016). Gene flow across genus barriers - conjugation of *Dinoroseobacter shibae*'s 191-kb killer plasmid into *Phaeobacter inhibens* and AHL-mediated expression of type IV secretion systems. *Front. Microbiol.* 7:742. doi: 10.3389/fmicb.2016.00742

Patzelt, D., Wang, H., Buchholz, I., Rohde, M., Grobe, L., Pradella, S., et al. (2013). You are what you talk: quorum sensing induces individual morphologies and cell division modes in *Dinoroseobacter shibae*. *ISME J.* 7, 2274–2286. doi: 10.1038/ismej.2013.107

Paul, D., Gopal, J., Kumar, M., and Manikandan, M. (2018). Nature to the natural rescue: silencing microbial chats. *Chem. Biol. Interact.* 280, 86–98. doi: 10.1016/j.cbi.2017.12.018

Pesci, E. C., Milbank, J. B., Pearson, J. P., McKnight, S., Kende, A. S., Greenberg, E. P., et al. (1999). Quinolone signaling in the cell-to-cell communication system of *Pseudomonas aeruginosa*. *Proc. Natl. Acad. Sci. U.S.A.* 96, 11229–11234. doi: 10.1073/pnas.96.20.11229

Pukatzki, S., Ma, A. T., Revel, A. T., Sturtevant, D., and Mekalanos, J. J. (2007). Type VI secretion system translocates a phage tail spike-like protein into target cells where it cross-links actin. *Proc. Natl. Acad. Sci. U.S.A.* 104, 15508–15513. doi: 10.1073/pnas.0706532104

Qian, G., Zhou, Y., Zhao, Y., Song, Z., Wang, S., Fan, J., et al. (2013). Proteomic analysis reveals novel extracellular virulence-associated proteins and functions regulated by the diffusible signal factor (DSF) in *Xanthomonas oryzae* pv. *oryzicola*. *J. Proteome Res.* 12, 3327–3341. doi: 10.1021/pr4001543

Rai, N., Rai, R., and Kareenhalli, V. (2015). "Quorum sensing in competence and sporulation", in *Quorum Sensing vs Quorum Qenching: A Battle with No End in Sight*, ed. K. Vipin Chandra (New Delhi: Springer), 61–64.

Rhoades, E. R., Archambault, A. S., Greendyke, R., Hsu, F. F., Streeter, C., and Byrd, T. F. (2009). *Mycobacterium abscessus* Glycopeptidolipids mask underlying cell wall phosphatidyl-myo-inositol mannosides blocking induction of human macrophage TNF-alpha by preventing interaction with TLR2. *J. Immunol.* 183, 1997–2007. doi: 10.4049/jimmunol.0802181

Riedel, K., Ohnesorg, T., Krogfelt, K. A., Hansen, T. S., Omori, K., Givskov, M., et al. (2001). N-acyl-L-homoserine lactone-mediated regulation of the lip secretion system in *Serratia liquefaciens* MG1. *J. Bacteriol.* 183, 1805–1809. doi: 10.1128/JB.183.5.1805-1809.2001

Robert, V., Filloux, A., and Michel, G. P. (2005). Subcomplexes from the Xcp secretion system of *Pseudomonas aeruginosa*. *FEMS Microbiol. Lett.* 252, 43–50. doi: 10.1016/j.femsle.2005.08.029

Rojas-Lopez, M., Zorgani, M. A., Kelley, L. A., Bailly, X., Kajava, A. V., Henderson, I. R., et al. (2017). Identification of the autochaperone domain in the type va secretion system (T5aSS): prevalent feature of autotransporters with a beta-helical passenger. *Front. Microbiol.* 8:2607. doi: 10.3389/fmicb.2017.02607

Ruer, S., Ball, G., Filloux, A., and de Bentzmann, S. (2008). The 'P-usher', a novel protein transporter involved in fimbrial assembly and TpsA secretion. *EMBO J.* 27, 2669–2680. doi: 10.1038/emboj.2008.197

Russell, A. B., Hood, R. D., Bui, N. K., LeRoux, M., Vollmer, W., and Mougous, J. D. (2011). Type VI secretion delivers bacteriolytic effectors to target cells. *Nature* 475, 343–347. doi: 10.1038/nature10244

Russell, A. B., Peterson, S. B., and Mougous, J. D. (2014). Type VI secretion system effectors: poisons with a purpose. *Nat. Rev. Microbiol.* 12, 137–148. doi: 10.1038/nrmicro3185

Ruwandeepika, H. A., Karunasagar, I., Bossier, P., and Defoirdt, T. (2015). Expression and quorum sensing regulation of type III secretion system genes of *Vibrio harveyi* during infection of gnotobiotic brine shrimp. *PLoS One* 10:e0143935. doi: 10.1371/journal.pone.0143935

Ryan, R. P., Monchy, S., Cardinale, M., Taghavi, S., Crossman, L., Avison, M. B., et al. (2009). The versatility and adaptation of bacteria from the genus *Stenotrophomonas*. *Nat. Rev. Microbiol.* 7, 514–525. doi: 10.1038/nrmicro2163

Sana, T. G., Hachani, A., Bucior, I., Soscia, C., Garvis, S., Termine, E., et al. (2012). The second type VI secretion system of *Pseudomonas aeruginosa* strain PAO1 is regulated by quorum sensing and Fur and modulates internalization in epithelial cells. *J. Biol. Chem.* 287, 27095–27105. doi: 10.1074/jbc.M112.376368

Sato, K., Naito, M., Yukitake, H., Hirakawa, H., Shoji, M., McBride, M. J., et al. (2010). A protein secretion system linked to bacteroidete gliding motility and pathogenesis. *Proc. Natl. Acad. Sci. U.S.A.* 107, 276–281. doi: 10.1073/pnas.0912010107

Schauder, S., Shokat, K., Surette, M. G., and Bassler, B. L. (2001). The LuxS family of bacterial autoinducers: biosynthesis of a novel quorum-sensing signal molecule. *Mol. Microbiol.* 41, 463–476. doi: 10.1046/j.1365-2958.2001.02532.x

Schiano, C. A., Koo, J. T., Schipma, M. J., Caulfield, A. J., Jafari, N., and Lathem, W. W. (2014). Genome-wide analysis of small RNAs expressed by *Yersinia pestis* identifies a regulator of the Yop-Ysc type III secretion system. *J. Bacteriol.* 196, 1659–1670. doi: 10.1128/JB.01456-13

Schulthess, B., Bloes, D. A., and Berger-Bachi, B. (2012). Opposing roles of sigmaB and sigmaB-controlled SpoVG in the global regulation of *esxA* in *Staphylococcus aureus*. *BMC Microbiol.* 12:17. doi: 10.1186/1471-2180-12-17

Schuster, M., Lostroh, C. P., Ogi, T., and Greenberg, E. P. (2003). Identification, timing, and signal specificity of *Pseudomonas aeruginosa* quorum-controlled genes: a transcriptome analysis. *J. Bacteriol.* 185, 2066–2079. doi: 10.1128/JB.185.7.2066-2079.2003

Seed, P. C., Passador, L., and Iglewski, B. H. (1995). Activation of the *Pseudomonas aeruginosa lasI* gene by LasR and the *Pseudomonas* autoinducer PAI: an autoinduction regulatory hierarchy. *J. Bacteriol.* 177, 654–659. doi: 10.1128/jb.177.3.654-659.1995

Shanker, E., and Federle, M. J. (2017). Quorum sensing regulation of competence and bacteriocins in *Streptococcus pneumoniae* and *mutans*. *Genes* 8:E15. doi: 10.3390/genes8010015

Shao, Y., and Bassler, B. L. (2014). Quorum regulatory small RNAs repress type VI secretion in *Vibrio cholerae*. *Mol. Microbiol.* 92, 921–930. doi: 10.1111/mmi.12599

Sharma, I. M., Petchiappan, A., and Chatterji, D. (2014). Quorum sensing and biofilm formation in mycobacteria: role of c-di-GMP and methods to study this second messenger. *IUBMB Life* 66, 823–834. doi: 10.1002/iub.1339

Sheng, L., Gu, D., Wang, Q., Liu, Q., and Zhang, Y. (2012). Quorum sensing and alternative sigma factor RpoN regulate type VI secretion system I (T6SSVA1) in fish pathogen *Vibrio alginolyticus*. *Arch. Microbiol.* 194, 379–390. doi: 10.1007/s00203-011-0780-z

Sheng, L., Lv, Y., Liu, Q., Wang, Q., and Zhang, Y. (2013). Connecting type VI secretion, quorum sensing, and c-di-GMP production in fish pathogen *Vibrio alginolyticus* through phosphatase PppA. *Vet. Microbiol.* 162, 652–662. doi: 10.1016/j.vetmic.2012.09.009

Sloup, R. E., Konal, A. E., Severin, G. B., Korir, M. L., Bagdasarian, M. M., Bagdasarian, M., et al. (2017). Cyclic Di-GMP and VpsR induce the expression of type II secretion in *Vibrio cholerae*. *J. Bacteriol.* 199:e00106-17. doi: 10.1128/JB.00106-17

Soto-Aceves, M. P., Cocotl-Yanez, M., Merino, E., Castillo-Juarez, I., Cortes-Lopez, H., Gonzalez-Pedrajo, B., et al. (2019). Inactivation of the quorum-sensing transcriptional regulators LasR or RhlR does not suppress the expression of virulence factors and the virulence of *Pseudomonas aeruginosa* PAO1. *Microbiology* 165, 425–432. doi: 10.1099/mic.0.000778

Sperandio, V., Mellies, J. L., Nguyen, W., Shin, S., and Kaper, J. B. (1999). Quorum sensing controls expression of the type III secretion gene transcription and protein secretion in enterohemorrhagic and enteropathogenic *Escherichia coli*. *Proc. Natl. Acad. Sci. U.S.A.* 96, 15196–15201. doi: 10.1073/pnas.96.26.15196

Stanley, S. A., Raghavan, S., Hwang, W. W., and Cox, J. S. (2003). Acute infection and macrophage subversion by *Mycobacterium tuberculosis* require a specialized secretion system. *Proc. Natl. Acad. Sci. U.S.A.* 100, 13001–13006. doi: 10.1073/pnas.2235593100

Stintzi, A., Evans, K., Meyer, J. M., and Poole, K. (1998). Quorum-sensing and siderophore biosynthesis in *Pseudomonas aeruginosa*: *lasR/lasI* mutants exhibit reduced pyoverdine biosynthesis. *FEMS Microbiol. Lett.* 166, 341–345. doi: 10.1111/j.1574-6968.1998.tb13910.x

Surette, M. G., Miller, M. B., and Bassler, B. L. (1999). Quorum sensing in *Escherichia coli*, *Salmonella typhimurium*, and *Vibrio harveyi*: a new family of genes responsible for autoinducer production. *Proc. Natl. Acad. Sci. U.S.A.* 96, 1639–1644. doi: 10.1073/pnas.96.4.1639

Teschler, J. K., Zamorano-Sanchez, D., Utada, A. S., Warner, C. J., Wong, G. C., Linington, R. G., et al. (2015). Living in the matrix: assembly and control of *Vibrio cholerae* biofilms. *Nat. Rev. Microbiol.* 13, 255–268. doi: 10.1038/nrmicro3433

Thomas, S., Holland, I. B., and Schmitt, L. (2014). The Type 1 secretion pathway - the hemolysin system and beyond. *Biochim. Biophys. Acta* 1843, 1629–1641. doi: 10.1016/j.bbamcr.2013.09.017

Trastoy, R., Manso, T., Fernandez-Garcia, L., Blasco, L., Ambroa, A., Perez Del Molino, M. L., et al. (2018). Mechanisms of bacterial tolerance and persistence in the gastrointestinal and respiratory environments. *Clin. Microbiol. Rev.* 31:e00023-18. doi: 10.1128/CMR.00023-18

Tseng, T.-T., Tyler, B. M., and Setubal, J. C. (2009). Protein secretion systems in bacterial-host associations, and their description in the Gene Ontology. *BMC Microbiol.* 9:S2. doi: 10.1186/1471-2180-9-S1-S2

Tsirigotaki, A., De Geyter, J., Sostaric, N., Economou, A., and Karamanou, S. (2017). Protein export through the bacterial Sec pathway. *Nat. Rev. Microbiol.* 15, 21–36. doi: 10.1038/nrmicro.2016.161

Tsou, A. M., Cai, T., Liu, Z., Zhu, J., and Kulkarni, R. V. (2009). Regulatory targets of quorum sensing in *Vibrio cholerae*: evidence for two distinct HapR-binding motifs. *Nucleic Acids Res.* 37, 2747–2756. doi: 10.1093/nar/gkp121

Van den Bergh, B., Fauvart, M., and Michiels, J. (2017). Formation, physiology, ecology, evolution and clinical importance of bacterial persisters. *FEMS Microbiol. Rev.* 41, 219–251. doi: 10.1093/femsre/fux001

Vilches, S., Jimenez, N., Tomas, J. M., and Merino, S. (2009). *Aeromonas hydrophila* AH-3 type III secretion system expression and regulatory network. *Appl. Environ. Microbiol.* 75, 6382–6392. doi: 10.1128/AEM.00222-09

Virmani, R., Hasija, Y., and Singh, Y. (2018). Effect of homocysteine on biofilm formation by mycobacteria. *Indian J. Microbiol.* 58, 287–293. doi: 10.1007/s12088-018-0739-8

Wagner, V. E., Bushnell, D., Passador, L., Brooks, A. I., and Iglewski, B. H. (2003). Microarray analysis of *Pseudomonas aeruginosa* quorum-sensing regulons: effects of growth phase and environment. *J. Bacteriol.* 185, 2080–2095. doi: 10.1128/JB.185.7.2080-2095.2003

Waters, C. M., and Bassler, B. L. (2005). Quorum sensing: cell-to-cell communication in bacteria. *Annu. Rev. Cell Dev. Biol.* 21, 319–346. doi: 10.1146/annurev.cellbio.21.012704.131001

Waters, C. M., Wu, J. T., Ramsey, M. E., Harris, R. C., and Bassler, B. L. (2010). Control of the type 3 secretion system in *Vibrio harveyi* by quorum sensing through repression of ExsA. *Appl. Environ. Microbiol.* 76, 4996–5004. doi: 10.1128/AEM.00886-10

Watve, S. S., Thomas, J., and Hammer, B. K. (2015). CytR is a global positive regulator of competence, type VI secretion, and chitinases in *Vibrio cholerae*. *PLoS One* 10:e0138834. doi: 10.1371/journal.pone.0138834

Whiteley, M., Diggle, S. P., and Greenberg, E. P. (2017). Progress in and promise of bacterial quorum sensing research. *Nature* 551, 313–320. doi: 10.1038/nature24624

Wilhelm, S., Gdynia, A., Tielen, P., Rosenau, F., and Jaeger, K. E. (2007). The autotransporter esterase EstA of *Pseudomonas aeruginosa* is required for rhamnolipid production, cell motility, and biofilm formation. *J. Bacteriol.* 189, 6695–6703. doi: 10.1128/JB.00023-07

Wood, T. K., Knabelm, S. J., and Kwan, B. W. (2013). Bacterial persister cell formation and dormancy. *Appl. Environ. Microbiol.* 79, 7116–7121. doi: 10.1128/AEM.02636-13

Xiao, G., Déziel, E., He, J., Lépine, F., Lesic, B., Castonguay, M. H., et al. (2006). MvfR, a key *Pseudomonas aeruginosa* pathogenicity LTTR-class regulatory protein, has dual ligands. *Mol. Microbiol.* 62, 1689–1699. doi: 10.1111/j.1365-2958.2006.05462.x

Yang, Z., Zhou, X., Ma, Y., Zhou, M., Waldor, M. K., Zhang, Y., et al. (2018). Serine/threonine kinase PpkA coordinates the interplay between T6SS2 activation and quorum sensing in the marine pathogen *Vibrio alginolyticus*. *Environ. Microbiol.* 20, 903–919. doi: 10.1111/1462-2920.14039

Zhang, L. H., and Dong, Y. H. (2004). Quorum sensing and signal interference: diverse implications. *Mol. Microbiol.* 53, 1563–1571. doi: 10.1111/j.1365-2958.2004.04234.x

Zhang, Y., Sass, A., Van Acker, H., Wille, J., Verhasselt, B., Van Nieuwerburgh, F., et al. (2018). Coumarin reduces virulence and biofilm formation in *Pseudomonas aeruginosa* by affecting quorum sensing, type III secretion and C-di-GMP levels. *Front. Microbiol.* 9:1952. doi: 10.3389/fmicb.2018.01952

Zhao, X., and Drlica, K. (2014). Reactive oxygen species and the bacterial response to lethal stress. *Curr. Opin. Microbiol.* 21, 1-6. doi: 10.1016/j.mib.2014.06.008

Zheng, J., Shin, O. S., Cameron, D. E., and Mekalanos, J. J. (2010). Quorum sensing and a global regulator TsrA control expression of type VI secretion and virulence in *Vibrio cholerae*. *Proc. Natl. Acad. Sci. U.S.A.* 107, 21128–21133. doi: 10.1073/pnas.1014998107

Zoued, A., Brunet, Y. R., Durand, E., Aschtgen, M. S., Logger, L., Douzi, B., et al. (2014). Architecture and assembly of the Type VI secretion system. *Biochim. Biophys. Acta* 1843, 1664–1673. doi: 10.1016/j.bbamcr.2014.03.018

Conflict of Interest Statement: The authors declare that the research was conducted in the absence of any commercial or financial relationships that could be construed as a potential conflict of interest.

Copyright © 2019 Pena, Blasco, Ambroa, González-Pedrajo, Fernández-García, López, Bleriot, Bou, García-Contreras, Wood and Tomás. This is an open-access article distributed under the terms of the Creative Commons Attribution License (CC BY). The use, distribution or reproduction in other forums is permitted, provided the original author(s) and the copyright owner(s) are credited and that the original publication in this journal is cited, in accordance with accepted academic practice. No use, distribution or reproduction is permitted which does not comply with these terms.

INFORME DE LABORES 2019

Received: 14 December 2017 | Revised: 15 May 2018 | Accepted: 15 May 2018

DOI: 10.1002/mbo3.675

Check for updates

ORIGINAL ARTICLE

WILEY MicrobiologyOpen Open Access

Wolbachia pipientis grows in *Saccharomyces cerevisiae* evoking early death of the host and deregulation of mitochondrial metabolism

Cristina Uribe-Alvarez[1]* | Natalia Chiquete-Félix[1]* | Lilia Morales-García[1] | Arlette Bohórquez-Hernández[2] | Norma Laura Delgado-Buenrostro[3] | Luis Vaca[2] | Antonio Peña[1] | Salvador Uribe-Carvajal[1]

[1]Depto. de Genética Molecular, Instituto de Fisiología Celular, Universidad Nacional Autónoma de México, Ciudad de México, México

[2]Depto. de Biología Celular y del Desarrollo, Instituto de Fisiología Celular, Universidad Nacional Autónoma de México, Ciudad de México, México

[3]Unidad de Biomedicina UBIMED, Facultad de Estudios Superiores Iztacala, Universidad Nacional Autónoma de México, Tlanepantla, Edo. de México, México

Correspondence
Antonio Peña and Salvador Uribe-Carvajal
Depto. de Genética Molecular, Instituto de Fisiología Celular, Universidad Nacional Autónoma de México, Ciudad de México, México.
Emails: apd@ifc.unam.mx; suribe@ifc.unam.mx

Funding information
Dirección General de Asuntos del Personal Académico, Universidad Nacional Autónoma de México, Grant/Award Number: IN204015 and IN2114; Consejo Nacional de Ciencia y Tecnología, Grant/Award Number: 239487 and 344726

Abstract

Wolbachia sp. has colonized over 70% of insect species, successfully manipulating host fertility, protein expression, lifespan, and metabolism. Understanding and engineering the biochemistry and physiology of *Wolbachia* holds great promise for insect vector-borne disease eradication. *Wolbachia* is cultured in cell lines, which have long duplication times and are difficult to manipulate and study. The yeast strain *Saccharomyces cerevisiae* W303 was used successfully as an artificial host for *Wolbachia w*AlbB. As compared to controls, infected yeast lost viability early, probably as a result of an abnormally high mitochondrial oxidative phosphorylation activity observed at late stages of growth. No respiratory chain proteins from *Wolbachia* were detected, while several *Wolbachia* F_1F_0-ATPase subunits were revealed. After 5 days outside the cell, *Wolbachia* remained fully infective against insect cells.

KEYWORDS

bioenergetics, endosymbiosis, oxidative phosphorylation, *Saccharomyces cerevisiae*, *Wolbachia pipientis*

1 | INTRODUCTION

Construction of artificial ecosystems mimicking symbiotic relationships have been proposed to study ecology and evolution of symbioses (Hosoda et al., 2011; Momeni, Chen, Hillesland, Waite, & Shou, 2011), to engineer microbial consortia (Brenner, You, & Arnold, 2008; French, 2017; Frey-Klett et al., 2011; Mee & Wang, 2012), and to host uncultivable bacteria (Stewart, 2012). Synthetic mutualism of species that do not interact naturally has been established in co-culture between bacteria, yeast, amoeba, alga, cell lines, and tissues (Buchsbaum & Buchsbaum, 1934; Hosoda & Yomo, 2011; Hosoda et al., 2011; Kubo et al., 2013; Lőrincz et al., 2010; Shou, Ram, & Vilar, 2007). Several bacterial endosymbionts have been found in yeast (Kang, Jeon, Hwang, & Park, 2009; Saniee & Siavoshi, 2015) as

*Cofirst authors.

This is an open access article under the terms of the Creative Commons Attribution License, which permits use, distribution and reproduction in any medium, provided the original work is properly cited.
© 2018 The Authors. *MicrobiologyOpen* published by John Wiley & Sons Ltd.

INFORME DE LABORES 2019

well as in fungal hyphae and spores (Bertaux et al., 2003; Bianciotto et al., 2004; de Boer et al., 2004; Hoffman & Arnold, 2010; Lumini, Ghignone, Bianciotto, & Bonfante, 2006; Partida-Martinez & Hertweck, 2005; Sato et al., 2010). In this work, we cultured the obligate endosymbiont bacterium *Wolbachia* in an artificial host: the nonpathogenic yeast *Saccharomyces cerevisiae*.

Wolbachia pipientis is an exceedingly successful obligate endoparasite/endosymbiont in nematodes and arthropods (Taylor & Hoerauf, 1999; Werren, 1997; Werren, Baldo, & Clark, 2008). The size of the *Wolbachia* genome varies widely depending on the strain. Arthropod endoparasites have much larger genomes than nematode endosymbionts (Bandi, Slatko, & O'Neill, 1999; Darby et al., 2012; Foster et al., 2005; Klasson et al., 2008; Salzberg, Puiu, Sommer, Nene, & Lee, 2009; Wu et al., 2004). In regard to a possible aerobic metabolism, the *Wolbachia* from the plant hopper *Leodelphax stratellus* (*wStr*) is ten times more sensitive to paraquat than the insect host cell, suggesting that *wStr* does not possess the enzymes needed for reactive oxygen species (ROS) detoxification and thus it may be anaerobic or microaerophilic (Fallon, Kurtz, & Carroll, 2013). In contrast, eliminating *Wolbachia* with tetracycline in filaria, increases respiratory-chain gene expression in the host and causes an early death. This result, lead to the hypothesis that at least in filariae *Wolbachia* contributes as an energy generator for the host (Strübing, Lucius, Hoerauf, & Pfarr, 2010; Darby et al., 2012, 2014).

Culturing obligate intracellular bacteria is a challenge. Insect cells support *Wolbachia* growth, but culture times are long and cells are difficult to manipulate. Alternative systems such as mammalian blood have proven helpful to grow intracellular organisms such as *Sodalis* (Dale & Maudlin, 1999). However, *Wolbachia* did not seem to grow in blood and this was not pursued further (Result not-shown; see Methods). In contrast, *Saccharomyces cerevisiae* did support the growth of *Wolbachia* strain *w*AlbB.

As it can be extensively manipulated, *S. cerevisiae* is widely used as a model organism in biochemistry and molecular biology. In *S. cerevisiae*, it is possible to study processes such as the Crabtree effect observed in tumor cells (Diaz-Ruiz, Rigoulet, & Devin, 2011) and to model cell death in response to anoxia or ischemia/reperfusion (Stella, Burgos, Chapela, & Gamondi, 2011). In addition, it is used as a host to study DNA and RNA viral replication (Alves-Rodrigues, Galão, Meyerhans, & Díez, 2006), to identify and characterize bacterial effectors and toxins (Siggers & Lesser, 2008) and to analyze the function of heterologously expressed proteins such as the *Yarrowia lipolytica* and the mammalian brown-fat mitochondrial uncoupling proteins (UCPs) (Guerrero-Castillo et al., 2011). Thus, when it was observed that *Wolbachia* grew in *S. cerevisiae*, the system was characterized and the effects of *Wolbachia* infection on its host were analyzed.

Growing *Wolbachia* in insect cell cultures or in live hosts presents difficulties that have precluded detailed biochemistry and physiology studies (Baldridge et al., 2014; Khoo, Venard, Fu, Mercer, & Dobson, 2013). Here, we used the *S. cerevisiae* strain W303 as an alternative host for *Wolbachia* *w*AlbB and analyzed the host/endosymbiont system. Infected yeasts died earlier than controls. This probably resulted from an abnormally high mitochondrial oxidative phosphorylation activity observed at late stages of growth. Understanding *Wolbachia* and host-*Wolbachia* interactions holds great promise for medical, parasitological, and biotechnological applications.

2 | EXPERIMENTAL PROCEDURES

2.1 | Aa23 cell line maintenance

Aa23 cell line (*Aedes albopictus* infected with *w*AlbB) (O'Neill et al., 1997) was kindly donated by Professor Anne Fallon (U. Minnesota) and maintained in Eagle's minimal essential medium (MEM, Sigma Chemical Co. M0643). MEM was supplemented as indicated elsewhere (Shih, Gerenday, & Fallon, 1998). The medium was filter-sterilized (Millipore, 0.22 μm) and stored in 200 ml aliquots at 4°C. Prior to use, heat-inactivated fetal bovine serum (FBS; 30 min at 56°C) was added to a final concentration of 10% (Shih et al., 1998). The insect cell line was grown on True Line TR 4003 140 mm sterile petri dishes at 27°C in a 5% CO_2 atmosphere (ESCO CelCulture CO_2 incubator or in Corning culture flasks, Shanghai, China). Subcultures were performed in a 1:10 split at 90% confluence. A sample from this cell line was treated with tetracycline to eliminate *Wolbachia* infection (Aa23Tet) (Dobson, Marsland, Veneti, Bourtzis, & O'Neill, 2002).

2.2 | Cell viability assays

Viability of Aa23 cell line, *Wolbachia* or yeast was assessed using the BacLight live-dead staining kit (Molecular Probes, Carlsbad, CA). Ten microliters of cell suspension were stained according to the manufacturer suggested protocol and viewed in an epifluorescence NIKON microscope.

2.3 | Failed attempts to grow *Wolbachia* ex-vivo and a serendipitous finding

The original idea was to find a system where *Wolbachia* would grow ex-vivo. To do this, diverse protocols used for other endosymbionts such as *Sodalis* and *Coxiella* were followed (Dale & Maudlin, 1999; Omsland et al., 2009, 2013). It was found that some components did improve survival in isolated *Wolbachia*, even if we never observed substantial growth. Some of these agents were: (1) Trehalose and other compatible solutes such as mannitol, glycerol and sucrose, known to stabilize pollen (Crowe, Reid, & Crowe, 1996; Leslie, Israeli, Lighthart, Crowe, & Crowe, 1995) and isolated proteins (Sampedro & Uribe, 2004) (2) Actin, which supports binding and movements of some endosymbionts in vivo. (3) Catalase which deactivates hydrogen peroxide (Dale & Maudlin, 1999) and (4) Blood from large mammals, which has been used to grow *Sodalis* (Dale & Maudlin, 1999) and increases *Wolbachia* titers (Amuzu, Simmons, & McGraw, 2015; McMeniman, Hughes, & O'Neill, 2011). Human blood was also effective.

First, we tried growing *Wolbachia* using sheep blood. However, it was easily contaminated at the sites of extraction, so cultures

INFORME DE LABORES 2019

had to be discarded often. On one occasion we obtained positive *wsp* gene amplification from a yeast colony grown in one of the agar plates. Out of curiosity, we studied the host, which turned out to be *S. cerevisiae*. From this accidental finding we decided to test a known strain of *S. cerevisiae* as an alternative host. We learned that, in order to support growth of *Wolbachia*, yeast culture media needed to be supplemented with blood, which eventually was substituted with ammonium ferric citrate with excellent results and none of the contamination problems. Neither compatible solutes, nor catalase nor actin enhanced growth. The second addition needed was bovine fetal serum, which was present in all original growth media but not in yeast culture media. FBS was titrated and we ended up using 1%.

Among laboratory strains, infection was successful in W303 and NB40, while infection % in BY was milder (Figure 1). The *S. cerevisiae* strain W303-1A (MATα; ura3-1; trp1Δ 2; leu2-3,112; his3-11,15; ade2-1; can1-100) (Gutierrez-Aguilar et al., 2014), where *Wolbachia* was abundant at 10 days of infection was chosen for further experiments (See Results).

2.4 | *Wolbachia* wAlbB infection of the *Saccharomyces cerevisiae* W303 yeast strain (*wScW303*)

A first yeast infection was performed following a modified cell line infection protocol (Dobson et al., 2002). All procedures were performed under sterile conditions. The Aa23 cell line (containing *Wolbachia*) was grown in Corning cell culture flasks (225 cm^2) as described in (Shih et al., 1998). After 20 days of culture, cells were scrapped and concentrated by centrifugation at 3,000*g* for 5 min. For homogenization, ~$1*10^7$ cells were resuspended in 10 ml Eagles medium and vortexed for 10 min with (50% v/v) 3 mm sterile borosilicate glass beads (Rasgon, Gamston, & Ren, 2006). The homogenate was centrifuged at 3,000*g* for 10 min to remove unbroken cells. The supernatant was passed through a 2.7 μm syringe filter and the filtrate containing bacteria was centrifuged at 16,500*g* for 10 min. The pellet was resuspended in 2 ml of Mitsuhashi-Maramorosch medium (MM) supplemented with 1 mmol L^{-1} ammonium ferric citrate and 20% fetal bovine serum (FBS) (MM Fe FBS). In parallel, yeasts were

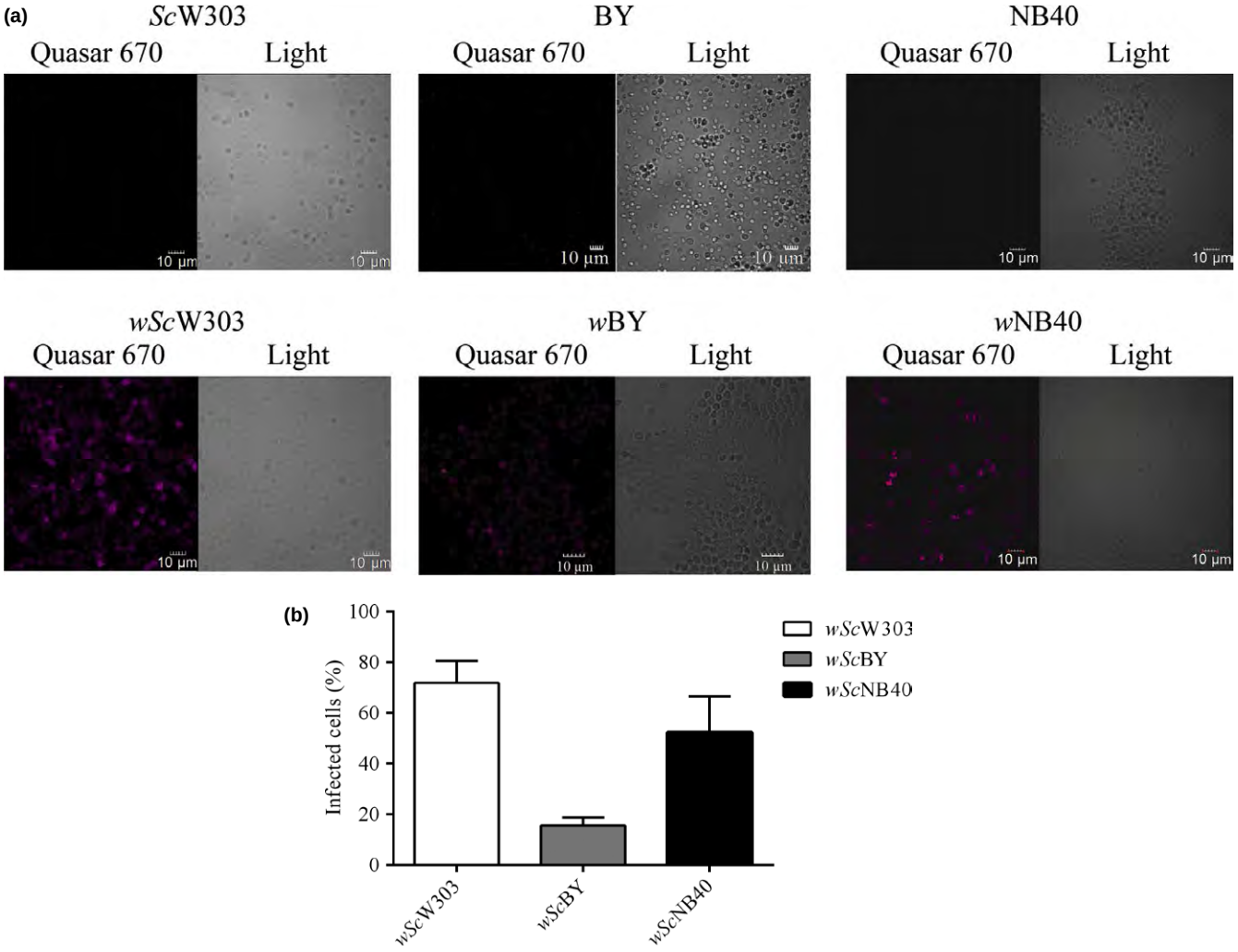

FIGURE 1 Infection of *Saccharomyces cerevisiae* with *Wolbachia*. (a) FISH using a *Wolbachia* 16S rDNA specific probe labeled with Quasar 670 (pink) was performed on 14 day old cultures of infected and control *S. cerevisiae strains* W303 (*Sc*W303), BY (*Sc*BY), and NB40 (*Sc*NB40) (b) After 14 days postinfection, the percentage of infected cells were counted as those with positive hybridization.

INFORME DE LABORES 2019

grown in a liquid YPD culture for 3 hr, harvested and centrifuged at 3,000*g* for 3 min. Culturing yeast in low oxygen environments prevents thickening of the cell wall (Aguilar-Uscanga & Francois, 2003; Smith et al., 2000; Avrahami-Moyal, Braun, & Engelberg, 2012). To induce contact between bacteria and yeast both bacteria (the whole 2 ml sample) and yeast (60 mg ww) were mixed and centrifuged at 2,500*g* for 1 hr at 20°C (Dobson et al., 2002). Bacteria-infected yeast were plated (all 2 ml) on a Petri dish containing MM supplemented with 1 mmol L^{-1} ammonium ferric citrate plus 25% v/v outdated human packaged erythrocytes and 2% agar (MM Fe-blood) and incubated at 27°C in a 5% CO_2 chamber (ESCO, Cell Culture CO_2 incubator, Singapore) for 14 days (Dale & Maudlin, 1999). Infection was confirmed by FISH and PCR. Infected yeast was transferred to a fresh agar plate every month for up to 6 months, then yeast was discarded and a new sample was used. Some aliquots were added with 40% glycerol, frozen and stored at −80°C, these samples have remained infective for nearly 10 months.

To transfer *Wolbachia* from yeast to yeast, slight modifications to the protocol were made: An aliquot of 100 µl of yeast taken from a glycerol-frozen sample or a loophole of infected yeast cells was diluted in 2 ml YPD Fe 20% FBS and plated in YPD Fe-blood agar plates, which were grown in 5% CO_2. After 14 days, all cells grown in a Petri dish were collected and washed by centrifugation at 3,000*g* for 3 min at 20°C with sterile water and the pellet was suspended in 10 ml MM. The suspension was vortexed for 10 min in the presence of 0.425–0.600 mm sterile borosilicate glass beads (60% v/v) to disrupt yeast cells (note that beads were smaller than those used for insect cell lines). Disrupted yeasts were centrifuged at 3,000*g* for 10 min and the supernatant was centrifuged again 3,000*g* for 10 min. The washed supernatant was filtered through different 0.8–0.65–0.45 µm syringe filters. Again, we used filters with smaller pores than those used for cell lines due to the small size of yeast cells. The last filtrate was centrifuged at 16,500*g* for 10 min. The pellet (~60 mg ww) was suspended in 2 ml MM Fe FBS and used to infect yeast from 3-h cultures as described above. The yeast–bacterium mixture was plated in a YPD Fe agar plate and incubated at 27°C with 5% CO_2 for at least 7 days. Infection was evaluated using FISH and PCR.

2.5 | Culture and maintenance of *w*AlbB-infected *Saccharomyces cerevisiae* W303

Infected *S. cerevisiae* strains were kept in YPD plus 1 mmol L^{-1} ammonium ferric citrate agar plates. When transferring to liquid medium, a loophole from the desired strain was suspended in 100 ml of sterile YPDS and incubated at 28°C, 130 rpm for 48 hr. Precultures were decanted in one liter YPDS and incubated at the same conditions for up to 14 days. When transferring from solid to solid media, a loophole of yeast was suspended in 1 ml YPD supplemented with 1 mmol L^{-1} ammonium ferric citrate plus 20% FBS and plated on YPD agar. A cell passage every 2–3 weeks was performed in order to maintain the infection. When it was desired to eliminate *Wolbachia* from yeast, tetracycline 30 µg/ml was added five consecutive times to the medium as passages were performed (Dobson et al., 2002).

2.6 | *Wolbachia* wAlbB infection of the C6C36 *Aedes albopictus* cell line

To determine whether *Wolbachia* cells retained its infective ability after all treatments, *Wolbachia* were isolated from *S. cerevisiae* grown in liquid YPD Fe 1% FBS and they were tested for infection against a C6C36 insect cell line.

2.7 | *Wolbachia* surface protein (*wsp*) gene PCR identification

The *Wolbachia wsp* gene was amplified using the following primers: *wsp* 81F (5′ TGGTCCAATAAGTGATGAAGAAAC 3′) and *wsp* 691R (5′ AAAAATTAAACGCTACTCCA 3′) (Braig, Zhou, Dobson, & O'Neill, 1998) in a 25 µl reaction volume using recombinant Taq DNA polymerase (Thermo Fisher Scientific). PCR amplification was performed as reported elsewhere (Braig et al., 1998; Xi, Khoo, & Dobson, 2006). The PCR product was electrophoresed on a 1% agarose gel and stained with ethidium bromide. PCR product was purified using a GeneJET PCR purification Kit (Thermo Fisher Scientific) and sequenced in the Molecular Biology Unit at the Institute of Cellular Physiology, UNAM.

2.8 | Fluorescence in-situ hybridization (FISH)

Wolbachia 16S rDNA oligonucleotide probe labeled with Quasar 670 dye (λ_{em}647, λ_{ex}670) W1, 5′-AATCCGGCCGARCCGACCC-3′ was used for FISH assays (Heddi, Grenier, Khatchadourian, Charles, & Nardon, 1999). One milliliter of the desired culture was centrifuged at 3,000*g* for Aa23, C6C36 and yeast, and 18,500*g* for purified *Wolbachia* for 5 min. Protocol was followed as reported elsewhere (Genty, Bouchon, Raimond, & Bertaux, 2014). Samples were viewed in a FluoView FV-1,000 Olympus confocal microscope, NA 1.4 with a 100X objective. Images were analyzed with the FV-Viewer Olympus software.

2.9 | Z-cut images for cell reconstruction

Fourteen day old infected and noninfected yeast samples were visualized with a Olympus-FV1000 or FV-3000 microscopes. Z-cut images were reconstructed using Imaris 7.2.1 and Image J software. Calcofluor-white (0.05 mmol L^{-1} in 20% DMSO-20 mmol L^{-1} Bicine Buffer) was used to stain fungus cell wall.

2.10 | Antibodies

Primary antibodies: Mouse monoclonal Anti-*Wolbachia* Surface Protein NR-31029 was from BEI Resources, NIAID, NIH. Mouse monoclonal Anti-VDAC was from Abcam. Secondary antibody: HRP

INFORME DE LABORES 2019

coupled Anti-mouse antibody from Jackson ImmunoResearch (West Grove, PA).

2.11 | Western blot

A loophole from yeast grown in solid media was suspended in 200 µl of water; otherwise, 200 µl from liquid culture samples were centrifuged at 3,000*g* for 5 min and washed twice in water. The pellet was solubilized in 200 µl RIPA buffer (25 mmol L^{-1} Tris•HCl pH 7.6, 150 mmol L^{-1} NaCl, 1% NP-40, 1% sodium deoxycholate, 0.1% SDS) supplemented with protease inhibitors 1 mmol L^{-1} PMSF (Sigma-Aldrich) and Complete protease inhibitor cocktail (Roche-CO-RO) as recommended by the abcam protocol. Samples were lysed in a Sonics VibraCell sonicator (Sonics & materials, Inc., Newtown, CT) at 80% amplitude for 10 s and left under agitation in a Multi-Vortex V-32 (Biosan, Riga, Latvia) for 30 min at 4°C. Samples were centrifuged at 15,160*g* for 5 min. The supernatant was recovered and protein concentration was measured by Bradford in a PolarStar Omega (BMG labtech, Ortenberg, Germany) [(Bradford, 1976) #64]. Samples were diluted in a 4X buffer (500 mmol L^{-1} Tris, pH 6.8, 10% glycerol, 10% SDS, 0.05% beta-mercapto-ethanol, and 0.01% bromophenol blue) and boiled for 5 min. SDS/PAGE was performed in 10% polyacrylamide gels and electrotransferred to poly(vinylidenedifluoride) membranes as reported elsewhere (Chiquete-Felix et al., 2009). Membranes were blocked with 5% Blotto nonfat dry milk in TBS-T (50 mmol L^{-1} Tris, 104 mmol L^{-1} NaCl, pH 7.6, 0.1% Tween 20) for 1 hr, and incubated overnight at 4°C with the primary antibody. Membranes were washed with TBS-T and incubated at 37°C for 1 hr with secondary antibody. Membranes were washed again and the bands were developed by chemiluminescence using an ECL kit (Amersham Biosciences, GE, Healthcare) (Chiquete-Felix et al., 2009). PVDF membranes were stripped as indicated by abcam protocol using a mild-stripping buffer, blocked with 5% Blotto nonfat dry milk in TBS-T and reprobed with a different antibody as indicated.

2.12 | Transmission electron microscopy of *wSc*W303

Infection was assessed by transmission electron microscopy (TEM) following a protocol from (Sun et al., 2015). Briefly, 500 µl of cells were harvested from 100 ml cultures of infected and uninfected *Saccharomyces cerevisiae* cultures form the first unintentional infection (*wSc*) at 10 days and *wSc*W303 of fourteen days. Yeast and *Wolbachia* samples were washed twice in distilled water at 740 g for 5 min for yeast and 23400 g for 10 min for bacteria in an Eppendorff Centrifuge 5415C. Samples were fixed in 2% $KMnO_4$ at 4°C overnight. Next day, samples were washed for 15 min with deionized water six times and dehydrated with sequential 10-minute washes with 50%, 70%, 80%, 90% ethanol and three washes with 100% ethanol. Samples were washed with ethanol-propanone (1: 1) for 8 min, then with anhydrous propanone for 5 min, then with propanone-EPON 821 (3: 1) for 1 hr and left in propanone-EPON 821 (1 : 3) overnight. Next day, samples were concentrated and resuspended in propanone-EPON 821 (1: 1) for 1 hr. Then, samples were concentrated again and left in resin for 24 hr. Then they were incubated for 12 hr at 37°C and then further incubated for 36 hr at 60°C. Resins were cut into 70 nm slices on an ultra-microtome (Ultracut Reicheit-jung) and observed in a JEOL JEM-1200 EXII electron microscope. Data were processed using Gatan Digital Micrograph Software.

2.13 | Mitochondrial (or Mitochondria/*Wolbachia* mixture) isolation

Yeast were centrifuged at 3,000*g* for 5 min, washed twice in water and resuspended in MES-mannitol buffer (5 mmol L^{-1} MES, 0.6 mol L^{-1} mannitol, 0.1% BSA pH 6.8 adjusted with triethanolamine). Yeast were disrupted using a Bead Beater cell homogenizer (Biospec Products, OK, USA, final volume 50 ml) with 0.425–0.6 mm glass beads during three 20 s pulses separated by 40 s resting periods in ice (Uribe, Rangel, Espínola, & Aguirre, 1990). The homogenate was differentially centrifuged to isolate mitochondria similar to described in (Peña, Piña, Escamilla, & Piña, 1977). Briefly, cells were centrifuged at 1,100*g* for 5 min. The supernatant was centrifuged at 9,798*g* for 10 min and the pellet was resuspended in MES-mannitol buffer and centrifuged at 3,000*g* for 5 min. Finally, the supernatant was centrifuged at 17,500*g* for 10 min. The resulting pellet was resuspended in minimal volume and protein concentration was measured by Biuret (Gornal, 1957) using a Beckman Coulter spectrophotometer at 540 nm.

2.14 | Oxymetry

Mitochondrial high resolution respirometry was assessed in an Oroboros oxygraph (Oroboros Intrs Corp, Innsbruck, Austria) using 5 mmol L^{-1} MES, 0.6 mol L^{-1} mannitol pH 6.8, 10 mmol L^{-1} KCl and 4 mmol L^{-1} Pi at 30°C. Final volume in the closed chamber was 1.5 ml with a protein concentration of 0.5 mg prot/ml. Bacterial protein concentration of 0.5 mg prot/ml was used. The trace was started by the addition of 5 mmol L^{-1} of the indicated substrate: glycerol-3-phosphate, ethanol, NADH, pyruvate-malate, succinate, glutamine or glutamate. For Complex IV evaluation, 5 mmol L^{-1} ascorbate (pH 7.6)- 0.05 mmol L^{-1} TMPD was used (Uribe, Ramirez, & Peña, 1985). Respiratory control was measured using 0.5 µl/ml ethanol to induce state II respiration and 1 mmol L^{-1} ADP to induce the phosphorylated state (Uribe et al., 1985). Respiratory chain inhibitors were used in the following concentrations: 0.1 µmol L^{-1} rotenone, 0.15 mmol L^{-1} flavone, 0.1 µmol L^{-1} antimycin A, and 2 mmol L^{-1} cyanide (Uribe et al., 1985).0.5 µmol L^{-1} CCCP was added as an uncoupler. Data were analyzed using the Oroboros Lab software.

2.15 | Electrophoretic techniques and in-gel activities

Blue native gel electrophoresis (BN-PAGE) and high-resolution clear native electrophoresis (hrCN-PAGE) were performed as in (Wittig,

INFORME DE LABORES 2019

Braun, & Schägger,2006; Wittig, Karas, & Schägger, 2007). Whole cells were solubilized with 2 mg dodecylmaltoside/mg protein plus 1 mmol L^{-1} PMSF and Complete protease inhibitor cocktail (Roche-CO-RO) and shaken for 30 min at 4°C. Membranes were centrifuged at 23,680*g* at 4°C for 1 hr. Protein concentration in the supernatants was determined by Bradford (1976). Between 0.1 and 0.15 mg of protein were loaded in 5%–15% polyacrylamide gradient gels. When hr-CN PAGE electrophoresis was performed 0.01% Lauryl maltoside and 0.05% sodium deoxycholate were added to the cathode buffer [(Wittig et al., 2007) #69]. Gels were run for about an hour at 15 mA/gel in a Bio-rad electrophoresis chamber. In-gel NADH-NBT oxido-reductase (100 μg protein), succinate-NBT oxido-reductase (150 μg protein), cytochrome *c* oxidase (100 μg protein), and in-gel ATPase (100 μg protein) activities were done as reported previously (Uribe-Alvarez et al., 2016). 20 μg protein of solubilized Bovine Heart Mitochondria (BHM) were loaded in each gel as controls.

2.16 | LC-MALDI-MS/MS

Indicated bands from hr-CN PAGE or BN-PAGE were enzymatically digested, separated on a HPLC EkspertnanoLC 425 (Eksigent, Redwood City CA) and analyzed in a MALDI-TOF/TOF 4800 Plus mass spectrometer (ABSciex, Framingham MA) (Shevchenko, Tomas, Havli, Olsen, & Mann, 2006) in the Unidad de Genómica, Proteómica y Metabolómica, CINVESTAV-IPN. Generated MS/MS spectra were compared using Protein Pilot software v. 4.0 (ABSciex, Framingham MA) against the *Saccharomyces cerevisiae* ATCC 204508 database (downloaded of Uniprot, 6721 protein sequences) and *Wolbachia* genus database (downloaded of Uniprot, 47781 protein sequences) using Paragon algorithm.

3 | RESULTS

3.1 | At the expense of its own viability, the artificial host *Saccharomyces cerevisiae* W303 supports growth of *Wolbachia* wAlbB

To study *Wolbachia* (wAlbB) large biomass yields plus a host that is easy to manipulate are needed. After testing different alternatives (see Methods), it was discovered that different *S. cerevisiae* strains were susceptible to infection and supported active *Wolbachia* proliferation. At 14 days of infection, *Wolbachia* grew efficiently in *S. cerevisiae* strains W303 (*Sc*W303) and NB40 (*Sc*NB40), while strain BY (*Sc*BY) supported only a weak infection (Figure 1a). After 14 days the percentage of infected cells counted by FISH using probes against the *Wolbachia* 16S rDNA was 71.8% ± 8.7% for *Sc*W303 and 52.3% ± 14.3% for *Sc*NB40, while in *Sc*BY less than 20% cells were positive for FISH (Figure 1b). Strain *Sc*W303 was chosen for further studies. *Sc*W303 maintains high rate of oxidative phosphorylation regardless of the carbon source, it is highly resistant to oxidative stress (Ocampo, Liu, Schroeder, Shadel, & Barrientos, 2012) and it has a weak cell wall (Avrahami-Moyal et al., 2012). Strains used in this study are detailed in Table S1.

3.2 | Proliferation of *Wolbachia* in *Sc*W303 was further confirmed using different independent methods as follows (Figure 2)

3.2.1 | PCR of the *Wolbachia* outer surface protein gene (*wsp*)

Both the Aa23 cell line (Figure 2a) and infected *S. cerevisiae* (*wSc*W303) (Figure 2b) amplified 650 bp fragments exhibiting sequences 100% identical to the surface protein of the *Wolbachia* endosymbiont of *Aedes albopictus* (NCBI database: KC242223.1) (Table S2). PCR amplification bands were not observed in the tetracycline-treated Aa23 cell line (Figure 2a, Aa23 Tet) and in the noninfected yeast (Figure 2b, *Sc*W303). Tetracycline used continuously in cell cultures is reported to kill *Wolbachia* (Dobson et al., 2002).

3.2.2 | Western Blot analysis detected *Wolbachia* wsp in *S. cerevisiae*

In the Aa23 cell line, a ~37 kDa protein corresponding to the *Wolbachia* Surface protein (wsp) was revealed with anti wsp antibodies (Bei resources, NIH, MD) (Figure 2c, Aa23). This band disappeared after growth in the presence of tetracycline (Aa23 Tet). VDAC (Voltage dependent anionic channel) protein was used as a loading control. In non–infected yeast wsp was not detected, (Figure 2c, *Sc*W303), while in infected yeast the wsp western blot signal was first detected at day 3 and increased gradually up to day 10, remaining stable until day 14 (Figure 2c, *wSc*W303). (For images of original Western Blots, see Figure S1a). When tetracycline was added to the medium, the wsp signal decreased, disappearing by day 10 (Figure S1b, *wSc*W303Tet).

3.2.3 | Normal growth and early death were observed in infected *S. cerevisiae*

During the first 12 days of culture, growth curves of infected *wSc*W303 were similar to the controls (Figure 3a). Then, beginning at day 14, *wSc*W303 absorbance decreased. Cell wall degradation (Figure S2) and viability staining (Figure 3b) confirmed that *wSc*W303 viability was rapidly lost during the late stages of the stationary phase, from 14 to 18 days of culture.

In addition, during growth the transcriptional activity of both *S. cerevisiae* 18S rRNA and the *Wolbachia wsp* were tested. Transcription was high in *S. cerevisiae* from the first day, decreased at day fourteen and became negligible at days 16 and 18 (Figure 3c). In contrast, transcription of the *wsp* from *Wolbachia* became detectable only after 3 days, increased exponentially until day 10 and remained constant until day 14. Then, at days 16 and 18, transcription decreased abruptly (Figure 3c). Transcription data in the *Wolbachia/S. cerevisiae* system indicated that *Wolbachia* activity grew later than *S. cerevisiae*, reaching a maximum at 10 days. Later, beginning at 14 days both transcription activities decreased abruptly in parallel with the death of the host.

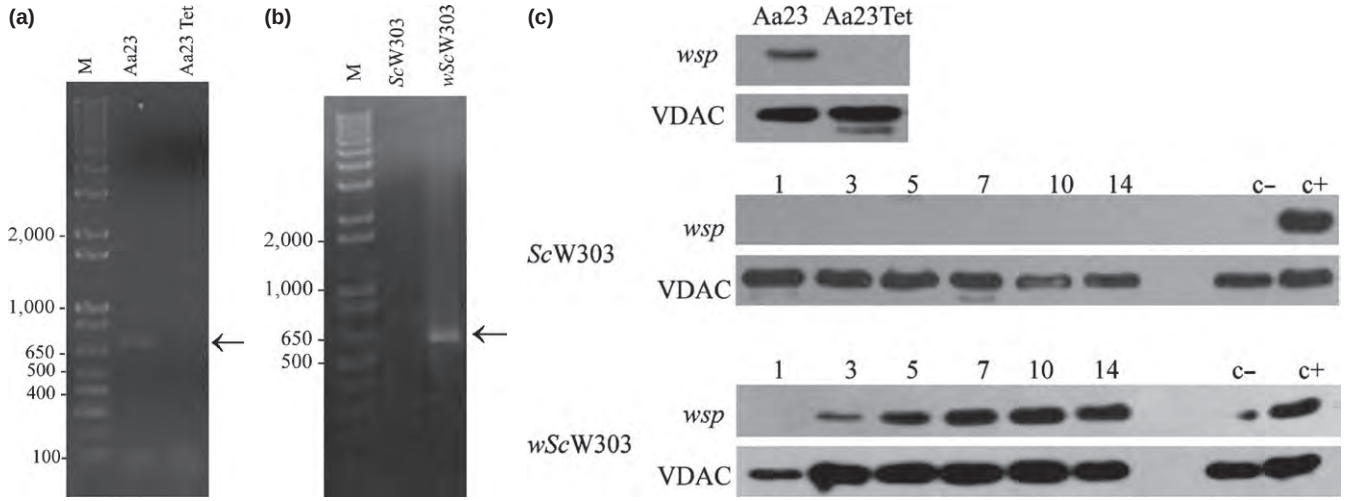

FIGURE 2 Detection of *Wolbachia* in *Saccharomyces cerevisiae* W303. (a) Agarose gel electrophoresis of the *wsp* PCR products predicted as a ~600 bp band in the Aa23 cell line. Lanes: M, Invitrogen 1 kb plus DNA ladder; Aa23, infected cell line; Aa23 Tet, noninfected cell line. (b) Agarose gel electrophoresis of the *wsp* PCR products for *S. cerevisiae*. Lanes: M, Invitrogen 1 kb plus DNA ladder; *Sc*W303, uninfected original yeast; *wSc*W303, infected yeast. (c) Western blot against the wsp and VDAC proteins. First row, first lane Aa23 infected cell line and second lane Aa23Δw tetracycline-cured cell line. Yeast samples were taken at 1, 3, 5, 7, 10, and 14 days postinfection. A positive control was taken from a 20 day YPD-2% agar culture infected-*wSc*W303. Negative control was a noninfected sample *Sc*W303

3.2.4 | Yeast cell/endosymbiont images were observed by staining *S. cerevisiae* with Calcofluor white and *w*AlbB with Quasar 670

Both the western blot and the RT-PCR experiments suggested that *Wolbachia* grew in the presence of *S. cerevisiae* becoming abundant at days 10–14. In order to determine whether *Wolbachia* was inside yeast, samples from infected and noninfected yeast cells from 14-day old cultures were hybridized using a *Wolbachia* specific 16S rDNA probe labeled with Quasar-670 (FISH). Then, the yeast cell wall was stained with Calcofluor white (Figure 4, Movie S1, Movie S2), Staining of the *S. cerevisiae* cell wall allowed observation of labeled bacteria inside yeast. Figure 4 shows that the Quasar-670 label was detectable only in *wSc*W303 and not in *Sc*W303. Merge of the Calcofluor, Quasar-670 and Clear field (Light) images show bacteria are inside the cell (Figure 4). Tridimensional reconstructions of z-cuts performed in a *wSc*W303 sample show the intracellular location of different bacteria (movies S1 and S2). In the periphery of movies S1 and S2, few independent bacterial labels were detected, which we speculate, may come from bacteria inside heavily deteriorated host cells whose cell wall was not stained by Calcofluor (movies S1 and S2).

3.2.5 | TEM images detected *Wolbachia* inside *S. cerevisiae*

Transmission electron microscopy images further suggested the intracellular location of *Wolbachia*. Cultures of 10 and 14 days of control and infected *S. cerevisiae* were analyzed. In infected yeast cells (Figure 5b–f, g), bacteria-like bodies (Figure 5, labeled *) that are not present in the uninfected yeast (Figure 5a and d) can be observed. At 10 days both infected and noninfected yeast present mitochondria, which can be identified by the presence of inner membrane cristae (Figure 5, labeled m). In contrast 14 day-old cultures of *Sc*W303 lost most mitochondrial structures, which suggest that these organelles are dysfunctional probably because cells are in late stationary phase. In contrast, 14 days-old infected *wSc*W303 show *Wolbachia* plus mitochondria where the typical cristae pattern may be observed, suggesting abnormal preservation of mitochondria in infected yeast (Figure 5e–g). In *wSc*W303 cultures, we can observe different cell images: most cells had an intact plasma membrane and contained mitochondria and bacteria-like bodies inside (Figure 5e). Other cells exhibited damaged membranes but the bacteria like structures were still present (Figure 5f). Among the whole population, we found some budding yeast, where bacteria-like bodies can be seem concentrated in the bud (Figure 5g). None of the latter populations was found in control *Sc*W303 cultures.

3.2.6 | *Wolbachia*-infected yeast retained high mitochondrial oxidative phosphorylation activity for abnormally long periods

A possible mechanism for the early death of infected yeast was explored in our infected *Sc*W303/*w*AlbB system. This system exhibited an abnormal preservation of mitochondria (Figure 5), so it was logical to explore aerobic metabolic activity. The relationship between *Wolbachia* and aerobic metabolism in the host is a matter of controversy. Some authors have proposed that these endo-cellular organisms possess an aerobic metabolism that contributes to overall activity (Strübing et al., 2010) while others suggest that *Wolbachia* optimizes aerobic metabolism by supplying heme groups for respiratory complexes (Darby et al., 2012; Fallon, Baldridge, Carroll, &

INFORME DE LABORES 2019

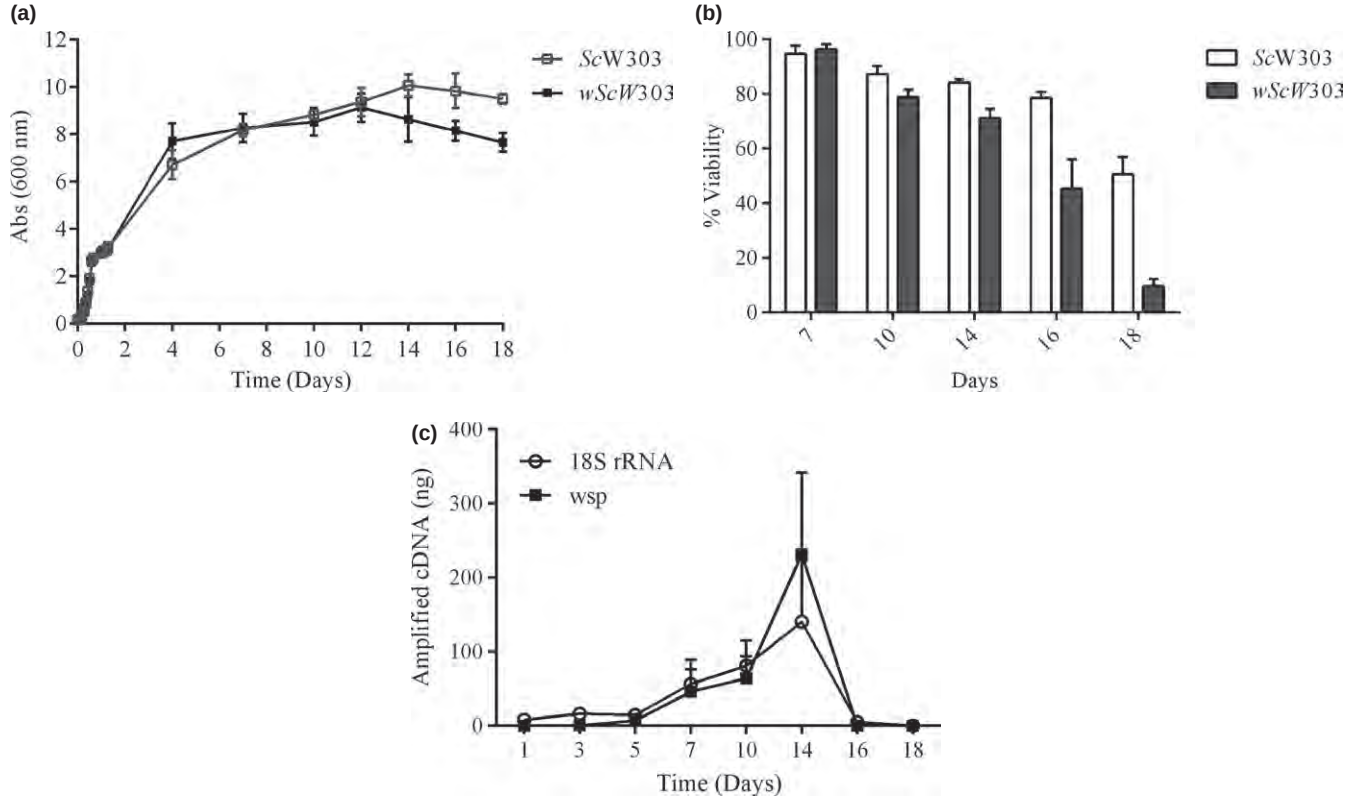

FIGURE 3 *S. cerevisiae* growth, viability, and transcriptional activity in the absence and presence of *Wolbachia*. (a) Growth curves of *Sc*W303 and *wSc*W303 grown in YPDS at 30°C, 130 rpm for 18 days. (b) Yeast cell viability in different days of culture quantified by microscopy with the BacLight viability kit. (c) Amplification of the *wsp* gene of *Wolbachia* and the 18S rRNA gene of *S. cerevisiae* of samples taken at different days of culture

Kurtz, 2014; Foster et al., 2005; Heddi et al., 1999; Strübing et al., 2010). Thus, we decided to evaluate oxidative phosphorylation activities in our system, which preserved mitochondrial structure beyond the stationary phase (Figure 5).

When isolation of *Wolbachia* was attempted, it was found that the bacterium and mitochondria migrated together (Baldridge et al., 2014; Uribe et al., 1985). Thus, it was decided to characterize oxidative phosphorylation activity in the mitochondria/*Wolbachia* mixture and then determine the contribution of each entity using different bioenergetics techniques. The rate of oxygen consumption was measured using ethanol as a substrate (Table 1). We isolated the mitochondria/*Wolbachia* fraction from either one-day cultures

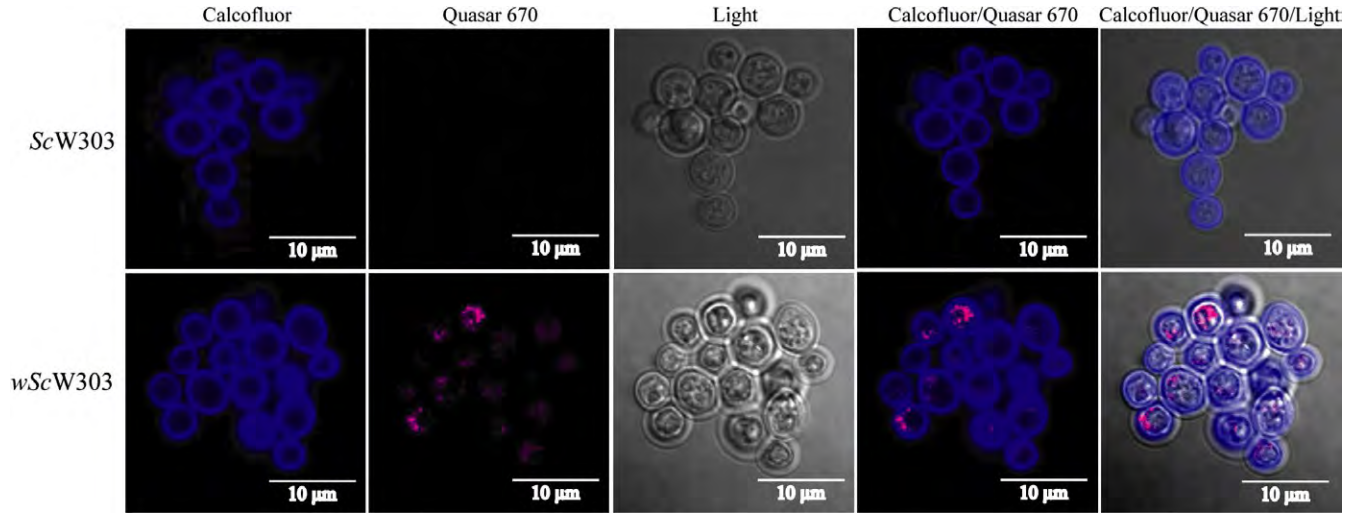

FIGURE 4 *Wolbachia* in calcofluor-labeled *S. cerevisiae*. Infected (*wSc*W303) and noninfected (*Sc*W303) *S. cerevisiae* cells were hybridized with the 16S rDNA *Wolbachia* probe (Quasar 670, pink). Then, the yeast cell wall was stained with calcofluor-white (Calcofluor, blue) to confirm the endosymbiosis. Merge images are shown to evaluate the presence of *Wolbachia* inside yeast

INFORME DE LABORES 2019

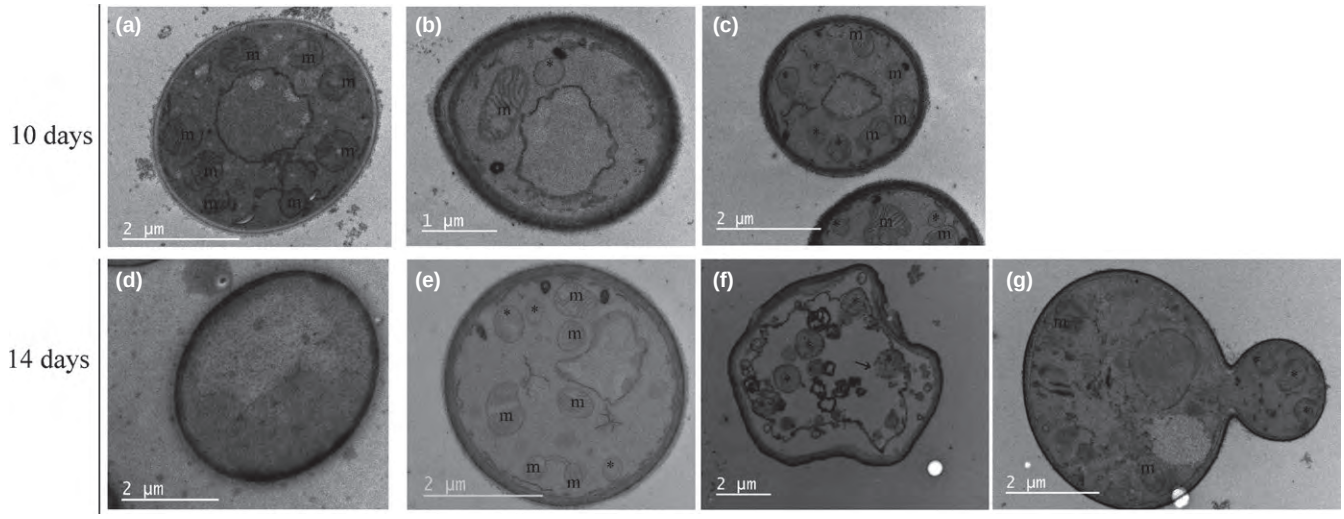

FIGURE 5 Electron microscopy images of infected and noninfected *Saccharomyces cerevisiae* at different times of incubation. Transmission electron microscopy images confirm the intracellular location of *Wolbachia*. 10-day images were taken with uninfected (a) *Sc* and infected (b–c) *wSc*; 14 day-old images were taken with (d) *Sc*W303 and (e–g) *wSc*W303. Images show the presence of bacteria-like bodies (*) that are not present in uninfected yeast and mitochondria (m) whose cristae can be easily identified

TABLE 1 Oxygen consumption rates of mitochondrial fractions from 1 and 14 day-old cultures of *Wolbachia*-infected (*wSc*W303) and noninfected (*Sc*W303) *Saccharomyces cerevisiae* cells

	State IV (natgO/min*mg prot)	State III (natgO/min*mg prot)	RCIII/IV
1 Day *Sc*W303	25.2 ± 3.1	52.5 ± 6.8	2.1 ± 0.15
1 Day *wSc*W303	27.4 ± 4.6	65.4 ± 9.0	2.4 ± 0.2
14 Days *Sc*W303	22.6 ± 5.1	29.0 ± 6.3	1.3 ± 0.2
14 Days *wSc*W303	34.2 ± 5.1	73.3 ± 11.1	2.1 ± 0.1

Reaction mixture: 0.6 mol L^{-1} mannitol, 5 mmol L^{-1} MES, pH 6.8, 4 mmol L^{-1} Pi, 10 mmol L^{-1} KCl. As substrate, 5 mmol L^{-1} ethanol. For state III, 1 mmol L^{-1} ADP.

where there are very few *Wolbachia* cells or from 14-day cultures, where *Wolbachia* numbers were high (Table 1). In one-day cultures from *Sc*W303 and *wSc*W303 respiratory activities were very similar. However, at 14 days the rates of oxygen consumption and respiratory controls (RC) were widely different as follows: In noninfected yeast, both the rate of oxygen consumption and respiratory control decreased at the expense of state 3 inhibition, while in contrast, *wSc*W303 retained high rates of oxygen consumption plus high respiratory controls, i.e. in 14-day old *Wolbachia*-infected yeast exhibited high oxidative phosphorylation activity, consistent with the presence of mitochondria observed by TEM in the infected cells (Table 1).

3.2.7 | In the presence of *Wolbachia* the activity of different mitochondrial respiratory complexes was preserved

In the isolated mitochondria/*Wolbachia* mixture, we tested specific substrates for each respiratory chain complex/enzyme (Table S3). In one-day cultures the rates of oxygen consumption were similar in infected and noninfected *S. cerevisiae* (Figure 6). In aged mitochondria from noninfected yeast, external NADH dehydrogenase (NDH2e, Pyruvate-Malate), succinate dehydrogenase (Succinate) and Complex IV (Ascorbate-TMPD) activities were strongly diminished. In contrast, in the 14 day-old mitochondrial fractions from *Wolbachia*-infected cells, respiratory activities in the presence of glycerol-3-phosphate, pyruvate-malate, and succinate were increased in comparison to 1-day cultures. Since *S. cerevisiae* does not have complex I and pyruvate-malate dependent respiration was insensitive to rotenone, redox activity was most likely from the mitochondrial NDH2 and not a bacterial complex I. Succinate oxidation was completely inhibited by antimycin A, indicating the absence of an alternative oxidase. Complex IV and NADH-dependent oxygen consumption rates were still decreased as compared to mitochondria from one-day cultures (Figure 6). Other respiratory substrates, namely glutamate and glutamine, which are used by Rickettsia (Winkler & Turco, 1988) where assayed and they did not support oxygen consumption. The respiratory activities measured indicate that the mitochondria/*Wolbachia* fractions from the infected and noninfected yeast consume the same substrates and are inhibited by the same respiratory chain inhibitors.

INFORME DE LABORES 2019

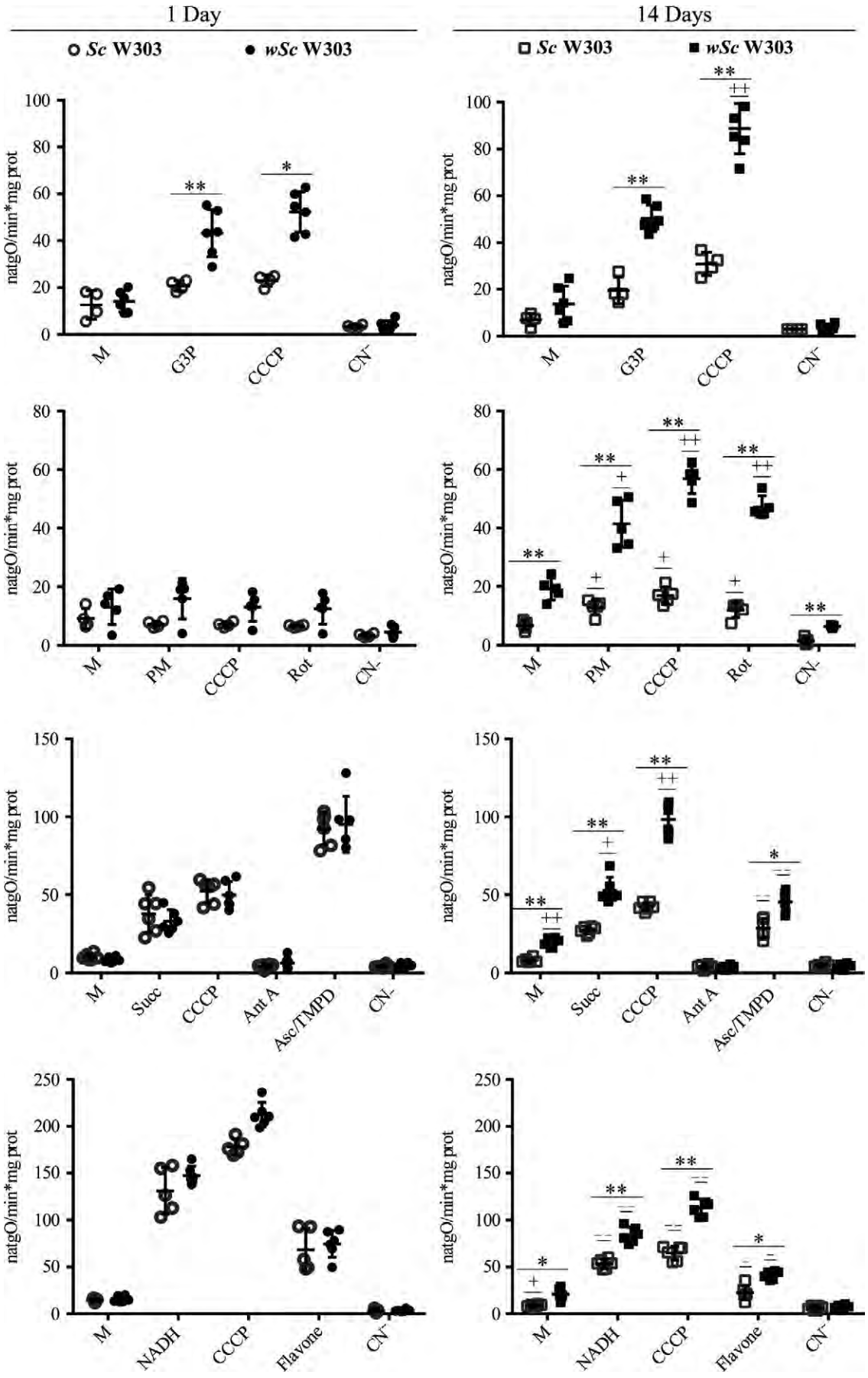

INFORME DE LABORES 2019

FIGURE 6 *Wolbachia*–mediated effects on the oxygen consumption activity of isolated yeast mitochondria. High-resolution respirometry. 1 day-old cultures of noninfected (1 Day *Sc*W303) and infected (1 Day *wSc*W303) yeast and 14 day-old cultures of noninfected (14 Days *Sc*W303) and infected (14 Days *wSc*W303) yeast. 5 mmol L^{-1} from each substrate was added as indicated: glycerol-3-phosphate (G3P), NADH, pyruvate-malate (Pyr-Mal), succinate (Succ), and ascorbate-TMPD (Asc/TMPD). Where indicated, 0.5 µmol L^{-1} CCCP, 0.1 µmol L^{-1} rotenone (Rot), 0.1 µmol L^{-1} antimycin A (Ant A), 1 mmol L^{-1} cyanide (CN-), and 0.15 mmol L^{-1} flavone. 0.5 mg prot/ml of mitochondria (M) were added. Data represent mean ± SEM. T test $^{*}p < .005$, $^{**}p < .001$ for *Sc*W303 versus *wSc*W303 yeast on the same day. *T* test $^{-/+}p < .05$ $^{--/++}p < .001$ ($^{-}$, decrease; $^{+}$, increase) for *Sc*W303 in day one versus day 14 cultures or *wSc*W303 in day one versus day 14 cultures

3.2.8 | Under the experimental conditions tested, infected *wSc*W303 oxygen consumption activity was mitochondrial

The experiments above suggested that either *Wolbachia* has the exact same electron transport chain as mitochondria or *Wolbachia* respiratory proteins may be damaged when the mitochondria/*Wolbachia* fraction is isolated and exposed to oxygen.

To explore this possibility further, we measured in-gel activities in the mitochondria/bacterium fraction. As eukaryote and prokaryote respiratory complexes I, II, III, and IV have different molecular masses the contribution from each organism to a given activity would be easily detected by native gel electrophoresis. The in-gel activities for each complex from infected and noninfected yeast from 1 and 14 day-old cultures were analyzed and, in all cases, activities were detected only at MWs corresponding to the mitochondrial enzymes (Table S3, Figure 7) suggesting that in the artificial *Sc*W303/*w*AlbB system and under the specific conditions of growth reported here, *Wolbachia* did not express any functional respiratory chain proteins. The above results suggest that mitochondria were responsible for all the observed oxygen consumption activity. Still, one NADH dehydrogenase (Table S4) was weakly expressed making it impossible to conclude on whether different *Wolbachia* strains may be aerobic or not.

3.2.9 | F_1F_0-ATPase subunits from *Wolbachia* were detected in *wSc*W303

In the in gel ATPase activity from the mitochondria/*Wolbachia* isolate no differential bands were observed. This was expected as the proposed MWs are similar for of both ATPases: 543 kDa for the eukaryote *S. cerevisiae* and 530 kDa for prokaryotes *Escherichia coli* and *Paracoccus denitrificans* (Bakhtiari, Lai-Zhang, Yao, & Mueller, 1999; Jonckheere, Smeitink, & Rodenburg, 2012; Morales-Rios, Montgomery, Leslie, & Walker, 2015; Robinson et al., 2013; Schagger, 2002). However, the ATPase activity band (Figure 7A1, Table S4) sequence exhibited a mixture of yeast and *Wolbachia* ATPase proteins. BN and hrCN-PAGE results indicate that if *Wolbachia* expresses any electron transport chain proteins (still a possibility), under our experimental conditions their concentration was negligible when compared to the mitochondrial proteins and to its own F_1F_0-ATPase.

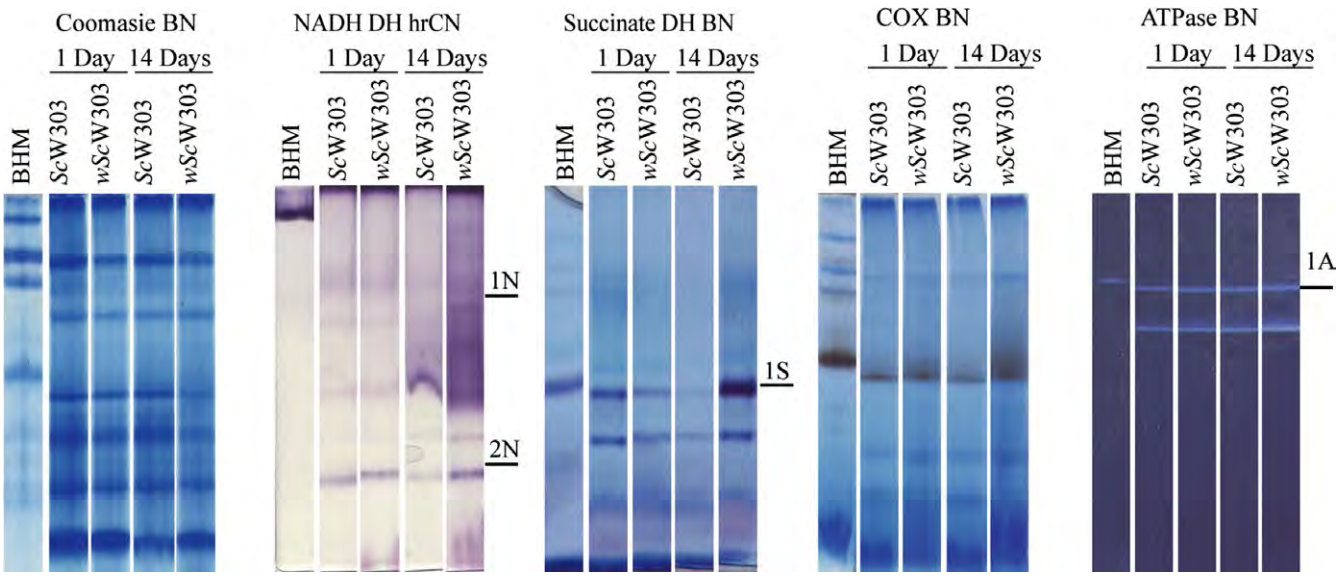

FIGURE 7 *Wolbachia*–mediated effects on the activity of each mitochondrial respiratory complex. BN-PAGE Coomassie-stained gel of *Sc*W303 and *wSc*W303 cells harvested at one and 14 days. In gel NADH-NBT oxido-reductase, succinate dehydrogenase, cytochrome *c* oxidase and ATPase enzyme activities in hrCN-PAGE or BN-PAGE, from 14 day old culture of *wSc*W303. Bands 1N, 2N, 1S, and 1A were sequenced (Table S4). Bovine heart mitochondria (BHM) were used as a control

INFORME DE LABORES 2019

3.2.10 | *Wolbachia* remains infective against insect cell lines

After being cultured in a yeast cell, the question arose on whether *Wolbachia* remained viable and infective when isolated. To test this, we extracted *Wolbachia* from *wSc*W303, incubated it in isolation for 5 days and then infected a C6C36 insect cell line which was previously reported to support bacterial infection (Baldridge et al., 2014). Aged *Wolbachia* infection was successful as assessed by specific staining using FISH (Figure 8 Movie S3).

4 | DISCUSSION

Growing obligate endosymbionts in cell lines yields low biomass at high costs (Baldridge et al., 2014; Khoo et al., 2013). To circumvent this problem, we built a synthetic host–endosymbiont system by artificially infecting the commonly used yeast *Saccharomyces cerevisiae* strain W303 with *Wolbachia* wAlbB from *A. albopictus* (Figures 1–5, Movies S1–S2). Culturing *Wolbachia* in yeast allowed us to study the complex relationship between the host and the bacterium. Using *S. cerevisiae* as an artificial host confers benefits such as a high resistance to changing environments (Gasch, 2002; Gasch & Werner-Washburne, 2002), use of inexpensive liquid cultures and most importantly, the ease of manipulating and genetically engineering the host cell. Following our approach, it may be possible to construct other synthetic parasite-mutualistic systems for obligate endosymbionts. Our system requirements for a successful infection were: supplementing YPD with iron and bovine fetal serum, plus low speed agitation of the nonbaffled Erlenmeyer flask and keeping the temperature between 28 and 30°C. These adjustments resulted in successful yeast infection and considerable *Wolbachia* yields in 14 days as compared with available methods that need up to 100 days. Even if the *Saccharomyces*/*Wolbachia* system is only a model of the interactions that occur in a naturally infected eukaryote cell, its manageability is outstanding and it may yield results that are not possible in cell lines.

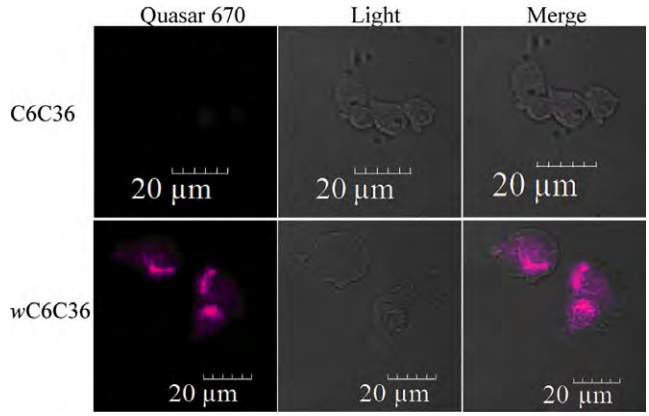

FIGURE 8 *Wolbachia* remains infective after being cultured in *S. cerevisiae*. FISH (Quasar 670-pink) of the *w*C6C36 cell line. Light/Quasar images show hybridization only inside the infected cell line. The noninfected cell line C6C36 does not have any of the pink hybridization mark identified as *Wolbachia*

Since *Wolbachia* is an alpha-proteobacterium closely related to mitochondria, it seemed likely that the aerobic metabolic machinery of *Wolbachia* might mimic, enhance, or supplement the respiratory activity from the host. (Strübing et al., 2010). However, under our conditions, *Wolbachia* respiratory chain proteins were not detectable, instead, we found an increase in host mitochondrial activity. Another obligate endosymbiont, the *Sytophilus oryzae* Principal Endosymbiont (SOPE), has also been reported to increase the mitochondrial activity in the host, probably by providing nutrients such as riboflavin (Heddi, Lefebvre, & Nardon, 1993; Heddi et al., 1999). Several authors suggest that *Wolbachia* provides riboflavin or heme groups to their arthropod and nematode hosts (Brownlie et al., 2009; Darby et al., 2012; Foster et al., 2005; Wu et al., 2009). This may vary with strains as *Wolbachia* from *Brugia malayi* (*wBm)* contains complete sets of riboflavin, heme and nucleotide biosynthesis genes the filarial host lacks (Darby et al., 2012; Foster et al., 2005; Klasson et al., 2008; Wu et al., 2004). In return, the host provides amino acid, proteins and a safe, stable environment (Brownlie et al., 2009; Darby et al., 2012; Foster et al., 2005; Wu et al., 2009). The possibility that *Wolbachia*, behaves as SOPE, donating riboflavin or heme groups to the host may be explored in auxotrophic yeast mutants. *S. cerevisiae* libraries have a mutant for almost every enzyme on the riboflavin and heme synthesis pathways e.g. *S. cerevisiae* genome database (https://www.yeastgenome.org/).

Under the conditions tested here, expression of *Wolbachia* electron transport proteins was not detected. The reported *Wolbachia pipientis* wAlbB genome (Mavingui et al., 2012) shows that some respiratory complex subunits are missing, e.g. *nuo*C and *nuo*D for a functional complex I (Sazanov, 2015); yet other *Wolbachia* sequenced genomes contain all the genes necessary for a functional electron transport chain (Klasson et al., 2008), so maybe under different growth conditions, hosts and *Wolbachia* strains, bacterial respiratory proteins may be detected. It is suggested that other *Wolbachia* strains should be tested in order to determine whether some consume oxygen.

In our hands, *Wolbachia* infection resulted in activation of mitochondria beyond the stationary growth phase. It may be speculated that such activation constitutes an advantage for *Wolbachia* either due to quenching of oxygen in the cytoplasm (Rosas-Lemus et al., 2016) or because *Wolbachia* needs high ATP that an active mitochondria provides (Potter, Badder, Hoade, Johnston, & Morten, 2016). It has already been suggested by experiments using paraquat that *Wolbachia* sensitivity to free radicals is higher than that of the host (Fallon et al., 2013) and it cannot survive outside a host cell unless it is kept in a 5% CO_2 atmosphere (Rasgon et al., 2006). Also, high agitation speeds, which would increase oxygen concentrations, lead to loss of the *Wolbachia* infection (Result not shown). Thus, it is possible that *Wolbachia* enters the cytoplasm to hide from high atmospheric oxygen and then it optimizes cell metabolism to both, use host metabolites and find low cytoplasmic oxygen concentrations.

INFORME DE LABORES 2019

Avoidance, i.e. hiding from oxygen, is a common behavior in oxyconformers (Rosas-Lemus et al., 2016). In air, oxygen saturation concentration is ~21% (200 μmol L^{-1}) while intracellular oxygen concentration ranges between 13.2% and 14% (126–133 μmol L^{-1}) for rhabdomyosarcoma (RD) cells (Potter et al., 2016) or HEK293T cells (Abcam, 2016). When cells are exposed to lower ambient oxygen, intracellular oxygen concentration is also decreased: HEK293T cells exposed to 6% oxygen (50 μmol L^{-1}) have an intracellular oxygen concentration below 2% (19 μmol L^{-1}) (Abcam, 2016); RD cells exposed to 10% or 5% ambient oxygen reduce their intracellular oxygen concentration to 5.4% and 2.1% respectively (Potter et al., 2016). In addition, there is an intracellular oxygen gradient in the area surrounding the mitochondria in rat heart and hepatocytes, where oxygen concentration ranges between 3 (Gnaiger, 2003) and 6 μmol L^{-1} (Jones & Kennedy, 1982; Tamura, Oshino, Chance, & Silver, 1978). Thus, a mitochondrion-containing host such as cell lines and yeast would probably provide the endosymbiont with a microaerobic environment. The mechanism for the increase in host mitochondrial activity needs to be defined.

In conclusion, we describe the infection of *S. cerevisiae* strain W303 by *Wolbachia w*AlbB. Infection led to premature death of the host and to an abnormal pattern of oxygen consumption. Further experiments using other yeast and other *Wolbachia* strains are needed to further explore oxidative phosphorylation patterns in the host/endosymbiont relationship. This system holds a large potential for different evaluations of biochemical and genetical processes in *Wolbachia*. Large biofermentors may be used to yield large amounts of biomass as required for different genomics and proteomics studies.

ACKNOWLEDGMENTS

Aa23 cell line was kindly donated by Dr. Ann Fallon from the University of Minnesota. The wsp antibody was a kind gift from Bei resources. CUA is a CONACYT PhD fellow enrolled in the Biochemistry PhD Program at UNAM. LMG is a CONACYT PhD fellow enrolled in the Biomedical Sciences PhD Program at UNAM. We received technical help from the Molecular Biology, the Microscopy and the Computation Units at IFC, UNAM. MALDI-TOF sequencing was performed by E. Ríos Castro from the Unidad de Genómica, Proteómica y Metabolómica, CINVESTAV-IPN, R Méndez-Franco, M. Contreras-Zentella, N.S. Sánchez and M. Calahorra are recognized for their technical assistance. M. Rigoulet, A. Devin (U-Bordeaux), D. González-Halphen, and G. Dreyfus-Cortés (IFC, UNAM) critically read the manuscript.

CONFLICT OF INTEREST

None declared.

REFERENCES

Abcam. (2016). ab197245 intracellular oxygen concentration assay. Retrieved from http://www.abcam.com/ps/products/197/ab197245/documents/ab197245%20Intracellular%20Oxygen%20Concentration%20Assay%20protocol%20v4%20(website).pdf.

Aguilar-Uscnaga, B., & Francois, J. M. (2003). A study of the cell wall composition and structure in response to growth conditions and mode of cultivation. *Letters in Applied Microbiology*, *37*(3), 268–274. https://doi.org/10.1046/j.1472-765X.2003.01394.x

Alves-Rodrigues, I., Galão, R. P., Meyerhans, A., & Díez, J. (2006). *Saccharomyces cerevisiae*: A useful model host to study fundamental biology of viral replication. *Virus Research*, *120*(1–2), 49–56. https://doi.org/10.1016/j.virusres.2005.11.018

Amuzu, H. E., Simmons, C. P., & McGraw, E. A. (2015). Effect of repeat human blood feeding on *Wolbachia* density and dengue virus infection in *Aedes aegypti*. *Parasit Vectors*, *8*, 246. https://doi.org/10.1186/s13071-015-0853-y

Avrahami-Moyal, L., Braun, S., & Engelberg, D. (2012). Overexpression of PDE2 or SSD1-V in *Saccharomyces cerevisiae* W303-1A strain renders it ethanol-tolerant. *FEMS Yeast Research*, *12*(4), 447–455. https://doi.org/10.1111/j.1567-1364.2012.00795.x

Bakhtiari, N., Lai-Zhang, J., Yao, B., & Mueller, D. M. (1999). Structure/function of the beta-barrel domain of F1-ATPase in the yeast *Saccharomyces cerevisiae*. *Journal of Biological Chemistry*, *274*(23), 16363–16369. https://doi.org/10.1074/jbc.274.23.16363

Baldridge, G. D., Baldridge, A. S., Witthuhn, B. A., Higgins, L., Markowski, T. W., & Fallon, A. M. (2014). Proteomic profiling of a robust *Wolbachia* infection in an *Aedes albopictus* mosquito cell line. *Molecular Microbiology*, *94*(3), 537–556. https://doi.org/10.1111/mmi.12768

Bandi, C., Slatko, B., & O'Neill, S. L. (1999). *Wolbachia* genomes and the many faces of symbiosis. *Parasitol Today*, *15*(11), 428–429. https://doi.org/10.1016/S0169-4758(99)01543-4

Bertaux, J., Schmid, M., Prevost-Boure, N. C., Churin, J. L., Hartmann, A., Garbaye, J., & Frey-Klett, P. (2003). In situ identification of intracellular bacteria related to *Paenibacillus* spp. in the mycelium of the ectomycorrhizal fungus *Laccaria* bicolor S238N. *Applied and Environment Microbiology*, *69*(7), 4243–4248. https://doi.org/10.1128/AEM.69.7.4243-4248.2003

Bianciotto, V., Genre, A., Jargeat, P., Lumini, E., Becard, G., & Bonfante, P. (2004). Vertical transmission of endobacteria in the arbuscular mycorrhizal fungus Gigaspora margarita through generation of vegetative spores. *Applied and Environment Microbiology*, *70*(6), 3600–3608. https://doi.org/10.1128/AEM.70.6.3600-3608.2004

de Boer, W., Leveau, J. H., Kowalchuk, G. A., Gunnewiek, P. J. K., Abeln, E. C., Figge, M. J., … van Veen, J. A. (2004). *Collimonas fungivorans* gen. nov., sp. nov., a chitinolytic soil bacterium with the ability to grow on living fungal hyphae. *International Journal of Systematic and Evolutionary Microbiology*, *54*(Pt 3), 857–864. https://doi.org/10.1099/ijs.0.02920-0

Bradford, M. M. (1976). A rapid and sensitive method for the quantification of microgram quantities of protein utilizing the principle of protein-dye binding. *Veterinary Parasitology*, *98*(1–3), 215–238.

Braig, H. R., Zhou, W., Dobson, S. L., & O'Neill, S. L. (1998). Cloning and characterization of a gene encoding the major surface protein of the bacterial endosymbiont *Wolbachia pipientis*. *Journal of Bacteriology*, *180*(9), 2373–2378.

Brenner, K., You, L., & Arnold, F. H. (2008). Engineering microbial consortia: A new frontier in synthetic biology. *Trends in Biotechnology*, *26*(9), 483–489. https://doi.org/10.1016/j.tibtech.2008.05.004

Brownlie, J. C., Cass, B. N., Riegler, M., Witsenburg, J. J., Iturbe-Ormaetxe, I., McGraw, E. A., & O'Neill, S. L. (2009). Evidence for metabolic provisioning by a common invertebrate endosymbiont, *Wolbachia pipientis*, during periods of nutritional stress. *PLoS Pathogens*, *5*(4), e1000368.

Buchsbaum, R., & Buchsbaum, M. (1934). An artificial symbiosis. *Science*, *80*(2079), 408–409.

Chiquete-Felix, N., Hernández, J. M., Méndez, J. A., Zepeda-Bastida, A., Chagolla-López, A., & Mujica, A. (2009). In guinea pig sperm, aldolase

INFORME DE LABORES 2019

A forms a complex with actin, WAS, and Arp2/3 that plays a role in actin polymerization. *Reproduction*, *137*(4), 669–678. https://doi.org/10.1530/REP-08-0353

Crowe, L. M., Reid, D. S., & Crowe, J. H. (1996). Is trehalose special for preserving dry biomaterials? *Biophysical Journal*, *71*(4), 2087–2093. https://doi.org/10.1016/S0006-3495(96)79407-9

Dale, C., & Maudlin, I. (1999). Sodalis gen. nov. and *Sodalis glossinidius* sp. nov., a microaerophilic secondary endosymbiont of the tsetse fly Glossina morsitans morsitans. *International Journal of Systematic Bacteriology*, *49* (Pt 1), 267–275. https://doi.org/10.1099/00207713-49-1-267

Darby, A. C., Armstrong, S. D., Bah, G. S., Kaur, G., Hughes, M. A., Kay, S. M., … Tanya, V. N. (2012). Analysis of gene expression from the *Wolbachia* genome of a filarial nematode supports both metabolic and defensive roles within the symbiosis. *Genome Research*, *22*(12), 2467–2477. https://doi.org/10.1101/gr.138420.112

Darby, A. C., Gill, A. C., Armstrong, S. D., Hartley, C. S., Xia, D., Wastling, J. M., & Makepeace, B. L. (2014). Integrated transcriptomic and proteomic analysis of the global response of *Wolbachia* to doxycycline-induced stress. *ISME Journal*, *8*(4), 925–937. https://doi.org/10.1038/ismej.2013.192

Diaz-Ruiz, R., Rigoulet, M., & Devin, A. (2011). The Warburg and Crabtree effects: On the origin of cancer cell energy metabolism and of yeast glucose repression. *Biochimica et Biophysica Acta*, *1807*(6), 568–576. https://doi.org/10.1016/j.bbabio.2010.08.010

Dobson, S. L., Marsland, E. J., Veneti, Z., Bourtzis, K., & O'Neill, S. L. (2002). Characterization of *Wolbachia* host cell range via the in vitro establishment of infections. *Applied and Environment Microbiology*, *68*(2), 656–660. https://doi.org/10.1128/AEM.68.2.656-660.2002

Fallon, A. M., Baldridge, G. D., Carroll, E. M., & Kurtz, C. M. (2014). Depletion of host cell riboflavin reduces *Wolbachia* levels in cultured mosquito cells. *In Vitro Cellular & Developmental Biology – Animal*, *50*(8), 707–713. https://doi.org/10.1007/s11626-014-9758-x

Fallon, A. M., Kurtz, C. M., & Carroll, E. M. (2013). The oxidizing agent, paraquat, is more toxic to *Wolbachia* than to mosquito host cells. *In Vitro Cellular & Developmental Biology – Animal*, *49*(7), 501–507. https://doi.org/10.1007/s11626-013-9634-0

Foster, J., Ganatra, M., Kamal, I., Ware, J., Makarova, K., Ivanova, N., … Vincze, T. (2005). The *Wolbachia* genome of *Brugia malayi*: Endosymbiont evolution within a human pathogenic nematode. *PLoS Biology*, *3*(4), e121. https://doi.org/10.1371/journal.pbio.0030121

French, K. E. (2017). Engineering mycorrhizal symbioses to alter plant metabolism and improve crop health. *Frontiers in Microbiology*, *8*, 1403. https://doi.org/10.3389/fmicb.2017.01403

Frey-Klett, P., Burlinson, P., Deveau, A., Barret, M., Tarkka, M., & Sarniguet, A. (2011). Bacterial-fungal interactions: Hyphens between agricultural, clinical, environmental, and food microbiologists. *Microbiology and Molecular Biology Reviews*, *75*(4), 583–609. https://doi.org/10.1128/MMBR.00020-11

Gasch, A. P. (2002). Yeast genomic expression studies using DNA microarrays. *Methods in Enzymology*, *350*, 393–414. https://doi.org/10.1016/S0076-6879(02)50976-9

Gasch, A. P., & Werner-Washburne, M. (2002). The genomics of yeast responses to environmental stress and starvation. *Functional & Integrative Genomics*, *2*(4–5), 181–192. https://doi.org/10.1007/s10142-002-0058-2

Genty, L. M., Bouchon, D., Raimond, M., & Bertaux, J. (2014). *Wolbachia* infect ovaries in the course of their maturation: Last minute passengers and priority travellers? *PLoS ONE*, *9*(4), e94577. https://doi.org/10.1371/journal.pone.0094577

Gnaiger, E. (2003). Oxygen conformance of cellular respiration. In R. C. Roach, P. D. Wagner, & P. H. Hackett (Eds.), *Hypoxia: Through the lifecycle* (pp. 39–55). Boston, MA: Springer. https://doi.org/10.1007/978-1-4419-8997-0

Gornal, A. G. (1957). Spectrophotometric and turbidimetric methods for mesuring proteins III: Biuret method. *Methods in Enzymology*, *3*, 447–454.

Guerrero-Castillo, S., Araiza-Olivera, D., Cabrera-Orefice, A., Espinasa-Jaramillo, J., Gutiérrez-Aguilar, M., Luévano-Martínez, L. A., … Uribe-Carvajal, S. (2011). Physiological uncoupling of mitochondrial oxidative phosphorylation. Studies in different yeast species. *Journal of Bioenergetics and Biomembranes*, *43*(3), 323–331. https://doi.org/10.1007/s10863-011-9356-5

Gutierrez-Aguilar, M., López-Carbajal, H. M., Uribe-Alvarez, C., Espinoza-Simón, E., Rosas-Lemus, M., Chiquete-Félix, N., & Uribe-Carvajal, S. (2014). Effects of ubiquinone derivatives on the mitochondrial unselective channel of Saccharomyces cerevisiae. *Journal of Bioenergetics and Biomembranes*, *46*(6), 519–527. https://doi.org/10.1007/s10863-014-9595-3

Heddi, A., Grenier, A. M., Khatchadourian, C., Charles, H., & Nardon, P. (1999). Four intracellular genomes direct weevil biology: Nuclear, mitochondrial, principal endosymbiont, and *Wolbachia*. *Proceedings of the National Academy of Sciences of the United States of America*, *96*(12), 6814–6819. https://doi.org/10.1073/pnas.96.12.6814

Heddi, A., Lefebvre, F., & Nardon, P. (1993). Effect of endocytobiotic bacteria on mitochondrial enzymatic activities in the weevil *Sitophilus oryzae* (Coleoptera: Curculionidae). *Insect Biochemistry and Molecular Biology*, *23*(3), 8.

Hoffman, M. T., & Arnold, A. E. (2010). Diverse bacteria inhabit living hyphae of phylogenetically diverse fungal endophytes. *Applied and Environment Microbiology*, *76*(12), 4063–4075. https://doi.org/10.1128/AEM.02928-09

Hosoda, K., Suzuki, S., Yamauchi, Y., Shiroguchi, Y., Kashiwagi, A., Ono, N., … Yomo, T. (2011). Cooperative adaptation to establishment of a synthetic bacterial mutualism. *PLoS ONE*, *6*(2), e17105. https://doi.org/10.1371/journal.pone.0017105

Hosoda, K., & Yomo, T. (2011). Designing symbiosis. *Bioengineered Bugs*, *2*(6), 338–341. https://doi.org/10.4161/bbug.2.6.16801

Jonckheere, A. I., Smeitink, J. A., & Rodenburg, R. J. (2012). Mitochondrial ATP synthase: Architecture, function and pathology. *Journal of Inherited Metabolic Disease*, *35*(2), 211–225. https://doi.org/10.1007/s10545-011-9382-9

Jones, D. P., & Kennedy, F. G. (1982). Intracellular oxygen supply during hypoxia. *American Journal of Physiology*, *243*(5), C247–C253. https://doi.org/10.1152/ajpcell.1982.243.5.C247

Kang, S. W., Jeon, B. Y., Hwang, T. S., & Park, D. H. (2009). Symbiotic relationship between *Microbacterium* sp. SK0812 and *Candida tropicalis* SK090404. *The Journal of Microbiology*, *47*(6), 721–727. https://doi.org/10.1007/s12275-009-0146-2

Khoo, C. C. H., Venard, C. M. P., Fu, Y., Mercer, D. R., & Dobson, S. L. (2013). Infection, growth and maintenance of *Wolbachia pipientis* in clonal and non-clonal *Aedes albopictus* cell cultures. *Bulletin of Entomological Research*, *103*(3), 251–260. https://doi.org/10.1017/S0007485312000648

Klasson, L., Walker, T., Sebaihia, M., Sanders, M. J., Quail, M. A., Lord, A., … Sinkins, S. P. (2008). Genome evolution of *Wolbachia* strain wPip from the *Culex pipiens* group. *Molecular Biology and Evolution*, *25*(9), 1877–1887. https://doi.org/10.1093/molbev/msn133

Kubo, I., Hosoda, K., Suzuki, S., Yamamoto, K., Kihara, K., Mori, K., & Yomo, T. (2013). Construction of bacteria-eukaryote synthetic mutualism. *Biosystems*, *113*(2), 66–71. https://doi.org/10.1016/j.biosystems.2013.05.006

Leslie, S. B., Israeli, E., Lighthart, B., Crowe, J. H., & Crowe, L. M. (1995). Trehalose and sucrose protect both membranes and proteins in intact bacteria during drying. *Applied and Environment Microbiology*, *61*(10), 3592–3597.

Lőrincz, Z., Preininger, É., Kósa, A., Pónyi, T., Nyitrai, P., Sarkadi, L., … Gyurján, I. (2010). Artificial tripartite symbiosis involving a green alga (*Chlamydomonas*), a bacterium (*Azotobacter*) and a fungus

INFORME DE LABORES 2019

(*Alternaria*): Morphological and physiological characterization. *Folia Microbiologica (Praha)*, *55*(4), 393–400. https://doi.org/10.1007/s12223-010-0067-9

Lumini, E., Ghignone, S., Bianciotto, V., & Bonfante, P. (2006). Endobacteria or bacterial endosymbionts? To be or not to be. *New Phytologist*, *170*(2), 205–208. https://doi.org/10.1111/j.1469-8137.2006.01673.x

Mavingui, P., Moro, C. V., Tran-Van, V., Wisniewski-Dyé, F., Raquin, V., Minard, G., … Lozano, L. (2012). Whole-genome sequence of *Wolbachia* strain wAlbB, an endosymbiont of tiger mosquito vector *Aedes albopictus*. *Journal of Bacteriology*, *194*(7), 1840. https://doi.org/10.1128/JB.00036-12

McMeniman, C. J., Hughes, G. L., & O'Neill, S. L. (2011). A *Wolbachia* symbiont in *Aedes aegypti* disrupts mosquito egg development to a greater extent when mosquitoes feed on nonhuman versus human blood. *Journal of Medical Entomology*, *48*(1), 76–84. https://doi.org/10.1603/ME09188

Mee, M. T., & Wang, H. H. (2012). Engineering ecosystems and synthetic ecologies. *Molecular BioSystems*, *8*(10), 2470–2483. https://doi.org/10.1039/c2mb25133g

Momeni, B., Chen, C. C., Hillesland, K. L., Waite, A., & Shou, W. (2011). Using artificial systems to explore the ecology and evolution of symbioses. *Cellular and Molecular Life Sciences*, *68*(8), 1353–1368. https://doi.org/10.1007/s00018-011-0649-y

Morales-Rios, E., Montgomery, M. G., Leslie, A. G., & Walker, J. E. (2015). Structure of ATP synthase from *Paracoccus denitrificans* determined by X-ray crystallography at 4.0 A resolution. *Proceedings of the National Academy of Sciences of the United States of America*, *112*(43), 13231–13236. https://doi.org/10.1073/pnas.1517542112

Ocampo, A., Liu, J., Schroeder, E. A., Shadel, G. S., & Barrientos, A. (2012). Mitochondrial respiratory thresholds regulate yeast chronological life span and its extension by caloric restriction. *Cell Metabolism*, *16*(1), 55–67. https://doi.org/10.1016/j.cmet.2012.05.013

Omsland, A., Cockrell, D. C., Howe, D., Fischer, E. R., Virtaneva, K., Sturdevant, D. E., … Heinzen, R. A. (2009). Host cell-free growth of the Q fever bacterium *Coxiella burnetii*. *Proceedings of the National Academy of Sciences of the United States of America*, *106*(11), 4430–4434. https://doi.org/10.1073/pnas.0812074106

Omsland, A., Cockrell, D. C., Howe, D., Fischer, E. R., Virtaneva, K., Sturdevant, D. E., … Heinzen, R. A. (2013). Bringing culture to the uncultured: *Coxiella burnetii* and lessons for obligate intracellular bacterial pathogens. *PLoS Pathogens*, *9*(9), e1003540. https://doi.org/10.1371/journal.ppat.1003540

O'Neill, S. L., M Pettigrew, M., Sinkins, S. P., Braig, H. R., Andreadis, T. G., & Tesh, R. B. (1997). In vitro cultivation of *Wolbachia pipientis* in an *Aedes albopictus* cell line. *Insect Molecular Biology*, *6*(1), 33–39. https://doi.org/10.1046/j.1365-2583.1997.00157.x

Partida-Martinez, L. P., & Hertweck, C. (2005). Pathogenic fungus harbours endosymbiotic bacteria for toxin production. *Nature*, *437*(7060), 884–888. https://doi.org/10.1038/nature03997

Peña, A., Piña, M. Z., Escamilla, E., & Piña, E. (1977). A novel method for the rapid preparation of coupled yeast mitochondria. *FEBS Letters*, *80*(1), 209–213.

Potter, M., Badder, L., Hoade, Y., Johnston, I. G., & Morten, K. J. (2016). Monitoring intracellular oxygen concentration: Implications for hypoxia studies and real-time oxygen monitoring. *Advances in Experimental Medicine and Biology*, *876*, 257–263. https://doi.org/10.1007/978-1-4939-3023-4

Rasgon, J. L., Gamston, C. E., & Ren, X. (2006). Survival of *Wolbachia pipientis* in cell-free medium. *Applied and Environment Microbiology*, *72*(11), 6934–6937. https://doi.org/10.1128/AEM.01673-06

Robinson, G. C., Bason, J. V., Montgomery, M. G., Fearnley, I. M., Mueller, D. M., Leslie, A. G., & Walker, J. E. (2013). The structure of F(1)-ATPase from *Saccharomyces cerevisiae* inhibited by its regulatory protein IF(1). *Open Biology*, *3*(2), 120164. https://doi.org/10.1098/rsob.120164

Rosas-Lemus, M., Uribe-Alvarez, C., Contreras-Zentella, M., Luévano-Martínez, L.A., Chiquete-Félix, N., Espinosa-Simón, E., … Uribe-Carvajal, S. (2016). Oxygen: from toxic waste to optimal (Toxic) fuel of life. In Free Radicals and Diseases. InTech.

Salzberg, S. L., Puiu, D., Sommer, D. D., Nene, V., & Lee, N. H. (2009). Genome sequence of the *Wolbachia* endosymbiont of *Culex quinquefasciatus* JHB. *Journal of Bacteriology*, *191*(5), 1725. https://doi.org/10.1128/JB.01731-08

Sampedro, J. G., & Uribe, S. (2004). Trehalose-enzyme interactions result in structure stabilization and activity inhibition. The role of viscosity. *Molecular and Cellular Biochemistry*, *256–257*(1–2), 319–327. https://doi.org/10.1023/B:MCBI.0000009878.21929.eb

Saniee, P., & Siavoshi, F. (2015). Endocytotic uptake of FITC-labeled anti-*H. pylori* egg yolk immunoglobulin Y in Candida yeast for detection of intracellular *H. pylori*. *Frontiers in Microbiology*, *6*, 113.

Sato, Y., Narisawa, K., Tsuruta, K., Umezu, M., Nishizawa, T., Tanaka, K., … Ohta, H. (2010). Detection of betaproteobacteria inside the mycelium of the fungus Mortierella elongata. *Microbes and Environments*, *25*(4), 321–324. https://doi.org/10.1264/jsme2.ME10134

Sazanov, L. A. (2015). A giant molecular proton pump: Structure and mechanism of respiratory complex I. *Nature Reviews Molecular Cell Biology*, *16*(6), 375–388. https://doi.org/10.1038/nrm3997

Schagger, H. (2002). Respiratory chain supercomplexes of mitochondria and bacteria. *Biochimica et Biophysica Acta*, *1555*(1–3), 154–159. https://doi.org/10.1016/S0005-2728(02)00271-2

Shevchenko, A., Tomas, H., Havli, J., Olsen, J. V., & Mann, M. (2006). In-gel digestion for mass spectrometric characterization of proteins and proteomes. *Nature Protocols*, *1*(6), 2856–2860.

Shih, K. M., Gerenday, A., & Fallon, A. M. (1998). Culture of mosquito cells in Eagle's medium. *In Vitro Cellular & Developmental Biology – Animal*, *34*(8), 629–630. https://doi.org/10.1007/s11626-996-0010-1

Shou, W., Ram, S., & Vilar, J. M. (2007). Synthetic cooperation in engineered yeast populations. *Proceedings of the National Academy of Sciences of the United States of America*, *104*(6), 1877–1882. https://doi.org/10.1073/pnas.0610575104

Siggers, K. A., & Lesser, C. F. (2008). The yeast *Saccharomyces cerevisiae*: A versatile model system for the identification and characterization of bacterial virulence proteins. *Cell Host & Microbe*, *4*(1), 8–15. https://doi.org/10.1016/j.chom.2008.06.004

Smith, A. E., Zhang, Z., Thomas, C. R., Moxham, K. E., & Middelberg, A. P. (2000). The mechanical properties of Saccharomyces cerevisiae. *Proceedings of the National Academy of Sciences of the United States of America*, *97*(18), 9871–9874.

Stella, C., Burgos, I., Chapela, S., & Gamondi, O. (2011). Ischemia–reperfusion: A look from yeast mitochondria. *Current Medicinal Chemistry*, *18*(23), 3476–3484. https://doi.org/10.2174/092986711796642553

Stewart, E. J. (2012). Growing unculturable bacteria. *Journal of Bacteriology*, *194*(16), 4151–4160. https://doi.org/10.1128/JB.00345-12

Strübing, U., Lucius, R., Hoerauf, A., & Pfarr, K. M. (2010). Mitochondrial genes for heme-dependent respiratory chain complexes are up-regulated after depletion of *Wolbachia* from filarial nematodes. *International Journal for Parasitology*, *40*(10), 1193–1202. https://doi.org/10.1016/j.ijpara.2010.03.004

Sun, X. Y., Zhao, Y., Liu, L. L., Jia, B., Zhao, F., Huang, W. D., & Zhan, J. C. (2015). Copper tolerance and biosorption of *Saccharomyces cerevisiae* during alcoholic fermentation. *PLoS ONE*, *10*(6), e0128611. https://doi.org/10.1371/journal.pone.0128611

Tamura, M., Oshino, N., Chance, B., & Silver, I. A. (1978). Optical measurements of intracellular oxygen concentration of rat heart in vitro. *Archives of Biochemistry and Biophysics*, *191*(1), 8–22. https://doi.org/10.1016/0003-9861(78)90062-0

Taylor, M. J., & Hoerauf, A. (1999). *Wolbachia* bacteria of filarial nematodes. *Parasitology Today*, *15*(11), 437–442. https://doi.org/10.1016/S0169-4758(99)01533-1

INFORME DE LABORES 2019

Uribe, S. A., Ramirez, J. O., & Peña, A. N. (1985). Effects of beta-pinene on yeast membrane functions. *Journal of Bacteriology*, *161*(3), 1195–1200.

Uribe, S., Rangel, P. A., Espínola, G. L., & Aguirre, G. A. (1990). Effects of cyclohexane, an industrial solvent, on the yeast *Saccharomyces cerevisiae* and on isolated yeast mitochondria. *Applied and Environment Microbiology*, *56*(7), 2114–2119.

Uribe-Alvarez, C., Chiquete-Félix, N., Contreras-Zentella, M., Guerrero-Castillo, S., Peña, A., & Uribe-Carvajal, S. (2016). *Staphylococcus epidermidis*: Metabolic adaptation and biofilm formation in response to different oxygen concentrations. *Pathogens and Disease*, *74*(1), ftv111. https://doi.org/10.1093/femspd/ftv111

Werren, J. H. (1997). Biology of *Wolbachia*. *Annual Review of Entomology*, *42*, 587–609. https://doi.org/10.1146/annurev.ento.42.1.587

Werren, J. H., Baldo, L., & Clark, M. E. (2008). *Wolbachia*: Master manipulators of invertebrate biology. *Nature Reviews Microbiology*, *6*(10), 741–751. https://doi.org/10.1038/nrmicro1969

Winkler, H. H., & Turco, J. (1988). Rickettsia prowazekii and the host cell: entry, growth and control of the parasite. *Current Topics in Microbiology and Immunology*, *138*, 81–107.

Wittig, I., Braun, H. P., & Schägger, H. (2006). Blue native PAGE. *Nature Protocols*, *1*(1), 418–428. https://doi.org/10.1038/nprot.2006.62

Wittig, I., Karas, M., & Schägger, H. (2007). High resolution clear native electrophoresis for in-gel funtional assays and fluorescence studies of membrane protein complexes. *Molecular & Cellular Proteomics: MCP*, *6*(7), 1215–1225. https://doi.org/10.1074/mcp.M700076-MCP200

Wu, B., Novelli, J., Foster, J., Vaisvila, R., Conway, L., Ingram, J., … Slatko, B. (2009). The heme biosynthetic pathway of the obligate *Wolbachia* endosymbiont of *Brugia malayi* as a potential anti-filarial drug target. *PLoS Neglected Tropical Diseases*, *3*(7), e475. https://doi.org/10.1371/journal.pntd.0000475

Wu, M., Sun, L. V., Vamathevan, J., Riegler, M., Deboy, R., Brownlie, J. C., … Wiegand, C. (2004). Phylogenomics of the reproductive parasite *Wolbachia pipientis* wMel: A streamlined genome overrun by mobile genetic elements. *PLoS Biology*, *2*(3), E69. https://doi.org/10.1371/journal.pbio.0020069

Xi, Z., Khoo, C. C., & Dobson, S. L. (2006). Interspecific transfer of *Wolbachia* into the mosquito disease vector *Aedes albopictus*. *Proceedings. Biological sciences Royal Society*, *273*(1592), 1317–1322. https://doi.org/10.1098/rspb.2005.3405

SUPPORTING INFORMATION

Additional supporting information may be found online in the Supporting Information section at the end of the article.

How to cite this article: Uribe-Alvarez C, Chiquete-Félix N, Morales-García L, et al. *Wolbachia pipientis* grows in *Saccharomyces cerevisiae* evoking early death of the host and deregulation of mitochondrial metabolism. *MicrobiologyOpen*. 2019;8:e675. https://doi.org/10.1002/mbo3.675

PLOS ONE

RESEARCH ARTICLE

Chronic exercise modulates the cellular immunity and its cannabinoid receptors expression

Salvador Valencia-Sánchez[1], Karen Elizabeth Nava-Castro[2☯], Margarita Isabel Palacios-Arreola[2☯], Oscar Prospéro-García[3‡], Jorge Morales-Montor[4]*, René Drucker-Colín[1†‡]

1 Instituto de Fisiología Celular, Departamento de Neuropatología Molecular, Universidad Nacional Autónoma de México, Circuito Exterior s/n, Ciudad Universitaria, Ciudad de México, México, **2** Genotoxicología y Mutagénesis Ambientales, Ciencias Ambientales, Centro de Ciencias de la Atmósfera, Ciudad de México, México, **3** Laboratorio de Cannabinoides, Departamento de Fisiología, Facultad De Medicina, Universidad Nacional Autónoma de México, Circuito Exterior s/n, Ciudad Universitaria, Ciudad de México, México, **4** Departamento de Inmunología, Instituto de Investigaciones Biomédicas, Universidad Nacional Autónoma de México, AP, Ciudad de México, México

☯ These authors contributed equally to this work.
† Deceased.
‡ These authors also contributed equally to this work.
* jmontor66@biomedicas.unam.mx

Check for updates

OPEN ACCESS

Citation: Valencia-Sánchez S, Nava-Castro KE, Palacios-Arreola MI, Prospéro-García O, Morales-Montor J, Drucker-Colín R (2019) Chronic exercise modulates the cellular immunity and its cannabinoid receptors expression. PLoS ONE 14 (11): e0220542. https://doi.org/10.1371/journal.pone.0220542

Editor: Junpeng Wang, Henan University, CHINA

Received: July 16, 2019

Accepted: November 1, 2019

Published: November 18, 2019

Peer Review History: PLOS recognizes the benefits of transparency in the peer review process; therefore, we enable the publication of all of the content of peer review and author responses alongside final, published articles. The editorial history of this article is available here: https://doi.org/10.1371/journal.pone.0220542

Copyright: © 2019 Valencia-Sánchez et al. This is an open access article distributed under the terms of the Creative Commons Attribution License, which permits unrestricted use, distribution, and reproduction in any medium, provided the original author and source are credited.

Data Availability Statement: All relevant data are within the paper.

Funding: This work was supported by IN-209719 Programa de Apoyo a Proyectos de Innovación

Abstract

The impact of performing exercise on the immune system presents contrasting effects on health when performed at different intensities. In addition, the consequences of performing chronic exercise have not been sufficiently studied in contrast to the effects of acute bouts of exercise. The porpoise of this work was to determine the effect that a popular exercise regimen (chronic/moderate/aerobic exercise) has on the proportion of different immune cell subsets, their function and if it affects the cannabinoid system with potentially functional implications on the immune system. A marked increase in several immune cell subsets and their expression of cannabinoid receptors was expected, as well as an enhanced proliferative and cytotoxic activity by total splenocytes in exercised animals. For this study male Wistar rats performed treadmill running 5 times a week for a period of 10 weeks, at moderate intensity. Our results showed a significant decrease in lymphocyte subpopulations (CD4+, Tγδ, and CD45 RA+ cells) and an increase in the cannabinoid receptors expression in those same cell. Although functional assays did not reveal any variation in total immunoglobulin production or NK cells cytotoxic activity, proliferative capability of total splenocytes increased in trained rats. Our results further support the notion that exercise affects the immunological system and extends the description of underlying mechanisms mediating such effects. Altogether, our results contribute to the understanding of the benefits of exercise on the practitioner´s general health.

INFORME DE LABORES 2019

Tecnológica (PAPIIT), Dirección General de Asuntos del Personal Académico (DGAPA), Universidad Nacional Autónoma de México (UNAM) to JMM; Grant FC-2016-2125 from Fronteras en la Ciencia, Consejo Nacional de Ciencia y Tecnología (CONACYT) Programa de Apoyo a Proyectos de Innovación Tecnológica (PAPIIT), Dirección General de Asuntos del Personal Académico (DGAPA), Universidad Nacional Autónoma de México (UNAM) to JMM; Grant IA202919 Programa de Apoyo a Proyectos de Innovación Tecnológica (PAPIIT), Dirección General de Asuntos del Personal Académico (DGAPA), Universidad Nacional Autónoma de México (UNAM) to KENC. The funders had no role in study design, data collection and analysis, decision to publish, or preparation of the manuscript.

Competing interests: The authors have declared that no competing interests exist.

Introduction

The beneficial impact of exercise on the practitioner's general health is a well-known fact [1–3]. Studies suggesting a connection between physical activity and the improvement of health have generated information that ranges from describing adipose tissue loss to changes in genetic expression [4,5]. It is well known that the proper composition of the immune system (IS) and its correct function will allow it to actively overcome challenges that otherwise would compromise the organism's health, such as infections, autoimmune diseases, cancer, etc. It is worth mentioning that the acknowledgment of those benefits conferred by the regular practice of exercise has led to its implementation as an alternative/complementary therapy against metabolic diseases [6,7], and in recent works even for the treatment of cancer [8].

Nonetheless, data regarding the changes induced by exercise in cell subpopulations of the IS and their function seems to be controversial [9–11]. This may be partly explained by the use of different exercise paradigms. Along with this, a classic idea has been established about such changes promoted by exercise, being those models of moderate/chronic exercise the promoters of an enhanced IS, while acute/high intensity models the responsible of hindering it. Finally, evidence suggesting a beneficial effect of the performance of exercise, on modalities previously described as detrimental, has been gathered and old data reinterpreted as in Campbell and Turner's review [12], so nowadays evidence debunking the previous conception of high intensity/long duration or chronic exercise evoked immune suppression increases, at least for several aspects of the immune function. On the same line, many studies document the immediate changes on the IS induced by a single bout of exercise, as opposed to the effects of its chronic performance, which suggest different outcomes and in some cases opposite effects over the IS [11,13,14]. Less attention has been paid to such studies and to the long-term alterations that it may produce on the IS. For instance, macrophages extracted from mice trained for 12 weeks exhibited increased phagocytic activity, superoxide anion production and glucose consumption when compared to macrophages obtained from sedentary mice [11]. Consistently other studies have shown that chronic exercise alters the function of T cells, affecting their production of pro- and anti-inflammatory cytokines, including the up-regulation of IL-2, an important cytokine related to proliferation and activation [14]. Likewise, trained rats presented increased glucose consumption, IL-2 production and IL-2R expression by their lymphocytic subpopulations. Furthermore, those changes obtained in trained animals seem to last days after the last exercise bout [14].

Many molecular pathways that are affected by exercise possess an immunoregulatory potential, ranging from variations in the energy substrates [15,16] to the activation of signaling pathways with direct immune-regulatory relevance, such as: the release of IL 6 by skeletal muscle [4,13], release of stress hormones, catecholamines [4,17] and neurotransmitters by the sympathetic and para-sympathetic system, among others. Hence, in order to contribute to the further understanding of these effects we decided to evaluate the cannabinergic system (CBS). Regarding this system, some studies have reported a subtle increase of anandamide, a widely studied molecule that acts as a CB1 and CB2 receptor agonist, after short bouts of aerobic exercise. Such increase was sustained up to several minutes after the conclusion of the physical activity [18–20]. Furthermore, both receptors are widely distributed in the immune cells and IS structures [21–23] and when activated, together or independently, produce changes in the function of several immune cells, suggesting that their activation is able to modulate the IS function. These modulatory actions have been explored *in vitro* [24,25] and *in vivo* [23]. Likewise, the expression of cannabinergic receptors (CBR) on the surface of immune cells, varies according to their activation and inflammatory status. Given that new data suggests its relevance as an immune-modulatory system, the expression of these receptors provides us with interesting and relevant information about the IS status.

INFORME DE LABORES 2019

Altogether, the objective of our study is to explore the long-term changes that chronic exercise (CE) produces in the proportion of splenocytes from the adaptive and innate immunity, and to assess the effects that it has on their function (by performing proliferation tests and cytotoxicity test with total splenocytes *in vitro*), and finally to determine if the expression of CBR in these cells is affected by this model of exercise. Furthermore, coherently with previous works on this topic, we expect that the changes evoked by CE will alter the composition of several of the immune cell subsets studied, mainly those from lymphoid origin. CE will also boost their cytotoxic activity and proliferative capacity. In terms of the cannabinoid receptor expression, we anticipate that CE will increase their expression in the entire cell subsets studied.

Finally, this study provide relevant information about those changes elicited on the IS by a way of exercising chosen by a big proportion of the society nowadays. Besides, our results further support the notion that exercise affects the IS and extends the description of underlying mechanisms mediating such effects.

Materials and methods

Ethic statement

Animal care and experimental practices were conducted at the Animal Facilities of the Instituto de Fisiología Celular (IFC), Universidad Nacional Autónoma de México (UNAM). All procedures in the experimental animals were approved by the Institutional Care and Animal Use Committee (CICUAL), adhering to Mexican regulation (NOM-062-ZOO-1999), in accordance with the recommendations from the National Institute of Health (NIH) of the United States of America (Guide for the Care and Use of Laboratory Animals). Euthanasia of experimental animals was performed in a humanitarian way.

Animals

For this study, male Wistar rats ranging between 250 to 300 g were used, proceeding from our own breeding at the animal facilities of IFC, UNAM. The animals were housed at IFC with controlled temperature (22˚C) and 12h light-dark cycles, with water and Purina LabDiet 5015 chow *ad libitum* (Purina, St. Louis MO). Sacrifice of those animals used exclusively for flow cytometry or samples extraction for cellular culture, was carried out by cervical dislocation after pentobarbital sodium (Pisabental®, México) anaesthesia. Animals that also were used for the extraction of the brain were sacrificed by an overdose of pentobarbital sodium (Purina, St. Louis MO). All procedures were carried out in a humanitarian way ensuring the maximisation of efforts in order to alleviate suffering.

Exercise protocol

Animals were set in one of three experimental groups: Exercised (EXE), Treadmill control (TC) and sedentary group (SED). Animals in the exercised group performed treadmill running 5 times a week for a period of 10 weeks, for which a previous habituation of one week was completed. During the habituation week, animals were placed inside the treadmill and then it was turned on at minimum capacity (4m/min) for 5 minutes per day. Once the habituation period was completed, animals started training. On the first day of training, rats ran at 7.5 m/min for 10 minutes, then speed and duration of exercise was escalated gradually each consecutive day, in order to achieve a daily exercise bout of 40 minutes at 15 m/min by the third week. Remaining weeks of training were kept constant in speed and duration until the sacrifice of the animals. It is noteworthy, that this training protocol equals to moderate chronic exercise, as it has been demonstrated in the works by Pilis and Carvalho [26,27] through the calculation

INFORME DE LABORES 2019

of the velocity at the lactate threshold. No electrical stimulus was used to incentive animals to run inside the treadmill.

Animals sited in the TC group were placed inside the treadmill at minimum capacity (4m/min) for 10 minutes, 5 times per week, for the same period of time than the exercised group (10 weeks). While being inside the treadmill, animals from TC group were exposed to the same context than animals from the EXE group without being exercised, reflecting any effect in the results prompted by sources other than exercise itself. Animals conforming the SED group were kept alive in standard conditions for the same amount of time than the other two groups.

At the end of the training period animals from every group were allowed to rest for one day in order to eliminate any possible effect of acute exercising. Afterwards, animals were sacrificed either by an overdose of pentobarbital sodium or by anesthesia with the same product followed by cervical dislocation (Pisabental®, México), afterwards the samples were taken.

Flow cytometry

Spleens were manually disaggregated using a 50μm nylon mesh, and cells resuspended in PBS. Erythrocytes in the solution were lysed using ACK buffer (150 mM NH_4Cl, 10mM $KHCO_3$, 0.1mM Na_2EDTA, pH 7.3) for 10 minutes and washed three times with PBS, then cells were resuspended in FACS buffer (PBS, FBS, 0.02% NaN_3).

Approximately $1x10^6$ cells were incubated with the following antibodies in order to characterize spleen immune subpopulations: Alexa Fluor® 488-conjugated- anti rat CD3 (IF4, Biolegend), PE Cy5-conjugated- anti rat CD4 (biolegend), PE-conjugated anti rat CD8a (Biolegend), PE-conjugated -anti rat CD45RA (Biolegend), Alexa Fluor® 647-conjugated-anti rat CD161 (biolegend), biotin-conjugated- anti rat CD11b (OX-42, Bioloegend), PE-conjugated anti rat TCR (V65, Biolengend). For the determination of macrophages, additionally to the use of anti CD11b antibody, a different gating was used, corresponding to bigger and more complex cells, in order to exclude other cells from the myeloid linage. Staining of the cell subpopulations was made by duplicate in order to additionally mark on each set one of the cannabinoid receptors.

For the staining of cannabinoid receptors, the polyclonal primary antibodies used were: rabbit anti Cannabinoid receptor I (abcam®) and rabbit anti Cannabinoid receptor II (abcam®), followed by the Secondary antibodies: AlexaFluor® 488- conjugated goat anti rabbit IgG (ThermoFisher Scientific) and DyLight® 649- conjugated- anti rabbit IgG (Vector laboratories).

In order to assess proliferation, a Cell Trace™ CFSE cell proliferation kit was used (Invitrogen™). Propidium iodide was used to determine viability of cells during cytotoxic assays. Attune Cytometer (life technologies) was used to obtain data which was further analyzed with FlowJo software (Treestar Inc.).

Proliferation assays

Total splenocytes were obtained as previously described and quantified on a Neubauer chamber. Subsequently, splenocytes were marked with CFSE cell tracer, which was used according to the manufacturer's protocol. Finally, cells were resuspended in RPMI-1640 medium (ATCC® 30 2001™). Splenocytes were cultivated in RPMI-1640 medium plus Ionomicyn (SIGMA-ALDRICH® 10634™) and PMA (SIGMA-ALDRICH® P8139-1MG™) at concentrations100 nm and and 25ng/ml for 72 hours. Proliferation was assessed using an Attune cytometer (Life Technologies) with blue and red lasers, obtained data was further analyzed with FlowJo software (Treestar Inc.).

INFORME DE LABORES 2019

Cell culture

Yac 1 cell line (ATCC® - TIB 160™) was cultivated in RPMI 1640 medium (ATCC® 30–2001™) supplemented with 10% Fetal bovine serum (FBS, ATCC® 30–2020™) and kept with air, 95%; carbon dioxide (CO^2), 5% at 37°C. Yac 1 cells were expanded for a week then counted on a Neubauer chamber and finally stained with CFSE kit for further use in cytotoxic assays.

In vitro cytotoxic assay

Yac 1 cells were stained with cell trace™ CFSE kit according to the manufacturer's protocol and used as target cells for the assay. A single cell splenocyte suspension was obtained from rats in the different experimental conditions as previously described, they were counted and used as the effector cells in the assay. Finally both, effector and target cells were co-cultivated in RPMI medium supplemented with 10% FBS for 4 hours, into 96 round well plates. Thereafter co-cultures were removed from the incubator and stained with Propidium Iodide and washed with Facs buffer. Acquisition was performed in an Attune Cytometer (life technologies) and data further analyzed with FlowJo software (Treestar Inc.).

Corticosterone and IgG levels assesssment

Animals were anesthetized and sacrificed one day after concluding their experimental condition, at the same time that they had been set for exercising (14:00–16:00 hr.). Cardiac puncture was performed in order to extract blood, which was immediately centrifuged at 4000rpm to collect the blood serum. Subsequently, blood serum was divided into two aliquots and stored at -70°C for later use. Corticosterone levels were assessed with a Corticosterone ELISA kit (Abcam® ab-108821) and procedures underwent according to manufacturer's protocol. Assessment of the levels of IgG in serum were carried out on a 96 flat bottom well plate. The plate was previously sensitized with a dilution of blood serum (1:1000), washed and blocked with a 1% albumin solution. Subsequently, the plate was incubated for 2 hours antibodies α IgG rat HRP were incubated, and once incubation finished, several washes were performed, chromogen was added to the wells, the reaction was stopped and the reading of the plate was carried out on a Stat Fax 4200 microplate reader (Awarness Technology).

Statistical analysis

For data regarding the changes of every cell subpopulation, a one-way ANOVA ($\alpha = 0.05$) was performed followed by a Tukey post-hoc test. Differences were considered significant when $p < 0.05$, with the actual p value and n being stated in each figure legend. Before the selection of the ANOVA test the normal distribution of the data was assessed via Shapiro-Wilk test. A similar process was carried out for the statistical analysis of the data regarding the proliferation and cytotoxicity tests, as well as for the data concerning the levels of corticosterone and IgG in serum. For the assessment of the expression of CBR, a two-way ANOVA ($\alpha = 0.05$) was performed, because of the consideration of two independent variables (group and CBR), followed by a Bonferroni post-hoc test with the same significant difference criterion. Data from all the experiments were charted as mean ± standard error, and analysed with Prism 5 software for Mac (GraphPad Software Inc.)

Results

Chronic-moderate exercise affects body composition parameters but not total ingestion of food or water

After ten weeks of rats being exposed to each experimental condition, animals were weighted, and results showed a significant gain of weight on those animals corresponding to both control

INFORME DE LABORES 2019

groups (SED, 490.8g; TC, 495.8g) against those from the EXE group (452g). ANOVA, $p = 0.0007$, $n = 6$, $P<0.05$. Accordingly, when samples were extracted, an observable difference in fat accumulation was perceived among the experimental groups, being those animals that performed the physical activity the ones with the lower amount of visceral fat. Interestingly water and food ingestion per week did not change among animals from the different experimental groups ($p = 0.3309$, $n = 6$, $P<0.05$, and $p = 0.3312$, $n = 6$, $P<0.05$ respectively).

Chronic-moderate exercise alters the composition of splenocyte subpopulations

Distribution of immune cells is a parameter that provides information about deficiencies or alterations from the IS, therefore we decided to evaluate several cell subpopulations from the innate and adaptive immune system in the spleen of rats that underwent different experimental conditions (S1 Fig). The immune cell subpopulations from the innate immune response that were analyzed corresponded to: NK cells (CD161+) and macrophages (CD11b+) for which flow cytometry analysis did not reflect a significant difference among groups (Fig 1). Analyzed cells from the adaptive immune response were: total T lymphocytes (CD3+), T helper lymphocytes (CD4+), cytotoxic T lymphocytes, Tγδ lymphocytes (Tγδ+) and B lymphocytes (CD45 RA+). For those cells studied, flow cytometry analysis reflected a decrease in the proportion of T helper lymphocytes (Fig 2) and in B lymphocytes (Fig 3) from the EXE group when compared to both control groups, SED and TC (Fig 2 and Fig 3), therefore considering such changes an effect of CE. On the other hand Tγδ lymphocytes showed an increase in the EXE group when compared to SED and TC groups (Fig 2), once more reflecting a change attributable to training. On the other hand, T cytotoxic cells decreased in TC and EXE groups in contrast to SED control group, reflecting an effect non attributable to exercise, but to the exposure to the treadmill (Fig 2). Total T lymphocytes (CD3+), did not show changes among the experimental groups (Fig 2).

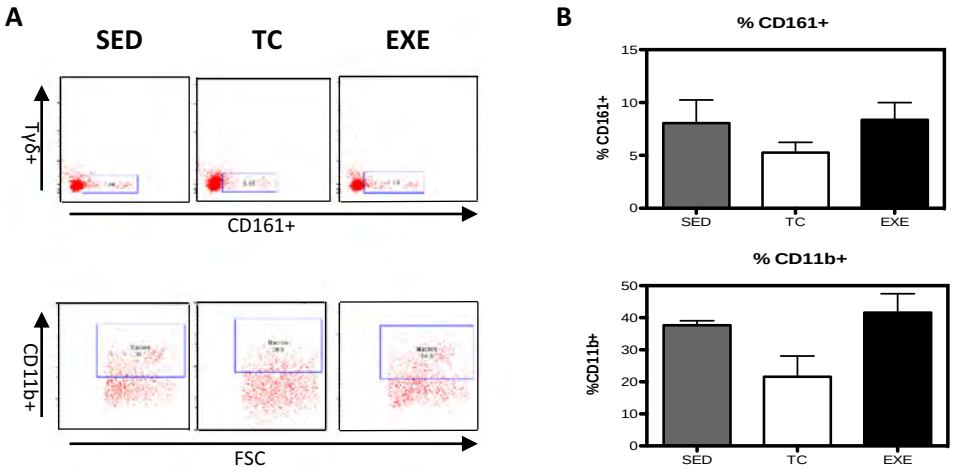

Fig 1. Changes in the composition of splenocyte populations related to the innate immune response. (A) Representative dot plot of the cytometric analysis of the subpopulation percentages. (B) Determination of splenocyte subpopulations from the innate immune response one day after being exposed to each condition in the different groups: SED, TC and EXE; data from 4 independent experiments are expressed as mean ± SE. No subpopulation showed statistically significant changes: Natural killer cells (ANOVA, $p = 0.0683$, $n = 10$), and Macrophages (ANOVA, $p = 0.0273$, $n = 10$).

https://doi.org/10.1371/journal.pone.0220542.g001

INFORME DE LABORES 2019

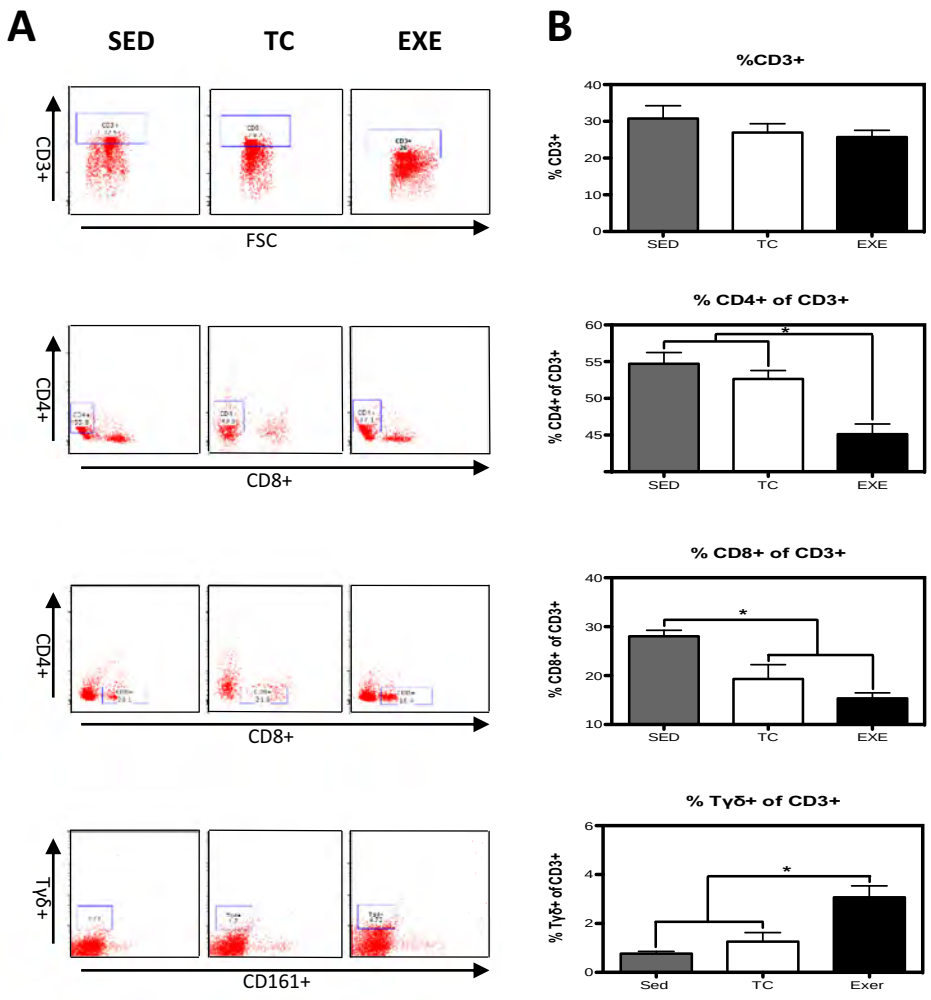

Fig 2. Changes in the composition of splenocyte populations related to the adaptive immune response. (A) Representative dot plot of the cytometric analysis of the subpopulation percentages. (B) Determination of splenocyte populations from the adaptive immune response in the different groups: SED, TC and EXE; data from 4 independent experiments are expressed as mean ± SE. Subpopulation that showed statistically significant changes were: T helper lymphocytes (ANOVA, p = 0.0008, n = 5) and Tγδ lymphocytes (ANOVA, p = 0.0002, n = 10). T lymphocytes (ANOVA, p = 0.3739, n = 12), cytotoxic T lymphocytes (ANOVA, p = 0.0016, n = 12). * Means statistically different from the two other groups, P<0.05.

https://doi.org/10.1371/journal.pone.0220542.g002

Modulation of CBR Expression in splenocytes after chronic exercise

CBR are widely distributed among immune cell subpopulations and structures from the IS. The expression of CBR on immune cells has been demonstrated to vary depending on activation or inflammatory profile, among other parameters. Thus, we decided to evaluate if CE would promote changes in the expression of CBR on splenocytes.

From the innate immune system, NK cells (CD161+) and macrophages were analyzed. NK cells from EXE and TC groups showed a decrease in CB2 expression, compared to SED, while no change was observed in CB1 expression. Macrophages (CD11b+) did not present changes in the expression of any CBR among groups (Fig 4). From the adaptive immune response, T helper lymphocytes (CD4+ cells) presented an increase in the expression of CB1 in animals from EXE group when compared to both control groups SED and TC, while no statistically

INFORME DE LABORES 2019

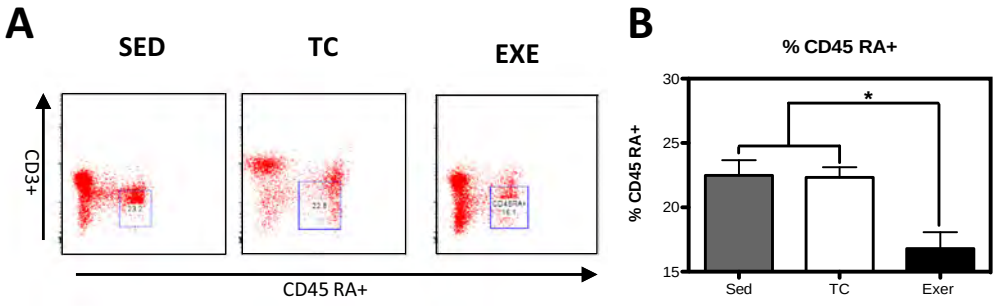

Fig 3. Changes in the composition of B-lymphocytes from spleen. (A) Representative dot plot of the cytometric analysis of the subpopulation percentages. (B) Determination of B-lymphocytes of spleen of rats in the different groups: SED, TC and EXE; data from 4 independent experiments are expressed as mean ± SE. B lymphocytes showed a statistically significant change (ANOVA, p = 0.3601, n = 10). * Means statistically different from the two other groups, P<0.05.

https://doi.org/10.1371/journal.pone.0220542.g003

significant difference was observed regarding CB2 expression. A similar phenomenon was observed in Tγδ subpopulation from EXE animals, which showed a higher expression of CB1 when compared to SED and TC groups (Fig 5), with no change in the expression of CB2. The expression of CBR did not vary in the subpopulations of T lymphocytes (CD3+) and cytotoxic T lymphocytes when experimental groups were compared (Fig 5).

On the other hand, B lymphocytes from the spleen of EXE animals showed a significant increase in CB2 expression, compared to those from SED and TC groups, whilst no change was reflected between groups in the expression of CB1 (Fig 6).

Immunoglobulin G levels are not altered by chronic exercising

Immunoglobulin G (IgG) is the most abundant type of immunoglobulins and a reliable parameter to assess the function of plasmatic cells. A change in the amount of IgG could represent an ongoing infectious process or an alteration on the normal function of plasmatic cells when observed in intact animals. We decided to assess if the total production of IgG would vary among our experimental groups. To do so, we performed a direct semi-quantitative ELISA. When data was analyzed statistically (ANOVA, n = 6, p = 0.0676) results did not show

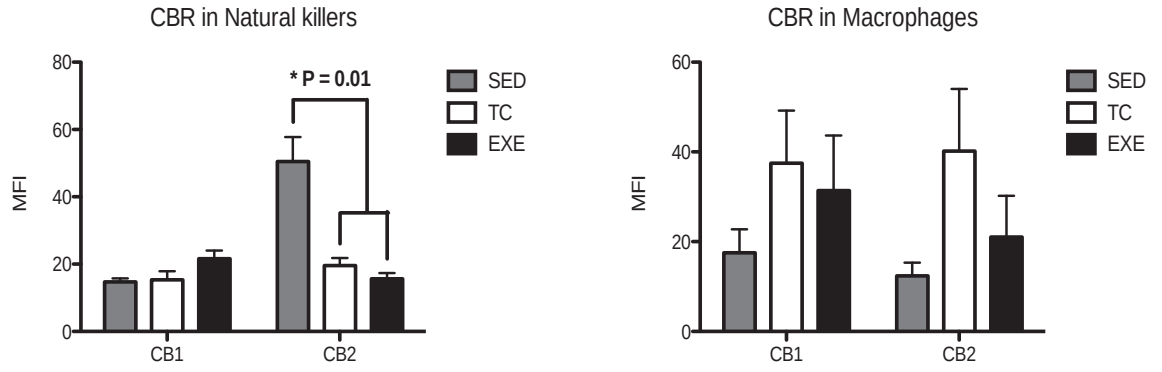

Fig 4. Expression of CBR in splenocyte populations related to the innate immune response. Analysis of the expression of CB1 and CB2 CBR in splenocyte populations from the innate immune response (NK's and macrophages) among experimental groups: SED (shaded bar), TC (white bar) and EXE (Solid bar); data from 4 independent experiments are expressed as mean ± SE. Lines connecting bars represent comparison among groups, * p<0.05. Two way ANOVA and Bonferroni post-test, n = 9.

https://doi.org/10.1371/journal.pone.0220542.g004

INFORME DE LABORES 2019

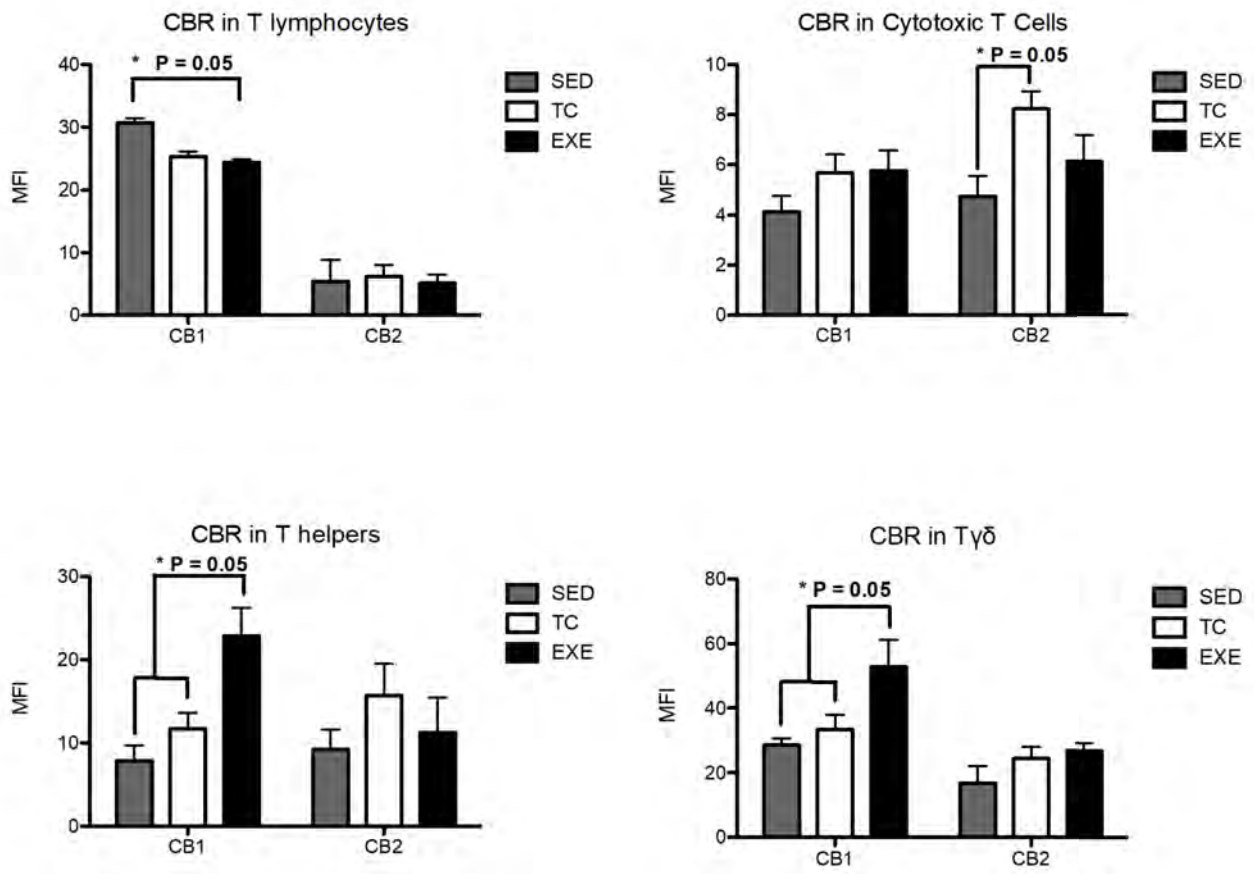

Fig 5. Expression of CBR in splenocyte populations related to the adaptive immune response. Analysis of the expression of CB1 and CB2 CBR in splenocyte populations from the adaptive immune response (T lymphocytes; n = 10, T helper lymphocytes; n = 8, cytotoxic T Lymphocytes; n = 10 and Tγδ n = 8) among experimental groups: SED (shaded bar), TC (white bar) and EXE (Solid bar); data from 4 independent experiments are expressed as mean ± SE. Lines connecting bars represent comparison among groups, * $p<0.05$. Two way ANOVA and Bonferroni post-test.

https://doi.org/10.1371/journal.pone.0220542.g005

any significant difference among the experimental groups: SED (optic density 2.731),TC and EXE (OD 2.973 and 2.871 respectively, S2 Fig).

Chronic exercise enhances proliferative capacity but not cytotoxic activity of total splenocytes

Proliferative capacity and cytotoxic activity have been tested before in order to assess the degree of competence of a subject's immune system. In order to observe if chronic exercise has any effect on both features we performed *in vitro* tests. For the proliferation assay we obtained total splenocytes and cultivated them on complete RPMI medium plus PMA and ionomycin for 72 hours. Data analyzed reflected no difference among groups in their proliferation index (Fig 7B). Nevertheless, total splenocytes from EXE group showed a higher proportion of dividing cells when compared to SED and TC groups (Fig 7C). Furthermore, we decided to test the proliferative capacity of the immune cell subpopulations and we found that B lymphocytes and NK cells from the EXE group exhibited a higher proportion of dividing cells than both SED and TC groups (Fig 7D).

INFORME DE LABORES 2019

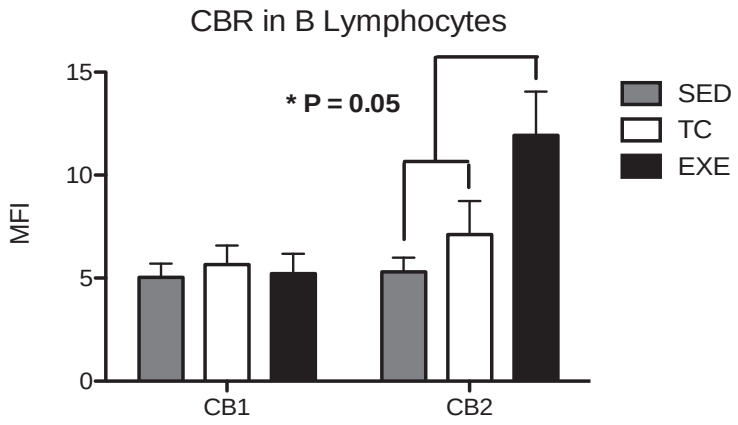

Fig 6. Expression of CBR in B lymphocytes from spleen. Analysis of the expression of CB1 and CB2 CBR in B lymphocytes from spleen among experimental groups: SED (shaded bar), TC (white bar) and EXE (Solid bar); data from 4 independent experiments are expressed as mean ± SE. Lines connecting bars represent comparison among groups, * $p<0.05$. Two way ANOVA and Bonferroni post-test, n = 10.

https://doi.org/10.1371/journal.pone.0220542.g006

In order to measure the cytotoxic capacity of splenocytes from the different groups, we performed a cytotoxicity test utilizing Yac1 cells as target cells and cultivating them with total splenocytes from animals of the different groups. Yac1 cells were previously marked with CFSE, and at the end of the test dead cells were dyed with propidium iodide, so double positive cells represented the target cells killed. The assay was carried out at three different effector/target ratios: 10:1, 50:1 and 100:1 and none showed any significant difference among treatments after the statistical analysis (Fig 8).

Corticosterone level is not altered by chronic exercise

Corticosterone level is considered a reliable stress marker in animals. In order to further comprehend the data obtained, we decided to analyze if corticosterone levels of blood serum differ among groups, reflecting a possible long-term effect of stress in exercised animals. When data was statistically analyzed (ANOVA, n = 6, p = 0.0473, Tukey's) results show a significant difference among the experimental groups. Nonetheless, The post hoc analysis did not show any significant interaction among the experimental groups. Means of the groups: TC and EXE (102.6 and 96.5 ng/ml respectively) were notoriously higher than that of the SED group (46.8 ng/ml, S3 Fig).

Discussion

Although widely studied, the consequences of physical activity over the IS remain as a promising field not only to expand our comprehension on basic physiology, but also on physiopathology and the different processes that take part on the orchestration of the immune response. At first instance, our investigation tries to emulate in rats a popular paradigm of exercising in modern times across the global population, which involves the chronic performance of medium intensity aerobic exercise. Such particularities in our model have led us to asses its raw impact over the IS composition and its function. Notwithstanding, the vast majority of studies have focused in the effects of short bouts of exercise over the immediate changes in composition and function of the IS [1,11,28,29], and neglecting those focused on the effect of CE and its long lasting effects over the IS [13,30]. In this study we observed that components

INFORME DE LABORES 2019

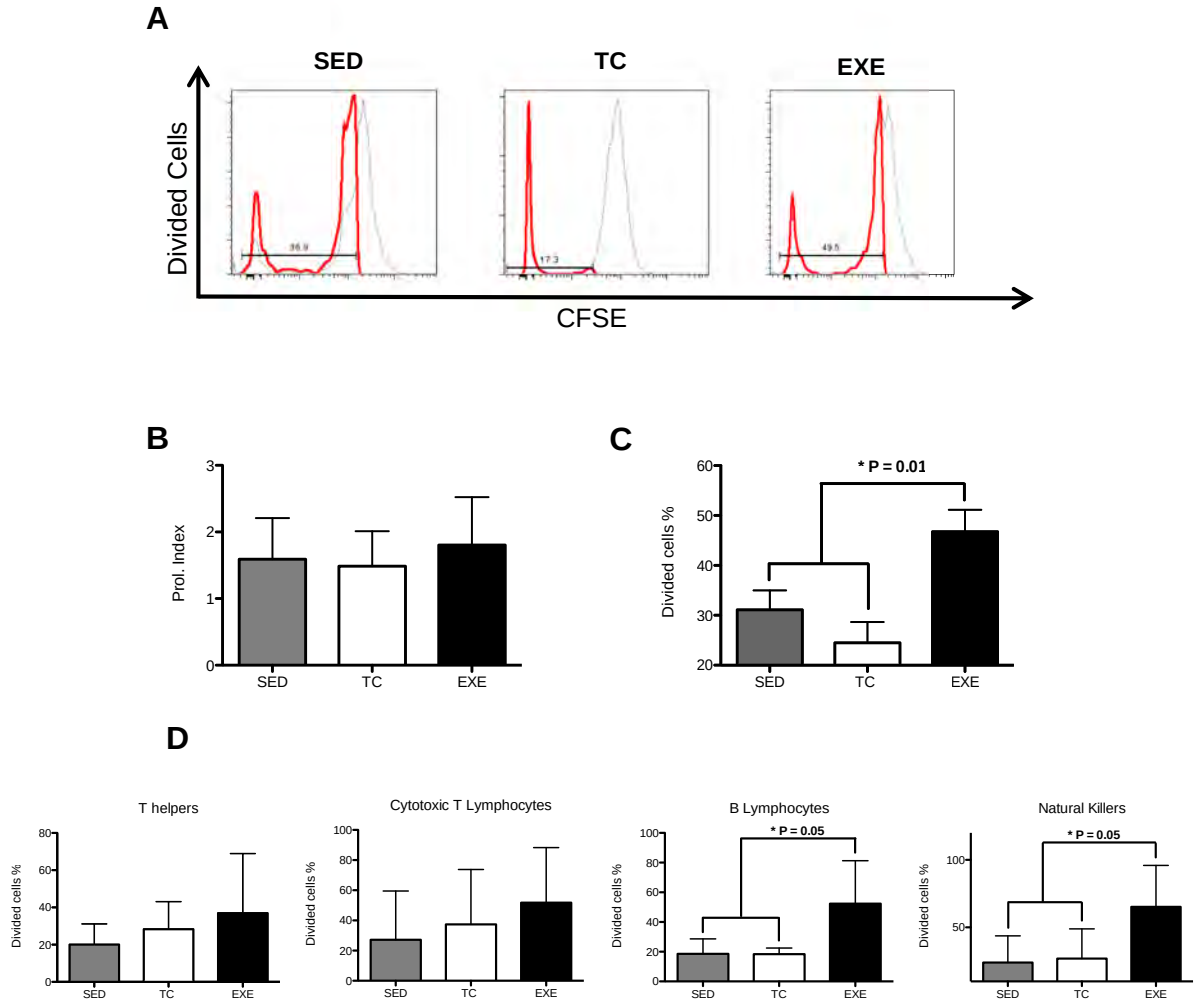

Fig 7. Effect of chronic exercise on splenocyte proliferation. (A) Representative histograms of cytometric analysis of dividing cells. Two parameters were considered to assess the proliferative capacity of splenocytes: (B) the proliferation index, which did not change due to chronic exercise and (C) the proportion of dividing cells, where we observed an increase in the exercised group when compared to both control groups (ANOVA, $p = 0.0092$, $n = 5$). (D) Analysis of proliferative capacity of specific splenocyte subpopulations: T helper lymphocytes (ANOVA, $p = 0.4543$, $n = 5$) and cytotoxic T lymphocytes (ANOVA, $p = 0.5248$, $n = 6$) did not show any change between groups; B lymphocytes (ANOVA, $p = 0.0006$, $n = 6$) and Natural killers (ANOVA, $p = 0.0191$, $n = 6$) from EXE did show an in increase in the proportion of dividing cells when compared to both control groups. In graphic bars SED is represented by shaded bar, TC by white bar and EXE by the solid bar.

https://doi.org/10.1371/journal.pone.0220542.g007

from the innate immune response were not affected by chronic-moderate exercise, while elements from the adaptive immune response did change in those animals that underwent physical training. T helper lymphocytes and B lymphocytes were decreased in trained animals, contrary to what would be expected according to the popular statement of moderate exercise enhancing a pro-inflammatory state [31,32]. On the other hand, Tγδ lymphocytes increased in animals from the EXE group, increase that could reflect an intensification in surveillance and protection of the upper respiratory tracts (URT) and mucosa tissue, idea that would be in accordance with the strengthened resistance against URT infections due to moderate exercising and opposite to the supposed effect of higher susceptibility to these infections in high performance athletes [29,33–37]. Nonetheless, the reduction of T helper and B lymphocyte populations was unexpected, since these cells play a major role at recognizing antigens and

INFORME DE LABORES 2019

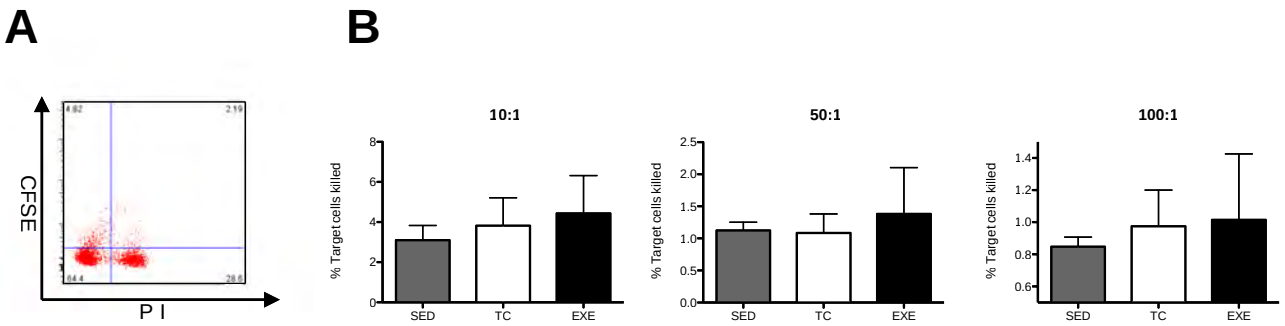

Fig 8. Cytotoxic activity of total splenocytes in vitro. (A) Representative dot plot of cytometric analysis of killed target cells percentage. (B) Cytotoxic activity of total splenocytes was assessed in vitro at three different ratios (effector cells: target cells, 10:1, 50:1 and 100:1); data from 2 independent experiments are expressed as mean ± SE, with an n = 6 for each condition. No differences were found among the groups at any of the different ratios. In bar graphics SED is represented by the shaded bar, TC by the white bar and EXE by the solid bar.

https://doi.org/10.1371/journal.pone.0220542.g008

therefore at orchestrating immune responses against new and already known threats and once activated they can polarize towards a pro-inflammatory or anti inflammatory state which modulates the activity of several other components from the innate and adaptive immune response. Consequently, the decrease of T helper lymphocytes as well as that of B lymphocytes made us wonder if it could be translated into a deficient immune response of animals of the EXE group.

Once we determined that our exercising paradigm did affect the composition of immune cells subpopulations, our next goal became to assess if those changes would be translated into functional alterations. To accomplish our purpose, we determined total IgG in serum among experimental groups and we also performed proliferation and cytotoxicity test *in vitro*. On the proliferation test, two parameters were evaluated: the proliferation index and the percentage of dividing cells. The first represents the mean of divisions that dividing cells underwent during the assay, which showed no difference among groups. In turn, the percentage of dividing cells among groups during the experiment showed statistical differences, being higher in splenocytes from the EXE group. Altogether, this data suggests that cells from EXE group are not more efficient at dividing once they have been activated but that more cells in proportion from EXE group are prone to proliferate once they have been exposed to PMA and ionomycine. These results made us wonder if this trend would be persistent in basal conditions, so we compared the percentage of proliferation in splenocytes among the experimental groups without activation by PMA and ionomycine and the statistical analysis showed no difference among them, reflecting a response produced by activation and not an anomaly that could reflect an inflammatory state that in turn could favor an autoimmune response. Thereafter, we evaluated the percentage of dividing cells from specific subpopulations, T helper cells, cytotoxic T cells, B lymphocytes and NK cells, showing an increase in the percentage of dividing cells in the last two subpopulations by effect of exercise. On the other hand, statistical analysis from the cytotoxicity test did not show variation among the experimental groups in any of the target/effector cell ratios tested, so data provided from this experiment does not suggest a higher cytotoxic activity from NK cells as a consequence from exercise. Nonetheless, exercise enhances the amount of NK cells that proliferate, which may indicate a higher immune-surveillance against transformed and virally infected cells in chronically exercised subjects.

Even though we found a decrease in major lymphocyte subpopulations (CD4+ and CD45 RA+ cells), which has been reported before for other immune cells in long term exercised individuals [32,38–40], we also determined that a bigger proportion of splenocytes is prone to

INFORME DE LABORES 2019

activate when stimulated, plus other functions of splenocytes from the EXE animals were not impaired. Given the fact that long-term exercised subjects do not report any kind of immune suppression, we have come to hypothesize that the decrease in the composition of some cell subpopulations may represent a more efficient IS, which requires less elements but presents a stronger reaction when needed. This idea is also supported by the results shown by the ELISA test, which showed that levels of IgG did not change among the groups, even though the subpopulation of B lymphocytes is decreased in EXE animals.

Finally, recent works have denominated the endocannabinoid system (ECS) as an immunomodulatory system; inhibiting the function of highly reactive and pro-inflammatory cells [25,41,42]. The ECS exerts its functions through the activation of its receptors, which expression vary greatly depending on cell subpopulation, activation or inflammatory status [24,41,43,44], being increased in the surface of more reactive cells. In this work we demonstrated that CE promotes changes in the expression of both CBR's in splenocytes, through the staining of each receptor on different cell suspension aliquots and due to the shared epitope for the secondary antibody. Our findings concur with previous works showing that during moderate exercise bouts there is an increase of circulating ECS agonists [18,19]. We must emphasize that changes in CBR's expression remained after one skipped day of training, which suggests that subjects exercising on a daily basis or in intervals of every two days might be maintaining this alterations. Our methodology allowed us to determine differences in the expression of CBR among cell subpopulations even between control groups. These differences might be explained by the intrinsic variability among cell subpopulations [21,45]. We also assessed an increased expression of CB1 receptor in the subpopulations of T helper and Tγδ lymphocytes and an increase in the expression of CB2 receptor in B lymphocytes of exercised animals. Therefore enhanced expression of CB1 in T helper, Tγδ, and CB2 in B lymphocytes could represent a mechanism to down regulate the activity of these probable high metabolic cells from EXE animals, as reflected by the proliferation tests. Some of these data differ from anterior reports concerning expression of CBR, nonetheless most of those reports used different techniques and did not measure the protein conforming CBR's but mostly mRNA [21,46,47], which highlights the novelty of the data presented in this work, by showing a direct measure of the expressed protein in question under this particularly conditions of exercise. On the same line, the increased expression of CBR in splenocytes, particularly in lymphocytes from the EXE group, concurs with previous data reporting changes in the expression of the protein through the assessment by different techniques, like western blot and immunofluorescense [21,48,49], adding validity to our results.

We would like to address those changes presented on this work that can not be attributable to CE, like the composition of cytotoxic T cells for which TC and EXE groups differ when compared against SED group, reflecting an effect relying probably on the stress produced by the placement of the animals inside the treadmill, being that, the one thing that those groups had in common. The same explanation seems plausible for the expression of CBR in NK and cytotoxic T cells. Nevertheless analysis of corticosterone did not showed significant difference among the experimental groups, different sensitivity to several molecules has been reported for the wide variety of cells from the IS, leaving the possibility of other molecular interactions that escaped our control and awareness.

Supporting information

S1 Fig. Gating strategy for the flow cytometric analysis of rat spleen subpopulations and their expression of CB1 and CB2 receptors. Single cell suspension was prepared and stained with fluorochrome-conjugated antibodies to separate splenocyte subpopulations and to mark

cannabinoid receptors (CB1 and CB2). Data was analyzed with FlowJo software 8.7 for Mac. Lymphocytes were identified by their scatter properties (FSC-A x SSC-A plot). Splenocyte subpopulations were characterized by surface staining and gated for their quantity assessment. Subsequently each cellular subpopulation was analyzed for their expression of both cannabinoid receptors in their surface.
(TIFF)

S2 Fig. Levels of IgG are not affected by chronic exercise. The analysis of total IgG was assessed for every experimental group with the use of a direct semi-quantitative ELISA. Statistical analysis did not show any significant difference among the experimental groups: SED (shaded bar), TC (white bar) and EXE (Solid bar). $P>0.05$. ANOVA, $p = 0.0676$, $n = 6$.
(TIF)

S3 Fig. Serum corticosterone concentration one day after the last exercising bout. Data is shown as mean (ng/ml) +- SE for each group. There was no significant difference among group values in concentration of serum corticosterone. Groups analyzed: SED (shaded bar), TC (white bar) and EXE (Solid bar). When data was statistically analyzed (ANOVA, $n = 6$, $p = 0.0473$, Tukey's) results show a significant difference among the experimental groups. Nonetheless, The post hoc analysis did not show any significant interaction among the experimental groups. Means of the groups: TC and EXE (102.6 and 96.5 ng/ml respectively) were notoriously higher than that of the SED group (46.8 ng/ml).
(TIF)

Acknowledgments

We thank M.V.Z Claudia Rivera-Cerecedo and her animal facility staff for assisting in the breeding of experimental animals. We also thank Diana Millán-Aldaco and Marcela Palomero-Rivero for their technical support.

Salvador Valencia-Sánchez is a doctoral student from Programa de Doctorado en Ciencias Biomédicas, Universidad Nacional Autónoma de México (UNAM) and received fellowship 223625 from CONACYT.

Author Contributions

Conceptualization: Salvador Valencia-Sánchez, Karen Elizabeth Nava-Castro, Oscar Prospéro-García, Jorge Morales-Montor, René Drucker-Colín.

Data curation: Karen Elizabeth Nava-Castro.

Formal analysis: Salvador Valencia-Sánchez, Karen Elizabeth Nava-Castro, Margarita Isabel Palacios-Arreola, Oscar Prospéro-García, Jorge Morales-Montor.

Funding acquisition: Karen Elizabeth Nava-Castro, Jorge Morales-Montor, René Drucker-Colín.

Investigation: Salvador Valencia-Sánchez, Margarita Isabel Palacios-Arreola, Oscar Prospéro-García, Jorge Morales-Montor.

Methodology: Salvador Valencia-Sánchez, Margarita Isabel Palacios-Arreola.

Project administration: Jorge Morales-Montor, René Drucker-Colín.

Resources: Oscar Prospéro-García, Jorge Morales-Montor.

INFORME DE LABORES 2019

Writing – original draft: Karen Elizabeth Nava-Castro, Margarita Isabel Palacios-Arreola, Oscar Prospéro-García, Jorge Morales-Montor, René Drucker-Colín.

Writing – review & editing: Jorge Morales-Montor.

References

1. Santos RVT, Caperuto É C, Costa Rosa LFBP. Effects of acute exhaustive physical exercise upon glutamine metabolism of lymphocytes from trained rats. Life Sci. 2007; 80(6):573–8. https://doi.org/10.1016/j.lfs.2006.10.015 PMID: 17123550
2. Freidenreich DJ, Volek JS. Immune responses to resistance exercise. Exerc Immunol Rev. 2012; 18:8–41. PMID: 22876721
3. Freidenreich DJ, Volek JS. The Immune Response to Exercise [Internet]. Nutrition and Enhanced Sports Performance. Elsevier Inc.; 2013. 95–101 p. Available from: http://linkinghub.elsevier.com/retrieve/pii/B9780123964540000096
4. Gleeson M, Bishop NC, Stensel DJ, Lindley MR, Mastana SS, Nimmo MA. The anti-inflammatory effects of exercise: mechanisms and implications for the prevention and treatment of disease. Nat Rev Immunol [Internet]. 2011 Sep 5; 11(9):607–15. Available from: https://doi.org/10.1038/nri3041 PMID: 21818123
5. Ropelle ER, Flores MB, Cintra DE, Rocha GZ, Pauli JR, Morari J, et al. IL-6 and IL-10 anti-inflammatory activity links exercise to hypothalamic insulin and leptin sensitivity through IKKβ and ER stress inhibition. PLoS Biol. 2010; 8(8):31–2.
6. Handschin C, Spiegelman BM. The role of exercise and PGC1α in inflammation and chronic disease. 2008; 454(7203):463–9. https://doi.org/10.1038/nature07206 PMID: 18650917
7. GROUP DPPR. Reduction in the Incidence of Type 2 Diabetes with Lifestyle Intervention or Metformin. N Engl J Med [Internet]. 2002 Feb 7; 346(6):393–403. Available from: https://doi.org/10.1056/NEJMoa012512 PMID: 11832527
8. Gustafson MP, DiCostanzo AC, Wheatley CM, Kim CH, Bornschlegl S, Gastineau DA, et al. A systems biology approach to investigating the influence of exercise and fitness on the composition of leukocytes in peripheral blood. J Immunother Cancer. 2017; 5(1):1–14.
9. LaVoy EC, Hussain M, Reed J, Kunz H, Pistillo M, Bigley AB, et al. T-cell redeployment and intracellular cytokine expression following exercise: effects of exercise intensity and cytomegalovirus infection. Physiol Rep [Internet]. 2017; 5(1):e13070. Available from: http://www.ncbi.nlm.nih.gov/pubmed/28087817%5Cnhttp://www.pubmedcentral.nih.gov/articlerender.fcgi?artid=PMC5256156%5Cnhttp://physreports.physiology.org/lookup/doi/10.14814/phy2.13070 PMID: 28087817
10. Pedersen BK, Hoffman-goetz L. Exercise and the Immune System: Regulation, Integration, and Adaptation. Society. 2000; 80(3):1055–81.
11. Sugiura H, Sugiura H, Nishida H, Inaba R, Mirbod SM, Iwata H. Effects of different durations of exercise on macrophage functions in mice Effects of different durations of exercise on macrophage functions in mice. J Appl Physiol. 2001;789–94.
12. Campbell JP, Turner JE, Campbell JP, Turner JE. Debunking the Myth of Exercise- Induced Immune Suppression: Redefining the Impact of Exercise on Immunological Health Across the Lifespan. 2018; 9 (April):1–21.
13. Lancaster G, Halson S, Khan Q, Drysadale P, Wallace F, Jeukendrup AE, et al. Effects of acute exhaustive exercise and chronic exercise training on type 1 and type 2 T lymphocytes. Exerc Immunol Rev [Internet]. 2004; 10:91–104. Available from: http://www.researchgate.net/publication/8096824_Effects_of_acute_exhaustive_exercise_and_chronic_exercise_training_on_type_1_and_type_2_T_lymphocytes/file/79e4150c59a6b1619f.pdf PMID: 15633589
14. Wang J, Song H, Tang X, Yang Y, Vieira VJ, Niu Y, et al. Effect of exercise training intensity on murine T-regulatory cells and vaccination response. Scand J Med Sci Sports [Internet]. 2012 Oct [cited 2012 Oct 10]; 22(5):643–52. Available from: http://www.ncbi.nlm.nih.gov/pubmed/21410542 https://doi.org/10.1111/j.1600-0838.2010.01288.x PMID: 21410542
15. Palmer CS, Cherry CL, Sada-Ovalle I, Singh A, Crowe SM. Glucose Metabolism in T Cells and Monocytes: New Perspectives in HIV Pathogenesis. EBioMedicine [Internet]. 2016 Apr; 6:31–41. Available from: https://doi.org/10.1016/j.ebiom.2016.02.012 PMID: 27211546
16. Palmer CS, Ostrowski M, Balderson B, Christian N, Crowe SM. Glucose metabolism regulates T cell activation, differentiation, and functions. Front Immunol. 2015; 6(JAN):1–6. https://doi.org/10.3389/fimmu.2015.00001 PMID: 25657648

17. Padgett D a. Glaser R. How stress influences the immune response. Trends Immunol. 2003; 24 (8):444–8. https://doi.org/10.1016/s1471-4906(03)00173-x PMID: 12909458

18. Sparling PB, Giuffrida a, Piomelli D, Rosskopf L, Dietrich a. Exercise activates the endocannabinoid system. Neuroreport [Internet]. 2003 Dec 2 [cited 2012 Aug 22]; 14(17):2209–11. Available from: http://www.ncbi.nlm.nih.gov/pubmed/14625449 https://doi.org/10.1097/00001756-200312020-00015 PMID: 14625449

19. Heyman E, Gamelin F, Goekint M, Piscitelli F, Roelands B, Leclair E, et al. Intense exercise increases circulating endocannabinoid and BDNF levels in humans——Possible implications for reward and depression. Psychoneuroendocrinology. 2012; 37:844–51. https://doi.org/10.1016/j.psyneuen.2011.09.017 PMID: 22029953

20. Galdino G, Romero TRL, Silva JFP, Aguiar DC, De Paula AM, Cruz JS, et al. The endocannabinoid system mediates aerobic exercise-induced antinociception in rats. Neuropharmacology [Internet]. 2014; 77:313–24. Available from: https://doi.org/10.1016/j.neuropharm.2013.09.022 PMID: 24148812

21. Galiègue S, Mary S, Marchand J, Dussossoy D, Carrikre D, Camyon P, et al. Expression of central and peripheral cannabinoid receptors in human immune tissues and leukocyte subpopulations. Eur J Biochem. 1995; 61(232):54–61.

22. Klein TW, Newton C, Friedman H. Cannabinoid receptors and immunity. Immunol Today [Internet]. 1998 Aug; 19(8):373–81. Available from: http://www.ncbi.nlm.nih.gov/pubmed/21873455 https://doi.org/10.1016/s0167-5699(98)01300-0 PMID: 9709506

23. Tanasescu R, Constantinescu CS. Cannabinoids and the immune system: an overview. Immunobiology [Internet]. 2010 Aug [cited 2012 Jul 23]; 215(8):588–97. Available from: http://www.ncbi.nlm.nih.gov/pubmed/20153077 https://doi.org/10.1016/j.imbio.2009.12.005 PMID: 20153077

24. Cencioni MT, Chiurchiù V, Catanzaro G, Borsellino G, Bernardi G, Battistini L, et al. Anandamide suppresses proliferation and cytokine release from primary human T-lymphocytes mainly via CB2 receptors. PLoS One. 2010; 5(1):2–11.

25. Malek N, Popiolek-Barczyk K, Mika J, Przewlocka B, Starowicz K. Anandamide, acting via CB2 receptors, alleviates LPS-induced neuroinflammation in rat primary microglial cultures. Neural Plast. 2015; 2015.

26. Pilis W., Zarzezny R., Langfort J., Kactuba-Uscitko H., Nazar K., Wojtyna J. Anaerobic treshold in rats. Comp Biochem Physiol. 1993;(106):285–9.

27. Carvalho JF, Masuda MO, Pompeu FAMS. Method for diagnosis and control of aerobic training in rats based on lactate threshold. 2005; 140:409–13. https://doi.org/10.1016/j.cbpb.2004.12.002 PMID: 15936699

28. Radom-Aizik S, Zaldivar F, Haddad F, Cooper DM. Impact of brief exercise on peripheral blood NK cell gene and microRNA expression in young adults. J Appl Physiol [Internet]. 2013; 114(5):628–36. Available from: https://doi.org/10.1152/japplphysiol.01341.2012 PMID: 23288554

29. Murphy E a, Davis JM, Brown a S, Carmichael MD, Van Rooijen N, Ghaffar a, et al. Role of lung macrophages on susceptibility to respiratory infection following short-term moderate exercise training. Am J Physiol Regul Integr Comp Physiol [Internet]. 2004; 287(6):R1354–8. Available from: http://www.ncbi.nlm.nih.gov/pubmed/15308485 https://doi.org/10.1152/ajpregu.00274.2004 PMID: 15308485

30. Syu G-D, Chen H-I, Jen CJ. Differential effects of acute and chronic exercise on human neutrophil functions. Med Sci Sports Exerc [Internet]. 2012; 44(6):1021–7. Available from: http://www.ncbi.nlm.nih.gov/pubmed/22130467 https://doi.org/10.1249/MSS.0b013e3182408639 PMID: 22130467

31. Sugiura H, Sugiura H, Nishida H, Inaba R, Mirbod SM, Iwata H. Effects of different durations of exercise on macrophage functions in mice Effects of different durations of exercise on macrophage functions in mice. J Appl Physiol. 2012;789–94.

32. Saito Y, Kusaka Y, Shimada M. Effects of exercise intensity on circulating leukocyte subpopulations. Environ Health Prev Med [Internet]. 2003; 8(1):18–22. Available from: http://www.pubmedcentral.nih.gov/articlerender.fcgi?artid=2723261&tool=pmcentrez&rendertype=abstract https://doi.org/10.1007/BF02897939 PMID: 21432111

33. Davis JM, Murphy E a, Brown a S, Carmichael MD, Ghaffar a, Mayer EP. Effects of moderate exercise and oat beta-glucan on innate immune function and susceptibility to respiratory infection. Am J Physiol Regul Integr Comp Physiol. 2004; 286(2):R366–72. https://doi.org/10.1152/ajpregu.00304.2003 PMID: 14551169

34. Slusher AL, Zúñiga TM, Acevedo EO. Maximal Exercise Alters the Inflammatory Phenotype and Response of Mononuclear Cells [Internet]. Medicine & Science in Sports & Exercise. 2017. 1 p. Available from: http://insights.ovid.com/crossref?an=00005768-900000000-97070

35. Matthews CE, Ockene IR a S, Freedson PS, Rosal MC, Merriam P a, Hebert JR. Moderate to vigorous physical activity and risk of upper-repiratory tract infection. Med Sci Sport Exerc. 2002; 34(8):1242–8.

36. Parsons LM, Denton D, Egan G, Mckinley M, Shade R, Lancaster J, et al. Neuroimaging evidence implicating cerebellum in support of sensorycognitive processes associated with thirst. 2000; 97(5). https://doi.org/10.1073/pnas.040555497 PMID: 10688891

37. MacKinnon LT. Special feature for the Olympics: effects of exercise on the immune system: overtraining effects on immunity and performance in athletes. Immunol Cell Biol [Internet]. 2000 Oct; 78(5):502–9. Available from: http://www.ncbi.nlm.nih.gov/pubmed/11050533 https://doi.org/10.1111/j.1440-1711.2000.t01-7-.x PMID: 11050533

38. Córdova A, Sureda A, Tur JA, Pons A. Immune response to exercise in elite sportsmen during the competitive season. J Physiol Biochem [Internet]. 2010 Mar 29; 66(1):1–6. Available from: http://link.springer.com/10.1007/s13105-010-0001-2 https://doi.org/10.1007/s13105-010-0001-2 PMID: 20428993

39. Lin YS, Jan MS, Chen HI. The effect of chronic and acute exercise on immunity in rats. / Effet de l ' exercice chronique et aigu sur l ' immunite chez des rats. Int J Sports Med [Internet]. 1993; 14(2):86–92. Available from: http://search.ebscohost.com/login.aspx?direct=true&db=sph&AN=SPH360924&site=ehost-live https://doi.org/10.1055/s-2007-1021151 PMID: 8463030

40. Blannin a K, Chatwin LJ, Cave R, Gleeson M. Effects of submaximal cycling and long-term endurance training on neutrophil phagocytic activity in middle aged men. Br J Sports Med [Internet]. 1996 Jun 1; 30(2):125–9. Available from: http://bjsm.bmj.com/cgi/doi/10.1136/bjsm.30.2.125%5Cnhttp://www.pubmedcentral.nih.gov/articlerender.fcgi?artid=1332375&tool=pmcentrez&rendertype=abstract https://doi.org/10.1136/bjsm.30.2.125 PMID: 8799596

41. Chiurchiu V, Battistini L, Maccarrone M. Endocannabinoid signalling in innate and adaptive immunity. Immunology. 2015; 144(3):352–64. https://doi.org/10.1111/imm.12441 PMID: 25585882

42. Greineisen WE, Turner H. Immunoactive effects of cannabinoids: considerations for the therapeutic use of cannabinoid receptor agonists and antagonists. Int Immunopharmacol [Internet]. 2010 May [cited 2013 Mar 7]; 10(5):547–55. Available from: http://www.ncbi.nlm.nih.gov/pubmed/20219697 https://doi.org/10.1016/j.intimp.2010.02.012 PMID: 20219697

43. Galgglje S, Mary S, Marchand J, Dussossoy D, Carrikre D, Camyon P, et al. Expression of central and peripheral cannabinoid receptors in human immune tissues and leukocyte subpopulations. Signals. 1995; 61:54–61.

44. Bouaboula M, Rinaldi M, Carayon P, Carillon C, Delpech B, Shire D, et al. Cannabinoid-receptor expression in human leukocytes. Eur J Biochem [Internet]. 1993; 214(1):173–80. Available from: http://content.febsjournal.org/cgi/content/abstract/214/1/173%5Cnhttp://onlinelibrary.wiley.com/doi/10.1111/j.1432-1033.1993.tb17910.x/full%5Cnhttp://www.ncbi.nlm.nih.gov/pubmed/8508790%5Cnhttp://www.ncbi.nlm.nih.gov/entrez/query.fcgi?cmd=Retrieve&db=PubM https://doi.org/10.1111/j.1432-1033.1993.tb17910.x PMID: 8508790

45. Graham ES, Angel CE, Schwarcz LE, Dunbar PR, Glass M. Detailed characterisation of CB2 receptor protein expression in peripheral blood immune cells from healthy human volunteers using flow cytometry. Int J Immunopathol Pharmacol. 2010; 23(1):25–34. https://doi.org/10.1177/039463201002300103 PMID: 20377992

46. Lee SF, Newton C, Widen R, Friedman H, Klein TW. Differential expression of cannabinoid CB 2 receptor mRNA in mouse immune cell subpopulations and following B cell stimulation. Eur J Pharmacol. 2001;235–41.

47. Noe SN, Newton C, Widen R, Friedman H, Klein TW. Anti-CD40, anti-CD3, and IL-2 stimulation induce contrasting changes in CB1 mRNA expression in mouse splenocytes. 2000; 110:161–7. https://doi.org/10.1016/s0165-5728(00)00349-0 PMID: 11024546

48. Amancio-Belmont O, Becerril Meléndez AL, Ruiz-Contreras AE, Méndez-Díaz M, Prospéro-García O. Opposed cannabinoid 1 receptor (CB1R) expression in the prefrontal cortex vs. nucleus accumbens is associated with alcohol consumption in male rats. Brain Res [Internet]. 2019; 1725(September):146485. Available from: https://doi.org/10.1016/j.brainres.2019.146485 PMID: 31568767

49. Piszcz J a, Lemancewicz D, Kloczko J, Dzieciol J, Rusak M, Dabrowska M. Cannabinoid receptors expression in bone marrow trephine biopsy of chronic lymphocytic leukaemia patients treated with purine analogues. Exp Oncol [Internet]. 2007 Sep; 29(3):221–5. Available from: http://www.ncbi.nlm.nih.gov/pubmed/18004250 PMID: 18004250

frontiers in Cellular Neuroscience

ORIGINAL RESEARCH
published: 21 May 2019
doi: 10.3389/fncel.2019.00215

Histamine Modulates Midbrain Dopamine Neuron Differentiation Through the Regulation of Epigenetic Marks

Fernanda Vargas-Romero[1†], Rodrigo González-Barrios[2†], Lissania Guerra-Calderas[3†], Itzel Escobedo-Avila[1,4], Daniel Cortés-Pérez[1,4], Adolfo López-Ornelas[1,4], Luisa Rocha[5], Ernesto Soto-Reyes[3] and Iván Velasco[1,4]**

[1] Instituto de Fisiología Celular – Neurociencias, Universidad Nacional Autónoma de México, Mexico City, Mexico, [2] Unidad de Investigación Biomédica en Cáncer, Instituto Nacional de Cancerología-Instituto de Investigaciones Biomédicas, Universidad Nacional Autónoma de México, Mexico City, Mexico, [3] Departamento de Ciencias Naturales, Universidad Autonoma Metropolitana, Unidad Cuajimalpa, Mexico City, Mexico, [4] Laboratorio de Reprogramación Celular, Instituto Nacional de Neurología y Neurocirugía "Manuel Velasco Suárez" – Instituto de Fisiología Celular, Universidad Nacional Autónoma de México, Mexico City, Mexico, [5] Departamento de Farmacobiología, Centro de Investigación y de Estudios Avanzados (Cinvestav), Mexico City, Mexico

OPEN ACCESS

Edited by:
Tommaso Pizzorusso, University of Florence, Italy

Reviewed by:
Maria Beatrice Passani, University of Florence, Italy
Yuriko Iwakura, Niigata University, Japan

***Correspondence:**
Ernesto Soto-Reyes
esotoreyes@correo.cua.uam.mx
Iván Velasco
ivelasco@ifc.unam.mx

† These authors have contributed equally to this work

Specialty section:
This article was submitted to Cellular Neurophysiology, a section of the journal Frontiers in Cellular Neuroscience

Received: *13 February 2019*
Accepted: *29 April 2019*
Published: *21 May 2019*

Citation:
Vargas-Romero F, González-Barrios R, Guerra-Calderas L, Escobedo-Avila I, Cortés-Pérez D, López-Ornelas A, Rocha L, Soto-Reyes E and Velasco I (2019) Histamine Modulates Midbrain Dopamine Neuron Differentiation Through the Regulation of Epigenetic Marks. Front. Cell. Neurosci. 13:215. doi: 10.3389/fncel.2019.00215

During midbrain development, dopamine neuron differentiation occurs before birth. Epigenetic processes such as DNA methylation and demethylation as well as post-translational modification of histones occur during neurogenesis. Here, we administered histamine (HA) into the brain of E12 embryos *in vivo* and observed significant lower immunoreactivity of Lmx1a+ and Tyrosine Hydroxylase (TH)+ cells, with parallel decreases in the expression of early (*Lmx1a*, *Msx1)* and late (*Th*) midbrain dopaminergic (mDA) genes. With MeDIP assays we found that HA decreases the percentage of 5-methylcytosine of *Pitx3* and *Th*, without changes in 5-hydroxymethylcytosine. Additionally, HA treatment caused a significant increase in the repressive epigenetic modifications H3K9me3 in *Pitx3* and *Th*, and also more H3K27me3 marks in *Th*. Furthermore, HA has a long-term effect on the formation of the nigrostriatal and mesolimbic/mesocortical pathways, since it causes a significant decrease in midbrain TH immunoreactivity, as well as alterations in dopaminergic neuronal fibers, and significant lower TH-positive area in the forebrain in whole-mount stainings. These findings suggest that HA diminishes dopaminergic gene transcription by altering several epigenetic components related to DNA and histone modifications, which affects mDA neuron progression during development.

Keywords: midbrain development, dopamine neuron differentiation, epigenetic modifications, neuroepigenetics, ultrasound-guided injection in utero

INTRODUCTION

Midbrain dopaminergic (mDA) neurons are essential for motor function control as well as for the regulation of reward and emotions (van Heesbeen et al., 2013). Development of mDA neurons can be divided into three stages: neural plate regionalization, midbrain cell fate determination and terminal differentiation to mDA neurons (Gale and Li, 2008). Each step presents activation of

different cascades of transcriptional factors triggered by extrinsic signals (Ang, 2006; Abeliovich and Hammond, 2007; Huang et al., 2015). During the specification stage, dopaminergic neural progenitors express specific genes such as *Lmx1a/b*, *Foxa2*, *Msx1/2*, and *Ngn2* (Ang, 2006; Gale and Li, 2008; Nakatani et al., 2010; Yan et al., 2011). At this stage neural progenitors acquire mDA neuronal fate and start the last stage to become post-mitotic neurons (Yi et al., 2014). The activation of *Nurr1* and *Pitx3* allows the expression of late-differentiation genes associated to the dopaminergic neuron phenotype, as they regulate the expression of enzymes such as Tyrosine Hydroxylase (TH), the rate limiting enzyme in the production of dopamine (Gale and Li, 2008; Jacobs et al., 2009; Kadkhodaei et al., 2009). Terminally differentiated mDA neurons extend their axons to reach the *striatum* (ST) and release dopamine to regulate motor function in the basal ganglia (Hegarty et al., 2013).

Histamine (HA) is a neurotransmitter/neuromodulator that participates in the sleep/awake cycle, motor activity, cognition, feeding and energy balance in the adult brain (Panula and Nuutinen, 2013). During rat embryonic development, the cerebral concentration of HA reaches higher levels than those observed in the adult; its highest concentration is found at embryonic days (E) 14–16 (Vanhala et al., 1994; Nissinen and Panula, 1995; Molina-Hernández et al., 2012). This amine has a cell proliferation and neuronal differentiation effect on cortical neural stem/progenitor cell (NSPC) cultures, through multiple effects, including: elevation of intracellular Ca^{2+}, up-regulation of FGF receptors and increased expression of proneural genes (Molina-Hernández and Velasco, 2008; Rodríguez-Martínez et al., 2012; Molina-Hernández et al., 2013). Similar effects of HA, have been observed on adult NSPC at the subventricular zone (Bernardino et al., 2012). In addition, the *in vivo* effects of HA injected at E12 include a decrease in NSPC proliferation in the ventricular zone and also a decrease in TH staining in the midbrain, without affecting serotoninergic nor GABAergic neurons; co-injection of HA with the H_1R antagonist chlorpheniramine prevented the decrease on TH induced by HA (Escobedo-Avila et al., 2014).

Recent studies describe different pathways to regulate neural stem cell differentiation via regulation of epigenetic modifications, which result in changes on gene expression. DNA demethylation has been related to the brain development control (Hahn et al., 2013; Wheldon et al., 2014). Particularly, the increase of 5-hydroxymethylcytosine (5hmC) along gene bodies has been associated with transcriptional activation during neuronal differentiation (Hahn et al., 2013; Kim et al., 2014). Furthermore, abundance of 5-methylcytosine (5mC) on gene body regions has been related to up-regulation of pre-mRNA splicing (Shukla et al., 2011; Guo et al., 2014; Yearim et al., 2015). These and other epigenetic modifications can be induced by environmental stimuli (Aguilera et al., 2010; van Heesbeen et al., 2013). For example, long-term exposure of cultured ventral midbrain (VM) NSPC to depolarizing potassium concentrations promotes mDA neuron differentiation, increasing binding of Nurr1 to the regulatory regions, and higher transcriptional activity, of *Th* and *Dat* genes, with parallel increases in H3K4me3 and decreased H3K9me3/H3K27me3, although the latter changes observed only in the *Th* promoter (He et al., 2011). Furthermore, VM NSPC treated with the neuropeptide urocortin increases mDA differentiation by inhibition of Histone Deacetylase 1 (HDAC1), resulting in hyperacetylation of histone H3, which allows the binding of Nurr1 to the upstream *Th* regulatory regions (Huang et al., 2015). This suggests that post-translational histone modifications participate in the regulation of the expression of genes involved in brain development.

In this work, we aimed to evaluate the effect of HA on several epigenetic marks on intragenic regions that regulate expression of genes involved in mDA development *in utero*, as well as its long-term effects *in vivo* before birth. We found an enrichment of repressive histone marks, H3K9me3 and H3K27me3, together with a decrease of 5mC at intergenic regulatory regions. Such modifications were associated to significantly lower mRNA levels of genes related to midbrain DA neuron fate specification. Injection of HA at E12 caused a decrease in the number of mDA neurons and modified the trajectory of its axons to the ST at late stages of midbrain development.

MATERIALS AND METHODS

Ultrasound-Guided Injections

All animal procedures were approved by the Institute of Cellular Physiology's Animal Care and Use Committee and conformed to National guidelines (*Norma Oficial Mexicana* NOM-062-ZOO-1999). We used timed-pregnant Wistar rats with embryos at gestational age E12 to perform ultrasound-guided injections as previously reported (Escobedo-Avila et al., 2014). Control (vehicle-injected) or experimental (HA-injected) conditions were performed by triplicate or quadruplicate in different embryos from the same rat, and repeated with six different pregnant dams. Each group was evaluated in a single uterine horn. Rats were deeply anesthetized in a chamber and then maintained with a facemask to administer inhaled sevoflurane (5% for induction and 1% for maintenance). We performed a midline laparotomy, the uterine horns were carefully exposed and the number of embryos was recorded. To visualize the embryos, we used an MHF-1 Ultraview UltraSound System (E-Technologies) with a focal distance of 7 mm. Intraventricular injections were performed through the uterine wall using pulled microcapillaries (borosilicate glass, Sutter Instruments). The glass needles were visualized in the ultrasound imaging system and when in the lateral ventricles, the injection of 2 μl was verified by observing the liquid going out of the needle with the aid of an automatic injector (Quintessential injector, Stoelting). Control embryos received injectable water and experimental embryos were injected with 50 μg of HA dihydrochloride (Sigma-Aldrich), a dose previously determined to decrease TH in the MB (Escobedo-Avila et al., 2014). The osmolarity of this HA solution was 348 mOsm, and HA decreased 0.6 pH units in relation to the vehicle. We have showed (Escobedo-Avila et al., 2014) that the injection of vehicle, or HA at this concentration, did not cause morphological abnormalities in the MB, ruing out damage caused by the osmolarity or pH.

After injection, the uterus was repositioned in its physiological site. The incisions of the abdominal muscle and skin were stitched with separate sutures. Finally, we applied Buprenorphine as analgesic (0.1 mg/kg, Pisa Laboratories) and animals were monitored and left to recover. Two or 6 days after the injections, pregnant rats were euthanized by an overdose of sodium pentobarbital (Pfizer), and identified embryos were recovered for analysis. We performed the following number of successfully injected E12 embryos: vehicle: 53; HA: 59. The number of dams used was 22.

Immunohistochemistry

Embryos were removed and transferred to PBS. Subsequently fixed by immersion in 4% paraformaldehyde solution in PBS at 4°C, overnight (for E14 embryos) and for 6 days (for E18 embryos). Afterward, tissues were cryoprotected overnight in 30% (v/v) sucrose, embedded in Tissue Freezing Medium (Tissue-Tek, Zakura Finetek) and frozen at −80°C. Coronal and sagittal sections of 20 μm were obtained on a cryostat (Leica). For immunohistochemistry, slides were rehydrated in PBS. Tissue sections were treated with immuno-retriever for 30 min at 65°C and subsequently, permeabilized and blocked for 1 ½ h at room temperature with 0.3% Triton X-100 and 5% horse serum in PBS. Slides were incubated overnight at 4°C with the following primary antibodies diluted in PBS containing 5% horse serum: rabbit polyclonal anti-TH (1:1000, Pel-freez), rabbit polyclonal anti-Lmx1a (1:1500, Millipore), mouse monoclonal anti-β-III Tubulin (1:500, Babco Covance). Then, the sections were washed three times for 5 min in PBS and incubated with the secondary antibodies Alexa-Fluor 488 anti-rabbit IgG and Alexa-Fluor 568 anti-mouse IgG (1:500; Molecular Probes) in PBS containing 5% horse serum for 2 h. Nuclei were stained with Hoechst 33258 (1 ng/mL). After three further washes in PBS, the sections were mounted in Aqua Poly/Mount (Polysciences, Inc.) Immunostainings were analyzed with an epifluorescence microscope (Nikon, Eclipse TE2000-U) and photographed with a Nikon digital camera (DMX1200 F). Some images were acquired with a FV1000 Olympus confocal microscope. Negative controls were performed in the absence of primary antibodies and showed no unspecific staining.

Immunohistochemistry of Whole-Mount Brains From Embryos

We perform immunohistochemistry of whole-mount brain as previously reported (Joyner and Wall, 2008). Embryos at E18 stage were incubated in 20% dimethyl sulfoxide (DMSO): 80% methanol (fixative solution) for 24 h at 4°C. Then, the embryos were transferred to 10% hydrogen peroxide diluted in fixative and incubated overnight at room temperature. This treatment effectively bleached the pigment of the embryo and blocked endogenous peroxidase activity. After bleaching, embryos were incubated in 100% methanol at −20°C for 4 h. For staining, bleached embryos were washed twice for 1 h with 2% skim milk and 0.5% Triton X-100 in PBS (PBSMT). Embryos were incubated overnight at 4°C with rabbit polyclonal anti-TH (1:1000, Pel-freez) in PBSMT. After this incubation, the embryos were washed seven times in PBSMT; each wash lasted 1 h. The embryos were then incubated overnight at 4°C with affinity-purified goat anti-rabbit immunoglobulin antibody conjugated to horseradish peroxidase (1:500, Santa Cruz) in PBSMT. The seven washes were repeated. Bound peroxidase-conjugated antibody was visualized using the DAB Substrate Kit for Peroxidase (VECTOR laboratories); reactions were carried out for 10 min at room temperature. Embryos were post-fixed in 4% paraformaldehyde in PBS at 4°C overnight and dehydrated in 50, 80, and 100% methanol (1 h each). Embryos were cleared by placing them in a 1:2 mixture of benzyl alcohol:benzyl benzoate. Immunostainings were visualized with a stereomicroscope (Nikon, SMZ1500) and photographed with a Nikon digital camera (Coolpix S10). This preparation allows to visualize the nigro-striatal as well as the mesolimbic and mesocortical pathways. We measured the area of TH+ staining with ImageJ software in: (a) the midbrain (including the *substantia nigra pars compacta* and the Ventral Tegmental Area); (b) the Medial Forebrain Bundle (MFB); and (c) the forebrain (striatum/cortex, including the Nucleus Accumbens). The average of four embryos was determined per treatment. Analysis is presented as the mean ± standard error of the mean (SEM) and statistical analysis by multiple *t*-test. Since the immunostaining with positive TH was tridimensional, the area of positive label was the preferred parameter to measure.

Quantitative RT-PCR (RT-qPCR) Analysis

Total RNA was extracted with TRIzol (Invitrogen) according to the manufacturer's specifications. The mRNA levels were determined by RT-qPCR performed with cDNA generated from 2 μg of total RNA using the Kit GeneAmp RNA PCR KIT (Applied Biosystems). Primers were synthetized based on the UCSC Genome Browse database from *Rattus norvegicus* (Gibbs et al., 2004; Havlak et al., 2004). Gene expression levels were determined using the following primers (all listed in 5′to 3′ orientation; Sense, S; Antisense, AS): *Lmx1a*, S: GCACGGAAGCTAGACTCAA; AS: GCTCTGCC CAGCAAAGAG; 143 bp. *Msx1*, S: CTGTTGGGGGACTCC TCAA; AS: GCCGCCTGGCTGGGGG; 119 bp. *Foxa2*, S: CAGAAAAAGGCCTGAGGTG; AS: CAGCATACTTTAACTC GCTG; 137 bp. *Nurr1*, S: GTCACAGAGAGACACGGG; AS: GGTAGTTGGGTCGGTTCAA; 121 bp. *Pitx3*, S: CTCGAAGCCCTGCGCTGT; AS: GCCTTCTCCGAGTC ACTGT; 100 bp. *Th*, S: CCACTGGAGGCTGTGGTATT; AS: CCGGGTCTCTAAGTGGTGAA; 145 bp. H_1 receptor, S: CTTCTACCTCCCCACTTTGCT; AS: TTCCCTTTCCC CCTCTTG; 292 bp. H_2 receptor S: TTCTTGGACTCCT GGTGCTGC; AS: CATGCCCCCTCTGGTCCC; 309 bp. *Gapdh*, S: GTGGACCTCATGGCCTACAT; AS: GGATGGAATT GTGAGGGAGA; 160 bp. *Gapdh* was used as an internal control. The qPCR reactions for 96-well plate format were performed using 50 ng of cDNA and the Thermo Maxima SYBR Green/ROX 1 PCR Master Mix (Thermo Fisher Scientific) with a StepOnePlus Real-Time PCR System (Applied Biosystems).

The fold change was calculated by the $2^{-\Delta\Delta Ct}$ method (Livak and Schmittgen, 2001).

Sodium Bisulfite Sequencing

Genomic DNA was isolated by phenol:chloroform:isoamyl alcohol (Sigma-Aldrich) extraction technique as reported (Clark et al., 2006). One microgram of genomic DNA was modified by sodium bisulfite using the EZ DNA methylation kit (ZYMO Research). For sequencing, modified DNA was amplified by PCR using the following primers recognizing *Th*, S: GTAGGTGTTTGTGATAGTGGATG; AS: AAAACCACTCCAACCCTAAATA, with a length of 439 bp. These primers were synthetized based on the UCSC Genome Browse database from *R. norvegicus* (Gibbs et al., 2004; Havlak et al., 2004). The PCR products were purified and cloned using the pGEM-T Easy Vector system (Promega). Eight clones were randomly chosen and sequenced individually. The percentage of modified cytosines was calculated for vehicle- and HA-treated embryos.

Methylated and Hydroxymethylated DNA Immunoprecipitation Assay (MeDIP and hMeDIP)

Genomic DNA was isolated as described above and processed by ultrasonic pulses (GENEQ, GEX500; Cole-Parmer). Initial experiments were set up to obtain fragments of an average size of 300 bp. Such conditions included 3 rounds of pulses of 30 s, with sequences of pulse-on for 5 s and pulse-off for 3 s at 35% amplitude. DNA was immunoprecipitated using a MeDIP/hMeDIP kit (Diagenode). Briefly, 1 μg of fragmented DNA was denatured for 3 min at 95°C and incubated with 2.5 μg of the company-validated mouse monoclonal anti-5 hmC (Diagenode) or 2 μg of mouse monoclonal anti-5mC (Diagenode). The antibody-bound DNA was recovered by immunoabsorption with anti-mouse IgG-coated magnetic beads (Diagenode) for 16 h at 4°C. The immunoprecipitated DNA was amplified by 30 cycles of PCR. Primers were designed from the sequences obtained in the UCSC Genome Browse database from *R. norvegicus* (Gibbs et al., 2004; Havlak et al., 2004). For the mDA differentiation genes, oligonucleotides were designed in exons, which represent regulatory regions for neurogenesis. Exons were chosen based on their higher percentage of CpG content or within a CpG island. Primers used are as follows: *Lmx1a*, exon 2, S: GGGTCATCTCGGATAGGTTT; AS: CAGGCACTTACTTCTCGTAG; 156 bp. *Msx1*, exon 1, S: CGAAACCCATGATCCAGGG; AS: GTCCTCCACTTTGA CACCG; 112 bp. *Foxa2*, exon 3, S: CGCTCATCACCAT GGCCAT; AS: GCCGGTAGAAAGGGAAGAG; 96 bp. *Nurr1*, exon 2, S: CAGTCCGAGGAGATGATGC; AS: GGAAG TTGTGAAGGGAGCC; 133 bp. *Pitx3*, exon 4, S: CTTAG TCCCTGCCAGTACG; AS: GCACCCCTTTTCAGACCCT; 149 bp. *Th*, exon1, S: GAGACAGAACTCGGGACC; AS: CGGGTGACAGCATATCCTC; 145 bp. The efficiency of MeDIP or hMeDIP products of a particular genomic locus was calculated from qPCR by a fast optical 96-well q PCR reaction plate (Applied Biosystems). The qPCR reaction was performed using Thermo Maxima SYBR Green/ROX 1 PCR Master Mix (Thermo Fisher Scientific) with a StepOnePlus Real-Time PCR System (Applied Biosystems). According to the manufacturer inset, data for each sample is reported as recovery of starting material: % MeDIP or hMeDIP/INPUT.

Chromatin Immunoprecipitation to Detect H3K9me3 and H3K27me3

Ventral midbrains were dissected and pooled from 7 embryos treated with HA or vehicle. Tissue was maintained in ice-cold PBS before crosslinking, which was carried out for 10 min, with 1% of formaldehyde. The crosslink reaction was stopped for 5 min with 125 mM glycine and the crosslinked tissue was washed three times with ice-cold PBS for 5 min. After the last wash, tissue was lysed with 500 μL of lysis buffer. Chromatin was sonicated using an Ultrasonic Processor (GENEQ, GEX500; SOVC505-00). After sonication, DNA was extracted and its length evaluated. Quantitation of chromatin was made by the Lowry reaction and 100 μg of material was used per IP. Immunoselection was performed according to the protocol of the OneDay ChIP kit (Diagenode, Kch-oned IP- 180), with anti-H3K9me3 or anti-H3K27me3 (Diagenode). Immunoprecipitation was performed by incubating 20 μL of magnetic beds (16-663 | Magna ChIP™ Protein A+G Magnetic Beads), with the antibody-chromatin complexes for 3 h in a rotating wheel; then the beads-antibody-chromatin complexes were washed three times with ice-cold ChIP buffer 1×. Finally, the DNA was decrosslinked overnight and purified employing the MinElute Reaction Cleanup Kit (Cat No./ID: 28204) following the manufacturer's instructions. ChIP assays were performed by qPCR in a fast optical 96-well qPCR reaction plate (Applied Biosystems) with the same primers used for MeDIP/hMeDIP for *Pitx3* and *Th*. The qPCR reaction was performed using Thermo Maxima SYBR Green/ROX1 PCR Master Mix (Thermo Fisher Scientific) with a StepOnePlus Real-Time PCR System (Applied Biosystems), according to the manufacturer's instructions.

Dopamine Quantification by High-Performance Liquid Chromatography (HPLC)

E18 embryos were recovered after vehicle or HA injection at E12. The striatum was dissected and individually homogenized with a mixture of 0.1 M perchloric acid (Baker), 4 mM $Na_2S_2O_3$ (Sigma), 0.1 mM EDTA (Sigma). The homogenate was centrifuged (12,600 rpm, 20 min at 4°C). Subsequently, the supernatant was filtered with 0.45 μm filters (Millex-HV) and 20 μl were mixed with 7.5 μL of antioxidant solution (0.1 N perchloric acid; 0.02% EDTA and 1% EtOH) and injected into the solvent stream of a HPLC system, using a reversed-phase column (C18, 3 μm; 2.1 × 50 mm; Atlantis, Waters) coupled to a pre-column (Nova-Pack, Waters) with a mobile phase solution containing 0.054 mM EDTA, 50 mM citric acid, and 0.1 mM octansulfonic acid, dissolved in milli-Q water and mixed with methanol in a proportion of 97:3, respectively. The pH was 2.9 and the flow rate 0.35 mL/min. Dopamine detection was performed by a

single-channel electrochemical amperometric detector (Waters model 2465) at 450 mV at a temperature of 30°C, and quantified by peak height measurements against standard solutions with know dopamine concentration, as described (Rocha et al., 2012).

Statistical Analysis

Data from four to six independent experiments are expressed as the mean ± SEM. The differences between groups were analyzed using the unpaired Student's *t*-test comparing the HA- with the vehicle-treated rat embryos. Differences between groups were considered statistically significant when $p < 0.05$.

RESULTS

Intrauterine Administration of HA Decreases TH and Lmx1a Immunoreactivity in the VM

We performed *in utero* microinjections of HA or vehicle, into the ventricular lumen close to the MB of E12 rat embryos, allowing them to develop to E14. Because it was previously reported that intrauterine injection of HA at E12 precludes mDA differentiation at E14 (Escobedo-Avila et al., 2014), we quantified the immunoreactivity of TH and Lmx1a in vehicle- or HA-injected embryos, confirming a significant decrease in TH (**Figure 1A**). We also assessed the effect of HA on VM dopamine progenitors positive to Lmx1a (Nakatani et al., 2010; Yan et al., 2011). We found that HA down-regulates Lmx1a reactivity, without altering β-III Tubulin, in contrast to the vehicle-treated embryos (**Figure 1B**).

Administration of HA Down-Regulates the Expression of Specification and Differentiation Dopaminergic Genes

Based on the Lmx1a-positive domain, we performed dissections selecting the VM of injected embryos 2 days after surgery. Subsequently, we analyzed the expression of DA specification (*Lmx1a, Msx1, and Foxa2*) and differentiation (*Nurr1, Pitx3, and Th*) genes by RT-qPCR. After normalization with *Gapdh*, we found that HA significantly decreases the expression of *Lmx1a*, *Msx1*, and *Th* compared to vehicle-injected embryos (**Figure 1C**). H_1 and H_2 receptors are expressed in the VM; we did not find significant changes in these receptors' expression after HA injection (data not shown).

HA Reduces 5mC at the Exons Regions of Genes Associated With DA Differentiation

Next, we asked if HA affected epigenetic modifications associated to DNA. By bisulfite sequencing, we evaluated the DNA methylation patterns in HA-treated embryos, after MB dissections (**Figure 2A**). We did not observe overall changes in the percentage of modified cytosines on *Th* gene, including exon 1, on HA-treated embryos, compared to vehicle-treated embryos, i.e., the percentages of modified bases were very similar (**Figure 2B**).

One limitation of bisulfite sequencing is that it does not allow discriminating between 5mC and 5hmC. Therefore, in order to evaluate both DNA modifications, we perform a MeDIP and hMeDIP, followed by qPCR in dissected VM (**Figure 2A**). Particularly, we focused on the intragenic regulatory regions of specification (*Lmx1a, Msx1, and Foxa2*) and differentiation (*Nurr1, Pitx3, and Th*) genes. We found that HA-injected embryos showed a significant decrease in 5mC at the exonic regions of the differentiation genes *Pitx3* and *Th*, compared to vehicle-treated embryos (**Figure 2C**). The 5hmC did not show significant changes on specification or differentiation genes neither in HA- nor in vehicle-treated embryos (**Figure 2D**).

HA Treatment Is Associated With an Increase in the H3K9me3 and H3K27me3 Histone Modifications

Due to the histone post-translational modifications may also participate in the modulation of gene expression, we decided to study two particular histone modifications the H3K9 trimethylation (H3K9me3) and H327 trimethylation (H3K27me3). In order to evaluate the effect of HA treatment in the histone modifications H3K9me3 and H3K27me3 we performed a chromatin immunoprecipitation assay (ChIP) after the HA or vehicle treatment, and then evaluate the immunoprecipitated DNA by qPCR analyzing the above-mentioned regions of *Pitx3* (**Figure 2E**) and *Th* (**Figure 2F**) genes. We found that HA-injected embryos showed a significant increase of H3K9me3 and H3K27me3, in contrast with vehicle-treated embryos (**Figures 2E,F**).

HA Injection Has a Long-Term Effect During the Formation of Midbrain Dopaminergic Pathways

We set out to investigate if the effect of HA on mDA 2-days after its injection has a long-term consequence, affecting the formation of nigrostriatal pathway. *In utero* injections of E12 embryos with either HA or vehicle were made, and the embryos were collected after 6 days, when normal development of the nigrostriatal pathway has reached the striatum. TH staining in sagittal sections or whole-mount immunohistochemistry was analyzed in E18 brains. A single injection of HA at early stages was enough to alter the formation of the nigrostriatal pathway; in vehicle-injected embryos, the MFB is apparently normal, whereas after HA administration a decrease in this bundle is observed and aberrant axons innervating the *thalamus* appeared (solid rectangles in **Figure 3A**). To comprehensively analyze the mesencephalic dopaminergic pathways, TH immunohistochemistry was performed in whole-brain mounts. Image analysis was used to quantify the indicated areas positive for TH within the dotted rectangles shown in **Figure 3B**. HA caused a significant reduction in the TH-positive area in the midbrain and the striatum/nucleus accumbens/cortex when compared to vehicle-injected embryos (**Figure 3C**). Also, the quantification of dopamine by HPLC assay in the striatal area

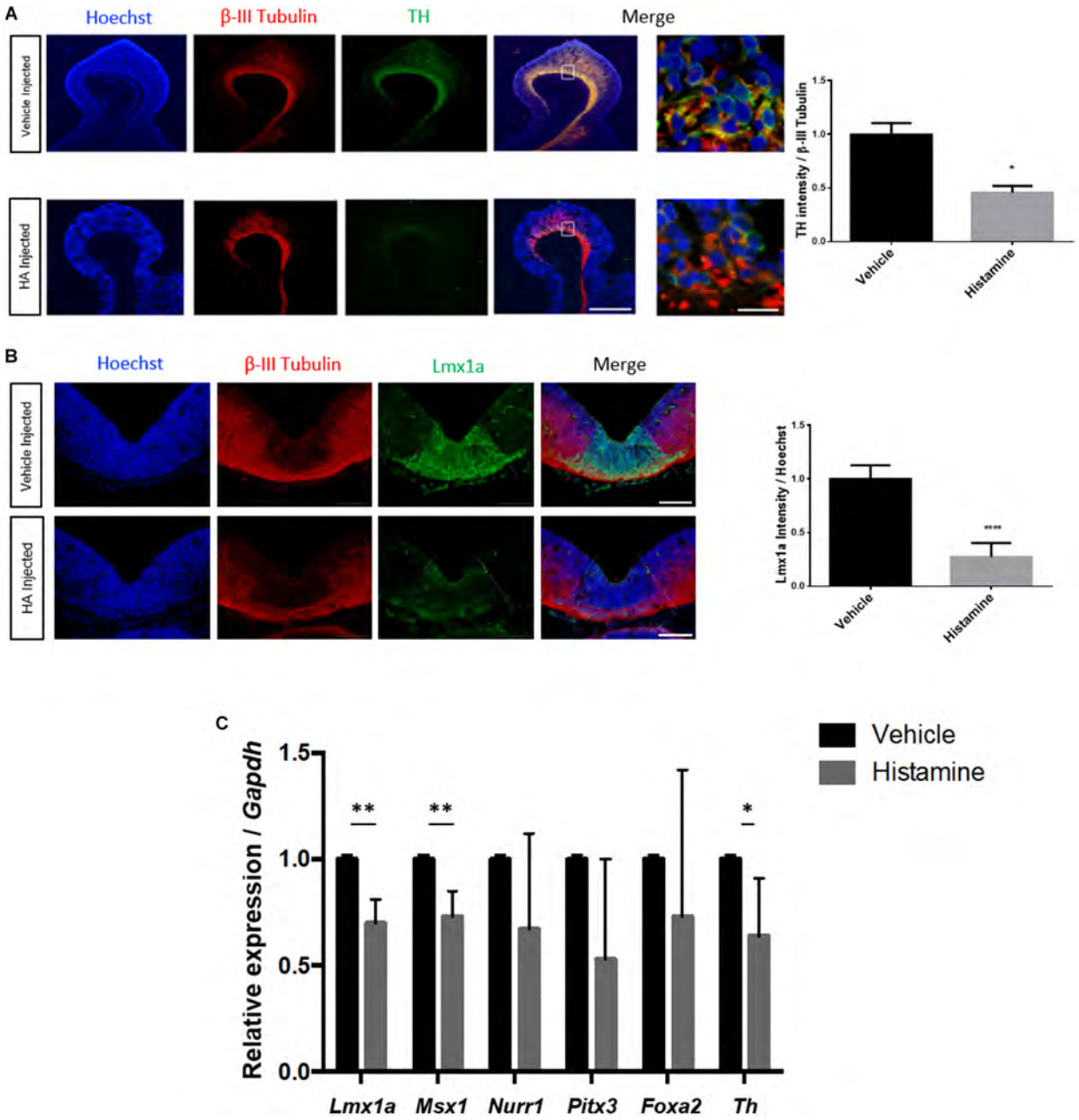

FIGURE 1 | HA decreases TH and Lmx1a immunoreactivity and down-regulates dopaminergic genes in the ventral midbrain (VM) after *in utero* injection. Rat embryos were injected at E12 and analyzed 2 days later. **(A)** Immunohistochemistry showing a significant decrease, caused by HA, in the DA marker TH, in sagittal sections. The neuronal marker β-III Tubulin was unaffected by HA, and was used to normalize TH immunoreactivity. Nuclei were detected with Hoechst. The white square in the merge image is expanded on the right. Scale bar: 150 μm in the low-magnification and 10 μm in the amplification. **(B)** HA significantly reduces the area positive for the dopaminergic progenitor marker Lmx1a, without affecting β-III Tubulin. The quantification of Lmx1a intensity was normalized by the Hoechst signal. The area of Lmx1a-positive DA progenitor cells is delimited by the dotted lines and was dissected to perform RT-qPCR. Scale bar: 200 μm. **(C)** Expression of genes involved in DA differentiation after intrauterine HA or vehicle administration, analyzed at day E14. Data was normalized by *Gapdh* expression. Vehicle-treated embryos were used as the reference for the $2^{-}\Delta\Delta Ct$ analysis. Graphs represent the mean values with SEM from 3 **(A,B)** to 5 **(C)** independent experiments. $^{*}p < 0.05$, $^{**}p < 0.01$, $^{****}p < 0.0001$.

shows a 19% non-significant reduction in HA injected animal compared to vehicle (**Figure 3D**). Together our data suggest that HA injection leads to a decrease in TH staining in the forebrain, which might result in lower dopamine release.

DISCUSSION

Brain development is initiated by formation of defined patterns in the neural ectoderm. As development proceeds, stem

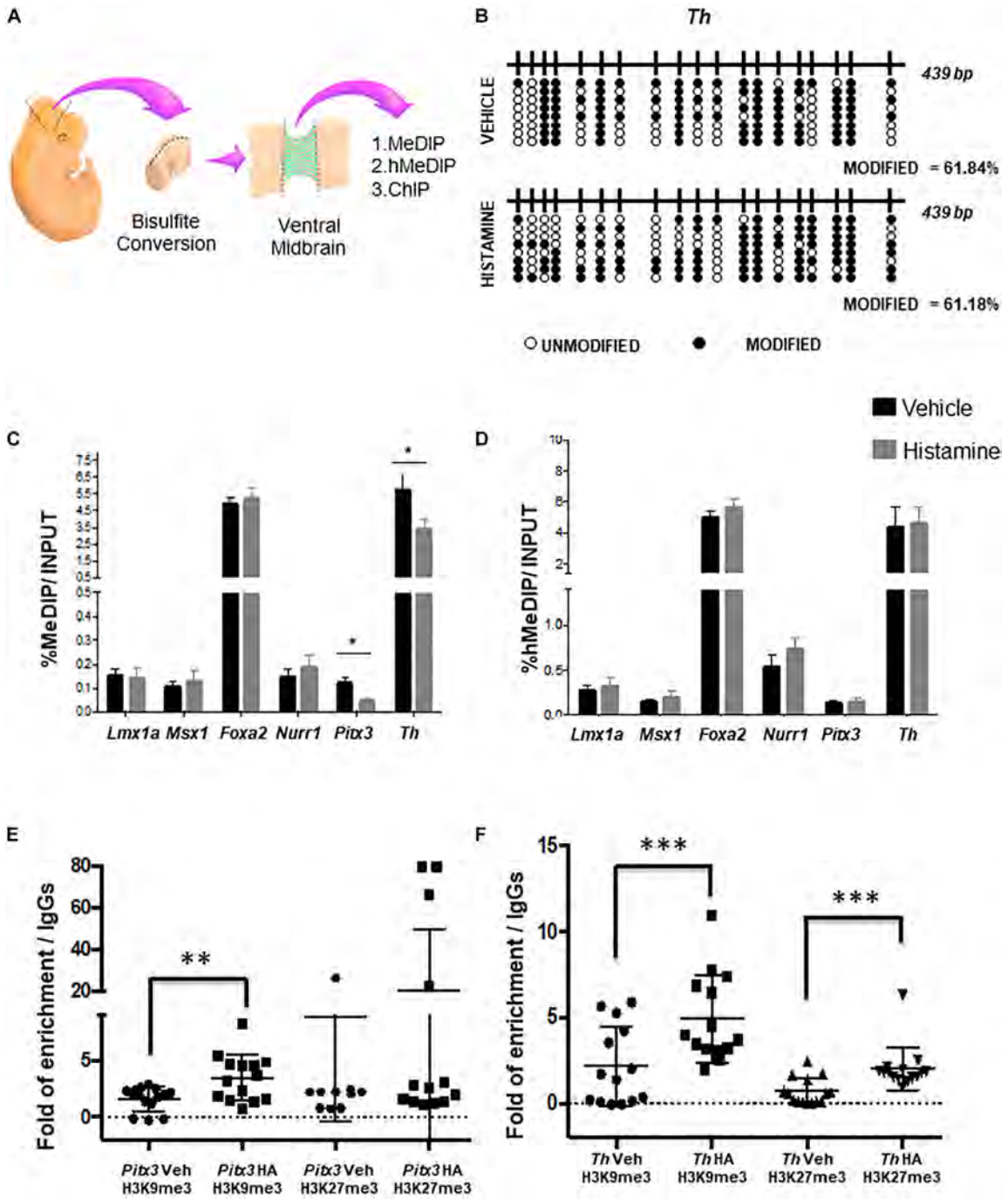

FIGURE 2 | Epigenetic modifications caused by HA *in utero*. **(A)** Scheme of the experimental design to dissect the midbrain and its ventral portion delimited by Lmx1a-positive cells, for the indicated analyses. **(B)** No changes were detected on modified cytosines, using sodium bisulfite and sequencing after HA administration in the MB, 2 days after intrauterine injection. Black circles represent modified CpGs, and white circles represent unmodified CpGs. **(C,D)** Enrichment analysis of 5-methylcytosine and 5-hydroxymethylcytosine in different genes involved in DA differentiation. qPCR analysis on DNA after immuno-precipitation with anti-5mC (**C**, MeDIP) and anti-5hmC (**D**, hMeDIP) antibodies in HA- or vehicle-injected embryos. Internal negative and positive controls were performed according to the manufacturer's specifications (Diagenode; mc-magme-048). Data was normalized against 10% INPUT. Chromatin immunoprecipitation analysis of H3K9me3 and H3K27me3 levels in *Pitx3* **(E)** and *Th* **(F)** genes. The box plots represent the qPCR amplifications of the fourth exon of *Pitx3* and the first exon *Th*, using the DNA obtained from the ChIP assay employing anti-H3K9me3 and anti-H3K27me3 antibodies, in tissue treated with either vehicle or HA. As a negative control, we used the IgG antibody included in the OneDay ChIP kit (Diagenode, NJ, United States, Kch-onedIP-180). $^{*}p < 0.05$, $^{**}p < 0.01$, $^{***}p < 0.005$ compared to the vehicle-treated tissue from 3 **(B)** to 4 **(C–F)** independent experiments.

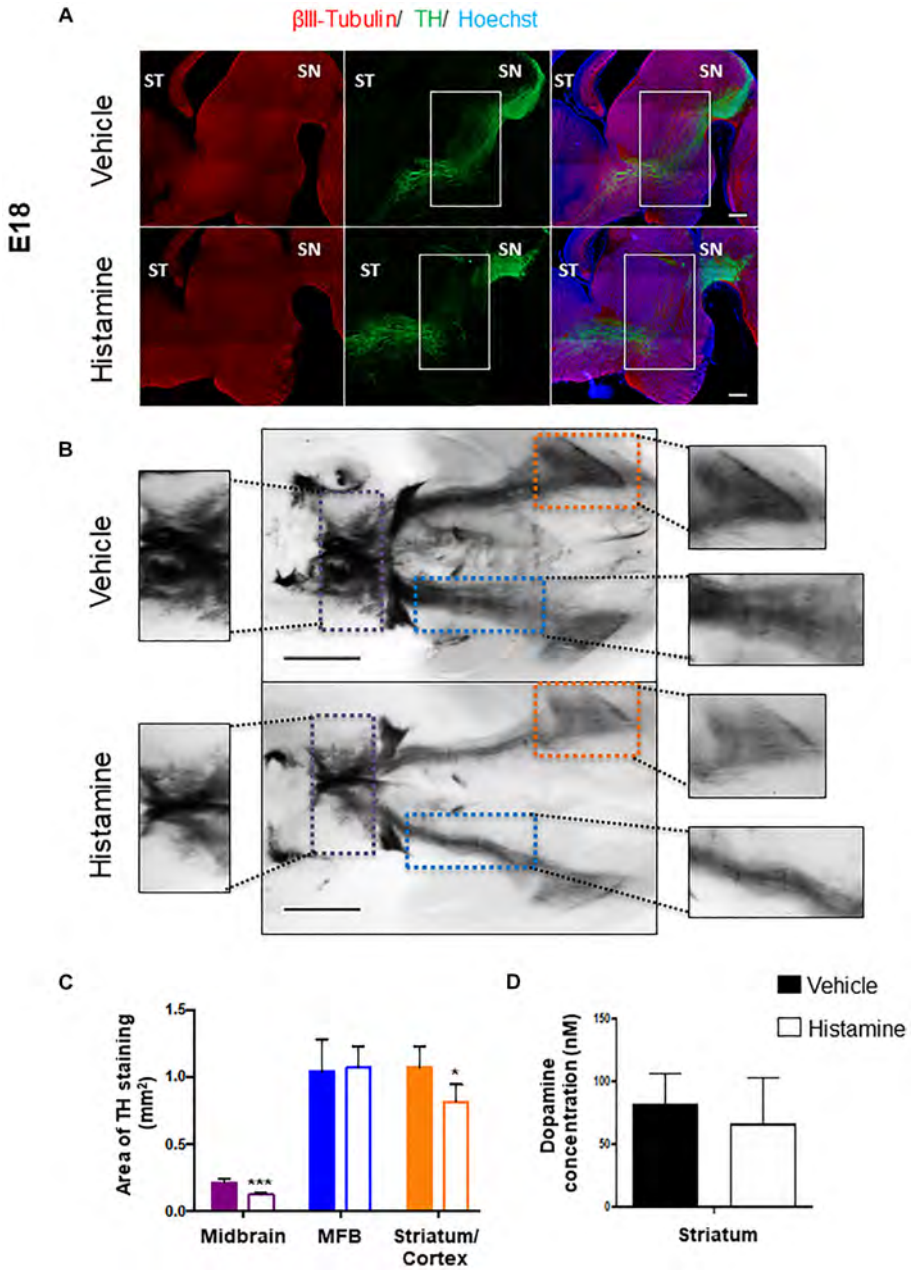

FIGURE 3 | Analysis of the midbrain dopaminergic projection pathways at E18, after injection of HA at E12. **(A)** Immunohistochemistry for the limiting enzyme in DA synthesis, TH, analyzed together with β-III Tubulin, in sagittal brain sections 6 days after injection of vehicle or HA. Regions with differences between the two experimental conditions in the nigrostriatal pathway are marked with the white rectangles. ST, *striatum*; SN, *substantia nigra*. Scale bar: 500 μm. **(B)** Ventral views of the whole-mount TH immunostainings of E18 brains from embryos injected with vehicle or HA. The midbrain area within the dotted purple lines, the Medial Forebrain Bundle (MFB) area within the dotted blue lines and the Striatum/Cortex area within the dotted orange lines, are amplified in the intermediate panels, and were used to measure the area of TH staining in 4 independent experiments. Scale bar: 1 mm. **(C)** Quantification of TH staining area of Midbrain, MFB and Striatum/Cortex (this region also includes the Nucleus Accumbens). $*p < 0.05$ and $***p < 0.005$. **(D)** Dopamine content quantification in the striatum of vehicle- or HA-injected embryos by HPLC. The dissection of this area was performed at E18 making sure to remove the cerebral cortex and the basal part of the brain. Solid and empty bars apply to panels **C,D**.

cell differentiation to neurons is defined by the action of morphogenic gradients and transcription factors, expressed in a temporal and sequential order (Gale and Li, 2008). In cultured cortical NSPC, HA has a neuronal-promoting action, involving up-regulation of proneural genes (Molina-Hernández and Velasco, 2008; Rodríguez-Martínez et al., 2012). However, HA administration *in vivo* diminishes proliferation of midbrain NSPC, down-regulating *Th* mRNA levels and the content of

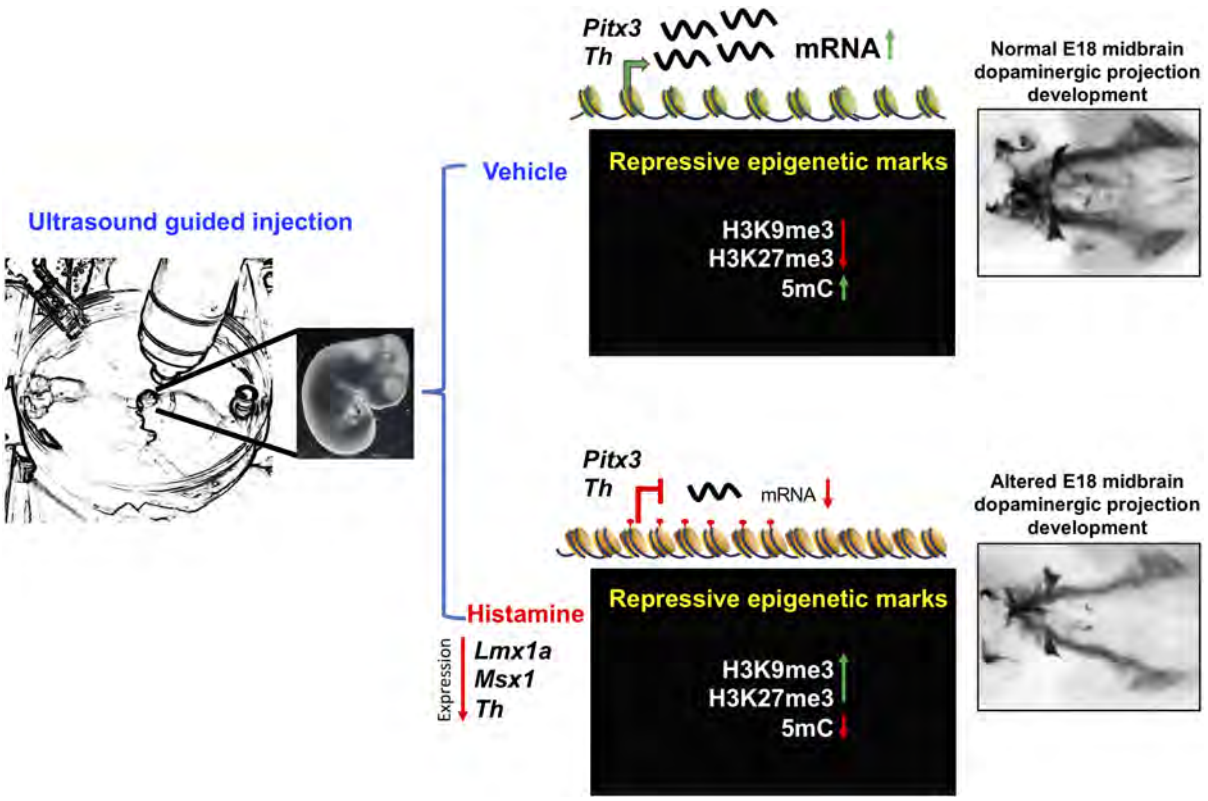

FIGURE 4 | Proposed mechanism of HA action on the regulation of late mDA differentiation genes. Intrauterine administration of HA into the MB of E12 rat embryos, decreases the expression of specification and differentiation dopaminergic genes, such as *Lmx1a*, *Msx1*, and *Th*. The decrease in *Th* expression induced by HA was correlated with the gain of histone repressive marks, H3K27me3 and H3K9me3, together with the loss of 5mC at intergenic regulatory regions. The down-regulation of these key dopaminergic differentiation genes, particularly *Th*, resulted on the alteration of the midbrain dopaminergic projection development at E18.

TH, Lmx1a, and Lmx1b assessed by western blot, 2 days after injection (Escobedo-Avila et al., 2014), but the mechanisms for these actions are just emerging (Molina-Hernández et al., 2013). In the current work, we administered embryos with either HA or vehicle, on a stage previous to the major production of DA neurons (Götz and Huttner, 2005), by ultrasound guided-injections. Injection of HA diminishes the presence of TH as well as the transcription factor Lmx1a in the VM.

Recently, studies about the influence of environment on epigenetics and its importance with regards to the expression of transcription factors during cell commitment have emerged. Regulation of the deposition of 5hmC in intragenic regions during progression of embryonic stem cells to NSPC is crucial for the development of mDA neurons (Kim et al., 2014). In dopaminergic neurons, methylation in one specific CpG site on the first exon of human *TH* gene down-regulates its transcription, allowing the binding of repressive transcription factors such as KAISO and NcoR and recruitment of HDACs, which might act as an additional modulator of *Th* expression (Arányi et al., 2005; van Heesbeen et al., 2013). We found that HA injection significantly decreased expression of early-differentiation genes (*Lmx1a* and *Msx1*) as well as in *Th*, a late canonical mDA differentiation gene.

Presence of 5mC and 5hmC within the exonic regions have been associated with up-regulation of gene expression, through different mechanisms (Hahn et al., 2013; Guo et al., 2014; Kim et al., 2014). Our findings reveal that injection of HA at early stages significantly diminish the percentage of enrichment of 5mC, but only on the differentiation genes *Pitx3* and *Th*. Although DNA methylation has been related to transcriptional repression, in recent years, some reports showed that 5mC within the gene body, specifically in exons, is associated to regulation of pre-mRNA splicing (Lev Maor et al., 2015). Other studies associated the gain of 5hmC at intergenic regions with transcriptional activation of neuronal differentiation genes (Hahn et al., 2013; Guo et al., 2014). We did not observe changes on 5hmC levels, indicating that HA induced gene repression independent of 5hmC, and suggesting that other epigenetic mechanisms participate in mDA gene regulation. Interestingly, many genes associated with neuronal differentiation can be negatively regulated by decreasing 5mC and a gain in histone repressive modifications, such as H3K27me3, at their regulatory regions (Hahn et al., 2013).

During mDA differentiation, epigenetic changes occur in cultured VM NSCP: Nurr1-controlled dopaminergic gene expression was precluded by the interaction of Nurr1 with CoREST and HDAC1, a complex that caused deacetylation of these promoters. Forced expression of Foxa2 allowed the formation of Nurr1-Foxa2 complexes with concomitant

acetylation of H3, associated to open chromatin, in *Th* and *Dat* promoters (Yi et al., 2014). *In vitro* expansion of VM NSCP caused decreased dopaminergic differentiation, which was associated with hypoacetylation on H3 and H4 and increased H3K27me3 in the Foxa2 promoter, as well as globally. Inhibition of HDAC activity up-regulates *Foxa2* transcripts, caused H3 acetylation, decreased methylation of H3K27 and restored dopaminergic induction (Bang et al., 2015). We observed significant increases in the repressive marks H3K27me3 and H3K9me3 in *Pitx3* and *Th* genes, although significant down-regulation was observed only in *Th*. Similar observations were recently reported by Hong et al. (2019), where they manipulated *in vitro* the levels of H3K27me3 in the promoter region of *Th*: treatment with EPZ005687, an inhibitor of histone methylase EZH2 reduces the levels of H3K27me3 and leads to an increase in TH levels; conversely, addition of GSK-J1, which affects the demethylase activity of Jmjd3, augmented H3K27me3 and decreased TH protein levels (Hong et al., 2019). Our data points that not only the H3K27me3 is involved in the regulation of *Th*, but also H3K9me3 participate.

We studied the long-term consequence of deregulation of such genes, in the formation of the MFB, and found that injection of HA caused disrupted and miss-oriented dopaminergic fibers in sagittal sections. Further, a significant reduction in TH-positive staining was found in the MB and the striatum/cortex after HA treatment, in whole-brain mounts. However, we did not observe a complete deterioration of the nigro-striatal, mesolimbic and mesocortical pathways, probably due to the plasticity of the developing brain; accordingly, dopamine level in the striatum were not reduced by HA. In newborn rats injected with 6-hydroxydopamine to degenerate mDA neurons, there is an increase in serotonergic projections (Snyder et al., 1986) and lesioned animals were hyperactive (Miller et al., 1981; Zhang et al., 2001; Avale et al., 2004). It will be of interest to analyze if embryos injected with HA at E12 show changes in locomotor activity at postnatal stages.

The precise mechanisms that link HA and the epigenetic changes reported here deserve further investigation. In cultured VM-NSPC, it has been shown that membrane depolarization and calcium influx is correlated with higher acetylation of Histone 3, trimethylation of K4 of H3 with reductions in the H3K9me3 and H3K27me3 marks (He et al., 2011). HA triggers intracellular calcium increases after receptor activation in VM-NSPC, through production of IP3 and Diacylglycerol by Phospholipase C, but the effects reported here are in the opposite direction: addition of the transcriptional repressive H3K9me3 and H3K27me3; additional signaling transduction mechanism to explore include Phospholipase A2/arachidonic acid production and nitric oxide production/cGMP increases (Molina-Hernández et al., 2012). On the other hand, the participation of the transient population of histaminergic neurons of the raphe nucleus or in the hypothalamus (Vanhala et al., 1994), and the activation of microglia after HA administration, as observed in adult mice (Rocha et al., 2016), cannot be ruled out in our experiments; therefore, it will be interesting to determine their roles in future experiments by ablating HA-producing neurons or microglial cells, respectively. All together, the data reported here describe molecular effects of HA on dopaminergic midbrain development. The reduction in expression of dopaminergic genes correlates with gain of the repressive modifications H3K9me3 and H3K27me3 and the loss of DNA methylation at intergenic regions in *Th*. Moreover, HA induced long-term alterations on mDA neurons, as shown in **Figure 4**. Our results suggest that HA promotes an epigenetic change related to significant reductions in the expression of important dopaminergic genes. Such alterations result in anatomical dysregulation and decreased TH staining in the dopaminergic neurons targets.

In conclusion, this study contributes to the understanding of the molecular actions of HA on mDA development, as well as chromatin structure regulation mediated by extracellular stimuli, during NPSC commitment in the midbrain; such knowledge may contribute to establish different roles of HA during brain development.

DATA AVAILABILITY

The datasets generated for this study are available on request to the corresponding author.

ETHICS STATEMENT

This study was carried out in accordance with Mexican guidelines and following recommendations of Instituto de Fisiologia Celular, UNAM Animal Care and Use Committee, which approved this protocol.

AUTHOR CONTRIBUTIONS

FV-R wrote the manuscript, analyzed the data and performed the majority of experiments, including epigenetics, whole mount stainings and dopamine quantification. LG-C and RG-B performed RT-qPCR and ChIP assays, contributed to the design of experiments and discussion of results. IE-A helped to perform intrauterine injections, data analysis and participated on discussion of results. DC-P contributed to set up techniques, performed results analysis and discussed results. AL-O and LR participated in dopamine quantification by HPLC. IV and ES-R contributed to the experimental design and supervision, reviewed the manuscript, and obtained funding. All authors read and approved the final manuscript.

FUNDING

This work was supported by grants from Dirección General de Asuntos del Personal Académico, Universidad Nacional Autónoma de México (PAPIIT IN213716 and IN213719), Consejo Nacional de Ciencia y Tecnología (CONACyT, CB09/131281), and Red Temática Células Troncales y Medicina

Regenerativa to IV. ES-R was supported by grants from Fondo Sectorial de Investigación en Salud y Seguridad Social (FOSISS, 0261181) and CONACyT (182997 and 284748). Fernanda Vargas-Romero and Lissania Guerra-Calderas received a graduate fellowship from CONACyT (662044 and 588391, respectively).

ACKNOWLEDGMENTS

We thank Dr. Alfredo Varela Echavarría, Dr. Luis A. Herrera Montalvo, and Jorge Landgrave-Gómez M.Sc., for continuous discussion and advice. We also thank the technical support of Francia Carmona B.Sc.

REFERENCES

Abeliovich, A., and Hammond, R. (2007). Midbrain dopamine neuron differentiation: factors and fates. *Dev. Biol.* 304, 447–454. doi: 10.1016/j.ydbio.2007.01.032

Aguilera, O., Fernández, A. F., Muñoz, A., and Fraga, M. F. (2010). Epigenetics and environment: a complex relationship. *J. Appl. Physiol.* 109, 243–251. doi: 10.1152/japplphysiol.00068.2010

Ang, S.-L. (2006). Transcriptional control of midbrain dopaminergic neuron development. *Development* 133, 3499–3506. doi: 10.1242/dev.02501

Arányi, T., Faucheux, B. A., Khalfallah, O., Vodjdani, G., Biguet, N. F., Mallet, J., et al. (2005). The tissue-specific methylation of the human tyrosine hydroxylase gene reveals new regulatory elements in the first exon. *J. Neurochem.* 94, 129–139. doi: 10.1111/j.1471-4159.2005.03173.x

Avale, M. E., Nemirovsky, S. I., Raisman-Vozari, R., and Rubinstein, M. (2004). Elevated serotonin is involved in hyperactivity but not in the paradoxical effect of amphetamine in mice neonatally lesioned with 6-hydroxydopamine. *J. Neurosci. Res.* 78, 289–296. doi: 10.1002/jnr.20245

Bang, S. Y., Kwon, S. H., Yi, S. H., Yi, S. A., Park, E. K., Lee, J. C., et al. (2015). Epigenetic activation of the Foxa2 gene is required for maintaining the potential of neural precursor cells to differentiate into dopaminergic neurons after expansion. *Stem Cells Dev.* 24, 520–533. doi: 10.1089/scd.2014.0218

Bernardino, L., Eiriz, M. F., Santos, T., Xapelli, S., Grade, S., Rosa, A. I., et al. (2012). Histamine stimulates neurogenesis in the rodent subventricular zone. *Stem Cells* 30, 773–784. doi: 10.1002/stem.1042

Clark, S. J., Statham, A., Stirzaker, C., Molloy, P. L., and Frommer, M. (2006). DNA methylation: bisulphite modification and analysis. *Nat. Protoc.* 1, 2353–2364. doi: 10.1038/nprot.2006.324

Escobedo-Avila, I., Vargas-Romero, F., Molina-Hernández, A., López-González, R., Cortés, D., De Carlos, J. A., et al. (2014). Histamine impairs midbrain dopaminergic development in vivo by activating histamine type 1 receptors. *Mol. Brain* 7:58. doi: 10.1186/s13041-014-0058-x

Gale, E., and Li, M. (2008). Midbrain dopaminergic neuron fate specification: of mice and embryonic stem cells. *Mol. Brain* 1, 1–10. doi: 10.1186/1756-6606-1-8

Gibbs, R. A., Weinstock, G. M., Metzker, M. L., Muzny, D. M., Sodergren, E. J., Scherer, S., et al. (2004). Genome sequence of the Brown Norway rat yields insights into mammalian evolution. *Nature* 428, 493–521. doi: 10.1038/nature02426

Götz, M., and Huttner, W. B. (2005). The cell biology of neurogenesis. *Nat. Rev. Mol. Cell Biol.* 6, 777–788.

Guo, J. U., Szulwach, K. E., Su, Y., Li, Y., Yao, B., Xu, Z., et al. (2014). Genome-wide antagonism between 5-hydroxymethylcytosine and DNA methylation in the adult mouse brain. *Front. Biol.* 9:66–74. doi: 10.1007/s11515-014-1295-1

Hahn, M. A., Qiu, R., Wu, X., Li, A. X., Zhang, H., Wang, J., et al. (2013). Dynamics of 5-hydroxymethylcytosine and chromatin marks in mammalian neurogenesis. *Cell Rep.* 3, 291–300. doi: 10.1016/j.celrep.2013.01.011

Havlak, P., Chen, R., Durbin, K. J., Egan, A., Ren, Y., Song, X.-Z., et al. (2004). The atlas genome assembly system. *Genome Res.* 14, 721–732. doi: 10.1101/gr.2264004

He, X.-B., Yi, S.-H., Rhee, Y.-H., Kim, H., Han, Y.-M., Lee, S.-H., et al. (2011). Prolonged membrane depolarization enhances midbrain dopamine neuron differentiation via epigenetic histone modifications. *Stem Cells* 29, 1861–1873. doi: 10.1002/stem.739

Hegarty, S. V., Sullivan, A. M., and O'Keeffe, G. W. (2013). Midbrain dopaminergic neurons: a review of the molecular circuitry that regulates their development. *Dev. Biol.* 379, 123–138. doi: 10.1016/j.ydbio.2013.04.014

Hong, F., Zhao, M., Zhang, L., and Feng, L. (2019). Inhibition of Ezh2 in vitro and the decline of Ezh2 in developing midbrain promotes dopaminergic neurons differentiation through modifying H3K27me3. *Stem Cells Dev.* doi: 10.1089/scd.2018.0258 [Epub ahead of print].

Huang, H.-Y., Chiu, T.-L., Chang, H.-F., Hsu, H.-R., Pang, C.-Y., Liew, H.-K., et al. (2015). Epigenetic regulation contributes to urocortin-enhanced midbrain dopaminergic neuron differentiation. *Stem Cells* 33, 1601–1617. doi: 10.1002/stem.1949

Jacobs, F. M. J., van Erp, S., van der Linden, A. J. A., von Oerthel, L., Burbach, J. P. H., and Smidt, M. P. (2009). Pitx3 potentiates Nurr1 in dopamine neuron terminal differentiation through release of SMRT-mediated repression. *Development* 136, 531–540. doi: 10.1242/dev.029769

Joyner, A., and Wall, N. (2008). Immunohistochemistry of whole-mount mouse embryos. *Cold Spring Harb. Protoc.* 3, 1–5.

Kadkhodaei, B., Ito, T., Joodmardi, E., Mattsson, B., Rouillard, C., Carta, M., et al. (2009). Nurr1 is required for maintenance of maturing and adult midbrain dopamine neurons. *J. Neurosci.* 29, 15923–15932. doi: 10.1523/JNEUROSCI.3910-09.2009

Kim, M., Park, Y.-K., Kang, T.-W., Lee, S.-H., Rhee, Y.-H., Park, J.-L., et al. (2014). Dynamic changes in DNA methylation and hydroxymethylation when hES cells undergo differentiation toward a neuronal lineage. *Hum. Mol. Genet.* 23, 657–667. doi: 10.1093/hmg/ddt453

Lev Maor, G., Yearim, A., and Ast, G. (2015). The alternative role of DNA methylation in splicing regulation. *Trends Genet.* 31, 274–280. doi: 10.1016/j.tig.2015.03.002

Livak, K. J., and Schmittgen, T. D. (2001). Analysis of relative gene expression data using real-time quantitative PCR and the $2^{-\Delta\Delta CT}$ method. *Methods* 25, 402–408. doi: 10.1006/meth.2001.1262

Miller, F. E., Heffner, T. G., Kotake, C., and Seiden, L. S. (1981). Magnitude and duration of hyperactivity following neonatal 6-hydroxydopamine is related to the extent of brain dopamine depletion. *Brain Res.* 229, 123–132. doi: 10.1016/0006-8993(81)90750-2

Molina-Hernández, A., Díaz, N. F., and Arias-Montaño, J.-A. (2012). Histamine in brain development. *J. Neurochem.* 122, 872–882. doi: 10.1111/j.1471-4159.2012.07863.x

Molina-Hernández, A., Rodríguez-Martínez, G., Escobedo-Ávila, I., and Velasco, I. (2013). Histamine up-regulates fibroblast growth factor receptor 1 and increases FOXP2 neurons in cultured neural precursors by histamine type 1 receptor activation: conceivable role of histamine in neurogenesis during cortical development in vivo. *Neural Devel.* 8:4. doi: 10.1186/1749-8104-8-4

Molina-Hernández, A., and Velasco, I. (2008). Histamine induces neural stem cell proliferation and neuronal differentiation by activation of distinct histamine receptors. *J. Neurochem.* 106, 706–717. doi: 10.1111/j.1471-4159.2008.05424.x

Nakatani, T., Kumai, M., Mizuhara, E., Minaki, Y., and Ono, Y. (2010). Lmx1a and Lmx1b cooperate with Foxa2 to coordinate the specification of dopaminergic neurons and control of floor plate cell differentiation in the developing mesencephalon. *Dev. Biol.* 339, 101–113. doi: 10.1016/j.ydbio.2009.12.017

Nissinen, M. J., and Panula, P. (1995). Developmental patterns of histamine-like immunoreactivity in the mouse. *J. Histochem. Cytochem.* 43, 211–227. doi: 10.1177/43.2.7822777

Panula, P., and Nuutinen, S. (2013). The histaminergic network in the brain: basic organization and role in disease. *Nat. Rev. Neurosci.* 14, 472–487. doi: 10.1038/nrn3526

Rocha, L., Alonso-Vanegas, M., Villeda-Hernández, J., Mújica, M., Cisneros-Franco, J. M., López-Gómez, M., et al. (2012). Dopamine abnormalities in the neocortex of patients with temporal lobe epilepsy. *Neurobiol. Dis.* 45, 499–507. doi: 10.1016/j.nbd.2011.09.006

Rocha, S. M., Saraiva, T., Cristóvão, A. C., Ferreira, R., Santos, T., Esteves, M., et al. (2016). Histamine induces microglia activation and dopaminergic neuronal

toxicity via H1 receptor activation. *J. Neuroinflam.* 13:137. doi: 10.1186/s12974-016-0600-0

Rodríguez-Martínez, G., Velasco, I., García-López, G., Solís, K. H., Flores-Herrera, H., Díaz, N. F., et al. (2012). Histamine is required during neural stem cell proliferation to increase neuron differentiation. *Neuroscience* 216, 10–17. doi: 10.1016/j.neuroscience.2012.04.049

Shukla, S., Kavak, E., Gregory, M., Imashimizu, M., Shutinoski, B., Kashlev, M., et al. (2011). CTCF-promoted RNA polymerase II pausing links DNA methylation to splicing. *Nature* 479, 74–79. doi: 10.1038/nature10442

Snyder, A. M., Zigmond, M. J., and Lund, R. D. (1986). Sprouting of serotoninergic afferents into striatum after dopamine-depleting lesions in infant rats: a retrograde transport and immunocytochemical study. *J. Comp. Neurol.* 245, 274–281. doi: 10.1002/cne.902450209

van Heesbeen, H. J., Mesman, S., Veenvliet, J. V., and Smidt, M. P. (2013). Epigenetic mechanisms in the development and maintenance of dopaminergic neurons. *Development* 140, 1159–1169. doi: 10.1242/dev.089359

Vanhala, A. N. U., Yamatodani, A., and Panula, P. (1994). Distribution of histamine-, 5-Hydroxytryptamine-, and tyrosine hydroxylase-immunoreactive neurons and nerve fibers in developing rat brain. *J. Comp. Neurol.* 347, 101–114. doi: 10.1002/cne.903470108

Wheldon, L. M., Abakir, A., Ferjentsik, Z., Dudnakova, T., Strohbuecker, S., Christie, D., et al. (2014). Transient accumulation of 5-carboxylcytosine indicates involvement of active demethylation in lineage specification of neural stem cells. *Cell Rep.* 7, 1353–1361. doi: 10.1016/j.celrep.2014.05.003

Yan, C. H., Levesque, M., Claxton, S., Johnson, R. L., and Ang, S.-L. (2011). Lmx1a and lmx1b function cooperatively to regulate proliferation, specification, and differentiation of midbrain dopaminergic progenitors. *J. Neurosci.* 31, 12413–12425. doi: 10.1523/JNEUROSCI.1077-11.2011

Yearim, A., Gelfman, S., Shayevitch, R., Melcer, S., Glaich, O., Mallm, J. P., et al. (2015). HP1 is involved in regulating the global impact of dna methylation on alternative splicing. *Cell Rep.* 10, 1122–1134. doi: 10.1016/j.celrep.2015.01.038

Yi, S.-H., He, X.-B., Rhee, Y.-H., Park, C.-H., Takizawa, T., Nakashima, K., et al. (2014). Foxa2 acts as a co-activator potentiating expression of the Nurr1-induced DA phenotype via epigenetic regulation. *Development* 141, 761–772. doi: 10.1242/dev.095802

Zhang, K., Tarazi, F. I., and Baldessarini, R. J. (2001). Role of dopamine D4 receptors in motor hyperactivity induced by neonatal 6-hydroxydopamine lesions in rats. *Neuropsychopharmacology* 25, 624–632. doi: 10.1016/s0893-133x(01)00262-7

Conflict of Interest Statement: The authors declare that the research was conducted in the absence of any commercial or financial relationships that could be construed as a potential conflict of interest.

Copyright © 2019 Vargas-Romero, González-Barrios, Guerra-Calderas, Escobedo-Avila, Cortés-Pérez, López-Ornelas, Rocha, Soto-Reyes and Velasco. This is an open-access article distributed under the terms of the Creative Commons Attribution License (CC BY). The use, distribution or reproduction in other forums is permitted, provided the original author(s) and the copyright owner(s) are credited and that the original publication in this journal is cited, in accordance with accepted academic practice. No use, distribution or reproduction is permitted which does not comply with these terms.

INFORME DE LABORES 2019

Biochemical Pharmacology 164 (2019) 283–288

Contents lists available at ScienceDirect

Biochemical Pharmacology

journal homepage: www.elsevier.com/locate/biochempharm

Lactate-stimulated ethanol oxidation: Revisiting an old hypothesis

Daniel Villalobos-García[a,b], Rolando Hernández-Muñoz[a,*]

[a] Departamento de Biología Celular y Desarrollo, Instituto de Fisiología Celular, Universidad Nacional Autónoma de México (UNAM). Ciudad de México 04510, Mexico
[b] Programa de Posgrado en Ciencias Químicas, UNAM, Mexico

ARTICLE INFO

Keywords:
Alcohol dehydrogenase
Catalase
H_2O_2
Peroxisomes
Lactate oxidase

ABSTRACT

Liver slices from starved rats and incubated without other substrates oxidized ethanol at a rate of 4.1 μmols • h^{-1} • g^{-1}. Addition of 10 mmols • L^{-1} lactate increased this rate 2-fold. 4-methylpyrazole (4-MP), an alcohol dehydrogenase (ADH) inhibitor, drastically decreased the rate of ethanol oxidation, but did not inhibit the stimulation due to lactate. In the same context, liver acetaldehyde production, as the main by-product of ethanol oxidation, appeared to be much less inhibited by 4-MP in the presence of lactate. Aminotriazole (a catalase inhibitor), however, completely inhibited the stimulation. Furthermore, 2-hydroxybut-3-ynoate, an alpha-hydroxy acid oxidase inhibitor, completely abolished the stimulated ethanol oxidation promoted by lactate. Moreover, to determine the origin of the H_2O_2 produced, we did liver subcellular fractionation and then analyzed their content in peroxisomes, mitochondria and catalase. We observed that cytoplasm and peroxisomes appears to be the main producers of H_2O_2, and that the acceleration of ethanol oxidation by lactate is completely dependent on catalase. In conclusion, the H_2O_2 necessary to boost the catalase-dependent oxidation of ethanol appears to come from cytoplasm and peroxisomes, and is produced by the enzyme lactate oxidase.

1. Introduction

Most of the oxidation of ethanol to acetaldehyde in the liver is catalyzed by the cytoplasmic enzyme alcohol dehydrogenase (ADH), with the concomitant reduction of $NAD^{\pm}$ to NADH [1,2]. It is well known that the dissociation of the ADH-NADH complex is the rate-limiting step in this reaction [1,3-5]. This has suggested that the rate of oxidation of NADH, mostly through the respiratory chain, is what determines the overall rate of ethanol metabolism [1].

In emergency medicine, in ethanol-intoxicated trauma the onset of metabolic acidosis is often attributed to serum ethanol. Despite ethanol intoxication being associated with acidosis, this event does not necessarily correlate with the rate of lactic acidosis [6]. During hemorrhage, ethanol blunts the respiratory and metabolic compensation resulting in a more severe lactic acidosis, and administration of additional lactate during intoxication and hypovolemia for hemodynamic stabilization may exacerbate a metabolic stress [7].

In turn, lactate has been known to increase the oxidation of ethanol both in vivo and in vitro [8,9]. However, the oxidation of lactate to pyruvate through lactate dehydrogenase (LDH) generates NADH, so it should be expected to slow the metabolism of ethanol, since the NADH produced would inhibit ADH [8]. This paradox has readily prompted two hypotheses to explain the lactate stimulation of ethanol oxidation:

i Lactate increases the concentration of the components of the malate-aspartate shuttle, which increases the rate of transport of reducing equivalents to the mitochondrial matrix [8,9], and
ii Lactate increases the ATP demand through gluconeogenesis, which increases the rate of oxidation of NADH in the respiratory chain [10,11].

In addition, we have demonstrated that an increased rate of hepatic ethanol metabolism resulting from purines administration is due to a coupled oxidation-reduction reaction between H_2O_2 and alcohol, where catalase activity plays a relevant role oxidizing ethanol by reducing hydrogen peroxide [12].

Indeed, our present results indicate that neither increased ATP demand nor increased malate-aspartate shuttle activity play a role on the lactate stimulation of ethanol oxidation in the liver. We instead found that lactate increases the oxidation of ethanol through catalase, coupled to a putative activity of a hepatic lactate oxidase (LOx).

* Corresponding author at: Departamento de Biología Celular y Desarrollo, Instituto de Fisiología Celular, Universidad Nacional Autónoma de México (UNAM). Apdo. Postal 70-243, 04510 CdMx, Mexico.
E-mail address: rhernand@correo.ifc.unam.mx (R. Hernández-Muñoz).

https://doi.org/10.1016/j.bcp.2019.04.012
Received 24 February 2019; Accepted 10 April 2019
Available online 11 April 2019
0006-2952/ © 2019 Published by Elsevier Inc.

INFORME DE LABORES 2019

2. Materials and methods

2.1. Substrates and inhibitors

Ethanol was used at a final concentration of 10 mM Aminotriazole was used at final concentration of 10 and 20 mM. 4-methylpyrazole (4-MP) was used at 1 mM. Lactate was used at concentrations between 5 and 20 mM in slices and at 20 mM in homogenate fractions and 2-hydroxybut-3-ynoate (2H3) was used at 1 mM. All chemicals were purchased from Sigma (Sigma-Aldrich México), except for 2-hydroxybut-3-ynoate, which was purchased from Enamine LLC (Monmouth, NJ).

2.2. Animals, incubation technique and determinations

Male Wistar rats (250–270 g) fed *ad libitum* were used for all experiments. Rats were anesthetized with sodium pentobarbital and the heart was perfused with cold Krebs buffer to remove the blood from the liver. The liver was then removed and sliced with a chopper, and about 500 mg of liver slices were placed in a 25 ml Erlenmeyer flask containing 5 ml of cold Krebs buffer, pH 7.4, to which ethanol was added to a final concentration of 10 mM. The flasks were placed in a shaking bath at 37 °C. After a pre-incubation period of 30 min, L-lactate was added to a final concentration of 5, 10 or 20 mM and the slices were incubated for a further 3 h. Samples of 160 µl were taken from each flask every hour. Perchloric acid at 16% was used to deproteinize the sample, which was later used for the enzymatic determination of ethanol and lactate. All procedures were performed according to the *Federal Regulations for Animals Care and Experimentation* (Ministry of Agriculture, SAGARPA).

2.3. Subcellular fractionation of liver

The homogenization buffer consisted of 250 mM sucrose, 5 mM MOPS and 1 mM EDTA. We homogenized and fractionated the liver into 4 fractions: A, B, C and P. Fraction A was the supernatant resulting from centrifuging the homogenate at 2,000 g to eliminate nuclei and cellular debris [13]; fraction B was the supernatant resulting from centrifuging fraction A at 25,000 g to eliminate peroxisomes [14]; fraction C was the supernatant resulting from centrifuging fraction B at 100,000 g to eliminate the rest of the mitochondria as well as microsomes, leaving only the cytosol [14,15]. The pellet resulting from the centrifugation at 25,000 g is called the crude peroxisomal fraction (CPF), and was used to isolate peroxisomes in an iodixanol gradient (fraction P), according to a manufacturer's indications of a Peroxisome isolation kit (Sigma Chemical Co.). In addition, we also used a hypotonic buffer with sucrose 25 mM to homogenize the liver with the intent of breaking organelle membranes, and it was centrifuged at 2000g to eliminate debris (the same as fraction A). The supernatant therefore represents 100% of the total activity of adenylate kinase [16]. For the incubation with ethanol and lactate (20 mM), fractions A, B and C were diluted in a 1:1 ratio with homogenization buffer, while fraction P was diluted to a final protein concentration of 1.3 mg/ml.

2.4. Enzymatic assays

The uricase activity was measured by incubating the respective fraction diluted in homogenization buffer in the presence of 1 mM potassium urate for 10 min at 37 °C. Samples were taken every 2 min and the remaining urate was measured with a kit. That of succinate dehydrogenase (SDH) was measured at room temperature in 1.25 ml of 75 mM potassium phosphate buffer, pH 7.4; succinate 48 mM; KCN 2 mM; dichlorophenolindophenol 0.06 mM and phenazine methosulfate 1.08 mM. The reaction was started by adding 5 µl of the respective fraction and lasted 5 min, and followed through DCPIP reduction at 600 nm [17]. The catalase activity was measured at room temperature by incubating the respective fraction in 1 ml of 75 mM potassium phosphate buffer, pH 7.4. The reaction was started by adding 30 mM H_2O_2. The incubation lasted 2 min. The reaction follows H_2O_2 disappearance at 240 nm [18]. In addition, adenylate kinase (AK) activity was measured at room temperature by incubating homogenate (5 µl) in 1 ml of 100 mM TEA buffer, pH 7.5; 130 mM KCl; 6.2 mM MgSO4; 1.7 mM glucose; 0.2 mM $NADP^{\pm}$; 5 U of hexokinase, and 4 U of G6PD. The reaction was started by adding 1.3 mM ADP. The incubation lasted 5 min. The reaction follows $NADP^{\pm}$ reduction at 340 nm [19].

2.5. Quantification of ethanol, lactate, and lipid peroxidation by-products

Lactate was measured enzymatically. Briefly, 20 µl of $NAD^{\pm}$ (100 mM) and 2 µl of rabbit LDH (9.3KU/ml) were added to 980 µl of hydrazine buffer (final volume of 1 ml; pH 9.5). After 60 min incubation, absorbance was read at 340 nm [20]. Ethanol was measured enzymatically with a spectrophotometer. Briefly, 20 µl of $NAD^{\pm}$ (100 mM), 100 µl of thiosemicarbazide (100 mM) and 20 µl of yeast alcohol dehydrogenase (ADH; 988 units/ml) were added to 860 ml of glycine buffer (final volume of 1 ml; pH 9.0). After 10 min incubation, absorbance was read at 340 nm [21].

2.6. Statistical analysis

All data were analyzed by the Program GraphPad Prism, by using an ordinary one-way ANOVA and by a post hoc Newman-Keuls analysis, considering $p < 0.01$ as significant.

3. Results

3.1. Effect of lactate on liver ethanol oxidation

As expected, lactate increased the oxidation of ethanol in liver slices. The relation between lactate concentration and ethanol oxidation is shown in the Fig. 1A. The mean peak increase in ethanol metabolism in the presence of 10 mmols • L^{-1} lactate was of 4.28 µmols • h^{-1} • g^{-1} of liver in the fasted state. In the fed state the lactate stimulation was somewhat weaker, an observation that has already been reported [10], and it was not abolished by 4-MP (1 mmol • L^{-1} [22]), an ADH inhibitor (Fig. 1B). This suggests that the lactate stimulation is completely independent of ADH and NADH. Moreover, as shown in Fig. 1C, the concentration of acetaldehyde increases when the oxidation of ethanol is increased with lactate even in the presence of 4-MP. These results suggest that the lactate stimulation is completely independent of ADH and by extension, independent of NAD+.

3.2. Effect of 3-aminotriazole on lactate-stimulated ethanol metabolism by liver slices from fasted rats

We next used 3-aminotriazole (3AT), an irreversible catalase inhibitor (20 mmols • L^{-1} [23]). As seen in the Fig. 2A, 3AT completely inhibited the stimulation by lactate. This points out to a mechanism mediated by catalase, which also suggests that lactate is somehow causing the production of H_2O_2. The concentration of lactate was also determined in the incubation with lactate 5 mmols • L^{-1} (Fig. 2B). During the 3 h of incubation, the concentration of lactate did not change. Since lactate seems to stimulate the ethanol oxidation by H_2O_2 production, this could suggest that a lactate oxidase (LOx) may be catalyzing the oxidation of lactate to pyruvate, reducing O_2 to H_2O_2. Two lactate oxidases have been reported in the liver: a peroxisomal L-alpha-hydroxy acid oxidase capable of oxidizing lactate to pyruvate, generating H_2O_2, was reported by de Duve & Baudhuin [24]; also, de Bari et al. has reported the existence of a mitochondrial L-lactate oxidase localized in the mitochondrial intermembrane space [25]. Since to our knowledge these two enzymes are the only known capable of producing H_2O_2 from lactate, our attention focused on these two organelles.

INFORME DE LABORES 2019

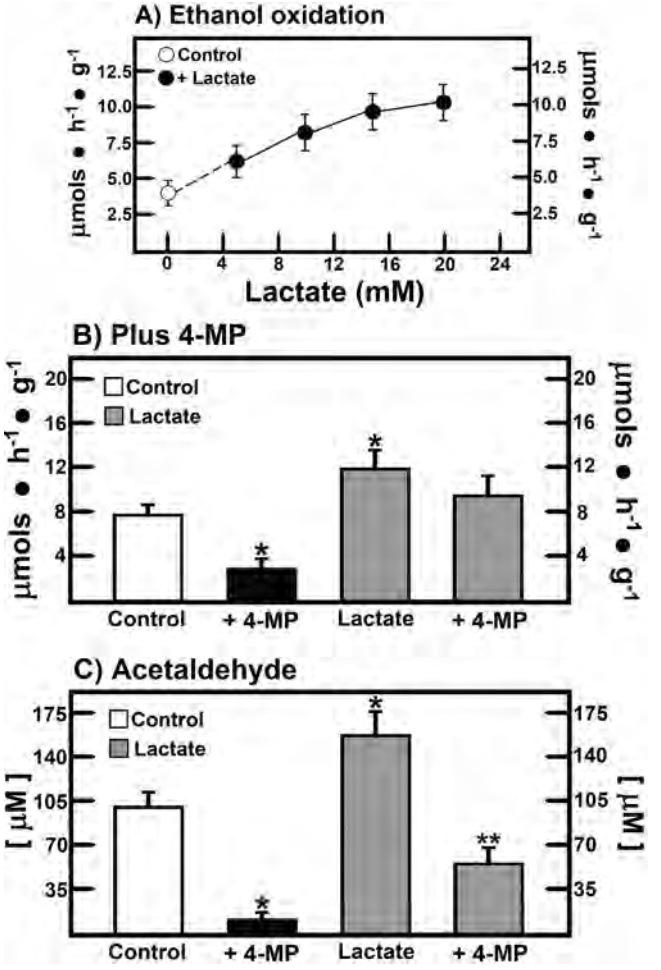

Fig. 1. Rates of ethanol oxidation in rat liver slices. Results are the mean ± SE of 4 individual observations per experimental group. In panel A, the time-curve for ethanol oxidation by liver slices from fasted rats in the presence of increasing concentrations of lactate. In panel B, the effect of 1 mmol • L^{-1} 4-methylpyrazole (4-MP) on ethanol metabolism by liver slices from fed rats in the presence or absence of lactate (20 mmols • L^{-1}); in panel C, the concentration of acetaldehyde produced from the slices is depicted. Experimental groups are designated by symbols at the upper of each panel. Statistical significance: *$p < 0.05$ vs. control group (no additions), and **$p < 0.05$ against the group with lactate.

3.3. Ethanol oxidation by liver subcellular fractions

To determine the origin of the H_2O_2 produced, we homogenized and fractionated the liver into 4 fractions: A, B, C and P. Every fraction was incubated in the presence of ethanol (10 mmols • L^{-1}), with or without lactate (20 mmols • L^{-1}). All fractions were analyzed for their content in peroxisomes, mitochondria, while fractions A, B, and C were analyzed for their catalase content, while fractions A and C were also analyzed for their content in adenylate kinase (Fig. 3A). Uricase was used as the marker of the peroxisomal fraction, succinate dehydrogenase was used as the mitochondrial marker, while adenylate kinase was used as the mitochondrial intermembrane space marker. We considered the enzyme activities of fraction A as 100% of the total. Interestingly, fraction B was very poor in peroxisome content compared to fraction A, though both fractions had similar content of mitochondria (Fig. 3A). Despite this, fraction B still showed a large stimulation in ethanol metabolism albeit smaller than that of fraction A (Fig. 3B). This suggests that peroxisomes are not the main producers of H_2O_2, and it also shows they are not needed for the stimulation (Fig. 3B). However, we wanted to know whether peroxisomes are able to oxidize ethanol by themselves in the presence of lactate.

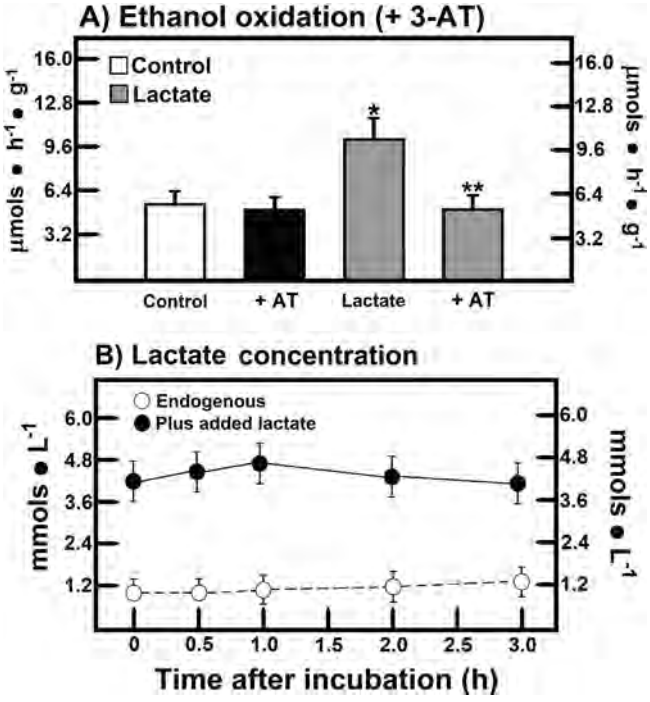

Fig. 2. Effects of lactate and aminotriazole on ethanol metabolism in liver slices from fasted rats. Results are the mean ± SE of 4 individual observations per experimental group in the presence of lactate (10 mmols • L^{-1}) and of 20 mmols • L^{-1} 3-aminotriazole (3-AT; panel A). In panel B, it is shown the lactate concentration from supernatant of liver slices from fasted rats in the presence or absence of lactate (5 mmols • L^{-1}). Abbreviations: 3-AT = 3-aminotriazole. Experimental groups are designated by symbols at the upper of each panel. Statistical significance as indicated in Fig. 1.

3.4. Rate of ethanol oxidation in purified peroxisomes (P)

From the CPF, peroxisomes were isolated using an iodixanol gradient. Purified peroxisomes (fraction P) were incubated with ethanol (10 mmols • L^{-1}) and lactate (20 mmols • L^{-1}) at a final concentration of 1.3 mg • ml^{-1} (at this concentration, the amount of peroxisomes is very similar to that of fraction A, as determined by the activity of uricase). As shown in Fig. 3B, peroxisomes by themselves showed a poor increase in ethanol metabolism in the presence of lactate. Even though the concentration of peroxisomes was much greater than in fraction B, and almost the same as fraction A (Fig. 3A), the lactate-induced increase in ethanol metabolism with purified peroxisomes was less than half that of fraction B. Once more, these results suggest that peroxisomes are not the main producers of H_2O_2, but it also shows that they, by themselves, can contribute somehow to the lactate stimulation of ethanol oxidation.

Fraction C showed negligible SDH and uricase activities, but it showed ample catalase activity (Fig. 3A). Strangely, this fraction also showed a stimulation of ethanol oxidation in the presence of lactate as large as fraction B (Fig. 3B). The putative mitochondrial LOx is localized in the intermembrane space [25], and because SDH is exclusively an internal membrane marker, it says nothing about the integrity of the outer membrane. Therefore, there existed the possibility that the outer membrane was broken during the fractionation, liberating the LOx into the cytosol [26]. To test this, we used AK as a marker of the intermembrane space. We used a hypotonic homogenizing buffer with a sucrose concentration of 25 mmols • L^{-1} to homogenize the liver and break the outer mitochondrial membrane [19]. The homogenate was centrifuged at 2000g (the same as A). As this fraction contains ruptured organelles, its content of AK is considered as 100% of the total. As

INFORME DE LABORES 2019

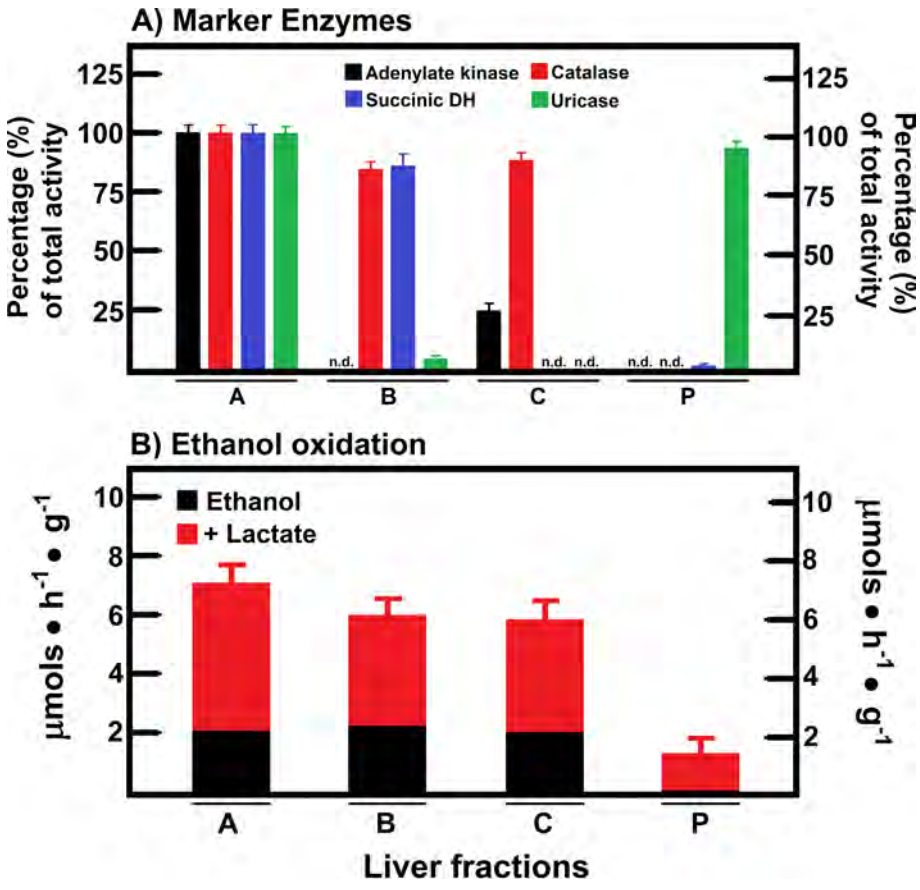

Fig. 3. Ethanol oxidation by liver subcellular fractions identified by "marker enzyme" activities. Results are the mean ± SE of 4 individual observations per experimental group. In panel A, there are shown enzyme activities (adenylate kinase, catalase, succinic dehydrogenase, and uricase) expressed in IU • g^{-1} of liver tissue, where an international unit is defined as the rate corresponding to catalysis of 1.0 µmole of substrate per min. Enzyme activities were to test purity of liver fractions: A) whole homogenate, B) Post-peroxisomes fraction, C) Cytosol, and P) Peroxisomal fraction. Panel B depicts ethanol metabolism by liver fraction B (Post-peroxisomes fraction) in the presence (red) or absence (black) of lactate (20 mmoles • L^{-1}). n.d. = non-determined. Experimental groups are designated by symbols at the upper of each panel. Statistical significance: *p < 0.05 vs. control group (no additions). (For interpretation of the references to colour in this figure legend, the reader is referred to the web version of this article.)

shown in Fig. 3A, the activity of AK from fraction C is 27.7% that of fraction A. Since around 20% of the total AK activity is localized in the cytoplasm and around 70% is located in mitochondria [19], our value of 28% is just above the expected level. Therefore we can conclude that the cytosolic fraction is largely uncontaminated with contents from the mitochondrial intermembrane space.

Since 3AT is not a specific inhibitor of catalase [27], we needed to rule out the possibility that it was inhibiting CYP450. We took advantage of the ability of ethanol to protect catalase from inhibition [28]. Fraction B was incubated in the presence of 20 mmols • L^{-1} of lactate and 10 mmols • L^{-1} 3AT for 20 min to eliminate all catalase present, after which 10 mmols • L^{-1} ethanol was added. Freshly prepared bovine catalase was then added to a final concentration of 4 mg • ml^{-1} (8–20 KU • ml^{-1}). Because there is ethanol present, it now prevents the inhibition of the bovine catalase. As seen in Fig. 4, the addition of catalase completely restored the lactate stimulation; while in the absence of lactate, catalase did not modify the rate of ethanol oxidation. Moreover, adding more catalase in the absence of 3AT does not cause a larger increase in the presence of lactate.

Finally, to show that the enzyme responsible for the lactate stimulation is indeed lactate oxidase, we used 2-hydroxybut-3-ynoate (2H3), a specific and potent irreversible inhibitor that only targets flavin-dependent α-hydroxy acid oxidases, including lactate oxidase [29-31]. Fraction B was incubated in the presence of 1 mM of 2H3 for 15 min to inhibit lactate oxidase, after which lactate and ethanol were added to a final concentrations of 20 and 10 mM, respectively. As seen in Fig. 5, the addition of 2H3 completely inhibited the lactate stimulation; while in the absence of lactate, 2H3 did not modify the rate of ethanol oxidation.

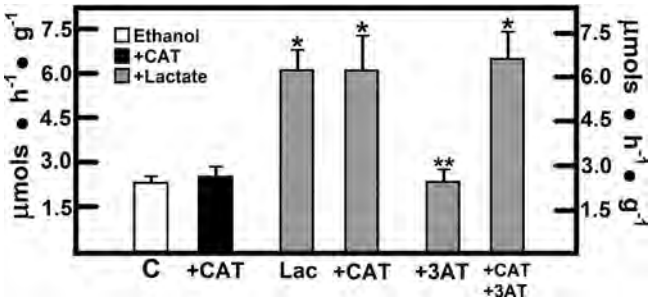

Fig. 4. Rate of ethanol oxidation by the liver post-peroxisomes fraction (B). Results are the mean ± SE of 4 individual observations per experimental group, indicated at the top of the Figure. The additions were: lactate (20 mmoles • L^{-1}), 3-aminotriazole (10 mmoles • L^{-1}), as well as of catalase (4 mg • ml^{-1}). Abbreviations: C = Control, Lac = lactate, CAT = catalase, and 3-AT = 3-aminotriazole. Statistical significance: *p < 0.05 vs. control group (no additions), and **p < 0.05 against the group with lactate.

4. Discussion

The addition of lactate doubled the oxidation of ethanol at 10 mmols • L^{-1} in slices from fasted liver. We found that the inhibition of ADH by 4-MP does not abolish the lactate stimulation. Therefore it can be concluded that the lactate stimulation is completely independent from ADH. On the other hand, 3AT did inhibit the lactate effect, suggesting that the effect is dependent on catalase.

3AT also inhibited the effect during the incubation of fraction B; however, the effect was completely restored when 8–20 KU • ml^{-1} of bovine catalase were added. The addition of catalase by itself (in the absence of 3AT) did not cause an increase in ethanol metabolism in both the absence or presence of lactate, showing that catalase is not rate-limiting. This confirms that catalase is the only ethanol-oxidizing

INFORME DE LABORES 2019

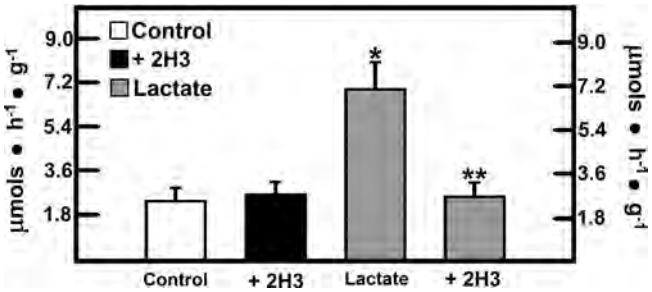

Fig. 5. Rate of ethanol oxidation by the liver post-peroxisomes fraction (B) in the presence of 2H3. Results are the mean ± SE of 4 individual observations per experimental group, indicated at the top of the Figure. The additions were: lactate (20 mmoles • L^{-1}) and 2H3 (1 mmoles • L^{-1}). Abbreviations: C = Control, Lac = lactate and 2H3 = 2-hydroxybut-3-ynoate. Statistical significance: *p < 0.05 vs. control group (no additions), and **p < 0.05 against the group with lactate.

enzyme involved in the lactate-stimulated ethanol oxidation and that aminotriazole is not interfering with any other part of the mechanism. Most importantly, the addition of 2H3 also inhibited the lactate stimulation during incubation of fraction B. 2H3 specifically inhibits flavin-containing α-hydroxy acid oxidases, meaning that this inhibitor can't target the NADH-requiring LDH [32]. This leaves lactate oxidase and membrane-attached lactate dehydrogenase as the only flavin-dependent enzymes capable of oxidizing lactate. However the latter is found only in mitochondria and can only oxidize D-lactate [33]. Since 2H3 by itself does not modify the rate of ethanol metabolism, this conclusively shows that lactate oxidase is responsible for the lactate stimulation observed in this study.

Peroxisomes were not able to oxidize ethanol by themselves, but in the presence of lactate they were able to, presumably due to the putative peroxisomal LOx. However, as evidenced by fraction B, which is almost free of peroxisomes, they are not required to stimulate the oxidation of ethanol. The difference in stimulation between fractions A and B can be attributed to the presence of peroxisomes in fraction A, since the sum of the effects from fractions B and P is very close to that of fraction A. Therefore, peroxisomes significantly contribute to the increased oxidation of ethanol by lactate; furthermore, as shown by fraction C, mitochondria are also not required for the stimulation. Therefore, the cytoplasm appears to produce the bulk of the H_2O_2 generated by lactate while peroxisomes may contribute around 30% of the total stimulation. These results potentially suggest the existence of a cytoplasmic lactate oxidase with a much higher activity than the ones found in both peroxisomes and mitochondria.

The apparent lack of lactate consumption implies that lactate is being replenished as fast as it disappears. Since LDH is the only known enzyme capable of producing lactate, this suggests the possibility that the pyruvate produced by LOx is being reduced back to lactate. The metabolism of ethanol inhibits the Krebs cycle as well as the enzyme pyruvate dehydrogenase [1]; therefore, the metabolism of pyruvate becomes limited to its reduction to lactate and gluconeogenesis. The high NADH concentration due to ethanol metabolism would enhance the already favorable reduction of pyruvate to lactate [1], constantly replenishing the oxidized lactate.

That lactate can increase the oxidation of ethanol is an old albeit largely ignored idea [8,34]. However, the fact that it can do so through catalase is unexpected. The normal concentration of lactate in blood is around 0.5–2 mmols • L^{-1} [33,35] and it increases considerably when there is alcohol in the body [36], reaching up to 15 mmols • L^{-1} during a condition known as alcohol-associated lactic acidosis [37], and may reach up to 25 mmols • L^{-1} during exercise [38]. Crow et al. [8] have shown that 1 mmol • L^{-1} of lactate is enough to significantly increase the oxidation of ethanol in isolated hepatocytes.

It has been shown that exercise can increase the rate of ethanol elimination in humans [1,39]; then, given the large increase in blood lactate due to exercise, it's possible that the increase in metabolism is due to an increase in H_2O_2 production. Since H_2O_2 is a reactive molecule and it is presumed to be deleterious to cells [40,41], one has to ask why the liver has an enzyme whose task is to produce it from such an abundant substrate. It is assumed that the main purpose of catalase is to eliminate H_2O_2 and keep it from building up [40]. However knockout mice and acatalasemic humans seem to develop normally and it is not clear whether they have increased sensitivity to oxidative stress [40,41]. It is known that H_2O_2 can function as a second messenger, including roles in insulin signaling and regeneration [42]; therefore lactate oxidase could be important for insulin signaling during exercise when the concentration of lactate is elevated or during hepatic regeneration. It is also known that besides eliminating H_2O_2, catalase also metabolizes various molecules, mainly xenobiotics, in a reaction dependent on H_2O_2, called the peroxidatic reaction [43,44]. Therefore, it is possible that the main role of catalase is to function as part of the metabolism of xenobiotics in the liver.

Authors disclosure statement

Authors declare that we do not have any conflict of interests.

Funding

DGV is supported by a fellowship from CONACYT.

References

[1] A.I. Cederbaum, Alcohol metabolism, Clin Liver Dis. 16 (2012) 667–685.
[2] C.S. Lieber, Microsomal Ethanol-Oxidizing System (MEOS): the first 30 years (1968–1998) - A review, Alcoholism: Clin Exp Res. 23 (1999) 991–1007.
[3] T.-K. Li, The absorption, distribution, and metabolism of ethanol and its effects on nutrition and hepatic function, in: B. Tabakoff, P.B. Sutker, C.L. Randall (Eds.), Medical and Social Aspects of Alcohol Abuse, Plenum Press, New York, 1983, pp. 64–67 Chapter 3.
[4] D. Mascord, J. Smith, G.A. Starmer, J.B. Whitfield, The effect of fructose on alcohol metabolism and on the [lactate]/[pyruvate] ratio in man, Alcohol Alcohol. 26 (1991) 53–59.
[5] N. Grunnet, B. Quistorff, H.I. Thieden, Rate-limiting factors in ethanol oxidation by isolated rat-liver parenchymal cells. Effect of ethanol concentration, fructose, pyruvate and pyrazole, Eur. J. Biochem. 40 (1973) 275–282.
[6] S. Zehtabchi, R. Sinert, B.J. Baron, L. Paladino, K. Yadav, Does ethanol explain the acidosis commonly seen in ethanol-intoxicated patients? Clin Toxicol (Phila) 43 (2005) 161–166.
[7] A.N. Swafford, D. Bidros, T.M. Truxillo, M.E. Giaimo, H.I. Miller, K.H. McDonough, Ethanol intoxication and lactated Ringer's resuscitation prolong hemorrhage-induced lactic acidosis, Shock 20 (2003) 237–244.
[8] K.E. Crow, N.W. Cornell, R.L. Veech, Lactate-stimulated ethanol oxidation in isolated rat hepatocytes, Biochem J. 172 (1978) 29–36.
[9] W.W. Westerfeld, E. Stotz, R.L. Berg, The coupled oxidation-reduction of alcohol and pyruvate in vivo, J. Biol. Chem. 49 (1943) 237–243.
[10] A.J. Meijer, G.M. van Woerkom, J.R. Williamson, J.M. Tager, Rate-limiting factors in the oxidation of ethanol by isolated rat liver cells, Biochem J. 150 (1975) 205–209.
[11] H.A. Krebs, R.A. Freedland, R. Hems, M. Stubbs, Inhibition of hepatic gluconeogenesis by ethanol, Biochem J. 112 (1969) 117–124.
[12] D. Villalobos-García, R. Hernández-Muñoz, Catalase increases ethanol oxidation through the purine catabolism in rat liver, Biochem. Pharmacol. 137 (2017) 107–112.
[13] G.H. Hogeboom, W.C. Schneider, Cytochemical studies of mammalian tissues. III. Isocitric dehydrogenase and triphosphopyridine nucleotide-cytochrome c reductase of mouse liver, J. Biol. Chem. 186 (1950) 417–427.
[14] A.K. Das, S. Horie, A.K. Hajra, Biosynthesis of glycerolipid precursors in rat liver peroxisomes and their transport and conversion to phosphatidate in the endoplasmic reticulum, J. Biol. Chem. 267 (1992) 9724–9730.
[15] J.M. Graham, Preparation of crude subcellular fractions by differential centrifugation, ScientificWorld J. 2 (2002) 1638–1642.
[16] W.E. Criss, G. Litwack, H.P. Morris, S. Weinhouse, Adenosine triphosphate: adenosine monophosphate phosphotransferase isozymes in rat liver and hepatomas, Cancer Res. 30 (1970) 370–375.
[17] T.E. King, Preparation of succinate dehydrogenase and reconstitution of succinate oxidase, Methods Enzymol. 10 (1967) 322–331.
[18] R. Singh, B. Wiseman, T. Deemagarn, V. Jha, J. Switala, P.C. Loewen, Comparative study of catalase-peroxidases (KatGs), Arch. Biochem. Biophys. 471 (2008) 207–214.
[19] W.E. Criss, Rat liver adenosine triphosphate: adenosine monophosphate

phosphotransferase activity. II. Subcellular localization of adenylate kinase isozymes, J. Biol. Chem. 245 (1970) 6352–6356.
[20] M. Olguín-Martínez, D.R. Hernández-Espinosa, R. Hernández-Muñoz, α-Tocopherol administration blocks adaptive changes in cell NAD/NAD+ redox sate and mitochondrial function leading to inhibition of gastric mucosa cell proliferation in rats, Free Radic. Biol. Med. 65 (2013) 1090–1100.
[21] A. Poklis, M.A. Mackell, Evaluation of a modified alcohol dehydrogenase assay for the determination of ethanol in blood, Clin. Chem. 28 (1982) 2125–2127.
[22] B.V. Plapp, K.G. Leidal, B.P. Murch, D.W. Green, Contribution of liver alcohol dehydrogenase to metabolism of alcohols in rats, Chem. Biol. Interact. 234 (2015) 85–95.
[23] K. Yamamoto, H.D. Fahimi, Three-dimensional reconstruction of a peroxisomal reticulum in regenerating rat liver: evidence of interconnections between heterogeneous segments, J. Cell. Biol. 105 (1987) 713–722.
[24] C. De Duve, P. Baudhuin, Peroxisomes (microbodies and related particles), Physiol Rev. 46 (1966) 323–357.
[25] L. de Bari, D. Valenti, A. Atlante, S. Passarella, L-lactate generates hydrogen peroxide in purified rat liver mitochondria due to the putative L-lactate oxidase localized in the intermembrane space, FEBS Lett. 584 (2010) 2285–2290.
[26] J.M. Graham, D. Rickwood, Subcellular Fractionation: A Practical Approach, Oxford University Press, New York, 2002, pp. 51–53.
[27] R.G. Thurman, J.A. Handler, New perspectives in catalase-dependent ethanol metabolism, Drug Metab. Rev. 20 (1989) 679–688.
[28] E. Margoliash, A. Novogrodsky, A. Schejter, Irreversible reaction of 3-amino-1:2:4-triazole and related inhibitors with the protein of catalase, Biochem J. 74 (1960) 339–348.
[29] T.H. Cromartie, C. Walsh, Mechanistic studies on the rat kidney flavoenzyme L-alpha-hydroxy acid oxidase, Biochemistry 14 (1975) 3482–3489.
[30] S. Ghisla, H. Ogata, V. Massey, A. Schonbrunn, R.H. Abeles, C.T. Walsh, Kinetic studies on the inactivation of L-lactate oxidase by [the acetylenic suicide substrate] 2-hydroxy-3-butynoate, Biochemistry 15 (1976) 1791–1797.
[31] T.H. Cromartie, C.T. Walsh, Rat kidney L-alpha-hydroxy acid oxidase: isolation of enzyme with one flavine coenzyme per two subunits, Biochemistry 14 (1975) 2588–2596.
[32] H.R. Kaback, J.P. Reeves, S.A. Short, F.J. Lombardi, Mechanisms of active transport in isolated bacterial membrane vesicles. 18. The mechanism of action of carbonylcyanide m-chlorophenylhydrazone, Arch. Biochem. Biophys. 160 (1974) 215–222.
[33] L. de Bari, A. Atlante, N. Guaragnella, G. Principato, S. Passarella, D-Lactate transport and metabolism in rat liver mitochondria, Biochem. J. 365 (2002) 391–403.
[34] K.E. Crow, K.M. Newland, R.D. Batt, Factors influencing rates of ethanol oxidation in isolated rat hepatocytes, Pharmacol. Biochem. Behav. 18 (Suppl 1) (1983) 237–240.
[35] J.A. Kraut, N.E. Madias, Lactic acidosis, New Engl. J. Med. 371 (2014) 2309–2319.
[36] R.A. Kreisberg, W.C. Owen, A.M. Siegal, Ethanol-induced hyperlacticacidemia: inhibition of lactate utilization, J. Clin. Invest. 50 (1971) 166–174.
[37] C.C. Yang, K.S. Chan, K.L. Tseng, S.F. Weng, Prognosis of alcohol-associated lactic acidosis in critically ill patients: an 8-year study, Sci Rep. 17 (6) (2016) 35368.
[38] M.L. Goodwin, J.E. Harris, A. Hernández, L.B. Gladden, Blood lactate measurements and analysis during exercise: a guide for clinicians, J. Diab. Sci. Technol. 1 (2007) 558–569.
[39] G.L. Pawan, Physical exercise and alcohol metabolism in man, Nature 218 (1968) 966–967.
[40] Y.S. Ho, Y. Xiong, W. Ma, A. Spector, D.S. Ho, Mice lacking catalase develop normally but show differential sensitivity to oxidant tissue injury, J. Biol. Chem. 279 (2004) 32804–32812.
[41] L. Góth, T. Nagy, Inherited catalase deficiency: is it benign or a factor in various age related disorders? Mutat. Res. 753 (2013) 147–154.
[42] H. Sies, Role of metabolic H2O2 generation: redox signaling and oxidative stress, J. Biol. Chem. 289 (2014) 8735–8741.
[43] E.J. Calabrese, A.T. Canada, Catalase: its role in xenobiotic detoxification, Pharmacol. Ther. 44 (1989) 297–307.
[44] M. Palese, T.R. Tephly, Metabolism of formate in the rat, J. Toxicol. Environ. Health 1 (1975) 13–24.

INFORME DE LABORES 2019

European Journal of Pharmacology 855 (2019) 267–275

Contents lists available at ScienceDirect

European Journal of Pharmacology

journal homepage: www.elsevier.com/locate/ejphar

Full length article

Receptor tyrosine kinase activation induces free fatty acid 4 receptor phosphorylation, β-arrestin interaction, and internalization

Sócrates Villegas-Comonfort[a], Alejandro Guzmán-Silva[a], M. Teresa Romero-Ávila[a], Yoshinori Takei[b], Gozoh Tsujimoto[b], Akira Hirasawa[b], J. Adolfo García-Sáinz[a,*]

[a] Instituto de Fisiología Celular, Universidad Nacional Autónoma de México, Ap. Postal 70-248, Ciudad de México, 04510, Mexico
[b] Graduate School of Pharmaceutical Sciences, Kyoto University: Sakyo-ku, Kyoto, 606-8501, Japan

ARTICLE INFO

Keywords:
FFA4
GPR120
Receptor tyrosine kinase
Receptor phosphorylation
Receptor internalization

ABSTRACT

FFA4 (Free Fatty Acid receptor 4, previously known as GPR120) is a G protein-coupled receptor that acts as a sensor of long-chain fatty acids, modulates metabolism, and whose dysfunction participates in endocrine disturbances. FFA4 is known to be phosphorylated and internalized in response to agonists and protein kinase C activation. In this paper report the modulation of this fatty acid receptor by activation of receptor tyrosine kinases. Cell-activation with growth factors (insulin, epidermal growth factor, insulin-like growth factor-I, and platelet-derived growth factor) increases FFA4 phosphorylation in a time- and concentration-dependent fashion. This effect was blocked by inhibitors of protein kinase C and phosphoinositide 3-kinase, suggesting the involvement of these kinases in it. FFA4 phosphorylation did not alter agonist-induced FFA4 calcium signaling, but was associated with decreased ERK 1/2 phosphorylation. In addition, insulin, insulin-like growth factor-I, epidermal growth factor, and to a lesser extent, platelet-derived growth factor, induce receptor internalization. This action of insulin, insulin-like growth factor I, and epidermal growth factor was blocked by inhibitors of protein kinase C and phosphoinositide 3-kinase. Additionally, cell treatment with these growth factors induced FFA4-β-arrestin coimmunoprecipitation. Our results evidenced cross-talk between receptor tyrosine kinases and FFA4 and suggest roles of protein kinase C and phosphoinositide 3-kinase in such a functional interaction.

1. Introduction

G Protein-Coupled Receptors (GPCR) and Receptor Tyrosine Kinases (RTK) participate in the normal function of organisms and are also involved in the pathogenesis of multiple diseases. Interestingly, there is intense cross-talk among these receptor families, involving both positive and negative modulations. The molecular mechanisms of such cross-talks include the following: GPCR-induced shedding of RTK ligands from the plasma membrane, triggering RTK activation; RTK activation through intracellular GPCR-associated signaling cascades; the formation of GPCR-RTK complexes with subsequent joint receptor signaling, and GPCR signaling attenuation involving direct tyrosine phosphorylation by RTK; GPCR serine/threonine phosphorylation catalyzed by different protein kinases (see (Chen et al., 2008; Doronin et al., 2002b; García-Sáinz et al., 2010; García-Sáinz et al., 2008; Gavi et al., 2006; Gschwind et al., 2001; Medina et al., 2000; Pyne et al., 2007; Sun et al., 2018; Vázquez-Prado et al., 2003) and references therein).

Free Fatty Acid receptor 4 (FFA4, previously known as GPR120), is a GPCR that functions as a free fatty acid sensor that increases incretin secretion by intestinal cells; this modulates insulin release, contributing to glycemic control (Hirasawa et al., 2005). FFA4-deficient mice develop glucose intolerance, obesity, and fatty liver (Ichimura et al., 2012); expression of a dysfunctional variant of this receptor (R270H) is associated with obesity and other metabolic disturbances in humans (Ichimura et al., 2012). FFA4 activation exerts insulin-sensitizing and anti-inflammatory effects on cells (adipocytes and macrophages, respectively) and mice. All these data point to FFA4 as an attractive target for the development of drugs with potential therapeutic action for these metabolic disturbances (obesity, metabolic syndrome, diabetes mellitus) (Liu et al., 2015; Milligan et al., 2015; Sparks et al., 2014; Sun et al., 2010).

Human FFA4 receptors couples with Gαq/11 and activates phospholipase C, leading to the hydrolysis of phosphatidylinositol 4, 5-bisphosphate, generating inositol trisphosphate and diacylglycerol (Hirasawa et al., 2005). Inositol trisphosphate triggers calcium release from intracellular stores, whereas diacylglycerol, together with calcium, activates protein kinase C. There is also evidence that the

* Corresponding author. Inst. Fisiología Celular, UNAM, Ap. Postal 70-248, Mexico City, 04510, Mexico.
E-mail address: agarcia@ifc.unam.mx (J.A. García-Sáinz).

https://doi.org/10.1016/j.ejphar.2019.05.018
Received 6 March 2019; Received in revised form 12 April 2019; Accepted 6 May 2019
Available online 10 May 2019
0014-2999/ © 2019 Elsevier B.V. All rights reserved.

INFORME DE LABORES 2019

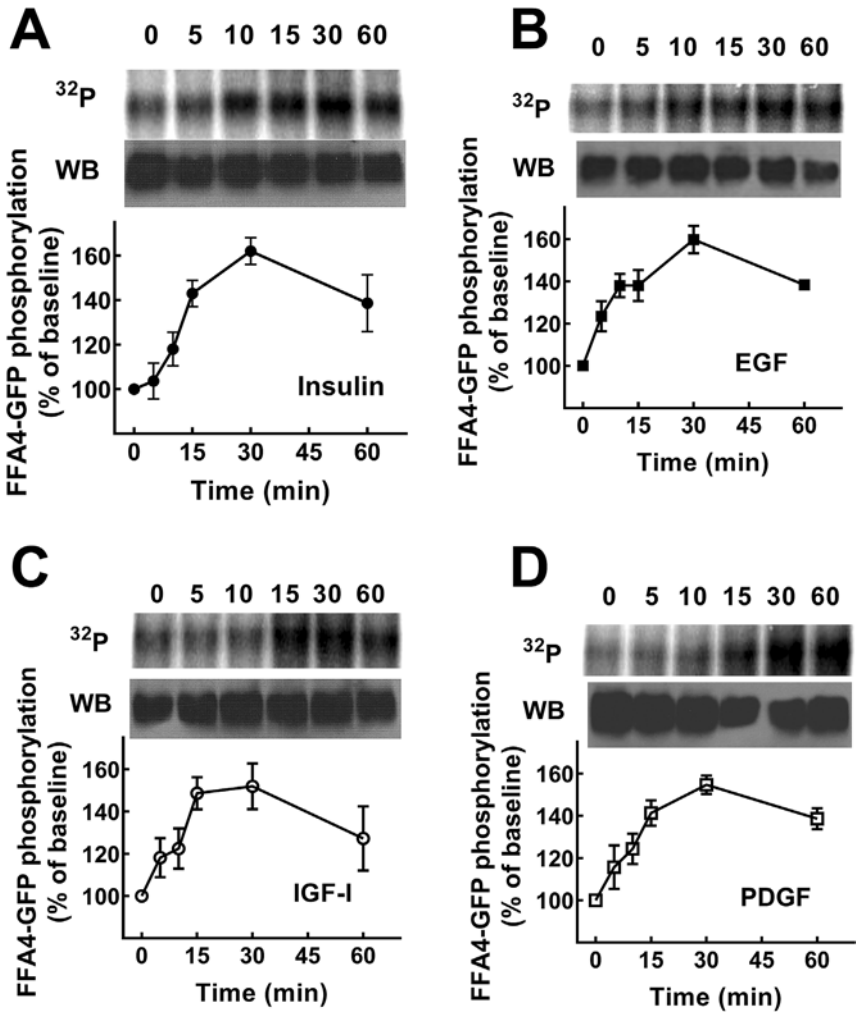

Fig. 1. Growth factor-induced FFA4 phosphorylation time-courses. Cells expressing GFP-tagged FFA4 receptors were incubated for the times indicated in the presence of 100 ng/ml of insulin (INS, panel A; n = 3), EGF (panel B; n = 4), IGF-I (panel C; n = 3) or PDGF (panel D; n = 3). Cells were lysed and receptor phosphorylation determined as indicated (section 2.4). In all cases the means are plotted with vertical lines indicating the S.E.M. of the indicated number (n) of independent experiments using different cell preparations. Representative autoradiographs (^{32}P) and Western blots (anti-GFP) are presented above each graph.

activation of FFA4 receptor induces extracellular signal-regulated kinases (ERK 1/2) activation. ERK 1/2 can be activated by a variety of signaling pathways, including those triggered by GPCR and RTK. The mitogen-activated protein kinase pathway is a master regulator that connects signals generated at the plasma membrane with the cell's nucleus, where cardinal events, such as differentiation and proliferation are controlled (Kolch, 2000). The FFA4 receptor interacts with β-arrestin (Watson et al., 2012), which participates in receptor desensitization and internalization.

Agonist stimulation and activation of protein kinase C induce FFA4 receptor phosphorylation and internalization (Burns and Moniri, 2010; Burns et al., 2014; Butcher et al., 2014; Sánchez-Reyes et al., 2014; Villegas-Comonfort et al., 2017). To the best of our knowledge, RTK-mediated modulation of the FFA4 phosphorylation state, cellular localization, and function has not been reported. In the present work, such a possibility was explored, and our data indicated that RTK-activation induces time- and concentration-dependent FFA4 phosphorylation and internalization and also affects its ability to induce ERK 1/2 activation.

2. Materials and methods

2.1. Materials

Docosahexaenoic acid, phorbol 12-myristate 13-acetate, insulin, insulin-like growth factor-I (IGF-I), wortmannin, and protease inhibitors were purchased from Sigma-Aldrich (St. Louis, MO, USA). Phosphate-free Dulbecco's modified Eagle's medium, fetal bovine serum, trypsin, antibiotics, and other reagents used for cell culture were from Life Technologies (Thermo Fisher Scientific; Carlsbad, CA, USA). Fura-2 AM and Dulbecco's Modified Eagle's Medium, were purchased from Invitrogen (Thermo Fisher Scientific; Carlsbad, CA, USA) and agarose-coupled protein A was from Upstate Biotechnology (Lake Placid, NY, USA). Bisindolylmaleimide I, Gö 6976, and LY294002 were obtained from Calbiochem (Merck-Millipore; Darmstadt, Germany) and platelet-derived growth factor (PDGF) and EGF were obtained from PreproTech (Rocky Hill, NJ, USA). [^{32}P]Pi (8,500–9,120 Ci/mmol) was obtained from PerkinElmer Life Sciences (Boston, MA, USA). Rabbit antisera against the Green Fluorescent Protein (GFP) were generated at our laboratory and have been previously characterized (Avendaño-Vázquez et al., 2005; Sánchez-Reyes et al., 2014). Rabbit polyclonal antibodies against total Extracellular signal-Regulated Kinases (ERK) 1/2 and phospho-ERK 1/2 were from Cell Signaling Technology (Danvers, MA, USA); anti β-arrestin 1/2 mouse monoclonal antibody was from Santa Cruz Biotechnology (Santa Cruz, CA, USA). Secondary antibodies were purchased from Zymed (Thermo Fisher Scientific; Carlsbad, CA, USA) or Jackson ImmunoResearch Laboratories (West Grove, PA, USA). Chemiluminescence kits were from Millipore Corporation (Merck-Millipore; Darmstadt, Germany). Other materials were from previously

INFORME DE LABORES 2019

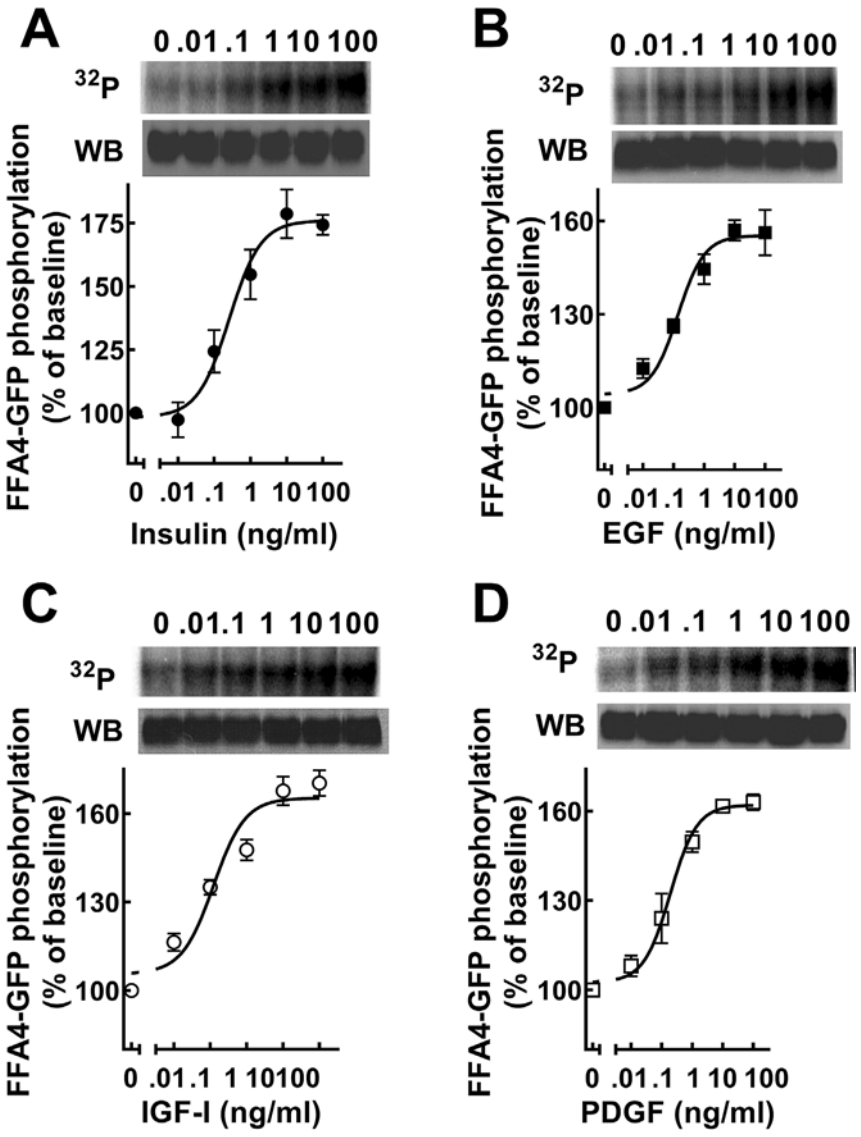

Fig. 2. Growth factor-induced FFA4 phosphorylation concentration-response curves. Cells expressing GFP-tagged FFA4 receptors were incubated for 30 min in the presence of the indicated concentration of insulin (INS, panel A; n = 3), EGF (panel B; n = 4), IGF-I (panel C; n = 3) or PDGF (panel D; n = 3). Cells were lysed and receptor phosphorylation determined as indicated (section 2.4). In all cases the means are plotted with vertical lines indicating the S.E.M. of the indicated number (n) of independent experiments using different cell preparations. Representative autoradiographs (^{32}P) and Western blots (anti-GFP) are presented above each graph.

published sources (Sánchez-Reyes et al., 2014; Villegas-Comonfort et al., 2017).

2.2. Cell lines

HEK 293-derived Flp-In T-Rex 293 cells were used to develop an inducible cell line expressing GFP-tagged human FFA4, as described previously (Hara et al., 2009; Hirasawa et al., 2005; Sánchez-Reyes et al., 2014; Villegas-Comonfort et al., 2017); receptor expression was induced by adding 1 μg/ml of doxycycline hyclate, 12–18 h before the experiments were performed. Cells were maintained in Dulbecco's modified Eagle's medium supplemented with fetal bovine serum and antibiotics, as described (Sánchez-Reyes et al., 2014; Villegas-Comonfort et al., 2017).

2.3. Intracellular free calcium concentration

This was determined fluorometrically as described previously (Sánchez-Reyes et al., 2014; Villegas-Comonfort et al., 2017). Briefly, cells were loaded with 2.5 μM Fura-2 AM in Krebs–Ringer–Hepes containing 0.05% fatty acid-free bovine serum albumin (pH 7.4) and then washed to eliminate unincorporated indicator with buffer without albumin. Determinations were carried out in an AMINCO-Bowman Series 2 luminescence spectrometer, employing 340- and 380-nm excitation wavelengths and an emission wavelength of 510 nm; the chopper interval was 0.5 s. The intracellular calcium concentration was calculated as described by Grynkiewicz et al. (1985).

2.4. FFA4 phosphorylation

The previously described procedure was used (Sánchez-Reyes et al., 2014; Villegas-Comonfort et al., 2017). In brief, cells were incubated in phosphate-free DMEM containing 50 μCi/ml [^{32}P]Pi for 3 h at 37 °C. Labeled cells were stimulated as described and then washed twice with ice-cold phosphate buffered saline solution and solubilized in detergent- and protease and phosphatase inhibitor-containing buffer (Sánchez-Reyes et al., 2014; Villegas-Comonfort et al., 2017). Lysates were incubated overnight with protein A-agarose and anti-GFP serum, with constant agitation at 4 °C. Samples were washed and the pellets were solubilized in Laemmli's sample buffer containing 130 mM

INFORME DE LABORES 2019

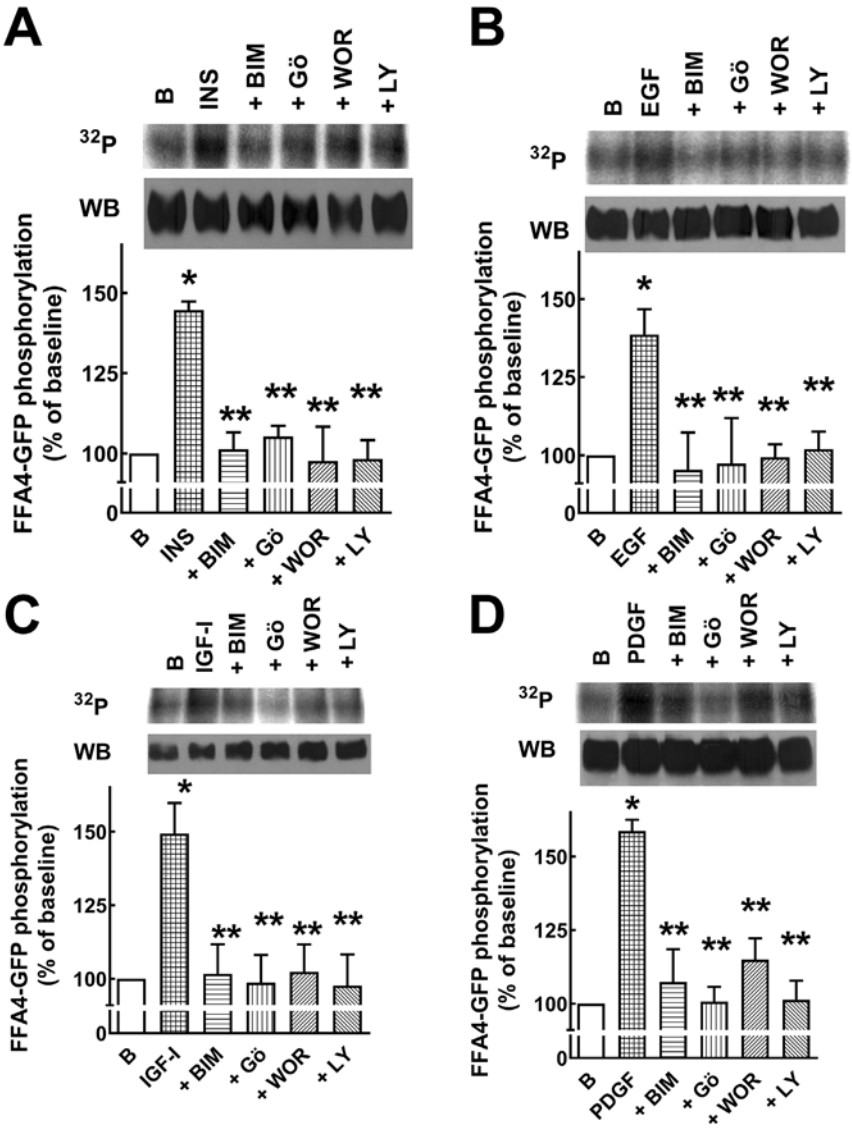

Fig. 3. Effect of protein kinase C and phosphoinositide 3-kinase inhibitors on growth factor-induced FFA4 phosphorylation. Cells expressing GFP-tagged FFA4 receptors were preincubated for 30 min in the absence or presence of 1 μM bisindolylmaleimide I (BIM), 1 μM Gö 6976 (Gö), 100 nM wortmannin (WOR) or 10 μM LY294002 (LY) and then challenged for an additional 30 min with 100 ng/ml of insulin (INS, panel A), EGF (panel B), IGF-I (panel C) or PDGF (panel D). Cells were lysed and receptor phosphorylation determined as indicated (section 2.4). In all cases the means are plotted with vertical lines indicating the S.E.M. of three independent experiments using different cell preparations. In all cases: $^{*}P < 0.005$ vs. baseline, and $^{**}P < 0.005$ vs. preincubation in the absence of inhibitor and presence of the growth factor. Representative autoradiographs (^{32}P) and Western blots (anti-GFP) are presented above each graph.

dithiothreitol. Proteins were separated employing 10% SDS-PAGE and the gels were dried. Receptor phosphorylation was analyzed with a Molecular Dynamics Typhoon PhosphorImager and the ImageJ software. Parallel samples were processed for detection of the receptor (employing anti-GFP antibodies) by Western blotting.

2.5. ERK 1/2 phosphorylation

Cells were incubated as indicated and cellular extracts were obtained by lysing the cells in detergent-, protease inhibitors-, and phosphatase inhibitors-containing buffer (Meizoso-Huesca et al., 2018). Cell extracts were subject to 10% SDS-PAGE and transferred onto nitrocellulose membranes. Samples obtained in parallel were incubated overnight at 4 °C, with anti-phospho-ERK 1/2 or anti-ERK 1/2. The following day, membranes were washed and incubated for 1 h at room temperature with a horseradish peroxidase-conjugated secondary antibody for enhanced chemiluminiscence detection. Densitometric analysis was performed using ImageJ software (http://rsb.info.nih.gov/ij/).

2.6. Confocal microscopy

Cells were seeded onto glass-bottomed Petri dishes and cultured overnight at 37 °C, and receptor expression was induced with doxycycline (1 μg/ml); the next day, cells were washed with medium without serum and further incubated for 3 h. Cells were treated as indicated and were washed with phosphate buffered saline and fixed with 4% paraformaldehyde in 0.1 M phosphate buffer for 20 min at room temperature; samples were then washed three additional times with phosphate buffered saline. Fluorescent images were acquired with an Olympus Fluoview FV10i confocal microscope with a water-immersion objective (60X). To determine receptor internalization, the plasma membrane was delineated utilizing differential interference contrast imaging and fluorescence within this region was excluded for quantification; the fluorescence present in intracellular structures was determined employing ImageJ software (http://rsb.info.nih.gov/ij/) (Collins, 2007; Hartig, 2013; Rasband, 1997–2004) as recommended (employing TFCC, total corrected cellular fluorescence (McCloy et al., 2014) and see also: (https://sciencetechblog.wordpress.com/2011/05/24/measuring-cell-fluorescence-using-imagej/)). At least five images of each of the four different cell cultures employed were taken for each condition. Data were normalized to baseline fluorescence (100%).

2.7. FFA4-β-arrestin coimmunoprecipitation

Experiments were carried out essentially as described previously (Villegas-Comonfort et al., 2017). In brief, cells were incubated in the absence or presence of 30 μM DHA for 15 min (Villegas-Comonfort

INFORME DE LABORES 2019

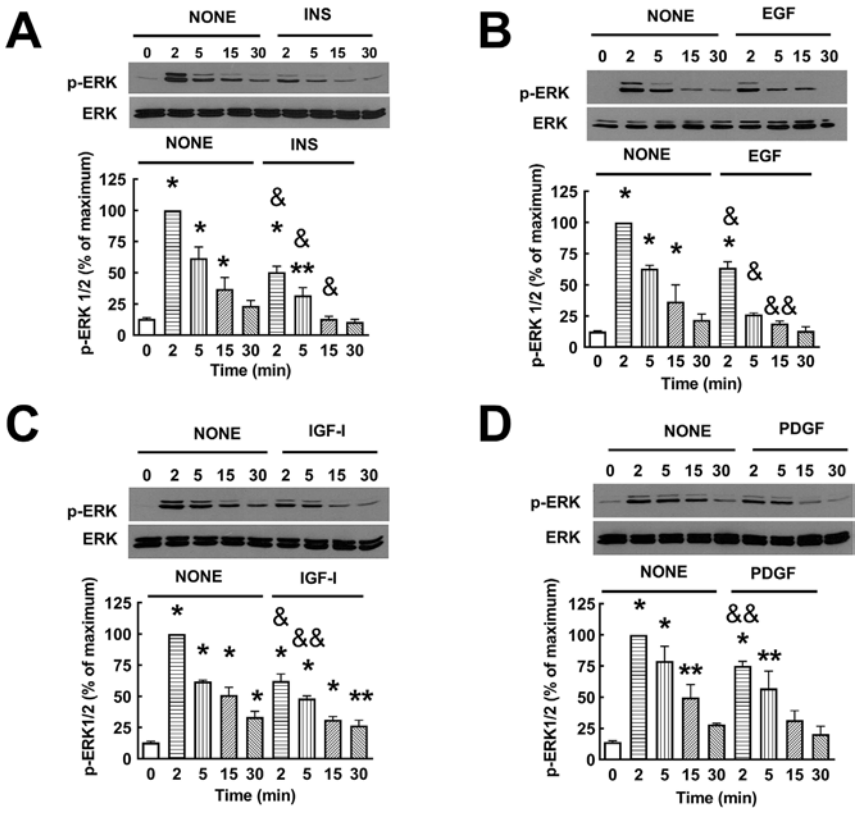

Fig. 4. Effect of preincubation with growth factors on docosahexaenoic acid-induced ERK 1/2 phosphorylation. Cells expressing GFP-tagged FFA4 receptors were incubated for 60 min in the absence (NONE) or in the presence of 100 ng/ml insulin (INS, panel A), EGF (panel B), IGF-I (panel C) or PDGF (panel D), and then were challenged for the times indicated with 30 μM docosahexaenoic acid. Cells were lysed and ERK 1/2 phosphorylation was determined as indicated (section 2.5). Data are presented as percentages of the maximal effect observed (preincubation without growth factor and challenged for 2 min with docosahexaenoic acid). In all cases the means are plotted with vertical lines indicating the S.E.M. of three independent experiments using different cell preparations. $^{*}P < 0.001$ vs. time 0 (baseline), $^{**}P < 0.05$ vs. time 0 (baseline), $^{\&}P < 0.001$ vs. same time, preincubation without growth factor, and $^{\&\&}P < 0.05$ vs. same time, preincubation without growth factor. Representative Western blots (anti-p(phospho)ERK 1/2 and anti-total ERK 1/2) are presented above each graph.

et al., 2017) or for 30 min in the presence of 100 ng/ml of the growth factors. After incubation, cells were washed with ice-cold phosphate buffered saline solution and solubilized in detergent containing buffer, as described for studying FFA4 phosphorylation. Lysates were incubated overnight with protein G-agarose and anti-β-arrestin 1/2 monoclonal antibody (1 μg/sample), with constant agitation at 4 °C. Samples were washed, solubilized, subjected to SDS-PAGE, and electrotransferred onto nitrocellulose membranes; Western blotting was performed using anti-β-arrestin 1/2 and anti-GFP antibodies.

2.8. Statistics

Statistical comparison between groups was performed using analysis of variance with the Bonferroni post-test using the software included in the GraphPad Prism 6 software program. A P value of < 0.05 was considered statistically significant.

3. Results

Cell incubation with 100 ng/ml of insulin (Fig. 1A), EGF (Fig. 1B), IGF-I (Fig. 1C), or PDGF (Fig. 1D) increased, in a time-dependent fashion, the phosphorylation state of FFA4; the time-course and magnitude of these FFA4 phosphorylations was very similar, i. e., these growth factors progressively increased receptor phosphorylation, reaching a maximum (~60% increase over baseline) in 30 min and decreasing at 60 min. Similarly, concentration-response analysis, utilizing 30 min incubation, indicated that the EC_{50} values for these growth factors were very similar (~0.2–0.5 ng/ml) (Fig. 2, panels A–D). Experiments comparing the FFA4 phosphorylation induced by the agonist DHA (30 μM) (Sánchez-Reyes et al., 2014; Villegas-Comonfort et al., 2017) and activation of the RTK receptors (growth factors were employed at a concentration of 100 ng/ml) were performed and are presented in Supplementary Fig. S1). As can be observed, DHA-induced FFA4 phosphorylation was of greater magnitude (2-fold) than those elicited by the growth factors (50–60% increase over baseline).

In order to investigate the signaling pathway(s) involved in RTK-induced FFA4 phosphorylation, the effect of protein kinase C (bisindolylmaleimide I (1 μM) and Gö 6976 (1 μM)) and phosphatidylinositol 3-kinase (wortmannin (100 nM) and LY294002 (10 μM)) inhibitors were tested. Cells were incubated with the inhibitors for 30 min and the peptide growth factors (100 ng/ml) were added (30 min incubation). As shown in Fig. 3, the FFA4-phosphorylations induced by insulin (panel A), EGF (panel B), IGF-I (panel C), and PDGF (panel D) were blocked by these inhibitors; the inhibitors by themselves did not alter baseline receptor phosphorylation at the concentrations tested (data not shown). It is noteworthy, that previous experiments have shown that protein kinase C inhibitors are unable to block agonist-stimulated FFA4 phosphorylation (Sánchez-Reyes et al., 2014).

The functional repercussion of incubation for 60 min with the peptide growth factors was explored next. None of the RTK agonists altered intracellular calcium (data not shown) or the effect of docosahexaenoic acid (30 μM) (Supplementary Fig. S2). The effect of the growth factors on ERK 1/2 phosphorylation was also examined. As depicted in Supplementary Fig. S3, the growth factor peptides by themselves increased ERK 1/2 phosphorylation; EGF was the most efficacious, followed by insulin and then by IGF-I and PDGF. In all cases, the effect of these growth factors was rapid, reaching their maximum at 2–5 min, and decreasing slowly afterward. A clear effect was still consistently observed after 15 min incubation with these agents but this effect further decreased at 30 min and had essentially vanished at 60 min. For this reason, the cells were incubated in parallel in the absence or presence of 100 ng/ml of these peptides for 60 min and then challenged with 30 μM DHA, in order to study whether RTK stimulation altered the response to FFA4 activation, and data were normalized to the maximal response observed (in all cases in cells preincubated without any agent and challenged for 2 min with the fatty acid, DHA (Fig. 4)). In cells preincubated in the absence of any growth factor, DHA induced marked ERK 1/2 phosphorylation that was maximal at 2 min and that decreased afterward (Fig. 4, first set of bars in each panel). As

INFORME DE LABORES 2019

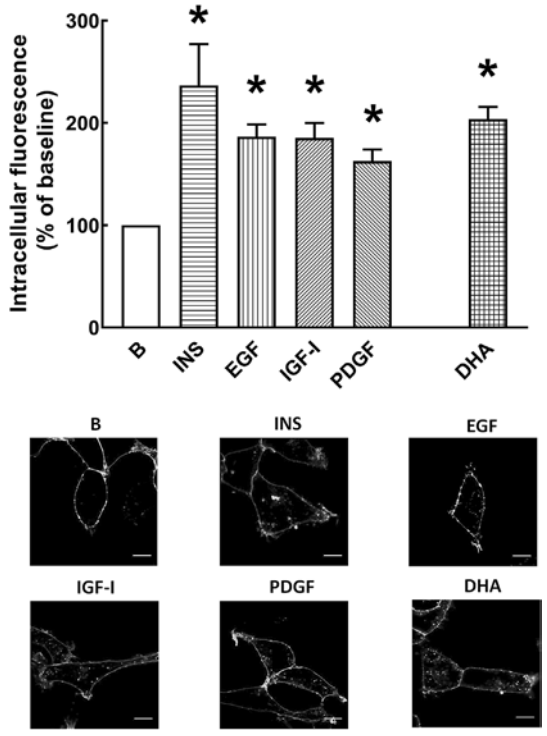

Fig. 5. Effect of growth factors and docosahexaenoic acid on FFA4 internalization (intracellular fluorescence). Cells expressing GFP-tagged FFA4 receptors were incubated for 30 min in the absence of any agent (B, baseline) or the presence of 100 ng/ml insulin (INS; n = 6), EGF (n = 10), IGF-I (n = 3), PDGF (n = 3), or 30 μM docosahexaenoic acid (DHA; n = 6) and then were fixed for observation with a confocal microscope as indicated (section 2.6). Data are presented as percentages of baseline intracellular fluorescence. In all cases the means are plotted with vertical lines indicating the S.E.M. of the indicated number (n) of independent experiments using different cell preparations; in each experiment five cells were analyzed per condition. $^{*}P < 0.001$ vs. baseline. Representative images are presented below the graph. Bar 10 μm.

can be observed, preincubation with any of the growth factors clearly decreased DHA-induced ERK 1/2 phosphorylation (Fig. 4A-D), PDGF being the least effective in this regard (Fig. 4D).

We next examined the possibility that activation of RTK could lead to FFA4 internalization. As illustrated in Fig. 5, the natural FFA4 agonist, docosahexaenoic acid, employed as a positive control, induced marked FFA4 internalization (30 min incubation) as previously reported (Sánchez-Reyes et al., 2014) (Fig. 5). Insulin, IGF-I, and EGF also increased FFA4 internalization after a 30 min incubation; PDGF also was able to induce FFA4 internalization, although the effect was smaller. The possibility that protein kinase C and PI3K could be involved in the internalization processes was tested by employing the inhibitors, bisindolylmaleimide I (1 μM) and wortmannin (100 nM). FFA4 internalization in response to insulin (Fig. 6A), EGF (Fig. 6B), and IGF-I (Fig. 6C) was blocked by the inhibitors. As indicated previously, PDGF-induced FFA4 internalization was of a smaller magnitude and the inhibitor's action was statistically insignificant (Fig. 6D). DHA-induced FFA4 internalization was clearly decreased by bisindolylmaleimide I but was only marginally decreased by wortmannin (Fig. 6E). The inhibitors by themselves did not alter FFA4 localization (Fig. 6F); representative images are presented in Supplementary Fig. S4.

β-Arrestin is known to associate with phosphorylated GPCR and to participate in receptor internalization (Alvarez-Curto et al., 2016; Butcher et al., 2014; DeFea et al., 2000; Kang et al., 2014; Shenoy and Lefkowitz, 2011). Therefore, the possibility that RTK activation might induce FFA4-β-arrestin interaction was hypothesized and experimentally explored through coimmunoprecipitation experiments. As shown in Fig. 7, the data indicated that FFA4 activation by DHA and also growth factor stimulation of endogenous RTK induced FFA4-β-arrestin coimmunoprecipitation.

4. Discussion

The present work shows that the activation of RTK, such as those of insulin, EGF, IGF-I, and PDGF, induced FFA4 phosphorylation in a time- and concentration-dependent fashion. This is consistent with what has been previously observed for other GPCR, including, but not limited to, the following: β_2-adrenoceptors (Doronin et al., 2002a, 2002b); α_{1B}- (Medina et al., 2000) and α_{1D}-adrenoceptors (Rodríguez-Pérez et al., 2009); δ-opioid receptors (Chen et al., 2008); dopamine D_1 receptors (Banday et al., 2007), and angiotensin II AT_1 receptors (García-Caballero et al., 2001); reviewed in (García-Sáinz et al., 2008, 2010; Gavi et al., 2006; Vázquez-Prado et al., 2003).

The ability of protein kinase C and PI3K inhibitors to block RTK-mediated FFA4 phosphorylation indicates that both enzymes are likely involved in such an effect. It is well-known that RTK auto-phosphorylation might lead to their association with the PI3K regulatory subunit, p85, resulting in activation of the catalytic subunit (Blume-Jensen and Hunter, 2001; Manning et al., 2002). Activation of protein kinase C could occur through a similar mechanism, i. e., the association with phospholipase C, triggering phosphatidylinositol 4,5-bisphosphate hydrolysis, generating diacylglycerol, or through other steps in the RTK-associated signaling pathways (Blume-Jensen and Hunter, 2001; García-Sáinz et al., 2010; Medina et al., 2000; Vázquez-Prado et al., 2003).

Roles of protein kinase C and phosphoinositide 3-kinases have been observed in RTK-induced phosphorylation and desensitization of other GPCR, such as α_{1B} and α_{1D}-adrenoceptors (Medina et al., 2000; Rodríguez-Pérez et al., 2009), angiotensin II AT_1 receptors (García-Caballero et al., 2001) and D_1 dopamine receptors (Banday et al., 2007). Other mechanisms involve direct RTK tyrosine phosphorylation of GPCR (for example, the β_2-adrenoceptor by insulin and insulin-like I receptors) (Doronin et al., 2002b; Gavi et al., 2006, 2007; Shumay et al., 2004) and EGF receptor-triggered tyrosine phosphorylation of GRK2, which phosphorylates and desensitizes δ-opioid receptors (Chen et al., 2008). Interestingly, a new mechanism for RTK desensitization of GPCR was recently proposed (Sun et al., 2018). In this study, EGF-induced D_3 dopamine receptor desensitization and down-regulation, involved the Src/Gβγ-dependent tyrosine phosphorylation of GRK2 and its binding to the T142 receptor's residue, which resulted in D_3 dopamine receptor uncoupling from G proteins, endocytosis, and lysosomal receptor degradation (Sun et al., 2018).

FFA4 phosphorylation sites have been identified by several groups (Alfonzo-Méndez et al., 2017; Burns et al., 2014; Butcher et al., 2014; Prihandoko et al., 2016). Five residues at the Ctail (Thr347, Thr349, Ser350, Ser357, and Ser360) were identified as the main agonist-induced phosphorylation sites of the human FFA4 receptor, employing mass spectrometry, mutagenesis, and phosphospecific antibodies (Butcher et al., 2014). Serine-to-alanine substitution of these receptors prevented FFA4 phosphorylation but did not alter ERK 1/2 activation, which appears to be associated with G protein activation (Prihandoko et al., 2016). Interestingly, the latter two serines seem to be particularly relevant for receptor internalization (Prihandoko et al., 2016). Mutagenesis of these five residues markedly reduced, but did not abolish, β-arrestin recruitment; further work by this group (Butcher et al., 2014) allowed identification of acidic residues in proximity to these sites, as structural elements relevant for FFA4-β-arrestin interaction. Mutagenesis/functional analysis have also shown that residues Thr347 and Ser350, are phosphorylation sites that are important for the recruitment of β-arrestin (Burns et al., 2014). We identified phosphorylated Thr242, Ser350, Ser357, and S360 in the FFA4 receptor using mass spectrometry (Alfonzo-Méndez et al., 2017). The sites phosphorylated in the FFA4 receptor in response to RTK activation remain to be determined.

The possibility that FFA4 receptor phosphorylation could entail

INFORME DE LABORES 2019

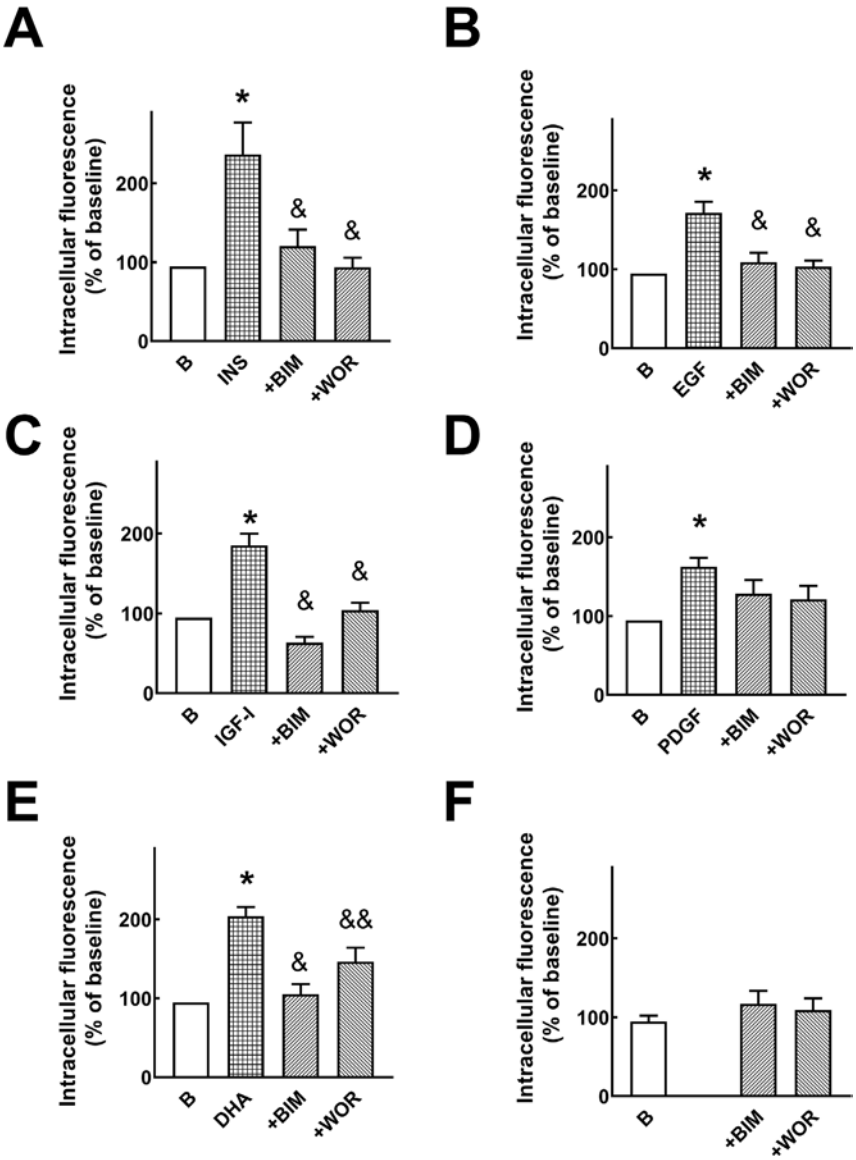

Fig. 6. Effect of bisindolylmaleimide I and wortmannin on growth factor- and docosahexaenoic acid-induced FFA4 internalization (intracellular fluorescence). Cells expressing GFP-tagged FFA4 receptors were preincubated for 30 min in the absence of any agent or in the presence of 1 μM bisindolylmaleimide (+BIM) or 100 nM wortmannin (+WOR) and then challenged with vehicle (B, baseline) or 100 ng/ml insulin (INS, panel A), EGF (panel B), IGF-I (panel C), PDGF (panel D), or 30 μM docosahexaenoic acid (DHA, panel E) (n = 5 in all cases) and then were fixed for observation with a confocal microscope as indicated (section 2.6). Absence of growth factor (panel F)(n= 5). Data are presented as percentages of baseline intracellular fluorescence. In all cases the means are plotted with vertical lines indicating the S.E.M. of the five independent experiments using different cell preparations; in each experiment five cells were analyzed per condition. $^{*}P < 0.001$ vs. baseline, $^{\&}P < 0.005$ vs. growth factor alone, and $^{\&\&}P < 0.05$ vs. growth factor alone.

functional consequences was studied. It was observed that treatment with the different growth factors did not alter the ability of a near-maximal concentration of DHA (30 μM) to increase intracellular calcium. These data indicate that receptor phosphorylation did not exert a direct impact on G protein-mediated signaling. A similar observation was made previously using phorbol myristate acetate to activate protein kinase C directly; i. e. phorbol 12-myristate 13-acetate induced FFA4 receptor phosphorylation without altering its ability to increase intracellular calcium upon agonist-activation (Sánchez-Reyes et al., 2014). RTK-induced FFA4 phosphorylation appears to involve protein kinase C which is consistent with the idea that this protein kinase does not regulate the immediate signaling of this free fatty acid receptor. Data from our laboratory have shown that DHA-induced FFA4 phosphorylation is not diminished by inhibitors of protein kinase C (Sánchez-Reyes et al., 2014). It is well-known that GPCR phosphorylation favors association with β-arrestin and internalization. (Alvarez-Curto et al., 2016; Butcher et al., 2014; DeFea et al., 2000; Kang et al., 2014; Shenoy and Lefkowitz, 2011). RTK activation induced FFA4 phosphorylation, interaction with β-arrestin and internalization; however, the causal relationship among these processes remains to be experimentally determined.

The possibility that other FFA4-triggered downstream processes could be altered by pretreatment with the growth factor evidenced a decrease in the magnitude of the ERK 1/2 phosphorylation response to DHA and an increase in agonist-independent FFA4 internalization. This is also interesting; particularly considering that calcium signaling was not altered. Both processes, that is, ERK 1/2 phosphorylation/activation and receptor internalization, were studied at relatively late times (60 or 30 min after RTK activation, respectively). The latter was studied in this manner, due to the fact that RTK activation induced ERK activation by itself, in the first case and, in the second case, because internalization is a rather complex cellular process that requires time to develop. It should be also borne in mind that ERK activation is a central process in cell physiology, as eloquently stated by Kolch: "… at the heart of signaling networks that govern proliferation, differentiation and cell survival" (Kolch, 2000). Consequently, it is not surprising that multiple pathways, modulated by a large variety of different receptor-activated and metabolic conditions, also involving a diversity of protein interactions, could participate in regulating its function (Kolch, 2000). Due to this time scale and the complexity involved, it is difficult to establish the direct relationship between RTK-induced FFA4 receptor phosphorylation and the effect of growth factors on FFA4-triggered ERK 1/2 phosphorylation. Although fatty acid receptor phosphorylation continues to be considered as a possible causal element, interaction of

INFORME DE LABORES 2019

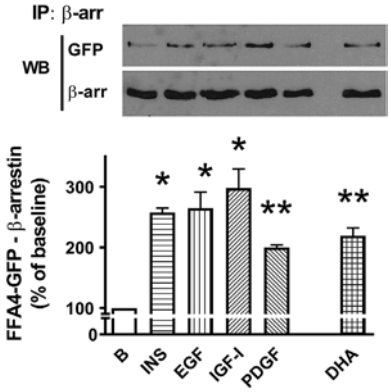

Fig. 7. Effect of growth factors and docosahexaenoic acid on FFA4-β-arrestin coimmunoprecipitation. Cells expressing GFP-tagged FFA4 receptors were incubated for 30 min with vehicle (B, baseline) or 100 ng/ml insulin (INS), EGF, IGF-I, PDGF, or 30 μM docosahexaenoic acid (DHA, 15 min) (n = 3 in all cases) and then coimmunoprecipitation was performed as indicated (section 2.7). Data are presented as percentages of baseline value. In all cases the means are plotted with vertical lines indicating the S.E.M. of the three independent experiments using different cell preparations. $^{*}P < 0.001$ vs. baseline and $^{**}P < 0.05$ vs. baseline. Representative Western blots are presented above the graph.

the signaling pathways modulated by RTK and the GPCR at downstream levels should also be considered. In the case of receptor internalization, there is already evidence indicating that the pharmacological activation of protein kinase C plays a role in the FFA4 internalization associated with receptor phosphorylation (Sánchez-Reyes et al., 2014). Therefore, it appears likely that the protein kinase C activation that participates in growth factor-triggered FFA4 phosphorylation might also lead to the internalization of the free fatty acid receptor.

The present experiments were performed in a cell model transfected with the FFA4 receptor and by stimulating a variety of endogenously expressed growth factor receptors. Although there is general consensus considering the overall response elicited by growth factors, there are many similarities among their actions, but also some differences. This could result of variances in the RTK themselves (specific tyrosine phosphorylation sites), the repertoire of associated signaling elements that are available in specific cells and other elements (Gschwind et al., 2004; Hubbard and Miller, 2007; Schlessinger, 2000). In other words, it is very cell-context-dependent. The expression of RTK varies among cells, tissues, and organs and in response to processes such as development or malignant transformation, and it is difficult to imagine cells devoid of such receptors. FFA4 expression appears to have a much more limited expression (Hirasawa et al., 2005; Miyauchi et al., 2009). Therefore, it is likely that cells expressing this free fatty acid receptor might also express some types of RTK. We hope our findings will promote exploration of this receptor cross-talk in physiological systems, particularly considering the many functions in which FFA4 appears to be involved and its therapeutic potential (Liu et al., 2015; Milligan et al., 2015).

Acknowledgments

The advice and technical support of Dr. Rocío Alcántara-Hernández, Dr. Héctor Malagón, Dr. Claudia Rivera, Juan Barbosa, and Aurey Hernández are gratefully acknowledged. Alejandro Guzmán-Silva is a Doctoral student from the Programa de Doctorado en Ciencias Bioquímicas, Universidad Nacional Autónoma de México, and received a Doctoral Fellowship from Consejo Nacional de Ciencia y Tecnología (CONACYT). Sócrates Villegas-Comonfort is a postdoctoral trainee, supported by a Fellowship from Consejo Nacional de Ciencia y Tecnología (CONACYT). The authors express their gratitude to Maggie Brunner, M.A., for editorial/style corrections. Funding information: This research was partially supported by Grants from Consejo Nacional de Ciencia y Tecnología (CONACYT) [Grant number 253156] and Dirección General de Personal Académico-UNAM [PAPIIT, Grant number IN200915].

Appendix A. Supplementary data

Supplementary data to this article can be found online at https://doi.org/10.1016/j.ejphar.2019.05.018.

References

Alfonzo-Méndez, M.A., Alcántara Hernández, R., García-Sáinz, J.A., 2017. Novel structural approaches to study GPCR regulation. Int. J. Mol. Sci. 18, 27.
Alvarez-Curto, E., Inoue, A., Jenkins, L., Raihan, S.Z., Prihandoko, R., Tobin, A.B., Milligan, G., 2016. Targeted elimination of G proteins and arrestins defines their specific contributions to both intensity and duration of G protein-coupled receptor signaling. J. Biol. Chem. 291, 27147–27159.
Avendaño-Vázquez, S.E., García-Caballero, A., García-Sáinz, J.A., 2005. Phosphorylation and desensitization of the lysophosphatidic acid receptor LPA1. Biochem. J. 385, 677–684.
Banday, A.A., Fazili, F.R., Lokhandwala, M.F., 2007. Insulin causes renal dopamine D1 receptor desensitization via GRK2-mediated receptor phosphorylation involving phosphatidylinositol 3-kinase and protein kinase C. Am. J. Physiol. Renal. Physiol. 293, F877–F884.
Blume-Jensen, P., Hunter, T., 2001. Oncogenic kinase signalling. Nature 411, 355–365.
Burns, R.N., Moniri, N.H., 2010. Agonism with the omega-3 fatty acids alpha-linolenic acid and docosahexaenoic acid mediates phosphorylation of both the short and long isoforms of the human GPR120 receptor. Biochem. Biophys. Res. Commun. 396, 1030–1035.
Burns, R.N., Singh, M., Senatorov, I.S., Moniri, N.H., 2014. Mechanisms of homologous and heterologous phosphorylation of FFA receptor 4 (GPR120): GRK6 and PKC mediate phosphorylation of Thr(3)(4)(7), Ser(3)(5)(0), and Ser(3)(5)(7) in the C-terminal tail. Biochem. Pharmacol. 87, 650–659.
Butcher, A.J., Hudson, B.D., Shimpukade, B., Alvarez-Curto, E., Prihandoko, R., Ulven, T., Milligan, G., Tobin, A.B., 2014. Concomitant action of structural elements and receptor phosphorylation determine arrestin-3 interaction with the free fatty acid receptor FFA4. J. Biol. Chem. 289, 18451–18465.
Chen, Y., Long, H., Wu, Z., Jiang, X., Ma, L., 2008. EGF transregulates opioid receptors through EGFR-mediated GRK2 phosphorylation and activation. Mol. Biol. Cell 19, 2973–2983.
Collins, T.J., 2007. ImageJ for microscopy. Biotechniques 43, 25–30.
DeFea, K.A., Zalevsky, J., Thoma, M.S., Dery, O., Mullins, R.D., Bunnett, N.W., 2000. beta-arrestin-dependent endocytosis of proteinase-activated receptor 2 is required for intracellular targeting of activated ERK1/2. J. Cell Biol. 148, 1267–1281.
Doronin, S., Shumay, E., Wang, H.Y., Malbon, C.C., 2002a. Akt mediates sequestration of the beta(2)-adrenergic receptor in response to insulin. J. Biol. Chem. 277, 15124–15131.
Doronin, S., Wang Hy, H.Y., Malbon, C.C., 2002b. Insulin stimulates phosphorylation of the beta 2-adrenergic receptor by the insulin receptor, creating a potent feedback inhibitor of its tyrosine kinase. J. Biol. Chem. 277, 10698–10703.
García-Caballero, A., Olivares-Reyes, J.A., Catt, K.J., García-Sáinz, J.A., 2001. Angiotensin AT(1) receptor phosphorylation and desensitization in a hepatic cell line. Roles of protein kinase c and phosphoinositide 3-kinase. Mol. Pharmacol. 59, 576–585.
García-Sáinz, J.A., Romero-Ávila, M.T., Medina, L.C., 2010. Dissecting how receptor tyrosine kinases modulate G protein-coupled receptor function. Eur. J. Pharmacol. 648, 1–5.
García-Sáinz, J.A., Romero-Ávila, M.T., Molina-Muñoz, T., García-Pasquel, M.-J., 2008. G-protein -coupled receptor-receptor tyrosine kinase crosstalk. Regulation of receptor sensitivity and roles of autocrine feedback loops and signal integration. Curr. Signal Transduct. Ther. 3, 174–182.
Gavi, S., Shumay, E., Wang, H.Y., Malbon, C.C., 2006. G-protein-coupled receptors and tyrosine kinases: crossroads in cell signaling and regulation. Trends Endocrinol. Metabol. 17, 48–54.
Gavi, S., Yin, D., Shumay, E., Wang, H.Y., Malbon, C.C., 2007. Insulin-like growth factor-I provokes functional antagonism and internalization of {beta}1-Adrenergic receptors. Endocrinology 148, 2653–2662.
Grynkiewicz, G., Poenie, M., Tsien, R.Y., 1985. A new generation of Ca2+ indicators with greatly improved fluorescence properties. J. Biol. Chem. 260, 3440–3450.
Gschwind, A., Fischer, O.M., Ullrich, A., 2004. The discovery of receptor tyrosine kinases: targets for cancer therapy. Nat. Rev. Canc. 4, 361–370.
Gschwind, A., Zwick, E., Prenzel, N., Leserer, M., Ullrich, A., 2001. Cell communication networks: epidermal growth factor receptor transactivation as the paradigm for interreceptor signal transmission. Oncogene 20, 1594–1600.
Hara, T., Hirasawa, A., Sun, Q., Sadakane, K., Itsubo, C., Iga, T., Adachi, T., Koshimizu, T.A., Hashimoto, T., Asakawa, Y., Tsujimoto, G., 2009. Novel selective ligands for free fatty acid receptors GPR120 and GPR40. Naunyn-Schmiedeberg's Arch. Pharmacol. 380, 247–255.
Hartig, S.M., 2013. Basic image analysis and manipulation in ImageJ. Curr Protoc Mol Biol Chapter 14, 15.11–15.12.
Hirasawa, A., Tsumaya, K., Awaji, T., Katsuma, S., Adachi, T., Yamada, M., Sugimoto, Y.,

INFORME DE LABORES 2019

Miyazaki, S., Tsujimoto, G., 2005. Free fatty acids regulate gut incretin glucagon-like peptide-1 secretion through GPR120. Nat. Med. 11, 90–94.
Hubbard, S.R., Miller, W.T., 2007. Receptor tyrosine kinases: mechanisms of activation and signaling. Curr. Opin. Cell Biol. 19, 117–123.
Ichimura, A., Hirasawa, A., Poulain-Godefroy, O., Bonnefond, A., Hara, T., Yengo, L., Kimura, I., Leloire, A., Liu, N., Iida, K., Choquet, H., Besnard, P., Lecoeur, C., Vivequin, S., Ayukawa, K., Takeuchi, M., Ozawa, K., Tauber, M., Maffeis, C., Morandi, A., Buzzetti, R., Elliott, P., Pouta, A., Jarvelin, M.R., Korner, A., Kiess, W., Pigeyre, M., Caiazzo, R., Van Hul, W., Van Gaal, L., Horber, F., Balkau, B., Levy-Marchal, C., Rouskas, K., Kouvatsi, A., Hebebrand, J., Hinney, A., Scherag, A., Pattou, F., Meyre, D., Koshimizu, T.A., Wolowczuk, I., Tsujimoto, G., Froguel, P., 2012. Dysfunction of lipid sensor GPR120 leads to obesity in both mouse and human. Nature 483, 350–354.
Kang, D.S., Tian, X., Benovic, J.L., 2014. Role of beta-arrestins and arrestin domain-containing proteins in G protein-coupled receptor trafficking. Curr. Opin. Cell Biol. 27, 63–71.
Kolch, W., 2000. Meaningful relationships: the regulation of the Ras/Raf/MEK/ERK pathway by protein interactions. Biochem. J. 351 Pt 2, 289–305.
Liu, H.D., Wang, W.B., Xu, Z.G., Liu, C.H., He, D.F., Du, L.P., Li, M.Y., Yu, X., Sun, J.P., 2015. FFA4 receptor (GPR120): a hot target for the development of anti-diabetic therapies. Eur. J. Pharmacol. 763, 160–168.
Manning, G., Whyte, D.B., Martinez, R., Hunter, T., Sudarsanam, S., 2002. The protein kinase complement of the human genome. Science 298, 1912–1934.
McCloy, R.A., Rogers, S., Caldon, C.E., Lorca, T., Castro, A., Burgess, A., 2014. Partial inhibition of Cdk1 in G 2 phase overrides the SAC and decouples mitotic events. Cell Cycle 13, 1400–1412.
Medina, L.C., Vázquez-Prado, J., García-Sáinz, J.A., 2000. Cross-talk between receptors with intrinsic tyrosine kinase activity and alpha1b-adrenoceptors. Biochem. J. 350, 413–419.
Meizoso-Huesca, A., Villegas-Comonfort, S., Romero-Ávila, M.T., Garcia-Sáinz, J.A., 2018. Free fatty acid receptor 4 agonists induce lysophosphatidic acid receptor 1 (LPA1) desensitization independent of LPA1 internalization and heterodimerization. FEBS Lett. 592, 2612–2623.
Milligan, G., Alvarez-Curto, E., Watterson, K.R., Ulven, T., Hudson, B.D., 2015. Characterizing pharmacological ligands to study the long-chain fatty acid receptors GPR40/FFA1 and GPR120/FFA4. Br. J. Pharmacol. 172, 3254–3265.
Miyauchi, S., Hirasawa, A., Iga, T., Liu, N., Itsubo, C., Sadakane, K., Hara, T., Tsujimoto, G., 2009. Distribution and regulation of protein expression of the free fatty acid receptor GPR120. Naunyn-Schmiedeberg's Arch. Pharmacol. 379, 427–434.
Prihandoko, R., Alvarez-Curto, E., Hudson, B.D., Butcher, A.J., Ulven, T., Miller, A.M., Tobin, A.B., Milligan, G., 2016. Distinct phosphorylation clusters determine the signaling outcome of free fatty acid receptor 4/G protein-coupled receptor 120. Mol. Pharmacol. 89, 505–520.
Pyne, N.J., Waters, C.M., Long, J.S., Moughal, N.A., Tigyi, G., Pyne, S., 2007. Receptor tyrosine kinase-G-protein coupled receptor complex signaling in mammalian cells. Adv. Enzym. Regul. 47, 271–280.
Rasband, W.S., 1997-2004. ImageJ, national institutes of health. http://rsb.info.nih.gov/ij/.
Rodríguez-Pérez, C.E., Calvo-Ochoa, E., Kalashnikova, E.V., Reyes-Cruz, G., Romero-Ávila, M.T., García-Sáinz, J.A., 2009. Receptor tyrosine kinases regulate alpha1D-adrenoceptor signaling properties: phosphorylation and desensitization. Int. J. Biochem. Cell Biol. 41, 1276–1283.
Sánchez-Reyes, O.B., Romero-Ávila, M.T., Castillo-Badillo, J.A., Takei, Y., Hirasawa, A., Tsujimoto, G., Villalobos-Molina, R., García-Sáinz, J.A., 2014. Free fatty acids and protein kinase C activation induce GPR120 (free fatty acid receptor 4) phosphorylation. Eur. J. Pharmacol. 723, 368–374.
Schlessinger, J., 2000. Cell signaling by receptor tyrosine kinases. Cell 103, 211–225.
Shenoy, S.K., Lefkowitz, R.J., 2011. beta-Arrestin-mediated receptor trafficking and signal transduction. Trends Pharmacol. Sci. 32, 521–533.
Shumay, E., Gavi, S., Wang, H.Y., Malbon, C.C., 2004. Trafficking of beta2-adrenergic receptors: insulin and beta-agonists regulate internalization by distinct cytoskeletal pathways. J. Cell Sci. 117, 593–600.
Sparks, S.M., Chen, G., Collins, J.L., Danger, D., Dock, S.T., Jayawickreme, C., Jenkinson, S., Laudeman, C., Leesnitzer, M.A., Liang, X., Maloney, P., McCoy, D.C., Moncol, D., Rash, V., Rimele, T., Vulimiri, P., Way, J.M., Ross, S., 2014. Identification of diarylsulfonamides as agonists of the free fatty acid receptor 4 (FFA4/GPR120). Bioorg. Med. Chem. Lett 24, 3100–3103.
Sun, N., Zhang, X., Guo, S., Le, H.T., Zhang, X., Kim, K.M., 2018. Molecular mechanisms involved in epidermal growth factor receptor-mediated inhibition of dopamine D3 receptor signaling. Biochim. Biophys. Acta 1865, 1187–1200.
Sun, Q., Hirasawa, A., Hara, T., Kimura, I., Adachi, T., Awaji, T., Ishiguro, M., Suzuki, T., Miyata, N., Tsujimoto, G., 2010. Structure-activity relationships of GPR120 agonists based on a docking simulation. Mol. Pharmacol. 78, 804–810.
Vázquez-Prado, J., Casas-González, P., García-Sáinz, J.A., 2003. G protein-coupled receptor cross-talk: pivotal roles of protein phosphorylation and protein-protein interactions. Cell. Signal. 15, 549–557.
Villegas-Comonfort, S., Takei, Y., Tsujimoto, G., Hirasawa, A., García-Sáinz, J.A., 2017. Effects of arachidonic acid on FFA4 receptor: signaling, phosphorylation and internalization. Prostaglandins Leukot. Essent. Fatty Acids 117, 1–10.
Watson, S.J., Brown, A.J., Holliday, N.D., 2012. Differential signaling by splice variants of the human free fatty acid receptor GPR120. Mol. Pharmacol. 81, 631–642.

INFORME DE LABORES 2019

Archives of Biochemistry and Biophysics 666 (2019) 107–115

Contents lists available at ScienceDirect

Archives of Biochemistry and Biophysics

journal homepage: www.elsevier.com/locate/yabbi

X-ray driven reduction of Cpd I of Catalase-3 from *N. crassa* reveals differential sensitivity of active sites and formation of ferrous state

Andrés Zárate-Romero[a], Vivian Stojanoff[b], Aina E. Cohen[c], Wilhelm Hansberg[d], Enrique Rudiño-Piñera[e,*]

[a] Cátedras CONACyT, Departamento de Bionanotecnología, Centro de Nanociencias y Nanotecnología, Universidad Nacional Autónoma de México, Ensenada, B. C., Mexico
[b] National Synchrotron Light Source II, Brookhaven National Laboratory, Upton, NY, USA
[c] Stanford Synchrotron Radiation Lightsource, Stanford University, Menlo Park, CA, USA
[d] Departamento de Biología Celular y del Desarrollo, Instituto de Fisiología Celular, Universidad Nacional Autónoma de México, Ciudad de México, Mexico
[e] Departamento de Medicina Molecular y Bioprocesos, Instituto de Biotecnología, Universidad Nacional Autónoma de México, Cuernavaca, Morelos, Mexico

ARTICLE INFO

Keywords:
Catalase
Composite datasets
Compound I
Ferrous heme
X-ray reduction

ABSTRACT

Catalases are biotechnologically relevant enzymes because of their applications in food technology, bioremediation, and biomedicine. The dismutation of hydrogen peroxide occurs in two steps; in the first one, the enzyme forms an oxidized compound I (Cpd I) and in the second one, the enzyme is reduced to the ferric state. In this research work, we analyzed the reduction of Cpd I by X-ray radiation damage during diffraction experiments in crystals of CAT-3, a Large-Size Subunit Catalase (LSC) from *Neurospora crassa*. A Multi-Crystal Data collection Strategy was applied in order to obtain the Cpd I structure at a resolution of 2.2 Å; this intermediate was highly sensitive to X-ray and was easily reduced at very low deposited radiation dose, causing breakage of the Fe=O bond. The comparison of the structures showed reduced intermediates and also evidenced the differential sensitivity per monomer. The resting ferric state was reduced to the ferrous state, an intermediate without a previous report in LSC. The chemically obtained Cpd I and the X-ray reduced intermediates were identified by UV-visible microspectrometry coupled to data collection. The differential sensitivity and the formation of a ferrous state are discussed, emphasizing the importance of the correct interpretation in the oxidation state of the iron heme.

1. Introduction

Heme-dependent catalases are ubiquitous enzymes present in most living organisms that play a fundamental role in response to oxidative stress. Catalases have multiple applications in the food industry [1–4], medicine [5,6] and fabrication of biosensors [7–9]. The origin of catalases is monophyletic and, they are grouped in three clades, clade 1 is distributed in bacteria, green algae and plants; clade 2 in bacteria, fungi and some archaea; and clade 3 in bacteria, fungi, animals and some archaea [10–12].

Large-Size Subunit Catalases (LSC) are enzymes with a MW ranging from 75 to 86 kDa and are grouped in clade 2 of the monofunctional heme-dependant catalases [13]. These enzymes dismutate hydrogen peroxide to molecular oxygen and two water molecules in two consecutive reactions. In the first reaction, the iron heme center in the ferric resting state is oxidized by a hydrogen peroxide molecule releasing a water molecule and forming the compound I (Cpd I) (reaction 1), an oxoferryl group associated to a cation-π radical of porphyrin. In the next reaction, a second hydrogen peroxide molecule acts as an electron donor reducing the oxoferryl group and restoring the resting ferric state (reaction 2). This set of reactions is named the catalatic pathway [14]. The Small-Size Subunit Catalases (SSC) are heme depending catalases which have subunits ranging between 50 and 55 kDa and are distributed in clades 1 and 3. The SSC can experience, added to the catalatic pathway, different reactions known as the peroxidant pathway. At low H_2O_2 flux, Cpd I can be reduced by a single electron donor resulting in the formation of compound II (Cpd II) [15], an oxoferryl without the cation-π porphyrin radical. This intermediate can restore the ferric state after a second single electron reduction (reaction 4) [16]. The Cpd II can also be further oxidized by H_2O_2 and form inactive compound III [17].

Catalatic pathway

* Corresponding author.
E-mail address: rudino@ibt.unam.mx (E. Rudiño-Piñera).

https://doi.org/10.1016/j.abb.2019.03.020
Received 14 February 2019; Received in revised form 21 March 2019; Accepted 29 March 2019
Available online 30 March 2019
0003-9861/ © 2019 Elsevier Inc. All rights reserved.

INFORME DE LABORES 2019

$$E-Fe^{III} + H_2O_2 \rightarrow E[\pi^+]-Fe^{IV}=O + H_2O \quad (1)$$

$$E[\pi^+]-Fe^{IV}=O + H_2O_2 \rightarrow E-Fe^{III} + H_2O + O_2 \quad (2)$$

Peroxidant pathway

$$E[\pi^+]-Fe^{IV}=O + AH \rightarrow E-Fe^{IV}=O + A^{\cdot} + H^+ \quad (3)$$

$$E\text{-}Fe^{IV}=O + AH + H^+ \rightarrow E\text{-}Fe^{III} + A + H_2O \quad (4)$$

Determination of structures through X-ray crystallography is pivotal to an understanding of enzyme function and characterization of molecular mechanisms. The preservation of the structural information, or the changes occurring while X-rays interact with the protein crystal, are critical for the correct interpretation of the three-dimensional structures. Nevertheless, during the data collection of diffraction patterns from protein crystals, the accumulation of high radiation doses affects several crystal parameters such as the unit cell dimensions, resolution, mosaicity and intensity of reflection spots as a direct consequence of the disorder in the structure [18]. At a molecular level, X-ray radiation damage occurs due to the photoelectric effect and inelastic scattering which cause the breakage of S-H, O-H, N-H, and C-H bonds as well as the production of solvated electrons (e^-aq), ·OH, and ·H radicals [19–21]. The presence of the radiolytic species lead to the breakage of other bonds in the protein, including disulfide bridges but also the reduction of metal centers, which are particularly sensitive to ionizing radiation [22].

X-ray radiation damage causes loss of information of the initial state of the crystal, but has also been used as a tool to determine structures of reduced catalytic intermediates that cannot be obtained through chemical procedures [23]. When crystals are reduced at low X-ray doses, the combination of composite datasets and spectroscopic techniques as UV-visible micro spectrometry, XAS and Raman [24–26] allow obtaining information of the reduction process. There are few studies showing crystal structures of oligomeric proteins with a different oxidation state in their monomers in which it has been suggested that these differences are due to the reduction of the initial state [27–29]. Until now we have no knowledge of any reports concerning structural studies that correlate the behaviour of a multimeric metalloenzyme with X-ray dosage.

Most LSC crystal structures deposited in PDB were determined for the ferric state [13,30–32]. There is only one crystal structure for the Cpd I intermediate of a LSC; the catalase from *Penicillium vitale* (PVC, PDB entry 2IUF) for which the prosthetic group is heme *d* [33]. The structures of Cpd I solved for catalases harboring a heme *b* only belong to SSC [16,33,34]. In this work, crystals of the homotetrameric LSC Catalase-3 from *N. crassa* (CAT-3), which harbors a heme *b* prosthetic group, were chemically oxidized to Cpd I and exposed to X-rays during data collection. We report the crystal structures obtained from crystals of CAT-3 describing the differential reduction of the active sites in response to the accumulation of radiation dose. Furthermore, the spectrophotometric analysis of the irradiated crystals reveals the existence of the ferrous state, described for the first time for LSC.

2. Materials and methods

2.1. Protein purification

Protein expression and purification was performed as described in Zarate-Romero et al. 2013 [35]. Briefly, a 5 L culture of *E. coli* BL21 DE3 (pLyss) in LB medium was grown to an OD_{600} of 0.5, supplemented with 30 μM hemin, and induced with 100 μM IPTG. The culture was incubated at 16 °C for 24 h. Cells were recovered by centrifugation at 3,500 × *g* for 15 min. The cell pellet was resuspended in 50 mM sodium phosphate buffer pH 8.0 containing 300 mM NaCl, and 15 mM imidazole, and lysed by sonication. The sonicated suspension was centrifuged for 40 min at 13,000 × *g*, and the supernatant was purified by Ni^{2+} affinity chromatography with a HisTrap column (GE Healthcare). The enzyme was eluted with the previous buffer but increasing imidazole concentration to 300 mM. The eluted protein was dialyzed against 20 mM Tris pH 8.0 at 4 °C employing a 12 kDa cut-off membrane. Anionic exchange chromatography was performed in a High-Q BioRad column using a 0–500 mM NaCl in 20 mM Tris pH 8.0 gradient. CAT-3 was eluted at ~200 mM NaCl. Gel filtration chromatography was performed in a Hi-Load 26/600 Superdex 200 pg column (GE Healthcare) using 20 mM Tris pH 8.0 and 100 mM NaCl at 3 mL/min and 0.1 MPa pressure in an AKTA prime liquid chromatography system (GE Healthcare). Fractions with a Soret's peak were analyzed in SDS-PAGE in non-reducing conditions and those containing most of the catalase activity were pooled. Buffer was exchanged with 10 mM HEPES by using an Amicon ultrafiltration unit with a 30 kDa cut-off membrane (Millipore). Finally, the protein was concentrated to 6 mg/mL in order to set crystallization trials. The concentration of the purified protein was determined by measuring A_{280}. Based on the CAT-3 sequence, the calculated extinction coefficient value was determined to be $\varepsilon_{280} = 321{,}320\ M^{-1}cm^{-1}$ for the tetrameric enzyme.

2.2. UV-visible spectrometry analysis in solution

CAT-3 was resuspended in 100 mM sodium acetate-acetic acid buffer pH 5.5 at a concentration of 0.2 mg/mL. The UV-visible spectrum ranging from 250 to 850 nm was measured using an *Evolution 300* spectrometer (Thermo Scientific). To form Cpd I, 50 μL of the CAT-3 solution was treated with 1 mM peracetic acid (PAA) previously treated with commercial bovine liver catalase (BLC, Sigma Aldrich) to eliminate H_2O_2. After a colour shift from brown to green, the UV- visible spectra was measured.

2.3. Protein crystallization and Cpd I obtaining

Crystals were obtained in space group $P2_12_12_1$ as in Zárate-Romero et al. 2013 [35]. Briefly CAT-3 at 3.5 mg/mL in 10 mM HEPES pH 7.0 was used to set droplets of 1 μL enzyme plus 1 μL of 200 mM ammonium dibasic tartrate and 20% w/v PEG 3350 (condition 38 of PEG/Ion screen, Hampton Research) in the microbatch method [36] and covered with 10 μL of paraffin oil. Crystals appeared 5 days after trial setting and were grown for 3 weeks.

Ferric CAT-3 crystals with an average dimension of 0.5 mm × 0.05 mm x 0.05 mm were soaked in a cryoprotectant solution containing 100 mM MES pH 6.6 and 40% w/v PEG 400. To obtain Cpd I, 100 mM PAA was added to the cryoprotectant solution and after 1 min, the crystal showed a colour shift from brown to green. After soaking in the cryoprotectant solution, the crystals were flash-cooled and stored in liquid nitrogen.

2.4. Data collection and structure determination

Data collection of all of the CAT-3 crystals was performed at X6A beamline of the NSLS. The X-ray deposited dose determination was performed by using *RADDOSE* [18], considering a Gaussian profile for the beam. To determine the CAT-3 soaked with PAA structure, a dataset of 360 frames was collected from one crystal with $\Delta\phi = 0.25^{\circ}$, t = 30 seg, $\lambda = 0.9796$ Å, d = 250 mm. Frames were indexed, integrated and scaled using the *XDS* suite [37]. Files were converted to mtz format using *F2mtz* in the CCP4i suite. Phases were solved by molecular replacement in *Phaser* [38], the search model had the coordinates for the peptide chains of the CAT-3 tetramer (PDB entry 3ZJ5 [35]). The model obtained was refined as a rigid body in *REFMAC5* [39]. Further refinement of coordinates, B-values and occupancies was performed in the *PHENIX* suite [40] and the subsequent construction of the model was performed in *Coot* [41]. CAT-3-PAA structure was deposited at PDB with code 4AJ9.

In order to produce composite datasets, 366 frames were collected from each crystal, with the following conditions, $\Delta\phi = 0.3^{\circ}$, t = 30 seg,

INFORME DE LABORES 2019

λ = 0.9764 Å, d = 210 mm. Each crystal was oriented with the longer axis perpendicular to the X-ray beam and with one of the faces in a plane normal to the beam. The next crystal was oriented in the same position and the initial angle ϕ was rotated 10° from the initial plane. For each new crystal, 10° were added to the initial angle ϕ. A total of 9 crystals were collected in order to cover the ϕ rotation needed (90°) to fulfil a 100% integrity for the composite datasets.

Every single crystal dataset was split in partial datasets, each one covering 10° of the collected data. The frames corresponding to each 10° section were indexed and integrated using *XDS* suite. The integrated partial datasets corresponding to the first 10° from each single crystal were scaled together and a composite dataset was obtained. This procedure was repeated for 10-20°, 20-30° and so on, until the 100-110° partial dataset. Furthermore, a composite dataset for the first 5° of data collection was obtained. All composite datasets were scaled in *XSCALE*; the phases for each composite structure were obtained by molecular substitution in *PHASER* [38] using PDB entry 4AJ9 as a search model. The resultant model was refined as a rigid body in *REFMAC5* [39] and subsequent refinement of coordinates, B-values and occupancies was performed in *PHENIX* suite [40]. The construction of the model was continued with *Coot*.

In order to analyze the presence of ligands near the heme prosthetic group, polder omit difference maps were calculated using *phenix.polder* [42] in the PHENIX suite by eliminating the heme prosthetic group and the neighbouring water molecules. All the structure figures were generated using *CCP4MG* [43]. Coordinates of the determined structures were deposited at PDB with codes 6NSW, 6NSY, 6NSZ, 6NT0 and 6NT1 for 5°, 10°, 20°, 50° and 110° respectively.

2.5. UV-visible spectroscopy coupled to data collection

Collection of UV-visible absorbance spectra from CAT-3 crystals in native state or soaked in PAA was done in beamline BL11-1 at SSRL. Crystals were rotated 360° and a UV-visible spectrum was collected each 10° after an area with strong signal was identified. Rotation was changed to 2° in that area until the orientation with the highest signal was located. The angular position of the crystal was fixed, and then X-ray exposure was done collecting a spectrum every two seconds. The conditions for X-ray irradiation were: slits 0.05 mm × 0.05 mm, λ = 0.9795 Å. The flux conditions were adjusted in order to deposit a dose of 7.7×10^{-4} MGy/s.

3. Results

3.1. CAT-3 compound I in solution

The UV-visible spectra of a solution of CAT-3 in the resting state or incubated with 1 mM PAA were measured. A colour change from brown to green was observed in the sample with PAA added. The resultant spectra of both samples (Fig. 1a) showed the characteristic Soret's band at 406 nm. The 280/406 nm ratio for the resting state is 1, while in the sample treated with PAA this ratio is 2. There were also two peaks observed at 500 nm and 535 nm which slightly decrease in the Cpd I spectrum. The charge-transfer band appears at 619 nm in the resting state, but in the sample that reacted with PAA, this band was displaced to 670 nm. These changes correlate with the presence of Cpd I as has been described for several catalases, e.g. the PVC [33] which is an ortholog of CAT-3 [12], as well as for the SSCs of *Aspergillus niger* (ANC) [15] *Proteus mirabilis* [44], *Helicobacter pylori* [33] and BLC [45].

3.2. Cpd I structure is reduced under data collection of a single dataset

One crystal of CAT-3 (Fig. 1b) was soaked in a cryoprotectant supplied with 100 mM PAA. As in solution, a colour shift was observed (Fig. 1c) and the crystal was immediately flash-cooled in liquid nitrogen. After X-ray diffraction, the exposed area changed to a brown

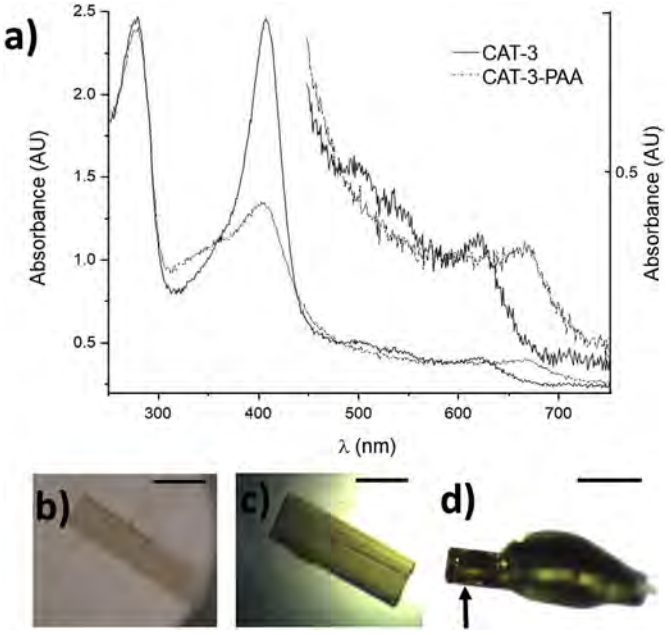

Fig. 1. UV-visible spectra of CAT-3 in solution. a) Spectra of CAT-3 in solution with the Soret's band at 402 nm and the characteristic peaks of the ferric state at 502 nm, 535 nm and the charge-transfer band at 615 nm (line). The CAT-3 treated with PAA (dashed) has decreased in the Soret's band and a shift of the charge-transfer band to 665 nm, the 450–750 nm region is rescaled according to the scale shown in the right for absorbance. b) Crystal of CAT-3 in the ferric state. c) Crystal of CAT-3 treated with PAA, colour shift to green. d) Crystal of CAT-3-PAA after diffraction, the arrow points toward the path of X-ray beam, the green colour shift back to brown after X-ray exposure. The scale bar in b-d) represents 100 μm. (For interpretation of the references to colour in this figure legend, the reader is referred to the Web version of this article.)

colour (Fig. 1d). A structure was determined and deposited in the PDB with the entry 4AJ9 at 1.85 Å resolution, and a calculated dose of 1.18 MGy.

The electron density map $2F_o$-F_c of the structure and a polder omit map lacking the heme moiety were analyzed looking for continual electron density at 1.8 Å from the iron atom. The expected peak, characteristic for the Fe = O bond in Cpd I, was not present in any of the maps. In comparison to the structure collected from a crystal in ferric state [35] (Fig. 2a), an acetate ion was found in the access tunnel of each monomer, interacting with the carboxyl group of Asp 155 and the isopropyl group of Val 195. Both the colour shift and presence of acetate suggest that Cpd I was obtained, however, as shown by the lack of continual electron density, it was reduced during data collection.

The PVC is the only LSC with a crystal structure determined for Cpd I (PDB entry 2IUF at 1.71 Å resolution) [33]. The intermediate was obtained by the same method described here and the acetate ions were also observed in the tunnel, additionally showing the oxidation of two methionine residues in the middle of the tunnel (Fig. 2a). The methionine in position 153 is the only of these which is conserved in CAT-3 (Met 231). PVC is also in the G2C group of LSC and among the enzymes with a three-dimensional crystal structure has the highest sequence identity to CAT-3 [13]. The active site of PVC is highly conserved with CAT-3, however instead of heme *b*, the prosthetic group of this catalase is a heme *d*. It is assumed that heme *d* increases the stability of Cpd I in LSC [46]. A serine residue located near the heme site at position 388 has an alternate conformation (Fig. 2b) that was only observed in one crystal structure of CAT-3 crystallized under the same conditions (PDB entry 3ZJ5 at 2.1 Å resolution), but not in any other LSC or SSC structure determined so far. Among the LSC with a known structure, the residue Ser 388 is conserved; in those with heme *d*, the hydroxyl group interacts with the C6 hydroxyl of the heme *d* at ring III.

INFORME DE LABORES 2019

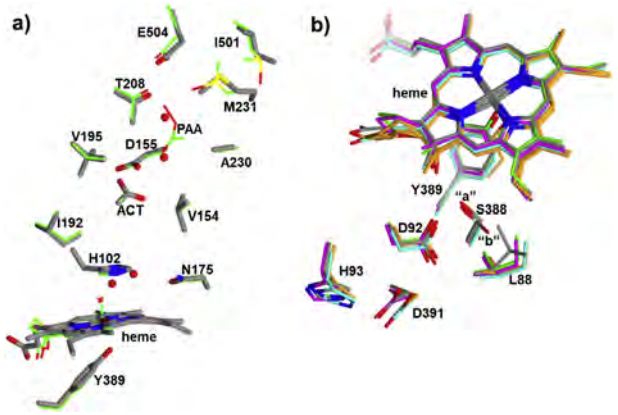

Fig. 2. CAT-3 soaked with PAA in comparison with other LSC. a) Superposition of CAT-3 soaked in PAA (PDB entry 4AJ9) with PVC Cpd I (PDB entry 2IUF) b) Ser 388 and residues forming a hydrogen bond network until the central channel. Conformation "a" is observed in other structures of LSC and in those with heme *d* is hydrogen bonded to the hydroxyl group of heme, alternative conformation "b" is present only in CAT-3 which has Leu 88 instead of isoleucine. Leu 88, D92 and H93 belong to the P-related subunit. In both panels oxygen atoms are presented in red, nitrogen in blue and the carbon atoms are shown in gray for CAT-3 and green for PVC. In panel b), the carbon atoms are shown in cyan for *Scytalidum thermophilum* CATPO, orange for *N. crassa* CAT-1 and magenta for *E. coli* HPII. The water molecules in panel a) are represented as red spheres for CAT-3. Figures were drawn using CCP4MG [43]. (For interpretation of the references to colour in this figure legend, the reader is referred to the Web version of this article.)

The alternate conformation of Ser 388 is not found in any of those structures probably due a steric hindrance with the sidechain of a conserved leucine from the monomer related in P found in all other LSC and substituted by the Val 88 in CAT-3. It has also been proposed that in the catalase HPII from *E. coli*, this residue participates in the oxidation of heme *b* to heme *d* in the first cycles of catalysis of hydrogen peroxide [46]. Both conformations of Ser 388 are hydrogen bonded to Asp 92 of the P-related subunit. These residues together with Asp 391 and His 91 from P-related subunit form a hydrogen bond network that connects to the central channel present in every tetrameric catalase described to date.

3.3. Composite datasets and UV-visible spectroscopy of Cpd I and its reduction by X-rays

Through the Multi-Crystal Data collection Strategy [24] and processing of composite datasets, a series of crystal structures with increasing absorbed dose were determined. Data collection and refinement statistics are presented in Table 1. Additionally, in an independent experiment the UV-visible spectra of a CAT-3 crystal soaked in PAA were recorded before the X-ray exposure and at different cumulative dose of X-rays. The first spectrum at 0 MGy (Fig. 3) shows the characteristic peaks for the ferric state, but also for the Cpd I, as was described in the previous section for solutions. Peaks at 498, 532, 565, 615 and 665 nm were observed; the Soret's band is found at 402 nm but the ratio 280/402 nm is ~1 instead of ~2 as occurred in solution. A small shoulder at 344 nm is also present, as was described for ANC. Except for the peak at 565 nm, all other observed peaks correlate with those previously reported in ferric or Cpd I intermediates of heme *b* catalases [15,45]. This absorbance spectrum suggests that there is a mixture of the Cpd I and the ferric resting state in the heme moiety at the beginning of the experiment; the mixed state could be explained by partial reaction of the active sites with PAA during soaking experiments.

The structure with the lowest dose (0.135 MGy) was solved using the frames comprising the first 5° of each collected crystal. A polder omit map of the heme moiety and the neighbouring region was obtained. The polder omit map shows continual electron density surrounding the heme prosthetic group and the bonded oxygen modeled in the final structure for each one of the four monomers (Fig. 4). The Fe = O bond lengths are 1.74 Å, 1.77 Å, 1.76 Å and 1.77 Å for monomer A, B, C and D respectively, correlating with those observed for Cpd I of LSC and SSC (reviewed in Alfonso-Prieto et al. [33]). Occupancies for the oxygen atoms are 0.66, 0.71, 0.60 and 0.57 for monomers A, B, C and D respectively. The water molecule W1 is present in all monomers at a distance between 1.9 Å and 2.7 Å from the bonded oxygen and forms hydrogen bonds with the atom N2 of His 102 and the nitrogen atom from the heme pyrrolic ring III.

The changes in spectra from 0 MGy to 0.127 MGy are shown in Fig. 3; both peaks at 615 nm and 665 nm decrease in a dose dependent manner, however there is also an increment in the absorbance of the small peak at 565 nm and the appearance of a new peak at 594 nm. The Soret's band stretches with increasing dose and its maximum is displaced from 402 nm to 407 nm. All spectra at this dose range describe mixtures of oxidation states which could explain why the Soret's band is wider than in the spectra recorded in solution for the Cpd I or the ferric state. The decrease in the charge-transfer band at 615 nm (from 0.550 AU to 0.480 AU) and at 665 nm (from 0.242 AU to 0.155 AU) was unexpected and unexplained because the reduction of Cpd I at (665 nm) should cause a gradual increase in the absorbance of the ferric resting state (615 nm) after the reduction by two electrons of Cpd I.

The second composite structure was determined by processing the first 10° of each data collection, accumulating a total dose of 0.263 MGy. The polder omit difference maps shows that the continual electron density corresponding to the Fe = O bond of Cpd I of the monomers A and B have disappeared. For both C and D monomers, the continual electron density that belong to the Fe = O bond of Cpd I is still present. The occupancies of the oxygen atoms are 0.61 and 0.62 respectively and the bond lengths are 1.85 Å and 1.82 Å. The increase in the length of bonds can be correlated to the formation of a Fe-OH intermediate as has been shown for catalases through different X-ray crystal structures [16,34] and QM/MM calculations [33,47]. The measured distances and the continual electron density of the 5° and 10° structures confirm the presence of the iron-oxygen bond, but are not enough to distinguish between the Fe = O and the Fe-OH intermediates. The spectrum with the dose closest to that of the 10° structure was acquired at 0.176 MGy. In this spectrum the peak at 665 nm has decreased from 0.242 AU to 0.137 AU which accounts to 50% of its initial absorbance. The peak at 615 nm decreased from 0.550 AU to 0.465 AU, 84.5% from the initial absorbance. At 0.36 MGy, which is the next spectrum with an absorbed dose closer to that of the three-dimensional structure of 10°, the ferric charge-transfer band at 615 nm decreased to 0.43 UA and the Cpd I charge-transfer band at 665 nm decreased to 0.095 UA.

The structure obtained with the data of the 20° section of the collected data has 0.526 MGy of accumulated dose. The F_o-F_c polder omit maps of the active sites show, instead of the continuity in the electron density for the Fe = O bond, a second peak separated from the heme position for all the monomers in the enzyme (Fig. 4), those maps confirmed the reduction of Cpd I in the whole structure. The position of the separated peak supports the presence of both molecules W0 and W1 that correlates with the resting ferric state in catalases [48], peroxidases [24] and myoglobin [26,48].

The structures for 50° and 110° (1.31 MGy and 2.89 MGy respectively) did not show changes in the active sites of the four monomers. In all structures the F_o-F_c polder omit map show two separated peaks as was observed in the 20° structure and in the structures deposited in PDB for the resting enzyme (entries 3EJ6 and 3ZJ5). The UV-visible spectra of the Cpd I crystal at doses of 0.71, 1.07 and 1.27 MGy did not followed the same trend that previous spectra, the absorbance of the charge-transfer band at 615 nm and at 665 nm stopped decreasing in the spectrum at 0.71 MGy at values of 0.413 UA and 0.077 UA

INFORME DE LABORES 2019

Table 1
Data Collection and refinement statistics of crystal structures.

	CAT-3-PAA	5° (0.135 MGy)	10° (0.263 MGy)	20° (0.526 MGy)	50° (1.31 MGy)	110° (2.89 MGy)
PDB entry	4AJ9	6NSW	6NSY	6NSZ	6NT0	6NT1
Resolution range	29.70–1.85 (1.91–1.85)	29.60–2.10 (2.15–2.10)	29.60–2.20 (2.26–2.20)	29.60–2.20 (2.26–2.20)	29.65–2.20 (2.26–2.20)	29.65–2.20 (2.26–2.20)
Space group	P 2_1 2_1 2_1	P 2_1 2_1 2_1	P 2_1 2_1 2_1	P 2_1 2_1 2_1	P 2_1 2_1 2_1	P 2_1 2_1 2_1
a, *b*, *c* (Å)	130.7, 154.1, 160.3	131.1, 154.4, 160.9	131.1, 154.5, 160.9	131.1, 154.5, 160.9	131.1, 154.5, 160.9	131.1, 154.5, 160.9
α, β, γ (°)	90, 90, 90	90, 90, 90	90, 90, 90	90, 90, 90	90, 90, 90	90, 90, 90,
Unique reflections	268553 (24084)	153203 (11159)	158332 (11654)	160372 (11717)	149236 (14510)	159994 (11710))
Multiplicity	3.6(2.6)	2.02 (1.92)	3.35 (3.31)	3.27 (3.29)	3.07 (3.14)	3.15 (3.19)
Completeness (%)	97.77 (84.80)	80.52 (79.94)	95.61 (95.88)	96.83 (96.36)	90.11 (88.34)	96.60 (96.24)
Mean I/sigma(I)	15.9 (4.3)	4.39 (2.03)	6.77 (3.41)	7.12 (3.46)	7.36 (3.79)	6.80 (3.21)
Wilson B-factor	10.10	16.55	14.21	15.08	13.42	14.92
R_{merge} (%)	8.90 (34.10)	15.70 (37.30)	14.50 (35.20)	14.00 (37.10)	13.00 (32.20)	14.90 (37.20)
R-meas (%)	11.30 (44.50)	19.80 (48.00)	17.10 (41.50)	16.60 (47.10)	15.40 (37.90)	17.70 (44.10)
$CC_{1/2}$ (%)	99.30 (81.20)	96.4 (73.90)	97.90 (81.20)	98.00 (79.70)	98.30 (85.90)	97.90 (80.60)
R_{work} (%)	17.75 (24.94)	17.00 (22.14)	15.40 (19.38)	15.67 (20.93)	15.14 (19.35)	15.01 (19.39)
R_{free} (%)	21.76 (29.49)	21.95 (28.45)	20.22 (25.64)	20.41 (27.19)	19.99 (25.37)	19.84 (26.32)
Number of atoms	24066	23892	23879	23972	23902	23938
protein	21614	21575	21552	21599	21576	21564
Heme	172	172	172	172	172	172
Oxigen	0	4	2	0	0	0
Acetate	32	32	32	32	32	32
PEG	144	142	155	155	160	161
solvent	2116	1967	1966	2014	1962	2009
Protein residues	2720	2719	2720	2720	2720	2720
RMSD bond lengths (Å)	0.007	0.003	0.004	0.003	0.004	0.007
RMSD bond angles (°)	1.07	0.64	0.74	0.57	0.68	0.86
Ramachandran favored (%)	96.94	96.82	96.90	96.90	96.94	97.05
Ramachandran allowed (%)	3.06	3.18	3.10	3.10	3.06	2.95
Average *B*-values (Å^2)	11.00	18.39	15.93	16.68	14.86	16.87
protein	12.00	17.59	17.64	18.22	16.29	16.97
Heme	3.90	10.70	8.05	8.40	7.13	8.35
Oxigen	–	11.96	9.02	–	–	–
Acetate	11.60	18.34	16.5	18.93	15.29	17.1
PEG	27.80	25.94	28.63	28.99	26.72	26.00
solvent	15.53	21.07	18.57	20.2	18.14	21.18

The values for the highest resolution shell are given within parenthesis.

respectively. The last collected spectra had accumulated a dose of 1.27 MGy which is approximately the dose of the 50° crystal structure. Additionally, while the peak at 565 nm still increased in the last three spectra, the peak at 594 nm reached its maximum with a value of 0.692 AU at 0.36 MGy, after this dose, the peak decrease gradually in the last three spectra. In summary, from 0 MGy to 1.27 MGy the peaks at 615 nm and 665 nm decrease its height as the absorbed dose increase, and those at 565 nm and 594 nm increased. The spectra reported for the Cpd II in ANC [15], has two peaks at 539 nm and 570 nm respectively. In our spectra, the peak at 565 nm is in a zone near to 570 nm but the absence of the 539 nm peak cannot allow confirming the formation of Cpd II. The peak at 594 nm is not present in the UV-visible spectra of the catalytic intermediates of any catalase; this peak does not correlate with Cpd I, Cpd II or ferric states. In LSC there are no evidences for the production of the ferrous state in the heme moiety, however in SSC the ferrous state has been obtained by chemical reduction in the BLC, the UV-visible spectra of the intermediate presented peaks at 567 nm and 600 nm [49] or 561 nm and 595 nm [50]. At the beginning of X-ray data collection there were mixed states for the CAT-3 crystal and there are not enough evidences that correlate the increase in the peak at 594 nm to the formation of Cpd II, nevertheless the reduction of the pure ferric state could contribute to clarify the identity of both peaks at 565 nm and 594 nm.

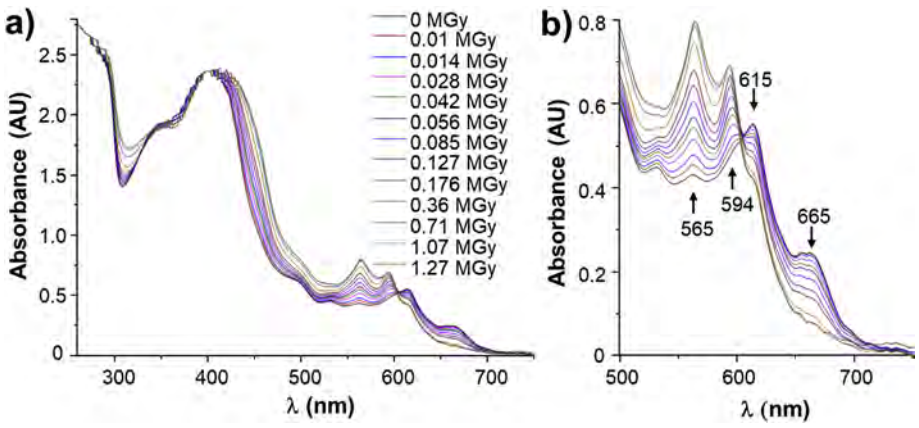

Fig. 3. UV visible spectra of the X-ray reduction of Cpd I CAT-3. a) Spectra of a single crystal treated with PAA. Soret's band and peaks related to Cpd I (665 nm) and ferric state (502 nm, 535 nm and 615 nm) are present before X-ray exposure (0 MGy) at increasing dose peaks at 565 and 594 nm are present. b) Zoom at the 500 nm-700 nm visible spectra.

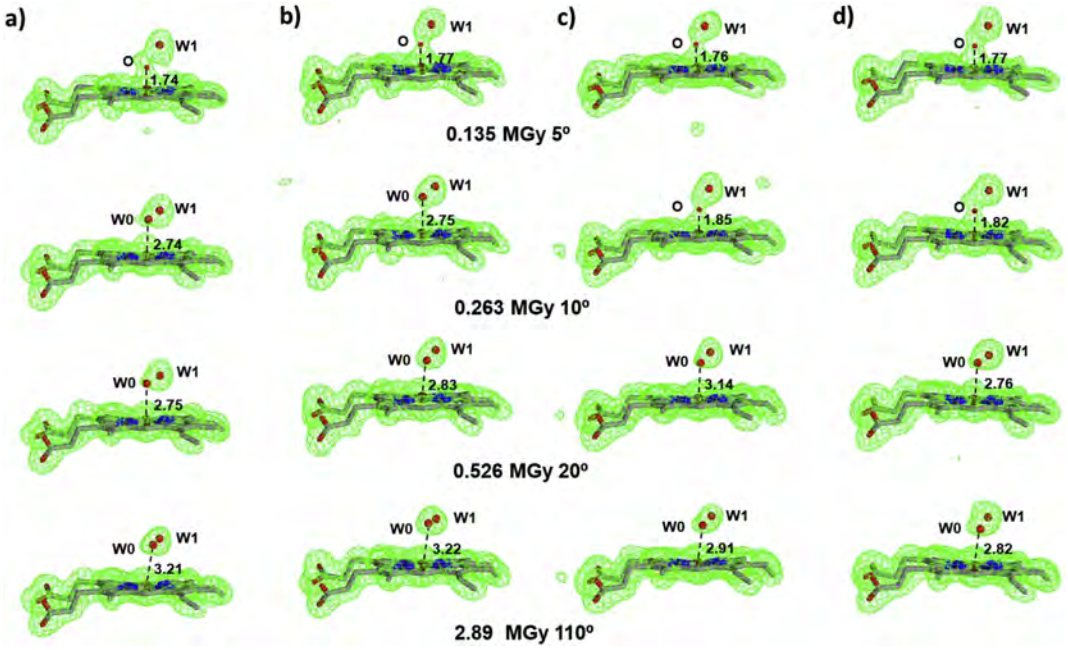

Fig. 4. Structural changes in the reduced intermediates. a) to d); Polder omit maps of CAT-3 of the active sites of monomers A to D respectively, for crystal structures determined at the given dose. O (oxygen atom), W0 (water molecule in the sixth coordination site), W1 (water molecule hydrogen bonded to His 102 and Asn 175). Polder omit map contoured at 4σ, figure drawn with CCP4MG [43].

3.4. X-ray driven reduction of the CAT-3 in the resting ferric state

One crystal of CAT-3 was exposed to X-rays in similar conditions to the used for structural determination. UV-visible spectra of the unexposed and of the irradiated crystal at different absorbed doses were acquired. The initial spectrum, at 0 MGy shows the same peaks that were observed in the CAT-3 solution for the ferric state (Fig. 5), the Soret's band appeared at 400 nm instead of 406 nm, the 280/400 ratio is 1. The peak at 500 nm is present, but the peak expected at 535 nm is displaced at 537 nm in the crystal. The charge-transfer band of the ferric state is observed at 620 nm as in solution. After X-ray exposure at a final dose 1.63 MGy, the peak at 620 nm decreased from 0.368 AU, at 0 MGy, to 0.214 AU, but there was a proportional increase in a peak at 565 nm from 0.220 AU to 0.475 AU, similar to the behaviour in the crystal of Cpd I when was reduced. There was also a small shoulder at 599 nm. In the course of X-ray exposure, the Soret's band was displaced from 400 nm to 406 nm; and a shoulder in 446 nm appeared and increased in a dose dependent manner. At the end of the exposure, the absorbance intensity in the peak at 500 nm decreased from 0.394 AU to 0.342 UA and the peak at 537 nm can be observed as a small shoulder of the peak at 565 nm. The presence of both peaks at 565 nm and 594–599 nm in the X-ray driven reduction of the Cpd I and the resting enzyme confirms the reduction to the ferrous state.

4. Discussion

4.1. Differential reduction in CAT-3 monomers

In both monomers of the crystallographic structure of PVC in the Cpd I state (PDB entry 2IUF at 1.71 Å resolution) [33] the Fe = O bond is clearly defined by the electron density map and the occupancies of the bonded oxygen have a value of 1. In this structure the dose accumulated during data collection was not reported, but in the PDB report for the entry is annotated that it was collected at a rotating anode X-ray source, so it is highly probable that the deposited dose radiation was lower in comparison to crystals collected at a synchrotron beamline, where the flux is generally $\sim 10^3$ times higher. The presence of the unreduced Cpd I in both monomers of the dimer present in the asymmetric unit of the PVC structure is probably due to the lower dose. The sensitivity of metal atoms to X-ray driven reduction in the active sites have been discussed

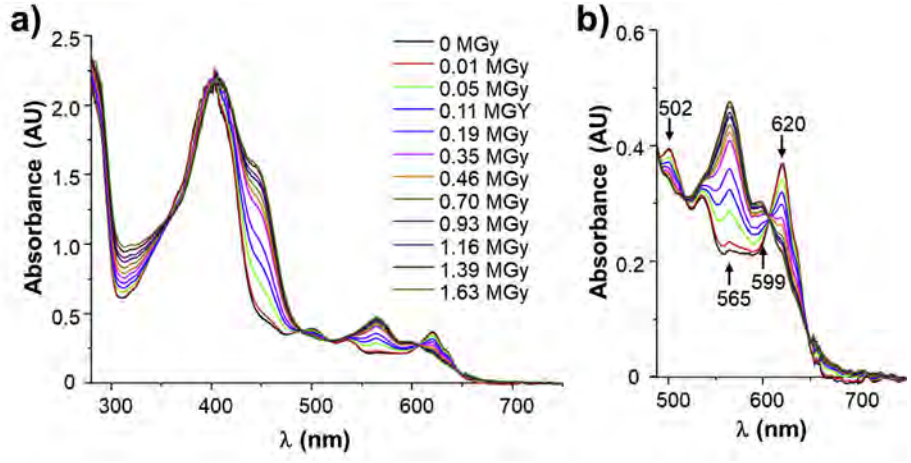

Fig. 5. UV visible spectra of the X-ray reduction of ferric CAT-3. a) Spectra of a single crystal of CAT-3 in the ferric state. Soret's band and peaks related to ferric state (502 nm, 535 nm and 620 nm) are present before X-ray exposure (0 MGy) at increasing dose, a shoulder in the Soret's band at 446 nm, one peak at 565 nm and a shoulder at 599 nm are present. b) Zoom at the 500 nm-700 nm visible spectra.

INFORME DE LABORES 2019

in several research works [23,51,52]. The oxidation state, coordination or even atom occupancy are the parameters affected. Nevertheless, it is not a requirement to report the dose deposited in a crystal when a structure is determined and deposited in the PDB.

There are only a few reports for crystallographic experiments in which the structure of an intermediate of a metalloenzyme is associated to an absorbed dose [23,24,26]. In those, the changes occurred at different rates, but in the most sensitives it is impossible to collect the complete data without affecting the original information, e.g. in horse myoglobin after a crystal accumulated 0.010 MGy the protein is reduced in 10% in comparison to the original oxidation state of the crystal. Furthermore, the use of radioprotectants as ascorbate has minimal effects in protecting the reduced intermediates [26].

In this work, the oxygen bonded to the iron heme in the Cpd I of CAT-3 presents partial occupancies for all monomers in the structure at 0.135 MGy, although at 0.263 MGy the oxygen is bonded to the iron only in monomers C and D with very similar occupancies to that observed in the previous structure, these monomers are related in R and apparently there are not structural relationships that makes the oxidation state to be dependent from each other. The results for UV-visible microspectrometry in the crystal at 0 MGy suggest that there is a partial occupancy since the beginning of the data collection. At this point, the resistance to reduction that has been observed for both C and D monomers, in comparison with the two other monomers cannot be attributed to a higher transformation of them during soaking in PAA, because the occupancy values in the 5° structure were very similar to those at 10°, however only monomers A and B were reduced.

Differential reduction states have been observed in some other enzymes, e.g. the ribonucleotide reductase (R2F) from *Corynebacterium ammoniagenes* [27]. This enzyme is also a homotetramer with two iron atoms in each of the active sites. Authors showed that the sites which were more sensitive to X-ray driven reduction correlated to those with more accessibility to iron during soaking of the apoenzyme in a solution with Fe^{2+} ions, proposing the dependence of a diffusion component during the X-ray reduction process. At temperatures below 110 K solvated electrons are the only species which can diffuse [53,54], the electron are able to migrate through the solvent to the metallic center, as in this case the iron heme. In the CAT-3 structures analyzed in this work (which were crystallized in the space group $P2_12_12_1$) each one of the four monomers has a different surface of contact with the copies of the molecules that forms the crystal. In monomer D the surface contact is 493 $Å^2$, for A is 406.5 $Å^2$, for B is 741 $Å^2$, and for C is 898 $Å^2$. The access to active sites from the surface through the main tunnel is not blocked in any monomer, and the intermolecular contacts do not affect the flux through it, also there is a continual water network which confirms that the tunnels to active site are accessible. If CAT-3 would have the same behaviour that R2F, it would be expected that the oxygen atom in Cpd I of monomers A and D would have a similar occupancy values or the same reduction rate at a given dose. However, as is shown in the structures presented in this work, the reduction of Cpd I occurred before in the A and B monomers. There is not a correlation, at least in our experiments, between the initial occupancy of the Cpd I or the sensitivity to reduction, and the solvent accessibility.

The migration of solvated electrons depends on the accessibility of a water network to the neighbouring of the metallic centers or to residues involved in coordination that allow electron transference through the backbone. As there are only subtle differences between the monomers in the access tunnel (Fig. S1), it is not possible to identify specific structural determinants that control the reactivity of the each monomer. It is possible that this differential sensitivity is tuned by some other specific feature of LSC. LSCs from *N. crassa* (CAT-1 and CAT-3) show cooperativity in kinetic studies, their saturation kinetics fit to a double Hill equation [13]. Molecular dynamic studies of CAT-1 has shown that an “interconnecting channel”, also present in CAT-3, can communicates the P-related subunits in the CAT-3 tetramer, allowing the transportation of substrate molecules between subunits [55]. The interconnecting channel could explain the cooperativity observed in the LSCs kinetic, this hypothesis has not been proven experimentally.

The two subunits that remain oxidized as Cpd I in the 5° structure (C and D) are the R-related subunits; there is no tunnel for solvent communication between the active sites of those subunits but, as previously mentioned, Ser 388 (Fig. 2b) is part of a hydrogen bond network that is connected to the water molecules of the main central channel. This network is communicated to the R-related subunit through the Asp 391, forming a hydrogen bond with a water molecule; this molecule has the same interaction with Asp 391 of the R-related subunit (Fig. S2), being the R-related dimers A-B or C-D. We hypothesize that after the reduction of Cpd I, by means of a proton coupled-electron transfer process, the electrons from one active site can be transferred to Ser 388 and travel through the hydrogen bond network to the R-related metal center. It has been well characterized that proteins are able to transport charge in a controlled way using the protein matrix (backbone, side-chains or hydrogen bonds with solvent) thus defining electron transfer pathways that connect along different protein regions. The role of those pathways has been demonstrated for several proteins by computational and experimental approaches [56,57].

The monomer A is the subunit with lower crystal contacts and may possibly be the more prone to be reduced, and then transfer the exceeding electrons to the heme moiety of B through this electron transfer pathway. This hypothesis could be tested by obtaining of mutants that disrupt the hydrogen bond network. Also it would be interesting to perform an experiment of X-ray driven reduction of CAT-3 in any of the other space groups in which the enzyme has been crystallized [35], in order to analyze if the crystal contacts determine the first R-related dimer which is reduced by X-rays.

4.2. Differences in ferrous state structures

In the structure of CAT-3 in ferric state at 1.95 Å resolution (PDB entry 3ZJ5) [35], there are differences in the position of water molecules of the active site. The monomer B is the only one with 2 water molecules in positions W0 and W1. Every one of the other monomers possesses only one water molecule in position W1 but lack the water in position W0. In the HRP the absence of the water in position W0 has been correlated with the ferrous state [24], on the other hand, for horse Mb has been described an aquo ferrous state, in which there is a water molecule in the sixth coordination site (W0 position) obtained also by X-ray reduction [26].

The identification of the ferrous state in this work establish that CAT-3, and likely all LSC can be found in 4 different oxidation states (Fe^{II} to Fe^{IV+}). The catalysis mediated by CAT-3 occurs in the Fe^{III} and the Fe^{IV+}, an active site of CAT-3 can receive 3 electrons when is in the Fe^{IV+} state. The ferrous state occurs naturally in cytochrome p450, and Mb, but in SSC catalases has been only obtained artificially, chemically with NO [58] or CO [59] as a ligand, or by photoreduction of BLC in a deoxyferrous state [49,50], this photoreduced intermediate was not stable. The mechanisms that allow the catalase to recover the ferric state have not been established. As our experiments were performed at 100 K, it is not possible to make assumptions about its stability at room temperature. It has been reported that in X-ray driven reduction of horse Mb after annealing of reduced crystals, most of the properties in UV-visible and Raman spectra of Mb in the ferric state (MetMb) were recovered [26]. When the CAT-3 crystals of this work were annealed after X-ray exposure, those break immediately after gas release, making impossible the further UV-visible analysis of the crystal (Data not shown). It has been demonstrated that molecular hydrogen (H_2) is the main produced gas in irradiated ethylene glycol samples [60], is important to consider that the precipitant agent in CAT-3 crystals and also the cryoprotectant are PEGs molecules with different lengths (PEG 3350 from the mother liquor and PEG 400 from the cryoprotectant), glycerol was also assayed as cryoprotectant but the crystals lost resolution. On the other hand, water radiolysis produces H_2O_2 [21]. When the crystal

INFORME DE LABORES 2019

was annealed, if there was H_2O_2 present, the enzyme could catalyze the production of O_2 immediately. As annealing procedures for the crystal presented here are destructive, the stability of the ferrous state could be evaluated by performing the UV-visible spectrometric analysis on irradiated samples of CAT-3 in solution.

The UV-visible spectra obtained in the X-ray reduced CAT-3 presented in this work are very similar to that of the deoxyferrous BLC. In the structure of BLC in the ferric state (PDB entry 4BLC at 2.3 Å) the iron heme is pentacoordinated and there are no water molecules in the vicinity of heme moiety, for the ferrous state there is not an associated structure. In the structures of CAT-3 presented here, for those of the reduced Cpd I there is a water W0 at 2.9 Å from the iron heme in the partially reduced structure (monomers A and B of 10° structure) or at 3.3 Å when is fully reduced (110° structure). The structure 3ZJ5 can be associated to the ferrous spectra of X-ray reduced enzyme obtained from the ferric crystals, in this structure, the W0 water molecule is at 3.05 Å of the iron heme in one monomer, while in the three other monomers only the water molecule W1 is present at 4.5 Å.

The behaviour of the peak at 565 nm in both Cpd I and ferric crystals spectra suggest that the reduced intermediates have common features. The reduction of Cpd I to the ferrous state apparently occurs very fast, then both Cpd II and ferric are immediately reduced. As shown in Fig. 4, there are not spectroscopic evidences of presence of Cpd II in the visible spectra. The differences in the absorbance of the peak at 594 nm or 599 nm could be interpreted as differences between the ferrous states obtained from the reduced Cpd-I and the obtained from the ferric, the structural evidence presented here point towards a role for the position of W0 for the high absorbance of the peak at 594–599 nm when is at 3.3 Å from the iron heme, this peak is observed as a shoulder when occupancy of W0 is low (as in the ferric reduced structure), also the presence of a shoulder at 446 nm that is observed in the reduced ferric crystal could be related to the lack of W0 in three of the four monomers. The breakage of heme bonds could also affect the UV-visible spectra of the enzyme, e.g. the peak at 594 nm, however in the analysis of the polder maps of the structures (Fig. 4), there are no changes in the electron density that can be related to alterations of heme structure. Nevertheless, in order to shed light on the role of water W0 in the UV-visible spectra of the ferrous state, the use of techniques which are non-dependant from crystal resolution as EXAFS or Raman spectroscopy would be of great utility.

5. Conclusions

The Cpd I of CAT-3 was totally reduced at a dose lower than 0.263 MGy, this is the dose needed to collect 2/9 of a complete orthorhombic crystallographic dataset, as was supported by X-ray crystallography and UV-visible spectrometry. Reduction of this tetrameric enzyme did not occur simultaneously in the four monomers, but independently. Half of the sites seem to be more sensitive to chemical reduction, which we hypothesized could be due to electron transference between R-related subunits. The ferrous state in heme *b* LSC can be obtained by X-ray reduction, and considering the doses measured here for reduction of ferric catalase, it is probable that several deposited crystal structures, in the PDB, describing a ferric state belong actually to the ferrous state of the enzyme.

Acknowledgment

This work was financed by Consejo Nacional de Ciencia y Tecnología (CONACyT) through project 102370 and by Universidad Nacional Autónoma de México through PAPIIT IN204611. Authors thank the staff at NSLS beamline X6A for data-collection facilities. Beamline X6A is funded by NIGMS (GM-0080) and the U.S. Department of Energy (No. DE-AC02-98CH10886). Authors thank also the staff at SSRL beamline BL11-1 for data collection facilities. Use of the Stanford Synchrotron Radiation Lightsource, SLAC National Accelerator Laboratory, is supported by the U.S. Department of Energy, Office of Science, Office of Basic Energy Sciences under Contract No. DE-AC02-76SF00515. The SSRL Structural Molecular Biology Program is supported by the DOE Office of Biological and Environmental Research, and by the National Institutes of Health, National Institute of General Medical Sciences (including P41GM103393). The contents of this publication are solely the responsibility of the authors and do not necessarily represent the official views of NIGMS or NIH. AZR thank the program Cátedras from Consejo Nacional de Ciencia y Tecnología (CONACyT) for the project No. 27. The authors thank Sonia P. Rojas Trejo for technical assistance in the crystallization of the enzyme.

Appendix A. Supplementary data

Supplementary data to this article can be found online at https://doi.org/10.1016/j.abb.2019.03.020.

References

[1] J. Röcker, M. Schmitt, L. Pasch, K. Ebert, M. Grossmann, The use of glucose oxidase and catalase for the enzymatic reduction of the potential ethanol content in wine, Food Chem. 210 (2016) 660–670.
[2] J. Geciova, D. Bury, P. Jelen, Methods for disruption of microbial cells for potential use in the dairy industry - a review, Int. Dairy J. 12 (6) (2002) 541–553.
[3] J. Kaushal, S. Mehandia, G. Singh, A. Raina, S.K. Arya, Catalase enzyme: application in bioremediation and food industry, Biocatal. Agric. Biotechnol. 16 (April) (2018) 192–199.
[4] W.L. Boatright, Hydrogen peroxide generation from hydrated protein drink mixes, J. Food Sci. 78 (11) (2013).
[5] H.M. Abdel-Mageed, H.M. El-Laithy, L.G. Mahran, A.S. Fahmy, K. Mäder, S.A. Mohamed, Development of novel flexible sugar ester vesicles as carrier systems for the antioxidant enzyme catalase for wound healing applications, Process Biochem. 47 (7) (2012) 1155–1162.
[6] X. Shi, et al., PEGylated human catalase elicits potent therapeutic effects on H1N1 influenza-induced pneumonia in mice, Appl. Microbiol. Biotechnol. 97 (23) (2013) 10025–10033.
[7] H.M. Özcan, T. Aydin, A new PANI biosensor based on catalase for cyanide determination, Artif. Cells, Nanomed. Biotechnol. 44 (2) (2016) 664–671.
[8] E. Akyilmaz, G. Oyman, E. Cınar, G. Odabas, "A new poly-aniline–catalase–glutaraldehyde-modified biosensor for hydrogen peroxide detection, Prep. Biochem. Biotechnol. 47 (1) (2017) 86–93.
[9] B. Elsebai, M.E. Ghica, M.N. Abbas, C.M.A. Brett, Catalase based hydrogen peroxide biosensor for mercury determination by inhibition measurements, J. Hazard Mater. 340 (2017) 344–350.
[10] M.G. Klotz, P.C. Loewen, The molecular evolution of catalatic hydroperoxidases: evidence for multiple lateral transfer of genes between prokaryota and from bacteria into eukaryota, Mol. Biol. Evol. 20 (7) (2003) 1098–1112.
[11] M.G. Klotz, G.R. Klassen, P.C. Loewen, Phylogenetic relationships among prokaryotic and eukaryotic catalases, Mol. Biol. Evol. 14 (9) (Sep. 1997) 951–958.
[12] W. Hansberg, R. Salas-Lizana, L. Domínguez, Fungal catalases: function, phylogenetic origin and structure, Arch. Biochem. Biophys. 525 (2) (Sep. 2012) 170–180.
[13] A. Díaz, V.-J. Valdés, E. Rudiño-Piñera, E. Horjales, W. Hansberg, Structure-function relationships in fungal large-subunit catalases, J. Mol. Biol. 386 (1) (Feb. 2009) 218–232.
[14] P. Nicholls, I. Fita, P.C. Loewen, Enzymology and Structure of Catalases vol 51, Academic Press, 2000, pp. 51–106.
[15] O. Lardinois, P. Rouxhet, Characterization of hydrogen peroxide and superoxide degrading pathways of Aspergillus Niger catalase: a steady-state analysis, Free Radic. Res. 20 (I) (1994) 29–50.
[16] P. Andreoletti, A. Pernoud, G. Sainz, P. Gouet, H.M. Jouve, Structural studies of Proteus mirabilis catalase in its ground state, oxidized state and in complex with formic acid, Acta Crystallogr. Sect. D Biol. Crystallogr. 59 (12) (Nov. 2003) 2163–2168.
[17] O.M. Lardinois, Reactions of bovine liver catalase with superoxide radicals and hydrogen peroxide, Free Radic. Res. 22 (3) (Mar. 1995) 251–274.
[18] J.W. Murray, E. Rudiño-Piñera, R.L. Owen, M. Grininger, R.B.G. Ravelli, E.F. Garman, Parameters affecting the X-ray dose absorbed by macromolecular crystals, J. Synchrotron Radiat. 12 (Pt 3) (May 2005) 268–275.
[19] R. Henderson, Cryo-protection of protein crystals against radiation damage in electron and X-ray diffraction, Proc. R. Soc. 241 (1300) (1990) 6–8.
[20] R. Henderson, The potential and limitations of neutrons, electrons and X-rays for atomic resolution microscopy of unstained biological molecules, Q. Rev. Biophys. 28 (02) (1995) 171–193.
[21] A. Hiroki, S.M. Pimblott, J. a. LaVerne, Hydrogen peroxide production in the radiolysis of water with high radical scavenger concentrations, J. Phys. Chem. A 106 (40) (Oct. 2002) 9352–9358.
[22] M. Weik, et al., Specific chemical and structural damage to proteins produced by synchrotron radiation, Proc. Natl. Acad. Sci. U. S. A. 97 (2) (Jan. 2000) 623–628.
[23] H. Serrano-Posada, B. Valderrama, V. Stojanoff, E. Rudiño-Piñera, Thermostable multicopper oxidase from Thermus thermophilus HB27: crystallization and

INFORME DE LABORES 2019

preliminary X-ray diffraction analysis of apo and holo forms, Acta Crystallogr. Sect. F. Struct. Biol. Cryst. Commun. 67 (Pt 12) (Dec. 2011) 1595–1598.
[24] G.I. Berglund, G.H. Carlsson, A.T. Smith, H. Szöke, A. Henriksen, J. Hajdu, The catalytic pathway of horseradish peroxidase at high resolution, Nature 417 (6887) (May 2002) 463–468.
[25] C.M. Wilmot, T. Sjögren, G.H. Carlsson, G.I. Berglund, J. Hajdu, Defining redox state of X-ray crystal structures by single-crystal ultraviolet-visible microspectrophotometry, Methods Enzymol. 353 (2000) 301–18, Jan. 2002.
[26] H.-P. Hersleth, K.K. Andersson, How different oxidation states of crystalline myoglobin are influenced by X-rays, Biochim. Biophys. Acta 1814 (6) (Jun. 2011) 785–796.
[27] J.J. Griese, M. Högbom, X-ray reduction correlates with soaking accessibility as judged from four non-crystallographically related diiron sites, Metallomics 4 (9) (Aug. 2012) 894–898.
[28] J. Wuerges, J.-W. Lee, Y.-I. Yim, H.-S. Yim, S.-O. Kang, K. Djinovic Carugo, Crystal structure of nickel-containing superoxide dismutase reveals another type of active site, Proc. Natl. Acad. Sci. U. S. A. 101 (23) (Jun. 2004) 8569–8574.
[29] M. a Hough, S.S. Hasnain, Crystallographic structures of bovine copper-zinc superoxide dismutase reveal asymmetry in two subunits: functionally important three and five coordinate copper sites captured in the same crystal, J. Mol. Biol. 287 (3) (Apr. 1999) 579–592.
[30] A. Díaz, E. Horjales, E. Rudiño-Piñera, R. Arreola, W. Hansberg, Unusual Cys-Tyr covalent bond in a large catalase, J. Mol. Biol. 342 (3) (Sep. 2004) 971–985.
[31] W. Melik-Adamyan, et al., Substrate flow in catalases deduced from the crystal structures of active site variants of HPII from Escherichia coli, Proteins 44 (3) (Aug. 2001) 270–281.
[32] Y. Yuzugullu, et al., Structure, recombinant expression and mutagenesis studies of the catalase with oxidase activity from Scytalidium thermophilum, Acta Crystallogr. D. Biol. Crystallogr. 69 (Pt 3) (Mar. 2013) 398–408.
[33] M. Alfonso-Prieto, et al., The structures and electronic configuration of compound I intermediates of Helicobacter pylori and Penicillium vitale catalases determined by X-ray crystallography and QM/MM density functional theory calculations, J. Am. Chem. Soc. 129 (14) (Apr. 2007) 4193–4205.
[34] G.N. Murshudov, et al., The structures of Micrococcus lysodeikticus catalase, its ferryl intermediate (compound II) and NADPH complex, Acta Crystallogr. Sect. D Biol. Crystallogr. 58 (12) (Nov. 2002) 1972–1982.
[35] A. Zárate-Romero, V. Stojanoff, S.P. Rojas-Trejo, W. Hansberg, E. Rudiño-Piñera, Conformational stability and crystal packing: polymorphism in Neurospora crassa CAT-3, Acta Crystallogr. Sect. F Struct. Biol. Cryst. Commun. 69 (7) (2013) 753–758.
[36] N.E. Chayen, Comparative studies of protein crystallization by vapour-diffusion and microbatch techniques, Acta Crystallogr. Sect. D Biol. Crystallogr. 54 (1) (Jan. 1998) 8–15.
[37] W. Kabsch, Integration, scaling, space-group assignment and post-refinement, Acta Crystallogr. D. Biol. Crystallogr. 66 (Pt 2) (Feb. 2010) 133–144.
[38] A.J. McCoy, R.W. Grosse-Kunstleve, P.D. Adams, M.D. Winn, L.C. Storoni, R.J. Read, Phaser crystallographic software, J. Appl. Crystallogr. 40 (Pt 4) (Aug. 2007) 658–674.
[39] G.N. Murshudov, et al., REFMAC5 for the refinement of macromolecular crystal structures, Acta Crystallogr. Sect. D Biol. Crystallogr. 67 (4) (2011) 355–367.
[40] P. V Afonine, et al., Towards automated crystallographic structure refinement with phenix.refine, Acta Crystallogr. D. Biol. Crystallogr. 68 (Pt 4) (Apr. 2012) 352–367.
[41] P. Emsley, B. Lohkamp, W.G. Scott, K. Cowtan, Features and development of Coot, Acta Crystallogr. D. Biol. Crystallogr. 66 (Pt 4) (Apr. 2010) 486–501.
[42] D. Liebschner, et al., Polder maps: improving OMIT maps by excluding bulk solvent, Acta Crystallogr. Sect. D 73 (2) (Feb. 2017) 148–157.
[43] S. McNicholas, E. Potterton, K.S. Wilson, M.E.M. Noble, Presenting your structures: the CCP4mg molecular-graphics software, Acta Crystallogr. Sect. D Biol. Crystallogr. 67 (4) (2011) 386–394.
[44] P. Gouet, et al., Ferryl intermediates of catalase captured by time resolved Weissenberg crystallography and UV-vis spectroscopy, Nat. Struct. Biol. 3 (11) (1996) 951–956.
[45] D.C. Deluca, R. Dennis, W.G. Smith, Inactivation of an animal and a fungal catalase by hydrogen peroxide, Arch. Biochem. Biophys. 320 (1) (Jun. 1995) 129–134.
[46] C. Obinger, M. Maj, P. Nicholls, P. Loewen, Activity, peroxide compound formation, and heme d synthesis in Escherichia coli HPII catalase, Arch. Biochem. Biophys. 342 (1) (Jun. 1997) 58–67.
[47] M. Alfonso-Prieto, P. Vidossich, C. Rovira, The reaction mechanisms of heme catalases: an atomistic view by ab initio molecular dynamics, Arch. Biochem. Biophys. 525 (2) (Sep. 2012) 121–130.
[48] H.-P. Hersleth, U. Ryde, P. Rydberg, C.H. Görbitz, K.K. Andersson, Structures of the high-valent metal-ion haem-oxygen intermediates in peroxidases, oxygenases and catalases, J. Inorg. Biochem. 100 (4) (Apr. 2006) 460–476.
[49] N. Shimizu, K. Kobayashi, K. Hayashi, Studies on the equilibria and kinetics of the reactions of ferrous catalase with ligands, J. Biochem. 140 (1988) 136–140.
[50] D.M.I. Bandara, M. Sono, G.S. Bruce, A.R. Brash, J.H. Dawson, Coordination modes of tyrosinate-ligated catalase-type heme enzymes: magnetic circular dichroism studies of Plexaura homomalla allene oxide synthase, Mycobacterium avium ssp. paratuberculosis protein-2744c, and bovine liver catalase in their ferric and fe, J. Inorg. Biochem. 105 (12) (Dec. 2011) 1786–1794.
[51] E. De la Mora, J.E. Lovett, C.F. Blanford, E.F. Garman, B. Valderrama, E. Rudino-Pinera, Structural changes caused by radiation-induced reduction and radiolysis: the effect of X-ray absorbed dose in a fungal multicopper oxidase, Acta Crystallogr. D. Biol. Crystallogr. 68 (Pt 5) (May 2012) 564–577.
[52] S. V Antonyuk, M. a Hough, Monitoring and validating active site redox states in protein crystals, Biochim. Biophys. Acta 1814 (6) (Jun. 2011) 778–784.
[53] R.L. Owen, E. Rudiño-Piñera, E.F. Garman, Experimental determination of the radiation dose limit for cryocooled protein crystals, Proc. Natl. Acad. Sci. U. S. A. 103 (13) (Mar. 2006) 4912–4917.
[54] R.J. Southworth-Davies, E.F. Garman, Radioprotectant screening for cryocrystallography, J. Synchrotron Radiat. 14 (Pt 1) (Jan. 2007) 73–83.
[55] L. Domínguez, A. Sosa-Peinado, W. Hansberg, Catalase evolved to concentrate H2O2 at its active site, Arch. Biochem. Biophys. 500 (1) (Aug. 2010) 82–91.
[56] A. Vidal-Limón, S. Águila, M. Ayala, C.V. Batista, R. Vazquez-Duhalt, Peroxidase activity stabilization of cytochrome P450BM3 by rational analysis of intramolecular electron transfer, J. Inorg. Biochem. 122 (2013) 18–26.
[57] J.R. Winkler, H.B. Gray, Electron flow through biological molecules: does hole hopping protect proteins from oxidative damage? Q. Rev. Biophys. 48 (04) (2015) 411–420.
[58] O.M. Lardinois, M.M. Mestdagh, P.G. Rouxhet, Reversible inhibition and irreversible inactivation of catalase in presence of hydrogen peroxide, Biochim. Biophys. Acta Protein Struct. Mol. Enzymol. 1295 (2) (Jul. 1996) 222–238.
[59] J.R. Kincaid, Resonance Raman Studies of the Carbonmonoxy Form of Catalase Evidence for and Effects of Phenolate Ligation vol. 3, (1992), pp. 293–296.
[60] A. Meents, S. Gutmann, A. Wagner, C. Schulze-Briese, Origin and temperature dependence of radiation damage in biological samples at cryogenic temperatures, Proc. Natl. Acad. Sci. U. S. A. 107 (3) (Jan. 2010) 1094–1099.

Journal of Helminthology

cambridge.org/jhl

Hippocampal sclerosis induced in mice by a *Taenia crassiceps* metacestode factor

N. Zepeda[1], N. Copitin[1], J.L. Chávez[2], F. García[3], F. Jaimes-Miranda[3], R. Rincón-Heredia[3], R. Paredes[3], S. Solano[4], A.M. Fernández[4] and J.L. Molinari[1]

[1]Departamento de Bioquímica y Biología Estructural, Instituto de Fisiología Celular, Universidad Nacional Autónoma de México, Ciudad de México, C.P. 04510 A.P. 70-242; [2]Departamento de Neurociencia Cognitiva, Instituto de Fisiología Celular, Universidad Nacional Autónoma de México, Ciudad de México, C.P. 04510 A.P. 70-242; [3]Unidad de Imagenología, Instituto de Fisiología Celular, Universidad Nacional Autónoma de México, Ciudad de México, C.P. 04510 A.P. 70-242 and [4]Departamento de Microbiología y Parasitología, Facultad de Medicina, Universidad Nacional Autónoma de México, Ciudad de México, 04510

Research Paper

Cite this article: Zepeda N *et al* (2019). Hippocampal sclerosis induced in mice by a *Taenia crassiceps* metacestode factor. *Journal of Helminthology* **93**, 690–696. https://doi.org/10.1017/S0022149X18000755

Received: 8 February 2018
Accepted: 26 July 2018
First published online: 23 August 2018

Key words:
apoptosis; Barnes maze; hippocampal sclerosis, metacestode factor (Fac); mouse model; neurocysticercosis; *Taenia crassiceps*; *Taenia solium*

Author for correspondence:
J.L. Molinari, E-mail: jmolinar@ifc.unam.mx

Abstract

An experimental *Taenia crassiceps* mouse model was used to assess the role of *Taenia solium* metacestode factor (Fac) in human neurocysticercosis. Intraperitoneal infection with *T. crassiceps* metacestodes or subcutaneous inoculation with a *T. crassiceps* metacestode factor (Fac) produced significant impairment of performance (learning) in the Barnes maze and induced bilateral hippocampal sclerosis in mice. Several staining techniques revealed important cell dispersion, extensive apoptosis and cell loss in the dentate gyrus, hilus and CA1-CA3 regions of both hippocampi, as well as intense deterioration of the adjacent cortex. An outstanding disruption of its histoarchitecture in the surrounding tissue of all these regions and apoptosis of the endothelial cells were also observed.

Introduction

Human beings acquire neurocysticercosis (NCC) by ingesting foods contaminated with *Taenia solium* eggs. The acidic gastric juice breaks up the inter-embryophore cement of the eggs. Then, the sheath-covered embryos are carried to the duodenum, where the pancreatic juice and bile dissolve the external lipid layer of the sheath, allowing the entrance of water and nutrients, which activate the previously dormant embryos. The activated embryos rip their envelopes with the help of their six sharp hooks, and they promptly leave these broken structures, as described in an *in vitro* study (Molinari *et al.*, 1993). Released from their envelopes, activated embryos invade the intestine, as with *Hymenolepis nana* (Miyasato *et al.*, 1977), migrate through the bloodstream and implant in several tissues, such as the striated muscles and central nervous system, where they develop into the metacestode stage.

Neurocysticercosis is considered to be the most common parasitic infestation of the central nervous system and the single most common cause of epilepsy. Seizures, headaches and neurological deficits are described in human neurocysticercosis. Signs of psychiatric disease (65.8%), cognitive decline (87%), altered memory (25%) and attention deficits (100%) among others were reported in a heterogeneous sample of 38 patients (Forlenza *et al.*, 1997). Other features are hydrocephalous, chronic meningitis, and impairment in executive functions, verbal and non-verbal memory, praxis and verbal fluency (Varghese *et al.*, 2016).

Hippocampal atrophy without seizures in patients with calcified neurocysticercosis (cNCC) has been observed, suggesting inflammatory-mediated mechanisms provoked by cysticercosis, which may contribute or even lead to refractory mesial temporal lobe epilepsy with hippocampal sclerosis (MTLE-HS) by mechanisms that need to be clarified (Bianchin *et al.*, 2015; Griper and Welburn, 2017). To address the role that *T. solium* metacestode factor (Fac) (Molinari *et al.*, 1990) could play in the production of hippocampal sclerosis, whose cause in human neurocysticercosis is poorly understood, we developed an experimental *Taenia crassiceps*-mouse model to study and understand the effects of an infection of mice with *T. crassiceps* metacestodes and the subcutaneous inoculation of mice with a *T. crassiceps* factor on hippocampal cells; results showed an extensive and significant apoptosis of dentate gyrus, CA1, CA2, CA3 and hilus cells compared with intact control cells (Zepeda *et al.*, 2017).

In the current research, we extended the time of infection and the inoculation with Fac for 110 days to try to induce a more severe hippocampal injury than that reported recently (Zepeda *et al.*, 2017). Histopathologically, temporal lobe epilepsy (TLE) associated with HS has been characterized by cell death and neuronal cell loss, which is most severe in the CA1 and CA3 regions and in the hilus of the dentate gyrus (DG), volume loss, reactive gliosis, and dispersion of the dentate gyrus granule cells (Sloviter, 1994; Lurton *et al.*, 1998).

© Cambridge University Press 2018

CAMBRIDGE UNIVERSITY PRESS

Downloaded from https://www.cambridge.org/core. CDC de la AtmosferaAv: Universidad No. 3000, on 20 Oct 2020 at 08:09:37, subject to the Cambridge Core terms of use, available at https://www.cambridge.org/core/terms. https://doi.org/10.1017/S0022149X18000755

INFORME DE LABORES 2019

Materials and methods

Treatment of mice

BALB/c mice (28 days old, 20–22 g) were maintained under standard animal housing conditions with access to Purina chow and water *ad libitum*. *Taenia crassiceps* metacestodes (WFU strain) were maintained in our laboratory via peritoneal passage in female mice, as described (Everhard *et al.*, 2004). Peritoneal fluid from healthy female controls (CPF) and *T. crassiceps* metacestode-infected mice, as well as *T. crassiceps* metacestode factor (Fac), were obtained according to Zepeda *et al.* (2011). To determine the effects of infection with *T. crassiceps* metacestodes and Fac treatment on hippocampal cells and the surrounding tissue, 18 female mice were divided into three groups. The control (Con) group (n = 6) and Factor (Fac) group (n = 6) were inoculated subcutaneously with 0.1 ml CPF, or Fac containing 50 µg of carbohydrates, as determined by the anthrone method (Ashwell, 1957) every 4 days for 100 days. The infected (Inf) group (n = 6) was infected intraperitoneally with up to 40 *T. crassiceps* metacestodes, measuring 2–3 mm in diameter and suspended in 0.2 ml phosphate buffered saline (PBS).

Barnes maze

At 110 days post infection with intraperitoneal *T. crassiceps* metacestodes or subcutaneous inoculation with *T. crassiceps* Fac, the Barnes maze procedure for small rodents was followed to estimate cognitive impairment in learning and memory (Rosenfeld and Ferguson, 2014), with minor modifications. Briefly, a bright illumination overhead was used. The maze was centred below the lights. Mice were tested without the use of a wall or cues. The maze was 90 cm in diameter and 90 cm in height, with 20 escape holes that each had a diameter of 5 cm, and there was only one hole with an escape cage. No hole was plugged in this test. After 30 minutes of habituation, each mouse was gently removed from his home cage and placed onto the maze centre. Then, the overhead lights were turned on. Every mouse's performance was recorded using a Canon VIXIA HF R70 camera (Canon, Melville, NY, USA). If the mouse failed to enter the escape cage within 5 minutes, it was guided gently to the correct location and into the escape cage, where it remained for 2 minutes. Each mouse was tested for two trials/day with an inter-trial interval of approximately 30 minutes. All mice were tested for five consecutive days. Videos were analysed carefully. The Barnes maze test was used to study the behaviour of the control, experimental cysticercotic and Fac treated-mice.

Histology and cellular apoptosis

At 115 days post treatment and infection, all mice were anaesthetized with pentobarbital and perfused transcardially with saline followed by phosphate-buffered 10% formalin. Then, the brains were carefully removed, and intraperitoneal metacestodes were obtained and counted. Two coronal cuts were made in each brain: an anterior cut was made at Bregma −1.43 mm and the other at Bregma −5.19 mm (Paxinos and Franklin, 2013). The intermediate fragments of each brain were fixed with 2.5% paraformaldehyde in PBS for 12 h at room temperature. Next, the fragments of each brain were embedded in paraffin. Coronal sections that were 5 µm thick were prepared on a rotary microtome, placed on poly-L-lysine-coated microscopic slide, and subjected to haematoxylin/eosin (H/E) and DAPI staining to analyse the cellular morphology and histoarchitecture of the dentate gyrus and CA1-CA3 regions. Sections stained with H/E were analysed with an Olympus IX71 microscope and IMAGE PRO-PCUS 60 software. Sections stained with DAPI were analysed with a Zeiss LSM 800 confocal microscope and ZEN version 2.1 software. The presence of DNA strand breaks was evaluated using an *in situ* cell death detection kit (Roche). TUNEL assays were analysed with a confocal microscope Leica TCS-SPS (Carl Zeiss de México-División Microscopía, Ciudad de México).

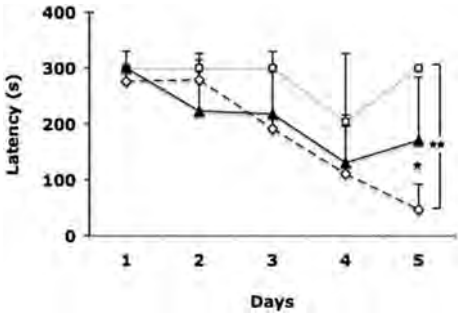

Fig. 1. Mean escape latency in seconds as a measure of performance of mice in the Barnes maze. Values of the second trials for 5 days. Control group (◇); Infected group (□); Factor group (▲). ** $P < 0.01$ Control vs Infected. * $P < 0.05$ Control vs Factor.

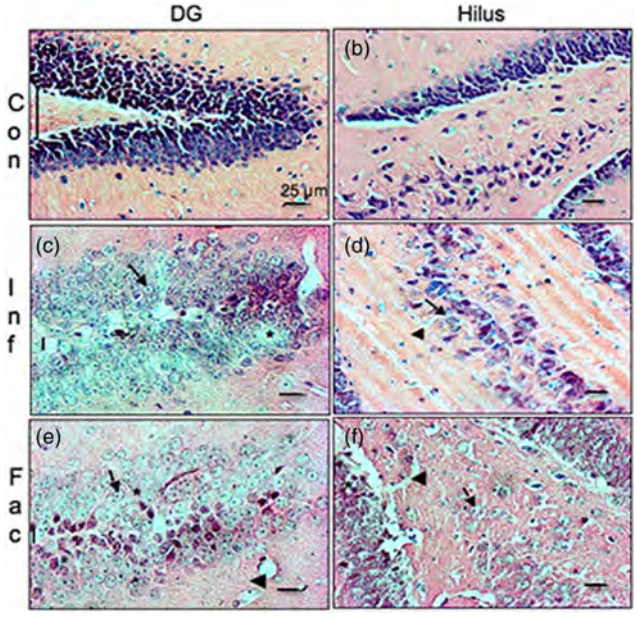

Fig. 2. Haematoxylin/eosin-stained brain section that contains part of the dentate gyrus and hilus from a control mouse (a & b), a mouse infected with *T. crassiceps* metacestodes (c & d), and a mouse inoculated with *T. crassiceps* Fac (e & f). Cell loss (*); bleached nuclei (arrows); tears (arrowheads); gyrus branches angle (vertical bar). Scale bar = 25 µm. 40×.

Data analysis

The numbers of haematoxylin/eosin-stained and TUNEL-positive cells were measured by manual counting (area in μm^2) with the aid of Image J software (National Institutes of Health, Bethesda, MD, USA). For statistical data, one-way analyses of variance and Tukey's test were performed using GraphPad software

Downloaded from https://www.cambridge.org/core. CDC de la AtmosferaAv: Universidad No. 3000, on 20 Oct 2020 at 08:09:37, subject to the Cambridge Core terms of use, available at https://www.cambridge.org/core/terms. https://doi.org/10.1017/S0022149X18000755

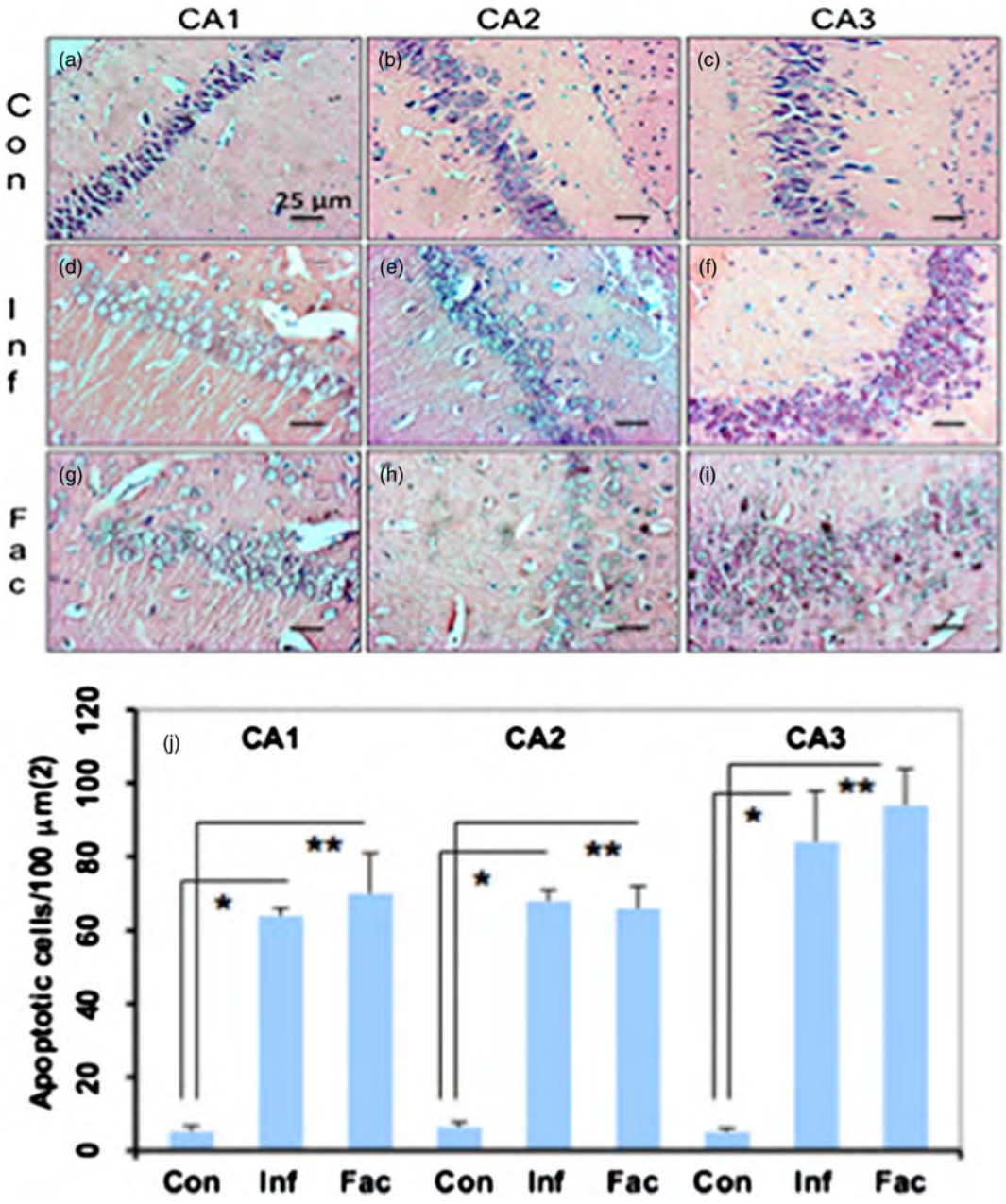

Fig. 3. Haematoxylin/eosin-stained brain sections that contain portions of CA1, CA2 and CA3 regions from a control mouse (a–c), a mouse infected with *T. crassiceps* metacestodes (d–f) and a mouse inoculated with *T. crassiceps* Fac (g–i). Scale bar = 25 µm. 40×. (j) Number of apoptotic cells/100 µm^2. Bars represent the mean ± SD. * $P < 0.001$ Infected vs Control. ** $P < 0.001$ Factor vs Control.

(GraphPad Instat, San Diego, CA, USA). Data are presented as the mean ± SD. $P < 0.05$ was considered significant.

Results

Barnes maze

Both intraperitoneal infection with *Taenia crassiceps* metacestodes and subcutaneous inoculation with a *T. crassiceps* metacestode factor (Fac) produced significant impairment on performance in the Barnes maze and induced bilateral hippocampal sclerosis in mice. The performance in the Barnes maze was mainly assessed by the escape latency parameter (mean ± SD), measured in the number of seconds it took to reach and completely hide in the escape hole.

During all time (second trial) to learn this task, both infected and factor mice were significantly slower in reaching and hiding in the escape hole, in comparison with control mice. On the fifth day, all control mice (n = 6) were able to hide in the escape hole in 28 ± 44 s after reaching it. Latency values of control mice were significantly less than those of experimental mice ($P < 0.05$ Con vs Fac, and $P < 0.01$ Con vs Inf.; fig. 1). Infected mice (n = 4) showed difficulty in moving in the maze; on the fourth day only one (25%) was able to hide at 151 s after reaching the escape hole. On the fifth day only one reached the escape hole in 73 s, and stayed there the rest of time without hiding in the hole. On

Downloaded from https://www.cambridge.org/core. CDC de la AtmosferaAv: Universidad No. 3000, on 20 Oct 2020 at 08:09:37, subject to the Cambridge Core terms of use, available at https://www.cambridge.org/core/terms. https://doi.org/10.1017/S0022149X18000755

INFORME DE LABORES 2019

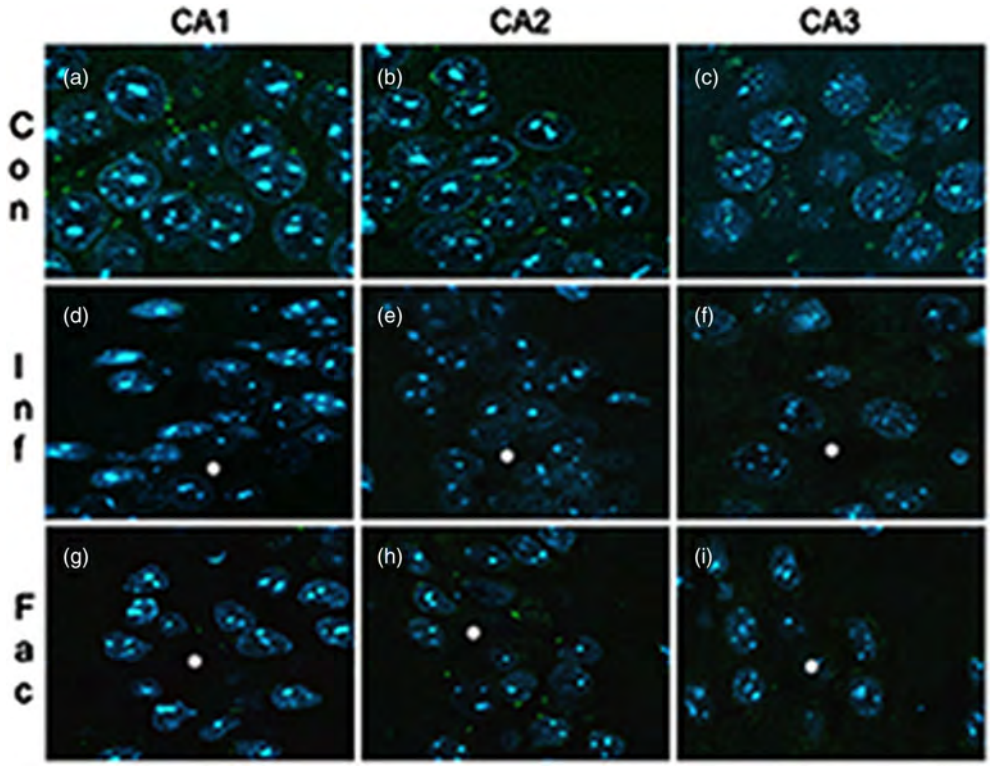

Fig. 4. DAPI-stained brain sections that contain portions of CA1, CA2 and CA3 from a control mouse (a–c), a mouse infected with *T. crassiceps* metacestodes (d–f) and a mouse inoculated with *T. crassiceps* Fac (g–i). Scale bar = 25 μm. 40×.

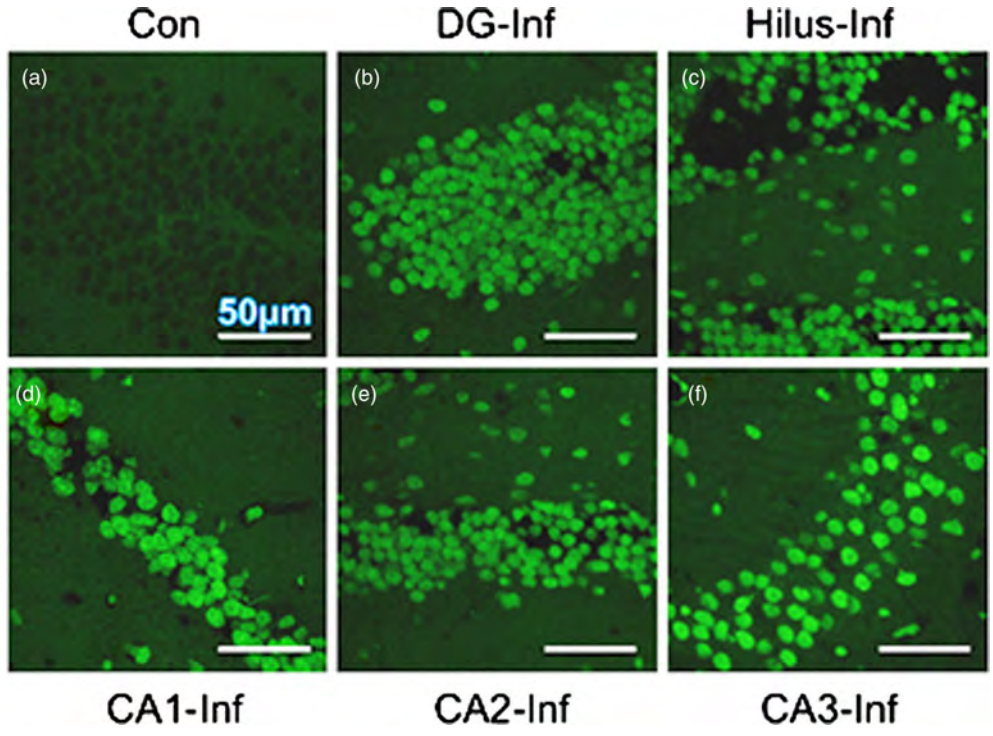

Fig. 5. TUNEL-stained brain sections that contain a portion of the dentate gyrus from a control mouse (a), and a portion of the dentate gyrus, hilus, CD1, CD2 and CD3 from a mouse infected with *T. crassiceps* metacestodes (b–f). Scale bar = 50 μm. 60×.

Downloaded from https://www.cambridge.org/core. CDC de la AtmosferaAv: Universidad No. 3000, on 20 Oct 2020 at 08:09:37, subject to the Cambridge Core terms of use, available at https://www.cambridge.org/core/terms. https://doi.org/10.1017/S0022149X18000755

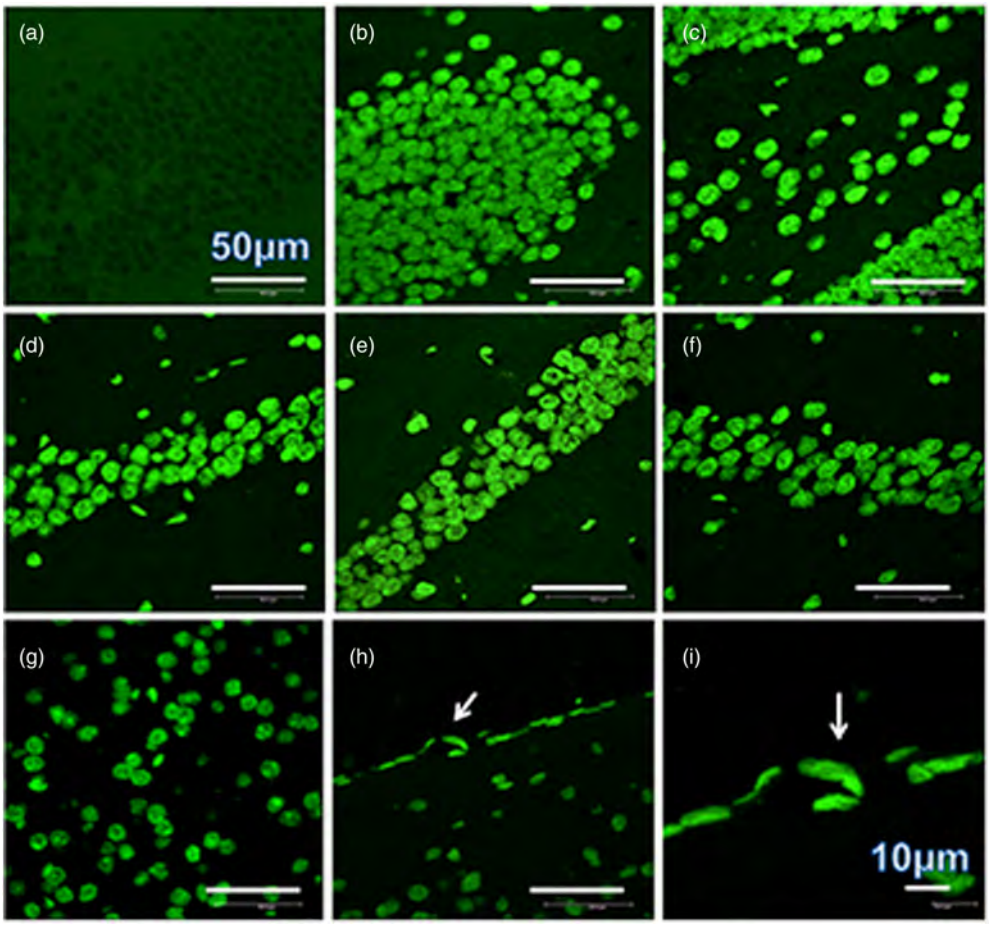

Fig. 6. TUNEL-stained brain sections that contain a portion of dentate gyrus from a control mouse (a), a portion of dentate gyrus and hilus from a mouse infected with *T. crassiceps* Fac (b and c), a portion of CD1, CD2 and CD3 from a mouse inoculated with *T. crassiceps* Fac (d–f), a portion of the adjacent cortex from a mouse inoculated with Fac (g), and the border of the adjacent cortex showing apoptotic endothelial cells within sections of the capillary (arrow) (h). Scale bar = 50 μm. 60×. (i) is an amplification of (h). Scale bar = 10 μm. 200×.

the fifth day Factor mice (n = 6) showed hyperactivity, reaching the escape hole at 67 ± 38 s. Only five mice had hidden at 73 ± 85 s after reaching the escape hole. The sixth mouse did reach the escape hole at 99 s, then left the hole four times to explore several holes and came back, but it never hid (fig. 1).

Histopathological studies

A heavy parasite load was found in the peritoneal cavity of mice infected with *T. crassiceps* metacestodes (485 ± 78 metacestodes per mouse). Haematoxylin/eosin staining showed that all sub-regions of hippocampi from experimental animals were affected in their tissue architecture either in the cellular morphology or in the surrounding tissue. The dentate gyri, as well as the hilus, CA1, CA2 and CA3 cells displayed dispersion, bleached nuclei, cell loss and many tears in the surrounding white matter, compared with the integrity of the cells and the white matter of the control hippocampi. Dentate gyrus branches from experimental mice (fig. 2c, e) formed a smaller angle compared to those of the control hippocampi (fig. 2a). The number of cells that had altered morphology and staining were statistically ($P < 0.001$) more than those of the control mice (fig. 3). DAPI staining displayed generalized pyknosis or hypercondensation of the chromatin of the CA1, CA2 and CA3 nuclei from *T. crassiceps* infected and Fac-treated mice. Apparently, all nuclei in these sub-regions were collapsed, and their number was less than those of the control mice. Additionally, numerous empty spaces among the reduced number of pyknotic nuclei of these sub-regions were observed, which suggested cell loss (fig. 4). Pyknosis is the accepted sign of programmed cell death (Burgoyne, 1999). To evaluate DNA fragmentation, DNA strand breaks were labelled using fluorescein-dUTP. This staining showed generalized and significant TUNEL-positive cells in the three layers of the dentate gyrus, hilus and in cells from the CA1, CA2 and CA3 regions, including the adjacent cortex ($P < 0.01$ Inf and Fac vs. Con). In all these places, many fragmented nuclei were observed, compared to TUNEL-negative nuclei of the control hippocampi. The intensity of the fluorescence of the nuclei in the above-mentioned regions was not homogeneous, suggesting that apoptosis was induced at different times. Nuclei with a lower fluorescence intensity and of reduced size could be among the first in developing apoptosis. Dispersion and cell loss were also observed (figs 5 and 6). Numerous TUNEL-positive cells were also found in the neighbouring cortex. A remarkable finding was the observation of apoptosis of endothelial cells in several places in all the studied regions (figs 6 and 7).

Discussion

In the current research, the experimental *T. crassiceps* mouse model (Zepeda *et al.*, 2017) was used to investigate parasite mechanisms involved in the production of hippocampal sclerosis

Downloaded from https://www.cambridge.org/core. CDC de la AtmosferaAv: Universidad No. 3000, on 20 Oct 2020 at 08:09:37, subject to the Cambridge Core terms of use, available at https://www.cambridge.org/core/terms. https://doi.org/10.1017/S0022149X18000755

INFORME DE LABORES 2019

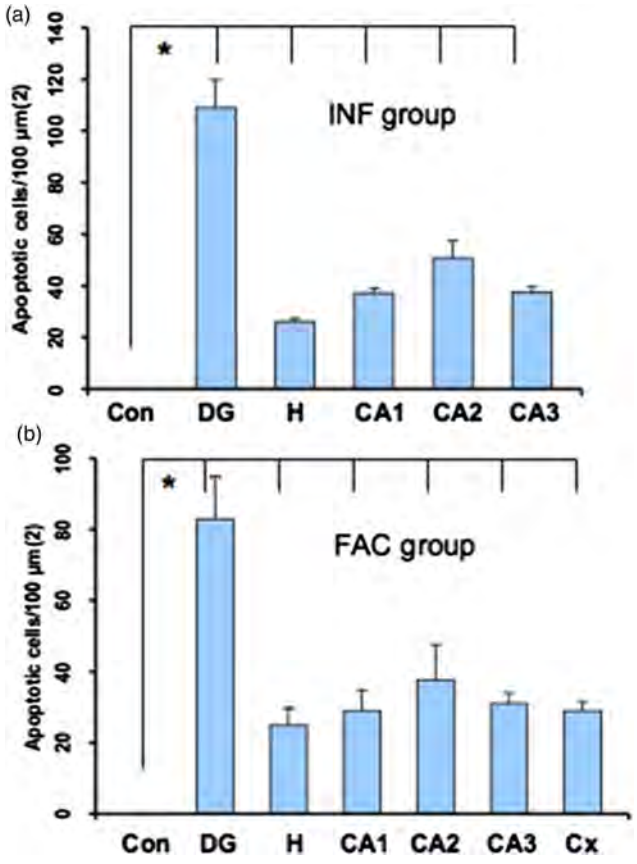

Fig. 7. Statistical data from the sections stained with TUNEL. Bars represent the mean ± SD of the dentate gyrus from control mice (a & b), dentate gyrus (DG), hilus (H), CA1, CA2 and CA3 from infected mice (a), and DG, H, CA1, CA2, CA3 and Cortex (Cx) from factor mice (b). * $P < 0.01$ DG, H, CA1, CA2, CA3 and Cx vs Con.

(HS), in which some patients suffer from neurocysticercosis. A deficit in learning and memory functions was observed using the Barnes maze. This deficit was more pronounced in mice infected with *T. crassiceps* metacestodes, perhaps due to a heavy parasitic load and an intense intraperitoneal inflammatory reaction as described (Zepeda *et al.*, 2010), as well as structural damage of the histoarchitecture of the hippocampi from experimental mice. This damage was characterized by significant cell death (apoptosis), cell dispersion and cell loss, in all sub-regions of the hippocampus either in the infected group or the Fac-treated animals, such as dentate gyrus, hilus, CA1, CA2, CA3, and the adjacent cortex, compared with the integrity of the cells in control mice. Structural damage was also observed in the neighbouring white matter.

The Barnes maze has been used to relate memory loss and long-term potentation (LTP) dysfunction in the hippocampus, which are involved in Alzheimer's disease. Using the Barnes maze, Hadipour *et al.* (2018) found that administration of crocin in rats significantly improves spatial memory indicators such as latency time. The learning deficit in Aβ (beta-amyloid)-treated animals correlated with a reduction of LTP in hippocampal synapses. Crocin significantly reduced the number of TUNEL-positive cells in the CA1 sub-region compared to the Aβ-group. Barbe *et al.* (2016) utilized the Barnes maze to test for long-term memory deficits, with good success. Their results showed in the CA1-3 regions of the hippocampus of mice significantly reduced numbers of neuronal cell bodies overall, and reduced numbers of Pur-alpha+ neuronal cell bodies and dendrites in heterozygous Pur-alpha (+/-) mice, compared to wild-type (+/+) littermates.

Here, in every sub-region studied, a very interesting finding was the observation of apoptotic endothelial cells dispersed in the white matter near the neuronal packages and in the border of the adjacent cortex. This finding suggests that the Fac apoptogenic activity on endothelial cells could impair the blood–brain barrier, allowing the entry of the Fac (that migrated via the bloodstream when the peritoneal cavity of the mouse was infected with *T. crassiceps* metacestodes or the abdominal skin of the mouse was inoculated with Fac) into the brain, so that it can reach the hippocampal cells and other regions of the brain, such as thalamic nuclei (Zepeda *et al.*, 2017). The apoptogenic activity of Fac seems to have been cumulative, as was observed with the TUNEL staining.

The pathological characteristic produced by *T. crassiceps* metacestode infection or by *T. crassiceps* Fac in all sub-regions of the hippocampus resembles human hippocampal sclerosis, such as volume loss, which indicates atrophy (Jeniffer *et al.*, 2015). The learning deficit and hyperactivity are neurological manifestations of structural damage in the hippocampus, which rely on other functions, such as attention, language and spatial memory. Another feature of hippocampal sclerosis described in the literature is the increase of astrocytes during the scarring process in places where there has been cell loss due to some injury (Sloviter, 1994). We looked for this feature using a rabbit antibody anti-GFAP fluorescein mouse, but we could not obtain positive results in this way. So, in the next study, we intend to test this hypothesis.

In humans, NCC damage to the hippocampus caused by the *T. solium* Fac must be a very chronic process, proportional to the number of living parasites; thus, when the neurological deficits are apparent, including epilepsy, the parasites are probably already calcified. Molinari *et al.* (1987) reported that in porcine cysticercosis, the suppression of T-cells was proportional to the number of cysticerci per 1 kg of parasitized meat. Human neurocysticercosis has been associated with hippocampal atrophy, and the results of a study by Del Brutto *et al.* (2017) suggested that NCC-related hippocampal atrophy takes a long time to develop.

Taenia crassiceps Fac are chromatographic Sephadex G-50 fractions containing substances of low molecular weight (< 1250 Da) obtained by ultrafiltration of the peritoneal fluid from female mice infected intraperitoneally with *T. crassiceps* metacestodes (Zepeda *et al.*, 2011). The complete chemical characterization of these substances has not been possible. By preliminary NMR and infrared studies, these Sephadex G-50 fractions contain at least three aromatic components, carbohydrates such as glucose, and can induce a specific antibody response in rabbits and mice, which indicate that this factor is produced by the parasite (data not published). The non-specific way this Fac induces apoptosis in different types of cells, such as testis cells (Zepeda *et al.*, 2011), ovary cells (Solano *et al.*, 2015), spleen cells (Zepeda *et al.*, 2016), and hippocampal cells (Zepeda *et al.*, 2017) is unknown. The learning deficit and the extensive apoptosis of hippocampal cells of experimental mice indicate a close relationship between both structure and function. Thus, it may be reasonable to assume *T. solium* metacestode factor is the causative agent of brain injuries such as hippocampal sclerosis in human neurocysticercosis. It will be important to contrast these results with relevant studies in human neurocysticercosis, as has been noted by Del Brutto *et al.* (2016).

Downloaded from https://www.cambridge.org/core. CDC de la AtmosferaAv: Universidad No. 3000, on 20 Oct 2020 at 08:09:37, subject to the Cambridge Core terms of use, available at https://www.cambridge.org/core/terms. https://doi.org/10.1017/S0022149X18000755

Using the Barnes maze, experimental mice showed a learning deficit closely related to hippocampal injury and very similar to that observed in patients with neurocysticercosis. Apoptosis of hippocampal endothelial cells suggested that *T. crassiceps* metacestode factor was able to break the BBB, enter the brain and produce hippocampal sclerosis.

Acknowledgments. We are grateful to Teresa Cortés and Daniela Rodríguez for performing histological procedures, and Claudia Rivera and Héctor Malagón for providing the healthy mice. Nadia Zepeda was supported for her graduate studies by the Posgrado en Ciencias Biológicas, Universidad Nacional Autónoma de México (UNAM) and CONACyT (scholarship number 262633).

Financial support. This research was supported by Universidad Nacional Autónoma de México.

Conflict of interest. None.

Ethical standards. The authors assert that all procedures contributing to this work comply with the ethical standards of the laws of Mexico on the care and use of laboratory animals. Animal studies were performed under an institutional protocol similar to that of the U.S. Public Health Service's *Guide for the Care and Use of Laboratory Animals*. From the Secretariat of Agriculture (SAGARPA NOM-062-ZOO-1999).

References

Ashwell G (1957) Colorimetric analysis of sugars. In Colowick SP and Kaplan NO (eds), *Methods in Enzymology*. III. New York, NY: Academic Press, pp. 73–84.

Barbe MF *et al.* (2016) Memory deficits, gait ataxia and neuronal loss in the hippocampus and cerebellum in mice that are heterozygous for Pur-alpha. *Neuroscience* **337**, 177–190.

Bianchin MM *et al.* (2015) Neuroimaging observations linking neurocysticercosis and mesial temporal lobe epilepsy with hippocampal sclerosis. *Epilepsy Research* **116**, 34–39.

Burgoyne LA (1999) The mechanisms of pyknosis: hypercondensation and death. *Experimental Cell Research* **248**, 214–222.

Del Brutto OH *et al.* (2016) Update on cysticercosis epileptogenic: the role of the hippocampus. *Current Neurology Neuroscience Reports* **16**, 1.

Del Brutto OH *et al.* (2017) The association between neurocysticercosis and hippocampal atrophy is related to age. *American Tropical Medicine and Hygiene* **96**, 243–248.

Everhard ME, Kuhn RE and Zelmer DA (2004) Infrapopulation dynamics of a wild strain of *Taenia crassiceps* (WFU) (Cestoda Taeniidae) in BALB/cJ mice. *Journal of Parasitology* **90**, 79–84.

Forlenza OV *et al.* (1997) Psychiatric manifestations of neurocysticercosis: a study of 38 patients from a neurology clinic in Brazil. *Journal of Neurology, Neurosurgery and Psychiatry* **62**, 612–616.

Griper LB and Welburn SC (2017) The causal relationship between neurocysticercosis infection and the development of epilepsy – a systematic review. *Infectious Diseases of Poverty* **6**, 31.

Hadipour M *et al.* (2018) Crocin improved amyloid beta induced long-term potentiation and memory deficits in the hippocampal CA1 neurons in freely moving rats. *Synapse* **72**, e22026.

Jeniffer VN, Udayakumar S and Pushpalatha K (2015) A clinical study to identify the possible etiology of complex partial seizures using magnetic resonance imaging brain findings and its implications on treatment. *Journal of Pediatric Neurosciences* **10**, 350–354.

Lurton D *et al.* (1998) Granule cell dispersion is correlated with early epileptic events in human temporal lobe epilepsy. *Journal of Neurological Science* **154**, 133–136.

Miyasato T *et al.* (1977) Electron microscopic observations on the penetration of *Hymenolepis nana* into the intestine of the mouse. *Acta Medica Kinki University* **2**, 1–18.

Molinari JL, Tato P and Valles Y (1987) Immunosuppression T-lymphocytes in swine, modulated by *Cysticercus cellulosae*. *Revista Latinoamericana de Microbiología* **29**, 293–300.

Molinari JL *et al.* (1990) Depressive effect of a *Taenia solium* cysticercus factor on cultured human lymphocytes stimulated with phytohaemagglutinin. *Annals of Tropical Medicine and Parasitology* **84**, 205–208.

Molinari JL *et al.* (1993) Effects of serum from neurocysticercosis patients on the structure and viability of *Taenia solium* oncospheres. *Journal of Parasitology* **79**, 124–127.

Paxinos G and Franklin KBJ (2013) *The Mouse Brain in Stereotaxic Coordinates*. 4th Edn. Oxford: Elsevier.

Rosenfeld CS and Ferguson SA (2014) Barnes maze testing strategies with small and large rodent models. *Journal of Visualized Experiments* **84**, 51194–51219.

Sloviter RS (1994) The functional organization of the hippocampal dentate gyrus and its relevance to the pathogenesis of temporal lobe epilepsy. *Annals of Neurology* **35**, 640–654.

Solano S *et al.* (2015) A *Taenia crassiceps* metacestode factor enhance ovarian follicle atresia and oocyte degeneration in female mice. *Journal of Helminthology* **89**, 49–59.

Varghese V *et al.* (2016) Cognitive dysfunction and its determinants in patients with neurocysticercosis. *Indian Journal of Psychological Medicine* **38**, 142–146.

Zepeda N *et al.* (2010) Decrease of peritoneal inflammatory CD4+, CD8+, CD19+ lymphocytes and apoptosis of eosinophils in a murine *Taenia crassiceps* infection *Parasitology Research* **127**, 1129–1135.

Zepeda N *et al.* (2011) *Taenia crassiceps*: a secretion substance of low molecular weight leads to disruption and apoptosis of seminiferous epithelium cells in male mice. *Experimental Parasitology* **128**, 184–191.

Zepeda N *et al.* (2016) A *Taenia crassiceps* factor induces apoptosis of spleen CD4 + T cells and TGF-β and Foxp3 gene expression in mice. *Journal of Helminthology* **90**, 223–231.

Zepeda N *et al.* (2017) Apoptosis of mouse hippocampal cells induced by *Taenia crassiceps* metacestode factor. *Journal of Helminthology* **91**, 215–221.

Downloaded from https://www.cambridge.org/core. CDC de la AtmosferaAv: Universidad No. 3000, on 20 Oct 2020 at 08:09:37, subject to the Cambridge Core terms of use, available at https://www.cambridge.org/core/terms. https://doi.org/10.1017/S0022149X18000755

Vaccine 37 (2019) 1928–1937

Contents lists available at ScienceDirect

Vaccine

journal homepage: www.elsevier.com/locate/vaccine

Incorporation of ORF2 from Porcine Circovirus Type 2(PCV2) into genetically encoded nanoparticles as a novel vaccine using a self-aggregating peptide

Jesús Zepeda-Cervantes [a,b,1], Adolfo Cruz-Reséndiz [a,1], Alicia Sampieri [a], Rosalba Carreón-Nápoles [c], José Iván Sánchez-Betancourt [c], Luis Vaca [a,*]

[a] Instituto de Fisiología Celular, Universidad Nacional Autónoma de México, Ciudad Universitaria, CDMX, Coyoacán 04510, Mexico
[b] Programa de Doctorado en Ciencias Biomédicas, Universidad Nacional Autónoma de México, Ciudad Universitaria, México, CDMX, Coyoacán 04510, Mexico
[c] Departamento de Medicina y Zootecnia de Cerdos, Facultad de Medicina Veterinaria y Zootecnia, Universidad Nacional Autónoma de México, Ciudad Universitaria, CDMX, Coyoacán 04510, Mexico

ARTICLE INFO

Article history:
Received 1 October 2018
Received in revised form 11 February 2019
Accepted 17 February 2019
Available online 26 February 2019

Keywords:
Nanoparticles
Subunit vaccine
Porcine Circovirus Type 2
Polyhedrin
Self-aggregating peptide

ABSTRACT

Porcine Circovirus Type 2 (PCV2) is one of the most important pathogens in pigs around the world. PCV2 is a non-enveloped virus and its capsid is formed by a single protein known as open reading frame 2 (ORF2). The aim of this study was to evaluate the antigenicity and immunogenicity of genetically-encoded protein nanoparticles (NPs) containing ORF2 from PCV2 fused to the first 110 amino acids of the N-terminus of polyhedrin from the insect virus Autographa californica nucleopolyhedrovirus (PH (1 −1 1 0)). Our group has previously described that some polyhedrin fragments self-aggregate forming polyhedra-like particles. We identified a self-aggregating signal within the first 110 amino acids from polyhedrin (PH(1 −1 1 0)). Fusing the ORF2 from PCV2 to the carboxyl terminus from PH(1 −1 1 0) results in the formation of NPs which incorporate the antigen of interest. Using this system we synthesized NPs containing PH(1 −1 1 0) fused to ORF2 (PH(1 −1 1 0)PCV2) and purify them to immunize pigs and evaluate the humoral immune response generated by these NPs comparing them to a commercially available vaccine. Pigs immunized with PH(1 −1 1 0)PCV2 NPs produced antibodies against ORF2 from PCV2 as indicated by western blot and ELISA analysis. Antibodies obtained with PH(1 −1 1 0)PCV2 NPs were comparable to those obtained using a commercial PCV2 vaccine. These antibodies neutralized the infection of a recombinant PCV2 expressing the green fluorescent protein (GFP). These results together suggest that the self-aggregating peptide PH(1 −1 1 0) can be used for the synthesis of subunit vaccines against PCV2.
© 2019 Elsevier Ltd. All rights reserved.

1. Introduction

Porcine circoviruses (PCV) are small DNA viruses showing worldwide distribution. Nowadays, at least 3 types of PCV have been identified. PCV1 was reported as a non-cytopathic virus contaminant of porcine kidney cells [1]. PCV2 was described for the first time in pigs affected by post-weaning multisystemic wasting syndrome (PMWS) in 1991 in Canada [2–4]. PCV2 is associated to porcine dermatitis and nephropathy syndrome (PDNS), reproductive disorders [3,5–7], respiratory diseases, hepatitis, enteropathy and neurologic syndrome [8]. PCV2 infects monocytes/macrophages and enters to host cells via clathrin-mediated endocitosis [9]. PCV2 also induces lymphocyte depletion, and therefore, facilitates many infectious diseases by bacteria and other viruses [10]. PCV2 contains 2 main genes: open reading frame 1 (ORF1) implicated in viral DNA replication and ORF2 responsible for the formation of the capsid. The ORF2 protein has a molecular weight of 30 kDa [11] and binds to heparan sulfate from the target cells [12]. Antibodies against ORF2 are sufficient to neutralize the infection [4,13]. PCV3 is a novel circovirus species associated to PDNS, reproductive failure and systemic inflammation, which has been isolated recently in the United States, Italy [14], China [15], and Poland [16].

PCV2 is one of the most important pathogens in the pig industry around the world because it causes important economic losses [3,4,17,18]. There are several commercially available vaccines against PCV2 and all of them are based on the ORF2 [4,19]. The first

* Corresponding author.
E-mail addresses: asampier@ifc.unam.mx (A. Sampieri), rcarreonn@prodigy.net.mx (R. Carreón-Nápoles), lvaca@ifc.unam.mx (L. Vaca).
[1] These authors contributed equally to this study.

https://doi.org/10.1016/j.vaccine.2019.02.044
0264-410X/© 2019 Elsevier Ltd. All rights reserved.

vaccine against PCV2 was Circovac® (Merial) which is based on an inactivated PCV2 [4]. Recent advances in vaccine development allowed the production of virus-like particles (VLPs) [20]. VLPs are self-assembling nanoparticles (NPs) formed by capsid proteins but without nucleic acids [21,22]. The baculovirus system is preferred to produce VLPs because it allows produce high protein yield with posttranslational changes [23,24]. Currently, there are three VLPs-based vaccines against PCV2, which induce a strong humoral immune response against PCV2: Circoflex® (Boehringer Ingelheim), Circumvent® (Intervet/Merck) and Porcilis PCV® (Shering Plough/Merk). Another PCV2 vaccine is Fostera® PCV which is based on chimeric PCV1/2 containing the genomic backbone of PCV1 with the ORF2 from PCV2 (Zoetis) [4].

Although PCV2 vaccines have been shown to induce antibodies that can neutralize the PCV2 infection [25] and increase the daily weight gain in growing pigs [25,26], the drawbacks of some of them are of special concern. For instance, the purification process of VLPs is time-consuming and specialized laboratory instruments are needed which may increase the cost of vaccination [20,27]. Previously, we reported that a peptide of 110 amino acids derived of the N-terminus of polyhedrin protein (PH(1 1 0)) from *Autographa californica nucleopolyhedrovirus* (AcNPV) self-aggregates forming nanoparticles (NPs) [28]. These NPs can be easily produced and purified by simple centrifugation. Furthermore, producing a fusion protein of PH(1 1 0) with an antigen of interest facilitates the purification of such antigen by centrifugation [29]. These PH (1 1 0)-antigen NPs can be produced with the baculovirus expression system, resulting in very high yields [29].

In this work, we generated NPs containing ORF2 fused to PH (1 1 0) (PH(1 1 0)PCV2 NPs) by the infection of Sf9 cells using a recombinant baculovirus and we characterized these NPs. We immunized pigs with these NPs and evaluated the antibody production against ORF2 by western blot and ELISA. Finally, we evaluated if these antibodies could neutralize the PCV2 infection in PK-15 cells using a recombinant PCV2 expressing the green fluorescence protein (GFP) as reporter of infection.

2. Materials and methods

2.1. Regents

Grace medium (catalog no. 11300-043 or 11605102), Antibiotic-antimycotic 100X containing 10,000 UI of penicilin/ml, 10,000 μg of streptomicin/ml and 25 μg of amphotericin B/ml (catalog no. 15240-062), Dulbecco's Modified Eagle Medium (DMEM) (catalog no. 12800082), Optimem™ (catalog no. 22600134), yeastolate (catalog no. 292805), Platinum® Pfx polymerase (catalog no. 11708039), X-gal (5-bromo-4-chloro-3-indolyl-β-D-galactopyranoside) (catalog no. 15520018), IPTG (Isopropyl ß-D-1-thiogalactopyranoside) (catalog no. 15529019), the Pierce™ BCA Protein Assay (catalog no. 10741395), TMB (3,3′,5,5′-Tetramethylbenzidine) (catalog no. N301), Proteinase K (catalog no. 25530015), DAPI(4′, 6-diamino-2-phenylindole) (catalog no. D3571), sodium dodecyl sulfate (SDS) (catalog no. 18220), the Cyanine3 (Cy3)-conjugated goat anti-mouse IgG (catalog no. A10521), the SuperSignal® West Femto Maximum Sensitivity Substrate (catalog no. 34095), and the baculovirus Bac-to-Bac™ system (catalog no. 10359-016) which contains: pFastBac™ vector, DH10Bac™ *E. coli* competent cells, and Cellfectin® II reagent, an additional pFastBac™ Dual Expression vector (catalog no. 10712-024), and the Lipofectamine® 2000 (catalog no. 11668019) were from Thermo Fisher Scientific (Waltham, MA, USA). Lactalbumin (catalog no. L9010), pluronic acid F-68 (catalog no. P1300), the anti-mouse HRP-conjugated antibody (catalog no. A9044), the anti-pig HRP-conjugated antibody (catalog no. A5670), the bovine serum albumin (BSA) (catalog no. A5611), D-glucosamine hydrocloride (catalog no. G4875), and LB broth, Miller medium (catalog no. L3152) were from Sigma-Aldrich (St. Louis, MO, USA). The fetal bovine serum (FBS) (catalog no. 081105) was from Biowest (Rue du Vieux Bourg, Nuaillé, France). Nitrocellulose membrane (catalog no. HATF00010), pET-28a-c(+) (69864), BL21 cells (69386-3) were from Merck Millipore, Ltd. (Tullagreen, Carrigtwohill. Co. Cork, Ireland). The Qiagen plasmid Midi Kit (catalog no. 12143) was from QIAGEN (Hilden, Germany). The pGEM® T Easy vector (A1360) were from promega (Madison, WI, USA). The Precision Plus Protein™ Dual Color Standards (catalog no. 1610374) was from Bio-Rad (Hercules, CA, USA). The Dako Fluorescent Mounting Medium (catalog no. S3023) was from Agilent (Santa Clara, CA, USA). The following vaccines were used: Fostera® PCV (lote no. 14075700). Circoflex® (lote no. 1601035B) and Circovac® (lote no. L433873). Syringes were 1 and 3 ml and needles were 26G × 1/2″ (0.45 × 12 mm) (brown needles) and 22G × 1 1/4″ (0.7 × 30 mm) (black needles) (for their use in mice and pigs, respectively).

2.2. Cells and virus

Sf9 cells (*Spodoptera frugiperda*) (catalog no. B82501) were obtained from Thermo Fisher Scientific (Waltham, MA, USA) and were maintained in Grace medium supplemented with 10% heat-inactivated FBS (56 °C 30 min), containing 3.33 g/l yeastolate, 3.33 g/l lactalbumin hydrolysate, antibiotic-antimycotic containing 100 UI of penicilin/ml, 100 μg of streptomicin/ml and 0.25 μg of amphotericin B/ml and pluronic acid F-68 to a final concentration of 0.1%. The baculovirus Bac-to-Bac™ system was used for the construction of three recombinant baculoviruses: PH(1 1 0)PCV2, PH (1 1 0)GFP (which induce the expression of GFP or ORF2 from PCV2 fused to PH(1 1 0), respectively), and PH(2 4 5) (which contains the full-length polyhedrin protein). All the recombinant baculoviruses were propagated in Sf9 cells. For the neutralization assay against PCV2, PK15-C1 cells (American Type Culture Collection, ATCC® number PTA-8244™; University Boulevard Manassas, VA 20110-2209 USA) and a recombinant PCV2 expressing GFP were used.

2.3. Recombinant PCV2 viruses

All the recombinant baculoviruses were produced similarly using the Bac-to-Bac™ system following the manufacturer's instructions. Briefly, the recombinant baculovirus PH(1 1 0)PCV2 was produced by a PCR flanking ORF2 from PCV2 isolated from an PCV2-infected Mexican pig. The primers 5′-CCATGGCTATGACGTATCCAAG GAGGCG-3′ and 5′-GTCGACTTAGGGTTTAAGTGGGGGG-3′ and the Platinum® Pfx polymerase were used for the PCR reaction. Baculovirus PH(1 1 0)PCV2 was designed similarly to baculovirus PH (1 1 0)GFP with slight modifications. The stromal interaction molecule 1 (STIM1, a protein localized to the endoplasmic reticulum) was fused to the yellow fluorescent protein (YFP) gene and was inserted under p10 promoter (Pp10) to easily visualize the infected cells. The baculovirus PH(2 4 5) was designed by inserting the full-length *polyhedrin* gene under polyhedrin promoter (PpH).

A recombinant PCV2 was designed by using the plasmid pGEM® T easy vector and the GFP. GFP was inserted into pGEM® T easy vector under the cytomegalovirus earlier promoter (CMV). The complete genome from PCV2 was linearized and inserted into the modified pGEM® T easy vector. PK-15 cells were transfected with the recombinant plasmid with Lipofectamine® 2000.

2.4. Production of specific sera against polyhedrin and ORF2 from PCV2

Sf9 cells were infected with a multiplicity of infection (MOI) of 20 from baculovirus PH(2 4 5). At 72 h postinfection (hpi), infected

INFORME DE LABORES 2019

Sf9 cells were sonicated and polyhedra were recovered and washed 3 times with PBS containing 0.1% of SDS to eliminate residual debris [30]. Finally, polyhedra were washed with PBS to eliminate residual SDS and protein concentration was measured. Five 6-week-old BALB/c female mice were immunized with 50 μg of polyhedra with complete Freund adjuvant coadministration intramuscularly into the leg muscle, 2 and 4 weeks later mice received two booster doses of 50 μg of polyhedra with incomplete Freund adjuvant coadministration subcutaneously at the base of a fold of loose skin (area at the neck). Similarly, five 6-week-old BALB/c female mice were immunized with 50 μl of vaccine Fostera® PCV and two booster doses were given 2 and 4 weeks later, intramuscularly into the leg muscle. Injections had a final volume of 50 μl for both groups of mice and sera were collected for both groups 8 weeks after prime doses.

2.5. Production of PH(1 1 0)PCV2 NPs

In order to produce the PH(1 1 0)PCV2 NPs, the first step was to determine the MOI of the baculovirus PH(1 1 0)PCV2. To do this, Sf9 cells were infected with the recombinant baculovirus PH (1 1 0)PCV2 with a MOI of 0.2, 2 and 20. At 72 hpi, infected Sf9 cells were centrifugated at 3000*g* for 10 min and the pellet was resuspended in PBS. The infected Sf9 cells were lysed by sonication (Qsonica 700, USA) at 500 J/min for 1 min in ice bath (20% of amplitude using a microprobe). PH(1 1 0)PCV2 NPs were purified using three cycles of sonication, and centrifugation at 11,300*g* for 2 min and a wash after each cycle. The PH(1 1 0)PCV2 NPs were resuspended in PBS and were analyzed by SDS-polyacrylamide gel electrophoresis (SDS-PAGE) using a 12% acrylamide gel. After electrophoresis, the gel was stained with Coomassie blue for 2 h and then was destained overnight. The MOI of 20 was selected to produce PH(1 1 0)PCV2 NPs. The second step was to determine the time for recovering PH(1 1 0)PCV2 NPs. Briefly, Sf9 cells were infected with a MOI of 20. Aliquots of infected Sf9 cells were taken at 48 and 72 hpi and the infected cells were sonicated for recovering PH(1 1 0)PCV2 NPs as we previously mentioned. PH(1 1 0)PCV2 NPs were resuspended in a volume of 100 μl of PBS and 50 μl of a 1:1000 dilution of these NPs were added to each well of a polystyrene ELISA microplate. The presence of PH(1 1 0)PCV2 NPs was evaluated using hyperimmune sera against PCV2 obtained from mice immunized with Fostera® PCV. The complete ELISA protocol is showed below. The time for recovering PH(1 1 0)PCV2 NPs was 72 hpi. Finally, 100 ml of Sf9 cells were infected with a MOI of 20 of the recombinant baculovirus PH(1 1 0)PCV2 in Erlenmeyer 250-ml flasks and recovered at 72 hpi, sonicated and purified as we mentioned above. All the Sf9 cell cultures contained 2×10^6 cells/ml and were incubated at 27 °C at 100 rpm. PH(1 1 0)GFP NPs were synthesized similarly and protein concentration was determined by the BCA method. NPs were stored at −70 °C.

2.6. Western blot analysis

The recombinant ORF2 from PCV2 was produced by inducing BL21 bacteria transformed with the modified plasmid pET-28a. The recombinant ORF2 from PCV2 was used in western blot for detecting anti-PCV2 antibodies in the vaccinated pigs (see below). 30 μg of PH(1 1 0)PCV2NPs, PH(1 1 0)GFP NPs, lysed Sf9 cells or 20 μg of recombinant ORF2 from PCV2 were boiled for 5 min in Laemmli buffer and run by SDS-PAGE using 10 and 12% acrylamide gels. Antigens were electrophoresed at 50 V for 40 min and then 2 h at 100 V. Proteins were transferred to nitrocellulose membranes at 80 V for 1 h 20 min. The nitrocellulose membranes were blocked in tris-buffered saline (TBS) with 5% of low fat milk overnight. A dilution of 2:4000 of a serum from a PCV2-infected pig was used to detect ORF2 from PCV2 in the denatured PH(1 1 0)PCV2 protein. Similarly, a dilution of 2:4000 of a serum from a mouse immunized with polyhedra was used to detect PH(1 1 0) in the denatured PH(1 1 0)PCV2 and PH(1 1 0)GFP proteins. The sera from pigs immunized with Circoflex® or PH(1 1 0)PCV2 NPs were used to detect specific antibodies against ORF2 from PCV2. Anti-pig or anti-mouse antibodies, both HRP-conjugated, were used at a dilution of 1:5000. The membranes were scanned with C-Digit blot scanner (LI-COR) after the substrate was added.

2.7. Immunofluorescence assay

Sf9 cells were grown in 6-well microplates with sterilized coverslips. The Sf9 cells were infected with the recombinant baculovirus PH(1 1 0)PCV2 or PH(1 1 0)GFP with a MOI of 20. An indirect immunofluorescence assay was realized to visualize the PH(1 1 0) PCV2 NPs. Sf9 cells infected with the recombinant baculovirus PH (1 1 0)GFP also were treated for immunofluorescence against PCV2 and were used as a negative control. At 72 hpi, the Sf9 cells infected by the recombinant baculoviruses PH(1 1 0)PCV2 or PH (1 1 0)GFP were washed 2 times with PBS, fixed with 4% paraformaldehyde for 20 min and permeabilized with PBS containing 0.3% Triton X-100 for 15 min. After each procedure, the coverslips were washed three times. PBS containing 50 mM glycine was added for 10 min. Cells were blocked with 5% BSA in PBS at room temperature for 1 h and hyperimmune sera against ORF2 from PCV2 from mice immunized with Fostera® PCV were used at a dilution of 1:500 and incubated for 1 h at room temperature with 2% BSA in PBS. The secondary antibody anti-mouse Cy3-conjugated was added at a dilution of 1:1000. The cells were incubated with DAPI at a dilution of 1:1000 for 5 min. Finally, the coverslips were mounted with DAKO on microscope slides. The infected Sf9 cells were observed with the Fluoview FV10i microscope (Olympus®) and the images were analyzed with the ImageJ program.

2.8. Transmission electron microscopy (TEM) in infected Sf9 cells

Sf9 cells were infected with the recombinant baculovirus PH (1 1 0)PCV2 using a MOI of 20. At 72 hpi, the infected Sf9 cells were centrifuged, and the pellet was resuspended in PBS. Then, particles were included into an epoxic resin and slices of 90 nm were obtained. Infected Sf9 cells were contrasted with uranil acetate 1% and lead citrate. Samples were observed with the JEOL JEM 12,000 EXII at 80 kv. Three different stocks of Sf9 cells infected with the recombinant baculovirus PH(1 1 0)PCV2 were analyzed.

2.9. Nanoparticle tracking analysis (NTA)

PH(1 1 0)PCV2 NPs were produced as mentioned above. After purification, 0.3 μg of PH(1 1 0)PCV2 NPs were resuspended in 1 ml of sterile water and analyzed with the NanoSight instrument (Malvern Panalytical, Malvern, United Kingdom). Three independent measurements for each condition were conducted and the NP size was obtained from these recordings using the NanoSight software.

2.10. Pig immunization

9 PCV2-free 8-week-old Pietrain/York males and females pigs were obtained from a Mexican farm (the absence of PCV2 was corroborated by PCR, and the absence of antibodies against PCV2 was corroborated by ELISA). Three groups of 3 pigs each were used to evaluate the antibody production against ORF2 from PCV2. All the groups of pigs used in this experiment were isolated in filtered air rooms and maintained with water and food *at libitum* during all

INFORME DE LABORES 2019

the experiment. All the pigs were intramuscularly injected in the muscle of neck as following: the first group was immunized with Circoflex® according to manufacurer's instructions; the second was immunized with 200 μg of PH(1 1 0)PCV2 NPs with emulsion coadministration; and the third was immunized with 2000 μg of PH(1 1 0)PCV2 NPs with emulsion coadministration. This emulsion is based on light paraffin oil (1:1 vol/vol). Blood samples were taken in all the groups of pigs each week and sera were collected by means of centrifugation at 3000*g* for 15 min. Two booster doses were given to all the groups of pigs at 14 and 28 days after the prime dose in all the groups. The sera were stored at −70 °C until their use.

2.11. Indirect ELISA assay for antibodies against PCV2

96-well polystyrene microplates were coated with 50 μl of a dilution of 0.33 μg/ml of the recombinant protein ORF2 from PCV2. Microplates were incubated at 37 °C for 1 h, washed with 350 μl of PBS containing 0.2% Triton X-100 and blocked with PBS-BSA(2% BSA) at 37 °C for 1 h. 50 μl of a 1:200 dilution of sera from pigs diluted to in PBS-BSA were added each well and microplates were incubated at 37 °C for 1 h. After 5 washes, 50 μl of anti-pig antibody (HRP-conjugated) diluted 1:5000 in PBS-BSA were added to each well and microplates were incubated at 37 °C for 1 h. After washes, 50 μl of TMB were added to each well. Microplates were incubated at room temperature for 20 min and the reaction was stopped with 50 μl of a 0.16 M sulfuric acid solution. The microplates were read with an ELISA reader (SkanIt for Multiskan FC 3.1) using a filter of 450 nm. An ELISA positive value was the two-fold mean of the preimmune sera and the antibody titers were determined with the highest sera dilution that gave a positive value in ELISA as reported previously [31].

2.12. Virus seroneutralization assay and flow cytometry

PK-15 cells were maintained in DMEM supplemented with 10% of FBS in 35 mm tissue culture dishes until 90% of confluence and were washed with PBS and incubated with 500 μl Optimem™. PK-15 cells were transfected with 2 μg of the plasmid pGEM® T easy vector containing PCV2 expressing GFP. The supernatant was recovered 72 h post-transfection. 50,000 PK-15 cells were added to each well in 96-well microplates and were incubated for 24 h. 50 μl of the supernatant containing PCV2 expressing GFP (a MOI of 1 of the recombinant PCV2) were mixed with 50 μl of preimmune sera, or a serum from a PCV2-infected pig, or sera from pigs immunized with Circoflex® or PH(1 1 0)PCV2 NPs diluted 1:500 in Optimem™ (after complement inactivation 30 min at 56 °C). The mixtures were incubated for 1 h at 37 °C and were added to each well to allow to PCV2 attach to target cells. 1 h later, the PK-15 cells were washed twice with 200 μl of PBS. Then, 200 μl of Optimem™ supplemented with 1% FBS were added to each well. PK-15 cells were incubated at 37 °C with 5% CO_2 and were recovered at 72 hpi and analyzed by flow cytometry (Attune™). For the flow cytometry, PK-15 cells were recovered in 1.5-ml microtubes and analyzed individually by triplicate. 10,000 events were analyzed, and each event represents a PK-15 cell infected with the recombinant PCV2. Data were obtained with the Attune® Cytometer Software v2.1 (life technologies) and were graphed as histograms. The percentage of inhibition of infection by the recombinant PCV2 was calculated according to the difference between the average intensity of fluorescence of the PK-15 cells infected with the recombinant PCV2 and the average intensity of fluorescence of the PK-15 cells incubated with the mixture of the recombinant PCV2 and sera from different groups of pigs. Cells infected with the recombinant PCV2 were used as a reference for 100% of infection whereas non-infected cells were used to adjust the histograms before analysis.

2.13. Ethics statement and animal welfare

Mice used in this study were housed on a 12 h light/dark cycle with food and purified water *ad libitum*, following the protocol LVD74-5 approved by the Internal Committee for the Care and Use of Laboratory Animals (CICUAL) from Instituto de Fisiología Celular-UNAM. Pigs were fed with an age-based diet and purified water *ad libitum* at the National Center for Diagnostic Services in Animal Health (CENASA) from the National Health Service, Food Safety and Food Quality from Mexico (SENASICA) following the statements of the official Mexican standard NOM-062-ZOO-1999 for the ethical use of animals.

2.14. Statistic analysis

The absorbance of sera from pigs immunized with Circoflex® or PH(1 1 0)PCV2 NPs were compared with the absorbance of preimmune sera from pigs obtained by ELISA. An ELISA positive value was the two-fold mean of the preimmune sera. Data were recorded as mean and standard error. Statistic analysis of the virus seroneutralization assay was carried out by comparing the fluorescence of PK-15 cells incubated with PCV2 expressing GFP mixed with sera from pigs immunized with Circoflex® or PH(1 1 0)PCV2 NPs with the fluorescence of PK-15 cells incubated with PCV2 expressing GFP mixed with preimmune sera. For data with normality, a one-way ANOVA test following by a Tukey's test were used to determine differences with preimmune sera. If not, a Kruskal-Wallis test followed by a Dunn's Multimple Comparison test were used. The statistical significance was $p < 0.05$.

3. Results

3.1. Simple purification of PH(1 1 0)PCV2 NPs

Most of the PCV2 commercial vaccines are based on VLPs [4], and they have been important tools to control diseases associated to PCV2 [32], but their purification process is time-consuming and expensive [20,27]. In this work, we developed a system based on the self-aggregating peptide PH(1 1 0), which forms NPs that are easily purified by centrifugation. This system uses recombinant baculovirus as expression vectors [28,29]. We produced two main recombinant baculoviruses: a baculovirus containing GFP fused to PH(1 1 0) to be used as control and a second baculovirus carrying ORF2 from PCV2 fused to PH(1 1 0) (for generating PH(1 1 0)GFP and PH(1 1 0)PCV2 NPs, respectively) (Fig. 1A). For the production of recombinant proteins using baculoviruses we explored different multiplicities of infection (MOI). A MOI of 20 produced the largest amount of recombinant protein at 72 h postinfection, and a single band of 42-kDa was detected in SDS-PAGE analysis (Fig. 1B). This band corresponds to the expected molecular weight for PH(1 1 0) PCV2.

3.2. PH(1 1 0)PCV2 NPs are recognized by specific sera against PCV2

The next step was to determine if specific sera anti-polyhedrin or anti-PCV2 could identify the antigens PH(1 1 0) and ORF2 from PCV2 present in the PH(1 1 0)PCV2 NPs. Briefly, PH(1 1 0)GFP and PH(1 1 0)PCV2 NPs were run by SDS-PAGE and transferred to nitrocellulose membranes. Then, we evaluated whether the denatured PH(1 1 0)PCV2 protein was recognized by a specific sera against polyhedrin. The serum from a mouse immunized with polyhedra recognized both PH(1 1 0)GFP and PH(1 1 0)PCV2 proteins as

INFORME DE LABORES 2019

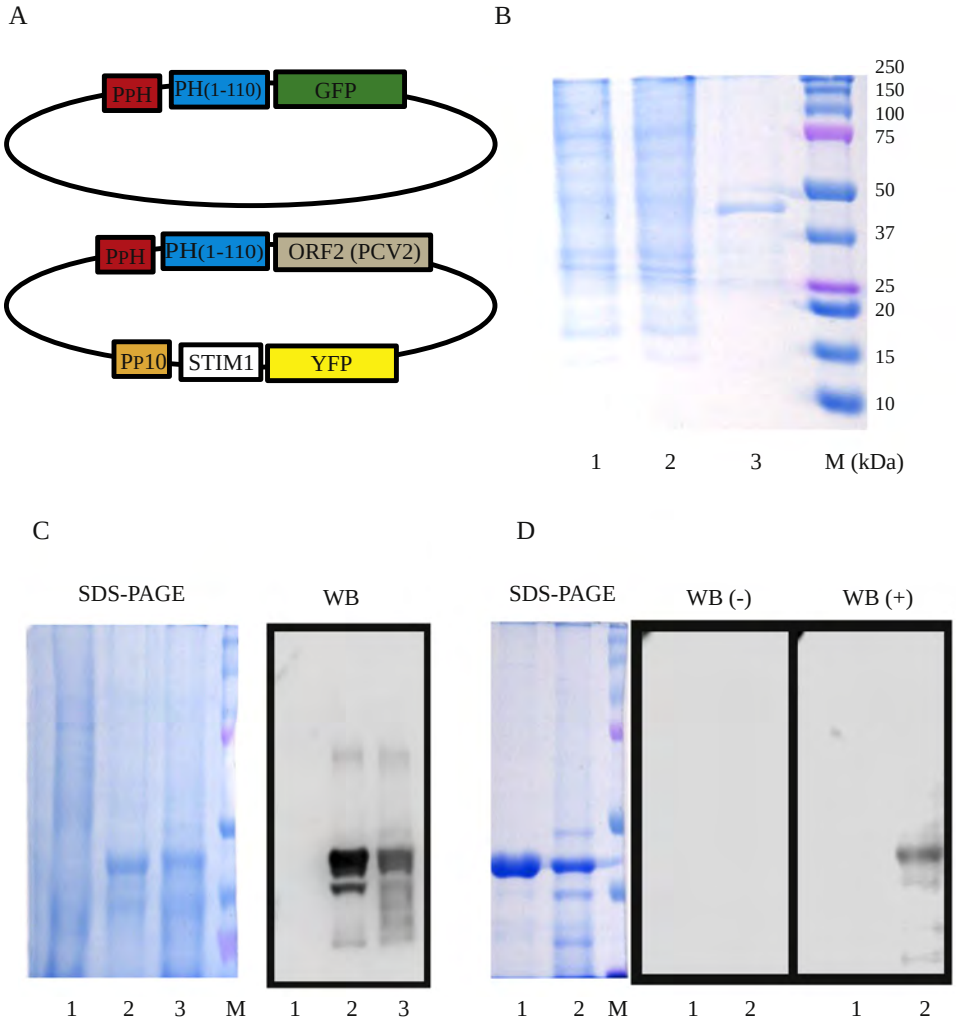

Fig. 1. Design of recombinant baculoviruses carrying the gene for the production of PH(1 1 0)PCV2 nanoparticles (NPs). (A) Cartoon illustrating the distribution of the genes carried by the recombinant baculoviruses genome with PH(1 1 0)GFP (upper panel) and PH(1 1 0)PCV2 (lower panel). (B) Multiplicity of infection (MOI) optimization was carried out by infecting Sf9 cells with 0.2 (lane 1), 2 (lane 2) and 20 (lane 3) MOI of the recombinant baculovirus PH(1 1 0)PCV2. PH(1 1 0)PCV2 and PH(1 1 0)GFP NPs were purified by simple sonication of infected Sf9 cells at 72 h postinfection (hpi), centrifugation and washes with phosphate saline buffered (PBS). Electrophoresis on a 12% polyacrylamide gel under denaturing conditions, gel was stained with Coomassie blue. A 42-kDa protein was observed in Sf9 cells infected with 20 MOI of the recombinant baculovirus PH(1 1 0)PCV2. (C) Evaluation of antigenicity of PH(1 1 0). Non-infected Sf9 cell lysates, PH(1 1 0)GFP NPs and PH(1 1 0)PCV2 NPs (lanes1, 2, and 3, respectively) were run on a 10% polyacrylamide gel under denaturing conditions. Gel was stained with Coomassie blue (SDS-PAGE, left side) and transferred to a nitrocellulose membrane for western blot analysis (right side). A hyperimmune serum of a mouse immunized with polyhedra was used to detect PH(1 1 0) in PH(1 1 0)GFP and PH(1 1 0)PCV2 proteins in the western blot. A 42-kDa protein was observed in both PH(1 1 0)GFP and PH(1 1 0)PCV2 denatured proteins, but it was not observed in non-infected Sf9 cell lysates. (D) Evaluation of antigenicity of ORF2 contained into the PH(1 1 0)PCV2 fusion protein. PH(1 1 0)GFP (lane 1) and PH(1 1 0)PCV2 (lane 2) NPs were run on a 10% polyacrylamide gel under denaturing conditions. Gel stained with Coomassie blue (SDS-PAGE, left side) sows all the proteins loaded, while western blot analysis (right side) illustrates the selective recognition of PH(1 1 0) by the hiperimmune serum. The western blot analysis was conducted by using a PCV2-free pig serum (WB (−)) and a PCV2-infected pig serum (WB (+)). Serum of the PCV2-infected pig recognized a 42-kDa protein only in PH(1 1 0)PCV2 which was not observed in PH(1 1 0)GFP. The molecular weight marker (M) is the same for all the gels and indicates the molecular weight (10–250 kDa). (See the full-length blots in the supplementary Fig. S1). (For interpretation of the references to color in this figure legend, the reader is referred to the web version of this article.)

expected (Fig. 1C, right side). Both PH(1 1 0)GFP and PH(1 1 0)PCV2 proteins had the expected molecular weight of 42 kDa as indicated by SDS-PAGE (Fig. 1C, left side). A lysate of non-infected Sf9 cells showed several protein bands with different molecular weights by SDS-PAGE, but none of these were recognized by the anti-polyhedrin serum, indicating high specificity. Most importantly, PH(1 1 0)PCV2 protein was recognized by a serum obtained from a PCV2-infected pig. PH(1 1 0)GFP protein was not recognized by this serum (Fig. 1D). A serum from a PCV2-free pig was used as negative control, which did not recognize PH(1 1 0)GFP nor PH (1 1 0)PCV2 proteins. These results demonstrate that antibodies from PCV2-infected pigs recognize the ORF2 antigen present in the PH(1 1 0)PCV2 NPs.

3.3. The ORF2 from PCV2 fused to PH(1 1 0) self-aggregates and forms particles located in the nucleus of infected Sf9 insect cells

Previously, we reported that the peptide PH(1 1 0) derived from the N-terminus of the polyhedrin protein from the baculovirus AcNPV self-aggregates forming NPs into the nuclei of infected cells [28]. This event occurs even when the full-length GFP is fused to the C-terminus of PH(1 1 0) [28]. The PH(1 1 0)GFP particles have a size of 500 nm to 3 μm when observed by confocal microscopy inside the nuclei of infected Sf9 cells [28]. In order to evaluate if PH(1 1 0) retains the capacity of self-aggregation when fused to ORF2 from PCV2, we conducted indirect immunofluorescence assays. Immunofluorescence also allowed us to evaluate the local-

INFORME DE LABORES 2019

ization and morphology of the PH(1 1 0)PCV2 NPs in the infected Sf9 cells.

The PH(1 1 0)PCV2 NPs were amorphous and were located inside the nuclei of the infected Sf9 cells as indicated by the colocalization with the fluorescent DNA marker DAPI (Fig. 2A, upper part). The immunofluorescence was specific for the PH(1 1 0)PCV2 particles, since the serum from mice immunized with Fostera® PCV recognized only these NPs, but not PH(1 1 0)GFP NPs (Fig. 2A, lower part).

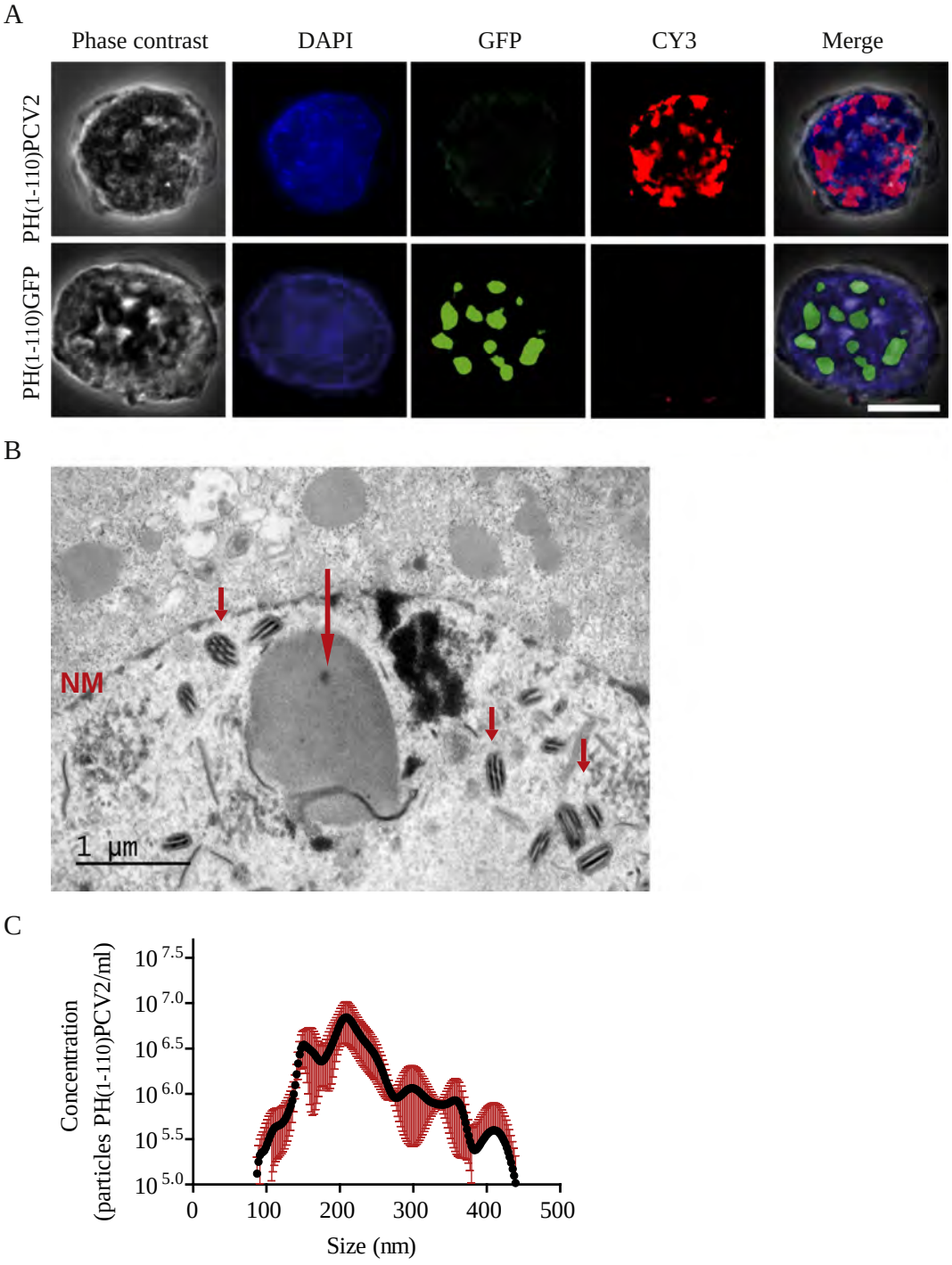

Fig. 2. Characterization of PH(1 1 0)PCV2 NPs: morphology, localization and size. (A) Confocal microscopy images of PH(1 1 0)PCV2 NPs. Sf9 cells were infected with the recombinant baculoviruses PH(1 1 0)PCV2 or PH(1 1 0)GFP. At 72 hpi, cells were processed for specific immunofluorescence against ORF2 from PCV2 using an anti-PCV2 hyperimmune sera from a mouse and a Cy3-conjugated antibody (Section 2). PH(1 1 0)GFP NPs were treated in the same way using the same serum and secondary antibody. The nuclei of cells are stained with 4′, 6-diamino-2-phenylindole (DAPI) dye. Protein PH(1 1 0)PCV2 self-aggregated and formed NPs located in the nucleus of Sf9 cells infected by the recombinant baculovirus PH(1 1 0)PCV2. PH(1 1 0)PCV2 NPs were recognized by a specific serum against PCV2, unlike PH(1 1 0)GFP NPs. All the confocal microscopy images have the same scale. The bar indicates 6 μm. (B) Transmission electron microscopy (TEM) of Sf9 cells infected by the recombinant baculovirus PH(1 1 0)PCV2. Red big arrows indicate the particles produced by the recombinant baculovirus PH(1 1 0)PCV2 and the red short arrows indicate baculoviruses near but outside the particles. NM = nuclear membrane. Barr indicates 1 μm. (C) Nanoparticle tracking analysis (NTA) of PH(1 1 0)PCV2 NPs. Fresh PH(1 1 0)PCV2 NPs were analyzed with the NanoSight instrument (Section 2) in triplicate. The dotted line is the mean value of the particle concentration/ml and the error bars are the standard error. Size of NPs is indicated in nanometers (nm). (For interpretation of the references to color in this figure legend, the reader is referred to the web version of this article.)

INFORME DE LABORES 2019

3.4. The PH(1 1 0)PCV2 NPs do not contain occluded baculoviruses

The natural role of polyhedron is to form the polyhedra, a crystal structure in which thousands of baculoviruses are occluded, forming what is known as the occluded bodies [33]. Polyhedra is formed in the nuclei of infected cells, and provides stability to occluded baculovirus [30]. We have previously shown by TEM that PH(1 1 0)GFP particles do not occlude baculoviruses [28] unlike wild type polyhedra [33]. Similarly to PH(1 1 0)GFP NPs, PH(1 1 0)PCV2 NPs do no occlude baculovirus inside them, as demonstrated by TEM analysis (Fig. 2B). This observation is particularly relevant for vaccines, since the immunization with contaminating baculoviruses is not desirable for vaccination.

3.5. The PH(1 1 0)PCV2 NPs are polydisperse

Particle size may play an important role in the vaccine development, since NPs between 20 and 200 nm appear to be more immunogenic than larger particles [34]. To further evaluate the dimensions of PH(1 1 0)PCV2 NPs we conducted nanoparticle tracking analysis (NTA) [35]. NTA of PH(1 1 0)PCV2 indicated that these NPs are polydisperse. PH(1 1 0)PCV2 NPs showed three main components: 150, 210 and 300 nm (Fig. 2C).

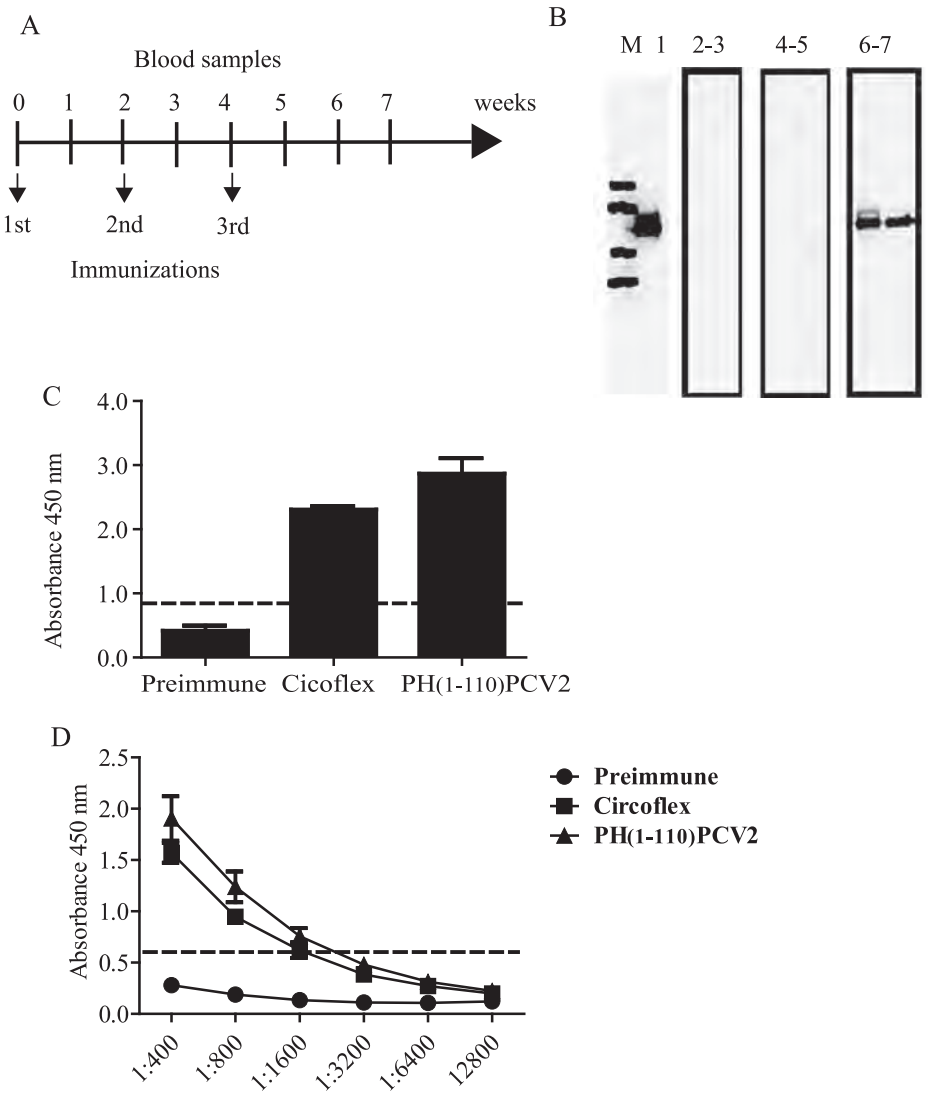

Fig. 3. Immunization of pigs with PH(1 1 0)PCV2 NPs. (A) Diagram illustrating the immunization and bleeding schedules. PCV2-free pigs were immunized with the commercial vaccine Circoflex® or PH(1 1 0)PCV2 NPs with emulsion co-administration based on light paraffin oil. Two booster doses were given to each pig with an interval of 2 weeks. Sera samples were taken every week until 7th week. (B) Western blot analysis of sera from vaccinated pigs. A recombinant ORF2 was produced in bacteria and purified to use as antigen for western blot. The recombinant ORF2 was run by PAGE at 10% and transferred to nitrocellulose membrane strips. Each strip was incubated with a different serum from pigs: infected (lane 1), pre-immune (lane 2 and 3), vaccinated with Circoflex (lane 4 and 5) and vaccinated with PH(1 1 0)PCV2 NPs (lane 6 and 7). M = molecular weight marker representing from top to bottom: 50, 37, 25 and 20 kDa proteins. A sera from a PCV2-infected pig and sera from pigs vaccinated with PH(1 1 0) PCV2 NPs recognized a protein of approximately 30 kDa corresponding to the molecular weight of ORF2 from PCV2 (See the full-length blots in the supplementary Fig. S2). (C) Evaluation of specific antibodies against ORF2 from PCV2 by an indirect ELISA. Sera from 3 pigs for each condition were evaluated for duplicate. All the sera evaluated in this experiment belong at 7 weeks after immunization and were used at a dilution of 1:200. Bars show the mean and standard error. (D) Specific antibody titters against ORF2 from PCV2 from pigs vaccinated with Circoflex® or PH(1 1 0)PCV2 NPs determined by an indirect ELISA. Dilutions of sera were from 1:400 to 1:12,800. Symbols (rhombs, squares and circles) are the mean of the absorbance obtained from the sera and the error bars are the standard error. The dotted line indicates the breaking point of twice the mean of the pre-immune sera and represents the cutoff value for positive pigs. The antibody titers were determined with the highest sera dilution that gave a positive value in ELISA.

INFORME DE LABORES 2019

3.6. Pigs immunized with PH(1 1 0)PCV2 NPs induced neutralizing antibodies against PCV2

To evaluate the efficiency of PH(1 1 0)PCV2 NPs as vaccines we immunized pigs with these NPs and compared them with the commercially available vaccine Circoflex® (Fig. 3A). Pigs immunized with 200 μg of PH(1 1 0)PCV2 NPs generated antibodies based on IgG against ORF2 from PCV2 detected by western blot and ELISA, whereas pigs immunized with Circoflex® induced antibodies against ORF2 from PCV2 detected only by ELISA. These results strongly suggested that PH(1 1 0)PCV2 NPs induced antibodies that recognize both conformational and non-conformational epitopes whereas Circoflex predominantly produced antibodies recognizing conformational epitopes (Fig. 3B and C). Antibody titers generated with PH(1 1 0)PCV2 NPs and Circoflex® were indistinguishable, with titers of 1:1600 (Fig. 3D). PCV2 antibody titers were indistinguishable in pigs immunized with 200 or 2000 μg of PH(1 1 0)PCV2 NPs (Supplementary Fig. S3-D).

In order to determine if the antibodies produced by our vaccine PH(1 1 0)PCV2 contained neutralizing antibodies, we conducted an *in vitro* neutralization assay using the pig kidney cell line PK-15.

To evaluate the infection of PK-15 cells with PCV2, we produced a recombinant virus carrying the gene for the green fluorescent protein (GFP) under the strong CMV promoter (Section 2). In this way we could quantify infection by PCV2 following the fluorescence from GFP by cell cytometry (Section 2).

With this *in vitro* neutralization assay we compared the sera from pigs vaccinate with our PH(1 1 0)PCV2 NPs, pigs vaccinated with Circoflex® and control pigs (pigs vaccinate with saline solution). We also used the serum from a naturally infected pig with PCV2 as positive control.

Preimmune sera did not inhibit PCV2 infection in PK-15 cells. Most interestingly, the sera from pigs immunized with Circoflex® and the sera from the pigs immunized with PH(1 1 0)PCV2 NPs showed neutralizing antibody titers of 1:500 as indicated by the reduction in fluorescence intensity from GFP (Fig. 4A and B). Additionally, the fluorescence intensity of PK-15 cells induced by the infection of the recombinant PCV2 decreased 25–35% when the recombinant PCV2 was mixed with sera from pigs immunized with Circoflex® (Fig. 4A and B). Fluorescence intensity of PK-15 cells decreased 50–60% when the recombinant PCV2 was mixed with sera from pigs immunized with our PH(1 1 0)PCV2 NPs. These results show that the sera from pigs vaccinated with Circoflex® or PH(1 1 0)PCV2 NPs contained neutralizing antibodies against PCV2. These antibodies were as efficient as those found in pigs naturally infected with PCV2 (Fig. 4B).

4. Discussion

PCV2 is one of the most important pathogens in the pig industry around the world causing serious economic losses [3,4,17,18]. Even trough there are several vaccines available in the market today, the need for simpler, easier to produce and less expensive vaccines is always required.

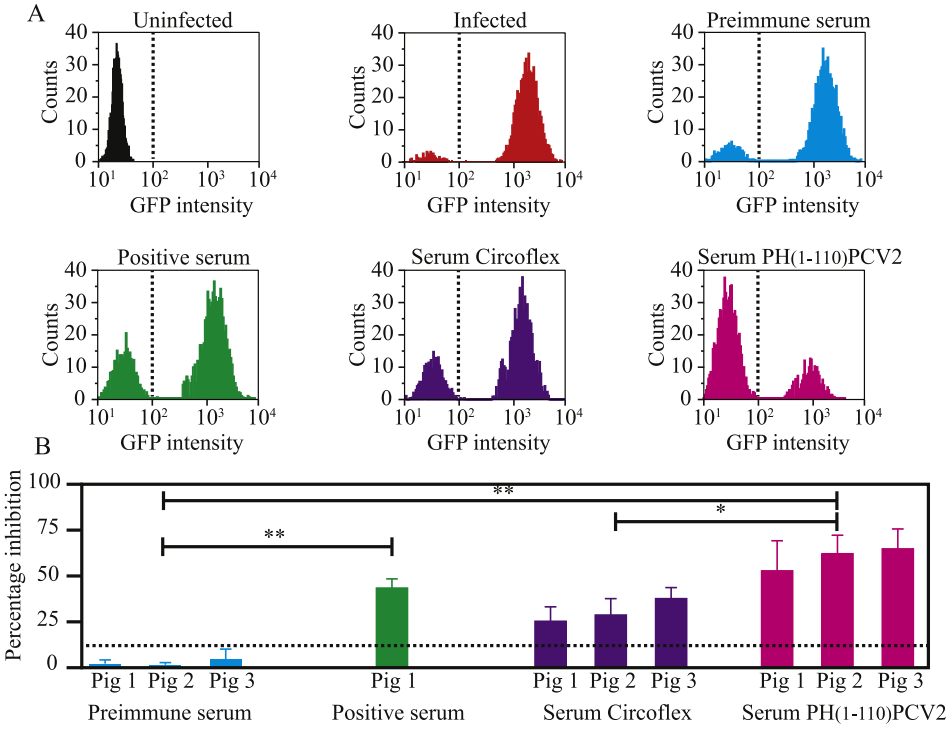

Fig. 4. Neutralization assay against a recombinant PCV2 expressing GFP. (A) Representative histograms obtained form the cell cytometer after counting 10,000 cells for each condition. Fluorescence shows the expression of GFP by a recombinant PCV2 expressing soluble GFP (Section 2). PK-15 cells were transfected with DNA from the recombinant PCV2 and supernatant was recovered 72 h later and used for the neutralization assay. Pre-immune sera and sera from vaccinated pigs with PH(1 1 0)PCV2 NPs or Circoflex® as well as a serum from a positive pig (naturally infected by PCV2) were diluted 1:500 and mixed individually with the recombinant PCV2 using a MOI of 1. PK-15 cells were added to microplates and incubated 24 h. Each mix was added to each well and incubated for 72 h. PK-15 cells were analyzed by flow cytometry. Each sample was analyzed in triplicate and 10,000 events were recorded. Data are the counts of PK-15 cells with different fluorescence intensities of GFP, indicating PK-15 cells infected with the recombinant PCV2. (B) Percentage of inhibition of the fluorescent intensity of GFP in PK-15 cells in the neutralization assay. The percentage of inhibition of fluorescence of GFP was calculated considering the baseline from non-infected PK-15 cells (indicated in black as uninfected) and the infected PK-15 cells with a standard quantity of recombinant PCV2 without sera (indicated as infected in the red histogram). The titers of neutralizing antibodies were 1:500 (since the sera were previously diluted 1:500). Data are presented in percentage and based on the number of cells positive to GFP. Bars show the mean and standard error. The asterisk indicates conditions different from the group injected with PBS ($^{*}p < 0.05$ and $^{**}p < 0.01$). A one-way ANOVA test following by a Tukey's test were used to determine differences with the pre-immune sera. (For interpretation of the references to color in this figure legend, the reader is referred to the web version of this article.)

INFORME DE LABORES 2019

In an attempt to explore novel pathways for vaccine production, we produced nanoparticles by fusing the ORF2 from PCV2 to the fragment PH(1 1 0) from polyhedron obtained from the baculovirus *Autographa californica*. Polyhedrin is the main constituent from the polyhedral, a crystal structure that occludes baculoviruses and protects them from the environment for years [33].

The use of polyhedra as carriers for vaccines has been recently proposed [36,37]. Nevertheless, polyhedra can withstand acidic pH of the endolysosome of antigen presenting cells such as dendritic cells (DCs), avoiding the maturation process for presenting antigens [36]. However, the peptide PH(1 1 0) derived from the first 110 amino acids from polyhedrin protein retains the self-aggregate property of polyhedra and forms NPs [28], and is processed by antigen presenting, generating antibodies [29]. In the present study we evaluated the use of PH(1 1 0)PCV2 NPs as a PCV2 vaccine candidate.

The main advantages of our system are the downstream processes such as recovery and purification of the PH(1 1 0)PCV2 NPs, because these nanoparticles can be purified using a single centrifugation step, while yielding large amounts of pure protein (Fig. 1D). In addition, our vaccine does not require refrigeration for storage; since these NPs are stable a room temperature for several months. These properties are not met by other vaccines such as VLPs, because they need to be purified by different methods from ultracentrifugation using sucrose or cesium chloride gradients to chromatography [27,38–40]. Thus, the recovery and purification of VLPs-based vaccines are time-consuming and often yields are not very good [20,27]. Therefore, our system based on PH(1 1 0) PCV2 NPs is not only easy to produce and faster than other methods, but also less expensive because requires a simple centrifugation step and yields large amounts of protein.

However, our method is not without some limitations. The main limitations of our system based on PH(1 1 0)PCV2 NPs are the lack of experience in molecular biology for the design of the recombinant baculovirus and the lack of knowledge in genetics and proteomics of some pathogens to adequately identify the antigen (or segment of the antigen) to be used in the fusion protein.

On the other hand, the use of NPs has gained attention for the production of novel antigen delivery systems. NPs have been designed based on proteins [21,22], peptides [41–45] or lipopeptides [46–48] which self-assemble generating NPs with different dimensions. The particle formation is a process that involves the self-interaction among molecules of the same type to form supramolecular assemblies, which may improve the immunogenicity of fused/conjugated antigens [29]. The size of antigens is also important because it plays an important role in the antibody production. Current research has indicated that NPs between 20 and 200 nm are more immunogenic than larger particles because are easily endocyted by DCs and/or enter directly through the lymphatic vessels whereas larger particles cannot [34]. The PH(1 1 0) PCV2 protein generated NPs range from 90 to 450 nm (Fig. 2C). Additionally, these NPs do not contain occluded baculovirus and generate high antibody titers against ORF2 from PCV2.

We also evaluated the *in vitro* protection of the PH(1 1 0)PCV2 NPs through an seroneutralization assay, because a challenge experiment is difficult due to the well known fact that PCV2 infection in pigs is often asymptomatic [49]. In addition, Porcine circovirus disease (PCVD) is not lethal and coinfection by other viruses are required to trigger symptoms in infected animals [3]. The use of immunostimulants has also been suggested before the PCV2 challenge to trigger the development of PCVD, but this has given controversial results, since with this methodology, up to 70% of pigs develop PCVD [50], whereas other similar methodologies do not trigger the PCVD [49]. On the other hand, it has been shown that neutralizing antibodies against PCV2 correlate well with *in vivo* protection [51,52]. For this reason, we decided to develop an *in vitro* neutralization assay using a recombinant PCV2 carrying the gen for GFP. Our results indicated that the pigs immunized with PH(1 1 0)PCV2 NPs or Circoflex® generated antibodies against PCV2 that can neutralize the PCV2 infection in PK-15 cells.

5. Conclusions

Here we show the development of a novel technology to produce vaccines by encapsulating antigens into genetically encoded NPs. Because the antigen and the self-aggregating peptide used for encapsulation are a fusion protein, the incorporation efficiency is 100%. Given the fact that particles can be precipitated by centrifugation, purification of the NPs carrying the antigen of interest is easy, fast and inexpensive. Furthermore, we have shown that the NPs produced with this technology are stable for years at room temperature, preventing the use of a cold chain and extending the life shelf of the vaccine.

Acknowledgements

This work was partially supported by Laboratorios Sanfer (Boulevard Adolfo López Mateos No 314. 2nd floor, Tlacopac, Alvaro Obregón, 01049, Mexico City). Luis Vaca received the grant Secretaria de Ciencia y Tecnología e Innovación de la Ciudad de México. Jesús Zepeda-Cervantes is a doctoral student from Programa de Doctorado en Ciencias Biomédicas, Universidad Nacional Autónoma de México (UNAM) and received fellowship 282604 from Consejo Nacional de Ciencia y Tecnología (CONACyT), México. We would like to thank M.Sc. Liliana Suárez Ramírez from Facultad de Medicina Veterinaria y Zootecnia-UNAM and Dr. Josué Orlando Ramírez Járquin from Instituto de Fisiología Celular-UNAM for his critical review of this manuscript and valuable comments.

Author contribution

JZC and LV conceived the study, standardized the production of PH(110)PCV2 NPs, conducted western blots, ELISA, NTA and neutralization assays, produced figures of the paper and wrote the paper. AS designed the recombinant baculoviruses and plasmids and ACR synthesized the recombinant ORF2 from PCV2, conducted ELISAs and western blots. JISB and RCN isolated PCV2 from infected animals and conducted PCR for cloning. All the authors analyzed and interpreted data, and approved the final manuscript.

Declaration of interest

The pharmaceutical company Sanfer supported partially this research by providing the pigs used in this study.

Appendix A. Supplementary material

Supplementary data to this article can be found online at https://doi.org/10.1016/j.vaccine.2019.02.044.

References

[1] Tischer I, Vettermann H, Gelderblom W, Koch MA. A very small porcine virus with circular single-stranded DNA. Nature 1982;295:64–6.
[2] Grau-Roma L, Fraile L, Segalés J. Recent advances in the epidemiology, diagnosis and control of diseases caused by Porcine Circovirus Type 2. Vet J 2011;187:23–32. https://doi.org/10.1016/j.tvjl.2010.01.018.
[3] Segalés J, Allan GM, Domingo M. Porcine circovirus diseases. Anim Heal Res Rev 2005;6:119–42. https://doi.org/10.1079/AHR2005106.
[4] Chae C. Commercial Porcine Circovirus Type 2 vaccines: efficacy and clinical application. Vet J 2012;194:151–7. https://doi.org/10.1016/j.tvjl.2012.06.031.

[5] An DJ, Song DS, Park JY, Park BK. A DNA miniarray system for simultaneous visual detection of Porcine Circovirus Type 1 (PCV1) and 2 (PCV2) in pigs. Vet Res Commun 2009;33:139–47. https://doi.org/10.1007/s11259-008-9080-8.
[6] Segalés J, Rosell C, Domingo M. Pathological findings associated with naturally acquired Porcine Circovirus Type 2 associated disease. Vet Microbiol 2004;98:137–49. https://doi.org/10.1016/j.vetmic.2003.10.006.
[7] Chae C. A review of porcine circovirus 2-associated syndromes and diseases. Vet J 2005;169:326–36. https://doi.org/10.1016/j.tvjl.2004.01.012.
[8] Segalés J. Porcine Circovirus Type 2 (PCV2) infections: clinical signs, pathology and laboratory diagnosis. Virus Res 2012;164:10–9. https://doi.org/10.1016/j.virusres.2011.10.007.
[9] Misinzo G, Delputte PL, Lefebvre DJ, Nauwynck HJ. Porcine circovirus 2 infection of epithelial cells is clathrin-, caveolae- and dynamin-independent, actin and Rho-GTPase-mediated, and enhanced by cholesterol depletion. Virus Res 2009;139:1–9. https://doi.org/10.1016/j.virusres.2008.09.005.
[10] Nauwynck HJ, Sanchez R, Meerts P, Lefebvre DJ, Saha D, Huang L, et al. Cell tropism and entry of porcine circovirus 2. Virus Res 2012;164:43–5. https://doi.org/10.1016/j.virusres.2011.11.003.
[11] Nawagitgul P, Morozov I, Bolin SR, Harms PA, Sorden SD, Paul PS. Open reading frame 2 of Porcine Circovirus Type 2 encodes a major capsid protein. J Gen Virol 2000;81:2281–7. https://doi.org/10.1099/0022-1317-81-9-2281.
[12] Misinzo G, Delputte PL, Meerts P, Lefebvre DJ, Nauwynck HJ. Porcine circovirus 2 uses heparan sulfate and chondroitin sulfate B glycosaminoglycans as receptors for its attachment to host cells. J Virol 2006;80:3487–94. https://doi.org/10.1128/JVI.80.7.3487-3494.2006.
[13] Blanchard P, Mahé D, Cariolet R, Keranflec'h A, Baudouard MA, Cordioli P, et al. Protection of swine against post-weaning multisystemic wasting syndrome (PMWS) by Porcine Circovirus Type 2 (PCV2) proteins. Vaccine 2003;21:4565–75. https://doi.org/10.1016/S0264-410X(03)00503-6.
[14] Faccini S, Barbieri I, Gilioli A, Sala G, Gibelli LR, Moreno A, et al. Detection and genetic characterization of Porcine Circovirus Type 3 in Italy. Transbound Emerg Dis 2017;64:1661–4. https://doi.org/10.1111/tbed.12714.
[15] Ku X, Chen F, Li P, Wang Y, Yu X, Fan S, et al. Identification and genetic characterization of Porcine Circovirus Type 3 in China. Transbound Emerg Dis 2017;64:703–8. https://doi.org/10.1111/tbed.12638.
[16] Stadejek T, Woźniak A, Miłek D, Biernacka K. First detection of Porcine Circovirus Type 3 on commercial pig farms in Poland. Transbound Emerg Dis 2017;64:1350–3. https://doi.org/10.1111/tbed.12672.
[17] Afghah Z, Webb B, Meng XJ, Ramamoorthy S. Ten years of PCV2 vaccines and vaccination: is eradication a possibility? Vet Microbiol 2017;206:21–8. https://doi.org/10.1016/j.vetmic.2016.10.002.
[18] Karuppannan AK, Opriessnig T. Porcine Circovirus Type 2 (PCV2) vaccines in the context of current molecular epidemiology. Viruses 2017;9:1–15. https://doi.org/10.3390/v9050099.
[19] Bucarey SA, Noriega J, Reyes P, Tapia C, Sáenz L, Zuñiga A, et al. The optimized capsid gene of Porcine Circovirus Type 2 expressed in yeast forms virus-like particles and elicits antibody responses in mice fed with recombinant yeast extracts. Vaccine 2009;27:5781–90. https://doi.org/10.1016/j.vaccine.2009.07.061.
[20] Vicente T, Roldão A, Peixoto C, Carrondo MJT, Alves PM. Large-scale production and purification of VLP-based vaccines. J Invertebr Pathol 2011;107:S42–8. https://doi.org/10.1016/j.jip.2011.05.004.
[21] Zhao L, Seth A, Wibowo N, Zhao CX, Mitter N, Yu C, et al. Nanoparticle vaccines. Vaccine 2014;32:327–37. https://doi.org/10.1016/j.vaccine.2013.11.069.
[22] Castro-Acosta RM, Revilla AL, Ramírez OT, Palomares La. Separation and quantification of double- and triple-layered rotavirus-like particles by CZE. Electrophoresis 2010;31:1376–81. https://doi.org/10.1002/elps.200900558.
[23] Pijlman GP. Enveloped virus-like particles as vaccines against pathogenic arboviruses. Biotechnol J 2015;10:659–70. https://doi.org/10.1002/biot.201400427.
[24] Harrison RL, Jarvis DL. Protein N-glycosylation in the baculovirus-insect cell expression system and engineering of insect cells to produce "mammalianized" recombinant glycoproteins. Adv Virus Res 2006;68:159–91. https://doi.org/10.1016/S0065-3527(06)68005-6.
[25] Jeong J, Park C, Choi K, Chae C. Comparison of three commercial one-dose Porcine Circovirus Type 2 (PCV2) vaccines in a herd with concurrent circulation of PCV2b and mutant PCV2b. Vet Microbiol 2015;177:43–52. https://doi.org/10.1016/j.vetmic.2015.02.027.
[26] Kristensen CS, Baadsgaard NP, Toft N. A meta-analysis comparing the effect of PCV2 vaccines on average daily weight gain and mortality rate in pigs from weaning to slaughter. Prev Vet Med 2011;98:250–8. https://doi.org/10.1016/j.prevetmed.2010.11.015.
[27] Morenweiser R. Downstream processing of viral vectors and vaccines. GeneTher 2005;12:S103–10. https://doi.org/10.1038/sj.gt.3302624.
[28] Sampieri A, Luz-Madrigal A, Zepeda J, Vaca L. Identification of fragments from Autographa Californica polyhedrin protein essential for self-aggregation and exogenous protein incorporation. BMC Biochem 2015;16:1–12. https://doi.org/10.1186/s12858-015-0034-9.
[29] Zepeda-Cervantes J, Vaca L. Induction of adaptive immune response by self-aggregating peptides. Expert Rev Vaccines 2018. https://doi.org/10.1080/14760584.2018.1507742. 00:14760584.2018.1507742.
[30] Nazli-Huda. Stability of Spodoptera litura nucleopolyhedrovirus in sodium dodecyl sulphate. African J Biotechnol 2012;11:3877–81. https://doi.org/10.5897/AJB11.2848.
[31] Hedge V, Venkatesh Y. Generation of antibodies specific to d-mannitol, a unique haptenic allergen, using reductively aminated d-mannose-bovine serum albumin conjugate as the immunogen. Immunology 2007;2012:119–28. https://doi.org/10.1016/j.imbio.2006.10.002.
[32] Franzo G, Tucciarone CM, Cecchinato M, Drigo M. Porcine Circovirus Type 2 (PCV2) evolution before and after the vaccination introduction: a large scale epidemiological study. Sci Rep 2016;6:1–10. https://doi.org/10.1038/srep39458.
[33] Slack J, Arif BM. The baculoviruses occlusion-derived virus: virion structure and function. Adv Virus Res 2006;69:99–165. https://doi.org/10.1016/S0065-3527(06)69003-9.
[34] Bachmann MF, Jennings GT. Vaccine delivery: a matter of size, geometry, kinetics and molecular patterns. Nat Rev Immunol 2010;10:787–96. https://doi.org/10.1038/nri2868.
[35] Tian X, Nejadnik MR, Baunsgaard D, Henriksen A, Rischel C, Jiskoot W. A comprehensive evaluation of nanoparticle tracking analysis (nanosight) for characterization of proteinaceous submicron particles. J Pharm Sci 2016;105:3366–75. https://doi.org/10.1016/j.xphs.2016.08.009.
[36] Molina GN, Tavarone E, Taboga O, Molinari P. Two distinctive phenotypes of AcMNPV display different immune abilities and intracellular destiny. PLoS One 2016;11:1–14. https://doi.org/10.1371/journal.pone.0168939.
[37] Lee KS, Sohn MR, Kim BY, Choo YM, Woo SD, Yoo SS, et al. Production of classical swine fever virus envelope glycoprotein E2 as recombinant polyhedra in baculovirus-infected silkworm larvae. Mol Biotechnol 2012;50:211–20. https://doi.org/10.1007/s12033-011-9431-5.
[38] Li T-C, Yamakawa Y, Suzuki K, Tatsumi M, Azeez Razak MA, Uchida T, et al. Expression and self-assembly of empty virus-like particles of hepatitis E virus. J Virol 1997;71:7207–13. doi: 0022-538X/97.
[39] Cook JC, Joyce JG, George HA, Schultz LD, Hurni WM, Jansen KU, et al. Purification of virus-like particles of recombinant human papillomavirus type 11 major capsid protein L1 from Saccharomyces cerevisiae. Protein Expr Purif 1999;17:477–84. https://doi.org/10.1006/prep.1999.1155.
[40] Chung Y, Huang J, Lai C, Sheng H, Shih S, Ho M, et al. Expression, purification and characterization of enterovirus-71 virus-like particles 2006;12:921–7.
[41] Chen J, Pompano RR, Santiago FW, Maillat L, Sciammas R, Sun T, et al. The use of self-adjuvanting nanofiber vaccines to elicit high-affinity B cell responses to peptide antigens without inflammation. Biomaterials 2013;34:8776–85. https://doi.org/10.1016/j.biomaterials.2013.07.063.
[42] Rudra JS, Tian YF, Jung JP, Collier JH. A self-assembling peptide acting as an immune adjuvant. Proc Natl Acad Sci 2010;107:622–7. https://doi.org/10.1073/pnas.0912124107.
[43] Rudra JS, Mishra S, Chong AS, Mitchell RA, Nardin EH, Nussenzweig V, et al. Self-assembled peptide nanofibers raising durable antibody responses against a malaria epitope. Biomaterials 2012;33:6476–84. https://doi.org/10.1016/j.biomaterials.2012.05.041.
[44] Chesson CB, Huelsmann EJ, Lacek AT, Kohlhapp FJ, Webb MF, Nabatiyan A, et al. Antigenic peptide nanofibers elicit adjuvant-free CD8+ T cell responses. Vaccine 2014;32:1174–80. https://doi.org/10.1016/j.vaccine.2013.11.047.
[45] Rudra JS, Tripathi PK, Hildeman DA, Jung JP, Collier JH. Immune responses to coiled coil supramolecular biomaterials. Biomaterials 2010;31:8475–83. https://doi.org/10.1016/j.biomaterials.2010.07.068.
[46] Trent A, Ulery BD, Black MJ, Barrett JC, Liang S, Kostenko Y, et al. Peptide amphiphile micelles self-adjuvant group A streptococcal vaccination. AAPS J 2015;17:380–8. https://doi.org/10.1208/s12248-014-9707-3.
[47] Hamley IW, Kirkham S, Dehsorkhi A, Castelletto V, Reza M, Ruokolainen J. Toll-like receptor agonist lipopeptides self-assemble into distinct nanostructures. Chem Commun 2014;50:15948–51. https://doi.org/10.1039/C4CC07511K.
[48] Mandal D, Nasrolahi Shirazi A, Parang K. Self-assembly of peptides to nanostructures. Org Biomol Chem 2014;12:3544–61. https://doi.org/10.1039/C4OB00447G.
[49] Resendes A, Segalés J, Balasch M, Calsamiglia M, Sibila M, Ellerbrok H, et al. Lack of an effect of a commercial vaccine adjuvant on the development of postweaning multisystemic wasting syndrome (PMWS) in Porcine Circovirus Type 2 (PCV2) experimentally infected conventional pigs. Vet Res 2004;35:83–90.
[50] Krakowka S, Ellis J, McNeilly F, Waldner C, Rings DM, Allan G. Mycoplasma hyopneumoniae bacterins and Porcine Circovirus Type 2 (PCV2) infection: Induction of postweaning multisystemic wasting syndrome (PMWS) in the gnotobiotic swine model of PCV2-associated disease. Can Vet J 2007;48:716–24. https://doi.org/10.3233/JAD-140231.
[51] Fort M, Olvera A, Sibila M, Segalés J, Mateu E. Detection of neutralizing antibodies in postweaning multisystemic wasting syndrome (PMWS)-affected and non-PMWS-affected pigs. Vet Microbiol 2007;125:244–55. https://doi.org/10.1016/j.vetmic.2007.06.004.
[52] Meng X-J. Porcine Circovirus Type 2 (PCV2): pathogenesis and interaction with the immune system. Annu Rev Anim Biosci 2013;1:43–64. https://doi.org/10.1146/annurev-animal-031412-103720.